Tandem Wessely oxidation and intramolecular Diels–Alder reactions. III. Synthesis of isotwistanes[1]

PETER YATES AND TADAS S. MACAS[2]

Lash Miller Chemical Laboratories, University of Toronto, Toronto, Ont., Canada M5S 1A1

Received June 24, 1987

PETER YATES and TADAS S. MACAS. Can. J. Chem. **66**, 1 (1988).

Wessely oxidation of *o*-(3-alkenyl) phenols (**5**) with lead tetraacetate gives 6-acetoxy-6-(3-alkenyl)-2,4-cyclohexadien-1-ones (**6**), which undergo intramolecular Diels–Alder reactions to give isotwistene (hexahydro-1,5-methanoindene) derivatives (**7**). These, on hydrolysis followed by oxidation with periodic acid, give hexahydro-1-oxo-1*H*-indene-5-carboxylic acids (**41**, **46**). Compounds **5** were prepared either by Grignard coupling of *o*-methoxybenzyl chloride with allyl halides followed by de-*O*-methylation with sodium thioethoxide or via reduction of dihydrocoumarins (**18**–**20**) to 2-chromanols (**21**–**23**) with diisobutylaluminum hydride, followed by Wittig reaction of these with ethyl (triphenylphosphoranylidene)acetate.

PETER YATES et TADAS S. MACAS. Can. J. Chem. **66**, 1 (1988).

L'oxydation de Wessely des *o*-(alcène-3 yl) phénols (**5**) par le tétraacétate de plomb conduit aux acétoxy-6 (alcène-3 yl)-6 cyclohexadiène-2,4 ones-1 (**6**) qui subissent des réactions de Diels–Alder intramoléculaires conduisant à des dérivés de l'isotwistène (hexahydro méthano-1,5 indène) (**7**). Ceux-ci, soumis à une réaction d'hydrolyse suivie d'une oxydation par de l'acide periodique, conduisent aux acides hexahydro oxo-1 1*H*-indènecarboxyliques-5 (**41** et **46**). On a préparé les composés **5** soit par un couplage de Grignard du chlorure d'*o*-méthoxybenzyle avec des halogénures allyliques suivi d'une *O*-déméthylation par le thioéthylate de sodium soit par une réduction, par l'hydrure de diisobutylaluminium, des dihydrocoumarines (**18**–**20**) en chromanols (**21**–**23**) suivie d'une réaction de Wittig de ces derniers avec le (triphénylphosphoranylidène)acétate d'éthyle.

[Traduit par la revue]

Can. J. Chem. Downloaded from www.nrcresearchpress.com by 213.222.148.141 on 09/07/12
For personal use only.

The oxidation of *ortho*-substituted phenols with lead tetraacetate LTA to give 6-acetoxy-2,4-cyclohexadien-1-ones (*o*-quinol acetates; **1**), which was first reported by Wessely and his co-workers in 1950 (4), is the simplest general method for the synthesis of the latter class of compounds. Wessely early recognized (5) the potential utility of *o*-quinol acetates in intermolecular Diels–Alder reactions leading to bicyclo[2.2.2]octenones and bicyclo[2.2.2]octadienones (e.g., **2** (R = CH_3)[3]) (Scheme 1).

Work in these laboratories (1, 2) has shown that an intramolecular version of the latter reaction can be effected by Wessely oxidation products that incorporate a dienophilic group in the ester moiety (e.g., **3**). This provides a route to tricyclic lactones of type **4**, as exemplified in Scheme 2.

It occurred to us that a related reaction sequence involving Wessely oxidation of an *o*-(3-alkenyl) phenol (**5**) to give a 2,4-cyclohexadienone of type **6**, followed by intramolecular Diels–Alder reaction, could provide a viable route to tricarbocyclic analogues of **4**, i.e., isotwistene (hexahydro-1,5-methanoindene) derivatives of type **7** (Scheme 3). Other workers (7) have already demonstrated the practicability of the synthesis of tricyclic systems via intramolecular reactions of alkenyl 1,3-cyclohexadiene derivatives, but none to our knowledge has coupled this reaction with the Wessely oxidation reaction.

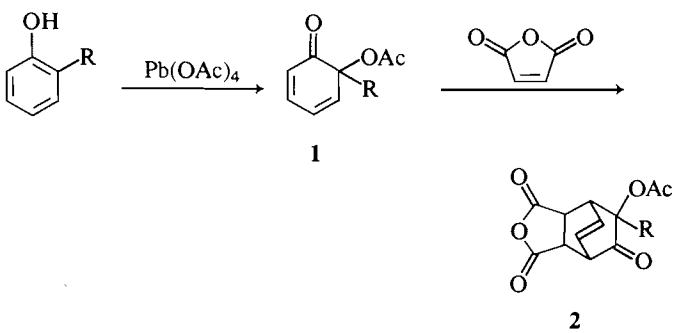

SCHEME 1

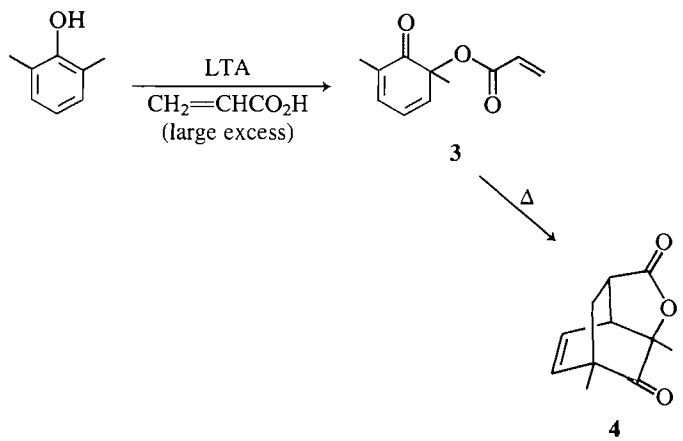

SCHEME 2

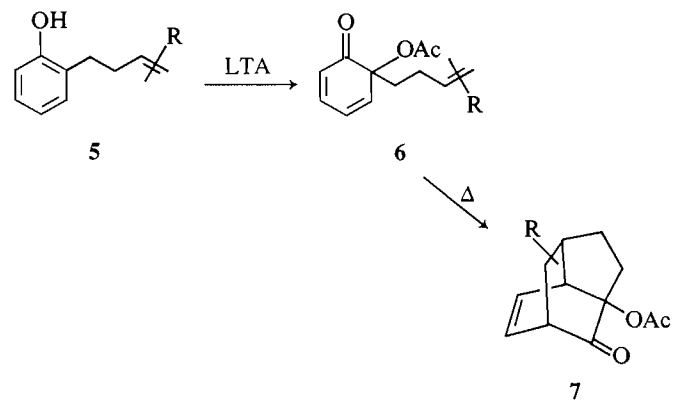

SCHEME 3

[1]References 1*a* and 2*a* are considered to be parts I and II of this series; for a preliminary communication describing part of this work, see ref. 3.

[2]Present address: C-I-L Research Centre, 2101 Hodwen Road, Mississauga, Ontario L5K 2L3.

[3]The stereochemistry of the adducts was not assigned; for recent work on the stereochemistry of this type of adduct, see ref. 6.

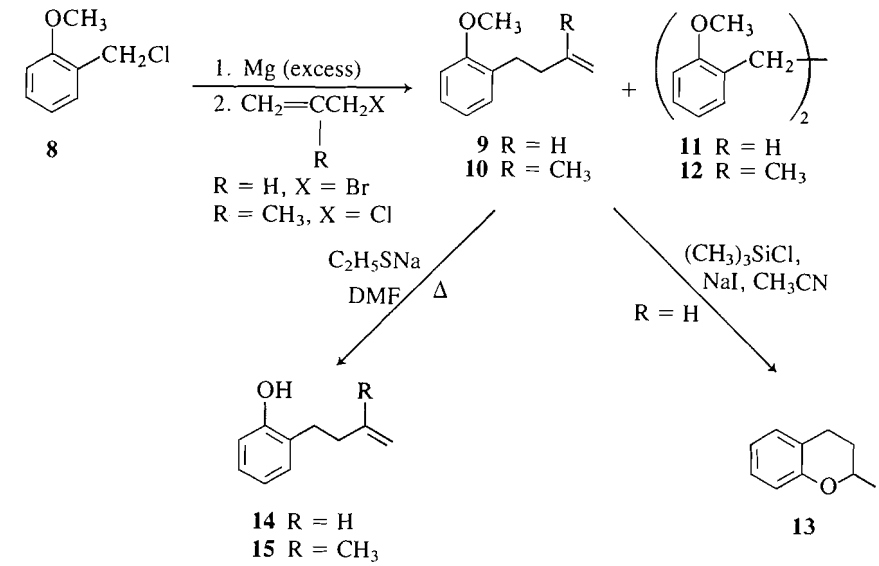

SCHEME 4

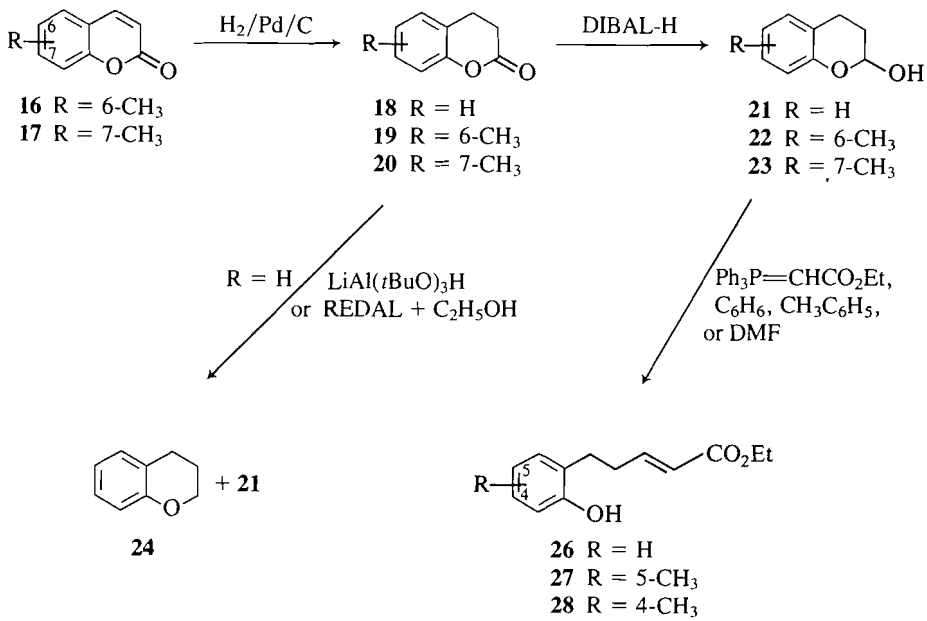

SCHEME 5

Synthesis of o*-(3-alkenyl) phenols*

Although in intermolecular Diels–Alder reactions of ethylenic dienophiles an activating, electron-withdrawing substituent is required for facile reaction, this is less true of intramolecular Diels–Alder reactions because of a favorable entropic factor. We therefore chose to develop two general routes for the synthesis of *o*-(3-alkenyl) phenols, one leading to 3-alkenyl side chains without electron-withdrawing substituents and the other to 3-alkenyl side chains with a 4-alkoxycarbonyl substituent.

The first route (Scheme 4) is based on earlier work by Oki and Iwamura (8). *o*-Methoxybenzyl chloride (**8**) was prepared by treatment of *o*-methoxybenzyl alcohol with thionyl chloride (9). The alcohol was obtained by reduction of anisaldehyde with sodium borohydride or methylation of *o*-hydroxybenzyl alcohol with dimethyl sulfate in dry dimethylformamide (10). In the latter case the product was contaminated with *o*-methoxybenzyl methyl ether; however, we found that this too was converted to **8** by thionyl chloride. Coupling of the Grignard reagent devised from **8** with allyl bromide and with methallyl chloride gave the *o*-(3-alkenyl) anisoles **9** and **10**, respectively. Not surprisingly, these reactions also gave rise to significant amounts of the symmetrical coupling products **11** and **12**, which were isolated and identified.

Attempted demethylation of **9** with trimethylsilyl chloride and sodium iodide in acetonitrile (11) gave the chromane **13**, indicating that although demethylation was occurring, adventitious acid was promoting ring closure. Resort was therefore had to demethylation of **9** and **10** under basic conditions with sodium thioethoxide in dimethylformamide (12) to give phenols **14** and **15**, respectively.

The second route (Scheme 5) entailed reduction of the dihydrocoumarins **18–20** to the 2-chromanols **21–23**. Compound **18** is commercially available and compounds **19** and **20** were prepared by hydrogenation of the coumarins **16** and **17**, respec-

Can. J. Chem. Downloaded from www.nrcresearchpress.com by 213.222.148.141 on 09/07/12
For personal use only.

tively.[4] Reduction of **18** with lithium tri-(*tert*-butoxy)aluminum hydride (14) or sodium bis(2-methoxyethoxy)aluminum hydride (REDAL) plus one equivalent of ethanol (15) has previously been reported to give **21** in yields of 50%. We obtained similar yields but found that a persistent problem was the formation of chroman (**24**), an impurity that was found to be difficult to remove. However, compounds **18**–**20** were smoothly reduced by diisobutylaluminum hydride (DIBAL-H) in 84–93% yield.

It is known that 2-chromanol **21** is in mobile equilibrium with the corresponding phenolic aldehyde **25** (15), and it was

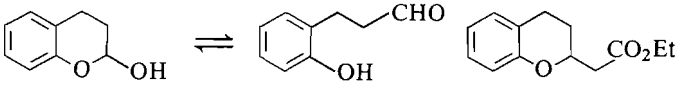

21 **25** **29**

therefore expected that the 2-chromanols **21**–**23** would undergo the Wittig reaction via their aldehydic tautomers. An analogous reaction has already been carried out with tetrahydro-2-pyranol (16). Treatment of the 2-chromanols with ethyl (triphenylphosphoranylidene)acetate in benzene or dimethylformamide (16, 17) gave the 5-(*o*-hydroxyphenyl)-2-pentenoic esters **26**–**28**. In all cases the *E* isomer was the major product; this was obtained in admixture with a small amount of the *Z* isomer and the by-product, triphenylphosphine oxide. Separation of the phenol from the triphenylphosphine oxide proved to be difficult.[5] Molecular distillation or extraction of crude **27** with dilute aqueous base led to ring closure to give the chroman **29**. Molecular distillation of the acetylated mixture was only partially successful and subsequent hydrolysis under either basic or acidic conditions led to the formation of **29**. The mixture of **26**, its *Z* isomer, and triphenylphosphine oxide could be separated by chromatography, but not without some reduction in yield because of the formation of **29**. Ultimately it was found that the mixture could be subjected successfully to Wessely oxidation and that the optimum point for the removal of triphenylphosphine oxide was after the intramolecular Diels–Alder reaction. Recourse was also had to this *modus operandi* in the cases of the phenols **27** and **28**.

The second route could also be utilized for the preparation of *o*-(3-butenyl) phenol (**14**) via treatment of 2-chromanol (**21**) with methylenetriphenylphosphorane, but the first route was found to be preferable. It is not possible, of course, to use the first route for the synthesis of the phenols **26**–**28**.

The assignments of structure to the compounds discussed above are based on their provenance and spectra. The 2-chromanols **21**–**23** show in their ^{1}H nmr spectra two-proton multiplets at δ 1.7–2.2 and 2.5–3.1 for the C-3 methylene protons and C-4 benzylic protons, respectively. The C-2 protons of **21** and **22** give rise to doublets of triplets (J = 4, 3 Hz), at δ 5.46 and 5.56, which collapse to triplets (J = 3 Hz) after D_2O treatment; compound **23** gives rise to a triplet (J = 3 Hz) at δ 5.47. All show a one-proton signal for the hydroxyl proton in the δ 3–4 region that is absent after D_2O treatment. In the case of **23** this is a broad singlet and in the cases of **21** and **22** it is a doublet (J = 4 Hz). All 2-chromanols show multiplets for the aromatic protons, and compounds **22** and **23** show three-proton singlets for their aromatic methyl groups at δ 2.25. The phenols **26**–**28** show in their ^{1}H nmr spectra four-proton multiplets at δ 2.3–3.0 for their benzylic and allylic methylene groups, one-proton doublets of triplets (J = 15, 2 Hz) at δ 5.8 for their C-2 vinylic protons, singlets at δ 5.5–7 for their phenolic protons, and multiplets at δ 6.5–7.4 arising from the overlap of signals of their C-3 vinylic and their aromatic protons. The methyl protons of compounds **27** and **28** give rise to three-proton singlets at δ 2.1–2.2 and all three compounds show appropriate signals for the protons of their ethoxycarbonyl groups. The 15-Hz vicinal coupling constants of the C-2 vinylic protons establish that all compounds isolated have the *E* configuration about their ethylenic bonds. The ^{1}H nmr spectra of the phenols **14** and **15** resemble those of the phenols **26**–**28**, *mutatis mutandis*. The ^{13}C spectra of the dihydrocoumarins, 2-chromanols, and phenols (Tables 1 and 2) are in accord with the structural assignments.

Wessely oxidation and intramolecular Diels–Alder reactions

The Wessely oxidation of *o*-substituted phenols with lead tetraacetate has been carried out under a wide variety of conditions, especially with respect to the solvent used (19). The yields of *o*-quinol acetates and the distribution of oxidized products are often markedly sensitive to the conditions used. We therefore first oxidized the phenol **26** with lead tetraacetate in a number of solvents (and catalysts) that had been reported to give good yields of *o*-quinol acetates in other cases. This phenol was chosen for the purpose because we anticipated that of the two types of *o*-(3-alkenyl) phenol we had prepared, the one with a 4-ethoxycarbonyl substituent might be more susceptible to side reactions involving the side chain than those without such a substituent. The solvents (and catalysts) used were acetic acid (4*b*, 5*a*), dichloromethane (2*a*, 20), chloroform (21), chloroform and pyridine (22), dioxane, tetrahydrofuran (−60°C), and methanol/ethyl acetate/boron trifluoride (23). The efficiency of the reaction conditions was judged by the yield of the *o*-quinol acetate **30** as indicated by the ^{1}H nmr spectra of the crude reaction products. The use of acetic acid was judged to be the most effective; dioxane and methanol/ethyl acetate/boron trifluoride also gave satisfactory results.

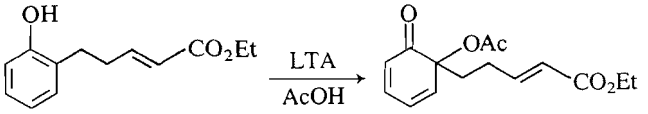

26 **30**

The Wessely oxidation – Diels–Alder sequence was then investigated with the simplest *o*-(3-alkenyl) phenol, **14**. Treatment of **14** with lead tetraacetate in acetic acid gave a crude product whose ^{1}H nmr spectrum was dominated by a sharp methyl singlet at δ 2.01, assigned to the acetoxyl protons of the *o*-quinol acetate **31**; in addition, signals for the terminal alkene were evident at δ 4.8–5.8. Its ir spectrum showed strong peaks at 5.71 and 5.9 μm, consonant with the acetoxyl and 2,4-dienone functions of **31**.[6] This product was heated in boiling benzene and the progress of the intramolecular Diels–Alder reaction was followed by ^{1}H nmr spectroscopy. The formation of the tricyclic product **32** was evidenced by the appearance of a new acetoxyl proton signal at δ 1.97 and the diminution of the acetoxyl proton signal of **31** at δ 2.01. After 54

[4]Coumarin **16** is commercially available and coumarin **17** was prepared from *m*-cresol, malic acid, and sulfuric acid by a modification of the method of Bailey and Boethner (13).

[5]This difficulty may stem from the propensity for triphenylphosphine oxide to form very stable complexes with phenols (18).

[6]Each of these bands occurs at shorter wavelength than the wavelengths characteristic of the individual carbonyl functions; this is not uncommon for α-acyloxy ketones and results most probably from dipole–dipole interactions (24).

Can. J. Chem. Downloaded from www.nrcresearchpress.com by 213.222.148.141 on 09/07/12
For personal use only.

TABLE 1. ^{13}C nuclear magnetic resonance spectra of 3,4-dihydrocoumarins and 2-chromanols[a]

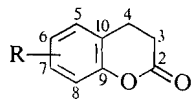

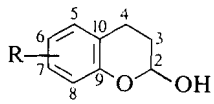

	18 R = H	**19** R = 6-Me	**20** R = 7-Me	**21** R = H	**22** R = 6-Me	**23** R = 7-Me
C-2	168.2	168.6	168.5	92.2	92.2	92.3
C-3	29.1	29.2	29.3	27.1	27.2	27.3
C-4	23.6	23.6	23.3	20.4	20.4	20.0
C-5	128.1	128.5	127.8	129.3	129.6	129.0
C-6	124.3	133.9	125.0	120.9	129.9	121.8
C-7	128.1	128.6	138.3	127.4	128.0	137.4
C-8	116.7	116.4	117.2	116.9	116.5	117.3
C-9	152.1	149.9	152.0	152.1	149.8	151.8
C-10	122.9	122.4	119.6	122.1	121.7	118.9
R	—	20.6	21.0	—	20.4	21.0

[a]In $CDCl_3$; the assignments are in accord with the signal multiplicities in single-frequency off-resonance decoupled spectra.

TABLE 2. ^{13}C nuclear magnetic resonance spectra of (4-*o*-hydroxyphenyl)-butenes[a]

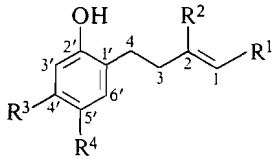

	14	**15**	**26**	**27**	**28**
R^1	H	H	CO_2Et	CO_2Et	CO_2Et
R^2	H	Me	H	H	H
R^3	H	H	H	H	Me
R^4	H	H	H	Me	H
C-1	115.0	110.3	121.4	121.5	121.4
C-2	138.3	145.8	149.5	149.0	149.4
C-3	33.8	37.8	32.4	32.5	32.6
C-4	29.5	28.5	28.8	28.8	28.4
C-1′	128.2	128.5	127.4	127.0	124.0
C-2′	153.3	153.5	154.0	151.5	153.8
C-3′	115.5	115.4	115.4	115.2	116.2
C-4′	127.2	127.1	127.5	127.8	137.3
C-5′	121.0	120.9	120.5	129.8	121.3
C-6′	130.3	130.1	130.1	130.8	129.9
R^1	—	—	167.5	167.1	167.3
	—	—	60.5	60.3	60.4
	—	—	14.2	14.2	14.2
R^2	—	22.6	—	—	—
R^3	—	—	—	—	20.9
R^4	—	—	—	20.4	—

[a]See footnote *a*, Table 1.

hours the ratio of these peaks remained constant. The lethargy of the Diels–Alder reaction was not unexpected since the dienophilic ethylenic bond was unactivated in this case. When the cyclization was carried out in boiling toluene or xylene, the rate of the reaction was increased but the yield and purity of **32** were not significantly improved. Since it is known that *o*-quinol acetates dimerize via an intermolecular Diels–Alder reaction at elevated temperatures (21), reaction conditions were then chosen so as to minimize the concentration of the Wessely product during the ring-closure reaction and thus favor the

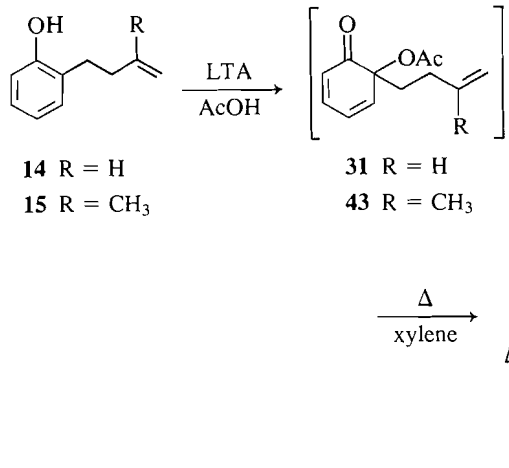

SCHEME 6

monomolecular ring closure reaction over the intermolecular Diels–Alder reaction. Thus the slow addition of a solution of **31** in xylenes to the reaction flask containing boiling xylenes gave the highest, albeit still modest (*vide infra*), yield of **32**.

The structure of the Diels–Alder reaction product was provisionally assigned as **32** in analogy to structures of type **4** that had previously been assigned to the analogous tricyclic lactones (Scheme 2) (1, 2). This assumes that the addition is of the quasi "ortho" type (25). However, there is sufficient precedent to suggest that the product might possibly arise by the less usual quasi "pene" type of reaction (25), resulting in a twistane derivative **33** rather than the isotwistane derivative **32**.

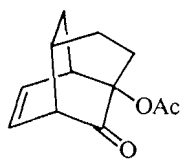

33

Thus, for example, Greuter and Schmid (7*d*) have found that a mixture of both types of product, **35** and **36**, are formed from compound **34** (Scheme 7). Although it has been demonstrated that in the case of the lactones only the "ortho" products of type

Can. J. Chem. Downloaded from www.nrcresearchpress.com by 213.222.148.141 on 09/07/12
For personal use only.

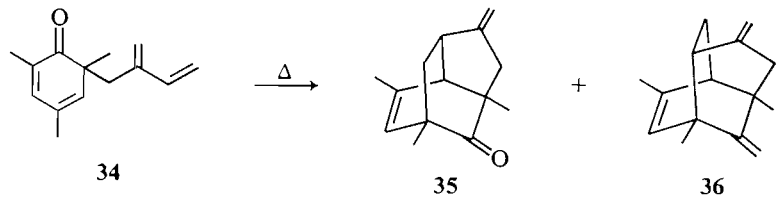

SCHEME 7

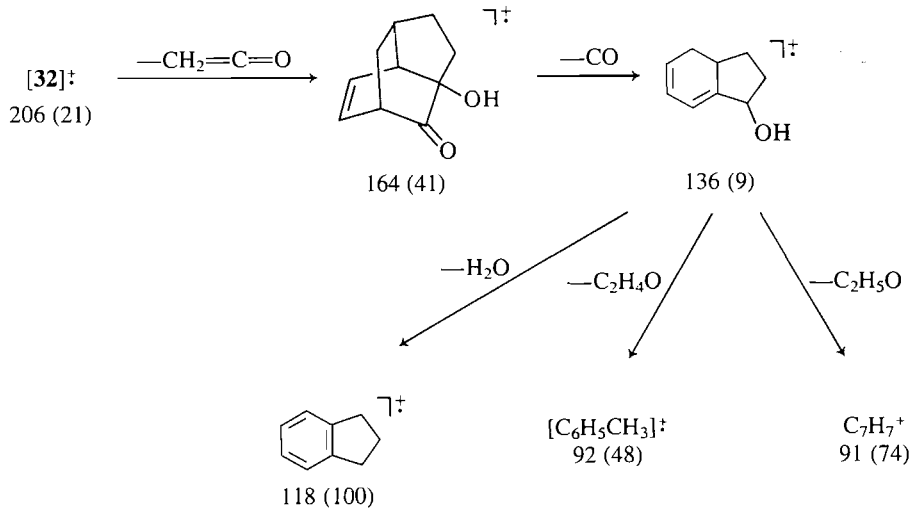

SCHEME 8

4 are formed (2), it could not be excluded *a priori* that the tricarbocyclic products in the present work were of type **33**. Their spectra and chemistry in fact establish that they are of type **32** rather than **33**. Nevertheless, several facets of their spectra can be interpreted in terms of either. We shall discuss the spectra in terms of structure **32**, emphasizing those aspects that distinguish it from **33**.

The ir spectrum shows carboxyl-stretching bands at 5.70 (sh) and 5.76 μm in accord with the α-acyloxy ketone function.[6] The mass spectrum shows several prominent peaks in addition to the molecular ion peak at *m/z* 206; the fragmentation is interpretable as shown in Scheme 8.

The 400-MHz ^{1}H nmr spectrum is given in Table 3 together with the assignments for structure **32**.[7] These are based on the chemical shifts and coupling constants and comparison of these with those in the spectra of **4** and its congeners (2). They are ambiguous in the cases of the C-9 and C-10 protons, but otherwise appear to be secure. In particular, decoupling experiments confirmed that the protons that give rise to signals at δ 3.47 and 6.12 are coupled, as are those giving rise to signals at δ 3.11 and 6.21. Thus irradiation at the frequencies corresponding to δ 3.47 and 3.11 led to collapse of the signals at δ 6.12 and 6.21 to doublets of doublets with J = 6 and 1.5 Hz, and J = 6.5 and 2 Hz, respectively.

It is important to note that this ^{1}H nmr spectrum does not of itself unambiguously distinguish structures **32** and **33**. However, from its relation to the spectrum of **31**, formed by mild hydrolysis of **32** (Scheme 9), such a distinction can be reached. The allylic bridgehead proton signals of **32** at δ 3.11 and 3.47 appear at δ 3.18 and 3.02, respectively, in the spectrum of **37**. The large upfield shift of Δδ −0.45 clearly

TABLE 3. The 400-MHz ^{1}H nmr spectrum of compound **32**[a]

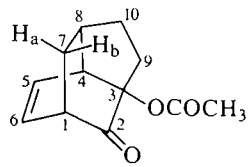

H-1	3.11 (m, 1H)
H-4	3.47 (ddd, J = 6, 4.5, 2 Hz, 1H)
H-5	6.12 (ddd, J = 8, 6, 1.5 Hz, 1H)
H-6	6.21 (ddd, J = 8, 6.5, 2 Hz, 1H)
H-7a	1.64 (ddd, J = 13, 10.5, 2 Hz, 1H)
H-7b	1.37 (ddd, J = 13, 3, 2 Hz, 1H)
H-8	2.20 (m, 1H)
H-9	2.39 (dddd, J = 14, 12, 3, 1.5 Hz, 1H)
	1.47 (ddd, J = 12, 9, 2.5 Hz, 1H)
H-10	2.02 (m, 1H)
	1.84 (m, 1H)
CH_3COO-	1.96 (s, 3H)

[a]In $CDCl_3$.

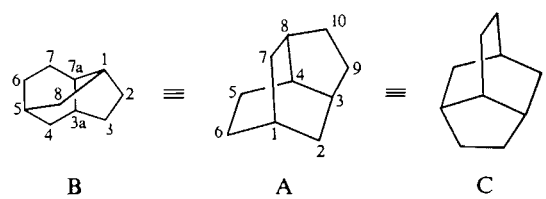

[7]The numbering system *A* used in Table 3 and in the ensuing discussion here is based on the numbering system for bicyclo[2.2.2]oct-5-en-2-one since we have used this previously for the lactones of type **4** (3). The *Chemical Abstracts* numbering of the 1,5-methanoindene system (*B*) is used in the experimental section. A further representation of this system is given in *C*.

Can. J. Chem. Downloaded from www.nrcresearchpress.com by 213.222.148.141 on 09/07/12
For personal use only.

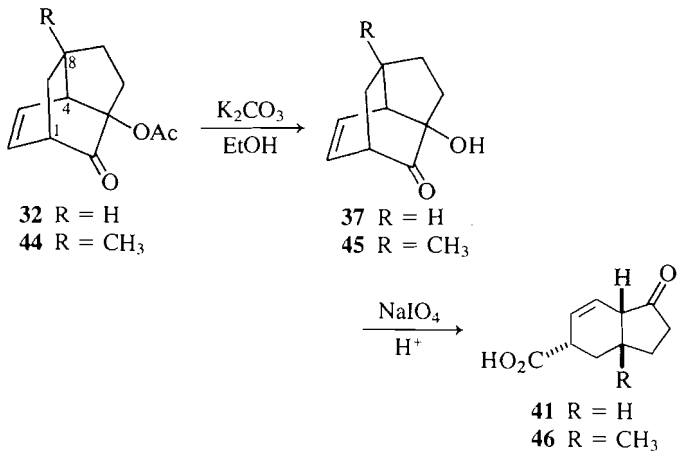

32 R = H
44 R = CH_3

37 R = H
45 R = CH_3

41 R = H
46 R = CH_3

SCHEME 9

demonstrates that the protons giving rise to the δ 3.47 and 3.02 signals must be on carbon atoms adjacent to those bearing the acetoxyl and hydroxyl groups (cf., for example, the upfield shift of Δδ −0.51 previously observed for the corresponding proton signal in the alcohol **39** (δ 3.53) vs. the acetate **38** (δ 4.04) (6)). This excludes the possibility that the structure of the Diels–Alder product is **33** and that of its hydrolysis product is **40** and that the δ 3.11 and 3.47 signals are assignable to the C-1 and C-4 protons, respectively, in **33**.

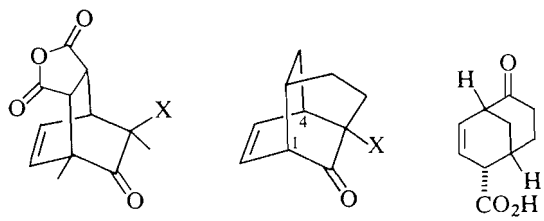

38 X = OAc
39 X = OH

33 X = OAc
40 X = OH

42

Related evidence is provided by the ^{13}C nmr spectra of compounds **32** and **37** (experimental section). The signals for C-1 and C-4 in the former occur at δ 47.4 and 46.3, respectively, while they appear at δ 47.0 and 49.0, respectively, in the latter. The larger effect of conversion of the acetoxyl to a hydroxyl group (Δδ 3.7) is expected for the bridgehead carbons adjacent to the carbons bearing these groups, i.e., C-4 in **32** and **37**. The differential shift has the opposite sign to that observed in the proton spectra: this can readily be attributed to a γ-effect that is operative in the acetoxy but not in the hydroxy compound (26). A similar effect may be noted in the ^{13}C nmr spectra of compounds **38** and **39**, where Δδ = 1.6. The remainder of the ^{13}C nmr spectra of **32** and **37** are also in consonance with the structural assignments.[8]

A further piece of evidence that confirms the assignment of structure **32** rather than **33** to the Diels–Alder product comes from the ir spectrum of the product formed on treatment of the hydrolysis product **37** with periodic acid. This is a keto acid, as expected for either structure **32** or **33**. Its ir spectrum shows carbonyl peaks at 5.74 and 5.83 μm, demonstrating that the ketonic group is in a five-membered ring as in **41**, the product derived from **37**, and excluding the cyclohexanone derivative **42** that would be formed from **40**.

The spectra of the Diels–Alder product **44** derived from the Wessely oxidation product **43** of phenol **15** (Scheme 6) bear the expected relationship to those of **32**, as do the spectra of its hydrolysis product **45** and the periodic acid oxidation product, **46** (Scheme 9). In particular, the methyl group at C-8 shields the C-4 proton (Δδ −0.36) and deshields the C-4 carbon (Δδ 5.8) of **44**, and conversion of **44** and **45** results in a shielding of the C-4 proton (Δδ −0.52) and a deshielding of C-4 itself (Δδ 2.9). Analogy for the former effect is found in the effect of the C-8 methyl group in the tricyclic lactone **47** on the chemical shifts of the C-4 proton (Δδ −0.50) and of C-4 (Δδ 6.5) of the parent lactone **4** (2, 27). Again the ir spectrum of the periodic acid product **4***b* shows the presence of a cyclopentanone rather than a cyclohexanone moiety.

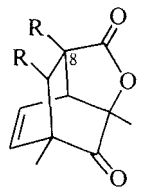

47 R = CH_3
4 R = H

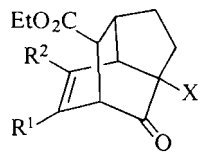

48 $R^1 = R^2 = H$, X = OAc
49 $R^1 = H$, $R^2 = CH_3$, X = OAc
50 $R^1 = CH_3$, $R^2 = H$, X = OAc
51 $R^1 = R^2 = H$, X = OH
52 $R^1 = H$, $R^2 = CH_3$, X = OH
53 $R^1 = CH_3$, $R^2 = H$, X = OH

Wessely oxidation of the *o*-(3-alkenyl) phenols **26–28** bearing an ethoxycarbonyl group at the terminal carbon of the ethylenic double bond gave 6-acetoxy-2,4-cyclohexadienones that were not isolated but were directly subjected to Diels–Alder cyclization. As expected, the presence of the ethoxycarbonyl groups increased the dienophilicity of the side chain ethylenic double bonds, and the Diels–Alder reactions in boiling xylenes under the same conditions as previously described were complete in 12 h giving the tricarbocyclic acetoxy ketones **48–50**, which were converted to the corresponding alcohols **51–53** with potassium carbonate in boiling methanol. Comparison of their ir and ^1H and ^{13}C nmr spectra (see experimental section) with each other and with those of the acetoxy and hydroxy ketones discussed previously established that the Diels–Alder reactions had again given the "ortho" products **48–50**.

The feasibility of the synthesis of isotwistane derivatives of type **7** by tandem Wessely oxidation – Diels–Alder reaction sequences of *o*-(3-alkenyl) phenols has thus been established. Although the overall yields were modest (20–35%), we consider that this disadvantage is offset by the brevity of the synthetic sequence. Furthermore, this sequence, unlike some related sequences involving intramolecular reactions of 6-alkenyl-2,4-cyclohexadien-1-ones (7), results in isotwistane derivatives with both carbonyl and hydroxyl functions, a feature that is of potential importance in their further synthetic elaboration.

Experimental

Melting points were determined on a Fisher–Johns apparatus and are uncorrected. Infrared (ir) spectra were recorded in $CHCl_3$ solution; the appearance of bands, where noted, is designated as strong (s), medium (m), weak (w), and broad (br). Proton nuclear magnetic resonance (^1H nmr) spectra were recorded at 60 MHz in $CDCl_3$ solution unless otherwise specified. Carbon-13 nuclear magnetic resonance (^{13}C nmr) spectra were recorded in $CDCl_3$ solution; signal multiplicities were determined from single-frequency off-resonance decoupled spectra. Mass spectra were recorded at 70 eV with a Bell and Howell CEC 21-490 single-focussing mass spectrometer and molecular ion peak

[8]It is planned to discuss these spectra in detail elsewhere.

Can. J. Chem. Downloaded from www.nrcresearchpress.com by 213.222.148.141 on 09/07/12
For personal use only.

Can. J. Chem. Downloaded from www.nrcresearchpress.com by 213.222.148.141 on 09/07/12
For personal use only.

positions are reported in mass-to-charge (m/z) units followed by the relative abundance in parentheses. Exact mass measurements were determined from high resolution mass spectra obtained on an AEI-MS 902 double-focussing mass spectrometer.

Preparative thin-layer chromatography (tlc) was carried out on 200 × 200 × 2.0 mm silica gel "G" plates containing a fluorescent indicator. The bands were extracted with ether or methanol. Column chromatography was carried out with MN-Kieselgel 60 (70–270 mesh ASTM). Unless otherwise indicated, all organic solvents were evaporated by means of a Buchi "Rotovapor ⟨R⟩" rotary evaporator at water aspirator pressure. Solvents were distilled immediately before use. Where required, dry hydrocarbons and ethers were obtained by boiling the solvent under reflux over, and distilling from, sodium ribbon. Dry diethyl ether for the Grignard coupling reactions was distilled from $LiAlH_4$. Dry ethanol was obtained by boiling absolute ethanol over, and distilling from, magnesium. Anhydrous experiments were carried out under dry nitrogen that had been passed through concentrated H_2SO_4, followed by KOH. Brine refers to a saturated aqueous solution of NaCl.

*o-Methoxybenzyl chloride (**8**)*

An ice-cooled solution of *o*-anisaldehyde (31.9 g, 0.23 mol) in methanol (120 mL) was treated with a solution of $NaBH_4$ (7.68 g, 0.20 mol) in aqueous 5% NaOH (150 mL). The reaction mixture was stirred for 12 h and the methanol was evaporated under reduced pressure. The residue was taken up in ethyl acetate (150 mL), and the solution was washed with water (100 mL) and brine (100 mL) and dried over Na_2SO_4. Evaporation of the solvent left *o*-methoxybenzyl alcohol (25.9 g, 80%); ^{1}H nmr δ: 2.77 (bs, 1H), 3.79 (s, 3H), 4.63 (bs, 2H), 6.7–7.3 (m, 4H).

The crude alcohol (10.0 g, 72 mmol) in benzene (80 mL) and pyridine (0.2 mL) was treated dropwise with $SOCl_2$ (15 g, 126 mmol) over a period of 20 min. The solution was heated to reflux for 2.5 h, cooled, and evaporated under reduced pressure. The residue was taken up in ether (250 mL), and the organic solution was washed with water (100 mL) and brine (100 mL) and dried over Na_2SO_4. After evaporation of the solvent, **8** was distilled, bp 57°C/0.15 Torr (lit. (9) bp 64–65°C/0.3 Torr; 1 Torr = 133.3 Pa) as a colorless liquid (7.91 g, 51 mmol, 70%); ^{1}H nmr δ: 3.82 (s, 3H), 4.63 (s, 2H), 6.6–7.3 (m, 4H).

*4-(2-Methoxyphenyl)-1-butene (**9**)*

A solution of **8** (29.9 g, 0.190 mol) in dry ether (150 mL) was added to magnesium turnings (6.1 g, 0.25 mol) in 25 mL of ether at a rate that maintained reflux. The mixture was heated for a further 30 min, cooled to ambient temperature, and decanted under a nitrogen atmosphere through a glass wool plug into a three-necked flask equipped with an addition funnel and a reflux condenser. The filtrate containing the Grignard reagent was treated dropwise with allyl bromide (33.5 g, 0.280 mol) in ether (50 mL) at a rate that sustained reflux. The solution was heated for a further 2 h, cooled with an ice bath, and treated with aqueous NH_4Cl (25 mL). The mixture was diluted with water (100 mL) and the organic layer was separated. The aqueous layer was extracted with ether (3 × 100 mL) and the combined extracts were dried (K_2CO_3) and evaporated to give a pale yellow oil, which was distilled to give **9** as a colorless liquid (15.2 g, 0.094 mol, 49%), bp 89–90°C/14 Torr (lit. (8) bp 120–123°C/18 Torr); ^{1}H nmr δ: 2.3–3.0 (m, 4H), 3.82 (s, 3H), 4.9–5.3 (m, 2H), 5.7–6.3 (m, 1H), 6.8–7.3 (m, 4H).

*4-(2-Hydroxyphenyl)-1-butene (**14**)*

*(a) From **9***

Under a nitrogen atmosphere, a 50% dispersion of NaH (1.68 g, 350 mmol) in oil was washed with dry hexanes (10 mL) and dry ether (10 mL), and then the NaH was suspended in dry DMF (20 mL). A solution of ethanethiol (2.10 mL, 40 mmol) in DMF (40 mL) was added and when gas evolution had ceased, **9** (2.56 g, 15.2 mmol) in DMF (20 mL) was added. The mixture was heated at reflux for 2 h, cooled in an ice bath, and carefully neutralized with aqueous 10% HCl. The neutralized solution was extracted with ether (5 × 50 mL) and the ethereal extracts were washed with water (150 mL) and brine (3 × 50 mL). The resulting pale yellow solution was dried and evaporated to leave an orange oil. Consecutive molecular distillations (38°C/0.01 Torr; lit. (8) bp 78°C/2.5 Torr) gave **14** (1.63 g, 11.2 mmol, 74%) as a colorless liquid; ir λ_{max}: 2.88, 3.10, 3.51, 6.10, 6.29 μm; ^{1}H nmr δ: 2.3–2.9 (m, 4H), 4.8–5.3 (m, 3H), 5.18 (bs, 1H, absent after D_2O treatment), 5.5–6.2 (m, 1H), 6.5–7.2 (m, 4H); ms m/z: 148 (32).

*(b) From **21***

Under a nitrogen atmosphere, a 50% dispersion of NaH (2.16 g, 45 mmol) in oil was washed with dry pentanes and ether and then treated with DMSO (20 mL). The mixture was heated at 80°C until gas evolution ceased. To the deep gray solution was added methyl triphenylphosphonium bromide (15.72 g, 44 mmol) in DMSO (75 mL) at room temperature. After 15 min a solution of 2-chromanol (**21**) (3.23 g, 21 mmol) in DMSO (5 mL) was added. After a further 30 min the reaction mixture was quenched with water (50 mL), and the solution was neutralized (dilute aqueous HCl) and extracted with ether (4 × 50 mL). The organic extracts were washed with water (100 mL) and brine (100 mL) and dried over $MgSO_4$. The solution was evaporated and the residual yellow oil was purified by molecular distillation (110°C/0.10 Torr) to give **14** (1.06 g, 7.25 mmol, 35%) as a colorless oil. Its spectral data were identical to those of the product from route (*a*).

*4-(2-Methoxyphenyl)-2-methyl-1-butene (**10**)*

The Grignard reagent was prepared from **8** (7.82 g, 0.0482 mol) and magnesium (1.82 g, 0.078 mol) in ether (25 mL) as in the preparation of **9** above; in this case a crystal of iodine was added to initiate the reaction. The solution was cooled in a Dry Ice – acetone bath and treated with freshly distilled methallyl chloride (9.06 g, 0.100 mol) in ether (20 mL). The mixture was then warmed to reflux and maintained at reflux for 1 h. Work-up as in the case of **9** gave **10** as a colorless liquid (4.54 g, 0.0258 mol, 53.5%), bp 107–108°C/10 Tor; ^{1}H nmr δ: 1.77 (s, 3H), 2.1–2.4 (m, 2H), 2.6–2.9 (m, 2H), 3.77 (s, 3H), 4.68 (s, 2H), 6.6–7.2 (m, 4H).

*4-(2-Hydroxyphenyl)-2-methyl-1-butene (**15**)*

Compound **15** was prepared by treatment of **10** (2.95 g, 0.0167 mol) with sodium thioethoxide (from NaH (50% dispersion; 19.3 g, 0.0444 mol) and ethanol (293 g, 0.0471 mol)) in DMF was in the preparation of **14** from **10** above. Molecular distillation (80°C/0.005 Torr) of the crude product gave **15** as a colorless liquid (2.25 g, 0.0141 mol, 84.5%); ^{1}H nmr δ: 1.72 (s, 3H), 2.1–2.4 (m, 2H), 2.6–2.9 (m, 2H), 4.73 (s, 2H), 5.67 (bs, 1H, absent after D_2O treatment), 6.6–7.1 (m, 4H).

*2-Chromanol (**21**)*

Dihydrocoumarin (**18**) (14.6 g, 0.10 mol) in dry toluene (250 mL) was cooled to −78°C and treated over a period of 2 h with diisobutylaluminum hydride (25% in toluene; 74.6 mL, 0.110 mol). The reaction mixture was stirred for a further 2 h at −78°C, treated dropwise with water (50 mL), warmed to room temperature, treated with Celite, and suction filtered. The filtrate was extracted with ether (5 × 100 mL) and the combined organic solutions were washed with water (200 mL) and brine (200 mL) and dried over Na_2SO_4. The Celite and filtered salts were shaken with ether (200 mL) and the mixture was filtered. The filtrate was washed with water (100 mL) and brine (100 mL) and dried as above. Evaporation of the combined organic solutions left a pale yellow liquid, which was distilled (bp 95–96°C/0.10 Torr; lit. (14) bp 88–89°C/0.05 Torr) to give **21** as a colorless liquid (12.6 g, 0.84 mol, 84%); ir λ_{max}: 2.86, 3.02, 3.48, 6.33 μm; ^{1}H nmr δ: 1.8–2.2 (m, 2H), 2.5–3.1 (m, 2H), 3.44 (d, 1H, J = 4 Hz, absent after D_2O treatment), 5.56 (dt, 1H, J = 4, 3 Hz; t, J = 3 Hz after treatment with D_2O), 6.6–7.2 (m, 4H).

*Ethyl 5-(2-hydroxyphenyl)-2-pentenoate (**26**)*

2-Chromanol (**21**) (1.30 g, 8.65 mmol) in benzene (25 mL) was treated with carboethoxymethylenetriphenylphosphorane (3.05 g, 9.00 mmol) in benzene (25 mL). After 12 h the solvent was evaporated to leave a colorless, viscous oil that was a mixture of **26** and triphenylphosphine oxide. The crude mixture was used without

Can. J. Chem. Downloaded from www.nrcresearchpress.com by 213.222.148.141 on 09/07/12
For personal use only.

purification in the subsequent Wessely oxidation. The phenol **26** could be isolated by preparative tlc (hexanes/ethyl acetate, 4:1) as a colorless oil; ir λ_{max}: 5.85 μm; ^{1}H nmr δ: 1.17 (t, J = 8 Hz, 3H), 2.3–3.0 (m, 4H), 4.18 (q, J = 8 Hz, 2HO), 5.84 (dt, J = 15, 2 Hz, 1H), 6.35 (s, 1H, absent after D_2O treatment), 6.6–7.4 (m, 5H); ms m/z: 220 (52). *Exact Mass* calcd. for $C_{13}H_{16}O_3$: 220.1100; found: 220.1101.

*3,4-Dihydro-6-methylcoumarin (**19**)*

6-Methylcoumarin (**16**) (10.54 g, 65.8 mmol) in ethyl acetate (250 mL) was added slowly to 10% Pd/C (1.20 g) in a Parr hydrogenation flask. The mixture was shaken under a hydrogen atmosphere (57 psi; 1 psi = 6.9 kPa) for 3 h, after which time no further uptake of hydrogen could be observed. The reaction mixture was filtered through a layer of Celite in a sintered glass funnel and, after evaporation of the solvent, a colorless oil was left, which crystallized on standing. Drying under vacuum (0.10 Torr) overnight left **19** as white crystals (10.51 g, 64.8 mmol, 98.5%), mp 80–81°C (lit. (28) mp 81°C); ir λ_{max}: 5.68 μm; ^{1}H nmr δ: 2.30 (s, 3H), 2.5–3.1 (m, 4H), 6.3–7.1 (m, 3H).

*6-Methyl-2-chromanol (**22**)*

3,4-Dihydro-6-methylcoumarin (**19**) (15.9 g, 98.0 mmol) in dry toluene (250 mL) under a nitrogen atmosphere was treated dropwise at −78°C (Dry Ice – acetone) with diisobutylaluminum hydride (70.0 mL, 104 mmol, 25% solution in toluene) over a period of 2 h. After a further 2 h at −78°C, water (50 mL) was added slowly to the stirred, cold solution. The mixture was allowed to warm to room temperature and more water (50 mL) was added, followed by ether (250 mL). The mixture was treated with Celite and filtered, and the precipitated salts were further extracted with ether (2 × 250 mL). The combined organic extracts were washed with brine (250 mL) and dried over Na_2SO_4. Removal of solvent left **22** as a colorless oil (14.6 g, 88.9 mmol, 90.7%); ir λ_{max}: 2.85 (w), 3.00 (w), 3.46 (w), 6.35 (m) μm; ^{1}H nmr δ: 1.7–2.1 (m, 2H), 2.23 (s, 3H), 2.5–3.0 (m, 2H), 3.75 (d, 1H, J = 4 Hz, absent after D_2O treatment), 5.46 (dt, 1H, J = 4, 3 Hz; t, J = 3 Hz, after D_2O treatment), 6.5–7.0 (m, 3H); ms m/z: 164 (29). *Exact Mass* calcd. for $C_{10}H_{12}O_2$: 164.0837; found: 164.0845.

*Ethyl 5-(2-hydroxy-5-methylphenyl)-2-pentenoate (**27**)*

6-Methyl-2-chromanol (**22**) (2.03 g, 12.3 mmol) in benzene (30 mL) was treated with carboethoxymethylenetriphenylphosphorane (4.40 g, 13.0 mmol) in benzene (30 mL) and the solution was stirred for 12 h. Evaporation of solvent left a pale yellow, viscous oil, which was used without purification in the Wessely oxidation. A sample of **27** was isolated by preparative tlc (hexanes/ethyl acetate, 4:1) as a colorless oil; ir λ_{max}: 5.85 μm; ^{1}H nmr δ: 1.25 (t, J = 7 Hz, 3H), 2.10 (s, 3H), 2.5–2.9 (m, 4H), 4.18 (q, J = 7 Hz, 2H), 5.77 (dt, J = 15.2 Hz, 1H), 6.5–7.2 (m, 4H), 6.80 (br s, 1H); ms m/z: 234 (43). *Exact Mass* calcd. for $C_{14}H_{18}O_3$: 234.1256; found: 234.1259.

*7-Methylcoumarin (**17**)*

A solution of *m*-cresol (54.1 g, 0.50 mol) in concentrated H_2SO_4 (125 mL) was heated to 110°C and treated over a 3-h period with malic acid (80.5 g, 0.60 mol). After being heated for a further 3 h, the reaction mixture was allowed to cool to room temperature and was then treated slowly with water (50 mL). After the reaction mixture had again cooled to room temperature, the dark solution was poured into ice (250 g) and the precipitate that formed was removed by filtering the mixture through a sintered glass funnel. The resulting tan solid was dissolved in boiling aqueous 50% ethanol (300 mL) and the solution was cooled slowly to −30°C. The cream-colored, shiny leaves that formed were recrystallized from aqueous 50% ethanol to give **17** (38.1 g, 0.24 mol, 48%) as white needles, mp 129–130°C (lit. (13) mp 128–130°C); ir λ_{max}: 5.78, 6.16 μm; ^{1}H nmr δ: 2.43 (s, 3H), 6.27 (d, J = 9.5 Hz, 1H), 6.9–7.5 (m, 3H), 7.60 (d, J = 9.5 Hz, 1H); ^{13}C nmr δ: 160.8 (s), 154.0 (s), 143.1 (s), 142.9 (d), 127.4 (d), 125.4 (d), 116.8 (d), 116.3 (d), 115.3 (d), 21.4 (q); ms m/z: 160 (11).

*3,4-Dihydro-7-methylcoumarin (**20**)*

7-Methylcoumarin (**17**) (10.0 g, 62.4 mmol) in ethyl acetate (250 mL) was added to 10% Pd/C (1.5 g) in a Parr hydrogenation vessel. The mixture was shaken under a hydrogen atmosphere (57 psi) for 6 h, at which time no further uptake of H_2 could be observed. The reaction mixture was filtered through Celite in a sintered glass funnel and evaporation of the solvent under reduced pressure left a colorless oil that crystallized upon standing. The crystalline mass was pulverized and dried *in vacuo* overnight to yield **20** (10.0 g, 61.7 mmol, 99%), mp 45–47°C (lit. (27) mp 44.5°C); ir λ_{max}: 5.67 μm; ^{1}H nmr δ: 2.31 (s, 3H), 2.5–3.1 (m, 4H), 6.7–7.2 (m, 3H).

*7-Methyl-2-chromanol (**23**)*

3,4-Dihydro-7-methylcoumarin (**20**) (1.62 g, 10.0 mmol) in dry toluene (40 mL) under a nitrogen atmosphere was treated at −78°C over a period of 90 min with diisobutylaluminum hydride (25% in toluene; 7.40 mL, 11.0 mmol). After a further 90 min the reaction mixture was quenched by the slow addition of water (50 mL). The solution was allowed to warm to room temperature. Celite was added to the mixture, which was then filtered and the filtrate was extracted with ether (4 × 100 mL). The extracts were washed with water (50 mL) and brine (50 mL) and dried over Na_2SO_4, and the solvent was evaporated to leave a pale yellow solid (1.42 g, 87%), which was recrystallized from hexanes – ethyl acetate to give **23** as white crystals, mp 103–103.5°C; ir λ_{max}: 2.86, 3.02, 3.47, 6.33 μm; ^{1}H nmr δ: 1.8–2.1 (m, 2H), 2.26 (s, 3H), 2.5–3.0 (m, 2H), 3.6 (br s, 1H), 5.47 (t, J = 3 Hz, 1H), 6.5–7.0 (m, 3H); ms m/z: 164 (65). *Exact Mass* calcd. for $C_{10}H_{12}O_2$: 164.0837; found: 164.0842. *Anal.* calcd. for $C_{10}H_{12}O_2$: C 73.14, H 7.37; found: C 73.08, H 7.43.

*Ethyl 5-(2-hydroxy-4-methylphenyl)-2-pentenoate (**28**)*

7-Methyl-2-chromanol (**23**) (2.75 g, 16.8 mmol) in benzene (30 mL) was mixed with carboethoxymethylenetriphenylphosphorane (6.09 g, 18.0 mmol) in benzene (30 mL). After 12 h the solvent was evaporated to leave a crude mixture of **28** and triphenylphosphine oxide as a colorless, viscous oil that was used without purification in the subsequent Wessely oxidation. Compound **28** could be purified by preparative tlc (hexanes/ethyl acetate, 5:2) to give a colorless oil that crystallized upon standing. Recrystallization from hexanes–$CHCl_3$ gave **28**, mp 63.5–64.5°C; ir λ_{max}: 5.79 μm; ^{1}H nmr δ: 1.26 (t, J = 7 Hz, 3H), 2.24 (s, 3H), 2.4–2.9 (m, 4H), 4.16 (q, J = Hz, 2H), 5.68 (br s, 1H), 5.78 (dt, J = 15, 2 Hz, 1H), 6.5–7.1 (m, 4H); ms m/z: 234 (48). *Anal.* calcd. for $C_{14}H_{18}O_3$: C 71.77, H 7.74; found: C 71.57, H 7.75.

*3a-Acetyloxy-1,2,3,3a,5,7a-hexahydro-1,5-methano-4*H*-inden-4-one (**32**)*

To a suspension of lead tetraacetate (14.5 g, 32.8 mmol) in acetic acid (100 mL) was added **14** (2.96 g, 20.0 mmol) in acetic acid (25 mL). The reaction mixture was stirred under nitrogen for 12 h and then treated with water (100 mL), stirred briefly, and evaporated to a viscous dark oil. The oil was extracted with ether (3 × 100 mL), the extracts were gravity filtered and washed with water (100 mL), saturated aqueous $NaHCO_3$ (100 mL), water (100 mL), and brine (100 mL). After being dried over Na_2SO_4, the solution was evaporated to a dark orange oil (2.52 g). The oil was taken up in freshly distilled xylenes (100 mL) and added over a 4-h period to boiling xylenes (200 mL). After 24 h at reflux, the bulk of the solvent was distilled at atmospheric pressure, and the residual solvent was distilled under vacuum (1.0 Torr), to leave a viscous yellow oil (1.40 g). This was molecularly distilled (45°C/0.01 Torr) to give **32** as a colorless solid (1.14 g, 5.51 mmol, 28%), mp 44–50°C, which was further purified by column chromatography (hexanes/ethyl acetate, 9:1), mp 51–53°C; ir λ_{max}: 5.70, 5.76 μm; ^{1}H nmr δ: 1.4–2.6 (m, 7H), 2.00 (s, 3H), 3.15 (m, 1H), 3.51 (m, 1H), 6.18 (m, 2H); ^{13}C nmr δ: 208.2 (s), 169.9 (s), 131.7 (d), 129.8 (d), 84.4 (s), 47.4 (d), 46.3 (d), 34.3 (d), 31.2 (t), 29.8 (t), 28.9 (t), 21.7 (q); ms m/z: 206 (21). *Exact Mass* calcd. for $C_{12}H_{14}O_3$: 206.0943; found: 206.0934.

*3a-Hydroxy-1,2,3,3a,5,7a-hexahydro-1,5-methano-4*H*-inden-4-one (**37**)*

Compound **32** (210 mg, 1.02 mmol) in ethanol (15 mL) was stirred with anhydrous K_2CO_3 (10 mg, 0.07 mmol) for 12 h. The mixture was filtered, the filtrate was evaporated, and the residue was extracted with

Can. J. Chem. Downloaded from www.nrcresearchpress.com by 213.222.148.141 on 09/07/12
For personal use only.

ether (3 × 50 mL). The ether was evaporated to leave **37** as a colorless crystalline solid (0.12 g, 0.83 mmol, 82%), mp 101–104°C; ir λ_{max}: 2.79 (w), 5.77 (s) μm; ^{1}H nmr δ: 1.2–2.5 (m, 7H), 3.02 (m, 1H), 3.07 (br s, 1H, absent after D_2O treatment), 3.18 (m, 1H), 6.26 (m, 2H); ^{13}C nmr δ: 214.6 (s), 133 (d), 129.1 (d), 79.3 (s), 49.0 (d), 47.0 (d), 34.5 (d), 33.0 (t), 31.7 (t), 29.0 (t); ms *m/z*: 164 (5). *Exact Mass* calcd. for $C_{10}H_{12}O_2$: 164.0837; found: 164.0834.

*2,3,3a,4,5,7a-Hexahydro-1-oxo-1*H*-indene-5-carboxylic acid (**41**)*

Compound **37** (100 mg, 0.61 mmol) in THF (20 mL) was treated with $NaIO_4$ (150 mg, 0.70 mmol) in water (10 mL). The solution was acidified to pH 4 with dilute aqueous HCl and left to stand for 12 h. The solution was then diluted with water (20 mL) and the THF was evaporated. The aqueous solution was extracted with ether (2 × 50 mL), the ethereal extracts were dried over Na_2SO_4, filtered, and evaporated to give **41** as a pale yellow resin (71 mg, 39 mmol, 65%); ir λ_{max}: 5.74, 5.83 μm; ^{1}H nmr δ: 1.3–3.0 (m, 7H), 3.10 (m, 1H), 3.24 (m, 1H), 5.98 (s, 2H), 8.77 (br s, 1H, absent after D_2O treatment); ms *m/z*: 180 (8).

*3a-Acetyloxy-1,2,3,3a,5,7a-hexahydro-1-methyl-1,5-methano-4*H*-inden-4-one (**44**)*

Lead tetraacetate (32.8 g, 74.0 mmol) was mixed with acetic acid (200 mL), and **15** (6.00 g, 37.0 mmol) was added over a 2-h period. After a further 2 h, water (50 mL) was added and the mixture was evaporated to a dark oil. The oil was treated with water (200 mL) and extracted with ether (4 × 200 mL). The combined organic extracts were washed with water (100 mL), aqueous 5% $NaHCO_3$ (100 mL), water (100 mL), and brine (100 mL). After being dried over Na_2SO_4, the ethereal solution was evaporated to a dark, viscous oil. The oil was taken up in xylenes (50 mL) and added to boiling xylenes (250 mL) over a 4-h period. After 36 h at reflux, the solvent was evaporated to leave a dark oil, which was distilled (72–100°C/0.10 Torr) to give a yellow oil. This was purified by column chromatography (hexanes/ethyl acetate, 9:1) to give **44**, after recrystallization from pentane, as colorless crystals (1.79 g, 8.14 mmol, 22%), mp 87.5–90.5°C; ir λ_{max}: 5.71, 5.77 μm; ^{1}H nmr δ: 1.11 (s, 3H), 1.3–2.5 (m, 6H), 2.02 (s, 3H), 3.15 (m, 2H), 6.22 (m, 2H); ^{13}C nmr δ: 208.1 (s), 169.9 (s), 131.7 (d), 129.2 (d), 84.5 (s), 52.1 (d), 48.1 (d), 41.9 (s), 37.3 (t), 36.7 (t), 30.0 (t), 27.5 (q), 21.8 (q); ms *m/z*: 220 (60). *Exact Mass* calcd. for $C_{31}H_{16}O_3$: 220.1099; found: 220.1101.

*3a-Hydroxy-1,2,3,3a,5,7a-hexahydro-1-methyl-1,5-methano-4*H*-inden-4-one (**45**)*

Compound **44** (110 mg, 0.50 mmol) was stirred with anhydrous K_2CO_3 (10 mg, 0.07 mmol) in ethanol (15 mL) for 12 h. The mixture was filtered and the filtrate was evaporated to dryness. The residue was extracted with ether (3 × 50 mL) and the ether was evaporated to leave **45** as a colorless crystalline solid (86 mg, 0.48 mmol, 96%), mp 112–116°C; ir λ_{max}: 2.78 (w), 5.77 (s), μm; ^{1}H nmr δ: 1.10 (s, 3H), 1.1–2.0 (m, 6H), 2.63 (m, 1H), 3.12 (m, 1H), 3.41 (s, 1H, absent after D_2O treatment), 6.19 (m, 2H); ^{13}C nmr δ: 214.5 (s), 133.1 (d), 128.7 (d), 79.2 (s), 55.0 (d), 47.5 (d), 41.9 (s), 37.7 (t), 37.0 (t), 33.0 (t), 27.7 (q); ms *m/z*: 178 (4). *Exact Mass* calcd. for $C_{11}H_{14}O_2$: 178.0994; found: 178.0988.

*2,3,3a,4,5,7a-Hexahydro-3a-methyl-1-oxo-1*H*-indene-5-carboxylic acid (**46**)*

The hydroxy ketone **45** (145 mg, 81.3 mmol) was taken up in THF (20 mL) and treated with $NaIO_4$ (0.19 g, 0.87 mmol) in water (10 mL) and acidified with dilute HCl to pH 4. After 12 h the solution was reduced in volume to 10 mL and extracted with ether (4 × 25 mL). The ethereal extracts were dried over Na_2SO_4 and evaporated to give **46** as a light yellow oil (106 mg); ir λ_{max}: 5.76, 5.85 μm; ^{1}H nmr δ: 1.10 (s, 3H), 1.0–2.5 (m, 6H), 3.0–3.4 (m, 2H), 5.96 (s, 2H), 9.42 (br s, 1H, absent after D_2O treatment).

*Ethyl 1-acetyloxy-2,3,3a,4,5,7a-hexahydro-4-oxo-1,5-methano-1*H*-indene-8-carboxylate **48***

A mixture of **26** and triphenylphosphine oxide, prepared from **21** (1.30 g, 8.65 mmol), was taken up in acetic acid (50 mL) and added over a period of 2 h to lead tetraacetate (5.75 g, 13.0 mmol) in acetic acid (25 mL). After a further 2 h, water (100 mL) was added, and the mixture was evaporated to dryness. The residue was extracted with ether (5 × 50 mL), and the combined extracts were washed with water (2 × 100 mL), aqueous 5% $NaHCO_3$ (100 mL), and brine (100 mL). The organic solution was dried over Na_2SO_4 and evaporated to leave a deep orange resin. This was taken up in xylenes (100 mL) and the solution was slowly dripped into boiling xylenes (200 mL) over a period of 4 h. After a further 12 h, the solvent was evaporated and the residue was eluted with ether from a silica gel plug (10 g). The fractions containing **48** were combined and evaporated and the residue was purified by column chromatography (hexanes/ethyl acetate, 9:1) to give **48** (0.63 g, 2.25 mmol, 26%) as colorless crystals, mp 42–43°C; ir λ_{max}: 5.78 μm; ^{1}H nmr δ: 1.26 (t, J = 7 Hz, 3H), 1.5–2.6 (m, 5H), 2.05 (s, 3H), 2.83 (m, 1H), 3.64 (m, 2H), 4.16 (q, J = 7 Hz, 2H), 6.26 (m, 2H); ^{13}C nmr δ: 206.0 (s), 171.7 (s), 169.8 (s), 132.6 (d), 126.9 (d), 83.6 (s), 61.2 (t), 49.9 (d), 42.3 (d), 46.4 (d), 39.3 (d), 30.4 (t), 28.5 (t), 21.6 (q), 14.2 (q); ms *m/z*: 278 (4). *Anal.* calcd. for $C_{15}H_{18}O_5$: C 64.73, H 6.52; found: C 64.70, H 6.62.

*Ethyl 1-hydroxy-2,3,3a,4,5,7a-hexahydro-4-oxo-1,5-methano-1*H*-indene-8-carboxylate **51***

Compound **48** (73.2 mg, 0.26 mmol) in ethanol (10 mL) was stirred with anhydrous K_2CO_3 (10 mg, 0.07 mmol) for 12 h. The solvent was evaporated and the residue was extracted with ether (3 × 25 mL). The ethereal solution was filtered and evaporated to give **51** as a colorless oil (56.7 mg, 0.23 mmol, 88%); ir λ_{max}: 5.77 μm; ^{1}H nmr δ: 1.25 (t, J = 7 Hz, 3H), 1.5–2.3 (m, 4H), 2.5–3.0 (m, 2H), 3.15 (s, 1H), 3.63 (m, 2H), 4.17 (q, J = 7 Hz, 2H), 6.24 (m, 2H); ^{13}C nmr δ: 212.3 (s), 171.9 (s), 134.1 (d), 126.1 (d), 78.9 (s), 61.2 (t), 49.3 (d), 48.9 (d), 47.6 (d), 39.6 (t), 33.4 (t), 28.6 (t), 14.2 (q); ms *m/z*: 236 (10). *Exact Mass* calcd. for $C_{13}H_{16}O_4$: 236.1048; found: 236.1047.

*Ethyl 1-acetyloxy-2,3,3a,4,5,7a-hexahydro-7-methyl-4-oxo-1,5-methano-1*H*-indene-8-carboxylate **49***

The crude product **27** from the Wittig reaction of **22** (2.03 g, 12.3 mmol) in acetic acid (50 mL) was added to a suspension of lead tetraacetate (7.98 g, 18.0 mmol) in acetic acid (50 mL). After 12 h water (100 mL) was added, the reaction mixture was stirred for 15 min, and the solvents were evaporated. The residue was extracted with ether (5 × 50 mL) and the extracts were washed with water (2 × 100 mL), aqueous 5% $NaHCO_3$ (100 mL), and brine (100 mL). After being dried with Na_2SO_4, the ether was evaporated to leave a dark oil. The oil was taken up in xylenes (100 mL) and added slowly to boiling xylenes (200 mL). After 12 h, the solvent was evaporated and the residue was eluted with ether from a silica gel plug and then further purified by column chromatography (hexanes/ethyl acetate, 9:1) to give **49** as a colorless solid (1.19 g, 4.1 mmol, 33%), which was recrystallized from hexanes – ethyl acetate to give colorless crystals, mp 71.5–73°C; ir λ_{max}: 5.77 μm; ^{1}H nmr δ: 1.22 (t, J = Hz, 3H), 1.79 (d, J = 1.5 Hz, 3H), 1.5–2.6 (m, 5H), 2.02 (s, 3H), 2.80 (m, 1H), 3.42 (m, 2H), 4.14 (q, J = 7 Hz, 2H), 5.71 (m, 1H); ^{13}C nmr δ: 205.9 (s), 171.8 (s), 169.7 (s), 142.7 (s), 118.1 (d), 84.0 (s), 61.1 (t), 51.6 (d), 49.6 (d), 47.4 (d), 38.7 (d), 30.5 (t), 28.4 (t), 21.5 (q), 21.2 (q), 14.2 (q); ms *m/z*: 292 (15). *Exact Mass* calcd. for $C_{16}H_{20}O_5$: 292.1311; found: 292.1296. *Anal.* calcd. for $C_{16}H_{20}O_5$: C 65.74, H 6.90; found: C 65.38, H 7.01.

*Ethyl 1-hydroxy-2,3,3a,4,5,7a-hexahydro-7-methyl-4-oxo-1,5-methano-1*H*-indene-8-carboxylate **52***

The acetoxy ketone **49** (5.1 mg, 0.17 mmol) was treated with anhydrous K_2CO_3 (10.0 mg, 0.07 mmol) in ethanol (10 mL). After 12 h the solvent was evaporated and the residue extracted with ether (3 × 25 mL). The ethereal solution was filtered, dried with Na_2SO_4, and evaporated to leave a colorless solid (40.3 mg), which was recrystallized from hexanes – ethyl acetate to give **52** as a colorless crystalline solid (34.9 mg, 0.14 mmol, 83%), mp 105–106°C; ir λ_{max}: 5.77 μm; ^{1}H nmr δ: 1.22 (t, J = 7 Hz, 3H), 1.4–2.4 (m, 4H), 1.88 (s, 3H), 2.56 (m, 1H), 2.85 (m, 2H), 2.18 (s, 1H, absent after D_2O treatment), 3.52 (dd, J = 7, 3.5 Hz, 1H), 4.12 (q, J = Hz, 2H), 5.68 (m, 1H); ^{13}C nmr δ: 212.4 (s), 172.1 (s), 144.5 (s), 117.3 (d), 79.2 (s),

61.1 (s), 54.0 (d), 49.0 (d), 47.9 (d), 38.8 (d), 33.3 (t), 28.6 (t), 21.6 (q), 14.2 (q); ms *m/z*: 250 (8). *Exact Mass* calcd. for $C_{14}H_{18}O_4$: 250.1205; found: 250.1205. *Anal.* calcd. for $C_{14}H_{18}O_4$: C 67.18, H 7.25; found: C 67.06, H 7.25.

*Ethyl 1-acetyloxy-2,3,3a,4,5,7a-hexahydro-6-methyl-4-oxo-1,5-methano-1*H*-indene-8-carboxylate* ***50***

A mixture of phenol **78** and triphenylphosphine oxide, prepared from **23** (6.22 g, 37.9 mmol), in acetic acid (50 mL) was added to lead tetraacetate (33.7 g, 76.0 mmol) in acetic acid (50 mL). After 12 h the solvent was evaporated and the residue was extracted with ether (250 mL) and water (250 mL). The aqueous solution was extracted with ether (2 × 250 mL) and the combined organic extracts were washed with water (150 mL), aqueous 5% $NaHCO_3$ (3 × 150 mL), water (150 mL), and brine (150 mL). The deep orange solution was dried over Na_2SO_4 and evaporated. The red residue was taken up in xylenes (150 mL), added slowly to boiling xylenes (250 mL), and heated for 12 h. The solvent was evaporated and the residue was passed through a silica gel (10 g) plug with ether. The fractions containing **50** were combined and evaporated, and the dark, viscous resin that remained was purified by column chromatography (hexanes/ethyl acetate, 9:1) to give **50** as a colorless oil (3.88 g, 13.3 mmol, 35%). This was molecularly distilled to give a solid that was recrystallized from hexanes – ethyl acetate to give colorless crystals, mp 77–78°C; ir λ_{max}: 5.77, 5.79 μm; ^{1}H nmr δ: 1.26 (t, *J* = 8 Hz, 3H), 1.6–2.7 (m, 5H), 1.85 (d, *J* = 1.5 Hz, 3H), 2.02 (s, 3H), 2.82 (m, 1H), 3.47 (m, 2H), 4.16 (q, *J* = 8 Hz, 2H), 5.86 (m, 1H); ^{13}C nmr δ: 205.5 (s), 171.8 (s), 169.7 (s), 136.4 (s), 124.7 (d), 83.8 (s), 61.1 (t), 55.0 (d), 47.1 (d), 46.1 (d), 39.8 (t), 30.4 (t), 28.6 (t), 21.6 (q), 20.5 (q), 14.3 (q); ms *m/z*: 292 (15). *Exact Mass* calcd. for $C_{16}H_{20}O_5$: 292.1311; found: 292.1304. *Anal.* calcd. for $C_{16}H_{20}O_5$: C 65.74, H 6.90; found: C 65.77, H 6.94.

*Ethyl 1-hydroxy-2,3,3a,4,5,7a-hexahydro-6-methyl-4-oxo-1,5-methano-1*H*-indene-8-carboxylate* ***53***

Compound **50** (242.9 mg, 0.83 mmol) in ethanol (50 mL) was stirred with anhydrous K_2CO_3 for 12 h. The solvent was then evaporated and the residue was extracted with ether (3 × 50 mL). The ethereal solution was filtered and evaporated to a white crystalline solid. This was recrystallized from pentanes – ethyl acetate to give **53** (172 mg, 0.69 mmol, 83%), mp 110–112°C; ir λ_{max}: 5.77 μm; ^{1}H nmr δ: 1.26 (t, *J* = 7 Hz, 3H), 1.5–3.2 (m, 7H), 1.83 (d, *J* = 1.5 Hz, 3H), 3.11 (br s, 1H, absent after D_2O treatment), 3.39 (m, 1H), 4.19 (q, *J* = 7 Hz, 2H), 2.87 (m, 1H); ^{13}C nmr δ: 211.8 (s), 172.0 (s), 135.6 (s), 126.2 (d), 78.7 (s), 61.1 (t), 54.4 (d), 48.4 (d), 47.4 (d), 40.1 (d), 33.3 (t), 28.7 (t), 20.4 (q), 14.3 (q); ms *m/z*: 250 (7). *Exact Mass* calcd. for $C_{14}H_{18}O_4$: 250.1205; found: 250.1208.

Acknowledgments

We thank the Natural Sciences and Engineering Research Council of Canada for support of this work. One of us (T.M.) thanks the Government of Ontario for an Ontario Postgraduate Scholarship.

1. (*a*) D. J. Bichan and P. Yates. Can. J. Chem. **53**, 2054 (1975); (*b*) J. Am. Chem. Soc. **94**, 4773 (1972).
2. (*a*) P. Yates and H. Auksi. Can. J. Chem. **57**, 2853 (1979); (*b*) Chem. Commun. 1016 (1976).
3. T. S. Macas and P. Yates. Tetrahedron Lett. **24**, 147 (1983).
4. (*a*) F. Wessely, G. Lauterbach-Keil, and F. Schmid. Monatsh. Chem. **81**, 811 (1950); (*b*) F. Wessely and F. Sinwel. Monatsh. Chem. **81**, 1055 (1950).
5. (*a*) W. Metlesics, F. Wessely, and H. Budzikiewicz. Monatsh. Chem. **89**, 102 (1958); (*b*) F. Wessely and H. Budzikiewicz. Monatsh. Chem. **90**, 62 (1959).
6. H. Auksi and P. Yates. Can. J. Chem. **59**, 2510 (1981).
7. (*a*) A. Krantz and C. Y. Lin. J. Am. Chem. Soc. **95**, 5662 (1973); Chem. Commun. 1287 (1971); (*b*) F. Naf and G. Ohloff. Helv. Chim. Acta, **57**, 1868 (1974); (*c*) H. Greuter, G. Frater, and H. Schmid. Helv. Chim. Acta, **55**, 526 (1972); (*d*) H. Greuter and H. Schmid. Helv. Chim. Acta, **55**, 2382 (1972).
8. M. Oki and H. Iwamura. Bull. Chem. Soc. Jpn. **39**, 681 (1960).
9. R. Grice and L. N. Owens. J. Chem. Soc. 1947 (1963).
10. T. M. Cresp and M. Sargeant. J. Chem. Soc. Perkin Trans. 1, 2435 (1974).
11. G. A. Olah, S. C. Narang, B. G. Gupta, and R. Malhotra. J. Org. Chem. **44**, 1247 (1979); M. E. Jung and M. A. Lyster. J. Org. Chem. **42**, 3761 (1977); T.-L. Ho and G. A. Olah. Angew. Chem. Int. Ed. Engl. **15**, 774 (1976).
12. G. L. Feutrill and R. N. Mirrington. Aust. J. Chem. **25**, 1719 (1972).
13. (*a*) G. C. Bailey and F. Boettner. J. Ind. Eng. Chem. **13**, 905 (1921); (*b*) K. Fries and W. Klosterman. Chem. Ber. **39**, 871 (1906).
14. W. P. Parham and L. D. Huestis. J. Am. Chem. Soc. **84**, 813 (1962).
15. T. Tokorogama and R. Kanazawa. Synthesis, 526 (1976).
16. L. D. Bergel'son, E. V. Dyatlovitskaya, and M. M. Shemyakin. Izv. Akad. Nauk SSSR, Ser. Khim. 2003 (1964); Engl. 1904 (1964).
17. O. Isler, H. Gutman, M. Montavon, R. Ruegg, R. Ryser, and P. Zeller. Helv. Chim. Acta, **40**, 1242 (1957).
18. G. Akones and P. Albriktaen. Acta Chem. Scand. **22**, 1866 (1968); H. Schindlbauer and H. Stensenbergh. Monatsh. Chem. **79**, 2468 (1968).
19. (*a*) G. W. Rotermund. *In* Methoden der Organischen Chemie (Houben-Weyl). *Edited by* E. Muller. Georg Thieme Verlag, Stuttgart. 1975. pp. 243–251.
20. H. Auksi. Ph.D. Thesis, University of Toronto, Toronto, Ont. 1978.
21. K. Holmberg, H. Kirudd, and G. Westin. Acta Chem. Scand. Ser. B: **28**, 913 (1974).
22. H. C. Bell, J. T. Pinhey, and S. Sternhell. Aust. J. Chem. **32**, 1551 (1979).
23. F. Takacs. Monatsh. Chem. **95**, 961 (1964).
24. R. N. Jones and C. Sandorfy. *In* Chemical applications of spectroscopy. *Edited by* W. West. Interscience, New York. 1956. pp. 479–481.
25. G. Brieger and J. N. Bennett. Chem. Rev. **80**, 63 (1980).
26. J. B. Stothers. Carbon-13 nmr spectroscopy. Academic Press, New York. 1972. pp. 149–151.
27. G. E. Langford, H. Auksi, J. A. Gosbee, F. N. MacLachlan, and P. Yates. Tetrahedron, **17**, 1091 (1981).
28. T. Nakabayashi. J. Pharm. Soc. Jpn. **74**, 23 (1954).

Can. J. Chem. Downloaded from www.nrcresearchpress.com by 213.222.148.141 on 09/07/12
For personal use only.

Rate constants for abstraction of bromine from bromotrichloromethane by butyl, cyclopropylmethyl, and phenyl radicals in solution

LUKOSE MATHEW AND JOHN WARKENTIN[1]

Department of Chemistry, McMaster University, Hamilton, Ont., Canada L8S 4M1

Received July 15, 1987

LUKOSE MATHEW and JOHN WARKENTIN. Can. J. Chem. **66**, 11 (1988).

The radical chain decomposition of cyclopropylmethyl (1-hydroxy-1-methylethyl)-diazene ($(CH_3)_2C(OH)N{=}NCH_2$—◁ **1**) at 253–341 K in hexafluorobenzene or in dichloromethane solution containing bromotrichloromethane affords cyclopropylmethyl bromide, 4-bromo-1-butene, 1-bromo-5,5,5-trichloro-2-pentene, and 3,5-dibromo-1,1,1-trichloropentane from the cyclopropylmethyl portion of **1**. Other major products are nitrogen, acetone, and chloroform. The rate constant for formation of cyclopropylmethyl bromide by attack of cyclopropylmethyl free radicals from **1** at bromine of $BrCCl_3$ (k_{Br}^{cpm}) was calculated from the product composition using the known rate constant for rearrangement of cyclopropylmethyl radicals to 3-buten-1-yl radicals. At 25°C, $k_{Br}^{cpm} = 6.5 \times 10^8\ M^{-1}\ s^{-1}$ and the temperature dependence is given by $\log (k_{Br}^{cpm}/M^{-1}\ s^{-1}) = (10.6 \pm 0.3) - (2.4 \pm 0.4)/\theta$, where $\theta = 2.3RT\ \text{kcal/mol}^{-1}$. Non-chain decomposition of $(CH_3)_2C(OH)N{=}N$—R (**2**, R = Bu, and **3**, R = Ph) in the presence of excess 1,1,3,3-tetramethylisoindolin-2-yloxyl (**4**) and bromotrichloromethane afforded BuBr and PhBr, respectively, in yields determined by the relative concentrations of **4** and $BrCCl_3$. Rate constants for coupling (k_c) of Bu· and Ph· with **4** were assumed to be proportional to rate constants for diffusion controlled reactions, k_d, which were estimated from measured viscosities. Values of k_{Br}^{Bu} and k_{Br}^{Ph}, calculated from k_c and product yields for reactions at 80°C, are 0.26×10^9 and $1.55 \times 10^9\ M^{-1}\ s^{-1}$, respectively. The relative radical reactivities toward $BrCCl_3$ at 80°C are Ph, 6; cpm, 5; Bu, 1.

LUKOSE MATHEW et JOHN WARKENTIN. Can. J. Chem. **66**, 11 (1988).

La décomposition radicalaire en chaîne du cyclopropylméthyl (hydroxy-1 méthyl-1 éthyl) diazène ($(CH_3)_2C(OH)N{=}NCH_2CH(CH_2)_2$, **1**), à des températures allant de 253 à 341 K, dans des solutions d'hexafluorobenzène ou de dichlorométhane contenant du bromotrichlorométhane, conduit au bromure de cyclopropylméthyle, au bromo-4 butène-1, au bromo-1 trichloro-5,5,5 pentène-2 et au dibromo-3,5 trichloro-1,1,1 pentane qui dérivent tous de la portion cyclopropylméthyle du composé **1**. Les autres produits importants sont l'azote, l'acétone et le chloroforme. On a calculé la constante de vitesse pour la formation du bromure de cyclopropylméthyle par attaque des radicaux libres cyclopropylméthyles, provenant du composé **1**, au niveau du brome du $BrCCl_3$ (k_{Br}^{cpm}); pour ce faire, on a fait appel à la composition des produits et on a utilisé la constante de vitesse connue pour la transposition des radicaux cyclopropylméthyles en radicaux butène-3 yles. À 25°C, $k_{Br}^{cpm} = 6{,}5 \times 10^8\ M^{-1}\ s^{-1}$ et la variation avec la température est donnée par l'équation suivante : $\log (k_{Br}^{cpm}/M^{-1}\ s^{-1}) = (10{,}6 \pm 0{,}3) - (2{,}4 \pm 0{,}4)/\theta$, dans laquelle $\theta = 2{,}3RT\ \text{kcal/mol}^{-1}$. Les décompositions des composés $(CH_3)_2C(OH)N{=}N$—R (**2**, R = Bu, et **3**, R = Ph) par un processus qui n'implique pas de chaînes, en présence d'un excès de tétraméthyl-1,1,3,3 isoindolinyl-2 oxyl (**4**) et de bromotrichlorométhane, fournissent respectivement du BuBr et du PhBr, avec des rendements qui ont été déterminés par les concentrations du composé **4** et du $BrCCl_3$. On a fait l'hypothèse que les constantes de vitesses pour les couplages (k_c) des radicaux Bu· et Ph· avec le composé **4** sont proportionnelles aux constantes de vitesse des réactions contrôlées par la diffusion, k_d, qui ont été évaluées à partir des viscosités mesurées. Pour les réactions à 80°C, les valeurs de k_{Br}^{Bu} et k_{Br}^{Ph}, calculées à partir des valeurs de k_c et des rendements en produits, sont respectivement égales à $0{,}26 \times 10^9$ et $1{,}55 \times 10^9\ M^{-1}\ s^{-1}$. À 80°C, les réactivités relatives des radicaux pour le $BrCCl_3$ sont Ph, 6; cpm, 5; Bu, 1.

[Traduit par la revue]

Introduction

Although it is well known that bromotrichloromethane reacts rapidly, by bromine atom transfer, with a large variety of free radicals, there are relatively few reports in the literature concerning rate constants for attack on $BrCCl_3$ by primary, secondary, and tertiary alkyl radicals in solution. A recent study (1) gave $k_{Br}^{25°C} = 3.4 \times 10^5\ M^{-1}\ s^{-1}$ for the reaction of the methyl radical with $BrCCl_3$ in the gas phase. Much larger values were reported recently for corresponding reactions of phenyl (2) and of cyclopropyl radicals (3) in solution, rate constants having values 1.7×10^9 (45°C) and $(2.8–3.7) \times 10^9$ (25°C) $M^{-1}\ s^{-1}$, respectively. In abstraction of Cl from CCl_4 at about 298 K, the phenyl radical (2, 4) reacts 6.5×10^2, 1.3×10^2, and 1.4×10^3 times faster than the neophyl radical (5), the butyl radical (6), and the 5-hexenyl radical (7) respectively.[2] Cyclopropyl radical is also more reactive toward CCl_4 (3*a*) than the above mentioned primary radicals; corresponding rate factors are 1.2×10^2, 26, and 2.8×10^2. It seemed likely, therefore, that the reported rate constants for abstraction of Br from $BrCCl_3$ by phenyl (2) and cyclopropyl radicals (3) are significantly higher than that for a primary alkyl radical, but not by a factor as large as the gas phase rate constant for the methyl radical (see above) would suggest. We now report the Arrhenius equation for abstraction of Br from $BrCCl_3$ by the cyclopropylmethyl radical, and rate constants at 80°C for the same reaction by butyl and by phenyl radicals.

Method

The method based on the determination of relative rates from product analysis (8) is simple, requiring only that the chosen radical must undergo a competitive "clocking" reaction (8) with a known rate constant of suitable magnitude and that the total chemistry be understood and clean enough for the reliable quantitative assay of products. The ring-opening reaction of the cyclopropylmethyl radical (eq. [1]) was chosen because it

$$[1] \quad c\text{-}C_3H_5CH_2\cdot \xrightarrow{k^{25°C} = 2.1 \times 10^8\ s^{-1}} H_2C{=}CH_2CH_2$$

occurs with a rate constant (9*a*, 10) large enough to clock a

[1]Author to whom correspondence may be addressed.

[2]The quoted reactivity ratios are for phenyl radical data from ref. 4. Somewhat smaller ratios result from use of the data of Lorand and co-workers (2).

Can. J. Chem. Downloaded from www.nrcresearchpress.com by 213.222.148.141 on 09/07/12
For personal use only.

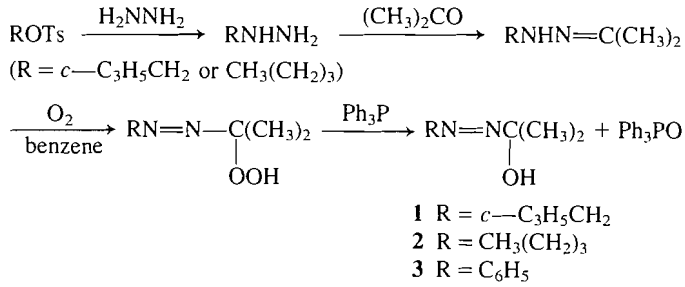

SCHEME 1

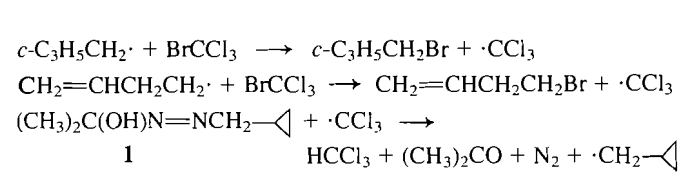

SCHEME 2

bimolecular competing reaction with a rate constant between about 10^7 and 10^{10} M^{-1} s^{-1}. Moreover, although the ring opening is known to be reversible, the rate constant for the reverse reaction is small (ca. 4.9×10^3 s^{-1} at 25°C) (9*b*) and reclosure should therefore be suppressed effectively in the presence of $BrCCl_3$.

α-Hydroxydiazene **1**, prepared by the sequence of reactions in Scheme 1, was chosen as the radical precursor for three reasons. First, α-hydroxydiazenes decompose thermally at temperatures near room temperature (11), offering the potential advantage of measured, rather than extrapolated, rate constants in that important temperature range. Second, their decomposition was known to be induced by a number of radicals (11) including the trichloromethyl radical. Therefore, for decomposition of **1** in $BrCCl_3$, a radical chain reaction with the following chain propagating steps seemed likely (Scheme 2). Even modest chain lengths would facilitate analysis by minimizing the importance of radical pair chemistry. Third, the by-products of induced decomposition ($HCCl_3$ and $(CH_3)_2CO$) should cause minimal problems during analysis by glpc or by ^1H nmr spectroscopy, and it seemed unlikely that they would undergo complicating chemical reactions to a detectable extent under the conditions of their formation.

Solutions of **1** in hexafluorobenzene or dichloromethane containing excess $BrCCl_3$ were degassed and sealed into nmr tubes. The tubes were irradiated (in low temperature experiments) or they were kept in a constant temperature bath until the *gem*-dimethyl signal of **1** could no longer be detected in the ^1H nmr spectrum. The contents of the tubes were then analyzed by glpc.

Butyl and phenyl radicals were generated by thermolysis of **2** and **3**, respectively. Coupling of the radicals with 1,1,3,3-tetramethylisoindolin-2-yloxyl (**4**) was used as the competing

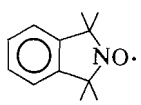

4

reaction for clocking abstraction of Br from $BrCCl_3$. Coupling rate constants were estimated from those for diffusion control and the latter were calculated from measured viscosities (10). Coupling with **4** occurred under pseudo first-order conditions, with **4** in about 12-fold excess.

Results and discussion

Products

The nmr spectra of spent solutions of **1** indicated a simple mixture of $CHCl_3$, $(CH_3)_2CO$, *c*-$C_3H_5CH_2Br$ (**5**), CH_2=$CHCH_2CH_2Br$ (**6**), and $Cl_3CCH_2CH(Br)CH_2CH_2Br$ (**7**) and acetone azine (**8**), up to 8% from thermal runs and ca. 3% from photo-initiated reactions. The azine, giving ^1H nmr signals of equal intensities at δ 1.71 and 1.85 in the crude reaction mixture, was distinguished from the mixed azine ($(CH_3)_2C$=N—N=CH—◁) by comparison (^1H nmr and gc) with an authentic sample of the latter, synthesized independently from acetone hydrazone and cyclopropane carboxyaldehyde. Although the origin of acetone azine is not understood at this time, the possibility that it was a contaminant in the starting material (**1**) could be excluded. The ^1H nmr spectra of **1** from different batches did not show the azine singlets that are visible after thermolysis or photolysis. We assume that the mixed azine, formed by catalyzed dehydration of **1**, is an initial minor product that is subsequently equilibrated with acetone (a major product) to form mostly **8** at equilibrium.

Only trace amounts of additional uncharacterized products were registered by gc analysis[3] except for a material (**9**) with a long retention time that was eluted just before **7**. Examination of the reaction mixture by gc/ms gave (for **9**) m/z = 256, 254, 252, and 250, with intensity ratios appropriate for $C_5H_6BrCl_3$. Compound **9** is therefore the result of dehydrobromination (formally) of **7**. Partial dehydrobromination of **7**, to form **9**, was achieved by injection of **7** onto an old gc column. New columns, under the same conditions, gave only sharp symmetric peaks for **7**, indicating that **7** is thermally stable and that dehydrobromination was caused by residues present in the old column.[4]

The most likely structure for **9** is *trans*-1-bromo-5,5,5-trichloro-2-pentene, formed, in the $BrCCl_3$ medium, by disproportionation between 1-(2-bromoethyl)-3,3,3-trichloroprop-1-yl radicals (**10**) and trichloromethyl radicals. For the present purposes it is not critical that the mechanism of its formation, or its exact structure for that matter, be known. The important point is that **9** must be counted with **6** and **7**, as a product from 3-butene-1-yl radical, in calculating k_{Br}.

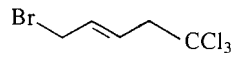

9

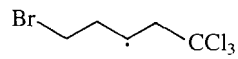

10

The source of 3–8% of **8** aside, the chemistry of **1** is adequately accounted for with the chain mechanism of Scheme 2 and with the subsequent reactions of Scheme 3. The large ratio (>70) of chain transfer product ($CHCl_3$) to chain termination product (C_2Cl_6) in the thermal runs was particularly satisfying, indicating an average kinetic chain length large enough to minimize complications from radical pair chemistry. Although photochemical initiation for the low temperature runs led to smaller ratios of $CHCl_3/C_2Cl_6$ (≃30), reaction products from the procedure were the same, but the yield of **8** was reduced.

Analysis of the relevant products from thermolysis of **2** in media containing both **4** and $BrCCl_3$ was achieved by straightforward gc analysis, after calibration of the detector response toward authentic 1-bromobutane and 2-(1-butoxy)-1,1,3,3-

[3]One of these, hexachloroethane, was identified by injection of a solution of authentic hexachloroethane in hexafluorobenzene.

[4]Repeated use of the new column for analyses of products from **1** did not result in deterioration of its performance. Pure **7** was not dehydrohalogenated and pure **5** was not isomerized to **6**.

Can. J. Chem. Downloaded from www.nrcresearchpress.com by 213.222.148.141 on 09/07/12
For personal use only.

Can. J. Chem. Downloaded from www.nrcresearchpress.com by 213.222.148.141 on 09/07/12
For personal use only.

$$CH_2{=}CHCH_2CH_2Br + \cdot CCl_3 \longrightarrow Cl_3CCH_2\dot{C}HCH_2CH_2Br$$
6 **10**

$$\mathbf{10} + BrCCl_3 \longrightarrow Cl_3CCH_2CH(Br)CH_2CH_2Br$$
7

$$\mathbf{10} + \cdot CCl_3 \longrightarrow Cl_3CCH_2CH{=}CHCH_2Br + HCCl_3$$
9

SCHEME 3

tetramethylisoindoline (**11**). The product of coupling between **4** and $\cdot CCl_3$ (**12**) was eluted late and its presence did not interfere. Analysis of the important products from thermolysis of **3** in similar media was not straightforward. While it was easy to analyze for bromobenzene, it was not possible to determine the relative yield of the expected 2-phenoxy-1,1,3,3-tetramethylisoindoline (**13**) from coupling of phenyl radicals with **4**. Presumably, **13** is unstable[5] and undergoes thermolysis, either

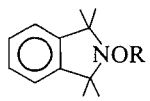

11 R = Bu
12 R = CCl_3
13 R = Ph

under the conditions of its formation (80°C) or in the gc column. The initial ratio of products was therefore determined as follows. The absolute yield of bromobenzene was determined by gc and that yield was corrected to take into account the fact that the yield of bromobenzene was 95%, instead of 100%, from thermolysis of **3** in $BrCCl_3$ without added **4**.[6] The phenyl moieties not accounted for with the corrected yield of bromobenzene were assumed to have gone, initially at least, to **13**. This determination of the product ratio by difference is not likely to be subject to serious error because it is very unlikely that phenyl radicals could be involved significantly in reactions that could compete with abstraction of Br from $BrCCl_3$ or with coupling to **4**. Moreover, it is not conceivable that **13**, in subsequent reactions, could lead to bromobenzene.

Rate constants

From the analytical results in Table 1, values of k_{Br}^{cpm}, for the reaction $c\text{-}C_3H_5CH_2\cdot + BrCCl_3 \rightarrow c\text{-}C_3H_5CH_2Br + \cdot CCl_3$, were calculated from eq. [2].

$$[2] \quad k_{Br}^{cpm} = \frac{k_i[\mathbf{5}]}{([\mathbf{6}] + [\mathbf{7}] + [\mathbf{9}])[BrCCl_3]}$$

In eq. [2], the symbols [**5**]–[**9**] represent the relative yields, $[BrCCl_3]$ is the initial concentration of that reagent, and k_i is the rate constant for ring opening of cyclopropylmethyl, calculated from the equation (10) $\log (k_i/s^{-1}) = 13.9\text{–}7.6/\theta$ where $\theta = 2.3RT$ kcal mol^{-1}. The rate constants so calculated for the 253–341 K temperature range gave $\log (k_{Br}^{cpm}/M^{-1}\,s^{-1}) = (10.6 \pm 0.3) - (2.4 \pm 0.4)/\theta$ where $\theta = 2.3RT$ kcal mol^{-1}, and $k_{Br}^{cpm} = 6.9 \times 10^8\,M^{-1}\,s^{-1}$ at 25°C.

Rate constants for the reactions of Bu· and Ph· with $BrCCl_3$ were calculated from eq. [3], where k_c is the rate constant for

$$[3] \quad k_{Br} = k_c\left(\frac{[\mathbf{4}]}{[BrCCl_3]} \times \frac{[RBr]}{[CP]}\right)$$

coupling between Bu· or Ph· and **4**, where [CP] is the relative yield of coupling product, and where [RBr] is the relative yield of 1-bromobutane or bromobenzene. The concentrations of **4** and of $BrCCl_3$ were calculated from their weights and from volumes of their solutions in C_6F_6 determined at room temperature. Corrections for thermal expansion at the reaction temperature (80°C) or for consumption of **4** and $BrCCl_3$ were not applied because the former cancel (eq. [3]). The latter cancel in part and are in any case very small because of the large stoichiometric excess of **4** and $BrCCl_3$ over the radical sources (**2** or **3**).

From the data in Tables 2 and 3, $k_{Br}^{Bu} = (2.61 \pm 0.38) \times 10^8\,M^{-1}\,s^{-1}$ and $k_{Br}^{Ph} = (1.55 \pm 0.64) \times 10^9\,M^{-1}\,s^{-1}$ at 80°C. The latter is in good agreement with the literature value (2), $k_{Br}^{Ph} = 1.7 \times 10^9\,M^{-1}\,s^{-1}$ at 45°C, considering that the effect of the temperature difference (35°C) corresponds to a rate factor[7] of only 1.5. At 80°C, $k_{Br}^{cpm} = 1.30 \times 10^9\,M^{-1}\,s^{-1}$ and the relative reactivities are therefore Ph, 5.9; cpm, 5.0; Bu, 1.0. Phenyl radical is expected to be more reactive than either of the primary alkyls and the higher reactivity of cpm over that of Bu probably reflects a polar transition state, depicted below.

$$\overset{\delta^+}{RCH_2}\text{----}\overset{}{Br}\text{----}\overset{\delta^-}{CCl_3}$$

The fact that rate constants in CH_2Cl_2 are ca. 10% larger than those for C_6F_6 solvent (Table 1) suggests a dipolar contributor. Moreover, a polar effect is known to be important in determining rate constants for Cl abstraction from CCl_4 and $CHCl_3$. For example, 1,1-dimethylethyl is about six times as reactive as methyl toward $CHCl_3$ (12) and 1-methylcyclopropyl is 10-fold more reactive than cyclopropyl toward CCl_4 (3*b*). Those factors presumably reflect minimum values of the polar enhancement factor because steric effects must operate in the opposite sense. Recent evidence indicates that a polar effect may operate also in the case of $BrCCl_3$, for 1-methylcyclopropyl is ca. 1.3 times as reactive as cyclopropyl, in Br abstraction (3*b*). A larger net enhancement for cyclopropylmethyl, compared to a simple 1° alkyl radical, is likely because of the effect of conjugative stabilization of the cyclopropylmethyl cation. However, the discrepancy between the gas- and solution-phase results (see Introduction) appears to be much too large to be explained away in terms of the effects of transition state solvation in solution.

It is interesting that the polar factor, which presumably is rate retarding[8] in the case of the phenyl analogue, can account for the fact that Ph and cpm are, within experimental error, equally reactive toward $BrCCl_3$. A similar argument can be used to accommodate the apparently higher reactivity ($k_{Br}^{cp} = 2.8 \times 10^9\,M^{-1}\,s^{-1}$) at 25°C of cyclopropyl radicals (cp) (3*b*) relative to that of phenyl radicals, toward $BrCCl_3$. That is, cp may be more polarizable than Ph, in the sense depicted above, by virtue of the four β hydrogens in cp. It must be emphasized, however, that the relative reactivities of cyclopropyl and phenyl radicals toward $BrCCl_3$ are based on different methodologies and that conclusions from the numbers available at this stage are necessarily tentative.

[5]The N—O bond strength of **13** probably falls between that of the N—N bond of phenylhydrazine and the O—O bond of an alkyl phenyl peroxide. Compounds of the latter class are not isolable.

[6]This small shortfall of the yield of PhBr is probably indicative of slightly impure **3**.

[7]The temperature dependence of k_{Br} for the change from 45 to 80°C is that of cpm. A similar factor has been assumed for Ph.

[8]The transition state for abstraction by phenyl is expected to be even less polar than that for abstraction by methyl, because of the higher electronegativity of sp^2-carbon compared to that of sp^3-carbon.

Can. J. Chem. Downloaded from www.nrcresearchpress.com by 213.222.148.141 on 09/07/12
For personal use only.

TABLE 1. Product ratios and rate data

Method	T, K[a]	Solvent	[**1**], M[b]	[$BrCCl_3$], M[c]	[**5**]/([**6**] + [**7**] + [**9**])[d]	k_i, s^{-1}[e]	k_{Br}, M^{-1} s^{-1}[f]
Δ	341.6	C_6F_6	0.159	2.26	1.11	1.09×10^9	5.35×10^8
Δ	341.6	C_6F_6	0.159	2.26	1.01[g]	1.09×10^9	4.87×10^8
Δ	322.8	C_6F_6	0.159	2.31	1.78	5.70×10^8	4.39×10^8
Δ	322.8	CH_2Cl_2	0.051	0.652	0.659	5.70×10^8	5.76×10^8
Δ	322.8	CH_2Cl_2	0.051	0.652	0.600	5.70×10^8	5.25×10^8
Δ	321.8	C_6F_6	0.185	2.31	1.97	5.50×10^8	4.69×10^8
Δ	321.8	C_6F_6	0.217	2.79	2.10[h]	5.50×10^8	4.14×10^8
hν	303.0	C_6F_6	0.023	0.682	1.11	2.63×10^8	4.28×10^8
hν	303.0	C_6F_6	0.008	0.889	1.61	2.63×10^8	4.76×10^8
Δ	302.8	C_6F_6	0.185	2.37	3.58	2.61×10^8	3.94×10^8
Δ	302.2	CH_2Cl_2	0.030	0.789	1.51	2.54×10^8	4.86×10^8
Δ	302.2	CH_2Cl_2	0.030	0.789	1.52	2.54×10^8	4.89×10^8
hν	273.5	CH_2Cl_2	0.051	0.693	2.19	6.74×10^7	2.13×10^8
hν	273.5	CH_2Cl_2	0.051	0.693	2.01	6.74×10^7	1.94×10^8
hν	273.5	CH_2Cl_2	0.051	0.693	1.99	6.74×10^7	1.93×10^8
Δ	273.0	C_6F_6	0.159	2.51	6.80	6.57×10^7	1.78×10^8
hν	258.0	CH_2Cl_2	0.030	0.820	6.25	2.91×10^7	2.22×10^8
hν	256	C_6F_6[i]	0.106	1.44	9.99	2.59×10^7	1.80×10^8
hν	253	CH_2Cl_2	0.097	1.06	9.55[j]	2.17×10^7	1.95×10^8

[a] ±0.2° for T = 323 K, ±0.5° for T = 273 K, and ±1.0° for T < 273 K.
[b] Initial concentration.
[c] Initial concentration in solution prepared at ambient temperature, corrected for thermal expansion or contraction of the solvent and for the presence of **1**.
[d] Ratio determined by gas chromatography. Each number represents the average value for at least three injections. Detector response factors for **5** and **6** were indistinguishable; that for **7** was within 5% of the response factor for **5** and **6** and a correction was not applied. The response factor for **9** was assumed to be the same as that for **7**.
[e] Calculated from the Arrhenius equation (10) $\log (k_i/s^{-1}) = (13.9 \pm 0.4) - (7.6 \pm 0.1)/\theta$, where $\theta = 2.3RT$ kcal mol^{-1}.
[f] Calculated by use of eq. [2].
[g] Actual yields for this experiment: $CHCl_3$ (90%), Me_2CO (ca. 80%), **5** (45.6%), **6** (25.5%), **7** (19.4%), **9** (0.4%), **8** (ca. 3%).
[h] Actual yields for this experiment: $CHCl_3$ (90%), Me_2CO (95%), **5** (63.3%), **6** (16.8%), **7** (13.2%), **9** (below detection limit), **8** (ca. 1%).
[i] CCl_4 (33% by vol.) added to prevent freezing.
[j] Actual yields for this experiment: $CHCl_3$ (ca. 80%), Me_2CO (not determined), **5** (81.4%), **6** (7.3%), **7** (1.2%), **9** (below detection limit), **8** (<1%).

TABLE 2. Product ratios and rate data for 1-butyl radicals (80°C)

Reactant concentrations, M[a]		Product ratio[b]	Rate constants[c]
4	$BrCCl_3$	BuBr/CP[d]	k_{Br}^{Bu}, M^{-1} s^{-1}
0.848	9.15	1.15	2.24×10^8
0.566	9.44	2.43	3.07×10^8
0.364	9.64	2.96	2.36×10^8
0.283	9.72	4.47	2.75×10^8
		Mean (sd)	$(2.61 \pm 0.38) \times 10^8$

[a] Solutions of **4** in $BrCCl_3$. Initial concentration of **2** = 0.08–0.02 M.
[b] Corrected for detector response. The actual ratio of gc integrator counts from three or more injections has been divided by 0.32 to yield the numbers in this column. The material balance on butyl groups ranged from 91 to 96%.
[c] Calculated from eq. [3], with $k_c = 0.2k_d = 2.11 \times 10^9$ M^{-1} s^{-1}, where k_d, the diffusion controlled rate constant, was calculated from the viscosity of $BrCCl_3$ at 80°C (0.735 cP) as described earlier (10). The viscosity was not corrected for the presence of **4**, **2**, and the products of decomposition of **2**.
[d] CP signifies the coupling product, 2-(1-butoxy)-1,1,3,3-tetramethylisoindoline (**11**).

In summary, the reactivities of relatively unhindered carbon-centered radicals toward $BrCCl_3$ span a narrow range. The low sensitivity of k_{Br} toward radical structure suggests that abstraction of Br from $BrCCl_3$ might be used, without risk of serious error, as a clock to estimate rate constants for other fast reactions of a variety of carbon-centered free radicals.[9] For example, it is now possible to estimate a minimum rate constant for ring closure of radical **14**, an intermediate in the radical chain addition of $BrCCl_3$ to *cis,trans*-1,5-cyclodecadiene (13), eq. [4]. The reaction afforded the stereoisomers **15** (from initial

[4] 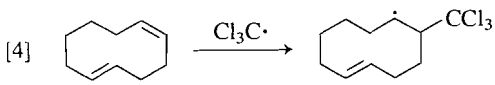

14

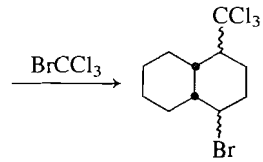

15

attack on the *cis* double bond) and 6-bromo-5-trichloromethyl-*cis*-1-cyclodecene (**16**, from initial attack on the *trans* double bond) in the ratio 24:1. The isomer of **16**, with a *trans* double bond, was not found. If it is assumed that the upper limit for its yield was *no more* than 1 part in 25 (more is unlikely because **16**

[9] Including tertiary radicals, probably, although there are no data yet for their reactivities toward $BrCCl_3$. The combined effects of polar rate enhancement and steric retardation are likely to place rate constants for 3° radicals between those for 1° and phenyl radicals.

TABLE 3. Product ratios and rate data for phenyl radicals (80°C)

Reactant concentrations, M [a]		Product ratio[b]	Viscosity,[c]	Rate constant[d]
4	$BrCCl_3$	PhBr/CP[e]	cP at 80°C	k_{Br}^{Ph}, M^{-1} s^{-1}
1.32	8.47	4.56	0.735	1.50×10^9
0.558	4.79	2.62	0.500	1.18×10^9
0.558	4.79	3.55	0.500	1.30×10^9
0.530	2.07	1.31	0.485	1.13×10^9
0.530	2.07	1.03	0.485	8.80×10^8
0.576	0.588	0.705	0.475[f]	2.28×10^9
0.576	0.588	0.806	0.475	2.61×10^9
			Mean (st)	$(1.55 \pm 0.64) \times 10^9$

[a]Solutions of **4** and $BrCCl_3$ in C_6F_6 except for the first entry, where C_6F_6 was absent.
[b]The product ratio was determined from the absolute yield of PhBr; the yield of coupling product was determined by difference (see text).
[c]Viscosities were measured at 77°C, on solvents not containing **4**, **3**, or products from **3**. The viscometer was calibrated against CCl_4 and measured viscosities were extrapolated from 77 to 80°C.
[d]Calculated from eq. [3], where k_c is derived from k_d, which in turn is derived from the viscosity, see footnote *c*, Table 2.
[e]CP signifies the coupling product, 2-phenoxy-1,1,3,3-tetramethylisoindoline (**13**). See also footnote *b* of this table. Yields of PhBr: 77.9, 68.8, 74.1, 53.9, 48.2, 39.3, and 42.4%, in order from the top.
[f]Viscosity of neat C_6F_6 at 80°C.

was *isolated* from a 24:1 mixture), then the rate constant for cyclization of **14** must be at least 1.4×10^{11} s^{-1}.[10]

Experimental

The synthesis and spectra of **1** have been reported (10). Hydroxydiazenes **2** and **3** were prepared by analogous procedures, from 1-butylhydrazine and phenylhydrazine, respectively. Spectra of intermediates (Scheme 1) and of the final products are listed below.

Acetone (1-butyl)hydrazone: ^{1}H nmr ($CDCl_3$, 90 MHz) δ: 0.93 (t, 3H), 1.19–1.63 (m, 4H), 1.75 (s, 3H), 1.95 (s, 3H), 3.14 (t, 2H), 4.08 (s, br, 1H).

(1-Butyl)(1'-hydroperoxy-1'-methylethyl)diazene: ^{1}H nmr ($CDCl_3$, 90 MHz) δ: 0.97 (t, 3H), 1.12–1.71 (m) with 1.45 (s) superimposed, total 8H, 1.65–1.93 (m, 2H), 3.87 (t, 2H), 9.40 (s, br, 1H); ^{13}C nmr ($CDCl_3$, 62.90 MHz) δ: 13.95, 20.60, 21.80, 29.79, 68.82, 102.86. Iodometric titration, 96.9%, average of three.

(1-Butyl)(1'-hydroxy-1'-methylethyl)diazene (2): ^{1}H nmr ($CDCl_3$, 90 MHz) δ: 0.93 (t, 3H), 1.15–1.58 (m) with 1.42 (s) superimposed, total 8H, 1.70–1.88 (m, 2H), 3.92 (t, 2H), 4.80 (s, br, 1H); ^{13}C nmr ($CDCl_3$, 62.90 MHz) δ: 13.80, 20.38, 26.95, 29.66, 66.48, 93.55; tlc (0.2 mm, neutral alumina on plastic) R_f 0.53, 50% petroleum ether, 50% ether, one spot.

Acetone phenylhydrazone: ^{1}H nmr ($CDCl_3$, 90 MHz) δ: 1.83 (s, 3H), 2.03 (s, 3H), 6.7–7.6 (m, 5H).

(1-Hydroperoxy-1-methylethyl)phenyldiazene: ^{1}H nmr ($CDCl_3$, 90 MHz) δ: 1.47 (s, 6H), 7.32–7.88 (m, 5H), 8.5 (s, br, 1H); tlc (0.2 mm, neutral alumina) R_f 0.51, 50% petroleum ether, 50% ether, one spot.

(1-Hydroxy-1-methylethyl)phenyldiazene (3): ^{1}H nmr ($CDCl_3$, 90 MHz) δ: 1.53 (s, 6H), 4.97 (s, 1H), 7.3–7.9 (m, 5H), no extraneous signals.

2-(1-Butoxy)-1,1,3,3-tetramethylisoindoline (11)

This product of coupling between **4** and the butyl radical was prepared by thermolysis of **2** at 80°C in C_6F_6 containing **4**. It was isolated by preparative tlc on silica coated plates and the fraction thus obtained was purified by chromatography on a rotating, alumina-coated, plate (Chromatotron apparatus); ^{1}H nmr ($CDCl_3$, 90 MHz) δ: 0.89 (t, 3H), 1.20–2.67 (m, 16H), 3.88 (t, 2H), 6.96–7.32 (m, 4H); ^{13}C nmr ($CDCl_3$, 62.90 MHz) δ: 14.23, 19.92, 22–31 (broad signal for the four ring methyl groups), 31.67, 67.32, 77.38, 121.61, 127.25, 145.59; ms (ei) *m/z*: 247 (M^+), 232 ($M^+ - CH_3$, 100%), 176 (90%).

Cyclopropylmethyl bromide (5), 4-bromo-1-butene (6), 1-bromobutane, and bromobenzene

Authentic samples of these compounds, for identification of the reaction products and for calibration of the gc detector, were purchased from Aldrich.

3,5-Dibromo-1,1,1-trichloropentane (7)

4-Bromo-1-butene (2.7 g, 0.017 mol), benzoyl peroxide (0.2 g, 0.8 mmol), and bromotrichloromethane (5.0 g, 0.025 mol) were heated in a sealed, evacuated tube at 80°C for 4 days. The ^{1}H nmr spectrum of the resulting solution was nearly free from vinyl proton signals. A portion of the product was isolated by preparative tlc (silica gel-60, F_{254}, 1 mm thick, on glass) with petroleum ether (80 parts) and ether (20 parts) as the solvent system. The pure product had R_f = 0.46 on silica gel-60 (0.2 mm, on plastic), with the same solvent system; ^{1}H nmr ($CDCl_3$, 500 MHz) δ: 2.38 (m, 1H), 2.59 (m, 1H), 3.23 (dd, 1H), 3.52 (dd, 1H), 3.59 (m, 2H), 4.53 (m, 1H); ms (ei) *m/z*: 338, 336, 334, 332, 330 (M^+); 301, 299, 297, 295 ($M^+ - Cl$); 263, 261, 259 ($M^+ - 2Cl$); 255, 253, 251 ($M^+ - Br$); 221, 219, 217, 215 ($M^+ - Br - Cl$); 111, 109 ($C_2H_4Br^+$); 77, 75 ($C_3H_4Cl^+$); 40 (100%, $C_3H_4^+$).

Mixed azine of acetone and cyclopropanecarboxaldehyde

A solution of cyclopropanecarboxaldehyde and acetone hydrazone (1:1) in CCl_4 at room temperature was examined periodically by ^{1}H nmr spectroscopy. When the aldehyde signal was no longer visible, solid potassium carbonate was added and the supernatant solution was passed through a short column of magnesium sulfate. Evaporation of most of the solvent and chromatography on a rotating disk (Chromatotron apparatus) gave fractions containing the unsymmetric azine contaminated with symmetric aldazine. The latter was obtained in pure form by preparative tlc (Al_2O_3 on plastic), permitting assignment of the gc signals from the mixture of azines and the assignment of ^{1}H nmr signals of the mixture. For the mixed azine, ^{1}H nmr ($CDCl_3$) δ: 0.67–1.08 (m, CH_2), 1.53–1.92 (m, CH), 2.00 (s, CH_3), 2.03 (s, CH_3), 7.18 (d, J = 8 Hz, CH=N); gc retention time (conditions described below) 25.3 min. For the symmetric aldazine, ^{1}H nmr ($CDCl_3$) δ: 0.67–1.08 (m, 4H), 1.53–1.92 (m, 2H), 7.35 (d, J = 8 Hz, 2H); gc retention time 28.9 min.

[10]Additional assumptions are (*a*): temperature 35°C (Rayonet, 1 h (13)); (*b*) $k_{Br}^{14} \simeq 2 \times 10^8$ s^{-1} at 35°C, which is 4-fold lower than k_{Br}^{cpm} at 35°C; (*c*) $[BrCCl_3] = 7.5$ *M*, calculated from data in ref. 13 by using 0.90 and 1.96 g mL^{-1} for the densities of the diene and of $BrCCl_3$, respectively.

Can. J. Chem. Downloaded from www.nrcresearchpress.com by 213.222.148.141 on 09/07/12
For personal use only.

Thermolysis of 1 and product analysis

Stock solutions of $BrCCl_3$ and **1** in C_6F_6 or in CH_2Cl_2 were prepared. Solutions for thermolysis were prepared by measuring the appropriate volumes of the stock solutions with small pipettes or syringes into nmr tubes sealed to ground glass joints. The contents were freed from dissolved gases prior to sealing by means of several freeze–pump–thaw cycles, care being taken to warm the sample gently, and only until melting was complete. A sealed tube was then heated or photolysed (Table 1) until starting material could not be detected in the ^1H nmr spectrum. Thermal decompositions at 0°C and 30°C were complete in 10 days and 4 days, respectively. At higher temperatures, 2 days was sufficient. Photolyses with 300-nm light were carried out with a Rayonet apparatus. The sample tube was inside a quartz Dewar flask containing the thermostating fluid and a magnetic stirring bar. The photolyses were interrupted frequently to check and to adjust the temperature so as to maintain a $\pm 1°$ or better range (Table 1). Photolyses were complete (^1H nmr) in 2–3 h.

Analyses were carried out on the untreated reaction solution using a Varian Vista 6000 instrument fitted with a flame ionization detector and with a OV-17 column (8 ft × 1/8 in., 3% stationary phase) operating with a flow rate of 10 mL min^{-1} (N_2). The temperature was held at 35°C for 15 min before it was increased to 210°C at 10°C min^{-1}. The order of elution was acetone, $CHCl_3$ and C_6F_6 (together), **6** (8.5 min), $BrCCl_3$ (12.2 min), **5** (14 min), **8** (20.4 min), C_2Cl_6 (24.8 min), **9** (32.5 min), and 7 (33 min). The yield of **8** was estimated by integration of the ^1H nmr spectra because dibromodichloromethane, a minor (ca. 0.3%) contaminant in the $BrCCl_3$, eluted together with **8** from the gc column. Chloroform was fully separated from other volatile components on Carbowax (8 ft × 1/8 in., 5%) under similar conditions. The response factors of the flame ionization detector were determined by injection of standard solutions of **5**, **6**, 7, $CHCl_3$, and C_2Cl_6. Compounds **5**–7 and C_2Cl_6 gave the same response, to within ±5%, but signal intensities for $CHCl_3$ had to be multiplied by 3.6. The response factor for minor component **9** was assumed to be the same as that of **5**–7.

Thermolysis of 2 and 3

Solutions of these substrates and **4** in $BrCCl_3$, with or without C_6F_6, were prepared in volumetric flasks and portions were transferred into small Pyrex tubes for freeze–pump–thaw degassing prior to sealing. Tubes were immersed in an oil bath kept at 80 ± 0.2°C. Spent solutions were analyzed with the gc column and instrument described earlier (10).

For the 1-butyl system the temperature program was 35°C for 15 min, increased at 10°C min^{-1} to 300°C. Retention times, for a flow rate of 10 mL min^{-1} were (min) acetone (1.8), chloroform (2.9), 1-BuBr (5.8), $BrCCl_3$ (8.7), **4** (29.7), **4**-Bu (30.8), **4**-CCl_3 (35.7, broad), where **4**-Bu and **4**-CCl_3 are the coupling products.

In the case of the phenyl system the column temperature program was the same except for a shorter interval (10 min) at 35°C. Retention times were acetone (1.8), $CHCl_3$ (2.9), $BrCCl_3$ (8.7), PhBr (16.9), **4** (24.8), **4**-CCl_3 (32, broad). The expected product, **4**-Ph, was not eluted as such (see text) but a complex series of peaks was observed instead.

2-Hydroxy-1,1,3,3-tetramethylisoindoline was not separated from excess **4** by the gc column (10).

Acknowledgement

This work was financed from a grant provided by the Natural Sciences and Engineering Research Council of Canada.

1. K. V. Macken and H. W. Sidebottom. Int. J. Chem. Kinet. **11**, 511 (1979).
2. R. G. Kryger, J. P. Lorand, N. R. Stevens, and N. R. Herron. J. Am. Chem. Soc. **99**, 7589 (1977).
3. (*a*) L. J. Johnston, J. C. Scaiano, and K. U. Ingold. J. Am. Chem. Soc. **106**, 4877 (1984); (*b*) L. J. Johnston and K. U. Ingold. J. Am. Chem. Soc. **108**, 2343 (1986).
4. J. C. Scaiano and L. C. Stewart. J. Am. Chem. Soc. **105**, 3609 (1983).
5. D. A. Lindsay, J. Lusztyk, and K. U. Ingold. J. Am. Chem. Soc. **106**, 7087 (1984).
6. J. A. Hawari, S. Davis, P. S. Engel, B. C. Gilbert, and D. J. Griller. J. Am. Chem. Soc. **107**, 4721 (1985).
7. D. R. Jewell, L. Mathew, and J. Warkentin. Can. J. Chem. **65**, 311 (1987).
8. D. Griller and K. U. Ingold. Acc. Chem. Res. **13**, 317 (1980).
9. (*a*) B. Maillard, D. Forrest, and K. U. Ingold. J. Am. Chem. Soc. **98**, 7024 (1976); (*b*) A. Effio, D. Griller, K. U. Ingold, A. L. J. Beckwith, and A. K. Serelis. J. Am. Chem. Soc. **102**, 1734 (1980).
10. L. Mathew and J. Warkentin. J. Am. Chem. Soc. **108**, 7981 (1986).
11. (*a*) P. Knittel and J. Warkentin. Can. J. Chem. **53**, 2275 (1975); (*b*) D. W. K. Yeung and J. Warkentin. Can. J. Chem. **54**, 1345 (1976); (*c*) Can. J. Chem. **54**, 1349 (1976); (*d*) Can. J. Chem. **58**, 2386 (1980); (*e*) Y.-M. Chang, R. Profetto, and J. Warkentin. J. Am. Chem. Soc. **103**, 7189 (1981).
12. H.-R. Dutsch and H. Fischer. Int. J. Chem. Kinet. **13**, 527 (1981).
13. J. G. Traynham and H. H. Hsieh. J. Org. Chem. **38**, 868 (1973).

Can. J. Chem. Downloaded from www.nrcresearchpress.com by 213.222.148.141 on 09/07/12
For personal use only.

The rapid synthesis of organic compounds in microwave ovens

RICHARD N. GEDYE, FRANK E. SMITH, AND KENNETH CHARLES WESTAWAY
Chemistry Department, Laurentian University, Sudbury, Ont., Canada P3E 2C6

Received June 19, 1987

RICHARD N. GEDYE, FRANK E. SMITH, and KENNETH CHARLES WESTAWAY. Can. J. Chem. **66**, 17 (1988).

This work demonstrates that organic compounds can be synthesized up to 1240 times faster in sealed Teflon vessels in a microwave oven than by conventional (reflux) techniques. It is shown that all polar molecules absorb microwave energy rapidly and that the rate of energy absorption varies with the dielectric constant. The rates of reaction of polar molecules in nonpolar solvents are not increased appreciably by the microwave method. Also, the homogeneity of the reaction does not affect the rate enhancement. The rate enhancement arises predominantly because the oven superheats the solvent rapidly. Finally, pressure (temperature) measurements have shown that the maximum rate enhancement is achieved when the proper power level and volume of solvent are used. It appears that rate enhancements of approximately 200 are possible for many reactions if the reaction conditions are optimized.

RICHARD N. GEDYE, FRANK E. SMITH et KENNETH CHARLES WESTAWAY. Can. J. Chem. **66**, 17 (1988).

Dans ce travail, on démontre que les composés organiques peuvent être synthétisés 1240 fois plus rapidement dans des récipients de Téflon scellés, dans des fours à micro-ondes, que par les techniques conventionnelles de reflux. On démontre que toutes les molécules polaires absorbent rapidement l'énergie des micro-ondes et que les vitesses d'absorption de l'énergie varient avec la constante diélectrique. La méthode des micro-ondes ne provoque pas en une augmentation substantielle des vitesses des réactions impliquant des molécules polaires dans des solvants qui ne sont pas polaires. De plus, l'homogénéité du milieu réactionnel n'influence pas le taux d'augmentation des vitesses des réactions. L'augmentation des vitesses des réactions provient principalement du fait que le four provoque une surchauffe rapide du solvant. Enfin, des mesures de pression (température) ont permis de démontrer que le taux maximal d'augmentation des vitesses de réaction est atteint lorsqu'on utilise un niveau de puissance et un volume de solvant appropriés. Il semble que l'on puisse atteindre des taux d'augmentation des vitesses de réactions d'environ 200 si les conditions des réactions sont optimisées.

[Traduit par la revue]

Can. J. Chem. Downloaded from www.nrcresearchpress.com by 213.222.148.141 on 09/07/12
For personal use only.

Introduction

Although several chemical applications of microwave heating have been reported (1–5), it is only recently that microwave ovens have been used in organic synthesis (6, 7). In a preliminary communication (6) we described the use of microwave ovens for synthesizing esters from carboxylic acids, carboxylic acids from alkyl benzenes and amides, and ethers from alkyl halides. In fact, these organic reactions occurred up to 1240 times more rapidly in sealed Teflon containers in the microwave oven than by classical reflux methods. Since then, Giguere *et al.* (7) reported dramatic reductions in reaction time in microwave syntheses using the Diels–Alder, Claisen, and ene reactions.

The present paper extends the scope of this new synthetic method and reports our investigations of several of the factors that affect the rate enhancements found in organic syntheses in microwave ovens.

Results and discussion

Several different types of organic reactions were carried out both in sealed Teflon vessels in a microwave oven and under traditional reflux conditions. In the reactions described previously (6), approximate rate enhancements of between 5 and 1240 times were observed. Some representative reactions are given in Table 1. Carrying out reactions in the microwave oven was also found to be very useful for the preparation of derivatives for the identification of organic compounds. This approach was particularly useful for preparing derivatives that require relatively long reflux periods. For example, derivatives that normally required up to 2.5 h to prepare can be synthesized effectively in 2–2.5 min in a microwave oven. This reduces the time required for the preparation of the derivatives by between 24 and 60 times. The results of some of these syntheses are shown in Table 2.

Heating rates

Once it had been demonstrated that this rapid new synthetic method could be used to synthesize a wide range of organic compounds, attention was turned to an examination of the factors that affected these syntheses. The first experiment involved heating 50 mL of several organic compounds in open vessels[1] in a microwave oven for 1 min at 560 watts to determine the types of molecules that absorb microwave energy. It was found, Table 3, that all polar compounds absorbed significant amounts of microwave energy. For example, all the polar compounds with boiling points of less than 100°C reached their boiling point within 1 min. While polar molecules such as acids, esters, alkyl halides, primary alcohols and amines, and carbonyl compounds absorb microwave energy readily, the less polar ether, tertiary amine, and higher molecular weight alcohols were poorer absorbers. As expected, little or no microwave energy was absorbed by the nonpolar carbon tetrachloride and hydrocarbon solvents.

The above results suggested that the rate at which a molecule absorbs microwave energy depends on the polarity of the molecule. This relationship was confirmed by an examination of the rate of energy absorption for a fairly wide range of polar organic liquids. The data in Table 4 and Fig. 1 suggest that the ability to absorb microwave energy is related to the dielectric constant (polarity) of the solvent. Although two out of the 13 compounds are not near the least-squares straight line, the correlation coefficient for the plot of the temperature increase found when 0.5 mol of each compound is heated for 15 s at 560 watts versus the dielectric constant is still 0.920. Since the correlation coefficient for the other 11 compounds is 0.985, it appears that one can use a solvent's dielectric constant to estimate a compound's ability to absorb microwave energy.

[1]See "Safety precautions", experimental section.

TABLE 1. A comparison of reaction times and yields in representative reactions using classical and microwave procedures

Compound synthesized	Procedure followed	Reaction time	Average[b] yield (%)	$\left[\frac{k_{microwave}}{k_{classical}}\right]$
Hydrolysis of benzamide to benzoic acid in water				
C_6H_5COOH	Classical	1 h	90	
C_6H_5COOH	Microwave	10 min	99	6
Oxidation of toluene to benzoic acid in water				
C_6H_5COOH	Classical	25 min	40	
C_6H_5COOH	Microwave[a]	5 min	40	5
Esterification of benzoic acid with methanol				
$C_6H_5COOCH_3$	Classical	8 h	74	
$C_6H_5COOCH_3$	Microwave	5 min	76	96
S_N2 reaction of 4-cyanophenoxide ion with benzyl chloride in methanol				
$NCC_6H_4OCH_2C_6H_5$	Classical	16 h	89	
$NCC_6H_4OCH_2C_6H_5$	Microwave	4 min[c]	93	240
$NCC_6H_4OCH_2C_6H_5$	Classical	12 h	65	
$NCC_6H_4OCH_2C_6H_5$	Microwave	35 sec[c,d]	65	1240

[a]Very high pressures developed and the study of this reaction was halted.
[b]The average yields are based on isolated yields and represent the average of at least two experiments. The S_N2 reaction was followed by titrating the chloride ion (8).
[c]Value for one run only.
[d]This reaction was done in a 50-mL Teflon bomb.

TABLE 2. A comparison of reaction times and yields for classical and microwave procedures in the preparation of derivatives

Substrate	Derivative	Reaction time		Yield (%)		Reduction in reaction time[a]
		Classical	M-wave	Classical	M-wave	
Cinnamic acid	4-Nitrobenzyl ester	1.5 h	2 min	26	39	×45
2-Naphthol	Aryloxyacetic acid	1.0 h	2 min	14	13	×30
Methyl benzoate	Carboxylic acid	1.0 h	2.5 min	95	84	×24
Benzophenone	Oxime	2.0 h	2 min	68	71	×60

[a]These values are not rate enhancements but should be similar to them. The reductions in reaction time are the time used for the classical syntheses/the time used for the microwave synthesis. The classical times were taken from the literature (10, 11).

Sample volume

The effect of the amount of material in the oven on the heating rate was determined by heating 0.51 and 1.2 mol of methanol and 1-propanol in an open vessel in the microwave oven at 560 watts. Since the smaller sample is always at a higher temperature after the same heating time, Fig. 2, both the methanol and the 1-propanol are heated more rapidly when less material is in the reaction vessel. This presumably occurs because the microwave energy entering the oven has to heat fewer molecules. This suggests that the fastest heating and greatest rate enhancements will be observed when small (less than one mole) amounts of material are in the Teflon reaction vessel.

Reactions in nonpolar solvents

An experiment was performed to determine if the rate of reaction of a polar substrate in a nonpolar solvent would be increased in the microwave oven. A comparison of the heating rate of a 1.6 M solution of 1-propanol in octane with that of 1-propanol in an open vessel in the microwave oven at 560 watts, Fig. 3, shows that dilute solutions of polar substrates in nonpolar solvents are heated very slowly in the microwave oven. This occurs because only the polar molecules in the solution absorb the microwave energy. Thermal energy is then transferred to the nonpolar solvent by molecular collisions. Because the heating rate is much slower and the reaction times for microwave syntheses are short, it appears that microwave heating will only cause significant rate enhancements in organic syntheses in polar solvents.

Heterogeneous and homogeneous reactions

Another interesting question, from a synthetic point of view, is whether the rate enhancements are similar in homogeneous and heterogeneous reactions. Almost identical rate enhancements of 5 and 6 were found in the heterogeneous aqueous oxidation of toluene to benzoic acid and in the homogeneous hydrolysis of benzamide, respectively, Table 1. This suggests that the microwave technique is equally effective in enhancing the rates of both homogeneous and heterogeneous reactions.

This hypothesis was confirmed by comparing the rate enhancement for the hydrolysis of isopropyl benzoate in aqueous KOH, a heterogeneous reaction, with that found under

Can. J. Chem. Downloaded from www.nrcresearchpress.com by 213.222.148.141 on 09/07/12
For personal use only.

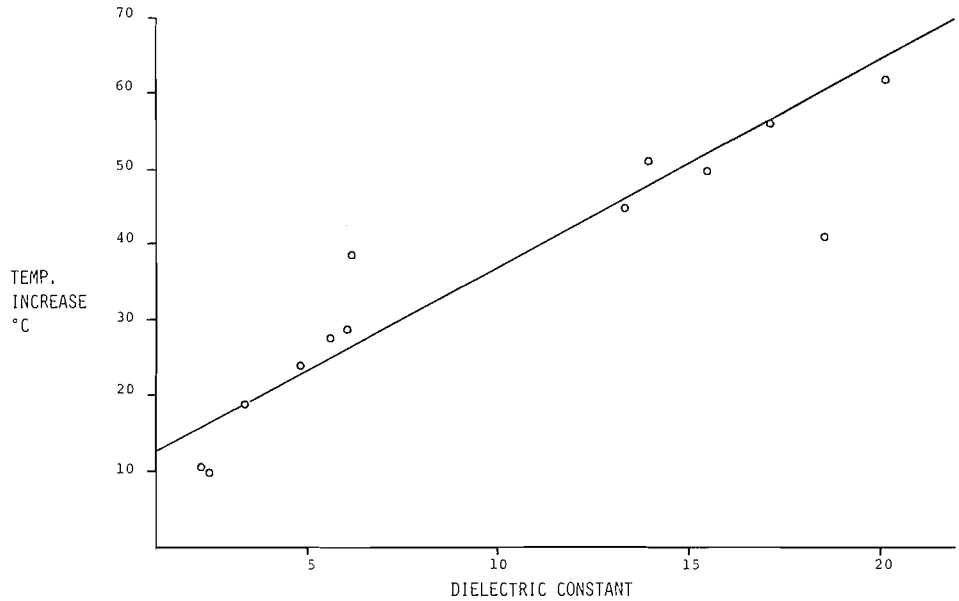

FIG. 1. The effect of the dielectric constant on the heating rate of various organic liquids.

TABLE 3. The temperature of 50 mL of several solvents after heating for 1 min at 560 watts in an open vessel in a microwave oven

Solvent	Temperature (°C) after 1 min	Boiling point (°C)
Water	81	100
Methanol	65	65
Ethanol	78	78
1-Propanol	98	97
1-Butanol	109	117
1-Pentanol	106	137
1-Hexanol	92	158
1-Chlorobutane	76	78
1-Bromobutane	95	101
Acetic acid	110	119
Ethyl acetate	73	77
Methylene chloride	41	41
Chloroform	49	61
Acetone	56	56
N,*N*-Dimethylformamide	131	153
Diethyl ether	32	35
1,4-Dioxane	53	101
1-Butylamine	70	77
Tripropylamine	56	157
Hexane	25	68
Heptane	26	98
Carbon tetrachloride	28	77

TABLE 4. The increase in temperature found when 0.5 mol of organic liquids is heated for 15 s at 560 watts in an open vessel in a microwave oven

Alcohol	Temperature increase after 15 s (°C)	Boiling point (°C)	Dielectric constant
1,4-Dioxane	11	101	2.2
Tripropylamine	10	156	2.4
Propanoic acid	19	141	3.3
Chloroform	24	62	4.8
n-Propyl acetate	28	102	5.6
Ethyl acetate	29	77	6.0
Acetic acid	38	118	6.2
1-Hexanol	45	158	13.3
1-Pentanol	51	137	13.9
2-Pentanone	49	102	15.4
1-Butanol	56	117	17.8
2-Butanone	41	80	18.5
1-Propanol	62	97	20.1

homogeneous conditions in alcoholic KOH. The results, Table 5, show that the rate enhancement is almost identical, i.e., 2.5 times and 3.0 times, in the heterogeneous and homogeneous reactions, respectively. Obviously the homogeneity of the reaction has little effect on the rate enhancement, and the microwave technique can be used to increase the rates of both types of reactions.

Safety

Although the observed rate enhancements of between 5 and 1240 are impressive, some problems were encountered in our early investigations. The chief obstacle in the use of microwaves for routine organic synthesis is that very high pressures can develop in the Teflon reaction vessels when the reactions are carried out in the microwave oven. The reactions described in this study were carried out in sealed 120-mL or 300-mL Berghof[2] or 150-mL Savillex[3] Teflon bottles. In some cases, the increase in pressure led to deformation of the Berghof vessels. In a few reactions, Berghof bottles exploded, destroying the Teflon bottle and in two cases damaging the microwave oven. The problem arises because the hot reaction mixture transfers heat to the Teflon container. This softens the Teflon and the pressure in the reaction vessel causes the walls of the vessel to deform and (or) explode. This problem is much less severe with the Savillex containers, which are made from a more temperature resistant type of Teflon, and should be absent when one uses a Savillex bottle with a pressure-release cap[3] that vents at approximately 100 psi (1 psi = 6.9 kPa). However,

[2]These bottles were purchased from Berghof/America Inc., Main St., Raymond, NH 03770, U.S.A.

[3]These bottles were purchased from the Savillex Corporation, 5325 Hwy 101, Minnetonka, MI 55343, U.S.A.

Can. J. Chem. Downloaded from www.nrcresearchpress.com by 213.222.148.141 on 09/07/12
For personal use only.

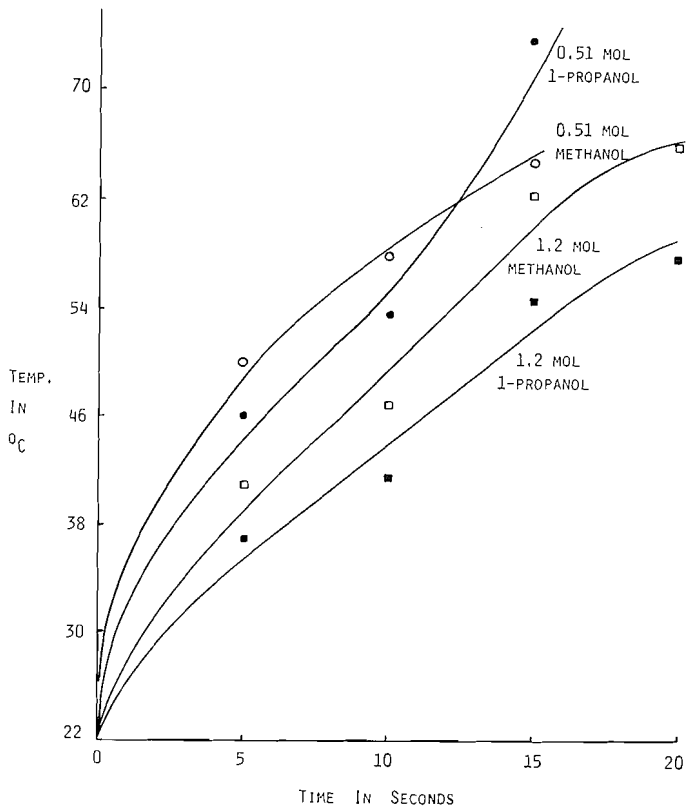

FIG. 2. The effect of the amount of solvent on the heating rate at 560 watts in open vessels.

long heating times and reactions using a large volume of reactants should be avoided because these conditions generate very high pressures in the Teflon vessels in some reactions. In practice, if the volume of the reaction mixture is kept to between 10 and 15% of the volume of the container, the pressure will not exceed safe limits.[1]

However, if this new synthetic method is to be useful, it is imperative that these syntheses be done safely. The following experiments were undertaken in an effort to understand why (*i*) the rates and (*ii*) the pressures are significantly greater when an organic reaction is carried out in a microwave oven.

Boiling point of the solvent

The results in Table 1 show that the most dramatic rate enhancements were obtained in methanol. Reactions in water and higher boiling alcohols, on the other hand, showed smaller rate increases. In the esterification of benzoic acid with a homologous series of alcohols, Table 6, the rate enhancement decreased with increasing boiling point of the alcohol, i.e., the rate enhancement decreased from 96 in the lowest boiling solvent, methanol, to a low of 1.3 in the highest boiling solvent, 1-pentanol.

The rate enhancement decreases with an increase in the boiling point of the solvent because the rates of the microwave and the classical reactions are affected differently by a change in solvent. The rate of the classical (reflux) reaction increases as the reaction temperature (the boiling point of the solvent) increases. Two pieces of evidence, on the other hand, suggest that the rate constants for the microwave reactions are almost identical in the different solvents. First, the esterifications in methanol, 1-propanol, 1-butanol, and 1-pentanol, Table 6, are all 78 ± 2% complete in approximately 6 min. Secondly, the final temperatures of the reaction mixtures in these four solvents

TABLE 5. The rate enhancements found for the heterogeneous and homogeneous saponification of isopropyl benzoate[a]

Classical method		Microwave at 560 watts		
Average[b] % yield $C_6H_5CO_2H$	Reaction time	Average[b] % yield $C_6H_5CO_2H$	Reaction time	$\left[\frac{k_{microwave}}{k_{classical}}\right]$
Heterogeneous reaction with aqueous NaOH				
15 ± 2	10 min	17 ± 1	4 min	2.5
Homogeneous reaction with alcoholic NaOH				
68 ± 2	3 min	63 ± 1	1 min	3.0

[a]The reactions were carried out on 10 mL of solution in a 300-mL Berghof reaction vessel.

[b]The averages are for at least three separate experiments.

were virtually identical, i.e., they varied from 134°C in methanol to 137°C in 1-pentanol. The almost identical rate constants for the microwave reactions are probably found because all the solvents reach the same final temperature when the same amount of microwave energy (560 watts) is used. Finally, the rate enhancement decreases when a higher boiling solvent is used because the rate of the slower (reflux) reaction increases with the boiling point of the solvent while the rate of the microwave reaction does not change significantly.

While the major cause of the decreasing rate enhancements with higher boiling solvents appears to be the almost constant reaction rates in the microwave oven, the dielectric constant of the solvent may also affect the magnitude of the rate enhancement. Since the dielectric constants decrease from methanol to 1-pentanol, methanol will heat up more rapidly and reach the final temperature sooner than the higher alcohols. Thus, the microwave reaction in methanol should be faster than in the higher alcohols. Although the errors in the yield are too large to be certain, the reaction in methanol, which takes 5 min, seems to be slightly faster than that in 1-propanol, which takes 6 min, and those in 1-butanol and 1-pentanol, which take 7.5 min to reach 78 ± 2% of completion, Table 6.

The above results suggest that the microwave technique is only successful in increasing the rates of reactions that are carried out in low boiling solvents. This is not the case, however. The rate constant of a reaction in a high boiling solvent can, in fact, be increased in two ways: by adjusting the volume of the solvent in the container used in the microwave experiment (*vide infra*) and by increasing the amount of microwave energy used in the synthesis. For example, the rate enhancement for the esterification of benzoic acid with 1-pentanol is increased from 1.3 to 6.1 when the power level is increased from 560 to 630 watts, Table 6. It is worth noting that a small increase in the amount of microwave energy has a marked effect on the reaction temperature, i.e., the final temperature of the reaction mixture increased by approximately 20°C when the power level was increased by 10%. The important observation, however, is that the microwave technique can be used to increase the rates of reactions in both high and low boiling solvents.

Size of the reaction vessel

In another set of experiments, the rate enhancement in an S_N2 reaction between 4-cyanophenoxide ion and benzyl chloride in methanol was determined by reacting identical amounts of reagents to 65% completion in 50-mL, 120-mL, and 300-mL

Can. J. Chem. Downloaded from www.nrcresearchpress.com by 213.222.148.141 on 09/07/12
For personal use only.

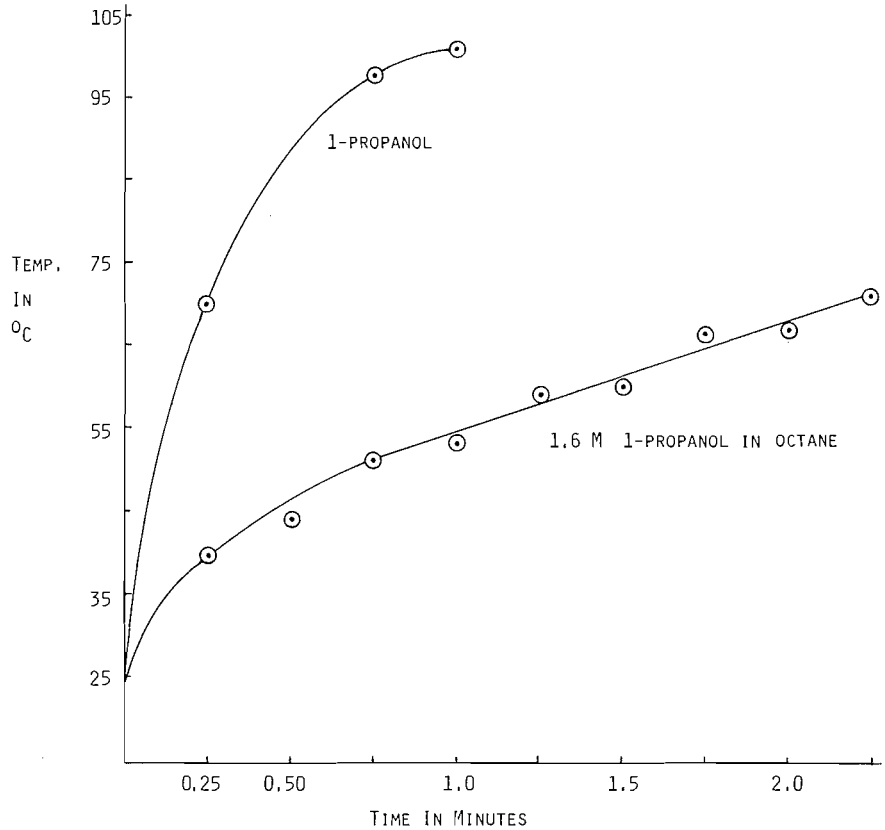

FIG. 3. Microwave heating of a polar solute in a nonpolar solvent at 560 watts in an open vessel.

TABLE 6. Reaction times and rates for the esterification of benzoic acid with different alcohols under classical and microwave conditions[a]

Alcohol	Approximate reaction temperature (°C)	Reaction time	Average[b] yield (%)	$\left[\frac{k_{\text{microwave}}}{k_{\text{classical}}}\right]$
Methanol	65	8 h (reflux)	74	
	134	5 min (M-wave)	76	96
1-Propanol	97	4 h (reflux)	78	
	135	6 min (M-wave)	79	40
1-Butanol	117	1 h (reflux)	82	
	135	7.5 min (M-wave)	79	8
1-Pentanol	137	10 min (reflux)	83	
	137	7.5 min (M-wave)	79	1.3
1-Pentanol at 630 watts	162	1.5 min (M-wave)	77	6.1

[a]All reactions were done using 10 mL of the alcohol in a 300-mL Berghof bottle. With the exception of the 1-pentanol reaction at 630 watts, all the reactions were done at 560 watts.
[b]The yields are the averages from at least two separate experiments.

Teflon vessels. The results in Table 7 show that the rate of reaction increases markedly when the volume of the Teflon container is reduced. In fact, the linear relationship, Fig. 4, between 1/volume of the Teflon bottle and 1/the time it took for the reaction to go to 65% completion is excellent, with a correlation coefficient of 0.996. The reciprocal of the time to take the reaction to 65% completion is directly related to the rate of the reaction because the same amounts of reagents were used in each experiment. Thus, the rate of reaction varies inversely with the volume of the container. Since the pressure in the Teflon bottle is related to 1/volume of the container (*vide infra*), the rate of reaction increases when the pressure in the Teflon bottle increases. In fact, this relationship is reasonable because the boiling point of a liquid is greater when it is under pressure (9).

The above experiment suggested that the increased rates of reaction found in the microwave oven syntheses were the result of a pressure increase in the reaction vessel rather than the result

Can. J. Chem. Downloaded from www.nrcresearchpress.com by 213.222.148.141 on 09/07/12
For personal use only.

TABLE 7. Time required to obtain 65% yield of benzyl-4-cyanophenyl ether using equal amounts of sodium 4-cyanophenoxide, benzyl chloride, and methanol in vessels of different sizes

Volume of the Teflon vessel (mL)	Time[a] for 65% reaction (min)	$\left[\frac{1}{\text{Vol. of Teflon vessel in mL}}\right]$	$\left[\frac{1}{\text{Time for 65\% reaction}}\right]$	$\left[\frac{k_{\text{microwave}}}{k_{\text{classical}}}\right]$
50	35 s	20.0	1.71	1240
120	1.33 min	8.33	0.75	540
300	3.0 min	3.33	0.33	240

[a]All reactions were done using the same concentrations and volumes.

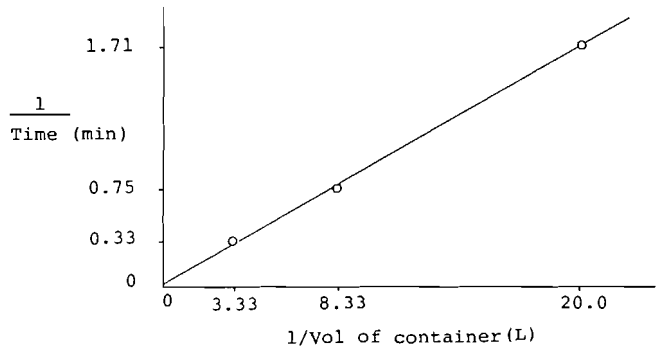

FIG. 4. The effect of the volume of container on the rate of an S_N2 reaction.

TABLE 8. Percent yield of *n*-propyl benzoate after heating equal amounts of reactants for 4 min in an oil bath at 160°C and in the microwave oven in an open vessel

Conditions	Percent ester	Percent acid	Percent total recovery
Oil bath, 4 min at 160°C	29	64	94
Microwave, 4 min (atmos. pressure)	25	69	94

of any special effect of the microwaves. An experiment was carried out to test this hypothesis. *n*-Propyl benzoate was synthesized by heating identical mixtures of benzoic acid, sulfuric acid, and 1-propanol in an open vessel in the microwave oven and in an oil bath at 160°C for 4 min. The yield of *n*-propyl benzoate in these two reactions was identical within experimental error, Table 8. This clearly illustrates that the microwaves only heat the molecules but do not activate them in any other way. Thus, the faster rate of reaction in the microwave oven is observed because the high pressure in the sealed Teflon vessels allows the microwaves to superheat the reaction mixture.

Pressure measurements, power levels

The above experiments demonstrated that the rate enhancements observed in the microwave oven were the result of the increased pressure that is generated in the Teflon bottles when they are heated in the microwave oven. Thus, it was important to determine the parameters that affected the pressure (temperature) of different solvents (reaction mixtures) in the Teflon containers. The first experiment was done to determine the effect of the power setting on the amount of microwave radiation that is absorbed by a fixed amount of liquid in the Teflon bottles. The results, Fig. 5, indicate that the pressure (temperature) of the liquid in the Teflon containers increases more rapidly when the power level is higher. Also, the final pressure (temperature) is higher when a higher power level is used with a particular solvent. These results were expected since more microwave energy will be absorbed by the solvent in the Teflon vessel when the power level is higher.

Volume of the reaction mixture

The next set of experiments involved examining the effect of the ratio of the volume of the reaction mixture/the volume of the Teflon container. In these experiments, different volumes of solvents were heated at 560 watts in the same Teflon vessel and the pressures (temperatures) of the solvents were determined at various times. The results are shown graphically in Figs. 6–8. When the volume of solvent is small, the pressure (temperature) increases as the volume of the solvent in the container increases. However, as the volume of solvent in the Teflon bottle increases, this trend is eventually reversed, i.e., a point is reached where the larger volume of solvent is not heated more quickly. In fact, this trend is found with every solvent that has been tested. It is worth noting, however, that the final pressure (temperature) reached with the larger volumes of solvent is at least as high as that found with smaller amounts of solvent, Fig. 7. This probably occurs because it takes longer to heat the larger volume of solvent to the same temperature at the same power level.

The point at which the maximum amount of microwave energy retained by the solvent (the maximum heating rate) is observed occurs at different volumes for different solvents. For example, the most rapid temperature increase is found with 15 mL of water, 20 mL of 1-propanol, and 30 mL of 1-butanol in a 150-mL Savillex bottle. Thus, the volume of a particular solvent that should be used to obtain the fastest increase in temperature (the maximum rate enhancement) is different for each solvent. This maximum increase in pressure (temperature) with a particular amount of solvent is found because the amount of microwave energy absorbed by the thicker layer of solvent in the Teflon container (the rate of increase in pressure) increases until the amount of solvent is too great to be heated by the available microwave energy.

The volume for which the maximum heating rate is observed seems to depend on the molecular weight and the heat capacity of the liquid. In water, the greatest increase in pressure occurs at 15 mL (0.83 mol) and a smaller rate of increase is found at 20 mL (1.11 mol), Fig. 6. Because 15 mL of 1-propanol and 1-butanol are only 0.20 and 0.16 mol, respectively, the greatest heating rate occurs with larger volumes of these solvents. In

Can. J. Chem. Downloaded from www.nrcresearchpress.com by 213.222.148.141 on 09/07/12
For personal use only.

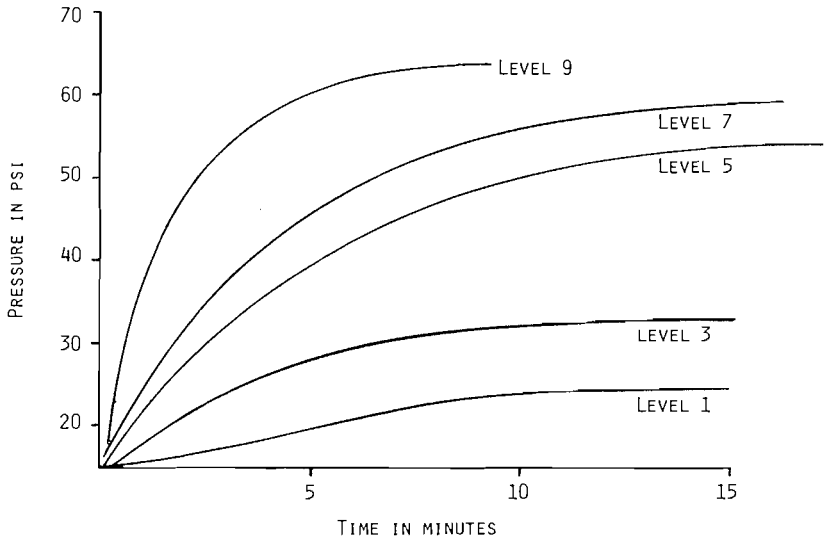

FIG. 5. The effect of the power setting on the microwave heating of 1-propanol.

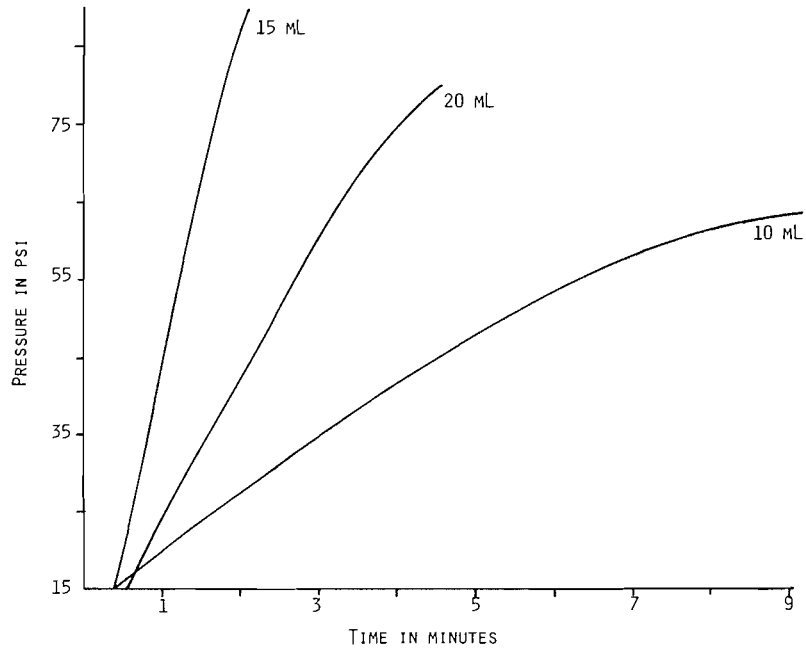

FIG. 6. The effect of the volume of water in a sealed 150-mL Savillex bottle on the heating rate.

fact, the most rapid increase in pressure for 1-propanol and 1-butanol occurs at 20 mL (0.27 mol) and 30 mL (0.32 mol), respectively. The maximum increase in pressure for 1-butanol presumably occurs at only 0.32 mol rather than the 0.83 mol found for water because the heat capacity of 1-butanol is approximately twice that of water. Thus, the amount of energy that is required to heat 15 mL of water and 30 mL of 1-butanol is almost identical and it is not surprising that these volumes have the maximum heating rate.

An experiment was carried out to learn if the volume of solvent/volume of the container or the amount of solvent in the container was important in determining the fastest heating rate and maximum rate enhancement. The volume (amount) of solvent in the bottle was important in determining the maximum heating effect. The maximum heating rate for water is at 15 mL in both a small (50-mL) and in a larger (150-mL) Savillex Teflon bottle, Fig. 9. This is not too surprising because the Teflon containers are made of the same material and should absorb and radiate similar amounts of energy.

However, the results in Fig. 9 also show that the pressure (temperature) increases faster in the smaller reaction vessel. Although we are unable to explain this phenomenon, the same trend is observed in our study of the S_N2 reaction between 4-cyanophenoxide ion and benzyl chloride in methanol (*vide supra*).

Optimization of conditions

Finally, the information that had been collected was used to try to increase the rate acceleration observed in the esterification of benzoic acid in 1-propanol, a reaction that had a fairly small rate enhancement in the microwave oven (6). The results in Table 9 show that the rate enhancement could indeed be

Can. J. Chem. Downloaded from www.nrcresearchpress.com by 213.222.148.141 on 09/07/12
For personal use only.

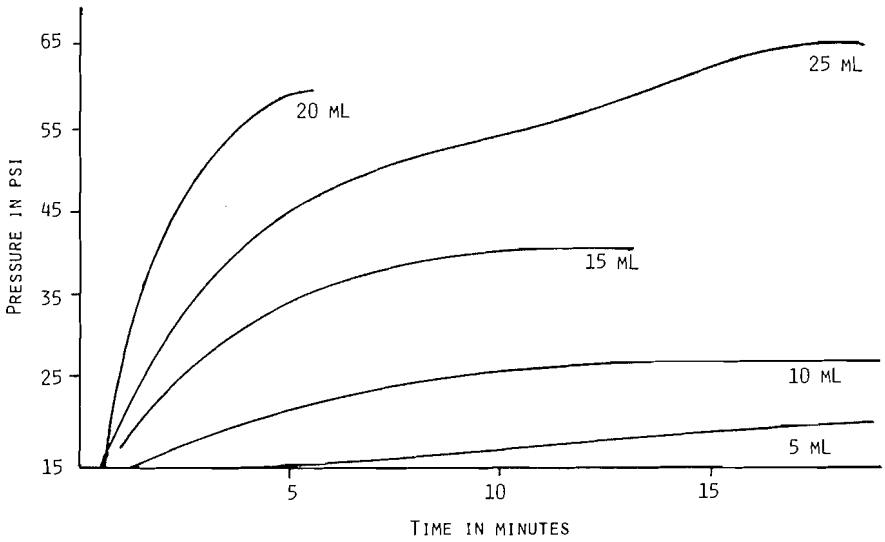

FIG. 7. The effect of the volume of 1-propanol in a sealed 150-mL Savillex bottle on the heating rate.

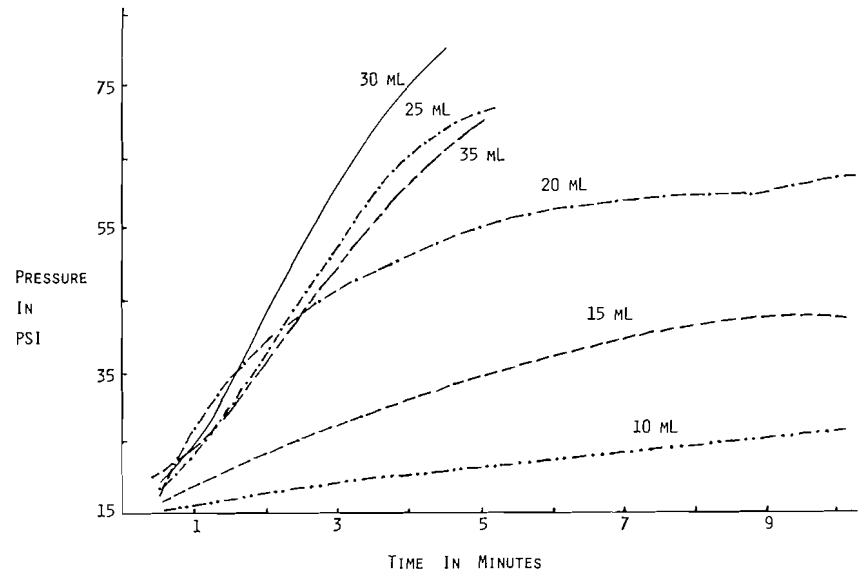

FIG. 8. The effect of the volume of 1-butanol in a sealed 150-mL Savillex bottle on the heating rate.

increased by varying the reaction conditions. For example, the rate enhancement for the esterification was increased from 18 to 60 when the volume of the reaction mixture was altered to maximize the heating rate. Increasing the power level from 560 watts to 630 watts increased the rate enhancement for the microwave reaction from 60 to 180 (*vide supra*). These results are important because they demonstrate that a rate enhancement of approximately 200 is possible if the conditions are optimized for the reaction in the microwave oven.

Conclusion

The nonoptimized rate enhancements of between 5 and 1240 found for several different classes of organic reactions, Table 10, show that organic reactions in polar solvents can be carried out quickly and conveniently in a microwave oven. However, rate enhancements of approximately 200 appear possible for many reactions when the reaction conditions are optimized. These syntheses can be carried out safely if the reaction volumes are limited to approximately 10% of the volume of the Teflon bottle used for the synthesis and if a pressure-release Savillex Teflon reaction vessel is used.[1] The rate enhancing properties of the microwave oven are predominantly due to its ability to superheat the solvent rapidly in the sealed Teflon vessels.

Experimental

Apparatus

The microwave oven used for this study was a domestic Toshiba model ER-8000 BTC with nine power settings, starting at 72 watts and increasing by 81-watt increments to 720 watts. Power setting 7 (a nominal 560 watts) was used unless otherwise stated. The Teflon vessels used for the reactions in the microwave oven were (*i*) 120- and 300-mL Teflon bottles manufactured by Berghof/America Inc.,[2] (*ii*) 50- and 150-mL PFA vessels manufactured by the Savillex Corporation,[3] and (*iii*) a Savillex 150-mL PFA vessel fitted with a pressure-releasing device designed to vent at approximately 100 psi.[3]

Product analysis

Reaction products were identified by their melting or boiling points (uncorrected) and by nmr and ir spectroscopy. The nmr spectra were recorded with a Varian T-60 nmr spectrometer and the ir spectra with a Beckman Acculab I double beam spectrophotometer.

Can. J. Chem. Downloaded from www.nrcresearchpress.com by 213.222.148.141 on 09/07/12
For personal use only.

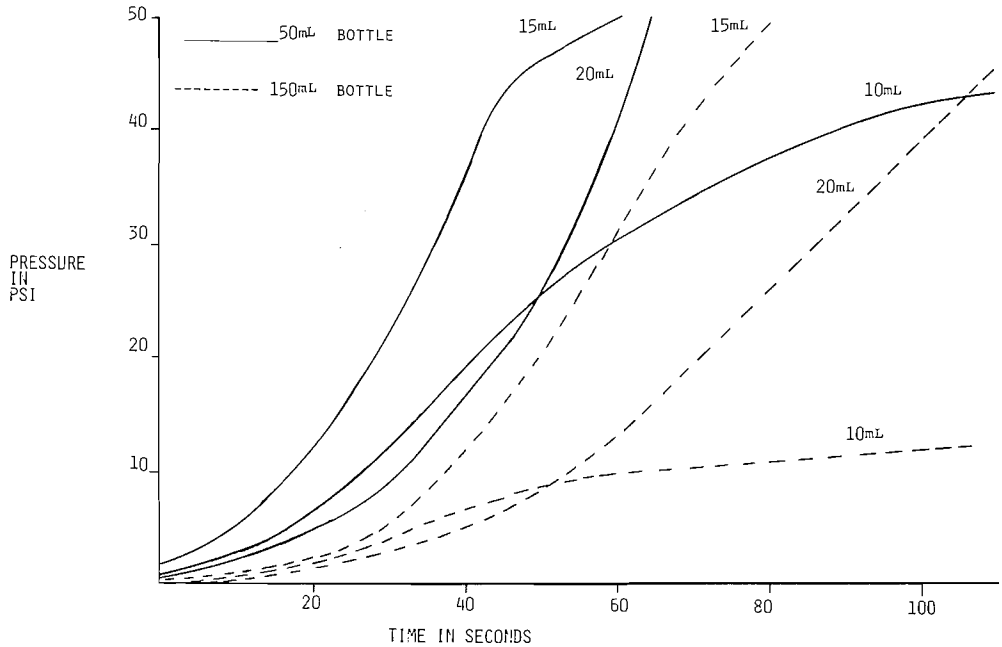

FIG. 9. Increase in pressure with time when various volumes of water were heated at 560 watts in 50-mL and 150-mL Savillex bottles.

TABLE 9. The optimization of reaction rates in the formation of *n*-propyl benzoate

$\left[\frac{\text{Volume of reaction mixture}}{\text{Volume of the Teflon bottle}}\right]$	Percent reaction	$\left[\frac{\text{Time (classical)}}{\text{Time (microwave)}}\right]$	$\left[\frac{k_{\text{microwave}}}{k_{\text{classical}}}\right]$
10/300 at 560 watts	46	$\frac{180}{10}$	18
20/160 at 560 watts	41	$\frac{180}{3}$	60
20/160 at 630 watts	40	$\frac{180}{1.0}$	180

TABLE 10. Rate enhancements found for eight different reactions using the microwave technique

Reaction	Solvent	$\left[\frac{k_{\text{microwave}}}{k_{\text{classical}}}\right]$
1. Amide hydrolysis	H_2O	6
2. Permanganate oxidation	H_2O	5
3. Esterification	ROH	1.3–180
4. S_N2 reaction	MeOH	240–1240
5. Ester saponification	H_2O	25[a]
6. Phenol derivatization	H_2O	30[a]
7. S_N2 esterification	EtOH–H_2O	45[a]
8. Oxime formation	EtOH	60[a]

[a]These are not as accurate as the other rate enhancements, see Table 2.

General procedure

Each experiment was carried out by both the classical (reflux) method and in the microwave oven. In each case, the same quantities of reagents were used and the products were worked up and purified in the same way. Each reaction was carried out several times to find the reaction times that gave the same yields by the classical and microwave techniques. This allowed the relative rate constants for each experiment (the rate enhancement) to be calculated.

In all the microwave preparative experiments, the reagents were mixed in a Teflon vessel, the lid screwed on tightly, and the mixture heated in the oven for the specified time (Tables 1 and 2). After the heating was completed, the vessel was left to stand in the oven for 2 min to reduce the pressure in the bottle. Then the bottle, which was still hot, was removed from the oven and cooled in ice-water for 5 min before the top was unscrewed.

Safety precautions

Increasing the volume of solvent and (or) the power level or decreasing the size of the container can cause an increase in pressure and temperature that can lead to deformation of the reaction vessels or even to an explosion. To ensure a safe experiment, the solvent volumes should not exceed 10% of the volume of the container and heating times of more than 5 min at a power of 560 watts should be avoided. Higher power levels should be avoided regardless of the heating times or the volume of the container. It is possible, however, that these recommended volumes and power levels may be different for other microwave ovens. In any case, excess pressure is usually not a problem if small volumes of reagents are used and if the experiments are carried out in Savillex bottles with a pressure-releasing cap.

Flammable organic solvents have been heated in open vessels in microwave ovens in this study. Although one might be concerned that a spark from the oven might ignite the organic vapours, this has never occurred because a stream of air constantly blows any vapour out of the oven. In any case, these experiments were done in a fume hood to ensure that the vapours were carried away from the electronics. It is recommended that this procedure be followed when organic solvents are heated in microwave ovens.

Can. J. Chem. Downloaded from www.nrcresearchpress.com by 213.222.148.141 on 09/07/12
For personal use only.

Can. J. Chem. Downloaded from www.nrcresearchpress.com by 213.222.148.141 on 09/07/12
For personal use only.

Pressure and temperature measurements

Pressure measurements were carried out by connecting the cap of a pressure-release 150-mL Savillex bottle to a pressure gauge outside the microwave oven. The bottle was connected to the pressure gauge by a 1/4-in. to 1/8-in. Swagelok reducing adapter, a 1/8-in. Teflon tube that passed through a small hole drilled in the back of the oven, and a Swagelok fitting. The pressure was recorded every 30 s for the duration of the experiment. The final temperature in the sealed bottle was estimated by pointing a Williamson 600 infrared sensor at the mixture in the bottle immediately after the heating was completed. The temperature readings obtained on the infrared sensor were in good agreement with those predicted from the pressure in the Teflon bottles (9).

Synthetic procedures

Esterification of benzoic acid

In all of the esterifications, benzoic acid was reacted with 10 mL (approximately a tenfold excess) of the alcohol. A typical microwave procedure is described. A mixture of 1.6 g (13 mmol) of benzoic acid, 10 mL (0.13 mol) of 1-propanol, and 0.1 mL of concentrated H_2SO_4 was sealed in a 300-mL Teflon bottle and heated in the microwave oven for several minutes. After cooling (see General procedure), the mixture was made basic with 20% Na_2CO_3 and the ester extracted with ether. The aqueous layer was acidified with 10% H_2SO_4 and the unreacted benzoic acid extracted with ether. Both ether extracts were dried over anhydrous $MgSO_4$ and the ester and benzoic acid isolated by evaporation of the solvent under reduced pressure.

Hydrolysis of benzamide

A mixture of 1.0 g (8.4 mmol) of benzamide and 10 mL of a 20% sulfuric acid solution in the sealed 300-mL Teflon bottle was placed in the microwave oven and heated for several minutes. After cooling, the reaction mixture was made basic with 20% sodium carbonate and the unchanged amide isolated by extraction with chloroform, drying over anhydrous $CaCl_2$, and evaporation of the solvent. The aqueous layer was acidified with 20% H_2SO_4 and the benzoic acid extracted with ether. The ether extracts were dried with anhydrous $MgSO_4$ and the benzoic acid isolated by evaporation of the ether.

Oxidation of toluene

A mixture of 0.92 g (10 mmol) of toluene, 3.0 g (19 mmol) of $KMnO_4$ in 50 mL of water, and 13 mL of 6 M KOH were sealed in the 300-mL Teflon bottle and heated in the microwave oven for several minutes. After cooling, the reaction mixture was extracted with ether to remove the unchanged toluene. The aqueous layer was acidified with 20% H_2SO_4 and sufficient $NaHSO_3$ added to decolourize the solution. The solution was extracted with ether, the extracts dried with anhydrous $MgSO_4$, and the benzoic acid isolated by evaporation of the ether.

The reaction of sodium 4-cyanophenoxide with benzyl chloride

A mixture of 0.22 g (1.5 mmol) of sodium 4-cyanophenoxide, 0.19 g (1.4 mmol) of benzyl chloride, and 15 mL of methanol in the sealed 300-mL Teflon bottle was heated in the microwave oven for a few minutes. The reaction mixture, after cooling, was poured into 90 mL of water and extracted with ether. The yield of 4-cyanophenyl benzyl ether was determined by titrating the chloride ion in the aqueous phase with a standard silver nitrate solution (8).

Preparation of derivatives

The derivatives were synthesized both by the classical methods outlined in standard laboratory manuals (10, 11) and in sealed Teflon containers in the microwave oven. Typical examples of the preparation of each derivative using the microwave procedure are described. The reaction times and yields obtained in the preparation of the derivatives by microwave and by classical methods are listed in Table 2.

4-Nitrobenzyl esters from carboxylic acids

A mixture of 1.5 g (10 mmol) of cinnamic acid and 1 mL of water was neutralized with a 10% solution of NaOH. A solution of 1.5 g (9 mmol) of 4-nitrobenzyl chloride in 7 mL of ethanol was added and the mixture heated for 2 min in a sealed 150-mL Teflon bottle in the microwave oven. After cooling, 2 mL of water was added. The precipitated ester was collected by filtration and washed with a 5% Na_2CO_3 solution. Recrystallization from ethanol gave 0.67 g (26%) of 4-nitrobenzyl cinnamate, mp 115–116°C (lit. (11) mp 116°C).

Aryloxyacetic acids from phenols

A mixture of 0.2 g (1.4 mmol) of 2-naphthol in 3 mL of 6 M NaOH and 0.5 mL of 50% aqueous chloroacetic acid were sealed in the 150-mL Teflon bottle and heated in the microwave oven for 2 min. After cooling, 2 mL of water was added and the solution acidified with dilute HCl. The mixture was extracted with ether, and the ether extracts were washed with water and extracted with a 5% sodium carbonate solution. The sodium carbonate extract was acidified with dilute HCl and the precipitated acid collected by filtration. Recrystallization from water gave 0.04 g (14%) of the 2-naphthoxyacetic acid, mp 154–156°C (lit. (10) mp 154°C).

Oximes from aldehydes and ketones

A mixture of 1.0 g (5.5 mmol) benzophenone, 1.0 g (14.4 mmol) of hydroxylamine hydrochloride, 5 mL of pyridine, and 5 mL of absolute ethanol in a 150-mL sealed Teflon bottle was heated in the microwave oven for 2 min. After cooling, the solvents were removed under reduced pressure, the residue stirred with 5 mL of cold water, and the crude oxime collected by filtration. Recrystallization from ethanol gave 0.74 g (68%) of the benzophenone oxime, mp 139–140°C (lit. (11) mp 141°C).

Carboxylic acids from esters

A mixture of 1.0 g (7.4 mmol) of methyl benzoate and 10 mL of a 25% aqueous NaOH solution in a sealed 150-mL Teflon bottle was heated for 2.5 min in the microwave oven. Then the solution was cooled and acidified with dilute HCl. The acid was extracted with ether, and the extracts dried over anhydrous $MgSO_4$ and evaporated, giving 0.76 g (84%) of benzoic acid, mp 121–122°C (lit. (10) mp 122°C).

Acknowledgements

The authors gratefully acknowledge the financial assistance provided by the Laurentian University Research Fund, the Natural Sciences and Engineering Research Council of Canada, and the SEED project funded by the Government of Canada. We would also like to thank Ms. H. Ali, Ms. L. Baldisera, Mr. J. Duhaime, Ms. B. Gleason, and Ms. E. Robitaille for their assistance. Donations from Inco Metals Co. and the Savillex Corporation are also acknowledged.

1. F. Smith, B. Cousins, J. Bozic, and W. Flora. Anal. Chim. Acta, **177**, 243 (1985).
2. J. K. S. Wan, K. Wolf, and R. D. Heyding. *In* Catalysis on the energy scene. *Edited by* S. Kaliaguine and K. Mahay. Elsevier, Amsterdam. 1984. p. 561.
3. J. A. Hesek and R. C. Wilson. Anal. Chem. **46**, 1160 (1974).
4. R. A. Nadkarni. Anal. Chem. **56**, 2233 (1984).
5. M. Bacci, M. Bini, A. Checcucci, A. Ignesti, L. Millanta, N. Rubino, and R. Vanni. J. Chem. Soc. Faraday Trans. 1, **77**, 1503 (1981).
6. R. Gedye, F. Smith, K. Westaway, H. Ali, L. Baldisera, L. Laberge, and J. Rousell. Tetrahedron Lett. **27**, 279 (1986).
7. R. J. Giguere, T. L. Bray, S. M. Duncan, and G. Majetich. Tetrahedron Lett. **27**, 4945 (1986).
8. D. A. Skoog and D. M. West. *In* Fundamentals of analytical chemistry. 4th ed. Holt Rinehart and Winston, New York, NY. 1982. p. 185.
9. A. S. Foust, L. A. Wenzel, C. W. Clump, L. Maus, and L. B. Andersen. *In* Principles of unit operations. 2nd ed. J. Wiley and Sons, New York, NY. 1980. pp. 728–732.
10. D. J. Pasto and R. L. Johnson. *In* Laboratory text for organic chemistry. Prentice–Hall Publishers, Englewood, NJ. 1979.
11. R. L. Shriner, R. C. Fuson, D. R. Curtin, and T. C. Morrill. *In* The systematic identification of organic compounds. 6th ed. J. Wiley and Sons, New York, NY. 1980.

Studies of the synthesis of 8a-hydroxy-4a-methyloctahydronaphthalen-1(2*H*)-ones and their 2α-deutero derivatives

SHIRLEY STIVER, PETER D. CLARK, AND PETER YATES
Lash Miller Chemical Laboratories, University of Toronto, Toronto, Ont., Canada M5S 1A1

Received June 19, 1987

SHIRLEY STIVER, PETER D. CLARK, and PETER YATES. Can. J. Chem. **66**, 27 (1988).

Two syntheses of the bicyclic α-ketols, 8a-hydroxy-4a-methyl-*trans*- and -*cis*-octahydronaphthalen-1(2*H*)-ones (**1** and **2**), have been effected. One involves epoxidation of 4a-methyl-1,2,3,4,4a,5,6,7-octahydronaphthalene (**4**), followed by hydrolysis and oxidation; direct "hydroxy ketonization" of **4** was found not to be practicable. The second involves treatment of 3,4,5,6,7,8-hexahydronaphthalen-1(2*H*)-one (**14**) with lithium dimethylcuprate, trimethylsilylation of the resulting enolate, oxidation of the enol ether, and hydrolysis. Syntheses of the 2α-deutero derivatives of **1** and **2** are also described.

SHIRLEY STIVER, PETER D. CLARK et PETER YATES. Can. J. Chem. **66**, 27 (1988).

On a effectué deux synthèses des α-cétols bicycliques, hydroxy-8a méthyl-4a octahydronaphtalène-1 (2*H*) ones-*trans* et -*cis* (**1** et **2**). Une de ces synthèses implique l'époxydation du méthyl-4a octahydro-1,2,3,4,4a,5,6,7 naphtalène (**4**), suivie d'une hydrolyse et d'une oxydation; on a trouvé que l'«hydroxy-cétonisation» directe du composé **4** n'est pas pratique. La deuxième synthèse implique une réaction de l'hexahydro-3,4,5,6,7,8 naphtalène-1 (2*H*) one (**14**) avec du diméthylcuprate de lithium, une triméthylsilylation de l'énolate qui en résulte, une oxydation de l'éther énolique et une hydrolyse. On décrit aussi les synthèses des dérivés deutéro-2α des composés **1** et **2**.

[Traduit par la revue]

Can. J. Chem. Downloaded from www.nrcresearchpress.com by 213.222.148.141 on 09/07/12
For personal use only.

In a previous paper (1) we discussed the synthesis of 5-hydroxy 6-keto steroids and their 7α-deutero derivatives. We have also undertaken studies on the synthesis of the analogous bicyclic ketols **1** and **2** and their 2α-deutero derivatives, which, like the steroidal ketols, were required for our photochemical investigations (2). These studies have led to observations of intrinsic interest and are reported here; it is planned to report the full details of the photochemical work subsequently.

Syntheses of the bicyclic ketols

Application of different approaches furnished two syntheses of the *trans* and *cis* bicyclic ketols **1** and **2**. A "classical" synthesis analogous to that employed for the related steroidal ketols (1) provided a reliable, albeit not elegant, method for the preparation of **1**. An efficient synthesis of the olefin **4** was essential to the success of this route. Direct reduction of the bicyclic enone **3** with lithium aluminum hydride and aluminum chloride gave a mixture of three olefins, despite reports of the sole formation of unrearranged olefin from similar reaction of the analogous steroidal enone system (3). The target $\Delta^{8,8a}$ olefin **4** was the major product (~60%). The two additional products are considered to be *trans* and *cis* $\Delta^{7,8}$ olefins **5** and **6**, because of the presence of an additional vinyl signal at δ 5.50 and two additional methyl singlets at δ 0.80 and 0.93 in the ^{1}H nmr spectrum of the crude reaction product. Notorious difficulties associated with separations of double-bond isomers led us to investigate an alternative synthesis of **4**. Conversion of **3** to its thioketal **7** and reduction of this with sodium or lithium in liquid ammonia gave the olefin **4** without the formation of its isomers **5** and **6** (Scheme 1).

The lure of a one-stage transformation of olefin **4** to the *trans* and *cis* bicyclic ketols **1** and **2** led us to study its "hydroxy ketonization" with catalytic quantities of molybdenum hexacarbonyl and a large excess of anhydrous *tert*-butyl hydroperoxide in boiling benzene (4). This yielded a crude product in which the presence of the *trans* ketol **1** was evidenced as the major constituent by ^{1}H nmr spectroscopy. The spectrum also indicated the presence of *tert*-butyl-containing side products considered to arise from further reaction of *tert*-butoxy and *tert*-butylperoxy radicals, formed by a metal-catalyzed

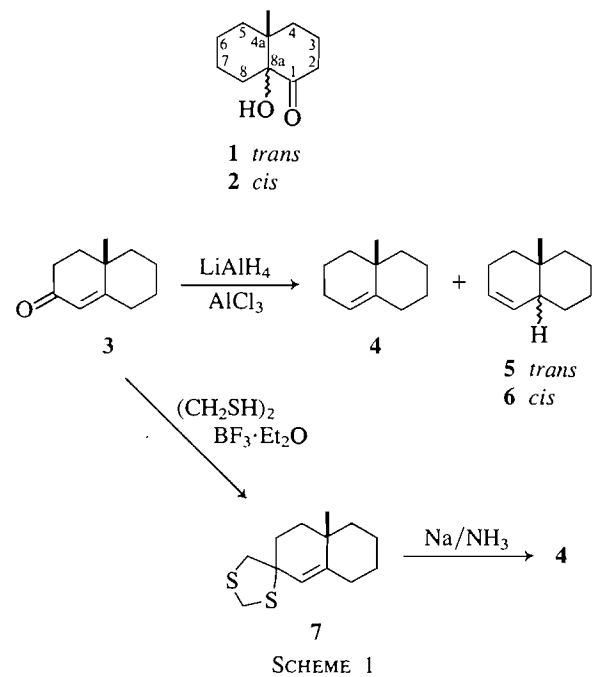

SCHEME 1

decomposition of the *tert*-butyl hydroperoxide (5). Extensive chromatography led to the isolation of **1**, the *cis* ketol **2**, and the *trans* and *cis* 1-decalones **10** and **11** (Scheme 2), which were identified by direct comparison with authentic samples. The ketones **10** and **11** are thought to arise from isomerization of the A/B *trans* and *cis* epoxides **8** and **9**, which are considered to be intermediates in the hydroxy ketonization of **4** (6), via catalysis by a molybdenum species acting as a Lewis acid. The addition of disodium hydrogen phosphate or barium oxide to the reaction mixture retarded the metal-induced decomposition of the hydroperoxide, as reported in other cases (7, 8); however, even upon prolonged reaction, oxidation stopped at the stage of the epoxides **8** and **9**. Interestingly, the A/B-*cis* epoxide **9** proved to be the major isomer, in contrast to the preference for formation of the A/B-*trans* epoxide **8** from peracid epoxidation

Can. J. Chem. Downloaded from www.nrcresearchpress.com by 213.222.148.141 on 09/07/12
For personal use only.

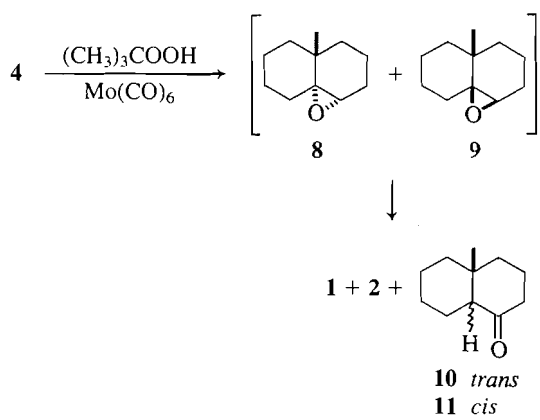

SCHEME 2

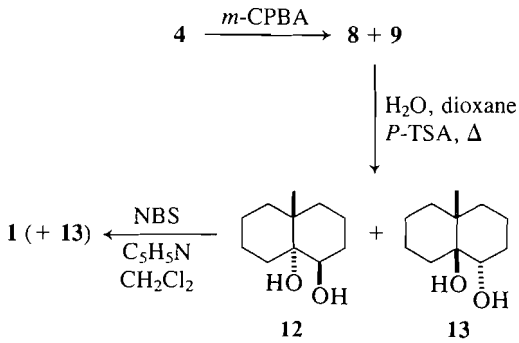

SCHEME 3

of **4** (*vide infra*).[1] The difficulties encountered during purification of the ketols and the resulting low yields render this one-stage hydroxy ketonization a procedure of limited synthetic utility.

A practicable synthesis of **1** from olefin **4** was attained by the sequence of reactions in Scheme 3. Epoxidation of **4** with *m*-chloroperoxybenzoic acid by the procedure of Marshall and Hochstetler (10) gave in 91% yield a 3:2 mixture of the epoxides **8** and **9**, whose stereochemistry has been established by these workers (10). In our hands, reaction of this mixture with aqueous perchloric acid in tetrahydrofuran (11) gave a mixture of diols, olefins, and unconsumed **9**. We found that the mixture of epoxides underwent selective epoxide opening upon treatment with catalytic quantities of *p*-toluenesulfonic acid in boiling aqueous dioxane to give a 4:1 mixture of *trans* and *cis* fused diols **12** and **13** in 89% yield. In the ^{1}H nmr spectrum of this mixture the C*H*OH proton signal of **12** was observed as a narrow multiplet at δ 3.50, while a broad multiplet at δ 3.83 is ascribed to the corresponding proton of **13**, evidencing the preference of the *cis* fused diol for the steroid-like decalin conformation **13***A* rather than for **13***B*. Among other features **13***A* permits intramolecular hydrogen bonding, which is not possible in the nonsteroidal conformer **13***B*. By analogy with the acid-catalyzed reactions of steroidal oxirane systems (1), the A/B-*trans* and A/B-*cis* epoxides **8** and **9** are considered to open with *trans* diaxial selectivity. Thus, the *cis* fused diol **13** is postulated to arise from such opening of the nonsteroidal conformer **9***B*, rather than from the steroidal conformer **9***A*.

Oxidation of the mixture of diols **12** and **13** with *N*-bromo-

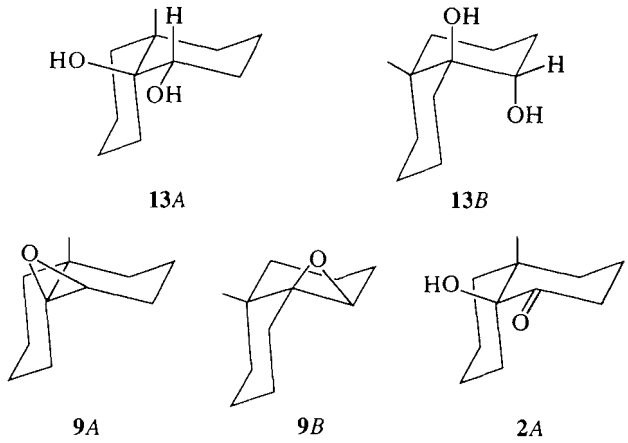

succinimide and pyridine in dichloromethane (12), a procedure that we found superior to the more frequently used *N*-bromosuccinimide in aqueous dioxane, gave a mixture of **1** and unconsumed diol **13** (Scheme 3), which were separated chromatographically. As observed in the ^{1}H nmr spectra of the steroidal 5α-ketols (1), the C-2 proton in **1** with a 1,3-diaxial relationship to the hydroxyl group is deshielded and gives rise to a multiplet at δ 3.04–3.13.

Equilibration of the *trans* ketol **1** with its *cis* epimer **2** was effected with methanolic potassium hydroxide (cf. ref. 13) (Scheme 4). The *cis* ketol **2** was isolated by flash chroma-

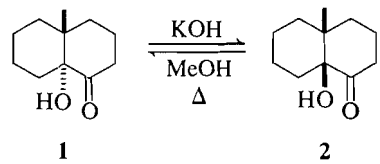

SCHEME 4

tography. The equilibrium ratio of **1** and **2** is 7:93, as shown by equilibration of either ketol under these conditions. In the ^{1}H nmr spectrum of *cis* ketol **2**, the sharp signal of the hydroxyl proton at δ 3.81 witnesses the presence of a strong intramolecular hydrogen bond (14) and thus the preference of **2** for the steroid-like conformation **2***A*. The mass spectra of **1** and **2** are essentially identical. Both exhibit base peaks at *m/z* 112 attributed to an ion arising from cleavage of the molecular ion followed by fragmentation (Scheme 5). Peaks at *m/z* 98 are

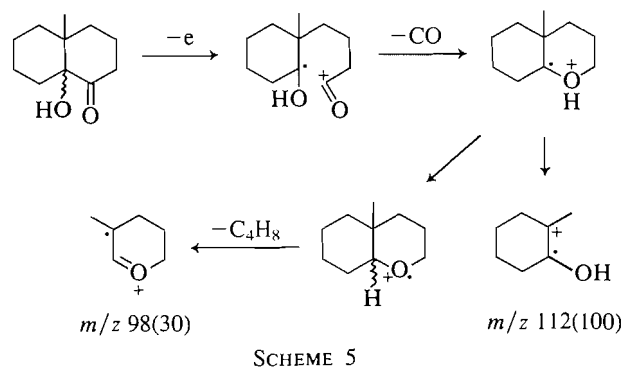

SCHEME 5

assigned to the bicyclic analogue of the ion considered to give rise to the base peak in the mass spectra of the corresponding steroidal 5β-ketols (1). While the steroidal 5α-ketols do not fragment in this manner, both the *trans* and *cis* bicyclic α-ketols exhibit *m/z* 98 peaks in their spectra. In the uv spectra of α-hydroxycycloalkanones, the position of the maximum depends on the spatial relationship between the carbonyl and hydroxyl

[1]Differences between metal catalyst and peroxy acid reagents in the stereoselectivity of olefin epoxidations have been observed previously (7, 9).

Can. J. Chem. Downloaded from www.nrcresearchpress.com by 213.222.148.141 on 09/07/12
For personal use only.

groups (15). Comparison of the uv and photoelectron spectra of 2-hydroxy- and 2-methoxycyclohexanone led Brown (16) to conclude that a marked blue shift of the $n \rightarrow \pi^*$ transition in the uv spectrum of the former is attributable to intramolecular hydrogen bonding. Consistent with this conclusion, the uv spectrum of the *cis* ketol **2** exhibits a maximum at 280 nm, hypsochromically shifted from that observed at 298 nm for the *trans* ketol **1**.

In a more contemporary approach, the *trans* and *cis* ketols **1** and **2** were also synthesized by the use of cuprate methodology. The pivotal intermediate, enone **14**, was prepared by a slight modification of the procedure of Rae and Umbrasas (17). The previous successful trapping of ketone enolates by benzoyl peroxide (18)[2] prompted us to treat enone **14** with lithium dimethylcuprate (19)[3] and to add the enolate thus formed to a suspension of benzoyl peroxide. However, the anticipated benzoyloxy ketones **17** and **18** constituted only a minor fraction of the crude reaction product, the major components being the *trans* and *cis* bromo ketones **15** and **16** (Scheme 6).

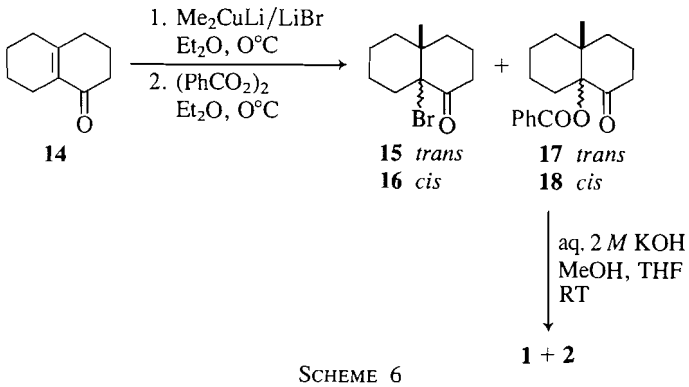

SCHEME 6

The epimeric bromo ketones **15** and **16** were separated chromatographically. The *trans* isomer **15** exhibits a carbonyl-stretching band at 5.84 μm in its ir spectrum and the position of this band, relative to that at 5.85 μm for the mixture of *trans* and *cis* 1-decalones **10** and **11**, establishes the axial orientation of the bromine substituent (20). The chemical shift of the methyl singlet (δ 1.03; $\Delta\nu$ 62 Hz) in the ^{1}H nmr spectrum of **15** correlates well with the predicted (21) 19-Hz deshielding of the methyl singlet of *trans* 1-decalone **10** (δ 0.77; $\Delta\nu$ 46 Hz). A multiplet at δ 3.30–3.90 (width ~ 36 Hz) is attributed to the C-2 proton that is 1,3-diaxial to the bromine substituent (22). The *cis* bromo ketone **16** exhibits a carbonyl-stretching band at 5.86 μm in its ir spectrum. As this is again indicative of an axial bromine substituent, it establishes the preference of the *cis* bromo ketone for the nonsteroidal decalin conformation **16***A*.

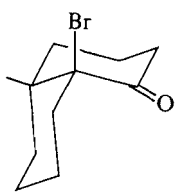

16*A*

[2]The synthetic utility of the trapping of enolate intermediates was first exploited by P. Deslongchamps (University of Toronto Chemistry Club Lecture, 1981).

[3]Cuprous bromide was used for the preparation of the cuprate reagent since the more commonly used cuprous iodide would have led to the reduction of the benzoyl peroxide.

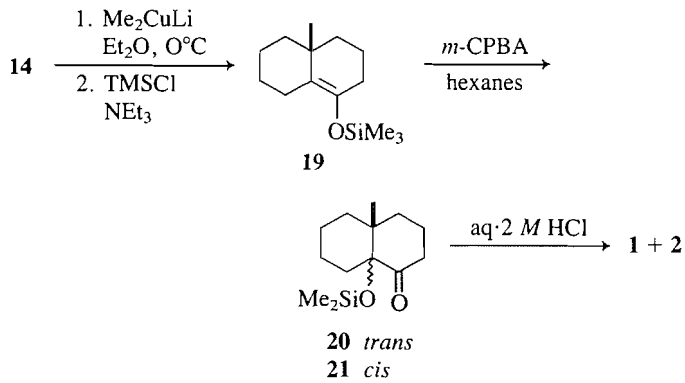

SCHEME 7

Low-halide lithium dimethylcuprate solutions (23) were employed in the above reaction in attempts to circumvent the formation of the bromo ketones. However, the yields of the benzoyloxy ketones **17** and **18** were not improved. These were not separated, but the methyl singlets at δ 0.98 and 1.27 in the ^{1}H nmr spectrum of the mixture of **17** and **18** can be assigned to the *trans* and *cis* isomers, respectively, since the methyl signal of the *trans* ketol **1** (δ 0.86) is expected to be less affected by benzoylation than that of the *cis* ketol **2** (δ 0.80). Hydrolysis of the mixture of **17** and **18** (Scheme 6) gave the *trans* and *cis* ketols **1** and **2** in 34 and 32% yield, respectively.

Since direct trapping of the enolate derived from cuprate addition to **14** had not proven efficient, the stepwise sequence shown in Scheme 7 was used for the preparation of **1** and **2**. The enolate formed by reaction of lithium dimethylcuprate with enone **14** was treated *in situ* with chlorotrimethylsilane and triethylamine to give the enol silyl ether **19** in quantitative yield. Treatment of this with *m*-chloroperoxybenzoic acid in anhydrous hexanes (cf. ref. 24)[4] yielded a crude mixture considered to consist largely of the *trans* and *cis* trimethylsiloxy ketones **20** and **21**, which were not fully characterized. Hydrolysis with aqueous acid gave the *trans* and *cis* ketols **1** and **2** in 53 and 16% yield, respectively (based on the enol silyl ether **19**).

Synthesis of 2α-deutero bicyclic ketols

Bromination of the *trans* ketol **1** and reductive cleavage of the resulting 2-bromo ketol **22** with zinc and *O*-deuteroacetic acid provided a highly stereoselective synthesis of the 2α-deutero *trans* ketol **23** (Scheme 8). Spectrometric analysis evidenced

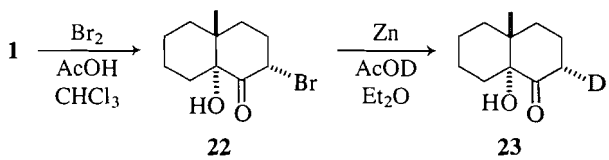

SCHEME 8

excellent incorporation of a single deuterium label into the ketol: d_0 6%, d_1 92%, d_2 2%.

The α stereochemistry of the deuterium atom in **23** was ascertained from its 400-MHz ^{1}H nmr spectrum. The intensity of the weak, broad multiplet at δ 3.00–3.18, which is assigned to the C-2α proton in **1**, relative to the methyl singlet indicated that the C-2α position was 84% deuterated in **23**. Given the

[4]Hexanes proved to be a better solvent than dichloromethane for this reaction; cf. the earlier report of a remarkable solvent effect of ether vs. dichloromethane (25).

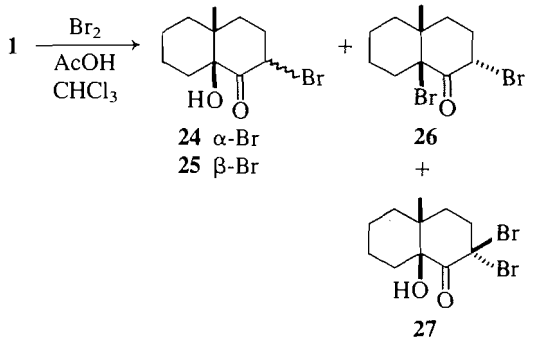

SCHEME 9

margin of error of the method, the 92% d_1 content calculated from the mass spectrum correlates well with that calculated from the ^{1}H nmr spectrum, and establishes that essentially all the deuterium label was incorporated into the C-2α site.

Bromination of the *cis* ketol **2** under the same reaction conditions led to a complex mixture comprised of the 2α- and 2β-bromo *cis* ketols **24** and **25**, the dibromo ketone **26**,[5] and the dibromo *cis* ketol **27** (Scheme 9).[6]

The structural assignments for the bromo compounds **24–27** rely heavily on the positions of the carbonyl-stretching bands in their ir spectra and known equatorial and axial bromine effects on such bands (20), the width and chemical shifts[7] of low-field C*H*Br multiplets (when present) in the ^{1}H nmr spectra, the chemical shifts of carbonyl carbon signals in the ^{13}C nmr spectra, and the characteristic relative intensities of isotopic clusters associated with the molecular ions in the mass spectra.

The 2α- and 2β-bromo *cis* ketols **24** and **25** exhibit carbonyl-stretching bands in their ir spectra at 5.87 and 5.79 μm, respectively, reflecting the effects of axial and equatorial bromine substituents, as present in the preferred steroidal conformers **24***A* and **25***A* on the position of the carbonyl band relative to that of the parent *cis* ketol **2** (5.85 μm). The α epimer **24** also exhibits a weaker band at 5.77 μm suggestive of the presence of the nonsteroidal conformer **24***B*, in which the bromine is equatorial. These assignments for the bromo ketols **24** and **25** were confirmed by the width of the C*H*Br multiplets in their ^{1}H nmr spectra. That of the 2α-bromo ketol **24** displays a triplet-like multiplet of width 12 Hz, which lies between the widths considered to be indicative of axial and equatorial bromine substitution (27, 28). This intermediate width for the C*H*Br multiplet is in accord with the postulated equilibrium between the two conformers **24***A* and **24***B*. A sharp singlet at δ 3.72 assigned to the hydroxyl proton (14) and a broad C*H*Br multiplet (width = 20 Hz) demonstrate the preference of the 2β-bromo ketol **25** for the hydrogen-bonded conformer **25***A*. In the ^{13}C spectra of **24** and **25**, both give rise to signals at δ 206, shielded relative to the carbonyl carbon signal of **2** (δ 215).

The presence of two bromine atoms in ketone **26** is indicated by the high-field carbonyl carbon signal at δ 196 in its ^{13}C nmr spectrum (29) and by the 1:2:1 ratio of the isotopic cluster

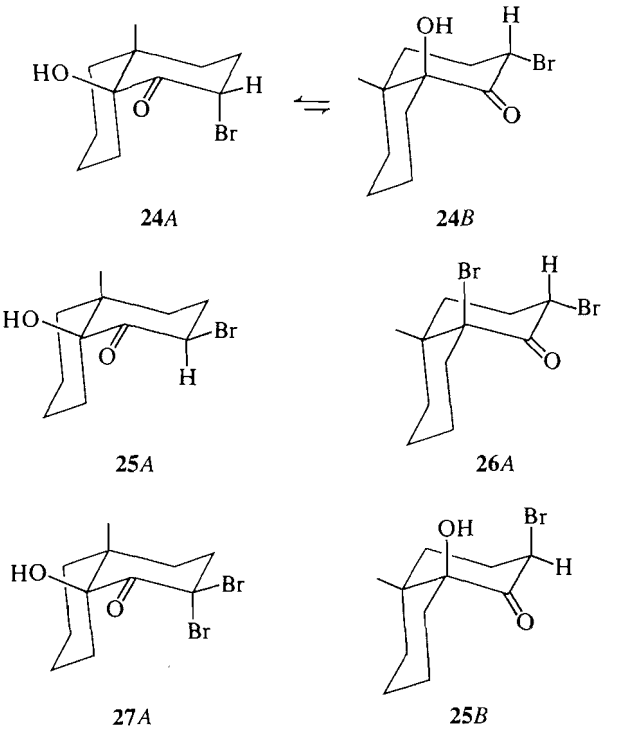

associated with the molecular ion in its mass spectrum. Comparison of the carbonyl-stretching band at 5.78 μm in its ir spectrum with that of the mixture of *trans* and *cis* 1-decalones **10** and **11** at 5.86 μm indicates that one bromine atom is equatorial, the other axial. In the ^{1}H nmr spectrum of **26**, the chemical shift of the methyl singlet (δ 1.33) compared to the chemical shifts of the methyl singlets of the *trans* and *cis* fused 8α-bromo ketones **15** and **16** (δ 1.03 and 1.32, respectively) indicates the *cis* fusion of the dibromo ketone **26**. Since the *cis* bromo ketone **16** exists in the nonsteroidal decalin conformation (*vide supra*), the excellent correlation between the chemical shifts of the pertinent methyl singlets noted above, together with the broad multiplet (width = 20 Hz) given by the C*H*Br proton, provides compelling evidence that **26** prefers to exist as the nonsteroidal decalin conformer **26***A*.

The gross structural assignment for the dibromo ketol **27** is based on the characteristic two-bromine 1:2:1 ratio of peaks related to the molecular ion in its mass spectrum and the absence of a low-field C*H*Br signal in its ^{1}H nmr spectrum. A sharp singlet at δ 3.27, in the latter signifying a hydrogen-bonded hydroxyl proton (14), indicates the *cis* ring fusion and the preference for the steroid-like decalin conformation **27***A*.

The ^{1}H nmr spectrum of the crude product obtained from bromination of the *cis* ketol **2** (Scheme 9) indicates that the predominant brominated product is the 2α-bromo *cis* ketol **24**. This was partially converted to its thermodynamically more stable epimer **25** during silica gel chromatography, and the close similarity of the R_f values of **24** and **25** rendered purification of the former difficult. Consequently, the ~4:1 mixture of 2α- and 2β-bromo ketols was stirred with a silica gel slurry to give a mixture rich in the β epimer **25**. Chromatographic purification of this proved much easier than that of **24**.

Reaction of **25** with zinc and *O*-deuteroacetic acid gave the 2α-deutero *cis* ketol **28**. As zinc and acetic acid mediated reductive cleavage of α-bromo ketones is known to occur with greater facility for axial than for equatorial orientations of the bromine (30), this reaction may be envisioned to proceed

[5]Replacement of the hydroxyl group by bromine with retention of configuration has been observed in the reactions of 5-hydroxy-5α-cholestan-4- and -6-ones with hydrobromic acid (26).

[6]In contrast, bromination of the related 5-hydroxy-5β-cholestan-6-one occurs stereoselectively to give the 7α-bromo derivative (1).

[7]An equatorial C*H*Br proton in an axial bromo ketone resonates in general at higher field than an axial C*H*Br proton in an equatorial bromo ketone (ref. 22, pp. 73–75).

Can. J. Chem. Downloaded from www.nrcresearchpress.com by 213.222.148.141 on 09/07/12
For personal use only.

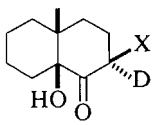

28 X = H
29 X = D

via one or both the following pathways: (*i*) a less favorable reductive cleavage of the equatorial bromine substituent from the preferred steroidal conformer **25***A* and (*ii*) reaction of a small equilibrium concentration of the less favored conformer **25***B* in which the bromine is axial. The equilibrium of **25***A* with **25***B* may be catalyzed by the *O*-deuteroacetic acid in the medium. As evidenced by the mass spectrum of **28**, excellent incorporation of deuterium into the *cis* ketol was achieved by this method: d_0 7%, d_1 91%, d_2 1%.

The α stereochemistry of the deuterium label in **28** is indicated by its ^{1}H nmr spectrum, which differs from that of the undeuterated *cis* ketol **2** by the greatly reduced intensity of the multiplet at δ 2.56–2.74, whose width (35 Hz) suggests that it corresponds to the C-2α proton. Verification of the assignment of this signal to the C-2α proton was achieved from the ^{1}H nmr spectrum of the α,α-dideutero ketol **29**, prepared by two successive treatments of **2** with deuterium oxide in the presence of potassium carbonate. Relative to the spectrum of the undeuterated **2**, that of **29** lacks two multiplets, δ 2.34–2.45 (width = 23 Hz) and δ 2.56–2.74 (width = 35 Hz), assigned on the basis of their widths to the C-2β (equatorial) and C-2α (axial) protons, respectively, in **2**.

The intensity of the weak multiplet at δ 2.56–2.74 in the ^{1}H nmr spectrum of the monodeutero ketol **28**, indicates that 83% of the deuterium label has been incorporated into the α site. In comparison with the total deuterium content calculated from the mass spectrum (91%), the ^{1}H nmr spectrum indicates that essentially all of the label has the α stereochemistry. Furthermore, the multiplet at δ 2.28–2.44, comprising the C-2β proton signal and an overlapping signal that was not assigned, corresponds to two protons (relative to the methyl singlet), demonstrating that negligible deuteration has occurred at this site. Thus deuterium is incorporated with high stereoselectivity at the α site in **28**.

Experimental[8]

*Reduction of **3** with lithium aluminum hydride and aluminum chloride. Formation of 4a-methyl-1,2,3,4,4a,5,6,7-octahydronaphthalene (**4**) and 4a-methyl-*trans- *and* -cis-*3,4,4a,5,6,7,8,8a-octahydronaphthalene (**5** and **6**)*

Anhydrous aluminum chloride (2.69 g, 20.2 mmol) under argon was cooled to −97°C in a dichloromethane – Dry Ice bath and anhydrous ether (25 mL) was added with stirring over a period of 20 min. The grey, gummy mixture was allowed to warm slowly to room temperature to give a grey solution. Lithium aluminum hydride (0.387 g, 10.2 mmol) was added in portions over a period of 20 min. The resulting grey-white suspension was stirred and treated dropwise with a solution of **3** (31, 32) (0.946 g, 5.77 mmol) in ether (10 mL), and the mixture was boiled under reflux for 30 min. The colorless solution containing a brown-black precipitate was allowed to cool and was filtered. Ether – ethyl acetate (1:1 v/v; 30 mL) was added dropwise to the filtrate, and the resulting cloudy mixture was cooled in an ice bath and treated cautiously with water (10 mL). The organic layer was separated, washed with saturated aqueous $NaHCO_3$ (15 mL) and water (3 × 5 mL), and dried (Na_2SO_4). The solvent was removed by distillation at atmospheric pressure leaving a pale yellow liquid residue (0.87 g, 100%) shown by its ^{1}H nmr spectrum to be composed of **4** (~60%) and a 75:25 mixture of **5** and **6** (~40%); ^{1}H nmr δ: 0.80 (s, $\Delta^{7,8}$ Me—minor isomer), 0.93 (s, $\Delta^{7,8}$ Me—major isomer), 1.10 (s, **4** Me), 5.28 (m, **4** vinyl proton), 5.50 (m, $W_{1/2}$ = 4 Hz, $\Delta^{7,8}$ vinyl protons).

*4a-Methyl-1,2,3,4,4a,5,6,7-octahydronaphthalene (**4**)*

Sodium (20.7 g, 0.902 mol) was added over a period of 1.5 h to a stirred suspension of **7** (33) (10.1 g, 0.042 mol) in liquid ammonia (1.2 L) containing anhydrous ether (50 mL) and anhydrous *tert*-butyl alcohol (50 mL) at −33°C. The blue reaction mixture was maintained at reflux for 1 h and ethanol (200 mL) was added slowly; the ammonia was allowed to evaporate overnight. The residue was treated with ether (450 mL) and the mixture was filtered through Celite into water (200 mL). The Celite was washed with a further 100 mL of ether, and the aqueous phase was extracted with ether (4 × 25 mL). The combined organic phases were washed with saturated aqueous NaCl (30 × 25 mL) and dried ($MgSO_4$), and the ether was removed by distillation at atmospheric pressure. Hexanes (1 L) were added and the ethanol and *tert*-butyl alcohol were removed by azeotropic distillation at atmospheric pressure. Distillation of the residue using a Kugelrohr (92–94°C/14 Torr; 1 Torr = 133.3 Pa) gave **4** (4.74 g, 76%) as a colorless liquid; ir λ_{max}(neat): 5.98 (w) μm; ^{1}H nmr δ: 1.07 (s, 3H), 1.30–2.17 (m, 14H), 5.30 (m, $W_{1/2}$ = 7 Hz, 1H); ms *m/z*: 150 (70), 135 (100).

Preparation of anhydrous tert*-butyl hydroperoxide in benzene*

A 125-mL separatory funnel was charged with benzene (50 mL) and 70% *tert*-butyl hydroperoxide (13 mL). The mixture was swirled for 1 min, and the organic layer was transferred to a 250-mL round-bottomed flask. Boiling chips were added and the benzene–water azeotrope was distilled from a steam bath; the distillation was terminated when the boiling point of the distillate remained constant at 80°C. An estimate of the *tert*-butyl hydroperoxide concentration in benzene was obtained from the ^{1}H nmr spectrum by comparison of the areas of the *tert*-butyl and benzene proton signals; typical values were in the range of 1.4–1.8 *M*.

*Oxidation of **4** with molybdenum hexacarbonyl and* tert*-butyl hydroperoxide. Formation of 8a-hydroxy-4a-methyl-*trans- *and* -cis-*octahydronaphthalen-1-(2*H*)-one (**1** and **2**) and 4a-methyl-*trans- *and* -cis-*octahydronaphthalen-1(2*H*)-ones (**10** and **11**)*

A solution of freshly prepared anhydrous *tert*-butyl hydroperoxide in benzene (1.76 *M*; 35.0 mL, 61.6 mmol) was added dropwise over a period of 2 h to a stirred mixture of **4** (405 mg, 2.70 mmol) and molybdenum hexacarbonyl (54 mg, 0.20 mmol) in anhydrous benzene (35 mL) in an oil bath at 80°C under a nitrogen atmosphere. The mixture was heated for a further 4 h, and the resulting yellow solution was cooled and added to a stirred solution of aqueous 10% Na_2SO_3 (150 mL) cooled in ice. After starch–KI test paper acidified with aqueous 2 *M* HCl gave a negative test, the benzene – *tert*-butyl alcohol – water azeotrope was distilled at atmospheric pressure and the residue was extracted with ether (75 mL, 3 × 25 mL). The combined ethereal extracts were washed with saturated aqueous NaCl (4 × 20 mL), dried ($MgSO_4$), and concentrated. The residue (420 mg) was flash chromatographed on a 2.5 × 15 cm silica gel column with hexanes–ether (4:1 v/v) as eluent. A mixture of *cis* ketol **2** and ketones **10** and **11** (100 mg) was eluted first followed by *trans* ketol **1** (220 mg, 45%), contaminated with a small amount of *tert*-butyl-containing impurity. Sublimation (90–92°C/760 Torr) gave **1** (86 mg, 18%) as white needles, mp 105–114°C. The mixture of compounds **2**, **10**, and **11** was flash chromatographed again on a 1 × 14 cm silica gel column using dichloromethane–hexanes (1:1 v/v) as eluent to give first a mixture (~85:15)[9] of ketones **10** and **11** (25 mg, 5%) as a colorless liquid; ir λ_{max}: 5.86 μm; ^{1}H nmr δ: 0.80 (s, *trans* Me), 1.0 (s, *cis* Me); vpc retention time (3% OV-17; 140°C): 2.26 min, *cis* and *trans* isomers not separated. Further elution with dichloromethane gave the *cis* ketol **2**

[8]For a general description of the experimental procedures used, see refs. 1 and 2*b*.

[9]This ratio was estimated from the relative heights of the methyl singlets in the ^{1}H nmr spectrum.

Can. J. Chem. Downloaded from www.nrcresearchpress.com by 213.222.148.141 on 09/07/12
For personal use only.

Can. J. Chem. Downloaded from www.nrcresearchpress.com by 213.222.148.141 on 09/07/12
For personal use only.

(29 mg, 6%) as a colorless liquid; vpc retention time (3% OV-17; 140°C): 2.68 min.

*4a-Methyl-*trans- *and* -cis-*decahydronaphthalene-*trans-*1,8a-diols (12 and 13)*

A solution of the mixture of epoxides **8** and **9** (10) (1.19 g, 7.16 mmol) and *p*-toluenesulfonic acid monohydrate (76 mg, 0.40 mmol) in 9:1 (v/v) dioxane–water (50 mL) was boiled at reflux for 1.5 h, cooled, and poured into aqueous 10% Na_2CO_3 (50 mL). The dioxane was removed as a dioxane–water azeotrope using a rotary evaporator fitted with a cold trap condenser under water aspirator pressure. The residue was extracted with ether (80 mL, 3 × 20 mL), and the combined ether phases were washed with saturated aqueous NaCl (3 × 20 mL), dried (Na_2SO_4), and concentrated to give a 4:1[9] mixture of diols **12** and **13** (1.18 g, 89%) as a white solid; ir λ_{max}: 2.76 (sh, w), 2.86 (br, w) μm; ^{1}H nmr δ: 0.87–2.47 (m), 0.97 (s, *cis* Me), 1.23 (s, *trans* Me), 1.35 (m, OH, exchanges with D_2O), 3.50 (nar m, $W_{1/2}$ = 6 Hz, *trans* C*H*OH), 3.83 (br m, *cis* C*H*OH); ms *m/z*: 184 (20), 112 (100).

*8a-Hydroxy-4a-methyl-trans-octahydronaphthalen-1(2*H*)-one (1)*

A solution of a 4:1 mixture of diols **12** and **13** (329 mg, 1.79 mmol) in dichloromethane (20 mL) was treated with pyridine (175 μL, 2.16 mmol) and *N*-bromosuccinimide (341 mg, 1.92 mmol), and the mixture was allowed to stand with occasional swirling at room temperature for 3.5 h. The resultant orange solution was added to aqueous 10% $NaHSO_3$ (25 mL). The aqueous phase was extracted with ether (3 × 30 mL), and the combined organic phases were washed with aqueous 2 *M* HCl (2 × 20 mL), saturated aqueous $NaHCO_3$ (20 mL), and saturated aqueous NaCl (3 × 15 mL), dried (Na_2SO_4), and concentrated to give a mixture of *trans* ketol **1** and unconsumed *cis* fused diol **13** as a pale yellow solid (358 mg). Chromatography on neutral alumina with chloroform–ether (4:1 v/v) as eluent gave **1** (242 mg, 74%) as a white solid. Crystallization from hexanes gave white needles, mp 112–114°C. Sublimation (85°C/15 Torr) followed by crystallization from hexanes raised the melting point to 115–115.5°C; ir λ_{max}: 2.78 (sh, w), 2.90 (br, w), 5.83 μm; uv λ_{max}(EtOH): 298 nm (ε 31); ^{1}H nmr (400 MHz) δ: 0.86 (s, 3H), 1.05–1.20 (m, 2H), 1.41–1.64 (m, 5H), 1.76–1.91 (m) and 1.87 (br s, OH, exchanges with D_2O) (5H), 2.05–2.16 (m, 2H), 3.04–3.13 (m, width = 34 Hz, 1H); ms *m/z*: 182 (24), 112 (100). *Anal.* calcd. for $C_{11}H_{18}O_2$: C 72.49, H 9.96; found: C 72.47, H 9.88.

Further elution gave unconsumed **13** (44 mg, 13%) as a pale yellow oil; ^{1}H nmr δ: 0.80–2.13 (m), 0.97 (s), 1.87 (m, OH), 3.83 (br m, $W_{1/2}$ = 20 Hz, 1H).

Epimerization of 1. Formation of 2

A solution of **1** (2.96 g, 16.3 mmol) in methanol (25 mL) was added dropwise over a period of 10 min to a stirred solution of methanolic 10% KOH (250 mL), and the solution was heated at reflux under an argon atmosphere for 18 h. The resultant orange-red solution was shown by gas chromatography (3% OV-17; 140°C) to contain **2** and **1** in a ratio of 93:7. Ether (200 mL) was added, and the mixture was poured into water (200 mL). The aqueous phase was extracted with ether (2 × 100 mL, 4 × 50 mL). The combined ethereal phases were washed with saturated aqueous NaCl (6 × 10 mL), dried (Na_2SO_4), and concentrated. The residual orange liquid (2.82 g) was flash chromatographed on silica gel (4 × 19 cm) with dichloromethane–ether (98:2) to give **2** (2.20 g, 74%) as a yellow liquid. Molecular distillation (134°C/20 Torr) gave **2** (1.82 g, 61%) as a colorless liquid, which solidified on the cold finger of the molecular distillation apparatus (water temperature 20°C) and melted as the cold finger was allowed to warm to room temperature; ir λ_{max}(neat): 2.88 (sh, m), 5.83, 8.04 (m), 8.70 (m), 9.41 (m), 9.80 (m), 10.62 (m) μm; uv λ_{max}(EtOH): 280 nm (ε 33); ^{1}H nmr (200 MHz) δ: 0.80 (s, 3H), 1.14–2.16 (m, 11H), 2.28–2.45 (m, 2H), 2.56–2.74 (m, width = 35 Hz, 1H), 3.81 (m, OH, exchanges slowly with D_2O, 1H); ms *m/z*: 182 (19), 112 (100). *Accurate Mass* calcd. for $C_{11}H_{18}O_2$: 182.1307; found: 182.1294. *Anal.* calcd. for $C_{11}H_{18}O_2$: C 72.49, H 9.96; found: C 72.34, H 9.98.

Further elution with dichloromethane–ether (95:5 v/v) gave **1** (0.54 g, 18%) as a white solid.

*3,4,5,6,7,8-Hexahydronaphthalen-1(2*H*)-one (14)*

Compound **14** was prepared by a modification of the method of Rae and Umbrasas (17). Colorless polyphosphoric acid (Aldrich; 27.9 g), stirred and heated in an oil bath at 105°C, was treated dropwise with 4-cyclohexylidenebutyric acid (17) (2.73 g, 16.3 mmol). The mixture was heated at 110–115°C under argon for 4 h, and the cooled, brown syrup was poured with stirring onto ice-water (100 g). The mixture was stirred under argon at 0°C overnight and extracted with ether (150 mL, 4 × 50 mL, 3 × 20 mL). The combined ethereal phases were washed with saturated aqueous $NaHCO_3$ (50 mL, 20 mL) and saturated aqueous NaCl (3 × 20 mL), dried (Na_2SO_4), and concentrated to give **14** as an orange liquid (2.96 g). The ^{1}H nmr spectrum indicated that **14** was contaminated with 3% of tetralin. Distillation (oil bath 120°C/15 Torr) first removed the tetralin as a colorless liquid; ir λ_{max}(neat): 3.37 (w), 6.70 (m), 6.88 (m), 12.37 (w), 13.40 (v br) μm; ^{1}H nmr δ: 1.77 (m, 4H), 2.77 (m, 4H), 7.33 (s, 4H); ms *m/z*: 132 (70), 104 (100). Compound **14** (2.08 g, 85%) then distilled as a colorless liquid, bp 132°C/15 Torr (lit. (17) bp 120°C/14 Torr); ir λ_{max}(neat): 5.99, 6.11, 7.31, 7.77, 8.35 μm; ^{1}H nmr δ: 1.47–2.53 (m, maxima at δ 1.60 and 2.20); ms *m/z*: 150 (82), 122 (100).

*Reaction of lithium dimethylcuprate with 14 and trapping of the resulting enolate with benzoyl peroxide. Formation of 8a-bromo-4a-methyl-*trans- *and* -cis-*octahydronaphthalen-1(2*H*)-one (15 and 16) and 8a-benzoyloxy-4a-methyl-*trans- *and* -cis-*octahydronaphthalen-1(2*H*)-one (17 and 18)*

Cuprous bromide (0.97 g, 6.8 mmol), prepared by the reduction of cupric bromide with Na_2SO_3 according to the method of Theis and Townsend (34), was stirred in anhydrous ether (24 mL) under argon and cooled in an ice bath. A solution of methyllithium – lithium bromide complex in ether (1.82 *M*; 7.0 mL, 13 mmol) was added dropwise, followed by a solution of compound **14** (0.400 g, 2.67 mmol) in anhydrous ether (3 mL), also added dropwise. The resulting mixture was stirred at 0°C for 24 h and added via cannula to a stirred suspension of anhydrous benzoyl peroxide (Aldrich; 2.58 g, 10.7 mmol) in anhydrous ether (45 mL) cooled in an ice bath. After the mixture had been stirred at 0°C for 2.5 h, the reddish-brown color that initially formed faded, and the resulting brown suspension was added to aqueous 10% NH_3 (75 mL) cooled in an ice bath. The two-phase mixture was stirred and allowed to warm to room temperature overnight, when it was poured with stirring into cold (10°C) aqueous 10% Na_2SO_3 (300 mL). When starch–KI paper acidified with aqueous 2 *M* HCl gave a negative test, the layers were separated, and the blue aqueous phase was extracted with ether (3 × 25 mL). The ethereal phases were combined, washed with saturated aqueous NaCl (5 × 10 mL), dried (Na_2SO_4), and concentrated to a yellow oil (636 mg). Flash chromatography on silica gel (2 × 11 cm) with hexanes – ethyl acetate (9:1 v/v) as eluent gave a 3:2[9] mixture of bromo ketones **15** and **16** (416 mg, 64%) as a white solid. Further elution gave a yellow oil comprised of a 45:55[9] mixture of benzoyloxy ketones **17** and **18** (183 mg, 23%), which could not be separated; ir λ_{max}: 5.79 μm; ^{1}H nmr δ: 0.98 (s, *trans* Me), 1.27 (*cis* Me), 1.40–2.80 (m, 14H), 7.40–7.60 (m, 3H), 7.93–8.17 (m, 2H); ms *m/z*: 286 (3), 105 (100). *Accurate Mass* calcd. for $C_{18}H_{22}O_3$: 286.1569; found: 286.1569.

Partial separation of the bromo ketones **15** and **16** was achieved by flash silica gel chromatography with hexanes – ethyl acetate (97:3 v/v). Compound **16** was eluted first, and crystallization from pentane gave a white powder, mp 91–94°C; ir λ_{max}: 5.86 μm; ^{1}H nmr δ: 1.32 (s, 3H), 1.40–3.63 (m, 14H); ms *m/z*: 246 (4), 244 (4), 165 (100). *Accurate Mass* calcd. for $C_{11}H_{17}OBr$: 246.0444, 244.0463; found: 246.0465, 244.0464.

Following a mixed fraction, **15** was eluted. Crystallization from pentane gave white needles, mp 118–120°C; ir λ_{max}: 5.84 μm; ^{1}H nmr δ: 1.03 (s, 3H), 1.10–2.57 (m, 13H), 3.13–3.90 (m, 1H); ms *m/z*: 246 (15), 244 (15), 165 (100). *Accurate Mass* calcd. for $C_{11}H_{17}OBr$: 246.0444, 244.0463; found: 246.0456, 244.0459. *Anal.* calcd. for $C_{11}H_{17}OBr$: C 53.87, H 6.99, Br 32.61; found: C 53.93, H 7.04, Br 32.58.

Hydrolysis of the mixture of 17 and 18. Formation of 1 and 2

A 45:55[9] mixture of **17** and **18** (74 mg, 0.26 mmol) was dissolved in

Can. J. Chem. Downloaded from www.nrcresearchpress.com by 213.222.148.141 on 09/07/12
For personal use only.

tetrahydrofuran–methanol (2:1 v/v; 4 mL), and the solution was stirred with aqueous 2 *M* KOH (3 mL) at room temperature for 48 h. Water (10 mL) was added, and the mixture was extracted with ether (25 mL, 4 × 10 mL). The ethereal extracts were washed with saturated aqueous NaCl (3 × 10 mL), dried (Na_2SO_4), and concentrated to a colorless oil (40 mg), the ^1H nmr spectrum of which showed it to be a 45:55[9] mixture of **1** and **2**. Flash chromatography on silica gel (1.5 × 11 cm) with dichloromethane–ether (98:2 v/v) as eluent gave **2** (15 mg, 32%) as a colorless liquid. Further elution afforded **1** (16 mg, 34%), crystallized from hexanes as white needles, mp 113–114°C.

*4a-Methyl-8-(trimethylsiloxy)-1,2,3,4,4a,5,6,7-octahydronaphthalene (**19**)*

A solution of lithium dimethylcuprate in ether under argon was prepared by the dropwise addition of a solution of methyllithium – lithium bromide complex in ether (1.53 *M*; 13.0 mL, 19.9 mmol) to a cold (0°C), stirred suspension of cuprous iodide (1.90 g, 9.97 mmol) in anhydrous ether (35 mL). A solution of **14** (0.60 g, 4.0 mmol) in anhydrous ether (5 mL) was added dropwise over a period of 20 min, and the mixture was stirred at 0°C for 28 h. In a septum-capped centrifuge tube, anhydrous chlorotrimethylsilane (10.4 mL, 0.082 mmol) was added to anhydrous triethylamine (9.0 mL, 0.065 mmol); the white precipitate that formed was centrifuged, and the clear liquid was added via cannula to the yellow cuprate suspension. The mixture was stirred at 0°C under argon for 1 h, and cold (0°C) saturated aqueous $NaHCO_3$ (10 mL) was added dropwise over a period of 15 min. The gummy greyish-white precipitate that formed was filtered and washed with ether (3 × 20 mL). Water (50 mL) was added to the filtrate, the layers were separated, and the aqueous phase was extracted with ether (5 × 50 mL). The combined ethereal phases were washed with cold (0°C) aqueous 2% NH_3 (6 × 20 mL) and cold water (12 × 20 mL), dried (Na_2SO_4), and concentrated, with a drying tube containing self-indicating 6–20 mesh silica gel inserted between the aspirator and the rotary evaporator, to give the silyl enol ether **19** (0.97 g, quantitative) as a yellow liquid. Its ir and ^1H nmr spectra showed that this was essentially pure, and it was used without further purification in the following epoxidation procedure. Compound **19** could be obtained as a colorless liquid by molecular distillation (105°C/0.4 Torr); ir λ_{max}(neat): 5.97, 7.36, 8.81, 9.31, 9.71 μm; ^1H nmr δ: 0.17 (s, 9H), 1.07 (s, 3H), 1.23–2.27 (m, 13H), 2.68 (br d, J = 14 Hz, 1H).

*Epoxidation of **19** and hydrolysis of the resulting trimethylsiloxy ketones **20** and **21**. Formation of **1** and **2***

A solution of **19** (968 mg, 4.07 mmol) in anhydrous hexanes (5 mL) was added to a stirred suspension of *meta*-chloroperoxybenzoic acid (85%; 903 mg, 4.45 mmol) in anhydrous hexanes under argon and cooled to −13°C in an ice–methanol bath. The suspension became more flocculent during the addition. The cold bath was removed, and the suspension was stirred for 2 h following which a starch–KI test was negative. The suspension was filtered, and the solid was washed with hexanes (2 × 75 mL). The combined filtrate and washings were poured into aqueous 10% Na_2SO_3 (50 mL), and the organic layer was washed with saturated aqueous $NaHCO_3$ (2 × 10 mL) and saturated aqueous NaCl (4 × 10 mL), dried (Na_2SO_4), and concentrated to an off-white solid (1.4 g), considered to be a mixture of the trimethylsiloxy ketones **20** and **21**. The ir spectrum of the product exhibited a band at 5.84 μm, and the ^1H nmr spectrum displayed a distinctive singlet at δ 0.40. The solid was dissolved in ether (75 mL) and the solution was stirred with aqueous 2 *M* HCl (25 mL) at room temperature for 2 h. The aqueous phase was separated and extracted with ether (3 × 10 mL). The combined ethereal phases were washed with saturated aqueous $NaHCO_3$ (30 mL, 5 mL) and saturated aqueous NaCl (3 × 5 mL), dried (Na_2SO_4), and concentrated to give a yellow solid (742 mg). Flash chromatography on a silica gel column (3.5 × 15 cm) with the use of dichloromethane–pentane (95:5 v/v) as eluent gave **2** (116 mg, 16%) as a colorless liquid. Further elution with dichloromethane–ether (93:7 v/v) afforded **1** (393 mg, 53%) as a slightly off-white solid. Crystallization from hexanes gave **1** as white needles, mp 112–114°C.

*2α-Bromo-8a-hydroxy-4a-methyl-*trans*-octahydronaphthalen-1(2H)-one (**22**)*

A solution of **1** (136 mg, 0.75 mmol) in chloroform (5 mL) was treated with 2.28 mL of a solution of bromine (0.4 mL) in acetic acid (1 mL) and chloroform (20 mL). The red solution was allowed to stand at room temperature for 2 h, and the resulting gold colored reaction mixture was poured into aqueous 10% Na_2SO_3 (10 mL) and extracted with benzene (25 mL, 4 × 10 mL). The combined organic phases were washed with saturated aqueous $NaHCO_3$ (10 mL) and water (4 × 10 mL), dried (Na_2SO_4), and concentrated to a yellow solid (197 mg). Flash chromatography on silica gel (2 × 20 cm) with pentane–ether (4:1 v/v) as eluent gave **22** (145 mg, 75%) as a white solid. Crystallization from pentane afforded white needles, mp 79–80°C; ir λ_{max}: 2.93 (sh, w), 3.07 (br, w), 5.82 μm; ^1H nmr δ: 0.88 (s, 3H), 0.93–2.73 (m), 2.27 (s, OH), 4.28 (nar m, $W_{1/2}$ = 8 Hz, 1H); ms m/z: 262 (1), 260 (1), 112 (100). *Anal.* calcd. for $C_{11}H_{17}O_2Br$: C 50.57, H 6.56, Br 30.61; found: C 50.63, H 6.56, Br 30.66.

*2α-Deutero-8a-hydroxy-4a-methyl-*trans*-octahydronaphthalen-1(2H)-one (**23**)*

A solution of **22** (126 mg, 0.48 mmol) in ether (24 mL) was washed with D_2O (99.8%; 4 × 2 mL) and added via cannula to zinc dust (728 mg, 11.13 mmol) in a D_2O-pretreated flask under argon. The stirred suspension was treated dropwise with *O*-deuteroacetic acid (98%; 1.30 mL, 22.6 mmol), stirred at room temperature for 2.5 h, and neutralized by the addition of anhydrous Na_2CO_3 (12 g). The mixture was filtered, and the precipitate was washed with ether (3 × 15 mL). The filtrate was washed with 5% $NaHCO_3$ in D_2O (4 mL) and saturated aqueous NaCl (4 × 10 mL), dried over Na_2SO_4, and concentrated to give a pale yellow solid (85 mg). Sublimation (86°C/15 Torr) and crystallization from hexanes gave **23** (61 mg, 69%) as white needles, mp 113–114°C; ir λ_{max}: 2.94 (br, w), 5.83, 10.10 (w) μm; ^1H nmr (200 MHz) δ: 0.87 (s, 3H), 1.00–1.94 (m), 1.72 (s), 1.99–2.17 (m, 2H), 3.00–3.18 (m, 0.16H); ms m/z: 183 (24), 112 (100); d_0 6%, d_1 92%, d_2 2%.

*Bromination of **2**. Formation of 2α-bromo- and 2β-bromo-8a-hydroxy-4a-methyl-*cis*-octahydronaphthalen-1(2H)-one (**24** and **25**), 2α,8a-dibromo-4a-methyl-*cis*-octahydronaphthalen-1(2H)-one (**26**), and 2,2-dibromo-8a-hydroxy-4a-methyl-*cis*-octahydronaphthalen-1(2H)-one (**27**)*

A solution of **2** (217 mg, 1.19 mmol) in chloroform (8 mL) was treated with 3.64 mL of a solution of bromine (0.4 mL) in acetic acid (1 mL) and chloroform (20 mL). The red solution was allowed to stand at room temperature for 2 h, and the resulting colorless solution was poured into aqueous 10% Na_2SO_3 (10 mL). The mixture was extracted with benzene (40 mL), and the combined organic phases were washed with saturated aqueous $NaHCO_3$ (15 mL) and water (3 × 10 mL), dried over Na_2SO_4, and concentrated to give a pale yellow oil (359 mg), whose ^1H nmr spectrum showed the 2α-bromo *cis* ketol **24** to be the major product. Flash silica gel chromatography of the oil on a 2 × 19 cm column with pentane–ether (85:15 v/v) as eluent gave first the 2α,8a-dibromo ketone **26** (57 mg, 15%) as a white solid. Crystallization from pentane–methanol gave **26** as fine, white needles, mp 72–73.5°C; ir λ_{max}: 5.78, 8.79 (m) μm; ^1H nmr δ: 1.33 (s, 3H), 1.42–2.87 (m, 12H), 5.50–5.83 (m, width = 20 Hz, 1H); ms m/z: 326 (3), 324 (5), 322 (3), 245 (100). *Anal.* calcd. for $C_{11}H_{16}OBr_2$: C 40.75, H 4.98, Br 49.34; found: C 40.74, H 5.11, Br 49.34.

The 2,2-dibromo *cis* ketol **27** was eluted next and obtained as a colorless oil (37 mg, 9%). Molecular distillation (80°C/25 Torr) gave **27** as a colorless gummy solid that solidified on standing at 0°C; mp 60–62°C; ir λ_{max}: 2.96 (sh, m), 5.82, 8.87 (m), 9.78 (m), 10.19 (m), 11.47 (m) μm; ^1H nmr δ: 0.90 (s, 3H), 1.07–3.33 (m), 3.27 (s, OH); ms m/z: 342 (0.5), 340 (1), 338 (0.5), 112 (100). *Anal.* calcd. for $C_{11}H_{16}O_2Br_2$: C 38.83, H 4.74, Br 47.01; found: C 39.18, H 4.77, Br 46.73.

Further elution gave an 80:20[9] mixture of the bromo ketols **24** and **25** (224 mg, 72%). The β epimer **25** was eluted first and a fraction free of α epimer was isolated as a white solid (46 mg). Sublimation (70°C/25 Torr) gave fine white needles of **25**, mp 64–65.5°C; ir λ_{max}: 2.99 (sh, w), 5.79 μm; ^1H nmr δ: 0.86 (s, 3H), 1.13–2.80 (m, 12H), 3.72 (s, OH, 1H), 4.87–5.13 (m, width = 20 Hz, 1H); ms m/z: 262 (<1), 260 (<1), 135 (100). *Anal.* calcd. for $C_{11}H_{17}O_2Br$: C 50.57, H 6.56, Br 30.61; found: C 50.56, H 6.65, Br 30.89.

Can. J. Chem. Downloaded from www.nrcresearchpress.com by 213.222.148.141 on 09/07/12
For personal use only.

The mixture of **24** and **25** was repeatedly chromatographed as above with removal of the fractions containing **25**. In this manner, **24** (43 mg) contaminated by only a small amount of **25** could be isolated. Crystallization from pentane gave pure **24** as fine white needles, mp 74–76°C; ir λ_{max}: 3.00 (sh, m), 5.77, 5.87, 8.78 (m), 9.78 (m), 10.39 (m) μm; ^{1}H nmr δ: 0.92 (s, 3H), 1.33–2.67 (m, 12H), 2.93 (br s, OH, 1H), 4.73 (m, width = 12 Hz, 1H); ms *m/z*: 262 (2), 260 (2), 112 (100). *Anal.* calcd. for $C_{11}H_{17}O_2Br$: C 50.57, H 6.56, Br 30.61; found: C 50.62, H 6.63, Br 30.40.

*Epimerization of **24**. Formation of **25***

A solution of a ~75:25 mixture[9] of **24** and **25** (265 mg, 1.02 mmol) in pentane–ether (85:15 v/v; 10 mL) was added to a stirred suspension of 230–400 mesh silica gel (2.0 g) in pentane–ether (85:15 v/v; 10 mL). After 24 h the mixture was filtered through Celite and concentrated to give a mixture (~20:80)[9] of **24** and **25** (249 mg). Flash silica gel chromatography on silica gel (2 × 24 cm) with pentane–ether (85:15 v/v) as eluent gave **25** (187 mg, 71%) as a white solid followed by a colorless oil (43 mg, 16%), which was a mixture of **24** and **25**.

*2α-Deutero-8a-hydroxy-4a-methyl-*cis*-octahydronaphthalen-1(2*H*)-one (**28**)*

A solution of **25** (137 mg, 0.52 mmol) in ether (25 mL) was washed with D_2O (99.8%; 4 × 2 mL), and the organic phase was added via cannula to zinc dust (791 mg, 12.09 mmol) in a D_2O-pretreated flask under argon. The grey suspension was treated dropwise with *O*-deuteroacetic acid (98%; 1.45 mL, 25.1 mmol), stirred at room temperature for 2 h, and neutralized by the addition of anhydrous Na_2CO_3 (12 g). The mixture was filtered, and the grey-white solid was washed with ether (6 × 5 mL). The combined ethereal phases were washed with 5% $NaHCO_3$ in D_2O (4 mL) and saturated aqueous NaCl (4 × 20 mL), dried (Na_2SO_4), and concentrated. The residue on molecular distillation (92°C/15 Torr) gave **28** (79 mg, 82%) as a colorless liquid; ir λ_{max}: 3.00 (sh, m), 5.86, 8.74, 10.06 (w), 10.23 (w) μm; ^{1}H nmr (200 MHz) δ: 0.81 (s, 3H), 1.15–2.16 (m, 12H), 2.28–2.44 (m, 2H), 2.56–2.74 (m, 0.21H), 3.81 (s, 1H); ms *m/z*: 183 (29), 112 (100); d_0 7%, d_1 91%, d_2 1%.

*2,2-Dideutero-8a-hydroxy-4a-methyl-*cis*-octahydronaphthalen-1(2*H*)-one (**29**)*

A stirred solution mixture of **2** (70 mg, 0.38 mmol), anhydrous K_2CO_3 (202 mg, 1.46 mmol), and D_2O (99.8%; 2 mL) was heated under reflux in an argon atmosphere for 18 h. The reaction mixture was cooled and extracted with ether (30 mL), and the organic phase was washed with D_2O (5 × 1 mL), dried (Na_2SO_4), and concentrated. The concentrate was heated under reflux again with K_2CO_3 (213 mg, 1.54 mmol) and D_2O (2 mL) for 66 h, and the reaction mixture was subjected to the above work-up procedure. Molecular distillation (115°C/20 Torr) of the resulting residue (49 mg) gave **29** (28 mg, 40%) as a colorless liquid; ir λ_{max}: 3.01 (sh, w), 5.87, 8.73, 9.15 (w), 9.96 (w), 10.07 (w) μm; ^{1}H nmr (200 MHz) δ: 0.80 (s, 3H), 1.15–2.16 (m, 12H), 2.28–2.44 (dt, J = 13, 5 Hz, 1H), 3.81 (s, 1H); ms *m/z*: 184 (32), 112 (100); d_1 3%, d_2 95%, d_3 1%.

Acknowledgments

We thank the Natural Sciences and Engineering Research Council of Canada for financial support of this work and for the award of a postgraduate fellowship to S.S., and Imperial Oil Limited for the award of a Graduate Research Fellowship to S.S.

1. P. Yates and S. Stiver. Can. J. Chem. **65**, 2203 (1987).
2. (*a*) S. Stiver and P. Yates. Tetrahedron Lett. **25**, 3289 (1984); **26**, 5501 (1985); **27**, 2215 (1986); (*b*) S. Stiver. Ph.D. thesis, University of Toronto. 1985.
3. J. Broome, B. R. Brown, A. Roberts, and A. M. S. White. J. Chem. Soc. 1406 (1960); B. R. Brown and A. M. S. White. J. Chem. Soc. 3755 (1957).
4. G. A. Tolstikov, U. M. Dzhemilev, and V. P. Yur'ev. Zh. Org. Khim. **8**, 1190 (1971).
5. R. A. Sheldon and J. A. Van Doorn. J. Catal. **31**, 427 (1973).
6. U. M. Dzhemilev, V. P. Yur'ev, G. A. Tolstikov, F. B. Gershanov, and S. R. Rafikov. Dokl. Akad. Nauk SSSR, **196**, 588 (1971).
7. K. B. Sharpless and T. R. Verhoeven. Aldrichimica Acta, **12**, 63 (1979).
8. C. Y. Wu and H. E. Swift. J. Catal. **43**, 383 (1976).
9. G. A. Tolstikov, V. P. Yur'ev, I. A. Gailyunas, and U. M. Dzhemilev. Zh. Obshch. Khim. **44**, 215 (1974); G. A. Tolstikov, V. P. Yur'ev, and U. M. Dzhemilev. Russ. Chem. Rev. **44**, 319 (1975).
10. J. A. Marshall and A. R. Hochstetler. J. Org. Chem. **31**, 1020 (1966).
11. J. M. Coxon and J. R. Gibson. Aust. J. Chem. **34**, 2577 (1981).
12. Y. Kitahara, M. Oda, and H. Ogawa. Jpn. Kokai Tokkyo Koho, 77-131547 (1977); Chem. Abstr. **88**, 104909m (1978).
13. Y. Mazur and M. Nussim. Tetrahedron Lett. 817 (1961).
14. L. M. Jackman and S. Sternhell. Applications of nuclear magnetic resonance spectroscopy in organic chemistry. 2nd ed. Pergamon, New York. 1969. p. 103.
15. R. C. Cookson and S. H. Dandegaonker. J. Chem. Soc. 352 (1955).
16. R. S. Brown. Can. J. Chem. **54**, 3203 (1976).
17. I. D. Rae and B. N. Umbrasas. Aust. J. Chem. **28**, 2669 (1975).
18. A. E. Greene, J. C. Muller, and G. Ourisson. Tetrahedron Lett. 3375 (1972).
19. R. K. Boeckman, Jr. and S. M. Silver. J. Org. Chem. **40**, 1755 (1975).
20. L. J. Bellamy. The infra-red spectra of complex molecules. 3rd ed. Chapman Hall, London. 1975. pp. 157–158.
21. (*a*) J. C. Jacquesy, J. M. Lehn, and J. Levisalles. Bull. Soc. Chim. Fr. 2444 (1961); (*b*) A. D. Cross and I. T. Harrison. J. Am. Chem. Soc. **85**, 3223 (1963).
22. N. S. Bhacca and D. H. Williams. Applications of NMR spectroscopy in organic chemistry. Holden–Day. London. 1964. pp. 186–190.
23. H. O. House and W. F. Fischer, Jr. J. Org. Chem. **33**, 949 (1968).
24. G. M. Rubottom and J. M. Gruber. J. Org. Chem. **43**, 1599 (1978).
25. R. K. Boeckman, Jr. and M. Ramaiah. J. Org. Chem. **42**, 1581 (1977).
26. W. J. Rodewald, W. J. Szczepek, and J. Gumulka. Pol. J. Chem. **53**, 797 (1979); C. W. Shoppee, M. E. H. Howden, R. W. Killick, and G. H. R. Summers. J. Chem. Soc. 630 (1959).
27. C. W. Shoppee, T. E. Bellas, R. E. Lack, and S. Sternhell. J. Chem. Soc. 2483 (1965).
28. E. W. Garbisch, Jr. J. Am. Chem. Soc. **86**, 1780 (1964).
29. G. C. Levy and G. L. Nelson. Carbon-13 nuclear magnetic resonance for organic chemists. Wiley–Interscience, New York. 1972. pp. 112–113.
30. H. O. House. Modern synthetic reactions. 2nd ed. Benjamin, Menlo Park, CA. 1972. pp. 158–161.
31. R. A. Moss and D. J. Smudin. J. Org. Chem. **41**, 611 (1976).
32. C. H. Heathcock and J. E. Ellis. Tetrahedron Lett. 4995 (1971).
33. F. Sondheimer and D. Rosenthal. J. Am. Chem. Soc. **80**, 3995 (1958).
34. A. B. Theis and C. A. Townsend. Synth. Commun. **11**, 157 (1981).

The electrochemical oxidation of silver and tetraethylammonium salts of formamides and imides. *N,N*-Coupling of formanilidyl radicals

JEAN-YVES HUOT,[1] DENIS SERVE,[2] SYLVIE DESJARDINS, AND JEAN LESSARD[3]

Département de chimie, Université de Sherbrooke, Sherbrooke (Québec), Canada J1K 2R1

Received April 30, 1987

JEAN-YVES HUOT, DENIS SERVE, SYLVIE DESJARDINS, and JEAN LESSARD. Can. J. Chem. **66**, 35 (1988).

The electrochemical oxidation of [amide-Ag-amide]Ag, [amide-Ag-amide]Et_4N, and [amide]Et_4N salts of imides and formanilides, in acetonitrile containing tetraethylammonium tetrafluoroborate, at platinum and vitreous carbon electrodes, is a one-electron and irreversible ($\alpha n < 1$) process leading to an amidyl radicals that preferentially abstracts hydrogen from the medium to give the parent amide. *N,N*-Coupling (formation of hydrazine derivatives) was observed in the oxidation of the amide-Ag-amide anions of formanilide and *p*-methoxyformanilide. No coupling was observed in the oxidation of the amide-Ag-amide anion of *p*-cyanoformanilide and of imides, and in the oxidation of any of the tetraethylammonium salts (amidyl anions) studied. The formanilidyl radical was trapped by *N-tert*-butyl-α-phenylnitrone. Attempts to trap the succinimidyl radical by addition to olefins were unsuccessful.

JEAN-YVES HUOT, DENIS SERVE, SYLVIE DESJARDINS et JEAN LESSARD. Can. J. Chem. **66**, 35 (1988).

L'oxydation électrochimique des sels [amide-Ag-amide]Ag, [amide-Ag-amide]Et_4N, et [amide]Et_4N d'imides et formanilides, dans l'acétonitrile contenant du tétrafluoroborate de tétraéthylammonium sur des électrodes de platine et carbone vitreux est irréversible ($\alpha n < 1$) et fait intervenir un électron. Le radical amidyle formé réagit surtout avec le milieu par arrachement d'hydrogène pour donner l'amide parent. L'oxydation de l'anion amide-Ag-amide du formanilide et de son dérivé paraméthoxy a donné des dérivés hydrazines résultant du couplage azote–azote du radical amidyle. Aucun produit de couplage n'a été obtenu à partir d'un anion amide-Ag-amide dérivé du *p*-cyanoformanilide ou des imides, ou à partir du sel de tétraethylammonium (anion amidyle) d'aucun des amides étudiés. Le radical formanilidyle a été piégé par la *N-tert*-butyl α-phénylnitrone. Le radical succinimidyle n'a pu être piégé par addition à une oléfine.

Introduction

The oxidation of amidyl and imidyl anions should lead to the corresponding radicals (eq. [1]) and further oxidation of the radical to an acyl or diacyl nitrenium ion (eq. [2]) should be much more difficult.

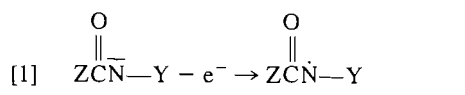

[1] $ZC(=O)\overset{\cdot}{N}-Y - e^- \rightarrow ZC(=O)\overset{\cdot}{N}-Y$

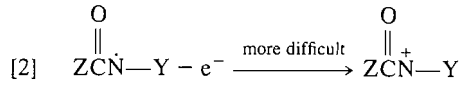

[2] $ZC(=O)\overset{\cdot}{N}-Y - e^- \xrightarrow{\text{more difficult}} ZC(=O)\overset{+}{N}-Y$

Dimerization of imidyl or amidyl radicals has been observed in the anodic oxidation of the imido-disulfonate trisanion, $[N(SO_3)_2]^{3-}$, in water (~80% current yield) (1, 2), of the lithium and sodium salts of diaryl sulfimides, $[(ArSO_2)_2N]M$, in THF (2), and of the lithium salts of *N,N'*-disubstituted sulfamides, [RNHSO$_2$NR]Li, in methanol (intramolecular coupling with subsequent loss of SO_2 to give the azo compound) (3). In the latter case, the yield of *N–N* coupling derived products, diaryldisulfones, was low and the main reaction was hydrogen abstraction from THF regenerating the parent imide. The same authors (2) studied also the anodic oxidation of succinimide and phthalimide salts in THF and in methanol and no hydrazine derivative was formed. They obtained the parent imides only as a result of H-abstraction from the solvent.

N,N-Coupling has been reported to occur in high yields in the oxidation of *N*-alkoxycarboxamides, ZCONHOR (Z = alkyl or aryl), with lead tetraacetate and other oxidants (4, 5), and in the silver oxide (6) and anodic oxidation (7) of *N*-alkoxycarbamates (Z = O-alkyl). In the anodic oxidation of *N*-alkoxycarbamates (7), the dimerization was observed only in the presence of a base such as γ-collidine. The intermediate *N*-alkoxycarboxamidyl radical has been observed by esr in the chemical oxidation of *N*-alkoxy-acylcarboxamides (5).

No coupling was observed in the electrochemical oxidation of the sodium salt of acetanilide (8). The intermediate acetanilidyl radical was trapped with *N-tert*-butyl-α-phenylnitrone. Very recently, *N,N*-coupling (~60% of hydrazine derivative) was reported in the oxidation of the lithium salt of *N*-methylphenylacetamide in benzene with tetracyanoethylene (9). In THF solution, no hydrazine derivative was formed, the amidyl radical abstracting hydrogen from the solvent to afford the parent amide (9).

The electrochemical oxidation of enolate anions, which are closely related to amidyl anions, was shown to give the corresponding carbon radicals, which also undergo *C,C*-coupling and abstract hydrogen from the solvent (10–13). Addition to olefins has been observed in some cases (14). Correlations between the pK_a of the parent acid, the structure of the enolate anion, and the half-wave potential were discussed by Fern and Federlin (15).

This paper is concerned with the anodic oxidation of the silver (**1**), the mixed silver–tetraethylammonium (**2**), and the tetraethylammonium (**3**) salts of imides and carboxamides. The structure determination and the general electrochemical behavior of these salts have been reported (16). The electrochemical behavior is summarized here. The linear voltammogram of salts **1** on a platinum or a vitreous carbon electrode, in acetonitrile containing tetraethylammonium tetrafluoroborate (TEAFB) as supporting electrolyte, shows three diffusion controlled waves having nearly the same amplitude: two cathodic waves and one anodic wave. The first cathodic wave ($E_{1/2} \sim 0.2$ V vs. Ag^0/Ag^+ 0.01 M) corresponds to the reduction of the loosely bound silver ion of salts **1** (eq. [3]), and the second cathodic wave ($E_{1/2} \sim -1.4$ V), to the reduction

[1]NSERC of Canada (1978–1980) and "Ministère de l'Éducation du Québec" (1978–1980) predoctorate fellow.

[2]France–Québec visiting scientist (Sept–Dec 1977). Present address: Laboratoire de photochimie, Université scientifique et médicale de Grenoble, 38041 Grenoble CEDEX, France.

[3]Author to whom correspondence may be addressed.

Can. J. Chem. Downloaded from www.nrcresearchpress.com by 213.222.148.141 on 09/07/12
For personal use only.

Can. J. Chem. Downloaded from www.nrcresearchpress.com by 213.222.148.141 on 09/07/12
For personal use only.

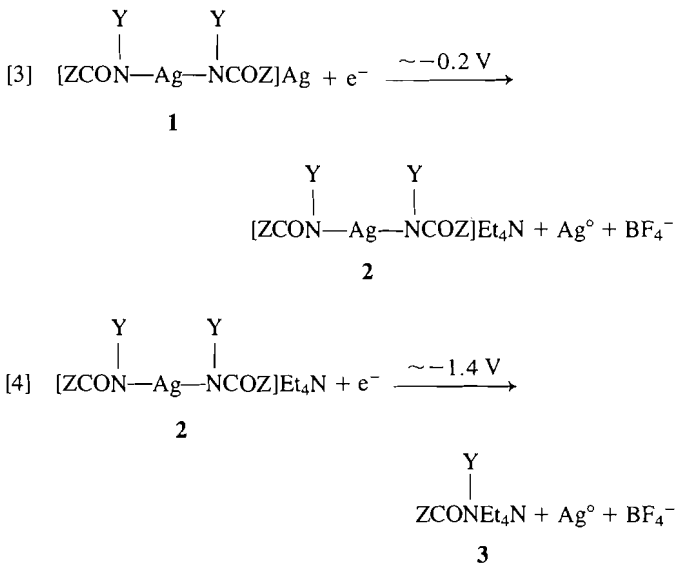

of the tightly bound silver ion of salts **2** (eq. [4]). The linear voltammogram of salts **2** shows the second cathodic wave only and the anodic wave as expected. The second cathodic wave and the anodic wave are irreversible (28).

We studied the oxidation of salts **1**, **2**, and **3** to compare the anodic behaviour of an amide-Ag-amide[4] anion (salts **1** and **2**) with that of an amidyl anion (salts **3**) and to see if amidyl radicals could be generated from amide-Ag-amide anions. As summarized above, amidyl radicals have been generated by oxidation of amidyl anions (1–8) and we were interested to see if the oxidation of an amide-Ag-amide anion would give a higher proportion of *N*,*N*-coupling (for instance by producing two amidyl radicals complexed to a silver ion) than the oxidation of an amidyl anion, and if an electrochemically generated

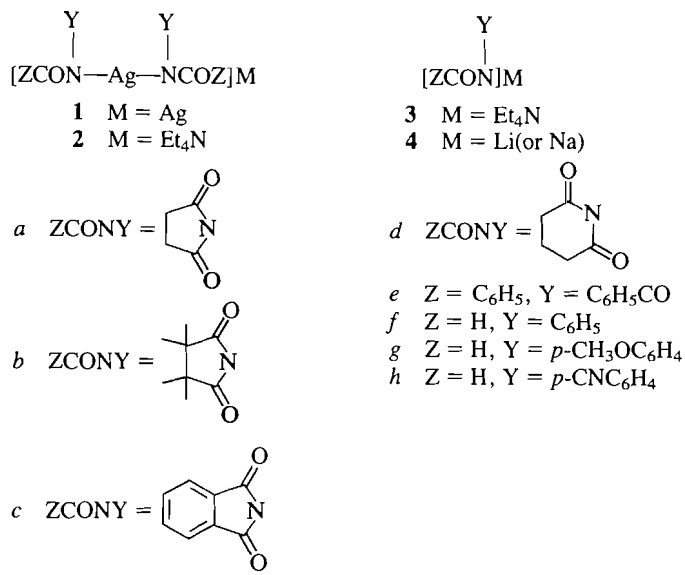

amidyl could be added to olefins. Amidyl radicals generated from *N*-haloamides have been shown to add efficiently to olefins in a chain reaction (17–27).

Results and discussion

As seen from Table 1, the half-wave potential of the anodic wave, on a platinum electrode in acetonitrile–TEABF, is about the same for salts **1** and **2** since the same species, the amide-Ag-amide anion, is oxidized. The amidyl anion (salt **3**) is either more easily oxidized (entries 2, 5, 6, 8) or more difficult to oxidize (entries 1, 3, 4) than the amide-Ag-amide anion (salts **1** and **2**); there is no general trend. The oxidation wave of the tetraethylammonium salts **3***a–d* shows a hysteresis effect (Fig. 1): the forward scan is more anodic than the backward scan for salts **3***a*, **3***c*, and **3***d* (entries 1, 3, 4) whereas the forward scan is less anodic in the case of salt **3***b* (entry 2).

Table 2 gives the oxidation potentials of the silver salts **1** measured at a vitreous carbon electrode in acetonitrile–TEABF. They are generally less anodic than those measured at a platinum electrode (Table 1). The same is true for the mixed silver–tetraethylammonium salt **2***e* ($E_{1/2}$ = 0.81 V at C vs. 1.01 V at Pt) and the tetraethylammonium salts **3***e* ($E_{1/2}$ = 0.71 V at C vs. 0.93 V at Pt) and **3***a* (see Fig. 1). The potential differences reflect differences in the strength of adsorption of the amide salts and (or) the parent amide on the two electrode materials. These adsorption differences can be seen also on the reduction potential of succinimide in acetonitrile–TEABF (0.1 M): $E_{1/2} = -1.85$ V vs. Ag^0/Ag^+ 0.01 M at platinum; no reduction wave before the reduction of the medium at vitreous carbon.

In methanol containing tetraethylammonium perchlorate (TEAP) (Table 3), the half-wave oxidation potential is now higher at carbon (entry 2) than at platinum (entry 1), contrary to the oxidation in acetonitrile–TEABF. The oxidation wave of **3***a* shows no hysteresis effect in methanol–TEAP either at platinum (entry 1) or at carbon (entry 2) and the half-wave potential is much lower than in acetonitrile–TEABF considering the fact that *E* vs. SCE ≅ E. vs. Ag^0/Ag^+ + 0.3 V (29) (compare entries 1 of Tables 1 and 3, entry 2 of Table 3, and footnote *f* of Table 2). In THF (Table 3), the anodic half-wave potentials of alkali metal salts of succinimide and phthalimide measured at carbon (entries 5 and 10) are the same as those measured at platinum (entries 6 and 11) and there is no mention of a hysteresis effect (2).

Table 3 also shows that the lithium (or sodium, see footnote *f*) salts of succinimide and phthalimide (entries 3 and 8 respectively) have more anodic half-wave potentials in methanol at carbon than the corresponding tetraethylammonium salts (entries 2 and 7). This could reflect a difference in ion-pairing strength between the amidyl anion and a lithium (or sodium) cation on the one hand, and a tetraethylammonium cation on the other hand, and (or) an effect of the cation adsorption on the double layer structure. However, the possibility of a surface effect being involved in the small potential differences observed cannot be excluded since the electrode material and (or) electrode conditioning are probably different in this work (entries 2 and 7) and in that reported by Wendt and co-workers (2) (entries 3 and 8).

The range of $E_{1/2}$ values obtained with different solutions of a given salt (see Tables 1, 2, and 3) is not due to concentration effects or to different preparations of the salt (e.g., **3***a* has been prepared by electrochemical reduction of **2***a* and of succinimide, and by a chemical route (16)) but to the difficulty of reproducing exactly the same electrode surface.

The structure of the imide moiety has little influence on the anodic potentials of the silver salts **1** and **2** of the four cyclic imides studied (*a*, *b*, *c*, and *d*) either at platinum (Table 1) or at carbon (Table 2) in acetonitrile–TEABF. The same is true for the lithium (sodium) salts **4** and tetraethylammonium salts **3** of succinimide (*a*) and phthalimide (*c*) in methanol–TEAP or in

[4]Amide = carboxamide or imide.

TABLE 1. Electrochemical data[a] for the oxidation salts **1**, **2**, and **3**, in acetonitrile–TEAFB (0.1 M),[b] on a Pt electrode[c]

Entry	Salt	$E_{1/2}$[d] (V)	αn[e]	n_{app}[f] (F/mol)	Salt	$E_{1/2}$[d] (V)	αn[e]	Salt	$E_{1/2}$[d] (V)	αn[e]	n_{app}[f] (F/mol)
1	**1***a*	1.37–1.48	0.2–0.3	0.97	**2***a*	1.48	0.3	**3***a*	1.90–2.25[g]	0.5–0.7	1.2
									1.70–1.95[h]	1.0–1.2	
2	**1***b*	1.50–1.54	0.2	0.90	**2***b*	1.56	0.2	**3***b*	1.16[g]	0.3	
									1.46[h]	0.3	
3	**1***c*	1.50–1.52	0.3	1.04	**2***c*	1.52	0.3	**3***c*	2.02[g]	0.8	
									1.50[h]	0.7	
4	**1***d*	1.32–1.45	0.3	0.86	**2***d*	1.47	0.2	**3***d*	1.71[g]	0.3	
									1.64[h]	0.3	
5	**1***e*	1.01–1.04	0.4–0.5	0.95	**2***e*	1.01	0.4	**3***e*	0.93	0.6	
6	**1***f*	0.48[i]	1.0	0.9[j]	**2***f*	0.45	0.9	**3***f*	0.14–0.16[k]	0.4	0.9
7	**1***g*	0.27[l]	—[m]	1.0							
8	**1***h*	0.65	—[m]	1.0				**3***h*	0.45–0.50		—[m]

[a]When the voltammetric analyses were carried out on two or more different solutions, the range of values obtained for $E_{1/2}$ and αn values (the latter were generally quite reproducible) is given. In the case of salt **3***a* (entry 1), two sets of $E_{1/2}$ values were obtained, either 1.9 and 1.7 V or 2.2 and 1.9 V for forward and backward scan respectively.

[b]The salt concentration ranged from 1.2 mM (e.g., salts *f*) to 5.7 mM (e.g., salts *a*). In the case of salts *a*, the concentration had no effect on $E_{1/2}$ (up to 14.7 mM).

[c]Rotating disk electrode, ω = 660 rpm.

[d]*E* vs. Ag^0/Ag^+ 0.01 M.

[e]Obtained by plotting log $[(i_1 - i)/i]$ vs. potential according to the relationship given in ref. 28 for irreversible processes.

[f]Working potential (E_w) = $E_{1/2}$ + 0.1 to 0.2 V.

[g]Forward scan.

[h]Backward scan.

[i]In samples of the salt where formanilide was present, there was a peak with $E_{max} \simeq$ 1.4–1.5 V.

[j]The electrolysis stopped after the uptake of 0.5 F/mol. Acidification of the solid residue led to the recovery of 45% of formanilide, thus showing that 55% of **1***f* was oxidized.

[k]A solution of **3***f* prepared by electroreduction of formanilide in the cell at −2.26 V gave $E_{1/2}$ = 0.22 V.

[l]Additional wave at $E_{1/2}$ = 1.0 V due to the presence of *p*-methoxyformanilide.

[m]Not determined.

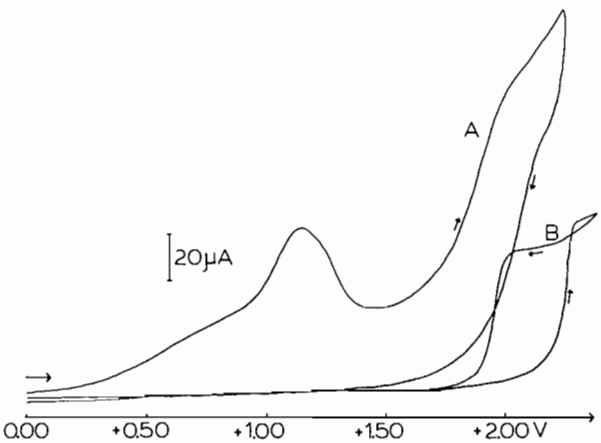

FIG. 1. Linear voltammetry of the tetraethylammonium salt of succinimide (**3***a*) (4.40 mM) in acetonitrile–TEABF (0.1 M) (ω = 660 rpm, sweep rate = 16 mV/s): A, on a vitreous carbon electrode; B, on a Pt electrode.

TABLE 2. Electrochemical data for the oxidation of salts **1**, in acetonitrile–TEAFB (0.1 M), on a vitreous carbon electrode[a]

Entry	Salt[b]	$E_{1/2}$[c] (V)	αn[d]	n_{app}[e] (F/mol)
1	**1***a*[f]	0.95–1.12	0.3–0.4	1.3
2	**1***b*	1.09	0.3	1.3
3	**1***c*	1.13	0.3	1.2
4	**1***d*	0.92	0.5	0.9
5	**1***e*[g]	0.78–0.83	0.8–0.9	1.1
6	**1***f*[h]	0.38	1.0	—[i]

[a]Rotating disk electrode, ω = 660 rpm.

[b]Salt concentration: from 1.2 mM (salt **1***f*) to 4.8 mM (salt **1***a*).

[c]*E* vs. Ag^0/Ag^+ 0.01 M.

[d]See footnote *e* of Table 1.

[e]$E_w = E_{1/2}$ + 0.1 to 0.7 V.

[f]Reduction at −1.5 V (1 F/mol of Ag^+) gave salt **3***a* with $E_{1/2}$ (ox.) at 1.60 V (forward scan) and 2.05 V (backward scan).

[g]Reduction of the solution at −0.3 V (0.5 F/mol of Ag^+) gave salt **2***e* ($E_{1/2}$ = 0.81 V, αn = 0.9), and further reduction at −0.9 V (another 0.5 F/mol of Ag^+) gave salt **3***e* ($E_{1/2}$ = 0.71 V, αn = 1.2). The voltammogram shows a non-diffusion-controlled wave at $E_{1/2}$ = 1.1 V for **1***e* and **2***e*, and at $E_{1/2}$ = 0.9 V for **3***e*.

[h]Peak at 1.50 V due to the oxidation of formanilide.

[i]It was not possible to carry out a coulometric determination due to a strong passivation of the electrode.

THF–TEAP (Table 3). However, for the tetraethylammonium salts **3***a–d* in acetonitrile–TEABF, the voltammogram of which shows a hysteresis effect as already pointed out, the anodic potential and the importance and direction of the hysteresis effect do vary with the structure of the imide moiety (Table 1). Surface effects seem therefore more important in acetonitrile–TEABF than in methanol–TEAP and more important for the tetraethylammonium salts **3** than for the silver salts **1** and **2**, and the lithium (sodium) salts **4**.

The silver salts **1***e* and **2***e* as well as the tetraethylammonium salt **3***e* of dibenzoylimide, an acyclic imide (Tables 1 and 2, entry 5), are more easily oxidized than those of cyclic imides (*a–d*). In the case of the imide-Ag-imide anions (salts **1** and **2**), this can be accounted for by the fact that an acyclic imidyl anion binds Ag^+ less tightly than a cyclic amidyl anion, as

Can. J. Chem. Downloaded from www.nrcresearchpress.com by 213.222.148.141 on 09/07/12
For personal use only.

TABLE 3. Electrochemical data for the oxidation of salts of succinimide, phthalimide, and formanilide in methanol and tetrahydrofuran

Entry	Salt: Anion	Salt: Cation	Salt: No.	Electrode[a]	Solvent	Supporting electrolyte[b]	$E_{1/2}$[c] (V)	αn[d]	n_{app} (F/mol)	Ref.
1	Succinimide	Et_4N	(**3***a*)	Pt	CH_3OH	TEAP	0.85	—	—	This work
2	Succinimide	Et_4N	(**3***a*)	C	CH_3OH	TEAP	1.07–1.12[e]	0.3	—	This work
3	Succinimide	(Li)[f]	(**4***a*)	C	CH_3OH	—[f]	1.220	—	1.1	2
4	Succinimide	Li[g]	(**4***a*)	C	THF	$LiClO_4$	1.08	0.2	—	This work
5	Succinimide	(Li)[f]	(**4***a*)	C	THF	—[f]	0.915	—	1.1	2
6	Succinimide	(Li)[f]	(**4***a*)	Pt	THF	—[f]	0.910	—	1.1	2
7	Phthalimide	Et_4N[h]	(**3***c*)	C	CH_3OH	TEAP	1.08	0.5	—	This work
8	Phthalimide	(Li)[f]	(**4***c*)	C	CH_3OH	—[f]	1.170	—	1.1	2
9	Phthalimide	Li[i]	(**4***c*)	C	THF	$LiClO_4$	1.14	—	—	This work
10	Phthalimide	(Li)[f]	(**4***c*)	C	THF	—[f]	0.895	—	1.1	2
11	Phthalimide	(Li)[f]	(**4***c*)	Pt	THF	—[f]	0.885	—	1.1	2
12	Formanilide	Et_4N	(**3***f*)	C	CH_3OH	TEAP	0.50	—	—	This work

[a]Rotating disk electrode, ω = 660 rpm in this work (not given in ref. 2).
[b]Tetraethylammonium perchlorate (TEAP) 0.1 M; $LiClO_4$ 0.3 M.
[c]E vs. SCE $\simeq$ E vs. Ag^0/Ag^+ + 0.3 V (29).
[d]See footnote *e* of Table 1.
[e]Range observed with three different solutions.
[f]The cation is not given in ref. 2 and there is no mention of the use of a supporting electrolyte. Presumably the authors have studied the lithium and (or) the sodium salts.
[g]Prepared *in situ* by reacting succinimide with 1 equiv. of *n*-BuLi.
[h]Solution (4.3 mM) of the potassium salt of phthalimide in a 0.1 M solution of TEAP in methanol.
[i]Solution (4.3 mM) of the potassium salt of phthalimide in a 0.3 M solution of $LiClO_4$ in THF.

shown by the reduction potential of the mixed silver–tetraethylammonium salts **2**, which is less negative for the dibenzoylimide salt **2***e* ($E_{1/2}$ = −0.5 V vs. Ag^0/Ag^+ 0.01 M) than for salts **2***a–d* ($E_{1/2}$ = −1.3 to −1.5 V) (16). The weaker N—Ag bonds of the acyclic imide salts **1***e* and **2***e*, when compared to the cyclic analogues **1***a–d* and **2***a–d*, must result mainly from a greater loss of entropy upon binding Ag^+ in the case of an acyclic imidyl anion. As for the tetraethylammonium salts **3**, the association between Et_4N^+ and the imidyl anion should involve mainly the oxygen atoms where the negative charge density should be the highest and such an association should be relatively weak. The lower oxidation potential of the dibenzoylimide salt **3***e*, when compared to that of salts **3***a–d*, probably reflects primarily a difference in charge delocalization between an acyclic imidyl anion having the *cis–trans* and (or) the *trans–trans* (or U) conformation and a cyclic imidyl anion having necessarily the *cis–cis* (or W) conformation (16).

Interestingly, in the case of lithium enolates of β-dicarbonyl compounds, an acyclic enolate is now more difficult to oxidize than a cyclic enolate: E_{ox} of lithium acetylacetonate = 0.49 V vs. Ag^0/AgCl 0.1 M in DMSO; E_{ox} of the lithium salt of dimedone = 0.14 V (15). This is primarily due to the fact that the acyclic enolate anion in the U conformation is bonded more strongly to Li^+ (bonding involving the two oxygens) than the cyclic enolate ion in the W conformation (bonding to one oxygen only).

The oxidation potential of the tetraethylammonium salt of *N*-benzoyl-3-cyclohexenecarboxamide (**5**), both at platinum ($E_{1/2}$ = 0.72 V vs. Ag^0/Ag^+ 0.01 M) and at carbon ($E_{1/2}$ = 0.57 V), in acetonitrile–TEABF, is about 200 mV lower than that of the tetraethylammonium salt of dibenzoylimide (**3***e*) (see Table 1, entry 5, and Table 2, footnote *g*). This probably reflects the fact that a phenyl ring is more electron attracting than a cyclohexyl ring. As a result, the highest occupied molecular orbital (HOMO) from which the electron is removed (30) is lower in energy in the case of **3***e* than in the case of **5** (31). Similarly, and for the same reasons, the oxidation potential of enolates of aliphatic β-carbonyl nitriles (RCH(CN)COR′) is slightly lower (40–60 mV lower) than that of enolates of the aromatic analogues (ArCH(CN)COR′) (15).

The oxidation of the silver salts (**1***f* and **2***f*) and the tetraethylammonium salt (**3***f*) of formanilide, a carboxamide, is much easier than that of the same salts of imides (Tables 1 and 2), again because the energy of the HOMO of the amide-Ag-amide anion (salts **1** and **2**) and of the amidyl anion (salts **3**) should be lower when there are two electron-withdrawing carbonyl groups attached to the nitrogen (imide) than when there is only one (carboxamide) (31). For the same reason, the oxidation half-wave potentials of the silver (**1***h*) and tetraethylammonium (**3***h*) salts of paracyanoformanilide (Table 1, entry 8) are more anodic (CN is electron withdrawing) than those of formanilide salts (**1***f* and **3***j*, entry 6). Since CH_3O is electron donating and raises the energy of the HOMO (31), the oxidation potential of the silver salt of paramethoxyformanilide (**1***g*, entry 7) is less anodic than that of formanilide (**1***f*). Similarly, the oxidation potential of lithium enolates of the *p*-methoxy derivative of aromatic β-carbonyl nitriles is more anodic than that of the unsubstituted analogues (15).

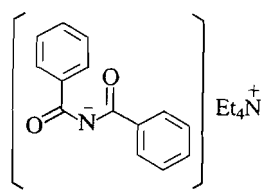

3*e*

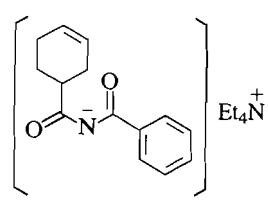

5

According to the αn values of Tables 1 and 2, the oxidation of the salts of formanilide (**1***f*, **2***f*, **3***f*) would be more reversible than that of the imide analogues, and the oxidation of the acyclic imide salts (**1***e*, **2***e*, **3***e*) slightly more reversible than that of the cyclic ones (*a–d*).

Can. J. Chem. Downloaded from www.nrcresearchpress.com by 213.222.148.141 on 09/07/12
For personal use only.

TABLE 4. Preparative electrooxidation of imide salts in acetonitrile–TEABF (0.1 M)[a]

Entry	Salt	Electrode	Olefin added[b]	E_W[c] (V)	F/mol	Parent imide **6** (%)[d]	Coulometric yield (%)	Material balance (%)[d,e]
1	**1***a*	Pt	None	1.5	1.13	83	73	95–100
2	**1***a*	Pt	None	1.85	1.46	86	59	95–100
3	**1***a*	C[f]	None	1.6	0.54	30	56	95–100
4	**1***a*	C[f]	None	2.1	0.71	71	100	95–100
5	**1***a*	Pt	3,3-Dimethyl-1-butene	1.5	1.16	88	76	95–100
6	**1***a*	C[f]	3,3-Dimethyl-1-butene	1.6	0.63	25	40	95–100
7	**1***a*	Pt	3-Sulfolene	1.5	0.67	65[g]	97	90
8	**3***a*	Pt	None	2.2	1.07	100	93	100
9	**1***a*	Pt	3,3-Dimethyl-1-butene	2.0	1.09	93[h]	85	93
10	**1***c*	Pt	None	1.6	1.05	75	81	92
11	**1***e*	Pt	None	1.3	1.01	81[i]	80	92
12	**5**[j]	Pt	None	1.0	—[k]	—		—
13	**5**[j]	C[f]	None	1.0	0.80	80[i]	100	≥90[l]

[a]The electrolyses were carried out on 14–20 mM solutions in a two-compartment cell using a platinum auxiliary electrode (see Experimental) until zero current. In most cases, some imide salt was still present according to voltammetric analyses. Acid hydrolysis of the solid residue after extraction of the products with ether followed by extraction with ether gave the parent imide.

[b]An excess of olefin was used: 10–15 mol per mol of salt.

[c]Working potential vs. Ag^0/Ag^+ 0.01 M.

[d]Determined by vapor phase chromatography (vpc) unless otherwise stated.

[e]The material balance includes the parent imide recovered after acid hydrolysis of the residue (see footnote *a*).

[f]Vitreous carbon. The current density was low.

[g]Beside succinimide, another product, presumably a dimer of sulfolene (see text), was formed in small amount.

[h]Yield of succinimide isolated by preparative layer chromatography (plc) on silica gel. Five other products present in very small amounts were detected and were not investigated further.

[i]Yield of parent imide isolated by plc on silica gel.

[j]The tetraethylammonium salt **5** was prepared in the cell by electrochemical reduction of a 4.2 mM solution of the parent amide in acetonitrile–TEABF (0.1 M) at −2.1 V vs. Ag^0/Ag^+ 0.01 M using 1.2 F/mol. The voltammogram of the resulting solution showed an anodic wave at ca. 0.5 V, both on Pt and C, and no cathodic wave.

[k]The current intensity dropped to zero a few seconds after applying the potential and it was not possible to carry out the electrolysis.

[l]There was still some salt left according to voltammetric analysis but it was not hydrolysed into the parent imide.

Both the αn values and the coulometric determinations of Tables 1, 2, and 3 show that the oxidation of salts **1**, **2**, **3**, and **4**, in acetonitrile–TEABF, in methanol–TEAP, and in tetrahydrofuran–TEAP, is a one-electron process. Removal of one electron from an amidyl (imidyl) anion should lead to an amidyl (imidyl) radical (eq. [1]), which could then abstract hydrogen from the medium to generate the parent amide or imide **6** (eq. [7]) and (or) undergo nitrogen–nitrogen coupling to give an hydrazine derivative **7** (eq. [8]).

[7] $ZCO\dot{N}Y + SH \longrightarrow \underset{\mathbf{6}}{ZCONHY} + S^{\cdot}$

[8] $ZCO\dot{N}Y + ZCO\dot{N}Y \longrightarrow \underset{\mathbf{7}}{ZCON(Y)-(Y)NCOZ}$

The results of preparative electrooxidations of the silver salts of succinimide (**1***a*), phthalimide (**1***c*), and benzoylimide (**1***e*), and of the tetraethylammonium salt of succinimide (**3***a*), at platinum, in acetonitrile–TEABF, are reported in Table 4. The working potential is generally close to the half-wave potential except in entries 2 and 11 where it is more anodic by about 300–350 mV. At vitreous carbon, electrooxidation of **1***a* at a potential near the half-wave potential was very slow due to electrode passivation and stopped when about 30% of the silver salt was oxidized (entries 3 and 6). It was possible to obtain a higher conversion rate at a more anodic potential (entry 4). The sole product obtained from these oxidations was the parent imide. Thus an imidyl radical prefers to abstract hydrogen from the medium (eq. [7]) rather than to dimerize (eq. [8]). This was observed also by Wendt and co-workers (2) in the electrooxidation of the lithium (sodium) salts **4***a* (of succinimide) and **4***c* (of phthalimide) at platinum or carbon, in methanol or tetrahydrofuran: the parent imide was the sole product obtained. From the oxidation in methanol, small amounts of formaldehyde were detected and the authors (2) took this as evidence for hydrogen abstraction from methanol by the imidyl radical followed by oxidation of the resulting hydroxymethyl radical ($\cdot CH_2OH$). Hydrogen abstraction from acetonitrile would give a cyanomethyl radical ($\cdot CH_2CN$), which, among other things, could undergo carbon–carbon coupling to give succinonitrile.[5] We could not detect any succinonitrile in the oxidations of Table 4.

Imidyl radicals are known to be good hydrogen abstractors (34–38) but they are also known to add efficiently to a variety of olefins (17, 23, 24, 26, 27) and, among them, to 3,3-dimethyl-1-butene (23, 24, 26) and sulfolene (17). However, no product resulting from the addition of the succinimidyl radical to the olefin was detected in the electrooxidation of **1***a* and **3***a* in the presence of either 3,3-dimethyl-1-butene (Table 4, entries 5, 6, and 9) or 3-sulfolene (entry 4). From the oxidation in the presence of sulfolene, a compound was obtained in minute amounts to which structure **8** was tentatively assigned (see the Experimental). 3-Sulfolene, with its allylic hydrogens, should

[5]The formation of high yields of succinonitrile was reported by O'Donnell and Mann (32) in the electrochemical oxidation of carboxamides in dry acetonitrile. However, this work was repeated by Genies (33) and he was not able to detect any succinonitrile.

Can. J. Chem. Downloaded from www.nrcresearchpress.com by 213.222.148.141 on 09/07/12
For personal use only.

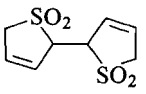

8

be a good hydrogen-atom donor, most probably better than acetonitrile, and dimer **8** would result from allylic hydrogen abstraction by the imidyl radical followed by coupling of two allylic radicals.[6]

Since the intramolecular addition of amidyl radicals to a double bond can be a very efficient process, as in the radical cyclization of *N*-chloro-*N*-methyl-3-cyclohexenecarboxamide (19, 20, 22), we investigated the electrooxidation of the tetraethylammonium salt of *N*-benzoyl-3-cyclohexenecarboxamide (**5**) (Table 4, entries 12 and 13). Salt **5** was prepared by electrochemical reduction of the parent amide in acetonitrile–TEABF. The voltammogram at platinum and at vitreous carbon showed no cathodic wave and an anodic wave at ca. 0.5 V vs. Ag^0/Ag^+ 0.01 M. It was not possible to carry out the oxidation of **5** on platinum because of electrode passivation (entry 12). On vitreous carbon, at a working potential of 1.0 V (entry 13), the electrolysis was successful but the current density was low. No product resulting from intramolecular trapping of the imidyl radical could be detected; again the sole product obtained was the parent amide.

Unequivocal evidence for the generation of an amidyl radical in the electrooxidation of an amide salt was obtained when the mixed silver–tetraethylammonium salt of formanilide (**2***f*) was oxidized in the presence of *N*-*tert*-butyl-α-phenylnitrone at 0.5 V on a platinum electrode, in acetonitrile–TEABF, in the cavity of an epr (electron paramagnetic resonance) spectrometer. The epr spectrum recorded is shown in Fig. 2. It corresponds to the nitroxide **9** resulting from the addition of the formanilidyl radical to the nitrone: $g = 2.0057$; $a^{N\alpha} = 13.9$ G, $a^{H} = 3.6$ G, $a^{N\gamma} = 1.7$ G (±0.1 G). This spectrum differs somewhat from that obtained by Bacon (8) upon oxidizing the sodium salt of acetanilide in the presence of the same nitrone: $a^{N\alpha} = 14.4$ G, $a^{H} = 1.5$ G, $a^{N\gamma} = 2.9$ G. In nitroxide **9**, a^{H} is larger than $a^{N\gamma}$, whereas in the nitroxide resulting from the trapping of the acetanilide radical (8), a^{H} is smaller than $a^{N\gamma}$. An acetyl group being larger than a formyl group, the preferred conformation around the C—N_α and C—N_γ bonds as well as the extent of delocalization of the N_γ electrons into the carbonyl group and the phenyl ring (hybridization of N_γ) are probably not the same in the two nitroxides, and these differences could account for the fact that the hyperfine coupling constants a^{H} and $a^{N\gamma}$ have different values in the two nitroxides.

The formation of *N*,*N*′-diformyl-*N*,*N*′-diphenylhydrazine (**7***f*; Z = H, Y = C_6H_5), in the preparative electrooxidation of the silver salts **1***f* and **2***f* of formanilide (see Table 5, entries 1 to 5), must result from the head-to-head coupling of two formanilidyl radicals and constitutes further evidence of the formation of amidyl radicals by electrooxidation of amide salts. No product resulting from head-to-tail or tail-to-tail coupling could be detected.

As mentioned in the introduction, high yields of *N*,*N*-coupling were reported for the oxidation of *N*-alkoxy derivatives of carboxamides and carbamates (4–7) where the intermediate

[6]Bicyclohexenyl, resulting from the coupling of two cyclohexenyl radicals, is formed when radicals are generated in the presence of cyclohexene (18).

TABLE 5. Preparative electrooxidation of formanilide salts at Pt in acetonitrile–TEAFB (0.1 M)[a]

				Products[c]		
Entry	Salt	E_W[b] (V)	F/mol	Hydrazine derivative **7** (%)	Parent amide **6** (%)	Material balance (%)
1	**1***f*	0.5	0.67	14	39	85
2	**1***f*	0.7	0.67	12	38	83
3[d]	**1***f*	0.7	0.60	8	37	85
4[e]	**1***f*	0.7	0.71	9	34	72
5	**2***f*[f]	0.8	0.66	7	40	81
6	**3***j*[g]	0.6	0.57	0	46	89
7	**3***j*[g]	0.7	0.81	0	59	78
8	**3***j*[h]	0.7	0.80	0	41	46
9	**1***g*	0.4	0.52	7	34	85
10	**1***h*	0.8	0.74	0	32	32[i]
11	**2***h*[f]	1.0	0.74	0	43	43[i]
12	**3***h*[g]	1.0	0.81	0	51	51[i]

[a]See footnote *a* of Table 4. The electrolyses were carried out on 10 mM solutions.

[b]Working potential vs. Ag^0/Ag^+ 0.01 M.

[c]Yield of products isolated by preparative layer chromatography.

[d]Water (4%) was added.

[e]In the presence of 1 mol of γ-collidine per mol of **1***f*.

[f]Salts **2***f* and **2***h* were prepared in the cell by electrochemical reduction of **1***f* and **1***h* respectively at −0.4 V.

[g]Salts **3***j* and **3***h* were prepared in the cell by electrochemical reduction of **1***j* and **1***h* respectively at −1.6 V.

[h]Salt **3***j* was prepared in the cell by electrochemical reduction of formanilide at −2.6 V.

[i]The residue after extraction with ether was not hydrolysed with acid (see footnote *a* of Table 4).

amidyl radical, having a π electronic configuration (4, 39),[7] is a capto-dative radical stabilized by the synergistic effect of resonance electron-donating methoxyl and electron-withdrawing acyl or acyloxyl groups (42).[8] We therefore studied the electrooxidation of the silver salts of *p*-methoxyformanilide (**1***g*) and of *p*-cyanoformanilide (**1***h* and **2***h*). No coupling was observed in the electrooxidation of **1***h* and **2***h* (Table 5, entries 10 and 11) where the *p*-cyanoformanilidyl radical is not a capto-dative radical since it is stabilized by two electron-withdrawing groups. However, contrary to expectation, no enhancement of *N*,*N*-coupling was observed in going from the formanilidyl radical (entries 1–5) to the *p*-methoxyformanilidyl radical (entry 9). The phenyl ring can be considered as electron donating and the formanilidyl radical becomes a capto-dative radical. But the capto-dative stabilization should be larger in the *p*-methoxy formanilidyl radical and this did not translate into a more effective *N*,*N*-coupling.

N,*N*-Coupling of the formanilidyl radical was observed only in the electrochemical oxidation of the silver salts **1***f* and **2***f* (Table 5, entries 1–5). There was no *N*,*N*-coupling in the electrooxidation of the tetraethylammonium salt **3***f* (entries 6–8). In the latter oxidation, an electron is removed from the

[7]*N*-Alkylcarboxamidyl radicals have been shown to have the π electronic configuration in their ground state (40, 41) and the π structure should be energetically even more favourable in *N*-alkoxyamidyl radicals (4).

[8]Such a resonance stabilization of a radical center has been described also as "push–pull" stabilization (43) and "merostabilization" (44).

Can. J. Chem. Downloaded from www.nrcresearchpress.com by 213.222.148.141 on 09/07/12
For personal use only.

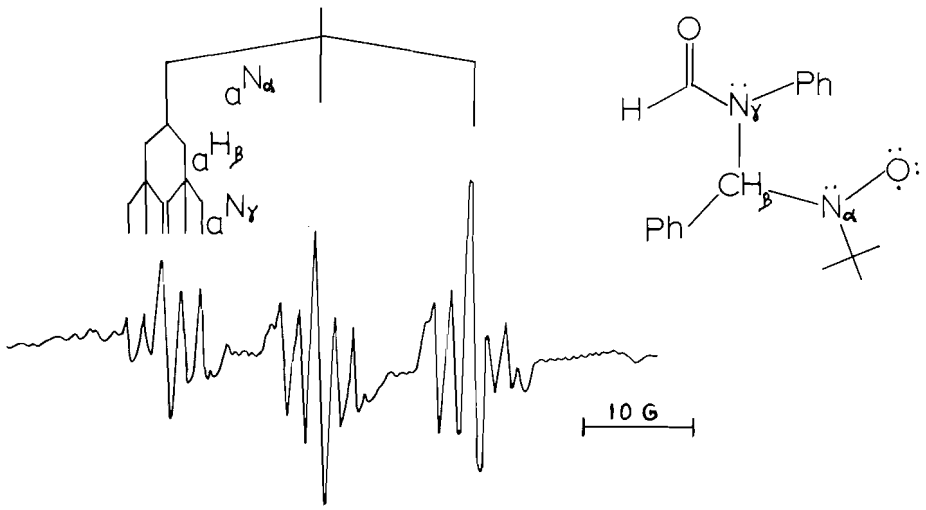

FIG. 2. The epr spectrum obtained in the electrochemical oxidation of the mixed silver–tetraethylammonium salt of formanilide (**2***f*), at a Pt electrode, in acetonitrile–TEABF(0.1 M), in the presence of *N*-*tert*-butyl-α-phenylnitrone: $a^{N\alpha} = 13.9$ G, $a^{H\beta} = 3.6$ G, $a^{N\gamma} = 1.7$ G; $g = 2.0057$.

amidyl anion to give an amidyl radical (eq. [1]), which abstracts hydrogen from the medium (eq. [7]). But, in the oxidation of the silver salts **1** and **2**, the electron is removed from an amide-Ag-amide anion (eq. [9]). The resulting radical could collapse to the silver salt and a free amidyl radical (eq. [10]), which would then abstract hydrogen from the medium (eq. [7]). However, the lifetime of the amide-Ag-amide radical could be long enough to allow further oxidation to occur to some extent to give a solvated radical pair and a silver ion and (or) a radical pair still complexed to the silver ion (eq. [11]). *N*,*N*-Coupling would then occur in the solvent cage and (or) the complex (eq. [12]) (45). Escape from the solvent cage and (or) the complex (eq. [13]) would give a free amidyl radical abstracting hydrogen

[9] $[ZCO(Y)N—Ag—N(Y)COZ]^- \xrightarrow{-e^-} [ZCO(Y)N—Ag—N(Y)COZ]^\cdot$

[10] $[ZCO(Y)N—Ag—N(Y)COZ]^\cdot \longrightarrow [ZCO(Y)N—Ag] + ZCO\dot{N}Y$

$\downarrow$

$1/2[(ZCO(Y)N)_2Ag]Ag$

1

[11] $[ZCO(Y)N—Ag—N(Y)COZ]^\cdot \xrightarrow{-e^-} [ZCO\dot{N}Y \quad Y\dot{N}COZ] + Ag^+$

and/or

$[ZCON^\cdot \ldots Ag^+ \ldots {}^\cdot NCOZ]$ (Y substituents)

[12] $[ZCO\dot{N}Y \quad Y\dot{N}COZ] \longrightarrow ZCON—NCOZ$ (Y substituents)

7

and (or)

$[ZCON^\cdot \ldots Ag^+ \ldots {}^\cdot NCOZ]$ (Y substituents) $\xrightarrow{-Ag^+}$

[13] $[ZCO\dot{N}Y \quad Y\dot{N}COZ] \longrightarrow 2ZCO\dot{N}Y$

and (or)

$[ZCON^\cdot \ldots Ag^+ \ldots {}^\cdot NCOZ]$ (Y substituents) $\xrightarrow{-Ag^+}$

from the medium (eq. [7]). In the case of the electrooxidation of silver salts of *p*-cyanoformanilide (**1***h* and **2***h*) and of an imide (**1***a–e* and **2***a–e*), the lifetime of the amide-Ag-amide radical would be too short (electron-withdrawing groups only on nitrogen, N—Ag bond weaker) to allow further oxidation to occur before its breakdown to a free amidyl radical and the silver salt **1** (eq. [10]). Thus, the absence of *N*,*N*-coupling product in the electrooxidation of the silver salts of *p*-cyanoformanilide (**1***h* and **2***h*) and of imides (**1***a–e* and **2***a–e*), as well as in the electrooxidation of the tetraethylammonium salt of formanilide (**3***f*), is accounted for. Interestingly, the combination of the solvated and (or) complexed radical pair (eq. [12]) could be slightly slower in the case of the *p*-methoxyformanilidyl radical than in the case of the less stable formanilidyl radical, which would explain the smaller proportion of *N*,*N*-coupling obtained in the oxidation of the silver salt of *p*-methoxyformanilide (**1***g*) (15%) as compared to the oxidation of salts **1***f* and **2***f* of formanilide (21–26%).

Conclusion

The oxidation potential of an imidyl anion with two electron-attracting carbonyl groups attached to the nitrogen is higher than that of a carboxamidyl anion that has only one carbonyl group and therefore has a higher energy HOMO. The same is true for the oxidation of amide-Ag-amide anions (amide = imide or carboxamide).

The oxidation of these anions at platinum and at vitreous carbon is a one-electron process and gives rise to an irreversible wave ($\alpha n < 1$). It leads to an amidyl radical. *This electrochemically generated amidyl preferentially abstracts hydrogen from the medium to give the parent amide*. Attempts to trap the succinimidyl radical by intermolecular addition to an olefin were unsuccessful. The oxidation of the anion of *N*-benzoyl-3-cyclohexenecarboxamide (salt **5**) led to the parent amide only, and intramolecular addition of the imidyl radical to the

Can. J. Chem. Downloaded from www.nrcresearchpress.com by 213.222.148.141 on 09/07/12
For personal use only.

Can. J. Chem. Downloaded from www.nrcresearchpress.com by 213.222.148.141 on 09/07/12
For personal use only.

double bond was not observed. Spin trapping of the formanilidyl radical was achieved by oxidizing the formanilide-Ag-formanilide anion (salt **2***f*) in the presence of *N-tert*-butyl-α-phenylnitrone.

In the oxidation of the amide-Ag-amide anion derived from formanilide (salts **1***f* and **2***f*) and *p*-methoxyformanilide (salt **2***g*), *N*,*N*-coupling does occur to some extent, the hydrazine derivative accounting for 15–26% of the oxidation products. However, no *N*,*N*-coupling product was detected in the oxidation of the corresponding formanilidyl anions (salts **3***f* and **3***g* respectively). This suggests that, in the oxidation of amide-Ag-amide anions, the presence of silver favors the formation of two amidyl radicals in a solvent cage and (or) complexed to a silver ion (see eqs. [9] and [11]). When the nitrogen radical bears two electron-attracting groups on the nitrogen such as in an imidyl radical or in the *p*-cyano-formanilidyl radical, no *N*,*N*-coupling was detected, suggesting that the amide-Ag-amide radical (eq. [9]) breaks down to an amidyl radical and silver salt **1** (eq. [10]) faster than it is oxidized (eq. [11]).

Experimental

The general information is the same as that given in ref. 16. Information concerning solvents, electrolytes, electrochemical instrumentation, and methods that is the same as that given in ref. 16 is not repeated here.

Solvents and electrolytes

Methanol was dried by refluxing over magnesium, then distilled, and THF was distilled over $LiAlH_4$. Tetraethylammonium perchlorate (TEAP), prepared from perchloric acid and Et_4NBr, was recrystallized from water until a negative silver ion test and was dried in vacuum for 2 days at 80°C. Commercially available $LiClO_4$ (Alfa Inorganic) was dried in vacuum for 24 h at 100°C.

Electrochemical instrumentation and methods

The voltammetric analysis and the electrodeposition of silver were carried out as described in ref. 16.

The preparative electrolyses were performed under a nitrogen atmosphere, at room temperature, in a two-compartment cell, either a cell of concentric construction with the cathode in a central compartment separated by a fritted glass disc (medium porosity) from the exterior anolyte (containing 50–70 mL), or a standard H-cell with a fritted glass disc as separator. A three-electrode system controlled by a Tacussel potentiostat, model ASA-100, having both an integrator, Tacussel type IG-5, and an ammeter connected in series with the auxiliary circuit, was used. The working electrode was either an 18-cm^2 platinum plate or a 19-cm^2 vitreous carbon plate. They were treated with concentrated nitric acid, thoroughly rinsed with water, and dried in an oven before each use. The auxiliary electrode was an 18-cm^2 platinum plate. The reference electrode was an Ag^0/Ag^+ (0.01 M) electrode (46).

For the spin-trapping experiments, the electrolyses were carried out at room temperature, in the cavity of a Varian E-9 epr spectrometer and in a Varian electrolytic cell, model E256, with a platinum anode, while flowing the solution through the cell. The epr spectrometer was equipped with an E-101 microwave module and a 9.6-GHz Klystron. A dispersion of manganese sulfide in zinc sulfide was used as external standard to determine the g value (g = 2.0054) and to check the magnetic field calibration (3rd and 4th peak, Δ = 67.5 G).

Amides

Succinimide, phthalimide, and glutarimide were obtained from commercial sources. The preparation of tetramethylsuccinimide, benzoylimide, and formanilide has been described in ref. 16.

p-*Methoxyformanilide*

It was prepared as described for formanilide (16) in 78% yield after recrystallization from chloroform–hexane, mp 78–79°C; ir ($CHCl_3$) ν_{max}: 3450, 3420, 1695, 1515, 1255 cm^{-1}; ^{1}Hmr ($CDCl_3$) δ: 3.79 (s, OCH_3), 6.77, 6.99, 7.38, 7.53 (AA′BB′ quartet, 4H), 8.28, 8.31 (two s, CHO) ppm; ms (70 eV) *m/e*: 151 (M^+).

p-*Cyanoformanilide*

It was prepared as described for formanilide (16) in 70% yield after recrystallization from benzene, mp 189–190°C; ir (CH_2Cl_2) ν_{max}: 3400, 2230, 1710, 1610, 1515 cm^{-1}; ^{1}Hmr (CD_2Cl_2) δ: 7.53 (m, 4H), 8.29 (m, CHO), 8.7 (br m, NH) ppm; ms (70 eV) *m/e*: 146 (M^+). *Exact Mass* calcd. for $C_8H_6N_2O$: 146.0480; found (ms): 146.0482.

N-*Benzoyl-3-cyclohexene-carboxamide*

Benzamide (3.645 mg, 30 mmol) was added to a solution of 3-cyclohexene-carbonyl chloride (4.128 g, 30 mmol) in dry THF (50 mL) containing dry pyridine (2.4 mL, 30 mmol). The mixture was stirred at room temperature for seven days. Pyridinium chloride was removed by filtration and the solvent evaporated to dryness. The crystalline residue was washed with water and recrystallized from methylene chloride to afford the pure amide (4.00 g, 58% yield), mp 142–143°C; ir ($CHCl_3$) ν_{max}: 3400, 1700 cm^{-1}; ^{1}Hmr ($CDCl_3$) δ: 2.27 (m, 6H), 3.59 (m, 1H), 5.74 (s, 2H), 7.69 (m, 5H), 8.69 (s, 1H) ppm; ms (70 eV) *m/e*: 229 (M^+). *Anal.* calcd. for $C_{14}H_{15}NO_2$: C 73.33, H 6.61, N 6.11; found: C 73.09, H 6.68, N 6.02.

Silver salts 1

The general procedure for preparing the silver salts of imides and formanilides has been given in ref. 16, as well as the characterization of the silver salts **1***a* (succinimide), **1***b* (tetramethylsuccinimide), **1***c* (phthalimide), **1***d* (glutarimide), **1***e* (benzoylimide), and **1***f* (formanilide).

*Salt 1*g (p-*methoxyformanilide)*

This salt was isolated as a brown solid, mp 160–163°C (87% yield), which was contaminated with Ag_2O, according to the elemental analysis. *Anal.* calcd. for $C_8H_8NO_2Ag \cdot 1/2H_2O$ + 0.1 Ag_2O: C 33.11, H 2.78, N 4.83, Ag 44.60; found: C 33.07, H 2.78, N 5.53, Ag 46.3.

*Salt 1*h *(*p-*cyanoformanilide)*

This salt was isolated as a beige solid, mp 225–227°C (85% yield), which was contaminated with Ag_2O, according to the elemental analysis. *Anal.* calcd. for $C_8H_5N_2OAg \cdot 1/2H_2O$ + 0.1 Ag_2O: C 33.69, H 1.77, N 9.82, Ag 45.39; found: C 33.31, H 1.72, N 10.15, Ag 45.8.

Silver salt of N-*benzoyl-3-cyclohexene carboxamide*

This salt was isolated as a brown solid (62% yield), which was contaminated with Ag_2O, according to the elemental analysis. *Anal.* calcd. for $C_{14}H_{14}NO_2 \cdot 1/2H_2O$ + 1/6 Ag_2O: C 43.70, H 3.93, N 3.64, Ag 37.38; found: C 43.47, H 3.86, N 3.46, Ag 37.0.

Mixed silver–tetraethylammonium salts 2

The chemical preparation of salt **2***a* (succinimide) has been described in ref. 16. Salts **2***a*, **2***b* (tetramethylsuccinimide), **2***c* (phthalimide), **2***d* (glutarimide), and **2***f* (formanilide) were prepared in the electrolysis cell by electrodeposition of Ag^0 at −0.5 vs. Ag^0/Ag^+ (0.01 M) from a solution of the silver salts **1**, in acetonitrile–TEABF, until the current dropped to 2% or less of its initial value. The yield of Ag^0 varied from 48 to 54%. For salt **2***e* (dibenzoylimide), the electrodeposition of Ag^0 was carried out at −0.25 V and the yield of Ag^0 was 54%.

Tetraethylammonium salts 3

The chemical preparation of salt **3***a* (succinimide) has been described in ref. 16. Salts **3***a*, **3***b* (tetramethylsuccinimide), **3***c* (phthalimide), **3***d* (glutarimide), **3***f* (formanilide), and **3***h* (*p*-cyano-formanilide) were prepared in the electrolysis cell by electrodeposition of Ag^0 at −1.5 to −1.6 V vs. Ag^0/Ag^+ (0.01 M), from a solution of the silver salts **1**, in acetonitrile–TEABF (0.1 M), until the current dropped to 2% or less of its initial value. The yield of electrodeposited Ag^0 varied from 97 to 105%. For salt **3***e* (dibenzoylimide), the electrodeposition of Ag^0 was carried out at −0.90 V and the yield of Ag^0 was 104%.

A solution of **3***c* in methanol was prepared by dissolving the commercially available potassium salt of phthalimide (0.6 mmol) in a 0.1 M solution of TEAP in methanol (100 mL).

Can. J. Chem. Downloaded from www.nrcresearchpress.com by 213.222.148.141 on 09/07/12
For personal use only.

Salts **3***a* and **3***f* were also prepared in the electrolysis cell by electrochemical reduction of the parent amide in acetonitrile–TEABF (0.1 M): at −2.00 V for **3***a*; at −2.26 V for **3***f*.

Tetraethylammonium salt **5** *(*N*-benzoyl-3-cyclohexene-carboxamide)*

This salt was prepared in the electrolysis cell by electrochemical reduction of the parent amide, 4.2 mM solution in acetonitrile–TEABF, at −2.10 V vs. Ag^0/Ag^+ (0.01 M), until the current dropped to 3% of its initial value (1.24 F/mol consumed). The voltammogram of the resulting solution showed an anodic wave at 0.5 V both at Pt and C, and no cathodic wave.

Lithium salts **4**

The lithium salt **4***a* (succinimide) was prepared by adding succinimide to a solution of LiOH in absolute methanol. Addition of ether caused the precipitation of **4***a*, which was filtered, washed with ether, and dried. The resulting precipitate contained 20% of succinimide, according to the ^{1}Hmr spectrum.

Lithium salt **4***a* was also prepared in the electrochemical cell by treating a solution of succinimide in dry THF with 1 equiv. of *n*-BuLi.

A solution of **4***c* (phthalimide) was prepared by dissolving the potassium salt of phthalimide (0.6 mmol) in a 0.3 M solution of $LiClO_4$ in THF (100 mL).

Authentic samples

N,N′-*Diformyl*-N,N′-*diphenylhydrazine (***7***, Z = H, Y = C_6H_5)*

A mixture of hydrazobenzene and azobenzene (2.40 g) in methylene-chloride (25 mL) was treated with the mixed acetic formic anhydride (47) in excess (54 mmol) at 25°C. After 3 days, more formic anhydride (54 mmol) was added. After 5 days, the reaction mixture was passed through a short column of silica gel and the solvent evaporated. The residue was recrystallized from CH_2Cl_2–ether, mp 95–96°C (0.56 g); ir ($CHCl_3$) ν_{max}: 1710, 1680, 1600 cm^{-1}; ^{1}Hmr (CD_3COCD_3) δ: 7.42 (m, 10H), 8.55 (s, 0.5 H), 8.91 (s, 1H), 9.14 (s, 0.5 H) (mixture of three rotational isomers) ppm; ms (70 eV) *m/e*: 240 (M^+), 212, 183. *Anal.* calcd. for $C_{14}H_{12}N_2O_2$: C 70.00, H 5.05, N 11.66; found: C 69.84, H 4.93, N 11.86.

N,N′-*Diformyl*-N,N′-*di*-p-*methoxyphenylhydrazine (***7***, Z = H, Y = p-CH_3O C_6H_4)*

N,*N*-Di-*p*-methoxyphenylhydrazine was prepared by the electrochemical reduction of *p*-methoxyazoxybenzene as described by Hazard and Tallec (48). It was reacted with the mixed acetic formic anhydride as described above to afford **7** (Z = H, Y = *p*-$CH_3OC_6H_4$) as a viscous oil; ir ($CHCl_3$) ν_{max}: 2825, 1715, 1680, 1605, 1510, 1250, 1035, 835 cm^{-1}; ^{1}Hmr ($CDCl_3$) δ: 3.77, 3.80, and 3.81 (three s, OCH_3), 6.82, 6.93, 7.16, 7.26 (AA′BB′ quartet, aromatic protons), 8.46, 8.62, and 8.65 (three s, CHO) (mixture of three rotational isomers) ppm; ms (70 eV) *m/e*: 300 (M^+). *Exact Mass* calcd. for $C_{16}H_{16}N_2O_4$: 300.1140; found (ms): 300.1128.

Preparative electrolyses

Typical electrolyses are described below.

*Electrooxidation of the silver salt of succinimide (***1***a) in the presence of 3-sulfolene* (Table 4, entry 7)

Salt **1***a* (253 mg, 1.18 mmol), in acetonitrile–TEABF (0.1 M) (60 mL) containing sulfolene (2.35 g, 19.8 mmol), was electrolysed on a platinum electrode in the concentric cell, at an anodic potential of 1.5 V until zero current (0.67 F/mol) (45 min). The cathode compartment contained 10 mL of the 0.1 M electrolyte solution. The anolyte was evaporated to dryness *in vacuo* and the residue was extracted with refluxing ether (5 × 40 mL). The yield of succinimide determined by vpc was 65%. The chromatograms showed the presence of a small amount of another product, which was isolated by preparative vpc as a colorless liquid (15 mg); ir ($CHCl_3$) ν_{max}: 1610 (C=C), 1140, and 1300 (SO_2) cm^{-1}; ^{1}Hmr ($CDCl_3$) δ: 3.14 (m) and 6.70 (m) ppm in a 3:2 ratio plus weak absorptions due to the presence of succinimide (detected by vpc also); ms (70 eV) *m/e*: 118 and ms (CI) *m/e*: 119. These spectral characteristics are consistent with structure **8**.

The solid residue after extraction with ether was treated with nitric acid (1.2 mmol) and extracted again with refluxing ether (3 × 40 mL) to yield an additional 25% of succinimide (by vpc) (total yield, 90%).

The catholyte solution was treated in the same way as the anolyte solution and it did not contain any organic product, according to vpc analysis.

*Electrooxidation of the silver salt of formanilide (***1***f)* (Table 5, entry 1)

Salt **1***f* (155 mg, 0.66 mmol), in acetonitrile–TEABF (0.1 M) (70 mL), was electrolysed on a platinum electrode, in the concentric cell, at an anodic potential of 0.50 V until zero current (0.66 F/mol) (6 h). The cathode compartment contained 10 mL of the 0.1 M electrolyte solution. Work-up of the anolyte was carried out as above and the crude product was separated by preparative layer chromatography (plc) on silica gel (ether–hexane 4:1) to yield two main fractions. The less polar fraction consisted of N,N′-*diformyl*-N,N′-*diphenylhydrazine* (**7**, Z = H, Y = C_6H_5), mp 93–95°C (11 mg, 14% yield), identical (ir, ^{1}Hmr, ms) to the authentic sample. The more polar fraction consisted of formanilide (31 mg, 39%).

The solid residue after ether extraction was treated with nitric acid (0.7 mmol) and extracted with refluxing ether to yield an additional 32% of formanilide (by vpc) (total yield, 71%).

Electrooxidation of the tetraethylammonium salt of N*-benzoyl-3-cyclohexenecarboxamide (***5***)* (Table 4, entry 13)

N-Benzoyl-3-cyclohexenecarboxamide (24 mg, 0.11 mmol), in acetonitrile–TEABF (0.1 M) (25 mL), was reduced on a platinum electrode in a concentric cell (central compartment: 5 mL of the 0.1 M electrolyte solution), at a cathodic potential of −2.10 V. The electrolysis was stopped after 1.24 F/mol. The auxiliary electrode was a magnesium rod. The voltammogram of the solution showed the absence of the cathodic wave of the parent imide and an anodic wave at $E_{1/2}$ = 0.5 V due to the oxidation of salt **5**.

The platinum and magnesium electrodes were removed and replaced by a vitreous carbon and a platinum electrode respectively. The solution of **5** was oxidized at an anodic potential of 1.00 V (0.8 F/mol) (90 min). The usual work-up followed by plc on silica gel (ether–hexane 2:1) gave the parent imide as the sole product, mp 138–140°C (19 mg, 80% yield).

Acknowledgements

We are grateful to the Natural Sciences and Engineering Research Council of Canada and to the "Fonds pour la Formation de Chercheurs et l'Aide à la Recherche" of Québec for their financial support, and to Mrs. Solange Thériault for typing the manuscript. We thank Mr. Y. Couture and Mr. A. Cyr for the preparation of authentic samples.

1. R. R. GRINSTEAD. J. Inorg. Nucl. Chem. **4**, 287 (1957).
2. Z. ALI, R. BAUER, W. SCHÖN, and H. WENDT. J. Appl. Electrochem. **10**, 97 (1980).
3. R. BAUER and H. WENDT. Angew. Chem. Internat. Ed. Engl. **17**, 202 (1978).
4. J. H. COOLEY, M. W. MOSHER, and M. A. KAHN. J. Am. Chem. Soc. **90**, 1867 (1968).
5. A. R. FORRESTER, E. M. JOHANSON, and R. H. THOMSON. J. Chem. Soc. Perkin Trans. 1, 1112 (1979).
6. R. J. CRAWFORD and R. RAAP. J. Org. Chem. **28**, 2419 (1963).
7. S. OZAKI and M. MASUI. Chem. Pharm. Bull. **27**, 357 (1979).
8. A. J. BACON. Ph.D. thesis, University of Kansas, 1970.
9. G. ASENSIO, E. GONZALEZ-NUNEZ, and M. J. RODRIGO. J. Chem. Soc. Chem. Commun. 263 (1987).
10. T. OKUBO and S. TSUTSUMI. Bull. Chem. Soc. Jpn. **37**, 1794 (1964).
11. K. M. JOHNSTON and J. D. STRIDE. Chem. Commun. 325 (1966); R. G. COOKS, D. H. WILLIAMS, K. M. JOHNSTON, and J. D. STRIDE. J. Chem. Soc. C, 2199 (1968).
12. R. T. BINNS and R. BRETTLE. J. Chem. Soc. C, 336 (1966); R. BRETTLE and J. G. PARKIN. J. Chem. Soc. C, 1352 (1967); R. BRETTLE and D. SEDDON. J. Chem. Soc. C, 1153 (1970); R. BRETTLE, J. G. PARKIN, and R. SEDDON. J. Chem. Soc. C, 1317 (1970).

13. J. M. FERN and P. FEDERLIN. J. Electroanal. Chem. **96**, 209 (1979).
14. H. SCHÄFER and A. ALAZRAK. Angew. Chem. Int. Ed. Engl. **7**, 474 (1968).
15. J. M. FERN and P. FEDERLIN. Tetrahedron, **34**, 661 (1978).
16. J. Y. HUOT, D. SERVE, and J. LESSARD. Can. J. Chem. **61**, 1890 (1983).
17. J. M. LANDERSBERG and M. SIEGEL. J. Org. Chem. **35**, 1674 (1970).
18. D. TOUCHARD and J. LESSARD. Tetrahedron Lett. 4425 (1971); Tetrahedron Lett. 3827 (1973).
19. Y. L. CHOW and R. A. PERRY. Tetrahedron Lett. 531 (1972); Can. J. Chem. **63**, 2203 (1985).
20. M. E. KUEHNE and D. HORNE. J. Org. Chem. **40**, 1287 (1975).
21. H. DRIGUEZ, J. M. PATON, and J. LESSARD. Can. J. Chem. **55**, 700 (1977); H. DRIGUEZ and J. LESSARD. Can. J. Chem. **55**, 720 (1977).
22. P. MACKIEWICZ, R. FURSTOSS, B. WAEGELL, R. CÔTÉ, and J. LESSARD. J. Org. Chem. **43**, 3746 (1978); J. LESSARD, R. CÔTÉ, P. MACKIEWICZ, R. FURSTOSS, and B. WAEGELL. J. Org. Chem. **43**, 3750 (1978).
23. J. C. DAY, M. G. KATSAROS, W. D. KOCHER, A. E. SCOTT, and P. S. SKELL. J. Am. Chem. Soc. **100**, 1950 (1978); U. LÜNING, D. S. MCBAIN, and A. S. SKELL. J. Org. Chem. **51**, 2077 (1986).
24. F. L. LU, Y. M. A. NAGUIB, M. KITADANI, and Y. L. CHOW. Can. J. Chem. **57**, 1967 (1979).
25. J. LESSARD, M. MONDON, and D. TOUCHARD. Can. J. Chem. **59**, 431 (1981).
26. J. TUAILLON and J. LESSARD. J. Org. Chem. **47**, 5013 (1982).
27. J. LESSARD, Y. COUTURE, M. MONDON, and D. TOUCHARD. Can. J. Chem. **62**, 105 (1984).
28. Z. GALUS. Fundamentals of electrochemical analysis. Ellis Horwood Ltd., Westergate, G.B. 1976. p. 249.
29. R. C. LARSONS, R. T. IWAMOTO, and R. N. ADAMS. Anal. Chim. Acta, **25**, 371 (1961); L. EBERSON and J. H. P. UTLEY. *In* Organic electrochemistry. *Edited by* M. M. Baizer and H. Lund. Marcel Dekker Inc., New York, NY. 1983. p. 414; G. SCHIAVON, S. ZECCHIN, G. ZOTTI, and S. CATTARIN. J. Electroanal. Chem. **213**, 53 (1986).
30. G. CAUQUIS. *In* Organic electrochemistry. *Edited by* M. M. Baizer and H. Lund. Marcel Dekker Inc., New York, NY. 1983. pp. 64–67.
31. I. FLEMING. Frontier orbitals and organic chemical reactions. John Wiley and Sons Ltd., New York, NY. 1976.
32. J. F. O'DONNELL and C. K. MANN. J. Electroanal. Chem. **13**, 157 (1967).
33. M. GENIES. Bull. Soc. Chim. Fr. 389 (1985).
34. J. C. DAY, M. J. LINDSTROM, and P. S. SKELL. J. Am. Chem. Soc. **96**, 5616 (1974); U. LÜNING, S. SESHADRI, and P. S. SKELL. J. Org. Chem. **51**, 2071 (1986), and references therein.
35. J. G. TRAYNHAM and Y. S. LEE. J. Am. Chem. Soc. **96**, 3590 (1974).
36. M. W. MOSHER and G. W. ESTES. J. Am. Chem. Soc. **99**, 6928 (1977).
37. D. D. TANNER, D. W. REED, S. L. TAN, C. P. MEINTZER, C. WALLING, and A. SOPCHIK. J. Am. Chem. Soc. **107**, 6576 (1985), and references therein.
38. Y. L. CHOW and Y. M. A. NAGUIB. J. Am. Chem. Soc. **106**, 7557 (1984).
39. A. R. FORRESTER, J. HENDERSON, E. M. JOHANSON, and R. H. THOMSON. Tetrahedron Lett. 5139 (1978); A. R. FORRESTER and H. IRIKAWA. J. Chem. Soc. Chem. Commun. 253 (1981).
40. J. LESSARD, D. GRILLER, and K. U. INGOLD. J. Am. Chem. Soc. **102**, 3262 (1980); R. SUTCLIFFE, D. GRILLER, J. LESSARD, and K. U. INGOLD. J. Am. Chem. Soc. **103**, 624 (1981); R. SUTCLIFFE, K. U. INGOLD, and J. LESSARD. J. Am. Chem. Soc. **103**, 7685 (1981).
41. W. C. DANEN and R. W. GELLERT. J. Am. Chem. Soc. **102**, 3264 (1980).
42. L. STELLA, Z. JANOUSEK, R. MERENYI, and H. G. VIEHE. Angew. Chem. Int. Ed. Engl. **17**, 691 (1978); H. G. VIEHE, R. MERENYI, L. STELLA, and Z. JANOUSEK. Angew. Chem. Int. Ed. Engl. **18**, 917 (1979); H. G. VIEHE, Z. JANOUSEK, R. MERENYI, and L. STELLA. Acc. Chem. Res. **18**, 148 (1985).
43. A. T. BALABAN, P. T. FRANGOPOL, M. FRANGOPOL, and N. NEGOITA. Tetrahedron, **23**, 4661 (1967); A. T. BALABAN. Rev. Roum. Chim. **16**, 725 (1971).
44. R. W. BALDOCK, P. HUDSON, A. R. KATRITZKY, and F. SOTI. J. Chem. Soc. Perkin Trans. 1, 1422 (1974).
45. C. REICHARDT. Solvent effects in organic chemistry. Verlag Chemie, New York, NY. 1978. pp. 180–182.
46. J. P. BILLON. J. Electroanal. Chem. **1**, 486 (1950/60).
47. C. W. HUFFMAN. J. Org. Chem. **23**, 727 (1958).
48. R. HAZARD and A. TALLEC. Bull. Soc. Chim. Fr. 2197 (1971).

Can. J. Chem. Downloaded from www.nrcresearchpress.com by 213.222.148.141 on 09/07/12
For personal use only.

Biologically active metabolites from *Agelas mauritiana*

R. FATHI-AFSHAR AND T. M. ALLEN
Department of Pharmacology, University of Alberta, Edmonton, Alta., Canada T6G 2H7

Received June 15, 1987

R. FATHI-AFSHAR and T. M. ALLEN. Can. J. Chem. **66**, 45 (1988).

Two novel bicyclic diterpenoides, agelasimine-A (**9**), and agelasimine-B (**10**), have been isolated from the orange sponge *Agelas mauritiana*. Also, a new bromine-containing alkaloid, 5-debromomidpacamide (**12**), along with midpacamide (**13**) and methyl *N*-methyl-4,5-dibromopyrrole-2-carboxylate (**11**), has been isolated. The structures were determined by interpretation of their spectral data. Agelasimine-A and -B exhibit a wide range of interesting biological activities such as cytotoxicity, inhibition of adenosine transfer into rabbit erythrocytes, Ca^{2+}-channel antagonistic action, and α_1 adrenergic blockade.

R. FATHI-AFSHAR et T. M. ALLEN. Can. J. Chem. **66**, 45 (1988).

On a isolé deux nouveaux diterpénoïdes bicycliques, les agélasimines-A (**9**) et -B (**10**), de l'éponge orange *Agelas mauritiana*. On a aussi isolé du *N*-méthyl dibromo-4,5 pyrrolecarboxylate de méthyle et un nouvel alcaloïde contenant du brome, le débromo-5 midpacamide (**12**), aux côtés du midpacamide (**13**). Les agélasimines-A et -B présentent un grand nombre de propriétés biologiques intéressantes comme de la cytotoxicité, une inhibition du transfert de l'adénosine dans les érythrocytes de lapin, une action antagoniste dans le canal du Ca^{2+} et un effet bloqueur adrénergique α_1.

[Traduit par la revue]

Introduction

Some time ago Cullen and Devlin (1) reported the isolation and partial structure determination of agelasine (**1**), a mixture of diterpenes each bearing a novel 9-methyladenine group, from the sea sponge *Agelas dispar*. No attempts have been made on the complete structure determination of agelasine (**1**). However, recently the isolation of several quaternary 9-methyladenine derivatives of bicyclic diterpenes, agelasines A–D (**2–5**) (2), ageline B (**6**) (3), and also 9-methyladenine derivatives of the monocyclic diterpenes, agelasine E (**7**) (4) and ageline A (agelasine F)[1] (**8**) (3, 4), has been reported.

In our continuing search for new antineoplastic compounds from marine organisms, we have examined the cytotoxicity and antineoplastic properties of numerous species (5). In this paper we present the isolation and structure determination of two novel non-quaternary adenine derivatives of a bicyclic diterpene, agelasimine-A (**9**) and agelasimine-B (**10**), along with three bromine-containing alkaloids from the sponge *Agelas mauritiana*.

Specimens of the sponge were collected from Enewetak Atoll at 15-m depths, and maintained frozen (−20°C) until needed. The sponge was partially thawed, and homogenized in 95% ethanol. The chloroform-soluble portion of the crude extract was chromatographed on Sephadex LH-20. The resulting fractions were screened (in vitro) against the L1210 mouse leukemia cell line for cytotoxic activity. The major metabolites isolated from the most active fractions (after repeated chromatography over alumina[2]) are two non-quaternary adenine

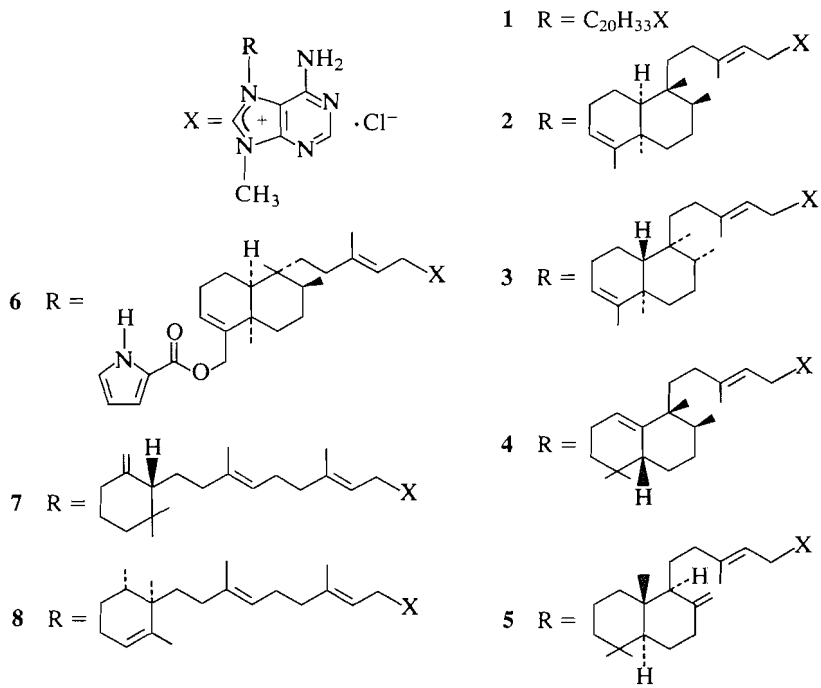

[1]Ageline A and agelasine F refer to the same compound.

[2]Chromatography using silica gel gave fractions with diminished cytotoxicity.

Can. J. Chem. Downloaded from www.nrcresearchpress.com by 213.222.148.141 on 09/07/12
For personal use only.

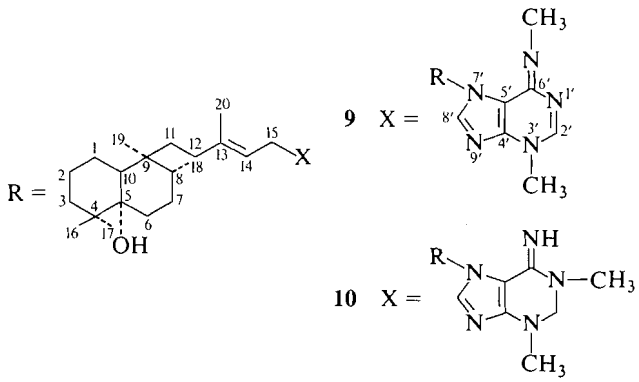

derivatives, agelasimine-A (**9**) ($C_{27}H_{43}N_5O$) and agelasimine-B (**10**) ($C_{27}H_{45}N_5O$), and methyl *N*-methyl-4,5-dibromopyrrole-2-carboxylate (**11**). The inactive fractions, after chromatography over alumina and silica gel, afforded 5-debromomidpacamide (**12**) and midpacamide (**13**) (6).

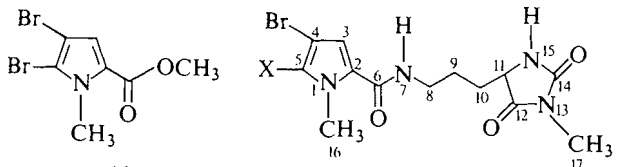

11 **12** X = H; **13** X = Br

The molecular formula $C_{27}H_{43}N_5O$ for agelasimine-A (**9**) was established by a combination of chemical ionization mass spectrometry (cims, molecular weight 453), and high resolution electron impact mass spectroscopy (hrms). Inspection of the fragmentation pattern of this compound in the hrms reveals that the compound fragments into two different portions: a nitrogen-containing heterocyclic nucleus ($C_7H_8N_5$), and an oxygen-containing hydrocarbon portion ($C_{20}H_{35}O$). The ultraviolet (uv) spectrum of the compound has absorptions at 227 nm (10 000) and 285 nm (10 277), similar to the values reported (7) for an adenine type molecule. The infrared (ir) spectrum of the compound shows strong absorption at 1642 cm^{-1} characteristic of the C=N group (8). The ^1H nmr spectrum (Table 1) exhibits two N-methyl singlets at δ 3.22 and 3.66, and two aromatic singlets at δ 7.5 and 7.65. These signals in the ^1H nmr spectrum account for the eight protons present in the $C_7H_8N_5$ nucleus. These observations suggest a dimethyladenine derivative for the heterocyclic portion of the agelasimine-A. Of the several ways of arranging the alkyl ($C_{20}H_{35}O$) and the two methyl groups on the adenine nucleus, we prefer the one shown in the partial structure **A**, on the following grounds. The possibility of

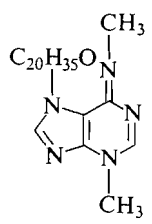

A

having a quaternary 9-methyladenine is rejected, since the characteristic proton signals (1–4) are absent in the ^1H nmr spectrum of the agelasimine-A. The presence of the two aromatic protons at unusually high field (δ 7.5, 7.65), compared to the reported values for *N*-methyl-7-alkyladenine derivatives (δ 7.85, 8.53) (3, 9), suggests the existence of an exocyclic double bond. The different chemical shifts observed (δ 3.22 and 3.66) for the two N-methyl singlets rule out the possibility that both methyl groups are located on the same or fairly similar nitrogen atom(s). Furthermore, irradiation of the C-2′ aromatic proton signal at δ 7.65 sharpens the methyl singlet at δ 3.22; on the other hand, no effect is observed when the other aromatic singlet at δ 7.5 is irradiated. This implies that the methyl group at δ 3.22 is attached to one of the nitrogens on the six-membered ring.

The suggested partial structure also accounts for the ^{13}C nmr signals at 113.8 (C), 137.8 (CH), 143.2 (C), 145.2 (CH), and 150.5 (C), as well as the two signals at δ 34.1 and 34.9 (2 NCH_3) (Table 1).[3]

The nitrogen-containing portion of the molecule is thus established, leaving a $C_{20}H_{35}O$ alkyl residue to be characterized.

The ^1H nmr spectrum of the agelasimine-A contains the spin system depicted in the partial structure **B**; a broad singlet at

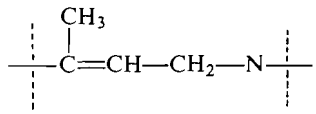

B

δ 1.8 (C=CCH_3), a doublet at 5.17 (NCH_2, J = 7.5 Hz), and a triplet at 5.44 (HC=C, J = 7.5 Hz). This partial structure is supported by corresponding carbon signals observed in the ^{13}C nmr at δ 17.4 (CH_3), 44.8 (CH_2), 118.1 (CH), and 143.3 (C).

Inspection of the mass spectrum of agelasimine-A and analysis of the major peaks at m/z 209 ($C_{14}H_{25}O$), 216 ($C_{11}H_{14}N_5$), 230 ($C_{12}H_{16}N_5$), and 244 ($C_{13}H_{18}N_5$) suggests that a C_6H_{10} chain links the heterocyclic nucleus (partial structure **A**) to a $C_{14}H_{25}O$ hydrocarbon portion. This gives rise to a partial structure **C**, as an expansion of the structures **A** and **B**. The facile loss of $C_{12}H_{27}O$ giving rise to the base peak at m/z 230 is explained by the cleavage of a bond allylic to the olefin bond.

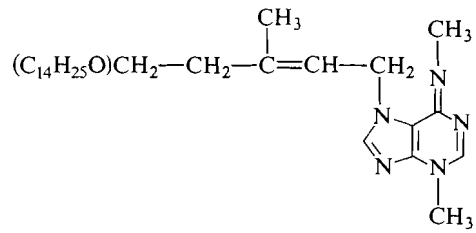

C

The remaining portion of the molecule ($C_{14}H_{25}O$) is defined as the partial structure **D** by comparison of the nmr spectral

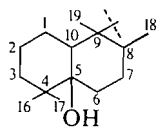

D

data with those reported for similar structures (2). The mass spectrum shows a fragment at m/z 191 ($C_{14}H_{23}$) arising from the loss of H_2O from the $C_{14}H_{25}O$ fragment. The ^1H nmr spectrum indicates the presence of an exchangeable proton (presumably an OH) at δ 1.2 ppm, and this is confirmed by the absorption shown at 3400 cm^{-1} in the ir spectrum and the ^{13}C nmr spectrum, which displays a singlet at δ 76.2 (C)

[3]Assignment of the diterpene substituent at N-7′ is not unambiguous. We prefer N-7′ to N-9′ since previously reported metabolites of sea sponge are substituted at N-7′.

Can. J. Chem. Downloaded from www.nrcresearchpress.com by 213.222.148.141 on 09/07/12
For personal use only.

TABLE 1. ^{1}H (400 MHz) and ^{13}C (100 MHz) data for agelasimine-A and -B (**9**, **10**)

	Agelasimine-A		Agelasimine-B	
Position	δH	δC	δH	δC
4	—	38.9[a] (s)	—	38.9[a] (s)
5	—	76.2 (s)	—	76.3 (s)
6	—	—	—	—
7	—	—	—	—
8	—	36.5[b] (d)	—	36.6[b] (d)
9	—	38.8[a] (s)	—	38.95[a] (s)
10	—	40.9[b] (d)	—	41.4[b] (d)
13	—	143.3 (s)	—	143.3 (s)
14	5.44 (t, 7.5)	118.1 (d)	5.4 (t, 7.5)	118.1 (d)
15	5.17 (d, 7.5)	44.8 (t)	4.89 (d, 7.5)	45.1 (t)
16	0.98[a] (s)	—	0.98[a] (s)	—
17	0.87[a] (s)	—	0.88[a] (s)	—
18	0.84 (s)	—	0.83 (s)	—
19	0.81 (d, 7)	—	0.79 (d, 7)	—
20	1.8 (s)	17.4 (q)	1.8 (s)	17.4 (q)
2′	7.65 (s)	145.2 (d)	4.17 (s)	71.1 (t)
4′	—	150.5 (s)	—	155.2 (s)
5′	—	133.8 (s)	—	115.9 (s)
6′	—	143.2 (s)	—	143.2 (s)
8′	7.5 (s)	137.8 (d)	7.26 (s)	138.2 (d)
=N—Me	3.66 (s)	34.9[c] (q)	—	—
3′-Me	3.22 (s)	34.1[c] (q)	2.90 (s)	35.3[c] (q)
1′-Me	—	—	3.02 (s)	33.8[c] (q)
OH	1.2 (s)	—	1.2 (s)	—
Other		15.9 (q), 16.7 (q), 24 (q), 24.4 (q), 21.7 (t), 22.1 (t), 26.4 (t), 32 (t), 33 (t), 36.1 (t), 36.9 (t)		16 (q), 16.8 (q), 24.1 (q), 24.5 (q), 21.8 (t), 22.2 (t), 26.5 (t), 32.1 (t), 33.1 (t), 36.1 (t), 37 (t)

[a–c]Values with identical superscript within a column may be interchanged.

characteristic of a tertiary alcohol carbon (10). The ^{1}H nmr spectrum contains a methyl doublet (δ 0.8, J = 7 Hz), methyl singlet (δ 0.84), and a *gem*-dimethyl group at δ 0.87 and 0.98 (irradiation at 0.98 clearly enhances the signal at δ 0.87). The chemical shifts of the methyl signals imply that none of the four methyl groups are attached to the carbon bearing the hydroxyl group.

Thus we propose structure **9** for agelasimine-A. The main proof for this assignment comes from the comparison of the spectral data of **9** with that of the purino-diterpene (**14**), isolated by Nakatsu and Faulkner (11). This compound has been isolated

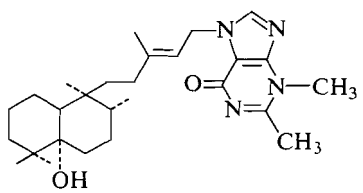

14

from the acetylated[4] mixture of the crude extract of the same sponge (*Agelas mauritiana*), and identified by X-ray analysis.

Another major metabolite isolated (compound **10**), which is biologically active, has a molecular formula of $C_{27}H_{45}N_5O$ as determined by cims and hrms. Analysis of the hrms shows that this compound also consists of two portions: a heterocyclic nucleus ($C_7H_{10}N_5$) and a hydrocarbon portion ($C_{20}H_{35}O$).

[4]Acetic anhydride in pyridine.

Inspection of the mass spectrum fragmentation and ^{1}H and ^{13}C nmr spectra (Table 1) reveals that the $C_{20}H_{35}O$ portion of this compound is very similar to the diterpene portion of the agelasimine-A (**9**).

The infrared spectrum displays absorption at 3400–3300 cm^{-1} (OH and (or) NH) and also exhibits the C=N— absorption at 1619 cm^{-1}. The presence of two exchangeable protons (OH at δ 1.2 and NH at δ 5.3) was detected in the ^{1}H nmr. Also, two methyl singlets are observed at δ 2.9 with 3.02, implying that they are attached to two nitrogens with very similar electronic environments. The presence of only one aromatic proton is observed at δ 7.26, as well as a singlet at δ 4.17 for two hydrogens. These data suggest the partial structure **E** for the heterocyclic portion of this molecule.

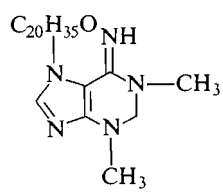

E

These changes in the structure of compound **10** compared with that of agelasimine-A are also reflected in the ^{13}C nmr spectrum (Table 1) of this compound. Most of the signals remain fairly unchanged; however, the C-2′ signal changes from δ 145.2 (CH) in agelasimine-A to δ 71.1 (CH_2) in this

Can. J. Chem. Downloaded from www.nrcresearchpress.com by 213.222.148.141 on 09/07/12
For personal use only.

compound. At this stage we proposed the structure **10** for this metabolite, which was called agelasimine-B. Complete assignments for the ^1H and ^{13}C nmr spectra of compounds **9** and **10** are given in Table 1.

To study the relationship between the agelasimines and the purino-diterpene **14**, and to obtain more information regarding the stereochemistry of these two molecules, we investigated the reactions of the compounds **9** and **10** with acetic anhydride in pyridine.

Agelasimine-A, after purification, gave a product that, although its exact nature has not been firmly established (mixture of isomers), showed mass spectral fragmentation and ^1H nmr spectra in support of the formation of the diacetate (**15**). Acetylation reaction of agelasimine-B, on the other hand, produced one major product, which was characterized as *N*-acetylagelasimine-B (**16**) based on the following data. The

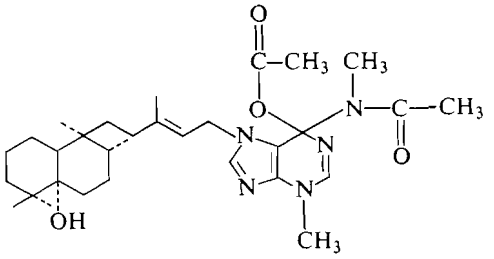

15

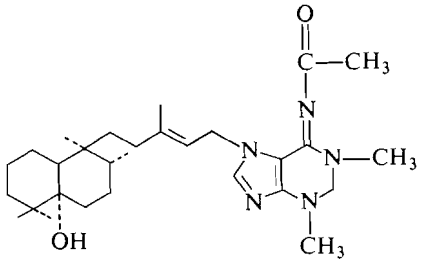

16

^1H nmr of this product exhibited all the signals observed for agelasimine-B plus a singlet at δ 2.15 representing the newly introduced acyl methyl group. This compound was also isolated by Dr. Faulkner and co-workers from their original acetylated mixture, along with the purino-diterpene **14**. The ^1H nmr spectrum for this compound provided us by Dr. Faulkner[5] is identical to the one recorded in our laboratory. Since this product has the same relative stereochemistry as compound **14**, one could also infer the same stereochemistry for the diterpene portion of the agelasimine-A and -B.

In addition to the agelasimines, a minor compound $C_7H_7Br_2NO_2$ was isolated as yellow crystals (mp 87–90°C) from the less polar fractions of the alumina column. This compound belonged to a different class of compounds and was identified as methyl *N*-methyl-4,5-dibromopyrrole-2-carboxylate (**11**) based on its ^1H and ^{13}C nmr spectra. This methyl ester is known as a synthetic product (12). It is possible that the ester is an artefact derived from the free acid, since similar observations have been made for 4,5-dibromopyrrole-2-carboxylic acid (13).

Several of the fractions (see Experimental) from the initial Sephadex chromatography were combined and evaporated. The orange solid was then chromatographed over alumina and silica gel[6] to yield two highly uv-active white solids, $C_{13}H_{16}Br_2N_4O_3$, and $C_{13}H_{17}BrN_4O_3$. The dibromo compound was identified as midpacamide (**13**), a known sponge alkaloid of the "oroidin group." The structure of this compound was confirmed by the comparison of its ^1H and ^{13}C data (Table 2) with the reported values (6).

TABLE 2. ^1H (400 MHz) and ^{13}C (100 MHz) data for compounds **12** and **13**

	Midpacamide (**13**)		5-Debromomidpacamide (**12**)	
Position	δH	δC	δH	δC
2	—	127.4 (s)	—	126 (s)
3	6.66 (s)	113.7 (d)	6.54 (d, 1.7 Hz)	113.5 (d)
4	—	98 (s)	—	94.5 (s)
5	—	111.9 (s)	6.72 (d, 1.7 Hz)	127.4 (d)
6	—	157.6 (s)	—	157.6 (s)
7	6.2[a] (bt, 5.5 Hz)	—	6.07[a] (bt, 5.5 Hz)	—
8	3.4 (m)	38.8 (t)	3.39 (m)	38.4 (t)
9	1.6–2.02 (m)	28.7[b] (t)	1.6–2 (m)	28.7[b] (t)
10		25.1[b] (t)		25.3[b] (t)
11	4.12 (m)	56.7 (d)	4.1 (m)	56.8 (d)
13	—	160.7 (s)	—	161.2 (s)
14	—	174.1 (s)	—	174.1 (s)
15	6.52[a] (s)	—	6.26[a] (s)	—
16	3.95 (s)	35.8 (q)	3.89 (s)	36.8 (q)
17	3.02 (s)	24.6 (q)	3.02 (s)	24.6 (q)

[a]Exchangeable protons.
[b]Values within a column may be interchanged.

The small coupling constant (1.7 Hz) observed between the two aromatic protons at δ 6.54 and 6.72 (W-coupling) supports the substitution pattern on the pyrrole ring (15, 16).

Identification of the monobrominated metabolite, 5-debromomidpacamide (**12**), was greatly facilitated by the structural resemblance of the compound to midpacamide. Structure **12** was assigned to this compound based on the ^1H and ^{13}C nmr (14) spectral data (Table 2).

The agelasimines have been tested for a variety of pharmacological activities. Both compounds show cell growth inhibition properties when tested against L1210 mouse leukemia cells in vitro (ED_{50} = 2–4 μg/mL). Their effect on the smooth muscle relaxation of rabbit gut and beef coronary artery was studied, and both compounds appear to be equipotent in causing relaxation in these tissues (ED_{50} = 3–10 μM). These compounds also showed ability to inhibit nucleoside transport into rabbit erythrocytes (IC_{50} = 6–14 μM). The most interesting biological activity was their ability to reverse the effects on rat aorta ring preparations of a variety of neurotransmitter and other substances. Both agelasimines (**9**, **10**) may act as Ca^{2+}-channel antagonists as well as α_1 adrenergic blockers. Pharmacological activities of agelasimines will be reported elsewhere in detail.

Experimental

General methods

All solvents were distilled prior to use. Camag aluminium oxide (neutral, activity III) was used for column chromatography. Analytical thin-layer chromatography (tlc) was carried out on aluminium oxide F254 (EM Reagents precoated tlc plates, 0.25 mm), and silica gel 60 F254 (Merck precoated tlc plates, 0.2 mm). Preparative thin-layer chromatography (ptlc) was carried out on silica gel 60 F254 (EM Reagents precoated ptlc plates 2 mm). Materials were detected

[5]Private communication.

[6]Several elutions (≈13) on preparative plate were required for this separation.

Can. J. Chem. Downloaded from www.nrcresearchpress.com by 213.222.148.141 on 09/07/12
For personal use only.

Can. J. Chem. Downloaded from www.nrcresearchpress.com by 213.222.148.141 on 09/07/12
For personal use only.

by visualization under an ultraviolet lamp or by using the phosphomolybdic acid (3%) – cerric sulfate (1%) in 5% aqueous sulfuric acid solution followed by heating.

Mass spectra (ms) were recorded on an A.E. ± MS-50 mass spectrometer, or an A.E.I. MS-90 mass spectrometer (chemical ionization), and are reported as m/z (relative intensity). Infrared spectra were recorded on a Nicolet 7199 FT interferometer, ultraviolet spectra on a Hewlett Packard 8450A ultraviolet spectrophotometer, and optical rotations on a Perkin–Elmer Model 241 polarimeter. The ^{1}H and ^{13}C nmr spectra were measured on a Bruker WH-200 spectrometer or a Bruker WH-400 spectrometer. All nuclear magnetic resonance measurements employed tetramethylsilane as an internal standard.

Most of the fractionation and purification stages were monitored by testing the fractions for their activities against L1210 (mouse leukemia) cell line in vitro.

Collection, extraction, and separation

Agelas mauritiana was collected by hand using SCUBA (−15 m) at Enewetak Atoll and frozen for transport to Edmonton.

The finely cut sponge (0.8 kg wet weight) was extracted with 95% ethanol (1 L × 3). The solvent was evaporated under reduced pressure to give a crude extract (23.47 g), which was then dissolved in methanol. The methanol-soluble portion (22 g) was triturated with chloroform, then evaporated to yield 10 g of dark red oil (the most active fraction). This fraction was dissolved in 20 mL of ethanol and chromatographed on Sephadex LH-20 (40 × 4 cm) with ethanol at a flow rate of 1.2 mL/min. Fractions (8 mL) were collected with the aid of an automatic fraction collector. The cytotoxic fractions (fractions 31–50) were combined to give 6.94 g of a mixture of compounds, which was further chromatographed over a larger (48 × 5 cm) Sephadex LH-20 column (ethanol, 0.5 mL/min, 7-mL fractions). The most active fractions (90–124) gave 3.72 g of a mixture of several compounds, which after further chromatography over alumina (300 g), using chloroform–methanol as solvent for elution (7-mL fractions), yielded agelasimine-A (**9**) and agelasimine-B (**10**). Also, methyl *N*-methyl-4,5-dibromopyrrole-2-carboxylate (**11**) was isolated from one of the less polar fractions after this chromatography.

Several inactive fractions (51–63) from the first Sephadex column were combined to give 2.39 g of an orange solid. This was further chromatographed over alumina, and the fractions eluted with chloroform gave 0.5 g of a mixture that, upon further purification employing preparative thin-layer chromatography (10–13 elutions, eluent:ethyl acetate), furnished the brominated pyrroles **12** and **13**.

*Isolation of agelasimine-A (**9**)*

Agelasimine-A was obtained as a yellowish oil (300 mg, 0.038% of the wet weight of the sponge) when the alumina column was being eluted with chloroform–methanol (97:3) in fractions 320–340. This was freed from the trace of colored impurities using another alumina column; $[\alpha]_D^{25}$ +2.3 (CH_3OH); uv (CH_3OH) $\lambda_{max}(\varepsilon)$: 209 (7911 sh), 227 (10 000 sh), 285 (10 277) nm; ir ($CHCl_3$): 3400, 2930, 2840, 2780, 1710, 1642, 1600, 1510, 1460, 1380, 760 cm^{-1}; ^{1}H and ^{13}C nmr ($CDCl_3$), see Table 1; hrms, m/z calcd. for $C_{27}H_{43}N_5O$ (M^+): 453.3467; found: 453.3462, 438, 420, 244, 230 (100), 217, 209, 189, 163, 135. Chemical ionization (NH_3) ms shows an $M + 1$ (m/z 454) peak.

*Isolation of agelasimine-B (**10**)*

When the preliminary alumina column of the active fraction was eluted with chloroform–methanol (99:1), agelasimine-B was obtained (tubes 141–240) as a viscous yellowish oil (160 mg, 0.02% of the wet sponge weight). Another purification over alumina eliminated the minor impurities; $[\alpha]_D^{25}$ +2.46 (CH_3OH); uv (CH_3OH) $\lambda_{max}(\varepsilon)$: 214 (10 965), 245 (5687 sh), 286 (3629) nm; ir ($CHCl_3$): 3350, 2940, 2860, 2800, 1720, 1619, 1570, 1520, 1460, 1380, 760 cm^{-1}; ^{1}H and ^{13}C nmr ($CDCl_3$), see Table 1; hrms, m/z calcd. for $C_{27}H_{45}N_5O$ (M^+): 455.3623; found: 455.3618, 440, 438, 291, 273, 246, 232, 209, 191, 165, 122 (100%). Chemical ionization (NH_3) ms shows a peak at m/e 456 ($M + 1$).

Reaction of agelasimine-A with acetic anhydride in pyridine

A mixture of agelasimine-A (**9**, 10 mg, 0.022 mmol), pyridine (0.2 mL), and acetic anhydride (0.1 mL) was stirred for 44 h at room temperature. Evaporation to dryness *in vacuo*, followed by column chromatography over silica gel (5 g, methanol–chloroform (1:99)) gave 7 mg of the diacetylagelasimine-A as an oil; ^{1}H nmr ($CDCl_3$) δ: 0.83 (3H, d, J = 7 Hz), 0.87 (3H, s), 0.89 (3H, s), 1.00 (3H, s), 1.76 (3H, bs), 2.2 (3H, s), 2.22 (3H, s), 3.2 (3H, s), 3.27 (3H, s), 4.61 (2H, d, J = 7.5 Hz), 5.36 (1H, t, J = 7.5 Hz), 7.48 (1H, s), 8.25 (1H, s); hrms, m/z calcd. for $C_{31}H_{49}N_5O_4$ (M^+): 555.3773; found: 555.3784, 541, 527, 513, 304, 290, 265, 248, 244, 222, 209, 195, 178, 165, 122.

Reaction of agelasimine-B with acetic anhydride in pyridine

N-*Acetylagelasimine-B (**16**)*

Agelasimine-B (20 mg, 0.044 mmol) was stirred with pyridine (0.4 mL), and acetic anhydride (0.2 mL) at room temperature for 50 h. The mixture was then evaporated to dryness and the residue was chromatographed over silica gel (flash, methanol–chloroform (1:99)) to give 10 mg of *N*-acetylagelasimine-B; ^{1}H nmr ($CDCl_3$) δ: 0.77 (3H, d, J = 7 Hz), 0.81 (3H, s), 0.84 (3H, s), 0.96 (3H, s), 1.16 (s, OH), 1.74 (3H, bs), 2.15 (3H, s), 2.94 (3H, s), 3.04 (3H, s), 4.4 (2H, s), 4.77 (2H, d, J = 7.5 Hz), 5.36 (1H, t, J = 7.5 Hz), 7.32 (1H, s); hrms m/z calcd. for $C_{29}H_{47}N_5O_2$ (M^+): 497.3719; found: 497.3722, 482, 480, 454, 289, 288, 274, 165.

*Isolation of methyl N-methyl-4,5-dibromopyrrole-2-carboxylate (**11**)*

The ester (**11**) was isolated as a yellow solid (80 mg, 0.01% of the wet weight) from the active fraction when the alumina column was eluted with chloroform. Traces of colored impurities were removed by preparative thin-layer chromatography, after which the ester (**11**) was crystallized from hexane to give white needles, mp 87–90°C (lit. (12) mp 87°C); ^{1}H nmr ($CDCl_3$) δ: 3.82 (3H, s), 3.98 (3H, s), 7.01 (1H, s); ^{13}C nmr ($CDCl_3$) δ: 160.2, 123.9, 119.3, 113.7, 98.8, 51.5, 35.8; hrms, m/z calcd. for $C_7H_7Br_2NO_2$ (M^+): 296.8821; found: 296.8837 (100), 265, 237.

*Isolation of 5-debromomidpacamide (**12**)*

This compound was obtained from the inactive fraction the same way as the midpacamide (**13**). This afforded white crystals, mp 116–119°C (0.02% wet weight); ir ($CHCl_3$): 3120, 1740, 1710, 1170 cm^{-1}; ^{1}H and ^{13}C nmr ($CDCl_3$), see Table 2; hrms m/z calcd. for $C_{13}H_{17}BrN_4O_3$ (M^+): 356.0476; found: 356.0479, 197 (100), 170, 153.

*Isolation of midpacamide (**13**)*

Midpacamide (**13**) was isolated from the inactive portion of the original Sephadex column, after chromatography over alumina followed by preparative plate, and recrystallized from acetonitrile as a white powder (0.05% of wet sponge), mp 93–95°C (lit. (6) mp 97°C); ir ($CHCl_3$): 3320, 1764, 1740, 1610 cm^{-1}; ^{1}H nmr ($CDCl_3$) and ^{13}C nmr ($CDCl_3$–MeOD), see Table 2; hrms, m/z calcd. for $C_{13}H_{16}Br_2N_4O_3$ (M^+): 435.9509; found: 435.9560, 436, 265, 197 (100), 153.

Acknowledgements

We wish to thank Dr. P. Colin from the University of Papua New Guinea for the help in the sample collection, the technical staff of the Department of Chemistry for the determinations of spectra and for their helpful suggestions, and Dr. L. M. Browne for proof reading and her constructive criticisms of this manuscript. We thank Professor D. John Faulkner, Scripps Institution of Oceanography, for reading this manuscript. We gratefully acknowledge the financial support of the Alberta Cancer Board and National Cancer Institute.

1. E. Cullen and J. P. Devlin. Can. J. Chem. **53**, 1690 (1975).
2. H. Nakamura, H. Wu, Y. Ohizumi, and Y. Hirata. Tetrahedron Lett. **25**, 2989 (1984).
3. R. J. Capon and D. J. Faulkner. J. Am. Chem. Soc. **106**, 1819 (1984).

4. H. WU, H. NAKAMURA, J. KOBAYASHI, Y. OHIZUMI, and Y. HIRATA. Tetrahedron Lett. **25**, 3719 (1984).
5. (*a*) T. M. ALLEN, A. SHARMA, and R. E. DUBIN. Bull. Mar. Sci. **38**, 4 (1986); (*b*) R. FATHI-AFSHAR and T. M. ALLEN. Proc. West. Pharmacol. Soc. **30**, 131 (1987).
6. L. CHEVOLOT, S. PADUA, B. N. RAVI, P. C. BLYTH, and P. J. SCHEUER. Heterocycles, **7**, 891 (1977).
7. A. I. SCOTT. Interpretation of the ultraviolet spectra of natural products. Pergamon Press, Oxford. 1964. pp. 191–203.
8. K. NAKANISHI and P. H. SALOMON. Infrared absorption spectroscopy. 2nd ed. Holden–Day, San Francisco. 1977.
9. L. M. JACKMAN and S. STERNHELL. Application of nuclear magnetic resonance spectroscopy in organic chemistry. 2nd ed. Pergamon Press, Oxford. 1969.
10. F. W. WEHRLI and T. WIRTHLIN. Interpretation of carbon-13 nmr spectra. Heyden and Son Ltd., New York. 1976. p. 311.
11. T. NAKATSU and D. J. FAULKNER. Tetrahedron Lett. **25**, 935 (1984).
12. P. HODGE and R. W. RICHARDS. J. Chem. Soc. 459 (1965).
13. S. FORENZA, L. MINALE, and R. RICCIO. Chem. Commun. 1129 (1971).
14. J. B. STOTHERS. Carbon-13 nmr spectroscopy. Academic Press, New York. 1972.
15. R. M. SILVERSTEIN and G. CLAYTON BASSLER. Spectrometric identification of organic compounds. 4th ed. Wiley, New York. 1981.
16. H. NAKAMURA, Y. OHIZUMI, and J. KOBAYASHI. Tetrahedron Lett. **25**, 2475 (1984).

Can. J. Chem. Downloaded from www.nrcresearchpress.com by 213.222.148.141 on 09/07/12
For personal use only.

Thujin, a novel lactone isolated from the discolored heartwood of *Thuja plicata* Donn.

LEHONG JIN AND JACK W. WILSON
Faculty of Forestry, University of British Columbia, Vancouver, B.C., Canada

AND

ERIC P. SWAN[1]
Forintek Canada Corporation, Vancouver, B.C., Canada

Received June 29, 1987

LEHONG JIN, JACK W. WILSON, and ERIC P. SWAN. Can. J. Chem. **66**, 51 (1988).

The chemical structure of a novel lactone isolated from the discolored heartwood of living western red cedar (WRC) (*Thuja plicata* Donn.) trees has been determined as 3,3,4,7,7,8-hexamethyl-2,6-dioxa-1,5-anthracene-dione, and given the trivial name thujin (**1**). The isolation, purification, and determination of the structure were carried out by a combination of chemical, chromatographic, and spectroscopic methods.

LEHONG JIN, JACK W. WILSON et ERIC P. SWAN. Can. J. Chem. **66**, 51 (1988).

On a déterminé que la structure chimique d'une nouvelle lactone, qui a été isolée du bois dur décoloré de cèdres rouges de l'ouest (cro) (*Thuja plicata* Donn.), est l'hexaméthyl-3,3,4,7,7,8 dioxa-2,6 anthracènedione-1,5 et que son nom trivial est thujine (**1**). On a isolé et purifié le produit et on a déterminé sa structure en faisant appel à une combinaison de méthodes chimiques, chromatographiques et spectroscopiques.

[Traduit par la revue]

Can. J. Chem. Downloaded from www.nrcresearchpress.com by 213.222.148.141 on 09/07/12
For personal use only.

Introduction

During the past three decades, the large-scale chemical investigation of western red cedar (WRC) (*Thuja plicata* Donn.) heartwood extractives has led to identification of more than a dozen biologically active phenolic compounds (1). These heartwood extractives can be separated readily into volatile and nonvolatile fractions by steam distillation. The volatile fraction consists partly of compounds that are tropolone derivatives, the thujaplicins. The nonvolatile WRC heartwood extractives are mainly lignans (2–12). WRC is recognized as one of the world's most durable woods. It has long been understood from chemical and biological studies that the above two major groups of compounds in WRC heartwood extractives give the wood its durability. It is observed, however, that in certain areas of British Columbia (B.C.) there is a serious WRC heartwood decay problem, especially in living mature and over-mature trees. Questions arise on the biological roles of WRC heartwood extractives in response to microorganism attacks in living trees. In this study, a comparison of differences in extractive composition between healthy and discolored heartwood within the same growth zones in the tree was made. The discoloration of healthy wood was due to infection by microorganism attacks. We now report a novel lactone compound isolated from discolored heartwood extractives that was not present in healthy WRC heartwood extractives. Associated biological tests (13) in this study positively demonstrated that this lactone compound was a biodegradation product of the thujaplicins during infection by a fungus, *Sporothrix* sp., in the heartwood of a once living WRC tree.

Results and discussion

Isolation, purification, and elucidation of the chemical structure of this lactone compound were carried out by chemical, chromatographic, and spectroscopic methods. On the basis of the following results, the compound structure has been determined as 3,3,4,7,7,8-hexamethyl-2,6-dioxa-1,5-anthracene-dione, and given the trivial name thujin (**1**).

Thujin was preliminarily separated by extracting WRC discolored heartwood meal with a benzene–ethanol (2:1) solvent. After evaporation of this solvent, the crude material was liquid extracted by a series of solvents. The solvents used were ethyl ether, ethyl acetate, and ethanol. Thujin was found by thin-layer chromatography (tlc) to occur mainly in the ethyl acetate solubles. Removal of the ethyl acetate insoluble material from the extractives separated thujin from the more strongly polar components, such as plicatic acid, a most important lignin in WRC extractives. After the ethyl acetate solubles passed through a gradient elution chromatographic column, thujin was found to be present in the fraction eluted by a benzene–ethanol (85:15) solvent mixture. The final purified thujin was obtained by using a preparative tlc method with a benzene–ethanol (9:1) solvent system, and crystallization was achieved.

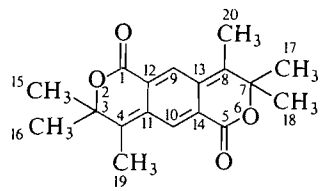

1

On the silica gel tlc plates, thujin had an R_f value of 0.79, which was considerably higher than R_f values for most known tropolone derivatives and lignans in WRC heartwood extractives (14). The blue fluorescence under shortwave ultraviolet (uv) light indicated that the chemical structure of thujin contained some chromophores or auxochromes, such as conjugated double bonds and carbonyl groups, or -OH and -OR groups.

Both low and high resolution mass spectra of thujin were recorded. The parent ion was observed at *m/e* as 300 (*m/z*). The isotopic peak of it was at *m/e* as 301. The intensity of the isotopic peak was 19.3% of the parent ion peak. From the natural isotopic abundance of carbon-13, this indicated approximately 18 carbons present in the structure. The high resolution mass spectrum gave a molecular weight of 300.1368 with an empirical formula of $C_{18}H_{20}O_4$. The elemental analysis for carbon and hydrogen further confirmed the molecular composition.

[1]Author to whom correspondence may be addressed.

Can. J. Chem. Downloaded from www.nrcresearchpress.com by 213.222.148.141 on 09/07/12
For personal use only.

TABLE 1. Carbon-13 proton decoupled and APT nmr spectral data and assignments for thujin (**1**)

Chemical shift (ppm)	APT data	Assignment
167.95	Quaternary	C-1 or C-5
138.45	Methine	C-9 or C-10
135.63	Quaternary	{C-4, C-11, and C-12, or
123.57	Quaternary	C-8, C-13, and C-14}
122.93	Quaternary	
62.02	Quaternary	C-3 or C-7
35.14	Methyl	C-19 or C-20
26.22	Methyl	C-15 and C-16, or C-17 and C-18

The pattern of fragmentation in the mass spectra showed a very clear symmetry in the compound. The examples of such were those fragments with m/e at 300 (parent ion, M), $M/2$, $M - 15$, $M - (2 \times 15)$, $M - 44$, $M - (2 \times 44)$, and $M - (2 \times 14 - 2 \times 44)$. The peak with m/e at 149.0609 with an empirical formula of $C_9H_9O_2$ was half of the parent ion, with the additional loss of one hydrogen. The peak with mass of $M - (2 \times 15)$ may be assigned to the loss of two CH_3 groups while the peak with the mass of $M - (2 \times 44)$ can be assigned to the loss of two CO_2 groups in the molecule.

The proton nuclear magnetic resonance (nmr) spectrum of thujin was rather simple with only three singlet peaks. Their chemical shifts were 1.28, 2.3, and 7.3 ppm. Therefore there were only three types of protons with different environments present in the molecule. None of these protons had any neighbouring protons, since no coupling was observed. Integration of the peak areas showed that the relative numbers of the three types of protons present in the compound were 1:3:6 for the signals at 7.3, 2.3, and 1.28 ppm, respectively.

Carbon-13 Broad Band (BB) proton decoupled and Attached Proton Test (APT) nmr spectral data and assignments for thujin (**1**) are listed in Table 1.

An APT carbon-13 nmr spectrum determined the numbers of protons bonded to a carbon in the molecule (Table 1).

Evidence from mass spectral fragments showed that thujin had a symmetric dimer structure. According to proton and carbon-13 nmr information, it was assumed that the molecule had 2×9 carbons and 2×10 protons. The carbon at 167.95 ppm in the carbon-13 nmr spectrum was assigned to an acid, ester, or lactone carbonyl, which meant that this carbonyl carbon bonded directly to two oxygens in the molecule. Since thujin was a symmetric compound, it would have 2×2 oxygen atoms. Therefore, the empirical formula $C_{18}H_{20}O_4$ for thujin (**1**) was also strongly supported by the nmr spectral evidence.

Information provided by the infrared (ir) spectrum was quite conclusive. The lack of absorption peaks (3650–3200 cm^{-1}) in the ir spectrum of thujin indicated absence of an -OH group in the structure. One of the most distinctive bands in the ir spectrum of thujin was that arising from the carbonyl group at 1733 cm^{-1}, which was a characteristic peak for six-membered ring lactones.

Experimental

The WRC wood sample used for this study was obtained from a 420-year-old living tree that was infected by microorganisms (13). On the tree cross section, there was a discolored pocket that was surrounded by straw-colored healthy heartwood. Healthy and discolored WRC heartwood samples were collected within the same growth zones of the tree, air dried, and ground to pass a 50-mesh screen.

The wood meals were Soxhlet extracted with a benzene–ethanol (2:1) solvent. The evaporated benzene–ethanol extractives were fractionated with ether, ethyl acetate, and ethanol. The fractions were monitored by tlc with benzene–ethanol (9:1) as a developing solvent. The ethyl acetate solubles that contained thujin were chromatographed on a silica gel (Bio-sil A, 200–400 mesh) column (3 cm × 40 cm). The eluting solvents were chosen by trial experiments. The column was eluted with solvent mixtures of increasing polarity, starting with pure benzene and gradually increasing the percentage of ethanol to give an equal mixture of benzene–ethanol (50:50). The tlc result indicated that thujin was present mainly in the fraction eluted with a benzene–ethanol mixture at the ratio of 85:15. The final purification of thujin was achieved by using preparative tlc with Whatman PLK5F silica gel plates, 20 × 20 cm, 1000 μm thickness by benzene–ethanol (9:1) solvent. Thujin was found under shortwave uv light as a blue fluorescent band at an R_f value of 0.79. Shortwave uv light fluorescence was used to locate the thujin band, which was then scraped from the plate with care. The thujin–silica scraped from the plate was ground to very fine particles and then **1** was leached from the absorbent by ethanol. Crystallization of thujin was achieved by dissolving it in an ethyl acetate – heptane mixture (1:3) and keeping it in a freezer for about 5 weeks. The uncorrected melting range for thujin was 88–91°C.

Both proton and carbon-13 nmr spectra were taken on a Varian XL-300 machine. The samples were prepared in deuterochloroform solution with tetramethylsilane (TMS) as an internal standard. The ir spectrum was recorded on a Perkin–Elmer 137 spectrophotometer. The low resolution mass spectrum was determined on a MAT CH-4 spectrometer, while the high resolution mass spectrum was recorded on a Kratos MS-50 spectrometer. Elemental analysis was done by the Microanalytical Laboratory, Department of Chemistry, U.B.C. A Beckman model 24 spectrometer was used for uv and visible spectral measurements.

The important spectral data were: (*a*) ir: λ_{max} (cm^{-1}), no hydroxyl band, 2962 and 2878 (methyl C—H stretching), 1459 and 1381 (methyl C—H bending), 3016 (double bonding =C—H), 1733 (lactone), 1599, 1574, 1500, and 1459 (conjugated double bonds); (*b*) uv: λ_{max}, 285 nm (extended conjugation system including a carbonyl group); (*c*) proton nmr: 1.28 (6H, singlet, for CH_3 at C-15 and C-16, or at C-17 and C-18), 2.3 (3H, singlet, for CH_3 at C-19 or at C-20), 7.3 (1H, singlet, for CH at C-9 or at C-10); and (*d*) mass spectra: m/e, 300 (parent ion), 285, 270, 256, 212, 184 and 149. *Mol. Wt.* calcd. for $C_{18}H_{20}O_4$: 300.1362; found (hrms): 300.1368. *Anal.* calcd. for $C_{18}H_{20}O_4$: C 71.89, H 6.71%; found: C 72.14, H 6.78%.

Acknowledgments

We wish to thank the Department of Chemistry, U.B.C., for generously providing the spectroscopic and elemental analysis services. We also would like to thank the Ministry of Education, People's Republic of China, and the University of British Columbia for financial support in the form of scholarships towards L. Jin's Ph.D. program.

1. G. M. BARTON and B. F. MACDONALD. For. Serv. Publ. No. 1023. Dept. Fish and For. Can. 1971. pp. 1–31.
2. J. A. F. GARDNER, G. M. BARTON, and H. MACLEAN. Can. J. Chem. **37**, 1703 (1959).
3. J. A. F. GARDNER, G. M. BARTON, and H. MACLEAN. Can. J. Chem. **38**, 2387 (1960).
4. J. A. F. GARDNER, E. P. SWAN, S. A. SUTHERLAND, and H. MACLEAN. Can. J. Chem. **44**, 52 (1966).
5. H. MACLEAN and K. MURAKAMI. Can. J. Chem. **44**, 1541 (1966).
6. H. MACLEAN and K. MURAKAMI. Can. J. Chem. **44**, 1827 (1966).

7. H. MACLEAN and K. MURAKAMI. Can. J. Chem. **45**, 305 (1967).
8. H. MACLEAN and B. F. MACDONALD. Can. J. Chem. **45**, 739 (1967).
9. H. MACLEAN and B. F. MACDONALD. Can. J. Chem. **47**, 457 (1969).
10. H. MACLEAN and B. F. MACDONALD. Can. J. Chem. **47**, 4495 (1969).
11. B. F. MACDONALD and G. M. BARTON. Can. J. Chem. **48**, 3144 (1970).
12. B. F. MACDONALD and G. M. BARTON. Can. J. Chem. **51**, 482 (1973).
13. L. JIN. Ph.D. thesis. Faculty of Forestry, University of British Columbia, Vancouver, B.C. 1987.
14. B. F. MACDONALD and E. P. SWAN. J. Chromatogr. **51**, 553 (1970).

Can. J. Chem. Downloaded from www.nrcresearchpress.com by 213.222.148.141 on 09/07/12
For personal use only.

Selenium-77 nuclear magnetic resonance studies of selenols, diselenides, and selenenyl sulfides

KHOON-SIN TAN, ALAN P. ARNOLD,[1] AND DALLAS L. RABENSTEIN[2]
Department of Chemistry, University of Alberta, Edmonton, Alta., Canada T6G 2G2

Received May 27, 1987

KHOON-SIN TAN, ALAN P. ARNOLD, and DALLAS L. RABENSTEIN. Can. J. Chem. **66**, 54 (1988).

^{77}Se and ^{1}H nuclear magnetic resonance spectra have been measured for selenols (RSeH), diselenides (RSeSeR), and selenenyl sulfides (RSeSR′), including selenenyl sulfides formed by reaction of glutathione and penicillamine with selenocystine and related diselenides. Exchange processes strongly affect the ^{77}Se and ^{1}H nuclear magnetic resonance spectra of all three classes of compounds. Sharp, exchange-averaged resonances are observed in the ^{1}H nuclear magnetic resonance spectra of selenols; however, selenol proton exchange causes the ^{77}Se resonances to be extremely broad over the pH range where the selenol group is titrated. Selenol/diselenide exchange ($\overset{*}{R}SeH + RSeSeR \rightleftarrows \overset{*}{R}SeSeR + RSeH$) also results in exchange-averaged ^{1}H resonances for solutions containing RSeH and RSeSeR; however, the ^{77}Se resonances were too broad to detect. Exchange reactions have similar effects on nuclear magnetic resonance spectra of solutions containing selenols and selenenyl sulfides. The results indicate selenol/diselenide exchange is much faster than thiol/disulfide exchange. The ^{77}Se chemical shift depends on the chemical state of the selenium, e.g., titration of the selenol group of selenocysteamine causes the ^{77}Se resonance to be shielded by 164 ppm, oxidation of the selenol to form the diselenide selenocystamine causes a deshielding of 333 ppm, and oxidation to form the selenenyl sulfide $\overset{+}{H_3}NCH_2CH_2SeSCH_2CH_2\overset{+}{N}H_3$ results in a deshielding of 404 ppm. ^{77}Se chemical shifts were found to be in the range -240 to -270 ppm (relative to $(CH_3)_2Se$) for selenolates, approximately -80 ppm for selenols, 230–360 ppm for diselenides, and 250–340 ppm for selenenyl sulfides. The ^{77}Se chemical shift is also affected by titration of neighboring carboxylic acid and ammonium groups, and their pK_A values can be calculated from ^{77}Se chemical shift data.

KHOON-SIN TAN, ALAN P. ARNOLD et DALLAS L. RABENSTEIN. Can. J. Chem. **66**, 54 (1988).

On a déterminé les spectres en résonance magnétique nucléaire du ^{77}Se et du ^{1}H de sélénols (RSeH), de disélénures (RSeSeR) et de disulfures de sélénényles (RSeSR′), y compris des sulfures de sélénényles qui se forment au cours de la réaction du glutathion et de la pénicillamine avec la sélénocystéine et des disélénures apparentés. Les processus d'échange affectent beaucoup les spectres en résonance magnétique nucléaire du ^{77}Se et du ^{1}H de ces trois classes de composés. Avec les sélénols, les spectres en résonance magnétique nucléaire du ^{1}H présentent des raies bien définies qui résultent de moyennes; toutefois, l'échange du proton du sélénol fait que les résonances du ^{77}Se sont extrêmement larges à tous les pH où le groupement sélénol peut être titré. Dans le cas des solutions qui contiennent du RSeH et du RSeSeR, l'échange sélénol/disélénure ($R^*SeH + RSeSeR \rightleftarrows R^*SeSeR + RSeH$) conduit aussi à des résonances du ^{1}H qui résultent de moyennes; toutefois, les résonances du ^{77}Se sont trop élargies pour être détectées. Les réactions d'échange ont des effets semblables sur les spectres en résonance magnétique nucléaire de solutions contenant des sélénols et des sulfures de sélénényles. Les résultats indiquent que l'échange sélénol/disélénure est beaucoup plus rapide que l'échange thiol/disulfure. Le déplacement chimique du ^{77}Se dépend de l'état chimique du sélénium; par exemple, le titrage du groupement sélénol de la sélénocystamine provoque un blindage de la résonance du ^{77}Se de 164 ppm, l'oxydation du sélénol conduisant au disélénure de sélénocystamine provoque un déblindage de 330 ppm et l'oxydation conduisant au sulfure de sélénényle $\overset{+}{H_3}NCH_2CH_2SeSCH_2CH_2\overset{+}{N}H_3$ provoque en déblindage de 404 ppm. On a trouvé que les déplacements chimiques sont de l'ordre de -240 à -270 ppm (par rapport au $(CH_3)_2Se$) pour les sélénolates, de -80 ppm pour les sélénols, de 230 à 360 ppm pour les disélénures et de 250 à 340 ppm pour les sulfures de sélénényles. Le déplacement chimique du ^{77}Se est aussi influencé par le titrage des groupements acide carboxylique et ammonium voisins et leurs pK_A peuvent être calculés à partir des déplacements chimiques du ^{77}Se.

[Traduit par la revue]

Introduction

Reactions of selenium-containing functional groups with thiols and disulfides are important in the biological chemistry of seleno compounds and the mechanism of action of seleno enzymes (1–4). For example, reaction of the diselenide RSeSeR with the thiol R′SH to form the selenol RSeH and the selenenyl sulfide RSeSR′, which in turn reacts with R′SH to form RSeH and the disulfide R′SSR′ (eqs. [1] and [2]), provides

[1] $R'SH + RSeSeR \rightleftarrows R'SSeR + RSeH$

[2] $R'SH + R'SSeR \rightleftarrows R'SSR' + RSeH$

a pathway for reduction of diselenide (5). The reaction of thiols with selenenyl sulfides (eq. [2]) is of particular interest because such a reaction (eq. [3]) is the third step in a proposed

[3] $GSH\text{-}Px\text{-}SeSG + GSH \rightleftarrows GSH\text{-}Px\text{-}SeH + GSSG$

mechanism for the glutathione peroxidase (GSH-Px-SeH) catalyzed reduction of hydroperoxides by glutathione (GSH) (2, 3). The selenium of a selenocysteine residue is the active site of glutathione peroxidase (2, 3).

Although the importance of reactions [1] and [2] in the biological chemistry of selenium is well established, little is known about their kinetics and equilibria, or about the chemistry of the intermediate selenenyl sulfides. As the first part of a study of the reduction of diselenides by thiols and of the oxidation of selenols by disulfides, we have investigated the feasibility of using ^{77}Se nmr to study the selenium-containing reactants and products in such reactions. The high sensitivity of ^{77}Se chemical shifts to electronic environment (6) suggests that ^{77}Se nmr is potentially a powerful technique for characterizing the solution chemistry of such compounds. We are particularly interested in characterizing selenenyl sulfides formed by reaction of glutathione with selenocystine and related diselenides as models for the selenenyl sulfide intermediate in the proposed

[1]Present address: Department of Chemistry, University College, Australian Defence Force Academy, Campbell, Australia 2600.

[2]Address correspondence to this author at: Department of Chemistry, University of California, Riverside, CA 92521, U.S.A.

Can. J. Chem. Downloaded from www.nrcresearchpress.com by 213.222.148.141 on 09/07/12
For personal use only.

Can. J. Chem. Downloaded from www.nrcresearchpress.com by 213.222.148.141 on 09/07/12
For personal use only.

mechanism for glutathione peroxidase activity (2, 3). Luthra *et al.* have demonstrated that ^{77}Se nmr spectra can be obtained for selenenyl sulfides formed from phenyl- and nitrophenylselenenyl moieties and several thiol compounds (7, 8). However, phenylselenium may not be an appropriate model for the alkyl selenium in glutathione peroxidase and other biological selenium compounds. Also, the effect of the reactions in eqs. [1] and [2] on the measurement of ^{77}Se nmr spectra of selenols, diselenides, and selenenyl sulfides has not been established.

Experimental

D,L-Selenocystine and selenocystamine dihydrochloride were used as received from Sigma Chemical Company. They contained no impurities that could be detected by ^{1}H nmr. Bis(2-hydroxyethyl)diselenide was prepared by hydrolysis of 2-hydroxyethaneselenosulfate, which was prepared from 2-hydroxyethylbromide and potassium selenosulfate in water (9). The bis(2-hydroxyethane)diselenide was fractionally distilled under reduced pressure as an orange oil. The diselenodialkanoic acids $(HO_2C(CH_2)_nSe)_2$, $n = 1-3$, were prepared as described previously (10). Selenols were prepared from the diselenides by reduction over a Hg pool cathode (10), or by reduction with sodium borohydride.

L-Cysteine, D-penicillamine, and glutathione (Sigma Chemical Company) were used as received. Cysteamine hydrochloride (Aldrich Chemical Company) was sublimed *in vacuo* to purify it from the disulfide, cystamine, which was detected in the ^{1}H nmr spectrum of a 10 m*M* solution in D_2O.

pH measurements were made at 25°C with an Orion Model 701A pH meter equipped with a standard glass electrode (Philips GAT 130) and a double-junction saturated calomel reference electrode (Philips R44/2-SD/1); the outer junction solution was 0.3 *M* KNO_3 in D_2O. The pH meter was calibrated with pH 4.008 (0.05 *m* phthalate) and pH 6.865 (0.05 *m* phosphate) standard buffers prepared according to NBS specifications. Sample solutions were either in D_2O or 90%/10% H_2O/D_2O. pH measurements for D_2O solutions were corrected for deuterium isotope effects with the relation pD = pH meter reading + 0.40 (11). No correction was applied to the pH readings for the 90% H_2O solutions.

The ^{1}H nmr spectra were obtained at 360 MHz with a Bruker WM 360 nmr spectrometer operating in the pulse/Fourier transform mode. Measurements were made at a probe temperature of 25 ± 2°C. ^{1}H chemical shifts were measured relative to the methyl resonance of internal *tert*-butyl alcohol (TBA), but are reported relative to the methyl resonance of sodium-2,2-dimethyl-2-silapentane-5-sulfonate (DSS). The ^{77}Se nmr spectra were measured at 68.68 MHz with proton decoupling. The variable temperature unit was set to 25°C and spectra were measured with the decoupler on only during acquisition to minimize sample heating. ^{77}Se chemical shifts were measured relative to the resonance for an 8.4 *M* H_2SeO_3 solution; the chemical shift of this resonance is 1282 ppm relative to that for $(CH_3)_2Se$ (12). The 90° pulse width for ^{77}Se was 24 μs. Typically, spectra were measured with a repetition time of ~2 s, an acquisition time of ~0.2 s, and 60–90 min of signal averaging. Spin-lattice relaxation times were measured by the inversion–recovery pulse sequence, with relaxation delays of at least $5T_1$ between inversion–recovery pulse sequences and the decoupler gated on only during acquisition. Solutions used in the measurement of ^{77}Se nmr spectra had concentrations of 20 m*M* – 0.2 *M*. In most cases, solutions were made up in 90% v/v aqueous D_2O containing 0.3 *M* KNO_3. Solutions used for the measurement of relaxation times were degassed by bubbling with argon, and the nmr tubes were sealed under an argon atmosphere.

Results

The ^{77}Se and ^{1}H nmr spectra were measured for selenols, diselenides, and selenenyl sulfides with the objectives of establishing conditions under which spectra can be obtained for such compounds in aqueous solution and of identifying the chemical shift ranges for ^{77}Se in such compounds.

TABLE 1. ^{77}Se chemical shifts for selenols and diselenides

Compound	pH	Chemical shift, ppm[a]
$H_3\overset{+}{N}CH_2CH_2SeH$	2.68	−81.6
$H_3\overset{+}{N}CH_2CH_2Se^-$	8.40	−245.6
$^-O_2CCHCH_2Se^-$ $\quad\quad\vert$ $\quad NH_3^+$	8.86	−268.5
$^-O_2CCHCH_2Se^-$ $\quad\quad\vert$ $\quad NH_2$	11.68	−266.8
$^-O_2CCH_2Se^-$	8.79	−131.5
$(H_3\overset{+}{N}CH_2CH_2Se)_2$	3.72	251.3
$(H_2NCH_2CH_2Se)_2$	12.23	234.3
$(HO_2CCHCH_2Se)_2$ $\quad\quad\vert$ $\quad NH^+$ $\quad\quad 3$	1.57 	268.2 264.0
$(^-OCCHCH_2Se)_2$ $\quad\quad\vert$ $\quad NH^+$ $\quad\quad 3$	6.64 	266.4 259.6
$(^-OCCHCH_2Se)_2$ $\quad\quad\vert$ $\quad NH_2$	11.63 	254.9 252.3
$(HO_2CCH_2Se)_2$	2.09	353.9
$(^-O_2CCH_2Se)_2$	10.00	314.9
$(HO_2C(CH_2)_2Se)_2$	2.09	287.3
$(^-O_2C(CH_2)_2Se)_2$	6.02	286.1
$(HO_2C(CH_2)_3Se)_2$	2.21	266.1
$(^-O_2C(CH_2)_3Se)_2$	7.83	267.3
$(HOCH_2CH_2Se)_2$	7.80	238.4

[a]Relative to $(CH_3)_2Se$.

Selenols

The ^{77}Se and ^{1}H nmr spectra were measured for selenocysteine, selenocysteamine, and selenoethanoic acid in aqueous solution as a function of pH. Selected ^{77}Se chemical shifts are listed in Table 1. Sharp, exchange-averaged resonances were observed in the ^{1}H nmr spectra, whereas the lineshape of the exchange-averaged ^{77}Se resonances is strongly dependent on pH. ^{77}Se resonances could be observed at low and high pH where the selenol is present as RSeH and RSe^-, respectively; however, the ^{77}Se resonance generally was too broad to observe in the pH region 4–7 where the selenol group is titrated (13). For example, the width at half-height of the ^{77}Se resonance for selenocysteine was 21, 28, 52, and >200 Hz at pH values of 11.68, 10.00, 7.60, and 6.36 respectively, and was too broad to observe at lower pH. The ^{77}Se resonance for selenocysteamine also broadened over the pH range 4–7; however, not so much that it could not be observed. At pH 3, selenocysteamine is present as **I** and its chemical shift was determined to be −81.6 ppm. As the pH is increased and the selenol group titrated to give **II**, the ^{77}Se resonance shifts to lower frequency,

[4] $H_3\overset{+}{N}CH_2CH_2SeH \rightleftarrows H_3\overset{+}{N}CH_2CH_2Se^- + H^+$
I **II**

reaching a limiting chemical shift of −245.6 ppm at pH 8. From the dependence of the chemical shift of the exchange-averaged ^{77}Se resonance on pH, the p*K* of the selenol group

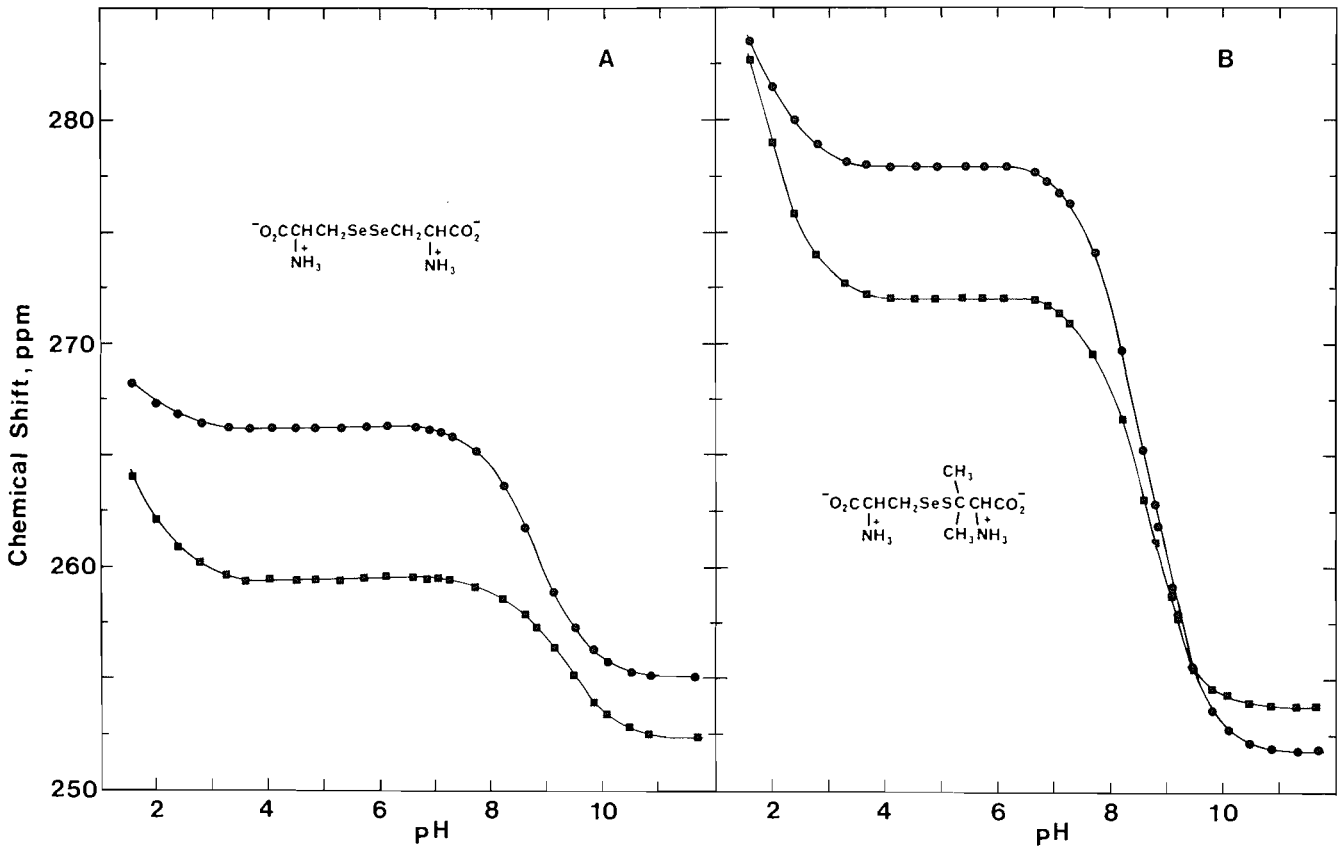

FIG. 1. pH dependence of the chemical shifts of the ^{77}Se resonances for D,L-selenocystine (A) and the selenenyl sulfide formed from D-penicillamine and D,L-selenocystine (B). The selenenyl sulfide was prepared by reacting 50 m*M* D-penicillamine with 50 m*M* D,L-selenocystine as described in the text. Ionic strength 0.3 *M* (KNO_3) and 25°C.

was estimated to be 5.31 ± 0.14. Because the change in the ^{77}Se chemical shift accompanying titration of the selenol group is so large (164 ppm for the ^{77}Se of selenocysteamine vs. 0.25 ppm for the methylene protons next to the selenol group of selenocysteamine), exchange broadening makes difficult or impossible the measurement of ^{77}Se spectra for selenol groups at pH values within ±2 pH units of the selenol pK_A at the spectrometer frequency used in this work.

Diselenides

The ^{77}Se and ^{1}H nmr spectra were measured as a function of pH for the diselenodialkanoic acids $(HO_2C(CH_2)_nSe)_2$, n = 1–3, selenocystamine $(H_3\overset{+}{N}CH_2CH_2Se)_2$, D,L-selenocystine $(^{-}O_2CCH(\overset{+}{N}H_3)CH_2Se)_2$, and bis(2-hydroxyethane)diselenide $(HOCH_2CH_2Se)_2$. The chemical shifts of the ^{77}Se and ^{1}H resonances for all but the last diselenide are pH dependent, changing over the pH region where carboxylic acid and (or) ammonium groups are titrated. ^{77}Se chemical shifts are reported in Table 1 for the diselenides at various stages of protonation.

Two resonances of equal intensity are observed for D,L-selenocystine, one for seleno-D,D-cystine and seleno-L,L-cystine, and one for seleno-D,L-cystine (14). The chemical shifts of the two resonances are plotted vs. pH in Fig. 1A. As the pH is increased from 6.5 to 11, the chemical shifts change due to titration of the ammonium group; however, the chemical shifts for the two diastereomers change by significantly different amounts (11.3 and 7.1 ppm), and by somewhat smaller amounts than the ^{77}Se resonance for selenocystamine (17.0 ppm). These results suggest that the chemical shift changes accompanying titration of the two ammonium groups of selenocystine are due to a combination of inductive and conformational effects. Acid dissociation constants for the ammonium groups of the two diastereomers, obtained by fitting the two sets of chemical shift data by nonlinear least-squares methods to a diprotic acid model (15), are different (pK_1 = 8.62 ± 0.04 and pK_2 = 9.81 ± 0.13 for the high frequency resonance and pK_1 = 8.32 ± 0.15 and pK_2 = 9.50 ± 0.06 for the low frequency resonance), which supports the conclusion that their conformations are different. pK values of 9.65 ± 0.03 and 10.77 ± 0.11 were obtained from the pH dependence of the ^{77}Se chemical shift data for selenocystamine.

Titration of the carboxylic acid groups of the diselenodialkanoic acids $(HO_2C(CH_2)_nSe)_2$ also causes the ^{77}Se chemical shift to change (Table 1). The magnitude of the change for diselenodiethanoic acid (n = 1) is somewhat larger than observed for titration of the ammonium groups of selenocystamine and selenocystine; however, the magnitude of the change decreases rapidly as n increases from 1 to 3, and in fact the direction of the change is reversed when n = 3. pK values of 3.47 ± 0.02 and 4.32 ± 0.03 were obtained by fitting the ^{77}Se chemical shift data for diselenodiethanoic acid to a diprotic acid model. For comparison, pK values of 3.49 ± 0.02 and 4.30 ± 0.01 were obtained from ^{1}H chemical shift data. The change in ^{77}Se chemical shifts accompanying titration of the carboxylic acid groups of diselenodipropanoic and diselenodibutanoic acids was too small for precise determination of their

Can. J. Chem. Downloaded from www.nrcresearchpress.com by 213.222.148.141 on 09/07/12
For personal use only.

TABLE 2. ^{77}Se spin-lattice relaxation times for selected diselenides and selenenyl sulfides

Compound	pH	T_1 (s)
$(H_2NCH_2CH_2Se)_2$	9.38	2.2 ± 0.2
$(^-O_2CCHCH_2Se)_2$	7.62	1.7 ± 0.3
NH_3^+		1.0 ± 0.2
$(^-O_2CCH_2Se)_2$	7.0	7.8 ± 0.6
$(^-O_2C(CH_2)_2Se)_2$	7.80	6.1 ± 0.6
$(^-O_2C(CH_2)_3Se)_2$	7.67	3.4 ± 0.5
$HO(CH_2)_2SeSC(CH_3)_2CHCO_2H$	1.12	1.8 ± 0.1
NH_3^+		
$^-O_2CCHCH_2SeSC(CH_3)_2CHCO_2^-$	3.68	1.3 ± 0.1
NH_3^+ NH_3^+		1.1 ± 0.2

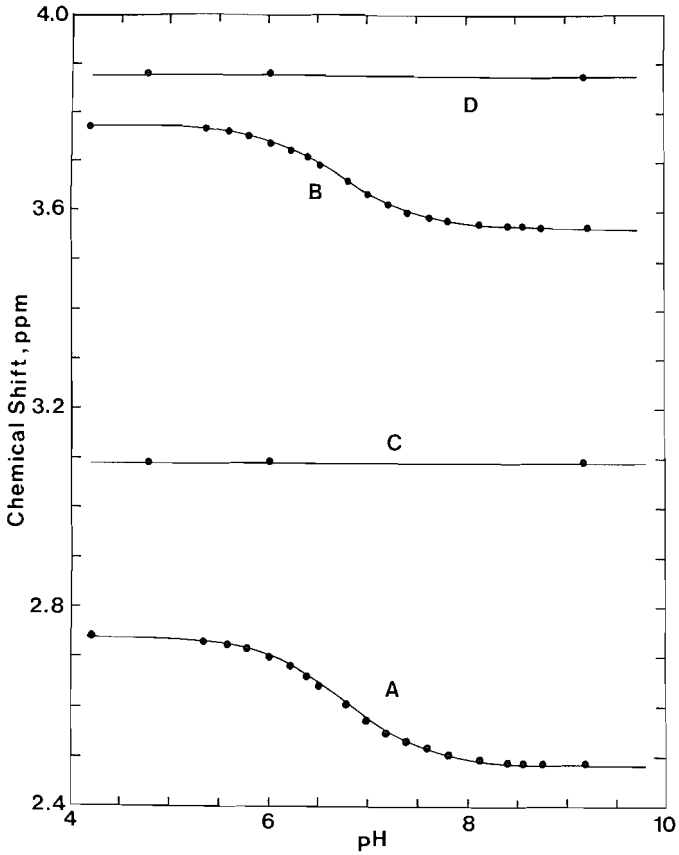

FIG. 2. pH dependence of the chemical shifts of the CH_2Se (A) and OCH_2 (B) protons of 0.020 *M* 2-hydroxyethaneselenol and of the CH_2Se (C) and OCH_2 (D) protons of bis(2-hydroxyethane)diselenide. Both solutions were in 90% H_2O/10% D_2O and contained 0.3 *M* KNO_3 for ionic strength control. The smooth curves through A and B are theoretical curves for a pK_A of 6.75.

p*K* values. The values obtained from ^1H chemical shift data are 3.88 ± 0.05 and 4.62 ± 0.04 for diselenodipropanoic acid and 4.29 ± 0.08 and 5.67 ± 0.03 for diselenodibutanoic acid.

^{77}Se spin-lattice relaxation times for several of the diselenides are reported in Table 2. Previous studies have shown that the spin rotation mechanism dominates ^{77}Se spin-lattice

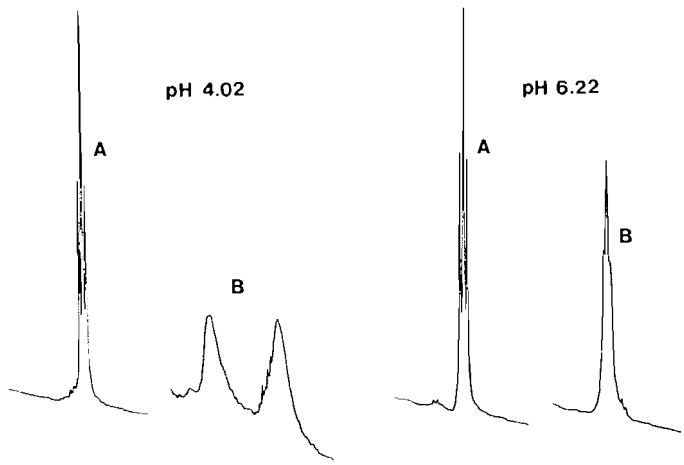

FIG. 3. The ^1H nmr spectra for the CH_2Se protons of a 20 m*M* solution of 2-hydroxyethaneselenol (A) and of the CH_2Se protons of a solution containing 20 m*M* 2-hydroxyethaneselenol and 12 mM bis(2-hydroxyethane)diselenide (B). At pH 4.02, selenol/diselenide exchange is slow, and separate resonances are observed for selenol and diselenide; at pH 6.22 a broad, exchange-averaged triplet is observed.

relaxation in small diselenides at low magnetic fields, with the chemical shift anisotropy mechanism becoming more important as the magnetic field strength and the size of the diselenide increase (13, 14, 16, 17). The decrease in ^{77}Se spin-lattice relaxation times for the diselenodialkanoic acids as their size increases is consistent with increased relaxation by the chemical shift anisotropy mechanism.

Selenol/diselenide exchange

Nuclear magnetic resonance measurements were also made on solutions containing both selenol and diselenide. By analogy with results from ^1H and ^{13}C nmr studies of thiol/disulfide exchange reactions (18–20), we expected to observe separate resonances for selenol and diselenide. However, ^1H resonances were either broadened or exchange-averaged, depending on pH and the relative concentrations of selenol and diselenide, and ^{77}Se resonances could not be detected for selenol/diselenide mixtures. To illustrate, ^1H nmr results for the 2-hydroxyethaneselenol (HES)/bis(2-hydroxyethane)diselenide (HEDS) system are presented in Figs. 2–4. The ^1H nmr spectrum of a solution containing HES alone consists of two triplets for the two methylene groups, the chemical shifts of which are pH dependent due to titration of the selenol group. The chemical shifts are plotted vs. pH in Fig. 2 (A is for CH_2Se and B for OCH_2). Sharp triplets were observed over the entire pH range, e.g., the resonances for the CH_2Se protons are shown in Fig. 3 at pH 4.02 (A) and 6.22 (A). The ^1H nmr spectrum of HEDS alone also consists of two sharp triplets whose chemical shifts are independent of pH as shown by C (for CH_2Se) and D (for OCH_2) in Fig. 2. However, in mixtures of HES and HEDS, resonances for the CH_2Se protons and for the OCH_2 protons of the two compounds are either exchange-broadened or exchange-averaged. For example, the spectra in Fig. 3 show that, at pH 4.02, separate, broadened resonances are observed at 2.740 and 3.090 ppm for the CH_2Se protons of HES and HEDS, respectively, in a mixture of the two. However, at pH 6.22, a single, broadened triplet (B) is observed at a chemical shift (2.857 ppm) intermediate between those of the CH_2Se protons of HES and HEDS. Exchange-averaged resonances were also observed at higher pH, and they were sharper the higher the

Can. J. Chem. Downloaded from www.nrcresearchpress.com by 213.222.148.141 on 09/07/12
For personal use only.

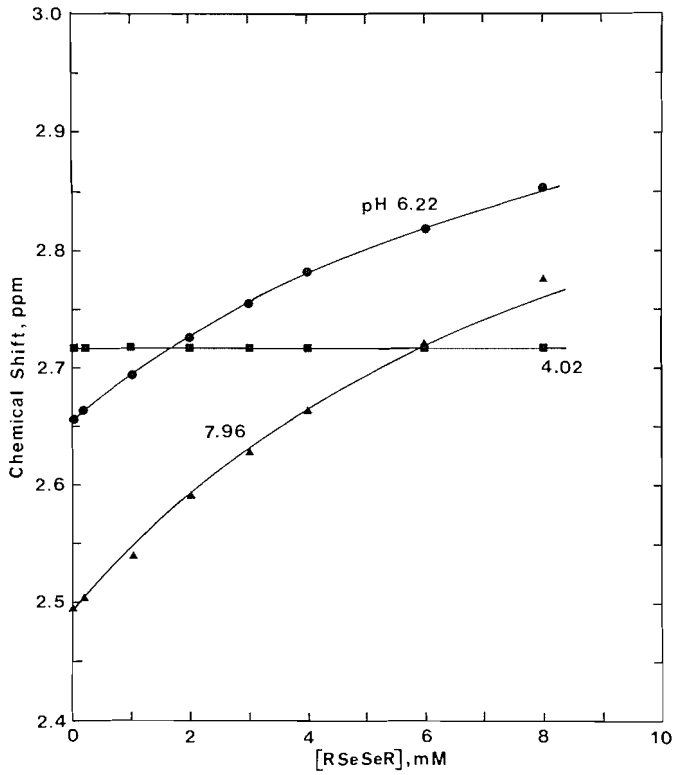

FIG. 4. Dependence of the chemical shift of the resonance for the CH_2Se protons of 2-hydroxyethaneselenol (20 m*M*) at pH 4.02 and the exchange-averaged resonance for the CH_2Se protons of 2-hydroxyethaneselenol and of bis(2-hydroxyethane)diselenide at pH 6.22 and 7.96 as a function of the diselenide concentration. The smooth curves through the experimental points at pH 6.22 and 7.96 are theoretical curves calculated assuming fast exchange.

pH. The chemical shifts of the exchange-averaged resonances depend on the concentrations of HES and HEDS and on the pH as shown in Fig. 4 for the results at pH 6.22 and 7.96. The chemical shifts are pH independent at pH 4.02 because exchange is slow, and separate, broadened resonances are observed for HES and HEDS.

Selenenyl sulfides

Solutions containing selenenyl sulfides were prepared by reaction of thiol with diselenide (eqs. [1] and [2]) or by chemical reduction of diselenide with $NaBH_4$ to give the selenol, and then addition of disulfide. Below pH 7, thiol groups are protonated and no reaction of thiol with diselenide was observed. Above pH 8, where the thiol group is partially or completely deprotonated, reaction proceeds rapidly. Selenols reacted more rapidly with disulfides, and at lower pH values as a result of the lower pK_A of the selenol group.

Resonances in ^1H nmr spectra for such reaction mixtures were broad while no resonances could be detected in the ^{77}Se spectra. As a result of exchange by eqs. [1] and [2], the solutions contained selenol, which, as discussed above, causes broadening of the ^1H resonances and loss of the ^{77}Se resonances for diselenide due to selenol/diselenide exchange. The observation of similar effects in nmr spectra for R′SSeR suggests that the reaction of selenol with R′SSeR also occurs on a similar time scale. ^{77}Se resonances could be observed for R′SSeR only after eliminating selenols from the solution. In the procedure generally followed, thiol and diselenide, or selenol and disulfide, were allowed to react for at least 4 h, and then the solution was bubbled with oxygen for 6–8 h to oxidize the selenol.

The ^{77}Se nmr spectra of several reaction mixtures prepared as described above are shown in Fig. 5. Resonances are observed for the selenenyl sulfide and the diselenide; diselenide resonances were assigned using chemical shift data from Table 1. ^{77}Se chemical shift data for selenenyl sulfides are presented in Table 3, and spin-lattice relaxation times for two selenenyl sulfides are reported in Table 2. Two resonances are observed in Fig. 5A for PSSeC due to formation of the diastereomers, D-PSSeC-D and D-PSSeC-L. Their chemical shifts are pH dependent (Fig. 1B) due to titration of the acidic functional groups.

Discussion

Exchange processes strongly affect nmr spectra of aqueous solutions of selenols, selenenyl sulfides, and diselenides. Sharp, exchange-averaged ^1H nmr spectra are observed for the carbon-bonded protons of selenols over the entire pH range; however, proton exchange between the selenol and selenolate forms causes the ^{77}Se resonance to be so broad over the pH range $pK_A \pm 2$ that it cannot be observed in most cases. No rate constants have been reported for selenol proton exchange; however, the results of this study indicate that it is fast relative to the chemical shift change in ^1H nmr spectra accompanying titration of the selenol proton but not compared to that in ^{77}Se spectra (~90 and ~11 000 Hz, respectively, at the spectrometer frequencies used in this work).

The exchange-averaged ^1H resonances observed for solutions containing selenol and diselenide are in sharp contrast with the separate resonances observed for thiol and for disulfide in both ^1H and ^{13}C spectra of solutions containing thiol and disulfide (18–20), indicating that selenol/diselenide exchange is much faster than thiol/disulfide exchange.

$$[5] \quad \overset{*}{R}SeH + RSeSeR \rightleftarrows \overset{*}{R}SeSeR + RSeH$$

The ^1H nmr results indicate that the rate of selenol/diselenide exchange increases as the pH is increased through the pH region where the selenol group is titrated, which suggests that the deprotonated selenolate, RSe^-, is the reactive form of the selenol. The ^{77}Se nmr spectra could be obtained for selenols only if the solution did not contain diselenides or selenenyl sulfides. Likewise, ^{77}Se spectra could be obtained for diselenides and selenenyl sulfides only in the absence of selenols. Exchange-averaged ^1H resonances are observable, whereas ^{77}Se resonances are not, because the chemical shift change on going from selenol to diselenide or selenenyl sulfide is much larger in the ^{77}Se spectra, and thus much faster exchange is necessary to observe exchange-averaged ^{77}Se resonances. For example, the chemical shift of protons on carbons bonded to selenium changes by ~0.4–0.6 ppm, depending on pH, when the selenium is converted from the selenol to the diselenide form. However, the results in Tables 1 and 3 indicate that the ^{77}Se resonance is deshielded by ~500 ppm and ~600 ppm on going from RSe^- to $(RSe)_2$ and from RSe^- to RSeSR′, respectively. It is of interest to note, however, that ^{77}Se resonances can be obtained for selenenyl sulfides formed by reaction of 6,6′-diselenobis(3-nitrobenzoic acid) with cysteine, acetylcysteine, and glutathione in the presence of the selenol (8). The exchange kinetics in this system are presumably slow due to steric effects.

The ^{77}Se chemical shift depends on the chemical state of the selenium. The most complete set of data in Tables 1 and 3 is for

Can. J. Chem. Downloaded from www.nrcresearchpress.com by 213.222.148.141 on 09/07/12
For personal use only.

Can. J. Chem. Downloaded from www.nrcresearchpress.com by 213.222.148.141 on 09/07/12
For personal use only.

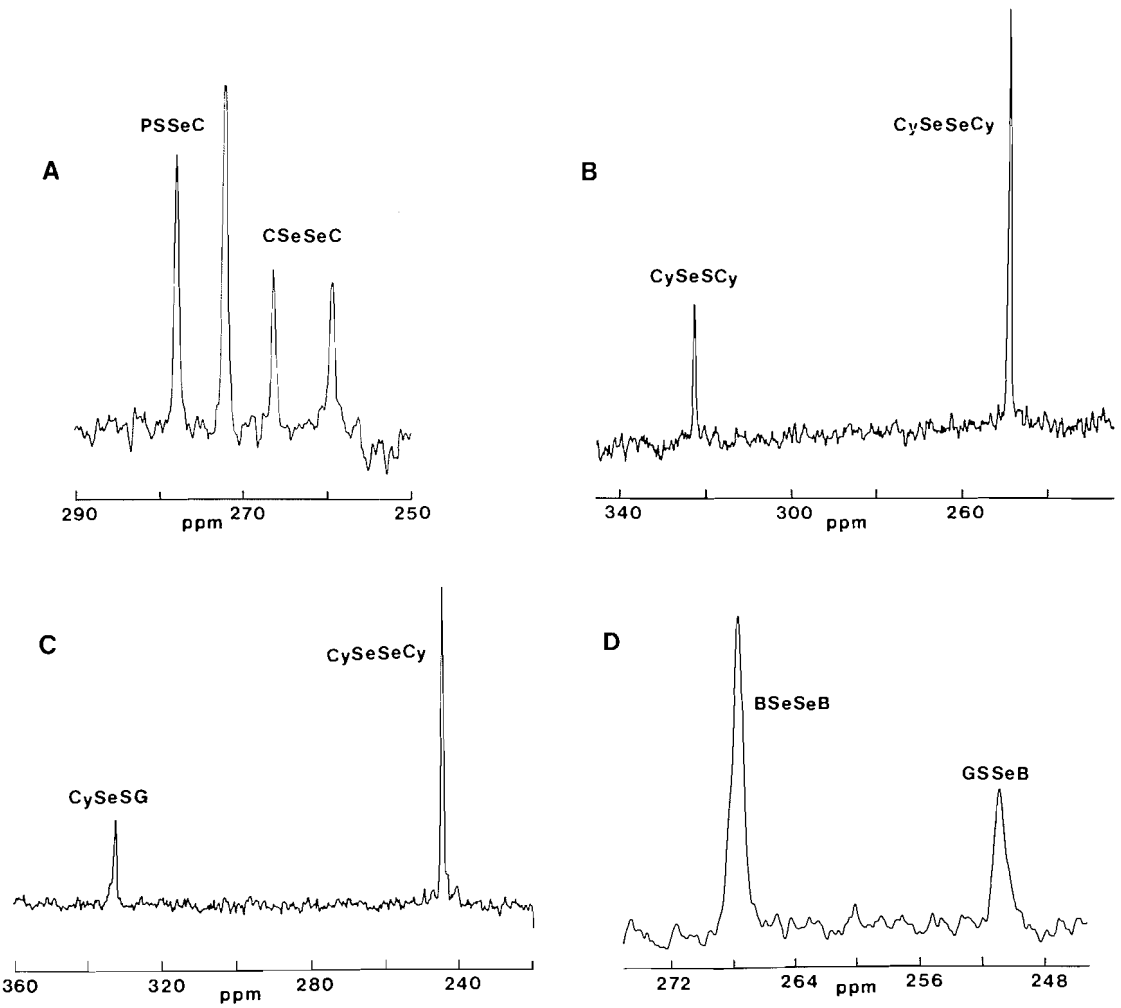

FIG. 5. The ^{77}Se nmr spectra of solutions containing diselenides and selenenyl sulfides. Selenenyl sulfides were prepared *in situ* from the appropriate disulfides as described in the text. Selenium concentration was 0.1–0.2 *M* in each solution. The compounds are identified in footnote *a* of Table 3.

TABLE 3. ^{77}Se chemical shifts of selenenyl sulfides

Compound[a]	pH	Chemical shift, ppm[b]
CySeSCy	8.75	322.7
CySeSG	9.38	332.8
CySeSP-D	7.80	282.0
D,L-CSeSC-L	9.39	334.4
		327.9
D,L-CSeSG	3.65	333.1
		326.7
D,L-CSeSP-D	1.57	283.4
		282.8
D,L-CSeSP-D	6.64	277.9
		272.0
D,L-CSeSP-D	11.71	252.0
		253.4
D,L-CSeSCy	9.73	310.5
ESeSP-D	1.12	275.4
BSeSG	Acidic	250.7

[a]Cy = $H_3\overset{+}{N}CH_2CH_2$—; C = $^-O_2CCH(\overset{+}{NH_3})CH_2$—; P = $^-O_2CCH(NH_3^+)C(CH_3)_2$—; G = $^-O_2CCH(NH_3)$-$CH_2CH_2CONHCH(CH_2$—$)CONHCH_2CO_2^-$; E = $HOCH_2CH_2$—; B = $^-O_2CCH_2CH_2CH_2$—.

[b]Relative to $(CH_3)_2Se$.

selenocysteamine ($H_3N^+CH_2CH_2SeH$, CySeH). Titration of the selenol proton causes the shielding to increase by 164 ppm; increased shielding is expected due to the increased electron density at the selenium. Oxidation of the selenol group to form CySeSeCy causes a deshielding of 332.9 ppm, while oxidation by reaction with cystamine to form CySeSCy causes an even larger deshielding of 404.3 ppm, consistent with the relative electronegativities of sulfur and selenium (7). The magnitude of the additional deshielding upon replacement of selenium in diselenides by sulfur in selenenyl sulfides depends on the nature of the sulfide and the protonation state of carboxylic acid and ammonium groups. For example, the ^{77}Se resonance of CySeSCy is deshielded 71.4 ppm relative to that of CySeSeCy and the two ^{77}Se resonances of D,L-CSeSC-L are deshielded by 70–80 ppm relative to those of D,L-CSeSeC. However, the ^{77}Se resonance of CySeSP-D is deshielded by only 31 ppm relative to that of CySeSeCy while the resonances of D,L-CSeSP-D are deshielded by 15–18 ppm, 11–13, and ~0 ppm relative to those of D,L-CSeSeC at pH values of 1.57, 6.64, and 11.71. It also is of interest to note that the selenium in phenylselenenyl sulfides experiences even greater deshielding than the selenium in alkylselenenyl sulfides. For example, ^{77}Se chemical shifts for phenylselenenyl sulfides are in the range of 420–740 ppm (7, 8) while those reported here for alkylselenenyl sulfides are in

the range 250–340 ppm. The additional deshielding of ^{77}Se in phenylselenenyl sulfides is consistent with the expected ring current effects from the phenyl ring.

The change in ^{77}Se chemical shift accompanying titration of a neighboring carboxylic acid or ammonium group also depends on the chemical state of the selenium, with the changes for selenium in selenide, diselenide, and selenenyl sulfide forms being somewhat larger than for selenium in the selenolate form. For example, the ^{77}Se resonance of the selenolate form of selenocysteine (CSe^-) is deshielded by 1.7 ppm when the ammonium group is titrated, whereas the ^{77}Se resonances of the diastereomers of selenocystine (CSeSeC) are shielded by 11.5 and 7.3 ppm, and those of the diastereomers of the selenenyl sulfide PSSeC are shielded by 25.9 and 18.6 ppm. For comparison, titration of the ammonium group of selenomethionine causes the ^{77}Se resonance to be shielded by 5.4 ppm.

$$^{-}O_2CCHCH_2CH_2SeCH_3 \rightleftarrows {}^{-}O_2CCHCH_2CH_2SeCH_3 + H^{+}$$
$$\quad\quad\quad

Synthesis of cyclopentane analogs of 1-(2′,3′-dideoxy-β-*glycero*-pentofuranosyl)pyrimidine nucleosides

LUCJAN J. J. HRONOWSKI AND WALTER A. SZAREK
Department of Chemistry, Queen's University, Kingston, Ont., Canada K7L 3N6

Received November 10, 1986[1]

LUCJAN J. J. HRONOWSKI and WALTER A. SZAREK. Can. J. Chem. **66**, 61 (1988).

Synthesis of new carbocyclic analogs of 1-(2′,3′-dideoxy-*glycero*-pentofuranosyl)pyrimidine nucleosides having the uracil (**34**), 2-thiouracil (**33**), 2-thiothymine (**31**), cytosine (**44**), and 5-methylcytosine (**43**) bases is described. The nucleoside analogs having the uracil, 2-thiouracil, and 2-thiothymine bases were prepared by coupling *cis*-3-aminocyclopentanemethanol (**8**) with 3-ethoxypropenoyl isocyanate (**26**), 3-ethoxypropenoyl isothiocyanate (**25**), and 3-methoxy-2-methylpropenoyl isothiocyanate (**23**), respectively, to give the corresponding acyl urea (**30**) and acyl thioureas (**29** and **27**). The acyl urea was cyclized in 2 *N* H_2SO_4 and the acyl thioureas in 15 *N* aqueous ammonia to give the corresponding nucleoside analogs. The nucleoside analogs containing the cytosine (**44**) and 5-methylcytosine (**43**) bases were prepared from the uracil and thymine nucleoside analogs, respectively, by way of the 4-chloropyrimidinone intermediates (**42** and **41**). The synthesis of *cis*-3-aminocyclopentanemethanol (**8**) from norbornene by way of *cis*-1,3-cyclopentanedicarboxylic acid anhydride (**3**) is also described. In addition, the ease of nucleophilic opening of compound **3** is compared to the opening of camphoric anhydride (**9**), which contains a *cis*-vicinal substituent at position 2. The relative ease of opening of compound **3** is discussed with respect to the effect, observed in an earlier study, that a *cis*-vicinal acetoxy group has on the course of the nucleophilic opening of such anhydrides. The ^1H magnetic resonance spectra at 200 MHz of all of the synthetic intermediates and of the nucleoside analogs have been determined and discussed. The nucleoside analogs were screened for cell-growth inhibition using K-562 cells. Nucleoside analogs having the 2-thiouracil (**33**), 2-thiothymine (**31**), cytosine (**44**), and 5-methylcytosine (**43**) bases showed some growth inhibition with activity 150 to 300 times lower than that shown by 5-fluorouracil in this test system.

LUCJAN J. J. HRONOWSKI et WALTER A. SZAREK. Can. J. Chem. **66**, 61 (1988).

On décrit la synthèse de nouveaux analogues carbocycliques des nucléosides de la (didésoxy-2′,3′ *glycéro*-pentofuranno-syl)pyrimidine contenant de l'uracil (**34**), du thio-2 uracil (**33**), de la thio-2 thymine (**31**), de la cytosine (**44**) et de la méthyl-5 cytosine (**43**). On a préparé les analogues des nucléosides contenant les bases uracil, thio-2 uracil et thio-2 thymine en procédant au couplage de l'amino-3-*cis* cyclopentaneméthanol avec respectivement l'isocyanate d'éthoxy-3 propènoyle (**26**), l'isothiocyanate d'éthoxy-3 propènoyle (**25**) et l'isothiocyanate de méthoxy-3 méthyl-2 propènoyle (**23**); on obtient ainsi l'acyl urée **30** et les acyl thiourées **29** et **27** correspondantes. La cyclisation de l'acyl urée en présence de H_2SO_4 2 *N* et des acyl thiourées en présence d'ammoniac aqueux 15 *N* conduit aux analogues de nucléosides correspondants. On a préparé les analogues de nucléosides contenant de la cytosine (**44**) et de la méthyl-5 cytosine (**43**) à partir de leurs analogues de nucléosides correspondants contenant de l'uracil et de la thymine et en procédant par leurs intermédiaires chloropyrimidinones (**42** et **41**). On décrit aussi la synthèse de l'amino-3-*cis* cyclopentaneméthanol (**8**) à partir du norbornène, en passant par l'anhydride de l'acide cyclopentanedicarboxylique-1,3-*cis* (**3**). De plus, on compare la facilité d'ouverture du produit **3**, sous l'influence d'agents nucléophiles, avec celle observée pour l'anhydride de l'acide camphorique (**9**) qui contient un substituant vicinal-*cis* en position 2. On discute de la facilité relative d'ouverture du composé **3** en fonction de l'effet, observée dans une étude antérieure, qu'un groupement vicinal-*cis* peut avoir sur le cours de l'ouverture de tels anhydrides. On a déterminé les spectres en résonance magnétique du ^1H à 200 MHz de tous les intermédiaires de synthèse et de tous les analogues de nucléosides et on les discute. Utilisant des cellules K-562, on a évalué l'utilité des analogues de nucléosides comme inhibiteurs de la croissance des cellules. Comparées à l'activité du fluoro-5 uracil dans ce système, les analogues de nucléosides contenant les bases thio-2 uracil (**33**), thio-2 thymine (**31**), cytosine (**44**) et méthyl-5 cytosine (**43**) présentent des effets qui sont de 150 à 300 fois plus faibles.
[Traduit par la revue]

Introduction

The synthesis of 2′,3′-dideoxynucleosides was first described in 1955 by Michelson and Todd (1), who synthesized a variety of 3′-deoxythymidines. Nine years later Pfitzner and Moffatt (2) described the synthesis of various 2′,3′-dideoxyuridines. The importance of the 2′,3′-dideoxynucleosides as possible chain terminators of DNA synthesis was pointed out by Robins *et al.* (3), who synthesized 2′,3′-dideoxyadenosine. 2′,3′-Dideoxyadenosine was subsequently shown by Doering *et al.* (4) to be lethal to *Escherichia coli* cultures with activity at concentrations as low as 10^{-7} *M*; however, the 2′,3′-dideoxy derivatives of uridine and cytidine were found to be inactive in their test systems. 2′,3′-Dideoxyadenosine was shown to irreversibly inhibit DNA synthesis, possibly by adding to the end of a growing polydeoxynucleotide and thus blocking further chain elongation. Such a mechanism of action was shown for 3′-deoxythymidine in a cell-free system (5). 2′,3′-Dideoxy-5-fluorouridine was shown by Khwaja and Heidelberger (6) to be lethal to *E. coli* at a concentration of 2×10^{-4} *M* and it also inhibited the growth of HeLa cells at 10^{-4} *M*. An important recent use of the 2′,3′-dideoxynucleotides is in DNA sequencing, in which they are used as specific, chain-terminating inhibitors of DNA polymerase (7).

In contrast to the relatively large number of 2′,3′-dideoxynucleosides that have been synthesized (1–3, 6–8, and references therein), there have been described relatively few syntheses of the carbocyclic analogs of the 2′,3′-dideoxynucleosides and most of these were of analogs of purine nucleosides. Schaeffer *et al.* (9), in their studies on the structural requirements in inhibitors of the enzyme adenosine deaminase, have synthesized several *cis*-3-(6-substituted-9-purinyl)cyclopentylmethanols in which the substituent was the Cl, SH, OH, NH_2, $NHCH_3$, or $N(CH_3)_2$ group. Montgomery and Hewson (10) synthesized the carbocyclic analog of 2′,3′-dideoxytubercidin.

[1]Revision received August 20, 1987.

Can. J. Chem. Downloaded from www.nrcresearchpress.com by 213.222.148.141 on 09/07/12
For personal use only.

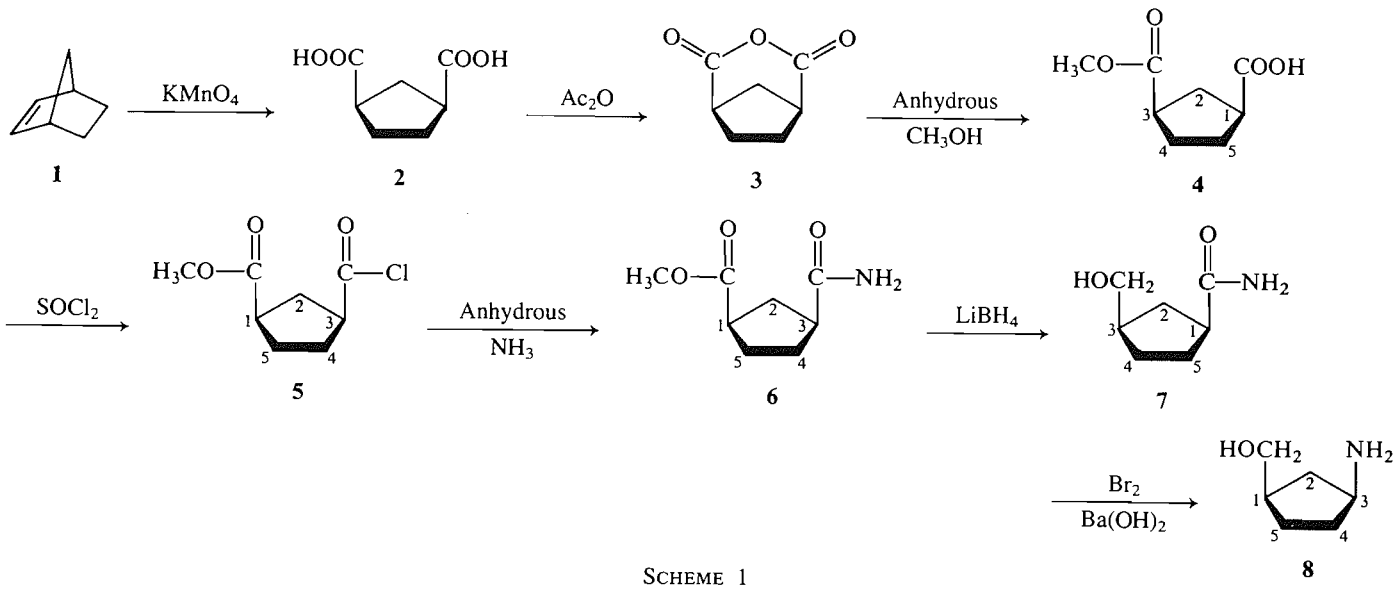

SCHEME 1

This compound, although somewhat cytotoxic, showed no activity against leukemia L1210. Shealy *et al.* (11) have synthesized the 2′,3′-dideoxy carbocyclic analogs of 8-aza-hypoxanthine and 8-azaadenine nucleosides; only the carbocyclic analog of 2′,3′-dideoxy-8-azaadenosine showed cytotoxicity to H. Ep./2 cells in culture (ED_{50} = 42 μg/mL), and both analogs showed no activity against leukemia L1210 in mice. The only carbocyclic analog synthesized of the 2′,3′-dideoxypyrimidine nucleosides is the analog of 3′-deoxythymidine (12). This compound was shown to be noncytotoxic to human epidermoid carcinoma cells and also showed no activity against L1210 leukemia in mice. The present paper describes the synthesis of the carbocyclic analogs of 2′,3′-dideoxypyrimidine nucleosides having the uracil, 2-thiouracil, 2-thiothymine, cytosine, and 5-methylcytosine bases. In addition, preliminary results are presented on their effects on the growth of K-562 cells in culture.

Results and discussion

cis-3-Aminocyclopentanemethanol (**8**), used in the synthesis of the carbocyclic analogs of 2′,3′-dideoxynucleosides, was prepared previously by Schaeffer *et al.* (9) from 3-oxocyclopentanecarboxylic acid (13). Shealy *et al.* (12) reported the synthesis of **8** from *cis*-1,3-cyclopentanedicarboxylic acid (**2**) without giving experimental details. In the present work **8** has been prepared from norbornene as shown in Scheme 1.

*Synthesis of (±)-*cis*-3-aminocyclopentanemethanol (8)*

The *cis* configuration of the two substituents in the cyclopentane derivatives shown in Scheme 1 is determined by the starting material, bicyclo[2.2.1]hept-2-ene (**1**), which, in the first step, is oxidized to *cis*-1,3-cyclopentanedicarboxylic acid (**2**) using potassium permanganate by the procedure described by Birch *et al.* (14). The *cis*-diacid (**2**) was then converted into (±)-*cis*-3-aminocyclopentanemethanol (**8**) by the same series of reactions that was used by O'Dell and Shealy (15) for the preparation of the cyclopentane analogs of 2′- and 3′-deoxy-*erythro*-pentofuranosylamine. The diacid was converted first into the anhydride (**3**) by heating at reflux temperature in acetic anhydride. The anhydride (**3**) was then opened with anhydrous methanol to give an intermediate (**4**)[2] having two different functional groups at positions 1 and 3 of the cyclopentane ring. The carboxylic acid and the ester functional groups were then converted selectively into the amino and the hydroxymethyl substituents, respectively, as shown in Scheme 1. In the final reaction shown in Scheme 1 the carbamoyl group was converted into the amino substituent by the Hofmann hypobromite reaction, in which the configuration of the original carbamoyl group is retained (16–18).

The ^{1}Hmr spectra of the compounds shown in Scheme 1 were determined on a 200-MHz spectrometer. However, even with this instrument, the signals of the methylene protons at positions 4 and 5 show complex second-order patterns, and thus only the ranges of their signals are given. The chemical shifts of the protons at positions 1, 2, and 3 could be more easily determined, although the signals of these protons often overlapped other signals to make the measurement of the exact chemical shifts difficult. The chemical-shift assignments were made with the aid of spin–spin decoupling experiments.

Nucleophilic opening of cis*-1,3-cyclopentanedicarboxylic acid anhydrides*

It was observed previously that nucleophilic opening of *cis*-1,3-cyclopentanedicarboxylic acid anhydrides, substituted at position 4 with an acetoxy group, gives a mixture of isomers when this group is in the *trans* configuration (16) and a single isomer when it is in the *cis* configuration (19). In the latter case only one isomer was isolated when ammonia or methanol was used as the nucleophile. With each of these nucleophiles the attack occurred at the carbonyl carbon farthest away from the acetoxy substituent. It was of interest, therefore, to study the effect of substituents at position 2. Scheme 2 shows a series of reactions using *dl*-camphoric anhydride (**9**) as the model compound. In contrast to compound **3**, which is converted

[2]The solvolysis of *cis*-1,3-cyclopentanedicarboxylic acid anhydride (**3**) generates a racemic mixture, since the attack by methanol is equally probable at both carbonyl carbons. Consequently, all of the subsequent cyclopentane derivatives are racemates, although only one enantiomer is shown in Schemes 1, 3, and 4.

Can. J. Chem. Downloaded from www.nrcresearchpress.com by 213.222.148.141 on 09/07/12
For personal use only.

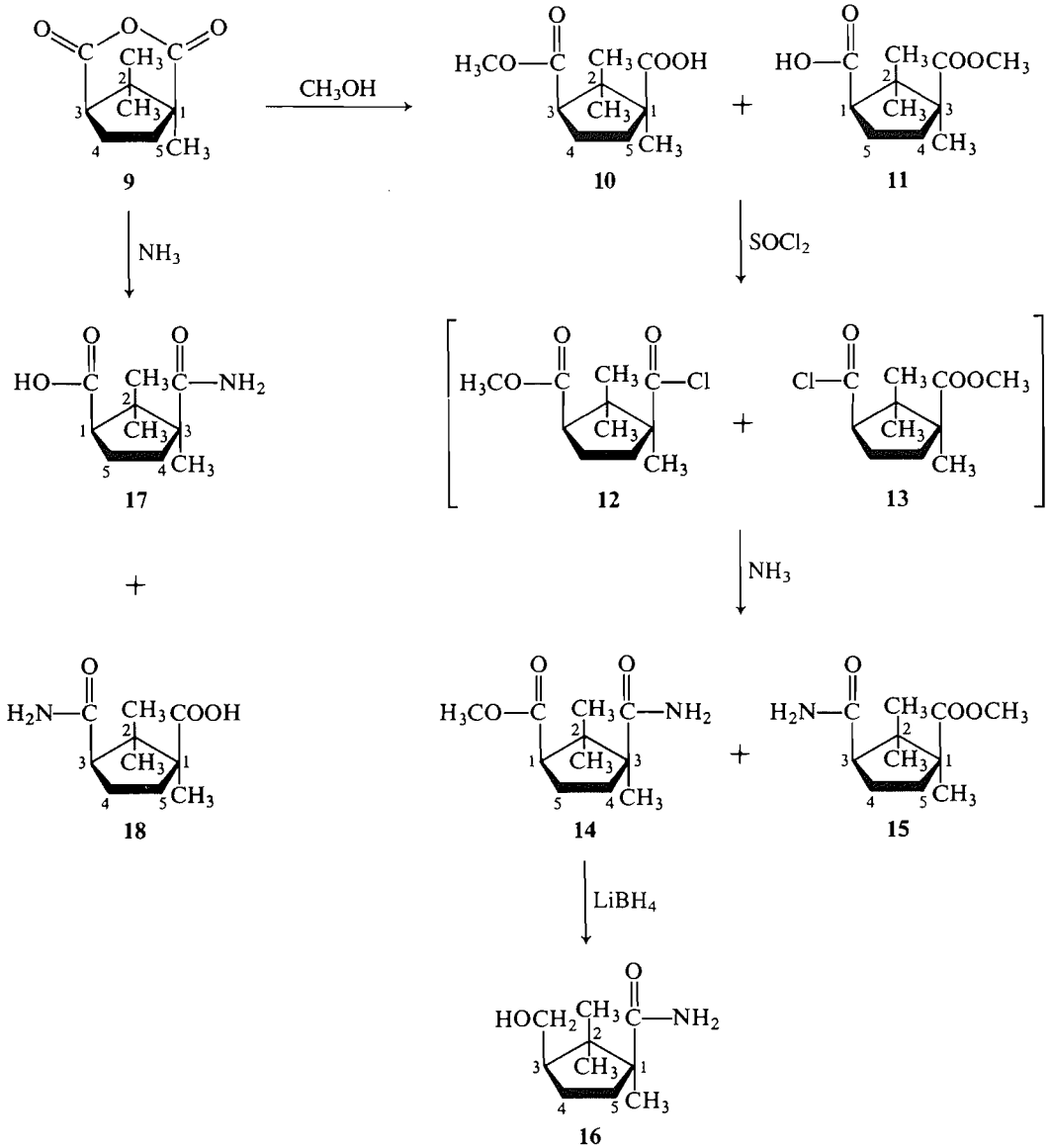

SCHEME 2

into compound **4** by stirring in anhydrous methanol at room temperature for 19 h, camphoric anhydride (**9**) is very resistant to methanolysis; no reaction was observed after 10 days of stirring in anhydrous methanol at room temperature. Moreover, even after being heated at reflux temperature for 2 days in methanol, over 81% of **9** was recovered and only a 12% yield of the solvolysis products, as a mixture of compounds **10** and **11**, was obtained. However, the opening of camphoric anhydride (**9**) was relatively rapid, when anhydrous ammonia in benzene was used, to give a mixture of compounds **17** and **18** in over 95% yield. The above observations and those with the acetoxy substituents (16, 19) indicate that steric interactions between *cis*-vicinal substituents in these compounds greatly reduce the rate of nucleophilic attack at the adjacent carbonyl carbon, thus accounting for the production of a single isomer in the nucleophilic opening of the anhydride containing the *cis*-acetoxy substituent at position 4 (19).

Assignment of the ^{1}Hmr signals in the spectra of the compounds shown in Scheme 2 was made after preparation of compound **16** from **14**. The signals of the protons in compound **16** were unambiguously assigned with the aid of spin–spin decoupling experiments. In general, the signals in the spectra of compounds **10**–**18** are much better resolved than those in the spectra of compounds **4**–**7**.

Synthesis of pyrimidine nucleoside analogs shown in Scheme 3

The base moiety of the 2-thiothymine nucleoside analog (**31**) was synthesized from 3-methoxy-2-methylpropenoyl isothiocyanate (**23**), which was prepared using the method of Shaw and Warrener (20). Compound **23** was coupled with (±)-*cis*-3-aminocyclopentanemethanol (**8**) to give compound **27**; this product was then cyclized in 15 *N* aqueous ammonia to give nucleoside analog **31**. The corresponding thymine nucleoside analog (**32**) was prepared as described previously (12).

The 2-thiouracil nucleoside analog (**33**) was prepared by coupling compound **8** with 3-ethoxypropenoyl isothiocyanate (**25**) (20) to give **29**, which was then cyclized in 15 *N* aqueous ammonia to give the nucleoside analog (**33**). The uracil

Can. J. Chem. Downloaded from www.nrcresearchpress.com by 213.222.148.141 on 09/07/12
For personal use only.

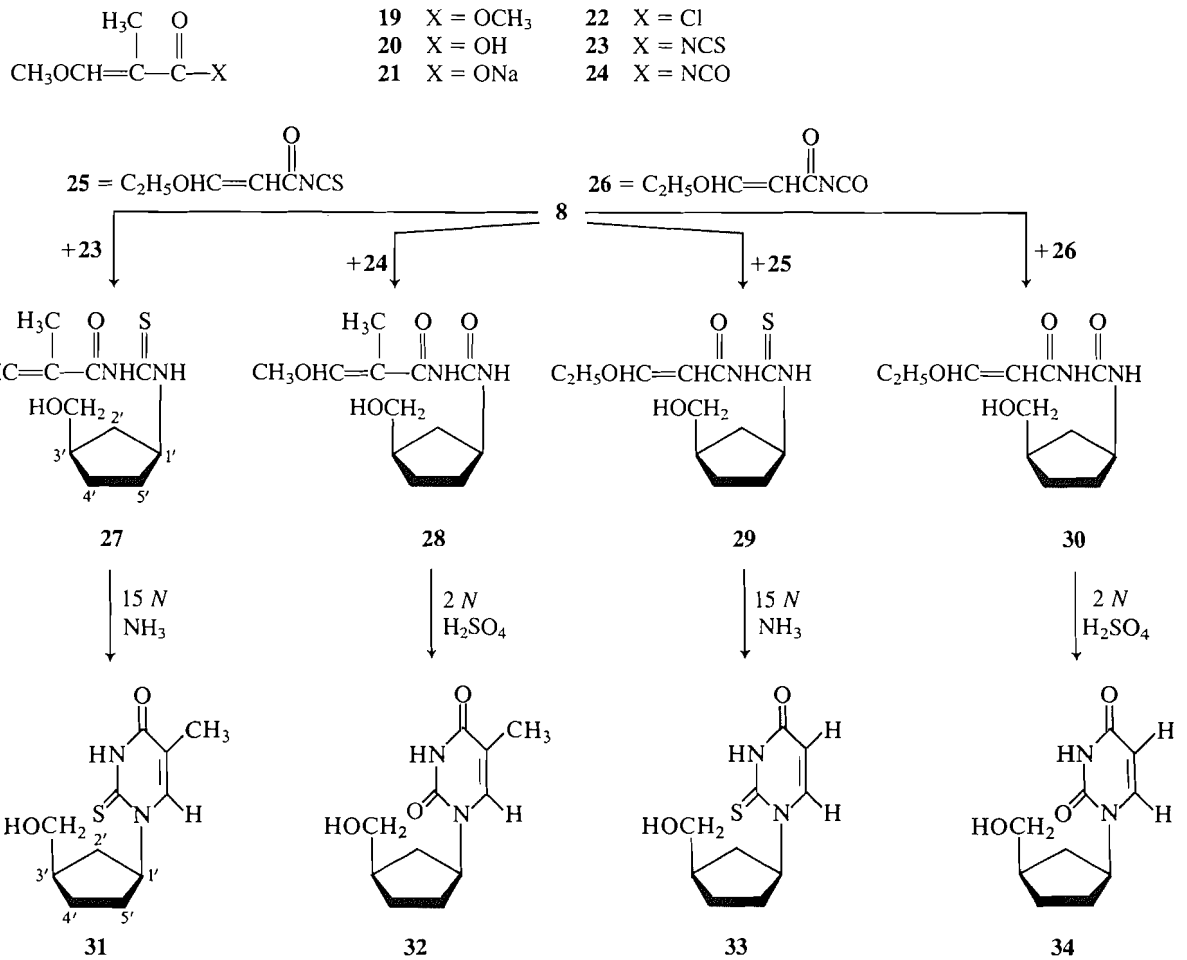

SCHEME 3

nucleoside analog (**34**) was prepared by coupling compound **8** with 3-ethoxypropenoyl isocyanate (**26**) (21) to give **30**, which was then cyclized in 2 *N* H_2SO_4 to give the nucleoside analog (**34**).

The signals of the protons on the cyclopentane rings in compounds **27**–**30** show complex patterns with many of the signals overlapping in a narrow region of the ^{1}Hmr spectrum. The signals of the other protons in each of these compounds are well resolved and allow relatively easy characterization of the different compounds (**27**–**30**). Also, as was observed previously (19, 22), the protons in the sulfur-containing compounds, in general, resonate further downfield than the corresponding protons in the oxygen-containing analogs. The only significant exception to this trend occurs for H-3 in compounds **29** and **30**; in the case of the oxygen-containing compound (**30**) this proton resonates at lower field than in the case of the sulfur-containing compound (**29**).

In the case of nucleoside analogs **31**–**34**, in a 200-MHz field all of the protons on the cyclopentane ring in each of these compounds, except for H-1′, have complex overlapping signals in the δ 1.2–2.2 region. The signals for the other protons in these nucleosides are easily resolved even at 60 MHz, and, as was seen above, protons in the sulfur-containing compounds resonate at lower fields than the corresponding protons in the oxygen-containing compounds. Also, as was seen previously (19, 22), this difference is largest for the protons nearest the sulfur atom. Thus, H-1′ and H-3 resonate 1.0 and 1.3 ppm, respectively, further downfield in the case of the sulfur-containing nucleosides (**31** and **33**) than in the case of the oxygen-containing nucleosides (**32** and **34**), whereas the methylene protons of the hydroxymethyl group have virtually the same chemical shifts in all four compounds. The chemical shifts of the protons in compound **32** were previously reported by Shealy *et al.* (12) using a 100-MHz spectrometer and agree with those observed in the present study to within ±0.02 ppm.

Synthesis of carbocyclic analogs of cytosine nucleosides

The cytosine nucleosides shown in Scheme 4 were synthesized using the method described by Žemlička and Šorm (23); however, the protection of the hydroxyl groups was performed as described by Shealy and O'Dell (24). Nucleosides **32**–**34** were treated first with an excess of benzoyl chloride in pyridine to give compounds **35**–**37**. The benzoyl group on the pyrimidine rings was then selectively removed using dilute hydrochloric acid solution to give the monobenzoyl derivatives (**38**–**40**). The protected nucleosides **38** and **40** were converted into the 4-chloropyrimidinone intermediates **41** and **42**, respectively, using a catalytic amount of *N*,*N*-dimethylformamide and an excess of thionyl chloride in chloroform; compounds **41** and **42** were then converted into the cytosine nucleosides **43** and **44**, respectively, using anhydrous ammonia in methanol. However, an attempt to prepare the 4-amino analog of the 2-thiouracil nucleoside (**33**) by the above method gave instead nucleoside **44**.

In the case of the nucleosides shown in Scheme 4, at 200 MHz the signals of the methylene protons occur as complex groups

Can. J. Chem. Downloaded from www.nrcresearchpress.com by 213.222.148.141 on 09/07/12
For personal use only.

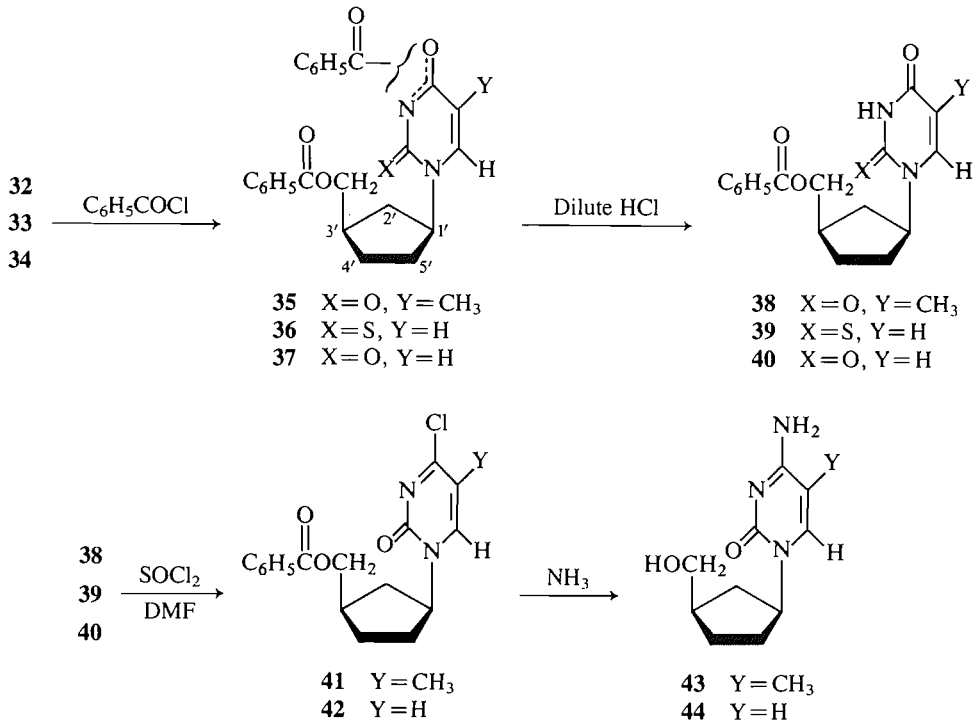

SCHEME 4

of overlapping multiplets, and thus only their chemical-shift ranges are given. The signals of the protons at C-1′, C-2′, and C-3′ are more resolved in the spectra of most of the nucleosides and, as was observed previously, the signals of the protons in the sulfur-containing nucleosides occur further downfield than those of the corresponding protons in the oxygen-containing nucleosides. The signals for the amino protons show different patterns in the two cytosine nucleosides (**43** and **44**). In the case of the nucleoside analog **44** these protons give rise to a single broad peak, whereas in the case of the 5-methylcytosine analog **43** they give rise to two broadened singlets at δ 6.66 and 7.04, suggesting that rotation of the amino group in the 5-methylcytosine analog **43** may be restricted.

Ultraviolet spectra of nucleoside analogs 31–34

The ultraviolet spectra of the uracil-nucleoside analog **34** closely resemble the spectra of 1-methyluracil (25) at the corresponding pH's. The absorption maxima in the spectra of the thymine analog **32** occur at slightly longer wavelengths (λ = 272–273 nm) than in the case of the uracil analog **34** (λ = 266–268 nm); otherwise, the spectra closely resemble those of **34** at the corresponding pH's. The absorption spectra of the 2-thiouracil- (**33**) and of 2-thiothymine- (**31**) -nucleoside analogs are more complex than those of **32** and **34**; however, they resemble closely the behavior of 1-methyl-2-thiouracil and 1-methyl-2-thiothymine, respectively, at the corresponding pH's (25). The absorption maximum at longer wavelength in the spectrum of **33** is relatively constant in both acidic and basic solvents; however, in the case of **31** the maximum shifts from 276 nm in acidic media to 266 nm in basic media. A similar behavior had been observed in the cases of 1-methyl-2-thiouracil and 1-methyl-2-thiothymine (25).

Biological evaluation

Compounds **31–34**, **43**, and **44** were tested for cell-growth inhibition using cultured K-562 cells by methods described previously (26). Nucleoside analogs having the 2-thiouracil (**33**), 2-thiothymine (**31**), cytosine (**44**), and 5-methylcytosine (**43**) bases showed some growth inhibition, with activity 150–300 times lower (higher values of ED_{50}) than that shown by 5-fluorouracil in this test system. Compounds **31–34** have also been tested for activity against the HSV-1 and the HSV-2 viruses. None of these compounds demonstrated antiviral activity in the 0.24–500 μg/mL concentration range.

Conclusion

The synthesis of (±)-*cis*-3-aminocyclopentanemethanol (**8**) from norbornene has been described. In addition, the effect of *cis*-vicinal substituents on the nucleophilic opening of *cis*-1,3-cyclopentanedicarboxylic acid anhydrides has been studied using *dl*-camphoric anhydride as a model. The results obtained with this anhydride, together with those obtained with the *cis*-1,3-cyclopentanedicarboxylic acid anhydrides having acetoxy substituents at position 4 (19, 22), show that *cis*-vicinal substituents greatly decrease the rate of nucleophilic attack at the adjacent carbonyl carbon. In the anhydride containing the 4-*cis*-acetoxy substituent, nucleophilic attack occurred only at the carbonyl carbon farthest away from the acetoxy group, thus allowing regiospecific opening of this anhydride (19).

(±)-*cis*-3-Aminocyclopentanemethanol was utilized for the synthesis of carbocyclic analogs of nucleosides having uracil, 2-thiouracil, 2-thiothymine, thymine, cytosine, and 5-methylcytosine bases. The 200-MHz ^{1}Hmr spectra of all of these nucleosides, as well as of the cyclopentane derivatives, have also been determined and discussed.

Experimental

Melting points were determined on a Fisher–Johns apparatus and are uncorrected. The ^{1}Hmr spectra were recorded on a Bruker CXP-200 spectrometer at 200 MHz. The proton chemical shifts (δ) are given relative to Me_4Si (δ = 0). Assignments of chemical shifts and coupling constants were made with the aid of spin-decoupling experiments. The following abbreviations are used in describing ^{1}Hmr signals: singlet (s), doublet (d), triplet (t), quartet (q), quintuplet (qu), sextuplet (se),

Can. J. Chem. Downloaded from www.nrcresearchpress.com by 213.222.148.141 on 09/07/12
For personal use only.

Can. J. Chem. Downloaded from www.nrcresearchpress.com by 213.222.148.141 on 09/07/12
For personal use only.

multiplet (m), and broadened (br). Ultraviolet spectra were recorded on a Perkin–Elmer 552 spectrophotometer. Thin-layer chromatography (tlc) was performed using silica gel 60 F-254 plates and column chromatography on silica gel 60. The plates and silica gel 60 were purchased from BDH Chemicals. The developed plates were dried and sprayed with a solution of ceric sulfate (1%) and molybdic acid (1.5%) in 10% aqueous sulfuric acid, and heated at ~150°C. Unless otherwise indicated, the same solvent was used for both tlc and column chromatography.

cis-1,3-Cyclopentanedicarboxylic acid (2)

Compound **2** was prepared from bicyclo[2.2.1]hept-2-ene (**1**) by the procedure of Birch *et al.* (14) using potassium permanganate instead of sodium permanganate. A solution of norbornene (**1**) (28.2 g, 0.30 mmol) in 2,2,4-trimethylpentane (200 mL) was added to water (1 L). To the stirred mixture, a solution of $KMnO_4$ (147 g, 0.93 mol) in water (2.5 L) was added over a period of 5 h (temperature 25–37°C), during which time CO_2 was vigorously bubbled through the reaction mixture. Immediately after the permanganate addition was complete, SO_2 was passed through the reaction mixture until it became colorless. The volume of the reaction solution was reduced to 825 mL. The solution was then cooled in an ice bath and acidified with concentrated HCl (90 mL). Extraction with diethyl ether (9 × 200 mL) gave a white solid (33.26 g, 70%), mp 104–114°C. After recrystallization of this material from diethyl ether – hexanes, the mp was 120°C (lit. (14) mp 119.9–120.6°C (corr.)); ^{1}Hmr (200 MHz, Me_2SO-d_6), δ: 1.67–1.94 (5H, m, H-2, H-4, H-4′, H-5, and H-5′), 2.11 (1H, d of t, J_{gem} = 13.2, ^3J = 8.0 Hz, H-2′), 2.64–2.80 (2H, m, H-1 and H-3), 12.1 (2H, br s, CO_2H). *Anal.* calcd. for $C_7H_{10}O_4$: C 53.16, H 6.37; found: C 53.19, H 6.45.

cis-1,3-Cyclopentanedicarboxylic acid anhydride (3)

Compound **2** (36.4 g, 230 mmol) was dissolved in acetic anhydride (100 mL) and 31 mL of solvent were removed by distillation. The reaction solution was heated at reflux temperature for a further 0.5 h and cooled. The solvent was removed under vacuum and the residue was recrystallized from tetrahydrofuran–hexanes to give a light-grey solid (25.56 g, 79%); in a melting point determination, this material turned from an opaque solid to a stiff, clear gel in the range 128–145°C and melted at 159–160°C (lit. (27) mp 161°C). Repeated recrystallizations from tetrahydrofuran–hexanes gave a white solid but did not alter the above melting behavior; ^{1}Hmr (200 MHz, $CDCl_3$), δ: 1.77 (1H, d of t, J_{gem} = 12.8, ^3J = 4.2 Hz, H-2), 1.98–2.33 (5H, m, H-2′, H-4, H-4′, H-5, and H-5′), 3.21–3.33 (2H, m, H-1 and H-3); ^{1}Hmr (200 MHz, Me_2SO-d_6), δ: 1.69 (1H, d of t, J_{gem} = 12.5, ^3J = 4.2 Hz, H-2), 1.82–2.21 (4H, m, H-4, H-4′, H-5, and H-5′), 2.36 (1H, br d, J_{gem} = 12.5 Hz, H-2′), 3.18 (2H, m, H-1 and H-3); spin–spin decoupling was performed at δ 1.69 and 2.36. *Anal.* calcd. for $C_7H_8O_3$: C 60.00, H 5.75; found: C 59.99, H 5.99.

(±)-Methyl hydrogen cis-1,3-cyclopentanedicarboxylate (4)

A solution of **3** (19.34 g, 138 mmol) in anhydrous methanol (400 mL) was stirred at room temperature for 19 h and left in the cold room (2°C) for 12 days. The solvent was removed on a rotary evaporator to give **4** as a light-brown oil (23.6 g); ^{1}Hmr (200 MHz, Me_2SO-d_6), δ: 1.68–2.05 (5H, m, H-2, H-4, H-4′, H-5, and H-5′), 2.13 (1H, d of t, J_{gem} = 12.7, ^3J = 8.0 Hz, H-2′), 2.66–2.97 (2H, m, H-1 and H-3), 3.60 (3H, s, OMe), 12.1 (1H, br s, CO_2H); ^{1}Hmr (200 MHz, $CDCl_3$), δ: 1.9–2.5 (6H, m, H-2, H-2′, H-4, H-4′, H-5, and H-5′), 2.8–3.0 (2H, m, H-1 and H-3), 3.71 (3H, s, OMe), 11.3 (1H, br s, CO_2H).

(±)-Methyl cis-3-(chloromethanoyl)cyclopentanecarboxylate (5)

Compound **4** (23.6 g) was dissolved in benzene (550 mL) and 50 mL were removed by distillation to remove traces of water. To the hot, benzene solution, thionyl chloride (50 mL, 0.68 mol) was added dropwise, and the solution was stirred for 5 min. Two drops of pyridine were then added and stirring was continued until the vigorous evolution of gases subsided; then 2 drops of *N*,*N*-dimethylformamide were added and the solution was heated at reflux temperature for 2 h. The mixture was kept at room temperature overnight, and the solvent was removed on a rotary evaporator to give **5** as a yellow oil (26.2 g); ^{1}Hmr (200 MHz, $CDCl_3$), δ: 1.95–2.48 (6H, m, H-2, H-2′, H-4, H-4′, H-5, and H-5′), 2.87 (1H, qu, ^3J = 8.1 Hz, H-1), 3.30 (1H, m, H-3), 3.70 (3H, s, OMe).

(±)-Methyl cis-3-carbamoylcyclopentanecarboxylate (6)

Compound **5** (26.2 g) was dissolved in dry benzene (450 mL) and anhydrous ammonia was bubbled through the reaction solution for 0.5 h. The resulting mixture was purged with nitrogen for 10 min. It was then diluted with ethyl acetate (400 mL), heated to boiling, and treated with charcoal. The hot mixture was filtered and the solid residue was washed with hot ethyl acetate. The combined filtrate and washings were cooled and the white crystalline solid was collected by filtration to give **6** (13.56 g), mp 122–123°C. The volume of the filtrate was reduced to 75 mL and additional **6** (2.21 g), mp 122–123°C, was collected by filtration. A final third crop of **6** (0.24 g) was obtained and had mp 117–121°C (total yield of 16.01 g, 67.8%, from **3**); ^{1}Hmr (200 MHz, Me_2SO-d_6), δ: 1.61–1.89 (5H, m, H-2, H-4, H-4′, H-5, and H-5′), 2.04 (1H, d of t, J_{gem} = 12.6, ^3J = 7.6 Hz, H-2′), 2.59 (1H, m, H-3), 2.78 (1H, m, H-1), 3.59 (3H, s, OMe), 6.78 (1H, br s, $CONH_2$), 7.29 (1H, br s, $CONH_2$). *Anal.* calcd. for $C_8H_{13}O_3N$: C 56.13, H 7.65, N 8.18; found: C 56.07, H 7.98, N 8.32.

(±)-cis-3-(Hydroxymethyl)cyclopentanecarboxamide (7)

A solution containing lithium borohydride (3.58 g, 164 mmol) in tetrahydrofuran (200 mL) was heated at reflux temperature for 1 h; heating was discontinued, compound **6** (14.09 g, 82 mmol) was added to the hot tetrahydrofuran solution, and heating at reflux temperature was then continued for 2 h. The reaction solution was cooled in an ice bath and diluted slowly with water (150 mL), then a slow addition of Amberlite CG-120 (H^+) cation-exchange resin (90 g) was made. The mixture was stirred overnight at room temperature. The resin was removed by filtration and washed with water (3 × 90 mL). The combined filtrate and washings were treated with Dowex 1-X8 (^-OH) anion-exchange resin to adjust the pH to 7. The resin was removed by filtration and washed with water (3 × 90 mL). The combined filtrate and washings were evaporated and the residue was evaporated with methanol (3 × 30 mL) to give a white solid (11.6 g), mp 112–117°C. This material was recrystallized from methanol–tetrahydrofuran to give **7** in two crops (9.14 g, mp 121–123°C, and 0.91 g, mp 119–122°C) for a total yield of 10.05 g (85.7%); R_f 0.49 (9:1 (v/v) acetonitrile–water), component visualized using iodine vapor; ^{1}Hmr (200 MHz, Me_2SO-d_6), δ: 1.15–1.76 (5H, m, H-2, H-4, H-4′, H-5, and H-5′), 1.78–2.09 (2H, m, H-2′ and H-3), 2.55 (1H, m, H-1), 3.29 (2H, d of d, $^3J_{to\ H\text{-}3}$ = 6.4, $^3J_{to\ CH_2OH}$ = 5.3 Hz, CH_2OH), 4.46 (1H, t, ^3J = 5.3 Hz, CH_2OH), 6.68 (1H, br s, $CONH_2$), 7.21 (1H, br s, $CONH_2$); the $CONH_2$ and OH protons exchanged with D_2O. *Anal.* calcd. for $C_7H_{13}O_2N$: C 58.72, H 9.15, N 9.78; found: C 59.16, H 9.17, N 10.28.

(±)-cis-3-Aminocyclopentanemethanol (8)

To a solution at 5°C containing $Ba(OH)_2 \cdot 8H_2O$ (95.4 g, 0.302 mol) in water (1.9 L), bromine (3.8 mL, 74 mmol) was added. Immediately after the bromine had dissolved, a solution of compound **7** (9.63 g, 67.2 mmol) in water (50 mL) was added in one portion, and the reaction solution was allowed to warm to room temperature over a period of 2 h. The solution was then heated at 50–65°C for 1.25 h, cooled to ice-bath temperature, and acidified with 3 *M* H_2SO_4 (85 mL). The mixture was stirred for 1 h and the precipitate was removed by centrifugation. The solution was stored in the cold room (2°C) overnight and then passed through Amberlite CG-120 (H^+) cation-exchange resin (150 g). The resin was washed with water (1.5 L) and then eluted with 2 *N* NH_3 in water; the elution was monitored by tlc (5:3:2 (v/v/v) *n*-butanol–water–acetic acid). No product was eluted in the first 2 L; an additional 2.5 L of 2 *N* NH_3 in water was required to elute the product from the column. The solvent was evaporated and the residual oil was dissolved in ethanol; the mixture was filtered to remove small amounts of insoluble matter. The solvent was evaporated to afford **8** as a yellow oil (5.70 g, 74%). The ^{1}Hmr spectrum showed no signals attributable to impurities; ^{1}Hmr (200 MHz, Me_2SO-d_6), δ: 0.95 (1H, d of t, J_{gem} = 12.4, ^3J = 7.0 Hz, H-2), 1.17–1.73 (4H, m, H-4, H-4′, H-5,

Can. J. Chem. Downloaded from www.nrcresearchpress.com by 213.222.148.141 on 09/07/12
For personal use only.

and H-5'), 1.79–2.11 (2H, m, H-2' and H-1), 3.17 (1H, m, H-3), 3.28 (2H, d, J = 6.0 Hz, HOCH_2); spin–spin decoupling was performed at δ 0.95 and 3.17.

*(±)-3-Methyl hydrogen 1,2,2-trimethyl-*cis*-1,3-cyclopentanedicarboxylate (**10**) and (±)-3-methyl hydrogen 2,2,3-trimethyl-*cis*-1,3-cyclopentanedicarboxylate (**11**)*

A mixture of *dl*-camphoric anhydride (**9**, 50 g, 274 mmol) in anhydrous methanol (650 mL) was heated at reflux temperature for 2 days, cooled to room temperature, and a white solid (28.6 g) was collected by filtration, which was shown by ^{1}Hmr spectroscopy and a melting-point determination to be starting material (**9**). The volume of the filtrate was reduced to 150 mL, the solution was cooled to 4°C, and additional **9** (11.72 g) was collected by filtration. The solvent was evaporated and the resulting oil was fractionated by column chromatography on silica gel to give a component (6.96 g, 12%), R_f = 0.43 (9:1 (v/v) toluene–2-propanol), which was shown by ^{1}Hmr spectroscopy to be a mixture of compounds **10** and **11**, with compound **10** being the major isomer. Compound **10**, ^{1}Hmr (200 MHz, $CDCl_3$), δ: 0.84 (3H, s, Me), 1.25 (3H, s, Me), 1.27 (3H, s, Me), 1.52 (1H, m, J_{gem} = 13.5, $^3J_{5,4}$ = 9.6, $^3J_{5,4'}$ = 3.9 Hz, H-5), 1.72–1.94 (1H, m, H-4), 2.08–2.30 (1H, m, H-4'), 2.47–2.67 (1H, m, H-5'), 2.78–2.88 (1H, m, H-3), 3.70 (3H, s, OMe); compound **11**, ^{1}Hmr (200 MHz, $CDCl_3$), δ: 0.82 (3H, s, Me), 1.21 (3H, s, Me), 1.29 (3H, s, Me), 1.52 (1H, m, J_{gem} = 13.5, $^3J_{4,5}$ = 9.6, $^3J_{4,5'}$ = 3.9 Hz, H-4), 1.72–1.94 (1H, m, H-5), 2.08–2.30 (1H, m, H-5'), 2.47–2.67 (1H, m, H-4'), 2.78–2.88 (1H, m, H-1), 3.69 (3H, s, OMe); spin–spin decoupling was performed at δ 1.52 and 2.83.

*(±)-Methyl 2,2,3-trimethyl-*cis*-3-carbamoylcyclopentanecarboxylate (**14**) and (±)-methyl 1,2,2-trimethyl-*cis*-3-carbamoylcyclopentanecarboxylate (**15**)*

A solution of compounds **10** and **11** (6.64 g, 31.0 mmol) in benzene (100 mL) was treated with thionyl chloride (11 mL, 153 mmol), as described above for the preparation of **5**, to give an oily mixture of compounds **12** and **13**. The oil was dissolved in dry benzene (100 mL) and anhydrous ammonia was bubbled through the reaction solution for 0.5 h. The reaction mixture was then flushed with nitrogen for 10 min, heated to boiling, and filtered. The filtrate was evaporated to give a pale-yellow solid (5.68 g), which was fractionated by column chromatography on silica gel to give **14** (3.024 g) and a mixture of **14** and **15** (0.584 g), with **14** as the major component, for a total yield of 3.608 g (55% from **10** and **11**). An analytical sample of **14** was prepared by recrystallization from ethyl acetate – hexanes, mp 135°C, R_f 0.35 (tlc) (7:2:1 (v/v/v) toluene – ethyl acetate – 2-propanol); ^{1}Hmr (200 MHz, $CDCl_3$), δ: 0.83 (3H, s, Me), 1.22 (3H, s, Me), 1.30 (3H, s, Me), 1.55 (1H, m, H-4), 1.75–1.95 (1H, m, H-5), 2.16–2.48 (2H, m, H-4' and H-5'), 2.82 (1H, d of d, ^3J = 10.5, ^3J = 7.6 Hz, H-1), 3.69 (3H, s, OMe), 5.55 (2H, br s, $CONH_2$); ^{1}Hmr (200 MHz, Me_2SO-d_6), δ: 0.66 (3H, s, Me), 1.08 (3H, s, Me), 1.16 (3H, s, Me), 1.35 (1H, m, J_{gem} = 12.6, $^3J_{4,5}$ = 9.3, $^3J_{4,5'}$ = 3.2 Hz, H-4), 1.74 (1H, m, H-5), 1.99 (1H, m, H-5'), 2.33 (1H, t of d, J = 12.2, ^3J = 8.6 Hz, H-4'), 2.79 (1H, d of d, ^3J = 10.2, ^3J = 8.0 Hz, H-1), 3.60 (3H, s, OMe), 6.86 (1H, br s, $CONH_2$), 6.91 (1H, br s, $CONH_2$); spin–spin decoupling was performed at δ 2.79. *Anal.* calcd. for $C_{11}H_{19}O_3N$: C 61.95, H 8.98, N 6.57; found: C 61.86, H 9.00, N 7.04.

The mixture of **14** and **15** was fractionated again by column chromatography on silica gel to give a sample of **15**. An analytical sample of **15** was prepared by recrystallization from ethyl acetate – hexanes, mp 116–118°C, R_f 0.24 (tlc); ^{1}Hmr (200 MHz, $CDCl_3$), δ: 0.82 (3H, s, Me), 1.20 (3H, s, Me), 1.27 (3H, s, Me), 1.51 (1H, m, J_{gem} = 13.8, $^3J_{5,4}$ = 9.6, $^3J_{5,4'}$ = 4.3 Hz, H-5), 1.81 (1H, m, J_{gem} = 13.6, ^3J = 9.6, $^3J_{4,5'}$ = 6.9 Hz, H-4), 2.18 (1H, m, J_{gem} = 13.6, $^3J_{4',5'}$ = 11.6, $^3J_{4',3}$ = 9.1, $^3J_{4',5}$ = 4.3 Hz, H-4'), 2.61 (1H, m, H-5'), 2.63 (1H, t, ^3J = 9.3 Hz, H-3), 3.68 (3H, s, OMe), 5.35 (1H, br s, $CONH_2$), 5.54 (1H, br s, $CONH_2$); ^{1}Hmr (200 MHz, Me_2SO-d_6), δ: 0.63 (3H, s, Me), 1.11 (6H, s, Me), 1.38 (1H, m, J_{gem} = 13.3, $^3J_{5,4}$ = 9.4, $^3J_{5,4'}$ = 4.0 Hz, H-5), 1.62 (1H, m, J_{gem} = 12.9, $^3J_{4,5}$ = $^3J_{4,3}$ = 9.6, $^3J_{4,5'}$ = 6.8 Hz, H-4), 1.97 (1H, m, H-4'), 2.42 (1H, t of d, J = 12.8, $^3J_{5',4}$ = 6.8 Hz, H-5'), 2.62 (1H, t, ^3J = 9.6 Hz, H-3), 3.59 (3H, s, OMe), 6.88 (1H, br s, $CONH_2$), 7.13 (1H, br s, $CONH_2$). *Anal.* calcd. for $C_{11}H_{19}O_3N$: C 61.95, H 8.98, N 6.57; found: C 62.05, H 9.16, N 6.91.

*(±)-1,2,2-Trimethyl-*cis*-3-(hydroxymethyl)cyclopentanecarboxamide (**16**)*

Compound **14** (1.43 g, 6.70 mmol) was treated with lithium borohydride (0.5 g, 23 mmol) in tetrahydrofuran (100 mL) as described for the preparation of **7**. After treatment with cation- and anion-exchange resins, the solvent was evaporated and the residue was evaporated with methanol (10 × 2 mL). The residue was then stirred in tetrahydrofuran–hexanes, and the resulting white solid was collected by filtration to give 0.84 g of material. This material was fractionated by column chromatography on silica gel to give **16** (0.102 g, 8.2%), mp 159°C, R_f 0.26 (tlc) (4:1 (v/v) toluene–2-propanol). An analytical sample was prepared by recrystallization from ethyl acetate – methanol–hexanes, mp 162–163°C; ^{1}Hmr (200 MHz, Me_2SO-d_6), δ: 0.65 (3H, s, Me), 1.05 (6H, s, Me), 1.15–1.38 (2H, m, H-4 and H-5), 1.68–1.99 (2H, m, H-3 and H-4'), 2.27 (1H, t of d, J = 13.2, ^3J = 6.9 Hz, H-5'), 3.24 (1H, d of d of d, J_{gem} = 10.2, $^3J_{\text{to H-3}}$ = 7.6, $^3J_{\text{to HOCH}_2}$ = 5.0 Hz, HOCH_2), 3.47 (1H, m, J_{gem} = 10.2, ^3J = 5.1 Hz, HOCH_2), 4.27 (1H, t, ^3J = 5.0 Hz, HOCH$_2$), 6.76 (1H, br s, $CONH_2$), 6.79 (1H, br s, $CONH_2$); spin–spin decoupling was performed at δ 2.27, 3.47, and 4.27. *Anal.* calcd. for $C_{10}H_{19}O_2N$: C 64.83, H 10.34, N 7.56; found: C 64.92, H 10.12, N 7.81.

*(±)-2,2,3-Trimethyl-*cis*-3-carbamoylcyclopentanecarboxylic acid (**17**) and (±)-1,2,2-trimethyl-*cis*-3-carbamoylcyclopentanecarboxylic acid (**18**)*

Dry ammonia was bubbled through a solution of *dl*-camphoric anhydride (**9**, 40.0 g, 220 mmol) in tetrahydrofuran (500 mL) (which had been cooled initially to 5°C) for 40 min. The mixture was left at 0°C overnight and then flushed with nitrogen for 30 min. The ice-cold mixture was filtered and the solid was dissolved in water (250 mL). Insoluble material was removed by filtration, and the filtrate was cooled to ice-bath temperature and acidified to pH 2. The solution was kept in the cold room (2°C) for 2 days; the crystalline solid was collected by filtration and washed with ice-cold water to give a mixture of **17** and **18** (39.2 g) that, by integration of the ^{1}Hmr signals, was shown to contain **17** and **18** in a 1:3 ratio, respectively. Compound **18**, ^{1}Hmr (200 MHz, Me_2SO-d_6), δ: 0.72 (3H, s, Me), 1.11 (3H, s, Me), 1.13 (3H, s, Me), 1.28–2.46 (4H, m, H-4, H-4', H-5, and H-5'), 2.61 (1H, t, ^3J = 9.4 Hz, H-3), 6.83 (1H, br s, $CONH_2$), 7.06 (1H, br s, $CONH_2$), 12.1 (1H, br s, CO_2H). The volume of the filtrate was reduced to 50 mL, the solution was cooled for 8 h at 0°C, and an additional crop of a mixture of **17** and **18** (2.62 g) was obtained for a total yield of 41.82 g (95.4%); the second crop contained compounds **17** and **18** in a 4:1 ratio, respectively. Compound **17**, ^{1}Hmr (200 MHz, Me_2SO-d_6), δ: 0.72 (3H, s, Me), 1.08 (3H, s, Me), 1.18 (3H, s, Me), 1.28–2.46 (4H, H-4, H-4', H-5, and H-5'), 2.69 (1H, d of d, ^3J = 10.0, ^3J = 8.0 Hz, H-1), 6.85 (1H, br s, $CONH_2$), 6.89 (1H, br s, $CONH_2$), 12.1 (1H, br s, CO_2H).

*3-Methoxy-2-methylpropenoic acid (**20**)*

Compound **20** was prepared from methyl 2-methylpropenoate by way of the intermediacy of methyl 2,3-dibromo-2-methylpropanoate and methyl 3-methoxy-2-methylpropenoate (**19**) as described previously (12, 20). Compound **20**, ^{1}Hmr (200 MHz, $CDCl_3$), δ: 1.73 (3H, d, $^4J_{\text{to H-3}}$ = 1.2 Hz, Me), 3.86 (3H, s, OMe), 7.40 (1H, q, ^4J = 1.2 Hz, H-3); ^{1}Hmr (200 MHz, Me_2SO-d_6), δ: 1.59 (3H, d, $^4J_{\text{to H-3}}$ = 1.4 Hz, Me), 3.80 (3H, s, OMe), 7.31 (1H, q, ^4J = 1.4 Hz, H-3), 11.8 (1H, br s, CO_2H).

*3-Methoxy-2-methylpropenoyl chloride (**22**)*

Compound **20** was converted into its sodium salt (**21**) as described by Shaw and Warrener (20); ^{1}Hmr (200 MHz, Me_2SO-d_6), δ: 1.54 (3H, d, $^4J_{\text{to H-3}}$ = 1.3 Hz, Me), 3.60 (3H, s, OMe), 6.91 (1H, q, ^4J = 1.3 Hz, H-3). The sodium salt was then treated with $SOCl_2$ in ether as described previously (20); distillation gave **22**, ^{1}Hmr (200 MHz, $CDCl_3$), δ: 1.74 (3H, d, Me), 3.96 (3H, s, OMe), 7.66 (1H, q, ^4J = 1.2 Hz, H-3).

Can. J. Chem. Downloaded from www.nrcresearchpress.com by 213.222.148.141 on 09/07/12
For personal use only.

*(±)-*N*-{N′-[*cis*-3-(Hydroxymethyl)cyclopentyl]thiocarbamoyl}-3-methoxy-2-methylpropenamide (27)*

3-Methoxy-2-methylpropenoyl isothiocyanate (**23**) was prepared from equivalent amounts of compound **22** and potassium thiocyanate in acetonitrile as described previously (20). Compound **23** was purified by distillation under vacuum and used immediately for the preparation of **27**. Compound **23** (0.28 g, 1.8 mmol) was added to a solution of **8** (0.21 g, 1.8 mmol) in methanol (5 mL) and diethyl ether (5 mL) and the reaction solution was kept at room temperature overnight; the mixture was filtered and the solvent was evaporated. The residue was fractionated by column chromatography on silica gel to give **27** (0.337 g, 77%) as a colorless oil, R_f 0.50 (8:8:1 (v/v/v) toluene – ethyl acetate – 2-propanol). The ^{1}Hmr spectrum showed minor signals attributable to impurities; ^{1}Hmr (200 MHz, Me_2SO-d_6), δ: 1.14–2.23 (7H, m, H-2′, H-2″, H-3′, H-4′, H-4″, H-5′, and H-5″), 1.61 (3H, d, $^4J_{\text{to H-3}}$ = 1.1 Hz, Me), 3.29–3.36 (2H, m, HOCH_2), 3.85 (3H, s, OMe), 4.50 (1H, se, ^3J = 7.0 Hz, H-1′), 4.61 (1H, t, ^3J = 5.3 Hz, *H*OCH$_2$), 7.52 (1H, q, ^4J = 1.1 Hz, H-3), 10.40 (1H, br s, CON*H*CSNH), 10.97 (1H, br d, $^3J_{\text{to H-1′}}$ = 7.3 Hz, CONHCSN*H*); spin–spin decoupling was performed at δ 4.50.

*(±)-*N*-{N′-[*cis*-3-(Hydroxymethyl)cyclopentyl]carbamoyl}-3-methoxy-2-methylpropenamide (28)*

A solution of 3-methoxy-2-methylpropenoyl isocyanate (**24**) in benzene was prepared from **22** and silver cyanate as described by Shealy *et al.* (12) and was used immediately for the preparation of **28** without further purification. To a solution of **8** (0.67 g, 5.8 mmol) in dry *N*,*N*-dimethylformamide (12.2 mL), cooled to −15°C, a solution of **24** (1.22 equiv., theoretical) in benzene was added dropwise; the temperature of the reaction solution was maintained below −10°C with a cooling bath. After the addition of **24** was complete, the reaction solution was kept at room temperature overnight; the mixture was filtered and the solvent was evaporated. The residue was fractionated by column chromatography on silica gel to give **28** (1.05 g, 71%) as a white solid, R_f 0.44 (3:3:1 (v/v/v) toluene – ethyl acetate – 2-propanol). The ^{1}Hmr spectrum revealed only minute signals attributable to impurities; ^{1}Hmr (200 MHz, Me_2SO-d_6), δ: 1.02–1.18 (1H, m, H-2′), 1.29–2.11 (6H, m, H-2″, H-3′, H-4′, H-4″, H-5′, and H-5″), 1.61 (3H, d, $^4J_{\text{to H-3}}$ = 1.3 Hz, Me), 3.30 (2H, t, ^3J = 5.2 Hz, HOCH_2), 3.79 (3H, s, OMe), 3.99 (1H, se, ^3J = 6.9 Hz, H-1′), 4.55 (1H, t, ^3J = 5.2 Hz, *H*OCH$_2$), 7.45 (1H, q, ^4J = 1.3 Hz, H-3), 8.65 (1H, br d, $^3J_{\text{to H-1′}}$ = 7.3 Hz, CONHCON*H*), 9.67 (1H, br s, CON*H*CONH); spin–spin decoupling was performed at δ 1.10, 3.30, and 3.99.

*(±)-3-Ethoxy-*N*-{N′-[*cis*-3-(hydroxymethyl)cyclopentyl]thiocarbamoyl}propenamide (29)*

3-Ethoxypropenoyl isothiocyanate (**25**) was prepared as described previously (20) and used immediately after distillation for the preparation of **29**. Compound **25** (1.41 g, 8.97 mmol) was added to a solution of **8** (0.934 g, 8.11 mmol) in methanol (13 mL) and diethyl ether (20 mL), and the reaction solution was kept at room temperature overnight; the mixture was filtered and the solvent was evaporated. The resulting oil was fractionated by column chromatography on silica gel to give **29** (1.54 g, 70%) as a pale yellow-green oil; R_f 0.50 (8:8:1 (v/v/v) toluene – ethyl acetate – 2-propanol). The ^{1}Hmr spectrum showed minor signals attributable to impurities; ^{1}Hmr (200 MHz, Me_2SO-d_6), δ: 1.10–2.23 (6H, m, H-2′, H-2″, H-4′, H-4″, H-5′, and H-5″), 1.24 (3H, t, ^3J = 7.0 Hz, Me), 1.85–2.23 (1H, m, H-3′), 3.32 (2H, t, ^3J = 5.6 Hz, HOCH_2), 3.98 (2H, q, ^3J = 7.0 Hz, CH_3CH_2O), 4.48 (1H, se, ^3J = 6.9 Hz, H-1′), 4.56 (1H, t, ^3J = 5.0 Hz, *H*OCH$_2$), 5.70 (1H, d, $^3J_{2,3}$ = 12.2 Hz, H-2), 7.59 (1H, d, $^3J_{3,2}$ = 12.2 Hz, H-3), 10.84 (1H, br s, CON*H*CSNH), 10.96 (1H, br d, $^3J_{\text{to H-1′}}$ = 7.2 Hz, CONHCSN*H*); spin–spin decoupling was performed at δ 3.32, 4.48, and 10.96.

*(±)-3-Ethoxy-*N*-{N′-[*cis*-3-(hydroxymethyl)cyclopentyl]carbamoyl}propenamide (30)*

A solution of 3-ethoxypropenoyl isocyanate (**26**) in benzene was prepared as described previously (21, 28). A solution of compound **26** (26.6 mmol, theoretical) in benzene (60 mL) was added to a solution of **8** (2.73 g, 23.7 mmol) in *N*,*N*-dimethylformamide (60 mL) that had been cooled to −15°C; the temperature was maintained below −10°C during the addition. The reaction solution was kept at room temperature overnight. The mixture was filtered and the solvent was evaporated with ethanol (2 × 20 mL); fractionation of the residue by column chromatography on silica gel gave **30** (2.59 g, 43%) as a semisolid, R_f 0.57 (2:2:1 (v/v/v) toluene – ethyl acetate – 2-propanol). The ^{1}Hmr spectrum showed minor signals attributable to impurities; ^{1}Hmr (200 MHz, Me_2SO-d_6), δ: 1.05–2.15 (7H, m, H-2′, H-2″, H-3′, H-4′, H-4″, H-5′, and H-5″), 1.26 (3H, t, ^3J = 7.0 Hz, Me), 3.32 (2H, t, ^3J = 5.6 Hz, HOCH_2), 3.98 (1H, se, ^3J = 7.0 Hz, H-1′), 4.02 (2H, q, ^3J = 7.0 Hz, CH_3CH_2O), 4.53 (1H, t, ^3J = 5.3 Hz, *H*OCH$_2$), 5.59 (1H, d, $^3J_{2,3}$ = 12.7 Hz, H-2), 7.69 (1H, d, $^3J_{3,2}$ = 12.7 Hz, H-3), 7.98 (1H, br d, $^3J_{\text{to H-1′}}$ = 7.4 Hz, CONHCON*H*); spin–spin decoupling was performed at δ 3.32 and 4.00.

*(±)-2,3-Dihydro-1-{*cis*-3-(hydroxymethyl)cyclopentyl}-5-methyl-2-thioxo-4(1*H*)-pyrimidinone (31)*

A solution of compound **27** (0.359 g, 1.32 mmol) in 15 *N* aqueous ammonia (15 mL) was heated at 100°C in an oil bath for 30 min. After the reaction solution had cooled to room temperature, the solvent was evaporated and the residue was evaporated with ethanol (2 × 10 mL). The resulting material was fractionated by column chromatography on silica gel to give **31** (0.195 g, 62%). Recrystallization from ethanol–hexanes gave **31** (0.116 g) as a white crystalline solid, mp 138.5–139.5°C, R_f 0.39 (4:4:1 (v/v/v) toluene – ethyl acetate – 2-propanol); uv λ_{max} (C_2H_5OH): 221 (ε 15 300), 276 (15 400) nm; λ_{max} (0.01 *M* HCl in C_2H_5OH): 221 (ε 15 300), 276 (15 300) nm; λ_{max} (0.01 *M* NaOH in C_2H_5OH): 242 (ε 20 300), 255 (17 800), 266 (17 600) nm; ^{1}Hmr (200 MHz, Me_2SO-d_6), 1.26–2.21 (7H, m, H-2′, H-2″, H-3′, H-4′, H-4″, H-5′, and H-5″), 1.85 (3H, m, Me), 3.40 (2H, m, HOCH_2), 4.61 (1H, t, ^3J = 5.2 Hz, *H*OCH$_2$), 5.74 (1H, m, H-1′), 7.76 (1H, m, H-6), 12.51 (1H, br s, H-3). *Anal.* calcd. for $C_{11}H_{16}O_2N_2S$: C 54.98, H 6.71, N 11.66, S 13.34; found: C 55.19, H 6.96, N 11.73, S 13.52.

*(±)-1-{*cis*-3-(Hydroxymethyl)cyclopentyl}-5-methyl-2,4(1*H*,3*H*)-pyrimidinedione (32)*

A solution of **28** (1.106 g, 3.96 mmol) in aqueous ammonia (35 mL) was heated at 100°C in an oil bath for 65 min. After the solution had cooled to room temperature, the solvent was evaporated and the residue was then evaporated with ethanol (2 × 10 mL). The resulting material was fractionated by column chromatography on silica gel to give **32** (0.724 g, 82%) as a white solid. Recrystallization from ethanol–hexanes gave **32** (0.596 g) having mp 165–168°C (lit. (12) mp 173–174°C). Repeated recrystallization gave material having mp 166–168°C; R_f 0.34 (2:2:1 (v/v/v) toluene – ethyl acetate – 2-propanol); uv λ_{max} (C_2H_5OH): 210 (ε 9990), 272 (9980) nm; λ_{max} (0.01 *M* HCl in C_2H_5OH): 210 (ε 9960), 272 (9930) nm; λ_{max} (0.01 *M* NaOH in C_2H_5OH): 220 (ε 9590), 272 (7400) nm; ^{1}Hmr (200 MHz, Me_2SO-d_6), δ: 1.29–2.18 (7H, m, H-2′, H-2″, H-3′, H-4′, H-4″, H-5′, and H-5″), 1.79 (3H, d, $^4J_{\text{to H-6}}$ = 0.9 Hz, Me), 3.38 (2H, m, HOCH_2), 4.58 (1H, t, ^3J = 5.3 Hz, *H*OCH$_2$), 4.73 (1H, m, H-1′), 7.56 (1H, m, H-6), 11.19 (1H, br s, H-3). *Anal.* calcd. for $C_{11}H_{16}O_3N_2$: C 58.91, H 7.19, N 12.49; found: C 59.04, H 7.30, N 12.44.

*(±)-2,3-Dihydro-1-{*cis*-3-(hydroxymethyl)cyclopentyl}-2-thioxo-4(1*H*)-pyrimidinone (33)*

A solution of **29** (1.491 g, 5.47 mmol) in 15 *N* aqueous ammonia (50 mL) was heated at 100°C in an oil bath for 25 min. After the reaction solution had cooled to room temperature, the solvent was evaporated and the residue was then evaporated with ethanol (2 × 10 mL). The resulting material was fractionated by column chromatography on silica gel to give **33** (1.001 g, 81%) as a white solid, R_f 0.41 (3:3:1 (v/v/v) toluene – ethyl acetate – 2-propanol). An analytical sample was prepared by recrystallization from ethanol–hexanes, mp 145–147°C; uv λ_{max} (C_2H_5OH): 219 (ε 16 000), 272 (13 600) nm; λ_{max} (0.01 *M* HCl in C_2H_5OH): 219 (ε 16 700), 273 (13 700) nm;

Can. J. Chem. Downloaded from www.nrcresearchpress.com by 213.222.148.141 on 09/07/12
For personal use only.

λ_{max} (0.01 *M* NaOH in C_2H_5OH): 240 (ε 18 500), 273 (16 000) nm; ^{1}Hmr (200 MHz, Me_2SO-d_6), δ: 1.23–2.19 (7H, m, H-2′, H-2″, H-3′, H-4′, H-4″, H-5′, and H-5″), 3.39 (2H, t, ^3J = 5.1 Hz, $HOCH_2$), 4.62 (1H, t, ^3J = 5.2 Hz, $HOCH_2$), 5.73 (1H, m, H-1′), 5.99 (1H, br d, $^3J_{5,6}$ = 7.8 Hz, H-5), 7.90 (1H, d, $^3J_{6,5}$ = 7.8 Hz, H-6), 12.63 (1H, br s, H-3). *Anal.* calcd. for $C_{10}H_{14}O_2N_2S$: C 53.08, H 6.24, N 12.38, S 14.17; found: C 53.13, H 6.40, N 12.20, S 13.95.

*(±)-1-{*cis*-3-(Hydroxymethyl)cyclopentyl}-2,4(1*H*,3*H*)-pyrimidinedione (**34**)*

A solution of **30** (2.47 g, 9.64 mmol) in 2 *N* H_2SO_4 (65 mL) was heated at reflux temperature for 30 min. After the solution had cooled to room temperature, it was treated with charcoal and the mixture was filtered. The filtrate was cooled to ice-bath temperature and neutralized with 2 *M* NaOH. The solvent was evaporated and the residue was extracted with ethanol (4 × 30 mL). The ethanol was then evaporated and the residue was fractionated by column chromatography on silica gel to give **34** (1.401 g, 69%) as a pale-yellow solid, mp 150–155°C, R_f 0.43 (1:1:1 (v/v/v) toluene – ethyl acetate – 2-propanol). An analytical sample was prepared by recrystallization from ethanol–hexanes, mp 158–159°C; uv λ_{max} (C_2H_5OH): 209 (ε 9490), 268 (10 400) nm; λ_{max} (0.01 *M* HCl in C_2H_5OH): 209 (ε 9460), 268 (10 300) nm; λ_{max} (0.01 *M* NaOH in C_2H_5OH): 220 (ε 8220), 266 (7490) nm; ^{1}Hmr (200 MHz, Me_2SO-d_6), δ: 1.27–2.18 (7H, m, H-2′, H-2″, H-3′, H-4′, H-4″, H-5′, and H-5″), 3.38 (2H, t, ^3J = 5.6 Hz, $HOCH_2$), 4.57 (1H, t, ^3J = 5.1 Hz, $HOCH_2$), 4.74 (1H, m, H-1′), 5.57 (1H, d of d, $^3J_{5,6}$ = 8.1, $^4J_{5,3}$ = 2.2 Hz, H-5), 7.69 (1H, d, $^3J_{6,5}$ = 8.1 Hz, H-6), 11.24 (1H, br s, H-3). *Anal.* calcd. for $C_{10}H_{14}O_3N_2$: C 57.13, H 6.71, N 13.32; found: C 57.18, H 6.83, N 13.35.

*(±)-1-{*cis*-3-(Hydroxymethyl)cyclopentyl}-5-methyl-2,4(1*H*,3*H*)-pyrimidinedione benzoate (**38**)*

A solution of benzoyl chloride (0.66 mL, 5.7 mmol) in pyridine (5 mL) was added to a solution of compound **32** (0.424 g, 1.89 mmol) in pyridine (20 mL). The reaction solution was kept at 55°C in a water bath for 48 h and then poured into a water–ice mixture (150 mL). An oil separated, which was extracted with chloroform (3 × 25 mL). The solvent was evaporated and the residue was evaporated with ethanol–water (1:1 (v/v), 2 × 20 mL). The resulting oil was fractionated by column chromatography on silica gel to give **35** (0.822 g) as a colorless solid foam, R_f 0.56 (3:2 (v/v) toluene – ethyl acetate). The ^{1}Hmr spectrum showed this sample to be contaminated by a small amount of benzoic acid; ^{1}Hmr (200 MHz, Me_2SO-d_6), δ: 1.58–2.12 (5H, m, H-2′, H-4′, H-4″, H-5′, and H-5″), 1.88 (3H, m, Me), 2.22 (1H, d of t, J_{gem} = 12.4, ^3J = 7.0 Hz, H-2″), 2.45 (1H, m, H-3′), 4.24–4.41 (2H, m, OCH_2C), 4.83 (1H, m, H-1′), 7.47–8.02 (10H, m, C_6H_5), 7.88 (1H, m, H-6); spin–spin decoupling was performed at δ 1.88. Compound **35** (0.758 g) was dissolved in hot ethanol (70 mL), and to this solution water (25 mL) and 1 *M* hydrochloric acid (6 mL) were added; the reaction solution was heated at reflux temperature for 24 h. The solution was cooled and the solvent was evaporated. The residue was fractionated by column chromatography on silica gel to give **38** (0.429 g, 75% from **32**) as a white crystalline solid, R_f 0.46 (8:8:1 (v/v/v) toluene – ethyl acetate – 2-propanol). An analytical sample was prepared by recrystallization from ethanol, mp 159–161°C; uv λ_{max} (C_2H_5OH): 202 (ε 17 300), 224 (16 600), 273 (10 800) nm; λ_{max} (0.01 *M* HCl in C_2H_5OH): 202 (ε 16 500), 224 (16 500), 273 (10 800) nm; λ_{max} (0.01 *M* NaOH in C_2H_5OH): 228 (ε 20 400), 272 (8170) nm; ^{1}Hmr (200 MHz, Me_2SO-d_6), δ: 1.47–2.00 (5H, m, H-2′, H-4′, H-4″, H-5′, and H-5″), 1.78 (3H, m, Me), 2.12 (1H, d of t, J_{gem} = 12.0, ^3J = 6.9 Hz, H-2″), 2.43 (1H, m, H-3′), 4.21–4.37 (2H, m, OCH_2), 4.82 (1H, m, H-1′), 7.50–8.02 (5H, m, C_6H_5), 7.63 (1H, m, H-6), 11.26 (1H, br s, H-3); spin–spin decoupling was performed at δ 1.78, 2.43, and 4.82. *Anal.* calcd. for $C_{18}H_{20}O_4N_2$: C 65.84, H 6.14, N 8.53; found: C 66.19, H 6.10, N 8.57.

*(±)-2,3-Dihydro-1-{*cis*-3-(hydroxymethyl)cyclopentyl}-2-thioxo-4(1*H*)-pyrimidinone benzoate (**39**)*

A solution of benzoyl chloride (0.60 mL, 5.2 mmol) in pyridine (5 mL) was added dropwise to a solution of compound **33** (0.338 g, 1.49 mmol) in pyridine (15 mL). The reaction solution was treated as for the preparation of **35**, and, after fractionation by column chromatography on silica gel, two major components were isolated, namely **36** (0.386 g) as a solid foam, R_f 0.54 (3:2 (v/v) toluene – ethyl acetate), and **39** (0.192 g) as a crystalline solid that, after recrystallization from ethanol–water, gave a sample of **39** (0.111 g) having mp 179–182°C, R_f 0.34. Compound **36**, ^{1}Hmr (200 MHz, Me_2SO-d_6), δ: 1.42–2.50 (7H, H-2′, H-2″, H-3′, H-4′, H-4″, H-5′, and H-5″), 4.22–4.42 (2H, m, OCH_2), 5.72 (1H, m, H-1′), 6.32 (1H, d, $^3J_{5,6}$ = 8.3 Hz, H-5), 7.46–8.02 (10H, m, C_6H_5), 8.22 (1H, d of d, $^3J_{6,5}$ = 8.3, J = 1.3 Hz, H-6); spin–spin decoupling was performed at δ 6.32 and 5.72. To a solution of compound **36** (0.362 g, 0.83 mmol) in hot ethanol (50 mL) were added water (25 mL) and 1 *M* hydrochloric acid (5 mL), and the reaction solution was heated at reflux temperature for 4 h. After the solution had cooled to room temperature, a white solid precipitated that, after reduction of the volume of the reaction mixture to 20 mL, was collected by filtration to give **39** (0.244 g), mp 179–182°C, for a total yield of 0.355 g (75% from **33**). An analytical sample was prepared by recrystallization from ethanol, mp 180–182°C; uv λ_{max} (C_2H_5OH): 203 (ε 17 200), 223 (26 700), 273 (15 600) nm; λ_{max} (0.01 *M* HCl in C_2H_5OH): 203 (ε 16 700), 223 (26 700), 273 (15 400) nm; λ_{max} (0.01 *M* NaOH in C_2H_5OH): 234 (ε 29 600), 273 (18 100) nm; ^{1}Hmr (200 MHz, Me_2SO-d_6), δ: 1.51 (1H, m, H-2′), 1.62–2.13 (4H, m, H-4′, H-4″, H-5′, and H-5″), 2.26 (1H, d of t, J_{gem} = 11.9, ^3J = 6.9 Hz, H-2″), 2.46 (1H, m, H-3′), 4.21–4.38 (2H, m, OCH_2), 5.82 (1H, m, H-1′), 6.01 (1H, d of d, $^3J_{5,6}$ = 8.1, $^4J_{5,3}$ = 1.3 Hz, H-5), 7.50–8.02 (5H, m, C_6H_5), 7.96 (1H, d, $^3J_{6,5}$ = 8.1 Hz, H-6), 12.62 (1H, br s, H-3); spin–spin decoupling was performed at δ 4.30 and 6.01. *Anal.* calcd. for $C_{17}H_{18}O_3N_2S$: C 61.80, H 5.49, N 8.48, S 9.70; found: C 62.17, H 4.97, N 8.46, S 10.17.

*(±)-1-{*cis*-3-(Hydroxymethyl)cyclopentyl}-2,4(1*H*,3*H*)-pyrimidinedione benzoate (**40**)*

Compound **34** (0.448 g, 2.13 mmol) was treated with benzoyl chloride (0.75 mL, 6.5 mmol) as described for the preparation of **35**, and, after fractionation by column chromatography on silica gel, **37** (0.85 g) was obtained as a colorless solid foam, R_f 0.44 (3:2 (v/v) toluene – ethyl acetate); ^{1}Hmr (200 MHz, Me_2SO-d_6), δ: 1.57–2.15 (5H, m, H-2′, H-4′, H-4″, H-5′, and H-5″), 2.24 (1H, d of t, J_{gem} = 12.2, ^3J = 7.0 Hz, H-2″), 2.43 (1H, m, H-3′), 4.22–4.38 (2H, m, OCH_2), 4.81 (1H, m, H-1′), 5.88 (1H, d, $^3J_{5,6}$ = 7.9 Hz, H-5), 7.50–8.01 (10H, m, C_6H_5), 8.03 (1H, d, $^3J_{6,5}$ = 7.9 Hz, H-6); spin–spin decoupling was performed at δ 2.43, 4.81, and 5.88. Compound **37** (0.81 g) was treated as described for the preparation of **38**, and, after fractionation by column chromatography on silica gel, **40** (0.449 g, 70% from **34**) was obtained as a white crystalline solid, mp 153–155°C, R_f 0.56 (4:4:1 (v/v/v) toluene – ethyl acetate – 2-propanol). An analytical sample was prepared by recrystallization from ethanol, mp 154–155°C; uv λ_{max} (C_2H_5OH): 202 (ε 17 700), 226 (14 700), 268 (11 000) nm; λ_{max} (0.01 *M* HCl in C_2H_5OH): 203 (ε 15 800), 227 (14 500), 268 (10 900) nm; λ_{max} (0.01 *M* NaOH in C_2H_5OH): 227 (ε 19 400), 266 (8040) nm; ^{1}Hmr (200 MHz, Me_2SO-d_6), δ: 1.47–2.02 (5H, m, H-2′, H-4′, H-4″, H-5′, and H-5″), 2.14 (1H, d of t, J_{gem} = 12.1, ^3J = 7.0 Hz, H-2″), 2.43 (1H, m, H-3′), 4.20–4.36 (2H, m, OCH_2), 4.79 (1H, m, H-1′), 5.59 (1H, d of d, $^3J_{5,6}$ = 8.0, $^4J_{5,3}$ = 2.0 Hz, H-5), 7.49–8.00 (5H, m, C_6H_5), 7.77 (1H, d, $^3J_{6,5}$ = 8.0 Hz, H-6), 11.28 (1H, br d, $^4J_{3,5}$ = 2.0 Hz, H-3); spin–spin decoupling was performed at δ 2.43, 4.79, and 5.59. *Anal.* calcd. for $C_{17}H_{18}O_4N_2$: C 64.96, H 5.77, N 8.91; found: C 64.93, H 6.02, N 8.87.

*(±)-4-Amino-1-{*cis*-3-(hydroxymethyl)cyclopentyl}-5-methyl-2(1*H*)-pyrimidinone (**43**)*

A solution of **38** (0.315 g, 0.96 mmol), thionyl chloride (1 mL, 13.8 mmol), *N*,*N*-dimethylformamide (55 mg, 0.75 mmol), and chloroform (16 mL) was heated at reflux temperature for 6 h. The solution was cooled and the solvent evaporated; the residue was dried overnight using a vacuum pump. The residue was transferred to a Teflon-lined steel bomb with dry methanol (11 mL). The steel bomb

Can. J. Chem. Downloaded from www.nrcresearchpress.com by 213.222.148.141 on 09/07/12
For personal use only.

was cooled by immersion in crushed Dry Ice for a few min, and then anhydrous ammonia (11 mL) was added. The bomb was sealed and kept in an oil bath at 100°C for 21 h. The bomb was then cooled with Dry Ice, opened, and allowed to warm to room temperature. The contents were transferred with the aid of methanol and, after reduction of the volume using a rotary evaporator, the material was fractionated by column chromatography on silica gel to give **43** (0.158 g, 74%) as a light-yellow oil, R_f 0.33 (5:3:1 (v/v/v) acetonitrile – 1,2-dimethoxyethane – 15 *N* aqueous ammonia). An analytical sample was prepared by crystallization from ethanol–acetonitrile – diethyl ether, mp 217–220°C; ^{1}Hmr (200 MHz, Me_2SO-d_6), δ: 1.24–2.16 (7H, m, H-2′, H-2″, H-3′, H-4′, H-4″, H-5′, and H-5″), 1.84 (3H, s, Me), 3.39 (2H, t, ^3J = 5.8 Hz, HOCH_2), 4.54 (1H, t, ^3J = 5.4 Hz, HOCH$_2$), 4.79 (1H, m, H-1′), 6.66 (1H, br s, NH_2),[3] 7.04 (1H, br s, NH_2),[3] 7.46 (1H, s, H-6). *Anal.* calcd. for $C_{11}H_{17}O_2N_3$: C 59.16, H 7.67, N 18.82; found: C 58.89, H 7.55, N 18.73.

*(±)-4-Amino-1-{*cis*-3-(hydroxymethyl)cyclopentyl}-2(1*H*)-pyrimidinone (**44**)*

A solution of **40** (0.375 g, 1.19 mmol), thionyl chloride (1 mL, 13.8 mmol), *N*,*N*-dimethylformamide (51 mg, 0.70 mmol), and chloroform (17 mL) was treated as described for the preparation of **43**. After having been dried in a vacuum, compound **42** was dissolved in methanol – anhydrous ammonia (20 mL, 1:1 (v/v)) and the solution was heated in a Teflon-lined steel bomb at 100°C for 8.5 h. The bomb was opened as described for the preparation of **43**, and the material was fractionated by column chromatography on silica gel to give **44** (173 mg, 69%) as an oil, R_f 0.35 (5:3:1 (v/v/v) acetonitrile–1,2-dimethoxyethane – 15 *N* aqueous ammonia). An analytical sample was prepared by recrystallization from ethanol – diethyl ether, mp 200–202°C; ^{1}Hmr (200 MHz, Me_2SO-d_6), δ: 1.23–2.18 (7H, m, H-2′, H-2″, H-3′, H-4′, H-4″, H-5′, and H-5″), 3.3–3.45 (2H, m, HOCH_2), 4.58 (1H, br t, HOCH$_2$), 4.80 (1H, m, H-1′), 5.69 (1H, d, $^3J_{5,6}$ = 7.3 Hz, H-5), 7.05 (2H, br s, NH_2), 7.64 (1H, d, $^3J_{6,5}$ = 7.3 Hz, H-6). *Anal.* calcd. for $C_{10}H_{15}O_2N_3$: C 57.40, H 7.23, N 20.08; found: C 57.16, H 7.50, N 19.70.

Treatment of compound **39** as described for the preparation of **44** gave material having mp 195–199°C and an ^{1}Hmr spectrum identical to that obtained for compound **44**.

Acknowledgements

The authors are grateful to the Natural Sciences and Engineering Research Council of Canada for its support of this work in the form of a grant (to W.A.S.). They also thank Dr. K. Rosenthal of McMaster University for permitting the cell-growth inhibition studies using K-562 cells to be performed in his laboratory. The antiviral screening of the nucleoside analogs **31**–**34** was performed by the Bristol–Myers Company.

1. A. M. Michelson and A. R. Todd. J. Chem. Soc. 816 (1955).
2. K. E. Pfitzner and J. G. Moffatt. J. Org. Chem. **29**, 1508 (1964).
3. (*a*) M. J. Robins and R. K. Robins. J. Am. Chem. Soc. **86**, 3585 (1964); (*b*) M. J. Robins, J. R. McCarthy, and R. K. Robins. Biochemistry, **5**, 224 (1966); (*c*) M. J. Robins, F. Hansske, N. H. Low, and J. I. Park. Tetrahedron Lett. **25**, 367 (1984).
4. A. M. Doering, M. Jansen, and S. S. Cohen. J. Bacteriol. **92**, 565 (1966).
5. M. R. Atkinson, M. P. Deutscher, A. Kornberg, A. F. Russell, and J. G. Moffatt. Biochemistry, **8**, 4897 (1969).
6. T. A. Khwaja and C. Heidelberger. J. Med. Chem. **10**, 1066 (1967).
7. F. Sanger, S. Nicklen, and A. R. Coulson. Proc. Natl. Acad. Sci. U.S.A. **74**, 5463 (1977).
8. J. P. Horwitz, J. Chua, M. A. Darooge, M. Noel, and I. L. Klundt. J. Org. Chem. **31**, 205 (1966).
9. H. J. Schaeffer, D. D. Godse, and G. Liu. J. Pharm. Sci. **53**, 1510 (1964).
10. J. A. Montgomery and K. Hewson. J. Med. Chem. **10**, 665 (1967).
11. Y. F. Shealy, J. D. Clayton, and C. A. O'Dell. J. Heterocycl. Chem. **10**, 601 (1973).
12. Y. F. Shealy, C. A. O'Dell, and M. C. Thorpe. J. Heterocycl. Chem. **18**, 383 (1981).
13. A. P. Arendaruk, E. I. Budovskii, B. P. Gottikh, M. Ya. Karpeiskii, L. I. Kudryashov, A. P. Skoldinov, N. V. Smirnova, A. Ya. Khorlin, and N. K. Kochetkov. Zh. Obshch. Khim. **27**, 1312 (1957); Chem. Abstr. **52**, 4508d (1958).
14. S. F. Birch, W. J. Oldham, and E. A. Johnson. J. Chem. Soc. 818 (1947).
15. C. A. O'Dell and Y. F. Shealy. *In* Nucleic acid chemistry. Part I. *Edited by* L. B. Townsend and R. S. Tipson. John Wiley and Sons, Inc., New York. 1978. pp. 161–167.
16. Y. F. Shealy and C. A. O'Dell. Tetrahedron Lett. 2231 (1969).
17. Y. F. Shealy, C. A. O'Dell, M. C. Thorpe, and W. C. Coburn, Jr. J. Heterocycl. Chem. **20**, 655 (1983).
18. E. S. Wallis and J. F. Lane. *In* Organic reactions. Vol. III. *Edited by* R. Adams. John Wiley and Sons, Inc., New York. 1946. pp. 267–306.
19. L. J. J. Hronowski and W. A. Szarek. Can. J. Chem. **63**, 2787 (1985).
20. G. Shaw and R. N. Warrener. J. Chem. Soc. 153 (1958).
21. G. Shaw and R. N. Warrener. J. Chem. Soc. 157 (1958).
22. L. J. J. Hronowski and W. A. Szarek. Can. J. Chem. **64**, 1620 (1986).
23. J. Žemlička and F. Šorm. Collect. Czech. Chem. Commun. **30**, 2052 (1965).
24. Y. F. Shealy and C. A. O'Dell. J. Heterocycl. Chem. **17**, 353 (1980).
25. M. Sano. Chem. Pharm. Bull. **10**, 320 (1962).
26. L. J. J. Hronowski and W. A. Szarek. J. Med. Chem. **25**, 522 (1982).
27. Dictionary of organic compounds. 5th ed. Vol. 2. Chapman and Hall, New York. 1982. p. 1404.
28. Y. F. Shealy and C. A. O'Dell. J. Heterocycl. Chem. **13**, 1015 (1976).
29. E. D. Becker, H. T. Miles, and R. B. Bradley. J. Am. Chem. Soc. **87**, 5575 (1965).
30. Y. F. Shealy, C. A. O'Dell, G. Arnett, W. M. Shannon, M. C. Thorpe, J. M. Riordan, and W. C. Coburn, Jr. J. Med. Chem. **29**, 1720 (1986).

[3]The observation of two broadened singlets arising from the amino group of 5-substituted cytosines has been documented previously (see refs. 29 and 30).

Semiempirical calculation of ^{13}C nuclear magnetic resonance chemical shifts of acyclic hydrocarbons. Application to the stereochemical analysis of steroidal side chains

MANUEL GONZALEZ-SIERRA, DANIEL A. BUSTOS, AND EDMUNDO A. RUVEDA
Instituto de Quimica Organica de Sintesis (CONICET–UNR), Facultad de Ciencias Bioquimicas y Farmaceuticas, Casilla de Correo 991, 2000 Rosario, Argentina

AND

ALEJANDRO C. OLIVIERI AND MARIANO GRASSELLI
PRIBIOR–CONICET, Facultad de Farmacia y Bioquimica, Junin 956, 1113 Buenos Aires, Argentina

Received April 14, 1987

MANUEL GONZALEZ-SIERRA, DANIEL A. BUSTOS, EDMUNDO A. RUVEDA, ALEJANDRO C. OLIVIERI, and MARIANO GRASSELLI. Can. J. Chem. **66**, 71 (1988).

A semiempirical approach for predicting ^{13}C nuclear magnetic resonance chemical shifts of acyclic hydrocarbons has been adapted to a microcomputer program. A series of methyl and dimethyl substituted cholesterols has been studied using this program, and the predicted shifts are in agreement with literature reports. Preferred conformations of the steroidal side chains have been also predicted and agree with previous studies. A simple rule for analyzing the trends in the chemical shift of the carbon C-20, which is sensitive to changes in the configuration at C-22, is also given, not only for hydrocarbon side chains but also for hydroxy substituted compounds.

MANUEL GONZALEZ-SIERRA, DANIEL A. BUSTOS, EDMUNDO A. RUVEDA, ALEJANDRO C. OLIVIERI et MARIANO GRASSELLI. Can. J. Chem. **66**, 71 (1988).

Une approche semi-empirique permettant de prédire les déplacements chimiques en résonance magnétique nucléaire du ^{13}C d'hydrocarbures acycliques a été adaptée à une programme de micro-ordinateurs. Utilisant ce programme, on a étudié une série de cholestérols substitués par des méthyles ou diméthyles; les déplacements chimiques prévus sont en accord avec ceux rapportés dans la littérature. On a aussi prédit les conformations privilégiées des chaînes latérales des stéroïdes et ces conformations correspondent à celles prévues dans des études antérieures. On présente aussi une règle simple pour analyser les tendances dans le déplacement chimique du carbone C-20, qui est sensible aux changements de configuration en C-22; cette règle s'applique tant aux chaînes latérales hydrocarbonées qu'aux composés portant des groupements hydroxyles.

[Traduit par la revue]

Can. J. Chem. Downloaded from www.nrcresearchpress.com by 213.222.148.141 on 09/07/12
For personal use only.

Introduction

^{13}C nuclear magnetic resonance spectroscopy is well established as a powerful tool in the structure elucidation of organic molecules. The range of ^{13}C chemical shifts is large (about 250 ppm in common organic compounds), and therefore this parameter is able to reflect subtle structural changes. However, the physical background of the factors influencing the position of ^{13}C resonances is not yet fully understood. A survey of the literature on substituent effects reveals that sp^2 carbons have been widely studied (1–7), and correlations have been found with known physicochemical properties. For aliphatic systems, on the other hand, there is no comprehensive treatment of the structural features involved in ^{13}C chemical shifts. Nevertheless, the number of empirical studies in this field is continually growing. Several rules for evaluating chemical shifts of sp^3 carbons have been proposed (8–12), but they cannot deal with molecular asymmetry or conformationally rigid molecules. The semiempirical method developed by Beierbeck *et al.* (13, 14) allows us to predict, with a satisfactory degree of accuracy, ^{13}C chemical shifts of saturated aliphatic hydrocarbons and rigid cyclohexanes having different substituents, and has been recently extended to epoxides (15).

Whereas in fixed substrates the calculations can be easily performed, the analysis of acyclic compounds requires considerable effort. In this report we use a microcomputer program to calculate conformer populations, ^{13}C chemical shifts of individual conformers, and conformationally averaged resonances according to the method of Beierbeck and Saunders (14). A comparison is presented between the observed shifts for a series of steroidal side chains and those calculated with the program. The implications of the results regarding the use of ^{13}C nmr spectroscopy in the structure elucidation of related steroids are discussed, and the predicted preferred conformations are compared with previous studies involving ^{1}H nmr spectroscopy.

Results and discussion

One of the earliest rules for predicting ^{13}C chemical shifts was that of Grant and Paul (8), later improved by Lindeman and Adams (9) to account for highly branched hydrocarbons. The latter rule has been extended to substituted alkanes by relating them to analogously constituted hydrocarbons in which the substituent heteroatoms are replaced by carbons (e.g., OH, Cl, Br, I by CH_3; -COO- by $-CH(CH_3)CH_2-$, etc.) (10–12). Since the parameters used in these analyses were based on conformational averages, they were not able to deal with molecular asymmetry or fixed structures.

In the approach of Beierbeck and Saunders (14), conformer populations are estimated prior to the ^{13}C chemical shift study, using experimentally determined rotational energies and steric contributions. The conformer statistical weights Ω_j are taken as products of m contributions E_{ij} to the energy of the conformer j:

$$[1] \quad \Omega_j = \prod_{i=1}^{m} \exp(-E_{ij}/RT)$$

The conformer populations are then obtained according to

$$[2] \quad p_j = \Omega_j \Big/ \left(\sum_{j=1}^{n} \Omega_j \right)$$

where n is the total number of conformers. Details on the values of the contributions E_{ij} are given in ref. 14. Individual ^{13}C resonances are predicted using the substituent parameter set derived for rigid cyclic systems (13), and are conformationally averaged using the populations p_j.

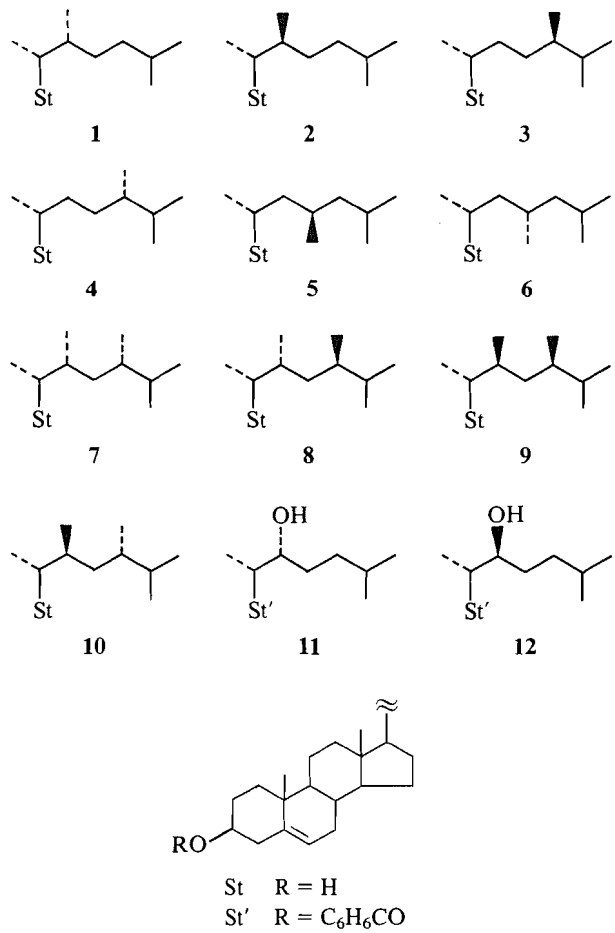

Since the number of conformers grows exponentially with the number of rotated C—C bonds, the calculation of a medium size hydrocarbon requires considerable work. Therefore, we have devised a program written in ISOPASCAL for the microcomputer Sinclair QL, which calculates the conformer populations, their ^{13}C chemical shifts, and the final weighted values predicted for solution resonances. The user may select some bonds to remain fixed, allowing the others to rotate every 120°. This proves useful in the study of aliphatic side chains attached to rigid frameworks, as will be illustrated below. The output of the program consists of the averaged ^{13}C chemical shifts, a computer drawing of the most abundant conformer, and its relative population.

As an example of the potential application of this approach, the series of methyl and dimethyl substituted cholesterols **1–10** was studied. The ^{13}C nmr chemical shifts of these compounds are available from the literature, having attracted attention in recent years due to their biological significance (16–18). Compounds **3** and **4** exist in marine environments (19), and the rest are expected to be also naturally occurring.

To undertake the study of ^{13}C chemical shifts of the side chains of **1–10**, we choose as a convenient model the compound shown in Fig. 1, in which some bonds are maintained fixed by the computer program, while the others are allowed to rotate every 120° during the calculations. In Table 1 a comparison is shown between the experimental data and the values calculated with the program. The standard deviation is within the expected values (13, 14) although the errors may accumulate in some unfavourable cases. However, the power of the method rests in the prediction of relative shieldings or deshieldings, and is not intended to give reliable absolute values.

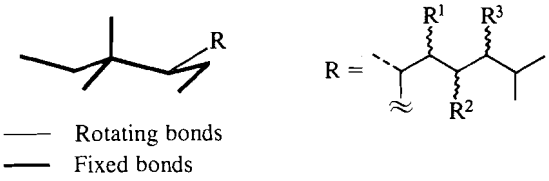

FIG. 1. Model compound used to study ^{13}C chemical shifts with the semiempirical method developed by Beierbeck *et al.*

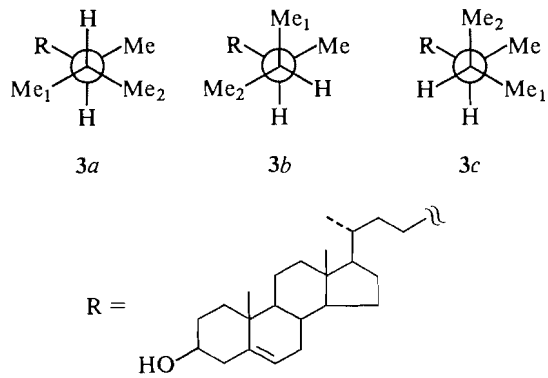

	Predicted values				Observed values
	3*a*	**3***b*	**3***c*	Average[a]	
δ_{Me_1}	21.99	16.54	21.99	19.99	20.2
δ_{Me_2}	21.99	21.99	16.54	19.10	18.2

[a]Conformationally averaged chemical shifts according to the analysis of Beierbeck *et al.*

FIG. 2. Conformations of compound **3** obtained by rotating the 24,25 bond, and analysis of the chemical shifts of the C-25 methyls.

As shown in Table 1, the method is also able to deal with the nonequivalence of the methyls C-26 and C-27, induced by nearby chiral centers (20). Consider compound **3**, whose conformations around the 24,25 bond are depicted in Fig. 2. In the most favourable one (**3***a*), both methyls are predicted to have the same chemical shift, since they have the same number of HC interactions (associated with 1,3-diaxial-like H/H interactions, the dominant deshielding mode assumed by the method). In **3***b*, one of the methyls should be shielded relative to the other (one HC interaction has been removed), whereas the reverse situation is found in **3***c* (see Fig. 2). Since the population of **3***c* is larger than that of **3***b*, where two unfavourable R/Me interactions are seen, a small difference is expected in the averaged chemical shifts of C-26 and C-27. The nonequivalence is therefore accounted for by the chirality of C-24, which perturbs the energies of the rotamers **3***b* and **3***c*. In this way, molecular asymmetry is taken into account without postulating additional parameters than those required for rigid systems.

Another interesting feature to be found in Table 1 is the success of the method in predicting the chemical shift of C-20, since the values estimated with the aid of the Lindeman–Adams rule (9) are too low, although the latter has been especially devised to analyze highly branched alkanes. This can be explained on the basis of a restricted rotation about the 17,20 bond. In fact, the most abundant conformers predicted by the program are those that show an antiperiplanar relation between H-17 and H-20. Furthermore, in C-22 substituted compounds the 20,22 bond is predicted to adopt a conformation in which

Can. J. Chem. Downloaded from www.nrcresearchpress.com by 213.222.148.141 on 09/07/12
For personal use only.

TABLE 1. Comparison between observed and predicted ^{13}C nmr chemical shifts of the steroids studied[a,b,c,d]

Carbon	Compound	$\delta_{obs.}$	$\delta_{calc.}$	Carbon	Compound	$\delta_{obs.}$	$\delta_{calc.}$
20	**1**	41.44	42.53	20	**4**	36.1	37.28
21	**1**	12.90	12.52	21	**4**	18.9	16.63
22	**1**	34.80	36.41	22	**4**	33.8	31.75
23	**1**	26.90	28.59	23	**4**	30.6	31.39
24	**1**	37.70	37.10	24	**4**	39.1	41.12
25	**1**	28.33	29.92	25	**4**	31.5	33.69
26	**1**	22.32	22.98	26	**4**	17.6	18.97
27	**1**	23.06	23.28	27	**4**	20.5	20.06
28	**1**	18.82	16.54	28	**4**	15.5	15.63
20	**2**	38.55	40.42	20	**5**	33.68	33.46
21	**2**	12.95	12.22	21	**5**	19.01	16.86
22	**2**	34.59	36.08	22	**5**	45.33	42.91
23	**2**	33.51	32.34	23	**5**	25.38	28.34
24	**2**	37.15	37.13	24	**5**	45.84	44.73
25	**2**	28.22	29.92	25	**5**	27.76	26.18
26	**2**	22.59	23.13	26	**5**	21.42	21.06
27	**2**	22.59	23.12	27	**5**	21.63	21.72
28	**2**	12.27	14.39	28	**5**	24.16	25.09
20	**2**	35.9	36.99	20	**6**	33.61	33.17
21	**3**	18.7	16.61	21	**6**	19.47	16.60
22	**3**	33.8	31.59	22	**6**	44.02	41.01
23	**3**	30.3	31.18	23	**6**	25.16	28.13
24	**3**	38.9	40.89	24	**6**	48.44	48.42
25	**3**	32.4	33.95	25	**6**	27.34	26.19
26	**3**	18.2	19.10	26	**6**	22.69	23.46
27	**3**	20.2	19.99	27	**6**	22.99	23.30
28	**3**	15.4	15.54	28	**6**	18.62	18.98
20	**7**	41.92	42.36	20	**9**	35.17	39.32
21	**7**	12.98	12.65	21	**9**	12.09	12.08
22	**7**	31.78	32.88	22	**9**	32.10	31.90
23	**7**	34.21	35.80	23	**9**	39.50	38.44
24	**7**	35.70	36.81	24	**9**	36.92	37.02
25	**7**	28.87	31.29	25	**9**	31.12	33.84
26	**7**	19.37	17.49	26	**9**	20.12	19.98
27	**7**	21.38	20.65	27	**9**	17.91	18.88
28	**7**	15.33	16.65	28	**9**	15.56	15.62
29	**7**	15.67	16.97	29	**9**	14.04	15.39
20	**8**	41.68	42.62	20	**10**	40.77	41.46
21	**8**	12.85	12.41	21	**10**	12.71	12.22
22	**8**	33.78	32.22	22	**10**	32.25	32.06
23	**8**	33.18	34.08	23	**10**	40.13	38.33
24	**8**	35.70	37.11	24	**10**	35.80	37.03
25	**8**	31.47	35.07	25	**10**	31.59	33.99
26	**8**	19.84	19.53	26	**10**	17.80	18.95
27	**8**	18.79	19.67	27	**10**	20.18	19.45
28	**8**	15.39	15.14	28	**10**	15.44	15.62
29	**8**	18.79	16.46	29	**10**	12.51	15.39

[a]In ppm downfield from TMS.

[b]The data for compounds **1**, **2**, **3**, and **4** have been taken from ref. 16, those for **5** and **6** from ref. 17, and those for **7**, **8**, **9**, and **10** from ref. 18.

[c]Root mean square deviation between calculated and observed shifts is 1.51 ppm.

[d]In compounds **1**, **2**, **7**, **8**, **9**, and **10** the original assignments of carbons 20 and 22 have been interchanged.

interactions between the C-22 substituents and the methylene C-16 are avoided. These results, illustrated in Fig. 3 by computer drawings of the preferred conformations of **1** and **10**, are in agreement with previous studies performed by ^1H nmr spectroscopy (21). If the conformation around the 17,20 bond is somewhat fixed, then the failure of the Lindeman–Adams rule is not surprising, since its parameters are derived through conformational averages.

We now focus our attention on the determination of the configuration at C-22, a subject of great biological relevance (18). From the data presented in Table 1, it is clear that the chemical shift of C-23 is of diagnostic value: both predicted and observed values are upfield in the 22(*R*) substituted compounds. The resonance of C-20 seems also to be sensitive to changes in the configuration of C-22, being consistently shielded in the 22(*S*) series relative to the 22(*R*). The study of the chemical shift of C-20 is particularly interesting, since it can be analyzed in a simple way by assuming a fixed conformation

Can. J. Chem. Downloaded from www.nrcresearchpress.com by 213.222.148.141 on 09/07/12
For personal use only.

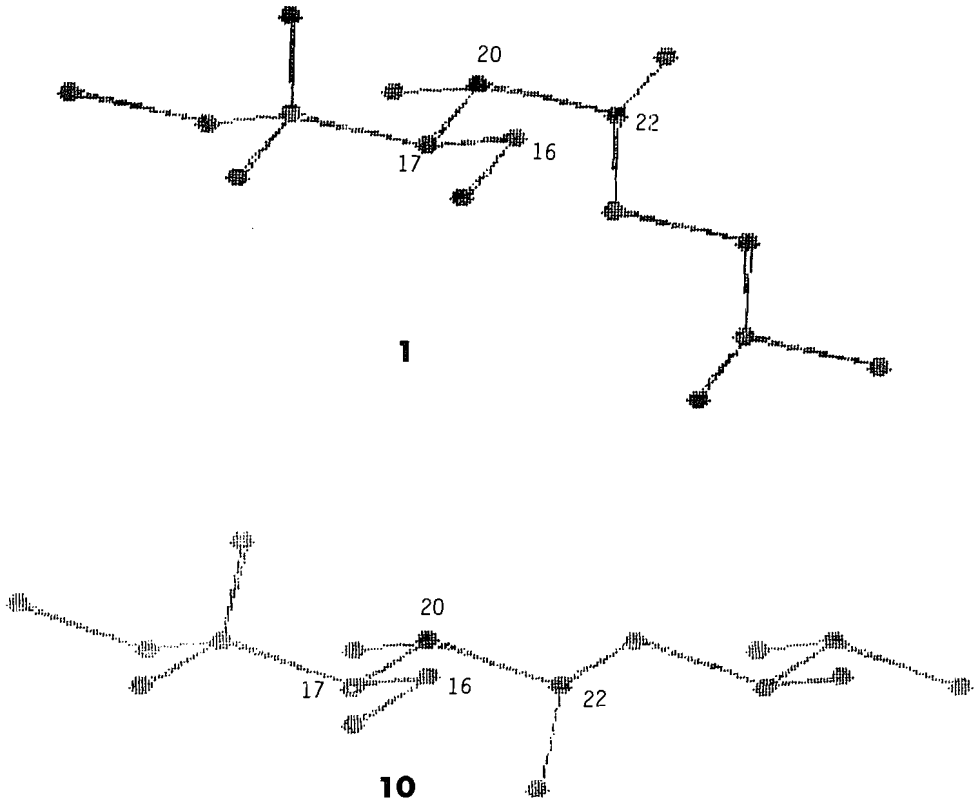

FIG. 3. Computer drawings of the preferred conformations of the side chains of **1** and **10** as predicted by analysis of model compounds (see Fig. 1) using a microcomputer program based on the method of Beierbeck *et al.* (only the carbons belonging to the model are shown). In both **1** and **10** the *anti* relationship between H-17 and H-20 is apparent, as well as the parallel 1,3 interaction between H-22 and the methylene C-16.

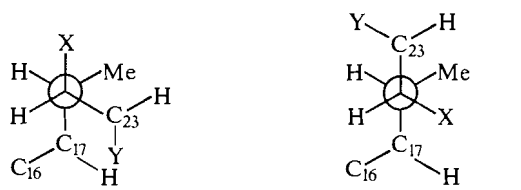

1	X = Me; Y = H	**2**	X = Me; Y = H
11	X = OH; Y = H	**12**	X = OH; Y = H
16	X = Br; Y = OH	**15**	X = OH; Y = Br
17	X = OH; Y = Br	**18**	X = Br; Y = OH

FIG. 4. Preferred conformations of **1**, **2**, **11**, **12**, **15**, **16**, **17**, and **18** used to analyze the substituent effects on C-20.

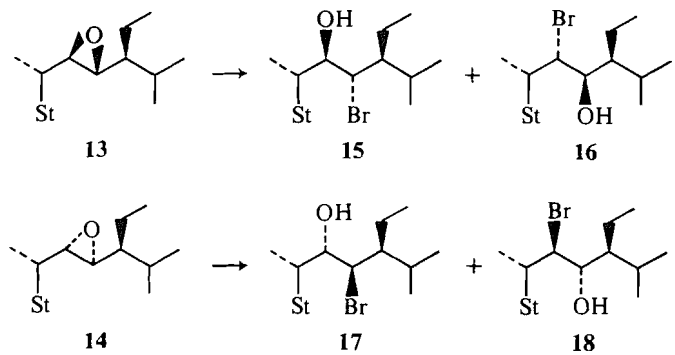

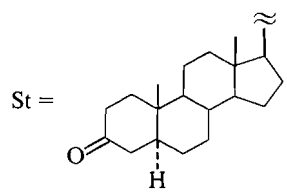

SCHEME 1

around the 17,20 bond, as stated above. Shown in Fig. 4 are the preferred conformations of **1** and **2**, which we assume to be fixed except for a rotation around the 22,23 bond. In both of them C-20 is predicted to have the same chemical shift. However, a rotation about the 22,23 bond in **2** will remove one parallel 1,3 interaction H-20/H-23, and this contribution will produce an average shielding on C-20. The possibility of a similar rotation exists in **1**, but in this case the number of HC interactions affecting C-20 is unchanged. An analogous situation is found in C-22 hydroxy substituted molecules, such as **11** and **12**. The set of parameters derived by Beierbeck *et al.* for rigid cyclohexane alcohols, applied to the preferred conformations shown in Fig. 4, gives nearly equal values for C-20 in both cases. Again, a rotation about the 22,23 bond is expected to lead to an average shielding in the 22(*S*) compound **12**, in agreement with the experimental data (22). Remarkably, this effect appears to be independent of the nature of the group attached to C-22, as has been observed in steroids substituted with halogens, amino, etc. (22).

An additional example is provided by the bromohydrins **15**–**18**. They have been obtained from the epoxides **13** and **14** (23), whose configurations are known from ^{13}C nmr studies (24) (Scheme 1). Table 2 shows ^{13}C chemical shifts of some selected carbons of these compounds, where the assignments have been confirmed by subsequent chemical transformation (25). The

Can. J. Chem. Downloaded from www.nrcresearchpress.com by 213.222.148.141 on 09/07/12
For personal use only.

TABLE 2. The ^{13}C nmr chemical shifts of selected carbons of bromohydrins **15–18** and calculated values for C-20[a,b]

Carbon	Compound	$\delta_{obs.}$	$\delta_{calc.}$
20	**15**	37.7	37.6
22	**15**	73.3	
23	**15**	60.6	
20	**16**	42.9	41.5
22	**16**	63.2	
23	**16**	73.2	
20	**17**	40.9	41.5
22	**17**	77.4	
23	**17**	61.8	
20	**18**	36.3	37.6
22	**18**	65.4	
23	**18**	72.8	

[a]In ppm downfield from TMS.
[b]Assuming preferred conformations shown in Fig. 4.

diagnostic value of C-20 is apparent, being upfield in the 22(*R*) compounds.[1] This trend in the chemical shift of C-20 can be accounted for by analyzing the preferred conformations shown in Fig. 4 (22). The calculated values for C-20, assuming that Br induces β and γ effects similar to OH, are also included in Table 2, and are in good agreement with the observed ones. Similar values have been reported for C-20 in related chlorohydrins derived from naturally occurring epoxides (26). It should be noted that attempts to predict the values of C-22 and C-23 in this type of compound may fail due to nonadditive effects that are observed when two substituents are at vicinal positions (27, 28).

In conclusion, we have used a method for the derivation of ^{13}C chemical shifts in rigid systems, which is equally applicable to the calculation of chain conformer resonances. With the aid of a microcomputer program we have obtained an estimate of conformer populations and conformationally averaged chemical shifts for a series of steroidal side chains of biological interest. The results are in good agreement with the values reported in the literature. In addition, the configuration at C-22 has been shown to be monitored by the chemical shift of C-20, and rules have been given to analyze the effects produced by C-22 substitution on this resonance, on the basis of a preferred conformation around the 17,20 and 20,22 bonds.

Acknowledgments

This work was supported by CONICET (Consejo Nacional de Investigaciones Cientificas y Tecnicas). A.C.O. and D.A.B. thank CONICET for fellowships. Fruitful discussions with Dr. Helmut Duddeck (Univ. Bochum) are also gratefully acknowledged.

[1]Care should be taken when introduction or removal of a group changes the *R* or *S* notation.

1. J. B. STOTHERS. Carbon-13 NMR spectroscopy. Academic Press, New York. 1972.
2. G. C. LEVY, R. L. LICHTER, and G. L. NELSON. Carbon-13 nuclear magnetic resonance spectroscopy. 2nd ed. Wiley, New York. 1980.
3. F. W. WEHRLI and T. WIRTHLIN. Interpretation of carbon-13 nuclear magnetic resonance spectra. Heyden, London. 1976.
4. E. BREITMAIER and W. VOELTER. ^{13}C NMR spectroscopy. 2nd ed. Verlag Chemie, Weinheim. 1978.
5. G. L. NELSON and E. A. WILLIAMS. Electronic structure and ^{13}C NMR. *In* Progr. Phys. Org. Chem. *Edited by* R. W. Taft. Wiley, New York. 1976.
6. G. J. MARTIN, M. L. MARTIN, and S. ODIOT. Org. Magn. Reson. **7**, 2 (1975).
7. D. F. EWING. Org. Magn. Reson. **12**, 499 (1979).
8. D. M. GRANT and E. G. PAUL. J. Am. Chem. Soc. **86**, 2984 (1964).
9. L. P. LINDEMAN and J. Q. ADAMS. Anal. Chem. **43**, 1245 (1971).
10. J. D. ROBERTS, F. J. WEIGERT, J. I. KROSCHWIRTZ, and H. J. REICH. J. Am. Chem. Soc. **92**, 1338 (1970).
11. A. EJCHART. Org. Magn. Reson. **13**, 368 (1980).
12. A. EJCHART. Org. Magn. Reson. **10**, 263 (1977).
13. H. BEIERBECK, J. K. SAUNDERS, and J. W. APSIMON. Can. J. Chem. **55**, 2813 (1977).
14. H. BEIERBECK and J. K. SAUNDERS. Can. J. Chem. **58**, 1258 (1980).
15. M. I. COLOMBO, D. A. BUSTOS, M. GONZALEZ-SIERRA, A. C. OLIVIERI, and E. A. RUVEDA. Can. J. Chem. **64**, 552 (1986).
16. J. ZIELINSKI, H. LI, and C. DJERASSI. J. Org. Chem. **47**, 620 (1982).
17. H. LI, I. J. MASSEY, D. C. SWENSON, W. L. DUAX, and C. DJERASSI. J. Org. Chem. **48**, 48 (1983).
18. T. GEBREYESUS and C. DJERASSI. J. Org. Chem. **49**, 987 (1984).
19. L. J. GOAD. *In* Biochemical and biophysical perspectives in marine biology. *Edited by* D. C. Malins and J. R. Sargent. Academic Press, New York. 1976. pp. 213–218.
20. J. L. C. WRIGHT, A. G. MCINNES, S. SHIMIZU, D. G. SMITH, and J. A. WALTER. Can. J. Chem. **56**, 1898 (1978).
21. M. NAKANE and N. IKEKAWA. J. Chem. Soc. Perkin Trans. 1, 1426 (1977).
22. Y. LETOURNEAUX, Q. KHUONG-HUU, M. GUT, and G. LUKACS. J. Org. Chem. **40**, 1674 (1975).
23. M. NAKANE, N. MORISAKI, and N. IKEKAWA. Tetrahedron, **31**, 2755 (1975).
24. M. GONZALEZ-SIERRA, D. A. BUSTOS, M. E. ZUDENIGO, and E. A. RUVEDA. Tetrahedron,**42**, 755 (1986).
25. D. A. BUSTOS. PhD Dissertation, Facultad de Ciencias Bioquimicas y Farmaceuticas, Universidad Nacional de Rosario, Argentina. 1986.
26. L. MINALE, R. RICCIO, F. DE SIMONE, A. DINI, and C. PIZZA. Tetrahedron Lett. 645 (1979).
27. D. K. DALLING and D. M. GRANT. J. Am. Chem. Soc. **94**, 5318 (1972).
28. Y. SENDA, J. ISHIYAMA, and S. IMAIZUMI. Tetrahedron, **31**, 1601 (1975).

Can. J. Chem. Downloaded from www.nrcresearchpress.com by 213.222.148.141 on 09/07/12
For personal use only.

An electron spin resonance spin trapping investigation of azide oxidation on TiO_2 powder suspensions

ANDREA MALDOTTI,[1] ROSSANO AMADELLI, AND VITTORIO CARASSITI

Centro di Studio sulla Fotochimica e Reattività degli Stati Eccitati dei Composti di Coordinazione del C.N.R. and Dipartimento di Chimica dell'Università degli Studi di Ferrara, 44100 Ferrara, Italy

Received March 24, 1987

ANDREA MALDOTTI, ROSSANO AMADELLI, and VITTORIO CARASSITI. Can. J. Chem. **66**, 76 (1988).

The oxidation of azide has been studied on TiO_2 powder suspensions in water, methanol, and mixtures of the two solvents. The esr spin trapping technique has been employed to provide evidence for the formation of azidyl radicals $N_3^{\bullet}$. The results show that an aqueous alkaline medium is necessary to obtain a high production of $N_3^{\bullet}$ radicals. A mechanism is proposed whereby the oxidation of N_3^- is mainly due to reaction with $OH^{\bullet}$ radicals which are in turn generated upon capture of holes by OH^- groups adsorbed on TiO_2. Azidyl anions adsorb weakly on TiO_2 and do not displace adsorbed OH^- from the surface.

ANDREA MALDOTTI, ROSSANO AMADELLI et VITTORIO CARASSITI. Can. J. Chem. **66**, 76 (1988).

On a étudié l'oxydation de l'azoture sur des poudres de TiO_2 en suspension dans l'eau, le méthanol et des mélanges des deux solvants. On a utilisé la technique du piégeage de spin par rpe pour obtenir des indications relatives à la formation des radicaux azidyles $N_3^{\bullet}$. Les résultats démontrent qu'il est nécessaire d'opérer dans un milieu aqueux alcalin pour obtenir une production élevée de radicaux $N_3^{\bullet}$. On propose un mécanisme selon lequel l'oxydation des ions N_3^--provient principalement d'une réaction avec des radicaux $OH^{\bullet}$ qui sont à leur tour générés par la capture de trous par les groupements OH^- adsorbés sur le TiO_2. Les anions azidyles ne s'adsorbent que faiblement sur le TiO_2 et ils ne déplacement pas les OH^- qui sont adsorbés sur la surface.

[Traduit par la revue]

Introduction

Considerable interest has recently been shown in the oxidation of azide, especially with a view to studying the addition of anodically generated radicals to olefins (1–3). The oxidation of N_3^- produces $N_3^{\bullet}$ radicals whose addition to an olefin competes with their dimerization. Interest has also been focused on the use of $N_3^{\bullet}$ as a selective oxidant of organic (4) and inorganic (5) compounds. It has been pointed out, in this respect, that $N_3^{\bullet}$ as opposed to, for example, $OH^{\bullet}$, reacts primarily by electron transfer.

We were interested in the possibility of using $N_3^{\bullet}$ radicals as oxidation mediators between a semiconductor surface at which they are photogenerated and species of interest, in particular organic compounds in the solution phase. In this work, we describe an esr spin trapping investigation on the formation of $N_3^{\bullet}$ radicals in a photoactivated TiO_2 suspension. The esr spin trapping technique is a powerful tool for detecting the formation of short-lived radicals and has been fruitfully employed in work with semiconductors (6–8). The spin trapping of electrochemically generated azidyl radicals has been previously described (9, 10).

Experimental

Titanium dioxide (99.99%) was obtained from Strem Chemicals. Sodium azide (Fluka), *N-tert*-butyl-α-phenylnitrone (PBN) (Janssen), 5,5-dimethyl-pyrrolinyl-1-oxy (DMPO), and Fe tetra-4-sulfonatophenyl porphine (Fluka) were used as received. Methanol and ethanol were Fluka spectroscopic grade reagents and were dried according to standard procedures (11). Sodium azide and PBN were added to the ultrasonically dispersed TiO_2 in water. Triply distilled water was used in all experiments.

Electron spin resonance measurements were carried out with a Bruker ER 200 D spectrometer. Calibration was achieved as described in ref. 12. The suspension containing the required reagents was introduced into a Spectrosil flat cell and irradiated directly in the esr cavity using a medium pressure mercury lamp (Hanau Q 600). Light of wavelength lower than 360 nm was cut off using suitable glass filters.

Before each experiment with illumination, runs were performed in the dark to check for possible radicals formed thermally. The kinetic data were obtained by recording the esr signal intensity I at a fixed value of the magnetic field.

Results

Radical trapping under continuous irradiation

Irradiation ($\lambda > 360$) of a TiO_2 suspension in water containing sodium azide and PBN leads to the formation of a paramagnetic species whose esr spectrum, shown in Fig. 1*a*, is characteristic of the spin adduct (N_3PBN) (13). This implies that oxidation of azide produces azidyl radicals which are subsequently trapped according to reaction [1].

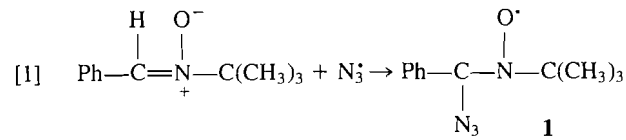

[1] $Ph{-}C(H)(O^-){=}N^+{-}C(CH_3)_3 + N_3^{\bullet} \rightarrow Ph{-}C(O^{\bullet})(N_3){-}N{-}C(CH_3)_3$ **1**

It is worthwhile mentioning the possible occurrence of the following reaction, in competition with the trapping process:

[2] $N_3^{\bullet} + N_3^- \rightarrow N_6^-$

There are controversial data in the literature concerning this reaction. According to Hayon and Simic (14) it does not occur at all, but Kremers and Singh (15) present evidence that it does take place at the higher N_3^- concentrations. The latter authors, however, state that there is no concentration effect on the esr signal intensity due to the adduct of the azidyl radicals with the spin trap; they conclude that $N_3^{\bullet}$ and N_6^- form adducts having the same esr spectral pattern. This is an important conclusion for the consistency of the experimental results reported in this work.

Figure 2 shows the different behavior of the kinetics curves in air and O_2-saturated TiO_2 aqueous suspensions. In the latter case, the signal intensity regains its initial value when light is switched on after a period in the dark. Harbour and Hair (7) observe a similar effect of O_2 in a study of the DMPO—OH adduct decay. We attribute the observed behavior to the fact that increasing the concentration of O_2 makes more efficient the

[1]To whom correspondence should be addressed.

Printed in Canada / Imprimé au Canada

Can. J. Chem. Downloaded from www.nrcresearchpress.com by 213.222.148.141 on 09/07/12
For personal use only.

Can. J. Chem. Downloaded from www.nrcresearchpress.com by 213.222.148.141 on 09/07/12
For personal use only.

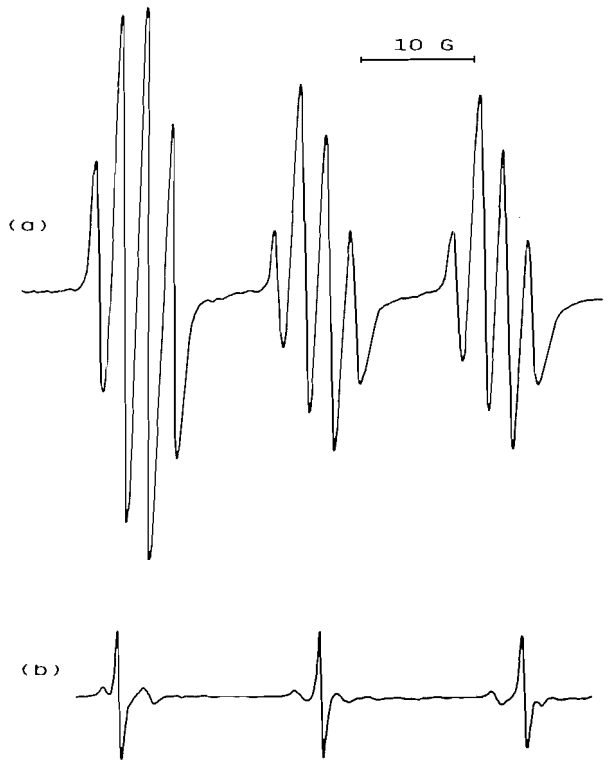

FIG. 1. (*a*) Electron spin resonance spectrum of the adduct between PBN and $N_3^{\cdot}$ obtained after 60 s irradiation of a TiO_2 aqueous suspension containing 0.1 *M* NaN_3 and 0.1 *M* PBN; (*b*) esr spectrum of di-*t*-butyl nitroxide (DTN) obtained in the dark after a prolonged irradiation of the suspension.

removal of conduction band electrons, which, in turn, gives longer life to the photogenerated holes.

Figure 3 shows a plot of the initial rate, r, of growth of the esr signal due to (N_3PBN) adduct vs. the concentration of N_3^-. The form of this curve is strongly reminiscent of a Langmuir isotherm, which means that the reaction leading to $N_3^{\cdot}$ occurs in the adsorbed phase. The rate[2] is then proportional to the surface coverage by adsorbed N_3^-. Indeed, a plot of $1/r$ vs. $1/C_{N_3^-}$ is linear (Fig. 4).

A prolonged irradiation leads to the appearance of another signal superimposed on the spectrum of the (N_3PBN) adduct. After light is switched off, the signal due to (N_3PBN) disappears and only the signal shown in Fig. 1*b* remains. The spectrum is characteristic of di-*t*-butyl nitroxide (DTN) (16).

Iron porphyrin induced oxidation of azide in homogeneous solution

In order to verify whether the decay of the esr signal is due to a reaction occurring in the homogeneous phase or on the photoactivated semiconductor, we have looked for a system in which it is possible to produce N_3^- radicals in the homogeneous solution.

The irradiation of deaerated solutions of Fe(III)$TPPS_4$ in ethanol/water solutions containing NaN_3 and PBN leads to the

[2]The true rate constant for $N_3^{\cdot}$ formation, R, is certainly higher than that we derived from the growth of the esr signal, r, which correspond to the formation of (N_3PBN). The reason for this is that not all $N_3^{\cdot}$ radicals are trapped by PBN. However, the purpose of this work is not to determine R; for our purposes it is sufficient that a linear proportionality exists between R and r. That this is the case is substantiated by the linearity of the plots in Fig. 4.

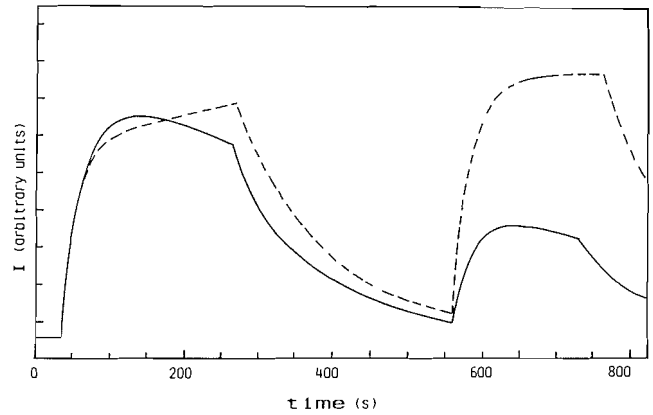

FIG. 2. Electron spin resonance signal intensity of the adduct (N_3PBN) as a function of illumination at a fixed field position. Solid line: air-saturated suspension; dashed line: O_2-saturated suspension.

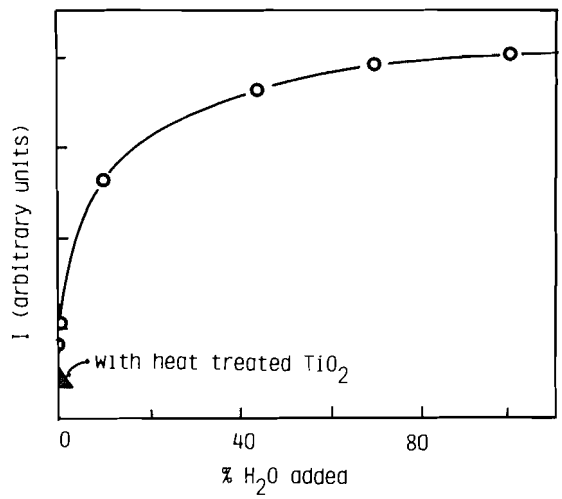

FIG. 3. Initial rate r of (N_3PBN) formation as a function of the N_3^- concentration at different pH values. The signal is measured within 5 min from switching on the light.

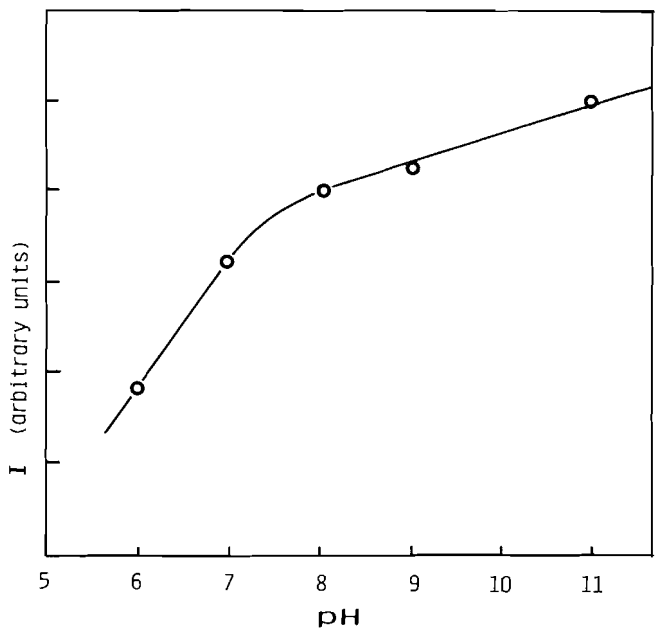

FIG. 4. Plots of $1/r$ vs. $1/C_{N_3^-}$ constructed from the data of Fig. 3.

formation of both the (N_3PBN) adduct and DTN as seen from the esr spectra. The behavior is the same as that observed with the semiconductor suspension, and we can conclude that the decay of the spin adduct is not appreciably affected by the heterogeneous phase.

Irradiation in the presence of catalase

It is known that hydrogen peroxide is formed when TiO_2 is irradiated in aqueous solution (17). To examine the possibility that H_2O_2 might be involved in reactions with $N_3^{\cdot}$ according to

[3] $H_2O_2 + N_3^{\cdot} \rightarrow HN_3 + HO_2^{\cdot}$

We carried out experiments with catalase added to the suspensions. In these conditions, H_2O_2 should be decomposed by the enzyme to H_2O and O_2. Since we did not observe any effect on the rate of the esr signal intensity, we conclude that reaction [3] does not occur to an appreciable extent. The same conclusion is arrived at by Singh *et al.* (18) in their pulse radiolysis studies.

Solvent and pH effect

We observed a marked influence of solvent on the yield of (N_3PBN) formation. Figure 5 shows the change in the intensity of the esr signal due to (N_3PBN) on passing from methanol to water through mixtures of the two solvents. It is evident that a decrease in the water content leads to a marked decrease in the amount of $N_3^{\cdot}$ produced. Besides, if TiO_2 is evacuated at high temperature (300 to 400°C) to remove the surface OH groups and then suspended in dry methanol, a further decrease in the yield of $N_3^{\cdot}$ formation is observed with respect to unheated TiO_2.

A signal due to the formation of a PBN–CH_2OH adduct is observed immediately upon irradiation of a TiO_2 suspension in pure methanol in the absence of azide. With azide present, the formation of $\dot{C}H_2OH$ radicals is apparent only after prolonged irradiation. This suggests that the observed decrease in $N_3^{\cdot}$ formation on changing the solvent from water to methanol cannot be ascribed to the preferential oxidation of the organic solvent.

The influence of the solution pH on the yield of the N_3PBN spin adduct formation is displayed in Fig. 6. The esr signal increases as the solution is made more alkaline, the higher increase being found between pH = 6 and 9. Lower pH's were not tested to avoid protonation of N_3^-. The experiments were carried out with both buffered solutions or with solutions whose pH was adjusted to the desired value by addition of $HClO_4$ or NaOH.

Irradiation in the absence of azide

Irradiation of TiO_2 in water with PBN but without NaN_3 leads to the appearance of an esr spectrum consisting of a triplet of doublets with coupling constants $a_N = 16.2$ G and $a_H = 3.0$ G. This spectrum is ascribed to the formation of a PBN–OH adduct. The values of the coupling constants do not fit well into the equation given by Janzen *et al.* (19), i.e.,

[4] $a_H = 0.604a_N - 6.53$

On the other hand, a difference between the experimental values of a_H and those calculated from eq. [4] is also observed using the coupling constants for the PBN–OH reported in the literature (8). In experiments carried out with an aqueous semiconductor suspension and DMPO as a spin trap we unequivocally proved the formation of $OH^{\cdot}$ in the absence of azide (1:2:2:1 quartet $a_N = a_H = 15.2$ G) (20).

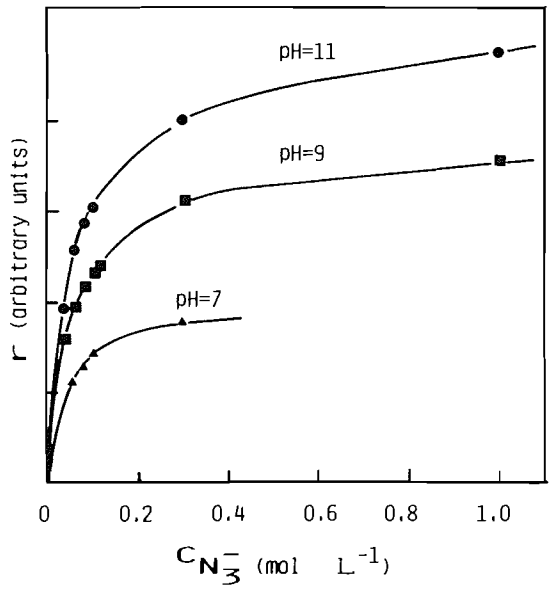

FIG. 5. Electron spin resonance signal intensity of the (N_3PBN) adduct formed by oxidation of N_3^- on TiO_2 suspended in a mixed solvent methanol/water. The dark triangle refers to dry methanol but with TiO_2 evacuated at 400°C.

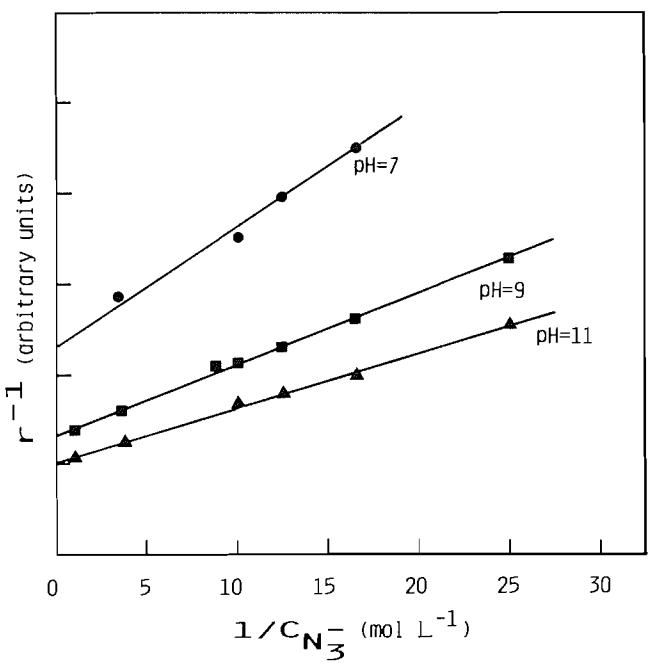

FIG. 6. Electron spin resonance signal intensity of the (N_3PBN) adduct as a function of pH.

Discussion

Surface interaction of N_3^- with TiO_2

The results reported in this work indicate that an aqueous alkaline medium is necessary to increase the amount of azidyl radicals formed upon N_3^- oxidation. It is also evident that the surface OH groups of TiO_2 play a fundamental part in the oxidation process.

As far as the pH dependence is concerned (Fig. 6), note that by virtue of the dissociation equilibrium

[5] $TiOH + OH^- \rightarrow TiO^- + H_2O$

Can. J. Chem. Downloaded from www.nrcresearchpress.com by 213.222.148.141 on 09/07/12
For personal use only.

Can. J. Chem. Downloaded from www.nrcresearchpress.com by 213.222.148.141 on 09/07/12
For personal use only.

The surface becomes negative as the pH increases. This would lead to the repulsion of N_3^- to the outer Helmholtz layer and one would thus expect a decrease in the formation of $N_3^{\cdot}$ as the pH increases. Indeed, this occurs in the oxidation of, e.g., I^- on TiO_2 (21) but contrasts with the data reported herein for N_3^-. A possible explanation for the data obtained with our system is that the azidyl ion may not compete significantly with OH^- for adsorption; the coverage by N_3^- would then be consistently low but the negatively charged surface would represent a less critical factor on the $N_3^{\cdot}$ formation as the pH increases.

Figure 4 shows that straight lines with different slopes and intercepts are obtained from the plot of $1/r$ vs. $1/C_{N_3^-}$ at different solution pH values. This means that the concentration of hydroxyl ions has an important role in the mechanism, in accordance with the reported pH dependence (Fig. 6).

The type of behavior illustrated in Fig. 4 is indicative of a Langmuir–Hinshelwood mechanism where OH^- and N_3^- are adsorbed on different sites (22). Under these conditions, the reaction rate for N_3^- oxidation is given by

$$[6] \quad R = \frac{kK_{OH^-}K_{N_3^-}[OH^-][N_3^-]}{(1 + K_{OH^-}[OH^-])(1 + K_{N_3^-}[N_3^-])}$$

and

$$[7] \quad 1/R = \frac{1}{kK_{OH^-}K_{N_3^-}}\left(K_{OH^-} + \frac{1}{[OH^-]}\right)\left(K_{N_3^-} + \frac{1}{[N_3^-]}\right)$$

The data in Fig. 4 allow us to calculate the equilibrium constant of adsorption $K_{N_3^-}$ at a constant pH from the ratio of the intercept to the slope. The calculation provides a value of $K_{N_3^-} = 16.5\ dm^3\ mol^{-1}$.

The surface coverage by N_3^- is given by

$$[8] \quad \theta_{N_3^-} = \frac{K_{N_3^-}[N_3^-]}{1 + K_{N_3^-}[N_3^-]}$$

From this one obtains a coverage $\theta_{N_3^-} = 14\%$ of the maximum coverage for $(N_3^-) = 0.01\ M$. The coverage by N_3^- is indeed low, as anticipated above, and should be compared with the coverage $\theta = 76\%$ for the adsorption of I^- (21) and $\theta = 98\%$ by oxalic acid (23) on TiO_2, for the same concentration of species in solution.

Mechanism of oxidation of azide

The relevant reactions at the TiO_2 interface in our system are as follows

$$[9] \quad TiO_2 \xrightarrow{h\nu} TiO_2(h^+/e_{cB}^-)$$

$$[10] \quad O_2 + e_{cB}^- \longrightarrow (O_2)^-$$

$$[11] \quad N_3^- + h^+ \longrightarrow N_3^{\cdot}$$

$$[12] \quad TiOH^- + h^+ \longrightarrow TiOH^0$$

$$[13] \quad TiOH^0 + N_3^- \longrightarrow TiOH^- + N_3^{\cdot}$$

Reaction [11] is the direct (isoenergetic) capture of photoproduced holes by N_3^-, while reaction [13] represents a mediated (inelastic) oxidation by surface states. The latter type of reaction appears in a number of cases to be operative with TiO_2, including the oxidation of halides (21, 24), the oxidation of methyl orange (25) and a number of organic compounds (26).

The data recorded in Fig. 5, showing that the removal of the surface OH groups leads to a dramatic decrease in trapped N_3^-, seem to indicate that the oxidation of N_3^- proceeds significantly via a reaction of type [13], although a contribution by the direct oxidation (reaction [11]) cannot be ruled out.

On the basis of the data reported herein we propose the following mechanism for the oxidation of N_3^- on TiO_2

$$[14] \quad TiOH^0 + (N_3^-)_{ads} \longrightarrow Ti{-}\square + (N_3OH)^{\cdot-}$$

$$[15] \quad Ti{-}\square + OH^- \longrightarrow Ti{-}OH^-$$

$$[16] \quad (N_3OH)^- \longrightarrow (N_3^{\cdot})_{aq} + (OH^-)_{aq}$$

The reaction sequence [14]–[16] is essentially a modification of reaction [13]. The formation of $(N_3OH)^-$ from $OH^{\cdot}$ and N_3^- and its dissociation (reaction [16]) is also proposed by Singh *et al.* (18) on the basis of pulse radiolysis measurements.

It has been reported that the OH^0 surface radicals are more loosely bound than OH^- (27). Their surface mobility makes the encounter with $(N_3^-)_{ads}$ (reaction [14]) easier despite a low coverage by N_3^-.

(N_3PBN) adduct reactivity

The decrease in the intensity of the signal due to (N_3PBN) after light is switched off (Fig. 2) allows some considerations to be made on the kinetics and mechanism by which this species decomposes thermally.

The decay of the (N_3PBN) adduct fits first order kinetics with $k = (8.13 \pm 0.9) \times 10^{-3}\ s^{-1}$ and $t_{1/2} = 83 \pm 8$ s. This latter figure is at variance with the $t_{1/2}$ reported by Rehorek *et al.* (13) of 20 s.

Reaction [18] represents a likely pathway for the (N_3PBN) adduct decay:

$$[18] \quad Ph{-}\underset{\displaystyle N_3}{\overset{\displaystyle H}{\overset{|}{C}}}{-}\overset{\displaystyle O^{\cdot}}{\overset{|}{N}}{-}C(CH_3)_3 \longrightarrow Ph{-}\underset{\displaystyle N_3}{\overset{\displaystyle H}{\overset{|}{C^{\cdot}}}} + (CH_3)_3{-}C{-}N{=}O$$

2

It is known that spin adducts with PBN tend to fragment thermally according to reactions of the type shown above (28). It is also known that methylnitrosopropane (**2**) (MNP) is photolyzed by visible light into nitric oxide and *t*-butyl radicals (16). These can be scavenged, in turn, by another MNP molecule

$$[19] \quad Bu^t{-}NO \xrightarrow{h\nu} NO + Bu^{t}\cdot \xrightarrow{MNP} Bu^t_2NO$$

In fact, we observed the growth of the signal due to Bu^tNO under prolonged illumination (Fig. 1). This behavior is the same as that observed with iron porphyrin in homogeneous solution, and we conclude that reaction [18] is not appreciably affected by the heterogeneous phase.

The possibility that reaction [18] is assisted by light cannot be ruled out *a priori* since the adduct (**1**) could be sensitive to visible light despite the fact that PBN is not. However, we did not observe any transient absorption above 360 nm, which seems to exclude the possibility that **1** absorbs an appreciable amount of visible light.

Acknowledgements

We wish to thank Mr. O. Zerlotin for technical help in the experiments. We are greatly indebted to Professor F. Scandola for a helpful discussion. Support by the Ministry of Education is gratefully acknowledged.

1. V. PLZÀK and H. WENDT. Ber. Bunsenges. Phys. Chem. **83**, 481 (1979).
2. H. WENDT and V. PLZÀK. J. Electroanal. Chem. **154**, 13 (1983).
3. V. PLZÀK and H. WENDT. J. Electroanal. Chem. **154**, 29 (1983).
4. Z. B. ALFASSI and R. H. SCHULER. J. Phys. Chem. **89**, 3359 (1985).
5. G. V. BUXTON and I. JANOVSKY. J. Chem. Soc. Faraday Trans. I, **72**, 1884 (1976).
6. J. R. HARBOUR, M. L. HAIR, and S. L. ISSLER. Can. J. Chem. **60**, 1523 (1982).
7. J. R. HARBOUR and M. L. HAIR. J. Phys. Chem. **83**, 652 (1979).
8. B. AURIAN-BLAJENI, M. HALMANN, and J. MANASSEN. Photochem. Photobiol. **35**, 157 (1982).
9. E. G. JANZEN, H. J. STRONKS, D. E. NUTTER, JR., E. R. DAVIS, H. N. BLOUNT, J. L. POYER, and P. B. MCCAY. Can. J. Chem. **58**, 1596 (1980).
10. T. H. WALTER, E. E. BANCROFT, G. L. MCINTIRE, E. R. DAVIS, L. M. GIERASCH, H. N. BLOUNT, H. J. STRONKS, and E. G. JANZEN. Can. J. Chem. **60**, 1621 (1982).
11. C. K. MANN. *In* Electroanalytical chemistry. Vol. 3. *Edited by* A. J. Bard. M. Dekker. p. 110.
12. J. CUNNINGHAM and H. ZAINAL. J. Phys. Chem. **76**, 2362 (1972).
13. D. REHOREK, P. THOMAS, and H. HENNIG. Inorg. Chim. Acta, **32**, L1 (1979).
14. E. HAYON and M. SIMIC. J. Am. Chem. Soc. **92**, 7486 (1970).
15. W. KREMERS and A. SINGH. Can. J. Chem. **58**, 1592 (1980).
16. M. J. PERKINS. *In* Adv. Phys. Org. Chem. Vol. 17. *Edited by* V. Gold and D. Bethel. Academic Press. p. 1.
17. P. CLECHET, C. MARTELET, J. R. MARTIN, and R. OLIER. Electrochim. Acta, **24**, 457 (1979).
18. A. SINGH, G. KOROLL, and R. B. CUNDALL. Radiat. Phys. Chem. **19**, 137 (1982).
19. E. G. JANZEN, D. E. NUTTER, E. R. DAVIES, B. J. BLACKBURN, J. L. POYER, and P. B. MCCAY. Can. J. Chem. **56**, 2237 (1978).
20. J. R. HARBOUR and M. L. HAIR. Can. J. Chem. **52**, 3549 (1974).
21. J. M. HERRMANN and P. PICHAT. J. Chem. Soc. Faraday Trans. I, **76**, 1138 (1980).
22. H. MOZZANEGA, J. M. HERRMANN, and P. PICHAT. J. Phys. Chem. **83**, 2251 (1979).
23. J. M. HERRMANN, H. M. MOZZANEGA, and P. PICHAT. J. Photochem. **22**, 333 (1983).
24. C. GUTIERREZ and P. SALVADOR. J. Electrochem. Soc. **133**, 924 (1986).
25. G. T. BROWN and J. R. DARWENT. J. Phys. Chem. **88**, 4955 (1984).
26. I. IZUMI, F. R. F. FAN, and A. J. BARD. J. Phys. Chem. **85**, 218 (1981).
27. P. SALVADOR. J. Electrochem. Soc. **128**, 1985 (1981).
28. K. SOMMERMEYER, W. SEIFFERT, and W. WILKER. Tetrahedron Lett. **20**, 1821 (1974).

Can. J. Chem. Downloaded from www.nrcresearchpress.com by 213.222.148.141 on 09/07/12
For personal use only.

Reactions between Co(II) and bis(diphenylphosphino)methane in the presence of $NaBH_4$ or $NaBH_3CN$

DAVID J. ELLIOT, DAVID G. HOLAH, ALAN N. HUGHES, AND STANISLAW MACIASZEK
Department of Chemistry, Lakehead University, Thunder Bay, Ont., Canada P7B 5E1

AND

VINCENT R. MAGNUSON AND KENNETH O. PARKER
Department of Chemistry, University of Minnesota-Duluth, Duluth, MN 55812 U.S.A.

Received June 19, 1987

DAVID J. ELLIOT, DAVID G. HOLAH, ALAN N. HUGHES, STANISLAW MACIASZEK, VINCENT R. MAGNUSON, and KENNETH O. PARKER. Can. J. Chem. **66**, 81 (1988).

Reactions between Co(II) and bis(diphenylphosphino)methane (dppm) in the presence of $NaBH_4$ or $NaBH_3CN$ are described. The main products are the Co(I) complex, $CoCl(dppm)_3$, and Co(III) complexes of the type $[CoHX(dppm)_2]Y$ (where X = Cl, Y = Cl or BPh_4; X = Y = Br; X = Y = I; X = BH_3CN, Y = BH_3CN, ClO_4, or BPh_4). The former has been shown by X-ray crystallography to contain a Co atom tetrahedrally coordinated by a Cl and three P atoms from three monodentate dppm ligands. Possible mechanisms for the formation of Co(III) are discussed.

DAVID J. ELLIOT, DAVID G. HOLAH, ALAN N. HUGHES, STANISLAW MACIASZEK, VINCENT R. MAGNUSON et KENNETH O. PARKER. Can. J. Chem. **66**, 81 (1988).

On décrit les réactions entre le Co(II) et le bis(diphénylphosphino)méthane (dppm), en présence de $NaBH_4$ ou de $NaBH_3CN$. Les produits principaux sont le complexe du Co(I), $CoCl(dppm)_3$ et des complexes du Co(III) du type $[CoHX(dppm)_2]Y$ (dans lesquels X = Cl, Y = Cl ou BPh_4; X = Y = Br; X = Y = I; X = BH_3CN, Y = BH_3CN, ClO_4 ou BPh_4). Utilisant la diffraction des rayons-X, on a pu démontrer que le premier complexe comporte un atome de Co qui est tétracoordonné par un Cl et par trois atomes de P provenant de trois ligands dppm monodentates. On discute des mécanismes qui peuvent expliquer la formation du Co(III).

[Traduit par la revue]

Introduction

For a number of years we have been interested in reactions between metal ions and $NaBH_4$ (and some of its derivatives) in the presence of a variety of phosphines (1, 2). During the course of our studies (2) on Co(II)–$Ph_2P(CH_2)_nPPh_2$–$NaBH_4$ systems, it became clear that there is a fundamental difference between the type of product formed when n = 2–6 than when n = 1 (dppm). Isolated from the former reactions (2) were Co(I) hydrides and, with phosphines for which n = 4, 5, $[Co(BH_4)(phosphine)]_2$, containing a most unusual mode of attachment of the BH_4 group. A previous communication (3) on the latter (dppm) reactions reported the formation of not only Co(I) but also, unexpectedly, Co(III) compounds of which no trace was found in the n = 2–6 cases. An explanation of this may well rest with the more versatile coordination abilities of dppm (4) compared to the n = 2–6 phosphines. This paper reports more details of the Co(II)–dppm–$NaBH_4$ (or $NaBH_3CN$) reactions.

Results and discussion

Reactions between Co(II), dppm, and $NaBH_4$ are very complex, sensitive to reaction conditions, and difficult to control (as is the case with other phosphines). While the syntheses described in the Experimental section have been performed many times, the expected product is not always formed, even when the conditions have apparently been duplicated as closely as possible. Reactions involving $NaBH_3CN$ are slower and, generally, easier to handle. The routes to the various complexes to be described are summarized in Scheme 1.

A dark green precipitate **1**, was obtained as the first identifiable product from benzene–ethanol mixtures of $CoCl_2.6H_2O$, dppm, and $NaBH_4$. In order to stabilize this product and to prevent it from undergoing further reaction, it is important that, after its filtration, all traces of unreacted $NaBH_4$ be removed from the solid. The product has little solubility in all but the most polar of solvents and has only been recrystallized successfully from dmf–ether mixtures. In a previous communication (3), we tentatively identified **1** as $Co_2X_3(dppm)_2.xS$ (S = dmf, X = Cl) on the basis of total chemical analysis. The amount of solvent appears to increase from $x \sim 1$ after one recrystallization to $x \sim 2.5$ after two recrystallizations, with the Co:Cl:P ratio remaining constant. Blue crystals invariably formed along with the product during these recrystallizations but these were easily removed by washing the mixture with ethanol. Although the crystals of **1** (X = Cl) appeared to be well formed, all those examined by X-ray diffraction methods proved to be twinned and, therefore, unsuitable for data collection. For this reason the related compound **1**, X = Br, was made by an analogous reaction. However, recrystallizations of the initially formed product from dmf–ether produced only blue crystals of $CoBr_2.3dmf$ (presumably, $[Co(dmf)_6][CoBr_4]$ (5)) together with mixtures of **2** and **3**. Successful recrystallization was achieved from acetophenone–ether but again, no crystals suitable for X-ray work could be obtained. Without X-ray work it is clearly not possible to be definitive about the structure of **1**. Given, however, the apparent empirical formula, the propensity of dppm to bridge and the fact that all three chlorides of **1** appear to be coordinated (no ready reaction with $NaBPh_4$), it is tempting to suggest an A-frame type arrangement. On the other hand, the magnetic moment in the solid state measured as 6.1 BM (X = Cl, $x \sim 1.0$), i.e., a total of five unpaired electrons, would be surprising in such a structure. Another uncertainty is the role of the potentially strongly coordinating solvent dmf in the structure of **1**. The characteristic reflectance spectra of **1** (X = Cl, Br) are shown in Fig. 1, the peaks occurring at (for X = Cl) 7 800, 14 100, 16 900 (sh), and

Can. J. Chem. Downloaded from www.nrcresearchpress.com by 213.222.148.141 on 09/07/12
For personal use only.

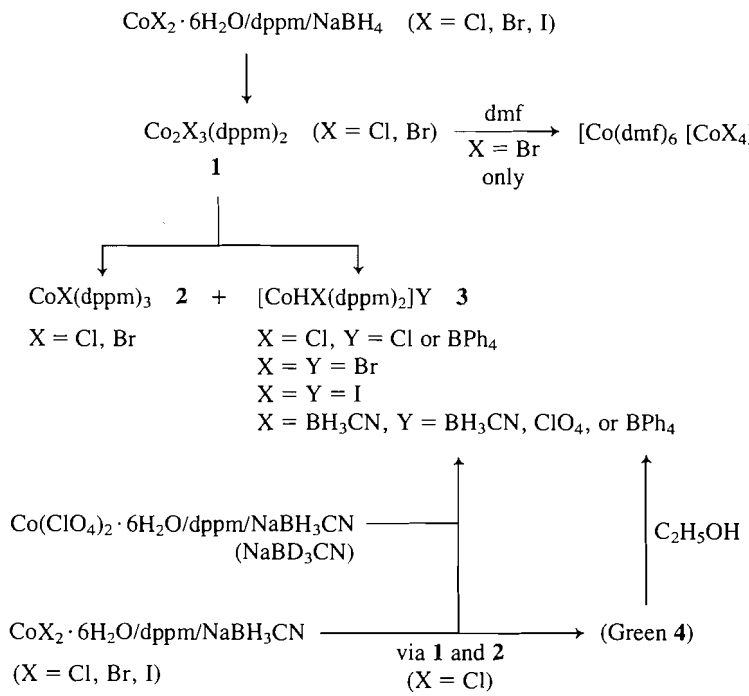

SCHEME 1

21 100 cm^{-1}. In dmf solution, the relative intensities change significantly; the lowest energy peak now occurs at 7 100 cm^{-1} ($\epsilon \sim 90$) while the 14 100 cm^{-1} signal shifts to 14 900 ($\epsilon \sim 560$). The solution spectrum is consistent with those of either tetrahedral d^8 or d^7 complexes (6). A related, neutral, mixed oxidation state Co(II)–Co(I) complex has recently been characterized (7), although in this case the molecule is low spin (one unpaired electron) and the Co atoms are square planar.[1]

Compound **2** (X = Cl, Br) forms a beautiful deep green cube-shaped crystals and, therefore, it is very easily recognizable in the various reaction product mixtures. It has been synthesized in two ways. Firstly, during attempts to obtain single crystals of **1** (X = Cl) from dmf–ethanol mixtures, large cubic crystals were obtained. Remarkably, this is a very convenient route to **2** in good yields. Secondly, **2** has been obtained as crystals from the filtrates of reactions between Co(II) chloride, dppm, and both $NaBH_4$ and $NaBH_3CN$. In these, **1** is recognizable as the first (insoluble) product which, if not removed by filtration, slowly dissolves as the reaction proceeds and **2** can be obtained from the resulting yellow–green solutions. It is easily separated from **1** because of its ready solubility in benzene, toluene, or dichloromethane.

The magnetic moment of 3.1 BM in the solid state is consistent with high spin Co(I). The reflectance spectrum shows (Fig. 1) peaks at 5 800, ~9 000 (sh), 10 400, 14 200, and 17 500 (weak sh) cm^{-1}, which very closely resemble those in the spectrum (8) of the high spin, tetrahedral $CoCl(PPh_3)_3$. Considering the stoichiometry of **2**, the implication is that the three dppm ligands are bound to the Co(I) atom in a monodentate fashion.

This has been confirmed by X-ray crystallography, which shows the Co(I) atom on a three-fold axis of symmetry in a tetrahedral environment of one Cl atom and three P atoms from three crystallographically equivalent monodentate dppm ligands. Although the structure is incomplete, the results indicate that the Cl—Co—P bond angle is 112°, the distances of the Co, non coordinated P and methylene C atoms from the plane formed by the three bonded P atoms are +0.86, +0.79, and +1.71 Å, respectively, and the Co—Cl and Co—P distances are 2.14 and 2.28 Å, respectively. Attempts to resolve the apparently disordered phenyl ring on the coordinated P atom continue. However, the fact remains that, with $Z = 2$, in either space group $R32$ or $R\bar{3}$, the Co must be tetrahedral from which it follows that each ligand is monodentate.

Complexes which contain one (4) and two (refs. 4, 9*a*, 9*b*, and, more recently, $Ni(CO)_2(dppm)_2$ (9*c*)) monodentate dppm ligands are well known but this appears to be the first example of three such ligands on one metal ion. There is considerable interest in using complexes containing monodentate dppm as precursors to bimetallic systems (9*b*, 10) and we are currently examining the potential of **2** in this respect.

Another interesting feature of this work is the fact that the filtrates of CoX_2/dppm/$NaBH_4$ reactions which produce **2** also produce Co(III) compounds of the type $[CoHX(dppm)_2]^+Y^-$, i.e. **3**. Similar compounds are also produced from analogous reactions in which $NaBH_3CN$ is used instead of $NaBH_4$ and, as mentioned earlier, we have also positively identified **1** and **2** (X = Cl) from the $NaBH_3CN$ reactions. Thus, Co(III) compounds are being produced in significant amounts in reducing environments (more strongly so in the case of $NaBH_4$ than $NaBH_3CN$).

The well characterized Co(III) complexes, **3**, are all bright yellow crystalline solids. They all show a terminal ν_{Co-H} in their ir spectra at ~1 970 cm^{-1} which shifts to ~1 700 cm^{-1} on deuteration. The hydride signal appears in the ^1H nmr spectra as a quintet at $\delta -17$ ppm with $J_{PH} \sim 50$ Hz. In addition, the two P—CH_2—P protons appear as separate signals 0.5–0.8 ppm

[1]A referee has suggested that it may be more attractive to describe the structure of **1** in terms of a "cradle" structure as found in $Ni_2(CO)_3(dppm)_2$ and $Ni_2(CH_3NC)_3(dppm)_2$ (17). While this is possible, the magnetic properties of **1** require that there are no spin interactions between the Co atoms, and this would be unexpected in such an arrangement.

Can. J. Chem. Downloaded from www.nrcresearchpress.com by 213.222.148.141 on 09/07/12
For personal use only.

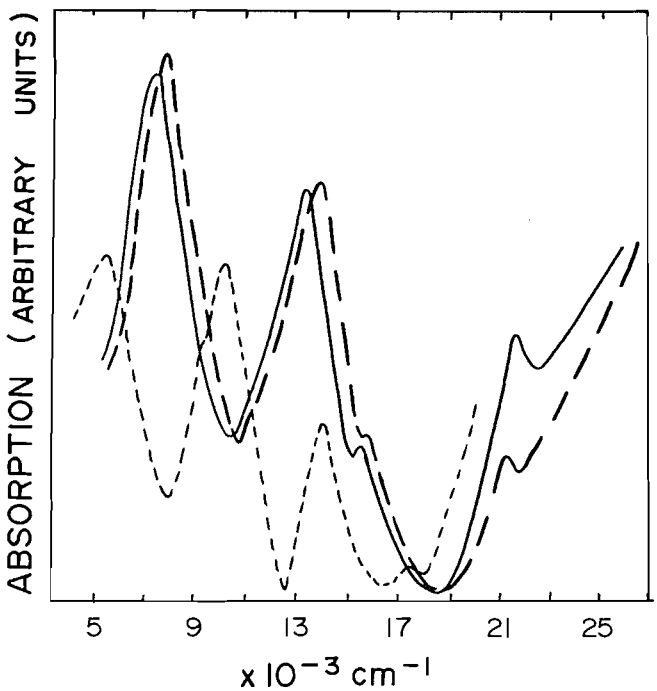

FIG. 1. Reflectance spectra: —, compound **1** (X = Cl); – – –, compound **1** (X = Br); ---, compound **2** (X = Cl).

apart in the δ 4.0–5.2 range depending upon the nature of X and Y and the solvent used for the nmr measurements. These signals are very well resolved in certain instances (e.g. with X = Cl or BH_3CN, Y = BPh_4 and with X = Y = I) and are typical (11) of the AA′A″A‴ MX pattern in which A, A′, A″, and A‴ are the P atoms of two chelating dppm ligands, while M and X are the magnetically non-equivalent protons of the P—CH_2—P unit. Such a pattern would be expected from a diamagnetic octahedral $[CoHX(dppm)_2]^+$ ion in which H and X are *trans*. Thus, each proton appears as a doublet of quintets and J_{HH} is essentially constant at ~15 Hz for all examples of **3**. The line separations (the apparent J_{PH}, i.e., the average of $^2J_{PH}$ and $^4J_{PH}$) are also remarkably constant for these signals with values of, for example, 5.2 Hz and 3.5 Hz for the lower and higher field CH_2 proton signals, respectively, in the spectrum of **3** (X = Cl, Y = BPh_4). In all cases, the line separation is larger in the lower field proton signal of the CH_2 group.

In the ^{31}P nmr spectra, the P singlet occurs close to δ = 0, consistent with chelating dppm (12). Electronic spectra of **3** show a strong, broad peak at 22 – 25 000 cm^{-1} (ε ~ 1 000 cm^{-1} M^{-1} L) similar to those of related Co(III) species (13). Thus, the Co(III) compounds appear to be analogous to $[RhHCl(dppm)_2](BPh_4)$ which has been shown by X-ray crystallography (14) to contain a Rh(III) atom surrounded by a slightly distorted octahedron. The hydrido and chloro ligands occupy *trans* positions with the phosphines in the equatorial positions. The space group and unit cell dimensions of **3** (X = Cl, Y = BPh_4) and the above Rh(III) complex are so close (see Experimental section) that the two complexes may be presumed to be isostructural.

Before discussing possible mechanisms for the formation of Co(III) in these reactions, it should be recalled that in our work (2) on Co(II)–$Ph_2P(CH_2)_nPPh_2$–$NaBH_4$ or $NaBH_3CN$, production of Co(III) has been observed only when n = 1. In all other cases, n = 2–6, either Co(II) or reduced cobalt compounds were the only ones isolated, with no evidence for Co(III) formation being observed at any time. Three possible mechanisms for Co(III) formation can be considered, namely, disproportionation, hydride abstraction, and oxidative addition. For example, the recent extensive study by Socol and Verkade (15) on the properties of phosphines which affect the disproportionation reaction

$$Co(II) + phosphine \rightarrow Co(I) + Co(III)$$

concluded that factors such as shape, bulk, and basicity all play a role. Unfortunately, bidentate phosphines of the type used in the work described here were not included. Secondly, it is possible that Co(III) is formed in a way similar to that proposed (14) for the formation of $[RhHCl(dppm)_2]^+$ from $[RhCl(CO)_2]_2$, namely by abstraction of hydride from the ethanol–water solvent. In related work (16) it has been observed that reactions between $Co(BF_4)_2.6H_2O$ and $HP(C_2H_5)Ph$ in 2-propanol lead immediately to $Co[HP(C_2H_5)Ph]_5^{2+}$, but when these are stirred for 4 days, they produce the Co(III) species $CoH[HP(C_2H_5)Ph]_5^{2+}$. Whether this too occurs by hydride abstraction from the alcohol or by disproportionation is not clear but it is difficult to see why either of these two mechanistic possibilities would be unique to dppm with the bidentate phosphines. Thirdly, we speculated (3) that, since **1** appears to be unique to the dppm reactions, Co(III) may be formed by oxidative addition of H_2 from $NaBH_4$ to the two Co centers of **1**. Accordingly, several attempts to react **1** with H_2 were made but all failed to yield any Co(III).

Some light has been thrown upon the reaction by experiments aimed at growing single crystals of **1**. In these, we obtained good yields of Co(III) by allowing ethanol to diffuse into concentrated solutions of **1**, in dmf in a freezer over 24 h. In this connection, it should also be remembered that, while **1** can be recrystallized unchanged from dmf–ether, when it is recrystallized from dmf–ethanol, crystals of **2** are also obtained. These points are consistent with our original observations that in reactions where **1** is not isolated, it slowly dissolves and reacts to produce mixtures of **2** and **3**. A further complication is that compounds of type **3** are readily produced from $Co(ClO_4)_2.6H_2O$–dppm–$NaBH_3CN$ reactions (Scheme 1) in which ethanol is present but in which **1** cannot occur as an intermediate (although a different dppm bridged binuclear Co intermediate may occur). It is therefore possible that it is indeed reactions between alcohol and the partially reduced cobalt species **1** which produce the Co(III) hydrides, as in the case with rhodium (14). It is unfortunate that solutions containing **1** and **2** are so strongly paramagnetic that nmr studies are impossible.

We have been unsuccessful in characterizing bright emerald green, highly crystalline compounds **4** (Scheme 1) obtained from CoX_2–dppm–$NaBH_3CN$ reactions (X = Cl, Br). In spite of repeated attempts and several recrystallizations, consistent chemical analyses were not obtained. The compounds contain halide (X-ray fluorescence) and coordinated BH_3CN and H (ir), exhibit a strong broad peak at ~25 500 cm^{-1}, (with additional peaks at ~7 000 and ~15 500 cm^{-1}), dissolve in dmf to give bright green unstable solutions which show a quintet δ −15 (J_{PH} ~ 47 Hz) and a singlet in the ^1H and ^{31}P nmr spectra, respectively, and turn yellow instantly in ethanol to produce **3**. It appears that each attempted recrystallization of **4** results in further decomposition.

Experimental

Materials

Dppm was obtained from Strem Chemicals Inc. and was used without further purification. The reducing agents $NaBH_4$, $NaBH_3CN$

Can. J. Chem. Downloaded from www.nrcresearchpress.com by 213.222.148.141 on 09/07/12
For personal use only.

Can. J. Chem. Downloaded from www.nrcresearchpress.com by 213.222.148.141 on 09/07/12
For personal use only.

TABLE 1. Summary of crystal data and intensity collection for $CoCl(dppm)_3$

Formula	$C_{75}H_{66}ClP_6Co$
Formula weight	1247.6
Space group	$R\bar{3}$ or $R32$
Cell parameters	
a, Å	16.256 (10)
α, deg	69.74 (1)
V, Å^3	3654
Crystal size, mm	0.5 × 0.2 × 0.3
Molecules/cell	2
Density	
Calculated, g cm^{-3}	1.13
Observed, g cm^{-3}	1.20
Temperature	Ambient
Diffractometer	CAD-4
Radiation	Mo K_α (λ = 0.71069 Å)
Total reflections	9022
Observed reflections	2726 $I \geq 3\sigma(I)$

(and their deuterated analogues), and $NaBPh_4$ were obtained from the Aldrich Chemical company and stored over $CaCl_2$ in a desiccator to protect them from hydrolysis. Even so, it was found that samples from freshly opened bottles can behave differently from samples which have been stored for periods of time, even under apparently dry conditions.

Analyses and measurements

The air-sensitive samples were protected from atmospheric oxidation or hydrolysis during weighing or data collection. Microanalytical data for C, H, and N, ir spectra and both ^{31}P and ^1H nmr spectra were measured as described previously (1). (For $^{31}P-\{^1H\}$ spectra, recorded at 32.3 MHz, chemical shifts of signals downfield of external 85% H_3PO_4 are positive.) Analyses for Co, Cl, and P were performed by Galbraith Laboratories Inc., Knoxville, TN. Magnetic momements were measured using the Gouy method, the tube being calibrated with $HgCo(SCN)_4$ and $Nien_3(S_2O_3)$.

Syntheses and X-ray crystallography

All synthetic work was carried out under pure nitrogen.

Crystals of $CoCl(dppm)_3$, **2**, and $[CoHCl(dppm)_2](BPh_4)$ were selected for X-ray data analysis on the basis of a polarizing microscope examination and precession photographs (the former compound was sealed under nitrogen in a quartz capillary). Data collection on **2**, using MoK_α radiation was on a CAD-4 Enraf-Nonius diffractometer using the θ–2θ scan. The compound was found to crystallize in the rhombohedral crystal class using the Enraf-Nonius CAD-4 SDP peak search centering and indexing programs. A tabulation of the crystal and intensity data is presented in Table 1. The Co, Cl, and the coordinated P atom were located using conventional heavy atom techniques. Successive full-matrix least-squares refinement and difference Fourier maps were used to find the non-coordinated P atom, the methylene C atom, and 18 of the C atoms in the phenyl rings. We have so far been unsuccessful in locating the C atoms of a phenyl ring on the P atom coordinated to Co. Attempts to refine the structure in the non-centrosymmetric space group $R32$ have also proven unsuccessful. In either case, the Co and Cl atoms are restricted to being on the three-fold axis of rotation. Accordingly, the Co(I) atom is tetrahedrally coordinated to one Cl and the three P atoms.

The hydrido complex was found to crystallize in the monoclinic space group $P2_{1/c}$. Unit cell dimensions are a = 19.464, b = 15.168, c = 22.165 Å, β = 107.08° with 4 formula units per unit cell. (Corresponding data (14) for $[RhHCl(dppm)_2](BPh_4)$, $P2_{1/c}$, a = 19.477, b = 15.266, c = 22.282 Å, β = 106.85, Z = 4.)

*$Co_2X_3(dppm)_2 \cdot xS$, **1***

(*a*) X = Cl. To a mixture of $CoCl_2.6H_2O$ (0.51 g, 2.1 mmol) dissolved in ethanol (20 mL) and dppm (1.81 g, 4.7 mmol) in benzene (10 mL) was added, over a ~7 min period, a suspension of $NaBH_4$ (0.025 g, 0.66 mmol) in ethanol (10 mL). The mixture was stirred for 1 h, when the green solid which formed was filtered off, washed with ethanol (20 mL), benzene (20 mL), ethanol (20 mL), water (10 mL), ethanol (20 mL), and finally ether (30 mL), and dried under reduced pressure. The extensive washings are necessary to remove any free phosphine and, particularly, residual $NaBH_4$ which may react during recrystallization. The product was recrystallized, at 0°C over ~48 h, from dmf–ether. Blue crystals, which may contaminate the product at this point, were removed by washing with ethanol until the washings were colorless. The remaining green crystals were washed with ether and dried under reduced pressure. Yield 30%.

The following results were obtained after one recrystallization. *Anal.* calcd. for $Co_2Cl_3(dppm)_2.dmf$: C 59.71, H 4.82, N 1.31, Co 11.06, P 11.62, Cl 9.98; found: C 59.49, H 4.78, N 1.68, Co 10.27, P 10.69, Cl 9.93. Infrared $\nu_{CO(dmf)}$ 1670(s) cm^{-1}. The following results were obtained after a second recrystallization. *Anal.* calcd. for $Co_2Cl_3(dppm)_2.2.5dmf$: C 58.74, H 5.27, N 2.98, Co 10.02, P 10.54, Cl 9.05; found: C 58.03, H 5.20, N 3.12, Co 9.90, P 10.38, Cl 9.06. Infrared $\nu_{CO(dmf)}$ 1670(vs) cm^{-1}.

The compound has slight solubility in CH_2Cl_2 but recrystallization from this results in a finely powdered form of the sample along with some decomposition. Recrystallization from dmf–ethanol is discussed below. The compound is insoluble in benzene, toluene, and ethanol.

(*b*) X = Br. A crude green product was filtered off from reactions which were carried out in analogous ways to those in (*a*) above. This product was washed with small amounts of benzene, ethanol, acetophenone, and finally ether, and recrystallized from acetophenone–ether (1:1) at 0°C overnight as green crystals. Yield 10%. *Anal.* calcd. for $Co_2Br_3(dppm)_2.0.5C_6H_5COCH_3$: C 54.67, H 4.08; found: C 54.33, H 4.09. Infrared ν_{CO} 1670 cm^{-1}. Attempts to recrystallize the compound from dmf–ether produced blue crystals. *Anal.* calcd. for $CoBr_2.3dmf$: C 24.68, H 4.83, N 9.60; found: C 25.25, H 4.91, N 9.76.

*Chlorotris[bis(diphenylphosphino)methane]cobalt(I), $CoCl(dppm)_3$, **2***

$CoCl_2.6H_2O$ (0.36 g, 1.5 mmol) was dissolved in ethanol (20 mL) and mixed with dppm (1.77 g, 4.6 mmol) in toluene (10 mL). To this stirred mixture was added slowly (10 min) a suspension of $NaBH_4$ (0.044 g, 1.2 mmol) in ethanol (10 mL). The stirring was continued for a further 10 min. Any green solid remaining at this point was removed by filtration. The dark green filtrate produced large green crystals after 3 days at 0°C. These were filtered off, washed with ethanol (20 mL) and hexane (20 mL), and dried under vacuum. Yield 30%. *Anal.* calcd. for $CoCl(dppm)_3$: C 72.20, H 5.33, Cl 2.84, Co 4.72; found: C 72.15, H 5.60, Cl 2.99, Co 4.25.

Alternatively, $Co_2Cl_3(dppm)_2$ was recrystallized from dmf–ethanol (1:2) overnight at 0°C to produce well-formed crystals of the product. *Anal.* calcd. for $CoCl(dppm)_3.dmf$: C 70.94, H 5.57, N 1.06; found: C 70.84, H 5.62, N 1.07. Infrared $\nu_{CO(dmf)}$ 1670 cm^{-1}.

This compound forms striking, perfectly formed crystals in the shape of cubes, and as such, is easily recognizable. It is readily soluble in benzene, toluene, CH_2Cl_2, and dmf to give green solutions. It is insoluble in ethanol.

*Hydridohalogenobis[(bis(diphenylphosphino)methane]cobalt(III) chloride, bromide, iodide, or tetraphenylborate $[CoHX(dppm)_2]^+Y^-$, **3***

(*a*) X = Cl, Y = Cl. $CoCl_2.6H_2O$ (0.52 g, 2.2 mmol) in ethanol (20 mL) and dppm (1.9 g, 4.9 mmol) in toluene (10 mL) were mixed and to the stirred solution was added $NaBH_4$ (0.037 g, 1.0 mmol) in ethanol (10 mL) over a period of ~2 h. A green solid was filtered off, washed with ethanol (20 mL) until the washings were colorless and the washings were added to the yellow–green filtrate. Hexane (15 mL) was added and the solution produced yellow crystals after ~12 h at 0°C. These were filtered off, washed with toluene and hexane, and dried under reduced pressure. Yield 25%. *Anal.* calcd. for $[CoHCl(dppm)_2]Cl.2C_2H_5OH$: Co 5.94, Cl 7.15, P 12.49, C 65.40, H 5.79; found: Co 6.00, Cl 7.11, P 12.10, C 64.29, H 5.95. Infrared ν_{Co-H} 1968, ν_{OH} (from C_2H_5OH) 1680, 3340 cm^{-1}; ^{31}P nmr ($CHCl_3$)

Can. J. Chem. Downloaded from www.nrcresearchpress.com by 213.222.148.141 on 09/07/12
For personal use only.

δ −1.8(s); ^{1}H nmr ($CDCl_3$) hydridic hydrogen at δ −17.5 (quintet), $^2J_{PCoH}$ 51 Hz; C_2H_5OH at δ 1.25(t), 3.75(q); integration C_2H_5OH: dppm = 1:1; —CH_2— at δ 4.38 and 4.98 (with each signal as a poorly resolved doublet of quintets), $^2J_{HH}$ ~ 14 Hz.

(*b*) X = Cl, Y = BPh_4. Compound (*a*) above reacts smoothly with $NaBPh_4$ in ethanol to produce the orange-colored $[CoHCl(dppm)_2](BPh_4)$ which was recrystallized from dmf–ethanol. Yield 80%. *Anal.* calcd. for $[CoHCl(dppm)_2](BPh_4)$: C 75.10, H 5.54; found: C 74.86, H 5.61. Infrared ν_{Co-H} 1968 cm^{-1}; ^{31}P nmr (dmf) δ −1.5(s); ^{1}H nmr (CD_2Cl_2) hydridic hydrogen at δ −16.95 (quintet), J_{PH} 52 Hz; —CH_2— at δ 4.18 (doublet of quintets, line separation i.e. the average of $^2J_{PH}$ and $^4J_{PH}$ 3.5 Hz) and 4.95 (doublet of quintets, line separation 5.3 Hz), $^2J_{HH}$ 14.8 Hz. Electronic spectrum (acetone) λ_{max} 22 700 cm^{-1}, ϵ ~ 1250.

(*c*) X = Br, Y = Br. This yellow compound was prepared from $CoBr_2.6H_2O$ in a way analogous to (*a*) above. Yield 40%. *Anal.* calcd. for $[CoHBr(dppm)_2]Br.2C_2H_5OH$: C 60.02, H 5.32; found: C 59.65, H 5.39. Infrared ν_{Co-H} 1965, ν_{OH} (from C_2H_5OH) at 1675 and 3330 cm^{-1}; ^{31}P nmr (CH_2Cl_2) δ −2.6(s); ^{1}H nmr (CD_2Cl_2) hydridic hydrogen at δ −14.7 (quintet) $^2J_{PCoH}$ 51 Hz; —CH_2— at δ 4.41 (doublet of quintets, line separation 3.5 Hz) and 5.05 (doublet of quintets, line separation 5.3 Hz), $^2J_{HH}$ 14.9 Hz.

(*d*) X = I, Y = I. This yellow compound was prepared from $CoI_2.6H_2O$ as in (*a*) above. Reactions were run for 1.4 and 12 h and, in each case, the yellow Co(III) was rapidly produced. No green intermediates were obtained. Yield 45%. *Anal.* calcd. for $[CoHI(dppm)_2]I.2C_2H_5OH$: C 55.21, H 4.89; found: C 55.28, H 4.72. Infrared ν_{Co-H} 1962, ν_{OH} (from C_2H_5OH) at 1670 and 3350 cm^{-1}; ^{31}P nmr (CH_2Cl_2) δ −2.8(s); ^{1}H nmr (CD_2Cl_2) hydridic hydrogen at δ −10.9 (quintet), $^2J_{PCoH}$ 51 Hz; —CH_2— at δ 4.58 (doublet of quintets, line separation ~3 Hz) and 5.14 (doublet of quintets, line separation 5.1 Hz) $^2J_{HH}$ 14.9 Hz.

*Hydrido(cyanotrihydroborato)bis[bis(diphenylphosphino)methane]-cobalt(III) perchlorate, tetraphenylborate, or cyanotrihydroborate [CoH(BH$_3$CN)(dppm)$_2$]Y (**3**), Y = ClO$_4$, BPh$_4$, or BH$_3$CN*

(*a*) Y = ClO_4. To the stirred pink solution obtained by mixing $Co(ClO_4)_2.6H_2O$ (0.45 g, 1.25 mmol) and dppm (1.44 g, 3.75 mmol) in toluene–ethanol (2.5:1, 15 mL) a solution of $NaBH_3CN$ (0.08 g, 1.25 mmol) in ethanol (10 mL) was added dropwise over a period of 10 min. The colour turned to dark green with the formation of some precipitate. The mixture was stirred for 24 h during which time a yellow solid was slowly precipitated from a brown solution. The solid was filtered off, washed with benzene (20 mL), ethanol (10 mL), and hexane (5 mL), dried, and finally, recrystallized from hot methanol as bright yellow crystals. Yield 45%. *Anal.* calcd. for $[CoH(BH_3CN)(dppm)_2]ClO_4$: C 63.28, H 5.00, N 1.45; found: C 63.96, H 5.26, N 1.49. Infrared ν_{BH} 2340(s), ν_{CN} 2200, ν_{Co-H} 1987, ν_{ClO_4} 1100(b) cm^{-1}; ^{31}P nmr (dmf) δ 1.8(s); ^{1}H nmr (dmf d_7) hydridic hydrogen at δ −15.5 (quintet), $^2J_{PCoH}$ 48 Hz; —CH_2— at δ 4.65 and 5.20 (with each signal as a poorly resolved doublet of quintets) $^2J_{HH}$ ~ 15 Hz.

This complex decomposes in CH_2Cl_2, $CHCl_3$, tetrahydrofuran, CH_3CN, and dimethylsulfoxide. It can be recrystallized from dmf–C_2H_5OH, although some dmf is retained in the lattice.

The analogous reaction was carried out with $NaBD_3CN$, and the resulting deuterated product was purified as described above. *Anal.* calcd. for $[CoD(BD_3CN)(dppm)_2]ClO_4$: C 63.02, H 5.39, N 1.44; found: C 64.36, H 5.24, N 1.36. Infrared ν_{CN} 2200, ν_{BD} 1752(m), 1678(w), 1638(w), ν_{CoD} was not observed.

(*b*) Y = BPh_4. The yellow hydride from (*a*) was dissolved in hot methanol and a solution containing a slight molar excess of $NaBPh_4$ in methanol added. The yellow crystals which slowly formed were filtered off and recrystallized from CH_2Cl_2/hexane. Yield 75%. *Anal.* calcd. for $[CoH(BH_3CN)(dppm)_2]BPh_4$: C 74.84, H 5.77, N 1.18; found: C 76.40, H 5.92, N 1.10. Infrared ν_{BH} 2380(s.b.), 2230(sh), ν_{CN} 2200, ν_{Co-H} 1987 cm^{-1}. ^{1}H nmr (CD_2Cl_2) hydridic hydrogen at δ −15.0 (quintet), $^2J_{PCoH}$ 51 Hz; —CH_2— at δ 4.08 (doublet of quintets, line separation, i.e., the average of $^2J_{PH}$ and $^4J_{PH}$ 4.3 Hz) and 4.66 (doublet of quintets, line separation 4.8 Hz).

(*c*) Y = BH_3CN. A mixture of $CoCl_2.6H_2O$ (0.3 g, 1.25 mmol) and dppm (1.5 g, 3.8 mmol) was dissolved in benzene–ethanol (15 mL, 2.5:1) to give a dark blue–green solution to which $NaBH_3CN$ (0.3 g, 5 mmol) in ethanol (10 mL) was added dropwise, with stirring, over a period of 10 min. During the addition, the color changed to dark green and finally to dark brown–green. The precipitate which formed started to redissolve after ~20 min. The mixture was stirred for ~24 h after which a brown solid was filtered off. The solid turns instantly to bright yellow when brought into contact with methanol, in which it dissolves and from which a yellow solid crystallized. Yield 30%. *Anal.* calcd. for $[CoH(BH_3CN)(dppm)_2](BH_3CN).CH_3OH$: C 67.79, H 5.90, N 2.98; found: C 67.81, H 5.90, N 3.02. Infrared ν_{BH} 2310, ν_{CN} (coordinated) 2190, ν_{CN} (ionic) 2162, ν_{CoH} 1980, ν_{OH} (from CH_3OH) 3360 cm^{-1}. ^{31}P nmr (dmf) δ 1.76(s); ^{1}H nmr (CD_3OD) hydridic hydrogen at δ −15.3 (quintet), $^2J_{PCoH}$ 49 Hz; —CH_2— at δ 4.64 and 5.18 (with each signal a poorly resolved doublet of quintets), $^2J_{HH}$ ~ 15 Hz.

Similar reactions using $CoBr_2.6H_2O$ lead to the production of a dark brown crude product. Recrystallization from dichloromethane/hexane produced (from the brown solution), green plates of variable composition (C 55–61, H 4.7–5.2, N 1.8–2.5). Infrared ν_{BH} 2330, ν_{CN} 2190, ν_{CoH} 1990; ^{31}P nmr (dmf) δ 0.71; ^{1}H nmr ($CDCl_3$) δ −15.3 (quintet), J_{PH} ~ 47 Hz. Repeated recrystallizations from either CH_2Cl_2 or CH_3CN failed to produce a pure compound. There is no immediate reaction between a solution of the green crystals and $NaBPh_4$, but addition of ethanol results in an immediate color change to yellow and the crystallization from solution of **3**, X = BH_3CN, Y = BPh_4.

Acknowledgments

We thank the Natural Sciences and Engineering Research Council of Canada, the Lakehead University Senate Research Committee, and the University of Minnesota-Duluth Computer Center for generous financial support.

1. D. G. Holah, A. N. Hughes, and N. I. Khan. Can. J. Chem. **62**, 1016 (1984).
2. D. G. Holah, A. N. Hughes, S. Maciaszek, V. R. Magnuson, and K. O. Parker. Inorg. Chem. **24**, 3956 (1985).
3. D. J. Elliot, D. G. Holah, A. N. Hughes, S. I. Khan, and S. Maciaszek. Inorg. Chim. Acta, **96**, L29 (1985).
4. R. J. Puddephatt. Chem. Soc. Rev. **12**, 199 (1983) and references cited therein.
5. F. A. Cotton and R. Francis. J. Am. Chem. Soc. **82**, 2986 (1960).
6. F. A. Cotton and G. Wilkinson. Advanced inorganic chemistry. 4th ed. Wiley-Interscience, New York. 1980.
7. F. Arena, C. Floriani, and P. F. Zanazzi. J. Chem. Soc. Chem. Commun. 183 (1987).
8. M. Aresta, M. Rossi, and A. Sacco. Inorg. Chim. Acta, **3**, 227 (1969).
9. (*a*) P. W. A. Dean and R. S. Srivastava. Can. J. Chem. **63**, 2829 (1985); (*b*) A. Blagg and B. L. Shaw. J. Chem. Soc. Dalton Trans. 221 (1987); (*c*) D. G. Holah, A. N. Hughes, and H. A. Mirza. To be published.
10. G. B. Jacobsen, B. L. Shaw, and M. Thornton-Pett. J. Chem. Soc. Chem. Commun. 13 (1986).
11. A. Balch. *In* Homogeneous catalysis with metal phosphorus complexes. *Edited by* L. H. Pignolet. Plenum, New York, NY. 1984. p. 183.
12. P. E. Garrou. Chem. Rev. **81**, 229 (1981).
13. B. Bosnich, W. G. Jackson, and S. T. D. Lo. Inorg. Chem. **14**, 1460 (1975).
14. M. Cowie and S. K. Dwight. Inorg. Chem. **18**, 1209 (1979).
15. S. M. Socol and J. G. Verkade. Inorg. Chem. **25**, 2658 (1986).
16. P. Rigo and M. Bressan. Inorg. Chim. Acta, **33**, 39 (1979).
17. D. L. DeLaet, P. E. Fanwick, and C. P. Kubiak. Organometallics, **5**, 1807 (1986).

The electrochemical behavior of flavin adenine dinucleotide in neutral solutions

V. I. BIRSS,[1] H. ELZANOWSKA, AND R. A. TURNER
Department of Chemistry, University of Calgary, Calgary, Alta., Canda T2N 1N4

Received February 20, 1987[2]

V. I. BIRSS, H. ELZANOWSKA, and R. A. TURNER. Can. J. Chem. **66**, 86 (1988).

A detailed investigation of the electrochemical behavior of flavin adenine dinucleotide (FAD) in neutral solutions has been carried out at Hg and glassy carbon electrodes. At FAD concentrations of about 10^{-4} *M*, cyclic voltammetry (CV) shows a pair of anodic and cathodic peaks having a peak separation at low sweep rates indicative of a two-electron transfer process and yielding a formal redox potential for FAD of -0.206 ± 0.003 V vs. NHE at pH 7. Evidence for FAD adsorption was obtained in experiments at high sweep rates, from the effect of time of exposure of the electrode surface to FAD in solution and from the effect of the potential limits on the cyclic voltammetric response. The process of FAD adsorption was studied in detail in dilute FAD solutions (ca 10^{-6} *M*) using a hanging mercury drop electrode and the techniques of CV and ac voltammetry. Three distinct stages of FAD adsorption were observed and a model of the orientation of FAD on the electrode surface as a function of time and potential is presented. In addition, the kinetics of oxidation and reduction of adsorbed FAD was studied for each of the stages of FAD deposition, and a surface standard rate constant of ca. 40 s^{-1} was obtained for Stages II and III of FAD adsorption.

V. I. BIRSS, H. ELZANOWSKA et R. A. TURNER. Can. J. Chem. **66**, 86 (1988).

Opérant en solutions neutres et à des électrodes de Hg ainsi que de verre, on a réalisé une étude détaillée du comportement électrochimique du dinucléotide de la flavine et de l'adénine (DFA). A des concentrations de DFA d'environ 10^{-4}, la voltamétrie cyclique (VC) présente une paire de pics anodique et cathodique qui possèdent, à des vitesses de balayage lentes, une séparation entre les pics qui suggère qu'il s'agit d'un processus de transfert de deux électrons et qui, à un pH de 7, fournit pour le DFA un potentiel redox formel de $-0{,}206 \pm 0{,}003$ V vs. NHE. On a obtenu des indications relatives à l'adsorption du DFA au cours d'expériences à des vitesses élevées de balayage; ces indications découlent de l'effet du temps d'exposition de la surface de l'électrode au DFA en solution ainsi que de l'effet des limites de potentiel sur la réponse voltamétrique cyclique. On a étudié en détail le processus d'adsorption du DFA en solutions diluées (environ 10^{-6} *M*) en utilisant un électrode à goutte tombante de mercure ainsi que les techniques de VC et de voltamétrie à c.a. On a observé trois stages distincts d'adsorption du DFA et on présente un modèle de l'orientation du DFA sur la surface de l'électrode en fonction du temps et du potentiel. De plus, on a étudié la cinétique de l'oxydation et de la réduction du DFA adsorbé pour chacun des stages de la déposition du DFA; on a obtenu une constante de vitesse standard d'environ 40 s^{-1} pour les stages II et III de l'adsorption du DFA.

[Traduit par la revue]

Introduction

The redox-active flavoproteins play a particularly important biological role in the electron transfer reactions of all living systems. These proteins utilize the cofactor flavin adenine dinucleotide (FAD) to dehydrogenate (oxidize) pyridine nucleotides and hydrogenate (reduce) the cytochromes (1, 2). This valuable cofactor, which is derived from riboflavin (RF) (Vitamin B_2), is unique in that, depending on the conditions, it can undergo either two separate one-electron transfer reactions or one essentially simultaneous two-electron transfer reaction. The flavin coenzymes occur in a variety of proteins and interface between organic oxidation and reduction reactions, which are usually two-electron processes, and electron transfer reactions to/from metal centers, often requiring only one electron. The two one-electron reactions are shown below involving a proton and producing neutral molecules (Fl = flavin).

[1] $\mathrm{Fl} + \mathrm{H}^+ + \mathrm{e}^- \rightleftharpoons \mathrm{FlH}$

[2] $\mathrm{FlH} + \mathrm{H}^+ + \mathrm{e}^- \rightleftharpoons \mathrm{FlH_2}$

All flavins share the isoalloxazine moiety, which is the electroactive part of the molecule (Fig. 1). Attached to this ring system is another group, depicted as R in Fig. 1, which aids in apoprotein–cofactor binding and specificity (1, 2). The isoalloxazine ring system can exist in an oxidized form (quinone), the radical semiquinone form, after the acceptance of the first electron, and the reduced hydroquinone form, after a second electron transfer. Therefore, all compounds derived from flavin, e.g., lumiflavin (LF), riboflavin, flavin mononucleotide (FMN), and FAD, which vary only in the nature of the R group (Fig. 1), are expected to have similar formal potentials to that of the isoalloxazine ring system. It should also be noted that depending on the solution pH, each of these species can exist in either neutral or ionic forms (1).

In biological systems, the factors which govern the mechanism of FAD reduction and oxidation, as well as its redox potential, are related to the microenvironment of the cofactor–apoprotein interaction site. For example, steric hindrance, solution pH, and ionic strength all give rise to unique microenvironments (2, 3), and therefore may affect the redox potential of the flavin.

It is also known that, in solution, the oxidized flavins are expected to have a planar structure, while the reduced flavin resembles a butterfly in conformation (2), with atoms 1 to 5 and 10, and 5 to 9 and 10 (Fig. 1) constituting two planes or wings intersecting the N(5)—N(10) axis, with a dihedral angle of 21° (4). Therefore, enforced flattening of the reduced flavin should increase its reducing power, and conversely, enhanced bending should increase the oxidizing power. Selectivity for a one- or two-electron reaction could conceivably be assisted in this manner (4). This may occur in the protein and could perhaps also occur at the surface of an electrode.

The electrochemical behavior of the flavins, particularly of RF, has been studied at Hg electrodes, primarily with the use of dc and ac polarographic and also chronopotentiometric methods (5–9). It has been reported that in acidic solutions, both the oxidized and the reduced forms of RF are strongly adsorbed on a Hg surface (5, 6, 10). One monolayer of oxidized RF oriented parallel to the electrode surface and two layers (a bilayer) of the reduced RF ($\mathrm{RFH_2}$) are thought to adsorb (8, 9). Despite the

[1]To whom correspondence should be addressed.
[2]Revision received September 14, 1987.

Can. J. Chem. Downloaded from www.nrcresearchpress.com by 213.222.148.141 on 09/07/12
For personal use only.

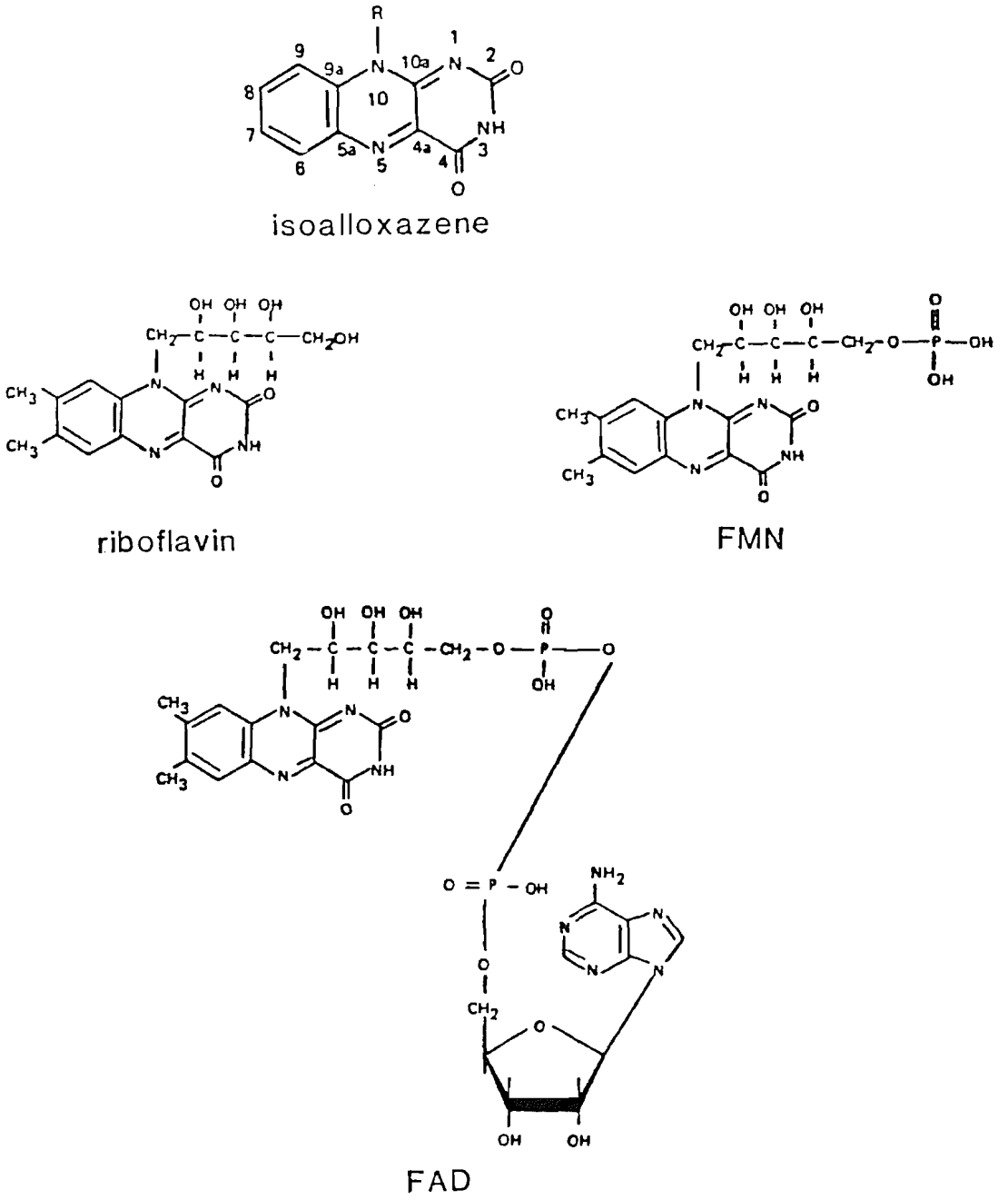

FIG. 1. Structure of isoalloxazine moiety and of the R groups for RF, FMN, and FAD.

presence of these adsorbed layers, the reduction of RF from solution was found to occur via a reversible two-electron transfer reaction (9).

A study of the adsorption behavior of FMN at Hg electrodes in acid solutions has also been reported (11). As in the case of RF, strong adsorption of both the oxidized and reduced forms of FMN are observed electrochemically. Also, a bilayer (1.2×10^{-10} mol/cm^2) of the reduced form is presumed to be present, while only a single layer (0.6×10^{-10} mol/cm^2) of the oxidized form of FMN is found to adsorb at the Hg electrode (11).

In a more recent work (12), it was shown that both the oxidized and the reduced forms of FMN are strongly adsorbed at a Hg drop electrode in buffered solutions of pH 4.9 and 6.9. The quantity of adsorbed FMN, as measured by cyclic voltammetry, was estimated to be in the range of 7 to 9×10^{-11} mol/cm^2, close to the predicted amount of FMN (7.5×10^{-11} mol/cm^2) having the isoalloxazine ring system parallel to the electrode surface (12).

The same authors also carried out a similar study using a Hg electrode in dilute FAD solutions buffered to a pH of 6.9 (13), and again, both the oxidized and reduced forms of the flavin were found to be strongly adsorbed. In concentrated FAD solutions, another investigation (14), carried out over the entire range of pH, has dealt in detail with the mechanism of reduction of FAD in solution, but did not discuss FAD adsorption.

An area of current interest which is of relevance to studies of flavin adsorption involves the attachment of various important redox materials to electrode surfaces, producing chemically modified electrodes. This has been carried out recently for FAD, which has been successfully attached to various graphite

Can. J. Chem. Downloaded from www.nrcresearchpress.com by 213.222.148.141 on 09/07/12
For personal use only.

Can. J. Chem. Downloaded from www.nrcresearchpress.com by 213.222.148.141 on 09/07/12
For personal use only.

and carbon electrode surfaces (15–20). At glassy carbon electrodes, a single layer of FAD can be attached, while at porous graphite electrodes, up to 50 to 100 monolayers of FAD have apparently been adsorbed (18, 20). However, it appears that the roughness factor of these porous graphite electrodes was not taken into account in estimating the number of FAD layers adsorbed, and therefore, it is likely that only ca. one layer is also deposited on these electrodes. In all of this work at carbon electrodes, it was found that glucose oxidase activity in solution could be restored with the use of the FAD-coated electrode. FAD has also been attached to an indium – tin oxide electrode via the adenine amino group (20).

While most of the papers described above have reported that the flavins do indeed adsorb at electrode surfaces, none of them has investigated the actual mechanism of build-up of adsorbed flavin layers or the kinetics of their oxidation and reduction. The present investigation has involved the use of cyclic voltammetry to study the oxidation and reduction of FAD at mercury electrodes in neutral solutions and to discover whether two separate one-electron transfer steps can be distinguished at rapid sweep rates. Also, a detailed examination of the process of FAD adsorption, the oxidation and reduction of adsorbed FAD and layer reorientation has been carried out using cyclic voltammetry (CV) and alternating current (ac) voltammetry.

Experimental

(a) Equipment

Standard three-electrode potentiostatic circuitry was employed, utilizing either a PAR 173 potentiostat and a PAR 175 universal programmer, or a PAR 273 digital potentiostat/function generator for the cyclic voltammetry experiments. I/E curves were usually plotted on a HP 7044A X/Y recorder at slow potential sweep rates (s), and on either a Nicolet 3091 digital oscilloscope or a HP 7090A digital recorder at s greater than about 200 mV/s.

The ac voltammetry experiments were carried out using a PAR 273 potentiostat in conjunction with a PAR 5206 Lock-in Amplifier. For most experiments, a voltage amplitude of 5 mV, a frequency of 329 Hz, and phase angles of either 0° or 90° were employed.

(b) Electrodes

The working electrodes (WE) utilized in this work were either a Hg pool electrode, a PAR 303A HMDE, or a glassy carbon electrode. The HMDE was utilized only on the medium drop size setting, producing a drop having a surface area of 1.3×10^{-2} cm^2. The Hg pool electrode, contacted with a Pt wire, had a surface area of 2 cm^2. The surface areas were determined by measuring the minimum capacity in a flavin-free buffer solution and comparison with the reported double layer capacity minimum of 15.4 μF/cm^2 for Hg in phosphate solutions (21). In this paper, all current and charge densities are given with respect to the electrode areas measured by this method.

The glassy carbon (GC) electrode (5 mm radius) consisted of a GC disc placed into the end of some shrinkable Teflon tubing, which was then heated, leaving only the end of the disc exposed to the solution. Electrical contact was made at the back of the GC disc by a Ni wire embedded into a drop of Hg. The GC electrode surface was prepared by polishing with γ alumina, followed by ultrasonic cleaning in acetone for about 1 min and then a thorough rinse with distilled water.

The counter electrode (CE) used in these experiments was either a Pt gauze or Pt wire electrode. The reference electrodes (RE) were either a Ag/AgCl electrode or an SCE. All potentials are given vs. the NHE in this paper.

(c) Cells and solutions

All experiments were carried out in either a two compartment cell or in the standard polarographic cell used with the PAR 303A HMDE. Both cells were constructed so that the cell solution could be thoroughly deoxygenated by bubbling argon or nitrogen either through the solution or passing it above the solution during the experimental runs.

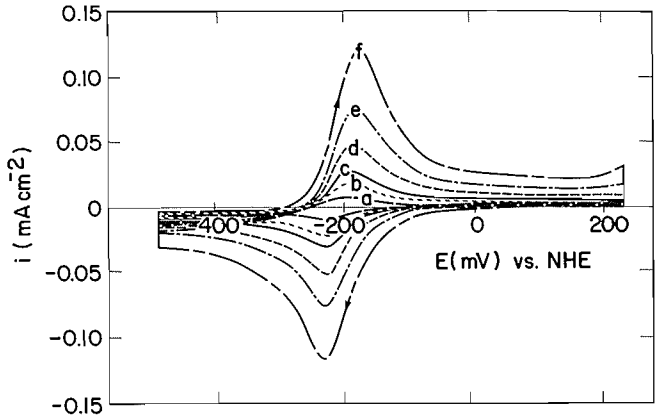

FIG. 2. Cyclic voltammograms obtained at a Hg pool electrode in 1.1×10^{-4} M FAD solution (pH = 7). s = 2 (a), 10 (b), 20 (c), 50 (d), 100 (e), and 200 (f) mV/s.

The experiments were carried out in buffered (sodium phosphate or potassium hydrogen phthalate) solutions. FAD was obtained as its sodium salt from Sigma Chemicals Co. The flavin solution concentrations ranged from about 2×10^{-6} to 1×10^{-4} M. All chemicals utilized were of reagent grade and all water was thrice distilled. All experiments were carried out at room temperature.

Results and discussion

(a) General electrochemical behavior of FAD at Hg electrodes

Initial experiments were carried out with the use of cyclic voltammetry (CV) to establish whether a single two-electron or two one-electron transfer steps would be observed for FAD reduction and oxidation over a wide range of s. A Hg pool electrode was used for these early experiments (at sweep rates less than or equal to ca. 500 mV/s), primarily as it was anticipated that in the subsequent adsorption studies, it would be desirable to transfer the Hg electrode from one solution to another and it was considered that a Hg pool electrode would facilitate this process.

Figure 2 shows a family of CVs for a range of s from 2 to 200 mV/s and a FAD concentration of 1.1×10^{-4} M (pH = 7). This rather high FAD concentration was selected so that the diffusion currents would be significantly larger than the current due to the reaction of adsorbed FAD. However, despite this, the peaks are somewhat non-ideal in shape, having a greater peak separation and being wider at half-height than theoretically predicted (22).

Figure 3a (□) shows that at low s, the difference in the anodic and cathodic peak potentials (ΔE_p) is constant at about 35 mV for the Hg pool electrode. This is somewhat larger than the expected value for a reversible two-electron transfer reaction, $57/z$ mV, where z is the number of electrons transferred in the process (2). At sweep rates greater than about 20 mV/s, the peak separation begins to increase, as is predicted for the onset of kinetic irreversibility.

When the peak current density (i_p) is plotted vs. $s^{1/2}$ (Fig. 3b), a linear relationship is observed up to a sweep rate of about 20 mV/s. However, rather than observing a decrease in the slope of this plot at high s, as might have been expected when a diffusion-controlled process becomes irreversible (22), the slope of the plot increases. This is indicative of the presence of adsorbed flavin, as the current due to the oxidation and reduction of adsorbed species is expected to vary linearly with s, rather than with $s^{1/2}$ (22). This result implies that the increased peak separation at higher sweep rates, shown in Fig. 3a, is

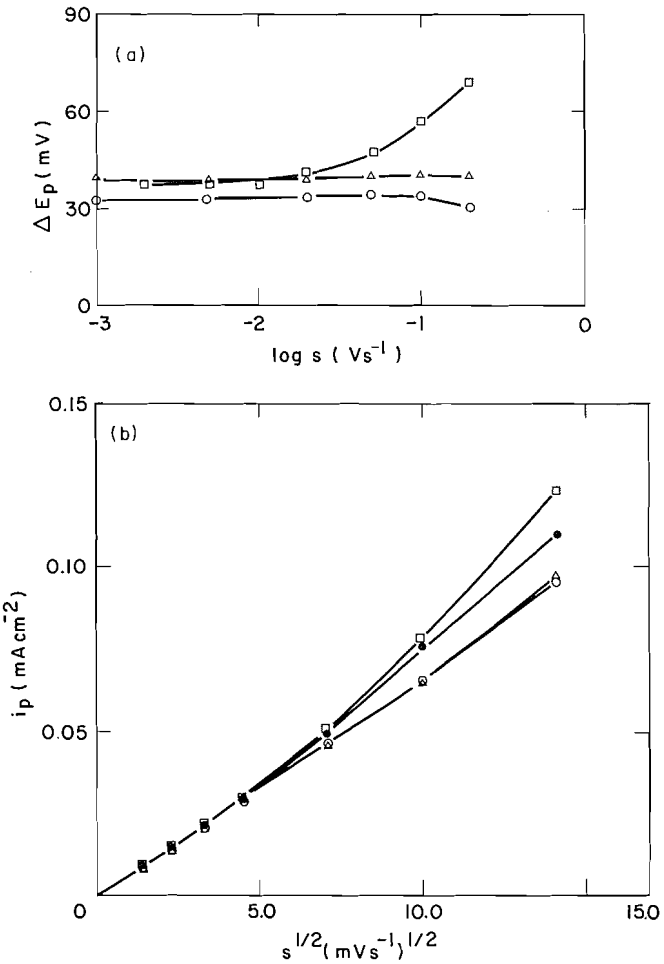

FIG. 3. (*a*) ΔE_p vs. log s; 1.1×10^{-4} *M* FAD solution (pH = 7), using a Hg pool electrode (□) or a HMDE, where (○) represents the "first scan" of potential and (△) scans nos. 2, 3, and 4. (*b*) The dependence of $i_{p,c}$ (●, ○) and $i_{p,a}$ (□, △) on $s^{1/2}$ for 1.1×10^{-4} *M* FAD solution (pH = 7) at a Hg pool electrode (●, □) and the HMDE (○, △).

related to contributions to the current peak from the reaction of both adsorbed flavin and flavin molecules diffusing to the surface from the solution. Therefore, a simple estimation of the rate constant for the reaction cannot be obtained from the results of Fig. 3. It can be seen in Fig. 3*b* that the anodic peak is influenced more by adsorption than is the cathodic peak. This is in agreement with the findings (reported below) that the adsorption peaks are centered at a somewhat more positive potential than the diffusion peaks (Table 1).

It should be noted that even at sweep rates greater than 500 mV/s, no evidence for the splitting of the main FAD reduction and oxidation peaks into those for the individual one-electron transfer steps was observed, notwithstanding the difficulty in avoiding the current response to adsorbed FAD at high sweep rates. This is consistent with the reported E^0 values for reactions [1] and [2], −240 and −130 mV, respectively (23), measured by the coulometric titration of flavin bound to a benzoate substrate. Anderson (24) utilized pulse radiolysis and obtained E^0 values of −314 and −124 mV for the two reactions. These values indicate that as soon as the first electron is transferred in the reduction process, the second should pass immediately thereafter. As stated earlier, in biological systems, it is possible that binding and local environment effects could

TABLE 1. Characteristics of FAD adsorption peaks (HMDE, 1.8×10^{-6} *M* FAD, pH = 7)

Stage	q (μC cm^{-2})	E_f' (mV vs. NHE)*	ΔE_p (mV)†
I	8–9	−189	16–20
II	12.5–13	−202	8–10
III	13–13.5	−189	14–17

*Determined as the potential midway between the anodic and cathodic peak (cf. with E_f = ca. −206 mV).
†Measured at s = 100 mV/s.

cause the second step to become more difficult than the first, or the first to become more facile, so that the two one-electron steps could become more readily separated (23). The observation of a two-electron transfer process has been reported previously for FAD (14, 25–27), although two overlapping one-electron steps have sometimes been reported for RF (28), FMN (29, 30), and for FAD (14), particularly in acid solutions. It has also been reported that flavins coordinated to particular metal centers, e.g. $Ru^{2+/3+}$, undergo electron transfer in discreet one-electron steps, rather than in one two-electron step, in both aqueous and non-aqueous solutions, e.g. DMF (31–33).

Efforts were made to determine the formal potential, E_f, of the reaction from CVs such as those shown in Fig. 2. The potential midway between the anodic and cathodic peaks, −0.208 ± 0.002 V vs. NHE, was taken as E_f at pH = 7 at the Hg pool electrode. There are numerous values reported in the literature for this potential, e.g. −0.205 V (14), −0.210 V (26), −0.213 V (29), −0.219 V (34) etc. Our value is well within this range.

The strong adsorption of FAD at Hg electrodes has been demonstrated by replacing the FAD solution with buffer solution only and then monitoring the electrochemical response. A matching pair of peaks were observed in the same potential range as the diffusion peaks had been. These peaks were seen both when the Hg electrode was at open-circuit during the exchange of solutions as well as when potential control was maintained and the transfer of solutions was done in a flow-through cell. These peaks contain a charge equivalent to about one layer of adsorbed FAD (see below) and demonstrate conclusively the strong adsorption of both the oxidized and the reduced forms of FAD on the Hg surface.

It was also found that when the FAD solution was removed from the cell, the Hg was shaken/rinsed with water, and the pool electrode was replaced in the cell containing only the buffer solution, the small adsorption peaks were still present. The only absolute method for removing the adsorbed flavin was by washing the Hg electrode in HCl, after which only a small fraction of the adsorption peaks could still be seen. Very similar effects were seen with GC electrodes after exposure to FAD solutions. The only method by which the adsorbed FAD could be removed was by a mechanical polishing of the GC surface. These experiments indicate clearly why a simple kinetic analysis could not be carried out for the reduction and oxidation of FAD from solution at these Hg pool electrodes.

An interesting effect observed at the Hg pool electrode in phosphate buffered FAD solutions was that when the potential was extended to potentials more negative than about −0.800 V vs. NHE, a new pair of peaks was observed at ca. −0.85 V (Fig. 4). If the potential was held just negative of these peaks for several minutes, the next complete anodic run (Fig. 4) displayed a new peak on the positive side of the main FAD oxidation

Can. J. Chem. Downloaded from www.nrcresearchpress.com by 213.222.148.141 on 09/07/12
For personal use only.

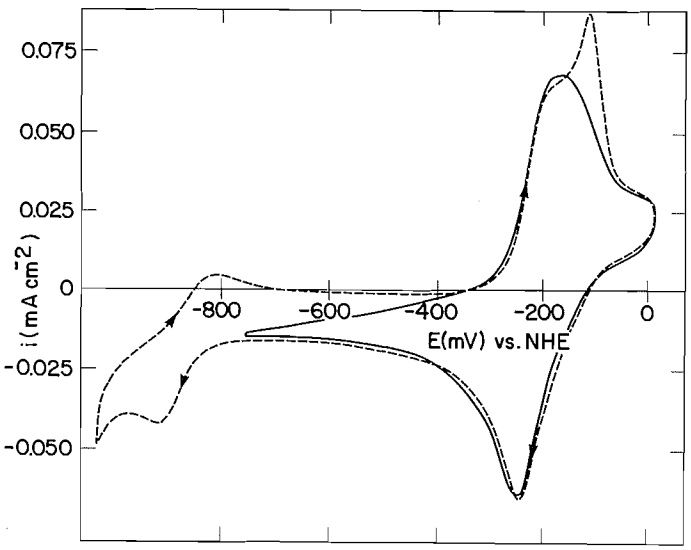

FIG. 4. Cyclic voltammogram at Hg pool electrode in 1×10^{-4} *M* FAD solution (pH = 7), s = 100 mV/s. The dashed line shows the influence of extended negative potential limit on anodic peak.

peak. This new peak was quite sharp and exceeded the anodic diffusion peak in magnitude. This was observed at both Hg and GC electrodes in this work. This is a similar effect to that reported for FMN at Hg electrodes in pH 1 solutions (11), in which an anodic "post-peak", considered to be due to $FMNH_2$ adsorption, splits to give a second, rather sharp post-peak at more positive potentials after time spent at potentials cathodic of the main reduction peak.

The behavior observed in Fig. 4 is therefore also likely to be indicative of FAD adsorption at the Hg pool electrodes. It will be shown below that it represents a reorientation within the underlying adsorbed FAD film. In the case of FMN (11), no small peaks such as those at negative potentials in Fig. 4 were reported.

It should be noted that at pH 4, neither the small peaks at ca. −0.85 V nor the new anodic spike are observed. It is probably significant that at pH 7, the anion form of both the semiquinone (FlH) and the hydroquinone (FlH_2) may be present in reasonable quantities, while at pH 4, all forms of FAD are neutral. Therefore, it is likely that the new anodic spike is related to reorientation of adsorbed negatively-charged FAD at negative potentials. It will be shown below that similar effects of holding the potential at the negative limit of the potential range are seen in the electrochemical response of adsorbed FAD. The small peaks at negative potentials in Fig. 4 will be shown below to be due to the capacitive change caused by the desorption and reorientation of FAD (see ac results below).

From the results presented above, it was concluded that the Hg pool electrode becomes covered with a strongly adsorbed FAD film which clearly influences the shape and position of the peaks observed by CV and which may influence the kinetics of the oxidation and reduction of FAD from solution. For these reasons, and also in order to produce a fresh, reproducible Hg electrode surface readily, all subsequent studies were carried out with the HMDE. The use of the HMDE also enabled a thorough study of the mechanism of the build-up of adsorbed FAD to be carried out.

(b) FAD electrochemistry at the HMDE

The CVs of FAD reduction and oxidation at the HMDE were generally similar to those in Fig. 2 for the Hg pool electrode. However, the extent of FAD adsorption could be more readily controlled by extruding a fresh Hg drop just before recording the CV, and comparing this result to those at later times. Figure 3*a* (○) shows ΔE_p as a function of the sweep rate for the first sweep at a fresh Hg drop as well as for later sweeps. A fresh Hg drop was extruded for the measurements at each sweep rate. For the first sweep at a fresh Hg drop, it can be seen that at sweep rates less than about 100 mV/s, ΔE_p is about 31 mV, close to the theoretically predicted peak separation of 28.5 mV (22). However, for the first sweep at sweep rates greater than 100 mV/s, a more ideal peak separation (29 mV) was observed, indicating that the electron transfer reaction is relatively rapid. It also indicates the probable influence of adsorption at low s (long times). This point is discussed further below.

These results indicate that FAD adsorption is a fast process at this high FAD concentration, causing an increased peak separation at low sweep rates. Only at high sweep rates, when little time is available for adsorption to occur, is the peak separation more ideal. The peak separation in the subsequent few sweeps at low s (Fig. 3*a*, △) is more similar to that at the Hg pool electrode, while at high s, the peak separation is smaller as less time has elapsed in the experiment and less FAD has adsorbed.

Figure 3*b* (○, △) also shows that less FAD is adsorbed at a Hg drop electrode in the first few sweeps of potential than at the Hg pool electrode, which remains exposed to the FAD solution for the duration of the experiment. This is seen by the fact that the $i_p/s^{1/2}$ relationship remains essentially linear, even at high s. In comparison, the results at the pool electrode in Fig. 3*b* (□, ●) show a significant deviation towards a linear i_p/s relationship at high s, indicative of a greater extent of current response from adsorbed FAD.

The formal potential of FAD reduction/oxidation, E_f, determined from these results at the HMDE, is −0.205 ± 0.002 V vs. NHE, again within the reported range of potentials for this reaction. It should be noted that by using the "first sweep" results at greater than ca. 100 mV/s at a freshly extruded Hg drop, it is likely that the potential is not influenced significantly by adsorption effects. Much of the older literature, e.g. ref. 29, shows non-ideal polarographic waves and has reported formal potentials from these waves. These potentials are likely to be more negative than those at a fresh Hg surface, when adsorption effects can be minimized.

(c) FAD adsorption at the HMDE in pH = 7 solutions

The study of the adsorption of FAD has been carried out in dilute FAD solutions (less than 5×10^{-6} *M*) and at relatively high s (greater than 100 mV/s). The purpose of this was to enhance the FAD adsorption currents relative to the diffusion controlled currents. The HMDE was used in all of this work because a fresh reproducible Hg surface could be produced at controlled intervals of time.

(i) General electrochemical behavior

The gradual build-up with time of adsorbed FAD at a fresh HMDE surface has been monitored using both CV and the out-of-phase (ϕ = 90°) "capacitive" current response to an ac signal. Figure 5*a* shows the ac response of the HMDE, first in the phosphate buffer supporting electrolyte solution only, with no FAD added, and then in a 1.8×10^{-6} *M* FAD solution in the buffer solution at s = 5 mV/s in the range of voltage between −0.650 and +0.250 V vs. NHE. The ac response is seen to reach a steady-state after the second scan. Figure 5*b* shows the analogous experiment, starting with a fresh Hg drop, using CV and s = 100 mV/s. The progression of time of cycling is

Can. J. Chem. Downloaded from www.nrcresearchpress.com by 213.222.148.141 on 09/07/12
For personal use only.

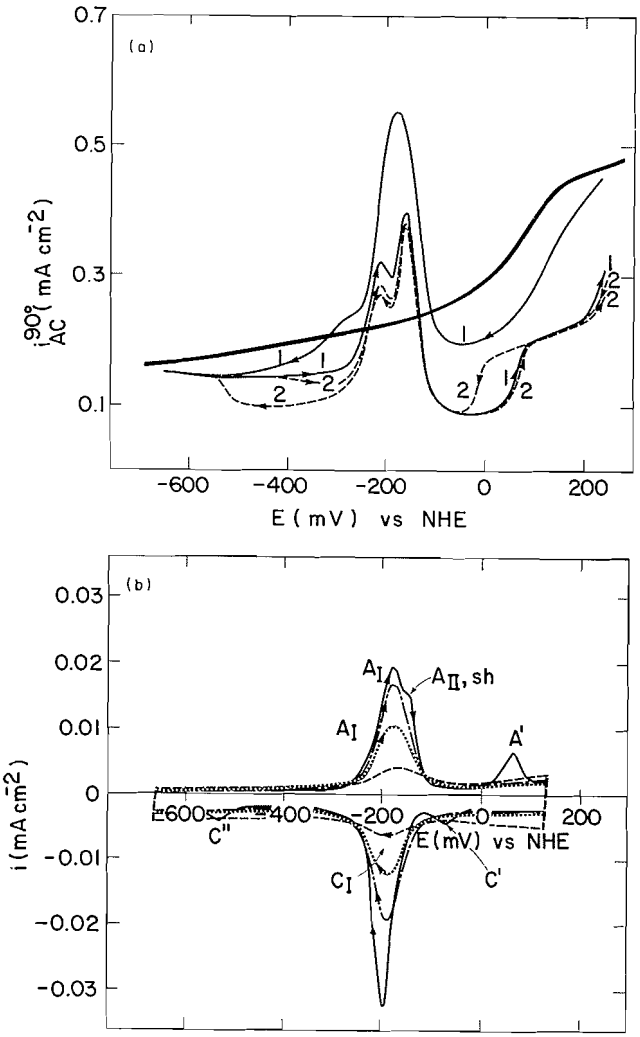

FIG. 5. Adsorption of FAD (Stages I and II) at fresh HMDE; 1.8×10^{-6} *M* FAD solution (pH = 7, 0.08 *M* phosphate buffer). (*a*) ac voltammograms where ΔE = 5 mV, ν = 329 Hz, s = 5 mV/s. (—) buffer solution only (no FAD); (—) first sweep in FAD solution (curve 1); (---) second sweep in FAD solution (curve 2). Note the "capacitance pit" between −0.55 V and +0.05 V. (*b*) Cyclic voltammograms in FAD solution; s = 100 mV/s. (---) sweep no. 1; (···) sweep no. 8; (-·-) sweep no. 16; (—) sweep no. 21. Note that peaks A′, C′, and C″ are related to the sudden changes of double layer capacitance seen in Fig. 5*a*.

indicated by the number of each of the runs (each run is equivalent to 16 s), given in the figure caption. It should be noted that because of the different sweep rates used in the ac and CV experiments, the time which elapses in one complete ac cycle is about 20 times that in one CV cycle.

In Fig. 5*a*, the first scan with FAD present was commenced at a potential of 0.250 V vs. NHE. The ac response shows a fairly broad peak, due to the pseudocapacity of the adsorbed electroactive material, and the double layer capacity on either side of the peak. At the start of the first negative sweep, the ac current is already lower than that of the supporting electrolyte alone, indicative of the onset of an adsorption process (34). The capacitance peak appears at a potential very close to the formal potential for FAD reduction, i.e. about −0.205 V vs. NHE. It will be shown below that the appearance of a single broad ac peak in the first few scans is indicative of Stage I of the adsorption of FAD.

It can be seen in Fig. 5*a* that the ac current obtained in the FAD-containing solution is closer to that for the buffer alone at potentials negative of the capacitance peak than at positive potentials. At pH = 7, the reduced form is expected to be partly anionic (1) and therefore it is likely that the negatively charged electrode would "destabilize" the anionic reduced form of the FAD layer.

On the first positive-going sweep in Fig. 5*a*, the ac peak appears as two smaller, but sharper ac peaks. Only one peak is seen at lower frequencies or if the solution is made substantially more conductive. After crossing these peaks, the current reaches its lowest value, before rising sharply at about +0.050 V. On the second cathodic sweep, the current drops sharply at about −0.030 V. After crossing the two peaks in this direction, the current remains low, increasing suddenly at about −0.550 V. Therefore, a type of capacitance "pit" or "well", also seen in the adsorption of nucleosides (35, 36), is observed between ca. −0.550 and ca. 0 V. The presence of this "pit" and the two sharp peaks is characteristic of "Stage II" of FAD adsorption. It is interesting to note that the centre of the capacitance "pit" is close to the pzc of Hg in phosphate solutions, i.e. about −0.200 V vs. NHE (21).

"Stage III" of FAD adsorption is observed after several hours of potential cycling over the range of potential in Fig. 5*a*. The ac response of this stage is shown in Fig. 6*a*, and it can be seen that now, the two ac peaks have again partly merged into one and that the capacitance "pit" has disappeared.

The development of Stages I to Stages III of FAD adsorption can also be followed by CV, as seen in Figs. 5*b* and 6*b*. It should be recalled that as s (used in the CV experiments) is 100 mV/s, much less time elapses per cycle as compared to a single cycle in the ac experiment. In the first few cycles of potential in Fig. 5*b*, a pair of broad peaks having a width at half height of ca. 70 mV (Peaks A_I and C_I, respectively) are seen. Both of these increase in magnitude with each cycle, and are centered near the expected potential for FAD reduction and oxidation. The charging current which flows on either side of the peaks decreases with continued cycling of the potential, consistent with the ac results of Fig. 5*a*. These broad peaks, A_I and C_I, are considered to depict "Stage I" of FAD adsorption. When a critical charge density of about 8 to 9 $\mu C/cm^2$ has passed, Stage I is complete and Stage II commences.

As seen in Fig. 5*b*, a sudden change in the appearance of the CV occurs as Stage II of FAD adsorption ensues. This is seen by the fact that within one or two sweeps of potential, and as the charge continues to increase, the cathodic peak (C_{II}) becomes sharp and narrow (width at half height about 40 mV) and a small, sharp shoulder ($A_{II,sh}$) appears on the positive side (at about −0.150 V) of the anodic peak. In addition, several small peaks appear at about +0.050 V (peak A′), at about −0.080 V (peak C′) and at about −0.530 V (peak C″), precisely the same potentials as where the capacitance "pit" is entered and exited in Fig. 5*a*. These peaks will be referred to as "capacitance peaks" here, as they depict the sudden changes in the double layer capacitance with potential, as seen clearly in the ac results of Figs. 5*a* and 6*a*.

"Stage III" of FAD adsorption occurs after long times of potential cycling between the extended potential limits of Figs. 5 and 6, and the CV response for "Stage III" is shown in Fig. 6*b*. Now, only a single broad pair of anodic and cathodic peaks (Peaks A_{III} and C_{III}) are observed, having a width at half height of about 70 mV. It should also be noted that the capacitance peaks A′, C′, and C″ are all now absent, consistent with the disappearance of the "pit" in Stage III in Fig. 6*a*. The relative narrowness of the peaks for Stage II as compared to Stages I and

Can. J. Chem. Downloaded from www.nrcresearchpress.com by 213.222.148.141 on 09/07/12
For personal use only.

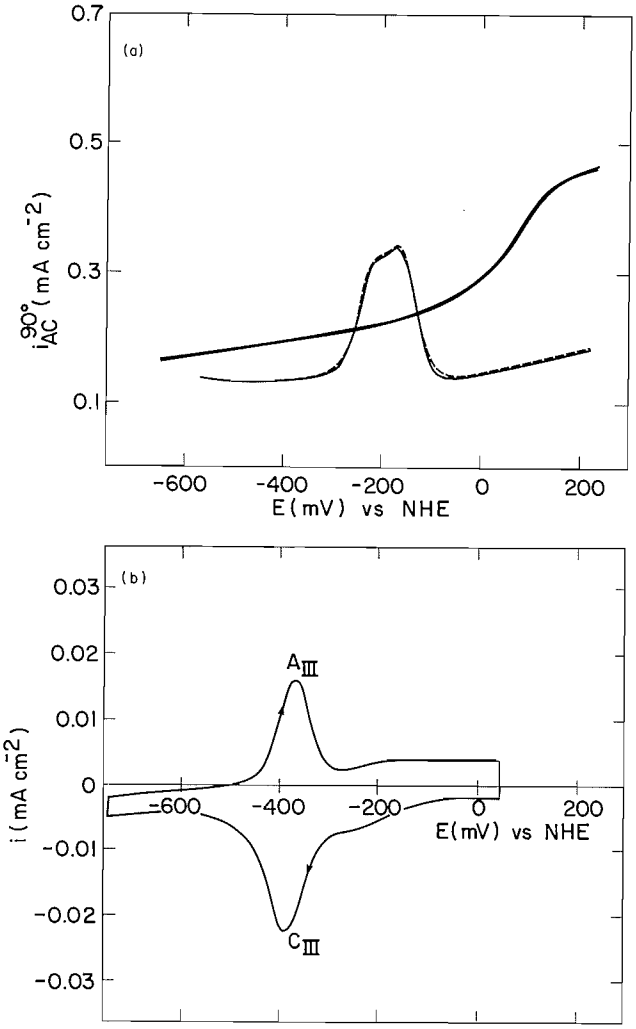

FIG. 6. Adsorption of FAD (Stage III) at the HMDE in 1.8×10^{-6} *M* FAD solution (pH = 7, 0.08 *M* phosphate buffer), after 1.5 h of continuous potential cycling to $E_- = -0.65$ V. (*a*) ac voltammogram where $\Delta E = 5$ mV, $\nu = 329$ Hz, $s = 5$ mV/s. (—) buffer solution only (no FAD); (—) cathodic sweep in FAD solution; (- - -) anodic sweep in FAD solution. (*b*) Cyclic voltammogram obtained immediately after recording the ac voltammogram in Fig. 6*a*; $s = 100$ mV/s.

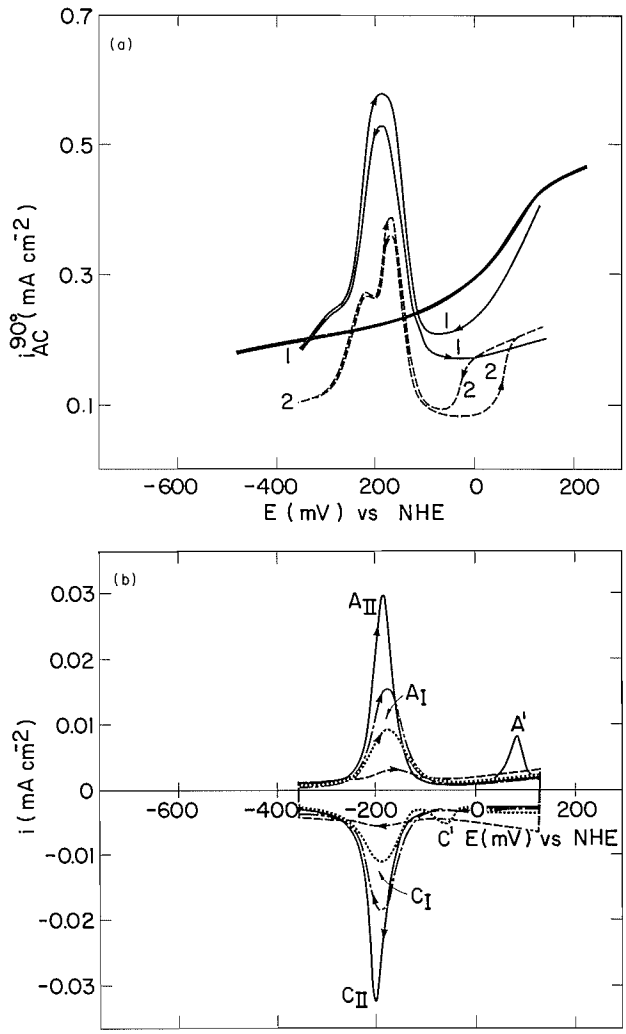

FIG. 7. Adsorption of FAD at a fresh HMDE over a less extended potential range than Fig. 5 ($E_- = -0.35$ V vs. -0.65 V); 1.8×10^{-6} *M* FAD solution (pH = 7). (*a*) ac voltammograms where $\Delta E = 5$ mV, $\nu = 329$ Hz, $s = 5$ mV/s. (—) buffer solution only (no FAD); (—) first sweep in FAD solution (curve 1); (- - -) third sweep in FAD solution (curve 2). (*b*) Cyclic voltammograms at $s = 100$ mV/s. (- - -) sweep no. 1; (···) sweep no. 10; (-·-) sweep no. 24; (—) sweep no. 38.

III is probably an indication of the presence of relatively strong lateral attractive forces within the adsorbed FAD layers in Stage II (37).

At higher FAD concentrations than 1.8×10^{-6} *M* (Figs. 5 and 6), the three stages of FAD deposition described above are also still seen, although in significantly fewer cycles, i.e. diffusion-controlled adsorption of FAD is observed. The i/E relationships for FAD adsorption are not in any way affected or controlled by the electrochemical technique utilized, e.g. CV, AC voltammetry or potential holding. However, the orientation of FAD on the electrode surface does depend strongly on time and on the potential.

(ii) Effect of potential limits

The effect of the potential limits on the mechanism of FAD adsorption can be seen most clearly from the results of the following two experiments. In Fig. 7, both the ac (Fig. 7*a*) and the CV (Fig. 7*b*) response is displayed for a fresh Hg drop when the negative voltage limit (E_-) is -0.350 V (rather than -0.650 V, as in Figs. 5 and 6), i.e. E_- is kept within the range of the capacitance "pit" during the adsorption of FAD. It is seen that when the transformation to Stage II commences, both the cathodic and anodic peaks become sharp and narrow (Fig. 7*b*), as opposed to the case when the potential is extended negatively outside of the "pit" in each scan (Fig. 5*b*) and the anodic peak remains broad. A further change observed in Fig. 7*b* vs. Fig. 5*b* is that the sharp shoulder ($A_{II,sh}$), seen previously at about -0.150 V at the positive side of A_I, now has only a transient existence. The effects shown in Fig. 7 are independent of whether or not the positive potential limit, E_+, is extended positively of the "pit".

The result of a second important experiment involving the effect of the potential limits is shown in Fig. 8. Here, Stage II of FAD adsorption has been reached after a number of cycles of potential (not shown in Fig. 8) in which E_- has been extended outside of the capacitance "pit" to -0.650 V, as in Figs. 5 and 6. The sharp cathodic peak (C_{II}), broad anodic peak (A_I), shoulder ($A_{II,sh}$), and the three capacitance peaks are all observed. By varying E_+ for each sweep as shown in Fig. 8, it is seen that when E_+ is kept negative of the potential of $A_{II,sh}$, the

Can. J. Chem. Downloaded from www.nrcresearchpress.com by 213.222.148.141 on 09/07/12
For personal use only.

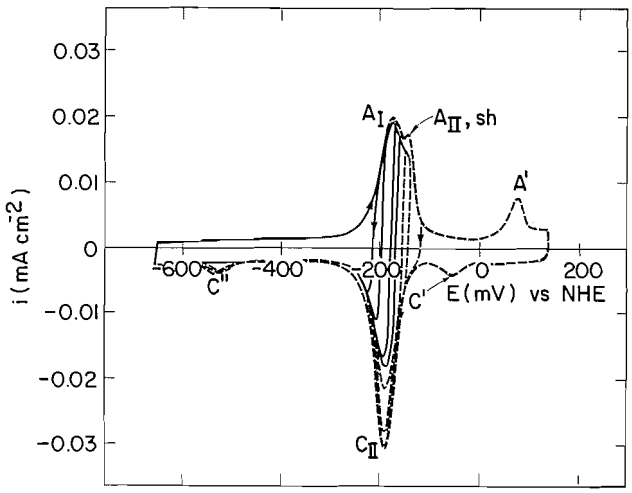

FIG. 8. Cyclic voltammograms of adsorbed FAD at HMDE after 24 cycles of potential at $s = 100$ mV/s; 1.8×10^{-6} M FAD solution (pH = 7). E_+ is increased with each potential cycle (nos. 1 to 8). Note that C'' appears only after cycle no. 5, when peak $A_{II,sh}$ has been reached.

principal cathodic peak is broad (C_I) and C'' is not observed. When E_+ reaches and crosses $A_{II,sh}$, the cathodic peak is narrower and C'' is clearly present, depicting Stage II of FAD adsorption.

These results show that if E_+ is not extended positively of the anodic shoulder, the "system" is not yet "within the capacitance pit". This confirms the ac results of Fig. 5*a*, which show that in Stage II, the capacitance drops as the two ac peaks are crossed when scanning positively. This experiment (Fig. 8) shows clearly that $A_{II,sh}$ is probably the indicator of this sudden change of the system capacitance as Stage I transforms to Stage II.

The results shown in Fig. 8 also give an indication of the kinetics of the oxidation and reduction of adsorbed FAD. When the potential is reversed within the range of peak A_{II}, the current immediately reverses in sign, indicative of a very fast process, particularly as the potential sweep rate is already reasonably high (100 mV/s). Also, the small peak separation indicates the rapid kinetics of adsorbed FAD oxidation and reduction. A more detailed kinetic discussion is presented later in this paper.

(iii) Surface formal potentials and charge densities – Stages I to III of FAD adsorption

Table 1 contains the surface formal potentials (E_f', the potential midway between the anodic and cathodic peaks) and the charge densities at the completion of each of the three stages of FAD adsorption described above. The table also lists the magnitude of the peak separation as well as the peak width at half height, all given at a potential sweep rate of 100 mV/s. It can be seen that Stages I and III, characterized by broad peaks having a width at half height of about 70 mV, have a E_f' about 20 mV more positive than does Stage II. Also, the formal potential of Stage II is closest to that obtained from the diffusion peaks (Fig. 2) at high FAD concentrations and low s. The peak separations given in Table 1 for the three stages of FAD adsorption also indicate that Stages I and III are similar, while Stage II is clearly different.

The variation of E_f' which occurs with time as the adsorption of FAD progresses through its stages points out clearly why it is difficult to reliably measure the formal potential (E_f) for FAD reduction and oxidation from the diffusion peaks (Fig. 2). At low s and high FAD concentrations, FAD adsorption would probably be complete by the time the reduction peak is reached in the first scan of potential. It is possible that Stage III would already be reached, which would lead to a positive shift of the measured E_f. At higher s, FAD adsorption would probably still be in Stage II, leading to a more negative measured E_f, while at very high s, Stage I could very well still be present in the first few sweeps. As the current response to adsorption would dominate at high s, a positive shift of the measured E_f might again be observed. This discussion stresses the difficulties associated with the measurement of a formal potential from a polarographic wave or a voltammetric peak when adsorption of the reactant and/or the product is occurring at the electrode surface as a function of time.

Significant disagreement exists in the literature regarding the quantity of RF and FMN which adsorbs at Hg electrodes and also how much charge constitutes a single layer of adsorbed flavin. For example, refs. 8 and 9 report that one molecule of adsorbed RF, with the isoalloxazine moiety parallel to the surface, would occupy an area of 150 Å^2, but observe 15 μC/cm^2 (212 Å^2) and 30 μC/cm^2 for one layer of oxidized RF and two layers of the reduced form of RF, respectively. Tedoradze *et al.* (10) have reported 22 μC/cm^2 (150 Å^2) as the charge for one monolayer of adsorbed oxidized RF and 30 μC/cm^2 for reduced RF on the electrode surface. The charge measured experimentally may depend on many variables such as solution pH, composition, and time of exposure of the electrode to the flavin solution. Some of these factors may account for the range in the reported values. Also, for bulkier molecules such as FAD, containing the phosphate and sugar groups of FMN, and also the rather large adenine group (Fig. 1), significantly more electrode surface area may be coupled per molecule, resulting in lower charge densities.

Overall, it appears that a value of 15 to 20 μC/cm^2 is a reasonable estimate of the charge equivalent to a single layer of flavin adsorbed with its isoalloxazine ring system flat on the electrode surface. Table 1 shows that Stage I of FAD adsorption is complete after 8 to 9 μC/cm^2 have passed, while Stages II and III involve a charge density of about 13 to 14 μC/cm^2. This latter charge density is consistent with the complete coverage of the Hg surface by FAD with its isoalloxazine system parallel to the electrode surface (the adenine ring can be assumed to lie above the surface, perhaps parallel to the isoalloxazine ring system, in a "stacked" configuration). The lower charge density observed for Stage I indicates a less tightly packed structure than for Stages II and III.

(iv) Kinetics of oxidation and reduction of adsorbed FAD

Figure 9*a* and *b* show plots of the peak current densities of Stages II and III as a function of potential sweep rate. In Fig. 9*a*, a linear relationship can be seen up to a sweep rate less than ca. 1 V/s, while Fig. 9*b* confirms that the deviation from linearity commences at a sweep rate greater than ca. 1 to 2 V/s. Although the charge density is the same for Stages II and III (Table 1), the currents are larger for Stage II (sharp, narrow peaks), as compared to Stage III (broad peaks), at any s.

The linear i_p/s relationship further confirms that Peaks II and III are due to the reduction/oxidation of adsorbed FAD. Because both the oxidized and the reduced form of FAD are strongly adsorbed on the Hg electrode surface, similar to the formation of a two-dimensional surface compound, it is probable that the reduction/oxidation reaction is activation controlled. Using CV, it is then anticipated that the i/E relationship should be exponential (38). However, the reaction

Can. J. Chem. Downloaded from www.nrcresearchpress.com by 213.222.148.141 on 09/07/12
For personal use only.

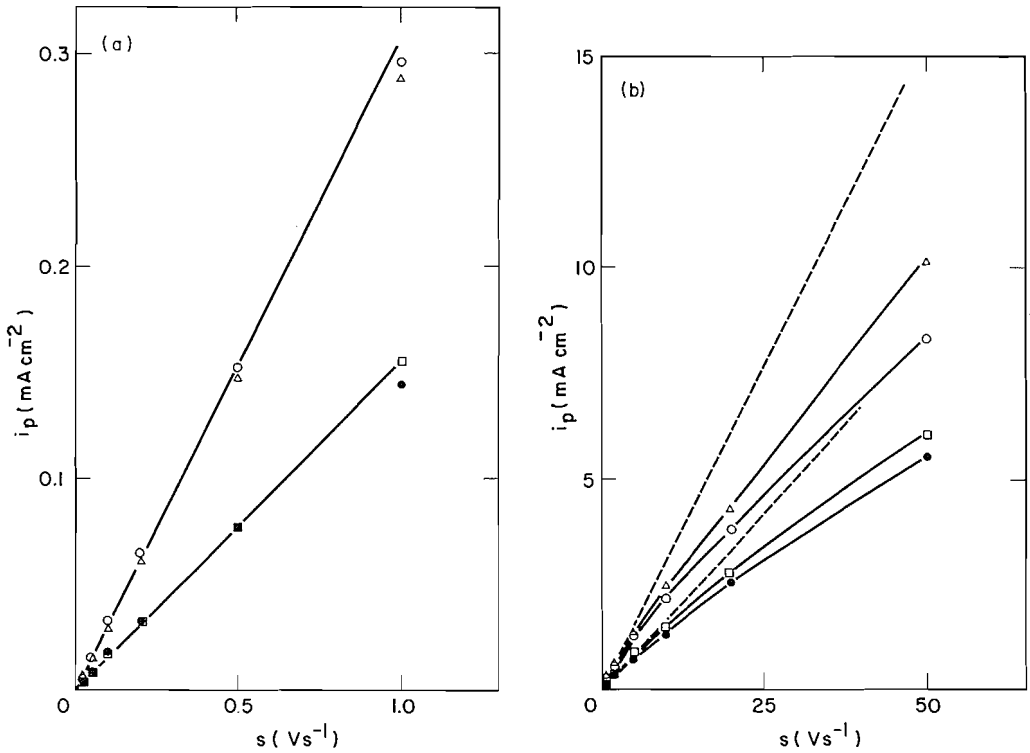

FIG. 9. Dependence of $i_{p,c}$ (○, ●) and $i_{p,a}$ (△, □) of adsorbed FAD on s; 1.8×10^{-6} M FAD solution (pH = 7); HMDE. Stage II (○, △); Stage III (●, □). (*a*) s less than 1 V/s. (*b*) s up to 50 V/s. The dashed lines represent the slope of the plots obtained at lower s (Fig. 9*a*).

rate will also depend on the number of available sites. Therefore, as the reaction progresses, e.g. cathodically, the tendency for the current to increase as the potential is made more negative will be offset by the decreasing number of reducible sites remaining. This then leads to a characteristic peak-shaped i/E response, such as seen in Figs. 5*b* and 6*b*. The same is true in the reverse (anodic) sweep.

As long as the ratio of i_p to s is constant (i.e. at a sweep rate less than 1 V/s in Fig. 9*a*), the reaction can be considered to be at equilibrium. Under these conditions, the peak potential should be constant and ΔE_p should be zero, as the concentration of oxidized and reduced species should adjust to the equilibrium values at each potential. As the sweep rate is increased, the reaction will become irreversible, as evidenced by the change of the slope of the i_p/s plot. By varying s over a reasonably wide range, the reversibility parameter, s_0, i.e. the point at which the reaction becomes irreversible, can be determined (39). s_0 is directly linked to the surface reaction standard rate constant, $k^{0'}$, according to eq. [3] (39):

$$[3] \quad k^{0'} = s_0 zF/2RT$$

where F, R, and T have their usual meaning, and z (= 2) is the number of electrons transferred per molecule of adsorbed species.

As is well known (39), the magnitude and shape of the current peaks should be independent of the concentration of reactants in solution when the surface reaction is activation controlled, and hence no bulk concentration terms appear in eq. [3]. Using an s_0 of 1 V/s, the surface standard rate constant is found to be 40 s^{-1}, which is indicative of a relatively fast surface reaction, similar to the rate of H^+ reduction at Pt electrodes in alkaline solutions (40).

Figure 10 shows a plot of ΔE_p vs. log s for Stages I to III. In this dilute FAD solution, there are no contributions from the reaction of FAD in solution, i.e. only adsorbed FAD is involved, as is seen by the constant charge for each Stage at all s. Contrary to the prediction above that ΔE_p should be equal to zero when the reaction is kinetically reversible (i.e. $s < 1$ V/s), the plot shows a peculiar rise in ΔE_p at $s < 0.5$ V/s, although it does show a sharp increase in ΔE_p at $s > 1$ V/s, at least for Stages II and III, which were examined in Fig. 9. Considering first the plot at high sweep rates, it is important to note that for Stage I, ΔE_p increases significantly only when $s > 10$ V/s, i.e. the reaction of FAD in Stage I is much faster than in the later stages. Stages II and III appear to behave similarly kinetically, apparently becoming kinetically irreversible at $s > 1$ V/s.

The unusual increase in ΔE_p at low sweep rates can only be understood by assuming that the oxidized and reduced forms of adsorbed FAD are thermodynamically different. This is consistent with a previous report regarding the lack of true reversibility seen in the diffusion waves for FAD in solutions of high FAD concentration (14). It is possible that this implies that at low sweep rates, there is adequate time for the conversion of FAD from its flat to its "butterfly" conformation as it is reduced, and vice versa, so that the oxidized and reduced forms are thermodynamically different (by 10 to 20 mV). At higher s, there may simply be too little time for this change to take place. It should be noted in Fig. 10 that this thermodynamic difference is more pronounced for Stage I than for Stages III and II.

It is also possible that the difference in peak potentials, and hence of E_f', at low s, depicts the fact that the reduced form of FAD is partly anionic, while the oxidized form is neutral, and that these two different chemical forms of FAD have somewhat different redox potentials. This would imply that at high sweep rates, both the oxidized and reduced forms of FAD would be anionic or both would be neutral.

Can. J. Chem. Downloaded from www.nrcresearchpress.com by 213.222.148.141 on 09/07/12
For personal use only.

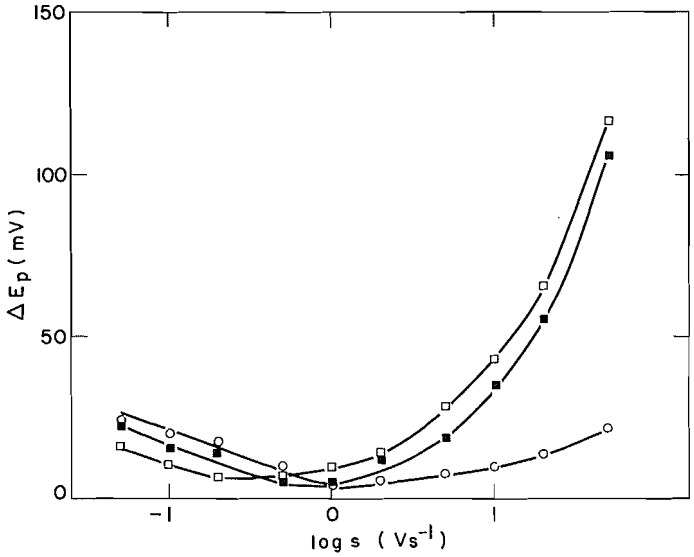

FIG. 10. ΔE_p vs. log s for adsorbed FAD; 1.8×10^{-6} M FAD solution (pH = 7). Stages of adsorption: (○) Stage I; (□) Stage II; (■) Stage III.

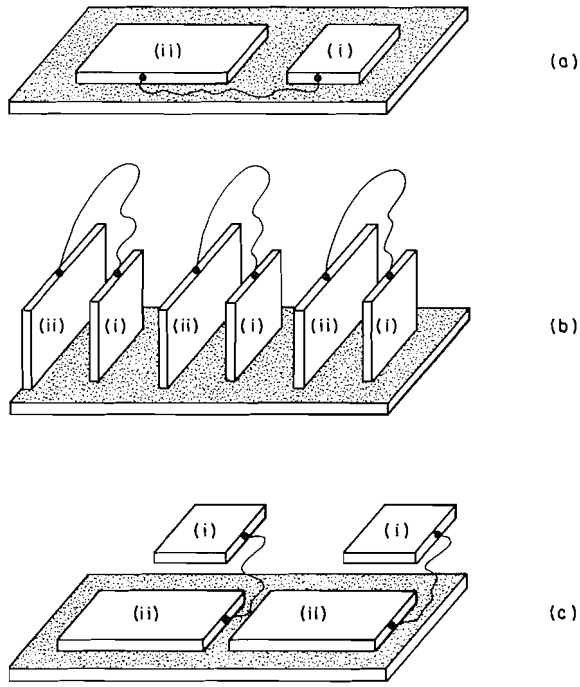

FIG. 11. Schematic of proposed orientation of adsorbed FAD at Hg electrodes, pH = 7; (*a*) Stage I; (*b*) Stage II; (*c*) Stage III. (*i*) Depicts the adenine group connected via the sugar–phosphato linkage to the isoalloxazine system (*ii*).

(v) Model of FAD adsorption at Hg electrodes

On the basis of all of the results presented above, the following model for the formation of an adsorbed FAD layer at Hg electrodes in pH 7 solutions is presented. When a fresh Hg drop is exposed to the FAD solution, FAD molecules adsorb as a function of time, as seen by the gradually increasing adsorption peaks with continuous potential sweeping (Fig. 5*b*). A time- and concentration-dependent loading of FAD on the surface of carbon electrodes has also been reported by Miyawaki and Wingard (19). It is proposed that the initial mode of adsorption (Peaks A_I/C_I) in the present work is such that the isoalloxazine moiety is approximately parallel to the electrode surface and the adenine groups are also on the Hg surface, as shown schematically in Fig. 11. This structure, having a large area per molecule (estimated to be about 400 Å^2), would be consistent with the relatively low charge densities of about 8 to 9 μC/cm^2 seen at this stage of deposition (Table 1). It should be noted that a "flat" orientation is actually more likely to be somewhat tilted, to enhance the overlap of the electron orbital on the N site on the isoalloxazine system with the Hg surface. A tilted structure has been suggested for the adsorption of pyridine on Pt electrode surfaces (41). The lack of significant lateral interactions between adjacent FAD molecules, due to the relatively loose structure of the layer and as the principal forces are probably between the Hg surface and the π electrons in the ring system would be consistent with the relatively broad nature of peaks A_I and C_I.

As the surface concentration of the loose FAD structure of Fig. 11*a* increases, a critical surface coverage is reached. Surface crowding then leads to a sudden change in orientation, represented by Stage II, for which it is suggested that the isoalloxazine ring system (and the adenine group) orients itself perpendicularly to the Hg surface, probably with the long end of the isoalloxazine moiety in contact with the electrode surface (Fig. 11*b*), similar to the vertical orientation assigned to adsorbed nucleosides when a "capacitance pit" is observed (35, 36). This suggestion is also supported by the larger surface coverage obtained in this orientation, as the π electrons of adjacent rings can overlap, leading to strong lateral interactions within the FAD layer. This leads to a more tightly packed layer, i.e. charge densities of about 13 to 14 μC/cm^2 and much sharper, narrower peaks (A_{II}, C_{II}) having a peak width of 35 to 40 mV (see Fig. 7). It should be pointed out that this perpendicular orientation is very stable when the potential is maintained within the region of the "capacitance pit", i.e. between $E = -0.550$ and 0.000 V. As long as the potential is kept within this range, the peaks will remain sharp and narrow and this orientation remains undisturbed.

When the potential is extended positively of the "pit", it is hypothesized that the now positively charged Hg surface provokes the isoalloxazine ring system to take on a parallel FAD orientation once again. This results in the observed increase in capacitance positive of the "pit". When the potential is scanned negatively, the FAD layer reorients itself again to the perpendicular orientation at $E = -0.050$ V (C′), resulting in a narrow cathodic peak (C_{II}) indicative of a perpendicular orientation with strong lateral interactions.

Figure 7 shows that when the potential is reversed during the cathodic sweep at a potential more positive than −0.550, i.e. inside the "pit", the FAD layer remains in the perpendicular orientation and a very sharp and narrow anodic peak, A_{II}, is observed. However, the extension of E_- to potentials negative of −0.550 V, i.e. out of the "pit", produces a broad anodic peak having a sharp shoulder in the next positive-going scan. On the basis of the above model, it appears that the reduced FAD layer, being at least partly anionic at pH 7, is not stable in the perpendicular orientation at negative electrode potentials and that the parallel orientation dominates at more negative potentials. This change to the parallel orientation at negative potentials is seen by the sudden increase of capacitance in Fig. 5*a* (i.e. C″ in Fig. 5*b*) at these potentials. The subsequent anodic sweep reveals a broad anodic peak, characteristic of a parallel orientation. However, as the FAD layer is oxidized,

Can. J. Chem. Downloaded from www.nrcresearchpress.com by 213.222.148.141 on 09/07/12
For personal use only.

it becomes neutral again, and therefore the perpendicular orientation is again favored. This transformation from parallel to perpendicular orientation occurs in the potential range of $A_{II,sh}$. This interpretation is consistent with the results of Fig. 5*a*, showing that the system is "inside the pit" after electro-oxidation, while it was "outside the pit" before the anodic reaction commenced.

After several hours of potential cycling over the full range of potential of Figs. 5 and 6, Stage III is reached. It is suggested that because of the broad nature of peaks A_{III} and C_{III} (Fig. 6*b*) and the similarity of these peaks to those seen in Stage I, the last stage of FAD adsorption again involves a parallel orientation of the isoalloxazine system to the Hg surface. This is supported by the absence of the capacitance peaks in CV experiments, i.e. the absence of the "pit". However, in order to make space for the equivalent of 13 $\mu C/cm^2$, the adenine group now positions itself directly above the isoalloxazene moiety in a "condensed structure" (Fig. 11*c*).

From Fig. 10, it is seen that the oxidation/reduction kinetics of adsorbed FAD are the most rapid for Stage I, when the principal interactions are thought to be between the isoalloxazine system and the Hg surface. For Stages II and III, when the strongest forces will be present between the isoalloxazine rings and the adenine system (Stage II and III) as well as between adjacent FAD molecules (Stage II), the redox reaction is somewhat slower.

Based on the above model (Fig. 11), it is also reasonable that Stage I, having no inter- or intra-molecular forces, other than to the electrode surface, would most readily take on the "butterfly" configuration in the reduced form at low s. This is consistent with the greatest thermodynamic difference being seen in Fig. 10 at low s for this stage, as compared to Stages II and III, which would be more constrained due to the presence of attractive forces between the isoalloxazine and adenine groups. Also, the observed negative shift of E_f' for Stage II vs. Stages I and III would be consistent with the predicted increase in the reducing power of the flavin, i.e. the negative shift of the redox potential, when the isoalloxazine ring system is held in the flat (vs. butterfly) orientation in the reduced state. This is more likely to be possible in Stage II than in the other Stages, as the strong lateral interactions between the FAD molecules (Fig. 11*c*) would tend to prevent any bending of the ring system during its oxidation and reduction.

Acknowledgements

Grateful acknowledgement is made to the Natural Sciences and Engineering Research Council of Canada for support of this work. Thanks are also extended to D. A. Armstrong for supplying the flavin salt and for numerous helpful discussions, and to Eileen Clarke for technical assistance.

1. G. Dryhurst, K. M. Kadish, F. Scheller, and F. Renneberg. *In* Biological electrochemistry. Vol. 1. Academic Press, Toronto. 1982. Chap. 7.
2. P. Hemmerich, C. Veeger, and H. C. S. Wood. Angew. Chem. Inter. Edit. **4**, 671 (1965).
3. B. Janik and P. J. Elving. Chem. Rev. **68**, 295 (1968).
4. T. C. Bruice. Prog. Bioinorg. Chem. **4**, 2 (1976).
5. B. Breyer and T. Biegler. J. Electroanal. Chem. **1**, 453 (1959/60).
6. B. Breyer and T. Biegler. Czech. Chem. Commun. **25**, 3348 (1960).
7. S. V. Tatwawadi and A. J. Bard. Anal. Chem. **36**, 2 (1964).
8. M. L. Foresti, F. Pergola, G. Aloisi, and R. Guidelli. J. Electroanal. Chem. **137**, 341 (1982).
9. M. L. Foresti, F. Pergola, G. Aloisi, and R. Guidelli. J. Electroanal. Chem. **137**, 355 (1982).
10. G. A. Tedoradze, E. Khmel'nitskaya, and Ya. M. Zolotovitskii. Sov. Electrochem. **3**, 200 (1967).
11. A. M. Hartley and G. S. Wilson. Anal. Chem. **38**, 681 (1966).
12. T. Kakutani, K. Kano, S. Ando, and M. Senda. Bull. Chem. Soc. Jpn. **54**, 884 (1981).
13. T. Kakutani, I. Katasho, and M. Senda. Bull. Chem. Soc. Jpn. **56**, 1761 (1983).
14. R. D. Braun. J. Electrochem. Soc. **124**, 1342 (1977).
15. O. Miyawaki and L. B. Wingard, Jr. Biotechnol. Bioeng. **26**, 1364 (1984).
16. L. Gorton and G. Johansson. J. Electroanal. Chem. **113**, 151 (1980).
17. L. B. Wingard, Jr. Trends Anal. Chem. **3**, 235 (1984).
18. O. Miyawaki and L. B. Wingard, Jr. Biochim. Biophys. Acta, **838**, 60 (1985).
19. O. Miyawaki and L. B. Wingard, Jr. Enzyme Eng. 7, Vol. **434**, 520 (1984).
20. K. Narasimham and L. Wingard, Jr. App. Biochem. Biotech. **11**, 221 (1985).
21. E. R. Gonzalez, A. Carubelli, and S. Srinivasan. Electrochim. Acta, **30**, 191 (1985).
22. A. J. Bard and L. R. Faulkner. Electrochemical Methods. John Wiley and Sons. 1980. pp. 218, 219, 522.
23. S. Van den Berghe-Snorek and M. T. Stankovich. J. Am. Chem. Soc. **106**, 3683 (1984).
24. R. F. Anderson. Biochim. Biophys. Acta, **722**, 158 (1983).
25. C. Walsh, J. Fisher, R. Spencer, D. W. Graham, W. T. Ashton, J. E. Brown, R. D. Brown, and E. F. Rogers. Biochemistry, **17**, 1942 (1978).
26. Y. Asahi. J. Pharm. Soc. Jpn. **76**, 378 (1956).
27. O. S. Ksenzhek, S. A. Petrova, and I. D. Pinielle. Sov. Electrochem. **11**, 1603 (1975).
28. Z. Brdicka. Zeit. Elektrochem. **48**, 278 (1942).
29. B. Ke. Arch. Biochem. Biophys. **68**, 330 (1957).
30. M. T. Stankovich. Anal. Biochem. **109**, 295 (1980).
31. M. J. Clarke, M. G. Dowling, A. R. Garafalo, and T. F. Brennan. J. Am. Chem. Soc. **101**, 223 (1979).
32. M. J. Clarke and M. G. Dowling. Inorg. Chem. **20**, 3506 (1981).
33. M. G. Dowling and M. J. Clarke. Inorg. Chim. Acta, **78**, 153 (1983).
34. B. B. Damaskin, O. A. Petrii, and V. V. Batrakov. *In* Adsorption of organic compounds on electrodes. Plenum Press, New York. 1971.
35. W. T. Bresnahan, J. Moiroux, Z. Samec, and P. J. Elving. Bioelectrochem. Bioeng. **7**, 125 (1980).
36. V. Vetterl, K. Kovarikova, and R. Zaludova. Bioelectrochem. Bioeng. **4**, 389 (1977).
37. E. Laviron. Electroanalytical chemistry. Vol. 12. *Edited by* Allen J. Bard. Marcel Dekker Inc. 1982. p. 53.
38. H. Angerstein-Kozlowska, J. Klinger, and B. E. Conway. J. Electroanal. Chem. **75**, 45 (1977).
39. H. Angerstein-Kozlowska and B. E. Conway. J. Electroanal. Chem. **95**, 1 (1979).
40. H. Angerstein-Kozlowska and B. E. Conway. J. Electroanal. Chem. **87**, 321 (1978).
41. A. L. Johnson and E. L. Muetterties. J. Phys. Chem. **89**, 4071 (1985).

Can. J. Chem. Downloaded from www.nrcresearchpress.com by 213.222.148.141 on 09/07/12
For personal use only.

Crystal and molecular structure of the di-μ-hydroxo-dimolybdenum compound, $[Mo(CO)_2(OH)(C_4H_7)(3,5\text{-diMepzH})]_2.C_6H_6$

STEVEN J. RETTIG, ALAN STORR,[1] AND JAMES TROTTER[1]

Department of Chemistry, University of British Columbia, Vancouver, B.C., Canada V6T 1Y6

Received April 3, 1987

STEVEN J. RETTIG, ALAN STORR, and JAMES TROTTER. Can. J. Chem. **66**, 97 (1988).

The synthesis and X-ray crystal analysis of a hydroxy-bridged molybdenum dimer are described. Crystals of di-μ-hydroxo-bis[dicarbonyl(3,5-dimethylpyrazole)(η^3-2-methylallyl)molybdenum(II)] benzene solvate are monoclinic, $P2_1/c$, $a = 7.508(1)$, $b = 20.747(1)$, $c = 20.717(3)$ Å, $\beta = 99.536(6)°$, $Z = 4$. The structure was determined by Patterson and Fourier methods and refined by full-matrix least-squares procedures to $R = 0.022$ for 3197 observed reflections. The dimeric molecule contains two distorted Mo coordination octahedra sharing an OH...OH edge to form a central folded four-membered $Mo(\mu\text{-}OH)_2Mo$ ring. The pyrazole ligands form bent N—H...O intramolecular hydrogen bonds to the bridging OH groups, and the other ligands occupy positions which result in approximate C_2 molecular symmetry. Two sets of Mo—OH bonds differ significantly in length, 2.237(2) and 2.140(2) Å; other molecular dimensions are within expected ranges. Molecules are linked into chains along *a* by O—H...OC hydrogen bonds, and benzene solvate molecules are well defined.

STEVEN J. RETTIG, ALAN STORR et JAMES TROTTER. Can. J. Chem. **66**, 97 (1988).

On décrit la synthèse et la cristallographie de rayons-X d'un dimère du molybdène pont d'hydroxyle. Les cristaux de di-μ-hydroxo-bis[dicarbonyl(diméthyl-3,5 pyrazolé)(η^3-méthyl-2 allyl)molybdène(II)] solvaté par la benzène sont monocliniques, $P2_1/c$, $a = 7{,}508(1)$, $b = 20{,}747(1)$, $c = 20{,}717(3)$ Å, $\beta = 99{,}536(6)°$, $Z = 4$. On a résolu la structure par les synthèses de Patterson et de Fourier et on l'a affinée par la méthode des moindres carrés (matrice entière) jusqu'à $R = 0{,}022$ pour 3197 réflexions observées. La molécule dimère comprend deux coordinations octaèdres déformés du molybdène qui partagent une arête OH...OH, en formant un cycle central plié à quatres membres, $Mo(\mu\text{-}OH)_2Mo$. Les ligands de pyrazol forment des liaisons hydrogène intramoléculaires et pliés, N—H...O, aux groupes pontés d'OH, et les autres ligands occupent les positions qui aboutent approximativement à la symétrie moléculaire C_2. Les longueurs des deux ensembles des liaisons Mo—OH sont significativement différentés, 2,237(2) et 2,140(2) Å; les autres dimensions moléculaires sont en dedans des domaines attendus. Les molécules s'articulent dans les chaînes le long de l'axe *a* par les liaisons d'hydrogène, et les molécules du solvant de benzène sont bien précises.

Can. J. Chem. Downloaded from www.nrcresearchpress.com by 213.222.148.141 on 09/07/12
For personal use only.

Introduction

In an earlier publication (1) we described the syntheses and properties of a number of manganese, molybdenum, and tungsten carbonyl derivatives incorporating the dimethylbis(1-pyrazolyl)gallate ligand, $[Me_2Gapz_2]^-$. These included the complex $[Me_2Gapz_2]Mo(CO)_2(\eta^3\text{-}C_3H_5)(pzH)$. Attempts to prepare the analogous $[Me_2Ga(3,5\text{-diMepz})_2]Mo(CO)_2(\eta^3\text{-}C_4H_7)(3,5\text{-diMepzH})$, however, were unsuccessful, but yielded instead a yellow crystalline complex since characterized as $[Mo(CO)_2(OH)(C_4H_7)(3,5\text{-diMepzH})]_2.C_6H_6$. The present account details the X-ray crystal analysis of this compound and describes the $Mo(\mu\text{-}OH)_2Mo$ bridging feature central to the dimeric molecule.

Experimental

Synthesis

The title complex resulted from the reaction of $Mo(MeCN)_2(\eta^3\text{-}C_4H_7)(CO)_2Cl$ (2) with the organogallate ligand $[Me_2Ga(3,5\text{-diMepz})_2]^-$ (3) in acetonitrile solvent, followed by recrystallization of the product mixture from benzene, and may have arisen via the attack of water on the coordinatively unsaturated species $[Me_2Ga(3,5\text{-diMepz})_2]Mo(CO)_2(\eta^3\text{-}C_4H_7)$ expected from the reaction. *Anal.* calcd. for $[Mo(CO)_2(OH)(C_4H_7)(3,5\text{-diMepzH})]_2.C_6H_6$: C 46.81, H 5.29, N 7.80; found: C 46.58, H 5.18, N 7.86%. Infrared (Nujol): ν_{OH} 3590, ν_{NH} 3200 br, ν_{CO} 1920, 1790 cm^{-1}. ^1H nmr (d_6-acetone $\delta = 2.11$) $\delta = 1.72$ (*Me*-allyl); 2.38, 2.50 (*Me*-pz); 5.81 (OH); 6.02 (pz-H[4]); 7.41 (C_6H_6).

Spectra

The infrared spectrum was recorded on a Perkin-Elmer 467 spectrometer, the ^1H nmr spectrum on a Varian 100 MHz spectrometer using FT technique, and the elemental analyses were performed by Mr. P. Borda of the UBC Microanalytical Laboratory.

X-ray crystal analysis of di-μ-hydroxo-bis[dicarbonyl(3,5-dimethylpyrazole)(η^3-2-methylallyl)molybdenum(II)] benzene solvate

A crystal of dimensions 0.39 × 0.17 × 0.06 mm, with {1 0 0}, {0 1 0}, {0 0 1} faces, was mounted in a general orientation. Unit cell parameters were determined from the settings of 25 reflexions measured on a diffractometer with Mo$K\alpha$ radiation ($\lambda\alpha_1 = 0.70930$ Å). Crystal data at 295 K are as follows:

$C_{22}H_{32}Mo_2N_4O_6.C_6H_6$ fw = 718.51

Monoclinic, $a = 7.508(1)$, $b = 20.747(1)$, $c = 20.717(3)$ Å, $\beta = 99.536(6)°$, $V = 3182.5(6)$ Å^3, $Z = 4$, $D_x = 1.499$ g cm^{-3}, $F(000) = 1464$, μ(Mo$K\alpha$) = 8.1 cm^{-1}. Absent reflections: $h0l$, $l \neq 2n$, $0k0$, $k \neq 2n$, space group $P2_1/c$ (C_{2h}^5, No. 14).

Intensities were measured with graphite-monochromatized Mo$K\alpha$ radiation on an Enraf-Nonius CAD4-F diffractometer. An ω–2θ scan was used, at 1.0–10.0° min^{-1} over a range of (0.65 + 0.35 tan θ) deg in ω (extended 25% on both sides for background measurement). Data were measured to $2\theta = 50°$. The intensities of three check reflections, measured every 3600 s throughout the data collection, showed small variations of ±3%. Lorentz and polarization factors were applied, and absorption corrections were made (4, 5), and transmission factors ranged from 0.873 to 0.956.[2] Of the 5565 independent reflections measured, 3197 (57.5%) had intensities $\geq 3\sigma(I)$, where $\sigma^2(I) = S + 2B + (0.04(S - B))^2$, where S = scan count and B = normalized background count.

[1]Authors to whom correspondence should be addressed.

[2]The computer programs used include locally written programs for data processing and locally modified versions of the following: AGNOST, absorption correction, J. A. Ibers; ORFLS, full-matrix least-squares, and ORFFE, function and errors, by W. R. Busing, K. O. Martin, and H. A. Levy; FORDAP, Patterson and Fourier syntheses, by A. Zalkin; ORTEPII, illustrations, by C. K. Johnson.

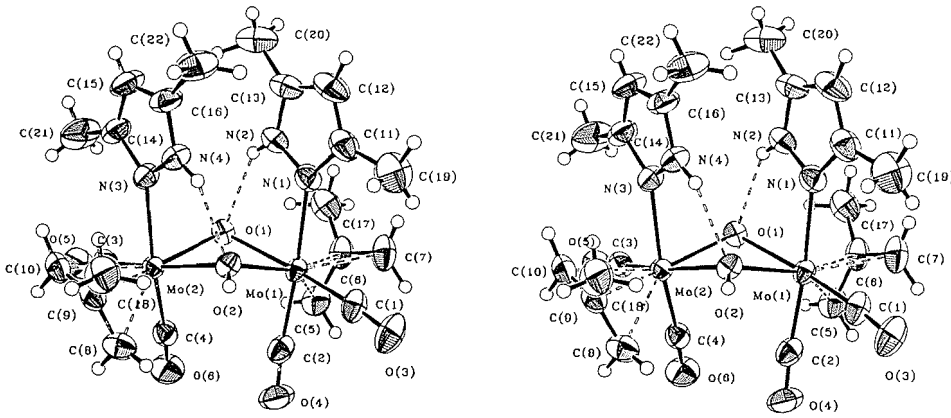

FIG. 1. View of the molecule, with 50% probability thermal ellipsoids.

TABLE 1. Final positional (fractional × 10^4, Mo × 10^5) and isotropic thermal parameters ($U \times 10^3$ Å^2) with estimated standard deviations in parentheses

Atom	x	y	z	U_{eq}
Mo(1)	23390(4)	43821(2)	30746(2)	32
Mo(2)	43580(4)	48356(2)	17888(2)	30
O(1)	4963(4)	4739(1)	2831(1)	34
O(2)	1818(4)	4955(1)	2206(1)	34
O(3)	−1594(4)	3985(2)	3139(2)	63
O(4)	1390(4)	3159(2)	2221(2)	65
O(5)	8213(4)	4576(2)	1512(2)	63
O(6)	4895(5)	3365(2)	1632(2)	66
N(1)	2511(5)	5377(2)	3545(2)	43
N(2)	4079(5)	5709(2)	3602(2)	44
N(3)	4516(4)	5897(2)	2072(2)	40
N(4)	3043(5)	6199(2)	2220(2)	41
C(1)	−120(6)	4168(2)	3126(2)	45
C(2)	1832(5)	3618(2)	2524(2)	46
C(3)	6786(6)	4706(2)	1629(2)	43
C(4)	4596(5)	3903(2)	1703(2)	42
C(5)	3947(7)	3503(2)	3536(2)	53
C(6)	3879(6)	3982(2)	4011(2)	50
C(7)	2141(8)	4103(3)	4158(3)	61
C(8)	2568(8)	4461(2)	848(2)	54
C(9)	2865(6)	5124(2)	801(2)	45
C(10)	4661(7)	5298(3)	784(2)	56
C(11)	1418(6)	5759(2)	3828(2)	53
C(12)	2325(8)	6312(3)	4055(3)	60
C(13)	4021(7)	6274(2)	3903(2)	51
C(14)	5775(6)	6366(2)	2115(2)	51
C(15)	5048(7)	6939(2)	2292(3)	60
C(16)	3301(6)	6830(2)	2355(2)	47
C(17)	5511(8)	4345(3)	4326(3)	63
C(18)	1361(9)	5603(3)	767(3)	62
C(19)	−465(9)	5554(4)	3883(5)	82
C(20)	5608(11)	6718(3)	4033(4)	74
C(21)	7627(9)	6232(4)	1983(5)	83
C(22)	1879(10)	7254(3)	2531(4)	68
C(23)	8629(14)	3099(3)	598(4)	93
C(24)	7016(13)	3026(3)	199(5)	96
C(25)	6953(14)	2707(4)	−381(4)	100
C(26)	8483(18)	2466(4)	−556(4)	111
C(27)	10072(16)	2535(4)	−144(5)	112
C(28)	10147(12)	2859(3)	424(4)	96

The coordinates of the Mo atoms were determined from the Patterson function and those of the remaining non-hydrogen atoms from a subsequent difference map. Full-matrix least-squares refinement of the non-hydrogen atoms with anisotropic thermal parameters gave R = 0.034. A difference map at this point gave the coordinates of all 38 hydrogen atoms, which were included in all subsequent cycles of refinement with isotropic thermal parameters. The scattering factors used were those of ref. 6; the weighting scheme $w = 1/\sigma^2(F)$ gave uniform average values of $w\Delta F^2$, and was employed in the final stages of refinement of 513 variables. Convergence was reached at $R = 0.022$ and $R_w = 0.026$ for 3197 reflections with $I \geq 3\sigma(I)$; for all 5565 reflections $R = 0.080$. On the final cycle of refinement parameter shifts were 0.13σ (mean) and 2.8σ (maximum, for y of H(20b)); the mean error in an observation of unit weight was 0.81. A final difference map showed maximum fluctuations of ±0.3 e Å^{-3}. Final positional parameters are listed in Table 1, and a summary of the molecular dimensions is given in Table 2; thermal parameters, and full listings of bond lengths, bond angles, torsion angles, and structure factors have been placed in the Depository of Unpublished Data.[3] Analysis of the thermal parameters of all non-H atoms of the organometallic molecule, excluding the pyrazole carbon atoms, gave physically reasonable rigid body parameters, rms $\Delta U_{ij} = 0.0052$ Å^2; bond distance increases for libration are of the order of only 1σ, and have not been applied.

Results and discussion

The origin of the hydroxy species is not known with certainty, but the material must have resulted from the presence of water, most probably contained in the acetonitrile solvent, even though the solvent was carefully dried. Previous examples of water accidentally entering similar reactions have been documented. Thus the 3,5-dimethylpyrazolyl based ligand [MeGa(3,5-diMepz)$_3$]$^-$ is very prone to conversion to the hydroxy species [MeGa(3,5-diMepz)$_2$(OH)]$^-$ in sterically demanding situations, even when rigorous attempts to eliminate water are made (7). It is also reported that the reaction of $Mo_2(CH_3CO_2)_4$ with $Na^+Et_2Bpz_2^-$ results in the incorporation of [Et$_2$B(pz)(OH)]$^-$ ligands in the dimolybdenum product, an unexpected result attributed to the "adventitious" entry of water into the reaction mixture (8). A related reaction involving the gallate ligand [MeGapz$_3$]$^-$ gives an equally unexpected product (9).

The molecule (Fig. 1) is dimeric, with two distorted Mo

[3]Complete set of data may be purchased from the Depository of Unpublished Data, CISTI, National Research Council of Canada, Ottawa, Ont., Canada K1A 0S2.

Can. J. Chem. Downloaded from www.nrcresearchpress.com by 213.222.148.141 on 09/07/12
For personal use only.

TABLE 2. Selected bond lengths (Å) and angles (deg), with standard deviations in parentheses

Bonds			Mo(1)	Mo(2)
Mo—OH			2.239(3)	2.235(3)
			2.138(3)	2.142(3)
Mo—N			2.277(3)	2.277(3)
Mo—C (allyl, central)			2.246(4)	2.245(4)
Mo—C (allyl, terminal)			2.306(5)	2.311(5)
			2.346(5)	2.337(5)
Mo—CO (axial, *trans* to N)			1.952(5)	1.954(4)
Mo—CO (eq., *trans* to O)			1.918(4)	1.925(4)
Mo...Mo			3.408(1)	
Angles				
O—Mo—O			70.9(1)	70.9(1)
Mo—O—Mo			102.1(1)	
			102.4(1)	
Torsion angles about Mo—O bonds				
Mo(1)—O(1)	−28.7(1)	Mo(2)—O(2)	−28.8(1)	
O(1)—Mo(2)	27.3(1)	O(2)—Mo(1)	27.4(1)	

Hydrogen bonds

Intramolecular

	H...O	N...O	N—H...O	H...O—Mo
N(2)—H(N2)...O(1)	2.14(4)	2.719(5)	137(3)	120, 89(1)
N(4)—H(N4)...O(2)	2.15(3)	2.738(5)	133(3)	122, 90(1)

Intermolecular

	H...O	O...O	O—H...O	H...O—C
O(1)—H(01)...O(3)[a]	2.33(3)	2.998(4)	164(4)	131(1)
O(2)—H(02)...O(5)[b]	2.27(4)	2.954(4)	169(5)	132(1)

[a] $1 + x, y, z$.
[b] $x - 1, y, z$.

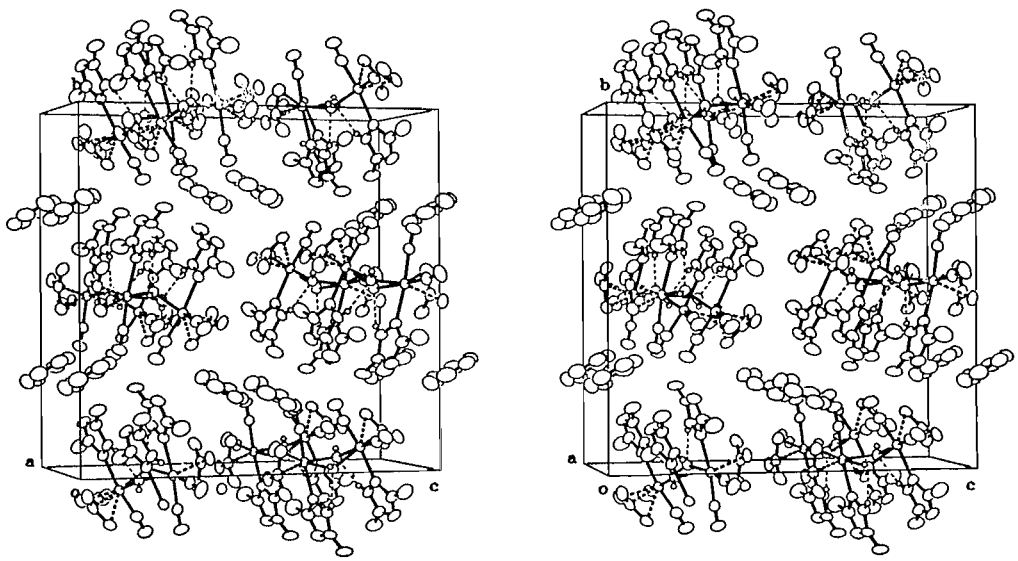

FIG. 2. Packing diagram.

coordination octahedra (taking the allyl ligand as occupying one coordination position) sharing an OH...OH edge to form a central folded four-membered Mo(μ-OH)$_2$Mo ring (bond dihedral angles 28°, Table 2). The pyrazole ligands are in axial positions, and form bent N—H...O intramolecular hydrogen bonds to the bridging OH groups, N...O = 2.719 and 2.738(5) Å, N—H...O = 137, 133(3)° (Table 2). The other ligands occupy positions which give the molecule close to overall C_2 symmetry (Fig. 1).

The two sets of Mo—OH bonds differ significantly in length; the two bonds in the five-membered hydrogen-bonded rings average 2.237(2) Å, while the two Mo—OH bonds not bridged by hydrogen bonding are 2.140(2) Å. A similar difference was found in an Mo_2S_2 ring in a related compound (10), with

Can. J. Chem. Downloaded from www.nrcresearchpress.com by 213.222.148.141 on 09/07/12
For personal use only.

Mo—S bonds of 2.687(1) Å, which are part of a chelate ring, and other Mo—S bonds of 2.558(1) Å. The O—Mo—O angles are 70.9(1)°, with Mo—O—Mo 102.3(1)°, and a Mo...Mo cross-ring distance of 3.408(1) Å indicating no significant metal–metal interaction.

The η^3-C_4H_7 ligands are in equatorial sites, *cis* to one OH and *trans* to the second OH; Mo—C(allyl) = 2.246(3) (central C), 2.306–2.346(5) Å (terminal C). Mo—CO (axial, *trans* to N) = 1.953(4), Mo—CO (equatorial, *trans* to O) = 1.922(4), Mo—N = 2.277(2) Å. These and other molecular dimensions are similar to those in related compounds (7, 10).

Molecules are linked into O(5)(x − 1)...H—O(2)—Mo_2—O(1)—H...O(3)(x + 1) chains along a by O—H...OC hydrogen bonds, O...O = 2.998 and 2.954(4) Å, O—H...O = 164(4), 169(5)°; the acceptor oxygen atoms belong to the equatorial CO groups. The benzene solvate molecule, C(23)—C(28), is well defined, with slightly large, but not unreasonable thermal parameters. The benzene molecules occupy channels along a (Fig. 2).

Acknowledgements

We thank the Natural Sciences and Engineering Research Council of Canada for financial support, and the University of British Columbia Computing Centre for assistance.

1. S. E. ANSLOW, K. S. CHONG, S. J. RETTIG, A. STORR, and J. TROTTER. Can. J. Chem. **59**, 3123 (1981).
2. R. G. HAYTER. J. Organomet. Chem. **13**, P1 (1968).
3. K. R. BREAKALL, D. J. PATMORE, and A. STORR. J. Chem. Soc. Dalton Trans. 749 (1975).
4. P. COPPENS, L. LEISEROWITZ, and D. RABINOVICH. Acta Crystallogr. **18**, 1035 (1965).
5. W. R. BUSING and H. A. LEVY. Acta Crystallogr. **22**, 457 (1967).
6. International Tables for X-ray Crystallography. Vol. IV. Kynoch Press, Birmingham. 1974. pp. 99–102, 149.
7. K. R. BREAKALL, S. J. RETTIG, A. STORR, and J. TROTTER. Can. J. Chem. **57**, 139 (1979).
8. F. A. COTTON, B. W. S. KOLTHAMMER, and G. N. MOTT. Inorg. Chem. **20**, 3890 (1981).
9. K. R. BREAKALL, S. J. RETTIG, A. STORR, and J. TROTTER. Can. J. Chem. **61**, 1659 (1983).
10. D. A. COOPER, S. J. RETTIG, A. STORR, and J. TROTTER. Can. J. Chem. **64**, 1643 (1986).

Can. J. Chem. Downloaded from www.nrcresearchpress.com by 213.222.148.141 on 09/07/12
For personal use only.

Coordination compounds containing a novel tridentate pyrazolylgallate ligand. X-ray structures of $Me_2Ga(\mu\text{-}OH)(\mu\text{-}Me_2pz)GaMe_2 \cdot HOCH_2Me_2pz$ and $[Me_2Ga(pz)(OCH_2pz)]_2Ni$ (pz = $N_2C_3H_3$)

ARTHUR MAR, STEVEN J. RETTIG, ALAN STORR,[1] AND JAMES TROTTER[1]

Department of Chemistry, University of British Columbia, 2036 Main Mall, Vancouver, B.C., Canada V6T 1Y6

Received June 22, 1987

ARTHUR MAR, STEVEN J. RETTIG, ALAN STORR, and JAMES TROTTER. Can. J. Chem. **66**, 101 (1988).

The syntheses of the novel anionic tridentate dimethyl(pyrazol-1-yl)(1-oxymethylpyrazolyl)gallate ligand and representative transition metal complexes thereof are reported. The direct reaction of Me_3Ga with 1-hydroxymethyl-3,5-dimethylpyrazole leads to the isolation of $Me_2Ga(\mu\text{-}OH)(\mu\text{-}Me_2pz)GaMe_2 \cdot HOCH_2Me_2pz$. Crystals of ($\mu$-hydroxy)($\mu$-3,5-dimethylpyrazolyl)bis(dimethylgallium) 1-hydroxymethyl-3,5-dimethylpyrazole solvate are monoclinic, a = 33.105(2), b = 7.3048(7), c = 8.8336(6) Å, β = 97.474(7)°, Z = 4, space group $P2_1/n$, and those of bis[dimethyl(pyrazol-1-yl)(1-oxymethylpyrazolyl)gallato-$N^2,N^{2\prime},O$]nickel(II) are monoclinic, a = 9.6345(3), b = 14.2731(6), c = 18.6356(7) Å, β = 99.660(3)°, Z = 4, space group $P2_1/c$. Both structures were solved by conventional heavy atom methods and were refined by full-matrix least-squares procedures to R = 0.044 and 0.037 for 2660 and 3904 reflections with $I \geq 3\sigma(I)$, respectively. Mean bond lengths in $Me_2Ga(\mu\text{-}OH)(\mu\text{-}Me_2pz)GaMe_2 \cdot HOCH_2Me_2pz$ are Ga—O = 1.918(11), Ga—N = 2.001(5), and Ga—C = 1.955(5) Å. *Fac*-$[Me_2Ga(pz)(OCH_2pz)]_2Ni$ crystallizes as an all-*cis* isomer with normal bond lengths and angles at Ga and Ni—O = 1.918(3) and 1.927(3), Ni—N = 2.030(4)–2.111(4) Å. The coordination geometry about Ni is irregular pseudo-octahedral with evidence of both steric and structural *trans* effects.

ARTHUR MAR, STEVEN J. RETTIG, ALAN STORR et JAMES TROTTER. Can. J. Chem. **66**, 101 (1988).

On rapporte les synthèses du nouveau ligand anionique tridentate diméthyl (pyrazolyl-1)(oxyméthyl-1 pyrazolyl) gallate et de complexes représentatifs de métaux de transition. La réaction directe du Me_3Ga avec l'hydroxyméthyl-1 diméthyl-3,5 pyrazole conduit au $Me_2Ga(\mu\text{-}OH)(\mu\text{-}Me_2pz)GaMe_2$. Les cristaux du ($\mu$-hydroxy)($\mu$-diméthyl-3,5 pyrazolyl)bis(diméthylgallium) solvaté par de l'hydroxyméthyl-1 diméthyl-3,5 pyrazole sont monocliniques avec a = 33,105(2), b = 7,3048(7) et c = 8,8336(6)], β = 97,474(7)°, Z = 4 et groupe d'espace $P2_1/n$ alors que ceux du bis [diméthyl(pyrazolyl-1)(oxyméthyl-1 pyrazolyl) gallato-$N^2,N^{2\prime},O$] nickel(II) sont monocliniques avec a = 9,6345(3), b = 14,2731(6) et c = 18,6356(7) Å, β = 99,660(3)°, Z = 4 et groupe d'espace $P2_1/c$. On a résolu les deux structures en faisant appel aux méthodes conventionnelles aux atomes lourds et on les a affinées par la méthodes des moindres carrés (matrice entière) jusqu'à des valeurs respectives de R de 0,044 et 0,037 pour 2660 et 3904 réflexions avec $I \geq 3\sigma(I)$. Les longueurs moyennes des liaisons dans le $Me_2Ga(\mu\text{-}OH)(\mu\text{-}Me_2pz)GaMe_2 \cdot HOCH_2Me_2pz$ sont Ga—O = 1,918(11), Ga—N = 2,001(5) et Ga—C = 1,955(5) Å. Le $[Me_2Ga(pz)(OCH_2pz)]_2Ni$-*Fac* cristallise sous la forme de l'isomère complètement *cis* et les longueurs et les angles sont normaux au niveau du Ga et Ni—O = 1,918(3) et 1,927(3), Ni—N = 2,030(4)–2,111(4) Å. La géométrie de coordination autour du Ni est du type pseudo-octaédrique irrégulier et l'on a relevé des données à l'effet qu'il existe des effets stériques ainsi que des effets structuraux *trans*.

[Traduit par la revue]

Introduction

Recently Driessen reported a straightforward synthesis of 1-hydroxymethylpyrazole compounds (1). These compounds have been condensed with various primary and secondary amines and with ammonia to give a series of novel chelating ligands (2–6). The 1-oxymethyl-3,5-dimethylpyrazolate anion itself has shown interesting properties as a chelating ligand, having been incorporated into a number of transition metal cubane-type cluster compounds (7). More recently the reaction of 1-hydroxymethyl-3,5-dimethylpyrazole with a series of Ru complexes has resulted in the substitution of the 1-hydroxymethyl group by a hydrogen in the resulting coordination complex (8). Our continuing interest in unsymmetrical tridentate ligands of the type **1** (ref. 9 and references therein)

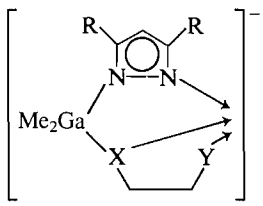

1 (R = H or Me, X and Y = donor atoms)

and the comparative dearth of information available on the coordination chemistry of the 1-oxymethylpyrazolyl moiety has prompted us to synthesize a novel organogallate ligand, L^-, which includes the 1-oxymethylpyrazolyl in addition to a gallium-substituted pyrazolyl ring system:

L^- =

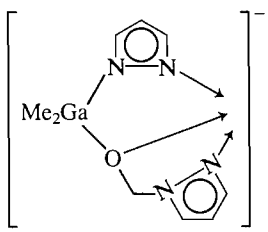

The present paper describes the synthesis of representative transition metal complexes incorporating this ligand, and, through an X-ray crystallographic analysis of the L_2Ni complex, definitively establishes the expected tridenticity and chelating character of the organogallate ligand. Direct reaction of Me_3Ga and 1-hydroxymethylpyrazoles gave unexpected products; the structure of one of these has also been established by crystal analysis.

Experimental

Starting materials

Air-sensitive materials were handled in a nitrogen atmosphere.

[1]Authors to whom correspondence should be addressed.

Can. J. Chem. Downloaded from www.nrcresearchpress.com by 213.222.148.141 on 09/07/12
For personal use only.

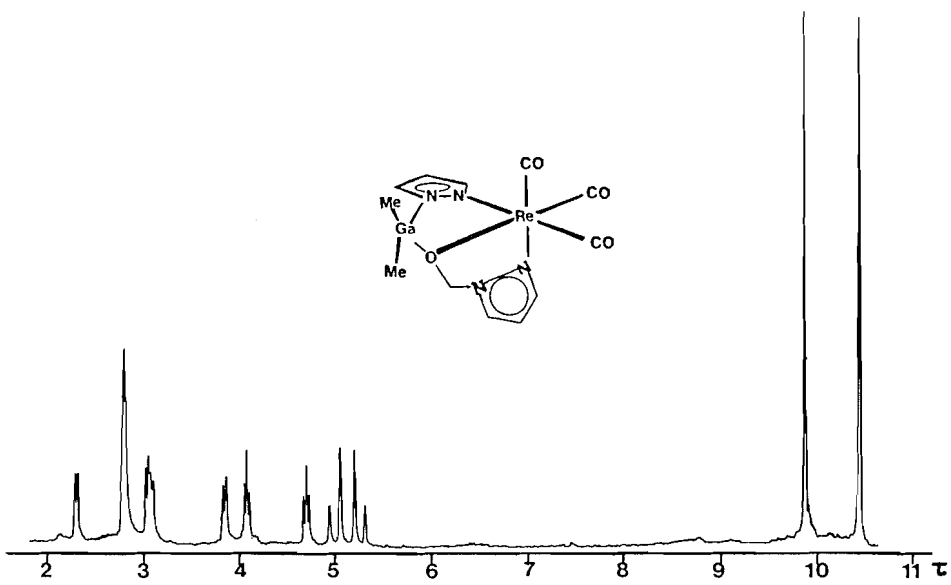

FIG. 1. Nuclear magnetic resonance spectrum of $[Me_2Ga(pz)(OCH_2pz)]Re(CO)_3$.

Tetrahydrofuran (THF), benzene, and CH_2Cl_2 were dried by refluxing over Na/benzophenone, potassium, and calcium hydride respectively, followed by distillation. $[Re(CO)_4Cl]_2$ (10), $Mn(CO)_5Br$ (11), Ni(NO)I (12), and Me_3Ga (13) were prepared as previously described. Sodium pyrazolides were prepared by reacting sodium hydride (Alfa) with the appropriate pyrazole (K and K Laboratories) in THF. The 1-hydroxymethylpyrazoles were prepared by the method described by Driessen (1).

Preparation of $Na^+[Me_2Ga(pz)(OCH_2pz)]^-$ (Na^+L^-)

$$Na^+pz^- + Me_3Ga \xrightarrow{THF} Na^+Me_3Gapz^-$$

$$Na^+Me_3Gapz^- + HOCH_2pz \xrightarrow[\Delta]{THF} Na^+L^- + CH_4$$

An equimolar amount of 1-hydroxymethylpyrazole (0.502 g, 5.12 mmol) in THF was added to a THF solution of $Na^+Me_3Gapz^-$ (14) and the mixture was refluxed overnight. The resultant clear solution was cooled and made up to standard volume with THF for use in subsequent reactions.

Preparation of $[Me_2Ga(pz)(OCH_2pz)]_2Ni$ (L_2Ni)

$$NiBr_2 + 2Na^+L^- \xrightarrow[rt]{THF} L_2Ni + 2NaBr$$

To a stirred slurry of $NiBr_2$ (0.112 g, 0.51 mmol) in THF was added a two molar equivalent of a THF solution of the ligand Na^+L^-. The reaction mixture was stirred for 2–3 days and the solvent was then removed *in vacuo*. The residue was extracted with benzene and the solvent allowed to evaporate from the filtered solution. Purple and blue crystals of the desired product, L_2Ni, were obtained in ~60% yield. *Anal.* calcd. for $[Me_2Ga(pz)(OCH_2pz)]_2Ni$: C 36.86, H 4.81, N 19.10; found: C 36.97, H 4.96, N 19.09. Analytical data for the blue and purple crystals are virtually identical. The X-ray structure of the purple crystals is described below.

In addition, a small quantity of orange crystals, identified as the previously characterized $[Me_2Gapz_2]_2Ni$ complex (15, 16), was obtained.

Preparation of $[Me_2Ga(pz)(OCH_2pz)]Re(CO)_3$ ($LRe(CO)_3$)

$$[Re(CO)_4Cl]_2 + 2Na^+L^- \xrightarrow[\Delta]{THF} 2LRe(CO)_3 + 2CO + 2NaCl$$

A two molar equivalent of the Na^+L^- ligand in THF solutuion was added to $[Re(CO)_4Cl]_2$ (0.082 g, 0.12 mmol) in the same solvent. The mixture was refluxed for ~3 h and the solvent then removed *in vacuo*. The residue was extracted with CH_2Cl_2 and the mixture filtered. On concentration, the filtrate yielded colorless crystals of the desired product. *Anal.* calcd. for $[Me_2Ga(pz)(OCH_2pz)]Re(CO)_3$: C 26.98, H 2.64, N 10.49; found: C 26.92, H 2.68, N 10.32. ^1H nmr (C_6D_6, 80 MHz, see Fig. 1) τ = 10.39 s, 9.84 s ($GaMe_2$), A = 5.26, B = 5.04, J = 8 Hz (—CH_2—), 4.71 t, 4.10 t (pz-H^4), 3.86 d, 3.13 d, 3.06 d, 2.32 d (pz-H^3, pz-H^5) ($\tau_{C_6H_6}$ = 2.84 ppm; $J \approx 2$ Hz for pz protons). Infrared (cyclohexane solution) ν_{CO} 2038, 1931, 1914 cm^{-1}. Mass spectrum: strong signals due to the monomer parent ion (P^+), P − Me^+, P − CO^+, P − $2CO^+$, P − CO − $2Me^+$, P − $3CO^+$, and P − Me − OCH_2^+ were observed with the signals arising from the latter ion being the most intense in the spectrum.

Preparation of $[Me_2Ga(pz)(OCH_2pz)]Mn(CO)_3$ ($LMn(CO)_3$)

$$Mn(CO)_5Br + Na^+L^- \xrightarrow[\Delta]{THF} LMn(CO)_3 + NaBr + 2CO$$

$Mn(CO)_5Br$ (0.423 g, 1.54 mmol) in THF was refluxed with a molar equivalent of the ligand Na^+L^- in the same solvent for ~4 h. The solvent was then removed and the residue extracted with benzene. An orange solid was obtained from the filtrate which was recrystallized from CH_2Cl_2. A yellow orange product was obtained. *Anal.* calcd. for $[Me_2Ga(pz)(OCH_2pz)]Mn(CO)_3$: C 35.76, H 3.48, N 13.91; found: C 35.58, H 3.41, N 13.83. ^1H nmr (C_6D_6, 80 MHz) τ = 10.39 s, 9.34 s ($GaMe_2$), A = 5.23, B = 5.15, J = 8 Hz (—CH_2—), 4.58 t, 3.96 t (pz-H^4), 3.79 d, 2.91 d, 2.91 d, 2.29 d (pz-H^3, pz-H^5). Infrared (cyclohexane solution) ν_{CO} 2045, 1951, 1930 cm^{-1}.

Preparation of $[Me_2Ga(pz)(OCH_2pz)]Ni(NO)$ ($LNiNO$)

$$Ni(NO)I + Na^+L^- \xrightarrow[rt]{THF} LNi(NO) + NaI$$

One molar equivalent of the ligand Na^+L^- in THF was added to a solution of Ni(NO)I (0.221 g, 1.02 mmol) in the same solvent. The resulting mixture was stirred at room temperature for ~3 h after which the solvent was removed to yield a dark blue oily residue. This was extracted with benzene and the solid recovered from the filtrate was recrystallized from CH_2Cl_2/hexane to yield a dark blue crystalline material. *Anal.* calcd. for $[Me_2Ga(pz)(OCH_2pz)]Ni(NO)$: C 30.65, H 3.97, N 19.86; found: C 30.90, H 4.00, N 19.88. ^1H nmr (C_6D_6, 80 MHz) τ = 10.14 s ($GaMe_2$), 5.74 s (—CH_2—), 4.31 t, 3.84 t

Can. J. Chem. Downloaded from www.nrcresearchpress.com by 213.222.148.141 on 09/07/12
For personal use only.

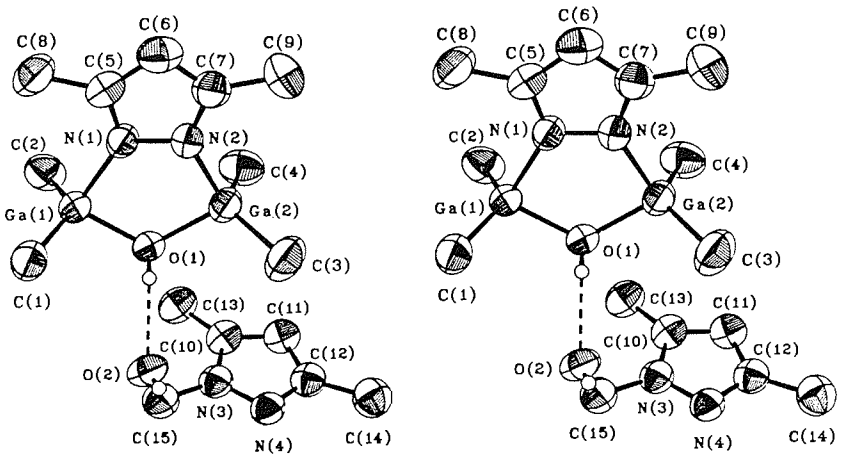

FIG. 2. Stereoscopic diagram of $Me_2Ga(\mu\text{-}OH)(\mu\text{-}Me_2pz)GaMe_2 \cdot HOCH_2Me_2pz$.

(pz-H^4), 3.29 d, 3.20 d, 2.90 d, 2.40 d (pz-H^3, pz-H^5). Infrared (Nujol) ν_{NO} 1793 cm^{-1}.

Reaction of Me_3Ga with 1-hydroxymethylpyrazoles

Anticipated reaction

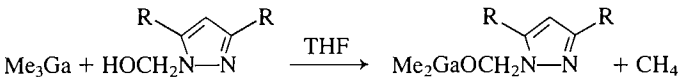

R = H or Me

Equimolar amounts of Me_3Ga (0.225 g, 1.96 mmol) and 1-hydroxymethylpyrazole (0.192 g, 1.96 mmol) in THF solution were refluxed for ~5 h. The solvent was then removed to yield an intractable oily residue which we were unsuccessful in characterizing. In a second reaction, Me_3Ga (0.225 g, 1.96 mmol) and 1-hydroxymethyl-3,5-dimethylpyrazole (0.247 g, 1.96 mmol) dissolved in THF were refluxed for 5 h, and the solvent was then removed *in vacuo*. The residue was recrystallized from CH_2Cl_2 to yield a waxy crystalline material which has been characterized by X-ray crystallography (see Fig. 2), elemental analysis, and ^1H nmr spectroscopy. *Anal.* calcd. for $Me_2Ga(\mu\text{-}OH)(\mu\text{-}Me_2pz)GaMe_2 \cdot HOCH_2Me_2pz$: C 41.15, H 6.86, N 12.80; found: C 40.88, H 6.66, N 12.61. ^1H nmr (C_6D_6, 80 MHz) τ = 10.09 s (12H, $GaMe_2$), 8.14 s (3H), 8.04 s (6H), 7.84 s (3H) (pz-Me groups), 4.78 s (2H, —CH_2—), 4.44 s (1H), 4.39 s (1H) (pz-H^4 protons), 2.53 br (OH). Infrared (Nujol) ν_{OH} 3800 cm^{-1} br.

Spectra

^1H nmr spectra were recorded on a Bruker WP-80 instrument using FT techniques. Mass spectra were recorded on a Kratos AES MS-50 mass spectrometer, infrared spectra on a Perkin-Elmer 598 spectrometer. Elemental analyses were performed by Mr. P. Borda of the UBC microanalytical laboratory.

X-ray crystallographic analyses

Crystallographic data for $Me_2Ga(\mu\text{-}OH)(\mu\text{-}Me_2pz)GaMe_2 \cdot HOCH_2Me_2pz$ and $[Me_2Ga(pz)(OCH_2pz)]_2Ni$ appear in Table 1. Unit-cell parameters were refined by least-squares on 2 sin θ/λ values for 25 carefully centered reflections (2θ = 60–80° and 80–100°, respectively) measured with Cu-$K\alpha_1$ radiation. The intensities of three standard reflections, measured each hour of X-ray exposure time, showed only small random variations in each case. Data were reduced,[2] and corrected for absorption (analytical method (17)).

Both structures were solved by conventional heavy atom methods, the coordinates of the heavy atoms being determined from the Patterson functions and those of the remaining atoms from subsequent difference maps. Non-hydrogen atoms were refined with anisotropic thermal parameters. The OH hydrogen atoms of $Me_2Ga(\mu\text{-}OH)(\mu\text{-}Me_2pz)GaMe_2 \cdot HOCH_2Me_2pz$ and all hydrogen atoms of $[Me_2Ga(pz)(OCH_2pz)]_2Ni$ were refined with isotropic thermal parameters. The remaining hydrogen atoms in $Me_2Ga(\mu\text{-}OH)(\mu\text{-}Me_2pz)GaMe_2 \cdot HOCH_2Me_2pz$ were fixed in positions idealized from observed positions (C(sp^2)—H = 0.97 Å, C(sp^3)—H = 0.98 Å, $U_H \propto U_{\text{bonded atom}}$). Neutral atom scattering factors and anomalous scattering corrections (Ga and Ni) were taken from ref. 18. Isotropic type I extinction corrections were applied (19–21), the final values of g being 0.13(2) × 10^4 and 0.87(5) × 10^4, respectively.

Final positional and isotropic thermal parameters appear in Table 2. Bond lengths, bond angles, and intra-annular torsion angles are given in Tables 3–5, respectively. Calculated hydrogen atom parameters for $Me_2Ga(\mu\text{-}OH)(\mu\text{-}Me_2pz)GaMe_2 \cdot HOCH_2Me_2pz$, anisotropic thermal parameters, bond lengths and angles involving hydrogen, complete listings of torsion angles (Tables 6–10), and measured and calculated structure factor amplitudes have been placed in the Depository of Unpublished Data.[3]

Results and discussion

Alkane elimination from trimethylgallium and compounds containing active hydrogen has been well documented (9). The reaction of Me_3Ga with 1-hydroxymethylpyrazoles released the expected methane but did not yield the predicted products, "$pzCH_2OGaMe_2$". The reaction of Me_3Ga with 1-hydroxymethylpyrazole yielded an intractable oil. However, the reaction of Me_3Ga with 1-hydroxymethyl-3,5-dimethylpyrazole did yield a characterizable product. The crystal structure determination revealed an arrangement in which two "Me_2Ga" moieties are bridged by a 3,5-dimethylpyrazolyl fragment and an OH group (see Fig. 2). The structure is completed by a hydrogen-bonded 1-hydroxymethyl-3,5-dimethylpyrazole molecule. Evidently facile loss of the —CH_2OH group from a molecule of the starting pyrazole compound has occurred, a phenomenon well documented in a recent publication (8). The present structure can be compared with that of an earlier complex, $Me_2Ga(\mu\text{-}OH)(\mu\text{-}Me_2pz)GaMe_2 \cdot 2Me_2pzH$ (22), the primary difference between the two being the involvement of the μ-OH group of the previous complex in two hydrogen bonds, one to each of

[2]The computer programs used include locally written programs for data processing and locally modified versions of the following: AGNOST, absorption corrections, by J. A. Ibers; ORFLS, full-matrix least-squares, and ORFFE, function and errors, by W. R. Busing, K. O. Martin and H. A. Levy; FORDAP, Patterson and Fourier syntheses, by A. Zalkin; ORTEP II, illustrations, by C. K. Johnson.

[3]Supplementary material mentioned in the text may be purchased from the Depository of Unpublished Data, CISTI, National Research Council of Canada, Ottawa, Ont., Canada K1A 0S2.

Can. J. Chem. Downloaded from www.nrcresearchpress.com by 213.222.148.141 on 09/07/12
For personal use only.

TABLE 1. Crystallographic data[a]

Compound	$Me_2Ga(\mu\text{-}OH)(\mu\text{-}Me_2pz)GaMe_2 \cdot HOCH_2Me_2pz$	$[Me_2Ga(pz)(OCH_2pz)]_2Ni$
Formula	$C_{15}H_{30}Ga_2N_4O_2$	$C_{18}H_{28}Ga_2N_8NiO_2$
fw	437.9	586.6
Crystal system	Monoclinic	Monoclinic
Space group	$P2_1/n$	$P2_1/c$
a (Å)	33.105(2)	9.6345(3)
b (Å)	7.3048(9)	14.2731(6)
c (Å)	8.8336(6)	18.6356(7)
β (deg)	97.474(7)	99.660(3)
V (Å^3)	2118.0(3)	2526.3(2)
Z	4	4
ρ_c (g/cm^3)	1.373	1.542
F(000)	904	1192
μ(Cu-Kα) (cm^{-1})	31.95	35.77
Crystal dimensions (mm)	0.32 × 0.35 × 0.55	0.37 × 0.37 × 0.53
Transmission factors	0.303–0.496	0.259–0.430
Scan type	ω–2θ	ω–2θ
Scan range (deg in ω)	0.90 + 0.14 tan θ	0.90 + 0.14 tan θ
Scan speed (deg/min)	1.5–10.0	1.5–10.0
Data collected	$+h, +k, \pm l$	$+h, +k, \pm l$
$2\theta_{max}$ (deg)	150	150
Crystal decay	Negligible	Negligible
Unique reflections	4348	5176
Reflections with $I \geq 3\sigma(I)$	2660	3904
Number of variables	217	393
R	0.044	0.037
R_w	0.052	0.048
S	0.969	1.056
Mean Δ/σ (final cycle)	0.02	0.03
Max Δ/σ (final cycle)	0.14	0.32
Residual density (e/Å^3)	−1.1 to +0.55	−1.1 to +0.42

[a]Temperature 295 K, Enraf-Nonius CAD4-F diffractometer, Cu-K_α radiation ($\lambda_{K\alpha_1}$ = 1.540562, $\lambda_{K\alpha_2}$ = 1.544390 Å), nickel filter, takeoff angle 2.7°, aperture (2.0 + tan θ) × 4.0 mm at a distance of 173 mm from the crystal, scan range extended by 25% on both sides for background measurement $\sigma^2(I) = C + 2B + [0.04(C - B)]^2$ (C = scan count, B = normalized background count), function minimized: $\Sigma w(|F_o| - |F_c|)^2$ where $w = 1/\sigma^2(F)$, $R = \Sigma||F_o| - |F_c||/\Sigma|F_o|$, $R_w = (\Sigma w(|F_o| - |F_c|)^2/\Sigma w|F_o|^2)^{1/2}$, $S = (\Sigma w(|F_o| - |F_c|)^2/(m - n))^{1/2}$. Values given for R, R_w, and S are based on those reflections with $I \geq 3\sigma(I)$.

the two Me_2pzH solvate molecules. In $Me_2Ga(\mu\text{-}OH)(\mu\text{-}Me_2pz)GaMe_2 \cdot HOCH_2Me_2pz$ the μ-OH group is hydrogen bonded only to the oxygen atom of the $HOCH_2Me_2pz$ molecule (O(1)—H(O1)···O(2), H···O = 2.03(6), O···O = 2.754(6) Å, O—H···O = 156(6)°). These 1:1 molecular complexes form well-separated dimeric units via O—H···N hydrogen-bonding of pairs of $HOCH_2Me_2pz$ molecules across centres of symmetry (O(2)—H(O2)···N(4)($-x$, $1 - y$, $1 - z$), H···N = 2.00(5), O···N = 2.721(7) Å, O—H···N = 165(6)°). The μ-OH group in the present structure acts only as a hydrogen bond donor while that in the earlier complex functions as both a donor and an acceptor. The Ga—O bonds are shorter and the Ga—N and Ga—C bonds longer in $Me_2Ga(\mu\text{-}OH)(\mu\text{-}Me_2pz)GaMe_2 \cdot HOCH_2Me_2pz$; respective mean[4] values of 1.918(11), 2.001(5), and 1.955(5) Å compared with corresponding values of 1.934(2), 1.989(6), and 1.948(8) Å for the bis(3,5-dimethylpyrazole) solvate. The five-membered Ga_2ON_2 ring has a flattened and twisted O-envelope conformation (see Table 5) similar to that noted previously (22). The Ga···Ga distance of 3.307(1) Å is slightly shorter than the earlier value of 3.316(1) Å. The pyrazolyl rings are both planar to within experimental error.

The successful synthesis of the ligand Na^+L^- is reflected in the subsequent incorporation of the ligand into a number of transition metal complexes. Thus reaction of Na^+L^- with $[Re(CO)_4Cl]_2$ resulted in a good yield of the rhenium tricarbonyl product, $[Me_2Ga(pz)(OCH_2pz)]Re(CO)_3$. The occurrence of three strong ν_{CO} bands in the ir spectrum and the ^{1}H nmr pattern (see Fig. 1) for this complex indicated that the tridentate organogallate ligand is *facially* coordinated. *Meridional* coordination would lead to a single peak for the $GaMe_2$ protons (2 signals are observed) and a singlet for the —CH_2— protons (an AB quartet is observed) in the ^{1}H nmr spectrum. In addition, for a *mer* coordination the ir spectrum should show two weak ν_{CO} bands and one strong ν_{CO} band. The analogous $LMn(CO)_3$ complex has been synthesized and the spectroscopic results again indicate quite clearly an octahedral arrangement of the ligating atoms about the transition metal with a *facial* coordination of the L^- ligand and concomitantly of the three CO groups.

The reaction of Ni(NO)I with Na^+L^- yielded a dark blue crystalline product characterized as LNi(NO). The room temperature solution ^{1}H nmr spectrum of the complex indicates a *mer* coordination of L^- in a square-planar arrangement about the Ni centre, the fourth coordination site being occupied by the NO group. Thus the ^{1}H nmr spectrum gives singlets for both the —$GaMe_2$ and —CH_2— protons, a pattern inconsistent with a *fac* coordination for the ligand. However, a square-planar Ni centre is unlikely in the light of previous studies which have shown that square-planar $\{MNO\}^{10}$ complexes should have an M—N—O bond angle of 120° (23, 24) which is contrary to the linear M—N—O group suggested by the ν_{NO} value of

[4]Here and elsewhere in this report mean values refer to weighted means with rms deviations from the mean in parentheses.

Can. J. Chem. Downloaded from www.nrcresearchpress.com by 213.222.148.141 on 09/07/12
For personal use only.

Can. J. Chem. Downloaded from www.nrcresearchpress.com by 213.222.148.141 on 09/07/12
For personal use only.

TABLE 2. Final positional (fractional × 10^4, Ga and Ni × 10^5, H × 10^3) and isotropic thermal parameters ($U \times 10^3$ Å^2) with estimated standard deviations in parentheses[a]

Atom	x	y	z	U_{eq}/U_{iso}
	$Me_2Ga(\mu\text{-}OH)(\mu\text{-}Me_2pz)GaMe_2 \cdot HOCH_2Me_2pz$			
Ga(1)	12884(2)	51212(10)	10838(8)	57
Ga(2)	14804(2)	45297(11)	48201(8)	61
O(1)	1121(1)	4237(7)	2940(5)	63
O(2)	296(1)	4505(7)	3067(6)	72
N(1)	1749(1)	6506(6)	2253(5)	55
N(2)	1821(1)	6303(7)	3815(5)	59
N(3)	275(2)	2078(7)	4821(6)	63
N(4)	164(2)	2640(7)	6166(6)	61
C(1)	879(2)	6864(10)	170(7)	78
C(2)	1521(2)	3030(11)	106(8)	88
C(3)	1179(2)	5758(12)	6280(8)	97
C(4)	1796(2)	2287(10)	5255(9)	91
C(5)	2027(2)	7643(9)	1837(8)	64
C(6)	2277(2)	8221(10)	3097(9)	76
C(7)	2141(2)	7356(9)	4325(8)	67
C(8)	2031(2)	8134(11)	174(8)	89
C(9)	2292(2)	7477(11)	5993(8)	91
C(10)	585(2)	823(8)	5014(8)	64
C(11)	666(2)	571(9)	6569(8)	68
C(12)	399(2)	1723(9)	7230(8)	64
C(13)	757(2)	−38(9)	3723(8)	81
C(14)	355(2)	1955(11)	8876(8)	85
C(15)	88(2)	2912(10)	3408(8)	71
H(O1)	91(2)	462(8)	300(7)	64(21)
H(O2)	20(2)	531(7)	338(6)	41(20)
	$[Me_2Ga(pz)(OCH_2pz)]_2Ni$			
Ga(1)	19742(6)	31994(5)	9045(3)	66
Ga(2)	50994(6)	37539(4)	36689(3)	53
Ni	19591(8)	30592(5)	27383(4)	52
O(1)	1734(3)	2382(2)	1698(2)	60
O(2)	4175(3)	2992(2)	2884(2)	51
N(1)	2028(4)	4357(3)	1501(2)	64
N(2)	1953(4)	4312(3)	2222(2)	59
N(3)	−604(4)	2366(3)	1889(2)	64
N(4)	−249(4)	2928(3)	2469(2)	62
N(5)	3354(4)	3970(3)	4089(2)	61
N(6)	2087(4)	3688(3)	3736(2)	60
N(7)	3697(4)	1483(2)	3250(2)	57
N(8)	2341(4)	1726(3)	3207(2)	58
C(1)	210(9)	3279(8)	199(4)	98
C(2)	3859(9)	3004(8)	664(6)	103
C(3)	2034(6)	5275(4)	1311(4)	77
C(4)	1960(6)	5817(4)	1899(4)	76
C(5)	1929(5)	5201(4)	2455(3)	67
C(6)	−1986(7)	2469(6)	1621(4)	84
C(7)	−2542(7)	3070(5)	2037(4)	84
C(8)	−1421(5)	3361(4)	2561(3)	71
C(9)	531(6)	1830(4)	1638(3)	72
C(10)	6419(7)	3015(6)	4366(4)	84
C(11)	5644(10)	4930(5)	3256(4)	74
C(12)	3156(7)	4375(5)	4712(3)	91
C(13)	1758(7)	4396(5)	4758(4)	100
C(14)	1152(6)	3933(5)	4154(3)	81
C(15)	4001(6)	685(4)	3627(3)	74
C(16)	2798(7)	400(5)	3842(4)	84
C(17)	1782(7)	1064(4)	3572(3)	71
C(18)	4560(5)	2056(3)	2834(3)	60
H(1a)	−41(9)	348(6)	41(5)	133(33)
H(1b)	27(13)	399(9)	−7(8)	275(65)
H(1c)	33(8)	278(5)	0(4)	120(30)
H(2a)	410(10)	231(7)	79(5)	199(41)
H(2b)	375(8)	280(6)	31(4)	115(35)
H(2c)	435(9)	352(6)	89(5)	164(39)
H(3)	197(7)	540(5)	78(4)	122(24)
H(4)	193(5)	645(4)	194(3)	65(15)
H(5)	180(6)	532(4)	302(3)	96(18)
H(6)	−206(7)	218(4)	134(3)	77(23)
H(7)	−335(7)	319(4)	201(3)	96(22)
H(8)	−131(6)	382(4)	289(3)	84(19)
H(9a)	31(7)	170(4)	114(3)	108(21)
H(9b)	68(5)	120(4)	202(3)	79(16)
H(10a)	636(8)	240(5)	450(4)	124(27)
H(10b)	709(8)	286(5)	407(4)	120(29)
H(10c)	700(9)	336(6)	470(5)	159(34)
H(11a)	646(7)	489(5)	329(4)	121(28)
H(11b)	509(6)	503(4)	282(3)	96(21)
H(11c)	540(8)	532(6)	346(4)	123(35)
H(12)	405(7)	467(5)	503(4)	126(23)
H(13)	122(5)	470(4)	512(3)	88(17)
H(14)	33(5)	383(4)	406(3)	68(17)
H(15)	496(5)	31(4)	355(3)	78(16)
H(16)	273(8)	−10(5)	411(4)	124(26)
H(17)	92(7)	111(4)	366(3)	102(22)
H(18a)	441(5)	184(3)	235(2)	56(13)
H(18b)	560(5)	195(3)	306(2)	52(12)

[a] U_{eq} = (1/3)trace (diagonalized U).

TABLE 3. Bond lengths (Å) with estimated standard deviations in parentheses

Bond	Length (Å)	Bond	Length (Å)
	$Me_2Ga(\mu\text{-}OH)(\mu\text{-}Me_2pz)GaMe_2 \cdot HOCH_2Me_2pz$		
Ga(1)—O(1)	1.910(4)	N(3)—N(4)	1.352(6)
Ga(1)—N(1)	2.001(5)	N(3)—C(10)	1.372(8)
Ga(1)—C(1)	1.956(7)	N(3)—C(15)	1.452(8)
Ga(1)—C(2)	1.961(7)	N(4)—C(12)	1.320(7)
Ga(2)—O(1)	1.925(4)	C(5)—C(6)	1.365(9)
Ga(2)—N(2)	2.000(5)	C(5)—C(8)	1.514(9)
Ga(2)—C(3)	1.949(7)	C(6)—C(7)	1.381(9)
Ga(2)—C(4)	1.953(7)	C(7)—C(9)	1.495(9)
O(2)—C(15)	1.405(7)	C(10)—C(11)	1.377(8)
N(1)—N(2)	1.377(6)	C(10)—C(13)	1.479(8)
N(1)—C(5)	1.327(7)	C(11)—C(12)	1.403(8)
N(2)—C(7)	1.339(7)	C(12)—C(14)	1.489(9)
	$[Me_2Ga(pz)(OCH_2pz)]_2Ni$		
Ga(1)—O(1)	1.927(3)	N(2)—C(5)	1.343(6)
Ga(1)—N(1)	1.987(4)	N(3)—N(4)	1.344(5)
Ga(1)—C(1)	1.970(7)	N(3)—C(6)	1.350(7)
Ga(1)—C(2)	1.961(8)	N(4)—C(8)	1.323(6)
Ga(2)—O(2)	1.918(3)	N(5)—N(6)	1.347(5)
Ga(2)—N(5)	1.995(4)	N(5)—C(12)	1.339(6)
Ga(2)—C(10)	1.965(6)	N(6)—C(14)	1.334(6)
Ga(2)—C(11)	1.955(6)	N(7)—N(8)	1.341(5)
Ni—O(1)	2.144(3)	N(7)—C(15)	1.344(6)
Ni—O(2)	2.109(3)	N(8)—C(17)	1.330(7)
Ni—N(2)	2.030(4)	C(3)—C(4)	1.355(9)
Ni—N(4)	2.111(4)	C(4)—C(5)	1.362(8)
Ni—N(6)	2.049(4)	C(6)—C(7)	1.329(11)
Ni—N(8)	2.100(4)	C(7)—C(8)	1.392(8)
O(1)—C(9)	1.390(6)	C(12)—C(13)	1.364(9)
O(2)—C(18)	1.393(5)	C(13)—C(14)	1.351(8)
N(1)—N(2)	1.361(5)	C(15)—C(16)	1.351(8)
N(1)—C(3)	1.357(7)	C(16)—C(17)	1.394(8)

TABLE 4. Bond angles (deg) with estimated standard deviations in parentheses

Bonds	Angle (deg)	Bonds	Angle (deg)
O(1)—Ga(1)—N(1)	90.8(2)	N(4)—N(3)—C(10)	112.2(5)
O(1)—Ga(1)—C(1)	108.1(2)	N(4)—N(3)—C(15)	119.7(5)
O(1)—Ga(1)—C(2)	106.8(3)	C(10)—N(3)—C(15)	128.0(6)
N(1)—Ga(1)—C(1)	109.0(3)	N(3)—N(4)—C(12)	105.7(5)
N(1)—Ga(1)—C(2)	107.7(2)	N(1)—C(5)—C(6)	109.7(6)
C(1)—Ga(1)—C(2)	128.0(3)	N(1)—C(5)—C(8)	120.7(6)
O(1)—Ga(2)—N(2)	90.6(2)	C(6)—C(5)—C(8)	129.6(6)
O(1)—Ga(2)—C(3)	108.0(3)	C(5)—C(6)—C(7)	105.9(6)
O(1)—Ga(2)—C(4)	109.3(3)	N(2)—C(7)—C(6)	108.8(6)
N(2)—Ga(2)—C(3)	111.3(3)	N(2)—C(7)—C(9)	120.9(6)
N(2)—Ga(2)—C(4)	108.2(3)	C(6)—C(7)—C(9)	130.3(7)
C(3)—Ga(2)—C(4)	124.2(3)	N(3)—C(10)—C(11)	105.0(6)
Ga(1)—O(1)—Ga(2)	119.2(2)	N(3)—C(10)—C(13)	123.1(6)
Ga(1)—N(1)—N(2)	119.0(4)	C(11)—C(10)—C(13)	131.9(7)
Ga(1)—N(1)—C(5)	133.1(4)	C(10)—C(11)—C(12)	106.5(6)
N(2)—N(1)—C(5)	108.0(5)	N(4)—C(12)—C(11)	110.7(6)
Ga(2)—N(2)—N(1)	118.7(4)	N(4)—C(12)—C(14)	121.0(6)
Ga(2)—N(2)—C(7)	133.6(4)	C(11)—C(12)—C(14)	128.3(7)
N(1)—N(2)—C(7)	107.6(5)	O(2)—C(15)—N(3)	111.5(5)
		$[Me_2Ga(pz)(OCH_2pz)]_2Ni$	
O(1)—Ga(1)—N(1)	94.00(15)	Ga(1)—N(1)—N(2)	120.8(3)
O(1)—Ga(1)—C(1)	110.2(3)	Ga(1)—N(1)—C(3)	131.1(4)
O(1)—Ga(1)—C(2)	108.9(4)	N(2)—N(1)—C(3)	107.9(4)
N(1)—Ga(1)—C(1)	105.3(4)	Ni—N(2)—N(1)	120.9(3)
N(1)—Ga(1)—C(2)	107.9(4)	Ni—N(2)—C(5)	132.7(4)
C(1)—Ga(1)—C(2)	125.7(5)	Ni(1)—N(2)—C(5)	106.3(4)
O(2)—Ga(2)—N(5)	94.17(14)	N(4)—N(3)—C(6)	109.5(5)
O(2)—Ga(2)—C(10)	111.4(3)	Ni—N(4)—N(3)	110.8(3)
O(2)—Ga(2)—C(11)	107.9(2)	Ni—N(4)—C(8)	140.8(4)
N(5)—Ga(2)—C(10)	108.6(3)	N(3)—N(4)—C(8)	106.1(4)
N(5)—Ga(2)—C(11)	108.7(3)	Ga(2)—N(5)—N(6)	121.1(3)
C(10)—Ga(2)—C(11)	122.3(3)	Ga(2)—N(5)—C(12)	131.2(4)
O(1)—Ni—O(2)	92.43(12)	N(6)—N(5)—C(12)	107.7(4)
O(1)—Ni—N(2)	88.67(14)	Ni—N(6)—N(5)	119.1(3)
O(1)—Ni—N(4)	78.46(14)	Ni—N(6)—C(14)	134.6(4)
O(1)—Ni—N(6)	177.51(14)	N(5)—N(6)—C(14)	106.3(4)
O(1)—Ni—N(8)	87.25(14)	N(8)—N(7)—C(15)	112.1(4)
O(2)—Ni—N(2)	91.37(13)	Ni—N(8)—N(7)	111.1(3)
O(2)—Ni—N(4)	170.04(14)	Ni—N(8)—C(17)	143.0(4)
O(2)—Ni—N(6)	89.86(13)	N(7)—N(8)—C(17)	105.0(4)
O(2)—Ni—N(8)	78.59(13)	N(1)—C(3)—C(4)	109.7(5)
N(2)—Ni—N(4)	92.43(15)	C(3)—C(4)—C(5)	104.9(5)
N(2)—Ni—N(6)	92.2(2)	N(2)—C(5)—C(4)	111.2(5)
N(2)—Ni—N(8)	168.97(15)	N(3)—C(6)—C(7)	108.9(6)
N(4)—Ni—N(6)	99.18(15)	C(6)—C(7)—C(8)	105.1(6)
N(4)—Ni—N(8)	96.77(15)	N(4)—C(8)—C(7)	110.4(6)
N(6)—Ni—N(8)	92.27(15)	N(5)—C(12)—C(13)	110.5(5)
Ga(1)—O(1)—Ni	114.46(15)	C(12)—C(13)—C(14)	103.3(5)
Ga(1)—O(1)—C(9)	119.1(3)	N(6)—C(14)—C(13)	112.1(6)
Ni—O(1)—C(9)	106.5(3)	N(7)—C(15)—C(16)	106.7(5)
Ga(2)—O(2)—Ni	113.75(14)	C(15)—C(16)—C(17)	105.9(6)
Ga(2)—O(2)—C(18)	120.0(3)	N(8)—C(17)—C(16)	110.3(5)
Ni—O(2)—C(18)	108.1(3)		

1793 cm^{-1} recorded for the LNi(NO) complex. In addition, previous studies on related complexes have established that even though room temperature ^1H nmr data indicate square-planar NiNO complexes, these are in fact tetrahedral Ni species undergoing fluxional processes at ambient temperatures (14, 25–27).

The reaction of the Na^+L^- ligand with anhydrous $NiBr_2$ in THF resulted in the isolation of purple and blue crystalline forms of the L_2Ni complex together with a small amount of the previously characterized $[Me_2Gapz_2]_2Ni$ complex (15, 16). The X-ray crystal structure of the purple crystals has been determined (Fig. 3) and confirms the arrangement of the tridentate ligands which are *facially* coordinated in the monomeric pseudo-octahedral complex. The crystal structure of *fac*-L_2Ni consists of discrete molecules separated by normal van der Waals distances. Unlike the symmetric all-*trans*

Can. J. Chem. Downloaded from www.nrcresearchpress.com by 213.222.148.141 on 09/07/12
For personal use only.

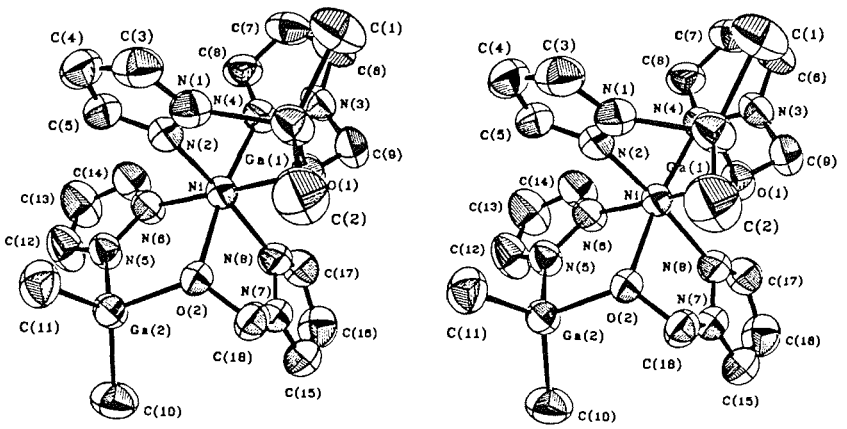

FIG. 3. Stereoscopic diagram of $[Me_2Ga(pz)(OCH_2pz)]_2Ni$.

TABLE 5. Intra-annular torsion angles (deg) with standard deviations in parentheses

Atoms	Torsion angle (deg)
$Me_2Ga(\mu\text{-}OH)(\mu\text{-}Me_2pz)GaMe_2 \cdot HOCH_2Me_2pz$	
N(1)—Ga(1)—O(1)—Ga(2)	−12.5(3)
N(2)—Ga(2)—O(1)—Ga(1)	13.7(3)
O(1)—Ga(2)—N(2)—N(1)	−9.8(4)
Ga(1)—N(1)—N(2)—Ga(2)	3.2(5)
O(1)—Ga(1)—N(1)—N(2)	5.3(4)
$[Me_2Ga(pz)(OCH_2pz)]_2Ni$	
N(1)—Ga(1)—O(1)—Ni	−8.4(2)
N(2)—Ni—O(1)—Ga(1)	10.2(2)
O(1)—Ni—N(2)—N(1)	−9.3(3)
Ga(1)—N(1)—N(2)—Ni	5.5(5)
O(1)—Ga(1)—N(1)—N(2)	2.3(3)
N(4)—Ni—O(1)—C(9)	−30.9(3)
Ni—O(1)—C(9)—N(3)	44.2(5)
N(4)—N(3)—C(9)—O(1)	−38.5(6)
C(9)—N(3)—N(4)—Ni	10.4(5)
O(1)—Ni—N(4)—N(3)	11.1(3)
N(5)—Ga(2)—O(2)—Ni	13.4(2)
N(6)—Ni—O(2)—Ga(2)	−13.8(2)
O(2)—Ni—N(6)—N(5)	9.3(3)
Ga(2)—N(5)—N(6)—Ni	−1.7(5)
O(2)—Ga(2)—N(5)—N(6)	−7.7(4)
N(8)—Ni—O(2)—C(18)	29.7(3)
Ni—O(2)—C(18)—N(7)	−43.7(4)
N(8)—N(7)—C(18)—O(2)	39.2(6)
C(18)—N(7)—N(8)—Ni	−13.1(5)
O(2)—Ni—N(8)—N(7)	−8.9(3)

isomer observed for the related molecule *fac*-$[Me_2Ga(pz)(OCH_2CH_2NH_2)]_2Ni$ (28), *fac*-L_2Ni exists in the solid state as an all-*cis* isomer. High steric strain is noted for the NiOCNN chelate rings, evidenced by small angles at Ni and differences of 30° or more between the Ni—N—N and Ni—N—C angles. The Ni—N bonds in these highly strained chelate rings are significantly longer than those in the less-strained NiOGaNN chelate rings. There is one Ni—O bond *trans* to each type of pyrazolyl ligand, that opposite the more strained Ni—N bond being 0.009(4) Å shorter than the other. The mean Ni—O distance of 1.923(6) Å is significantly shorter than the corresponding values of 2.086(2) and 2.040(4) Å in *fac*- and *mer*-$[Me_2Ga(pz)OCH_2CH_2NH_2)]_2Ni$ (28) and 2.049(3) Å in *mer*-$[Me_2Ga(pz)(OC_6H_4NH_2)]_2Ni$ (29), which all have the oxygen donors *trans* to one another. A structural *trans* effect is noted for the Ni—N bonds: those *trans* to O are longer (by 0.019(6) and 0.011(6) Å for the less and more strained types, respectively) than those *trans* to N. The Ni—N distances of 2.030(4) and 2.049(4) Å in the NiOGaNN chelate rings of *fac*-L_2Ni may be compared with corresponding distances of 2.057(5)–2.098(4) Å (mean 2.08(2) Å) in the above-mentioned related molecules (28, 29). Other details of the molecular geometry (Tables 3–5) are normal.

We speculate that the blue crystals probably contain *meridionally* coordinated ligands as was shown in the crystal structure of the blue form of the analogous complex $[Me_2Ga(pz)(OCH_2CH_2NH_2)]_2Ni$. The purple form of this compound was shown to have *facially* coordinated tridentate ligands (28).

Acknowledgments

We thank the Natural Sciences and Engineering Research Council of Canada for financial support and the University of British Columbia Computing Centre for assistance.

1. W. L. DRIESSEN. Recl. Trav. Chim. Pays-Bas, **101**, 441 (1982).
2. J. W. F. M. SCHOONHOVEN, W. L. DRIESSEN, J. REEDIJK, and G. C. VERSCHOOR. J. Chem. Soc. Dalton Trans. 1053 (1984).
3. G. J. VAN DRIEL, W. L. DRIESSEN, and J. REEDIJK. Inorg. Chem. **24**, 2919 (1985).
4. H. L. BLONK, W. L. DRIESSEN, and J. REEDIJK. J. Chem. Soc. Dalton Trans. 1699 (1985).
5. G. J. KLEYWEGT, W. G. R. WIESMEIJER, G. J. VAN DRIEL, W. L. DRIESSEN, J. REEDIJK, and J. H. NOORDIK. J. Chem. Soc. Dalton Trans. 2177 (1985).
6. J. B. J. VELDHUIS, W. L. DRIESSEN, and J. REEDIJK. J. Chem. Soc. Dalton Trans. 537 (1986).
7. F. PAAP, E. BOUWMAN, W. L. DRIESSEN, R. A. G. DE GRAAFF, and J. REEDIJK. J. Chem. Soc. Dalton Trans. 737 (1985).
8. A. ROMERO, A. VEGAS, A. SANTOS, and A. M. CUADRO. J. Chem. Soc. Dalton Trans. 183 (1987).
9. D. J. COOPER, S. J. RETTIG, A. STORR, and J. TROTTER. Can. J. Chem. **64**, 1643 (1986).
10. G. DOLCETTI and G. R. NORTON. Inorg. Synth. **16**, 35 (1976).
11. R. B. KING. Organometallic synthesis. Vol. 1. Academic Press, New York. 1965. p. 174.
12. B. HAYMORE and R. D. FELTHAM. Inorg. Synth. **14**, 81 (1973).
13. A. STORR and B. S. THOMAS. Can. J. Chem. **48**, 3667 (1970).
14. S. J. RETTIG, A. STORR, J. TROTTER, and K. URICH. Can. J. Chem. **62**, 2788 (1984).

Can. J. Chem. Downloaded from www.nrcresearchpress.com by 213.222.148.141 on 09/07/12
For personal use only.

15. D. F. RENDLE, A. STORR, and J. TROTTER. J. Chem. Soc. Dalton Trans. 176 (1975).
16. K. R. BREAKELL, D. J. PATMORE, and A. STORR. J. Chem. Soc. Dalton Trans. 749 (1975).
17. J. DE MEULENAER and H. TOMPA. Acta Crystallogr. **19**, 1014 (1965).
18. International tables for X-ray crystallography. Vol. IV. Kynoch press, Birmingham. 1974. pp. 99–102 and 149.
19. P. J. BECKER and P. COPPENS. Acta Crystallogr. Sect. A, **30**, 129 (1974); **30**, 148 (1974); **31**, 417 (1975).
20. P. COPPENS and W. C. HAMILTON. Acta Crystallogr. Sect. A, **26**, 71 (1970).
21. F. R. THORNLEY and R. J. NELMES. Acta Crystallogr. Sect. A, **30**, 748 (1974).
22. D. F. RENDLE, A. STORR, and J. TROTTER. Can. J. Chem. **53**, 2944 (1975).
23. K. J. HALLER and J. H. ENEMARK. Inorg. Chem. **17**, 3552 (1978).
24. J. H. ENEMARK and R. D. FELTHAM. Coord. Chem. Rev. **13**, 339 (1974).
25. K. S. CHONG, S. J. RETTIG, A. STORR, and J. TROTTER. Can. J. Chem. **57**, 3107 (1979).
26. K. S. CHONG and A. STORR. Can. J. Chem. **59**, 1331 (1981).
27. S. J. RETTIG, A. STORR, and J. TROTTER. Can. J. Chem. **59**, 2391 (1981).
28. K. S. CHONG, S. J. RETTIG, A. STORR, and J. TROTTER. Can. J. Chem. **56**, 1212 (1978).
29. G. D. GRACEY, S. J. RETTIG, A. STORR, and J. TROTTER. Can. J. Chem. **65**, 2469 (1987).

Can. J. Chem. Downloaded from www.nrcresearchpress.com by 213.222.148.141 on 09/07/12
For personal use only.

Balance between van der Waals and coordination bond energies — Unified Model of coordination bond length in lanthanide complexes[1]

XI-ZHANG FENG[2] AND YING-TING XU

Application Department, Institute of High Energy Physics, Academia Sinica, P.O. Box 2732, Beijing, The People's Republic of China

AND

PENG-NIAN SUN

University of Science and Technology of China, Hefei, Anhui Province, The People's Republic of China

Received March 30, 1987

XI-ZHANG FENG, YING-TING XU, and PENG-NIAN SUN. Can. J. Chem. **66**, 109 (1988).

This paper presents the variation of coordination bond lengths in lanthanide complexes as a balance between van der Waals and coordination bond energies. Each coordination atom moves in a unified potential well that is a combination of the Morse potential of its coordination bond and the van der Waals potentials of its neighboring coordination atoms. This is termed the Unified Model of coordination bond length.

XI-ZHANG FENG, YING-TING XU et PENG-NIAN SUN. Can. J. Chem. **66**, 109 (1988).

Dans ce travail, on présente la variation des longueurs des liaisons de coordination dans des complexes de lanthanides qui est due à une balance entre les énergies de van der Waals et les énergies des liaisons de coordination. Chaque atome de coordination se déplace dans un puits de potentiel unifié qui est la combinaison du potentiel de Morse de sa liaison de coordination et les potentiels de van der Waals de ses atomes de coordination voisins. Ceci est le modèle unifié de la longueur des liaisons de coordination.

[Traduit par la revue]

I. Introduction

An analysis of the crystal structure of about 280 lanthanide and actinide complexes (1) shows that the coordination bond lengths vary appreciably. Even bond lengths from two identical coordination atoms of two identical ligands to the central metal ion are significantly different. For instance, in $Ln(C_2H_5SO_4)_3 \cdot 9H_2O$ (Ln represents the trivalent cations of 14 rare earth elements) (2), each metal ion is coordinated with the nine water molecules to form nine Ln—O coordination bonds. Six of them are identical and shorter, three of them are identical but longer, and the difference in bond lengths is far outside the experimental error. This phenomenon, resulting from the balance between van der Waals and coordination bond energies, merits extensive study. We propose the Unified Model of coordination bond length to explain this phenomenon.

II. Theory

The total potential appropriate to a given system may be considered as a sum of several potentials. In the present paper, for each coordination atom, a unified potential well that is a combination of the Morse potential of its coordination bond and the van der Waals (Lennard–Jones) potentials of its neighboring coordination atoms is sufficient to describe its motion.

If the bond length of a coordination atom k is $|\vec{R}| = R$ and that of its neighboring coordination atom i is $|\vec{R}_i| = R_i$ ($i = 1, 2, \ldots$), and the angle between $\vec{R}$ and $\vec{R}_i$ is θ_i, then the distance between k and i is

$$[1] \quad r_i = (R^2 + R_i^2 - 2RR_i \cos\theta_i)^{1/2}$$

the Morse potential at k is

$$[2] \quad V(R) = V_0\{\exp[-2(R - R_0)/a] - 2\exp[-(R - R_0)/a]\}$$

the sum of the van der Waals potentials at k is

$$[3] \quad \sum_i U_i(R) = \sum_i 4E_j\left[\left(\frac{r_{0j}}{r_i}\right)^{12} - \left(\frac{r_{0j}}{r_i}\right)^{6}\right]$$

and the unified potential at k is

$$[4] \quad V_T(R) = V(R) + \sum_i U_i(R)$$

where j represents the kind of coordination atom, V_0 and E_j are the energy parameters, r_{0j} and R_0 are the length parameters, and a is the width of the Morse potential. Because k is in its ground state, $V_T(R)$ is very near its minimum. Therefore, due to the effect of van der Waals potentials, the bond length of k is perturbed slightly from R_0 to R. This is the essence of the Unified Model of coordination bond length. By studying $V_T(R)$, we can also obtain the ratio between V_0 and E_j, and the value of a.

III. Analysis of experimental data

Using $Lu(C_2H_5SO_4)_3 \cdot 9H_2O$ as an example, we see that the central metal ion is coordinated with nine oxygen (j) atoms from nine water molecules. From the results of our Packing Model calculations (1), we choose the minimum van der Waals potential ($-E_j$) at a separating distance (r_{min}) of about twice the van der Waals radius of the oxygen atom, i.e., 2.800 Å, and r_{0j} = 2.4945 Å. We choose one oxygen atom k with a longer bond length whose R = 2.497 Å (long bond). The atom k has four neighboring oxygen coordination atoms with R_i = 2.318 Å (i = 1, 2, 3, 4; short bonds), $\theta_1 = \theta_2 = 66.1785°$ and $\theta_3 = \theta_4 = 72.5943°$. In order to minimize $V_T(R)$ with the condition of having both a unique a and a unique V_0, we use the following procedure. Choose $R_0 = R_i$ (the effect of van der Waals potentials on R_i is expected to be small) and θ_i to remain constant. Then, by using eqs. [1], [2], [3], and [4], we obtain $V_T(R)$, $V_T(R + 0.01$ Å), and $V_T(R - 0.01$ Å). If a = 0.10 Å is used, $V_0 = 1.068E_j$ is obtained from $V_T(R) = V_T(R + 0.01$ Å), and $V_0 = 1.070E_j$ is obtained from $V_T(R) = V_T(R - 0.01$ Å). If a = 0.09 Å is used, $V_0 = 1.139E_j$ is obtained from $V_T(R) =$

[1]Project is supported by the Science Fund of Academia Sinica.

[2]To whom correspondence should be addressed. Present address: INC-11, MS-H824, Los Alamos National Laboratory, Los Alamos, NM 87545, U.S.A.

Can. J. Chem. Downloaded from www.nrcresearchpress.com by 213.222.148.141 on 09/07/12
For personal use only.

TABLE 1. The potential well depth (V_0) and width (a) of the Morse potential of fourteen $Ln(C_2H_5SO_4)_3 \cdot 9H_2O$ compounds and their r_{min}'s and solid angle factor sums (SAS) (1)

$Ln(C_2H_5SO_4)_3 \cdot 9H_2O$	r_{min} (Å)	a (Å)	V_0 (E_j)	SAS
Lu	2.800	0.10	1.1	0.854
Yb	2.808	0.10	1.1	0.855
Tm	2.816	0.10	0.9	0.850
Er	2.824	0.10	0.9	0.849
Ho	2.832	0.10	0.9	0.847
Dy	2.840	0.10	0.9	0.846
Tb	2.850	0.10	0.8	0.844
Gd	2.864	0.09	0.8	0.840
Eu	2.878	0.09	0.7	0.840
Sm	2.892	0.09	0.7	0.839
Nd	2.920	0.09	0.7	0.838
Pr	2.928	0.09	0.7	0.839
Ce	2.952	0.09	0.7	0.834
La	2.980	0.09	0.7	0.833

$V_T(R + 0.01$ Å), and $V_0 = 1.126E_j$ is obtained from $V_T(R) = V_T(R - 0.01$ Å). Therefore, the results $a = 0.10$ Å and $V_0 = 1.1E_j$ are found.

To check the effect of van der Waals potentials on R_i, we have carried out the same analysis for the short bond. The bond angle between two neighboring short bonds is 75.3123°. Each short bond has two long bonds and two short bonds as its neighbors. The result is that when $R_0 = 2.315$ Å, V_T of the short bond reaches a minimum. The long bond is analyzed again with $R_0 = 2.315$ Å. The same results, $a = 0.10$ Å and $V_0 = 1.1E_j$, are obtained. In view of the symmetry of the molecule, three long bonds are identical and six short bonds are identical. Therefore, the whole analysis is self-consistent and complete.

The analysis of all fourteen $Ln(C_2H_5SO_4)_3 \cdot 9H_2O$ compounds shows that r_{min} increases slightly as the atomic number Z of the lanthanides decreases. The results are summarized in Table 1.

The lengths of both long and short bonds increase, their differences decrease, and thus the errors of the calculated results increase, all as the atomic number Z of Ln decreases. Generally, the errors are between ±5% and ±20%.

IV. Discussion

1. A plot of the short Ln—O bond lengths of the fourteen $Ln(C_2H_5SO_4)_3 \cdot 9H_2O$ compounds against the ionic radii of 14 lanthanide (3+) ions is a straight line. If the normal bond length is equal to the sum of the ionic radii of the lanthanides ion and oxygen (2−), then the ionic radius of oxygen (2−) is 1.29 Å, which is close to the literature value of 1.32 Å (see ref. 2). Therefore, the short bond lengths are normal bond lengths and the long bonds are elongated due to the balance between the van der Waals and the coordination bond energies.

2. Table 1 shows that V_0 decreases from $1.1E_j$ to $0.7E_j$, a decreases from 0.10 to 0.09 Å, and r_{min} increases from 2.800 to 2.980 Å as Z of Ln decreases from 71 to 57. This is in accordance with what we would have expected from the lanthanide contraction.

3. V_c is close to E_j. This is an important character of weak coordination bonds.

4. The solid angle factor sums (SAS) (1) in Table 1 are calculated by setting the van der Waals radius to be $\frac{1}{2}r_{min}$. They are between 0.855 and 0.833 and are all located within the packing saturation region. These results are closer to one another than those between 0.854 and 0.739, which would have been obtained had a constant $r_{min} = 2.800$ Å been used. The magnitudes of their solid angle factor vector sums ($|\Sigma\vec{S}\vec{A}\vec{F}|$) (1) are all equal to zero. Thus, all results are in agreement with the packing saturation rule and the uniform packing rule of the Packing Model (1).

5. The phenomena of packing saturation and uniform packing are the direct results of V_0 being close to E_j in complex compounds of the lanthanides and actinides. Therefore, the balance between van der Waals and coordination bond energies is the foundation of the Packing Model.

6. The Unified Model of the coordination bond length explains the difference between the bond lengths of the oxygen coordination bonds in each of the fourteen $Ln(C_2H_5SO_4)_3 \cdot 9H_2O$ compounds, which was not explained before.

1. X. F. LI, X. Z. FENG, Y. T. XU, P. N. SUN, and J. SHI. Acta Chim. Sin. **43**, 502 (1985).
2. R. E. GERKIN and W. J. REPPART. Acta Crystallogr. C**40**, 781 (1984).

Can. J. Chem. Downloaded from www.nrcresearchpress.com by 213.222.148.141 on 09/07/12
For personal use only.

Studies on density, viscosity, dielectric constant, and refractive index of binary mixtures of esters in benzene and carbon tetrachloride

SHANTILAL OSWAL
Department of Chemistry, South Gujarat University, Surat – 395 007, India

Received May 27, 1986[1]

SHANTILAL OSWAL. Can. J. Chem. **66**, 111 (1988).

Densities, viscosities, dielectric constants, and refractive indices have been determined for six binary mixtures of propyl acetate, butyl acetate, and ethyl butyrate in benzene and carbon tetrachloride at different mole fractions and temperatures. The excess volumes V^E, apparent excess values of viscosity $\delta\eta$, excess Gibbs energy of activation of flow ΔG^{*E}, excess molar polarizations P_m^E, excess molar refraction R_m^E, and excess dielectric constants ϵ^E have been calculated from the experimental data. The results for these binary mixtures are compared with those of ethyl acetate with benzene, carbon tetrachloride, and cyclohexane and of propyl acetate, butyl acetate, and ethyl butyrate with cyclohexane. The results for V^E, ΔG^{*E}, P_m^E, and ϵ^E indicate specific molecular interaction between unlike molecules in ester + benzene and ester + carbon tetrachloride. The specific molecular interaction for mixtures of esters with benzene may be due to n–π complex formation between the free electrons of carboxylic group and aromatic ring while with carbon tetrachloride it may be due to dipole – induced dipole interactions. The molar refractions for all six mixtures vary linearly with mole fraction of components. Comparison between experimental excess volume V^E and excess viscosity $\Delta \ln \eta$ and that calculated from Flory theory for ethyl acetate + benzene and ethyl acetate + carbon tetrachloride has also been made.

SHANTILAL OSWAL. Can. J. Chem. **66**, 111 (1988).

Opérant à diverses fractions molaires et à diverses températures, on a déterminé les densités, les viscosités, les constantes diélectriques et les indices de réfraction de six mélanges binaires d'acétate de propyle, d'acétate de butyle et de butyrate d'éthyle dans le benzène et le tétrachlorure de carbone. À partir de ces données expérimentales, on a calculé les volumes en excès, V^E, les valeurs apparentes d'excès de viscosité, $\delta\eta$, les énergies de Gibbs en excès pour l'activation de l'écoulement, ΔG^{*E}, les polarisations molaires en excès, P_m^E, les réfractions molaires en excès, R_m^E et les constantes diélectriques en excès, ϵ^E. On a comparé les résultats obtenus avec ces mélanges binaires avec ceux obtenus pour l'acétate d'éthyle dans le benzène, le tétrachlorure de carbone et le cyclohexane ainsi que pour l'acétate de propyle, l'acétate de butyle et le butyrate d'éthyle dans le cyclohexane. Les valeurs des V^E, ΔG^{*E}, P_m^E et ϵ^E suggèrent qu'il existe des interactions moléculaires specifiques entre les molécules qui ne sont pas semblables dans les mélanges ester + benzène et ester + tétrachlorure de carbone. Il est possible que les interactions moléculaires spécifiques observées dans les mélanges d'esters + benzène soient dues à des interactions dipôle – dipôle induit. Les réfractions molaires des six mélanges varient d'une façon linéaire avec les fractions molaires des composants. On a aussi fait une comparaison entre les valeurs expérimentales des volumes en excès, V^E, et des viscosités en excès, $\Delta \ln \eta$, et les valeurs calculées par la théorie de Flory pour l'acétate d'éthyle + benzène et pour l'acétate d'éthyle + tétrachlorure de carbone.

[Traduit par la revue]

Introduction

We are engaged in a systematic study of the thermodynamic, dielectric, and transport properties of binary mixtures of esters with various solvents. We have determined excess volumes, molar polarizations, molar refractions, viscosities, and excess Gibbs energy of activation of flow for ethyl acetate (EA) in cyclohexane, benzene, toluene, ethylbenzene, *p*-xylene, carbon tetrachloride, chloroform, and *p*-dioxane (1–5). It is found that specific interactions are present between ethyl acetate and aromatic hydrocarbons; and between ethyl acetate and carbon tetrachloride. These observations are in agreement with the findings of Loiseleur, Merlin, and Paris (6), Grolier, Ballet, and Viallard (7), and Dusart, Grolier, and Viallard (8) from the study of excess volumes and excess enthalpies of such mixtures. Studies on viscosities (9), excess volumes (9), and excess enthalpies (10, 11) have been reported for binary mixtures of propyl acetate (PA), butyl acetate (BA), and ethyl butyrate (EB) with cyclohexane, whereas no such work seems to exist for mixtures of these esters with benzene and carbon tetrachloride.

In this paper, I report the densities, viscosities, dielectric constants, and refractive indices for six binary mixtures of PA, BA, and EB with benzene and carbon tetrachloride at different mole fractions. From the experimental results the excess volumes V^E, apparent excess values of the viscosity $\delta\eta$, excess Gibbs energy of activation of flow ΔG^{*E}, excess molar polarizations P_m^E, excess molar refractions R_m^E, and excess dielectric constants ϵ^E have been calculated using appropriate relations. A comparison between experimental excess volume V^E and excess viscosity $\Delta \ln \eta$ and those evaluated from Flory theory (12) has also been made.

[1]Revision received August 18, 1987.

Experimental

Densities were determined with single stem pycnometer, having a bulb volume of about 11 cm^3 and capillary of internal diameter of 1 mm. Viscosities were determined with a modified Ubbelohde Viscometer calibrated with doubly distilled water and benzene. Dielectric constants were measured using modified Toshniwal Dipolemeter (Type RL09) which operates at 300 kHz. Refractive indices for the sodium D line of the pure components and of the mixtures were measured with Abbe's research refractometer. The details of the apparatus and procedures have been described in earlier papers (1–3). In these determinations both pycnometer and viscometer were suspended vertically for sufficient time in constant temperature bath maintained within ±0.02 K. The temperature for dielectric constant and refractive index measurements was maintained within ±0.05 K by a circulating water thermostat. The temperatures were read with certified thermometers. All the weighings were made on a monopan analytical balance (MERA-WAG-GDANSK, Poland) accurate to 0.1 mg. Densities, viscosities, dielectric constants, and refractive indices are accurate to ±0.0001, ±0.003, ±0.004, and ±0.0002 units, respectively.

Materials and solutions

Propyl acetate (Fluka AG), butyl acetate (Sarabhai GR), and ethyl butyrate (Fluka AG) were dried over potassium carbonate for 15 days

Can. J. Chem. Downloaded from www.nrcresearchpress.com by 213.222.148.141 on 09/07/12
For personal use only.

Can. J. Chem. Downloaded from www.nrcresearchpress.com by 213.222.148.141 on 09/07/12
For personal use only.

and were fractionally distilled (13). Benzene (BDH Analar) and carbon tetrachloride (BDH, spectroscopic) were of the same origin and purity as in ref. 3. Mixtures were prepared by weighing the liquids in ground stoppered weighing bottles, taking due precautions to minimise evaporation.

Results

The measured densities ρ and viscosities η at 303.15 and 313.15 K; dielectric constants ϵ and refractive indices n_D at 303.15 K for pure components and for binary mixtures: PA + C_6H_6, EB + C_6H_6, PA + CCl_4, BA + CCl_4, and EB + CCl_4 and densities, viscosities, dielectric constants, and refractive indices at 308.15 K for BA + C_6H_6, over entire range of mole fractions were measured.[2] The values of properties ρ, η, ϵ and n_D of pure liquids are in agreement with those available in the literature (13).

The values of the excess volume V^E, the apparent excess value of the viscosity $\delta\eta$, and the excess Gibbs energy of activation of flow ΔG^{*E} were calculated from the experimental data with the following equations (14)[2]

$$[1] \quad V = (x_1M_1 + x_2M_2)/\rho$$

$$[2] \quad V^E = V - (x_1V_1^0 + x_2V_2^0)$$

$$[3] \quad \delta\eta = \eta - (x_1\eta_1^0 + x_2\eta_2^0)$$

$$[4] \quad \Delta G^{*E} = RT[\ln \eta V - (x_1 \ln \eta_1^0 V_1^0 + x_2 \ln \eta_2^0 V_2^0)]$$

where ρ, η, and V are the density, viscosity, and molar volume of the mixture, M_1 and M_2 are the molar masses, η_1^0 and η_2^0 the viscosities, V_1^0 and V_2^0 the molar volumes, x_1 and x_2 the mole fractions of the first and second component, respectively. It is preferred to define $\eta - x_1\eta_1^0 - x_2\eta_2^0$ as the apparent excess value of viscosity $\delta\eta$ instead of excess viscosity η^E (15, 16) as it does not represent true excess function as per the definitions of excess functions (17).

The molar polarization P_m, the molar refraction R_m, the excess molar polarization P_m^E, and the excess dielectric constants ϵ^E were obtained from the following expressions from [5] to [8]:

$$[5] \quad P_m = V(\epsilon - 1)/(\epsilon + 2)$$

$$[6] \quad R_m = V(n_D^2 - 1)/(n_D^2 + 2)$$

$$[7] \quad P_m^E = P_m - (x_1P_{m,1}^0 + x_2P_{m,2}^0)$$

$$[8] \quad \epsilon^E = \epsilon - (\theta_1\epsilon_1^0 + \theta_2\epsilon_2^0)$$

where ϵ and n_D are the dielectric constant and refractive index of the mixture, $P_{m,1}^0$ and $P_{m,2}^0$ are the molar polarizations, ϵ_1^0 and ϵ_2^0 the dielectric constants, and θ_1 and θ_2 the dielectric fractions of the first and second component, respectively. The dielectric fraction $\theta_1 = 1 - \theta_2$ is given by eq. [9] as shown earlier (4)

$$[9] \quad \theta_1 = \frac{x_1V_1^0/(\epsilon_1^0 + 2)}{x_1V_1^0/(\epsilon_1^0 + 2) + x_2V_2^0/(\epsilon_2^0 + 2)}$$

The excess quantities Y^E (V^E, $\delta\eta$, ΔG^{*E}, P_m^E, and ϵ^E) over the entire range of composition have been fitted to empirical equation [10]

$$[10] \quad Y^E = x_1x_2 \sum_{i=0}^{3} A_i(x_1 - x_2)^i$$

The coefficients A_i of these fitting equations together with the standard deviations σ are summarized in Table 1.

It seems that there are no literature data on densities, viscosities, dielectric constants, refractive indices, and other derived excess properties of these binary mixtures with which the present data can be compared. Figures 1, 2, and 3 show the dependence of the values of V^E, ΔG^{*E}, and P_m^E on x_2 at 303.15 K for these mixtures.

Discussion

For the analysis of results the experimental values of V^E, ΔG^{*E}, P_m^E, and ϵ^E for binary mixtures of EA, PA, BA, and EB with C_6H_6 and CCl_4 at equimolar composition are summarised in Table 2. A close examination of Table 2 and Figs. 1 to 3 yields the following information.

Values of V^E for ester + C_6H_6 and ester + CCl_4 series are very small and decrease in the order: EA > PA > BA > EB. Values of V^E for ester + C_6H_6 mixtures are greater than those of corresponding ester + CCl_4 mixture. Thus by increasing —CH_2— group in the aliphatic chains of esters, V^E of their mixtures with C_6H_6 and CCl_4 regularly decreases. The results obtained indicated similarity to the behaviour of esters mixed with n-C_7H_{16} and c-C_6H_{12} (7, 9). The decrease in V^E from ethyl acetate through butyl acetate is apparently due to a weakening of the molecular interactions in the pure esters by the aliphatic chains of the esters. It is interesting to compare results of mixtures of alkyl alkanoates in C_6H_6, CCl_4, c-C_6H_{12}, and n-C_7H_{16} with those of ethyl acetate in n-alkanes and benzene in n-alkanes (n-hexane through n-dodecane). The values of V^E increase with the increase in chain length of n-alkanes (7, 18) but decrease with the increase in chain length of esters. Hence, —CH_2— group in the presence of —COO— group contributes differently to V^E than that in n-alkanes.

Values of $\delta\eta$ are small and negative for all the mixtures, the highest value of $\delta\eta$ is for EB + C_6H_6 ($\delta\eta = -0.012$ cP at 313.15 K) and lowest for EA + CCl_4 ($\delta\eta = -0.060$ cP at 303.15 K). The values of $\delta\eta$ increase with the increase in temperature for all these mixtures. It indicates that in these binary mixtures, the forces between pairs of unlike molecules are a little less than the forces between pairs of like molecules and that is why the mixture is less viscous.

Values of ΔG^{*E} are small and negative for all the mixtures of esters with C_6H_6 and CCl_4. It is observed that as the chain length increases, either in alkyl or alkanoates group in the esters the values of ΔG^{*E} increase for both the series of esters + C_6H_6 and esters + CCl_4, that is to say, the order for ΔG^{*E} values is ethyl < propyl < butyl in alkyl acetates mixtures and acetate < butyrate in ethyl alkanoates. Similar trends were observed by Dusart, Piekarski, and Piekarski (19) and Memmi and Piekarski (9) for esters + n-heptane and esters + cyclohexane, respectively. This effect arises from the varying size ratios of unlike components in the mixtures, as molar volume ratios of ester/C_6H_6 and ester/CCl_4 gradually increase by replacing ethyl acetate either with propyl acetate, butyl acetate, or ethyl butyrate. Similar results were also found for mixtures of trialkylamines + C_6H_6 and trialkylamines + c-C_6H_{12} (20). Present results are also consistent with the finding that the difference in the sizes of two unlike components in the binary mixture makes positive contribution to the values of ΔG^{*E}.

The values of V^E, $\delta\eta$, and ΔG^{*E} for esters with C_6H_6 and CCl_4 show relatively small deviations from ideal values, suggesting that either the different contributions arising from the mixing of the components are small or that opposite

[2]All numerical results may be purchased from the Depository of Unpublished Data, CISTI, National Research Council of Canada, Ottawa, Ont., Canada K1A 0S2.

TABLE 1. Coefficients for least-square fit results for eq. [10]

Property	Temperature (K)	A_0	A_1	A_2	A_3	σ
		(*i*) Propyl acetate + benzene				
V^E, cm^3 mol^{-1}	303.15	0.504	0.253	−0.552	−0.961	0.019
	313.15	0.239	−0.290	−0.290	0.594	0.003
δη, cP	303.15	−0.092	0.045	−0.046	−0.018	0.002
	313.15	−0.072	0.020	−0.012	0.031	0.001
ΔG^{*E}, J mol^{-1}	303.15	−345.3	196.7	−168.2	−168.2	5.6
	313.15	−306.8	92.1	−133.4	20.7	6.2
P_m^E, cm^3 mol^{-1}	303.15	18.98	−7.88	9.82	−1.19	0.22
ϵ^E	303.15	2.130	−0.122	0.819	0.565	0.028
		(*ii*) Butyl acetate + benzene				
V^E, cm^3 mol^{-1}	308.15	0.262	−0.250	0.065	0.029	0.007
δη, cP	308.15	−0.056	0.065	0.004	0.004	0.001
ΔG^{*E}, J mol^{-1}	308.15	−68.9	251.7	154.0	190.2	2.6
P_m^E, cm^3 mol^{-1}	308.15	22.64	3.16	20.71	13.75	0.39
ϵ^E	308.15	2.197	0.883	2.245	1.933	0.042
		(*iii*) Ethyl butyrate + benzene				
V^E, cm^3 mol^{-1}	303.15	0.011	−0.230	0.081	0.031	0.006
	313.15	−0.013	−0.096	−0.049	0.287	0.01
δη, cP	303.15	−0.065	0.033	0.004	−0.015	0.001
	313.15	−0.047	0.023	0.008	−0.028	0.000
ΔG^{*E}, J mol^{-1}	303.15	−84.3	97.0	−9.3	135.6	4.5
	313.15	−16.6	82.7	68.4	−34.9	1.2
P_m^E, cm^3 mol^{-1}	303.15	14.60	−6.11	1.31	2.72	0.155
ϵ^E	303.15	1.427	−0.179	−0.031	0.293	0.015
		(*iv*) Propyl acetate + carbon tetrachloride				
V^E, cm^3 mol^{-1}	303.15	−0.322	0.164	−0.038	−0.235	0.002
	313.15	−0.294	0.080	−0.013	−0.292	0.004
δη, cP	303.15	−0.168	0.020	−0.163	−0.163	0.006
	313.15	−0.125	0.055	−0.006	−0.013	0.001
ΔG^{*E}, J mol^{-1}	303.15	−293.2	499.9	−73.0	−561.4	20.9
	313.15	−196.4	199.8	19.3	−201.1	3.3
P_m^E, cm^3 mol^{-1}	303.15	20.55	−9.00	5.51	2.63	0.11
ϵ^E	303.15	2.188	0.0412	0.411	0.659	0.015
		(*v*) Butyl acetate + carbon tetrachloride				
V^E, cm^3 mol^{-1}	303.15	−0.584	0.299	0.386	−0.209	0.015
	313.15	−0.471	0.694	−0.085	−1.647	0.013
δη, cP	303.15	−0.074	0.048	−0.017	0.046	0.001
	313.15	−0.068	0.068	0.005	−0.109	0.001
ΔG^{*E}, J mol^{-1}	303.15	−35.8	169.6	−55.2	140.5	5.0
	313.15	−50.8	233.5	−5.1	−382.7	3.0
P_m^E, cm^3 mol^{-1}	303.15	16.52	−9.36	3.15	3.12	0.12
ϵ^E	303.15	1.633	−0.409	1.046	1.613	0.015
		(*vi*) Ethyl butyrate + carbon tetrachloride				
V^E, cm^3 mol^{-1}	303.15	−0.650	0.128	0.409	−0.098	0.006
	313.15	−0.580	0.018	0.332	0.213	0.004
δη, cP	303.15	−0.102	0.0524	−0.055	0.042	0.001
	313.15	−0.090	−0.047	0.009	−0.040	0.001
ΔG^{*E}, J mol^{-1}	303.15	−99.3	134.3	−165.1	119.0	4.2
	313.15	−139.2	161.9	55.3	−24.2	3.8
P_m^E, cm^3 mol^{-1}	303.15	16.43	−5.56	−1.65	−0.85	0.12
ϵ^E	303.15	1.546	0.015	−0.378	−0.158	0.010

contributions largely balance each other (21). It is interesting to compare present results of V^E, $\Delta\eta$, and ΔG^{*E} for mixtures of esters in C_6H_6 or CCl_4 with those of corresponding esters in c-C_6H_{12} (1, 3, 8, 9). The values of V^E for EA, PA, BA, and EB with c-C_6H_{12} are large and positive in the range 0.8 to 1.2 cm^3 mol^{-1} and the values of ΔG^{*E} are large and negative in the range −375 to −510 J mol^{-1} which are attributable to strong ester–ester interaction through dipole–dipole interaction and dispersion interaction between ester + c-C_6H_{12}. In the mixtures of esters with C_6H_6 and with CCl_4, these large contribution to V^E and ΔG^{*E} are reduced too much. This suggests that the specific molecular interactions between unlike molecules are

Can. J. Chem. Downloaded from www.nrcresearchpress.com by 213.222.148.141 on 09/07/12
For personal use only.

TABLE 2. Experimental V^E, $\delta\eta$, ΔG^{*E}, P_m^E, and ϵ^E at equimolar composition EA, PA, BA, and EB with C_6H_6, CCl_4, and c-C_6H_{12}

Mixture	Temperature (K)	V^E ($cm^3\ mol^{-1}$)	$\delta\eta$ (cP)	ΔG^{*E} ($J\ mol^{-1}$)	P_m^E ($cm^3\ mol^{-1}$)	ϵ^E
EA + C_6H_6[a,b]	303.15	0.104	−0.030	−124.9	4.6	0.556
PA + C_6H_6	303.15	0.126	−0.023	−86	4.7	0.533
	313.15	0.052	−0.018	−77		
BA + C_6H_6	308.15	0.066	−0.014	−17	5.7	0.549
EB + C_6H_6	303.15	0.003	−0.016	−21	3.6	0.357
	313.15	−0.003	−0.012	−4		
EA + CCl_4[b,c,d]	303.15	+0.039	−0.060	−97	5.1	0.574
PA + CCl_4	303.15	−0.081	−0.042	−73	5.1	0.547
	313.15	−0.074	−0.031	−49		
BA + CCl_4	303.15	−0.146	−0.019	−9	4.1	0.408
	313.15	−0.118	−0.017	−13		
EB + CCl_4	303.15	−0.163	−0.026	−25	4.1	0.387
	313.15	−0.145	−0.022	−35		

[a]Reference 1.
[b]Reference 3.
[c]Reference 2.
[d]Reference 18.

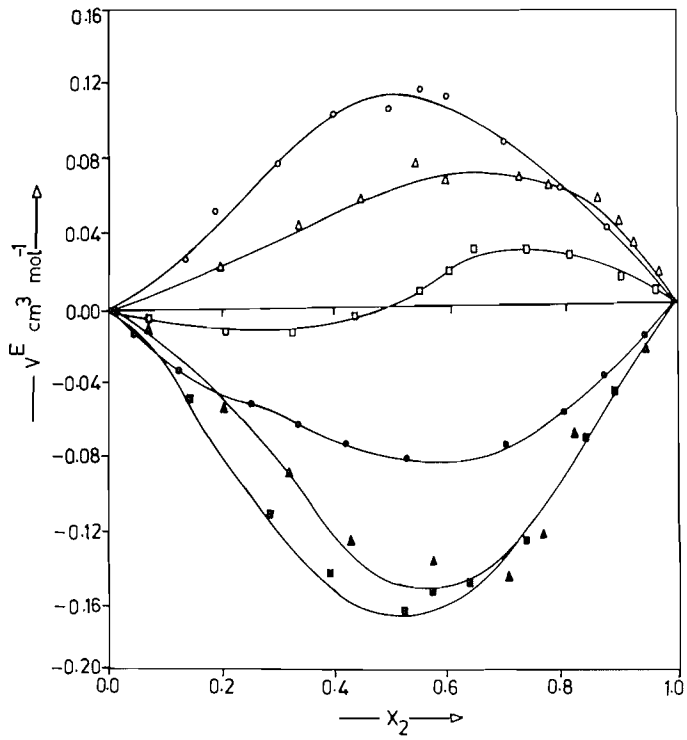

FIG. 1. Excess volumes V^E at 303.15 K for PA + C_6H_6, ○; BA + C_6H_6, △; EB + C_6H_6, □; PA + CCl_4, ●; BA + CCl_4, ▲; and EB + CCl_4, ■.

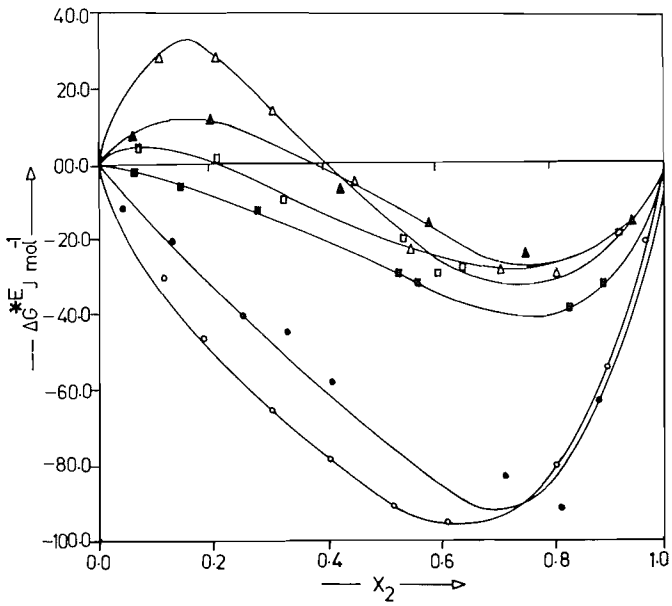

FIG. 2. Excess Gibbs energy of activation of flow ΔG^{*E} at 303.15 K for PA + C_6H_6, ○; BA + C_6H_6, △; EB + C_6H_6, □; PA + CCl_4, ●; BA + CCl_4, ▲; and EB + CCl_4, ■.

present. The specific interaction in mixtures of esters with C_6H_6 may be due to the formation of n–π complex between the free electrons of the carboxylic group and those of the aromatic ring. On the other hand, specific interaction with CCl_4 mixtures may be due to dipole – induced dipole interaction because of high polarizability of CCl_4 molecule. The similar conclusions were reached after analyzing available H^E results of these mixtures (6–8, 10, 11).

The values of P_m^E and ϵ^E are positive for all the mixtures investigated. From P_m of the mixtures the molar polarization P_1 of ester was determined in the manner described by Earp and Glasstone (22) using the relation $P_m = x_1P_1 + x_2P_2$. The polarization P_2 of the other component (C_6H_6 or CCl_4) is assumed to be equal to that in the pure liquid state and to remain constant throughout. When the molar polarization P_1 of ester in mixtures of C_6H_6 or CCl_4 was plotted against its mole fraction, a definite increase in P_1 at high dilution was observed and it was much greater than that of ester mixtures in c-C_6H_{12}. This exaltation of polarization further supports the specific interaction of esters with C_6H_6 and CCl_4. Earp and Glasstone (22) suggested that such results indicate formation of new coordinate link joining the two molecules. In this case the oxygen atom of esters acts as a donor while C_6H_6 and CCl_4 act as acceptors.

The molar refractions R_m calculated by eq. [6] are close to

Can. J. Chem. Downloaded from www.nrcresearchpress.com by 213.222.148.141 on 09/07/12
For personal use only.

TABLE 3. Physicochemical data (ρ, α, γ), equation of state parameters ($\tilde{v}$, P^*, V^*, T^*) for pure liquids at 303.15 K

Compound	ρ (g cm^{-3})	$10^3\,\alpha$ (K^{-1})	γ (J cm^3 K^{-1})	$\tilde{v}$	V^* (cm^3 mol^{-1})	P^* (J cm^{-3})	T^* (K)
Ethyl acetate	0.8885	1.394	1.119	1.3274	74.70	607	4467
Benzene	0.8684	1.233	1.221	1.2975	69.33	623	4730
Carbon tetrachloride	1.5748	1.245	1.103	1.2998	75.16	565	4708

TABLE 4. Experimental and calculated results from Flory theory related to excess enthalpy, volume, and viscosity

Mixtures	H^E (J mol^{-1})	X_{12} (J cm^{-3})	V^E_{cal} (cm^3 mol^{-1})	δV^E (cm^3 mol^{-1})	ln η_H	ln η_S	ln $\eta_{f.v.}$	ln η_{cal}	ln η_{exp}	δ
EA + C_6H_6	86[a]	1.7	0.091	0.013	−0.033	+0.021	−0.038	−0.052	−0.052	0.000
EA + CCl_4	−82[b]	−3.8	−0.091	0.130	+0.033	−0.016	+0.001	+0.018	−0.040	−0.058

[a]Reference 7.
[b]Reference 8.

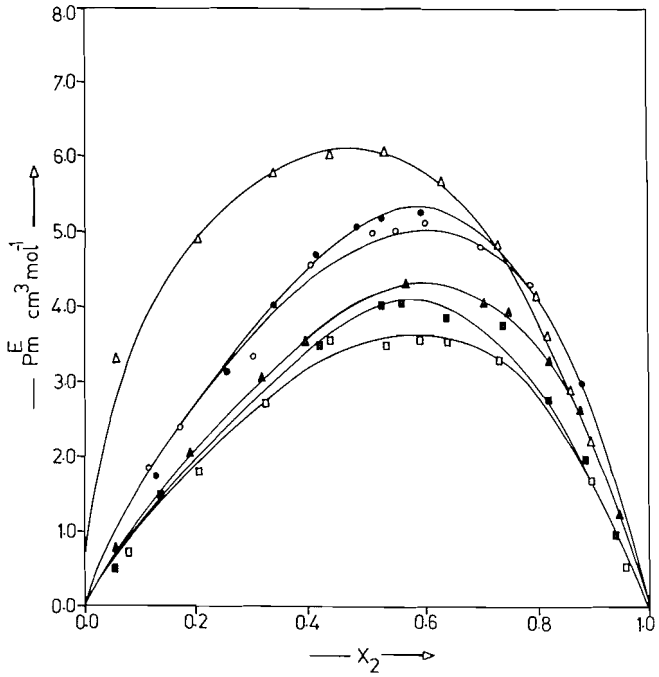

FIG. 3. Excess molar polarization P^E_m at 303.15 K for PA + C_6H_6, ○; BA + C_6H_6, △; EB + C_6H_6, □; PA + CCl_4, ●; BA + CCl_4, ▲; and EB + CCl_4, ■.

those calculated from the mole fraction mixture rule, the slight differences may be attributed to the experimental error. This is to be expected as per Clausius–Mosotti theory, that the molar refraction represents the true volume of the matter in a mole (23).

Flory theory

A further comparison between experimental excess volume V^E and excess viscosity $\Delta \ln \eta$ and that calculated theoretically from Flory theory (12, 24–26) has been made for representative mixtures EA + C_6H_6 and EA + CCl_4. Excess viscosity $\Delta \ln \eta$ is obtained from the experimental viscosity of mixture and pure components through eq. [11]

$$[11]\quad \Delta \ln \eta = \ln \eta - (x_1 \ln \eta_1^0 + x_2 \ln \eta_2^0)$$

Following the Flory theory and original notations (12, 26), excess enthalpy H^E, excess entropy S^E, excess volume V^E, and excess viscosity $\Delta \ln \eta$ are given by

$$[12]\quad H^E = x_1P_1^*V_1^*(\tilde{v}_1^{-1} - \tilde{v}^{-1}) + x_2P_2^*V_2^*(\tilde{v}_2^{-1} - \tilde{v}^{-1}) + x_1\theta_2V_1^*X_{12}\tilde{v}^{-1}$$

$$[13]\quad S^E = -\frac{3x_1P_1^*V_1^*}{T_1^*}\ln\left(\frac{\tilde{v}_1^{1/3}-1}{\tilde{v}^{1/3}-1}\right) - \frac{3x_2P_2^*V_2^*}{T_2^*}\ln\left(\frac{\tilde{v}_2^{1/3}-1}{\tilde{v}^{1/3}-1}\right)$$

$$[14]\quad V^E = (\tilde{v} - \phi_1\tilde{v}_1 - \phi_2\tilde{v}_2)(x_1V_1^* + x_2V_2^*)$$

$$[15]\quad \Delta \ln \eta = -\frac{H^E}{RT} + \frac{S^E}{R} + \left\{\frac{1}{\tilde{v}-1} - \left(\frac{x_1}{\tilde{v}_1-1} + \frac{x_2}{\tilde{v}_2-1}\right)\right\}$$

or

$$[16]\quad \Delta \ln \eta = \ln \eta_H + \ln \eta_S + \ln \eta_{f.v.}$$

Equations [15] and [16] were developed by Bloomfield and Dewan (26). ln η_H, ln η_S, and ln $\eta_{f.v.}$ are the enthalpy, entropy, and free volume contributions, respectively, to the total excess viscosity $\Delta \ln \eta$. The equation of state parameters of pure liquids needed in the use of Flory theory are given in Table 3. Contact interaction parameter X_{12} is obtained from experimental H^E (12). The values of H^E, X_{12}, V^E_{cal}, δV^E ($= V^E_{exp} - V^E_{cal}$), ln η_H, ln η_S, ln $\eta_{f.v.}$, $\Delta \ln \eta_{cal}$, $\Delta \ln \eta_{exp}$, and δ ($= \Delta \ln \eta_{exp} - \Delta \ln \eta_{cal}$) are summarised in Table 4.

The differences 0.013 and 0.130 cm^3 mol^{-1} for EA + C_6H_6 and EA + CCl_4, respectively, between experimental V^E and that calculated from Flory theory are not very large. A perfect prediction of V^E for these mixtures would be somewhat surprising with such a simple van der Waals model for energy. A better agreement may be obtained by taking into account the order in pure ethyl acetate due to dipole–dipole interaction which is destroyed by the presence of C_6H_6 or CCl_4 molecules in the mixture.

A very good agreement between the experimental $\Delta \ln \eta$ and that calculated from Flory theory is obtained for EA + C_6H_6 and EA + CCl_4. The values of ln η_H and ln $\nu_{f.v.}$ contributions are small and negative while ln η_S is small and positive for EA + C_6H_6. The values of ln η_H and ln η_S contributions for EA + CCl_4 reflect that specific interactions are stronger in it than that in EA + C_6H_6.

Can. J. Chem. Downloaded from www.nrcresearchpress.com by 213.222.148.141 on 09/07/12
For personal use only.

Comparison of present results with those of EA + c-C_6H_{12} throws some more light on order, disorder, and specific molecular interactions which are operating in these mixtures. There is a large difference ($\delta = 0.333$) between the values of experimental excess viscosity and that predicted by Flory theory for EA + c-C_6H_{12}. This large positive difference for EA + c-C_6H_{12} is attributable to the effect of disorder (deorientation) which occurs due to the breaking of order in ester dipoles by the presence of c-C_6H_{12} molecules as suggested by Delmas, Purves, Saint Romain (27). Therefore, it can be safely said that in case of mixtures EA + C_6H_6 and EA + CCl_4, the effect of disorder of esters molecules is counter balanced by the formation of complex between unlike molecules due to specific interactions, thus leading to a very good agreement between the experiment and theory.

Acknowledgements

The author is thankful to Mr. M. V. Rathnam for his help in experimental measurements and to the Council of Scientific and Industrial Research, New Delhi, for the financial support to carry out this work.

1. S. L. Oswal and K. G. Pathak. Indian J. Chem. **21**A, 712 (1982).
2. S. L. Oswal and M. V. Rathnam. J. Indian Chem. Soc. **61**, 269 (1984).
3. S. L. Oswal and M. V. Rathnam. Can. J. Chem. **62**, 2851 (1984).
4. S. L. Oswal and M. V. Rathnam. Indian J. Chem. **26**A, 29 (1987).
5. S. L. Oswal and M. V. Rathnam. J. Indian Chem. Soc. **63**, 674 (1986).
6. H. Loiseleur, J. C. Merlin, and R. A. Paris. J. Chim. Phys. **62**, 1380 (1965).
7. J. P. E. Grolier, D. Ballet, and A. Viallard. J. Chem. Thermodyn. **6**, 895 (1974).
8. O. Dusart, J. P. E. Grolier, and A. Viallard. Bull. Soc. Chim. Fr. 587 (1977).
9. A. Memmi and S. Piekarski. J. Chem. Res. (s) 98 (1982).
10. D. D. Deshpande and C. S. Prabhu. Indian J. Chem. **16**A, 95 (1978).
11. D. D. Deshpande and C. S. Prabhu. J. Phys. Chem. **85**, 1261 (1981).
12. P. J. Flory. J. Am. Chem. Soc. **87**, 1833 (1965).
13. J. R. Riddick and W. B. Bunger. Organic solvents: physical properties and method of purification. Wiley Interscience, New York. 1970.
14. P. K. Katti and M. Chaudri. J. Chem. Eng. Data, **9**, 442 (1964).
15. R. K. Nigam and B. S. Mahl. Indian J. Chem. **9**, 1255 (1971).
16. R. J. Fort and W. R. Moore. Trans. Faraday Soc. **62**, 112 (1966).
17. J. S. Rowlinson. Liquid and liquid mixtures. 2nd ed. Butterworths, London. 1969.
18. R. G. Rubio, C. Menduina, M. DiazPena, and J. A. R. Renuncio. J. Chem. Soc. Faraday Trans. I, **80**, 1425 (1984).
19. O. Dusart, C. Piekarski, and S. Piekarski. J. Chim. Phys. **75**, 919 (1978).
20. S. L. Oswal and A. V. Rao. Indian J. Chem. **24**A, 1026 (1985).
21. L. Pikkarainen. Finn. Chem. Lett. 63 (1983).
22. D. P. Earp and S. Glasstone. J. Chem. Soc. 1709 (1935).
23. A. N. Campbell and E. M. Kartzmark. Can. J. Chem. **47**, 619 (1969).
24. P. J. Flory. Discuss. Faraday Soc. **49**, 7 (1970).
25. D. Patterson and G. Delmas. Discuss. Faraday Soc. **49**, 98 (1970).
26. V. A. Bloomfield and R. K. Dewan. J. Phys. Chem. **75**, 3113 (1971).
27. G. Delmas, P. Purves, and P. De Saint Romain. J. Phys. Chem. **79**, 1970 (1975).

Can. J. Chem. Downloaded from www.nrcresearchpress.com by 213.222.148.141 on 09/07/12
For personal use only.

Ruthenium(II) complexes of 4-nitroimidazoles: their characterization, solution chemistry, and radiosensitizing activity

PETER K. L. CHAN, PAUL K. H. CHAN, DAVID C. FROST,[1] AND BRIAN R. JAMES[1]
Department of Chemistry, University of British Columbia, Vancouver, B.C., Canada V6T 1Y6

AND

KIRSTEN A. SKOV
Medical Biophysics Unit, British Columbia Cancer Research Centre, 601 West 10th Avenue, Vancouver, B.C., Canada V5Z 1L3

Received July 14, 1987

PETER K. L. CHAN, PAUL K. H. CHAN, DAVID C. FROST, BRIAN R. JAMES, and KIRSTEN A. SKOV. Can. J. Chem. **66**, 117 (1988).

A series of ruthenium(II) complexes of formulation $RuCl_2(dmso)_2L_n$, where dmso = S-bonded dimethylsulfoxide, L is a 4-nitroimidazole derivative, and n = 1 or 2, have been synthesized and characterized by spectroscopic methods, particularly ^1H nmr and X-ray photoelectron spectroscopy. With L = 4-nitroimidazole itself (4-NO_2Im), RSU-1170,[2] -3083 or -3100, n = 2 and the six-coordinate complexes are considered to be of *cis,cis,cis*-geometry. The *N*-methyl-4-nitroimidazole (NMe-4-NO_2Im) ligand (n = 1) chelates through the imidazole-*N* and the oxygen of NO_2. The RSU-3159 ligand (n = 1) binds through the sulfur and may be chelated. The complexes are of interest because of their radiosensitizer properties toward hypoxic tumour cells; the $RuCl_2(dmso)_2$(NMe-4-NO_2Im) complex has a higher sensitizing enhancement ratio than the free imidazole ligand, and shows no cytoxicity *in vitro*, and these data are compared to those reported previously for $RuCl_2(dmso)_2$(4-NO_2Im)$_2$. Some aspects of the aqueous solution chemistry of the complexes (aquation via loss of chloride, pK_a of coordinated water) are discussed in relation to their biological activities.

PETER K. L. CHAN, PAUL K. H. CHAN, DAVID C. FROST, BRIAN R. JAMES et KIRSTEN A. SKOV. Can. J. Chem. **66**, 117 (1988).

On a synthétisé une série de complexes du ruthénium(II), $RuCl_2(dmso)_2L_n$, dans lesquels dmso = diméthylsulfoxyde lié par le S, L = un dérivé nitro-4 imidazole et n = 1 ou 2; de plus, on les a caractérisés par des méthodes spectroscopiques, en particulier par rmn du ^1H et par spectroscopie photoélectronique des rayons-X. Lorsque L = nitro-4 imidazole (4-NO_2Im), RSU-1170,[2] -3083 ou -3100, n = 2 et on considère que les complexes hexacoordonnés possèdent la géométrie *cis,cis,cis*. Le ligand *N*-méthyl nitro-4 imidazole (NMe-4-NO_2Im) (n = 1) se chélate par le biais du N de l'imidazole et le O du NO_2. Le ligand RSU-3159 (n = 1) se lie par le soufre et il est possible qu'il soit chélaté. Les complexes sont intéressants à cause de leurs propriétés comme radiosensibilisateurs par rapport aux cellules tumorales hypoxiques. Le complexe de $RuCl_2(dmso)_2$(NMe-4-NO_2Im) possède un caractère sensibilisateur qui est plus élevé que celui du ligand imidazole libre et il ne présente aucune cytotoxicité *in vitro*; de plus, on compare ces données avec celles rapportées antérieurement pour le $RuCl_2(dmso)_2$(4-NO_2Im)$_2$. On discute de quelques aspects de la chimie en solution aqueuse de ces complexes (aquation par le biais d'une perte de chlorure et pK_a de l'eau qui est coordonnée) en relation avec leurs activités biologiques.

[Traduit par la revue]

Introduction

Many tumours contain cells which are low in dioxygen content (hypoxic) and consequently are relatively resistant to radiation treatment (1). This radioresistance may be significantly reduced through the identification of chemical radiosensitizers which enhance radiation-induced damage. Classic radiosensitizers are the so-called "electron-affinic" agents such as nitroimidazoles (2) and nitrofurans (3). The rationale is that the electron-affinic nitro group may mimic dioxygen (which is known to interact with damage on DNA induced by radiation) and lead to effective treatment (4). However, maximum sensitization cannot be achieved owing to the serious side-effects of the nitro-compound drugs (5).

Studies on DNA as a radiation target may well lead to the development of new species having radiosensitizing and DNA-binding properties. In this regard, attachment of a radiosensitizer to metals that bind to DNA may be of value. As a consequence of binding to DNA, the metal could act as a carrier, increase the local concentration of radiosensitizer at the target, and thus decrease the deleterious side-effects (6). In this respect, the strong binding of ruthenium to purine and pyrimidine bases (7) and their anti-neoplastic activity (8) suggested that ruthenium complexes containing known radiosensitizers could have interesting biological properties.

We have recently assessed the radiosensitizing ability of some ruthenium(II) complexes of nitroimidazoles (9, 10), and shown that $RuCl_2(dmso)_2$(4-nitroimidazole)$_2$, **1**, has a good sensitizing enhancement ratio (SER = 1.6) in hypoxic Chinese hamster ovary (CHO) cells (SER is defined as the ratio of X-ray doses between hypoxic control and drug at 1% cell survival), and also gives low genotoxicity (11).

In the present study, we report details on the synthesis, characterization, and solution chemistry of complex **1**, as well as related work on other Ru(II) complexes containing a range of 4-nitroimidazoles. Their biological properties are also reported on briefly. The general formula of the species can be represented as $RuCl_2(dmso)_2L_n$, where dmso = S-bonded dimethylsulfoxide, L is a 4-nitroimidazole (Fig. 1), and n = 1 or 2. In the absence of X-ray structural data, X-ray photoelectron spectroscopy (XPS) (12–15) has been particularly useful in elucidation of the structures of the complexes.

[1]Authors to whom correspondence should be addressed.

[2]The RSU terminology is used by Drs. I. J. Stratford and T. C. Jenkins (Medical Research Council, Harwell, Didcot, England), the suppliers of these ligands whose structures are given in Fig. 1; see, for example, I. J. Stratford, G. E. Adams, C. Hardy, S. Hoe, P. O'Neill, and P. W. Sheldon. Int. J. Radiat. Biol. **46**, 731 (1984).

Can. J. Chem. Downloaded from www.nrcresearchpress.com by 213.222.148.141 on 09/07/12
For personal use only.

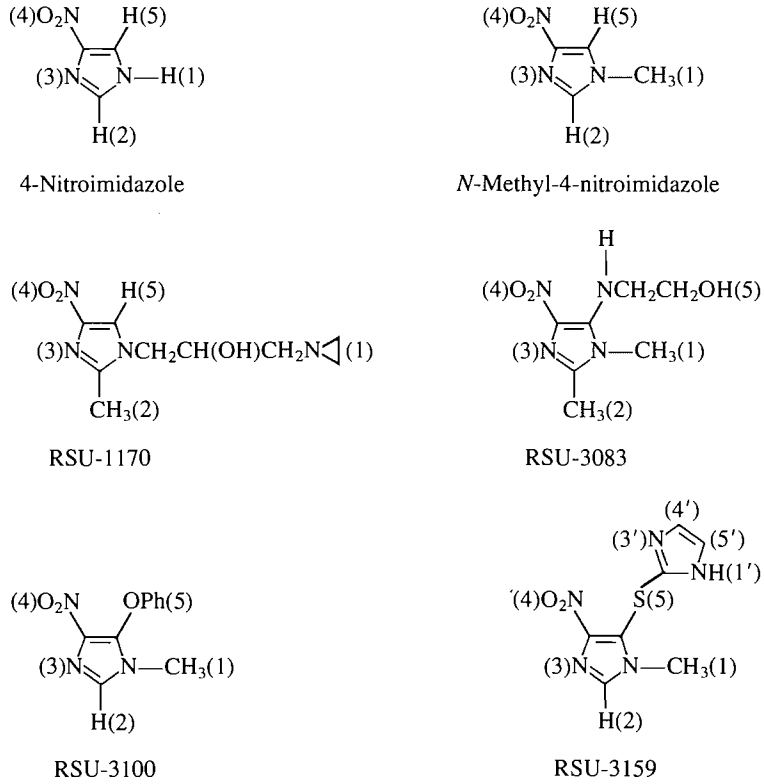

FIG. 1 Structure formulae and numbering scheme for the 4-nitroimidazole ligands.

Experimental section

Chemicals and complexes

$RuCl_3 \cdot 3H_2O$ was received on loan from Johnson Matthey Ltd. and 4-nitroimidazole (4-NO_2Im) was purchased from Sigma. Of the nitroimidazole ligands (Fig. 1), RSU-1170, RSU-3100, and RSU-3159 were kindly supplied by Dr. T. C. Jenkins,[2] and RSU-3083 by Dr. I. J. Stratford.[2] All these chemicals were used without further purification. All other common reagents were at least reagent grade. The precursor complex *cis*-$RuCl_2(dmso)_4$, which contains one O-bonded and three S-bonded sulfoxides (16), was prepared by a literature procedure (17), as was *N*-methyl-4-nitroimidazole, NMe-4-NO_2Im (18).

*$RuCl_2(dmso)_2$(4-NO_2Im)$_2$, **1***. Dry MeOH (15 mL) was added to $RuCl_2(dmso)_4$ (483 mg, 1 mmol) and 4-NO_2Im (382 mg, 2.5 mmol), and the mixture refluxed for 4 h under N_2. The resulting brown solution was cooled to room temperature and diethylether (40 mL) added slowly to precipitate out a brown product, which was filtered off, washed with acetone and diethylether, and dried *in vacuo* at room temperature (65% yield). *Anal.* calcd. for $C_{10}H_{18}O_6N_6S_2Cl_2Ru$: C 21.66, H 3.25, N 15.16; found: C 22.0, H 3.1, N 15.4. Ultraviolet/visible, see text. Infrared (Nujol): ν_{SO} 1127, 1090, ν_{NO_2} 1559, 1535 cm^{-1}.

*$RuCl_2(dmso)_2$(NMe-4-NO_2Im), **2***. The complex $RuCl_2(dmso)_4$ (483 mg, 1 mmol) was suspended in an isopropanol solution (20 mL) of NMe-4-NO_2Im (254 mg, 2 mmol), and the mixture refluxed for 4 h under N_2. The resulting blue solution was cooled to RT, when a blue precipitate formed. This was collected, dissolved in CH_2Cl_2 (10 mL), reprecipitated with diethylether (20 mL), and dried *in vacuo* at room temperature (80% yield). *Anal.* calcd. for $C_8H_{17}O_4N_3S_2Cl_2Ru$: C 21.06, H 3.73, N 9.22; found: C 21.0, H 3.9, N 9.25. λ_{max} nm (log ϵ), H_2O: 303(4.32), 427(3.06). Infrared (Nujol): ν_{SO} 1112, 1085, ν_{NO_2} 1543, 1523 cm^{-1}.

*$RuCl_2(dmso)_2$(RSU-1170)$_2$, **3***. The nitroimidazole (226 mg, 1 mmol) was mixed with $RuCl_2(dmso)_4$ (242 mg, 0.5 mmol) in dry MeOH (10 mL), and the mixture refluxed for 4 h under N_2. The resulting green solution was cooled to RT, and diethylether (30 mL) added slowly to precipitate out a green product, which was filtered off, washed with acetone, and dried *in vacuo* at room temperature (65% yield). *Anal.* calcd. for $C_{22}H_{40}O_8N_8S_2Cl_2Ru$: C 33.85, H 5.13, N 14.35; found: C 33.5, H 5.4, N 13.9. λ_{max} nm (log ϵ), H_2O: 310(4.39). Infrared (Nujol): ν_{SO} 1123, 1087, ν_{NO_2} 1560, 1522 cm^{-1}.

*$RuCl_2(dmso)_2$(RSU-3083)$_2$, **4***. The compound RSU-3083 (200 mg, 1 mmol) was added to $RuCl_2(dmso)_4$ (242 mg, 0.5 mmol) in dry EtOH (10 mL), and the mixture refluxed for 4 h under N_2. The resulting red solution was cooled to RT and filtered; slow addition of diethylether (30 mL) yielded a red solid, that was filtered off, washed with EtOH and acetone, and dried *in vacuo* at room temperature (70% yield). *Anal.* calcd. for $C_{16}H_{36}O_8N_8S_2Cl_2Ru$: C 29.67, H 4.98, N 15.37; found: C 29.3, H 4.6, N 15.7. λ_{max} nm (log ϵ), H_2O: 385(4.40), 450(4.12). Infrared (Nujol): ν_{SO} 1167, 1086, ν_{NO_2} 1627, 1599 cm^{-1}.

*$RuCl_2(dmso)_2$(RSU-3100)$_2$, **5***. The complex $RuCl_2(dmso)_4$ (242 mg, 0.5 mmol) was suspended in an isopropanol (10 mL) solution of RSU-3100 (219 mg, 1 mmol), and the mixture refluxed for 6 h under N_2. The resulting brown solution yielded a brown product as in the synthesis of **1** (65% yield). *Anal.* calcd. for $C_{22}H_{30}O_8N_6S_2Cl_2Ru$: C 37.58, H 3.92, N 10.96; found: C 37.7, H 4.3, N 10.7. λ_{max} nm (log ϵ), H_2O: 350(4.13), 396(4.09). Infrared (Nujol): ν_{SO} 1137, 1091, ν_{NO_2} 1614, 1583 cm^{-1}.

*$RuCl_2(dmso)_2$(RSU-3159), **6***. The complex $RuCl_2(dmso)_4$ (242 mg, 0.5 mmol) was added to RSU-3159 (225 mg, 1 mmol) in MeOH (15 mL), and the mixture refluxed for 3 h under N_2. The resulting dark green solution was filtered hot, and diethylether (30 mL) added slowly to the cooled filtrate to precipitate a green solid; this was filtered off, washed with acetone and diethylether, and dried *in vacuo* at room temperature (75% yield). *Anal.* calcd. for $C_{11}H_{19}O_4N_5S_3Cl_2Ru$: C 23.87, H 3.46, N 12.65; found: C 24.1, H 3.8, N 12.5. λ_{max} nm (log ϵ), H_2O: 325(4.22). Infrared (Nujol): ν_{SO} 1125, 1085, ν_{NO_2} 1684, 1653 cm^{-1}.

Microanalyses were performed by Mr. P. Borda of the Department of Chemistry, UBC.

Physical techniques and methods

Optical spectra were recorded on a Perkin Elmer 552A, and infrared (KI discs or Nujol nulls) on a Nicolet DX FTIR; ^1H and $^{13}C\{^1H\}$ nmr

Can. J. Chem. Downloaded from www.nrcresearchpress.com by 213.222.148.141 on 09/07/12
For personal use only.

TABLE 1. XPS data for Ru(II) compounds and free ligands[a]

Atom	Compound[b]	Group	BE[c]	Peak width[c]
N (1*s*)	**1**, *Ru*(4-NO_2Im)$_2$	—NO_2	405.80(405.35)	2.6(2.6)
		N(3)	400.20(399.70)[d]	2.4(2.6)
		N(1)	399.00(398.10)[d]	2.4(2.5)
	2, *Ru*(NMe-4-NO_2Im)	—ONO	405.60(404.90)	2.5(2.3)
		N(3)	400.60(399.80)[d]	2.3(2.4)
		N(1)	399.30(397.90)[d]	2.3(2.4)
O (1*s*)	*cis*-$RuCl_2$(dmso)$_4$	—S(O)Me_2	532.00[d]	3.7
		—OSMe_2	533.70[d]	3.7
	1, *Ru*(4-NO_2Im)$_2$	NO_2	531.70(531.70)	2.9(2.9)
		—S(O)Me_2	532.00	3.6
	2, *Ru*(NMe-4-NO_2Im)	—ONO	531.70[d](531.70)	3.8(4.0)
			530.80[d]	3.8
		—S(O)Me_2	532.00	3.8
	6, *Ru*(RSU-3159)	NO_2	530.10(530.10)	3.6(3.6)
		—S(O)Me_2	532.01	3.8
Cl ($2p_{1/2,3/2}$)	*cis*-$RuCl_2$(dmso)$_4$	Cl	197.5	3.0
	1, **2**, and **6**	Cl	197.5–197.6	3.1
S ($2p_{1/2,3/2}$)	*cis*-$RuCl_2$(dmso)$_4$	SO	166.3[e]	2.8
	6, *Ru*(RSU-3159)	—S(O)Me_2	166.3	2.7
		—S	164.2(163.0)	2.7(2.7)
	1 and **2**	—S(O)Me_2	166.4–166.5	2.9

[a]Binding energy and peak width given in eV; estimated maximum error ±0.15 eV.
[b]*Ru* represents $RuCl_2$(dmso)$_2$, both dmso ligands being S-bonded.
[c]Number in parentheses gives data for corresponding group in the free ligand; the ranges of BE values for atoms are given in ref. 23.
[d]Our deconvolution method assumes the same intensity and shape for each particular type of atom; the error in these particular assignments could be as high as ±0.3 eV.
[e]The XPS peaks for sulfurs of the one O-bonded and three S-bonded ligands are not resolved.

Can. J. Chem. Downloaded from www.nrcresearchpress.com by 213.222.148.141 on 09/07/12
For personal use only.

spectra (in $CDCl_3$ wrt TMS) were recorded on a Varian XL-300 operating in the Fourier transform mode. Conductivities were measured in water using a Beckman Serfass Conductance Bridge. pH-titrations were carried out in aqueous media under N_2 using a Corning 12 pH-meter using a combination glass-electrode: typically, 25 mL of aq. HCl (2 m*M*) in the absence and presence of added complex (2 m*M*), was titrated with standard 4 m*M* NaOH solution — differences between the two titration curves allow for a simple determination of pK_a values (19).

XPS spectra were taken on a Varian IEE-15 spectrometer, at a background pressure $< 10^{-7}$ Torr, using MgK_α radiation (1253.60 eV) at 280 W and an analyzer pass energy of 100 eV. Resolution was 1.6 eV at full width half maximum on Au($4f_{7/2}$). Each sample was lightly dusted onto single-sided 3M scotch tape and introduced into the spectrometer on a rapid insertion probe cooled by liquid N_2. All binding energies (BE) were calibrated with reference to the C_{1s} peak (284.0 eV) of graphite. There was no evidence for any sample deterioration during irradiation.

Results and discussions

Complexes of formulation $RuCl_2(dmso)_2L_2$ (L = 4-NO_2Im, RSU-1170, RSU-3083, and RSU-3100) and $RuCl_2(dmso)_2L$ (L = NMe-4-NO_2Im and RSU-3159) are readily synthesized from the precursor complex *cis*-$RuCl_2(dmso)_4$, of known structure (16), by substitution of two sulfoxide ligands. The XPS, ^{1}H nmr and ir data (see below) are consistent with the diamagnetic, hexacoordinate products (**1**, **3**–**5**) having a purely *cis* structure (i.e. *cis*,*cis*,*cis*), with both dmso ligands being S-bonded. The syntheses proceed via reaction [1]:

[1] 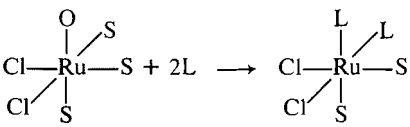

(O or S implies oxygen- or sulfur-bonded dmso)

Complex **2** of formulation $RuCl_2(dmso)_2L$ is again hexacoordinate, L binding via an imidazole nitrogen, and oxygen of the NO_2 group; the S-bonded dmso ligands may be *trans*. Complex **6**, $RuCl_2(dmso)_2$(RSU-3159), has S-bonded dmso ligands and a coordinated thioether of RSU-3159, this ligand probably being chelated via the nitrogen of the NMe group.

X-ray photoelectron spectroscopy data

XPS can be used for determining bonding configurations because the technique detects changes in the electronic environment of an atom, as evidenced by shifts in the BE of core electrons. Data for N, O, Cl and S atoms within complexes **1**, **2**, **6**, and *cis*-$RuCl_2(dmso)_4$, and for some of the free ligands, are summarized in Table 1. Coordination of imidazole ligands via the tertiary nitrogen N(3) is well established for metal ions, including Ru(II) (20–22), and the XPS and ^{1}H nmr data (see below) are consistent with this. The shift to higher BE for all the N atoms present in **1** and **2**, compared to the energies within the free ligands, indicates delocalization of electrons within the systems; in the free ligands 4-NO_2Im and NMe-4-NO_2Im, N(3), adjacent to the electron-withdrawing NO_2 group, will have a

Can. J. Chem. Downloaded from www.nrcresearchpress.com by 213.222.148.141 on 09/07/12
For personal use only.

binding energy higher than that of N(1), and in the complex the coordinated N(3) might be expected to have an even higher BE, although d^6, low-spin Ru(II) has a quite remarkable π-donor ability toward unsaturated N-atom donors (22). The perhaps greater shift to higher BE for N(3) of **2** (0.8 eV) as compared to **1** (0.5 eV) would be consistent with chelation (and therefore further loss of electron density) via an oxygen of NO_2. Stronger evidence for coordinated nitrito is provided by the doublet seen for the O 1*s* of the NO_2 group. This is not seen for **1** where the corresponding O 1*s* BE is the same as that of the free ligand. The 531.70 and 530.80 eV BE's for O in **2** are assigned to the coordinated and uncoordinated (23) oxygens, respectively. Chelating ligands utilizing a nitrito moiety are uncommon (24), and we are unaware of any other examples involving nitroimidazole ligands. On comparison of the N 1*s* and O 1*s* BE's of 4-NO_2Im and NMe-4NO_2Im, the lower values for the latter reflect the electron-donating properties of the methyl group which likely promote the chelation (25). The possibility of **2** being a chloride-bridged dimer with monodentate imidazole ligands is ruled out by the Cl $2p_{1/2,3/2}$ datum which is essentially identical to that for *cis*-$RuCl_2(dmso)_4$ (this is also true for complexes **1** and **6**).

Of interest, *cis*-$RuCl_2(dmso)_4$ shows two O 1*s* (and two S $2p_{1/2,3/2}$ peaks) in an intensity ratio of about 3:1, entirely consistent with structural data for the complex (16), see eq. [1]. The corresponding O 1*s* and S $2p_{1/2,3/2}$ data available for **1** and **2** (and **6**), on comparison with those for *cis*-$RuCl_2(dmso)_4$, reveal the presence of only sulfur-bonded dmso ligands in these complexes. Previous work using XPS to distinguish O- and S-bonded dmso ligands has generally been less definitive (26).

The BE for the S $2p_{1/2,3/2}$ level of the thioether sulfur atom of RSU-3159 (163.0 eV) is increased by 1.2 eV within **6**, strongly implying coordination via this sulfur; models suggest that chelation of RSU-3159 via the lone pair of N(1), the methylated nitrogen is plausible. However, the N 1*s* BE data for **6** (and for **4**) are insufficiently resolved to give information about binding to a nitrogen; ^{1}H nmr data (see below) provide some support for the chelation.

Nuclear magnetic resonance and infrared data

^{1}H nmr and ir spectroscopy have been widely used to distinguish between O- and S-bonded sulfoxide ligands, especially in Ru(II) complexes (17, 26–29). The Me protons of free dmso occur at δ 2.60, while those for O- and S-bonded dmso are found at δ ~2.7 and ~3.2–3.5, respectively; ν_{SO} for free dmso is seen at 1050 cm^{-1}, while coordination via O decreases this by about 100 cm^{-1} and coordination via S increases the value by about 40–100 cm^{-1}.

The ir data for all the complexes **1–6** (see Experimental) reveal ν_{SO} bands in both the 1085–1091 and 1112–1167 cm^{-1} regions, consistent with S-bonded dmso ligands. All the free nitroimidazole ligands reveal ir bands at about 1560–1565 and at 1545–1550 cm^{-1}, attributable to asymmetric and symmetric ν_{NO_2}, respectively (30). Values within complex **2**, 1543 and 1523 cm^{-1}, are both some 20 cm^{-1} lower than the free ligand values, presumably reflecting the coordinated nitrito group. Changes in ν_{NO_2} on coordination of the other nitroimidazoles are smaller. A 2815 cm^{-1} band of free NMe-4-NO_2Im (attributed to $\nu_{NCH_2—H}$) is found at 2800 cm^{-1} within **2**, while corresponding bands at 2724, 2730, and 2724 cm^{-1} for complexes **4–6**, respectively, are ~10 cm^{-1} lower than that found in the free ligands; the data provide no support for chelation of RSU-3159 via N(1) within **6**. Bands due to $\nu_{Ru—Cl}$ are not assigned because of uncertainty in the multi-band far-ir region. Even for *cis*-$RuCl_2(dmso)_4$, only one band at 344 cm^{-1} has been definitely assigned (31), and there are certainly bands in this region for complexes **1–6**.

Table 2 lists the relevant ^{1}H nmr data. Data for *cis*-$RuCl_2(dmso)_4$, discussed previously (17, 29, 31), are complex because of formation of isomers from dissolution of the complex that initially has three S- and one O-bonded dmso ligands (eq. [1]), but resonances at δ 2.60 and 2.73 are due to free and O-dmso, while the group of peaks at δ 3.3–3.5 results from S-dmso. Corresponding data for **1–6** show only S-bonded dmso: there is no dissociation of dmso in $CDCl_3$ solution, and even in D_2O **1** generates no free dmso. Oxygen-bonded dmso is known to be labile, relative to S-bonded dmso (26), and this has been demonstrated for *cis*-$RuCl_2(dmso)_4$ (17, 29, 31); thus, as seen in eq. [1], substitution of O-bonded dmso and a S-bonded dmso *cis* to it (necessarily so for the chelating ligand NMe-4-NO_2Im) would lead to the *cis,cis,cis*-geometry of the product. The presence of four major, equal intensity resonances, these occurring as partly resolved multiplets centred at the shifts listed in Table 2, for complexes **1**, and **3–5**, reveals inequivalent Me groups for each of the two inequivalent dmso ligands, and only the low symmetry all *cis*-structure of 6-coordinate complexes can give rise to such an nmr pattern (29). A model of **1** shows that free rotation about the Ru—S bonds for *cis*-dmso ligands is restricted because of steric interaction between methyl groups, but this is not a requirement for the magnetic inequivalence of the methyls (29). Proton decoupling experiments did simplify the observed multiplet patterns of the methyls, but this provided no further information on the structures. For the chelated complex **2**, the two Me resonances (again of equal intensity) are consistent with *trans* dmso ligands (and thus *cis*-chlorides) (29). The presence of four Me resonances within **6** is again consistent with a chelated 6-coordinate complex with *cis* arrangements for both chloride and dmso ligands.

On comparison with the free imidazole ligands, the H(2) and H(5) resonances in the complexes are generally shifted slightly to lower field, although the effects are more marked for **2**, presumably resulting from the chelation. Similar small shifts have been observed with other imidazole and *N*-methylimidazole complexes of, for example, Ru(II) (22) and Pt(II) (33). The somewhat larger downfield shift (0.13 ppm) for the NMe protons of RSU-3159 on coordination, and a surprising upfield shift of 0.28 ppm for H-2, provide evidence for interaction of the Ru(II) with the nitroimidazole ring, presumably via the nitrogen of the NMe. Thus, together with the ESCA data, the nmr data suggest formation of a five-membered chelate ring through the sulfur and nitrogen.

The $^{13}C\{^1H\}$ nmr spectrum of **1** shows four peaks for the inequivalent methyls (δ 35.40, 36.63, 44.77, 45.13) and imidazole carbons at 112.69 (C-2), 116.48 (C-5), and 120.49 (C-4). For **2**, consistent with the ^{1}H nmr, two ^{13}C shifts were seen at δ 38.13 and 45.02 for the methyls of the two equivalent dmso ligands; other assigned peaks were 112.41 (C-2), 116.18 (C-5), 119.94 (C-4), and 122.24 (N-Me).

Considerable efforts to grow suitable crystals of any of the complexes have thus far proved fruitless.

Aqueous solution chemistry

On dissolution in water under N_2, complex **1**, $RuCl_2(dmso)_2(4\text{-}NO_2Im)_2$, instantly gives a molar conductivity (100.8 ohm^{-1} mol^{-1} cm^2) corresponding to a 1:1 electrolyte (34), that results from loss of a single chloride ligand; no further chloride loss occurs over 2*d*. Further, the resulting solution

TABLE 2. Selected ^{1}H nmr chemical shifts for the Ru(II) compounds and free ligands[a]

Compound[b]	H-2[c]	H-5[c]	NMe[c]	Me(dmso)	
cis-$RuCl_2(dmso)_4$	—	—	—	2.60	2.73[d]
				3.32	3.43
				3.48	3.50
1, *Ru*(4-NO_2Im)$_2$	8.35(8.25[e])	7.87(7.80[e])		3.37	3.38
				3.40	3.47
2, *Ru*(NMe-4-NO_2Im)	7.96(7.54[f])	8.78(7.87[f])	3.93(3.90[f])	3.48	3.52
3, *Ru*(RSU-1170)$_2$	—	7.91(7.90)		3.20	3.25
				3.33	3.35
4, *Ru*(RSU-3083)$_2$	—	—	3.60(3.60)	3.37	3.42
				3.46	3.52
5, *Ru*(RSU-3100)$_2$	7.18(7.16)	—	3.62(3.60)	3.20	3.30
				3.39	3.50
6, *Ru*(RSU-3159)	7.64(7.92)	[g]	3.62(3.49)	3.18	3.20
				3.25	3.28

[a] δ in ppm wrt TMS, in $CDCl_3$ at room temperature. In each case the integrations are consistent with the assignment.
[b] As for Table 1.
[c] Shift values given in parentheses are for the free nitroimidazole ligand.
[d] Values are in good agreement with literature data (17, 29).
[e] 4-NO_2Im was dissolved in $CDCl_3$ with 5% CF_3CO_2H; the NH protons are not seen because of proton exchange. Values agree well with literature data (32).
[f] Values agree well with literature data (32).
[g] Shift values for 4′ and 5′ protons are 7.05(7.02).

is weakly acidic, implying loss of a proton from coordinated water. Standard pH-titration experiments (19) yield data that analyze well for a pK_a value of 4.10 ± 0.10:

$$[2]\quad \mathbf{1} \xrightarrow[+H_2O]{-Cl^-} \underset{\mathbf{1}b}{[RuCl(H_2O)(dmso)_2(4\text{-}NO_2Im)_2]^+} \rightleftharpoons \underset{\mathbf{1}c}{RuCl(OH)(dmso)_2(4\text{-}NO_2Im)_2} + H^+$$

The pK_a value seems resonable for H_2O coordinated at a Ru(II) centre (35). A second proton loss measured at higher pH (pK_a = 8.90 ± 0.10) is attributed to loss of the pyrrolic-N hydrogen to form coordinated 4-nitroimidazolate; a corresponding value for imidazole itself within $Ru(NH_3)_5(imidazole)^{2+}$ is also 8.90 (22). A uv/vis spectrum recorded for **1** at pH 7.0 (λ_{max} 338 nm, log ε = 4.63) thus refers to species **1***c*; minor differences are noted at pH 3.0 (species **1***b*, λ_{max} 343 nm) and at similar acidity in the presence of added Cl^- (0.1 *M*) (species **1**, λ_{max} 345 nm)). Titration with base of the other complexes **2–6** shows no titratable protons are present at least up to pH ~ 11 and consistent with this, molar conductivity values measured within 10 min of dissolution are much lower (15.5–37.4), showing little replacement of Cl^- ligand by H_2O. Ultraviolet/visible spectra for **2–6** (see Experimental) are dominated by charge transfer bands in the 300–450 nm region, and offer little insight into the coordination geometry.

Clearly, the aqueous solution chemistry of the complexes is germane for an understanding of their biological properties. Of the complexes **1–6** synthesized thus far, only **1** demonstrates high lability according to eq. [2].

Biological activities

The techniques used for determination of SER values in hypoxic CHO cells, toxicity, and DNA binding capabilities, as well as reduction potentials for the complexes and ligands, are not given in the Experimental section, because they have been described in detail previously for complex **1** elsewhere (9, 10). Identical procedures were used to test **2–6**.

Both **1** and **2** have increased SER values and reduced toxicity properties compared to the free nitroimidazole ligands for CHO cells *in vitro*, the SER value for **1**, 1.6 at 2×10^{-4} *M* (9), being higher than that for **2** (1.35) at corresponding conditions. SER values for **3–6**, and the corresponding free nitroimidazole ligands are lower, 1.20 ± 0.1 (10), implying marginal effect. Further, of all the complexes, only **1** binds to DNA, as tested for by a DNA-binding enzyme inhibition assay (9, 10).

Binding of a nitroimidazole ligand to a metal centre results in an increase in reduction potential *of the ligand*, i.e., increases electron affinity, a property often correlated with effectiveness of radiosensitizer ability (2, 9, 10, 36). For **1**, this increase in potential (in H_2O vs. SCE) is ~70 mV (from −685 to −615 mV (9)), but for the other complexes the increase is ≤20 mV (10) and the corresponding potentials are significantly higher (−560 to −370 mV). Clearly then, all the properties of complex **1** (including lability) are "different" to those of **2–6**.

The better radiosensitizing ability of **1** may depend on some or all of the following factors: (*a*) increased reduction potential of the coordinated 4-NO_2Im ligand, (*b*) hydrolysis to a species capable of binding to DNA, as demonstrated for other Ru(II) species (37), and (*c*) the presence of the pyrrolic proton of imidazole, N—H(1), which could be involved in H-bonding that stabilizes a DNA–Ru interaction — as demonstrated for Pt(II) systems (33, 38, 39). As regards (*a*), a higher reduction potential will certainly favour thermodynamically abstraction of an electron from irradiation-damaged DNA; electron-donor substituents on the nitroimidazole (e.g. the N—CH_3, and the amino and thioether substituents of **4** and **6**, respectively) lower the reduction potentials. The effect of having the —NO_2 substituent coordinated, as in **2**, is less clear.

Acknowledgements

The work was financially supported by the Natural Sciences and Engineering Research Council of Canada (operating grants to D.C.F. and B.R.J.), the Medical Research Council of Canada (operating grant to K.A.S., and UBC Fellowship to

Can. J. Chem. Downloaded from www.nrcresearchpress.com by 213.222.148.141 on 09/07/12
For personal use only.

P.K.L.C.), and the British Columbia Cancer Foundation (grant to K.A.S.). Johnson Matthey, Ltd. kindly loaned the Ru.

1. R. H. THOMLINSON and L. H. GRAY. Br. J. Cancer, **9**, 539 (1955); B. C. MILLAR, E. M. FIELDEN, and J. L. MILLAR. Int. J. Radiat. Biol. **33**, 599 (1978).
2. J. L. FOSTER and R. L. WILLSON. Br. J. Radiol. **46**, 234 (1973).
3. G. E. ADAMS, E. D. CLARKE, I. R. FLOCKHART, R. S. JACOB, D. S. SEHMI, I. J. STRATFORD, P. WARDMAN, M. E. WATTS, J. PARRICK, R. G. WALLACE, and C. E. SMITHEN. Int. J. Radiat. Biol. **35**, 133 (1979).
4. G. E. ADAMS and D. L. DEWEY. Biochem. Biophys. Res. Commun. **12**, 473 (1963).
5. C. CLARKE, K. B. DAWSON, P. W. SHELDON, and I. AHMED. Int. J. Radiat. Oncol. Biol. Phys. **8**, 787 (1982).
6. N. P. FARRELL and K. A. SKOV. Radiat. Res. **91**, 378 (1982).
7. M. J. CLARKE. *In* Chemistry and biochemistry of platinum, gold and other chemotherapeutic agents. *Edited by* S. J. Lippard. Am. Chem. Soc. Symposium Series, No. 209, Am. Chem. Soc., Washington. 1983. p. 335.
8. N. P. FARRELL. *In* Chemistry and biochemistry of platinum, gold and other chemotherapeutic agents. *Edited by* S. J. Lippard. Am. Chem. Soc. Symposium Series, No. 209, Am. Chem. Soc., Washington. 1983. p. 279.
9. P. K. L. CHAN, K. A. SKOV, B. R. JAMES, and N. P. FARRELL. Int. J. Radiat. Oncol. Biol. Phys. **12**, 1059 (1986).
10. P. K. L. CHAN, K. A. SKOV, and B. R. JAMES. Int. J. Radiat. Biol. **52**, 49 (1987).
11. P. K. L. CHAN, K. A. SKOV, B. R. JAMES, and N. P. FARRELL. Chem. Biol. Interact. **59**, 247 (1986).
12. K. SIEGBAHN, C. NORDING, A. FAHLMAN, R. NORDBERG, K. HAMRIN, J. HEDMAN, G. JOHANSSON, S. E. KARLSSON, I. LINDGREN, and B. J. LINDBERG. Nova Acta Regial Soc. Sci. Upsal. 20 (1967).
13. W. L. JOLLY. Coord. Chem. Rev. **13**, 47 (1974).
14. L. A. CASPER and C. J. POWELL (*Editors*). Industrial applications of surface analysis. Am. Chem. Soc. Symposium Series, No. 199, Am. Chem. Soc. Washington. 1982.
15. P. K. H. CHAN, D. C. FROST, and K. VENKATESWARAN. Spectrosc. Lett. **19**, 1071 (1986), and references therein.
16. A. MERCER and J. TROTTER. J. Chem. Soc., Dalton Trans. 2480 (1975).
17. I. P. EVANS, A. SPENCER, and G. WILKINSON. J. Chem. Soc. Dalton Trans. 204 (1973).
18. R. G. FARGHER and F. L. PYMAN. J. Chem. Soc. Trans. **115**, 217 (1919).
19. B. R. JAMES and R. J. P. WILLIAMS. J. Chem. Soc. 2007 (1961).
20. T. G. FAWCETT, E. E. BERNARDUCCI, K. KROGH-JESPERSEN, and H. J. SCHUGAR. J. Am. Chem. Soc. **102**, 2599 (1980).
21. C. R. JOHNSON, R. E. SHEPHERD, B. MARR, S. O'DONNELL, and W. DRESSICK. J. Am. Chem. Soc. **102**, 6227 (1980).
22. R. J. SUNDBERG, R. F. BRYAN, I. F. TAYLOR JR., and H. TAUBE. J. Am. Chem. Soc. **96**, 381 (1974).
23. T. A. CARLSON. Photoelectron and Auger spectroscopy. Plenum Press, New York. 1975. p. 349.
24. R. G. LITTLE. Acta Crystallogr. Sect. B, **35**, 2398 (1979).
25. R. S. BERMAN and J. K. KOCHI. Inorg. Chem. **19**, 248 (1980).
26. J. A. DAVIES. Adv. Inorg. Chem. Radiochem. **24**, 115 (1981).
27. R. S. MCMILLAN, A. MERCER, B. R. JAMES, and J. TROTTER. J. Chem. Soc. Dalton Trans. 1006 (1975).
28. A. R. DAVIES, F. W. B. EINSTEIN, N. P. FARRELL, B. R. JAMES, and R. S. MCMILLAN. Inorg. Chem. **17**, 1965 (1978).
29. J. R. BARNES and R. J. GOODFELLOW. J. Chem. Res. Synop. 350 (1979); J. R. BARNES, P. L. GOGGIN, and R. J. GOODFELLOW. J. Chem. Res. Synop. 118 (1979).
30. K. NAKAMOTO. Infrared spectra of inorganic and coordination compounds. John Wiley and Sons, Inc., New York. 1970. p. 160.
31. B. R. JAMES, E. OCHIAI, and G. L. REMPEL. Inorg. Nucl. Chem. Lett. **7**, 781 (1971); R. S. MCMILLAN. Ph.D. Dissertation, University of British Columbia. 1976.
32. G. B. BARLIN and T. J. BATTERHAM. J. Chem. Soc. (B), 516 (1967).
33. C. G. VAN KRALINGEN, J. K. DE RIDDER, and J. REEDIJK. Inorg. Chim. Acta, **36**, 69 (1979).
34. W. J. GEARY. Coord. Chem. Rev. **7**, 81 (1971).
35. Z. HARZION and G. NAVON. Inorg. Chem. **19**, 2236 (1980), and references therein.
36. G. E. ADAMS, I. R. FLOCKHART, C. E. SMITHEN, I. J. STRATFORD, P. WARDMAN, and M. E. WATTS. Radiat. Res. **67**, 9 (1976).
37. M. J. CLARKE, B. JANSEN, K. A. MARX, and R. KRUGER. Inorg. Chim. Acta, **124**, 13 (1986).
38. S. E. SHERMAN, D. GIBSON, A. H. J. WANG, and S. J. LIPPARD. Science, **230**, 412 (1985).
39. K. A. SKOV and N. P. FARRELL. Int. J. Radiat. Biol. **52**, 289 (1987)

Can. J. Chem. Downloaded from www.nrcresearchpress.com by 213.222.148.141 on 09/07/12
For personal use only.

Physical and structural studies of *N*-substituted-3-hydroxy-2-methyl-4(1*H*)-pyridinones

WILLIAM O. NELSON, TIMOTHY B. KARPISHIN, STEVEN J. RETTIG, AND CHRIS ORVIG[1]

Department of Chemistry, University of British Columbia, 2036 Main Mall, Vancouver, B.C., Canada V6T 1Y6

Received May 15, 1987

WILLIAM O. NELSON, TIMOTHY B. KARPISHIN, STEVEN J. RETTIG, and CHRIS ORVIG. Can. J. Chem. **66**, 123 (1988).

A series of 3-hydroxy-2-methyl-4(1*H*)-pyridinones has been prepared with the substituents H, CH_3, n-C_6H_{11}, and $CH_2CH_2NH_2$ at the ring N. The dipyridinone 1,6-bis(3-hydroxy-2-methyl-4(1*H*)-pyridinon-1-yl)hexane has also been synthesized. The products with H and CH_3 substituents have been studied by single crystal X-ray diffraction. Crystals of 3-hydroxy-2-methyl-4-pyridinone are monoclinic, a = 6.8351(4), b = 10.2249(4), c = 8.6525(4) Å, β = 105.215(4)°, Z = 4, space group $P2_1/n$ and those of 3-hydroxy-1,2-dimethyl-4-pyridinone are orthorhombic, a = 7.3036(4), b = 13.0490(6), c = 13.7681(7) Å, Z = 8, space group *Pbca*. Both structures were solved by direct methods and were refined by full-matrix least-squares procedures to R = 0.037 and 0.044 for 914 and 857 reflections with $I \geq 3\sigma(I)$, respectively. Bond lengths and angles in the two compounds were normal. All the compounds have been studied by mass spectrometry, and by infrared and proton nmr spectroscopies. The importance of hydrogen bonding to both the solution and solid state properties of these compounds has been confirmed by these techniques.

WILLIAM O. NELSON, TIMOTHY B. KARPISHIN, STEVEN J. RETTIG et CHRIS ORVIG. Can. J. Chem. **66**, 123 (1988).

On a préparé une série d'hydroxy-3 méthyl-2 (1*H*)-pyridones-2 portant des substituants H, CH_3, n-C_6H_{11} et $CH_2CH_2NH_2$ sur l'azote du cycle. On a aussi synthétisé la dipyridone bis(hydroxy-3 méthyl-2 (1*H*)-pyridone-4 yl-1)-1,6 hexane. On a fait une étude par diffraction des rayons-X des produits portant des substituants soit H soit CH_3. Les cristaux de l'hydroxy-3 méthyl-2 pyridone-4 sont monocliniques avec a = 6,8351(4), b = 10,2249(4) et c = 8,6525(4) Å, β = 105,215(4)°, Z = 4, et groupe d'espace $P2_1/n$; par ailleurs, ceux de l'hydroxy-3 diméthyl-1,2 pyridone-4 sont orthorhombiques avec a = 7,3036(4), b = 13,0490(6) et c = 13,7681(7) Å, Z = 8 et groupe d'espace *Pbca*. On a résolu les deux structures par des méthodes directes et on les a affinées par la méthode des moindres carrés (matrice entière) jusqu'à des valeurs respectives de R de 0,037 et 0,044 pour 914 et 857 réflexions avec $I \geq 3\sigma(I)$. Les angles et les longueurs des liaisons sont normaux dans chacun des composés. On a étudié tous les composés par spectrométrie de masse ainsi que par infrarouge et par rmn. A l'aide de ces techniques, on a pu confirmer l'importance des liaisons hydrogènes pour les propriétés de ces composés tant en solution qu'à l'état solide.

[Traduit par la revue]

Introduction

There is considerable literature on 4-pyridinones (1) but a limited amount of information is available on the 3-hydroxy-4-pyridinones. Much of the preparative work on the latter is scattered and inaccessible, having been reported in the form of patents, and we discovered when we became interested in them, that a considerable effort was required before we had the requisite compounds for further study.

As part of a project to examine neutral water soluble complexes of aluminum, gallium, and other metals, we have prepared and characterized a series of *N*-substituted-3-hydroxy-2-methyl-4-pyridinones (**1**) to be used as ligands for these metals in aqueous solution. Recently, there has been significant interest in these compounds, and the related pyrones (e.g. maltol **2**), as binding groups for various metal ions. This

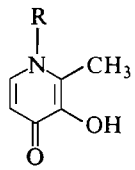

1

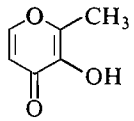

2

includes our work with Al and Ga (2–4), that of Kontoghiorghes and co-workers (5) with Fe and Pu, and that of Raymond and co-workers who have been extensively involved in the area studying the related 1-hydroxy-2-pyridinones (6–8) and 3-hydroxy-2-pyridinones (8) as sequestering agents for various metal ions including the actinides and iron. There has also been considerable attention focussed on mimosine (a 3-hydroxy-4-pyridinone amino acid derivative with depilatory properties) and its isomers as chelating agents for various divalent (9, 10) and trivalent metals (11).

The reaction of primary amines with 4-pyrones to form *N*-substituted-4-pyridinones has been known for more than eighty years (12). It has been utilized for the preparation of a variety of these pyridinones (1, 12–17), despite the fact that this reaction is somewhat limited in scope, being reliable only for small alkyl (15), and aryl (16, 17) amines. Attempts at *N*-alkylation to synthesize one pyridinone from another sometimes yields a mixture of *N*- and *O*-alkylated products (18). We were particularly interested in a variety of these compounds where there were alkyl or alkylamino substituents in order to prepare Al and Ga complexes with some lipophilicity, but also some water solubility. As a result of the rather unusual hydrogen-bonding observed in some of the Al and Ga complexes (4), we became interested in the preparation, complete characterization, and solid state structures of the 3-hydroxy-4-pyridinones themselves. Herein we report our studies of some of these pyridinones using various physical techniques including single crystal X-ray crystallography.

Experimental

Materials and methods

Melting points were recorded with a Mel-Temp apparatus and are uncorrected. Infrared spectra were determined as KBr pellets in the range 4000–200 cm^{-1} with a Perkin Elmer PE 783 and were referenced to polystyrene film. The proton nmr spectra were recorded in the indicated solvent with one of a Bruker WP-80, Varian XL-300, or Bruker WH-400 instrument. Elemental analyses (C, H, Cl, N) were performed by Mr. Peter Borda of the Microanalytical Laboratory of this Department. Electron impact mass spectra were recorded with a Kratos MS 50 spectrometer.

All chemicals were reagent grade (or better) and were used as received. The starting material 3-benzyloxy-2-methyl-4-pyrone (Bzma)

[1]Author to whom correspondence should be addressed.

Can. J. Chem. Downloaded from www.nrcresearchpress.com by 213.222.148.141 on 09/07/12
For personal use only.

Can. J. Chem. Downloaded from www.nrcresearchpress.com by 213.222.148.141 on 09/07/12
For personal use only.

TABLE 1. Crystallographic data[a]

Compound	Hmpp	Hdpp
Formula	$C_6H_7NO_2$	$C_7H_9NO_2$
fw	125.1	139.2
Crystal system	Monoclinic	Orthorhombic
Space group	$P2_1/n$	*Pbca*
a (Å)	6.8351(4)	7.3036(4)
b (Å)	10.2249(4)	13.0490(6)
c (Å)	8.6525(4)	13.7681(7)
β (deg)	105.215(4)	
V (Å^3)	583.51(6)	1312.2(1)
Z	4	8
D_c (g/cm^3)	1.424	1.409
D_m (g/cm^3)[b]	1.41	1.39
$F(000)$	264	592
μ(Cu-K$_\alpha$) (cm^{-1})	8.65	8.21
Crystal dimensions (mm)	0.14 × 0.20 × 0.41	0.18 × 0.25 × 0.33
Transmission factors	0.708–0.886	0.789–0.864
Scan type	ω–2θ	ω–2θ
Scan range (deg in ω)	0.60 + 0.14 tan θ	0.90 + 0.14 tan θ
Scan speed (deg/min)	1.3–10.0	1.5–10.0
Data collected	$+h, +k, \pm l$	$+h, +k, \pm l$
$2\theta_{max}$ (deg)	150	150
Crystal decay	Negligible	Negligible
Unique reflections	1201	1343
Reflections with $I \geq 3\sigma(I)$	914	857
Number of variables	111	128
R	0.037	0.044
R_w	0.046	0.046
S	2.349	1.014
Mean Δ/σ (final cycle)	0.005	0.005
Max Δ/σ (final cycle)	0.05	0.05
Residual density (e/Å^3)	0.20	0.32

[a]Temperature 295 K, Enraf-Nonius CAD4-F diffractometer, Cu-K$_\alpha$ radiation ($\lambda_{K\alpha_1}$ = 1.540562, $\lambda_{K\alpha_2}$ = 1.544390 Å), nickel filter, takeoff angle 2.7°, aperture (2.0 + tan θ) × 4.00 mm at a distance of 173 mm from the crystal, scan range extended by 25% on both sides for background measurement, $\sigma^2(I) = C + 2B + [0.04(C - B)]^2$ (C = scan count, B = normalized background count), function minimized: $\Sigma w(|F_o| - |F_c|)^2$ where $w = 1/\sigma^2(F)$, $R = \Sigma||F_o| - |F_c||/\Sigma|F_o|$, $R_w = (\Sigma w(|F_o| - |F_c|)^2/\Sigma w|F_o|^2)^{1/2}$, $S = (\Sigma w(|F_o| - |F_c|)^2/(m - n))^{1/2}$. Values given for R, R_w, and S are based on those reflections with $I \geq 3\sigma(I)$.

[b]Measured by flotation in aqueous KI.

was made from commercially available (Aldrich) 3-hydroxy-2-methyl-4-pyrone (maltol – Hma) by the method of Harris (19). It is a viscous yellow liquid that is used without further purification (TLC pure). Yield >95%. Water was deionized (Barnstead D8902 and D8904 cartridges) and distilled (Corning MP-1 Megapure still). Thin layer chromatography (TLC) was performed on silica gel plates.

*3-Benzyloxy-2-methyl-4(1*H*)-pyridinone*, Bzmpp. This intermediate is made by the treatment of Bzma with a solution of ammonia in ethanol according to the method of Harris (19). Pale yellow crystals were obtained from ethanol in 60% yield. *Anal.* calcd. for $C_{13}H_{13}NO_2$: C 72.53, H 6.10, N 6.51; found: C 72.71, H 6.07, N 6.49. Melting point: 166–167°C.

*3-Hydroxy-2-methyl-4(1*H*)-pyridinone*, Hmpp. The final product is obtained by acid hydrolysis with HBr in acetic acid (19). The crude product was redissolved in water and brought to pH 7–8 by addition of aqueous ammonia. Chilling produced pale pink single crystals (suitable for X-ray diffraction) in 82% yield. Overall yield (from Hma) was 48%. *Anal.* calcd. for $C_6H_7NO_2$: C 57.57, H 5.65, N 11.24; found: C 57.58, H 5.70, N 11.23. Melting point 263°C dec.

*3-Hydroxy-1,2-dimethyl-4(1*H*)-pyridinone*, Hdpp. To a solution of Bzma (10.0 g, 46.0 mmol) in 50 mL ethanol was added 40% aqueous methylamine (100 mL, 130 mmol) and the mixture was stirred at 25°C for 72 h. The excess amine was removed under reduced pressure and the oily residue was taken up in 100 mL water. The organic phase was extracted into methylene chloride (2 × 100 mL). Removal of solvent in vacuum gave 8.64 g (82% yield) of a pure (TLC) oil (Bzdpp). The benzyl ether was dissolved in THF (50 mL) and subjected to hydrogenolysis under ambient conditions over 5% Pd/C catalyst (1 g) until hydrogen uptake ceased. The solution was filtered and the solid extracted with boiling water (3 × 100 mL). The aqueous solution was concentrated until crystallization commenced and then chilled (15°C) overnight. The product was recrystallized from hot methanol to yield 3.46 g, 65% based on Bzdpp. Single crystals suitable for X-ray diffraction were grown from methanol/ether by a liquid diffusion method (20). The overall yield based on Hma is 51%. *Anal.* calcd. for $C_7H_9NO_2$: C 60.41, H 6.53, N 10.07; found: C 60.45, H 6.49, N 10.00. Melting point 260°C dec.

*3-Hydroxy-2-methyl-1-(β-aminoethyl)-4(1*H*)-pyridinone*, Hmapp·2HCl. To a solution of Bzma (15.0 g, 69.4 mmol) in 100 mL ethanol was added ethylenediamine (21.5 g of a 98% aqueous solution, 351 mmol). After stirring at room temperature overnight, the solvent and excess ethylenediamine were removed under reduced pressure to give an amber coloured oil which was triturated with water to give a pale yellow solid and this was dried at room temperature. The solid was treated with charcoal in THF twice and triturated again to give a white solid. This solid was then treated with 100 mL 6 *M* HCl at room temperature overnight to remove the benzyl group. The acid was removed under reduced pressure and the resulting white solid was washed with methanol to give crude Hmapp·2HCl (3.00 g, 20% yield). Recrystallization was from 6 *M* HCl/ethanol. *Anal.* calcd. for

Can. J. Chem. Downloaded from www.nrcresearchpress.com by 213.222.148.141 on 09/07/12
For personal use only.

$C_8H_{14}Cl_2N_2O_2$: C 39.85, H 5.85, Cl 29.41, N 11.62; found: C 39.57, H 5.90, Cl 29.19, N 11.40. Melting point 250°C dec.

3-Hydroxy-2-methyl-1-hexyl-4(1H)-pyridinone, Hmhpp. Bzma (7.1 g, 32.8 mmol) and hexylamine (16.6 g, 164 mmol) were dissolved in 100 mL methanol and left stirring at 25°C for 72 h. The excess amine was removed under vacuum and 100 mL 12 *M* HCl added to the oily residue. After heating on a steambath for 1 h, the excess acid was removed under vacuum. To the residue was added 100 mL water and the pH adjusted to 8 with 2.0 *M* NaOH at which time a precipitate formed. Subsequent sublimation (*in vacuo* at 120°C) of this beige solid gave 3.40 g of a pale yellow powder in an overall yield (from Hma) of 48%. *Anal.* calcd. for $C_{12}H_{19}NO_2$: C 68.87, H 9.15, N 6.69; found: C 68.56, H 9.01, N 6.61. Melting point 123–125°C with slight discoloring.

1,6-Bis(3-hydroxy-2-methyl-4(1H)-pyridinon-1-yl)hexane, H_2exn. Bzma (3.0 g, 14.0 mmol) and 1,6-diaminohexane (8.0 g, 69.0 mmol) were stirred in 25 mL methanol for 2 days at room temperature and the solvents were removed at reduced pressure. The oily residue was treated with 50 mL concentrated HCl and heated for 30 min on a steambath. The acid was then removed by rotary evaporation, the residue dissolved in 50 mL water, and the pH was adjusted to 7–8 with 2 *N* KOH. Crude H_2exn precipitates and the filtrate may be extracted with $CHCl_3$ to increase the yield. The yield is 0.43 g (18% based on Hma). Sublimation (280–300°C at 3×10^{-2} Torr) gave an analytically pure sample. *Anal.* calcd. for $C_{18}H_{24}N_2O_4$: C 65.03, H 7.29, N 8.43; found: C 64.81, H 7.19, N 8.40. Melting point 270°C dec.

X-ray crystallographic analyses

Crystallographic data appear in Table 1. Unit-cell parameters were refined by least-squares on 2 sin θ/λ values for 25 reflections with $2\theta = 70–100°$ for Hmpp and $2\theta = 50–91°$ for Hdpp. The intensities of three standard reflections, measured each hour of X-ray exposure time, showed only small random fluctuations. The data were reduced[2] and corrected for absorption (numerical integration). Both structures were solved by direct methods, the positions of the non-hydrogen atoms being determined from *E*-maps and those of the hydrogen atoms from subsequent difference maps. The non-hydrogen atoms were refined with anisotropic thermal parameters and the hydrogen atoms with isotropic thermal parameters. Neutral atom scattering factors and anomalous dispersion corrections (O, N, and C) were taken from ref. 21. Isotropic type I extinction corrections were applied (22–24), the final values of g being $0.31(8) \times 10^4$ for Hmpp and $0.28(3) \times 10^4$ for Hdpp. Final positional and anisotropic thermal parameters appear in Tables 2 and 8,[2] respectively. Measured and calculated structure factors have been placed in the Depository of Unpublished Data.[3]

The thermal motion in both molecules has been analyzed in terms of rigid-body modes of translation, libration, and screw-motion (25). The rms errors in the temperature factors σU_{ij} (derived from the least-squares analyses) are 0.0008 and 0.0016 Å^2 for Hmpp and Hdpp respectively. Analysis of all non-hydrogen atoms gave physically reasonable results and rms ΔU_{ij} values of 0.0010 Å^2 for Hmpp and 0.0019 Å^2 for Hdpp. The appropriate bond distances have been corrected for libration (25, 26), using shape parameters q^2 of 0.08 for all atoms involved. Corrected bond lengths appear in Table 3 along with the uncorrected values; corrected bond angles do not differ by more than 1σ from the uncorrected values given in Table 4. Bond

[2]The computer programs used include locally written programs for data processing and locally modified versions of the following: AGNOST, absorption corrections, by J. A. Ibers; ORFLS, full-matrix least-squares, and ORFFE, function and errors, by W. R. Busing, K. O. Martin, and H. A. Levy; FORDAP, Patterson and Fourier syntheses, by A. Zalkin; and ORTEP II, illustrations, by C. K. Johnson.

[3]The structure factor table, Table 8 (anisotropic thermal parameters) and other material mentioned in the text may be purchased from the Depository of Unpublished Data, CISTI, National Research Council of Canada, Ottawa, Ont., Canada K1A 0S2.

TABLE 2. Final positional (fractional $\times 10^4$, H $\times 10^3$) and isotropic thermal parameters ($U \times 10^3$ Å^2) with estimated standard deviations in parentheses

Atom	x	y	z	U_{eq}/U_{iso}
		Hmpp		
O(1)	3723(2)	5273(1)	1896(2)	45
O(2)	6775(2)	3876(1)	1100(2)	42
N	4178(2)	2509(2)	4498(2)	38
C(1)	1726(3)	4302(3)	4114(3)	49
C(2)	3487(2)	3640(2)	3729(2)	34
C(3)	4409(3)	4120(2)	2618(2)	34
C(4)	6022(2)	3433(2)	2203(2)	33
C(5)	6679(3)	2281(2)	3085(2)	40
C(6)	5729(3)	1841(2)	4189(2)	41
H(O1)	405(4)	537(3)	97(3)	88(9)
H(N)	344(3)	216(2)	514(2)	48(6)
H(1a)	118(4)	376(3)	479(4)	99(10)
H(1b)	62(5)	444(3)	316(4)	96(10)
H(1c)	217(5)	514(4)	466(4)	119(12)
H(5)	784(3)	176(2)	291(2)	47(6)
H(6)	611(3)	100(2)	475(2)	48(6)
		Hdpp		
O(1)	4783(4)	−564(2)	3507(2)	45
O(2)	3734(3)	971(2)	4746(1)	49
N	3596(4)	1432(2)	1821(2)	36
C(1)	4659(6)	−323(3)	1475(3)	42
C(2)	4157(4)	502(2)	2174(2)	33
C(3)	4234(4)	364(2)	3163(2)	33
C(4)	3708(4)	1144(2)	3837(2)	35
C(5)	3144(5)	2074(3)	3415(2)	39
C(6)	3112(5)	2197(3)	2431(2)	41
C(7)	3536(7)	1628(3)	762(2)	51
H(O1)	503(6)	−53(3)	408(3)	108(19)
H(1a)	360(5)	−45(3)	108(3)	66(12)
H(1b)	572(5)	−14(3)	107(3)	71(12)
H(1c)	498(5)	−91(3)	177(3)	59(12)
H(5)	276(4)	267(2)	380(2)	38(9)
H(6)	272(4)	286(2)	213(2)	33(8)
H(7a)	475(5)	144(3)	50(2)	65(13)
H(7b)	264(5)	117(3)	48(2)	63(12)
H(7c)	318(5)	236(3)	67(3)	73(13)

TABLE 3. Bond lengths (Å) with estimated standard deviations in parentheses

	Length			Length	
Bond	Uncorr.	Corr.	Bond	Uncorr.	Corr.
		Hmpp			
O(1)—C(3)	1.358(2)	1.363	C(2)—C(3)	1.371(2)	1.375
O(2)—C(4)	1.280(2)	1.284	C(3)—C(4)	1.431(2)	1.436
N—C(2)	1.356(2)	1.362	C(4)—C(5)	1.411(2)	1.417
N—C(6)	1.345(2)	1.350	C(5)—C(6)	1.365(2)	1.369
C(1)—C(2)	1.493(2)	1.497			
		Hdpp			
O(1)—C(3)	1.360(3)	1.364	C(1)—C(2)	1.489(4)	1.493
O(2)—C(4)	1.272(3)	1.276	C(2)—C(3)	1.376(4)	1.381
N—C(2)	1.369(4)	1.376	C(3)—C(4)	1.430(4)	1.435
N—C(6)	1.352(4)	1.356	C(4)—C(5)	1.407(4)	1.414
N—C(7)	1.482(4)	1.486	C(5)—C(6)	1.364(4)	1.368

TABLE 4. Bond angles (deg) with estimated standard deviations in parentheses

Bonds	Angle (deg)	Bonds	Angle (deg)
		Hmpp	
C(2)—N—C(6)	121.8(2)	C(2)—C(3)—C(4)	121.8(2)
N—C(2)—C(1)	118.3(2)	O(2)—C(4)—C(3)	120.0(2)
N—C(2)—C(3)	119.0(2)	O(2)—C(4)—C(5)	124.4(2)
C(1)—C(2)—C(3)	122.7(2)	C(3)—C(4)—C(5)	115.5(2)
O(1)—C(3)—C(2)	117.8(2)	C(4)—C(5)—C(6)	120.7(2)
O(1)—C(3)—C(4)	120.4(2)	N—C(6)—C(5)	121.1(2)
		Hdpp	
C(2)—N—C(6)	120.8(2)	O(1)—C(3)—C(4)	119.2(2)
C(2)—N—C(7)	120.7(3)	C(2)—C(3)—C(4)	122.5(3)
C(6)—N—C(7)	118.4(3)	O(2)—C(4)—C(3)	120.5(3)
N—C(2)—C(1)	119.0(3)	O(2)—C(4)—C(5)	124.3(3)
N—C(2)—C(3)	118.6(3)	C(3)—C(4)—C(5)	115.2(3)
C(1)—C(2)—C(3)	122.3(3)	C(4)—C(5)—C(6)	121.1(3)
O(1)—C(3)—C(2)	118.2(3)	N—C(6)—C(5)	121.7(3)

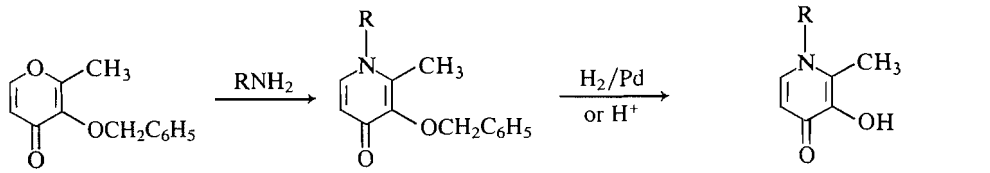

Bzma

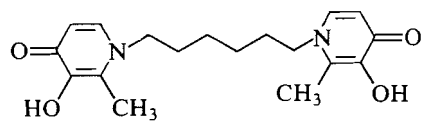

H_2exn

SCHEME 1

lengths and angles involving hydrogen and a complete listing of torsion angles (Tables 9–11) are included as supplementary material.

Results and discussion

It is possible to prepare, in varying yields from benzylated maltol (Bzma), a series of 3-hydroxy-2-methyl-4(1*H*)-pyridinones with a number of different substituents on the ring nitrogen atom. The preparations of Bzma, and its ammoniated deprotected product Hmpp, are analogous to those published by Harris (19). The preparation of Hmpp from Bzma is simpler than that of Hodge and Nelson (27) which involves methyl-protection of the hydroxyl functionality. The synthesis of Hdpp has been reported by the reaction of methylammonium acetate with any of lactose, maltose, maltol, or isomaltol (28). The preparation of Hmapp·2HCl was analogous to that of mimosinamine dihydrochloride (19). The *N*-hexyl species Hmhpp has been reported previously from maltol protected with D-glucose (29). To our knowledge the doubly inserted amine product H_2exn has never been reported. Our interest in a compound of this type arose from a desire to prepare potentially four coordinating ligands based on the 3-hydroxy-4-pyridinone binding group.

The structures of Hmpp and Hdpp were established by single crystal X-ray diffraction. Stereoviews of the two molecules are shown in Fig. 1. Both structures contain centrosymmetric O—H···O=C hydrogen-bonded dimeric units (O(1)—H(O1)···O(2) ($1-x, 1-y, -z$ for Hmpp; $1-x, -y, 1-z$ for Hdpp), H···O = 1.90(3), 1.94(5) Å, O···O = 2.670(2), 2.692(3) Å, O—H···O = 144(3), 154(4)°). Stereodiagrams of the unit cell packing are shown for Hmpp in Fig. 2 and for Hdpp in Fig. 3. In the *N*-substituted compound Hdpp, interleaving dimeric units form stacks of pyridinone rings with interplanar spacings[4] of 3.435 and 3.462 Å along the *a* axis (see Fig. 3). All distances between the H-bonded dimers in Hdpp correspond to normal van der Waals contacts. In Hmpp each dimer is linked to four others by N—H···O=C hydrogen bonds (N—H(N)···O(2) ($x-\frac{1}{2}, \frac{1}{2}-y, \frac{1}{2}+z$), H···O = 1.90(2) Å, N···O = 2.796(2) Å, N—H···O = 166(2)°) to form a three-dimensional network (Fig. 2).

The six-membered rings in both Hmpp and Hdpp are significantly non-planar, maximum deviations from the mean

[4]Calculated as the displacement of the centroid of the neighboring ring from the mean plane of the reference ring.

Can. J. Chem. Downloaded from www.nrcresearchpress.com by 213.222.148.141 on 09/07/12
For personal use only.

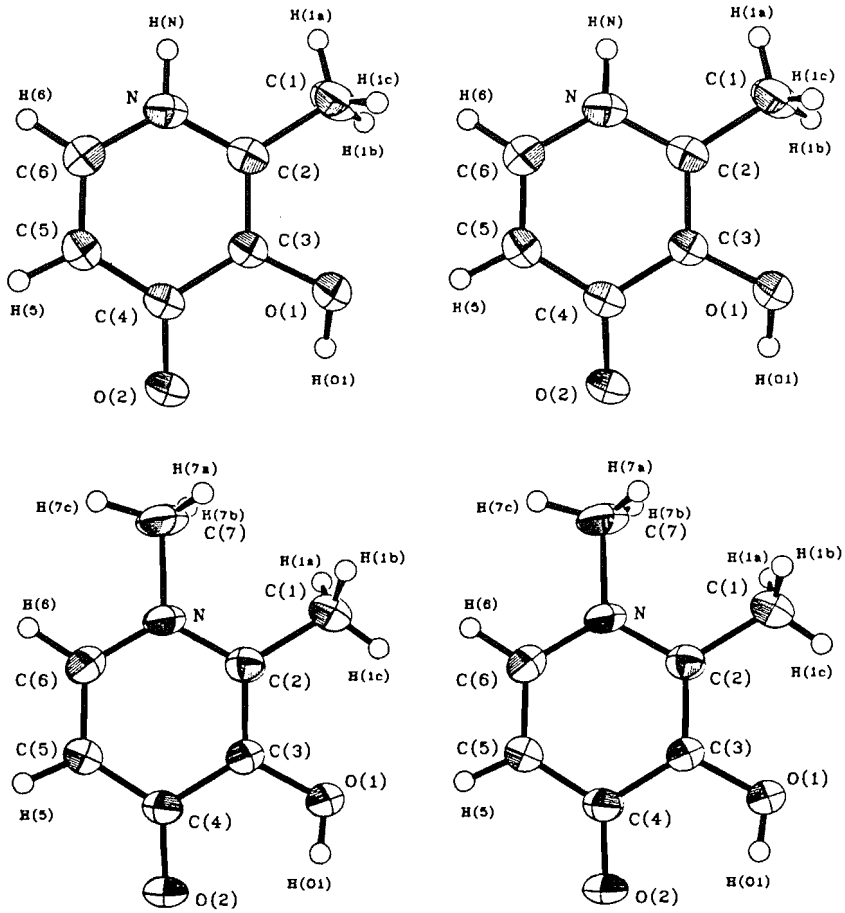

FIG. 1. Stereoscopic views of the Hmpp (top) and Hdpp (bottom) molecules; 50% probability thermal ellipsoids are shown. Hydrogen atoms have been assigned artificially small thermal parameters for the sake of clarity.

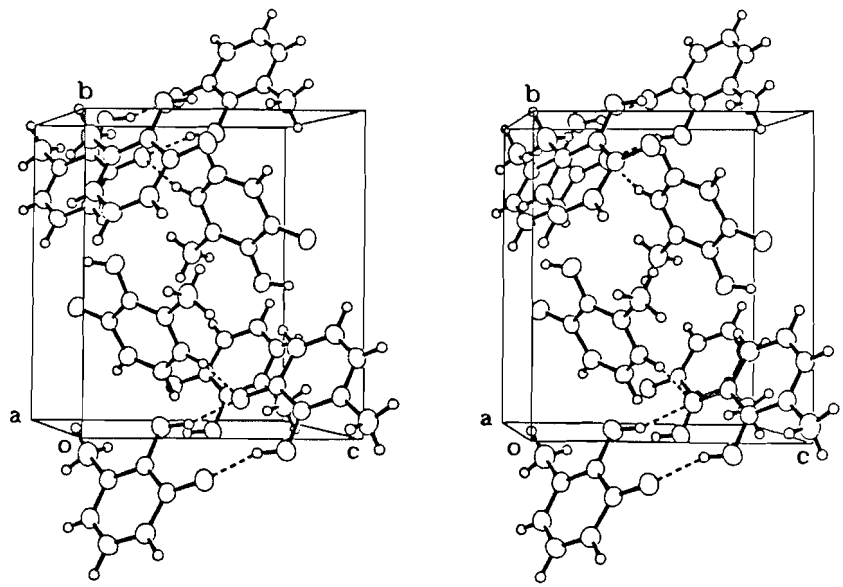

FIG. 2. Stereoscopic view of the packing arrangement in Hmpp.

planes being 0.019(2) Å in the former and 0.009(3) Å in the latter. The distortions from planarity are toward a C(4)-envelope in Hmpp and a C(2), C(5)-boat in Hdpp. Bond lengths and angles in the two compounds are very similar, *N*-methylation resulting in a significantly longer N—C(2) bond and a significantly smaller intra-annular bond angle at nitrogen. The only other significant difference between the two molecules is the O(1)—C(3)—C(4) angle, 1.23(25)° larger in Hmpp than in Hdpp. The nitrogen coordination is planar to within experimental error in both compounds and bond lengths indicate partial delocalization of the formal double bonds. The extent of the delocalization is greater than that observed in the

Can. J. Chem. Downloaded from www.nrcresearchpress.com by 213.222.148.141 on 09/07/12
For personal use only.

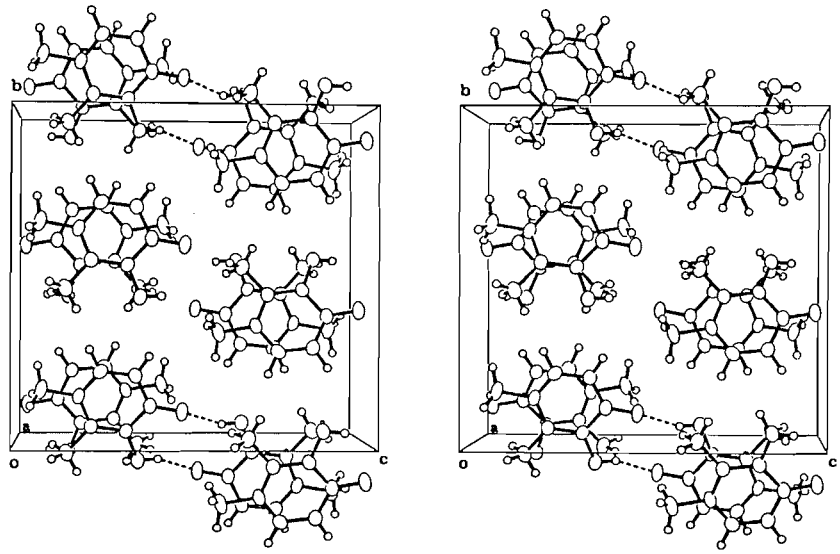

FIG. 3. Stereoscopic view of the packing arrangement in Hdpp.

isoelectronic molecule 4-pyrone (30). The structures of the diphenylboron chelates of the anions derived from Hmpp (mpp^-) and Hdpp (dpp^-) have been compared with that of Hmpp (31). Of note is the fact that in dpp^- complexed to $(Ph)_2B$ a marked bond length alternation is observed, unlike in the free ligands Hmpp and Hdpp or mpp-coordinated in $(Ph)_2B$mpp, all of which only show a slight alternation.

The mass spectra for all the compounds are reproduced in Fig. 4.[3] Some assignments have been made by comparison with the literature on 2-pyridinones because of the scant work available on the 4-pyridinones and their 3-hydroxy congeners (32). The spectrum of Hmpp shows the molecular radical cation $M^{+\cdot}$ as the base peak (m/z 125 (relative intensity = 100)) and peaks due to loss of CO (m/z 97(9)) and loss of HCO$^\cdot$ (m/z 96(47)). The stability of the m/z 125 radical cation is shown by the fact that it occurs in all five spectra and is the base peak in three. It is no doubt a result of the ability of the ring nitrogen to localize positive charge and the great stability of a (di)hydroxypyridinium moiety which should be favored in the gas phase (33). The basic ring fragments exclusively by loss of CO or HCO$^\cdot$ without any loss of HCN or CH_3CN. This is not surprising since there are two CO groups to lose. Loss of CO and HCO$^\cdot$ accounts for the m/z 111(25) and 110(100) peaks, respectively, in the spectrum of Hdpp ($M^{+\cdot}$ = m/z 139).

The H_2exn spectrum has a molecular ion at m/z 332(15) which fragments through loss of one ring (m/z 208(64)) followed by successive losses of methylene moieties (m/z 194(38), 180(8.2), 166(37), and 152(30)). The m/z 139 peak is the $Hdpp^{+\cdot}$ fragment and the subsequent peaks are exactly as previously observed for Hmpp and Hdpp. The spectrum of Hmhpp shows a parent at 209(38) plus the same methylene cascade as in H_2exn and the same 139, 125, 110, and 96 peaks as the other spectra. The Hmapp spectrum has been renormalized to make the m/z 153 peak the base peak since HCl serves that function in the salt. The molecular ion is observed at 168(29) and the new base peak is the loss of a methyl radical (60% relative to HCl). The m/z 126 peak in this spectrum and the others is most likely the 1-methyl-3,4-dihydroxypyridinium cation (from high resolution studies). In short, the ring fragments are dominated by CO loss and the longer chain substituents show the expected fragmentation patterns.

The infrared spectral bands of the five hydroxypyridinone compounds are listed in Table 5; infrared bands in Hmpp and selected analogues are listed in Table 6. These analogues, which were prepared to facilitate the ir assignments, are the dideuterated d_2-Hmpp, the benzyl-protected intermediate Bzmpp, and the aluminum complex $Al(mpp)_3$ (34).

The assignment of νOH in Hmpp is confirmed by Bzmpp where the 3270 cm^{-1} band disappears and by d_2-Hmpp, where it shifts to 2420 cm^{-1}. This gives a $\nu OH/\nu OD$ of 1.35, indicative of a relatively weak H-bond. The theoretical ratio is 1.375 (from the reduced masses) and for free OH it is 1.355 (35). This ratio falls systematically as the strength of the H-bond increases and can reach unity for very short H-bonds (36). A combination of a lower zero point energy for H than D, and a weaker O···D···O than O···H···O interaction explains this low ratio (36). The stretches are indicative of normal polymeric intermolecular hydrogen-bonding systems (37, 38). In Hdpp, the νOH drops further to 3170 cm^{-1}. The suggestion of stronger hydrogen bonding in this compound can be made on consideration of this and the lower νC=O.

The assignment of νNH is again confirmed by Bzmpp, deuteration, and Hdpp: the band is at 2800 cm^{-1} in Hmpp, shifts to 2650 cm^{-1} on benzylation, shifts to 2210–2150 cm^{-1} (split, mean = 2180 cm^{-1}) on deuteration, and finally disappears on methylation. The ratio ($\nu NH/\nu ND$) is 1.28 and splitting of the νND is not without precedent, as it is reported in deuterio-2-pyridinone (39). These authors list a 3100 cm^{-1} band (in KBr) for the protio compound which supports our assignment. They also state that the 2885 cm^{-1} νNH band seen for 2-thiapyridone is the strongest NH H-bonding yet recorded for other than zwitterionic structures. The deuteration ratio for the thiapyridone is 1.29, and the typical N···H···S stretch appears at 3160 cm^{-1}. The packing diagram in Fig. 3 shows that there is considerable N—H···O=C hydrogen-bonding which binds the dimeric units to each other in this compound but not in the N—CH_3 compound Hdpp.

It is impossible to separate the νC=O and the higher energy νring (C=C) stretches in any of the compounds, hence the assignments in Tables 5 and 6. Numerous authors have come to this same conclusion in their considerations of 4-pyridinone and related compounds (40, 41). The bands which do appear are

Can. J. Chem. Downloaded from www.nrcresearchpress.com by 213.222.148.141 on 09/07/12
For personal use only.

TABLE 5. Selected infrared absorption bands and their assignments (cm^{-1})[a]

Assignment	Infrared absorption band				
	Hmpp	Hdpp	Hmapp	Hmhpp	H_2exn
νOH(b,s)	3270	3150	3300–2600 vb	3195	3195
νCH_{ring}	3100	3010	3300–2600 vb	3060	3060
$\nu CH_{3(2)}$	2920	2940	3300–2600 vb	2960, 2935	2960
				2860	2890
νC=O	1645	1630	1635 s	1630 s	1630 s
and	1620	1565 s	1535	1580 s	1580 s
νRing	1540	1530	1510 s	1530	1530
	1500 s	1515 s	1470	1510 s	1505 s
	1420 w	1400 w	1400 w	1405 w	1400 m
$\delta_{as}CH$	1450 w	1460–50 sh	1450 sh	1465 w	1460 w
$\delta_{sy}CH$	1380 s	1380 m	1380 w	1380 w	1380 w
		1335 s	1345 m	1350 s	1360 m
νCN		1250	1240	1230 sh	1250
νCO and	1300, 1270	1280	1325 s	1270 sh	1300, 1280 sh
δOH	1245	1250 b, s	1270	1240 b, s	1235 b, s
δRing	1225	1230	1200	1220	1220
	1110	1125	1140	1170	1170
	1045	1055	1060	1130	1040
		1030	1030	1040	
πRing(s)	830	820	830	850	850

[a]Abbreviations are as follows: ν, stretching; δ, in-plane bend; π, out-of-plane bend; as, asymmetric mode; sy, symmetric mode; s, strong absorption; m, medium absorption; w, weak absorption; b, broadened band; sh, shoulder; v, very; sp, split band.

TABLE 6. Infrared bands for Hmpp and substituted analogues (cm^{-1}; abbreviations are the same as in Table 5)

Assignment	Infrared band			
	Hmpp	d_2-Hmpp	Bzmpp	Al(mpp)$_3$
νOH(D)	3270	2420	—	—
νNH(D)	2800 b	2180 sp	2650 vb	3280
νC=O	1645	1630	1630 sh	1620
and	1620	1550	1620	1595
νRing	1540	1540 sh	1535	1540 sh
	1500 s	1490 s	1500 s	1505 b, s
	1420 w	1420 w	1410	1400
νCO and	1300, 1270	1325	1190 s(νCOC)	1310
δOH(D)	1245	900 b		1270
δRing	1225	1245 sp	1215 sp	1220
	1110	1150	1110	1100
	1045	1090	1050	1060

coupled and there is no mode which is localized in any one of these frequencies (42). There is a reproducible series of four ring stretching modes which appears in many pyridinones (43) and the fact that some of these bands are coupled to νC=O makes individual assignments impossible. Because Hmpp is the only one of the compounds capable of assuming a dihydroxypyridine-type tautomer, the separate modes contributing to each band in this region may be different in Hmpp than in the *N*-substituted compounds.

In the δCH region, weak to medium intensity bands are observed with additional bands for the compounds with *N*-substitution consistent with the presence of additional methyl and methylene groups. There is extensive mechanical coupling of the δOH and νCO modes in the region 1325 to 1235 cm^{-1} (36, 44, 45) and the presence of three bands in metal complexes of these species has been noted (34). Since the assignments in Table 6 for the other compounds are exactly analogous to those for Hmpp and Hdpp, they are given without further discussion. The deuteration and O-substitution studies corroborate the assignments of the infrared spectra of the compounds which we have given here.

The results of the proton nmr spectra are shown in Table 7. All the chemical shifts were recorded on the 400 MHz instrument except those of the NH and OH protons which were from the 80 MHz instrument. Generally, one observed two doublets for the ring protons with $J_{5,6}$ of 7 to 8 Hz, $J_{7,8}$ values of 7 to 8 Hz (when they could be resolved), a singlet for the ring methyl group, and a series of peaks for the R substituent with the OH proton detectable when the spectra were recorded in non-aqueous solution. Both Hmapp and Hmhpp were quite insoluble and these spectra were recorded in acidic solution, hence the absence of resonances for the hydroxyl protons. Samples (Hmpp and analogues, Hdpp, and Hmhpp) and solvents were rigorously dried to allow the observation of the NH/OH peaks. The NH resonance could be assigned based on a peak in Bzmpp at 11.30 ppm in d_6-DMSO and a peak in the spectra of M(mpp)$_3$ very near 12 ppm (M = Al, Ga) (34). Addition of a drop of water to solutions of the complexes resulted in a loss of the 12 ppm peak and the loss of the second order coupling to ^{6}H which appears as a less well resolved doublet in Hmpp and its complexes than in Hdpp or the other compounds. The presence of an NH chemical shift of 12.05 ppm in 2-pyridinone has been taken to suggest that the compound exists as hydrogen-bonded dimers in solution (46) just as it does in the solid state (47). The Hmpp crystal structure clearly shows the N—H···O=C bonds which hold the aggregates of dimers together so the 11.35 ppm shift may suggest that this same bond persists in solution.

The chemical shift of the OH proton is markedly dependent on the concentration of water in the system and also on the concentration of the nmr sample. The variation is considerable (from 6.90 ppm at 0.09 *M* to 5.64 ppm at 0.03 *M*) indicating

Can. J. Chem. Downloaded from www.nrcresearchpress.com by 213.222.148.141 on 09/07/12
For personal use only.

TABLE 7. Proton nmr spectral data[a]

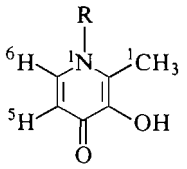

R = -^{1}H

-$^{7}CH_3$

-$^{7}CH_2{}^{8}CH_2NH_2$

-$^{7}CH_2{}^{8}CH_2{}^{9}CH_2\ {}^{10}CH_2{}^{11}CH_2{}^{12}CH_3$

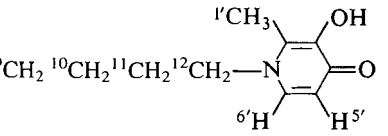

Assignment	Hmpp in D_2O	Hdpp in D_2O	In D_2O/trifluoroacetic acid		
			Hmapp	Hmhpp	H_2exn[e]
^{1}NH	11.35[b]	—	—	—	—
OH	6.90[b]	6.35[b]	—	5.96[c]	—
^{6}H(d)	7.58	7.58	7.69	7.57	7.55
^{5}H(d)	6.51	6.46	6.77	6.71	6.69
$^{1}CH_3$(s)	2.34	2.36	2.20	2.16	2.13
$^{7}CH_2$	—	3.73(s)[d]	3.10(t)	3.87(t)	3.87(t)[f]
$^{8}CH_2$	—	—	4.29(t)	1.37(q)	1.37(s)[g]
$^{9,10,11}CH_2$	—	—	—	0.85(m)	0.93(s)[h]
$^{12}CH_3$	—	—	—	0.38(t)	—

[a]s = singlet; d = doublet; t = triplet; q = quintet; m = multiplet.
[b]In D_2O/DMSO-d_6.
[c]In D_2O/$CDCl_3$.
[d]Read CH_3 rather than CH_2.
[e]For the dimer, the rings are apparently equivalent, e.g. integral equal to two protons.
[f]Read $^{7,12}CH_2$ with integral equal to four protons.
[g]Read $^{8,11}CH_2$ with integral equal to four protons.
[h]Read $^{9,10}CH_2$ with integral equal to four protons.

that in solution there is considerable intermolecular hydrogen-bonding in Hmpp.

The structural, infrared, and nmr studies show how important hydrogen-bonding is to the properties of the 3-hydroxy-4-pyridinones, a feature which we have observed in their complexes as well. Amine, hydroxl, and ketone functionalities contribute a number of hydrogen-bonding sites to each of the molecules discussed herein and the solution and solid state properties and structures reflect these interactions. Every one of these potential hydrogen-bonding sites is used in the solid state structures and the solution properties suggest that the same situation obtains therein as well.

Acknowledgements

The authors acknowledge support from NSERC and from the B.C. Health Care Research Foundation in the form of operating grants. C.O. acknowledges NSERC for a University Research Fellowship, as well as an Undergraduate Student Research Award to T.B.K. We also thank U.B.C. for a University Graduate Fellowship to W.O.N., and Professor J. Trotter for the use of his crystallographic facilities.

1. A. R. KATRITZKY (*Editor*). Handbook of heterocyclic chemistry. Pergamon, New York. 1985.
2. M. M. FINNEGAN, S. J. RETTIG, and C. ORVIG. J. Am. Chem. Soc. **108**, 5033 (1986).
3. M. M. FINNEGAN, T. G. LUTZ, W. O. NELSON, A. SMITH, and C. ORVIG. Inorg. Chem. **26**, 2171 (1987).
4. W. O. NELSON, S. J. RETTIG, and C. ORVIG. J. Am. Chem. Soc. **109**, 4121 (1987).
5. G. J. KONTOGHIORGHES. Inorg. Chim. Acta, **135**, 145 (1987) and references contained therein.
6. P. E. RILEY, K. ABU-DARI, and K. N. RAYMOND. Inorg. Chem. **22**, 3940 (1983).
7. R. C. SCARROW, D. L. WHITE, and K. N. RAYMOND. J. Am. Chem. Soc. **107**, 6540 (1985).
8. R. C. SCARROW, P. E. RILEY, K. ABU-DARI, D. L. WHITE, and K. N. RAYMOND. Inorg. Chem. **24**, 954 (1985).
9. H. STUNZI, D. D. PERRIN, T. TEITEI, and R. L. N. HARRIS. Aust. J. Chem. **32**, 21 (1979).
10. H. STUNZI, R. L. N. HARRIS, D. D. PERRIN, and T. TEITEI. Aust. J. Chem. **33**, 2207 (1980).
11. W.-C. TSAI and K.-H. LING. J. Chinese Biochem. Soc. **2**, 70 (1973).
12. A. PERATONER. Gazz. Chim. Ital. **36**, I, 52 (1906).
13. F. BRODY and P. R. RUBY. *In* The chemistry of heterocyclic compounds. Vol. 14. Pyridine and its derivatives. Part one. *Edited by* E. Klingsberg. Interscience, New York. 1960. pp. 90–589.
14. H. MEISLICH. *In* The chemistry of heterocyclic compounds. Vol. 14. Pyridine and its derivatives. Part three. *Edited by* E. Klingsberg. Interscience, New York. 1962. pp. 509–890.
15. R. J. C. KLEIPOOL and J. P. WIBAUT. Rec. Trav. Chim. Pays Bas, **69**, 1041 (1950).
16. K. JAKOPCIC, B. TAMHINA, F. ZORKO, and M. J. HERAK. J. Inorg. Nucl. Chem. **39**, 1201 (1977).
17. J. H. LOOKER and M. D. CLIFFTON. J. Heterocyclic Chem. **23**, 5 (1986).
18. M. HAYASHI, K. YAMAUCHI, and M. KINOSHITA. Bull. Chem. Soc. Jpn. **50**, 1510 (1977) and references contained therein.
19. R. L. N. HARRIS. Aust. J. Chem. **29**, 1329 (1976).
20. C. ORVIG. J. Chem. Ed. **62**, 84 (1985).
21. International tables for X-ray crystallography. Vol. IV. Kynoch press, Birmingham. 1974. pp. 99–102 and 149.
22. P. J. BECKER and P. COPPENS. Acta Crystallogr. Sect. A, **30**, 129 (1974); **30**, 148 (1974); **31**, 417 (1975).
23. P. COPPENS and W. C. HAMILTON. Acta Crystallogr. Sect. A, **26**, 71 (1970).
24. F. R. THORNLEY and R. J. NELMES. Acta Crystallogr. Sect. A, **30**, 748 (1974).
25. V. SCHOMAKER and K. N. TRUEBLOOD. Acta Crystallogr. Sect. B, **24**, 63 (1968).
26. D. W. J. CRUIKSHANK. Acta Crystallogr. **9**, 747 (1956); **9**, 754 (1956); **14**, 896 (1961).
27. B. E. FISHER and J. E. HODGE. J. Org. Chem. **29**, 776 (1964).
28. TH. SEVERIN and A. LOIDL. Z. Lebensm. Unter.-Forsch. **161**, 119 (1976).
29. M. YASUE, N. KAWAMURA, and J. SAKAKIBARA. Yakugaku Zasshi, **90**, 1222 (1970).
30. C. L. NORRIS, R. C. BENSON, P. BEAK, and W. H. FLYGARE. J. Am. Chem. Soc. **95**, 2766 (1973).
31. W. O. NELSON, C. ORVIG, S. J. RETTIG, and J. TROTTER. Can. J. Chem. In press.
32. Q. N. PORTER. Mass spectrometry of heterocyclic compounds. 2nd ed. Wiley, New York. 1985. Chap. 14.
33. A. MAQUESTIAU, Y. VAN HAVERBEKE, C. DE MEYER, A. R. KATRIZKY, M. J. COOK, and A. D. PAGE. Can. J. Chem. **53**, 490 (1975).
34. W. O. NELSON, T. B. KARPISHIN, S. J. RETTIG, and C. ORVIG. Inorg. Chem. In press.
35. S. E. ODINOKOV, A. A. NABIULLIN, A. A. MASHKOVSKY, and V. P. GLAZUNOV. Spectrochim. Acta, **39A**, 1055 (1983).

Can. J. Chem. Downloaded from www.nrcresearchpress.com by 213.222.148.141 on 09/07/12
For personal use only.

36. L. J. BELLAMY. The infrared spectra of complex molecules. Vol. 2. 2nd ed. Chapman and Hall, New York. 1980. pp. 240–280.
37. L. J. BELLAMY. The infrared spectra of complex molecules. Vol. 1. 3rd ed. Chapman and Hall, New York. 1975.
38. A. NOVAK. Struct. Bond. (Berlin) **18**, 177 (1974).
39. L. J. BELLAMY and P. E. ROGASCH. Proc. R. Soc. **257**A, 98 (1960).
40. B. D. BATTS and E. SPINNER. Aust. J. Chem. **22**, 2581 (1969).
41. D. COOK. Can. J. Chem. **41**, 2575 (1963).
42. A. R. KATRITZKY and P. J. TAYLOR. Physical methods in heterocyclic chemistry. Vol. IV. *Edited by* A. R. Katritzky. Academic Press, New York. 1971. pp. 265–434.
43. A. R. KATRITZKY and R. A. JONES. J. Chem. Soc. 2947 (1960).
44. D. HADZI and N. SHEPPARD. Proc. R. Soc. **216**A, 247 (1953).
45. R. C. LORD and F. A. MILLER. Appl. Spectrosc. **10**, 115 (1956).
46. R. H. COX and A. A. BOTHNER-BY. J. Phys. Chem. **73**, 2465 (1969).
47. B. R. PENFOLD. Acta Crystallogr. **6**, 591 (1953).

Can. J. Chem. Downloaded from www.nrcresearchpress.com by 213.222.148.141 on 09/07/12
For personal use only.

Structural studies of organoboron compounds. XXVII.[1] (3-Hydroxy-2-methyl-4-pyridinonato)diphenylboron and (3-hydroxy-1,2-dimethyl-4-pyridinonato)diphenylboron

WILLIAM O. NELSON, CHRIS ORVIG, STEVEN J. RETTIG, AND JAMES TROTTER

Department of Chemistry, University of British Columbia, 2036 Main Mall, Vancouver, B.C., Canada V6T 1Y6

Received March 11, 1987

WILLIAM O. NELSON, CHRIS ORVIG, STEVEN J. RETTIG, and JAMES TROTTER. Can. J. Chem. **66**, 132 (1988).

Details of the preparation and crystal structures of the title compounds are given. Crystals of (3-hydroxy-2-methyl-4-pyridinonato)diphenylboron, **1**, are orthorhombic, $a = 13.4010(6)$, $b = 15.005(1)$, $c = 14.833(1)$ Å, $Z = 8$, space group *Pbca*, and those of (3-hydroxy-1,2-dimethyl-4-pyridinonato)diphenylboron, **2**, are monoclinic, $a = 8.2617(5)$, $b = 12.374(1)$, $c = 16.104(1)$ Å, $\beta = 92.741(5)°$, $Z = 4$, space group $P2_1/n$. Both structures were solved by direct methods and were refined by full-matrix least-squares procedures to $R = 0.047$ and 0.071 for 1654 and 1831 reflections with $I \geq 3\sigma(I)$, respectively. Both molecules contain five-membered C_2O_2B chelate rings, that in **2** being nearly planar. Structural data indicate weaker overall binding of the ligand oxygen atoms to boron in **1** than in **2**. Bond lengths (corrected for libration) are O—B = 1.497(5) and 1.650(5), C—B = 1.600(5) and 1.599(5) Å for **1**; O—B = 1.542(5) and 1.569(5), C—B = 1.607(6) and 1.609(6) Å for **2**.

WILLIAM O. NELSON, CHRIS ORVIG, STEVEN J. RETTIG et JAMES TROTTER. Can. J. Chem. **66**, 132 (1988).

On rapporte les détails relatifs à la préparation et à la détermination des structures cristallines des composés mentionnés dans le titre. Le (hydroxy-3 méthyl-2 pyridinonato-4) diphénylbore, **1**, est orthorhombique avec $a = 13,4010(6)$, $b = 15,005(1)$ et $c = 14,833(1)$ Å, $Z = 8$ et groupe d'espace *Pbca*; par ailleurs, ceux du (hydroxy-3 diméthyl-1,2 pyridinonato-4) diphénylbore, **2**, sont monocliniques avec $a = 8,2617(5)$, $b = 12,374(1)$ et $c = 16,104(1)$ Å, $\beta = 92,741(5)°$, $Z = 4$ et groupe d'espace $P2_1/n$. On a résolu les deux structures par des méthodes directes et on les a affinées par la méthode des moindres carrés (matrice entière) jusqu'à des valeurs respectives de R de 0,047 et 0,071 pour 1654 et 1831 réflexions avec $I \geq 3\sigma(I)$. Les deux molécules contiennent chacune des noyaux à cinq chaînons de chélate C_2O_2B; celui que l'on retrouve dans le composé **2** est pratiquement plan. Les données structurales indiquent que, dans l'ensemble, la liaison avec bore des atomes d'oxygène du ligand est plus faible dans le composé **1** que dans le composé **2**. Les longueurs des liaisons (corrigées pour la libration) sont les suivantes : O—B = 1,497(5) et 1,650(5), C—B = 1,600(5) et 1,599(5) Å pour le composé **1**; O—B = 1,542(5) et 1,569(5), C—B = 1,607(6) et 1,609(6) Å pour le composé **2**.

[Traduit par la revue]

Introduction

(Maltolato)diphenylboron ((3-hydroxy-2-methyl-4-pyronato)diphenylboron) was characterized in a previous report (1). It was established that the binding of the maltolate oxygen atoms to boron is weaker than that to aluminum in the neurotoxin tris(maltolato)aluminum (1, 2). In parallel with a study of neutral water-soluble Al and Ga compounds of neurological interest (2, 3) the diphenylboron complexes of the maltol analogs (by replacement of the ring oxygen by NR, R = H and Me) 3-hydroxy-2-methyl-4(1*H*)-pyridinone and 3-hydroxy-1,2-dimethyl-4(1*H*)-pyridinone have been synthesized and their crystal structures determined.

Experimental

(3-Hydroxy-2-methyl-4-pyridinonato)diphenylboron, 1

A solution of diphenylborinic acid was prepared by acid hydrolysis of (2-aminoethanolato)diphenylboron (1.30 g, 5.8 mmol, Aldrich Chemical) and was extracted with diethyl ether (4 × 50 mL). To the organic layer was added a solution of 3-hydroxy-2-methyl-4(1*H*)-pyridinone (0.73 g, 5.8 mmol, prepared according to the literature (4)) in 100 mL methanol. After stirring 1 h and reduction of volume to 100 mL, a white precipitate formed. Overnight cooling at 20°C, filtering and washing with water and ethanol produced 1.43 g (4.9 mmol, 85% yield). Analytically pure compound was obtained by recrystallization from acetone/water, mp (dec.) 225–228°C. *Anal.* calcd. for $C_{18}H_{16}BNO_2$: C 74.76, H 5.59, N 4.85; found: C 74.54, H 5.67, N 4.79. Infrared (KBr, all strong): 3320 cm^{-1} (NH); 1650 (CO); 1590, 1550, 1500 (pyridinone ring). ^1H nmr (d_6-acetone, 25°C, 80 MHz) δ (ppm): 2.50 (s, 3H, CH_3); 6.73 (d, 6.6 Hz, 1H, CHC(O)); 7.25 (m, 10H, 2 C_6H_5); 7.80 (d, 6.6 Hz, 1H, CHC*H*N). Crystals used for the X-ray analysis were obtained by liquid–liquid diffusion (5) from acetone/water.

(3-Hydroxy-1,2-dimethyl-4-pyridinonato)diphenylboron, 2

The procedure is essentially the same as that described above for **1**. A solution of (0.58 g, 4.2 mmol) 3-hydroxy-1,2-dimethyl-4(1*H*)-pyridinone (prepared according to the literature (6)) in 100 mL ethanol was added to Ph_2BOH (from acid hydrolysis of 5.2 mmol $Ph_2BOCH_2CH_2NH_2$) in 150 mL diethyl ether. Precipitate started to form within 10 min; the solution was heated (30°C) overnight to reduce volume and digest the precipitate. After cooling, the white solid mass was collected and recrystallized from acetone/water. This produced 0.78 g (2.6 mmol, 62% yield) of analytically pure compound, mp (dec.) 220–222°C. *Anal.* calcd. for $C_{19}H_{18}BNO_2$: C 75.26, H 6.00, N 4.62; found: C 75.40, H 6.01, N 4.54. Infrared (KBr, all strong): 1640 cm^{-1} (CO); 1580, 1530, 1500 (pyridinone ring). ^1H nmr (d_6-acetone, 25°C, 80 MHz) δ (ppm): 2.50 (s, 3H, NC(CH_3)); 3.94 (s, 3H, CN(CH_3)); 6.73 (d, 6.6 Hz, 1H, *CH*CHN); 7.25 (m, 10H, 2 C_6H_5); 7.80 (d, 6.6 Hz, 1H, CHC*H*N). Crystals used for the X-ray study were obtained by slow evaporation from acetone/ethanol.

Infrared spectra were recorded as KBr pellets on a Perkin-Elmer 783 from 4000–200 cm^{-1} and ^1H nmr spectra on a Bruker WP-80.

X-ray crystallographic analyses

Crystallographic data for **1** and **2** appear in Table 1. Unit-cell parameters were refined by least-squares on 25 reflections with $2\theta = 60–91°$ for **1** and $2\theta = 40–79°$ for **2**. The intensities of three check reflections, measured each hour of X-ray exposure time throughout the data collections, showed only small random variations in each case. The data were reduced[2] and, for **2**, corrected for absorption. No absorption correction was applied for **1** in view of the crystal dimensions (Table 1) and the low coefficient of absorption.

[1]Part XXVI: ref. 17.

[2]The computer programs used include locally written programs for data processing and locally modified versions of the following: AGNOST, absorption corrections, by J. A. Ibers; ORFLS, full-matrix least-squares, and ORFFE, function and errors, by W. R. Busing, K. O. Martin, and H. A. Levy; FORDAP, Patterson and Fourier syntheses, by A. Zalkin; ORTEP II, illustrations, by C. K. Johnson.

Can. J. Chem. Downloaded from www.nrcresearchpress.com by 213.222.148.141 on 09/07/12
For personal use only.

TABLE 1. Crystallographic data[a]

Compound	**1**	**2**
Formula	$C_{18}H_{16}BNO_2$	$C_{19}H_{18}BNO_2$
fw	289.14	303.17
Crystal system	Orthorhombic	Monoclinic
Space group	*Pbca*	$P2_1/n$
a	13.4010(6)	8.2617(5)
b	15.005(1)	12.374(1)
c (Å)	14.833(1)	16.104(1)
β (deg)	90	92.741(5)
V (Å^3)	2982.7(3)	1644.4(2)
Z	8	4
ρ_c (g/cm^3)	1.288	1.225
F(000)	1216	640
μ(Cu-K_α) cm^{-1}	6.2	5.8
Crystal dimensions (mm)	0.29 × 0.35 × 0.38	0.13 × 0.28 × 0.58
Transmission factors	—	0.756–0.938
Scan type	ω–2θ	ω–2θ
Scan range (deg in ω)	1.00 + 0.14 tan θ	0.90 + 0.14 tan θ
Scan speed (deg/min)	1.55–10.06	1.18–10.06
Data collected	$+h, +k, +l$	$\pm h, +k, +l$
$2\theta_{max}$ (deg)	150	150
Unique reflections	3073	3377
Reflections with $I \geq 3\sigma(I)$	1654	1831
Number of variables	257	280
R	0.047	0.071
R_w	0.056	0.076
S	0.996	1.330
Mean Δ/σ (final cycle)	0.01	0.01
Maximum Δ/σ (final cycle)	0.10	0.08
Maximum residual density (e/Å^3)	0.22	0.80

[a]Temperature 22°C, Enraf-Nonius CAD4-F diffractometer, Cu-K_α radiation ($\lambda_{K\alpha 1}$ = 1.540562, $\lambda_{K\alpha 2}$ = 1.544390 Å), nickel filter, takeoff angle 2.7°, aperture (2.0 + tan θ) × 4.00 mm at a distance of 173 mm from the crystal, scan range extended by 25% on both sides for background measurement, $\sigma^2(I) = S + 2B + [0.04(S - B)]^2$ (*S* = scan count, *B* = normalized background count), function minimized $\Sigma w(|F_o| - |F_c|)^2$ where $w = 1/\sigma^2(F)$, $R = \Sigma||F_o| - |F_c||/\Sigma|F_o|$, $R_w = (\Sigma w(|F_o| - |F_c|)^2/\Sigma w|F_o|^2)^{1/2}$, $S = (\Sigma w(|F_o| - |F_c|)^2/(m - n))^{1/2}$. Values given for *R*, R_w, and *S* are based on those reflections with $I \geq 3\sigma(I)$.

Both structures were solved by direct methods, the coordinates of the non-hydrogen atoms being determined from *E*-maps. Early in the refinement of the structure of **1** it was apparent that the pyridinone ligand was twofold disordered, the two orientations being related by a 180° rotation about the C(3)···B vector (see Fig. 1). Site occupancy factors were initially estimated as 0.75 and 0.25 from relative Fourier peak heights for the well-resolved atom pairs. Simultaneous refinement of both the thermal and site occupancy factors resulted in a poorly-conditioned matrix. The occupancy factors for the atom pairs O(1), O(2), C(2), C(4), and C(5) were refined with the thermal parameters fixed at equal values. The resulting normalized average occupancy factors were kept fixed in subsequent cycles of refinement. In the final stages of the refinement of **1**, all non-hydrogen atoms were refined with anisotropic thermal parameters except for the low-occupancy atoms N(b), C(1b), and C(6b) which were refined with isotropic thermal parameters due to their proximity to atoms of the high-occupancy ligand. Hydrogen atoms were included as fixed contributors to the structure of **1** in idealized positions (N—H = 0.90, C(sp^2)—H = 0.97, C(sp^3)—H = 0.98 Å, methyl group orientation based on observed hydrogen positions), with the exception of those associated with the low-occupancy methyl group. In the case of **2** all non-hydrogen atoms were refined with anisotropic thermal parameters and the hydrogen atoms with isotropic thermal parameters. Neutral atom scattering factors were taken from ref. 7. An isotropic type I extinction correction was applied for **1** (Thornley–Nelmes definition of mosaic anisotropy with a Lorentzian distribution) (8–10), the final value of *g* being 0.73(10) × 10^4. The F_o and F_c values for the intense reflections of **2** were in good agreement thus no extinction correction was necessary.

The relatively high final *R* value and the unusually large residual densities (located near O) for **2** are probably due to poor crystal quality. It was difficult to grow good crystals of **2**, most samples growing as multiple twins. The best crystal found was used for data collection but had ω peak widths of 0.4°, twice as large as those usually observed for compounds of this type.

Final positional and anisotropic thermal parameters appear in Tables 2, 6,[3] and 7,[3] respectively. Measured and calculated structure factors have been placed in the Depository of Unpublished Data.[3]

The thermal motion in both compounds has been analysed in terms of rigid-body modes of translation, libration, and screw motion (11). The rms errors in the temperature factors ΔU_{ij} (derived from the least-squares analyses) are 0.0025 Å^2 for **1** (excluding the low-occupancy atoms) and 0.0030 Å^2 for **2**. Three subunits were considered for each molecule (2 PhB, pyridinone-B), rms ΔU_{ij} = 0.0023–0.0048 Å^2 for **1** and 0.0027–0.0059 Å^2 for **2**. The appropriate bond distances have been corrected for libration (11, 12), using shape parameters q^2 of 0.08 for all atoms involved. Corrected bond lengths appear in Table 3 along with the uncorrected values; corrected bond angles do not differ by more than 1 σ from the uncorrected values given in Table 4. Intra-annular torsion angles defining the conformations of the five-membered chelate rings are listed in Table 5. Hydrogen atom parameters (Table 6) have been deposited. Bond lengths and

[3]The structure factor table, Table 7 (anisotropic thermal parameters) and other material mentioned in the text may be purchased from the Depository of Unpublished Data, CISTI, National Research Council of Canada, Ottawa, Ont., Canada K1A 0S2.

Can. J. Chem. Downloaded from www.nrcresearchpress.com by 213.222.148.141 on 09/07/12
For personal use only.

Can. J. Chem. Downloaded from www.nrcresearchpress.com by 213.222.148.141 on 09/07/12
For personal use only.

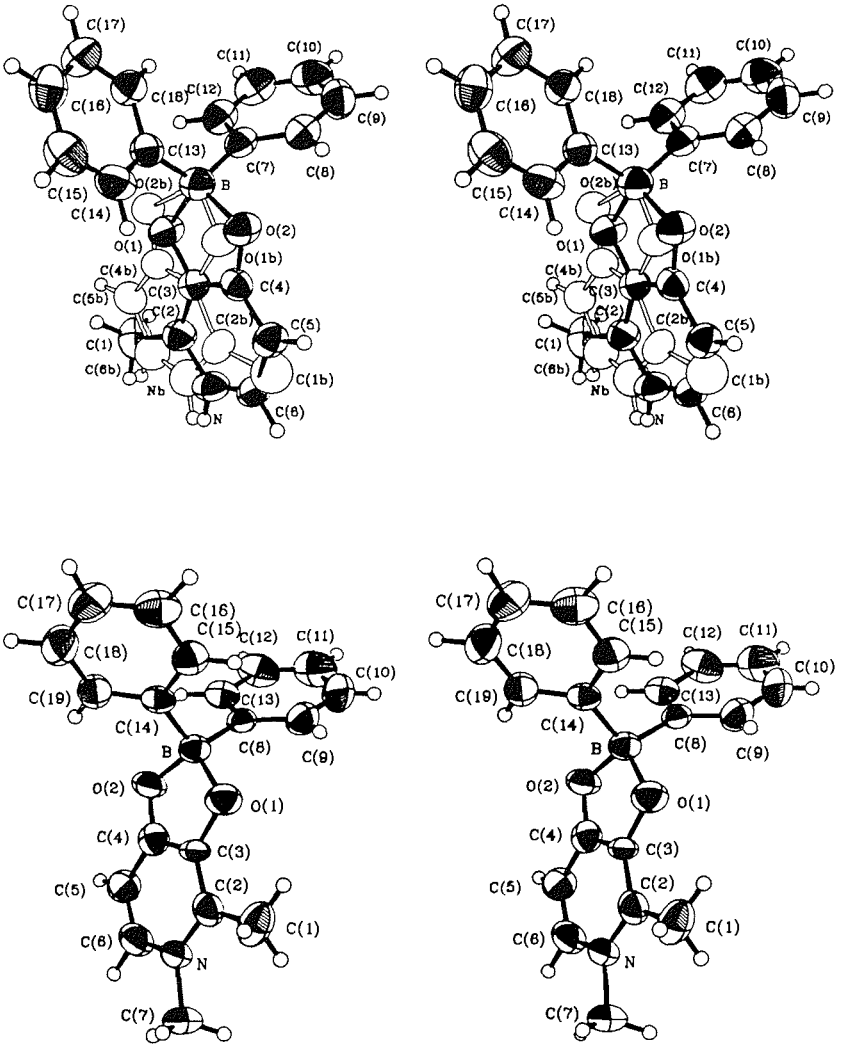

FIG. 1. Stereoscopic views of the (3-hydroxy-2-methyl-4-pyridinonato)diphenylboron (top) and (3-hydroxy-1,2-dimethyl-4-pyridinonato)diphenylboron (bottom) molecules; 50% probability thermal ellipsoids are shown for the non-hydrogen atoms. Hydrogen atoms have been assigned arbitrary thermal parameters for the sake of clarity.

angles involving hydrogen and a complete listing of torsion angles (Tables 8–10) are included as supplementary material.

Results and discussion

Both crystal structures consist of discrete molecules separated by normal van der Waals distances. In the case of the disordered structure of **1**, only the major component will be considered for the discussion of molecular geometry. Bond lengths and angles involving the minor component suggest that the Ph_2B moiety in **1** is also disordered although the disorder was not resolvable.

The molecular structures of **1** and **2** (Fig. 1) each feature central fused-ring systems and closely resemble that of the isoelectronic (maltolato)diphenylboron molecule, **3** (1). The pyridinone rings in **1** and **2** are both slightly, but significantly, non-planar (maximum deviations from the C_5N mean planes are 0.018(5) Å in **1** and 0.015(5) Å in **2**) as are those in the free ligands (6). The five-membered C_2O_2B ring is non-planar in **1** but nearly planar in **2** (maximum deviations from the mean planes are 0.067(4) Å in **1** and 0.011(5) Å in **2**). The C_2O_2B ring in **3** was found to have a non-planar conformation intermediate between those in **1** and **2**. The phenyl rings in both structures are planar within experimental error and have normal geometry (13).

Compound **1** contains both the shortest and longest O—B bonds yet observed for an *O,O*-chelate of Ph_2B containing a five-membered chelate ring, but the disorder in the structure may lead to some uncertainty in the O—B distances. The average O—B and C—B distances[4] (which should be less sensitive to the effects of the disorder) of 1.574 and 1.600 Å in **1** represent the weakest overall binding of ligand oxygen atoms to boron observed for this type of compound (see Table 5 of ref. 1). The isoelectronic compound **3** previously exhibited the weakest overall O—B binding with average O—B and C—B distances of 1.567 and 1.603 Å. The ligand binding is stronger in **2** with corresponding average values of 1.556 and 1.608 Å, respectively. The structures of five other molecules of this

[4]Libration corrected bond lengths (esd's assumed equal to those of the uncorrected values) are employed in the discussion and are compared with similarly treated (11) distances unless otherwise stated.

TABLE 2. Final positional (fractional × 10^4) and isotropic thermal parameters ($U \times 10^3$ Å^2) with estimated standard deviations in parentheses[a]

Atom	x	y	z	U_{eq}/U_{iso}
		1		
O(1)[1]	1298(3)	1228(2)	5837(2)	58
O(2)[1]	1375(2)	210(2)	7083(2)	58
N[1]	−1277(4)	572(3)	5923(3)	60
C(1)[1]	−598(8)	1678(5)	4837(5)	71
C(2)[1]	−464(4)	1026(3)	5601(4)	58
C(3)	407(3)	833(2)	6028(2)	49
C(4)[1]	470(4)	267(3)	6751(3)	50
C(5)[1]	−389(4)	−179(3)	7061(3)	58
C(6)[1]	−1248(5)	−2(4)	6614(5)	59
C(7)	2774(2)	133(2)	5864(2)	52
C(8)	2934(2)	−744(2)	6131(2)	60
C(9)	3510(3)	−1331(2)	5621(3)	77
C(10)	3941(3)	−1050(3)	4838(3)	83
C(11)	3801(3)	−190(3)	4558(2)	79
C(12)	3233(3)	387(2)	5059(2)	65
C(13)	2613(2)	1537(2)	7029(2)	53
C(14)	2101(3)	1972(2)	7720(3)	67
C(15)	2533(3)	2617(3)	8251(2)	77
C(16)	3514(4)	2856(2)	8122(2)	73
C(17)	4052(3)	2437(2)	7455(3)	70
C(18)	3605(3)	1792(2)	6927(2)	59
B	2084(3)	808(3)	6410(3)	62
O(1b)[2]	1173(10)	484(8)	6583(8)	66
O(2b)[2]	1666(8)	1489(7)	5408(8)	58
N(b)[2]	−1198(17)	898(12)	5522(12)	71(6)
C(1b)[2]	−932(25)	−223(22)	6818(24)	83(12)
C(2b)[2]	−596(17)	485(12)	6125(13)	66
C(4b)[2]	722(12)	1354(10)	5392(11)	52
C(5b)[2]	97(14)	1745(12)	4791(12)	58
C(6b)[2]	−845(25)	1413(19)	4873(25)	68(10)
		2		
O(1)	3171(4)	1413(2)	4185(2)	60
O(2)	2172(3)	3211(2)	4363(2)	58
N	986(4)	981(3)	6044(2)	52
C(1)	2564(9)	−365(5)	5324(5)	74
C(2)	1922(5)	729(4)	5408(3)	55
C(3)	2240(4)	1554(3)	4858(2)	40
C(4)	1673(5)	2583(4)	4937(3)	53
C(5)	654(6)	2815(4)	5602(3)	62
C(6)	354(6)	2018(5)	6114(3)	67
C(7)	584(10)	213(6)	6696(4)	81
C(8)	2321(4)	2518(3)	2865(2)	43
C(9)	2158(6)	1611(4)	2375(3)	63
C(10)	1405(8)	1661(7)	1580(4)	90
C(11)	837(7)	2601(7)	1262(4)	92
C(12)	963(7)	3513(6)	1733(4)	77
C(13)	1709(5)	3470(4)	2523(3)	56
C(14)	5019(5)	2998(3)	3768(2)	44
C(15)	6191(6)	2524(4)	3298(3)	57
C(16)	7757(6)	2930(5)	3278(4)	72
C(17)	8167(6)	3844(5)	3734(4)	77
C(18)	7048(6)	4328(5)	4198(4)	81
C(19)	5503(6)	3905(4)	4211(3)	61
B	3209(6)	2531(4)	3769(3)	47

[a]Superscripts 1 and 2 refer to occupancy factors of 0.77 and 0.23, respectively.

Can. J. Chem. Downloaded from www.nrcresearchpress.com by 213.222.148.141 on 09/07/12
For personal use only.

TABLE 3. Bond lengths (Å) with estimated standard deviations in parentheses

Bond	Length		Bond	Length	
	Uncorr.	Corr.		Uncorr.	Corr.
			1		
O(1)—C(3)	1.362(5)	1.366	C(9)—C(10)	1.364(5)	1.373
O(1)—B	1.493(5)	1.497	C(10)—C(11)	1.370(5)	1.382
O(2)—C(4)	1.311(6)	1.315	C(11)—C(12)	1.372(5)	1.380
O(2)—B	1.645(5)	1.650	C(13)—C(14)	1.396(4)	1.408
N—C(2)	1.372(7)	1.377	C(13)—C(18)	1.392(4)	1.405
N—C(6)	1.338(9)	1.342	C(13)—B	1.594(5)	1.599
C(1)—C(2)	1.508(10)	1.512	C(14)—C(15)	1.374(5)	1.380
C(2)—C(3)	1.359(6)	1.364	C(15)—C(16)	1.376(5)	1.389
C(3)—C(4)	1.371(5)	1.375	C(16)—C(17)	1.376(5)	1.388
C(3)—O(1b)	1.417(14)		C(17)—C(18)	1.381(4)	1.387
C(3)—C(2b)	1.45(2)		B—O(1b)	1.339(13)	
C(3)—C(4b)	1.30(2)		B—O(2b)	1.889(11)	
C(4)—C(5)	1.409(7)	1.413	O(2b)—C(4b)	1.28(2)	
C(5)—C(6)	1.355(9)	1.359	C(2b)—N(b)	1.35(3)	
C(7)—C(8)	1.390(4)	1.403	C(2b)—C(1b)	1.55(4)	
C(7)—C(12)	1.397(4)	1.407	C(4b)—C(5b)	1.36(2)	
C(7)—B	1.593(5)	1.600	C(5b)—C(6b)	1.36(4)	
C(8)—C(9)	1.394(5)	1.402	N(b)—C(6b)	1.32(3)	
			2		
O(1)—C(3)	1.370(4)	1.374	C(8)—C(13)	1.386(6)	1.398
O(1)—B	1.537(5)	1.542	C(8)—B	1.600(6)	1.607
O(2)—C(4)	1.289(5)	1.292	C(9)—C(10)	1.399(7)	1.408
O(2)—B	1.560(5)	1.569	C(10)—C(11)	1.346(9)	1.358
N—C(2)	1.349(5)	1.354	C(11)—C(12)	1.361(8)	1.374
N—C(6)	1.392(6)	1.400	C(12)—C(13)	1.388(7)	1.396
N—C(7)	1.465(6)	1.467	C(14)—C(15)	1.388(6)	1.398
C(1)—C(2)	1.462(7)	1.466	C(14)—C(19)	1.379(6)	1.392
C(2)—C(3)	1.385(5)	1.388	C(14)—B	1.603(6)	1.609
C(3)—C(4)	1.366(4)	1.374	C(15)—C(16)	1.390(6)	1.396
C(4)—C(5)	1.423(6)	1.428	C(16)—C(17)	1.381(7)	1.395
C(5)—C(6)	1.316(6)	1.319	C(17)—C(18)	1.355(7)	1.364
C(8)—C(9)	1.375(6)	1.389	C(18)—C(19)	1.381(6)	1.387

Can. J. Chem. Downloaded from www.nrcresearchpress.com by 213.222.148.141 on 09/07/12
For personal use only.

type having unsaturated five-membered chelate rings have been determined (1, 14–16). The average O—B distances are shortest (1.550–1.555 Å) when the chelate rings are planar (15, 16) and longer (1.565–1.567 Å) when the chelate rings are non-planar (1, 14). Packing effects are probably responsible for deviations of the unsaturated chelate rings from planarity (14) and may influence the O—B distances in this type of compound. The ν_{CO} bands in the solid state ir spectra of **1–3** occur at 1650, 1640, and 1640 cm^{-1}, respectively, consistent with the weakest O(2)—B bond in **1**.

The geometry of the coordinated ligands in **1** and **2** differs from that of the free ligands (6) in the same way as discussed for the maltolate **3** (1). The ligand bite (O(2)···O(3)) is reduced from 2.761(2) and 2.740(3) Å in the free ligands to 2.400(5) Å in **1** and 2.394(5) Å in **2** (the corresponding distance in **3** is 2.384(2) Å) via angular distortions about the ring-junction atoms C(3) and C(4). Bond lengths do not change significantly upon coordination except in the O(1)—C(3)—C(4)—O(2) fragment which is part of the chelate ring. Both C—O distances increase (C(3)—O(1) and C(4)—O(2) by 0.007(5) and 0.031(6) Å in **1** and by 0.010(5) and 0.016(6) Å in **2**) and the C(3)—C(4) distance decreases significantly from 1.436(2) to 1.375(5) Å in **1** and from 1.435(4) to 1.374(5) Å in **2**. Comparison of the ligand geometries of **1** and **2** shows the effect of the *N*-methyl substitution. Except for the C(3)—C(4) distances which are the same in **1** and **2**, all pyridinone ring bonds in **2** are alternately shorter and longer than those in the unsubstituted molecule **1**. The largest differences occur for the N—C(6) and C(5)—C(6) bonds (see Table 3). This substituent effect may also account in part for the substantially different bonding to boron in **1** and **2** along with the steric effects discussed above and σ-hybridization effects.

TABLE 4. Bond angles (deg) with estimated standard deviations in parentheses

Bonds	Angle (deg)	Bonds	Angle (deg)
	1		
C(3)—O(1)—B	108.5(3)	C(13)—C(14)—C(15)	122.9(3)
C(4)—O(2)—B	105.7(3)	C(14)—C(15)—C(16)	120.4(3)
C(2)—N—C(6)	124.2(6)	C(15)—C(16)—C(17)	118.7(4)
N—C(2)—C(1)	119.3(6)	C(16)—C(17)—C(18)	120.1(3)
N—C(2)—C(3)	114.5(6)	C(13)—C(18)—C(17)	123.0(3)
C(1)—C(2)—C(3)	126.2(5)	O(1)—B—O(2)	99.7(3)
O(1)—C(3)—C(2)	124.3(4)	O(1)—B—C(7)	112.9(3)
O(1)—C(3)—C(4)	112.2(4)	O(1)—B—C(13)	110.6(3)
C(2)—C(3)—C(4)	123.3(4)	O(2)—B—C(7)	107.3(3)
O(1b)—C(3)—C(2b)	118.7(10)	O(2)—B—C(13)	106.4(3)
O(1b)—C(3)—C(4b)	114.2(9)	C(7)—B—C(13)	118.1(3)
C(2b)—C(3)—C(4b)	126.3(12)	C(7)—B—O(1b)	113.3(6)
O(2)—C(4)—C(3)	113.0(5)	C(7)—B—O(2b)	96.6(4)
O(2)—C(4)—C(5)	127.0(4)	C(13)—B—O(1b)	123.0(6)
C(3)—C(4)—C(5)	120.0(4)	C(13)—B—O(2b)	102.3(4)
C(4)—C(5)—C(6)	116.2(4)	O(1b)—B—O(2b)	94.4(7)
N—C(6)—C(5)	121.7(5)	C(3)—O(1b)—B	114.5(8)
C(8)—C(7)—C(12)	115.7(3)	B—O(2b)—C(4b)	102.8(12)
C(8)—C(7)—B	123.1(3)	C(3)—C(2b)—N(b)	109(2)
C(12)—C(7)—B	121.1(3)	C(3)—C(2b)—C(1b)	126(2)
C(7)—C(8)—C(9)	121.9(3)	N(b)—C(2b)—C(1b)	125(3)
C(8)—C(9)—C(10)	120.1(4)	C(3)—C(4b)—O(2b)	114(2)
C(9)—C(10)—C(11)	119.5(4)	C(3)—C(4b)—C(5b)	122.5(15)
C(10)—C(11)—C(12)	120.4(4)	O(2b)—C(4b)—C(5b)	124(2)
C(7)—C(12)—C(11)	122.4(3)	C(4b)—C(5b)—C(6b)	111(2)
C(14)—C(13)—C(18)	114.8(3)	C(2b)—N(b)—C(6b)	122(3)
C(14)—C(13)—B	121.8(3)	C(5b)—C(6b)—N(b)	128(3)
C(18)—C(13)—B	123.4(3)		
	2		
C(3)—O(1)—B	104.7(3)	C(8)—C(9)—C(10)	121.1(6)
C(4)—O(2)—B	108.6(3)	C(9)—C(10)—C(11)	121.2(6)
C(2)—N—C(6)	120.4(4)	C(10)—C(11)—C(12)	119.3(6)
C(2)—N—C(7)	123.5(5)	C(11)—C(12)—C(13)	119.9(6)
C(6)—N—C(7)	116.2(5)	C(8)—C(13)—C(12)	122.3(5)
N—C(2)—C(1)	120.6(5)	C(15)—C(14)—C(19)	115.7(4)
N—C(2)—C(3)	116.6(4)	C(15)—C(14)—B	121.6(4)
C(1)—C(2)—C(3)	122.8(5)	C(19)—C(14)—B	122.7(4)
O(1)—C(3)—C(2)	122.9(4)	C(14)—C(15)—C(16)	122.3(5)
O(1)—C(3)—C(4)	113.6(3)	C(15)—C(16)—C(17)	119.3(5)
C(2)—C(3)—C(4)	123.5(4)	C(16)—C(17)—C(18)	119.9(5)
O(2)—C(4)—C(3)	111.8(4)	C(17)—C(18)—C(19)	119.8(5)
O(2)—C(4)—C(5)	129.7(4)	C(14)—C(19)—C(18)	123.1(5)
C(3)—C(4)—C(5)	118.5(4)	O(1)—B—O(2)	101.2(3)
C(4)—C(5)—C(6)	117.1(5)	O(1)—B—C(8)	111.7(3)
N—C(6)—C(5)	123.9(5)	O(1)—B—C(14)	111.3(3)
C(9)—C(8)—C(13)	116.3(4)	O(2)—B—C(8)	108.8(3)
C(9)—C(8)—B	123.9(4)	O(2)—B—C(14)	110.2(3)
C(13)—C(8)—B	119.7(4)	C(8)—B—C(14)	112.9(3)

Can. J. Chem. Downloaded from www.nrcresearchpress.com by 213.222.148.141 on 09/07/12
For personal use only.

TABLE 5. Intra-annular torsion angles (deg) standard deviations in parentheses

Atoms	Value (deg)
1	
B—O(1)—C(3)—C(4)	7.8(4)
O(1)—C(3)—C(4)—O(2)	−1.8(5)
B—O(2)—C(4)—C(3)	−4.4(4)
C(4)—O(2)—B—O(1)	8.2(4)
C(3)—O(1)—B—O(2)	−9.3(4)
C(4b)—C(3)—O(1b)—B	5.5(13)
O(1b)—C(3)—C(4b)—O(2b)	−2.9(15)
B—O(2b)—C(4b)—C(3)	0.0(13)
O(1b)—B—O(2b)—C(4b)	2.8(11)
O(2b)—B—O(1b)—C(3)	−4.4(10)
2	
B—O(1)—C(3)—C(4)	0.2(4)
O(1)—C(3)—C(4)—O(2)	−1.3(5)
B—O(2)—C(4)—C(3)	1.8(4)
C(4)—O(2)—B—O(1)	−1.6(4)
C(3)—O(1)—B—O(2)	0.8(4)

Acknowledgments

We thank the Natural Sciences and Engineering Research Council of Canada for financial support and the University of British Columbia Computing Centre for assistance. We also thank Mr. P. Borda for the C,H,N analyses.

1. C. ORVIG, S. J. RETTIG, and J. TROTTER. Can. J. Chem. **65**, 590 (1987).
2. M. M. FINNEGAN, S. J. RETTIG, and C. ORVIG. J. Am. Chem. Soc. **108**, 5033 (1986).
3. M. M. FINNEGAN, T. G. LUTZ, W. O. NELSON, A. SMITH, and C. ORVIG. Inorg. Chem. **26**, 2171 (1987).
4. R. L. N. HARRIS. Aust. J. Chem. **29**, 1329 (1976).
5. C. ORVIG. J. Chem. Ed. **62**, 84 (1985).
6. W. O. NELSON, T. KARPISHIN, S. J. RETTIG, and C. ORVIG. Can. J. Chem. **66**, 123 (1988).
7. International tables for X-ray crystallography. Vol. IV. Kynoch press, Birmingham. 1974. pp. 99–102 and 149.
8. P. J. BECKER and P. COPPENS. Acta Crystallogr. Sect. A, **30**, 129 (1974); **30**, 148 (1974); **31**, 417 (1975).
9. P. COPPENS and W. C. HAMILTON. Acta Crystallogr. Sect. A, **26**, 71 (1970).
10. F. R. THORNLEY and R. J. NELMES. Acta Crystallogr. Sect. A, **30**, 748 (1974).
11. V. SCHOMAKER and K. N. TRUEBLOOD. Acta Crystallogr. Sect. B, **24**, 63 (1968).
12. D. W. J. CRUICKSHANK. Acta Crystallogr. **9**, 747 (1956); **9**, 754 (1956); **14**, 896 (1961).
13. A. DOMENICANO, P. MURRAY-RUST, and A. VACIAGO. Acta Crystallogr. Sect. B, **39**, 457 (1983) and references therein.
14. W. KLIEGEL, D. NANNINGA, S. J. RETTIG, and J. TROTTER. Can. J. Chem. **61**, 2493 (1983).
15. S. J. RETTIG and J. TROTTER. Can. J. Chem. **60**, 2957 (1982).
16. S. J. RETTIG, J. TROTTER, W. KLIEGEL, and D. NANNINGA. Can. J. Chem. **56**, 1676 (1978).
17. W. KLIEGEL, U. LAUTERBACH, S. J. RETTIG, and J. TROTTER. Can. J. Chem. **65**, 1457 (1987).

Can. J. Chem. Downloaded from www.nrcresearchpress.com by 213.222.148.141 on 09/07/12
For personal use only.

Trace analysis for aluminum by furnace atomic absorption spectroscopy and differential pulse polarography

KEITH E. JOHNSON, A. KAREN BRICHTA, AND KATHY-LYNN HOLTER
Department of Chemistry, University of Regina, Regina, Sask., Canada S4S 0A2

Received March 2, 1987

KEITH E. JOHNSON, A. KAREN BRICHTA, and KATHY-LYNN HOLTER. Can. J. Chem. **66**, 139 (1988).

The determination of total aluminum in water by furnace atomic absorption spectrometry is best performed with a prior sample treatment with 1% HNO_3 + 2% H_2O_2 or Acid Alizarin Violet N: detection limits of a few $\mu g\ L^{-1}$ are reliably obtained. Ionic aluminum may be measured at levels down to 25 $\mu g\ L^{-1}$ by differential pulse polarography of the aluminum complex with Acid Alizarin Violet N; excesses of Fe^{3+}, Cl^-, and EDTA interfere.

KEITH E. JOHNSON, A. KAREN BRICHTA et KATHY-LYNN HOLTER. Can. J. Chem. **66**, 139 (1988).

Pour déterminer l'aluminium total dans l'eau en utilisant la spectrométrie d'absorption atomique, il y a lieu de soumettre l'échantillon à un traitement préalable avec du HNO_3 à 1% + du H_2O_2 à 2% ou de l'Alizarine Violet N Acide; on peut ainsi obtenir des limites de détection de quelques $\mu g\ L^{-1}$ qui sont faibles. On peut mesurer l'aluminium ionique à des niveaux allant jusqu'à 25 $\mu g\ L^{-1}$ en faisant appel à la polarographie pulsée différentielle du complexe de l'aluminium avec l'Alizarine Violet N Acide; des excès de Fe^{3+}, de Cl^- ou d'EDTA interfèrent dans cette réaction.

[Traduit par la revue]

Can. J. Chem. Downloaded from www.nrcresearchpress.com by 213.222.148.141 on 09/07/12
For personal use only.

Acid rain (rain with a pH of less than 5.6) is able to leach several metals from sediments and soils; among the metals that pass into groundwater and, sometimes, surface water is aluminum which is believed to be toxic to fish, other aquatic organisms, and several plant species (1). The forms of aluminum in water included the hydrated ion, $Al(H_2O)_6^{3+}$, relatively weak inorganic complexes, and strong organic complexes and there is evidence that the toxicity *de*creases in this sequence. The aluminum levels of concern are $\mu g/L$ (ppb).

Any study of the aluminum toxicity of water would be aided if one could determine the ionic aluminum rather than simply the total aluminum. The approach of Campbell *et al.* (2) was to equilibrate with a chelating ion exchange resin and determine the non-exchanged aluminum remaining in solution: the exchanged or ionic aluminum amounted to the difference between the first value and the total. Most of their actual aluminum determinations were made by furnace atomic absorption spectroscopy (FAAS) although the Lumogallion spectrofluorometric method was also found to be satisfactory. They noted rapid exchange of inorganic aluminum species, slow exchange in the presence of fulvic and humic acids, and an intermediate rate of exchange for natural samples.

We have considered an alternative characterization of free ionic aluminum which might be susceptible to direct measurement, i.e., an electrochemical approach. Since most groups will probably continue to use FAAS or ICP spectrometry, if available, as a routine method for determining total aluminum, we have carried out a cursory statistical study of various FAAS preliminary sample treatments.

The obvious electrochemical technique to consider for an ion at trace levels in solution is some form of polarography but the aluminum reduction wave is obscured by that of hydrogen in the simple dc mode; although some resolution was obtainable by the differential pulse technique (3), the detection limit was in the mg/L range whilst many ions found in natural waters interfere in such an analysis. Willard and Dean (4), meanwhile, showed that aluminum could be determined at the 0.1 mg/L level by dc polarography of its complex(es) with an azo-dye such as Alizarin Violet N (Solochrome Violet RS). The next step was to apply the more sensitive variations of linear sweep polarography (5), derivative polarography (6, 7) and differential pulse polarography[1] to the aluminum–dye system: sensitivities of 20, 10, and 25 $\mu g/L$, respectively, were obtained. We elected to test differential pulse polarography of the aluminum–dye complex for sensitivity, for iron interference and for other chelon interactions. It should be noted that in utilizing the reduction (or oxidation!) of the aluminum–dye complex (6, 7), we are not changing the Al^{3+}/Al potential by complexing Al^{3+} with dye but, rather, the dye reduction potential by differential complexing of Al^{3+} with dye (—N=N—) and reduced dye (—NH—NH—) or the dye oxidation potential by differential complexing of Al^{3+} with dye (—N=N—) and oxidized dye (—N=N—). Any metal ion – dye wave should occur at

approximately RT/nF ln K_2K_1 from the dye wave where the K's are the corresponding stability constants of metal ion with dye in its different oxidation states.

Experimental

(a) Furnace atomic absorption spectroscopy

The primary standard aluminum solution (1 g/L) was obtained from Fisher Scientific Company: it had been made by dissolving high purity metal in dilute HCl. Acid Alizarin Violet N (sodium 4-hydroxy-3-[(2-hydroxy-1-naphthalenyl)azo]benzenesulfonate) (60%) was used as obtained from Aldrich Chemical Company.

All samples were prepared daily and stored in polypropylene flasks (8) (glass absorbs a significant proportion of aluminum ions when they are only present at the $\mu g/L$ level), Nalgene pipettes were used for transfers. Unused flasks and pipettes were kept in contact with HNO_3 and, when required, were repeatedly rinsed with acid and water.

Measurements were made on an Hitachi 180-80 Polarized Zeeman Atomic Absorption Spectrophotometer equipped with graphite furnace, high temperature sensor, and auto-sampler and Hitachi 180-0205 Data Processing Unit. The instrument parameters are given in Table 1. The graphite tubes only gave reproducible results if limited to 80 runs each and the plastic sample holders could not be adequately cleaned between runs and so were disposed of after each run. The sample volume was 10 μL, each sample was injected thrice and all measurements were made in the peak height mode.

(b) Differential pulse polarography

The aluminum stock solution was prepared from $AlK(SO_4)_2 \cdot 12H_2O$

[1]Metrohm instruments, courtesy of J. G. Dick.

Can. J. Chem. Downloaded from www.nrcresearchpress.com by 213.222.148.141 on 09/07/12
For personal use only.

TABLE 1. FAAS instrument parameters

Instrument	Hitachi 180-80	Processor 180-0205	
Analytical report	Lamp current	7.5 mA	
	Wavelength	309.3 nm	
	Slit width	1.3 nm	
	Cuvette type	Tube pyrolytically coated	
	Carrier gas	200 mL/min	
	Sample volume	10 μL	
Measurement report	Analytical mode	AAS (ABS)	
	Measurement mode	Peak height	
	Equation type	Linear fit (N/A)	
	Zeeman AA mode	ZAA	
	Recorder output	Direct (0.5 s)	
	Scale expansion	1.0×	
	Repeat times	3	
Heating program	Stage	Temperature (°C)	Time (s)
	Dry	80–120	30.0
	Ash	700	30.0
	Atomize	2800	7.0
	Clean	2800	3.0

(BDH). Acid Alizarin Violet N and Solochrome Violet RS are two names given to the same formulated dye. Acid Alizarin Violet N, ostensibly 60% from Aldrich, was either used as supplied (200 mg in 100 mL water to give 120 mg "pure" dye in 100 mL) or recrystallized to ~90% purity from absolute ethanol (130 mg of material in 100 mL water taken to yield 120 mg "pure" dye). Solochrome Violet RS from ICN Pharmaceuticals Inc. was taken, as supplied, to be 100% pure (an incorrect assumption as we shall see). Other chemicals were from BDH or Fisher. Flasks, pipettes, and vials were of polypropylene (Cole-Parmer) and were acid- and water-washed prior to use.

pH values were measured with a Corning Scientific pH Meter, Model 7. Polarograms were obtained with a Metrohm Polarecord 626 (with 60 Hz filter added) and a vintage (pre-1965) E354 Metrohm Polarography stand bearing a mercury electrode with electronically controlled drop knocker. The auxiliary electrode was platinum and the reference sce.

(c) Ultraviolet–visible spectroscopy

Dilute dye solutions were studied by means of a Beckman Model 26 UV/Visible spectrophotometer.

(d) Ion chromatography

Chloride determinations were performed on a Dionex 4002i ion chromatograph using an AS4A column in the HPIC mode with $NaHCO_3$ eluant.

(e) Natural water samples

Samples were collected from several sites in Southern Saskatchewan in 1983 and 1987.

Results and discussion

The average aluminum concentrations obtained by furnace AAS for several sample sets (a sample set is a set of samples derived from the standard and measured on a particular occasion) in the 4 matrices: distilled water, 1% HNO_3, 1% HNO_3 + 2% H_2O_2, and Acid Alizarin Violet N were compared. The statistical summary appears in Table 2. Although one might argue that distilled water and 1% HNO_3 give adequate sensitivity and lowest detection limits respectively, the decidedly better variance and coefficient of variation data obtained with the dye present or with 1% HNO_3 + 2% H_2O_2, particularly neglecting low concentrations in the latter case, suggest that *furnace AAS for aluminum be carried out either in the presence of a complexing agent or a mildly oxidizing acid solution of* $HNO_3 + H_2O_2$. This conclusion is consistent with the practices of some groups but no definitive study of the relative merits of different procedures has appeared.

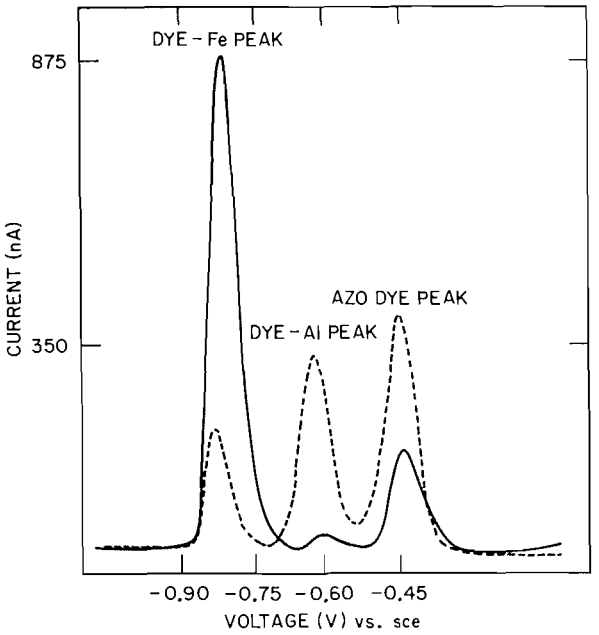

FIG. 1. Differential pulse polarograms of Acid Alizarin Violet N in the presence of different ratios of Fe^{3+} to Al^{3+}. Solid line represents 10-fold Fe^{3+} excess, broken line equal concentrations.

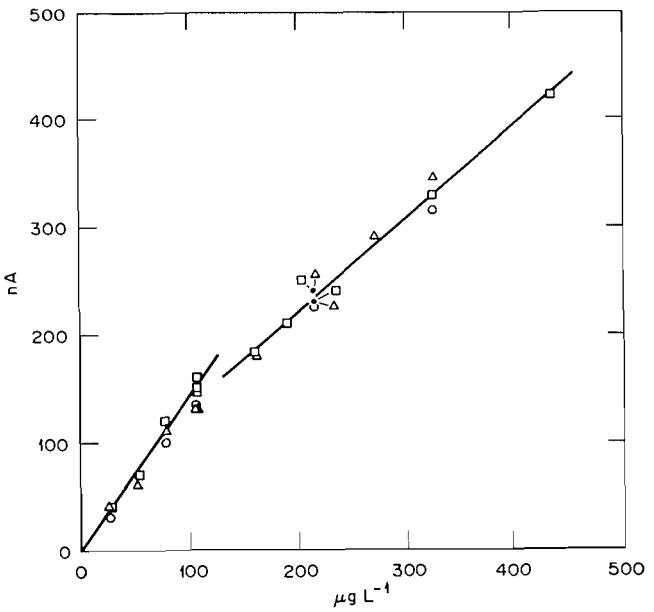

FIG. 2. Calibration graph for DPP of the aluminum–dye complex. AAVN concentration (unpurified) ~67 m*M*. SRVS concentration (actual) 45 m*M*. □, AAVN; △, AAVN recrystallized; ○, SRVS.

Acid Alizarin Violet N (AAVN) or Solochrome Violet RS (SVRS) in aqueous solution gave a differential pulse reduction peak at −0.44 V vs. sce (Fig. 1). Addition of aluminum ions reduced the size of the AAVN peak concurrent with the growth of a new peak at −0.60 V.

The peak current was least sensitive to pH in the range 4 to 4.5 so this condition was imposed. The peak current vs. concentration relation appears as Fig. 2. Two linear regions are apparent (25 to 120 μg L^{-1}, correlation coefficient 0.9971 and

TABLE 2. Summary of FAAS statistical results

Matrix	H_2O	1% HNO_3	1% HNO_3/H_2O_2	AAVN
Number of measurements	24	45*	36	31
Range	1–15 μg/L	1–15	1–15	1–15
Variances ≥5	8	5	4	0
Coefficient of variation ≥25%	7	12	6	0
C.V. excluding lower concentrations, ≥25%	2	5	1	0
Sensitivity range of sample set	1–2 μg/L	1–3	1–3	1–4
Detection limit range of sample set	1–3 μg/L	1–4	2–4	1–4

*5 sets of samples in this matrix, 4 otherwise.

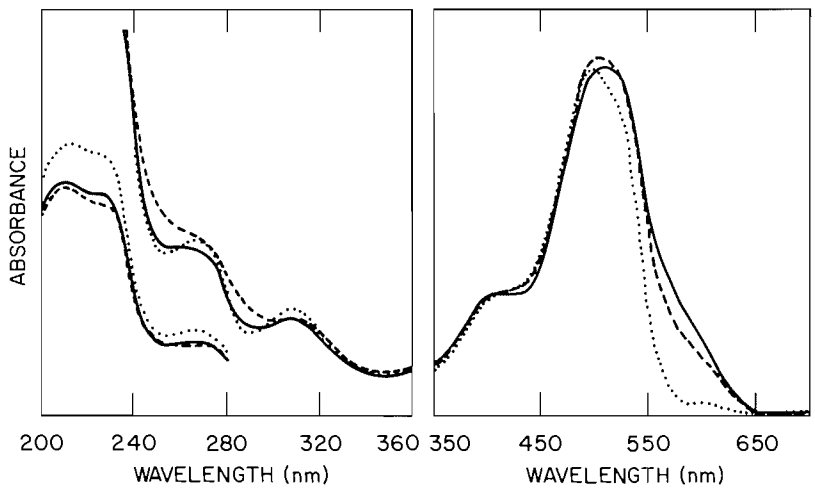

FIG. 3. Normalized (by 500 nm peak) spectra of AAVN (—), AAVN recrystallized (- - -) and SRVS (····) in water at 22°C dye concentrations 0.07 m*M* for visible and 0.035 m*M* for uv region.

TABLE 3. Al concentrations in natural waters

Site	Location	AA (1987)	AA (1983)	DPP (1987)
1	Estevan Gen. Stn., Souris	28.4± 3.9 ppb	64.5	
2	Boundary Dam CW Inlets	341.5±27.7	170	340
3	Poplar River Gen. Stn. CW Inlet	34.0± 3.3		
4	Sask River at Nipawin	6.2± 0.6	3.2	
5	Weyburn, Souris	3.7± 0.4		
6	Q.E. Gen. Stn., Saskatoon	24.2± 2.4	1.4	
7	Regina Beach-boat dock	97.9± 8.6	63	19.3
8	Buffalo Pound L-boat dock	12.5± 2.0	118	

140 to 400 μg L^{-1}, correlation coefficient 0.9988). The change-over concentration corresponded to a dye:aluminum molar ratio of 14. The formal stability constants of the [Al(AAVN)] and $[Al(AAVN)_2]^{3-}$ complexes were determined (9) as log K_1 = 18.4 and log K_2 = 13.2 so that complete conversion to the second complex would be anticipated. Recrystallization of AAVN did not substantially change the lines.

In the presence of Fe^{3+}, both the AAVN and Al—AAVN reduction peaks were reduced in size and a new Fe—AAVN peak appeared (Fig. 1). Provided the iron concentration did not exceed the aluminum concentration, the Al—AAVN peak still gave a satisfactory measure of the aluminum; a 10-fold Fe^{3+} excess virtually eliminated the Al—AAVN peak.

EDTA was examined as an organic ligand competitor of AAVN for the aluminum with the result that no Al—AAVN peak was obtained in the presence of a many-fold excess of EDTA.

Thus, electroactive or ionic aluminum can be determined by differential pulse polarography without interference from moderate iron concentration. However, calibration over a broad concentration range is essential for the obtaining of precise results.

Can. J. Chem. Downloaded from www.nrcresearchpress.com by 213.222.148.141 on 09/07/12
For personal use only.

The spectral study showed that the SVRS is also impure (~66% purity). The gross impurity in the manufactured products was identified by HPIC as sodium chloride from the "salting out" step. The finer structure of the spectra (Fig. 3) suggests that AAVN and SVRS are not exactly the same dyes (cf. especially the 600 nm region).

Table 3 gives the approximate locations of the 1987 sampling locations, together with the aluminum concentrations determined by FAAS with the AAVN matrix. The aluminum levels at or near some of these locations in 1983 are included for interest. When the AA standard solutions were examined by differential pulse polarography, aluminum levels <50 ppb were not measurable but solutions with ≥ 50 ppb Al gave the same pulse currents as those prepared from $AlK(SO_4)_2$ standards. This indicates that the Cl^- in the AA standards interferes with pulse polarography at low levels; the Cl^- inadvertently added with impure dye was insufficient in quantity to interfere. Only samples 2 and 7 contained sufficient aluminum to test the DPP method. As shown, all of the Al found by AA in sample 2 was electroactive but only some of that in sample 7 responded to DPP. No chloride was detected in sample 7. When the chloride content of sample 2 was increased to ~1300 times the Al content, ~90 ppb Al (of the 340 ppb) was found in sample 2 by DPP.

We conclude that the differential pulse polarographic determination of ionic aluminum holds promise provided the reagent chloride level is low. Further studies would be required to discern whether chloride would prevent aluminum uptake by live organisms and, if so, without killing them.

Acknowledgements

This work was supported in part by Environment Canada and the Alcoa Foundation. A.K.B. is grateful for the award of a Herzberg Scholarship.

1. J. W. Robinson and P. M. Deano. Am. Lab. July 1986. p. 17.
2. P. C. G. Campbell, M. Bisson, R. Bougie, A. Tessier, and J.-P. Villeneuve. Anal. Chem. **55**, 2246 (1983).
3. G. S. P. Ritchie, A. M. Posner, and I. M. Ritchie. Anal. Chim. Acta, **117**, 233 (1980).
4. H. H. Willard and J. A. Dean. Anal. Chem. **22**, 1264 (1950).
5. T. M. Florence and D. B. Izard. Anal. Chim. Acta, **25**, 386 (1961).
6. T. M. Florence, F. J. Miller, and W. E. Zittel. Anal. Chem. **38**, 1065 (1966).
7. T. M. Florence and W. L. Belew. J. Electroanal. Chem. **21**, 157 (1969).
8. K. E. Johnson, F. W. Yerhoff, J. Robinson, and C. Dehm. Anal. Chim. Acta, **149**, 129 (1983).
9. E. Coates and B. Rigg. Trans. Faraday Soc. **58**, 2058 (1962).

Can. J. Chem. Downloaded from www.nrcresearchpress.com by 213.222.148.141 on 09/07/12
For personal use only.

The He(I) photoelectron spectra of 2-butynal and related oxyalkynes

DIETER KLAPSTEIN[1] AND ROBERT T. O'BRIEN
Department of Chemistry, St. Francis Xavier University, Antigonish, N.S., Canada B2G 1C0

Received May 11, 1987

DIETER KLAPSTEIN and ROBERT T. O'BRIEN. Can. J. Chem. **66**, 143 (1988).

The He(I), λ = 58.4 nm, photoelectron spectra of 2-butynal and the related compounds 2-butynol, 2-butynoic acid, 2-butynoyl fluoride, and 2-butynoyl chloride were obtained. The lower ionization energy bands may be assigned to photoionization from specific orbitals by comparison within the series, with related species and with the use of semi-empirical MO calculations. The energy variation of the more localized orbitals with substituent variation may be rationalized in terms of the inductive and resonance effects of the substituents.

DIETER KLAPSTEIN et ROBERT T. O'BRIEN. Can. J. Chem. **66**, 143 (1988).

On a déterminé les spectres photoélectroniques He(I), à une longueur d'onde de 58,4 nm, du butyne-2 al et des composés suivants qui lui sont apparentés : le butyne-2 ol, l'acide butyne-2 oïque, les fluorure et chlorure de butyne-2 oyle. En se basant sur des comparaisons, à l'intérieur de séries, avec des espèces apparentées et en utilisant des calculs d'OM semi-empiriques, on peut attribuer les bandes d'énergies d'ionisation plus faibles à des orbitales spécifiques. Pour rationaliser la variation d'énergie des orbitales plus localisées en fonction de la nature des substituants, on fait appel aux effets inductifs et de résonance des substituants.

[Traduit par la revue]

Introduction

In a previous paper (1) the valence shell helium(I) photoelectron spectra of a series of α,β-unsaturated carbonyl compounds of the general structure (**I**):

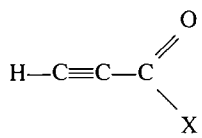

I

with X = H, F, Cl, OH, and CH_3 were presented and interpreted. These species are of interest in the investigation of the electronic structure of molecules since their small size results in generally resolvable bands in the photoelectron spectra and also makes the species attractive for computational modelling of the electronic interactions.

This work extends the investigation to the methyl-substituted analogues of **I**:

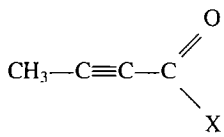

II

where X = H, F, Cl, OH and the related alcohol, 2-butynol, the spectra of which have not previously been reported. The aim of the study was to determine (*i*) the relative energies and identities of the higher occupied molecular orbitals, and their variation with the carbonyl substituents, (*ii*) the degree of interaction of the out-of-plane orbitals in these planar species (C_s symmetry), and (*iii*) compare these results with those observed for the terminal alkynyl compounds (1) to deduce the influence of the methyl group.

Experimental

The spectra were obtained with a photoelectron spectrometer incorporating a helium high voltage d.c. discharge lamp (54.8 nm, 21.22 eV) and a 127° cylindrical sector electron analyzer operated in a constant resolution mode. Signals were acquired with a Nicolet 1170 Signal Averager and Apple IIe microcomputer data acquisition system. The ionization energies were calibrated with Ar, N_2, CH_3I, H_2O, and HCl. The full spectra were obtained with a resolution of 30 meV, while structured bands were recorded with a resolution of 20–25 meV. Sharp bands have an ionization energy uncertainty of ±0.02 eV, while for broad bands it is ±0.1 eV. Vibrational intervals are ±80 cm^{-1}.

Semi-empirical MO calculations were carried out using CNDO/2 (2) and HAM/3 (3) programs adapted for use on a VAX-11/780 computer. The HAM/3 program was not parameterized for chlorine. The CNDO/2 MO eigenvalues have been divided by a factor of 1.35 for comparison with the vertical ionization energies (for the low IE region this corresponds to the 4 eV correction factor (4) commonly used).

As no structural parameters have been determined experimentally for these species, the relevant parameters were transferred from propynal (5), propynoyl fluoride (6), propynoyl chloride (7), and propynoic acid (8). Vibrational assignments in the photoelectron spectra were made by comparison with the frequencies for the neutral molecules (9), when available, and considering the bonding characteristics of the source molecular orbitals.

Commercial samples of 2-butynol (Aldrich) and 2-butynoic acid (Farchan) were used. 2-Butynal was prepared by the oxidation of 2-butynol using aqueous CrO_3 (10). 2-Butynoyl fluoride was prepared by reacting 2-butynoic acid with benzoyl fluoride (11). 2-Butynoyl chloride was prepared by reacting 2-butynoic acid with thionyl chloride. Sample purities were checked by infrared spectroscopy (9).

Results and discussion

The photoelectron spectra are shown in Figs. 1 to 5. The measured vertical ionization energies and observed vibrational structure are given in Tables 1 to 5, along with the predicted ionization energies and orbital symmetries from the semi-empirical MO calculations, and the band assignments. The latter are only possible in the lower IE regions of the spectra where most of the bands are at least partially resolvable and for which comparisons with structurally related molecules may be made. The following discussions of the individual spectra are limited to the lower IE bands. The C_s symmetry of the molecular species results in MO classifications of *a'* (in-plane) or *a"* (out-of-plane). However, the higher occupied MOs are usually quite localized in specific areas of the molecules (e.g. n_O', π_{CC}''). The discussion uses this latter concept as it provides more chemically useful information.

2-Butynol

The full spectrum is shown in Fig. 1. The low IE bands are

[1]Author to whom correspondence should be addressed.

Can. J. Chem. Downloaded from www.nrcresearchpress.com by 213.222.148.141 on 09/07/12
For personal use only.

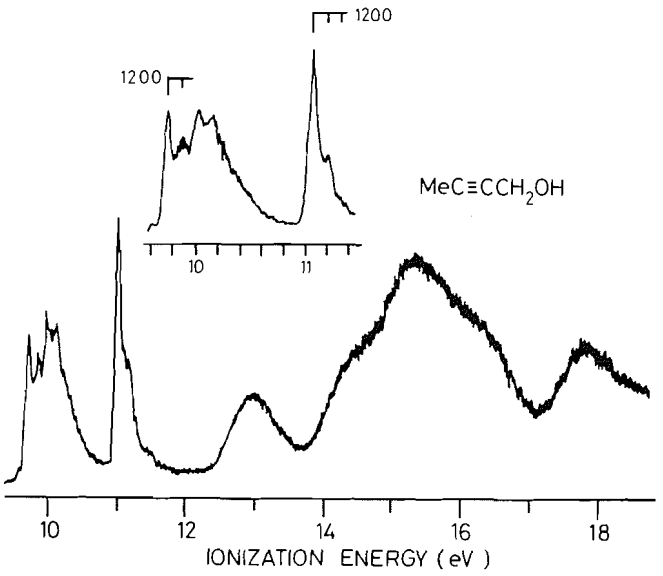

FIG. 1. The He(I) photoelectron spectrum of 2-butynol. The inset shows some of the vibrational structure (cm^{-1}).

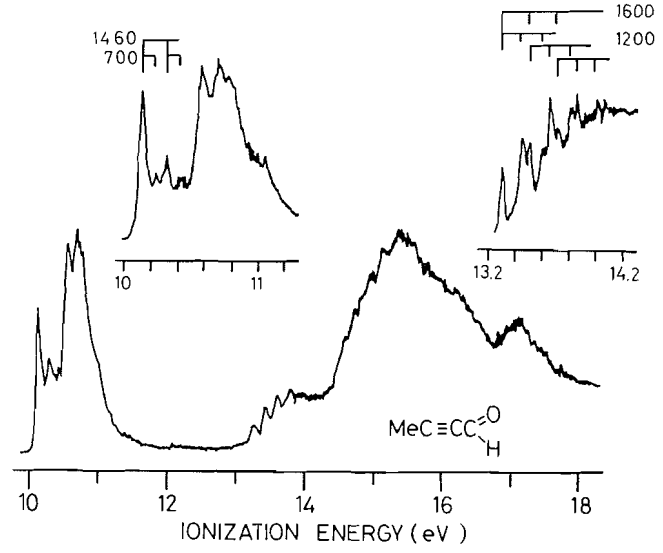

FIG. 2. The He(I) photoelectron spectrum of 2-butynal. The insets show some of the vibrational structure (cm^{-1}).

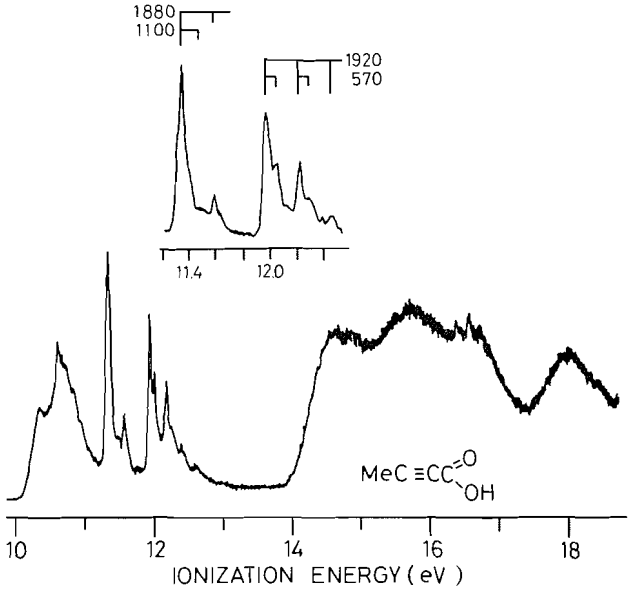

FIG. 3. The He(I) photoelectron spectrum of 2-butynoic acid. The inset shows some of the vibrational structure (cm^{-1}).

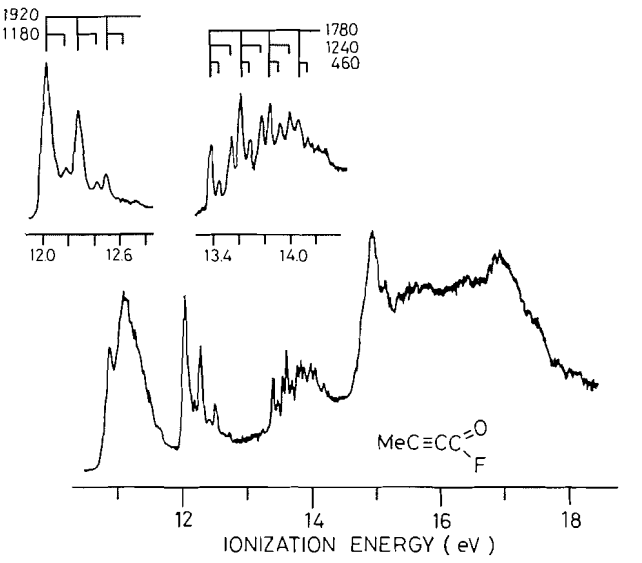

FIG. 4. The He(I) photoelectron spectrum of 2-butynoyl fluoride. The insets show some of the vibrational structure (cm^{-1}).

expected to arise from ionization from orbitals which may be described as π'_{CC}, π''_{CC}, and n''_O. Considering related molecules, the (degenerate) π_{CC} band of 2-butyne appears at 9.56 eV (12), while the n''_O bands of CH_3OH (13) and $HC{\equiv}CCH_2OH$ (14) appear at 10.96 and 11.37 eV, respectively. The π_{CC} bands of 2-butynol are thus expected to be found at lower IEs than the n''_O band. The lowest IE band, at 9.74 eV, is assigned as $(\pi''_{CC})^{-1}$ and is overlapping with the second band at 10.01 eV, assigned as $(\pi'_{CC})^{-1}$. While both π_{CC} orbitals have been stabilized slightly relative to 2-butyne by the inductive effect of the alcohol group, the π''_{CC} orbital is also destabilized by conjugation with the energetically close n''_O orbital of the alcohol group. The energy difference of 0.27 eV between the $(\pi_{CC})^{-1}$ bands is twice that observed for 2-butynal (below), for which the other a'' orbitals (π''_{CH_3} and π''_{CO}) are much further away in energy. The first band shows some initial vibrational structure of 1200 cm^{-1} which is then lost due to overlap with the second band. The $(n''_O)^{-1}$ band is located at 11.06 eV; the weak cationic vibrational progression of 1200 cm^{-1} is probably excitation of the ν(C—O) stretching mode.

The broad band observed at 12.96 eV ionization energy is assigned to ionization from an in-plane orbital which the MO calculations predict to be centered mainly on the oxygen atom. Similar bands are assigned for methanol at 12.62 eV (13), ethanol at 12.18 eV (13), and prop-2-yn-1-ol at 13.22 (14).

2-Butynal

The structure of 2-butynal consists of the planar aldehyde functional group attached to a propynyl group. The low IE orbitals are predicted by the MO calculations to be n'_O and the acetylenic π''_{CC} and π'_{CC} orbitals. Figure 2 shows that the spectrum has only two distinct bands in the 9 to 13 eV region but the second has roughly twice the intensity of the first.

The location of the $(n'_O)^{-1}$ band can be predicted by considering the results for related molecules. The $(n'_O)^{-1}$ band of propynal has an IE of 10.70 eV (1). Substitution of the

Can. J. Chem. Downloaded from www.nrcresearchpress.com by 213.222.148.141 on 09/07/12
For personal use only.

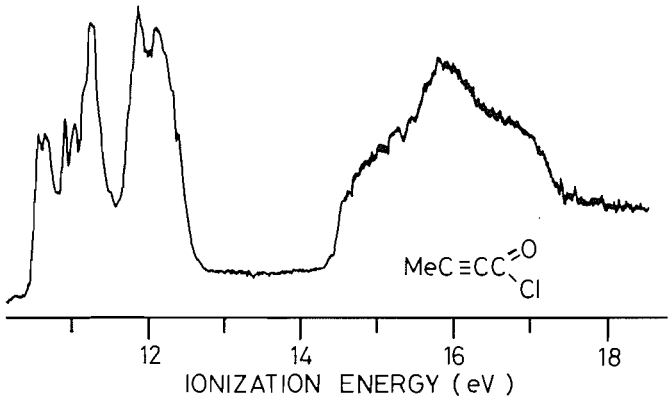

FIG. 5. The He(I) photoelectron spectrum of 2-butynoyl chloride.

TABLE 1. Results and assignments for 2-butynol, $CH_3C{\equiv}CCH_2OH$

IE (eV)	Vibrational structure (cm^{-1})	Assignment	CNDO/2[a]	HAM/3
9.74	1200	$4a'' : \pi''_{CC}$	9.91 a''	9.25 a''
10.01		$15a' : \pi'_{CC}$	10.39 a'	9.84 a'
11.06	1200	$3a'' : n''_O$	12.12 a''	10.23 a''
12.96		$14a' : \sigma_{COH}$	12.26 a'	12.21 a'
14.7			14.33 a'	13.94 a''
				14.04 a'
15.4			15.52 a'	14.26 a'
			16.02 a''	15.08 a'
16.4			16.75 a'	15.50 a''
				16.55 a'
17.8			18.44 a''	
			18.55 a'	
				19.95 a'
			22.59 a'	

[a]Calculated eigenvalues divided by 1.35.

terminal hydrogen with a methyl group should result in a shift to lower ionization energy, similar to the 0.41 eV shift observed for propionaldehyde (15) relative to acetaldehyde (16). Thus the first band of the 2-butynal spectrum at 10.15 eV, is assigned as $(n'_O)^{-1}$. Some vibrational structure is observed on this band (Fig. 2): the 1460 cm^{-1} main progression could be the cationic carbonyl stretching mode while the weaker 700 cm^{-1} progression could be the ν(C—C) stretching mode.

The second prominent band of the spectrum is assigned to ionization from the π''_{CC} and π'_{CC} orbitals. For propynal (1), these bands are observed at 11.52 and 11.57 eV, respectively, the out-of-plane orbital being slightly destabilized relative to the in-plane by interaction with the carbonyl π-orbital at higher binding energy. Close examination of the 2-butynal spectrum (Fig. 2) shows two distinct maxima on the second band, at 10.59 and 10.73 eV IE, which are assigned as the vertical IEs of the $(\pi''_{CC})^{-1}$ and $(\pi'_{CC})^{-1}$ bands. The substantial shift to lower IEs for these bands, compared to propynal, results from the electron-donating ability of the methyl group. The energy difference of the $(\pi_{CC})^{-1}$ bands reflects the relative degree of interaction of π''_{CC} with the other out-of-plane localized orbitals π''_{CH_3} and π''_{CO}, both of which are more stable. Since this difference is small, it is concluded that the interaction is also small (on the photoelectron energy scale).

The next band of the spectrum has a broad Franck–Condon profile, with an adiabatic IE of 13.30 eV, a vertical IE of

TABLE 2. Results and assignments for 2-butynal, $CH_3C{\equiv}CCHO$

IE (eV)	Vibrational structure (cm^{-1})	Assignment	CNDO/2[b]	HAM/3
10.15	1460, 700	$14a' : n'_O$	10.22 a'	9.84 a'
10.59		$3a'' : \pi''_{CC}$	10.42 a''	10.57 a'
10.73		$13a' : \pi'_{CC}$	11.00 a'	10.58 a''
13.64[a]	1600, 1200	$2a'' : \pi''_{CO}$	14.41 a''	13.44 a''
14.8			14.58 a'	14.47 a'
15.4			15.50 a'	14.54 a''
				14.58 a'
16.2			16.70 a'	15.19 a'
				16.6 a'
17.1			17.49 a''	
			19.11 a'	19.61 a'

[a]Adiabatic IE = 13.30 eV.
[b]Calculated eigenvalues divided by 1.35.

TABLE 3. Results and assignments for 2-butynoic acid, $CH_3C{\equiv}CCOOH$

IE (eV)	Vibrational structure (cm^{-1})	Assignment	CNDO/2[a]	HAM/3
10.36		$18a' : n'_O$	10.41 a''	10.35 a'
10.63	(1060)	$4a'' : \pi''_{CC}$	10.45 a'	10.39 a''
11.35	1880, 1100	$17a' : \pi'_{CC}$	11.01 a'	10.76 a'
11.96	1920, 570	$3a'' : n''_O$	12.04 a''	11.56 a''
			12.76 a'	13.77 a'
14.61				14.30 a''
				14.37 a'
15.5			15.38 a'	15.03 a'
				15.07 a''
			16.03 a'	15.59 a'
				16.85 a'
16.53	1340		16.06 a''	
			17.03 a'	
18.0			17.84 a'	
			18.07 a''	19.65 a'
			21.44 a'	

[a]Calculated eigenvalues divided by 1.35.

TABLE 4. Results and assignments for 2-butynoyl fluoride, $CH_3C{\equiv}CCOF$

IE (eV)	Vibrational structure (cm^{-1})	Assignment	CNDO/2[b]	HAM/3
10.84		$18a' : n'_O$	10.93 a''	10.77 a'
11.06		$4a'' : \pi''_{CC}$	11.12 a'	10.82 a''
12.03	1920, 1180	$17a' : \pi'_{CC}$	11.40 a'	11.27 a'
13.62[a]	1780, 1240, 460	$3a'' : \pi''_{CO}$	13.34 a''	13.29 a''
14.93		$16a' : n'_F$	13.59 a'	14.53 a''
15.5			15.68 a'	14.56 a'
15.9			16.34 a'	14.75 a'
				15.37 a'
16.73				
				16.09 a'
			16.73 a''	17.04 a''
			17.59 a'	
			18.61 a''	18.37 a'
			18.89 a'	

[a]Adiabatic IE = 13.39 eV.
[b]Calculated eigenvalues divided by 1.35.

Can. J. Chem. Downloaded from www.nrcresearchpress.com by 213.222.148.141 on 09/07/12
For personal use only.

TABLE 5. Results and assignments for 2-butynoyl chloride, $CH_3C{\equiv}CCOCl$

IE (eV)	Vibrational structure (cm^{-1})	Assignment	CNDO/2[a]
10.59		$22a' : n'_O$	9.78 a'
10.92	830	$4a'' : \pi''_{CC}$	10.51 a''
11.26		$21a' : \pi'_{CC}$	10.69 a'
11.87		$3a'' : n''_{Cl}$	11.12 a''
12.13		$20a' : n'_{Cl}$	11.44 a'
14.80		$2a'' : \pi''_{CO}$	15.01 a'
15.17			15.36 a''
15.90			15.72 a'
			16.70 a'
16.9			17.63 a''
			17.94 a'
			20.73 a'

[a]Calculated eigenvalues divided by 1.35.

13.64 eV, and some resolved vibrational structure (Fig. 2). This band is assigned to the $(\pi''_{CO})^{-1}$ ionization on the basis of its energy and characteristic structure. The $(\pi''_{CO})^{-1}$ band of propynal is found at 14.22 eV (vertical), the shift to lower IE for 2-butynal resulting from both the positive inductive and resonance effects of the methyl group. While the vibrational structure is not completely resolved, the observed 1600 cm^{-1} progression could be the cationic $\nu(C{\equiv}C)$ mode while the 1200 cm^{-1} interval might be excitation of the $\nu(C{=}O)$ mode. As found for propynal and the propynoyl halides (1), the Franck–Condon profile of the $(\pi''_{CO})^{-1}$ band indicates a considerable change in geometry between the neutral ground state and the resulting doublet state of the cation.

2-Butynoic acid

For the interpretation of the photoelectron spectrum, 2-butynoic acid may be thought of as a hybrid of 2-butynol and 2-butynal, the alcohol and aldehyde groups combining to produce the acid group. The full spectrum is shown in Fig. 3. Four bands are expected with IEs less than 14 eV: ionization from the n'_O (carbonyl), π''_{CC}, π'_{CC}, and n''_O (hydroxyl) orbitals.

The $(n'_O)^{-1}$ band of 2-butynal is found at 10.15 eV. For the acid it should be shifted to higher IE by the inductive effect of the hydroxyl group. The first band of the spectrum, at 10.36 eV IE, is assigned as $(n'_O)^{-1}$. The next two bands, at 10.63 and 11.35 eV, are assigned as $(\pi''_{CC})^{-1}$ and $(\pi'_{CC})^{-1}$, respectively. The out-of-plane orbital energy is destabilized considerably relative to the in-plane by interaction with the n''_O orbital of the hydroxyl oxygen. The $(\pi''_{CC})^{-1}$ band is partially overlapping with the $(n'_O)^{-1}$ band but has a considerably broader profile than the $(\pi'_{CC})^{-1}$ band. This could be a result of delocalization of the out-of-plane system. The $(\pi'_{CC})^{-1}$ band has the characteristically sharp Franck–Condon profile of an acetylenic π-band (Fig. 3). The short vibrational progression of 1800 cm^{-1} results from excitation of the cationic $\nu(C{\equiv}C)$ stretching mode. A weaker progression of 1100 cm^{-1} could be a $\nu(C{-}C)$ stretching mode.

The fourth band, vertical IE 11.96 eV, arises from ionization from the n''_O orbital, centered on the hydroxyl oxygen atom. The corresponding band of 2-butynol appears at 11.06 eV while for methanol it is found at 10.96 eV (13). In this case, the n''_O orbital energy is lowered substantially (IE increased) by its interaction with the other out-of-plane orbitals, most importantly with π''_{CC}. The $(n''_O)^{-1}$ band has been shifted to higher IE while the $(\pi''_{CC})^{-1}$ band has been shifted to lower IE relative to the $(\pi'_{CC})^{-1}$ band as a result of this interaction. This delocalization is also evident from the extensive vibrational structure observed on the $(n''_O)^{-1}$ band, shown in Fig. 3, compared to the corresponding band of 2-butynol. The main progression of 1920 cm^{-1} is probably the $\nu(C{\equiv}C)$ stretching mode while the weaker 570 cm^{-1} progression could be a bending mode. An alternative band assignment scheme would be to assign the 11.35 eV band as (n''_O) and the 11.96 eV band as $(\pi'_{CC})^{-1}$. However, this gives a low IE for $(n''_O)^{-1}$ compared to other simple carboxylic acids: CH_3COOH, 12.05 eV (17); CH_3CH_2COOH, 12.04 eV (17); $HC{\equiv}CCOOH$, 12.46 eV (1); and $CH_2{=}CHCOOH$, 12.00 eV (18).

The $(\pi''_{CO})^{-1}$ band, clearly discernible for 2-butynal at 13.64 eV, has been shifted to higher IE by the inductive effect of the hydroxyl group and is probably one of at least two bands overlapping at 14.61 eV.

2-Butynoyl fluoride

Substitution of the aldehyde hydrogen of 2-butynal by fluorine results in two effects. The strong electron-withdrawing ability of fluorine should result in a general shift of ionization energies to higher values. Secondly the "lone-pair" orbitals of the halogen are of the correct symmetry and similar size to interact with other localized orbitals; this is especially true for the out-of-plane orbitals.

The spectrum of 2-butynoyl fluoride is shown in Fig. 4. The similarities in the electronic effects of the OH and F groups is demonstrated by the similarity of the shapes and relative positions of the first three bands of the acid and the acid fluoride. The $(n'_O)^{-1}$ band of the acid fluoride is the first band at 10.84 eV. No vibrational structure is observable as there is considerable overlap with the second band, vertical IE 11.06 eV, which is assigned to the $(\pi''_{CC})^{-1}$ ionization. The lack of vibrational structure on the second band might be the result of delocalization of the π''_{CC} orbital over the molecular out-of-plane π-system or simply due to the overlap of the first two bands.

The third band, at 12.03 eV, must be assigned to ionization from the π'_{CC} orbital. The well-resolved vibrational structure (Fig. 4) has a main progression of 1920 cm^{-1} which is the cationic $\nu(C{\equiv}C)$ stretching mode; a weaker excitation of 1180 cm^{-1} may be one of the combinations of C—C and C—F stretching modes. The relatively large energy difference of the π''_{CC} and π'_{CC} bands, 0.97 eV, implies a substantial degree of interaction of π''_{CC} with the other a'' orbitals with higher IEs. This was also found in the case of propynoyl fluoride (1).

The fourth band, maximum 13.62 eV, has complex vibrational structure (Fig. 4). The position of this band and the similarity of its structure with bands observed for 2-butynal (above) and the propynoyl halides (1) leads to its assignment as $(\pi''_{CO})^{-1}$. This band has essentially the same IE as in 2-butynal (13.64 eV); the strong inductive effect of fluorine is offset by the resonance interaction of π''_{CO} with the halogen out-of-plane lone pair orbital. The vibrational structure consists of intervals of 1780, 1240, and 460 cm^{-1}. The 1780 cm^{-1} value is too large to correspond to the $\nu(C{=}O)$ stretching mode since an electron has been removed from an orbital which is strongly π-bonding in the C=O internuclear region. A more likely assignment is to excitation of the $\nu(C{\equiv}C)$ stretching mode, as

Can. J. Chem. Downloaded from www.nrcresearchpress.com by 213.222.148.141 on 09/07/12
For personal use only.

Can. J. Chem. Downloaded from www.nrcresearchpress.com by 213.222.148.141 on 09/07/12
For personal use only.

the out-of-plane delocalization extends to the acetylenic group. Excitation of the carbonyl stretching mode is assigned to the 1240 cm^{-1} interval. The 460 cm^{-1} interval could be excitation of a bending mode.

The intense band at 14.93 eV results from ionization of a fluorine in-plane "lone-pair" electron. Bands with this characteristic shape are observed for formyl fluoride at 15.45 eV (19) and propynoyl fluoride at 15.42 eV (1). In this case there is a shift to lower IE due to the positive inductive effect of the methyl group.

2-Butynoyl chloride

The spectrum of 2-butynoyl chloride, Fig. 5, is congested in the low IE region due to the bands arising from the $(n'_{Cl})^{-1}$ and $(n''_{Cl})^{-1}$ processes, in addition to the $(n'_O)^{-1}$ and $(\pi'_{CC})^{-1}$, $(\pi''_{CC})^{-1}$ bands. The relative ordering of the bands can be deduced from the spectra of similar species. The $(n_{Cl})^{-1}$ bands should be at higher IE values than the $(\pi_{CC})^{-1}$ bands since the former appear at 11.29 eV for CH_3Cl (20) and 11.69 eV for $HC{\equiv}CCH_2Cl$ (14), while the latter appear at 10.37 eV for propyne (21) and 10.76 and 10.98 eV for $HC{\equiv}CCH_2Cl$ (14). The relative placement of the $(n'_O)^{-1}$ band can be rationalized by considering the corresponding assignments for the aldehyde (10.15 eV) and the acid fluoride (10.84 eV). For both propynoyl chloride (1) and propenoyl chloride (22), the $(n'_O)^{-1}$ band is at an IE intermediate to that of the respective aldehydes and acid fluorides. This follows from a simple relative electronegativity argument. As there is only one band observed for 2-butynoyl chloride in this range, the first band at 10.59 eV, it must be assigned to the $(n'_O)^{-1}$ ionization.

The $(\pi''_{CC})^{-1}$ and $(\pi'_{CC})^{-1}$ ionizations are assigned to the bands at 10.92 and 11.26 eV, respectively. The $(\pi''_{CC})^{-1}$ band shows initial vibrational structure of 830 cm^{-1} before overlapping with the $(\pi'_{CC})^{-1}$ band. This value is too low to be excitation of the cationic $\nu(C{\equiv}C)$ stretching mode; a probable assignment is to the symmetric C—C stretching mode as there is some delocalization of the source orbital, as shown by the MO calculations and the energy difference of the π''_{CC} and π'_{CC} bands. This difference, 0.34 eV, is more than that of the aldehyde but less than that observed for the acid or the acid fluoride.

The broad bands with maxima at 11.87 and 12.13 eV are due to ionization from the chlorine 3*p* orbitals (lone pairs). It is not clear which should be the lower IE band, $(n''_{Cl})^{-1}$ or $(n'_{Cl})^{-1}$. This depends, in part, on the relative magnitudes of the interaction of the n''_{Cl} orbital with π''_{CC} (at lower binding energy) and π''_{CO} (at higher binding energy). It is felt that the interaction with π''_{CO} is more important, thus destabilizing n''_{Cl} relative to n'_{Cl}. The latter could also be stabilized somewhat by interaction with n'_O; the CNDO/2 MO calculation predicts a significant interaction. These arguments lead to the assignment of the lower IE band as $(n''_{Cl})^{-1}$ and the higher as $(n'_{Cl})^{-1}$.

Compared to the aldehyde and acid fluoride, the inductive and resonance effects of the chlorine in the acid chloride both shift the π''_{CO} orbital to a higher ionization energy. Unfortunately, the resultant band is lost in the multitude of overlapping bands beginning at about 14.5 eV. It could be the first maximum observed, 14.80 eV, as this is consistent with the expected shift based on the spectra of the propynoyl halides (1).

General trends

Only the lower IE bands are generally resolvable and assignable to ionizations from specific orbitals. The higher IE regions of the spectra contain a pseudo-continuum of bands owing to the number of accessible occupied σ-type orbitals. For the lower IE bands, Fig. 6 illustrates the general trends observed within the series. Within the approximation of Koopmans' Theorem (23), equating the measured ionization energies with the negative of the source orbital energies, Fig. 6 shows the variation of the orbital energies with substituent changes. Several comments are in order. For the carbonyl compounds the n'_O orbital energy changes as expected with the electronegativity of the carbonyl substituent, i.e. H > OH > Cl > F. The difference between the energies of the in- and out-of-plane π_{CC} orbitals indicates the degree of delocalization of the out-of-plane orbitals. For the carbonyl compounds the relative size of this splitting is H < Cl < OH < F. Both the OH and F substituents have out-of-plane orbitals of appropriate size to enable good π-type overlap with the adjacent carbonyl π-system. The size disparity between the chlorine 3*p* orbital and the 2*p* orbitals of the other atoms makes this less favourable. A large splitting is also observed for the alcohol; in this case the OH out-of-plane n''_O orbital is both physically and energetically close to the π''_{CC} localized orbital.

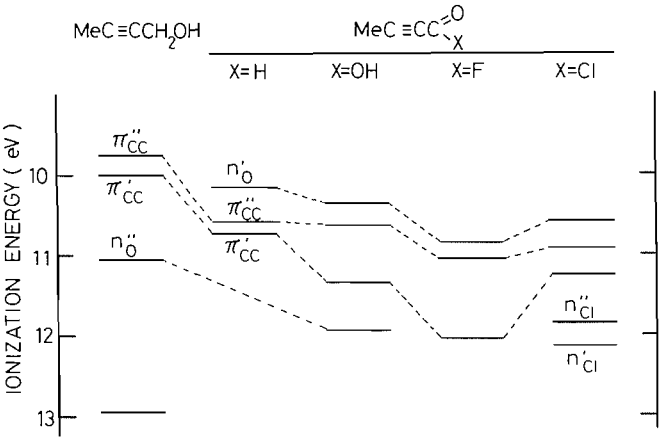

FIG. 6. Ionization energy correlation diagram for the higher occupied molecular orbitals.

The effect of the alkynyl methyl substituent, when compared to the corresponding results of the terminal alkynyl compounds (1), is mainly an inductive effect. There is a general shift to lower IEs for correlated bands between the two series. There is only a small effect on the interactions of the out-of-plane orbitals. The $(\pi''_{CH_3})^{-1}$ bands could not be identified as they are in the congested parts of the spectra.

The semi-empirical MO calculations were used to predict the ionization energies and bonding character of the occupied MOs giving rise to bands in the low ionization energy region of the spectra. The CNDO/2 method provided ionization energies from the MO eigenvalues by Koopmans' Theorem. In contrast, the HAM/3 method gave ionization energies directly by removing electron density diffusely. Comparison of the calculated results from the two methods with the experimental values shows that the HAM/3 method gives more satisfactory values. As noted previously, both sets of calculation were performed with structural parameters transferred from structurally similar molecules and without optimization. The experimental energies for these relatively simple molecular systems should be of use for more rigorous quantum chemical calculations, both for binding energies in the molecular species and for energy

differences between the molecules and the various electronic states of the cations.

Acknowledgements

This work was supported by the Natural Sciences and Engineering Research Council of Canada and the St. Francis Xavier University Council for Research.

1. D. KLAPSTEIN. J. Electron Spectrosc. Relat. Phenom. **42**, 149 (1987).
2. P. DOBOSH and N. S. OSTLUND. Quantum Chemistry Program Exchange, **11**, 281 (1975).
3. L. ÅSBRINK, C. FRIDH, and E. LINDHOLM. Quantum Chemistry Program Exchange, **13**, 393 (1981).
4. D. W. DAVIES. Chem. Phys. Lett. **1**, 649 (1968).
5. C. C. COSTAIN and J. R. MORTON. J. Chem. Phys. **31**, 389 (1959).
6. R. W. DAVIS and M. C. L. GERRY. J. Mol. Spectrosc. **57**, 118 (1975).
7. R. W. DAVIS, M. C. L. GERRY, S. VISAISOUK, and W. J. BALFOUR. Chem. Phys. Lett. **26**, 561 (1974).
8. D. G. LISTER and J. K. TYLER. Spectrochim. Acta, Part A, **28**, 1423 (1972).
9. (*a*) J. C. BRAND and R. A. POWELL. J. Mol. Spectrosc. **43**, 342 (1972); (*b*) W. J. BALFOUR, K. BEVERIDGE, and J. C. M. ZWINKELS. Spectrochim. Acta, **35**A, 163 (1979); (*c*) E. AUGDAHL, E. KLOSTER-JENSEN, and A. ROGSTAD. Spectrochim. Acta, **30**A, 399 (1974).
10. J. C. SAUER. Org. Synth. Collect. **4**, 813 (1963).
11. G. A. OLAH, R. J. SPEAR, P. W. WESTERMAN, and J.-M. DENIS. J. Am. Chem. Soc. **96**, 5855 (1974).
12. F. BROGLI, E. HEILBRONNER, V. HORNUNG, and E. KLOSTER-JENSEN. Helv. Chim. Acta, **56**, 2171 (1973).
13. M. B. ROBIN and N. A. KUEBLER. J. Electron Spectrosc. Relat. Phenom. **1**, 13 (1972/73).
14. M. V. ANDREOCCI, P. BITCHEV, P. CARUSI, and A. FURLANI. J. Electron Spectrosc. Relat. Phenom. **16**, 25 (1979).
15. K. KIMURA, S. KATSUMATA, T. YAMAZAKI, and H. WAKABAYASHI. J. Electron Spectrosc. Relat. Phenom. **6**, 41 (1975).
16. D. CHADWICK and A. KATRIB. J. Electron Spectrosc. Relat. Phenom. **3**, 39 (1974).
17. K. KIMURA, S. KATSUMATA, Y. ACHIBA, T. YAMAZAKI, and S. IWATA. Handbook of He I photoelectron spectra of fundamental organic molecules. Halsted, New York. 1981. pp. 164, 165 and references therein.
18. A. KATRIB and J. W. RABALAIS. J. Phys. Chem. **77**, 1358 (1973).
19. K. WITTEL. J. Electron Spectrosc. Relat. Phenom. **8**, 245 (1976).
20. J. L. RAGLE, I. A. STENHOUSE, D. C. FROST, and C. A. MCDOWELL. J. Chem. Phys. **53**, 178 (1970).
21. D. C. FROST, F. G. HERRING, C. A. MCDOWELL, and I. A. STENHOUSE. Chem. Phys. Lett. **4**, 533 (1970).
22. D. KLAPSTEIN and R. T. O'BRIEN. Can. J. Chem. **65**, 683 (1987).
23. T. A. KOOPMANS. Physica, **1**, 104 (1933).

Can. J. Chem. Downloaded from www.nrcresearchpress.com by 213.222.148.141 on 09/07/12
For personal use only.

Energy maxima in anionic nucleophilic additions to carbonyl groups: The location of a saddle point for the addition of hydride to formaldehyde

C. I. BAYLY AND F. GREIN[1]

Department of Chemistry, University of New Brunswick, Fredericton, N.B., Canada E3B 6E2

Received June 16, 1987

C. I. BAYLY and F. GREIN. Can. J. Chem. **66**, 149 (1988).

The reaction profile of the anionic nucleophilic addition of hydride to formaldehyde giving methanolate was re-investigated using theoretical *ab initio* methods. A variety of basis sets (including 4-31G and 6-31G with and without polarization and diffuse functions) were used, and electron correlation calculations were performed at the MP2, MP3, and MP4 levels with geometry optimizations at the MP2 level. Upon the addition of diffuse functions to the basis set, a local energy maximum was introduced into the SCF reaction profile, a major change in the character of the profile compared to the entirely attractive potential energy curve found in previous studies. On the reactants side of the barrier a local minimum 4.56 kcal/mol lower in energy was found, corresponding to an ion–dipole complex. With the inclusion of electron correlation, the local barrier almost disappeared, with the energy difference between the ion–dipole complex and the barrier maximum decreasing to less than 1 kcal/mol. Furthermore, the location of the energy maximum along the reaction coordinate changed by 0.4 Å. These results are used to critically re-evaluate some prevalent viewpoints on the nature of the reaction profiles of this type of anionic nucleophilic addition.

C. I. BAYLY et F. GREIN. Can. J. Chem. **66**, 149 (1988).

Faisant appel à des méthodes théoriques ab initio, on a réétudié le profil de la réaction d'addition nucléophile anionique de l'hydrure sur le formaldéhyde pour donner le méthanolate. On a utilisé divers ensembles de base (y compris 4-31G et 6-31G, avec et sans fonctions diffuse ou de polarisation) et on a réalisé des calculs de corrélations électroniques aux niveaux MP2, MP3 et MP4 avec des optimisations de géométries au niveau MP2. Par addition des fonctions diffuses aux ensembles de base, on a introduit une énergie locale maximale dans le profil de la réaction en champ auto-cohérent; ceci correspond à un changement majeur dans le caractère du profil par rapport à la courbe d'énergie potentielle entièrement attractive qui avait été trouvée dans les études antérieures. Du côté des réactifs, on a trouvé qu'il existe un minimum local dont l'énergie est 4,56 kcal/mol plus basse que la barrière et ce minimum correspond à un complexe ion-dipôle. Avec l'inclusion de la corrélation électronique, la barrière locale disparaît pratiquement complètement alors que la différence d'énergie entre le complexe ion-dipôle et la barrière maximale diminue à moins de 1 kcal/mol. De plus, la position du maximum d'énergie le long des coordonnées de la réaction est déplacée de 0,4 Å. On utilise ces résultats pour réévaluer d'une façon critique quelques points de vue qui prévalent actuellement sur la nature des profils réactionnels pour ce type d'addition nucléophile anionique.

[Traduit par la revue]

Can. J. Chem. Downloaded from www.nrcresearchpress.com by 213.222.148.141 on 09/07/12
For personal use only.

Introduction

Anionic nucleophilic additions to carbonyl groups play a major role in key biochemical processes as well as being of great strategic importance in synthetic organic chemistry. The mechanism of this type of reaction has been studied intensively, with much interest focussing on the formation of the tetrahedral intermediate generally agreed to result from the initial (and normally rate-determining) step. In a "landmark" paper (1) published in 1974, SCF *ab initio* calculations were carried out on a prototype model reaction, the nucleophilic addition of hydride to formaldehyde to form methanolate. An important feature of the SCF potential energy (PE) profile in this study was the absence of energy maxima — the PE was always attractive as the hydride approached the carbonyl reaching a minimum only at the final equilibrium bonded distance. A number of subsequent theoretical studies (refs. 2 to 4, for example), simulating various anionic gas phase additions of similar types, verified this trend, leading to a general view that in the gas phase there are no PE local maxima as an anionic nucleophile attacks a carbonyl group (4). The above theoretical work was performed prior to the general use of diffuse functions (ref. 5 and references therein) by chemists, now widely accepted as being essential for the proper description of anions.

In contrast to the above results, in a recent *ab initio* study by Madura and Jorgensen (6) on the addition of hydroxide to formaldehyde, using a basis set containing diffuse functions, a small local maximum was found in the potential energy profile of the reaction. It is therefore of interest to establish whether or not reaction profiles in general for this class of reaction exhibit such an energy "hump". The effect of including electron correlation in the energy claculations would further indicate if the local maximum is a real feature of the potential energy profile of this reaction, or an artifact of the Hartree–Fock method.

In this paper we present the results of a theoretical reinvestigation of the original prototype reaction, the nucleophilic addition of hydride to formaldehyde to form methanolate. Diffuse functions were included in the basis set, and geometry optimizations were performed at both the Hartree–Fock and electron correlation levels. The strategy of the investigation was to determine the reaction profile of the hydride–formaldehyde system with basis sets of increasing sophistication, finding out at what basis set level the profile changed in character, and how further improvements of the basis set and the inclusion of electron correlation influenced the new profile.

Calculations

Calculations were carried out at the RHF (Restricted Hartree–Fock) and MP (Møller–Plesset) levels using the GAUSSIAN 80 (7*a*) and GAUSSIAN 82 (7*b*) computer programs. Several basis sets were tested, with polarization and diffuse functions added as described below. At each SCF level the geometry was fully optimized (using the GAUSSIAN 82 gradient-searching algorithms). MP2, MP3, and MP4 calculations with a very good basis set were performed with geometry optimization at the MP2 level. C_s symmetry was always enforced. The geometry was specified as follows: the formaldehyde H—C—H plane was chosen as the frame of reference, and a dummy atom X

[1]Author to whom all correspondence should be addressed.

TABLE 1. Relative energies at several basis set levels for the $H^- + H_2CO$ addition

R (Å) C—H$^-$	E(rel)[a] (kcal/mol)					
	STO-3G	4-31G	4-31G*p	4-31Gd	4-31G*pd	6-31G**d
E_{min}	0.00	0.00	0.00	0.00	0.00	0.00
(R)	(1.1330)	(1.1218)	(1.1373)	(1.1074)	(1.1205)	(1.1223)
1.6000	36.13	21.90	19.59	25.05	21.79	21.29
2.0000	69.77	34.59	30.97	33.96	28.50	27.85
E_{max}	—	—	—	34.10	28.50	27.85
(R)				(2.0803)	(2.0036)	(2.0070)
2.2500	84.63	38.23	34.04	33.68	27.59	27.03
2.5000	95.31	40.61	36.13	32.43	26.11	25.70
3.0000	108.09	43.49	38.93	29.90	23.65	23.65
E_{min}	—	—	—	29.65	23.29	23.35
(R)				(3.2014)	(3.2492)	(3.2254)
3.500	—	—	—	30.004	23.526	23.632
10.000	120.47	62.98	56.97	39.78	32.31	32.45
∞	121.40	64.85	58.63	41.82	34.14	34.26

[a]The energy (in hartree) of the global minimum for each basis set is STO-3G, −112.70637; 4-31G, −114.21841; 4-31G*p, −114.27294; 4-31Gd, −114.25220; 4-31G*pd, −114.30507; 6-31G**d, −114.41622.

TABLE 2. 6-31++G** optimized geometries and relative energies for the $H^- + H_2CO$ addition

Distance (Å)			Angle (deg)			E(rel)[a] (kcal/mol)
C—H$^-$	C—H	C—O	H$^-$—C—X	H—C—H	O—C—H$^-$	
1.1226	1.1226	1.3298	111.70	103.24	115.10	0.000
1.6000	1.1002	1.2632	97.10	109.52	116.00	21.226
1.7000	1.0954	1.2494	92.50	111.08	116.40	24.441
1.8000	1.0914	1.2372	87.60	112.48	116.60	26.465
1.9000	1.0885	1.2270	82.50	113.66	117.30	27.494
2.0071	1.0864	1.2184	77.00	114.44	118.30	27.799
2.1000	1.0853	1.2129	72.40	114.86	119.70	27.641
2.2500	1.0846	1.2067	65.20	115.34	122.50	26.975
2.5000	1.0848	1.2012	53.10	115.34	129.90	25.630
3.0000	1.0874	1.1978	0.00	114.08	180.00	23.548
3.2268	1.0880	1.1967	0.00	114.34	180.00	23.243
3.5000	1.0887	1.1956	0.00	114.70	180.00	23.518
10.000	1.0916	1.1876	0.00	116.28	180.00	32.256
∞	1.0922	1.1861	0.00	116.34	180.00	34.057

[a]The energy at the global minimum is −114.41606 hartree.

placed bisecting this angle. The formaldehyde C—H bond lengths, and bond angles H—C—X were allowed to vary during optimization. Oxygen and hydride were allowed movement only in the plane perpendicular to the H—C—H plane and containing the line C—X. The hydride–carbon distance was used as the reaction coordinate.

Basis sets labeled with a *d* were augmented with *s* and *p* diffuse functions (8*a*) on oxygen (exponent 0.0845 with 6-31G, exponent 0.0680 with 4-31G) and hydride (exponent 0.0360). Basis sets labeled with a *p* were augmented with polarization *p* functions (8*b*) on hydride (exponent 0.110). Other basis set notation is according to standard practice: * for polarization functions and + for diffuse functions on all nuclei other than hydrogen; ** for polarization functions and ++ for diffuse functions on all nuclei including hydrogen. The notation *x*//*y* refers to a calculation with basis set *x* on geometries optimized with basis set *y* (e.g. 6-31G//4-31G means "the 6-31G energy calculated at the 4-31G optimized geometry"). For all SCF calculations involving a PE local maximum, the geometry for the structure at the maximum had a single negative eigenvalue in the Hessian matrix, showing it to be a true saddle point on the potential energy hypersurface.

Results

The minimal basis set STO-3G was used as a starting point, followed by split-valence basis sets. The effect of adding special functions was tested at the 4-31G level. First, polarization functions were added to carbon, oxygen, and hydride (4-31G*p), then diffuse functions only were added to oxygen and hydride (4-31Gd), and finally both polarization and diffuse functions were added (4-31G*pd). The relative energies at various carbon–hydride distances, including the local maximum and the secondary minimum, are given in Table 1. The effect of further basis set improvement was tested in calculations using the 6-31G**d basis set (Table 1, last column). These results are shown graphically in Fig. 1. The final basis set used was 6-31++G**, having both polarization and diffuse functions on all nuclei. In Table 2, the optimized geometry for each

Can. J. Chem. Downloaded from www.nrcresearchpress.com by 213.222.148.141 on 09/07/12
For personal use only.

TABLE 3. MP2/6-31**d optimized geometries and RHF, MP2, MP3, and MP4 relative energies for the H^- + H_2CO addition

Distance (Å)			Angle (deg)			E(rel)[a] (kcal/mol)			
C—H^-	C—H	C—O	H^-—C—X	H—C—H	O—C—H^-	RHF	MP2	MP3	MP4SDQ
1.1257	1.1242	1.3571	111.80	103.54	115.00	0.000	0.000	0.000	0.000
1.9000	1.0976	1.2668	85.86	113.22	117.04	28.539	31.207	31.938	30.639
2.0100	1.0950	1.2584	80.48	114.26	117.62	28.942	33.046	33.500	32.262
2.1000	1.0935	1.2527	75.90	114.84	118.40	28.814	34.042	34.222	33.054
2.2500	1.0922	1.2453	68.40	115.38	120.60	28.151	34.999	34.722	33.680
2.3600	1.0918	1.2416	63.19	115.56	122.91	27.556	35.354	34.787	33.826
2.4000	1.0919	1.2404	61.15	115.56	123.95	27.332	35.437	34.773	33.842
2.4330	1.0918	1.2396	59.47	115.58	124.93	27.150	35.494	34.755	33.846
2.5000	1.0919	1.2381	56.34	115.56	126.76	26.803	35.579	34.703	33.835
2.6000	1.0921	1.2363	51.28	115.46	130.32	26.313	35.655	34.597	33.783
2.7500	1.0925	1.2347	42.09	115.24	137.91	25.670	35.694	34.417	33.670
3.0000	1.0940	1.2327	0.50	114.08	179.50	24.622	35.595	34.032	33.405
3.1298	1.0942	1.2323	0.00	114.30	180.00	24.379	35.506	33.904	33.263
3.1750	1.0942	1.2322	0.00	114.32	180.00	24.353	35.515	33.902	33.255
3.2500	1.0943	1.2320	0.00	114.48	180.00	24.354	35.566	33.933	33.276
3.5000	1.0945	1.2312	0.00	114.88	180.00	24.648	35.963	34.259	33.574
4.0000	1.0948	1.2300	0.00	115.42	180.00	25.922	37.214	35.410	34.669
4.5000	1.0950	1.2290	0.00	115.78	180.00	27.346	38.529	36.668	35.890
10.000	1.0968	1.2246	0.00	116.52	180.00	33.621	44.326	42.484	41.699
∞	1.0975	1.2232	0.00	116.54	180.00	35.454	45.922	44.097	43.308

[a]The energy (hartree) of the global minimum for each basis set is RHF, −114.41563; MP2, −114.77923; MP3, −114.78569; MP4, −114.79550.

Can. J. Chem. Downloaded from www.nrcresearchpress.com by 213.222.148.141 on 09/07/12
For personal use only.

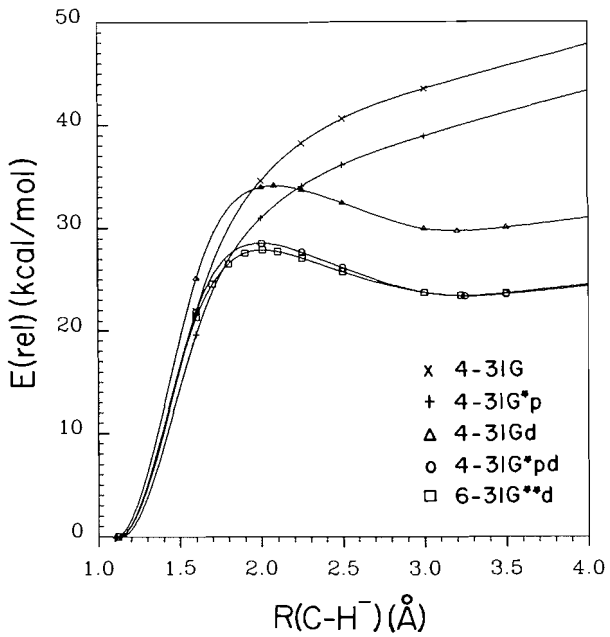

FIG. 1. Energy profiles of the H^- + H_2CO addition calculated using various basis sets.

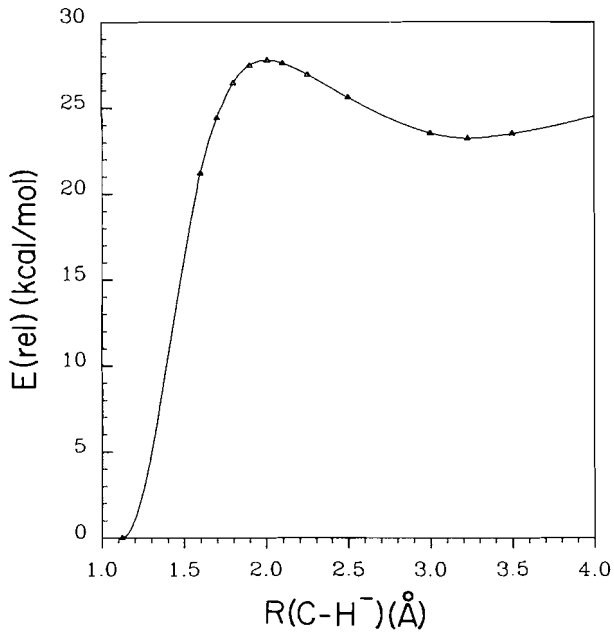

FIG. 2. Energy profile of the H^- + H_2CO addition calculated using the 6-31++G** basis set.

carbon–hydride distance, including the local maximum and the secondary minimum, is given together with the corresponding energy relative to the global minimum (methanolate). The potential curve is shown in Fig. 2.

Møller–Plesset calculations were performed using the 6-31G**d basis set with geometry optimization at the MP2 level. The resulting geometries and the RHF, MP2, MP3, and MP4 energies are given in Table 3 and the energies are plotted in Fig. 3. Zero-point energy (ZPE) corrections were made at the geometry of methanolate and the intermediate minimum. Several structures from Table 2 are superimposed in Fig. 4 to indicate the changes in geometry taking place over the course of the reaction.

Discussion

The STO-3G and 4-31G results (Table 1) gave a reaction profile in agreement with the literature, indicating no PE maximum in the addition reaction. The minimal basis set drastically overestimated ΔE_{reac} (the energy difference between the separated reactants and the global minimum) to be 121 kcal/mol, while for the unaugmented 4-31G basis ΔE_{reac} was 65 kcal/mol, still much larger than the best RHF energy of 34 kcal/mol from the 6-31++G** basis set (Table 2).

Can. J. Chem. Downloaded from www.nrcresearchpress.com by 213.222.148.141 on 09/07/12
For personal use only.

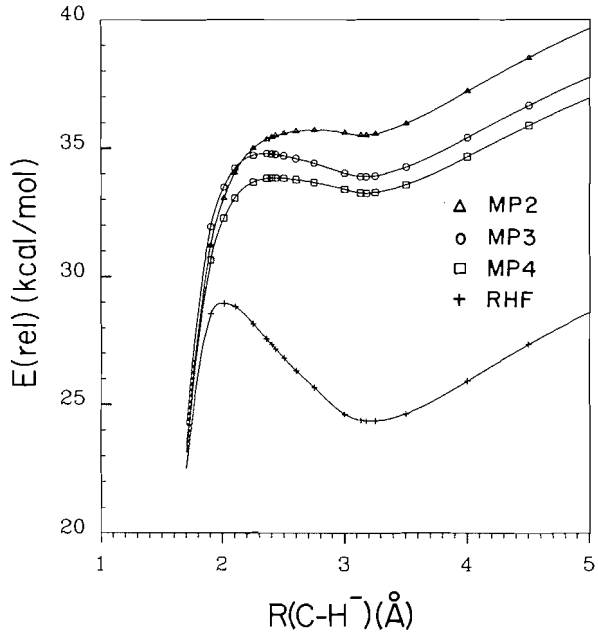

FIG. 3. Energy profiles of the MP2/6-31G**d optimized structures for the H^- + H_2CO addition.

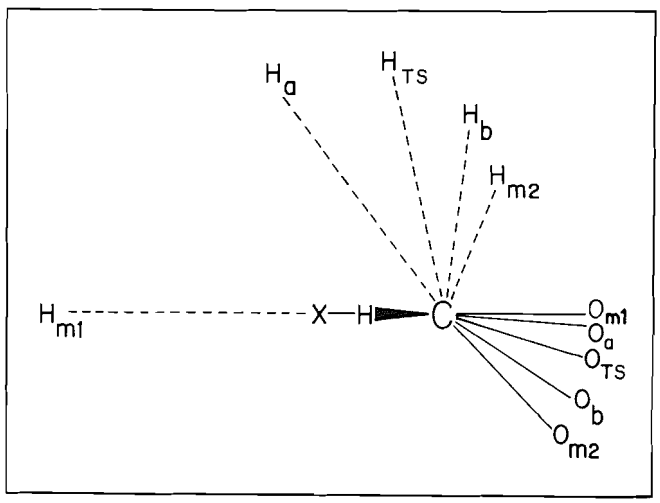

FIG. 4. Several structures of the H^- + H_2CO addition, superimposed to show geometry changes over the course of the reaction. Geometries (6-31++G**//6-31++G** calculations) are labelled as follows (with the C—H^- distance given): m1: charge dipole complex (C_{2v}), 3.2268 Å; *a*: 2.5 Å; TS: transition state, 2.0071 Å; *b*: 1.6 Å; m2: global minimum, methanolate (C_{3v}), 1.1226 Å.

It is interesting to compare the results for different kinds of extra functions added to the 4-31G basis set. The first step was to put polarization functions on those nuclei involved in polar bonding during the reaction process, viz. carbon, oxygen, and hydride (4-31G*p). While this did lower the total energies and improve the ΔE_{reac} by a few kcal/mol, the reaction profile was unchanged. The next basis set modification was the further addition of diffuse functions to hydride and to oxygen (the 4-31G*pd basis). These diffuse functions allow for a better description of extra electron density from the anionic electron, which is found on the hydride in the reactants and on the oxygen in the product.

It was upon the addition of diffuse functions that the reaction profile underwent its change of character. A potential energy hump appeared, giving a local energy minimum on the reactants side of the barrier (Fig. 1). Since the introduction of the diffuse functions into the 4-31G*p basis set caused such a radical change in the reaction profile, we decided to remove the polarization functions and recalculate the profile with only diffuse functions added (the 4-31Gd basis (Table 1)). While the resulting total energies were higher than those for the 4-31G*p basis set, the new reaction profile did contain the barrier. Furthermore, ΔE_{reac} for 4-31Gd was 42 kcal/mol, much closer to the 4-31G*pd value of 34 kcal/mol than the 4-31G*p value of 59 kcal/mol. This led us to conclude that the inclusion of polarization functions to accompany the diffuse functions was not necessary for an adequate SCF description of this reaction. In an *ab initio* study by Spitznagel *et al.* (8), using the standard 4-31G and 6-31G basis sets to investigate methyl anions, these authors also added diffuse functions with and without polarization functions, and found that diffuse functions alone were sufficient.

The qualitative difference in the reaction profile brought by diffuse functions is probably due to the large energy lowering given to hydride. Using differences between 4-31G and 4-31Gd energies, diffuse functions stabilize hydride by 40.6 kcal/mol, whereas they lower the energy of H_2CO by only 3.7 kcal/mol, and that of methanolate by 21.2 kcal/mol. Therefore, ΔE_{reac} decreases by 23.1 kcal/mol as a result of the introduction of diffuse functions, most of this decrease being due to hydride. It is likely that the energy maximum is hidden by the large value of ΔE_{reac} when diffuse functions are not used.

The SCF study was concluded with the increase of the basis set first to the 6-31G**d and finally to the 6-31++G** level. In the latter basis, all hydrogens received diffuse functions, not only the hydride, resulting in all C—H distances of methanolate (C_{3v}) to be identical. These two basis sets gave virtually identical profiles that were also very similar to those of the 4-31G*pd basis set (see Fig. 1), and it was felt that further basis set extension would not qualitatively change the reaction profile at the RHF level.

While the trajectory of the minimum energy pathway does not differ significantly from that found in previous studies, the RHF energy profile has major differences. The trajectory and profile can be summarised together (using data from Table 2) in the following way: the initial approach of the hydride (from the separated reactants having ΔE_{reac} = 34.1 kcal/mol) is along the C_{2v} symmetry axis of formaldehyde towards the carbon. A planar charge dipole complex is formed at a distance of 3.23 Å, representing a local energy minimum (the energy difference relative to the global minimum E(rel) = 23.2 kcal/mol). Further approach of the hydride, now rising out of the H—C—H plane of formaldehyde, requires the overcoming of a small (4.6 kcal/mol) energy barrier whose energy maximum (E(rel) = 27.8 kcal/mol) is lower than the energy of the separated reactants. At the barrier maximum the carbon–hydride distance is 2.007 Å, the hydride is 77° above the H—C—H plane, and the carbon is pyramidalizing, with the carbon–oxygen bond 15° below the H—C—H plane and lengthening. From here on the potential energy is highly attractive, with the nuclei completing their trajectories to take up their equilibrium positions in the product (E(rel) = 0 kcal/mol).

In the previously mentioned study by Madura and Jorgensen (6) on the addition of hydroxide to formaldehyde using the 6-31+G* basis set, a small local maximum in the potential

Can. J. Chem. Downloaded from www.nrcresearchpress.com by 213.222.148.141 on 09/07/12
For personal use only.

energy was found in a similar area of the reaction coordinate. The hydroxide traces a similar trajectory to that outlined above in its approach to the carbonyl carbon, with the potential energy hump occurring at 2.39 Å for an O—C—O bond angle of 126.9°. This energy maximum is only 1.1 kcal/mol higher than the energy of the corresponding planar ion–dipole complex (formed at a C—OH distance of 2.47 Å), a quantity the authors claim could disappear upon the inclusion of electron correlation and zero-point energy, or basis set extension. In comparing the global minimum with the separated reactants, the authors also noted that the correlation and zero-point correction tended to cancel each other.

Møller–Plesset claculations were carried out on the hydride–formaldehyde system to check the effect of electron correlation on the SCF results. With geometry optimization done at the MP2/6-31G**d level, the resulting MP2, MP3, and MP4 energies (given in Table 3 and plotted in Fig. 3) showed a pronounced change in the reaction profile in that the potential energy barrier flattened greatly on the reactant side. Starting from the charge–dipole complex, the energy change in going to the top of the PE barrier decreased to less than 1 kcal/mol for all MP levels compared to 4.6 kcal/mol at the RHF level. In contrast, the MP results otherwise indicated a general increase in the relative energies, such as those between the product and the barrier maximum, and the barrier maximum and the separated reactants. The three levels of MP treatment gave very similar results.

These changes in the energy profile cannot be due to geometry differences between the RHF and MP2 optimized geometries because the RHF energies given in Table 3 calculated for MP2/6-31G**d optimized geometries show a 4.6 kcal/mol energy difference between the charge–dipole complex and the barrier maximum, in agreement with the RHF optimized 6-31G**d results. The differences between the RHF and MP2 reaction profile must therefore be attributed to the correlation energy changes during the course of the reaction.

Perhaps the most interesting feature of the changes caused by the introduction of electron correlation is the movement of the saddlepoint location on the reaction coordinate. The RHF results placed the saddlepoint at a carbon–hydride distance of 2.0 Å, whereas the saddlepoint was found at around 2.7 Å at the MP2 level, and around 2.4 Å at the MP3 and MP4 levels. This is presumably a consequence of having such a shallow maximum in this region, where small changes in the energy distribution result in large changes in internuclear distance.

In the study of closed-shell singlet state reactions such as the one investigated here, the inclusion of electron correlation is frequently considered to be unnecessary, since the RHF relative energies should be adequate to properly describe the reaction profile. From the above results, however, we see that not only is the character of the potential energy curve changed substantially, but the location of the saddlepoint changes by about 0.4 Å. At the RHF level the barrier, while not steep, would not lead one to expect such a large change.

The effect of the zero-point energy on the two minima found on the 6-31++G** profile was checked. The methanolate global minimum (ZPE/6-31++G**//6-31++G** total energy −114.37793 hartree) had a ZPE correction 4.93 kcal/mol higher than that for the charge dipole complex (ZPE/6-31++G**//6-31++G** total energy −114.34396 hartree). In agreement with the findings of Madura and Jorgensen (*vide infra*), this indicates a trend of the ZPE correction opposite to that of the correlation energy correction, so they would tend to cancel. In our case the ZPE correction reduces the MP4 relative energy difference between the global minimum and the charge dipole complex from 33.26 to 28.33 kcal/mol, still 3.98 kcal/mol above the RHF relative energy of 24.35 kcal/mol (Table 3).

Conclusions

For the gas-phase addition of hydride to formaldehyde, *ab initio* calculations indicate that at the RHF level the reaction profile does contain a potential energy local maximum, in contrast to previous studies. This maximum is sensitive to the choice of basis set. It is essential to include diffuse functions on centers having anionic character in reactants and product (to allow for proper distribution of the extra charge). Basis sets tried without diffuse functions, even those with polarization functions, showed no energy barrier.

Possibly the reason that local maxima are not commonly found for anionic nucleophilic reactions with carbonyl functionalities is that the basis sets used lack diffuse functions; this can be seen as forcing the anionic centers to be extraordinarily "hard". For calculations involving large anionic systems, the omission of diffuse functions might be considered necessary to avoid prohibitively large computations. This is understandable, since it is common practice to include polarization functions when adding diffuse functions (6), which together can correspond to a large increase in the total number of basis functions. While adding both kinds of extra functions is the better avenue, our results indicate that alternatively a basis set including only diffuse functions (even if they are on only the anionic centers – c.f. 6-31G**d vs. 6-31++G** results) might describe adequately the reaction profile; this could not be said of the results when no extra functions or only polarization functions were included.

Contrary to expectations, we found that the inclusion of electron correlation significantly changed the results for the closed-shell singlet-state addition reaction of hydride to formaldehyde. The local barrier found at the RHF level was flattened into a broad, shallow maximum, and the position of the saddlepoint changed by about 0.4 Å along the reaction coordinate.

It is unlikely that the differences between the new humped profile presented in this work and the barrier-less profile of previous studies would be experimentally measurable for the hydride–formaldehyde addition reaction. However, considering this reaction to be a prototype of anionic nucleophilic attack on carbonyl groups, a small increase in the barrier height on the order of a few kcal/mol could measurably influence the behaviour of larger systems at the experimental level. Our results suggest that such a barrier could pass entirely undetected at the RHF level without the inclusion of diffuse functions in the basis set. Furthermore, even for closed-shell singlet-state reactions the RHF energy profile might be significantly altered by the inclusion of electron correlation, with accompanying large changes in the geometries associated with the various intermediates along the reaction path.

Acknowledgements

We would like to thank NSERC Canada for our operating grant, and a postgraduate award to C.I.B. Generous financial support by the Leonard and Kathleen O'Brien Humanitarian Foundation to C.I.B. is much appreciated. Equipment grants by the MPHEC and the University of New Brunswick Research Fund, as well as plentiful allocation of computer time by the University of New Brunswick are gratefully acknowledged.

1. H. B. BURGI, J. M. LEHN, and G. WIPFF. J. Am. Chem. Soc. **96**, 1956 (1974).
2. H. B. BURGI, J. D. DUNITZ, J. M. LEHN, and G. WIPFF. Tetrahedron, **30**, 1563 (1974).
3. S. SCHEINER, W. N. LIPSCOMB, and D. A. KLEIER. J. Am. Chem. Soc. **98**, 4770 (1976).
4. I. H. WILLIAMS, G. M. MAGGIORA, and R. L. SCHOWEN. J. Am. Chem. Soc. **102**, 7831 (1980).
5. T. CLARK, J. CHANDRASEKHAR, G. W. SPITZNAGEL, and P. R. SCHLEYER. J. Comp. Chem. **4**, 294 (1983); P. C. HARIHARAN and J. A. POPLE. Theor. Chim. Acta, **28**, 213 (1973).
6. J. D. MADURA and W. L. JORGENSEN. J. Am. Chem. Soc. **108**, 2517 (1986).
7. (*a*) J. S. BINKLEY, R. A. WHITESIDE, R. KRISHNAN, R. SEEGER, D. J. DE FREES, H. B. SCHLEGEL, S. TOPIOL, L. R. KAHN, and J. A. POPLE. QCPE, **13**, 406 (1981); (*b*) J. S. BINKLEY, M. J. FRISCH, D. J. DE FREES, K. RAGHAVACHARI, R. A. WHITESIDE, H. B. SCHLEGEL, E. M. FLUDER, and J. A. POPLE. GAUSSIAN 82 Release H; Carnegie-Mellon University: Pittsburg. 1986.
8. (*a*) G. W. SPITZNAGEL, T. CLARK, J. CHANDRASEKHAR, and P. R. SCHLEYER. J. Comp. Chem. **3**, 363 (1983); (*b*) P. C. HARIHARAN and J. A. POPLE. Theor. Chim. Acta, **28**, 213 (1973).

Can. J. Chem. Downloaded from www.nrcresearchpress.com by 213.222.148.141 on 09/07/12
For personal use only.

Enaminic reactions of 4-*tert*-butyl-3,3-dimethyl-5-methylene-Δ^1-1,2,4-triazoline. Novel heterocycles by sequential [2 + 2] cycloaddition and ylide-forming [3 + 2] cycloreversion[1]

ADRIAN L. SCHWAN[2] AND JOHN WARKENTIN[3]

Department of Chemistry, McMaster University, Hamilton, Ont., Canada L8S 4M1

Received May 21, 1987

ADRIAN L. SCHWAN and JOHN WARKENTIN. Can. J. Chem. **66**, 155 (1988).

Triazoline **1**, which is formally an α azoenamine, reacts with dimethyl acetylenedicarboxylate, acrylonitrile, methacrylonitrile, methyl methacrylate, phenylisocyanate, and sulfene to form products that appear to be derived from a common first step, the formation of a dipolar intermediate (e.g., **5**). That intermediate may close to form either a 4-membered ring (**6**, **8**) or ring-open to **7** with subsequent closure to a 5-membered ring (**4**). Alternatively it may lead to an enamine with extended conjugation (**10**, **11**) by a sequence of proton transfers. The spirotriazolines (e.g., **6**) are unstable and decompose by loss of N_2 to form spiro aziridines (e.g., **3**). Hydrogen cyanide, from acetone cyanohydrin, converts **1** to the cyanoaziridine **13** while methanol adds reversibly under acidic conditions to form **17**.

ADRIAN L. SCHWAN et JOHN WARKENTIN. Can. J. Chem. **66**, 155 (1988).

La triazoline **1**, qui est formellement une α-azoènamine, réagit avec l'acétylènedicarboxylate de diméthyle, l'acrylonitrile, le méthacrylonitrile, le méthacrylate de méthyle, l'isocyanate de phényle et le sulfène pour conduire à des produits qui semblent tous provenir d'une première étape commune, soit la formation d'un intermédiaire dipolaire (à savoir **5**). Cet intermédiaire peut soit se refermer pour former un cycle à 4 chaînons (**6**, **8**) soit s'ouvrir pour donner **7** qui subit une fermeture ultérieure conduisant à un composé cyclique à cinq chaînons (**4**). Par ailleurs, il peut aussi conduire à une ènamine comportant une conjugaison étendue (**10**, **11**) et provenant d'une séquence de transferts protoniques. Les spirotriazolines (comme **6**) sont instables et se décomposent, par perte de N_2, pour former des spiroaziridines (comme **3**). L'acide cyanhydrique, provenant de la cyanohydrine de l'acétone, transforme le composé **1** en cyanoaziridine **13**; par ailleurs, le méthanol s'additionne d'une façon réversible, dans des conditions acides, pour former le composé **17**.

[Traduit par la revue]

Introduction

The synthetic utility of enamines is well documented (1, 2). Stork's methodology (3) is still one of the most reliable procedures for overall monoalkylation of a ketone. Nucleophilic addition of an enamine to an electron-deficient unsaturated compound, on the other hand, often leads to formation of a [2+2] cycloadduct (eq. [1]), which in many cases is the final

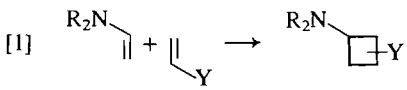

[1]

product (4). Electron-deficient unsaturated compounds that form [2+2] cycloadducts with enamines include sulfenes (5), ketenes (6), isocyanates (7), acetylenic compounds (8, 9), acrylic acid derivatives (10), tetracyanoethylene (11), and maleimide (12).

Recently, we reported (13) the synthesis of triazoline **1**, in which enamine and α,β-unsaturated azo functionalities are combined. Triazoline **1** showed enaminic reactivity toward sulfene and acrylonitrile (13) but the products (Scheme 1), although they had the expected 4-membered ring (eq. [1]), were also spiroaziridines. A likely mechanism for their formation, shown in the first line of Scheme 1, involves [2+2] cycloaddition followed by [3+2] cycloreversion to form an azomethine ylide, which undergoes electrocyclic ring closure to the final product.

Azomethine ylides are useful intermediates for the synthesis of alkaloids (14, 15) and the preparation and reactivity of such ylides are the topics of two recent reviews (16, 17). The

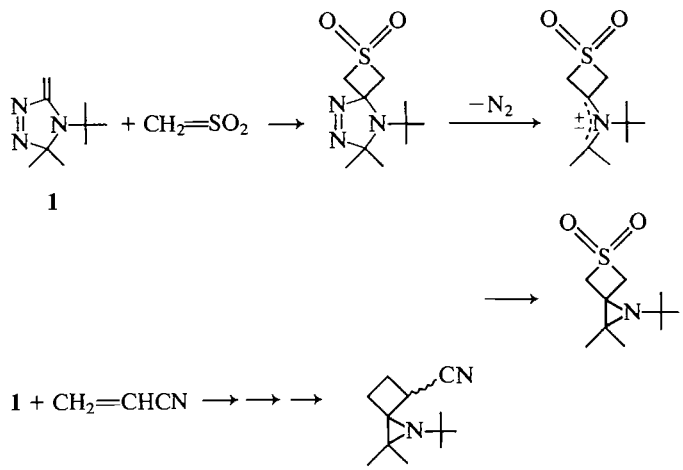

SCHEME 1

thermolysis (or photolysis) of Δ^1-1,2,4-triazolines (eq. [2]), as a route to azomethine ylides, has been considered (18) but the only examples of ylide generation by that general approach seem to be the two given in Scheme 1 (13).

We now report additional chemistry of **1** as well as details of the results that were presented earlier in the form of a preliminary communication (13).

Results and discussion

Heating of **1** in neat acrylonitrile (**2***a*) at temperatures between 50 and 80°C afforded the diastereomers of **3** in 1:1

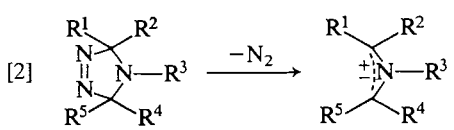

[2]

[1]Presented in part at the 14th Ontario–Quebec Physical Organic Minisymposium, Toronto, November, 1986.

[2]Holder of an NSERC Postgraduate Scholarship, 1983–1987.

[3]Author to whom correspondence may be addressed.

Can. J. Chem. Downloaded from www.nrcresearchpress.com by 213.222.148.141 on 09/07/12
For personal use only.

Can. J. Chem. Downloaded from www.nrcresearchpress.com by 213.222.148.141 on 09/07/12
For personal use only.

TABLE 1. Spectroscopic data

Compound	^{1}H nmr (δ, $CDCl_3$, 500 MHz)	^{13}C nmr (δ, $CDCl_3$, 22.62 MHz)[a]	Mass spectrum (*m/z*, (%), ei, lr)[b]	Ultraviolet (λ_{max}, nm (log ε))	Infrared (cm^{-1})
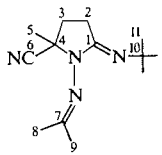 **4*b***	1.19 (s, 9H), 1.52 (s, 3H), 1.83 (s, 3H), 1.93 (m, 1H), 2.11 (s, 3H), 2.47 (m, 1H), 2.60 m, 2H)	21.59, 24.69, 25.09 (5, 8, 9), 25.43 (3 or 2), 31.05 (11), 32.89 (2 or 3), 53.33 (10), 58.89 (4), 120.97 (6), 150.61 (1 or 7); 172.83 (7 or 1)	234 (2), 219 (24), 163 (67), 95 (24), 57 (100), 56 (19). 234.1848 (hr, obsd.); 234.1844 (calcd. for $C_{13}H_{22}N_4$)	234 (3.52), methanol	2980, 2920, 2866, 2225 (vw), 1674 (br), 1449, 1371, 1358, 1254, 1217, 1166, 853, 736, film
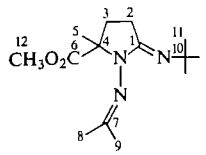 **4*c***	1.21 (s, 9H), 1.42 (s, 3H), 1.85 (s, 3H), 2.05 (s, 3H), 2.17 (m, 1H), 2.41 (m, 1H), 2.54 (m, 1H), 2.66 (m, 1H), 3.71 (s, 3H)	21.21, 21.53, 24.96 (5, 8, 9); 28.53 (3 or 2), 29.46 (2 or 3), 30.79 (11), 51.86 (12), 53.11 (10), 66.34 (4), 154.16 (1 or 7), 174.49 (7 or 1), 177.60 (6)	267 (3), 252 (28), 197 (49), 196 (100), 152 (29), 112 (45), 87 (37), 57 (77). 267.1949 (hr, obsd.); 267.1949 (calcd. for $C_{14}H_{25}N_3O_2$)	240 (3.87), $CHCl_3$	2949, 2899, 1739, 1670 (br), 1459, 1372, 1359, 1258, 1220, 1192, 1095, film
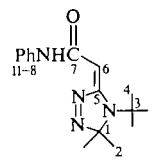 (8–11 in order, C8═CN) **10**	1.50 (s, 9H), 1.69 (s, 6H), 5.17 (s, 1H), 7.38 (m, br, 5H), 10.45 (s, br, 1H)[c]	25.31 (2), 28.06 (4), 54.43 (3), 94.03 (6), 105.15 (1), 120.00 (9), 123.21 (11), 128.89 (10), 139.37 (8), 159.07 (5 or 7), 164.91 (7 or 5)	258 (11), 129 (18), 166 (12), 110 (100), 93 (30), 71 (21), 70 (20), 57 (78), 55 (26). 258.1748 (hr, obsd.); 258.1732 (calcd. for $C_{16}H_{22}N_2O$, $M^+ - N_2$). ci (NH_3) 289 (100), ci (CH_4), 289 (9), 288 (8), 287 (32)	226 (3.85), 256 (4.32), 310 (3.53), 392 (3.83), ethanol	3345, 3017, 2982, 2942, 2900, 1632, 1617, 1594, 1540, 1499, 1442, 1373, 1317, 1296, 1263, 1202, 1159, $CHCl_3$
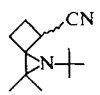 **3*a***	1.13 (s, 3H), 1.14 (s, 9H), 1.19 (s, 9H), 1.21 (s, 3H), 1.24 (s, 3H), 1.45 (s, 3H), 2.14 (m, 3H), 2.31 (m, 3H), 2.52 (m, 1H), 2.94 (q, 1H), 3.07 (m, 1H), 3.33 (t, 1H)	17.93, 20.26, 21.08, 24.67, 25.81, 27.69, 30.61, 30.87, 31.14, 32.15, 40.12, 41.62, 48.56, 49.31, 54.80, 55.26, 120.43, 122.06[d]	192 (10), 177 (8), 135 (46), 121 (20), 109 (20), 109 (20), 82 (48), 81 (37), 57 (100). 192.1625 (hr, obsd.); 192.1626 (calcd. for $C_{12}H_{20}N_2$)	212 (2.01), hexane	2990, 2978, 2967, 2923, 2221, 1450, 1396, 1384, 1366, 1355, 1256, CCl_4

Can. J. Chem. Downloaded from www.nrcresearchpress.com by 213.222.148.141 on 09/07/12
For personal use only.

TABLE 1 (*concluded*)

Compound	^{1}H nmr (δ, $CDCl_3$, 500 MHz)	^{13}C nmr (δ, $CDCl_3$, 22.62 MHz)[a]	Mass spectrum (*m/z*, (%), ei, lr)[b]	Ultraviolet (λ_{max}, nm (log ε))	Infrared (cm^{-1})
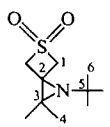 **15***a*	1.16 (s, 9H), 1.25 (s, 6H), 4.22 (AB-q, 4H)	22.04 (4), 30.26 (6), 41.35 (2), 53.46 (3 or 5), 55.68 (5 or 3), 68.55 (1)	217 (4), 216 (4), 202 (22), 160 (30), 97 (43), 96 (97), 57 (100). 202.0898 (hr, obsd.); 202.0902 calcd. for $C_9H_{16}NO_2S$, $M^+ - CH_3$)	no max. above 200 nm	2964, 2927, 1450, 1385, 1377, 1368, 1358, 1325, 1200, $CDCl_3$
14	1.13 (s, 3H), 1.18 (s, 9H), 1.36 (s, 3H), 1.45 (s, 3H)[c]	19.67, 20.19, 23.68, (4, 5, 8), 29.34 (7), 46.08, 52.18, 55.89, (2, 3, 6), 122.12 (9)	151 (9), 110 (25), 109 (25), 83 (53), 57 (100), ci (NH_3), 167 (100), 111 (31). 151.1243 (hr, obsd.); 151.1235 (calcd. for $C_9H_{15}N_{27}$, $M^+ - CH_3$)	no max. above 200 nm	3000, 2962, 2931, 2866, 2210, 1455, 1386, 1378, 1364, CCl_4
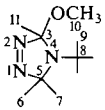 **17**	1.34 (s, 9H), 1.49 (s, 3H), 1.64 (s, 3H), 1.72 (s, 3H), 2.97 (s, 3H)[c]	28.24, 28.40, 25.63 (6, 7, 11), 31.04 (9), 47.95 (10), 51.67 (8), 104.00 (5), 126.18 or 128.85 (3)[e,f]			

[a]The numbers in brackets after the chemical shifts are tentative assignments. See structures for arbitrary numbering schemes.
[b]Abbreviations: ei = electron impact, lr = low resolution, hr = high resolution, ci = chemical ionization. The numbers in parentheses are the relative intensities as percentages of the base peak (100%).
[c]At 90 MHz.
[d]Some signals in the spectrum of this 1:1 mixture of diastereomers overlap.
[e]Impurity other than **1** present. Signals from **1** are not coincident with any of those from **17**.
[f]In methanol.

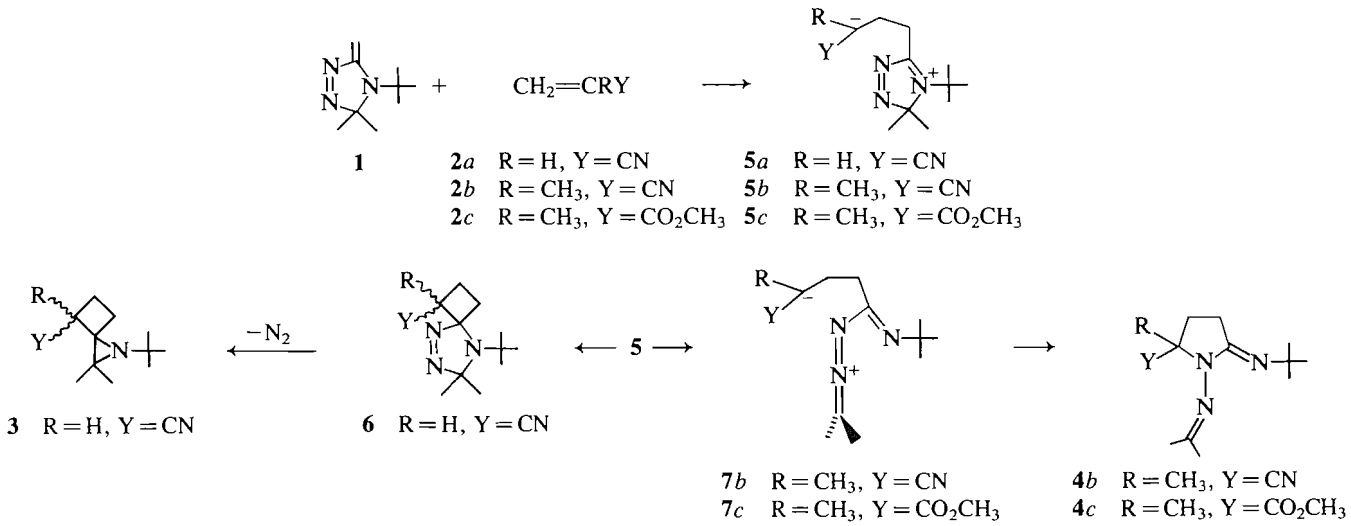

SCHEME 2

ratio and in 88% isolated yield. The diastereomers were barely separable by analytical glpc but separation on a preparative scale was unsuccessful. The ^{13}C nmr spectra (Table 1) indicate clearly that diastereomers **6** cannot be considered as alternatives to **3**. Triazolines **6** would give rise to a signal in the 100–110 ppm range for the *gem*-dimethyl bearing carbon, as in **1**, **11**, and **17**. Moreover, the ^{13}C nmr signals in the range 41–55 ppm suggest quaternary carbon atoms bonded to one nitrogen atom, while the ^1H nmr spectrum (500 MHz, Table 1), although not fully resolved, requires that the methylene and methine protons are attached to a rigid carbon framework.

Surprisingly, the reaction of **1** with methacrylonitrile (**2***b*) did not afford the analogues of **3** but gave, instead, compound **4***b* in 70% yield. Methyl methacrylate (**2***c*) behaved like **2***b*, affording **4***c* in about 70% yield. The hydrazone functional group of **4** follows from the methyl group singlets characteristic of the ^1H nmr spectra of hydrazones of acetone, and the five-membered ring is indicated by the fact that all four methylene protons are magnetically nonequivalent and coupled to one another. All of the additional spectroscopic evidence (Table 1) is fully consistent with the structures labelled **4**.

The above results can be rationalized as follows. Initial interaction of **1** with the acceptor involves formation of one C—C bond, to generate zwitterion **5** (Scheme 2). That species cyclizes, in the 4-*exo* sense, to form spiro compound **6**, or it undergoes ring opening to form intermediate **7**. The latter undergoes ring closure[4] to **4**. Steric effects on the rate constant for 4-*exo* cyclization are probably large because closure to **6** involves eclipsing interactions between neighbouring substituents of the developing cyclobutane ring. One of those substituents is the large N—$C(CH_3)_3$ group. Ring opening to **7**, on the other hand, is probably accompanied by a reduction of nonbonded interactions. Moreover, the stereoelectronic requirements for forming **7** are well provided for in **5** and there is precedent for such reactions in the [2,3]-sigmatropic rearrangement of allenic sulfonium ylides (19). Although we were not able to detect both **3** and **4** from a given **2**, the possibility that minor amounts of the appropriate coproduct were formed in each case has not been ruled out.

Geometric isomers of **4***b* and **4***c* were not observed. The *E* configuration at the C=NC$(CH_3)_3$ group is required by the proposed mechanism and it is also the least sterically congested of the possible configurations.

Reaction of **1** with phenyl isocyanate in chloroform at room temperature afforded neither **8** nor **9** but, instead, the β-amino-α,β-unsaturated amide (**10**) in 62% yield. Compound **10** is analogous to the *E* and *Z* isomers **11** formed, together with **12**, from reactions of **1** with dimethylacetylene dicarboxylate (8).

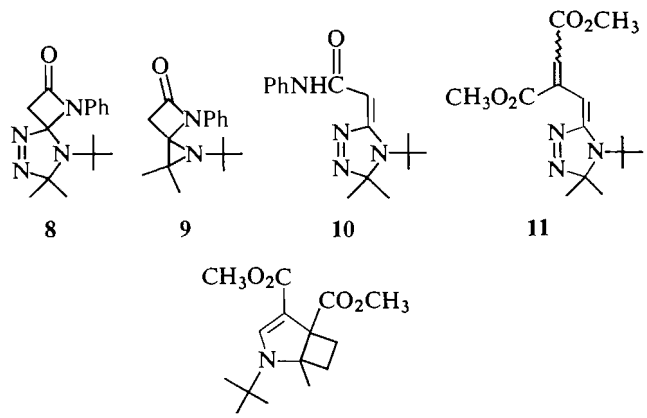

8 **9** **10** **11**

12

The mass spectrum of **10** deserves brief mention. Under ei conditions the molecular ion peak was not observed but there was, instead, a peak at *m/z* 258 corresponding to $M^+ - N_2$. Chemical ionization (ci) mass spectra (NH_3 or CH_4), on the other hand, led to a signal at *m/z* 289, corresponding to $M + 3)^+$. In the ci (NH_3) mass spectrum, the signal for *m/z* 289 was the most intense one, while in the case of ci (CH_4) the relative intensity for *m/z* 289 was 9% (base peak, *m/z* 110) and there were additional signals at *m/z* 288 (8%) and 287 (32%). Similar ci mass spectra of diethyl azodicarboxylate and of **11** (*E* isomer) revealed that they too had significant signals at *m/z* $(M + 3)^+$. Apparently reduction of such azo compounds is a significant process under the conditions for ci mass spectrometry. Although the low reduction potential of azocarbonyl compounds is well known (20), the apparent reduction of **10** and **11** by NH_3 or by CH_4 in the mass spectrometer was surprising.

Triazoline **10** is the type of product expected from the reaction of phenyl isocyanate with an enanime that has at least one hydrogen at the nucleophilic carbon. Enamines that are

[4]The intermediacy of **7** is postulated because the alignment of orbitals for concerted formation of **4** from **5** is poor.

Can. J. Chem. Downloaded from www.nrcresearchpress.com by 213.222.148.141 on 09/07/12
For personal use only.

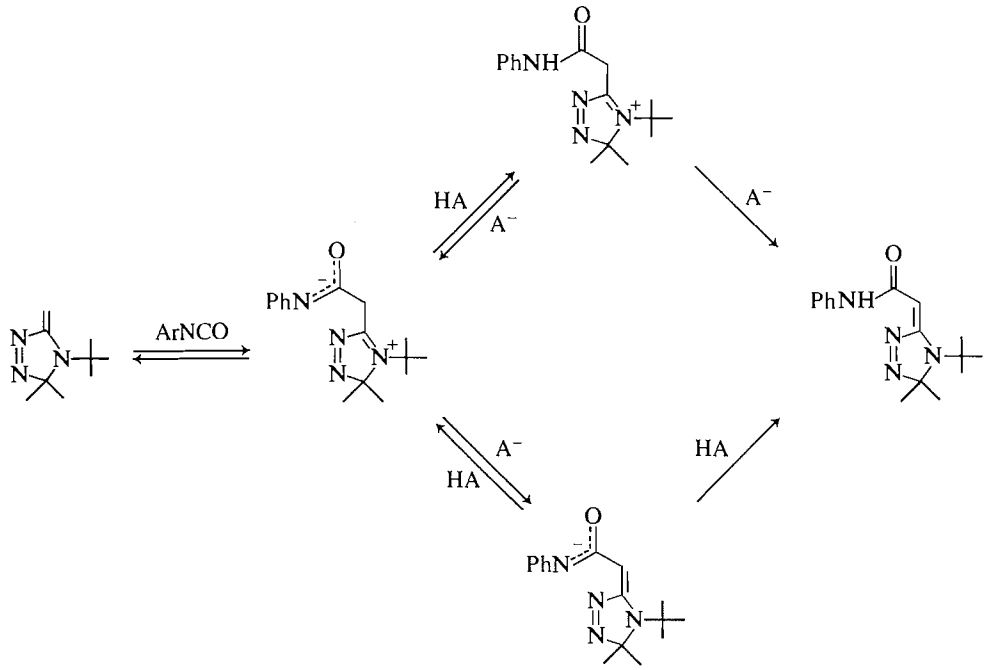

SCHEME 3

disubstituted at the β-carbon give isolable β-lactams when treated with phenyl isocyanate (7). The *E* configuration of **10** was assigned on the basis of signal intensity enhancements in the ^{1}H nmr spectrum of **10** (nuclear Overhauser effects) attributable to the proximity of the *tert*-butyl group and the vinyl proton of **10** (see Experimental).

There are at least two mechanisms by which **10** could be formed. First there is the sequential proton transfer mechanism (Scheme 3) by which compounds **11** appear to be formed from **1** and dimethyl acetylenedicarboxylate (8). Second is a mechanism usually postulated for reactions of enamines with isocyanates (7) but which, in fact, is not supported by any hard evidence, insofar as we are aware. That mechanism is the [2 + 2] cycloaddition, enolization, and [2 + 2] cycloreversion sequence of Scheme 4. At this time there is insufficient evidence to rule out either mechanism and we note only that the acid–base pair HA/A^- required for Scheme 3 is unidentified and that there is a problem with Scheme 4. It was not possible to detect any intermediates by ^{1}H nmr spectroscopy, implying that the β-lactam of Scheme 4 would have to be surprisingly reactive, either in the ring-opening sense or in the enolization sense. In Scheme 3, on the other hand, there are no intermediates that would be expected to accumulate to readily detectable concentrations.

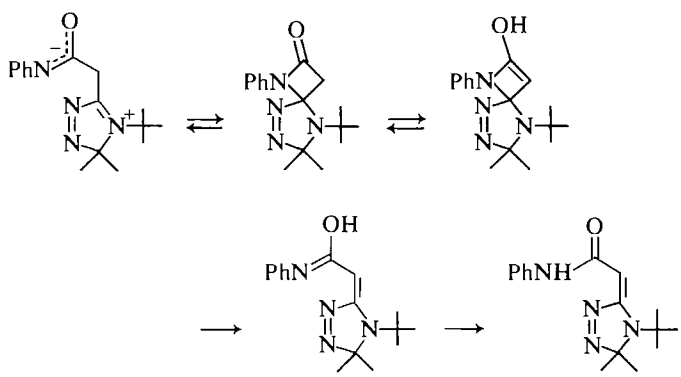

SCHEME 4

Acetone cyanohydrin in CH_3OH, CH_2Cl_2, or CH_2=CHCN reacted with **1** to afford **14** in 42–47% yield (eq. [3]). The

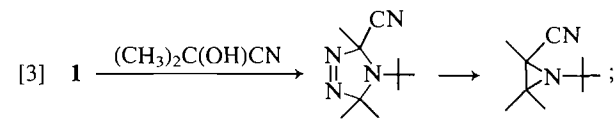

[3]

13 **14**

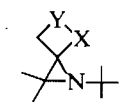

15*a* X = CH_2, Y = SO_2
15*b* X = SO_2, Y = CH_2

structure of **14** was inferred from its ^{1}H and ^{13}C nmr spectra (Table 1) and from its simple ci mass spectrum, with base peak at *m/z* 167 corresponding to $(M + 1)^+$. As in the case of **4** (above) the absence of ^{13}C nmr signals in the range 100–110 ppm, characteristic of 1,2,4-triazolines, excluded **13** from consideration.

Treatment of **1** with sulphene (CH_2=SO_2), generated *in situ* from methanesulfonyl chloride and triethylamine, gave **15***a* in 40% yield. In keeping with previous experience (5, 21) and with FMO analysis of the reacting double bonds (22), the regioisomer **15***b* was not observed. The structure of **15***a* followed from its ms and nmr data (Table 1). In the ^{13}C nmr spectrum the absence of signals near 105 ppm indicated that the azo function had been lost. Moreover, the signal at δ 70 is characteristic of the α-carbon of a thietane-1,1-dioxide (21). The ^{1}H nmr spectrum included a clean AB pattern centered at δ 4.22 (21). The clean AB pattern suggests that inversion of the aziridine nitrogen of **15***a* is fast enough, on the nmr time scale, to give the molecule an effective plane of symmetry passing through the aziridine ring atoms and through the S-atom of the thietane-1,1-dioxide ring. Facile inversion of a pentasubstituted

Can. J. Chem. Downloaded from www.nrcresearchpress.com by 213.222.148.141 on 09/07/12
For personal use only.

Can. J. Chem. Downloaded from www.nrcresearchpress.com by 213.222.148.141 on 09/07/12
For personal use only.

aziridine is not surprising because eclipsing between C and N substituents can be expected to drive the geometry at nitrogen towards planarity, thereby reducing the barrier to inversion (23).

A remarkable result that emerges from the present study is that the azomethine ylide intermediates that are necessary to account for the transformations of **1** into **3** (Scheme 2) and of **1** into **14**, by reaction with acetone cyanohydrin, are not readily intercepted. The yield of **3** in neat acrylonitrile was 88%, and the yield of **14** (42–47%) was essentially independent of the solvent (CH_2Cl_2 or CH_3OH or $CH_2{=}CHCN$). Although the failure of acrylonitrile to trap the ylide could be rationalized in terms of steric hindrance, methanol is known to capture ylides very rapidly (24), and therefore we are forced to conclude that the azomethine ylides in question cyclize to aziridines with very large rate constants.

The reason for very rapid ring closure may be complex, but an identifiable component has its roots in steric factors. In the ylides, the large *N-tert*-butyl substituent and the terminal *exo* substituents should be eclipsed to maximize π-bonding (25). In the transition structures for cyclization, those eclipsing interactions are relieved by twisting. The new steric interactions that develop should not be as large because all three C—N bonds must lengthen as N is rehybridized from a planar to a shallow pyramidal geometry. Moreover, the geminal and vicinal substituent separations are large because of the compressed internal angles of a small ring. An equivalent rationale begins with the assumption that the ylides cannot adopt the all-planar structure that is the ground state of less congested ylides (25) and that they are already substantially twisted in their most stable conformations. Whichever view is taken, the very fast ring closures of the ylides encountered here are attributed to a raised ground state energy level, as proposed by others (26, 27).

Triazoline **1** adds methanol reversibly in the presence of a protic acid (eq. [4]). Although the overall addition of methanol

[4] **1** $\overset{H^+}{\rightleftharpoons}$ **16** $\overset{CH_3OH}{\rightleftharpoons}$ **17**

to **1** is normal enamine chemistry, the survival of **17** is surprising in view of the apparent instability of analogous triazolines with quaternary ring carbons (**6**, **8**, **13**, for example). There was no evidence for appreciable decomposition of **17** even after weeks at room temperature in methanol. Although increased solvent polarity decreases rate constants for decomposition of *cis* azo compounds (28), the stability of **17** in methanol cannot be attributed to the solvent polarity because **13** does not accumulate during conversion of **1** to **14** in methanol at room temperature (eq. [3]). The ratio (**17**:**1**) at equilibrium at room temperature was 0.6 at a total concentration (**17** + **1**) near 0.2 *M*.

Experimental

Melting points were determined on a Thomas Hoover capillary melting point apparatus and are uncorrected. Proton nuclear magnetic resonance (^{1}H nmr) spectra were recorded on a Bruker AM-500 or a Varian EM-390 spectrometer using TMS or residual $CHCl_3$ in $CDCl_3$ as internal standard. Carbon nuclear magnetic resonance (^{13}C nmr) spectra were obtained on a Bruker WP 80/90 spectrometer. Infrared (ir) spectra, obtained with a Perkin–Elmer model 283 instrument, are reported in wavenumbers (cm^{-1}) calibrated against the 1601.4 cm^{-1} band of polystyrene. Ultraviolet (uv) spectra were obtained with a Hewlett–Packard model 8451A diode array spectrophotometer. Mass spectra (ms) were recorded on a VG 70-70F double focussing or a VG ZAB-E triple focussing mass spectrometer.

Centrifugal chromatography was carred out on silica (Merck, Kieselgel 60 PF_{254}) coated glass plates (coating 2 mm thick) spinning in a Chromatotron model 7924T apparatus. Plastic-backed, Merck Kieselgel 60 F_{254}, 0.2-mm silica plates or plastic-backed Polygram ALOX, N/UV_{254}, 0.2-mm neutral alumina plates were used for analytical thin-layer chromatography (tlc).

The following materials are commercially available and were distilled before use: CH_3SO_2Cl, Et_3N (from KOH), methacrylonitrile, and acrylonitrile. Also commercially available, but used as received, were methyl methacrylate, methanol (Baker Analyzed), anhydrous ether (Allied), phenyl isocyanate, acetone cyanohydrin, and methanol-OD (Aldrich). Methylene chloride (Caledon) and chloroform (Caledon) were distilled from P_2O_5 and stored over 4 Å molecular sieves.

The synthesis of triazoline **1** has been described (13).

Nuclear Overhauser enhancement (nOe) measurement

The substrate (10 mg) in 0.4 mL of $CDCl_3$ with a trace of added MeOH was sealed into a medium-walled nmr tube after three cycles of freeze–pump–thaw degassing at 0.3 Torr (1 Torr = 133.3 Pa). Eight scans on a Bruker WH250 nmr spectrometer with off-resonance irradiation were followed by eight scans taken with irradiation directed at the substrate's *t*-Bu signal. Each signal was integrated against the CH_3 signal of the internal MeOH. No correction was made for enhancement, if any, of the reference signal during double irradiation.

*Reactions of **1** with acrylonitrile, methacrylonitrile, and methyl methacrylate*

Triazoline **1** (0.120 g) in 10 mL of acrylonitrile was sealed into a tube that had been evacuated at 0.1 Torr. The tube and contents were heated with an oil bath at 80°C (8 h) or at 50°C (14.5 h). After cooling, the tube was opened and the excess acrylonitrile was removed under reduced pressure (aspirator). The residue, in ether, was applied to a neutral Al_2O_3(II) column from which it was eluted with 40% ether in light petroleum. The first fraction collected contained the diastereomeric 2-aza-2-(*tert*-butyl)-4-cyano-3,3-dimethyl-spiro[2.3]hexanes, **3** (R_f = 0.61, Al_2O_3, ether) isolated as an oil, 139 mg (88%).

Similar heating of **1** (0.127 g) in methacrylonitrile (9 mL) at 80°C for 26 h, and analogous work-up except for elution with ethyl acetate (10%) in light petroleum, afforded amidrazone **4***b* (0.128 g, 70%), R_f = 0.08 (Al_2O_3, ether). Recrystallization from light petroleum gave **4***b* as a colourless solid, mp 60–61.5°C.

Analogous treatment of **1** (0.260 g) with methyl methacrylate (10 mL) at 80°C for 26 h led to significant polymer formation. The contents of the tube were added to dry methanol (20 mL), the precipitate was filtered off, and the residue was concentrated to afford crude **4***c*, which is very easily hydrolyzed. The ^{13}C nmr spectrum was obtained directly with the crude sample. For other spectra (Table 1) pure samples were collected by preparative glpc (6 ft × 1/4 in. column packed with OV-17, 10% on Chromosorb W) at 172°C. With a helium flow rate of 18 mL min^{-1}, the retention time for **4***c* was 7 min.

*Reaction of **1** with acetone cyanohydrin*

A solution of triazoline **1** (210 mg) in 2.5 mL of a solvent (see below) and 0.25 mL of acetone cyanohydrin was stirred at room temperature until the triazoline was consumed (5 h for CH_2Cl_2 solvent, 3 h for methanol or acrylonitrile). Once the reaction was complete, CH_2Cl_2 (10 mL) and dilute aqueous base (20 mL) were added. After five minutes more of stirring, the layers were separated. The aqueous portion was extracted (3 × 10 mL) with CH_2Cl_2. The organic layers were combined and dried over $MgSO_4$.

After filtration and concentration (aspirator) the residue was applied to a column of 10 g of Al_2O_3(II) and eluted with 50% ether in light petroleum. The first fraction (R_f = 0.57, ether) was 1-(*tert*-butyl)-2-cyano-2,3,3-trimethylaziridine (**14**, 88–99 mg, 42–47%) obtained as an oil.

*Reaction of **1** with phenyl isocyanate*

A solution of triazoline **1** (0.158 g) in 6 mL of dry chloroform containing 0.25 mL of phenyl isocyanate was stirred at room tempera-

ture for 48 h. More isocyanate (0.25 mL) was added and stirring was continued for a further 48 h. Dry chloroform (20 mL) was added and the resulting solution was washed twice with aqueous NaOH (20 mL, 0.5 *M*). The organic layer was dried over $MgSO_4$. Concentration and chromatography of the residue on a silica column (ether) led to separation of an orange compound with R_f = 0.22 (SiO_2, ether). Fractions containing the orange material were concentrated and the residues were subjected to centrifugal chromatography (Chromatotron, SiO_2 plate) with ethyl acetate (25%) in light petroleum. The viscous orange product would not crystallize. The yield of triazoline **10** was 168 mg (62%). Irradiation at the frequency of the *tert*-butyl signal (^{1}H nmr) increased the intensity of the vinyl signal of **10** by 26%.

*Reaction of **1** with sulfene*

A 50-mL round-bottomed flask was charged with **1** (0.280 g, 1.7 mmol), triethylamine (0.350 g, 3.5 mmol), and 10 mL of anhydrous ether. The solution was stirred and cooled with ice while methanesulfonyl chloride (0.379 g, 3.3 mmol) was added dropwise in 20 min. The ice bath was removed and stirring was continued for 4 h. Dichloromethane (10 mL) was added, the precipitated amine salt was filtered off, and the filtrate was concentrated. The residue was applied to a column of Al_2O_3(II) from which the product was eluted with ether (50%) in light petroleum (R_f = 0.17, ether). Further chromatographic purification of the product from the first column gave 2-aza-2-(*tert*-butyl)-3,3-dimethyl-5-thiaspiro[2.3]hexane-5,5-dioxide (0.104 g, 40% based on 0.20 g of triazoline consumed), mp 78.5–80°C (from petroleum).

Methylenetriazoline–methoxytriazoline equilibrium

Triazoline **1** (0.20 g) in methanol (2 mL) containing a few crystals of toluenesulfonic acid hydrate was kept at room temperature for 5 h. Analysis of the solution by ^{1}H nmr and ^{13}C nmr spectroscopy showed the presence of unreacted **1** and 4-(*tert*-butyl)-3,5,5-trimethyl-3-methoxy-Δ^1-1,2,4-triazoline (**17**). The ratio **17**:**1** = 0.6, estimated by integration of the ^{1}H nmr spectrum, remained constant with time for several weeks. Spectra of **17** are in Table 1.

Acknowledgements

This work was financed from a grant provided by the Natural Sciences and Engineering Research Council of Canada. We are indebted to Professor J. F. King for some very helpful comments and we acknowledge also the assistance of D. R. Myers, B. G. Sayer, and G. Timmins, who provided nmr spectra, and of J. Kapron and F. Ramelan, who obtained the mass spectrometric data.

1. A. G. Cook. Enamines: synthesis, structure, and reactions. Dekker, New York. 1969.
2. P. W. Hickmott. (*a*) Tetrahedron, **38**, 1975 (1982); (*b*) Tetrahedron, **38**, 3363 (1982).
3. G. Stork, A. Brizzolara, H. Landesman, J. Szmuszkovicz, and R. Terrell. J. Am. Chem. Soc. **85**, 207 (1963).
4. D. N. Reinhoudt. Adv. Heterocycl. Chem. **21**, 253 (1977).
5. J. F. King. Acc. Chem. Res. **8**, 10 (1975).
6. P. W. Hickmott. Chem. Ind. 731 (1974).
7. H. Ulrich. Cycloaddition reactions of heterocumulenes. Academic Press, New York, 1967. Chap. 4.
8. A. L. Schwan and J. Warkentin. Can. J. Chem. **65**, 1200 (1987).
9. D. N. Reinhoudt, W. Verboom, G. W. Visser, W. P. Trompenaars, S. Harkema, and G. J. van Hummel. J. Am. Chem. Soc. **106**, 1341 (1984).
10. K. C. Brannock, A. Bell, R. D. Burpitt, and C. A. Kelly. J. Org. Chem. **26**, 625 (1961).
11. S. R. Tanny and F. W. Fowler. J. Org. Chem. **39**, 2715 (1974).
12. R. H. Rynbrandt. J. Heterocycl. Chem. **11**, 787 (1974).
13. A. L. Schwan and J. Warkentin. J. Chem. Soc. Chem. Commun. 1721 (1986).
14. R. Smith and T. Livinghouse. Tetrahedron, **41**, 3559 (1985).
15. E. Vedejs, S. Larsen, and F. G. West. J. Org. Chem. **50**, 2170 (1985).
16. J. W. Lown. *In* 1,3-Dipolar cycloaddition chemistry. Vol. 1. *Edited by* A. Padwa. Wiley–Interscience, New York. 1984. Chap. 6.
17. E. Vedejs and F. G. West. Chem. Rev. **86**, 941 (1986).
18. R. M. Kellogg. Tetrahedron, **32**, 2165 (1976).
19. H. Hopf. *In* The chemistry of allenes. Vol. 2. *Edited by* S. R. Landor. Academic Press, New York. 1982. p. 226.
20. F. Yoneda, K. Suzuki, and Y. Nitta. J. Am. Chem. Soc. **88**, 2328 (1966).
21. D. C. Dittmer and T. C. Sedergran. *In* The chemistry of heterocyclic compounds. Small ring heterocycles. Part 3. *Edited by* A. Hassner. Interscience, Toronto. 1985. p. 488.
22. I. Fleming. Frontier orbitals and organic chemical reactions. Wiley–Interscience, New York. 1976.
23. J. B. Lambert. Top. Stereochem. **6**, 19 (1971).
24. (*a*) N. Shimizu and P. D. Bartlett. J. Am. Chem. Soc. **100**, 4260 (1978); (*b*) S. W. Ege, J. E. Gess, A. Thomas, P. Umrigar, S. W. Griffin, P. K. Das, A. M. Trozzolo, and T. M. Leslie. J. Chem. Soc. Chem. Commun. 1263 (1980); (*c*) M. Bekhazi and J. Warkentin. J. Am. Chem. Soc. **103**, 2473 (1981).
25. K. N. Houk, N. G. Rondan, C. Santiago, C. J. Gallo, R. W. Gandour, and G. W. Griffin. J. Am. Chem. Soc. **102**, 1504 (1980).
26. J. A. Deyrup and W. A. Szabo. J. Org. Chem. **40**, 2048 (1975).
27. C. W. Martin, H. S. Gill, and J. A. Landgrebe. J. Org. Chem. **48**, 1898 (1983).
28. (*a*) A. Schulz and C. Rückhart. Tetrahedron Lett. 3883 (1976); (*b*) W. Duismann and C. Rückhardt. Chem. Ber. **111**, 596 (1978); (*c*) P. S. Engel. Chem. Rev. **80**, 99 (1980).

Can. J. Chem. Downloaded from www.nrcresearchpress.com by 213.222.148.141 on 09/07/12
For personal use only.

Methylation of polymethylbenzenesulfonic acids by hexamethylbenzene and pentamethylbenzenesulfonic acid in concentrated sulfuric acid[1]

HANS CERFONTAIN[2] AND ANKIE KOEBERG-TELDER

Laboratory for Organic Chemistry, University of Amsterdam, Nieuwe Achtergracht 129, 1018 WS Amsterdam, The Netherlands

Received May 25, 1987

HANS CERFONTAIN and ANKIE KOEBERG-TELDER. Can. J. Chem. **66**, 162 (1988).

The methylation of a series of polymethylbenzenes (PoMB's) or their sulfonic acids by added hexamethylbenzene (HMB) and pentamethylbenzene-1-sulfonic acid (PeMB-1-S) as reagents in 95.5 and 98.4% H_2SO_4 as solvent has been studied under homogeneous conditions. HMB effects methylation of 2,4,6-trimethylbenzene-1-sulfonic acid (2,4,6-TrMB-1-S), 2,3,4,6-tetramethylbenzene-1-sulfonic acid (2,3,4,6-TeMB-1-S), and 2,3,5,6-TeMB-1-S, but not of the sulfonic acids of 1,3-dimethylbenzene (1,3-DMB), 1,2,3-TrMB, 1,2,4-TrMB, and 1,2,3,4-TeMB. PeMB-1-S is less reactive as methylating reagent than HMB. The observed substrate reactivity towards methylation by HMB was observed to decrease in the order 2,3,4,6-TeMB-1-S $\approx$ 2,3,5,6-TeMB-1-S $>$ 2,4,6-TrMB-1-S $\gg$ 2,3,4,5-TeMB-1-S, and towards methylation by PeMB-1-S to decrease in the order PeMB-1-S $\gg$ 2,4,6-TrMB-1-S. On the basis of a comparison of these orders of substrate reactivities with those predicted for the series of the PoMB-1-sulfonates and the corresponding PoMB's, it is concluded that the substrate species undergoing methylation are the PoMB's and not the corresponding sulfonates.

HANS CERFONTAIN et ANKIE KOEBERG-TELDER. Can. J. Chem. **66**, 162 (1988).

Utilisant des conditions homogènes, dans du H_2SO_4 à 95,5 et 98,4%, on a étudié la méthylation d'une série de polyméthylbenzènes (PoMB) ou de leurs acides sulfoniques par de l'hexaméthylbenzène (HMB) et de l'acide pentaméthylsulfonique-1 (PeMBS-1) agissant comme réactifs. Le HMB provoque la méthylation des acides triméthyl-2,4,6 (TrM-2,4,6 BS-1), tétraméthyl-2,3,4,6 (TeM-2,3,4,6 BS-1) et tétraméthyl-2,3,5,6 (TeM-2,3,5,6 BS-1) benzènesulfoniques; toutefois, il ne provoque pas la méthylation des acides sulfoniques du diméthyl-1,3 (DM-1,3 B), des triméthyl-1,2,3 ou 1,2,4 (Tr-1,2,3 B ou Tr-1,2,4 B) et du tétraméthyl-1,2,3,4 (TeM-1,2,3,4 B) benzène. Comme agent de méthylation, l'acide PeMBS-1 est moins réactif que le HMB. On a observé que la réactivité des substrats, par rapport à la méthylation par le HMB, diminue dans l'ordre TeM-2,3,4,6 BS-1 $\approx$ TeM-2,3,5,6 BS-1 $>$ TrM-2,4,6 BS-1 $\gg$ TeM-2,3,4,5 BS-1; par ailleurs, par rapport à la méthylation par le PeMBS-1, la réactivité diminue dans l'ordre PeMBS-1 $\gg$ TrM-2,4,6 BS-1. En se basant sur une comparaison de ces ordres de réactivités des substrats avec ceux prédits pour des séries de PoMBsulfonates-1 ainsi que les PoMB correspondants, on en conclut que les espèces des substrats qui subissent la méthylation sont les PoMB et non pas les sulfonates correspondants.

[Traduit par la revue]

As a continuation of our studies on the behaviour of polyisopropyl- (1) and polyethylbenzenes (2) in sulfuric acid as solvent, we recently reported on the reactions of various polymethylbenzenes (PoMB's) and their sulfonic acids in that solvent system (3), reactions generally referred to as the Jacobsen reaction (for reviews see ref. 4). Whereas the 2,3,4,6- and 2,3,5,6-tetraethylbenzene-1 sulfonic acids isomerize to the (stable) 2,3,4,5-isomer *intra*-molecularly, as appears from the simple first-order kinetics (2), the corresponding tetramethyl homologues indeed yield the stable 2,3,4,5-tetramethylbenzene-1-sulfonic acid (2,3,4,5-TeMB-1-S), but not by first-order kinetics (3). The conversions of both the 2,3,4,6- and 2,3,5,6-TeMB-1-S are characterized by an induction period, illustrating autocatalysis. The induction period for 2,3,5,6-TeMB-1-S is in line with its observed initial slow disproportionation to the sulfonic acids of pentamethylbenzene (PeMB) and 1,2,4-trimethylbenzene (1,2,4-TrMB) and the subsequent partial methylation of PeMB (initially mainly by protonated 1,2,4,5-TeMB) to hexamethylbenzene (HMB). The isomerization of the 2,3,5,6- into the 2,3,4,6-TeMB-1-S then proceeds via *inter*-molecular *trans*-methylations involving PeMB-1-S and HMB as the methylating reagents. The isomerization of 2,3,4,6-TeMB-1-S into the stable 2,3,4,5 isomer was proposed to proceed in a similar mechanistic fashion by initial disproportionation of the substrate to the sulfonic acids of PeMB and 1,3,5-TrMB and subsequent *inter*-molecular *trans*-methylations involving PeMB and 1,3,5-TrMB as intermediates, although the presence of PeMB-1-S and 2,4,6-TrMB-1-S in the reaction mixtures could not be established beyond the limits of the ^{1}H nmr analysis, which in the presence of 2,3,4,6-TeMB-1-S was, however, 10% at the least.

To obtain more information on the various reactions of the intermediates possibly occurring in the Jacobsen reaction of the PoMB's, in particular on the proposed intermediacy of 1,3,5-TrMB and PeMB and their sulfonic acids in the conversion of 2,3,4,6- into 2,3,4,5-TeMB-1-S, we have studied the methylation of a series of polymethylbenzenes and their sulfonic acids in concentrated sulfuric acid by added HMB and PeMB-1-S.

Results

Varying amounts of a given PoMB or its monosulfonate have been treated in concentrated aqueous sulfuric acid with HMB and PeMB-1-S at 25°C under homogeneous conditions. The reaction mixtures have been analyzed as such by multicomponent ^{1}H nmr analysis. The pertinent data are compiled in Table 1. HMB effects methylation of 2,4,6-TrMB-1-S, 2,3,4,6-TeMB-1-S, and 2,3,5,6-TeMB-1-S, but not of (the sulfonic acids of) 1,2,3,4-TeMB (3), 1,2,3-TrMB, 1,2,4-TrMB, and 1,3-dimethylbenzene (1,3-DMB). The latter three hydrocarbons, upon addition to 98.4% H_2SO_4, are only sulfonated, and those of the resulting sulfonic acids, which contain a hydrogen atom *meta* to the sulfo group, are relatively slowly sulfonated in part further to the corresponding *meta*-disulfonic acids (6, 7). The sulfonic acids formed upon dissolving the TeMB's in 98.4% H_2SO_4 at 25°C are not further sulfonated.[3]

The methylation product of 2,4,6-TrMB-1-S is 2,3,4,6-

[1]Aromatic isomerizations and related reactions, part 7. Preceding paper, see ref. 3.

[2]Author to whom correspondence may be addressed.

[3]In fact, the TeMB disulfonic acids in concentrated aqueous sulfuric acid undergo desulfonation yielding the monosulfonic acids (8).

Printed in Canada / Imprimé au Canada

Can. J. Chem. Downloaded from www.nrcresearchpress.com by 213.222.148.141 on 09/07/12
For personal use only.

Can. J. Chem. Downloaded from www.nrcresearchpress.com by 213.222.148.141 on 09/07/12
For personal use only.

TeMB-1-S and that of both 2,3,4,6- and 2,3,5,6-TeMB-1-S is PeMB-1-S. The resulting three sulfonic acids are not stable in concentrated sulfuric acid and undergo Jacobsen type conversions. The equilibrium content of 1,3,5-TrMB present in a solution of 2,4,6-TrMB-1-sulfonic acid in 95.5 and 98.4% H_2SO_4 was determined at 25°C to be 0.03 and ≤0.006% respectively. These values compare with the value of 0.01% for 96.1% H_2SO_4 at 12°C, calculated from the extrapolated sulfonation and desulfonation rate coefficients (9).

Discussion

Relative reactivities of reagents and substrates

As appears from the initial rate of substrate conversion, the methylating reactivity is greater for HMB than PeMB-1-S (cf. entry 2 with 4 and entry 8 with 9). In aqueous sulfuric acid more concentrated than 95% H_2SO_4, HMB is for the greater part protonated (5) and the resulting hexamethylbenzenonium ion is in fact the active methyl transferring species (see later). In the study on the Jacobsen reaction of PeMB-1-, 2,3,4,6-TeMB-1-, and 2,3,5,6-TeMB-1-S we showed that the *trans*-methylating entity is the ring-protonated polymethylbenzene and not its ring-protonated sulfonate or sulfonic acid (3). Accordingly, on using the PeMB-1-S/PeMB methylating system the greater part of the reagent is present in the unreactive, mainly unionized (10), sulfonic acid form and this is the main reason for the observed lower methylating reactivity of PeMB as compared with HMB.

The rate of substrate conversion for the methylation by HMB in 98.4% H_2SO_4 is very similar on starting with 1,3,5-TrMB and 2,4,6-TrMB-1-S (cf. entries 1 and 3). Apparently for 98.4% H_2SO_4 the rate of methylation is slow relative to the time required to establish the 1,3,5-TrMB $\rightleftharpoons$ 2,4,6-TrMB-1-S equilibrium (9). However, for 95.5% H_2SO_4 the initial rates of conversion of both the substrate and the HMB reagent are significantly greater for 1,3,5-TrMB than 2,4,6-TrMB-1-S (entries 6 and 5), indicating that the rate of methylation of 1,3,5-TrMB in 95.5% H_2SO_4 is no longer negligibly small relative to its rate of sulfonation. In fact, the observed rate difference strongly suggests that the substrate species undergoing methylation is the polymethylbenzene and not the corresponding sulfonate or sulfonic acid (see also later).

Based on the foregoing discussion, the *trans*-methylation of an aromatic substrate $ArR^1R^2R^3$ by the PeMB-1-S/PeMB system and HMB is thought to proceed by steps [1]–[5] in which Ar stands for C_6Me_3 and R^1, R^2, and R^3 may be Me, H, SO_3^-, or SO_3H. In cases where R^3 = H, sulfonation of R^2R^3ArMe will take place (step [6]) to yield $R^2MeArSO_3H$ (step [6]).

[1] $PeMB\text{-}1\text{-}S + H_2SO_4 \rightleftharpoons PeMB + H_2S_2O_7$

[2] $ArR^1R^2Me + HB \rightleftharpoons R^1R^2Ar^+(Me)(H) + B^-$

[3] $R^1R^2Ar^+(Me)(H) + R^2R^3ArH \rightleftharpoons R^1R^2ArH + R^2R^3Ar^+(Me)(H)$

[4] $R^2R^3Ar^+(Me)(H) + B^- \rightleftharpoons R^2R^3ArMe + HB$

[5] $R^1R^2ArH + H_2S_2O_7 \rightleftharpoons R^1R^2ArSO_3H + H_2SO_4$

[6] $R^2MeArH + H_2S_2O_7 \rightleftharpoons R^2MeArSO_3H + H_2SO_4$

The substrate R^2R^3ArH being methylated by steps [3] and [4] may be the polymethylbenzenesulfonic acid, its sulfonate anion, or the corresponding polymethylbenzene. The methylation rate coefficient of the unionized sulfonic acid, which is the majority species in aqueous sulfuric acid more concentrated than 95% H_2SO_4 (10), will be very much smaller than that of the corresponding sulfonate anion (because of the difference in charge) and the rate coefficient of the latter will be a factor of at least 10^5 smaller than that of the corresponding hydrocarbon (11, 12). Presuming additivity of the methyl and sulfonate substituent effects,[4] the reactivity order of the polymethylbenzenes proper towards a given methylating reagent will increase in the order 1,3-DMB [0.1] < 1,2,4-TrMB [0.3] = 1,2,3-TrMB [0.3] < 1,2,4,5-TeMB [0.7] < 1,2,3,4-TeMB [1.3] < 1,3,5-TrMB [6] < 1,2,3,5-TeMB [15] < PeMB [30], and those of the corresponding polymethylbenzenesulfonates will increase in the order 2,3,5-TrMB-1-S [0.04] ≈ 2,3,4,5-TeMB-1-S [0.06] ≈ 2,3,5,6-TeMB-1-S [0.07] < 2,4-DMB-1-S [0.25] < 2,4,5-TrMB-1-S [0.35] < 2,3,4-TrMB-1-S [0.6] ≪ 2,4,6-TrMB-1-S [15] < 2,3,4,6-TeMB-1-S [30] in which the data in square brackets for a given series of compounds give a relative measure of the overall rate of methylation within that series. The actually observed reactivity order for methylation by HMB increases in the order 2,4-DMB-1-S, 2,3,4-TrMB-1-S, 2,4,5-TrMB-1-S, 2,3,4,5-TeMB-1-S (all nonreactive) ≪ 2,4,6-TrMB-1-S < 2,3,4,6-TeMB-1-S ≈ 2,3,5,6-TeMB-1-S (cf. Table 1, entries 2, 7, and 8). This order does not at all fit in with the order predicted for the polymethylbenzenesulfonate substrate species (compare, e.g., the position of 2,3,5,6-TeMB-1-S within the two series). The differences in the degree of ionization of the various polymethylbenzenesulfonic acids are only small[5] and cannot explain the apparent discrepancy.

Accordingly, the polymethylbenzenesulfonates can be ruled out as the substrate species being methylated. This then leaves the polymethylbenzenes as the species undergoing methylation. The observed order deviates to some degree from the one predicted for these type of species, but it should be realized that the relatively small amount of free hydrocarbon in equilibrium with its sulfonic acid and sulfonate in the sulfuric acid solvent system differs strongly for the various polymethylbenzenesulfonic acids; it increases in the order 1,2,4-TrMB ≈ 1,2,3,4-TeMB ≪ 1,3,5-TrMB < 1,2,3,5-TeMB < 1,2,4,5-TeMB < PeMB (cf. results and ref. 3).[6]

The absence of methylation of 2,3,4,5-TeMB-1-S is ascribed to the very low (equilibrium) content of 1,2,3,4-TeMB in the reaction mixture, if any (≪0.01% in 96.1% H_2SO_4 (3)).

Upon reaction of 2,4,6-TrMB-1-S with an equimolar amount of PeMB-1-S in 98.4% H_2SO_4 (entry 4), the initial decrease is

[4]The partial rate factors employed in the calculations of the relative rate coefficients were those reported for sulfonation by the $H_2S_2O_7$ mechanism in concentrated aqueous sulfuric acid (3, 11).

[5]The ionization of arenesulfonic acids in sulfuric acid is governed by the H^a acidity function (13). The $|ArSO_3^-|/|ArSO_3H|$ ratios for the various PoMB-1-S's in 98.4% H_2SO_4 (H^a = −8.24 (13)) were calculated taking pK_a ($C_6H_5SO_3H$) = −6.65 (14) and applying the principle of additivity of the methyl substituents with ΔpK_a for *o*-, *m*-, and *p*-Me = 0.10 (14), 0.04 (15), and 0.10 (15) respectively. The ionization ratios thus calculated, given in square brackets, increase (but in total only 30%) in the order 2,3,4,6-TeMB-1-S [0.012], 2,4,6-TrMB-1-S [0.013], 2,3,4,5-TeMB-1-S = 2,3,5,6-TeMB-1-S [0.014], 2,3,4-TrMB-1-S = 2,4,5-TrMB-1-S [0.015], 2,4-DMB-1-S [0.016].

[6]The equilibrium content of polymethylbenzene increases with increasing steric hindrance between the sulfo group and the adjacent methyls in the PoMB-1-S.

Can. J. Chem. Downloaded from www.nrcresearchpress.com by 213.222.148.141 on 09/07/12
For personal use only.

TABLE 1. Methylation of polymethylbenzenes and their sulfonic acids in sulfuric acid at 25°C

Entry	Substrate (M)	H_2SO_4 (wt.%)	Methylating reagent (M)	Method[a]	Reaction time (h)	Composition (%, ±2)						Methyl balance (%)[c]
						2,4,6-TrMB-		2,3,4,5-	2,3,4,6-	2,3,5,6-		
						-1-S	-1,3-S_2	-TeMB-1-S			PeMBS	HMB[b]
1	1,3,5-TrMB	98.4	HMB	A	0.	50						50	100
	(0.20)		(0.20)		1.3	41		3	14		14	28	95
					3.3	33		11	14		22	20	95
					4.6	28		18	10		29	15	97
					6.8	20		26	7		38	9	97
					26.8	—	3	47 ± 5	—		50 ± 5	—	99
2	2,4,6-TrMB-1-S	98.4	HMB	B	0	50						50	100
	(0.20)		(0.20)		1.8	35		4	12		30	19	96
					4.3	23		16	15		36	10	98
					21.4	—		55 ± 5	—		45 ± 5	—	98
3	2,4,6-TrMB-1-S	98.4	HMB	A	0	50						50	100
	(0.20)		(0.20)		1.8	44		3	3		21	29	97
					2.5	38		4	5		29	23	96
					4.8	30		15	5		35	16	98
					5.3	24		21	3		38	14	98
					27.3	—		52 ± 5	—		48 ± 5	—	100
4	2,4,6-TrMB-1-S	98.4	PeMB-1-S	B	0	50						50	100
	(0.20)		(0.20)		1.5	48		10	14		23	6	100
					4.0	38		22	18		20	3	98
					21.0	22	3	50	9		16	—	98
					46.5	17	6	56	4		17		99
					69.0	16	7	60	—		17		99
					166	9	12	61			18		99
5	2,4,6-TrMB-1-S	95.5	HMB	A	0	64						36	100
	(0.07)		(≃0.04)		2.4	44		3	21		15	17	99
					4.4	29		13	36		13	9	99
					6.0	21		21	38		14	6	99
					26.3	12		76	12		—	—	95
6	1,3,5-TrMB	95.5	HMB	A	0	64						36	100
	(0.07)		(≃0.04)		1.7	36		3	28		14	19	102
					3.3	26		17	37		8	12	100
					6.8	19		39	31		6	6	99
					26.3	10		75	10		5	—	97

Can. J. Chem. Downloaded from www.nrcresearchpress.com by 213.222.148.141 on 09/07/12
For personal use only.

TABLE 1 (*concluded*)

Entry	Substrate (M)	H_2SO_4 (wt.%)	Methylating reagent (M)	Method[a]	Reaction time (h)	Composition (%, ±2)							Methyl balance (%)[c]
						2,4,6-TrMB-		2,3,4,5-	2,3,4,6-	2,3,5,6-			
						-1-S	-1,3-S_2	-TeMB-1-S			PeMBS	HMB[b]	
7	2,3,4,6-TeMB-1-S (0.25)	98.4	HMB (0.25)	B	0				50			50	100
					0.6			1–2	17–16		61	21	100
					2.2			6	12		62	20	99
					4.2			9	11		—82—		—
					6.0			12	6		—82—		—
8	2,3,5,6-TeMB-1-S (0.20)	98.4	HMB (0.20)	B	0					50		50	100
					0.2					29	47	24	99
					0.6			1	5	20	54	20	99
					1.5			5	24	6	44	21	97
					4.1			21	22	1	33	23	96
9	2,3,5,6-TeMB-1-S (0.20)	98.4	PeMB-1-S (0.20)	B	0					50	50		100
					0.2				3	50	44	3	98
					0.6			2	4	51	39	4	99
					1.6			4	13	44	32	5	97
					4.0			13	27	18	33	5	95
					7.0			26	31	5	29	5	93
10	PeMB-1-S (0.20)	98.4	—		0						100		100
					0.6			3	15		64	18	100
					2.1			7	11		65	17	100
					4.9			10	8		64	18	100
					6.4			14	4		64	18	100
					18.8			18	<2		—81—		—

[a]Method A: The mixture of HMB and sulfuric acid was stirred for 30 min and then added to the substrate. Method B: The sulfuric acid was added to the mixture of the reactants.
[b]HMB is present predominantly as $C_6Me_6H^+$ (3, 5).
[c]The initial average number of methyl groups per benzene ring was set to be 100%.

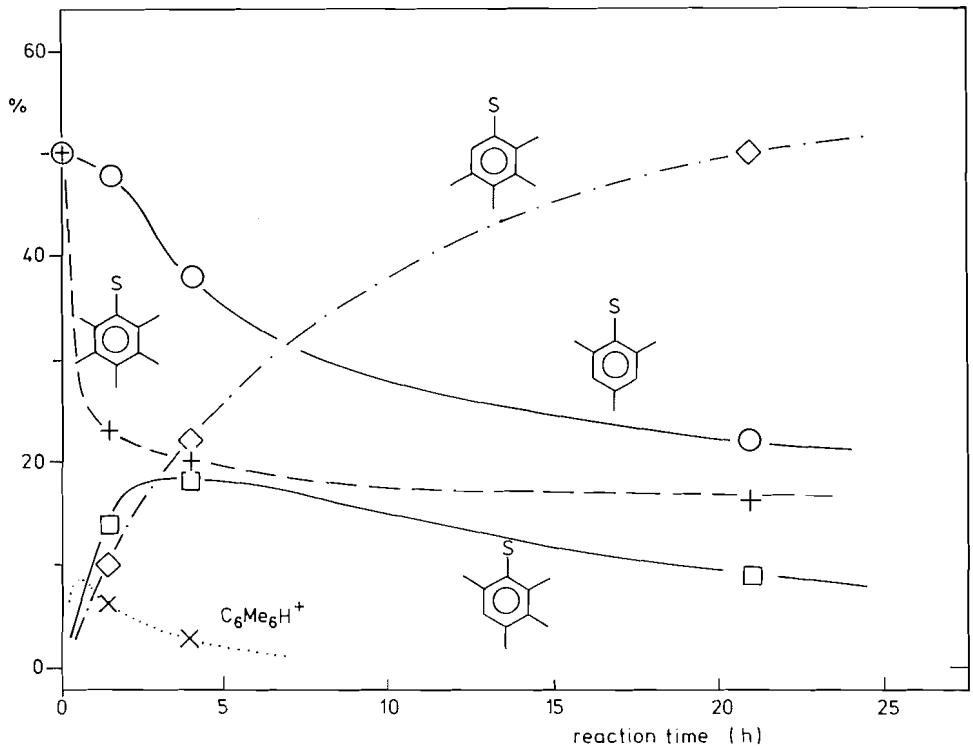

FIG. 1. Reaction of 2,4,6-TrMB-1-S (0.20 M) with PeMB-1-S (0.20 M) in 98.4% H_2SO_4 at 25°C.

far greater for PeMB-1-S than for 2,4,6-TrMB-1-S (Fig. 1). This is ascribed to methylation of PeMB in addition to that of 1,3,5-TrMB, of which the former is apparently very much faster (by a factor of 30–100) than the latter. The higher reactivity of PeMB is mainly due to the higher relative equilibrium content of this hydrocarbon in the system.

trans-*Methylation equilibrium*

Upon dissolving PeMB-1-S in 98.4% H_2SO_4, PeMB acts both as methylating agent and as substrate, the products of the rapid initial partial conversion being HMB and a (8:1) mixture of 2,3,4,6- and 2,3,4,5-TeMB-1-S formed in equal amounts (entry 10). The reverse reaction occurs on mixing equimolar amounts of HMB and 2,3,4,6-TeMB-1-S (entry 7). After 0.6 h of reaction, about the same compositions are obtained for the two experiments and the equilibrium constant for the apparent overall interconversion [7] is $K_7 = 12 \pm 2$. The initial

[7] HMB + 2,3,4,6-TeMB-1-S $\rightleftharpoons$ 2 PeMB-1-S

equilibrium is subsequently broken up as a result of the relatively slow, irreversible, conversion of the 2,3,4,6- into 2,3,4,5-TeMB-1-S.

Isomerization of tetramethylbenzenesulfonic acids

In the presence of HMB the substrates 2,3,4,6- and 2,3,5,6-TeMB-1-S, in addition to being methylated, are found to isomerize to the stable 2,3,4,5 isomer (entries 7 and 8). These isomerizations were shown to proceed *inter*-molecularly with PeMB-1-S and HMB as the *trans*-methylating agents involving the substrate hydrocarbons as the entities being methylated (see preceding discussion and ref. 3). In essence, the methyl transfers in these conversions proceed similarly to the isomerizations and disproportionations of the TrMB's and TeMB's induced by Brønsted acid catalysts other than sulfuric acid, such as $HF–BF_3$ (16) and methanesulfonic acid (17), in that they all involve polymethylbenzenonium ions as intermediates effecting the *trans*-methylations. As emphasized by Kilpatrick and Meyer (18), the outcome of the *inter*-molecular *trans*-methylation reactions of a given TeMB in sulfuric acid differs from the results obtained on using other acids, as a result of the partial or complete sulfonation of the hydrocarbon substrates, intermediates, and products. For that reason, upon starting with, e.g., 2,3,4,6- or 2,3,5,6-TeMB-1-S, the cycle of desulfonation, *inter*-molecular methyl transfer, and resulfonation leads eventually to the stable 2,3,4,5-TeMB-1-S as the only product, whereas on starting with any of the three TeMB's in, e.g., methanesulfonic acid the final thermodynamic equilibrium mixture contains all the PoMB's with the exception of toluene (17). Interestingly, sodium di- and trimethylbenzenesulfonates, containing at least one methyl *ortho* to the sulfonate group, upon fusion with an excess of aluminium chloride at elevated temperatures isomerize as such by migration of the *o*-methyl(s) (19). In the absence of a suitable proton donor in the system these isomerizations in all likelihood proceed *intra*-molecularly.

Experimental

The polymethylbenzenes were high-quality commercial compounds and were used without further purification. The preparations of the various potassium polymethylbenzenesulfonates have been described (6, 8, 20).

The ^1H nmr spectra of the various sulfuric acid solutions were recorded using a Varian HA-100 spectrometer. The quantitative analyses of the reaction mixtures in concentrated aqueous sulfuric acid were performed applying ^1H nmr multicomponent analysis based on the specific hydrogen absorptions of the various components (3). The equilibrium content of 1,3,5-TrMB present in a solution of 2,4,6-TrMB-1-S in sulfuric acid was determined as described previously (3).

1. H. CERFONTAIN, A. KOEBERG-TELDER, and C. RIS. J. Chem. Soc. Perkin Trans. 2, 729 (1977).
2. A. KOEBERG-TELDER and H. CERFONTAIN. J. Chem. Soc. Perkin Trans. 2, 717 (1977).

Can. J. Chem. Downloaded from www.nrcresearchpress.com by 213.222.148.141 on 09/07/12
For personal use only.

3. A. KOEBERG-TELDER and H. CERFONTAIN. Recl. Trav. Chim. Pays-Bas, **106**, 85 (1987).
4. H. SHINE. Aromatic rearrangements. Elsevier, London. 1987. pp. 23–32 and 51–55; H. CERFONTAIN. Mechanistic aspects in aromatic sulfonation and desulfonation. Interscience, New York. 1968. pp. 214–226.
5. L. S. SINGER and I. C. LEWIS. J. Am. Chem. Soc. **87**, 4695 (1961).
6. A. J. PRINSEN, A. KOEBERG-TELDER, and H. CERFONTAIN. Tetrahedron, **26**, 1953 (1970); A. KOEBERG-TELDER and H. CERFONTAIN. J. Chem. Soc. Perkin Trans. 2, 633 (1973).
7. H. CERFONTAIN, A. KOEBERG-TELDER, C. RIS, and Z. R. H. SCHAASBERG-NIENHUIS. J. Chem. Soc. Perkin Trans. 2, 970 (1975).
8. A. KOEBERG-TELDER and H. CERFONTAIN. Recl. Trav. Chim. Pays-Bas, **101**, 41 (1982).
9. M. KILPATRICK, M. W. MEYER, and M. L. KILPATRICK. J. Phys. Chem. **65**, 1189 (1961).
10. A. KOEBERG-TELDER and H. CERFONTAIN. J. Chem. Soc. Perkin Trans. 2, 226 (1975), and cited papers.
11. H. CERFONTAIN and Z. R. H. SCHAASBERG-NIENHUIS. J. Chem. Soc. Perkin Trans. 2, 1780 (1976).
12. R. B. MOODIE, K. SCHOFIELD, and T. YOSHIDA. J. Chem. Soc. Perkin Trans. 2, 788 (1975).
13. T. G. BROUWER and J. PHILLIPS. J. Chem. Soc. (B), 650 (1966); P. K. MAARSEN and H. CERFONTAIN. J. Chem. Soc. Perkin Trans. 2, 921 (1977).
14. H. CERFONTAIN and B. W. SCHNITGER. Recl. Trav. Chim. Pays-Bas, **91**, 199 (1972).
15. P. K. MAARSEN, R. BREGMAN, and H. CERFONTAIN. Tetrahedron, **30**, 1211 (1974).
16. D. A. MCCAULEY. *In* Friedel–Crafts and related reactions. Vol. II, part 2. *Edited by* G. A. Olah. Interscience, New York. 1964. pp. 1049–1073.
17. E. G. WILLARD and H. CERFONTAIN. Recl. Trav. Chim. Pays-Bas, **92**, 739 (1973).
18. M. KILPATRICK and M. W. MEYER. J. Phys. Chem. **65**, 1312 (1961).
19. G. HOLT and B. PAGDIN. J. Chem. Soc. 4514 (1961).
20. A. KOEBERG-TELDER and H. CERFONTAIN. J. Chem. Soc. Perkin Trans. 2, 633 (1973).

Can. J. Chem. Downloaded from www.nrcresearchpress.com by 213.222.148.141 on 09/07/12
For personal use only.

Synthèses des alkyl-1 cyclanols fonctionnalisés aux positions α, β et γ de la chaîne hydrocarbonée

P. CANONNE, M. BELLEY, G. FYTAS ET J. PLAMONDON

Département de chimie, Faculté des sciences et de génie, Université Laval, Québec (Québec), Canada G1K 7P4

Reçu le 16 mars 1987

P. CANONNE, M. BELLEY, G. FYTAS et J. PLAMONDON. Can. J. Chem. **66**, 168 (1988).

Nous avons mis au point une synthèse générale, efficace et à hauts rendements des *N*,*N*-dialkylaminoalkyl-, chloroalkyl-, phénoxyalkyl-, thiophénoxyalkyl-, diéthoxyalkyl- et dithiolane-1,3 alkylcyclanols par action des α,ω-bis(bromomagnésio)alkanes sur les esters fonctionnalisés correspondants.

P. CANONNE, M. BELLEY, G. FYTAS, and J. PLAMONDON. Can. J. Chem. **66**, 168 (1988).

We have developed a general and versatile synthesis of *N*,*N*-dialkylaminoalkyl-, 1-chloroalkyl-, 1-phenoxyalkyl-, 1-thiophenoxyalkyl-, 1-diethyoxyalkyl-, and 1-(1,3-dithiolane)alkylcyclanols in good yields by the reaction of α,ω-bis(bromomagnesio)alkanes with the corresponding functionalized carboxylic acid esters.

Plusieurs méthodes de synthèses d'aminoalkyl-1 cyclanols ont été raportées dans la littérature (1, 2), mais ces méthodes mettent en jeu des transformations subséquentes des cyclanones correspondantes nécessitant parfois des réactifs coûteux.

Généralement, l'introduction du groupement amino s'effectue par trois voies différentes, selon la longueur de la chaîne aminoalkylée désirée. Par exemple, les α-aminoalkylcyclanols sont plus facilement accessibles par modification des cyanhydrines (3) ou des énamines (4) que les β-aminoalkylcyclanols, car ces derniers ne peuvent être formés que par des réactions plus élaborées effectuées sur la chaîne hydrocarbonée (5). Enfin, la synthèse des γ-aminoalkylcyclanols semble être encore plus difficile, car les résultats obtenus, lors des études précédemment réalisées, montrent que les rendements réactionnels sont faibles (6).

Nous avons alors pensé que notre méthode, basée sur l'utilisation des α,ω-bis(bromomagnesio)alcanes (7), conduirait aux composés désirés avec des bons rendements. L'examen de l'ensemble des résultats que nous avons obtenus par l'action de ces organodimagnésiens sur les lactones (8) et anhydrides des acides dicarboxyliques (9), nous suggère de ne pas vouloir tenir compte de ceux déjà rapportés dans la littérature (10) en utilisant quelques aminoesters avec ces mêmes réactifs. En effet, les rendements obtenus par ces auteurs sont anormalement trop faibles et il nous est difficile d'attribuer un rôle important à la présence de l'azote ou à la basicité de l'amine qui auraient influencé grandement le cours de cette réaction. Rappelons que dans une récente publication nous avons démontré que les isoxazolones-5 encombrées fournissent les β-hydroxyoximes α,α-bisubstituées (11) avec de très bons rendements par la réaction du bis(bromomagnésio)-1,4 butane.

La question se posa alors à savoir, si les dialkylaminoalkylesters utilisés dans les conditions des réactions d'annélation que nous avons mises au point, fourniraient d'aussi bons résultats ou s'ils présenteraient des particularités distinctes qui diminueraient l'efficacité de notre méthode.

Dans ce but, nous avons alors entrepris la présente étude en utilisant systématiquement divers types d'aminoesters (**1–10**) constituant ainsi une série homogène. Nous avons repris certains α- et β-*N*,*N*-dialkylaminoalkylesters que ces auteurs avaient utilisés mais aussi des γ-aminoalkylesters afin de démontrer l'influence éventuelle de la position de l'azote et de la basicité de l'amine sur les réactions de Grignard inter- et intramoléculaires (Schéma 1).

La synthèse des α- et β-aminoesters a été effectuée, d'une

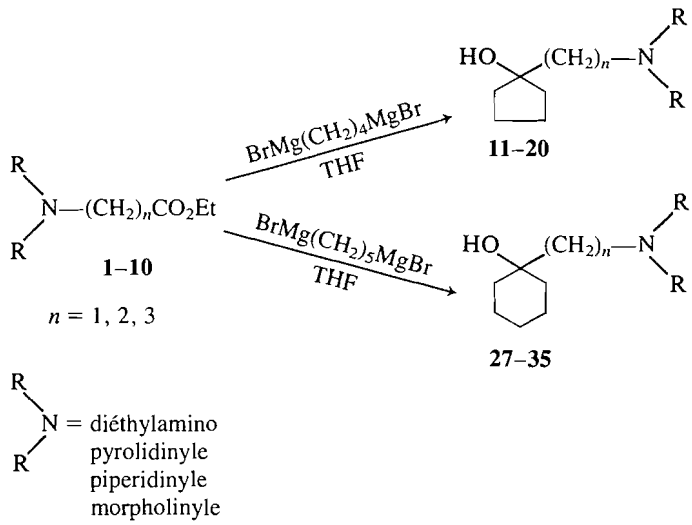

SCHÉMA 1

part, à partir des halogénoesters par substitution nucléophile (12) et, d'autre part, à partir du propénoate d'éthyle par addition conjuguée d'amines secondaires (13).

Le bis(bromomagnesio)-1,4 butane a été préparé dans le THF en présence d'un excès de tournures de magnésium et ses réactions avec les aminoesters ont fourni les aminoalkyl-1 cyclopentanols **11–20** avec des meilleurs rendements que celles rapportées précédemment (10). Nous constatons que les facteurs ci-haut mentionnés n'ont pas une influence considérable et ainsi nous démontrons que la différence de rendements trouvés ne peut être attribuée qu'aux conditions expérimentales que ces auteurs ont choisies, plutôt qu'à la structure des esters. Ces résultats suggèrent d'effectuer quelques réactions sur des aminoesters encombrés tels que (pyrrolidinyl-1)-2 propanoate d'éthyle (**21**), méthyl-2 (pyrrolidinyl-1)-2 propanoate d'éthyle (**22**) et (morpholinyl-4)-2 propanoate d'éthyle (**23**) afin de cerner les limites de notre méthode, à ce qui a trait l'influence de l'encombrement stérique sur la formation des cyclopentanols. Nous avons alors fait réagir le bis(bromomagnesio)-1,4 butane sur les esters **21**, **22** et **23** et avons constaté que les aminocyclopentanols **24**, **25**, **26** correspondants sont obtenus aussi avec des bons rendements. Nous rappelons que les rendements n'ont pas été optimisés et ont été calculés à partir des composés déjà purifiés (Schéma 2).

Il apparaît ainsi que l'encombrement stérique influence peu le

Can. J. Chem. Downloaded from www.nrcresearchpress.com by 213.222.148.141 on 09/07/12
For personal use only.

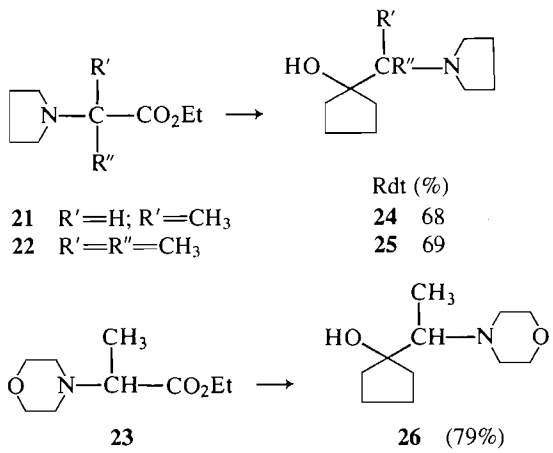

SCHÉMA 2

cours de la réaction au niveau de la cyclisation. Les réactions compétitives intermoléculaires ou intramoléculaires sont peu favorisées. En effet, nous n'avons pas trouvé en quantité appréciable ni les cétones intermédiaires, provenant de la réaction d'énolisation, ni les aminoalcools secondaires à chaîne ouverte provenant d'une réaction de réduction intramoléculaire. Nous pouvons en déduire que la réaction d'annélation à l'aide de bis(bromomagnesio)-1,4 butane est générale et applicable aux *N*,*N*-dialkylalkylaminoesters quelle que soit leur structure.

La question se posa encore une fois à savoir si notre méthode est aussi générale pour la formation des cyclohexanols correspondants en utilisant le bis(bromomagnesio)-1,5 pentane, sachant que le cycle à six membres est plus difficile à former par notre méthode (11).

Nous avons alors entrepris d'étudier les réactions de cet organodimagnésien avec les aminoesters **1**–**10** dans les mêmes conditions expérimentales et avons observé que les dialkylaminoalkyl-1 cyclohexanols **27**–**35** sont formés avec des rendements légèrement plus faibles que ceux trouvés lors de la préparation des dialkylaminoalkylcyclopentanols mais de loin supérieurs à ceux trouvés dans la littérature (10) pour l'ensemble des composés (tableau 1). Cette différence est principalement due à l'encombrement stérique au niveau du carbonyle qui se traduit par la formation d'une faible quantité d'alcools secondaires à chaîne ouverte (2–18%) formés par la réaction de réduction intramoléculaire (Schéma 3). De l'ensemble des résultats obtenus, il ressort que les réactions organodimagnésiennes effectuées dans le tétrahydrofuranne, en utilisant les conditions expérimentales précédemment décrites (3), sont applicables aux α-, β- et γ-aminoesters.

Ce travail démontre que notre méthodologie peut facilement être utilisée pour la synthèse de divers alkyl-1 cyclanols fonctionnalisés.

Il nous a semblé intéressant d'étendre les réactions de ces organodimagnésiens bis-primaires aux esters fonctionnalisés sur la chaîne hydrocarbonée par d'autres groupements importants pour leurs applications synthétiques (Schéma 4). Nous avons alors décidé d'utiliser comme substrats, d'une part, le phénoxyacétate d'éthyle (**36**), le phénylthioacétate d'éthyle (**37**), le chloro-2 propionate d'éthyle (**38**), le phénoxy-2 propanoate d'éthyle (**39**) et, d'autre part, le diéthoxyacétate d'éthyle (**40**) et le dithiolane-1,3 acétate d'éthyle (**41**). Les résultats obtenus consignés au tableau 2 montrent que les cyclanols correspondants **42**–**51** sont formés avec des rendements très satisfaisants. Les organomagnésiens attaquent sélectivement la fonction ester plutôt que les autres fonctions.

TABLEAU 1. Action des α,ω-bis(bromomagnesio)alcanes sur les esters *N*,*N*-dialkylaminoalkylcarboxyliques

$R_2N(CH_2)_nCO_2C_2H_5$			$R_2N(CH_2)_nCO_2C_2H_5$ + $BrMg(CH_2)_4MgBr$ Aminocyclopentanol		$R_2N(CH_2)_nCO_2C_2H_5$ + $BrMg(CH_2)_5MgBr$ Aminocyclohexanol	
N°	R_2N	*n*	N°	Rdt (%)	N°	Rdt (%)
1	Pyrrolidinyle	1	**11**	70	**27**	66
2	Diperidinyle	1	**12**	72	**28**	68
3	Diéthylamino	1	**13**	68	—	—
4	Morpholinyle	1	**14**	73	**29**	70
5	Pyrrolidinyle	2	**15**	75	**30**	65%
6	Piperidinyle	2	**16**	76	**31**	70
7	Morpholinyle	2	**17**	83	**32**	68
8	Pyrrodinyle	3	**18**	82	**33**	67
9	Piperidinyle	3	**19**	84	**34**	68
10	Morpholinyle	3	**20**	82	**35**	75

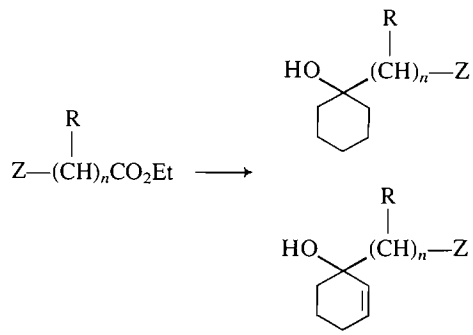

SCHÉMA 3

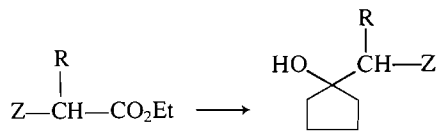

SCHÉMA 4

TABLEAU 2. (*a*) Action du bis(bromomagnésio)-1,4 butane sur les esters (**36**–**41**); (*b*) action du bis(bromomagnésio)-1,5 pentane sur les esters **37** et **39**

Esters	Cyclopentanols N°	Cyclopentanols Rdt (%)
(*a*)		
36 Phénoxyacétate d'éthyle	**42**	80
37 Phénylthioacétate d'éthyle	**43**	84
38 Chlorométhylacétate d'éthyle	**44**	67
39 Phénoxy-2 propanoate d'éthyle	**45**	87
40 Diéthoxyacétate d'éthyle	**46**	76
41 Dithiolane-1,3 acétate d'éthyle	**49**	67
(*b*)		
37 Phénylthioacétate d'éthyle	**50**	55
39 Phénoxy-2 propanoate d'éthyle	**51**	60

Can. J. Chem. Downloaded from www.nrcresearchpress.com by 213.222.148.141 on 09/07/12
For personal use only.

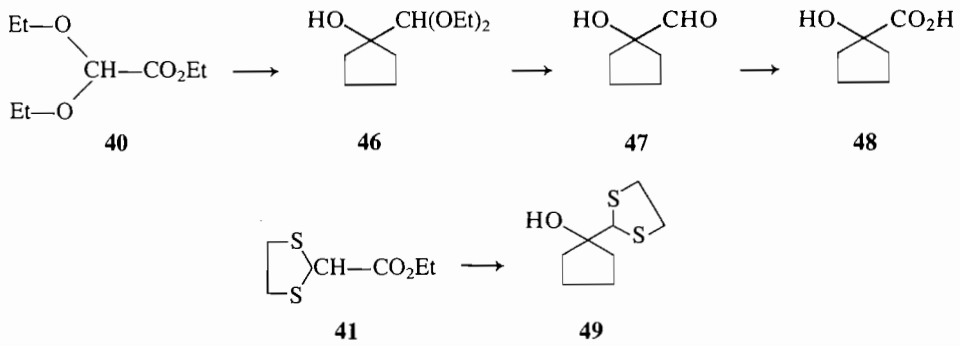

40 46 47 48

41 49

SCHÉMA 5

Les rendements ne sont pas optimisés; nous supposons qu'à une température plus basse ils peuvent être améliorés, surtout dans les expériences réalisées avec le bis(bromomagnésio)-1,5 pentane (Schéma 3).

Par la présente étude, nous pouvons obtenir plusieurs cyclanols substitués, à la position 1, par une chaîne fonctionnalisée (Schéma 5). De tels hydroxyaldéhydes, chlorocyclopentanols, sont plus difficilement accessibles par d'autres méthodes (14, 20). Nous concluons en nous basant sur les résultats des aminoalkylesters que cette méthode est très générale et applicable à la synthèse des divers α, β ou γ-hydroxycétones, hydroxyacides, chloroalkyl-1 cyclopentanols et hydroxyalkyl-1 cyclopentanols. En effet la déthioacétalisation de dithialanes-1,3 a été réalisée récemment (21).

Partie expérimentale

Les spectres ir ont été enregistrés à l'aide d'un appareil Beckman IR 4250 (sous forme de films ou en solution dans CCl_4 et CH_2Cl_2), les spectres rmn ^1H sur un appareil Bruker 90 MHz et sur un appareil Varian XL-200 (200 MHz). Les spectres rmn ^{13}C ont été effectués sur un appareil Bruker WP-80 (20 MHz). Les spectres de masse ont été effectués sur un appareil Hewlett–Packard 5992 (gs/mg). Les séparations chromatographiques sur colonne sous pression «flash» ont été effectuées sur gel de silice. Les esters **34**, **35**, **38** sont commercialement accessibles chez Aldrich. Les microanalyses ont été effectuées chez Galbraith Laboratories.

Matériel de départ

Le tétrahydrofuranne a été distillé sur sodium et gardé sous atmosphère d'azote. Les dialkylaminoacétates et dialkylamino-4 butanoates d'éthyle ont été préparés par les réactions précédemment décrites basées sur la transformation des halogénoalkylesters par les amines correspondantes (12*a*, 15). Les dialkylaminopropénoates d'éthyle ont été préparés à partir du propénoate d'éthyle (13).

N,N-*Dialkylaminoacétates,* N,N-*dialkylamino-4 butanoates d'éthyle et* N,N-*dialkylamino-2 propanoate d'éthyle*[1]

À une solution de 65 mmol de chloroacétate, bromo-2 propanoate, bromo-2 méthyl-2 propanoate ou bromo-4 butanoate d'éthyle dans 25 mL de benzène anhydre, on ajoute goutte à goutte 140 mmol d'amine dans 25 mL de benzène anhydre.

*(Pyrrolidinyl-1) acétate d'éthyle (**1**)* : Rdt = 79% (8,067 g); Eb = 95–96°C (20 Torr) (litt. (15) Eb 77°C (16 Torr)) (1 Torr = 133,3 Pa).

*(Pipéridinyl-1) acétate d'éthyle (**2**)* : Rdt = 79% (8,781 g); Eb = 102–104°C (15 Torr) (litt. (12*b*) Eb 102–103°C (12 Torr)).

*Diéthylaminoacétate d'éthyle (**3**)* : Rdt = 79% (7,847 g); Eb = 78–80°C (20 Torr).

*(Morpholinyl-4) acétate d'éthyle (**4**)* : Rdt = 90% (10,138 g); Eb = 102–103°C (8 Torr) (litt. (12*b*) Eb 112–114°C (13 Torr)).

*(Pyrrolidinyl-1)-4 butanoate d'éthyle (**8**)* : Rdt = 68% (8,235 g); Eb = 107–109°C (9 Torr).

1. Tous les composés ont donné des spectres satisfaisants.

*(Pipérydinyl-1)-4 butanoate d'éthyle (**9**)* : Rdt = 88% (22,433 g); Eb = 110–111°C (15 Torr).

*(Morpholinyl-4)-4 butanoate (**10**)* : Rdt = 89% (11,625 g); Eb = 140–142°C (15 Torr).

*(Pyrrolidinyl-1)-2 propanoate d'éthyle (**21**)* : Rdt = 76% (8,478 g); Eb = 102–103°C (21 Torr) (litt. (13*a*) 84°C (12 Torr)).

*Méthyl-2 (pyrrolidinyl-1)-2 propanoate d'éthyle (**22**)* : Rdt = 70% (8,3 g); Eb = 108–110°C (22 Torr) (litt. (19) Eb 114°C (26 Torr)).

*(Morpholinyl-4)-2 propanoate d'éthyle (**23**)* : Rdt = 68% (8,232 g); Eb = 123–125°C (20 Torr) (litt. (18) Eb 110–113°C (15 Torr)).

Dialkylaminopropanoates d'éthyle

Dans un ballon de 50 mL, on introduit 10,012 g (100 mmol) de propénoate d'éthyle et 100 mmol d'amine et on chauffe à reflux sous agitation magnétique pendant 3 h. Le produit est purifié par distillation sous pression réduite.

*(Pyrrolidinyl-1)-3 propanoate d'éthyle (**5**)* : Rdt = 96% (16,386 g); Eb = 108–109°C (20 Torr) (litt. (15) Eb 82°C (8 Torr)).

*(Pipéridinyl-1)-3 propanoate d'éthyle (**6**)* : Rdt = 89% (16,577 g); Eb = 120–122°C (20 Torr) (litt. (13*b*) Eb 115–117°C (17 Torr)).

*(Morpholinyl-4)-3 propanoate d'éthyle (**7**)* : Rdt = 96% (18,065 g); Eb = 133–134°C (19 Torr) (litt. (13*c*) Eb 138–140°C (25 Torr)).

*Phénoxyacétate d'éthyle (**36**)*

En utilisant le mode opératoire décrit par Munch-Peterson (16*a*) on transforme 16,30 g (133 mmol) de chloroacétate d'éthyle en présence de 3,105 g (135 mmol) de sodium et de 12,545 g (133 mmol) de phénol en phénoxyacétate d'éthyle; Rdt = 69% (16,688 g); Eb = 84°C (0.05 Torr) (litt. (16) Eb 250–251°C).

*Phénylthioacétate d'éthyle (**37**)*

En utilisant le mode opératoire ci-dessus, nous avons opéré avec 11,011 g (100 mmol) de thiophénol, 2,415 g (0,105 mmol) de sodium et 12,255 g (100 mmol) de chloroacétate d'éthyle; Rdt = 90% (18,062 g); Eb = 90–93°C (0,05 Torr) (litt. (17) Eb 118°C (3 Torr)).

*Phénoxy-2 propanoate d'éthyle (**39**)*

En utilisant le mode opératoire général (16*a*), on ajoute 12,545 g (13,3 mmol) de phénol, 3,105 g de sodium et 27,2 g (15 mmol) de bromo-3 propionate d'éthyle et on recueille, par distillation, l'ester **39**; Rdt = 68%; Eb = 86°C (0.05 Torr).

Préparation des organodimagnésiens

Dans un tricol de 500 mL, sous atmosphère inerte, muni d'une agitation magnétique, d'une ampoule à additionner et d'un réfrigérant surmonté d'un tube de garde à $CaCl_2$, on introduit 1,07 g de Mg et on chauffe à l'aide d'un brûleur à gaz pour chasser l'humidité et activer le Mg. Après refroidissement de l'appareillage, on couvre le Mg d'une quantité de 3 mL de solution de dibromure dilué dans le THF. La réaction démarre rapidement et on poursuit l'addition de 0,0253 mol de dibromure dans 50 mL de THF. Après la fin de l'addition, on laisse agiter durant 4 h à la température ambiante, puis on y ajoute goutte à goutte, à la même température, une solution d'ester (0,02 mol). Après hydrolyse, à l'aide d'une solution saturée de chlorure d'ammonium,

Can. J. Chem. Downloaded from www.nrcresearchpress.com by 213.222.148.141 on 09/07/12
For personal use only.

Can. J. Chem. Downloaded from www.nrcresearchpress.com by 213.222.148.141 on 09/07/12
For personal use only.

on obtient le cycloalcanol par extraction à l'éther et évaporation du solvant sous vide.

Préparation des N,N-*dialkylaminoalkylcyclopentanols*

À une solution de bis(bromomagnésio)-1,4 butane (1,2 équivalent), on ajoute goutte à goutte un équivalent d'ester dissous dans 10 équivalents de THF anhydre à 0°C sous atmosphère d'azote, puis on laisse la réaction se poursuivre durant 1 h à 20–25°C. On hydrolyse à froid par une solution saturée de chlorure d'ammonium. On extrait à l'éther, on sépare la couche éthérée, on sèche sur sulfate de magnésium et on distille sous pression réduite.

*(Pyrrolidinyl-1)méthyl-1 cyclopentanol (10) (**11**)*

En utilisant 4 g (26 mmol) d'ester **1** on obtient 3,2 g de (pyrrolidinyl-1)méthyl-1 cyclopentanol par distillation fractionnée; Rdt = 70%; Eb = 122–124°C (20 Torr) (litt. (10) Eb 70°C (2 Torr)); ir ν_{max} (film) : 3430, 2957, 2865, 2792 cm^{-1}; rmn ^1H ($CDCl_3$) δ : 1,47–1,95 (12H, m, CH_2 cycl.), 2,60–2,90 (6H, s, CH_2-NCH_2, -NCH_2), 3,70 (1H, s, OH) ppm; rmn ^{13}C δ : 80,0 (C-1), 65,3 (C-1′), 55,8 (C-2′ et C-5″), 39,7 (C-2 et C-5), 24,1 (C-3, C-4, C-3′, C-4″) ppm; sm *m/e* : 169,15 (M^+, 3,9), 84,20 ($C_4H_8NCH_2$, 100%), 58,05 (11), 55,05 (12).

*(Pipéridinyl-1)méthyl-1 cyclopentanol (10) (**12**)*

La réaction a été effectuée en utilisant 3,363 g (19,6 mmol) d'ester. Après distillation, on recueille 2,5 g (72%) de (pipéridinyl-1)méthyl-1 cyclopentanol; Eb = 47–49°C (24 Torr) (litt. (4) Eb 80°C (2 Torr)); ir ν_{max} (CCl_4) : 3415, 2939 cm^{-1}; rmn ^1H ($CDCl_3$) δ : 1,37–1,85 (14H, m, CH_2 cycl.), 2,36 (2H, s, NCH_2), 2,40–2,65 (4H, m, CH_2N-), 3,12 (1H, s, OH) ppm; rmn ^{13}C ($CDCl_3$) δ : 79,5 (C-1), 67,5 (C-1′), 56,3 (C-2″, C-6″), 39,8 (C-2, C-5), 26,5 (C-3″, C-5″), 24,2 (C-4″), 24 (C-3, C-4) ppm; sm *m/e* : 183,25 (M^+, 1,6), 99,15 (7), 98,15 ($C_5H_{10}NCH_2$, 100%), 55,05 (7).

*Diéthylaminométhyl-1 cyclopentanol (10) (**13**)*

En utilisant 3,243 g (20,4 mmol) de l'ester **3**, après distillation on obtient 2,350 g de cyclopentanol **13**; Rdt = 68%; Eb = 105–107°C (20 Torr); rmn ^1H (CH_2Cl_2) δ : 1,03 (6H, t, *J* = 7 Hz, CH_3), 1,40–1,83 (8H, m, CH_2 cycl.), 2,53 (2H, s, NCH_2), 2,60 (4H, q, *J* = 7 Hz, CH_2-CH_3), 2,70 (1H, s, OH); rmn ^{13}C ($CDCl_3$) δ : 79,4 (C-1), 62,6 (C-1′), 48,5 (CH_3CH_2), 39,6 (C-2, C-5), 23,9 (C-3, C-4), 12,2 (CH_3); sm *m/e* : 171,20 (M^+, 4,9), 142,15 (M − C_2H_5, 12), 86,15 ($C_2H_5NCH_2^+$, 100%), 58,10 (32).

*(Morpholinyl-4)méthyl-1 cyclopentanol (**14**)*

En utilisant 2,882 g (16,7 mmol) d'ester **4**, après distillation on obtient 2,258 g de cyclopentanol **14**; Rdt = 73%; Eb = 60–62°C (0,02 Torr) (litt. (4) Eb 77°C (3 Torr)); ir ν_{max} (CH_2Cl_2) : 3405, 2955, 2850, 2870, 1117 cm^{-1}; rmn ^1H ($CDCl_3$) δ : 1,40–1,95 (8H, m, CH_2 cycl.), 2,48 (2H, s, NCH_2O), 2,49–2,75 (4H, m, CH_2N), 3,50 (1H, s, OH), 3,62–3,85 (4H, m, CH_2CH_2O) ppm; rmn ^{13}C ($CDCl_3$) δ : 80,0 (C-1), 67,6 (C-1′), 67,2 (C-2″, C-6″), 55,3 (C-3″, C-5′), 39,7 (C-2, C-5), 23,9 (C-3, C-4) ppm; sm *m/e* : 185,20 (M^+, 3,1), 101,15 (11), 100,15 ($C_4H_8ONCH_2^+$, 100%), 56,16 (11).

*(Pyrrolidinyl-1)-2 éthylcyclopentanol (**15**)*

En utilisant 1,748 g (10,2 mmol) d'ester **5** on obtient, après distillation, 1,450 g de cyclopentanol **15**; Rdt = 75%; Eb = 68–70°C (0,03 Torr); *F* = 67–68°C; ir ν_{max} (CH_2Cl_2) : 3190, 2945, 2870, 2803, 1335, 1133 cm^{-1}; rmn ^1H ($CDCl_3$) δ : 1,57–1,93 (14H, m, CH_2 cycl.), 2,43–2,93 (6H, m, CH_2N), 6,30 (1H) ppm; rmn ^{13}C ($CDCl_3$) δ : 82,6 (C-1), 54,1 (C-2″, C-5″), 53,9 (C-2′), 40,1 (C-2, C-5), 37,3 (C-1′), 23,8 (C-3, C-4), 23,6 (C-3″, C-4″) ppm; sm *m/e* : 183,25 (M^+, 2,3), 84,10 ($C_4H_8NCH_2^+$, 100%), 71,10 (12), 70,00 (9). *Anal.* calcd. pour $C_{11}H_{21}NO$: C 72,08, H 11,55, N 7,64; tr. : C 72,14, H 11,51, N 7,61.

*(Pipéridinyl-1)-2 éthyl-1 cyclopentanol (**16**)*

En utilisant 1,81 g (9,80 mmol) de l'ester **6** on obtient, après distillation, 76% (1,466 g) de (pipéridinyl-1)-2 éthyl-1 cyclopentanol (**16**); Eb = 62–64°C (0,02 Torr) (litt. (10) Eb 104°C (25 Torr)); *F* = 38,5–39,5°C; ir ν_{max} (film) : 3206, 2922, 2841, 2798, 1119 cm^{-1}; rmn ^1H ($CDCl_3$) δ : 1,23–1,91 (16H, m, CH_2 cycl.), 2,30–2,77 (6H, m, CH_2N), 6,63 (1H, s, OH) ppm; rmn ^{13}C ($CDCl_3$) δ : 82,6 (C-1), 56,9 (C-2′), 54,7 (C-2″, C-6″), 40,1 (C-2, C-5), 35,2 (C-1′), 26,2 (C-3″, C-5″), 24,4 (C-4″), 23,8 (C-3, C-4) ppm; sm *m/e* : 197,20 (M^+, 4), 98,10 ($C_5H_{10}NCH_2$, 100%), 85,10 (14), 84,10 (11).

*(Morpholinyl-4)-2 éthyl-1 cyclopentanol (**17**)*

En utilisant 1,872 g (10,00 mmol) d'ester **7** on obtient, après de distillation, 1,660 g de cyclopentanol **17**; Rdt = 83%; Eb = 72–73°C (0.02 Torr); ir ν_{max} (film) : 3295, 2945, 2842, 2809, 1121 cm^{-1}; rmn ^1H (CCl_4) δ : 1,26–1,90 (10H, m, CH_2 cycl.), 2,37–2,77 (6H, m, CH_2N-O), 3,53–3,83 (4H, m), 4,97 (1H, s, OH) ppm; rmn ^{13}C ($CDCl_3$) δ : 82,7 (C-1),67,0 (C-2″, C-6″), 56,6 (C-2′), 53,8 (C-3″, C-5″), 40,1 (C-2, C-5), 35,0 (C-1′), 23,8 (C-3, C-4) ppm; sm *m/e* : 199,20 (*M* − 15), 100,15 ($C_4H_8ONCH_2^+$, 100%), 87,10 (16), 57,05 (10), 55,95 (13). *Anal.* calc. pour $C_{11}H_{12}NO_2$: C 66,29, H 10,62, N 7,02; tr. : C 66,32, H 10,75, N 7,11.

*(Pyrrolidinyl-1)-3 propyl-1 cyclopentanol (**18**)*

En utilisant 1,839 g (9,92 mmol) d'ester **8** on obtient, après distillation, 1,611 g de cyclopentanol **18**; Rdt = 82%; Eb = 78–80°C (0,02 Torr); *F* = 33,5–35,0°C; ir ν_{max} (film) : 3390, 2950, 2867, 2787, 1137 cm^{-1}; rmn ^1H ($CDCl_3$) δ : 1,43–1,97 (16H, m, CH_2 cycl.), 2,40–2,73 (6H, s, CH_2N), 6,77 (1H, s, OH) ppm; rmn ^{13}C ($CDCl_3$) δ : 80,3 (C-1), 57,1 (C-3′), 53,8 (C-2″, C-5″), 41,6 (C-1′), 40,3 (C-2), 24,7, 24,3, 23,5 ppm; sm *m/e* : 197,25 (M^+, 1,3), 85,10 (7), 84,20 ($C_4H_8NCH_2^+$, 100%), 70,10 (7), 55,05 (11). *Anal.* calc. pour $C_{12}H_{23}NO$: C 73,05, H 11,75, N 7,09; tr. : C 72,98, H 11,71, N 6,98.

*(Pipéridinyl-1)-3 propyl-1 cyclopentanol (**19**)*

En utilisant 2,018 g (10,2 mmol) d'ester **9** on obtient, après distillation, 1,811 g de cyclopentanol **19**; Rdt = 84%; Eb = 75–77°C (0,03 Torr) (litt. (14*a*) Eb 107–109°C (2 Torr)); *F* = 40–41°C; ir ν_{max} (film) : 3380, 3110, 2918, 2842, 2787, 2757 cm^{-1}; rmn ^1H ($CDCl_3$) δ : 1,25–1,90 (18H, m, CH_2 cycl.), 2,24–2,60 (6H, m, CH_2), 6,78 (1H, s, OH) ppm; rmn ^{13}C ($CDCl_3$) δ : 80,3, 59,9, 54,5, 41,9, 40,3, 25,6, 24,4, 24,3, 22,8 ppm; sm *m/e* : 215,15 (M^+, 1,7), 98,15 ($C_5H_{10}NCH_2^+$, 100%), 84,15 (8), 55,10 (9).

*(Morpholinyl-4)-3 propyl-1 cyclopentanol (10) (**20**)*

En utilisant 2,0240 (10,1 mmol) d'ester **10** on obtient, après distillation, 1,770 g de cyclopentanol **20**; Rdt = 82%; Eb = 92–94°C (0,03 Torr); *F* = 49,5–50°C; ir ν_{max} (film) : 3420, 3150, 2948, 2862, 2844, 2802, 1269, 1132 cm^{-1}; rmn ^1H ($CDCl_3$) δ : 1,30–1,35 (12H, m, CH_2 cycl.), 2,30–2,67 (6H, m, CH_2N), 3,60–3,87 (4H, m, CH_2-O), 5,50 (1H, s, OH) ppm; rmn ^{13}C ($CDCl_3$) δ : 80,7, 66,7, 59,6, 53,6, 41,0, 40,2, 24,1, 22,0 ppm; sm *m/e* : 213,30 (M^+, 2,0), 100,20 ($C_4H_8ONCH_2^+$, 100%), 56,10 (13), 55,10 (14). *Anal.* calc. pour $C_{12}H_{23}NO_2$: C 67,57, H 10,87, N 6,56; tr. : C 67,52, H 10,83, N 6,62.

*(Pyrrolidinyl-1)-1 éthyl-1 cyclopentanol (**24**)*

En utilisant 2,917 g (17,8 mmol) d'ester **21** on obtient, après distillation, 2,128 g de cyclopentanol **24**; Rdt = 71%; Eb = 56–58°C (0,03 Torr); ir ν_{max} (film) : 3375, 3060, 2875, 2805 cm^{-1}; rmn ^1H ($CDCl_3$) δ : 0,93 (3H, d, *J* = 7 Hz, CH_3), 1,27–2,97 (12H, m, CH_2 cycl.), 2,43–2,83 (4H, s, CH_2), 2,97 (1H, q, CHN), 4,73 (1H, s, OH) ppm; rmn ^{13}C ($CDCl_3$) δ : 82,4 (C-1), 61,5 (C-1), 49,5 (C-2″, C-5″), 39,1 (C-5), 35,8 (C-2), 25,2 (C-4), 24,2 (C-3), 24,0 (C-3″, C-4″), 7,4 (C-2′) ppm; sm *m/e* : 183,25 (M^+, 0,8), 28,20 ($C_4H_8NCH^+CH_3$, 100%), 55,10 (11). *Anal.* calc. pour $C_{11}H_{21}NO$: C 78,08, H 11,55, N 7,64; tr. : C 71,95, H 11,59, N 7,55.

*(Méthyl-1)-pyrrolidinyl-1 éthyl-1 cyclopentanol (**25**)*

En utilisant 1,995 (10,9 mmol) de méthyl-2 pyrrolidinyl-2 propanoate d'éthyle (**22**), on obtient après distillation, 1,446 g de (méthyl-1)-pyrrolidinyl-1 éthyl-1 cyclopentanol (**24**); Rdt = 72%; Ed = 58–60°C (0,05 Torr); ir ν_{max} (film) : 3360, 2978, 2869, 2812, 1173, 1013 cm^{-1}; rmn ^1H ($CDCl_3$) δ : 1,07 (6H, s, CH_3), 1,23–1,87 (12H, m, CH_2 cycl.), 2,50–2,83 (4H, m, CH_2O), 4,65 (1H, s, OH) ppm; rmn ^{13}C ($CDCl_3$) δ : 85,2 (C-1), 60,8 (C-1′), 47,6 (C-2″, C-5″), 37,5 (C-2, C-5), 24,4 (C-3, C-4), 19,1 (CH_3); sm *m/e* : 197,35 (M^+, 0,1), 113,20 (7), 112,10 ($C_4H_8NC^+(CH_3)_2$, 100%), 70,15 (17), 55 (8).

Can. J. Chem. Downloaded from www.nrcresearchpress.com by 213.222.148.141 on 09/07/12
For personal use only.

(Morpholinyl-4)-1 éthyl-1 cyclopentanol (26)

En utilisant 2,706 g (14,0 mmol) d'ester **23** on obtient après purification 2,280 g de cyclopentanol **26**; Rdt = 80%; Eb = 81–83°C (0,03 Torr); ir ν_{max} (film) : 3955, 2955, 2845, 1118 cm^{-1}; rmn ^1H ($CDCl_3$) δ : 1,00 (3H, d, J = 7 Hz, CH_3CH), 1,33–1,90 (8H, m, CH_2 cycl.), 2,30–2,90 (5H, m, CH_2N, CH_2N), 3,73 (4H, t, J = 4,5 Hz, CH_2O), 4,63 (1H, s, OH) ppm; rmn ^{13}C ($CDCl_3$) δ : 82,3 (C-1), 67,5 (C-2″, C-6″), 66,4 (C-1′), 50,5 (C-3″, C-5″), 39,2 (C-5), 35,7 (C-2), 25,2 (C-4), 23,6 (C-3), 7,4 (C-2′) ppm; sm *m/e* : 199,25 (M^+, 1,0), 115,20 (7), 114,10 ($C_4H_8ONCH^+CH_3$, 100%), 70,15 (6). *Anal.* calc. pour $C_{11}H_{21}NO_2$: C 66,29, H 10,62, N 7,02; tr. : C 66,19, H 10,72, N 7,15.

Préparation des N,N-*dialkylaminoalkylcyclohéxanols*

En suivant le même mode opératoire que pour la préparation des *N,N*-dialkylcyclopentanols, on constate que le produit brut contient des quantités variant de 2 à 18% d'alcools secondaires insaturés. La séparation s'est avérée difficile dans certains cas. La spectroscopie de rmn ^1H montre des faibles quantités d'alcool insaturé même après purification des aminoalkylcyclopentanols liquides.

(Pyrrolidinyl-1)méthyl-1 cyclohexanol (10) (27)

En utilisant 1,852 (11,9 mmol) de l'ester **1** on obtient, après distillation, 1,356 g de cyclohexanol **27**; Rdt = 66%; Eb = 62–65°C (0,2 Torr); ir ν_{max} (CH_2Cl_2) : 3420, 2930, 2848, 2800 cm^{-1}; rmn ^1H ($CDCl_3$) δ : 1,10–1,93 (14H, m, CH_2), 2,45 (2H, s, NCH_2COH), 2,50–2,83 (4H, m, CH_2N), 3,47 (1H, s, OH) ppm; rmn ^{13}C ($CDCl_3$) δ : 70,0 (C-1), 66,6 (C-1′), 56,9 (C-2″, C-5″), 37,2 (C-2, C-6), 26,0 (C-4), 24,3 (C-3″, C-4″), 22,3 (C-3, C-5); ms *m/e* : 183,20 (M^+, 3,1), 85,15 (9), 84,15 ($C_4H_8NCH_2$, 100%), 55,15 (9).

(Pipéridinyl-1)méthyl-1 cyclohexanol (10) (28)

En utilisant 3,802 g (22,2 mmol) de l'ester **2** on obtient, après distillation, 1,601 g de cyclohexanol **28**; Rdt = 68%; Eb = 56–58°C (0,02 Torr); ir ν_{max} (film) : 3440, 2922, 2847, 2790, 1110 cm^{-1}; rmn ^1H ($CDCl_3$) δ : 1,46 (16H, m, CH_2 cycl.), 2,27 (2H, s, CH_2N), 2,43–2,70 (4H, m, CH_2N), 3,45 (1H, s, OH) ppm; rmn ^{13}C ($CDCl_3$) δ : 70,00 (C-1), 68,4 (C-1′), 57,5 (C-2″, C-6″), 37,2 (C-2, C-6), 26,6 (C-3″, C-5″), 26,1 (C-4), 24,1 (C-4″), 22,4 (C-3, C-5) ppm; sm *m/e* : 197,30 (M^+, 2), 99,15 (8), 98,15 ($C_5H_{10}NCH_2^+$, 100%), 55,05.

(Morpholinyl-4)méthyl-1 cyclohexanol (29)

En utilisant 1,732 g (10,0 mmol) de l'ester **4** on recueille 1,366 g de composé **29**; Rdt = 70%; Eb = 77–78°C (0,03 Torr); ir ν_{max} (film) : 3460, 2923, 2844, 2802, 1120, 1010 cm^{-1}; rmn ^1H ($CDCl_3$) δ : 1,33–1,70 (10H, m, CH_2 cycl.), 2,33 (2H, s, NCH_2), 2,50–2,73 (4H, m, CH_2N), 3,03 (1H, s, OH), 3,60–3,90 (4H, m, CH_2O) ppm; rmn ^{13}C ($CDCl_3$) δ : 70,6 (C-1), 68,5 (C-1′), 67,4 (C-2″, C-6″), 56,3 (C-3″, C-5″), 37,0 (C-2, C-6), 26,0 (C-4), 22,2 (C-3, C-5) ppm; sm *m/e* : 199,30 (M^+, 2,5), 101,15 (12), 100,15 ($C_4H_8ONCH_2^+$, 100%), 56,05 (14). *Anal.* calc. pour $C_{11}H_{21}NO_2$: C 66,29, H 10,62, N 7,02; tr. : C 66,20, H 10,49, N 6,98.

(Pyrrolidinyl-1)-2 éthyl-1 cyclohexanol (30)

En utilisant 2,002 g (11,7 mmol) de l'ester **5** on recueille, après distillation, 1,410 de l'aminocyclohexanol **30**; Rdt = 65%; Eb = 71–72°C (0,04 Torr); F = 46,5–47,5°C; ir ν_{max} (CH_2Cl_2) : 3200, 2936, 2860, 2809 cm^{-1}; rmn ^1H ($CDCl_3$) δ : 1,17–1,93 (16H, m, CH_2 cycl.), 2,42–2,90 (6H, m, CH_2N), 6,27 (1H, s, OH) ppm; rmn ^{13}C ($CDCl_3$) δ : 71,6 (C-1), 54,1 (C-2″, C-5″), 51,7 (C-2′), 38,3 (C-2, C-6), 37,6 (C-1′), 26,3 (C-4), 23,6 (C-3″, C-4″), 22,4 (C-3, C-5) ppm; ms *m/e* : 197,25 (M^+, 3,7), 85,05 (6), 84,15 ($C_4H_8NCH_2^+$, 100%), 71,70 (5), 70,10 (6), 55,15 (7). *Anal.* calc. pour $C_{12}H_{23}NO$: C 73,04, H 11,75, N 7,10; tr. : C 72,98, H 11,79, N 7,11.

(Pipéridinyl-1)-2 éthyl-1 cyclohexanol (31)

En utilisant 1,927 g (10,4 mmol) de l'ester **6** on obtient après purification 1,406 g de cristaux blancs; Rdt = 70%; Eb = 67–69°C (0,03 Torr) (litt. (10) Eb 115°C (2,9 Torr)); F = 46,0–48,0°C; ir ν_{max} (film) : 3220, 2923, 2848, 2810, 2758, 1119 cm^{-1}; rmn ^1H ($CDCl_3$) δ : 1,28–1,87 (18H, m, CH_2 cycl.), 2,33–2,77 (7H, m, CH_2N) ppm; rmn ^{13}C ($CDCl_3$) δ : 71,6 (C-1), 54,8 (C-2′, C-2″, C-6″), 38,5 (C-2, C-6), 35,5 (C-1′), 26,2 (C-4, C-3″, C-5″), 25,1 (C-4″), 22,5 (C-3, C-5) ppm; sm *m/e* : 211,5 (M^+, 2,1), 99,15 (7), 98,15 ($C_5H_{10}NCH_2^+$, 100%).

(Morpholinyl-4)-2 éthyl-1 cyclohexanol (32)

En utilisant 1,872 g (10,0 mmol) de l'ester **7** on obtient après purification 68% (1,670 g) d'aminocyclohexanol **32**; Eb = 91–93°C (0,08 Torr); F = 37,5–39,0°C; ir ν_{max} (film) : 3350, 2921, 2845, 2810, 1436, 1135, 1020, 1008 cm^{-1}; rmn ^1H ($CDCl_3$) δ : 1,23–1,77 (12H, CH_2 cycl.), 2,43–2,77 (7H, m, CH_2N), 3,64–3,86 (4H, m, CH_2O) ppm; rmn ^{13}C ($CDCl_3$) δ : 71,6 (C-1), 67,0 (C-2″, C-6″), 54,6 (C-2′), 53,8 (C-3″, C-5″), 38,3 (C-2, C-6), 35,3 (C-1′), 26,2 (C-4), 22,3 (C-3, C-5); sm *m/e* : 213,20 (M^+, 3,0), 100,20 ($C_4H_8ONCH_2^+$, 100%), 56,10 (10). *Anal.* calc. pour $C_{12}H_{23}NO_2$: C 67,57, H 10,87, N 6,56; tr. : C 67,6, H 10,79, N 6,61.

(Pyrrolidinyl-1)-3 propyl-1 cyclohexanol (33)

En utilisant 1,872 g (10,0 mmol) de l'ester **8** on obtient après purification 1,460 g d'aminocyclohexanol **33**; Rdt = 67%; Eb = 85–87°C (0,03 Torr); ir ν_{max} (film) : 3100, 3025, 2928, 2870, 2833, 2799, 1458, 1442 cm^{-1}; rmn ^1H ($CDCl_3$) δ : 1,17–1,97 (18H, m, CH_2 cycl.), 2,33–2,77 (6H, m, CH_2N), 5,70 (1H, s, OH) ppm; rmn ^{13}C ($CHCl_3$) δ : 69,3 (C-1), 57,1 (C-3′), 53,9 (C-2″, C-5″), 41,4 (C-1′), 38,2 (C-2, C-6), 26,3 (C-4), 23,5 (C-3″, C-4″), 22,6 (C-3, C-5, C-2′) ppm; sm *m/e* : 211,15 (M^+, 1,9), 84,15 ($C_4H_8NCH_2^+$, 100%), 55,10 (10). *Anal.* calc. pour $C_{13}H_{25}NO$: C 73,88, H 11,92, N 6,62; tr. : C 73,80, H 11,98, N 6,67.

(Pipéridinyl-1)-3 propyl-1 cyclohexanol (34)

En utilisant 1,955 g (10,0 mmol) de l'ester **9** on recueille, après distillation, 68% de cyclohexanol **34**; Eb = 86–87°C (0,05 Torr) (litt. (14*a*) Eb 122–123°C (2 Torr)); ir ν_{max} (film) : 3380, 3120, 2922, 2843, 2795, 2760, 729 cm^{-1}; rmn ^1H ($CDCl_3$) δ : 1,20–1,80 (20H, m, CH_2 cycl.), 2,20–2,57 (6H, m, CH_2N), 5,95 (1H, s, OH) ppm; rmn ^{13}C ($CDCl_3$) δ : 69,1 (C-1), 59,9 (C-3′), 54,6 (C-2″, C-6″), 41,7 (C-1), 38,3 (C-2, C-6), 26,3 (C-4), 25,6 (C-3″, C-5″), 24,4 (C-4″), 22,6 (C-3, C-5), 20 (C-2′) ppm; sm *m/e* : 225,25 (M^+, 2,1), 99,15 (6), 98,15 ($C_5H_{10}CH_2^+$, 100%), 84,15 (6), 55,10 (8). *Anal.* calc. pour $C_{14}H_{27}NO$: C 74,61, H 12,08, N 6,21; tr. : 74,59, H 12,05, N 6,17.

(Morpholinyl-4)-3 propyl-1 cyclohexanol (35)

En utilisant 2,088 g (10,4 mmol) de l'ester **10** on recueille, après distillation, 2,086 g de cyclohexanol **35**; Rdt = 75%; Eb = 106–107°C (0,03 Torr); ir ν_{max} (film) : 3440, 2929, 2850, 2804, 1120 cm^{-1}; rmn ^1H ($CDCl_3$) δ : 1,10–1,85 (14H, m, CH_2 cycl.), 2,30–2,67 (6H, m, CH_2N), 3,60–3,87 (4H, m, CH_2O), 5,00 (1H, s, OH); rmn ^{13}C ($CDCl_3$) δ : 69,8 (C-1), 66,7 (C-2″, C-6″), 59,8 (C-3′), 53,8 (C-3″, C-5″), 41,0 (C-1′), 38,1 (C-2, C-5), 26,1 (C-4), 22,5 (C-3, C-5), 20,0 (C-2′) ppm. *Anal.* calc. pour $C_{13}H_{25}NO_2$: C 68,68, H 11,08, N 6,16; tr. : C 68,45, H 11,16, N 6,11.

Phénoxyméthylcyclopentanol (42)

En utilisant 1,915 g (10,6 mmol) d'ester **36** on obtient 1,526 g de cyclopentanol **42**; Rdt = 80%; Eb = 80–81°C (0,05 Torr); F = 47–48°C; ir ν_{max} (film) : 3430, 2960, 2862, 1602, 1590, 1498, 1249, 1044, 757, 694 cm^{-1}; rmn ^1H ($CDCl_3$) δ : 1,87 (8H, m, CH_2 cycl.), 2,30 (1H, s, OH), 3,93 (2H, s, CH_2O), 6,83–7,53 (5H, m, 4 aromatiques) ppm; rmn ^{13}C ($CDCl_3$) δ : 159,3 (C-1″), 129,7 (C-3″, C-6″), 121,2 (C-4″), 115,0 (C-2″, C-6″), 81,4 (C-1), 75,0 (C-1′), 37,5 (C-2, C-5), 24,4 (C-3, C-4); ms *m/e* : 193,20 (M + 1, 7,8), 192,30 (M^+, 15,7), 108,10 ($C_6H_5OCH_3$, 100%), 94,20 ($C_6H_5OH^+$, 71), 85, 77,15, 67,15, 65,20, 51,20. *Anal.* calc. pour $C_{12}H_{16}O_2$: C 74,96, H 8,39; tr. : C 74,81, H 8,28.

Phénylthiométhyl-1 cyclopentanol (43)

En utilisant 2,085 g (10,6 mmol) d'ester **37** on recueille 1,856 g de cyclopentanol **43**; Rdt = 84%; Eb = 108–110°C (0,03 Torr); ir ν_{max} (film) : 3427, 2958, 2862, 1579, 1474, 1000, 737, 688 cm^{-1}; rmn ^1H ($CDCl_3$) δ : 1,70 (8H, m, CH_2 cycl.), 2,20 (1H, s, OH), 3,27 (2H, s, CH_2S), 7,20–7,63 (5H, m, aromatiques) ppm; rmn ^{13}C ($CDCl_3$) δ : 137,3 (C-1), 129,9 (C-3″, C-5), 129,1 (C-2″, C-6″), 126,4 (C-4′), 81,9

(C-1), 46,8 (C-1'), 39,5 (C-2, C-5), 24,1 (C-3, C-4) ppm; sm *m/e* : 209,15 (*M* + 1, 2), 208,15 (M^+, 14), 124,15 ($C_6H_5CH_3^+$, 21), 78,15 ($C_6H_5^+$, 11), 77,15 (C_6H_5, 13), 67,15 (21), 65,20 ($C_6H_5^+$, 15), 57,20 (11), 51,20 (14). *Anal.* calc. pour $C_{12}H_{16}OS$: C 69,18, H 7,74; tr. : C 69,27, H 7,70.

*Chlorométhyl-1 cyclopentanol (**44**)*

En utilisant 4,80 g (39,2 mmol) de chloroacétate d'éthyle (**38**) on obtient 3,203 g de cyclopentanol **44**; Rdt = 67%; Eb = 60–62°C (7 Torr) (litt. (14*b*) Eb 57–58°C (6 Torr)); ir ν_{max} (film) : 3400, 2955, 2869, 1437, 1322, 1285, 1249, 1217, 1188, 1066, 990, 727 cm^{-1}; rmn ^1H ($CDCl_3$) δ : 1,55–1,90 (8H, m, CH_2 cycl.), 2,23 (1H, s, OH), 3,62 (2H, s, CH_2Cl) ppm; rmn ^{13}C ($CDCl_3$) δ : 81,9 (C-1), 54,2 (C-1'), 38,3 (C-2, C-5), 24,4 (C-3, C-4) ppm; sm *m/e*: 136,5 (M^+ + 2, 0,4), 134,25 (M^+, 1,4), 107,10 ($C_4H_6O_{37}Cl$, 12), 105,10 ($C_4H_6O_{35}Cl$, 37), 92,10 (27), 85,25 ($C_3H_8OH^+$, 100%), 67,15 ($C_5H_7^+$, 44), 57,10, 55,10, 53,10. *Anal.* calc. pour $C_6H_{11}OCl$: C 53,53, H 8,23; tr. : C 53,43, H 8,15.

*(Phénoxy-1 éthyl)-1 cyclopentanol (**45**)*

En utilisant 5,00 g (26 mmol) de phénoxy-2 propanoate d'éthyle (**39**) on obtient, après distillation, 4,043 g de cyclopentanol **45**; Rdt = 87%; Eb = 125°C (0,03 Torr); ir ν_{max} (film) : 3450, 2960, 2885, 1595, 1488, 1447, 1288, 1240, 1170, 1050, 740 cm^{-1}; rmn ^1H ($CDCl_3$) δ : 1,32 (3H, d, CH_3), 1,74 (8H, m, CH_2 cycl.), 2,11 (1H, s, OH), 4,27 (1H, q, $CHCH_3$), 6,72–7,45 (5H, m, 4 aromatiques) ppm. *Anal.* calc. pour $C_{13}H_{18}O_2$: C 75,69, H 8,79; tr. : C 75,52, H 8,74.

*Diéthoxyméthyl-1 cyclopentanol (**46**)*

En utilisant 5,00 g (28 mmol) de diéthoxyacétate d'éthyle (**40**) on recueille, après distillation, 4,039 g de diéthoxyméthyl-1 cyclopentanol **46**; Rdt = 76%; Eb = 48°C (0,08 Torr); ir ν_{max} (film) : 3460, 2970, 2865, 1100, 1065 cm^{-1}; rmn ^1H δ : 1,25 (6H, t, CH_2-CH_3), 1,44–2,00 (8H, m, CH_2 cycl.), 2,18 (1H, s, OH), 1,47–4,10 (4H, m, CH_3CH_2), 4,38 (1H, s, OH) ppm. *Anal.* calc. pour $C_{10}H_{20}O_3$: C 63,79, H 10,71; tr. : C 63,71, H 10,76.

*(Dithiolane-1,3)-1 cyclopentanol (**49**)*

En utilisant 3 g (27 mmol) de dithiolane-1,3 acétate d'éthyle **41** on obtient, après distillation, 2,131 g de cyclopentanol **49**; Rdt = 67%; Eb = 92–94°C (0,05 Torr); ir ν_{max} (film) : 3440, 2950, 2865, 1355, 1278, 1000 cm^{-1}; rmn ^1H ($CDCl_3$) δ : 1,79 (8H, m, CH_2 cycl.), 2,28 (1H, s, OH), 3,27 (4H, s, CH_2-CH_2), 4,72 (1H, s, CH) ppm. *Anal.* calc. pour $C_8H_{14}OS_2$: C 50.49, H 7.41; tr. : C 50.42, H 7.46.

*Phénylthiométhyl-1 cyclohexanol (**50**)*

En utilisant 2,085 g (10,6 mmol) de l'ester **37** on recueille, après distillation, 1,080 g de cyclohexanol **50**; Rdt = 55%; Eb = 112°C (0,02 Torr); ir ν_{max} (film) : 3440, 2930, 2860, 1587, 1483, 1442, 1032, 987, 741, 695 cm^{-1}; rmn ^1H ($CDCl_3$) δ : 1,17–1,70 (10H, m, CH_2 cycl.), 2,23 (1H, s, OH), 3,10 (2H, s, CH_2S), 7,24 (5H, m, H aromatiques) ppm. *Anal.* calc. pour $C_{13}H_{18}OS$: C 70,22, H 8,16; tr. : C 70,21, H 8,14.

*(Phénoxy-1 éthyl-1)-1 cyclohexanol (**51**)*

En utilisant 4,00 g (21 mmol) de phénoxy-2 propanoate d'éthyle (**39**) on recueille, après distillation, 3,291 g de liquide incolore. D'après le spectre de rmn ^1H nous obtenons une quantité appréciable de phénoxy-2 heptène-6 ol-3. Le rendement approximatif en (phénoxy-1 éthyl-1)-1 cyclohexanol (**51**) est de 38%; Eb = 90–104°C (0,02 Torr); ir ν_{max} (film) : 3430, 2940, 2865, 1605, 1500, 1245, 918, 758, 700 cm^{-1}; rmn ^1H ($CDCl_3$) δ : 1,30 (3H, d, CH_3), 1,62 (10H, m, OH cycl.), 2,10 (1H, s, OH), 3,71 (1H, m, $CHCH_3$), 4,03–4,43 (1H, m, $CHCH_3$), 6,73–7,56 (5H, m, aromatiques) ppm. *Anal.* calc. pour $C_{14}H_{20}O_2$: C 76,32, H 9,15; tr. : C 76,28, H 9,03.

Remerciements

Nous remercions le Conseil de recherches en sciences naturelles et en génie du Canada et le Ministère de l'éducation du gouvernement du Québec pour l'aide financière apportée sous forme de subventions et bourses.

1. (*a*) A. G. Cook et E. K. Fields. J. Org. Chem. **27**, 3686 (1962); (*b*) J. Maillard, M. Vincent, P. Delaunay, M. Rapin et Vo Van-Tri. Bull. Soc. Chim. Fr. 1683 (1966); (*c*) G. F. Hennion et L. Price. J. Org. Chem. **27**, 1587 (1962).
2. (*a*) K. Miescher et A. Marxer. U.S. Appl. 2,590,638, 25 mars 1952; Chem. Abstr. **46**, 11236b (1952).
3. M. A. Kira, M. N. Aboul-Enein et G. Tammam. J. Chem. U.A.R. **11**, 51 (1968); Chem. Abstr. **70**, 19753 q (2969).
4. T. Kudo et A. Nose. Chem. Abstr. **82**, 125255m (1975).
5. B. V. Shetty et T. L. Thomas. Ger. Offen. 250953 (Cl,C07C), 11 sept. 1975; U.S. Appl. 447804, 04 Mars 1974; Chem. Abstr. **84**, P.58889x (1976).
6. (*a*) M. A. Galbraith, J. J. Hobbs et R. A. Massy-Westropp. Aust. J. Chem. **16**, 112 (1963); (*b*) R. I. Kruglikova et N. A. Kamennov. Zh. Org. Khim. **2**, 1227 (1966).
7. P. Cannone, H. Caron et G. Foscolos. Tetrahedron, **40**, 865 (1984).
8. P. Cannone, G. B. Foscolos et D. Bélanger. J. Org. Chem. **45**, 1828 (1980).
9. P. Cannone, D. Bélanger, G. Lemay et G. B. Foscolos. J. Org. Chem. **46**, 3091 (1981).
10. S. Hayashi, M. Furakawa, Y. Fujino et T. Ohkawara. Chem. Pharm. Bull. **17**, 1054 (1969).
11. P. Cannone, D. Thibeault et G. Fytas. Tetrahedron, **42**, 4203 (1986).
12. (*a*) M. Viscontini et J. Meier. Helv. Chim. Acta, **33**, 1773 (1950); (*b*) J. Schmutz, R. Hirt, F. Kunzle, E. Eichenberger et H. Lauener. Helv. Chim. Acta, **36**, 620 (1953); (*c*) R. A. Henry et W. M. Dehn. J. Am. Chem. Soc. **72**, 2280 (1950); (*d*) W. V. Drake et S. M. McElvain. J. Am. Chem. Soc. **56**, 697 (1934) et références citées.
13. (*a*) R. B. Moffett. J. Org. Chem. **14**, 862 (1949); (*b*) D. W. Adamson. J. Chem. Soc. S, 144 (1949); (*c*) C. A. Weisel, R. B. Taylor, H. S. Mosher et F. C. Whitmore. J. Am. Chem. Soc. **67**, 1071 (1945).
14. (*a*) I. N. Nazarov, R. I. Kruglikova et G. M. Nikolaev. Zh. Obshch. Khim. **30**, 462 (1960); Chim. Abstr. **54**, 22634b (1960); (*b*) J. G. Traynham et O. S. Pascual. Tetrahedron, **7**, 165 (1959).
15. B. C. Barrass, R. W. Brimblecombe, D. C. Parkes et P. Rich. Br. J. Pharmacol. **34**, 345 (1968).
16. (*a*) J. Munch-Peterson. Acta Chem. Scand. **5**, 519 (1951); (*b*) A. Morel. Bull. Soc. Chim. Fr. **21**, 968 (1899).
17. W. E. Truce et R. J. Steltenkamp. J. Org. Chem. **27**, 2816 (1962).
18. J. Attenburrow, J. Elks, B. A. Hems et K. N. Speyer. J. Chem. Soc. 510 (1949).
19. R. Ripps, C. Derappe, M. Dupont et M. Crucifix. Chim. Ther. **6**, 45 (1971).
20. B. M. Trost and H. Hiemstra. Tetrahedron, **42**, 3323 (1986).
21. H. J. Cristeau, A. Bazhovs, Ph. Morand et E. Tonelles. Tetrahedron Lett. **27**, 3009 (1986).

Can. J. Chem. Downloaded from www.nrcresearchpress.com by 213.222.148.141 on 09/07/12
For personal use only.

Dosage du Sr-90 dans l'eau des lacs et des rivières du Québec par précipitation avec l'oxine et comptage β

E. HADDAD ET L. ZIKOVSKY

École Polytechnique de Montréal, C.P. 6079, succursale A, Montréal (Québec), Canada H3C 3A7

Reçu le 17 juin 1987

E. HADDAD et L. ZIKOVSKY. Can. J. Chem. **66**, 174 (1988).

Une nouvelle méthode de dosage du Sr-90 dissout dans les eaux de surface a été mise au point. Elle est basée sur la précipitation du Sr avec l'hydroxy-8 quinoléine à pH de 11,3 et le comptage des particules β dont l'énergie dépasse 150 keV. La limite de détection qu'on peut obtenir est de 0,5 mBq/L et le rendement global de séparation est de 28%. Les facteurs de décontamination des principales interférences β sont supérieurs à 10 000. La méthode a été utilisée pour doser le Sr-90 dans 5 lacs et 5 rivières du Québec et les activités de 3 à 15 mBq/L ont été mesurées. La nouvelle méthode est moins onéreuse et aussi fiable et performante que la méthode conventionnelle.

E. HADDAD and L. ZIKOVSKY. Can. J. Chem. **66**, 174 (1988).

A new method for the determination of Sr-90 dissolved in surface waters has been developed. It is based on the precipitation of Sr with 8-hydroxyquinoline at pH 11.3 and counting of β particles with energy above 150 keV. The detection limit obtained is 0.5 mBq/L and the mean yield is 28%. The decontamination factors from other β emitters achieved are better than 10 000. This method has been used to measure the Sr-90 in 5 lakes and 5 rivers in Québec and activities ranging from 3 to 15 mBq/L were obtained. This new method is as efficient and reliable as conventional techniques while being less tedious.

Can. J. Chem. Downloaded from www.nrcresearchpress.com by 213.222.148.141 on 09/07/12
For personal use only.

Introduction

Le Sr-90 avec le Cs-137 constituent les deux radioéléments anthropogènes les plus importants. Ils ont été introduits dans l'environnement terrestre en grande quantité par les essais nucléaires dans les années 50 et 60. On a estimé (1) leur déposition globale en 1971 à 574 GBq (Sr-90) et à 920 GBq (Cs-137).

L'importance du Sr-90 provient de sa longue demi-vie (29 ans), de sa radiotoxicité élevée et de ses propriétés chimiques et biologiques similaires au calcium. Une fois introduit dans l'organisme, il se fixe dans les os où il présente un danger pour la santé.

Étant un émetteur β pur, le Sr-90 est difficile à doser. En 1984, Suchny (2) a présenté les résultats d'une étude comparative de dosage des radioéléments de 50 laboratoires de différents pays. Cette étude montre qu'il y avait un tiers des résultats à rejeter sans doute à cause des difficultés du dosage de cet isotope.

Sa concentration dans l'eau est très faible (0,16–10 mBq/L) et il est difficile à séparer d'autres émetteurs β qui sont présents dans l'eau.

Il existe (3, 4) plusieurs méthodes de dosage du Sr-90. Mais elles sont généralement très onéreuses et longues. Par conséquent, nous avons entrepris de mettre au point une nouvelle méthode de dosage du Sr-90 dans l'eau qui serait plus rapide que les méthodes existantes.

Partie théorique

Le Sr-90 est un émetteur β pur et, par conséquent, il ne peut pas être dosé directement par les méthodes instrumentales (spectrométrie).

Un dosage fiable du Sr-90 demande une séparation la plus complète possible de tous les émetteurs β du Sr-90. Les radioéléments qui risquent d'interférer avec le dosage du Sr-90 sont les radioéléments naturels primordiaux (U, Th et leurs descendants, K-40, etc.), les radioéléments produits par les rayons cosmiques (Na-22, Be-10, P-32, etc.) et les produits de fission ou d'activation (Fe-59, Co-60, Zn-65, etc.). Sur le plan chimique, il s'agit d'isoler sélectivement le Sr de tous les autres éléments. Grâce au fait que le Sr-90 forme rapidement un équilibre radioactif avec le Y-90, un émetteur β très énergétique (E_{max} = 2280 keV), on peut simplifier cette tâche difficile en coupant, au cours du comptage, les émetteurs β d'énergie faible. C'est cette approche que nous avons adoptée en choisissant un absorbeur en Al d'une épaisseur de 45 μm qui arrête tous les β dont l'énergie est plus faible que 100 keV.

La séparation se simplifie davantage en excluant les radioéléments dont la demi-vie est courte et nous avons choisi 1 mois comme la frontière entre les radioéléments qu'il faut étudier en détails et le reste.

À l'aide de ces deux critères, nous avons identifié les radioéléments (tableau 1) dont le comportement chimique doit être étudié et qui doivent être séparés du Sr-90. Nous avons inclus également quelques émetteurs α (Ra, U, Th) qui possèdent des émetteurs β parmi leurs descendants et les membres de la même famille chimique (Ba, Ca).

En sachant la concentration moyenne des éléments dans l'eau et l'activité spécifique des radioéléments primordiaux, on peut calculer facilement l'activité spécifique des émetteurs β dans l'eau. Egalement en connaissant les taux des effluents radioactifs provenant des installations nucléaires, on peut évaluer grossièrement la teneur des produits de fission dans l'eau. Suivant ce raisonnement, on conclut que le Ba-140, K-40, Ra-226, U-238, Zn-65 et Zr-95 sont les radioéléments qui sont les plus susceptibles de gêner le dosage du Sr-90. Pour augmenter la sélectivité de la séparation du Sr-90, nous avons ajouté une préconcentration sur une résine cationique. Ceci permet d'éliminer les anions qui pourraient interférer (I-129, Tc-99) et d'améliorer la limite de détection. Comme il est onéreux de transporter 100 litres d'eau au laboratoire, la préconcentration se fait sur le terrain.

Partie expérimentale

Notre méthode est basée sur la précipitation en milieu basique du Sr par hydroxy-8 quinoléine (oxine) et le comptage des particules β d'une énergie supérieure à 150 keV. Des études menées dans les années soixante (5, 6) ont montré qu'il est possible d'extraire le Sr avec l'oxine dans le chloroforme à pH plus élevé que 11,0. Cette approche malheureusement ne s'applique pas directement aux eaux de surface où la concentration du Ca est très supérieure à celle du Sr de manière que la capacité d'extraction est rapidement atteinte. Après nombreux essais, nous avons adopté la procédure suivante :

1. Préconcentration du Sr-90 : passer 100 L d'eau à travers une

TABLEAU 1. Propriétés nucléaires des émetteurs β qui peuvent interférer avec le Sr-90

RE	T (ans)	E_β (keV)	MF	CER (ng/g)	AS (Bq/g, mBq/L)	ASE	Réf.
Ba-140	0,035	1030	F	12	—	11*	11, 14
Ca-45	0,442	257	A	15 000	—		8
Cd-113	14,6	590	F	80	—	2E-3$	8, 14
Ce-144	0,778	316	F	0,17	—	~6*	11, 14
Co-60	5,27	318	A	0,9	—	0,04	8, 13
Cs-137	30	516	F	0,2	—	3,2	8, 12
Eu-152	13	727	F	0,01	—	0,5$	11, 15
Fe-59	0,13	467	A	670	—	2,2*	8, 14
K-40	$1{,}28 \times 10^9$	1310	P	2300	31,6	73	8, 9
Lu-176	$2{,}9 \times 10^{10}$	570	P	~0,003	5,5	2E-5	9
Na-22	2,6	545	C	6300	3E-4	2E-3	8, 9
Ra-226	1620	—	P	3,9E-7	3,9E-10	14	8, 9
Rb-87	$4{,}9 \times 10^{10}$	273	P	1,5	888	1,3	8, 9
Sb-125	2,7	300	F	0,6	—	0,3$	10, 15
Sn-121	50	354	F	0,04	—	0,01$	8, 15
Th-232	$1{,}4 \times 10^{10}$	—	P	0,02	4070	0,08	8
Tl-204	3,8	763	P	—	—	—	—
U-238	$4{,}4 \times 10^9$	—	P	1	12 346	12	8
Zn-65	0,67	325	A	10	—	11*	8, 14
Zr-95	0,20	400	A,F	2,6	—	9*	8, 14

MF = mode de formation (A = activation, C = rayons cosmiques, F = produit de fission, P = radioélément primordial).

CER = concentration moyenne d'élément correspondant dans les rivières.

AS = activité spécifique des radioéléments primordiaux.

ASE = activité spécifique des radioéléments dans l'eau évaluée à partir des concentrations moyennes, des activités spécifiques et des débits des effluents radioactifs.

* = activité dans la rivière Outaouais calculée à partir des effluents radioactifs (14) et du débit de la rivière (1260 m^3/s).

$ = activité évaluée à partir de la composition du combustible irradié (15) en utilisant l'activité du Zr-95 comme la base de comparaison.

colonne (rayon : 5 cm, hauteur : 1,3 cm, débit : 3 L/min) d'échange cationique (Dowex 50W-X8). Le Sr et autres cations sont absorbés sur la résine.

2. Elution du Sr avec 2 L de l'acide nitrique 2 M (3 élutions consécutifs).

Les deux étapes d'échange–élution se font sur place : l'eau à doser est prise à l'aide d'une pompe qui fonctionne avec une batterie d'auto. La quantité d'eau est mesurée après son passage à travers la colonne dans un tonneau gradué.

3. Neutraliser la solution avec le NaOH à pH 7.

4. Ajouter 0,5 g de $Sr(NO_3)_2$ comme entraîneur et précipiter les sulfates avec 250 mL de H_2SO_4 (96%).

Le but principal de cette étape est de séparer le Sr des métaux alcalins (Na, K, Rb et Cs), ces derniers pouvant coprécipiter avec l'oxine à pH 11,2.

5. Laisser reposer et séparer le précipité par filtration (papier Whatman 41).

6. Dissoudre le précipité dans 400 mL de HNO_3 (1 M), ajouter 45 mg de $FeCl_3$ et précipiter les hydroxydes à l'aide de l'ammoniac concentrée (0,4 M). On réduit ainsi la concentration du Co, Sn, V, Th, Zn et Zr.

7. Séparer le précipité et garder la solution.

8. Ajuster le pH à 9,5 avec le NaOH, ajouter 50 mL d'oxine 0,5 M dans le chloroforme et agiter 2 h.

L'oxine (C_9H_7ON) est un réactif organique très versatile, qui réagit facilement avec presque tous les métaux de la table périodique pour donner des chelates neutres : le cation métallique est pris entre deux ou plusieurs ions oxinates pour donner un complexe insoluble dans l'eau.

9. Laisser reposer, séparer et garder la phase aqueuse (à cette étape on enlève une partie du Ca).

Notons que la formation du complexe dépend fortement du pH du milieu. Nous profitions de cette propriété pour séparer le Sr, puisqu'il ne forme d'oxinate qu'à pH > 10,5.

10. Ajuster le pH à 11,3, ajouter 50 mL d'oxine 0,1 M, agiter 2 h et laisser reposer. Le Sr précipite tandis que le Ba et Ra restent en solution.

11. Sécher le précipité à l'aide d'une lampe infrarouge; carboniser le précipité sec avec un brûleur à gas pendant 2 min et compter tout de suite le Sr-90 et Sr-89.

12. Attendre 2 semaines et compter le Sr-90 et Y-90.

Pour compter nos échantillons, on utilise un compteur proportionnel Tennelec LB 1000 conçu pour le comptage des radiations α et β à un faible niveau. Il est formé de 2 chambres de gaz à circulation, l'une au-dessus de l'autre. Celle d'en haut détecte les radiations cosmiques, qui sont à haute énergie et les élimine grâce à un signal de coïncidence qu'elles déclenchent dans les 2 chambres. L'autre partie (plus basse) compte les radiations émises par l'échantillon à analyser, avec une fenêtre de 5,6 cm et de 50 $\mu g/cm^2$ d'épaisseur. Le détecteur est placé entre deux plaques de cuivre et le tout est entouré avec des briques de plomb formant un écran de 10 cm d'épaisseur. L'échantillon à compter est déposé sur une rondelle d'acier de 4,5 cm de diamètre qui a une position précise devant le détecteur, ce qui garde un facteur de géométrie constant et nous permet de comparer les échantillons aux étalons.

Comme efficacité de comptage (nombre de coups par désintégration d'un atome de Sr-90) nous avons trouvé 79 ± 1% pour Sr-90 et Y-90 une fois à l'équilibre et 39,5 ± 0,5% pour le Sr-90 seul.

Pour éliminer toute interférence possible des émetteurs α et des β des faible énergie (< 150 keV), on utilise un absorbeur (Al) qui assure l'arrêt des α < 8 MeV et des β < 100 keV, puis on met un seuil sur la fenêtre d'entrée de l'amplificateur pour arrêter les β de < 150 keV. De cette façon on réduit aussi le bruit de fond de 3 coups à 1,7 coups/min.

Après l'emploi de l'absorbeur (45 μm de Al) et du seuil de l'amplificateur, l'efficacité de comptage baisse à 21%.

Résultats et discussion

Les rendements de diverses opérations chimiques sont

Can. J. Chem. Downloaded from www.nrcresearchpress.com by 213.222.148.141 on 09/07/12
For personal use only.

Can. J. Chem. Downloaded from www.nrcresearchpress.com by 213.222.148.141 on 09/07/12
For personal use only.

TABLEAU 2. Comportement chimique des radioéléments qui pourraient interférer avec le dosage du Sr-90

	SS	FC	PS	PH	PO1	PO2	FD
RI	g/L		(%)	(%)	(%)	(%)	
Ba-140	0,0022	Ba^{2+}	>99*	11,0	<0,1	<0,2	>500
Ca-45	2	Ca^{2+}	<1*	25	>99	>99	>6000
Cd-113	750	Cd^{2+}	<1*	85	>98	>99	>60 000
Ce-144	100	Ce^{3+}	<1*	65	>98	>99	>28 000
Co-60	360	Co^{2+}	<1*	95	>98	>99	>200 000
Cs-137	1670	Cs^{+}	<1*	0,1	1,2	1,5	>6000
Eu-152	25	Eu^{3+}	<1*	67	P	—	>30 000
Fe-59	3240	Fe^{3+}	<1*	96	>98	>99	>120 000
K-40	120	K^{+}	<1*	<1	<1	<1	>10 000
Lu-176	420	Lu^{3+}	<1*	71	P	—	>30 000
Ra-226	0,002	Ra^{2+}	>99*	11	<0,1	<0,1	>1100
Sb-125	f	Sb^{3+}	>99*	85	P	—	>60 000
Sn-121	330	Sn^{2+}	<1*	85	P	—	>60 000
Sr-90	0,13	Sr^{2+}	>99*	21	25	98	
Th-232	94	Th^{4+}	<1*	95	>90	>98	>20 000
Tl-204	48	Tl^{+}	<1*	23	>97	>98	>4800
U-238	230	U^{4+}	<1*	98	>95	>98	>100 000
Zn-65	380	Zn^{2+}	<1*	75	>96	>98	>10 000
Zr-95	e	Zr^{4+}	<1*	98	>96	>98	>120 000

FD = facteur de décontamination.
FC = forme chimique.
P = précipite pendant ajustement du pH.
PS = précipitation des sulfates.
e = elevée.
f = faible.
PH = précipitation des hydroxydes.
PO1 = précipitation des oxinates à pH 9,5.
PO2 = précipitation des oxinates à pH 11,3.
* calculé à partir des solubilités.
SS = solubilité des sulfates.

déterminés à l'aide de traceurs radioactifs émetteurs γ. Les traceurs ont été préparés par irradiation dans le réacteur SLOWPOKE II de l'École Polytechnique de Montréal, avec un flux de 10^{12} n cm^{-2} s^{-1}.

Afin de vérifier le rendement du Sr et calibrer le compteur, un traceur (Sr-90, émetteur β pur) a été utilisé. Il a été fournit par la compagnie New England Nuclear Ltd.

Nous avons choisi la résine Dowex 50-X8 pour préconcentrer le Sr. Cette résine a fait ses preuves dans plusieurs études précédentes (7). La rétention du strontium sur la résine a été étudiée en fonction du débit de l'eau et de la quantité de résine dans la colonne. Pour réduire le temps de passage de l'eau dans la colonne, et maximiser le taux d'échange, nous avons choisi 100 g de résine et un débit de 2,5 L/m, la rétention étant de 56 ± 3%.

Malheureusement, cette approche ne permet pas de doser le Sr-90 qui se trouve dans l'eau sous forme des particules fines et insolubles. Par contre, ces particules devraient être peu absorbées par le système digestif et par conséquent, moins dangereuses pour la santé.

Pour l'élution du Sr, nous avons préféré l'acide nitrique aux acides sulfurique et chlorhydrique : les sulfates sont peu solubles et les chlorures risquent de former des complexes avec les réactifs organiques.

Pour améliorer le rendement d'élution avec un volume minimal d'acide, la solution éluante a été repassée plusieurs fois à travers la résine. Après 3 passages consécutifs de la même solution, le rendement atteint 90 ± 3%.

Toutes les étapes ont été vérifiées au moins 3 fois et les moyennes ont été prises.

Comme résultat on a réussi à diminuer le volume d'un facteur de 50 (100 L à 2 L) et la concentration de Sr a été augmentée d'un facteur de 25 (100 L × 90% × 56%/2 L).

La contamination possible des produits chimiques utilisés par Sr-90 a été vérifiée en utilisant l'eau distillée comme échantillon. La valeur ainsi obtenue est inférieure à 9 mBq à niveau de confiance de 90%.

Comme application de la procédure, le Sr-90 a été dosé dans 5 lacs et cinq rivières du Québec.

Les lacs choisis sont (1) Champlain et Memphrémagog, à côté de la frontière des Etats-Unis (état de New-York); (2) Manitou, Tremblant et Simon, qui sont loin des agglomérations et des usines.

Les cinq sites de prélèvements sur les rivières sont l'Outaouais, au nord-ouest de Montréal et qui reçoit des déversements des laboratoires de Chalk River; le fleuve Saint-Laurent à Beauharnois en amont de Montréal pour déterminer le Sr-90 qui provient de l'extérieur de la ville; à Montréal, près du centre-ville; à Varennes en aval de Montréal et à 20 km de la centrale Gentilly II, pour voir l'effet de ses déversements.

La valeur d'une méthode de séparation radiochimique dépend des facteurs de décontamination qui quantifient le degré auquel on réussit à purifier le mélange initial. Pour notre méthode, ces facteurs sont très élevés (tableau 2) et par conséquent, l'activité finale représente bien celle du Sr-90. Une purification supplémentaire s'effectue au cours de la préconcentration et au

TABLE 3. Concentration du Sr-90 dans les rivières et les lacs du Québec

Rivières du Saint-Laurent	Concentration (mBq/L)
Beauharnois	14 ± 0,7*
Montréal	5 ± 0,5
Varennes	11 ± 0,6
L'Outaouais, Montebello	12 ± 0,6
Gentilly, St-Pierre-Les-Besquets	15 ± 0,7
Lacs	
Memphremagog	7,4 ± 0,6
Champlain	5,4 ± 0,5
Manitou	5,9 ± 0,6
Tremblant	3,7 ± 0,5
Simon	3,2 ± 0,5

*Erreur statistique à un niveau de confiance de 90%. Les concentrations ont été calculées de la façon suivante :

$$\text{Concentration (Bq/L)} = \frac{\text{Taux de comptage (coups/s)}}{100 \times 0{,}28 \times 0{,}21}$$

cours du comptage quand on favorise aussi très fortement la détection du Sr-90 au dépens d'autres émetteurs β.

Il est intéressant de comparer les résultats obtenus (tableau 3) avec les mesures du Sr-90 faites par d'autres chercheurs. Les chercheurs canadiens du Ministère de la Santé et du Bien-être social (12) ont trouvé les concentrations du Sr-90 dans le fleuve St-Laurent allant de 3 à 21 mBq/L et dans le lac Ontario de 1 à 20 mBq/L. Dans la mer baltique en 1972, les chercheurs Vakulskij *et al.* (16) ont trouvés 27 mBq/L du Sr-90. Dans l'eau de mer du Golfe du Mexique on a trouvé (17) 3 mBq/L et dans l'eau potable dans les iles Faroe on a mesuré (18) 5.5 mBq/L.

On constate que les concentrations mesurées au Québec sont assez semblables aux valeurs déterminées ailleurs. Le rendement global de notre méthode est de 28% et la limite de détection est de 0,5 mBq/L avec un bruit de fond de 1,7 coups/min et le temps de comptage de 600 min. Cette limite se compare bien avec celle (1 mBq/L) obtenue par d'autres chercheurs (19).

Le rendement pourrait être déterminé pour chaque analyse en utilisant un traceur radioactif comme le Sr-85. Nous n'avons pas adopté l'emploi d'un traceur à cause des frais additionnels.

Notre méthode est plus courte (10 étapes) que la technique utilisée présentement par les autorités canadiennes (19) qui comporte 34 étapes et nous cryons qu'elle est aussi sélective que les méthodes compétitives.

La durée totale d'une analyse (sans prélèvement) est de 9 h, mais elle comporte des périodes d'attente qui totalisent 6 h et, par conséquent, on peut faire plusieurs analyses simultanément.

Conclusions

Nous avons mis au point une nouvelle méthode de dosage du Sr-90 dissout dans l'eau des lacs et des rivières. Cette méthode est moins onéreuse et aussi performante que la méthode conventionnelle et, nous croyons, aussi fiable. Cette méthode a été utilisée pour doser le Sr-90 dissout dans les lacs et les rivières du Québec et les activités variant de 3 à 15 mBq/L ont été mesurées.

Remerciements

Nous remercions sincèrement la Conseil de recherches en sciences naturelles et en génie du Canada pour une subvention qui a rendu la réalisation de ce travail possible. Nous exprimons notre gratitude au personnel du laboratoire SLOWPOKE de l'École Polytechnique pour la fabrication des traceurs radioactifs utilisés dans cette recherche.

1. Nations Unies. Ionizing radiation: Levels and effects. United Nations Publ. E.72.IX.17. New York, 1970.
2. J. SUSCHNY. Nucl. Instrum. Methods Phys. Res. **223**, 477 (1984).
3. V. T. BOWEN. Reference methods for marine radioactivity studied. IAEA, TRS-118. 1970. p. 93.
4. D. SUNDERMAN et C. TOWNLEY. The radiochemistry of Ca, Sr and Ba. NAS-NS 3010, National Academy of Sciences. 1960.
5. J. STARY. The solvent extraction of metal chelates. Macmillan, New York. 1964. p. 80.
6. G. H. MORRISON. Solvent extraction in analytical chemistry. Wiley, New York. 1957.
7. B. TREMILLON. Les résines échangeuses d'ions. Gautier-Villards, Paris. 1965. p. 5.
8. H. J. M. BOWEN. Trace elements in biochemistry. Academic Press, New York. 1966. p. 31.
9. M. EISENBUD. Environmental radioactivity. Academic Press, New York. 1973. pp. 161–162.
10. S. H. HARRISON, P. D. LAFLEUR et W. H. ZOLLER. Anal. Chem. **47**, 1685 (1975).
11. B. SALBU et E. STEINNES. Anal. Chem. **47**, 1011 (1975).
12. Santé et Bien-être social Canada. La radioactivité ambiante au Canada—1984. Rapport 86-DMM-125. 1986.
13. L. ZIKOVSKY et J. L. GALINIER. Energie nucléaire et pollution de l'eau par les radioisotopes. Rapport IGN-302. 1978.
14. Atomic Energy Control Board. Radioactive releases from Canadian installations in 1975 and 1976. Rapport AECB-1115, AECB, Ottawa. Sept. 1977.
15. R. E. BURN et E. R. IRISH. AIChE Symp. Ser. **72**, 18 (1976).
16. S. M. VAKULSKIJ, I. Y. KATRICH et S. G. MALAKHOV. At. Energ. **39**, 183 (1975).
17. P. H. PAYTON, S. B. HILD, C. V. OERTTI et A. D. SUTTLE, JR. Health Phys. **33**, 143 (1977).
18. A. AARKROG *et al.* Risoe-R-488, 1983.
19. Ministry of National Health and Welfare. Chemical procedures for the determination of ^{89}Sr, ^{90}Sr and ^{137}Cs in surface waters, fresh water algae and fresh water fish. Rapport 77-EMD-14, 1977.

Can. J. Chem. Downloaded from www.nrcresearchpress.com by 213.222.148.141 on 09/07/12
For personal use only.

Étude cinétique et thermodynamique de l'interaction d'un complexe de Pd(II) avec l'inosine et l'acide polyinosinique

ROBERT MÉNARD[1] ET MIKLOS ZADOR[2]

Département de chimie, Université de Montréal, C.P. 6128, succursale A, Montréal (Québec), Canada H3C 3J7

Reçu le 26 mai 1987

ROBERT MÉNARD et MIKLOS ZADOR. Can. J. Chem. **66**, 178 (1988).

Les réactions du complexe (dien)Pd(II) avec l'inosine et l'acide polyinosinique ont été étudiées à l'aide de méthodes spectroscopiques et de flux-stoppé. Dans les deux cas, le métal se lie initialement au site N7 de la base hypoxanthine. Les résultats des études cinétiques indiquent que le mécanisme implique deux voies réactionnelles : une substitution nucléophile directe ainsi qu'une réaction via un intermédiaire aquo. Les réactions sont plus rapides dans le cas du poly(I), due à la forte densité de charges négatives de ce polymère. La réaction initiale au site N7 est suivie d'une redistribution lente du métal vers le site N1 thermodynamiquement plus stable. La fixation du (dien)Pd(II) au poly(I) induit la formation d'une structure multi-hélicoïdale stable du polymère. Cette structure a été caractérisée par des mesures d'absorbance et de dichroïsme circulaire ainsi que par la détermination de la courbe de fusion du polymère. Il a aussi été observé qu'en présence du complexe de Pd(II), le poly(I) peut être hydrolysé à pH alcalin, dans des conditions relativement douces.

ROBERT MÉNARD and MIKLOS ZADOR. Can. J. Chem. **66**, 178 (1988).

Reactions of the (dien)Pd(II) complex with inosine and polyinosinic acid were studied by spectroscopic and stopped-flow methods. In both cases, the metal initially binds at the N7 site of the hypoxanthine base. The results of kinetic studies indicate the existence of a two-path mechanism: a direct nucleophilic substitution and a solvent path with formation of an aquo intermediate. The reactions are faster for poly(I), due to the high density of negative charges for this polymer. The initial reaction at N7 is followed by a slow redistribution of the metal towards the thermodynamically more stable N1 site. Binding of (dien)Pd(II) to poly(I) leads to formation of a stable, multistranded helicoidal structure of the polymer. This structure was characterized by absorption and circular dichroism measurements and by the melting curve of the polymer. It was also observed that in presence of the Pd(II) complex, poly(I) can be hydrolyzed at relatively mild conditions at high pH.

Introduction

À cause de la complexité des polynucléotides, les premiers travaux fondamentaux sur l'interaction des acides nucléiques avec les complexes de Pd(II) et de Pt(II) ont été orientés vers l'étude des unités constituantes plus simples, tels les bases nucléiques et les nucléosides (1–4). La plupart de ces travaux ont pour but la détermination des sites de liaison et de la stabilité des complexes formés. Parmi les divers nucléosides étudiés, l'inosine s'est avéré être un cas relativement complexe dû à la présence de deux sites potentiels de liaison pour le palladium et le platine : les azotes N1 et N7 (5–9). Le site N1 est protoné en solution neutre et la liaison à ce site dépend du pH. Divers types de complexes peuvent alors exister et, pour un composé tel (en)$PdCl_2$, des espèces polymériques sont connues (7). La formation d'un chélate entre les sites N7 et O6 a aussi été proposée à quelques reprises (10, 11) mais son existence est contestée (3).

Le complexe (dien)Pd(II), qui a l'avantage de ne posséder qu'un seul groupe labile, a fait l'objet d'études exhaustives (6, 8, 9, 12–14). Martin et coll. ont utilisé la rmn pour étudier l'importance des liaisons à chacun des sites en fonction du pH. Les résultats pour l'inosine indiquent que la liaison au site N7 est prédominante à pH < 4, tandis qu'à pH > 8, la liaison se fait presque exclusivement à N1. En solution neutre, les espèces Pd–N1, Pd–N7 ainsi que l'espèce binucléaire sont présentes. Avec l'inosine monophosphate, la distribution des espèces est similaire sauf que la présence du groupe phosphate tend à favoriser la liaison à N7. De plus, la présence du palladium en N7 cause une diminution du pK_a du site N1, ce qui conduit à une redistribution des ions métalliques et à la formation de liens avec le site N1 déprotoné (8).

Bien que l'importance des facteurs cinétiques ne soit pas mise en doute, très peu d'études quantitatives ont cependant été consacrées à cet aspect. Quelques études cinétiques ont été publiées impliquant la réaction de complexes de Pd(II) avec l'inosine, le poly(I)·poly(C) ainsi que la cytidine et ses dérivés (12, 15–18). Les résultats ont permis de démontrer l'existence de deux voies réactionnelles principales conduisant au produit final : une substitution nucléophile directe ainsi qu'une réaction via un ou des intermédiaires aquo. Il a aussi été observé, dans le cas des polynucléotides, que les facteurs de type électrostatique ont un effet prédominant sur la cinétique des réactions ainsi que sur la stabilité des complexes formés.[3]

Le but de ce travail est de définir avec précision le mécanisme de la réaction entre le (dien)Pd(II) et l'inosine, et de vérifier si ce mécanisme s'applique dans le cas du polynucléotide correspondant, le poly(I). Nous examinerons aussi comment la structure de ce polymère est affectée lors de la fixation de l'ion métallique.

Partie expérimentale

L'inosine (In) et l'inosine-5′-monophosphate (IMP, sel de sodium) ont été obtenus de Sigma Chemical Co. tandis que l'acide polyinosinique (poly(I), sel de potassium) provenait de Miles Laboratories Inc. La concentration du poly(I) est donnée en termes d'unité mononucléotide. Tous ces produits sont de haute pureté et furent utilisés sans purification supplémentaire. Les complexes [(dien)PdCl]Cl et [(dien)Pd(H_2O)](ClO_4)$_2$ (dien : diéthylènetriamine) ont été préparés tel que décrit précédemment (16). La force ionique est fixée par addition de $NaClO_4$, préparé à partir de $HClO_4$ (Biopharm) et de NaOH (Fisher Scientific Co.), étant donné que le $NaClO_4$ commercial contient souvent des impuretés pouvant interférer avec nos résultats. Le pH a été ajusté à l'aide de solutions concentrées de $HClO_4$ et de NaOH. Aucun tampon n'a été utilisé, de façon à éviter les interactions possibles avec les complexes de Pd(II).

Les mesures d'absorbance ont été effectuées à l'aide d'un spectro-

1. Adresse présente : Institut de recherche en biotechnologie, 6100, avenue Royalmount, Montréal (Québec), Canada H4P 2R2.

2. Auteur à qui toute correspondance doit être envoyée.

3. R. Ménard et M. Zador, article soumis pour publication.

Can. J. Chem. Downloaded from www.nrcresearchpress.com by 213.222.148.141 on 09/07/12
For personal use only.

Can. J. Chem. Downloaded from www.nrcresearchpress.com by 213.222.148.141 on 09/07/12
For personal use only.

photomètre Perkin–Elmer modèle 552, équipé d'un système électronique de contrôle de la température permettant la détermination de la courbe de fusion d'un polynucléotide (vitesse d'accroissement de température utilisée : 1°C/min). Les réactions rapides ont été suivies par spectrophotométrie à flux-stoppé en utilisant un système décrit précédemment (16). Les spectres de dichroïsme circulaire ont été enregistrés au moyen d'un spectropolarimètre Cary modèle 61 à la température de la pièce (21–23°C), en utilisant des cellules circulaires de chemin optique l = 1 cm. Les conditions standards pour ce travail sont : pH 7,0, force ionique 0,20 M, température 25,0°C. Les conditions expérimentales différentes seront spécifiées.

Résultats et discussion

Inosine

La cinétique de la réaction entre le (dien)PdCl$^+$ et l'inosine a d'abord été étudiée en mélangeant les réactifs à un pH initial de 7. On observe la présence de deux signaux distincts à 300 nm, le premier étant une augmentation relativement rapide ($t_{1/2}$ = 0,4 s) et importante de l'absorbance et attribuée à la fixation du (dien)Pd(II) au site N7 de l'inosine. Cette réaction est suivie

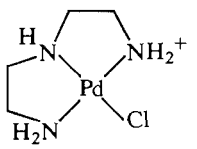

(dien)PdCl$^+$

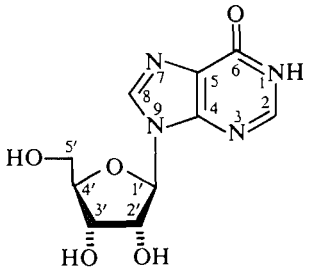

Inosine

d'une autre, beaucoup plus lente ($t_{1/2}$ = 120 s), produisant une très faible augmentation d'absorbance et correspondant à la formation du complexe Pd–N1 à partir de Pd–N7 avec libération de protons. Ce transfert a lieu entre pH 4 et 8, tel qu'illustré à la figure 1(a). Le mécanisme de ce processus lent n'a pas été étudié, à cause du faible signal dans ces conditions. Par ailleurs, des travaux antérieurs (6, 8) ont démontré que ce processus résulte d'une série de réactions impliquant plusieurs espèces. À λ = 350 nm, où les espèces Pd–N1 et Pd–N7 possèdent pratiquement la même absorbance, un seul signal est observé, correspondant à la formation du complexe Pd–N7. La cinétique de la réaction au site N7 a donc été étudiée en suivant les variations d'absorbance à 350 nm. On considère que la variation du pH durant cette réaction n'affecte pas la cinétique de la fixation en N7. Cette variation est d'autant plus faible que la concentration d'inosine en excès est importante.

La figure 1(b) montre l'influence du pH sur la constante de vitesse de cette réaction. On note une augmentation de la constante de vitesse à pH > 7 suivie d'une importante diminution à pH > 9. À pH élevé, la déprotonation du site N1 de l'inosine (pK_a = 8,7 (3)) conduit à l'apparition de concentrations importantes d'inosine déprotonée [InH$_{-1}$]. Avec k_{i7} et k_{i1} comme constantes de vitesse pour la réaction du (dien)Pd(II) aux sites N7 et N1 déprotoné respectivement, on obtient l'équation [1] :

$$[1] \quad k_{exp} = k_{i7}[In] + k_{i1}[InH_{-1}]$$

À pH élevé, la contribution du deuxième terme devient importante et les résultats indiquent que la réaction au site N1 déprotoné est plus rapide que celle au site N7. À partir de pH ≈ 8, on a maintenant apparition du dérivé (dien)Pd(OH)$^+$. Cette espèce, moins réactive, conduit à un ralentissement de la

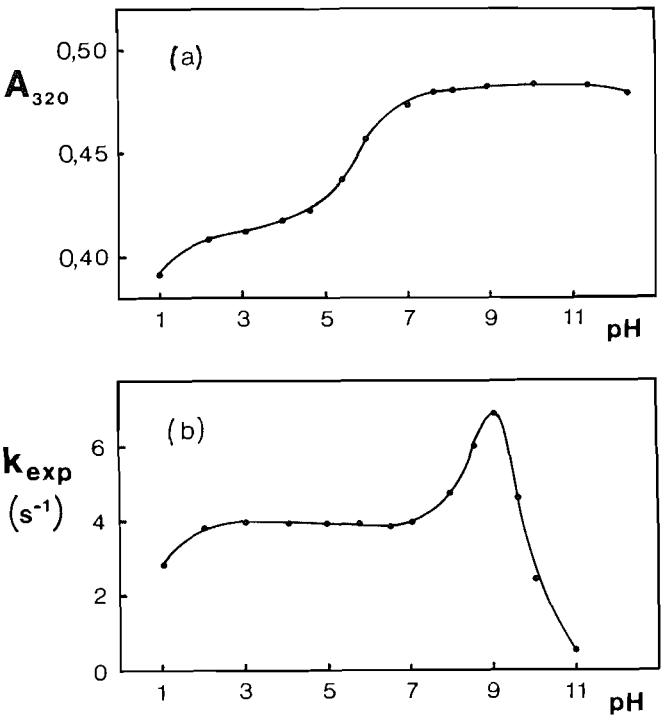

FIG. 1. Influence du pH sur l'absorbance (a) et sur la constante de vitesse de réaction (b) du système (dien)Pd(II)–inosine. Conditions : (a) inosine 1,0 × 10^{-2} M, [(dien)PdCl]Cl 1,0 × 10^{-3} M, NaCl 0,10 M, $NaClO_4$ 0,10 M; (b) inosine 5,0 × 10^{-3} M, [(dien)PdCl]Cl 5,0 × 10^{-4} M, NaCl 0,10 M, $NaClO_4$ 0,10 M.

réaction, tel qu'observé à pH > 9. La combinaison de ces deux effets permet d'expliquer l'allure de la courbe à pH > 7. La vitesse maximum se situe aux environs de pH 9, position qui est relativement sûre étant donné que la variation du pH durant la réaction devient négligeable à pH > 8. Entre pH 3 et 7, la valeur de k_{exp} est constante et reflète la réaction du (dien)Pd(II) au site N7 de l'inosine. La diminution de vitesse observée à pH < 2 peut être expliquée en considérant la protonation du site N7 à ce pH (pK_a ≈ 1,0 (3)).

La cinétique de la réaction à pH 7 a aussi été étudiée en fonction de la concentration en inosine et à diverses concentrations en ions chlorure ajoutés. Les résultats sont donnés à la figure 2. On remarque que la réaction est inhibée par l'addition d'ions chlorure et que l'ordre par rapport à l'inosine est inférieur à un à faible concentration en ion Cl$^-$. Les résultats sont semblables à ceux obtenus précédemment pour la réaction du (dien)Pd(II) avec la cytidine (16). On peut donc proposer un mécanisme similaire pour la formation du complexe Pd–N7 de l'inosine. Deux voies réactionnelles sont possibles : une substitution nucléophile directe ainsi qu'une réaction via un intermédiaire aquo.

$$[2] \quad In + (dien)PdCl^+ \underset{k_{-1}}{\overset{k_1}{\rightleftharpoons}} (dien)Pd(In)^{2+} + Cl^- \quad \Big\} \text{ voie directe}$$

$$[3] \quad (dien)PdCl^+ + H_2O \underset{k_{-2}}{\overset{k_2}{\rightleftharpoons}} (dien)Pd(H_2O)^{2+} + Cl^- \quad \Big\} \text{ voie du solvant}$$

$$[4] \quad In + (dien)Pd(H_2O)^{2+} \underset{k_{-3}}{\overset{k_3}{\rightleftharpoons}} (dien)Pd(In)^{2+} + H_2O \quad \Big\}$$

La constante d'équilibre pour la réaction du (dien)PdCl$^+$ au site N7 de l'inosine (équation [2] du mécanisme) a été évaluée par titrage spectrophotométrique en présence d'ions chlorure et

Can. J. Chem. Downloaded from www.nrcresearchpress.com by 213.222.148.141 on 09/07/12
For personal use only.

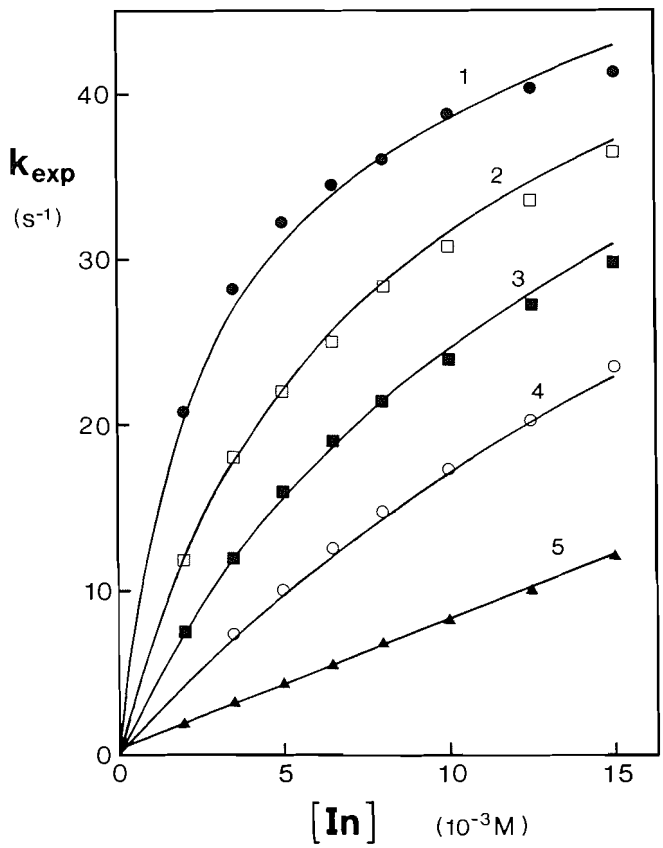

FIG. 2. Variation de la constante de vitesse expérimentale en fonction de la concentration en inosine, à diverses concentrations en ion Cl^- ajouté. Conditions : [(dien)PdCl]Cl 5,00 × 10^{-4} M, force ionique constante (0,20 M NaCl + $NaClO_4$), pH 7, NaCl ajouté : (1) 0, (2) 0,0030 M, (3) 0,0080 M, (4) 0,020 M, (5) 0,10 M. Les courbes sont calculées, d'après le mécanisme décrit par les équations [2]–[4].

TABLEAU 1. Paramètres cinétiques pour la réaction du (dien)$PdCl^+$ au site N7 de l'inosine à pH 7

k_1	450 M^{-1} s^{-1}
k_{-1}	1,88 M^{-1} s^{-1}
k_2	42 s^{-1}
k_{-2}	29 000 M^{-1} s^{-1}
k_3	27 000 M^{-1} s^{-1}
k_{-3}	0,16 s^{-1}

à pH 4 afin d'éliminer l'interférence du complexe Pd–N1. Une valeur de K_1 = 240 ± 40 a été obtenue. Les constantes de vitesse individuelles ont pu être évaluées en procédant tel que décrit précédemment pour la cytidine. Les résultats sont donnés au tableau 1.

La plus grande réactivité du dérivé aquo du (dien)Pd(II) permet d'expliquer l'inhibition par l'ion Cl^- observée. Les constantes de vitesse k_1 et k_3 sont comparables à celles obtenues pour le système analogue impliquant le (dien)$PdBr^+$ (12). Les différences sont dues à la force ionique plus élevée ainsi qu'à la contribution de l'espèce (dien)$Pd(OH)^+$ en l'absence d'ion Cl^- pour les expériences réalisées avec le (dien)$PdBr^+$. Les valeurs des constantes de vitesse individuelles diffèrent beaucoup cependant de celles obtenues pour la cytidine. En particulier, la valeur de k_1 pour l'inosine est six fois plus élevée que celle pour

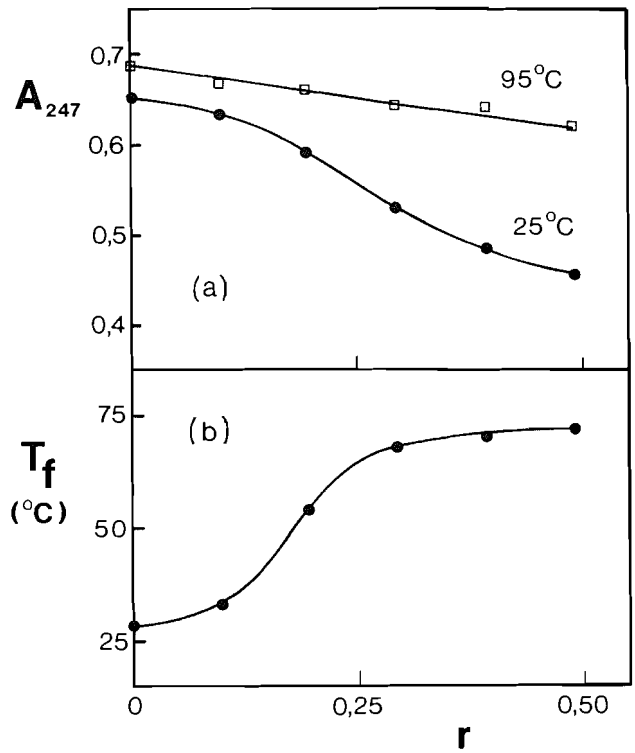

FIG. 3. Influence du (dien)Pd(II) sur l'absorbance (*a*) et sur la température de fusion (*b*) du poly(I). Conditions : poly(I) 6,14 × 10^{-5} M, $NaClO_4$, 0,20 M, pH 7. r = [(dien)PdCl]Cl/[poly(I)].

la cytidine (450 M^{-1} s^{-1} vs. 75 M^{-1} s^{-1}) tandis que pour k_3, le rapport est de neuf (27 000 M^{-1} s^{-1} vs. 2900 M^{-1} s^{-1}). L'inosine est donc un meilleur nucléophile pour les réactions de substitution des complexes du (dien)Pd(II) et, en présence de cytidine, la réaction au site N7 de l'inosine serait cinétiquement favorisée.

Induction d'une forme hélicoïdale du poly(I) par le (dien)Pd(II)

Le complexe formé entre le (dien)Pd(II) et le poly(I) a été caractérisé à l'aide de mesures d'absorbance, de dichroïsme circulaire et de température de fusion. Pour les mesures d'absorbance, la bande d'absorption du polynucléotide, dont le maximum se situe à 247 nm, a été utilisée. L'addition du complexe de palladium cause un léger déplacement du maximum vers 249 nm, accompagné d'une importante diminution de l'absorbance. L'importance de cette diminution est inhabituelle pour un système (dien)Pd(II)–polynucléotide et suggère la formation d'une structure hélicoïdale ordonnée avec recouvrement des bases hypoxanthine. La valeur de l'absorbance à 247 nm à 25°C en fonction du rapport r = [(dien)Pd(II)]/[poly(I)] est donnée à la figure 3(*a*). La diminution d'absorbance est de type coopératif, caractéristique des systèmes impliquant des polynucléotides hélicoïdaux. La complexation du Pd(II) à l'inosine produit une très légère diminution de l'absorbance à 247 nm (de 0,78 à 0,74) comparativement à celle observée pour le poly(I) (de 0,65 à 0,45).

Pour vérifier l'existence d'une telle structure, la variation de l'absorbance en fonction de la température a été étudiée. Les courbes obtenues à divers rapports r sont représentées à la figure 4. Pour r = 0, une très légère transition peu coopérative est observée à basse température, indiquant la présence de faibles proportions de poly(I) associé en l'absence de Pd(II). Lors de l'addition de concentrations croissantes de (dien)Pd(II), la transition est déplacée à des températures plus élevées

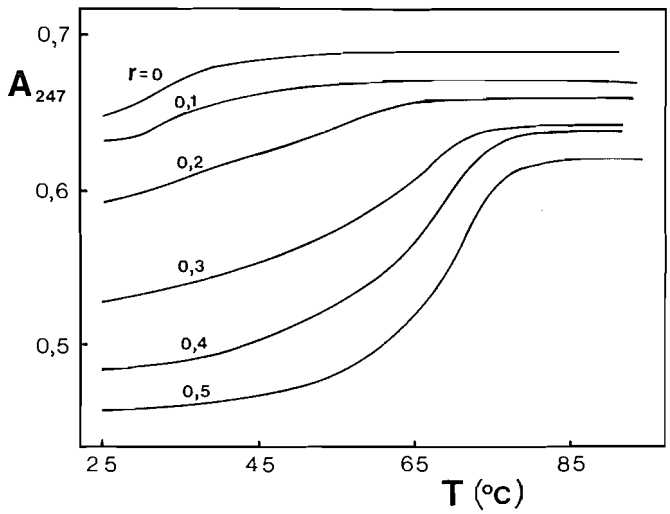

FIG. 4. Courbe de fusion du poly(I) en présence de diverses concentrations de (dien)Pd(II). Conditions : poly(I) 6,14 × 10^{-5} M, $NaClO_4$ 0,20 M, pH 7. r = [[(dien)PdCl]Cl]/[poly(I)].

et devient plus importante et coopérative. Ce comportement indique la formation d'une structure hélicoïdale de stabilité croissante avec l'addition du (dien)Pd(II). La température de fusion, correspondant au maximum de la courbe différentielle dA_{247}/dT en fonction de T, est représentée à la figure 3(b) en fonction du rapport r. La courbe obtenue démontre clairement l'effet coopératif de la fixation du (dien)Pd(II) sur la stabilité du produit formé. La température de fusion passe de 28°C en l'absence de Pd(II) à 72°C pour r = 0,49. À température élevée, où le polynucléotide est sous forme de pelote statistique, l'absorbance à 247 nm décroît aussi lorsque le rapport r augmente (figure 3(a)). Cette faible diminution est non-coopérative et reflète la fixation du Pd(II) à la base hypoxanthine du poly(I). D'ailleurs, le minimum de la bande d'absorption du poly(I) à 95°C se situe toujours à 249 nm en présence de (dien)Pd(II), comparativement à 247 nm pour le poly(I) libre, ce qui montre que le Pd(II) est complexé au poly(I) dans ces conditions. La diminution graduelle de la température conduit à une renaturation très lente du polymère, caractéristique du poly(I) (19). La vitesse de renaturation semble augmenter cependant avec la concentration en (dien)Pd(II). Le système est seulement partiellement réversible pour des temps courts (<1 h).

En l'absence du complexe de palladium, le poly(I) peut s'auto-associer en solution à force ionique élevée et à basse température (19–23). Les deux structures proposées pour ce polymère contiennent trois et quatre brins respectivement tenus ensemble par des ponts hydrogène N1—H···O6 (21, 23). Un modèle alternatif implique des ponts hydrogène N1—H···N7 (19). L'addition du complexe de Pd(II) peut faciliter la formation de la multiple hélice. Comme le site de fixation du (dien)Pd(II) se situe à N7 ou N1, la dernière structure proposée semble improbable. Pour les deux structures à ponts hydrogène N1—H···O6, le site N7 est suffisamment accessible pour permettre la complexation du (dien)Pd(II). Une fois fixé, le complexe de Pd(II), chargé positivement, neutralise les charges négatives des phosphates voisins, réduisant les répulsions interchaîne et favorisant ainsi l'association de plusieurs brins. Comme le (dien)Pd(II) est fixé plus fortement que des cations tels Na^+, l'effet structurant est plus important (T_f = 72°C à une force ionique de 0,20 M $NaClO_4$) et est rencontré à des

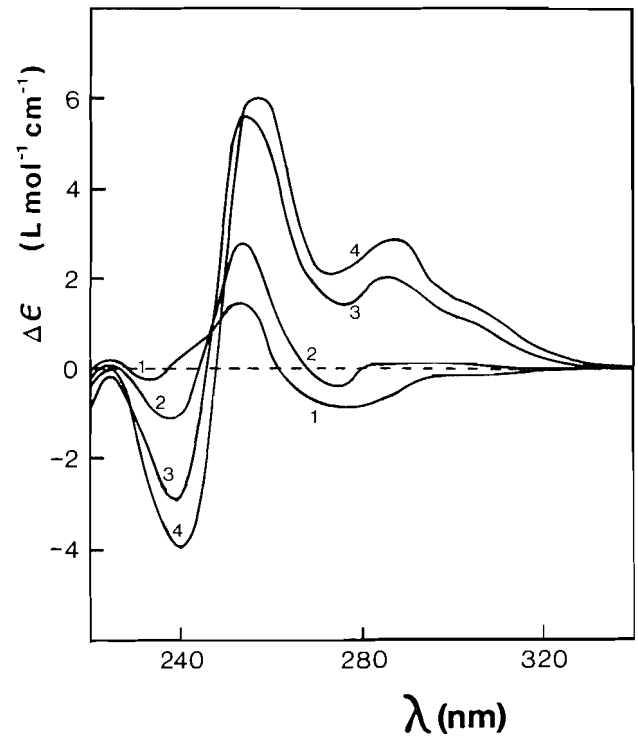

FIG. 5. Spectre de dichroïsme circulaire du poly(I) en présence de diverses concentrations de (dien)Pd(II). Conditions : poly(I) 8,02 × 10^{-5} M, NaCl 1,0 × 10^{-4} M, $NaClO_4$ 0,20 M, pH 7. r = [[(dien)PdCl]Cl]/[poly(I)] = (1) 0, (2) 0,1, (3) 0,3, (4) 0,5.

concentrations plus basses en métal (3,0 × 10^{-5} M). Ackermann et coll. ont déjà suggéré que la formation de la multiple hélice du poly(I) était due principalement à la diminution des répulsions électrostatiques entre les brins à force ionique élevée (22). De plus, comme la fixation du (dien)Pd(II) en N7 accroît l'acidité du proton en N1 pour l'inosine (6, 8), un effet similaire avec le poly(I) contribuerait à la stabilisation des ponts hydrogène N1—H···O6.

La stabilisation de la multiple hélice est possible avec des ions métalliques bivalents possédant une affinité reconnue pour le groupe phosphate, tels Mg^{2+} et Ca^{2+} (24). Il y a peu d'exemples similaires impliquant un métal qui se fixe préférentiellement aux bases nucléiques. L'ion Ag^+ peut conduire à la formation d'une multiple hélice avec le poly(I) (25). Cependant, cette structure est formée à l'aide de ponts interchaîne, avec l'ion Ag^+ lié simultanément aux sites N1 et O6 de deux hypoxanthines. Un tel complexe est impossible avec le (dien)Pd(II) possédant un seul groupe labile.

Lors de l'étude de l'interaction du poly(I)·poly(C) et du poly(I) avec le (dien)Pt(II), une autre hypothèse a été avancée qui implique des ponts hydrogène entre les groupes amino du dien et les sites N7 des bases hypoxanthines voisines du site de complexation du métal (26). Ces ponts hydrogène contribueraient à la stabilisation du poly(I)·poly(C) et existeraient aussi dans le cas du poly(I), bien que le degré de structuration ne soit pas quantifiable. Bien que de telles interactions puissent être présentes, nous croyons que les facteurs de type électrostatique jouent un rôle prédominant, tel que démontré précédemment lors de l'étude du système (dien)Pd(II)–poly(I)·poly(C) (17).

Les spectres de dichroïsme circulaire du poly(I) libre et en présence de (dien)Pd(II) sont représentés à la figure 5. Le spectre du poly(I) est relativement peu intense. L'addition du

Can. J. Chem. Downloaded from www.nrcresearchpress.com by 213.222.148.141 on 09/07/12
For personal use only.

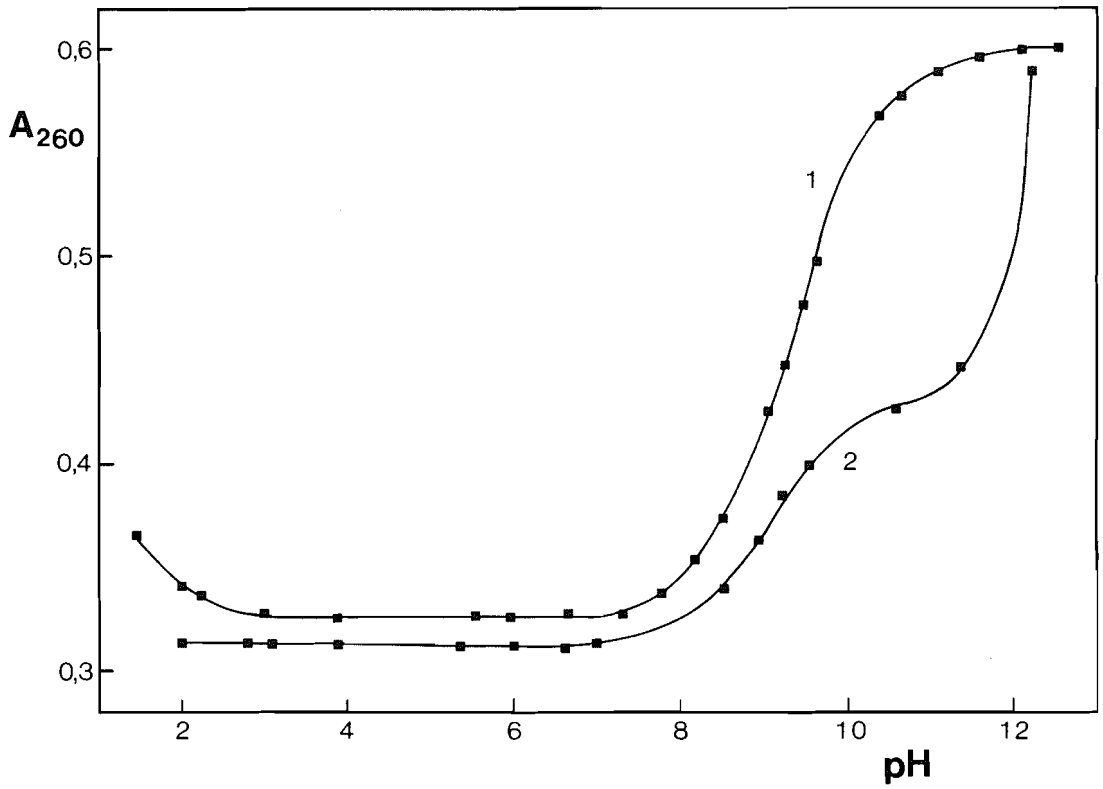

FIG. 6. Influence du pH sur l'absorbance du poly(I) libre (1) et du complexe (dien)Pd(II)–poly(I) (2). Conditions : (1) poly(I) $5{,}04 \times 10^{-5}$ M; (2) poly(I) $5{,}04 \times 10^{-5}$ M, [(dien)PdCl]Cl $2{,}50 \times 10^{-5}$ M. Dans les deux cas : $NaClO_4$ 0,20 M.

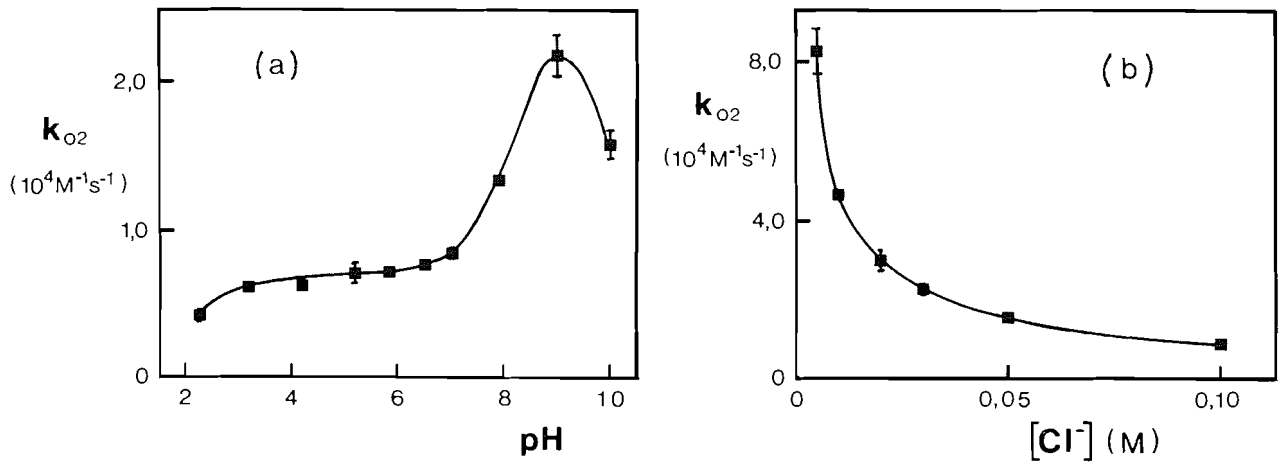

FIG. 7. Influence du pH (*a*) et de la concentration en ion chlorure (*b*) sur la constante de vitesse d'ordre 2 de la réaction du (dien)Pd(II) avec le poly(I). Conditions : (*a*) poly(I) $3{,}08 \times 10^{-5}$ M, [(dien)PdCl]Cl $1{,}00 \times 10^{-5}$ M, NaCl 0,10 M, $NaClO_4$ 0,10 M; (*b*) poly(I) $3{,}07 \times 10^{-5}$ M, [(dien)PdCl]Cl $1{,}00 \times 10^{-5}$ M, force ionique constante (0,20 M NaCl + $NaClO_4$), pH 7.

complexe de Pd(II) modifie profondément le spectre et accroît l'intensité des bandes. Un tel accroissement de l'intensité peut être attribué à la formation d'une structure hélicoïdale ordonnée. La forme de ce spectre est différente cependant de celles généralement attribuées à la multiple hélice du poly(I) à force ionique élevée ou à basse température (19, 20). En particulier, la bande négative vers 280 nm pour le poly(I) libre est remplacée par une bande positive en présence du (dien)Pd(II). Une bande négative, absente dans le cas de la multiple hélice du poly(I) libre, est aussi rencontrée vers 240 nm. Ces résultats suggèrent, pour le complexe poly(I)–Pd(dien), une géométrie différente de celle de la multiple hélice du poly(I). Une inversion de la bande positive, lors de l'addition de complexes de Pt(II), a déjà été remarquée (27). Cette inversion a été attribuée à une modification de l'empilement des bases et de la structure secondaire du polymère lors de la fixation du métal aux bases nucléiques.

La figure 6 illustre l'influence du pH sur l'absorbance à 260 nm du poly(I) et de son complexe avec le (dien)Pd(II). Pour le polynucléotide libre, la déprotonation du site N1 cause une importante augmentation de l'absorbance à pH $> 7{,}5$, correspondant à un pK_a de 9,3. Un début de transition à pH < 3 est aussi visible, attribué à la protonation du site N7 dont le pK_a est voisin de 1.

La valeur de l'absorbance à 260 nm est légèrement plus faible en présence du complexe de palladium. Deux transitions sont maintenant observées en milieu alcalin. La première, possédant un pK_a apparent de 9,2, correspond probablement à la déproto-

Can. J. Chem. Downloaded from www.nrcresearchpress.com by 213.222.148.141 on 09/07/12
For personal use only.

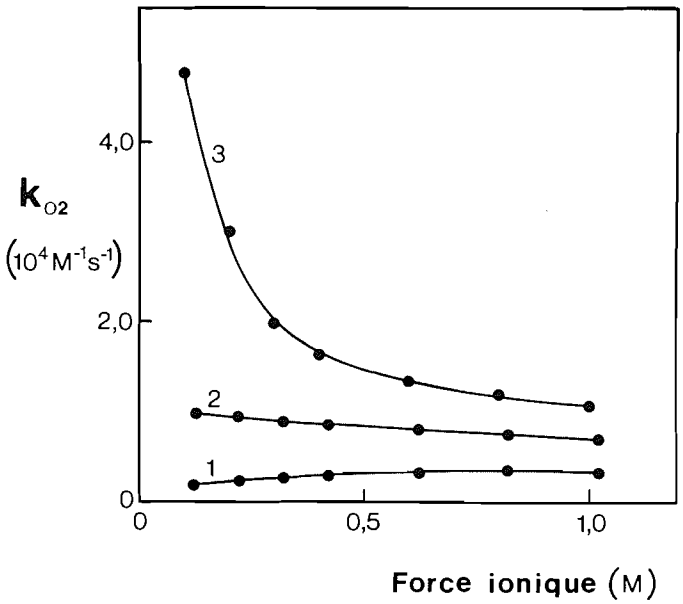

FIG. 8. Influence de la force ionique sur la constante de vitesse d'ordre 2 de la réaction du (dien)Pd(II) avec l'inosine (1), IMP (2) et poly(I) (3). Conditions : (1) inosine $2,5 \times 10^{-3}$ M, [(dien)PdCl]Cl $2,5 \times 10^{-4}$ M; (2) IMP $2,5 \times 10^{-3}$ M, [(dien)PdCl]Cl $2,5 \times 10^{-4}$ M; (3) poly(I) $3,10 \times 10^{-5}$ M, [(dien)PdCl]Cl $1,0 \times 10^{-5}$ M. Dans les trois cas : NaCl 0,020 M, pH 7. La force ionique a été ajustée par addition de $NaClO_4$.

nation des sites N1 des bases hypoxanthine non-complexées par le palladium. À pH > 11, une augmentation abrupte et importante de l'absorbance est aussi observée. Cette transformation est irréversible et très lente, nécessitant au minimum 3 h. Le spectre de la solution ramenée à pH 7 correspond à celui du complexe (dien)Pd–IMP, suggérant l'hydrolyse du poly(I). Le poly(I) libre peut être dégradé en milieu fortement basique (KOH, 0,2 M, 40°C, 4 h) et il a déjà été observé que certains ions métalliques pouvaient conduire à sa dégradation en milieu moins basique (28). Toutefois, contrairement aux ions interagissant fortement au phosphate (tels Mn(II), Zn(II), Cu(II), etc.), un pH relativement élevé est requis dans le cas du palladium.

Cinétique de l'interaction (dien)Pd(II)–poly(I)

La cinétique de la réaction du complexe de Pd(II) avec le poly(I) a été étudiée en fonction du pH, de la concentration en ion chlorure et de la force ionique. En plus de la réaction rapide habituelle au site N7, on observe subséquemment des variations d'absorbance lentes. Ces phénomènes lents, qui n'affectent pas la détermination des constantes de vitesse, peuvent être attribués à des réarrangements conformationnels du polymère après la fixation du (dien)Pd(II) ainsi qu'au transfert du complexe Pd–N7 au complexe Pd–N1. Le transfert ou fixation du Pd(II) au groupement phosphate ne devrait pas avoir une influence significative, dû à la faible stabilité par rapport au complexe Pd(II)–N (16).

L'influence du pH sur la constante de vitesse d'ordre deux de la réaction au site N7 du poly(I) (figure 7(*a*)) est très similaire au cas de l'inosine (voir figure 1(*b*)). Les effets observés peuvent donc être attribués aux mêmes facteurs : diminution de la vitesse à pH < 3, due à la protonation du site N7, et augmentation de la constante de vitesse à pH > 7, due à la contribution du site N1 déprotoné, suivie d'une diminution à pH > 9 attribuable à la présence du complexe $(dien)Pd(OH)^+$ peu réactif. Il est à noter que le maximum de réactivité se situe aux environs de pH 9, tout comme dans le cas de l'inosine. L'inhibition par l'ion chlorure à pH 7 est aussi observée avec le poly(I) (figure 7(*b*)). La constante de vitesse en l'absence d'ion Cl^- ajouté est très élevée, $k_{02} = 4,1 \times 10^5 M^{-1} s^{-1}$ (non-représenté sur la figure). Le comportement est identique à celui de l'inosine et des autres systèmes étudiés (16) et indique que le mécanisme général est le même dans tous les cas.

L'influence de la force ionique est représentée à la figure 8 pour les réactions du (dien)Pd(II) avec le poly(I), l'IMP est l'inosine. Le poly(I) réagit beaucoup plus rapidement avec les complexes de Pd(II) à faible force ionique, dû au champ électrostatique fort de ce polyélectrolyte. La vitesse de cette réaction est, de plus, fortement influencée par la force ionique de la solution, à cause de l'effet d'écran et de la condensation des ions autour du polymère, facteurs très importants pour un polyélectrolyte. La grande accélération, en passant de l'inosine à l'IMP, est attribuée à la proximité du site N7 et du groupe phosphate dans la conformation *anti* favorisée de l'IMP (3). Ceci conduit à un effet catalytique plus important du phosphate dans ce cas que dans le cas du CMP (16).

Remerciements

Nous tenons à remercier le Conseil de recherches en sciences naturelles et en génie du Canada et le Fonds pour la formation de chercheurs et l'aide à la recherche du Québec pour l'aide financière et les bourses d'études supérieures (R.M.) accordées.

1. L. G. MARZILLI. Prog. Inorg. Chem. **23**, 255 (1977).
2. R. W. GELLERT et R. BAU. Met. Ions Biol. Syst. **8**, 1 (1979).
3. R. B. MARTIN et Y. H. MARIAM. Met. Ions Biol. Syst. **8**, 57 (1979).
4. J. K. BARTON et S. J. LIPPARD. Met. Ions Biol. **1**, 31 (1980).
5. G. Y. H. CHU et R. S. TOBIAS. J. Am. Chem. Soc. **98**, 2641 (1976).
6. K. H. SCHELLER, V. SCHELLER-KRATTIGER et R. B. MARTIN. J. Am. Chem. Soc. **103**, 6833 (1981).
7. U. K. HÄRING et R. B. MARTIN. Inorg. Chim. Acta, **80**, 1 (1983).
8. R. B. MARTIN. ACS Symp. Ser. **209**, 231 (1983).
9. S.-H. KIM et R. B. MARTIN. Inorg. Chim. Acta, **91**, 11 (1984).
10. G. PNEUMATIKAKIS, N. HADJILIADIS et T. THEOPHANIDES. Inorg. Chem. **17**, 915 (1978).
11. G. PNEUMATIKAKIS. Inorg. Chim. Acta, **66**, 131 (1982).
12. J.-Y. SÉGUIN et M. ZADOR. Inorg. Chim. Acta, **20**, 203 (1976).
13. F. D. ROCHON, P.-C. KONG, B. COULOMBE et R. MELANSON. Can. J. Chem. **58**, 381 (1980).
14. I. SOVAGO et R. B. MARTIN. Inorg. Chem. **19**, 2868 (1980).
15. W. KADIMA et M. ZADOR. Inorg. Chim. Acta, **78**, 97 (1983).
16. R. MÉNARD, M. LACHAPELLE et M. ZADOR. Biophys. Chem. **20**, 29 (1984).
17. R. MÉNARD et M. ZADOR. Inorg. Chim. Acta, **123**, L23 (1986).
18. R. MÉNARD, M. T. PHAN VIET et M. ZADOR. Inorg. Chim. Acta, **136**, 25 (1987).
19. D. THIELE et W. GUSCHLBAUER. Biophysik, **9**, 261 (1973).
20. J. C. MAURIZOT et G. BOUBAULT. Biochimie, **55**, 1209 (1973).
21. A. RICH. Biochim. Biophys. Acta, **29**, 502 (1958).
22. H.-J. HINZ, W. HAAR et T. ACKERMANN. Biopolymers, **9**, 923 (1970).
23. C. H. CHOU, G. J. THOMAS, JR., S. ARNOTT et P. J. CAMPBELL SMITH. Nucleic Acids Res. **4**, 2407 (1977).
24. Y. A. SHIN. Biopolymers, **12**, 2459 (1973).
25. Y. A. SHIN et G. L. EICHHORN. Biopolymers, **19**, 539 (1980).
26. D. HERMANN, G. V. FAZAKERLEY et W. GUSCHLBAUER. Biopolymers, **23**, 973 (1984).
27. Y. A. SHIN et G. L. EICHHORN. Biopolymers, **16**, 225 (1977).
28. J. J. BUTZOW et G. L. EICHHORN. Biopolymers, **3**, 95 (1965).

Can. J. Chem. Downloaded from www.nrcresearchpress.com by 213.222.148.141 on 09/07/12
For personal use only.

An unlikely coincidence in coupled ^{13}C nuclear magnetic resonance spectra. ^{2}J(C,H) in 2,6-dichlorotoluene and related molecules

TED SCHAEFER AND JAMES PEELING
Department of Chemistry, University of Manitoba, Winnipeg, Man., Canada R3T 2N2

Received July 21, 1987

TED SCHAEFER and JAMES PEELING. Can. J. Chem. **66**, 184 (1988).

Although as many as 13 peaks are observable in each half of the ^{13}C nuclear magnetic resonance spectrum of C-4 in 2,6-dichlorotoluene at 22.6 MHz, the iterative analysis yields an incorrect value of ^{2}J(C,H). Theoretical spectra for two values of this coupling constant are essentially identical under normal linewidth conditions. At 75.5 MHz, the ^{13}C spectrum displays most of the 48 peaks expected for the X part of an AB_2XR_3 spectrum, yielding the correct choice for ^{2}J(C,H). The theoretical spectrum at 125 MHz is similar to that at 22.6 MHz but only for the correct ^{2}J(C,H). Correct values of ^{2}J(C-4,H) are given for the 2,6-dichloro derivatives of toluene, ethylbenzene, benzyl alcohol, benzyl bromide, and chloride; these were given incorrectly previously.

TED SCHAEFER et JAMES PEELING. Can. J. Chem. **66**, 184 (1988).

Même si on peut observer jusqu'à 13 bandes dans chacune des moitiés du spectre en résonance magnétique nucléaire ^{13}C du C-4 du dichloro-2,6 toluène mesuré à 22,6 MHz, l'analyse itérative conduit à une valeur incorrecte pour la constante ^{2}J(C,H). Les spectres théoriques pour deux valeurs de cette constante de couplage sont essentiellement identiques dans les conditions normales de largeur de raies. À 75,5 MHz, le spectre du ^{13}C comporte la plupart des 48 bandes que l'on peut attendre pour la partie X d'un spectre AB_2XR_3 et il conduit à un choix correct pour la valeur de la constante ^{2}J(C,H). Le spectre théorique à 125 MHz est semblable à celui à 22,6 MHz, mais uniquement pour la valeur correcte de ^{2}J(C,H). Les valeurs correctes pour ^{2}J(C-4,H) sont rapportées pour les dérivés dichloro-2,6 du toluène, de l'éthylbenzène, de l'alcool benzylique et des chlorure et bromure de benzyle; les valeurs rapportées antérieurement n'étaient pas correctes.

[Traduit par la revue]

Can. J. Chem. Downloaded from www.nrcresearchpress.com by 213.222.148.141 on 09/07/12
For personal use only.

Introduction

The analysis of second order or tightly coupled high resolution nuclear magnetic resonance spectra is generally considered to be straightforward (1), although it is probable that analyses of high precision are not as common as sometimes assumed in the deduction of molecular properties from isotropic chemical shifts and spin–spin coupling constants. The complexity of ^{1}H nmr spectra at relatively low magnetic fields is often such that a precise, or even an approximate, analysis is impractical. In a proton-coupled ^{13}C nmr spectrum the so-called second-order effects arise because, while the ^{13}C nucleus is an X nucleus in the sense that its chemical shift is far removed from the chemical shifts of the protons, the protons are tightly coupled. These effects are often considered a nuisance both in one- and two-dimensional spectra. Recipes (2, 3) have been given for their amelioration, one being the use of high magnetic fields. In principle, of course, a first-order spectrum will be observed if the spectrometer frequency is sufficiently high. It does not follow, however, that the ^{13}C nmr spectrum of a particular ^{13}C nucleus in a molecule will be most informative at highest field.

If second-order effects in ^{13}C nmr are treated as informative phenomena, then, as shown by Jakobsen and co-workers (4, 5) and by Ernst *et al.* (6), for example, both the signs and magnitudes of relatively small proton–carbon coupling constants, J(C,H), are extractable. This conclusion is as expected, particularly for spectra of the type ABC...X, where ABC... represents the protons and X the ^{13}C nucleus.

A few years ago, a paper from this laboratory reported (7) on the conformational applications of the five-bond coupling constants between protons on the side chain and the C-4 or *para* ^{13}C nucleus in toluene derivatives. The symmetries of the molecules entailed the analysis of AB_2XR_n (n = 1–3) spectra. For example, for **1** the analyses of spectra, recorded at 22.63 MHz for ^{13}C and at 90.02 MHz for ^{1}H, also yield ^{2}J(C,H), and these were tabulated (7) but not used in the discussion. ^{2}J(C,H) varies between roughly −5 and +5 Hz in benzene derivatives (6, 8, 9). For monosubstituted benzenes, correlations of ^{2}J with substituent electronegativities or with Hammett σ constants exist (6, 10). In polysubstituted benzene derivatives, ^{2}J(C,H) is less easily predicted. Theoretical values (6) are unreliable.

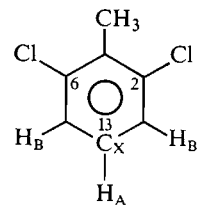

1

In 2,6-dichlorobenzene, ^{2}J(C-4,H) is 0.67 Hz (11), while it is 1.07 Hz in toluene (4). ^{2}J(C,H) in benzene is reported as 1.15 Hz (4), so that a simple additivity scheme implies ^{2}J(C-4,H) as about 0.6 Hz in 2,6-dichlorotoluene, **1**. Indeed, the iterative analysis (7) gives ^{2}J(C-4,H) as 0.627 ± 0.006 Hz. This number is wildly incorrect, as illustrated below.

Results and discussion

Figure 1 displays half of the ^{13}C nmr spectrum of C-4 for **1** at 22.63 MHz. As discussed in the caption to this figure, the two halves have the same appearance at this frequency. The two theoretical spectra at 22.63 MHz in Fig. 1 assume different values for ^{2}J(C-4,H), 0.627 and 0.271 Hz. All other spectral parameters are identical for the two simulations, as are the appearances of the latter. The X region of an AB_2XR_3 spectrum can display 48 peaks, that is, 24 in each half of the spectrum. This result is easily ascertainable from the theoretical structure (12) of the simpler AB_2X arrangement. Only 13 discernible peaks appeared in the half-spectrum in Fig. 1, yet the analysis was deemed reliable. ^{5}J(C-4,H), the desired parameter (7), is 0.89 Hz, as expected from its value in toluene (4). Fortunately,

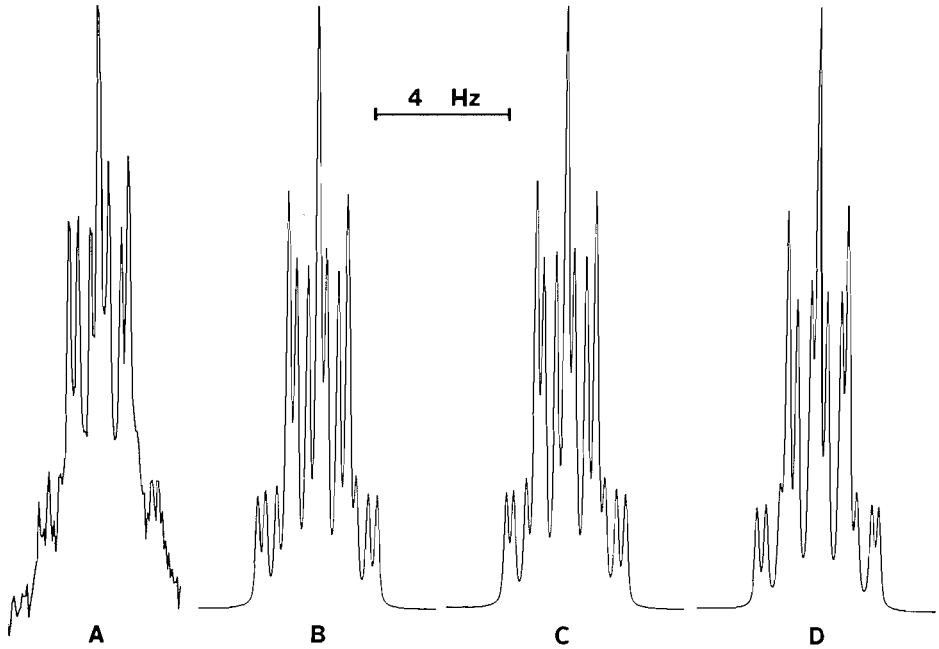

FIG. 1. The high-frequency half of the ^{13}C nmr spectrum of C-4 in 2,6-dichlorotoluene is shown in (A) for a relatively dilute solution described in Fig. 2. The spectrum was obtained with the INEPT sequence and is not of high quality. The low-frequency part of the spectrum has essentially the same appearance, also displaying evidence for 13 peaks. The computed spectra with ^2J(C,H) as 0.627 and 0.271 Hz are also shown in (B) and (C), respectively, and use the parameters indicated in Fig. 2, except for the internal proton chemical shifts, of course. The computed spectrum at 125 MHz (500-MHz spectrum) is displayed in (D) for the correct value of ^2J(C,H), 0.27 Hz. This spectrum alters markedly if ^2J(C,H) is set at 0.627 Hz.

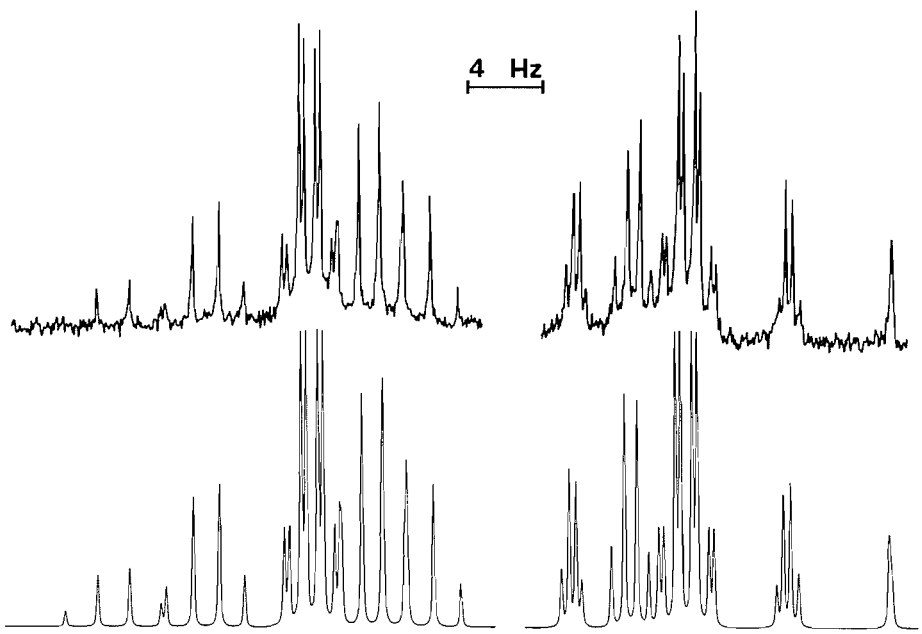

FIG. 2. The observed and computed ^{13}C nmr spectrum of C-4 at 75.477 MHz of 2,6-dichlorotoluene at 300 K. The solution consists of 20% v/v of the toluene in benzene-d_6, which itself contains 20% v/v of acetone-d_6. The difference between the chemical shifts of the protons in the AB_2XR_3 spectrum is 86.1 Hz, J_{AB} is 8.07 Hz, J_{AR} is -0.61 Hz, and J_{BR} is 0.43 Hz. ^1J(C,H), ^2J(C,H), and ^5J(C,H) are 164.92, 0.27, and 0.89 Hz, respectively. Each half of the spectrum consists, in principle, of 6 quartets. The half on the right at low frequency (high field) displays all six quartets because the outermost broad peak is a collapsed quartet. The spectrum was accumulated without polarization transfer procedures, the linewidth at half height is 0.15 Hz in the computed spectrum, and no resolution enhancement was done on the experimental spectrum.

this number does not change in the iterative analysis of the ^{13}C nmr spectrum of C-4 at 75.477 MHz in Fig. 2.

In this figure most of the 48 peaks are observable if it is noted that, in the part at low frequency, the broad band at the right is a collapsed quartet. The signs of ^2J(C,H) and ^3J(H,H) relative to ^1J(C,H) follow from the spectrum, as can be shown easily by simulation. In fact, the relative sign of ^5J(C-4,H) also follows. Note that ^2J(C,H) is unequivocally deduced as $+0.27$ Hz.

The ^{13}C nmr spectrum of C-3 in **1** is displayed in Fig. 3, corresponding to the X part of an $ABCXR_3$ pattern. The

Can. J. Chem. Downloaded from www.nrcresearchpress.com by 213.222.148.141 on 09/07/12
For personal use only.

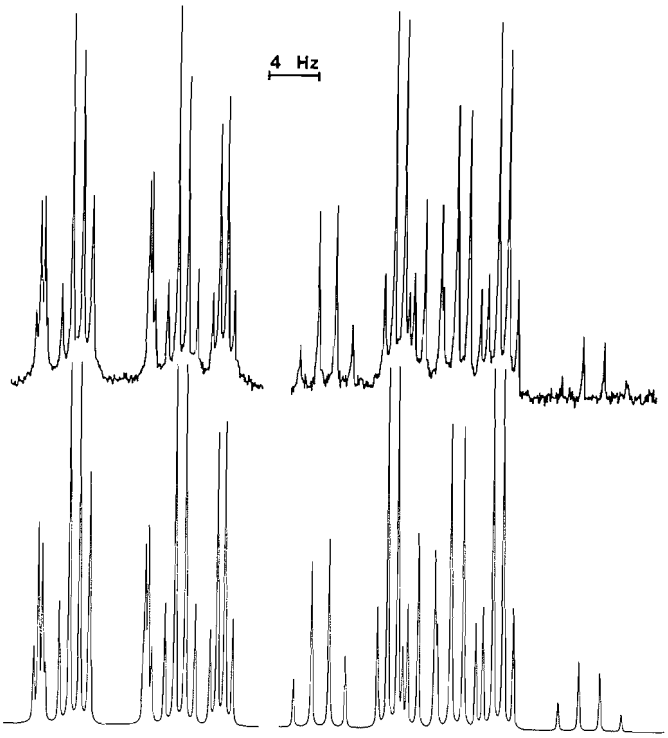

FIG. 3. The ^{13}C nmr spectrum of C-3 in 2,6-dichlorotoluene at 75.477 MHz is compared with the computed spectrum. Most of the peaks of the 12 quartets are apparent. $^1J(C,H)$, $^2J(C,H)$, $^3J(C,H)$, and $^4J(C,H)$ are 166.67, 1.27, 8.13, and −0.78 Hz, respectively. The computed peak widths are 0.15 Hz. The $^{13}C,^{12}C$ isotope shift on H-3, relative to H-5, is 0.37 Hz at 300.135 MHz (shift to low frequency, high field). The other ^1H nmr parameters are the same as for C-4 in Fig. 2, except that $^4J(H-3,H-5)$ is 1.30 Hz. The low-frequency half of the spectrum occurs on the right.

chemical shifts of H-3 and H-5 are not the same, of course, H-5 being more shielded by 0.37 Hz or 1.2 ppb. Again, the spectrum is sensitive to the relative signs of the coupling constants, $^4J(C-3,H)$ being −0.78 Hz, compared to −0.39 Hz in toluene (4). In the ^{13}C nmr spectrum at 22.63 MHz (not shown) this fact is not apparent.

Returning to Fig. 1, the computed ^{13}C nmr spectra of C-4 of **1** is also shown at a ^{13}C resonance frequency of 125 MHz. The number of peaks is reduced relative to those in the spectrum at 75.477 MHz, but the spectra at 125 MHz would allow a decision between the two values of $^2J(C,H)$. Whether the correct value would be obtained from an experimental spectrum is another matter.

Without going into great detail, the reason for the spectral complexity of the C-4 spectrum at 75.477 MHz in Fig. 2 is closely connected to the fact that, at this field intensity, twice the chemical shift difference between the *meta* and *para* protons of **1** is near $^1J(C-4,H)$. Such spectral coincidences have been described for the ABX spectrum (2).

In conclusion, the $^2J(C,H)$ values for C-4 in the 2,6-dichloro derivatives of toluene, ethylbenzene, benzyl bromide, benzyl chloride, and benzyl alcohol are 0.27, 0.31, 0.26, 0.31, and 0.31 Hz, respectively, as extracted from the ^{13}C nmr spectra at 75.477 MHz and, of course, from the ^1H nmr data at 300.135 MHz on the *same* nmr samples. Consequently, the reported $^2J(C-4,H)$, all near 0.6 Hz (7), are incorrect.

Experimental

The procedure for the accumulation of the ^{13}C nmr spectra at 22.63 MHz of the compound above has been described (7). The nmr samples described there (7) were later also used to accumulate ^{13}C and ^1H nmr spectra on an AM300 Bruker spectrometer at 300 K. The ^1H nmr spectra were recorded with the decoupler coil on the 10-mm ^{13}C probe. For 2,6-dichlorotoluene, the INEPT sequences (13) were not employed. Instead, 400 FIDs were stored in 32 K of memory, with acquisition times of 21.4 s and a spectral window of 766 Hz. No resolution enhancement was used for the spectra in Fig. 2, which had peak widths of about 0.15 Hz.

Iterative spectral analyses were performed with the computer program NUMARIT (14), as modified by R. Sebastian in this laboratory. Standard deviations of the spectral parameters were computed as 0.01 Hz or less and the rms errors in the analyses were 0.02 Hz or less.

Acknowledgements

We are grateful to Rudy Sebastian for some spectral simulations and other help and to the Natural Sciences and Engineering Research Council of Canada for financial assistance.

1. R. J. ABRAHAM. Analysis of high resolution nmr spectra. Elsevier, Amsterdam. 1971.
2. A. J. JONES, G. A. JENKINS, and M. L. HEFFERNAN. Aust. J. Chem. **33**, 1275 (1980).
3. A. W. DOUGLAS and M. SHAPIRO. Org. Magn. Reson. **14**, 38 (1980).
4. M. HANSEN and H. J. JAKOBSEN. J. Magn. Reson. **10**, 74 (1973); **20**, 520 (1975).
5. M. HANSEN, R. S. HANSEN, and H. J. JAKOBSEN. J. Magn. Reson. **13**, 386 (1974).
6. L. ERNST, V. WRAY, V. A. CHERTKOV, and N. M. SERGEYEV. J. Magn. Reson. **25**, 123 (1977).
7. T. SCHAEFER, J. PEELING, and G. H. PENNER. Can. J. Chem. **61**, 2773 (1983).
8. P. E. HANSEN. Prog. Nucl. Magn. Reson. Spectrosc. **14**, 175 (1981).
9. D. F. EWING. Annu. Rep. NMR Spectrosc. **6**, 389 (1975).
10. A. R. TARPLEY and J. H. GOLDSTEIN. J. Phys. Chem. **76**, 515 (1972).
11. A. R. TARPLEY and J. H. GOLDSTEIN. J. Mol. Spectrosc. **39**, 275 (1971).
12. P. DIEHL and J. A. POPLE. Mol. Phys. **3**, 557 (1960).
13. G. A. MORRIS and R. J. FREEMAN. J. Am. Chem. Soc. **101**, 760 (1979).
14. A. R. QUIRT and J. S. MARTIN. J. Magn. Reson. **5**, 318 (1971); J. S. MARTIN, A. R. QUIRT, and K. E. WORVILL. The NMR program library, Daresbury Laboratory, Daresbury, U.K.

Can. J. Chem. Downloaded from www.nrcresearchpress.com by 213.222.148.141 on 09/07/12
For personal use only.

Synthesis and biological activity of (*S*)-2′-fluorodaunorubicin

HANS H. BAER AND LISA SIEMSEN

Ottawa–Carleton Institute for Research and Graduate Studies in Chemistry, Department of Chemistry, University of Ottawa, Ottawa, Ont., Canada K1N 9B4

Received June 22, 1987

HANS H. BAER and LISA SIEMSEN. Can. J. Chem. **66**, 187 (1988).

Methyl 3-amino-2,3,6-trideoxy-2-fluoro-β-L-galactopyranoside was hydrolyzed to the free sugar, (*S*)-2-fluorodaunosamine hydrochloride, which was converted into the α,β-1,4-di-*O*-acetyl-*N*-trifluoroacetyl derivative and thence into the corresponding glycosyl bromide. The latter was condensed with daunomycinone, and the product was deprotected to give the title compound. The fluoroanthracycline displayed significant cytotoxicity against a number of tumor cell lines in vitro. Antitumor activity against L1210 murine leukemia in vivo was lower than that of the parent daunorubicin, but toxicity appeared to be reduced.

HANS H. BAER et LISA SIEMSEN. Can. J. Chem. **66**, 187 (1988).

On a hydrolysé l'amino-3 tridésoxy-2,3,6 fluoro-2 β-L-galactopyrannoside de méthyle en sucre libre, le chlorhydrate de la fluoro-2-(*S*) daunosamine, que l'on a transformé en dérivé di-*O*-acétyl-α,β-1,4 *N*-trifluoroacétyle et finalement en bromure de glycosyle correspondant. On a condensé ce dernier avec la daunomycinone et on a déprotégé le produit pour obtenir le composé mentionné dans le titre. La fluoroanthracycline présente une cytotoxicité in vitro importante contre un certain nombre de lignes de cellules tumorales. L'activité antitumorale in vivo contre les cellules de murine leucémique L1210 est plus faible que celle de la daunorubicine parente; toutefois, la toxicité semble être réduite.

[Traduit par la revue]

Introduction

In the course of a project aimed at procuring modified anthracycline antitumor agents that are substituted by fluorine in the amino sugar moiety we have described (1) a synthesis of methyl 3-amino-2,3,6-trideoxy-2-fluoro-β-L-galactopyranoside (**1**, methyl (*S*)-2-fluoro-β-L-daunosaminide). We now wish to record the coupling of that carbohydrate component with daunomycinone (**6**), which afforded (*S*)-2′-fluorodaunorubicin hydrochloride (**11**). While this work was in progress, various derivatives of **1** were also obtained elsewhere (2–5), and a coupling reaction with **6** was described (5), similar to ours in principle but different in detail.

Results and discussion

Although hydrolysis of the 2-fluoro glycoside **1** predictably was quite difficult, it succeeded by use of 4 M hydrochloric acid (6 h, reflux) and gave (*S*)-2-fluorodaunosamine hydrochloride (**2**) in 90% yield. Trifluoroacetylation of **2**, followed by methanolysis of the crude product to effect selective *O*-deacylation, furnished the trifluoroacetamido sugar **3** in yields of ~70–90%. Acetylation of **3** gave the 1,4-diacetate **4** as a crystalline mixture of anomers (93%) from which was obtained, by fractional crystallization, the pure α-anomer and sublimable, mixed crystals of the anomers (α:β = 2:1). Treatment of **4** in dichloromethane with hydrogen bromide in acetic acid generated the bromo sugar **5**, a reactive compound that was too unstable for storage and was therefore used without delay as a glycosyl donor for the subsequent operation. However, a sample of **5** was crystallized and characterized by its ^{1}H nmr spectrum; $J_{1,2}$ = 3.9 Hz indicated α-L stereochemistry. For chemical characterization, a sample was allowed to react with methanol in the presence of silver triflate, and the product was shown by its ^{1}H nmr spectrum to be an anomeric mixture of methyl glycosides, proving the bromide to act as a glycosyl donor (see Experimental).

For the condensation of **5** with daunomycinone (**6**) we tried several of the procedures commonly employed in anthracycline synthesis (6), but were unable to achieve high α-selectivity. Best results were obtained when **6** and 1.2 mol equivalents of **5** were allowed to react in boiling toluene in the presence of mercuric cyanide and mercuric bromide; chromatographic isolation then gave the desired α-glycoside **7** in 41%, and its β-anomer **8** in 29% yield (based on **6**). Treatment of **5** with 1.75 mol equiv. of **6** in 1:1 dichloromethane–nitromethane solution in the presence of silver triflate proved less satisfactory; **7** and **8** could be isolated in yields (based on **5**) of 15 and 16.5% only.

Zemplén *O*-deacetylation of **7** gave crystalline (*S*)-2′-fluoro-*N*-trifluoroacetyldaunorubicin (**9**), which was then *N*-deacylated with aqueous barium hydroxide at room temperature to furnish the target compound as the free base **10**, obtained in the form of dark-red microscopic needles in 35% overall yield based on the amount of aglycon used. The hydrochloride **11** crystallized as a (nonhygroscopic) sesquihydrate showing strong dextrorotation, $[\alpha]_D$ +218° (in methanol). The product obtained by Castillon *et al.* (5), named 2′-*C*-fluoro-β-daunomycin, was isolated as a highly hygroscopic hydrochloride monohydrate that was accorded formula **11** but showed $[\alpha]_D$ −37° (in methanol).[1]

Biological activity

Tests to evaluate antitumor activity of **11** in comparison with parent daunorubicin were performed by Bristol–Myers

[1]The authors (5) prepared their compound by silver triflate-promoted condensation of aglycon **6** with the 4-*O*-benzoyl analog of **5** (compound **17** in ref. 5, erroneously depicted as the β-anomer), followed by sequential deacylation at positions 4′ and 3′. The reported (5) ^{1}H nmr data are in fair agreement with our values for **11**, but the reason for the discrepancy in optical rotation is unclear. The molecular rotation of our product **11**, $[M]_D$ +133 000°, is close to that of parent daunorubicin hydrochloride ($[M]_D$ +143 000°, from $[\alpha]_D$ +253° (7)) and to that of adriamycin hydrochloride ($[M]_D$ +144 000°, from $[\alpha]_D$ +248° (8)). In this series of aminoglycoside hydrochlorides, β-L anomers exhibit *higher* dextrorotation than their α-L counterparts. Although values for the β-anomers (9) of the daunorubicin and adriamycin hydrochlorides have apparently not been published, for the latter compound a value of $[\alpha]_D$ +472° (*c* 0.07, methanol) was communicated to us privately by Dr. S. Penco (Farmitalia Carlo Erba, Milan). Similarly, 4′-epi-daunorubicin hydrochloride and its β-anomer show $[\alpha]_D$ +314° and +357°, respectively (10), and their 6′-hydroxy analogs show $[\alpha]_D$ +388° and +412°, respectively (11).

Can. J. Chem. Downloaded from www.nrcresearchpress.com by 213.222.148.141 on 09/07/12
For personal use only.

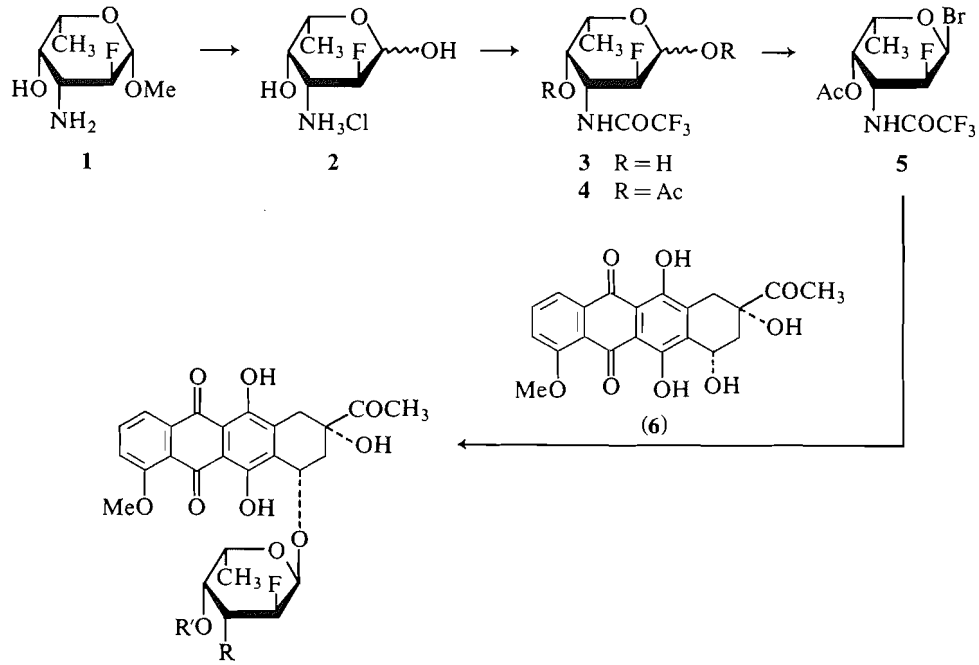

1 **2** **3** R = H, **4** R = Ac **5** **(6)**

7 R = $NHCOCF_3$, R′ = Ac
8 as for **7**, but inverted at C-1′
9 R = $NHCOCF_3$, R′ = H
10 R = NH_2, R′ = H
11 R = NH_3Cl, R′ = H

Can. J. Chem. Downloaded from www.nrcresearchpress.com by 213.222.148.141 on 09/07/12
For personal use only.

Company, Wallingford, Connecticut. Although in vitro cytotoxicity tests with mouse melanoma B16-F10 and human colon tumor HCT-116, respectively, indicated a 5- to 8-fold lower potency for **11** than for daunorubicin (IC_{50} = 4.92 and 3.87 μg/mL versus 0.64 and 0.72 μg/mL), the two antibiotics showed comparable potency (IC_{50} = 17.30 vs. 21.40, 10.06 vs. 16.95, and 8.48 vs. 8.00 μg/mL) against the cell lines HCT/VP35, Moser, and SW900 (average values from four test series). Tests in vivo against L1210 murine leukemia in the dose range 0.8–16 mg/kg showed median survival time increases (T/C values) of 117–133% for **11**, whereas daunorubicin gave values of 133–167% in parallel tests with the dose range of 1–12 mg/kg. In subsequent tests compound **11** was dosed as high as 64 mg/kg; at that dose it achieved a maximum T/C of 129%. No toxicity was observed in **11** at the dose levels tested, which considerably exceeded the toxic limit for daunorubicin. Even though antitumor activity was but modest, this point encourages further study and we are currently engaged in the synthesis of similar fluoroanthracyclines for biological evaluation.

Experimental

General preparative and instrumental methods were the same as those previously employed (1). The following solvent combinations (v/v) were used for thin-layer chromatography (tlc) and column chromatography (medium pressure) on silica gel: methanol–chloroform, 1:3 (A) and 1:6 (B); methanol–acetone, 1:1 (C); acetone–dichloromethane, 1:4 (D); and ethyl acetate – hexanes in the proportions 3:1 (E), 3:2 (F), 1:1 (G), 1:2 (H), 1:3 (I), and 1:5 (J). Proton magnetic resonance spectra were taken at 300 MHz, with tetramethylsilane as internal standard. Infrared spectra were taken from Nujol mulls. Optical rotations were measured at ~25°C.

3-Amino-2,3,6-trideoxy-2-fluoro-L-galactose ((S)-2-fluoro-L-daunosamine) hydrochloride (2)

A solution of compound **1** (1) (1.08 g) in 4 M hydrochloric acid (108 mL) was boiled under reflux for 6 h. Complete conversion into the more slowly moving sugar **2** was indicated by tlc (solvent A). The acid was removed by coevaporation with added water, and the residual aqueous solution was decolorized with charcoal and brought to dryness at 35°C, to give **2** as a crystalline solid (1.10 g after drying *in vacuo* over KOH; 90%); mp ~190°C (dec.); $[\alpha]_D$ −70° (*c* 0.9, H_2O) (lit. (3) $[\alpha]_D$ −69.7°); ν_{max}: 3400 (br), 2700–2500 (several weak bands), 1600, 1580, 1530 (strong), 1300–990 (numerous sharp bands), 890, and 740 cm^{-1}. The ^1H nmr revealed the product to be the pure *β-anomer*; δ(DMSO-d_6): 8.45 (bs, 3H, exchangeable, H_3N^+), 7.18 and 5.74 (d, J = 6.7 and 5.9 Hz, exchangeable, 2 OH), 4.67 (td, collapsing to dd on D_2O exchange, $J_{1,F}$ = 3, $J_{1,2} \approx J_{1,OH} \approx$ 7.3 Hz, H-1), 4.40 and 4.23 (2 dd, 0.5H each, $J_{2,F}$ = 51.7, $J_{1,2}$ = 7.8, $J_{2,3}$ = 10.2 Hz, H-2), 3.75 (nm, H-4), 3.72 (q, $J_{5,Me}$ = 6.25, $J_{4,5}$ < 0.5 Hz, H-5), 3.52 (~td, $J_{3,4}$ = 2.4, $J_{2,3}$ = 10, $J_{3,F}$ = 12 Hz, H-3), and 1.12 (d, 3H, J = 6.25 Hz, *C*-Me).

When **2** was recovered from its aqueous solution by *freeze-drying*, it was obtained as a crystalline, 1:1 mixture of anomers; mp 182–185°C (dec.); $[\alpha]_D$ −85° (*c* 1.1, H_2O). The ir spectrum, similar to that of the pure β-anomer, was distinguished by additional, prominent peaks at 1495, 860, 807, and 755 cm^{-1}. The ^1H nmr spectrum, in addition to showing all the β-anomer signals listed above, contained the following set of signals, of equal strength, for the *α-anomer*; δ(DMSO-d_6): 7.00 and 5.69 (d, J = 3.5 and 6 Hz, exchangeable, 2 OH), 5.22 (~t, collapsing to ~d on D_2O exchange, $J_{1,2} \approx J_{1,OH} \approx$ 3.5, $J_{1,F} \approx$ 0.5 Hz, H-1), 4.76 and 4.59 (2 dd, 0.5H each, $J_{2,F}$ = 51, $J_{1,2}$ = 3.5, $J_{2,3}$ = 10.5 Hz, H-2), 4.05 (q, $J_{5,Me}$ = 6.5, $J_{4,5}$ < 0.5 Hz, H-5), 3.82 (nm, H-4), 3.58 (td, similar to, and partially overlapped by, the corresponding signal of the anomer, H-3), and 1.06 (d, 3H, J = 6.5 Hz, *C*-Me). *Anal.* calcd. for $C_6H_{13}ClFNO_3$ (201.5): C 35.76, H 6.50, Cl 17.59; found: C 35.66, H 6.50, Cl 17.71.

2,3,6-Trideoxy-2-fluoro-3-trifluoroacetamido-D-galactose (3)

A suspension of **2** (1.00 g) in dry ether (70 mL) containing triethylamine (0.7 mL) was stirred for 0.5 h, and for a further 2.5 h following the addition of trifluoroacetic anhydride (2.1 mL, 3 mol equiv.). The solution then showed a double spot, R_f ~ 0.8 (tlc, solvent D), for the α,β-ditrifluoroacetate of **3**; a small proportion of suspended

Can. J. Chem. Downloaded from www.nrcresearchpress.com by 213.222.148.141 on 09/07/12
For personal use only.

solid gave a double spot at $R_f \sim 0.25$ and proved to be α,β-**3**. (Starting **2** had R_f 0). The mixture was evaporated, with added portions of ether, to give a yellow residue that was dissolved in dry methanol (50 mL). After 2 days at room temperature, all of the diester had been methanolized to α,β-**3** (tlc). The solvent was removed and a solution of the residue in EtOAc was washed once with a small amount of ice water, dried (Na_2SO_4), and evaporated. Trituration of the material with ether gave crystalline **3** (0.84 g), mp 162–165°C, and chromatographic processing of the mother liquor augmented the yield to 1.015 g (68%); $[\alpha]_D$ −129° (*c* 0.5, acetone). In one experiment (50-mg scale), direct crystallization gave a 93% yield of **3**, mp 153–156°C; ν_{max}: 3540, 3400, 1700, 1550 cm^{-1}. Different preparations showed variable anomeric composition, according to ^1H nmr, e.g., α:β ratio ~ 10:1 and 3:2. (The latter sample was a crystalline solvate containing ½ mol of diethyl ether, not removed by drying *in vacuo*; the former sample was solvent free.) The ^1H nmr data (DMSO-d_6; low-field OH and NH resonances removed by D_2O exchange) for the *α-anomer*, δ: 5.17 (~d, $J_{1,2} = 4$, $J_{1,F} \approx 0.5$ Hz, H-1), 4.81 and 4.64 (2 dd, 0.5H each, $J_{1,2} = 4$, $J_{2,3} = 10.6$, $J_{2,F} = 50$ Hz, H-2), 4.30 (m, H-3), 4.06 (qd, $J_{4,5} = 1$, $J_{5,Me} = 7$ Hz, H-5), 3.60 (~nt, H-4), and 1.04 (d, 3H, $J = 7$ Hz, *C*-Me); for the *β-anomer*, δ: 4.64 (m, H-1), 4.50 and 4.33 (2 dd, 0.5H each, $J_{1,2} = 8$, $J_{2,3} = 10$, $J_{2,F} = 51$ Hz, H-2), 4.3 (m, H-3), 3.74 (qd, $J_{4,5} = 1$, $J_{5,Me} = 6.5$ Hz, H-5), 3.56 (~nt, H-4), and 1.09 (d, $J = 6.5$ Hz, *C*-Me). The hemietherate showed a quartet (2H, $J = 6.5$ Hz) at δ 3.37 and a matching triplet that was superposed on the sugar *C*-Me signals for a total intensity of 6H. *Anal.* calcd. for $C_8H_{11}F_4NO_4 \cdot 0.5\ C_4H_{10}O$ (298.2): C 40.27, H 5.41; found: C 40.47, H 5.64.

1,2-Di-O-acetyl-2,3,6-trideoxy-2-fluoro-3-trifluoroacetamido-L-galactose (4)

Compound **3** (1.01 g) was acetylated with acetic anhydride and pyridine (23°C, 1 h), and the crude diacetate **4** (R_f 0.4, tlc with solvent H) was isolated by exhaustive evaporation of added toluene from the mixture. Crystallization from ethyl acetate – hexane gave two crops (670 and 90 mg, mp 165–168 and 161–164°C) of **4**, with the first one representing the pure *α-anomer*, $[\alpha]_D$ −178° (*c* 0.4, $CHCl_3$); ν_{max}: 3300, 1750 (doublet), 1700, 1540 cm^{-1}; δ ($CDCl_3$): 6.41 (d, $J_{1,2} = 3.4$ Hz, H-1), 5.36 (~td, $J_{4,5} = 1.5$, $J_{3,4} \approx J_{4,F} \approx 3.5$ Hz, H-4), 4.86 and 4.69 (2 dd, 0.5H each, $J_{1,2} = 3.4$, $J_{2,3} = 11$, $J_{2,F} = 52$ Hz, H-2), 4.76 (m, H-3), 4.23 (qd, $J_{4,5} = 1.4$, $J_{5,Me} = 6.5$ Hz, H-5), 2.19 and 2.17 (s, 3H each, 2 OAc), and 1.11 (d, 3H, $J = 7$ Hz, *C*-Me).

The mother liquor of crystallization was purified by passage over a column of silica gel with solvent I, to give another crop of **4** (480 mg), for a total yield of 1.24 g (93%). This crop gave a double spot in tlc ($R_f \sim 0.6$, solvent H) and was shown to be an anomer mixture (α:β = 2:1, by ^1H nmr). On heating at 110°C in an oil-pump vacuum for 16 h it sublimed almost without residue, and the sublimate showed unchanged spectral and tlc patterns; mp 130–134°C, $[\alpha]_D$ −138° (*c* 0.6, $CHCl_3$); ^1H nmr ($CDCl_3$) signals attributable to the *β-anomer*, δ: 5.79 (dd, $J_{1,F} = 3.5$, $J_{1,2} = 7.5$ Hz, H-1), 5.30 (td, $J_{4,5} = 1.7$, $J_{3,4} \approx J_{4,F} = 3.3$ Hz, H-4), 4.59 and 4.41 (2 dd, 0.5H each, $J_{1,2} = 7.5$, $J_{2,3} = 10.7$, $J_{2,F} = 54$ Hz, H-2), 4.48 (m, H-3), 3.99 (qd, $J_{4,5} = 1.7$, $J_{5,Me} = 6.5$ Hz, H-5), 2.18 and 2.17 (2 s, 3H each, 2 OAc), and 1.18 (d, 3H, $J = 6.5$ Hz, *C*-Me). *Anal.* calcd. for $C_{12}H_{15}F_4NO_6$ (345.3): C 41.74, H 4.38, N 4.06; found: C 41.33, H 4.54, N 3.98.

4-O-Acetyl-2,3,6-trideoxy-3-trifluoroacetamido-α-L-galactopyranosyl bromide (5)

To a solution of **4** (780 mg) in CH_2Cl_2 (20 mL, distilled from CaH_2) was added 30% hydrogen bromide in acetic acid (17 mL), at room temperature. After 30 min all of the **4** was consumed (tlc), and the mixture was processed by evaporation of the CH_2Cl_2, removal of the acid by coevaporation with added toluene, decolorization of the product with activated carbon, and brief drying *in vacuo* of the syrupy, almost colorless **5** so obtained. The crude **5** was homogeneous in tlc (R_f 0.5, solvent H) except for the presence of trace impurities, and, being rather unstable, it was used without delay for the intended condensation reaction.

For characterization, a sample of the syrup was crystallized from ether–hexane (0°C, overnight), whereby the trace impurities were removed and no change in the R_f value was observed. The crystals were immediately taken to ^1H nmr analysis; δ ($CDCl_3$): 6.59 (d, $J_{1,2} = 3.9$ Hz, H-1), 6.3 (br d, NH), 5.39 (td, $J_{4,5} = 1.25$, $J_{3,4} = J_{F,4} = 3.3$ Hz, H-4), 4.82 (symm. m, 10 lines, width 32 Hz, $J_{3,4} \approx J_{3,NH} \approx 4$, $J_{2,3} \approx 11$, $J_{3,F} \approx 13$ Hz, H-3), 4.73 and 4.57 (2 dd, 0.5H each, $J_{1,2} = 3.9$, $J_{2,3} = 10.8$, $J_{2,F} = 49.9$ Hz, H-2), 4.40 (qdd, $J_{5,Me} = 6.6$ and $J_{4,5} = 1.2$ Hz, with additional splitting due to long-range coupling, H-5), 2.17 (s, 3H, OAc), and 1.17 (d, 3H, $J = 6.6$ Hz, *C*-Me).

A 10-mg sample of **5** was allowed to react with methanol (0.5 mL) in the presence of a few milligrams of silver triflate. After 1 h at 25°C, **5** (R_f 0.5) had been converted into a new product, R_f 0.4 (tlc with solvent H). The mixture was filtered through Celite, which was washed with CH_2Cl_2, and the filtrate was washed once with aqueous $NaHCO_3$ and twice with water, dried (Na_2SO_4), and evaporated. The foamy residue of *methyl glycoside* was passed through a small column of silica gel with solvent J but still failed to crystallize. The eluate contained mainly the β-anomer; δ ($CDCl_3$): 6.3 (br m, NH), 5.29 (nm, H-4), 4.52–4.36 (m, 2.5H, H-1,3, and downfield part of H-2), 4.25 (dd, 0.5H, $J_{1,2} = 7.3$, $J_{2,3} = 10.5$ Hz, H-2, upfield part), 3.85 (qd, $J_{4,5} = 1$, $J_{5,Me} = 6.5$ Hz, H-5), 3.59 (s, 3H, OMe), 2.16 (s, 3H, OAc), and 1.19 (d, 3H, $J = 6.5$ Hz, C-Me). A small *C*-Me doublet at δ 1.11 indicated the presence of some α-anomer (< 10%).

7-O-(4-O-Acetyl-2,3,6-trideoxy-2-fluoro-3-trifluoroacetamido-β-L-galactopyranosyl)-daunomycinone (7) and its β-anomer 8

Procedure A

The syrupy glycosyl bromide (**5**) obtained from 100 mg (0.29 mmol) of diacetate **4** was dissolved in dry toluene (10 mL, distilled from Na), and $HgBr_2$ (200 mg, 2 mol equiv.), $Hg(CN)_2$ (145 mg, 2 mol equiv.), and daunomycinone (**6**; 100 mg, 0.25 mmol) were added. The mixture was boiled under reflux for 5 h, with exclusion of moisture and light. Thin-layer chromatography (solvent F) indicated complete consumption of **5** (R_f 0.9) but incomplete consumption of **6** (R_f 0.2); two ill-separated spots (R_f 0.4–0.5) representing **7** and **8** were seen. The filtered solution was evaporated and the resultant residue dissolved in $CHCl_3$. The solution was washed with water (3×), dried (Na_2SO_4), and evaporated to give a red solid that still contained some inorganic material and was, therefore, triturated with $CHCl_3$ (2 mL). The filtered solution gave 180 mg of product, which was subjected to preparative tlc (triple irrigation with solvent G), furnishing slower moving **7** (71 mg, 41.4%) and faster moving **8** (49 mg, 28.5%).

Compound **7** showed mp 194–196°C (with gradual darkening from 160°C); $[\alpha]_D$ +149°C (*c* 0.6, $CHCl_3$); ν_{max}: 3500, 3300, 1745, 1700, 1615, 1570 cm^{-1}; δ ($CDCl_3$): 8.03, 7.77, and 7.38 (d, t, and d, $J \approx 8$ Hz, H-1,2,3), 6.18 (d, $J_{3',NH} = 7.9$ Hz, NH), 5.70 (d, $J_{1',2'} = 3.9$ Hz, H-1'), 5.43 (sx, $J_{4',5'} = 1.5$, $J_{3',4'} \approx J_{4',F} \approx 3$ Hz, H-4'), 5.40 (nm, H-7), 4.73 and 4.565 (2 dd, 0.5H each, $J_{1',2'} = 4$, $J_{2',3'} = 11$, $J_{2',F} = 49.5$ Hz, H-2'), 4.50 (m, H-3'), 4.39 (qd, $J = 1.5$ and 6.2 Hz, H-5'), 4.07 (s, 3H, OMe), 4.01 (s, exchangeable, OH-9), 3.26 and 3.00 (2 d, $J_{gem} = 19$ Hz, H-10e,10a), 2.41 (s, 3H, Me-14), 2.33 and 2.22 (2 dd, $J_{gem} = 16$, $J_{vic} = 1.5$ and 4 Hz, H-8e,8a), 2.16 (s, 3H, OAc), and 1.16 (d, $J_{5',Me} = 6.2$ Hz, *C*-Me). *Anal.* calcd. for $C_{31}H_{29}F_4NO_{12}$ (683.5): C 54.47, H 4.28, F 11.12; found: C 54.38, H 4.51, F 10.91.

Compound **8** showed mp 105–110°C; $[\alpha]_D$ +116° (*c* 0.6, $CHCl_3$); ν_{max}: 3500, 3300 (strong), 3090, 1740–1700, 1615 (weak), 1560 cm^{-1}; δ ($CDCl_3$): 8.03, 7.78, and 7.39 (d, t, and d, $J \sim 8$ Hz, H-1,2,3), 6.25 (d, $J_{3',NH} = 8$ Hz, NH), 5.54 (nm, width 6 Hz, H-4'), 5.22 (nm, width 6 Hz, H-7), 5.10 (dd, $J_{1',F} = 3$, $J_{1',2'} = 7.5$ Hz, H-1'), 4.50 (m, H-3'), 4.42 and 4.25 (2 dd, 0.5H each, $J_{1',2'} = 7.8$, $J_{2',3'} = 10.5$, $J_{2',F} = 51$ Hz, H-2'), 4.08 (s, 3H, OMe), 3.83 (qd, $J_{4',5'} = 1.2$, $J_{5',Me} = 6.4$ Hz, H-5'), 3.26 and 3.06 (2 d, $J_{gem} = 19$ Hz, H-10e,10a), 2.40 (s, 3H, Me-14), 2.15–2.0 (m, 2H, H-8e,8a), 2.11 (s, 3H, OAc), and 0.99 (d, $J_{5',Me} = 6.3$ Hz, *C*-Me). *Anal.* calcd. for $C_{31}H_{29}F_4NO_{12} \cdot 3.5\ H_2O$ (746.6): C 49.87, H 4.86; found: C 49.87, 49.74; H 4.80, 4.79.

Procedure B

Daunomycinone **6** (278 mg, 0.7 mmol) in dry CH_2Cl_2 (20 mL) and nitromethane (20 mL) was stirred for 1 h with powdered molecular sieve (4 Å; 1 g). Silver triflate (180 mg, 0.8 mmol) was then added,

followed after 1 h by bromide **5** (obtained from 137 mg of diacetate **4** (0.4 mmol) and dissolved in a small volume of CH_2Cl_2). The bromide was completely consumed after 1 h (tlc with solvent F). The inorganic material was removed and washed exhaustively with CH_2Cl_2, and the filtrate was shaken with concentrated aqueous NaI solution followed by water, dried, and evaporated. The crude product mixture was chromatographed, first on a column (9 g of SiO_2) eluted with solvent I followed by solvent H, which separated **7** and **8** from most of the residual **6**, and then on preparative tlc plates (double irrigation with solvent G), which furnished pure **7** (41 mg, 15%) and **8** (45 mg, 16.5%).

*7-O-(2,3,6-Trideoxy-2-fluoro-3-trifluoroacetamido-α-L-galactopyranosyl)-daunomycinone (**9**)*

A sample of **7** (35 mg) in dry methanol (2 mL) was treated at room temperature under N_2 with methanolic 1 M sodium methoxide solution (0.5 mL). Clean conversion of **7** (R_f 0.6) into **9** (R_f 0.4) occurred within 20 min (tlc with solvent E). The dark blue to violet solution was deionized with a weak-acid ion exchange resin (Amberlite IRC-50, H^+). The orange-red solution was evaporated to give crystalline **9** (31 mg, 93%), decomposing at 160–165°C after recrystallization from ethyl acetate – hexane; $[\alpha]_D$ +177.5 ± 1.5° (*c* 0.3, $CHCl_3$); ν_{max}: 3500 (bd), 1710, 1610, 1570 cm^{-1}; δ($CDCl_3$): 8.02, 7.77, and 7.37 (d, t, and d, $J \approx 8$ Hz, H-1,2,3), 6.68 (d, $J_{3',NH} = 8.1$ Hz, NH), 5.66 (d, $J_{1',2'} = 3.8$ Hz, H-1′), 5.42 (dd, $J = 2.7$, 4.0 Hz, H-7), 4.69 and 4.53 (2 dd, 0.5H each, $J_{1',2'} = 4$, $J_{2',3'} = 10.5$, $J_{2',F} = 49$ Hz, H-2′), 4.45–4.3 (m, 2H, H-3′,5′), 4.09 (nm, H-4′), 4.06 (s, 3H, OMe), 3.92 (nm, exchangeable, OH), 3.27 and 2.99 (dd and d, $J_{gem} \approx 18$ Hz, H-10e,10a), 2.40 (s, 3H, Me-14), 2.34 and 2.21 (dt and dd, $J_{gem} = 15$, $J_{vic} = 4$ Hz, H-8e,8a; small long-range coupling present in H-8e), 2.03 (d, exchangeable, $J = 6$ Hz, OH), and 1.30 (d, 3H, $J_{5',Me} = 7$ Hz, *C*-Me). *Anal.* calcd. for $C_{29}H_{27}F_4NO_{11} \cdot 0.5\ H_2O$ (650.5): C 53.54, H 4.34, F 11.68; found: C 53.34, H 4.45, F 11.49.

*7-O-(3-Amino-2,3,6-trideoxy-2-fluoro-α-L-galactopyranosyl)-daunomycinone (**10**, (S)-2′-fluorodaunorubicin) and its hydrochloride **11***

Acetate **7** (310 mg) was *O*-deacetylated in methanol (5 mL) with $NaOCH_3$ as just described, and the crude **9** so obtained was dissolved under N_2 in a saturated, aqueous $Ba(OH)_2$ solution (10 mL) at 25°C. After 20 min, tlc (solvent C) indicated absence of **9** (R_f 1.0) and the presence of **10** (R_f 0.5), and after 30 min the blue solution was diluted with some water and neutralized by addition of solid CO_2. The red solution was filtered by suction through a layer of Celite from the precipitated $BaCO_3$, and the product was extracted from the filtrate into $CHCl_3$. The extract was washed once with water, and evaporated to give **10** as dark-red microscopic needles that were dried over KOH in a desiccator; yield, 221 mg (89.5%). The product charred at 209–210°C and melted indistinctly at 212–216°C; tlc (solvent C): R_f 0.5, with trace contaminant, R_f 0.9; ν_{max}: 3500, 3400, 3330 (3 weak bands), 1715 with shoulder at 1750, 1615, 1580, 1410, 1285, 1260–1030 (several sharp, medium intensity bands), 990, 820, 767, 745 cm^{-1}; δ($CDCl_3$): 8.02, 7.72, and 7.38 (d, t, and d, $J = 7$–8 Hz, H-1,2,3), 5.63 (d, $J_{1',2'} = 3.9$ Hz, H-1′), 5.43 (nm, H-7), 4.54 and 4.38 (2 dd, 0.5H each, $J_{1',2'} = 4$, $J_{2',3'} = 10$, $J_{2',F} = 49$ Hz, H-2′), 4.17 (~q, width 20 Hz, H-5′), 4.07 (s, 3H, OMe), 3.66 (nm, H-4′), 3.3–3.2 (m, 2H, H-3′,10e), 3.00 (d, $J_{gem} = 19$ Hz, H-10a), 2.39 (s, 3H, Me-14; partially obscuring downfield part of H-8e signal), 2.35 (dd, H-8e), 2.16 (dd, $J_{7,8a} = 4$, $J_{8a,8e} = 14$ Hz, H-8a), 1.34 (d, 3H, $J_{5',Me} = 6.2$ Hz, *C*-Me).

For preparing the *hydrochloride* **11**, a solution of **10** (210 mg) in 0.1 M HCl (15 mL) was first extracted with EtOAc for removal of the aforementioned impurity (R_f 0.9), and then evaporated to dryness with additions of ethanol and benzene. The solid **11** was crystallized from ethanol–ether and dried *in vacuo* over KOH; it was not noticeably hygroscopic, and gave a single spot (R_f 0.2) in tlc (solvent B). Yield after recrystallization, 193 mg (86%); mp 224°C (with prior darkening from 217°C); $[\alpha]_D$ +218° (*c* 0.32, CH_3OH); ν_{max}: 3600–3200 (br), 1705, 1615, 1575, 1410, 1285, 1230–1030 (several medium intensity bands), 990, and 960–720 cm^{-1} (several weak bands); δ(DMSO-d_6): 7.92 (m, 2H, H-1,3), 7.65 (t, H-2), 5.72 and 5.58 (d of 5.8 Hz, and s, exchangeable, 2 OH), 5.46 (d, $J_{1',2'} = 3.7$ Hz, H-1′), 5.08 (nm, H-7), 4.80 and 4.63 (2 dd, 0.5H each, $J_{1',2'} = 3.7$, $J_{2',3'} = 10.5$, $J_{2',F} = 49.5$ Hz, H-2′), 4.33 (~q, width 20 Hz, H-5′), 3.98 (s, 3H, OMe), 3.81 (m, narrowed after D_2O exchange, H-4′), 3.40 (m, H-3′), 2.97 (s, 2H, H-10a,e), 2.27 (s, 3H, Me-14), 2.22 (dd, H-8e), 2.11 (dd, $J_{7,8a} \approx 4$, $J_{8a,8e} = 14$ Hz, H-8a), and 1.14 (d, 3H, $J_{5',Me} = 6.6$ Hz, *C*-Me). *Anal.* calcd. for $C_{27}H_{29}ClFNO_{10} \cdot 1.5\ H_2O$ (609.0): C 53.25, H 5.13, Cl 5.82, F 3.12, N 2.30; found: C 53.00, H 5.17, Cl 5.67, F 3.45, N 2.29.

Acknowledgments

This work was financially supported by grant GM 35244 from the United States Public Health Service. The authors are grateful to Dr. T. W. Doyle, Director, Antitumor Chemistry, Bristol–Myers Company, for providing a generous sample of daunomycin from which the aglycon **6** used in this synthesis was prepared, and for kindly arranging the biological tests. Drs. W. Rose and S. Mamber are thanked for performing the in vivo tests, and Dr. Schurig and Ms. Farwell for determining in vitro cytotoxicity.

1. H. H. Baer and A. Jaworska-Sobiesiak. Carbohydr. Res. **140**, 201 (1985).
2. M. K. Gurjar, V. J. Patil, J. S. Yadav, and A. V. Rama Rao. Carbohydr. Res. **135**, 174 (1984).
3. D. Picq and D. Anker. J. Carbohydr. Chem. **4**, 113 (1985).
4. L. H. B. Baptistella, A. J. Marsaioli, J. D. de Souza Filho, G. G. de Oliveira, A. B. de Oliveira, A. Dessinges, S. Castillon, A. Olesker, T. T. Ton, and G. Lukacs. Carbohydr. Res. **140**, 51 (1985).
5. S. Castillon, A. Dessinges, R. Faghih, G. Lukacs, A. Olesker, and T. T. Ton. J. Org. Chem. **50**, 4913 (1985).
6. F. Arcamone. Doxorubicin, anticancer antibiotics (Medicinal Chemistry monograph series, vol. 17). Academic Press, New York. 1981.
7. F. Arcamone, G. Franceschi, P. Orezzi, G. Cassinelli, W. Barbieri, and R. Mondelli. J. Am. Chem. Soc. **86**, 5334 (1964).
8. F. Arcamone, G. Franceschi, S. Penco, and A. Selva. Tetrahedron Lett. 1007 (1969).
9. F. Arcamone, S. Penco, and A. Vigevani. Cancer Chemother. Rep. Part 3, **6**, 123 (1975).
10. F. Arcamone, S. Penco, A. Vigevani, S. Redaelli, G. Franchi, A. Di Marco, A. M. Casazza, T. Dasdia, F. Formelli, A. Necco, and C. Soranzo. J. Med. Chem. **18**, 703 (1975).
11. F. Arcamone, A. Bargiotti, G. Cassinelli, S. Redaelli, S. Hanessian, A. Di Marco, A. M. Casazza, T. Dasdia, A. Necco, R. Reggiani, and R. Supino. J. Med. Chem. **19**, 733 (1976).

Can. J. Chem. Downloaded from www.nrcresearchpress.com by 213.222.148.141 on 09/07/12
For personal use only.

The biosynthesis of caerulomycins in *Streptomyces caeruleus*. Isolation of a new caerulomycin and incorporation of picolinic acid and glycerol into caerulomycin A[1]

LEO C. VINING
Biology Department, Dalhousie University, Halifax, N.S., Canada B3H 4J1

AND

A. GAVIN MCINNES, ARCHIBALD W. MCCULLOCH, DONALD G. SMITH, AND JOHN A. WALTER
Atlantic Research Laboratory, National Research Council of Canada, Halifax, N.S., Canada B3H 3Z1

Received June 15, 1987

LEO C. VINING, A. GAVIN MCINNES, ARCHIBALD W. MCCULLOCH, DONALD G. SMITH, and JOHN A. WALTER. Can. J. Chem. **66**, 191 (1988).

Oxidation with permanganate of caerulomycin A labeled biosynthetically from [U-^{14}C]lysine in cultures of *Streptomyces caeruleus* yielded picolinic acid with the same specific activity as the antibiotic. [^{3}H]Picolinic acid was incorporated into caerulomycin A with high efficiency and the label was also found exclusively in picolinic acid after oxidation, implicating free picolinic acid as an intermediate in the pathway from lysine. The substituted pyridyl ring of caerulomycin was labeled by [2-^{13}C, 1,3-^{14}C]glycerol. ^{13}C nuclear magnetic resonance analysis located the ^{13}C predominantly at C-6, suggesting that C-5, C-6, and C-7 were derived from glycerol as an intact three-carbon precursor. Since no incorporation of [1-^{13}C]glyceric acid was detected and [3-^{13}C, 3-^{14}C]methylglyoxal labeled the antibiotic only marginally, these compounds are probably not biosynthetic intermediates en route from glycerol. A new caerulomycin possessing an aldehyde in place of the aldoxime substituent at C-6 was isolated from culture broths and is postulated to be a late intermediate in the formation of caerulomycin A.

LEO C. VINING, A. GAVIN MCINNES, ARCHIBALD W. MCCULLOCH, DONALD G. SMITH et JOHN A. WALTER. Can. J. Chem. **66**, 191 (1988).

On a préparé de la caerulomycine A marquée par biosynthèse dans des cultures de *Streptomyces caeryleus*, à partir de [U-^{14}C]-lysine; l'oxydation de ce composé par du permanganate fournit de l'acide picolinique possédant la même activité spécifique que l'antibiotique. On a incorporé de l'acide [^{3}H]-picolinique dans de la caerulomycine A avec une haute spécificité et, lors de son oxydation, on n'a retrouvé le marqueur que dans l'acide picolinique; ce résultat suggère que l'acide picolinique libre est un intermédiaire dans la synthèse à partir de la lysine. On a procédé au marquage du cycle pyridyle substitué de la caerulomycine par du [^{13}C-2, ^{14}C-1,3]-glycérol. Une analyse par résonance magnétique nucléaire du ^{13}C a permis de déterminer que le ^{13}C se trouve principalement en position C-6; ce résultat suggère que les carbones C-5, C-6 et C-7 proviennent d'une molécule de glycérol agissant comme un précurseur à trois atomes de carbones qui est intact. Puisqu'on n'a pas détecté d'incorporation d'acide [^{13}C-1]-glycérique et que le [^{13}C-3, ^{14}C-3]-méthylglyoxal ne marque l'antibiotique que d'une façon marginale, on peut en déduire que ces composés ne sont probablement pas des intermédiaires dans la biosynthèse à partir du glycérol. Des bouillons de culture, on a isolé une nouvelle caerulomycine qui possède un aldéhyde à la place du substituant aldoxime en position C-6; on fait l'hypothèse qu'il s'agit d'un des derniers intermédiaires dans la formation de la caerulomycine A.

[Traduit par la revue]

Introduction

Caerulomycin A (**1**) is a member of the 2,2′-dipyridyl group of antibiotics produced by *Streptomyces caeruleus* (1–4), *Actinomyces* (*Streptomyces*) *coerulescens* (5), and *Nocardiopsis cirriefficiens* (6). An earlier study of its biosynthesis showed [U-^{14}C]lysine to be the most efficiently incorporated precursor tested and ^{13}C nmr analysis of the labelling patterns obtained with [^{13}C]acetate were consistent with formation of the unsubstituted pyridyl moiety (ring B) and bridging 2,2′-carbons from this amino acid (7). Although the results indicated that free picolinic acid could be an intermediate in the route from lysine to the antibiotic, as observed in the biosynthesis of proferrorosamine A (**2**) by *Pseudomonas fluorescens* (8), no direct evidence for this was obtained. The ^{13}C labelling experiments demonstrated that acetate also supplied C-3 and C-4 of the substituted pyridyl moiety (ring A) of caerulomycin but failed to identify a source of the remaining three carbons at C-5, C-6, and C-7. The possibility that these might be derived from serine could be discounted because [3-^{13}C]serine, although efficiently incorporated into the methoxyl substituent, did not enrich the ring or aldoxime carbons. Pyruvate could be excluded as a source of C-5, C-6, and C-7 because these carbon atoms were not labeled by ^{13}C-enriched precursors that labeled the carbon atoms of ring B derived from pyruvate via lysine.

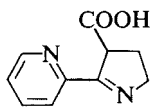

2

In the present paper, we provide evidence that free picolinic acid is specifically incorporated into ring B of caerulomycin A and that glycerol serves as a precursor of C-5, C-6, and C-7. We also report the isolation of a new product, caerulomycin E, from culture broths and show that it has the structure **3**.

Experimental

Culture

The origin and maintenance of *Streptomyces caeruleus* strain 4/2, used throughout these studies, has been described (7). Cultures supplemented with isotopically labeled potential biosynthetic precursors or used for isolating caerulomycins were grown in 250-mL Erlenmeyer flasks containing 50 mL of medium 1 which contained (per liter): soluble starch (20 g), $NaNO_3$ (2.0 g), $CaCO_3$ (2.0 g), K_2HPO_4 (1.0 g),

[1]NRCC No. 28306.

Can. J. Chem. Downloaded from www.nrcresearchpress.com by 213.222.148.141 on 09/07/12
For personal use only.

KCl (0.5 g), and $MgSO_4 \cdot 7H_2O$ (0.5 g). Where different nitrogen sources were tested they replaced $NaNO_3$ at equivalent nitrogen concentration. Growth conditions were as reported previously (7).

Labeled supplements

[U-^{14}C]Lysine, [1,3-^{14}C]glycerol, and [^{3}H]water were purchased from New England Nuclear Corporation, Boston, MA; [2-^{13}C]glycerol (90 at.% ^{13}C) was from Merck Sharp and Dohme Canada Ltd., Pointe Claire, P.Q. [^{3}H]Picolinic acid was prepared from unlabeled compound by catalytic exchange in [^{3}H]water.

[1-^{13}C]Glyceric acid was prepared by a modification of the method of Ashworth (9). Glycolaldehyde was converted to the dibenzoylated cyanohydrin by reaction with potassium [^{13}C]cyanide and benzoyl chloride. The product was washed well with petroleum ether. The acid hydrolysate was evaporated under high vacuum below 40°C and the residue was purified by trituration with diethyl ether (solubles discarded) and acetone (insolubles discarded). The labeled glyceric acid was obtained as a pale yellow syrup (46% overall yield) and was characterized by ^{1}H and ^{13}C nmr spectroscopy.

[3-^{13}C, 3-^{14}C]Methylglyoxal was prepared as required by acid hydrolysis of the diethyl acetal (10). The latter was synthesized by the method of Wohl and Lange (11). Thus ethyl diethoxyacetate was converted to the piperide (74%) and subjected to Grignard reaction using [1-^{13}C, 1-^{14}C]methyl iodide to give the desired acetal (46%).

All supplements were sterilized by filtration; times of addition and concentrations varied and are reported for each experiment.

Caerulomycin assay

Samples (2.0 mL) of culture broth were mixed with 10 m*M* ferrous ammonium sulfate (2.0 mL), basified with 1% sodium carbonate (1.0 mL), and extracted with *n*-butanol (5.0 mL). The absorbance of the clarified butanolic extract was measured at 532 nm and related to that of similarly treated reference solutions of caerulomycin A.

Isolation of caerulomycins

Cultures were harvested by filtration after reaching stationary phase (9–12 days from inoculation). Caerulomycins were extracted as described (7). In experiments with radioactive precursors, the products from 100 mL of broth were separated by thin-layer chromatography (tlc) on silica gel (Silicar T7G, Analabs, Inc., NJ) using successive development with chloroform and chloroform–acetone (19:1). Zones were located as quenched areas under ultraviolet (254 nm) irradiation, scraped from the plate, and extracted with ethanol. Where radioactivity was measured, the radiochemical purity of the product was confirmed by scanning after tlc of the eluted material in two additional systems (silica gel GHLF; chloroform–methanol – 6 *M* ammonium hydroxide, 20:3:10, lower phase; benzene – acetic acid – water, 42:24:1). In ^{13}C labelling experiments and for the isolation of caerulomycin E, the products from 1 L of broth were separated on a column of cross-linked dextran (Sephadex LH20, Pharmacia Limited, Uppsala) equilibrated with the solvent mixture benzene – ethyl acetate – acetic acid – water (1:6:2:6). Caerulomycins E and A were collected at elution volumes of 320–360 and 380–560 mL, respectively, during development with the organic phase. Caerulomycin A was purified for ^{13}C nmr examination as described previously (7).

Fractions containing caerulomycin E were evaporated and the residue was crystallized successively from hexane and aqueous methanol as colourless needles, mp 83°C. These were sublimed under high vacuum at 55°C to give clusters of prisms of the same mp (yield, 12.6 mg). The high resolution electron-impact mass spectrum showed two prominent peaks at m/z 213.0664 ± 0.0007 and 214.0738 ± 0.0007, corresponding to $C_{12}H_9N_2O_2$ (calculated m/z 213.0664) and $C_{12}H_{10}N_2O_2$ (calculated m/z 214.0742), respectively. The ^{1}H nmr spectrum in dimethyl sulfoxide-d_6 contained resonances at δ (ppm) 8.12 (H-3), 7.45 (H-5), 10.08 (H-7), 8.46 (H-3′), 7.99 (H-4′), 7.51 (H-5′), 8.71 (H-6′), and 3.98 (4-OCH_3); $J_{H,H}$ (±0.1 Hz): 2.5 (H-3,H-5), 7.8 (H-3′,H-4′), 1.2 (H-3′,H-5′), 0.9 (H-3′,H-6′), 7.5 (H-4′,H-5′), 1.8 (H-4′,H-6′), 4.7 (H-5′,H-6′). All values were obtained by simulation. The ^{13}C nmr spectrum of a sample in dimethyl sulfoxide-d_6 gave signals at δ (ppm) (J_{CH} (Hz)): 157.6 (m, C-2), 109.8 (dd, C-3, ^1J 166.3, $^3J_{3,5}$ 3.9), 167.3 (bm, C-4), 107.7 (ddd, C-5, ^1J 167.1, $^3J_{3,5}$ 4.2, $^3J_{5,7}$ 2.7), 153.8 (d, C-6, $^2J_{6,7}$ 23.3), 193.2 (d, C-7, ^1J 183.1), 153.9 (bm, C-2′), 120.8 (dddd, C-3′, ^1J 166.8, $^3J_{3',5'}$ 7.0, $^2J_{3',4'}$ 1.4, $^4J_{3',6'}$ 0.8), 137.4 (dd, C-4′, ^1J 165.7, $^3J_{4',6'}$ 6.1), 124.8 (ddd, C-5′, ^1J 165.5, $^2J_{5',6'}$ 8.6, $^3J_{3',5'}$ 6.5), 149.3 (ddd, C-6′, ^1J 179.2, $^2J_{5',6'}$ 3.8, $^3J_{4',6'}$ 7.0), 56.0 (q, 4-OCH_3, ^1J 146.2).

Oxidation of caerulomycin A

Caerulomycin A (20 mg) dissolved in 10% H_2SO_4 (5 mL) was heated on a steam bath with $KMnO_4$ (200 mg; 12.5 mol) until the permanganate color disappeared. The filtered reaction mixture was evaporated and the residue was extracted with ethanol. The extract, diluted with water, was applied to a column (1 × 5 cm) of cation exchange resin (Dowex 50W, H^+, 200–400 mesh size) and washed with water. Picolinic acid was recovered by further elution with water and sublimed under high vacuum at 65°C to give prisms, mp 142°C (2).

Instrumentation

Radioactivity on tlc plates was located with a gas-flow windowless detector linked to a recorder (model 7200 radiochromatogram scanner, Packard Instruments Limited). For quantitative measurements a liquid scintillation counter (model 1215, LKB Wallac, Helsinki) was used.

Carbon-13 nmr spectra at 25.2 MHz of caerulomycin A samples (approximately 40 mg in 0.5 mL of dimethyl sulfoxide-d_6) at natural abundance or labeled with ^{13}C were recorded at 25°C with a Varian XL-100 spectrometer. Conditions were as follows: spectral width 5120 Hz, acquisition time 0.8 s, flip angle approximately 40°C, relaxation reagent $Cr(acac)_3$ (10 mg mL^{-1}) added to solution, ^{1}H broadband decoupling switched off for 1.2 or 3.2 s between acquisition periods for further suppression of nuclear Overhauser enhancement (nOe), internal ^{2}H lock, 5-mm sample tubes. Carbon-13 enrichments were calculated by comparing integrated resonance intensities from the [^{13}C]-supplemented and natural abundance compounds as described previously (12).

The same conditions were used for ^{13}C nmr spectra of caerulomycin E (22 mg in 0.5 mL of dimethyl sulfoxide-d_6) except that $Cr(acac)_3$ was not added and the acquisition time was 1.6 s for broadband ^{1}H-decoupled spectra and 3.2 s for ^{1}H-coupled spectra with nOe maintained by ^{1}H irradiation between acquisition periods. Continuous-wave ^{1}H spectra of this compound were obtained with a Varian HA-100 spectrometer.

Electron-impact mass spectra were obtained with a Dupont/CEC model 21-110B mass spectrometer.

Results

Origin of ring B

Although the very high specific incorporation of 40.7% reported previously (7) was not reproduced under the culture conditions used in the present investigation, [U-^{14}C]lysine was an efficient precursor of caerulomycin A (Table 1). Oxidation of the labeled product with permanganate gave picolinic acid with virtually unchanged specific activity (Table 2). Cultures supplemented with [^{3}H]picolinic acid produced 32% more caerulomycin than unsupplemented control cultures and the specific incorporation of ^{3}H was 51.4%. All of the radioactivity in [^{3}H]caerulomycin A from this experiment was recovered in the picolinic acid obtained after permanganate oxidation.

Origin of ring A

Supplementation of cultures with [1,3-^{14}C]glycerol under a variety of regimens gave an optimum specific incorporation of 70.4% when aliquots of the precursor were fed at intervals in an overall concentration of 10 m*M*. An isotopic enrichment of 4–10%, adequate for ^{13}C nmr analysis of the labelling pattern, was obtained with successive supplementation to an aggregate of 1 m*M*. Under the latter conditions, a sample of [2-^{13}C, 1,3-^{14}C]glycerol exhibiting a specific radioisotopic incorporation of 4.4% preferentially labeled caerulomycin A with ^{13}C at C-6 (0.7% above natural abundance). The methoxyl carbon (0.2%), C-2′ (0.3%), C-4 (0.4%), C-4′ (0.5%), and

Can. J. Chem. Downloaded from www.nrcresearchpress.com by 213.222.148.141 on 09/07/12
For personal use only.

TABLE 1. Incorporation of radioactivity into caerulomycin A from ^{14}C-labeled compounds

Compound administered	Caerulomycin A		
	μCi/mmol	μCi/mmol	%
[^{3}H]Picolinic acid	0.167	0.086	51.4
[U-^{14}C]Lysine	65.7	6.72	10.2
[2-^{13}C, 1,3-^{14}C]Glycerol	17.4	0.767	4.41
[3-^{13}C, 3-^{14}C]Methylglyoxal	1.89	0.006	0.31

TABLE 2. Recovery of radioactivity in picolinic acid after oxidation of caerulomycin A

Caerulomycin A		Picolinic acid	
Labeled from	μCi/mmol	μCi/mmol	%
[U-^{14}C]Lysine	8.50	8.11	95
[^{3}H]Picolinic acid	0.086	0.085	99
[1,3-^{14}C]Glycerol	1.05	0.223	21

C-6′ (0.4%) were labeled to lesser extents (error, ±0.1%). In contrast, when cultures were supplemented under the same conditions with [1-^{13}C]glyceric acid, no ^{13}C enrichment of caerulomycin A carbons was detected. With [3-^{13}C, 3-^{14}C]-methylglyoxal, the incorporation of radioisotope was extremely low (Table 1) and ^{13}C enrichment was below detectable limits. Although unused supplement was identified in the broth at harvest, a 33% depletion of radioactivity during growth of the culture indicated that the labeled compound was taken up slowly by the mycelium. In support of this conclusion, an increase in the concentration of the supplement to 5 m*M* severely inhibited antibiotic production. Methylglyoxal has been shown to exert toxic effects in other organisms (13).

Isolation of caerulomycin E

Radiochromatogram scans after tlc of the basic ether-extractable product from cultures supplemented with [1,3-^{14}C]glycerol showed several minor radioactive, fluorescence-quenching components less polar than caerulomycin A. The most prominent of these (R_f 0.63; Silicar 7GF; chloroform–acetone, 19:1) gave an orange-brown color when the chromatogram was sprayed with $FeSO_4$ and could be identified by these properties in fractions obtained when culture extracts were chromatographed on partition columns on Sephadex LH20. With a solvent system modified from that used previously (7) to increase resolution of the less polar metabolites, the new product was separated from caerulomycin A and other components. It was then purified by crystallization and fractional sublimation for structural analysis by nmr.

Structure of caerulomycin E

The structure of caerulomycin E (**3**) was determined from its mass spectrum and comparison of its ^{13}C and ^{1}H nmr spectra with those of caerulomycin A (**1**) and the nitrile (**4**) for which ^{13}C and ^{1}H nmr resonances and spin–spin couplings have been assigned previously (3). The spectral data were in accord with a 2,2′-dipyridyl derivative in which the respective oxime and nitrile substituents of **1** and **4** were replaced by an aldehyde group. In particular, the chemical shifts for H-7 and C-7 as well as the $^{1}J_{CH}$ and $^{2}J_{CH}$ values for C-7 and C-6, respectively, were consistent with an aldehyde at the C-6 position. The ^{13}C substituent effects when a nitrile at C-6 is replaced by an aldehyde group are obtainable from the work of Retcofsky and Friedel (14). The predicted shifts (δ_C) based on known values for caerulomycin A nitrile (3) are C-2, 157.2; C-3, 109.7; C-4, 166.1; C-5, 108.7; and C-6, 152.5 ppm, all in close agreement with the measured values.

TABLE 3. Effect of nitrogen source on the production of caerulomycins by *S. caeruleus* 4/2*

Nitrogen source	Caerulomycins (mg L^{-1})
Sodium nitrate	226
Glutamate	68
Asparagine	68
Soytone	29
Ammonium sulfate	15
Serine	6

*Cultures were grown in medium 1 with the different nitrogen sources replacing nitrate at a concentration of 24 m*M* N L^{-1}. Broths were assayed for total caerulomycins after 10 days.

To ascertain whether generation of hydroxylamine as an intermediate in the assimilation of nitrate was a factor in the biosynthesis of caerulomycins containing the oxime substituent, cultures of *S. caeruleus* were grown in medium 1 with nitrate replaced by alternative nitrogen sources (Table 3). When the basic ether-extractable products from each culture were examined by tlc in system A, caerulomycin A was found to be the principal component. In addition, the relative amounts of minor components, including caerulomycin E, were not appreciably altered by changing the nitrogen source.

Discussion

The specificity with which [U-^{14}C]lysine is incorporated into the segment of caerulomycin A that is recovered as picolinic acid after oxidative degradation of the molecule is consistent with the pattern of ^{13}C labelling from [1-^{13}C]- and [1,2-^{13}C]-acetate found earlier (7), as well as with the high specific incorporation of the amino acid. That lysine is incorporated into the antibiotic after initial conversion to picolinic acid can be assumed from the significantly higher specific incorporation of [^{3}H]picolinic acid into the same structural segment. The results parallel those obtained in studies of proferrorosamine biosynthesis in *Pseudomonas roseus fluorescens* (8, 15). It is noteworthy that lysine is also known to be metabolized to 3-hydroxypicolinic acid before incorporation into etamycin by *Streptomyces griseoviridus* (16), and the structural relationships between caerulomycins, proferrorosamine, and the actinomycete-derived siderochelin (**5**, ref. 17) and siderochelin C (18) suggest that lysine may also be metabolized to 6-hydroxypicolinic acid in some species.

It is apparent from the 70% level of specific ^{14}C incorporation achieved with [1,3-^{14}C]glycerol at a supplement concentration much below that of the principal carbon source that glycerol is preferentially used to form the caerulomycins. The evidence from ^{13}C nmr analysis of the product obtained when [2-^{13}C]glycerol was combined with the radioactive precursor indicates that one glycerol molecule was incorporated as a unit into positions C-5, C-6, and C-7. The small ^{13}C enrichments at positions other than C-6 are explained by partial metabolic conversion of glycerol to products that are incorporated elsewhere in the antibiotic molecule. Thus the formation of [2-^{13}C]pyruvate and [2-^{13}C]aspartate semialdehyde would lead to [2,6-^{13}C]picolinic

Can. J. Chem. Downloaded from www.nrcresearchpress.com by 213.222.148.141 on 09/07/12
For personal use only.

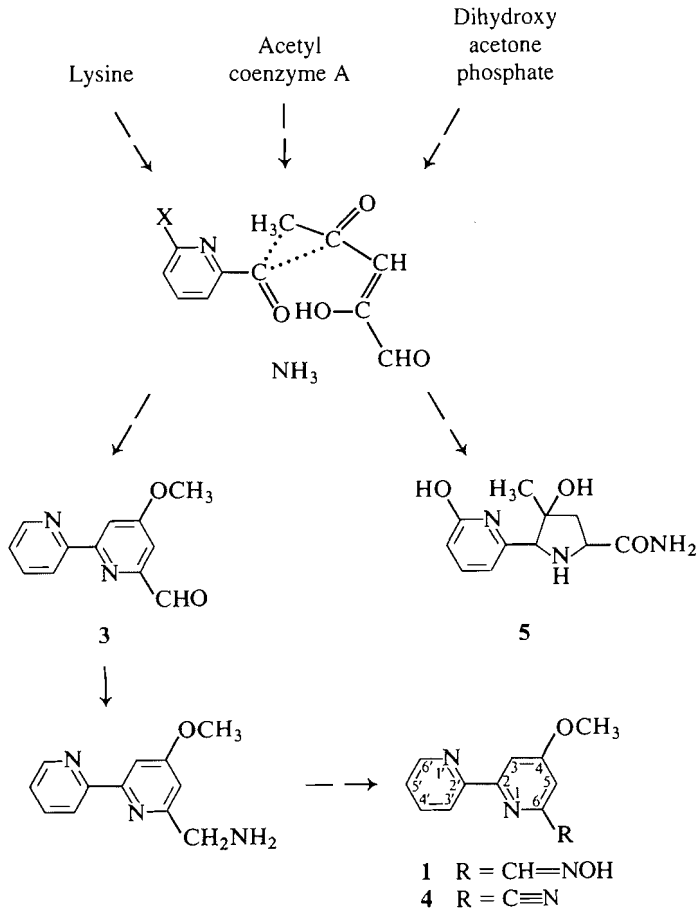

FIG. 1. Proposed biosynthesis of caerulomycins and siderochelin.

acid and generate caerulomycin A labeled at C-2′ and C-6′. Likewise, [1-^{13}C]acetyl coenzyme A formed from the labeled glycerol would introduce isotopic carbon into C-2, C-4, and C-4′. The earlier experiments with [1-^{13}C]acetate (7) showed much higher enrichments at C-4 and C-4′ than at C-2, accounting for the detection of small amounts of ^{13}C at the former two positions whereas incorporation at C-2 was below detectable limits. Labelling of the methoxyl carbon probably occurred through ^{13}C enrichment of the one-carbon pool via glycine.

Although glycerol itself is unlikely to be the immediate metabolic precursor, neither [1-^{13}C]glyceric acid nor [3-^{13}C, 3-^{14}C]-methylglyoxal, the two potential candidates tested, labeled the antibiotic to an appreciable extent. [1-^{13}C]Glyceric acid may not have been taken into the cells, but phosphoglycerates or phosphoenolpyruvate are not attractive intermediates since the carboxyl group they would introduce at C-7 would subsequently have to be reduced to an aldoxime or equivalent in caerulomycin A. The low incorporation of radioactivity from the methylglyoxal supplement cannot be attributed wholly to poor uptake since approximately one third of the radioactivity added to the culture was removed from the broth but less than 1% of this found its way into the antibiotic. If methylglyoxal is thus excluded as a precursor, it is likely that dihydroxyacetone phosphate, derived from glycerol when this supplement is fed, enters the secondary metabolic pathway directly. This could occur by condensation with acetyl or malonyl coenzyme A, either before or after the thioester had reacted with an activated form of picolinic acid. Alternative modes of condensation might lead to the caerulomycins or siderochelin. Proferrorosamine, which as neopurpuratin has recently been discovered as a product of *Streptomyces purpuratus* (19), might be similarly derived.

The isolation of caerulomycin E as a minor component of the caerulomycin complex produced by *S. caeruleus* raises the possibility that introduction of the oxime group is a terminal biosynthetic step. One route by which the oxime might be generated is by reaction of the aldehyde with hydroxylamine formed as an intermediate in the assimilation of nitrate. Nitrate supports the highest production of caerulomycins when supplied as the sole nitrogen source for growth of *S. caeruleus*; nevertheless, it is not an absolute requirement for biosynthesis of the secondary metabolite. Since generation of free hydroxylamine from organic nitrogen sources is questionable, a more likely origin for the oxime group of caerulomycin A and related products is through hydroxylation and dehydrogenation of an amino group. A mechanism of this kind probably accounts for formation of the oxime group in nocardicin from the amino group of *p*-hydroxyphenylglycine (20). With all of the above considerations in mind, we suggest the route shown in Fig. 1 for the biosynthesis of caerulomycins and related compounds.

Acknowledgements

We thank D. J. Embree for the mass spectra and C. Mofford for valuable technical assistance. The work was supported by a research grant from the Natural Sciences and Engineering Research Council of Canada.

1. A. FUNK and P. V. DIVEKAR. Can. J. Microbiol. **5**, 317 (1959).
2. P. DIVEKAR, G. READ, and L. C. VINING. Can. J. Chem. **45**, 1215 (1967).
3. A. G. MCINNES, D. G. SMITH, J. L. C. WRIGHT, and L. C. VINING. Can. J. Chem. **55**, 4159 (1977).
4. A. G. MCINNES, D. G. SMITH, J. A. WALTER, J. L. C. WRIGHT, L. C. VINING, and G. P. ARSENAULT. Can. J. Chem. **56**, 1836 (1978).
5. M. G. BRAZHNIKOVA, T. S. BOBKOVA, V. A. SHORIN, and O. K. ROSSOLIMO. Antibiotiki (Moscow), **2**, 16 (1957).
6. TAKEDA. Jpn. Kokai Tokkyo Koho, JP 59 51,797 (1984).
7. A. G. MCINNES, D. G. SMITH, J. A. WALTER, L. C. VINING, and J. L. C. WRIGHT. Can. J. Chem. **57**, 3200 (1979).
8. M. POUTEAU-THOUVENOT, J. PADIKKALA, M. BARBIER, A. HELBLING, and M. VISCONTINI. Helv. Chim. Acta, **59**, 2284 (1976).
9. J. M. ASHWORTH. J. Chem. Soc. 2563 (1963); Biochem. Prep. **11**, 50 (1966).
10. J. MEISENHEIMER. Ber. **45**, 2635 (1912).
11. A. WOHL and M. LANGE. Ber. **41**, 3612 (1908).
12. J. L. C. WRIGHT, L. C. VINING, A. G. MCINNES, D. G. SMITH, and J. A. WALTER. Can. J. Biochem. **5**, 678 (1977).
13. W. B. FREEDBERG, W. S. KISTLER, and E. C. C. LIN. J. Bacteriol. **108**, 137 (1971).
14. H. L. RETCOFSKY and R. A. FRIEDEL. J. Phys. Chem. **72**, 2619 (1968).
15. M. POUTEAU-THOUVENOT, J. PADIKKALA, M. BARBIER, and M. VISCONTINI. Helv. Chim. Acta, **56**, 1067 (1973).
16. D. J. HOOK and L. C. VINING. Can. J. Biochem. **51**, 1630 (1973).
17. W. C. LIU, S. M. FISHER, J. S. WELLS, JR., C. S. RICCA, P. A. PRINCIPE, W. H. TREJO, D. P. BONNER, J. Z. GOUGOUTOS, B. K. TOEPLITZ, and R. B. SYKES. J. Antibiot. **34**, 791 (1981).
18. L. A. MITSCHER, T. HOGBERG, S. D. DRAKE, A. W. BURGSTAHLER, M. JACKSON, B. LEE, R. I. SHELDON, H. E. GRACEY, W. KOHL, and R. J. THERIAULT. J. Antibiot. **37**, 1260 (1984).
19. M. OHSHIMA, N. ISHIZAKI, and Y. TONOOKA. J. Ferment. Technol. **63**, 79 (1985).
20. C. A. TOWNSEND and A. M. BROWN. J. Am. Chem. Soc. **103**, 2873 (1981).

Can. J. Chem. Downloaded from www.nrcresearchpress.com by 213.222.148.141 on 09/07/12
For personal use only.

Synthesis of rigid, chiral 1,5-diamino-3-oxapentanes and incorporation into chiral macrocyclic polyether ligands

JEAN-MARIE LEHN AND PIERRE G. POTVIN[1]

Institut Le Bel, Université Louis-Pasteur, 4, rue Blaise Pascal, 67000 Strasbourg, France

Received June 18, 1987

JEAN-MARIE LEHN and PIERRE G. POTVIN. Can. J. Chem. **66**, 195 (1988).

The syntheses of 2,5-anhydro-1,6-di-*C*-amino-1,6-dideoxy-3,4-di-*O*-methyl-D-mannitol **11** and its *N*,*N'*-dimethyl analogue **15** are described, as are couplings to bis-tartaro-18-crown-6 **1** to give a macrobicyclic cryptand **16**, and macrocycles **17** and **18** bearing four lateral groups, which are potential precursors of a cylindrical stacked macrocyclic system such as **6**.

JEAN-MARIE LEHN et PIERRE G. POTVIN. Can. J. Chem. **66**, 195 (1988).

Les synthèses du 2,5-anhydro-1,6-di-*C*-amino-1,6-didéoxy-3,4-di-*O*-méthyle-D-mannitol **11** et de son analogue *N*,*N'*-diméthylé **15** sont décrites, ainsi que leurs réactions de couplage avec le bis-tartaro-18-couronne-6 **1** pour former le cryptand macrobicyclique **16** et les macrocycles à quatre «bras» latéraux **17** et **18**, qui sont des précurseurs possibles à un système macropolycyclique cylindrique tel que **6**.

Can. J. Chem. Downloaded from www.nrcresearchpress.com by 213.222.148.141 on 09/07/12
For personal use only.

Introduction

The design of polyfunctional molecular receptors, catalysts, and carriers involves the judicious combination of design elements of well-defined size, shape, and stereochemistry. Functionalized macrocycles with side chains of defined stereochemistries have found use as such design elements (1). The optically active 18-crown-6 **1**,[2] incorporating two *R*,*R*-tartaric acid residues (2), is a particularly attractive one because its carboxyl groups can be readily modified, via tetra-acid chloride **2** (2, 3), dianhydride (4), and *anti* diester-diacid chlorides **3***a* and **4***a* (5), or via the face-differentiated *syn* diester-diacid chlorides **3***b* and **4***b* (5), and may serve for introducing various side chains (3, 4). Furthermore, it and its derivatives form stable complexes with a variety of cations (3) through anchoring at the macrocycle and interaction with the side chains held in quasi-axial orientations (3, 4, 6).

To avoid problems of positional isomerism and diastereomerism in preparing complex macropolycyclic structures based on **1** using nonspecific linkage reactions, we chose to use C_2-symmetric linkage subunits. We describe herein the syntheses of two C_2-symmetric chiral 1,5-diamino-3-oxapentanes from D-glucosamine and the incorporation of one of them into chiral macrocyclic polyether ligands as a "bridge" in a macrobicycle and as a "spacer" unit in work toward the synthesis of a potential ion channel (*vide infra*). Many chiral macrocycles have been prepared that incorporate sugar or sugar-derived chiral ethylene glycol (for an earlier compilation, see ref. 7; see also ref. 8), diethylene glycol (9), or 1,4-butanediol (10) moieties or, although not of carbohydrate origin, 2*S*,5*S*-bis(hydroxymethyl)tetrahydrofuran (11) or another chiral 1,5-diamino-3-oxa-pentane, 2*S*,5*S*-bis(aminomethyl)tetrahydrofuran (12).

Chiral macrobicyclic polyethers

Recently, four novel macrobicyclic cryptands (exemplified by **5**) were prepared using 1,5-diamino-3-oxapentane to stereospecifically bridge over the face of **1** (5). The dianion of the diacid derived from **5** binds NH_4^+ and NH_3OH^+ as well as does the tetra-anion of **1**. This would imply a participation of the ether oxygen along the bridge in the stabilization of the complexes. The title diamines are conformationally more rigid than their achiral parent and, as bridges in structures analogous to **5**, would be expected to form more highly organized structures allowing better control of binding stabilities and selectivities.

Approaches to ion channels

Trans-membrane ion channels or "canals" have been implicated in the modes of action of the gramicidins (13), of alamethicin (14), and of amphotericin B and other polyene antifungals (15). Few synthetic channels have been reported. A polymer consisting of 4 helically-twisted "stacks" of closely-spaced 18-crown-6 moieties centred about the polymer backbone has been reported (16). The stacks are, on average, 40 Å long and composed of 10 monomer units each. The polymer extracts picrate salts from aqueous solutions more efficiently but less selectively than 18-crown-6. A 19–20 Å long half-canal has been based on a β-cyclodextrin unit bearing 4 hydrophobic chains and presenting 3 metal-ion binding sites (17). This model enables the passage of Cu^{2+} and Co^{2+} through vesicular membranes. The X-ray structure of the KBr complex of the tetra-*N*,*N*-dimethylamide of **1** (6*b*) shows a canal-like stack of disconnected macrocycles with half of the complexed K^+ ions bound in the plane of macrocycles and the other half frozen in mid-jump between two macrocycles. Such "jumps" between binding sites had been demonstrated in 1:1 Ca^{2+}, Ba^{2+}, and Sr^{2+} complexes of a cylindrical binuclear macrocycle (18).

We were interested in the possibility of using the title amines as C_2-symmetric spacers to link units of **1** into polynucleating stacks or canals such as **6** that may enable the transfer of a metal ion from one macrocyclic subunit to another and thus constitute operational models of an ion channel. The ether-type oxygens in **11** and **15** would facilitate that transfer, and the rigidity afforded by the backbone would help prevent the collapse of the internal cavities in **6**.

Results and discussion

Synthesis of the chiral linear diamines 11–15

The transformations of D-glucosamine to 2,5-anhydro-D-mannitol **7** (19), and thence to the tetraolditosylate **8** (20), are established procedures. We wished to methylate the secondary hydroxyl groups and to transform the tosyloxy functions to amino groups. However, electrophilic methylation of **8** (Ag_2O, CH_3I, THF) (19*b*) failed, as did nucleophilic conditions ($SO_2(OMe)_2$, aqueous NaOH). The problem could be avoided

[1]Present address: Department of Chemistry, York University, 4700 Keele Street, North York, Ont., Canada M3J 1P3.

[2]2*R*,3*R*,11*R*,12*R*-1,4,7,10,13,16-Hexaoxacyclooctadecane2,3,11,12-tetracarboxylic acid.

Printed in Canada / Imprimé au Canada

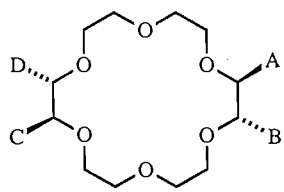

1 A = B = C = D = COOH

2 A = B = C = D = COCl

3a A = D = COCl B = C = $COOCH_3$

3b A = C = COCl B = D = $COOCH_3$

4a A = D = COCl B = C = $COOCH_2$-

4b A = C = COCl B = D = $COOCH_2$-

17 A = B = C = D = 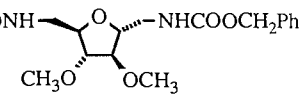

18 A = B = C = D = 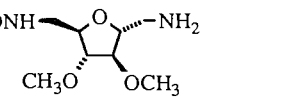

by reversing the order of the reactions. Displacement of the tosyloxy groups of **8** with azide ion (2.2 equiv. NaN_3, DMSO, 24 h at 80°C) (21) provided **9** in 94% yield as a stable oil.[3] During the course of our work, Guthrie *et al.* (22) reported a slightly different, lower yielding preparation of **9**. The reported ^1H nmr data differ significantly from ours, however. Our spectrum and other data are both internally consistent and as expected for **9**. Hence, the previous report must clearly be in error. Methylation of **9** (2.5 equiv. NaH, 2.2 equiv. CH_3I, cat. n-$Bu_4N^+Br^-$ (23), THF, overnight at room temperature) proceeded smoothly to afford an 86% yield of **10**, as an initially slightly yellow oil that darkened over a period of weeks. Decomposition was only slight, however, and **10** could be chromatographed before use. Hydrogenation of **10** in acidic solution (3.0 equiv. H_2, cat. 10% Pd/C, EtOH containing 2.1 equiv. concentrated HCl, 24 h at RT) afforded crystalline **11**·2HCl in 72% yield. Neutralization gave a quantitative yield of oily free base **11**.

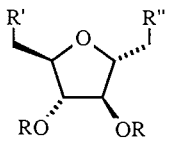

7 R = H R' = R'' = OH

8 R = H R' = R'' = OTs

9 R = H R' = R'' = N_3

10 R = CH_3 R' = R'' = N_3

11 R = CH_3 R' = R'' = NH_2

12 R = CH_3 R' = NH_2 R'' = $NHCOOCH_2Ph$

13 R = CH_3 R' = R'' = $NHCOOCH_2Ph$

14 R = CH_3 R' = R'' = $N(CH_3)COOCH_2Ph$

15 R = CH_3 R' = R'' = $NHCH_3$

[3]Although no problems of explosive instability were encountered in our work, special care should be taken when preparing and handling organic polyazides. In particular, they should not be heated in large batches in the absence of solvents, and crystallization may release dangerous amounts of heat (21).

Our approach to the synthesis of "trimeric stack" **6** called for a high dilution coupling of two face-differentiated units (such as **3***a* (5)) with one bearing four spacers as a central unit. Alternatively, two face-differentiated units of **1**, each bearing two spacers, could be coupled to the central unit (e.g., **2**). In both cases, we wished to link diamine **11** to macrocycles via only one of the amine functions and therefore required a mono-protected form of **11**. As could be expected, mono-protection in homogeneous solution of diamine **11** by benzyloxycarbonyl (BzOC) groups proved to be nonselective. Treatment of **11**·2HCl with 1.0 equiv. benzyl chloroformate (BzOCCl) in 4:15 H_2O–EtOH (containing 1.0 equiv. Et_3N, 1 h at RT) produced a mixture of mono-BzOC **12**·HCl, di-BzOC **13**, and unreacted **9**·2HCl. Nevertheless, successive extractions in acidic and basic media resolved the statistical mixture of products (see Experimental) affording oily free base mono-BzOC **12** in 31% yield (ca. 49% based on converted **11**) and di-BzOC **13** in ca. 30% yield as an oil that slowly crystallized. Compound **13** could also be produced deliberately from free base **11** with 2 or more equiv. each of benzyl chloroformate and Et_3N. Substituting CH_3CN for EtOH, or NaOH for Et_3N, in the above procedure did not improve the yield of mono-BzOC **12**. When two phases were present in the reaction mixture, higher proportions of di-BzOC **13** were produced by virtue of the H_2O-insolubility of BzOCCl and the appreciable solubility of mono-BzOC **12**·HCl in organic media. Using free base **11** instead of the dihydrochloride salt gave only **13** for the same reason. The solvent mixture used in this preparation of **12** appeared to maintain homogeneity throughout the reaction.

Reduction of the protecting groups in **13** ($LiAlH_4$, THF, 2 days at reflux; basic work-up) produced a complex mixture from which a small amount of crystalline **15**·2HCl was isolated. Alternatively, methylation of **13**, in the same way as was done with **9**, produced oily **14** in quantitative yield. The room temperature nmr spectrum of **14** is complex, but a well-resolved spectrum could be obtained by heating to 60°C, where rotation about the carbonyl nitrogen bond of the tertiary amide groups becomes fast on the nmr timescale. Deprotection of **14** (excess HBr in HOAc, overnight at RT; ion exchange with Dowex 1X8 OH^- form) afforded oily free base **15**.

Can. J. Chem. Downloaded from www.nrcresearchpress.com by 213.222.148.141 on 09/07/12
For personal use only.

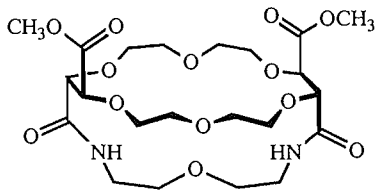

5

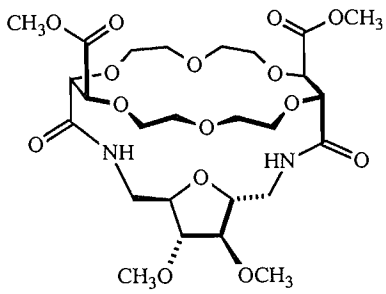

16

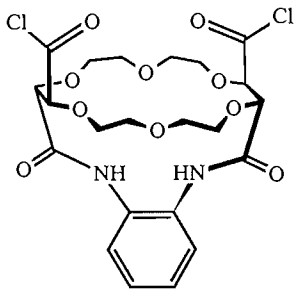

19

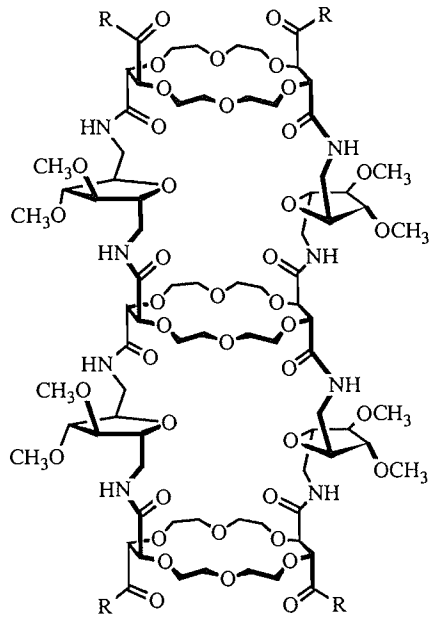

6 R = 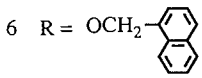

20 R, R = 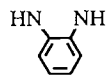

*Combination of diamine **11** with macrocycles*

syn-Dimethyl ester-diacid chloride **3***a* (5) and **11** were coupled under high dilution conditions, where equimolar CH_2Cl_2 solutions of **11** (containing 2 equiv. Et_3N) and of **3***a* were slowly pumped from syringes into rapidly stirred CH_2Cl_2 such that the initial reactant concentrations were ca. 10^{-6} M. Work-up afforded a crude mixture that consisted largely of **16** (according to nmr, ir, and tlc). However, this material did not well survive chromatography on Al_2O_3 or SiO_2, and pure **16** was isolated in only 5% yield as a thick oil.[4] The ^1H nmr spectrum (taken in $CDCl_3$) displays two singlets for the asymmetric crown (OCH-type) protons at 4.41 and 4.27 ppm, a single ester-type methoxyl peak at 3.77 ppm, and a single ether-type methoxyl peak at 3.37 ppm. Similarly, the ^1H nmr spectrum of the related macrobicycle **5** (taken in CD_3CN) also displays two singlets at 4.30 and 4.18 ppm for the corresponding asymmetric crown protons (5, 24). The ^{13}C nmr spectrum of **16** also showed single peaks for each of the structurally distinct carbons, analogous to those displayed by **5** (5, 24).

Tetra-acid chloride **2** (2, 3) and 4.0 equiv. of **12** were coupled in the presence of excess Et_3N (CH_2Cl_2, 0.5 h at RT) to provide, after chromatography on Al_2O_3, a 77% yield of oily tetra-"armed" crown **17**.[4] This could be deprotected in the same manner as was **14** to give a 92% yield of tetra-amine **18** as a slightly yellow foam.[4] Apart from characteristic signals assignable to asymmetric crown OCH, there was strong overlap in the region near 3.6 ppm of the ^1H nmr spectra of **17** and **18**. The ^{13}C spectra were more useful, but they also showed some accidental overlap and assignments were made by analogy. For instance, the signal at 86.6 ppm assigned to C2′ and C5′ of **17** was analogous to a signal also at 86.6 ppm for C2(C5) of **13**. Similarly, a signal at 87.1 ppm was assigned to C2′ and C5′ of **18** by analogy to peaks at 87.1 and 86.9 ppm for C2 and C5 of **12**. Further, the spectrum of **17** showed a taller peak at 81.6 ppm, with an upfield shoulder, which was attributed to C3′, C4′, and macro-ring O*C*H by analogy to the signal at 81.7 ppm for C3(C4) of **13** and to a signal at 81.8 ppm for O*C*H of the tetra(*N*-methyl)amide of **1** (2). This overlap was partially resolved in the spectrum of **18**, where two signals appeared for the corresponding nuclei at 83.8 and 81.4 ppm (in ca. 1:2 intensity ratio), analogous to signals at 84.3 and 81.1 ppm (in ca. 1:1 ratio) for C3 and C4 of **12**.

A high dilution coupling of **18** with two equivalents of *syn*-dimethyl ester-diacid chloride **3***a* (5) provided a complex mixture of products. Column chromatographic separation was unsuccessful, however. When *syn*-bis(naphth-1-yl)methyl ester-diacid chloride **4***a* (5) was used instead, a small amount

[4]The compounds **16**, **17**, and **18** were obtained as thick oils or foams. Although they appeared chromatographically homogeneous, the reader should be aware that, in the absence of crystalline materials, indications of their purity and proofs of their structure rely entirely on nmr and ir data.

Can. J. Chem. Downloaded from www.nrcresearchpress.com by 213.222.148.141 on 09/07/12
For personal use only.

Can. J. Chem. Downloaded from www.nrcresearchpress.com by 213.222.148.141 on 09/07/12
For personal use only.

of the chromatographically most mobile product (on tlc plates) could be isolated (ca. 6.5% yield) by column chromatography on basic Al_2O_3 (act. II/III). This material, largely homogeneous on tlc plates, unfortunately decomposed even at room temperature to liberate naphthalene-1-methanol. Exposure to basic alumina seemed to accelerate this process. Column chromatography on neutral Al_2O_3 (act. I), preparative tlc on Al_2O_3, or reverse-phase hplc, using 3–8:10 CH_3CN – 0.01 M $NH_4^+HCOO^-$ as eluent, failed to effect purification without decomposition. Coupling of **4***a* and **18** at 0°C or in the presence of CsOTf at −10°C failed to provide cleaner product mixtures. The ^1H nmr spectrum of the product displayed chemical shifts and integration ratios consistent with a "trimeric" macropentacyclic structure **6**. In particular, the spectrum, taken in $CDCl_3$, featured a single, well-resolved AB pattern at 5.69 ppm for the benzylic protons, 2 singlets of unequal intensity (ca. 1:2 integration ratio) at 4.37 and 4.30 ppm for the asymmetric crown protons, and a single peak for methoxyl protons at 3.34 ppm. Although there are three structurally distinct protons at the asymmetric centres of the macrocycles, viz. those α to the carboxamides on the central ring, those α to the carboxamides on the outer rings, and those α to ester groups, one may expect little difference in chemical environments between the first two types, and expect the signals from the latter type to occur at a lower field position than the first two. As well, one may expect overlap of the two structurally distinct methoxyl protons for the same reason. Recently, attempts at forming a macroheptacyclic entity **20** were made via high dilution condensation of 2 equiv. of *o*-phenylenediamine-bridged 18-crown-6 diacid chloride **19** (25) with one of tetra-amine **18** (24). The spectrum of this condensation product (taken in CD_3OD) displayed a signal at 4.50 ppm (assigned to four macro-ring OC*H*), a mass of signals near 4.3 ppm (assigned to the eight remaining macro-ring OC*H* and to eight H2′ and H5′), and two methoxyl peaks centred near 3.5 ppm. These and other similarities with the spectra of **16**, **17**, **18**, and **5** lend support to our assignment of the ^1H nmr peaks of our condensation product, but an unequivocal synthesis of **6** remains to be performed.

In conclusion, the 1,5-diamino-3-oxapentanes **11** and **15** are readily prepared from D-glucosamine, and are versatile structural units that, in addition to the couplings described here, may find use in other applications where rigidity, chirality, and C_2 symmetry are desired. From the results of our high dilution reactions, however, it would appear that, although the ester linkages of macrocycles **3***a* and **4***a* may be more amenable to conversion to other functionalities, amide-linked side chains such as in **19** are more stable and, hence, likely more preparatively useful in condensation reactions.

Experimental

General

The nmr spectra were run on 60 MHz Varian A-360 or 200 MHz Bruker Aspect 2000 instruments. Internal references were either TMS or the signal due to the protio-solvent in ^1H spectra, or the deuterio-solvent peak in ^{13}C spectra. A Beckman 197 instrument was used for ir spectra. Optical rotations were measured at room temperature on a Perkin–Elmer 110 polarimeter. Melting points are uncorrected. Column grade silica was type 60, and alumina was basic, with activity II/III, or neutral, with activity I. Flash chromatography used silica of 43–60 Å particle size. Thin-layer chromatography (tlc) was performed on Macherey–Nagel plastic-backed plates of Al_2O_3. Solvents were distilled over appropriate drying agents before use. 2,5-Anhydro-D-mannitol **7** was prepared from D-glucosamine hydrochloride (20), omitting the acetylation, chromatography, and deacetylation purification steps (19*b*). The product, a thick yellow syrup, was used directly in the preparation of 2,5-anhydro-1,6-di-*O*-tosyl-D-mannitol **8** (19*b*, 20). However, we replaced the chromatographic purification of **8** with a trituration with hot toluene, from which the product crystallizes upon cooling. The overall yield of **8** was ca. 37% from D-glucosamine hydrochloride.

*2,5-Anhydro-1,6-di-*C*-azido-1,6-dideoxy-*D*-mannitol* ***9***

A mixture of ditosyl ester **8** (21.39 g, 45.3 mmol) and NaN_3 (6.48 g, 2.2 equiv.) in 225 mL of dry DMSO was stirred at 80°C for 24 h. After cooling, the reaction mixture was diluted with H_2O (1 L) and extracted with EtOAc (6 × 500 mL). Each organic layer was separately washed with a series of five volumes of H_2O (100 mL), then evaporated to dryness and analysed by nmr. The first four were found to be free by DMSO, and were combined to give 9.07 g (94% yield) of slightly yellow oil. An analytical sample was obtained by flash chromatography of the combined fifth and sixth extracts, using 40% EtOAc in hexane as eluent; $[\alpha]_D$ +117.6° (0.037 M, $CHCl_3$); ir (thin film): 3400 (b), 2100 (s) cm^{-1}; ^1H nmr ($CDCl_3$) δ: 4.14–3.94 (m, 4H), 3.67 (bs, 2H, OH), 3.51 (ddd, 4H, J = 3.7, 4.2, 13.2 Hz) ppm; ^{13}C nmr ($CDCl_3$) δ: 81.1 (C2, C5), 78.0 (C3, C4), 51.8 (C1, C6) ppm.

*2,5-Anhydro-1,6-di-*C*-azido-1,6-dideoxy-3,4-di-*O*-methyl-*D*-mannitol* ***10***

A two-necked flask, flushed with Ar, equipped with an outlet to a gas bubbler and an additional funnel, and cooled in a water bath, was charged with NaH (4.67 g of ca. 55% oil dispersion, ca. 107 mmol) and a trace of tetra-*N*-butylammonium bromide. This was suspended in dry THF (25 mL), and a solution of diazide **9** (9.17 g, 42.8 mmol) and CH_3I (5.86 mL, 2.2 equiv.) in dry THF (50 mL) was added over 5–10 min, avoiding internal reflux of the THF. After complete addition and flushing with Ar, the mixture was stirred overnight at RT. After quenching with a little H_2O, most of the THF was removed *in vacuo*, and the mixture was twice extracted with ether. The ether layers were separately washed with H_2O, then combined, dried ($MgSO_4$), and evaporated to dryness. Most of the oil was removed by partitioning the residue between CH_3CN and hexane. The CH_3CN layer was evaporated to give 9.0 g of crude product as a light yellow oil. This was chromatographed on a short column of SiO_2, using 20% EtOAc in hexane to elute 8.91 g (86%) of pure dimethoxy diazide **10** as a colourless, mobile liquid. The major impurity, eluted with 40% EtOAc in hexane, was the product of monomethylation; $[\alpha]_D$ +67.4° (0.089 M, $CHCl_3$); ir (thin film): 3430 (b), 2490 (s) cm^{-1}; ^1H nmr ($CDCl_3$) δ: 4.18–4.10 (m, 2H, H2, H5), 3.72 (q, 2H, J = 1.1, 2.9 Hz, H3, H4), 3.40 (d, 4H, J = 5.6 Hz, H1, H6), 3.40 (s, 6H, OCH_3) ppm; ^{13}C nmr ($CDCl_3$) δ: 86.5 (C2, C5), 81.6 (C3, C4), 57.6 (CH_3), 52.2 (C1, C6) ppm.

*2,5-Anhydro-1,6-di-*C*-amino-1,6-dideoxy-3,4-di-*O*-methyl-*D*-mannitol* ***11***

A 500-mL stainless steel bomb was loaded with a solution of diazide **10** (8.93 g, 36.9 mmol) in EtOH (100 mL), to which was added 10% Pd on C (ca. 1.0 g) and 6.5 mL concentrated HCl (ca. 2.1 equiv.). After flushing with H_2, the bomb was charged with 6 atm H_2 (ca. 3.0 equiv.) and shaken overnight. After discharging the pressure, the solid mass deposited at the bottom was taken up in MeOH and the catalyst was filtered off. The filtrate was concentrated to give crude crystalline product. Recrystallization from MeOH–CH_3CN afforded 7.02 g of colourless crystals of the pure dihydrochloride salt of **11** (72% yield), mp 260°C; $[\alpha]_D$ +69.2° (0.019 M, H_2O); ^1H nmr (CD_3OD) δ: 4.39 (td, 2H, J = 1, 6.5 Hz, H2, H5), 3.84 (dd, 2H, J = 1.1 Hz, H3, H4), 3.43 (s, 6H, OCH_3), 3.15 (ddd, 4H, J = 1, 1, 6.5 Hz, H1, H6) ppm; ^{13}C nmr (D_2O) δ: 86.0 (C2, C5), 80.1 (C3, C4), 57.6 (OCH_3), 41.1 (C1, C6) ppm. *Anal.* calcd. for $C_8H_{20}N_2O_3Cl_2$: C 36.51, H 7.66, N 10.64%; found: C 36.52, H 7.61, N 10.67%. The free diamine was generated as needed by treating a MeOH solution of the salt with a slight excess of 1 M NaOH solution, evaporating to dryness, and triturating with dry CH_2Cl_2. Filtration of the triturate and evaporation of the filtrate afforded quantitative yields of the pure diamine as a slightly yellow oil that slowly carbonated in air; ^1H nmr ($CDCl_3$) δ:

Can. J. Chem. Downloaded from www.nrcresearchpress.com by 213.222.148.141 on 09/07/12
For personal use only.

3.84 (m, 2H, J = 1.6, 4.7 Hz, H2, H5), 3.54 (q, 2H, J = 1.0, 3.2 Hz, H3, H4), 3.34 (s, 6H, OCH_3), 2.80 (dd, 4H, J = 1.1, 3.2 Hz, H1, H6), 1.25 (s, 4H, NH_2) ppm; ^{13}C nmr ($CDCl_3$) δ: 87.2 (C2, C5), 83.4 (C3, C4), 57.1 (OCH_3), 43.8 (C1, C6) ppm.

2,5-Anhydro-1-C-(N-benzyloxycarbonyl)amino-6-C-amino-1,6-dideoxy-3,4-di-O-methyl-D-mannitol ***12*** *and 2,5-anhydro-1,6-di-C-(N-benzyloxycarbonyl)amino-1,6-dideoxy-3,4-di-O-methyl-D-mannitol* ***13***

A solution of **11**·2HCl (1.00 g, 3.80 mmol) in H_2O (4 mL) was diluted with EtOH (15 mL) and treated with Et_3N (0.53 mL, 1.0 equiv.). Then technical grade benzyl chloroformate (85% pure, 0.53 mL, ca. 1.0 equiv.) was added dropwise to the vigorously stirred solution. The mixture was allowed to stir at RT a further hour, then rid of solvents. Trituration with several volumes of CH_2Cl_2 left 0.75 g of insoluble residue, containing unreacted **11**·2HCl. The CH_2Cl_2-soluble portion was washed twice with dilute HCl (containing at least 4 mmol HCl per wash), and the aqueous phases were separately reextracted with CH_2Cl_2. The combined CH_2Cl_2 layers were evaporated to give impure bis-protected diamine **13**. The combined aqueous phases were concentrated and treated with NaOH pellets to bring the pH to about 12. The resulting turbid solution was extracted twice with CH_2Cl_2. The combined organic layers were evaporated to afford 0.378 g of mono-amine **12** (31% yield); $[\alpha]_D$ of the HCl salt +57.9° (0.047 M, H_2O); ir (thin film): 3410–3300 (b), 1695 (s) cm^{-1}; ^1H nmr ($CDCl_3$) δ: 7.35 (bs, 5H, Ph), 5.31 (bt, 1H, NH), 5.11 (s, 2H, CH_2Ph), 4.03 (m, 1H, H2), 3.90 (m, 1H, H5), 3.59 (bs, 2H, H3, H4), 3.43 (m, 2H, H1), 3.37, 3.36 (2s, 6H, OCH_3), 2.81 (m, 4H, H6) ppm; ^{13}C nmr ($CDCl_3$) δ: 156.4 (C=O), 136.5, 128.3, 127.9 (Ph), 87.1 (C2), 86.9 (C5), 84.3 (C3), 81.1 (C4), 66.6 (CH_2Ph), 57.5 (C1), 57.2 (C6), 43.8, 42.9 (OCH_3) ppm. The crude by-product **13** was purified by column chromatography on SiO_2, using 40% EtOAc in hexane as eluent. This afforded a colourless oil that crystallized in the cold. Suspending the solid in 1:1 ether–hexane, followed by filtration and washing with cold toluene, afforded white crystals (ca. 30% yield) that could not be recrystallized, mp 69–71°C; $[\alpha]_D$ +37.8° (0.063 M, $CHCl_3$); ir ($CHCl_3$): 3580, 3565, 3445, 1705 cm^{-1}. ^1H nmr ($CDCl_3$) δ: 7.33 (s, 10H, Ph), 5.28 (bt, 2H, NH), 5.09 (s, 4H, CH_2Ph), 4.04 (bm, 2H, H2, H5), 3.58 (bs, 2H, H3, H4), 3.38 (m, 4H, H1, H6), 3.33 (s, 6H, OCH_3) ppm; ^{13}C nmr ($CDCl_3$) δ: 156.4 (C=O), 136.5, 128.4, 128.0 (Ph), 86.6 (C2, C5), 81.7 (C3, C4), 66.7 (CH_2Ph), 57.4 (C1, C6), 42.7 (OCH_3) ppm. *Anal.* calcd. for $C_{24}H_{30}N_2O_7$: C 62.87, H 6.59, N 6.11%; found: C 62.98, H 6.66, N 6.15%. The original CH_2Cl_2-insoluble residue was extensively triturated with CH_3CN to rid it of most of the Et_3N·HCl before recovery, as described above, of **11** as its free base.

2,5-Anhydro-1,6-di-C-(N-benzyloxycarbonyl-N-methyl)amino-1,6-dideoxy-3,4-di-O-methyl-D-mannitol ***14***

The di-*N*-benzyloxycarbonyl diamine **13** was methylated in the same manner as was diazide **9** to afford a quantitative yield of di-*N*-benzyloxycarbonyl di-*N*-methyl diamine **14** as a slightly yellow oil that could be purified by column chromatography on SiO_2 using 40% EtOAc in hexane as eluent; $[\alpha]_D$ +32.9° (0.139 M, $CHCl_3$); ir (thin film): 1690 cm^{-1}; ^1H nmr ($CDCl_3$, 60°C) δ: 7.30 (m, 10H, Ph), 5.10 (s, 4H, CH_2Ph), 4.11 (bq, 2H, H2, H5), 3.55–3.30 (m, 6H), 3.24 (bs, 6H, OCH_3), 2.95 (s, 6H, NCH_3) ppm; ^{13}C nmr ($CDCl_3$, RT) δ: 156.1, 155.6 (C=O), 136.3, 133.7, 133.4 (Ph), 86.8 (C2, C5), 84.1 (C3, C4), 66.8 (CH_2Ph), 56.9 (C1, C6), 50.9, 50.6 (OCH_3), 35.5 (NCH_3) ppm. *Anal.* calcd. for $C_{26}H_{34}N_2O_7 \cdot \frac{1}{2}H_2O$: C 63.02, H 7.12, N 5.65%; found: C 63.17, H 6.99, N 5.83%.

2,5-Anhydro-1,6-di-C-(N-methyl)amino-1,6-dideoxy-3,4-di-O-methyl-D-mannitol ***15***

A solution of **14** in HOAc was treated with 4 equiv. 37% HBr in HOAc and the solution was allowed to stand overnight. After evaporating to dryness, the crude product was dissolved in H_2O, then passed through a column of Dowex 1X8 resin (OH^- form). After evaporating to dryness, the residue was dissolved in EtOH and treated with a slight excess of 1 M HCl solution, then rid of solvents to afford **15**·2HCl, mp 220°C (dec.); $[\alpha]_D$ +61.0° (0.024 M, H_2O); ^1H nmr of free base ($CDCl_3$) δ: 3.85 (m, 2H, H2, H5), 3.60 (m, 2H, H3, H4), 3.45 (s, 6H, OCH_3), 2.85 (m, 4H, CH_2), 1.55 (s, 6H, NCH_3) ppm.

Macrobicycle ***16***

A flame-dried, three-necked, invaginated round-bottom flask, equipped with a mechanical stirrer and two stopcocks, was flushed with Ar and loaded with 5 mL of dry CH_2Cl_2. In an oven-dried gas-tight syringe was placed 24 mL of a CH_2Cl_2 solution of **3***a* (120 mg, 0.237 mmol). A second, identical syringe held an equal volume of CH_2Cl_2 containing free base diamine **11** (45 mg, 0.237 mmol) and Et_3N (67 μL, 2.02 equiv.). Identical 12 in. long needles (delivering ca. 5-μL drops of CH_2Cl_2) were fitted to the syringes, and these were mounted on a syringe pump. The needles were passed through the opened stopcocks and dipped just below the surface of liquid. Vigorous stirring was applied and the pumping rate of the syringe pump was adjusted to deliver ca. 1 drop/s. After complete addition, fresh solvent was drawn into the syringes and the rinses pumped into the reaction mixture. The resulting greenish solution was washed with H_2O (3×) and the aqueous layers extracted once with fresh CH_2Cl_2. The combined organic layers were concentrated and treated with toluene to precipitate an amorphous reddish solid that contained no desired product (as determined by tlc using 2.5–5% MeOH in CH_2Cl_2 as developer). The yellow supernatant was filtered and freed of solvents. The residue was chromatographed on a column of basic Al_2O_3, eluting with CH_2Cl_2 containing, firstly, 1% v/v MeOH, then 2% MeOH, and finally 3% MeOH. The yield of the combined fractions containing the desired product was ca. 8 mg. Similar preparations chromatographed on silica or neutral Al_2O_3 gave similar yields; $[\alpha]_D$ +66.3° (0.021 M, $CHCl_3$); ir (thin film): 3360 (b, shoulder at 3410), 1740 (s), 1642 (s), 1532 (m) cm^{-1}; ^1H nmr ($CDCl_3$) δ: 8.45 (bm, 2H, NH), 4.41, 4.27 (2s, 4H, OCH), 4.04–3.52 (m, 28H), 3.77 (s, 6H, $COOCH_3$), 3.37 (s, 6H, $ROCH_3$) ppm; ^{13}C nmr ($CDCl_3$) δ: 169.8, 169.3 (C=O), 88.3 (C2′, C5′), 80.9 (C3′, C4′), 79.6, 79.0 (OCH), 70.5, 69.2, 68.3, 68.1 (OCH_2), 57.6 (C1′, C6′), 51.8 ($COOCH_3$), 41.6 ($ROCH_3$) ppm.

Tetra-N-benzyloxycarbonyl tetra-amine ***17***

Under an Ar atmosphere, a solution of tetra-acid chloride **2** (123 mg, 0.24 mmol) in dry CH_2Cl_2 (4 mL) was added over 0.5 h to a stirred solution of mono-*N*-benzyloxycarbonyl diamine **12** (310 mg, 4 equiv.) and Et_3N (133 μL, 4.4 equiv.) in dry CH_2Cl_2 (5 mL). The mixture was stirred a further 0.5 h, then evaporated to dryness. The crude product was purified on a column of Al_2O_3 by eluting first with 1% MeOH in CH_2Cl_2, then with 2% MeOH in CH_2Cl_2, to afford 305 mg (77%) of slightly yellow oily material; $[\alpha]_D$ +83.1° (0.018 M, $CHCl_3$); ir (thin film): 3305 (b), 1700 (s), 1660 (s), 1520 (s) cm^{-1}; ^1H nmr ($CDCl_3$) δ: 7.30 (bs, 20H, Ph), 5.57 (bt, 4H, NH), 5.06 (s, 8H, CH_2Ph), 4.35 (bs, 4H, OCH), 4.05 (bq, 8H, H2′, H5′), 3.62, 3.56 (2bm, 24H), 3.34, 3.29 (2s+bm, 40H, OCH_3) ppm; ^{13}C nmr ($CDCl_3$) δ: 170.1 (RCONH), 156.3 (OCONH), 136.3, 128.2, 127.8 (Ph), 86.6 (C2′, C5′), 81.6 (C3′, C4′, OCH), 71.2, 69.2 (OCH_2), 66.4 (CH_2Ph), 57.3, 56.9 (C1′, C6′), 42.7, 40.7 (OCH_3) ppm.

Tetra-amine ***18***

A solution of tetra-*N*-benzyloxy tetra-amine **17** (354 mg, 0.213 mmol) in glacial HOAc (3.5 mL) was treated with a 33% solution of HBr in HOAc (0.30 mL, 8 equiv.) and allowed to stand overnight at RT. A reddish, oily second phase formed. The mixture was rid of solvent and the crude salt was partitioned between H_2O and CH_2Cl_2. The organic phase was washed once with H_2O and the aqueous layers were separately washed with fresh CH_2Cl_2. The combined aqueous phases were concentrated, then stirred with an excess of Dowex 1X8 resin (OH^- form) for 15 min. The resin was filtered off, washed with H_2O, and the combined filtrates were evaporated to dryness, leaving 220 mg of slightly yellow foam (92% yield); $[\alpha]_D$ of the tetra HCl salt +100.35° (0.029 M, MeOH); ^1H nmr (CD_3CN) δ: 7.54 (bm, 4H, amide NH), 4.22 (bs, 4H, OCH), 3.99, 3.84 (bm+q, 8H, J = 5.8, 9.7 Hz, H2′, H5′), 3.66, 3.61, 3.40 (3bm, 36H), 3.36, 3.34 (2s, 24H, OCH_3), 2.69 (d, 8H, J = 5.9 Hz, H6′) ppm; ^{13}C nmr ($CDCl_3$) δ: 170.0 (C=O), 87.1 (C2′, C5′), 83.8, 81.4 (1:2 ratio, C3′, C4′,

OCH), 71.2, 69.4 (OCH_2), 57.3, 57.1 (C1′, C6′), 43.8, 41.3 (OCH_3) ppm.

Attempted preparation of "trimer" 6

A procedure identical to that used in the preparation of **16** was employed in the condensation of 12 mL of CH_2Cl_2 solutions of **4***a* (92 mg, 0.121 mmol) with **18** (69 mg, 0.060 mmol) and Et_3N (28 μL, 4.55 equiv.) in 25 mL of CH_2Cl_2. After washing with H_2O and evaporation of solvent, the residue was chromatographed on a column of Al_2O_3 eluted firstly with $CHCl_3$, then with CH_2Cl_2 containing increasing amounts of MeOH (1–30%). As judged by tlc (using 2.5–5% MeOH in CH_2Cl_2 or 4% EtOH in $CHCl_3$ as developer), the fractions containing the chromatographically most mobile product were combined, freed of solvent, and loaded onto a second, similar column eluted with 2% MeOH in CH_2Cl_2. The fractions containing desired product were combined and evaporated to dryness to afford ca. 10 mg of an oil (ca. 6.5% yield); ^{1}H nmr ($CDCl_3$) δ: 8.06, 7.82, 7.57–7.28 (3m, 36H, Ar, NH), 5.69 (ABq, 8H, CH_2Ar), 4.37, 4.30 (2s, 12H, asymmetric crown H), 4.22–3.03 (m, 80H), 3.34 (s, 24H, OCH_3) ppm.

Acknowledgement

P.G.P. wishes to thank the Natural Sciences and Engineering Research Council of Canada for a Post-Doctoral Fellowship (1982–1984).

1. J. M. LEHN. Pure Appl. Chem. **51**, 979 (1979); Science, **227**, 849 (1985); P. G. POTVIN and J. M. LEHN. *In* Synthesis of macrocycles. The design of selective complexing agents. *Edited by* R. M. Izatt and J. J. Christensen. Wiley–Interscience, New York. 1987. p. 167.
2. J. P. BEHR, J. M. GIRODEAU, R. C. HAYWARD, J. M. LEHN, and J. P. SAUVAGE. Helv. Chim. Acta, **63**, 2096 (1980).
3. J. P. BEHR, J. M. LEHN, and P. VIERLING. Helv. Chim. Acta, **65**, 1853 (1982).
4. J. P. BEHR, J. M. LEHN, D. MORAS, and J. C. THIERRY. J. Am. Chem. Soc. **103**, 701 (1981).
5. J. P. BEHR, C. J. BURROWS, R. HENG, and J. M. LEHN. Tetrahedron Lett. 215 (1985).
6. (*a*) J. J. DALY, P. SCHÖNHOLZER, J. P. BEHR, and J. M. LEHN. Helv. Chim. Acta, **64**, 1444 (1981); (*b*) J. P. BEHR, J. M. LEHN, A. C. DOCK, and D. MORAS. Nature, **295**, 526 (1982); (*c*) J. P. BEHR, P. DUMAS, and D. MORAS. J. Am. Chem. Soc. **104**, 4540 (1982).
7. S. T. JOLLEY, J. S. BRADSHAW, and R. M. IZATT. J. Heterocycl. Chem. **19**, 3 (1982).
8. B. L. ALLWOOD, S. E. FULLER, P. C. Y. K. NING, A. M. Z. SLAWIN, J. F. STODDART, and D. J. WILLIAMS. J. Chem. Soc. Chem. Commun. 1356 (1984); M. PIETRASZKIEWICZ, P. SATANSKI, and J. JURCZAK. J. Chem. Soc. Chem. Commun. 1184 (1984); Tetrahedron, **40**, 2967 (1984); P. BAKO, L. FENICHEL, and L. TOKE. Acta Chim. Hung. **116**, 323 (1984); Chem. Abstr. **101**, 192332 (1984); B. WALZ and G. SCHRODER. Liebigs Ann. Chem. 426 (1985); R. ELLINGHAUS and G. SCHRODER. Liebigs Ann. Chem. 418 (1985); H. GRUBER and G. SCHRODER. Liebigs Ann. Chem. 421 (1985); U. ELBEN. Liebigs Ann. Chem. 210 (1985); S. SASAKI, M. KAWASAKI, and K. KOGA. Chem. Pharm. Bull. (Tokyo), **33**, 4247 (1985); M. PIETRASKIEWICZ and J. JURCZAK. J. Carbohydr. Chem. **4**, 429 (1985).
9. J. A. HASLEGRAVE, J. F. STODDART, and D. J. THOMPSON. Tetrahedron Lett. 2278 (1979).
10. D. A. LAIDLER and J. F. STODDART. Tetrahedron Lett. 453 (1979); D. G. ANDREWS, P. R. ASHTON, D. A. LAIDLER, J. F. STODDART, and J. B. WOLSTENHOLME. Tetrahedron Lett. 2629 (1979).
11. M. NAKAZAKI, K. NAEMURA, M. MAKIMURA, A. MATSUDA, T. KAWANO, and Y. OHTA. J. Org. Chem. **47**, 2429 (1982); K. NAEMURA, I. EBASHI, and A. MATSUDA. Bull. Chem. Soc. Jpn. **56**, 3057 (1985).
12. K. NAEMURA, Y. HOKURA, Y. KANDA, and M. NAKAZAKI. Chem. Lett. 615 (1985).
13. D. W. URRY. Proc. Natl. Acad. Sci. U.S.A. **68**, 672 (1971); **68**, 1907 (1971); W. R. VEATCH, E. T. FOSSEL, and E. R. BLOUT. Biochemistry, **13**, 5249 (1974).
14. R. O. FOX, JR. and F. M. RICHARDS. Nature, **300**, 325 (1985).
15. B. DE KRUIJFF and R. A. DEMEL. Biochim. Biophys. Acta, **339**, 57 (1974).
16. A. J. W. VAN BEIJNEN, R. J. M. NOLTE, J. W. ZWIKKER, and W. DRENTH. Recl. Trav. Chim. Pays-Bas, **101**, 409 (1983).
17. I. TABUSHI, Y. KURODA, and Y. YOKOTA. Tetrahedron Lett. 4601 (1982).
18. J. M. LEHN and M. E. STUBBS. J. Am. Chem. Soc. **96**, 4011 (1974).
19. (*a*) D. HORTON and K. D. PHILLIPS. Methods Carbohydr. Chem. **7**, 168 (1976), and references cited therein; (*b*) D. PARKER. Doctoral thesis, University of Durham, U.K. 1980.
20. S. AKIYA and T. OSAWA. Yakugaku Zasshi, **74**, 1259 (1954); Chem. Abstr. **49**, 14649i (1955).
21. R. L. MARTIN and B. E. NORCROSS. J. Org. Chem. **40**, 523 (1975).
22. R. D. GUTHRIE, I. D. JENKINS, J. J. WATTERS, M. W. WRIGHT, and R. YAMASAKI. Aust. J. Chem. **35**, 2169 (1982).
23. S. CZERNECKI, C. GEORGOULIS, and C. PROVELENGHIOU. Tetrahedron Lett. 3535 (1976).
24. R. HENG. Thèse de Doctorat ès Sciences, Université Louis Pasteur, Strasbourg, France. 1985.
25. J. P. BEHR, M. BERGDOLL, B. CHEVRIER, P. DUMAS, J. M. LEHN, and D. MORAS. Tetrahedron Lett. 1989 (1987).

Can. J. Chem. Downloaded from www.nrcresearchpress.com by 213.222.148.141 on 09/07/12
For personal use only.

Anodic and cathodic reactions in acetonitrile/tetra-*n*-butylammonium tetrafluoroborate: an electrochemical and infrared spectroelectrochemical study

JOHN K. FOLEY,[1] CAROL KORZENIEWSKI, AND STANLEY PONS[2]
Department of Chemistry, University of Utah, Salt Lake City, UT 84112, U.S.A.

Received February 3, 1987

JOHN K. FOLEY, CAROL KORZENIEWSKI, and STANLEY PONS. Can. J. Chem. **66**, 000 (1988).

In situ infrared spectroelectrochemistry has been used to observe electrolyte/solvent breakdown processes in TBAF/acetonitrile at a platinum electrode. Anodic breakdown gives the adduct CH_3CNBF_3 as the major product. Cathodic breakdown gives the anion of 3-aminocrotonitrile as the major product in the absence of water, and the formation of this product is a consequence of reduction of hydrogen dissolved in the metal. In the presence of water the anion of acetamide is also formed, and breakdown commences at much less negative potentials.

JOHN K. FOLEY, CAROL KORZENIEWSKI et STANLEY PONS. Can. J. Chem. **66**, 000 (1988).

On a utilisé de la spectroélectrochimie infrarouge in situ pour observer les processus de décomposition électrolyte/solvant dans le TBAF/acétonitrile, à une électrode de platine. Le produit principal de la décomposition anodique fournit l'adduit CH_3CNBF_3. En absence d'eau, la décomposition cathodique fournit de l'amino-3 crotonitrile comme produit principal; la formation de ce produit une conséquence de la réduction de l'hydrogène dissous dans le métal. En présence d'eau, il y a aussi formation de l'anion acétamide et la décomposition commence à des potentiels beaucoup moins négatifs.

[Traduit par la revue]

Introduction

Acetonitrile is one of the most widely used aprotic solvents in electrochemistry. It has a high dielectric constant and a very wide useful potential window. Under ideal conditions the usable potential range of this solvent is determined by the potentials at which the supporting electrolyte breaks down. Half-wave potentials of up to +3.9 V have been measured for the oxidation of aliphatic hydrocarbons in acetonitrile (2), using a platinum ultramicroelectrode to eliminate the need for supporting electrolyte. Tetra-*n*-butylammonium tetrafluoroborate (TBAF) is a common supporting electrolyte which also has a wide usable potential range; the *n*-Bu_4N^+ cation is reduced at potentials more negative than is Li^+, for example, while the BF_4^- anion is oxidized at potentials more positive than is ClO_4^- (1). The acetonitrile/TBAF system is therefore in common use, and it is of interest to identify the solvent and electrode breakdown processes which limit its useful potential range under normal laboratory conditions.

The anodic breakdown of wet acetonitrile solutions at platinum electrodes has been studied with tetra-*n*-propylammonium tetrafluoroborate supporting electrolyte (3). No significant reaction was observed at potentials up to +2.4 V unless water was present (in about 0.1 *M* concentration), in which case the electrolysis products observed were mainly CO_2 and acetamide.

Pons and Khoo (4) have investigated the cathodic limiting reaction at platinum with TBAF as electrolyte. Short periods of electrolysis at −3.3 V gave 3-aminocrotonitrile (diacetonitrile) as the major product, and some 2,4,6-trimethyl-1,3,5-triazine (a trimer of acetonitrile) was formed at longer electrolysis times. With water present, acetamide was the major product of electrolysis at −2.2 V.

In this paper we report an *in situ* infrared spectroelectrochemical investigation of electrode reactions at high positive and negative potentials in nominally dry acetonitrile/TBAF. The reduction of pyrene, which takes place close to the negative potential limit, has been studied in the absence and in the presence of water, to examine the effect of cathodic solvent breakdown on this process.

Experimental

Infrared spectra were obtained by subtractively normalized interfacial FTIR spectroscopy (SNIFTIRS), which has been described in detail elsewhere (5). The FTIR spectrometer was an IBM 98 instrument equipped with a cooled 77 K HgCdTe solid-state detector. A specular reflectance attachment was used to control the angle of incidence of the beam on the cell window for maximum sensitivity. The cell itself was situated outside the spectrometer in a nitrogen purged box, so that the spectrometer could be evacuated to minimize the amount of water vapor and CO_2 in the optical path. The beam passed out of, and returned into, the spectrometer through a KBr window.

The spectroelectrochemical cell was constructed of Pyrex. The working electrode was a 7 mm diameter metal disk, mounted on the end of a brass shaft which was press fitted in a 9 mm diameter Kel-F tube. The tube, which could be moved in a direction perpendicular to the window, was held in place by expanding an O-ring located on the electrode barrel. The secondary electrode was a platinum wire loop. The reference electrode was a silver wire in contact with an acetonitrile solution of $AgNO_3$ (0.01 *M*) and TBAF (0.1 *M*), and all potentials reported herein are with respect to this electrode. A flat silicon infrared transparent window was used, which allowed the spectral region down to 800 cm^{-1} to be investigated. The angle of incidence of the beam on the window was 70°. The electrode potential was controlled with a potentiostat, and potential–time waveforms for cyclic voltammetry were supplied by a waveform generator (Hi Tek Instruments DT2101 and PPR1, respectively). Cyclic voltammograms were recorded on a Houston Instruments Omnigraphic 2000 X-Y recorder.

Before each experiment the electrode was polished to a mirror finish with alumina of successively smaller particle sizes, starting with 1 μm and ending with 0.05 μm. The solution was deaerated by bubbling purified nitrogen through the cell. After deaeration cyclic voltammograms were run with the electrode pulled back from the window. For spectroelectrochemical experiments, the electrode was pushed forward and the plane surface located about 1–2 μm from the window. Single beam spectra, each the average of 128 scans at 4 cm^{-1} resolution, were collected first at 0.0 V (E_1) and then at a series of increasing positive or negative potentials (E_2). Ratioing any pair of spectra gave a difference spectrum for the two potentials. Results are plotted as $\Delta R/R = (R_2 - R_1)/R_1$ vs. wavenumber, where R_1 and R_2 are the reflectivities at E_1 and E_2. Bands with positive $\Delta R/R$ values are

[1]Present address: Department of Chemistry, Box 4260, Texas Tech University, Lubbock, TX 79409, U.S.A.

[2]To whom correspondence should be addressed.

Can. J. Chem. Downloaded from www.nrcresearchpress.com by 213.222.148.141 on 09/07/12
For personal use only.

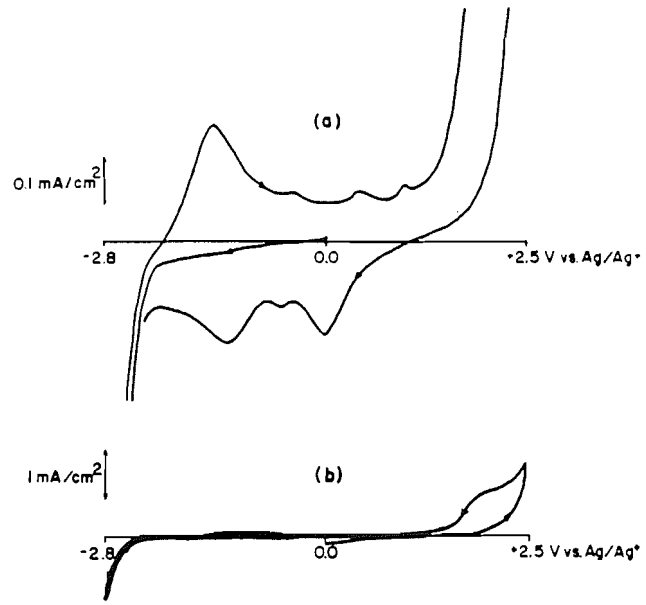

FIG. 1. Cyclic voltammograms for acetonitrile solution of TBAF (0.1 *M*) at a platinum electrode. The potential was swept negative from 0.0 to −2.8 V vs. Ag/Ag^+ (0.01 *M*), then positive to +2.5 V, and then negative again. The sweep rate was 100 mV s^{-1}. The current scale in (*a*) is 10 times more sensitive than in (*b*).

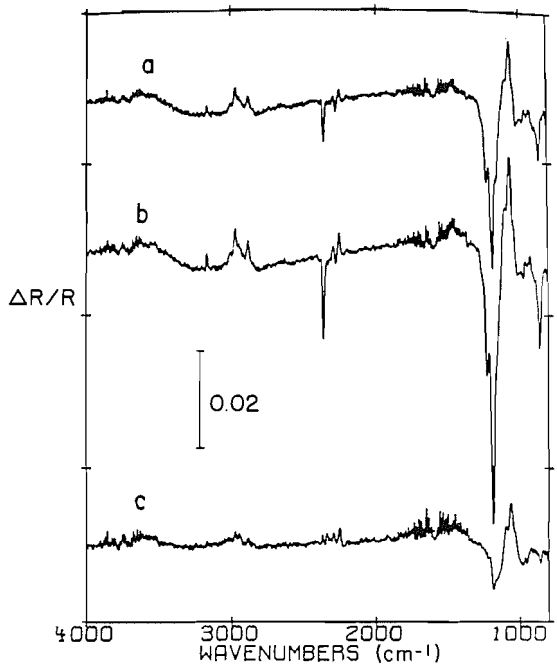

FIG. 2. SNIFTIRS spectra for TBAF (0.1 *M*) in acetonitrile at Pt. Reference spectrum taken at 0.0 V, sample spectra at (*a*) +2.0 V, then (*b*) 0.0 V, then (*c*) −2.0 V.

due to species in the solution at E_1 that are not present at E_2, while the converse is the case for bands with negative values of $\Delta R/R$.

Acetonitrile (Burdick and Jackson, nominal water content <0.005%) was used as received. TBAF (Chem-Biochem Research) was recrystallized from dichloromethane/diethyl ether. Anthracene (Aldrich) and pyrene (Eastman) were sublimed before use. Water was triply distilled.

Results and discussion

(i) Anodic reactions in dry TBAF/acetonitrile

Figure 1 shows cyclic voltammograms of the TBAF (0.1 *M*)/acetonitrile electrolyte system, including the potential region where anodic and cathodic breakdown commence. The potentials at which current densities of 1 mA cm^{-2} of anodic or cathodic current flows, E_f^c and E_f^a, are ca. −2.9 and +2.5 V. E_f^a is rather lower than the +2.91 V measured by Fleischmann and Pletcher (6) for oxidation of BF_4^-, and in fact two processes seem to be taking place at positive potentials. There is a broad plateau between ca. +1.5 and +2.3 V, and this is followed by a current which increases steadily with potential beyond +2.3 V.

A series of SNIFTIRS spectra were taken with base potential 0.0 V where, in a fresh solution, no electrochemical reaction occurs. A potential step to +1.0 V resulted in no new infrared bands, which indicates that there is no electrochemical reaction occurring at this potential. A potential step to +2.0 V, however, gave the difference spectrum shown in Fig. 2*a*. This spectrum includes vibrational bands from the Bu_4N^+, BF_4^-, and CH_3CN species, and the observed frequencies are compared with frequencies and assignments from the literature in Table 1. There are four bands in the C—H stretching region with positive $\Delta R/R$ values. Three of these (2966, 2943, and 2800 cm^{-1}) belong to the *n*-Bu_4N^+ species. The positive values of the absorbances indicate that there is less of this species at this potential (+2.0 V) relative to 0.0 V. The reason for this is well known: any anodic reaction will generate an excess of positive charge in the region close to the electrode surface. To maintain electroneutrality positive ions then must migrate out of the thin layer and negative ions into it. One might therefore expect to observe corresponding bands (negative $\Delta R/R$ values) from BF_4^-, but the bands for this species that are observed have positive values of $\Delta R/R$ indicating that the BF_4^- is being consumed in the electrode reaction at +2.0 V. (BF_4^- is tetrahedral, with only one fundamental ir-active stretching mode, but three or more bands are observed around 1000–1100 cm^{-1} because of the 20% and 80% natural abundances of ^{10}B and ^{11}B, and because of Fermi resonance with the overtone of the antisymmetric BF_2 deformation near 520 cm^{-1} (8, 9)). Positive absorption bands in the difference spectrum at 3163, 2999, 2287, 2249, and 918 cm^{-1} indicate that acetonitrile also reacts at +2.0 V. The frequencies of the 2287 and 2249 cm^{-1} bands are probably affected slightly by the negative band at 2272 cm^{-1}.

The products formed at +2.0 V absorb in the C≡N and B—F stretching regions. In particular, there is a sharp negative band at 2257 cm^{-1} and very strong negative bands at 1227, 1190, 1163, and 856 cm^{-1}. Although CO_2 has been detected as one of the major oxidation products of wet acetonitrile/BF_4^- (3), this cannot be the origin of the 2357 cm^{-1} band observed here, because bubbling CO into the solution and oxidizing it at potentials above +2.0 V gave the negative band for CO_2 formation at 2341 cm^{-1}, as expected. The high C≡N stretch frequency and loss of BF_4^- suggest that the 2357 cm^{-1} band arises instead from the adduct of CH_3CN and BF_3, and the negative bands from Fig. 2*a* indeed agree quite well with the literature infrared (10–12) and Raman (10) spectra of this adduct (Table 2).

The C≡N stretch frequency of the complex in acetonitrile is very close to that of the complex in benzene (11) and in methylene chloride (12). The large (100 cm^{-1}) increase in C≡N stretch frequency due to coordination has been attributed to an increase in the C—N force constant upon donation of the somewhat antibonding nitrogen lone pair to the empty BF_3 π orbital (12). The increase in intensity of this band upon coordination has been attributed to a contribution to the C≡N

Can. J. Chem. Downloaded from www.nrcresearchpress.com by 213.222.148.141 on 09/07/12
For personal use only.

TABLE 1. Frequencies and assignments of positive bands in Fig. 2*a*

Species	Infrared frequency/cm^{-1} SNIFTIRS[a]	Literature[b]	Vibration
Bu_4N^+	2966m	2970	C—H str
	2943w	2942	C—H str
	2880m	2881	C—H str
BF_4^-	1096sh	1098	asym B—F str (?)
	1065s	1062	asym B—F str (?)
	1042sh	1037	asym B—F str (?)
CH_3CN	3163w	3165	sym C—N str + sym C—C str
	2999w	3001	asym C—H str
	2287w	2293	sym C—H def + sym C—C str
	2249w	2254	sym C—N str
	918w	918	sym C—C str

[a]This work.
[b]From ref. 7. Transmission spectra in 50 mm solution cell.

TABLE 2. Vibrational frequencies of H_3CCNBF_3 (cm^{-1})

Infrared solid[a]	Raman solid[a]	Infrared C_6H_6[b]	Infrared CH_2Cl_2[c]	Infrared CH_3CN[d]	Mode[e]
2956m	2954vs		2935		ν_1
2376s	2373vs	2359	2355	2357m	ν_2
1374mw	1372s		1362		ν_3
1208s				1227s	ν_{11}
1188s, sh				1190vs	ν_{11}
1157vs				1163sh	$\nu_6 + \nu_{13}$
1127mw					$\nu_6 + \nu_7$
	1038w				ν_{12}
979m	972m		965	972vw	ν_4
904s				891vw	?
884s					?
	856s			856s	ν_5

[a]Reference 10. Annealed sample at −196°C. Weak ir bands not listed.
[b]Reference 11. Benzene solution.
[c]Reference 12. Dichloromethane solution.
[d]This work. Acetonitrile solution.
[e]ν_1, sym CH_3 str; ν_2, sym C≡N str; ν_3, sym CH_3 def; ν_4, sym C—C str; ν_5, sym BF_3 str; ν_6, sym B—N str; ν_7, sym BF_3 def; ν_{11}, asym BF_3 str; ν_{12}, asym CH_3 rock; ν_{13}, asym BF_3 def.

stretch vibration from stretching of the highly polar B—N bond. The C≡N stretch frequency of the complex in solution is 20 cm^{-1} lower than that of the solid adduct at −196°C (10), because of the difference in temperature, and because of lattice interactions and symmetry changes in the solid state.

There are also some differences between the solution and solid state spectra in the B—F stretching region. In particular, the solid adduct has a strong Raman band at 856 cm^{-1}, assigned to the ν_5 symmetric BF_3 stretching mode, which could not be observed in the infrared (10). Instead there were strong infrared bands at 904 and 884 cm^{-1}, which were assigned to factor group splitting of the ν_5 mode. The adduct in solution has a strong infrared band at 856 cm^{-1}, but no strong bands around 900 cm^{-1}, which would seem to confirm that the solid state ir spectrum is affected by interactions between neighboring adducts, and that the assignment of the 856 cm^{-1} band to ν_5 in ref. 10 is correct. The variation in frequency of the ν_{11} antisymmetric BF_3 stretching mode (1208 cm^{-1} in the solid, 1227 cm^{-1} in solution) may have the same origin.

It is clear that CH_3CN and BF_4^- react at +2.0 V to form CH_3CNBF_3. Determining the nature of the other products, and the reason for breakdown of the solvent/electrolyte system at such a low potential, is more difficult. It is well known that BF_4^- acts as a fluorinating agent in acetonitrile at +2.0 V (13). The initial step in the reaction is believed to be the reaction of any previously formed cation radical which then reacts with BF_4^-, or with another fluorinating agent derived from it. The negative bands at 2272 cm^{-1} and at 959 cm^{-1} are shifted from the corresponding actonitrile modes in a direction that would be expected the cation of acetonitrile. Fluoroacetonitrile is most likely formed in the reaction; the ir spectrum of this species is so similar to acetonitrile (14, 15) that at the resolutions required in this technique we do not expect to see the difference spectrum for it. (The C≡N stretch frequencies are the same to within 0.5 cm^{-1}.) However, HF should be a product of this reaction, and the weak characteristic 3475 cm^{-1} absorption (16) for this species has been observed in experiments where several thousand spectra are signal averaged.

The evidence is strong that hydrogen sorbed in the platinum electrode plays the dominant role in the reaction mechanism of the solvent/electrolyte oxidation at positive potentials, just as it is known to do in the solvent/electrolyte reduction at negative potentials (*vide infra*). Hydrogen in platinum electrodes is oxidized at potentials greater than about +1.0 V to H^+ which diffuses into the reaction/diffusion layer near the surface of the electrode. The electrode then serves as Brønsted acid strong enough to protonate even the very weakly basic acetonitrile. The protonated acetonitrile then can extract F^- from BF_4^-, under the same mechanism as described above (13).

[1] $H(Pt) \rightarrow H^+ + e^-$

[2] $H^+ + CH_3CN \rightarrow CH_3CNH^+$

[3] $CH_3CNH^+ + BF_4^- \rightarrow CH_3CN + HF + BF_3$

[4] $BF_3 + CH_3CN \rightarrow CH_3CNBF_3$

Direct removal of F^- from BF_4^- by the strong acid H^+ at the electrode surface must also be considered. A product of this reaction is also HF, which as mentioned above, is observed.

Figure 2*b* shows the SNIFTIRS spectrum obtained by returning the potential to 0.0 V, the reference spectrum being that of Fig. 1*a*, also taken at 0.0 V. The bands from Bu_4N^+,

Can. J. Chem. Downloaded from www.nrcresearchpress.com by 213.222.148.141 on 09/07/12
For personal use only.

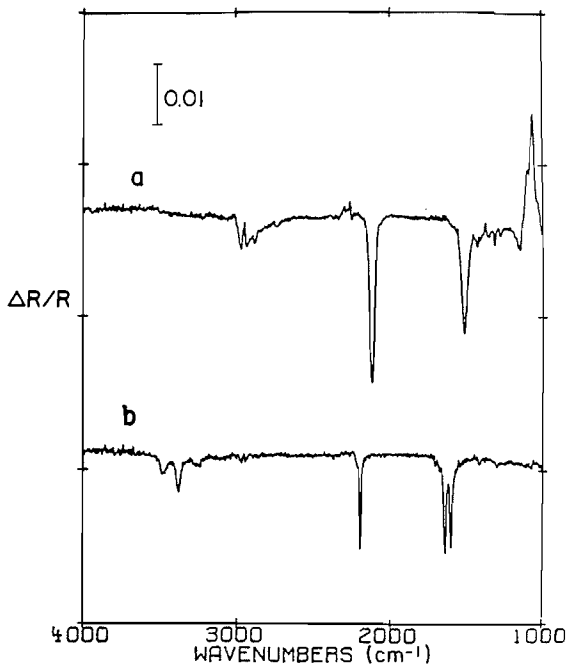

FIG. 3. SNIFTIRS spectra for TBAF (0.1 *M*) in acetonitrile at Pt. Reference spectrum taken at 0.0 V, sample spectra at (*a*) −3.0 V, then (*b*) 0.0 V.

BF_4^-, CH_3CN, and CH_3CNBF_3 have increased in intensity, even though electron transfer is not taking place at this potential. This is a typical finding that results when an electron transfer reaction (such as that at +2.0 V) generates a species which reacts slowly with another species (cf. BF_4^-) in solution, and in which the reaction continues for some time after electron transfer has stopped. Making the electrode potential as negative as −2.0 V reverses the reaction to some extent (Fig. 2*c*).

(ii) Cathodic reactions in dry TBAF/acetonitrile

The single beam reference spectra shown in Fig. 3*a* and *b* were taken at 0.0 V in nominally dry acetonitrile/TBAF (0.1 *M*). The potential was changed to −3.0 V, where the sample spectrum in Fig. 3*a* was taken, and then changed back to 0.0 V, where the sample spectrum in Fig. 3*b* was taken. The spectrum in Fig. 3*b* shows only negative bands, at 3479(m), 3373(s), 3250(w), 2193(s), 1645(s), 1607(s), 1420(w), 1384(vw), and 1306(w) cm^{-1}, which correspond to the literature spectrum (17) of 3-aminocrotonitrile (3450, 3370, 3250, 2180, 1650, 1600, 1430, 1370, 1320, 1130, and 1030 cm^{-1}, KBr wafer). This agrees with the results of Pons and Khoo (4), who found mostly 3-aminocrotonitrile after isolating the products of bulk electrolysis at −3.3 V. In that work, it was proposed that the 3-aminocrotonitrile anion is formed at −3.3 V, and is protonated during workup. Figure 3*a* corroborates this result. The most prominent features of the spectrum are very strong negative bands at 2116 and 1516 cm^{-1}. There are weaker negative bands at 1427, 1315, 1275, and 1145 cm^{-1}. The 2116 cm^{-1} band can be assigned to the C≡N stretch of the 3-aminocrotonitrile anion,

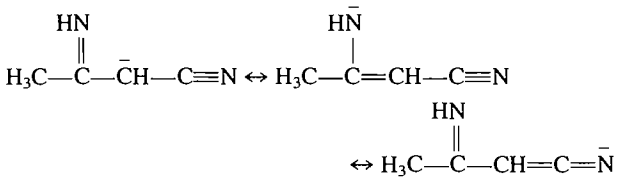

the frequency of which is lowered by delocalization of the negative charge. A Nujol mull of the sodium salt of 3-aminocrotonitrile gives a band at 2120 cm^{-1} (18), and in DMSO solution it absorbs at 2110 cm^{-1} (18).

The reaction mechanism was shown (4) to involve deprotonation of acetonitrile by hydride ion followed by nucleophilic attack of the resulting anion on another molecule of acetonitrile:

[5] $H(Pt) + e^- \rightarrow H^-$

[6] $H^- + CH_3CN \rightarrow H_2 + \bar{C}H_2CN$

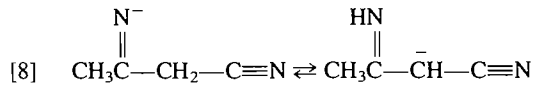

(It is well known that hydride ion is formed by reduction of hydrogen absorbed in the metal lattice; this is common in palladium, platinum, and nickel electrodes.) When the potential is returned to 0.0 V the 3-aminocrotonitrile anion is protonated, probably by oxidized hydrogen:

[9] $H_2 \rightarrow 2H^+ + 2e^-$

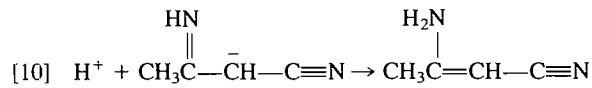

The intense band at 1516 cm^{-1} in Fig. 3*a* is probably due to the conjugated C=N stretch of the 3-aminocrotonitrile anion (there are no literature values for the spectrum of the anion below 1800 cm^{-1}). The band disappears upon addition of water to the system (see below), while the 2116 cm^{-1} band remains. The 1516 cm^{-1} band is most likely due to a product formed by a nucleophilic attack on the nitrogen of the acetonitrile anion (4):

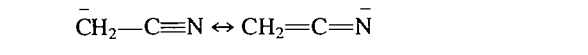

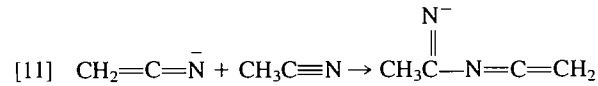

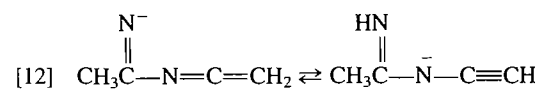

This species decomposes to acetonitrile upon protonation since the only product at 0.0 V is 3-aminocrotonitrile.

At −3.0 V (Fig. 3*a*) there are also bands from both of the electrolyte ions and from the solvent (c.f. Table 1), which disappear when the potential is returned to 0.0 V (Fig. 3*b*). There are negative bands from Bu_4N^+ at 2964, 2928, and 2881 cm^{-1}, positive bands from BF_4^- at 1097, 1063, and 1036 cm^{-1}, and positive bands from CH_3CN at 2945, 2293, 2257, and 1377 cm^{-1}. The directions of all of these bands are consistent with the migration of BF_4^- out of, and of Bu_4N^- into, the thin optical reaction layer at the negative potential limit.

(iii) Cathodic reactions in a dry pyrene/TBAF/acetonitrile solution

The effect of adding pyrene (0.5 m*M*) to the TBAF (0.1 *M*) solution is shown in Fig. 4. The reference potential is again 0 V. At −2.0 V no difference spectrum is be observed (Fig. 4*a*), indicating no faradaic reaction occurring. At −2.5 V, which is 0.1 V negative of the half-wave potential of the pyrene/pyrene anion radical couple, negative bands appear at 1529, 1294, 1234, and 1159 cm^{-1}, which are due to absorption by the anion

Can. J. Chem. Downloaded from www.nrcresearchpress.com by 213.222.148.141 on 09/07/12
For personal use only.

Can. J. Chem. Downloaded from www.nrcresearchpress.com by 213.222.148.141 on 09/07/12
For personal use only.

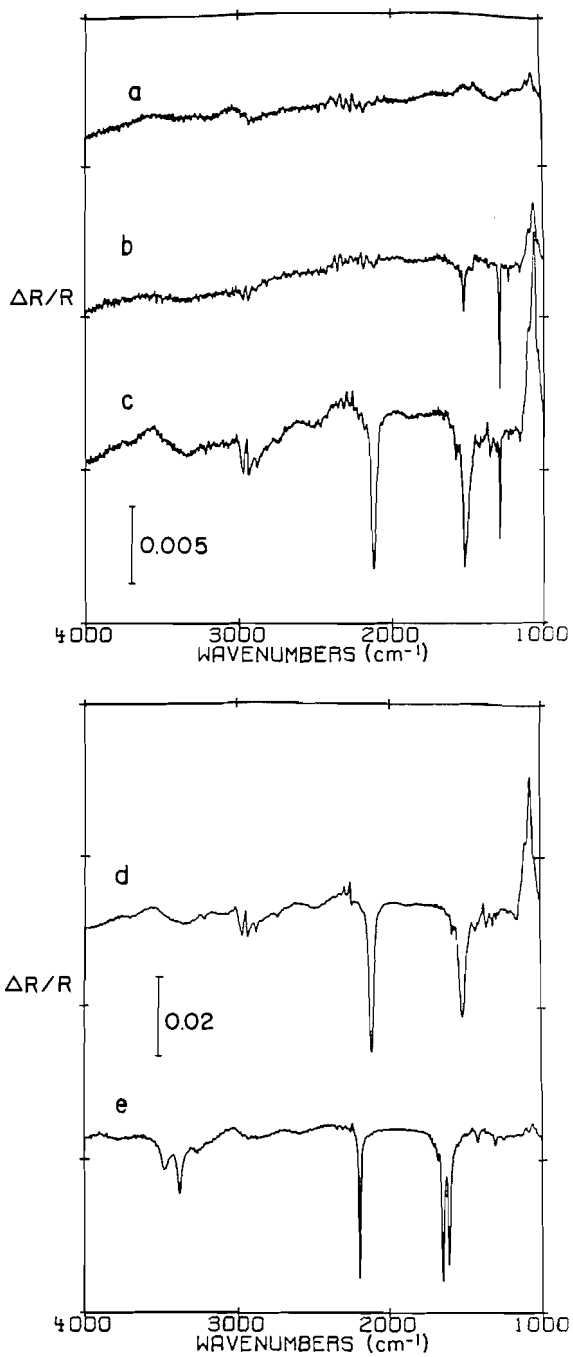

FIG. 4. SNIFTIRS spectra for pyrene (0.5 mM) and TBAF (0.1 M) in acetonitrile at Pt. Reference spectrum taken at 0.0 V, sample spectra at (a) −2.0 V, then (b) −2.5 V, then (c) −2.8 V, then (d) −3.0 V, then (e) 0.0 V.

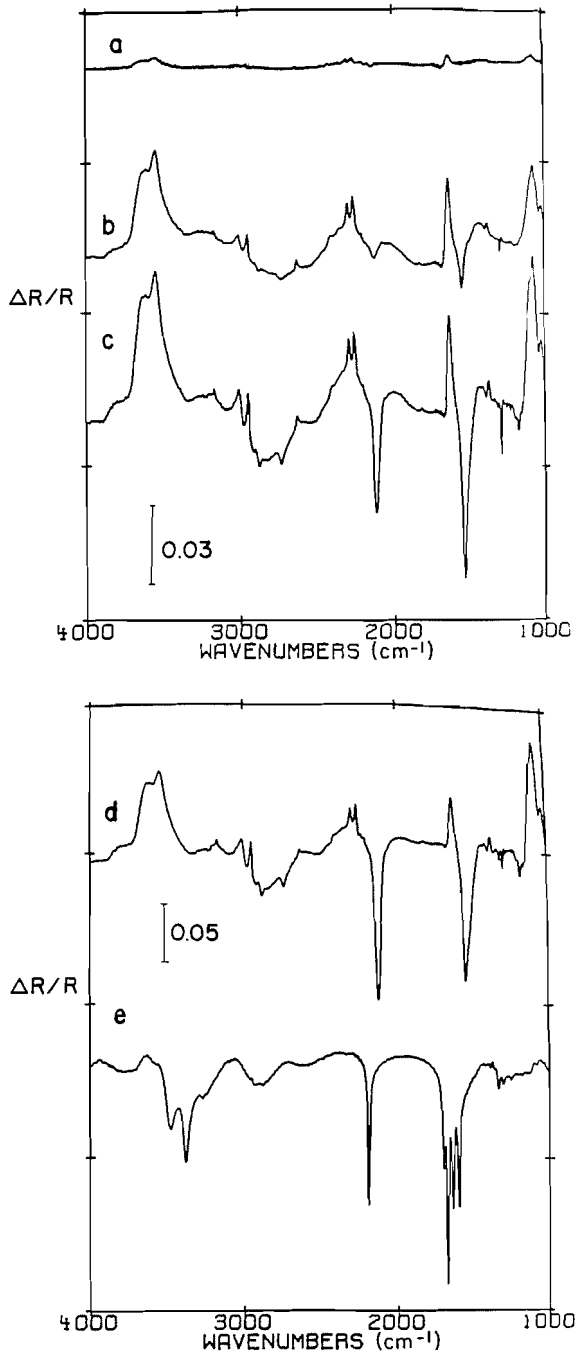

FIG. 5. SNIFTIRS spectra for acetonitrile solution of water (~0.1 M), pyrene (0.5 mM), and TBAF (0.1 M) at Pt. Reference spectrum taken at 0.0 V, sample spectra at (a) −2.0 V, then (b) −2.5 V, then (c) −2.8 V, then (d) −3.0 V, then (e) 0.0 V.

radical. Bands for acetonitrile, TBA^+, and BF_4^- also appear (Fig. 4b) due to differential migration as discussed above. At −2.8 V (Fig. 4c) solvent breakdown commences and strong negative bands at 2118 and 1528 cm^{-1} appear. There is a slight decrease in the intensities of the anion radical bands at 1294, 1234, and 1159 cm^{-1}. At −3.0 V the 2118 and 1528 cm^{-1} bands are very intense, and the bands from the pyrene anion radical have virtually disappeared. Returning the potential to 0.0 V results in the appearance of the spectrum for the acetonitrile reduction product 3-aminocrotonitrile, as in the system that did not contain pyrene. The disappearance of $pyrene^-$ at negative potentials is due to reduction of the anion to the dianion; the half-wave potential of the second reduction wave of pyrene is about 0.4 V more negative than the first (19).

(iv) Cathodic reactions in a wet pyrene/TBAF/acetonitrile solution

The spectra of a solution that is 0.1 M water, 0.5 mM pyrene, and 0.1 M TBAF in acetonitrile is shown in Fig. 5. The same reference spectrum, taken at 0.0 V, was used for all of the difference spectra. The spectra show that even at potentials as low as −2.0 V faradaic reaction is occurring, and the strong positive bands at 3610, 3540, and 1643 cm^{-1} indicate that water is one of the reactants. The main negative features are a

broad band around 2900 cm^{-1} and strong bands at 2120 and 1543 cm^{-1}. A negative band at 1294 cm^{-1} indicates that the pyrene anion radical is stable on the timescale of the experiment in the presence of water at −2.8 V. When the potential is returned to 0.0 V there are strong negative bands at 1709 and 1682 cm^{-1}, as well as the ubiquitous bands indicating 3-aminocrotonitrile formation.

The new bands at 1709 and 1682 cm^{-1} are assigned to acetamide, the literature values in acetonitrile solution having been reported at 1709 and 1684 cm^{-1} (20). The rest of the acetamide spectrum is very similar to that of 3-aminocrotonitrile, and will not be observed in these results. The strong negative band at 1543 cm^{-1} which appears at negative potentials is assigned to the anion of acetamide, the literature value of which is around 1500 cm^{-1} (20, 21). These spectra again confirm the results of Pons and Khoo (4), who found acetamide to be the major isolated product after bulk electrolysis in the presence of water, and suggested that the acetamide anion is formed at negative potentials by nucleophilic attack of OH^- on acetonitrile. The OH^- is formed in the reduction of water:

[13] $H_2O + e^- \rightarrow \frac{1}{2}H_2 + OH^-$

[14] $OH^- + CH_3C{\equiv}N \rightarrow CH_3C(N^-)—OH \rightleftarrows CH_3C(HN^-)=O$

When the potential is returned to 0.0 V, reoxidation of H_2 to H^+ and protonation of the anion form acetamide occurs (4). It can be seen by comparing Figs. 4 and 5 that the anion of 3-aminocrotonitrile is formed at less negative potentials in the presence of water. This suggests that OH^- acts as a base toward CH_3CN as well as a nucleophile, generating $[CH_3CN]^-$, which goes on to form $[CH_3C(NH)CHCN]^-$.

Acknowledgement

The authors thank the Office of Naval Research for support of this work.

1. H. Lund. *In* Organic electrochemistry. *Edited by* M. M. Baizer and H. Lund. Marcel Dekker, New York. 1983. Chapt. 5.
2. J. F. Cassidy, S. B. Khoo, S. Pons, and M. Fleischmann. J. Phys. Chem. **89**, 3933 (1985).
3. L. C. Portis, J. C. Roberson, and C. K. Mann. Anal. Chem. **44**, 294 (1972).
4. S. Pons and S. B. Khoo. Electrochim. Acta, **27**, 1161 (1982).
5. (*a*) A. Bewick and S. Pons. *In* Advances in infrared and Raman spectroscopy. Vol. 12. *Edited by* R. J. H. Clark and R. E. Hester. Wiley, New York. 1985. p. 1; (*b*) S. Pons, J. K. Foley, J. Russel, and M. Severson. *In* Modern aspects of electrochemistry. Vol. 17. *Edited by* J. O'M. Bockris and B. E. Conway. Plenum, New York. 1986; (*c*) J. K. Foley, C. Korzeniewski, J. L. Daschbach, and S. Pons. *In* Electroanalytical chemistry. Vol. 14. *Edited by* A. J. Bard. Marcel Dekker, New York. 1986.
6. M. Fleischmann and D. Pletcher. Tetrahedron Lett. 6255 (1968).
7. T. Davidson. M.S. Thesis; University of Alberta, Edmonton, Alta. 1983.
8. N. N. Greenwood. J. Chem. Soc. 3811 (1959).
9. H. A. Bonadeo and E. Silberman. Spectrochim. Acta, **26**, 2337 (1970).
10. B. Swanson and D. F. Shriver. Inorg. Chem. **9**, 1406 (1970).
11. H. J. Coerver and C. Curran. J. Am. Chem. Soc. **80**, 3522 (1958).
12. K. F. Purcell and R. S. Drago. J. Am. Chem. Soc. **88**, 919 (1966).
13. V. R. Koch, L. L. Miller, D. B. Clark, M. Fleischmann, T. Joslin, and D. Pletcher. J. Electroanal. Chem. **43**, 318 (1973).
14. R. G. Jones and W. J. Orville-Thomas. J. Chem. Soc. 4632 (1965).
15. G. Butt, J. Cilmi, P. M. Hoobin, and R. D. Topsom. Spectrochim. Acta, **36**A, 521 (1980).
16. H. Tauhara, H. Shimoda, K. Nakanishi, and N. Watanabe. J. Phys. Chem. **75**, 2222 (1971).
17. Sadtler Standard Infrared Grating Spectra; Sadtler Research Laboratories: Philadelphia. 1972. No. 48343P.
18. I. N. Juchnovski and I. G. Binev. J. Organomet. Chem. **99**, 1 (1955).
19. H. Siegerman. *In* Techniques of electroorganic synthesis. Part II. *Edited by* N. L. Weinberg. Wiley, New York. 1975. p. 699.
20. W. Kutzelnigg and R. Mecke. Spectrochim. Acta, **18**, 549 (1962).
21. P. D. Crispin and R. L. Werner. Aust. J. Chem. **20**, 2589 (1967).

Can. J. Chem. Downloaded from www.nrcresearchpress.com by 213.222.148.141 on 09/07/12
For personal use only.

H. M. Jemson, W. Lewis-Bevan, and M. C. L. Gerry. Can. J. Chem. **65**, 2478 (1987). The microwave spectrum and structure of bromine thiocyanate, BrSCN.

Page 2480. On the right hand table the observed frequency for $11_{3,8}$–$10_{3,7}$, 25/2–23/2 transition should read 39666.155.

Page 2484. On the left hand table, the residuals without χ_{ab} for $12_{3,10}$–$11_{3,9}$ 27/2–25/2 transition should read −6.461 and for $12_{3,10}$–$11_{3,9}$ 23/2–21/2 transition should read −7.110.

Page 2486. The second sentence in Fig. 2 caption should read "Three transitions are indicated for each isotopic species".

Page 2487. Structure **I** should read

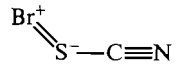

I

Can. J. Chem. Downloaded from www.nrcresearchpress.com by 213.222.148.141 on 09/07/12
For personal use only.

Chelation vs. non-chelation control in addition reactions of ethylmetallic reagents to acrolein dimer

SHANKAR M. SINGH AND ALLAN C. OEHLSCHLAGER
Department of Chemistry, Simon Fraser University, Burnaby, B.C., Canada V5A 1S6

Received August 13, 1987

SHANKAR M. SINGH and ALLAN C. OEHLSCHLAGER. Can. J. Chem. **66**, 209 (1988).

Reactions of 3,4-dihydro-2*H*-pyran-2-carboxaldehyde (acrolein dimer) with ethylmetallics based on lithium, titanium, and copper were examined for stereoselectivity. High selectivity (92:8) was found for non-chelation controlled addition yielding the *erythro* product when ethyllithium was employed in the presence of $BF_3 \cdot OEt_2$. High selectivity (89:11) for products of chelation controlled addition (*threo*) was observed for ethylcopper reagents in the presence of magnesium salts. Titanium reagents yielded mixtures rich in products of either chelation or non-chelation controlled addition depending on the titanium substituents. In no cases were stereoselectivities obtained with titanium reagents better than those obtained by use of the aforementioned lithium and copper reagents.

SHANKAR M. SINGH et ALLAN C. OEHLSCHLAGER. Can. J. Chem. **66**, 209 (1988).

Dans le but d'évaluer leurs stéréosélectivités, on a étudié les réactions du dihydro-3,4 2*H*-pyrannecarboxaldéhyde-2 (dimère de l'acroléine) avec des dérivés éthylmétalliques du lithium, du titane et du cuivre. Lorsqu'on utilise de l'éthyllithium en présence de $BF_3 \cdot OEt_2$, on observe une sélectivité élevée (92:8) pour cette addition qui n'est pas contrôlée par la chélation et qui conduit au dérivé *érythro*. Lorsqu'on utilise des réactifs d'éthyl-cuivre en présence de sels de magnésium, on observe aussi une sélectivité élevée (89:11) pour les produits de cette addition qui est contrôlée par la chélation (*thréo*). Les réactifs du titane fournissent des mélanges qui sont riches en produits provenant d'additions qui sont (ou qui ne sont pas) contrôlées par la chélation; les résultats dépendent de la nature des substituants portés par le titane. Les sélectivités observées avec les dérivés du titane ne sont jamais supérieures à celles obtenues avec les réactifs du lithium ou du cuivre qui ont été mentionnés antérieurement.

[Traduit par la revue]

Can. J. Chem. Downloaded from www.nrcresearchpress.com by 213.222.148.141 on 09/07/12
For personal use only.

The *exo*- and *endo*-brevicomins, **1** and **2** respectively, are aggregation pheromones for several species of economically important bark beetles in the genus *Dendroctonus* (1) and *Dryocetes*.[1] For all species except *Dendroctonus frontalis*, the southern pine beetle, racemic formulations of the brevicomins are attractive in the field.[2]

Although there are many reported syntheses of racemic **1** (2) and **2** (2*b*,*h*,*i*,*v*, 3) as well as the chiral isomers of **1** (4, 5) and **2** (4*c*,*p*, 5), few rival the approach of Bhupathy and Cohen (2*aa*, 3*d*) in simplicity and versatility. In this approach acrolein dimer, **3**, is reacted with ethylmetallic reagents, **4**. Under the conditions of chelation, control mixtures of **5** and **6** are formed that are rich in **5**. When non-chelation conditions are utilized, **6** is the principal isomer. They were able to obtain mixtures rich in **5** with Et_2Zn (**5**:**6** = 85:15) and EtMgBr (**5**:**6** = 70:30) while reaction of **3** with EtLi in ether (**5**:**6** = 28:72), alone or with added HMPA (**5**:**6** = 12:88) or TMEDA (**5**:**6** = 20:80), gave mixtures rich in **6**. In the latter reaction subsequent deprotonation at C-6 and alkylation with methyl iodide to yield **7** could be conducted in the same flask. Isomeric alcohol **8** was similarly produced from **5** isolated by flash chromatography.

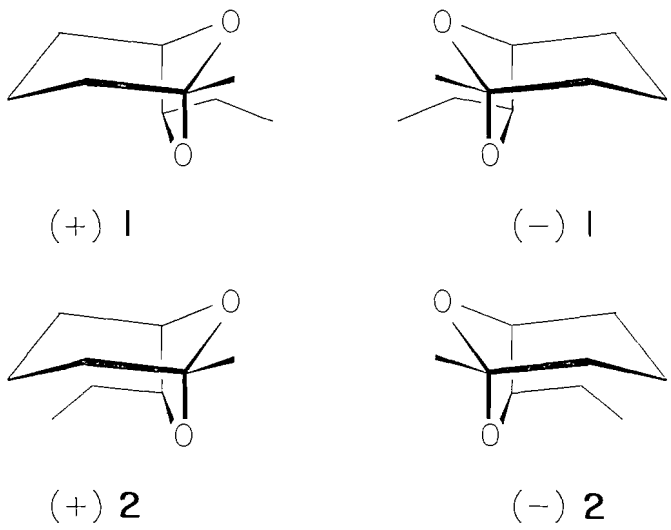

The purpose of the present investigation was to examine the effect of organometallic reagents and reaction conditions on the proportion of **5** and **6** obtained from reaction of **3**. The goal was to achieve conditions wherein **5** was the only diastereoisomer and wherein **6** was the only diastereoisomer.

Results and discussion

We carried out addition of ethylmetallic reagents **4** to acrolein dimer **3**, using various reaction conditions. Products **5** and **6** were isolated and the ratio of **5** to **6** was determined by capillary gas chromatographic analysis. The results are summarized in Table 1.

Addition of organometallic reagents to α-alkoxycarbonyls such as **3** is most easily induced to yield *threo* products **5** by conducting the reaction in the presence of Lewis-acidic reagents that are capable of forming a chelate between the substrate oxygens (*TS* **1**). Attack by the organometallic reagent from the least hindered side of the chelated carbonyl favors the formation of **5** (chelation control, ref. 6).

Attack of α-alkoxycarbonyl compounds from the least hindered side of the conformation in which the polar groups are *anti* (*TS* **2**) would yield **6** (non-chelation control, ref. 7).

Attainment of high stereoselectivity under non-chelation control requires conditions that induce a dramatic preference for the *anti* conformation of dipolar substrates (8). With few

[1] *exo*-Brevicomin is an aggregation pheromone from *Dryocetes confusus*, western balsam bark beetle, a pest of subalpine fir in the Pacific Northwest of America, ref. 12. *endo*-Brevicomin is an aggregation pheromone for *Dryocetes autographus*, a serious pest of Norway spruce, ref. 5*a* and references cited therein.

[2] *Dendroctonus frontalis* utilizes (+) **2** as an aggregation pheromone and (−) **2** as an antiaggregation pheromone, ref. 13.

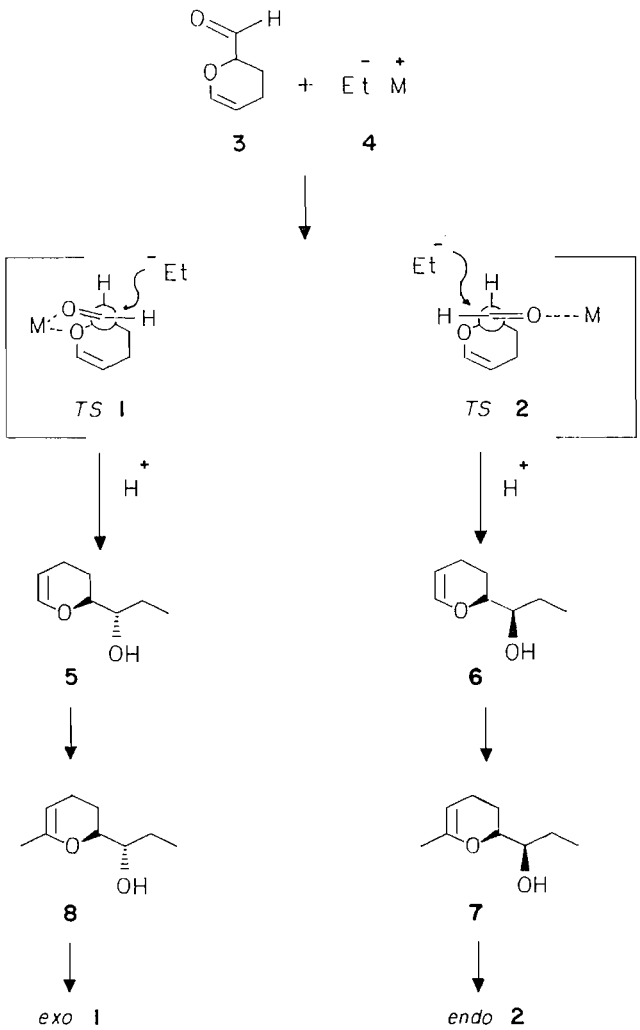

SCHEME 1

exceptions alkyllithiums add to α-alkoxycarbonyl compounds to yield products of non-chelation control. We found that addition of ethyllithium to **3** in THF proceeded in a stereoselective fashion to yield **5** and **6** in a ratio of 11:89 (entry 1).

Addition of TMEDA to the reaction had little effect on the stereoselectivity (**5**:**6** = 19:81, entry 2). These results compare favorably with those of Bhupathy and Cohen (2*aa*). They achieved a **5**:**6** ratio of 28:72 in ether, and using HMPA (**5**:**6** = 12:88) or TMEDA (**5**:**6** = 20:80) as cosolvent did not improve selectivity.

Next we conducted the reaction of ethyllithium with **3** in the presence of $BF_3 \cdot OEt_2$ (entry 3). This reaction gave a significantly improved stereoselectivity (**5**:**6** = 8:92), presumably due to increased preference for the *anti* conformation of **3**.

Strong chelation control has been reported for alkyltitanium addition to α-alkoxycarbonyls wherein the titanium has significant Lewis acid character (8). Thus alkyltitanium trichlorides and dialkyltitanium dichlorides readily form octahedral complexes with donor atoms of solvent or substrate (8) and are very effective in delivering alkyl residues under conditions of chelation control.

In the present study we found that **3** reacted with ethyltitanium trichloride (**9**) in CH_2Cl_2 at −78°C to give only polymeric products (entry 4). Treatment of **3** with diethyltitanium dichloride (**10**) gave a good yield of product in which the isomer

$C_2H_5TiCl_3$ **9** $(C_2H_5)_2TiCl_2$ **10** $C_2H_5Ti(OiPr)_3$ **11**

of chelation control predominated (**5**:**6** = 76:24) but selectivity was not outstanding (entry 5).

Changing the ligands of alkyltitaniums from chloride to alkoxide produces reagents significantly reduced in Lewis acid properties. Such reagents deliver alkyl residues to α-alkoxycarbonyl compounds under conditions of non-chelation control (8, 9). Because of the steric bulk of alkylalkoxy reagents such as **11** we felt they would efficiently produce **6** from **3**. Reaction of **11** with **3** in both THF and ether (entries 6 and 7) gave only low (30–35%) yields of addition (**5**:**6** ≈ 20:80) because of competing reduction of **3** to 3,4-dihydro-2*H*-pyran-2-methanol. The two most attractive mechanisms for this latter reaction are a Merwein–Pondorff type reaction or elimination of ethylene followed by titanium hydride reduction. The yields and stereoselectivities of addition of **11** to **3** did not warrant further investigation.[3]

$(C_2H_5)_2Cu(I)Li$ **12** $(C_2H_5)_2Cu(I)MgBr$ **13** $C_2H_5Cu(I)Li$ **14**

$C_2H_5Cu(I)MgBr$ **15** $C_2H_5Cu(CN)MgBr$ **16**

Cuprate addition to α-alkoxycarbonyls gives products expected of chelation control (9, 10). Addition of the diethyl cuprates (**12** and **13**) as well as ethylcoppers (**14**, **15**, and **16**) to **3** gave products of chelation control (entries 8–22).

We prepared the diethylcuprates **12** and **13** and ethylcoppers **14–16** by treatment of ethyllithium or ethylmagnesium bromide with CuI or CuCN. Treatment of **3** with **12** in THF yielded **5** and **6** in a 1:1 ratio (entry 8). Addition of HMPA to this reaction (entry 9) gave, as expected, a higher proportion of non-chelation control product (**6**). Addition of $BF_3 \cdot OEt_2$ to the reaction of **12** with **3** (entry 10) surprisingly increased the proportion of chelation control product. A possible explanation for this effect is that the species in this solution is the boron "ate" complex **17** as suggested by Yamamoto (11). In this reaction, the copper cation would be the presumptive chelating ion.

Reaction of magnesium cuprate **13** with **3** gave higher proportions of products of chelation control than the corresponding lithium cuprate **12** (compare entry 8 with 11 and 12). Addition of magnesium bromide (9) to the reaction of **13** and **3** only

$$(C_2H_5)_2CuLi + BF_3 \rightleftharpoons (C_2H_5\bar{B}F_3)(LiCu^+C_2H_5)$$
12 **17**

slightly increased the proportion of product of chelation control (entry 13).

Finally we investigated the addition of ethylcopper reagents **14–16** to **3**. As with diethyl lithium cuprate (**12**), the ethylcopper lithium reagent (**14**) showed very low selectivity (**5**:**6** = 1:1, entry 14). Addition of $BF_3 \cdot OEt_2$ to this reaction increased the selectivity in favor of chelation controlled addition (**5**:**6** = 74:26, entry 15).

Changing the metal cation from lithium to magnesium dramatically increased the proportion of products of chelation control. Thus, reaction of **3** with **15** gave **5**:**6** = 88:12 (entry 16). Addition of $BF_3 \cdot OEt_2$ (entry 17) or magnesium bromide

[3]Bhupathy and Cohen reported that addition of titanium reagents to **3** gave low yields of addition products, but did not report formation of other products, ref. 2*aa*.

Can. J. Chem. Downloaded from www.nrcresearchpress.com by 213.222.148.141 on 09/07/12
For personal use only.

TABLE 1. Reaction of ethylmetallic reagents with 3,4-dihydro-2*H*-pyran-2-carboxaldehyde (**3**)

Entry	EtM	Solvent	Temperature (°C)	Yield[a] (%)	Product ratio[b] (**5**:**6**)
1	EtLi	THF	−78→0	(81)	11:89
2	EtLi, TMED	THF	−78→0	(85)	19:81
3	EtLi, $BF_3 \cdot OEt_2$	THF	−78→0	(66)	8:92
4	$EtTiCl_3$	CH_2Cl_2	−78→−20	—	—
5	Et_2TiCl_2	CH_2Cl_2	−78→−20	(56)	76:24
6	$EtTi(OiPr)_3$	THF	−50→RT	(35)[c]	21:79
7	$EtTi(OiPr)_3$	Ether	−50→RT	(30)[c]	19:81
8	$(Et)_2Cu(I)Li$	THF	−78→0	89	55:45
9	$(Et)_2Cu(I)Li$	THF, HMPA	−78→0	88	25:75
10	$(Et)_2Cu(I)Li$, $BF_3 \cdot OEt_2$	THF	−78→0	64	72:28
11	$(Et)_2Cu(I)Mg$	THF, Me_2S	−78→0	91	68:32
12	$(Et)_2Cu(I)Mg$	Ether, Me_2S	−78→0	88	71:29
13	$(Et)_2Cu(I)Mg$, $MgBr_2$	THF, Me_2S	−78→0	75	80:20
14	EtCu(I)Li	THF, Me_2S	−78→0	75	50:50
15	EtCu(I)Li, $BF_3 \cdot OEt_2$	THF, Me_2S	−78→0	50	74:26
16	EtCu(I)MgBr	THF, Me_2S	−78→0	(80)	88:12
17	$EtCu(I)MgBr \cdot BF_3$	THF, Me_2S	−78→0	81	86:14
18	EtCu(I)Mg, $MgBr_2$	THF, Me_2S	−78→0	81	89:11
19	EtCu(I)MgBr	Ether, Me_2S	−78→0	76	83:17
20	EtCu(I)MgBr	CH_2Cl_2	−78→0	82	76:24
21	EtCu(I)MgBrCN	THF, Me_2S	−78→0	78	76:25

[a]Capillary gc yield. Yield in the parentheses refers to isolated yield.
[b]The product ratios were determined by capillary gc.
[c]The reaction of ethyltitanium triisopropoxide with **3** also gave 3,4-dihydro-2*H*-pyran-2-methanol in 30 and 40% yields in THF and ether, respectively, along with the desired product.

(entry 18) to this reaction did not dramatically alter the preference for formation of products of chelation control, whereas changing the solvent from THF to ether or CH_2Cl_2 lowered preference for this mode of reaction (entries 19 and 20). Finally, comparison of entries 16 and 21 reveals that the presence of cyanide counterion **16** has a deleterious effect on chelation control. Overall, the simplest procedure for obtaining chelation control addition is that described in entries 16–18. These results are equivalent to those reported by Jefford *et al.* (10) for the addition of the *n*-decyl analog of **15** to **3** in which the chelation control to non-chelation control product ratio was 90:10. The present results are marginally better in favor of chelation control than those reported by Bhupathy and Cohen (2*aa*) for addition of diethylzinc to **3** (**5**:**6** = 85:15).

Experimental

Hewlett–Packard 5880A and 5890A gas chromatographs fitted with capillary inlet systems, flame-ionization detectors, and WCOT columns (15 or 30 m × 0.25 mm i.d.) of glass or fused silica were employed for analyses by gas–liquid chromatography (gc). Columns were coated with OV-101, SP-2100, or DB-1 liquid phases. Injection port and detector temperatures were 260 and 275°C, respectively. Helium was the carrier gas.

Low resolution mass spectra were obtained on a Hewlett–Packard 5985B coupled gas chromatograph – mass spectrometer using electron-impact ionization at 70 eV or chemical ionization (CI) with isobutane as the ionizing gas. The ^{1}H nmr spectra were recorded in $CDCl_3$ on a Bruker 400 WM spectrometer. The gc–ir spectra were recorded on a Bruker IFS-85 spectrophotometer. All reactions were run in flame-dried glassware under a positive pressure of nitrogen.

Rotary evaporation at water aspirator pressure was employed to concentrate or remove solvent from solutions obtained by extractive work-up of reactions. Column chromatography was performed by the flash chromatography method on silica gel (Kieselgel 60, 40–63 μm, E. Merck, Darmstadt). Solvents were distilled before use. Tetrahydrofuran (THF) was distilled from sodium benzophenone ketyl prior to use. Dichloromethane was distilled over P_2O_5 and stored over 4 Å molecular sieves. Hexamethylphosphoramide (HMPA), *N,N,N′,N′*-tetramethylethylenediamine (TMEDA), and $BF_3 \cdot OEt_2$ were distilled over calcium hydride. Diethylzinc and chlorotitanium triisopropoxide were purchased from Aldrich Chemical Co., and 3,4-dihydro-2*H*-pyran-2-carboxaldehyde (**3**) was purchased from Fluka, AG Chem.

*Reaction of ethyllithium with 3,4-dihydro-2*H*-pyran-2-carboxaldehyde (**3**)*

The following procedure is representative. To a mixture of **3** (0.7 g, 6.25 mmol) in THF (15 mL) was added $BF_3 \cdot OEt_2$ (1.15 mL, 9.37 mmol) at −78°C and the reaction mixture was stirred for 15 min. Ethyllithium (1.4 M in ether) (6.7 mL, 9.37 mmol) was added dropwise along the inner wall of the flask. After addition, the reaction mixture was stirred for 1 h at −78°C, then warmed to 0°C over 1 h. Ice-cold 1 M NaOH solution was added until the reaction mixture became basic. The organic layer was separated and the aqueous layer was extracted with ether (5 × 25 mL). The combined organic layers were washed twice with brine, dried (Na_2SO_4), and 0.5 mL of triethylamine added to prevent cyclization. Solvent was removed under partial vacuum (10–20 Torr; 1 Torr = 133.3 Pa). The crude product was flash chromatographed (ethyl acetate: *n*-hexane, 1:4) to provide pure **5** and **6** in 66% yield (0.57 g). The gc/ir of **6** gave (vapor): 3628, 3072, 2970, 2937, 1651, 1387, 1242, 1074, 970, and 729 cm^{-1}; ^{1}H nmr ($CDCl_3$) δ: 1.0 (t, 3H, methyl, J = 7.5 Hz), 1.41–1.60 (m, 2H, methylene), 1.68–1.87 (m, 2H, C(3)), 1.95–2.13 (m, 3H, C(4), OH), 3.65 (dt, 1H, methine, J = 8.5, 4 Hz), 3.73 (ddd, 1H, C(2), J = 10.5, 4, 2.5 Hz), 4.68 (m, 1H, C(5)), 6.38 (dt, 1H, C(6), J = 6, 2 Hz); for product **5**, δ: 3.47 (1H, methine), 3.65 (1H, C(2); ms, *m/e* (%, rel. int.): 142(14.5%), 124(2%), 114(5%), 95(27%), 83(100%), 70(23%), 55(59%).

Can. J. Chem. Downloaded from www.nrcresearchpress.com by 213.222.148.141 on 09/07/12
For personal use only.

Can. J. Chem. Downloaded from www.nrcresearchpress.com by 213.222.148.141 on 09/07/12
For personal use only.

Reaction of diethyltitanium dichloride with 3

Diethylzinc (1.15 mL, 11.25 mmol) was added dropwise to a solution of titanium tetrachloride (1.2 mL, 11.25 mmol) in CH_2Cl_2 (75 mL). After addition, the reaction mixture was stirred for 15 min. Aldehyde **3** (0.56 g, 7.5 mmol) in CH_2Cl_2 (10 mL) was added dropwise and the reaction mixture was stirred for 7 h at −78°C to −20°C. The reaction mixture was poured into excess 1 M NaOH solution, filtered through Celite, and the aqueous layer was extracted with ether (5 × 30 mL). The combined ether extract was washed with brine and dried (Na_2SO_4). The crude product obtained from the removal of ether was flash chromatographed to yield **5** and **6** (0.41 g, 56%).

Reaction of ethyltitanium triisopropoxide with 3

To a solution of chlorotitanium triisopropoxide (4.8 mL, 20 mmol) in THF (40 mL) was added ethyllithium (1.4 M in ether) (14.28 mL, 20 mmol) at −50°C. The reaction was stirred for 0.5 h, then aldehyde **3** (1 g; 8.92 mmol) in THF (10 mL) was added at −50°C. The reaction mixture was warmed to room temperature over 12 h, then poured into excess ice-cold NaOH and filtered through Celite. The organic layer was separated and the aqueous layer was extracted with ether (5 × 30 mL). The combined organic layer was washed with brine and dried (Na_2SO_4). Solvent was removed to give crude product, which was flash chromatographed to provide **5** and **6** (0.45 g, 35%) as well 3,4-dihydro-2*H*-pyran-2-methanol (0.3 g, 30%). The identity of the products was confirmed by ir and nmr spectra, and gc coinjection with authentic samples.

Reaction of diethyl cuprates with 3

Diethyl cuprates were prepared by the addition of either ethyllithium or ethylmagnesium bromide to copper(I) iodide.

The following procedure is representative. To a mixture of copper(I) iodide (1.42 g, 7.5 mmol) in THF (16 mL) and Me_2S (4 mL) was added ethylmagnesium bromide (5 mL, 15 mmol) at −78°C. After addition, the reaction mixture was stirred for 10 min and then **3** (0.56 g, 5 mmol) in THF (6 mL) was added dropwise and the contents were stirred for 2 h at −78°C to 0°C. The reaction was poured into an excess of ice-cold 1 M NaOH. The aqueous layer was extracted with ether (5 × 30 mL). The combined organic layer was washed with brine, dried (Na_2SO_4), and analyzed by gas chromatography.

Reaction of ethylcoppers with 3

The following method is representative. Ethylmagnesium bromide (5 mL, 15 mmol) was added dropwise to a mixture of copper(I) iodide (3.22 g, 17 mmol) in THF (32 mL) and dimethylsulfide (8 mL) at −78°C. After addition, the reaction mixture was stirred for 15 min. Acrolein dimer (1.12 g, 10 mmol) in THF (10 mL) was added and the reaction mixture was stirred for 3 h at −78°C to 0°C. The mixture was poured into ice-cold 1 M NaOH. The aqueous layer was extracted with ether (5 × 30 mL). The combined extract was washed with brine, dried (Na_2SO_4), and the solvent removed to afford a crude product, which was purified by flash column chromatography to provide **5** and **6** in 80% yield (1.14 g). For product **5**, gc/ir (vapor): 3626, 3074, 2937, 1653, 1394, 1240, 1070, and 980 cm^{-1}; ^1H nmr ($CDCl_3$) δ: 1.0 (t, 3H, methyl, J = 7.5 Hz), 1.42–1.68 (m, 2H, methylene), 1.68–1.89 (m, 2H, C(3)), 1.95–2.15 (m, 2H, C(4)), 2.23 (d, 1H, OH, J = 5 Hz), 3.47 (dt, 1H, methine, J = 8.5, 5.8 Hz), 3.65 (ddd, 1H, C(2), J = 10.5, 5.8, 2.5 Hz), 4.68 (m, 1H, C(5)), 6.37 (dt, 1H, C(6), J = 6, 2 Hz); product **6**, δ: 3.65 (1H, methine) and 3.74 (1H, C(2)); ms, m/e (%, rel. int.): 142(21%), 124(2%), 114(5%), 95(30%), 83(100%), 70(31%), and 55(38%).

Acknowledgement

This work was funded through N.S.E.R.C. Operating (ACO) and N.S.E.R.C. Strategic grants.

1. J. H. Borden. *In* Comprehensive insect physiology, biochemistry and pharmacology. Vol. 9. *Edited by* G. A. Kerkut and L. I. Gilbert. Pergamon Press, Oxford. 1985. pp. 257.
2. (*a*) H. H. Wasserman and E. H. Barber. J. Am. Chem. Soc. **91**, 3674 (1969); (*b*) T. E. Bellas, R. G. Brownlee, and R. M. Silverstein. Tetrahedron, **25**, 5149 (1969); (*c*) B. P. Mundy, R. D. Otzenberger, and A. R. Debernarois. J. Org. Chem. **36**, 2390 (1971); (*d*) J. O. Rodin, C. A. Reese, R. M. Silverstein, V. H. Brown, and J. I. Degraw. J. Chem. Eng. Data, **16**, 382 (1971); (*e*) K. B. Lipkowitz, B. P. Mundy, and D. Greesman. Synth. Commun. **3**, 453 (1973); (*f*) J. Knolle and H. J. Schafer. Angew. Chem. Int. Ed. Engl. **14**, 758 (1975); (*g*) B. P. Mundy, K. B. Lipkowitz, and G. W. Dirks. Synth. Commun. **5**, 7 (1975); (*h*) P. J. Kocienski and R. W. Ostrow. J. Org. Chem. **41**, 398 (1976); (*i*) N. T. Byrom, R. Grigg, and B. Kong-Rathip. J. Chem. Soc. Chem. Commun. 216 (1976); (*j*) K. B. Lipkowitz and B. P. Mundy. J. Org. Chem. **41**, 373 (1976); (*k*) P. Chaquin, J. P. Morizur, and J. Kossanyi. J. Am. Chem. Soc. **99**, 903 (1977); (*l*) J. L. Coke, H. J. Williams, and S. Natarajan. J. Org. Chem. **42**, 2380 (1977); (*m*) G. Cahiez, A. Alexakis, and J. F. Normant. Tetrahedron Lett. 1433 (1980); (*n*) L. T. Cohen and J. R. Matz. J. Am. Chem. Soc. **102**, 6900 (1980); (*o*) P. G. M. Wuts and S. S. Bigelow. Synth. Commun. **12**, 779 (1982); (*p*) R. W. Hoffmann and B. Kemper. Tetrahedron Lett. 845 (1982); (*q*) Y. Yamamoto, Y. Saito, and K. Maruyama. Tetrahedron Lett. 4959 (1982); (*r*) M. N. Joshi, V. R. Mamdapur, and M. S. Chadha. J. Chem. Soc. Perkin Trans. 1, 2963 (1983); (*s*) P. S. Reddy, V. Vidyasagar, and J. S. Yadhav. Synth. Commun. **14**, 197 (1984); (*t*) S. J. Danishefsky, W. H. Pearson, and D. F. Harvey. J. Am. Chem. Soc. **106**, 2455 (1984); (*u*) N. T. Byrom, R. Grigg, B. Kongathip, G. Reimer, and A. R. Wade. J. Chem. Soc. Perkin Trans. 1, 1643 (1984); (*v*) D. P. Wiesler, F. J. Schwende, M. Carmack, and M. Novotny. J. Org. Chem. **49**, 882 (1984); (*w*) B. P. Mundy and W. B. Bornmann. J. Org. Chem. **49**, 5264 (1984); (*x*) S. J. Danishefsky, W. H. Pearson, D. F. Harvey, C. J. Maring, and J. P. Springer. J. Am. Chem. Soc. **107**, 1256 (1985); (*y*) M. Jatczak, R. Amouroux, and M. Chastrette. Tetrahedron Lett. 2315 (1985); (*z*) T. Sato, T. Oikawa, and K. Kobayashi. J. Org. Chem. **50**, 1646 (1985); (*aa*) M. Bhupathy and T. Cohen. Tetrahedron Lett. 2619 (1985); (*bb*) R. W. Hoffmann, B. Kemper, and R. Metternich. Justus Liebigs Ann. Chem. 2246 (1985); (*cc*) M. Koreeda and Y. Tanaka. Tetrahedron Lett. 143 (1987).
3. (*a*) M. Look. J. Chem. Ecol. **2**, 83 (1976); (*b*) K. Mori. Agric. Biol. Chem. **40**, 2499 (1976); (*c*) P. E. Sum and L. Wieler. Can. J. Chem. **57**, 1475 (1979); T. Cohen and M. Bhupathy. Tetrahedron Lett. 4163 (1983); (*e*) C. Meister, Z.-P. Shen, and H.-D. Scharf. Justus Liebigs Ann. Chem. 147 (1984).
4. (*a*) K. Mori. Tetrahedron, **30**, 4223 (1974); (*b*) H. H. Meyer. Justus Liebigs Ann. Chem. 732 (1977); (*c*) R. Bernardi, C. Fuganti, and P. Grasselli. Tetrahedron Lett. 4021 (1981); (*d*) A. E. Sherk and B. Fraser-Reid. J. Org. Chem. **47**, 932 (1982); (*e*) B. D. Johnston and A. C. Oehlschlager. J. Org. Chem. **47**, 5384 (1982); (*f*) Y. Masaki, K. Nagata, Y. Serizawa, and K. Kaji. Tetrahedron Lett. 5553 (1982); (*g*) C. Fuganti, P. Grasselli, G. Pedrocchi-Fantoni, S. Servi, and C. Zirotti. Tetrahedron Lett. 3753 (1983); (*h*) M. Asami and T. Mukaiyama. Chem. Lett. 93 (1983); (*i*) R. J. Ferrier and P. Prasit. J. Chem. Soc. Perkin Trans. 1, 1645 (1983); (*j*) D. S. Matteson and K. M. Shadu. J. Am. Chem. Soc. **105**, 2077 (1983); (*k*) P. G. M. Wuts and S. S. Bigelow. J. Chem. Soc. Chem. Commun. 736 (1984); (*l*) R. J. Ferrier, P. Schmidt, and P. C. Tyler. J. Chem. Soc. Perkin Trans. 1, 301 (1985); (*m*) M. Larcheveque and J. Lalonde. J. Chem. Soc. Chem. Commun. 83 (1985); (*n*) F. Sato, O. Takahashi, T. Kato, and Y. Kobayashi. J. Chem. Soc. Chem. Commun. 1638 (1985); (*o*) D. S. Matteson, K. M. Sadhu, and M. L. Peterson. J. Am. Chem. Soc. **108**, 810 (1986); (*p*) J. Mulzer, A. Angermann, and W. Munch. Justus Liebigs Ann. Chem. 825 (1986).
5. (*a*) K. Mori and Y.-B. Sew. Tetrahedron, **41**, 3429 (1985); (*b*)

S. HATAKEYAMA, K. SAKURAI, and S. TAKANO. J. Chem. Soc. Chem. Commun. 1759 (1985); (*c*) A. YUSUFOGLU, S. ANTONS, and H.-D. SCHARF. J. Org. Chem. **51**, 3485 (1986); (*d*) B. D. JOHNSTON and A. C. OEHLSCHLAGER. J. Org. Chem. **52**, 940 (1987).

6. D. J. CRAM and D. R. WILSON. J. Am. Chem. Soc. **85**, 1245 (1963).
7. (*a*) J. W. CORNFORTH, R. H. CORNFORTH, and K. K. MATHEW. J. Chem. Soc. 112 (1959); (*b*) M. CHÉREST, H. FELKIN, and N. PRUDENT. Tetrahedron Lett. 2199 (1968); (*c*) N.-T. AHN. Top. Curr. Chem. **88**, 145 (1980).
8. (*a*) M. T. REETZ. Organotitanium reagents in organic synthesis. Springer, Berlin. 1986; (*b*) Pure Appl. Chem. **57**, 1781 (1985).
9. M. T. REETZ. Angew. Chem. Int. Ed. Engl. **23**, 556 (1984).
10. C. W. JEFFORD, D. JAGGI, and J. BOUKOUVALAS. Tetrahedron Lett. 4011 (1986).
11. Y. YAMAMOTO. Angew. Chem. Int. Ed. Engl. **25**, 947 (1986).
12. J. H. BORDEN, A. M. PIERCE, H. D. PIERCE, JR., L. J. CHONG, A. O. STOCK, and A. C. OEHLSCHLAGER. J. Chem. Ecol. **13**, 823 (1987).
13. J. P. VITÉ, R. F. BILLINGS, C. W. WARE, and K. MORI. Naturwissenschaften, **72**, 99 (1985).

Can. J. Chem. Downloaded from www.nrcresearchpress.com by 213.222.148.141 on 09/07/12
For personal use only.

Photochemistry of cyclic α-hydroxy ketones. I. The nature and genesis of the photoproducts from steroidal 5-hydroxy 6-keto steroids and related compounds[1]

SHIRLEY STIVER AND PETER YATES
Lash Miller Chemical Laboratories, University of Toronto, Toronto, Ont., Canada M5S 1A1

Received September 9, 1987

SHIRLEY STIVER and PETER YATES. Can. J. Chem. **66**, 214 (1988).

Photolyses of 5-hydroxy-5α- and 5β-cholestan-6-one and their 3β-acetoxy- and 3β-benzyloxy derivatives in benzene or ethanol proceed stereospecifically with retention of configuration at C-5 to give the corresponding lactones, 6-oxa-B-homocholestan-7-ones. Photolyses of 3β-acetoxy-7α-deutero-5-hydroxy-5α- and 5β-cholestan-6-ones also proceed stereospecifically to give the corresponding 5-deutero lactones. 3β-Acetoxy-5-deuteroxy-5α- and 5β-cholestan-6-one give on irradiation 1:3 and 7:1 mixtures, respectively, of the corresponding 7aα- and 7aβ-deutero lactones. Irradiation of 3β-acetoxy-5-methoxy-5α-cholestan-6-one in ethanol leads to the stereoselective formation of ethyl 3β-acetoxy-5-methoxy-5,6-seco-5α-cholestan-6-oate, while that of 3β-acetoxy-5α-cholestan-6-one gives mainly photoreduction products. These observations are interpreted in terms of α-cleavage of the C-5—C-6 bond of the ketols to give alkyl acyl diradicals that undergo hydrogen transfer to give hydroxy ketenes, which then form the lactones. It is proposed that retention of configuration at C-5 results from two major factors—the nonplanar geometry of the hydroxyalkyl radical center, and fast hydrogen transfer in the diradical, the latter resulting from restricted rotation about the C-9—C-10 bond. The specific transfer of the 7α-deuterium atom in the 7α-deutero ketols is attributed to these factors and to the preferred direction of opening to the diradical on α-cleavage. The *O*-deuterium labelling results are interpreted in terms of product development control in the conversion of the hydroxy ketenes to the lactones and are in accord with restricted rotation about the C-9—C-10 bond. The photolysis of 3β-acetoxy-5-amino-5α-cholestan-6-one proceeds stereoselectively to give the 5β-lactam analogue of the 5β-lactone formed from the analogous 5α-ketol.

SHIRLEY STIVER et PETER YATES. Can. J. Chem. **66**, 214 (1988).

La photolyse des hydroxy-5 5α- et 5β-cholestanones-6 et de leurs dérivés acétoxy-3β et benzyloxy-3β, dans le benzène ou l'éthanol, se produit d'une façon stéréospécifique, avec rétention de configuration en C-5, pour conduire aux lactones correspondantes, oxa-6 B-homocholestanones-7. La photolyse des acétoxy-3β deutéro-7α hydroxy-5 5α- et 5β-cholestanones-6 se produit aussi d'une façon stéréospécifique pour conduire aux lactones correspondantes deutéro-5. Par irradiation, les acétoxy-3β deutéroxy-5 5α- et 5β-cholestanones-6 conduisent respectivement à des mélanges 1:3 et 7:1 des lactones correspondantes deutéro-7aα et -7aβ. L'irradiation de l'acétoxy-3β méthoxy-5 5α-cholestanone-6, dans l'éthanol, conduit à la formation stéréosélective de l'acétoxy-3β méthoxy-5 séco-5,6 5α-cholestanoate-6 d'éthyle alors que celles de l'acétoxy-3β 5α-cholestanone-6 donne principalement des produits de photoréduction. On interprète ces résultats en fonction d'un clivage-α de la liaison C-5/C-6 des cétols qui fournit des diradicaux alkyle acyle qui subissent des transferts d'hydrogène conduisant des hydroxy-cétènes qui forment alors des lactones. On suggère que la rétention de configuration en C-5 provient de deux facteurs principaux—la géométrie non-planaire du centre radicalaire hydroxyalkyle et le transfert rapide d'hydrogène dans le diradical; ce dernier facteur proviendrait d'une rotation empêchée autour de la liaison C-9/C-10. Le transfert spécifique de l'atome de deutérium 7α des cétols-7α est aussi attribué à ces facteurs ainsi qu'à la direction privilégiée de l'ouverture en diradical par clivage α. On interprète les résultats du marquage au deutérium de l'hydroxyle en fonction d'un contrôle au développement du produit lors de la conversion des hydroxy cétènes en lactones; cette interprétation est en accord avec une rotation empêchée autour de la liaison C-9/C-10. La photolyse de l'acétoxy-3β amino-5 5α-cholestanone-6 conduit d'une façon stéréospécifique à la lactame-5β analogue de la lactone-5β qui se forme à partir du cétol-5α analogue.

[Traduit par la revue]

Introduction

Although the photochemistry of cyclic ketones has been investigated exhaustively (2), comparatively few studies have focused on the photochemistry of cyclic α-hydroxy ketones. Hamer (3) and Padwa and Au (4) have studied the photoreactions of several 2-hydroxy-1-indanones of type **1** and have observed that they can give epimerization products (**2**), keto aldehydes (**3**), and isochromenes (**4**), depending on the nature of the substituents and the solvent. The formation of all of these can be interpreted in very similar terms to those that have been used in the case of cyclic ketones lacking an α-hydroxyl substituent (2). Thus Norrish type I cleavage (α-cleavage) gives the alkyl acyl diradical **5**, which closes to give **1** and **2**, or undergoes 1,6 hydrogen transfer from the hydroxyl group to give **3** or 1,4 hydrogen transfer from the benzylic carbon to give **6**, which then cyclizes or reacts with solvent methanol to give **4**. Deuterium labeling results were in accord with the two postulated types of hydrogen transfer.

Our attention was first drawn to the photochemistry of cyclic α-hydroxy ketones by the report of Cookson *et al.* (5) that the steroidal α-hydroxy ketones **7** and **8** on photolysis in either benzene or ethanol give the lactones **9** and **10**, respectively. The general course of these reactions again appears to be closely analogous to the known photochemical reactions of cyclic ketones not bearing an α-hydroxyl group, viz., α-cleavage to give **11** followed by 1,5 hydrogen transfer to give a ketene **12** that can undergo intramolecular reaction with the hydroxyl group to give the lactones **9** and **10**. However, in detail two features appear to be extraordinary. First, the reactions of **7** and **8** are reported to be stereospecific, i.e., **7** gives only **9**, and **8** only **10**, whereas it would have been anticipated that C-5 in the diradical **11** would undergo configurational change and that stereospecificity would not be observed. Second, when the reaction is carried out in ethanol, intramolecular reaction of the ketene group of **12** with the hydroxyl group occurs to the

[1]For a preliminary communication concerning part of this work, see ref. 1.

Can. J. Chem. Downloaded from www.nrcresearchpress.com by 213.222.148.141 on 09/07/12
For personal use only.

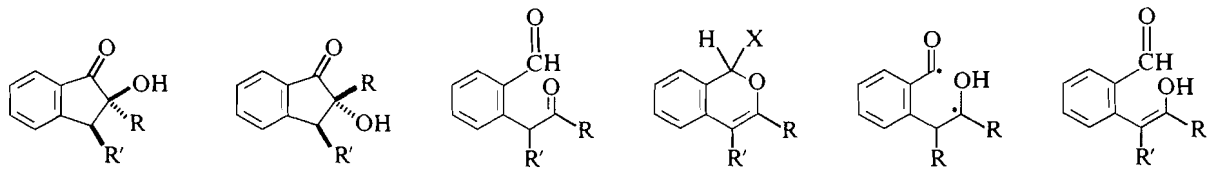

1
R = Me, Ph or CO_2Me
R′ = H or Me

2 3 4
X = OH or OMe

5 6

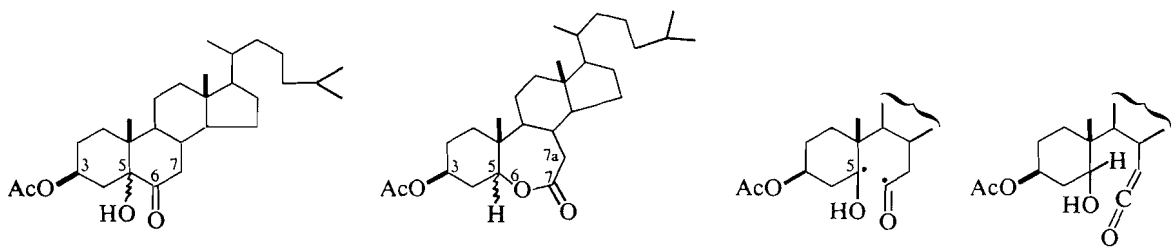

7 α-OH
8 β-OH

9 5β-H
10 5α-H

11 12

exclusion of intermolecular reaction with the solvent. With respect to the former feature it may be noted that photoepimerization at the α-carbon of a cyclic ketone that undergoes photocleavage is well known. In addition to the case of the compounds of type **1** referred to above, it has been well documented, for example, in the cases of 17-keto steroids (**13**) (6), octahydro-7a-methylinden-1-one (**14**), and octahydro-8a-methylnaphthalen-1(2*H*)-one (**15**) (7).

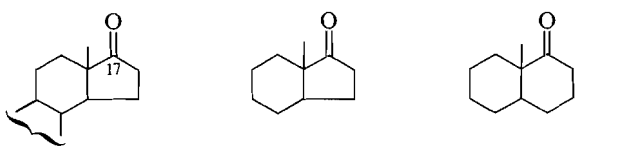

13 14 15

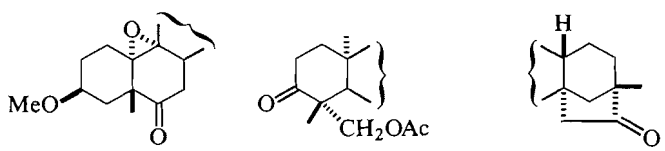

16 17 18

In rare cases retention of configuration has been reported (8–10). Photolysis of compounds with part-structures **16**–**18**, in alcohols, gives the corresponding ketene-derived esters via α-cleavage of the cycloalkanone moiety with retention of configuration at the α-carbon. However, in none of these cases was the photochemistry of the corresponding α-epimer examined. To the best of our knowledge compounds **7** and **8** represent the only case where the reaction has been shown to be *stereospecific*.

In the present work we have sought to define both the generality and the major controlling factors of this stereospecificity. Towards this end we have reexamined the photochemistry of **7** and **8** and have synthesized (11) and studied the photochemistry of a number of steroids related to them.

Results

Photolysis of 5α- and 5β-hydroxy 6-keto steroids

We first repeated the photolyses of **7** and **8** to determine whether the stereospecificity reported by Cookson *et al.* (5) would withstand the more searching scrutiny made possible by recent advances in instrumentation.

The total photolysates from irradiation of **7** and **8** in benzene or in ethanol were concentrated and analyzed by high performance liquid chromatography. In either solvent, ketone **7** gave only lactone **9** and ketone **8** only lactone **10**. The original stereochemical assignments (5) for the lactones were confirmed by ^1H nmr spectroscopy. In the 5β-lactone **9** equatorial–equatorial and axial–equatorial interactions of the C-5 methine proton with the C-4 α- and β-methylene protons, respectively, result in a narrow multiplet at δ 4.33 for the C-5 proton. In contrast the signal of the C-5 methine proton of **10** appears as a doublet of doublets (J = 11, 5 Hz) at δ 4.30; the 11-Hz splitting, indicative of an axial–axial type coupling, confirms the 5α-stereochemistry (Scheme 1).

Further confirmation of the stereospecificity of the reactions derives from the ^{13}C nmr spectra of the photolysates, which in each case showed the presence of only one of the epimeric lactones. These spectra again showed that the reactions proceeded with retention of configuration at the C-5 center.[2]

An attempt was made to promote epimerization at this center during photolysis by irradiation of **7** in *n*-butanol at 100°C. However, the effect of temperature was negligible and the only product obtained was lactone **9**.

To determine the effect, if any, of the 3-acetoxy group in **7** and **8** on the course of reaction we next investigated the photolysis of the 3-deoxy (**19** and **20**) and 3-benzyloxy analogues (**21** and **22**) of **7** and **8** in both benzene and ethanol. As shown by ^{13}C nmr spectroscopy, in all cases the stereospecificity of the reactions was maintained, with **19** and **21** giving only the lactones **23** and **25**, respectively, and **20** and **22** giving only the lactones **24** and **26**, respectively. The stereochemistry of the lactones was established by ^1H nmr spectroscopy as in the case of their 3-acetoxy analogues, and these stereospecific reactions were again found to proceed with retention of configuration at the C-5 center (Scheme 1).

Photolysis of deuterated 5α- and 5β-hydroxy 6-keto steroids

To obtain information concerning the hydrogen transfer reactions involved in the photoconversion of the hydroxy ketones to the lactones, we investigated the photolysis of the

[2]It is planned to discuss in detail elsewhere the ^{13}C nmr spectra of these lactones and of other compounds obtained in the present investigation.

Can. J. Chem. Downloaded from www.nrcresearchpress.com by 213.222.148.141 on 09/07/12
For personal use only.

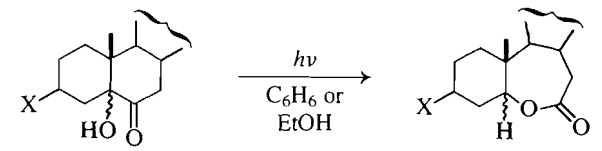

7 X = OAc, α-OH
8 X = OAc, β-OH
19 X = H, α-OH
20 X = H, β-OH
21 X = OBn, α-OH
22 X = OBn, β-OH

9 X = OAc, β-H
10 X = OAc, α-H
23 X = H, β-H
24 X = H, α-H
25 X = OBn, β-H
26 X = OBn, α-H

SCHEME 1

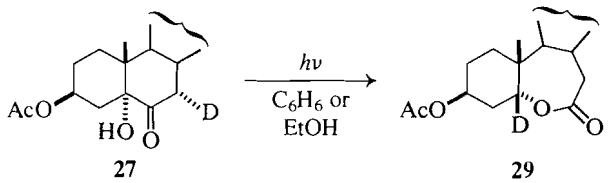

27 29

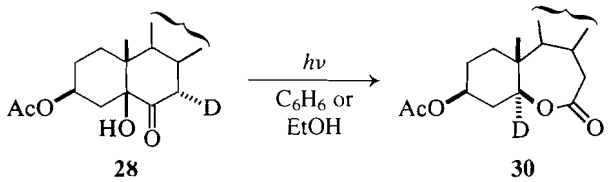

28 30

SCHEME 2

7α-deutero-5α- and 5β-hydroxy 6-keto steroids **27** and **28** (11) in benzene and in ethanol. These reactions were found to proceed stereoselectively to give the 5-deutero lactones **29** and **30**, respectively (Scheme 2). The C-5 position of the deuterium label was made manifest by the ^{1}H nmr spectra of the product lactones by the greatly diminished intensities of the C-5 methine proton signals. The extent of deuterium incorporation at C-5, as determined from the relative areas of the C-5 and the C*H*OAc proton signals when compared with the deuterium content calculated from the mass spectra of the products, showed that the deuterium label was present essentially exclusively at the C-5 site and thus established the highly stereoselective nature of the deuterium transfer reactions.

The photolysis of the *O*-deuterated 5α- and 5β-hydroxy 6-keto steroids **31** and **32** was also investigated, to throw further light on the mechanism of lactone formation. Irradiation of **31** and **32** in benzene was carried out in the presence of deuterium oxide, the latter being added to improve the extent of deuterium incorporation. To exclude the possibility that, under these conditions, deuterium incorporation into the product lactones occurred *after* their formation, ε-caprolactone was similarly irradiated for a prolonged period. There was no evidence of any deuterium incorporation into this lactone.

Irradiation of **31** gave a ~1:3 mixture of the 7aα- and 7aβ-deutero 5β-lactones **33** and **34**, while **32** gave a ~7:1 mixture of the 7aα- and 7aβ-deutero 5α-lactones **35** and **36** (Scheme 3). The mass spectrum of the product mixture from **31** evidenced a d_1 content of 68%, an acceptable level of incorporation in the light of the well-known difficulties associated with the manipulation of compounds labelled at a heteroatom (12). In the case of **32** the mass spectrum of the product mixture showed excellent incorporation (d_1 88%) of the label.

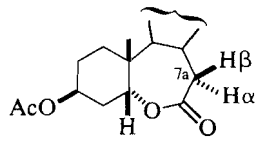

9
H 7aα δ = 2.44 (br d, J = 14 Hz)
H 7aβ δ = 2.96 (dd, J = 14, 10 Hz)

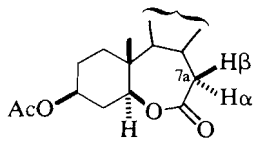

10
H 7aα δ = 2.39 (dd, J = 14, 11 Hz)
H 7aβ δ = 2.54 (dd, J = 14, 2 Hz)

FIG. 1

The conclusions concerning the location of the deuterium label in the product lactones are dependent on the assignments for the C-7a methylene protons in the ^{1}H nmr spectra of the undeuterated lactones **9** and **10**. The task of making these assignments proved not to be a simple one, because of the conformational flexibility of the seven-membered lactone rings. In order not to interrupt unduly our discussion of the photochemical results, we give only our conclusions regarding these assignments here and give a separate account of the basis for them in an Appendix. The assignments are shown in Fig. 1.

The 200-MHz ^{1}H nmr spectrum of the mixture of **33** and **34** exhibited a narrow multiplet ($W_{1/2}$ = 6 Hz) at δ 2.42 and a much weaker, broad doublet at δ 2.94 (J = 10 Hz). These must correspond to the C-7a methylene protons of the undeuterated lactone **9** shifted slightly upfield by the presence of deuterium at C-7a (13). The narrow multiplet at δ 2.42 is assigned to the C-7a α-proton of the 7aβ-deutero lactone **34**, and the broad doublet at δ 2.94 to the C-7a β-proton of the 7aα-deutero lactone **33**. The relative intensities of these peaks show that the **33**/**34** product ratio is ~1:3. In the case of the irradiation of **32** the spectrum of the mixture of **35** and **36** showed a broad singlet at δ 2.52, assigned to the C-7a β-proton of the 7aα-deutero lactone **35** and a very weak doublet at δ 2.38, assigned to the C-7a α-proton of the 7aβ-deutero lactone **36**. The relative intensities of these peaks showed that the reaction of **32** was somewhat more stereoselective than that of **31**, with a **35**/**36** product ratio of ~7:1.

Photolysis of other 6-keto steroids

The photolysis of 3β-acetoxy-5-methoxy-5α-cholestan-6-one (**37**) in methanol has been investigated previously by Morand and Samad (14). They assigned structure **38** to the single product isolated. Although the configuration at C-5 could not be assigned directly from the ^{1}H nmr spectrum of the product because of overlap of the methoxyl proton signal with that of the C-5 proton, they were able to assign the α configuration of the C-5 proton as shown in **38** (Scheme 4) after a series of chemical transformations.

To confirm the stereochemical assignment and to determine whether there is any evidence for the formation of other products, we have investigated the photolysis of **37** in ethanol. The ethyl ester **39** was found to be the sole photoproduct, as shown by both the ^{1}H and ^{13}C nmr spectra of the crude

Can. J. Chem. Downloaded from www.nrcresearchpress.com by 213.222.148.141 on 09/07/12
For personal use only.

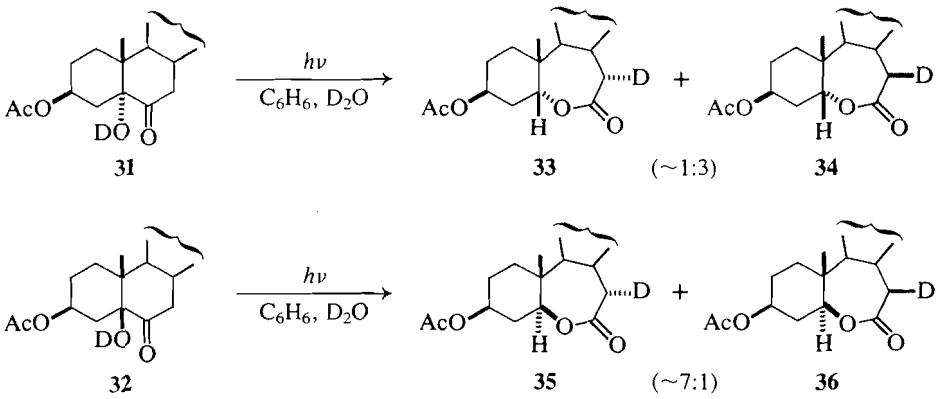

SCHEME 3

photolysate. In its ^{1}H nmr spectrum, the broad signal arising from the C*H*OAc proton evidenced the preference for the conformation **39***A*. The configuration at C-5 was established directly from the 200-MHz ^{1}H nmr spectrum in benzene-d_6, in which the coincidence of the C-5 methine and methoxyl proton signals observed in the spectrum in deuterochloroform was resolved. A narrow multiplet ($W_{1/2}$ = 8 Hz) at δ 3.36, assigned to the C-5 methine proton, established the 5α configuration of the methoxyl group, thus corroborating the earlier results (14).

Unfortunately, we were unable to examine the photochemistry of 3β-acetoxy-5-methoxy-5β-cholestan-6-one (**40**), the C-5 epimer of **37**, because of problems in its synthesis (11). However, it is likely that this would have undergone preferential Norrish type II cleavage (15, 16) to give 3β-acetoxy-5α- (**41**) and (or) 5β-cholestan-6-one (**42**) (Scheme 5), and its photolysis would not have shed light on the α-cleavage reactions under study.

An exploratory study was made of the photolysis in ethanol of a steroidal 6-ketone lacking any substituent at C-5, viz. 3β-acetoxy-5α-cholestan-6-one (**41**). Under the conditions

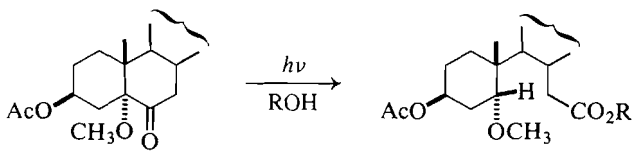

37

38 R = CH_3
39 R = C_2H_5

SCHEME 4

used previously (Pyrex tube; Rayonet apparatus; 300-nm lamps) photoreaction was slow, but irradiation in a quartz tube with this apparatus with 254-nm lamps or in Pyrex with a Hanovia 450-W medium pressure lamp proceeded much more rapidly, giving very similar product mixtures. The photolysis was much less clean than in the previous cases and thin-layer and vapor phase chromatography showed that the crude photolysate comprised a number of compounds. In the ^{1}H nmr spectrum of this photolysate a prominent broad multiplet at δ 3.5 and narrow multiplet at δ 3.8 indicated that the major constituents were hydroxyl

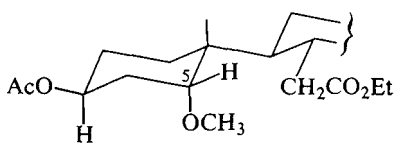

39*A*

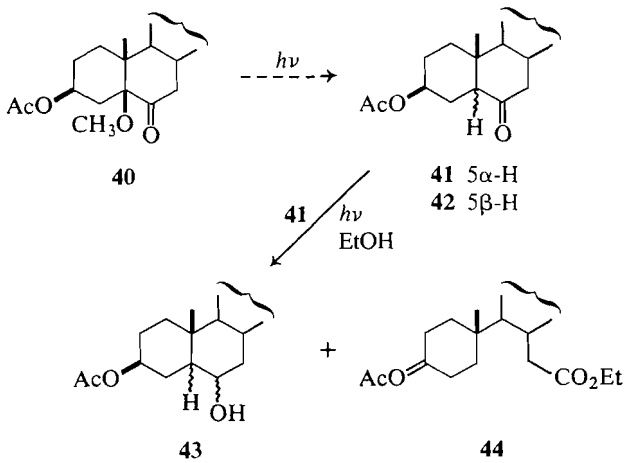

SCHEME 5

compounds. These are considered to be alcohols of type **43** (Scheme 5), arising by photoreduction of **41**, and were not examined further. A second type of product isolated was the ester **44**. Although this was isolated in only 7% yield, the ^{1}H nmr spectrum of the crude photolysate suggested that this could account for ~30% of the photoproduct. Its structure was readily assigned on the basis of its spectra and analogy with the photochemistry of other simple cyclohexanones.

We have also examined the photochemistry of an amino analogue of the hydroxy steroids discussed above. 3β-Acetoxy-5-amino-5α-cholestan-6-one (**45**), prepared by hydrolysis of the corresponding (*E*)-oxime (17), on irradiation in benzene gave the 5β-lactam **46** in 69% yield (Scheme 6). The 60-MHz ^{1}H nmr spectrum of the crude photolysate gave no indication of the presence of another product; thus the epimeric 5α-lactam can be, at most, a very minor constituent of the reaction mixture. The lactam functionality of the product was readily apparent from its ir spectrum, which showed bands at 2.97 and 6.02 μm. The stereochemical assignment at C-5 derives from comparison of its ^{1}H nmr spectrum with that of its 5α-epimer **47**, which was prepared previously by Beckmann rearrangement of 3β-acetoxy-5α-cholestan-6-one (*E*)-oxime (**48**) (18) and as a minor product in the irradiation in methanol of **49**, the acetate of **48** (19) (Scheme 6). These spectra were similar, as expected, but exhibited well-defined differences. Thus the C-19 CH_3, C-5 CH, and C*H*OAc proton signals of **46** appeared at δ 1.03 (s), 3.23 (m, $W_{1/2}$ = 20 Hz), and 5.10 (m, $W_{1/2}$ = 16 Hz), respectively, while the corresponding signals of **47** appeared at δ 0.93 (s), 3.42 (ddd, J = 10, 5, 5 Hz), and 4.67 ($W_{1/2}$ = 24 Hz). It is of interest that the C*H*OAc signal of **46** ($W_{1/2}$ =

Can. J. Chem. Downloaded from www.nrcresearchpress.com by 213.222.148.141 on 09/07/12
For personal use only.

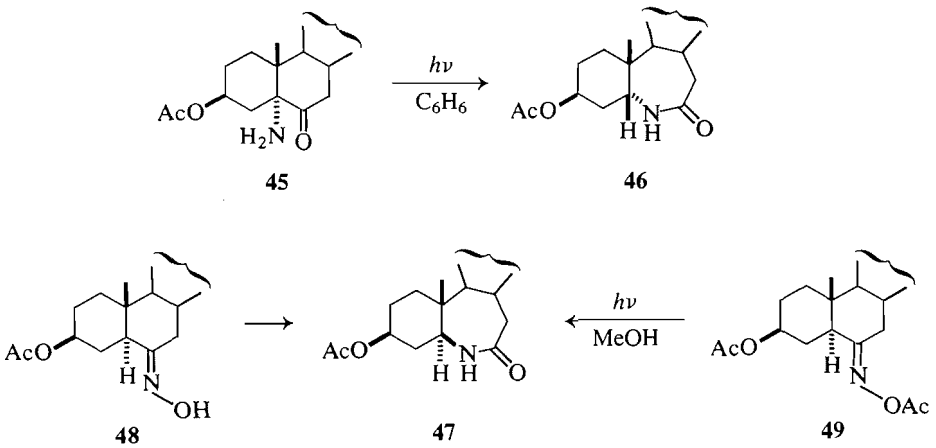

SCHEME 6

16 Hz) is narrower than usual for an axial proton at C-3 ($W_{1/2}$ = 20 Hz). This may reflect some distortion in ring A of this epimer resulting from planarity of the lactam function in ring B.

Discussion

Modes of photoreaction of α-ketols and related compounds

Irradiation of the steroidal α-hydroxy ketones **7** and **8** in benzene or ethanol gave photoproducts **9** and **10**, whose structures are consistent with exclusive α-cleavage of the excited ketone to give acyl alkyl diradicals of type **11** that undergo intramolecular hydrogen transfer to give ketene intermediates of type **12**. The regiochemistry of the α-cleavage corresponds to that yielding the more stable, oxygen-substituted alkyl radical (or to that involving cleavage of the weaker α bond) in accord with expectation (20, 21). Photolyses in ethanol gave no indication of the formation of any products attributable to photoreduction.

Norrish II cleavage does not intervene as a competitive reaction pathway to α-cleavage in the irradiation of the 5α-methoxy ketone **37** in ethanol, which gives the ketene-derived ester **39** (Scheme 4). This is presumably because the hydrogens of the methoxyl group are held distant from the *n*-orbitals of the carbonyl group and thus do not satisfy the strict geometrical requirements for Norrish II cleavage (22).

Irradiation of the 5α-amino ketone **45** afforded the lactam **46** as the predominant photoproduct. As for the related oxygen-substituted ketones, a mechanism comprising α-cleavage and hydrogen abstraction in the resulting diradical **50** and intramolecular addition to the ketene intermediate **51** is considered to account best for the formation of **46** (Scheme 7). α-Dialkylamino cyclohexanone systems have been observed to undergo direct β-cleavage of the C—N bond (23), while hydrogen abstraction becomes a competitive process for α-dialkylamino ketones, where α-hydrogens that are geometrically favorably disposed (22) are available (24). To the best of our knowledge, the formation of amide **46** from irradiation of amino ketone **45** represents the first example of an α-cleavage reaction of an α-amino ketone.

In contrast to the selective α-cleavage photoreactivity exhibited by the α-hetero-substituted ketones studied, irradiation of the C-5 unsubstituted ketone **41** in ethanol induced photoreduction, via intermolecular hydrogen abstraction, as the predominant reaction (Scheme 5). The ketene-derived ester **44**, formed as a minor photoproduct, is considered to originate from α-cleavage of the C-5—C-6 bond, generating the more stable diradical intermediate, as in the cases of the major products from the α-hetero-substituted ketones.

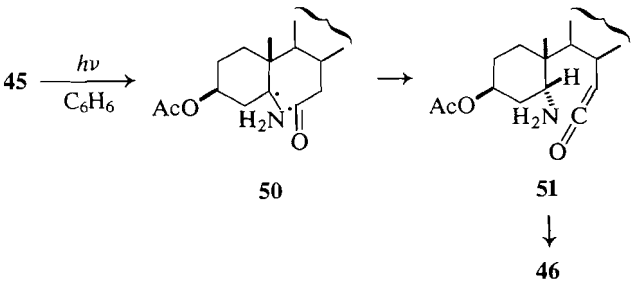

SCHEME 7

The pronounced increase in the extent of α-cleavage upon introduction of a heteroatom α to the carbonyl group is considered to be primarily attributable to the increase in the rate of α-cleavage concomitant with the increased stability of the diradical intermediate (*vide supra*). In addition, the planar geometry of the cyclohexyl radical may not be as geometrically well disposed for hydrogen abstraction as the nonplanar radical centers of α-hetero-substituted cyclohexyl radicals (*vide infra*). Consequently, reclosure of the diradical to **41** may compete more effectively with hydrogen abstraction, resulting in a decrease in the apparent efficiency of α-cleavage for the unsubstituted ketone **41**.

Stereochemistry of α-ketol photolyses

We have shown that in steroidal systems the photolyses of 5α- and 5β-ketols proceed stereospecifically to give lactones wherein the stereochemistry of the C-5 carbon atom has been retained (Scheme 1). The stereospecificity observed for the irradiations of the C-3 deoxy steroidal ketols **19** and **20** excludes the possibility that the configuration of the radical center at C-5 is maintained during photolysis by interaction with the C-3 substituent.

Hydrogen bonding in the intermediate diradical (25) is discounted as a source of the stereospecific steroidal α-ketol photolyses on the basis of the stereoselectivity in the irradiation of the 5α-methoxy ketone **37** (Scheme 4).

We propose that two major factors, the shape of the hydroxyl-substituted carbon radical and fast hydrogen transfer in the diradical intermediate, are the source of the stereospecificity of the steroidal α-ketol photolyses.[3] We first discuss the radical site geometry. Simple alkyl radicals (26) (with the possible exception of the *tert*-butyl radical (27)) and cyclohexyl

[3]These factors are considered to account also for the stereoselective nature of the photolyses of the 5α-methoxy ketone **37** and the 5α-amino ketone **45**.

Can. J. Chem. Downloaded from www.nrcresearchpress.com by 213.222.148.141 on 09/07/12
For personal use only.

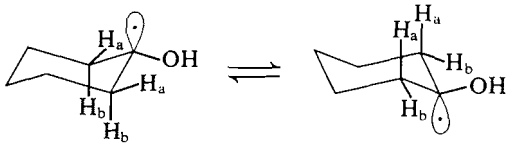

SCHEME 8

radicals (28) are generally considered to have a planar radical geometry.[4] Introduction of oxygen functionality at the carbon radical center induces deviation from planarity (30, 31). This deviation from planarity has been attributed primarily to delocalization involving a lone pair on the oxygen atom and the unpaired electron (30, 32).

A nonplanar geometry for the 1-hydroxycyclohexyl radical has been predicted by calculation (33) and supported by variable temperature esr spectroscopy (34). The activation barrier, E_a, for chair $\rightleftharpoons$ chair inversion of the 1-hydroxycyclohexyl radical was determined to be 6.6 kcal/mol. The higher value of this barrier relative to that measured for ring inversion of the cyclohexyl radical (4.9 kcal/mol) (28) has been interpreted as evidence for nonplanarity at the hydroxyl-substituted carbon radical (34).

The low temperature esr spectrum of the 1-hydroxycyclohexyl radical is consistent only with a species in which the unpaired electron is in an axial orientation. At higher temperatures, the esr spectrum evidences the equivalence of all four β-protons. Lloyd *et al.* (33, 34) have concluded that a mechanism involving both chair $\rightleftharpoons$ chair inversion and simultaneous inversion of the nonplanar carbon radical center (Scheme 8) best accounts for the observed spectra. Consistent with this mechanism, the calculated activation barrier for inversion of the 1-hydroxyl-substituted radical center (3.5 kcal/mol) (33) is lower than that measured for ring inversion.

With regard to the ease of radical site inversion, Malatesta and Ingold (35) have observed that carbon radicals in cyclic systems with one or two oxygen substituents invert their nonplanar radical centers rapidly, and only in cases where the radical is flanked by three oxygen substituents was radical inversion observed to be "frozen" on the esr time scale.

Models demonstrate that an analogous nonplanar geometry of the hydroxycyclohexyl radical center in the diradicals formed from the steroidal α-ketols holds the unfilled orbital in a favorable orientation for hydrogen abstraction. In contrast, if the radical center at C-5 were planar, the unfilled orbital in the case of the 5α-ketols is not suitably disposed for hydrogen abstraction to give the observed stereochemistry of the lactone photoproducts. Moreover, a planar radical geometry would project the hydroxyl substituent into close proximity with the acyl radical; products derived from abstraction of the hydroxyl hydrogen atom that would then be anticipated were not observed in the cases of the steroidal α-ketols. Thus our results support a nonplanar geometry for the hydroxyl-substituted cyclohexyl radical and indicate that this geometry plays a significant role in the stereospecificity of the steroidal α-ketol irradiations.

However, we have found that photolyses of bicyclic α-ketol analogues of the steroidal α-ketols are not stereospecific (36). Thus the nonplanar geometry of the radical center is not of itself the controlling factor for the stereospecificity of the steroid ketol photolyses. As detailed in the following discussion, rapid hydrogen abstraction in the diradical is also considered to be critical for stereospecificity.

[4]A slight deviation from planarity has also been proposed for the cyclohexyl radical (29).

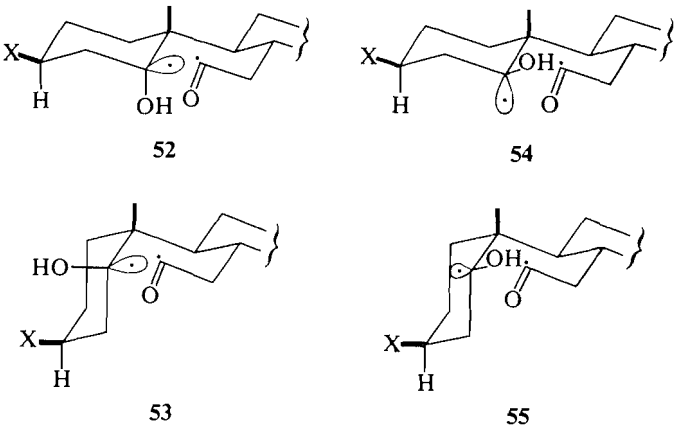

X = OAc, H, OBn

Hydrogen abstraction leading to ketene formation in the photolyses of the 5α- and 5β-steroidal ketols is postulated to occur from the diradicals **52** and **53**, respectively, first formed upon α-cleavage. Hydrogen transfer in these diradicals gives lactone photoproducts in which the configuration of the C-5 center is maintained.

Consideration of the consequences of ring inversion and (or) inversion at the radical carbon center in diradicals **52** and **53** with respect to the configuration of the C-5 center in the resulting lactone photoproduct leads us to propose that hydrogen transfer occurs in diradicals **52** and **53** more rapidly than such ring inversion or radical center inversion. The persistence of the stereospecific character of the steroidal α-ketol photolyses with changes in the nature of the C-3 substituent indicates that conformational effects in the diradicals **52** and **53** are not important to the stereochemical course of the irradiations. This lends credence to the suggestion that ring inversion does not occur prior to hydrogen abstraction in these two diradicals.

Inversion of the radical center without concomitant chair inversion (i.e., **52** $\rightleftharpoons$ **54** and **53** $\rightleftharpoons$ **55**) is considered unlikely to be competitive with hydrogen abstraction, since it would require that hydrogen transfer occur selectively in the diradicals **52** and **53** and not in the inverted forms **54** and **55**. While this would be expected for the diradical **55**, where hydrogen transfer is geometrically not feasible, models indicate that hydrogen transfer should occur in both the diradicals **52** and **54**, leading to lactones with both the α and β stereochemistry at C-5. The fact that this is not observed precludes inversion of the radical center prior to hydrogen abstraction.

Further, we interpret the absence of the formation of keto aldehydes, products that would arise from abstraction of the hydrogen of the hydroxyl group, in the photolysis of the 5α- and 5β-steroidal ketols as evidence that inversion of the radical center is not competitive with hydrogen abstraction. In diradicals **52** and **53**, the hydroxyl groups are axial and, as models indicate, their hydrogen atoms are not readily accessible for abstraction by the acyl radicals. However, if the radical centers invert, the hydroxyl groups in the resultant diradicals **54** and **55** become equatorial and favorably disposed for abstraction of their hydrogen atoms by the acyl radicals. This argument is corroborated by the observation that photolyses of the corresponding bicyclic α-ketols proceed to some extent by abstraction of the hydroxyl hydrogen to afford the corresponding keto aldehyde (36).

Our conclusion that radical center inversion does not compete with hydrogen abstraction in the steroidal α-ketol photolyses, in spite of the very rapid rate of such inversion observed by Lloyd and Ingold and their co-workers (33–35), raises the possibility

Can. J. Chem. Downloaded from www.nrcresearchpress.com by 213.222.148.141 on 09/07/12
For personal use only.

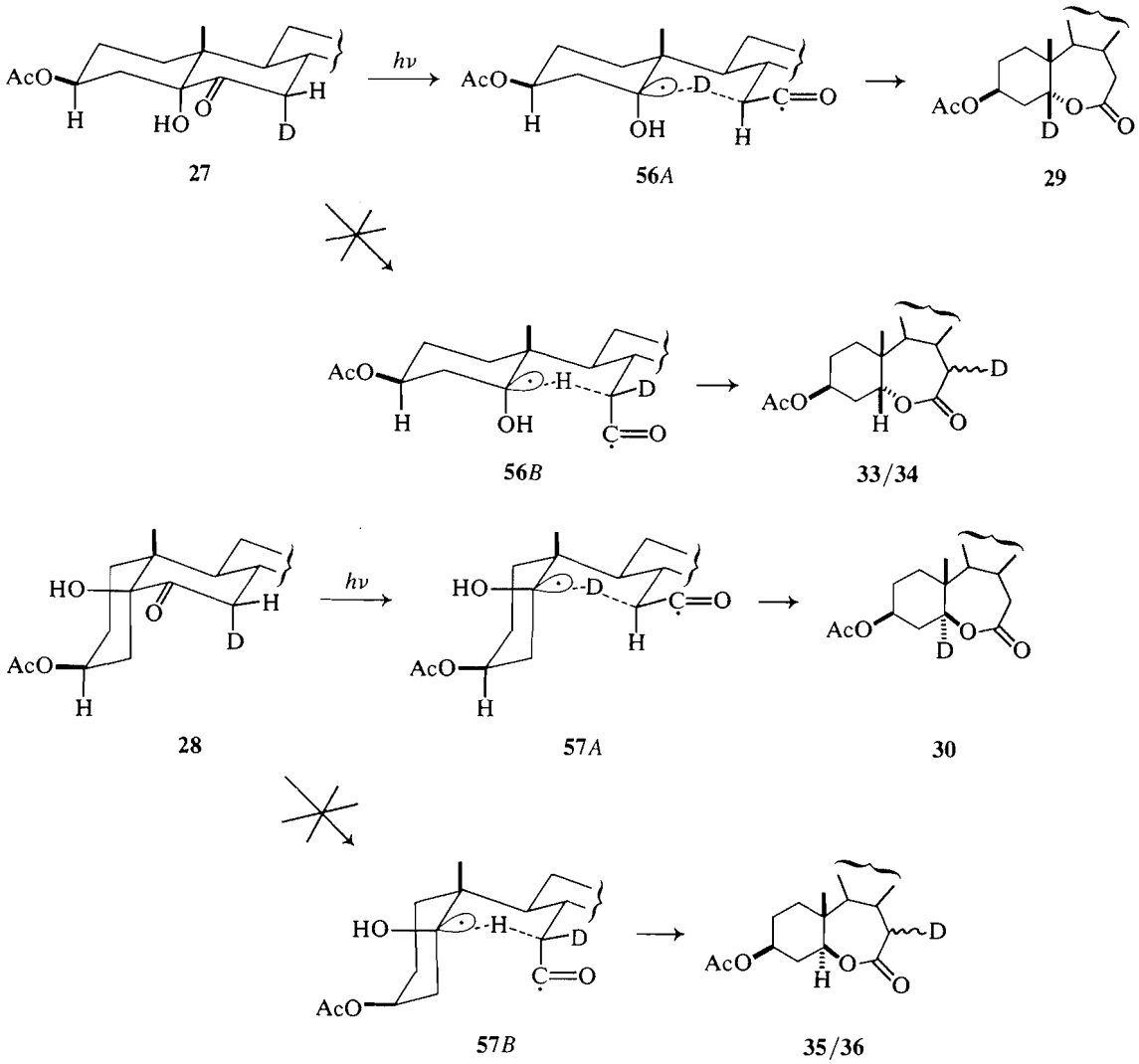

SCHEME 9

that the hydrogen abstraction process leading to ketene formation is concerted with α-cleavage. However, our C-7 deuterium labelling results contraindicate this. If the photolyses were concerted, the 7β-hydrogen in both the 5α- and 5β-steroidal ketols should, by affording better orbital overlap with the incipient acyl radical during α-cleavage, be transferred to the alkyl radical center. Contrary to this, the deuterium labeling studies showed that stereoselective transfer of the 7α-hydrogen occurs (1) (Scheme 2). Moreover, given a concerted reaction, the bicyclic α-ketol photolyses would also be expected to be stereospecific.

The fast hydrogen abstraction that we have invoked as the source of the stereospecificity of the steroidal α-ketol photolyses can be accounted for by the presence of the CD ring system in the steroid, which restricts the rotational motions of the acyl side chain in the diradicals **52** and **53**. This holds the alkyl radical center at C-5 and the hydrogen α to the acyl radical in close proximity, thus favoring fast hydrogen abstraction and preempting inversion of the radical center and (or) cyclohexyl ring inversion.

Evidence for this again comes from the deuterium labeling results involving irradiations of the 7α-deutero ketols **27** and **28**. As shown in Scheme 9, abstraction via the chair-like transition states **56***A* and **57***A* accounts for the completely stereoselective formation of the C-5 deutero lactones **29** and **30**, respectively. The preference of the diradicals **52** and **53** (R = OAc, 7α-D) for the ketene-forming transition states **56***A* and **57***A* is considered to result from the preferred direction of opening of the diradicals upon α-cleavage.[5]

Newman projections show that as the C-5—C-6 bond cleaves in the excited 5α- and 5β-ketols, clockwise rotation (as viewed along the C-7—C-8 bond) of the incipient acyl radical minimizes eclipsing interactions (Scheme 10). As the acyl group rotates clockwise, the 7α-deuterium atom approaches the electron-deficient orbital. This arrangement represents transition states **56***A* and **57***A* and results in favored abstraction of the deuterium atom.

As the rotation of the acyl group occurs about the C-7—C-8 bond, the C-8—C-9 framework is held by ring C and rotation about the C-9—C-10 bond is considered to be frozen relative to the time scale for hydrogen abstraction. The activation barrier to rotation about the C-9—C-10 bond is expected to be higher than that for rotation about the C-7—C-8 bond because of the greater eclipsing interactions involved in the former. Furthermore, the

[5]The direction of ring opening in α-cleavage reactions of cycloalkanones has been previously invoked to rationalize stereoselective hydrogen abstractions leading to ketene formation (37, 38).

Can. J. Chem. Downloaded from www.nrcresearchpress.com by 213.222.148.141 on 09/07/12
For personal use only.

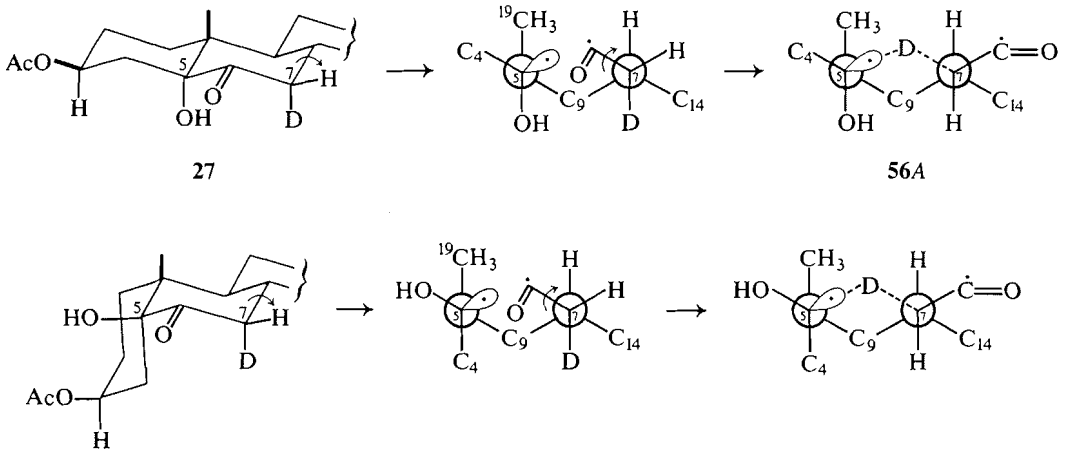

SCHEME 10

rotamer of the C-9—C-10 bond first formed upon α-cleavage is considered to be the preferred rotamer about this bond.

Thus, the presence of ring C is suggested to hold the C-8—C-9—C-10 framework in the diradicals **52** and **53** in an arrangement that mimics the one in their steroidal ketol precursors. This then maintains the alkyl and acyl radical centers in close proximity, facilitating rapid hydrogen abstraction.

We also note that the above clockwise opening upon α-cleavage affords the thermodynamically favored rotamers about the C-7—C-8 bond. In contrast, transition states **56*B*** and **57*B*** leading to hydrogen abstraction giving **33**/**34** and **35**/**36**, respectively (Scheme 9), incorporate unfavorable 1,3-diaxial interactions of the acyl radical with ring A and *gauche* interactions with C-9 and C-14.

In summary, in the photolyses of both the 5α and 5β steroidal ketols, a clockwise rotation of the acyl radical about the C-7—C-8 bond without concomitant rotation of the C-9—C-10 bond is postulated to give directly a favorable transition state for hydrogen abstraction leading to ketene formation. The fast hydrogen abstraction that results precludes competitive inversion of the ring conformation and (or) radical configuration in the intermediate diradicals and thereby gives rise to the stereospecificity of the steroidal α-ketol photolyses.

Reactions of the ketene intermediates

We conclude by discussing the addition reactions of the ketene intermediates. Although these are "dark" reactions, they are of importance in determining the nature of the products isolated from the photolytic reactions of the α-ketols. Intramolecular addition of the hydroxyl group to the ketene group in these intermediates formed in the steroidal photolyses gives rise to the lactone photoproducts. Deuterium labelling studies have provided us with information concerning the transition state for this addition.

Photolyses of the 5α- and 5β-deuteroxy 6-keto steroids **31** and **32** exhibited preferences for the formation of the C-7aβ-deutero 5β-lactone **34** and the C-7aα-deutero 5α-lactone **35**, respectively (Scheme 3). Concerted reactions involving four-membered ring transition states are considered to be involved in the addition of the deuteroxyl group to the ketene intermediate (39). In the case of **31**, transition state **58** leads to the formation of the C-7aβ-deutero lactone **34**. Models show that **34** is first formed in its preferred conformation, whereas addition to the other face of the ethylenic bond would give rise to the C-7aα-deutero lactone initially in a nonpreferred conformation. For the 5β-ketol **32**, transition state **59** leads to initial formation of the C-7aα-deutero lactone **35** in its preferred conformation, whereas addition to the other face of the ethylenic bond would give rise to a nonpreferred conformation of the C-7aβ-deutero lactone **36**.

In the photolyses of **31** and **32** selective formation of the lactones **34** and **35**, respectively, is observed (Scheme 11). Since these products correspond to the transition states that lead directly to the preferred conformations of these lactones (*vide* Appendix), the addition of the C-5 hydroxyl groups to the ketene groups is considered to be under product development control, with the transition states for the additions being formed relatively late on the reaction coordinate. The importance of product development control in these additions is considered to be fostered by the maintenance of the C-8—C-9—C-10 framework in the ketene in an arrangement that approximates the backbone of the preferred conformation of the lactone ring.

Finally we note that the maintenance of this framework in the ketenes accounts for the exclusive formation of intramolecular addition products when the photolyses of the steroidal α-ketols are carried out in ethanol. The presence of ring C is considered to hold the C-5 hydroxyl group and the ketene system in close proximity, thus leading to lactone photoproducts rather than the esters that would arise if the ketenes reacted with the solvent ethanol.

Conclusions

Our studies of the photochemistry of a variety of α-ketols and related ketones have shown that introduction of an oxygen, and in one case a nitrogen, function α to the carbonyl group induces a highly efficient and highly regioselective α-cleavage reaction of the excited state of cycloalkanones. The efficiency and regioselective nature of these photolyses is attributed primarily to the increase in the stability of the diradicals, formed on α-cleavage, as a result of heteroatom substitution.

We have established that stereospecificity is a general feature of the photolyses of the steroidal 5α- and 5β-ketols (Scheme 1). The stereospecific nature of these photolyses is attributed to a relatively rapid hydrogen transfer in the diradicals first formed from α-cleavage (Scheme 9). Efficient hydrogen abstraction in these diradicals is fostered by the preferential clockwise rotation (viewed along the C-7—C-8 bond) of the acyl radical following α-cleavage. This rotation directs the C-7a hydrogen towards the electron-deficient alkyl radical center. This, together with the nonplanar geometry of this center, generates directly favorable

Can. J. Chem. Downloaded from www.nrcresearchpress.com by 213.222.148.141 on 09/07/12
For personal use only.

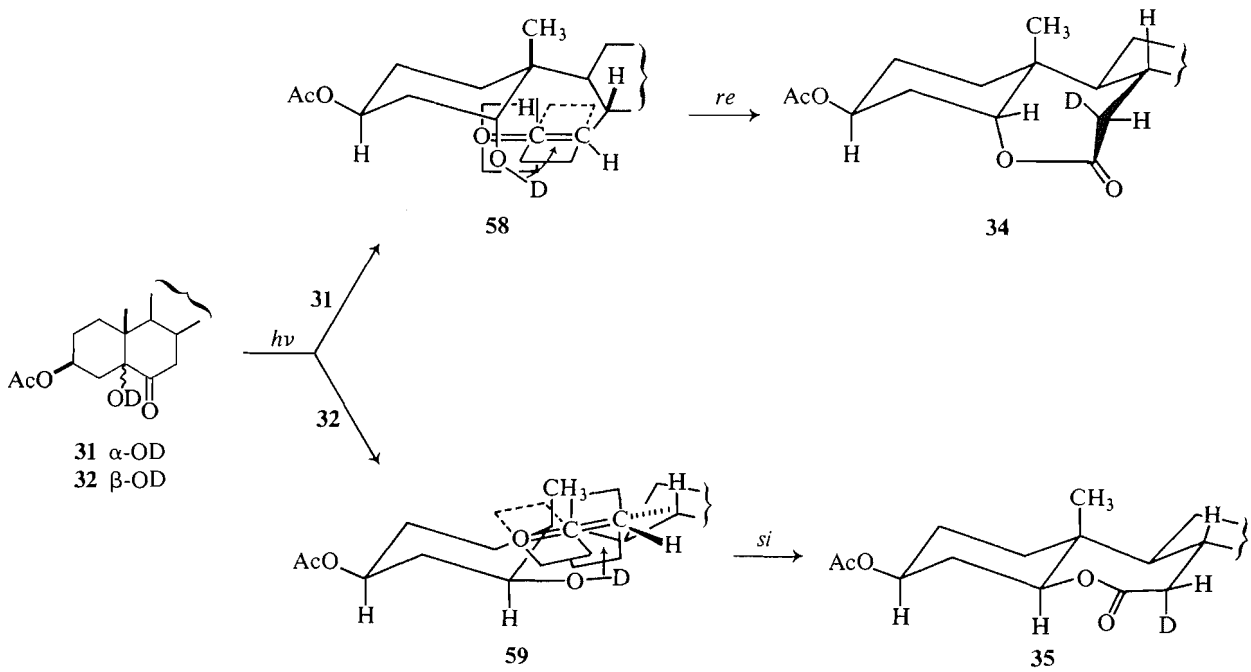

SCHEME 11

chair-like transition states for hydrogen abstraction leading to ketene formation in these photolyses. As the acyl radical rotates, the presence of the CD ring system in the steroid is considered to hinder rotational movement in the C-8—C-9—C-10 framework of the diradical, thereby maintaining the alkyl and acyl portions of the diradical in close proximity. This facilitates rapid hydrogen abstraction from the diradicals first formed from α-cleavage, precluding inversion of the ring conformation or of the configuration of the radical center prior to hydrogen transfer, and thereby giving rise to the stereospecificity of the steroidal α-ketol photolyses.

Thus, the stereospecificity of the photolyses of 5-hydroxy 6-keto steroids is not a general attribute of all α-ketol irradiations, but neither is it necessarily limited to these steroidal cycloalkanones. It is considered to arise from an unusual confluence of special circumstances. In principle, other cycloalkanones giving rise to diradicals wherein hydrogen transfer is a fast process compared to competitive processes may also be expected to be highly stereoselective or possibly stereospecific. However, in general, ring and radical inversion motions in the diradical are expected to be strongly competitive with hydrogen abstraction, and the relative stabilities of the diradicals that result from these inversions are then expected to determine the stereochemistry of the photoproducts. Thus, studies of the stereochemical fate of the alkyl radical center can provide interesting insights into the intricacies of α-cleavage reactivity in the photochemistry of cycloalkanones.

Experimental

Melting points were recorded on a Fisher–Johns melting point apparatus and are uncorrected. The ir spectra were recorded in chloroform and the ^{1}H nmr spectra at 60 MHz in deuterochloroform unless otherwise specified. For symmetrical multiplets in the latter, the width at half height ($W_{1/2}$) is recorded while for unsymmetrical multiplets the total width is given. Low resolution mass spectra were recorded with a Bell and Howell CEC 21-490 mass spectrometer. For the deuterium content calculations, 10–20 scans of the region of the spectrum containing the isotopic cluster associated with the molecular ion or, where appropriate, of the (M − AcOH) fragment were obtained at a high signal-to-noise ratio and averaged. Exact mass measurements were made with an AEI MS-3074 spectrometer with a DS-50 data system.

Organic solutions were dried over $MgSO_4$ or Na_2SO_4 and concentrated on a rotary evaporator under water aspirator pressure. Column chromatography was carried out on silica gel (Grace Davison, grade 923, 100–200 mesh), neutral alumina (Merck, activity 1, 70–230 mesh, 90 Å mean pore diameter), or Florisil (Aldrich, 100–200 mesh). Flash chromatography was performed on 40- to 60-μm silica gel (Merck, grade 60, 230–400 mesh, 60 Å mean pore diameter) under air, nitrogen, or argon pressure so that the drop in solvent height was ~5 cm/min. Analytical high performance chromatography was carried out on a Waters Associates Model ALC 100 liquid chromatograph equipped with a μ-Porasil column (4.2 mm × 30 cm). The eluates were monitored with a differential ultraviolet absorption detector.

Deuterium-labeling experiments were carried out in glassware that had been washed three times in D_2O and flame dried while subjected to an argon flow.

General procedure for irradiation of the steroidal 5α- and 5β-hydroxy ketones ***7***, ***8***, ***19***, ***20***, ***21***, *and* ***22***

A solution (diameter × height dimensions of the solution enclosed in parentheses) of the hydroxy ketone in anhydrous ethanol or anhydrous benzene in a Pyrex tube was degassed with argon or nitrogen for 1 h and irradiated at 300 nm in a Rayonet photochemical reactor. The progress of the photolysis was monitored by thin-layer chromatography, and the irradiation was carried out typically for 6–24 h depending on the age of the lamps. The temperature inside the reactor rose to 50–53°C during the photolysis. The photolysate was concentrated on a rotary evaporator under water aspirator pressure, and the crude product was analyzed by ^{13}C nmr spectroscopy for stereochemical purity. In all cases, the ^{13}C spectra of lactone pairs epimeric at C-5 were distinct, and the concentrated photolysate was shown, within the limits of detection of the ^{13}C nmr spectrum, to contain only one epimer. Although the epimeric acetoxy lactones **9** and **10** could not be separated by thin-layer chromatography, analytical high performance liquid chromatography of the crude photolysates on a μ-Porasil column (4.2 mm × 30 cm) with hexanes – ethyl acetate (9:1 v/v) as eluent further evidenced the stereospecificity of the photolyses in the acetoxy series. For the deoxy ketols **19** and **20**, thin-layer chromatography with chloroform–acetone (95:5 v/v) indicated, in addition to the ^{13}C nmr spectra, that each photolysis gave only one lactone epimer. Thin-layer chromatography

Can. J. Chem. Downloaded from www.nrcresearchpress.com by 213.222.148.141 on 09/07/12
For personal use only.

Can. J. Chem. Downloaded from www.nrcresearchpress.com by 213.222.148.141 on 09/07/12
For personal use only.

with hexanes – ethyl acetate (4:1 v/v) gave further evidence of stereospecificity in the photolyses of the benzyloxy ketols **21** and **22**. The ir, ^{1}H nmr, and ^{13}C nmr spectra of the lactones obtained from photolyses in benzene were identical to those obtained by irradiation in ethanol.

Irradiation of 3β-acetoxy-5-hydroxy-5α-cholestan-6-one (7). Formation of 3β-acetoxy-6-oxa-B-homo-5β-cholestan-7-one (9)

(i) In ethanol

A solution (2 × 5 cm) of **7** (56 mg, 0.12 mmol) in ethanol (8 mL) was irradiated under argon for 6 h. Thin-layer chromatography (chloroform–acetone (9:1 v/v)) showed that the starting ketol had completely reacted. The photolysate was concentrated to give **9** (58 mg) as a white solid in quantitative yield. Crystallization from methanol gave **9** as white needles, mp 230–231°C (lit. (5) mp 228–229°C); ir λ_{max}: 5.78 μm; ir λ_{max} (KBr): 5.80, 8.10, 9.66 μm; ^{1}H nmr (200 MHz) δ: 0.66 (s, C-18 Me), 0.86 (d, J = 6 Hz, C-26,27 Me), 0.90 (d, J = 7 Hz, C-21 Me), 1.00 (s, C-19 Me), 2.02 (s), 2.44 (br d, J = 14 Hz, 1H), 2.96 (dd, J = 14, 10 Hz, 1H), 4.33 (nar m, $W_{1/2}$ = 8 Hz, 1H), 5.02 (br m, $W_{1/2}$ = 23 Hz, 1H); ^{1}H nmr (benzene-d_6, 200 MHz) δ: 0.46 (s), 0.49 (s), 0.95 (d, J = 7 Hz, C-21,26,27 Me), 1.75 (s), 2.12 (br d, J = 14 Hz, 1H), 2.32 (nar m, $W_{1/2}$ = 11 Hz, 2H), 3.68 (nar m, $W_{1/2}$ = 10 Hz, 1H), 4.30 (br m, $W_{1/2}$ = 24 Hz, 1H); ms m/z: 460 (1), 318 (100).

(ii) In benzene

A solution (1.5 × 7 cm) of **7** (42 mg, 0.09 mmol) in benzene (8 mL) was irradiated under argon for 8 h, and the photolysate was concentrated to give **9** (40.5 mg, 96%) as a pale yellow solid.

(iii) In butanol at 100°C

A solution (4 × 9 cm) of **7** (84 mg, 0.18 mmol) in freshly distilled *n*-butanol (100 mL) in a Pyrex tube was degassed with nitrogen for 1 h. The photolysis tube was fitted with a condenser, and the solution was stirred, heated to 100°C with a heating mantle, and irradiated at 300 nm under a nitrogen atmosphere for 14 h. Thin-layer chromatography (chloroform–acetone (9:1 (v/v)) evidenced complete reaction of the starting material, and the cooled photolysate was concentrated to give **9** (80 mg, 95%) as a white solid. The ir, ^{1}H nmr, and ^{13}C nmr spectra were superimposable with those of the lactone **9** obtained by photolysis of ketol **7** in ethanol.

Irradiation of 3β-acetoxy-5-hydroxy-5β-cholestan-6-one (8). Formation of 3β-acetoxy-6-oxa-B-homo-5α-cholestan-7-one (10)

(i) In ethanol

A solution (1.5 × 9 cm) of **8** (62 mg, 0.13 mmol) in ethanol (12 mL) was irradiated under argon, and the photolysis was followed by thin-layer chromatography (chloroform – ethyl acetate (9:1 v/v)). After 24 h, when the starting material had completely reacted, the photolysate was concentrated to give **10** (62 mg) as a white solid in quantitative yield. Crystallization from hexanes gave lactone **10** as fine white needles, mp 175–177°C (lit. (5) mp 178°C); ir λ_{max}: 5.80 μm; ir λ_{max} (KBr): 5.76, 8.05, 9.68 (m) μm; ^{1}H nmr (200 MHz) δ: 0.69 (s, C-18 Me), 0.86 (d, J = 6 Hz, C-26,27 Me), 0.89 (d, J = 7 Hz, C-21 Me), 0.93 (s, C-19 Me), 2.05 (s), 2.39 (dd, J = 14, 11 Hz, 1H), 2.54 (dd, J = 14, 2 Hz, 1H), 4.30 (dd, J = 11, 5 Hz, 1H), 4.63 (tt, J = 12, 4 Hz, 1H); ms m/z: 460 (2), 318 (100).

(ii) In benzene

Lactone **10** (49 mg) was obtained as a white solid in quantitative yield by irradiation of a solution (1.5 × 8 cm) of **8** (49 mg, 0.11 mmol) in benzene (12 mL) under argon for 24 h.

Irradiation of 5-hydroxy-5α-cholestan-6-one (19). Formation of 6-oxa-B-homo-5β-cholestan-7-one (23)

(i) In ethanol

A solution (1.5 × 4 cm) of **19** (26.5 mg, 0.07 mmol) in anhydrous ethanol (5 mL) was irradiated under argon. After 6 h, thin-layer chromatographic analysis (hexanes – ethyl acetate (4:1 v/v)) indicated complete reaction of the starting ketol, and the photolysate was concentrated to give **23** (25 mg, 94%) as a white solid. Flash chromatography on a silica gel column (0.5 × 14 cm) with dichloromethane as eluent gave **23** (18 mg, 69%) as a white solid. Crystallization from methanol afforded **23** as long, colorless needles, mp 122–123.5°C; ir λ_{max}: 5.79 μm; ^{1}H nmr δ: 0.67 (s, C-18 Me), 0.97 (s, C-19 Me), 2.42 (br d, J = 14 Hz, 1H), 3.00 (dd, J = 14, 9 Hz, 1H), 4.20 (nar m, $W_{1/2}$ = 8 Hz, 1H); ms m/z: 402 (7), 318 (100). *Exact Mass* calcd. for $C_{27}H_{46}O_2$: 402.3498; found: 402.3480. *Anal.* calcd. for $C_{27}H_{46}O_2$: C 80.54, H 11.52; found: C 80.72, H 11.55.

(ii) In benzene

A solution (1.5 × 6 cm) of **19** (43 mg, 0.11 mmol) in anhydrous benzene (7 mL) was degassed with nitrogen and irradiated for 19 h. The progress of the reaction was monitored by thin-layer chromatography (chloroform–acetone (9:1 v/v)) and, following completion of the reaction, the photolysate was concentrated to give **23** (42 mg, 98%) as a pale yellow solid.

Irradiation of 5-hydroxy-5β-cholestan-6-one (20). Formation of 6-oxa-B-homo-5α-cholestan-7-one (24)

(i) In ethanol

A solution (1.5 × 7 cm) of **20** (51.5 mg, 0.13 mmol) in anhydrous ethanol (9 mL) was irradiated under argon, and the photolysis was monitored by thin-layer chromatography (hexanes – ethyl acetate (4:1 v/v)). After 6 h, thin-layer chromatography showed that the starting ketol had completely reacted, and the photolysate was concentrated to give **24** (50 mg, 97%) as a white solid. Crystallization from methanol afforded lactone **24** as colorless plates, mp 159.5–160.5°C (lit. (40) mp 143–144°C; lit. (41) mp 155°C (light petroleum)); ir λ_{max}: 5.81 μm; ^{1}H nmr δ: 0.67 (s, C-18 Me), 0.90 (s, C-19 Me), 2.40–2.53 (m, 2H), 4.17 (dd, J = 10, 5 Hz, 1H); ms m/z: 402 (7), 318 (100). *Exact Mass* calcd. for $C_{27}H_{46}O_2$: 402.3498; found: 402.3507. *Anal.* calcd. for $C_{27}H_{46}O_2$: C 80.54, H 11.52; found: C 80.54, H 11.52.

(ii) In benzene

A solution (1.5 × 5 cm) of **20** (30 mg, 0.08 mmol) in benzene (5 mL) was irradiated under nitrogen for 11 h. Concentration of the photolysate gave **24** (28 mg, 94%) as a white solid.

Irradiation of 3β-benzyloxy-5-hydroxy-5α-cholestan-6-one (21). Formation of 3β-benzyloxy-6-oxa-B-homo-5β-cholestan-7-one (25)

(i) In ethanol

A solution of **21** (121 mg, 0.24 mmol) in ethanol (20 mL) was irradiated under argon, and the photolysis was monitored by thin-layer chromatography (hexanes – ethyl acetate (9:1 v/v)). After 17 h of irradiation, when the starting material was shown to have completely reacted, the photolysate was concentrated to give **25** (132 mg) as a white solid in quantitative yield. Flash chromatography of the solid on a silica gel column (1.5 × 15 cm) with chloroform – ethyl acetate (97:3 v/v) as eluent gave **25** (111 mg, 92%). Crystallization from methanol gave **25** as fine white needles, mp 154–155°C; ir λ_{max}: 5.79 μm; ^{1}H nmr δ: 0.67 (s, C-18 Me), 0.98 (s, C-19 Me), 2.98 (dd, J = 14, 9 Hz, 1H), 3.75 (br m, $W_{1/2}$ = 24 Hz, 1H), 4.32 (nar m, $W_{1/2}$ = 8 Hz, 1H), 4.53 (s, 2H), 7.32 (s, 5H); ms m/z: 91 (100). *Anal.* calcd. for $C_{34}H_{52}O_3$: C 80.26, H 10.30; found: C 80.46, H 10.33.

(ii) In benzene

A solution (1.5 × 14 cm) of **21** (93 mg, 0.18 mmol) in benzene (20 mL) was irradiated under argon for 17 h, and the photolysate was concentrated to give **25** (93 mg) as a white solid in quantitative yield.

Irradiation of 3β-benzyloxy-5-hydroxy-5β-cholestan-6-one (22). Formation of 3β-benzyloxy-6-oxa-B-homo-5α-cholestan-7-one (26)

(i) In ethanol

A solution (1.5 × 14 cm) of **22** (155 mg, 0.30 mmol) in anhydrous ethanol (20 mL) was irradiated under argon for 6 h. A thin-layer chromatography plate spotted with the photolysate was eluted twice with hexanes – ethyl acetate (85:15 v/v) and evidenced complete reaction of the starting ketol. The photolysate was concentrated to give **26** (153 mg, 99%) as a white solid. Crystallization from methanol gave **26** as very fine white needles, mp 171–173°C; recrystallization from

Can. J. Chem. Downloaded from www.nrcresearchpress.com by 213.222.148.141 on 09/07/12
For personal use only.

methanol gave an analytical sample, mp 174.5–175.5°C. Lactone **26**, ir λ_{max}: 5.81 μm; ^{1}H nmr δ: 0.68 (s, C-18 Me), 0.93 (s, C-19 Me), 3.32 (br m, $W_{1/2}$ = 24 Hz, 1H), 4.20 (dd, J = 11, 5 Hz, 1H), 4.56 (s, 2H), 7.33 (s, 5H); ms m/z: 508 (1), 91 (100). *Anal.* calcd. for $C_{34}H_{52}O_3$: C 80.26, H 10.30; found: C 80.25, H 10.32.

(ii) In benzene

A solution (1.5 × 12 cm) of **22** (79.5 mg, 0.16 mmol) in benzene (15 mL) was irradiated under argon for 6 h. Concentration of the photolysate gave **26** (76 mg, 96%) as a pale yellow solid.

Irradiation of the 7α-deutero 5α-ketol 27. Formation of 3β-acetoxy-5-deutero-6-oxa-B-homo-5β-cholestan-7-one (29)

(i) In benzene

A solution (1.5 × 6 cm) of **27** (38.1 mg, 0.083 mmol) in anhydrous benzene (6 mL) was irradiated in Pyrex at 300 nm under an argon atmosphere for 22 h. Concentration of the photolysate gave **29** (37 mg, 97%) as an off-white solid; ir λ_{max}: 5.79 μm; ^{1}H nmr (200 MHz) δ: 0.66 (s, C-18 Me), 0.86 (d, J = 7 Hz, C-26,27 Me), 0.90 (d, J = 7 Hz, C-21 Me), 1.00 (s, C-19 Me), 2.02 (s), 2.44 (br d, J = 14 Hz, 1H), 2.96 (dd, J = 14, 10 Hz, 1H), 4.33 (nar m, 0.21H), 5.02 (br m, $W_{1/2}$ = 23 Hz, 1H); ms m/z: 461 (2), 319 (97), 318 (100); d_0 21%, d_1 76%, d_2 3% (based on M − AcOH).

(ii) In ethanol

The 7α-deutero 5α-ketol **27** (ms: d_0 36%, d_1 62%, d_2 2%; 18.0 mg, 0.039 mmol) was irradiated in anhydrous ethanol (5 mL) in a Pyrex tube under a nitrogen atmosphere at 300 nm for 23 h. The photolysate was concentrated to give the 5β-deutero lactone **29** (16 mg, 89%) as a white solid; ^{1}H nmr (200 MHz) δ: 4.33 (nar m, 0.38H; C-5 methine); ms: d_0 42%, d_1 55%, d_2 3%.

Irradiation of the 7α-deutero 5β-ketol 28. Formation of 3β-acetoxy-5-deutero-6-oxa-B-homo-5α-cholestan-7-one (30)

(i) In benzene

A solution (1.5 × 3 cm) of **28** (18.0 mg, 0.039 mmol) in anhydrous benzene (4.5 mL) was irradiated in Pyrex under argon at 300 nm for 24 h. The photolysate was concentrated to give **30** (17 mg, 95%) as a white solid; ir λ_{max} (KBr): 5.76, 7.68 (w), 9.29 (m) μm; ^{1}H nmr (200 MHz) δ: 0.69 (s, C-18 Me), 0.86 (d, J = 6 Hz, C-26,27 Me), 0.89 (d, J = 7 Hz, C-21 Me), 0.93 (s, C-19 Me), 2.05 (s), 2.39 (dd, J = 13, 11 Hz, 1H), 2.54 (dd, J = 14, 2 Hz, 1H), 4.30 (dd, J = 11, 5 Hz, 0.13H), 4.63 (tt, J = 12, 4 Hz, 1H); ms m/z: 461 (3), 319 (89), 318 (100); d_0 11%, d_1 86%, d_2 3% (based on M − AcOH).

(ii) In ethanol

A solution of **28** (16.5 mg, 0.036 mmol) in anhydrous ethanol (3 mL) was irradiated in Pyrex under argon at 300 nm for 27 h. Concentration of the photolysate gave the 5α-deutero lactone **30** (14 mg, 86%) as a white solid; ^{1}H nmr (200 MHz) δ: 4.30 (dd, J = 11, 5 Hz, 0.14H, C-5 methine); ms: d_0 11%, d_1 87%, d_2 2% (based on M − AcOH); d_0 9%, d_1 87%, d_2 4% (based on M).

Irradiation of 3β-acetoxy-5-deuteroxy-5α-cholestan-6-one (31). Formation of 3β-acetoxy-7aα- and 7aβ-deutero-6-oxa-B-homo-5β-cholestan-7-one (33 and 34)

In a separatory funnel, a solution of 3β-acetoxy-5-hydroxy-5α-cholestan-6-one (**7**) (20.4 mg, 0.044 mmol) in benzene (15 mL) was washed with deuterium oxide (99.8%, Aldrich; 5 × 1 mL), and deuterium oxide (1 mL) was added to the organic layer. The two-phase mixture was added via cannula under argon to a Pyrex photolysis tube pretreated with deuterium oxide. The mixture (1.5 × 13 cm) was degassed with argon for 1 h, and stirred and irradiated at 300 nm for 22 h. The deuterium oxide layer of the photolysate was extracted with benzene (2 × 5 mL), and the combined benzene phases were concentrated to give a 26:74 mixture of **33** and **34** (19.8 mg, 97%) as a white solid; ir λ_{max}: 5.77 μm; ^{1}H nmr (200 MHz) δ: 0.66 (s, C-18 Me), 0.86 (d, J = 7 Hz, C-26,27 Me), 0.89 (d, J = 7 Hz, C-21 Me), 1.00 (s, C-19 Me), 2.02 (s), 2.42 (nar m, $W_{1/2}$ = 6 Hz, 0.58H), 2.94 (br d, J = 10 Hz, 0.20H), 4.33 (nar m, $W_{1/2}$ = 8 Hz, 1H), 5.03 (br m, $W_{1/2}$ = 24 Hz, 1H); ms m/z: 461 (1), 319 (100); d_0 28%, d_1 68%, d_2 3% (based on M − AcOH).

Irradiation of 3β-acetoxy-5-deuteroxy-5β-cholestan-6-one (32). Formation of 3β-acetoxy-7aα- and 7aβ-deutero-6-oxa-B-homo-5α-cholestan-7-one (35 and 36)

A solution (1.5 × 16 cm) of **32** (25.3 mg, 0.055 mmol) in benzene (20 mL) was prepared by the procedure used for the analogous 5α-deuteroxy ketol **31** (*vide supra*). Deuterium oxide (1 mL) was added, and the stirred two-phase mixture was irradiated at 300 nm for 24 h. The organic phase of the photolysate was washed with saturated aqueous sodium bicarbonate (1 × 2 mL) and water (5 × 2 mL), dried over anhydrous sodium sulfate, and concentrated to give an 88:12 mixture of **35** and **36** (24 mg, 94%) as a white solid; ir λ_{max} (KBr): 5.77, 5.81 (sh), 5.84 (sh), 7.66 (m), 8.52 (w) μm; ^{1}H nmr (200 MHz) δ: 0.69 (s, C-18 Me), 0.86 (d, J = 6 Hz, C-26,27 Me), 0.89 (d, J = 7 Hz, C-21 Me), 0.93 (s, C-19 Me), 2.05 (s), 2.38 (br d, J = 12 Hz, 0.12H), 2.52 (br s, $W_{1/2}$ = 3 Hz, 0.91H), 4.30 (dd, J = 11, 5 Hz, 1H), 4.63 (tt, J = 12, 4 Hz, 1H); ms m/z: 461 (2), 319 (100); d_0 9%, d_1 88%, d_2 3% (based on M − AcOH); d_0 8%, d_1 88%, d_2 4% (based on M).

Irradiation of the 5α-methoxy ketone 37 in ethanol. Formation of 3β-acetoxy-5-methoxy-5,6-seco-5α-cholestan-6-oic acid ethyl ester (39)

A solution of **37** (153 mg, 0.32 mmol) in anhydrous ethanol (100 mL) in a Pyrex tube was degassed with nitrogen for 1.5 h. The Pyrex tube was fitted with a cold finger insert, and the solution was irradiated at 300 nm in a Rayonet photochemical reactor at 22°C for 4.5 h. The photolysate was concentrated to give **39** (169 mg) as a yellow oil in quantitative yield. A ^{13}C nmr spectrum of the crude photolysate evidenced only one component. Flash chromatography of the oil on a silica gel column (2 × 13 cm) with hexanes – ethyl acetate (85:15 v/v) as eluent gave the seco ester **39** as a colorless oil that resisted crystallization; ir λ_{max}: 5.78 μm; ^{1}H nmr δ: 0.67 (s, C-18 Me), 1.02 (s, C-19 Me), 1.25 (t, J = 7 Hz), 2.03 (s), 3.32 (overlapping s and m, 4H), 4.13 (q, J = 7 Hz, 2H), 4.80 (br m, $W_{1/2}$ = 24 Hz, 1H); ^{1}H nmr (benzene-d_6, 200 MHz) δ: 0.69 (s, C-18 Me), 0.92 (d, J = 6 Hz, C-26,27 Me), 0.95 (s, C-19 Me), 0.98 (d, J = 7 Hz, C-21 Me), 0.98 (t, J = 7 Hz), 1.73 (s), 3.26 (s, 3H), 3.36 (nar m, $W_{1/2}$ = 8 Hz, 1H), 3.89–4.09 (m, width = 39 Hz, 2H), 5.10 (br m, $W_{1/2}$ = 24 Hz, 1H); ms m/z: 520 (4), 460 (55), 84 (100). *Exact Mass* calcd. for $C_{30}H_{52}O_3$ (M − AcOH): 460.3916; found: 460.3922. *Anal.* calcd. for $C_{32}H_{56}O_5$: C 73.80, H 10.84; found: C 73.81, H 10.83.

Irradiation of 3β-acetoxy-5α-cholestan-6-one (41) in ethanol. Formation of 3β-acetoxy-5,6-seco-cholestan-6-oic acid ethyl ester (44)

A solution of **41** (308 mg, 0.69 mmol) in anhydrous ethanol (30 mL) was degassed with nitrogen for 1 h in a quartz photolysis tube. The solution was irradiated at 254 nm in a Rayonet photochemical reactor for 3.5 h, and the photolysate was concentrated to give a pale yellow oil (290 mg). The ^{1}H nmr spectrum of the oil evidences complete reaction of the starting material. Flash chromatography of the oil on a silica gel column (2.5 × 15 cm) with hexanes – ethyl acetate (95:5 v/v) gave 3β-acetoxy-5,6-seco-cholestan-6-oic acid ethyl ester **44** (23 mg, 7%) as a colorless oil that resisted crystallization; ir λ_{max}: 5.76, 5.79 μm; ^{1}H nmr δ: 0.65 (s, C-18 Me), 0.97 (s, C-19 Me), 1.22 (t, J = 7 Hz), 2.00 (s), 2.48 (m, $W_{1/2}$ = 6 Hz, 2H), 4.10 (q, J = 7 Hz, 2H), 4.70 (br m, $W_{1/2}$ = 22 Hz, 1H); ms m/z: 490 (<1), 95 (100).

Irradiation of 3β-acetoxy-5-amino-5α-cholestan-6-one (45) in benzene. Formation of 3β-acetoxy-6-aza-B-homo-5β-cholestan-7-one (46)

A solution of **45** (20 mg, 0.43 mmol) in anhydrous benzene (5 mL) was irradiated in Pyrex under a nitrogen atmosphere at 300 nm in a Rayonet photochemical reactor for 14 h. The photolysate was concentrated to give **46** (22 mg) as a pale yellow oil in quantitative yield. Flash chromatography of the oil on a silica gel column (0.5 × 14 cm) with dichloromethane removed a small amount (2 mg) of high R_f materials. Further elution with dichloromethane–methanol (95:5 v/v) gave the lactam **46** (14 mg, 69%) as a colorless oil, which crystallized on standing, mp 84–91°C; ir λ_{max}: 2.97 (sh, w), 5.75, 6.02 μm; ^{1}H nmr δ:

0.67 (s, C-18 Me), 1.03 (s, C-19 Me), 2.03 (s), 3.23 (br m, $W_{1/2}$ = 20 Hz, 1H), 5.10 (br m, $W_{1/2}$ = 16 Hz, 1H), 6.27 (br d, J = 8 Hz, 1H); ms m/z: 459 (20), 399 (100). *Exact Mass* calcd. for $C_{29}H_{49}O_3N$: 459.3712; found: 459.3714.

Acknowledgments

We thank the Natural Sciences and Engineering Research Council of Canada for financial support of this work and for the award of a postgraduate fellowship to S.S., and Imperial Oil Limited for the award of a Graduate Research Fellowship to S.S.

1. S. STIVER and P. YATES. Tetrahedron Lett. **25**, 3289 (1984).
2. D. S. WEISS. Org. Photochem. **5**, 347 (1981), and references cited therein.
3. N. K. HAMER. J. Chem. Soc. Perkin Trans. 1, 1285 (1979).
4. A. PADWA and A. AU. J. Am. Chem. Soc. **98**, 5581 (1976).
5. R. C. COOKSON, R. P. GANDHI, and R. M. SOUTHAM. J. Chem. Soc. C, 2494 (1968).
6. A. BUTENANDT and A. WOLFF. Chem. Ber. **72**, 1121 (1939); H. WEHRLI and K. SCHAFFNER. Helv. Chim. Acta, **45**, 385 (1962).
7. N. C. YANG and R. H. K. CHEN. J. Am. Chem. Soc. **93**, 530 (1971).
8. R. J. CHAMBERS and B. A. MARPLES. J. Chem. Soc. Chem. Commun. 1122 (1972).
9. E. L. GHISALBERTI, P. R. JEFFERIES, and M. A. SEFTON. Tetrahedron, **34**, 3337 (1978).
10. G. ADAM and T. V. SUNG. Proc. 7th I.U.P.A.C. Symp. Photochem. 1978. p. 7; Chem. Abstr. **90**, 39062e (1979).
11. P. YATES and S. STIVER. Can. J. Chem. **65**, 2203 (1987).
12. A. F. THOMAS. Deuterium labeling in organic chemistry. Appleton–Century–Crofts, New York. 1971. Chap. 1.
13. C. G. MACDONALD, J. S. SHANNON, and S. STERNHELL. Aust. J. Chem. **17**, 38 (1964), and references cited therein.
14. P. MORAND and S. A. SAMAD. Bangladesh J. Sci. Ind. Res. **12**, 3 (1977).
15. J. C. ARNOULD and J. P. PETE. Tetrahedron Lett. 2415 (1972); Tetrahedron, **31**, 815 (1975).
16. N. J. TURRO. Modern molecular photochemistry. Benjamin Cummings, Menlo Park, CA. 1978. Chap. 10.
17. Y. KOMEICHI, S. TOMIOKA, T. IWASAKI, and K. WATANABE. Tetrahedron Lett. 4677 (1970); Y. KOMEICHI, T. IWASAKI, and F. AIDA. Steroids, **19**, 47 (1972).
18. L. KNOF. Justus Liebigs Ann. Chem. **642**, 194 (1961).
19. M. ONDA and K. TAKEUCHI. Chem. Pharm. Bull. **23**, 677 (1975).
20. O. L. CHAPMAN and D. S. WEISS. Org. Photochem. **3**, 197 (1973).
21. N. J. TURRO, J. C. DALTON, K. DAWES, G. FARRINGTON, R. HAUTALA, D. MORTON, M. NIEMCZYK, and N. SCHORE. Acc. Chem. Res. **5**, 92 (1972).
22. J. C. DALTON, K. DAVIES, N. J. TURRO, D. S. WEISS, J. A. BARLTROP, and J. D. COYLE. J. Am. Chem. Soc. **93**, 7213 (1971); N. J. TURRO and D. S. WEISS. J. Am. Chem. Soc. **90**, 2185 (1968).
23. J. J. HLAVKA and P. BITHA. Tetrahedron Lett. 3843 (1966).
24. J. HILL and J. TOWNEND. J. Chem. Soc. Chem. Commun. 1108 (1972).
25. W. M. HORSPOOL. *In* Photochemistry. Vol. 1. *Edited by* D. Bryce-Smith. Chemical Society, London. 1970. p. 146.
26. J. K. KOCHI. Adv. Free-Radical Chem. **5**, 189 (1975); D. C. NONHEBEL and J. C. WALTON. Free-radical chemistry. Cambridge University Press, London. 1974. Chap. 4.
27. D. GRILLER, K. U. INGOLD, P. J. KRUSIC, and H. FISCHER. J. Am. Chem. Soc. **100**, 6750 (1978).
28. S. OGAWA and R. W. FESSENDEN. J. Chem. Phys. **41**, 994 (1964); R. W. FESSENDEN. J. Phys. Chem. **71**, 74 (1967).
29. A. HUDSON, H. A. HUSSAIN, and J. N. MURRELL. J. Chem. Soc. (A), 2336 (1968).
30. A. J. DOBBS, B. C. GILBERT, and R. O. C. NORMAN. J. Chem. Soc. A, 124 (1971).
31. A. J. DOBBS, B. C. GILBERT, and R. O. C. NORMAN. J. Chem. Soc. Perkin Trans. 2, 786 (1972); A. L. J. BECKWITH and P. K. TINDAL. Aust. J. Chem. **24**, 2099 (1971).
32. P. J. KRUSIC and R. C. BINGHAM. J. Am. Chem. Soc. **98**, 230 (1976).
33. R. V. LLOYD, J. G. CAUSEY, and F. A. MOMANY. J. Am. Chem. Soc. **102**, 2260 (1980).
34. R. V. LLOYD and J. G. CAUSEY. J. Chem. Soc. Perkin Trans. 2, 1143 (1981).
35. V. MALATESTA and K. U. INGOLD. J. Am. Chem. Soc. **103**, 609 (1981).
36. S. STIVER and P. YATES. Tetrahedron Lett. **26**, 5501 (1985).
37. J. MEINWALD, R. A. SCHNEIDER, and A. F. THOMAS. J. Am. Chem. Soc. **89**, 70 (1967).
38. R. O. DUTHALER and C. GANTER. Helv. Chim. Acta, **59**, 415 (1976).
39. W. T. BRADY, W. L. VAUGHN, and E. F. HOFF. J. Org. Chem. **34**, 843 (1969).
40. G. J. FONKEN and H. M. MILES. J. Org. Chem. **28**, 2432 (1963).
41. M. S. AHMAD, G. MOINUDDIN, and I. A. KHAN. J. Org. Chem. **43**, 163 (1978).
42. N. K. HALL, JR. and R. ZBINDEN. J. Am. Chem. Soc. **80**, 6428 (1958).
43. G. E. BACHERS and T. SCHAEFER. Chem. Rev. **71**, 617 (1971); R. A. BELL and J. K. SAUNDERS. Can. J. Chem. **48**, 1114 (1970).

Appendix

For the interpretation of the photochemistry of the *O*-deuteroxy ketols, the resonances for the C-7a methylene protons in the ^{1}H nmr spectra of the undeuterated lactones **9** and **10** had to be assigned. This proved not to be a simple task since the seven-membered lactone rings were conformationally flexible.

In the case of the acetoxy 5β-lactone **9**, two lactone conformers, **9***A* and **9***B*, are consistent with the 200-MHz ^{1}H nmr spectrum, but predicted coupling constants for the dihedral angles measured from Dreiding models led to opposite assignments for the C-7a methylene protons. The preference of

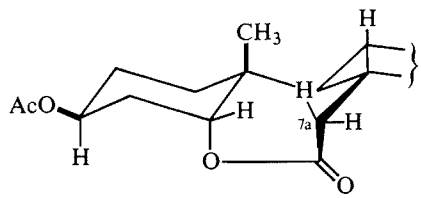

9*A*

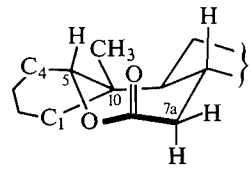

9*B*

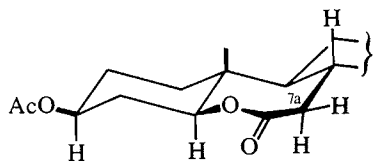

10*A*

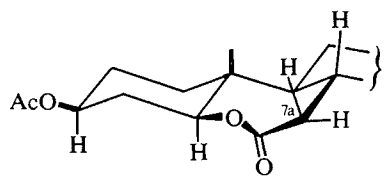

10*B*

Can. J. Chem. Downloaded from www.nrcresearchpress.com by 213.222.148.141 on 09/07/12
For personal use only.

9 to exist as conformer **9***A* was established as follows. In the ir spectrum of **9**, a carbonyl stretching band at 5.79 μm, viewed relative to the band at 5.79 μm recorded in carbon tetrachloride for ε-caprolactone (42), is consistent with conformer **9***A*, wherein a lone pair on the ring oxygen is aligned with the carbonyl π-bond so as to allow favorable overlap. However, in conformer **9***B* the disposition of the oxygen lone pairs and carbonyl π-orbitals of the lactone group prohibits good overlap, and the carbonyl stretching band for **9***B* would be expected to occur at shorter wavelength than the band position observed for **9**.

Direct evidence for the preference of **9** to exist as conformer **9***A* was procured by a nuclear Overhauser enhancement (nOe) study. Dreiding models show that the C-5 methine and C-7a β protons in conformer **9***A* are approximately 1.3 Å apart, ideally disposed to exhibit an nOe effect. The C-7a methylene protons in conformer **9***B* were each estimated to be ~3.5 Å distant from the C-5 methine proton, a distance considered too remote for any nOe enhancement between these protons (43). Irradiation of the doublet of doublets at δ 2.96 induced a 12% enhancement of the area of the C-5 methine proton signal in the ^{1}H nmr spectrum of **9**, thereby confirming that **9***A* is the preferred conformation. Thus, the doublet of doublets at δ 2.96 and the broad doublet at δ 2.44 could be assigned unequivocally to the C-7a β- and C-7a α-protons, respectively.

There are also two conformations, **10***A* and **10***B*, available to the 5α-lactone **10**, both of which are consistent with the coupling pattern observed for the C-7a methylene protons in the 200-MHz ^{1}H nmr spectrum. Measurement of the dihedral angles in Dreiding models in conjunction with estimated coupling constants led to opposite assignments of the C-7a methylene protons for the two conformers.

The ir spectrum of **10** exhibits a carbonyl stretching band at 5.80 μm ($CHCl_3$), indicative of effective orbital overlap in the lactone group, thus favouring conformation **10***A*. Again, the preference of **10** to exist in conformation **10***A* was verified by an nOe experiment. Irradiation of the doublet of doublets at δ 2.39 gave rise to a 13% increase in the area of the C-5 methine proton signal of **10**. The observation of an nOe effect is in accord only with conformer **10***A*, for which a Dreiding model indicates that the C-7a α-proton is situated ~1.5 Å from the C-5 methine proton. Thus the doublet of doublets at δ 2.39 can be assigned unambiguously to the C-7a α-proton and that at δ 2.54 to the C-7a β-proton.

Can. J. Chem. Downloaded from www.nrcresearchpress.com by 213.222.148.141 on 09/07/12
For personal use only.

Synthesis of maytenoquinone

ROBERT H. BURNELL,[1] MICHEL JEAN, AND SONIA MARCEAU
Département de chimie, Université Laval, Québec (Québec), Canada G1K 7P4

Received July 29, 1987

ROBERT H. BURNELL, MICHEL JEAN, and SONIA MARCEAU. Can. J. Chem. **66**, 227 (1988).
A synthesis of maytenoquinone (**11**) from natural podocarpic acid (**1**) is described.

ROBERT H. BURNELL, MICHEL JEAN et SONIA MARCEAU. Can. J. Chem. **66**, 227 (1988).
Nous avons transformé l'acide podocarpique naturel (**1**) en maytenoquinone (**11**).

Can. J. Chem. Downloaded from www.nrcresearchpress.com by 213.222.148.141 on 09/07/12
For personal use only.

Following our synthesis of taxodione (1) we turned our attention to the positional isomer maytenoquinone **11** (2). The straightforward sequence described below enabled us to obtain several hundred milligrams of this interesting extended quinone, and while the unoptimized yields of some of the steps are low, this is normal in this area of synthesis (3).

We chose, as has become a tradition, to use podocarpic acid **1** as our naturally available chiral starting material, which led to the natural maytenoquinone **11**. After modifying the carboxyl group at C.4 to establish the *gem*-dimethyl moiety by well-documented methods (4), a Duff reaction was used to introduce a formyl residue at C.13 and this product **3** was oxidized to the *O*-formyl derivative **4***a*. Hydrolysis of the latter afforded the catechol monoether **4***b*.

Of several attempts to introduce useful substituents at C.14, none was successful, presumably for steric reasons. A small amount of the 14-formyl derivative was obtained when the dimethoxy compound **4***d* was subjected to the conditions used to prepare **3***a* but the best yield was only 3%. By directed lithiation of the carbamate **4***c* by the Snieckus procedure (5) we were unable to introduce even deuterium at C.14, so an intramolecular route was employed. Williamson type alkylation of **4***b* with crotyl bromide gave the allylic ether **5**, which rearranged smoothly but not too efficiently to the 14-substituted compound **6**. At this stage a superfluous chiral centre had been formed (wavy line in **6** and **7**) but no attempt was made to separate the epimers since this asymmetry would disappear in subsequent steps. The nmr spectra of **6** and **7** show the presence of two diastereomers in each case.

After methylating the phenolic hydroxyl in **6***a*, the double bond in the product **6***b* was cleaved by the osmium tetroxide/periodate procedure to afford the aldehyde **7** and the latter was reduced under Huang–Minlon conditions to afford the 14-isopropyl derivative **8***a*. The dimethoxy aldehyde **7** suffered some partial demethylation during the reduction, as evidenced by the isolation of a small quantity of dispermol (the 13-methoxy-12-hydroxy compound **8***b*, 7% yield). These compounds were described by Matsumoto, Ohmura, and Usui (6) in their earlier synthesis of maytenoquinone **11**.

The diether **8***a* was demethylated with boron tribromide and the resulting catechol **8***c* promptly oxidized with silver oxide, which should have given the *o*-quinone **9** according to published precedent. The latter was not the product isolated. As in our previous taxodione synthesis, the *o*-quinone enolized to the methylene-quinone **10**, as seen from the spectral characteristics of the material obtained. Slow column chromatography of the latter gave maytenoquinone **11** showing identical uv, ir, and nmr spectra with those described by Matsumoto (6). We were unable to isolate the intermediate with a hydroxyl or a hydroperoxyl group at C.6, which is probably on the reaction path from **10** to **11**. Presumably its ready oxidation precludes its isolation.

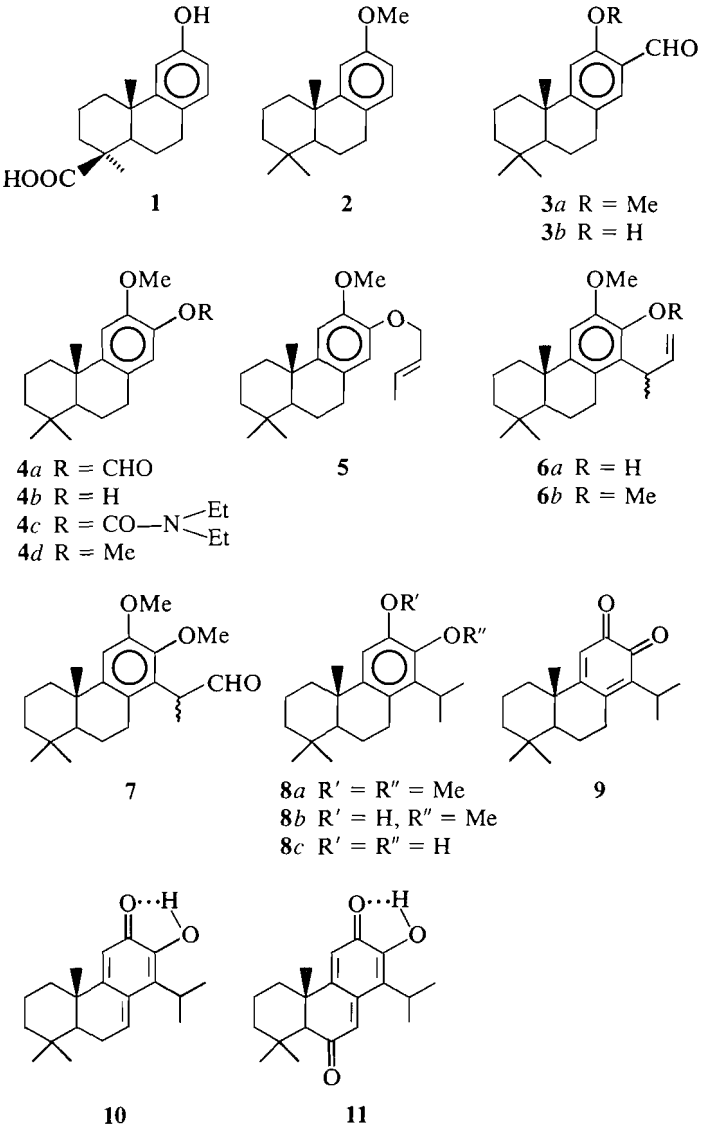

1 **2** **3***a* R = Me; **3***b* R = H

4*a* R = CHO; **4***b* R = H; **4***c* R = CO—N(Et)(Et); **4***d* R = Me

5 **6***a* R = H; **6***b* R = Me

7 **8***a* R′ = R″ = Me; **8***b* R′ = H, R″ = Me; **8***c* R′ = R″ = H **9**

10 **11**

Experimental

Unless otherwise stated the conditions and instruments used to characterize the products were as follows: melting points, Electrothermal, uncorrected; ultraviolet spectra, ethanol solutions (ε in parentheses), Hewlett Packard 8450 A; infrared spectra, carbon tetrachloride solutions, Beckman 4250 and Perkin Elmer 457; 200-MHz proton and 50-MHz carbon-13 magnetic resonance spectra, deuteriochloroform solutions, TMS internal standard (and, where relevant, multiplicity, integrated peak areas, coupling constants, and assign-

[1]Author to whom correspondence may be addressed.

TABLE 1. ^{13}C nuclear magnetic resonance data[a]

Carbon	Compound											
	3*a*	**3***b*	**4***b*	**5**	**6***a*	**6***b*	**7**	**8***a*	**8***b*	**8***c*	**10**	**11**
1	38.85	38.56	37.53	37.45	39.68	39.27	39.16	39.55	39.47	39.42	37.79	37.18
2	18.95	18.94	19.07	19.30	19.33	19.20	19.16	19.45	19.50	19.41	18.74	18.26
3	41.56	41.46	41.64	41.60	41.54	41.29	41.26	41.47	41.55	41.53	41.42	42.42
4	33.58	33.65	33.36	33.33	33.29	33.03	33.11	33.16	33.23	33.20	29.71	29.74
5	49.97	49.62	50.59	50.55	49.82	49.53	49.64	49.57	49.59	49.61	48.79	62.01
6	29.19	29.14	29.85	30.11	19.47	24.59	27.14	27.83	27.56	27.50	26.69	199.60
7	33.22	33.25	33.27	33.27	28.25	28.02	27.67	28.25	28.09	28.21	130.19	161.51
8	127.90	127.17	128.13	130.02	127.95	136.17	131.42	125.30	25.55	125.22	144.99	130.97
9	159.00	159.16	143.12	145.72	145.18	150.44	149.80	150.56	146.67	142.10	116.93	119.92
10	38.85	38.84	39.18	38.98	39.63	37.96	37.89	38.11	38.13	37.56	36.91	37.18
11	107.56	112.89	106.91	108.07	105.20	107.09	108.14	106.78	109.98	109.18	143.96	128.73
12	160.17	160.66	144.64	147.09	142.64	143.15	143.96	138.43	138.14	131.48	181.56	181.32
13	129.00	133.77	141.84	142.12	142.53	143.23	146.00	145.25	144.10	140.94	127.57	120.02
14	122.85	118.69	114.21	113.02	125.92	125.43	125.49	106.78	109.98	109.18	162.31	146.27
15	—	—	—	—	36.74	37.91	45.88	19.45	19.50	19.50	26.56	26.09
16	—	—	—	—	17.79	19.14	13.48	21.57	21.68	20.36	23.54	22.74
17	—	—	—	—	141.72	145.40	200.73	21.47	21.68	20.30	22.76	21.63
18	24.36	24.34	24.88	24.76	33.20	32.96	32.98	33.23	33.38	33.20	32.49	32.85
19	21.66	21.77	21.55	21.56	25.11	24.78	24.78	24.96	24.84	25.03	26.56	26.76
20	19.24	19.19	19.32	19.14	21.55	21.35	21.36	21.39	21.42	21.56	20.47	20.17
Others	55.61		55.99	56.01	55.91	55.26	55.32	55.46	—			
	189.36	195.69		69.36	112.52	60.04	60.17	60.26	61.28			
				126.31		111.77						
				127.04								
				17.83								

[a]In ppm from TMS.

Can. J. Chem. Downloaded from www.nrcresearchpress.com by 213.222.148.141 on 09/07/12
For personal use only.

ments in parentheses), Varian XL-200; mass spectra, Hewlett Packard 5992. Elemental analyses were by Galbraith Laboratories, Knoxville. The high resolution mass spectra were recorded at the Centre Régional de Spectrométrie de masse, Université de Montréal. Unless otherwise stated, dry column chromatography implies the use of Merck Kieselgel 60F (70–230 mesh) and elution with hexane – ethyl acetate (proportions determined by prior thin-layer chromatography using Baker-flex Silica gel 1B2-F precoated plastic sheets).

Formylation of 12-methoxypodocarpa-8,11,13-triene

Following the method described by Smith (7), the methoxy derivative **2** (13.5 g) was dissolved in trifluoroacetic acid (150 mL) and hexamethylenetetramine (16 g) was added. The mixture was well stirred and heated under reflux for 10 h and then, after cooling, the acid was neutralized with sodium bicarbonate and the product obtained by ether extraction. The crude material was chromatographed over silica gel, affording first the aldehyde **3***a*: *12-methoxy-13-formylpodocarpa-8,11,13-triene* (8) (9.3 g; 62%), as a colorless oil; uv (MeOH): 264 (13 800) and 334 (4800) nm; ir: 3060, 1685, 1610, and 1490 cm^{-1}; ^1H nmr δ: 0.93, 0.95, and 1.20 (3s, Me-C at C.4 and C.10), 3.88 (s, Me-O-Ar), 6.85 and 7.49 (2s, arom. H at C.11 and C.14 respectively), and 10.36 (s, Ar-CHO); ^{13}C nmr, see Table 1; ms *m/z*: 286 (86, M^+), 271 (28), 215 (23), 203 (58), 201 (47), and 189 (100). *Exact Mass* calcd. for $C_{19}H_{26}O_2$: 286.1934; found (hrms): 286.1925. *Anal.* calcd. for $C_{19}H_{24}O_2$: C 79.68, H 9.15; found: C 79.67, H 9.48. Further elution of the column gave the phenolic aldehyde **3***b*: *12-hydroxy-13-formylpodocarpa-8,11,13-triene* (3.50 g; 25%), mp 133–134°C (from ether–hexane); ir: 3140, 3060, 1650, 1570, and 1475 cm^{-1}; ^1H nmr δ: 0.93, 0.95, and 1.18 (3s, Me-C), 6.87 (s, H-C.11), 7.19 (s, H-C.14), 9.77 (s, CHO), and 10.64 (s, Ar-OH, diss. D_2O); ^{13}C nmr, see table. *Exact Mass* calcd. for $C_{18}H_{24}O_2$: 272.1777; found (hrms): 272.1754. *Anal.* calcd. for $C_{18}H_{24}O_2$: C 79.37, H 8.88; found: C 79.70, H 8.93.

The phenol **3***b* (5.2 g) was dissolved in acetone (200 mL), and potassium bicarbonate (1.5 g) and methyl iodide (2.3 mL) were added. The mixture was refluxed for 48 h. After cooling, the bicarbonate was filtered off and the residue remaining after evaporating the solvent was chromatographed as above, affording the methoxy compound **3***a* (5.4 g; 99%).

*Baeyer–Villiger oxidation of the aldehyde 3*a

m-Chloroperbenzoic acid (4 g; 85%) was added to a solution of the aldehyde **3***a* (4.6 g) in dichloromethane (70 mL) and the mixture was refluxed for 18 h. The cooled solution was well washed with sodium bicarbonate solution, saturated sodium chloride, dried, and the crude formate **4***a* (4.8 g; 98%) obtained by evaporation. In the ir spectrum it showed bands at 1745 (formate), 1620, and 1500 cm^{-1}, and the following ^1H nmr singlets were measured at 60 MHz: 0.95 (6H), 1.20 (Me-C), 3.80 (Me-O-Ar), 6.75 and 6.90 (H-Ar), and 8.25 (formate). The product was not purified further but was hydrolysed by dissolving in methanol (70 mL) to which was added aqueous potassium hydroxide (15 mL of 10%) and the solution was refluxed for 4 h. The cooled mixture was evaporated to remove most of the solvent, diluted with water, and the product obtained by ether extraction. Chromatography afforded the phenol **4***b*: *12-methoxy-13-hydroxypodocarpa-8,11,13-triene* (9) (3.5 g; 79%), mp 109–110°C (from ether–hexane); uv: 286 (3700) nm; ir: 3510, 3420, 1620, 1590, and 1500 cm^{-1}; ^1H nmr δ: 0.91, 0.94, 1.17 (Me-C at C.4 and C.10), 3.83 (s, Me-O-Ar), 5.43 (s, OH, diss. D_2O), 6.57 and 6.73 (2s, arom. H); ^{13}C nmr, see table; ms *m/z*: 274 (M^+, 45), 259 (100), 203 (18), 189 (54), 177 (44), and 163 (74). *Exact Mass* calcd. for $C_{18}H_{26}O_2$: 274.1934; found (hrms): 274.1924. *Anal.* calcd. for $C_{18}H_{26}O_2$: C 78.79, H 9.55; found: C 78.82, H 9.62.

N,N-*Diethylcarbamate of phenol 4*b

The literature method (10) was modified. The phenol **4***b* (83 mg) was dissolved in acetone (20 mL), and potassium carbonate (120 mg) and *N*,*N*-diethylcarbamoyl chloride (0.2 mL) were added and the mixture

heated under reflux for 24 h. The solution was filtered and evaporated and the crude material chromatographed to afford the derivative **4***c* (103 mg; 91%), mp 76–78°C (from ethanol); uv (MeOH): 221 (9500), 267 (1700), and 279 (3800) nm; ir ($CHCl_3$): 1700, 1610, 1500, 1260, and 1150 cm^{-1}; ^1H nmr δ: 0.91, 0.94, and 1.17 (3s, Me-C), 1.25 (m, 6H, CH_3CH_2-N), 3.40 (m, 4H, CH_3CH_2-N), 3.77 (s, Me-O-Ar), 6.73 and 6.81 (2s, arom. H); ms *m/z*: 373 (M^+, 16), 301 (29), 300 (100), and 285 (34). *Exact Mass* calcd. for $C_{23}H_{35}NO_3$: 373.2619; found (hrms): 373.2634. *Anal.* calcd. for $C_{23}H_{35}NO_3$: C 73.96, H 9.45, N 3.75; found: C 74.09, H 9.81, N 3.64. *Note*: Under the conditions described by Snieckus *et al.* (5) we were unable to introduce substituents at the C.14 position via the lithiated species. Neither acetone, 2-bromopropane, nor carbon dioxide gave even traces of substituted products.

Methylation of phenol **4**b *to dimethoxy compound* **4**d

Potassium carbonate (2 g) and methyl iodide (1.05 mL) were added to a solution of phenol **4***b* (2.3 g) in acetone (75 mL). After 24 h at reflux, the cooled solution was filtered and evaporated, and the product obtained by chromatography: *12,13-dimethoxypodocarpa-8,11,13-triene* (9) (**4***d*) (2.25 g; 93%), colourless oil; ir: 1605 and 1505 cm^{-1}; ^1H nmr δ: 0.92, 0.95, and 1.18 (3s, Me-C), 3.82 and 3.84 (2s, Me-O-Ar), 6.52 and 6.77 (2s, arom. H); ms *m/z*: 288 (56), 273 (100), 203 (56), and 191 (69). *Exact Mass* calcd. for $C_{19}H_{28}O_2$: 288.2090; found (hrms): 288.2062.

Formylation of the dimethoxy compound **4**d

The dimethoxy product **4***d* (1.35 g) was formylated in exactly the same manner as used to prepare **3***a*. Chromatography of the mixture obtained gave the starting material (1.28 g) and then the formyl derivative: *12,13-dimethoxy-14-formylpodocarpa-8,11,13-triene* (40 mg; 3%) ir: 2845, 1690, 1610, and 1480 cm^{-1}; ^1H nmr δ: 0.92, 0.95, and 1.20 (3s, Me-C), 3.88 and 3.90 (2s, Me-O-Ar), 7.10 (s, arom. H at C.11), and 10.56 (s, CHO); ms *m/z*: 316 (97), 301 (30), 245 (28), 231 (74), 219 (63), and 305 (100). *Exact Mass* calcd. for $C_{20}H_{28}O_3$: 316.2039; found (hrms): 316.2101.

Note of this compound was obtained in several versions of the Vilsmeier–Haack procedure.

Allylic ether **5**

To a solution of phenol **4***b* (3.02 g) in acetone (75 mL) was added potassium bicarbonate (3 g), and then, with efficient stirring, crotyl bromide (3.4 mL). After refluxing for 24 h, the cooled mixture was poured into aqueous hydrochloric acid (100 mL) and most of the acetone was removed at the pump. Ether extraction and chromatography afforded the ether **5**: *12-methoxy-13-but-2-enyloxypodocarpa-8,11,13-triene* (3.12 g; 86%); uv: 222 (10 500) and 281 (4100) nm; ^1H nmr δ: 0.92, 0.94, and 1.18 (3s, Me-C), 1.74 (d, CH_3-CH), 3.82 (s, Me-O-Ar), 4.44 (dd, J = 3.8 and 1.3 Hz, CH_2-O), 5.78 (m, vinyl H in side chain), 6.52 and 6.76 (2s, arom. H); ^{13}C nmr, see table; ms *m/z*: 328 (M^+, 10), 274 (14), 259 (34), 203 (12), 189 (17), and 177 (22). *Exact Mass* calcd. for $C_{22}H_{32}O_2$: 328.2404; found (hrms): 328.2448. *Anal.* calcd. for $C_{22}H_{32}O_2$: C 80.44, H 9.83; found; C 79.92, H 10.09.

Claisen rearrangement of ether **5**

The ether **5** (2.0 g) was refluxed in dimethylaniline (100 mL) during 48 h with efficient stirring. After cooling, the solution was diluted with ether and washed exhaustively with 10% hydrochloric acid, and the product was then obtained in the normal manner. Chromatography using CCl_4 gave the product **6***a*: *12-methoxy-13-hydroxy-14-(1-methylallyl)-podocarpa-8,11,13-triene* (1.60 g; 80%); uv: 285 (3300) nm; ir: 3540, 3060, 1630, 1610, and 1485 cm^{-1}; ^1H nmr δ: 0.91 and 0.95 (2s, Me-C and C.4), 1.17 and 1.19 (2s, Me-C.10, two epimers), 1.44 and 1.46 (2d, J = 7.0 Hz, Me in side chain, two epimers), 2.81 (m, H-C.15), 3.83 (s, Me-O-Ar), 5.01 (dd, J = 10.3 and 1.9 Hz, *cis* coupled terminal vinyl), 5.09 (dd, J = 17.1 and 1.9 Hz, *trans* coupled terminal vinyl), 5.62 (s, OH, diss. D_2O), 6.34 (ddd, J = 6.7, 10.2, and 16.8 Hz, vinyl), and 6.69 (s, arom. H); ^{13}C nmr, see table; ms *m/z*: 328 (M^+, 56), 314 (21), 313 (100), 257 (17), 243 (44), and 231 (25). *Exact Mass* calcd. for $C_{22}H_{32}O_2$: 328.2404; found (hrms): 328.2395.

12,13-Dimethoxy-14-(1-methylallyl)podocarpa-8,11,13-triene **6**b

The phenol **6***a* (2.77 g) was dissolved in ethanol (100 mL), and aqueous sodium hydroxide (20 mL of 50%) was added. After 10 min stirring, dimethyl sulfate was introduced (15 mL) and the mixture was refluxed for 48 h. The cooled solution was acidified with dilute hydrochloric acid and the product obtained by either extraction was chromatographed to afford the methylated compound **6***b* (2.55 g; 88%) as a colorless oil; ir: 3070, 1630, and 1590 cm^{-1}; ^1H nmr δ: 0.92, 0.94, and 1.20 (3s, Me-C), 1.39 and 1.41 (2d, J = 7.0 Hz, Me in side chain, two epimers), 2.84 (m, H-C.15), 3.77 and 3.80 (2s, Me-O-Ar), 4.94 (dd, J = 10.3 and 1.9 Hz, *cis* coupled terminal vinyl), 5.04 (dd, J = 16.3 and 1.9 Hz, *trans* coupled terminal vinyl), 6.20 (ddd, J = 16.2, 10.5, and 1.9 Hz, vinyl), and 6.74 (s, arom. H); ^{13}C nmr, see table; ms *m/z*: 342 (M^+, 46), 327 (60), 313 (11), 271 (16), 257 (43), 245 (29), 231 (62), and 218 (24). *Exact Mass* calcd. for $C_{23}H_{34}O_2$: 342.2560; found (hrms): 342.2560.

Double bond cleavage to give the aldehyde **7**

Following essentially the method of Graham and Williams (11), the olefin **6***b* (1.42 g) was dissolved in dioxane (100 mL) and water (30 mL). Osmium tetroxide (200 mg) was added, and then small portions of sodium metaperiodate (total 2.5 g). Stirring was continued at room temperature for 3 h and, after dilution with water, the product was obtained by ether extraction. Chromatography afforded the aldehyde **7**: *12,13-dimethoxy-14-(1-formylethyl)-podocarpa-8,11,13-triene* (774 mg; 54%) as a colorless oil; ir: 2700, 1720, 1595, and 1485 cm^{-1}; uv: 284 (2300) nm; ^1H nmr δ: 0.93 and 0.96 (2s, Me-C), 1.21 and 1.22 (2s, Me-C.10, two epimers), 1.31 and 1.35 (2d, J = 7.0 Hz, Me in side chain, two epimers), 3.49 (m, H-C.15), 3.76 and 3.81 (2s, Me-O-Ar), 6.82 (s, arom. H), and 9.65 (CHO, two epimers); ^{13}C nmr, see table; ms *m/z*: 344 (M^+, 34), 329 (23), 315 (7), 287 (13), 273 (13), 259 (18), 247 (20), 233 (42), and 203 (43). *Exact Mass* calcd. for $C_{22}H_{32}O_3$: 344.2353; found (hrms): 344.2345.

Reduction of the aldehyde **7**

Hydrazine hydrate (1.8 mL of 85%) was added to a solution of the aldehyde **7** (1.25 g) in diethylene glycol (50 mL) and the mixture was heated at 100°C for 2.5 h. After cooling to room temperature, potassium hydroxide (1.3 g) was added, the solution was distilled until the flask contents boiled at 210°C, and then refluxing was continued for 1 h. The cooled reaction mixture was acidified to pH 2 with 6 M hydrochloric acid and the product was recovered by ether extraction. Chromatography gave first the dimethoxy compound **8***a*: *12,13-dimethoxy-14-isopropylpodocarpa-8,11,13-triene* (0.833 g; 74%), mp 75–76°C (from ether–hexane); uv: 284 (2000) nm; ir: 1590 and 1480 cm^{-1}; ^1H nmr δ: 0.91, 0.94, and 1.21 (3s, Me-C), 1.32 and 1.33 (2d, J = 7.0 Hz, iso-Pr Me), 2.78 (m, 2H, H-C.7), 3.23 (m, H-C.15), 3.81 and 3.82 (2s, Me-O-Ar), and 6.72 (s, arom. H); ^{13}C nmr, see table; ms *m/z*: 300 (M^+, 29), 315 (29), 259 (10), 245 (36), 233 (24), 231 (28), and 219 (91). *Exact Mass* calcd. for $C_{22}H_{34}O_2$: 330.2560; found (hrms): 330.2565. *Anal.* calcd. for $C_{22}H_{34}O_2$: C 79.95, H 10.37; found: C 79.84, H 10.46.

Further elution of the column afforded the monomethoxy derivative **8***b*: *13-methoxy-12-hydroxy-14-isopropylpodocarpa-8,11,13-triene or dispermol* (75 mg; 7%), colorless oil; ir: 3540, 3390, 1590, and 1480 cm^{-1}; ^1H nmr δ: 0.91, 0.94, and 1.17 (3s, Me-C), 1.32 and 1.35 (2d, J = 7.0 Hz, iso-Pr Me), 2.80 (m, 2H, H-C.7), 3.34 (m, H-C.15), 5.32 (s, OH, diss. D_2O), and 6.72 (s, arom. H); ^{13}C nmr, see table; ms *m/z*: 316 (21), 301 (9), 259 (11), 245 (43), 231 (27), and 219 (83). *Exact Mass* calcd. for $C_{21}H_{32}O_2$: 316.2404; found (hrms): 316.2399.

Demethylation to the catechol **8**c

A solution of the dimethoxy compound **8***a* (875 mg) in dichloromethane (50 mL) was cooled in an ice bath. The reaction was conducted under rigorously dry nitrogen. After pouring the mixture into water, the product was extracted into ether, affording a crude yield of 98% (788 mg) of **8***c*: *12,13-dihydroxy-14-isopropyl-podocarpa-8,11,13-triene*; uv: 285 (3650) nm; ir: 3420, 1610, and 1490 cm^{-1};

Can. J. Chem. Downloaded from www.nrcresearchpress.com by 213.222.148.141 on 09/07/12
For personal use only.

^{1}H nmr δ: 0.89, 0.93, and 1.13 (3s, Me-C), 1.35 and 1.36 (2d, J = 7.0 Hz, iso-Pr Me), 2.78 (m, 2H, H-C.7), 3.24 (sept, J = 7.0 Hz, iso-Pr CH), 5.35 (br s, 2H, OH, diss. D_2O), and 6.64 (s, arom. H); ^{13}C nmr, see table; ms m/z: 302 (M^+, 37), 299 (18), 287 (43), 245 (12), 231 (12), 217 (60), 205 (39), 203 (31), 201 (12), and 191 (100). *Exact Mass* calcd. for $C_{20}H_{30}O_2$: 302.2247; found (hrms): 302.2245. *Note*: This catechol was understandably unstable and attempts to purify the material were counterproductive. The same mass spectroscopy sample described above showed that the catechol (37% relative intensity) was accompanied by the oxidation product **10** (300.2057, 6%) and maytenoquinone **11** (314.2248, 7%) after vacuum sublimation!

Oxidation of catechol ***8****c* *to intermediate* ***10*** *and maytenoquinone* ***11***

To a solution of catechol ***8****c* (465 mg) in chloroform (50 mL) was added silver oxide (700 mg) and the mixture was refluxed for 4 h. After filtering, the solvent was evaporated and the residue quickly chromatographed to afford the product **10** (402 mg; 87%): *12-oxo-13-hydroxy-14-isopropylpodocarpa-7,9(11),13-triene*, as a reddish oil; uv: 289 (5600) and 312 (5700) nm; ir: 3520, 3440, 1720, 1670, 1620, and 1550 cm^{-1}; ^{1}H nmr δ: 0.92, 0.99, and 1.08 (3s, Me-C), 1.34 and 1.37 (2d, J = 7.3 Hz, Me-C.15), 3.13 (sept, J = 7.3 Hz, iso-Pr CH), 6.32 (s, H-C.11), 6.98 (s, OH, diss. D_2O), and 7.21 (dd, J = 3.8 and 2.0 Hz, H-C.7; ^{13}C nmr, see table; ms m/z: 300 (M^+, 19), 258 (19), 257 (21), 232 (76), 228 (49), 215 (43), and 204 (44). *Exact Mass* calcd. for $C_{20}H_{28}O_2$: 300.2090; found (hrms): 300.2056.

The intermediate **10** (69 mg) was adsorbed on a small quantity of silica gel by evaporation of the solvent and the resulting powder was introduced at the top of a chromatographic column. Slow elution of the column with benzene afforded some of the starting intermediate **10** (45 mg) followed by maytenoquinone (18.8 mg; 26% rising to 75% if the recovery of the starting material is taken into account), orange glass; uv: 318 (11 650), 326 (11 000), and 410 (1700) nm; ir: 3370, 1670, and 1625 cm^{-1}; ^{1}H nmr δ: 1.17 (3H) and 1.26 (6H, 2s, Me-C), 1.31 and 1.37 (2d, J = 7.0 Hz, iso-Pr Me), 2.49 (s, H-C.5), 3.07 (sept, J = 7.0 Hz, iso-Pr CH), 6.40 (d, J = 1.3 Hz, H-C.7), 6.61 (d, J = 1.3 Hz, H-C.11), and 7.14 (s, OH); ^{13}C nmr, see table; ms m/z: 314 (M^+, 41), 299 (13), 271 (20), 257 (12), 243 (11), 229 (20), 217 (19), and 215 (19). *Exact Mass* calcd. for $C_{20}H_{26}O_3$: 314.1883; found (hrms): 314.1911. *Anal.* calcd. for $C_{20}H_{26}O_3$: C 76.40, H 8.33; found: C 76.63, H 9.06.

Acknowledgments

We thank the Natural Sciences and Engineering Research Council of Canada and the Ministère de l'éducation du Québec for operating and equipment grants.

1. R. H. Burnell, M. Jean, and D. Poirier. Can. J. Chem. **65**, 775 (1987).
2. J. D. Martin. Tetrahedron, **29**, 2553 (1973).
3. (*a*) K. Mori and M. Matsui. Tetrahedron, **26**, 3467 (1970); (*b*) T. Matsumoto, Y. Tachibana, J. Uchida, and K. Fukui. Bull. Chem. Soc. Jpn. **44**, 2766 (1971); (*c*) T. Matsumoto, S. Usui, and T. Morimoto. Bull. Chem. Soc. Jpn. **50**, 1575 (1977); (*d*) T. Matsumoto, T. Ohmura, and S. Usui. Bull. Chem. Soc. Jpn. **52**, 1957 (1979); (*e*) D. L. Snitman, R. J. Himmelsbach, R. C. Haltiwanger, and D. S. Watt. Tetrahedron Lett. 2477 (1979); (*f*) R. V. Stevens and G. S. Bisacchi. J. Org. Chem. **47**, 2396 (1982); (*g*) A. K. Bannerjee and M. C. Carrasco. Synth. Commun. **13**, 281 (1983).
4. T. Matsumoto, Y. Oshuga, S. Harada, and K. Fukui. Bull. Soc. Chim. Jpn. **50**, 2676 (1977).
5. (*a*) V. Snieckus and P. Beak. Acc. Chem. Res. **15**, 306 (1982); (*b*) V. Snieckus and M. Sibi. J. Org. Chem. **48**, 1937 (1983).
6. T. Matsumoto, T. Ohmura, and S. Usui. Bull. Chem. Soc. Jpn. **52**, 1957 (1979).
7. W. E. Smith. J. Org. Chem. **37**, 3973 (1972).
8. T. Matsumoto, S. Imai, S. Yuki, M. Mitsuki, and S. Sunaoka. Bull. Chem. Soc. Jpn. **56**, 290 (1983).
9. H. Akita and T. Oishi. Chem. Pharm. Bull. **29**, 1567 (1981).
10. E. Lustig, W. R. Benson, and N. Duy. J. Org. Chem. **32**, 851 (1967).
11. S. H. Graham and A. J. S. Williams. J. Chem. Soc. 4066 (1959).

Can. J. Chem. Downloaded from www.nrcresearchpress.com by 213.222.148.141 on 09/07/12
For personal use only.

Cinétique et mécanisme des réactions bromate–chlorite et bromate – dioxyde de chlore[1]

GUY SCHMITZ ET HENRI ROOZE

Faculté des sciences appliquées, Université libre de Bruxelles, 50 Avenue F. Roosevelt, 1050 Bruxelles, Belgique

Reçu le 3 juillet 1987

GUY SCHMITZ et HENRI ROOZE. Can. J. Chem. **66**, 231 (1988).

Dans une solution acide contenant initialement de l'acide chloreux et un excès de bromate on observe deux réactions consécutives, l'oxydation de l'acide chloreux en dioxyde de chlore suivie de l'oxydation du dioxyde de chlore : $BrO_3^- + 4ClO_2 + 2H_2O = 4ClO_3^- + 3H^+ + HOBr$. Nous avons étudié la cinétique de cette réaction et proposé un mécanisme en accord avec celui accepté pour la réaction apparentée entre le bromate et le Ce(III). Ce mécanisme, complété par des réactions de l'acide chloreux, permet de reproduire les courbes expérimentales d'évolution du dioxyde de chlore dans les solutions d'acide chloreux et de bromate. Les valeurs des constantes d'équilibres et des constantes cinétiques sont discutées.

GUY SCHMITZ and HENRI ROOZE. Can. J. Chem. **66**, 231 (1988).

In an acidic solution, containing initially chlorous acid and bromate in excess, two consecutive reactions are observed, the oxidation of chlorous acid to chlorine dioxide followed by the oxidation of chlorine dioxide: $BrO_3^- + 4ClO_2 + 2H_2O = 4ClO_3^- + 3H^+ + HOBr$. The kinetics of this reaction has been studied and a mechanism proposed. It agrees with the one accepted for the related reaction between bromate and Ce(III). Extended by reactions of chlorous acid, the mechanism reproduces the experimental curves of chlorine dioxide evolution in chlorous acid – bromate solutions. The values of the equilibrium and kinetic constantes are discussed.

Introduction

L'intérêt pour les réactions périodiques en phase homogène a suscité de nombreuses études de sous-systèmes et de réactions apparentées, en particulier celles du bromate et du chlorite. La compréhension de leurs mécanismes a fortement progressé ces 15 dernières années. Cependant celui de la réaction entre le bromate et le chlorite n'a jamais été entièrement élucidé. La figure 1 donne un exemple de nos résultats confirmant l'allure générale observée par Thompson (1) dans l'acide perchlorique 0,2–2 M. On utilise l'alcool allylique pour capter l'acide hypobromeux produit avant qu'il ne réagisse avec le chlorite. Ceci évite une série de réactions secondaires compliquant fortement la stoechiométrie et la cinétique du système. Avec un excès de bromate on observe deux périodes : l'oxydation du chlorite en dioxyde de chlore suivie d'une réaction entre le dioxyde de chlore et le bromate. Thompson a établi les caractéristiques stoechiométriques et cinétiques de la première période et a proposé un mécanisme qui en rend compte. Par contre il n'a pas trouvé d'interprétation de la cinétique de la réaction entre le dioxyde de chlore et le bromate. Effectivement, dans ses conditions expérimentales, la cinétique de cette réaction ne se laisse pas représenter par une loi simple. En élargissant le domaine de concentrations étudié nous avons pu établir son mécanisme et montrer qu'il est en accord avec celui admis pour la réaction apparentée bromate–Ce(III).

Partie expérimentale

Le dioxyde de chlore est préparé par la méthode de Bray (2), lavé dans une solution acide de chlorite (pour éliminer des traces éventuelles de chlore), dans une solution de nitrate d'argent (pour éliminer des traces éventuelles d'acide chlorhydrique) et dissout dans l'eau distillée. Les autres réactifs sont de la qualité «pour analyse».

Lors de l'étude cinétique de la réaction entre le dioxyde de chlore et un excès de bromate on mélange les réactifs dans la cuvette thermostatisée à 25°C d'un spectrophotomètre Spectronic 2000 et on suit la diminution de l'absorbance à 355 nm, maximum du spectre du dioxyde de chlore. Son coefficient d'absorption molaire a été remesuré et vaut 1265 M^{-1} cm^{-1}. Nous avons constaté que l'alcool allylique n'a pas d'effet sur les vitesses de cette réaction, ce qui indique que le HOBr n'induit pas de réaction secondaire en absence de chlorite. Les résultats présentés ont donc été obtenus sans addition d'alcool.

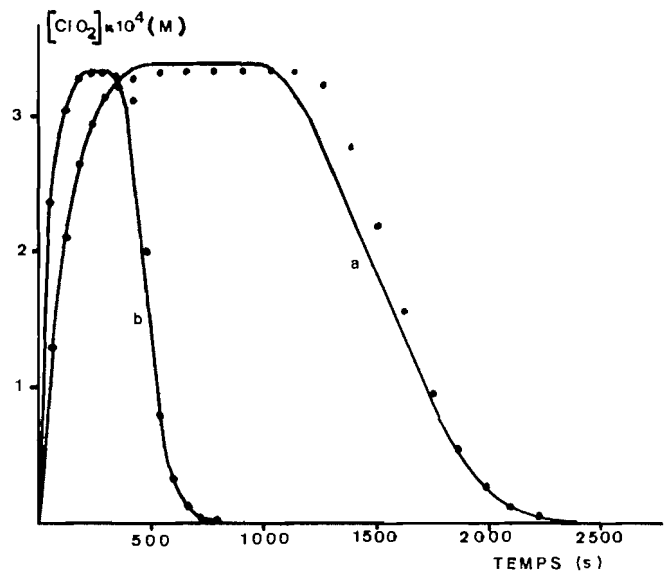

FIG. 1. Réaction bromate–chlorite. $[HClO_4] = 1$ M; $[NaClO_2] = 6{,}3 \times 10^{-4}$ M; $[C_3H_5OH] = 5 \times 10^{-3}$ M; $[KBrO_3] = 2 \times 10^{-3}$ (a) et 5×10^{-3} M (b). Résultats expérimentaux (—) et calculés (●).

Lorsque tout le dioxyde de chlore a été consommé, le spectre de la solution correspond à celui d'un mélange d'halogénates et de HOBr. En utilisant les coefficients d'absorption molaire mesurés par Betts et MacKenzie (3), on obtient $[HOBr]/[ClO_2]_0 = 0{,}245 \pm 0{,}005$. On vérifie donc la stoechiométrie [1].

$$[1] \qquad BrO_3^- + 4ClO_2 + 2H_2O = 4ClO_3^- + 3H^+ + HOBr$$

La figure 2 montre qu'après une période d'induction, les courbes expérimentales présentent une partie linéaire dont les pentes donnent les vitesses reprises dans le tableau 1. Si la concentration en ClO_2 est suffisamment grande, les vitesses n'en dépendent pas et on obtient la loi cinétique [2]. Par contre lorsque la concentration en ClO_2 est faible il n'existe pas de loi cinétique simple.

$$[2] \qquad -\frac{d[ClO_2]}{dt} = k_{exp}[KBrO_3]^2[HClO_4]^2$$

1. Article n° 6 de la série «Mécanisme des réactions du chlorite et du dioxyde de chlore». Article n° 5, voir la référence 28.

Printed in Canada / Imprimé au Canada

Can. J. Chem. Downloaded from www.nrcresearchpress.com by 213.222.148.141 on 09/07/12
For personal use only.

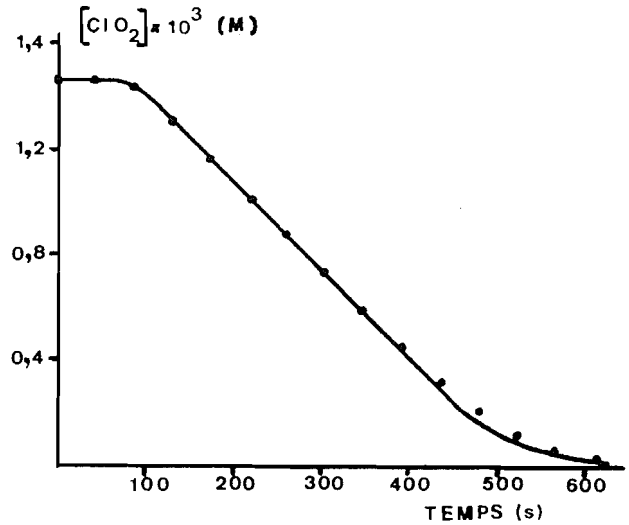

FIG. 2. Réaction bromate – dioxyde de chlore. $[HClO_4] = 1$ M; $[KBrO_3] = 5 \times 10^{-3}$ M; $[ClO_2]_0 = 1{,}46 \times 10^{-3}$ M. Résultats expérimentaux (—) et calculés (●).

TABLEAU 1. Effet des concentrations du bromate et du dioxyde de chlore

$[ClO_2]_0$ (10^{-3} M)	$[KBrO_3]$ (10^{-3} M)	Vitesse (10^{-6} M s)	k_{exp} (M^{-3} s^{-1})
1,6	1,0	0,147	0,139
1,6	2,0	0,592	0,140
0,4	2,5	0,850	0,128
1,6	2,5	0,840	0,127
3,2	2,5	0,877	0,132
1,6	5,0	3,64	0,137
1,6	10,0	13,86	0,131

$[HClO_4] = 1{,}03$ M.

TABLEAU 2. Effet de l'acidité et de la force ionique

$[HClO_4]$ (M)	k_{exp} (M^{-3} s^{-1})	k_{cor} (M^{-3} s^{-1})
0,103	0,460	0,493
0,103[a]	0,315	0,338
0,206	0,320	0,368
0,206[a]	0,245	0,281
0,515[a]	0,178	0,247
1,03	0,133	0,244
2,06	0,113	0,330

$[ClO_2]_0 = (0{,}4\text{–}3{,}2) \times 10^{-3}$ M; $[KBrO_3] = 10^{-3}$–10^{-2} M.

[a]Force ionique ajustée à 1 M avec du $NaClO_4$.

La variation de k_{exp} en fonction de l'acidité résulte, au moins en partie, de la différence entre la concentration en bromate $[KBrO_3]$ correspondant à la quantité de réactif utilisée et les concentrations réelles en solution $[BrO_3^-]$ et $[BrO_3H]$ calculées en tenant compte de l'équilibre [3].

[3] $\quad BrO_3^- + H^+ = BrO_3H$

Avec la valeur $K_3 = 2{,}9$ admise antérieurement (4) on obtient les valeurs de k_{cor} reprises dans le tableau 2.

$$k_{cor} = \left[1 + \frac{[H^+]}{K_3}\right]^2 k_{exp}$$

On déduit des séries de mesures faites sans ajuster la force ionique que la constante cinétique passe par un minimum aux environs de $I = 1$ M. Il est classique d'observer ce type de variation des coefficients d'activités.

Mécanisme de la réaction bromate – dioxyde de chlore

Les observations précédentes peuvent être expliquées par les réactions [R1]–[R3]. On obtient la stoechiométrie [1] en faisant la somme 2[R1] + 4[R2] + [R3].

[R1] $\quad BrO_3^- + H^+ + HBrO_2 \rightleftharpoons 2BrO_2 + H_2O$

[R2] $\quad BrO_2 + ClO_2 + H_2O \rightarrow ClO_3^- + H^+ + HBrO_2$

[R3] $\quad 2HBrO_2 \rightarrow BrO_3^- + H^+ + HOBr$

Tant que la concentration $[ClO_2]$ est suffisamment grande pour avoir $r_{+2} \gg r_{-1}$, la quasi-stationnarité des concentrations des intermédiaires BrO_2 et $HBrO_2$ donne

$$[HBrO_2] = \frac{k_1}{2k_3}[BrO_3^-][H^+]$$

$$[4] \qquad -\frac{d[ClO_2]}{dt} = \frac{k_1^2}{k_3}[BrO_3^-]^2[H^+]^2$$

On retrouve la loi expérimentale avec $k_{cor} = k_1^2/k_3$. Lorsque la concentration $[ClO_2]$ diminue, la réversibilité de [R1] cesse d'être négligeable. La concentration quasi stationnaire de $HBrO_2$ est alors donnée par une équation du troisième degré et la loi cinétique ne peut plus être mise sous une forme analytique simple.

Période d'induction de la réaction bromate – dioxyde de chlore

La durée t_i de cette période, en secondes, ne dépend pas de la concentration initiale en ClO_2 et varie comme l'inverse des concentrations en acide et en bromate. L'addition initialement de 2×10^{-5} mol L^{-1} de Br^- allonge notablement la période d'induction mais n'a pas d'effet sur la vitesse de disparition du ClO_2. L'addition de 2×10^{-5} mol L^{-1} de Cl^- n'a aucun effet.

$$t_i = \frac{0{,}4 \pm 0{,}05}{[BrO_3^-][H^+]}$$

Montrons que l'on peut justifier cette relation en admettant que la période d'induction correspond au temps nécéssaire pour que la concentration $[HBrO_2]$ atteigne sa valeur quasi stationnaire. Si on peut faire l'approximation $2r_{+1} = r_{+2} \gg r_{-1}$ on obtient :

$$\frac{d[HBrO_2]}{dt} = k_1[BrO_3^-][H^+][HBrO_2] - 2k_3[HBrO_2]^2$$

On pose $X = [HBrO_2]/[HBrO_2]_s$, où l'indice s désigne la valeur quasi stationnaire de la concentration, et on intègre.

$$k_1[BrO_3^-][H^+]t = \ln\frac{(1 - X_0)X}{X_0(1 - X)}$$

Le temps nécessaire pour atteindre une valeur donnée de X, pour X_0 donné, varie comme l'inverse de $[BrO_3^-][H^+]$. Ceci peut expliquer la variation observée de t_i. L'intégration des équations générales associées aux réactions [R1]–[R3] (cf. *infra*) a confirmé cette interprétation de la période d'induction.

La réaction bromate–chlorite

Ses caractéristiques ont été établies par Thompson (1) dans l'acide perchlorique 0,2–2 M en présence d'alcool allylique. Elles peuvent se résumer comme suit.

Can. J. Chem. Downloaded from www.nrcresearchpress.com by 213.222.148.141 on 09/07/12
For personal use only.

Can. J. Chem. Downloaded from www.nrcresearchpress.com by 213.222.148.141 on 09/07/12
For personal use only.

En présence d'un large excès de chlorite la réaction principale est [5]. Elle est accompagnée de la dismutation du chlorite (14).

[5] $BrO_3^- + 3HClO_2 = 2ClO_2 + ClO_3^- + HOBr + H_2O$

En présence d'un excès de bromate on obtient des courbes du type de celles de la figure 1. Lorsque la concentration $[ClO_2]$ est maximale le chlorite a été entièrement consommé. Les réactions bromate–chlorite et bromate – dioxyde de chlore sont donc consécutives et bien séparées dans le temps. Le palier de la concentration du ClO_2 correspond à la période d'induction de la réaction bromate – dioxyde de chlore. Le rapport $\Delta[ClO_2]/\Delta[HClO_2]$ dépend des conditions expérimentales. Pour $[BrO_3^-]_0 = (1{,}7–7{,}9) \times 10^{-3}$ M et $[HClO_2]_0 = (0{,}7–8{,}6) \times 10^{-4}$ M, il vaut 0,48 dans l'acide perchlorique 1,9 M et augmente si la concentration de l'acide diminue. Il diminue si la concentration en ClO_2 augmente. La vitesse de formation du ClO_2 est proportionnelle à la concentration du bromate et à celle du chlorite. Elle augmente plus que proportionnellement à la concentration de l'acide.

Thompson a interprété ces observations en considérant les réactions [R2] et [R4]–[R6].

[R4] $BrO_3^- + H^+ + HClO_2 \rightarrow BrO_2 + ClO_2 + H_2O$

[R5] $BrO_2 + HClO_2 \rightarrow HBrO_2 + ClO_2$

[R6] $HBrO_2 + HClO_2 \rightarrow ClO_3^- + H^+ + HOBr$

Lorsque la concentration en chlorite est grande le BrO_2 réagit principalement suivant [R5] et la somme [R4] + [R5] + [R6] donne la stoechiométrie expérimentale [5]. Si par contre le BrO_2 réagit également suivant [R2] on obtient également [6] = [R4] + [R2] + [R6] et un rapport $\Delta[ClO_2]/\Delta[HClO_2]$ inférieur à 2/3.

[6] $BrO_3^- + 2HClO_2 = 2ClO_3^- + H^+ + HOBr$

La compétition entre [R2] et [R5] explique que ce rapport diminue si la concentration $[ClO_2]$ augmente. Elle explique qu'il augmente si la concentration en acide diminue à condition d'écrire [R5] sous la forme [R5′].

[R5′] $BrO_2 + ClO_2^- \rightarrow BrO_2^- + ClO_2$

Les réactions [R1] et [R3] sont négligeables pendant la réaction bromate–chlorite car la concentration $[HBrO_2]$ est beaucoup plus faible que pendant la réaction bromate – dioxyde de chlore. La simulation numérique ci-après précisera ce point.

Constantes d'équilibre des réactions [R1]–[R6] à 25°C

Les enthalpies libres de formation, en kJ/mol, des différents composés intervenant dans ces réactions peuvent être estimées comme suit.

$$\Delta G_f^0(ClO_2\ aq.) = 119 \pm 3$$

Cette valeur a été déduite (5) de celle mesurée en phase gazeuse (6). Le potentiel standard du couple ClO_2/ClO_2^- vaut 0,935 ± 0,005 V et sa valeur apparente en milieu perchlorique de force ionique 1 M est 0,950 V (7–13). Cette différence est compatible (14) avec l'effet de la force ionique sur la constante d'acidité du $HClO_2$ (15). Avec $K_a^0\ (HClO_2) = 1{,}1 \times 10^{-2}$ on obtient :

$$\Delta G_f^0(HClO_2) = \Delta G^0(ClO_2\ aq.) - 101{,}4 \pm 0{,}5$$

Pour le chlorate et le bromate, nous adoptons les valeurs, et les estimations d'erreurs, de Johnson *et al.* (16). Latimer (17) avait admis respectivement −2,6 et 21 kJ/mol. La valeur 1,7 kJ/mol pour le bromate proposée récemment (18) est peu vraisemblable.

TABLEAU 3. Constantes d'équilibres et constantes cinétiques dans $HClO_4$ 1 M

Réactions	K_q	k_+	k_-
[R1]	10^{-6}	21	$2{,}1 \times 10^7$
[R2]	$1{,}2 \times 10^6$	$1{,}2 \times 10^5$	[a]
[R3]	5×10^{10}	$3{,}3 \times 10^3$	[a]
[R4]	80	1,15	[a]
[R5]	K_4/K_1	$3{,}8 \times 10^5$	[a]
[R6]	$K_2K_3K_4$	5×10^4	[a]

Unités : mol L^{-1} s.

[a]Les vitesses correspondantes sont négligeables dans les conditions étudiées.

$$\Delta G_f^0(ClO_3^-) = -7{,}95 \pm 0{,}75$$

$$\Delta G_f^0(BrO_3^-) = 19{,}0 \pm 0{,}6$$

L'enthalpie libre de formation du HOBr semble bien établie (17, 18).

$$\Delta G_f^0(HOBr) = -83 \pm 0{,}5$$

La constante d'équilibre de [R1] a été mesurée par Field et Försterling (19) :

$$K_1 = 10^{-6} \text{ à } 20°C \text{ dans } H_2SO_4\ 1\ M$$

Pour en déduire une relation entre les enthalpies libres de formation de BrO_2 et de $HBrO_2$ il faut tenir compte de la formation de $HBrO_3$, en multipliant K_1 par $(1 + [H^+]/K_3)$, et de la force ionique. Il faudrait également tenir compte de l'effet de la température mais on n'a aucune indication concernant celui-ci. Avec $K_3 = 2{,}9$ et $\gamma_\pm = 0{,}7$ on obtient :

$$2\Delta G_f^0(BrO_2) - \Delta G_f^0(HBrO_2) = 239{,}17 + 19 - RT \ln (2.7 \times 10^{-6}) = 290$$

Une estimation $\Delta G_f^0(BrO_2)$ a été déduite (20) des mesures de vitesses d'échange isotopique de Betts et MacKenzie (21). Cependant les calculs impliquent que lors de ces mesures le système était à l'équilibre chimique. Betts et MacKenzie ayant souligné (réf. 21, p. 664) que ce n'était pas le cas, nous préférons nous baser sur des données récentes permettant d'estimer la constante d'équilibre de la réaction [7].

[7] $Ce(III) + BrO_2 + H^+ = Ce(IV) + HBrO_2$

Field et Försterling (réf. 19, note 33) ont obtenu $k_7 = 8 \times 10^4\ M^{-2}\ s^{-1}$ à 20°C dans H_2SO_4 1 M. Une courte extrapolation des mesures de Sullivan et Thompson (22) donne $k_{-7} = 9 \times 10^3$ à 25°C dans H_2SO_4 1 M. Le rapport des deux constantes vaut 12. D'autre part Försterling *et al.* (23) ont observé que dans une solution 1 M en H_2SO_4 et 1 M en BrO_3^-, l'équilibre de [7] correspond à 80% du cerium sous la forme Ce(IV) lorsque $[BrO_2] = 4{,}7 \times 10^{-6}$. On en déduit $K_7 = (1{,}9 \times 10^{-5})/K_1$ en parfait accord avec l'estimation précédente. Sachant que dans l'acide sulfurique 1 M le potentiel du couple Ce(IV)/Ce(III) vaut 1,44 V (18), on obtient 1,51 V pour le potentiel du couple $BrO_2/HBrO_2$ et

$$\Delta G_f^0(BrO_2) - \Delta G_f^0(HBrO_2) = 146$$

On dispose ainsi de toutes les données nécessaires pour calculer les constantes d'équilibre des réactions [R1]–[R6]. À 25°C dans l'acide perchlorique 1 M, en incluant l'effet de l'équilibre [3] dans les constantes apparentes, on obtient les valeurs du tableau 3. Il faut cependant souligner qu'une erreur de 2 kJ sur les ΔG_f^0 entraine une erreur d'un facteur 2 sur

Can. J. Chem. Downloaded from www.nrcresearchpress.com by 213.222.148.141 on 09/07/12
For personal use only.

TABLEAU 4. Exemples de valeurs calculées dans les conditions de la figure 1*b*

Temps (s)	$[ClO_2]$ (10^{-4} M)	$[HClO_2]$ (10^{-4} M)	$[HBrO_2]$ (10^{-6} M)	$[BrO_2]$ (10^{-6} M)	r_{-1}/r_{+1}
28,3	1,55	3,89	0,116	0,014	—
56,6	2,40	2,45	0,116	0,012	—
141,4	3,22	0,68	0,119	0,007	—
226,3	3,32	0,21	0,128	0,003	—
311,1	3,32	0,07	0,163	0,002	0,004
396,0	3,27	0,01	0,862	0,005	0,005
480,9	1,85	—	13,55	0,107	0,169
565,7	0,47	—	8,656	0,151	0,530
650,6	0,11	—	4,260	0,131	0,810
735,4	0,03	—	2,310	0,103	0,916

ces constantes. Ceci constitue certainement une estimation optimiste de l'incertitude relative aux valeurs adoptées. Elles permettent cependant d'établir que lors de nos expériences les réversibilités des réactions [R2]–[R6] étaient négligeables. L'interprétation des résultats est donc insensible à la valeur exacte des constantes d'équilibre correspondantes.

Constantes cinétiques à 25°C dans $HClO_4$ 1 M

La réaction [R1] n'est pas élémentaire et résulte de $BrO_3^- + H^+ + HBrO_2 = Br_2O_4 + H_2O$ et $Br_2O_4 = 2BrO_2$. La cinétique de la réaction inverse, l'hydrolyse du BrO_2, a été étudiée par Buxton et Dainton (24). Si on admet qu'au cours de leurs expériences de radiolyse la réaction $BrO_2 + OH \rightarrow BrO_3^- + H^+$ (25) était négligeable et si les valeurs obtenues en milieu neutre sont valables en milieu acide, on peut montrer qu'au cours des expériences considérées içi, Br_2O_4 est en équilibre avec BrO_2 et qu'on a $r_{-1} = 2{,}1 \times 10^7[BrO_2]^2$. Avec $K_1 = 10^{-6}$ on en déduit $k_1 = 21$.

Nous avons mesuré $k_1^2/k_3 = 0{,}133$ dans l'acide perchlorique 1 M. Cette valeur apparente comprend, comme celle de k_1 ci-dessus, l'effet de la formation de $HBrO_3$. On en déduit $k_3 = 3{,}3 \times 10^3$. L'accord avec les autres déterminations de k_3 (19, 23, 26, 27) est excellent : $1{,}4 \times 10^3$ (24°C, H_2SO_4 0,15 M), $2{,}2 \times 10^3$ (24°C, H_2SO_4 0,5 M), $3{,}8 \times 10^3$ (24°C, H_2SO_4 1 M) et $3{,}5 \times 10^9$ K_1 (20°C, H_2SO_4 1 M). Cet accord confirme indirectement la valeur de k_1 ci-dessus, deux fois plus faible[2] que celle adoptée par Field et Försterling (19).

La valeur de k_2 peut être déduite de notre étude de la cinétique de la réaction bromate – dioxyde de chlore. Tant que $[ClO_2]$ est assez grand pour que la réaction [R1] soit irréversible, la vitesse est donné par [4]. Soit r_0 cette vitesse et $[ClO_2]_{1/2}$ la concentration telle que suite à la réversibilité de [R1] la vitesse soit tombée à la moitié de cette valeur.

$$0{,}5r_0 = 2k_1[BrO_3^-][H^+][HBrO_2] - 2k_{-1}[BrO_2]^2$$
$$= k_2[BrO_2][ClO_2]_{1/2}$$
$$= 4k_3[HBrO_2]$$

En éliminant $[HBrO_2]$ et $[BrO_2]$ on obtient

$$k_2^2 = 2{,}41k_{-1}\frac{r_0}{[ClO_2]_{1/2}^2}$$

Avec $k_{-1} = 2{,}1 \times 10^7$, nos mesures dans l'acide perchlorique 0,5–2 M donnent $k_2 = (1{,}2 \pm 0{,}2) \times 10^5$.

Nous avons mesuré antérieurement (4) la valeur de k_4. Celle de k_5 est déduite des mesures par Thompson (1) du rapport k_2/k_5. Il dépend de l'acidité et vaut 0,32 dans l'acide perchlorique 1 M. La constante k_6 n'a d'effet que sur le temps écoulé entre les périodes de production et de consommation du ClO_2 lors de la réaction bromate–chlorite. C'est le seul paramètre ajustable du modèle. La valeur adoptée doit être considérée comme une limite supérieure car elle inclut l'effet éventuel de réactions de disparition du $HClO_2$ que nous avons négligées.

Les équations différentielles associées aux réactions [R1]–[R6] ont été intégrées par une méthode de Gear en utilisant les valeurs des constantes cinétiques reprises dans le tableau 3. Les figures 1 et 2 montrent que l'accord avec les résultats expérimentaux est excellent. Le tableau 4 donne les valeurs des concentrations à quelques moments caractéristiques de l'évolution du système. Au palier de la concentration $[ClO_2]$ on a bien consommé tout le $HClO_2$ et on voit augmenter la concentration $[HBrO_2]$ vers sa valeur quasi stationnaire correspondant à la réaction bromate – dioxyde de chlore. Avec les constantes d'équilibre données dans le tableau 3 on peut vérifier que les réversibilités des réactions [R2]–[R6] sont négligeables. On voit par contre que lorsque la concentration $[ClO_2]$ diminue, la réversibilité de la réaction [R1] devient importante.

Conclusions

Les réactions [R1]–[R3] suffisent pour expliquer la cinétique de la réaction bromate – dioxyde de chlore. Ce ne sont pas des réactions élémentaires mais, mis à part l'effet de l'acidité, les ordres correspondent aux coefficients stoechiométriques. Lorsque la concentration en dioxyde de chlore est assez grande pour que la réaction [R1] soit irréversible on obtient la loi cinétique [4]. Sinon il n'existe pas de loi cinétique simple. En y ajoutant les réactions [R4]–[R6] on peut reproduire les courbes de production et de consommation du ClO_2 lors de la réaction bromate–chlorite. Les constantes cinétiques utilisées provenant de diverses séries de mesures indépendantes, l'accord entre les courbes expérimentales et calculées place ce travail dans le cadre d'un ensemble cohérent ayant permis ces dernières années de mieux comprendre le mécanisme des réactions des dérivés oxygènés des halogènes.

2. Un rapporteur nous a demandé de préciser l'origine de cette différence. Les calculs de Field et Försterling s'enchaînent comme suit. Ils adoptent $k_1^2/k_3 = 0{,}60$ et $k_3 = 3000$ et en déduisent $k_1 = 42$, ensuite $K_1 = 10^{-6}$ donne $k_{-1} = 4{,}2 \times 10^7$. Par contre nous partons de $k_{-1} = 2{,}1 \times 10^7$ (24) et $K_1 = 10^{-6}$ ce qui donne $k_1 = 21$. Ensuite la valeur $k_1^2/k_3 = 0{,}133$, déduite de notre étude cinétique de la réaction $BrO_3^- + ClO_2$, donne $k_3 = 3300$. Aucune des valeurs que nous avons adoptées n'est basée sur les mesures de vitesses d'échanges isotopiques de Betts et MacKenzie (21), ces auteurs ayant clairement précisé que toute corrélation entre ces mesures et la loi d'action des masses serait injustifiable.

1. R. C. THOMPSON. Inorg. Chem. **12**, 1905 (1973).
2. W. C. BRAY. Z. Phys. Chem. **54**, 569 (1906).
3. R. H. BETTS et N. MACKENZIE. Can. J. Chem. **29**, 666 (1951).
4. G. SCHMITZ et H. ROOZE. Can. J. Chem. **64**, 1747 (1986).
5. G. SCHMITZ. J. Chim. Phys. **76**, 209 (1979).
6. M. A. CLYNE et R. T. WATSON. J. Chem. Soc. Faraday 1, **73**, 1169 (1977).
7. G. HOLST. Svensk. Papperstidn. **48**, 23 (1945).
8. I. E. FLIS. Zh. Fiz. Khim. **32**, 573 (1958).
9. N. V. TROITSKAYA, K. P. MISCHENKO et I. E. FLIS. Russ. J. Phys. Chem. **33**, 77 (1959).
10. T. NAITO. Kogyo Kagaku Zasshi, **65**, 749 (1962); Chem. Abstr. **57**, 16326e (1962).
11. V. M. ZOLOTUKHIN, I. E. FLIS et K. P. MISCHENKO. Zh. Prikl. Khim. **38**, 369 (1965); Chem. Abstr. **62**, 12494a (1965).
12. O. SCHWARZER et R. LANDSBERG. J. Electroanal. Chem. **14**, 339 (1967).

13. F. PERGOLA, R. GUIDELLI et G. RASPI. J. Am. Chem. Soc. **92**, 2645 (1970).
14. G. SCHMITZ et H. ROOZE. Can. J. Chem. **63**, 975 (1985).
15. C. C. HONG et W. H. RAPSON. Can. J. Chem. **46**, 2053 (1968).
16. G. K. JOHNSON, P. N. SMITH, E. H. APPELMAN et W. N. HUBBARD. Inorg. Chem. **9**, 119 (1970).
17. W. M. LATIMER. Oxidation potentials. 2e éd. Prentice–Hall, New York. 1952.
18. A. J. BARD, R. PARSONS et J. JORDAN (*Éditeurs*). Standard potentials in aqueous solutions. IUPAC monographs, M. Dekker, New York. 1985.
19. R. J. FIELD et H. D. FÖRSTERLING. J. Phys. Chem. **90**, 5400 (1986).
20. R. J. FIELD, E. KOROS et R. M. NOYES. J. Am. Chem. Soc. **94**, 8649 (1972).
21. R. H. BETTS et N. MACKENZIE. Can. J. Chem. **29**, 655 (1951).
22. J. C. SULLIVAN et R. C. THOMPSON. Inorg. Chem. **18**, 2375 (1979).
23. H. D. FÖRSTERLING, H. J. LAMBERZ et H. SCHREIBER. Z. Naturforsch A: Phys. Phys. Chem. Kosmophys. **40A**, 368 (1985).
24. G. V. BUXTON et F. S. DAINTON. Proc. R. Soc. A, **304**, 427 (1968).
25. R. J. FIELD, N. V. RAGHAVAN et J. G. BRUMMER. J. Phys. Chem. **86**, 2443 (1982).
26. Z. NOSZTICZIUS, E. NOSZTICZIUS et Z. A. SCHELLY. J. Phys. Chem. **87**, 510 (1983).
27. F. ARIESE et Z. NAGY-UNGVARAI. J. Phys. Chem. **90**, 1 (1986).
28. G. SCHMITZ et H. ROOZE. Can. J. Chem. **65**, 497 (1987).

Can. J. Chem. Downloaded from www.nrcresearchpress.com by 213.222.148.141 on 09/07/12
For personal use only.

Étude des complexes fluorés et chlorés du cadmium dans les mélanges eau–HF

RÉJEAN BEAUDOIN ET HUGUES MÉNARD

Département de chimie, Faculté des sciences, Université de Sherbrooke, Sherbrooke (Québec), Canada J1K 2R1

Reçu le 7 avril 1987

RÉJEAN BEAUDOIN et HUGUES MÉNARD. Can. J. Chem. **66**, 236 (1988).

L'étude des complexes fluorés et des complexes chlorés du cadmium dans les mélanges eau–HF a été effectuée par polarographie. La diminution de l'ordre des complexes fluorés de CdF_3^- à CdF^+ est en accord avec la diminution de l'activité en ions fluorure, $R_0(F)$, mesurée en augmentant la concentration en HF. À plus de 60% en HF, le déplacement du potentiel de demi-vague ne peut plus être expliqué par les complexes de l'ion fluorure libre. La formation de complexes chlorés de degré trois et quatre a été observée en augmentant la concentration de HF jusqu'à 60% en poids.

RÉJEAN BEAUDOIN and HUGUES MÉNARD. Can. J. Chem. **66**, 236 (1988).

The formation of fluoride and chloride complexes in water – hydrogen fluoride mixtures has been studied using polarography. The reduction of the complexation by the fluoride ions from CdF_3^- down to CdF^+ is in good agreement with the reduction of the fluoride ion activity, $R_0(F)$ with increasing HF concentration. At higher HF concentration than 60%, the half-wave potential for the reduction of cadmium is shifted in a pattern that cannot be explained by fluoride in complexation. The formation of $CdCl_3^-$ and $CdCl_4^{2-}$ has been observed in H_2O–HF–KCl mixtures when the HF concentration was increased to 60%.

Can. J. Chem. Downloaded from www.nrcresearchpress.com by 213.222.148.141 on 09/07/12
For personal use only.

Introduction

L'étude des complexes métalliques du cadmium dans les mélanges eau–HF a été réalisée à l'aide de la polarographie classique. Une bonne connaissance des différentes espèces ioniques et moléculaires présentes dans les mélanges eau–HF (1–5) permet de calculer les constantes de formation des divers complexes du fluor en solution. L'utilisation d'un système de référence indépendant du solvant est une condition nécessaire (6) à cause de la variation de la force ionique et de l'acidité très élevée de ces mélanges.

Dans les solutions aqueuses, Bond et O'Donnell (7, 8) ont observé le complexe CdF^+ et le complexe CdF_2 à haute concentration en ions fluorure. Eliezer et Moreno (9) ont étudié le comportement du cadmium face aux autres halogènes. On a la possibilité de trois complexes chlorés alors que le brome et l'iode forment quatre complexes avec le cadmium. Bond et O'Donnell (10, 11) ont obtenu une vague réversible pour la réduction du cadmium dans les solutions aqueuses de HF.

Cette étude a permi de déterminer les complexes fluorés du cadmium dans les mélanges eau–HF et d'examiner la formation des complexes chlorés dans ces mélanges jusqu'à 60% en poids de HF. Les constantes de formation permettent de calculer la distribution des différents complexes en fonction de la proportion de HF dans le mélange.

Partie expérimentale

Les solutions ont été préparées à partir de HF 48% en poids (J. T. Baker) et à partir de HF 100% (Matheson) dilué à la concentration voulue avec de l'eau distillée. Les autres produits sont de grade ACS. Un potentiostat modèle PAR 174 A (Princeton Applied Research) a été utilisé avec un système à trois électrodes. L'électrode de référence au calomel saturé est séparée de la solution par une jonction en Teflon poreux jusqu'à environ 60% en poids de HF. À partir de 50% en poids de HF, l'électrode Cu/CuF_2 séparée de la solution par une jonction en Teflon poreux a été utilisée (12). Le capillaire polarographique est recouvert de polyéthylène (13) et l'électrode auxiliaire est faite d'un fil de platine. La cellule a été fabriquée dans nos ateliers à partir de $KelF^-$ et de Teflon. La diffraction des rayons-X a été effectuée avec un appareil Philips PW 1140/1139.

La méthode expérimentale consiste à mesurer le potentiel de demi-vague du cadmium par rapport à l'électrode de référence ECS ou Cu/CuF_2. Le potentiel de demi-vague du système de référence indépendant du solvant, le système ferricinium/ferrocène, est ensuite mesuré dans la même solution, lorsque c'est possible. Si les vagues polarographiques sont trop près l'une de l'autre, on prend les mesures séparément mais l'une après l'autre.

L'étude du cadmium en présence d'ions chlorure se fait en ajoutant du KCl à une solution de 10^{-3} M en cadmium. L'activité en ions chlorure est mesurée à l'aide d'une électrode sélective Ag/AgCl, de façon à s'assurer que l'activité est près de la concentration. Jusqu'à 55% en HF, la correspondance est suffisamment bonne pour assumer l'activité égale à la concentration.

Résultats et discussion

Les résultats pour les complexes fluorés sont présentés en rapport avec la fonction $R_0(F)$ et les constantes de formation des complexes chlorés ont été calculées selon la théorie de DeFord et Hume (5, 14, 15).

Les complexes fluorés du cadmium

Les potentiels de réduction du cadmium en fonction de la concentration en HF sont présentés au tableau 1. Le tableau montre les mesures par rapport au système ferricinium/ferrocène et les résultats calculés par rapport au potentiel de l'électrode réversible aux ions fluorure. Les valeurs de $R_0(F)$ et de E_{F^-} sont les mêmes que celles publiées par Vaillant *et al.* (2) et Ménard *et al.* (3).

La figure 1 présente le graphique du potentiel de demi-vague réversible aux ions fluorure en fonction de $R_0(F)$. On peut calculer la pente $E_{1/2}$ versus $R_0(F)$ et déterminer les complexes fluorés en solution. La fonction $R_0(F)$ est définie selon l'équation [1].

$$[1] \quad R_0(F) = -\log a_{F^-}$$

Pour confirmer les résultats obtenus par polarographie, nous avons mesuré le potentiel d'oxydation d'une électrode de cadmium dans les mélanges eau–HF. Les résultats sont présentés au tableau 2 et à la figure 2. Le potentiel d'oxydation du cadmium est donné par rapport au système de référence ferricinium/ferrocène et calculé par rapport au potentiel de l'électrode réversible aux ions fluorure. On peut calculer la pente du potentiel réversible aux ions fluorure et déterminer les complexes fluorés en solution. La pente est donnée en fonction de $\log a_{F^-}$.

L'interprétation des résultats se fait à partir de la pente du graphique de $E_{1/2}$ versus $R_0(F)$ pour la polarographie et de

Can. J. Chem. Downloaded from www.nrcresearchpress.com by 213.222.148.141 on 09/07/12
For personal use only.

TABLEAU 1. Potential de réduction du cadmium

%HF (poids)	$E_{1/2}$ Cd^{2+}/Cd Fc^+/Fc (volt)	R_0(F)	$E_{1/2}$ Cd^{2+}/Cd E_{F^-} (volt)	E_{F^-} Fc^+/Fc (volt)
2	−0,767	2,1	−0,716	−0,051
5	−0,739	2,4	−0,706	−0,030
10	−0,705	2,9	−0,692	−0,013
15	−0,664	3,4	−0,668	+0,020
20	−0,620	4,0	−0,671	+0,051
25	−0,585	4,5	−0,664	+0,079
30	−0,560	5,0	−0,669	+0,109
35	−0,525	5,6	−0,667	+0,142
40	−0,480	6,2	−0,657	+0,177
45	−0,420	7,3	−0,660	+0,240
47	−0,385	8,0	−0,664	+0,279
50	−0,345	9,0	−0,680	+0,335
55	−0,270	9,8	−0,652	+0,382
60	−0,220	10,3	−0,626	+0,406
65	−0,175	10,7	−0,600	+0,425
70	−0,135	11,1	−0,580	+0,445
75	−0,095	11,6	−0,565	+0,470
80	−0,055	12,0	−0,545	+0,490
85	−0,025	12,4	−0,537	+0,512
90	+0,010	12,8	−0,524	+0,534
95	+0,060	13,2	−0,494	+0,554
100	+0,130	13,6	−0,445	+0,575

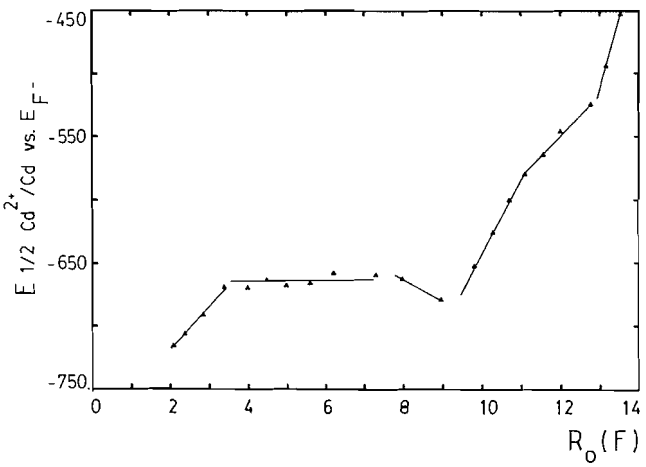

FIG. 1. Déplacement du $E_{1/2}$ de la réduction du Cd^{2+} en fonction de R_0(F).

la même façon pour l'oxydation de l'électrode de cadmium. Les tableaux 3 et 4 donnent les pentes et les complexes correspondants.

Nous allons diviser les mélanges eau–HF en trois sections. Les solutions de KF dans l'eau représentent la première partie, les solutions aqueuses de HF jusqu'à 60% représenteront la deuxième partie et les mélanges contenant plus de 60% en HF représenteront la troisième partie.

Les solutions aqueuses contenant Cd^{2+} et l'ion fluorure ont été étudiées par plusieurs auteurs. Mesaric et Hume (16) ont mesuré la constante de formation du complexe CdF^+. Ils ont donné une valeur de $\beta_1 = 6{,}4$. Le cadmium forme un complexe faible avec l'ion fluorure. Bond et O'Donnell (7, 8) ont mesuré les constantes de formation de deux complexes; $\beta_1 = 5{,}8$ pour le complexe CdF^+ et $\beta_2 = 4$ pour le complexe CdF_2 qui apparaît

TABLEAU 2. Potentiels d'oxydation d'une électrode de cadmium

%HF (poids)	E Cd/Cd^{2+} Fc^+/Fc (volt)	R_0(F)	E Cd/Cd^{2+} E_{F^-} (volt)	E_{F^-} Fc^+/Fc (volt)
2	−0,925	2,1	−0,869	−0,056
5	−0,902	2,4	−0,862	−0,040
10	−0,845	2,9	−0,834	−0,011
20	−0,759	4,0	−0,810	+0,051
26	−0,718	4,6	−0,803	+0,085
30	−0,675	5,0	−0,784	+0,109
40	−0,602	6,25	−0,779	+0,177
46	−0,521	7,8	−0,789	+0,268
47	−0,517	8,1	−0,796	+0,279
52,5	−0,472	9,5	−0,832	+0,360
60	−0,389	10,3	−0,795	+0,406
65	−0,254	10,7	−0,689	+0,435
71,5	−0,213	11,3	−0,668	+0,455
80	−0,152	12,0	−0,642	+0,490
90	−0,055	12,8	−0,589	+0,534
100	+0,030	13,6	−0,545	+0,575

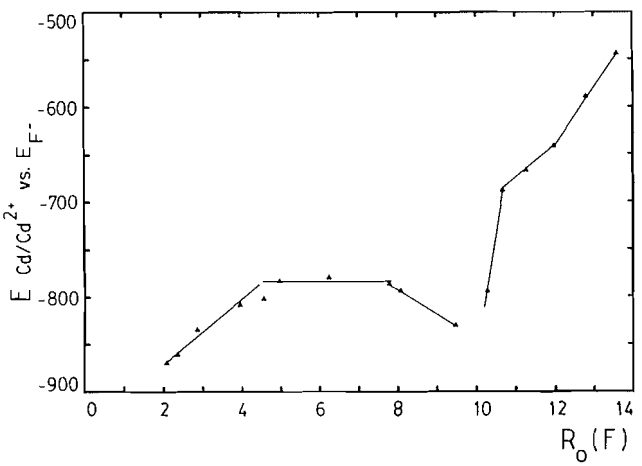

FIG. 2. Potentiel d'oxydation d'une électrode de cadmium à courant nul.

TABLEAU 3. Pentes tirées du graphique de la réduction du cadmium

Domaine de % en HF (poids)	Pente (volt)	Complexe	Pente calculée (volt)
KF	+0,029	CdF^+	+0,029
2– 20	−0,031	CdF_3^-	−0,029
20– 45	−0,001	CdF_2	0
45– 55	+0,016	$\sim CdF^+$	+0,029
55– 80	−0,056		
80– 90	−0,027		
90–100	Négative		

à plus grande concentration en ions fluorure. Les mesures que nous avons effectuées dans les solutions contenant du KF nous permettent de conclure à l'existence du complexe CdF^+. La pente de $E_{1/2}$ versus le logarithme de l'activité en ions fluorure est de +0,031 volt. Lorsque nous passons aux solutions contenant du HF, la pente passe par zéro puis devient négative. On peut donc dire qu'à faible concentration en ions fluorure on

TABLEAU 4. Pentes tirées du graphique de l'oxydation d'une électrode de cadmium

Domaine de % en HF (poids)	Pente (volt)	Complexe	Pente calculée (volt)
2– 20	−0,031	CdF_3^-	−0,029
20– 45	~0	CdF_2	0
45– 55	+0,027	CdF^+	+0,029
55– 70	−0,220		
70– 90	−0,052		
90–100	Négative		

a le complexe CdF^+, ensuite CdF_2 lorsque la concentration de ligand augmente.

Eliezer et Moreno (9) ont étudié le comportement du cadmium face aux autres halogènes. On a la possibilité de trois complexes chlorés alors que le brome et l'iode forment quatre complexes avec le cadmium. Même si le fluor est moins complexant que les autres halogènes, il est raisonnable que le cadmium forme des complexes de degrés supérieurs à un avec l'ion fluorure.

Bond et O'Donnell (10, 11) ont étudié le cadmium dans des solutions aqueuses de HF. La vague polarographique est réversible. Ils concluent à partir du déplacement du potentiel de demi-vague que la solvatation ou la coordination n'est pas la même qu'en solution aqueuse. Nos résultats montrent que la réduction du cadmium est réversible sur tout le domaine de concentration en HF.

Dans le domaine de 2 à 60% en HF, il y a formation de trois complexes fluorés différents. Les pentes mesurées sur la figure 1 et données au tableau 3 permettent de dire qu'on a le complexe CdF_3^- entre 2 et 20% en HF. De 20 à 45% en HF on a le complexe CdF_2. De 45 à 60% en HF, il est difficile de mesurer de façon précise la pente. Cependant on voit qu'elle est positive et on conclut au complexe CdF^+.

Les écarts entre les valeurs de potentiels de demi-vague étant petits, nous avons mesuré le potentiel d'oxydation d'une électrode de cadmium pour appuyer les résultats obtenus par polarographie. Les résultats obtenus confirment et même précisent ceux mesurés par polarographie. On a le complexe CdF_3^- de 2 à 20% en HF, CdF_2 de 20 à 45% en HF et CdF^+ de 45 à 60% en HF. Dans la dernière région, la pente est de +0,027 volt. Le tableau 4 montre les pentes obtenues pour l'oxydation du cadmium métallique.

On peut écrire les équilibres suivants pour la réduction du cadmium dans les mélanges eau–HF de 2 à 60 :

[2] $CdF_3^- + 2\acute{e} \rightleftarrows Cd_{Hg} + 3F^-$

[3] $CdF_2 + 2\acute{e} \rightleftarrows Cd_{Hg} + 2F^-$

[4] $CdF^+ + 2\acute{e} \rightleftarrows Cd_{Hg} + F^-$

Dans le domaine de 60 à 100% en HF, il n'est pas possible de traiter les résultats à partir des mêmes hypothèses de départ. L'évolution du potentiel de demi-vague ressemble à une courbe de titrate. La formation de l'ion HF_2^- serait responsable du déplacement rapide du potentiel de demi-vague. On peut postuler un équilibre du type suivant :

[5] $CdF^+ + xHF_2^- \rightleftarrows CdF(HF_2^-)_x^{(1-x)}$

L'activité de l'ion HF_2^- n'étant pas connue, il n'est pas possible d'évaluer l'ordre des complexes formés avec cet ion.

TABLEAU 5. Constantes d'équilibre et de formation successive des complexes fluorés du cadmium

Complexe	log K	log β
CdF^+	9,3	9,3
CdF_2	7,8	17,1
CdF_3^-	3,6	20,7

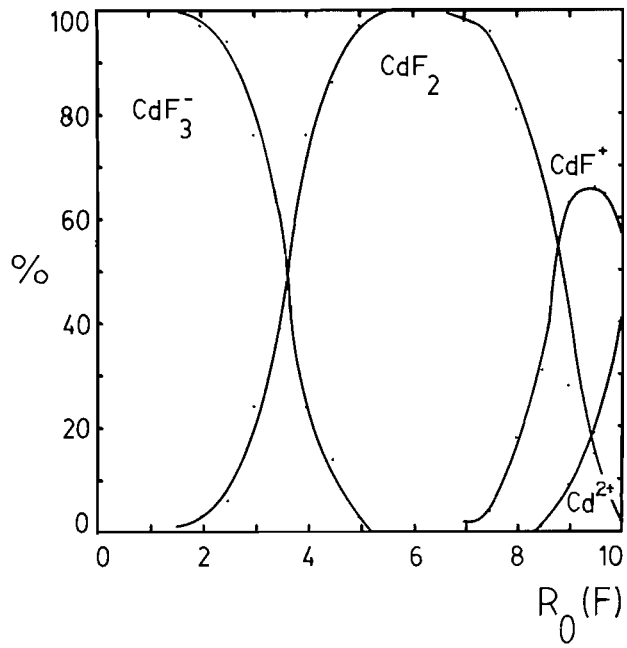

FIG. 3. Distribution des complexes fluorés dans les mélanges eau–HF jusqu'à 60% en poids.

Il est possible d'évaluer les constantes de formation des complexes fluorés à partir du changement de pente du potentiel de demi-vague réversible aux ions fluorure en fonction de l'activité en ions fluorure, R_0(F) (17). Si on établit l'équilibre suivant :

[6] $CdF_2 \overset{K_2}{\rightleftharpoons} CdF^+ + F^-$

La constante d'équilibre s'établit comme suit :

[7] $$K_2 = \frac{[a_{F^-}][a_{CdF^+}]}{[a_{CdF_2}]}$$

Au point d'inflection, à la figure 1, on peut faire l'approximation que la concentration des deux complexes fluorés est équivalente. L'équilibre est alors contrôlé par l'activité en ions fluorure du milieu. La constante d'équilibre du complexe peut alors être exprimée de la façon suivante :

[8] $K_2 = 1/a_{F^-}$

[9] $\log K_2 = -\log a_{F^-} = R_0(F)$

Le tableau 5 montre les constantes d'équilibre K_1, K_2 et K_3 et le log des constantes de formation β_1, β_2 et β_3. La figure 3 présente la distribution des complexes fluorés du cadmium jusqu'à 60% en HF calculés à partir des constantes successives de formation.

Can. J. Chem. Downloaded from www.nrcresearchpress.com by 213.222.148.141 on 09/07/12
For personal use only.

TABLEAU 6. Constantes de formation des complexes chlorés du cadmium

% HF (poids)	β_1	β_2	β_3	β_4
61	0	$(1,2\times10^8)\pm(0,2\times10^8)$	$(4,1\times10^8)\pm(0,1\times10^8)$	$(7\times10^8)\pm(1\times10^8)$
52	~0	$(1,1\times10^6)\pm(1,0\times10^6)$	$(2,2\times10^7)\pm(0,5\times10^7)$	$(5\times10^7)\pm(1\times10^7)$
46	200±20	$(2,1\times10^5)\pm(0,2\times10^5)$	$(3,0\times10^6)\pm(0,2\times10^6)$	$(1,4\times10^7)\pm(0,2\times10^7)$
40	380±10	4500±500	$(3,3\times10^5)\pm(0,1\times10^5)$	$(7,0\times10^5)\pm(0,5\times10^5)$
30	100±5	1000±200	$(1,0\times10^4)\pm(0,1\times10^4)$	9000±2000
20	55±5	300±20	1100±100	400±100
10	44±4	170±10	60±10	~60±10
5	22±2	50±5	40±10	
	$CdCl^+$	$CdCl_2$	$CdCl_3^-$	$CdCl_4^{2-}$

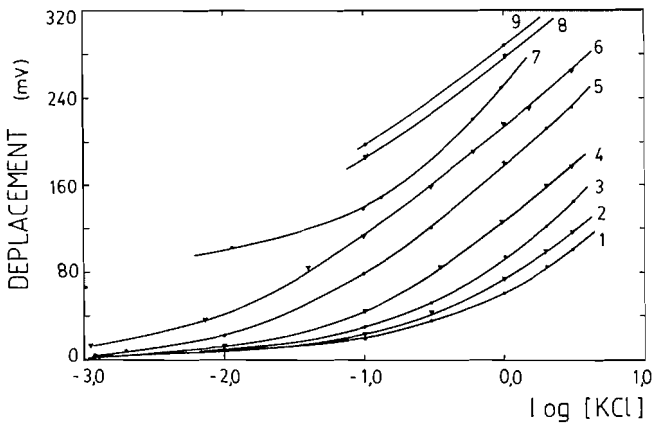

FIG. 4. Déplacement du potentiel de demi-vague du cadmium en fonction de la concentration en HF. 1, 5%; 2, 10%; 3, 20%; 4, 30%; 5, 40%; 6, 46%; 7, 52%; 8, 55%; 9, 61%.

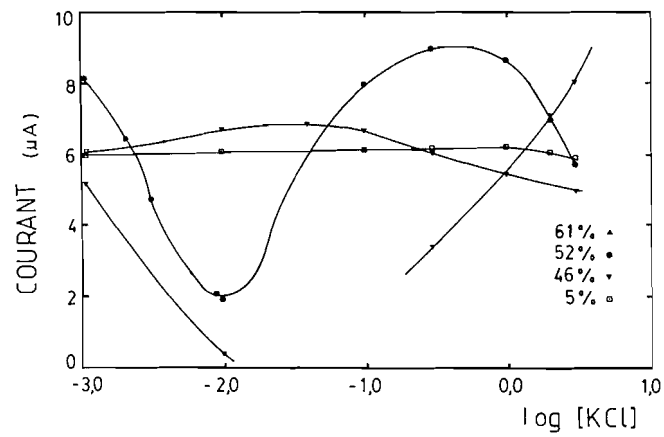

FIG. 5. Évolution du courant de diffusion du cadmium en fonction de la concentration en HF.

Les complexes chlorés du cadmium

L'addition de KCl à une solution de cadmium cause un déplacement du potentiel de demi-vague et dans certains cas des changements importants du courant de diffusion. La figure 4 montre le déplacement du potentiel de réduction du cadmium à plusieurs concentrations en HF et la figure 5 montre le courant de réduction du cadmium en fonction de la concentration en KCl pour différentes solutions de HF. La diminution très importante du courant de diffusion pour les solutions de 52 et 61% en HF

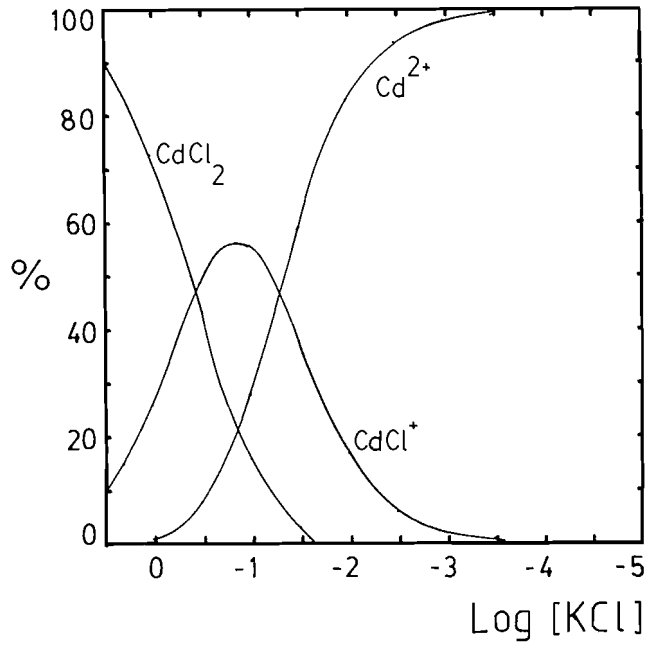

FIG. 6. Distribution des complexes chlorés dans HF 5%.

est due à la précipitation de chlorure de cadmium sous forme hydratée $CdCl_2 \cdot H_2O$. Le précipité a été identifié par diffraction des rayons-X et comparé avec les valeurs ASTM.

Les constantes de formation des complexes chlorés ont été calculées à partir de la théorie de DeFord et Hume (15). Le tableau 6 présente les constantes de formation jusqu'à 61% en HF. À plus grande concentration en HF, le KCl se transforme en HCl et l'activité en ions chlorure ne suit donc plus la concentration en KCl ajouté. À partir des constantes de formation données au tableau 6, on peut calculer la proportion de chaque complexe chloré dans les mélanges eau–HF. Les figures 6–10 montrent la distribution des complexes en fonction de la concentration en KCl dans la solution. La figure 11 montre la distribution des complexes chlorés en solution aqueuse calculée à partir des constantes de formation de Eliezer et Moreno (9).

En solution aqueuse, le cadmium donne deux complexes chlorés. Il donne cependant dans les mêmes conditions quatre complexes avec le brome et l'iode (9). On peut soupçonner qu'à plus grande concentration en ions chlorure et à force ionique plus élevée, on aurait un quatrième complexe chloré. Dans le

Can. J. Chem. Downloaded from www.nrcresearchpress.com by 213.222.148.141 on 09/07/12
For personal use only.

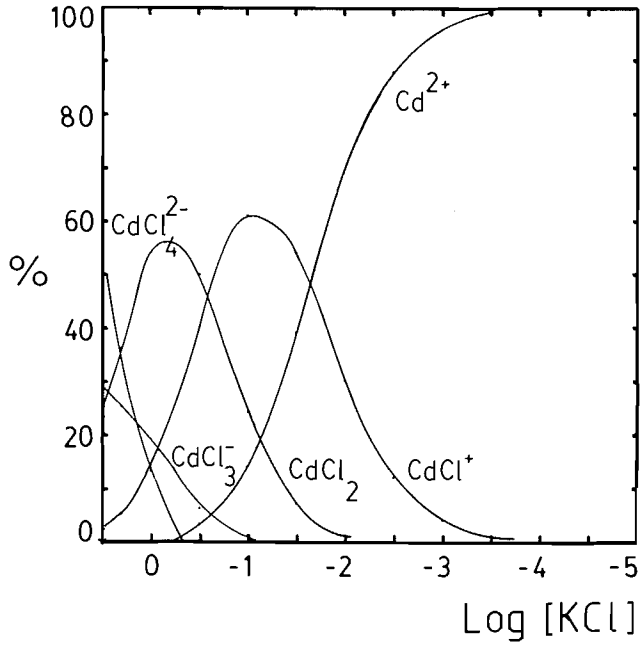

FIG. 7. Distribution des complexes chlorés dans HF 10%.

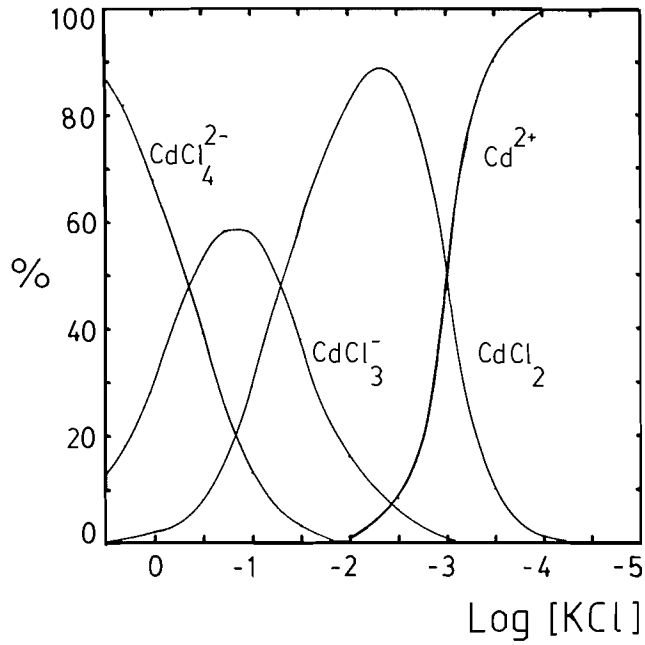

FIG. 9. Distribution des complexes chlorés dans HF 52%.

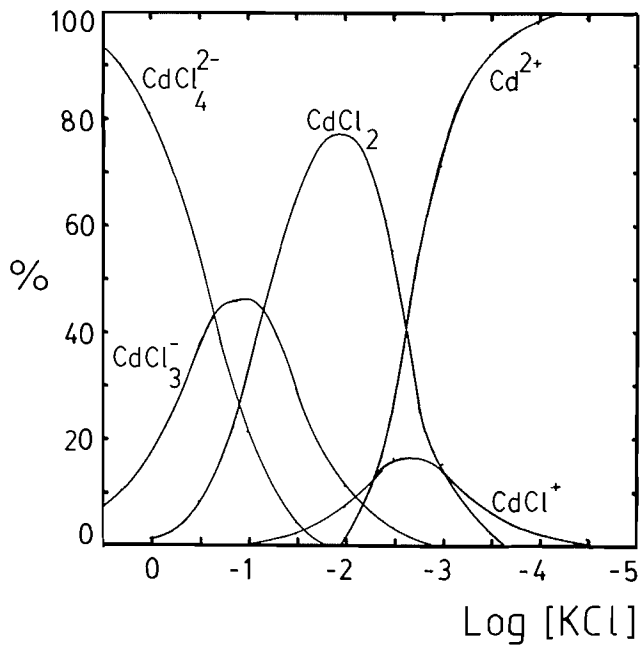

FIG. 8. Distribution des complexes chlorés dans HF 46%.

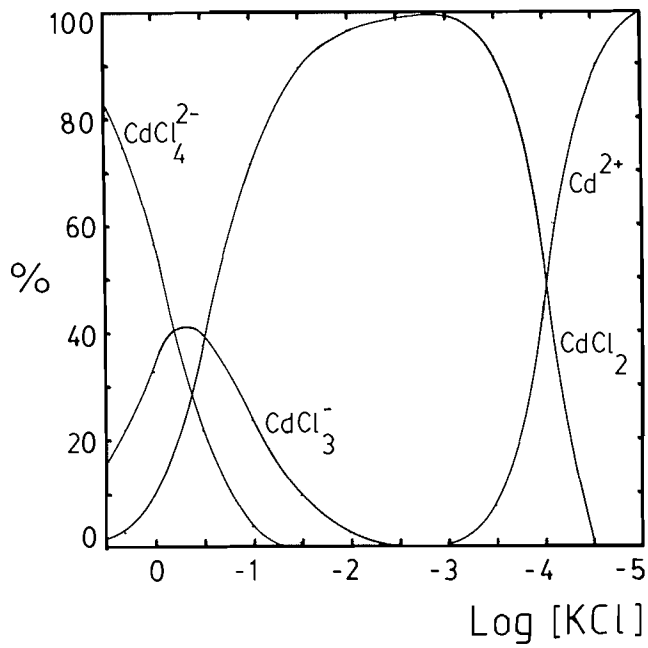

FIG. 10. Distribution des complexes chlorés dans HF 61%.

mélange eau–HF à 5%, on observe seulement trois complexes chlorés. À cette concentration en HF, on a en solution CdF_3^-. La compétition entre les complexes fluorés et les complexes chlorés empêche probablement l'obtention de complexes de degrés supérieurs dans ce domaine de concentration en KCl. En solution aqueuse (9), on observe le complexe $CdCl_3^-$ à des concentrations en KCl supérieures à 0,1 M ce qui indique que le complexe n'est pas très fort. La compétition due aux ions fluorure est suffisante dans notre cas pour empêcher la formation de $CdCl_3^-$ en quantité appréciable. Dans les mélanges eau–HF à 10%, on peut observer quatre complexes chlorés. La force ionique est beaucoup plus grande qu'en solution aqueuse. Il suffit de mentionner que l'activité en ions hydrogène est supérieure à un molaire. Les deux complexes de degré supérieur apparaissent à des concentrations en KCl de un molaire et plus. On a cependant une incertitude très grande sur les constantes de formation. Dans les mélanges eau–HF de 20 à 40%, les quatre complexes chlorés évoluent de façon à peu près régulière. Le complexe fluoré dans le solvant pur est CdF_2 sur tout le domaine; les complexes chlorés de degré supérieur apparaissent à plus faible concentration en KCl que dans HF à 5%. Dans les mélanges eau–HF à 46%, la distribution des complexes commence à changer de façon importante. La proportion du premier complexe $CdCl^+$ diminue de façon importante. La constante de formation β_1 est beaucoup plus faible que dans HF 40%. Le second complexe $CdCl_2$ prend une très grande

Can. J. Chem. Downloaded from www.nrcresearchpress.com by 213.222.148.141 on 09/07/12
For personal use only.

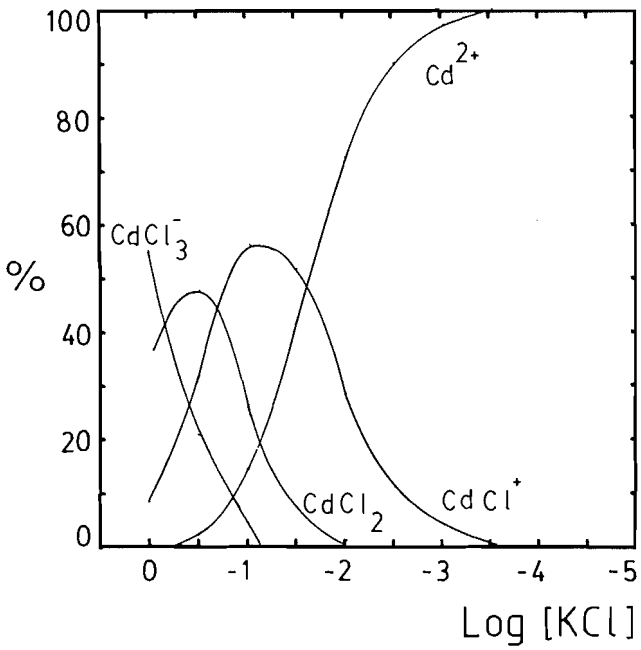

FIG. 11. Distribution des complexes chlorés en solution aqueuse.

importance. Dans les mélanges contenant 52–61% en HF, on voit que le domaine de concentration en KCl où $CdCl_2$ prédomine est de plus en plus important. La constante de formation du premier complexe chloré β_1 est à zéro. Si on considère la distribution des complexes fluorés dans les mélanges eau–HF telle que définie précédemment, on voit qu'à HF 50% le complexe CdF^+ prédomine. En ajoutant des ions chlorure, on peut avoir formation de CdClF dans la solution. La formation de $CdCl_2$ semble cependant beaucoup plus rapide et on a précipitation du complexe hydraté, selon l'équilibre [10].

[10] $Cd^{2+} + 2Cl^- + H_2O \rightleftarrows CdCl_2 \cdot H_2O$

Conclusion

L'étude des vagues polarographiques du cadmium dans les mélanges eau–HF a conduit à la détermination de trois complexes fluorés, le CdF_3^- à faible concentration en HF, le CdF_2 entre 20 et 45% en poids de HF et le CdF^+ jusqu'à 60% en HF. À plus grande concentration en HF, la connaissance précise des espèces présentes en solution n'est pas suffisante pour établir le type de complexe présent.

La précipitation de $CdCl_2 \cdot H_2O$ et la formation de complexes de degré trois et quatre, lorsque la proportion du HF augmente, indique que le mélange eau–HF est un milieu où la solvatation est faible et que les complexes du fluor avec le cadmium sont aussi très faibles par rapport aux complexes chlorés.

Remerciements

Les auteurs sont reconnaissants des octrois de recherche du Conseil de recherches en sciences naturelles et en génie du Canada et du Ministère de l'Éducation du Québec qui ont rendu ce travail possible.

1. A. VAILLANT, J. DEVYNCK et B. TRÉMILLON. Anal. Lett. **6**, 1095 (1973).
2. A. VAILLANT, J. DEVYNCK et B. TRÉMILLON. J. Electroanal. Chem. **57**, 219 (1974).
3. H. MÉNARD, J. P. MASSON, J. DEVYNCK et B. TRÉMILLON. J. Electroanal. Chem. **63**, 163 (1975).
4. P. A. GIGUÈRE et S. TURRELL. J. Am. Chem. Soc. **102**, 5473 (1980).
5. R. BEAUDOIN. Thèse de doctorat. Université de Sherbrooke, Sherbrooke, Canada (1985).
6. H. STREBLOW. *Dans* The chemistry of nonaqueous solvents. Vol. 1. *Edité par* J. J. Lagowski. Academic Press, New York, NY. 1966, Chap. 4.
7. A. M. BOND. J. Electroanal. Chem. **20**, 223 (1969).
8. A. M. BOND et T. A. O'DONNELL. J. Electroanal. Chem. **26**, 137 (1970).
9. I. ELIEZER et A. MORENO. J. Chem. Eng. Data, **19**, 226 (1974).
10. A. M. BOND et T. A. O'DONNELL. Anal. Chem. **41**, 1801 (1969).
11. A. M. BOND et T. A. O'DONNELL. Anal. Chem. **44**, 590 (1972).
12. B. BURROW et R. JOSINSKI. J. Electrochem. Soc. **115**, 348 (1968).
13. H. MÉNARD et F. LEBLOND-ROUTHIER. Anal. Chem. **50**, 687 (1980).
14. R. BEAUDOIN et H. MÉNARD. Can. J. Chem. **65**, 528 (1986).
15. D. D. DEFORD et D. N. HUME. J. Am. Chem. Soc. **83**, 4699 (1961).
16. S. S. MESARIC et D. N. HUME. Inorg. Chem. **2**, 1063 (1963).
17. J. DEVYNCK, A. VAILLANT, B. TRÉMILLON, F. LEBLOND-ROUTHIER et H. MÉNARD. J. Electrochem. Soc. **100**, 885 (1979).

Can. J. Chem. Downloaded from www.nrcresearchpress.com by 213.222.148.141 on 09/07/12
For personal use only.

Mixed alkali effect in sodium thiosulfate pentahydrate melt

SHAKIRA S. ISLAM AND KOCHI ISMAIL[1]

Department of Chemistry, North-Eastern Hill University, Bijni Campus, Laitumkhrah, Shillong – 793003, India

Received January 5, 1987[2]

SHAKIRA S. ISLAM and KOCHI ISMAIL. Can. J. Chem. **66**, 242 (1988).

Density and electrical conductance measurements of $0.35[X\text{NaNO}_3 + (1 - X)\text{KNO}_3] + 0.65\text{Na}_2\text{S}_2\text{O}_3.5\text{H}_2\text{O}$ melt were made as functions of temperature and X. Molar volume, V, is found to be additive. The percent deviation of V_{ext} (extrapolated V of the pure solute from the plot of V vs. total added alkali ion fraction) from V_{cal} (calculated V of the pure solute from its high temperature density data) increases monotonically as the amount of NaNO_3 in the hydrate melt increases, thereby manifesting a "structure-forming" tendency of NaNO_3. The non-Arrhenius temperature dependence of molar conductance, Λ is analyzed in terms of the Vogel–Tammann–Fulcher (VTF) equation. Mixed alkali effect (MAE) has been observed on Λ and T_0 (ideal glass transition temperature). A competitive polarization model has been used to explain the MAE on Λ.

SHAKIRA S. ISLAM et KOCHI ISMAIL. Can. J. Chem. **66**, 242 (1988).

On a effectué des mesures de densité et de conductivité électrique sur des mélanges fondus de $0{,}35[X\text{NaNO}_3 + (1 - X)\text{KNO}_3] + 0{,}65\text{Na}_2\text{S}_2\text{O}_3.5\text{H}_2\text{O}$, en fonction de la température et de la valeur de X. On a trouvé que le volume molaire, V, est une propriété additive. Le pourcentage de déviation de la valeur V_{ext} (la valeur de V du soluté pur extrapolée à l'aide du courbe de V en fonction de la fraction totale des ions alcalins ajoutés) par rapport à la valeur V_{cal} (la valeur V calculée du soluté pur obtenue à partir de ses données de densité à haute température) augmente d'une façon monotone avec l'augmentation de la quantité de NaNO_3 dans la phase hydratée fondue; ces résultats suggèrent que le NaNO_3 a tendance à former des structures. La relation entre conductivité molaire, Λ, et la température ne suit pas la loi d'Arrhénius; on analyse ce fait en fonction de l'équation de Vogel–Tamman–Fulcher (VTF). On a observé l'effet des sels alcalins mixtes (EAM) sur Λ et sur T_0 (température de transition vitreuse idéale). On a utilisé un modèle de polarisation compétitive pour expliquer l'EAM sur Λ.

[Traduit par la revue]

Introduction

The mixed alkali effect (MAE) is an established phenomenon which has long been known to occur in a glassy or molten medium (1–6). It refers to deviations from additivity in isotherms of various physical properties as a function of composition which is being varied by progressively replacing one alkali ion by another in a glass or melt. In a more general term this effect is known as a mixed monovalent cation effect. Normally the MAE is most pronounced for properties related to ionic transport. In contrast to transport properties, equilibrium properties such as molar volume are additive or sometimes nearly additive functions of composition even when transport properties show a large MAE.

Continuing interests are being shown on MAE mainly because of the following reasons. Firstly, it has a direct relevance to glass industry (5, 7). A knowledge about the MAE helps a glass technologist in deciding about the glass compositions for achieving glasses with specific properties. Secondly, the problem of providing a completely satisfactory explanation for the existence of MAE is not yet settled (2–4, 8–11). Thirdly, curiosity has recently arisen among workers to look for MAE in media other than glass or melt of rigid network structure. One such convenient medium for testing the existence of MAE is hydrate melt. A few reports (11–14) have been made on the study of MAE in hydrate melts. In all these studies made up till now only calcium nitrate tetrahydrate has been used as the medium.

Recently we have reported (15) the feasibility of using $\text{Na}_2\text{S}_2\text{O}_3.5\text{H}_2\text{O}$ melt as a molten solvent for physicochemical studies. This melt has been found to dissolve about 60 mol% of KNO_3. Therefore in the present study we have made an attempt to look for MAE in molten sodium thiosulfate pentahydrate medium by measuring the density and electrical conductance of $0.35[X\text{NaNO}_3 + (1 - X)\text{KNO}_3] + 0.65\text{Na}_2\text{S}_2\text{O}_3.5\text{H}_2\text{O}$ system.

Experimental section

The solutes, NaNO_3 and KNO_3 (BDH, LR grade), were recrystallized twice from distilled water and dried over P_2O_5 in a vacuum desiccator for several days before use. Sodium thiosulfate pentahydrate (SMerck, GR grade) was used as molten solvent without further purification. The actual H_2O/Na^+ mole ratio in the sodium thiosulfate pentahydrate sample used was determined to be 5 ± 0.01 (0.2% error on the molality scale) from iodometric titration.

Although sodium thiosulfate pentahydrate melt dissolves ~60% mol% of KNO_3, it dissolves only ~35 mol% of NaNO_3. Therefore the total solute alkali ion concentration in the samples was kept constant at 0.35 mole fraction. The crystallization temperature of the melt increased with increase in the amount of NaNO_3.

Methods of density and conductance (at 1 kHz) measurements are the same as described earlier (14, 16). For the conductivity measurement the samples were taken in a closed Corning glass container attached with the conductivity cell to prevent water loss. The temperature control of the thermostat was improved ($< \pm 0.02$°C) by connecting an additional voltage divider to the heating element of the NBE Type Ultra Thermostat.

Results and discussion

Volumetric property

Measured density of the system under study is a linear function of temperature and is presented in Table 1. Composition dependence of molar volumes of systems containing hydrate melts is rather more interesting. Previous studies (15–18) on the composition dependence of molar volumes of binary systems containing anhydrous solute and hydrate melt have led to treat these systems as a mixture of hydrate melt and hypothetical supercooled solute. This general feature of such binary melts is, however, expected only in systems containing anhydrous solutes whose cations do not get hydrated by the water molecules of the hydrate melt. The water–anion interaction is normally not taken into consideration.

[1]To whom correspondence should be addressed.

[2]Revision received October 19, 1987.

Can. J. Chem. Downloaded from www.nrcresearchpress.com by 213.222.148.141 on 09/07/12
For personal use only.

Can. J. Chem. Downloaded from www.nrcresearchpress.com by 213.222.148.141 on 09/07/12
For personal use only.

TABLE 1. Parameters for the density equation, $\rho = a - bt(°C)$ for $0.35[X NaNO_3 + (1 - X)KNO_3] + 0.65Na_2S_2O_3.5H_2O$ melt

X	$a/(g\,cm^{-3})$	$b \times 10^4/(g\,cm^{-3}\,deg^{-1})$	rms dev., $\sigma \times 10^4$
0.0	1.7509	7.4642	4.05
0.2	1.7529	7.6771	3.41
0.4	1.7517	7.3176	3.69
0.6	1.7519	7.4392	2.04
0.8	1.7554	7.9281	3.39
1.0	1.7499	7.1504	3.21

$\rho(Na_2S_2O_3.5H_2O) = 1.6958 - 7.7097 \times 10^{-4}t$

$(\sigma \times 10^4 = 2.58)$

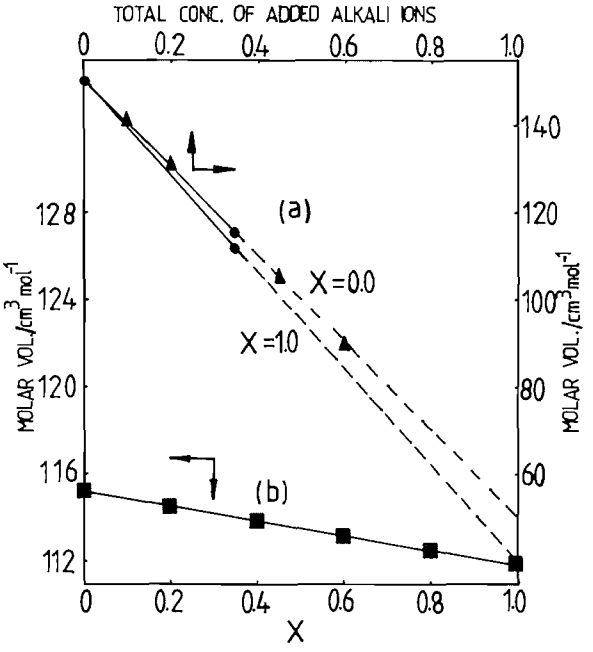

FIG. 1. Plots of molar volume of $0.35[X NaNO_3 + (1 - X)KNO_3] + 0.65Na_2S_2O_3.5H_2O$ melt as functions of (a) total concentration of added alkali ion and (b) X. (▲: data from ref. 15).

In the present system of interest there is an opportunity to examine the above aspect for the two types of solutes, viz., one having cation which competes and the other having cation which does not compete for the water of hydration of the solvent molecule. Although we have here only two concentration points (0 and 0.35 mole fraction of solute) to draw the molar volume vs. mole fraction isotherms, an attempt to draw such isotherms and then to extrapolate them to the pure solute concentration is justifiable in view of the fact that the linearity of this type of isotherms is already established for $Na_2S_2O_3.5H_2O + KNO_3$ system (15). Two such exemplary plots at 60°C are illustrated in Fig. 1. It may be noted that in those systems containing both $NaNO_3$ and KNO_3 the mixture of these two with the respective proportion is considered to be the solute of 0.35 mole fraction. The molar volumes, V_{ext}, of the pure solutes at 60°C obtained by extrapolating the plots of the type shown in Fig. 1 are listed in Table 2 along with the corresponding values of the molar volume, V_{cal}, evaluated from the high temperature density data (19) of these molten solutes. The interesting point to note from Table 2 is the % deviation of V_{ext} from V_{cal}. This deviation is minimum (0.87%) for the case of pure KNO_3 which is in accordance with our earlier result (15). The % deviation monotonically increases as the solute contains more and more amounts of $NaNO_3$ and is maximum (4.45%) for the case of pure $NaNO_3$. Similar trend in the % deviation was observed at other ambient temperature also. Since the experimental uncertainties involved are the same at all compositions, such a monotonic increase in the % deviation of V_{ext} from V_{cal} with increase in the amount of $NaNO_3$ is not attributable to experimental errors. Another possible source of error is the uncertainty in the high temperature density data from which V_{cal} is evaluated. We found that the monotonic increase in the % deviation exists even after accounting for the uncertainty (0.5%) in the high temperature density data (19).

Since the K^+ ion has a smaller ionic potential than the Na^+ ion, it does not compete with the Na^+ ion of the solvent for the water of hydration. Therefore KNO_3 appears to behave like an inert solute in molten sodium thiosulfate pentahydrate. On the other hand, as K^+ ions are replaced by Na^+ ions, these added Na^+ ions also compete with the solvent Na^+ ion for the water of hydration. This "structure-forming" tendency of the Na^+ ion added to molten sodium thiosulfate pentahydrate appears to cause a decrease in the volume of the system and may thereby account for the increase in the % deviation of V_{ext} from V_{cal} with increase in the amount of $NaNO_3$. In Fig. 1 we have also plotted the molar volume (at 60°C) of the system of interest against X. This plot is linear as is the case with other similar systems (13, 14). The linearity of this particular plot reveals that the above referred "structure-forming" tendency of the added Na^+ ion does not seem to cause an observable amount of non-ideality in the molar volume of the system.

Conductance property

The measured values of Λ in the temperature range 20–90°C are represented in Fig. 2 in the form of Arrhenius plots. From Fig. 2 it is apparent that the temperature dependence of Λ is non-Arrhenius which is normally the case with systems containing hydrate melts. The molar conductances are therefore least-squares fitted using an iterative least-squares method to the VTF equation of the form

$$[1] \quad \ln \Lambda = A - B/(T - T_0)$$

A, B, and T_0 are temperature independent parameters. The best-fit values of A, B, and T_0 obtained thus are listed in Table 3. It is interesting to note the variation in T_0 with the concentration of one of the added alkali ions. The plot (Fig. 3) of T_0 vs. X passes through a minimum around $X = 0.5$. Such a behaviour of T_0 with X may be attributed to the MAE. Although similar trends in the variation of experimental glass transition temperature, T_g with the ion fraction of either of the alkali ions were reported for mixed alkali systems in hydrate (12, 13) as well as anhydrous melts (2, 20), to date no report of T_0 of mixed alkali system varying in this fashion with composition has been made. However, it may be pointed out that since in the temperature ranges of this study the conductance varies by only factors of 3 to 6 the computed values of the T_0 parameter may not be very precise. As a consequence the minimum in the T_0 vs. X plot in Fig. 3 could be illusory. Therefore, in order to assess the uncertainties in T_0 we also analyzed the conductance data using the procedure adopted by Moynihan (21). The best-fit values (corresponding to minimum average |% dev.| in Λ) of A, B, and T_0 thus obtained are found to be in agreement with the values given in Table 3. In the light of the percent deviations of

TABLE 2. Molar volumes of $0.35[X NaNO_3 + (1 - X)KNO_3] + 0.65Na_2S_2O_3.5H_2O$ melts (V) and of pure solutes (V_{ext} and V_{cal}) at 60°C

X	Solute	$V/(cm^3\ mol^{-1})$	$V_{ext}/(cm^3\ mol^{-1})$	$V_{cal}/(cm^3\ mol^{-1})$	% dev. between V_{ext} and V_{cal}
0.0	KNO_3	115.30	49.98	50.42	0.87
0.2	$0.8KNO_3 + 0.2NaNO_3$	114.59	47.96	48.78	1.68
0.4	$0.6KNO_3 + 0.4NaNO_3$	113.87	45.90	47.15	2.65
0.6	$0.4KNO_3 + 0.6NaNO_3$	113.24	44.10	45.51	3.10
0.8	$0.2KNO_3 + 0.8NaNO_3$	112.54	42.13	43.88	3.99
1.0	$NaNO_3$	111.94	40.38	42.26	4.45

$V(Na_2S_2O_3.5H_2O) = 150.47$

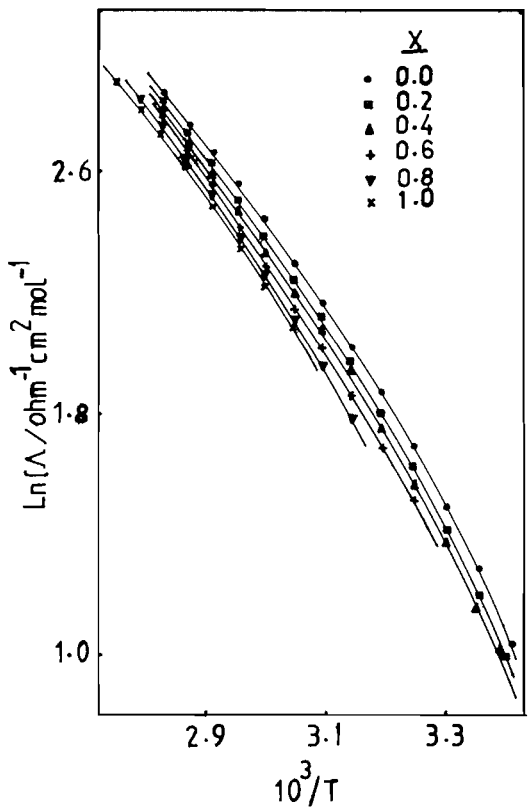

FIG. 2. Plots of ln Λ of $0.35[X NaNO_3 + (1 - X)KNO_3] + 0.65Na_2S_2O_3.5H_2O$ melt against $1/T$ for different X.

experimental values of the conductance from the least-squares curve for various values of T_0, the uncertainties involved in T_0 are estimated and are included in Table 3. For the T_0 values lying within the uncertainty range the least-squares fit of the conductance data is found to be very close to the best-fit. Since the uncertainties involved in the T_0 values are almost the same (6–8 K) for all the compositions, the nature of the T_0 vs. X plot (Fig. 3) does not seem to be very much affected.

The composition dependence of Λ is illustrated in Fig. 3. There is a negative deviation of Λ from additivity at temperatures below ~338 K. At temperatures higher than this Λ appears to approach additive behaviour. Increase in the amount of non-ideality of conductance with decreasing temperature is a general phenomenon observed in mixed alkali systems. The negative deviation of Λ from ideal behaviour therefore reveals the presence of MAE in the present system of study. The above

TABLE 3. Best-fit parameters of eq. [1] for molar conductance of $0.35[X NaNO_3 + (1 - X)KNO_3] + 0.65Na_2S_2O_3.5H_2O$ melt

X	A	B	T_0/K	rms dev. in ln Λ
0.0	5.6711 ∓ 0.2	427.48 ∓ 40	200.66 ∓ 6	0.0072
0.2	5.7729 ∓ 0.2	449.61 ∓ 45	200.00 ∓ 6	0.0086
0.4	6.1167 ∓ 0.2	545.37 ∓ 50	188.15 ∓ 6	0.0126
0.6	6.1504 ∓ 0.2	554.93 ∓ 60	188.68 ∓ 8	0.0112
0.8	6.1374 ± 0.2	535.09 ∓ 60	195.14 ∓ 8	0.0107
1.0	5.7233 ∓ 0.2	434.81 ∓ 55	208.33 ∓ 8	0.0156

referred "structure-forming" tendency of the Na^+ ion added to molten $Na_2S_2O_3.5H_2O$ may also be causing, superimposed on MAE, non-ideality of Λ of the present system.

However, since the solvent used in this study contains also alkali ion, it is worthwhile to make a comment on the presence of MAE. It may be noted that in $0.35[X NaNO_3 + (1 - X)KNO_3] + 0.65Na_2S_2O_3.5H_2O$ system although X varies from 0 to 1, the mole fraction, $K^+/(Na^+ + K^+)$ varies from 0 to 0.21 only unlike the case with other similar systems studied (11–14) containing solvent free from alkali ion. Consequently, for systems of the present type a complete estimation of MAE may not be possible. On the other hand, it is interesting to note that the maximum negative deviation of conductance from additivity observed in this study and that reported (14) in $0.3[X KSCN + (1 - X)NaSCN] + 0.7Ca(NO_3)_2.4.06H_2O$ are of the same order (~4% at 328 K). Therefore, in this work the presence of alkali ion in the solvent does not seem to affect the MAE significantly. A probable explanation to this may be that the hydration sheath around the Na^+ ions of the solvent makes the interaction with the K^+ ion very weak, thereby causing negligible MAE. This view is further supported by the above mentioned fact that the added K^+ ion does not compete for the water of hydration of the solvent. About 11% negative deviation from ideality is however reported (13) in $0.45[X LiNO_3 + (1 - X)KNO_3] + 0.55Ca(NO_3)_2.4.09H_2O$ at 298 K which is attributable to the higher alkali ion concentration, the lower temperature, and to the larger difference in the radii of the two alkali ions. The small amount of MAE generally observed in hydrate melts is attributed to the absence of rigid type structure in these melts.

Numerous explanations have been proposed for the MAE on electrical conductivity. The structural/mechanistic theories appear to be more successful in systems of rigid network structure which exhibit normally large MAE. On the other hand,

Can. J. Chem. Downloaded from www.nrcresearchpress.com by 213.222.148.141 on 09/07/12
For personal use only.

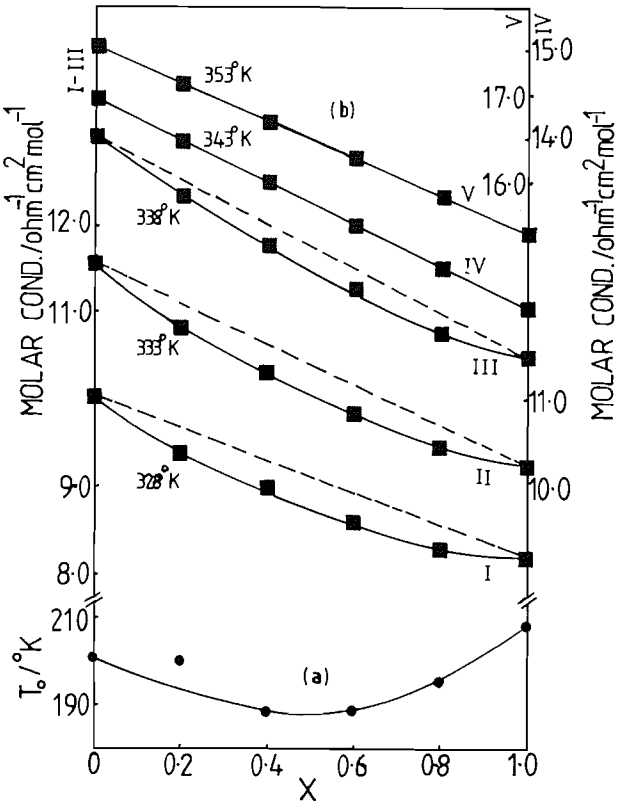

FIG. 3. Variation of (*a*) T_0 and (*b*) Λ of $0.35[X\text{NaNO}_3 + (1 - X)\text{KNO}_3] + 0.65\text{Na}_2\text{S}_2\text{O}_3.5\text{H}_2\text{O}$ melt with X.

in mixed alkali systems containing hydrate melts which do not show large MAE as seen above, the cationic interaction theories seem to be more appropriate.

Moynihan and Laity (22, 23) explained the negative deviations of conductance from additivity observed in molten binary systems like LiCl + KCl, LiNO_3 + KNO_3, etc. in terms of an anion polarization model. Such a polarization model applicable to binary melts may also be employed to explain the MAE observed in the present system of interest. The following two factors seem to provide support to this view. (1) The NaNO_3 + KNO_3 mixture behaves nearly like a hypothetical supercooled mixture in molten $\text{Na}_2\text{S}_2\text{O}_3.5\text{H}_2\text{O}$ as mentioned above which is, of course, more true when the interactions between the added alkali ions and the water molecule of the hydrate melt are negligible. (2) Negative deviations of Λ from additivity are observed in the cases of both binary NaNO_3 + KNO_3 melt (19) and the present system. Easteal (13) also made a similar attempt to compare the electrical conductance behaviour of $0.45[X\text{LiNO}_3 + (1 - X)\text{KNO}_3] + 0.55\text{Ca}(\text{NO}_3)_2.4.09\text{H}_2\text{O}$ with that of molten (Na + Tl)NO_3 system and then to use the anion polarization model to explain the MAE observed in the former molten system.

According to the anion polarization model the NO_3^- ion is considered to experience an average symmetrical field when the hydrate melt medium contains either NaNO_3 or KNO_3. When Na^+ ions are partially replaced by K^+ ions, some of the NO_3^- ions find themselves between electric fields of differing intensities. Due to this a competitive polarization of the anion occurs and the NO_3^- ion gets more polarized towards the smaller ion, i.e., Na^+. Consequently, in a hydrate melt medium addition of KNO_3 to NaNO_3 results in a decrease of the internal mobility of the Na^+ ion whereas addition of NaNO_3 to KNO_3 increases the internal mobility of K^+ ion. Presuming that the degrees of ionization of NaNO_3 and KNO_3 in the hydrate melt are equal and do not change with X we may write, $\Lambda = F[X|u_{\text{Na}^+}| + (1 - X)|u_{\text{K}^+}|]$, where F is the Faraday constant and the u terms refer to the internal mobilities of cations with respect to the NO_3^- ion. Therefore, the observed negative deviation of Λ from additivity implies that in the hydrate melt when both NaNO_3 and KNO_3 are present the decrease caused in $|u_{\text{Na}^+}|$ is always greater than the increase in $|u_{\text{K}^+}|$. Considering linear composition dependences of cationic internal mobilities it is possible to write the excess molar conductance as $\Delta\Lambda = KX(1 - X)$, where $\Delta\Lambda = \Lambda - \Lambda_{\text{id}}$ and K is a constant. A similar equation for $\Delta\Lambda$ was reported by Timmermann (24). In the present case it has, however, been found that the plot of $\Delta\Lambda$ vs. X is not exactly a symmetric parabola in X thereby indicating that in the system under study the cationic mobilities vary non-linearly with composition as is the case with binary mixtures of molten nitrates (22).

Acknowledgement

We acknowledge the financial support received from the Council of Scientific and Industrial Research (New Delhi) to carry out this work.

1. R. M. HAKIM and D. R. UHLMANN. Phys. Chem. Glasses, **8**, 174 (1967).
2. J. O. ISARD. J. Non-Cryst. Solids, **1**, 235 (1969).
3. R. TERAI. J. Non-Cryst. Solids, **6**, 121 (1971).
4. D. E. DAY. J. Non-Cryst. Solids, **21**, 343 (1976).
5. J. E. SHELBY. J. Appl. Phys. **46**, 193 (1975).
6. A. A. AHMED and A. F. ABBAS. J. Non-Cryst. Solids, **80**, 371 (1986).
7. S. YUZHEN, S. YOUAN, and H. BAOYE. J. Non-Cryst. Solids, **80**, 335 (1986).
8. W. M. RISEN, JR., G. B. ROUSE, and J. M. GORDON. *In* Non-crystalline solids. *Edited by* G. H. Frischat. Trans. Tech. Publ., Switzerland. 1977. p. 473.
9. M. D. INGRAM, C. T. MOYNIHAN, and A. V. LESIKAR. J. Non-Cryst. Solids, **38/39**, 371 (1980).
10. C. T. MOYNIHAN and A. V. LESIKAR. J. Am. Ceram. Soc. **64**, 40 (1981).
11. C. T. MOYNIHAN. J. Electrochem. Soc. **126**, 2144 (1979).
12. A. J. EASTEAL and M. C. EMSON. J. Phys. Chem. **84**, 3330 (1980).
13. A. J. EASTEAL. Aust. J. Chem. **34**, 1853 (1981).
14. P. SANGMA, S. MAHIUDDIN, and K. ISMAIL. J. Phys. Chem. **88**, 2378 (1984).
15. C. BHATTACHARJEE, S. ISMAIL, and K. ISMAIL. J. Chem. Eng. Data, **31**, 117 (1986).
16. N. ISLAM and K. ISMAIL. J. Phys. Chem. **79**, 2180 (1975).
17. J. BRAUNSTEIN, L. ORR, and W. MACDONALD. J. Chem. Eng. Data, **12**, 415 (1967).
18. S. MAHIUDDIN and K. ISMAIL. Bull. Chem. Soc. Jpn. **54**, 2525 (1981).
19. G. J. JANZ, U. KREBS, H. F. SIEGENTHALER, and R. P. T. TOMKINS. J. Phys. Chem. Ref. Data, **1**, 581 (1972).
20. C. T. MOYNIHAN, A. J. EASTEAL, D. C. TRAN, J. A. WILDER, and E. P. DONOVAN. J. Am. Ceram. Soc. **59**, 137 (1976).
21. C. T. MOYNIHAN. J. Phys. Chem. **70**, 3399 (1966).
22. C. T. MOYNIHAN and R. W. LAITY. J. Phys. Chem. **68**, 3312 (1964).
23. C. T. MOYNIHAN. *In* Ionic interactions. Vol. 1. *Edited by* S. Petrucci. Academic Press, New York. 1971. p. 261.
24. E. O. TIMMERMANN. Ber. Bunsenges. Phys. Chem. **83**, 263 (1979).

Can. J. Chem. Downloaded from www.nrcresearchpress.com by 213.222.148.141 on 09/07/12
For personal use only.

The crystal structure and stereochemistry of 2-acetyl-3,5,6-trihydroxy-5,6-dimethyl-2-cyclohexenones

GIORGIO ADEMBRI, MIRELLA SCOTTON, AND ALESSANDRO SEGA
Istituto di Chimica Organica, Piano dei Mantellini, 44 – 53100 Siena, Italy

Received June 3, 1987

GIORGIO ADEMBRI, MIRELLA SCOTTON, and ALESSANDRO SEGA. Can. J. Chem. **66**, 246 (1988).

The stereochemistry of **3***a*, one of the 2-acetyl-3,5,6-trihydroxy-5,6-dimethylcyclohexenones, obtained by rearrangement of 2,3-diacetyl-4-hydroxy-4-methylcyclopentenone, **2***a*, under basic conditions, was determined by an X-ray crystal structure analysis. An ORTEP plot shows the configuration of (5*RS*,6*RS*)-2-acetyl-3,5,6-trihydroxy-5,6-dimethylcyclohexenone and the presence of a conjugated chelated system involving the H-bonding between O(3)...H(31) and H(31)...O(2).

Crystals of **3***a* are triclinic, $a = 10.979(4)$, $b = 7.766(3)$, $c = 6.382(3)$ Å, $\alpha = 86.23(2)$, $\beta = 72.86(1)$, $\gamma = 88.23(2)°$, $Z = 2$, space group $P\bar{1}$. The structure was solved by direct methods and was refined by full-matrix least-squares procedures to $R = 0.036$ and $R_w = 0.039$ for 1324 reflections with $I > 3\sigma(I)$.

The structure of **3***a* consists of centrosymmetric dimers which contain a nearly planar bicyclic system of a cyclohexenone moiety and a chelated system (Scheme 2).

The pathway of the reaction allows one to put forward some hypothesis on the stereochemistry of some analogues of the cyclohexenones **3***a* and **3***b*.

GIORGIO ADEMBRI, MIRELLA SCOTTON et ALESSANDRO SEGA. Can. J. Chem. **66**, 246 (1988).

Faisant appel à la diffraction des rayons-X, on a déterminé la stéréochimie du composé **3***a*, une des acétyl-2 trihydroxy-3,5,6 diméthyl-5,6 cyclohexénones obtenues par une transposition de la diacétyl-2,3 hydroxy-4 méthyl-4 cyclopenténone, **2***a*, en milieu alcalin. Une courbe ORTEP démontre que la configuration est (5*RS*,6*RS*) pour l'acétyl-2 trihydroxy-3,5,6 diméthyl-5,6 cyclohexénone et qu'il existe un système de chélation conjugué impliquant des liaisons hydrogènes entre O(3)...H(31) et H(31)...O(2).

Les cristaux du composé **3***a* sont tricliniques avec $a = 10{,}979(4)$, $b = 7{,}766(3)$ et $c = 6{,}382(3)$ Å, $\alpha = 86{,}23(2)$, $\beta = 72{,}86(1)$ et $\gamma = 88{,}23(2)°$, $Z = 2$ et groupe d'espace $P\bar{1}$. On a résolu la structure par des méthodes directes et on l'a affinée par la méthode des moindres carrés (matrice entière) jusqu'à des valeurs de $R = 0{,}036$ et $R_w = 0{,}039$ pour 1324 réflexions avec $I \geq 3\sigma(I)$.

La structure du composé **3***a* comporte des dimères centrosymétriques qui contiennent un système bicyclique pratiquement plan d'une portion cyclohexénone et un système chélaté (Schéma 2).

Le chemin réactionnel permet de suggérer quelques hypothèses concernant la stéréochimie de quelques analogues des cyclohexénones **3***a* et **3***b*.

[Traduit par la revue]

Introduction

Our previous research has shown that with bases in non-hydroxylic solvents compounds **1***a–c* gave functionalized cyclopentenones **2** (1), whereas in hydroxylic solvents **1***a* led to the isomers **3***a* and **3***b* in a 4:1 ratio (2).

That **3***a* and **3***b* had cyclohexenone structures followed from their ir, ^{1}H, and ^{13}C nmr spectra. With these data we could establish neither the relative configuration of C(5) and C(6) of the two isomers nor the site of the enol bond. The most relevant signals in the nmr experiments are overlapped or too near to each other to allow a selective irradiation of significant resonances even with a 200 MHz instrument. Moreover, the nmr analysis shows, besides a very strong intramolecular hydrogen bond, strong intermolecular hydrogen bonds even in dilute solutions. Thus we undertook a X-ray crystal structure analysis on the more abundant isomer (mp 108–110°C).

Experimental

Crystal data of compound **3***a* are as follows:

$C_{10}H_{14}O_5$ mw = 214.22

Triclinic, $a = 10.979(4)$, $b = 7.766(3)$, $c = 6.382(3)$ Å, $\alpha = 86.23(2)$, $\beta = 72.86(1)$, $\gamma = 88.23(2)°$,[1] $V = 518.82$ Å^3, $\rho_c = 1.37$ g cm^{-3}, $Z = 2$, $F(000) = 228$ (20°C, graphite monochromated Mo-Kα, $\lambda = 0.71069$ Å), μ(Mo-Kα) = 0.69 cm^{-1}. Space group $P\bar{1}$.

Single crystals of **3***a* were obtained from a cyclohexane solution at room temperature. An irregular prism shaped fragment (0.6 × 0.4 × 0.3 mm) was mounted on a Philips PW 1100 four circle automated diffractometer. Cell constants were determined by least squares treatment of angles of 25 reflections in the range $8.2 < 2\theta < 16.6°$: the reflections were collected within $2\theta < 50°$ by ω–2θ step-scan technique at a scan speed of 0.07° s^{-1} and a scan width of $(0.90 + 0.3 \tan\omega)°$ in ω. The intensities of three standard reflections monitored periodically showed no significant variation. After correction for Lorentz and polarization effects, 1324 reflections with $I > 3\sigma(I)$ were considered significant and used in the structure solution and refinement. The total number of unique reflections measured were 1764. No absorption correction was applied. The structure was solved by using the phasing program SHELX 76 (3) and the *E* map showed all non-hydrogen atoms. The refinement was pursued using the SHELX 76 program system. Two cycles of full-matrix least-squares refinement with isotropic temperature factors reduced the *R* value to 0.20. Subsequently, three full-matrix least-squares cycles with anisotropic temperature factors converged at $R = 0.10$. All the hydrogen atoms were located on the difference Fourier map and all were isotropically refined. The final disagreement indexes obtained were $R = 0.036$ and

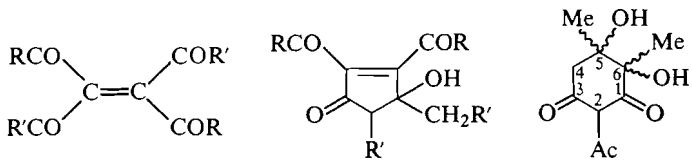

1*a* R = R′ = Me
1*b* R = Me, R′ = OEt
1*c* R = Et, R′ = OEt

2*a* R = Me, R′ = H
2*b* R = OEt, R′ = H
2*c* R = OEt, R′ = Me

3*a*, **3***b*

SCHEME 1

[1]The reduced cell has the following parameters: $a = 6.382$, $b = 7.766$, $c = 10.953$ Å, $\alpha = 89.58$, $\beta = 73.31$, $\gamma = 86.23°$, and the transformation matrix is (001, 010, −101) (see International Tables Vol. A, p. 737).

Printed in Canada / Imprimé au Canada

Can. J. Chem. Downloaded from www.nrcresearchpress.com by 213.222.148.141 on 09/07/12
For personal use only.

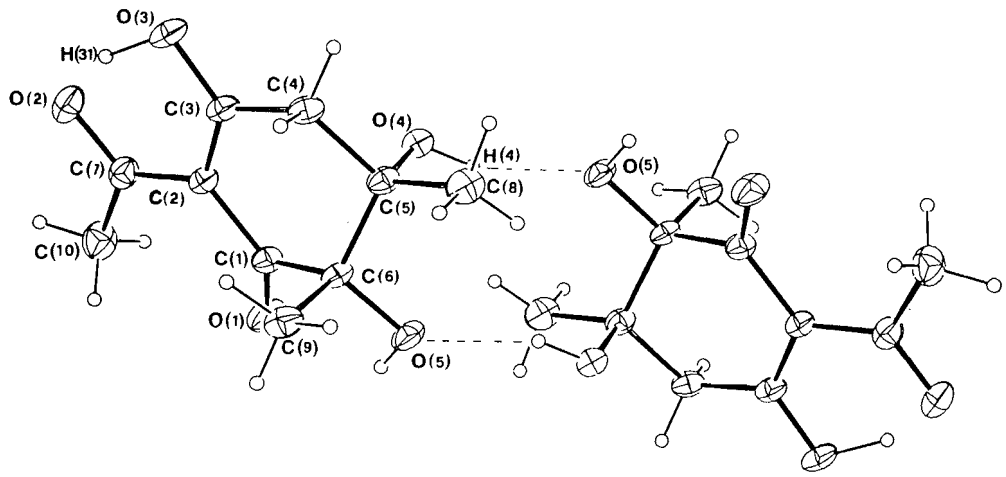

FIG. 1. ORTEP drawing of **3***a*, showing interaction between two molecules of **3***a*: dashed lines show the hydrogen bonds.

TABLE 1. Fractional atomic coordinates and temperature parameters[a]

Atom	x/a	y/b	z/c	U_{eq}
C(1)	1951(2)	6597(2)	535(3)	46
C(2)	1501(2)	8365(2)	1041(3)	44
C(3)	2315(2)	9726(2)	73(3)	47
C(4)	3604(2)	9477(2)	−1482(4)	52
C(5)	4145(2)	7659(2)	−1357(3)	45
C(6)	3127(2)	6370(2)	−1443(3)	44
C(7)	255(2)	8748(3)	2438(3)	53
C(8)	5402(2)	7440(3)	−3141(4)	66
C(9)	2707(3)	6575(3)	−3527(4)	62
C(10)	−685(2)	7412(4)	3577(5)	73
O(1)	1424(1)	5305(2)	1532(2)	71
O(2)	−98(1)	10316(2)	2708(2)	66
O(3)	1979(2)	11320(2)	446(2)	64
O(4)	4341(1)	7458(2)	769(2)	50
O(5)	3625(1)	4669(2)	−1248(2)	56

[a]Coordinates × 10^4, estimated standard deviations are given in parentheses; U_{eq} is the equivalent isotropic temperature parameter; temperature parameters × 10^3; $U_{eq} = (1/3)\sum_i\sum_j U_{ij}a_i^*a_j^*(a_i\cdot a_j)$.

$R_w = 0.039$. The maximum fluctuation of the residual electron density was 0.16 e Å^{-3}. The weighting scheme used was $w = [\sigma^2(F_o)]^{-1}$, where $\sigma(F_o)$ is the individual standard deviation for each reflection from the diffractometer counting statistics.

The final atomic positional parameters and the equivalent isotropic temperature factors are listed in Table 1, bond distances and angles are listed in Tables 2 and 3, respectively.

Anisotropic temperature parameters, C—H and O—H distances and a list of observed and calculated structure factors are available from the Depository of Unpublished Data.[2]

Discussion

An ORTEP plot (4), shown in Fig. 1, clearly shows the configuration of (5*RS*,6*RS*)-2-acetyl-3,5,6-trihydroxy-5,6-dimethyl-2-cyclohexenone and the presence of an enolic group at C(3). The cyclohexenone system shows an envelope-like conformation with the methyl groups at 5 and 6 positions in a pseudo-axial and pseudo-equatorial position respectively. The

[2]These tables may be purchased from the Depository of Unpublished Data, CISTI, National Research Council of Canada, Ottawa, Ont., Canada K1S 0S2.

TABLE 2. Bond lengths (Å)

Bond	Length	Bond	Length
C(1)—C(2)	1.468(2)	C(6)—C(9)	1.529(3)
C(1)—C(6)	1.532(2)	C(7)—C(10)	1.482(3)
C(2)—C(3)	1.394(2)	C(1)—O(1)	1.217(2)
C(2)—C(7)	1.430(3)	C(3)—O(3)	1.297(2)
C(3)—C(4)	1.485(3)	C(5)—O(4)	1.433(2)
C(4)—C(5)	1.521(2)	C(6)—O(5)	1.426(2)
C(5)—C(6)	1.538(2)	C(7)—O(2)	1.274(2)
C(5)—C(8)	1.521(3)		

sequence of torsion angles of the ring is C(1)—C(2)—C(3)—C(4) = 1.4(2), C(2)—C(3)—C(4)—C(5) = −19.6(2), C(3)—C(4)—C(5)—C(6) = 49.2(2), C(4)—C(5)—C(6)—C(1) = −61.0(2), C(5)—C(6)—C(1)—C(2) = 45.5(2), and C(6)—C(1)—C(2)—C(3) = −15.3(2)°.

The C(2)—C(3), C(3)—O(3), C(2)—C(7), and C(7)—O(2) distances are intermediate between the respective single and double bonds. These atoms (and H(31)) lie on a plane with maximum and minimum deviations of 0.037(3) and −0.03(3) Å, respectively. These data show the presence of a conjugated chelated system as already inferred from nmr analysis (2, 5). The O(2)...O(3) distance is 2.432(3) Å and the O(2)...H(31)...O(3) angle is 157(3)°. The O(3)...H(31) = 1.22(3) and O(2)...H(31) = 1.26(3) Å distances are also in agreement with this system shown by **3***a* in Scheme 2.

In the solid state **3***a* is present as a dimer with two molecules centrosymmetrical correlated, connected by two hydrogen bonds between H(4) and O(5)* (H(4)—O(4) = 0.90(3) Å, O(4)...O(5)* = 2.81(4) Å, and O(4)—H(4)...O(5)* = 161(1)°) as shown in Fig. 1.

The isomeric cyclohexanone **3***b* has been assigned the structure of (5*RS*,6*SR*)-2-acetyl-3,5,6-trihydroxy-5,6-dimethyl-2-cyclohexenone. The alternative structure having the enolic group at position 1 was discarded by the strict analogy of the spectral data (ir, uv, ^{1}H and ^{13}C nmr spectra) with those of **3***a*. Since isomers **3***a* and **3***b* can be obtained from cyclopentenone **2***a* under the same conditions as from **1***a* and the presence of a carbonyl group at 3 position seems essential, whereas **2***b* and **2***c* behave in a different way, the most reasonable mechanism is outlined below. It cannot explain the stereoselectivity of the reaction. A Dreiding model of **3***a* shows some interaction

Can. J. Chem. Downloaded from www.nrcresearchpress.com by 213.222.148.141 on 09/07/12
For personal use only.

TABLE 3. Bond angles (deg)

Bonds	Angle (deg)	Bonds	Angle (deg)
C(2)—C(1)—C(6)	117.5(1)	C(1)—C(6)—C(5)	108.7(1)
C(2)—C(1)—O(1)	124.3(2)	C(1)—C(6)—C(9)	108.2(2)
C(6)—C(1)—O(1)	118.1(2)	C(1)—C(6)—O(5)	108.1(1)
C(1)—C(2)—C(3)	118.4(2)	C(5)—C(6)—C(9)	114.4(2)
C(1)—C(2)—C(7)	122.7(2)	C(5)—C(6)—O(5)	108.1(1)
C(3)—C(2)—C(7)	118.8(2)	C(9)—C(6)—O(5)	109.3(1)
C(2)—C(3)—C(4)	123.2(2)	C(2)—C(7)—C(10)	123.7(2)
C(2)—C(3)—O(3)	121.7(2)	C(2)—C(7)—O(2)	119.4(2)
C(4)—C(3)—O(3)	115.1(2)	C(10)—C(7)—O(2)	116.9(2)
C(3)—C(4)—C(5)	114.0(1)	C(3)—O(3)—H(31)	100(1)
C(4)—C(5)—C(6)	108.4(2)	C(7)—O(2)··H(31)	103(1)
C(4)—C(5)—C(8)	111.3(2)	O(2)··H(31)—O(3)	157(3)
C(4)—C(5)—O(4)	104.9(1)		
C(6)—C(5)—C(8)	113.1(2)		
C(6)—C(5)—O(4)	108.5(1)		
C(8)—C(5)—O(4)	110.2(2)		

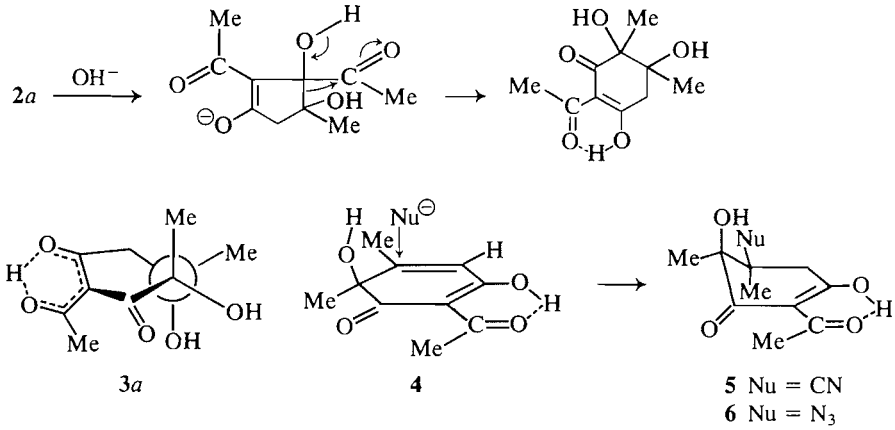

SCHEME 2

between the pseudo-axial methyl group at position 6 and the pseudo-axial hydrogen atom at 4. Since the isomer **3***b* has the methyl groups *trans*, it could assume an ee or an aa conformation. The corresponding Dreiding models show that the aa conformation offers a less steric hindrance, even if there is interaction between the methyl group at 6 and the pseudo-axial hydrogen atom of the methylene group. We have to bear in mind that a methyl group of cyclohexene, as in our case, is opposed by one less 1,3-diaxial interaction than in cyclohexane.

As we observed earlier (6), the presence of an allyl carbon atom substituted with a methyl and a hydroxyl group affects addition reactions in a highly stereoselective manner. Thus the cyclohexene **4**, obtained by facile dehydration of **3***a* or **3***b*, adds nucleophiles giving rise to only one of the expected stereoisomers. So the ions CN^- or N_3^- led, respectively, to compounds **5** or **6**, whose stereochemistry were assigned on the basis of the following considerations: (*i*) the Dreiding model of the cyclohexadienone **4** shows that the less hindered face is the si face; (*ii*) the selectivity of the attack is enhanced by the anchimeric assistance on the behalf of the OH group; (*iii*) this kind of attack leads to the less hindered isomer. On the basis of these observations we suggest that compounds **5** and **6** have the stereochemistry *5RS,6RS*.

Acknowledgements

We thank Professor A. Vacca of the University of Florence for the use of the diffractometer at the "Istituto del C.N.R. per lo studio della Stereochimica ed Energetica dei Composti di Coordinazione". Financial support by C.N.R. (Roma) is gratefully acknowledged.

1. G. ADEMBRI, C. ANSELMI, A. CAMPARINI, A. M. CELLI, and M. SCOTTON. Gazz. Chim. Ital. **113**, 489 (1983).
2. A. M. CELLI, S. CHIMICHI, L. R. LAMPARIELLO, R. NESI, and M. SCOTTON. Can. J. Chem. **60**, 1327 (1982).
3. G. M. SHELDRICK. SHELX-76, a program for crystal structure determination. Anorganisch-Chemisches Institut der Universitat Gottingen. 1976.
4. C. K. JOHNSON. ORTEP. A Fortran thermal ellipsoid plot program for crystal structure illustrations. ORNL-3794, Revised. Oak Ridge National Laboratory, Oak Ridge, TN. 1965.
5. S. FORSÉN, F. MERÉNYI, and M. NILSSON. Acta Chem. Scand. **18**, 1208 (1964).
6. G. ADEMBRI, D. DONATI, L. R. LAMPARIELLO, and M. SCOTTON. J. Heterocyclic Chem. **19**, 353 (1982).

Can. J. Chem. Downloaded from www.nrcresearchpress.com by 213.222.148.141 on 09/07/12
For personal use only.

Spectroscopic studies of some Pd(II), Pt(II), Ag(I), and Au(III) complexes of 4,6-diamino-2-thiopyrimidine and 4,6-diamino-2-methylthiopyrimidine. Structure and binding site determination

M. D. GUTIÉRREZ, R. LÓPEZ, M. A. ROMERO,[1] AND J. M. SALAS

Departamento de Química Inorgánica, Universidad de Granada, 18071 Granada, Spain

Received April 24, 1987

M. D. GUTIÉRREZ, R. LÓPEZ, M. A. ROMERO, and J. M. SALAS. Can. J. Chem. **66**, 249 (1988).

Interaction of Pd(II), Pt(II), Ag(I), and Au(III) with 4,6-diamino-2-thiopyrimidine (DATP) and 4,6-diamino-2-methylthiopyrimidine (DAMTP) in aqueous medium resulted in the formation of new complexes which have been characterized by elemental analysis, ir, ^{1}H-nmr spectroscopic techniques, magnetic susceptibility measurements in the solid state, and conductivity measurements in DMF solution. The ir and ^{1}H-nmr spectra were consistent with coordination involving the non-protonated ring nitrogen atom, the exocyclic sulphur atom, or *N*,*S*-chelation.

M. D. GUTIÉRREZ, R. LÓPEZ, M. A. ROMERO et J. M. SALAS. Can. J. Chem. **66**, 249 (1988).

La réaction, en milieu aqueux, de sels de Pd(II), Pt(II), Ag(I) et Au(III) avec de la diamino-4,6 thio-2 pyrimidine (DATP) et de la diamino-4,6 méthylthio-2 pyrimidine (DAMTP) conduit à la formation de nouveaux complexes qu'on a caractérisés par analyse élémentaire, par spectroscopies ir et rmn du ^{1}H, par des mesures de susceptibilité magnétique à l'état solide et par des mesures de conductivité en solution dans le DMF. Les spectres ir et rmn du ^{1}H suggèrent la présence d'une coordination impliquant l'atome d'azote du cycle qui n'est pas protoné, l'atome de soufre exocyclique ou un chélation-*N*,*S*.

[Traduit par la revue]

Introduction

Pyrimidine derivatives with sulphur in their structures are known to act as potent inhibitors (1, 2) and as antimetabolites (3, 4). Some authors (5) have explained the cytotoxicity of 2-thiocytosine and 2-thiouracil on the basis of the interference of these compounds in ARN synthesis. Furthermore, the effect of 2-thiocytosine on the mytosis of human lymphocytes has been described as well (6). The compound 2-thiopyrimidine shows a pronounced "*in vitro*" bacteriostatic activity (7), whereas 6-amino-2-thiouracil exhibits antiviral activity (8) besides acting chemotherapeutically (8–10). For these reasons, the interactions between metal ions and this type of ligand have been widely investigated (11).

Some of our earlier papers discussed the interactions of some thiopyrimidine and thiopurine derivatives with metal ions both in solution and in the solid phase (12–21). In this paper we report the characterization of two thiopyrimidine derivatives: 4,6-diamino-1,2-dihydro-2-thiopyrimidine (DATP) and 4,6-diamino-2-methyl-thiopyrimidine (DAMTP) and the synthesis and characterization of their Pd(II), Pt(II), Ag(I), and Au(III) complexes.

Experimental

Preparations

DATP and DAMTP. Thiopyrimidine derivatives were synthesized using methods previously described (22, 23).

Palladium(II) and platinum(II) complexes. The corresponding thiopyrimidine derivative (2 mmol) was added to a hot solution of $PdCl_2$ or $PtCl_2$ (1 mmol) dissolved in the minimum amount of saturated aqueous NaCl or NaBr. The resulting solutions were kept in a thermostatic bath at 40°C until the initial volume was reduced to 1/4. By cooling these solutions a precipitate was obtained in all cases. The complexes were washed with cold water, ethanol, and ether, and dried over P_4O_{10}.

Silver(I) complexes. A thiopyrimidine derivative (2 mmol) was dissolved in the minimum amount of water at 60–70°C, and an $AgNO_3$ aqueous solution was added until a 1:1 ligand–metal ratio was achieved. The complexes precipitated immediately and were then washed with water, ethanol, and ether, and dried over P_4O_{10}.

Gold(III) complexes. The corresponding pyrimidine derivative (2 mmol) was dissolved in 150 mL hot water (60°C). An aqueous solution of 2 mmol of $H[AuCl_4].3H_2O$ was neutralized with 0.1 *M* NaOH and added, with stirring, to the former solution. After a few minutes, the precipitation was complete and the solids were washed and dried as before.

Methods

Infrared spectra were obtained with Beckman 4250 and Perkin-Elmer 983 G spectrophotometers, using KBr and polyethylene discs in all cases. ^{1}H-nmr spectra were recorded on a Hitachi Perkin-Elmer R-600 FT NMR spectrometer using DMSO-d_6 and D_2O as solvents, and TMS as internal standard.

Magnetic measurements at room temperature were realized on a Faraday Bruker Magnet B-E15 using $HgCo(NCS)_4$ as standard. Microanalyses of C, H, and N, were performed in the Instituto de Química Bio-orgánica, C.S.I.C. (Barcelona), and Technical Services of University of Granada.

Thermal studies have been carried out on a Mettler TA-3000 system consisting of a thermobalance (Mettler TG-50) and a differential scanning calorimeter (model DSC-20); TG studies were realized in a dynamic atmosphere of pure air (100 mL min^{-1}). The determination of the acidity constants of both thiopyrimidine derivatives was carried out by potentiometric titration using a Radiometer TTT-60. The measurements were performed at 20, 25, 30, 40, and 50°C. The ionic strength was adjusted to 0.1 mol L^{-1} with potassium nitrate. To obtain the distribution diagrams we used the data treatment generally recommended (24).

Results and discussion

Ligands

Infrared, uv-visible, and ^{1}H-nmr data of the ligands are given in Table 1. These assignments are based on a comparison of the ligand spectra with those of several 2-thiopyrimidine derivatives (25–29), their complexes (30–34), and those with the —NH—CS—NH— grouping (11, 35, 36).

The infrared spectrum of DATP supports the preponderance of the thione form in the solid phase with the presence of ν(NH) bands (ca. 3100 cm^{-1}), the absence of ν(SH) (ca. 2500 cm^{-1}), and the production of the characteristic "thioamide" bands (see Table 1) due to extensive coupling of (CH), (NH), (CN), and

Printed in Canada / Imprimé au Canada

Can. J. Chem. Downloaded from www.nrcresearchpress.com by 213.222.148.141 on 09/07/12
For personal use only.

TABLE 1. Spectral data of the ligands

Source	Band: DATP.½H₂O	Band: DAMTP	Band assignment
Infrared data (cm^{-1})	3460		ν(OH)
	3410, 3390	3440, 3400 h	ν(NH)
	3320, 3270	3300, 3170	ν(NH)
	1635	1625	δ(NH)
	1615, 1565	1565, 1540, 1465	ν(C=C) + ν(C=N)
	1510[a]		ν(N—C=S)
	1420		δ(N1—H)
	1315, 1240, 1195[b]	1285, 1235	ν(CN) + ν(NCS) + ν(CS)
Electronic spectra (nm)	291 (log ε = 4.1) } [c] DATP	267 (log ε = 3.9) } [d] DAMTP	π—π*
	262 (log ε = 4.0) } DATP	[218] (log ε = 4.5) } DAMTP	π—π*
	244 (log ε = 4.3) } DATP		π—π*
	284 (log ε = 4.4) } $DATP^+$	274 (log ε = 4.1) } $DAMTP^+$	π—π*
	235 (log ε = 4.1) } $DATP^+$	236 (log ε = 4.3) } $DAMTP^+$	π—π*
		[215] (log ε = 4.3) } $DAMTP^+$	π—π*
	270 (log ε = 4.2) $DATP^-$		π—π*
^{1}H-nmr data (ppm)		2.5	S—CH_3
	3.30		H_2O
	5.05	5.30	C_5—H
	6.60	6.20	NH_2
	11.00		N1—H

[a]Thioamide I.
[b]Thioamide III.
[c]DATP pH = 7.1, $DATP^+$ pH = 2.0, $DATP^-$ pH = 12.1.
[d]DAMTP pH = 8.4; $DAMTP^+$ pH = 1.7.

TABLE 2. Acidic dissociation constants for DATP at KNO_3 = 0.1 *M*

	pK_a	
T (°C)	Bjerrum's method	Chaberek and Martell's method
20	10.1	9.9
25	9.8	9.8
30	9.6	9.6
40	9.5	9.4
50	9.2	9.1

(CS) vibrational activity (11). On the other hand, the uv and ^{1}H-nmr spectra of both pyrimidine derivatives show the normal bands and signals, respectively, for these type of compounds (37–43). Proton nmr measurements for DATP support the presence of a tautomeric equilibrium between the thione and mercapto forms in DMSO solution, and therefore, C_s symmetry has been proposed for both molecules.

In aqueous solution, DATP can be considered a weak acid. The pK_A values at various temperatures were obtained by applying Bjerrum's (44) and Chaberek-Martell's (45) methods, and are given in Table 2. These values are in good agreement with those previously reported for 4-amino-2,6-dioxo-3-methyl-5-nitroso-1,2,3,6-tetrahydro-pyrimidine (46), and several nucleic bases (47). The values of ΔH and ΔS accompanying the dissociation process of DATP were calculated by plotting log K_A vs. $1/T$ (ΔH = 46.8 kJ mol^{-1} and ΔS = 31.5 J K^{-1} mol^{-1}).

The protonation constants (K_B) of DATP and DAMTP have been determined in aqueous medium at 25°C (I = 0.1 *M* KNO_3) by the Pease-Williams spectrophotometric method (pK_B = 5.3 and 4.9, respectively). From pK_A and pK_B values, the distribution diagrams of the different forms as a function of pH were obtained (Fig. 1).

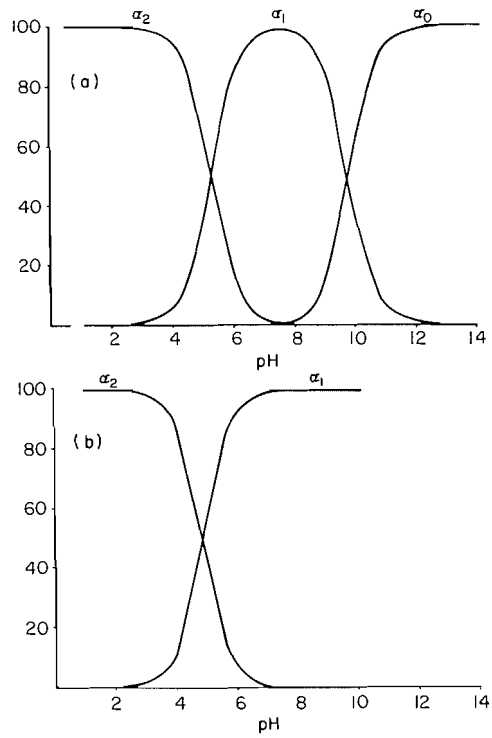

FIG. 1. Distributión diagrams of ionic forms for (*a*) DATP, (*b*) DAMTP.

Palladium(II) complexes. Four new DATP and DAMTP palladium complexes have been isolated, according to the

Can. J. Chem. Downloaded from www.nrcresearchpress.com by 213.222.148.141 on 09/07/12
For personal use only.

TABLE 3. Colour and analytical data, and proposed formulae for the complexes

Colour	Analysis (%) (calculated values in parentheses) C	H	N	M	Proposed formula
Dark red	21.04(20.83)	3.26(3.25)	23.96(24.30)	22.9(23.09)	$Pd(DATP)(DATP^-)Cl.2H_2O$
Dark brown	16.57(16.89)	2.37(2.46)	20.47(19.71)	18.7(18.73)	$Pd(DATP)_2Br_2.H_2O$
Light yellow	21.73(22.07)	3.31(3.21)	24.97(25.74)	23.5(22.42)	$Pt(DATP)_4Cl_22H_2O$
Orange yellow	9.72(9.32)	1.35(1.55)	11.20(10.88)	37.2(37.89)	$Pt(DATP)Br_2.H_2O$
White	14.75(14.55)	2.25(2.43)	20.72(21.27)	33.3(32.70)	$Ag(DATP)NO_3.H_2O$
Dark blue	11.82(11.73)	1.35(1.22)	13.25(13.69)	48.7(48.17)	$Au(DATP^-)Cl_2$
Orange	24.51(24.52)	3.36(3.27)	22.28(22.88)	21.6(21.74)	$Pd(DAMTP)_2Cl_2$
Dark brown	21.25(20.75)	2.79(2.77)	19.36(19.37)	17.0(18.4)	$Pd(DAMTP)_2Br_2$
Light yellow	19.98(20.44)	2.79(2.89)	18.61(19.07)	34.7(33.23)	$Pt(DAMTP)_2Cl_2.\frac{1}{2}H_2O$
Pale yellow	17.32(17.76)	2.40(2.52)	16.08(16.57)	27.9(28.86)	$Pt(DAMTP)_2Br_2.\frac{1}{2}H_2O$
White	22.55(22.39)	4.01(4.10)	23.26(23.51)	22.3(20.13)	$Ag(DAMTP)_2NO_3.3H_2O$
Brown	14.45(14.18)	1.81(1.65)	13.06(13.23)	47.8(46.57)	$Au(DAMTP^-)Cl_2$

preparative methods described in the experimental part of this paper. Analytical and colour data for these complexes are shown in Table 3. They all are soluble in water, DMSO, ethanol, and DMF, and exhibit a 2:1 ligand-to-metal ratio.

The molar conductivities in DMF solutions (10^{-3} *M*) of the Pd(II) complexes are in the 12.2–26.0 Ω^{-1} cm^2 mol^{-1} range, which suggest that these are non-electrolytes in solution (48).

In $Pd(DATP)(DATP^-)Cl.H_2O$ molecular and anionic forms of DATP are present as observed from the uv spectrum, which shows characteristic bands at 291, 262, 242, and 270 nm (see Table 1).

Although the ligand and the complexes show many ir absorption bands (Table 4) only the significant ones will be discussed here. The band assigned to δ(NH) is unusually broad in the complexes compared to the free ligand and we have tentatively assigned it as the hydrogen-bonded form NH—X (49). All Pd(II) complexes show one strong ν(Pd—X) band (X = Cl or Br), in the 250–355 cm^{-1} range, which corresponds to a *trans*-coordinated halogen atom. The frequency ratios ν(Pd—Br): ν(Pd—Cl) (0.87 for DATP and 0.82 for DAMTP complexes) are close to the values accepted for analogous structures (50). On the other hand, in the Pd(II)–DATP complexes the ν(C=S) band is slightly modified. From its position in the ir spectrum of free DATP. This is indicative of the involvement of sulphur atom in the coordination to the Pd(II) ion; analogous displacement has been observed in an other complex of DATP (solved by X-Ray) where the sulphur atom is involved in the coordination (21).

The most significant ^{1}H-nmr data for Pd(II) complexes have been collected in Table 5. The ^{1}H-nmr spectrum of $Pd(DATP)(DATP^-)Cl.H_2O$ shows two signals, at 5.00 and 5.25 ppm assigned to C5-H resonances in $DATP^-$ and DATP, respectively. Likewise in this complex, NH_2 signals of both DATP and $DATP^-$ ligands appear split between 6.50–7.60 ppm, although the low resolution of the spectrum suggests the hiding of some other signals. The non-equivalence of the H atoms of such groups could be attributed to hydrogen bonding interactions between the chlorine atom and NH_2 groups. The same behaviour has been found in the remaining Pd(II) complexes. Finally, the N1—H signal in Pd(II) complexes of DATP overlaps with that of water hydration, which can be explained by the increasing of acidic character due to the coordination of the aromatic ring to the Pd(II) ion. In spite of the above, another possible interpretation of the splitting of NH_2 signals supposes that the coordination takes place though the nitrogen atom of one of the two NH_2 groups which would give rise to a lowering of the electronic density of the two corresponding hydrogen atoms. In the complexes $Pd(DAMTP)_2Cl_2$ and $Pd(DAMTP)_2Br_2$, the S—CH_3 resonances are shifted downfield by 0.2 ppm, implying a possible coordination of Pd(II) via the sulphur atom.

From the above data and the consideration that the four Pd(II) complexes are diamagnetic, we propose for all of them a monomeric square-planar structure, where the halogen atoms are linked to Pd(II) ions in *trans* positions and DATP and DAMTP act as monodentate ligands through the S atom of the thione group; nevertheless, in $Pd(DATP)(DATP^-)Cl.2H_2O$, $DATP^-$ acts probably as (*N*,*S*) chelating ligand.

The most significant thermal data for the Pd(II) complexes, obtained from TG and DSC curves, have been collected in Table 6 showing the hydrated character of the $Pd(DATP)(DATP^-)Cl.2H_2O$ and $Pd(DATP)Br_2.H_2O$ complexes. The dehalogenation processes, in all cases, overlap with the pyrolytic decomposition of the pyrimidine ring, and suggest very strong palladium—halide bonds. For all the complexes the pyrolitic residue is PdO, identified by infrared spectroscopy. Experimental values are in good agreement with those expected theoretically.

Platinum(II) complexes. Analytical data of Table 3 show a great variation in the stoichiometries of the isolated Pt(II) complexes, varying between 4/1 and 1/1 (ligand-to-metal ratio).

DATP complexes show different ir spectra. For the $Pt(DATP)_4Cl_2.2H_2O$ complex a positive shift in the thioamide(I) band (20 cm^{-1}) is observed while the band at 1195 cm^{-1} (predominantly the ν(C=S) mode) remains unchanged. This is associated with cyclic nitrogen donation (11). However the ir spectrum of $Pt(DATP)Br_2.H_2O$ suggests the involvement of exocyclic sulphur in metal coordination due to the shift observed in the ν(C=S) band. In the 500–400 cm^{-1} range, the Pt(II)–DATP complexes show, besides some ligand bands, a new band assignable to the (Pt—N) mode. The bands at 320 cm^{-1} ($Pt(DAMTP)_2Cl_2.\frac{1}{2}H_2O$) and 235 cm^{-1} ($Pt(DAMTP)_2Br_2.\frac{1}{2}H_2O$) may be assigned to ν(Pt—Cl) and ν(Pt—Br), respectively. Pt–halogen bands have not been detected in Pt(II)—DATP complexes, which suggests that for $Pt(DATP)_4Cl_2.2H_2O$ (which is very water soluble) the halogen atoms are not coordinated; however, for $Pt(DATP)Br_2.H_2O$, whose stoichiometry implies

Can. J. Chem. Downloaded from www.nrcresearchpress.com by 213.222.148.141 on 09/07/12
For personal use only.

TABLE 4. Infrared spectral data of the complexes

Complex	ν(OH) + ν(N—H)	δ(OH) + δ(NH)	ν(C=C) + ν(C=N)	ν(N—C=S)[a]	ν(CN) + ν(NCS)[b] + ν(CS)[b]	ν(M—N)	ν(M—X)
$Pd(DATP)(DATP^-)Cl.2H_2O$	3330 3180	1635	1580 1535	1460	1330 1275 1200	—	355
$Pd(DATP)_2Br_2.H_2O$	3300 3180	1620(br)[c]	1590 1531	1467	1338 1285 1205	—	310
$Pt(DATP)_4Cl_2 2H_2O$	3410 3330 3180	1640	1620 1530	[d]	1335 1262 1195	485	—
$Pt(DATP)Br_2.H_2O$	3400 3310 3190	1630(br)[c]	1545 1470	[d]	1340 1260 1205	470	—
$Ag(DATP)NO_3.H_2O$	3400 3300 3200	1635(br)[c]	1545 1465	[d]	 1210	350	
$Au(DATP^-)Cl_2$	3300 3160	1635	1620 1535	1465	1340 1290 1200		
$Pd(DAMTP)_2Cl_2$	3400 3320 3200	1625	1580 1540 1470	—	1280 1250	—	305
$Pd(DAMTP)_2Br_2$	3400 3320 3200	1620	1580 1540 1465	—	1275 1250	—	250
$Pt(DAMTP)_2Cl_2.\frac{1}{2}H_2O$	3420 3320 3190	1620	1575 1540 1470	—	1270 1250	—	320
$Pt(DAMTP)_2Br_2.\frac{1}{2}H_2O$	3430 3325 3200	1620	1580 1540 1470	—	1270 1250	—	235
$Ag(DAMTP)_2NO_3.3H_2O$	3440 3300 3170	1625	1570 1540 1465		1290 1230	340	—
$Au(DAMTP^-)Cl_2$	3460 3350 3200	1625	1580 1545 1480	—	1270 1250	—	350

[a]Thioamide I.
[b]Thioamide III.
[c]br = broad band.
[d]Not observed due to overlapping with ν(C=C) + ν(C=N).

the presence of coordinated Br atoms, it can be supposed that ν(Pt—Br) bands, in this complex, may appear at lower values than 180 cm^{-1}.

^1H-nmr spectra of Pt(II) complexes show (*i*) a slight downfield shift of the C5-H signals which is probably due to the lowering in electronic density of the aromatic ring caused by the coordination to the metal ion; (*ii*) the splitting in four of the single signals of NH_2 groups could be explained by the hydrogen bond interactions between these groups and halogen or water molecules.

In agreement with the diamagnetic behaviour of these complexes, and from the above data, we propose for the $Pt(DAMTP)_2X_2.\frac{1}{2}H_2O$ (X = Cl, Br) complexes a monomeric structure with a *trans* square planar arrangement where the thiopyrimidine ligand is ring N cyclic coordinated. The same coordination is proposed for $PT(DATP)_4Cl_2.2H_2O$. In $Pt(DATP)Br_2.H_2O$ the ligand coordination takes place through the S atom of the thione group and the ring N atom.

From the TG and DSC curves three different steps can be clearly established for these complexes: (*a*) dehydration processes, where corresponding enthalpy values confirm the loss of coordinated water (see Table 6); (*b*) dehalogenation processes, with endothermic effects peaking at temperatures between 216–258°C; and (*c*) pyrolitic decomposition, ending at temperatures varying from 500–650°C.

Silver(I) complexes. The ir spectrum of $Ag(DATP)NO_3.H_2O$ is very similar to that of free DATP (Table 4) and to that of the $Cd(DATP)Cl_2.H_2O$ complex (21) with the exception of a new strong band at 1380 cm^{-1} (assigned to $\nu(NO_3^-)$) which proves

Can. J. Chem. Downloaded from www.nrcresearchpress.com by 213.222.148.141 on 09/07/12
For personal use only.

TABLE 5. ^{1}H-nmr data (δ in ppm)

Complex	Assignment				
	N1—H	S—CH_3	C5—H	H_2O	NH_2
Pd(DATP)(DATP$^-$)Cl.2H_2O	3.50	—	5.00, 5.25	3.50	6.50, 6.75, 7.20, 7.60
$Pd(DATP)_2Br_2.H_2O$	3.40	—	5.05	3.40	6.85,[a] 7.20[a]
$Pt(DATP)_4Cl_2.2H_2O$	11.90	—	5.35	3.55	6.70, 7.40,[b] 7.80
$Pt(DATP)Br_2.H_2O$	3.50	—	5.35[a]	3.50	6.95,[a] 7.05,[a] 7.35,[a] 7.70[a]
$Ag(DATP)NO_3.H_2O$	3.40	—	5.30	3.40	6.90
$Pd(DAMTP)_2Cl_2$	—	2.70	5.30	3.60	5.50, 6.20, 6.90, 7.40
$Pd(DAMTP)_2Br_2$	—	2.70	5.35	3.60	5.55, 6.20, 6.90, 7.30
$Pt(DAMTP)_2Cl_2.\frac{1}{2}H_2O$	—	2.50	5.50	3.40	6.40, 6.80, 7.10, 7.40
$Pt(DAMTP)_2Br_2.\frac{1}{2}H_2O$	—	2.50	5.40	3.35	6.40, 6.80, 7.10, 7.30
$Ag(DAMTP)_2NO_3.3H_2O$	—	2.50	5.40	3.50	6.70
Au(DAMTP$^-$)Cl_2	—	2.50[d]	5.50	—	7.10

[a]Not well resolved signal.
[b]Broad signal.
[c]Doublet.

TABLE 6. Thermal data

Complex	Dehydration			Dehalogenation		
	T (°C)	Wt. loss (%)	ΔH (kJ mol^{-1} H_2O)	T (°C)	Wt. loss (%)	ΔH (kJ mol^{-1})
Pd(DATP)(DATP$^-$)Cl.2H_2O	126	7.5(7.85)	22.8	315[a]	—	endo
$Pd(DATP)_2Br_2.H_2O$	89	4.2(3.17)	26.3	>300[a]	—	endo
$Pt(DATP)_4Cl_2.2H_2O$	102	4.2(4.13)	33.3	—	—	—
$Pt(DATP)Br_2.H_2O$	71	3.6(3.48)	23.4	240[a]	—	endo
$Ag(DATP)NO_3.H_2O$	97	5.6(5.45)	38.4	—	—	—
$Pd(DAMPTP)_2Cl_2$	—	—	—	250[a]	—	endo
$Pd(DAMTP)_2Br_2$	—	—	—	245[a]	—	endo
$Pt(DAMTP)_2Cl_2.\frac{1}{2}H_2O$	83	1.7(1.53)	26.0	219	13.6(12.09)	41.0
$Pt(DAMTP)_2Br_2.\frac{1}{2}H_2O$	120	1.4(1.33)	23.5	216	25.0(23.64)	54.2
$Ag(DAMTP)_2NO_3.3H_2O$	72	9.6(10.08)	50.7	—	—	—

[a]The endothermic process overlaps with the next exothermic process.

the presence of NO_3^- as a free ion in this complex. Likewise, in the 600–180 cm^{-1} range, a new strong band at 362 cm^{-1} was detected and assigned as ν(Ag—N) (50).

All these data suggest that DATP has a coordination pattern similar to that in the above cited $Cd(DATP)Cl_2.H_2O$ complex, acting as a bidentate ligand through the ring N and the S of the 2-thione group. We propose the structure showed in Scheme 1, similar to that found by other authors for a Ag(I)—1-methylthymine complex (51).

The signals corresponding to C5—H and NH_2 groups in the ^{1}H-nmr spectrum of this complex are slightly shifted to downfield values, arising from the lowering in electronic density of the aromatic ring. This also explains the acidic character of N1—H group whose signal is probably under that of water (3.4 ppm).

Finally, from TG and DSC data together with the ir spectrum, the following thermal decomposition mechanism has been proposed:

$$Ag(DATP)NO_3.H_2O \xrightarrow[endo]{97°C} Ag(DATP)NO_3 \xrightarrow[exo]{300°C} Ag(DATP) \xrightarrow[exo]{320\text{–}700°C} Ag$$

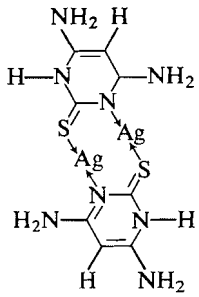

SCHEME 1. Possible structure for $Ag(DATP)NO_3 \cdot H_2O$.

$Ag(DAMTP)_2NO_3.3H_2O$. The ir spectrum of this complex shows the same bands as those of DAMTP at similar wavenumbers, plus two new bands at 1380 and 340 cm^{-1} which have been assigned to ν(NO_3^-) and ν(Ag—N), respectively.

The ^{1}H-nmr spectrum shows the same signals as those of DAMTP; those corresponding to NH_2 and C5-H groups being slightly shifted to downfield values while the remainder are unmodified value.

According to these data, we propose a monomeric linear structure for the complex in which the linking of DAMTP occurs via ring N atoms, as shown in Scheme 2.

Can. J. Chem. Downloaded from www.nrcresearchpress.com by 213.222.148.141 on 09/07/12
For personal use only.

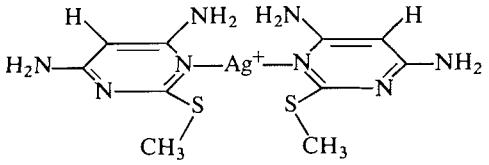

SCHEME 2. Possible structure for $Ag(DAMTP)_2NO_3 \cdot 3H_2O$.

The thermal decomposition of this complex takes place as follows:

$$Ag(DAMTP)_2NO_3.3H_2O \xrightarrow[endo]{72°C} Ag(DAMTP)_2NO_3$$

$$\xrightarrow[endo]{161°C} Ag(DAMTP)_2NO_3 \text{ (melting point)} \xrightarrow[exo]{260°C} Ag(DAMTP)_2$$

$$\xrightarrow[exo]{270-700°C} Ag$$

All the steps of this process were proven by ir spectroscopy.

Gold(III) complexes. The two Au(III) complexes are slightly soluble in water and the common organic solvents, and their anhydrous character was proved by TG and DSC data (see Table 6). The dehalogenation processes of both complexes have not been observed in the DSC curves due to the overlap with pyrolitic decomposition of the ligands, which finished at about 700°C giving Au.

The most significant ir data for both Au(III) complexes are the shifts to higher wavenumber observed for ν(C=C) and ν(C=N) vibration modes, indicating an increase in the double bond character of C=C and C=N linkages.

The ir of the $Au(DAMTP^-)Cl_2$ complex shows a new band at 350 cm^{-1} which is assigned to ν(Au—Cl); whereas the $Au(DATP)Cl_2$ ir spectrum exhibits two broad bands. The first one, between 300–400 cm^{-1} would be ν(Au—Cl), and the second between 470–550 cm^{-1} is assigned to ν(Au—N).

The ^{1}H-nmr spectrum of $Au(DAMTP^-)Cl_2$ shows the following features; (*a*) amino and imino group signals appear at 0.9 ppm, which are shifted downfield probably due to the presence of the imino group; (*b*) the signal of the C5-H group appears downfield shifted 0.2 ppm; (*c*) the SCH_3 signal is a doublet (J = 6 Hz) which could be explained by coupling to ^{197}Au, suggesting that the coordination occurs through the S atom. The ^{1}H-nmr spectrum of the $Au(DATP^-)Cl_2$ complex could not be obtained because of its insolubility in DMSO-d_6.

The two Au(III) complexes are diamagnetic, which indicates that the ligands define a square-planar arrangement around the Au(III) ions. Thus, in accord with the above data it could be assumed that in the $Au(DAMTP^-)Cl_2$ complex the thiopyrimidine derivatives are in the 4-iminic form acting as monoanionic bidentate ligands. The coordination positions are the S atom of the SCH_3 group and the negatively charged ring N atom. This implies that the two Cl atoms of each complex are cis, as shown in Scheme 3.

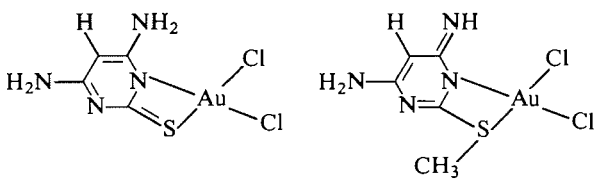

SCHEME 3. Possible structures for $Au(DATP^-)Cl_2$ and $Au(DAMTP^-)Cl_2$.

Acknowledgement

We thank a reviewer for his help in editorial work on this paper.

1. E. B. ASTWOOD, A. BISSELL, and A. M. HUGHES. Endocrinology, **37**, 456 (1945).
2. R. K. ROBINS. J. Med. Chem. **7**, 186 (1964).
3. R. HAMERS and C. HAMERS-CASTERMAN. J. Med. Biol. **3**, 166 (1972).
4. W. R. TROTTER. Nature, **164**, 63 (1949).
5. C. B. LOZZIO and P. W. WIGLER. J. Cell. Physiol. **78**, 25 (1971).
6. J. TIMSON and D. J. PRICE. Chromosomes Today, **3**, 118 (1972).
7. A. HOLY, I. VOTRUBA, and K. JOST. Coll. Czech. Chem. Commun. **39**, 634 (1974).
8. V. N. KRISHNAMURTHY, K. V. NAGLOWARA RAO, P. L. NARASIMHA RAO, and B. PRAPHULLA. Br. J. Pharmacol. Chemother. **31**, 1 (1967).
9. R. TRUHAUT and M. DECLERCQ. Rev. Ranc. Etudes Clin. Biol. **7**, 68 (1962).
10. R. H. LINDSAY, H. NAKAGAWA, and P. PHILIPCOHEN. Endocrinology, **76**, 728 (1965).
11. E. S. RAPER. Coord. Chem. Rev. **61**, 115 (1985).
12. C. VALENZUELA CALAHORRO, J. D. LÓPEZ GONZÁLEZ, R. LÓPEZ GARZÓN, and M. MELGAREJO SAMPEDRO. An. Quim. **77B**, 143 (1981).
13. C. VALENZUELA-CALAHORRO, J. D. LÓPEZ-GONZÁLEZ, and R. LÓPEZ-GARZÓN. An. Quim. **78B**, 184 (1982); **79B**, 467 (1983).
14. J. M. SALAS-PEREGRIN, M. A. ROMERO-MOLINA, E. COLACIO-RODRIGUEZ, and R. LÓPEZ-GARZÓN. An. Quim. **80B**, 465 (1984).
15. M. MORENO-CARRETERO, A. MARTINEZ-GARZÓN, R. LÓPEZ-GARZÓN, and J. M. SALAS-PEREGRÍN. Rev. Chim. Miner. **22**, 369 (1985).
16. A. MARTINEZ-GARZÓN, R. LÓPEZ-GARZÓN, and M. MORENO-CARRETERO. Thermochim. Acta, **80**, 143 (1984).
17. R. LÓPEZ-GARZÓN, A. MARTINEZ-GARZÓN, M. D. GUTIÉRREZ-VALERO, and M. DOMINGO-GARCÍA. Thermochim. Acta, **108**, 181 (1986).
18. M. P. SÁNCHEZ-SÁNCHEZ, J. M. SALAS-PEREGRÍN, M. A. ROMERO-MOLINA, and A. MATA-ARJONA. Thermochim. Acta, **88**, 355 (1985).
19. M. P. SÁNCHEZ-SÁNCHEZ, J. M. SALAS-PEREGRÍN, M. A. ROMERO-MOLINA, and E. COLACIO-RODRÍGUEZ. Thermochim. Acta, **89**, 165 (1985).
20. M. P. SÁNCHEZ-SÁNCHEZ, J. M. SALAS-PEREGRÍN, and M. A. ROMERO-MOLINA. J. Thermal Anal. **31**, 361 (1986); **31**, 573 (1986); Thermochim. Acta, **102**, 149 (1986).
21. M. A. ROMERO-MOLINA, M. D. GUTIÉRREZ-VALERO, R. LÓPEZ GARZÓN, J. M. SALAS-PEREGRÍN, M. I. ARRIORTUA, and F. J. ZÚÑIGA. Inorg. Chim. Acta, **136**, 87 (1987).
22. A. BENDICH, J. F. TINKER, and G. B. BROWN. J. Am. Chem. Soc. **70**, 3109 (1948).
23. E. C. TAYLOR and C. K. CAIN. J. Am. Chem. Soc. **74**, 1644 (1952).
24. H. S. ROSSOTTI. Talanta, **21**, 809 (1974).
25. R. SHUNMUGAM and D. N. SATHYANARAYANA. Bull. Soc. Chim. Belg. **92**, 11 (1983); **93**, 121 (1984).
26. A. LAUTIE, J. HERVIEN, and J. BELLOC. Spectrochim. Acta, **39A**, 367 (1983).
27. A. ARUNA and G. SHANMUGAM. Spectrochim. Acta, **41A**, 531 (1985).
28. M. GUPTA and M. N. SRIVASTAVA. Polyhedrom, **4**, 475 (1985).
29. R. K. GOEL, S. P. GUPTA, S. SHARMA, and C. GUPTA. J. Chem. Soc. Faraday Trans. 2, **82**, 123 (1986) and references therein.
30. R. BATTISTUZZI and G. PEYRONEL. Spectrochim. Acta, **36A**, 113 (1980); Transition Metal Chem. **3**, 345 (1978); Can. J. Chem. **59**, 591 (1981).

Can. J. Chem. Downloaded from www.nrcresearchpress.com by 213.222.148.141 on 09/07/12
For personal use only.

31. R. SHUNMUGAN and D. N. SATHYANARAYANA. Indian J. Chem. **23**A, 742 (1984).
32. G. C. STOCCO. Inorg. Chim. Acta, **78**, 57 (1983).
33. J. F. VILLA and H. C. NELSON. J. Indian. Chem. Soc. **55**, 631 (1978).
34. J. R. LUSTY, H. S. O. CHAN, and J. PEELING. Trans. Met. Chem. **8**, 343 (1983).
35. P. CASTAN. Transition Met. Chem. **6**, 14 (1981).
36. P. CASTAN and J. P. LAURENT. Transition Met. Chem. **5**, 154 (1980).
37. C. RODRÍGUEZ-MELGAREJO. Thesis. University of Granada. 1979.
38. A. ALBERT. J. Chem. Soc. 3129 (1962).
39. P. LARDENOIS, M. SELIM, and M. SELIM. Bull. Soc. Chim. Fr. **5**, 1958 (1971).
40. J. KISTER, D. BOUIN-ROUBAND, L. BOUSCASSE, and J. METZGER. Spectrosc. Lett. **13**(1), 1 (1980).
41. D. BOUIN-ROUBAND, J. KISTER, L. BOUSCASSE, and J. METZGER. Spectrosc. Lett. **14**(6), 431 (1981).
42. D. J. PASTO and C. R. JOHNSON. Determinación de Estructuras Orgánicas. Reverté. 1974. p. 109.
43. L. B. CLARK and J. TINOCO. J. Am. Chem. Soc. **87**, 11 (1965).
44. J. BJERRUM. Metal ammine formation in aqueous solutions. Haase and Son, Copenhagen. 1942.
45. S. CHABEREK and A. E. MARTELL. Organic sequestering agents. Wiley, New York. 1959.
46. J. D. LÓPEZ-GONZÁLEZ, J. M. SALAS-PEREGRÍN, J. GARCÍA-MINO, and C. VALENZUELA-CALAHORRO. An. Quim. **76**B, 256 (1980).
47. R. B. MARTÍN and Y. H. MARIAM. Met. Ions. Biol. Syst. **8**, 57 (1979).
48. W. J. GEARY. Coord. Chem. Rev. **7**, 81 (1971).
49. A. ADEYEMO, A. TURNER, and A. SHAMIM. Inorg. Chim. Acta, **67**, 67 (1982).
50. J. R. FERRARO. Low-frequency vibrations of inorganic and coordination compounds. Plenum Press, New York. 1971.
51. F. GUAY and A. L. BEAUCHAMP. J. Am. Chem. Soc. **101**, 6260 (1979).

Can. J. Chem. Downloaded from www.nrcresearchpress.com by 213.222.148.141 on 09/07/12
For personal use only.

Surface condensation products: their influence on the activity of carbon in cyclohexene conversion

M. M. SELIM AND TH. A. EL-NABARAWY
National Research Center, Dokki, Cairo, Egypt

AND

N. A. YOUSSEF
Faculty of Women, Ain Shams University, Cairo, Egypt

Received April 16, 1987

M. M. SELIM, TH. A. EL-NABARAWY, and N. A. YOUSSEF. Can. J. Chem. **66**, 256 (1988).

The catalytic conversion of cyclohexene was studied on steam-activated carbon using microcatalytic technique. Three sets of experiments were carried out to investigate the conversion of cyclohexene, depending on reaction temperature. The first set was conducted at a constant temperature while the other two sets were performed either by increasing the temperature from 300 to 400°C or by decreasing it from 400 to 300°C. In all cases, the activity of carbon in cyclohexene conversion was influenced by the nature of condensation products formed on the surface during conversion.

M. M. SELIM, TH. A. EL-NABARAWY et N. A. YOUSSEF. Can. J. Chem. **66**, 256 (1988).

Utilisant une technique microcatalytique, on a étudié la conversion catalytique du cyclohexène sur un charbon activé par de la vapeur d'eau. Dans le but d'étudier la conversion du cyclohexène et dépendant de la température de la réaction, on a réalisé trois séries d'expériences. La première série a été réalisée à température constante alors que les deux autres ont été réalisées soit en augmentant la température de 300 à 400°C ou en la diminuant de 400 à 300°C. Dans tous les cas impliquant la conversion du cyclohexène, l'activité du charbon est influencée par la nature des produits de condensation formés sur la surface au cours de la conversion.

[Traduit par la revue]

1. Introduction

Activated carbon possesses not only adsorption but also important catalytic properties which are the basis of many industrial applications. The catalytic activity may be attributed to the carbon surface and complexes formed on it. Active carbon catalysts comprise a number of oxidation, decomposition, and pyrolysis reactions. Little is known about the mechanism of their effects; however, probably the surface complexes of carbon and oxygen are mainly responsible for these effects. It is interesting to mention that in many cases (1–5) the activity and selectivity of some catalysts may depend on the cokes or condensation polymers formed on the surface. One of these catalysts has been active for conversion of cyclohexene with selective poisoning for cyclohexane conversion (6). The suggested mechanism through which the reaction proceeded in this case was a polymolecular one.

The objectives of this investigation have been to study the conversion of cyclohexene on activated carbon and to explain the effect of condensation products on the activity of the surface.

2. Experimental

2.1. Materials

A steam-activated carbon, OL (20 × 50), was kindly provided by the Pittsburgh Activated Carbon Division; Calgon Corporation, USA. The textural characteristics of the OL-activated carbon are given in the following table:

Textural characteristics of OL-activated carbon

S_{BET} m^2/g	S_t m^2/g	S_{cum} m^2/g	V_{cum} mL/g	V_p mL/g
808	793	850	1.1483	1.625

where S_{BET} = surface area obtained from BET method, S_t = surface area obtained from the V_{1-t} plots, S_{cum} = cumulative surface area, V_{cum} = cumulative pore volume are calculated from pore volume distribution curves, V_p = total pore volume is the volume adsorbed at saturated vapour pressure $P/p_0 = 1$ as taken from the adsorption isotherm.

The carbon material used in this investigation possesses high surface area, low ash content, and microporosity. The impurity, qualitatively estimated by emission spectroscopy, were mainly Ca, Mg, and Al.

2.2 Apparatus

The catalytic measurements were carried out using a microreactor followed closely the design of Emmett (7, 8). The reactor was a silica tube of 5 mm-inner diameter and about 30 cm long. A known weight of the carbon sample, (50–250 mg), was supported by a Pyrex wool plug midway through the reactor. The reactor was heated by means of a tube furnace. A control chromel–alumel thermocouple was placed between the furnace and the reactor tube. The hydrocarbons were introduced ($1–5 \times 10^{-3}$ mL) to the catalyst through an injection septum just upstream from the reactor. The reaction products were transferred directly by the carrier gas at a flow of 50 mL min^{-1} to a gas liquid chromatograph (Perkin Elmer Sigma 3B) equipped with hot wire detector. A column of 4 m was used, packed with chromosorb W-NAW 80/100 Mesh with 15% Apiezon L, which was suitable for the separation of hydrocarbons. The temperature of both column and detector was kept constant at 100°C. A valuable advantage of this method is that it can trace the first steps of the catalytic reactions, which cannot be obtained by the usual flow system.

3. Results

3.1. Preliminary investigations

A preliminary experiment was carried out using the silica reactor without carbon. It was found that even at 500°C, the conversion on the reactor wall was not significant.

Other preliminary experiments with cyclohexane and benzene were performed at different temperatures. These experiments revealed that carbon surface showed no conversion of any of

Printed in Canada / Imprimé au Canada

Can. J. Chem. Downloaded from www.nrcresearchpress.com by 176.9.209.113 on 09/07/12
For personal use only.

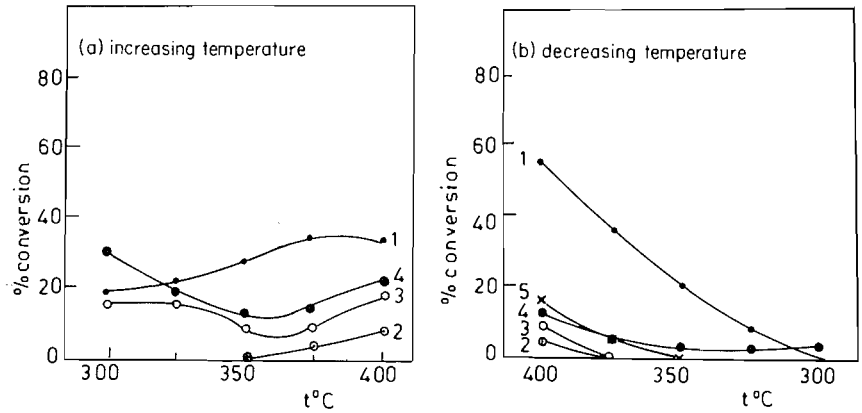

FIG. 1. Dependence of cyclohexene conversion on reaction temperature: (*a*) increasing reaction temperature; (*b*) decreasing reaction temperature. *1*, benzene; *2*, cyclohexane; *3*, methane; *4*, condensation products; *5*, toluene.

these substances. This reveals that the different kinds of active centers are not so active to convert cyclohexane or benzene.

3.2. Effect of reaction temperature on cyclohexene conversion

The results of cyclohexene conversion on activated carbon are represented in Fig. 1. These measurements were carried out by injection of 1 μL of cyclohexene into the micro-reactor charged with 50 mg of the carbon preheated at 450°C in a stream of helium for 2 h. Figure 1*a* shows the change in conversion when the starting reaction temperature increased from 300 to 400°C. Figure 1*b* shows a different trend when reaction temperature decreased from 400 to 300°C.

In the first case, at 300°C on a fresh catalyst, cyclohexene was converted into benzene (20%), methane (16%), and condensation products (34%); the remaining balance (30%) condensed on the carbon surface. Increasing reaction temperature was accompanied by an increase of percentage of benzene, a gradual increase in methane and condensation products.[1] The conversion percentages of the last two products passed through a minimum at 350–375°C and was followed by an increase in concentration up to 400°C. At 350°C, the conversion of cyclohexene to yield cyclohexane commenced and continued at higher temperatures.

On the other hand (Fig. 1*b*) starting at 400°C on a fresh sample catalyst, cyclohexene was converted into benzene (55%), cyclohexane (7%), methane (10%), toluene (17%), and condensation products (13%). Decreasing the temperature to 300°C was accompanied by a gradual decrease in all products. At 300°C, carbon showed almost no activity for cyclohexene conversion.

Figure 2 shows the effect of successive cyclohexene injections on its conversion at 400°C. For the first injection dose, cyclohexene was converted into benzene (55%), toluene (17%), methane (10%), cyclohexane (5%), and a very small quantity of condensation products. Successive injections of cyclohexene showed a gradual decrease in the percentages of all products except for cyclohexane; its percentage increased gradually reaching about 10% after the fifth injection.

4. Discussion

The first set of experiments (Fig. 1*a*) reveals that at 300°C carbon has moderate selectivity to form benzene (20%) and

[1]The condensation products were calculated by the difference between the quantity of injected cyclohexene and the sum of detected products.

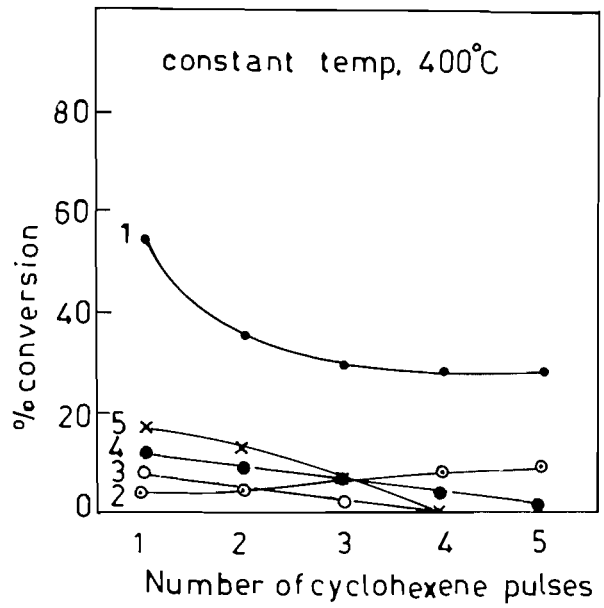

FIG. 2. Dependence of conversion on successive injections of cyclohexene at constant reaction temperature of 400°C. *1*, benzene; *2*, cyclohexane; *3*, methane; *4*, condensation products; *5*, toluene.

methane (16%). The condensation products remaining on the surface were 30% of the total injected cyclohexene. However, the second set of experiments (Fig. 1*b*) shows that at 300°C the catalyst is not active at all, and that only about 4% of cyclohexene was adsorbed at the surface. On the other hand, at 400°C (Fig. 1*a*) the percentages of benzene, methane, cyclohexane, and condensation products were 35, 17, 7, and 22, respectively. Starting from 400°C (Fig. 1*b*) the catalyst showed another behaviour; the percentages of benzene, methane, cyclohexane, and condensation products were 55, 10, 5, and 13, respectively. At this temperature a new product, toluene, was detected while it had not been observed when the reaction started at 300°C. This means that the nature of the condensation products, or the intermediate complexes formed on the surface at low temperatures, is different than those formed at high temperatures. In other words, at one and the same temperature, the conversion on a fresh carbon surface is not the same as on another surface on which the reaction has previously proceeded.

The formation of toluene at 400°C on a fresh carbon surface may be attributed to (*i*) the combination of benzene with

Can. J. Chem. Downloaded from www.nrcresearchpress.com by 176.9.209.113 on 09/07/12
For personal use only.

methane (alkylation) (1), (*ii*) the particular activity of the condensation products accumulated on the surface at high temperature, and (*iii*) the condensation of benzene on the fresh carbon surface with splitting of other products as toluene.

It remains now to confirm the mode of formation of toluene. An additional experiment was carried out to detect the mode of toluene formation when benzene was injected on a fresh carbon catalyst at 400°C, no products were observed, thus indicating that toluene is not formed from benzene. Another experiment was done by injecting benzene into a carbon bed previously exposed to cyclohexene at 400°C. The products had 10% toluene and the balance was unreacted benzene. These experiments indicate that the condensation products formed on the surface can participate with the reactant to produce a particular product. These results are confirmed with the results obtained by Hoffman *et al.* (9). They reported that, in propylene pyrolysis on graphitized carbon black, the carbon species were found to deposit on the active sites and become new active sites. The injection of cyclohexene at 300°C followed by benzene did not produce toluene. Again indicating that the condensation products formed at low temperature are not the same as those formed at high temperature. These results confirmed to those previously obtained on Ni catalyst (2). The successive injections of cyclohexene into the carbon bed at 400°C (Fig. 2) reveals that there is a gradual decrease in benzene formation. The formation of toluene and methane also decreased but that of cyclohexane increased. This means that the accumulated condensation products on the surface were subjected to a particular change in their nature due to the continuous splitting of products such as toluene and methane. The remaining condensation products on the surface are thus capable of converting cyclohexene into cyclohexane.

According to the mechanism mentioned above, the formation of toluene may also be a result of the dissociation of a certain type of the polymer–catalyst complexes formed at high temperature in the presence of benzene molecules.

1. M. M. SELIM and A. P. RUDENKO. Vestn. Moscow State Univ. Ser. Chim. **3**, 350 (1974).
2. M. M. SELIM and A. P. RUDENKO. Vestn. Moscow State Univ. Ser. Chim. **2**, 228 (1976).
3. M. M. SELIM and A. P. RUDENKO. Vestn. Moscow State Univ. Ser. Chim. **5**, 606 (1974).
4. M. M. SELIM, G. A. EL-SHOBAKY, and A. I. KIRA. J. Surf. Technol. **10**, 73 (1980).
5. M. M. SELIM, A. M. YOUSSEF, and G. F. EL-FAYOMY. J. Surf. Technol. **10**, 407 (1980).
6. M. M. SELIM and A. P. RUDENKO. Vestn. Moscow State Univ. Ser. Chim. **6**, 735 (1974).
7. R. I. KOKES, H. TOBIN, and P. H. EMMETT. J. Am. Chem. Soc. **77**, 5860 (1955).
8. D. W. BASSETT and H. W. HABGOOD. J. Phys. Chem. **64**, 769 (1960).
9. W. P. HOFFMAN, F. J. VASTOLA, and P. L. WALKER, JR. Carbon **23**, 151 (1985).

Can. J. Chem. Downloaded from www.nrcresearchpress.com by 176.9.209.113 on 09/07/12
For personal use only.

Anodic oxidation of UO_2. V. Electrochemical and X-ray photoelectron spectroscopic studies of film-growth and dissolution in phosphate-containing solutions

D. W. SHOESMITH, S. SUNDER, M. G. BAILEY, AND G. J. WALLACE

Atomic Energy of Canada Limited, Whiteshell Nuclear Research Establishment, Pinawa, Man., Canada R0E 1L0

Received March 27, 1987

D. W. SHOESMITH, S. SUNDER, M. G. BAILEY, and G. J. WALLACE. Can. J. Chem. **66**, 259 (1988).

The anodic oxidation of UO_2 has been studied in aqueous phosphate solutions over the pH range 4 to 11, using a combination of electrochemical and X-ray photoelectron spectroscopic techniques. The early stages of oxidation, leading to the formation of a film of composition $UO_{2.33}$, are unaffected by the presence of phosphate in the solutions. Phosphate concentrations $\gtrsim 10^{-1}$ mol L^{-1} prevent the formation of higher-oxide films that are present in phosphate-free solutions at higher oxidation potentials. Dissolution under steady-state conditions proceeds via a surface film of uranyl phosphate. For potentials $\gtrsim 200$ mV (vs. SCE), the rate of dissolution to yield $UO_2(HPO_4)_2^{2-}$ is controlled by charge-transfer kinetics. For potentials $\gtrsim 300$ mV, the rate-determining step is the chemical dissolution of the uranyl phosphate layer.

D. W. SHOESMITH, S. SUNDER, M. G. BAILEY et G. J. WALLACE. Can. J. Chem. **66**, 259 (1988).

Faisant appel à une combinaison de techniques électrochimiques et de spectroscopie photoélectronique des rayons-X, on a étudié l'oxydation anodique du UO_2, dans des solutions aqueuses de phosphate, à des pH allant de 4 à 11. Les étapes initiales de l'oxydation conduisent à la formation d'un film de composition $UO_{2.33}$ et elles ne sont pas affectées par la présence du phosphate dans les solutions. Des concentrations de phosphate $\gtrsim 10^{-1}$ mol L^{-1} empêchent la formation de films plus oxygénés qui sont formés, à des potentiels d'oxydation plus élevés, dans des solutions sans phosphate. La dissolution, dans des conditions d'état stationnaire, se produit par le biais d'un film à la surface du phosphate d'uranyle. A des potentiels $\gtrsim 200$ mV (vs. SCE), la vitesse de dissolution conduisant au $UO_2(HPO_4)_2^{2-}$ est contrôlée par la cinétique du transfert de charge. A des potentiels $\gtrsim 300$ mV, l'étape déterminant la vitesse de la réaction est la dissolution chimique de la couche de phosphate d'uranyle.

[Traduit par la revue]

Can. J. Chem. Downloaded from www.nrcresearchpress.com by 213.222.148.141 on 09/07/12
For personal use only.

Introduction

A knowledge of the mechanism and kinetics of the oxidative dissolution of UO_2 fuel from CANDU nuclear reactors is essential to the determination of the rate of release of radionuclides under waste-disposal conditions. The stability of UO_2 is controlled primarily by the redox conditions at the UO_2 surface and the chemical species present in the groundwaters to which it may be exposed. Previously, we have reported the mechanism of oxidative dissolution in neutral (1) and alkaline (2) solutions, determined by a combination of electrochemical techniques and X-ray photoelectron spectroscopy (XPS). We have also investigated the effect of carbonate, an anion known to complex the uranyl ion (UO_2^{2+}), which is the product of the dissolution process (3, 4). The dissolution of UO_2 in the presence of various oxidants has also been reported (5, 6).

In this paper, we report our results on the anodic dissolution of UO_2 in solutions containing phosphate, an anion known to complex both U(IV) and UO_2^{2+} (7). As in our previous studies, electrochemical techniques, complemented by XPS, have been used.

Experimental

The UO_2 electrodes used in our experiments were prepared from pellets of UO_2 taken from unused, CANDU fuel bundles. The design and preparation of the electrodes used in rotating-disk studies and those used for surface-analytical experiments have been described previously (8). A standard, three electrode, three compartment, electrochemical cell was used. All potentials were measured, and are quoted, against a saturated calomel reference electrode (SCE). The supporting electrolyte was either 0.5 mol L^{-1} Na_2SO_4 or 0.1 mol L^{-1} $NaClO_4$. No significant difference in UO_2 behaviour was observed between the two solutions.

For XPS studies, the electrochemical experiments were performed in the inert, oxygen-free (nitrogen) atmosphere of a glove box attached to the sample compartment of the McPherson ESCA-36 X-ray photoelectron spectrometer. Transfer of the electrode from the cell to the spectrometer was performed without exposing the electrode to atmospheric oxygen, using a fast-transfer probe, as described earlier (1, 9). All photoelectron spectra were excited using Al-Kα radiation.

Results

Preliminary information on the anodic oxidation process was obtained by cyclic voltammetry. Figure 1 shows sections of a series of voltammograms (from -2.0 V to $+0.8$ V and back) recorded in 0.1 mol L^{-1} $NaClO_4$ plus 0.1 mol L^{-1} Na_2HPO_4 over the range $4 \leq pH \leq 10$. To avoid confusion, only the potential range where anodic currents were obtained is shown. Although the voltammograms shown were recorded under stationary conditions, the effect of electrode-rotation rate was negligible, indicating that the anodic process is not transport-controlled. The corresponding reverse sweeps (limited to the cathodic-current regions) are shown in Fig. 2.

The position and size of the small oxidation peak occurring at negative potentials (~ -100 mV at pH = 4) are independent of phosphate concentration ($[PO_4]_T$). With increasing pH, this peak increases slightly in size and shifts to more cathodic potentials, as previously observed over a much narrower pH range, 10 to 12 (2). As discussed in our previous publications, this peak can be attributed to the formation of a thin layer of UO_{2+x} (Fig. 1).

The second oxidation peak, seen at positive potentials ($\sim +600$ mV at pH = 6.0), was not observed in the absence of phosphate. The position and size of this peak are independent of pH over the range $5 < pH \leq 10$ (Fig. 1). The majority of the charge consumed in this oxidation goes to the formation of a surface layer that is reduced at the more negative of the two reduction peaks (e.g., ~ -700 mV at pH = 7.1) observed in the subsequent reverse cathodic sweep (Fig. 2). As indicated in Fig. 2, this peak is attributed to the reduction of a layer of $UO_{2.33}$, by analogy to the reduction processes observed in sulphate, and sulphate plus carbonate solutions (1, 4). The XPS results discussed later confirm this assignment.

The first reduction process in the cathodic sweep (Fig. 2) is

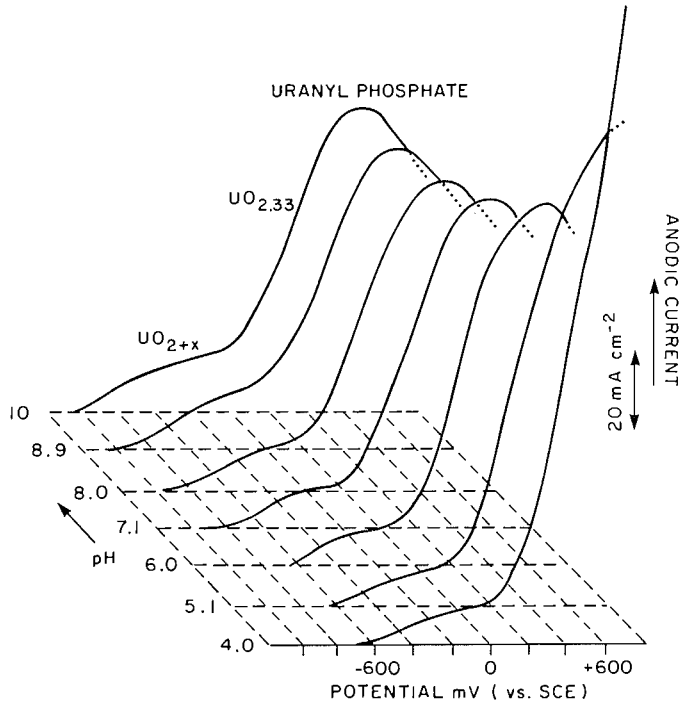

FIG. 1. Sections of a series of anodic sweeps at 20 mV s^{-1} from −2.0 V to +0.8 V recorded in a solution containing 0.1 mol L^{-1} $NaClO_4$ plus 0.1 mol L^{-1} Na_2HPO_4 for various pH values in the range $4.0 \leq pH \leq 10$.

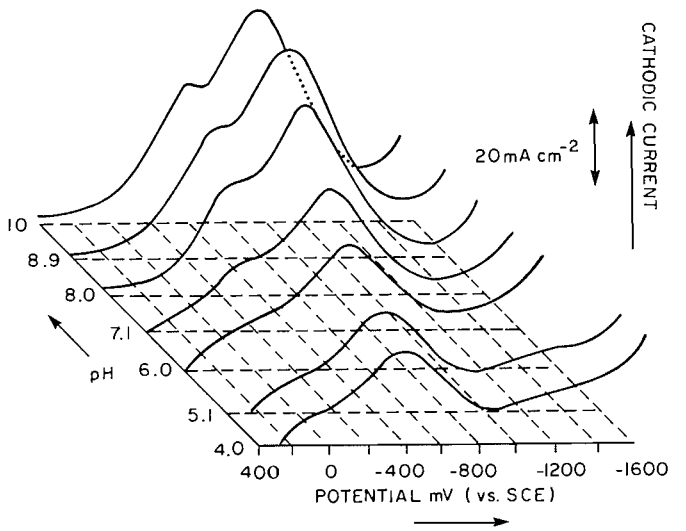

FIG. 2. Sections of the cathodic sweeps (20 mV s^{-1}) recorded after the corresponding anodic sweeps of Fig. 1.

only seen when the major anodic peak is observed in Fig. 1, and can be attributed to the reduction of a partially passivating layer formed at very positive potentials during the anodic sweep. This cathodic peak is absent at $pH \lesssim 5$ when no anodic peak is observed in Fig. 1. However, its size increases with increasing pH, indicating that this layer thickens at higher pH values despite the fact that the anodic peak in Fig. 1 does not vary in size or position with pH. As indicated, this partial-passivation process is tentatively attributed to the formation (Fig. 1) and reduction (Fig. 2) of a uranyl phosphate layer.

The surfaces of UO_2 electrodes subjected to potentiostatic oxidation in phosphate-containing solutions were analyzed using XPS. In addition to survey spectra recorded to determine

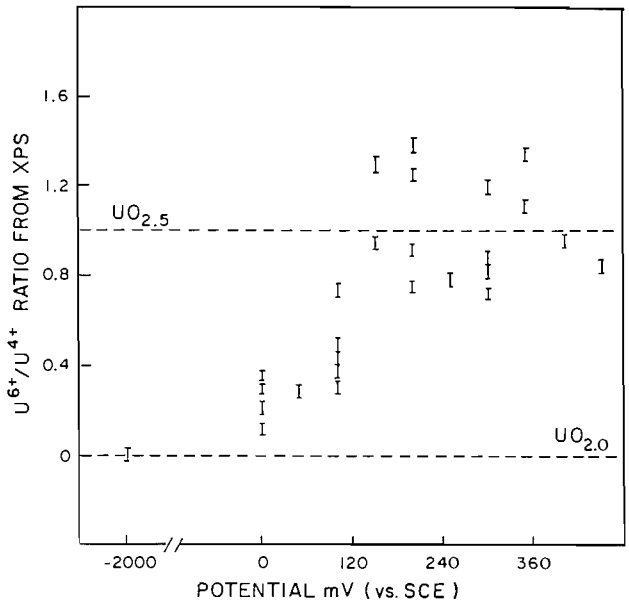

FIG. 3. Stoichiometry of the UO_2 electrode surface, expressed as the U^{6+} to U^{4+} ratio from XPS, after anodic oxidation for 20 min in 0.5 mol L^{-1} Na_2SO_4 + 0.1 mol L^{-1} Na_2HPO_4 solution, pH = 9.2, at various potentials.

the elemental composition of the surface layer, high-resolution spectra were recorded for U-4*f*, C-1*s*, O-1*s* and the valence region bands (0–20 eV) to determine the extent of oxidation of the UO_2 surface. The U-$4f_{7/2}$ band was resolved into U^{6+} and U^{4+} components according to procedures described earlier (1, 9). The results of this analysis were verified by the relative intensity of the bands in the valence region. The C-1*s* spectra were recorded to monitor any charging of the electrode surface.

Figure 3 shows the U^{6+} to U^{4+} ratio on the surface of the electrode after potentiostatic oxidation at various potentials for 20 min (1200 s) in a solution containing 0.1 mol L^{-1} Na_2HPO_4 plus 0.5 mol L^{-1} Na_2SO_4 (pH = 9.2). At −2.0 V, the U^{6+} to U^{4+} ratio is zero, consistent with a completely reduced electrode surface of composition UO_2. The ratio increases as the applied potential (E) increases, achieving a value of 1.0 ± 0.2 for $E \geq +200$ mV. A similar value of this ratio is obtained at these potentials in the absence of phosphate. This value is close to that expected for $UO_{2.5}$ (U_2O_5), as indicated in Fig. 3.

Figure 4 shows the U^{6+} to U^{4+} ratio achieved after potentiostatic oxidation at +300 mV for 20 min in 0.5 mol L^{-1} Na_2SO_4 containing various amounts of Na_2HPO_4 (pH = 9.2). For $[PO_4]_T \leq 10^{-2}$ mol L^{-1}, the ratio is ~1.0 and unaffected by the presence of phosphate. For $10^{-2} < [PO_4]_T < 10^{-1}$ mol L^{-1}, the ratio ranges from ~0.6 to ~1.5 with an average value close to 1, as observed at lower concentrations. For $[PO_4]_T > 10^{-1}$ mol L^{-1}, the ratio falls to a value of ~0.6, close to that expected for $UO_{2.33}$ (U_3O_7).

The voltammetric data of Figs. 1 and 2 indicate that a thin surface layer, possibly of uranyl phosphate, is formed at anodic potentials, and this could account for the high values of the U^{6+} to U^{4+} ratio (i.e., >1.0, the value expected) observed in the concentration range $10^{-2} < [PO_4]_T < 10^{-1}$ mol L^{-1}. Consequently, the survey spectra were analyzed in an attempt to determine whether phosphate anions were incorporated into the surface film during anodic oxidation. Unfortunately, it was not possible to directly distinguish between the phosphorus signal arising from phosphate incorporated in the oxidized surface

Can. J. Chem. Downloaded from www.nrcresearchpress.com by 213.222.148.141 on 09/07/12
For personal use only.

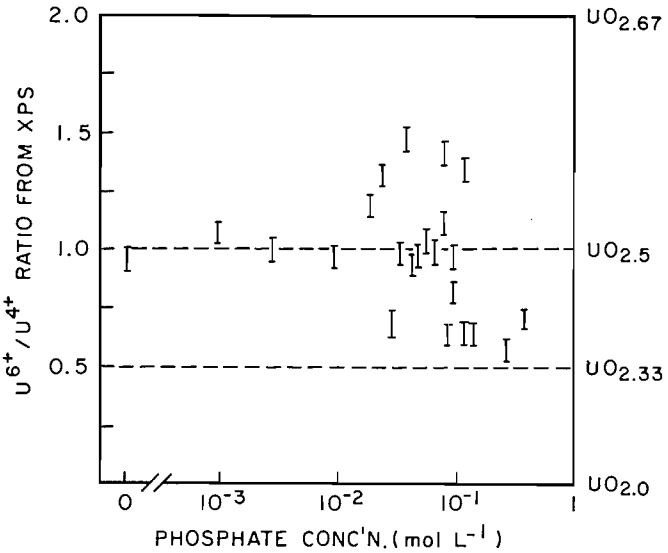

FIG. 4. Stoichiometry of the UO_2 electrode surface, expressed as the U^{6+} to U^{4+} ratio from XPS, after anodic oxidation at 300 mV for 20 min, in a solution of 0.5 mol L^{-1} Na_2SO_4 (pH = 9.2) containing various concentrations of Na_2HPO_4.

layer and that due to phosphate deposited from the solution, as a result of incomplete washing of the electrolyte from the electrode surface prior to transfer to the spectrometer vacuum chamber.

In an attempt to determine whether phosphate was incorporated into the oxidized surface layer, we measured the observed signal for phosphorus against that of sulphur, present as sulphate in the electrolyte. The intensities of the P-2*p* band (~133 eV) and the S-2*p* band (~168 eV) were normalized with respect to the intensity of the strongest uranium band (U-4$f_{7/2}$). An analysis of the relative intensity data of the P, S, and U indicated that a very thin, or incomplete, layer of "uranyl phosphate" is present (10). By lengthening the washing procedure and observing the corresponding disappearance of the P-2*p* band, we confirmed that redissolution of this layer did occur.

Consequently, we can attribute the high U^{6+} to U^{4+} ratios (>1.0), observed in Fig. 4 for $10^{-2} < [PO_4]_T < 10^{-1}$ mol L^{-1}, to the presence of a thin "uranyl phosphate" layer. The scatter in this concentration range suggests that, in some cases, we succeed in transfering the uranyl phosphate layer to the spectrometer ($U^{6+}/U^{4+} > 1.0$). In other cases, its redissolution in the electrolyte after the applied potential is switched off, or during the subsequent washing procedure, means that this layer is not observed by XPS analysis ($U^{6+}/U^{4+} < 1.0$, Fig. 4).

Figure 5 shows a series of logarithmic current–time plots recorded in 0.1 mol L^{-1} $NaClO_4$ plus 0.1 mol L^{-1} Na_2HPO_4 (pH = 9.5) for various potentials. For $E < 200$ mV, the plot is linear with a slope close to −1.0. This behaviour is consistent with a field-assisted, film growth process (4). For $E < 200$ mV, similar behaviour is observed at short times, indicating that the film-growth process is initially the same for all potentials. For longer times, the current deviates from this linear relationship. The potential range within which this deviation occurs ($E \geq 200$ mV, Fig. 5) coincides with the range over which the U^{6+} to U^{4+} ratio stabilizes around 1.0 ± 0.25, Fig. 3.

Figure 6 shows plots of Q_D (= $Q_A - Q_C$) and Q_C recorded at a potential of 300 mV for various phosphate concentrations as a function of the duration of oxidation, t_A. The anodic charge values, Q_A, were obtained by integration of potentiostatic

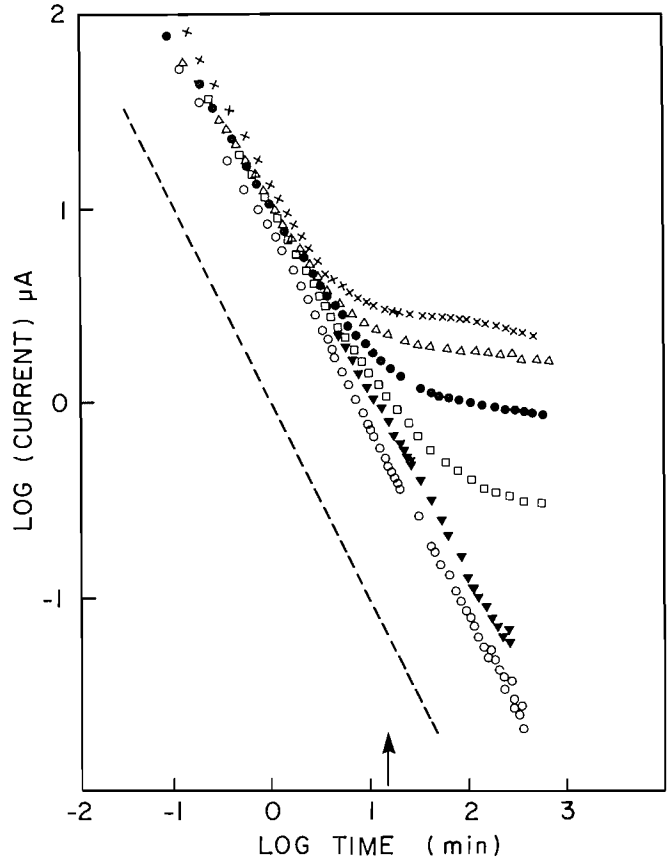

FIG. 5. Current–time curves obtained by potentiostatic oxidation in 0.1 mol L^{-1} $NaClO_4$ + 0.1 mol L^{-1} Na_2HPO_4 (pH = 9.5) for various potentials; ○, 100 mV; ▼, 150 mV; □, 200 mV; ●, 250 mV; △, 300 mV; ×, 400 mV; the dashed line represents a slope of −1.0.

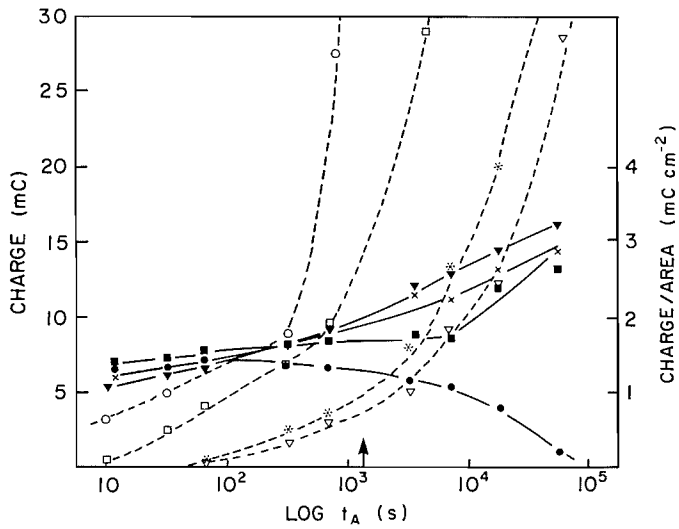

FIG. 6. Charge due to dissolution (○---△-), by integration of current–time curves obtained potentiostatically at 300 mV; and the charge due to film reduction (▼-×--●-), obtained by integration of CSV's (from +300 mV to −150 mV) recorded after oxidation, as a function of the duration of oxidation, t_A; 0.5 mol L^{-1} Na_2SO_4 (pH = 9.0) containing various amounts of phosphate; ▽▼, $[PO_4]_T$ = 10^{-3} mol L^{-1}; ×*, 10^{-2} mol L^{-1}; □■, 10^{-1} mol L^{-1}; ○●, 5 × 10^{-1} mol L^{-1}.

Can. J. Chem. Downloaded from www.nrcresearchpress.com by 213.222.148.141 on 09/07/12
For personal use only.

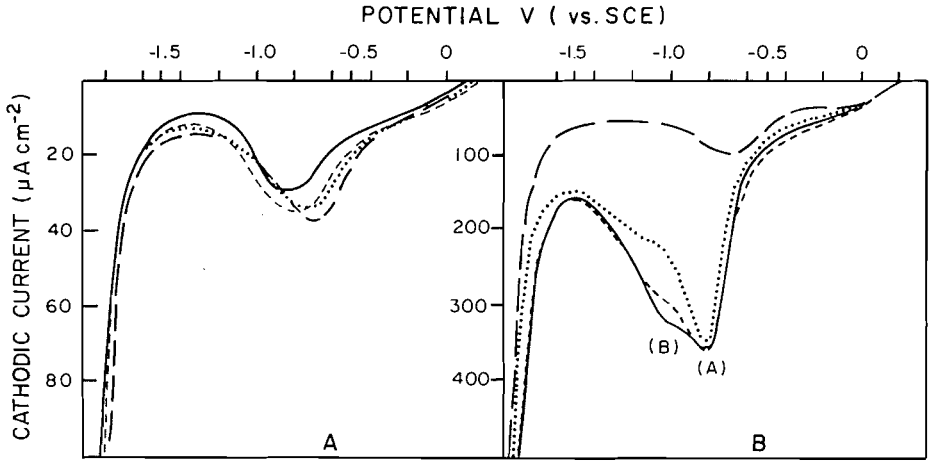

FIG. 7. Cathodic stripping voltammograms (20 mV s^{-1}) recorded after 10 s (A) and 17 h (B) of potentiostatic oxidation at 300 mV in a 0.5 mol L^{-1} Na_2SO_4 solution (pH = 9.0) containing various amounts of phosphate, $[PO_4]_T$; — 10^{-3} mol L^{-1}; ---- 10^{-2}; ··· 10^{-1}; --- 5×10^{-1}.

current–time curves, and Q_C values were obtained by integration of the subsequent cathodic stripping voltammograms (CSV). Q_D is a measure of the extent of dissolution up to the time t_A, and Q_C is a measure of the charge required to electroreduce the surface films formed during oxidation, and hence is a measure of film thickness.

For short times, $Q_C > Q_D$ since most of the anodic charge is consumed in film growth. This is consistent with the linear log i vs. log t plots of Fig. 5. For $[PO_4]_T = 10^{-1}$ mol L^{-1}, Q_D becomes substantial for $t_A > 10^2$ s. This is the time at which the log i vs. log t curve (for 300 mV) deviates from the initial linear relationship (indicated by the arrow in Fig. 5), showing that this deviation can be attributed to the predominance of dissolution over film growth. Similar cathodic stripping experiments at the other potentials used to construct Fig. 5 confirm that all the deviations from the linear log i vs. log t plots can be attributed to the onset of dissolution.

From Fig. 6, we can see that at +300 mV, for $[PO_4]_T < 10^{-1}$ mol L^{-1}, dissolution does not become extensive until $t > 10^3$ s. For these concentrations, the fast initial film formation is followed by a slower, second stage of film growth. Both the extent of dissolution, Q_D, and the film thickness, Q_C, are independent of $[PO_4]_T$. The arrow in Fig. 6 indicates the time for which the U^{6+} to U^{4+} ratios of Fig. 4 were measured. At $[PO_4]_T = 10^{-2}$ and 10^{-3} mol L^{-1}, a composition of $UO_{2.5}$ was achieved after 20 min.

For $[PO_4]_T = 0.5$ mol L^{-1}, dissolution is substantial even at short times ($t > 20$ s, Fig. 6), and the second stage of film growth is not observed. On the contrary, the initially formed film thins with time. The XPS data of Fig. 4 show that a composition close to $UO_{2.33}$ is achieved after 20 min. For $[PO_4]_T = 10^{-1}$ mol L^{-1}, the second stage of film growth is observed but only after $t > 10^4$ s, indicating that the switch from film thickening to film thinning occurs around this concentration. The U^{6+} to U^{4+} ratio (Fig. 4) is erratic in this region, consistent with a system balanced between film growth and dissolution. The XPS data indicate that for $[PO_4]_T > 10^{-1}$ mol L^{-1}, dissolution is occurring from a $UO_{2.33}$ surface covered with a thin uranyl phosphate layer. This conclusion is consistent with the voltammetric data of Figs. 1 and 2.

The forms of the CSVs for the shortest (10 s) and longest times (17 h) used to obtain the data of Fig. 6 are shown in Figs. 7*A* and 7*B* as a function of $[PO_4]_T$. The similar shape and size of the CSVs after 10 s of oxidation confirm that the first stage of oxidation is the same for all phosphate concentrations. This is consistent with the fast formation of a layer of $UO_{2.33}$ previously observed for sulphate and carbonate solutions (1, 4). After 17 h of oxidation, the size of this reduction peak (*A* in Fig. 7*B*) is increased, indicating a thickening of the $UO_{2.33}$ layer with time. For $[PO_4]_T \leq 0.5$ mol L^{-1}, this reduction peak observed after 17 h is much smaller than after 10 s since dissolution is much faster at this concentration, leading to a thinning of the $UO_{2.33}$ layer, Fig. 6.

The most marked difference between the CSV obtained after 10 s and that observed after 17 h of potentiostatic oxidation is the appearance of a second reduction peak (*B* in Fig. 7*B*) that increases in size as the phosphate concentration decreases. Similar CSVs for intermediate times, between 10 s and 17 h, show that this peak is due to the reduction of the oxide formed during the second stage of film growth observed for $t > 10^3$ s, Fig. 6. The U^{6+} to U^{4+} ratios recorded after 1.2×10^3 s (arrow in Fig. 6) show that the initially formed $UO_{2.33}$ layer is further oxidized to $UO_{2.5}$ at the beginning of this second stage of oxidation. This second oxidation process probably proceeds to the $UO_{2.67}$ stage after 17 h, as observed in solutions containing only sulphate (1).

The potentiostatic transients of Fig. 5 show that for long times at sufficiently anodic potentials, the current achieves a steady-state value. As discussed above, this current can be attributed to dissolution. Figure 8 shows steady-state currents recorded in a 0.1 mol L^{-1} Na_2SO_4 (pH = 9.4) solution and in the same solution containing either 0.1 mol L^{-1} $NaHCO_3$ or 0.1 mol L^{-1} Na_2HPO_4. The addition of phosphate to sulphate solutions accelerates dissolution for low anodic potentials, but inhibits the process at higher potentials. However, dissolution currents in phosphate solutions are always much lower than those in carbonate solutions.

Figure 9 shows steady-state currents as a function of potential for various phosphate concentrations at pH = 9.5. Two distinct regions of behaviour are observed. For potentials <300 mV, the current exhibits a Tafel region with a slope close to 60 mV^{-1}. For low potentials (<100 mV), steady-state is difficult to achieve. At higher potentials, the current becomes independent of potential, indicating a chemically, as opposed to electrochemically, controlled dissolution process. On the basis of the voltammetric data of Figs. 1 and 2 and the XPS data of Figs. 3

Can. J. Chem. Downloaded from www.nrcresearchpress.com by 213.222.148.141 on 09/07/12
For personal use only.

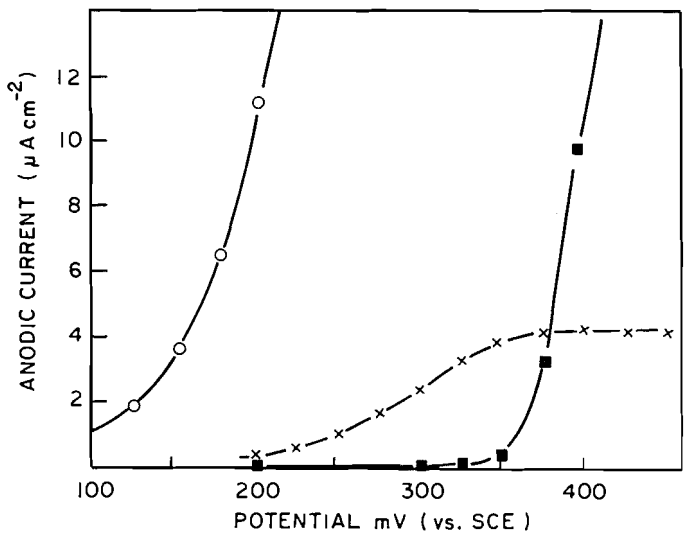

FIG. 8. Steady-state current voltage curves recorded in 0.1 mol L^{-1} Na_2SO_4 (pH = 9.4) (■) and in the same solution containing 0.1 mol L^{-1} $NaHCO_3$ (○) or 0.1 mol L^{-1} Na_2HPO_4 (×).

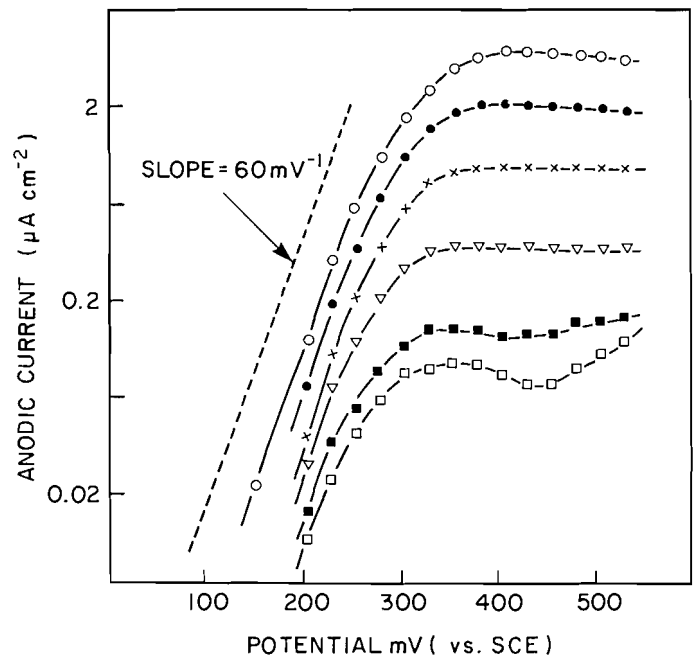

FIG. 9. Steady-state current–voltage curves recorded on a rotating-disk electrode (ω = 16.7 Hz) in 0.1 mol L^{-1} $NaClO_4$ (pH = 9.5) containing various amounts of Na_2HPO_4; □, $[PO_4]_T = 10^{-2}$ mol L^{-1}; ■, 2×10^{-2}; ▽, 5×10^{-2}; ×, 10^{-1}; ●, 2×10^{-1}; ○, 5×10^{-1}.

and 4, we can attribute chemical control to the potential-independent dissolution of a "uranyl phosphate" layer.

Chemical control of the dissolution process in the plateau region is confirmed by pulsing between potentials in this region. The current decay to a steady-state value after an anodic pulse is quite rapid (20–50 s) indicating that the formation of the uranyl phosphate layer is rapid. On pulsing back to the original, less positive potential, the current is depressed below the original value at this potential and only slowly recovers (200–500 s) to the steady-state value. This slow recovery confirms that the thick uranyl phosphate layer formed at the higher potential is only slowly dissolved.

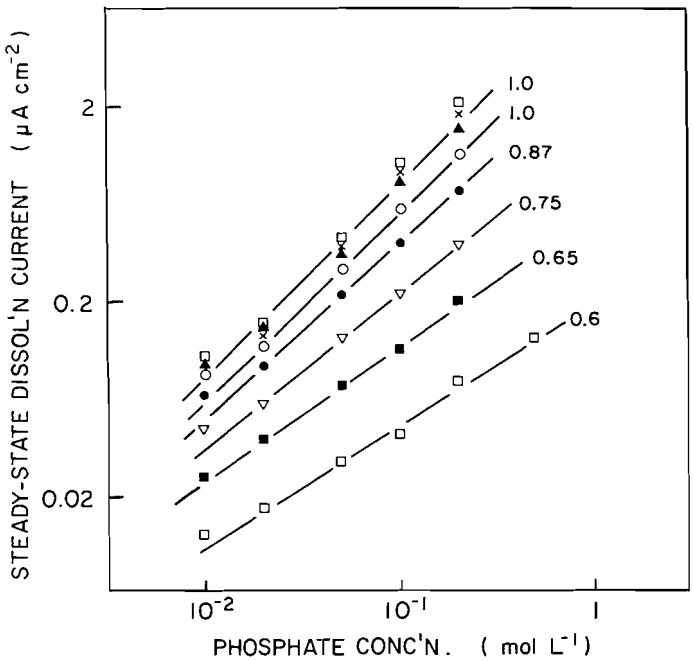

FIG. 10. Steady-state currents of Fig. 9 plotted as a function of phosphate concentration for various potentials; □, 200 mV; ■, 225 mV; ▽, 250 mV; ●, 275 mV; ○, 300 mV; ▲, 350 mV; ×, 375 mV; □, 400 mV. The numbers on the figure are the slopes of the various lines.

Figure 10 shows the steady-state currents plotted as a function of $[PO_4]_T$ for various potentials. These data show that the dissolution current is first order in phosphate concentration in the plateau region (i.e., for $E > 300$ mV), but the reaction order decreases with decreasing potential in the Tafel region. Also for $E \geq 400$ mV the dissolution current is independent of pH over the range $4 \leq$ pH ≤ 11.

Discussion

Figure 11 is an attempt to represent the different stages of oxidation and dissolution of UO_2 in phosphate-containing solutions. As previously determined in sulphate (1), and sulphate plus carbonate (4) solutions, the anodic oxidation of UO_2 proceeds in two stages.

The initial, fast stage of film formation, reaction [1] of Fig. 11, produces a layer of $UO_{2.33}$, approximately 4 nm thick,[1] in 10 s (Fig. 6).

[1] $UO_2 + 0.33H_2O \rightarrow UO_{2.33} + 0.66H^+ + 0.66e$

Under voltammetric conditions (Fig. 1) this process is preceded, in the potential range -600 mV $< E < 0$, by the formation of a very thin layer of undetermined composition, UO_{2+x}. It is likely that, under potentiostatic conditions, a layer of UO_{2+x} is also formed prior to further oxidation to $UO_{2.33}$. However, at the potential of 300 mV at which most of our studies were performed, the experimental techniques employed cannot resolve UO_{2+x} formation.

During the second, slower stage of film growth, the $UO_{2.33}$ layer thickens, and is partially oxidized to $UO_{2.5}$. Although not

[1]Film thicknesses are calculated assuming an initial composition of $UO_{2.33}$ and a final composition of $UO_{2.67}$. The volume per uranium atom is 0.0398 nm^3 for $UO_{2.33}$ and 0.0555 nm^3 for $UO_{2.67}$. These volumes are calculated by dividing the unit-cell volume with the number of uranium atoms per unit cell (4).

Can. J. Chem. Downloaded from www.nrcresearchpress.com by 213.222.148.141 on 09/07/12
For personal use only.

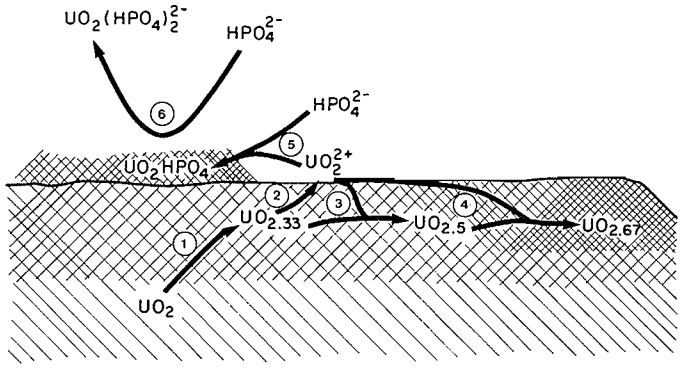

FIG. 11. Schematic of the mechanism of anodic film growth and dissolution of UO_2 in phosphate-containing solutions.

demonstrated in this paper, it is likely that $UO_{2.5}$ is simply a precursor (after a sufficient duration of oxidation) to the eventual formation of $UO_{2.67}$ as shown to occur in sulphate solutions (1). This second stage of film growth appears to be a recrystallization, because a significant structural rearrangement is required to convert the densely packed fluorite structure of $UO_{2.33}$ to the more open orthorhombic structure of $UO_{2.67}$. Since this second stage of oxidation is not observed when dissolution becomes extensive (Fig. 6) we have suggested previously (1) that dissolution and recrystallization proceed via a common intermediate and hence are in competition. In terms of Fig. 11, this represents a competition between reactions [2] and [5] (dissolution) and [2] and [3] (recrystallization). The nature of this intermediate has not been determined. It is assumed to be a UO_2^{2+} species, produced from the $UO_{2.33}$ layer and still partially coordinated to the electrode surface. This intermediate is then incorporated into the recrystallized oxide film;

$$[2] \quad UO_{2.33} + 0.33H^+ \rightarrow (UO_2^{2+})_{ads} + 0.33OH^- + 1.33e$$

$$[3] \quad (UO_2^{2+})_{ads} + 3UO_{2.33} + H_2O \rightarrow 4UO_{2.5} + 2H^+$$

Variations in phosphate concentration have no effect on the fast, initial film growth process, as previously demonstrated for carbonate (4). This is so even at the highest phosphate concentration employed, 0.5 mol L^{-1}. The formation of the $UO_{2.33}$ layer proceeds by the inclusion of oxide ions (O^{2-}) at interstitial sites in the UO_2 lattice, and hence is unaffected by the presence of complexing anions, such as phosphate and carbonate.

Since the second stage of film growth is in competition with dissolution, we would expect the addition of complexing anions, such as phosphate, to have an impact on the rate and extent of $UO_{2.5}/UO_{2.67}$ formation. The data of Fig. 6 show that the second stage of film growth can be prevented for $[PO_4]_T > 0.1$ mol L^{-1} and significantly retarded at a concentration of 0.1 mol L^{-1}. This is confirmed by the XPS data of Fig. 4. By comparison, in carbonate solutions the second stage of film growth is prevented for carbonate concentrations greater than $\sim 10^{-3}$ mol L^{-1}. This difference is consistent with the dissolution currents of Fig. 8, which show a much larger impact of carbonate than phosphate.

Compared to the behaviour in sulphate solutions, Fig. 8, phosphate is observed to accelerate dissolution over the potential range $200 < E < 380$ mV, but to inhibit the process for $E > 380$ mV. The equilibrium potential for the overall dissolution reaction

$$[4] \quad UO_2 \rightleftarrows UO_2^{2+} + 2e$$

will be decreased by complexation of the dissolution product

$$[5] \quad UO_2^{2+} + nA^- \overset{K}{\rightleftharpoons} UO_2A_n^{(n-2)-}$$

where K is the equilibrium constant. Thus, the extent by which the equilibrium potential for reaction [4] is shifted to more negative values, and hence the potentials at which dissolution is first observed will be determined by the value of K. On this basis, the observation of dissolution currents at lower potentials in phosphate than in sulphate is understandable, given the relative values of K for the specific equilibria involved

$$[6] \quad UO_2^{2+} + SO_4^{2-} \rightleftarrows UO_2SO_4(aq) \qquad (\log K = 2.9 \pm 0.5)$$

$$[7] \quad UO_2^{2+} + HPO_4^{2-} \rightleftarrows UO_2HPO_4(aq) \qquad (\log K < 8)$$

$$[8] \quad UO_2^{2+} + 2HPO_4^{2-} \rightleftarrows UO_2(HPO_4)_2^{2-} \qquad (\log K < 19)$$

The values of K are taken from the critical evaluation of Lemire and Tremaine (7). Complexation of UO_2^{2+} by carbonate is stronger than by phosphate and, hence, carbonate would cause dissolution of UO_2^{2+} even at lower potentials, as observed in Fig. 8.

The eventual inhibition of dissolution at higher potentials in phosphate solutions, Figs. 8 and 9, can be attributed to the stability of solid uranyl phosphates

$$[9] \quad (UO_2)_3(PO_4)_2 + 2H^+ \rightleftarrows 3UO_2^{2+} + 2HPO_4^{2-} \qquad (\log K = -24 \pm 3)$$

$$[10] \quad (UO_2)_2(HPO_4)_2 \rightleftarrows 2UO_2^{2+} + 2HPO_4^{2-} \qquad (\log K = -23 \pm 2)$$

$$[11] \quad UO_2HPO_4 \rightleftarrows UO_2^{2+} + HPO_4^{2-} \qquad (\log K = -12.33 \pm 0.06)$$

Here values of K for equilibria [9] and [10] are from ref. 7 and that for equilibrium [11] is from ref. 12. Our attempts to identify the "uranyl phosphate" layer formed in our experiments by XPS were only partially successful, due to redissolution of the layer during transfer of our electrode from cell to spectrometer vacuum chamber. However, the electrochemical evidence for the presence of a partially passivating surface layer (Figs. 1, 2, and 9) is overwhelming, and the dissolution of this layer eventually controls the overall process for $E > 300$ mV, Fig. 9.

The steady-state dissolution currents of Fig. 9 show two distinct regions: a Tafel region with a slope close to 60 mV^{-1}; and a region, at higher potentials, where the dissolution current is independent of potential and first order with respect to $[PO_4]_T$, Fig. 10. At these high potentials, if we assume the surface phase present is UO_2HPO_4, we can write the dissolution reaction as

$$[12] \quad UO_2HPO_4 + HPO_4^{2+} \rightarrow UO_2(HPO_4)_2^{2-}$$

corresponding to reactions [5] and [6] in Fig. 11. The data of Fig. 10 show that the thickness of the uranyl phosphate layer increases with potential in the plateau region of Fig. 9. This increase in thickness leads to an electric field in the surface film which does not vary with potential, thereby making the film dissolution/film replacement process potential-independent.

Can. J. Chem. Downloaded from www.nrcresearchpress.com by 213.222.148.141 on 09/07/12
For personal use only.

As written, this reaction is independent of pH, in agreement with our observations, which show that the dissolution current is independent of pH over the range $4 \leq pH \leq 11$. This suggests that the nature of the film present on the electrode surface does not vary with pH. This is not surprising since $UO_2(HPO_4)_2^{2-}$ is the predominant solution species over this whole pH range (11).

The 60 mV^{-1} slope obtained in the Tafel region of Fig. 9 indicates a direct, two-electron transfer process. Such processes are statistically unlikely. In the present case, it is probable that the two-electron process arises as a consequence of the stability of the "uranyl phosphate" surface layer. Any intermediate U^{5+} species formed must be rapidly, and irreversibly, converted into the U^{6+} species incorporated in the uranyl phosphate layer. Hence, in the Tafel region, dissolution proceeds via the reaction

$$[13] \quad UO_2 + HPO_4^{2-} \rightarrow UO_2HPO_4 + 2e$$

followed by reaction [11]. The intervening $UO_{2.33}$ layer exerts no kinetic influence on the dissolution process under steady-state conditions. Its rate of conversion to UO_2^{2+} (reaction [2]) is balanced by its rate of replacement (reaction [1]). Consequently, the overall charge transfer process can be taken as reaction [13].

The decrease in reaction order as the potential decreases, Fig. 10, is consistent with a switch at lower potentials from rate-control by chemical reaction [12] to rate-control by electrochemical reaction [2]. Since steady-state measurements were difficult to make below $E = 200$ mV, we did not measure the reaction order in the true Tafel region, where it would be expected to approach zero as the charge-transfer reaction, [2], assumed total rate control.

Summary

The anodic dissolution of UO_2 in phosphate solutions proceeds by the same basic mechanism as that observed previously in sulphate and carbonate solutions, except that the dissolution rate is limited at more anodic potentials (>300 mV) by the presence of a uranyl phosphate layer. This layer is formed by an irreversible, two-electron, charge-transfer process that controls the dissolution at potentials <200 mV. At potentials >300 mV, the dissolution process is controlled by chemical dissolution of the uranyl phosphate layer and is first order in total phosphate concentration.

1. S. SUNDER, D. W. SHOESMITH, M. G. BAILEY, F. W. STANCHELL, and N. S. MCINTYRE. J. Electroanal. Chem. **130**, 163 (1981).
2. S. SUNDER, D. W. SHOESMITH, M. G. BAILEY, and G. J. WALLACE. J. Electroanal. Chem. **150**, 217 (1983).
3. D. W. SHOESMITH, S. SUNDER, M. G. BAILEY, and D. G. OWEN. *In* Passivity of metals and semiconductors. *Edited by* M. Froment. Proc. 5th Intern. Symp. on Passivity. Bombannes, France. Elsevier, Amsterdam. 1983. p. 125.
4. D. W. SHOESMITH, S. SUNDER, M. G. BAILEY, G. J. WALLACE, and F. W. STANCHELL. Appl. Surf. Sci. **20**, 39 (1984).
5. D. W. SHOESMITH, S. SUNDER, L. H. JOHNSON, and M. G. BAILEY. Mat. Res. Soc. Symp. Vol. 50; Scientific Basis for Nuclear Waste Man. IX. *Edited by* L. O. Werme. 1985. p. 309.
6. S. SUNDER, D. W. SHOESMITH, L. H. JOHNSON, G. J. WALLACE, M. G. BAILEY, and A. P. SNAGLEWSKI. Mat. Res. Soc. Symp. Vol. 84 on Scientific Basis for Nuclear Waste Man. X. *Edited by* J. K. Bates and W. B. Seefeldt. 1986. p. 103.
7. R. J. LEMIRE and P. R. TREMAINE. J. Chem. Eng. Data, **25**, 361 (1980).
8. L. H. JOHNSON, D. W. SHOESMITH, G. E. LUNANSKY, M. G. BAILEY, and P. R. TREMAINE. Nucl. Technol. **56**, 238 (1982).
9. N. S. MCINTYRE, S. SUNDER, D. W. SHOESMITH, and F. W. STANCHELL. J. Vac. Sci. Technol. **18**, 714 (1981).
10. S. SUNDER, D. W. SHOESMITH, G. J. WALLACE, and M. G. BAILEY. Unpublished results.
11. D. LANGMUIR. Geochem. Cosmochim. Acta, **42**, 547 (1978).
12. M. MARKOVIĆ and N. PAVKOVIĆ. Inorg. Chem. **22**, 978 (1983).

Can. J. Chem. Downloaded from www.nrcresearchpress.com by 213.222.148.141 on 09/07/12
For personal use only.

Archaeometry of medieval Islamic glazed ceramics from North Yemen

JESSICA R. HALLETT AND MICHAEL THOMPSON[1]
Department of Chemistry, University of Toronto, 80 St. George Street, Toronto, Ont., Canada M5S 1A1

AND

EDWARD J. KEALL AND ROBERT B. MASON
West Asian Department, Royal Ontario Museum, 100 Queen's Park Crescent, Toronto, Ont., Canada M5S 2C6

Received October 17, 1986[2]

JESSICA R. HALLETT, MICHAEL THOMPSON, EDWARD J. KEALL, and ROBERT B. MASON. Can. J. Chem. **66**, 266 (1988).

Microscopic examination and electron microprobe analysis were employed to determine the materials and techniques used to decorate ten glazed types of medieval Islamic ceramics from North Yemen. Eight types were underglaze-painted, one was slip-painted, and one was monochrome glazed. The glazes were of two compositions, soda–silica and lead oxide – silica with annealing temperatures of approximately 835 and 640°C, respectively. The colourants used in the glazes and paints were cobalt (blue), iron (green), copper (green and blue), and antimony (yellow). Where clay slips or slip-paints were present, alumina enrichment of the glaze had occurred during application or firing, and pigment-paints on top of slip grounds masked enrichment. The Mellor ratio for the lead glazes ranges from 0.68 to 0.74 and is well above the acceptable safety limit of 0.5.

JESSICA R. HALLETT, MICHAEL THOMPSON, EDWARD J. KEALL et ROBERT B. MASON. Can. J. Chem. **66**, 266 (1988).

On a utilisé des examens microscopiques et des analyses à l'aide d'une micro-sonde électronique pour déterminer la nature des matériaux et des techniques qui ont été utilisés pour décorer dix types de céramiques islamiques médiévales émaillées provenant du Yémen du Nord. Huit types avaient été peints sous la glaçure, un avait été engobé et un portait une glaçure monochrome. Les glaçures sont de deux compositions, soude/silice et oxyde de plomb/silice, et les températures de recuisson étaient respectivement de 835 et de 640°C. Les colorants utilisés dans les glaçures et les peintures sont le cobalt (bleu), le fer (vert), le cuivre (vert et bleu) et l'antimoine (jaune). Dans les cas où des engobes d'argile ou des peintures par engobage sont présents, un enrichissement de l'aluminium de la glaçure s'est produit soit durant l'application ou durant la cuisson et les pigments de peinture présents sur les masses d'engobage masquent l'enrichissement. Dans les glaçures de plomb, le rapport de Mellor varie de 0,68 à 0,74 et se trouve bien au-dessus de la limite de 0,5 qui est considérée comme sécuritaire.

[Traduit par la revue]

Can. J. Chem. Downloaded from www.nrcresearchpress.com by 213.222.148.141 on 09/07/12
For personal use only.

Introduction

The Yemen Archaeological Project is concerned with the history and culture of a medieval Islamic university town, Zabid, and its interaction with neighboring settlements and the outside world, from A.D. 700 to 1750 (1). Zabid is 25 km inland, half-way between the Red Sea and the Yemeni highlands, on the Tihamah coastal plain. In the absence of any previous systematic archaeological work in the region, the initial surface reconaissance involved collection of pot sherds from abandoned sites in order to establish a ceramic typology, as a way of determining the nature, location, and period of settlements in the region. Sherds (2400) were collected and classified from a total of 73 sites within the 100 by 70 km study area. Almost all of the pottery is considered to be of local manufacture, and can be divided into separate *types* according to the colour of the fired clay, shape, and surface decoration treatment. The pottery can be tentatively dated by association with import pieces from other countries, such as 15th century "Ming" blue-and-white porcelain or 13th century Yuan celadons.

Neutron activation analysis of the clay bodies of 20 ceramic types supported the hypothesis that the ceramics were manufactured in the Tihamah coastal plain of Yemen (2). Petrographic analysis has indicated the presence of at least two production centres for the material, Hays and Zabid (3). Similar types appear to have been manufactured at both places in the heyday of the region between 12th–15th centuries, with Hays emerging as the dominant pottery producer once Zabid ceased to be a major administrative centre of the ruling dynasties.

Stylistically, there are no precise parallels for the Yemeni ceramics in the previously documented collections of Islamic pottery. In order to improve the initial visual classification of the material, it was considered essential to determine the physical components of decoration (glaze, slip, paint, etc.), their composition and order of application, and the firing temperature and kiln atmosphere used. Hence, consistency of composition among different types could indicate contemporaneity, and whether the glazing traditions remained constant throughout this 600 year period.

In the present paper, the application of electron microprobe analysis (EMPA) to selected Yemeni glaze samples is described. The advantages of this technique include the ability to obtain quantitative cross-sectional information, avoiding possible problems associated with glaze surface alteration caused by weathering, or by volatilization of components during manufacturing (4).

Experimental

(a) Microscopic analysis

Whole sherds were examined under a binocular microscope to observe the surface structure of the glaze, the state of preservation, degree of crazing[3] or peeling,[4] colour of the glazed areas, and presence of inclusions and of gases trapped in the glaze. Polished thin sections of two sherds per type were examined in reflected and transmitted light under a polarizing microscope to determine the components of decoration, size of slip and pigment particles, degree of vitrification[5] and of bonding between the glaze, slip, and body.

(b) Sample preparation

Resin impregnated polished thin sections of sherds from each of ten

[1]Author to whom correspondence should be addressed.
[2]Revision received October 9, 1987.

[3]Shrinkage cracks caused when glaze shrinks more than clay body; glaze is in tension and body in compression.
[4]Glaze separates from clay body; glaze is in compression and body in tension.
[5]Point at which raw materials fuse to form a *glass*.

TABLE 1. Geological standards

Soda–silica glaze		Lead oxide – silica glaze	
Standard	Element	Standard	Element
Scapolite	Si, Ca, Na, Cl	Crocoite	Pb
Orthoclase	K	Amphibole	Si, Al, Ti, Fe, Mg, Ca, Na, K
Pyroxene	Al, Mg, Fe, Ti		
Doped troilite	Co, Cu	Chalcopyrite	Cu

ceramic types were prepared as follows. Small slivers of the glaze and body were removed from the sherds using a diamond impregnated steel saw perpendicular to the glaze surface. The samples were impregnated with epoxy resin, and mounted on glass slides. This section was cut and ground to 30 μm using a thin section grinder, followed by treatment with 1000 mesh silicon carbide grains, and finally polished with 1 μm diamond compound on a nylon cloth.

(c) Electron microprobe analysis

Electron microprobe analyses were performed using an ETEC Autoprobe (ETEC Corp., USA) with an energy dispersive method of X-ray detection. A thin layer of carbon was vacuum deposited on the sample to prevent charging of local areas of the surface and subsequent distortion and deflection of the electron beam. The accelerating voltage was 20 kV; the probe current, approximately 200 picoamperes; take-off angle, 38°; beam size, 2 μm; and counting time, 100 s. Twelve elements were determined and the data were reduced with full ZAF correction. For Pb, the M α line was used; for Sn and Sb, the L α line; and for all other elements, the K α lines. Areas that appeared to be optically homogeneous glass, free from inclusions and devitrification products, were selected for analysis. The counts were checked throughout the analysis to detect wide variations which could indicate inhomogeneity. In addition to using a low probe current, the sample was slightly moved every 25 s to avoid problems associated with diffusion of the more mobile ions, like Na, under the effect of the beam. At least three analyses were made of the glaze, pigment-paint in solution with the glaze, or pigment particle. Elemental concentrations are reported here as equivalent oxide weight percent concentrations.

Peak overlaps occur with the EDS method which the software at our disposal could not resolve, in particular, the overlap of Pb and S. Hence, these two elements could not be analysed simultaneously. For Type J with a soda–silica glaze coloured with copper, the concentration of S was sought owing to the probability the pigment was CuS. In the case of the lead oxide – silica glaze of Type A, also coloured with a Cu pigment, Pb was determined as it was important to our understanding of the basic glaze composition. However, sulphur is usually present only in small concentrations in glazes owing to vaporization during firing (5).

Finally, the concentrations of the glass-forming oxides and colourants were not consistently similar to any one glass or mineral standard available. The standards used are listed in Table 1.

Results and discussion

Microscopic examination was used to refine the descriptions of the potting process for the ten types (Table 2). The process consists of the manufacture of a clay body, and the application of a slip, paint, and glaze. A slip is a mixture of clay in water and can be applied all over the surface as a ground for painting. Paint is either a slip-paint, where a slip is brushed on as a design, or a pigment-paint where either common ores, earthy materials, or ground coloured glass, with water as a vehicle, are used. The painted design can be applied beneath a transparent glaze (underglaze-painted) with or without colouring, or can be painted onto the wet glaze. A third method involving application of the paint on top of a vitrified glaze which is fixed in a second firing was not observed.

Microscopic examination identified four methods of glazed decoration (Fig. 1). Type A was "monochrome glazed"; types B, C, D, E, F, and I were "underglaze-painted" on a white slip ground over a red body; types G and H were underglaze-painted directly on a white clay body; and type J was underglaze "slip-painted".

For all ceramic types with pigment-painted decoration, the colourant transferred into solution with the glaze during firing, and only in green and brown paints were pigment particles identified. Where a slip ground was observed in types defined as underglaze-painted, the glaze is well fused with the slip. But, the slip poorly adheres to the body and is the weakest interface in the structure. Thus, the only function of an overall slip is to provide a white ground for painting.

The analyses for the glazes and paints are reported in Table 3. The sets of analyses are referred to by type, name, and number. In ancient times borax was not used in glazes. Boron could not be detected with the facilities available, but the fact that the analytical totals are reasonably close to 100% suggests that boron cannot be present in substantial amounts in these medieval glazes.

The general composition of all glaze samples with silica and soda as their major constituents (types D–J) are approximately 12 parts SiO_2, 2 parts Na_2O, and 1 part each of Al_2O_3, FeO, MgO, CaO, K_2O. Potash and soda are useful fluxes for a wide range of temperatures, however the alkaline earths, calcia, and magnesia are active fluxes only at high temperatures (6). The melting point of a soda–silica eutectic mixture (Na_2O–$4.579SiO_2$) with 18.4% soda and 81.6% silica, comparable to this general composition, is 860°C (7). The average of the calculated fusion temperature for these glazes, using West and Gerow's (5) coefficients, was 835 ± 24°C. Thus, these glazes should have been fired at a temperature of approximately 813°C for fusion of the glaze.

Silica was probably added to the glaze batch in the form of quartz sand, but no consistent stoichiometric relationships between Na_2O, K_2O, CaO, or MgO were observed that could conclusively identify plant ash ($Na_2CO_3.10H_2O + K_2CO_3.2H_2O$), dolomite ($CaCO_3.MgCO_3$), or carnallite ($MgCl_2.KCl.6H_2O$) as raw materials. The small concentrations of chlorine and sulphur detected suggest that part of the alkalis were added to the frit as chlorides and sulphides.

Calculations were performed to determine the coefficient of linear expansion for each of the glaze samples, using the empirical values established by English and Turner (6). The relationship between the thermal expansion coefficient of glass and composition is expressed by the Winkelmann and Shott equation (16):

$$P = p_1x_1 + p_2x_2 + p_3x_3$$

where P is the volume coefficient of expansion, p_1 ... are the percentages of the constituent oxides of the glass, and x_1 ... are values for the volume coefficients of expansion of the oxides (from English and Turner). The linear coefficient of expansion is one-third of P.

Dayton (6) calculates the linear expansion of a typical ancient alkaline glaze to be $10.54 \times 10^{-6}\,cm\,°C^{-1}$. For the soda–silica glazes the linear coefficient of expansion varies from 7.1 to 9.1 $\times 10^{-6}\,cm\,°C^{-1}$. A typical earthenware body has a value of 7.8 $\times 10^{-6}\,cm\,°C^{-1}$ (6). In cases where the glaze has a smaller factor than the body, the glaze would be compressed and thus

Can. J. Chem. Downloaded from www.nrcresearchpress.com by 213.222.148.141 on 09/07/12
For personal use only.

TABLE 2. Descriptions of ten types of Yemeni ceramics from microscopic examination of whole sherds, and of thin sections through glaze, paint, slip, and clay body

Type name	Clay*	Slip	Paint	Glaze
Monochrome glazed				
A. Monochrome Green	Red	No slip	No paint	Lead oxide – silica glaze, opaque green (CuO), abraded and pin-holed, partially devitrified, 0.07–0.12 mm thick
Underglaze-painted on white slip ground				
B. Green-on-White	Red	Continuous white clay slip, 0.04 mm thick	Green paint (CuO), pigment particles 0.02 mm in diameter	Lead oxide – silica glaze, colourless, abraded and pin-holed, partially devitrified, up to 0.07 mm thick
C. Green-on-Yellow	Red	Continuous white clay slip, 0.02 mm thick	Green paint (CuO), pigment particles 0.02 mm in diameter	Lead oxide – silica glaze, yellow (Sb_2O_3), slightly opaque, abraded and pin-holed, partially devitrified, 0.05–0.15 mm thick
D. Bleeding Green	Red	Continuous white clay slip, rich in quartz, 0.4–0.1 mm thick	Green paint (CuO), pigment particles 0.05 mm in diameter	Soda–silica glaze, transparent with yellow tinge, numerous bubbles, crazed and abraded, 0.11–0.20 mm thick
E. Brown-on-White	Red	Continuous white clay slip, rich in quartz, 0.08 mm thick	Brown pigment-paint, quartz grains in opaque ground mass, 0.05 mm thick	Soda–silica glaze, transparent with yellow tinge, numerous bubbles, crazed and abraded, pin-holing only above painted areas, 0.17 mm thick
F. Blue-on-White (red)	Red	Continuous white clay slip, rich in quartz, 0.08 mm thick	Blue paint (CoO), in solution with glaze	Soda–silica glaze, transparent (slight green tinge from FeO), numerous bubbles, crazed and abraded, 0.2 mm thick
I. Black-on-Blue	Red	Continuous white clay slip, quartz and mica inclusions, 0.04–0.08 mm thick	Black paint, opaque grains, non-vitreous, 0.05–0.08 mm thick	Soda–silica glaze, transparent turquoise (CuO) with green tinge from FeO, numerous bubbles, crazed and abraded, pin-holing above black paint only, 0.2 mm thick
Underglaze-painted on white clay body				
G. Blue and Green on White	White	No slip	Blue paint (CoO) and green stain (CuO?), in solution with glaze	Soda–silica glaze, transparent (slight green tinge from FeO), numerous bubbles, crazed and abraded, 0.1–0.16 mm thick
H. Blue-on-White	White	No slip	Blue paint (CoO), in solution with glaze	Soda–silica glaze, transparent (slight green tinge from FeO), numerous bubbles, crazed and abraded, 0.15 mm thick
Underglaze slip-painted				
J. Blue Tihamah	Red	No slip ground	White clay slip-paint, quartz and mica inclusions, 0.1 mm thick	Soda–silica glaze, transparent turquoise (CuO), numerous bubbles, crazed and abraded, 0.1–0.2 mm thick

*As designed by INAA (2).

grip the clay body (providing the tensile strength of the glaze is not exceeded). Hence, medieval Yemeni glaze technology is a definite advancement over the ancient composition.

Although soda in glazes acts as a strong flux, it has a very high coefficient of thermal expansion. In the case of the Yemeni glazes the coefficient is directly related to the concentration of soda. Glazes high in soda tend to craze, and are often soft and easily abraded (8). Re-examination of the glazes on the sherds themselves revealed that the degree of crazing discernable to the unaided eye reflects the extremes calculated (as noted by Lawrence (7)). The brilliance of the coloured soda–silica glazes and pigment-painted decoration can also be attributed to the high concentration of soda (9).

The blue pigment used in the blue painted designs is cobalt. The turquoise–green glaze of type I (Black-on-Blue) and the turquoise–blue glaze of type J (Blue Tihamah) are coloured with copper. The concentration of sulphur detected is too small to establish, on the basis of stoichiometry, that it is Copper Blue (CuS). However, one cannot rule out the possibility considering that sulphur could easily have vaporized during firing (5). Although both of these glazes are coloured with copper, they have slightly different colours. The iron oxide concentration in the type I glaze is higher (2.3%) than observed for type J (1.6%). This increased concentration of iron in the presence of an alkali glaze (9) is the reason for the green tinge in type I. The colourless glazes of types F, H (Blue-on-White) have a marked green tinge, unlike the glazes on types D, E (Bleeding Green; Brown-on-White), and have a higher FeO concentration than the latter. The green paint used in type D is also copper.

Rye and Evans (10) state that in order to characterize the compositional changes occurring in a glaze during firing, it would be necessary to have complete analytical data for glaze, slip, pigment, and body materials before firing. However, the nature of the decoration of the Yemeni ceramics provides a

Can. J. Chem. Downloaded from www.nrcresearchpress.com by 213.222.148.141 on 09/07/12
For personal use only.

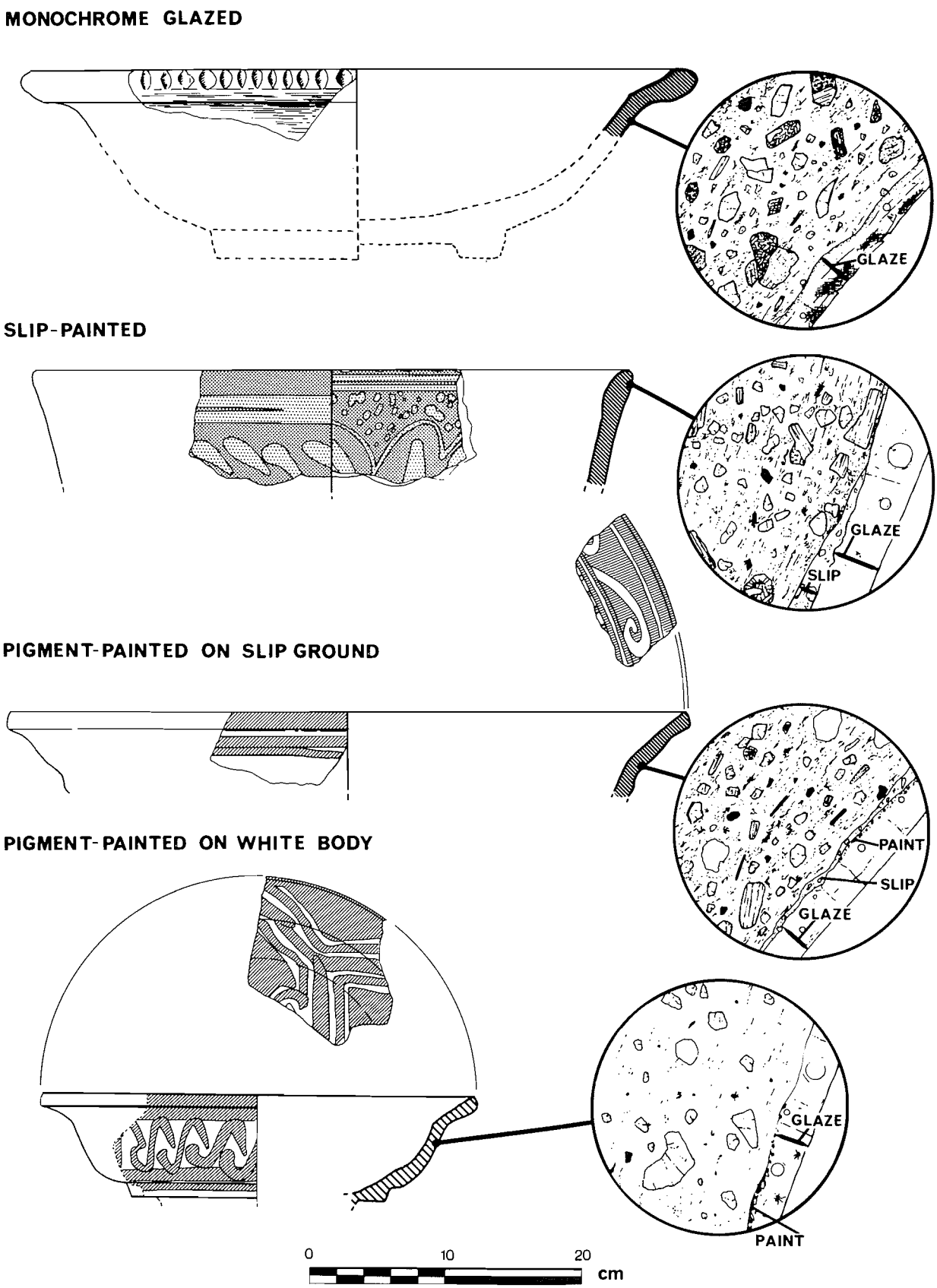

FIG. 1. Drawings of four methods of decorating Yemeni ceramics showing whole pottery sherd, vessel profile and reconstruction, and microscopic observation of decoration.

Can. J. Chem. Downloaded from www.nrcresearchpress.com by 213.222.148.141 on 09/07/12
For personal use only.

TABLE 3. Electron microprobe analysis of glazes and paints of eight types of Yemeni ceramics*

(*a*) Set 1

	Sample type and sherd number			
			D. Bleeding green	
Mineral composition	A. Monochrome green green glaze 33	C. Green-on-yellow yellow glaze 23	Clear glaze 30	Green paint 25
SiO_2	27.6±1.5	26.9±1.9	63±2	67.0±0.3
Al_2O_3	1.6±0.1	2.7±0.3	5.4±1.4	2.5±0.3
FeO	0.7±0.1	0.6±0.1	1.76±0.04	1.6±0.2
MgO	1.1±0.3	0.41±0.04	3.0±0.4	3.1±0.4
CaO	1.2±0.1	1.1±0.3	3.7±0.6	4.4±0.6
Na_2O	3.0±0.4	1.8±0.2	13.2±0.4	10.1±0.3
K_2O		0.25±0.09	3.6±0.2	3.23±0.03
TiO_2			0.30±0.08	0.34±0.01
Cl			0.72±0.06	0.5±0.1
CoO				
SnO_2	1.5±0.5	1.1±0.5		
CuO	1.2±0.2			2.3±0.2
PbO	61.0±1.1	62.2±1.8		
Sb_2O_5		0.8±0.3		
Total	98.9	97.0	94.7	95.0
coefficient of expansion ($\times 10^{-6}$ cm °C^{-1})	7.8	7.7	8.3	7.5
Fusion temperature (°C)	640	630	786	810

(*b*) Set 2

	Sample type and sherd number					
			F. Blue-on-White (red body)			
	E. Brown-on-White		Clear glaze		Blue paint	
Mineral composition	83	84	06	04	06	04
SiO_2	69.2±1.3	66.4±0.3	64±3	65.7±0.7	63.5±0.4	63±2
Al_2O_3	5.2±0.5	7.2±2.6	4.8±0.1	5.4±1.4	3.7±0.5	4.4±0.4
FeO	2.4±0.4	1.7±0.4	3.5±0.7	2.6±0.1	3.8±0.5	2.7±0.1
MgO	3.1±0.2	3.5±0.7	5.2±0.2	4.2±0.3	4.3±0.7	4.8±0.2
CaO	3.0±0.4	4.1±1.3	4.5±1.3	6.0±0.3	5.32±0.03	5.5±0.1
Na_2O	10.5±0.8	12.0±1.0	10.3±0.8	9.5±0.3	9.9±0.1	10.2±0.2
K_2O	3.29±0.03	3.4±0.3	3.5±0.3	3.6±0.2	3.38±0.09	3.0±0.10
TiO_2	0.3±0.1	0.36±0.08	1.3±0.6	0.6±0.08	0.52±0.06	0.7±0.1
Cl	0.41±0.03	0.6±0.2			0.17±0.07	0.19±0.07
CoO					0.42±0.05	0.5±0.2
SnO_2						
CuO						
PbO						
Sb_2O_5						
Total	97.4	99.3	97.6	97.7	95.0	95.5
Coefficient of expansion ($\times 10^6$ cm °C^{-1})	7.1	7.1	7.4	7.3	7.4	7.4
Fusion temperature (°C)	844	860	857	877	827	843

Can. J. Chem. Downloaded from www.nrcresearchpress.com by 213.222.148.141 on 09/07/12
For personal use only.

TABLE 3 (*concluded*)

(*c*) Set 3

Mineral composition	Sample type and sherd number				
	H. Blue-on-White clear gaze 111	I. Black-on-Blue turquoise–green glaze		J. Blue Tihamah turquoise–green glaze	
		105	104	No slip 07	Slip 07
SiO_2	66±2	66.4±0.3	64±3	65.7±0.7	63.5±0.4
Al_2O_3	5.6±0.9	5.5±0.3	6.9±0.6	3.2±0.5	3.9±0.2
FeO	2.4±0.4	2.34±0.06	2.3±0.1	1.51±0.08	1.7±0.1
MgO	3.9±0.1	4.2±0.6	3.6±0.2	4.6±0.1	4.8±0.4
CaO	3.9±0.3	4.5±0.2	4.1±0.3	3.4±0.1	3.5±0.1
Na_2O	15.0±0.8	13.5±0.3	12.73±0.06	16.4±0.6	16.2±0.7
K_2O	2.8±0.1	2.91±0.03	3.8±0.2	2.3±0.1	2.5±0.3
TiO_2	0.5±0.1	0.34±0.05	0.39±0.08	0.43±0.03	0.30±0.09
Cl	0.4±0.2	0.71±0.04	0.66±0.09	0.9±0.3	0.7±0.1
CoO					
SnO_2					
CuO		0.71±0.04	0.66±0.09	1.6±0.7	1.5±0.6
PbO					
Sb_2O_5					
Total	100.8	98.5	99.5	97.9	99.6
Coefficient of expansion ($\times 10^{-6}$ cm °C^{-1})	9.0	8.5	8.5	9.1	9.1
Fusion temperature (°C)	840	829	834	816	816

*Values are reported as percent equivalent oxide concentrations (where no value is given component was not detected above two standard deviations). Also shown are linear coefficients of expansion and temperature of fusion values.

means of establishing certain changes without prior knowledge of the original materials. For example, type J (Blue Tihamah) has a slip-painted decoration and samples of this type provide a direct means of determining how glaze and slip react, since the slip is discontinuous in this case. Alumina concentration is higher in the glaze area with slip (3.9%) than where the glaze was in contact with the body (3.2%).

All of the underglaze-painted ceramics with red bodies have an overall white slip to mask the clay colour, and enhance the pigment-painted decoration. The glazes of these types are consistently higher in alumina than types with white bodies which do not require an overall slip. The alumina concentration is higher in glaze directly above a slip than in areas where pigment-paint had been applied on top of the slip prior to the glaze. For example, in type D (Bleeding Green) the alumina concentration for the colourless glaze is 5.4% and for the green paint, 2.5%. Similarly, for type F (Blue-on-White) the alumina concentration for the clear glaze is 4.8% and for the blue paint, 3.7%. Thus, the level of alumina enrichment appears to be highest where an overall slip is present, masked by a pigment-paint on top of a slip, and lowest where no clay slip is present. It is not possible to extrapolate from this observation whether alumina migration occurred during application of the aqueous glaze mixture, or during firing.

Alumina enrichment is also observed for glazes applied over white firing pottery (types G, H). Neutron activation analysis determined the Al content in white pottery to be as high as 30%, in contrast to 8% for red pottery (2). Unfortunately, it is too difficult to cleanly separate slip from glaze in sufficient quantity to determine its trace element concentration for comparison with the data available for white pottery.

In general all glaze samples with lead oxide and silica as their major constituents (types A, C) have from approximately 1 part silica to 2 parts lead oxide. The calculated average temperature of fusion for these glazes is 640°C; this is 200°C lower than for the soda–silica glazes. The linear coefficient of thermal expansion is approximately 7.8×10^{-6} cm °C^{-1} for these glazes. Here too, the coefficient is directly related to the concentration of soda.

The lead oxide – silica glazes are mostly devitrified. This suggests that the glazes were cooled too slowly, or not fired at a sufficiently high temperature for annealing (just below the liquidus temperature the rate of crystal growth in glasses reaches a maximum). Since these ceramics were probably made at the same workshop as those with soda–silica glazes, it seems likely that a higher kiln temperature than necessary was used, along with too long a cooling period. Owing to devitrification, the glazes are more heterogeneous and the three analyses of each sample are not as consistent as observed for the soda–silica glazes.

The green colourant in the paints of types B, C (Green-on-Yellow; Green-on-White), and in the glaze of type A (Monochrome Green) is copper. The source of the yellow colouring of the glaze in Type C is antimony (lead antimonate). Tin was detected in these glazes but not in the soda–silica glazes. The intense colouring of the glazes and pigment-paints indicates that an oxidizing kiln atmosphere was used since lead glazes, if reduced, will turn grey or black (11).

The lead content in these glazes is sufficiently high that consistent use of these vessels for food storage and consumption could result in lead poisoning. Calculation of the Mellor ratio for the Yemeni glazes gives values from 0.68 to 0.74, above the

Can. J. Chem. Downloaded from www.nrcresearchpress.com by 213.222.148.141 on 09/07/12
For personal use only.

acceptable limit of 0.5 (8).[6] The solubility of lead into food or beverages stored in pottery is dependent on the type of lead compound used, its particle size, and the nature, pH and temperature of the chemical compounds present in the food or beverage. An increase in surface area and a decrease in lead compound particle size will increase lead solubility (12). The crazing due to the high soda content, and pitting due to escaping gases in the Yemeni glazes, would enhance the possibility of lead dissolving into the vessel contents. The presence of copper oxide in the paints and glazes of all of these types is also cause for concern, as a 2% addition of CuO to a low temperature lead glaze results in PbO release ten times that of the base glaze (8).

Conclusions

The results of this exploratory investigation have significantly extended understanding of glaze technology in medieval Yemen. What is apparent from the analysis of the pottery from this and other studies is that there was a viable ceramic industry, with a relatively wide variety of different decorative types being produced using four basic production techniques. Questions that are raised by the study involve comparison of the results with known data on ceramics from the high cultural centres of the Islamic world, notably from Egypt, Syria, Iraq, and Iran. Comparative data on Iranian ceramics is particularly significant. The "Monochrome Green", "Green-on-Yellow" and "Green-on-White" lead glazed ceramics are associated with Rasulid occupation of the region from the 13th–15th centuries. Contemporaneous Iranian lead glazes (13) contain much higher concentrations of tin oxide (13–20%) and lower concentrations of lead oxide (13–21%) than the Yemeni ceramics (less than 1% SnO_2, 52–62% PbO). However, Iranian glazes from the 9th–10th centuries (14) are similar to the Yemeni composition (less than 1% SnO_2, 28–36% PbO). Thus, the 13th–15th century Yemeni tradition of lead glazing may be perceived as similar to that of 9th–10th century Persia.

Lane (15) mentions that in the ninth century A.D., the potters of Samarkand (north of modern day Afghanistan) made the important discovery that "painted decoration, normally apt to "run" if the fluid lead glaze were applied over it, would stay if the metallic colouring agents were mixed with a paste of fine clay slip." The painted decoration in "Green-on-Yellow" and "Green-on-White" does not bleed in the lead glaze, and microscopic examination of thin sections of these types did not reveal the presence of clay in the paint. It has also been assumed that the tin present in Iranian glazes came into the region from the north, presumably by way of the Caucasus, as well as from the west (from Europe) and the east (from China) (11). Tin was detected in three Yemeni types. It is clear that, in the future, the composition of the glass-forming constituents and pigments identified must be compared with geological surveys of the area to determine whether these raw materials were locally available or imported. This investigation of the geology of the region, together with analysis of historic texts, may enhance our understanding of cultural diffusion, and how innovations in glaze technology migrated through the Middle East.

[6]Mellor ratio: $(RO + Al_2O_3)/RO_2 = 0.5$ maximum.

Acknowledgements

We are indebted to the Natural Sciences and Engineering Research Council of Canada for support (M.T.). The archaeological fieldwork was sponsored by the Royal Ontario Museum, and operated under license from the Office of Qadi Isma'il al-Akwa', General Organization for Libraries and Antiquities, Yemen Arab Republic. We are very grateful to C. Cermignani of the Department of Geology, University of Toronto, for valuable assistance with the analyses by the electron microprobe.

1. E. J. KEALL. World Archaeology, **14**, 378 (1983).
2. J. R. HALLETT, E. J. KEALL, V. VITALI, and R. G. V. HANCOCK. J. Radio-Nucl. An. Chem. Articles, **110**, No. 1, 293 (1987).
3. R. B. MASON, J. R. HALLETT, and E. J. KEALL. Proceedings of the International Symposium on Archaeometry, Athens. 1986.
4. I. C. FREESTONE. Archaeometry, **24**, 99 (1982).
5. R. WEST and J. V. GEROW. Trans. J. Brit. Ceram. Soc. **70**, 265 (1971).
6. J. DAYTON. Minerals, metals, glazing and man. Geo. G. Harrap and Co. Ltd., London. 1968. Chapt. 4. pp. 40–45.
7. W. G. LAWRENCE and R. R. WEST. Ceramic science for the potter. Chilton Book Co., Radnor, PA. 1982.
8. R. A. EPPLER. Glass: science and technology. *In* Glass forming systems. Vol. 1. *Edited by* D. R. Uhlmann and N. J. Kreidl. Academic Press, Toronto. 1983. Chapt. 4. pp. 301–310.
9. W. D. KINGERY and P. VANDIVER. Ceramic masterpieces. Free Press, New York. 1986. Chapt. 14. pp. 269–277.
10. O. S. RYE and C. EVANS. Smithsonian Contributions to Anthropology. **21**, 147 (1976).
11. J. W. ALLAN. Iran, **11**, 111 (1973).
12. D. DJURIC. Proceedings of the International Conference on Ceramic Foodware Society. World Health Organization, Geneva. 1974. pp. 40–45.
13. J. W. ALLAN, L. R. LLEWELLYN, and F. SCHWEIZER. Archaeometry, **15**, 165 (1973).
14. R. E. M. HEDGES and P. R. S. MOOREY. Archaeometry, **17**, 25 (1975).
15. A. LANE. Early Islamic pottery. Faber and Faber, London. 1947. Chapt. 4. p. 17.

Can. J. Chem. Downloaded from www.nrcresearchpress.com by 213.222.148.141 on 09/07/12
For personal use only.

The influence of water on the spectroscopic properties of a liposoluble magnesium porphyrin

CAMILLE CHAPADOS[1]

Centre de recherche en photobiophysique, Université du Québec à Trois-Rivières, Trois-Rivières (Qué.), Canada G9A 5H7

AND

DENIS GIRARD AND MICHEL RINGUET[1]

Département de chimie-biologie, Université du Québec à Trois-Rivières, Trois-Rivières (Qué.), Canada G9A 5H7

Received August 7, 1987

CAMILLE CHAPADOS, DENIS GIRARD, and MICHEL RINGUET. Can. J. Chem. **66**, 273 (1988).

Complexation of water by chlorophyll molecules in natural photosynthetic processes is a matter of great interest. In the present work the influence of water on a model porphyrin, magnesium 2,7,12,17-tetrahexyl-3,8,13,18-tetramethyl porphin (MgTHTMP) has been studied by infrared spectroscopy. A CCl_4 (spectroscopic grade) solution of MgTHTMP showed two small bands in the 3600 cm^{-1} infrared region. These bands are assigned to ν_3 and ν_1 vibrations of water coordinated to the Mg atom. For MgTHTMP in the solid state, either deposited on an infrared plate or suspended in a Nujol film, none of the OH bands is observed. An elemental analysis confirmed that the solid porphyrin was anhydrous. This evidence indicates that while no water is complexed with MgTHTMP in the solid state, this porphyrin is highly hygroscopic in a CCl_4 solution and will easily complex with the few water molecules (less than 0.01%) present in the spectro grade solvent by forming a coordinate bond between the central magnesium atom and the oxygen of water. Several other metallic porphyrins in CCl_4 solutions have been studied for comparison with the Mg porphyrin. The spectra of these substances did not show any complexed water. A model of the H_2O–MgTHTMP interaction is given and the implication of this model on the aggregation states of chlorophyll will be discussed.

CAMILLE CHAPADOS, DENIS GIRARD et MICHEL RINGUET. Can. J. Chem. **66**, 273 (1988).

Le complexation de l'eau par des molécules de chlorophylle, dans des processus naturels, est une question fondamentale. Dans le présent travail, on a étudié l'influence de l'eau sur une porphyrine modèle, la tétrahexyl-2,7,12,17 tétraméthyl-3,8,13,18 porphine – magnésium (THTMPMg), en faisant appel à la spectroscopie infrarouge. Une solution de THTMPMg dans du CCl_4 (qualité spectroscopique) présente deux petites bandes dans la région de 3600 cm^{-1} de l'infrarouge. On a attribué ces bandes aux vibrations ν_3 et ν_1 de l'eau coordonnée à l'atome de Mg. Dans le cas du THTMPMg à l'état solide, soit déposé sur une plaque infrarouge soit suspendu dans le Nujol, on n'observe aucune de ces bandes. Une analyse élémentaire a permis de confirmer que la porphyrine solide est anhydre. Ces données indiquent que, même s'il n'y a pas d'eau complexée avec la THTMPMg à l'état solide, cette porphyrine en solution dans le CCl_4 est tellement hygroscopique qu'elle se complexe facilement avec les quelques molécules d'eau présentes (moins que 0,01%) dans le solvant de qualité spectroscopique en formant une liaison de coordinence entre l'atome de magnésium central et l'oxygène de l'eau. Pour fins de comparaison avec la porphyrine de Mg, on a aussi étudié plusieurs autres porphyrines métalliques en solution dans le CCl_4. Les spectres de ces substances ne présentent pas de bandes correspondant à de l'eau complexée. On présente un modèle de l'interaction H_2O–THTMPMg et on discute des implications de ce modèle sur les états d'agrégation de la chlorophylle.

[Traduit par la revue]

1. Introduction

In algae and higher plants, water is being oxidized by photosynthetic process to produce oxygen at the reaction center of photosystem 2. Some chlorophyll *a* (Chl *a*) molecules are present in this reaction center as well as in the reaction center of photosystem 1 and in the antenna chlorophyll. These Chl *a* molecules are situated in the chloroplast where water is abundant. The aggregation state of chlorophyll within these systems is known to vary. The influence of water on these aggregation states is not fully understood because water can make several types of bonding with the chlorophyll at different sites: i.e. with the Mg atom, and with the carbonyl groups. No experimental technique has given a definitive answer for the structures of these organizations.

Infrared spectroscopy has been used in several occasions to study the influence of water on the chlorophyll molecules (1–8). Typical ir spectra of some chlorophylls and some Chl derivatives have been obtained by Katz *et al.* (1). Most of the spectra taken in CCl_4 solutions showed a broad featureless band in the 3400 cm^{-1} ir region. This band has been assigned to the OH stretch band of bonded water. Efforts to remove the water from the chlorophyll samples were mostly unsuccessful.

An infrared study of chlorophyll–chlorophyll and chlorophyll–water interactions in organic solutions (2) has shown in the OH stretch region a complex set of bands comprising some sharp bands in the 3700 cm^{-1} region and a broad band with unresolved features in the 3300 cm^{-1} region. An effort to dry the solutions did not remove those bands entirely. Pheophytin *a* in CCl_4 showed some sharp bands at 3397, 3538, 3622, and 3690 cm^{-1}. On exchange with D_2O, the first two bands were displaced to lower frequencies and the last two were replaced by one at 3665 cm^{-1}. The 3538 cm^{-1} band was assigned to enolic chlorophyll *a*.

Solutions of chlorophyll made up in undried solvents showed a broad, medium intensity band centered at ~3400 cm^{-1} (3). This absorption maximum appears to include the bands of free water dissolved in the solvent (ν_1 at 3620 cm^{-1} and ν_3 at 3710 cm^{-1}), of water coordinated to Mg at 3380 and 3665 cm^{-1}, and of water hydrogen bonded to the coordinated water molecule. Codistillation with dry solvents removes water to the point that no appreciable absorption can be detected in the OH stretch region although the spectrum is not coincident with the base line.

When a solution of Chl *a* hydrate in dry CCl_4 was studied by ir spectroscopy (4), the spectrum contained several peaks assigned to the symmetric (3620 cm^{-1}) and anti-symmetric

[1]To whom correspondence may be addressed.

Can. J. Chem. Downloaded from www.nrcresearchpress.com by 213.222.148.141 on 09/07/12
For personal use only.

Can. J. Chem. Downloaded from www.nrcresearchpress.com by 213.222.148.141 on 09/07/12
For personal use only.

(3715 cm^{-1}) stretch of free water, to OH stretch of water coordinated to the Mg atom of Chl (3665 cm^{-1}), and to hydrogen bonded water (3380 cm^{-1}). Two shoulders at 3300 and 3440 cm^{-1} are assigned to carbonyl overtones. Dry Chl *a* in dry CCl_4 showed three small bands (3280, 3365, and 3450 cm^{-1}) which are assigned to either carbonyl overtones following Ballschmiter and Katz (2) or to residual hydrogen bonded water (less than 3% mol relative to Chl).

Solid samples of anhydrous and hydrated chlorophyll species showed a broad, mostly featureless band in the 3350 cm^{-1} region (5). Depending on the hydration conditions, the band is more or less intense and the position of the maxima is slightly different for each aggregation species.

Microcrystalline Chl *a* hydrate deposited on a germanium ATR plate showed in the infrared a large structureless band centered ~3150 cm^{-1} indicative of bonded water molecules (unpublished results). To remove water, the sample is placed in a high vacuum of 10^{-7} Torr for more than 72 h. This treatment gave an amorphous dried species that showed no bands in the OH region (6). The dryness of the sample was further substantiated by a test with SO_2 vapor that showed no reaction (unpublished results), whereas, in the presence of water, Chl *a* reacts with SO_2 to give pheophytin *a* (7).

The influence of water on mono- and multilayers of Chl *a* obtained by the Langmuir–Blodgett technique have been reported previously (7, 8). A fresh multilayer kept in a moist atmosphere showed in the infrared a broad band centered at 3400 cm^{-1} which disappears rapidly under a vacuum of 10^{-3} Torr (7). A fresh monolayer deposited on a germanium ATR plate and placed in the dry sample compartment of the spectrometer showed no band in the OH stretch region (8).

The only study of the interaction of water with another metallic porphyrin is an X-ray diffraction study on a magnesium tetraphenylporphyrin (MgTPP) made by Timkovich and Tulinsky (9). The presence of water was confirmed by density measurements carried out by flotation in aqueous silver nitrate solution. The lack of other studies is probably due to the insolubility of most porphyrin molecules in ir organic solvents.

In order to understand the interaction of water with the Mg atom in a porphyrin environment, we studied by ir spectroscopy a model molecule, a synthetic liposoluble magnesium porphyrin, MgTHTMP (Fig. 1), in which the absence of other polar functional groups would limit the interactions of water to the Mg atom site and to the π electron system of the chromophore. This work was intended to verify the assignments reviewed above and to complement our knowledge of H_2O–Mg interactions in chlorophyll.

Several samples were made of MgTHTMP (Fig. 1): a suspension in Nujol, several solutions in CCl_4 of different dryness conditions, a solution in a mixture of pyridine and CCl_4, and a solid sample exposed to different moisture conditions. For comparison, we have obtained the ir spectra of several other metallic porphyrin compounds. The results of these experiments will be given and a model of the interaction between water and MgTHTMP will be presented.

2. Experimental

2.1. Synthesis

The synthesis of THTMP was made following the method used by Smith and Bisset for the synthesis of tetrapentyltetramethylporphin (10). The synthesis of ZnTHTMP was made by incorporating zinc in THTMP by the acetate method (11). The MgTHTMP compound was obtained by the reaction of propioxymagnesium bromide on THTMP at low heating temperature (70–75°C) (12). All manipulations of this compound have been done under red light because solutions of MgTHTMP are sensitive to white light. The samples were dried in a vacuum desiccator over $CaCl_2$ before recording the spectra.

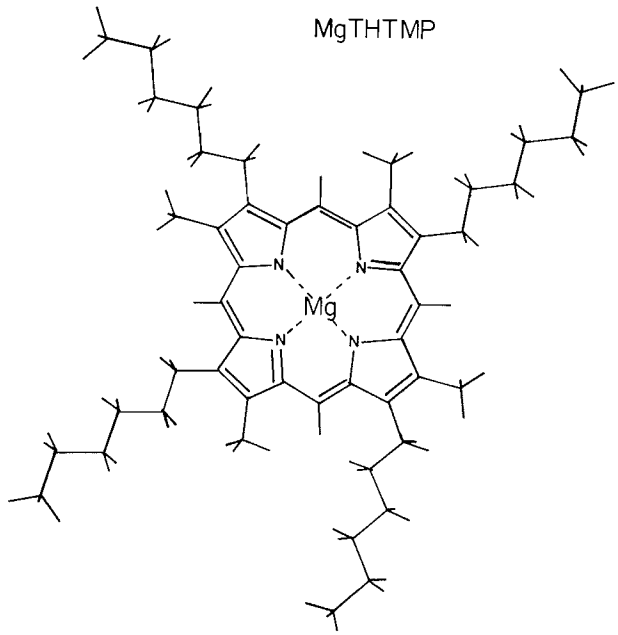

FIG. 1. Molecular model of MgTHTMP.

Elemental analyses were made by Guelph Chemical Lab., Guelph, Ont. and showed that these substances were pure and contained no water. *Anal.* calcd. for $C_{48}H_{68}N_4Zn$ (ZnTHTMP): C 75.54, H 9.05, N 7.03; found: C 75.22, H 8.94, N 7.31. *Anal.* calcd. for $C_{48}H_{68}N_4Mg$ (MgTHTMP): C 79.75, H 9.60, N 7.68; found: C 79.48, H 9.45, N 7.72.

2.2 Spectrum recording

The CCl_4 solutions of the porphyrin compounds were made using spectro grade solvent (Anachemia Chemicals Ltd.; water <0.01%) at a concentration of ~1×10^{-2} mol/L. The solutions were enclosed in a standard KBr cell with a pathlength of 1 mm. The Nujol suspension was made by the standard procedure. The solid sample was obtained from the CCl_4 solution in the following way: drops of the solution were put on a BaF_2 plate, when the solvent was evaporated, the plate was immediately transfered to an enclosed cell equipped with BaF_2 windows. Several spectra were taken successively. When no spectral modification was observed, the sample was put under vacuum of 10^{-3} Torr and several other spectra were recorded. The BaF_2 plate coated with MgTHTMP was then placed in a closed chamber and exposed to water vapor for 4 h. Thereafter, the plate was immediately transfered to the enclosed cell and successive spectra were taken. The sample was then put under vacuum and several other spectra were taken. Thereafter, the sample was dissolved in CCl_4, and more spectra were taken.

The spectra were recorded on a model 180 Perkin-Elmer spectrophotometer with a resolution of ~2 cm^{-1}. The calibration of the spectrophotometer was made with the water vapor bands; the precision of the bands was better than 1 cm^{-1} except for the broad bands. Three spectra were recorded for each sample except when successive spectra were needed to record the behavior of the OH stretch band with time. The spectral data were transfered to a computer where dedicated programs were used to obtain the figures given in this paper. For each spectra, the average of the original spectra were made, calibrated, and subtracted from the background.

3. Results and discussion

The spectra of ZnTHTMP and of MgTHTMP in CCl_4 solutions are given in Fig. 2*A* and *B*, respectively. On this

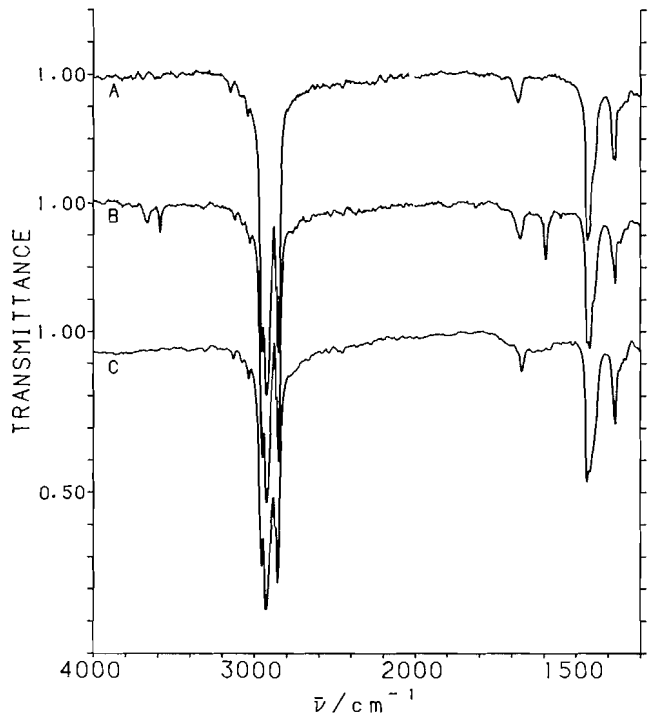

FIG. 2. Infrared spectra of *A*, ZnTHTMP in CCl_4 ($\sim 1 \times 10^{-2}$ mol/L); *B*, MgTHTMP in CCl_4 ($\sim 1 \times 10^{-2}$ mol/L); *C*, MgTHTMP solid.

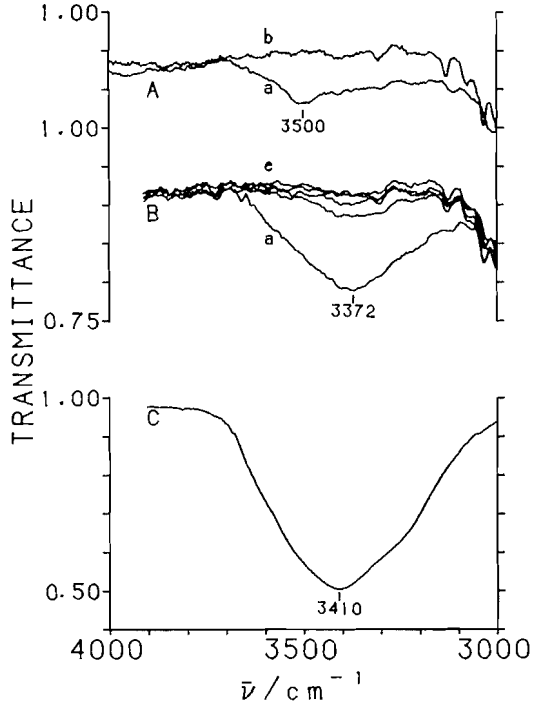

FIG. 3. Infrared spectra of MgTHTMP solid: *A*, obtained from CCl_4 solution: (*a*) immediately after evaporation of the solvent, (*b*) 2 min after; *B*, obtained after the solid was put in water vapors for 4 h: (*a*) immediately after transfering the ir plate in the closed cell, (*b*) 2 min after, (*c*) 5 min after, (*d*) 8 min after, (*e*) 11 min after; *C*, liquid water.

figure we present the OH stretch (3700 to 3200 cm^{-1}) and OH deformation (1650 to 1550 cm^{-1}) regions. In these regions, the zinc compound shows no bands whereas the magnesium compound shows two bands in the first region and one in the second one. The observation of these bands, which are typical of water bands, was surprising since other analyses of the magnesium compound (ir of the solid compound and elemental analysis) showed no evidence of water. The other metallic compounds (Co, Ni, Cu, Cd, Hg, MnCl, FeCl), and the free base of the same porphyrin substrate, in CCl_4 solutions did not show these bands (13). Solid MgTHTMP in a Nujol suspension did not show any bands in these regions, nor did the pure solid deposited directly on a BaF_2 plate (Fig. 2*C*). For reasons of clarity, only spectra of the pure solid sample are presented since those of the suspension in Nujol are identical. These last two results indicate that the original solid MgTHTMP is not hydrated.

Solid samples

To further access the hygroscopic nature of solid MgTHTMP, we have put the sample, obtained from a CCl_4 solution, in a closed cell and an ir spectrum was taken immediately after preparation. This spectrum is given in Fig. 3*Aa*. This figure shows a broad featureless band centered at 3500 cm^{-1}. A spectrum taken 5 min later (Fig. 3*Ab*) shows that the band has disappeared. Under vacuum, the sample showed no further modification. The same sample was then exposed to water vapor for 4 h and returned to the closed cell where five spectra were immediately taken in succession over a period of less than 15 min. The first spectrum of this series (Fig. 3*Ba*) shows a broad band centered at 3372 cm^{-1} which quickly disappears. After 5 min (Fig. 3*Bc*), the band is barely seen, and after 8 min (Fig. 3*Bd*) the band is gone. Another spectrum taken after 11 min (Fig. 3*Be*) and another one taken after pumping the sample to 10^{-3} Torr did not show any further modification. When the sample was dissolved again in CCl_4, the OH bands reappeared with the same intensity as observed previously.

The position of 3372 cm^{-1} for the OH band in solid hydrated MgTHTMP (Fig. 3*Ba*) indicates the presence of hydrogen bonded water, such a bond being possible with another water molecule. Therefore water is essentially aggregated to itself in liquid like form and is not bonded strongly to the Mg, that is the reason for its rapid evaporation. The position of this band is higher than that observed for hydrates of solid Chl *a* and for hydrated solid films of Chl *a* where the bands are observed at $\sim$3300 cm^{-1} (5). In these Chl *a* solid samples, the OH bands of water are difficult to remove requiring pumping and heating; beside the coordinate bond with the Mg, hydrogen bonds between the carbonyl groups of Chl *a* and water have been postulated. These two types of bands are necessary to hold strongly the water molecules in the chlorophyll environment.

In fresh multilayers, Chl *a* and water may aggregate in another way showing a band at 3400 cm^{-1} which disappears rapidly under vacuum (7). The special arrangement of the multilayer, where the ketone carbonyl of one molecule forms a coordinated bond with the Mg atom of another molecule, keeps the Mg from making a coordinate bond with water. Hence, the water molecules incorporated into the multilayers are essentially bonded to themselves and evaporate rapidly. Our results show that water in solid MgTHTMP behaves in the same fashion, and the position of the OH stretch band is indeed similar (3372 cm^{-1} for MgTHTMP and 3400 cm^{-1} for a fresh multilayer of Chl *a*). Therefore, in the solid state, MgTHTMP is not hygroscopic and does not retain water.

Solutions

The behavior of MgTHTMP in a CCl_4 solution is different from that in the solid state; the porphyrin molecule complexes

Can. J. Chem. Downloaded from www.nrcresearchpress.com by 213.222.148.141 on 09/07/12
For personal use only.

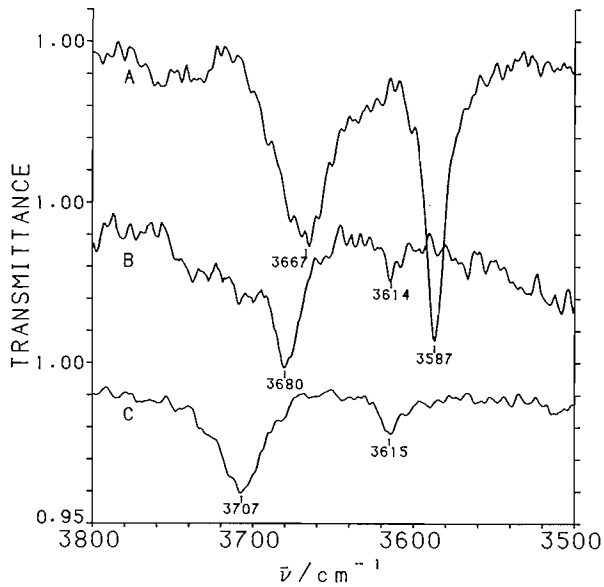

FIG. 4. Infrared spectra of *A*, MgTHTMP ($\sim 1 \times 10^{-2}$ mol/L) in a solution of CCl_4; *B*, MgTHTMP ($\sim 1 \times 10^{-2}$ mol/L) in a solution of CCl_4 where pyridine ($\sim 1 \times 10^{-2}$ mol/L) has been added; *C*, saturated solution of H_2O in CCl_4.

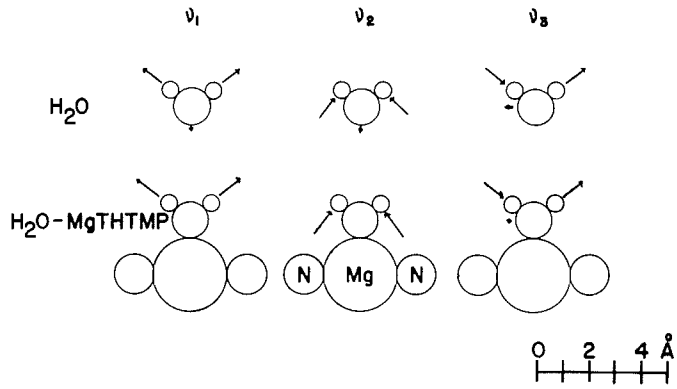

FIG. 5. Vibrations of H_2O complexed to MgTHTMP (bottom); pure water (top). The circles represent the covalent radii of each atom. The arrows indicate the approximate displacement (multiplied by a factor of 10) of atoms for each mode.

quickly the few water molecules present in the solution. To understand the nature of the interaction of water with MgTHTMP in a CCl_4 solution, we compare in Fig. 4 the OH stretch bands of a saturated solution of water in CCl_4 (Fig. 4*C*) with that of MgTHTMP in CCl_4 (water content less than 0.01%) (Fig. 4*A*).

The spectrum of water in a CCl_4 solution shows two bands situated at 3707 and 3615 cm^{-1} (Fig. 4*C*) and assigned to ν_3 and ν_1, respectively. These bands have been reported previously (2, 14–16). In Table 1, we have tabulated these values along with those of oligometric species of water (15, 16). The positions of the OH bands of water in a liquid crystal and those of a complex of water in benzonitrile (17) are listed in the same table. Also included are the positions of OH stretch bands of water interacting with Chl *a* in different aggregation states (2) and with MgTHTMP in CCl_4 solution and in the solid state.

MgTHTMP in CCl_4 gives two bands in the OH stretch region (Fig. 4*A*): one broad band centered at 3667 cm^{-1} and a sharper one situated at 3587 cm^{-1}. The positions of these bands is lower than those of water in CCl_4 and are an indication of the formation of a complex. The first band is assigned to ν_3 and the second one to ν_1 of water coordinated to the Mg atom. The shape of the ν_3 band of H_2O–MgTHTMP in CCl_4 is comparable to that of H_2O in CCl_4 (Fig. 4*A* and *C*). The ν_1 bands are different: in uncoordinated water the band is much weaker and broader than ν_3 but for the complex in solution, the ν_1 band is stronger and sharper than ν_3.

The increase in intensity of ν_1 of H_2O complexed to MgTHTMP in CCl_4 (3587 cm^{-1}) compared to that of H_2O in CCl_4 (3615 cm^{-1}) can be explained by looking at the different vibrations (Fig. 5). When the oxygen of water makes a coordinate bond with Mg of the porphyrin, the displacement of oxygen for ν_1 is inhibited and the whole movement of this mode is transfered to the hydrogens. Therefore the amplitude of this vibration will be greater in the complex than on pure water; since the intensity of a band is directly proportional to the square of variation of the dipole moment, if the amplitude of vibration is greater, then the variation of the dipole moment will be greater and so will be the intensity of the band. The same thing happens for the ν_2 band at 1593 which is stronger than ν_3 (Fig. 2). In uncomplexed water, ν_3 is stronger than ν_2. For ν_3, the situation is different because the movement of the oxygen is perpendicular to the axis of symmetry and so the displacement of the oxygen will not be much affected by the coordinate bond; therefore the intensity of the band will not vary as much as for ν_1 or ν_2. One must also remember that the Mg is bonded to the rest of porphyrin by the nitrogens, therefore not only the Mg inhibits the movement of the oxygen in ν_1 and ν_2 but that of the whole porphyrin molecule.

Another mechanism that could influence the intensity of the bands is the π electron cloud of the porphyrin molecule that could orient water molecules with its electric field. The effect of orientation on the ir bands of water has been observed with water in a liquid crystal under the influence of a magnetic field (17). When the electric vector is parallel to the magnetic field the ν_1 band is stronger than ν_3 and when the electric vector is perpendicular to the magnetic field the ν_1 band is less intense than ν_3. In the case of water bonded to MgTHTMP, the electric vector is perpendicular to the electric field of the π electron cloud. Since the influence of an electric field and a magnetic field are orthogonal, water bonded to MgTHTMP could be affected by the electric field very much like water in the liquid crystal.

A more intense ν_1 band compared to ν_3 band has also been observed in a crystal of cyclotriveratrylene with water included to form a clathrate (18). In this case the crystal field and the inclusion cavities orient the water molecules.

Although MgTHTMP is highly hygroscopic in CCl_4, the water molecules are not strongly coordinated to the magnesium atoms because the displacement of the bands is not great compared to that of H_2O in CCl_4. Also, as we have seen previously, once CCl_4 is evaporated from an MgTHTMP solution to obtain a solid, the water molecules rapidly evaporate. An additional proof of the coordination of water to MgTHTMP in CCl_4 solution has been obtained by a displacement experiment made by adding a small amount of pyridine to a CCl_4 solution of MgTHTMP. Pyridine is a stronger ligand than water and should replace it to form a new complex. The result of this experiment is given in Fig. 4*B*. Indeed the original spectrum (Fig. 4*A*) is modified and the bands that we observe are comparable to that of water in CCl_4 (Fig. 4*C*) although slightly displaced because of the presence of pyridine.

Can. J. Chem. Downloaded from www.nrcresearchpress.com by 213.222.148.141 on 09/07/12
For personal use only.

Can. J. Chem. Downloaded from www.nrcresearchpress.com by 213.222.148.141 on 09/07/12
For personal use only.

TABLE 1. Position (in cm^{-1}) of the water bands in different milieux[a]

Assignment	Gas (ref. 20)	CCl_4 solution			Liquid crystal (ref. 17)				Chl *a* – H_2O/CCl_4 (ref. 2)	Chl *a*/ CCl_4–H_2O (ref. 2)	Chl *a* in Nujol (ref. 2)	Conc. Chl *a*–H_2O in CCl_4 (ref. 2)	Chl *a* hydrate in CCl_4 (ref. 4)	H_2O–MgTHTMP in CCl_4 (this work)	MgTHTMP solid + H_2O (this work)
		This work	Ref. 15	Ref. 16	H_2O in BN	H_2O in BN + CCl_4	H_2O in 8CB $A_\parallel$	H_2O in 8CB $A_\perp$							
ν_3	3756														
Monomer		3707	3708	3709					3710	3710			3715[b]		
Dimer				3698											
Trimer				3687											
Free OH			3693	3680											
Hydrate									3665	3665		3660	3665		
1:1 complex						3689	3677	3658						3667	
2:1 complex					3650		3635								
ν_1	3657														
Monomer		3615	3616	3613					3615				3620[b]		
Dimer				3609											
Trimer				3600											
Hydrate											3590	3590			
Bonded OH			3552	3532											
1:1 complex						3560								3587	
2:1 complex					3549		3545	3545							
	liq.										3460	3450			
Hydrogen bond	3410								3380	3380			3380		3372
	(this work)										3240	3250			

[a]BN, benzonitrile; 8CB, 4′-*n*-octyl-4-cyanobiphenyl.
[b]This value is ~5 cm^{-1} too high.

Can. J. Chem. Downloaded from www.nrcresearchpress.com by 213.222.148.141 on 09/07/12
For personal use only.

The coordination number of magnesium in a porphyrin environment is mostly 5 because the energy of extra coordination of additional ligands is so small as to be almost negligible (19). Therefore only one molecule of water should be attached to MgTHTMP in CCl_4. In the solid state the coordination number should be 4 because water is not bonded to the porphyrin and no other ligand is available.

This result differs from that obtained for MgTPP by X-ray measurements (9) which showed that the crystal was hydrated. The presence of water in this crystal was determined by density measurements using flotation in aqueous silver nitrate solution. Our results show that for solid MgTHTMP maintained in a moist atmosphere, water is incorporated in the substance but is not bonded to the magnesium atom. Water disappears rapidly when the substance is removed from the moist atmosphere. It may possibly be due to the phenyl rings that MgTPP could be more hygroscopic than MgTHTMP.

Comparison with chlorophyll

The environment of the magnesium of chlorophyll molecule is similar to that of MgTHTMP. Therefore the interaction of water with Mg should be the same for both molecules. To have water strongly bonded to chlorophyll it is necessary to have the oxygen and at least one of the hydrogens of water attached to the Mg and the carbonyl of the chlorophyll molecules respectively, in a chain-like organization. When the ketone carbonyl of Chl *a* is unavailable for making a hydrogen bond with water the latter is not strongly attached to the chlorophyll molecule. Such is the case in fresh mono- and multilayer of Chl *a* where the special arrangement of the molecules have the ketone carbonyl either coordinate bonded to the magnesium of another molecule as in the case of the multilayer or free or bonded to the surface as in the case of the monolayer. With such arrangements, water is not retained in the layers of Chl *a* (7, 8).

Microcrystalline Chl *a* is a hydrate from which water is very difficult to remove. There is no free OH band, and the bonded OH band is situated at $\sim 3100\ cm^{-1}$; there is no free ketone carbonyl, and the bonded carbonyl band is situated at $1635\ cm^{-1}$ (unpublished results). The position of these bands which are displaced from the position of the free groups is indicative of strong intermolecular bonds which can be obtained from a coordinate bond between oxygen and magnesium on the one side, and between hydrogen and ketone carbonyl on the other side.

Microcrystalline Chl *a* dissolved in CCl_4 or Chl *a* dissolved in CCl_4 containing water give the same bands (Table 1) (2, 4). Beside the two free water bands seen in these solutions, two bands are observed: one at $3665\ cm^{-1}$ and a large band at $3380\ cm^{-1}$. No band is observed at the position of ν_1 of MgTHTMP in solution. We conclude from this observation that no water is bonded to Chl *a* in a fashion similar to that observed on MgTHTMP in solution, that is only bonded to the Mg site by oxygen. The band situated at $3665\ cm^{-1}$ is assigned to free OH and the one at $3380\ cm^{-1}$, to hydrogen-bonded OH. Such bands can be obtained if water is linked to Chl *a* by forming a coordinate bond between oxygen and magnesium on one side and by forming a hydrogen bond between hydrogen and carbonyl on the other side.

The visible spectrum of these species gives a strong band at 665 nm and minor absorptions at 680 and 700 nm (4). The position of 665 nm indicates that there is not much overlap of the π electron network of the two molecules; therefore there are probably not one but two molecules of water linked together by a hydrogen bond and sandwiched between two Chl *a* molecules. With one molecule of water between two molecules of Chl *a*, the distance between the porphyrin plane of the chlorophyll molecules would be too short to give the strong absorption at 665 nm.

Conclusion

We have showed that the presence of Mg is necessary for developing hygroscopicity of the porphyrin ring. This hygroscopicity is observed only in solution and water is lost rapidly with solid samples. If a carbonyl is present in the molecule and can lead to hydrogen bonds with the complexed water as in microcrystalline Chl *a*, the molecule is much more hygroscopic and can retain water even in the solid form.

Acknowledgements

This work was supported in part by the Fonds FCAR du Québec and in part by the Natural Sciences and Engineering Research Council of Canada. Denis Girard received a scholarship from the Fonds FCAR. The data manipulations were carried out by M. Trudel.

1. J. J. Katz, R. C. Dougherty, and L. J. Boucher. Infrared and nuclear magnetic resonance spectroscopy of chlorophyll. *In* The chlorophylls. *Edited by* L. P. Vernon and G. R. Seely. Academic Press, New York, NY. 1966. Chap. 7. pp. 185–251.
2. K. Ballschmiter and J. J. Katz. J. Am. Chem. Soc. **91**, 2661 (1969).
3. J. J. Katz, L. L. Shipman, T. M. Cotton, and T. R. Janson. Chlorophyll aggregation: coordination interactions in chlorophyll monomers, dimers, and oligomers. *In* The porphyrins. Vol. V. Part C. *Edited by* D. Dolphin. Academic Press, New York, NY. 1978. Chap. 9. pp. 401–458.
4. T. M. Cotton, P. A. Loach, J. J. Katz, and K. Ballschmiter. Photochem. Photobiol. **27**, 735 (1978).
5. K. Ballschmiter and J. J. Katz. Biochim. Biophys. Acta, **256**, 307 (1972).
6. J. P. Dodelet, J. Le Brech, C. Chapados, and R. M. Leblanc. Photochem. Photobiol. **31**, 143 (1980).
7. C. Chapados, D. Germain, and R. M. Leblanc. Biophys. Chem. **12**, 189 (1980).
8. C. Chapados and R. M. Leblanc. Biophys. Chem. **17**, 211 (1983).
9. R. Timkovich and A. Tulinsky. J. Am. Chem. Soc. **91**, 4430 (1969).
10. K. Smith and M. F. Bisset. J. Org. Chem. **44**, 2077 (1979).
11. J. H. Fuhrhop and K. M. Smith. *In* Porphyrins and metalloporphyrins. *Edited by* K. M. Smith. Elsevier, Amsterdam. 1975. p. 798.
12. I. H. Fisher, W. Neumann, and A. Treibs. Ann. **494**, 225 (1932).
13. D. Girard. Synthèses et étude spectroscopique de métalloporphyrines liposolubles. Mémoire de maîtrise, Université du Québec. 1986.
14. A. Cabana and C. Jolicoeur. Can. Spectrosc. **12**, 1 (1967).
15. L. B. Magnusson. J. Phys. Chem. **74**, 4221 (1970).
16. J. H. Keighley and A. Whitaker. Mol. Phys. **31**, 643 (1976).
17. N. Kimura, J. Umemura, S. Hayashi, and T. Takenaka. J. Mol. Struct. **116**, 153 (1984).
18. G. I. Birnbaum, D. D. Klug, J. A. Ripmeester, and J. S. Tse. Can. J. Chem. **63**, 3258 (1985).
19. B. D. Berezin. Coordination compounds of porphyrins and phthalocyanines. John Wiley and Sons, Chichester. 1981.
20. T. Shimanouchi. Nat. Stand. Ref. Data Ser. Nat. Bur. Stand. U.S. **39**, 10 (1972).

The synthesis and the nuclear magnetic resonance study of β-lactam derivatives of 1,5-benzothiazepines[1]

ARON SZÖLLÖSY[2] AND GEORGE KOTOVYCH
Department of Chemistry, University of Alberta, Edmonton, Alta., Canada T6G 2G2

GÁBOR TÓTH
NMR Laboratory of the Institute for General and Analytical Chemistry, Technical University, H-1521 Budapest, Hungary

AND

ALBERT LÉVAI
Department of Organic Chemistry, Kossuth Lajos University, H-4010 Debrecen, Hungary

Received June 15, 1987

This paper is dedicated to Professor C. A. McDowell

ARON SZÖLLÖSY, GEORGE KOTOVYCH, GÁBOR TÓTH, and ALBERT LÉVAI. Can. J. Chem. **66**, 279 (1988).

The synthesis and stereochemistry of seven β-lactam derivatives of 1,5-benzothiazepines are presented. The configurational and conformational analysis is based on nuclear Overhauser effect experiments, together with analysis of the vicinal proton–proton coupling constants. In the preferred conformation, the seven-membered ring is in a half-chair. Only for one compound, 2-aza-4-bromo-4-methyl-5,7-diphenyl-8-thiatricyclo[7.4.0.0^{2,5}]trideca-$\Delta^{1,9}$,10,12-trien-3-one, were two diastereomers isolated (compounds **6***a* and **6***b*). Six of the compounds have the 4*S**, 5*R**, 7*R** configuration while compound **6***b* has the 4*R**, 5*R**, 7*R** configuration.

ARON SZÖLLÖSY, GEORGE KOTOVYCH, GÁBOR TÓTH et ALBERT LÉVAI. Can. J. Chem. **66**, 279 (1988).

On rapporte la synthèse et la stéréochimie de sept dérivés β-lactames des benzothiazépines-1,5. Les analyses de configuration et de conformation sont basées sur des expériences d'effets Overhauser nucléaires ainsi que sur une analyse des constantes de couplage proton–proton vicinaux. Dans sa conformation privilégiée, le cycle à sept chaînons est dans un forme demi-chaise. On n'a isolé deux diastéréoisomères (les composés **6***a* et **6***b*) que dans le cas d'un seul composé, l'aza-2 bromo-4 méthyl-4 diphényl-5,7 thia-8 tricyclo[7.4.0.0^{2,5}]tridécatriène-1(9),10,12 one-3. Six des composés possèdent la configuration 4*S**, 5*R**, 7*R** alors que la configuration du composé **6***b* est 4*R**, 5*R**, 7*R**.

[Traduit par la revue]

Owing to their biological importance, numerous β-lactam compounds are discussed in the literature. A few examples of the β-lactam derivatives of benzoxazepines, benzothiazepines, and benzodiazapines have also been published (2, 3). The β-lactam moiety may modify the biological activity of the benzazepines or may result in new effects and, therefore, synthesis of new substances can be beneficial for pharmaceutical research. During the past decade we performed detailed investigations on the synthesis and stereochemistry of 2,3-dihydro-1,5-benzothiazepines (4–10). As a result, numerous compounds were obtained that are potential starting materials for the preparation of condensed β-lactams. In these compounds the C=N double bond can be attacked by suitable reactants to form β-lactam derivatives.

The synthesis of seven β-lactam derivatives is presented and their configurations and conformations are deduced based on proton and ^{13}C nuclear magnetic resonance experiments. In view of the fact that conformations of the conformationally flexible seven-membered ring (11), attached to the strained four-membered ring, have not been extensively studied, especially with different bulky substituents on the four-membered ring, we have proceeded with the configurational and conformational analysis of these systems. The spectra of 2,4-diphenyl-2,3-dihydro-2,3-dihydro-1,5-benzothiazepine have been previously analyzed (12).

Results and discussion

We report in this paper the reaction of 2,3-dihydro-2,4-diphenyl-1,5-benzothiazepine **1** with various acid halides, and the nmr investigation of the stereochemistry of the prepared compounds. According to the literature data (13–16), β-lactam formation may take place either by the addition of the acid halide to the imine to produce a reactive intermediate that cyclizes to β-lactam under the influence of a tertiary amine, or by the formation of a ketene from the acid halide and tertiary amine followed by a two-step formation of the β-lactam moiety. Since in our cases triethylamine was added first to the solution of compound **1**, the mechanism involving ketene formation seems most probable (16) (Fig. 1).

We have carried out the cycloaddition of compound **1** with several acid halides, namely with phenoxyacetyl chloride, thiophene-2-acetyl chloride, chloroacetyl chloride, dichloroacetyl chloride, α-bromopropionyl bromide, and α-bromobutyryl bromide. The reaction was monitored by thin-layer chromatography and the mixture was refluxed and stirred until the starting material disappeared. As a result of the incident side reactions and (or) decompositions, crude products were usually mixtures from which β-lactams (**2**–**7**) were isolated by column chromatography. All the β-lactams isolated (except **6**) were found to be stereochemically homogeneous according to spectroscopic evidence. Only in the case of the α-bromopropionyl bromide reagent were two β-lactams detected. One compound (**6***a*) was obtained by a further chromatographic procedure. The other product (**6***b*, minor product) was studied in a mixture with **6***a* where **6***a* was in excess (ca. 65%), and **6***b* was not isolated as a pure compound.

The configuration of the compounds was established by the application of several nmr methods. Since the racemic starting compound **1** has only one chiral centre, and the products contain three (ignoring the β-lactam nitrogen), four diastereomeric pairs of enantiomers should be considered (except for **5**, where

[1]For an application of the quantitative nuclear Overhauser effect, see ref. 1*a*. The previous synthetic paper is ref. 1*b*.

[2]On leave from the Technical University, Budapest, Hungary.

Can. J. Chem. Downloaded from www.nrcresearchpress.com by 176.9.209.113 on 09/07/12
For personal use only.

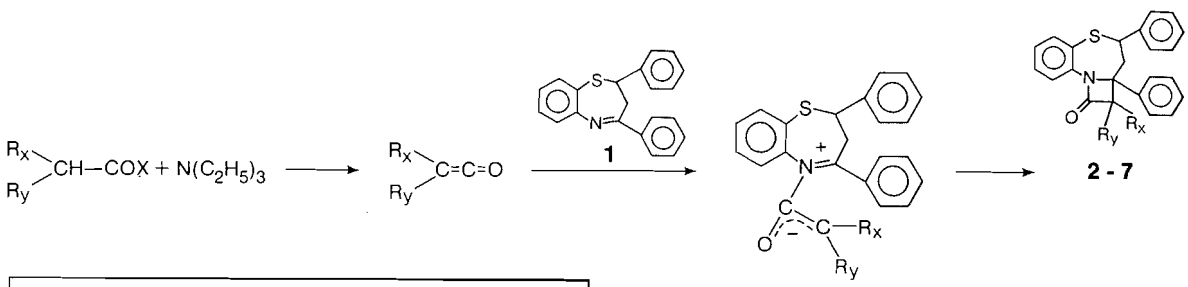

Compound	R_x	R_y
2	H	C_6H_5O
3	H	
4	H	Cl
5	Cl	Cl
6a	CH_3	Br
6b	Br	CH_3
7	CH_3CH_2	Br

FIG. 1. The synthesis of compounds **2–7**.

$R_x = R_y$ and consequently the number of possible diastereomeric pairs is two). By inspection of Dreiding models the possible relative stereochemistry and more stable conformations were established as depicted in Fig. 2. With three chiral centres, four products in racemic form are possible. In addition, a conformational equilibrium also should be considered. In structures of type I and II, boat ⇄ half-chair, and in structures of type III and IV, boat ⇄ boat conformational equilibria are represented. The twist-boat conformation was previously shown to be unimportant (12).

The conformational arguments will be presented first of all. The ^{1}H nmr chemical shift and coupling constants observed for compounds **2–7** in $CDCl_3$ solution are presented in Table 1. Concerning the tetrahydro-1,5-benzothiazepine ring conformation, the most valuable data are the ^3J coupling constants between the 6-H and 7-H protons. These form an ABX spin system, which was analysed to first-order as well as using the Bruker PANIC software for several cases. The coupling constants obtained were compared with those calculated using a modified Karplus curve taking into consideration the substituent effect (17). This analysis shows that the conformational equilibrium is shifted and structures Ia, IIb, IIIb, and IVa could be excluded. Conformations Ib and IIIa are more likely than the remaining two, IIa and IVb, on the basis of the $^3J_{6H,7H}$ coupling constants. The observed $^3J_{6,7}$ coupling constants (~11 Hz) also show that the 7-phenyl group occupies a quasi-equatorial position in the predominant conformation. This is in accordance with our previous results for several dihydro-1,5-benzothiazepine derivatives (10, 12). The data in Table 1 also show that compounds **2**, **3**, and **4** should have the same structure.

Configurational information can be found by comparison of the proton data (Table 1). There are two significant differences in the data for ***6a*** and ***6b***. First, the chemical shift of the 4-CH_3 methyl group signals differs considerably and in ***6b*** it is shielded by 0.66 ppm. This shielding arises from the aromatic ring current effect of the 5-phenyl group. It means that compounds ***6a*** and ***6b*** differ from each other in that the 5-phenyl and 4-methyl groups are *cis* in ***6b*** and *trans* in ***6a***. The second significant difference also confirms this conclusion. In compound ***6b*** the signal of the 6-H_{ax} proton is shifted downfield and $\delta H_{ax} > \delta H_{eq}$, which is opposite to the assignment for ***6a***, **2**, **3**, **4**, and **7**. Similar effects can be noticed by comparing the ^{1}H nmr data for **4** and **5**. Compounds **4** and **5** differ from each other in that **5** has an additional C—X bond (X = halogen) and this results in a downfield shift of the 6-H_{ax} signal. This very likely arises from the anisotropy of the C—X bond, and this effect is responsible for the downfield shifts (0.4 ppm) of 6-H_{ax} in ***6b*** and **5**.

Further evidence could be achieved from the one-dimensional proton–proton difference nOe (nuclear Overhauser enhancement) measurements. The magnitude of the nOe depends to a large extent on the intramolecular proton–proton distances (18, 19). Characteristic nOe data for compounds **4**, ***6a***, and **7** are summarized in Table 2. A characteristic feature of compound **4** is that the 6-H_{ax} and 6-H_{eq} protons differ from each other in steric proximity with respect to the other protons, which is clearly seen from the nOe data. Irradiation of 4-H resulted in a considerable nOe for the 6-H_{ax} signal while an nOe was not detectable at 6-H_{eq}. The irradiation of 6-H_{ax} and 6-H_{eq} also corroborates this different behaviour. Saturating the 7-H signal, an enhancement was only observed at 6-H_{eq} and in the aromatic region (H-2′,6′). Very similar effects can be observed for ***6a*** and **7**, which shows that the 4-H, 4-CH_3, and 4-Et groups occupy the same position in these compounds. The results of the nOe difference experiments are in accordance only with a Ib structure, where the 5-phenyl group and the halogen atom are *cis*.

These conclusions prove that compounds **2–*6a*** and **7** can be characterized as having conformation Ib_{cis} (4*S**, 5*R**, 7*R** configuration), while ***6b*** has the Ib_{trans} (4*R**, 5*R**, 7*R** configuration) conformation.

^{13}C chemical shifts and assignments for compounds **2–7** are summarized in Table 3. ^{13}C analysis of dihydro-1,5-benzothiazepines (9) together with the substituent effects were utilized for the assignments. For the β-lactam moiety, ^{13}C data for similar condensed derivatives of benzothiazines (16, 20) also were used. On the basis of the ^{1}H nmr conclusions, the chemical shift of the C-6 atom should be the best indicator of

Can. J. Chem. Downloaded from www.nrcresearchpress.com by 176.9.209.113 on 09/07/12
For personal use only.

TABLE 1. The ^1H nmr chemical shifts (ppm), multiplicities,[a] and coupling constants (Hz) for compounds **2**–**7** in $CDCl_3$ at ambient temperature

Compound	4-H	6-H_{ax}	6-H_{eq}	7-H	13-H	CH_3	CH_2	$J_{6,6'}$	$J_{6,7}$	$J_{6',7}$
2	5.41s	3.22dd	3.67dd	4.01dd	8.02m	—	—	−14.3	11.0	1.1
3	4.97s	3.28dd	3.64dd	3.99dd	8.04m	—	—	−13.7	10.9	1.1
4	5.05s	3.13dd	3.61dd	3.95dd	7.97m	—	—	−14.2	11.0	1.0
5	—	3.45dd	3.47dd	3.89dd	7.92m	—	—	−14.6	12.4	0.3
6*a*	—	3.16dd	3.37dd	3.86dd	7.99m	2.22s	—	−14.5	11.0	1.1
6*b*	—	3.55dd	3.36dd	3.88dd	7.92m	1.56s	—	−14.5	11.0	1.1
7	—	3.24dd	3.37dd	3.82dd	7.98m	1.31t	2.38 2.50	−13.6	10.3	<0.4

[a]s, singlet; dd, doublet of doublets; t, triplet; m, multiplet.

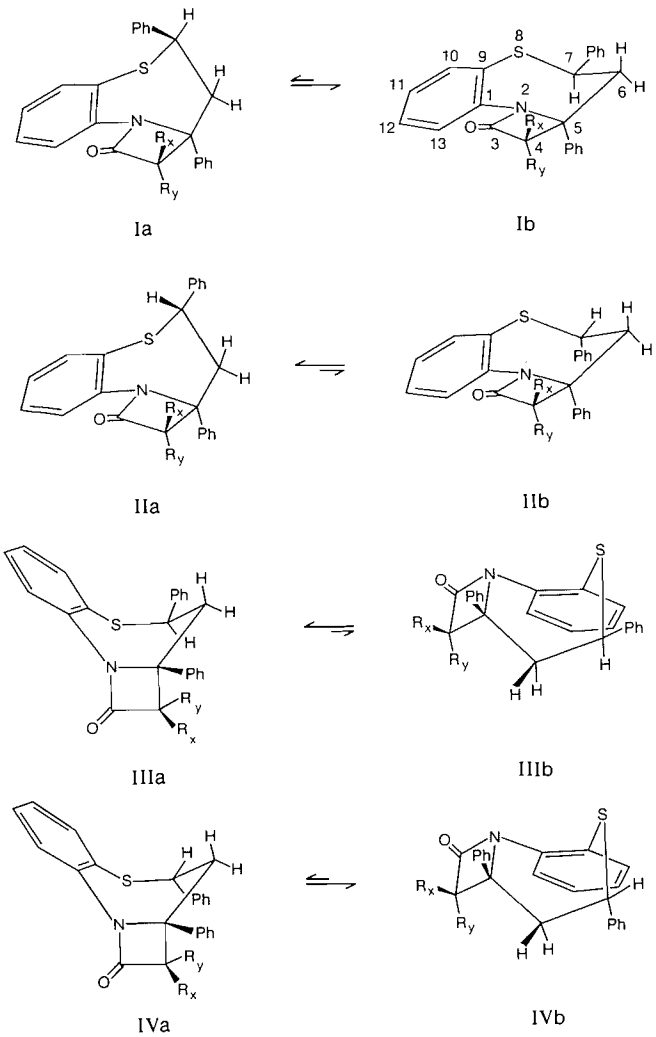

FIG. 2. The possible conformation and configurations of compounds **2**–**7**. Only in the case of compound **6** two racemic diastereomers were isolated. R_x and R_y are defined in Fig. 1.

structure. In compounds **2**–**4** the C-4 substituents cause a γ_{anti} effect on C-6, while for **5**, C-6 is affected by the superposition of the γ_{anti} and γ_{gauche} chlorine atoms. In compound **3**, this signal is quite distinct, possibly due to the thiaphenyl group. In compounds **6***a* and **6***b* a superposition of the methyl and bromine effect is observed. In **6***a* the bromine is *anti* and the methyl group is in a *gauche* position, and these are opposite in **6***b* so that the C-6 signal is shifted by ~4 ppm downfield. These

TABLE 2. Homonuclear Overhauser enhancements for irradiated protons of selected compounds

Compound	Nuclear Overhauser enhancement observed (%)				
4	6-H_{ax}	6-H_{eq}	4-H	7-H	Other
4-H	9	[a]	—	[a]	
6-H_{ax}	—	26	23	1	
6-H_{eq}	27.5	—	2	[a]	
7-H	[a]	2	[a]	—	H-2′,6′: 17
6*a*			4-CH_3		
4-CH_3	13	1.5	—	3	
6-H_{ax}	—	20.5	9.5	1	
6-H_{eq}	17	—	2	[a]	
7-H	[a]	1.5	[a]	—	H-2′,6′: 21
7			4-$EtCH_3$		
4-$EtCH_2$(x)	5.5	[a]	7		
4-$EtCH_2$(y)	9.0	[a]	11		
4-$EtCH_3$	[a]	2	—		$EtCH_2$: 14[c]
6-H_{ax}	—	[b]	6		$EtCH_2$: 13[c]
6-H_{eq}	[b]	—	7		$EtCH_2$: 2[c]

[a]Nuclear Overhauser enhancement could not be detected.
[b]Quantitative nOe data could not be observed with reasonable precision due to proximity of signals.
[c]The individual CH_2 protons were not distinguished in the integration.

data have less utility for the independent verification of the structures because data for more derivatives should be analyzed. Furthermore, the tetrahydro-benzothiazepine ring may not be rigid for the γ steric shifts to be applied for the stereochemical study.

Our studies have shown that most compounds obtained by the addition of acid halides to dihydro-1,5-benzothiazepines have the Ib_{cis} conformation. The structure of the intermediate is not known; the structure of the products, however, shows that its dominant conformation favours an arrangement where the 5-phenyl group and the halogen atom (or other bulky group) are on the same side. This arrangement should be governed by steric factors and, when the steric requirement for the R_x and R_y groups is nearly comparable (e.g., methyl and bromo groups), both *cis* and *trans* compounds appear. The conformation of the seven-membered ring is independent of the substituents present on the four-membered ring.

Experimental

(a) General

Melting points were determined on a Kofler hot stage and are

Can. J. Chem. Downloaded from www.nrcresearchpress.com by 176.9.209.113 on 09/07/12
For personal use only.

TABLE 3. Selected ^{13}C chemical shifts (ppm, relative to internal TMS) for compounds **2–7**

Compound	C-4	C-3	C-5	C-6	C-7	C-10	C-11	C-12	C-13	C-1	C-9
2	88.4	164.0	70.9	48.4	44.9	128.4	128.1	132.4	126.7	137.6	129.7
3	64.4	165.9	71.2	51.3	46.4	128.5	127.8	132.5	127.0	136.9	129.8
4	67.4	161.9	71.5	49.5	45.1	128.6	128.1	132.5	126.6	137.6	129.9
5	89.5	160.0	78.3	48.6	45.9	128.4	127.5	132.4	126.9	136.7	130.2
6[a]	71.2	165.7	74.2	47.3	46.2	128.4	127.8	132.2	126.6	139.6	129.5
	(70.7)		(73.9)	(51.6)	(46.4)						
7	78.3	165.5	75.0	47.7	46.2	128.6	127.9	132.2	126.6	139.8	129.6

[a]Data for **6***a*. Data for **6***b* (observed in a mixture with **6***a*) are in parentheses.

uncorrected. Thin-layer chromatography was performed on Merck Kieselgel foils using a petroleum ether:acetone (3:1 v/v) developing mixture. The spots were observed by uv light. Kieselgel 40 columns and petroleum ether:acetone (3:1 v/v) eluent were utilized for column chromatography.

(b) Synthesis

The general procedure for the preparation of compounds **2–7** is presented. A mixture of 2,3-dihydro-2,4-diphenyl-1,5-benzothiazepine (5 mmol), triethylamine (10.0 mmol), and anhydrous benzene (20.0 mL) was stirred and refluxed, and the appropriate acid halide (10.0 mmol) dissolved in anhydrous benzene (20.0 mL) was added dropwise for 15 min. Refluxing and stirring were continued for another 60 min, then the triethylamine salt was filtered off and the solvent evaporated. The residue was purified by column chromatography to produce compounds **2–7**. These are as follows: 2-Aza-4-phenoxy-5,7-diphenyl-8-thiatricyclo[7.4.0.0^{2,5}]trideca-$\Delta^{1,9}$,10,12-trien-3-one **2**. Yield 86.3%; mp 194–195°C. *Anal.* calcd. for $C_{29}H_{23}NO_2S$: N 3.11, S 7.12; found: N 3.05, S 7.78. 2-Aza-5,7-diphenyl-8-thia-4-thiaphenyltricyclo[7.4.0.0^{2,5}]trideca-$\Delta^{1,9}$,10,12-trien-3-one **3**. Yield 22.7%; mp 173–174°C. *Anal.* calcd. for $C_{27}H_{21}NOS_2$: N 3.18, S 14.57; found: N 3.08, S 14.72. 2-Aza-4-chloro-5,7-diphenyl-8-thiatricyclo[7.4.0.0^{2,5}]trideca-$\Delta^{1,9}$,10,12-trien-3-one **4**. Yield 27.8%; mp 214–215°C. *Anal.* calcd. for $C_{23}H_{18}NOSCl$: N 3.57, S 8.16; found: N 3.54, S 8.13. 2-Aza-4-dichloro-5,7-diphenyl-8-thiatricyclo-[7.4.0.0^{2,5}]trideca-$\Delta^{1,9}$,10,12-trien-3-one **5**. Yield 38.1%; mp 219–220°C. *Anal.* calcd. for $C_{23}H_{17}NOSCl_2$: N 3.28, S 7.51; found: N 3.24, S 7.81. 2-Aza-4-bromo-4-methyl-5,7-diphenyl-8-thiatricyclo[7.4.0.0^{2,5}]trideca-$\Delta^{1,9}$,10,12-trien-3-one **6***a*. Yield 19.1%; mp 239–240°C. *Anal.* calcd. for $C_{24}H_{20}NOSBr$: N 3.11, S 7.11; found: N 3.09, S 7.17. 2-Aza-4-bromo-4-ethyl-5,7-diphenyl-8-thiatricyclo-[7.4.0.0^{2,5}]trideca-$\Delta^{1,9}$,10,12-trien-3-one **7**. Yield 34.7%; mp 224–225°C. *Anal.* calcd. for $C_{25}H_{22}NOSBr$: N 3.01, S 6.89; found: N 3.03, S 6.94.

(c) Spectroscopy

The ^1H nmr spectra were obtained on a Bruker WM 360 nmr spectrometer equipped with an Aspect 2000 computer. Samples were prepared in chloroform solution using TMS as internal standard. For the 1-D and 2-D nOe measurements the solutions were degassed using the freeze–pump–thaw cycle several times.

Typical spectral conditions were as follows: The number of data points, 32K; flip angle, 30°; sweep width, 3200 Hz. For the nOe difference experiments, a preirradiation delay of 2–2.4 s, a relaxation delay of 6–7 s, and a 90° flip angle were applied. The lines of the multiplets were irradiated separately and several times during the preirradiation (21).

The ^{13}C nmr spectra were measured on a JEOL FX-100 spectrometer at 25.00 MHz. Typical spectral parameters were as follows: sweep width, 6000 MHz; data points, 16 K; repetition time, 2 s; flip angle, 30°. Broadband proton decoupled and the attached proton test (APT) (or DEPT) spectra were recorded for the determination of multiplicity.

Acknowledgements

The authors thank Dr. Susan E. Jensen for activity measurements, Dr. H. J. Liu for comments on the manuscript, and Dr. Albin Otter for valuable discussions. A.S. thanks the Alberta Heritage Foundation for Medical Research for a research fellowship, and G.T. the A.v. Humboldt Stiftung for a visiting fellowship (Ruhr-Universität, Bochum, Federal Republic of Germany). Technical assistance of Mrs. E. Hajnal is appreciated. The assistance of the Natural Sciences and Engineering Research Council of Canada, the Hungarian Academy of Sciences, and the University of Alberta is gratefully acknowledged.

1. (*a*) H. BEIERBECK, G. KOTOVYCH, and M. SUGIURA. Can. J. Chem. **63**, 1143 (1985); G. PUZICHA and A. LÉVAI. Synth. Commun. **15**, 623 (1985).
2. A. K. BOSE, W. A. HOFFMAN III, and M. S. MANHAS. J. Chem. Soc. Perkin Trans. 1, 2343 (1976).
3. T. E. GUNDA and C. ENEBACK. Acta Chem. Scand. B, **37**, 75 (1983).
4. A. LÉVAI and R. BOGNÁR. Acta Chim. Acad. Sci. Hung. **88**, 293 (1976).
5. A. LÉVAI and R. BOGNÁR. Acta Chim. Acad. Sci. Hung. **92**, 415 (1977).
6. A. LÉVAI. Pharmazie, **34**, 439 (1979).
7. A. LÉVAI, R. BOGNÁR, and J. KAJTÁR. Acta Chim. Acad. Sci. Hung. **103**, 27 (1980).
8. A. LÉVAI. Pharmazie, **36**, 449 (1981).
9. G. TÓTH, Á. SZÖLLÖSY, A. LÉVAI, and H. DUDDECK. Org. Magn. Reson. **20**, 133 (1982).
10. G. TÓTH, Á. SZÖLLÖSY, L. SCHULTZ, and A. LÉVAI. Acta Chim. Acad. Sci. Hung. **112**, 167 (1983).
11. J. B. HENDRICKSON, R. K. BOECKMAN, JR., J. D. GLICKSON, and E. GRUNWALD. J. Am. Chem. Soc. **95**, 494 (1973).
12. P. W. W. HUNTER and G. A. WEBB. Tetrahedron, **29**, 147 (1973).
13. H. BÖHME, S. EBEL, and K. HARTKE. Chem. Ber. **98**, 1463 (1965).
14. F. DURAN and L. GHOSEZ. Tetrahedron Lett. 245 (1970).
15. J. C. SHEEHAN and J. J. RYAN. J. Am. Chem. Soc. **73**, 1204 (1951); A. K. BOSE, G. SPIELGELMAN, and M. S. MANHAS. Tetrahedron Lett. 3167 (1971).
16. L. FODOR, J. SZABÓ, and P. SOHÁR. Tetrahedron, **37**, 963 (1981).
17. L. A. G. HAASNOOT, F. A. A. M. DE LEEUW, and C. ALTONA. Tetrahedron, **36**, 3783 (1980).
18. J. H. NOGGLE and R. E. SCHIRMER. The nuclear Overhauser effect. Academic Press, New York. 1971.
19. J. K. M. SAUNDERS and J. D. MERSH. Prog. Nucl. Magn. Reson. Spectrosc. **15**, 353 (1982).
20. P. SOHÁR, L. FODOR, J. SZABÓ, and G. BERNÁTH. Tetrahedron, **40**, 4387 (1984).
21. M. KINN and J. K. M. SAUNDERS. J. Magn. Reson. **56**, 518 (1984).

Can. J. Chem. Downloaded from www.nrcresearchpress.com by 176.9.209.113 on 09/07/12
For personal use only.

Régiosélectivité de la réaction des radicaux hydroxyle et hydroxy-2 propyle-2 avec l'hypoxanthine

JEAN ZYLBER, NICOLE ZYLBER ET DANIEL LEFORT

Laboratoire d'électrochimie catalyse et synthèse organique, Centre national de la recherche scientifique, 2, rue H. Dunant, 94320 Thiais, France

CHRISTIANE FERRADINI

Laboratoire de chimie physique, Université René Descartes, 45, rue des Saints-Pères, 75270 Paris CEDEX 06, France

ET

BERNARD HICKEL

Institut de recherche et de développement industriel – Département de physico-chimie – Service de chimie moléculaire – Unité associée au Centre national de la recherche scientifique, n° 331, Centre d'études nucléaires de Saclay, B.P. n° 2, 91190 Gif-sur-Yvette, France

Reçu le 17 février 1987 [1]

JEAN ZYLBER, NICOLE ZYLBER, DANIEL LEFORT, CHRISTIANE FERRADINI et BERNARD HICKEL. Can. J. Chem. **66**, 283 (1988).

La réactivité des radicaux ȮH et $(CH_3)_2\dot{C}OH$ avec l'hypoxanthine a été étudiée dans des conditions d'irradiation γ comparables. Une différence de régiosélectivité de l'attaque du radical ȮH, électrophile, et du radical $(CH_3)_2\dot{C}OH$, nucléophile, est mise en évidence. Ce dernier conduit au produit substitué en C-8 avec un rendement de 70%; la constante de vitesse d'addition du radical à l'hypoxanthine déterminée, en milieu acide, par radiolyse pulsée est $k = 1{,}4 \times 10^8\ M^{-1}\ s^{-1}$, et $k = 7 \times 10^5\ M^{-1}\ s^{-1}$ en milieu neutre. Le radical OH, beaucoup plus réactif, conduit essentiellement à des produits de dégradation dont le point de départ serait, entre autres, l'attaque en C-2 (donc formation de xanthine qui disparait rapidement); l'attaque en C-8, environ trois fois moins rapide, conduit à la dicéto-6,8 purine qui résiste aux réactions ultérieures et s'accumule dans le milieu.

JEAN ZYLBER, NICOLE ZYLBER, DANIEL LEFORT, CHRISTIANE FERRADINI, and BERNARD HICKEL. Can. J. Chem. **66**, 283 (1988).

The reactivity of ȮH and $(CH_3)_2\dot{C}OH$ radicals with hypoxanthine was studied under comparable γ-irradiation conditions. A difference in regioselectivity of attack by the electrophilic ȮH radical and the nucleophilic $(CH_3)_2\dot{C}OH$ radical is observed, the latter leading in 70% yield to a C-8 substituted product. The rate constants of the addition of the radical to hypoxanthine were determined by pulse radiolysis to be $k = 1.4 \times 10^8\ M^{-1}\ s^{-1}$ in acid medium, and in neutral medium $k = 7 \times 10^5\ M^{-1}\ s^{-1}$. The much more reactive ȮH radical leads essentially to degradation products arising, *inter alia*, from attack on C-2 (resulting in the formation of xanthine, which disappears rapidly), while attack at C-8, approximately three times less rapid, leads to the 6,8-diketo purine, which does not undergo further reactions and thus accumulates in the medium. [Journal translation]

L'action des radicaux hydroxyle produits par radiolyse de l'eau sur les bases puriques a fait l'objet de nombreux travaux dans le but de déterminer le mécanisme de dégradation des acides nucléiques soumis à l'irradiation γ (1).

La position 6 du noyau purique est le site privilégié d'attaque aussi bien des radicaux ·OH (2) que des radicaux carbonés (3). De nombreuses études ont montré que lorsque cette position 6 est substituée, la substitution par des radicaux carbonés se fait préférentiellement en 8 (4). La comparaison des résultats obtenus pour différents modèles a permis à certains auteurs (2, 5) de proposer la séquence de réactivité C6 > C8 > C2 en accord avec les conclusions d'une étude théorique (6).

La régiosélectivité de substitution des radicaux ·OH sur les bases puriques et en particulier sur l'hypoxanthine, premier maillon de la dégradation oxydative biochimique, n'est pas aussi évidente. En effet, selon certains auteurs, les radicaux ·OH produits lors de la radiolyse γ de l'eau, en solution oxygénée, réagissent quantitativement avec la double liaison centrale 4,5 pour conduire à des produits carbonylés de dégradation (7); d'autres auteurs ont montré que ·OH, obtenu à partir du réactif de Fenton, attaque l'hypoxanthine sur le cycle imidazole en position 8 pour donner la dicéto-6,8 purine (2).

Cette substitution en 8 a été établie également dans le cas de la radiolyse γ de l'adénine (8). Par ailleurs, l'un d'entre nous (9) a montré par une étude de radiolyse pulsée, que la réaction de ·OH sur l'hypoxanthine conduit principalement à la xanthine. Ni les études théoriques (10, 11), ni les analyses de spectres (résonance paramagnétique électronique) (12) ne permettent de prévoir ou d'expliquer sans ambiguïté les résultats expérimentaux; dans le premier cas l'ordre de réactivité d'un radical sur les différents atomes de carbone du noyau purique varie selon la méthode de calcul; dans le second, si le spectre du radical résultant de l'addition de ·OH en 8 est parfaitement défini pour le cas de la caféine, il n'en est pas de même pour ceux obtenus avec les purines non substituées en 2 ou 6.

Pour lever cette ambiguïté d'attaque par ·OH en 2 ou en 8 nous avons donc étudié les produits obtenus lors de la radiolyse γ d'une solution aqueuse d'hypoxanthine désaérée et saturée en N_2O. Les radicaux ·OH sont produits par les processus bien connus :

$$H_2O \rightsquigarrow \cdot OH,\ H\cdot,\ e^-_{aq.},\ H_2,\ H_2O_2$$

$$e^-_{aq} + N_2O \rightarrow N_2 + \cdot OH + {}^-OH$$

Puisque la réactivité et la régiosélectivité d'un radical dépendent, pour un substrat donné, de son caractère nucléophile ou électrophile (13, 14), il était intéressant de comparer les résultats obtenus, dans les mêmes conditions expérimentales, avec le radical ·OH électrophile et avec un radical nucléophile comme le radical **1** (hydroxy-2 propyle-2).

Celui-ci est formé lors de la radiolyse d'une solution aqueuse d'isopropanol; conformément aux travaux précédents (4), la

1. Revision reçue le 30 septembre 1987.

Can. J. Chem. Downloaded from www.nrcresearchpress.com by 213.222.148.141 on 09/07/12
For personal use only.

réaction avec l'hypoxanthine se déroule selon le schéma classique de substitution aromatique homolytique (14, 15) :

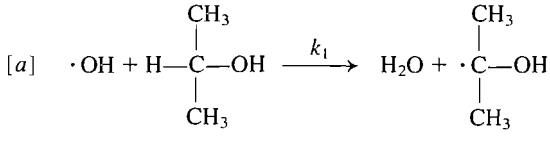

1

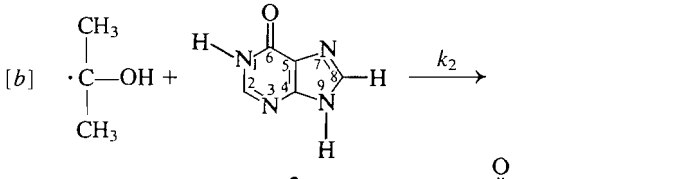

2

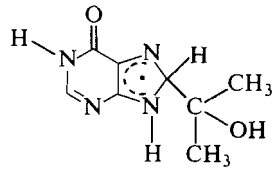

3

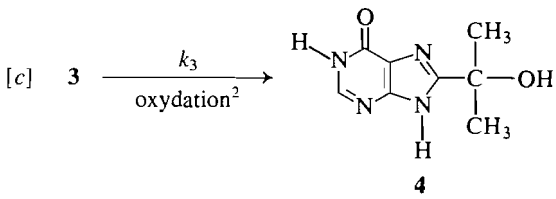

4

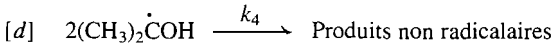

Le produit **4** a déjà été obtenu par d'autres méthodes photochimiques uv avec ou sans sensibilisateur (5, 16). De plus, par radiolyse pulsée, nous avons pu déterminer la constante de vitesse d'addition du radical **1** sur l'hypoxanthine et la comparer à celle obtenue précédemment pour ·OH (9).

Partie expérimentale

Le déroulement de la réaction est suivi par ccm (chromatographie sur couche mince) sur gel de silice (Kieselgel 60F254, Merck). Les points de fusion sont pris sous microscope. Les chromatographies hplc sont effectuées avec un appareil Varian 5000 muni d'un détecteur uv Shimadzu SPD/6A. Les spectres de masse sont obtenus avec un appareil de Ribermag 10-10. Les spectres de rmn sont enregistrés à 90 ou 200 MHz sur des appareils Bruker. Les déplacements chimiques sont exprimés en ppm avec le tétraméthylsilane comme référence interne. Les analyses sont exécutées par le Service central d'analyse du C.N.R.S. Toutes les expériences ont été effectuées sur des solutions aqueuses préalablement saturées en N_2O et irradiées à l'aide d'une source de ^{60}Co à une dose de 1055 rad/min.[3]

Matières premières

Les matières premières sont des produits commerciaux : hypoxanthine (Ega), acide urique (Aldrich), xanthine (Fluka), thymidine (Sigma).

Les solvants pour hplc sont des produits Carlo Erba.

*(Hydroxy-2' méthyl-2' éthyl)-8 hypoxanthine **4***

Une solution de 0,340 g (2,5 mmol) d'hypoxanthine et 30 g (0,5 mol) de propanol-2 dans 500 mL d'eau, saturée en N_2O, est irradiée pendant 16 h. La solution est ensuite lyophilisée; le résidu obtenu est chromatographié sur SiO_2 (70–230 mesh); par élution avec $CHCl_3$ à 10% MeOH on obtient une fraction brute de 219 mg dont le dosage par rmn ^1H permet de déterminer la présence de 100 mg de produit **4** (73% par rapport à l'hypoxanthine ayant réagi). La cristallisation dans l'acétate d'éthyle fournit 20 mg d'un échantillon pur d'(hydroxy-2' méthyl-2' éthyl)-8 hypoxanthine; F = décomposition au dessus de 350°C; uv (EtOH) : λ_{max} = 250 nm (log ε = 4,05); rmn 90 MHz (DMSO-d_6) δ : 1,53 (S, 6H, $2CH_3$, C-8 diméthylcarbinol), 7,93 (S, 1H, H en 2). Ce signal persiste après chauffage à reflux dans D_2O. Masse, m/e : 194. *Anal.* calc. pour $C_8H_{10}N_4O_2 + 1/2H_2O$: C 47,28, H 5,41, N 27,41; trouvé : C 48,08, H 5,25, N 27,58.

TABLEAU 1. Disparition de l'hypoxanthine **2** ($2{,}2 \times 10^{-3}$ *M* en solution aqueuse) par irradiation γ (1055 rad/min) au cours du temps

Temps (h)	**2** restant (%)	**7**/**2*** × 10^2	**7**/**2**† × 10^2
8	83	5,6	27
17	72	10	26
24	63	17	29
47	38	36	22

*2 restant.
†2 consommé.

*(Hydroxy-2' méthyl-2' éthyl)-8 caféine **5***

Une solution de 0,970 g (5 mmol) de caféine et 30 g (0,5 mol) de propanol-2 dans 500 mL d'eau, saturée en N_2O, est irradiée pendant 16 h. L'extraction avec $CHCl_3$ donne 1 g de produit. Par chromatographie sur silice (70–230 mesh) et élution par l'acétate d'éthyle on obtient 0,240 g de produit **5** chromatographiquement pur (95% par rapport à la caféine ayant réagi). La cristallisation dans un mélange acétate d'éthyle – méthanol fournit 170 mg de cristaux, pf 200–202°C (sublim. à 180°C) (lit. (5) pf 199–200°C); rmn 90 MHz (DMSO-d_6) δ : 1,8 (S, 6H, $2CH_3$, C-8 diméthylcarbinol), 3,4 (S, 3H), 3,6 (S, 3H), 4,25 (S, 3H) ($3CH_3$ en N-1, N-3 et N-7); masse, m/e : 252. *Anal.* calc. pour $C_{11}H_{16}N_4O_3$: C 52,37, H 6,39, N 22,21; trouvé : C 52,32, H 6,33, N 22,6. Par élution avec un mélange d'acétate d'éthyle – méthanol (99 : 1) on récupère 0,776 g (80%) de la caféine de départ.

*Irradiation de l'hypoxanthine dans H_2O. Dicéto-6,8 purine **7***

Une solution de 0,3 g (2,2 mmol) d'hypoxanthine dans 500 mL d'eau bidistillée, saturée en N_2O, est irradiée pendant 8, 16, 24 et 48 h. Pour chaque période la solution est lyophilisée; le produit obtenu est analysé par hplc; colonne Lichrosorb SRP 18, 150 × 46 mm; éluant eau/CH_3CO_2H/MeOH = 79,5 : 0,5 : 20. Détection à 270 nm. Dosage de l'hypoxanthine par rapport à la thymidine comme étalon interne. Résultats tableau 1. Temps de rétention (min) : acide urique, 3,3; dicéto-6,8 purine **7**, 3,5; xanthine, 3,9; hypoxanthine, 4,2. Débit 0,7 mL/min.

*Isolement et identification du produit **7***

Le mélange de produits obtenu après 48 h d'irradiation est chromatographié sur SiO_2 (200–400 mesh) sous pression (technique chromatographie «flash» et élué par $CHCl_3$/MeOH/NH_4OH 16 *M* : 40 : 10 : 1. On obtient 0,024 g de produit chromatographiquement pur (7% par rapport à l'hypoxanthine de départ). La cristallisation dans un mélange eau/MeOH fournit 8 mg de cristaux, pf : décomp. au délà de 350°C; les spectres uv sont différents de ceux de l'hypoxanthine et de la xanthine; aux pH 1 et 5, λ_{max} = 257 nm (log ε = 4,05) avec un épaulement caractéristique à 280 nm (log ε = 3,77); à pH 10, λ_{max} = 265 nm (log ε = 4,04), à pH 12, λ_{max} = 271 nm (log ε = 4,1) (17); rmn 90 MHz (DMSO-d_6) δ : 7,88 (S, 1H, H en 2), 11,07 (S, 1H, échangeable), 11,95 (S, 2H, échangeable); masse, m/e : 152, 124 (perte CO), 101 (pic métastable).

2. L'étape d'oxydation [c] peut se faire par différents processus selon la nature du milieu : dismutation avec un autre radical, oxygène de l'air, etc ...

3. Nous remercions M. Chapiro, C.N.R.S. à Thiais, d'avoir mis à notre disposition l'installation d'irradiation γ.

Can. J. Chem. Downloaded from www.nrcresearchpress.com by 213.222.148.141 on 09/07/12
For personal use only.

Can. J. Chem. Downloaded from www.nrcresearchpress.com by 213.222.148.141 on 09/07/12
For personal use only.

Réaction de l'hypoxanthine avec le propanol-2 en radiolyse pulsée

Une solution aqueuse à pH 0,95 d'hypoxanthine ($1,9 \times 10^{-3}$ *M*), de propanol-2 (0,75 *M*) et de $HClO_4$ (0,117 *M*) est soumise à la radiolyse pulsée.

La source d'électrons est un accélérateur type Febetron 707 situé au CEN de Saclay (DPC) (18). Dans cet appareil la décharge d'une série de modules comportant chacun deux résistances, deux condensateurs et un éclateur, est appliquée à une cathode à émission de champ contenue dans un tube sous vide. Une sélection magnétique des électrons de 1,8 MeV est alors utilisée pour réduire la durée de l'impulsion à environ 20 nanosecondes. Ces solutions sont contenues dans une cellule en Spectrosil (2,5 × 2,5 × 0,25 cm). À chaque impulsion l'énergie absorbée par la solution varie entre 70 et 700 Gray de sorte que la concentration initiale en radicaux libres ·OH est comprise entre 4×10^{-5} et 4×10^{-4} *M*.

L'analyse spectrophotométrique est effectuée par un montage optoélectronique classique incluant une lampe au xénon, un monochromateur et un photomultiplicateur. Le trajet optique est de 2,5 cm. Pour chaque longueur d'onde étudiée, le changement d'absorption est analysé en fonction du temps, le début de l'impulsion étant pris comme origine de l'échelle des temps.

Résultats et discussion

A. Réaction avec le propanol-2

1. Produit de réaction

Une solution aqueuse d'hypoxanthine (5×10^{-3} *M*) contenant de l'isopropanol (1 *M*) est irradiée sous N_2O à température ambiante pendant 16 h. Le taux de conversion est de 28%; le produit **4**, identifié par rmn et sm, est obtenu avec des rendements respectifs de 20 et 71% par rapport à l'hypoxanthine mise en oeuvre ou ayant réagi. Les 29% de produits secondaires formés n'ont pas été identifiés; toutefois aucun d'eux ne correspond au composé substitué en 2. Le produit disubstitué en 2 et 8 a été isolé en très petite quantité. Ce résultat montre que l'ordre de réactivité est bien C8 ≫ C2.

Dans ce système, le fait que les radicaux ·OH réagissent exclusivement avec l'isopropanol selon [*a*] pour conduire finalement au produit **4** plutôt qu'avec l'hypoxanthine (*vide infra*) n'est pas surprenant. En effet, les constantes de vitesse de ·OH avec l'hypoxanthine et avec l'isopropanol sont respectivement de $6,5 \times 10^9\ M^{-1}\ s^{-1}$ (9) et environ de $2 \times 10^9\ M^{-1}\ s^{-1}$ (19). Mais comme la concentration en isopropanol est 200 fois supérieure à celle de l'hypoxanthine, la réaction [*a*] de ȮH avec l'alcool est environ 60 fois plus rapide.

Dans les mêmes conditions réactionnelles nous avons obtenu avec la caféine le produit **5** substitué en 8, avec un rendement de

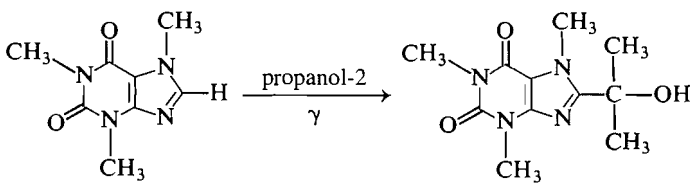

5

95% par rapport à la caféine ayant réagi et un taux de conversion analogue à celui obtenu avec l'hypoxanthine.

Un tel produit a déjà été obtenu par d'autres auteurs (5, 20) par irradiation uv ou γ. Nos résultats confirment la grande sélectivité du radical nucléophile hydroxypropyle **1** pour le sommet 8, en particulier dans le cas de la caféine où la transformation est pratiquement quantitative.

*2. Cinétique d'addition du radical **1** sur l'hypoxanthine*

L'étude a été faite en radiolyse pulsée; le spectre uv du radical intermédiaire **3** déterminé 10 μs après une impulsion délivrant une dose de 700 Gray environ, présente un maximum à 285 nm (fig. 1). Celui de l'hypoxanthine substituée **4** donne, en milieu neutre, deux maxima à 202 et 250 nm. Le déplacement bathochrome est donc conforme à ce que l'on sait des spectres uv des radicaux libres (15).

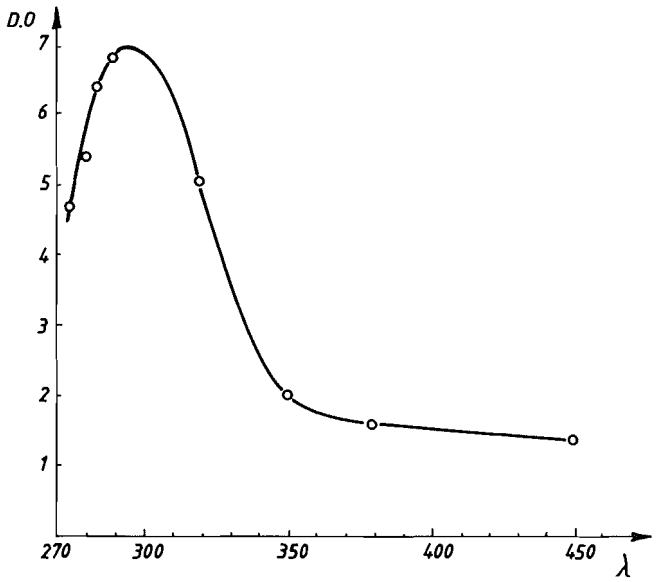

FIG. 1. Spectre différentiel d'absorption uv d'une solution aqueuse d'hypoxanthine ($1,9 \times 10^{-3}$ *M*) et de propanol-2 (0,75 *M*); 10 μs après l'impulsion; pH 0,95 ($HClO_4$ 0,117 *M*).

En milieu acide la réaction d'addition du radical hydroxypropyle **1** sur l'hypoxanthine est rapide. On peut suivre en fonction du temps l'apparition du radical **3** à 300 nm qui suit une cinétique de pseudo premier ordre avec un coefficient de corrélation de 0,999. En effet, la concentration initiale de l'hypoxanthine ($1,9 \times 10^{-3}$) est 40 fois supérieure à celle du radical hydroxypropyle **1**. La valeur de la constante de vitesse de la réaction [*b*] est alors $k_2^{(acide)} = 1,4 \times 10^8\ M^{-1}\ s^{-1}$.

Il est intéressant de comparer cette valeur à celles déjà connues pour des réactions de substitution homolytique de bases hétéroatomiques[4] dont la réactivité vis-à-vis de radicaux nucléophiles est plus élevée sous leur forme protonée que sous leur forme neutre (21) (dans le cas de la pyridine le facteur est de 70 environ).

En milieu neutre, une détermination directe de k_2 n'est pas possible car seulement une faible fraction de radicaux hydroxypropyle **1** réagissent sur l'hypoxanthine. Les autres disparaissent par dimérisation et dismutation selon la réaction [*d*], dont la valeur de la constante de vitesse est $k_4 = 7 \times 10^8\ M^{-1}\ s^{-1}$ (22). Néanmoins, en faisant l'hypothèse que l'absorption à 300 nm est due au radical **3** et que ε est du même ordre de grandeur en milieu acide et en milieu neutre (23), on peut calculer la fraction des radicaux hydroxypropyle **1** ayant réagi sur l'hypoxanthine et avoir ainsi une estimation de la valeur de k_2 en résolvant numériquement le système d'équations différentielles simultanées correspondant aux réactions [*b*] et [*d*]. On trouve alors k_2 (neutre) $\cong 7 \times 10^5\ M^{-1}\ s^{-1}$. Celle-ci, comparée à celle de ȮH, et déterminée également en milieu neutre (9) (*vide supra*), montre que le radical électrophile ȮH est

4. Les constantes de vitesse d'addition d'un radical primaire sur la quinoxaline et la pyridine protonées sont respectivement de $2,7 \times 10^7$ et $1,1 \times 10^5\ M^{-1}\ s^{-1}$ (21).

beaucoup plus réactif (environ 10 000 fois) que le radical hydroxypropyle **1** sur l'hypoxanthine.

On peut noter qu'en radiolyse γ la concentration stationnaire des radicaux hydroxypropyle **1** est de plusieurs ordres de grandeur plus faible qu'en radiolyse pulsée; par conséquent, dans le premier cas, la réaction [*d*] est négligeable par rapport à la réaction [*b*], même en milieu neutre.

B. Réaction avec les radicaux ·OH

L'action des radicaux ·OH sur l'hypoxanthine peut conduire soit à la xanthine **6** (attaque en 2), soit à la dioxo-6,8 purine **7** (attaque en 8):

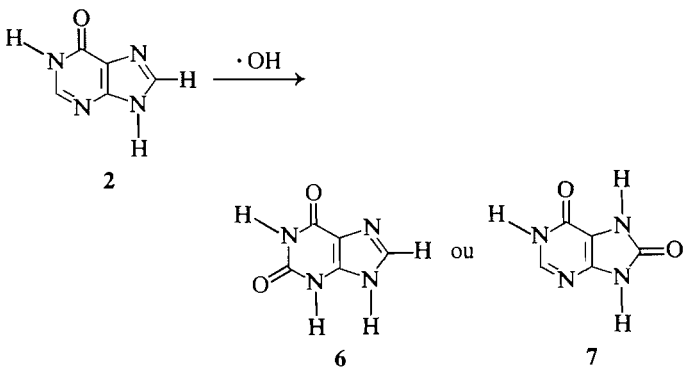

2 **6** **7**

Par ailleurs l'attaque sur la double liaison centrale selon Hollian et Garrison (7) conduirait à des produits de dégradation carbonylés. En régime permanent de production de ·OH, comme c'est le cas dans le présent travail, les produits **6** et **7** peuvent être oxydés en acide urique qui lui-même est dégradé.

L'irradiation pendant 48 h d'une solution 5×10^{-3} *M* d'hypoxanthine, saturée en N_2O, conduit à un mélange de 38% de produit de départ, 6% de dioxo-6,8 purine **7** (caractérisé par les spectres uv et de masse et par hplc) et 56% de produits non identifiés mais parmi lesquels nous n'avons pu mettre en évidence ni xanthine, ni acide urique.

Nous avons suivi au cours du temps la disparition de l'hypoxanthine par hplc en utilisant la thymine comme étalon interne. Par un traitement de lissage de courbe on trouve que la vitesse de disparition obéit à une loi d'ordre 0,80, ce qui traduit bien la complexité de la réaction. En l'absence d'un échantillon authentique de dioxo-6,8 purine nous n'avons pu faire de dosage exact de ce composé mais nous avons pu évaluer la quantité formée par rapport à celle de l'hypoxanthine restante. Les résultats donnés dans le tableau 1 permettent de faire deux constatations:

(*i*) La quantité de dioxopurine **7** croît au fur et à mesure de la disparition de l'hypoxanthine.

(*ii*) Le rapport de la quantité de dioxopurine **7** à celle de l'hypoxanthine consommée reste constant au cours de l'expérience.

Nous pouvons donc conclure que la dioxopurine **7** formée à partir de l'hypoxanthine ne subit pas ou peu de dégradation ultérieure par irradiation. À partir de cette déduction un raisonnement cinétique montre que ȮH est environ 3 fois plus réactif en position **2**, on peut-être sur d'autres sites, qu'en position 8.[5]

Les constantes de vitesse de réaction de ȮH sur la xanthine et sur l'hypoxanthine sont à peu près équivalentes (9). Néanmoins, nous avons voulu vérifier la vitesse de disparition de la xanthine dans nos conditions expérimentales.

Dans ce but nous avons irradié à la même dose que précédemment une solution aqueuse $0,87 \times 10^{-4}$ *M* de xanthine. Après 4 h, l'analyse par hplc montre qu'il reste seulement 5% de produit de départ; aucune trace d'acide urique n'a pu être détectée.

Conclusion

Les résultats de ce travail permettent de comparer la réactivité et la régiosélectivité des radicaux ȮH et hydroxy-2 propyle-2 **1** sur l'hypoxanthine dans des conditions expérimentales comparables.

Le radical hydroxy-2 propyle-2 **1**, nucléophile, conduit principalement au produit substitué en C-8 avec un rendement de 70%. Sa constante de vitesse d'addition sur l'hypoxanthine déterminée par radiolyse pulsée est $k = 1,4 \times 10^8 M^{-1} s^{-1}$ en milieu acide et environ $7 \times 10^5 M^{-1} s^{-1}$ en milieu neutre. Aucun produit de substitution en C-2 n'est décelable. Ceci confirme donc la plus grande réactivité d'un radical nucléophile en C-8 qu'en C-2 (cf. réf. 4 et réf. 5).

Le radical ·OH, électrophile, très réactif (environ 10 000 fois plus que **1**) conduit surtout à des produits de dégradation. Il y a tout lieu de penser (cf. réf. 9) que le premier intermédiaire est la xanthine, résultant de l'attaque en C-2, qui disparait rapidement par réaction avec ·OH. Néanmoins il se forme une certaine quantité de dicéto-6,8 purine qui résiste aux réactions ultérieures. Ce résultat suggère que la présence du carbonyle en C-8 diminue considérablement la réactivité du carbone C-2 ou d'autres sites vis-à-vis de ȮH.

Remerciements

Nous remercions vivement de Dr Jacques Fossey pour les discussions fructueuses que nous avons eues au cours de ce travail, Mme Andrée Druilhe pour les analyses qualitatives et quantitatives par hplc et J. Potier pour les expériences de radiolyse pulsée.

1. (*a*) L. Myers. *Dans* Free radicals in biology. Vol. IV. *Éditeur*: W. Pryor. Academic Press, New York. 1980. p. 95; (*b*) J. Cadet et M. Berger. Int. J. Radiat. Biol. **47**, 127 (1985).
2. C. Nofre, A. Lefier et A. Cier. C.R. Hebd. Seances Acad. Sci. **253**, 687 (1961).
3. (*a*) H. Linschitz et J. Connolly. J. Am. Chem. Soc. **90**, 2979

5. À partir du schéma:

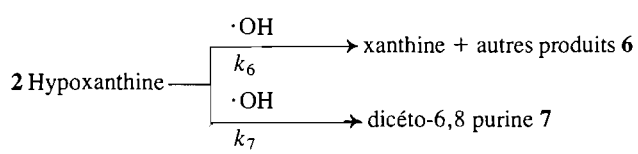

Supposons que le produit **7** ne disparait pas au cours de la réaction; en faisant le rapport des vitesses d'apparition de **7** et de disparition de **2** on obtient:

$$\frac{d|7|}{d|2|} = -\frac{1}{1 + k_6/k_7}$$

En intégrant entre le temps initial (0) et final (f)

$$\frac{|7|_f - |7|_0}{|2|_f - |2|_0} = -\frac{1}{1 + k_6/k_7}$$

au temps initial $|7|_0 = 0$, donc:

$$\frac{|7|_f}{|2|_0 - |2|_f} = -\frac{1}{1 + k_6/k_7} = a$$

En prenant $a = 0,26$ (tableau 1), on obtient $k_6/k_7 = 2,85$, c'est-à-dire que ȮH réagit environ 3 fois plus rapidement sur la position 2 (ou peut-être sur d'autres sites) qu'en position **8**.

Can. J. Chem. Downloaded from www.nrcresearchpress.com by 213.222.148.141 on 09/07/12
For personal use only.

(1968); (*b*) B. EVANS et R. WOLENDEN. J. Am. Chem. Soc. **92**, 4751 (1970).
4. (*a*) D. ELAD. *Dans* Photochemistry and photobiology of nucleic acids. Vol. 1. *Éditeur* : S. Y. Wang. Academic Press, New York. 1976. pp. 357–380; (*b*) D. LEONOV et O. ELAD. J. Org. Chem. **39**, 1470 (1974) (et références contenues); (*c*) M. ZADY et J. WONG. J. Org. Chem. **45**, 2373 (1980) (et références contenues).
5. H. STEINMAUS, I. ROSENTHAL et D. ELAD. J. Org. Chem. **36**, 3594 (1971).
6. B. PULLMAN. J. Chem. Soc. 1621 (1959).
7. (*a*) J. HOLLIAN et W. GARRISON. J. Phys. Chem. **71**, 462 (1967); (*b*) J. Chem. Soc. Chem. Commun. 676 (1967).
8. J. VAN HEMMEN et J. BLEICHRODT. Radiat. Res. **46**, 444 (1971).
9. J. SANTAMARIA, C. PASQUIER, C. FERRADINI et J. PUCHEAULT. Radiat. Res. **97**, 452 (1984).
10. Z. NEIMAN. Isr. J. Chem. **9**, 119 (1971).
11. T. MASUDA, H. SHINOHARA et M. KONDO. J. Radiat. Res. **16**, 153 (1975).
12. J. SCHMIDT et D. BORG. Radiat. Res. **65**, 220 (1976).
13. F. MINISCI et A. CITTERIO. *Dans* Advances in free-radical chemistry. Vol. 6. *Éditeur* : G. Williams. Heyden, London. 1980. p. 65.
14. F. MINISCI. Top. Curr. Chem. **62**, 1 (1976).
15. D. NONHEBEL et J. WALTON. Free-radical chemistry. Cambridge University Press, London. 1974.
16. S. BOSE et R. DAVIES. Photochem. Photobiol. **31**, 195 (1980).
17. S. MASON. J. Chem. Soc. 2071 (1954).
18. B. HICKEL. J. Phys. Chem. **82**, 1005 (1978).
19. B. BIELSKI et J. GEBICKI. *Dans* Free radicals in biology. Vol. III. *Éditeur* : W. Pryor. Academic Press, New York. 1977. p. 35.
20. J. SALOMON et D. ELAD. J. Org. Chem. **38**, 3420 (1973).
21. A. CITTERIO, F. MINISCI, O. PORT et G. SESANA. J. Am. Chem. Soc. **99**, 7960 (1977).
22. M. SIMIC, P. NETA et E. HAYON. J. Phys. Chem. **73**, 3794 (1969).
23. P. HOORTHY et E. HAYON. J. Am. Chem. Soc. **97**, 3345 (1975).

Can. J. Chem. Downloaded from www.nrcresearchpress.com by 213.222.148.141 on 09/07/12
For personal use only.

Comment: Limitations of the mixing rule proposed by Humffray for estimating the densities of aqueous mixed electrolyte solutions

ANIL KUMAR

Department of Sugar Chemistry, Deccan Sugar Institute, Manjari (Bk) Poona 412 307, India

Received July 21, 1987

ANIL KUMAR. Can. J. Chem. **66**, 288 (1988).

The recently proposed mixing rule by Humffray (Can. J. Chem. **65**, 833 (1987)) is examined using very precise experimental density data on aqueous mixed electrolytes. It is observed that the computed results deviate systematically from the experimental data, where the mixture densities are not linear with the component electrolyte densities.

ANIL KUMAR. Can. J. Chem. **66**, 288 (1988).

Utilisant des données très précises pour les densités expérimentales d'électrolytes mixtes en solutions aqueuses, on réexamine la règle des mélanges qui a été proposée récemment par Humffray (Can. J. Chem. **65**, 833 (1987)). On observe que les résultats calculés dévient systématiquement des données expérimentales lorsque les densités des mélanges ne sont pas linéaires avec les densités des composantes de l'électrolyte.

[Traduit par la revue]

Can. J. Chem. Downloaded from www.nrcresearchpress.com by 213.222.148.141 on 09/07/12
For personal use only.

In a recent article, Humffray (1) has derived a simple mixing rule for predicting the densities of aqueous mixed electrolyte solutions. He claimed excellent fits for the densities of aqueous NaCl–KBr (2), KCl–$CaCl_2$ (3), and satisfactory fits for NaCl–$CaCl_2$ (4, 5) systems using the mixing rule.

His equation for estimating the increments in density, Δd, is

$$[1] \quad \Delta d = \sum_j y_j \Delta d_j$$

where $\Delta d = d - d_0$; d and d_0 are densities of solution and water, respectively; y_j is ionic strength fraction of component j in mixture; and Δd_j is increment in density of a pure electrolyte solution.

In this note, I examine his mixing rule using very reliable density data for various systems and bring out the limitations, which restrict its application in estimating the densities of these mixtures.

The density data examined are listed in Table 1 along with their source and conditions. Equation [1], when applied to the systems with common and uncommon ions, yields results deviating systematically from the experimental densities. In Fig. 1 are plotted the deviations, δd, the differences obtained from the experimental and calculated densities ($d_{exp} - d_{calcd}$ by eq. [1]), as a function of y_2 the ionic strength fraction of second electrolyte in mixtures. One clearly observes large positive or negative systematic deviations. For example, for three ion systems like aq. $MgCl_2$–NaCl (6) at $I = 3$, δd reaches up to approximately +570 ppm and −671 ppm in the case of aq. NaCl–Na_2SO_4 (6) at $I = 3$. The similar situation can be observed for aq. NaCl–$CaCl_2$ (4) system, where Humffray quoted satisfactory standard deviations. However, one finds in Fig. 1 that for $I = 5$, the δd values pass a maximum of +273 ppm starting and ending at approximately −400 ppm. In general the deviation plots exhibit a symmetric parabola. The situations for four-ion systems are equally inferior extending δd to −603 ppm. The equation was also examined for aq. Li_2SO_4–LiCl, Na_2SO_4–NaCl, and Li_2SO_4–Na_2SO_4 reported by Wirth and Losurdo (7), yielding results with systematic deviations. In Table 1, the values of δd at $y_2 = 0.5$ are also listed. The equation also fails (maximum $\delta d = -169$ ppm) to predict the densities (8) of aq. KCl–K_2SO_4 at $I = 1.5$ where Δd for constituent electrolyte solutions differ only by 294 ppm. It is interesting that the equation overestimates the densities for the mixing of uncommon cations in the presence of common anion. In the case of uncommon anion mixing with common cation, the estimations are generally lower than the experimental data.

TABLE 1. Summary of experimental data used in testing the Hummfray mixing rule

Systems	Range of ionic strength (mol kg^{-1})	Maximum δd at $y_2 = 0.5$	No. of data points	Reference
NaCl–$CaCl_2$	0.3–5	+273	93	4, 5
NaCl–Na_2SO_4	1–3	−671	24	6, 8
Na_2SO_4–$MgSO_4$	1,3	+267	15	6
$MgSO_4$–$MgCl_2$	1,3	−333	18	6
$MgCl_2$–NaCl	1,3	+570	18	6
NaCl–$MgSO_4$	1,3	+363	18	6
$MgCl_2$–Na_2SO_4	1,3	−603	18	6
NaCl–KCl	1.5	+30	8	8
KCl–K_2SO_4	1.5	−169	8	8
K_2SO_4–Na_2SO_4	1.5	−20	8	8
NaCl–K_2SO_4	1.5	−214	8	8
KCl–Na_2SO_4	1.5	−186	8	8

Humffray reported the use of this equation with excellent accuracy in the cases of aq. NaCl–KBr and KCl–$CaCl_2$ systems. It is natural that the equation will fit experimental density data for the mixtures, where the variation of densities in mixture is linear with the component densities. This is the situation with the above two systems. But, as one can see that the densities do not always vary linearly, and thus this equation proposed by Humffray does not find extensive use in estimating the densities of mixtures. In general, the equations that predict the densities of the four-ion system, also do predict for the three-ion system with good accuracy, but this equation fails to do so.

Moreover, if the densities of mixture vary linearly with the component densities, it does not imply that the systems will obey the Young rule (9). A correction term, ΔV_m (excess volumes) is needed in order to fit the mixture data. This has been accomplished by several authors (6–12). It must be noted that whatever the δd values one obtains using eq. [1], these values will not indicate the magnitude of the correction term, ΔV_m.

Printed in Canada / Imprimé au Canada

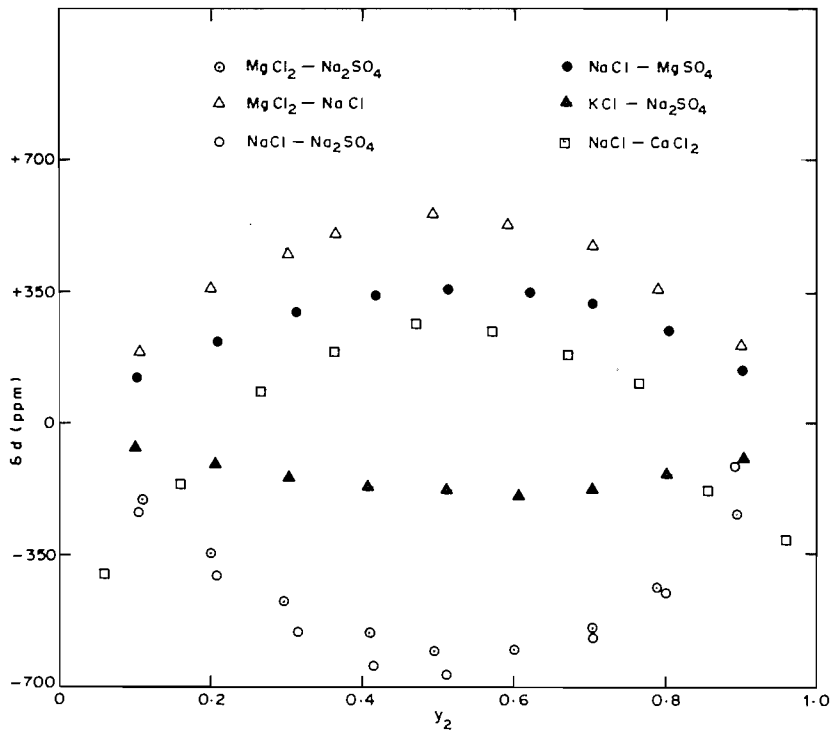

FIG. 1. Deviations, δd (experimental − calculated densities) against y_2 (ionic strength fraction of second electrolyte) for various electrolyte mixtures. Aqueous KCl–Na_2SO_4 and aq. NaCl–$CaCl_2$ are at $I = 1.5$ and 5 mol kg^{-1}; remaining systems are at $I = 3$ mol kg^{-1}.

1. A. A. HUMFFRAY. Can. J. Chem. **65**, 833 (1987).
2. A. KUMAR. Can. J. Chem. **63**, 3200 (1985).
3. A. KUMAR. J. Chem. Eng. Data, **31**, 21 (1986).
4. A. KUMAR, G. ATKINSON, and R. D. HOWELL. J. Solution Chem. **11**, 857 (1982).
5. A. KUMAR and G. ATKINSON. J. Phys. Chem. **87**, 5504 (1983).
6. F. J. MILLERO, L. M. CONNAUGHTON, F. VINOKUROVA, and P. V. CHETIRKIN. J. Solution Chem. **14**, 837 (1985).
7. H. E. WIRTH and A. LOSURDO. J. Chem. Eng. Data, **13**, 226 (1968).
8. S. SATOLONGO and F. J. MILLERO. J. Chem. Eng. Data, **31**, 470 (1986).
9. T. F. YOUNG. Rec. Chem. Prog. **12**, 81 (1951).
10. T. F. YOUNG and M. B. SMITH. J. Phys. Chem. **58**, 716 (1954).
11. T. F. YOUNG, Y. C. WU, and A. A. KRAWETZ. Discuss. Faraday Soc. **24**, 37 (1957).
12. Y. C. WU, M. B. SMITH, and T. F. YOUNG. J. Phys. Chem. **69**, 1868 (1965).

Can. J. Chem. Downloaded from www.nrcresearchpress.com by 213.222.148.141 on 09/07/12
For personal use only.

Thermodynamic investigation of molecular complexation in binary acetone + bromoform mixture

HARI P. DAHIYA, PREM P. SINGH, AND SHASHI DAGAR

Department of Chemistry, Maharshi Dayanand University, Rohtak-124001, India

Received July 7, 1987

HARI P. DAHIYA, PREM P. SINGH, and SHASHI DAGAR. Can. J. Chem. **66**, 290 (1988).

Molar excess volumes, V^E, and molar excess enthalpies, H^E, have been measured for acetone (A) + bromoform (B) mixtures at 298.15 and 308.15 K. Results of these measurements suggest the formation of a 1:1 acetone–bromoform molecular complex. The equilibrium constant, K, the enthalpy of formation, ΔH, of the AB complex as also the molar volume change, ΔV, accompanying the complexation reaction A + B $\rightleftarrows$ AB have been evaluated from the measured H^E and V^E data. The K value so obtained has further been substantiated by the K value determined for the AB molecular entity from nmr studies on this mixture. Partial molar enthalpy of B (at infinite dilution) in A and vice versa have also been evaluated from the measured H^E data at 298.15 K and used to calculate a consistent molar enthalpy of AB complex formation.

HARI P. DAHIYA, PREM P. SINGH et SHASHI DAGAR. Can. J. Chem. **66**, 290 (1988).

Opérant à 298,15 et 308,15 K, on a mesure les volumes molaires en excès, V^E, et les enthalpies molaires en excès, H^E, de mélanges d'acétone (A) et de bromoforme (B). Les résultats de ces mesures suggèrent qu'il y a formation d'un complexe moléculaire 1:1 acétone:bromoforme. En se basant sur les données de H^E et de V^E, on a calculé la constante d'équilibre, K, l'enthalpie de formation, ΔH, du complexe AB ainsi que le changement de volume molaire, ΔV, qui accompagne la réaction de complexation A + B $\rightleftarrows$ AB. La valeur de K ainsi déterminée a aussi été confirmée par la valeur de K déterminée pour l'entité moléculaire AB en se basant sur des études rmn sur le mélange. Sur la base des valeurs de H^E mesurées à 298,15 K, on a évalué l'enthalpie molaire partielle de B (à dilution infinie) dans A (et vice versa) et on a aussi calculé une enthalpie molaire consistante pour la formation du complexe AB.

[Traduit par la revue]

Introduction

Very few spectroscopic studies are available that yield precise equilibrium constant and molar enthalpy of formation data for weak molecular complexes in binary non-electrolyte mixtures. A number of workers (1–5) have, however, suggested that it is possible to determine both the equilibrium constant and the enthalpy of formation of such weak molecular complexes if molar excess enthalpy (H^E) data for these binary mixtures are available. Since acetone (A) is expected to undergo specific interactions with bromoform (B), the present studies were undertaken to first investigate the nature of the molecular complex and second evaluate equilibrium constant, K, the molar enthalpy of formation, ΔH, and the change in molar volume (ΔV) associated with the formation of the molecular moiety in this (A + B) mixture.

Experimental

Acetone and bromoform (Merck, Analar grade) were purified as suggested by Vogel (6). The purities of the final samples were checked by measuring their densities at 298.15 ± 0.01 K and these agreed to within ±0.00005 g cm^{-3} with their corresponding literature values (7, 8); the density of bromoform at 298.15 K was, however, evaluated from the density vs. temperature plot utilizing the relevant data reported in the literature (8).

Molar excess volume (V^E) data at 298.15 and 308.15 K were measured dilatometrically in the manner described earlier (9). In essence the two accurately weighed components were kept separated in a U shaped dilatometer by a thread of mercury. The dilatometer was then placed in a water bath maintained at 298.15 K or 308.15 ± 0.01 K and the position of the liquid in the calibrated dilatometer capillary and of the reference mark on the dilatometer capillary were noted with a cathetometer that could read to ±0.001 cm after thermal equilibrium. The contents of the dilatometer were then mixed thoroughly by tilting the dilatometer. To ensure that the liquid in the dilatometer capillary had the same composition as that of the bulk, the dilatometer was taken out of the water bath and cooled slightly so as to have a minimum amount of liquid in the capillary. The dilatometer was again placed in the water bath and this process was repeated three times before the dilatometer was finally clamped in the water bath for thermal equilibrium. The position of the liquid in the dilatometer capillary and that of the reference mark were again noted. From the change in position of the liquid level in the dilatometer capillary and the volume per cm length, V^E values were calculated (9). The capillary was calibrated by weighing a column of mercury thread (9). Uncertainties in the measured V^E values were about 0.5%.

Molar excess enthalpies, H^E, at 298.15 and 308.15 K were determined by an LKB flow microcalorimeter LKB-2107 (M/s LKB, Broma, Sweden) in the manner described by Monk and Wadso (10). The precision and stability of the instrument in terms of temperature is 0.1 K and ±0.01 K/24 h, respectively. Two identical Braun perfusor pumps (B. Braun Melsungen AG, W. Germany) and gas-tight Hamilton syringes were employed to pump liquids through the calorimeter. Using 10, 20, and 50 cm^3 syringes and 10 speed gear boxes of the perfusor pumps, different mixing ratios were achieved. The flow rates were determined by pumping distilled water through the calorimeter and weighing the amounts collected in a specific time interval. For each typical H^E measurement, different calibration constants were determined according to the flow rate, the amplification needed, and the composition of the mixture. The uncertainties in our measured H^E values are of the order of 1% or better. The performance of the calorimeter was checked (11) by measuring H^E data for benzene + carbon tetrachloride mixture at 298.15 K. Our measured H^E values (11) for this mixture agreed within the reported uncertainties with reliable literature values (12).

Samples for nmr studies were prepared by mixing bromoform with acetone (by weight) in nmr tubes followed by dilution with a fixed quantity of cyclohexane. Immediately after preparation, a fixed quantity of tetramethylsilane (TMS) was added to each tube and the spectra was recorded on a Varian 90 MHz spectrometer. The chemical shift of bromoform relative to TMS was then obtained using the side band method (13) and shifts for all the mixtures were averaged over three determinations and were reproducible to ±0.5 Hz.

Results

Molar excess volume, V^E, and molar excess enthalpy, H^E, data for this mixture as a function of composition at 298.15

Can. J. Chem. Downloaded from www.nrcresearchpress.com by 176.9.209.113 on 09/07/12
For personal use only.

Can. J. Chem. Downloaded from www.nrcresearchpress.com by 176.9.209.113 on 09/07/12
For personal use only.

TABLE 1. Measured molar excess volume V^E, various parameters of eq. [1] along with the standard deviation $\sigma(V^E)$ for the mixture acetone (A) + bromoform (B) for various mole fractions, x_A

x_A	V^E (cm^3 mol^{-1})	x_A	V^E (cm^3 mol^{-1})
Temperature = 298.15 K			
0.1775	0.065	0.5999	0.225
0.3372	0.123	0.6641	0.238
0.3549	0.131	0.7711	0.233
0.4631	0.176	0.8572	0.191
0.5097	0.195	0.9071	0.141
$V_0^{(0)} = 0.760$ cm^3 mol^{-1}, $V_0^{(1)} = 0.7737$ cm^3 mol^{-1}, $V_0^{(2)} = 0.4581$ cm^3 mol^{-1}, $\sigma(V^E) = 0.001$ cm^3 mol^{-1}			
Temperature = 308.15 K			
0.1230	−0.122	0.7151	−0.307
0.2504	−0.226	0.7852	−0.261
0.3911	−0.307	0.8552	−0.196
0.5005	−0.339	0.9250	−0.114
0.5775	−0.343	0.9733	−0.044
0.6350	−0.335		
$V_0^{(0)} = -1.36$ cm^3 mol^{-1}; $V_0^{(1)} = -0.317$ cm^3 mol^{-1}; $V_0^{(2)} = -0.0312$ cm^3 mol^{-1}, $\sigma(V^E) = 0.001$ cm^3 mol^{-1}			

TABLE 2. Measured molar excess enthalpy H^E, various parameters of eq. [1] along with the standard deviation $\sigma(H^E)$ for the mixture acetone (A) + bromoform (B) for various mole fraction, x_A

x_A	H^E (J mol^{-1})	x_A	H^E (J mol^{-1})
Temperature = 298.15 K			
0.0608	−289.5	0.7078	−1134.2
0.1171	−543.9	0.7387	−1042.1
0.2039	−899.0	0.8564	−607.0
0.3838	−1363.1	0.9229	−327.9
0.5346	−1447.7	0.9598	−171.0
$H_0^{(0)} = -5850.0$ J mol^{-1}, $H_0^{(1)} = 297.6190$ J mol^{-1}, $H_0^{(2)} = 1375.0$ J mol^{-1}, $\sigma(H^E) = 0.8$ J mol^{-1}			
Temperature = 308.15 K			
0.1062	−415.0	0.7067	−927.0
0.1956	−669.8	0.7374	−876.2
0.3196	−911.1	0.8484	−610.6
0.3822	−985.7	0.9186	−371.9
0.5331	−1055.8	0.9834	−83.2
$H_0^{(0)} = -4220.0$ J mol^{-1}, $H_0^{(1)} = -327.4$ J mol^{-1}, $H_0^{(2)} = -657.7$ J mol^{-1}, $\sigma(H^E) = 0.9$ J mol^{-1}			

and 308.15 K (recorded in Tables 1 and 2) were fitted to the equation.

$$[1] \quad X^E\,(X = V \text{ or } H) = x_A x_B \Sigma X_0^{(n)}(2x_A - 1)^n$$

where x_A is the mole fraction of acetone. Binary coefficients, $X_0^{(n)}$ ($X = V$ or H), were calculated by fitting X^E ($X = V$ or $H)/x_A x_B$ to eq. [1] by the method of least squares and are reported in Tables 1 and 2 along with the standard deviations, $\sigma(X^E)$.

The proton chemical shifts of bromoform in its mixture with acetone relative to pure bromoform are reported in Table 3.

TABLE 3. Proton resonance shifts δ of acetone (A) + bromoform (B) mixtures with respect to pure bromoform as a function of x_B

x_B	δ (Hz)
0.1126	−36.0
0.1244	−31.5
0.3833	−19.8
0.4381	−19.8
0.5065	−9.9
0.8247	4.5
0.9124	9.9

Discussion

We are unaware of any recent V^E data at 298.15 and 308.15 K with which to compare our results. Trew (14) determined densities of this mixture at 298.15 K but the resulting V^E data are of poor quality and are predominantly negative in contrast to the present results. For the two sets of older H^E results reported (15) for this mixture at 298.15 K, the data agree fairly well over the range $0.5 < x_A < 1.0$ and are considerably less negative than the present results.

Interestingly while the present V^E data are 298.15 K for this mixture are positive, they are negative at 308.15 K over the entire range of x_A. On the other hand, H^E data are negative at 298.15 and 308.15 K and $\partial H^E/\partial T$ is positive.

V^E and H^E values of acetone + bromoform may be explained if it is assumed that this mixture is characterized by (*i*) specific O---H interaction between the oxygen atom of A and the proton of B and (*ii*) steric repulsion between the bulky —CH_3 substituents and the bromine atoms. Consequently, the transition from negative V^E value at 308.15 to positive V^E values at 298.15 K should mean that although the lowering of temperature should cause A to interact strongly with B, the steric repulsion between the bulky —CH_3 substituents and the bromine atoms should also increase appreciably. Since V^E is a packing effect and its values are positive at 298.15 K and negative at 308.15 K, one may infer that steric repulsions (between the bulky —CH_3 subsituents and the bromine atoms) at 298.15 K outweigh specific interactions between A and B. To prove this one has to compare H^E data at 298.15 K with those at 308.15 K. The latter should be less negative. Experimental H^E data of this mixture tends to support this conjecture.

Since H^E data at 298.15 and 308.15 K are almost symmetrical about x_A, they suggest the following reaction for the formation of a single molecular complex.

$$[2] \quad A + B \rightleftharpoons AB$$

Matsui *et al.* (17), Singh and Sharma (3), and Fenby and Helper (2, 4) have shown that the equilibrium constant K, and the molar enthalpy of complex formation, ΔH, are related to the H^E data by

$$[3] \quad \frac{x_A x_B}{H^E} = -\left[\frac{(K+1)}{K(\Delta H)^2}\right]H^E + \frac{(K+1)}{K(\Delta H)}$$

provided the "physical" interactions between A and B are negligibly small compared to the "chemical" interactions. Matsui *et al.* (17) have further suggested that this requirement is met if the measured H^E value is greater than about 1.5 kJ/mol at

$x_A = 0.5$. The measured H^E for acetone + bromoform mixture fulfills this requirement, at 298.15 K and a linear plot of $x_A x_B/H^E$ versus H^E was observed.

The intercept (-2.18×10^{-4} J^{-1} mol) and the slope (-3.333×10^{-8} J^{-1} mol^2) then yielded $K = 2.35$ and $\Delta H = -6.54$ kJ mol^{-1}. Equation [3], however, could not be applied to H^E data at 308.15 K of this (A + B) mixtures since the measured $-H^E$ value at $x_A = 0.5$ is much less than 1.5 kJ.

To further supplement the numerical value for the equilibrium constant, we studied the proton chemical shift, δ, of bromoform relative to that of pure bromoform in its binary mixtures with acetone. The relevant δ data are recorded in Table 3 and it is clearly evident that there is a net shift of the bromoform proton towards low magnetic fields. Thus the protons of bromoform are deshielding in its interactions with acetone. The nmr data of binary acetone + bromoform mixture were then used to calculate the equilibrium constant.

If $\mathscr{C}_A$, $\mathscr{C}_B$, and $\mathscr{C}_{AB}$ denote the actual mole fractions of acetone, bromoform, and the complex AB, respectively, then

$$[4] \quad K = \mathscr{C}_{AB}/\mathscr{C}_A\mathscr{C}_B$$

Further $\mathscr{C}_A$, $\mathscr{C}_B$, and $\mathscr{C}_{AB}$ are related (18) to the stoichiometric mole fractions of A and B by

$$[5] \quad x_B = (\mathscr{C}_B + \mathscr{C}_{AB})/(\mathscr{C}_A + \mathscr{C}_B + 2\mathscr{C}_{AB})$$

and

$$[6] \quad x_A = (\mathscr{C}_A + \mathscr{C}_{AB})/(\mathscr{C}_A + \mathscr{C}_B + 2\mathscr{C}_{AB}) = (1 + K)\mathscr{C}_A/[1 + K\mathscr{C}_A(2 - \mathscr{C}_A)]$$

In deriving eq. [6] it has been assumed that $\gamma_A\gamma_B/\gamma_{AB} \approx 1$ and this assumption (19) does not seem to lead to serious errors in K. Now if the observed chemical shift δ_{obs}, of the bromoform proton in its mixture with acetone relative to that of the pure bromoform is assumed to be the weighted average of the shifts in the complexed state, δ_{AB}, and the uncomplexed state, δ_B, then

$$[7] \quad \delta_{obs} = \delta_B[\mathscr{C}_B/(\mathscr{C}_B + \mathscr{C}_{AB})] + \delta_{AB}[\mathscr{C}_{AB}/(\mathscr{C}_B + \mathscr{C}_{AB})] = \delta_B + C(\delta_{AB} - \delta_B)$$

where

$$[8] \quad C = \mathscr{C}_{AB}/(\mathscr{C}_B + \mathscr{C}_{AB}) = K\mathscr{C}_A/(1 + K\mathscr{C}_A)$$

To evaluate K from eqs. [4]–[8], a series of values were assumed for K and for each K value, $\mathscr{C}_A$ was evaluated from eq. [6] using the corresponding experimental x_A value. These $\mathscr{C}_A$ values were further utilized to obtain the values of C from eq. [8]. Only that particular value of K was retained that gave the best straight line of δ_{obs} against C. The criterion for the best value of K was that for which $\sigma = \Sigma(\delta_{obs} - \delta_{calc})^2$ is minimum. This analysis of our δ_{obs} data yielded $K = 2.38$. The uncertainty in our K value is of the order of ±0.05. This value of $K = 2.38 \pm 0.05$ obtained from nmr data is thus very close to the value of $K = 2.35$ evaluated from the measured enthalpy data at 298.15 K.

We next attempted a slightly different computational method for evaluating the molar volume change and molar enthalpy of complexation. If n_A, n_B, and n_{AB} are the stoichiometric number of moles of A, B, and AB entities then the equilibrium mixture contains $(n_A - n_{AB})$ mol of A, $(n_B - n_{AB})$ mol of B, and n_{AB} mol of AB. Again, if $\mathscr{C}_A$, $\mathscr{C}_B$, and $\mathscr{C}_{AB}$ are the equilibrium mole fractions of A, B, and AB then it has been shown (20) that these are related to the stoichiometric mol fractions of A and B by the following equations.

$$[9] \quad \mathscr{C}_A = (x_A - r)/(1 - r)$$

$$[10] \quad \mathscr{C}_B = (x_B - r)/(1 - r)$$

$$[11] \quad \mathscr{C}_{AB} = r/(1 - r)$$

where

$$[12] \quad r = n_{AB}/(n_A + n_B)$$

The mole fraction equilibrium constant K (for ideal associated solutions) therefore, can then be expressed as

$$[13] \quad K = r(1 - r)/(x_A x_B - r + r^2) = \frac{\mathscr{C}_{AB}}{\mathscr{C}_A\mathscr{C}_B}$$

thus by using $K = 2.38$ (obtained from nmr data), r can be evaluated for each x_A. This value of r was then used to calculate ΔX^0 from the relations (21) $X^E = r(\Delta X^0)$, where $X = H$ or V and ΔX^0 is the change in molar property X due to the complexation reaction [2].

The ΔH^0 and ΔV^0 values were then found to vary with x_A as

$$[14] \quad \Delta H^0(\text{kJ mol}^{-1}) = 0.857x_A - 7.00$$

$$[15] \quad \Delta V^0(\text{cm}^3\ \text{mol}^{-1}) = 0.3 + 0.21x_A + 2.076x_A^2$$

yielding $\Delta H^0 = -7.00$ kJ mol^{-1}. $\Delta V^0 = 0.3$ cm^3 mol^{-1} at $x_A = 0$; $\Delta H^0 = -6.57$ kJ mol^{-1}; $\Delta V^0 = 0.924$ cm^3 mol^{-1} at $x_A = 0.5$ and $\Delta H^0 = -6.14$ kJ mol^{-1}; $\Delta V^0 = 2.586$ cm^3 mol^{-1} at $x_A = 1.0$.

Again, Matsui *et al.* (17) have shown (for an ideal associated solution) that the molar enthalpy, ΔH, of AB complex formation is given by

$$[16] \quad \Delta H = \overline{\mathscr{L}}_B^0(1 + K)/K = \overline{\mathscr{L}}_A^0(1 + K)/K$$

where $\overline{\mathscr{L}}_B^0$ and $\overline{\mathscr{L}}_A^0$ represent the partial molar enthalpies of solution of B (at infinite dilution) in A and of solution of A (at infinite dilution) in B. To calculate ΔH from eq. [16] $\overline{\mathscr{L}}_B^0$ and $\overline{\mathscr{L}}_A^0$ values were first evaluated as suggested by Van Ness and Mrazek (22), i.e., by plotting $H^E/x_A x_B$ against x_A and extrapolating the intercepts to $x_A = 0$ and $x_A = 1$. This yielded $\overline{\mathscr{L}}_B^0 = -4.25$ kJ mol^{-1} and $\overline{\mathscr{L}}_A^0 = -4.95$ kJ mol^{-1} and the ΔH values obtained from eq. [16] with $K = 2.35$ range between -6.06 and -7.06 kJ mol^{-1}. On the other hand, an average value of $\overline{\mathscr{L}}_A^0$ and $\overline{\mathscr{L}}_B^0$ yielded $\Delta H = -6.56$ kJ mol^{-1} from eq. [16]. The ΔH values obtained from eqs. [16] and [3] are thus in reasonably good agreement with each other.

Acknowledgements

The authors thank the Head of the Chemistry Department and the authorities of Maharshi Dayanand University, Rohtak, for providing the necessary research facilities and a University Fellowship to S.D.

1. W. E. Acree Jr. *In* Thermodynamic properties of nonelectrolytes solutions. Academic Press, New York. 1984.
2. D. V. Fenby and L. G. Hepler. Chem. Soc. Rev. **3**, 193 (1974).
3. P. P. Singh and B. R. Sharma. Z. Phys. Chemie (Leipzig), **262**, 843 (1981).
4. D. V. Fenby and L. G. Hepler. J. Chem. Thermodyn. **6**, 185 (1974).
5. P. P. Singh, K. S. Sidhu, and B. R. Sharma. Aust. J. Chem. **30**, 1241 (1977).
6. A. I. Vogel. *In* A text book of practical organic chemistry. English Book Soc. Longmans, London. 1973. pp. 171, 299.
7. I. Brown and W. Fock. Aust. J. Chem. **8**, 361 (1955).
8. J. Timmerman. *In* Physico-chemical constants of pure organic compounds. Elsevier, Amsterdam. 1950. p. 221.

Can. J. Chem. Downloaded from www.nrcresearchpress.com by 176.9.209.113 on 09/07/12
For personal use only.

9. P. P. SINGH and S. P. SHARMA. J. Chem. Eng. Data, **30**, 477 (1985).
10. P. MONK and I. WADSO. Acta Chem. Scand. **22**, 1842 (1968).
11. H. P. DAHIYA, P. P. SINGH, and SHASHI DAGAR. Fluid Phase Equilibria, **33**, 191 (1987).
12. R. H. STOKES, K. N. MARSH, and R. P. TOMLINS. J. Chem. Thermodyn. **1**, 211 (1969).
13. C. M. HUGGINS, G. C. PIMENTAL, and J. N. SCHOOLERY. J. Chem. Phys. **23**, 1244 (1955).
14. V. C. G. TREW. Trans. Faraday Soc. **28**, 509 (1932).
15. J. J. CHRISTENSEN, R. W. HANKS, and R. M. IZATT. Handbook of heats of mixing. John Wiley and Sons. 1982. p. 1259.
16. K. W. MORCOM and D. N. TRAVERS. Trans. Faraday Soc. **62**, 2063 (1966).
17. T. MATSUI, L. G. HEPLER, and D. V. FENBY. J. Phys. Chem. **77**, 2397 (1973).
18. M. L. MCGLASHAN and R. P. RASTOGI. Trans. Faraday Soc. **54**, 496 (1958).
19. S. K. ALLEY and R. L. SCOTT. J. Phys. Chem. **67**, 1782 (1967).
20. L. G. HEPLER and D. V. FENBY. J. Chem. Thermodyn. **5**, 471 (1973).
21. H. P. DAHIYA, P. P. SINGH, and S. DAGAR. Ind. J. Chem. **25**A, 814 (1986).
22. H. C. VAN NESS and R. V. MRAZEK. AIChEJ. **5**, 209 (1959).

Can. J. Chem. Downloaded from www.nrcresearchpress.com by 176.9.209.113 on 09/07/12
For personal use only.

High pressure–temperature aqueous oxidations. III. A kinetic study of the enolization and oxidation of cyclohexanone

JOHN W. THOMAS[1] AND JAY E. TAYLOR[2]

Department of Chemistry, Kent State University, Kent, OH 44242, U.S.A.

Received July 22, 1987

JOHN W. THOMAS and JAY E. TAYLOR. Can. J. Chem. **66**, 294 (1988).

The rates of enolization of cyclohexanone have been determined at 145 and 172°C in D_2O and with buffers. The rates of oxidation were evaluated at temperatures of 145, 172, and 193.5°C with oxygen partial pressures of 20.4 to 131 atm. The rate of enolization was 10–160 times faster than the rate of oxidation thereby supporting the previously proposed concept of enol intermediacy for the oxidation of ketones. The oxidation was first order in cyclohexanone and 1/2 order in oxygen. The rate of oxidation was *increased* by the addition of traditional phenolic inhibitors. The products isolated were formic, acetic, butanedioic, pentanedioic, hexanedioic, and 5-oxohexanoic acids. The activation parameters were calculated to be $\Delta H^{\neq}$, 22 kcal/mol; $\Delta S^{\neq}$, −27 eu, log A, 7.6 for the oxidation and $\Delta H^{\neq}$, 12 kcal/mol; $\Delta S^{\neq}$, −42.3 eu, log A, 4.13 for the enolization. Based on these observations a mechanism has been postulated whereby an oxygen molecule forms a transitory adduct with two enolates of cyclohexanone. The latter may then split by a reversible reaction to form an intermediate which may then isomerize or oxidize to either 2-hydroxycyclohexanone or 1,3-cyclohexanedione. Upon further oxidation the former yields hexanedioic acid. The latter then undergoes a reverse condensation in the aqueous media to 5-oxohexanoic acid which upon further oxidation yields formic plus pentanedioic acid and acetic plus butanedioic acid.

JOHN W. THOMAS et JAY E. TAYLOR. Can. J. Chem. **66**, 294 (1988).

Opérant à 145 et à 172°C, dans le D_2O et des tampons, on a déterminé les vitesses d'énolisation de la cyclohexanone. Opérant à des températures de 145, 172 et 193,5°C et à des pressions partielles d'oxygène de 20,4 et 131 atm, on en a aussi évalué les vitesses d'oxydation. Les vitesses d'énolisation sont de 10 à 160 fois plus rapides que les vitesses d'oxydation; ces résultats supportent le concept proposé antérieurement selon lequel les énols sont des intermédiaires dans l'oxydation des cétones. L'oxydation est du premier ordre en cyclohexanone et d'ordre 1/2 en oxygène. Les vitesses d'oxydation sont *augmentées* par l'addition des inhibiteurs phénoliques traditionnels. Les produits isolés sont les acides formique, acétique, butanedioïque, pentanedioïque, hexanedioïque et oxo-5 hexanoïque. On a calculé que les paramètres d'activation sont $\Delta H^{\neq}$, 22 kcal/mol; $\Delta S^{\neq}$, −27 ue et log A, 7,6 pour l'oxydation et $\Delta H^{\neq}$, 12 kcal/mol; $\Delta S^{\neq}$, −42,3 ue et log A, 4,13 pour l'énolisation. Sur la base de ces observations, on propose un mécanisme par lequel une molécule d'oxygène forme un adduit transitoire avec deux énolates de cyclohexanone. Ce dernier adduit peut alors se décomposer, par une réaction réversible, pour former un intermédiaire qui peut alors s'isomériser ou s'oxyder soit en hydroxy-2 cyclohexanone ou en cyclohexanedione-1,3. Par oxydation subséquente, le premier conduit à de l'acide hexanedioïque. En milieu aqueux, le deuxième subit alors une condensation inverse qui transforme en acide oxo-5 hexanoïque dont l'oxydation subséquente conduit à la formation d'acide formique plus de l'acide pentanedioïque et d'acide acétique plus de l'acide butanedioïque.

[Traduit par la revue]

Introduction

That the enol is an intermediate in the aqueous oxidation of ketones at elevated temperatures and pressures was first postulated in an earlier study (1). This conclusion was based on the correlation of the rates of oxidation with the relative extents of enolization for several ketones. More recently the rates of enolization and oxidation of acetone were compared at 193.5°C in an aqueous media (2). Since the rate of enolization exceeded the rate of oxidation by a factor of ~75, the concept of the intermediacy of the enol was further supported.

Acetone oxidized very slowly at 193.5°C. Since this temperature was the practical upper limit for the constant temperature bath as previously described (2), the studies with acetone were necessarily limited. Cyclohexanone exhibited rates of oxidation and enolization which were appreciably faster than those of acetone; thus, a much broader and more complete survey of cyclohexanone has been possible and is herein described.

Experimental

The vapor pressure controlled constant temperature bath used for these experiments and the procedure for the determination of the rates of oxidation have been previously described (2).

Approximately 0.3 g of ketone was mixed with 10 mL water for both the enolization and oxidation experiments. Since in each case the ketone was sealed into a glass bulb as previously described (2) and the bulb was broken to initiate the reaction, the amount of ketone varied slightly with each experiment. The initial concentration for each experiment may be determined by extrapolation of the rate curve to zero time. For the enolization experiments a nitrogen pressure equal to the highest oxygen pressures was employed. Cyclohexane concentrations were determined by gas chromatographic analysis.

The cyclohexanone was from Eastman Kodak Company and was purified first by elution from an alumina column followed by double distillation through a 120 cm glass helix packed column. The fraction boiling at 153.5°C (735 Torr) was then used for these experiments.

In place of the mass spectrometric technique used with acetone (2), the rates of enolization of cyclohexanone were determined by following the substitution of deuterium on carbons 2 and 6 (H_α) using proton magnetic resonance, pmr, spectroscopy. Since only the α protons exchange, the remaining β and γ protons, whose signals were distinguishable from the α protons, provided a convenient internal standard for quantification of the rate of signal decay. At any time t the pmr signal was the resultant of the product of the instrument scale factor times the sum of the concentrations of the products multiplied by the number of remaining protons per cyclohexanone molecule.

Thus, the plots of ln $(H_\alpha/H_{\beta+\gamma})$ versus time were found to be linear, and slopes of these plots were equal to k, the rate constant. However, there were four α protons, and the replacement of one hydrogen by a deuterium introduced the possibility of a secondary isotope effect upon replacement of the second hydrogen on this same carbon. Since the reaction was not carried to completion, the probability of replacement of a second hydrogen on either side was small. Accordingly, the contribution of a secondary isotope effect was deemed negligible and was disregarded.

The rate of enolization of cyclohexanone was determined by

[1]Present address: Pfizer Inc., Terre Haute, IN 47808, U.S.A.

[2]Author to whom correspondence should be addressed.

Printed in Canada / Imprimé au Canada

Can. J. Chem. Downloaded from www.nrcresearchpress.com by 213.222.148.141 on 09/07/12
For personal use only.

Can. J. Chem. Downloaded from www.nrcresearchpress.com by 213.222.148.141 on 09/07/12
For personal use only.

substituting D_2O for water. Since enolization is a prototopic reaction, the rate was significantly altered by the presence of added base or acid. Buffers were employed in many of the reactions and consisted of acetic acid-D_4 with sodium acetate-D_3 or acetic acid with sodium acetate both in D_2O. Under the latter conditions there was difficulty in following the H_α decay signal due to the interference of the large proton signal from the CH_3 of the buffer acetate. The kinetic analysis was based on the growth of the DOH peak, thereby avoiding this difficulty.

Deuterium substituted for the protons in the methyl group of acetic acid at ordinary temperatures produces roughly a 3% change in acid strength (3). This effect was disregarded since it would be even smaller at elevated temperatures. However, isotope effects due to the solvent, D_2O, and to the substitution of D for H on the carboxyl group of acetic acid are more significant. Due to a lack of information about either of these effects with cyclohexanone, particularly at elevated temperatures, no explicit corrections have been made. A rough estimation suggests that the rate may be 10–30% greater in H_2O as compared to D_2O.

With acetone the only detectable products of oxidation were acetic acid and carbon dioxide. In contrast, cyclohexanone led to a variety of products including formic, acetic, butanedioic, pentanedioic, hexanedioic, and 5-oxohexanoic acids. Formic and acetic acids were identified by matching their gas chromatograph retention times with known samples of these acids.

The nonvolatile acids were identified by a combination of methods. Thin layer chromatography on silica gel-G and visualization with bromocresol blue revealed the presence of four nonvolatile carboxylic acids. The R_f values of three of these matched the R_f values of the three dibasic acids, hexanedioic, pentanedioic, and butanedioic acid. These acids were also identified by comparing gas chromatograph retention times of their methyl and trimethylsilyl esters against the corresponding esters of the known acids. The mass spectra of the methyl esters of these three acids also matched the corresponding methyl esters of the known acids.

The remaining acid was less easily characterized. Its methyl and trimethylsilyl esters showed gas chromatograph retention times close to those of pentanedioic acid. The mass was determined to be 144 from mass spectral data, and a prominent low energy fragment of mass 43, corresponding to the CH_3CO^+ ion, was observed thus strongly suggesting the 5-oxo isomer.

Since 6-oxohexanoic acid (adipic aldehyde or 5-formylvaleric acid) has been variously reported as a product of the oxidation of cyclohexanone (4, 5), both the 5- and 6-oxohexanoic acids were considered as possible identities of this acid. 6-Oxohexanoic was synthesized by the method of Baer (6) and 5-oxohexanoic acid was obtained from Aldrich Chemical Company. Thin layer chromatography was of little value since the R_f values were approximately the same. From gas chromatography methyl 5-oxohexanoate showed a retention time relative to dimethyl pentanedioate of 0.8 as did the unknown ester; whereas, methyl 6-oxohexanoate showed a relative retention time of 0.91. These various data served to identify the unknown acid as 5-oxohexanoic acid (4-acetylbutyric acid).

EDTA was added to many oxidations to minimize the effects of possible contamination by metal ion impurities from the reactor.

Data and discussion

Kinetics of enolization

The rates of enolization as determined from the rates of isotopic exchange were found to be sensitive to both pH and anions of weak bases. Some specific data are listed in Table 1. As may be seen there were marked changes in the rates of enolization as the conditions were altered. Typical first order rate curves using acetic acid-D_4 and sodium acetate-D_3 determined at 145°C and acetic acid – sodium acetate at 172°C are seen in Fig. 1.

Kinetics of oxidation

The first order rate constants for the oxidation of cyclohexanone were observed at three temperatures in a variety of oxygen pressures and with several buffer systems. The data are listed in Table 2. Typical rate curves demonstrating the first order character of the oxidation of cyclohexanone with constant oxygen partial pressures are seen in Fig. 2.

TABLE 1. First order rate constants for the substitution of the α-hydrogens of cyclohexanone by deuterium atoms from the deuterium oxide solvent

Temperature (°C)	Buffer HOAc (*M*)	Buffer NaOAc (*M*)	$OAc^-/HOAc$	$k \times 10^4$ (s^{-1})
172	—	—	—	3.7
172	0.284	0.50	1.76	20.
172	0.059	0.186	3.15	13.
145	0.228[a]	0.495[a]	8.4	2.2
145	0.234[a]	0.486[a]	7.7	2.1

[a]All hydrogens were replaced by deuterium. The product concentrations and overall pressures (nitrogen) were maintained as close as possible to the oxidation runs.

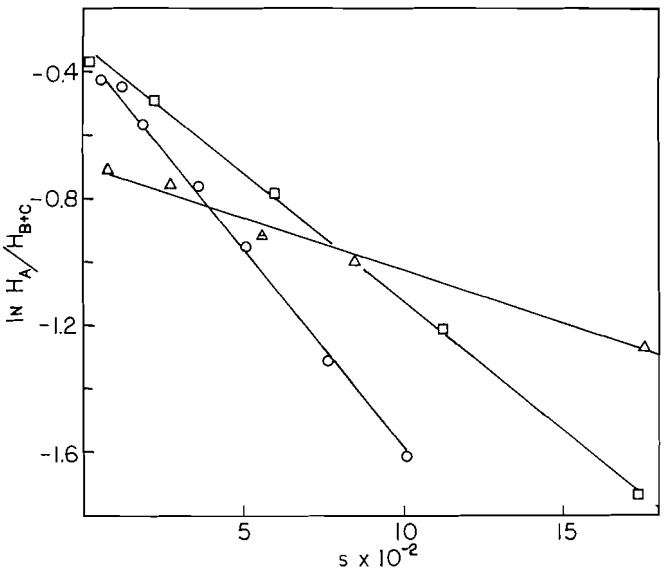

FIG. 1. Typical graphs of the rate of exchange of deuterium atoms with the hydrogen of cyclohexanone in deuterium oxide: △, no buffer, 172°C; ○, 0.059 *M* acetic acid, 0.186 *M* sodium acetate, 172°C; □, 0.234 *M* acetic acid-D_4, 0.486 *M* sodium acetate-D_3, 145°C. A, B, C are α, β, γ.

The relative rates of enolization and oxidation

The comparative rates of enolization and oxidation are listed in Table 3 at 145 and 172°C. As may be seen enolization was 10–160 times greater than oxidation, and the concept of the enol intermediate is thereby further supported. Thus, the rate of enol formation was more than adequate to maintain a constant source of the enol as an intermediate for the oxidation. However, the rate of enolization was dependent on pH and buffer concentrations; whereas the rate of oxidation was not. The simple oxidation is not a protonic reaction and should not be pH dependent. Since the rate of enolization is so much faster and is obviously a reversible reaction, an equilibrium concentration of the enol should be rapidly attained. The pH dependence of an enolization reaction lies in the rate of attainment of the equilibrium concentration, but there is no significant effect of pH on the concentrations of keto and enol forms once an equilibrium is attained. Thus the oxidation should show no pH dependency even if the enol is a precursor.

Can. J. Chem. Downloaded from www.nrcresearchpress.com by 213.222.148.141 on 09/07/12
For personal use only.

TABLE 2. First order rate constants for the oxidation of cyclohexanone at specified oxygen partial pressures

Temperature (°C)	Medium[a]	Partial pressure atom O_2	$k \times 10^5$ (s^{-1})
193.5	A	123	22.3
193.5	A	123	21.4
193.5	A	122	21.0
193.5	A	120	18.3
193.5	B	123	20.3
193.5	B	123	24.4
193.5	H_2O	123	18.1
193.5	H_2O	123	22.2
193.5	A	27.6	11.6
193.5	H_2O	26.2	8.8
193.5	A	22.5	10.3
172	B	128	8.1
172	B	128	7.8
172	B	128	7.5
172	B	128	7.6
172	B	59.9	4.98
172	B	59.9	4.81
172	C	44.2	4.18
172	C	35.7	3.91
172	C	35.3	4.22
172	H_2O	31.3	3.44
145	B	131	1.09
145	B	129	1.09
145	B	127	1.03
145	H_2O	127	0.99
145	B	44.2	0.62
145	B	44.2	0.64
145	B	26.5	0.54
145	B	20.4	0.51

[a]A, 0.0098 *M* EDTA; B, 0.5 *M* sodium acetate, 0.025 *M* acetic.

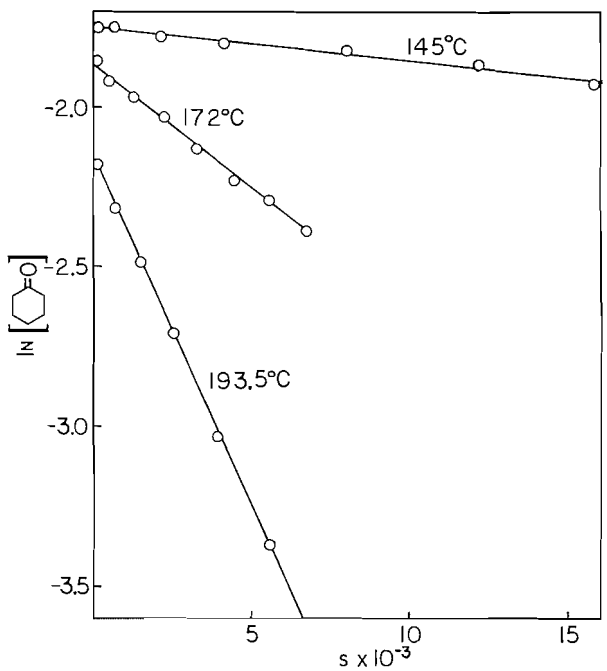

FIG. 2. Typical graphs of the rates of cyclohexanone oxidations: 0.05 *M* sodium acetate and 0.25 *M* acetic acid were added in each case.

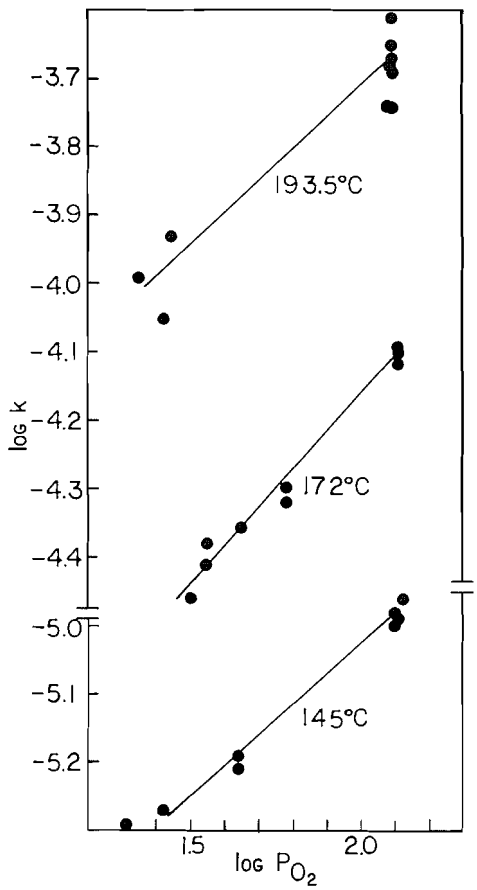

FIG. 3. Plots of log partial pressures of oxygen versus log rate constants demonstrating the one-half kinetic order with respect to oxygen concentration. The indicated slopes at the three temperatures are 0.46, 193.5°C; 0.53, 172°C; 0.44, 145°C.

Reaction order

The oxidation reaction is first order with respect to cyclohexanone since, as seen in Fig. 2, the rate of consumption of ketone clearly follows a first order relationship.

An earlier determination (1) of reaction order for several alcohols and ketones indicated that the reaction was first order in oxygen. However, only two pressures were compared, and these data were of a lower order of accuracy than the present work.

In Table 2 the pseudo first order rate constants are listed at varying oxygen partial pressures. These have been determined by correcting the gauge pressures for the partial pressures of water vapor and for temperatures. The applicability of Henry's law is assumed for the determination of the relative concentrations of oxygen in solution.

Data for the determination of the kinetic order of oxygen are listed in Table 2. The values of log *k* (first order rate constants) are plotted against the log partial pressures of oxygen at each of three temperatures in Fig. 3. As may be seen the slope is 0.5 in each case within experimental error. This relationship is further demonstrated in Fig. 4. For this experiment the oxygen partial pressure was changed from 26.5 to 123 atm during the course of a run by introducing additional oxygen. Upon calculation of the apparent order with respect to oxygen the value is 0.6 which is in good agreement with the above data in view of the magnitude of the experimental error.

Effects of added inhibitors

Since this is a reaction with elemental oxygen, a radical chain

TABLE 3. Comparative rates of enolization and oxidation for cyclohexanone

Reaction	Temperature (°C)	Medium[a]	Oxygen (atm)	$k \times 10^4$ (s^{-1})	Ratio enol/oxid
Enolization	172	D_2O	31.0	3.7	11
Oxidation	172	H_2O	31.3	0.34	
Enolization	172	C	36.0	20.0	51
Oxidation	172	C	36.0	0.39	
Enolization	145	E	20.0	8.0	160
Oxidation	145	B	20.4	0.051	

[a]C, 0.284 *M* acetic acid, 0.05 *M* sodium acetate, pH 5.4; E, 0.228 *M* acetic acid-D_4, 0.0495 *M* sodium acetate-D_3, pH 5.4; B, 0.25 *M* acetic acid, 0.05 *M* sodium acetate, pH 5.4.

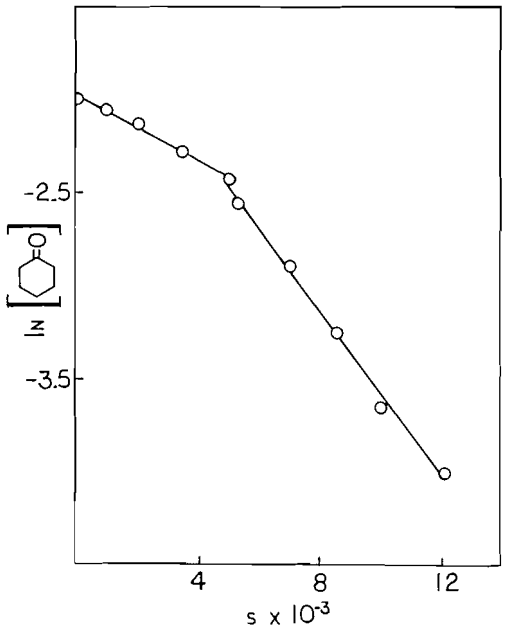

FIG. 4. A graph of the change in rate corresponding to a change in pressure from 26.5 to 123 atm during the course of an oxidation of cyclohexanone at 193.5°C. The observed first order rates are 8.8×10^{-5} and $22.0 \times 10^{-5}\ s^{-1}$. The determined oxygen order is 0.6.

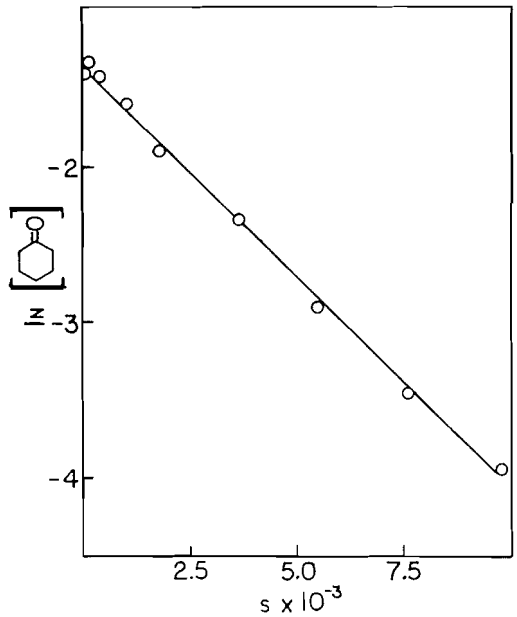

FIG. 5. Demonstration of the first order character of the oxidation of cyclohexanone in the presence of 10% 1-naphthol at 193.5°C. The rate constant is $2.8 \times 10^{-4}\ s^{-1}$.

mechanism must be considered. This possibility has been tested by the addition of typical inhibitors, 1-naphthol and 4-hydroxybenzoic acid. These were chosen because of their partial solubility in water. Other more efficient inhibitors such as *t*-butyl substituted phenols or anilines are less soluble in water and presumably would be very rapidly oxidized.

None of the 1-naphthol runs showed an induction period during the oxidation of cyclohexanone nor were there any reductions in the observed first order rate constants. There were minimal disturbances of the rates of oxidation since smooth first order plots were obtained as seen in Fig. 5. At 193.5°C the naphthol was 90% oxidized in 4000 s or about midway through the cyclohexanone run. In general there was a mild rate enhancement, 20–50%, for the seven experiments at 193.5°C and about 100% for the two runs at 172°C.

Two oxidations with added 0.04 *M* 4-hydroxybenzoic acid were made at 193.5°C. This compound has a solubility of about 1% at 25°C in water and has the position *para* to the hydroxyl group blocked. Again there was no evidence of an induction period, but there was an enhancement of the rate of oxidation of about twofold.

Thus, these experiments provide no evidence to indicate a radical chain mechanism.

TABLE 4. Activation parameters for cyclohexanone

Reaction	E_a (kcal/mol)	$\Delta H^{\ddagger}$ (kcal/mol)	$\Delta S^{\ddagger}$ (eu)	log *A*
Oxidation	23	22	−27	7.6
Enolization	12.7	11.9	−42.3	4.13

Activation parameters

The various constants of activation are listed in Table 4. These have been calculated using three-halves order rate constants for the oxidation and first order rate constants for the enolizations.

A proposed mechanism

The reaction of elemental oxygen with organic compounds is generally assumed to be a radical chain mechanism as typified by a general mechanism given for the oxidation of hydrocarbons (7). Ketones, exemplified by cyclohexanone, are deemed to react in a similar manner (8).

The data of this paper tend to distinguish aqueous oxidations (at least in part) from other typical neat or nonpolar solvent oxidations or autoxidations. No evidence for a radical-chain mechanism appeared since the phenols did not inhibit the

Can. J. Chem. Downloaded from www.nrcresearchpress.com by 213.222.148.141 on 09/07/12
For personal use only.

Can. J. Chem. Downloaded from www.nrcresearchpress.com by 213.222.148.141 on 09/07/12
For personal use only.

reaction. The multiplicity of products indicated a mechanism of appreciable complexity with a combination of successive and/or parallel reactions. Because the reaction was followed by the disappearance of cyclohexanone in a constant supply of oxygen, the only information presently available concerning the successive reactions is the identity of the products.

The reaction order suggests that a cyclohexanone molecule reacted with an O atom ($(1/2)O_2$). However, the activation energy is quite insufficient to accommodate a direct fission of an oxygen molecule whose bond strength is 118 kcal/mol (9).

Based on these considerations, it is suggested that the oxygen molecule can be split in a reversible reaction with two enolates of cyclohexanone. The resulting fragments, each containing only one oxygen atom from the original oxygen molecule, then react irreversibly to form intermediates which lead to the final products. Since the fracture of one oxygen molecule forms two reacting units, the bond dissociation energy of the oxygen fissure is divided by two for its contribution to the observed activation energy. Accordingly, a reduction in the O—O bond energy, resulting from its interaction with the enol, is needed to maintain the integrity of the observed activation energy with respect to this mechanism.

Although the data are insufficient to define this mechanism rigorously, a proposal will be advanced concerning how such a process may occur.

First the enol is formed.

[1] 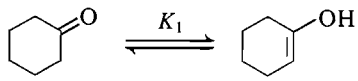

Two enol molecules then react reversibly with an oxygen molecule to form a transitory intermediate by interaction with the double bonds of the enol. This intermediate may take any of several forms, which due to insufficient evidence, are as yet not clearly defined. A possible mechanism is proposed below.

[2] 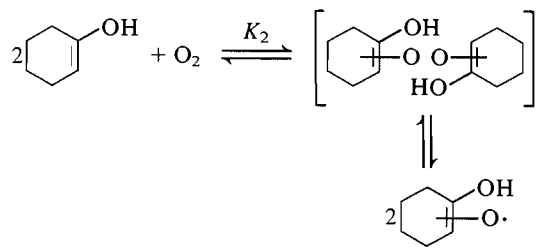

The resulting oxide intermediate then undergoes an irreversible change to a more stable configuration.

It should be emphasized that the interaction between an oxygen molecule and the enol as previously suggested can form only under extreme conditions of high pressure and temperature due to both the endothermic nature of the reaction and compression of the oxygen molecule onto the double bonds of the enols. Thus, under neat conditions with high pressure oxygen, the reaction may proceed with explosive violence since water[3] is not present to disperse the heat of reaction generated by the reactions which follow [2].

[3]We encountered two examples of the violence of this type of reaction in our earlier studies. For the first case the grease in a gauge reacted with tank pressure oxygen at room temperature. The resulting internal explosion made the gauge unusable. For the second case an attempt was made to use perfluorotoluene as a solvent for a ketone. After the reaction was heated the mixture ignited and emerged as a tongue of flame through the safety rupture disk. Because of the extra large safety factor allowed in design, the apparatus was reusable after minor internal replacements.

The mathematical relationships derived from the above proposal concur with the observed kinetic relationships. Treating step [1] and [2] as a single equilibrium where Cy is the original cyclohexanone molecule and RO· is the end product of step [2].

$$[3]\quad K = \frac{[RO\cdot]^2}{[Cy]^2[O_2]} \text{ and } [RO\cdot] = (K_1K_2)^{1/2}[Cy][O_2]^{1/2}$$

then assuming that the irreversible isomerization of RO· is the rate-determining step,

$$[4]\quad \frac{dx}{dt} = k[RO\cdot] = k(K_1K_2)^{1/2}[Cy][O_2]^{1/2}$$

In order that this mechanism apply, it is essential that the equilibria represented by [3] be rapidly formed, i.e., the forward reactions in steps [1] and [2] must be faster than the decomposition of RO· (step [4]) to maintain the equilibrium concentrations of the intermediates. The actual concentrations of these radical intermediates can only be very small.

As previously noted the sluggish reaction of acetone (2) as compared to cyclohexanone correlates with the relative ease of enol formation.

The enhancement of the rate of oxidation with added phenolics becomes explainable with this mechanism. Although the phenols were independently oxidized, they should also react with the oxide radical of step [2]. Such an interaction should shift the point of equilibrium of steps [1] and [2] to the right, thereby increasing the rate of consumption of cyclohexanone.

The variety of products: formic, acetic, butanedioic, pentanedioic, hexanedioic, and 5-oxohexanoic acids, indicate the complexity of the mechanism of the reaction. That the $—CH_3$ group of the latter acid was formed under oxidizing conditions from a molecule with only $—CH_2—$ bonding and that formic and acetic acid were also products require special consideration.

5-Oxohexanoic acid was a major component among the isolated products. Some specific analyses are shown in Table 5.

Proceeding from step [2] more stable intermediates may be formed by rearrangement of the oxygen radical.

[5] 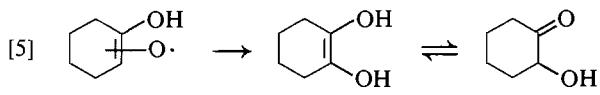

[5a] 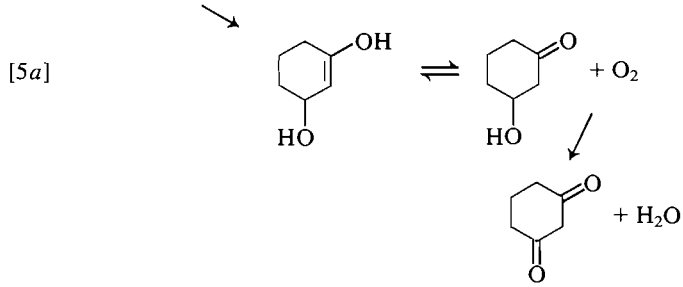

Both 2-hydroxycyclohexanone and its corresponding hydroperoxide have been isolated as products of oxidations of cyclohexanone at lower temperatures (10, 11). The peroxide has been reported to decompose at 120°C (12). Hexanedioic acid may then be rapidly formed by further oxidation of the 2-hydroxyketone.

[6] 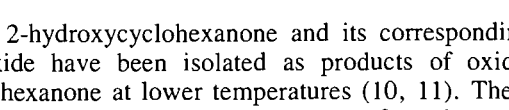

TABLE 5. Analysis of C_4–C_6 acid residues from selected oxidations at 193.5°C at the indicated reaction times

Reactant	Concentration when reaction time = 2850 s	3500 s	10000 s
Butanedioic acid	50	42	63
Pentanedioic acid	18	18	14
Hexanedioic acid	5	22	13
5-Oxohexanoic acid	27	18	10

5-Oxohexanoic acid is presumably formed from the 1,3-diketone by a reverse condensation. β-Diketones react with bases to form the corresponding acid and methyl ketone (13). That such a reaction could occur with water alone or with a near neutral buffer seems quite probable in view of the extreme conditions of elevated temperatures and pressures to which the oxidation of cyclohexanone was subjected. Also with the small concentrations of ions present the ionic or protonic character of the reaction would be greatly enhanced by the high temperature of the aqueous media.

[7] 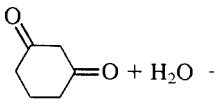

Upon further oxidation of 5-oxohexanoic acid, the shorter chain diacids should form along with formic and acetic acids.

[8] $$(3/2)O_2 + CH_3CO(CH_2)_3CO_2H \rightarrow HCO_2H + HO_2C(CH_2)_3CO_2H \rightarrow CH_3CO_2H + HO_2C(CH_2)_2CO_2H$$

Shorter chain diacids may also have been formed by direct oxidation of 1,3-cyclohexanedione. If propanedioic (malonic) acid were formed it would have decomposed to acetic acid and carbon dioxide, and could have served as another route to acetic acid.

As previously noted 6-oxohexanoic acid has been reported by several investigators, but only the 5-oxo isomer was observed in this study. The difference appears to be in the media. The 6-oxo isomer was obtained under neat or low polarity solvent conditions and the 5-oxo isomer from an aqueous media. Thus, upon formation of the 1,3-diketone this intermediate could rearrange to the 5-oxo isomer only in an aqueous environment since water is a reactant. Under less polar conditions the diketone would merely by oxidized to any of several diacids. The 6-oxo isomer, if formed in the aqueous media, must have been largely oxidized to hexanedioic acid. The 6-oxo isomer has been reported to be formed in the presence of 5% water with a copper ion catalyst (14).

Further work is needed in order to verify the proposed mechanism.

1. J. E. TAYLOR and J. C. WEYGANDT. Can. J. Chem. **52**, 1925 (1974).
2. J. W. THOMAS and J. E. TAYLOR. Can. J. Chem. **64**, 2235 (1986).
3. A. STREITWIESER, JR., and H. S. KLEIN. J. Am. Chem. Soc. **85**, 2759 (1963).
4. I. V. BEREZIN, E. T. DENISOV, and N. M. EMANUEL. The oxidation of cyclohexane. *Translated by* K. A. Allen. Pergamon Press, New York. 1966. pp. 136–160.
5. I. I. KORSAK, V. E. AGABEKOV, and N. I. MITSKEVICH. Vesti Akad. Navuk B. SSR, Ser. Khim. Navuk 1974, 28; c.f. Chem. Abstr. **83**, 9263j (1975).
6. E. BAER. J. Am. Chem. Soc. **64**, 1416 (1942).
7. N. M. EMANUEL. The oxidation of hydrocarbons in the liquid phase. *Translated by* K. R. Dobson and B. J. Hazard. Pergamon Press. New York. 1965. p. 48.
8. E. T. DENISOV, N. I. MITSKEVICH, and V. E. AGABEKOV. Liquid-phase oxidation of oxygen-containing compounds. *Translated by* D. A. Patterson. Consultants Bureau, New York. 1977. pp. 75–106.
9. R. C. WEAST. Handbook of chemistry and physics. 56th ed. CRC Press, Cleveland. 1975–6. p. F-216.
10. I. I. KORSAK, V. E. AGABEKOV, and N. I. MITSKEVICH. Neftekhimiya, **15**, 130 (1975); c.f. Chem. Abstr. **82**, 154900y (1975).
11. D. G. HENDRY, C. W. GOULD, D. SCHUETZLE, M. G. SYZ, and F. R. MAYO. J. Org. Chem. **41**, 1 (1976).
12. A. L. PERKEL and B. G. FREIDIN. Zh. Prikl. Khim. **54**, 1376 (1981); c.f. Chem. Abstr. **95**, 131980d (1981).
13. E. S. GOULD. Mechanisms and structure in organic chemistry. Holt, Rinehart, and Winston. New York. 1959. pp. 337–339.
14. Y. ISHIMOTO, H. TOGAWA, and S. NAKAHACHI. Japan, patent no. 72 26,768; c.f. Chem. Abstr. **77**, 139436e (1972).

Can. J. Chem. Downloaded from www.nrcresearchpress.com by 213.222.148.141 on 09/07/12
For personal use only.

Structure dependent regularities of zero-point plus heat content energies in organic molecules

S. FLISZÁR, F. POLIQUIN, I. BĂDILESCU, AND E. VAUTHIER[1]

Département de Chimie, Université de Montréal, C.P. 6128, Succ. A, Montréal (Qué.), Canada H3C 3J7

Received July 23, 1987

S. FLISZÁR, F. POLIQUIN, I. BĂDILESCU, and E. VAUTHIER. Can. J. Chem. **66**, 300 (1988).

A representative collection of heat content plus zero-point energies deduced in the harmonic oscillator approximation suggests a number of simple additivity rules which allow ZPE + $(H_T - H_0)$ to be related to structural features. Accurate evaluations are obtained for alkanes, alkenes, alkynes, cycloalkanes, chloroalkanes, and amines, as well as for large and small cycloalkanes in which CH_2 is replaced by O.

S. FLISZÁR, F. POLIQUIN, I. BĂDILESCU et E. VAUTHIER. Can. J. Chem. **66**, 300 (1988).

Une collection représentative d'enthalpies et d'énergies au point zéro qui ont été déduites en faisant appel à l'approximation de l'oscillateur harmonique suggère un certain nombre de règles simples d'additivité qui permettent d'établir une relation entre la valeur de ZPE + $(H_T - H_0)$ et des caractéristiques structurales. On a obtenu des évaluations précises pour les alcanes, les alcènes, les alcynes, les cycloalcanes, les chloroalcanes et les amines ainsi que pour les cycloalcanes à petits et à grands cycles dans lesquels le CH_2 a été remplacé par un O.

[Traduit par la revue]

Introduction

In our endeavour to understand the physics governing the energy of a molecule, traditional quantum mechanical energy minimization ends up describing a molecule at equilibrium, at its potential minimum. Thermochemistry, on the other hand, offers energy data (e.g., standard enthalpies of formation) for molecules possessing vibrational, rotational, and translational energies. This is where the problem lies. Vibrational energies are usually not as readily available as desired, thus rendering bona-fide comparisons between theory and experiment difficult, in spite of a wealth of thermochemical information. Indeed, the spectroscopic determination of the required complete sets of fundamental vibrational frequencies is usually far from being trivial, hence our interest in alternate rules which would allow the construction of reliable vibrational energies in a simple manner.

The sum of zero-point (ZPE) plus heat content $(H_T - H_0)$ energies is our target. It is fortunate that ZPE + $(H_T - H_0)$ energies can often be constructed to a good approximation by means of additivity rules (1). Theoretical foundation for this additivity, which has a long history (2), has been established (3). In the following, we calculate ZPE + $(H_T - H_0)$ energies from spectroscopic data and examine how these results can be related to structural features. In essence, this is a presentation of facts — a point worth remembering because, at times, the observed regularities exceed present theoretical expectations.

Calculations

The results were derived in the harmonic oscillator approximation using, whenever possible, observed infrared and Raman fundamental frequencies, ν_i. The inactive frequencies were taken from appropriate force field calculations. In this approximation we have

$$\text{ZPE} = \tfrac{1}{2}\sum_i h\nu_i$$

$$E_{\text{vibr}}(\text{therm}) = \sum_i h\nu_i \exp(-h\nu_i/kT)/[1 - \exp(-h\nu_i/kT)]$$

and

$$H_T - H_0 = E_{\text{vibr}}(\text{therm}) + 4RT$$

for nonlinear molecules. All the calculations were made for $T = 298.15$ K.[2]

Results

(a) Open chain alkanes, alkenes, and alkynes

A detailed study of the alkanes has revealed (1) that their ZPE + $(H_T - H_0)$ energies are satisfactorily described as follows, in kcal mol^{-1},

$$[1]\quad \text{ZPE} + (H_T - H_0) = 11.479 + 18.213n_C - 0.343n_{br}$$

where n_C is the number of carbon atoms and n_{br} is the number of branchings. The average deviation between the results deduced in this manner and their spectroscopic counterparts is 0.125 kcal mol^{-1}.

For the simple ethylenic compounds, C_nH_{2n}, it was shown (1) that eq. [2], in kcal mol^{-1},

$$[2]\quad \text{ZPE} + H_T - H_0 = 33.35 + 18.213(n_C - 2) - 0.343n_{br}$$

represents a valid approximation. Back calculations of enthalpies of formation using eqs. [1] and [2] and the appropriate atomization energies of molecules in their hypothetical vibrationless state at 0 K yields results which are well within experimental uncertainties (1).

Now we proceed with the conjugated and nonconjugated polyenic hydrocarbons indicated in Table 1. The ZPE + $H_T - H_0$ results can be estimated from those of their olefinic fragments, eq. [2], simply by subtracting 11.56 kcal mol^{-1} for each pair of hydrogen atoms eliminated in the condensation of the fragments. For example, the result predicted for 1,3-pentadiene follows from the values for ethene and propene less 11.56 kcal mol^{-1}. Similarly, the result for 1,3,5-hexa-

[1]Visiting scientist on temporary leave from the Université P. et M. Curie, Département de Recherches Physiques, 4, Place Jussieu, Paris, France.

[2]Planck's constant was taken as $h = 6.6256 \times 10^{-27}$ and Boltzmann's constant at $k = 1.38054 \times 10^{-16}$ erg K^{-1}. For the speed for light we have used 2.997925×10^{10} cm s^{-1}. Thus we obtain, for use with the usual wave number ω, in cm^{-1},

$$\tfrac{1}{2}h\nu_i = 1.42956 \times 10^{-3}\,\omega_i \quad \text{kcal mol}^{-1}$$

$$h\nu_i/kT = 4.82572 \times 10^{-3}\,\omega_i \quad \text{at 298.15 K}$$

Can. J. Chem. Downloaded from www.nrcresearchpress.com by 213.222.148.141 on 09/07/12
For personal use only.

Can. J. Chem. Downloaded from www.nrcresearchpress.com by 213.222.148.141 on 09/07/12
For personal use only.

TABLE 1. ZPE + $(H_T - H_0)$ for polyenic hydrocarbons

Molecule	ZPE + $(H_T - H_0)$, kcal mol^{-1} Exptl.[a]	Predicted
1,3-Butadiene	55.19 (4)	55.14
cis-1,3-Pentadiene	73.32 (5)	73.35
trans-1,3-Pentadiene	73.28 (5, 6)	73.35
Isoprene	72.85[b]	73.01
1,4-Pentadiene		73.35
1,5-Hexadiene		91.57
Dimethyl-1,3-butadiene	91.08 (6, 7)	90.88
trans-1,3,5-Hexatriene	76.70 (8)	76.93
cis-1,3,5-Hexatriene	76.99 (8)	76.93
1,3,5,7-*trans*,*trans*-Octatetraene	99.97 (9, 10)	98.72

[a]Numbers in parentheses indicate references reporting the vibrational frequencies used in this work.

[b]NOTE ADDED IN PROOF: This result follows from the spectral analyses given by Compton *et al.* (39*a*) (ir) and Kuznetsov *et al.* (39*b*) (Raman), reported by Bock *et al.* (39*c*).

TABLE 2. Experimental and predicted ZPE + $(H_T - H_0)$ results of selected alkynes

Molecule	ZPE + $(H_T - H_0)$, kcal mol^{-1} Exptl.[a]	Predicted
Ethyne	18.57 (11)	18.74
Propyne	37.05 (11)	36.87
1-Butyne	54.98 (12)	55.00
2-Butyne	55.17 (11)	55.00
1-Pentyne	72.98 (12)	73.13

[a]Numbers in parentheses indicate references reporting the vibrational frequencies.

triene corresponds to three times that of ethene less twice 11.56 kcal mol^{-1} or, alternatively, to the sum obtained from ethene and butadiene less 11.56 kcal mol^{-1}.

The alkynes (Table 2) are described by an equation similar to that given for the alkenes, i.e., in kcal mol^{-1},

$$[3]\quad \text{ZPE} + (H_T - H_0) = 18.74 + 18.13(n_C - 2) - 0.343n_{br}$$

Inspection of eqs. [1]–[3] indicates that the addition of one CH_2 group increases ZPE + $(H_T - H_0)$ by ~18.2 kcal mol^{-1}. In addition, the values of ethane (47.91), ethene (33.35), and ethyne (18.74 kcal mol^{-1}), from eqs. [1], [2], and [3], respectively, indicate that ZPE + $(H_T - H_0)$ decreases regularly by ~14.6 kcal mol^{-1} for each added multiple bond. Thus we can describe the alkanes, alkenes, and alkynes by a single equation, namely, in kcal mol^{-1},

$$[4]\quad \text{ZPE} + (H_T - H_0) = 47.77 + 18.30(n_C - 2) - 0.474n_{br} - 14.605n_{mb}$$

where n_{mb} is the number of multiple bonds (e.g., 1 in C_2H_4, 2 in C_2H_2). The validity of this approximation is illustrated in Table 3. The average deviation, 0.20 kcal mol^{-1}, is only slightly larger than what is obtained from separate correlations, confined to series of homologous compounds. Here, the striking feature lies in the remarkably regular decreases of vibrational energy in going from a single to a double and to a triple carbon—carbon bond.

The chloroalkanes follow the same general pattern as their

TABLE 3. Verification of eq. [4] describing the ZPE + $(H_T - H_0)$ energies of alkanes, alkenes and alkynes[a]

Molecule	ZPE + $(H_T - H_0)$, kcal mol^{-1} Eq. [4]	Exptl.
Methane	29.47	29.66
Ethane	47.77	48.02
Propane	66.07	65.94
Butane	84.37	84.38
Isobutane	83.90	83.89
Pentane	102.67	102.83
Isopentane	102.20	102.14
Hexane	120.97	120.99
2,3-Dimethylbutane	120.02	119.65
Heptane	139.27	139.29
Ethene	33.17	33.36
Propene	51.47	51.82
1-Butene	69.77	69.73
cis-2-Butene	69.77	69.91
trans-2-Butene	69.77	69.70
Isobutene	69.29	69.57
1,3-Butadiene	55.16	55.19
trans-1,3-Pentadiene	73.46	73.28
Isoprene	72.99	72.85
cis-1,3-Pentadiene	73.46	73.32
Dimethyl-1,3-butadiene	90.81	91.08
trans-1,3,5-Hexatriene	77.16	76.70
cis-1,3,5-Hexatriene	77.16	76.99
trans,*trans*-1,3,5,7-Octatetraene	99.15	99.97
Ethyne	18.56	18.57
Propyne	36.86	37.05
1-Butyne	55.16	54.98
2-Butyne	55.16	55.17
1-Pentyne	73.46	72.98
Allene	36.86	36.20

[a]The experimental results for the alkanes and alkenes are taken from ref. 1. The fundamental frequencies of allene are from ref. 11. The other results are those of Tables 1 and 2.

parent hydrocarbons (eq. [1]), i.e., in kcal mol^{-1},

$$[5]\quad \text{ZPE} + (H_T - H_0) = 25.27 + 18.213(n_C - 1) - 4.98(n_{Cl} - 1)$$

where n_{Cl} is the number of chlorine atoms. Although the possible verifications are presently limited in number, in essence because the vibrational analyses of haloalkanes are unfortunately often incomplete, it appears that our approximation, eq. [5], is reasonable (Table 4).

The ZPE + $(H_T - H_0)$ energies of amines and hydrazines also appear to follow simple additivity rules. For the amines, we predict ZPE + $(H_T - H_0)$ from NH_3 (22.94 kcal mol^{-1}) and the appropriate alkanes (eq. [1]), by subtracting 11.55 kcal mol^{-1} for each pair of H atoms lost during the condensation giving the amine. Dimethylamine, for example, is estimated by taking twice the value of CH_4 plus that of NH_3, less twice 11.55 kcal mol^{-1}. We proceed similarly with the alkyl-substituted hydrazines (Table 5). Our approximation is generally satisfactory. As regards diethylamine, we have to take into account that no provision was made in our estimate for the (at least partial) hindrance of internal rotations in the ethyl groups as a result of steric crowding. Earlier studies (1, 24) have revealed a systematic lowering of ZPE + $(H_T - H_0)$ by ~0.3 kcal mol^{-1} for one hindered internal rotation, suggesting

Can. J. Chem. Downloaded from www.nrcresearchpress.com by 213.222.148.141 on 09/07/12
For personal use only.

TABLE 4. ZPE + $(H_T - H_0)$ energies of chloroalkanes

Molecule	ZPE + $(H_T - H_0)$, kcal mol^{-1} Exptl.[a]	Predicted
Chloromethane	25.58 (11)	25.27
Dichloromethane	20.71 (11)	20.29
Chloroform	15.56 (11)	15.31
Carbon tetrachloride	10.02 (11)	10.33
Chloroethane	43.41 (13)	43.48
Chloropropane	61.38 (14)	61.70
Chlorobutane	79.61 (13)	79.91

[a]Number in parentheses indicate sources of the vibrational frequencies.

TABLE 5. Experimental and predicted ZPE + $(H_T - H_0)$ values of amines and hydrazines

Molecule	ZPE + $(H_T - H_0)$, kcal mol^{-1} Exptl.[a]	Predicted
Ammonia	22.94 (11)	(22.94)
Methylamine	41.48 (15)	41.08
Ethylamine	59.41 (16)	59.30
Propylamine	77.62 (16)	77.51
Isopropylamine	77.20 (16)	77.17
tert-Butylamine	95.21 (16)	95.38
Dimethylamine	59.44 (17)	59.22
Diethylamine	94.94 (18)	95.65
Trimethylamine	77.76 (19)	77.37
Hydrazine	33.94 (20)	(33.94)
Methylhydrazine	52.00 (21)	52.08
1,1-Dimethylhydrazine	69.98 (22)	69.88
1,2-Dimethylhydrazine	70.20 (23)	70.22

[a]The references, in parentheses, report the vibrational analyses used in this work.

that our estimate for diethylamine is possibly too high by $\sim$0.6 kcal mol^{-1}.

(b) Cyclic molecules

Cycloalkanes constructed from six-membered rings behave in essence like their noncyclic counterparts (eq. [1]) as regards their vibrational energies, provided that the suppression of internal rotations is adequately taken into account (1, 24). Their ZPE + $(H_T - H_0)$ energies can be evaluated by counting 18.213 kcal mol^{-1} for each C atom of the molecule (rule 1) and subtracting 0.343 kcal mol^{-1} for each tertiary C atom that is formed (rule 2). A number of H atoms are eliminated in the formation of polycyclic compounds, e.g., 2 H atoms in *trans*-decalin. The 11.479 kcal mol^{-1} term of eq. [1] represents roughly the contribution of two H atoms. Accordingly, we approximate the decrease in ZPE + $(H_T - H_0)$ due to the loss of one H atom by subtracting 5.74 kcal mol^{-1} per H atom that is removed (rule 3). Considering now that eq. [1] describes noncyclic molecules in which internal rotations are as free as possible and, moreover, that internal rotations are hindered in cyclic compounds, we tentatively subtract $RT/2$ = 0.296 kcal mol^{-1} (at 298.15 K) for each CC bond in the cycle (rule 4). These simple rules, modelled on eq. [1], as discussed elsewhere in detail (1, 24), lead to satisfactory estimates of

TABLE 6. ZPE + $(H_T - H_0)$ values of cycloalkanes[a]

Molecule	ZPE + $(H_T - H_0)$, kcal mol^{-1} Exptl.	Predicted
Cycloheptane	124.15	126.09
Cyclohexane	107.54	(107.54)
Cyclopentane	89.0	89.00
Cyclobutane	70.4	70.45
Cyclopropane	51.9	51.91
Ethylene	33.36	33.36

[a]The fundamental frequencies of cycloheptane are from ref. 25. The other results are given in ref. 1.

TABLE 7. ZPE + $(H_T - H_0)$ energies of oxygen containing cycles[a]

Molecule	ZPE + $(H_T - H_0)$, kcal mol^{-1} Exptl.	Predicted
Tetrahydropyran	92.87	93.04
Tetrahydrofuran	74.61 (26)	74.50
Oxetane	56.14 (27)	55.95
Ethylene oxide	37.25 (28)	37.41
Formaldehyde	18.62 (29)	18.86
1,4-Dioxane	78.48 (26)	78.54
1,3-Dioxolane		60.00
1,3,5-Trioxane	64.4 (30)	64.04
1,3-Dioxetane		41.45
1,3,5,7-Tetroxocane	86.2 (30)	86.63

[a]The result for tetrahydropyran is reported in ref. 1. The references, indicated in parentheses, report the vibrational analyses used in our calculations.

ZPE + $(H_T - H_0)$ energies for six-membered cycloalkanes. Here we examine the effect of ring size (Table 6).

The results indicate that any shrinking of a cycle accompanying the removal of one CH_2 group translates into a regular decrease of ZPE + $(H_T - H_0)$ by 18.545 kcal mol^{-1}. It is remarkable that this regularity includes the shrinking from cyclopropane to give the "two-membered cycle" ethylene.

Similar regularities are also observed for cycles containing one or more oxygen atoms (Table 7). It suffices to calculate the ZPE + $(H_T - H_0)$ value of the corresponding cycloalkane and to subtract 14.50 kcal mol^{-1} for each CH_2 which is replaced by an oxygen atom. The agreement with spectroscopic results is remarkable considering that this verification includes an eight-membered cycle with four oxygen atoms as well as small cycles such as ethylene oxide and the "two-membered cycle" formaldehyde.

The replacement of CH_2 by NH also translates into a lowering of ZPE + $(H_T - H_0)$. The few spectroscopic analyses which are presently available suggest a lowering of $\sim$7.1 kcal mol^{-1}. The values thus estimated for piperidine, pyrolidine, and ethyleneimine are 100.4, 81.9, and 44.8 kcal mol^{-1}, respectively, in moderate agreement with their experimental counterparts, namely, 100.53 (axial) and 100.25 (equatorial piperidine) (31), $\sim$81 (estimated for pyrolidine from an incomplete spectral analysis) (32), and 45.95 kcal mol^{-1} for ethyleneimine (33).

A tentative estimate for the loss in vibrational energy

TABLE 8. ZPE + $(H_T - H_0)$ results of selected azines

Molecule	ZPE + $(H_T - H_0)$, kcal mol^{-1} Exptl.	Predicted
Benzene	66.22 (11)	66.06
Pyridine	57.29 (34)	57.61
1,3-Diazine	49.40 (35)	49.16
1,4-Diazine	49.07 (35)	49.16
1,2-Diazine	49.16 (35)	49.16
1,3,5-Triazine	42.9 (36)	40.71

accompanying the replacement of an aromatic CH group by N follows from an unfortunately limited set of spectral data. ZPE + $(H_T - H_0)$ is approximately given by $66.06–8.45n_N$ kcal mol^{-1} with respect to benzene (with n_N = number of N atoms), but this approximation seems to be of limited validity (Table 8).

Conclusions

Simple additivity rules relating ZPE + $(H_T - H_0)$ energies to structural features have proven their usefulness in the past, namely for alkanes, six-membered cycloalkanes, alkenes (1), ethers (37), carbonyl compounds (37), and aromatic hydrocarbons (38) and were essentially examined because of the need to link thermochemical data to theoretical calculations made for molecules in their hypothetical vibrationless state. In this vein, it now appears that our arsenal of rules can be extended, giving access to additional classes of compounds amenable to simple evaluations. While certainly pleasing in problems requiring their application, the quality of the correlations obtained from bona fide spectral analyses at times exceeds what we might normally expect. This is, namely, the case with the remarkable regularities observed for the replacement of a single by a double or triple CC bond, the fundamental similarity between open chain and cyclic alkanes, the progressive shrinking of cycloalkanes and the replacement of CH_2 by O in a cycle. Thus, beyond any consideration of their practical merits, it is comforting to witness the surprising simplicity and the unifying trends governing ZPE + $(H_T - H_0)$ energies in relation to structural features although, admittedly, all of it is presently recognized only on an empirical basis.

Acknowledgement

The financial support received from the Natural Sciences and Engineering Research Council of Canada is gratefully acknowledged.

1. S. FLISZÁR. Charge distributions and chemical effects. Springer-Verlag, Heidelberg, New York. 1983.
2. K. S. PITZER and E. CATALANO. J. Am. Chem. Soc. **78**, 4844 (1956); T. L. COTTRELL. J. Chem. Soc. 1448 (1948); K. S. PITZER. Chem. Rev. **27**, 39 (1940); K. S. PITZER. J. Chem. Phys. **8**, 711 (1940); K. S. PITZER. J. Chem. Phys. **5**, 473 (1937).
3. T. OI, A. POPOWICZ, and T. ISHIDA. J. Phys. Chem. **90**, 3080 (1986).
4. YU. N. PANCHENKO. Spectrochim. Acta, **31**A, 1201 (1975).
5. D. A. C. COMPTON, W. O. GEORGE, and W. F. MADDAMS. J. Chem. Soc. Perkin II, 1311 (1977).
6. YU. N. PANCHENKO, V. I. MOCHALOV, P. CZÁSZÁR, F. TÖRÖK, E. BENEDETTI, and M. AGLIETTO. Acta Chim. Hung. **114**, 149 (1983).
7. J. R. DURIG and D. A. C. COMPTON. J. Phys. Chem. **83**, 2879 (1979).
8. C. W. BOCK, YU. N. PANCHENKO, S. V. KRASNOSHCHIOKOV, and V. I. PUPYSHEV. J. Mol. Struct. Theochem. **148**, 131 (1986).
9. B. S. HUDSON, B. E. KOHLER, and K. SCHULTEN. Excited states. Vol. 6. *Edited by* E. C. Lim. Academic Press, New York. 1982. pp. 1–95.
10. R. J. HEMLEY, B. R. BROOKS, and M. KARPLUS. J. Chem. Phys. **85**, 6550 (1986).
11. G. HERZBERG. Molecular spectra and molecular structure. II. Infrared and Raman spectra of polyatomic molecules. Van Nostrand Reinhold Co., New York. 1968.
12. G. A. CROWDER and H. FICK. J. Mol. Struct. **147**, 17 (1986).
13. R. G. SNYDER and J. H. SCHACHTSCHNEIDER. J. Mol. Spectrosc. **30**, 290 (1969).
14. K. TANABE and S. SAËKI. J. Mol. Struct. **27**, 79 (1975).
15. Y. HAMADA, N. TANAKA, Y. SUGAWARA, A. HIRAKAWA, M. TSUBOI, S. KATO, and K. MOROKUMA. J. Mol. Spectrosc. **96**, 313 (1982).
16. D. W. SCOTT. J. Chem. Thermodyn. **3**, 843 (1971).
17. G. GAMER and H. WOLFF. Spectrochim. Acta, **29**A, 129 (1973).
18. A. L. VERMA. Spectrochim. Acta, **27**A, 2433 (1971).
19. J. N. GAYLES. Spectrochim. Acta, **23**A, 1521 (1967).
20. P. A. GIGUÈRE and J. D. LIU. J. Chem. Phys. **20**, 136 (1952).
21. J. R. DURIG and W. C. HARRIS. J. Chem. Phys. **50**, 1457 (1969).
22. J. R. DURIG and W. C. HARRIS. J. Chem. Phys. **51**, 4463 (1969).
23. J. R. DURIG and W. C. HARRIS. J. Chem. Phys. **55**, 1745 (1971).
24. S. FLISZÁR and J.-L. CANTARA. Can. J. Chem. **59**, 1381 (1981).
25. D. F. BOCIAN and H. L. STRAUSS. J. Am. Chem. Soc. **99**, 2866 (1977).
26. A. T. BALABAN, S. BĂDILESCU, and I. BĂDILESCU. Infrared spectra of heterocyclic compounds. *In* Physical methods in heterocyclic chemistry. *Edited by* R. R. Gupta. John Wiley and Sons, Inc., New York. 1984.
27. GY. BÁNHEGYI, P. PULAY, and G. FOGARASI. Spectrochim. Acta, **39**A, 761 (1983).
28. N. W. CANT and W. J. ARMSTEAD. Spectrochim. Acta, **31**A, 839 (1975).
29. D. E. REISNER, R. W. FIELD, J. L. KINSAY, and H. L. DAI. J. Chem. Phys. **80**, 5968 (1984).
30. M. KOBAYASHI. J. Chem. Phys. **66**, 32 (1977).
31. KH. KH. MULDAGALIEV and J. S. IGNATEV. Z. Fiz. Khim. **57**, 1508 (1983).
32. J. C. EVANS and J. C. WAHR. J. Chem. Phys. **31**, 661 (1959).
33. H. T. HOFFMAN JR., G. E. EVANS, and J. GLOCKLER. J. Am. Chem. Soc. **73**, 3030 (1951).
34. D. P. DILALLA and H. D. STIDHAM. J. Raman Spectrosc. **9**, 103 (1980).
35. R. C. LORD, A. L. MARSTON, and F. A. MILLER. Spectrochim. Acta, **9**, 118 (1957).
36. W. PYCKHOUT, I. CALLAERTS, C. VAN ALSENOY, H. J. GEISE, A. ALMENNINGEN, and R. SEIP. J. Mol. Struct. **147**, 321 (1986).
37. S. FLISZÁR and M. T. BÉRALDIN. Can. J. Chem. **60**, 792 (1982).
38. S. FLISZÁR, G. CARDINAL, and N. A. BAYKARA. Can. J. Chem. **64**, 404 (1986).
39. (*a*) D. A. COMPTON, W. O. GEORGE, and W. F. MADDAMS. J. Chem. Soc. Perkin Trans. 2, 1666 (1976); (*b*) V. A. KUZNETSOV, S. DZHESSATI, A. R. KYAZIMOVA, and V. I. TYULIN. Moscow Univ. Chem. Bull. **26**(1), 29 (1971); (*c*) CH. W. BOCK, YU. N. PANCHENKO, S. V. KRASNOSHCHIOKOV, and R. AROCA. J. Mol. Struct. **160**, 337 (1987).

Can. J. Chem. Downloaded from www.nrcresearchpress.com by 213.222.148.141 on 09/07/12
For personal use only.

Oxidation of 3-alkylidene-β-lactams. A preparation of 3-alkenyl-3-hydroxy-β-lactams

WILLIAM W. OGILVIE AND TONY DURST

Ottawa–Carleton Chemistry Institute, Department of Chemistry, University of Ottawa, Ottawa, Ont., Canada K1N 9B4

Received August 4, 1987

WILLIAM W. OGILVIE and TONY DURST. Can. J. Chem. **66**, 304 (1988).

Hydroxylation of the enolates of several 3-alkylideneazetidin-2-ones with MoOPH leads to the formation of 3-hydroxy-3-alkenylazetidin-2-ones in fair to good yields. The products were formed with *trans* stereochemistry in the alkenyl moiety and a presumed *trans* relationship between the hydroxyl substituent and a 4-substituent. Hydrogenation leads to 3-alkyl-3-hydroxyazetidin-2-ones. The prerequisite 3-alkylideneazetidin-2-ones were formed from 3-trimethylsilylazetidin-2-ones and aldehydes via a Peterson olefin synthesis.

WILLIAM W. OGILVIE et TONY DURST. Can. J. Chem. **66**, 304 (1988).

L'hydroxylation des énolates de plusieurs alkylidène-3 azétidinones-2 par le MoOPH conduit à la formation d'hydroxy-3 alcènyl-3 azétidinones-2, avec des rendements qui vont de moyens à bons. Les produits qui se forment présentent une stéréochimie *trans* dans la portion alcènyle et une relation que l'on croit *trans* entre le substituant hydroxyle et un substituant en position 4. Une hydrogénation conduit à la formation d'alkyl-3 hydroxy-3 azétidinones-2. On a obtenu les alkylidène-3 azétidinones-2 de départ à partir des triméthylsilyl-3 azétidinones-2 et des aldéhydes par le biais d'une synthèse d'oléfine suivant Peterson.

[Traduit par la revue]

Introduction

Several monobactams have been described that contain a 3-hydroxy or 3-alkoxy-β-lactam moiety, such as Sulfazecin **1** (1), Tabtoxin **2** (2), and the related microbial product **3** (2*a*). As part of a study directed towards the synthesis of monobactams of this type, we required an entry into 3-hydroxy-3-alkyl-β-lactams, which we envisaged could be readily obtained from 3-hydroxy-3-alkenyl-β-lactams. Compounds of type **4** (R^1 = Me, Ph) had previously been produced by photolysis of α-oxo amides (3), photolytic reaction of benzoylformate in the presence of imines (4), and by the [2 + 2] cycloaddition of imines with ketenes derived with hydroxyacetic acid derivatives (5, 6) to give products of type **4** (R^1 = H, Ph). However, no general route to **4** (R^1 = alkenyl) was apparent in the literature.

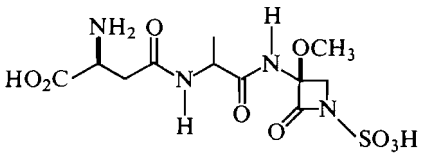

1

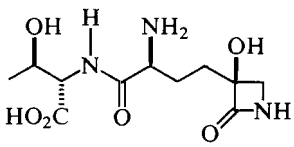

2

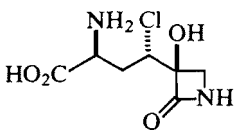

3

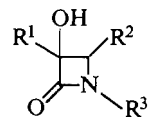

4

We would like to report a straightforward method for the preparation of 3-alkenyl-3-hydroxy-β-lactams via oxygenation of the anion derived from 3-alkenyl-β-lactams. Hydrogenation of these compounds should readily give the above mentioned 3-alkyl-3-hydroxy-β-lactams.

We briefly investigated the addition of organolithiums to 3-oxo-β-lactams as a route to 3-hydroxy-3-alkyl-β-lactam derivatives. Previous literature work indicated that such 3-oxo-β-lactam derivatives react with nucleophilic species such as hydride (7*a*), cyanide (7*a*), and Wittig reagents (7*b*,*c*) to give the expected products. In our hands the reaction of 3-oxo-4-phenyl-1-*p*-methoxyphenylazetidin-2-one, prepared from 3-ethylidene-4-phenyl-1-*p*-methoxyphenylazetidin-2-one, with several organolithiums gave complex mixtures of products, which were not further investigated.

Results and discussion

The formation of β-lactam enolates is a well-known and convenient method of introducing a variety of substituents onto position 3 of the azetidin-2-one ring. We therefore envisaged the formation of **4** by enolate hydroxylation of 3-alkylazetidin-2-ones (eq. [1]), since methods for hydroxylations

[1] 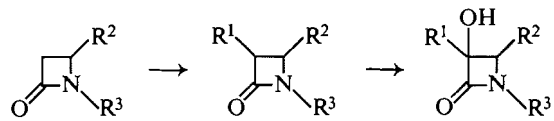

4

of carbanions have previously been described (8, 9). Initial attempts to hydroxylate 3-alkylazetidin-2-ones directly were unsuccessful, mainly due to difficulties in generating the required carbanions. Thus treatment of 3-methyl-4-phenylazetidin-2-one **5**, prepared in 70% yield from 4-phenyl-*N*-pyrrolidinomethyl-azetidin-2-one (10), with LDA at −78°C followed by quenching with methyl iodide resulted in recovery of the starting lactam. A similar result was observed using trimethylsilyl chloride as the electrophile, thus indicating that no enolate formation had taken place under these conditions.

Anion formation from **5** did occur upon treatment with LDA in the presence of one equivalent of tetramethylethylenediamine (TMEDA), based upon isolation of the *cis* 3,4-disubstituted lactam **6** and the formation of the 3,3-dimethylazetidin-2-one **7**.

Quenching of this enolate with CH_3I gave a mixture of 3,3-dimethyl product **7** (36%) as well as smaller amounts of **5** and **6**. The product **7** was characterized by the appearance of two methyl signals at δ 1.49 and 0.77 in the proton nmr. The signal

Can. J. Chem. Downloaded from www.nrcresearchpress.com by 213.222.148.141 on 09/07/12
For personal use only.

Can. J. Chem. Downloaded from www.nrcresearchpress.com by 213.222.148.141 on 09/07/12
For personal use only.

for the 3-methyl group in the *cis* isomer **6** was located 0.63 ppm upfield of the 3-methyl signal in **5**. Correspondingly, the signal for the α-hydrogen in **6** was 0.52 ppm downfield from the 3-hydrogen in **5**. These differences are explained by the anisotropic effect of the phenyl ring on the *cis* methyl group of **6** and on the *cis* H of **5**. In addition, the coupling constant for H-3 and H-4 of **6** was much larger (5.0 Hz) than the respective coupling in **5** (2.2 Hz), verifying that **6** had the *cis* 3,4 stereochemistry. This geometry was expected since **6** would arise by protonation of the enolate of **5**, which should preferentially occur *trans* to the 4-phenyl group.

Reaction of the enolate of **5**, generated as above, with TMS chloride gave no incorporation of a trimethylsilyl group, and resulted only in the recovery of starting material **5** and isomerization product **6**. Attempted oxidation of the **5** enolate with 2-sulfonyloxaziridine (11) or with molecular oxygen failed to give oxidation products and resulted only in the recovery of **5** and **6**.

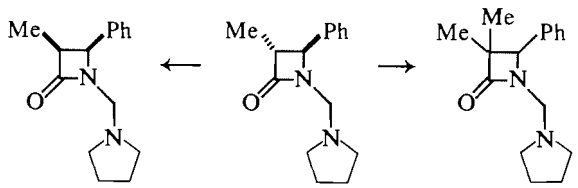

6 **5** **7**

To enhance anion formation at C-3 we decided to employ a vinylogous carbanion of type **8**. Since allyl anions are known to preferentially add hard electrophiles in the α position rather than at the γ-carbon (see ref. 12 for leading references), we felt that the control of regiochemistry in the hydroxylation reaction would not be a problem.

As an initial test of our hypothesis, we treated the lithium enolate of **9** (13) with oxodiperoxymolybdenum(pyridine)hexamethylphosphoramide (MoOPH) (8, 14, 15). After flash chromatography, 3-hydroxy-β-lactam **10** was isolated in 67% yield. The product **10** was also obtained in 30% yield upon treatment of the enolate of **9** with O_2. Compound **10** exhibited an infrared absorption at 1750 cm^{-1} indicating the presence of a β-lactam. The nmr spectrum showed a clear ABX pattern at δ 5.59 (H_A), δ 5.47 (H_B), and at δ 5.18 (H_X). Presumably the hydroxyl group and phenyl group are *trans*, since alkylations of β-lactam enolates at position 3 are known to proceed *anti* to any large group at position 4. Unfortunately, this conclusion could not be corroborated spectroscopically. This compound was smoothly hydrogenated over PtO_2 to give a highly crystalline solid, mp 129–130°C, which was identified as **11**.

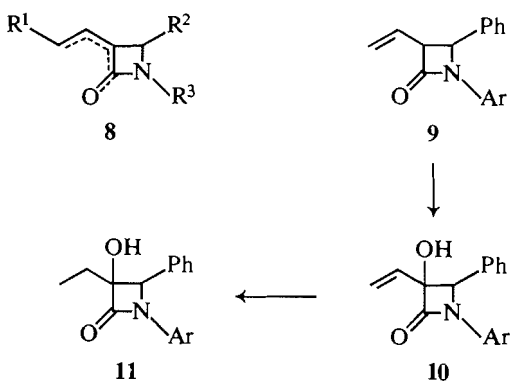

8 **9** **11** **10**

Ar = *p*-methoxyphenyl

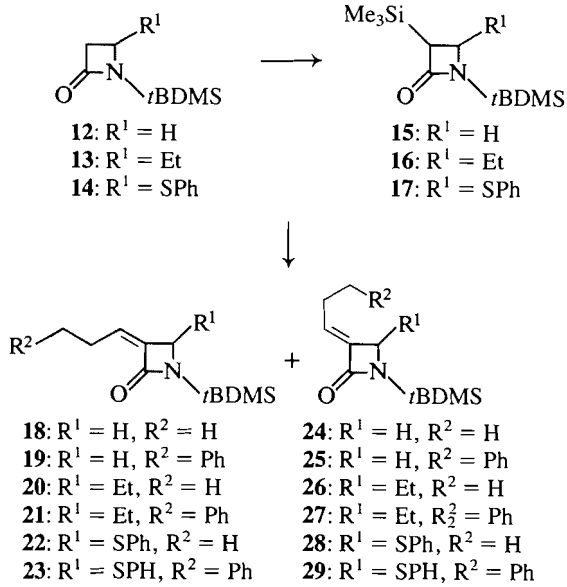

12: R^1 = H
13: R^1 = Et
14: R^1 = SPh
15: R^1 = H
16: R^1 = Et
17: R^1 = SPh

18: R^1 = H, R^2 = H
19: R^1 = H, R^2 = Ph
20: R^1 = Et, R^2 = H
21: R^1 = Et, R^2 = Ph
22: R^1 = SPh, R^2 = H
23: R^1 = SPH, R^2 = Ph
24: R^1 = H, R^2 = H
25: R^1 = H, R^2 = Ph
26: R^1 = Et, R^2 = H
27: R^1 = Et, R^2 = Ph
28: R^1 = SPh, R^2 = H
29: R^1 = SPH, R^2 = Ph

SCHEME 1

Compounds such as **11** are thus easily accessible via the route described above. The prerequisite 3-alkenylazetidin-2-ones are readily available via Peterson olefination starting with 3-trimethylsilylazetidin-2-ones and ketones (16), and presumably also aldehydes.

The preparation of the required alkenyl-β-lactams is shown in Scheme 1. The 4-unsubstituted β-lactam **12**, was obtained from the readily available 4-acetoxyazetidin-2-one **30** (17). Pfaendler and Hoppe (18) had reported that treatment of **30** with KBH_4 in H_2O gave **31** in 69% yield. We found that $NaBH_4$ in ethanol gave **31** in 84% yield from a nonaqueous work-up. This compound was readily protected as **12** with *tert*-butyldimethylsilyl chloride in DMF in 61% yield. 4-Ethylazetidin-2-one **13** was obtained by hydrogenation of 4-vinyl-1-*tert*-butyldimethylsilylazetidin-2-one **32** (19).

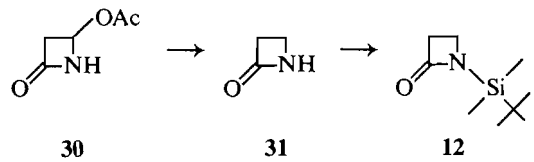

30 **31** **12**

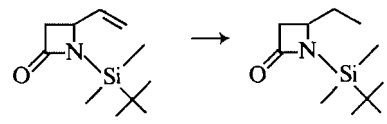

32 **13**

Both derivatives were smoothly converted to the 3-trimethylsilyl products **15** and **16** by treatment with LDA followed by addition of trimethylsilyl chloride. The thiophenyl derivative **17** was prepared in a similar manner from 4-thiophenylazetidin-2-one (20). Compounds **16** and **17** were obtained in pure form by flash chromatography while **15** was used without further purification.

The lithium enolate of **15**, prepared by treatment with LDA at −78°C, was reacted with propionaldehyde to give a mixture of **18** and **24** in 66% overall yield. These isomers could be easily separated by flash chromatography and were readily distinguished by ^1H nmr. The vinyl hydrogen of **18** appeared at δ 5.52, upfield of the vinyl hydrogen of **24** at δ 6.11.

Can. J. Chem. Downloaded from www.nrcresearchpress.com by 213.222.148.141 on 09/07/12
For personal use only.

Additionally, the vinylic methylene group of **18** was downfield of the analogous CH_2 group in **24**. The assignment of stereochemistry was based on observations noted previously (21). Reaction of **15** with hydrocinnamaldehyde gave **19** and **25** in 58% overall yield. As with **18** and **24**, the *Z*-isomer **19** was easily distinguished from the *E*-isomer **25** by the chemical shift differences in the olefinic hydrogens of each isomer.

In a similar manner, **16** and propionaldehyde gave **20** and **26** in yields similar to those obtained by the reaction of **15** with propionaldehyde. Reaction of the anion of **16** with hydrocinnamaldehyde gave a good yield of **21** and **27**. In all reactions, the *Z*-ene-lactams **18–21** were eluted before the corresponding *E*-isomers upon flash chromatography, and were obtained in higher proportions.

The reaction of the enolate of **17** with propionaldehyde at −78°C gave a disappointing yield of **22** and **28**. The reaction mixture smelled strongly of thiophenol and we isolated as the major product, in 30% yield, a crystalline material assigned structure **33** on the basis of spectroscopic data. An infrared spectrum showed signals at 1605 and 1551 cm^{-1} only, indicating that the β-lactam was no longer intact. Aside from signals for thiophenoxy, trimethylsilyl, and *tert*-butyldimethylsilyl groups, compound **33** showed only a doublet at δ 6.67 (J = 15.25) and a broad singlet at δ 9.0. A HOMCOR spectrum of this material indicated that the signals at δ 6.67 and δ 9.0 were coupled, as expected for a structure such as **33**.

This compound could arise by elimination of thiophenoxide to give the unsaturated β-lactam **34** followed by attack at the carbonyl group by thiophenoxide to afford thioester **33** (eq. [2]). The yield of desired products **22** and **28** could be

[2]

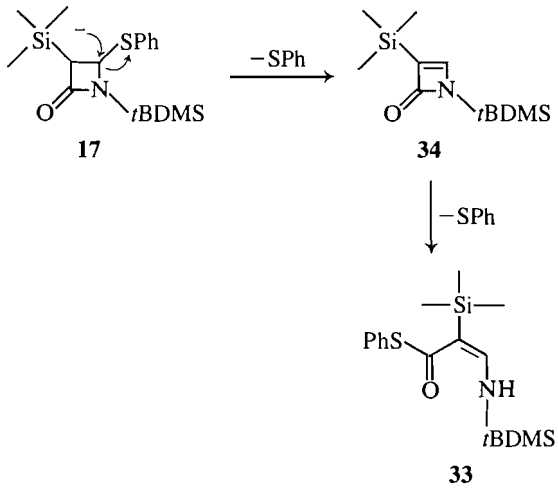

17 **34** **33**

increased to 37 and 28% respectively by allowing only 1 min for the formation of the enolate of **17**. The reaction of the enolate of **17** with hydrocinnamaldehyde using the normal reaction time gave **33** as the major product, with **23** and **29** being formed in smaller amounts. Using the short enolate formation time, **23** and **29** were obtained in 35 and 26% yield respectively.

Generation of the allylic enolates of **18–21** with LDA followed by addition of solid MoOPH at −78°C and subsequent warming until the solution had cleared gave crude products that were purified by flash chromatography to give the desired 3-hydroxy-3-alkenyl-β-lactams **35–38** in yields of 31–53%. Attempted oxidation of the 3-alkenyl-4-thiophenoxyazetidin-2-ones **22** and **23** was unsuccessful, possibly due to the instability of the anion. The crude reaction mixture smelled strongly of thiophenol.

In all cases the regenerated alkene moiety was shown to have an *E*-configuration as indicated by the large (approximately 15 Hz) coupling of the olefin protons. As mentioned above, the relative 3,4 stereochemistry could not be assigned on the basis of spectroscopic evidence. However, as with **10**, it is presumed that the hydroxyl group enters *trans* to the substituent at position 4.

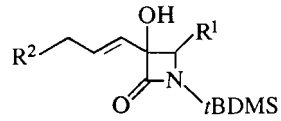

35: R^1 = H, R^2 = H
36: R^1 = H, R^2 = Ph
37: R^1 = Et, R^2 = H
38: R^1 = Et, R^2 = Ph

Experimental

Melting and boiling points are uncorrected. Nuclear magnetic resonance spectra were measured with a Varian XL-300 spectrometer in $CDCl_3$ solution. Values are given as δ values in ppm downfield from TMS. Infrared spectra were recorded with a Perkin–Elmer 783 spectrometer; values are given in cm^{-1}. Mass spectra were obtained on a VG 7070E. Column chromatography was performed using 60–200 mesh silica gel (Baker) and flash chromatography was done with Merck type 9385 silica gel (Terochem). In both cases ethyl acetate – hexane mixtures were used for elution.

CH_2Cl_2 was distilled from P_2O_5. THF was dried over benzophenone ketyl. DMF and diisopropylamine were distilled from CaH_2. Butyllithium was used as received from Aldrich after titration with diphenylacetic acid.

4-Phenyl-2-pyrrolidinomethylazetidin-2-one

4-Phenylazetidin-2-one (8.16 g) was refluxed in 45 mL of ethanol containing 6.4 mL of formalin and 5.5 mL of pyrrolidine for 7 h. The solvent was then removed under reduced pressure and the residue distilled (155°C/0.8 Torr; 1 Torr = 133.3 Pa) to give 9.6 g (75%) of 4-phenyl-2-pyrrolidinomethylazetidin-2-one as a pale yellow liquid; ir ($CHCl_3$): 1748; ^{1}H nmr δ: 7.40–7.36 (m, 5H), 4.72–4.69 (bs, 1H), 4.25 (d, J_{AB} = 13.12, 1H), 3.59 (d, J_{AB} = 13.12, 1H), 3.41 (dd, J = 5.25, 14.85, 1H), 2.85 (dd, J = 2.40, 15.00, 1H), 2.62–2.55 (m, 4H), 1.76–1.72 (m, 4H); ms: 230 (M^+), 70 (base peak) (M^+ − 160).

trans-*3-Methyl-4-phenyl-2-pyrrolidinomethylazetidin-2-one* ***5***

To a solution of 1.2 equivalents of LDA in THF at −78°C was added 3.0 g of 4-phenyl-2-pyrrolidinomethylazetidin-2-one in THF. The resulting deep orange solution was stirred at −78°C for 10 min and then 2 mL of MeI was added all at once. This solution was stirred at −78°C for an additional 10 min and then quenched with saturated NH_4Cl solution. The mixture was extracted with CH_2Cl_2, washed with water, and dried over $MgSO_4$. Removal of solvent followed by flash chromatography gave 2.2 g of **5** as a pale yellow oil (69%); ir (thin film): 1750; ^{1}H nmr δ: 7.25 (s, 5H), 4.21 (d, J_{AB} = 12.90, 1H), 3.55 (d, J_{AB} = 12.90, 1H), 4.22 (d, J = 2.2, 1H), 2.98 (dq, J_q = 7.4, J_d = 2.2, 1H), 2.70–2.41 (m, 4H), 1.90–1.52 (m, 4H), 1.41 (d, J = 7.4, 3H); ms: 244 (M^+).

cis-*3-Methyl-4-phenyl-2-pyrrolidinomethylazetidin-2-one* ***6***

To a solution of 1 equivalent of LDA and 1 equivalent of TMEDA in THF at −78°C was added 117 mg of **5** in THF. The solution was stirred for 10 min and 0.2 mL of freshly distilled trimethylsilyl chloride was added. Stirring was continued at −78°C for a further 20 min. Then the reaction mixture was quenched with saturated NH_4Cl, extracted with ether, washed with water, and dried over $MgSO_4$. Flash chromatography gave 38 mg of **6** as a pale yellow oil (33%); ir (thin film): 1745; ^{1}H nmr δ: 7.18 (m, 5H), 4.84 (d, J = 5.0, 1H), 4.28 (d, J_{AB} = 13.30, 1H), 3.50 (dq, J_q = 7.8, J_d = 5.0, 1H), 3.65 (d, J_{AB} = 13.30, 1H), 2.7–2.4 (m, 4H), 1.9–1.6 (m, 4H), 0.78 (d, J = 8.0, 3H); ms: 244 (M^+).

Can. J. Chem. Downloaded from www.nrcresearchpress.com by 213.222.148.141 on 09/07/12
For personal use only.

3,3-Dimethyl-4-phenyl-1-pyrrolidinomethylazetidin-2-one 7

Azetidin-2-one **5** (106 mg) in 2 mL of THF was added to a solution of 1 equivalent of LDA in 5 mL THF containing 1 equivalent of TMEDA at −78°C. The reaction mixture was stirred for 20 min, 0.2 mL of MeI was added, and the resulting solution stirred for a further 20 min at −78°C. The reaction mixture was then quenched with saturated NH_4Cl, extracted with ether, washed with water, and dried over $MgSO_4$. Removal of solvent and flash chromatography gave 40 mg of 7 as a pale yellow oil (36%); ir (thin film): 1750; ^{1}H nmr δ: 7.4–7.1 (m, 5H), 4.5 (s, 1H), 4.32 (d, J_{AB} = 12.25, 1H), 3.70 (d, J_{AB} = 12.25, 1H), 2.7–2.4 (m, 4H), 1.9–1.6 (m, 4H), 1.49 (s, 3H), 0.77 (s, 3H); ms: 258 (M^+).

Azetidin-2-one 31

To an ethanolic solution of 3.44 g of **30** at 0°C was added 1.01 g of $NaBH_4$ and the resulting solution stirred for 1 h at 0°C until the evolution of hydrogen had ceased. An excess of acidic Amberlite resin was then added at once and this suspension stirred for 1/2 h at 0°C. The resin was then filtered off and the ethanol removed under reduced pressure. The resulting white solid was washed with ethyl acetate to remove boron compounds, filtered, and the ethyl acetate removed under reduced pressure. This process was repeated with CH_2Cl_2 to give 1.60 g (84%) of **31** as white crystals, mp 72°C (lit. (22) mp 73–74°C).

*1-*tert*-Butyldimethylsilylazetidin-2-one 12*

A solution of 1.60 g of **31**, 3.72 g of *tert*-butyldimethylsilyl chloride and 3.76 mL of triethylamine in 20 mL DMF was stirred at 0°C for 1/2 h. The amine hydrochloride was filtered off and 40 mL of water added to the filtrate. This solution was extracted with ether (4 × 50 mL) and the combined ether fractions washed with water. Drying over $MgSO_4$ followed by removal of solvent under reduced pressure gave a pale yellow oil, which was distilled (75–77°C/1 Torr) to give 2.54 g (61%) of **12** as a colorless liquid; ir (thin film): 1745; ^{1}H nmr δ: 3.22 (t, J = 4.90, 2H), 3.00 (t, J = 4.90, 2H), 0.93 (s, 9H), 0.21 (s, 6H); ms: 185 (M^+), 128 (base peak) (M^+ − 57). *Anal.* calcd. for $C_9H_{19}NOSi$: C 58.38, H 10.27, N 7.57; found: C 58.02, H 10.24, N 7.33.

*4-Ethyl-1-*tert*-butyldimethylsilylazetidin-2-one 13*

4-Vinylazetidin-2-one **32** (2.87 g) was stirred in methanol with 100 mg of 10% Pd/C under H_2 at atmospheric pressure until 333 mL of H_2 had been consumed (2 h). The solution was then filtered and the methanol removed under reduced pressure. The pale yellow oil containing residual catalyst was purified by column chromatography to give 91% of **13** as a clear, colorless liquid; ir (thin film): 1750; ms: 213 (M^+), 156 (base peak) (M^+ − 57). *Anal.* calcd. for $C_{11}H_{23}NOSi$: C 61.97, H 10.80, N 6.57; found: C 62.07, H 10.66, N 6.44.

*General procedure for the preparation of 3-trimethylsilyl-1-*tert*-butyldimethylsilylazetidin-2-ones: 15, 16, 17*

A solution of *tert*-butyldimethylsilylazetidin-2-one (**12**, **13**, **11**) in THF was added to 1.2 equivalents of LDA generated *in situ* from diisopropylamine and *n*-butyllithium (ca. 2.5 M in hexane) in THF at −78°C. After 10 min, 1.2 equivalents of freshly distilled trimethylsilyl chloride was introduced and the mixture stirred at −78°C for an additional 10–20 min. The solution was then quenched with saturated NH_4Cl and extracted twice with ether. The combined extracts were washed with H_2O and dried over $MgSO_4$ before the solvent was removed under reduced pressure.

*3-Trimethyl-1-*tert*-butyldimethylsilylazetidin-2-one 15*

A portion of **12** (1.07 g) was treated as described above to give 1.49 g (96%) of **15** as a clear colorless oil. This material was used without further purification; ir (thin film): 1730; ^{1}H nmr δ: 3.26 (t, J = 5.93, 1H), 2.94–2.86 (m, 2H), 0.92 (s, 9H), 0.19 (s, 3H), 0.18 (s, 3H), 0.09 (s, 9H); ms: 257 (M^+), 242 (M^+ − 15), 200 (M^+ − 57).

*3-Trimethylsilyl-4-ethyl-1-*tert*-butyldimethylsilylazetidin-2-one 16*

Compound **13** (525 mg) gave 585 mg (83%) of **16** after flash chromatography; ir (thin film): 1730; ^{1}H nmr δ: 3.21–3.18 (m, 1H), 2.42 (d, J = 2.63, 1H), 1.90–1.80 (m, 1H), 1.40–1.30 (m, 1H), 0.93 (s, 9H), 0.85 (t, J = 7.44, 3H), 0.18 (s, 3H), 0.17 (s, 3H), 0.09 (s, 9H); ms (chemical ionization (CI)): 286 (base peak) (M^+ + 1). *Anal.* calcd. for $C_{14}H_{31}NOSi$: C 58.95, H 10.88, N 4.91; found: C 59.23, H 10.69, N 4.63.

*3-Trimethylsilyl-4-thiophenyl-1-*tert*-butyldimethylsilylazetidin-2-one 17*

Azetidin-2-one **11** (1.04 g) gave 980 mg (75%) of **17** after flash chromatography (75%); ir (thin film): 1740, 1580; ^{1}H nmr δ: 7.46–7.43 (m, 2H), 7.34–7.30 (m, 3H), 4.64 (d, J = 2.38, 1H), 2.89 (d, J = 2.39, 1H), 0.98 (s, 9H), 0.25 (s, 3H), 0.23 (s, 3H), −0.03 (s, 9H). *Exact Mass* (hrms) calcd. for $C_{12}H_{26}NOSi$: 256.1552; found: 256.1532 (M^+ − 109).

General procedure for the preparation of 3-alkylideneazetidine-2-ones 18–29

To a solution of 1.2 equivalents of LDA in THF (prepared as above) was added a solution of 3-trimethylsilyl-1-*tert*-butyldimethylsilyl-azetidin-2-one (**15**, **16**, **17**) in THF at −78°C. After stirring for 10 min, 1.5 equivalents of aldehyde was added to the golden yellow solution via syringe. The resulting mixture was stirred for 10–20 min and then quenched with saturated NH_4Cl, extracted twice with ether, washed with water, and dried over $MgSO_4$. Removal of solvent under reduced pressure gave a syrup, which was purified by flash chromatography. In all cases, the *Z*-isomers **18–23** were eluted before the *E*-isomers **24–29**.

From 664 mg of **15** and 50% excess propionaldehyde was obtained 203 mg (33%) of **18** and 181 mg (31%) of **24** as clear colorless oils. For **18**: ir (thin film): 1730; ^{1}H nmr δ: 5.52 (t, J = 8.4, 1H), 3.60 (s, 2H), 2.48 (quint, J = 8.5, 2H), 1.02 (t, J = 8.4, 3H), 0.92 (s, 9H), 0.20 (s, 6H); ms: 225.1 (M^+), 168 (base peak) (M^+ − 57). *Anal.* calcd. for $C_{12}H_{25}NOSi$: C 64.00, H 10.22, N 6.22; found: C 64.12, H 10.08, N 6.19. For **24**: ir (thin film): 1740; ^{1}H nmr δ: 6.11 (t, J = 7.5, 1H), 3.75 (s, 2H), 2.10 (quint, J = 7.5, 2H), 1.05 (t, J = 7.5, 3H), 0.95 (s, 9H), 0.24 (s, 6H); ms: 225.1 (M^+), 168 (base peak) (M^+ − 57). *Anal.* calcd. for $C_{12}H_{23}NOSi$: C 64.00, H 10.22, N 6.22; found: C 64.09, H 10.29, N 6.07.

From 164 mg of **15** and 50% excess hydrocinnamaldehyde was obtained 57.2 mg (35%) of **19** and 38.6 mg (23%) of **25**, both as clear colorless oils. For **19**: ir (CH_2Cl_2): 1720; ^{1}H nmr δ: 7.29–7.16 (m, 5H), 5.54 (t, J = 8.5, 1H), 3.59 (s, 2H), 2.84–2.75 (m, 4H), 0.93 (s, 9H), 0.22 (s, 6H); ms: 301 (M^+), 244 (89.2) (M^+ − 57). *Exact Mass* (hrms) calcd. for $C_{18}H_{27}NOSi$: 301.1860; found: 301.1870. For **25**: ir (CH_2Cl_2): 1730; ^{1}H nmr δ: 7.24–7.09 (m, 5H), 6.08 (t, J = 8.3, 1H), 3.44 (s, 2H), 2.71 (t, J = 8.4, 2H), 2.31 (q, J = 8.4, 2H), 0.87 (s, 9H), 0.16 (s, 6H); ms: 301 (M^+), 244 (base peak) (M^+ − 57). *Anal.* calcd. for $C_{18}H_{27}NOSi$: C 71.76, H 8.97, N 4.65; found: C 71.89, H 9.11, N 4.93.

From 547 mg of **16** and 50% excess propionaldehyde was obtained 180 mg (37%) of **20** and 145 mg (30%) of **26**, both as clear colorless oils. For **20**: ir (thin film): 1735; ^{1}H nmr δ: 5.53 (dt, J = 1.08, 7.70, 1H), 3.91 (dd, J = 2.39, 8.30, 1H), 2.48 (quint, J = 7.65, 2H), 1.80–1.77 (m, 1H), 1.60–1.53 (m, 1H), 1.03 (t, J = 7.52, 3H), 0.95 (s, 9H), 0.93 (t, J = 7.46, 3H), 0.24 (s, 3H), 0.19 (s, 3H); ms: 253 (M^+), 196.1 (base peak) (M^+ − 57). *Anal.* calcd. for $C_{14}H_{27}NOSi$: C 66.40, H 10.67, N 5.53; found; C 62.66, H 11.01, N 5.56. For **26**: ir (thin film): 1740; ^{1}H nmr δ: 6.03 (dt, J = 1.50, 7.66, 1H), 4.25 (b, 1H), 2.06 (quint, J = 7.56, 2H), 1.82–1.74 (m, 2H), 1.03 (t, J = 7.52, 3H), 0.948 (s, 9H), 0.90 (t, J = 7.37, 3H), 0.27 (s, 3H), 0.18 (s, 3H); ms: 253 (M^+), 196 (base peak) (M^+ − 57). *Exact Mass* (hrms) calcd. for $C_{14}H_{27}NOSi$: 253.1860; found: 253.1850.

From 214 mg of **16** and 50% excess hydrocinnamaldehyde was obtained 114 mg (46%) of **21** and 73 mg (29%) of **27**, both as clear colorless oils. For **21**: ir (thin film): 1730; ^{1}H nmr δ: 7.27 (m, 5H), 5.22 (t, J = 7.2, 1H), 3.84 (m, 1H), 2.81–2.75 (m, 4H), 1.75–1.70 (m, 1H), 1.45–1.40 (m, 1H), 0.94 (s, 9H), 0.869 (t, J = 7.4, 3H), 0.23 (s, 3H), 0.19 (s, 3H); ms: 329 (M^+), 272 (16) (M^+ − 57). *Anal.* calcd. for $C_{20}H_{31}NOSi$: C 72.95, H 9.42, N 4.26; found: C 72.25,

Can. J. Chem. Downloaded from www.nrcresearchpress.com by 213.222.148.141 on 09/07/12
For personal use only.

H 9.56, N 4.35. For **27**: ir (thin film): 1740; ^{1}H nmr δ: 7.29–7.20 (m, 5H), 6.06 (t, J = 7.8, 1H), 4.02 (s, 1H), 2.76–2.69 (m, 2H), 2.37–2.33 (m, 2H), 0.93 (s, 9H), 0.811 (t, J = 7.41, 3H), 0.24 (s, 3H), 0.16 (s, 3H); ms: 329 (M^+), 272 (base peak) ($M^+ - 57$). *Exact Mass* (hrms) calcd. for $C_{16}H_{22}NOSi$: C 272.1469; found: 272.1492 ($M^+ - 57$).

From 340 mg of **17** and 50% excess propionaldehyde was obtained 45 mg (15%) of **22** and 43 mg (14%) of **28**, both as clear colorless oils. Eluting in the fastest fractions was 102 mg (30%) of **33**, which was recrystallized from methanol, mp 102°C. For **22**: ir (thin film): 1740; ^{1}H nmr δ: 7.43–7.27 (m, 5H), 5.52 (t, J = 9.3, 1H), 5.30 (s, 1H), 2.34 (quint, J = 9.0, 2H), 0.97 (s, 9H), 0.91 (t, J = 7.51, 3H), 0.30 (s, 3H), 0.025 (s, 3H); ms (CI): 334 ($M^+ + 1$), 224 (60) ($M^+ - 109$). *Anal.* calcd. for $C_{18}H_{27}NOSSi$: C 64.86, H 8.11, N 4.20; found: C 64.69, H 8.35, N 4.20. For **28**: ir (thin film): 1750; ^{1}H nmr δ: 7.43–7.38 (m, 2H), 7.29–7.27 (m, 3H), 5.98 (t, J = 8.0, 1H), 5.40 (s, 1H), 2.17 (quint, J = 8.03, 2H), 0.99 (t, J = 7.45, 3H), 0.96 (s, 9H), 0.30 (s, 3H), 0.25 (s, 3H); ms (CI): 334 ($M^+ + 1$), 224 (63) ($M^+ - 109$). *Exact Mass* (hrms) calcd. for $C_{12}H_{22}NOSi$: 224.1469; found: 224.1493 ($M^+ - 109$). For **33**: ir ($CHCl_3$): 3600, 1605, 1551; ^{1}H nmr δ: 9.0 (b, 1H), 7.45–7.36 (m, 5H), 6.77 (d, J = 15.25, 1H), 0.86 (s, 9H), 0.30 (s, 9H), 0.14 (s, 3H); ms (CI): 366 ($M^+ + 1$). *Exact Mass* (hrms) calcd. for $C_{12}H_{26}NOSi_2$: 356.1552; found: 256.1532 ($M^+ - 109$).

From 468 mg of **17** and 50% excess hydrocinnamaldehyde was obtained 81 mg (15%) of **23** and 61 mg (12%) of **27**, both as clear colorless oils; 127 mg of **33** (27%) was also obtained in the fastest fractions. For **23**: ir (thin film): 1740; ^{1}H nmr δ: 7.42–7.36 (m, 5H), 7.28–7.20 (m, 5H), 5.54 (t, J = 7.8, 1H), 5.24 (s, 1H), 2.83–2.73 (m, 4H), 0.96 (s, 9H), 0.29 (s, 3H), 0.245 (s, 3H); ms (CI): 410 ($M^+ + 1$), 300 (base peak) ($M^+ - 109$). *Exact Mass* (hrms) calcd. for $C_{18}H_{26}NOSi$: 300.1782; found: 300.1760 ($M^+ - 109$). For **27**: ir (thin film): 1750; ^{1}H nmr δ: 7.42–7.36 (m, 10H), 6.00 (t, J = 8.1, 1H), 4.98 (s, 1H), 2.80–2.45 (m, 4H), 0.93 (s, 9H), 0.26 (s, 3H), 0.22 (s, 3H); ms (CI): 410 ($M^+ + 1$), 300 (base peak) ($M^+ - 109$). *Exact Mass* (hrms) calcd. for $C_{18}H_{26}NOSi$: 300.1782; found: 300.1775 ($M^+ - 109$).

General procedure for MoOPH hydroxylations

To a solution of LDA (1.2 equivalents) in THF at −78°C was added a solution of 3-alkylidene-1-*tert*-butyldimethylsilylazetidin-2-one **10**, **18**, **19**, **20**, **21** in THF. After stirring for 10 min, 1.5 equivalents of MoOPH was added at once. The solutions immediately turned orange or blue. Following MoOPH addition, the acetone bath was removed and the solution stirred until clear (10–15 min). Once MoOPH dissolution was complete, the solution was quenched with 10% Na_2SO_3, extracted twice with ether, washed with 10% HCl, dried over $MgSO_4$, and the solvent removed under reduced pressure. Products were purified by flash chromatography.

10: From 100 mg of **9** was obtained 71 mg (67%) of **10** as a white solid, which was recrystallized from ethyl acetate, mp 145°C; ir (thin film): 3600, 1750; ^{1}H nmr δ: 7.33–7.17 (m, 5H), 7.24 (d, J_{AB} = 9.07, 2H), 6.78 (d, J_{AB} = 9.07, 2H), 5.59 (dd, J_{AB} = 17.34, J_{AX} = 11.10, 1H), 5.47 (dd, J_{AB} = 17.34, J_{BX} = 0.92, 1H), 5.18 (dd, J_{AX} = 11.10, J_{BX} = 0.92, 1H), 5.10 (s, 1H), 3.74 (s, 3H); ms: 295 (M^+). *Exact Mass* (hrms) calcd. for $C_{18}H_{17}NO_3$: 295.1207; found: 295.1244.

35: From 95 mg of **18** was obtained 41.2 mg (41%) of **35** as a clear colorless oil; ir (CH_2Cl_2): 3550, 1642; ^{1}H nmr δ: 5.96 (dq, J_q = 6.47, J_d = 15.50, 1H), 5.67 (dd, J = 1.74, 15.50, 1H), 3.33 (d, J_{AB} = 6.05, 1H), 3.28 (d, J_{AB} = 6.05, 1H), 1.73 (dd, J = 1.59, 6.47, 3H), 0.93 (s, 9H), 0.24 (s, 3H), 0.21 (s, 3H); ms (CI): 242 (base peak) ($M^+ + 1$). *Anal.* calcd. for $C_{12}H_{23}NO_2Si$: C 59.75, H 9.54, N 5.81; found: C 59.86, H 9.56, N 6.00.

36: From 161.5 mg of **19** was obtained 52 mg (31%) of **36** as a clear colorless oil; ir ($CHCl_3$): 3500, 1740; ^{1}H nmr δ: 7.29–7.14 (m, 5H), 6.12 (dt, J_d = 15.57, J_t = 6.75, 1H), 5.72 (dt, J_d = 15.54, J_t = 1.54, 1H), 3.41 (dd, J = 6.05, 2H), 3.34 (d, J_{AB} = 6.11, 1H), 3.30 (d, J_{AB} = 6.11, 1H), 2.78 (s, 1H), 0.91 (s, 9H), 0.24 (s, 3H), 0.21 (s, 3H); ms (CI): 318 ($M^+ + 1$). *Anal.* calcd. for $C_{18}H_{27}NO_2Si$: C 68.14, H 8.52, N 4.42; found: C 67.99, H 8.93, N 4.38.

37: From 159 mg of **20** was obtained 90 mg (53%) of **37** as a white solid, mp 99°C. Recrystallization from hexanes did not change the melting point; ir ($CHCl_3$): 3500, 1740; ^{1}H nmr δ: 5.95 (dq, J_d = 15.62, J_q = 6.53, 1H), 5.59 (dd, J = 1.65, 15.62, 1H), 3.45 (dd, J = 3.17, 11.45, 1H), 2.64 (s, 1H), 1.77 (dd, J = 1.60, 6.51, 3H), 1.7–1.6 (m, 1H), 1.5–1.4 (m, 1H), 0.94 (s, 9H), 0.88 (t, J = 7.35, 3H), 0.25 (s, 3H), 0.22 (s, 3H); ms: 269 (M^+), 212 (9.3) ($M^+ - 57$). *Anal.* calcd. for $C_{14}H_{27}NO_2Si$: C 62.45, H 10.04, N 5.20; found: C 62.65, H 10.22, N 5.20.

38: From 290 mg of **21** was obtained 100 mg (33%) of **38** as a white solid, which was recrystallized from hexane, mp 101°C; ir ($CHCl_3$): 3300, 1730; ^{1}H nmr δ: 7.30–7.21 (m, 5H), 6.11 (dt, J_d = 15.56, J_t = 6.62, 1H), 5.61 (dt, J_d = 15.61, J_t = 1.55, 1H), 3.48–3.42 (m, 3H), 2.60 (s, 1H), 1.7–1.6 (m, 1H), 1.4–1.3 (m, 1H), 0.92 (s, 9H), 0.86 (t, J = 7.41, 3H), 0.24 (s, 3H), 0.21 (s, 3H); ms: 345 (M^+), 288 (10) ($M^+ - 57$). *Anal.* calcd. for $C_{20}H_{31}NO_2Si$: C 69.56, H 8.98, N 4.06; found: C 69.30, H 8.98, N 3.92.

3-Ethyl-3-hydroxy-4-phenyl-1-(4-methoxyphenyl)-azetidin-2-one ***11***

Compound **10** (71 mg) in THF was stirred with 21 mg of 10% PtO_2 under an atmosphere of H_2 at atmospheric pressure for 1 h. The solution was then filtered through a pad of Celite and the solvent removed under reduced pressure to give 73 mg (100%) of **11** as a white solid melting at 130°C. Recrystallization from ethyl acetate did not change the melting point; ir (KBr): 3400, 1720; ^{1}H nmr δ: 7.33–7.23 (m, 5H), 7.21 (d, J_{AB} = 9.04, 2H), 6.77 (d, J_{AB} = 9.04, 2H), 4.99 (s, 1H), 3.73 (s, 3H), 1.57 (sextet, J = 7.45, 1H), 1.37 (sextet, J = 7.27, 1H), 0.84 (t, J = 7.45, 3H); ^{13}C nmr δ: 168.68 (s), 156.20 (s), 134.27 (s), 130.45 (s), 128.67 (d), 128.25 (d), 126.98 (d), 119.15 (d), 114.19 (d), 87.93 (s), 69.50 (d), 55.33 (q), 25.08 (t), 6.84 (q). *Exact Mass* (hrms) calcd. for $C_{18}H_{19}NO_3$: 297.1363; found: 297.1367.

1. (*a*) A. Imada, K. Kitano, K. Kintata, M. Muroi, and M. Asai. Nature, **289**, 590 (1981); (*b*) K. Kamiya, M. Takamoto, Y. Wada, and M. Asai. Acta Crystallogr. Sect. B: Struct. Crystallogr. Cryst. Chem. **37**, 1262 (1981).
2. (*a*) W. W. Stewart. Nature, **229**, 174 (1971); (*b*) D. L. Lee and H. Rapaport. J. Org. Chem. **40**, 3491 (1975); (*c*) P. A. Taylor, H. K. Schnoes, and R. D. Durbin. Biochem. Biophys. Acta, **286**, 107 (1972); (*d*) J. P. Scannel, D. L. Pruess, J. F. Blount, H. A. Ax, M. Kellett, F. Weiss, T. C. Demny, T. H. Williams, and A. Stempel. J. Antibiot. **28**, 1 (1975); (*e*) D. W. Wolley, G. Schaffner, and A. C. Braun. J. Biol. Chem. **197**, 807 (1952).
3. (*a*) H. Aoyama, T. Hasegawa, M. Watabe, H. Shiraishi, and Y. Omote. J. Org. Chem. **43**, 419 (1978); (*b*) H. Aoyama, K. Miyazaki, M. Sakamoto, and Y. Omote. J. Chem. Soc. Chem. Commun. 333 (1983); (*c*) H. Aoyama, M. Sakamoto, K. Kuwabara, K. Yoshida, and Y. Omote. J. Am. Chem. Soc. **105**, 1958 (1983).
4. H. Aoyama, M. Sakamoto, K. Yoshida, and Y. Omote. J. Heterocycl. Chem. **20**, 1099 (1983).
5. M. S. Manhas, S. G. Amin, and R. D. Glazer. J. Heterocycl. Chem. **16**, 283 (1979).
6. F. P. Cossio and C. Palomo. Tetrahedron Lett. **26**, 4239 (1985).
7. (*a*) Y. S. Lo and J. C. Sheehan. J. Am. Chem. Soc. **94**, 8253 (1972); (*b*) J. C. Sheehan, A. Buku, E. Chackd, T. J. Commons, Y. S. Lo, S. Young, D. R. Ponzi, and W. C. Schwarzel. J. Org. Chem. **42**, 4045 (1971); (*c*) J. C. Sheehan, Y. S. Lo, J. Löliger, and C. C. Podewell. J. Org. Chem. **39**, 1444 (1974).
8. E. Vedejs, D. A. Engler, and J. E. Telschow. J. Org. Chem. **43**, 188 (1978).
9. F. A. Davis, L. C. Vishwakarma, J. M. Billmers, and J. Finn. J. Org. Chem. **49**, 3241 (1984).
10. A. B. Hamlet and T. Durst. Can. J. Chem. **61**, 411 (1982).
11. F. A. Davis, L. C. Vishwakarma, J. M. Billmers, and J. Finn. J. Org. Chem. **49**, 3243 (1984).

12. M. MAJEWSKI, G. B. MPANGO, M. T. THOMAS, A. WU, and V. SNIECKUS. J. Org. Chem. **46**, 2029 (1981).
13. A. K. BOSE, M. S. MANHAS, L. KRISHAN, M. GOSH, S. S. BARI, B. KURYS, J. M. VAN DER VEEN, and Z. KOSARYCH. American Chemical Society Division of Organic Chemistry National Meeting, Chicago, IL. September 1985.
14. M. MIMOUN, L. SEREE DE ROCH, and L. SAJUS. Bull. Soc. Chim. Fr. 1471 (1969).
15. E. VEDEJS and S. LARSON. Org. Synth. **64**, 127 (1986).
16. S. KANO, T. EBATA, K. FUNAKI, and S. SHIBUYA. Synthesis, 746 (1978).
17. (*a*) K. CLAUB, D. GRIMM, and G. PROSSEL. Liebigs Ann. Chem. 539 (1974); (*b*) S. J. MICKEL, C. N. HSIAO, and M. J. MILLER. Org. Synth. **64**, 135 (1986).
18. H. R. PFAENDLER and H. HOPPE. Heterocycles, **23**, 265 (1985).
19. F. A. BOUFFARD and B. G. CHRISTENSEN. J. Org. Chem. **46**, 2211 (1981).
20. A. YOSHIDA, T. HAYASHI, N. TAKEDA, S. OIDA, and E. OHKI. Chem. Pharm. Bull. **29**, 1854 (1981).
21. F. A. BOUFFARD, D. B. R. JOHNSTON, and B. G. CHRISTENSEN. J. Org. Chem. **45**, 1130 (1980).
22. R. W. HOLLEY and A. D. HOLLEY. J. Am. Chem. Soc. **71**, 2129 (1949).

Can. J. Chem. Downloaded from www.nrcresearchpress.com by 213.222.148.141 on 09/07/12
For personal use only.

α-Aminophosphonates. III.[1] Cycloaddition anionique-1,3 des esters α,β-insaturés : Préparation et transformations des Δ^1-pyrrolines[2]

ANDRÉ DEHNEL[3] ET JOLANTA M. KANABUS-KAMINSKA
Conseil national de recherches du Canada, Département de chimie, 100 Sussex Drive, Ottawa, Ont., Canada K1A 0R6

ET

GILBERT LAVIELLE
Institut de recherches Servier, 11, rue des Moulinaux, 92150 Suresnes, France

Reçu le 14 juin 1987

ANDRÉ DEHNEL, JOLANTA M. KANABUS-KAMINSKA et GILBERT LAVIELLE. Can. J. Chem. **66**, 310 (1988).

Les anions des aza-2 allylphosphonates **1** se combinent avec les esters α,β-insaturés **2** en donnant les intermédiaires chargés **4'**. Ces intermédiaires conduisent à la suite de protonation aux diéthoxyphosphonyl-2 éthoxycarbonyl-4 pyrrolidines **4**, ou bien à la suite de l'élimination de l'anion du diéthylphosphonate aux éthoxycarbonyl-4 Δ^1-pyrrolines **5**. Les proportions de ces deux produits dépendent des conditions de la réaction et de l'encombrement de substrats. La formation de produits cycliques a été étudiée pour de nombreux substrats et en présence de diverses bases. La réaction est régiosélective et stéréospécifique et l'obtention d'un diastéréoisomère cinétique plus encombré permet de déterminer que c'est une cycloaddition concertée. Les diastéréoisomères thermodynamiques moins encombrés **6** et **7** sont obtenus à partir de **4** et **5** respectivement par l'action d'une base dans un milieu protique. Les autres épimères de **4**, composés **8** et **9**, ont été obtenus par l'addition de diéthylphosphite sur les pyrrolines **5** et **7**. Les pyrrolines **5** ont été réduites pour donner les éthoxycarbonyl-3 pyrrolidines **12**. L'isomérisation de pyrrolines **5** possédant un substituant phényle dans la position 5 mène vers les éthoxycarbonyl-3 phényl-2 Δ^1-pyrrolines **10**. Ces dernières s'oxydent spontanément avec l'oxygène de l'air jusqu'au éthoxycarbonyl-3 hydroxy-3 phényl-2 Δ^1-pyrrolines **11**.

ANDRÉ DEHNEL, JOLANTA M. KANABUS-KAMINSKA, and GILBERT LAVIELLE. Can. J. Chem. **66**, 310 (1988).

The anions of the 2-azaallylphosphonates **1** react with the α,β-unsaturated esters **2** to yield the intermediates **4'**. These intermediates form the 2-diethoxyphosphonyl-4-ethoxycarbonylpyrrolidines **4** following a protonation while an elimination of the anion of the diethylphosphonate leads to the 4-ethoxycarbonyl-Δ^1-pyrrolines **5**. The proportions of these two products vary with the experimental conditions and the bulkiness of the substrates. The formation of the cyclic products has been studied for numerous substrates and in the presence of a number of bases. The reaction is regioselective and stereospecific and on the basis of the formation of the kinetically more strained diastereoisomer it is possible to conclude that the cycloaddition is a concerted one. The thermodynamically less strained diastereoisomers **6** and **7** are obtained from the compounds **4** and **5** respectively when they are subjected to the action of a base in a protic media. The other epimers of **4**, the compounds **8** and **9**, have been obtained by the addition of diethylphosphite to the pyrrolines **5** and **7**. The pyrrolines **5** have been reduced to the 3-ethoxycarbonylpyrrolidines **12**. The isomerization of the pyrrolines **5** with a phenyl substituent in position 5 leads to the formation of the 3-ethoxycarbonyl-2-phenyl-Δ^1-pyrrolines **10**. The latter spontaneously oxidize with atmospheric oxygen to yield the 3-ethoxycarbonyl-3-hydroxy-2-phenyl-Δ^1-pyrrolines **11**.

[Journal translation]

Introduction

Les aza-2 allylphosphonates **1** se sont avérés de précieux intermédiaires de synthèse. Grâce à la présence de deux groupes activants leurs anions se forment aisément sous l'action de diverses bases. Ces carbanions ont trouvé une première application dans une séquence, comprenant leur acylation, menant vers la synthèse de céphalosporines (1). Par la suite nous avons étudié leur alkylation (2, 3), leurs réactions de type Wittig–Horner avec les dérivés carbonylés (3, 4) et enfin les réactions avec les esters α,β-insaturés menant vers des composés cycliques (3, 5). Le présent travail est consacré à l'étude détaillée de cette dernière réaction. Elle donne, d'une manière régiosélective et stéréospécifique, accès aux diéthoxyphosphonyl-2 éthoxycarbonyl-4 pyrrolidines **4** ainsi qu'aux éthoxycarbonyl-4 Δ^1-pyrrolines **5** (cf. schéma 1) (3, 5). Les Δ^1-pyrrolines, intermédiaires de synthèse très intéressants, sont difficilement accessibles par une autre voie (5*a*, 6).

Dans ce travail, nous analyserons l'influence des conditions opératoires sur le déroulement de la réaction et, par ce moyen, le mécanisme réactionnel. D'autre part nous étudierons certaines transformations des Δ^1-pyrrolines.

Résultats

A. Cycloadditions

La réaction entre les carbanions formés à partir des imines **1** et les esters α,β-insaturés **2** (schéma 1) a été étudiée sur de nombreux exemples (tableau 1). Comme il est indiqué dans le schéma 1 elle peut mener vers trois produits : le composé linéaire **3** provenant de l'addition de Michael, la pyrrolidine **4** et la pyrroline **5**, obtenues à partir de l'intermédiaire **4'**, respectivement par sa protonation et par l'élimination de l'anion du diéthylphosphonate. L'obtention du composé **3** étant accessoire, nous nous concentrerons sur les conditions de synthèse des deux produits principaux.

À l'issue de la cycloaddition nous obtenons la pyrrolidine et tant que diastéréoisomère unique **4** possèdant les groupes éthoxycarbonyle et phosphonyle orientés mutuellement *cis* et également *cis* par rapport au substituant R^2 (s'il est plus encombrant que R^3). De même nous obtenons une seule Δ^1-pyrroline **5**. Or, si on tient compte de l'asymétrie uniquement dans les positions 2, 4 et 5, les pyrrolidines résultant

1. Partie I, cf. ref. 4; partie II, cf. ref. 2.
2. Publication du CNRC n° 27762.
3. Auteur à qui adresser toute correspondance. Adresse permanente : Institut universitaire de technologie d'Orléans, B.P. 6729, 45067 Orléans CEDEX 2, France.

Printed in Canada / Imprimé au Canada

Can. J. Chem. Downloaded from www.nrcresearchpress.com by 213.222.148.141 on 09/07/12
For personal use only.

TABLEAU 1. Conditions et résultats de cycloaddition d'anions lithiens formés au BuLi et LDA

							Résultants de cycloaddition							
							Anion obtenu au LDA				Anion obtenu au BuLi			
	Substituants						Temperature (°C)		Rdt (%)		Temperature (°C)		Rdt (%)	
Code	R^1	R^2	R^3	R^4	R^5	R^6	add.	hyd.	**4**	**5**	add.	hyd.	**4**	**5**
a	H	Ph	H	H	H	H	−72	−72	55*	0	−72	−72	63*	0
b	H	3-Pyr	H	H	H	H	‡							
c	H	Ph	H	H	H	Me	−105	−105	80	0	−70	−70	95*	0
							−75	−75	65	15			†	
d	H	Ph	H	H	Me	H	−72	−72	62	0	−72	−72	58	10
e	Me	Ph	H	H	H	H	−72	−10	76	0			†	
f	H	Ph	H	H	Ph	H	−72	0	42	0				
g	Ph	Ph	H	H	H	H	‡							
h	H	Ph	H	Me	Me	H	−72	−72	0	0	−70	0	13	45
							−72	−30	40	0				
i	Me	Ph	H	H	Me	H					−100	−100	60	10
											−72	−72	45	30
j	Me	Ph	H	H	H	Me					−72	0	15	62
k	Ph	Ph	H	H	H	Me	‡							
l	H	Ph	Me	H	Me	H	−72	0	12	68	−72	0	5	85†
m	H	Ph	H	—$(CH_2)_5$—		H	−72	−72	5	0	−70	−70	0	0
							−72	−10	30	30	−70	−10	5	85
n	H	Ph	H	H	—$(CH_2)_4$—		−72	−72	70	10				
o	H	—$(CH_2)_5$—		H	Ph	H					−72	−72	25	60
p	H	Me	Me	Me	Me	H					−70	15	22	65
q	H	*i*-Pr	Me	Me	Me	H					−70	15	0	77†
r	H	Ph	Me	Me	Me	H					−70	15	11	74
s	H	—$(CH_2)_5$—		Me	Me	H					−70	15	5	82
t	H	—$(CH_2)_5$—		—$(CH_2)_5$—		H					−78	−78	0	0
											−78	15	5	85
u	H	—$(CH_2)_5$—		H	—$(CH_2)_4$—						−78	−78	16	49

*Réaction réalisée en présence de 20% de base.
†Réaction commentée dans le texte.
‡Produit obtenu par une autre voie.
Les rendements inferieurs à 20% sont des estimations d'après les spectres de rmn. Les autres sont les rendements en produits purifiés.

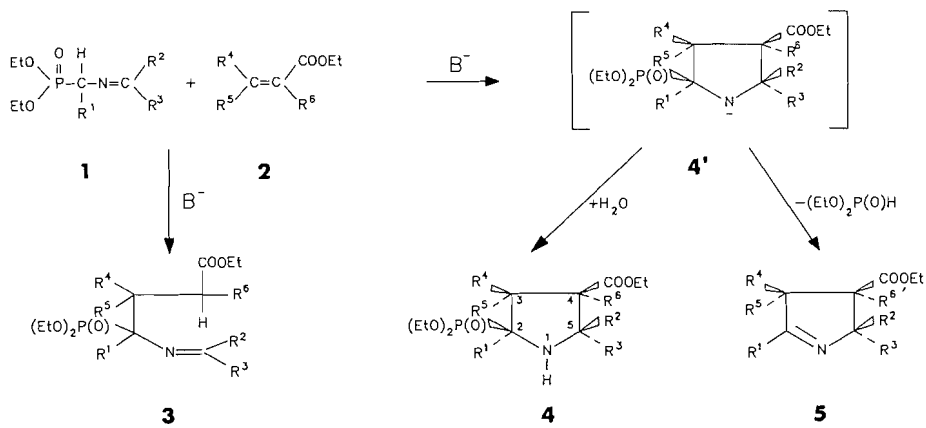

Les substituants sont indiqués par le code du tableau 1.
SCHÉMA 1

de la cycloaddition peuvent exister sous forme de quatre diastéréoisomères, et les pyrrolines sous forme de deux diastéréoisomères, visualisés dans le schéma 2. Par la suite nous appelerons les composés **4** et **5** produits *cis*, et **6** et **7**, *trans*. Les substituants seront indiqués par le code du tableau 1.

Les dérivés **6** et **7** sont obtenus respectivement à partir des composés **4** et **5**, si R^6 est un atome d'hydrogène, par l'épimérisation dans des conditions basiques (éthylate de sodium dans l'éthanol) menant vers l'équilibre thermodynamique. Remarquons donc que la cycloaddition donne des produits

Can. J. Chem. Downloaded from www.nrcresearchpress.com by 213.222.148.141 on 09/07/12
For personal use only.

TABLEAU 2. Résultats de cycloaddition en présence de l'hydrure de sodium et données analytiques de pyrrolidines **4**

Code	Cycloaddition en présence de NaH: Temps (min)	Temp (°C)	Rdt (%) **4**	Dérivé, *F* (°C)	Formule, M.M.	Analyse calculé/trouvé: C	H	N	P
a	5	0	82	Picrate	$C_{23}H_{29}N_4O_{12}P$	47,26	5,00	9,59	5,30
				123	584,47	47,08	4,98	9,56	5,44
c	30	10	85	Base	$C_{18}H_{28}NO_5P$	58,52	7,64	3,79	8,39
				70	369,39	58,21	7,65	3,70	8,09
d	10	10	85	Picrate	$C_{24}H_{31}N_4O_{12}P$	48,16	5,22	9,36	5,18
				140	598,50	48,15	5,18	9,20	5,39
e	10	20	77	Base	$C_{18}H_{28}NO_5P$	58,52	7,64	3,79	8,39
				53	369,39	58,46	7,72	3,76	8,07
f	30	20	81	Picrate	$C_{29}H_{33}N_4O_{12}P$	52,73	5,04	8,48	4,69
				168	660,57	52,89	5,03	8,46	4,48
g	10	15	90	Base	$C_{23}H_{30}NO_5P$	64,02	7,01	3,25	7,18
				121	431,46	63,95	6,96	3,14	7,15
h			*	Picrate	$C_{25}H_{33}N_4O_{12}P$	49,02	5,43	9,15	5,06
				140	612,53	49,39	5,55	9,23	5,08
i			*	Base	$C_{19}H_{30}NO_5P$	59,51	7,89	3,65	8,08
				84	383,42	59,56	8,01	3,63	7,93
j	15	20	87	Base	$C_{19}H_{30}NO_5P$	59,51	7,89	3,65	8,08
				105	383,42	59,77	7,94	3,74	8,04
k	60	10	89	Base	$C_{24}H_{32}NO_5P$	64,70	7,24	3,14	6,95
				115	445,48	64,80	7,18	2,99	6,53
l	20	20	85	Picrate	$C_{25}H_{33}N_4O_{12}P$	49,02	5,43	9,15	5,06
				98	612,53	48,97	5,57	9,31	5,12
o			*	Base	$C_{22}H_{34}NO_5P$	62,39	8,09	3,31	7,32
				87	423,48	62,52	8,31	3,15	6,99
p			*	HCl	$C_{15}H_{31}NO_5PCl$	48,45	8,40	3,77	
				219	371,84	48,25	8,32	3,87	
u			*	Base	$C_{20}H_{36}NO_5P$	59,83	9,04	3,49	7,72
				102	401,48	59,89	9,28	3,55	7,72

*Obtenu sur une autre voie. Les autres : rendements de produits purifiés.

cinétiques plus encombrés que les produits thermodynamiques obtenus par l'équilibration. C'est une information importante pour déterminer le mécanisme de la cycloaddition.

La structure de pyrrolidines obtenues dans ces réactions a été établie à l'aide de la spectroscopie de la rmn (*5b*).

1. Conditions de préparation de produits cycliques

La cycloaddition a été réalisée selon deux procédés différents présentés ci-dessous.

(*a*) La réaction entre les composés du type **1** et les composés du type **2** en présence de quantités catalytiques de l'hydrure de sodium à température ambiante et arrêtée par l'addition de l'eau donne les pyrrolidines **4** avec d'excellents rendements (cf. tableau 2). Elle reste cependant limitée aux substrats possèdant en tant que R^2 un substituant aromatique. Dans ces conditions on n'observe pas la formation de pyrrolines **5**.

(*b*) Les carbanions des imines **1** sont formés par l'action du butyllithium ou du diisopropylamidure de lithium, habituellement à −70°C. L'ester α,β-insaturé est ajouté à la même température. La réaction est arrêtée par l'addition de l'eau à la température indiquée. La composition du mélange résultant dépend de la nature des substrats et de cette température. Les conditions et les rendements de produits **4** et **5** dans ces réactions sont présentés dans le tableau 1.

De l'examen de ces résultats on peut tirer les conclusions suivantes :

(*i*) Le taux d'élimination du diéthylphosphite, menant vers la formation du produit **5**, est généralement plus élevé dans les

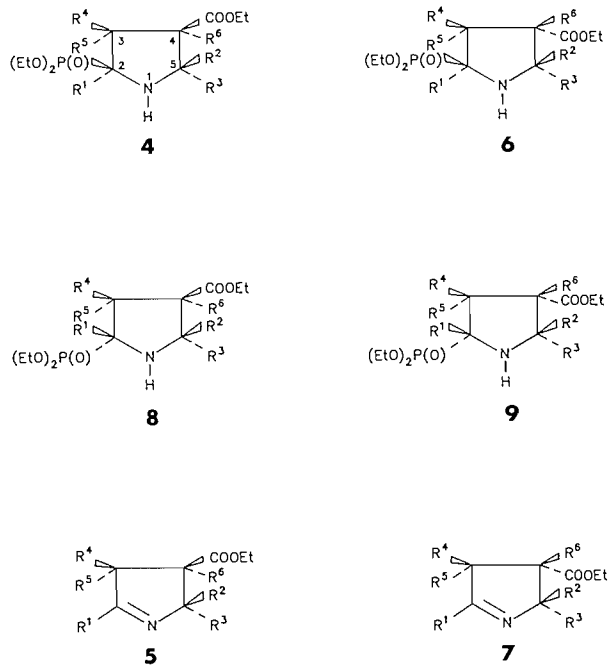

Dans les cas ou $R^2 = R^3$ et $R^4 = R^5$, l'isomérie *cis–trans* n'existant pas, les produits sont arbitrairement joints à la classe *cis*.

SCHÉMA 2

Can. J. Chem. Downloaded from www.nrcresearchpress.com by 213.222.148.141 on 09/07/12
For personal use only.

Can. J. Chem. Downloaded from www.nrcresearchpress.com by 213.222.148.141 on 09/07/12
For personal use only.

réactions où le carbanion est obtenu avec du butyllithium en comparaison au LDA (*h*, *l*, *m*).

(*ii*) Pour la même base, la proportion de produit d'élimination **5** croît avec la température d'hydrolyse (*c*, *i*).

(*iii*) D'une manière générale, les esters éthyléniques **2**, très encombrés en position β (par exemple, cyclohexénylacétate d'éthyle, cf. *m* et *t*), ne réagissent pas à la température de −70°C. La réaction a lieu dans ce cas entre −70°C et 0°C et la proportion de la pyrroline **5**, par rapport à la pyrrolidine **4**, est élevée.

(*iv*) L'encombrement de l'imine **1** semble être le facteur limitatif de la cycloaddition. Ainsi le produit **5***q* est obtenu avec le rendement de 77% accompagné de 18% du produit linéaire **3***q*, tandis que l'imine **1** avec R^2 = *tert*-butyle et R^3 = méthyle dans les mêmes conditions uniquement l'adduit de Michael **3**.

Dans certains cas nous avons réalisé des cycloadditions dans des conditions différentes :

(*i*) Les produits **4***a* et **4***c* sont obtenus, avec des bons rendements, en présence de défaut de base (environ 20% mol de BuLi ou LDA) par rapport à l'imine **1**. Les réactions, avec les mêmes substrats réalisées dans des conditions standard, donnent dans le cas *a* le mélange contenant des produits de polycondensation de l'acrylate d'éthyle, dans le cas *c* un mélange de produits dont nous parlerons dans le paragraphe suivant.

(*ii*) Si nous essayons de synthétiser le produit **4***l* en menant la réaction entièrement à −90°C, l'anion étant formé au butyllithium, nous obtenons essentiellement le produit linéaire **3***l*. Les produits cycliques sont cependant obtenus dans la réaction réalisée à température plus élevée.

(*iii*) Dans certains cas (*c* et *e*) de réactions réalisées à température comprise entre −70°C et −100°C (le carbanion étant préparé au butyllithium) nous obtenons à part les produits habituels **4** et **5** également leurs diastéréoisomères **6** et **7** ainsi que les produits linéaires **3**.

Le tableau 3 donne les résultats de synthèse de produits *c* dans des conditions variables.

Pour pouvoir expliquer ces anomalies nous avons réalisé quelques expériences qui ne sont pas des cycloadditions à proprement parler : (*i*) Le produit **4***c*, obtenu préalablement, en présence d'un équivalent de butyllithium à −100°C se transforme en produit linéaire **3***c* avec le rendement de 30%. On n'observe pas cette ouverture du cycle en présence de LDA. (*ii*) L'adduit de Michael **3***e*, obtenu sur une autre voie, soumis à l'action d'un équivalent de LDA à −70°C donne le produit *trans* **7***e* avec le rendement de 70%.

2. *Mécanisme de formation de produits cycliques*

Deux mécanismes peuvent expliquer la formation de produits cycliques : cycloaddition concertée ou bien la formation d'un intermédiaire linéaire **3** et sa cyclisation. La formation, dans la majeure partie des cas pour les trois bases utilisées, d'un produit unique cinétique semble indiquer un mécanisme concerté. Pour étayer cette hypothèse, en ce qui concerne les réactions en présence de l'hydrure de sodium, hous avons vérifié que les produits linéaires **3**, obtenus sur une autre voie, ne se cyclisent pas sous l'action de cette base.

La formation, dans certains cas particuliers, du mélange de produits comprenant les composés *trans* doit s'expliquer par la cyclisation d'un intermédiaire linéaire. L'exemple présenté dans le tableau 3 nous montre l'influence de la température sur la composition du mélange réactionnel. La pyrroline *trans* **7***c* obtenue à température élevée ne peut pas provenir directement

TABLEAU 3. Rendements de pyrrolidines et pyrrolines ayant les substituants *c* obtenues dans des conditions variables

Température (°C)		Rendement (%)				
		cis		*trans*		Linéaire
add.	hyd.	**4**	**5**	**6**	**7**	**3**
−100	−100	70	10*			10*
−100	+35		40		25	
−70	0	20	25	15	10	

*Les rendements estimés par la rmn. Les autres : rendements de produits purifiés.

de cyclisation car à basse température nous observons uniquement les produits *cis*. Elle ne peut non plus être le résultat d'une épimérisation, le substituant R^6 étant un méthyle. La seule explication de sa formation est donc l'ouverture de l'intermédiaire **4***c*′ et sa cyclisation en produit *trans*.

Pour certains substrats, à une température de l'ordre de −100°C, la formation de l'adduit de Michael est énergétiquement plus favorable que la cycloaddition. Dans ces cas les produits *trans* peuvent provenir de la cyclisation secondaire de ces intermédiaires.

Il nous faut donc conclure que les produits cycliques sont obtenus par deux voies différentes dont la première est unique dans le cas de l'hydrure de sodium et généralement prédominante :

(1) Cycloaddition concertée conduisant d'une façon stéréospécifique (7), avec un bon rendement, au produit unique cinétique, peu stable.

(2) Cyclisation d'un produit linéaire menant vers un mélange de produits. Le rendement est généralement faible car c'est une cyclisation du type 5-*endo*–*trig* qui est géométriquement défavorisée (8).

Quel que soit le mécanisme de la fermeture du cycle le produit formé possède toujours le groupe phosphonyle en position *cis* par rapport à R^2 plus volumineux que R^3. Ce fait explique par la stabilité de la conformation *trans*–*trans* du carbanion **1**′ (7) :

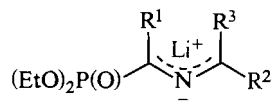

3. *Les transformations des amidures* **4**′

Dans les cas où le substituant R^2 est un phényle la cycloaddition peut avoir lieu en présence de quantités catalytiques de base. Ceci signifie que l'amidure cyclique **4**′, formé en petite quantité, est suffisamment basique pour déprotoner les molécules suivantes du substrat **1** et ainsi perpétuer la réaction (9).

Nous observons dans ce cas une réaction univoque car l'amidure **4**′ protoné par le substrat **1** ne peut plus évoluer dans le sens de l'élimination de l'anion phosphonate ou de l'ouverture du cycle.

D'une façon analogue, une plus faible tendance à l'élimination du diéthylphosphite et l'absence de produits *trans* dans le cas de réactions réalisées en présence de LDA indiquent que l'intermédiaire **4**′ est protoné par la diisopropylamine.

La β élimination des anions phosphoniques, que nous observons, est beaucoup mieux connue pour les esters des acides α-hydroxyalkylphosphoniques (10) que pour les composés azotés (11).

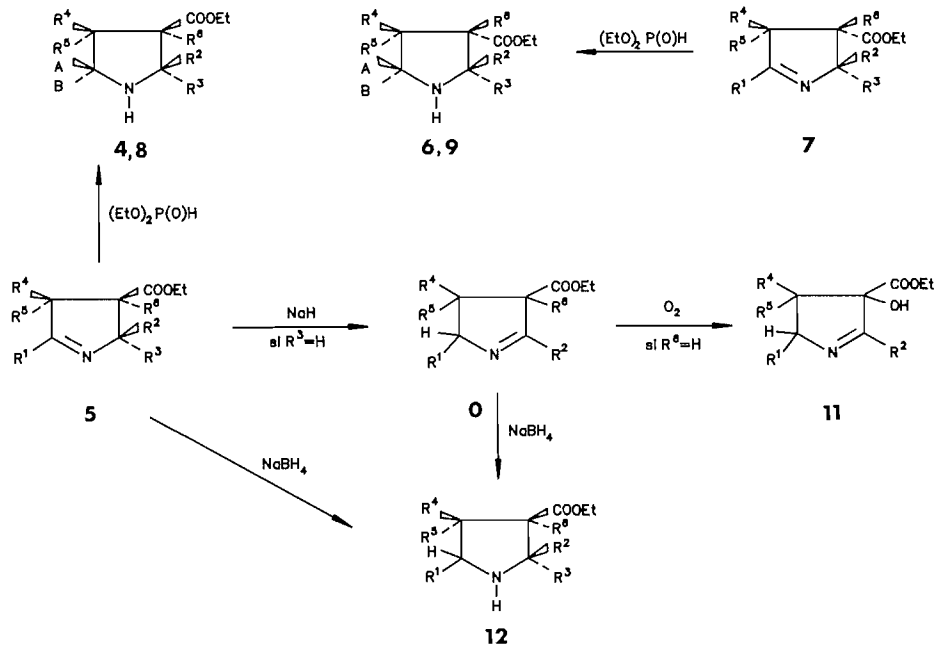

4 et **6** : A = $(EtO)_2P(O)$, B = R^1
8 et **9** : A = R^1, B = $(EtO)_2P(O)$

SCHÉMA 3

TABLEAU 4. Résultats d'addition de diéthylphosphite sur les pyrrolines **5** et **7**

	Addition sur **5**, rendement (%)		Addition sur **7**, rendement (%)	
Code	**4**	**6**	**8**	**9**
c	—	100	33	66
h	30	70	100	—
*j**	30	70		
l	—	100	50	50
m	50	50	100	—
p	50	50		

*Le rendement global 80%. Les rendements dans les cas de mélanges sont évalués d'après la rmn.

B. Transformations de Δ^1-pyrrolines 5 et 7

Les pyrrolines **5** et **7** peuvent subir certaines transformations qui soit présentent un intérêt théorique (éclaircissement de la structure de produits synthétisés), soit peuvent avoir une application pratique dans la synthèse. Les trois transformations que nous avons étudiées sont visualisées dans le schéma 3.

1. Addition du diéthylphosphite

Parmi quatres diastéréoisomères possibles de pyrrolidines étudiées deux seulement sont obtenus par la cycloaddition (ou cycloaddition suivie d'épimérisation). Afin de pouvoir déterminer indubitablement la structure des pyrrolidines, nous avons synthétisé les diastéréoisomères manquants en faisant réagir les pyrrolines **5** et **7** avec le diéthylphosphite. À l'issue de cette réaction nous avons obtenus les mélanges de pyrrolidines **4** et **8** (en partant de **5**) ou **6** et **9** (en partant de **7**) dont la composition est indiquée dans le tableau 4.

Le groupe phosphonyle a tendance à s'additionner sur la face opposée au carboxyle. Ainsi nous obtenons les pyrrolidines **6***c*, **6***l*, **8***h* et **8***m* en tant que produits uniques. Cette tendance peut être contrebalancée par la présence des autres substituants encombrants et nous constatons alors la formation de mélanges (cf. tableau 4).

2. Préparation de pyrrolines isomérisées 10 et leur oxydation

Sous l'action de l'excès de l'hydrure de sodium les pyrrolines **5** et **7**, si elles possèdent un atome d'hydrogène en tant que substituant R^3, sont transformées en pyrrolines **10**. Pratiquement nous réalisons plutôt une séquence ininterrompue de réactions qui en partant de **1** et **2**, en présence de l'hydrure de sodium, abouti à la formation de **10**. Le produit de cycloaddition **4** formé initialement s'épimérise jusqu'au **6**, celui-ci subit l'élimination du diéthylphosphonate de sodium pour donner la pyrroline **7**, qui à la suite de la migration de la double liaison donne la pyrroline **10**.

Dans des cas où le substituant R^1 est un phényle, cette séquence s'arrête au stade de l'élimination, la migration de la double liaison n'ayant pas lieu. Ainsi nous obtenons dans des conditions identiques le produit **7***g* avec le rendement de 60% et, dans une autre expérience, le mélange de 25% de produit **5***k* avec 42% de **7***k*.

Ces résultats signifient que la migration de la double liaison a lieu s'il en résulte un système plus stable où la double liaison C=N est conjuguée avec le noyau aromatique. Dans le cas où un tel système existe à l'origine, l'isomérisation ne se fait pas.

Les produits **10** obtenus ainsi sont des huiles. Exposés à l'air ils s'oxydent spontanément, si le substituant R^6 est un atome d'hydrogène, pour donner les dérivés hydroxylés cristallins **11**. Nous avons obtenu de cette manière les produits **11***a*, **11***b*, **11***d* et **11***m*.

L'oxydation spontanée de composés semblables est connue (12).

3. Réductions menant vers les pyrrolidines 12

La réduction de pyrrolines **5** et **10** au borohydrure de sodium donne, avec un excellent rendement, les pyrrolidines **12**. Ont été obtenus : les produits **12***p–u* par la réduction de pyrrolines **5** correspondantes, ainsi que **12***a* par la réduction du composé **10***a*. Dans tous ces cas on obtient le produit ayant le substituant

Can. J. Chem. Downloaded from www.nrcresearchpress.com by 213.222.148.141 on 09/07/12
For personal use only.

TABLEAU 5. Déplacements chimiques δ ^{1}H pour les pyrrolidines **4**, **6**, **8** et **9**

	δ ^{1}H/TMS (ppm)						COOEt		$P(O)(OEt)_2$	
Produit	R^1	R^2	R^3	R^4	R^5	R^6	OCH_2	CH_3	OCH_2	CH_3
4*f*	3,40	7,30	4,70	3,72	7,22	3,63	3,50	0,70	4,20	1,37
4*g*	7,10	7,10	4,40	2,6–3,1		3,22	3,50	0,72	4,43	1,43
4*k*	7,15	7,15	3,95	3,35	2,45	1,15	3,40	0,78	4,44	1,42
4*o*	3,51	—	—	3,60	7,11	2,65	3,90	1,11	4,15	1,35
4*p*	2,94	1,27	1,27	1,27	1,27	2,40	4,18	1,34	4,18	1,34
4*u*	3,20	—	—	3,30	—	—	4,11	1,25	4,13	1,36
5*f*	3–4	7,21	4,55	3–4	7,22	3–4	3,41	0,62	4,20	1,39
8*c*	3,82	7,23	4,01	2,21	1,90	1,31	3,72	0,82	4,21	1,36
8*h*	3,60	7,30	4,75	1,32	1,20	2,85	3,71	0,81	4,31	1,38
8*j*	1,50	7,05	4,32	2,05	2,45	1,35	3,53	0,88	4,20	1,38
8*p*	3,25	1,35	1,35	1,35	1,35	2,49	4,18	1,34	4,18	1,34
9*c*	3,51	7,21	4,61	1,80	2,31	0,90	4,02	1,31	4,32	1,41

R^2 en position *cis* par rapport au carboxyle. Dans le cas de la réduction de produits du type **5**, la stéréochimie est sauvegardée et la réduction de composés du type **10***a* conduit à des produits avec la même stéréochimie, l'approche du borohydrure se faisant du coté moins encombré, c'est-à-dire opposé au groupe carboxyle.

Conclusion

La nouvelle méthode de synthèse, présentée dans ce travail, permet d'obtenir un grand nombre de produits difficilement accessibles entre autres d'intéressants composés spiranniques ou polycycliques.

Le choix judicieux de conditions permet d'orienter la réaction vers des pyrrolidines ou des pyrrolines.

Les transformations de produits initialement obtenus offrent d'intéressants débouchés synthétiques.[4]

L'analyse détaillée de produits obtenus a permis de proposer un mécanisme réactionnel pour la cycloaddition.

Partie expérimentale

Les points de fusion ont été déterminés sur le banc de Kofler. Les analyses élémentaires ont été effectuées au Laboratoire central de microanalyse du Centre national de la recherches à Thiais ou par le Laboratoire de sciences biologiques du Conseil national de recherches du Canada à Ottawa. Les spectres rmn du proton ont été enregistrés sur le spectromètre Hitachi Perkin–Elmer R-24B, 60 MHz, et sur le spectromètre Bruker WP-80 FT, 80 MHz. Ce dernier appareil a servi également pour enregistrer les spectres du ^{13}C à 20.15 MHz. Les chromatographies sur couche mince (ccm) ont été réalisées sur gel de silice G type Merck 60 F-254 en plaques prêtes à l'emploi. L'éluant utilisé est un mélange chlorure de méthylène – méthanol 90 : 10 et le révélateur utilisé est le réactif de Dragendorff. Les chromatographies sur colonne ont été effectuées sur gel de silice 60 0,2–0,5 mm, Merck; l'éluant est habituellement le chlorure de méthylène pur ou mélangé avec 1–5% de méthanol.

Les α-aminoalkylphosphonates de diéthyle ont été préparés par des méthodes connues : aminométhylphosphonate de diéthyle (1), α-aminoéthylphosphonate de diéthyle (13) et phénylaminométhylphosphonate de diéthyle (14).

Les imines **1** ont été préparées par la réaction entre les α-aminoalkylphosphonates et dérivés carbonylés appropriés. Le composé **1** R^1 = H, R^2 = R^3 = Me est préparé par la réaction entre 1 mol de aminométhylphosphonate de diéthyle et 10 mol d'acétone à température ambiante pendant 48 h en présence de 30 g de tamis moléculaires du type 5Å. Les tamis sont filtrés, la solution évaporée et l'imine **1**, obtenue sous forme d'huile, est utilisée brute dans l'étape suivante. Dans tous les autres cas une mole de α-aminoalkylphosphonate est mise en présence d'une mole de dérivé carbonylé dans 500 mL de benzène. Dans le cas de l'acétophénone on ajoute 0,5 g de l'acide *p*-toluènesulfonique. La solution est chauffée à l'ébullition et l'eau formée séparée dans le séparateur de phases (Dean–Stark). Le temps de réaction varie de 0,5 jusqu'à 4 h. Le solvant est évaporé (si l'acide *p*-toluènesulfonique est employé la solution est lavée préalablement avec la solution saturée du bicarbonate de sodium, de l'eau et séchée). Les imines **1** obtenues, sous forme d'huile, avec un rendement de 92–98% sont utilisée brutes.

Cycloadditions en présence de l'hydrure de sodium

Une solution de 20 mmol de l'aza-2 allylphosphonate **1** et de 20 mmol de l'ester éthylénique **2** dans 30 mL de THF est ajoutée, sous agitation (cf. tableau 1 pour la température), en une seule fois, à une suspension de 0,2 g (4 mmol) d'hydrure de sodium dans 50 mL de THF. Une augmentation de température de l'ordre de 10°C est observée. Quand la température commence à diminuer, le mélange est refroidi à la glace et traité avec 50 mL d'une solution aqueuse de chlorure d'ammonium à 10%. La couche organique est séparée et la couche aqueuse extraite avec de l'éther. Les extraits réunis sont séchés sur sulfate de sodium et évaporés sous pression réduite. La pyrrolidine **4** est purifiée par recristallisation dans l'éther isopropylique ou transformée en picrate.

Les conditions de réaction, les rendements de pyrrolidines **4** et les données analytiques sont indiqués dans le tableau 2. Les données rmn des produits qui n'ont pas été publiées auparavant (5*b*) sont rapportées dans le tableau 5.

Cycloaddition des sels lithiens des carbanions de 1

Une solution de 20 mmol de l'aza-2 allylphosphonate **1** dans 30 mL de THF est ajoutée, goutte à goutte, à une solution dans le THF de 20 mmol (ou 4 mmol dans certains cas indiqués dans le tableau 1) de butyllithium, ou bien de LDA préparée préalablement. Cette addition est effectuée en atmosphère inerte, sous agitation, à la température indiquée dans le tableau 1. La solution devient rouge carmin. Ensuite, à la même température, est additionnée une solution de 20 mmol d'ester **2** dans 20 mL de THF. La réaction est suivie en rmn et terminée par l'addition de l'eau à la température indiquée dans le tableau 1. La couche organique est séparée et la couche aqueuse extraite avec de l'éther. Les extraits réunis sont séchés sur sulfate de sodium et évaporés sous pression réduite. Dans le cas où un des produits est nettement majoritaire il est séparé par la cristallisation dans l'éther isopropylique ou par la formation du picrate. Dans le cas contraire les produits sont séparés par la chromatographie sur silice. Les rendements sont indiqués dans le tableau 1, les donnés analytiques de pyrrolidines **4** dans le tableau 2, leurs données rmn dans le tableau 5, les données analytiques et rmn de pyrrolines **5** dans le tableau 6.

4. Les auteurs présenteront bientôt un travail concernant l'obtention des nitrones par l'oxydation des pyrrolidines **12**.

Can. J. Chem. Downloaded from www.nrcresearchpress.com by 213.222.148.141 on 09/07/12
For personal use only.

TABLEAU 6. Données rmn et analytiques des pyrrolines **5** et **7**

Produit	δ ^{1}H/TMS (ppm)						J (Hz)		Picrate	Formule	Analyse calculé/trouvé		
	R^1	R^2	R^3	R^4	R^5	R^6	$J_{R^1R^3}$	$J_{R^3R^6}$	F (°C)	M.M.	C	H	N
5*c*	7,65	7,22	4,95	3,62	2,38	1,45	2	—					
7*c*	7,65	7,18	5,45	2,42	3,18	0,65	3	—					
5*e*	2,00	7,19	5,15	2,3–3,5		2,65	—	10	150	$C_{20}H_{20}N_4O_9$	52,17	4,38	12,17
										460,39	52,47	4,33	11,99
7*e*	2,00	7,23	5,10	2,75	2,75	2,75	—	2					
5*g*	—	7,14	5,60	2,8–3,8		3,30	—	7	178	$C_{25}H_{22}N_4O_9$	57,47	4,24	10,72
										522,46	57,51	4,20	10,67
7*g*	—	7,19	5,35	2,8–3,3		3,05	—	8	182	$C_{25}H_{22}N_4O_9$	57,47	4,24	10,72
										522,46	57,59	4,11	10,88
5*h*	7,36	7,22	5,37	1,21 et 1,25		3,06	4	7,7					
7*h*	7,08	7,22	5,35	1,00 et 1,30		2,50	4	9,3					
5*i*	2,05	7,20	5,20	3,30	1,15	3,05	—	8					
5*j*	2,00	7,17	4,72	3,30	2,20	1,40	—	—	135	$C_{21}H_{22}N_4O_9$	53,16	4,67	11,81
										474,42	53,24	4,63	11,83
5*k*	—	7,14	5,05	3,70	2,70	1,45	—	—	179	$C_{26}H_{24}N_4O_9$	58,20	4,51	10,44
										536,48	58,45	4,34	10,31
7*k*	—	7,21	5,52	2,88	3,50	0,76	—	—	172	$C_{26}H_{24}N_4O_9$	58,20	4,51	10,44
										536,48	58,45	4,34	10,31
5*l*	7,35	7,19	1,80	3,25	1,15	2,45	—	—	152	$C_{21}H_{22}N_4O_9$	53,16	4,67	11,81
										474,42	53,47	4,72	11,76
7*l*	7,30	7,23	1,35	3,40	1,15	2,66	—	—					
5*m*	7,40	7,20	5,33	—	—	3,18	3	7	163	$C_{24}H_{26}N_4O_9$	56,03	5,09	10,89
										514,48	56,00	5,21	9,06
7*m*	7,46	7,21	5,28	—	—	2,37	3	9					
5*o*	7,33	—	—	4,40	—	2,45	—	—	152	$C_{24}H_{26}N_4O_9$	56,03	5,09	10,89
										514,48	56,04	5,14	10,94
5*p**	6,98	1,44	1,28	1,28	1,22	2,50	—	—	131	$C_{17}H_{22}N_4O_9$	47,88	5,20	13,14
										426,38	47,60	5,70	13,04
5*q**	7,06	2,27	1,26	1,26	1,21	2,55	—	—	138	$C_{19}H_{26}N_4O_9$	50,21	5,77	12,33
										454,43	50,12	5,68	12,20
7*q**	7,07	1,70	1,27	1,13	1,27	2,57	—	—	113	$C_{19}H_{26}N_4O_9$	50,21	5,77	12,33
										454,43	49,91	5,66	12,09
5*r**	7,34	7,26	1,76	1,32	1,15	2,94	—	—	168	$C_{22}H_{24}N_4O_9$	54,09	4,95	11,47
										488,44	54,82	4,78	11,37
5*s**	7,13	—	—	1,29	1,22	2,43	—	—	168	$C_{20}H_{26}N_4O_9$	51,50	5,62	12,01
										466,44	51,35	5,54	11,88
5*t*	7,08*	—	—	—	—	2,30*	—	—	165	$C_{23}H_{30}N_4O_9$	54,54	5,97	11,06
	7,34	—	—	—	—	2,50	—	—		506,50	54,53	6,13	11,09
5*u*	7,20	—	—	3,40	—	—	—	—	152	$C_{22}H_{28}N_4O_9$	53,65	5,73	11,38
										492,48	53,50	5,72	10,98

TABLEAU 6*a*. Les valeurs de δ pour les groupes éthoxycarbonyle

	R^2 = Ph		$R^2 \neq$ Ph
	5	**7**	**5** et **7**
δ CH_3	0,75	1,20	1,23
δ OCH_2	3,40	4,10	4,13

*Spectre enregistré dans $CDCl_3$. Tous les autres spectres enregistrés dans CCl_4.

Épimérisation de dérivés cis ***4*** *et* ***5***

La pyrrolidine **4** ou la pyrroline **5** est soumise à l'action d'une quantité équimolaire de la solution 1 M d'éthylate de sodium dans l'éthanol à température ambiante. La réaction est suivie en ccm. Le mélange réactionnel est concentré sous vide jusqu'à un tiers du volume initial et dilué avec l'éther. La solution résultante est lavée avec de l'eau, séchée sur du sulfate de sodium et le solvant évaporé sous pression réduite. Le résidu, pyrrolidine **6** ou pyrroline **7**, est purifié par recristallisation de l'éther isopropylique ou par formation du picrate. Les rendements sont de 80–90%. Le taux de transformation *cis–trans* est habituellement de 75 à 100%. Les données analytiques pour les pyrrolidines **6** sont rapportées dans le tableau 7, leur données rmn dans le tableau 5. Les données analytiques et rmn de pyrrolines **7** se trouvent dans le tableau 6.[5]

Préparation de l'adduit de Michael ***3***e

Une quantité (0,9 mL) de solution éthanolique de Triton B (2 mmol) est diluée avec 30 mL de benzène anhydre et on lui ajoute 20 mmol de l'imine **1** (R^1 = Me, R^2 = Ph, R^3 = H). Ensuite, une solution de 20 mmol d'acrylate d'éthyle dans 10 mL de benzène est ajoutée goutte à goutte, à la température de 15°C. Après 1 h le mélange réactionnel est traité par 15 mL de la solution saturée de chlorure d'ammonium et lavé à l'eau. La phase organique est séchée et le solvent est évaporé sous pression réduite. Le rendement est de 90%. Le produit ***3****e* obtenu

5. Les pyrrolines **7** se distinguent facilement des pyrrolines **5** grâce à la différence de déplacements chimiques de groupes éthyles d'ester respectivement *cis* et *trans* par rapport à R^2 si celui-ci est un phényle (*5b*); cf. tableau 6*a*.

Can. J. Chem. Downloaded from www.nrcresearchpress.com by 213.222.148.141 on 09/07/12
For personal use only.

Can. J. Chem. Downloaded from www.nrcresearchpress.com by 213.222.148.141 on 09/07/12
For personal use only.

TABLEAU 7. Données analytiques de pyrrolidines **6** et **8**

Produit	Dérivé, F (°C)	Formule M.M.	Analyse calculé/trouvé C	H	N	P
6*a*	Picrate	$C_{23}H_{29}N_4O_{12}P$	47,26	5,00	9,59	
	182	584,47	47,34	5,10	9,91	
6*d*	Picrate	$C_{24}H_{31}N_4O_{12}P$	48,16	5,18	9,36	
	178	598,50	48,29	5,39	9,78	
6*e*	Picrate	$C_{24}H_{31}N_4O_{12}P$	48,16	5,18	9,36	5,18
	140	598,50	48,15	5,17	9,45	5,40
6*f*	Picrate	$C_{29}H_{33}N_4O_{12}P$	52,73	5,04	8,48	4,69
	201	660,57	52,94	4,97	8,45	3,89
6*h*	Base	$C_{19}H_{30}NO_5P$	59,51	7,88	3,65	8,07
	101	383,42	59,76	7,72	3,67	7,98
6*m*	Base	$C_{22}H_{34}NO_5P$	62,39	8,09	3,30	7,31
	136	423,48	62,47	7,98	3,28	7,23
8*c*	Base	$C_{18}H_{28}NO_5P$	58,52	7,64	3,79	8,39
	65	342,18	58,64	7,42	4,01	8,22
8*l*	Picrate	$C_{25}H_{33}N_4O_{12}P$	49,02	5,43	9,15	5,06
	135	612,53	49,12	5,37	9,02	4,88
8*m*	Base	$C_{22}H_{34}NO_5P$	62,39	8,09	3,30	7,31
	Huile	423,48	62,64	8,23	3,07	7,18

contenant environ 5% de produit cyclique **6***e* est utilisé brut. δ H, ppm (CCl_4/TMS) : 1,0–1,4 (9H, m, 3 Me), 1,43 (3H, d $^3J_{HP}$ = 16 Hz, Me), 2,0–2,5 (4H, m, $(CH_2)_2$), 3,6–4,3 (6H, m, 3 OCH_2), 7,0–7,3 et 7,6–7,8 (2H et 3H, m, Ph), 8,20 (1H, d $^4J_{HP}$ = 5 Hz, HC=N).

Cyclisation de l'adduit de Michael **3**e

L'adduit de Michael **3***e* est additionné à une solution d'une quantité équimolaire de LDA dans le THF à −70°C. La température est remontée jusqu'à −10°C et l'eau est additionnée. La couche organique est séparée et la couche aqueuse extraite trois fois à l'éther. Les extraits réunis sont séchés et le solvant évaporé sous pression réduite. Le mélange obtenu, comprenant la pyrrolidine **6***e* et les pyrrolines **5***e* et **7***e*, est séparé par chromatographie. Le rendement en pyrroline **7***e* est de 70%.

Ouverture du cycle de la pyrrolidine **4**c

Une solution de 10 mmol de pyrrolidine **4***c* dans 30 mL de THF est ajoutée à une solution de 13 mmol de butyllithium dans 50 mL de THF à −100°C. Le spectre rmn d'un échantillon prélevé indique la présence du produit linéaire **3***c* (bande imine à 8,2 ppm). Le mélange est réchauffé progressivement (1,5 h) jusqu'à +35°C. La composition du mélange en fonction de la température, déterminée d'après les spectres rmn, est la suivante : température (°C), part de **4***c*, **5***c*, **6***c*, **7***c*, **3***c* (%) : −100, 70, 0, 0, 0, 30; −55, 60, 15, 5, 5, 15; −10, 45, 30, 10, 15, 0; +35, 20, 40, 20, 20, 0. Le traitement habituel donne 2,3 g de mélange qui est séparé par chromatographie.

Addition du diéthylphosphite sur les pyrrolines **5** *et* **7**

La pyrroline **5** ou **7** est chauffée avec cinq équivalents du diéthylphosphite à 130°C pendant 3 h. La réaction est suivie en ccm. Après être refroidi le mélange réactionnel est traité avec l'acide chlorhydrique à 5% et la solution ainsi obtenue est extraite avec deux portions d'éther. Ensuite elle est rendue basique par addition de carbonate de potassium et extraite trois fois à l'éther. L'extrait éthéré est séché sur sulfate de sodium et le solvant est évaporé sous pression réduite. Le résidu (comprenant les pyrrolidines, cf. tableau 4) est purifié par recristallisation de la base ou du picrate, ou bien par chromatographie. Les rendements de diastéréoisomères obtenus sont indiqués dans le tableau 4, les données analytiques dans le tableau 7 en rmn dans le tableau 5.

Préparation de pyrrolines ***10***

Une solution de 20 mmol de **1** et de 20 mmol d'ester éthylénique **2** dans 40 mL de THF est ajoutée à une suspension de 22 mmol

TABLEAU 8. Conditions de preparation de produits **10** et données rmn et analytiques de produits **10** et **11**

		Produit **10**									Produit **11**							
			δ ^{1}H/TMS (ppm) (CCl_4)					Analyse calculé/trouvé			δ ^{1}H/TMS (ppm) (CCl_4)					Analyse calculé/trouvé		
Code	Temps (min)	Rdt (%)	R^4	R^5	R^6	NCH_2	Picrate F (°C)	Formule M.M.	C	H	N	R^4	R^5	OH	NCH_2	F (°C)	Formule M.M.	C	H	N
a	90	60	2,2		4,0	3,8–4,1	140	$C_{19}H_{18}N_4O_9$	51,12	4,06	12,55	2,1–2,7		4,2	3,9–4,2	102	$C_{13}H_{15}NO_3$	66,93	6,48	6,01
					env.			446,37	51,09	4,09	12,43						233,26	67,30	6,73	6,47
b	120	29	2,2		4,0	3,8–4,1						2,0–2,7		4,1	3,9–4,2	113	$C_{12}H_{14}N_2O_3$	61,52	6,02	11,96
					env.												234,25	61,42	6,08	11,88
c	60	42	2,3	1,9	1,9	3,8–4,1	148	$C_{20}H_{20}N_4O_9$	52,17	4,38	12,17									
								460,39	52,07	4,44	12,32									
d	40	65	2,6	1,1	4,0	3,4–4,5						2,6	1,0	4,0	3,5; 4,2	130	$C_{14}H_{17}NO_3$	67,99	6,93	5,66
					env.												247,28	67,88	7,03	5,63
m	45	72	—	—	3,8	3,6; 3,8	135	$C_{24}H_{26}N_4O_9$	56,03	5,09	10,89	—	—	3,7	3,7; 4,1	152	$C_{18}H_{23}NO_3$	71,73	7,69	4,65
								514,48	56,10	5,21	10,82						301,37	71,80	7,42	4,63

Pour tous les produits : δ CH_3 = 1,1 ppm; δ OCH_2 env. 4,0 ppm; δ Ph = 7,2 (3H); 7,7 (2H) ppm. Rendements des produits purifiés.

d'hydrure de sodium dans 50 mL de THF. Après la fin de la réaction exothermique, le mélange est porté à l'ébullition (cf. tableau 8). Ensuite, il est refroidi et traité avec 50 mL d'une solution de chlorure d'ammonium à 10%. La couche organique est séparée et la couche aqueuse extraite avec de l'éther. Les extraits réunis sont séchés et le solvant évaporé sous pression réduite. Le résidu, pyrrolidine **10**, est transformé en picrate et celui-ci recristallisé. Les conditions de réaction ainsi que les résultats analytiques et rmn sont présentés dans le tableau 8.[6]

Les hydroxy pyrrolines **11** sont obtenues par oxydation spontanée de pyrrolines **10**. À la suite de l'exposition de ces dernières à l'action de l'air pendant plusieurs jours est observée la transformation de l'huile en masse semi-cristalline. Celle-ci est cristallisée dans l'éther isopropylique et recristallisée dans ce solvant ou l'acétate d'éthyle. Les rendements sont d'environ 85%. Les données analytiques et rmn sont rassemblées dans le tableau 8.[6]

Les pyrrolidines **12** sont préparées par réduction des pyrrolines **5** au borohydrure de sodium dans l'éthanol (pour éviter la transestérification).

12*l* : rendement 90%; δ H, ppm (CCl_4/TMS) : 0,88 (3H, t, Me), 1,05 (3H, d, R^5 = Me), 1,60 (3H, s, R^3 = Me), 2,3–3,3 (4H, m), 3,70 (2H, q, OCH_2), 7,25 (5H, m, Ph). Picrate, *F* (éthanol) 167°C. $C_{21}H_{24}N_4O_9$ (476,41) calculé/trouvé : C 52,94/52,77; H 5,08/5,04; N 11,76/11,74.

Ethoxycarbonyl-7 aza-15 dispiro[5.1.5.2]pentadecane **12***t*, rendement 87%; *F* (éther isopropylique) 51°C; δ H, ppm ($CDCl_3$/TMS) : 1,27 (3H, t, Me), 1,2–1,8 (20H, m, deux cyclohexyles), 2,32 (1H, s, NH), 2,38 (1H, s, CH), 2,86 (2H, d de d, CH_2), 4,11 (2H, q, OCH_2); δ ^{13}C ($CDCl_3$/TMS) : 14,45 (q, Me), 23,03, 23,36, 23,76, 24,05, 25,88 (double intensité), 33,32, 33,76, 39,23 (double intensité) (10t, deux cyclohexyles), 48,43 (s, C-8), 55,58 (t, C-14), 59,67 (t, OCH_2), 64,89 (d, C-7), 65,36 (s, C-6), 172,33 (s, C=O). $C_{17}H_{27}NO_2$ (279,41) calculé/trouvé : C 73,07/72,70; H 10,46/10,37; N 5,01/4,88.

12*u* : rendement 79%; δ H, ppm (CCl_4/TMS) : 1,27 (3H, t, Me), 1,2–2,0 (19H, m, deux cyclohexyles et NH), 2,7–3,0 (3H, m, CH—CH_2—N), 4,10 (2H, q, OCH_2). Chlorhydrate, *F* (éthanol, eau) 212°C. $C_{16}H_{27}NO_2 \cdot HCl$ (301,85); calculé/trouvé : C 63,66/63,70; H 9,35/9,38; N 4,64/4,69; Cl 11,75/11,89.

6. La forme du signal rmn du groupe phényle, deux multiplets centrés sur 7,2 et 7,7 ppm, indique la position α de la double liaison par rapport à ce substituant dans les produits **10** et **11**.

Réduction du picrate de ***10***a

Borohydrure de sodium (0.5 g) est ajouté progressivement en refroidissant, à une suspension de 1,5 g (3 mmol) de picrate de pyrroline **10***a* dans 20 mL de méthanol. Le mélange devient homogène. Quand l'addition est finie, le mélange est agité encore 20 min à température ambiante. Le solvant est évaporé sous pression réduite et le résidu repris avec une solution de soude à 5%. Cette solution est extraite 3 fois avec 30 mL de chlorure de méthylène. L'extrait est séché et le solvant évaporé sous pression réduite. On obtient 0,6 g d'huile claire, 85% de rendement de *cis*-éthoxycarbonyl-3 phényl-2 pyrrolidine **12***a*; δ H, ppm (CCl_4/TMS) : 0,80 (3H, t, Me), 2,0–2,4 (2H, m, H-4), 2,8–3,3 (3H, m, H-3 et H-5), 3,65 (2H, q, OCH_2), 4,35 (1H, d, H-2), 7,25 (5H, m, Ph). Picrate, *F* (ethanol) 181°C. $C_{19}H_{20}N_4O_9$ (448,38) calculé/trouvé : C 50,89/50,99; H 4,50/4,50; N 12,50/12,22.

1. R. W. Ratcliffe et B. G. Christensen. Tetrahedron Lett. 4645 (1973).
2. A. Dehnel et G. Lavielle. Bull. Soc. Chim. Fr. II, 95 (1978).
3. A. Dehnel. Thèse, Université d'Orléans, Orléans, France. 1983.
4. A. Dehnel, J. P. Finet et G. Lavielle. Synthesis, 474 (1977).
5. (*a*) A. Dehnel et G. Lavielle. Tetrahedron Lett. **21**, 1315 (1980); (*b*) C. Rabiller, A. Dehnel et G. Lavielle. Can. J. Chem. **60**, 926 (1982).
6. T. Saegusa, Y. Ito, H. Kinoshita et S. Tomita. J. Org. Chem. **36**, 3316 (1971).
7. Th. Kauffmann. Angew. Chem. Int. Ed. Engl. **13**, 627 (1974).
8. J. E. Baldwin. J. Chem. Soc. Chem. Commun. 734 (1976).
9. Th. Kauffmann et R. Eidenschink. Chem. Ber. **110**, 645 (1977).
10. D. Redmore. Chem. Rev. **71**, 333 (1971).
11. D. Redmore. *Dans* Topics in phosphorus chemistry. Vol. 8. *Édité par* E. J. Griffith et M. Grayson. Wiley, New York. 1976. pp. 515–585.
12. (*a*) D. St. C. Black et L. M. Johnstone. Angew. Chem. Int. Ed. Engl. **20**, 669 (1981); (*b*) K. Burger et S. Tremmel. Chem. Ztg. **106**, 302 (1982).
13. R. Tyka. Tetrahedron Lett. 677 (1970).
14. K. D. Berlin, R. T. Claunch et E. T. Gaudy. J. Org. Chem. **33**, 3090 (1968).

Can. J. Chem. Downloaded from www.nrcresearchpress.com by 213.222.148.141 on 09/07/12
For personal use only.

Electron transfer sensitized photolysis of 'onium salts

R. J. DeVoe, M. R. V. Sahyun,[1] and Einhard Schmidt[2]
Science Research Laboratory, 3M Corporate Research, St. Paul, MN 55133-3221 U.S.A.

and

N. Serpone and D. K. Sharma
Canadian Picosecond Laser Flash Photolysis Centre, Department of Chemistry, Concordia University, Montreal, Que., Canada H3G 1M8

Received June 15, 1987

R. J. DeVoe, M. R. V. Sahyun, Einhard Schmidt, N. Serpone, and D. K. Sharma. Can. J. Chem. **66**, 319 (1988).

We have studied the anthracene-sensitized photolyses of both diphenyliodonium and triphenylsulphonium salts in solution using both steady-state and laser flash photolysis techniques. Photoproducts, namely, phenylated anthracenes along with iodobenzene or diphenylsulphide, respectively, are obtained from both salts with quantum efficiencies of ca. 0.1 at 375 nm. We infer the intermediacy of diphenyliodo and triphenylsulphur radicals formed by single electron transfer from the singlet-excited anthracene. We have developed a quantitative model of this chemistry, and identify the principal sources of inefficiency as back electron transfer, which occurs at nearly the theoretically limiting rate, intersystem crossing from the initially formed sensitizer–'onium salt encounter complex, and in-cage radical recombination.

R. J. DeVoe, M. R. V. Sahyun, Einhard Schmidt, N. Serpone et D. K. Sharma. Can. J. Chem. **66**, 319 (1988).

Faisant appel aux techniques de l'état stationnaire et de la photolyse laser éclair, on a étudié la photolyse sensibilisée par l'anthracène des sels de diphényliodonium et de triphénylsulfonium en solution. Pour chacun des sels, à 375 nm, les efficacités quantiques en photoproduits, soit des anthracènes phénylés ainsi que respectivement de l'iodobenzène et du sulfure de diphényle, sont d'environ 0,1. On en déduit que les radicaux diphényliodo- et triphénylsoufre se forment comme intermédiaires par le transfert d'un électron de l'anthracène excité singulet. On a développé un modèle quantitatif de cette chimie et on a identifié que les principales causes de l'inefficacité sont un transfert en retour d'électron qui se produit à une vitesse proche de la limite théorique, un passage intersystème se produisant à partir du complexe de rencontre sensibilisateur–sel onium qui se forme initialement et une recombinaison radicalaire se produisant dans la cage.

[Traduit par la revue]

Introduction

'Onium cations, especially diaryliodonium and triarylsulphonium, are used in the photoinitiation of both radical and cationic polymerizations (1–3). Technologically useful spectral response requires that the photolyses of the 'onium salts are spectrally sensitized, as the 'onium salts themselves absorb light significantly only below ca. 280 nm. A photoinduced electron transfer mechanism is usually proposed for this sensitization (1–3), although recent results (4) indicate that a triplet energy transfer pathway is also feasible. In this study we concentrate on the electron transfer pathway, in which decomposition of the 'onium salts proceeds from the corresponding heteroatom-centered free radicals (1), vis-a-vis direct photolysis, in which reaction occurs from an excited state of the cation, thought to be the lowest triplet, at least in the case of diphenyliodonium cation (4).

We are specifically seeking to provide a mechanism for the initial steps of the photoreaction, which accommodates the observed discrepancies between reported (1) high quantum yields for solution photolyses and low quantum yields for photoinitiation of radical polymerization (5), and which identifies the photon energy-loss pathways, so they can be engineered out of applied photoinitiation systems. We employ both quantum yield and product studies on steady state photolyses, as well as photo-CIDNP (Chemically Induced Dynamic Nuclear Polarization) and picosecond laser flash spectroscopy, and concentrate our efforts on the diphenyliodonium and triphenylsulphonium hexafluorophosphate salts in acetonitrile (AN) with anthracene sensitization.

The fate(s) of the radicals formed subsequent to 'onium cation decomposition in the sensitized photolyses is beyond the scope of the present investigation.

Results and discussion

Photo-CIDNP studies

Photoinduced electron transfer yields singlet or triplet radical pairs. In studies on the model systems in acetonitrile-d_3, strong photo-CIDNP signals were observed,[3] similar to the photo-CIDNP spectra shown in Fig. 1. Iodonium salt, present at the 0.1 *M* level, appears as a strong emission (ca. 8.1 ppm), as does benzene (7.38 ppm). No signals are observed corresponding to iodobenzene, anthracene, or anthracene-derived photoproducts, owing in the latter two cases to exchange broadening by interaction of arene radical cations with the neutral hydrocarbons (6). Only benzene emission was observed when the sulphonium salt replaced iodonium under our conditions.

Photo-CIDNP results may be interpreted in accordance with Kaptein's Rules (7), whereby

$$\text{Net polarization} = \mu\epsilon\Delta g a_{\text{H}}$$

where μ is positive for a triplet radical pair precursor of the product in which the polarization is observed and negative for a singlet precursor, and ϵ is defined as positive for (in-cage) recombination products and negative for cage escape products. The other two factors in the vector model correspond to the difference between the so-called *g*-factors of the precursor radicals and the hyperfine coupling constant for the protons for

[1]Address correspondence to this author at 3M Center, 201-3N-05, St. Paul, MN 55144, U.S.A. This paper is contribution no. 1510 from the Corporate Research Laboratories, 3M.

[2]Undergraduate research participant, Department of Chemistry, University of Wisconsin, River Falls, WI 54022, U.S.A.

[3]We thank J. Hill, CRL Analytical and Properties Research Laboratories, for expert technical assistance with these experiments.

Can. J. Chem. Downloaded from www.nrcresearchpress.com by 213.222.148.141 on 09/07/12
For personal use only.

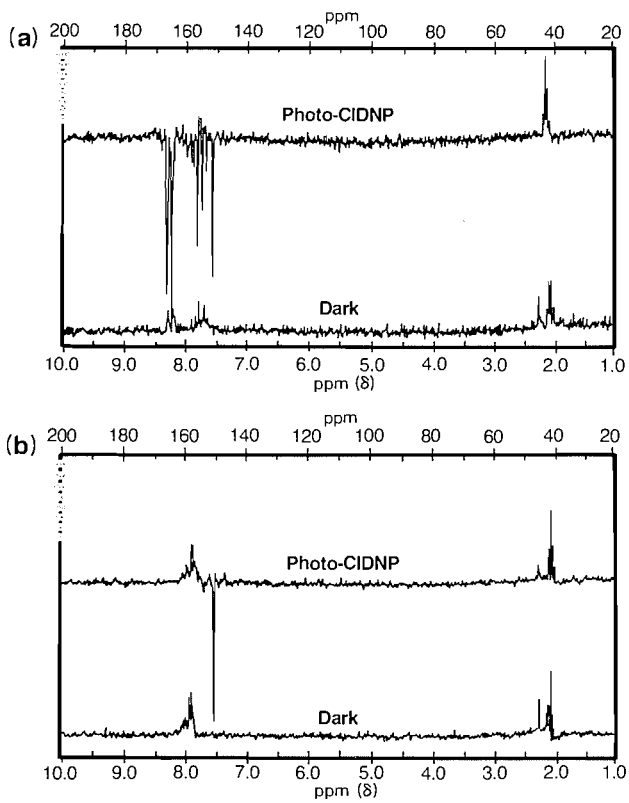

FIG. 1. Photo-CIDNP and dark spectra of electron transfer sensitized photodecompositions of (*a*) diphenyliodonium hexafluorophosphate and (*b*) triphenylsulphonium hexafluorophosphate in AN. For purpose of clarity, spectra shown here were obtained with 0.05 *M* perylene as sensitizer. (See Experimental section of text.)

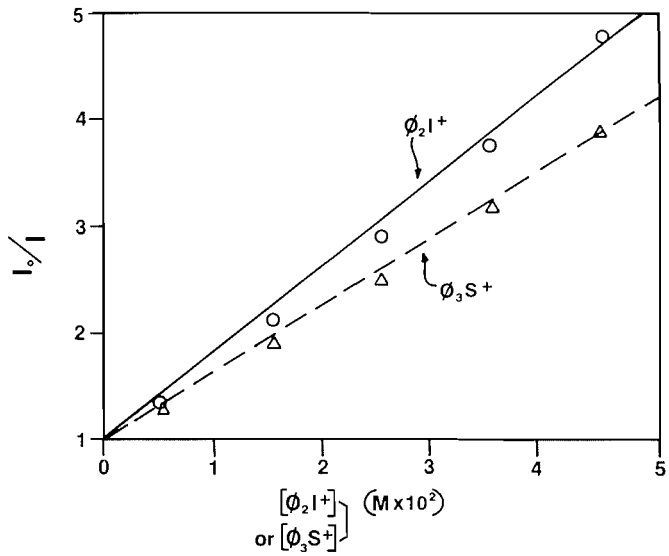

FIG. 2. Stern–Volmer plot for quenching of anthracene fluorescence by diphenyliodonium (○) and triphenylsulphonium (△) hexafluorophosphates in AN.

which the CIDNP signal is observed. As emission is observed for *both* the recombination product, iodonium salt, and the cage-escaped benzene, we infer from the opposite signs of ϵ in the two cases that these two products must result, at least in part, from radical pairs of opposite multiplicity. (Alternatively, the same signs for the two observed polarizations may reflect opposite signs for the product of Δg in the two precursor radical pairs and a_H in the corresponding emitters. This possibility was rendered unlikely by carrying out the photo-CIDNP experiment with Michler's Ketone, 4,4′-bis(*N*,*N*-dimethylamino)benzophenone, as sensitizer, which sensitizes exclusively from its triplet state (8), i.e. yields only triplet radical pairs. In this case net emission was again observed for the iodonium cation, but net absorption was observed for benzene, opposite to the result obtained with anthracene.

We accordingly hypothesize that the benzene is a cage-escaped product from a singlet radical pair ^{1}(anthracene$^{+\bullet}$/$C_6H_5^\bullet$). On the basis of the observed emission from *all* protons, we tentatively assign the iodonium salt polarization to back electron transfer by magnetic-field induced T_-–S_0 mixing (7) in the triplet radical pair, ^{3}(anthracene$^{+\bullet}$/$Ph_2I^\bullet$). To the extent that it competes with formation of ^{1}(anthracene$^{+\bullet}$/$C_6H_5^\bullet$) from ^{1}(anthracene$^{+\bullet}$/$Ph_2I^\bullet$), back electron transfer entirely within the singlet manifold would be expected to be transparent to CIDNP, insofar as it derives from hyperfine interactions. In this case we expect the in-cage decomposition of diphenyliodo (or triphenylsulphur) radical to be rapid compared to cage escape (see below), and no spin-sorting pathway is thus available (7*c*).

As the extent of the magnetic-field induced T_-–S_0 mixing is dependent on the magnitude of the spin–orbit coupling at the transition center (sulphur or iodine), the accessibility of the triplet pathway for recombination under photo-CIDNP conditions is greatly reduced in the sulphonium salt system compared to the iodonium (7*b*, 9). Apparently only the CIDNP-transparent recombination pathway is available to the (anthracene$^{+\bullet}$/$Ph_3S^\bullet$) pair.

Fluorescence quenching

Anthracene is an efficient fluorophore and the quenching of its fluorescence provides one probe of the sensitizing interactions with the 'onium salts. The quenching may occur by either or both of two pathways: (*a*) electron transfer to the 'onium salt (1), which on the basis of the relationship established by Rehm and Weller (10), we expect to occur at a diffusion limited rate; and (*b*) external heavy atom induced intersystem crossing, which is also thought to require contact between the excited molecule and the heavy atom containing species (9).

Quenching of anthracene fluorescence in acetonitrile (AN) solution in the presence of up to 0.05 *M* of either the iodonium or the sulphonium salt obeyed the Stern–Volmer relationship (11), as shown in Fig. 2. The slopes were 84 M^{-1} and 64 M^{-1}, respectively, compared with a theoretical value for diffusion control of 90 M^{-1}, calculated as the product of the bimolecular diffusion constant in AN, 2×10^{10} L s^{-1}, and the lifetime of the singlet excited state of anthracene, 4.5 ± 0.2 ns, as measured in our laboratory by time-correlated single photon counting.

On the other hand, with 1-iodopropane, which could quench *only* by the external heavy atom effect, a Stern–Volmer slope of 22 M^{-1} was found. Less than diffusion-controlled quenching implies a competition between intersystem crossing and escape of the reagents from the encounter complex of the excited sensitizer with the quencher, occurring at the characteristic solvent reorganization rate for AN, namely 5×10^8 s^{-1} (12). The intersystem crossing frequency in the encounter complex is accordingly ca. 1×10^8 s^{-1}. *If* a comparable intersystem crossing frequency also applies to the interaction of photoexcited anthracene with iodonium cation, the intersystem process is slow compared with exergonic electron transfer (10, 13).

Can. J. Chem. Downloaded from www.nrcresearchpress.com by 213.222.148.141 on 09/07/12
For personal use only.

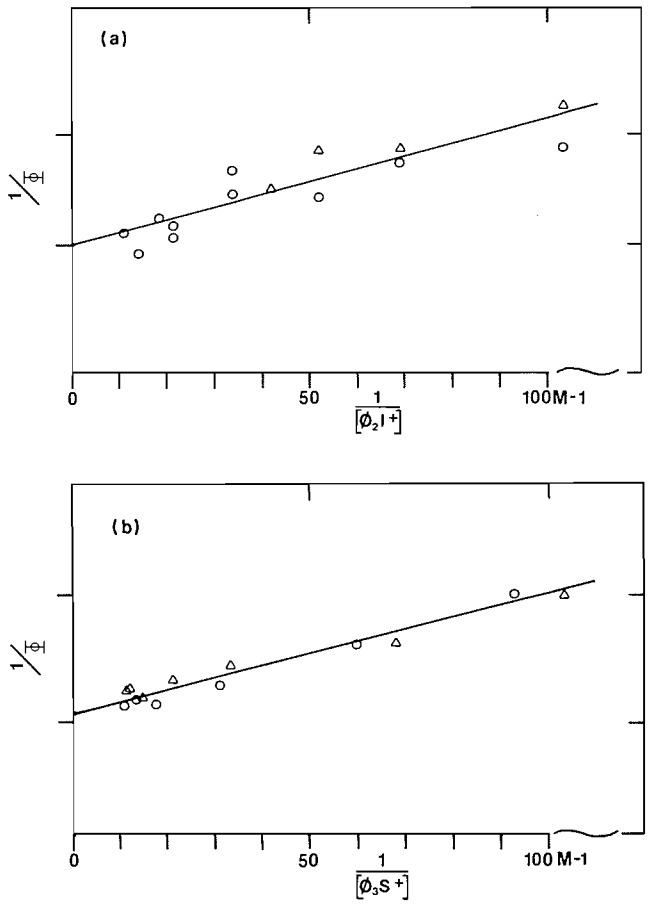

FIG. 3. Double reciprocal plots for anthracene sensitized photolyses of (*a*) diphenyliodonium and (*b*) triphenylsulphonium hexafluorophosphates in AN; (△) designates appearance of (*a*) iodobenzene or (*b*) diphenyl sulphide, and (○) designates disappearance of anthracene.

Accordingly we infer that sensitizer intersystem crossing, mediated by the heavy atom in the iodonium cation is a potential, though minor, source of inefficiency in the sensitized iodonium salt photolyses.

Quantum yields

Two probes proved useful in following the anthracene-sensitized photolyses at 375 ± 10 nm of either 'onium salt in AN: (*a*) iodobenzene or diphenyl sulphide could be quantitated by glc with reference to a dodecane internal standard: (*b*) alternatively, anthracene disappearance could be monitored spectrophotometrically, e.g. at 374 nm. Quantum yields obtained by the two methods were in agreement within experimental error for both salts; thus anthracene disappearance is stoichiometric with 'onium salt decomposition. Additionally, the photolyses were not oxygen sensitive; there was no difference in the quantum yields whether or not the solutions were deoxygenated by prolonged passage of dry argon prior to photolysis.

Double reciprocal plots of quantum yield data are shown in Figs. 3(*a*) and (*b*) for the iodonium and sulphonium salts, respectively. When sensitization (electron or energy transfer) occurs by diffusion controlled, collisional interaction of sensitizer and acceptor, the intercepts of such plots are the reciprocals of the limiting quantum yields, Φ_0, at infinite concentration of the acceptor (14), i.e., 'onium salt. These parameters are 0.10 ± 0.02 for the iodonium salt and 0.09 ± 0.01 for the sulphonium, and are substantially lower than reported by Pappas *et al.* (1) but in agreement with recent results of Timpe and Bah (28).[4]

The reciprocal of the product of the slope of the plot and Φ_0 should be equal to the slope of the Stern–Volmer plot from the quenching experiment under the same conditions, providing the photochemistry follows from collisional interaction of excited sensitizer with the 'onium acceptor. Accordingly the Stern–Volmer slopes estimated from the plots of Figs. 3(*a*) and (*b*) are 92 ± 24 M^{-1} and 109 ± 35 M^{-1}, in order-of-magnitude agreement with the values obtained by fluorescence quenching (Fig. 2).

Analysis of the reaction products (ca. 20% conversion) by capillary glc coupled with mass spectrometry[5] indicated that phenylanthracenes were the only *identifiable* anthracene products--one major isomer and small quantities of two others. The alteration of the absorption spectrum of the reaction mixture between 340 and 400 nm on irradiation with either salt could be accounted for by consumption of anthracene and generation of a product with a similar absorption spectrum but red-shifted by ca. 12 nm, consistent with 9-phenylanthracene (15). From the extinction coefficients, ca. 40% of the consumed anthracene appeared to become 9-substituted. On the other hand, quantitative glc (which did not separate the phenylanthracene isomers) indicated 55 ± 9% of the lost anthracene was present as the mixture of isomeric phenylanthracenes; the discrepancy between these two estimates represents the minor products, which must be the 1- and 2-phenylanthracenes. The fate of the rest of the anthracene consumed in the photoreaction was undetermined.

When anthracene-sensitized photolysis of the diphenyliodonium salt (0.05 M) was carried out in the presence of 1-iodopropane (1 M), Φ for iodobenzene formation was 0.0045 ± 0.0005. This concentration of 1-iodopropane reduced the anthracene fluorescence intensity to 4.3% by intersystem crossing, i.e., by the same factor as the photolysis quantum yield was reduced. We infer that sensitization occurs only from singlet photoexcited anthracene, even though electron-transfer sensitization of the iodonium cation by triplet anthracene may be energetically feasible (1). This interpretation is consistent with the absence of oxygen inhibition of the photochemistry.

Picosecond studies

Formation of the anthracene radical cation in the quenching of photoexcited anthracene by diphenyliodonium cation was followed on the ps time scale; a deoxygenated solution 4 × 10^{-4} M in anthracene and 0.10 M in the iodonium salt in AN was photolyzed with a ca. 30 ps pulse of 355 nm radiation from a mode-locked, frequency tripled Nd-YAG laser. Typical time-resolved absorption spectra of the quenching reaction over the continuum 425–675 nm are shown in Figs. 4(*a*) and (*b*).

The transient species absorbing at 565 and 610 nm is singlet-excited anthracene (16). It disappears with a pseudo-first order rate constant of ca. 3 (±1) × 10^9 s^{-1}, consistent with the diffusion-limited quenching of the anthracene fluorescence. An additional peak at close to 675 nm is consistent with the absorption of solvated electron, often observed in laser flash photolyses under these conditions (17); this species is also responsible for broad absorption across the visible region.

The absorption seen at ca. 430 nm is assigned to triplet

[4]We thank Professor S. P. Pappas for bringing this reference to our attention.

[5]We thank J. Schroepfer, CRL Analytical and Properties Research Lab, 3M, for these experiments.

Can. J. Chem. Downloaded from www.nrcresearchpress.com by 213.222.148.141 on 09/07/12
For personal use only.

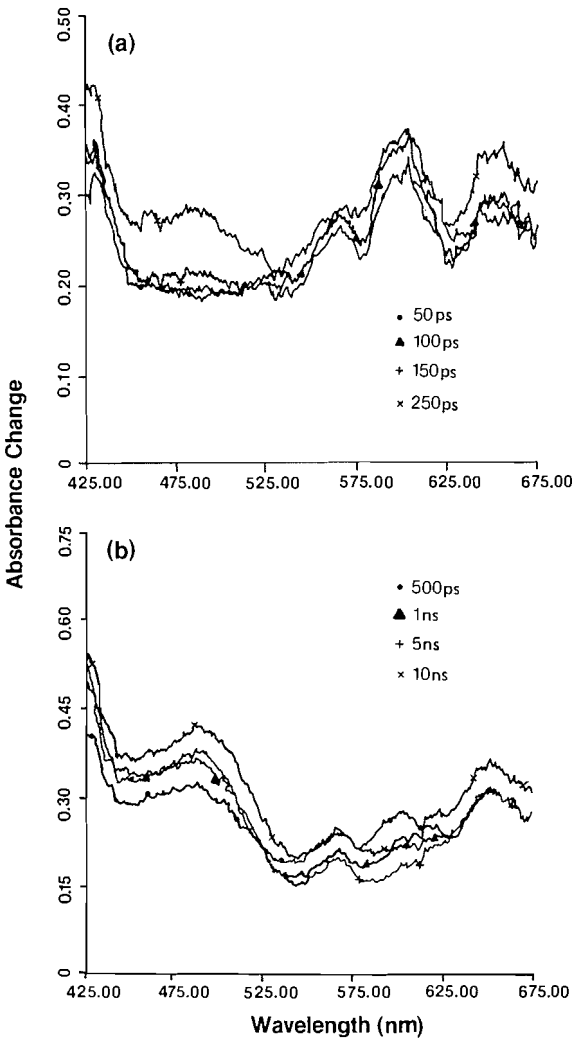

FIG. 4. Transient visible absorption spectra observed following anthracene sensitized laser flash photolysis of diphenyliodonium hexafluorophosphate in AN; (*a*) time scale 50–250 ps; (*b*) time scale 0.5–10 ns.

anthracene (18). A significant portion of this absorption apparently arises during the laser irradiation (<50 ps); the band does not grow in appreciably above the baseline of other overlapping absorptions after 500 ps, i.e. the apparent subsequent increase in absorbance at 430 nm appears to be more related to the increase in the broad-based absorbance underlying the sharp triplet band. This observation is consistent with the inference, above, that anthracene intersystem crossing is not a significant consequence of collisional interactions between photoexcited anthracene molecules and the iodonium cation. More to the point, the triplet does not appear to be consumed over the time scale of the observations. This observation supports the inference that triplet excited anthracene does not sensitize the 'onium salt photolysis, nor does a triplet exciplex (which would provide a deactivation pathway) form on diffusional encounter between triplet anthracene and iodonium cation.

Anthracene radical cation, generated by intense X-ray exposure of anthracene in a boric acid glass, absorbs primarily at 475 and 714 nm (19). In methylene chloride solution the anodically generated cation radical absorbs at 440 and 725 nm (20). The longer wavelength in both cases is outside the continuum probed in our experiment; however, we can assign the ca. 480 nm absorption to the radical ion. This transient grows in over the first 2 ns following the laser pulse, as shown in Fig. 5, with a

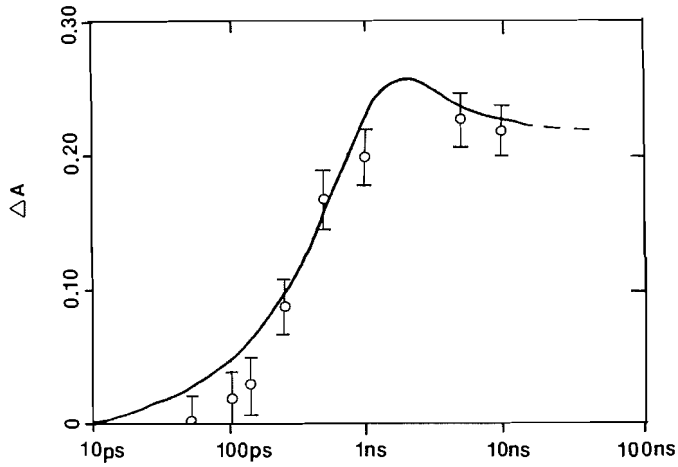

FIG. 5. Time evolution of 480 nm absorbing transient in anthracene-sensitized laser flash photolysis of diphenyliodonium hexafluorophosphate in AN; solid line is computer fit of the experimental data using parameters in Table 1 (see text).

pseudo-first order rate constant (evaluated from a plot of $\ln \Delta A$ vs. t, where ΔA is the absorbance at 480 nm above the absorbance minimum at 540 nm, read from the digital output of the vidicon (21)) of $1.9 \pm 0.3 \times 10^9\ s^{-1}$; conversion of photoexcited anthracene to its radical cation is thus diffusion controlled for a solution 0.10 *M* in the 'onium electron acceptor.

Preliminary experiments involving the laser flash photolysis of anthracene in the presence of the triphenylsulphonium cation indicate analogous results in this system.

Computer modelling

We propose the mechanistic scheme of Fig. 6 as containing all the elements necessary to rationalize the experimental results. The singlet-excited anthracene forms an encounter complex with the iodonium cation, from which the electron transfer photochemistry occurs.

Quantitative description of the system apparently requires specification of twelve rate constants: as the value for k_2 we take the estimate for the frequency of external heavy atom induced intersystem crossing inferred from the iodopropane quenching experiment, $1 \times 10^8\ s^{-1}$; k_{10} may be evaluated as "fast", i.e. $\geq 10^{10}\ s^{-1}$, on the basis of the Rehm–Weller treatment (10). (The triplet radical pair must, however, live for at least tens of ps for its reaction products to yield a CIDNP signal (22).) The processes described by k_7 and k_8 do not appear to contribute significantly to the observed chemistry, and they may be ignored; numerical evaluation (below) demonstrates that no more than 0.5% of the total excitation is dissipated by the pathway involving k_8. The constant k_1 is the rate constant for diffusional encounter and k_5, k_7, and k_{11} are the solvent cage relaxation rate constant, $5 \times 10^8\ s^{-1}$ for AN (12).

The problem then reduces to evaluation of four rate constants, k_3, k_4, k_6, and k_9, along with the product of the extinction coefficient for anthracene radical cation at 480 nm and the initial concentration of singlet photoexcited anthracene, $\epsilon[A^*]$ (cm^{-1}), in order to fit the time evolution of the six usable ΔA values of Fig. 5, as well as the quantum yields for iodobenzene and phenylanthracene formation. In the iodonium case, k_6 is a composite of the rate constants for the rate-determining steps of both direct and indirect (magnetic field-induced spin inversion) pathways leading to back electron transfer. In the absence of a heavy atom, the pathway involving a ground state spin flip in the radical pair should not contribute significantly, i.e. k_6 will be

Can. J. Chem. Downloaded from www.nrcresearchpress.com by 213.222.148.141 on 09/07/12
For personal use only.

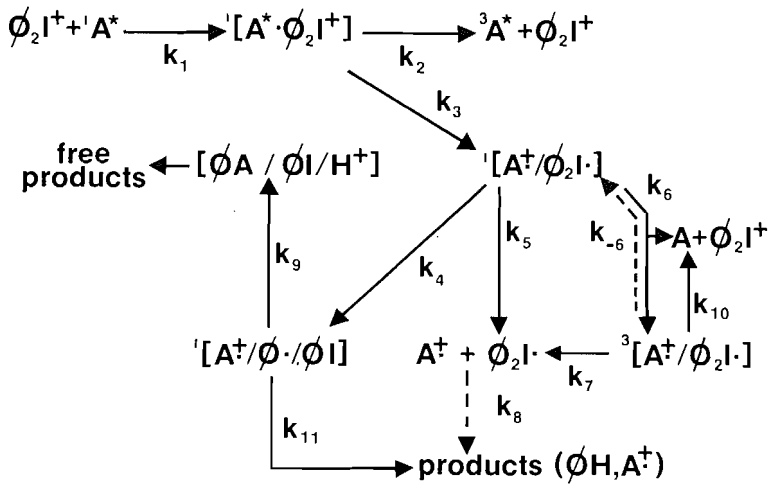

FIG. 6. Reaction scheme to account for the observations on anthracene-sensitized photolysis of diphenyliodonium cation. We propose that a similar scheme, without intervention of a triplet radical pair, applies to photolysis of triphenylsulphonium cation.

TABLE 1. Parameters of the mechanistic scheme of Fig. 6

Variable	Model value	Experimental value
Parameters		
k_1	2×10^{10} [Ph_2I^+] s^{-1}	
k_2	1×10^8	
k_3	1×10^9	
k_4	5×10^9	
k_5	5×10^8	
k_6	5×10^{10}	
k_9	1×10^9	
k_{11}	5×10^8	
ϵ[A*]	60 cm^{-1}	
Responses		
Φ_0 (PhI)	0.090	0.10 ± 0.02
Φ_0 (PhA)	0.054	0.055 ± 0.010
d ln [A^+]/dt	2.1×10^9 s^{-1}	$1.9 \pm 0.3 \times 10^9$ s^{-1}

dominated by the direct back electron transfer process. This inference is consistent with the CIDNP results, above, which indicate that no spin sorting is involved in back electron transfer from the sulphonium cation.

Differential equations describing the time dependence of the concentrations of the various intermediates in the scheme of Fig. 6 were numerically integrated for various values of the four adjustable rate constants in order to obtain "best fit" values. We assumed that both singlet radical pairs as well as the triplet pair, along with cage-escaped anthracene radical cation, contributed to the observed transient absorption, and that the lifetime of the cage-escaped species was long relative to the time scale of interest (≤ 10 ns). These "best fit" values and comparisons with experimental probes are reported in Table 1, and the evolution of the anthracene radical cation absorbance, with ϵ[A*] = 60 cm^{-1}, predicted by the model is shown in Fig. 5. The calculations proved quite sensitive to the *relative* values of the adjustable parameters, but less so to their *absolute* values; the numbers thus ought to be taken as order of magnitude estimates of the rate constants.

From the reciprocal of k_4, the upper-limiting lifetime under these conditions of the hypothetical (1) diphenyliodo radical intermediate, with respect to decomposition, is at most a few hundred picoseconds. In the photolysis of diphenyliodonium iodide (4), we observed a transient with broad absorption centering on 550 nm which lasted for ca. 250 ps after the laser pulse. On the basis of the present estimate for the lifetime of the diphenyliodo radical, we now suspect that a minor fraction of the *CT excited iodode salt dissociated to this radical and iodine atom, analogous to the known (23) photochemistry of triphenylsulphonium iodide, giving rise to the 550 nm transient. We estimate the energy of the lowest energy allowed transition in diphenyliodo radical to be approximately 2.25 eV (by analogy to the S_3–S_1 separation in the cation), consistent therewith.

Formation of iodobenzene in-cage at a rate much greater than cage escape is consistent with the lack of a photo-CIDNP signal from it (7, 22). The value of k_6 is in the range expected for exergonic, adiabatic electron transfers (13, 24) and observed in the radical pair formed from photolysis of the anthracene–TCNE complex (20). The value for k_9 likewise compares with the rate constant observed for in-cage combination in the anthracene–tetranitromethane system (20).

Conclusions

The anthracene-sensitized photolysis of either diphenyliodonium or triphenylsulphonium cation depends on collisional interaction between photoexcited anthracene and the 'onium cation; long range interactions, even though theoretically feasible (25), do not appear to contribute to the observed chemistry.

From the point of view of photogeneration of technologically useful free radicals, there are one major and two minor loss pathways: back electron transfer (k_6), which proceeds at close to the theoretically limiting rate with both salts; external heavy atom induced anthracene intersystem crossing (k_2); and in-cage combination of the phenyl radical and anthracene radical cation photoproducts (k_9).

Experimental

Materials and methods

Diphenyliodonium hexafluorophosphate (3), mp 136°C, and triphenylsulphonium hexafluorophosphate (3), mp 200–203°C, were purified by recrystallization from *iso*-propanol. The latter salt was shown to be free from thioether sulphonium salts.

Spectral quality, glass-distilled acetonitrile (EM Omni-Solv^R) was used for solution preparation. Scintillation grade anthracene, mp 214–217°C, exhibited a fluorescence lifetime of 4.5 ± 0.2 ns, as measured by time-correlated single photon counting (PRA System

Can. J. Chem. Downloaded from www.nrcresearchpress.com by 213.222.148.141 on 09/07/12
For personal use only.

3000), compared to the literature value of 4.9 ns (26). High resolution glc coupled with mass spectrometry (15) indicated low level (<1%) contamination with various alkylanthracenes, before and after irradiation experiments. The 1-iodopropane, bp 100–102°C, was used as received from MC&B, Ltd., as was the acetonitrile-d_3 (Cambridge Isotopes).

Fluorescence intensities were recorded on a Perkin Elmer MPF-44B fluorescence spectrophotometer. The data for the Stern–Volmer plots, Fig. 2, are based on emission intensities of 0.1 m*M* anthracene solutions at 403 nm, excited by 375 nm radiation; the photomultiplier was protected with a 390 nm cutoff filter.

Photo-CIDNP

The photo-CIDNP spectra were obtained using the proton probe on a Varian XL-100 magnetic resonance spectrometer, with the probe modified to allow direct irradiation of the sample at the receiver coil.[3] Typical sample composition was 0.01 *M* 'onium salt and ca. 0.05 *M* (saturated) anthracene or perylene in acetonitrile-d_3. The signals observed with these two sensitizers were qualitatively identical with respect to all features; stronger signals, hence better signal-to-noise characteristics in the spectra as recorded, were obtained using perylene, owing to the higher light absorptivity of its solutions. The light source was a 300 W Xe arc operating at full power, focused on the receiver coil using quartz optics on an optical rail. Heating of the sample was a problem, as infrared filtration decreased the light intensity too much to observe CIDNP. Consequently, photo-CIDNP spectra were recorded in the Fourier transform mode of the XL-100, collecting two transients over ca. 5 s exposure time, during which heating was minimal. Samples (2 mL volume) were deoxygenated by nitrogen purge, and dark spectra were taken before and after irradiation.

Quantum yields

Quantum yields were measured with no more than 10% conversion of anthracene on solutions 3×10^{-4} *M* in anthracene and 0.01–0.10 *M* in the 'onium salt. The solutions were deoxygenated by dry argon purge, as required. Aliquots (3 mL) in a 1 cm quartz spectrophotometer cell were irradiated at 375 ± 10 nm on an optical bench with light from the Xe arc lamp, passed through a monochromator with the slits adjusted to allow a 20 nm bandpass. The output of the source was calibrated by means of potassium ferrioxalate actinometry (27) and continuously monitored with a radiometer. Typical fluxes of 6×10^{17} photons s^{-1} required 2 min irradiation in order to yield ca. 10% conversion. Ultraviolet absorption spectra were recorded on the samples in the reaction vessel before and after irradiation.

The spectrophotometric quantum yields for anthracene disappearance were based on observed changes in optical density at 340, 356, and 374 nm, corrected for absorption at these wavelengths by the product 9-phenylanthracene (16), measured at ca. 10% conversion. For glc analyses, the photolysis mixtures obtained after up to 10% conversion were diluted with 5 mL of 1 *M* aq. sodium chloride and extracted with 1 mL cyclohexane containing 1×10^{-4} *M* dodecane as internal standard.

Laser flash photolyses

The instrumentation used for these experiments has already been described in detail (21). The double beam, mode-locked Nd-YAG laser system employed a silicon intensified target vidicon detector. Light pulses at 355 nm were obtained by frequency-tripling; typical irradiances were ca. 2 mJ per pulse focused to a 2 mm diameter spot on the face of a 2 mm quartz sample cuvette. The pulse width was 30 ps (FWHM). Individual experiments utilized 0.6 mL aliquots of solutions 4×10^{-4} *M* in anthracene and 0.10 *M* in the 'onium salt; the solutions were deoxygenated by dry argon purge prior to irradiation.

Acknowledgments

This work was supported *in part* by 3M Canada, Ltd., and *in part* by the Natural Sciences and Engineering Research Council of Canada. The expert technical assistance of Mr. Reza Danesh (Concordia University) is acknowledged with appreciation. We also thank Dr. Stefan Weigl, 3M Canada, and Dr. Tessa Godfrey, Minnesota 3M Research, Ltd., Harlow, Essex, UK, for helpful comments in the course of preparation of the manuscript.

1. S. P. PAPPAS. J. Imaging Technol. **11**, 146 (1985); S. P. PAPPAS, B. C. PAPPAS, L. R. GATECHAIR, and W. R. SCHNABEL. J. Polym. Sci. Polym. Chem. Ed. **22**, 69 (1984); S. P. PAPPAS, L. R. GATECHAIR, and J. H. JILEK. J. Polym. Sci. Polym. Chem. Ed. **22**, 77 (1984).
2. H. BAUMANN and H.-J. TIMPE. Acta Polymer. **37**, 309 (1986).
3. J. V. CRIVELLO and J. H. W. LAM. Macromolecules, **10**, 1307 (1977).
4. R. J. DEVOE, M. R. V. SAHYUN, N. SERPONE, and D. K. SHARMA. Can. J. Chem. **65**, 2342 (1987).
5. M. Z. ALI, R. J. DEVOE, and M. R. V. SAHYUN. Unpublished results.
6. H. D. ROTH and A. A. LAMOLA. J. Am. Chem. Soc. **96**, 6270 (1974).
7. (*a*) R. KAPTEIN. Adv. Free Radical Chem. **5**, 381 (1975); (*b*) N. J. TURRO. Modern molecular photochemistry. Benjamin-Cummings, Menlo Park, CA. 1978; (*c*) R. KAPTEIN. *In* Chemically induced magnetic polarization. *Edited by* L. T. Muus, P. W. Atkins, K. A. McLauchlan, and J. B. Petersen. D. Reidel, Boston, MA. 1977. pp. 13–14.
8. A. A. LAMOLA and G. S. HAMMOND. J. Am. Chem. Soc. **43**, 2129 (1965).
9. S. P. MCGLYNN, T. AZUMI, and M. KINOSHITA. Molecular spectroscopy of the triplet state. Prentice-Hall, Englewood Cliffs, NJ. 1969.
10. D. REHM and A. WELLER. Isr. J. Chem. **8**, 259 (1970).
11. P. J. WAGNER. Creation and detection of the excited state. Vol. I. Part A. Marcel Dekker, New York, NY. 1971. pp. 171ff, and references cited therein.
12. K. SCHULTEN, H. STAERK, A. WELLER, H.-J. WERNER, and B. NICKEL. Z. Phys. Chem. NF**101**, 371 (1976).
13. R. A. MARCUS. Int. J. Chem. Kinet. **13**, 865 (1981).
14. A. ALBINI, E. FASANI, and M. MELLA. J. Am. Chem. Soc. **108**, 4119 (1986) and references cited therein.
15. A. MIELERT, C. BRAIG, J. SAUER, J. MARTELLI, and R. SUSTMANN. Liebigs Ann. Chem. **1980**, 954 (1980).
16. D. BEBELAAR. Chem. Phys. **3**, 205 (1974).
17. N. SERPONE and M. Z. HOFFMAN. J. Phys. Chem. **91**, 1737 (1987).
18. D. S. KLIGER and A. C. ALBRECHT. J. Chem. Phys. **53**, 4059 (1970).
19. Z. H. ZAIDI and B. N. KHANNA. J. Chem. Phys. **50**, 3291 (1969).
20. J. M. MASNOVI, J. K. KOCHI, E. F. HILINSKI, and P. M. RENTZEPIS. J. Am. Chem. Soc. **108**, 1126 (1986) and references cited therein.
21. G. PONTERINI, N. SERPONE, M. A. BERGKAMP, and T. L. NETZEL. J. Am. Chem. Soc. **105**, 4639 (1983); N. SERPONE, T. L. NETZEL, and M. GOUTERMAN. J. Am. Chem. Soc. **104**, 246 (1982); T. L. NETZEL, M. A. BERGKAMP, and C.-K. CHANG. J. Am. Chem. Soc. **104**, 1952 (1982); N. SERPONE, D. K. SHARMA, J. MOSER, and M. GRAETZEL. Chem. Phys. Lett. **136**, 47 (1987).
22. X. SUN and J. ZHU. Bopuxue Zazhi, **3**, 47 (1986); for an English summary see Chem. Abstr. **105**, 143324f (1986).
23. S. L. NICKOL and J. A. KAMPMEIER. J. Am. Chem. Soc. **95**, 1908 (1973).
24. G. J. KAVARNOS and N. J. TURRO. Chem. Rev. **86**, 401 (1986).
25. A. I. BURSHTEIN. J. Luminesc. **34**, 167 (1985); M. C. PALAZZOTTO and M. R. V. SAHYUN. *In* Progress in basic principles of imaging systems. *Edited by* F. Granzer and E. Moisar. Vieweg, Wiesbaden. pp. 599ff.
26. I. B. BERLMAN. Handbook of fluorescence spectra of aromatic molecules. Academic Press, New York, NY. 1965. p. 123.
27. J. G. CALVERT and J. N. PITTS, JR. Photochemistry. John Wiley, New York, NY. 1966. pp. 785ff.
28. H.-J. TIMPE and A. BAH. Macromol. Chem. Rapid Commun. **8**, 353 (1987).

Can. J. Chem. Downloaded from www.nrcresearchpress.com by 213.222.148.141 on 09/07/12
For personal use only.

Surfactant–cyclodextrin interactions by conductance measurements

RAMAMURTHY PALEPU
Department of Chemistry, University College of Cape Breton, Sydney, N.S., Canada B1P 6L2

AND

VINCENT C. REINSBOROUGH
Chemistry Department, Mount Allison University, Sackville, N.B., Canada E0A 3C0

Received June 22, 1987

RAMAMURTHY PALEPU and VINCENT C. REINSBOROUGH. Can. J. Chem. **66**, 325 (1988).

Conductance measurements were used to identify and to obtain association constants for the complexes formed between cyclodextrins (CD) with emphasis on β-cyclodextrin (βCD), and surfactants such as sodium dodecylsulfate (SDS) and tetradecyltrimethyl ammonium bromide. With both anionic and cationic surfactants, αCD forms predominantly a 2:1 CD/surfactant complex while with both βCD and γCD the main species is 1:1. γCD binds much less strongly with surfactants than both αCD and βCD. Cyclodextrins destroy micelles by complexing the surfactant monomers more strongly than they are bound in self-association.

RAMAMURTHY PALEPU et VINCENT C. REINSBOROUGH. Can. J. Chem. **66**, 325 (1988).

On a utilisé des mesures de conductance pour identifier et pour obtenir les constantes d'association des complexes qui se forment entre des cyclodextrines (CD) et des agents de surface, principalement entre la β-CD et le dodécylsulfate de sodium (DSS), tant au-dessous qu'au-dessus de la concentration micellaire critique. Tant avec les agents de surface anioniques que cationiques, la α-CD forme principalement un complexe 2:1 de CD:agent de surface; par ailleurs, les β- et γ-CD forment principalement des complexes 1:1. La γ-CD se lie moins fortement que les α- et β-CD avec les agents de surface. Par comparaison avec leurs propres auto-associations, les cyclodextrines complexent avec les agents de surface monomères plus fortement que les monomères se complexent avec lui-mêmes et elles détruisent ainsi les micelles.

[Traduit par la revue]

Can. J. Chem. Downloaded from www.nrcresearchpress.com by 213.222.148.141 on 09/07/12
For personal use only.

Introduction

Cyclodextrins form inclusion complexes with a variety of solutes usually with a 1:1 stoichiometry (1). More recently, a number of 2:1 cyclodextrin-substrate complexes have been characterized (2). With surfactants, a 1:1 stoichiometry is usually presumed (3–5) but Hersey and co-workers (6) have demonstrated that α-cyclodextrin binds with alkylsulphate anions in a 2:1 ratio. The object of this study was to determine the binding ratio of β-cyclodextrin to various surfactants and to ascertain the effect this inclusion process had upon micellization. Conductance measurements were undertaken to determine the stoichiometry and association constants of cyclodextrin-surfactant inclusion complexes in the pre-cmc and post-cmc regions (cmc = critical micelle concentration). Most of the work was done with β-cyclodextrin (βCD) with some comparison results being also obtained with α-cyclodextrin (αCD) and γ-cyclodextrin (γCD). The chief surfactant studied was sodium dodecylsulphate (SDS) with sodium decylsulphate (SDeS), sodium octylsulphate (SOS), tetradecyltrimethylammonium bromide (TTAB) and dodecylammonium chloride (DAC) also receiving attention.

Experimental

Conductometric measurements were obtained with a Radiometer CDM83 Bridge together with a CDM 304 Immersion Cell thermostatted at 25.0°C. Cyclodextrins were obtained from Sigma Chemical and the surfactants were the best available commercially.

Results and discussion

Figure 1 shows the effect upon the molar conductances of pre-micellar sodium dodecylsulphate (SDS) solutions of adding β-cyclodextrin (βCD). Four SDS systems were studied in the pre-micellar region (cmc = 8×10^{-3} mol dm^{-3}) with one, 2.00×10^{-3} mol dm^{-3} SDS, being omitted from the diagram for the sake of clarity. The molar conductance decreased sharply as βCD was added presumably because the dodecyl sulfate ion having been complexed by βCD was less effective as a charge carrier. Na^+ ion is not thought to be complexed by βCD to any extent (7). At a certain concentration in βCD, this linear decrease of molar conductance with βCD concentration halted rather abruptly to show no or little further decrease with further βCD additions. The stoichiometry at which this halt occurred was 1.2:1 βCD:SDS for 1.00×10^{-3} mol dm^{-3} SDS; 1.1:1 for 2.00×10^{-3} mol dm^{-3} SDS; 1.1:1 for 3.0×10^{-3} mol dm^{-3}; and 1.1:1 for 5.00×10^{-3} mol dm^{-3}. This indicates that the chief inclusion complex of βCD with SDS in this range is 1:1 with possibly a little 2:1 complex also present. The plateau in the molar conductance beyond the 1:1 stoichiometry indicates that the SDS has been almost totally complexed. The molar conductance at this stage is due only to the charged inclusion complex and Na^+ ions originating from the surfactant.

Above the cmc, the molar conductance pattern for SDS solutions containing βCD is less simple, but consistent as a function of SDS concentration. Figure 2 demonstrates this for three post-cmc SDS systems. Again, one system, 1.50×10^{-3} mol dm^{-3} SDS, was omitted from the diagram. The consistent trend in all four systems was a sharply rising conductance with βCD addition to a maximum, which was more swiftly reached in more dilute micellar systems, followed afterwards by a drop in conductance in which two linear portions could be discerned as with the pre-cmc SDS systems. The addition of βCD to the micellar SDS thus appears to break up the micelles releasing monomeric SDS and gegen Na^+ ions. The former subsequently complex with βCD in the 1:1 stoichiometry observed in the pre-cmc range and the latter largely give rise to a marked increase in conductance. At the maximum of the curve, the micelles have disappeared and subsequent addition of βCD simply removes free SDS anions largely in a 1:1 complex (intersection of the two linear portions of the curve occurs at a CD to SDS ratio of 1.2 for all four

Can. J. Chem. Downloaded from www.nrcresearchpress.com by 213.222.148.141 on 09/07/12
For personal use only.

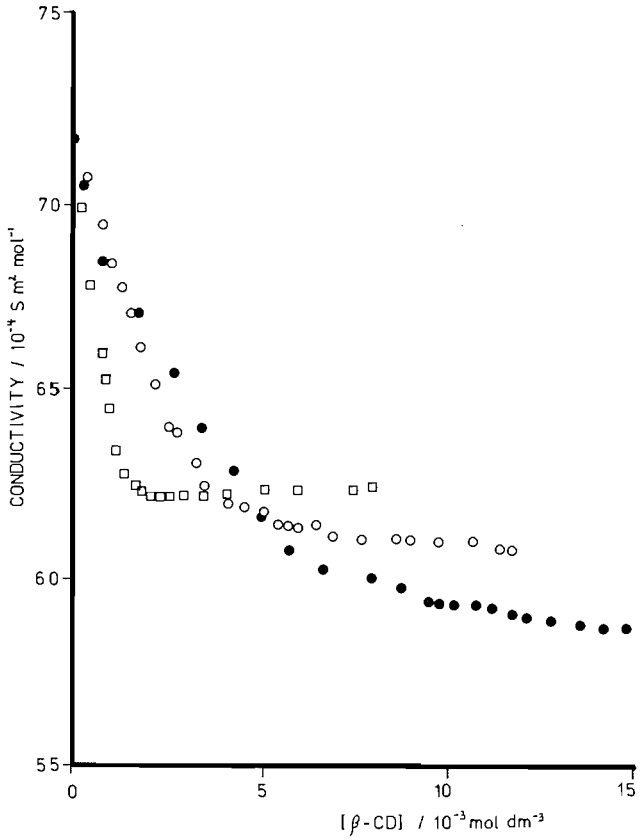

FIG. 1. Molar conductivity of SDS in βCD solutions below the cmc: open squares, 1.00×10^{-3} mol dm^{-3} SDS; closed circles, 5.00×10^{-3} mol dm^{-3} SDS.

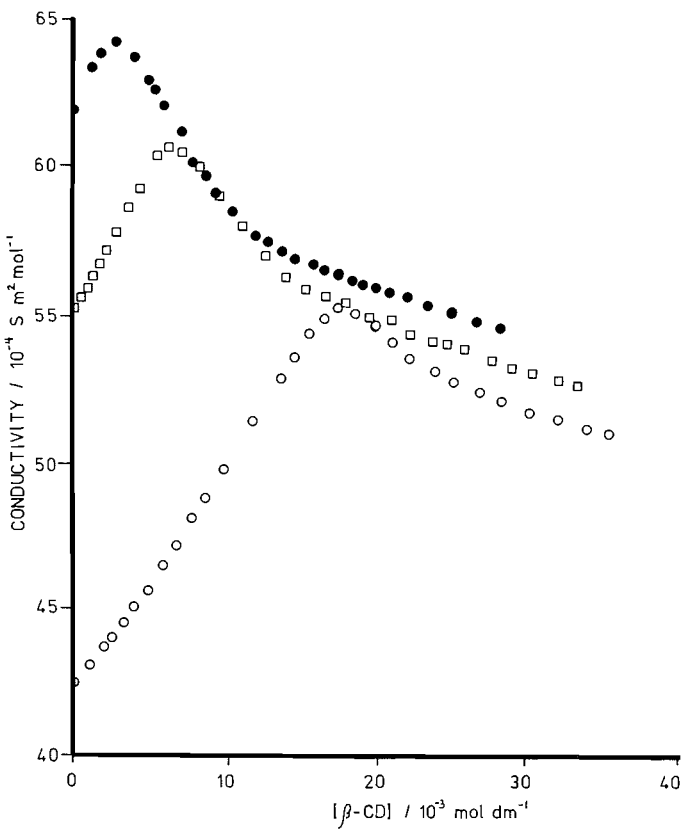

FIG. 2. Molar conductivity of SDS in βCD solutions above the cmc: closed circles, 0.95×10^{-2} mol dm^{-3} SDS; open squares, 1.20×10^{-2} mol dm^{-3} SDS; open circles, 2.00×10^{-2} mol dm^{-3} SDS.

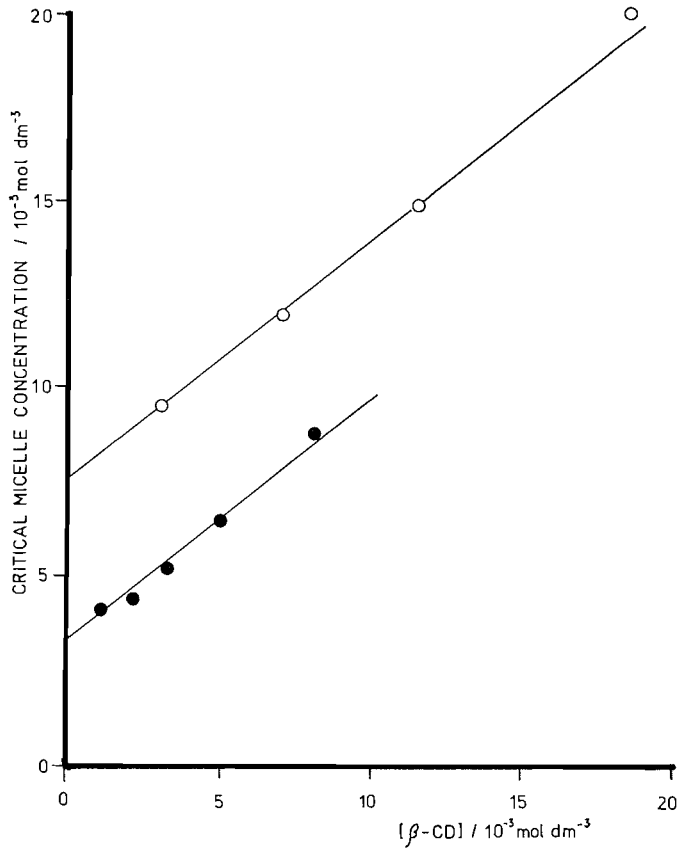

FIG. 3. Effect of βCD on the cmc values of SDS and TTAB.

post-cmc systems studied). The maximum of the curve may thus be interpreted as the cmc of the mixed surfactant system. These values are plotted in Fig. 3 and agree with the findings of Okubo *et al.* (3) that addition of cyclodextrins to SDS systems generally leads to an increase in the cmc. Extrapolation to zero βCD concentration yields the cmc of pure SDS as 7.5×10^{-3} mol dm^{-3}, in agreement with literature values.

An alternate explanation is that the initial βCD additions are incorporated into the SDS micelles as solubilizates and that the increase in conductance originates with the release of Na^+ ions with micelle swelling or increase in hydrophobicity. However, it is well known from solubilization studies that remarkably large quantities of hydrophobic solubilizates can oftentimes be incorporated within micelles with relatively little change in micellar size, structure, and effetive charge (8, 9). Thus, this explanation appears less likely.

When the chain length of the surfactant is shortened to 10 and 8 carbon atoms as in SDeS and SOS, the βCD concentration dependence of the conductance in the pre-cmc region differs little from SDS with the stoichiometry of the βCD–surfactant complex being 1.1:1 for SDeS and 1.2:1 for SOS (Fig. 4).

Even when the surfactant is cationic, the same behaviour and stoichiometry are found: 1.2:1 for both TTAB and DDAC. This suggests that it is the alkyl chain of the surfactant and not its polar head that is being fitted into the βCD torus. Fluorescence probes incorporated into cyclodextrins experience a more hydrophobic environment when surfactants are introduced (10, 11). This is consistent with the hydrocarbon tail of the surfactant being within the torus. Also, the maxima in the conductance curves appear again for cationic surfactants in the post-cmc range and, assuming these are in effect cmc values of the mixed cyclodextrin–surfactant systems, can be extrapolated to zero βCD concentration to yield the cmc of the pure surfactant. In

Can. J. Chem. Downloaded from www.nrcresearchpress.com by 213.222.148.141 on 09/07/12
For personal use only.

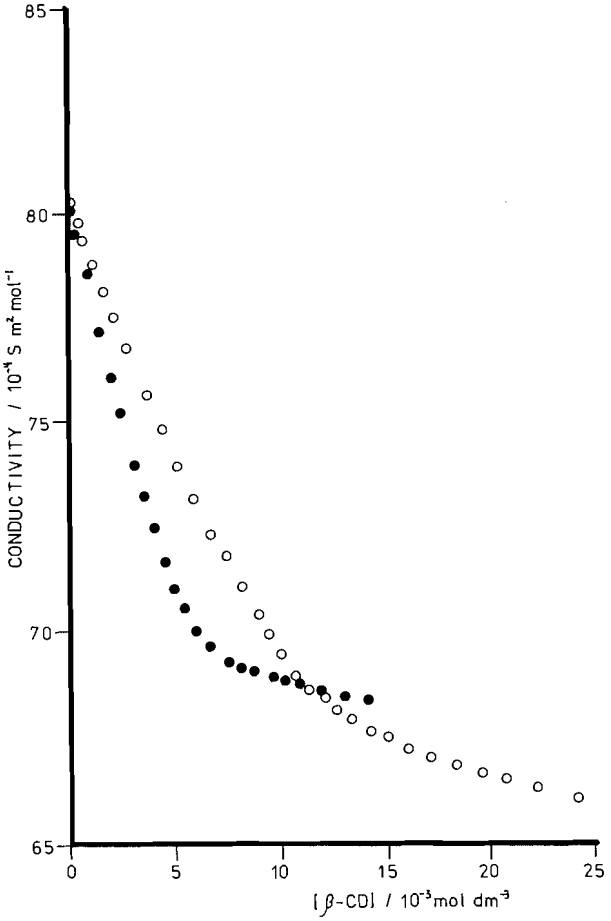

FIG. 4. Molar conductivity of 1.00×10^{-2} mol dm^{-3} sodium octylsulfate (open circles) and of 5.00×10^{-3} mol dm^{-3} sodium decylsulfate (closed circles) in βCD solutions.

Fig. 3 these maxima are plotted against βCD concentration of TTAB to yield a cmc of 3.5×10^{-3} mol dm^{-3} which is consistent with literature values.

When αCD or γCD rather than βCD is the additive, the conductance behaviour in the SDS and TTAB systems is similar with these important differences: αCD apparently forms a 2:1 complex with SDS and TTAB as well as 1:1 complex and γCD, although still forming a 1:1 inclusion complex with surfactants, binds much less strongly than the other cyclodextrins (Figs. 5, 6). With αCD, the conductance curves consist of three linear sections, the intersections of which indicate 2:1 and 1:1 stoichiometric species. The former is more distinct and is the ratio reported by Hersey, Robinson, and Kelly (6). If the first αCD encapsulates the hydrocarbon chain of the surfactant, then the second αCD probably envelopes the polar end in a CD/S/CD complex where S represents the surfactant monomer. Because of its wider annulus, βCD must fit too loosely over the polar heads of the surfactants to form a 2:1 complex, so that the 1:1 complex is the predominant inclusion form. When the annulus becomes even larger as with γCD, the hydrocarbon tail also is accommodated only loosely within the cyclodextrin torus. Above the cmc, αCD showed no major differences in conductance behaviour from βCD. For the 9.50×10^{-3} mol dm^{-3} SDS system which is just above the cmc for pure SDS, the same apparent destruction of micelles was observed as αCD was added. The maximum in the conductance curve occurred at 3.0×10^{-3} mol dm^{-3} αCD which indicates that 9.5×10^{-3} mol dm^{-3} is the cmc in the presence of 3.0×10^{-3} mol dm^{-3} αCD, exactly the same value as for βCD (Fig. 3).

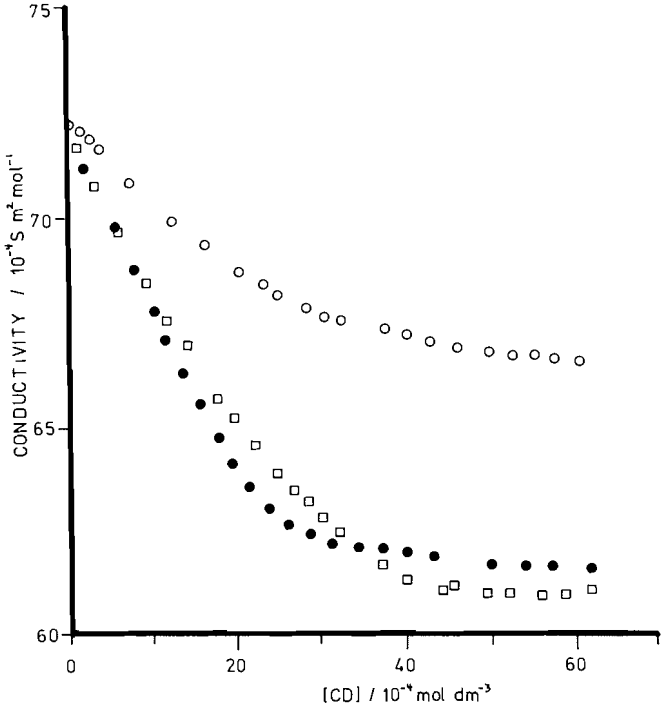

FIG. 5. Molar conductivity of 2.00×10^{-3} mol dm^{-3} SDS with added cyclodextrins: open squares, αCD; closed circles, βCD; open circles, γCD.

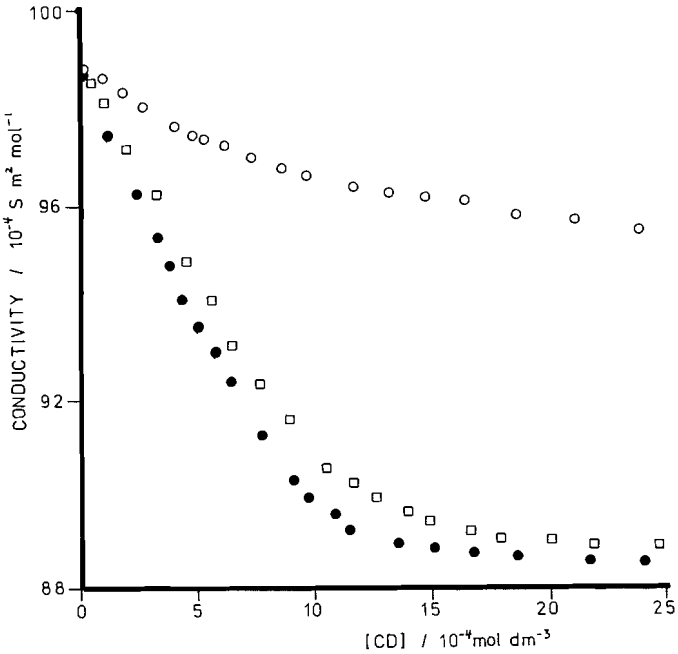

FIG. 6. Molar conductivity of 7.50×10^{-4} mol dm^{-3} TTAB with added cyclodextrins: open squares, αCD; closed circles, βCD; open circles, γCD.

The association constants for the formation of a 1:1 complex can be calculated with the equation given by Satake *et al.* (4, 5):

$$\Delta\Lambda = \frac{\Delta\lambda}{2KC_s}\left\{K(C_s + C_c) + 1 - ([K(C_s + C_c) + 1]^2 - 4K^2C_sC_c)^{1/2}\right\}$$

TABLE 1. Equilibrium constants for surfactant/cyclodextrin complexation

Complex	Surfactant concentration C_s (mmol dm^{-3})	Conductance difference $\Delta\lambda$ (10^{-4} S m^2 mol^{-1})	Equilibrium constant K (dm^3 mol^{-1})
βCD/SDS	1.00	10.5	7230
	2.00	11.6	4690
	3.00	11.3	3340
	5.00	12.5	1380
βCD/SDeS	5.00	12.7	2310
βCD/SOS	10.0	15.9	565
βCD/DDAC	5.00	14.5	1290
βCD/TTAB	0.800	11.1	11700
	5.00	10.3	9610
γCD/SDS	2.00	7.1	830
γCD/TTAB	0.800	4.3	2300
αCD/SDS	2.00	16.0	754
αCD/TTAB	0.800	11.8	4500

where $\Delta\Lambda$ is the decrease in molar conductivity brought about by the addition of CD; $\Delta\lambda$, the difference in the ionic conductivities of the unassociated and associated surfactant ions; C_s, the surfactant concentration and C_c, the CD concentration. The values of the association constant K were obtained by non-linear least-squares regression and are given in Table 1.

A point of comparison from the literature is 3630 for K for 2.60 mmol dm^{-3} SDS in βCD solutions (5) in excellent agreement with the present results. In the CD/SDS system, K is roughly inversely proportional to the total surfactant concentration. If the concentration of free surfactant is assumed to be proportional to the total surfactant concentration, then the ratio of bound βCD to free βCD will be constant over the entire pre-cmc range which is a reasonable expectation. As expected from the conductance curves, γCD forms much weaker complexes with SDS and TTAB than βCD. With αCD, the 1:1 complex is seen to be weakly formed compared to the corresponding βCD complexes with both SDS and TTAB.

In summary, below the cmc αCD appears to form predominantly a 2:1 complex while βCD and γCD form a 1:1 complex with both anionic and cationic surfactants. This is the situation even above the cmc where CDs act as micelle destroyers eventually complexing all of the surfactant if sufficient CD is available.

Acknowledgements

We wish to thank G. Maragoni for computer assistance and the Natural Sciences and Engineering Research Council of Canada for financial aid (V.C.R.).

1. W. SAENGER. Inclusion compounds. Vol. 2. *Edited by* J. L. Atwood, J. E. D. Davies, and D. D. MacNicol. Academic Press, London. 1984. p. 234.
2. D. W. ARMSTRONG, F. NOME, L. A. SPINO, and T. D. GOLDEN. J. Am. Chem. Soc. **108**, 1418 (1986).
3. T. OKUBO, H. KITANO, and N. ISE. J. Phys. Chem. **80**, 2661 (1976).
4. I. SATAKE, T. IKENOUE, T. TAKESHITA, K. HAYAKAWA, and T. MAEDA. Bull. Chem. Soc. Jpn. **58**, 2746 (1985).
5. I. SATAKE, S. YOSHIDA, K. HAYAKAWA, T. MAEDA, and Y. KUSUMOTO. Bull. Chem. Soc. Jpn. **59**, 3991 (1986).
6. A. HERSEY, B. H. ROBINSON, and H. C. KELLY. J. Chem. Soc. Faraday Trans. 1, **82**, 1271 (1986).
7. E. A. LEWIS and D. L. HANSEN. J. Chem. Soc. Perkin Trans. 2, 2081 (1973).
8. H. HØILAND, E. LJOSLAND, and S. BACKLUND. J. Coll. Interface Sci. **101**, 467 (1984).
9. S. OZEKI and S. IKEDA. J. Phys. Chem. **89**, 5088 (1985).
10. H. E. EDWARDS and J. K. THOMAS. Carbohydrate Res. **65**, 173 (1978).
11. R. A. FEMIA and L. J. CLINE LOVE. J. Coll. Interface Sci. **108**, 271 (1985).

Can. J. Chem. Downloaded from www.nrcresearchpress.com by 213.222.148.141 on 09/07/12
For personal use only.

Spectroscopic properties of SO_4 (and OH) in different molecular and crystalline environments. I. Infrared spectra of $Cu_4(OH)_6SO_4$, $Cu_4(OH)_4OSO_4$, and $Cu_3(OH)_4SO_4$[1,2]

ETALO A. SECCO
Chemistry Department, St. Francis Xavier University, Antigonish, N.S., Canada B2G 1C0

Received June 25, 1987

ETALO A. SECCO. Can. J. Chem. **66**, 329 (1988).

The infrared spectra over the range 4000–50 cm^{-1} of three copper basic sulfates, viz. $Cu_4(OH)_6SO_4$, $Cu_4(OH)_4OSO_4$, $Cu_3(OH)_4SO_4$ along with site group and factor group analysis for $Cu_4(OH)_6SO_4$ are reported for the first time. The observed absorption frequencies associated with OH and SO_4 activities show distinct individual structural features.

Three distinct types of OH groups are present in $Cu_4(OH)_6SO_4$ and $Cu_4(OH)_4OSO_4$ but only two types are evident in $Cu_3(OH)_4SO_4$. The two OH groups involved in the dehydroxylation reaction to give the oxycompound $Cu_4(OH)_4OSO_4$ are tentatively identified. The multiple frequencies involving Cu—O—H bending modes further reflect the varying degrees of H-bonding and OH coupling in $Cu(OH)_4O_2$ and $Cu(OH)_5O$ entities.

The SO_4 internal optic modes' multiplet structure and frequencies in the basic sulfates illustrate the different extent of dipolar coupling effects (OH and Cu) with respect to specific modes relative to Li_2SO_4 with same site symmetry. The SO_4 external optic modes relative to Li_2SO_4 are barely affected by neighboring OH groups.

The Cu—O mode frequencies show parallel behavior with minor interaction effects in all compounds.

ETALO A. SECCO. Can. J. Chem. **66**, 329 (1988).

On a déterminé les spectres infrarouges (de 4000 à 50 cm^{-1}) de trois sulfates basiques de cuivre, à savoir le $Cu_4(OH)_6SO_4$, le $Cu_4(OH)_4OSO_4$ et le $Cu_3(OH)_4SO_4$, et on a effectué une analyse de groupe des sites et des facteurs pour le $Cu_4(OH)_6SO_4$. Les fréquences d'absorption observées pour les activités du OH et du SO_4 présentent des caractéristiques structurales individuelles distinctes.

Il existe trois types distincts de groupements OH dans le $Cu_4(OH)_6SO_4$ et le $Cu_4(OH)_4OSO_4$; toutefois, seulement deux types sont évidents dans le $Cu_3(OH)_4SO_4$. On a identifié avec une certaine hésitation les deux groupements OH qui sont impliqués dans la réaction de déshydroxylation conduisant au composé oxy $Cu_4(OH)_4OSO_4$. Par ailleurs, les fréquences multiples impliquant les modes de déformation Cu—O—H indiquent aussi les degrés des liaisons hydrogènes et des couplages OH que l'on retrouve dans les entités $Cu(OH)_4O_2$ et $Cu(OH)_5O$.

La structure multiplet des modes optiques internes du SO_4 et les fréquences observées dans les sulfates basiques illustrent les degrés divers des effets de couplage dipolaire (OH et Cu) par rapport aux modes spécifiques relatifs au Li_2SO_4 possédant la même symétrie de site. Les modes optiques externes du SO_4 par rapport au Li_2SO_4 sont à peine affectés par les groupements OH voisins.

Pour tous les composés, les fréquences du mode Cu—O présentent un comportement parallèle qui n'est que faiblement influencé par les effets d'interaction.

[Traduit par la revue]

Introduction

Recent spectroscopic studies have investigated the nature and internal properties of the SO_4 ion in various crystalline environments (1–4). Interest in the SO_4 ion is based on (*i*) its simple tetrahedral symmetry which can undergo various steps of symmetry reduction and (*ii*) its proposed "rotational" coupling in promoting cation mobility in fast ion conductors of sulfates such as Li_2SO_4 (5, 6).

A polyatomic species such as the SO_4 ion in a crystal may be sited in different potential energy environments and therefore subjected to various interacting molecular forces. These intermolecular forces can yield a vibrational multiplet structure where a single vibrational frequency or no frequency is observed in the isolated molecular state. The observed multiplet structure can be attributed to three main effects: (*i*) *factor group* or *correlation field splitting*, (*ii*) *site group splitting*, and (*iii*) *multiple site splittings*. The observed spectrum may incorporate one or all of these multiplet contributions.

Frech and his group along with others (7–10) have analyzed the vibrational dynamics of internal optic modes in molecular crystals using the molecular dipole model. The dominant interaction of a normal internal optic mode in this model is the vibrationally induced dipole moment derivative $\partial\mu_\alpha/\partial q_j$ corresponding to the jth vibrational molecular normal coordinate q_j. The relation between the phonon frequency ν_j, the static crystal frequency ν_{0j}, and the dipolar coupling factor resulting from the interactions between vibrationally induced dipoles is given by

$$[1]\quad \nu_j^2(\kappa_\gamma) = \nu_{0j}^2 + \sum_\alpha S_{\alpha\alpha}(\kappa_\gamma)[I + \alpha_{0,\alpha\alpha}S_{\alpha\alpha}(\kappa_\gamma)]^{-1}\left(\frac{\partial\mu_\alpha}{\partial q_j}\right)^2$$

In this equation α is a Cartesian coordinate describing the polarization of the phonon, α_0 refers to the electronic polarizability, γ is the irreducible representation of the unit cell group, κ is the wave vector of the phonon, and $S_{\alpha\alpha}(\kappa_\gamma)$ is the unit cell symmetrized (γ) linear combination of dipole sums $S_{\alpha\alpha}$. The quantity $[I + \alpha_{0,\alpha\alpha}S_{\alpha\alpha}(\kappa_\gamma)]^{-1}$ is, therefore, a linear combination of functions of the various dipole sums and electronic polarizability components.

In an effort to extend our knowledge on the internal properties of the SO_4 ion in slightly modified crystalline environments an infrared study was carried out on two copper basic sulfates, $Cu_4(OH)_6SO_4$, also known as the mineral brochantite, and

[1]Preliminary results of this study, Paper No. 07L08, were presented at Symposium on Spectroscopy in Inorganic Chemistry, The 1984 International Congress of Pacific Basin Societies, Honolulu, Hawaii, December 16–21, 1984.

[2]This study received partial support from the Natural Sciences and Engineering Research Council of Canada.

Can. J. Chem. Downloaded from www.nrcresearchpress.com by 213.222.148.141 on 09/07/12
For personal use only.

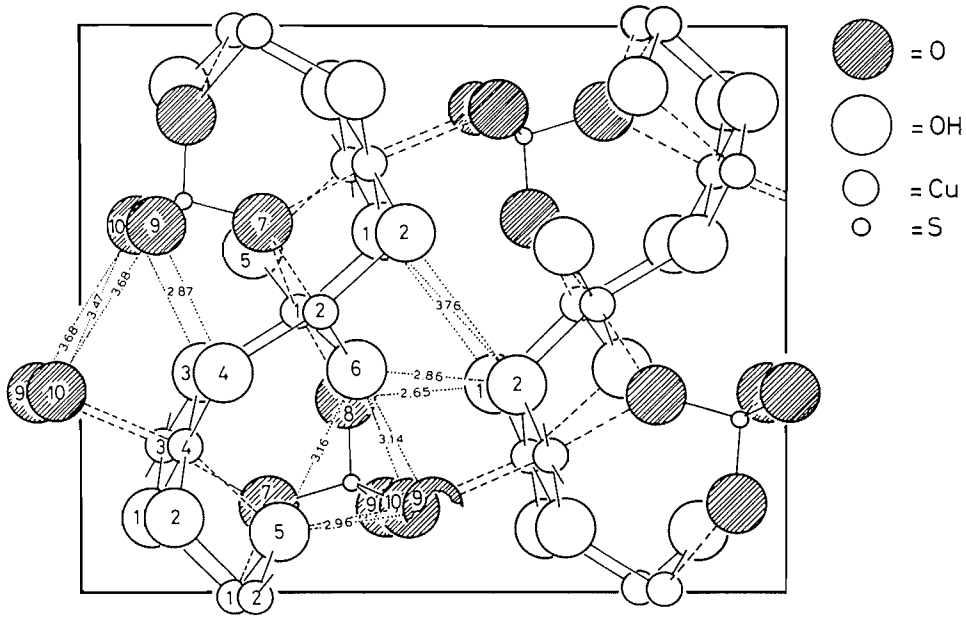

FIG. 1. Unit cell structure of brochantite $Cu_4(OH)_6SO_4$ taken from ref. 12.

$Cu_3(OH)_4SO_4$. These compounds were chosen because (*i*) a high potential for comparison and correlation in their spectral properties is expected and (*ii*) the existence of a stable decomposition intermediate $Cu_4(OH)_4OSO_4$ obtained from $Cu_4(OH)_6SO_4$ (11) should provide related but significant variations in the critical factors of dipole moment and electronic polarizability interactions as contained in eq. [1] which affect the SO_4 vibrational frequencies. The known crystal structure of brochantite should permit vibrational assignments on the basis of group and site effects. Furthermore, since the crystal structure of $Cu_4(OH)_6SO_4$ and Li_2SO_4 fit the same space group $P2_1/a$ (C_{2h}^5) with $Z = 4$ and SO_4 has the same site symmetry, the infrared spectra would provide a critical basis for comparison of SO_4 and OH interaction effects in $Cu_4(OH)_6SO_4$ with the known vibrational assignments for SO_4 external and internal optic modes in Li_2SO_4 obtained from Raman spectra (5). The crystal structures of the other compounds are unknown to us but can be assumed to be related to the brochantite structure.

While the main object of this study is intended to focus on the SO_4 ion (see following paper, Part II) these hydroxy-sulfates are expected to furnish fundamental structural knowledge on the nature of the OH species in related crystalline environments and their involvement in varying degrees of H-bridgings as discussed below.

Structure of $Cu_4(OH)_6SO_4$

The most recent structural assignment for brochantite, $Cu_4(OH)_6SO_4$ is monoclinic (12) with space group $P2_1/a = C_{2h}^5$ superseding earlier monoclinic assignments (13, 14). Using the notation given for the first setting of the C_{2h}^5 space group in the International tables for X-ray crystallography (15), we find that only the 4e sites (Wyckoff notation) with C_1 symmetry are occupied. The unit cell containing four molecular units, with dimensions $a_0 = 13.00$ Å, $b_0 = 9.85$ Å, $c_0 = 6.02$ Å, $\beta = 103° 22'$, shown in Fig. 1 is taken from Cocco and Mazzi (12) with the projection slightly tilted on the [001] plane to avoid masking superposed atoms along the [001]. The interatomic separation values noted on the figure are in Å units. The H atom of OH, not shown, forms Cu—O—H bond angles of 112 and 118°.

The disposition of the OH groups, their orientations, and their intermolecular distances as depicted in Fig. 1, suggest three classes of OH bridges. The first class is OH with no effective H-bonding, represented by O_6H and O_5H. The second class is strong H-bonded OH represented by $O_1H...O_8$. The third class is classified as medium strength H-bonded OH with slight variation in the degree of H-bonding, viz. $O_2H...O_6$, $O_3H...O_{10}$, $O_4H...O_9$.

It appears from Fig. 1 that Cu has a slightly distorted octahedral coordination with four equal coplanar Cu—OH bonds with interatomic separations 2.00 ± 0.02 Å and two Cu—O bonds. Both oxygens in one pair of Cu—O bonds are from the SO_4 ion forming the entity $Cu(OH)_4O_2$ while the second pair involves one oxygen from SO_4 and the other oxygen from OH to form the entity $Cu(OH)_5O$. There are three $Cu(OH)_4O_2$ and one $Cu(OH)_5O$ associated with each SO_4 in the unit cell. On the basis of Cu—O separations (12) two types of $Cu(OH)_4O_2$ are identified, (*i*) two equal Cu—O distances of 2.36 Å and (*ii*) one Cu—O separation of 2.32 Å and the other of 2.52 Å. $Cu(OH)_5O$ has one Cu—OH separation of 2.31 Å and one Cu—O separation of 2.52 Å. The octahedra are linked to form "layers" parallel to the cleavage plane [100] and these are held together by hydrogen bonds and Cu—O bonds.

Factor group analysis of $Cu_4(OH)_6SO_4$

A unit cell of $Cu_4(OH)_6SO_4$ containing 84 atoms gives rise to 252 degrees of freedom involving copper ion motion, OH group external and intramolecular motions, and sulfate external and intramolecular motions. A free sulphate ion belongs to the molecular point group T_d with irreducible representations for internal modes $\Gamma_{int} = A_1 + E + 2T_2$ which correspond to the intramolecular normal modes ν_1, ν_2, ν_3, ν_4, respectively. The low site symmetry C_1 of the SO_4 in the cell removes all the degeneracies of the T_d representations to yield the non-degenerate A representations. From correlation procedures (5, 16) each site group A representation is found to transfer to $A_g + B_g + A_u + B_u$ in the factor group C_{2h}. The number of irreducible representations of the modes for SO_4 is determined to be $9A_g + 9B_g + 9A_u + 9B_u$ for internal vibrational modes and 24 similar representations for translational and rotational

Can. J. Chem. Downloaded from www.nrcresearchpress.com by 213.222.148.141 on 09/07/12
For personal use only.

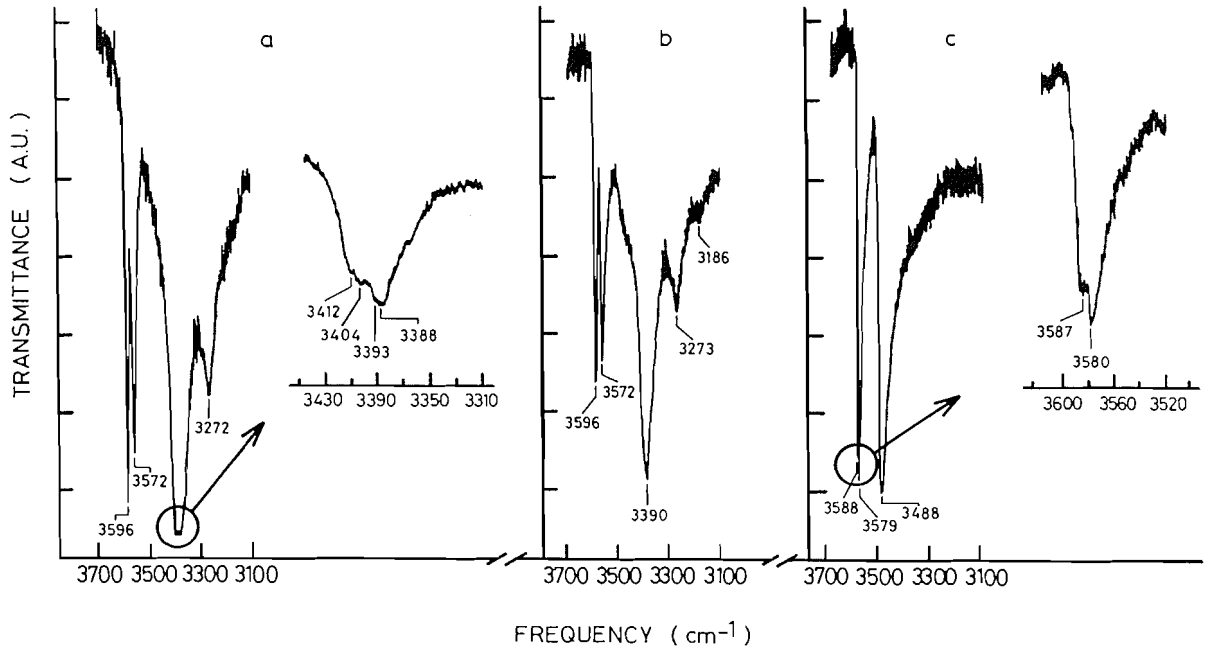

FIG. 2. Infrared spectra for region 3700–3100 cm^{-1}: (*a*) $Cu_4(OH)_6SO_4$, (*b*) $Cu_4(OH)_4OSO_4$, (*c*) $Cu_3(OH)_4SO_4$.

modes or external modes. The remaining representations are identified with 24 internal modes for OH, 48 Cu—O—H bending modes, 24 Cu—O stretching modes, 48 O—Cu—O angle deformation modes and 48 modes involving Cu ion motion.

Experimental

$Cu_4(OH)_6SO_4$ and $Cu_3(OH)_4SO_4$ were prepared according to accepted procedures and analyzed as described (11). The intermediate $Cu_4(OH)_4OSO_4$ was obtained from the parent $Cu_4(OH)_6SO_4$ according to the reaction, $Cu_4(OH)_6SO_{4(s)} \rightarrow Cu_4(OH)_4OSO_{4(s)} + H_2O_{(g)}$, by annealing in a Pt crucible placed in a well-type furnace maintained at 310 ± 5°C for 3–5 h. The sample color change was blue to olive green (11).

The infrared transmission spectra were recorded with a Perkin-Elmer 180 spectrophotometer using both the standard compressed KBr disc technique and Nujol mull samples between polyethylene windows. The observed absorption frequencies were reproducible within 2 cm^{-1} for most of the overlapping spectral regions using both sample techniques. Each compound was maintained in an oven at 150–160°C for 5–15 h before using.

Results and discussion

The infrared transmittance spectra recorded in this study are presented and interpreted with respect to OH and SO_4 optic modes in the compounds $Cu_4(OH)_6SO_4$, $Cu_4(OH)_4OSO_4$, and $Cu_3(OH)_4SO_4$. The spectral intensities are given in arbitrary units (A.U.). No HOH bending absorption was observed, in contrast to the assignment in other hydroxysulfates (17).

OH absorption

The fundamental vibrational frequency for OH was found to occur over the range 3600–3200 cm^{-1} depending on the degree of H-bonding, Fig. 2. Tarte (18) reported the range to be 3586–3270 cm^{-1} for $Cu_4(OH)_6SO_4$ and $Cu_3(OH)_4SO_4$.

Figure 2*a* shows a clearly resolved multiplet structure in the spectrum of $Cu_4(OH)_6SO_4$ indicating the three distinct classes of hydroxy groups known to exist in the crystal. The sharp peaks at 3596 and 3572 cm^{-1}, with fine splitting of 4 cm^{-1} in the 3572 cm^{-1} peak evident at higher resolution, are assigned to "free" non-hydrogen bonded OH identified as O_6H and O_5H, respectively. That is, three of the expected four components are observed. The 3596 cm^{-1} frequency is within range of 3600–3640 cm^{-1} and 3550–3570 cm^{-1} reported for "free" OH groups in weak alcohol solutions (19) and lanthanide (Gd, Nd) basic nitrates (20), respectively. The sharp band at 3272 cm^{-1} is assigned to strongly H-bonded $O_1H\ldots O_8$ with a separation of 2.65 Å. The slightly broader band centred at 3396 cm^{-1}, with fine structure 3412, 3404, 3393, 3388 cm^{-1} evident at higher resolution, is consistent with the different degrees of hydrogen bridging found for $O_2H\ldots O_6$, $O_3H\ldots O_{10}$, $O_4H\ldots O_9$ with separations of 2.86 and 2.87 Å.

Figure 2*b* is the spectrum of $Cu_4(OH)_4OSO_4$ obtained as a product from $Cu_4(OH)_6SO_4$ described above. The loss of two OH groups leaves the spectrum virtually unchanged relative to the parent spectrum Fig. 2*a*. The only discernible differences are the profile of the 3390 cm^{-1} which appears less broad and the appearance of a weak band at 3186 cm^{-1}. These features suggest dehydroxylation to involve group O_4H with either O_3H or O_2H from the $Cu(OH)_5O$ entity. This OH frequency parallels the dimer reported for alcohol solutions (19).

The spectrum of $Cu_3(OH)_4SO_4$ is given in Fig. 2*c*. The crystal structure of $Cu_3(OH)_4SO_4$ has yet to be determined, hence the disposition of the OH groups in the unit cell is unknown. The spectrum indicates two types of OH groups — a "free" (no H-bond) type and a medium strength H-bonded type as found in a dimer, viz. $OH_a\ldots OH_b$ where H_a is bridged but H_b is a terminal "free" entity. The $O—H_a\ldots O$ frequency of 3490 cm^{-1} agrees very well with the OH stretching frequency of 3485 cm^{-1} for the dimer observed in alcohol solutions (19). The splitting (site or LO-TO?) of 8 cm^{-1} for "free" OH, viz. 3588 and 3580 cm^{-1}, is evident.

The spectra of the three compounds in the 1300–50 cm^{-1} region are presented in Figs. 3, 4, and 5 with the absorption frequencies noted. The OH frequencies along with their assignments are tabulated in Table 1. The Cu—OH deformation

Can. J. Chem. Downloaded from www.nrcresearchpress.com by 213.222.148.141 on 09/07/12
For personal use only.

Can. J. Chem. Downloaded from www.nrcresearchpress.com by 213.222.148.141 on 09/07/12
For personal use only.

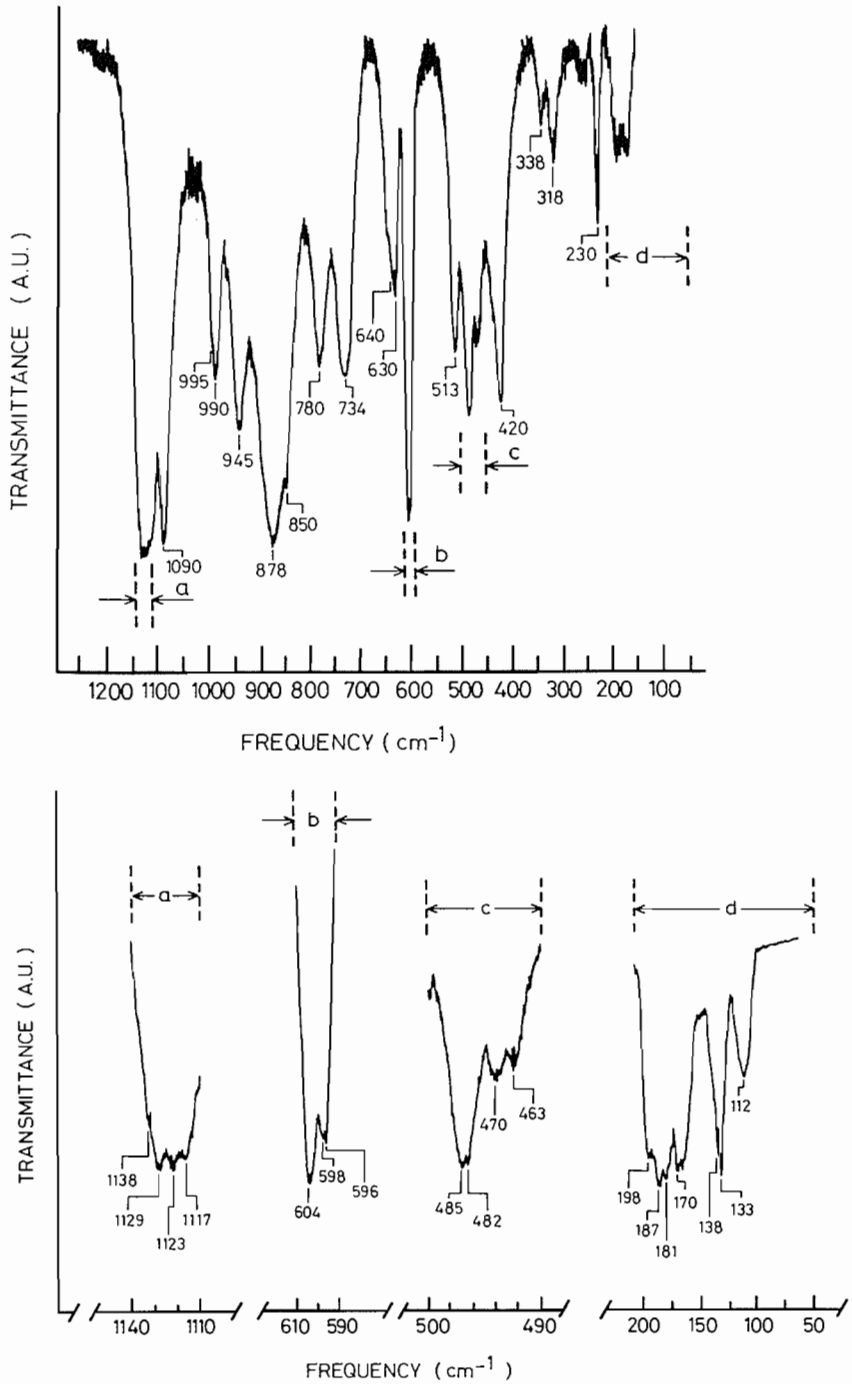

FIG. 3. Infrared spectrum of $Cu_4(OH)_6SO_4$ with expanded portions *a*, *b*, *c*, *d*.

assignments are based on the deuterium shift and these frequencies are within $\pm 2\,cm^{-1}$ of the values reported by Tarte (18). Again the frequencies involving the Cu—O—H bending modes reflect the disposition of the OH groups and the varying degrees of H-bonding. The larger shift of the bending mode frequencies, $\Delta\nu_b/\nu_b$, relative to the O—H stretching mode frequencies, $\Delta\nu_s/\nu_s$, by a factor ~4, usually $\Delta\nu_b/\nu_b < \Delta\nu_s/\nu_s$, implies that the bending modes involve coupling in the $Cu(OH)_4O_2$ and $Cu(OH)_5O$ entities discussed above. The additional frequencies in $Cu_4(OH)_6SO_4$ and $Cu_4(OH)_4OSO_4$ relative to $Cu_3(OH)_4SO_4$ correlate with the two extra CuOH units and the variation in CuO distances, 2.00–2.52 Å (21, 22). The assignment of the OH torsional and translational modes given in Table 2 is made on the basis of their absence in $CuSO_4$ and $Cu_3O_2SO_4$ spectra, as reported in Part II (23).

SO_4 absorption

The fundamental vibration frequencies for SO_4 of T_d symmetry observed in the infrared are $\nu_3(T_2)$ 1104 cm^{-1} and $\nu_4(T_2)$ 613 cm^{-1}. The fundamental vibration frequencies for SO_4 of reduced symmetry have been reported for infrared transmittance (2–5) to occur over a range of values, viz. $\nu_1(A_1)$ 971–993, $\nu_2(E)$ 445–490, $\nu_3(T_2)$ 1070–1190, and $\nu_4(T_2)$ 613–648 cm^{-1}.

The recorded spectra given in Figs. 3, 4, and 5 show the multiplet vibrational structure expected from factor group analysis for SO_4 in $Cu_4(OH)_6SO_4$ and assumed parallel consi-

Can. J. Chem. Downloaded from www.nrcresearchpress.com by 213.222.148.141 on 09/07/12
For personal use only.

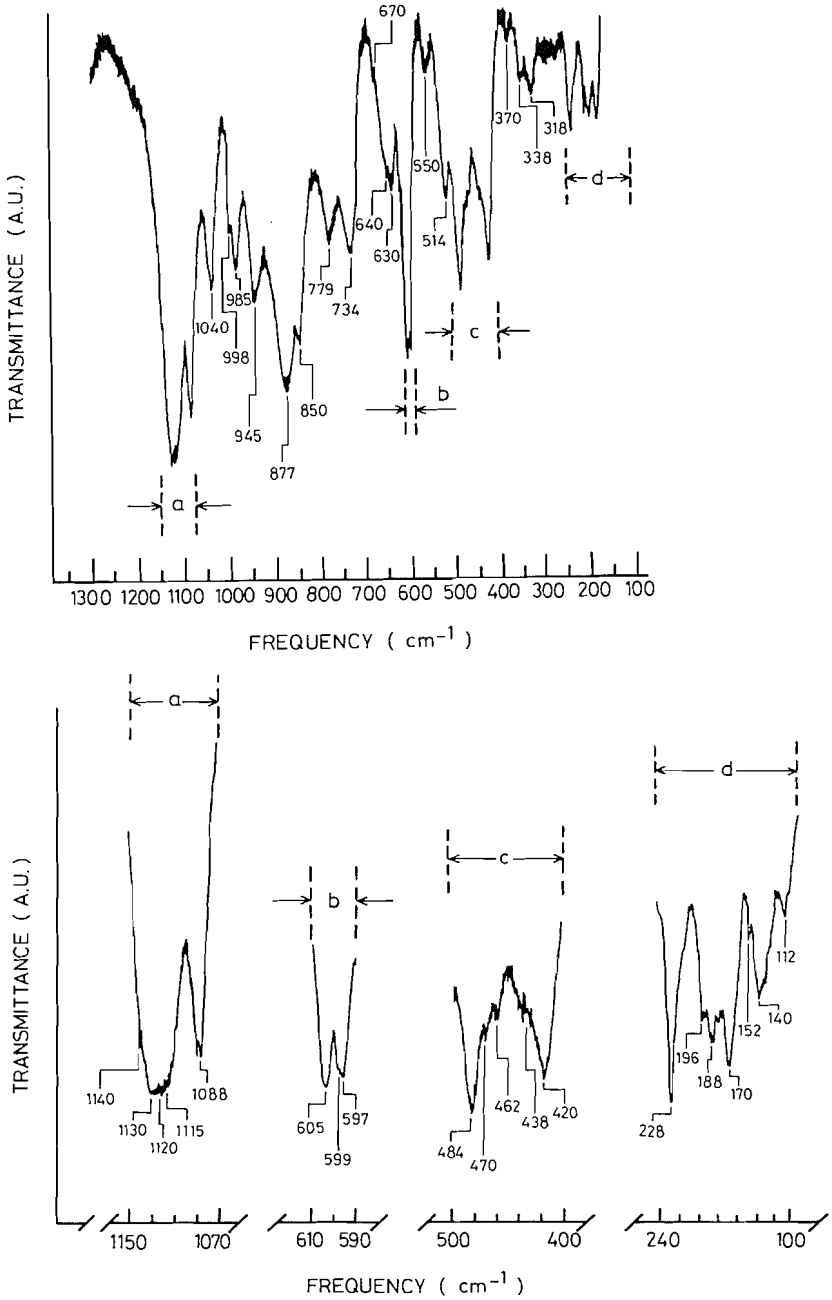

FIG. 4. Infrared spectrum of $Cu_4(OH)_4OSO_4$ with expanded portions *a*, *b*, *c*, *d*.

TABLE 1. Cu—O—H bending mode frequencies (cm^{-1})

Compounds	Frequency (cm^{-1})		
	$Cu_4(OH)_6SO_4$	$Cu_4(OH)_4OSO_4$	$Cu_3(OH)_4SO_4$
Assignment			
Strong H-bonded OH,	990 (989)[b]	985	
e.g. $O_1H\ldots O_3$[a]	945 (945)	945	
Medium H-bonded OH,	878 (874)	877	880 (889)
e.g. $O_2H\ldots O_6$[a]	850	850	850 (853)
Free OH, e.g. O_6H, O_5H[a]	780 (782)	779	807 796 (805)
	734 (736)	734	750 (757)

[a]OH identities from Fig. 1.
[b]Value taken from Tarte (18).

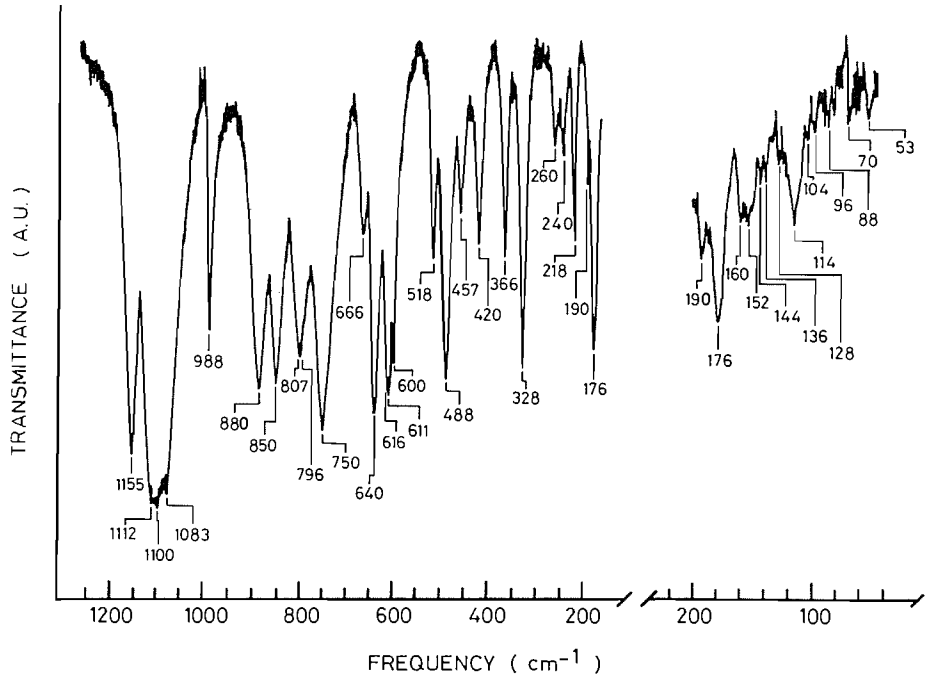

FIG. 5. Infrared spectrum of $Cu_3(OH)_4SO_4$.

TABLE 2. OH external/torsional mode frequencies (cm^{-1})

$Cu_4(OH)_6SO_4$	$Cu_4(OH)_4OSO_4$	$Cu_3(OH)_4SO_4$
—	370	366
289	285	—
254	255	260, 256
—	—	240
196	198	—
188	188	190
—	—	152
138	140	144, 136

derations for SO_4 in $Cu_4(OH)_4OSO_4$ and $Cu_3(OH)_4SO_4$. The pattern of infrared activity parallels the Raman activity of SO_4 for C_1 symmetry as expected. The internal optic mode frequencies of SO_4 noted on these spectra and their tentative correlated assignments are tabulated in Table 3 along with the Raman spectra frequencies and symmetry assignments for Li_2SO_4 (5) for comparison purposes. The frequencies noted on the main spectrum were taken from spectra with the abscissa expanded 2.5 or 5 times. The various absorption frequencies and splittings are discussed.

The weak $\nu_1(A_1)$ peak adjacent to the stronger OH deformation peak in $Cu_4(OH)_6SO_4$ and $Cu_3(OH)_4OSO_4$ is in contrast to the single sharp $\nu_1(A_1)$ absorption in $Cu_3(OH)_4SO_4$.

The multiplet and fine structure evident for $\nu_2(E)$ over a range of 100 cm^{-1} for the three compounds with splittings 20–65 cm^{-1} and 8 cm^{-1} indicates stronger site group or dipolar coupling effects relative to Li_2SO_4. Powers *et al.* assigned infrared frequencies of iron basic sulfates in the 412–550 cm^{-1} region to vibrations of FeO_6 octahedra (17). These frequencies are consistent with site group splitting of $\nu_2(E)$ in SO_4 rather than FeO_6 vibrations.

The $\nu_3(T_2)$ mode displays contrasting features in its multiplet structure for the three compounds. $Cu_4(OH)_6SO_4$ and $Cu_4(OH)_4OSO_4$ show similar absorption frequencies with the additional peak at 1040 cm^{-1}. Assuming the same site symmetry for SO_4 in both compounds, one might correlate the 1040 cm^{-1} absorption in $Cu_4(OH)_4OSO_4$ with different interactions of selective SO_4 units to permit extra splitting. The weak splitting observed for $Cu_3(OH)_4SO_4$ in the 1083–1112 cm^{-1} interval and the strong sharp peak at 1155 cm^{-1} are in distinct contrast to the profiles of the other two basic sulfates, suggesting effects originating with different site symmetry and/or dipolar coupling contributions as contained in eq. [1].

Most features in the multiplet structure of the $\nu_4(T_2)$ mode are common to the three compounds. The contrasting features of $Cu_3(OH)_4SO_4$ are (*i*) the lack of fine structure in the 600 cm^{-1} peak, (*ii*) the absence of the 628–630 cm^{-1} absorption, and (*iii*) the prominent and clearly resolved 666, 640, and 616 cm^{-1} peaks. $Cu_4(OH)_6SO_4$ does not show the 666–670 cm^{-1} absorption. The ν_2 of CO_2 appears sporadically as a distinct spike at 667 cm^{-1}.

The multiplets observed in the specific deformation modes ν_2 and ν_4, viz. 470–462, 604–597, 616–611, indicate either varied SO_4—OH interactions or selective site splittings.

The frequencies of the Cu—O stretching and O—Cu—O bending mode frequencies are presented in Table 5 along with those observed for $Cu_3O_2SO_4$ (23) and $Cu_4(OH)_6(NO_3)_2$ (24) for comparison purposes. The values 170–176 cm^{-1} also cited in Table 4 are also assigned to SO_4 external modes on the basis of possible coincident frequencies.

The frequencies of sulfate external optic modes of the basic sulfates are given in Table 4, along with those reported for Li_2SO_4 from Raman studies (5) for comparison purposes. The mode symmetries parallel assignments for Li_2SO_4. The high degree of agreement in their frequencies imply the sulfate external mode to be virtually unaffected by the surrounding OH groups.

Can. J. Chem. Downloaded from www.nrcresearchpress.com by 213.222.148.141 on 09/07/12
For personal use only.

TABLE 3. Sulfate internal optic mode frequencies (cm^{-1})

Compounds	Symmetry[a]	Frequency			
		Li_2SO_4[a]	$Cu_4(OH)_6SO_4$	$Cu_4(OH)_4OSO_4$	$Cu_3(OH)_4SO_4$
ν_1 region	$A_{g,u}-B_{g,u}$	1014	995	993	988
ν_2 region	$B_{g,u}$	516	513	514	518
	$A_{g,u}$	513	484	484	488
	$B_{g,u}$	451	462	470, 462	457
	$A_{g,u}$	447	420	420	420
ν_3 region	$B_{g,u}$	1204	1138	1140	1155
	$A_{g,u}$	1194	1129	1130	—
	$B_{g,u}$	1150	1123	1120	1112
	$A_{g,u}$	1127	1117	1115	1100
	$A_{g,u}$	1123	1090	1080	1083
	$B_{g,u}$	1116	—	1040	—
ν_4 region	$A_{g,u}-B_{g,u}$	665	—	670	666
	$B_{g,u}$	648	640	640	640
	$B_{g,u}$	622	630	630	—
	$A_{g,u}$	617	—	614	616, 611
			604, 598, 596	605, 597	600

[a]Reference 5, Raman data.

TABLE 4. Sulfate external optic modes

Symmetry[a]	Frequency (cm^{-1})			
	Li_2SO_4[a]	$Cu_4(OH)_6SO_4$	$Cu_4(OH)_4OSO_4$	$Cu_3(OH)_4SO_4$
$B_{g,u}$	176	172	170	176
$A_{g,u}$	162	166	—	160
$A_{g,u}$	134	133	—	136
$A_{g,u}$	119	112	112	114
$B_{g,u}$	108			104
$A_{g,u}$	94			96
$A_{g,u}$	89			88
$A_{g,u}$	81			80
$B_{g,u}$	73			70

[a]Reference 5, Raman data.

TABLE 5. Cu—O mode frequencies (cm^{-1})

Assignment	Frequency				
	$Cu_4(OH)_6SO_4$	$Cu_4(OH)_4OSO_4$	$Cu_3(OH)_4SO_4$	$Cu_3O_2SO_4$[a]	$Cu_4(OH)_6(NO_3)_2$[b]
ν_s(Cu—O)	338	338	328	338	328
	318	318	—	300	—
ν_b(O—Cu—O)	228	228	218	224	218
	172	170	176	—	172

[a]Data from ref. 23.
[b]Data from ref. 24.

Conclusions

The infrared spectra of three related basic sulfates, viz. $Cu_4(OH)_6SO_4$, $Cu_4(OH)_4OSO_4$, $Cu_3(OH)_4SO_4$, show the individual structural features and the binary interactions of the OH and SO_4 species. Three major types of OH groups are identified in $Cu_4(OH)_6SO_4$ whose structure is known. These are (*i*) "free" non H-bonded OH, (*ii*) medium strength H-bonded OH, and (*iii*) strong H-bonded OH. A separation of 4 cm^{-1} near the 3572 cm^{-1} peak is observed for the bifurcated OH hydrogen between two equidistant SO_4 oxygens. The two OH groups reacting in the dehydroxylation step to yield the oxycompound, via $Cu_4(OH)_6SO_{4(s)} \rightarrow Cu_4(OH)_4OSO_{4(s)} + H_2O_{(g)}$, are tentatively identified. Two types of OH groups are evident in $Cu_3(OH)_4SO_4$, structure unknown, namely (*i*) "free" OH and

Can. J. Chem. Downloaded from www.nrcresearchpress.com by 213.222.148.141 on 09/07/12
For personal use only.

(*ii*) medium strength H-bridged OH. Splittings are observed in the "free" OH stretching mode, 8 cm^{-1}, and the Cu—OH bending mode, 10 cm^{-1}.

The SO_4 internal optic modes show a general trend to lower frequencies in all modes accompanied by stronger splittings in ν_2 and ν_4 and weaker splittings in ν_3. The magnitude of these splittings emphasize the interplay of the dipole coupling, the correlation field, and the site group effects. The SO_4 external optic modes in the basic sulfates are barely affected by neighboring OH groups as indicated by the high degree of agreement between their frequencies and the analogous mode frequencies for SO_4 of the same site symmetry in Li_2SO_4.

Acknowledgments

I thank the National Research Council of Canada for an equipment grant to purchase the infrared spectrometer and Professor Roger Frech, University of Oklahoma, and Dr. Anthony Secco, University of Manitoba, for their generous assistance regarding interpretations.

1. G. J. Wu and R. Frech. J. Chem. Phys. **66**, 1352 (1977).
2. D. Teeters and R. Frech. J. Chem. Phys. **76**, 799 (1982).
3. M. Natarajan and E. A. Secco. J. Solid State Chem. **47**, 231 (1983).
4. E. A. Secco. J. Chem. Phys. **79**, 5208 (1983).
5. E. Cazzannelli and R. Frech. J. Chem. Phys. **79**, 2615 (1983).
6. L. Borjesson and L. M. Torrell. Phys. Rev. B **32**, 2471 (1985).
7. R. M. Hexter. J. Chem. Phys. **33**, 1833 (1960); **36**, 2285 (1962); **39**, 1608 (1963).
8. E. R. Nixon and F. D. Verderame. J. Chem. Phys. **41**, 1682 (1964).
9. J. C. Decius. J. Chem. Phys. **49**, 1387 (1968).
10. R. Frech. J. Chem. Phys. **58**, 5067 (1973).
11. P. Ramamurthy and E. A. Secco. Can. J. Chem. **48**, 3510 (1970).
12. G. Cocco and F. Mazzi. Period. Mineral. Rome, **28**, 121 (1959).
13. C. Palache. Am. Mineral. **24**, 463 (1939).
14. C. Lauro. Period. Mineral. Rome, **10**, 331 (1939).
15. International tables for X-ray crystallography. Vol. 1. Kynoch Press, Birmingham, England. 1952. p. 98.
16. J. R. Ferraro and J. S. Ziomek. Introductory group theory and its applications to molecular structure. Plenum, New York. 1975.
17. D. A. Powers, G. R. Rossman, H. J. Schugar, and H. B. Gray. J. Solid State Chem. **13**, 1 (1975).
18. P. Tarte. Spectrochim. Acta, **13**, 107 (1958).
19. L. Wilson, R. Bicca de Alencastro, and C. Sandorfy. Can. J. Chem. **63**, 40 (1985).
20. D. F. Mullica, E. L. Sappenfield, and D. A. Grossic. J. Solid State Chem. **63**, 231 (1986).
21. C. Cabannes-Ott. C.R. Acad. Sci. Paris, **242**, 355 (1956).
22. E. Hartert and O. Glemser. Z. Elektrochem. **60**, 746 (1956).
23. E. A. Secco. Can. J. Chem. **66**, 000 (1988).
24. E. A. Secco and G. G. Worth. Can. J. Chem. **65**, 2504 (1987).

Can. J. Chem. Downloaded from www.nrcresearchpress.com by 213.222.148.141 on 09/07/12
For personal use only.

Spectroscopic properties of SO_4 in different molecular and crystalline environments. II. Identification and infrared spectra of $Cu_3O_2SO_4$ and its hydroxylated derivative[1,2]

ETALO A. SECCO
Chemistry Department, St. Francis Xavier University, Antigonish, N.S., Canada B2G 1C0

Received June 25, 1987

ETALO A. SECCO. Can. J. Chem. **66**, 337 (1988).

The infrared spectra of $Cu_3O_2SO_4$, identified for the first time and obtained from three different preparations are reported. The proposed structure of $Cu_3O_2SO_4$ contains the copper oxysulfate anion $[(CuO)_2SO_4]^{2-}$ of C_s symmetry with each CuO attached by the Cu to two oxygens of the SO_4 group. Of the 21 infrared-active modes predicted for this anion 17 modes are discernible. Its hydroxylated derivative $Cu_3(OH)_4SO_4$ shows clearly resolved and evenly split peaks of the ν_3 mode of SO_4 in strong contrast to the strong overlap of this mode in its crystalline analog; the frequencies of the remaining SO_4 modes stay effectively unchanged.

ETALO A. SECCO. Can. J. Chem. **66**, 337 (1988).

On rapporte le spectre infrarouge du $Cu_3O_2SO_4$ qui a été identifié pour la première fois et qui a été préparé par trois méthodes différentes. La structure qui est proposée pour le $Cu_3O_2SO_4$ contient l'anion oxysulfate cuivre $[(CuO)_2SO_4]^{2-}$ qui possède la symétrie C_s et dans lequel chacun des CuO est attaché par le Cu à deux oxygènes du groupement SO_4. Des 21 modes qui d'après les prédictions devraient être actifs en infrarouge, on en discerne 17. Le dérivé hydroxylé $Cu_3(OH)_4SO_4$ présente les bandes bien résolues et bien séparées du mode ν_3 de SO_4 et ce résultat est en opposition avec l'important recouvrement de ce mode dans l'analogue cristallin; les fréquences des autres modes du SO_4 demeurent effectivement inchangées.

[Traduit par la revue]

Introduction

The SO_4 ion can undergo various steps of descent in symmetry from its simple isolated tetrahedral T_d symmetry to the low site symmetry C_1 in a crystalline lattice (1–4) and also by substitution to yield the monodentate sulfate group of C_{3v} symmetry or the bidentate sulfate group with C_{2v} symmetry (5–7). The infrared spectra of three copper basic sulfates have been reported in the preceding paper (4). In an effort to gain more insight into the intramolecular effects on the optic modes of SO_4 by the surrounding molecular units this paper extends the preceding study by reporting the infrared spectra of the compound $Cu_3O_2SO_4$, identified for the first time and obtained from three different preparations, along with its hydroxylated derivative $Cu_3(OH)_4SO_4$. This derivative shows physicochemical and spectral properties distinct from the crystalline compound $Cu_3(OH)_4SO_4$ presented in the preceding paper (4).

Experimental

$Cu_3O_2SO_4$ was obtained from three preparations: (*i*) solid state synthesis from $CuSO_4$ and CuO, (*ii*) dehydroxylation of $Cu_3(OH)_4SO_4$, and (*iii*) dehydroxylation of $Cu_4(OH)_6SO_4$.

The solid state synthesis of $Cu_3O_2SO_4$ was carried out by annealing the requisite composition of $CuSO_4$ and CuO, previously well ground manually, in a Pt crucible at <700°C for ca. 20 h. CuO was Fisher Certified ACS grade and $CuSO_4$ was from dehydrated $CuSO_4 \cdot 5H_2O$ Baker Analyzed Reagent grade.

The $Cu_3(OH)_4SO_4$ and $Cu_4(OH)_6SO_4$ used to obtain $Cu_3O_2SO_4$ were from the same origins as in the preceding paper (4). The dehydroxylation of $Cu_4(OH)_6SO_4$ as reported earlier (8) can occur via a single step,

$$[1] \quad Cu_4(OH)_6SO_{4(s)} \xrightarrow{>450°C} Cu_3O_2SO_{4(s)} + CuO_{(s)} + 3H_2O_{(g)}$$

or two separate steps [2*a*] and [2*b*],

$$[2a] \quad Cu_4(OH)_6SO_{4(s)} \xrightarrow{300°C} Cu_4(OH)_4OSO_{4(s)} + H_2O_{(g)}$$

and

$$[2b] \quad Cu_4(OH)_4OSO_{4(s)} \xrightarrow{>450°C} Cu_3O_2SO_{4(s)} + CuO_{(s)} + 2H_2O_{(g)}$$

The dehydroxylation of $Cu_3(OH)_4SO_4$ occurs in a single step [3],

$$[3] \quad Cu_3(OH)_4SO_4 \xrightarrow{510°C} Cu_3O_2SO_{4(s)} + 2H_2O_{(g)}$$

In the earlier report (8) the oxysulfate was assigned the formula Cu_2OSO_4 but this present study shows a more appropriate representation of the oxysulfate to be $Cu_3O_2SO_4$.

The infrared transmission spectra were recorded with a Perkin-Elmer 180 spectrometer using techniques described in the preceding paper (4).

Results and discussion

$Cu_3O_2SO_4$ from dehydroxylation

The infrared transmittance spectra of the dehydroxylated residue from reaction [1] and reaction [2*b*] are identical and presented as the full line in Fig. 1; the infrared spectrum of the dehydroxylated residue from reaction [3] is presented in Fig. 1 as the broken line. The vibrational frequencies from these spectra and the frequencies of SO_4 in the binuclear sulfate complex $[Co_2(NH_3)_8NH_2SO_4]^{3+}$ with C_{2v} molecular point group symmetry (6) are tabulated in Table 1 for comparison purposes. The $Cu_3O_2SO_4$ frequencies can also be compared with SO_4 frequencies tabulated in Tables 3 and 4 of the preceding paper (4).

The spectrum of the hydroxylated derivative of $Cu_3O_2SO_4$ from reaction [3], obtained by exposing it to H_2O vapor at room temperature, is given in Fig. 2. The hydroxylated derivative decomposes in a single step at 425°C as recorded by DSC. The ΔH of dehydroxylation is within 10% of the reported ΔH value determined for the dehydroxylation of the compound $Cu_3(OH)_4SO_4$, shown by TGA to correspond to the loss of two molecules of H_2O (8). This result confirms the derivative's composition to be $Cu_3(OH)_4SO_4$. The residue of the dehydroxylated derivative, i.e., $Cu_3O_2SO_4$, gives a spectrum identical to the broken line spectrum of Fig. 1. The dark brown color of $Cu_3O_2SO_4$ remained unchanged on hydroxylation, which is in

[1]Preliminary results of this study, Paper No. 07L08, were presented at Symposium on Spectroscopy in Inorganic Chemistry, The 1984 International Congress of Pacific Basin Societies, Honolulu, Hawaii, December 16–21, 1984.

[2]This study received partial support from the Natural Sciences and Engineering Research Council of Canada.

Can. J. Chem. Downloaded from www.nrcresearchpress.com by 213.222.148.141 on 09/07/12
For personal use only.

TABLE 1. Sulfate internal optic mode frequencies (cm^{-1})

Mode	Sources of $Cu_3O_2SO_4$			$\left[(NH_3)_4Co\begin{smallmatrix}NH_2\\SO_2\end{smallmatrix}Co(NH_3)_4\right]^{3+}$ C_{2v} modes	
	$Cu_4(OH)_6SO_4$	$Cu_3(OH)_4SO_4$	$CuSO_4 + 2CuO$		
$\nu_1 (A_1)$	1000	1000	996	995	(ν_2)
$\nu_2 (E)$	576	568	575	571	(ν_9)
	534	536	530		
	482	482	480	462	(ν_4)
	436	438	435		
$\nu_3 (T_2)$	1212	1196	1200	1170	(ν_8)
	1152	1153	1145	1105	(ν_6)
	1044	1050	1025	1055	(ν_1)
$\nu_4 (T_2)$	647, 643	654, 648	668, 640	641	(ν_3)
	630	642	630, 620	—	(ν_5)
	620	626, 620	608	610	(ν_7)

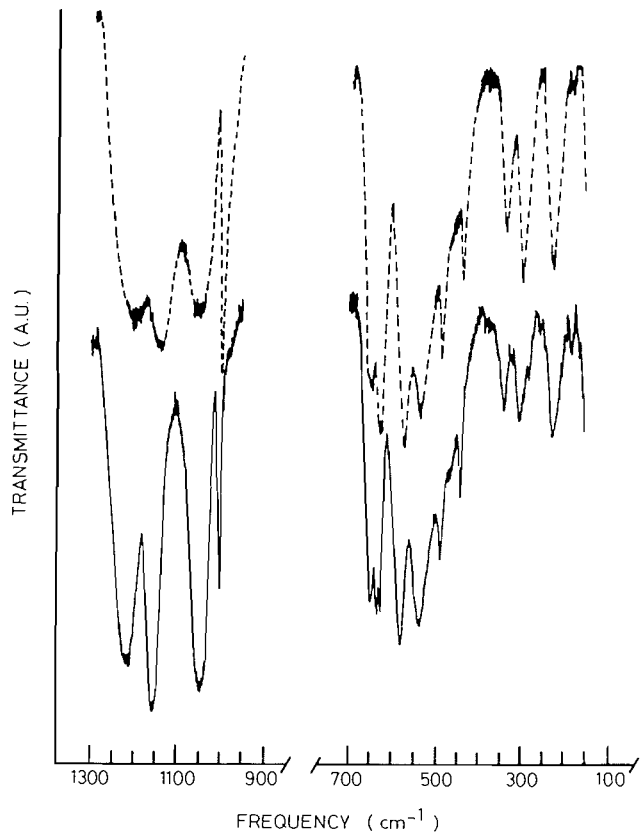

FIG. 1. Infrared spectra of $Cu_3O_2SO_4$; —, residue from reactions [1] and [2*b*], ---, residue from reaction [3].

strong contrast with the blue color of crystalline $Cu_3(OH)_4SO_4$, the parent compound from which $Cu_3O_2SO_4$ was obtained.

The hydroxylated solid residue from reaction [2*b*] gives virtually the same spectrum (not shown) as Fig. 2 displaying the same frequencies with minor variations in peak intensities. Spectra of the hydroxylated solid residue from reactions [2*b*] and [3] reveal the same essential features exhibited by $Cu_3(OH)_4SO_4$ of the preceding paper (4) except for the clearly resolved peaks in the 1070–1155 cm^{-1} region. The same spectrum for the hydroxylated derivative of reaction [2*b*] and [3] residues indicates a common oxysulfate reactant of composition $Cu_3O_2SO_4$ whose reaction with H_2O is described by

[4] $Cu_3O_2SO_{4(s)} + 2H_2O_{(g)} \rightarrow Cu_3(OH)_4SO_{4(s)}$

where the excess CuO from [2*b*] does not present any distinctive absorption peak.

The spectra in Fig. 1, displaying minor variations in absorption frequencies and in relative peak intensities in the 610–650 cm^{-1} and 1000–1250 cm^{-1} regions, show a high degree of internal consistency. These minor variations are not due to sample preparations but are reproducible and therefore genuine. The difference in the chemical composition of the full line spectrum, i.e. $Cu_3O_2SO_4$ + CuO relative to $Cu_3O_2SO_4$, may be responsible for the minor variations in these fundamental mode absorption regions. This fact suggests that molecularly dispersed non-chemically bonded CuO can affect the internal mode vibrations of $Cu_3O_2SO_4$. Since vibrational coupling is not confined to structural units contained within the unit cell one might expect weaker coupling effects with more distant vibrating neighbors (9).

The compound $Cu_3O_2SO_4$ is thought to incorporate the copper oxysulfate anion $[(CuO)_2SO_4]^{2-}$ of C_s point symmetry where the Cu of each CuO is attached to two oxygens of the SO_4 group with the O of the CuO extending out from the SO_4 tetrahedron, Fig. 4*a*. The anion $[(CuO)_2SO_4]^{2-}$ reacts with H_2O vapor to form the hydroxylated derivative by incorporating one OH group from the Cu extending to an opposite oxygen of SO_4 to form a weak H-bridge, i.e. Cu—O—H...OSO_3 while the other non-hydrogen bonded OH group projecting away from the SO_4 unit is effectively free as shown in Fig. 4*b*. The clearly resolved ν_3 peaks of SO_4 for the non-crystalline $Cu_3(OH)_4SO_4$, viz. 1150, 1112, 1078 cm^{-1}, are in strong contrast to the overlap between 1083–1112 cm^{-1} in the crystalline $Cu_3(OH)_4SO_4$. The clearly resolved peaks suggest the absence of any overlapping or crowding factor, and the specific modes of the molecule appear essentially unaffected by any near neighbors.

The space group of neither $Cu_3O_2SO_4$ nor of crystalline $Cu_3(OH)_4SO_4$ is known to us. Theoretically, the crystal structure could be derived from a unit cell group analysis of a complete infrared and Raman study of all the active normal modes but such an analysis would be far from unambiguous in view of a multiplicity of complications. Such a lack of site symmetry of SO_4 in $Cu_3O_2SO_4$ militates against the assignment of the infrared-active modes and the interpretation of the

Can. J. Chem. Downloaded from www.nrcresearchpress.com by 213.222.148.141 on 09/07/12
For personal use only.

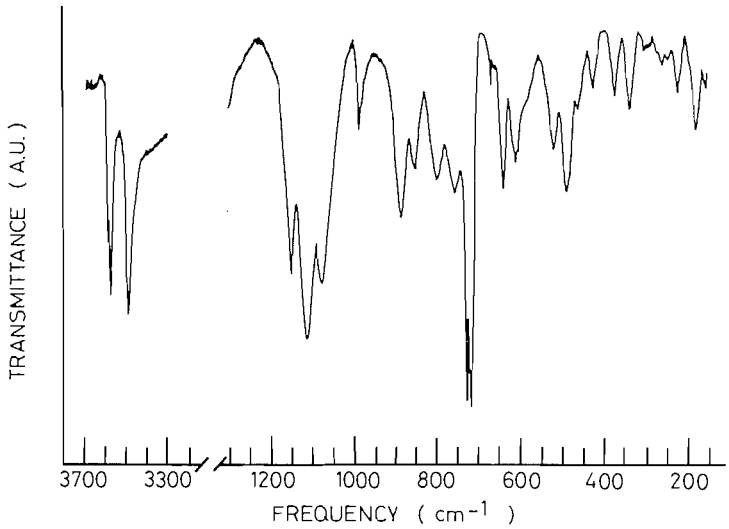

FIG. 2. Infrared spectrum of hydroxylated derivative of $Cu_3O_2SO_4$, i.e. $Cu_3(OH)_4SO_4$.

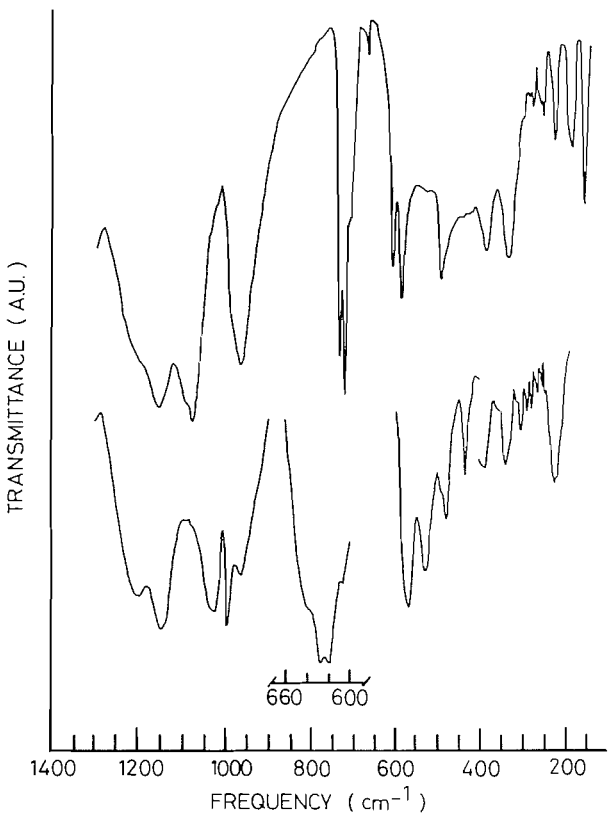

FIG. 3. Infrared spectra of 1:2 mole mixture $CuSO_4$:CuO; (*a*) upper line, unannealed, (*b*) lower line, annealed.

various splitting effects. The large number of absorption peaks, however, points to a low site symmetry consistent with the molecular point group symmetry C_s. The strong resemblance of $Cu_3O_2SO_4$ vibrational frequencies with those of the bidentate sulfate complex, Table 1, indicates the relative strength of the intra-molecular bonding in both species. Considering the $[(CuO)_2SO_4]^{2-}$ anion as an isolated unit of C_s point group the spectra show 15–17 of the possible 21 infrared-active internal modes.

The equally spaced weaker splitting, i.e. 36 ± 1 cm^{-1} in the asymmetric stretch of the $\nu_3(SO_4)$ in the hydroxylated derivative of $Cu_3O_2SO_4$, viz. $Cu_3(OH)_4SO_4$ relative to the uneven stronger splitting, i.e. 65 cm^{-1} and 110 cm^{-1}, in the original $Cu_3O_2SO_4$ indicates the moderating effect of OH presence and its H-bridging on the $\nu_3(SO_4)$ modes. However, the opposite trend in frequency shift with equal splitting occurs for the CuO modes involved in bending, viz. 340 and 300 versus 366 and 328 cm^{-1}. The effect of OH on the symmetric stretch of $\nu_1(SO_4)$ is minimal, a decrease of 12 cm^{-1}; a similar shift of 10 cm^{-1} is evident for the 227 cm^{-1} assigned to O—Cu—O bending mode.

The doublet at 730 and 720 cm^{-1} in Figs. 2 and 3*a* originating with polyethylene are presented as reference frequencies.

$Cu_3O_2SO_4$ from synthesis

The infrared spectrum of the CuO:$CuSO_4$ (2:1) unannealed mixture is given in Fig. 3*a*, upper line, along with the spectrum of the annealed product of CuO:$CuSO_4$ (2:1), Fig. 3*b* lower line. The infrared spectra of the annealed products of 1:1 and 3:1 mixtures of CuO:$CuSO_4$, not shown, were also recorded. The 1:1 product spectrum always contained intense peaks characteristic of SO_4 of unreacted $CuSO_4$ after twice the anneal time for the 2:1 mixture. The only distinct $CuSO_4$ internal fundamental in the annealed 2:1 product is the weak absorption at 965 cm^{-1}. There must be unreacted CuO present with unreacted $CuSO_4$. There is a striking similarity in the profiles of the spectrum of $Cu_3O_2SO_4$ + CuO, broken line Fig. 1, and of the spectrum of $Cu_3O_2SO_4$ from synthesis 2CuO:$CuSO_4$, lower Fig. 3, in the ν_3 region, excluding the $CuSO_4$ 965 cm^{-1} peak. This similarity lends further support to our interpretation that the brown residue is $Cu_3O_2SO_4$ from reaction [3] and $Cu_3O_2SO_4$ + CuO from reactions [1] and [2*b*]. The synthesized product's color is slightly dark olive-green which after exposure to H_2O vapor at room temperature hydroxylates and turns to light blue. The hydroxylated derivative of this synthesis product gives a complex spectrum which resembles a composite of spectral features found in $Cu_4(OH)_4OSO_4$, $Cu_3(OH)_4SO_4$, and $Cu_3O_2SO_4$. These multiple features suggest the sample contains partially hydroxylated products mixed with unreacted $Cu_3O_2SO_4$. The rate of hydroxylation of brown $Cu_3O_2SO_4$ is extremely fast relative to the olive–green 2:1 oxide–sulfate synthesized product $Cu_3O_2SO_4$. X-ray diffraction shows a complex pattern for the synthesized $Cu_3O_2SO_4$ whereas the dehydroxylated

Can. J. Chem. Downloaded from www.nrcresearchpress.com by 213.222.148.141 on 09/07/12
For personal use only.

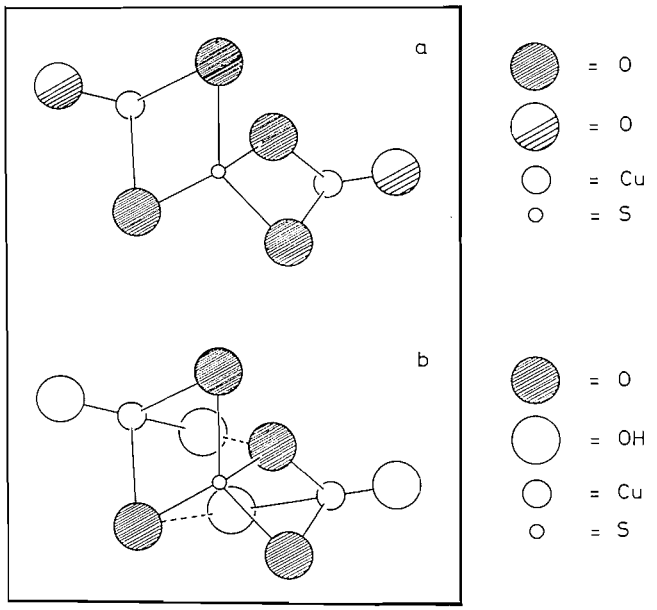

FIG. 4. Postulated configurations of (*a*) $Cu_3O_2SO_4$ and (*b*) $Cu_3(OH)_4SO_4$.

brown analog showed no discernible diffraction peaks. The brown $Cu_3O_2SO_4$ and its hydroxylated derivative $Cu_3(OH)_4SO_4$ required no grinding in making the Nujol mull whereas the synthesized analogous product required considerable grinding to obtain a consistently reproducible mull. All these distinctive features clearly indicate the brown $Cu_3O_2SO_4$ from dehydroxylation to be of high surface area and particle size of colloidal dimensions, possibly a non-crystalline state. It is worthwhile to contrast the infrared spectra of brown $Cu_3O_2SO_4$, Fig. 1, and its brown hydroxylated derivative $Cu_3(OH)_4SO_4$, Fig. 2, with the infrared spectrum of the crystalline compound $Cu_3(OH)_4SO_4$ in the far-infrared region, Fig. 5, Part I. No absorption is detected below 200 cm^{-1} for $Cu_3O_2SO_4$ and 176 cm^{-1} is the lowest absorption observed for its hydroxylated derivative $Cu_3(OH)_4SO_4$. However, crystalline $Cu_3(OH)_4SO_4$ exhibits high activity between 200 cm^{-1} and 60 cm^{-1}, see Part I. The absence of any SO_4 external optic mode activity in $Cu_3O_2SO_4$ and its hydroxylated derivative suggests a non-crystalline state or the $[(CuO)_2SO_4]^{2-}$ entity.

Conclusions

The infrared spectra of the compound $Cu_3O_2SO_4$, identified for the first time and observed from three different preparations, along with its hydroxylated derivative $Cu_3(OH)_4SO_4$ reveal contrasting spectral features and interactions of the SO_4 species. $Cu_3O_2SO_4$ obtained from the parent compounds $Cu_4(OH)_6SO_4$ or $Cu_3(OH)_4SO_4$ exhibits physicochemical properties distinctly different from the direct synthesis product from $2CuO:CuSO_4$. The proposed structure of $Cu_3O_2SO_4$ consists of the copper oxysulfate anion $[(CuO)_2SO_4]^{2-}$ of C_s symmetry with each CuO attached by the Cu to two oxygens of the SO_4 group. Of the 21 infrared-active modes predicted for this anion 17 modes are discernible.

The hydroxylated derivative $Cu_3(OH)_4SO_4$ shows physicochemical and spectral properties distinct from its crystalline analog $Cu_3(OH)_4SO_4$. The clearly resolved and evenly split peaks of the ν_3 mode of SO_4 for the derivative are in obvious contrast to the strong overlap of this mode in crystalline $Cu_3(OH)_4SO_4$ while the frequencies of the other SO_4 modes remain effectively unchanged. The OH frequencies and peak profiles remain unchanged except for the absence of the 750 cm^{-1} absorption peak in the derivative.

Acknowledgment

I am indebted to the National Research Council of Canada for an equipment grant to purchase the infrared spectrometer.

1. M. NATARAJAN and E. A. SECCO. J. Solid State Chem. **47**, 231 (1983).
2. E. A. SECCO. J. Chem. Phys. **79**, 5208 (1983).
3. E. CAZZANNELLI and R. FRECH. J. Chem. Phys. **79**, 2615 (1983).
4. E. A. SECCO. **66**, 000 (1988).
5. H. J. SHARP. J. Chem. Soc. 3761 (1957).
6. K. NAKAMOTO, J. FUJITA, S. TANAKA, and M. KOBAGASHI. J. Am. Chem. Soc. **79**, 4904 (1957).
7. A. PERKINS and M. K. WILSON. J. Phys. Chem. **20**, 1792 (1952).
8. P. RAMAMURTHY and E. A. SECCO. Can. J. Chem. **48**, 3510 (1970).
9. R. DURMAN, V. A. JAYASOORIYA, S. F. A. KETTLE, S. MAHASUVERACHAI, R. MORTIMER, and L.-J. NORRBY. J. Chem. Phys. **81**, 5247 (1984).

Can. J. Chem. Downloaded from www.nrcresearchpress.com by 213.222.148.141 on 09/07/12
For personal use only.

The methylenic sequence conformation in a series of isoelectronic molecules

SUZANNE DEGUIRE AND FRANÇOIS BRISSE

Département de Chimie, Université de Montréal, C.P. 6128, Succ. A, Montréal (P.Q.), Canada H3C 3J7

Received August 6, 1987

SUZANNE DEGUIRE and FRANÇOIS BRISSE. Can. J. Chem. **66**, 341 (1988).

The crystal structures of 1,4-dibenzoylbutane, 2DBC, and ethyleneglycol dithiobenzoate, 2DBS, have been solved by direct methods in order to follow the evolution of the geometry and the conformation of the Y—CH_2—CH_2—Y sequence in the isoelectronic series of C_6H_5—CO—Y—CH_2—CH_2—Y—CO—C_6H_5 where Y = CH_2, NH, O, and S. 2DBC is monoclinic, a = 7.750(4), b = 21.287(6), c = 8.905(2) Å, β = 100.55(3)°, Z = 4. 2DBS is also monoclinic, with a = 5.702(3), b = 16.171(15), c = 8.001(4) Å, β = 98.79(4)°, and Z = 2. Both compounds belong to the $P2_1/n$ space group. The weighted least-squares refinements converged to R_w = 0.049 (2DBC) and 0.043 (2DBS). The conformation of the methylenic sequence is all-*trans* (2DBC) and g^+tg^- for 2DBS (t = *trans*, g = *gauche*). The ir spectra have absorptions at 1467, 1308, and 931 cm^{-1} (2DBC) and at 1408, 1239, and 727 cm^{-1} (2DBS), respectively, characteristic of the *trans* conformation of the Y—CH_2—CH_2—Y sequence. The ^{13}C CP/MAS solid-state nmr spectra of these and other related compounds have been recorded. It is, in turn, possible to propose that the τ torsion angle between the amide group and the methylenic sequence, has a value of 85° in the aromatic polyamide, Nylon 2T.

SUZANNE DEGUIRE et FRANÇOIS BRISSE. Can. J. Chem. **66**, 341 (1988).

Dans le but de suivre l'évolution de la géométrie et de la conformation de la séquence Y—CH_2—CH_2—Y dans la série isoélectronique des composés C_6H_5—CO—Y—CH_2—CH_2—Y—CO—C_6H_5 (dans lesquels Y = CH_2, NH, O et S), on a résolu les structures cristallines du dibenzoyl-1,4 butane (2DBC) et du dithiobenzoate de l'éthylèneglycol (2DBS) par des méthodes directes. Le 2DBC est monoclinique avec a = 7,750(4), b = 21,287(6) et c = 8,905(2) Å, β = 100,55(3)° et Z = 4. Le 2DBS est aussi monoclinique avec a = 5,702(3), b = 16,171(15) et c = 8,001(4) Å, β = 98,79(4)° et Z = 2. Chacun des composés appartient au groupe d'espace $P2_1/n$. Les affinements par la méthode des moindres carrés (matrice entière) convergent vers des valeurs de R_w = 0,049 (2DBC) et 0,043 (2DBS). La conformation de la séquence des groupements méthylènes est complètement-*trans* pour le 2DBC et g^+tg^- pour le 2DBS. Les spectres ir présentent des absorptions à 1467, 1308 et 931 cm^{-1} pour le 2DBC et à 1408, 1239 et 727 cm^{-1} pour le 2DBS; ces absorptions sont caractéristiques de la conformation *trans* pour la séquence Y—CH_2—CH_2—Y. On a aussi enregistré les spectres rmn du ^{13}C CP/MAS à l'état solide de ces composés ainsi que d'autres composés apparentés. Ainsi, on peut proposer que, dans le polyamide aromatique Nylon 2T, l'angle de torsion τ entre le groupement amide et la séquence des groupements méthylènes est de 85°.

[Traduit par la revue]

Introduction

Brisse and co-workers (1–5) first studied the poly(oligomethylene terephthalates) and their model compounds, nDBO. They established that there are structural correlations between the conformation of the polyester and its model compounds. One of these, the polyethylene terephthalate, 2GT, studied by Astbury and Brown (6), Daubeny, Bunn, and Brown (7), Tomashpol'skii and Markova (8), and Arnott and Wonacott (9) has a fiber repeat shorter by 0.15 Å than expected for the all-*trans* zigzag conformation. To remedy this, a short CH_2—CH_2 distance was suggested by Daubeny and co-workers (7) but no clear justification was offered. On the other hand, the crystal structure of ethylene glycol dibenzoate, 2DBO, [C_6H_5—CO—O—$(CH_2)_2$—O—CO—C_6H_5] revealed some unusual geometrical features (1). First of all, the bond distance between methylene groups is significantly shorter than the expected distance for this type of bond and secondly, the two angles involving the CH_2—CH_2 bond are not as open as expected. As a result, the distance between the centers of the aromatic rings of ethylene glycol dibenzoate turns out to be identical to the fiber repeat, c, found by Daubeny *et al.* for poly(ethylene terephthalate). In these compounds, the only molecular interactions are of the van der Waals type.

In order to establish whether the same type of structural correlation exists between a polymer and its related model compounds when held by hydrogen bonds, Palmer and Brisse (10) determined the crystal structure of *N,N'*-ethylene bisbenzamide, 2DBN, [C_6H_5—CO—NH—$(CH_2)_2$—NH—CO—C_6H_5]. This molecule is isoelectronic with ethylene glycol dibenzoate and is a model compound for poly(ethylene terephthalamide) or Nylon 2T. To complete the series, we then decided to investigate two other isoelectronic molecules of ethylene glycol dibenzoate; 1,4-dibenzoylbutane, 2DBC, [C_6H_5—CO—CH_2—$(CH_2)_2$—CH_2—CO—C_6H_5] and ethylene glycol dithiobenzoate, 2DBS, [C_6H_5—CO—S—$(CH_2)_2$—S—CO—C_6H_5] where the oxygen atom is replaced by a CH_2 group and a sulfur atom, respectively. A comparative study of these four isoelectronic compounds will serve to show the influence of the adjacent atoms of the CH_2—CH_2 group upon the geometry and the conformation of the glycol segment.

Combining ^{13}C CP/MAS solid state nmr spectra of these and other related model compounds will yield some useful structural information on the parent polymers. In this manner 2DBO and poly(ethylene terephthalate) are related and so are 2DBN and the aromatic polyamide, Nylon 2T.

Experimental

1,4-Dibenzoylbutane was purchased from Aldrich Co. Ltd. Crystals were obtained by slow evaporation of a chloroform–ether 50:50 mixture.

Ethylene glycol dithiobenzoate was prepared by dissolving thiobenzoic acid and KOH in methanol (100 mL). The solution was cooled to 0°C. 1,2-Dibromoethane was then added. The solution was stirred under reflux for 8 h at 65°C. These steps are summarized by the equation:

$$2C_6H_5\text{-CO-SH} + 2KOH + \text{Br-}CH_2\text{-}CH_2\text{-Br} \rightarrow C_6H_5\text{-CO-S-}CH_2\text{-}CH_2\text{-S-CO-}C_6H_5 + 2H_2O + 2KBr$$

KBr was then filtered out and ethylene glycol dithiobenzoate was

Can. J. Chem. Downloaded from www.nrcresearchpress.com by 213.222.148.141 on 09/07/12
For personal use only.

Can. J. Chem. Downloaded from www.nrcresearchpress.com by 213.222.148.141 on 09/07/12
For personal use only.

TABLE 1. Crystal data of interest

Parameter	Value	
	2DBC	2DBS
Molecular formula	$C_{18}H_{18}O_2$	$C_{16}H_{14}O_2S_2$
Molecular weight	266.34	302.42
$F(000)$	552	316
Melting point (K)	382	366
Crystal system	Monoclinic	Monoclinic
a (Å)	7.750(4)	5.702(3)
b (Å)	21.287(6)	16.171(15)
c (Å)	8.905(2)	8.001(4)
β (deg)	100.55(3)	98.79(4)
V (Å^3)	1444.3	729.0
d_{obs} (g cm^{-3})	1.24	1.41
d_{calc}	1.225	1.377
Z	4	2
Space group	$P2_1/n$	$P2_1/n$
μ(Kα) (cm^{-1})	0.731	3.470
T (°C)	20	−140
Crystal size (mm)	0.55 × 0.22 × 0.11	0.60 × 0.24 × 0.03

TABLE 2. Summary of data collection and refinement

Parameter	Value	
	2DBC	2DBS
Scan range (deg)	1.0 + 0.35 tan θ	1.0 + 0.35 tan θ
Scan rate (deg min^{-1})	1.01	1.69
$2\theta_{max}$ (deg)	45.0	50.0
hkl ranges h	0, 8	0, 6
k	0, 22	0, 19
l	−9, 9	−9, 9
Number of reflections, measured	1892	1286
Number of reflections, observed	1058	898
when $I \geq k\sigma(I)$, k =	1.96	1.96
$R = \Sigma\|\Delta F\|/\Sigma\|F_o\|$	0.050	0.044
$R_w = [\Sigma w\Delta F^2/\Sigma F_o^2]^{1/2}$	0.049	0.043
$S = [\Sigma w\Delta F^2/(m-n)]^{1/2}$	1.46	1.20
$(\text{Displacement/error})_{max}$	0.20	0.08
$(\text{Displacement/error})_{average}$	0.07	0.02
Extreme fluctuations of residual electron density (e Å^{-3})	−0.14, 0.13	−0.26, 0.26

obtained by concentration of the filtrate. Good crystals of ethylene glycol dithiobenzoate were obtained by slow evaporation of an ethanol solution.

X-ray diffraction

A well-developed single crystal of each compound was mounted on a Nonius-CAD4 diffractometer. The unit cell dimensions and the orientation matrix have been obtained by a least-squares refinement of the angular settings of 25 well-centered reflections. Crystal data of interest are given in Table 1. The densities were measured by the flotation method using an aqueous $ZnCl_2$ solution. The intensities were collected by the $\omega/2\theta$ scan technique (Table 2). The intensities of seven reference reflections for 2DBC and of six reference reflections for 2DBS measured every hour showed a maximum random variation of 3.0% for 2DBC and 4.3% for 2DBS over the duration of the data collection. The orientation of the crystals was verified after every 100 measurements. The diffracted intensities were corrected for Lorentz and polarization effects, but since the absorption coefficient for the Mo radiation (λ = 0.71069 Å) was small, no absorption correction was applied to either set of data.[1]

TABLE 3.

(*a*) Fractional atomic coordinates and their esd's (×10^4 for O and C), U_{eq} (×10^4 for O and C) for 1,4-dibenzoylbutane

Atom	X	Y	Z	U_{eq}
O(1)	1675(4)	2177(1)	4281(3)	838
O(11)	−2328(3)	328(1)	−1972(3)	821
C(1)	2209(4)	1356(1)	6066(4)	503
C(2)	1890(4)	748(2)	6487(4)	611
C(3)	2532(5)	527(2)	7931(4)	759
C(4)	3550(5)	902(2)	8979(4)	788
C(5)	3897(5)	1507(2)	8596(4)	765
C(6)	3219(5)	1728(2)	7159(4)	630
C(7)	1533(5)	1616(2)	4513(4)	572
C(Y)	669(5)	1183(2)	3281(4)	576
C(8)	218(5)	1477(2)	1708(4)	653
C(11)	−2841(4)	1128(1)	−3818(4)	519
C(12)	−2775(5)	1764(2)	−4180(4)	677
C(13)	−3498(5)	1971(2)	−5626(4)	785
C(14)	−4291(5)	1558(2)	−6722(4)	800
C(15)	−4349(5)	927(2)	−6374(4)	785
C(16)	−3621(5)	717(2)	−4941(4)	662
C(17)	−2148(4)	882(2)	−2243(4)	569
C(1Y)	−1231(5)	1323(1)	−1039(4)	567
C(18)	−745(4)	1031(2)	522(4)	589

(*b*) Fractional atomic coordinates and their esd's (×10^5 for S; ×10^4 for O and C), U_{eq} (×10^4 for S, O, and C) for ethylene glycol dithiobenzoate

Atom	X	Y	Z	U_{eq}
S(1)	11711(16)	1338(6)	27371(11)	312
O(1)	4537(4)	864(2)	1370(3)	315
C(1)	4600(6)	1205(2)	4271(4)	230
C(2)	3503(6)	1143(2)	5705(4)	291
C(3)	4418(7)	1551(2)	7168(5)	354
C(4)	6432(7)	2037(2)	7220(5)	356
C(5)	7519(6)	2105(2)	5798(5)	318
C(6)	6621(6)	1691(2)	4334(4)	270
C(7)	3652(5)	779(2)	2646(4)	229
C(8)	748(6)	−284(2)	610(4)	272

The structures were solved using the multisolution program MULTAN. All non-hydrogen atoms were found on the first E-map. The hydrogen atoms were located on subsequent difference Fourier syntheses. The weighted least-squares refinement, minimizing $\Sigma w(|F_o| - |F_c|)^2$, was carried out with anisotropic temperature factors for S, O, and C atoms and isotropic temperature factors for H atoms. The details of the least-squares refinement are given in Table 2 for the two compounds.

The general position of the $P2_1/n$ space group requires that eight 2DBS molecules be present within a unit cell. However, since the observed density of 2DBS allows for only 4 molecules, these must sit on crystallographic centers of symmetry of the unit cell.

The scattering curves for non-hydrogen atoms were taken from ref. 15 and those for H-atoms from ref. 16. The anomalous dispersion correction for S was taken from ref. 17.

[1]The programs used here are modified versions of NRC-2, data reduction; NRC-10, bond distances and angles; and NRC-22, mean planes; FORDAP, Fourier and Patterson maps (A. Zalkin); MULTAN, multisolution program; NUCLS, least-squares refinement; and ORTEP, stereodrawings (11–14).

TABLE 4. Comparison of the bond distances and angles of the four isoelectronic molecules

	Distance (Å)					
Bond	2DBC Y = CH_2 esd = 0.004–0.006		2DBN Y = NH esd = 0.006	2DBO Y = O esd = 0.003		2DBS Y = S esd = 0.003–0.005
C(1)—C(2)	1.382	1.395	1.390	1.387	1.391	1.392
C(2)—C(3)	1.374	1.379	1.364	1.374	1.382	1.375
C(3)—C(4)	1.364	1.372	1.383	1.375	1.381	1.387
C(4)—C(5)	1.371	1.381	1.371	1.377	1.386	1.381
C(5)—C(6)	1.374	1.372	1.372	1.379	1.376	1.378
C(6)—C(1)	1.381	1.382	1.387	1.381	1.387	1.389
C(1)—C(7)	1.493	1.501	1.490	1.478	1.476	1.497
C(7)—O(1)	1.220	1.217	1.235	1.209	1.202	1.214
C(7)—Y	1.494	1.502	1.343	1.339	1.339	1.768
Y—C(8)	1.515	1.506	1.445	1.442	1.441	1.813
C(8)—C(8′)	1.512		1.522	1.499		1.506
	Angle (deg)					
Bonds	2DBC Y = CH_2 esd = 0.3–0.4		2DBN Y = NH esd = 0.4	2DBO Y = O esd = 0.2		2DBS Y = S esd = 0.2–0.3
C(1)—C(2)—C(3)	121.5	120.0	121.3	120.1	119.8	120.5
C(2)—C(3)—C(4)	120.3	120.8	120.4	120.3	120.3	120.1
C(3)—C(4)—C(5)	119.6	119.5	119.1	119.8	119.7	119.6
C(4)—C(5)—C(6)	119.6	120.1	120.7	120.5	120.5	120.4
C(5)—C(6)—C(1)	122.0	121.2	120.9	119.8	119.8	120.3
C(6)—C(1)—C(2)	116.9	118.5	117.7	119.8	119.9	119.1
C(1)—C(7)—O(1)	119.5	119.3	121.5	124.6	124.1	122.5
C(1)—C(7)—Y	119.1	119.4	117.7	113.1	112.8	114.9
O(1)—C(7)—Y	121.4	121.4	120.8	122.3	122.6	122.7
C(7)—Y—C(8)	114.9	114.0	122.4	115.9	115.5	100.0
Y—C(8)—C(8′)	112.8	113.2	112.0	104.7	105.2	111.2

Infrared spectroscopy

The ir spectra were recorded from KBr pellets on an FTIR Nicolet 7199 equipped with a He–Ne class II laser with a resolution of 2 cm^{-1} and 200 scans per spectra, while the background noise spectra were signal-averaged with 100 scans.

^{13}C CP/MAS nmr study

The ^{13}C CP/MAS solid-state nmr spectra were recorded with a Varian CXP 300 MHz spectrometer at a frequency of 75.431 MHz. A contact time of 2.0 to 2.5 μs was used with a delay of about 4 s between sequences (specific details are available as supplementary materials).[2] The number of contacts varied between 773 and 1500. The chemical shifts are given with respect to that of powdered hexamethylbenzene whose aromatic signal is at 132.1 ppm.

Results and discussion

Structural considerations

The final positional parameters and their standard deviations are presented in Table 3. The atomic numbering is shown in Fig. 1 and the molecular structures are presented as stereopairs in Fig. 2. The packing of the molecules is shown in Fig. 3. The bond distances and angles of the 2DBC and 2DBS are given in Table 4 and are compared to the corresponding quantities for 2DBO and 2DBN.

The benzoate groups

The C(sp^2)—C(sp^2) bond distances in the benzene rings average 1.374 and 1.380 Å for 2DBC, 1.378 Å for 2DBN, 1.379 and 1.384 Å for 2DBO, and 1.384 Å for 2DBS. They are very close to the mean bond length of 1.379 Å computed from 78 C(sp^2)—C(sp^2) distances by Brisse and Sygusch (18). The average angle in each of the six-membered rings is 120°. In the case of 2DBC, 2DBN, and 2DBS, it is observed that the angle C(6)—C(1)—C(2) deviates the most from the mean value. This feature may be explained by the geometry of the O=C—Y group. If we look at the value of the angle C(1)—C(7)—O(1), we see that it varies from 119.3 to 124.6° from one compound to another. The smaller this angle is, the closer the carbonyl oxygen and a phenyl hydrogen are. In order to minimize the interactions between the carbonyl group and the hydrogen atom on the C(6) atom, the C(6)—C(1)—C(2) angle tends to decrease. At the same time, the bond distances in the phenyl rings also reflect these repulsions between the H atom on C(6) and O(1). We observe that the bond distances C(1)—C(2) and C(6)—C(1) are the longest of all the aromatic ring bond distances. This is so in order to minimize the interactions between the hydrogen atom and the carbonyl group. In a

[2]Complete set of material may be purchased from the Depository of Unpublished Data, CISTI, National Research Council of Canada, Ottawa, Ont., Canada K1A 0S2.

Can. J. Chem. Downloaded from www.nrcresearchpress.com by 213.222.148.141 on 09/07/12
For personal use only.

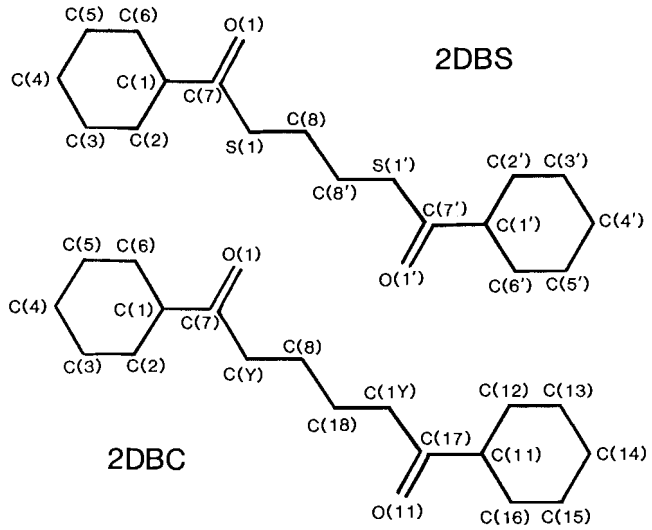

FIG. 1. Schematic representations of the molecules and atomic numbering.

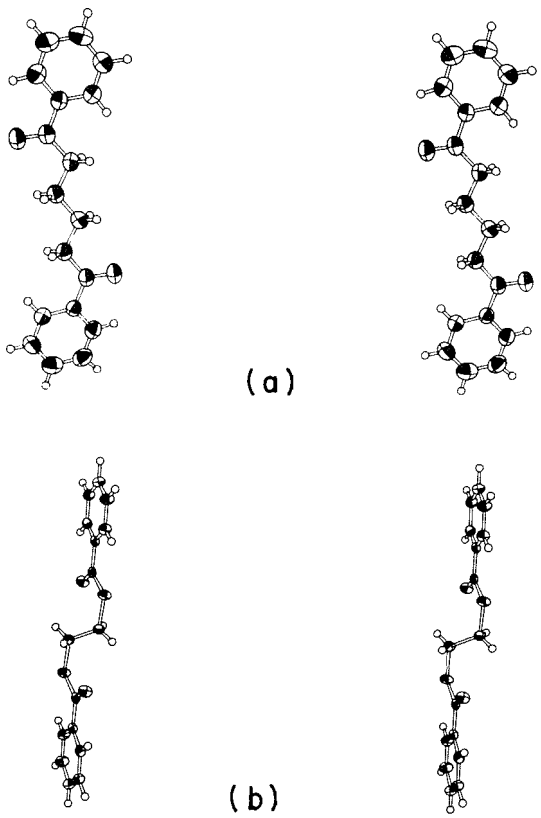

FIG. 2. Stereopairs of (*a*) 1,4-dibenzoylbutane (2DBC) and (*b*) ethyleneglycol dithiobenzoate (2DBS).

molecule of 2DBC, the two aromatic ring planes form an angle of 10° with each other while they are exactly parallel to one another in 2DBS since this molecule sits on a crystallographic center of symmetry.

The methylenic sequence

The observed CH_2—CH_2 bond lengths are significantly shorter than the expected C(sp^3)—C(sp^3) distance of 1.541(3) Å (19). A study undertaken by Brisse, Molhant, and Pérez (20) has shown the influence of the X and Y atoms on the CH_2—CH_2 distance in a sequence X—CH_2—CH_2—Y. When X = Y = O, X = O and Y = NH^+ or CH_3, X = S and Y = Cl, the CH_2—CH_2 bond length varies from 1.460 to 1.506 Å. In the case where X = NH_2 and Y = CH_3, no significant difference from the expected value of 1.541(3) Å was observed. The case of 2DBS, where X = Y = S, completes these results with a CH_2—CH_2 bond distance of 1.506(5) Å. For 2DBC, for which X = Y = CH_2, the observed CH_2—CH_2 bond length of 1.512(5) Å is also shorter than the expected one. For 2DBN, for which X = Y = NH, the CH_2—CH_2 bond distance of 1.522(6) Å is shorter than expected but it is the largest of all. The Y—CH_2—CH_2 bond angles is 2DBC, 2DBN, and 2DBS which average 112.2° are normal but differ significantly from the angle value of 2DBO whose average is 105.0°. These different effects seem to be independent of the value of the Y—C—C—Y torsion angle.

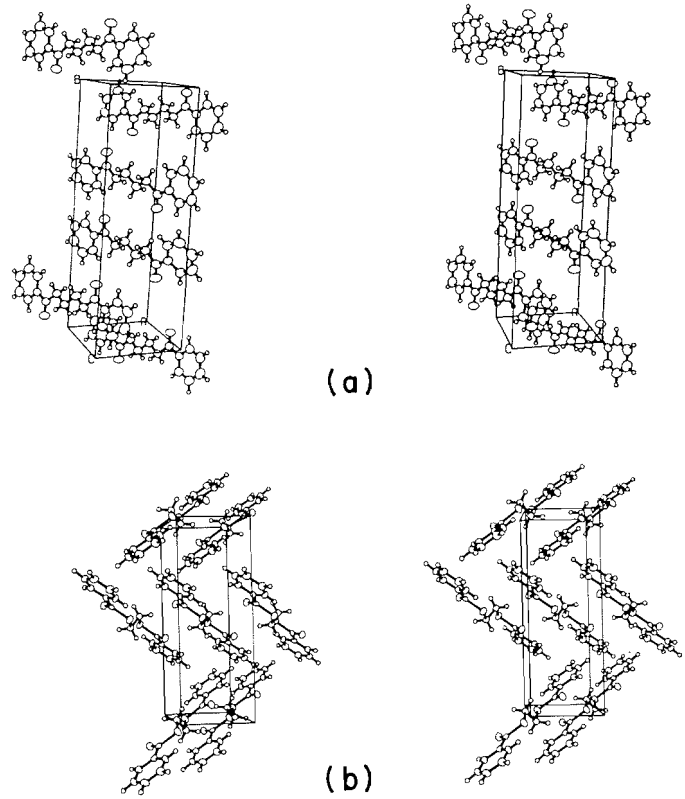

FIG. 3. Stereopairs showing the packing of the molecules (*a*) 2DBC and (*b*) 2DBS.

The conformational angles for the isoelectronic compounds correspond to the calculated conformations which are considered energetically stable. The torsional angles which characterize the methylenic sequence are defined by ϕ_1 = C(7)—Y—C(8)—C(8′), ϕ_2 = Y—C(8)—C(8′)—Y′, and ϕ_1' = C(8)—C(8′)—Y′—C(7′). The values of these torsional angles are given in Table 5. We observe two types of conformations: all-*trans* and *gauche*$^+$ *trans gauche*$^-$. Poulin-Dandurand (21) has calculated the conformational energy of an isolated molecule of ethylene glycol dibenzoate, 2DBO. The two conformations observed in the isoelectronic compounds correspond to some of the calculated energy minima. Indeed, the second energy minimum (21) is associated with the conformation observed for 2DBC (and 2DBO), while 2DBS (and 2DBN) have conformations near that calculated for the fifth energy minimum. At this point, it is worth noting that although the

Can. J. Chem. Downloaded from www.nrcresearchpress.com by 213.222.148.141 on 09/07/12
For personal use only.

TABLE 5. Comparison of the torsion angles of interest in the isoelectronic series of molecules

	2DBC Y = CH_2	2DBN Y = NH	2DBO Y = O	2DBS Y = S
ϕ_1 = C(7)—Y—C(8)—C(8′)	−176.7(3)	88.8(4)	175.6(5)	+85.5(3)
ϕ_2 = Y—C(8)—C(8′)—Y′	178.9(3)	180	−172.8(6)	180
ϕ_1' = C(8)—C(8′)—Y′—C(7′)	+178.5(3)	$-\phi_1$	176.1(4)	$-\phi_1$
Conformation	*ttt*	g^+tg^-	*ttt*	g^+tg^-
Equivalent fiber repeat (Å)	11.60	10.91	10.75	11.58

TABLE 6. Vibrational modes for the isoelectronic compounds

	CH_2 bending			CH_2 wagging			CH_2 rocking			
Compound	Observed	*trans*	*gauche*	Observed	*trans*	*gauche*	Observed	*trans*	*gauche*	Reference
2DBC	1467	1470	1450	1369	1375	1350	966	962	917	29
2DBN	1468	1464	1474	1348	1367	1360	888	877	817	26, 37
2DBO	1485	1470	1450	1339	1340	1370	856	845	898	29
2DBS	1408	1421	1425–1410	1239	1219	1294–1277	727	737	974–975	30

two halves of each molecule are chemically identical, they are crystallographically equivalent only for the two molecules with the *gauche*$^+$ *trans gauche*$^-$ conformation, i.e., 2DBN and 2DBS. The two moieties of the two other molecules, 2DBO and 2DBC, with the nearly all-*trans* conformation are only approximately equivalent.

We have undertaken a bibliographic search of the Cambridge Data File to locate molecules with the C—S—CH_2—CH_2—S—C segment. Only two of them were not macrocyclic polyethers or cyclic molecules: ethylene dithiodiacetic acid (22) and ethylene dithiocyanate (23). In both cases the conformations were *gauche*$^+$ *trans gauche*$^-$ similar to that of 2DBS.

Packing of the molecules

For 2DBC, 2DBO, and 2DBS, none of the intermolecular contacts are less than 3.30 Å, therefore these molecules are held in the crystal by van der Waals forces only. In 2DBN, each molecule is held to four other ones by hydrogen bonds.

In 2DBN, 2DBO, and 2DBS, the molecules are packed in a herring-bone manner while the molecules of 2DBC place themselves parallel to one another.

Infrared spectra

Since our interest was in the conformation of the methylenic sequence, the relevant absorption bands are those of methylene bending, wagging, and rocking. The FTIR bands observed for these vibrational modes for the isoelectronic compounds are compared in Table 6.

For the 2DBC, the band assignment follows the work of Snyder *et al.* (24, 25) for a *trans* conformation for the CH_2—CH_2—CH_2—CH_2 angle.

For the molecule 1,2-ethanediamine, NH_2—CH_2—CH_2—NH_2, Theophanides and Kong (26) observed absorption bands at 1464, 1367, and 877 cm^{-1} for a *trans* conformation of the molecule. They assigned them to the methylene bending, wagging, and rocking, respectively. The corresponding absorption bands for a *gauche* conformation have been identified by Borring and Rasmussen (35). For the 2DBN, the bond assignment and corresponds to the observed *trans* conformation.

For the 2DBO, the three bands observed were associated to the *trans* conformation as proposed by Boitsov and Gotlib (27), Schneider *et al.* (28), and Ward and Wilding (29). All of them assigned the absorption bands at 1470, 1340, and 845 cm^{-1} to the methylene bending, wagging, and rocking of a segment O—CH_2—CH_2—O with the *trans* conformation.

In the case of 2DBS, we compared the infrared spectrum with that of 1,2-ethanedithiol (30–32). All the authors assigned the absorption bands at 1421, 1219, and 737 cm^{-1} to the methylene bending, wagging, and rocking of the isomer with a *trans* conformation. Since the spectrum of 2DBS has absorption bands at 1408, 1239, and 727 cm^{-1}, it supports a *trans* conformation for the S—CH_2—CH_2—S segment.

Therefore, in the four cases, the absorptions for the vibration modes of the methylene groups support a *trans* conformation for the sequence Y—CH_2—CH_2—Y.

^{13}C CP/MAS nmr

The ^{13}C CP/MAS solid-state nmr spectra of 2DBC, 2DBO, 2DBN, and 2DBS are shown in Fig. 4 while the chemical shifts are listed in Table 7. Depending on the compound, the aromatic carbons appear with one to four peaks in the range 128.4–136.8 ppm. The signals for C(7) are either single (2DBS) or doubled peaks (2DBC, 2DBN, 2DBO). Since the 2DBS molecule lies on a crystallographic center of symmetry, there will be only one signal for each pair of centrosymmetrically related atoms. The nmr signals of C(7) and C(8) of the 2DBN molecule, which is also centrosymmetric, are doubled because of the quadrupolar moment of the adjacent nitrogen atom which is not averaged out entirely by the rotation of the sample. The other two molecules, 2DBC and 2DBO, do not have any symmetry element. Thus, the nmr signals for C(7) and C(8) will be doubled.

The chemical shift of a given atom may be affected by the γ-*gauche* effect and/or molecular packing interactions. In this series of compounds, the chemical shift of C(8) varies from 22.9 for 2DBC to 62.5 ppm for 2DBO but this is mostly due to the nature of the Y atom. Indeed, these values are linearly related to the electronegativity (33) of Y (see Fig. 5). The higher the electronegativity of Y the more deshielded C(8) will be. A similar relationship has already been reported (34) for

Can. J. Chem. Downloaded from www.nrcresearchpress.com by 213.222.148.141 on 09/07/12
For personal use only.

Can. J. Chem. Downloaded from www.nrcresearchpress.com by 213.222.148.141 on 09/07/12
For personal use only.

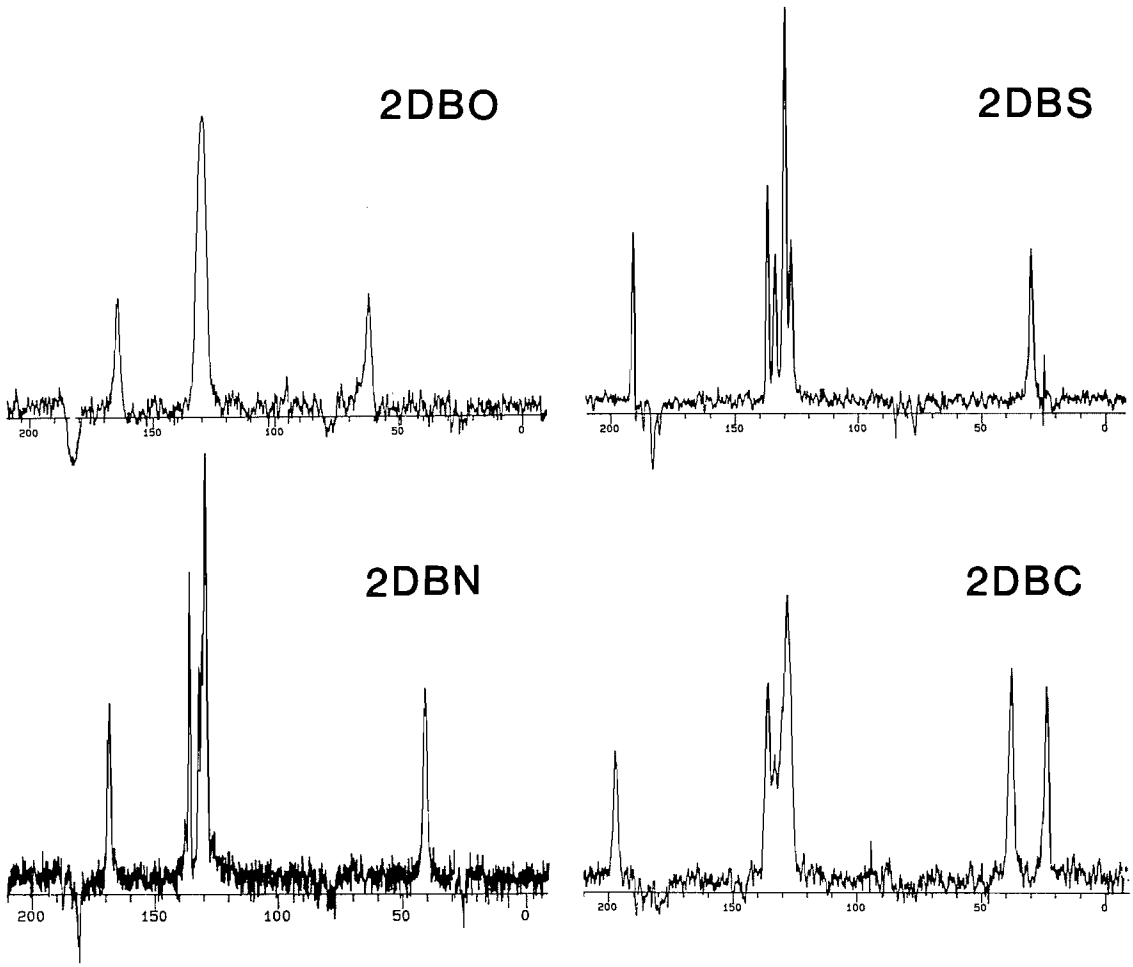

FIG. 4. ^{13}C CP/MAS nmr spectra of the four isoelectronic compounds.

TABLE 7. ^{13}C solid-state chemical shifts, ppm, for the four isoelectronic molecules

	Chemical shift			
Atoms	2DBC	2DBN	2DBO	2DBS
C(1)	135.9	135.5	129.4	133.4
C(2)	128.4	129.1	129.4	129.8
C(3)	128.4	130.3	129.4	127.0
C(4)	133.3	131.8	129.4	136.8
C(5)	128.4	130.3	129.4	127.0
C(6)	128.4	129.1	129.4	129.8
C(7)	196.9	167.9	163.4	190.6
	197.7	168.7	164.0	
C(8)	23.9	40.3	61.9	29.8
	22.9	41.0	62.5	
C(Y)	38.2			

the uracil molecule where the 5-position has been variously substituted.

However, we may compare the chemical shifts of C(8) in 2DBO with the values reported for a series of *para*-substituted 2DBO molecules whose structures have been established by single crystal X-ray diffractometry. The torsion angles that may affect the chemical shift of C(8) (γ-*gauche* effect) are all nearly *trans* no matter what the *para* substituent (X) may be. The chemical shifts vary between 60.2 (X = Ph) and 65.0 ppm (X = Cl). These values compare well with those recorded here for the unsubstituted molecule (61.9 and 62.5 ppm).

In the case of 2DBN, another related molecule, *N,N'*-ethylene bis(*para*-chlorobenzamide), and the parent polymer, Nylon 2T or poly(ethylene terephthalamide) have also been examined by solid state nmr. The crystal structure of the *para*-chloro derivative reveals that its molecular conformation is similar to that of 2DBN. The torsion angle of interest, τ, is 88.8(4)° for 2DBN and 82.0(5)° for the *para*-chloro derivative. Since these two compounds also have the same molecular packing, one may assign the chemical shift of 40.5 ppm (average) for C(8) to a τ torsion angle of about 85°.

By extrapolation to Nylon 2T, whose structure has not yet been established, we propose that in this aromatic polyamide, τ has a value near 85°. This is supported by the comparable value of the chemical shift of C(7). They are 168.3 and 167.7 ppm (average) in 2DBN and the *para*-chloro derivative, respectively, and 168.4 ppm for Nylon 2T. Furthermore, it is quite likely that the packing modes in the model compounds and the parent polyamide are similar.

Conclusion

The study of these four isoelectronic compounds had served to establish the following. (*1*) The CH_2—CH_2 bond length is always shorter than the expected C(sp^3)—C(sp^3) distance. Its value ranges from 1.499(3) to 1.522(6) Å. (*2*) The Y—CH_2—CH_2 bond angles average 112.2° for 2DBC, 2DBN,

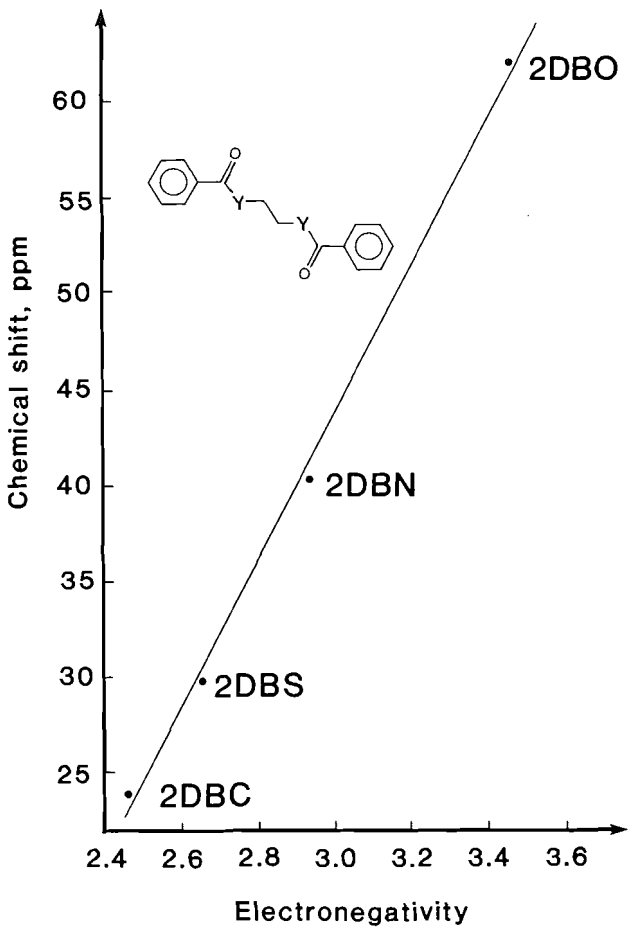

FIG. 5. Plot of the ^{13}C chemical shift of C(8) atom vs. the electronegativity of Y in —Y—CH_2—CH_2—Y—.

and 2DBS. In 2DBO, these angles average 105.0°. (*3*) We observe two types of conformation for the sequence C(7)—Y—C(8)—C(8′)—Y′—C(7′): all-*trans* and *gauche*$^+$ *trans gauche*$^-$.

Acknowledgements

We wish to thank the Natural Sciences and Engineering Research Council of Canada and the Fonds pour la Formation de Chercheurs et l'Aide à la Recherche for their financial support. We also thank Mr. M. J. Olivier for the X-ray data collections.

1. S. PÉREZ and F. BRISSE. Acta Crystallogr. Sect. B, **32**, 470 (1976).
2. S. PÉREZ and F. BRISSE. Can. J. Chem. **53**, 3551 (1975).
3. S. PÉREZ and F. BRISSE. Acta Crystallogr. Sect. B, **33**, 3259 (1977).
4. S. PÉREZ and F. BRISSE. Acta Crystallogr. Sect. B, **32**, 1518 (1976).
5. S. PÉREZ and F. BRISSE. Acta Crystallogr. Sect B, **33**, 1673 (1977).
6. W. T. ASTBURY and C. J. BROWN. Nature, **158**, 871 (1946).
7. R. P. DE DAUBENY, C. W. BUNN, and C. J. BROWN. Proc. R. Soc. A**226**, 531 (1954).
8. Y. Y. TOMASHPOL'SKII and G. S. MARKOVA. Polym. Sci. USSR, **6**, 316 (1964).
9. S. ARNOTT and A. J. WONACOTT. Polymer, **7**, 157 (1966).
10. A. PALMER and F. BRISSE. Acta Crystallogr. Sect. B, **36**, 1447 (1980).
11. F. R. AHMED, S. R. HALL, M. E. PIPPY, and C. P. HUBER. J. Appl. Crystallogr. **6**, 309 (1973).
12. P. MAIN, S. J. FISKE, S. E. HULL, L. LESSINGER, G. GERMAIN, J.-P. DECLERCQ, and M. M. WOOLFSON. MULTAN 80. A System of Computer Program for the Automatic Solution of Crystal Structures from X-ray Diffraction Data. Universities of York, England, and Louvain, Belgium. 1980.
13. R. J. DOEDENS and J. A. IBERS. Inorg. Chem. **6**, 204 (1967).
14. C. K. JOHNSON. ORTEP, Report ORNL-3794. Oak Ridge National Laboratory, Tennessee, 1965.
15. D. T. CROMER and J. B. MANN. Acta Crystallogr. Sect. A, **24**, 321 (1968).
16. R. F. STEWART, E. R. DAVIDSON, and W. T. SIMPSON. J. Chem. Phys. **42**, 3175 (1965).
17. D. T. CROMER and D. LIBERMAN. J. Chem. Phys. **53**, 1891 (1970).
18. F. BRISSE and J. SYGUSCH. Acta Crystallogr. Sect. B, **30**, 480 (1974).
19. Molecular structures and dimensions. International Union of Crystallography, Cambridge. 1972.
20. F. BRISSE, N. MOLHANT, and S. PÉREZ. Acta Crystallogr. Sect. B, **35**, 1825 (1979).
21. S. POULIN-DANDURAND. M.Sc. Thesis, Université du Québec à Montréal. 1978.
22. L. M. SHKOL'NIKOVA, T. N. SAFONOVA, M. A. PORAI-KOSHITS, N. M. DYATLOVA, and Y. PODLAGA. Zh. Strukt. Khim. **23**, 96 (1982).
23. R. BRINGELAND and O. FOSS. Acta Chem. Scand. **12**, 79 (1958).
24. R. G. SNYDER, S. L. HSU, and S. KRIMM. Spectrochim. Acta, Part A, **34**, 395 (1978).
25. R. G. SNYDER and J. H. SCHACHTSCHNEIDER. Spectrochim. Acta, **19**, 85 (1963).
26. T. THEOPHANIDES and P. C. KONG. Inorg. Chim. Acta, **5**, 485 (1971).
27. V. B. BOITSOV and Y. Y. GOTLIB. Opt. Spectrosc. **15**, 116 (1963).
28. B. SCHNEIDER, P. SEDLACEK, J. STOKR, D. DOSKOCILOVA, and J. LOVY. Collect. Czech. Chem. Commun. **46**, 1913 (1981).
29. I. M. WARD and M. A. WILDING. Polymer, **18**, 327 (1977).
30. K. NAHARA, S. NAKAYAMA, F. WATARI, and K. AIDA. J. Inorg. Nucl. Chem. **35**, 2610 (1973).
31. D. WELTI and D. WHITTAKER. J. Chem. Soc. 4372 (1962).
32. M. HAYASHI, Y. SHIRO, T. OSHIMA, and H. MURATA. Bull. Chem. Soc. Jpn. **38**, 1734 (1965).
33. R. T. SANDERSON. Chemical periodicity. Rheinhold Publishing Corporation, New York. 1960. p. 34.
34. A. R. TARPLEY and J. H. GOLDSTEIN. J. Am. Chem. Soc. **93**, 3573 (1971).
35. A.-L. BORRING and K. RASMUSSEN. Spectrochim. Acta, **31A**, 889 (1975).

Can. J. Chem. Downloaded from www.nrcresearchpress.com by 213.222.148.141 on 09/07/12
For personal use only.

Magnetism and structure in a series of halogen and hydroxo-bridged binuclear copper(II) diazine complexes. Structure of a dibromobridged derivative $[Cu_2(C_{14}H_{10}N_4S_2)Br_4]$[1]

LAURENCE K. THOMPSON[2] AND SANAT K. MANDAL
Department of Chemistry, Memorial University of Newfoundland, St. John's, Nfld., Canada A1B 3X7

AND

JEAN-PIERRE CHARLAND AND ERIC J. GABE
Division of Chemistry, National Research Council of Canada, Ottawa, Ont., Canada K1A 0R6

Received June 24, 1987

LAURENCE K. THOMPSON, SANAT K. MANDAL, JEAN-PIERRE CHARLAND, and ERIC J. GABE. Can. J. Chem. **66**, 348 (1988).

The ligand PTP (3,6-bis(2-pyridylthio)pyridazine) generates both hydroxo- and halogeno-bridged, square-pyramidal, binuclear copper(II) complexes ($[Cu_2(PTP)X_4]$ (X = Cl (**I**), Br (**II**)); $[Cu_2(PTP)(OH)X_3]$ (X = Cl (**IV**), Br (**V**)), which are antiferromagnetically coupled. The hydroxo-bridged derivatives are more strongly coupled than those with just halogen bridges and within each pair of complexes substantially increased spin exchange is observed for the bromo-derivatives ($-2J$ = 130.5 ± 0.4 (**I**), 243.5 ± 0.3 (**II**), 294 ± 3 (**IV**), 326 ± 6 (**V**) cm^{-1}). A related halogen-bridged derivative $[Cu_2(PAP46Me)Cl_4]$ (**III**) (PAP46Me = 1,4-di(4,6-dimethyl-2-pyridylamino)phthalazine) exhibits much weaker spin exchange associated with the diminished superexchange capacity of the phthalazine bridge compared with pyridazine ($-2J$ = 55 ± 0.1 cm^{-1}). An X-ray study on $[Cu_2(PTP)Br_4]$ reveals an asymmetric tribridged structure involving a pyridazine and two bromo-bridges with a copper–copper separation of 3.318(3) Å, one relatively short terminal copper–bromine bond (2.375(3), 2.398(3) Å), and a short and long copper–bromine bridging contact (2.380(3), 2.801(3); 2.414(3), 2.766(3) Å) per copper. The complex formed green crystals with a = 11.1042(18), b = 15.6554(10), c = 12.6058(14) Å, β = 113.485(11)°, $P2_1/c$, Z = 4, R_f = 0.045.

LAURENCE K. THOMPSON, SANAT K. MANDAL, JEAN-PIERRE CHARLAND et ERIC J. GABE. Can. J. Chem. **66**, 348 (1988).

Le ligand PTP (bis(pyridylthio-2)-3,6 pyridazine) fournit des complexes binucléaires du cuivre(II) ($[Cu_2(PTP)X_4]$ dans lesquels X = Cl (**I**) ou Br (**II**); $[Cu_2(PTP)(OH)X_3]$ dans lesquels X = Cl (**IV**) ou Br (**V**)) qui sont pyramidaux à base carrée, qui sont pontés par des groupements hydroxo ou halogéno et qui sont couplés d'une façon antiferromagnétique. Le couplage des dérivés qui sont pontés par le groupement hydroxy est plus fort que celui qu'on retrouve dans les dérivés qui ne sont pontés que par un halogène; de plus, dans chacune des paires de complexes, on observe une augmentation sensible de l'échange de spin pour les dérivés bromés ($-2J$ = 130,5 ± 0,4 (**I**), 243,5 ± 0,3 (**II**), 294 ± 3 (**IV**) et 326 ± 6 (**V**) cm^{-1}). Un dérivé apparenté ponté par un halogène, le $Cu_2(PAPMe\text{-}4,6)Cl_4$ (**III**) dans lequel le PAPMe-4,6 représente le di(diméthyl-4,6 pyridylamino-2)-1,4 phtalazine, présente un échange de spin qui est beaucoup plus faible et cette caractéristique est associée avec une capacité de superéchange qui est diminuée dans le cas de la phtalazine par rapport à la pyridazine ($-2J$ = 55 ± 0,1 cm^{-1}). Une étude par diffraction des rayons-X effectuée sur le $[Cu_2(PTP)Br_4]$ révèle la présence d'une structure asymétrique tripontée impliquant une pyridazine et deux bromes agissant comme ponts; la séparation cuivre–cuivre est de 3,318(3) Å et on observe une liaison cuivre–brome terminale relativement courte (2,375(3) et 2,398(3) Å) ainsi qu'un contact de pontage cuivre–brome court et un long (2,380(3), 3,801(3); 2,414(3), 2,766(2) Å) par cuivre. Le complexe forme des cristaux verts avec a = 11,1042(18), b = 15,6554(10) et c = 12,6058(14) Å, β = 113,485(11)°, $P2_1/c$, Z = 4 et R_f = 0,045.

[Traduit par la revue]

Introduction

Binucleating, tetradentate (N_4) phthalazine and pyridazine ligands in general preferentially form binuclear copper(II) complexes involving a hydroxide bridge, in addition to the diazine bridge, and in those cases where the ligand forms six-membered chelate rings a third ligand (e.g. halogen, NO_3, SO_4, IO_3) can act as a bridge between the two metal centres (1–16). Two such ligands, PTP and PAP46Me (Fig. 1), form not only hydroxo-bridged derivatives, $[Cu_2(PTP)(OH)X_3]$ (X = Cl, Br), $[Cu_2(PAP46Me)(OH)Cl_3]$ but also dihalogeno-bridged compounds $[Cu_2(PTP)X_4]$ (X = Cl, Br), $[Cu_2(PAP46Me)\text{-}Cl_4]$. The hydroxo-bridged complexes exhibit antiferromagnetic exchange between the two copper(II) centres, which is propagated by a superexchange mechanism via the ligand groups that bridge the copper magnetic orbitals (3–7, 9, 10). The hydroxide group acts as an important superexchange bridge, while the diazine bridges also contribute significantly to the total exchange with pyridazine being more efficient than phthalazine (16, 17).

The choice of metal magnetic orbital depends upon the ground state of the copper ion and the extent of magnetic exchange is influenced by such factors as metal–ligand bond lengths and bond angles, the identity of the bridge group(s) and also terminal ligand groups (16, 18), and by distortions at the metal centre from idealized geometries. Of these factors the ones that influence exchange for copper(II) systems to the largest extent are the identity of the bridge and the angle subtended at the bridge by the two metal centres. In a related series of dihydroxo-bridged, square planar or square pyramidal copper(II) complexes $[LCu(OH)_2CuL]^{2+}$ (L = aliphatic or heterocyclic N_2 donor) a linear relationship was observed between hydroxide bridge angle and exchange integral, with a critical changeover from antiferromagnetic to ferromagnetic behaviour occurring at a Cu—O—Cu angle of approximately 97.5° (19).

In the present study we compare a series of related binuclear copper(II) complexes involving both terminal and bridging halogens and examine the role of the halogen, in terms of how it influences exchange, both as a bridging and terminal ligand. The crystal structure of the complex $[Cu_2PTPBr_4]$ is reported and consists of a binuclear arrangement of two copper square pyramids bound to the tetradentate ligand and bridged by three

[1]NRCC No. 28289.

[2]Author to whom correspondence should be addressed.

Can. J. Chem. Downloaded from www.nrcresearchpress.com by 176.9.209.113 on 09/07/12
For personal use only.

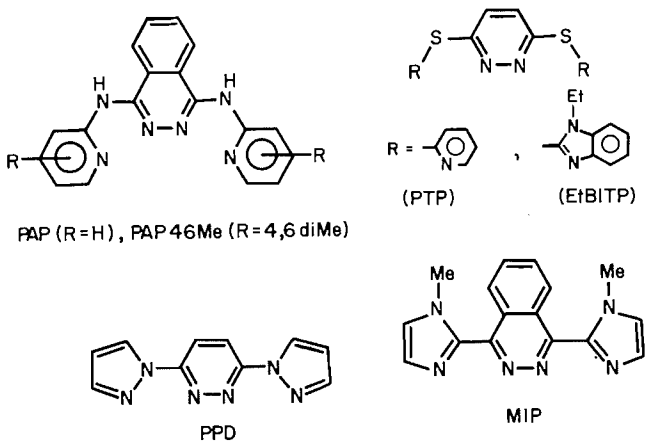

FIG. 1. Phthalazine and pyridazine ligands.

groups, the diazine (N_2) and two bromine atoms, which act as both equatorial and axial bridge groups to each copper centre. A similar structural arrangement has been observed for the analogous chloro-complex $[Cu_2(PTP)Cl_4].CH_3CH_2OH$. Variable temperature magnetic data indicate much stronger antiferromagnetic coupling in the case of the tetrabromo-derivative ($-2J$ = 243.5 (Br), 130.5 (Cl) cm^{-1}). Variable temperature magnetic data are also reported for $[Cu_2(PTP)(OH)X_3]$ (X = Cl, Br), which have stronger exchange than the tetrahalide derivatives, due to the presence of the hydroxide bridge.

Experimental

Synthesis of the ligands and complexes

PTP (11) and PAP46Me (21) were synthesized according to published procedures. Microanalyses were carried out by Canadian Microanalytical Service, Vancouver.

Cu_2PTPBr_4 (II)

$CuBr_2$ (1.8 g, 8.0 mmol) was dissolved in methanol (2 mL) and added to a solution of PTP (1.2 g, 4.0 mmol) in hot methanol (100 mL). A brown precipitate formed was filtered off, washed with methanol and chloroform, and air dried. The brown product was extracted with cold acetonitrile (300 mL) and the filtrate allowed to stand at room temperature for several weeks. Green crystals formed, which were filtered off, washed with acetonitrile, and air dried (yield 0.52 g). *Anal.* calcd. for $Cu_2(C_{14}H_{10}N_4S_2)Br_4$: C 22.55, H 1.34, N 7.52, Br 42.89; found: C 22.76, H 1.47, N 7.66, Br 39.49.

$[Cu_2PTP(OH)Cl_3]$ (IV)

PTP (1.2 g, 4.0 mmol) was dissolved in boiling methanol (80 mL). To this boiling solution an aqueous solution (40 mL) of $CuCl_2.2H_2O$ (1.4 g, 8.0 mmol) was added, with stirring, followed by a methanolic solution (10 mL) of triethylamine (0.41 g, 4.0 mmol) and the mixture refluxed for 20 min. The resulting green solution was filtered and the filtrate evaporated to a volume of approximately 40 mL on a steambath. On cooling green crystals formed and were filtered off, washed with methanol, and recrystallized from a DMF/ethanol/water mixture (yield 0.85 g). *Anal.* calcd. for $Cu_2(C_{14}H_{10}N_4S_2)(OH)Cl_3$: C 30.60, H 2.00, N 10.20, Cl 19.40; found: C 30.63, H 2.04, N 10.19, Cl 19.32.

$[Cu_2(PTP)Cl_4].CH_3CH_2OH$ (I) (20), $[Cu_2(PTP)(OH)Br_3]$ (V) (11) and $[Cu_2(PAP46Me)Cl_4]$ (III) (7) were prepared according to published procedures. $[Cu_2(PTP)(OH)Br_3]$ was also prepared by the same procedure used for IV. *Anal.* calcd. for $Cu_2(C_{14}H_{10}N_4S_2)(OH)Br_3$: C 24.65, H 1.61, N 8.21, Br 35.04; found: C 24.55, H 1.67, N 8.11, Br 35.61.

Magnetic measurements, infrared and electronic spectra

Variable temperature magnetic susceptibility data were obtained in the range 5–300 K (compounds II–IV) using an Oxford Instruments superconducting Faraday magnetic susceptibility system with a Sartorius 4432 microbalance. Main solenoid fields of 1.5 and 2.0 Telsa and a gradient field of 10 Tm^{-1} were employed. Susceptibility data are corrected for diamagnetism (Pascal corrections), temperature-independent paramagnetism, and for the presence of monomer impurity. $HgCo(NCS)_4$ was used as calibrant. Infrared spectra were obtained as Nujol mulls using a Perkin-Elmer 283 and electronic spectra (mull transmittance) using a Cary 17.

X-ray crystallographic analysis for $[Cu_2(PTP)Br_4]$ (II)

$C_{14}H_{10}N_4S_2Br_4Cu_2$ fw = 745.09

Monoclinic, $P2_1/c$, a = 11.1042(18), b = 15.6554(10), c = 12.6058(14) Å, β = 113.485(11)°, V = 2009.88 Å^3, Z = 4 (MoKα, λ = 0.70930 Å); μ = 10.21 mm^{-1}, D_{calcd} = 2.462 g cm^{-3}.

Crystals of II are green in colour. The diffraction intensities of an approximately 0.11 × 0.13 × 0.30 mm crystal were collected with graphite monochromatized MoKα radiation using the ω scan mode to $2\theta_{max}$ = 45° using a Nonius diffractometer. A total of 2869 reflections were measured, of which 2631 were considered unique, and 1580 reflections were considered significant with $I_{net} > 2.5\sigma(I_{net})$. Lorentz and polarization factors were applied but no correction was made for absorption. The cell parameters were obtained by the least-squares refinement of the setting angles of 44 reflections with 2θ in the range 38.0–43.1° (λMoKα = 0.70930 Å). The structure was solved by direct methods using MULTAN (22) and refined by full-matrix least-squares methods to final residuals of R_f = 0.045 and R_w = 0.033 for significant data (0.105 and 0.034 for all data) with weights based on counting statistics. The hydrogen atoms were fixed at calculated positions after the refinement of all the other atoms with anisotropic thermal motion. The refinement was then resumed including the hydrogen atoms. All calculations were performed with NRCVAX system of programs (23). Scattering factors were taken from ref. 24. The final atomic positional parameters and equivalent isotropic temperature factors are listed in Table 1, thermal parameters in Table 2,[3] and observed and calculated structure factors in Table 3.[3] Table 6[3] lists calculated atomic positional parameters for the hydrogen atoms and Table 7[3] lists detailed bond distances and angles for $[Cu_2(PTP)Br_4]$ (II). On the final difference map the deepest hole was $-0.840\bar{e}/Å^3$ and the highest peak $0.830\bar{e}/Å^3$. The maximum value of $|\Delta/\sigma|$ was 0.033.

Results and discussion

Description of the structure of $[Cu_2(PTP)Br_4]$ (II)

The molecular structure of II in the crystal is shown in Fig. 2 and consists of two somewhat distorted square-pyramidal copper centres bound to the tetradentate ligand, PTP, and bridged by the diazine nitrogen atoms (N2, N3) and two bromine atoms. Interatomic distances and angles relevant to the copper coordination spheres are listed in Table 4. The copper–nitrogen distances fall in the range 2.009–2.081 Å and are, on average, slightly longer than those found for the analogous complex, $[Cu_2(PTP)Cl_4].CH_3CH_2OH$ (I) (20). Terminal copper–halogen separations are longer than those observed for I, as would be expected, and, as in the case of I, the two bromine bridges are bound asymmetrically with respect to the two square-pyramidal copper centres, with each one occupying an axial and an equatorial ligand position. The axial interaction is weak with long copper–bromine bonds (2.766, 2.801 Å), while the equatorial ligands are much more strongly bound (2.380, 2.414 Å). The copper–copper separation (3.318 Å) is significantly longer than that observed for (I) (3.198 Å) and can be attributed to the presence of the more bulky bromine bridges in II. Another effect of replacing the chlorine bridges by bromine is to lengthen the diazine separation (N2—N3) which

[3]Photocopies of Tables 2, 3, 6, and 7 may be purchased from the Depository of Unpublished Data, CISTI, National Research Council of Canada, Ottawa, Ont., Canada K1A 0S2.

Can. J. Chem. Downloaded from www.nrcresearchpress.com by 176.9.209.113 on 09/07/12
For personal use only.

Can. J. Chem. Downloaded from www.nrcresearchpress.com by 176.9.209.113 on 09/07/12
For personal use only.

TABLE 1. Atomic positional parameters and equivalent isotropic temperature factors (esd's) for $[Cu_2(PTP)Br_4]$ (**II**)

Atom	X	Y	Z	B_{iso}
Br(1)	0.13721(19)	0.14557(12)	0.50836(16)	4.03(11)
Br(2)	−0.13516(18)	0.11790(10)	0.24979(15)	3.27(10)
Br(3)	−0.24373(16)	0.25057(12)	0.44390(13)	2.74(10)
Br(4)	−0.46820(18)	0.08662(11)	0.28583(14)	3.54(11)
Cu(1)	−0.03233(19)	0.23264(12)	0.37774(16)	2.36(12)
Cu(2)	−0.35431(19)	0.20417(12)	0.24581(17)	2.38(12)
S(1)	−0.5165(4)	0.3606(3)	0.0846(4)	2.78(24)
S(2)	0.0880(4)	0.3817(3)	0.2774(4)	2.88(27)
N(1)	−0.4655(12)	0.1942(9)	0.0735(11)	2.6(8)
N(2)	−0.2737(14)	0.3119(7)	0.2048(10)	2.6(9)
N(3)	−0.1399(12)	0.3168(7)	0.2464(10)	1.5(7)
N(4)	0.0554(12)	0.3369(8)	0.4688(10)	2.3(8)
C(1)	−0.4694(17)	0.1204(10)	0.0166(15)	3.1(11)
C(2)	−0.5418(19)	0.1113(11)	−0.0985(15)	4.1(12)
C(3)	−0.6108(17)	0.1795(13)	−0.1595(14)	3.5(12)
C(4)	−0.6117(14)	0.2546(11)	−0.1046(12)	2.4(9)
C(5)	−0.5307(14)	0.2602(10)	0.0090(14)	2.2(10)
C(6)	−0.3458(15)	0.3711(10)	0.1307(13)	2.3(9)
C(7)	−0.2887(16)	0.4388(10)	0.0917(13)	2.3(10)
C(8)	−0.1543(18)	0.4410(10)	0.1320(13)	2.9(11)
C(9)	−0.0875(16)	0.3790(10)	0.2134(13)	2.5(10)
C(10)	0.1097(14)	0.3966(10)	0.4234(13)	2.0(9)
C(11)	0.1766(16)	0.4663(10)	0.4863(16)	3.3(11)
C(12)	0.1925(16)	0.4736(10)	0.5999(15)	2.7(10)
C(13)	0.1388(15)	0.4143(11)	0.6477(13)	2.6(10)
C(14)	0.0683(16)	0.3470(11)	0.5795(14)	2.8(10)

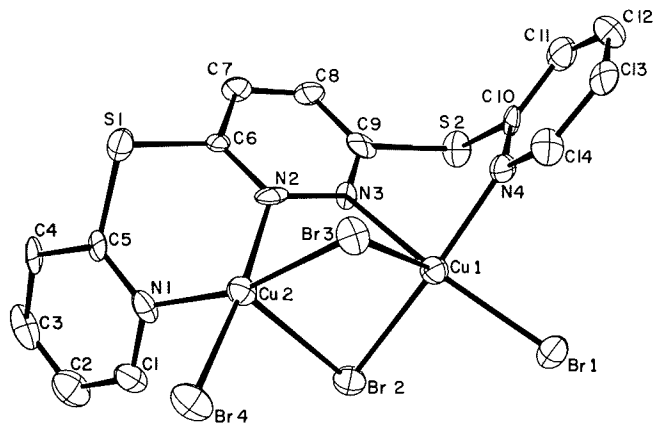

FIG. 2. Structural representation of $[Cu_2(PTP)Br_4]$ (**II**) with hydrogen atoms omitted (40% probability thermal ellipsoids). Bond distances (Å) and angles (deg): Cu(1)—Cu(2) 3.318(3), Cu(1)—Br(1) 2.375(3), Cu(1)—Br(2) 2.380(3), Cu(1)—Br(3) 2.801(3), Cu(1)—N(3) 2.081(12); Cu(2)—Br(4) 2.398(3), Cu(2)—Br(2) 2.766(3), Cu(2)—Br(3) 2.414(3), Cu(2)—N(2) 2.070(13); Br(2)—Br(3) 3.756(2); Cu(1)—Br(3)—Cu(2) 78.64(8), Cu(1)—Br(2)—Cu(2) 79.91(8); Cu(1)—Br(2)—Br(3) 48.16(8), Cu(1)—Br(3)—Br(2) 39.28(5), Cu(2)—Br(2)—Br(3) 39.94(5), Cu(2)—Br(3)—Br(2) 47.36(6).

increases from 1.316 Å in **I** to 1.366 Å in **II**. Very slight increases in the copper–nitrogen (diazine) bond lengths and bond angles (Cu—N—N) also occur.

The ligand in **II** is severely twisted with angles of 106.2° and 71.0°, respectively, between the pyridine mean planes 2 and 3 and the pyridazine mean plane (1) and an angle of 122.1° between the two pyridine mean planes (Fig. 2). Cu(1) is displaced by 0.202 Å above the mean plane of the four in plane donors N3, N4, Br1, Br2 (towards Br3) and Cu2 is displaced by 0.168 Å above the mean plane of the donors N1, N2, Br3, Br4 (towards Br2). The two N_2CuBr_2 mean planes are mutually inclined by 58.4°.

Magnetism, spectra, and structure

Variable temperature magnetic studies were carried out on **II**, **IV**, and **V** in the temperature range 5–300 K. The results are summarized in Table 5 along with data obtained previously for compounds **I** (25), **III** (16), $[Cu_2(EtBITP)(OH)Cl_3].DMF$ (**VI**) (26), and $[Cu_2(PAP)(OH)Cl_3].1.5H_2O$ (**VII**) (1). The best fit of the experimental data was calculated from the Van Vleck equation (27) for exchange coupled pairs of copper(II) ions (eq. [1]):

$$[1]\quad \chi_m = \frac{N\beta^2 g^2}{3kT}\left[1 + \frac{1}{3}\exp(-2J/kT)\right]^{-1}(1-\rho) + \left[\frac{N\beta^2 g^2}{4kT}\right]\rho + N\alpha$$

In this expression $2J$ (in the spin Hamiltonian $H = 2J\hat{s}_1.\hat{s}_2$) is the singlet–triplet splitting or exchange integral and other symbols have their usual meaning (ρ represents the fraction of a possible magnetically dilute copper(II) impurity). The temperature independent paramagnetism for a binuclear copper(II) complex, $N\alpha$, was taken as 120×10^{-6} cgs units/mol and the parameters giving the best fit were obtained by using a non-linear regression analysis (28) with ρ as a floating parameter. The experimental data and best fit lines for **II**, **IV**, and **V** are given in Fig. 3*a*, *b*, *c*, respectively. The complex $[Cu_2(PTP)(OH)Br_3]$ (**V**) contained significant amounts of paramagnetic impurity in different preparations and the sample chosen for magnetic study was analysed by non-linear, regression of the susceptibility–temperature data to a good fit with 7.5% monomeric, paramagnetic impurity (Fig. 3*c*).

A comparison of the magnetic data for **I** and **II** (Table 5) indicates greatly enhanced exchange in the case of the bromo-derivative. The structures of these two molecules are very similar with the dimensions of the binuclear centres differing slightly. The increased copper–copper separation in **II** is accompanied by increased copper–halogen distances and by a slight increase in the diazine N—N separation, which might be expected to weaken the exchange very slightly via the diazine bridge. The copper–nitrogen (diazine) separation and average Cu—N—N (diazine) angles are, however, essentially the same. The asymmetric halogen bridging arrangement in these two molecules effectively creates a situation where "no" magnetic exchange should occur via these bridge groups. This results because, on the assumption that the copper ion ground state is $d_{x^2-y^2}$, only one magnetic orbital lobe per copper is directed towards a bromine bridge. The other bridging interaction to each copper centre involves an axial orbital. This effectively orthogonal situation would, therefore, dictate that any spin-coupling should occur via the pyridazine bridge.[4] While

[4]A reviewer has suggested that, because the Br2—Br3 separation (3.756(2) Å) is slightly less than the sum of their van der Waals radii, a viable superexchange pathway could occur via this Br----Br bridge, which would contribute an antiferromagnetic term to the total exchange. Such interactions have been shown to occur between quite widely separated layers involving $CuCl_4^{2-}$ units (see, for example, ref. 30) but that deviations from linearity of the Cu—X----X—Cu bridge rapidly diminish this effect. The severely twisted bridging arrangement in **II** would, therefore, be unlikely to contribute such an exchange component.

TABLE 4. Selected bond distances (Å) and angles (deg) (esd's) for $[Cu_2(PTP)Br_4]$ (**II**)

Bond	Distance	Bond	Distance
Cu(1)—Cu(2)	3.318(3)	N(2)—N(3)	1.366(19)
Br(1)—Cu(1)	2.375(3)	N(2)—C(6)	1.332(20)
Br(2)—Cu(1)	2.3801(25)	N(3)—C(9)	1.286(21)
Br(2)—Cu(2)	2.766(3)	N(4)—C(10)	1.356(21)
Br(3)—Cu(1)	2.801(3)	N(4)—C(14)	1.355(20)
Br(3)—Cu(2)	2.4139(25)	C(1)—C(2)	1.357(24)
Br(4)—Cu(2)	2.398(3)	C(2)—C(3)	1.36(3)
Cu(1)—N(3)	2.081(12)	C(3)—C(4)	1.37(3)
Cu(1)—N(4)	2.009(12)	C(4)—C(5)	1.356(21)
Cu(2)—N(1)	2.032(12)	C(6)—C(7)	1.420(23)
Cu(2)—N(2)	2.070(13)	C(7)—C(8)	1.372(25)
S(1)—C(5)	1.813(17)	C(8)—C(9)	1.392(23)
S(1)—C(6)	1.754(16)	C(10)—C(11)	1.378(24)
S(2)—C(9)	1.788(17)	C(11)—C(12)	1.38(3)
S(2)—C(10)	1.774(16)	C(12)—C(13)	1.367(25)
N(1)—C(1)	1.351(22)	C(13)—C(14)	1.387(24)
N(1)—C(5)	1.336(21)	Br(2)—Br(3)	3.756(2)
		Br(1)—Br(2)	3.479(3)
		Br(3)—Br(4)	3.580(2)

Bonds	Angle	Bonds	Angle
Cu(1)—Br(2)—Cu(2)	79.91(8)	N(3)—N(2)—C(6)	119.2(13)
Cu(1)—Br(3)—Cu(2)	78.64(8)	Cu(1)—N(3)—N(2)	117.5(9)
Br(1)—Cu(1)—Br(2)	94.03(9)	Cu(1)—N(3)—C(9)	123.1(11)
Br(1)—Cu(1)—Br(3)	112.20(10)	N(2)—N(3)—C(9)	118.8(12)
Br(1)—Cu(1)—N(3)	163.8(4)	Cu(1)—N(4)—C(10)	121.0(10)
Br(1)—Cu(1)—N(4)	90.0(3)	Cu(1)—N(4)—C(14)	120.7(11)
Br(2)—Cu(1)—Br(3)	92.57(8)	C(10)—N(4)—C(14)	118.2(13)
Br(2)—Cu(1)—N(3)	88.3(3)	N(1)—C(1)—C(2)	122.5(15)
Br(2)—Cu(1)—N(4)	172.9(4)	C(1)—C(2)—C(3)	118.8(16)
Br(3)—Cu(1)—N(3)	83.7(4)	C(2)—C(3)—C(4)	120.4(15)
Br(3)—Cu(1)—N(4)	91.3(4)	C(3)—C(4)—C(5)	117.1(15)
N(3)—Cu(1)—N(4)	86.2(5)	S(1)—C(5)—N(1)	116.0(12)
Br(2)—Cu(2)—Br(3)	92.70(8)	S(1)—C(5)—C(4)	119.6(13)
Br(2)—Cu(2)—Br(4)	98.94(9)	N(1)—C(5)—C(4)	124.3(15)
Br(2)—Cu(2)—N(1)	97.9(4)	S(1)—C(6)—N(2)	115.8(13)
Br(2)—Cu(2)—N(2)	86.4(4)	S(1)—C(6)—C(7)	121.8(12)
Br(3)—Cu(2)—Br(4)	96.14(9)	N(2)—C(6)—C(7)	122.3(14)
Br(3)—Cu(2)—N(1)	166.1(4)	C(6)—C(7)—C(8)	117.5(13)
Br(3)—Cu(2)—N(2)	85.5(3)	C(7)—C(8)—C(9)	115.9(15)
Br(4)—Cu(2)—N(1)	91.1(4)	S(2)—C(9)—N(3)	115.1(12)
Br(4)—Cu(2)—N(2)	174.3(4)	S(2)—C(9)—C(8)	118.8(13)
N(1)—Cu(2)—N(2)	86.2(5)	N(3)—C(9)—C(8)	126.1(16)
C(5)—S(1)—C(6)	96.4(7)	S(2)—C(10)—N(4)	116.6(11)
C(9)—S(2)—C(10)	98.3(7)	S(2)—C(10)—C(11)	121.4(13)
Cu(2)—N(1)—C(1)	120.7(11)	N(4)—C(10)—C(11)	122.1(14)
Cu(2)—N(1)—C(5)	122.8(11)	C(10)—C(11)—C(12)	118.8(15)
C(1)—N(1)—C(5)	116.3(13)	C(11)—C(12)—C(13)	120.3(15)
Cu(2)—N(2)—N(3)	117.5(9)	C(12)—C(13)—C(14)	118.7(14)
Cu(2)—N(2)—C(6)	112.9(11)	N(4)—C(14)—C(13)	121.9(15)

it is known that symmetrically dibromo-bridged dicopper(II) compounds involving the anion $[Cu_2Br_6]^{2-}$ have significantly larger antiferromagnetic contributions to exchange than corresponding chloro-analogues (29) the bromine bridges in such compounds are poised appropriately to take part in magnetic exchange via the magnetic copper orbitals. For **I**, **II** this cannot be the case and so the difference in spin-exchange must be associated with other factors. A comparison of the magnetism for the isostructural pairs of compounds $[Cu_2(MIP)(OH)X_3(H_2O)].H_2O$ (MIP = 1,4-bis(1-methyl-2-imidazolyl)phthalazine (Fig. 1); X = Cl, Br) (4, 10) and $[Cu_2(PPD)(OH)X_3(H_2O)].nH_2O$ (PPD = 3,6-bis(1-pyrazolyl)pyridazine (Fig. 1); X = Cl, Br) (10) reveals in both cases that the bromo-complexes have considerably enhanced antiferromagnetic exchange. The difference in exchange is considered to be associated with the degree to which these terminal halogen ligands would polarize electron density in the copper magnetic orbital. The less electronegative bromine ligand would thus allow more unpaired spin to take part in the exchange process (16). The same criterion would explain the enhanced spin exchange in **II**, although in these two cases both terminal and bridging halogen ligands would be involved.

The pyridazine bridge is considerd to be the superexchange

Can. J. Chem. Downloaded from www.nrcresearchpress.com by 176.9.209.113 on 09/07/12
For personal use only.

Can. J. Chem. Downloaded from www.nrcresearchpress.com by 176.9.209.113 on 09/07/12
For personal use only.

TABLE 5. Magnetic and structural data

	Compound	$-2J$ (cm^{-1})	g	μ_{eff} (BM) (T, K)	Important bond lengths (Å), angles (deg)					
					Cu—Cu	Cu—N (diazine)	N—N	Cu—X (terminal)	Cu—X (bridge)	Cu—N—N
I	$[Cu_2(PTP)Cl_4].CH_3CH_2OH$	130.5±0.4[a]	2.029±0.004	1.61(300.7)	3.198(1)	2.075(6) 2.069(5)	1.316(9)	2.226(2) 2.227(2)	2.698(2) 2.269(2) 2.605(2) 2.268(2)	116.0(5) 118.0(5)
II	$[Cu_2(PTP)Br_4]$	243.5±0.3	2.072±0.002	1.43(295.4)	3.318(3)	2.081(12) 2.070(13)	1.366(19)	2.375(3) 2.398(3)	2.801(3) 2.414(3) 2.766(3) 2.380(3)	117.5(9) 117.5(9)
III	$[Cu_2(PAP46Me)Cl_4]$	55.2±0.1[b]	2.052±0.002	1.72(301.3)	3.251(1)	2.022(2)	1.385(5)	2.267(1)	2.277(1) 2.589(1)	117.5(2)
IV	$[Cu_2(PTP)(OH)Cl_3]$	294±3	2.02±0.02	1.31(300.2)						
V	$[Cu_2(PTP)(OH)Br_3]$	326±6	2.162±0.008	1.27(294.8)						
VI	$[Cu_2(EtBITP)(OH)Cl_3].DMF$	260±1[c]	2.01±0.01	1.37(302.8)	3.017(1)	2.130(3) 2.158(3)	1.352(4)	2.258(1) 2.261(1)	2.504(1) 2.538(1)	112.5(2) 113.2(2)
VII	$[Cu_2(PAP)(OH)Cl_3].1.5H_2O$	201[d]	2.28	1.66	3.001(2) 2.972(2)	2.020(4) 2.007(4) 2.000(4) 2.038(4)	1.372(6) 1.376(5)	2.279(2) 2.285(2) 2.293(2) 2.284(2)	2.635(2) 2.561(2) 2.566(2) 2.578(2)	113.7(3) 114.0(3) 113.5(3) 113.1(3)

[a]Reference 25.
[b]Reference 16.
[c]Reference 26.
[d]Reference 3.

Can. J. Chem. Downloaded from www.nrcresearchpress.com by 176.9.209.113 on 09/07/12
For personal use only.

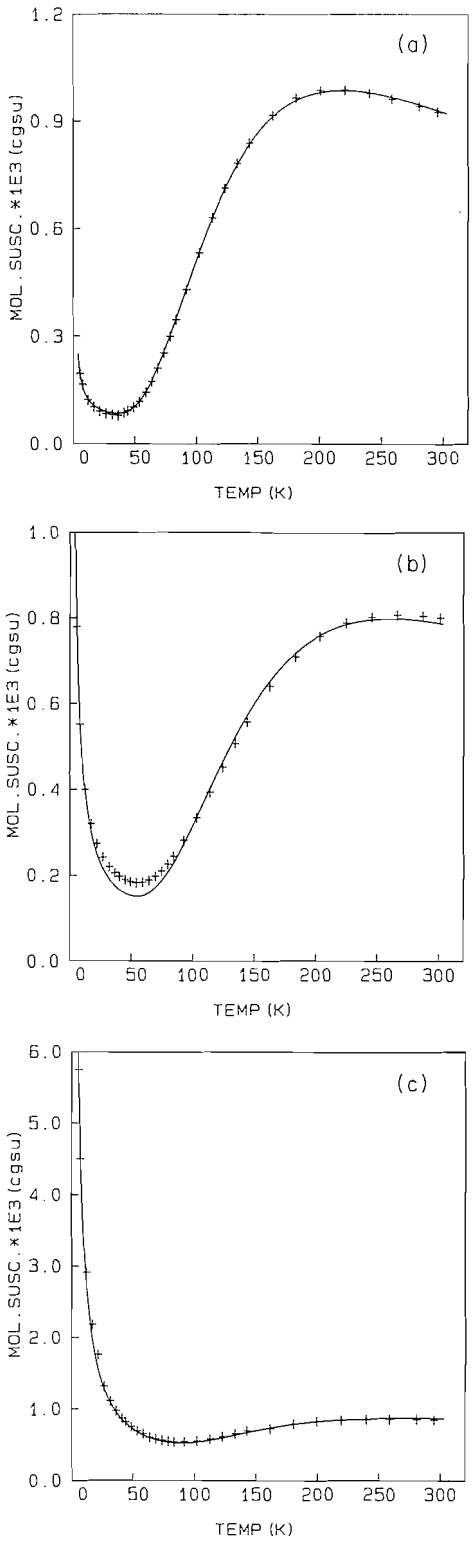

FIG. 3. (*a*) Magnetic susceptibility data for $[Cu_2(PTP)Br_4]$ (**II**). The solid line was calculated from eq. [1] with $g = 2.072 \pm 0.002$, $-2J = 243.5 \pm 0.3\ cm^{-1}$, and $N\alpha = 60 \times 10^{-6}$ cgs units ($cm^3\ mol^{-1}$)/Cu and assuming 0.19% paramagnetic impurity ($\rho = 0.0019$). (*b*) Magnetic susceptibility data for $[Cu_2(PAP)(OH)Cl_3]$ (**IV**). The solid line was calculated from eq. [1] with $g = 2.02 \pm 0.02$, $-2J = 294 \pm 3\ cm^{-1}$, and $N\alpha = 60 \times 10^{-6}$ cgs units ($cm^3\ mol^{-1}$)/Cu and assuming 1.1% paramagnetic impurity ($\rho = 0.011$). (*c*) Magnetic susceptibility data for $[Cu_2(PTP)(OH)Br_3]$ (**V**). The solid line was calculated from eq. [1] with $g = 2.162 \pm 0.008$, $-2J = 326 \pm 6\ cm^{-1}$, and $N\alpha = 60 \times 10^{-6}$ cgs units ($cm^3\ mol^{-1}$)/Cu and assuming 7.5% paramagnetic impurity ($\rho = 0.075$).

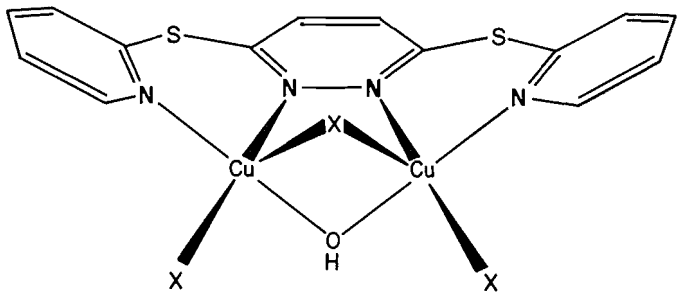

FIG. 4. Proposed structure for $[Cu_2(PTP)(OH)X_3]$ (X = Cl, Br).

pathway responsible for antiferromagnetic coupling in **I** and **II**, but it is not clear whether in the case of the bromo-derivative the bromine atoms have reduced the exchange capacity of the diazine bridge to a significant extent. No spin-coupled binuclear copper(II) complexes involving just pyridazine bridges have been characterized, to our knowledge, but the symmetrically chloro-bridged compound $[Cu_2(PTP)_2Cl](ClO_4)_3.CH_3CN$ exhibits strong antiferromagnetic coupling ($-2J = 480\ cm^{-1}$) (17). In this complex the two square pyramidal copper(II) centres are bridged equatorially by the pyridazines and axially by the chlorine, thus creating an effectively orthogonal situation in which no coupling should occur via the chlorine bridge. Each of the pyridazine rings, which bridge the two copper atoms via the magnetic $d_{x^2-y^2}$ orbital, can be considered to be responsible for half the total exchange observed for this complex. The close similarity between this value ($-2J = 240\ cm^{-1}$) and the value associated with **II** may be fortuitous but suggests that bromine may in fact have little influence on the exchange process and that the presence of more electronegative chlorine atoms bound to the copper magnetic orbitals leads to reduced exchange via the diazine bridge. A similar structural situation is found for $[Cu_2(PAP46Me)Cl_4]$ (**III**) (7) where exchange is effectively restricted to the phthalazine diazine bridge. However, the clear distinction between the exchange integrals of **I** and **III** indicates phthalazine to be a weaker exchange bridge, which may be associated with the extended delocalisation pathway present in the phthalazine group.

In a previous report the complex $[Cu_2(PTP)(OH)Cl_3].CH_3CH_2OH$ was described (11) with a room temperature magnetic moment (μ_{eff}) of 1.62 BM. Reexamination of this system suggests that this compound was in fact $[Cu_2(PTP)Cl_4].CH_3CH_2OH$ ($\mu_{eff}(RT) = 1.61$ BM; refs. 20, 25) and so compound **IV** is effectively reported here for the first time. The choice of an aqueous solvent medium for the synthesis of hydroxo-bridged copper(II) derivatives of this sort was based on the almost exclusive synthesis of such compounds from the pyridylphthalazine ligands in aqueous media (1, 3, 5, 7, 9). $[Cu_2(PTP)(OH)Br_3]$ (**V**) was, in fact, synthesized in this way (11). However, the use of triethylamine in this study ensures the formation of hydroxo-bridged species.

The hydroxo-bridged complexes $[Cu_2(PTP)(OH)X_3]$ (X = Cl, Br) (**IV**, **V**) are more strongly coupled than their tetrahalide counterparts and this clearly is a result of the presence of a hydroxide bridge disposed favorably with respect to the copper magnetic orbitals. Infrared spectra of these two complexes are virtually identical above 300 cm^{-1} with absorptions at 3460 cm^{-1} associated with OH stretch. Far infrared absorptions for **IV** at 290, 260 cm^{-1}, which are absent in **V**, are associated with terminal and bridging chloride groups, respectively. Electronic spectra (mull transmittance) have one major absorption with a low energy shoulder (15400, 11800 cm^{-1} (**IV**); 14900, 11600 cm^{-1} (**V**)) typical of square-pyramidal copper.

Structurally these complexes are assumed to resemble $[Cu_2(PAP)(OH)Cl_3].1.5H_2O$ (**VII**) (Table 5) (2) (PAP, Fig. 1) which involves two square-pyramidal copper(II) centres bound to the tetradentate pyridylphthalazine ligand and bridged equatorially by hydroxide and axially by chlorine. A proposed structural representation for these compounds is given in Fig. 4. The antiferromagnetic coupling would be the sum of the effects of both the pyridazine and hydroxide bridges, which are both bound to the magnetic orbital associated with the $d_{x^2-y^2}$ copper centres. Exchange integrals for $[Cu_2(PAP)(OH)X_3].1.5H_2O$ ($-2J$ = 201 (Cl), 191 (Br) cm^{-1}) (3) are much smaller than those observed for **IV** and **V** and again reflect the difference between pyridazine and phthalazine as a superexchange bridge. In the absence of structural data on these systems and, in particular hydroxide bridge angles, little can be said about the direct influence of the hydroxide bridge itself on exchange. However, the similarity between PTP and the pyridylphthalazine ligand PAP suggests that the binuclear centre dimensions for hydroxo-bridged derivatives of the two ligands would be comparable and in particular the hydroxide bridge angles. These angles are in the range 100–103° for $[Cu_2(PAP)(OH)X_3].1.5H_2O$ (X = Cl, Br) and comparable angles would seem reasonable for the PTP derivatives.

The copper ion ground state for **I**–**V** is $d_{x^2-y^2}$, associated with the square-pyramidal copper centres. Limited distortions from an idealized square-pyramidal situation do not seem to disrupt the effective ground state situation. However, major distortions do. The complex $[Cu_2(EtBITP)(OH)Cl_3].DMF$ (**VI**) (EtBITP, Fig. 1) has been shown to have a triple bridged structure involving pyridazine, hydroxide, and chloride bridges, but with trigonal bipyramidal copper centres (26). The hydroxide occupies an axial bridge position while the chlorine and pyridazine bridge equatorially. For a d_{z^2} ground state system exchange would involve both axial and equatorial interactions and so all three bridges would be involved in exchange, but the axial interaction would dominate since the major magnetic orbital lobe would coincide with this axis. The reduced exchange observed for this compound is consistent with a situation where the pyridazine bridge is involved in a magnetic interaction with the minor magnetic orbital lobe of the d_{z^2} ground state copper centre.

Acknowledgements

We thank the Natural Sciences and Engineering Research Council of Canada for financial support for this study and Dr. M. J. Newlands for graphics assistance.

1. L. K. Thompson, V. T. Chacko, J. A. Elvidge, A. B. P. Lever, and R. V. Parish. Can. J. Chem. **47**, 4141 (1969).
2. G. Marongiu and E. C. Lingafelter. Acta Crystallogr. B**38**, 620 (1982).
3. L. K. Thompson. Can. J. Chem. **61**, 579 (1983).
4. L. K. Thompson, F. W. Hartstock, and A. W. Hanson. Can. J. Chem. **62**, 2755 (1984).
5. L. K. Thompson, A. W. Hanson, and B. S. Ramaswamy. Inorg. Chem. **23**, 2459 (1984).
6. L. K. Thompson, T. C. Woon, D. B. Murphy, E. J. Gabe, F. L. Lee, and Y. LePage. Inorg. Chem. **24**, 4719 (1985).
7. S. K. Mandal, T. C. Woon, L. K. Thompson, M. J. Newlands, and E. J. Gabe. Aust. J. Chem. **39**, 1007 (1986).
8. L. Rosenberg, L. K. Thompson, E. J. Gabe, and F. L. Lee. J. Chem. Soc. Dalton Trans. 625 (1986).
9. S. K. Mandal, L. K. Thompson, and A. W. Hanson. J. Chem. Soc. Chem. Commun. 1709 (1985).
10. L. K. Thompson, S. K. Mandal, E. J. Gabe, F. L. Lee, and A. W. Addison. Inorg. Chem. **26**, 657 (1987).
11. T. C. Woon, R. McDonald, S. K. Mandal, L. K. Thompson, S. P. Connors, and A. W. Addison. J. Chem. Soc. Dalton Trans. 2381 (1986).
12. M. Ghedini, G. De Munno, G. Denti, A. M. Manotti Lanfredi, and A. Tiripicchio. Inorg. Chim. Acta, **57**, 87 (1982).
13. P. Dapporto, G. De Munno, G. Bruno, and M. Romeo. Acta Crystallogr. C**39**, 718 (1983).
14. P. Dapporto, G. De Munno, A. Sega, and L. Mealli. Inorg. Chim. Acta, **83**, 171 (1984).
15. G. De Munno and G. Denti. Acta Crystallogr. C**40**, 616 (1984).
16. L. K. Thompson, F. L. Lee, and E. J. Gabe. Inorg. Chem. In press.
17. S. K. Mandal, L. K. Thompson, E. J. Gabe, J.-P. Charland, and F. L. Lee. Inorg. Chem. In press.
18. S. K. Mandal, L. K. Thompson, K. Nag, J.-P. Charland, and E. J. Gabe. Can. J. Chem. **65**, 2815 (1987).
19. V. H. Crawford, H. W. Richardson, J. R. Wasson, D. J. Hodgson, and W. E. Hatfield. Inorg. Chem. **15**, 2107 (1976).
20. S. K. Mandal, L. K. Thompson, M. J. Newlands, F. L. Lee, Y. LePage, J.-P. Charland, and E. J. Gabe. Inorg. Chem. Acta, **122**, 199 (1986).
21. D. V. Bautista, G. Bullock, F. W. Hartstock, and L. K. Thompson. J. Heterocyclic Chem. **20**, 345 (1983).
22. G. Germain, P. Main, and M. M. Woolfson. Acta Crystallogr. A**27**, 368 (1971).
23. E. J. Gabe, F. L. Lee, and Y. LePage. Crystallographic computing III. *Edited by* G. Sheldrick, C. Kruger, and R. Goddard. Clarendon Press, Oxford. 1985. p. 167.
24. International tables for X-ray crystallography. Vol. IV. Kynoch Press, Birmingham, England. 1974. p. 99. Table 2.2B.
25. S. K. Mandal, L. K. Thompson, E. J. Gabe, F. L. Lee, and J.-P. Charland. Inorg. Chem. **26**, 2384 (1987).
26. L. K. Thompson, S. K. Mandal, L. Rosenberg, F. L. Lee, and E. J. Gabe. Inorg. Chim. Acta, **133**, 81 (1987).
27. J. H. Van Vleck. The theory of electric and magnetic susceptibilities. Oxford University Press, London. 1932. Chapt. 9.
28. R. G. Duggleby. Anal. Biochem. **110**, 9 (1981).
29. R. D. Willett. Inorg. Chem. **25**, 1918 (1986).
30. R. Block and L. Jansen. Phys. Rev. B, **26**, 148 (1982).

Can. J. Chem. Downloaded from www.nrcresearchpress.com by 176.9.209.113 on 09/07/12
For personal use only.

Crystal and molecular structure of [dimethyl(1-pyrazolyl)(2-pyridylmethoxy)gallato-N^2,O,N^3](η^3-allyl)dicarbonylmolybdenum(II)

STEVEN J. RETTIG, ALAN STORR,[1] AND JAMES TROTTER[1]

Department of Chemistry, University of British Columbia, 2036 Main Mall, Vancouver, B.C., Canada V6T 1Y6

Received April 7, 1987

STEVEN J. RETTIG, ALAN STORR, and JAMES TROTTER. Can. J. Chem. **66**, 355 (1988).

Crystals of [dimethyl(1-pyrazolyl)(2-pyridylmethoxy)gallato-N^2,O,N^3](η^3-allyl)dicarbonylmolybdenum(II) are triclinic, a = 9.632(2), b = 9.798(2), c = 10.255(2) Å, α = 80.16(1), β = 87.38(1), γ = 81.75(1)°, Z = 2, space group $P\bar{1}$. The structure was solved by conventional heavy-atom methods and was refined by full-matrix least-squares procedures to R = 0.033 and R_w = 0.037 for 3000 reflections with $I \geq 3\sigma(I)$. The molecule has pseudo-octahedral coordination geometry with the tridentate [$Me_2Ga(N_2C_3H_3)(OCH_2(C_5H_4N))$]$^-$ ligand *facially* coordinated and the η^3-allyl ligand occupying one coordination site *trans* to the pyridyl nitrogen atom. Important bond lengths are Mo—O = 2.219(2), Mo—N(py) = 2.212(3), Mo—N(pz) = 2.232(2), Mo—C(allyl) = 2.290(4), 2.189(4), 2.341(4), Mo—CO (*trans* to O) = 1.928(4), and Mo—CO (*trans* to N) = 1.952(4) Å.

STEVEN J. RETTIG, ALAN STORR et JAMES TROTTER. Can. J. Chem. **66**, 355 (1988).

Les cristaux du [diméthyl(pyrazolyl-1)(pyridyl-2 méthoxy)-gallato-N^2,O,N^3](η^3-allyl) dicarbonylmolybdène (II) sont tricliniques avec a = 9,632(2), b = 9,798(2) et c = 10,255(2) Å, α = 80,16(1), β = 87,38(1) et γ = 81,75(1)°, Z = 2 et groupe d'espace $P\bar{1}$. On a résolu la structure par les méthodes conventionnelles aux atomes lourds et on l'a affinée par la méthode des moindres carrés jusqu'à des valeurs de R et R_w de 0,033 et 0,037 pour 3000 réflexions avec $I \geq 3\sigma(I)$. La molécule possède une géométrie de coordination pseudo-octaédrique dans laquelle le ligand tridentate [$Me_2Ga(N_2C_3H_3)(OCH_2(C_5H_4N))$]$^-$ est coordonné d'une façon faciale alors que le ligand η^3-allyle occupe une site de coordination qui est *trans* par rapport à l'atome d'azote du pyridyle. Le longueurs importantes sont : Mo—O = 2,219(2), Mo—N(py) = 2,212(3), Mo—N(pz) = 2,232(2), Mo—C(allyle) = 2,290(4), 2,189(4), 2,341(4), Mo—CO (*trans* par rapport au O) = 1,928(4) et Mo—Co (*trans* par rapport au N) = 1,952(4) Å.

[Traduit par la revue]

Introduction

Earlier publications have reported the synthesis and complexation of the novel tridentate unsymmetric anionic organogallate ligand **1**, [$Me_2Ga(N_2C_3H_3)(OCH_2(C_5H_4N))$]$^-$ (1, 2).

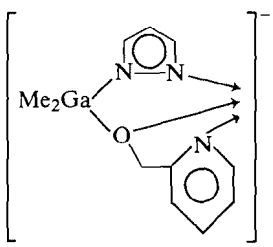

1

The flexibility of the tridentate ligand system has been demonstrated through the crystal structure determinations of the complexes [$Me_2Ga(N_2C_3H_3)(OCH_2(C_5H_4N))$]$Re(CO)_3$ and [$Me_2Ga(N_2C_3H_3)(OCH_2(C_5H_4N))$]$Rh(CO)$. In the former octahedral Re complex the ligand is *facially* coordinated whereas in the latter square planar Rh complex the ligand is in a *meridional* coordination mode. The present paper describes the crystal structure of the Mo complex, [$Me_2Ga(N_2C_3H_3)$-$(OCH_2(C_5H_4N))$]$Mo(CO)_2(\eta^3$-$C_3H_5)$. This complex was described in an earlier account at which time predictions were made about its most likely molecular stereochemistry (1). A *fac* coordination of the organogallate ligand was proposed with the allyl group positioned opposite the pyrazolyl moiety of the ligand. The X-ray structure described herein confirms the *facial* coordination of the organogallate ligand and also establishes the location of the allyl group in the pseudo-octahedral complex. The structural parameters obtained are discussed in conjunction with data available for similar Mo allyl complexes.

[1]Authors to whom correspondence may be addressed.

Experimental

The title compound was prepared and characterized as described previously (1). Crystals suitable for X-ray study were obtained by recrystallization from benzene. A crystal bounded by the eight faces (followed by their distances in mm from a common origin): {0 1 1}, 0.16, {1 1 −1}, 0.28, (−1 −1 3), 0.27, (1 5 0), 0.21, {1 0 0}, 0.04, was mounted in a general orientation. Unit-cell parameters were refined by least squares on 2 sin θ/λ values for 25 reflections (2θ = 35–40°) measured on a diffractometer with Mo-$K\alpha$ radiation ($\lambda(K\alpha_1)$ = 0.70930, $\lambda(K\alpha_2)$ = 0.71359 Å). Crystal data at 22°C are as follows:

$C_{16}H_{20}GaMoN_3O_3$ fw = 468.0

Triclinic, a = 9.632(2), b = 9.798(2), c = 10.255(2) Å, α = 80.16(1), β = 87.38(1), γ = 81.75(1)°, V = 943.6(3) Å^3, Z = 2, ρ_c = 1.647 Mg m^{-3}, $F(000)$ = 468, μ(Mo-$K\alpha$) = 20.9 cm^{-1}. Absent reflections: none, space group $P\bar{1}$ (Buerger reduced cell) from structure analysis.

Intensities were measured with graphite-monochromatized Mo-$K\alpha$ radiation on an Enraf-Nonius CAD4-F diffractometer. An ω-2θ scan at 0.87–10° min^{-1} over a range of (0.85 + 0.35 tan θ) degrees in ω (extended by 25% on both sides for background measurement) was employed. Data were measured to 2θ = 55°. The intensities of three check reflections, measured every hour throughout the data collection, decreased uniformly to final values of 0.96 times the initial values. The data were scaled accordingly. After data reduction,[2] an absorption correction was applied using the Gaussian integration method (3, 4). Transmission factors ranged from 0.482 to 0.759 for 128 integration points. Of the 4318 independent reflections measured, 3000 (69.5%) had intensities greater than or equal to $3\sigma(I)$ above background where $\sigma^2(I) = S + 2B + (0.04(S - B))^2$ with S = scan count and B = normalized background count.

The structure was solved by conventional heavy-atom methods in the

[2]The computer programs used include locally written programs for data processing and locally modified versions of the following: AGNOST, absorption corrections, by J. A. Ibers; ORFLS, full-matrix least-squares, and ORFFE, function and errors, by W. R. Busing, K. O. Martin, and H. A. Levy; FORDAP, Patterson and Fourier syntheses, by A. Zalkin; ORTEP II, illustrations by C. K. Johnson.

Can. J. Chem. Downloaded from www.nrcresearchpress.com by 176.9.209.113 on 09/07/12
For personal use only.

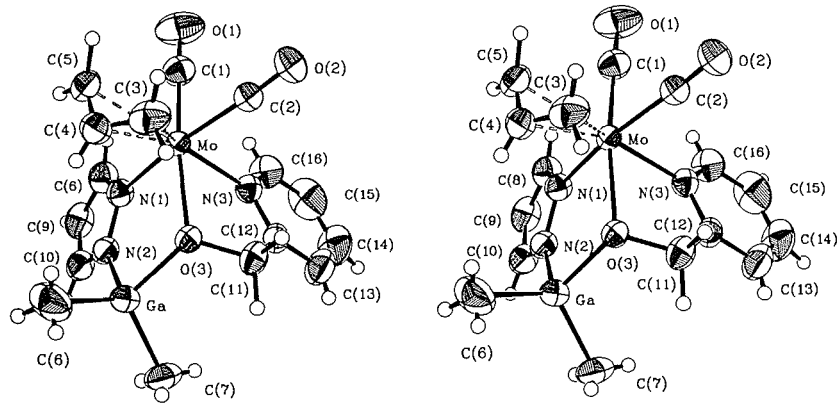

FIG. 1. Stereoscopic view of the $[Me_2Ga(N_2C_3H_3)(OCH_2(C_5H_4N))]Mo(CO)_2(\eta^3\text{-}C_3H_5)$ molecule; 50% probability thermal ellipsoids are shown for the non-hydrogen atoms. Hydrogen atoms have been assigned arbitrary thermal parameters for the sake of clarity.

TABLE 1. Final positional (fractional $\times 10^4$, Mo and Ga $\times 10^5$) and isotropic thermal parameters ($U \times 10^3$ Å^2) with estimated standard deviations in parentheses

Atom	x	y	z	U_{eq}
Mo	32158(3)	34757(3)	30787(3)	32
Ga	5900(4)	13658(4)	27270(4)	42
O(1)	4955(4)	5849(4)	1932(4)	86
O(2)	5574(3)	3172(4)	5108(3)	67
O(3)	2234(2)	1538(2)	3649(2)	37
N(1)	2030(3)	3582(3)	1236(3)	40
N(2)	1108(3)	2680(3)	1145(3)	42
N(3)	4566(3)	1812(3)	2225(3)	40
C(1)	4288(5)	4957(4)	2352(4)	50
C(2)	4677(4)	3232(4)	4389(4)	43
C(3)	2221(6)	3928(6)	5059(5)	60
C(4)	1387(5)	4584(5)	3986(5)	59
C(5)	1886(5)	5664(5)	3130(6)	63
C(6)	−1115(7)	2158(10)	3617(9)	79
C(7)	707(9)	−514(7)	2155(9)	58
C(8)	2178(5)	4308(5)	26(4)	51
C(9)	1369(5)	3908(5)	−852(4)	58
C(10)	706(5)	2893(5)	−123(4)	52
C(11)	3308(5)	356(4)	3856(4)	48
C(12)	4401(4)	484(4)	2768(4)	43
C(13)	5222(6)	−651(6)	2343(6)	65
C(14)	6212(6)	−439(7)	1374(6)	81
C(15)	6372(6)	903(8)	818(6)	83
C(16)	5546(5)	1993(6)	1268(5)	58

TABLE 2. Bond lengths (Å) with estimated standard deviations in parentheses

Bond	Length (Å)	Bond	Length (Å)
Mo—O(3)	2.219(2)	N(1)—N(2)	1.357(4)
Mo—N(1)	2.232(3)	N(1)—C(8)	1.333(5)
Mo—N(3)	2.212(3)	N(2)—C(10)	1.347(5)
Mo—C(1)	1.928(4)	N(3)—C(12)	1.354(5)
Mo—C(2)	1.952(4)	N(3)—C(16)	1.338(5)
Mo—C(3)	2.290(4)	C(3)—C(4)	1.400(7)
Mo—C(4)	2.189(4)	C(4)—C(5)	1.382(7)
Mo—C(5)	2.341(4)	C(8)—C(9)	1.359(6)
Ga—O(3)	1.924(2)	C(9)—C(10)	1.356(7)
Ga—N(2)	1.984(3)	C(11)—C(12)	1.500(6)
Ga—C(6)	1.968(6)	C(12)—C(13)	1.391(6)
Ga—C(7)	2.013(5)	C(13)—C(14)	1.357(8)
O(1)—C(1)	1.170(5)	C(14)—C(15)	1.368(9)
O(2)—C(2)	1.150(5)	C(15)—C(16)	1.370(8)
O(3)—C(11)	1.431(5)		

centrosymmetric space group $P\bar{1}$ which was confirmed by the success of the refinement. The heavy atoms were positioned from the Patterson function and all other atoms, including hydrogen, were positioned from subsequent difference Fourier syntheses. In the final stages of refinement the non-hydrogen atoms were refined with anisotropic thermal parameters and the hydrogen atoms with isotropic thermal parameters. Scattering factors for all atoms and anomalous dispersion corrections for Mo and Ga were taken from ref. 5. The weighting scheme $w = 1/\sigma^2(F)$, where $\sigma^2(F)$ is derived from the previously defined $\sigma^2(I)$, gave uniform average values of $w(|F_o| - |F_c|)^2$ over ranges of both $|F_o|$ and $\sin\theta/\lambda$ and was employed in the final stages of full-matrix refinement of 297 variables. Reflections with $I < 3\sigma(I)$ were not included in the refinement. Convergence was reached at $R = 0.033$ and $R_w = 0.037$ for 3000 reflections with $I \geq 3\sigma(I)$. The function minimized was $\Sigma w(|F_o| - |F_c|)^2$, $R = \Sigma||F_o| - |F_c||/\Sigma|F_o|$ and $R_w = (\Sigma w(|F_o| - |F_c|)^2/\Sigma w|F_o|^2)^{1/2}$.

On the final cycle of refinement the mean and maximum parameter shifts corresponded to 0.03 and 0.32σ, respectively. The mean error in an observation of unit weight, $(\Sigma w(|F_o| - |F_c|)^2/(m - n))^{1/2}$, was 1.568. A final difference Fourier synthesis showed maximum fluctuations of −1.2 to +0.8 e Å^{-3}, both near Mo, and was featureless away from the heavy atoms. The final positional parameters for the non-hydrogen atoms appear in Table 1. Bond lengths, bond angles, and intra-annular torsion angles are given in Tables 2–4, respectively. Hydrogen atom parameters, bond lengths and angles involving hydrogen, a complete listing of torsion angles, and structure factors have been deposited.[3]

Results and discussion

The crystal structure of [dimethyl(1-pyrazolyl)(2-pyridylmethoxy)gallato-N^2,O,N^3](η^3-allyl)dicarbonylmolybdenum(II) consists of discrete molecules separated by normal van der Waals distances, the shortest intermolecular contacts being O(2)···H(5a) = 2.59(5), O(1)···C(8) = 3.340(6), and O(1)···O(2) = 3.333(5) Å. The molecule (Fig. 1) contains a *facially* coordinated $[Me_2Ga(N_2C_3H_3)(OCH_2(C_5H_4N))]^-$ ligand, as expected (1). The η^3-allyl ligand occupies one coordination site of the pseudo-octahedral complex, *trans* to the pyridyl nitrogen atom rather than *trans* to the pyrazolyl nitrogen atom as predicted earlier (1) on the basis of the crystal structure of

[3]Supplementary material mentioned in the text may be purchased from the Depository of Unpublished Data, CISTI, National Research Council of Canada, Ottawa, Ont., Canada K1A 0S2.

Can. J. Chem. Downloaded from www.nrcresearchpress.com by 176.9.209.113 on 09/07/12
For personal use only.

TABLE 3. Bond angles (deg) with estimated standard deviations in parentheses

Bonds	Angle (deg)	Bonds	Angle (deg)
O(3)—Mo—N(1)	81.3(1)	N(2)—Ga—C(7)	106.2(3)
O(3)—Mo—N(3)	73.3(1)	C(6)—Ga—C(7)	120.7(4)
O(3)—Mo—C(1)	168.9(1)	Mo—O(3)—Ga	118.1(1)
O(3)—Mo—C(2)	102.3(1)	Mo—O(3)—C(11)	109.4(2)
O(3)—Mo—C(3)	81.8(2)	Ga—O(3)—C(11)	117.8(2)
O(3)—Mo—C(4)	87.6(2)	Mo—N(1)—N(2)	121.8(2)
O(3)—Mo—C(5)	120.1(2)	Mo—N(1)—C(8)	130.8(3)
N(1)—Mo—N(3)	81.5(1)	N(2)—N(1)—C(8)	106.8(3)
N(1)—Mo—C(1)	95.0(2)	Ga—N(2)—N(1)	120.6(2)
N(1)—Mo—C(2)	164.7(1)	Ga—N(2)—C(10)	131.9(3)
N(1)—Mo—C(3)	124.7(2)	N(1)—N(2)—C(10)	107.6(3)
N(1)—Mo—C(4)	90.8(2)	Mo—N(3)—C(12)	115.7(2)
N(1)—Mo—C(5)	83.1(2)	Mo—N(3)—C(16)	126.5(3)
N(3)—Mo—C(1)	95.9(1)	C(12)—N(3)—C(16)	117.7(4)
N(3)—Mo—C(2)	85.3(1)	Mo—C(1)—O(1)	178.7(4)
N(3)—Mo—C(3)	140.6(2)	Mo—C(2)—O(2)	175.0(4)
N(3)—Mo—C(4)	160.2(2)	Mo—C(3)—C(4)	67.9(3)
N(3)—Mo—C(5)	157.6(2)	Mo—C(4)—C(3)	75.8(3)
C(1)—Mo—C(2)	78.6(2)	Mo—C(4)—C(5)	78.4(3)
C(1)—Mo—C(3)	108.7(2)	C(3)—C(4)—C(5)	117.5(5)
C(1)—Mo—C(4)	103.0(2)	Mo—C(5)—C(4)	66.3(2)
C(1)—Mo—C(5)	69.4(2)	N(1)—C(8)—C(9)	111.1(4)
C(2)—Mo—C(3)	70.6(2)	C(8)—C(9)—C(10)	104.6(4)
C(2)—Mo—C(4)	104.2(2)	N(2)—C(10)—C(9)	110.0(4)
C(2)—Mo—C(5)	107.2(2)	O(3)—C(11)—C(12)	110.0(3)
C(3)—Mo—C(4)	36.3(2)	N(3)—C(12)—C(11)	114.9(3)
C(3)—Mo—C(5)	61.8(2)	N(3)—C(12)—C(13)	121.0(4)
C(4)—Mo—C(5)	35.3(2)	C(11)—C(12)—C(13)	124.0(4)
O(3)—Ga—N(2)	92.4(1)	C(12)—C(13)—C(14)	120.1(6)
O(3)—Ga—C(6)	110.4(3)	C(13)—C(14)—C(15)	118.9(5)
O(3)—Ga—C(7)	112.1(3)	C(14)—C(15)—C(16)	119.2(5)
N(2)—Ga—C(6)	111.3(3)	N(3)—C(16)—C(15)	123.0(6)

the related molecule $[Me_2Ga(N_2C_5H_7)(OCH_2CH_2NH_2)]Mo(CO)_2(\eta^3\text{-}C_4H_7)$, **2** (6). Inspection of Fig. 1 shows that a steric interaction with one of the hydrogen atoms bound to C(11) would result if the allyl ligand were located *trans* to the pyrazolyl nitrogen atom. The location of the allyl ligand in the present structure is analogous to that observed for the $\eta^3\text{-}C_7H_7$ ligands in the complexes $[Me_2Ga(N_2C_5H_7)(OCH_2CH_2NH_2)]Mo(CO)_2(\eta^3\text{-}C_7H_7)$ (7) and $[Me_2Ga(N_2C_5H_7)(OCH_2CH_2SEt)]Mo(CO)_2(\eta^3\text{-}C_7H_7)$ (8), *trans* to the amino nitrogen and alkyl sulphur atoms, respectively. The overall ligand shape and chelate ring conformations are very similar to those reported for $[Me_2Ga(N_2C_3H_3)(OCH_2(C_5H_4N))]Re(CO)_3$ (1).

The η^3-allyl ligand is oriented such that the central carbon atom is directed away from the carbonyl ligands. The central Mo—C(allyl) bond (2.189(4) Å) is significantly shorter than the two others (2.290(4) and 2.341(4) Å). These features are similar to those observed in related structures (refs. 9–13 and references therein). The Mo—N(pyrazolyl) bond length of 2.232(2) Å, *trans* to CO, is significantly shorter than corresponding distances ranging 2.276(4)–2.322(3) Å in related compounds (9–11). The Mo—N(pyridyl) bond at 2.212(3) Å and *trans* to the allyl group is, as expected, shorter than the Mo—N(pz) bond. The Mo—O distance of 2.219(2) Å is shorter than the corresponding distance of 2.269(2) Å in **2** (6) but is consistent with the relatively short metal—O distances observed for the rhenium analog $[Me_2Ga(N_2C_3H_3)(OCH_2(C_5H_4N))]Re(CO)_3$ (1). The Mo—C(O) distances reflect a structural *trans* effect, the bond *trans* to O (1.928(4) Å) being significantly shorter than that *trans* to N (1.952(4) Å). The corresponding C—O distances differ by 0.020(7) Å (in the opposite sense).

TABLE 4. Intra-annular torsion angles (deg) standard deviations in parentheses

Atoms	Value (deg)
N(1)—Mo—O(3)—Ga	−20.8(1)
N(2)—Ga—O(3)—Mo	24.9(1)
O(3)—Ga—N(2)—N(1)	−19.8(3)
Mo—N(1)—N(2)—Ga	7.7(4)
O(3)—Mo—N(1)—N(2)	7.4(3)
N(3)—Mo—O(3)—C(11)	33.9(2)
Mo—O(3)—C(11)—C(12)	−44.2(4)
O(3)—C(11)—C(12)—N(3)	29.3(5)
Mo—N(3)—C(12)—C(11)	0.8(4)
O(3)—Mo—N(3)—C(12)	−18.9(2)

The pyrazolyl and pyridyl rings are both planar to within experimental error. The Mo···Ga distance is 3.5552(5) Å. Other features of the molecular geometry (Tables 2–4) are as expected.

Acknowledgments

We thank the Natural Sciences and Engineering Research Council of Canada for financial support and the University of British Columbia Computing Centre for assistance.

Can. J. Chem. Downloaded from www.nrcresearchpress.com by 176.9.209.113 on 09/07/12
For personal use only.

1. S. J. RETTIG, A. STORR, J. TROTTER, and K. UHRICH. Can. J. Chem. **62**, 2783 (1984).
2. D. A. COPPER, S. J. RETTIG, and A. STORR. Can. J. Chem. **64**, 566 (1986).
3. P. COPPENS, L. LEISEROWITZ, and D. RABINOVICH. Acta Crystallogr. **18**, 1035 (1965).
4. W. R. BUSING and H. A. LEVY. Acta Crystallogr. **22**, 457 (1967).
5. International tables for X-ray crystallography. Vol. IV. Kynoch Press, Birmingham. 1974. pp. 99–102 and 149.
6. K. S. CHONG, S. J. RETTIG, A. STORR, and J. TROTTER. Can. J. Chem. **57**, 1335 (1979).
7. K. S. CHONG, S. J. RETTIG, A. STORR, and J. TROTTER. Can. J. Chem. **59**, 1665 (1981).
8. S. J. RETTIG, A. STORR, and J. TROTTER. Can. J. Chem. **59**, 2391 (1981).
9. K. R. BREAKELL, S. J. RETTIG, D. L. SINGBEIL, A. STORR, and J. TROTTER. Can. J. Chem. **56**, 2099 (1978).
10. K. R. BREAKELL, S. J. RETTIG, A. STORR, and J. TROTTER. Can. J. Chem. **57**, 139 (1979).
11. E. M. HOLT, S. L. HOLT, and K. J. WATSON. J. Chem. Soc. Dalton Trans. 2444 (1973).
12. C. F. PUTNIK, J. J. WELTER, G. D. STUCKY, M. J. D'ANIELLO, JR., B. A. SOSINSKY, J. F. KIRNER, and E. L. MUETTERTIES. J. Am. Chem. Soc. **100**, 4107 (1978).
13. J. A. KADUK, A. T. POULOS, and J. A. IBERS. J. Organomet. Chem. **127**, 245 (1977).

Can. J. Chem. Downloaded from www.nrcresearchpress.com by 176.9.209.113 on 09/07/12
For personal use only.

Vibrational analysis of the low resolution $\tilde{a} \leftarrow \tilde{X}$ absorption spectra of BrClCS and Br_2CS

B. SIMARD[1] AND R. P. STEER[2]

Department of Chemistry, University of Saskatchewan, Saskatoon, Sask., Canada S7N 0W0

AND

R. H. JUDGE AND D. C. MOULE

Department of Chemistry, Brock University, St. Catharines, Ont., Canada L2S 3A1

Received July 16, 1987

B. SIMARD, R. P. STEER, R. H. JUDGE, and D. C. MOULE. Can. J. Chem. **66**, 359 (1988).

The $\tilde{a} \leftarrow \tilde{X}$ absorption spectra of BrClCS and Br_2CS have been photographed under low resolution at room temperature. The electronic origins of BrClCS and Br_2CS have been placed at 17116 and 16859 cm^{-1}, respectively. Vibronic analyses show that the molecules are non-planar in their $\tilde{a}$ states. By fitting quadratic–Gaussian and quadratic–quartic double-minimum potentials to the observed vibrational levels of the out-of-plane manifolds, the equilibrium out-of-plane angles and the barrier heights to molecular inversion have been estimated to be 25 ± 1 deg and 541 ± 10 cm^{-1} for BrClCS, and 17.5 ± 1 deg and 524 ± 10 cm^{-1} for Br_2CS. In the case of BrClCS, all six $\tilde{a}$ state vibrational frequencies have been obtained. In the case of Br_2CS, only modes 1 (C—S stretch), 2 (symmetric C—Br stretch), 3 (in-plane Br—C—Br scissor), and 4 (out-of-plane bend) are active in the spectrum. Comparisons with other tetraatomic thiocarbonyls support the given assignments.

B. SIMARD, R. P. STEER, R. H. JUDGE et D. C. MOULE. Can. J. Chem. **66**, 359 (1988).

Les spectres d'absorption des transitions ($\tilde{a} \leftarrow \tilde{X}$ d'BrClCS et d'Br_2CS ont été photographiés dans des conditions de basse résolution à la température de la pièce. Les origines des transitions électroniques pures dans le BrClCS et le Br_2CS ont été respectivement placées à 17116 et 16859 cm^{-1}. Des analyses vibrationelles indiquent que les molécules sont non-planaires dans leurs états $\tilde{a}$. En modelant des potentiels à double minimum de types quadratique–Gaussien et quadratique–quartique aux niveaux vibrationel observés du mouvement hors du plan, les angles d'équilibre hors du plan et les hauteurs des barrières opposant l'inversion moléculaire ont été estimés à 25 ± 1° et 541 ± 10 cm^{-1} pour BrClCS, et 17.5 ± 1° et 524 ± 10 cm^{-1} pour Br_2CS. Dans le cas d'BrClCS, les fréquences vibrationelles des six modes de vibration ont pu être determinées. Dans le cas de Br_2CS, seulement les modes 1 (élongation C—S), 2 (élongation symmétrique C—Br), 3 (cisaillement dans le plan Br—C—Br), et 4 (repliement hors du plan) sont actifs dans le spectre. Des comparaisons avec d'autre thiocarbonyles tétra-atomiques appuient les attributions vibrationelles apportées.

Introduction

Interest in the spectroscopy, photophysics, and photochemistry of small thiocarbonyl molecules has grown rapidly in recent years. The initial interest in these compounds resulted partly from similarities with their carbonyl analogues whose spectroscopy and photochemistry have been relatively well-understood for many decades. However, it was soon realized that the thiocarbonyls are in many respects different from and more interesting than their carbonyl counterparts. One important reason for this lies in the fact that substitution of sulfur for oxygen shifts the excited electronic states of a molecule to lower energies. As a result, the low-lying excited states of the thiocarbonyls are bound, enabling one, in principle, to determine their excited state structures from their vibrationally and rotationally discrete absorption spectra.

The $\tilde{a}$–$\tilde{X}$ and $\tilde{A}$–$\tilde{X}$ band systems of most thiocarbonyls are found in the visible region of the spectrum. Both are associated with nominal $n \rightarrow \pi^*$ one electron promotions on the C=S moiety and are relatively weak (1). Their origins are separated by no more than ca. 1900 cm^{-1} and their oscillator strengths often differ by a factor of 10 or less, leading to extensive overlap of the two systems. The $\tilde{a}$–$\tilde{X}$ and $\tilde{A}$–$\tilde{X}$ spectra of H_2CS (2), HClCS (3), F_2CS (4, 5), FClCS (6, 7), and Cl_2CS (8, 9) have been analyzed to date.

Until recently, little has been known about the corresponding transitions in the heavier BrClCS and Br_2CS molecules. The $\tilde{A}$–$\tilde{X}$ band systems of these two thiocarbonyls were recently analyzed (10) using both conventional room temperature and jet-cooled excitation spectroscopy. These techniques failed to reveal observable emission from their lowest triplet states. In order to complete the characterization of the low-lying excited states of these molecules we therefore undertook to investigate their $\tilde{a}$–$\tilde{X}$ and systems using conventional room temperature photographic absorption spectroscopy. This method has been very successful in the past for studying such systems in spite of their relatively small oscillator strengths. We report here vibrational analyses of the low resolution $\tilde{a}$–$\tilde{X}$ absorption spectra of BrClCS and Br_2CS.

Experimental

BrClCS and Br_2CS were prepared by the method of Diderrich and Hass (11) by the direct reaction of boron tribromide with thiophosgene (Cl_2CS). Both reactants (Aldrich) were used as received. Purification of both BrClCS and Br_2CS was achieved by trap-to-trap vacuum distillation on a grease- and mercury-free vacuum line. Immediately following purification, the sample of BrClCS was analyzed by mass spectrometry which showed that the main contaminants were Br_2CS and Cl_2CS. In the case of Br_2CS, BBr_3, and BCl_3 (both non-emissive) were found to be the main contaminants; there was no evidence of residual Cl_2CS or BrClCS. No other spectral analyses were carried out before photographing the spectrum. When not in use the samples were kept in the dark at about −10°C to prevent dimerization and thermal decomposition.

A 2 m White-type multiple reflection cell was filled with either BrClCS or Br_2CS at its room temperature vapor pressure (ca. 17 and 6 Torr, respectively) and was illuminated with a 450 W high pressure Xe arc. The exit beam was then directed into a 1.5 m Bausch and Lomb grating spectrograph with a reciprocal dispersion of 15 nm/cm. The resulting spectrum was photographed with Kodak high speed infrared film. The absolute positions of the bands were determined by

[1]Present address: Laser Chemistry Group, Division of Chemistry, National Research Council of Canada, Ottawa, Ont., Canada K1A 0R6.

[2]To whom correspondence should be addressed.

Can. J. Chem. Downloaded from www.nrcresearchpress.com by 176.9.209.113 on 09/07/12
For personal use only.

Can. J. Chem. Downloaded from www.nrcresearchpress.com by 176.9.209.113 on 09/07/12
For personal use only.

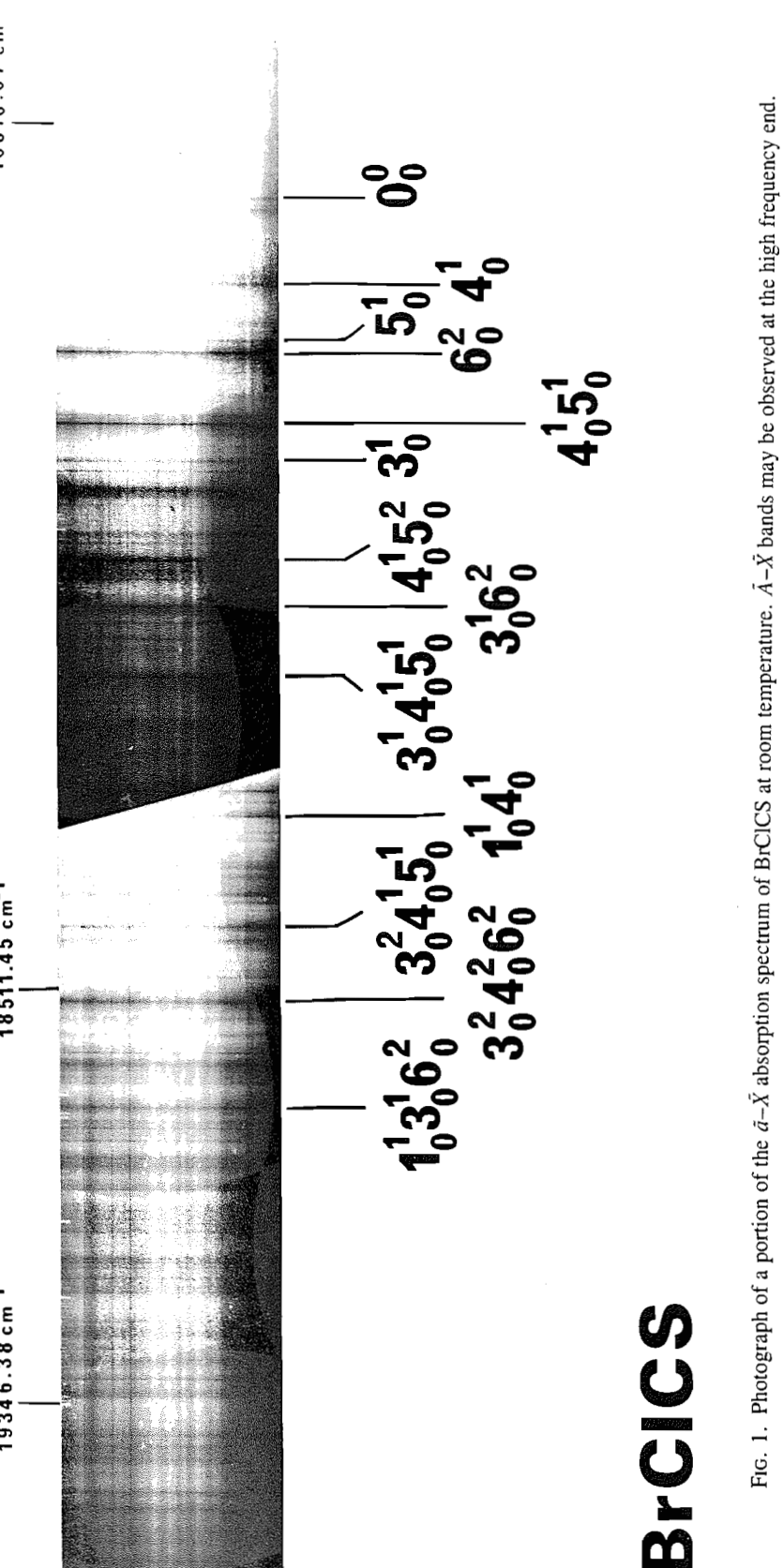

FIG. 1. Photograph of a portion of the $\tilde{a}$–$\tilde{X}$ absorption spectrum of BrClCS at room temperature. $\tilde{A}$–$\tilde{X}$ bands may be observed at the high frequency end.

TABLE 1. Separation between the $\tilde{A}$ and $\tilde{a}$ state origins of several thiocarbonyl compounds

Molecule	Separation (cm^{-1})	Reference
H_2CS	1888	2
Thioacetaldehyde	1629	19, 20
HClCS	1558	3
ClFCS	1467	5, 6
Thiopropynal	1397	21
Thioacetone	1380	19, 20
F_2CS	1286	4, 5
Cl_2CS	1224	8, 9
s-*trans*-Thioacrolein	1088	22

comparison with the simultaneously photographed emission lines of an Fe–Ne hollow cathode lamp.

Results and discussion

The $\tilde{a}$–$\tilde{X}$ and $\tilde{A}$–$\tilde{X}$ absorption systems of both BrClCS and Br_2CS are of comparable intensity and overlap substantially. Fortunately neither molecule phosphoresces strongly whereas both fluoresce with high quantum yield when excited at wavelengths below their dissociation thresholds (10). Thus, absorption bands due to the singlet systems may be identified from the laser-induced fluorescence excitation spectra. The remaining bands are assigned to the triplet systems.

Considerable photodecomposition of the samples occurred during the recording of the spectra. Fortunately, the most probable decomposition products either do not absorb in the same spectral region (e.g. dimer) or were not observed (e.g. Cl_2CS (9), Cl_2 (12), BrCl (13), Br_2 (14)).

The mechanism whereby the spin forbidden $\tilde{a}$–$\tilde{X}$ absorption systems gain intensity is well known (15–17). Assuming that the $\tilde{a}$–$\tilde{X}$ transitions in these molecules "borrow" intensity from the strong electric dipole allowed $\tilde{B}$–$\tilde{X}$ transitions, the origin bands should be observed, no restrictions should apply to Δv for transitions among totally symmetric vibrations, and Δv even is expected for transitions among non-totally symmetric vibrations (1, 15). Successful vibrational analysis (*vide infra*) of the $\tilde{a}$–$\tilde{X}$ systems in Br_2CS and BrClCS based upon these selection rules attest to the validity of the assumptions on which they are based.

1. The $\tilde{a}$–$\tilde{X}$ *absorption spectrum of BrClCS*

The low resolution $\tilde{a}(^3A'')$–$\tilde{X}(^1A')$ absorption spectrum of BrClCS was photographed in the 490–595 nm region. The 510–585 nm segment is shown in Fig. 1. Strong absorption begins at about 584 nm, and bands belonging to the $\tilde{A}(^1A'')$–$\tilde{X}(^1A')$ system can be observed in the blue part of the spectrum. The separations between the origins of the $\tilde{A}$ and $\tilde{a}$ states of thiocarbonyls for which data are already available is of immediate help in the analysis. The relevant data are given in Table 1, and from them an $\tilde{A}$–$\tilde{a}$ separation of the order of 1200 cm^{-1} is anticipated for BrClCS. Since the origin of the $\tilde{A}$ state is located at 18363 cm^{-1} (10), the origin of the $\tilde{a}$ state of BrClCS should therefore lie near 17160 cm^{-1}. The lowest energy strong absorption band lies at 17115.8 cm^{-1} and because progressions can be built on this band, this feature is assigned as the origin. The actual $\tilde{A}$–$\tilde{a}$ separation is therefore 1247 cm^{-1}.

The following band assignments were achieved on the basis that the $\tilde{a}$ state frequencies should be similar to those of the $\tilde{A}$ state, as is the case with other tetraatomic thiocarbonyls (see references in Table 1).

Modes 4 (Br—C—Cl rock) and 5 (Br—C—Cl scissor)

Excluding the anharmonic ν_6' stack, the lowest frequency mode is expected, by comparison with the $\tilde{A}$ state, to be ν_4'. The first strong band to the blue of the origin (17115.8 cm^{-1}) is located at 17259.0 cm^{-1}. The difference, 143.2 cm^{-1}, is attached to many hot and cold combination bands, and a progression extends to 4^3 in combination with 5_0^2. The band at 17259.0 cm^{-1} is therefore unambiguously assigned as 4_0^1. The frequency of $\nu_4' = 143.2\ cm^{-1}$ is only slightly smaller than the $\tilde{A}$ state value of 159 cm^{-1} (10).

The band located +237.0 cm^{-1} from the origin at 17352.9 cm^{-1} is assigned as the 5_0^1 band for two reasons. First, it is the first strong band to be detected to the blue of the 4_0^1 band and second, the combination bands $4_0^1 5_0^1$, and $4_0^1 5_0^2$ can be observed and are among the strongest bands of the spectrum.

A value of 237.0 cm^{-1} for ν_5' is nearly the same as the ground state frequency (235 ± 3 cm^{-1} from ref. 10). It was originally thought that the band at 17352.9 cm^{-1} was hot, but it was not possible to suitably assign the spectrum on this basis. Mode 5 is approximately described as the Br—C—Cl scissoring motion. As shown in Table 2, the ratio of ν_5':ν_5'' in the $\tilde{a}$:$\tilde{X}$ states for this vibration increases in the order F_2CS ($\tilde{a}$:$\tilde{X}$ = 0.74) > ClFCS ($\tilde{a}$:$\tilde{X}$ = 0.81) > Cl_2CS ($\tilde{a}$:$\tilde{X}$ = 0.84). The present value of

TABLE 2. Ratios of the frequencies of vibrational modes in the $\tilde{a}$:$\tilde{X}$ states of several tetraatomic thiocarbonyls

	Ratio			
Approximate description	H_2CS[b]	F_2CS[c]	ClFCS[d]	Cl_2CS[e]
C=S stretch	0.81	0.87	—	0.87
Symmetric Y—C—X stretch	—	0.93	0.94	0.94
Y—C—X scissor	0.94	0.74	0.81	0.84
Out-of-plane bend[a]	0.36	0.91	0.79	0.63
Antisymmetric Y—C—X stretch	—	—	—	—
Y—C—X rock	0.77	—	—	—

[a]The 0^+–1^+ separation is used as the $\tilde{a}$ state frequency.
[b]References 2, 23, 24, 25.
[c]References 4, 26.
[d]References 6, 27.
[e]Reference 9.

Can. J. Chem. Downloaded from www.nrcresearchpress.com by 176.9.209.113 on 09/07/12
For personal use only.

Can. J. Chem. Downloaded from www.nrcresearchpress.com by 176.9.209.113 on 09/07/12
For personal use only.

TABLE 3. Assignment of prominent bands of the $\tilde{a}(^3A'') \leftarrow \tilde{X}(^1A')$, absorption spectrum of BrClCS

Frequency (cm^{-1})	Intensity	Assignment
16825.5	w	$3_1^0 4_0^1$
16859.3	w	4_1^0
16879.0	w	5_1^0
16910.6	w	$3_1^0 5_0^1$, $5_0^1 6_1^1$
16954.2	w	6_1^3
17018.6	w	$4_0^1 5_1^0$
17076.6	w	$3_0^1 4_0^1 6_2^2$
17115.8	s	0_0^0
17137.7	s	$5_1^0 6_0^2$
17243.2	m	6_1^5
17250.2	m	$2_0^1 3_1^0$
17259.0	s	4_0^1
17353.8	m	5_0^1
17373.6	s	6_0^2
17496.0	s	$4_0^1 5_0^1$
17558.3	m	3_0^1
17578.3	m	6_0^4
17610.1	s	$5_0^1 6_0^2$
17686.1	m	2_0^1
17702.4	m	$3_0^1 4_0^1$
17731.9	s	$4_0^1 5_0^2$
17747.7	m	$4_0^1 5_0^1 6_0^2$
17763.4	m	$4_1^3 5_0^2$
17812.3	s	$3_0^1 6_0^2$
17819.6	m	6_0^6
17826.7	m	$2_0^1 4_0^1$
17842.7	m	$3_0^1 4_0^2$
17872.0	m	$4_0^2 5_0^2$
17939.7	s	$3_0^1 4_0^1 5_0^1$
18018.0	m	$4_0^3 5_0^2$
18050.6	m	1_0^1
18079.7	m	$3_0^1 4_0^2 5_0^1$
18144.9	m	$3_0^2 4_0^1$
18190.7	m	$1_0^1 4_0^1$
18220.2	w	$3_0^1 4_0^3 5_0^1$
18235.0	w	2_0^2
18286.1	w	$3_0^2 4_0^2$
18303.6	w	$1_0^1 6_0^2$
18380.6	m	$3_0^2 4_0^1 5_0^1$
18422.5	m	$1_0^1 4_0^1 5_0^1$
18493.6	w	$1_0^1 3_0^1$
18538.9	m	$3_0^2 4_0^2 6_0^2$
18666.4	m	$1_0^1 4_0^1 5_0^2$
18747.7	m	$1_0^1 3_0^1 6_0^2$
18866.7	w	$1_0^1 3_0^1 4_0^1 5_0^1$

nearly unity for BrClCS appears to be a continuation of this trend.

Mode 3 (Br—C—Cl symmetric stretch)

In the case of F_2CS (4, 5) and Cl_2CS (8, 9) the frequency of the X—C—Y symmetric stretch is observed to be somewhat higher in the $\tilde{a}$ state than in the $\tilde{A}$ state. The frequency of this mode in BrClCS is therefore expected to be higher than the $\tilde{A}$ state value of 423 cm^{-1} (10). The feature located +442.5 cm^{-1} from the origin is therefore assigned as the 3_0^1 band. This choice was motivated by the ability to assign several additional features in terms of combination bands involving this mode.

Again the ratio of $\nu_3':\nu_3''$ in the $\tilde{a}:\tilde{X}$ states is calculated to be very close to unity (1.01). This ratio is somewhat larger than the nearly constant ratio of 0.94 observed for F_2CS, ClFCS, and Cl_2CS (see Table 2).

Mode 1 (C—S stretch)

In the case of F_2CS (4, 5) and Cl_2CS (8, 9), the frequency of this mode is observed to be somewhat higher in the $\tilde{a}$ state than in the $\tilde{A}$ state. The same should apply for BrClCS. Thus, the $\tilde{a}$ state C—S stretching frequency is anticipated to be higher than the $\tilde{A}$ state value of 890 cm^{-1} (10). The feature located +934.7 cm^{-1} from the origin is assigned as the 1_0^1 band. Several combination bands involving this frequency can be found. The $\tilde{a}:\tilde{X}$ ratio of 0.83 compares well with those of other similar molecules listed in Table 2.

Mode 2 (Br—C—Cl asymmetric stretch)

There is a feature +570.3 cm^{-1} from the origin which could not be assigned in terms of bands involving modes 1, 3, 4, 5, or 6. This band is tentatively assigned as 2_0^1. On the grounds that most of the $\tilde{a}$ state frequencies of other tetraatomic thiocarbonyl halides are higher than the corresponding $\tilde{A}$ state values, the observed $\nu_2':\nu_2''$ ratio of 0.75 compares very well with the recently reported value of 0.71 in the $\tilde{A}:\tilde{X}$ states (10).

Mode 6 (out-of-plane bend)

By analogy with other similar systems (1), this mode is expected to be very active. In the $\tilde{A}$–$\tilde{X}$ system 6_0^2 is the strongest band. Because both the $\tilde{a}$–$\tilde{X}$ and the $\tilde{A}$–$\tilde{X}$ systems involve the same one electron, $n \rightarrow \pi^*$, promotion, the $\tilde{a}$ state structure is expected to be not too different from that of the $\tilde{A}$ state. Thus, the 6_0^2 band should also be very strong in the $\tilde{a}$–$\tilde{X}$ absorption spectrum. The strong feature +257.8 cm^{-1} from the origin is therefore assigned as the 6_0^2 band. This assignment is straightforward since this feature is the only strong band which could bear this assignment. The $\tilde{a}:\tilde{X}$ frequency ratio for this mode (see Table 2) decreases in the order F_2CS (0.91) > ClFCS (0.79) > Cl_2CS (0.63). The observed $\tilde{a}:\tilde{X}$ ratio of 0.58 for BrClCS fits very nicely into this pattern.

The complete analysis is given in Table 3; almost all the bands lying in the 528–595 nm region have been assigned. The frequencies of all six modes in each of the $\tilde{X}$, $\tilde{a}$, and $\tilde{A}$ states of BrClCS are summarized in Table 4.

2. The $\tilde{a}$–$\tilde{X}$ *absorption spectrum of* Br_2CS

The absorption spectrum of Br_2CS photographed at a pressure–path of 70 atm cm is shown in Fig. 2. The banded absorption system commences near 613 nm. Two types of features can be distinguished: (1) line-like features which lie in the blue part of the spectrum, and (2) broader bands which lie in the red part of the spectrum. Comparison with the recently reported fluorescence excitation spectrum of Br_2CS (10) shows that the line-like features belong to the $\tilde{A}(^1A_2)$–$\tilde{X}(^1A_1)$ singlet band system. As the broad features could not be associated with this system, these bands have been ascribed to the $\tilde{a}(^3A_2)$–$\tilde{X}(^1A_1)$ absorption.

Using the data of Table 1, together with the $\tilde{A}$–$\tilde{a}$ separation of 1247 cm^{-1} for BrClCS, and the origin of the $\tilde{A}$–$\tilde{X}$ system at 17992 cm^{-1} (10), the origin of the $\tilde{a}$–$\tilde{X}$ system of Br_2CS should be located in the 592–595 nm region. This appears to be reasonable at first sight since bands lying at $\lambda > 595$ nm are weak while those lying at $\lambda < 595$ nm are much stronger. The assignment was facilitated by the identification of progressions of 154 and 258 cm^{-1}. Both progressions converge to the weak band at 16859 cm^{-1}, which has been assigned to the electronic origin. The resulting $\tilde{A}$–$\tilde{a}$ separation of 1133 cm^{-1} compares very well with the data of Table 1.

TABLE 4. Ground, $\tilde{a}$, and $\tilde{A}$ state vibrational frequencies of BrClCS

Mode	Symmetry	Approximate description	Frequency (cm^{-1}) $\tilde{X}$		$\tilde{a}^c$	$\tilde{A}^b$
1	a'	C—S stretch	1130^a		934	890
2	a'	Br—C—Cl asym. stretch	764^a		570	540
3	a'	Br—C—Cl sym. stretch	438^a		442	423
4	a'	Br—C—Cl rock	256^a		143	159
5	a'	Br—C—Cl scissor	236^b		238	207
6	a''	Out-of-plane bend	441^b	$\nu' = 0$	0	0
				1	1.3	2
				2	258	273
				3	279	312
				4	462	483
				5	568	614
				6	703	780

[a]Reference 28.
[b]Reference 10.
[c]This work.

TABLE 5. Assignment of prominent bands of the $\tilde{a}(^3A_2) \leftarrow \tilde{X}(^1A_1)$ absorption spectrum of Br_2CS

Frequency (cm^{-1})	Intensity	Assignment
16312	w	3_3^0
16391	w	$2_0^1 3_4^0$
16411	w	3_5^3
16466	w	3_3^1
16496	w	$3_2^0, 2_1^0$
16545	w	$3_2^0 4_1^3$
16573	w	$2_0^1 3_3^0$
16596	w	3_4^3
16617	w	3_3^2
16649	w	$3_2^1, 3_3^0 4_0^2$
16679	w	3_1^0
16710	w	$2_1^1 3_1^1$
16727	w	$3_1^0 4_1^3, 2_0^1 3_3^1$
16751	w	$2_0^1 3_2^0$
16783	w	3_3^3
16804	m	$3_2^2, 4_0^2 3_3^1, 3_0^1 3_2^0 4_1^3$
16859	w	0_0^0
16913	w	4_1^3
16935	w	$2_0^1 3_1^0$
16966	w	3_2^3
16986	m	$3_1^2, 4_0^2 3_2^1, 2_0^1 3_1^0 4_1^3$
17012	s	$3_0^1, 4_0^2 3_1^0$
17081	s	$2_0^1 3_1^1$
17117	m	2_0^1
17146	w	3_1^3
17169	s	$3_0^2, 4_0^2 3_1^1, 2_0^1 4_1^3$
17195	s	4_0^2
17223	w	$2_0^1 3_2^3$
17240	w	$2_0^1 3_1^2$
17265	s	$2_0^1 3_0^1$
17300	w	3_1^4
17323	s	3_0^3
17348	w	$3_0^1 4_0^2$
17375	s	2_0^2
17421	s	$2_0^1 3_0^2, 4_1^5$
17453	w	$2_0^1 4_0^2$
17477	s	3_0^4
17530	s	$2_0^2 3_0^1$
17561	m	4_0^4

TABLE 5 (*concluded*)

Frequency (cm^{-1})	Intensity	Assignment
17583	s	$2_0^1 3_0^3$
17612	w	$2_0^3 3_1^1, 3_1^6$
17636	s	$2_0^3, 3_0^5$
17687	s	$2_0^2 3_0^2$
17754	m	1_0^1
17794	m	$2_0^3 3_0^1, 3_0^6$
17845	w	$2_0^2 3_0^3$

By comparison with the $\tilde{A}$–$\tilde{X}$ band system (10), the progressions of 154 and 258 cm^{-1} are attributed to activities in modes 3 (Br—C—Br scissor) and 2 (Br—C—Br symmetric stretch), respectively.

Only a few bands could not be assigned in terms of modes 2, 3, and their combinations. On the basis of the absorption spectra of other small thiocarbonyls (1), mode 1 (C—S stretch) should be active, and the band located +895 cm^{-1} from the origin could thus be 1_0^1. This assignment must be considered tentative because (1) the $\tilde{a}$:$\tilde{X}$ ratio (0.80) is somewhat smaller than the constant value of 0.87 observed for F_2CS and Cl_2CS (see Table 2), and (2) contrary to expectation no combination bands involving mode 1 could be positively identified.

Because the excited molecule exhibits a non-planar structure (*vide infra*), the out-of-plane bending mode is expected to be active. The band located +336 cm^{-1} from the origin is the strongest band in the spectrum and, by analogy with the previous analysis of the $\tilde{A}$–$\tilde{X}$ band system of BrClCS (10), this band is assigned as 4_0^2. The 4_1^3, 4_0^4, and 4_1^5 bands could also be observed and their positions have been listed in Table 5 together with the whole spectral assignment. Table 6 summarizes the vibrational frequencies of Br_2CS in its $\tilde{X}$, $\tilde{a}$, and $\tilde{A}$ states.

3. $\tilde{a}$ *state geometries*

The assignments of Tables 3 and 5 indicate that both BrClCS and Br_2CS are non-planar in their $\tilde{a}$ states. Whereas mildly anharmonic progressions are observed for most excited and ground state modes, one set of excited state frequencies in each

Can. J. Chem. Downloaded from www.nrcresearchpress.com by 176.9.209.113 on 09/07/12
For personal use only.

Can. J. Chem. Downloaded from www.nrcresearchpress.com by 176.9.209.113 on 09/07/12
For personal use only.

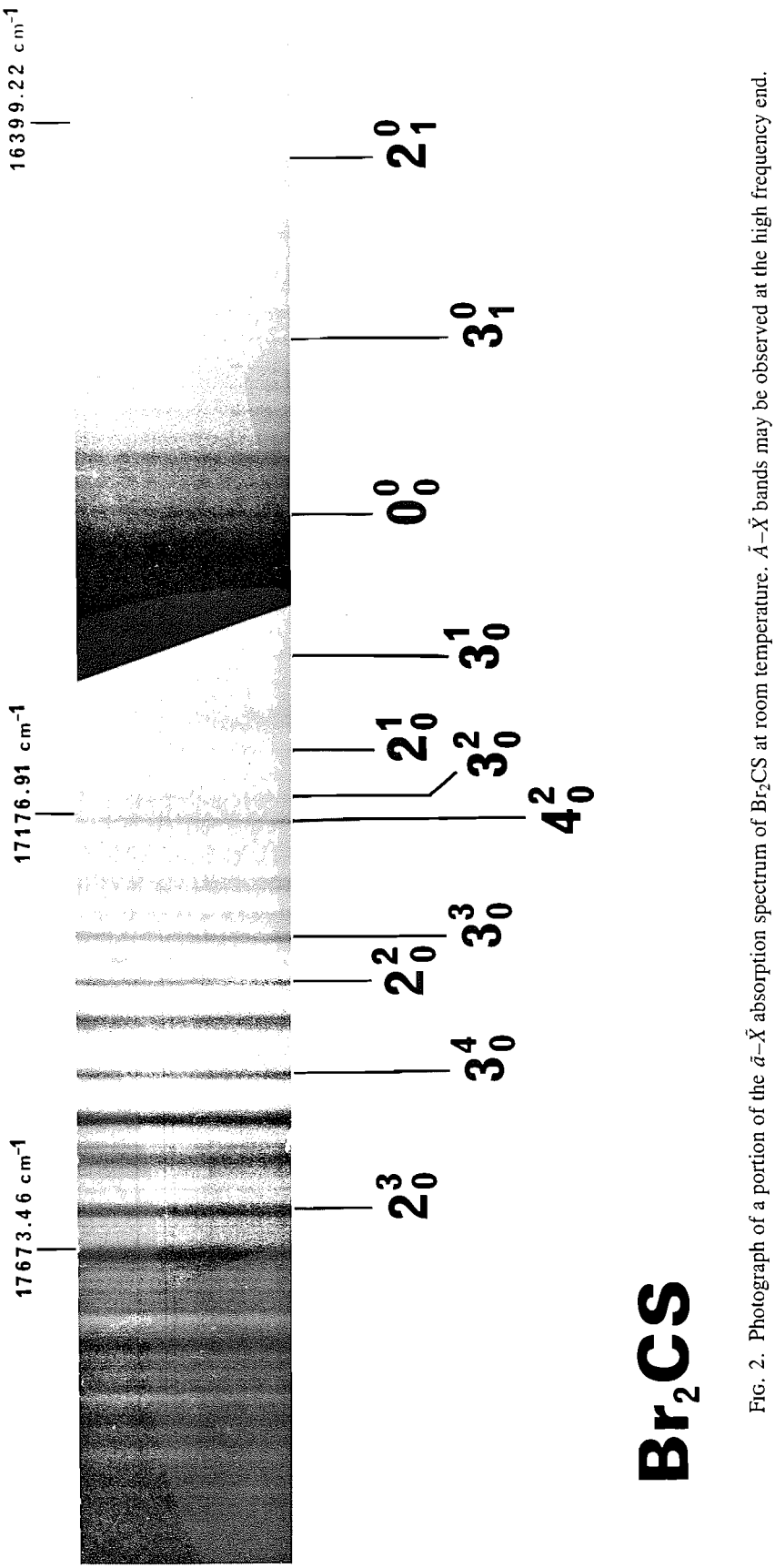

FIG. 2. Photograph of a portion of the $\tilde{a}$–$\tilde{X}$ absorption spectrum of Br_2CS at room temperature. $\tilde{A}$–$\tilde{X}$ bands may be observed at the high frequency end.

TABLE 6. Ground, $\tilde{a}$, and $\tilde{A}$ state vibrational frequencies of Br_2CS

Mode	Symmetry	Approximate description	Frequency (cm^{-1}) $\tilde{X}$		$\tilde{a}^b$	$\tilde{A}^c$
1	a_1	C—S stretch	1116		895[d]	890
2	a_1	Br—C—Br sym. stretch	367		258	250
3	a_1	Br—C—Br scissor	183		154	160
5	b_2	Br—C—Br asym. stretch	697		—	242
6	b_2	Br—C—Br rock	230		—	166
4	b_1	Out-of-plane bend	415	$v' = 0$	0	0
				1	—	9
				2	336	383
				3	469	389
				4	702	580
				5	977	791

[a]Reference 29.
[b]This work.
[c]Reference 10.
[d]Tentative.

TABLE 7. Observed and calculated levels of the out-of-plane bending mode of the $\tilde{a}$ state of BrClCS using the quadratic-Gaussian model

Parameter	Value			
ρ	0.9	1.2	1.5	1.8
B	2.3	2.7	3.1	3.5
ν_0 (cm^{-1})	227.6	195.6	174.6	160.6
$G(0^+)$ (cm^{-1})	144.5	143.9	143.1	142.9

	Frequency				
v_6'	Obs. (cm^{-1})	Calculated (cm^{-1})			
0	0	0	0	0	0
1	1.3	0.8	1.0	1.3	1.4
2	257.8	257.7	256.8	257.2	255.1
3	279.3	279.3	279.3	279.3	279.3
4	462.5	449.6	452.6	456.9	461.6
5	568.3	553.8	553.2	551.0	548.8
6	702.8	704.6	702.2	697.8	694.0
Barrier height (cm^{-1})		524	528	541	560
$Q_{min} \times 10^{20}$ ($g^{1/2}$ cm)		1.35	1.29	1.23	1.17
Out-of-plane angle (deg)		28.1	26.9	25.5	24.3

TABLE 8. Observed and calculated levels of the out-of-plane bending mode of the $\tilde{a}$ state of Br_2CS using the quadratic-Gaussian model

Parameter	Value			
ρ	0.6	0.9	1.2	1.5
B	1.20	1.47	1.70	1.90
ν_0 (cm^{-1})	443	355	304	270
$G(0^+)$ (cm^{-1})	220	214	208	204

	Frequency				
v_4'	Obs. (cm^{-1})	Calculated (cm^{-1})			
0	0	0	0	0	0
1	—	12	14	17	20
2	336	335	335	335	337
3	469	469	469	469	469
4	702	723	721	717	713
5	977	984	971	955	937
Barrier height (cm^{-1})		532	524	516	514
$Q_{min} \times 10^{20}$ ($g^{1/2}$ cm)		0.90	0.86	0.82	0.77
Out-of-plane angle (deg)		18.3	17.5	16.6	15.6

molecule does not fit this pattern. These are assigned to the excited state out-of-plane bending mode, and their extreme anharmonicity is therefore associated with the existence of an equilibrium non-planar nuclear conformation. This is in complete agreement with the observed behavior of the $\tilde{a}$ and $\tilde{A}$ states of all other thiocarbonyl halides investigated to date (1–9).

As shown previously for the $\tilde{A}$ states of these molecules (10, 18), either the quadratic–Gaussian or quartic–quadratic double-minimum potential models can be used to determine the out-of-plane angle and the barrier height opposing molecular inversion. The eigenvalues for the excited state out-of-plane bending levels in the quadratic–Gaussian model have been calculated and tabulated by Coon *et al.* (30) for various values of ρ, a shape factor, and B, a parameter directly proportional to the barrier height. The eigenvalues of the quartic–quadratic potential have been reported by Laane (31) but this model was found to provide a significantly poorer fit to the observed data. We take this as an indication that the shape of the inversion barrier is approximated better by a Gaussian function than a quadratic, a result which has often been observed in thiocarbonyl systems (1).

The results of the calculations for the quadratic-Gaussian model are summarized in Table 7 for BrClCS, and in Table 8 for Br_2CS. Following the technique of Coon *et al.* (30), these data were obtained by arbitrarily selecting a range of values of ρ (in increments of $\Delta\rho = 0.3$) and then determining the values of B (in increments of $\Delta B = 0.05$ or 0.10) which yielded reasonable agreement between the resulting calculated inversion vibrational energies and those oberved in the spectra. The "best" values of ρ and B were then selected from among several sets of such values. Because both the barrier height and the equilibrium out-of-plane angle exhibit only small differences for the set of nearly acceptable combinations of ρ and B (cf. Tables 7 and 8), we estimate the uncertainties to

Can. J. Chem. Downloaded from www.nrcresearchpress.com by 176.9.209.113 on 09/07/12
For personal use only.

Can. J. Chem. Downloaded from www.nrcresearchpress.com by 176.9.209.113 on 09/07/12
For personal use only.

be ca. $\pm 10\,cm^{-1}$ in the barrier heights and ca. $\pm 1°$ in the out-of-plane angles, within the limits imposed by the applicability of the model.

In the case of BrClCS, the best fit with the quadratic–Gaussian model is obtained using a shape factor of 1.5 and a B value of 3.1. This gives a barrier of 541 cm^{-1} and an equilibrium out-of-plane angle of 25°. A comparison of the above parameters with those of the $\tilde{A}$ state (10) indicates that both the $\tilde{A}$ and the $\tilde{a}$ states have nearly the same geometry. This result does not follow the trend established with other thiocarbonyls in which the barrier is somewhat higher in the $\tilde{a}$ state than in the $\tilde{A}$ state. A higher barrier would require a smaller separation between $\nu_6' = 2$ and $\nu_6' = 3$. The strong 6_0^2 band is undoubtedly correctly assigned. In order to obtain a smaller 2–3 splitting, the 6_1^3 band would have to lie to the red of its present position. Assuming that the 6_1^3 band can be observed in the present spectrum, careful examination of Fig. 1 reveals that there is no band which could be thus assigned.

The $\tilde{a}$–$\tilde{X}$ spectrum of Br_2CS consists of bands which are considerably broader than those of BrClCS, making the identification of closely spaced features difficult. The best fit to the ν_4' stack with the quadratic–Gaussian model is obtained using a shape factor of 0.9 and a B value of 1.475. This gives an out-of-plane angle and an inversion barrier height of 17.5° and 524 cm^{-1}, respectively. Unfortunately a definite assignment of a hot band transition terminating in $\nu_4' = 1$ could not be made, so a key datum on which to judge the quality of the calculated ν_4' levels is missing. Nevertheless, the calculated barrier and equilibrium out-of-plane angles are reasonable. The $\tilde{a}$ state inversion barrier is calculated to be about 60 cm^{-1} higher than that of the $\tilde{A}$ state, as expected on the basis of the structures of similar molecules.

The $\tilde{a}$–$\tilde{X}$ band systems of both BrClCS are associated with $n_S \rightarrow \pi^*_{CS}$ one electron promotions. Thus, the C—S bond order drops from 2 to 1.5 upon excitation and a substantial drop in the C—S stretching frequency must result. Our analyses assign ν_1' (BrClCS) = 934 cm^{-1} and ν_1' (Br_2CS) = 895 cm^{-1} which represent decreases of about 20% compared with the ground state values. Using Badger's empirical relationship (32), $r^2\omega$ = constant, Δr(C—S) = 0.10 and 0.12 Å are calculated for BrClCS and Br_2CS, respectively.

The decrease in frequency of the symmetric stretching mode, ν_2, in Br_2CS is similar to that observed upon excitation to the $\tilde{A}$ state (10), but is much larger than expected on the basis of a comparison with other tetraatomic thiocarbonyls. In the $\tilde{A}$ state (10, 18) the potential energy hypersurface along the C—Br symmetric stretching coordinate is highly perturbed by a dissociative process, most likely molecular fragmentation to form products in their ground electronic states (33). Such a process is also probably responsible for the lower than expected frequency of ν_2 in the $\tilde{a}$ state of Br_2CS.

Acknowledgements

This work was supported by the Natural Sciences and Engineering Research Council of Canada. One of us (B.S.) is grateful to the Government of Canada and the University of Saskatchewan for the award of NSERC and Province of Saskatchewan Postgraduate Scholarships, respectively.

1. R. P. Steer. Rev. Chem. Intermediates, **4**, 1 (1981).
2. D. J. Clouthier and D. A. Ramsay. Ann. Rev. Phys. Chem. **34**, 31 (1983).
3. R. H. Judge and D. C. Moule. J. Mol. Spectrosc. **113**, 77 (1985).
4. D. C. Moule. Can. J. Chem. **48**, 2623 (1970).
5. D. C. Moule and A. K. Mehra. J. Mol. Spectrosc. **35**, 137 (1970).
6. D. C. Moule and C. R. Subramaniam. J. Mol. Struct. **38**, 135 (1977).
7. C. R. Subramaniam and D. C. Moule. J. Mol. Spectrosc. **53**, 443 (1974).
8. D. J. Clouthier and D. C. Moule. J. Mol. Spectrosc. **87**, 471 (1981).
9. J. C. D. Brand, J. H. Callomon, D. C. Moule, J. Tyrell, and T. H. Goodwin. Trans. Faraday Soc. **61**, 2365 (1965).
10. B. Simard, P. A. Hackett, and R. P. Steer. J. Mol. Spectrosc. In press.
11. G. Diderrich and A. Hass. Chem. Ber. **109**, 3432 (1976).
12. M. A. A. Clyne and J. A. Coxon. Proc. R. Soc. London, **298**A, 425 (1967).
13. H. Okabe. Photochemistry of small molecules. John Wiley and Sons, New York. 1978.
14. K. P. Huber and G. Herzberg. Molecular spectra and molecular structure. Vol. 4. Constants of diatomic molecules. Van Nostrand Reinhold, New York. 1979.
15. J. M. Hollas. High resolution spectroscopy. Butterworths, London. 1982.
16. J. R. McDonald and L. E. Brus. Chem. Phys. Lett. **16**, 587 (1972).
17. H. Okabe. J. Chem. Phys. **66**, 2058 (1977).
18. B. Simard. Ph.D. Thesis, University of Saskatchewan. 1986.
19. A. E. Bruno, R. P. Steer, R. H. Judge, and D. C. Moule. Chem. Phys. Lett. **102**, 385 (1983).
20. A. E. Bruno. Ph.D. Thesis, University of Saskatchewan. 1984.
21. R. H. Judge and D. C. Moule. J. Mol. Spectrosc. **104**, 248 (1984).
22. D. C. Moule and R. H. Judge. J. Chem. Phys. **80**, 4646 (1984).
23. P. H. Turner, L. Halonen, and I. M. Mills. J. Mol. Spectrosc. **88**, 402 (1982).
24. J. W. C. Johns and W. B. Olson. J. Mol. Spectrosc. **39**, 479 (1971).
25. D. J. Clouthier, C. M. Kerr, and D. A. Ramsay. Chem. Phys. **56**, 73 (1981).
26. A. J. Downs. Spectrochim. Acta, **19**, 1165 (1963).
27. D. C. Moule and C. R. Subramaniam. Can. J. Chem. **47**, 1011 (1969).
28. J. L. Brema and D. C. Moule. Spectrochim. Acta, **28**A, 809 (1972).
29. W. Hauswirth and H. Willer. Spectrochim. Acta, **35**A, 263 (1979).
30. J. B. Coon, N. W. Naugle, and R. D. McKenzie. J. Mol. Spectrosc. **20**, 107 (1966).
31. J. Laane. Appl. Spectrosc. **24**, 73 (1970).
32. G. Herzberg. Molecular spectra and molecular structure. Vol. 1. Spectra of diatomic molecules. Van Nostrand Reinhold, New York. 1950.
33. B. Simard and R. P. Steer. Unpublished results.

Excess molar volumes and excess viscosities of 2-propanol + methylacetate + dichloromethane system at 298.15 K[1]

INÉS L. ACEVEDO, MIGUEL A. POSTIGO, AND MIGUEL KATZ[2]

Cátedra de Fisicoquímica, Instituto de Ingeniería Química e Instituto de Física, Facultad de Ciencias Exactas y Tecnología, Universidad N. de Tucumán, Avda. Independencia 1800, S.M. de Tucumán (4000), Argentina

Received July 17, 1987

INÉS L. ACEVEDO, MIGUEL A. POSTIGO, and MIGUEL KATZ. Can. J. Chem. **66**, 367 (1988).

Densities and viscosities were determined for the 2-propanol + methylacetate + dichloromethane system at 298.15 K. From the experimental results, molar excess volumes and excess viscosities were calculated. Different expressions exist in the literature to predict these excess properties from the binary mixtures. The empirical correlation of Tsao–Smith and Toop is the best for this system.

INÉS L. ACEVEDO, MIGUEL A. POSTIGO et MIGUEL KATZ. Can. J. Chem. **66**, 367 (1988).

Opérant à 298,15 K, on a déterminé les densités et les viscosités du système propanol-2 + acétate de méthyle + dichlorométhane. Utilisant les données expérimentales, on a calculé les volumes et les viscosités molaires en excès. Dans la littérature, on retrouve diverses expressions pour prédire ces propriétés en excès à partir de celles de mélanges binaires. La corrélation empirique de Tsao–Smith et Toop est la plus appropriée pour ce système.

[Traduit par la revue]

Can. J. Chem. Downloaded from www.nrcresearchpress.com by 176.9.209.113 on 09/07/12
For personal use only.

Introduction

In the chemical literature, properties of binary systems are relatively abundant, properties of ternary systems are scarce, and properties for high order multicomponent systems are very rare. For ternary systems we can find in the literature the works of Heric and Brewer (1), Rastogi *et al.* (2), Radojkovic *et al.* (3), Cibulka (4), Singh *et al.* (5), and Tsao and Smith (6).

It is the intention of this work to present molar excess volume (v^E) and excess viscosity (η^E) for the 2-propanol (*1*) + methylacetate (*2*) + dichloromethane (*3*) system at 298.15 K, and for the three corresponding binary systems as well as to consider some methods for empirical correlations if interactions in a ternary mixture are assumed to be closely dependent on the interactions of the constituent in binary mixtures.

Experimental

The methods used in our laboratory have been described previously (7, 8). Densities were determined with a digital densimeter A.P., model DMA 45. All weighings were made on a H315 Mettler balance. A thermostatically controlled bath (constant to 0.01°C) was used. Temperatures were read from calibrated thermometers. Calibration was done with doubly distilled water with an error of ± 0.1 kg m^{-3}.

Viscosities of the pure liquids and of the mixtures were determined with a Cannon–Fenske viscosimeter calibrated with doubly distilled water and benzene. Kinetic energy corrections were applied to viscosity data. The estimated error was ± 0.005 mPa s.

Materials and solutions

2-Propanol and dichloromethane Merck (puriss.) was fractionally distilled over calcium chloride and the middle colorless fractions collected. Methylacetate Mallinckrodt (puriss.) was heated by reflux with acetic anhydride and then distilled over potassium carbonate. Mixtures were prepared by mixing weighed amounts of the pure liquids. Caution was taken to prevent evaporation.

Results and discussion

The experimental results for the pure liquids are reported in Table 1, together with the values from the literature for comparison. Densities and viscosities of the binary mixtures can be calculated from the experimental data, knowing the mole fraction with the following equation:

TABLE 1. Properties characterizing the pure components at 298.15 K

	$\rho \times 10^{-3}$ (kg m^{-3})		η (mPa s)	
Substance	Exp.	Lit.	Exp.	Lit.
2-Propanol	0.7800	0.7804(9)	2.053	2.036(9)
Methylacetate	0.9274	0.9273(10)	0.361	0.360(9)
Dichloromethane	1.3163	1.3168(10)	0.420	0.412(10)

$$[1] \quad P = x_iP_i + x_jP_j + x_ix_j \sum_{\substack{k=0 \\ i<j}}^{n} a_k(x_i - x_j)^k$$

where P_i and P_j are the properties of the pure components. Table 2 shows the values of the coefficients a_k as well as their standard deviation, calculated by the method of least squares with a VAX 11/780 computer.

The excess function of the binary systems could be represented by a Redlich–Kister form of the type:

$$[2] \quad X^E = x_ix_j \sum_{k=0}^{n} a_k(x_i - x_k)^k$$

where X^E represents v^E or η^E, x_i and x_j the mole fractions of the components i and j, and a_k the polynomial coefficients. The method of least squares was used to determine the values of the coefficients. In each case, the optimum number of coefficients was ascertained from an examination of the variation of the standard error of estimate with n:

$$[3] \quad \epsilon = [\Sigma(X^E_{obs} - X^E_{cal})^2/(n_{obs} - n)]^{1/2}$$

The values adopted for the coefficients and the standard error of estimate associated with the use of eq. [3] are summarized in Table 3 for the three binary systems.

Figure 1 shows the experimental values of v^E and η^E for the three systems. The continuous curves were calculated from eq. [2] using these values for the coefficients.

The experimental values of densities and viscosities of the ternary system are obtained, adding the third component to

[1]Presented at the V Congreso Argentino de Fisicoquímica, Mar del Plata, Pcia. de Buenos Aires, Argentina, 1987.

[2]To whom correspondence should be addressed.

TABLE 2. Coefficients a_k for eq. [1] and standard deviations for the binary systems at 298.15 K

Systems	a_0	a_1	a_2	a_3	a_4	ϵ
(1) + (2)						
$\rho \times 10^{-3}$ (kg m^{-3})	−0.015	−0.005	−0.02	0.04	0.07	4×10^{-4}
η (mPa s)	−2.71	−2.3	−1.5	−0.4	—	5×10^{-3}
(1) + (3)						
$\rho \times 10^{-3}$ (kg m^{-3})	−0.123	0.034	0.038	0.02	−0.04	2×10^{-4}
η (mPa s)	−2.35	−1.40	−0.3	—	—	3×10^{-3}
(2) + (3)						
$\rho \times 10^{-3}$ (kg m^{-3})	−0.103	0.019	—	—	—	1×10^{-4}
η (mPa s)	0.056	0.01	—	—	—	7×10^{-4}

TABLE 3. Coefficients a_k from eq. [2] and standard deviations for the binary systems at 298.15 K

Systems	a_0	a_1	a_2	a_3	a_4	a_5	ϵ
(*1*) + (*2*)							
$v^E \times 10^6$ (m^3 mol^{-1})	1.829	−0.329	2.04	2.8	−6.7	−9.2	0.02
η^E (mPa s)	−1.33	−1.9	−1.4	−0.4	—	—	6×10^{-3}
(*1*) + (*3*)							
$v^E \times 10^6$ (m^3 mol^{-1})	1.972	−1.202	−3.29	−1.9	2.2	—	0.02
η^E (mPa s)	−1.12	−1.08	−0.2	—	—	—	4×10^{-3}
(*2*) + (*3*)							
$v^E \times 10^6$ (m^3 mol^{-1})	1.315	−0.29	—	—	—	—	4×10^{-3}
η^E (mPa s)	0.061	0.007	—	—	—	—	8×10^{-4}

a constant relation of the other two. Molar excess volume is calculated with the following equation:

$$[4] \quad v^E = \frac{x_1M_1 + x_2M_2 + x_3M_3}{\rho} - (x_1v_1 + x_2v_2 + x_3v_3)$$

where M_1, M_2, and M_3 are the molecular weights of the components; v_1, v_2, and v_3 are the molar volumes; and ρ the density of the solution. The excess viscosity is defined by the following equation:

$$[5] \quad \eta^E = \eta - \exp(x_1 \ln \eta_1 + x_2 \ln \eta_2 + x_3 \ln \eta_3)$$

where η, η_1, η_2, and η_3 are the viscosities of the mixture and of the pure components.

Table 4 shows the experimental values of densities and viscosities at different mole fractions.

Figures 2 and 3 show the experimental equal values of v^E_{123} and η^E_{123}.

If interaction in a ternary system $i + j + k$ is assumed to be closely dependent on the interactions of the constituent $i + j$, $j + k$, and $i + k$ mixtures, it should be possible to evaluate thermodynamic excess functions for ternary mixtures of non-electrolytes, when the corresponding functions for the binary $i + j$, $j + k$, and $i + k$ mixtures are known.

Rastogi *et al.* (2) suggested a form for predicting the excess volumes of a ternary solution:

$$[6] \quad v^E_{123} = \tfrac{1}{2}[(x_1 + x_2)v^E_{12} + (x_1 + x_3)v^E_{13} + (x_2 + x_3)v^E_{23}]$$

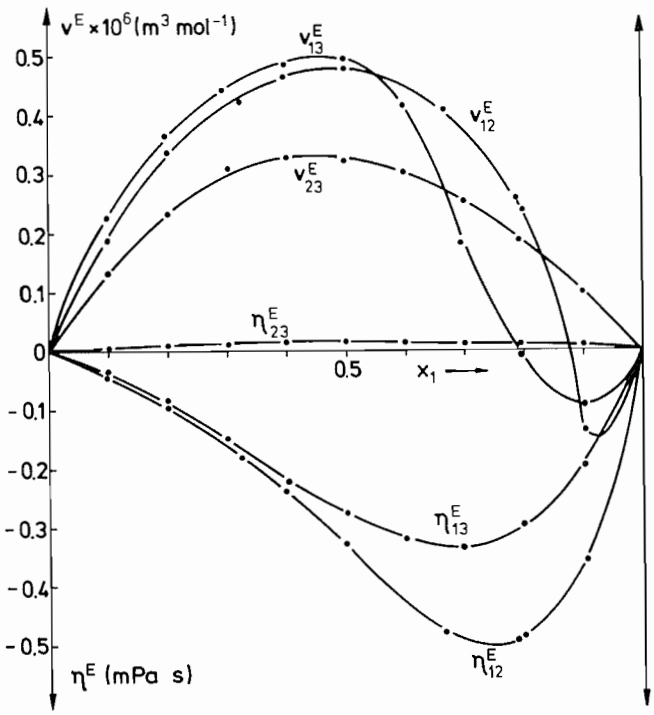

FIG. 1. Excess molar volumes and excess viscosities for binary systems at 298.15 K. Experimental results ····; continuous curves were calculated from eq. [2].

Can. J. Chem. Downloaded from www.nrcresearchpress.com by 176.9.209.113 on 09/07/12
For personal use only.

Can. J. Chem. Downloaded from www.nrcresearchpress.com by 176.9.209.113 on 09/07/12
For personal use only.

TABLE 4. Densities and viscosities for the 2-propanol (*1*) + methylacetate (*2*) + dichloromethane (*3*) system at 298.15 K

x_1	x_2	x_3	$\rho \times 10^{-3}$ (kg m^{-3})	η (mPa s)
0.0967	0.8235	0.0798	0.9353	0.396
0.0884	0.7528	0.1588	0.9616	0.402
0.0799	0.6799	0.2402	0.9897	0.407
0.0716	0.6095	0.3189	1.0179	0.410
0.0631	0.5370	0.3999	1.0481	0.413
0.1892	0.7344	0.0764	0.9192	0.421
0.1719	0.6671	0.1610	0.9488	0.424
0.1562	0.6062	0.2376	0.9764	0.426
0.1396	0.5417	0.3187	1.0070	0.428
0.1231	0.4776	0.3993	1.0382	0.429
0.2762	0.6426	0.0812	0.9068	0.449
0.2524	0.5873	0.1603	0.9359	0.450
0.2276	0.5296	0.2428	0.9670	0.450
0.2037	0.4739	0.3224	0.9980	0.459
0.1797	0.4181	0.4022	1.0201	0.450
0.3692	0.5489	0.0819	0.8925	0.482
0.3379	0.5023	0.1598	0.9227	0.481
0.3050	0.4534	0.2416	0.9548	0.479
0.2736	0.4067	0.3197	0.9863	0.477
0.2414	0.3589	0.3997	1.0196	0.476
0.4650	0.4530	0.0820	0.8781	0.530
0.4249	0.4139	0.1612	0.9099	0.526
0.3848	0.3748	0.2404	0.9424	0.522
0.3455	0.3366	0.3179	0.9748	0.516
0.3049	0.2970	0.3981	1.0092	0.509
0.6099	0.3059	0.0842	0.8590	0.658
0.5584	0.2801	0.1615	0.8907	0.625
0.5036	0.2526	0.2438	0.9255	0.602
0.4462	0.2238	0.3300	0.9635	0.582
0.7245	0.1931	0.0824	0.8429	0.836
0.6634	0.1768	0.1598	0.8751	0.775
0.5632	0.1501	0.2867	0.9306	0.701
0.5330	0.1421	0.3249	0.9480	0.680
0.4669	0.1245	0.4086	0.9864	0.628
0.8392	0.0921	0.0687	0.8229	1.180
0.7541	0.0828	0.1631	0.8635	0.993
0.6845	0.0752	0.2403	0.8981	0.872
0.6089	0.0669	0.3242	0.9364	0.762
0.5329	0.0585	0.4086	0.9767	0.681
0.0884	0.0792	0.8324	1.2175	0.449
0.0807	0.1591	0.7602	1.1871	0.442
0.0731	0.2388	0.6881	1.1583	0.436
0.0654	0.3188	0.6158	1.1302	0.428
0.0578	0.4000	0.5422	1.1026	0.418
0.1827	0.0791	0.7382	1.1600	0.478
0.1655	0.1658	0.6687	1.1345	0.471
0.1520	0.2338	0.6142	1.1149	0.459
0.1353	0.3180	0.5467	1.0914	0.448
0.1291	0.3495	0.5214	1.0828	0.444
0.2760	0.0780	0.6460	1.1060	0.507
0.2525	0.1564	0.5911	1.0887	0.490
0.2277	0.2393	0.5330	1.0709	0.474
0.2044	0.3171	0.4785	1.0543	0.461
0.1819	0.3924	0.4257	1.0383	0.451
0.3732	0.0771	0.5497	1.0526	0.552
0.3373	0.1659	0.4968	1.0383	0.529
0.3085	0.2371	0.4544	1.0286	0.509
0.2750	0.3199	0.4051	1.0162	0.489
0.2437	0.3973	0.3590	1.0045	0.467
0.4905	0.0807	0.4288	0.9898	0.633
0.4480	0.1603	0.3917	0.9836	0.590
0.4061	0.2388	0.3551	0.9781	0.553
0.3638	0.3181	0.3181	0.9720	0.521
0.3175	0.4049	0.2776	0.9651	0.493
0.5926	0.1090	0.2984	0.9299	0.728
0.5284	0.2055	0.2661	0.9294	0.640
0.4625	0.3046	0.2329	0.9284	0.569
0.3944	0.4069	0.1987	0.9274	0.515
0.3272	0.5080	0.1648	0.9263	0.479
0.7056	0.1031	0.1913	0.8792	0.877
0.6238	0.2071	0.1691	0.8835	0.717
0.5483	0.3031	0.1486	0.8878	0.618
0.4632	0.4112	0.1256	0.8926	0.543
0.3894	0.5050	0.1056	0.8969	0.498
0.8085	0.0990	0.0925	0.8347	1.092
0.7139	0.2045	0.0816	0.8443	0.848
0.6055	0.3253	0.0692	0.8554	0.657
0.5254	0.4145	0.0601	0.8630	0.572
0.5058	0.4364	0.0578	0.8651	0.556
0.1259	0.4369	0.4372	1.0519	0.433
0.2564	0.3717	0.3719	1.0072	0.480
0.3843	0.3078	0.3079	0.9652	0.534
0.5124	0.2437	0.2439	0.9244	0.620
0.6445	0.1777	0.1778	0.8835	0.766
0.7703	0.1148	0.1149	0.8463	1.007
0.9005	0.0497	0.0498	0.8094	1.458

in which v_{ij}^{E} represents the excess molar volume of the binary mixtures at composition x_i^0, x_j^0, such that:

$$[7] \quad x_i^0 = 1 - x_j^0 = \frac{x_i}{x_i + x_j}$$

This expression is inappropriate for describing the system near infinite dilution.

Radojkovič *et al.* (3) takes an expression proposed by Redlich and Kister (11) for the excess free energy:

$$[8] \quad v_{123}^{E} = v_{12*}^{E} + v_{23*}^{E} + v_{13*}^{E}$$

where v_{12*}^{E}, v_{23*}^{E}, and v_{12*}^{E} represent the excess molar volumes with x_1, x_2, and x_3 mole fractions of the ternary system calculated with eq. [2] using coefficients of Table 3.

Kohler (12) proposed an equation for a ternary solution of the following form:

$$[9] \quad v_{123}^{E} = (x_1 + x_2)^2 v_{12}^{E} + (x_1 + x_3)^2 v_{13}^{E} + (x_2 + x_3)^2 v_{23}^{E}$$

Kohler's equation is symmetrical in that all three binary systems are treated identically. In this equation v_{ij}^{E} refers to the excess volumes of x_i^0, x_j^0 in the binary mixtures using eq. [7].

Jacob and Fitzner (13) suggested an equation for estimating the properties of a ternary solution based on the binary data at composition nearest the ternary composition taking the form for excess molar volume:

$$[10] \quad v_{123}^{E} = \frac{x_1 x_2 v_{12}^{E}}{\left(x_1 + \frac{x_3}{2}\right)\left(x_2 + \frac{x_3}{2}\right)} + \frac{x_1 x_3 v_{13}^{E}}{\left(x_1 + \frac{x_2}{2}\right)\left(x_3 + \frac{x_2}{2}\right)} + \frac{x_2 x_3 v_{23}^{E}}{\left(x_2 + \frac{x_1}{2}\right)\left(x_3 + \frac{x_1}{2}\right)}$$

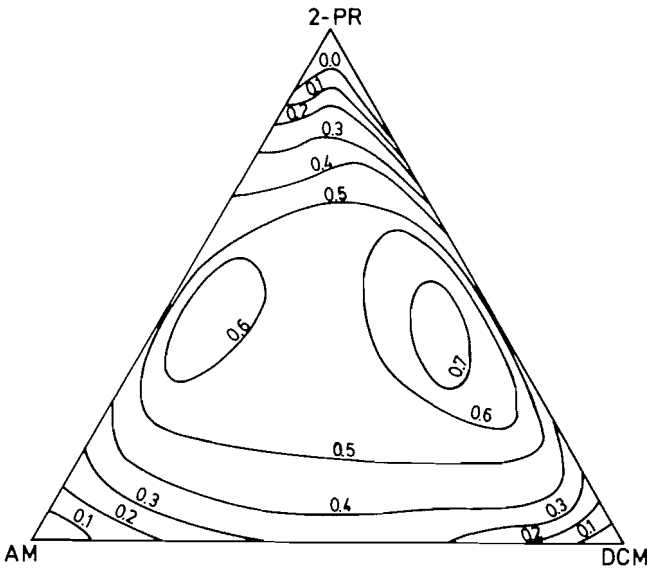

FIG. 2. Lines of constant excess molar volumes ($\times 10^6$ m^3 mol^{-1}) for 2-propanol (*1*) + methylacetate (*2*) + dichloromethane (*3*) system at 298.15 K.

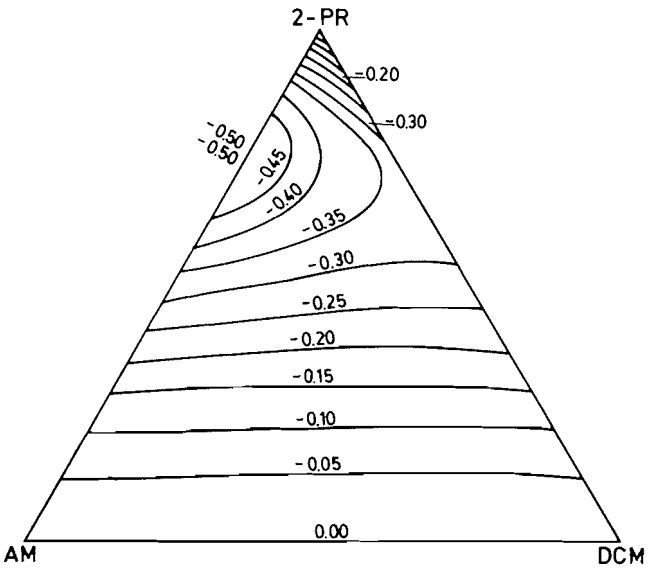

FIG. 3. Lines of constant excess viscosities (mPa s) for 2-propanol (*1*) + methylacetate (*2*) + dichloromethane (*3*) system at 298.15 K.

such that for the binary system at composition x_i^0, x_j^0:

[11] $$x_i - x_j = x_i^0 - x_j^0$$

Tsao and Smith (6) proposed an equation for predicting the excess enthalpy of a ternary system. For excess molar volume, it is

[12] $$v_{123}^E = \left(\frac{x_2}{1 - x_1}\right) v_{12}^E + \left(\frac{x_3}{1 - x_1}\right) v_{13}^E + (1 - x_1) v_{23}^E$$

in which the v_{ij}^E refer the excess volume for the binary mixtures at compositions x_i^0, x_j^0 such that $x_i^0 = x_i$ for the *1,2*, and *1,3* binary systems and $x_2^0 = x_2/(x_2 + x_3)$ for the *2,3* binary system.

TABLE 5. Standard deviations for 2-propanol (*1*) + methylacetate (*2*) + dichloromethane (*3*) system at 298.15 K

Equation	$\epsilon(v^E) \times 10^6$ (m^3 mol^{-1})	$\epsilon(\eta^E)$ (mPa s)
[8]	0.13	0.07
[9]	0.18	0.09
[10]	0.13	0.07
[12]	0.08	0.01
[13]	0.15	0.03

Toop (14) developed an equation for excess Gibbs free energy of mixture similar to that suggested previously by Tsao and Smith.

Singh *et al.* (5) proposed an equation of the following form:

[13] $$v_{123}^E = v_{12*}^E + v_{13*}^E + v_{23*}^E + Ax_1x_2x_3 + Bx_1(x_2 - x_3) + Cx_1^2(x_2 - x_3)^2$$

where A, B, and C are parameters characteristic of the mixtures evaluated by fitting this equation by the method of least squares, with a standard deviation defined as eq. [3].

The parameters obtained for this system are for v_{123}: $A = 1.6709$, $B = -13.032$, $C = 121.239$; for η_{123}: $A = 2.6439$, $B = -2.7820$, $C = 38.9507$.

Table 5 shows the standard deviations calculated from applications of eq. [8] of Radojkovič; eq. [9] of Kohler; eq. [10] of Jacob and Fitzner; eq. [12] of Tsao and Smith, and eq. [13] of Singh *et al.* for molar excess volumes and excess viscosities for the ternary system.

Equation [12] shows the best agreement with the experimental data.

Acknowledgment

The present work was financed by a CONICET and U.N.T. research grant.

1. E. L. HERIC and J. G. BREWER. J. Chem. Eng. Data, **14**, 55 (1969).
2. R. P. RASTOGI, J. NATH, and S. S. DAS. J. Chem. Eng. Data, **22**, 249 (1977).
3. N. RADOJKOVIČ, A. TASIČ, D. GROZDANIČ, B. DJORDJEVIČ, and M. MALIČ. J. Chem. Thermodyn. **9**, 349 (1977).
4. I. CIBULKA. Coll. Czech. Chem. Commun. **47**, 1414 (1982).
5. P. P. SINGH, R. K. NIGAM, S. P. SHARMA, and S. AGGARWAL. Fluid Phase Equilibria, **18**, 333 (1984).
6. C. C. TSAO and J. M. SMITH. Chem. Eng. Prog. Symp. N° **7**, 107 (1953).
7. M. A. POSTIGO, J. L. ZURITA, M. L. G. DE SORIA, and M. KATZ. Can. J. Chem. **64**, 1966 (1986).
8. J. L. ZURITA, M. L. G. DE SORIA, M. A. POSTIGO, and M. KATZ. J. Sol. Chem. **16**, 163 (1987).
9. I. WEI CHIEN and R. L. ROWLEY. J. Chem. Eng. Data, **29**, 336 (1984).
10. J. A. RIDDICK, W. B. BUNGER, and T. K. SAKANO. Organic solvents. 4th ed. J. Wiley and Sons. 1986.
11. O. REDLICH and A. T. KISTER. Ind. Eng. Chem. **40**, 345 (1948).
12. F. KOHLER. Monatsh. Chem. **91**, 738 (1960).
13. K. T. JACOB and K. FITZNER. Thermochim. Acta, **18**, 197 (1977).
14. W. E. ACREE, JR. Thermodynamic properties of nonelectrolyte solutions. Academic Press. 1984.

Can. J. Chem. Downloaded from www.nrcresearchpress.com by 176.9.209.113 on 09/07/12
For personal use only.

Temperature dependance of adiabatic compressibility, sound velocity, and specific acoustic impedance of water–cyclohexanone mixture

T. RAMANJAPPA AND E. RAJAGOPAL

Department of Physics, Sri Krishnadeveraya University, Anantapur – 515 003, India

Received July 6, 1987

T. RAMANJAPPA and E. RAJAGOPAL. Can. J. Chem. **66**, 371 (1988).

The temperature dependance of adiabatic compressibility minimum (TACM), sound velocity maximum (TSVM), and specific acoustic impedance (TSAIM) of water–cyclohexanone mixture has been studied by experimentally determining the sound velocity in and density of aqueous solution at different concentrations over a temperature range 36–77°C. The structural contribution to the shift in TACM, TSVM, and TSAIM has been evaluated. The shifts are negative and increase with concentration. The results indicate that cyclohexanone behaves as a structure breaker at higher temperature.

T. RAMANJAPPA et E. RAJAGOPAL. Can. J. Chem. **66**, 371 (1988).

Opérant à des températures allant de 36 à 77°C, on a mesuré les densités et les vitesses du son dans des solutions aqueuses, à diverses concentrations de cyclohexanone; on en a déduit la relation qui existe entre la température et la compressibilité adiabatique minimale (TCAM), la vélocité maximale du son (TCMS) et l'impédance acoustique spécifique (TIMAS). On a évalué le contribution de la structure au déplacement dans la TCAM, la TCMS et la TIMAS. Les déplacements sont négatifs et ils augmentent avec la concentration. Les résultats indiquent que, à des températures élevées, la cyclohexanone se comporte comme une substance qui brise les structures.

[Traduit par la revue]

Can. J. Chem. Downloaded from www.nrcresearchpress.com by 176.9.209.113 on 09/07/12
For personal use only.

Literature survey indicates that the thermodynamic behaviour of the system water–cyclohexanone has not been extensively studied but for a few measurements on excess heats of mixing and excess volumes of mixing (1, 2). Both the excess heats of mixing and excess volumes of mixing for this system have been found to be negative ($\Delta H = -5365$ cal mol^{-1} and $\Delta V = -4.5$ mL mol^{-1}). The magnitude and sign of ΔH and ΔV for this system fall in line with alcohols and amines (2). In general the contraction has been explained by the strong cohesive nature of water molecules. The behaviour of excess heats of mixing of this solute with water may be attributed to the formation of icebergs like alcohols and amines. However, no authentic evidence exists regarding the structural interaction of this solute with water. Since the studies on the effect of different solutes on temperature corresponding to velocity maximum (TSVM) and temperature corresponding to adiabatic compressibility minimum (TACM) of water have been found to characterize the structural propensity of any solute (3–7), the authors made an attempt to see how this solute modifies the hydrogen bonded structure of water by determining the structural contributions to the shift in TSVM and TACM. In addition to these studies, temperature corresponding to specific acoustic impedance maximum (TSAIM) studies of water have been also carried out and the results are reported in this paper.

Experimental

Triple distilled water was used to prepare stock solutions of aqueous cyclohexanone. Cyclohexanone was purified using standard procedures (8). The density of the purified liquid, determined using a bicapillary type pycnometer with an accuracy of 2 parts in 10^5, was found to be 942.77 kg m^{-3} at 25°C and is in good agreement with the literature data (9). Ultrasonic velocities in pure components and aqueous cyclohexanone solutions were determined using a single crystal variable path interferometer working at 3 MHz with an accuracy of ±0.003%. The details of the experimental technique were reported earlier (10) from our laboratory. Densities and ultrasonic velocities in the solutions were determined at ≃2°C intervals over a range of 5°C on either side of T_u, T_β, and T_z where T_β, T_u, and T_z are the temperatures corresponding to the adiabatic compressibility minimum, sound velocity maximum, and specific acoustic impedance maximum, respectively.

Results

The results of adiabatic compressibility, ultrasonic velocity, and specific acoustic impedance as a function of temperature at different concentrations of aqueous cyclohexanone are shown in Figs. 1, 2, and 3, respectively.

Discussion

The adiabatic compressibility minimum (T_β) of the solution is given (3) by

$$[1]\quad T_\beta = \left[64 - \frac{\phi_2}{\phi_1}\frac{\alpha_\beta}{0.0032}\right]\left[1 + \frac{\phi_2}{\phi_1}\frac{\alpha_\beta^1}{0.0016}\right]^{-1} - \left[\frac{d\beta^E}{dt}\right]\left[1 + \frac{\phi_2}{\phi_1}\frac{\alpha_\beta^1}{0.0016}\right]^{-1}[\phi_1 \times 0.0032]^{-1}$$

where ϕ_1 and ϕ_2 represent the volume fractions of pure water and organic solution, respectively, in the solutions. α_β and α_β^1 are the constants of organic solute involved in adiabatic compressibility versus temperature relation given by

$$[2]\quad \beta_2 = \beta_2^0 + \alpha_\beta t + \alpha_\beta^1 t^2$$

The sound velocity maximum (T_u) of the solution is given (3) by

$$[3]\quad T_u = 74 - \left[\frac{\phi_2}{\phi_1}\right]^2 \frac{w_1}{w_2}\frac{\alpha_u}{0.049}\left[\frac{u_1}{u_2}\right]^3 - \frac{w_1}{\phi_1^2}\frac{u_1^3}{0.098}\left[\rho\frac{d\beta^E}{dt} + \beta^E\frac{d\rho}{dt}\right]$$

where w_1 and w_2 represent weight fractions of pure water and organic solute, respectively, in the solution. α_u is the temperature coefficient of sound velocity in the relation

$$[4]\quad u_2 = u_2^0 - \alpha_u t$$

The specific acoustic impedance maximum (T_z) of the

Can. J. Chem. Downloaded from www.nrcresearchpress.com by 176.9.209.113 on 09/07/12
For personal use only.

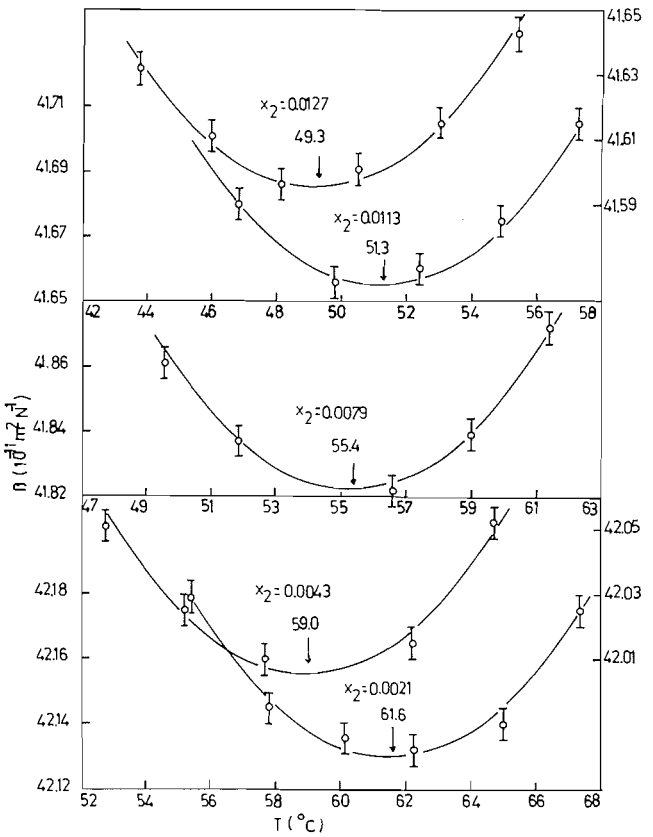

FIG. 1. Adiabatic compressibility versus temperature in aqueous solution at different mole fractions (X_2) of cyclohexanone.

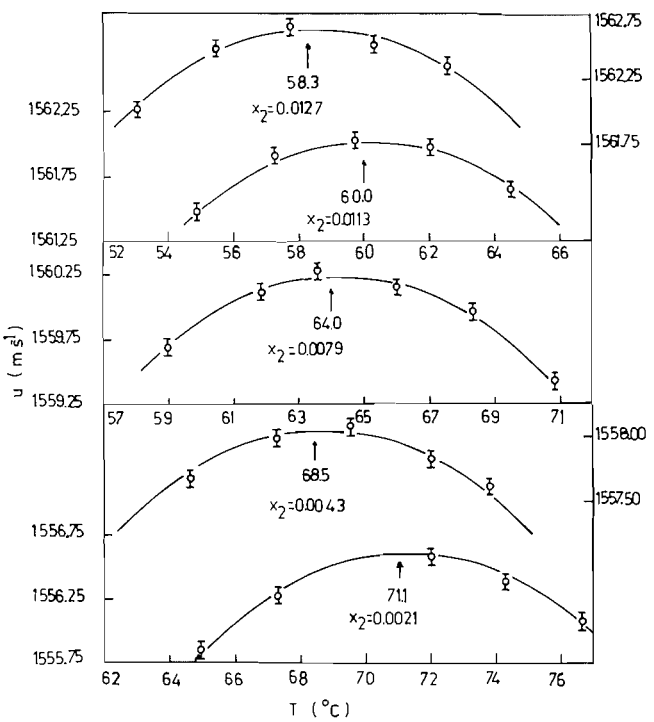

FIG. 2. Ultrasonic velocity versus temperature in aqueous solution at different mole fractions (X_2) of cyclohexanone.

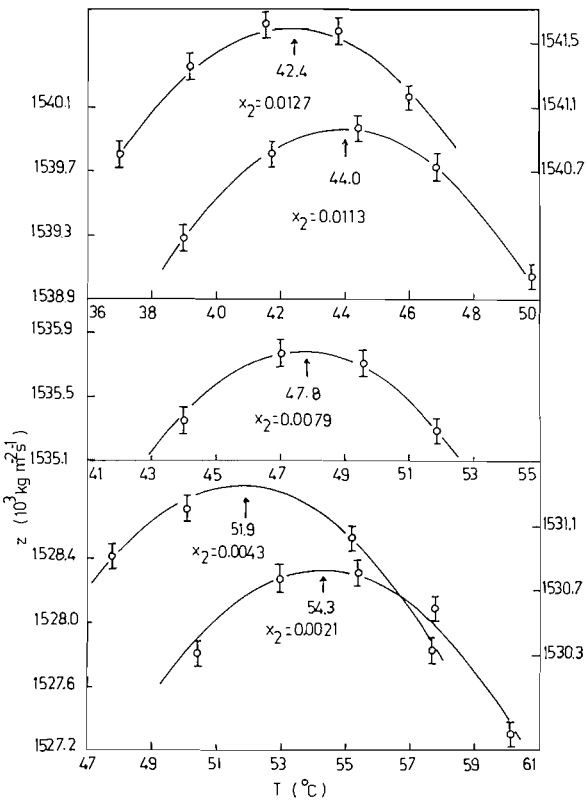

FIG. 3. Specific acoustic impedance versus temperature in aqueous solution at different mole fractions (X_2) of cyclohexanone.

TABLE 1. Pure liquid parameters of cyclohexanone

Parameter	Value
$\beta_2^0/(10^{-11}\ m^2\ N^{-1})$	46.510
$\alpha_\beta/(10^{-11}\ m^2\ N^{-1}\ °C^{-1})$	0.2298
$\alpha_\beta^1/(10^{-14}\ m^2\ N^{-1}\ °C^{-2})$	2.1757
$u_2^0/(m\ s^{-1})$	1505.84
$\alpha_u/(m\ s^{-1}\ °C^{-1})$	3.9400
$z_2^0/(10^3\ kg\ m^{-2}\ s^{-1})$	1453.68
$\alpha_z/10^3\ kg\ m^{-2}\ s^{-1}\ °C^{-1})$	−5.1651
$\alpha_z^1/(kg\ m^{-2}\ s^{-1}\ °C^{-2})$	3.564

solution is given (15) by

$$[5]\quad T_z = -\frac{\dfrac{7.5063w_1}{z_1^3}+\dfrac{2\alpha_z w_2}{z_2^3}}{\dfrac{-0.13404w_1}{z_1^3}+\dfrac{4\alpha_z^1 w_2}{z_2^3}} + \frac{\dfrac{1}{\rho}\left[\dfrac{d\beta^E}{dt}-\dfrac{\beta^E}{\rho}\dfrac{d\rho}{dt}\right]}{\dfrac{-0.13404w_1}{z_1^3}+\dfrac{4\alpha_z^1 w_2}{z_2^3}}$$

where α_z and α_z^1 are the temperature coefficients of specific acoustic impedance in the relation

$$[6]\quad z_2 = z_2^0 + \alpha_z t + \alpha_z^1 t^2$$

The values of β_2^0, α_β, α_β^1, u_2^0, α_u, z_2^0, α_z, α_z^1 for cyclohexanone are evaluated using the experimentally determined ultrasonic velocity and density data at different temperatures and the values are presented in Table 1.

In eqs. [1], [3], and [5], first term ($T_{\alpha\ or\ u\ or\ z\ id}$) represents the dilution effect and second term ($\Delta T_{\beta\ or\ u\ or\ z\ str}$) represents the structural contribution. ($\Delta T_{\beta\ or\ u\ or\ z\ str}$) can be evaluated experi-

TABLE 2. Experimental and theoretical values of $[\Delta T_{\beta\,str}]$, $[\Delta T_{u\,str}]$, and $[\Delta T_{z\,str}]$ for the system water–cyclohexanone

X_2	$[\Delta T_{\beta\,str}]_{exp}$ (°C)	$[\Delta T_{\beta\,str}]_{th}$ (°C)	$[\Delta T_{u\,str}]_{exp}$ (°C)	$[\Delta T_{u\,str}]_{th}$ (°C)	$[\Delta T_{z\,str}]_{exp}$ (°C)	$[\Delta T_{z\,str}]_{th}$ (°C)
0.0021	−0.5±0.4	−0.5	−0.7±0.2	0.7	−0.4±0.3	−1.3
0.0043	−1.1±0.4	−0.8	−1.0±0.2	0.5	−1.0±0.3	−1.5
0.0079	−1.6±0.4	−1.3	−2.0±0.2	−0.1	−2.3±0.3	−2.0
0.0113	−2.9±0.4	−2.2	−2.9±0.2	−1.4	−3.6±0.3	−2.8
0.0127	−3.8±0.4	−2.6	−3.4±0.2	−1.9	−4.2±0.3	−3.2

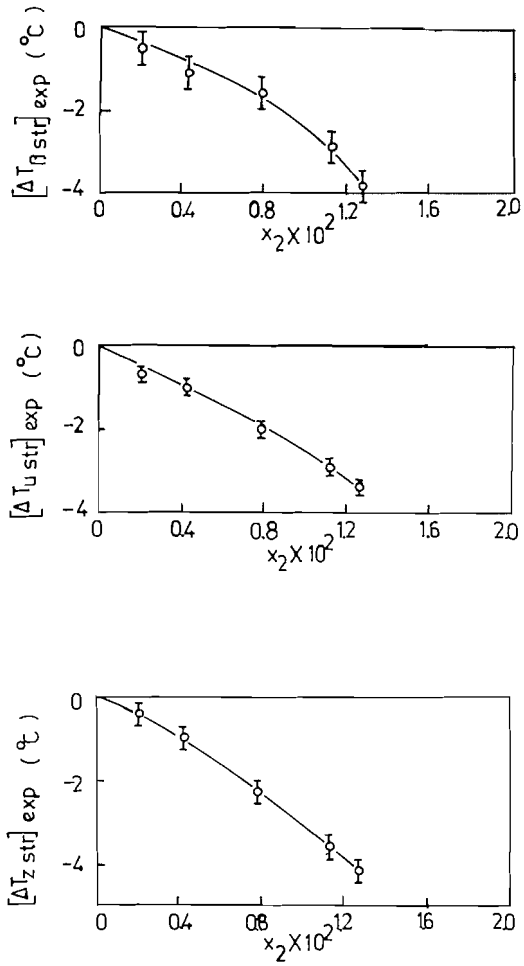

FIG. 4. (*a*) $[\Delta T_{\beta\,str}]_{exp}$ versus mole fraction (X_2) of cyclohexanone in aqueous solution; (*b*) $[\Delta T_{u\,str}]_{exp}$ versus mole fraction (X_2) of cyclohexanone in aqueous solution; (*c*) $[\Delta T_{z\,str}]_{exp}$ versus mole fraction (X_2) of cyclohexanone in aqueous solution.

mentally from the relation

$$[7]\quad (\Delta T_{\beta\,or\,u\,or\,z\,str})_{exp} = T_{\beta\,or\,u\,or\,z\,exp} - T_{\beta\,or\,u\,or\,z\,id}$$

The results of $[\Delta T_{\beta\,str}]_{exp}$, $[\Delta T_{u\,str}]_{exp}$, and $[\Delta T_{z\,str}]_{exp}$ are presented in Table 2 and are represented graphically against the mole fraction X_2 of cyclohexanone in Figs. 4*a*, *b*, and *c*, respectively. $[\Delta T_{\beta\,str}]_{exp}$, $[\Delta T_{u\,str}]_{exp}$ and $[\Delta T_{z\,str}]_{exp}$ for cyclohexanone are negative throughout the concentration range in the present study and increase with concentration. The negative values of structural shifts clearly demonstrate the structure disrupting nature of cyclohexanone. But carbonyl oxygen of ketone (1, 2, 11) is known to form hydrogen bond to water indicating this solute to behave as hydrophobic.

Excess heats of mixing and volumes of mixing (1, 2) indicate structure stabilization leading to iceberg formation around the solute molecule. It is worthwhile to note here that while excess heats and volumes of mixing data confined to 26.5°C, whereas the present studies are confined to high temperature range (36–77°C). Therefore it may be concluded that the structural propensity of a solute as revealed by physical property is dependent on temperature and literature survey (12, 13) indicates that structural interactions are sensitive to temperature and structure promoting interactions decrease with rise in temperature (14). The results of present study on water + cyclohexanone indicate that cyclohexanone loses its structure stabilizing character as temperature is increased and behaves as a structure breaker at higher temperature.

1. P. HEBERFIELD. J. Am. Chem. Soc. **96**, 761 (1974).
2. J. T. EDWARD, P. G. FARRELL, and F. SHAHIDI. J. Chem. Soc. Faraday Trans. I, **5**, 705 (1977).
3. N. MANOHARA MURTHY and S. V. SUBRAHMANYAM. Can. J. Chem. **56**, 2412 (1978).
4. N. MANOHARA MURTHY and S. V. SUBRAHMANYAM. Can. J. Chem. **58**, 1527 (1980).
5. N. MANOHARA MURTHY and S. V. SUBRAHMANYAM. Acustica. **40**, 263 (1978).
6. K. SUBBARANGAIAH, N. MANOHARA MURTHY, and S. V. SUBRAHMANYAM. Bull. Chem. Soc. Jpn. **54**, 2200 (1981).
7. K. SUBBARANGAIAH, N. MANOHARA MURTHY, and S. V. SUBRAHMANYAM. J. Chem. Soc. Faraday Trans. I, **78**, 165 (1982).
8. A. WEISSBERGER (*Editor*). Techniques of organic chemistry. Vol. VII. 1967.
9. B. CHAWLA, S. K. MEHTA, R. V. JASRA, and S. K. SURI. Can. J. Chem. **61**, 2147 (1983).
10. S. V. SUBRAHMANYAM and N. MANOHARA MURTHY. J. Solution Chem. **4**, 347 (1975).
11. K. R. BROWER, J. PESLAK JR., and J. ELROD. J. Phys. Chem. **73**, 207 (1969).
12. G. ROUX, G. PERRON, and J. E. DESNOYERS. J. Solution Chem. **7**, 639 (1978).
13. S. CABANI, P. GIANNI, V. MOLLICA, and L. LEPORI. J. Solution Chem. **10**, 563 (1981).
14. D. D. MACDONALD, M. D. SMITH, and J. B. HYNE. Can. J. Chem. **49**, 2817 (1971).
15. T. RAMANJAPPA. Ph.D. Thesis. Sri Krishnadevaraya University, Anantapur. 1985.

Can. J. Chem. Downloaded from www.nrcresearchpress.com by 176.9.209.113 on 09/07/12
For personal use only.

Remote steric effects on the disproportionation/recombination ratio of cumyl radicals[1]

KARL R. KOPECKY AND MEI-YUK YEUNG[2]
Department of Chemistry, University of Alberta, Edmonton, Alta., Canada T6G 2G2

Received August 14, 1987

KARL R. KOPECKY and MEI-YUK YEUNG. Can. J. Chem. **66**, 374 (1988).

The disproportionation/combination ratio in the reaction between two 3,5-di-*tert*-butylcumyl radicals, generated by thermolysis of the corresponding diazene, is 0.21 ± 0.03 at 60°C in benzene. This is much larger than the value of 0.06 found for the unsubstituted cumyl radicals. It is suggested that the *tert*-butyl groups hinder the formation of a parallel association complex, which has been proposed to account for the much smaller amount of disproportionation in the reaction between benzylic radicals as compared with alkyl radicals.

KARL R. KOPECKY et MEI-YUK YEUNG. Can. J. Chem. **66**, 374 (1988).

À 60°C, dans le benzène, on a évalué à 0,21 ± 0,03 le rapport dismutation/recombinaison pour la réaction de deux radicaux di-*tert*-butyl-3,5 cumyles provenant de la thermolyse du diazène correspondant. Cette valeur est beaucoup plus élevée que la valeur de 0,06 observée pour les radicaux cumyles qui ne sont pas substitués. On croit que les groupements *tert*-butyles empêchent la formation du complexe d'association parallèle dont la formation a été suggérée pour expliquer la faible quantité de produit de dismutation qui se forme au cours de la réaction entre radicaux benzyliques par opposition à ce qui est observé avec les radicaux alkyles.

[Traduit par la revue]

Can. J. Chem. Downloaded from www.nrcresearchpress.com by 176.9.209.113 on 09/07/12
For personal use only.

Introduction

The amount of coupling product formed upon reaction between two benzylic radicals with β-hydrogen atoms (1) is much larger than that between two alkyl radicals (2). For example, at 60°C the disproportionation/combination ratio for cumyl radicals is 0.06 while that for *tert*-butyl radicals is 5.4 (1*a*). It has been suggested that the reason for the difference is that benzylic radicals can form dimeric association complexes, such as **A** for cumyl radicals, which could easily collapse to coupling product but whose geometry would be unfavorable for disproportionation (3). If such a parallel association complex were an important entity, large substituents on the benzene ring should result in decreased stability and distortion of the complex. There is a bit more disproportionation between *p-tert*-butylcumyl radicals, but the effect of the *tert*-butyl group, if real, is small (1*b*). Inspection of molecular models suggests that there can be close association between two *p-tert*-butylcumyl radicals. The orientation can be nearly parallel and the benzylic carbon atoms could still be very close to bonding distance of one another.

In the present study, the disproportion/combination ratio of 3,5-di-*tert*-butylcumyl radicals was measured to explore further the effect of bulky ring substituents on this ratio. Inspection of molecular models suggests that there can still be a close association between two 3,5-di-*tert*-butylcumyl radicals but the orientation would be skewed toward that shown in **B** for closest approach. The benzylic radical centers would not be as close to each other as in **A** but would be closer to the benzylic methyl group of the partner in the complex. This should result in a higher disproportionation/combination ratio.

Results and discussion

The 3,5-di-*tert*-butylcumyl radicals were generated by thermolysis of the corresponding diazene **1**, Scheme 1. Degassed C_6D_6 solutions containing accurately known amounts of **1** (~0.05 *M*) and methyl triphenylmethyl ether as internal standard were kept at 60°C for 10 half-lives of decomposition. The rate of thermolysis of **1** was assumed to be equal to that of the corresponding diazene lacking *tert*-butyl groups (1*a*) since there is only a small effect of ring alkyl substituents on the rate of thermolysis (1*b*,*c*). The concentrations of the disproportionation products **2** and **3** were then determined by ^{1}H nmr, by comparing the areas of the benzylic proton of **2** and the allylic methyl group of **3** with the area of the methoxy group of the internal standard. As has been observed before (1*a*,*b*) there is more cumyl than α-methylstyryl disproportionation product, Table 1. This has been attributed to a possible polymerization of the latter product (1*a*) but its conversion to trimer, Scheme 2, seems more plausible. No attempt was made to isolate the trimer, which should be present in ~5% yield. The coupling reaction to give trimer will, of course, be accompanied by some disproportionation but the amount will be insignificant.

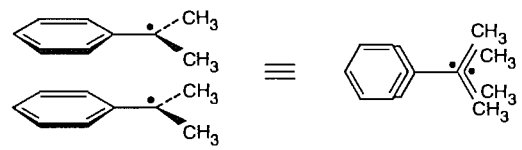

A

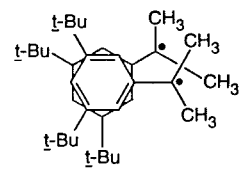

B

The nmr spectra of the reaction mixtures from thermolysis of **1** are very clean. Between the signals of the aromatic protons and the homobenzylic methyl groups there is only one unidentified signal. It is a singlet 25 Hz downfield from the signal of the allylic methyl group of **3** with an area about 5% of that of the methyl group.

[1]Research supported by a grant from the Natural Sciences and Engineering Research Council of Canada.

[2]Participant in the Summer Employment/Experience Development program sponsored by Employment and Immigration Canada in the summers of 1984 and 1985.

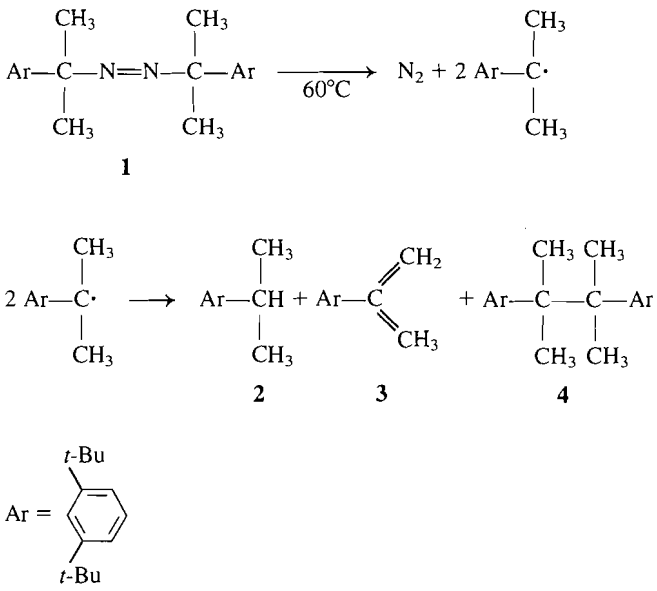

SCHEME 1

TABLE 1. Ratio k_{disp}/k_{comb} from thermolysis of **1** in C_6D_6 at 60°C

Initial moles × 10^6		^{1}H nmr peak areas				
1	Std[a]	Std[b]	**2**[c]	**3**[d]	k_{disp}/k_{comb}[e]	**2/3**
29.0	1.47	57	48	114	0.16	1.26
29.9	1.14	34	50	116	0.20	1.30
23.6	1.25	28	25	71	0.17	1.06
23.4	0.931	110	150	381	0.22	1.18
26.3	1.58	82	92	233	0.25	1.19
23.7	1.74	94	82	203	0.24	1.21
					Ave. 0.21 ± 0.03	

[a]Methyl triphenylmethyl ether was the internal standard.
[b]Area of the OCH_3 group.
[c]Area of the methine proton.
[d]Area of the allylic methyl group.
[e]Calculated according to eq. [1].

The reactions of Scheme 2 will have a negligible effect on the k_{disp}/k_{comb} ratio, calculated by eq. [1]. This ratio,

$$[1] \quad k_{disp}/k_{comb} = \frac{\%2}{100 - \%2}$$

0.21 ± 0.03, is much larger than that, 0.06, found for the reaction of unsubstituted cumyl radicals (1*a*) and cumyl radicals containing alkyl groups in the 4-position (1*b*,*c*). This lends support to the notion that the large amount of coupling found with benzylic radicals is the result of an association complex like **A**. However, it appears that the two *tert*-butyl groups in the 3 and 5 positions are not large enough to disrupt completely the formation of such a complex, since there is still much more coupling than with alkyl radicals.

Semibenzene dimers (4), formed by coupling of benzyl radicals at the α and *ortho* or *para* positions, probably play no role here. The α-*para* dimer, which is formed in ~20% yield by coupling of unsubstituted cumyl radicals, should be prevented from forming when two bulky *tert*-butyl groups flank the *para* position. Similarly, steric hindrance should greatly retard the formation of the α-*ortho* dimer, which is formed in lower yield than the α-*para* dimer from the unsubstituted cumyl radicals.

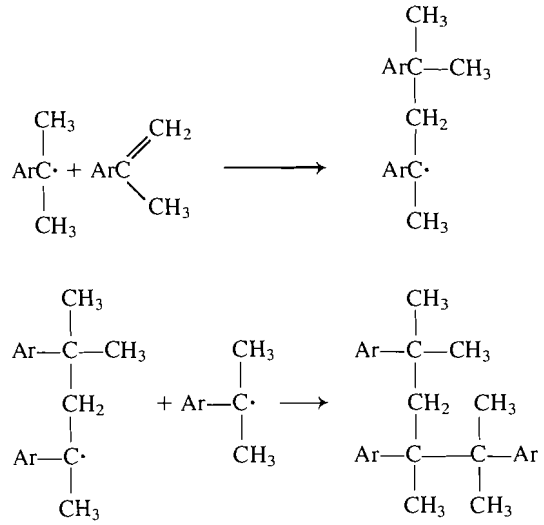

SCHEME 2

Experimental

Melting and boiling points are uncorrected. The nmr spectra were measured on Varian A50/60 and Bruker WP80 and WH200 spectrometers. Elemental analyses were performed in the Microanalytical Laboratories of the Chemistry Department under the supervision of Mrs. Darlene Mahlow.

*1-(Bromomethyl)-3,5-di-*tert*-butylbenzene*

A mixture of 146.8 g (0.718 mol) of 1,3-di-*tert*-butyl-5-methylbenzene (5), 127.8 g (0.718 mol) of *N*-bromosuccinimide, and 200 mL carbon tetrachloride was heated under reflux for 18 h, cooled, filtered, and the filtrate concentrated. The residual oil was distilled through a short Vigreux column to give 101 g (50%) of an oil, bp 122–126°C/5 Torr (1 Torr = 133.3 Pa), which crystallized on standing. The solid was recrystallized from ethyl acetate to give colorless crystals, mp 34–35°C; ^{1}H nmr ($CDCl_3$) δ: 7.30 (m, 3H), 4.38 (s, 2H), and 1.29 (s, 18H). *Anal.* calcd. for $C_{15}H_{23}Br$: C 68.61, H 8.18, Br 28.21; found: C 68.34, H 8.14, Br 28.02.

*1,3-Di-*tert*-butyl-5-(cyanomethyl)benzene*

The procedure for the preparation of phenylethanenitrile (6) was used starting with 100 g of the above bromide. The crude product, 75.5 g, was recrystallized four times from hexane to give 42.3 g colorless crystals. The mother liquors were combined, concentrated, and the residue was distilled through a 15-cm Vigreux column, collecting the fraction boiling at 94–101°C/0.3 Torr. This was crystallized from hexane. A total of 59.2 g (72.5%) of product was obtained, mp 49–50°C; ^{1}H nmr ($CDCl_3$) δ: 7.28 (m, 3H), 3.68 (s, 2H), and 1.30 (s, 18H). *Anal.* calcd. for $C_{16}H_{23}N$: C 83.78, H 10.11, N 6.11; found: C 83.71, H 10.11, N 6.01.

*2-(3,5-Di-*tert*-butylphenyl)-2-methylpropanenitrile*

A mixture of 59.2 g (0.26 mol) of the above cyanide and 119.5 g (0.84 mol) of iodomethane in 150 mL dimethylsulfoxide was added over 2 h to a stirred mixture of 64.0 g (1.14 mol) potassium hydroxide, 25 mL water, and 100 mL dimethylsulfoxide, which was cooled in an ice bath. Product precipitated during the addition. The resulting mixture was stirred at 22°C overnight and a large amount of ether and water were added. The organic layer was shaken three times with water, dried, and concentrated. The residue was recrystallized from hexane to give 44.2 g (66.5%) of colorless crystals, mp 70–71°C; ^{1}H nmr ($CDCl_3$) δ: 7.28 (m, 3H), 1.73 (s, 6H), and 1.35 (s, 18H). *Anal.* calcd. for $C_{18}H_{27}N$: C 83.99, H 10.57, N 5.44; found: C 84.05, H 10.71, N 5.54.

Can. J. Chem. Downloaded from www.nrcresearchpress.com by 176.9.209.113 on 09/07/12
For personal use only.

Can. J. Chem. Downloaded from www.nrcresearchpress.com by 176.9.209.113 on 09/07/12
For personal use only.

*2-(3,5-Di-*tert*-butylphenyl)-2-methylpropanamide*

A mixture of 44.2 g of the above cyanide and 763 g of 85% sulfuric acid was stirred at 50°C for 7 h (6) and poured onto crushed ice. The solid product was taken up in ether. The organic layer was dried, concentrated, and the residue recrystallized from ethyl acetate–hexane to give 27.6 g colorless crystals, mp 125–126°C; ^{1}H nmr ($CDCl_3$) δ: 7.28 (m, 3H), 5.52 (br, 2H), 1.55 (s, 6H), and 1.30 (s, 18H). *Anal.* calcd. for $C_{18}H_{29}NO$: C 78.49, H 10.61, N 5.08, O 5.81; found: C 78.56, H 10.76, N 5.04, O 5.87.

*Methyl 1-(3,5-di-*tert*-butylphenyl)-1-methylethylcarbamate*

Bromine, 17.1 g (0.11 mol), was added dropwise to a solution of 27.6 g (0.11 mol) of the above amide in 140 mL of methanol containing 0.28 mol of sodium methoxide at 0°C. The reaction mixture then was heated under reflux for 45 min and methanol removed. Water and ether were added to the residue, the organic layer was dried and concentrated, and the residual solid recrystallized from hexane to give 25.3 g (83%) of colorless crystals, mp 80–81°C; ^{1}H nmr ($CDCl_3$) δ: 7.30 (m, 3H), 5.07 (br, 1H), 3.58 (s, 3H), 1.68 (s, 6H), and 1.30 (s, 18H). *Anal.* calcd. for $C_{19}H_{31}NO_2$: C 74.71, H 10.23, N 4.58, O 10.48; found: C 74.89, H 10.24, N 4.57, O 10.30.

*2-Amino-2-(3,5-di-*tert*-butylphenyl)propane*

A solution of 4 g (0.013 mol) of the above carbamate and 2.1 g (0.052 mol) of sodium hydroxide in 40 mL methanol was heated at 155°C for 4 h, cooled, and then treated with excess hydrochloric acid at 0°C. A white precipitate formed, which was filtered and dissolved in methanol. The resulting solution was treated with excess 40% aqueous sodium hydroxide, and the resulting mixture was shaken with 100 mL and then with 3 × 20 mL ether. The combined extract was washed with water, dried, and concentrated to give 3.08 g (95%) of a colorless solid. Recrystallization from a variety of solvents did not produce analytically pure material. The product could be sublimed quantitatively to give material that analyzed correctly if the analysis was done immediately, mp 68–69°C; ^{1}H nmr ($CDCl_3$) δ: 7.33 (m, 3H), 1.58 (s, 2H), 1.48 (s, 6H), and 1.32 (s, 18H). *Anal.* calcd. for $C_{17}H_{29}N$: C 82.52, H 11.81, N 5.66; found: C 82.68, H 11.87, N 5.50.

*Bis[1-(3,5-di-*tert*-butylphenyl)-1-methylethyl]diazene* ***1***

A solution of 2.0 g (8.1 mmol) of the above amine in 10 mL dichloromethane was added dropwise to a stirred mixture of 4 mL pyridine and 0.60 mL (8.1 mol) of iodine pentafluoride in 16 mL dichloromethane at −78°C (7). The resulting mixture was stirred at 78°C for 1 h, allowed to warm to 22°C, and treated with 10 mL water. The organic layer was washed with 5% hydrochloric acid, 5% aqueous sodium bicarbonate, and brine. Removal of solvent left 1.66 g (83.7%) of a yellow oil, which soon solidified. The product was purified by chromatography on neutral alumina, followed by recrystallization from pentane to give light yellow crystals, mp 84–85°C (preheated melting point block); ^{1}H nmr ($CDCl_3$) δ: 7.27 (m, 3H), 1.58 (s, 6H), and 1.30 (s, 18H). *Anal.* calcd. for $C_{34}H_{53}N_2$: C 83.20, H 11.09, N 5.71; found: C 83.50, H 11.22, N 5.74.

*2,3-Di-(3,5-di-*tert*-butylphenyl)-2,3-dimethylbutane*

A solution of 0.2 g of the above diazene in 5 mL benzene was deoxygenated by bubbling a slow stream of argon through it for 15 min and was then heated under reflux for 18 h. Benzene was removed and the residual solid was recrystallized from petroleum ether to give colorless crystals, mp 211–212°C; ^{1}H nmr ($CDCl_3$) δ: 7.04 (m, 6H), 1.35 (s, 12H), and 1.23 (s, 36H). *Anal.* calcd. for $C_{34}H_{54}$: C 88.24, H 11.76; found: C 88.51, H 11.57.

*2-(3,5-Di-*tert*-butylphenyl)-2-(dimethylamino)propane*

A mixture of 2.25 g (9.1 mmol) of 1-(3,5-di-*tert*-butylphenyl)-1-methylethylamine, 2.32 g (45 mmol), and 1.72 g (20 mmol) of 35% formaldehyde was heated under reflux for 12 h, cooled, treated with 1 mL concentrated hydrochloric acid, and then evaporated to dryness. The residue was treated with aqueous sodium hydroxide, enough water was added to dissolve the precipitate, and the resulting mixture was extracted three times with ether. The oil (2.23 g; 89%) that was obtained from concentration of the combined extracts did not give a satisfactory analysis in spite of a variety of attempts at purification; ^{1}H nmr ($CDCl_3$) δ: 7.23 (m, 3H), 2.13 (s, 6H), 1.35 (s, 6H), and 1.32 (s, 18H). A portion of the amine was converted (8) to the picrate, mp 190–191°C; ^{1}H nmr ($CDCl_3$) δ: 8.82 (s, 2H), 7.40 (m, 3H), 2.75 (s, 6H), 1.93 (s, 6H), and 1.26 (s, 18H). *Anal.* calcd. for $C_{27}H_{36}N_3O_7$: C 59.51, H 7.19, N 11.10; found: C 59.49, H 7.25, N 11.14.

*2-(3,5-Di-*tert*-butylphenyl)propene*

A cold solution of 0.78 g (3.6 mmol) of *m*-chloroperbenzoic acid in 10 mL of chloroform was added gradually to 1.0 g (3.6 mmol) of the above amine in 6 mL of chloroform at 0°C. The reaction mixture was stirred for 3 h more, allowing it to come to room temperature, and then concentrated to ~5 mL. The residue was chromatographed on 35 g basic alumina using 1:3 methanol:chloroform as eluent. Concentration of the eluent gave 0.78 g (93%) of a colorless oil that contained no amine oxide and is extremely readily oxidized by air, bp 65–66°C/0.1 Torr; ^{1}H nmr ($CDCl_3$) δ: 7.23 (m, 3H), 5.27 (m, 1H), 5.00 (m, 1H), 2.16 (m, 3H), and 1.31 (s, 18H). *Anal.* calcd. for $C_{17}H_{26}$: C 88.62, H 11.38; found: C 88.13, H 11.36.

*2-(3,5-Di-*tert*-butylphenyl)propane*

The above alkene, 0.38 g, was hydrogenated over palladium on carbon in ethanol to give 0.33 g (86%) of colorless oil, bp 74–75°C/0.4 Torr; ^{1}H nmr ($CDCl_3$) δ: 7.20 (m, 3H), 2.85 (heptet, J = 6.5 Hz, 1H), 1.30 (s, 18H), and 1.24 (d, J = 6.5 Hz, 6H). *Anal.* calcd. for $C_{17}H_{28}$: C 87.86, H 12.14; found: C 87.89, H 12.05.

Yields of disproportionation products

C_6D_6 solutions of **1** and methyl triphenylmethyl ether, both of which had been accurately weighed out on a microbalance, in nmr tubes were degassed with three freeze–thaw cycles under 0.1 Torr, and the tubes sealed and placed in a 60°C bath for 12 h. The yields of **2** and **3** were determined by integration of the ^{1}H nmr spectra taken at 200 MHz as described in Results and discussion. The results are given in Table 1.

1. (*a*) S. F. Nelson and P. D. Bartlett. J. Am. Chem. Soc. **88**, 137 (1966); (*b*) J. R. Sheldon, C. K. Liang, and P. Kovacic. J. Am. Chem. Soc. **90**, 354 (1968); (*c*) P. Kovacic, R. R. Flynn, J. F. Gormish, A. H. Kappelman, and J. R. Shelton. J. Org. Chem. **34**, 3312 (1969); (*d*) F. D. Greene, M. A. Berwick, and J. C. Stowell. J. Am. Chem. Soc. **92**, 867 (1970); (*e*) J. R. Shelton and C. K. Liang. J. Org. Chem. **38**, 2301 (1973).
2. J. Kraus and J. Calvert. J. Am. Chem. Soc. **79**, 5921 (1957).
3. R. C. Neuman, Jr. and E. S. Alhadeff. J. Org. Chem. **35**, 3401 (1970).
4. K. J. Skinner, H. S. Hochster, and J. M. McBride. J. Am. Chem. Soc. **96**, 4301 (1974).
5. J. Gluze, C. Ruinard, J. Soeterbroek, P. E. Verkade, and B. M. Wepster. Recl. Trav. Chem. Pays-Bas, **75**, 301 (1956).
6. A. C. Cope, T. T. Foster, and P. H. Towle. J. Am. Chem. Soc. **71**, 3929 (1949).
7. T. S. Stevens. J. Org. Chem. **26**, 2531 (1961).
8. S. M. McElvain. The characterization of organic compounds. MacMillan, New York. 1949. p. 213.

Structural studies of organoboron compounds. XXVIII.[1] 5,5-Trimethylene-2,2-diphenyl-1,3-dioxa-5-azonia-2-boratacyclohexane and 5,5-dimethyl-2,2-diphenyl-1,3-dioxa-5-azonia-2-boratacyclohexane monohydrate

WOLFGANG KLIEGEL

Institut für Pharmazeutische Chemie, der Technischen Universität Braunschweig, 3300 Braunschweig, Beethovenstraße 55, Bundesrepublik Deutschland

AND

STEVEN J. RETTIG AND JAMES TROTTER

Department of Chemistry, University of British Columbia, 2036 Main Mall, Vancouver, B.C., Canada V6T 1Y6

Received June 2, 1987

WOLFGANG KLIEGEL, STEVEN J. RETTIG, and JAMES TROTTER. Can. J. Chem. **66**, 377 (1988).

The preparation of the title compounds demonstrates the bis-*N*-alkylation of secondary amines by formaldehyde, these labile ammonium inner salts being captured as diphenylboron chelates. Crystals of 5,5-trimethylene-2,2-diphenyl-1,3-dioxa-5-azonia-2-boratacyclohexane are orthorhombic, $a = 8.8461(3)$, $b = 10.7290(4)$, $c = 15.8773(5)$ Å, $Z = 4$, space group $P2_12_12_1$, and those of 5,5-dimethyl-2,2-diphenyl-1,3-dioxa-5-azonia-2-boratacyclohexane monohydrate are monoclinic, $a = 6.2432(3)$, $b = 17.1469(8)$, $c = 14.3701(5)$ Å, $\beta = 90.647(3)°$, $Z = 4$, space group $P2_1/n$. Both structures were solved by direct methods and were refined by full-matrix least-squares procedures to $R = 0.030$ and 0.047 for 1400 and 2258 reflections with $I \geq 3\sigma(I)$, respectively. Both compounds have a *B,N*-betaine structure, the six-membered chelate rings adopting chair conformations. Libration-corrected bond lengths, O—B = 1.508(3)–1.522(3) and C—B = 1.612(4)–1.637(4) Å, indicate relatively strong binding of the diphenylboron moiety to the oxygen atoms of the *O,O*-chelating ligands.

WOLFGANG KLIEGEL, STEVEN J. RETTIG et JAMES TROTTER. Can. J. Chem. **66**, 377 (1988).

La préparation des composés mentionnés dans le titre démontre que le formaldéhyde provoque une bis-*N*-alkylation des amines secondaires, alors que les sels d'ammonium internes qui sont labiles sont captés sous la forme de chélates de diphénylbore. Les cristaux du triméthylene-5,5 diphényl-2,2 dioxa-1,3 azonia-5 borata-2 cyclohexane sont orthorhombiques avec $a = 8{,}8461(3)$, $b = 10{,}7290(4)$ et $c = 15{,}8773(5)$ Å, $Z = 4$ et groupe d'espace $P2_12_12_1$ alors que ceux du monohydrate du diméthyl-5,5 diphényl-2,2 dioxa-1,3 azonia-5 borata-2 cyclohexane sont monocliniques avec $a = 6{,}2432(3)$, $b = 17{,}1469(8)$ et $c = 14{,}3701(5)$ Å, $\beta = 90{,}647(3)°$, $Z = 4$ et groupe d'espace $P2_1/n$. On a résolu les deux structures par des méthodes directes et on les a affinées par la méthode des moindres carrés jusqu'à des valeurs de R de 0,030 et 0,047 pour respectivement 1400 et 2258 réflexions avec $I \geq 3\sigma(I)$. Les deux composés présentent une structure *B,N*-bétaïne dans laquelle les cycles des chélates à six chaînons adoptent des conformations chaises. Les longueurs des liaisons corrigées pour la libration, O—B = 1,508(3)–1,522(3) et C—B = 1,612(4)–1,637(4) Å, indiquent que la portion diphénylbore est assez fortement liée aux atomes d'oxygène des ligands *O,O*-chélatants.

[Traduit par la revue]

Can. J. Chem. Downloaded from www.nrcresearchpress.com by 176.9.209.113 on 09/07/12
For personal use only.

Introduction

The alkylation of *N,N*-dialkylhydroxylamines **1** by formaldehyde leads to labile adducts **2** which can be trapped as diphenylboron chelates **3**, as shown for *N,N*-dimethylhydroxylamine (**1**, R = CH_3) by an X-ray crystallographic analysis (1). The formal insertion of methylene into **1** results in *N*-hydroxymethylamines **4** which are also described as zwitterionic primary adducts of formaldehyde and an amine (2). Formaldehyde adducts of dialkylamine (3) are known as very labile compounds[2] and exist generally as short-lived intermediates during the formation of enamines, aminals, iminium salts, Mannich bases, or similar compounds. Compared to the hydroxylamines **1**, the hydroxymethylamines **4** should be nucleophilic enough to add a second molecule of formaldehyde in a reversible reaction to give the labile intermediate **5** by *N*-alkylation of the tertiary amine, or an intermediate **7** by *O*-alkylation of the zwitterionic form. As reported in a preliminary communication (3), the dialkylamine–bisformaldehyde adducts can also be captured as diphenylboron chelates which are stable crystalline materials. A cyclic *B,N*-betaine structure **6**, derived from the *N,N*-bisalkylation product **5**, has been postulated for these compounds. The symmetric structure **6** is supported by evidence of two magnetically equivalent methylene groups in the ^{1}H nmr spectra. Compound **6** is also a ring-enlarged analog (by methylene insertion into the N—O bond) of **3**, the structure of which has been established (1). On the other hand, an intermediate like **7** could exist within the equilibrium reactions between the different formaldehyde–amine adducts[3] and could have been captured as the diphenylborinic acid derivative **8**. Compounds of structure **8** could be considered as "oxa-analogs" of the well-known diphenylborinates of 3-hydroxypropylamines (6) which possess a six-membered ring system **9** as a result of intramolecular N → B coordination (7).

In order to make an unambiguous decision between the alternate structures **6** and **8**, an X-ray crystallographic analysis of well-formed crystals of the azetidine derivative **6***a* (R_2 = —$(CH_2)_3$—) was undertaken. The dimethylamine derivative **6***b* was isolated as a monohydrate in every batch of crystals obtained during various preparations. This is indicated by elemental analysis and ^{1}H nmr data. Neither from nmr signals nor from ir data (which show bands for both associated and free O—H bonds) could a definite mode of binding be established

[1]Part XXVII: ref. 42.

[2]Only the formaldehyde adducts of weakly basic amines are known to be thermally stable, cf. ref. 4.

[3]"Macrozwitterions" such as **7** are supposed to be intermediates in amine-catalyzed formaldehyde polymerization reactions (5).

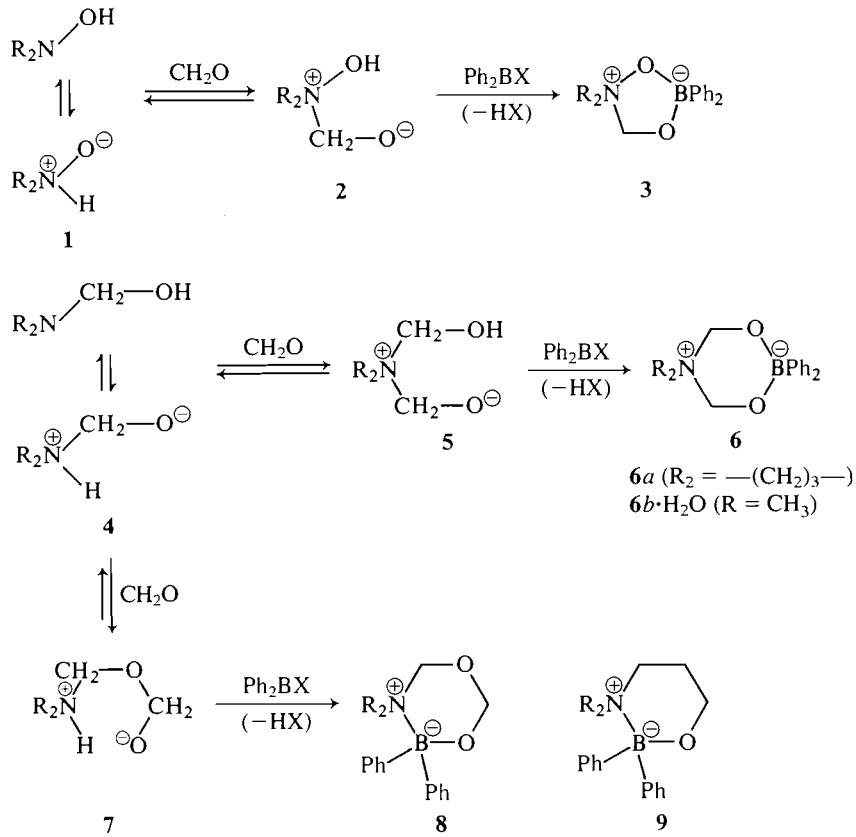

for the water molecule. Four-proton singlets in the ^1H nmr spectra of both the azetidine derivative **6***a* and **6***b*·H_2O indicate two (at least nearly) identical methylene groups, as realized in structures **A**–**D**. Less symmetrical structures that could derive from **8**·H_2O or structures like E or F should be ruled out. The most probable formulation of compound **6***b* appeared to be structure **A** with hydrogen-bonded water in the solid state. An alternative structure **B** represents a simple addition compound of **5** and diphenylborinic acid, which tends to form hydrogen bonds to nucleophilic centres such as an oxygen atom in a chelate ring system (7). Compound **C** with a cyclic diphenylborinate anion could result from condensation of two formaldehyde equivalents and diphenylborinic acid, and crystallization as a dimethylammonium salt, analogous to the formation of a tetramethylammonium salt of tetraphenylboroxinate (8). An open-chain betainic form **D** could derive from a ring-opening of **6** by water insertion. An X-ray crystallographic analysis of **6***b*·H_2O was also undertaken to provide a definitive structural assignment.

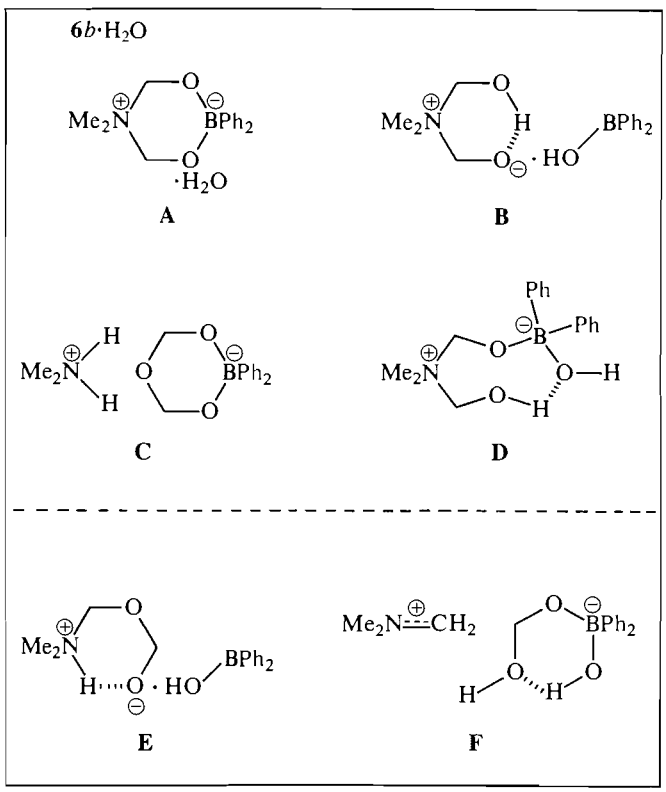

Experimental

5,5-Trimethylene-2,2-diphenyl-1,3-dioxa-5-azonia-2-boratacyclohexane, **6***a*

Azetidine (10 mmol) is dissolved in 5–10 mL ethanol and mixed with formaldehyde (20–25 mmol, 40% aqueous solution). After addition of (*a*) oxybisdiphenylborane (1.73 g, 5 mmol), or (*b*) (2-aminoethyloxy)diphenylborane (2.25 g, 10 mmol), or (*c*) triphenylborane (2.42 g, 10 mmol) the mixture is heated until the solution becomes clear. Crystallization begins to occur during the heating or after cooling down to room temperature. Yields: (*a*) 88%, (*b*) 85%, (*c*) 76%. Melting point (decomp) 157–159°C, literature (3) 157°C. *Anal.* calcd. for $C_{17}H_{20}BNO_2$: C 72.62, H 7.17, B 3.85, N 4.98; found: C 72.51, H 6.94, B 3.88, N 5.06. The substance gives a blue solution upon reaction with diphenylcarbazone in methanolic solution, indicating the presence of a diphenylboron moiety in the molecule (9). During the melting process the substance decomposes and the solution of the pyrolytic gases in water contains formaldehyde detectable by reaction with chromotropic acid (10) or dimedone (11). ^1H nmr (90 MHz, d_6-acetone/TMS): δ(ppm) = 2.34 (quint, J = 9 Hz, C—CH_2—C), 3.78 (t, J = 9 Hz, CH_2—C—CH_2), 4.68 (s, O—CH_2—N—CH_2—O), 6.8–7.4 (m, BPh_2); (60 MHz, CF_3COOH/

Can. J. Chem. Downloaded from www.nrcresearchpress.com by 176.9.209.113 on 09/07/12
For personal use only.

TABLE 1. Crystallographic data[a]

Compound	**6***a*	**6***b*·H_2O
Formula	$C_{17}H_{20}BNO_2$	$C_{16}H_{20}BNO_2 \cdot H_2O$
fw	281.2	287.2
Crystal system	Orthorhombic	Monoclinic
Space group	$P2_12_12_1$	$P2_1/n$
a (Å)	8.8461(3)	6.2432(3)
b (Å)	10.7290(4)	17.1469(8)
c (Å)	15.8773(5)	14.3701(5)
β (deg)		90.647(3)
V (Å^3)	1506.9(1)	1538.2(1)
Z	4	4
D_c (g/cm^3)	1.239	1.240
F(000)	600	616
μ(Cu-K$_\alpha$) (cm^{-1})	5.93	6.36
Crystal dimensions (mm)	0.14 × 0.17 × 0.55	0.30 × 0.30 × 0.35
Transmission factors	0.818–0.928	0.807–0.867
Scan type	ω–2θ	ω–2θ
Scan range (deg in ω)	0.70 + 0.14 tan θ	0.80 + 0.14 tan θ
Scan speed (deg/min)	0.9–10.0	1.3–10.0
Data collected	$+h, +k, +l$	$+h, +k, \pm l$
$2\theta_{max}$ (deg)	150	150
Crystal decay	Negligible	Negligible
Unique reflections	1782	3151
Reflections with $I \geq 3\sigma(I)$	1400	2258
Number of variables	271	275
R	0.030	0.047
R_w	0.034	0.056
S	0.665	1.146
Mean Δ/σ (final cycle)	0.001	0.04
Max Δ/σ (final cycle)	0.009	0.35
Residual density (e/Å^3)	0.15	0.17

[a]Temperature 295 K, Enraf-Nonius CAD4-F diffractometer, Cu-K$_\alpha$ radiation ($\lambda_{K\alpha_1}$ = 1.540562, $\lambda_{K\alpha_2}$ = 1.544390 Å), nickel filter, takeoff angle 2.7°, aperture (2.0 + tan θ) × 4.0 mm at a distance of 173 mm from the crystal, scan range extended by 25% on both sides for background measurement, $\sigma^2(I) = C + 2B + [0.04(C - B)]^2$ (C = scan count, B = normalized background count), function minimized: $\Sigma w(|F_o| - |F_c|)^2$ where $w = 1/\sigma^2(F)$, $R = \Sigma||F_o| - |F_c||/\Sigma|F_o|$, $R_w = (\Sigma w(|F_o| - |F_c|)^2/\Sigma w|F_o|^2)^{1/2}$, $S = (\Sigma w(|F_o| - |F_c|)^2/(m - n))^{1/2}$. Values given for *R*, R_w, and *S* are based on those reflections with $I \geq 3\sigma(I)$.

$CDCl_3$/TMS): δ(ppm) = 2.73 (quint, J = 8 Hz, C—CH_2—C), 4.30 (t, J = 8 Hz, CH_2—C—CH_2), 5.14 (s, O—CH_2—N—CH_2—O), 7.3–7.9 (m, BPh_2). ^{11}B nmr (32.1 MHz, DMSO/Et_2OBF_3): δ(ppm) = 2.4. Crystals suitable for X-ray analysis were obtained by recrystallization from ethanol.

5,5-Dimethyl-2,2-diphenyl-1,3-dioxa-5-azonia-2-boratacyclohexane monohydrate, **6**b·H_2O

Dimethylamine (10 mmol, aqueous solution) is reacted with formaldehyde (20–25 mmol) and (*a*) oxybisdiphenylborane (5 mmol), or (*b*) (2-aminoethyloxy)diphenylborane (10 mmol), or (*c*) triphenylborane (10 mmol), as described above for compound **6***a*. Yields: (*a*) 80%, (*b*) 75%, (*c*) 72%. Melting point (decomp) 121–125°C (slow heating) and 130–132°C (rapid heating). *Anal.* calcd. for $C_{16}H_{22}BNO_3$: C 66.93, H 7.72, B 3.77, N 4.88; found: C 67.37, H 7.61, B 3.67, N 4.86. As described above for **6***a*, the substance gives a blue color reaction with diphenylcarbazone and develops formaldehyde on pyrolysis. Infrared (KBr): 3630 cm^{-1} (sharp, O—H), 3400 (broad, O—H), 1630 (H_2O). ^{1}H nmr (90 MHz, d_6-DMSO/TMS): δ(ppm) = 2.72 (s, $N(CH_3)_2$), 3.30 (s, H—O—H, exchangeable), 4.53 (s, O—CH_2—N—CH_2—O), 6.8–7.4 (m, BPh_2). ^{11}B nmr (32.1 MHz, DMSO/Et_2OBF_3): δ(ppm) = 2.7. Crystals suitable for X-ray analysis were obtained by recrystallization from ethanol.

X-ray crystallographic analyses of **6**a *and* **6**b·H_2O

Crystallographic data for the two compounds appear in Table 1. Unit-cell parameters were refined by least-squares on 2 sin θ/λ values for 25 carefully centered reflections with 2θ = 60–87° for **6***a* and 2θ = 80–100° for **6***b*·H_2O. The intensities of three standard reflections, measured each hour of X-ray exposure time, showed only small random variations in each case. The data were reduced[4] and corrected for absorption (numerical integration). Both structures were solved by direct methods, the positions of all non-hydrogen atoms being determined from *E*-maps and those of the hydrogen atoms from subsequent difference maps. The non-hydrogen atoms were refined with anisotropic thermal parameters and the hydrogen atoms with isotropic thermal parameters. One hydrogen atom H(O3b), associated with the water molecule in **6***b* monohydrate, refined to an unreasonable position and was therefore kept fixed in its observed position and assigned a thermal parameter of 0.304 Å^2 in the final stages of refinement. Neutral atom scattering factors and anomalous scattering corrections (O, N, and C) were taken from ref. 12. Isotropic Type I extinction corrections (13–15) were applied, the final values of *g* being 0.49(5) × 10^4 for **6***a* and 1.48(10) × 10^4 for **6***b*. Parallel refinement of the mirror-image of the structure of **6***a* resulted in marginally higher residuals, the *R* and R_w value ratios of 1.0010 and 1.0006 being

[4]The computer programs used include locally written programs for data processing and locally modified versions of the following: MULTAN 80, multisolution program by P. Main, S. J. Fiske, S. E. Hull, L. Lessinger, G. Germain, J. P. Declercq, and M. M. Woolfson; AGNOST, absorption corrections, by J. A. Ibers; ORFLS, full-matrix least-squares, and ORFFE, function and errors, by W. R. Busing, K. O. Martin, and H. A. Levy; FORDAP, Patterson and Fourier syntheses, by A. Zalkin; ORTEP II, illustrations, by C. K. Johnson.

Can. J. Chem. Downloaded from www.nrcresearchpress.com by 176.9.209.113 on 09/07/12
For personal use only.

Can. J. Chem. Downloaded from www.nrcresearchpress.com by 176.9.209.113 on 09/07/12
For personal use only.

TABLE 2. Final positional (fractional × 10^4) and isotropic thermal parameters ($U \times 10^3$ Å^2) with estimated standard deviations in parentheses

Atom	x	y	z	U_{eq}
		6a		
O(1)	9224(2)	1060(2)	7112(1)	47
O(2)	8892(2)	−1172(2)	7273(1)	47
N	9456(2)	101(2)	8444(1)	48
C(1)	8955(4)	1238(3)	7953(2)	51
C(2)	8621(4)	−1029(3)	8116(2)	50
C(3)	11154(3)	−90(5)	8505(2)	67
C(4)	11036(4)	−170(5)	9464(2)	71
C(5)	9378(4)	216(4)	9402(2)	59
C(6)	9045(3)	−291(2)	5809(1)	42
C(7)	8902(4)	−1458(3)	5436(2)	56
C(8)	9355(5)	−1695(3)	4613(2)	68
C(9)	9953(4)	−751(4)	4135(2)	69
C(10)	10108(4)	411(4)	4478(2)	64
C(11)	9665(4)	629(3)	5306(2)	55
C(12)	6609(3)	118(3)	6762(1)	41
C(13)	5609(4)	−856(3)	6904(2)	50
C(14)	4046(4)	−700(4)	6870(2)	63
C(15)	3440(4)	439(4)	6690(2)	64
C(16)	4395(4)	1422(4)	6537(2)	66
C(17)	5947(4)	1273(3)	6574(2)	53
B	8442(3)	−61(3)	6751(2)	40
		***6b*·H_2O**		
O(1)	5422(2)	1692(1)	5174(1)	47
O(2)	1800(2)	1507(1)	5723(1)	42
O(3)	1898(5)	−30(2)	6548(2)	98
N	2598(3)	1371(1)	4109(1)	47
C(1)	991(4)	1631(2)	4844(2)	46
C(2)	4665(4)	1829(2)	4293(2)	50
C(3)	2989(7)	513(2)	4190(3)	68
C(4)	1744(6)	1571(2)	3164(2)	62
C(5)	3563(4)	2865(1)	5950(1)	40
C(6)	5269(4)	3363(2)	5771(2)	49
C(7)	5092(5)	4168(2)	5853(2)	61
C(8)	3182(6)	4496(2)	6122(2)	65
C(9)	1463(6)	4022(2)	6312(2)	62
C(10)	1664(5)	3217(2)	6229(2)	51
C(11)	4785(4)	1620(1)	6915(1)	38
C(12)	6851(4)	1337(1)	7052(2)	48
C(13)	7588(5)	1100(2)	7923(2)	60
C(14)	6268(5)	1147(2)	8684(2)	60
C(15)	4229(5)	1430(2)	8568(2)	56
C(16)	3497(4)	1664(2)	7700(2)	47
B	3890(4)	1925(2)	5925(2)	46

significant at approximately the 90 and 75% levels, respectively (ref. 12, pp. 288–292). Final positional parameters and equivalent isotropic thermal parameters for the non-hydrogen atoms are given in Table 2. Hydrogen coordinates and thermal parameters (Table 6), anisotropic thermal parameters (Table 7), and measured and calculated structure factors have been placed in the Depository of Unpublished Data.[5]

The thermal motion in both molecules has been analysed in terms of the rigid-body modes of translation, libration, and screw-motion (16). The rms errors in the thermal parameters σU_{ij} (derived from the least-squares analyses) are 0.0016 and 0.0014 Å^2 for **6***a* and **6***b*, respectively. The structural subunits PhB and the spiro-fused ring system for **6***a* and PhB and the six-membered heterocyclic ring along with the two *N*-methyl carbon atoms for **6***b* were separately analysed (rms ΔU_{ij} = 0.0014–0.0018 Å^2 for **6***a* and 0.0014–0.0024 Å^2 for **6***b*). The appropriate bond distances have been corrected for libration (16, 17), using shape parameters q^2 of 0.08 for all atoms involved. Corrected bond lengths appear in Table 3 along with the uncorrected values; corrected bond angles do not differ by more than 1σ from the uncorrected values given in Table 4. Intra-annular torsion angles defining the conformations of heterocyclic rings are listed in Table 5. Bond lengths and angles involving hydrogen and a complete listing of torsion angles (Tables 8–10) are included as supplementary material.

[5]The structure factor table and Tables 6–10 may be purchased from the Depository of Unpublished Data, CISTI, National Research Council of Canada, Ottawa, Ont., Canada K1A 0S2.

Results and discussion

5,5-Trimethylene-2,2-diphenyl-1,3-dioxa-5-azonia-2-boratacyclohexane and 5,5-dimethyl-2,2-diphenyl-1,3-dioxa-5-azonia-2-boratacyclohexane monohydrate both possess the general structure **6** (Fig. 1). The crystal structure of **6***a* consists of discrete molecules separated by normal van der Waals distances. Even though individual molecules of **6***a* are non-chiral, the crystal structure itself is chiral, probably with equal numbers of right- and left-handed crystals being formed. In **6***b*·H_2O each molecule of **6***b* is hydrogen-bonded to one water molecule (O(3)—H(O3a)···O(2), H···O = 1.51(8) Å, O···O = 2.891(3) Å, O—H···O = 164(5)°), these 1:1 molecular complexes forming centrosymmetric dimeric units via weak C—H···O interactions involving the water molecule (C(3)—H(3a)···O(3) (−*x*, −*y*, 1 − *z*), H···O = 2.39(4) Å, C···O = 3.324(5) Å, C—H···O = 157(3)°). The second hydrogen atom

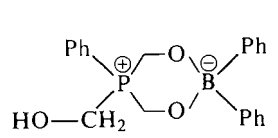

10

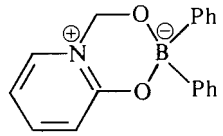

11

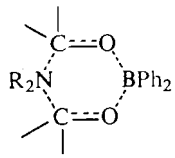

12

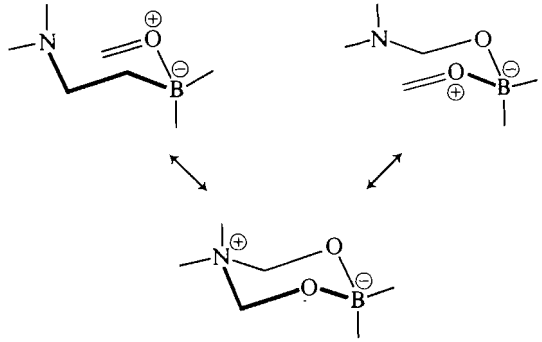

13

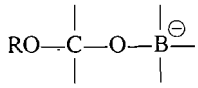

14

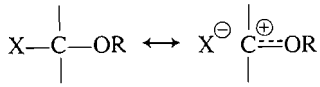

15

TABLE 3. Bond lengths (Å) with estimated standard deviations in parentheses

Bond	Length Uncorr.	Length Corr.	Bond	Length Uncorr.	Length Corr.
			6a		
O(1)—C(1)	1.370(3)	1.374	C(6)—B	1.608(4)	1.612
O(1)—B	1.501(3)	1.508	C(7)—C(8)	1.390(4)	1.394
O(2)—C(2)	1.367(3)	1.371	C(8)—C(9)	1.373(5)	1.382
O(2)—B	1.505(3)	1.512	C(9)—C(10)	1.367(5)	1.378
N—C(1)	1.514(4)	1.521	C(10)—C(11)	1.392(4)	1.396
N—C(2)	1.512(4)	1.519	C(12)—C(13)	1.388(4)	1.396
N—C(3)	1.519(4)	1.528	C(12)—C(17)	1.402(4)	1.411
N—C(5)	1.526(3)	1.530	C(12)—B	1.633(4)	1.637
C(3)—C(4)	1.528(4)	1.532	C(13)—C(14)	1.394(4)	1.398
C(4)—C(5)	1.527(5)	1.536	C(14)—C(15)	1.365(5)	1.374
C(6)—C(7)	1.391(4)	1.402	C(15)—C(16)	1.373(5)	1.381
C(6)—C(11)	1.382(4)	1.391	C(16)—C(17)	1.383(4)	1.387
			***6b*·H_2O**		
O(1)—C(2)	1.367(3)	1.372	C(6)—C(7)	1.390(4)	1.395
O(1)—B	1.505(3)	1.513	C(7)—C(8)	1.377(4)	1.385
O(2)—C(1)	1.371(3)	1.376	C(8)—C(9)	1.376(4)	1.384
O(2)—B	1.514(3)	1.522	C(9)—C(10)	1.391(4)	1.396
N—C(1)	1.532(3)	1.540	C(11)—C(12)	1.389(3)	1.399
N—C(2)	1.531(3)	1.539	C(11)—C(16)	1.396(3)	1.403
N—C(3)	1.495(3)	1.506	C(11)—B	1.609(3)	1.615
N—C(4)	1.494(3)	1.501	C(12)—C(13)	1.389(3)	1.395
C(5)—C(6)	1.392(3)	1.399	C(13)—C(14)	1.379(4)	1.386
C(5)—C(10)	1.393(3)	1.401	C(14)—C(15)	1.370(4)	1.380
C(5)—B	1.625(3)	1.630	C(15)—C(16)	1.383(3)	1.389

Can. J. Chem. Downloaded from www.nrcresearchpress.com by 176.9.209.113 on 09/07/12
For personal use only.

associated with the water molecule, H(O3b), is not involved in H-bonding. This is the first unequivocal proof of a cyclic *B*,*N*-betaine of this type, demonstrating the bis-*N*-alkylation of a secondary amine by formaldehyde via *N*-alkylation of the *N*-hydroxymethyl intermediate **4**. The addition of a second formaldehyde molecule to *N*-hydroxymethyl-*N*,*N*-dialkylamines had already been assumed by Künzel *et al.* (5*a*), but the product could not be isolated. The trapping of **5** by diphenylborinic acid (3) allowed the fixation of this labile ammonium inner salt within the *B*,*N*-betaine ring system **6**, the structure of which has now been established. A diphenylborinic ester of a tris-hydroxymethylated phenylphosphine, **10**, has been shown to contain an analogous *B*,*P*-betaine ring (18).

The six-membered heterocyclic rings in **6***a* and **6***b* adopt the sterically favorable chair conformation, as does that in compound **10** (18). In **6***b* the hydrogen bond to the water molecule occupies an axial position. The *B*-phenyl substituents in axial positions show significantly longer B—C bonds[6] than those in equatorial positions (see Table 3), the differences being 0.025(6) Å for **6***a* and 0.015(4) Å for **6***b*. Corresponding differences in the same range have been noted for **10** (18) and **11** (19), the substituents occupying pseudo-axial and pseudo-equatorial positions in the latter. Less pronounced differences are reported for six-membered diphenylboron chelates of salicylaldehyde (20) and acetylacetone (21), in which pseudo-axial and pseudo-equatorial B—C distances differ by 0.007 Å.

The N—C—O—B system in **6** is chemically the same as that in **3** (R = Me) (1) and similar to that in the corresponding *C*,*C*-dimethyl derivative (acetone analog) of **3** (22). The N—C(1) and N—C(2) distances of 1.521(4) and 1.519(4) Å in **6***a* and 1.540(3) and 1.539(3) Å in **6***b* lie between the corresponding distance of 1.505(10) Å (uncorrected) in **3** and the sterically lengthened N—C(1) distance of 1.591(3) Å in the *C*,*C*-dimethyl derivative of **3**. Bond lengths and angles in the non-planar (torsion angles of 8.0(3)°) azetidinium system in **6***a* show considerable steric strain. The higher nucleophilicity (basicity) of the azetidine component in **6***a* relative to that of the dimethylamine component in **6***b* may also be a cause of the difference between the N—C(1) and N—C(2) bond lengths in **6***a* and **6***b*, averaging 0.02 Å longer in the latter. The pK_a values of azetidine and dimethylamine are reported as 11.29 and 10.73, respectively, in aqueous solution at 25°C (23).

The average O—B and C—B distances in compounds **6** and **10** (1.510 and 1.625 Å in **6***a*, 1.518 and 1.623 Å in **6***b*, 1.514 and 1.621 Å (uncorr.) in **10**), which contain saturated six-membered chelate rings, are shorter and longer, respectively, than the corresponding averages of 1.528–1.538 and 1.606–1.607 Å reported for *O*,*O*-chelates of diphenylboron containing unsaturated six-membered chelate rings (19–21, 24). This is indicative of relatively strong binding of the ligand oxygen atoms to boron and is consistent with trends reported for analogous compounds containing five-membered chelate rings (24). The O(2)—B bond in **6***b* (1.522(3) Å) is longer than the O(1)—B bond in **6***b* and both O—B bonds in **6***a* (1.508(3)–1.513(3) Å), most likely as a result of the involvement of O(2) in the hydrogen bond to water in **6***b*·H_2O. The O—B bonds in compounds **6** (mean 1.514(6) Å), **3** (1.506(7) (uncorr.) and 1.507(3) Å), and **10** (1.514 Å (uncorr.)) are longer than those observed for diphenylboron chelates of aminoalcohols with five- and six-membered chelate rings (1.471–1.484 Å) (7,

[6]Libration corrected bond lengths (esd's assumed equal to those of the uncorrected values) are employed in the discussion and are compared with similarly treated (16) distances unless otherwise stated.

TABLE 4. Bond angles (deg) with estimated standard deviations in parentheses

Bonds	Angle (deg)	Bonds	Angle (deg)
		6*a*	
C(1)—O(1)—B	113.8(2)	C(8)—C(9)—C(10)	119.4(3)
C(2)—O(2)—B	113.8(2)	C(9)—C(10)—C(11)	120.1(3)
C(1)—N—C(2)	108.9(2)	C(6)—C(11)—C(10)	122.5(3)
C(1)—N—C(3)	115.5(3)	C(13)—C(12)—C(17)	115.7(3)
C(1)—N—C(5)	115.8(2)	C(13)—C(12)—B	123.1(2)
C(2)—N—C(3)	113.4(3)	C(17)—C(12)—B	121.1(2)
C(2)—N—C(5)	112.8(2)	C(12)—C(13)—C(14)	122.3(3)
C(3)—N—C(5)	89.6(2)	C(13)—C(14)—C(15)	120.4(4)
O(1)—C(1)—N	109.8(2)	C(14)—C(15)—C(16)	118.9(3)
O(2)—C(2)—N	110.0(2)	C(15)—C(16)—C(17)	120.9(4)
N—C(3)—C(4)	90.2(2)	C(12)—C(17)—C(16)	121.8(3)
C(3)—C(4)—C(5)	89.2(2)	O(1)—B—O(2)	107.6(2)
N—C(5)—C(4)	89.9(2)	O(1)—B—C(6)	108.9(2)
C(7)—C(6)—C(11)	115.7(3)	O(1)—B—C(12)	111.1(2)
C(7)—C(6)—B	120.3(2)	O(2)—B—C(6)	107.6(2)
C(11)—C(6)—B	124.0(2)	O(2)—B—C(12)	110.5(2)
C(6)—C(7)—C(8)	122.6(3)	C(6)—B—C(12)	111.0(2)
C(7)—C(8)—C(9)	119.7(3)		
		6*b*·H_2O	
C(2)—O(1)—B	113.8(2)	C(8)—C(9)—C(10)	119.8(3)
C(1)—O(2)—B	114.3(2)	C(5)—C(10)—C(9)	122.2(3)
C(1)—N—C(2)	106.8(2)	C(12)—C(11)—C(16)	116.5(2)
C(1)—N—C(3)	109.9(2)	C(12)—C(11)—B	123.5(2)
C(1)—N—C(4)	109.3(2)	C(16)—C(11)—B	120.0(2)
C(2)—N—C(3)	110.7(2)	C(11)—C(12)—C(13)	121.8(3)
C(2)—N—C(4)	109.3(2)	C(12)—C(13)—C(14)	120.1(3)
C(3)—N—C(4)	110.6(2)	C(13)—C(14)—C(15)	119.2(2)
O(2)—C(1)—N	110.7(2)	C(14)—C(15)—C(16)	120.6(3)
O(1)—C(2)—N	110.7(2)	C(11)—C(16)—C(15)	121.7(3)
C(6)—C(5)—C(10)	116.3(2)	O(1)—B—O(2)	106.9(2)
C(6)—C(5)—B	120.5(2)	O(1)—B—C(5)	111.1(2)
C(10)—C(5)—B	122.9(2)	O(1)—B—C(11)	109.3(2)
C(5)—C(6)—C(7)	122.2(3)	O(2)—B—C(5)	111.4(2)
C(6)—C(7)—C(8)	119.9(3)	O(2)—B—C(11)	107.8(2)
C(7)—C(8)—C(9)	119.6(3)	C(5)—B—C(11)	110.3(2)

25–27). This indicates a weaker oxygen atom nucleophilicity of the *N*-hydroxymethyl group relative to those of *N*-(2-hydroxymethyl) and *N*-(3-hydroxypropyl) groups.

Electronic differences are also reflected by the short C—O bonds in **6** and **3** (average 1.373 Å in **6**, 1.378(9) Å (uncorr.) and 1.387(3) Å in **3** (1, 22)) compared with an average of 1.428 Å in the 2- and 3-hydroxyalkylamine derivatives (7, 25–27). The C—O distances in **6** and **3** lie between the uncorrected distances of 1.209 Å in formaldehyde (28) and 1.430 Å in the formaldehyde trimer (trioxane) (29), and show a double bond character of approximately 20% (30) resulting from back-donation from oxygen to carbon in the formaldehyde moiety within the molecule **6**. The transition state of the thermally induced dissociation of **6**, which results in the formation of formaldehyde, may be represented by the structure **12**. The short C—O distances can also be described by the concept of "double bond – no bond" resonance (31), compound **6** being represented by a hybrid of the resonance structures **13**.

C=O bond lengthening during *nucleophilic* addition of amines to carbonyl groups has been observed in the course of a survey of crystal structures of compounds containing both functions (32). C—O bond lengths ranging from 1.209 to 1.38 Å demonstrate the approach of the nucleophilic nitrogen

TABLE 5. Intra-annular torsion angles (deg) standard deviations in parentheses

Atoms	Value (deg)
6*a*	
B—O(1)—C(1)—N	58.5(3)
C(2)—N—C(1)—O(1)	−57.9(3)
C(1)—N—C(2)—O(2)	57.8(3)
B—O(2)—C(2)—N	−58.2(3)
C(2)—O(2)—B—O(1)	54.7(3)
C(1)—O(1)—B—O(2)	−54.9(3)
C(5)—N—C(3)—C(4)	8.0(3)
N—C(3)—C(4)—C(5)	−8.0(3)
C(3)—C(4)—C(5)—N	7.9(3)
C(3)—N—C(5)—C(4)	−8.0(3)
6*b*·H_2O	
B—O(1)—C(2)—N	−60.3(3)
C(1)—N—C(2)—O(1)	58.4(3)
C(2)—N—C(1)—O(2)	−57.4(3)
B—O(2)—C(1)—N	58.5(3)
C(1)—O(2)—B—O(1)	−54.3(2)
C(2)—O(1)—B—O(2)	55.0(2)

Can. J. Chem. Downloaded from www.nrcresearchpress.com by 176.9.209.113 on 09/07/12
For personal use only.

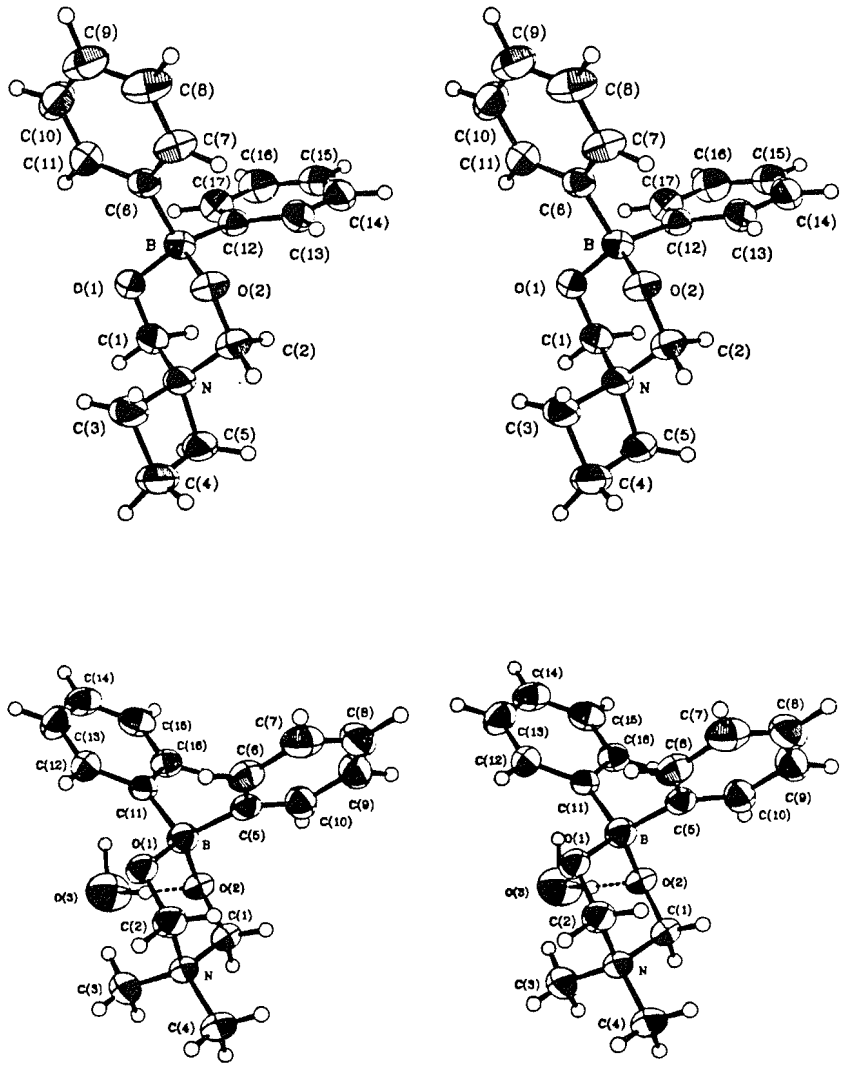

FIG. 1. Stereoscopic views of 5,5-trimethylene-2,2-diphenyl-1,3-dioxa-5-azonia-2-boratacyclohexane (top) and 5,5-dimethyl-2,2-diphenyl-1,3-dioxa-5-azonia-2-boratacyclohexane monohydrate (bottom); 50% probability thermal ellipsoids are shown for the non-hydrogen atoms. Hydrogen atoms have been assigned arbitrary thermal parameters for the sake of clarity.

centre to the electrophilic carbon centre at different stages of N···C=O interaction. C=O bond lengthening during *electrophilic* addition of Lewis acids to carbonyl groups is also documented by calculation and experiment, with C—O distances for C=O···A (A = Lewis acid) systems ranging from 1.244 to 1.33 Å (20, 21, 33–37). Nucleophilic and electrophilic forces both play a fundamental role in the formation and stability of **6** and **3**, adducts in which formaldehyde is trapped in a push–pull mechanism. Similar C—O distances are also found in the borate complex antibiotics boromycin (38) and aplasmomycin (39). These C—O bonds (uncorrected distances of 1.34 and 1.37 Å, respectively) are chemically similar to those in **3** and **6**: a carbonyl function participates as a nucleophilic ligand to the boron centre and as an electrophilic component in an acetal group, **14**. Comparable C—O distances of 1.37–1.38 Å are also found in acetal systems with halogen "leaving" groups, **15** (40).

The phenyl groups in both **6***a* and **6***b* are planar to within experimental error. Bond lengths and angles in the *B*-substituted phenyl rings show normal substituent-induced deviations from "ideal" values (41).

Acknowledgments

We thank the Natural Sciences and Engineering Research Council of Canada and the Fonds der Chemischen Industrie, Frankfurt am Main, for financial support, and the University of British Columbia Computing Centre for assistance. We are also grateful to Professor H. Nöth, University of Munich, for running the ^{11}B nmr spectra.

1. S. J. RETTIG, J. TROTTER, and W. KLIEGEL. Can. J. Chem. **52**, 2531 (1974).
2. (*a*) W. P. JENCKS. Catalysis in chemistry and enzymology. McGraw-Hill, New York. 1969. p. 463; (*b*) W. P. JENCKS. Chem. Rev. **72**, 705 (1972); (*c*) W. P. JENCKS. Acc. Chem. Res. **9**, 425 (1976); (*d*) J. HINE and F. C. KOKESH. J. Am. Chem. Soc. **92**, 4383 (1970); (*e*) M. A. SHOKHEN, D. A. TIKHOMIROV, and A. V. YEREMEYEV. Tetrahedron, **39**, 2975 (1983).
3. W. KLIEGEL. Angew. Chem. **80**, 614 (1968).
4. G. ZINNER, W. KLIEGEL, and W. RITTER. Chem. Ber. **99**, 1285 (1966), and references therein.
5. (*a*) E. KÜNZEL, A. GIEFER, and W. KERN. Makromol. Chem. **96**, 17 (1966); (*b*) K. BOEHLKE, M. J. HAN, V. JAACKS, N.

Can. J. Chem. Downloaded from www.nrcresearchpress.com by 176.9.209.113 on 09/07/12
For personal use only.

MATHES, and K. ZIMMERSCHIED. Angew. Chem. **81**, 336 (1969); (*c*) N. MATHES and V. JAACKS. Makromol. Chem. **135**, 49 (1970).
6. (*a*) H. K. ZIMMERMAN. Adv. Chem. Ser. **42**, 23 (1964); (*b*) W. KLIEGEL. Bor in biologie, medizin und pharmazie. Springer-Verlag, Berlin. 1980. pp. 474 and 785.
7. S. J. RETTIG and J. TROTTER. Can. J. Chem. **61**, 2334 (1983).
8. W. KLIEGEL, H.-W. MOTZKUS, S. J. RETTIG, and J. TROTTER. Can. J. Chem. **63**, 3516 (1985).
9. (*a*) R. NEU. Z. Anal. Chem. **176**, 334 (1960); (*b*) B. FRIESE and F. UMLAND. Anal. Chim. Acta, **96**, 303 (1978).
10. F. FEIGL. Spot tests in organic analysis. Elsevier, Amsterdam. 1960. p. 350.
11. (*a*) E. C. HORNING and H. G. HORNING. J. Org. Chem. **11**, 95 (1946); (*b*) HOUBEN-WEYL. methoden der organischen chemie. Vol. II. Thieme Verlag, Stuttgart. 1953. p. 456.
12. International tables for X-ray crystallography. Vol. IV. Kynoch Press, Birmingham. 1974. pp. 99–102 and 149.
13. P. J. BECKER and P. COPPENS. Acta Crystallogr. Sect. A, **30**, 129 (1974); **30**, 148 (1974); **31**, 417 (1975).
14. P. COPPENS and W. C. HAMILTON. Acta Crystallogr. Sect. A, **26**, 71 (1970).
15. F. R. THORNLEY and R. J. NELMES. Acta Crystallogr. Sect. A, **30**, 748 (1974).
16. V. SCHOMAKER and K. N. TRUEBLOOD. Acta Crystallogr. Sect. B, **24**, 63 (1968).
17. D. W. J. CRUICKSHANK. Acta Crystallogr. **9**, 747 (1956); **9**, 754 (1956); **14**, 896 (1961).
18. B. A. ARBUZOV, O. A. ERASTOV, G. N. NIKONOV, A. A. ESPENBETOV, A. I. YANOVSKII, and YU. T. STRUCHKOV. Izv. Akad. Nauk SSSR, Ser. Khim. 1545 (1981); Bull. Acad. Sci. USSR, Div. Chem. Sci. 1243 (1981).
19. W. KLIEGEL, H.-W. MOTZKUS, S. J. RETTIG, and J. TROTTER. Can. J. Chem. **64**, 507 (1986).
20. S. J. RETTIG and J. TROTTER. Can. J. Chem. **54**, 1168 (1976).
21. S. J. RETTIG and J. TROTTER. Can. J. Chem. **60**, 2957 (1982).
22. W. KLIEGEL, H.-W. MOTZKUS, S. J. RETTIG, and J. TROTTER. Can. J. Chem. **62**, 838 (1984).
23. D. D. PERRIN. Dissociation constants of organic bases in aqueous solution. Butterworths, London. 1965.
24. C. ORVIG, S. J. RETTIG, and J. TROTTER. Can. J. Chem. **65**, 590 (1987).
25. S. J. RETTIG and J. TROTTER. Can. J. Chem. **51**, 1288 (1973).
26. S. J. RETTIG and J. TROTTER. Acta Crystallogr. Sect. B, **30**, 2139 (1974).
27. S. J. RETTIG and J. TROTTER. Can. J. Chem. **54**, 3130 (1976).
28. C. KATO, S. KONAKA, T. IIJIMA, and M. KIMURA. Bull. Chem. Soc. Jpn. **42**, 2148 (1969).
29. V. BUSETTI. Z. Krist. **119**, 310 (1963).
30. G. HÄFELINGER. Chem. Ber. **103**, 2922 (1970).
31. P. DESLONGCHAMPS. Stereoelectronic effects in organic chemistry. Permagon Press, Oxford. 1983. p. 4.
32. H. H. BÜRGI, J. D. DUNITZ, and E. SHEFTER. J. Am. Chem. Soc. **95**, 5065 (1973).
33. D. J. RABER, H. K. RABER, J. CHANDRASEKHAR, and P. V. RAGUE SCHLEYER. Inorg. Chem. **23**, 4076 (1984).
34. D. R. CRIST, Z. H. HSIEH, C. O. QUICKSALL, and M. K. SUN. J. Org. Chem. **49**, 2478 (1984).
35. M. T. REETZ, M. HÜLLMANN, W. MASSA, S. BERGER, P. RADEMACHER, and P. HEYMANNS. J. Am. Chem. Soc. **108**, 2405 (1986).
36. R. BOESE, R. KÖSTER, and M. YALPANI. Chem. Ber. **118**, 670 (1985).
37. Y. P. SINGH, P. RUPANI, A. SINGH, A. K. RAI, R. C. MEHROTRA, R. D. ROGERS, and J. L. ATWOOD. Inorg. Chem. **25**, 3076 (1986).
38. J. D. DUNITZ, D. M. HAWLEY, D. MIKOS, D. N. J. WHITE, YU. BERLIN, R. MARUSIC, and V. PRELOG. Helv. Chim. Acta, **54**, 1709 (1971).
39. H. NAKAMURA, Y. IITAKA, T. KITAHARA, T. OKAZAKI, and Y. OKAMI. J. Antibiot. **30**, 714 (1977).
40. C. ROMERS, C. ALTONA, H. R. BUYS, and E. HAVINGA. *In* Topics in stereochemistry. Vol. 4. *Edited by* E. L. Eliel and N. L. Allinger. Wiley-Interscience, New York. 1969. p. 73.
41. A. DOMENICANO, P. MURRAY-RUST, and A. VACIAGO. Acta Crystallogr. Sect. B, **39**, 457 (1983) and references therein.
42. W. O. NELSON, C. ORVIG, S. J. RETTIG, and J. TROTTER. Can. J. Chem. **66**, 132 (1988).

Can. J. Chem. Downloaded from www.nrcresearchpress.com by 176.9.209.113 on 09/07/12
For personal use only.

Thermal intramolecular reactions of Δ^1-1,2,4-triazolines with extended exocyclic unsaturation

ADRIAN L. SCHWAN[1] AND JOHN WARKENTIN[2]

Department of Chemistry, McMaster University, Hamilton, Ont., Canada L8S 4M1

Received June 16, 1987

ADRIAN L. SCHWAN and JOHN WARKENTIN. Can. J. Chem. **66**, 385 (1988).

Fumaratotriazoline (**1**) and amidotriazoline (**3**) undergo thermal first-order transformations in solution at 65°C. The former affords the isomeric pyrrole **5** and its hydrolysis product **6**. A mechanism involving opening of the initial five-membered ring to form **8**, followed by closure to a new five-membered ring (**9**), is proposed. Amidotriazoline (**3**) loses N_2 on heating to form **19**. The experimental results are best accommodated in terms of a novel mechanism involving an electrocyclic ring closure, a [3 + 2] cycloreversion to form an ylide, a sigmatropic rearrangement of the ylide, and, finally, an electrocyclic ring-opening reaction.

ADRIAN L. SCHWAN et JOHN WARKENTIN. Can. J. Chem. **66**, 385 (1988).

En solution, à 65°C, la fumaratotriazoline (**1**) et l'amidotriazoline (**3**) subissent des transformations thermiques du premier ordre. Le premier composé fournit le pyrrole isomère **5** ainsi que son produit d'hydrolyse **6**. On propose un mécanisme impliquant dans une première étape l'ouverture du cycle à cinq chaînons qui se forme initialement; il s'en suit la formation du composé **8** qui est suivie d'une fermeture conduisant à un nouveau cycle à cinq chaînons (**9**). Par chauffage, l'amidotriazoline (**3**) perd du N_2 et forme le composé **19**. Pour expliquer les résultats expérimentaux, on doit faire appel à un nouveau mécanisme impliquant une cyclisation électrocyclique, une cycloréversion [3 + 2] conduisant à un ylure, une transposition sigmatropique de l'ylure et, finalement, une réaction électrocyclique d'ouverture de cycle.

[Traduit par la revue]

Introduction

The syntheses of fumaratotriazoline (**1**) (1) and of amidotriazoline (**3**) (2) from 4-(*tert*-butyl)-3,3-dimethyl-5-methylene-Δ^1-1,2,4-triazoline have been described. As cross-conjugated azoenamines with extended conjugation, **1** and **3** held promise for the generation of azomethine ylides (3, 4). Thus, **1** and **3** could conceivably lead to the spirotriazolines, **2** and **4**, respectively, by unimolecular cyclization, eqs. [1], [2]. With quaternary carbons at C3 and C5 of the Δ^1-1,2,4-triazoline ring, **2** and **4** might be susceptible to ylide-forming [3 + 2] cycloreversion, eqs. [1], [2]. We now report the results of thermal decomposition of **1** and **3**.

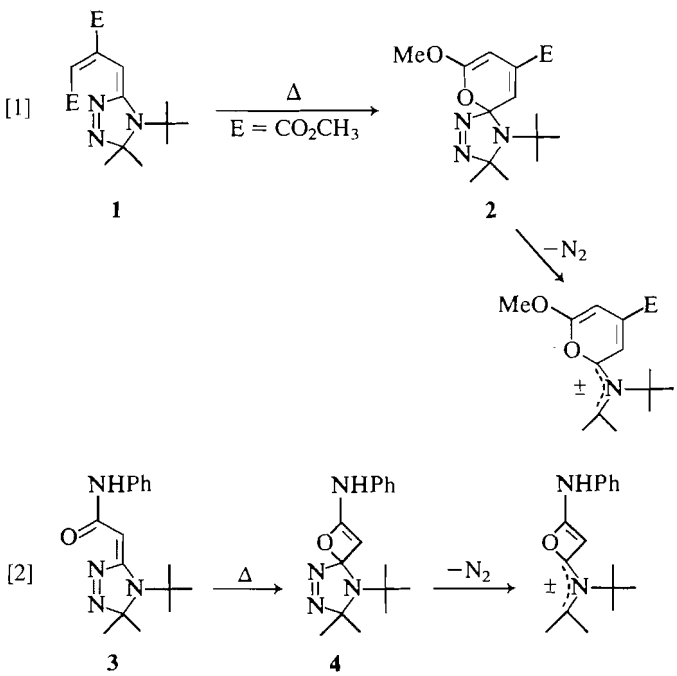

Results and discussion

Refluxing of a solution of fumaratotriazoline **1** in methanol for 48 h resulted in the consumption of **1**. Careful separation of the products by means of centrifugal chromatography under N_2 (Chromatotron) afforded pyrroles **5** and **6** in 91% combined yield, eq. [3]. Neat **5**, on exposure to the atmosphere, was

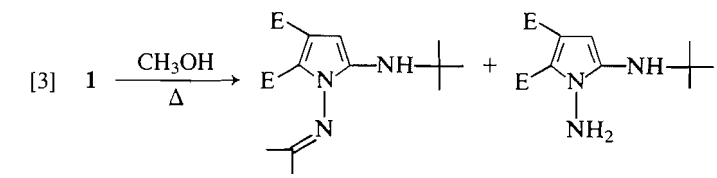

5 **6**

(E = CO_2CH_3)

converted to **6** at a remarkably high rate; the reaction was largely completed in 15 min. It is very likely, therefore, that **1** is converted to **5** in nearly quantitative yield and that **6** is a product of the hydrolysis of **5**, by traces of water in the solvent and (or) by contact with moisture during work-up.

The structures of **5** and **6** are based on spectroscopic data. Their infrared spectra are similar to the spectra of pyrroles bearing conjugating substituents (5) and both the ^1H (6) and ^{13}C nmr spectra support the assignments (Table 1).

A mechanism that can account for the results is shown in Scheme 1. According to this mechanism, **1** undergoes ring opening, probably reversibly, to the dipolar species **8**, which then cyclizes to **9**. Intermediate **9** may isomerize to **10** by prototropic shifts and either **9** or **10** isomerizes to the aromatic product **5**. In a slightly different version (Scheme 2), ring closure of **1** to **11** is the first step. Ylide **11**, which has a cyclopentadiene-like upper ring, rearranges to **12** by means of sequential 1,5-sigmatropic hydrogen shifts and **12** undergoes an electrocyclic ring-opening reaction to form **10**. The latter mechanism is considered less likely than that of Scheme 1 because the geometric requirements for 5-*exo* closure to **11** are not well met in **1**. An alternative and essentially equivalent rationale for preferring Scheme 1 is that the first step is an

[1] NSERC Postgraduate Scholarship holder, 1983–1987.

[2] Author to whom correspondence may be addressed.

Can. J. Chem. Downloaded from www.nrcresearchpress.com by 176.9.209.113 on 09/07/12
For personal use only.

TABLE 1. ^1H and ^{13}C nuclear magnetic resonance data

Compound	^1H nmr (δ for C3-H)	^{13}C nmr (ring protons) C-2	C-3	C-4	C-5
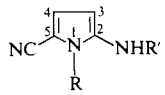					
7*a*, R = R′ = *t*-Bu	5.50				
7*b*, R = *t*-Bu, R′ = CH_2OCH_3	5.69				
5	5.71	137	93	112(119)	119(112)
6	5.54	142	91	113(121)	121(113)
Pyrrole	6.30	117	108	108	117

Can. J. Chem. Downloaded from www.nrcresearchpress.com by 176.9.209.113 on 09/07/12
For personal use only.

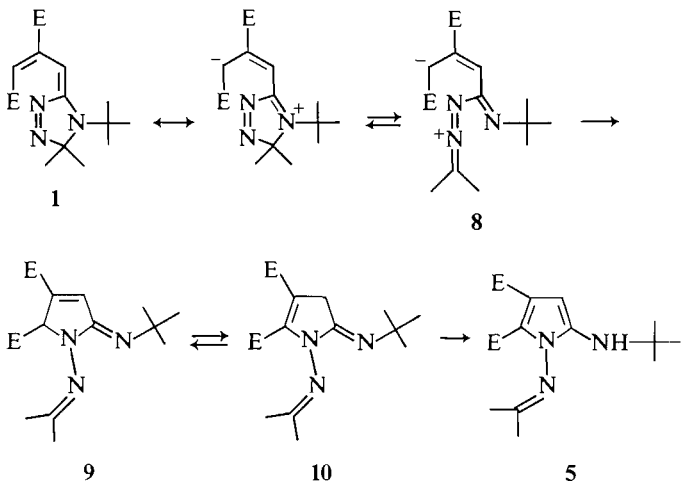

SCHEME 1

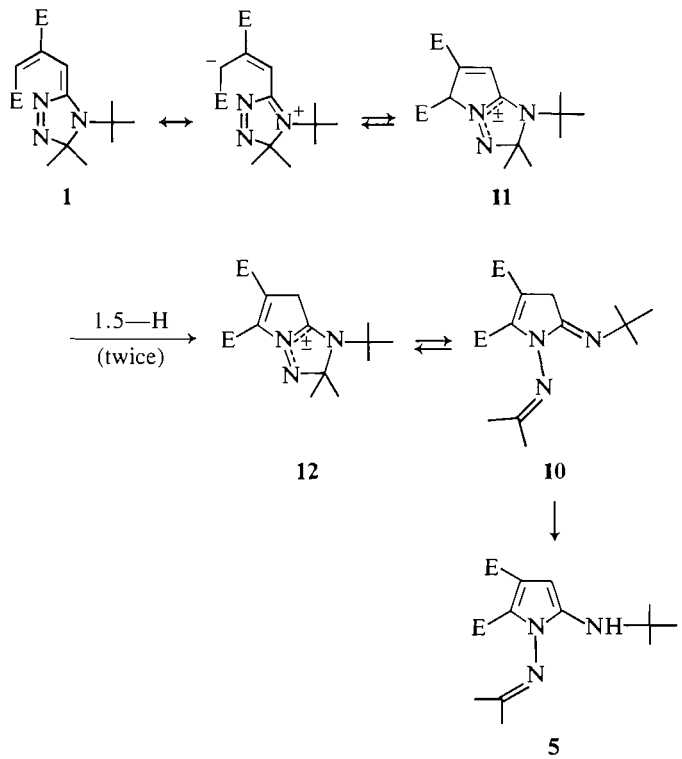

SCHEME 2

entropically favoured ring scission rather than a ring closure with accompanying increase of rigidity.

Although slightly different versions of the proposed mechanism can be put forward, it is clear from the high yield that the rearrangement of **1** to **5** is a clean process. Excluded specifically are the sequential reactions [1] and the electrocyclic rearrangement of **1** to **13**, reaction [4], as significant competitors. An

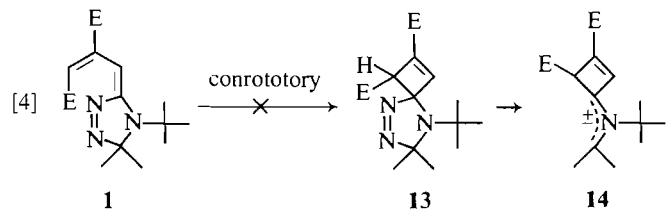

intermediate such as **13** is expected to lose N_2 rapidly, to form an azomethine ylide **14**, as demonstrated for a close analogue (1). Even the material not accounted for (compound X, 9%) has three nitrogen atoms per molecule, as indicated by the combined ms and ^1H nmr data (Experimental). The former, with highest m/z = 269, suggests that X is an isomer of **6** and the latter confirms that the isopropylidene portion is absent from X as it is from **6**. Although compound X remains an unknown, it is clearly not **13** and it cannot be derived from **14**. Thus, reaction [4] appears to be excluded.

Analogy for the proposed mechanism is found in the reactions of triazoline **15** with methacrylonitrile and with methyl methacrylate (2), reaction [5], except that the precursor of **17** and **18** is a true zwitterion (**16**) and not just a polar structure such as **1**.

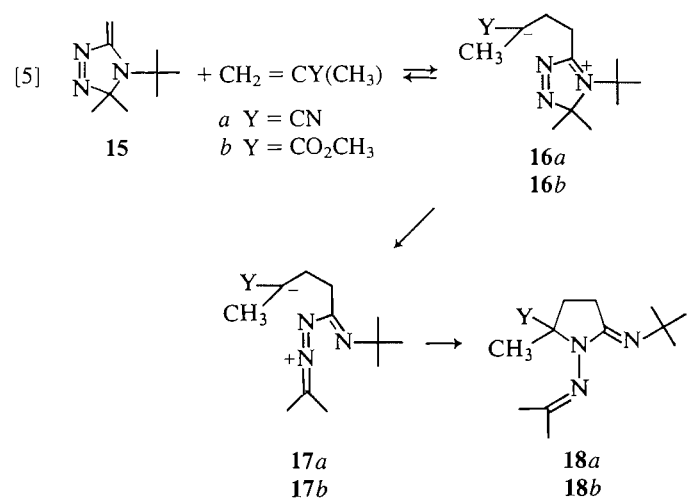

The very facile hydrolysis of **5** that was pointed out earlier is shared by **18***b* but not by **18***a*, suggesting that there may be bifunctional catalysis involving both the 2-substituent and the 5-carbomethoxy functional group of **5** and **18***b*.

3,4-Dicarboalkoxypyrroles are common while 4,5-dicarboalkoxypyrroles are rare. Methods for the synthesis of the less common 4,5 isomers (5*b*, 5*c*, 7–9) are unsuitable for the preparation of 2-alkylamino-4,5-dicarboalkoxypyrroles such as **5** and **6**, which seem to be the first members of that family. Reductive removal of the 1-amino substituent of **6** should be facile, as it is for other 1-aminopyrroles (10).

Thermolysis of **3** in solution led to formation of **19** (reaction [6]) in solvent-dependent yields. In methanol the yield was 53%

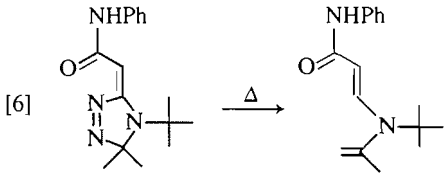

[6] **3** → **19**

but in benzene, or in methyl acrylate, the yields reached 85%. The *E*-configuration at the internal double bond of **19** was assigned on the basis of the 12-Hz coupling constant between the vinyl hydrogen atoms.

A mechanism that accounts for the transformation of **3** to **19** must accommodate the following observations. First, the decomposition of **3** occurs with first-order kinetics in both benzene and in methanol without the accumulation of intermediates to levels detectable by ^{1}H nmr spectroscopy. Second, the reaction is 2.3 times faster in benzene than in methanol at 80°C and both rate constants are probably larger than that for thermolysis of model compound **20** (11), which decomposes in 45–60 min at 165°C. From the activation parameters (log A = 13.6, E_a = 29.6 kcal mol^{-1}) for thermolysis of **3** in methanol (see Experimental), decomposition at 165°C would be complete (>98%) in less than 1.0 min. Fourth, thermolysis of **3** in CH_3OD affords **19**, which is fully deuterium labelled at C3 (Scheme 3). Finally, aniline and **21** are coproducts (10–21% each) of the thermolysis of **3** in methanol.

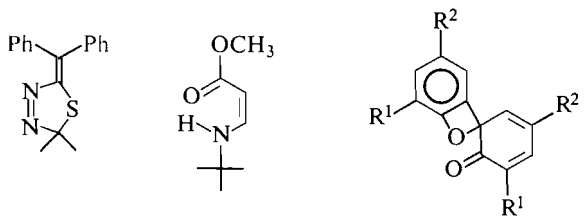

20 **21** **22**

The mechanism in Scheme 3 appears to fit the facts well. Electrocyclic ring closure of **3** and **4** is allowed thermally. Although analogous cyclizations of butadienes to cyclobutenes are rare, theoretical studies by Epiotis (12) indicate that closure of diene components that are "push–pull" polarized should be facilitated. Moreover, oxetes are recognized intermediates, or final products in favourable cases. Benzoxetes (**22**, for example) from oxidation of 2,4-disubstituted phenols, can be isolated (13). The solvent dependence of rates of electrocyclic reactions are small, in general (14), and the faster rate of decomposition of **3** in benzene, relative to that in methanol, can be explained readily in terms of greater solvation of the ground state **3** than of the transition state for going to **19**, by

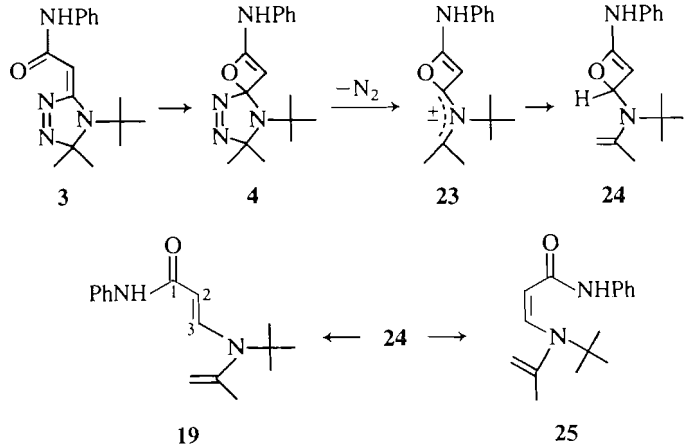

3 **4** **23** **24** **19** **25**

SCHEME 3

methanol. The entropy of activation ($\Delta S^{\ddagger} \simeq 1.5$ eu, methanol) is reasonable for a process involving a combination of decreased solvent ordering and increased substrate ordering as the oxete ring develops.

The remainder of Scheme **3** is relatively straightforward and well precedented. Facile cycloreversion of **4** to form **23** is analogous to loss of N_2 from some other Δ^1-1,2,4-triazolines with tetracoordinate C-3 and C-5 (2). Ylide **23** might well gain some stabilization from delocalization within the 4-membered ring, which is aromatic with respect to one of the ylide's contributing structures. The ylide must be slow to react with dipolarophiles, as yields of **19** from thermolysis of **3** in methyl acrylate were comparable to those obtained from thermolysis of **3** in benzene.

1,4-Sigmatropic shifts such as that which converts **23** to **24** are well known (15), as are electrocyclic ring openings of the type **24** to **19**. It is not surprising that the opening is unidirectional, although either **19** or **25** is allowed by (formal) conrotatory ring opening. Moreover, the deuterium labelling of **19**, when **3** is decomposed in CH_3OD, is readily explained in terms of interception of **23** by proton transfer from solvent (reaction [7]). Finally the formation of aniline and **21**, from

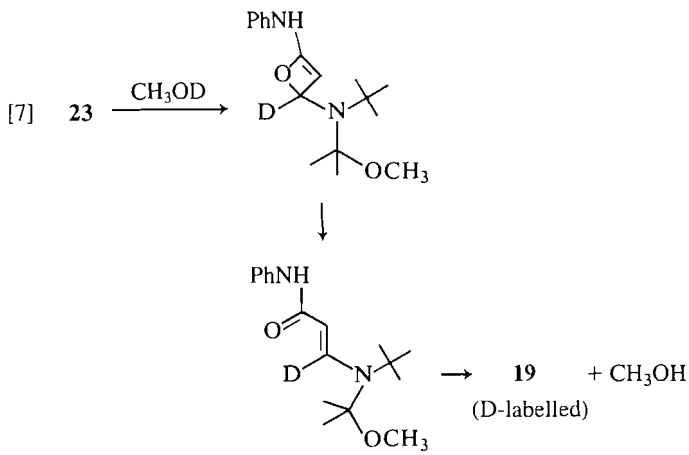

[7] **23** → **19** (D-labelled) + CH_3OH

heating of **3** in methanol, can be accommodated if it is assumed that an enaminic oxete like **24** can add methanol to the double bond. Such addition, followed by elimination of aniline and electrocyclic ring opening, constitutes formal anilide methanolysis (reaction [8]), and offers an explanation for the formation of **21** under conditions that **19** withstood in a control experiment. We see no reason why **19** should not serve as an

Can. J. Chem. Downloaded from www.nrcresearchpress.com by 176.9.209.113 on 09/07/12
For personal use only.

Can. J. Chem. Downloaded from www.nrcresearchpress.com by 176.9.209.113 on 09/07/12
For personal use only.

TABLE 2. Spectral data

Compound	^{1}H nmr (δ, $CDCl_3$, 90 MHz)	^{13}C nmr (δ, $CDCl_3$, 22.6 MHz)[a]	ms (*m/z*, %, ei, lr)[b]	uv (λ_{max}, nm, log ε)	ir ($CDCl_3$)
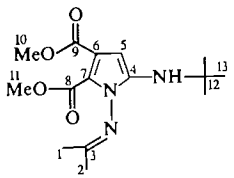 **5**	1.22 (s, 9H), 1.27 (s, NH), 1.80 (s, 3H), 2.21 (s, 3H), 3.68 (s, 3H), 3.77 (s, 3H), 5.71 (s, 1H)	20.29 (1 or 2), 24.93 (2 or 1), 29.53 (13), 51.28 (10 or 11), 51.74 (12, 11, or 10), 92.71 (5), 112.17 (6 or 7), 119.90 (7 or 6), 137.34 (4), 160.35 (8 or 9), 165.83 (9 or 8), 183.91 (3)	309 (54), 253 (25), 197 (100), 169 (28), 164 (23), 137 (20), 57 (100), 56 (86), 309.1687 (hr, obsd.), 309.1689 calcd. for $C_{15}H_{23}N_3O_4$)	240 (4.07) 328 (4.01) ($CHCl_3$)	3378, 2969, 2947, 1730, 1688, 1571, 1518, 1498, 1498, 1465, 1436, 1388, 1358, 1264, 1209, 1130, 1061
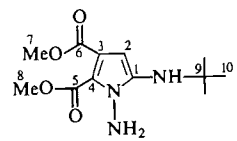 **6**	1.26 (s, 9H), 3.72 (s, 3H), 3.74 (s, 3H), 4.90 (s, br, 1H), 5.54 (s, 1H)	29.63 (10), 50.96 (9 and 7 or 8), 52.20 (8 or 7), 90.86 (2), 113.34 (3 or 4), 120.80 (4 or 3), 142.31 (1), 161.70 (5 or 6), 165.88 (6 or 5)	269 (83), 238 (22), 213 (83), 197 (100), 181 (62), 165 (30), 137 (35), 122 (43), 269.1379 (hr, obsd.), 269.1376 (calcd. for $C_{12}H_{19}N_3O_4$)	242 (3.96) 332 (4.03) ($CHCl_3$)	3384, 3353, 2963, 2945, 1730, 1678, 1640 (NH_2), 1567, 1530, 1497, 1435, 1399, 1352, 1253, 1222, 1210, 1134, 1065
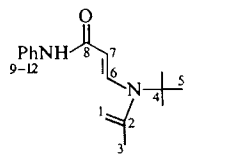 **19**	1.32 (s, 9H), 1.88 (s, 3H), 4.75 (d, J = 12.4 Hz, 1H), 4.83 (s, br, 1H), 5.18 (s, br, 1H), 6.80 (s, br, NH), 6.94–7.71 (m, 5H), 7.92 (d, J = 12.4 Hz, 1H)	21.12 (3), 30.05 (5), 57.52 (4), 90.10 (1), 116.73 (7), 119.50 (10), 122.76 (12), 128.95 (11), 139.89 (9), 144.29 (2), 145.64 (6), 167.70 (8)	258 (12), 182 (18), 166 (30), 112 (19), 110 (100), 105 (18), 93 (46), 82 (17), 77 (21), 70 (22), 57 (67), 258.1734 (hr, obsd.), 258.1732 (calcd. for $C_{16}H_{22}N_2O$)	200–270 (3.69, continuum) 302 (4.48) ($CHCl_3$)	3288, 3247, 3130, 3058, 3039, 2976, 2923, 2880, 1654, 1598, 1574, 1535, 1497, 1438, 1379, 1332, 1289, 1261, 1242, 1038, 1003, 981, 962, 897, 791, 747, 685[c]
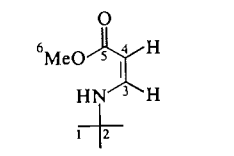 **21**	1.27 (s, 9H), 3.65 (s, 3H), 4.42 (d, J = 8.0 Hz, 1H), 6.80 (dd, J = 8.0, 14.0 Hz, 1H), 8.12 (s, v br, 1H)	30.31 (1), 50.14 (6), 52.01 (2), 81.42 (4), 148.19 (3), 165.50 (5)		280 (3.79) (CCl_4)	3334, 2978, 2917, 2883, 1668, 1618, 1480, 1461, 1371, 1307, 1196, 1140

[a]The numbers in parentheses are tentative assignments and refer to the arbitrary numbering schemes given with the structures.
[b]Abbreviations: ei = electron impact, lr = low resolution, hr = high resolution.
[c]Neat film.

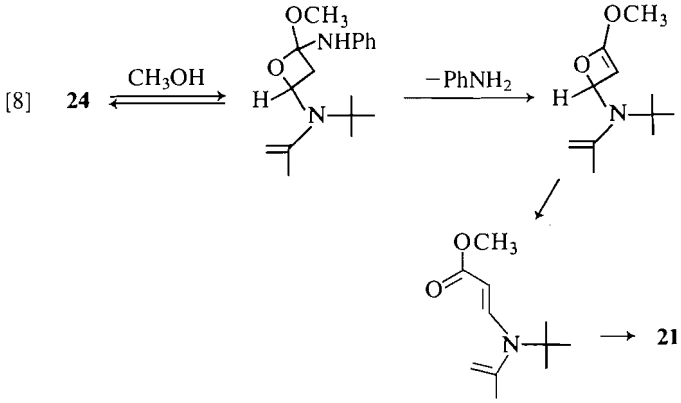

adequate model for estimating the rate of anilide methanolysis of **3**.

Although alternative mechanisms are conceivable, including initial C—N bond rupture as in Scheme 4, they fall short on several counts. First, and most telling, is the fact that analogous triazolines do not lose N_2 under similar conditions (1, 2), and that the thiadiazoline analogue (**20**) already mentioned above (11) decomposes with loss of N_2 only at a much higher temperature. Second, formation of a dipolar intermediate (**25**) in the rate-determining step (Scheme 4) should be facilitated, not retarded, in a more polar solvent. Third, an ylide of the type **26** (Scheme 4) would be expected to have an allenic structure with orthogonal π-systems as shown in that scheme. In benzene, where the H-transfer does not involve the solvent, 1,4-sigmatropic shifts to afford both **19** and its geometric isomer **27**, possibly with the latter predominating, would be required. For the above reasons, we favour the mechanism of Scheme 3.

Experimental

The ^1H and ^{13}C nmr spectra were recorded on a Varian EM-390 spectrometer and on a Bruker WP80/90 spectrometer, respectively. Infrared spectra were obtained with a Perkin–Elmer model 283 instrument. They are calibrated against the 1601.4 cm^{-1} band of polystyrene. Ultraviolet spectra were taken with a Hewlett–Packard model 8451A diode array spectrophotometer. Mass spectra were recorded on either a VG 70-70F or a VG-ZAB-E spectrometer. Centrifugal chromatography was carried out on a Chromatotron 7924T instrument equipped with silica coated glass plates (coating 2 mm thick, 12 cm in radius, Merck Kieselgel 60, PF_{254}) using distilled solvents. Analytical thin-layer chromatography (tlc) involved plastic backed silica plates (Merck Kieselgel 60, F_{254}) of 0.2 mm thickness. Benzene was distilled from P_2O_5 and stored over 4Å molecular sieves. Methanol, Baker Analyzed, was used as received. The synthesis and spectra of **1** and **3** have been described (1, 2).

*Thermolysis of **1***

Fumaratotriazoline **1** (369 mg, 1.2 mmol) was added to methanol (100 mL). Dissolution of **1** occurred during heating to the reflux temperature. Periodic withdrawal of aliquots of the boiling solution, and analysis by tlc, showed that no more **1** remained after 48 h. Cooling and evaporation of the solvent with a rotary evaporator was followed by centrifugal chromatography of the residue in two portions. Elution with ethyl acetate (15%) in light petroleum afforded pyrroles **6** and **5** in that order, combined yields (from both portions) of 13 and 78%, respectively. On silica tlc plates, developed with 50% ethyl acetate in light petroleum, **6** and **5** had R_f values of 0.40 and 0.22, respectively. Both were oils at room temperature. Spectroscopic data are in Table 2.

*Hydrolysis of **5***

Pyrrole **5** (10 mg) was dissolved in ether (0.5 mL) and the solution was transferred to a watch glass from which the ether was evaporated in ca. 5 min. Ten minutes after the ether had evaporated, analysis of the residue by ir revealed that little, if any, **5** remained and that **6** was the major product. For ir spectra, see Table 2.

*Thermolysis of **3** in methanol*

Amidotriazoline **3** (120 mg, 0.42 mmol) in methanol (5 mL) was heated at the reflux temperature for 6 days. Cooling, concentration, and centrifugal chromatography (15% ethyl acetate in light petroleum) afforded **19** (47 mg, 0.18 mmol), 43%, as a white solid, mp 163–164.5°C (from acetone in petroleum ether), R_f 0.58 (ethyl acetate), spectra in Table 2.

Direct analysis by gc of a similar thermolysate from **3** in methanol showed that both aniline and **21** were present in 11–14% yield. An authentic sample of **21** prepared from methylpropiolate and *tert*-butyl amine (16) had R_f 0.21 (10% ethyl acetate in petroleum) and gave the published ^1H nmr data (16). Crude **21**, from thermolysis of **3** and concentrated by chromatography, gave the ^1H nmr spectrum of authentic **21** except for extraneous signals from impurities in the former. Spectra of **21** are in Table 2.

*Thermolysis of **3** in benzene*

Heating of **3** (120 mg) in benzene (5 mL) at the reflux temperature for 3 days afforded **19** in 85% yield, estimated by integration of the ^1H nmr spectrum.

Unknown X

Properties of X: R_f 0.80 (15% ethyl acetate in petroleum); uv ($CHCl_3$), nm (log ε): 256 (4.03); ir ($CDCl_3$), cm^{-1}: 1702 (br); ^1H nmr (90 MHz, $CDCl_3$) δ: 1.53 (s, 9H), 2.69 (s, 3H), 3.72 (s, 3H), 6.37 (d, J = 3 Hz, 1H), 6.66 (d, J = 3 Hz, 1H); ms (ei), m/z (%): 269 (8), 219 (7), 195 (53), 149 (26), 139 (67), 124 (34), 108 (100), 107 (47), 69 (42).

*Kinetics of thermolysis of **3***

Medium-walled nmr tubes were charged with **3** and with enough solvent to give solutions at the concentrations given in Table 3. The

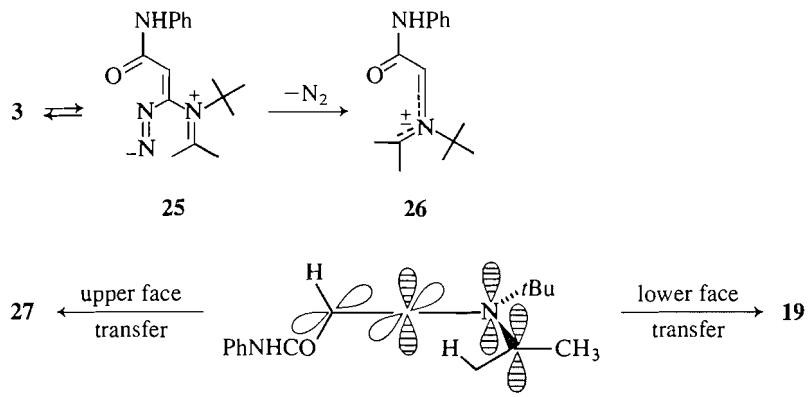

SCHEME 4

Can. J. Chem. Downloaded from www.nrcresearchpress.com by 176.9.209.113 on 09/07/12
For personal use only.

TABLE 3. Kinetics of thermolysis of **3**

Solvent	[**3**], M^a	T (°C)	k (s^{-1}) × 10^5
CH_3OH	0.055	58.5	0.143
CH_3OH	0.055	73.0	0.874
CH_3OH	0.103	80.0	2.09
CH_3OH	0.055	87.5	4.34
CH_3OH	0.055	102.0	27.2
C_6H_6	0.072	80.0	4.90

[a]Initial concentration at room temperature.

solutions were degassed by means of three freeze–pump–thaw cycles before the tubes were sealed and immersed in constant temperature baths controlled to ±0.1°C.

Progress of the decomposition was monitored by ^1H nmr spectroscopy. For samples in methanol, the internal standard for normalizing integrals of all methyl signals of remaining **3** was the sum of integrals from all *tert*-butyl and methyl signals except for the propenyl methyl group signal of **19**, which was doubled before entry into the summation. For samples in benzene, the methyl group signal from added toluene was used as internal standard. Decompositions were followed to at least 80% and usually to more than 85% conversion. Good fits of the data to the first-order rate law were obtained. From the temperature dependence of the rate constant in methanol (Table 3) the activation parameters calculated were as follows: Arrhenius equation, $\log A = 13.6$, $E_a = 29.6$ kcal mol^{-1}; Eyring equation, $\Delta H^{\neq} = 29$ kcal mol^{-1}, $\Delta S^{\neq} = 1.5$ eu.

Acknowledgements

Financial support for this work, from the Natural Sciences and Engineering Research Council of Canada, is gratefully acknowledged. We are indebted to Mr. J. Kapron and Mr. F. A. Ramelan for the mass spectral data.

1. A. L. SCHWAN and J. WARKENTIN. Can. J. Chem. **65**, 1200 (1987).
2. A. L. SCHWAN and J. WARKENTIN. Can. J. Chem. **66**, 155 (1988).
3. J. W. LOWN. *In* 1,3-Dipolar cycloaddition chemistry. Vol. 1. *Edited by* A. Padwa. Wiley–Interscience, New York, NY. 1984.
4. E. VEDEJS and F. G. WEST. Chem. Rev. **86**, 941 (1986).
5. (*a*) R. A. JONES and G. P. BEAN. The chemistry of pyrroles. Academic Press, New York, NY. 1977. p. 463; (*b*) S. K. KHETAN, J. G. HIRIYAKKANAVAR, and M. V. GEORGE. Tetrahedron, **24**, 1567 (1968); (*c*) S. K. KHETAN and M. V. GEORGE. Tetrahedron, **25**, 527 (1969).
6. M. TANTELAT and K. LEY. Synthesis, **70**, 593 (1970).
7. J. B. HENDRICKSON, R. REES, and J. F. TEMPLETON. J. Am. Chem. Soc. **86**, 107 (1964).
8. J. BARLUENGA, F. PALACIOS, and V. GATOR. Synthesis, **75**, 642 (1975).
9. G. L'ABBE, P. VAN STAPPEN, and J.-P. DEKERK. Chem. Commun. 784 (1982).
10. (*a*) M. SCOTTON and L. R. LAMPARIELLO. Chem. Ind. (Milan), **62**, 843 (1980); (*b*) R. A. JONES and G. P. BEAN. The chemistry of pyrroles. Academic Press, New York, NY. 1977. p. 399.
11. T. FURUHATA and W. ANDO. Tetrahedron Lett. **28**, 1179 (1987).
12. N. D. EPIOTIS. Angew. Chem. Int. Ed. Engl. **13**, 751 (1974).
13. (*a*) E. MULLER, R. MAYER, B. NARR, A. RIEKER, and K. SCHLEFFER. Ann. Chem. **645**, 25 (1961); (*b*) H.-D. BECKER. J. Org. Chem. **34**, 1198 (1969); (*c*) D. G. HEWITT. Chem. Commun. 227 (1970); (*d*) H.-D. BECKER and K. GUSTAFSSON. J. Org. Chem. **42**, 2966 (1977).
14. C. REICHART. Solvent effects in organic chemistry. Verlag Chemie, New York, NY. 1979. p. 101.
15. (*a*) R. SMITH and T. LIVINGHOUSE. Tetrahedron, **41**, 3559 (1985); (*b*) A. A. LEONE and P. S. MARIANO. Rev. Chem. Intermed. **4**, 81 (1981); (*c*) A. G. SCHULTZ. Acc. Chem. Res. **16**, 210 (1983).
16. R. HUISGEN, K. HERBIG, A. SIEGL, and H. HUBER. Chem. Ber. **99**, 2526 (1966).

Can. J. Chem. Downloaded from www.nrcresearchpress.com by 176.9.209.113 on 09/07/12
For personal use only.

Nuclear magnetic resonance and infrared study of lithium coordination by phosphonates and phosphine oxides $R_2P(O)CH_2COY$ and their carbanions. Comparison between ketone, ester, and amide COY groups

TEKLA STRZALKO AND JACQUELINE SEYDEN-PENNE
Unité associée n° 478 du Centre national de la recherche scientifique, Institut de chimie moléculaire d'Orsay, Université Paris-Sud, 91405 Orsay, France

FRANÇOISE FROMENT AND JACQUES CORSET
LASIR, Centre national de la recherche scientifique, BP 28, 94320 Thiais, France

AND

MARIE-PAULE SIMONNIN
Unité associée n° 403 du Centre national de la recherche scientifique, École nationale supérieure de chimie de Paris, 11, rue P. et M. Curie, 75231 Paris CEDEX 05, France

Received July 13, 1987

TEKLA STRZALKO, JACQUELINE SEYDEN-PENNE, FRANÇOISE FROMENT, JACQUES CORSET, and MARIE-PAULE SIMONNIN. Can. J. Chem. **66**, 391 (1988).

Lithiated carbanionic chelates α to P(O) groups are formed from four title compounds. Their infrared and ^{13}C and ^{31}P nuclear magnetic resonance spectra show that chelation induces peculiar structural perturbations that depend upon the nature of Y. The corresponding neutral precursors **1**–**4** are able to form bidentate coordinates with the Li cation, which can be observed in THF when Y = OMe or NMe_2 but in benzene only when Y = Me. They are probably intermediates in the lithiated base deprotonation of neutral compounds **1**–**4**.

TEKLA STRZALKO, JACQUELINE SEYDEN-PENNE, FRANÇOISE FROMENT, JACQUES CORSET et MARIE-PAULE SIMONNIN. Can. J. Chem. **66**, 391 (1988).

Les chélates anioniques lithiés en α d'un groupe P(O) sont formés à partir de quatre composés cités dans le titre. Leurs spectres infrarouge et résonance magnétique nucléaire du ^{13}C ou ^{31}P montrent que la chélation provoque des perturbations importantes du squelette organique qui dépendent de la nature de Y. Les précurseurs neutres **1**–**4** sont aptes à former des coordinats bidentés du cation lithium qui peuvent être mis en évidence dans le THF quand Y = OMe ou NMe_2 mais seulement dans le benzène quand Y = Me. Ceux-ci sont vraisemblablement les intermédiaires impliqués dans la déprotonation des composés **1**–**4** par les bases lithiées.

Can. J. Chem. Downloaded from www.nrcresearchpress.com by 176.9.209.113 on 09/07/12
For personal use only.

Phosphonates and phosphine oxides bearing a β-keto or a β-carbamoyl group $R_2P(O)CH_2COY$ are efficient extracting agents for heavy metal salts such as lanthanides (1, 2) and actinides (3–5). Their extracting ability is attributed to the formation of strong chelates between the two oxygens of the P=O and C=O bonds and the metal ions. During our previous studies on Wittig–Horner reagents we were able to show that neutral carbomethoxymethylphosphonate **1** can form, with the lithium cation, an analogous stable chelate (6), which can be an intermediate on the way to the anionic reagent.

$(EtO)_2P(O)CH_2COOMe$ **1**

It thus seemed worthy to examine whether such behaviour could also be observed with other P(O) related molecules, bearing β-keto or β-carbamoyl moieties. In the present work we report an nmr and ir study on the ability of ketophosphonate **2**, (dimethylcarbamoyl)methylphosphonate **3**, and carbomethoxymethyldiphenylphosphine oxide **4** to coordinate the lithium cation in tetrahydrofuran (THF) solution.

$(EtO)_2P(O)CH_2COMe$ **2**
$(EtO)_2P(O)CH_2CONMe_2$ **3**
$Ph_2P(O)CH_2COOMe$ **4**

We also examine the structure of the related lithiated anionic species in the same solvent, focusing our investigations on the modification of the organic framework in these systems, compared to that of the free neutral molecules.

Previous studies have been published on sodium (7) and magnesium (8) anionic chelates of **2** and on a sodium anionic chelate of the *N*-diethyl analog of **3** (9).

TABLE 1. Infrared frequencies and nuclear magnetic resonance chemical shifts for the neutral molecules in THF solution[a]

Parameter	2	3	1	4
ν(C2=O3)	1715	1652	1744	1738
ν(P=O)[b]	1260	1260	1268	1267
δ C2	199.3	164.8	166.7	167.8
δ C1	43.2	34.4	34.4	39.7
δ ^{31}P	19.6	20.9	19.6	21.9

[a]δ ^{13}C in ppm from internal Me_4Si; δ ^{31}P in ppm relative to external H_3PO_4 (85%). Positive δ values are in the direction of increasing frequency. ν in cm^{-1}.
[b]Mean value of the two components usually observed for this mode due to a Fermi resonance.

Results

The anionic species were generated from solutions of the neutral precursors in THF, using a slight excess of Bu"Li solution, under an inert and moisture-free atmosphere, as previously described for **1** (10) and **4** (11). The nmr and ir spectra of the solutions show the disappearance of the signals due to the neutral precursors (Table 1) and the total formation of carbanionic species, which coexist, as already discussed for **1** (6, 10), as monomeric chelated ion pairs (**AM**), aggregates $(\mathbf{AM})_n$, triple ions $(\mathbf{AMA})^-$, and free ions $(\mathbf{A})^-$ (Tables 2 and 3), in relative proportions depending on the concentration, where M stands for Li.

The carbanionic species, whatever their degree of association, will be designed $\mathbf{A}_1$, $\mathbf{A}_2$, $\mathbf{A}_3$, and $\mathbf{A}_4$ respectively.

Can. J. Chem. Downloaded from www.nrcresearchpress.com by 176.9.209.113 on 09/07/12
For personal use only.

TABLE 2. Infrared frequencies observed for the different anionic species formed in THF solution[a]

Frequency	A_2	A_3	A_1	A_4
ν(C2···O3)				
$(AMA)^-$		1591	1634	1630
(AM)	1530	(1528)	1594	1579
$(AM)_n$		1507	1578	1565
$(A)^-$			1525	1516
ν(P···O)				
(AM)	1197	1145	1185	1185
$(AM)_n$	1183			
ν(C1···C2)				
$(AM)_n$, (AM)	1431	1407	1376	1361

[a]In cm^{-1}, the total concentration is ≈0.25 M.

TABLE 3. Variations of the ir frequencies and nmr chemical shifts for the chelated ion pairs (AM) relative to the neutral parent molecule (THF solution)[a]

Parameter	(A_2M)	(A_3M)	(A_1M)	(A_4M)
$\Delta\nu$(C2=O3)	−185	−124	−150	−159
$\Delta\nu$(P=O)	−63	−115	−83	−82
$\Delta\delta$ C2	−13.0	10.2	9.0	6.7
$\Delta\delta$ C1	22.9[b]	7.4	6.6	5.0
$\Delta\delta$ ^{31}P	12.6	19.1	20.3	13.2

[a]Variations of ν or δ (ν or δ in (AM) minus ν or δ in the parent molecule); they are given in cm^{-1} or in ppm.
[b]This value is given in pyridine as solvent, the δ Cl for **2** being 43.5.

TABLE 4. Infrared frequencies and nuclear magnetic resonance chemical shifts for the intermediates (I) and their variations relative to the parent molecule (THF solution)[a]

Parameter	(I_2)	(I_3)	(I_1)	(I_4)
ν(C2=O3)	1687	1620	1675	1663
$\Delta\nu$	−28[b]	−32	−69	−75
δ C2		171.1	171.7	162.5
$\Delta\delta$		6.3	5.0	4.7
δ ^{31}P	30	16.3	28.5	33.2
$\Delta\delta$ ^{31}P	10.9[b]	−4.6	8.9	11.3

[a]Variations of ν or δ (ν or δ in (I) minus ν or δ in the parent molecule); they are given in cm^{-1} or in ppm.
[b]Benzene solutions (δ ^{31}P: 19.1 and 31.6 respectively for **2** and A_2).

When less than one equivalent of lithiated base was used to generate the anionic species from amide **3** and ester **4**, as well as from ester **1** (6), other sets of signals in the ^{31}P and ^{13}C nmr and other ir absorptions were observed: they were assigned, as in the case of **1** (6), to intermediates (I_3), and (I_4), in which neutral **3** or **4** act as ligands of a Li cation belonging to the different ionic species and coexist next to the neutral precursors (Table 4).

Thus L and L′ in (I) can be either the anionic part of (AM) or of $(AM)_n$, or solvent molecules; they could also be more or less aggregated Bu^{n}Li when present in the medium.

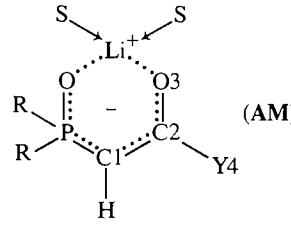

(AM)

(A_1M): R = EtO, Y = OMe
(A_2M): R = EtO, Y = Me
(A_3M): R = EtO, Y = NMe_2
(A_4M): R = Ph, Y = OMe

The same intermediates could also be observed by addition of neutral molecules to solutions of related anionic species, although their formation was slow in the amide case. However, from ketone **2**, we were not able to detect the signals corresponding to such (I_2) entities in THF, whatever the method used (Fig. 1, curve b). Interestingly, the corresponding signal could be observed using a solvent that poorly solvates the Li cation, i.e., in benzene solution when adding 0.4 equivalent of lithiated base to **2** (Table 4).

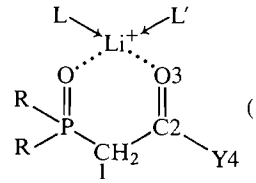

(I)

(I_1): R = EtO, Y = OMe
(I_2): R = EtO, Y = Me
(I_3): R = EtO, Y = NMe_2
(I_4): R = Ph, Y = OMe

To evaluate the relative stabilities of the anionic species and of the various intermediates, competition experiments were run: to solutions of the different carbanionic species **A**, increasing amounts of the other neutral compounds were added. Some of these experiments are illustrated in Figs. 1–3. The salient features of the spectra of such mixtures are the following:

(*i*) Concerning the ketophosphonate system, carbanionic species A_2 is always the predominating species, next to neutral **1** or **3**, whether A_2 is preformed (Fig. 1) or if neutral ketone **2** is added to a solution of carbanionic ester A_1 or amide A_3 (Fig. 3). In these solutions, intermediates (I_1) or (I_3) (Fig. 2) can also be observed. In all cases, equilibrium is quickly reached.

(*ii*) When ester **1** is added to a solution of carbanionic amide A_3 (Fig. 3), three species (A_1, A_3, and neutral **3**) coexist in slow exchange next to small amounts of intermediates (I_1) and (I_3). However, when adding neutral amide **3** to a solution of A_1 (Fig. 2), very small amounts of carbanionic species A_3 and of free ester **1** are seen; A_1 and **3** are the predominant species. In all cases, the amount of intermediates (I) is never greater than 20%.

Discussion

Neutral molecules 1–4

The ir spectra of the neutral molecules (Table 1) indicate that the keto and amide groups in **2** and **3** behave very similarly to the related ones in the unsubstituted aliphatic series: the main vibrations either of the $COCH_3$ group or of the $CONMe_2$ group are located at very close frequencies in both types of molecules. For instance, in THF, the ν(C2—N) frequency is located at 1410 cm^{-1} in $MeCONMe_2$ and at 1420 cm^{-1} in **3**. Esters **1** and **4** behave slightly differently as the ν(C2—O4) frequency is observed at 1118 cm^{-1} and 1121 cm^{-1} in **1** and **4** respectively instead of at 1248 cm^{-1} as in CH_3COOMe (12), thus showing a lengthening of this bond in **1** and **4** related to methyl acetate. It is known that the preferred conformation of methylacetate is *s-cis* (12); on the other hand, in a polar environment, ^{t}butyl formate adopts a predominating *s-trans* conformation, which corresponds to an ir ν(C—O) vibration at 1159 cm^{-1} (13). Intramolecular dipole interactions between the PO and COOMe moieties in THF might also induce an *s-trans* conformation of the ester group in neutral **1** and **4** as suggested by the value of the ν(C2—O4) elongation vibration. Assuming that, as in the case of malonates (14), the P=O and C=O bonds lie in approximately orthogonal planes, the conformations of neutral **1** and **4** should be represented by **5**.

Can. J. Chem. Downloaded from www.nrcresearchpress.com by 176.9.209.113 on 09/07/12
For personal use only.

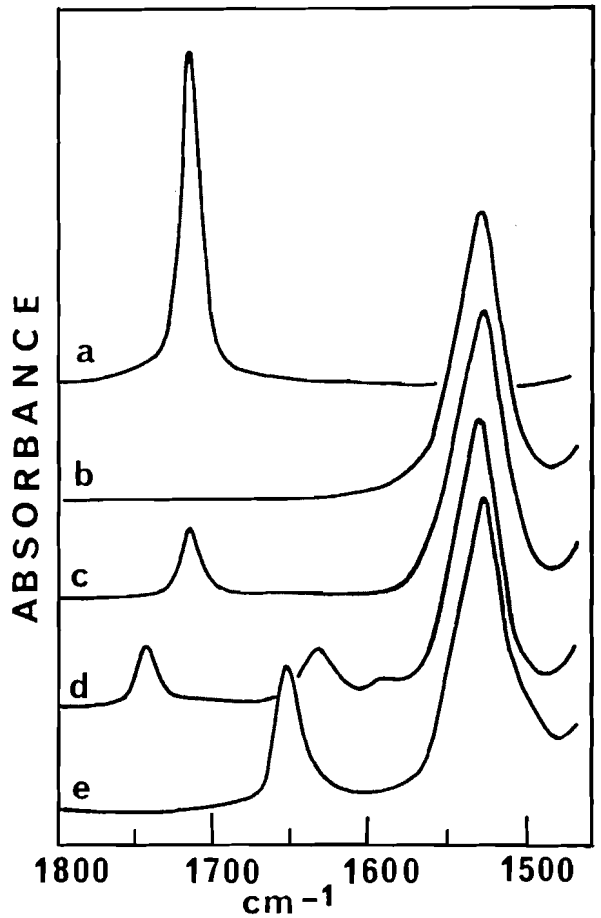

FIG. 1. Infrared spectra of neutral ketophosphonate **2** (a), anionic species A_2 (b), and mixtures of A_2 with **2** (c), A_2 with **1** (d), A_2 with **3** (e) in THF solution. (a) **2** 0.40 M; (b) A_2 0.21 M; (c) A_2 0.21 M + **2** 0.08 M; (d) A_2 0.21 M + **1** 0.08 M; (e) A_2 0.21 M + **3** 0.10 M.

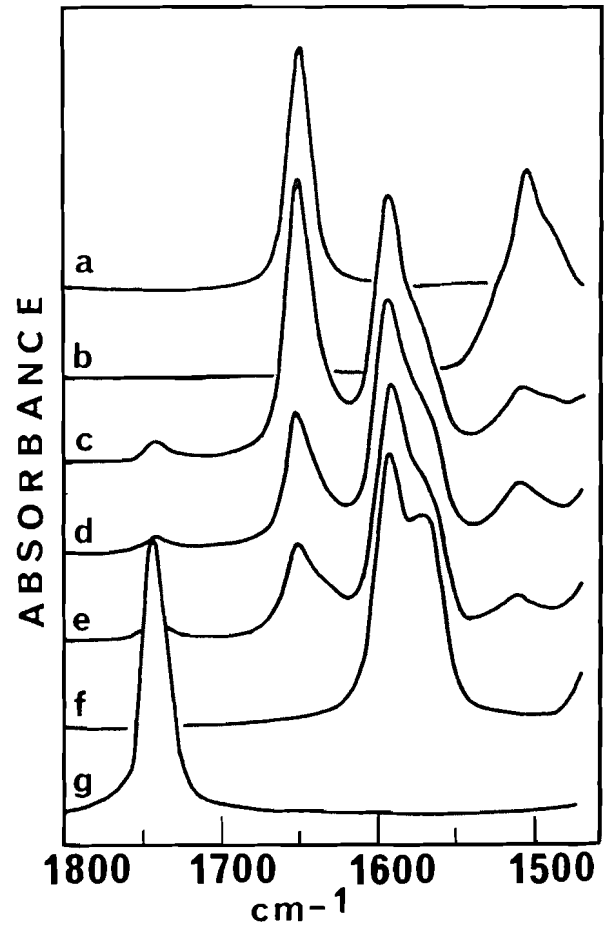

FIG. 2. Infrared spectra of neutral carbamoylmethylphosphonate **3** (a), phosphonate ester **1** (g), anionic species A_3 (b), A_1 (f), and mixtures of A_1 with decreasing amounts of **3** (c), (d), (e) in THF solution. (a) **3** 0.26 M; (b) A_3 0.21 M; (c) A_1 0.21 M + **3** 0.25 M; (d) A_1 0.21 M + **3** 0.13 M; (e) A_1 0.21 M + **3** 0.06 M; (f) A_1 0.21 M; (g) **1** 0.4 M.

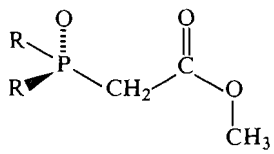

5

The ^{13}C chemical shifts of C1 in neutral molecules is in the expected range, related to unsubstituted analogs: replacement of a hydrogen in $(MeO)_2P(O)CH_3$ by a $COCH_3$ group induces a $\simeq +30$ ppm downfield shift similar to the difference between ethane and ethylmethylketone (15). A similar observation holds for the esters ($\simeq$22 ppm downfield shift).

Carbanionic lithiated chelates (**AM**) (Tables 2 and 3)

The structure of externally solvated monomeric species (**AM**) will be the only one discussed.

The chemical shifts variations of C1 and C2 in A_1, A_2, and A_4 related to **1**, **2**, and **4**, may be compared to those of lithium enolates related to the corresponding neutral precursors: C1 moves downfield from a ketone or an ester to their lithium enolates in THF by +50 and +36 ppm respectively, while C2 suffers a −44 or −3 ppm upfield shift (16). In our series, the variations are quite different: $\Delta\delta C1 = +22.9$ and $\simeq +5$ ppm in the keto and ester cases respectively. Those of C2, $\Delta\delta C2 = -13$ and $\simeq +8$ ppm, are, however, in the same range as observed in methylacetoacetate (17) and the related lithium chelate **6** (18) for which $\Delta\delta C2 = -13.3$ ppm and $\Delta\delta C2' = +4.4$ ppm.

In both cases, the shielding of the C2 ketocarbonyl and the deshielding of the C2′ ester reflect the electron-donating ability of the ester's extra heteroatom. Therefore, the formation of anionic lithiated bidentates induces a similar modification of the electronic distribution around the C2 or C2′ atoms as expressed by the ^{13}C chemical shift variations, whatever the group located in the position β to the carbonyl moiety—in the present cases either C_{sp^2} O or P^{IV} O. The chemical shift of C2 in the lithiated amide A_3 (δ = 175 ppm) is very close to that in A_1 (δ = 175.7 ppm) and in the corresponding sodium derivative (9).

The chemical shift variations of C1 in these systems ($\Delta\delta$ = +22.9 and +5–7 ppm) as well as in **6** ($\Delta\delta$ = +10 ppm) reflect

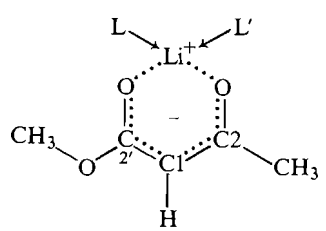

6

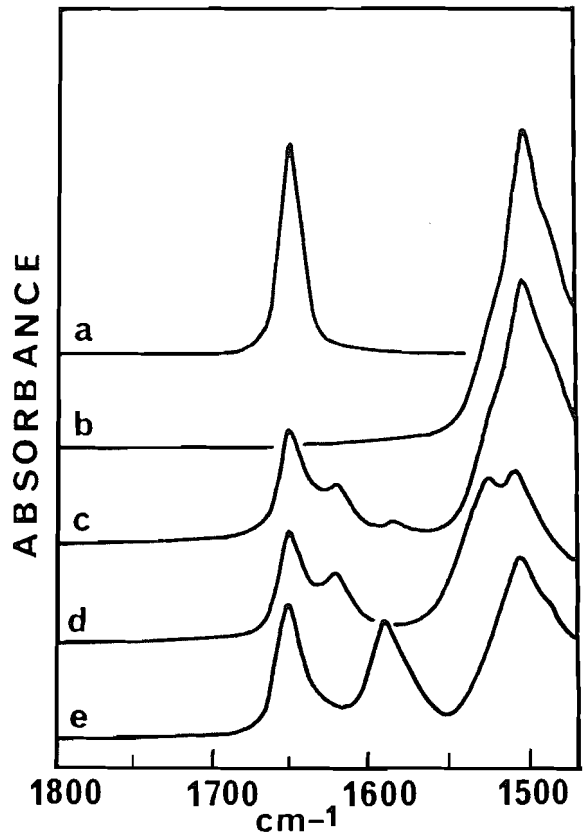

FIG. 3. Infrared spectra of carbamoylmethylphosphonate **3** (a), anionic species A_3 (b), and mixtures of A_3 with **3** (c), A_3 with **2** (d), and A_3 with **1** (e) in THF solution. (a) **3** 0.15 M; (b) A_3 0.21 M; (c) A_3 0.21 M + **3** 0.10 M; (d) A_3 0.21 M + **2** 0.10 M; (e) A_3 0.21 M + **1** 0.06 M.

two phenomena: the hybridization change from sp^3 to sp^2, which induces a large downfield shift, and the development of a negative charge, which increases the shielding. The resulting effect will depend upon the charge repartition: the experimental results suggest that the negative charge density on C1 is greater in chelated structures than in monodentate enolates. This effect can be due to the number and the strength of the oxygen lithium interactions in both types of species. Again, the presence on C2 of an extra heteroatom (Y = OMe or NMe_2) induces, as for C2, a stronger shielding of C1.

From the ir, the weakening of the C2=O3 bond in chelates (A_1M), (A_2M), and (A_4M) relative to that of **1**, **2**, and **4** is less important than in the case of acetylacetone or acetylacetonate (19). However, there is a noticeable difference in $\Delta\nu$(C2=O3) according to the nature of Y: when Y = Me, for (A_2M): $\Delta\nu = -185\ cm^{-1}$, the lengthening of this bond is the greatest in relation to a high ν(Cl···C2) frequency (1431 cm^{-1}). The $\Delta\nu$(C2=O3) decreases from (A_2M) to (A_1M): (−150) and (A_4M) (Y = OMe: $-159\ cm^{-1}$) and to (A_3M) (Y = NMe_2: $-124\ cm^{-1}$). These observations are strengthened by the value of ν(C2—O4) in (A_1M) (1118 cm^{-1}) and (A_4M) (1121 cm^{-1}), which increase by about 20 cm^{-1}, and of ν(C2—N) and ν_s(C—N—C) by 34 and 21 cm^{-1} respectively in (A_3M), thus showing that, as quoted previously, the heteroatom in Y participates in charge delocalization. An amide carbonyl being more basic than an ester carbonyl, the interaction with the lithium cation in (A_3M) will be stronger than in (A_1M), so that the carbonyl elongation in (A_3M) is less important than in (A_1M). Concurrently there is an increase in the low frequency shift of ν(P···O) when going from (A_2M) ($\Delta\nu$(P=O) = $-63\ cm^{-1}$) to (A_1M) ($-83\ cm^{-1}$) and (A_3M) ($-115\ cm^{-1}$); this sequence parallels the $\delta\ ^{31}P$ changes between (A_2M) on the one hand ($\Delta\delta$ = +12.6 ppm) and (A_1M) and (A_3M) on the other ($\Delta\delta$ = +20.3 and 19.1 ppm). All these trends probably reflect the asymmetrical charge repartition between the carbonyl and the phosphoryl oxygens, which is more important in the ketone (A_2M) than in the ester (A_1M) and the amide (A_3M). Such an asymmetry was already underlined by Brunette *et al.* (3) in β ketophosphonato thorium IV complexes. It also appears from the infrared results of Cotton *et al.* (7*a*) for ketonic sodium chelates, Guerchais and co-workers (7*b*) for zinc, and those of Kirilov *et al.* (8*a*) for magnesium chelates. X-ray structural determination shows that the formation of a magnesium anionic chelate from **2** (8*b*) induces a lengthening of the C2=O3 bond about twice that of the P=O bond; however, the latter bond is still longer than the former one. In the case of lanthanoid or thorium chelates formed from aroylphosphonates **7**, the lengthening of the two bonds is closer than in the previous cases ($\Delta\nu$(C2=O3) = −150 to $-165\ cm^{-1}$ and $\Delta\nu$(P=O) = −110 to $-100\ cm^{-1}$), as found by other authors (2*b*, 3).

$$(RO)_2P(O)CH_2COAr \qquad 7$$
$$1 \quad 2\,3$$

The results obtained for the phosphine oxide carbanionic species (A_4M) are similar to those obtained in ester (A_1M), except for the $\Delta\delta\ ^{31}P$, which is smaller (+13.2 ppm) (Table 3). As deduced from the aromatic ^{13}C chemical shifts (11), this is due to the fact that the P atom aryl substituents do not release electrons while the oxygens of the P-OEt groups in (A_1M) are able to do so (10).

Intermediate species (I)

Phosphine oxide ester **4** leads in THF to intermediate species (I_4) that are very similar to (I_1) (6) (Table 4), so that they do not deserve any further comment.

From carbamoylmethylphosphonate **3**, an intermediate species (I_3) is also generated: its peculiarities, related to (I_1) and (I_4), are the upfield ^{31}P shift related to its precursor **3** and the smaller ν(C=O) frequency shift ($\Delta\nu$(C=O) = $-32\ cm^{-1}$ instead of $-69\ cm^{-1}$ or $-75\ cm^{-1}$). Paine and co-workers (1, 2*a*) have described crystalline neutral bidentate complexes of various carbamoylmethylphosphonates and phosphine oxides with lanthanide salts: the observed $\Delta\nu$(C=O) values lie between −30 and $-56\ cm^{-1}$ according to the nature of the metal, i.e., the frequency shifts are always smaller than those observed in (I_1) and (I_4), as already quoted for the related anionic chelates (**AM**) (*vide supra*). A comparison between the ^{31}P shifts does not hold, due to the paramagnetism of the lanthanoid derivatives. Moreover, in the absence of reliable data for the ν(P=O) in (I_3), it seems difficult to discuss further the solvating ability of amide **3** towards lithium.

Intermediate species (I_2) was not detected[1] when starting from ketophosphonate **2** either in THF in the presence of lithiated bases or in acetonitrile in the presence of LiCl and diazabicycloundecene (DBU) (20), while similar intermediates were observed from ester **1** under the latter conditions (6, 21). However, in a solvent such as benzene, which has a poor solvating ability of the lithium cation, (I_2) was able to form in observable amounts as deduced from ^{31}P nmr and ir spectra. The low-field ^{31}P shift related to the nonchelated neutral ketone **2** ($\Delta\delta\ ^{31}P$ = +10.9 ppm) is nearly the same as the one observed

[1]T. Strzalko, F. Froment, J. Corset, J. Seyden-Penne, and M. P. Simonnin. Unpublished results.

Can. J. Chem. Downloaded from www.nrcresearchpress.com by 176.9.209.113 on 09/07/12
For personal use only.

for the esters (+8.9 and +11.3 ppm). However, the carbonyl perturbation ($\Delta\nu$(C=O) = -28 cm^{-1}) is less important than that for the esters (-69 or -75 cm^{-1}), similar to the one observed with amide **3** (-32 cm^{-1}), and in the range of that published by Lestas and Truter (22) for a solid phenacyldiphenylphosphine oxide – lithium bromide chelate **8** (-45 cm^{-1}).

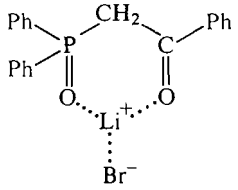

8

The lack of formation of ($\mathbf{I}_2$) in detectable amounts in THF and acetonitrile media can be ascribed to the better Li^+ solvating ability of these solvents and of esters **1** and **4** and amide **3** related to ketone **2**, and (or) to the high propensity of **2** to be deprotonated into anionic species $\mathbf{A}_2$ so that the concentration in ($\mathbf{I}_2$) is too low for observation. Furthermore, it was also noticed that the lithiated anionic species $\mathbf{A}_2$ has a high tendency to aggregation as it is less soluble in THF than the related ester anionic species $\mathbf{A}_1$: this propensity could also disfavor the solvation of Li^+ in ($\mathbf{A}_2\mathbf{M}$) by neutral **2** to give bidentate ($\mathbf{I}_2$).

From all these results, it appears that the lithium cation – carbonyl group interaction in all the observed intermediates is stronger in bidentates ($\mathbf{I}_1$), ($\mathbf{I}_2$), ($\mathbf{I}_3$), and ($\mathbf{I}_4$) than in the corresponding nonphosphorylated monodentate analogs such as $LiClO_4$/methylacetate ($\Delta\nu$(C=O) = 25 cm^{-1}) (23), $LiClO_4$/dimethylacetamide (11 cm^{-1}) (24), or $LiClO_4$/acetone (10 cm^{-1}) (25). The case of esters **1** and **4** is noteworthy, as the observed effects are the strongest. They are quite different from those observed with $LiClO_4$/dimethylmalonate (14) for which chelation within the 1:1 complex induces nearly no ν(C=O) mean frequency shift related to the uncoordinated diester. This difference might be due, to some extent, to a peculiar conformation of esters **1** and **4**, which deserves further investigation.

Exchange studies

The results obtained in THF when the ketophosphonate entity **2** is involved, i.e., the quantitative formation of the related anionic species $\mathbf{A}_2$, whatever the starting system, are quite in line with the well-known higher C-acidity of the ketones related to the ester (26, 27) or amide analogues (28). As expected, intermediate ($\mathbf{I}_2$) is never observed, while occasionally ($\mathbf{I}_1$) or ($\mathbf{I}_3$) are.

The exchange processes between ester (**1**, $\mathbf{A}_1$, ($\mathbf{I}_1$)) and amide entities (**3**, $\mathbf{A}_3$, ($\mathbf{I}_3$)) are more complex, the observations being dependent on the experimental procedure. Although the ester anionic species $\mathbf{A}_1$ is lower in energy than the related amide $\mathbf{A}_3$, the thermodynamic equilibrium is reached more slowly than in the previous case involving keto derivatives, and this is the reason why the relative concentrations of the various entities vary according to time. This indicates a small pK_a difference between **1** and **3**, **1** being slightly more acidic, which is in agreement with literature data on esters and amides in DMSO (28).

Conclusion

The formation of lithiated anionic species from ketophosphonate **2** and carbamoylmethylphosphonate **3**, as well as from related ester **1**, induces a strong perturbation of the carbonyl and phosphoryl bonds as seen from their nmr and ir spectra. Comparison between the neutral precursors and the related anionic species shows that the formation of the anion induces a lengthening of the C=O bond, which increases when going from the amide to the ester and finally to the ketone, while the phosphoryl elongation evolves in the reverse sequence.

All the neutral compounds studied, **1**–**4**, are able to act as bidentate chelates of the lithium cation, the formation of which gives rise to a noticeable perturbation of the organic framework. The strongest perturbation is observed with esters **1** and **4**; it is weaker with amide **3**, while from ketone *2* such a coordination only takes place in appreciable amount in a poorly Li^+-solvating medium such as benzene. These neutral bidentate intermediates (**I**) are probably involved, as already suggested by us (6), in the deprotonation of the β carbonyl phosphonates to their related anions **A**. Recently, Beak *et al.* also proposed coordination of neutral amides to Bu^{n}Li aggregates before deprotonation (31). The peculiarity observed with esters, which is reminiscent of recent results on zinc chelates (30), is probably due to conformational problems: this point is under current investigation.

Experimental

Materials

1: Methyl diethylphosphonoacetate (Janssen) was distilled under reduced pressure and kept under argon. **3**: Diethyl (*N*,*N*-dimethylcarbamoyl)methyl-phosphonate was prepared as described in ref. 29. **4**: Carbomethoxymethylenediphenylphosphine oxide was prepared according to ref. 11 (and references quoted).

Tetrahydrofuran (Merck pure) was distilled over $LiAlH_4$ and kept under argon. Benzene (Prolabo Normapur) was dried over molecular sieves Merck 4Å. Janssen *n*-butyllithium solutions (1.6 M in hexane) were standardized by acid–base titration before use.

Preparation of solutions

Solutions were prepared in a dry box or in a glove bag under argon.

Anionic species $\mathbf{A}_1$–$\mathbf{A}_4$ were obtained by adding one equivalent of Li^{n}Bu to a solution of starting material **1**–**4** (0.21 mol L^{-1} in THF). After 30 min, about 0.4–0.5 equiv. of **1**–**4** was added to the anionic solution, to observe the intermediate species (**I**), and in exchange experiments.

Infrared spectra

Infrared spectra were scanned on a Perkin–Elmer 983 spectrometer. The resolution was usually 3 cm^{-1} and the frequencies are given with a precision of at least ±1 cm^{-1}. The cell of 0.003 cm thickness was equipped with CaF_2 windows.

Nuclear magnetic resonance spectra

The ^{31}P spectra were recorded on a Bruker WP-80 spectrometer, using the FT mode and ^{1}H noise decoupling. A capillary filled with D_2O served as an ^{2}H internal lock. A spectral width of 10 000 Hz was used (digital resolution: 2.5 Hz/point).

The ^{13}C spectra were recorded at 62.9 MHz on a Bruker AM-250 spectrometer, using the FT mode and ^{1}H noise decoupling. The ^{2}H resonance of the solvent (THF-d_8) was used to provide an ^{2}H internal lock. A spectral width of 15 000 Hz was used (digital resolution: 1.85 Hz/point) for the 62.9-MHz spectra.

Acknowledgments

We are indebted to Drs. C. Charrier, B. Deschamps, and their colleagues (Laboratoire CNRS–SNPE, Thiais) for the ^{31}P spectra and to Mr. C. Mérienne (ICMO, Orsay) for the 62.9-MHz ^{13}C spectra. We thank Dr. Ph. Savignac for giving us a sample of ketophosphonate **2**.

1. (*a*) S. M. Bowen, E. N. Duesler, and R. T. Paine. Inorg. Chim. Acta, **61**, 155 (1982); (*b*) D. J. McCabe, E. N. Duesler, and R. T. Paine. Inorg. Chem. **24**, 4626 (1985), and quoted references.

Can. J. Chem. Downloaded from www.nrcresearchpress.com by 176.9.209.113 on 09/07/12
For personal use only.

2. (*a*) L. J. CAUDLE, E. N. DUESLER, and R. T. PAINE. Inorg. Chem. **24**, 4441 (1985), and quoted references; (*b*) M. BURGARD and B. CECCAROLI. J. Phys. Chem. **86**, 4817 (1982).
3. J. P. BRUNETTE, L. JURDY, M. J. F. LEROY, and B. ALLARD. Spectrochim. Acta, Part A, **37A**, 991 (1981).
4. T. YA MEDVED', M. K. CHMUTOVA, N. P. NESTEROVA, *et al.* Izv. Akad. Nauk SSSR, Ser. Khim. **9**, 2121 (1981).
5. E. I. MATROSOV, M. YU ANTIPIN, N. P. NESTEROVA, *et al.* Dokl. Akad. Nauk SSSR, **273**, 1419 (1983).
6. T. STRZALKO, J. SEYDEN-PENNE, F. FROMENT, J. CORSET, and M. P. SIMONNIN.J. Chem. Soc. Perkin Trans. 2, 783 (1987).
7. (*a*) A. COTTON and R. A. SCHUNN. J. Am. Chem. Soc. **85**, 2394 (1963); A. COTTON, R. HUGEL, and R. EISS. Inorg. Chem. **7**, 18 (1968); (*b*) M. T. YOUINOU and J. E. GUERCHAIS. J. Mol. Struct. **18**, 93 (1973); M. T. YOUINOU, J. E. GUERCHAIS, and G. STURTZ. J. Mol. Struct. **18**, 109 (1973).
8. (*a*) M. KIRILOV, M. ARNAUDOW, G. PETROV, and L. SHISHKOVA. Chem. Ber. **103**, 3190 (1970); (*b*) E. WEISS, J. KOPF, T. GARDEIN, S. CORBELIN, U. SCHUMANN, M. KIRILOV, and G. PETROV. Chem. Ber. **118**, 3534 (1985).
9. S. M. BOWEN, E. N. DUESLER, and R. T. PAINE. Inorg. Chim. Acta, **59**, 53 (1982).
10. T. BOTTIN-STRZALKO, J. CORSET, F. FROMENT, M. J. POUET, J. SEYDEN-PENNE, and M. P. SIMONNIN. J. Org. Chem. **45**, 1270 (1980).
11. T. BOTTIN-STRZALKO, G. ETEMAD-MOGHADAM, J. SEYDEN-PENNE, M. J. POUET, and M. P. SIMONNIN. Nouv. J. Chim. **7**, 155 (1983).
12. P. MATZKE, O. CHACOLN, and C. ANDRADE. J. Mol. Struct. **9**, 255 (1971).
13. (*a*) Y. OMURA, J. CORSET, and R. M. MORAVIE. J. Mol. Struct. **52**, 175 (1979); (*b*) Y. OMURA, J. CORSET, and P. BONNET. J. Mol. Struct. **66**, 93 (1980).
14. J. CORSET and M. L. JOSIEN. J. Chim. Phys. **75**, 620 (1978); M. L. JOSIEN. Short range order in non-aqueous solutions. Infrared and Raman study. Proceedings of the 12th European Congress on Molecular Spectroscopy: Molecular Spectroscopy of dense phases. Strasbourg, France. 1975.
15. J. B. STOTHERS. Carbon-13 NMR spectroscopy. Academic Press, New York, London. 1972. p. 146.
16. R. MEYER, L. GORRICHON, and P. MARONI. J. Organomet. Chem. **129**, C7 (1977); L. GORRICHON, P. MARONI, C. ZEDDE, and A. DOBREV. J. Organomet. Chem. **252**, 267 (1983); H. O. HOUSE, A. V. PRABHU, and W. V. PHILLIPS. J. Org. Chem. **41**, 1209 (1976); S. BRADAMANTE and G. A. PAGANI. J. Chem. Soc. Perkin Trans. 2, 1035 (1986).
17. H. H. VOGT and R. GOMPPER. Chem. Ber. **114**, 2884 (1981).
18. G. NEE, T. BOTTIN-STRZALKO, J. SEYDEN-PENNE, M. BEAUJEAN, and H. VIEHE. J. Org. Chem. **48**, 1111 (1983).
19. J. CORSET. Pure Appl. Chem. **58**, 1133 (1986), and quoted references.
20. D. BOSCHELLI, T. TAKEMASA, Y. NISHITANI, and S. MASAMUNE. Tetrahedron Lett. **26**, 5239 (1985).
21. M. A. BLANCHETTE, W. CHOY, J. T. DAVIS, A. P. ESSENFELD, S. MASAMUNE, W. R. ROUSH, and T. SAKAI. Tetrahedron Lett. **25**, 2183 (1984).
22. C. N. LESTAS and M. R. TRUTER. J. Chem. Soc. (A), 738 (1971).
23. R. M. MORAVIE and J. CORSET. J. Chim. Phys. 707 (1977); R. M. MORAVIE. Thèse d'Université Pierre et Marie Curie, Paris (1975).
24. M. H. BARON, H. JAESCHKE, R. M. MORAVIE, and C. DE LOZE. Metal–ligand interactions in organic chemistry and biochemistry. Part I. *Edited by* B. Pullman and N. Goldblum. D. Reidel Publishing Company, Dordrecht, Holland. 1977. pp. 171–191.
25. J. BORUCKA and Z. KECKI. Rocz. Chem. **45**, 2133 (1971).
26. E. M. ARNETT and J. A. HARRELSON JR. J. Am. Chem. Soc. **109**, 809 (1987).
27. A. J. DALE and P. FROYEN. Acta Chim. Scand. **24**, 3772 (1970); **25**, 1452 (1971).
28. F. G. BORDWELL and H. E. FRIED. J. Org. Chem. **46**, 4327 (1981).
29. V. I. LOMAKINA, YA. A. MENDEL'BAUM, and N. N. MEL'NIKOV. Zh. Obshch. Khim. **36**, 447 (1966).
30. M. R. P. VAN VLIET, G. VAN KOTEN, J. F. MODDER, J. A. M. VAN BEEK, W. J. KLAVER, K. GOUBITZ, and C. H. STAM. J. Organomet. Chem. **319**, 285 (1987).
31. P. BEAK, J. E. HUNTER, Y. M. JUN, and A. P. WALLIN. J. Am. Chem. Soc. **109**, 5403 (1987).

Can. J. Chem. Downloaded from www.nrcresearchpress.com by 176.9.209.113 on 09/07/12
For personal use only.

Molybdenum-95 nuclear magnetic resonance studies on disubstituted molybdenum(0) carbonyls

ELMER C. ALYEA[1] AND ARPAD SOMOGYVARI

Guelph–Waterloo Centre for Graduate Work in Chemistry, Guelph Campus, Department of Chemistry and Biochemistry, University of Guelph, Guelph, Ont., Canada N1G 2W1

Received March 6, 1987[2]

ELMER C. ALYEA and ARPAD SOMOGYVARI. Can. J. Chem. **66**, 397 (1988).

Molybdenum-95 nmr spectral data are reported for 40 *cis*- and *trans*-$Mo(CO)_4LL'$ compounds and the chemical shifts discussed in relation to a simplified Ramsey expression for the paramagnetic shielding term. The identification of mixtures of products of the type $Mo(CO)_{6-n}L_n$ is shown to be easily accomplished by ^{95}Mo nmr spectroscopy. The ^{95}Mo chemical shifts provide a sensitive probe of structural and electronic effects, as illustrated for several cyclic nitrogen ligands as well as a range of phosphine ligands in the $Mo(CO)_4LL'$ complexes.

ELMER C. ALYEA et ARPAD SOMOGYVARI. Can. J. Chem. **66**, 397 (1988).

On a déterminé les spectres rmn du ^{95}Mo de 40 composés *cis*- et *trans*-$Mo(CO)_4LL'$ et on discute des déplacements chimiques en fonction d'une expression de Ramsey simplifiée pour le terme d'écran paramagnétique. On démontre que'on peut facilement détecter la présence de mélanges d'entités du type $Mo(CO)_{6-n}L_n$ en faisant appel à la rmn du ^{95}Mo. Comme on a pu le mettre en évidence avec plusieurs ligands azotés cycliques ainsi qu'avec un certain nombre de phosphines agissant comme ligands dans des complexes du type $Mo(CO)_4LL'$, les déplacements chimiques du ^{95}Mo s'avèrent une sonde sensible pour examiner les effets de structure et électroniques.

[Traduit par la revue]

Introduction

The advent of Fourier transform nuclear magnetic resonance spectrometers with stable high magnetic fields has made possible investigations of a wide range of magnetic nuclei of the Periodic Table (1–8). Applications of some transition metal nuclei (e.g. ^{51}V(5) and ^{195}Pt(6)) have virtually reached the status of routine chemical probes of the steric and electronic environment of the metal nucleus. The numerous recent reports (7–11) of ^{95}Mo nmr chemical shifts, which describe at least 400 resonances over a 7000 ppm range, are quickly bringing ^{95}Mo nmr studies to the same status. Although attempts to observe ^{95}Mo resonances in molybdoenzymes have not yet been successful (9, 10) the technique has great potential for elucidating the structure and bonding situation in biologically relevant molybdenum species of high molecular weight (11).

Applications of ^{95}Mo nmr spectroscopy to new systems have proceeded more rapidly than an understanding of the factors that influence the nmr parameters of this quadrupolar nuclei ($I = 5/2$, 15.7% natural abundance, $Q = -0.015(4) \times 10^{-28}$ m^2 (1, 12)). We have undertaken a systematic study of several series of $Mo(CO)_{6-n}L_n$ (L = N, P, As, and Sb donor ligands) complexes to gain such information and herein report the ^{95}Mo nmr spectral data for 40 mononuclear *cis*- and *trans*-$Mo(CO)_4LL'$ complexes. Preliminary communications have appeared (7(*a*), 13(*a*)) as well as our results on $[Mo(CO)_4(L—L)]^-$ complexes with bidentate sulfur ligands (13(*b*)) and details of a companion study of $Mo(CO)_5L$ derivatives (13(*c*)). Other workers (8, 14, 15) reported ^{95}Mo nmr studies of several *cis*-$Mo(CO)_4(PR_3)_2$ species while our investigation was in progress.

Experimental

Molybdenum-95 nmr spectra were obtained from naturally abundant (15.7%) samples with a Bruker WH-400 nmr spectrometer in the pulsed Fourier transform mode. The probe was tuned for molybdenum-95 at 26.08 MHz using a field strength of 9.3956 T. All samples were measured at 293 ± 2 K with chemical shifts referenced to aqueous 2 *M* $K_2[MoO_4]$ at pH 11. Pulse widths of 75 μs (for a 90° pulse) were found to usually give a signal-to-noise ratio better than 100/1 for 500 to 1000 transients on saturated solutions. A spectral width of 10 kHz was normally used to collect one block of 4000 data points; digital resolution was typically better than 5 Hz per data point.

All compounds were prepared by literature methods (16) or slight modifications thereof. The complexes *cis*-$Mo(CO)_4(pip)L$ were prepared by stirring a stoichiometric amount of L and *cis*-$Mo(CO)_4(pip)_2$ under N_2 for several hours in the appropriate deoxygenated solvent (usually CH_2Cl_2). The *cis*-$Mo(CO)_4LL'$ species were prepared similarly by adding L′ to the $Mo(CO)_4(pip)L$ solution prepared *in situ*. The *trans* samples were prepared by refluxing the *cis* compounds for 1 h under N_2 in the appropriate solvent (usually deoxygenated toluene). Infrared spectra in the carbonyl region were used to confirm the stereochemistry of the species in solution subsequent to ^{95}Mo nmr analysis. In the case of complicated mixtures, ir could not confirm the stereochemistry and those cases are noted in Table 1; however, ^{95}Mo chemical shifts (particularly if coupling to phosphorus occurs) often allowed identification of the specific species present in the mixture (see text and Fig. 1).

Results and discussion

Table 1 summarizes the chemical shift and coupling constant data for the complexes in this study. Relatively narrow signals ($\Delta\nu_{1/2}$ = 5–250 Hz) are observed for these tetracarbonyl Mo(O) complexes in the chemical shift range −978 ppm to −1867 ppm. The phosphite complexes show ~60% greater ^{95}Mo–^{31}P coupling (*ca.* 210–260 Hz) than the phosphine complexes (*ca.* 130–160 Hz), as expected (1). No coupling to nitrogen was observed for the amine complexes, but it is worth noting that $^1J(^{95}Mo—^{14}N)$ is known to be about 46 Hz for $(C_5H_5)Mo(CO)_2(NO)$ and related complexes (17). No distinction may be made between the *cis* and *trans* complexes on the basis of coupling constants which contrasts sharply with the ^{195}Pt situation (6*c*)); however, the chemical shifts for the *trans* complexes are shielded relative to the corresponding values observed for the *cis* complexes. Variations in the shielding can be discussed in relation to the terms of a simplified Ramsey expression for the paramagnetic term applicable to quadrupolar nuclei (eq. [1])

[1]To whom all correspondence should be addressed. No reprints are available.

[2]Revision received November 6, 1987.

Can. J. Chem. Downloaded from www.nrcresearchpress.com by 176.9.209.113 on 09/07/12
For personal use only.

TABLE 1. Molybdenum-95 nmr spectral data for the $Mo(CO)_4LL'$ compounds

Geometry[a]	Ligand[d] L	Ligand[d] L'	Solvent	Chemical shift (ppm)	Linewidth (Hz)	Coupling constant (Hz)
trans	$SbPh_3$	$SbPh_3$	Toluene	−1867	150	—
trans	$P(OPr^i)_3$	$P(OPr^i)_3$	CH_2Cl_2	−1811	110	203
trans	PEt_3	PEt_3	CH_2Cl_2	−1810	110	151
cis	$SbPh_3$	$SbPh_3$	CH_2Cl_2	−1807	250	—
trans	$P(OPh)_3$	$P(OPh)_3$	CH_2Cl_2	−1792	30	231
trans[b]	PCy_3	PCy_3	CH_2Cl_2	−1765	90	134
trans	$AsPh_3$	$AsPh_3$	Toluene	−1757	5	—
cis	PEt_3	PEt_3	CH_2Cl_2	−1756	30	129
cis	$P(OPh)_3$	$P(OPh)_3$	CH_2Cl_2	−1754	40	250
cis[c]	PBu^n_3	PBu^n_3	CH_2Cl_2	−1742	90	123
trans[c]	PBu^n_3	PBu^n_3	Toluene	−1741	70	159
trans	$P(p\text{-}MeO\text{—}C_6H_4)_3$	$P(p\text{-}MeO\text{—}C_6H_4)_3$	CH_2Cl_2	−1739	60	139
cis[b]	$P(CH_2CH_2CN)_3$	$P(CH_2CH_2CN)_3$	DMF	−1737	210	128
cis[b]	$AsPh_2Me$	$P(OMe)_3$	CH_2Cl_2	−1729	120	208
trans	PPh_2Et	PPh_2Et	CH_2Cl_2	−1720	50	128
cis	PPh_2Et	PPh_2Et	CH_2Cl_2	−1657	80	130
trans	PPh_2Me	PPh_2Me	CH_2Cl_2	−1655	170	125
cis	PPh_2Me	PPh_2Me	CH_2Cl_2	−1637	60	133
trans	PPh_2Me	PPh_2Me	Toluene	−1631	90	134
cis	$AsPh_2Me$	$AsPh_2Me$	CH_2Cl_2	−1617	170	—
cis	$AsPh_3$	$AsPh_3$	CH_2Cl_2	−1577	190	—
cis	PPh_3	PPh_3	CH_2Cl_2	−1556	50	140
cis	$P(p\text{-}MeO\text{—}C_6H_4)_3$	$P(p\text{-}MeO\text{—}C_6H_4)_3$	CH_2Cl_2	−1552	90	127
cis	pip	$P(OMe)_3$	CH_2Cl_2	−1421	70	220
trans	quin	quin	CH_2Cl_2	−1401	180	—
cis[b]	pip	$P(OPr^i)_3$	CH_2Cl_2	−1396	210	208
cis[b]	pip	$P(OPh)_3$	CH_2Cl_2	−1362	110	257
cis[b]	pip	PEt_3	CH_2Cl_2	−1355	80	129
trans	2,6-Me_2pip	2,6-Me_2pip	CH_2Cl_2	−1351	10	—
trans	Et_3N	Et_3N	CH_2Cl_2	−1327	30	—
cis	MeCN	MeCN	MeCN	−1307	50	—
trans	pyr	pyr	DMF	−1155	60	—
cis	Et_3N	Et_3N	CH_2Cl_2	−1152	20	—
cis	pyr	pyr	CH_2Cl_2	−1140	60	—
cis	pip	pip	DMF	−1093	90	—
cis	4-Bu^{t}py	4-Bu^{t}py	DMF	−1077	210	—
cis[b]	py	py	CH_2Cl_2	−1046	80	—
cis	1-MeIm	1-MeIm	CH_2Cl_2	−1036	20	—
cis	2-NH_2Etpy	2-NH_2Etpy	DMF	−1002	70	—
cis	2-NH_2Mepy	2-NH_2Mepy	DMF	−978	90	—

[a]Assignment of geometry is based on synthetic method, ^{95}Mo nmr, and ir spectroscopy.
[b]Assignment of geometry is based on synthetic method and ^{95}Mo nmr spectroscopy only.
[c]*cis*-complex shows ν(CO) bands at 2062w, 2005w, 1975s, 1932vs cm^{-1}; *trans*-complex shows only a 1870 cm^{-1} band.
[d]Abbreviations: Me = methyl, Et = ethyl, Pr^i = isopropyl, Bu^n = *n*-butyl, Bu^t = *tert*-butyl, Cy = cyclohexyl, Ph = phenyl, pip = piperidine, py = pyridine, pyr = pyrrolidine, quin = quinoline, MeCN = acetonitrile, DMF = *N*,*N*-dimethylformamide, NH_2Etpy = 2-aminoethylpyridine, NH_2Mepy = 2-aminomethylpyridine, and MeIM = methylimidazole.

$$[1] \quad \sigma_{para} = -K \cdot \Delta E^{-1} \{r^{-3}\}_{4d} k^2$$

where ΔE is the mean excitation energy approximated by the HOMO-LUMO energy gap and the $\{r^{-3}\}_{4d}$ and k^2 terms are associated with the nephelauxetic effect and the covalency of the metal–ligand bond, respectively (1, 3, 5). Since the paramagnetic shielding term is negative, an increase in its magnitude corresponds to deshielding of the nucleus. The predominant term in eq. [1] is ΔE, assumed to involve mainly Mo 4*d* orbitals, because the other two terms can be considered constant for ligands of the same type (i.e. phosphines) and for molybdenum in the same oxidation state (1–3, 13(*c*)). Similarly, contributions to the total shielding by the diamagnetic term is normally ignored for quadrupolar nuclei as it is considered to be constant for a related series of compounds (1–3). Therefore, the relative *trans*-to-*cis* shielding order is explicable in terms of eq. [1]. The *trans* complexes have a greater HOMO-LUMO energy gap than the *cis* samples and consequently are considered to be more shielded because of the larger magnitude of the ΔE term of the Ramsey equation; in some instances, the chemical shifts approach those found for $Mo(CO)_5L$ complexes (13(*c*)).

A decrease in ΔE correlates qualitatively with a decrease in the amount of π-electron density accepted by the ligands (i.e. $(P(OR)_3 > PR_3 > NR_3)$. The resultant deshielding thus correlates with the spectrochemical series (19) and it is seen that chemical shifts for *cis*-$Mo(CO)_4$pipL complexes are predictable "averages" of the analogous $Mo(CO)_4pip_2$ and $Mo(CO)_4L_2$

Can. J. Chem. Downloaded from www.nrcresearchpress.com by 176.9.209.113 on 09/07/12
For personal use only.

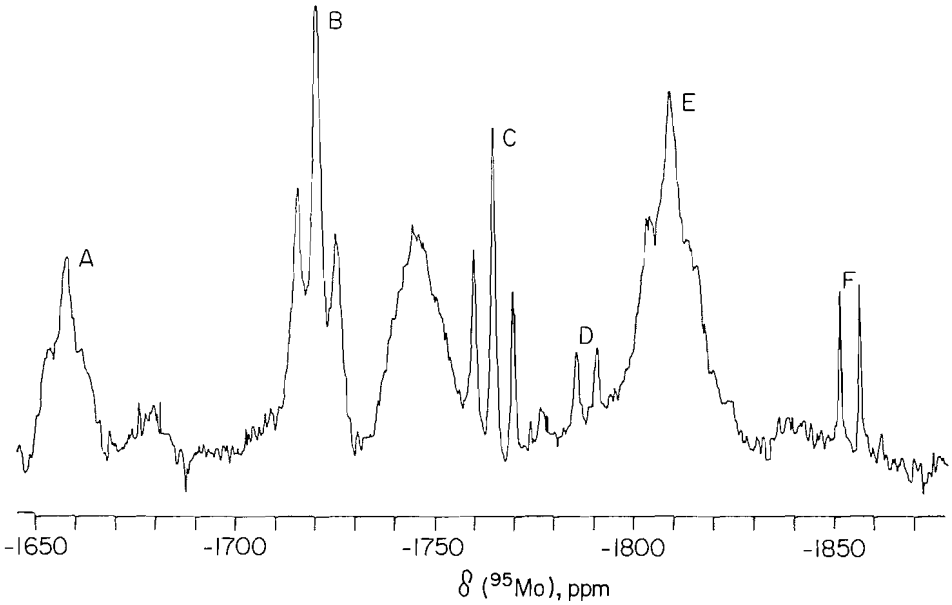

FIG. 1. The ^{95}Mo nmr spectrum of the reaction mixture following reflux of a dichloromethane solution of *cis*-{$Mo(CO)_4(PEtPh_2)(PEt_3)$}. The resonances are attributable to *cis*-$Mo(CO)_4(PEtPh_2)_2$ (A, −1657 ppm), *trans*-$Mo(CO)_4(PEtPh_2)_2$ (B, −1720 ppm), *cis*-$Mo(CO)_4(PEt_3)_2$ (C, −1765 ppm), $Mo(CO)_5(PEtPh_2)$ (D, −1788 ppm), *trans*-$Mo(CO)_4(PEt_3)_2$ (E, −1810 ppm), and $Mo(CO)_5(PEt_3)$ (F, −1854 ppm).

values. The same shielding order of the ligands (Sb > As > P > N) is found in $Mo(CO)_5L$ and $Mo(CO)_3L_3$ complexes (7, 8) and the factors influencing the order were previously discussed (13(*c*)).

Consideration of the factors influencing linewidths of resonances observed for quadrupolar nuclei (1, 5, 18) leads to a prediction of generally narrower linewidths for the *cis* as opposed to the *trans* complexes because the major parameter, the electric field gradient, is less for the former complexes (14). In practice, the linewidths for most of the *cis* complexes are considerably larger than those observed for the analogous *trans* complex. Such line-broadening might be attributed to the greater steric congestion and subsequent distortion expected for the *cis* complexes. Similarly, broad linewidths have been reported (9) for many *fac*-$Mo(CO)_3L_3$ complexes with bulky ligands even though the electric field gradient is theoretically zero for complexes with trigonal symmetry.

The identification of mixtures of products by ^{95}Mo nmr spectroscopy is readily effected without recourse to tedious column chromatographic separation. Not only can the presence of several species be inferred, as might be implied by the complexity of ir or ^{13}C nmr spectra, but each may be identified by its characteristic chemical shift, linewidth[2] and, for PR_3 and $P(OR)_3$ ligands, coupling constant. This useful application of ^{95}Mo nmr data was applied in the characterization of the products obtained during the attempted synthesis of *trans*-$Mo(CO)_4LL'$. Refluxing solutions of *cis*-$Mo(CO)_4LL'$ gave a variety of mono- and bis-substituted complexes, as expected (20). As an example, the ^{95}Mo nmr spectrum (Fig. 1) of the reaction mixture obtained by refluxing a dichloromethane solution of *cis*-$Mo(CO)_4(PEtPh_2)(PEt_3)$ illustrates dramatically how readily the "potpourri" of products can be analysed. All of the identified species were separately synthesized and characterized (Table 1 and ref. 13(*c*)) by ir and ^{95}Mo nmr spectroscopy. The only peak (at ~1745 ppm) that cannot be unambiguously assigned, due to the lack of resolution of the coupling, is nevertheless judged to be in the right location for *trans*-$Mo(CO)_4(PEtPh_2)(PEt_3)$. A range of such unsymmetrical *trans*-complexes, prepared by a "cleaner" synthetic route, is under investigation by ^{95}Mo nmr spectroscopy in order to provide further information on the relative *trans*-effect of phosphines and phosphites.[3]

In the case of cyclic nitrogen donor ligands, the chemical shift data demonstrate the effect of ring saturation (shielding from py to pip), ring contraction (shielding from pip to pyr), ring expansion to a double-ring system (shielding from py to quin), and the effect of electron donor substituents on the ring (shielding from py to 4-Bu^{t}py but deshielding from py to 2-NH_2Etpy and 2-NH_2Mepy). The need to change solvents to ensure sufficient solubility obviously complicates correlation of this data, though only a small chemical shift difference might be expected between DMF and CH_2Cl_2 (7(*a*)). The differing σ-donor/π-acceptor(donor) properties of the nitrogen ligands will influence the various terms of the Ramsey expression (eq. [1]) in a complicated fashion, as already discussed (13(*c*), 18), and thus no simple explanations of the observed chemical shifts are possible. Doubtless the ligand field strength and the polarizability of the donor atom as well as steric factors all play a role in determining the δ(^{95}Mo) values. We reserve further discussion of the complexes with N-donor ligands until completion of our ^{95}Mo nmr study of a range of related $Mo(CO)_3L_3$ compounds.

Acknowledgements

Support of this research by NSERC of Canada is gratefully acknowledged. The nmr spectra were obtained at the Southwestern Ontario NMR Centre funded by a Major Installation Grant from NSERC.

[3]McFarlane and co-workers (14) documented the expected changes in $\Delta\nu_{1/2}$ for $Mo(CO)_{6-n}(P(OMe)_3)_n$ (n = 0–6) species.

[4]Chemical shifts previously assigned (7(*a*)) to *trans*-$Mo(CO)_4(PPh_3)[P(OPh)_3]$ and *trans*-$Mo(CO)_4(PBu^n_3)[P(OPh)_3]$ are actually due to mixtures of the mono-substituted $Mo(CO)_5L$ derivatives (13(*c*)).

Can. J. Chem. Downloaded from www.nrcresearchpress.com by 176.9.209.113 on 09/07/12
For personal use only.

1. R. K. HARRIS and B. E. MANN (*Editors*). NMR and the Periodic Table. Academic Press, London. 1978.
2. C. BREVARD and P. GRANGER. Handbook of high resolution multinuclear NMR. Wiley-Interscience, New York. 1981.
3. J. B. LAMBERT and F. G. RIDDELL (*Editors*). The multinuclear approach to NMR spectroscopy. Reidel Publishing Company, Dordrecht. 1983.
4. D. G. BICKLEY, M. J. MCGLINCHEY, and G. J. SCHROBILGEN. Can. Chem. News, 19 (1984).
5. D. REHDER. Bull. Magn. Reson. **4**, 33 (1982).
6. (*a*) J. J. DECHTER. Progr. Inorg. Chem. **33**, 393 (1985); (*b*) R. HANI and R. G. GEANANGEL. Coord. Chem. Rev. **44**, 229 (1982); (*c*) P. S. PREGOSIN. Coord. Chem. Rev. **44**, 247 (1982).
7. (*a*) E. C. ALYEA and A. SOMOGYVARI. *In* Proc. Fourth Int. Conf. on the Chemistry and Uses of Molybdenum. *Edited by* H. F. Barry and P. C. H. Mitchell. Climax Molybdenum Company, Ann Arbor, MI. 1982. p. 46, and references cited therein; (*b*) E. C. ALYEA, A. MALEK, and J. MALITO. Polyhedron, **5**, 403 (1986); (*c*) C. G. YOUNG, MINELLI, J. H. ENEMARK, G. MIESSLER, N. JANIETZ, H. KAUERMANN, and J. WACHTER. Polyhedron, **5**, 407 (1986); (*d*) R. A. GRIEVES and J. MASON. Polyhedron, **5**, 415 (1986).
8. A. F. MASTERS, G. E. BOSSARD, T. A. GEORGE, R. T. C. BROWNLEE, M. J. O'CONNOR, and A. G. WEDD. Inorg. Chem. **22**, 908 (1983).
9. M. MINELLI, J. H. ENEMARK, R. T. C. BROWNLEE, M. J. O'CONNOR, and A. G. WEDD. Coord. Chem. Rev. **68**, 169 (1985).
10. (*a*) J. H. ENEMARK, C. G. YOUNG, M. MINELLI, and J. DILWORTH. Fifth Int. Conf. on the Chemistry and Uses of Molybdenum, University of Newcastle upon Tyne. July 1–5, 1985. Abstr. p. 83; (*b*) C. G. RODRIGUES, F. FARCHIONE, G. R. HANSON, G. L. WILSON, M. J. O'CONNOR, and A. G. WEDD. Fifth Int. Conf. on the Chemistry and Uses of Molybdenum, University of Newcastle upon Tyne. July 1–5, 1985. Abstr. p. 55.
11. S. BRISTOW, C. D. GARNER, S. K. HAGYARD, G. A. MORRIS, J. R. NICHOLSON, and C. F. MILLS. J. Chem. Soc. Chem. Commun. 479 (1985).
12. H. DUBKE, W. JITSCHIN, G. MEISEL, and W. J. CHILDS. Phys. Lett. **65**A, 109 (1978).
13. (*a*) E. C. ALYEA, R. E. LENKINSKI, and A. SOMOGYVARI. Polyhedron, **1**, 130 (1982); (*b*) E. C. ALYEA and A. SOMOGYVARI. Inorg. Chim. Acta, **83**, L49 (1984); (*c*) E. C. ALYEA and A. SOMOGYVARI. Trans. Met. Chem. In press.
14. G. T. ANDREWS, I. J. COLQUHOUN, W. MCFARLANE, and S. O. GRIM. J. Chem. Soc. Dalton Trans. 2353 (1982).
15. G. M. GRAY and C. S. KRAIHANZEL. Inorg. Chem. **22**, 2959 (1983).
16. D. J. DARENSBOURG and R. L. KUMP. Inorg. Chem. **17**, 2680 (1978).
17. M. MINELLI, J. L. HUBBARD, K. A. CHRISTENSEN, and J. M. ENEMARK. Inorg. Chem. **22**, 2652 (1983).
18. J. MASON. Adv. Inorg. Chem. Radiochem. **22**, 199 (1979).
19. W. D. HORROCKS, JR., and R. C. TAYLOR. Inorg. Chem. **2**, 723 (1963).
20. (*a*) S. O. GRIM, D. A. WHEATLAND, and P. R. MCALLISTER. Inorg. Chem. **7**, 161 (1968); (*b*) S. O. GRIM and D. A. WHEATLAND. Inorg. Chem. **8**, 1716 (1969).

Can. J. Chem. Downloaded from www.nrcresearchpress.com by 176.9.209.113 on 09/07/12
For personal use only.

On the spectrophotometric determination of UO_2^{2+} with 2-(5-bromo-2-pyridylazo)-5-diethylaminophenol

LUMÍR SOMMER AND EVA ŠAMLOTOVÁ

Department of Analytical Chemistry, J. E. Purkyně University, 61137 Brno, Czechoslovakia

Received October 22, 1986[1]

This paper is dedicated to Professor Douglas E. Ryan

LUMÍR SOMMER and EVA ŠAMLOTOVÁ. Can. J. Chem. **66**, 401 (1988).

2-(5-Bromo-2-pyridylazo)-5-diethylaminophenol (5-Br-PADAP) is a suitable reagent for the spectrophotometric determination of uranium but results are easily influenced by the reaction conditions as well as various common ions and masking agents. Optimum conditions, which must be carefully maintained, are 30% (v/v) dimethylformamide, 0.1% triton X-100, $\geq 8 \times 10^{-5}$ *M* 5-Br-PADAP, 8×10^{-2} *M* triethanolamine, 7×10^{-3} *M* sodium fluoride, 10^{-2} *M* 5-sulphosalicylic acid, and 579 nm. Sodium sulphate (10^{-2} *M*) and CDTA (5.7×10^{-3} *M*) may serve as additional masking agents. A previous separation of uranium by extraction with 0.1 *M* tri-*n*-octylamine in benzene from 4 *M* HCl and re-extraction of 0.3 *M* HCl is recommended for analysis of natural water samples.

LUMÍR SOMMER et EVA ŠAMLOTOVÁ. Can. J. Chem. **66**, 401 (1988).

Le (bromo-5 pyridyl-2 azo)-2 diéthylamino-5 phénol (Br-5 PADAP) est un réactif approprié pour la détermination spectrophotométrique de l'uranium; toutefois, les résultats sont facilement influencés par les conditions de la réaction ainsi que par divers ions communs et des agents masquants. Les conditions optimales, qui doivent être maintenues avec soins, sont les suivantes : 30% (v/v) de diméthylformamide, 0,1% de Triton X-100, $\geq 8 \times 10^{-5}$ *M* de Br-5 PADAP, 8×10^{-2} *M* de triéthanolamine, 7×10^{-3} *M* de fluorure de sodium, 10^{-2} *M* d'acide sulfo-5 salicylique et une longueur d'onde de 579 nm. On peut aussi utiliser du sulfate de sodium (10^{-2} *M*) et du CDTA ($5,7 \times 10^{-3}$ *M*) comme agents masquants. Pour l'analyse d'échantillons d'eaux naturelles, on recommande l'utilisation d'une méthode décrite antérieurement pour la séparation de l'uranium; elle implique une extraction d'une solution 4 *M* en HCl par de la tri *n*-octylamine 0,1 *M* dans le benzène suivie par une ré-extraction par du HCl à 0,3 *M*.

[Traduit par la revue]

The reaction of UO_2^{2+} belongs to the analytically most valuable reactions of pyridylazo dyes derived from *m*-aminophenol. These reagents, first introduced by Gusev and Schurova (1), show high sensitivity and adequate spectral contrast between the dye – metal ion chelate and the free dye. These properties result from intensive interaction of the lone electron pair of the alkylated amino group in the *para* position towards the azo group with the aromatic ring.

Several variants of spectrophotometric determination of UO_2^{2+} with the stable commercially available reagent 2-(5-bromo-2-pyridylazo)-5-diethylaminophenol (5-Br-PADAP) have been described in the presence of fluoride, *o*-phenolcarboxylic acids such as 5-sulfosalicylic acid, cyclohexandiaminetetraacetic acid (CDTA), triethanolamine (TEA), and borate buffer (2–6). Johnson and Florence (3) assumed three complexes formed depending on pH and composition of solution (*a*) UO_2L^+ (λ_{max} 554 and 586 nm), formed at pH 4.1 in the presence of an excess of UO_2^{2+} or sulphate and perchlorate and extractable in polar solvents; (*b*) an unstable 1:1 complex at pH 7.6, considered a hydroxocomplex, $UO_2L(OH)$ (λ_{max} 546 nm); (*c*) a stable and strongly absorbing ternary complex, UO_2LF (λ_{max} 578 nm) at pH 7.3 in the presence of limited concentrations of fluoride, which is, however, decomposed in the presence of excess fluoride (L is the anion of 5-Br-PADAP). The 1:1 stoichiometry of UO_2^{2+} with 5-Br-PADAP was also observed in extracts of TOPO, TOA, or TBP in cyclohexane, kerosine, or dimethylformamide–ethanol mixtures (11). The stability and absorptivity of the 1:1 chelate of UO_2^{2+} with 5-Br-PADAP increases considerably after transformation to a ternary species with fluoride or *o*-phenolcarboxylic acid. These reagents in combination with CDTA and TEA may serve as suitable masking agents for interferents. On the other hand, the effect of cationic and anionic surfactants is still uncertain (5–9, 13). In complex samples, UO_2^{2+} may be separated by extraction with trioctylphosphineoxide (TOPO) in cyclohexane (2, 4, 10), tri-*n*-alkylamines in kerosine (11), or tri-*n*-octylamine or tri-*n*-butylamine in kerosine (12) prior to the spectrophotometric determination with 5-Br-PADAP in the organic phase. The absorbance is, however, influenced by the composition of the mixed phase. Extraction chromatography has also been used for separation of uranium from various interferents, the UO_2^{2+} then being determined with 5-Br-PADAP in the acidic eluate (8). In spite of the slowness of the reaction of UO_2^{2+} with 5-Br-PADAP in the presence or absence of additional reactants, flow injection analysis has been successfully used for the automated continuous determination of UO_2^{2+} in ores or rocks after sample decomposition (13–15).

In this paper, the reaction of UO_2^{2+} with 5-Br-PADAP is re-examined and a modified procedure developed in aqueous dimethylformamide suitable for the determination of uranium in natural waters.

Experimental

Chemicals, solutions, instruments

2-(5-Bromo-2-pyridylazo)-5-diethylaminophenol (5-Br-PADAP) (E. Merck, Darmstadt, B.R.D.); stock solutions were 10^{-4} *M* in 95% ethanol or in 99.5% dimethylformamide. Solutions used were not older than 1 week.

A 0.189 *M* standard uranyl chloride dihydrate solution in 0.2 *M* HCl was prepared and standardized gravimetrically via 8-hydroxyquinolate; 2% aqueous stock solution of triton X-100 (octylphenolpolyethylene glycolether) (Koch-Light Labs., G.B.).

Septonex(1-ethoxycarbonylpentadecyltrimethylammonium bromide (Czech Pharmacopoia ČsL 3) (Slovakopharma, Hlohovec, ČSSR); 0.1 *M* aqueous stock solution.

Cetylpyridinium bromide (Lachema N.C., Brno); 5×10^{-2} *M* aqueous stock solution.

[1]Revision received September 16, 1987.

Can. J. Chem. Downloaded from www.nrcresearchpress.com by 176.9.209.113 on 09/07/12
For personal use only.

Dodecylsulphate, sodium salt; 0.05 *M* aqueous stock solution.

Ethanol 95%; commercial sample containing 4.1% methanol and 4.3% water was treated with EDTA and distilled under reflux.

Dimethylformamide 99.5% (Reachim, USSR) was distilled *in vacuo* at 51°C.

Tri-*n*-octylamine (E. Merck, Darmstadt, B.R.D.).

Triethanolamine (TEA) (E. Merck, B.R.D.); a 1 *M* aqueous buffer solution was prepared by dissolving 14.919 g of TEA in 50 mL, adjusting to pH 8.26 with concentrated $HClO_4$ and diluting with water to 100 mL.

Borate buffer: 13.09 g H_3BO_3 (E. Merck, Darmstadt) was dissolved in 50 mL of water, the pH adjusted to 9.0 with 1 *M* NaOH, and the solution diluted to 100 mL.

Sodium fluoride, 0.2 *M*.

Aqueous solution of CDTA (0.1 *M*) adjusted with sodium hydroxide to pH 7.0.

5-Sulphosalicylic acid dihydrate, 0.1 *M*.

Complexing and masking mixture: 7.1×10^{-2} *M* CDTA, 1.25×10^{-2} *M* 5-sulfosalicylic acid, 8.7×10^{-2} *M* sodium fluoride, 2.8×10^{-1} *M* sodium sulphate, i.e., 2.46 g of CDTA, 3.18 g of 5-sulfosalicylic acid, 0.365 g NaF and 4.03 g of anhydrous sodium sulphate were dissolved in water, adjusted to pH 7.3, and diluted to 100 mL.

All chemicals were of analytical grade or superpure quality. Water was doubly distilled.

Double beam spectrophotometer: Varian Techtron Superscan 3 controlled by Hewlett-Packard HP 9815 A computer, with 100 mm silica cells.

Single beam spectrophotometer: Unicam SP-500 with 10 mm glass cells. Absorbances were corrected by subtracting the blank containing all components except uranium under the same conditions.

Precision digital pH meter: Radelkis 208/1 with a combination electrode OP-0808 P. The pH meter was standardized with NBS buffers. pH values for solutions in 50% ethanol or 30% dimethylformamide in the presence of triton X-100 were not corrected.

The threshold interference of ions and components was defined as that causing ±2% relative absorbance change against the absorbance of a corresponding pure UO_2^{2+}–5-Br-PADAP complex solution.

Results

Stoichiometry of the complex

The 1:1 stoichiometry of UO_2^{2+} to 5-Br-PADAP has also been proved in 30% dimethylformamide containing 0.007 *M* fluoride, 0.01 *M* 5-sulfosalicylic acid, 5.7×10^{-3} *M* CDTA, 0.1% triton X-100, in the presence of TEA at pH 7.3 for the total concentration $c_L + c_M = 3 \times 10^{-4}$ *M* and 565–590 nm by the method of continuous variations. The customary 1:2 metal-to-ligand complex, which is usual between bivalent metal ions and 5-Br-PADAP, is not formed with UO_2^{2+}.

Effect of time and mixing of components

In 0.1 to 0.2% triton X-100 and 30% dimethylformamide, the absorbance of the complex between UO_2^{2+} and 5-Br-PADAP reaches a constant value in pure solutions containing excess reagent over the pH range 3 to 7 in 10 min. The same holds true for solutions containing fluoride, 5-sulfosalicylic acid, CDTA, and TEA. The most suitable order of mixing is acid sample solution, solvent (ethanol or dimethylformamide) surfactant, complexing and masking mixture, buffer solution, and 5-Br-PADAP reagent solution followed by pH adjustment to the desired value and dilution to the appropriate volume with water. The λ_{max} of 579 nm does not change with changes in the composition of solution or with time. Typical absorption spectra are shown in Fig. 1.

Effect of pH

The binary species of UO_2^{2+} with 5-Br-PADAP reaches its maximum absorbance at pH 3.5 in 50% ethanol or 30% dimethylformamide. The molar absorption coefficient with respect to UO_2^{2+} increases with increasing concentration of 5-Br-PADAP and even in the presence of excess nitrate, sulphate, or perchlorate. The optimum pH shifts to 6.5 in 10^{-2} *M* fluoride or to pH 7.1 in 0.05 *M* TEA, 50% ethanol, and 0.1% triton X-100. The optimum pH is 7.3 if 30% dimethylformamide is used instead of ethanol. Other components of the complexing and masking mixture do not influence the optimum pH value (Fig. 2).

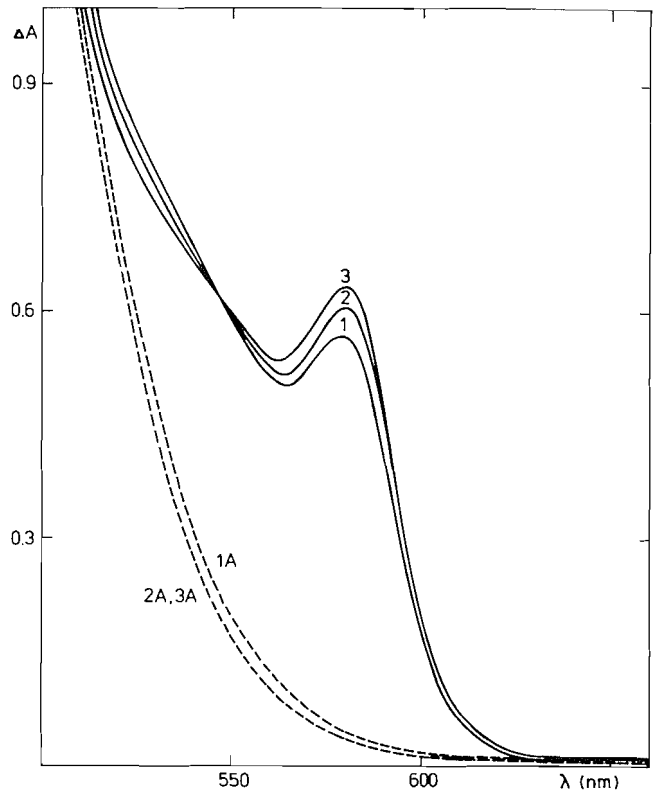

FIG. 1. Absorption curves of 8×10^{-4} *M* UO_2^{2+} and 8×10^{-5} *M* 5-Br-PADAP in 30% dimethylformamide at pH 9.7 (curve *1*), 6.0 (curve *2*), and 7.3 (curve *3*). The solutions also contain 0.1% triton X-100, 5×10^{-2} *M* TEA, 7×10^{-3} *M* NaF, 5.7×10^{-3} *M* CDTA, and 1×10^{-2} *M* sulfosalicylate; 1A to 3A show curves of the solutions without UO_2^{2+}; $\Delta A = A - A_{bl}$.

Effect of 5-Br-PADAP concentration

The maximum value of absorbance is reached for $c_l/c_M \geq 6.5$ at pH 7.0 and 579 nm, for solutions containing 8×10^{-6} *M* UO_2^{2+}, 0.01 TEA, 0.01 *M* fluoride, and 0.1% triton X-100 in 50% ethanol or 30% dimethylformamide. An 8×10^{-5} *M* 5-Br-PADAP concentration is sufficient for practical purposes.

Effect of buffers

The earlier recommended buffer mixture, triethanolamine–$HClO_4$ (2) is suitable in 0.08 *M* concentration over pH 7.0 to 7.3 in the presence of 8×10^{-5} *M* 5-Br-PADAP, 50% ethanol, or 30% dimethylformamide, 0.1% triton X-100, and 7×10^{-3} *M* fluoride. A 0.04 *M* borate buffer may also be used for the same conditions.

Effect of solvents

A 50% ethanol concentration is needed to keep the UO_2^{2+} complex with 5-Br-PADAP and the reagent excess in solution in the presence of 0.1% triton X-100. The ethanol can be replaced by 30% dimethylformamide, in which higher absorbance values are achieved under similar conditions.

Can. J. Chem. Downloaded from www.nrcresearchpress.com by 176.9.209.113 on 09/07/12
For personal use only.

Can. J. Chem. Downloaded from www.nrcresearchpress.com by 176.9.209.113 on 09/07/12
For personal use only.

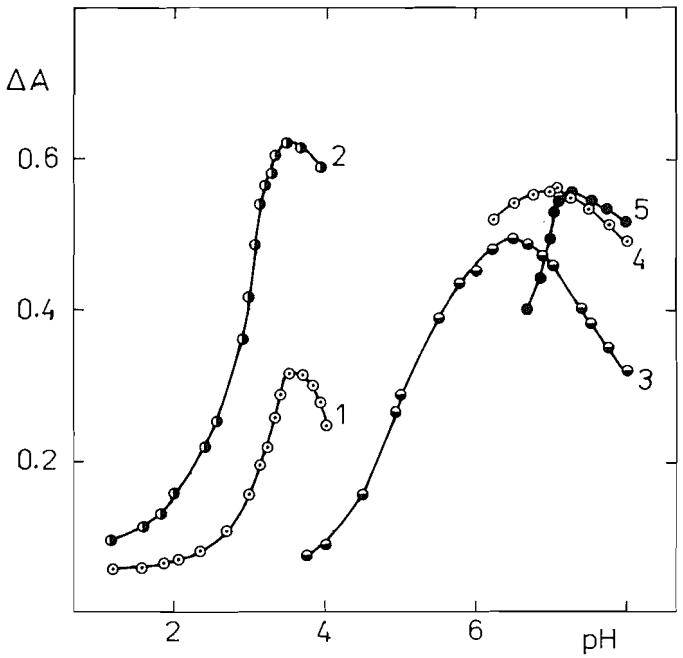

FIG. 2. Absorbance–pH plots at 579 nm for various ratios of UO_2^{2+} to 5-Br-PADAP under various conditions. 50% ethanol, 0.1% triton X-100; curve *1*, 2.1×10^{-5} *M* UO_2^{2+}, $c_L/c_M = 1$; curve *2*, $c_L/c_M = 3.0$; 3. 8×10^{-6} *M* UO_2^{2+}, $c_L = 1 \times 10^{-4}$ *M*, 1×10^{-2} *M* NaF; the same as for curves *3* and 5×10^{-2} *M* TEA; 5. 30% dimethylformamide, 0.1% triton X-100, 8×10^{-6} *M* UO_2^{2+}, $c_L = 8 \times 10^{-5}$ *M*, 7×10^{-3} *M* NaF, 5.7×10^{-3} *M* CDTA, 1×10^{-2} *M* 5-sulfosalicylate, 5×10^{-2} *M* TEA; $\Delta A = A - A_{bl}$.

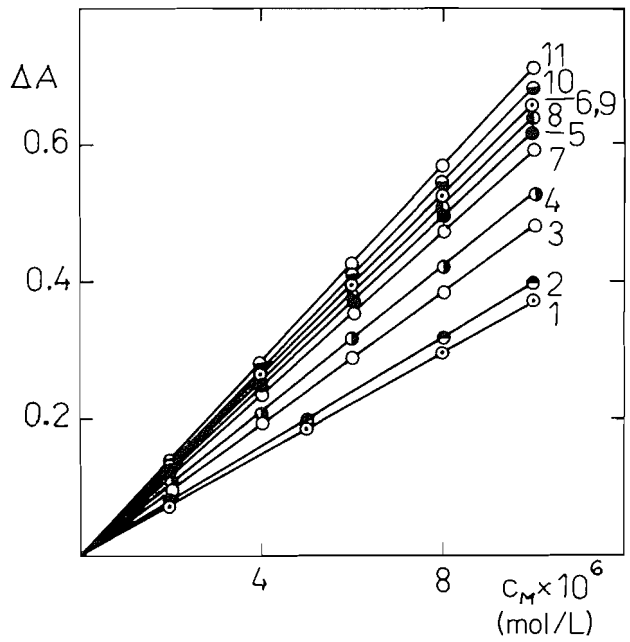

FIG. 3. Plots of absorbance vs. UO_2^{2+} concentration at 579 nm under various conditions used for spectrophotometric determination of UO_2^{2+}. All solutions contain 50% ethanol, 0.1% triton X-100, and 8×10^{-5} *M* 5-Br-PADAP at pH 7.3. Curve *1*, 9.5×10^{-3} *M* NaF, 5.7×10^{-3} *M* CDTA, 2×10^{-2} *M* sulphosalicylate, 8×10^{-2} *M* TEA; curve *2*, 7×10^{-3} *M* NaF, 8×10^{-2} *M* TEA; curve *5*, 7×10^{-3} *M* NaF, 5.7×10^{-3} *M* CDTA, 1×10^{-2} *M* sulfosalicylate, 5×10^{-2} *M* TEA; curve *6*, 7×10^{-3} *M* NaF, 5.7×10^{-3} *M* CDTA, 1×10^{-2} *M* sulfosalicylate, 8×10^{-2} *M* TEA. Particular values for $\epsilon \times 10^{-4}$ are 5.0, 5.1, 6.5, 6.6 L mol^{-1} cm^{-1}. All solutions contain 30% dimethylformamide, 0.1% triton X-100, pH 7.3, and 8×10^{-5} *M* 5-Br-PADAP. Curve *3*, 9.5×10^{-3} *M* NaF, 5.7×10^{-3} *M* CDTA, 2×10^{-2} *M* sulfosalicylate, 8×10^{-2} *M* TEA (pH 7.8); curve *4*, 7×10^{-3} *M* NaF, 8.1×10^{-3} *M* CDTA, 1×10^{-2} *M* sulfosalicylate, 5×10^{-2} *M* TEA; curve *7*, 7×10^{-3} *M* NaF, 5.7×10^{-3} *M* CDTA, 2×10^{-2} *M* sulfosalicylate, 8×10^{-2} *M* TEA; curve *8*, 7×10^{-3} *M* NaF, 8×10^{-2} *M* TEA, 4×10^{-5} *M* 5-Br-PADAP; curve *9*, 7×10^{-3} *M* NaF, 8×10^{-2} *M* TEA, 5.7×10^{-3} *M* CDTA, 1×10^{-2} *M* sulfosalicylate; curve *10*, 7×10^{-3} *M* NaF, 5.7×10^{-3} *M* CDTA, 1×10^{-2} *M* sulfosalicylate, 8×10^{-2} *M* TEA, 1×10^{-2} *M* sulphate; curve *11*, 7×10^{-3} *M* NaF, 8×10^{-2} *M* TEA; particular values for $\epsilon \times 10^{-4}$ are 5.6, 6.4, 6.9, 7.1, 7.2, 7.3, 7.4 L mol^{-1} cm^{-1}; $\Delta A = A - A_{bl}$.

Influence of various reactants

The concentration of various complexing agents is critical with respect to absorbance at 579 nm. Maximum absorbance is retained for 0.05 *M* TEA, 0.01 *M* fluoride, 5-sulfosalicylic acid, and not more than 6×10^{-3} *M* CDTA over pH 7.1 to 7.3 in 50% ethanol or 30% dimethylformamide containing 8×10^{-5} *M* ligand. Higher concentrations of the above components may considerably decrease the absorbance values of UO_2^{2+} solutions with 5-Br-PADAP and also shift the optimum pH to higher values. The effect of 5-sulfosalicylic acid on the binary UO_2^{2+}–5-Br-PADAP species is negligible in chloride medium and the conditional molar absorptivity of 3.5×10^4 L mol^{-1} cm^{-1} is similar to that of solutions without 5-sulfosalicylic acid. A chromogenic effect by 5-sulfosalicylic acid is only observed in 0.01 to 0.1 *M* nitrate (fluoride absent) containing 50% ethanol at pH 7.5. The observed molar absorptivity of 6.2×10^4 L mol^{-1} cm^{-1} is, however, considerably less than previously reported (6).

Effect of surfactants

Non-ionic surfactants such as triton X-100 in 0.1% concentration enhance the formation of the UO_2^{2+}–5-Br-PADAP complexes. A high concentration of surfactant is not desirable because of decreasing absorbance and foaming of solutions. In the presence of 1.0 to 3.2×10^{-3} *M* dodecylsulphate the resulting molar absorptivity is 5.5×10^4 L mol^{-1} cm^{-1} and the optimum pH is shifted to pH 8.1 in the presence of TEA if the chloride medium contains 50% ethanol, the complexing mixture, and 0.05 *M* TEA or 0.004 *M* borate at pH $\geq$7.3. The formation of the UO_2^{2+} complex with 5-Br-PADAP is hindered in solutions containing less than 10% ethanol, 3.2×10^{-3} *M* dodecylsulphate, and 5×10^{-3} *M* CDTA, which is in disagreement with ref. 9 and ref. 16 where the reagent 3,5-dibromo-PADAP was used for the determination of uranium. No stable ternary species is observed in the presence of 10^{-3} *M* cetylpyridinium bromide or septonex in 50% ethanol containing 0.1% triton X-100 and 1.44×10^4 *M* 5-Br-PADAP at pH 7.5. A small concentration of ternary species is formed only in the presence of 8×10^{-3} *M* 5-sulfosalicylic acid and cationic surfactant at pH 7.5 in the chloride medium (conditional $\epsilon = 2.1 \times 10^4$ L mol^{-1} cm^{-1} in the presence of septonex and 1.6×10^4 L mol^{-1} cm^{-1} in the presence of cetylpyridinium bromide at 579 nm). This negative result, which is in disagreement with ref. 7, may be the result of competition by the cationic surfactant for reagent anions bound in the UO_2^{2+}–complex.

UO^{2+}–concentration plots of absorbance

Absorbance vs. UO_2^{2+} plots are linear over the concentration range 0.4 to 3.2 μg U/mL in 30% dimethylformamide or 50% ethanol containing $\geq 8 \times 10^{-5}$ *M* 5-Br-PADAP and triton X-100, in the presence of fluoride, CDTA, TEA, sulfate, 5-sulfosalicylic acid at pH 7.3 and 579 nm. These plots, however,

TABLE 1. Limiting concentrations of selected anions in the determination of UO_2^{2+} with 5-Br-PADAP[a]

Ion	c_{Ion} (mol/L)	c_{Ion}/c_M (mol/L)	c_{Ion}/c_M (μg/mL)
PO_4^{3-}	3.5×10^{-4}	44	17
CO_3^{2-}	2.5×10^{-3}	312	79
SO_4^{2-}[b]	1.37×10^{-2}	1712	691
ClO_4^-	3.06×10^{-2}	3825	1597
SO_4^{2-}[c]	3.25×10^{-2}	4063	1639
NO_3^-	5.12×10^{-2}	6400	1667
Cl^-	1.04×10^{-1}	12962	1933

[a] $c_M = 8 \times 10^{-6}$ mol/L, $c_L = 8 \times 10^{-5}$ mol/L, 30% dimethylformamide, 0.1% triton X-100, $c_{NaF} = 7 \times 10^{-3}$ mol/L, $c_{CDTA} = 5.7 \times 10^{-3}$ mol/L, $c_{sulfosal} = 1 \times 10^{-2}$ mol/L, $c_{TEA} = 8 \times 10^{-2}$ mol/L, pH 7.3, 579 nm.
[b] Ammonium sulfate.
[c] Sodium sulfate.

yield various conditional values for the molar absorption coefficient (cf. Fig. 3). The highest value, 74000 L mol^{-1} cm^{-1}, was reached for 30% dimethylformamide, 0.1% triton X-100, 8×10^{-5} *M* 5-Br-PADAP, 8×10^{-3} *M* TEA, and 7×10^{-3} *M* fluoride, or 73000 L mol^{-1} cm^{-1} in a medium containing 5.7×10^{-3} *M* CDTA, 10^{-3} *M* 5-sulfosalicylic acid, 7×10^{-3} *M* sodium fluoride, 10^{-2} *M* sodium sulfate, and 0.08 *M* TEA. This enables partial masking of interfering ions by such mixture.

Interferences

The effect of various ions expected in natural waters on the UO_2^{2+} reaction with 5-Br-PADAP is summarized in Tables 1 and 2 for a medium of 30% dimethylformamide containing 8×10^{-5} *M* 5-Br-PADAP at pH 7.3. Unfortunately the masking capacity of the complexing mixture containing fluoride, 5-sulfosalicylic acid, CDTA, and sulphate is limited at pH 7.3. Unlike an earlier study (2), this work shows that Ca^{2+}, Mg^{2+} and several other ions interfere even in the presence of a masking–complexing mixture. The presence of 10^{-2} *M* sodium sulphate in this mixture often decreases interferences. The masking of Th(IV) is particularly effective. In contrast, 1×10^{-2} *M* ascorbic acid, 1×10^{-3} *M* oxalic acid, $\geq 5.6 \times 10^{-4}$ *M* dihydrogeneitrate, $\geq 9 \times 10^{-4}$ *M* acetate, and 4.25×10^{-4} *M* tartrate each interferes by causing a considerable absorbance decrease.

Optimized procedure

Add in succession 3.5 mL of dimethylformamide, 1.25 mL of 2% triton X-100, 2 mL of complexing and masking mixture, 2 mL of 1 *M* TEA, and 4 mL of 5×10^{-4} *M* 5-Br-PADAP in dimethylformamide to ≤10 mL of slightly acidic sample solution containing less than 65 μg UO_2^{2+} in chloride, nitrate, sulphate, or perchlorate medium. Adjust the pH to 7.3 with dilute sodium hydroxide, transfer the solution into a 25-mL volumetric flask and dilute to volume with water. Measure the absorbance 10 min after pH adjustment at 579 nm and subtract a blank measured under the same conditions. Prepare a calibration plot of 4 standard solutions of uranyl chloride in duplicate and measure each under optimized conditions. Linear regression of the plot between $0.196–1.370 \times 10^{-5}$ *M* (0.47–3.26 μg U/mL) gave $s_{xy(A)} = 0.008$, $\epsilon = (7.20 \pm 0.05) \times 10^4$ L mol^{-1} cm^{-1}, $A_{bl} = 0.043 \pm 0.005$. The determination limit, expressed from $A_{lim} = A_{bl} + 10\ s_{A(bl)}$ at 579 nm and evaluated from eight parallel solutions of the blank, is 0.02 μg U/mL.

Recommended procedure for the determination of uranium in drinking, surface, and waste waters

Evaporate 100 mL of water sample with 2 mL of concentrated HCl and 2 mL of 30% H_2O_2 in a porcelain dish to dryness. Repeat the evaporation with a second 2 mL portion of concentrated HCl. Dissolve the wet residue in a small portion of hot distilled water and continue with the spectrophotometric determination of uranium according to the above procedure. This direct method cannot be used for hard waters with high contents of Ca^{2+} and silicate since turbidity appears after dissolution of the residue and addition of the masking mixture. In this case, a previous separation of uranium by extraction with tri-*n*-octylamine in benzene is recommended (17). The modified procedure is as follows: Dissolve the residue after preconcentration of uranium in 10 mL of 10 *M* HCl and 15 mL of doubly distilled water. Transfer the solution quantitatively into a 50-mL pommel-form separation funnel with a 20-mm stem. Add 3 g of ascorbic acid to reduce Fe^{3+} to Fe^{2+} and 5 mL of 0.1 *M* tri-*n*-octylamine in benzene. Shake vigorously for 3 min. Discard the aqueous phase after complete separation of the phases, wash the organic phase twice with 5 mL of 4 *M* HCl, and re-extract the uranium twice with 5 mL of 0.3 *M* aqueous HCl. Transfer the aqueous phase quantitatively into a suitable

TABLE 2. Effect of selected cations on the determination of UO_2^{2+} with 5-Br-PADAP[a]

Ion	Salt used	c_{Ion} (mol/L)	c_{Ion}/c_M (mol/L)	Relative error (%) for $c_{Ion} = 10^{-3}$ (mol/L)
Mn^{2+}	$MnCl_2$	9×10^{-5}	43	+5.2
Mg^{2+}	$MgCl_2$	9×10^{-6}	4.3	−8.5
Fe^{2+}	$FeCl_2$	7.5×10^{-6}	3.5	+7.9
Al^{3+}	$AlCl_3$	8×10^{-5}	38	−3.3
Ca^{2+}	$CaCl_2$	5.5×10^{-6}	2.6	−12.4
Zn^{2+}	$Zn(NO_3)_2$	7×10^{-5}	33	+2.5
Th^{4+}	$Th(NO_3)_4$	4×10^{-4}	190	+2.5
Cu^{2+}	$CuCl_2$	4×10^{-5}	19	+9.4
Ni^{2+}	$Ni(NO_3)_2$	5×10^{-5}	24	+4.5
Co^{2+}	$Co(NO_3)_2$	7.5×10^{-6}	3.5	+7.9
Fe^{3+}	$FeCl_3$	6.5×10^{-6}	3	+8.0

[a] $c_M = 3 \times 10^{-6}$ mol/L, $c_L = 8 \times 10^{-5}$ mol/L, 30% dimethylformamide, 0.1% triton X-100, $c_{NaF} = 7 \times 10^{-3}$ mol/L, $c_{CDTA} = 5.7 \times 10^{-3}$ mol/L, $c_{sulfosal} = 1 \times 10^{-2}$ mol/L, $c_{TEA} = 8 \times 10^{-2}$ mol/L, pH 7.3, 579 nm.

Can. J. Chem. Downloaded from www.nrcresearchpress.com by 176.9.209.113 on 09/07/12
For personal use only.

TABLE 3. Analysis of water samples after extraction with 0.1 mol/L tri-*n*-octylamine in benzene and re-extraction (standard additions procedure)

Sample	Addition of standard solution (uranyl chloride) (μg/L U)	Found (μg/L U)
Drinking water (with spike of 499.8 μg/L U)	—	495[a]
	45	481[b]
	90	507[b]
	135	492[b]
	Average:[b]	493±9
Surface water	—	99.0[a]
	45	100.7[b]
	90	100.0[b]
	135	98.8[b]
	Average:[b]	99.8±0.7
Waste water	—	257[a]
	45	264[b]
	90	264[b]
	135	254[b]
	Average:[b]	261±4

[a]Graphical extrapolation procedure.
[b]Calculated from the following equation: $c_x = A_x c_{i(st)}/[A_{(x+c_{i(st)})} - A_x]$.

beaker and carry out the spectrophotometric determination of uranium according to the above procedure. Carry a 100-mL volume of pure water through the evaporation, extraction, and re-extraction procedure to serve as blank. Results evaluated by the method of standard additions, both graphically and numerically, are summarized in Table 3 for three practical samples.

1. S. J. GUSEV and L. M. SCHUROVA. Zh. Anal. Khim. **21**, 1042 (1966).
2. D. A. JOHNSON and T. M. FLORENCE. Anal. Chim. Acta, **53**, 73 (1971).
3. D. A. JOHNSON and T. M. FLORENCE. Talanta, **22**, 253 (1975).
4. P. PAKALNS. Anal. Chim. Acta, **69**, 211 (1974).
5. P. PAKALNS. Mikrochim. Acta, I, 339 (1980).
6. S. ABE and M. TAKAHASHI. J. Radioanal. Nucl. Chem. **90**, 247 (1985).
7. G. XUE. Huaxue Shiji, **6**, 48 (1984).
8. G. XUE. Fenxi Huaxue, **11**, 224 (1983); Anal. Abstr. **46**, 3B59 (1984).
9. D. XUE and Q. LIU. Fenxi Huaxue, **13**, 365 (1985); Anal. Abstr. **48**, 1B44 (1986).
10. I. BRČIC, E. POLLA, and M. RADOŠEVIC. Analyst, **110**, 1249 (1985).
11. S. J. LYLE and M. TAMIZI. Anal. Chim. Acta, **108**, 267 (1979).
12. P. PAKALNS and B. R. MACALLISTERS. Anal. Chim. Acta, **62**, 207 (1972).
13. T. P. LYNCH, A. F. TAYLOR, and J. N. WILSON. Analyst, **108**, 470 (1983).
14. E. A. JONES. Anal. Chim. Acta, **169**, 109 (1985).
15. C. SILFWERBRAND-LINDH, L. NORET, L. G. DANIELSSON, and F. INGMAN. Anal. Chim. Acta, **160**, 11 (1984).
16. S.-C. HUNG, C.-L. QU, and W. SHUI-SHENG. Talanta, **29**, 629 (1982).
17. M. PIŠTĚLKA, B. STOJEK, and J. HAVEL. Coll. Czech. Chem. Commun. **49**, 1974 (1984).

Can. J. Chem. Downloaded from www.nrcresearchpress.com by 176.9.209.113 on 09/07/12
For personal use only.

Cell growth inhibitory dihydrophenanthrene and phenanthrene constituents of the african tree *Combretum caffrum*[1]

GEORGE R. PETTIT,[2] SHEO BUX SINGH, MARGARET L. NIVEN,[3] AND JEAN M. SCHMIDT
Cancer Research Institute and Department of Chemistry, Arizona State University, Tempe, AZ 85287, U.S.A.

Received October 22, 1986[4]

GEORGE R. PETTIT, SHEO BUX SINGH, MARGARET L. NIVEN, and JEAN M. SCHMIDT. Can. J. Chem. **66**, 406 (1988).

Combretum caffrum, a tree in the family Combretaceae, has been found to contain three 9,10-dihydrophenanthrenes (6,7-dihydroxy-2,3,4-trimethoxy; 7-hydroxy-2,3,4,6-tetramethoxy; and 2,7-dihydroxy-3,4,6-trimethoxy) that inhibit (ED_{50} 2.2, 2.8, and 2.6 μg/mL) growth of the murine lymphocytic leukemia cell line. One phenanthrene (7-hydroxy-2,3,4,6-tetramethoxy) was also isolated with similar (ED_{50} 2.0 μg/mL) activity. Structures for each of these substances, including a dihydrophenanthrene (2-hydroxy-3,4,6,7-tetramethoxy-9,10-dihydrophenanthrene), were determined by detailed high resolution nuclear magnetic resonance and mass spectral studies and (or) X-ray crystal structure analysis.

GEORGE R. PETTIT, SHEO BUX SINGH, MARGARET L. NIVEN et JEAN M. SCHMIDT. Can. J. Chem. **66**, 406 (1988).

On a trouvé que le *Combretum caffrum*, un arbre de la famille des Combretaceae, contient trois dihydro-9,10 phénanthrènes (les dihydro-6,7 triméthoxy-2,3,4, hydroxy-7 tétraméthoxy-2,3,4,6 et dihydroxy-2,7 triméthoxy-3,4,6) qui inhibent (ED_{50} 2,2, 2,8 et 2,6 μg/mL) la croissance des cellules de la leucémie lymphocytaire de la murine. On a aussi isolé l'hydroxy-7 tétraméthoxy-2,3,4,6 phénanthrène qui possède une activité semblable (ED_{50} 2,0 μg/mL). Pour déterminer les structures de chacunes de ces substances, y compris celle de l'hydroxy-2 tétraméthoxy-3,4,6,7 dihydro-9,10 phénanthrène, on a fait appel à la résonance magnétique nucléaire à haute résolution, à des études par spectrométrie de masse ainsi que par des analyses de diffraction des rayons-X.

[Traduit par la revue]

Can. J. Chem. Downloaded from www.nrcresearchpress.com by 176.9.209.113 on 09/07/12
For personal use only.

In 1979 we began, in collaboration with the U.S. National Cancer Institute (NCI), a detailed investigation of the South African tree *Combretum caffrum* (Combretaceae) in respect to antineoplastic constituents. Two years later we isolated and determined the structure of combretastatin (**1**), a new substance that caused pronounced astrocyte reversal in the NCI astrocytoma bioassay (2–4). In 1985 the principal antineoplastic constituent of *Combretum caffrum* was found and designated combretastatin A-1 (5). The *cis* stilbene **2** proved to have in vivo activity against the murine P388 lymphocytic leukemia (6) and, most importantly, was found to be the most potent inhibitor of tubulin polymerization so far known, leading to complete inhibition at 1.5 μM concentrations. Some of the fractions accompanying combretastatin A-1 were found to inhibit growth of the PS cell line, and investigation of those leads forms the basis of this report.

As previously described (5), the stem-wood of *Combretum caffrum* was extracted with methylene chloride – methanol, and the methylene chloride fraction, prepared by dilution of the extract with water, was dissolved in 9:1 methanol–water and extracted with hexane. Next, the methanol–water solution was diluted to 3:2 with water and extracted with methylene chloride. The resulting methylene chloride fraction was employed for the original isolation of combretastatin A-1 (5) and as starting point for the present study of PS cell growth inhibitory components. The methylene chloride fraction was further separated by successive gel permeation chromatography in methanol on Sephadex-LH20, and gel partition chromatography on the same substrate using hexane–toluene–methanol (3:1:1), followed by chromatography in hexane – ethyl acetate (17:3) on silica gel. By this means dihydrophenanthrenes **3***a–d* were isolated in 6.49×10^{-4}, 7.14×10^{-4}, 1.3×10^{-5}, and 1.12×10^{-4}% yields respectively. In addition, phenanthrene **4***a* was isolated in 8.69×10^{-4}% recovery. Of these, all but dihydrophenanthrene **3***c* showed acceptable inhibition of the PS cell line with ED_{50} range 2–3 μg/mL.

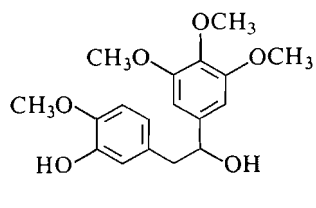

1, Combretastatin

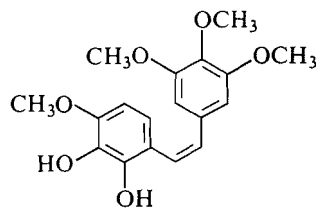

2, Combretastatin A-1

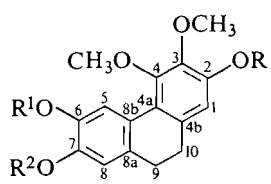

3*a*, R = CH_3, $R^1 = R^2$ = H
b, R = $R^1 = CH_3$, R^2 = H
c, R = H, $R^1 = R^2 = CH_3$
d, R = R^2 = H, $R^1 = CH_3$
e, R = CH_3, $R^1 = R^2 = COCH_3$
f, R = $R^1 = CH_3$, $R^2 = COCH_3$
g, R = $R^2 = COCH_3$, $R^1 = CH_3$

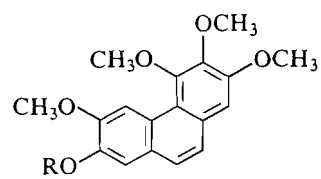

4*a*, R = H
b, R = $COCH_3$

In 1971–1972 Letcher *et al.* (7) at the University of Rhodesia (now Zimbabwe) reported isolation of a series of dihydrophenanthrenes from petroleum ether extracts of *Combretum apiculatum*, *molle*, and *psidioides*. Some of those dihydrophenanthrenes and associated phenanthrenes appeared closely related to the *Combretum caffrum* constituents **3***a–d* and **4***a*. However, we were unable to obtain authentic samples of phenanthrenes **3***a–d* and **4***a* and they had to be approached as new structural problems. A series of coordinated chemical transformations, nmr and mass spectral analyses, and X-ray crystal structure determinations were employed to unequivo-

[1]Antineoplastic Agents 129; for part 128, see ref. 1.

[2]Author to whom correspondence may be addressed.
[3]Department of Physical Chemistry, University of Cape Town, Rondebosch, 7700 South Africa.

[4]Revision received October 26, 1987.

TABLE 1. Dihydrophenanthrene and phenanthrene ^{1}H nmr (400 MHz) chemical shift assignments (δ and multiplicity) relative to tetramethylsilane in deuteriochloroform

Structure position	Compound no.											
	3*a*†	**3***b*	**3***c*	**3***d*	**3***e*	**3***f*	**3***g*	**4***a*‡	**4***b*	**5**	**6**	**7**
1	6.639	6.592	6.635	6.627	6.579	6.588	6.733	7.071	6.963	6.574	6.580	6.392
2	3.885	3.886	5.670	5.620*	3.899	3.889	2.331*	4.004	3.923	3.895	3.910	—
3	3.882	3.923	3.983	3.975	3.887	3.921	3.910	4.035	3.895	3.883	3.890	4.055*
4	3.771	3.773	3.748	3.746	3.773	3.786	3.762	4.023	3.923	3.769	3.780	3.890*
5	7.904	7.967	7.942	7.907	8.156	8.076	8.060	9.065	9.076	—	7.860	7.883
6	—	3.924	3.922*	3.924	2.230	3.865	3.867	4.093	3.923	2.298	5.950	3.901*
7	—	5.625	3.935*	5.700*	2.230	2.325	2.343*	5.950	2.277	2.298		—
8	6.739	6.787	6.738	6.779	7.035	6.886	6.907	7.713	7.385	—	6.720	6.239
9(10)	2.682 (m)	2.698 (m)	2.692 (brs)	2.660 (brs)	2.754 (brs)	2.710 (m)	2.704 (brs)	7.530	7.429	2.750	2.690	2.753
(10)	—	—	—	—	—	—	—	7.490 (d, 8.4)	7.383 (d, 8.7)	—	—	—

*Similar superscript in vertical column may be interchanged.
†Acetone-d_6 as solvent, OH signal could not be seen because of exchange.
‡$CDCl_3$ + C_6D_6.
All signals are singlet unless otherwise stated.

TABLE 2. Dihydrophenanthrene and phenanthrene ^{13}C nmr (100.6 MHz)‡ chemical shift (δ) assignments relative to tetramethylsilane in deuteriochloroform

Structure position	Compound no.										
	3*a*†	**3***b*	**3***c*	**3***d*	**3***e*	**3***f*	**3***g*	**4***a*	**4***b*	**5**	**7**
1	108.92	107.66	110.28[b]	110.42[a]	107.98	107.69	117.59	105.31	105.36	107.50	108.45
2	152.63[a]*	151.59[a]	147.42[a]	147.63	152.67[a]	152.37[a]	142.87	151.72[a]	152.55[a]	152.30[a]	180.28[a]
3	142.69	141.52	139.13	139.11	141.54	141.61	144.40	142.52	142.70	141.63	146.42
4	152.34[a]	151.39[a]	150.49	150.38	152.26[a]	152.02[a]	151.99	151.49[a]	152.05[a]	152.68[a]	153.23
4a	121.86	120.98	120.38	120.43	119.79	120.49	121.42	118.73	118.42	119.79	131.59
4b	130.73[d]	131.28[c]	130.59[c]	131.44[c]	131.22[d]	131.13[c]	131.13[a]	127.70[c]	128.89[b]	131.12	143.75
5	115.68[c]	110.52	111.21[b]	110.48[a]	122.41[c]	112.23	112.78	107.10	108.88	122.12[b]**	126.87[b]
6	144.51[b]	144.08[b]	147.70[a]	144.96[b]	140.34[b]	149.40	149.44	146.78[b]	150.18	139.88[c]	154.11
7	143.89[b]	144.96[b]	147.34[a]	144.05[b]	139.92[b]	137.88	138.58	144.63[b]	138.96	140.30[c]	182.50[a]
8	115.36[c]	113.67	111.00[b]	113.80	121.87[c]	121.54	121.71	111.98	120.94	121.57[b]**	125.15[b]
8a	134.85[d]	134.27[c]	134.05[c]	135.08[c]	136.18[d]	134.85[c]	134.84[a]	129.33[c]	130.28[b]	136.08	146.57
8b	125.27	124.62	130.95[c]	124.58	134.61	130.38	125.96	124.03	126.67	134.60	137.89
9, 10	31.35	29.15	29.38	29.12	29.31	28.84	28.60	124.87	125.03	29.25	29.74
	31.52	30.58	30.36	30.28	30.02	30.48	29.84	126.21	126.23	30.04	30.34
OCH_3C-2	56.31	56.98	—	—	55.89	56.19	—	56.60	55.88	56.01	—
OCH_3C-3	60.89	61.15	61.25	61.22	61.09	61.14	61.01	61.31	61.32	61.09	55.77
OCH_3C-4	60.53	60.57	60.17	60.12	60.73	60.76	60.52	60.37	60.51	60.73	61.12
OCH_3C-6	—	55.98	56.16	56.22	—	56.02	56.24	56.60	55.88	—	55.77
OCH_3C-7	—	—	55.89	—	—	—	—	—	—	—	—

*Chemical shifts with same sign in the vertical columns may be reversed and similar values for the methoxy groups may also be interchanged. Additional signals: acetates (**3***e*) 20.68, 20.70, 168.48, 168.55; (**3***f*) 20.75, 169.27; (**3***g*) 2 × 20.74, 2 × 169.15; (**4***b*) 20.74, 169.19. **t, J_{CD} = 50.0 Hz.
†Acetone-d_6 as solvent.
‡**3***a*, **3***b*, **3***d*, and **4***a* at 22.67 MHz and remainder at 100.62 MHz.

cally assign structures **3***a–d*, their acetate derivatives **3***e–g*, and phenanthrenes **4***a* and **4***b*. For example, dihydrophenanthrenes **3***a* and **3***d* appeared by high resolution electron impact mass spectrometry (HREIMS) to be isomeric with a molecular ion at *m/z* 302 corresponding to molecular formula $C_{17}H_{18}O_5$. No major fragmentation pathways were observed. Acetylation led to isomeric diacetates **3***e* and **3***g*. The high resolution (400 MHz) ^{1}H nmr spectra (Table 1) of phenols **3***a* and **3***d* suggested the presence of signals corresponding to benzylic, phenolic hydroxyl (2), methoxyl (3), and aromatic (3) protons. Detailed interpretation of the ^{1}H nmr (Table 1) and ^{13}C nmr (Table 2) spectra combined with the application of nuclear Overhauser enhancement difference spectroscopy (NOEDS) and 2D-NOESY nmr experiments (Fig. 1) suggested the structures **3***a* and **3***d*. The 6,7-dihydroxy assignment for dihydrophenanthrene **3***a* was further substantiated by a base (potassium *tert*-butoxide in D_2O) catalyzed deuterium exchange reaction that afforded, following acetylation, D-5, D-8-dihydrophenanthrene **5**. The ^{1}H nmr spectrum of deuterium derivative **5** showed absence of the H-5 and H-8 proton signals and the ^{13}C nmr displayed two very weak triplets due to deuterium coupling at δ 121.57 (C-8) and δ 122.12 (C-5) with J = 50 Hz, in the proton noise-decoupled

Can. J. Chem. Downloaded from www.nrcresearchpress.com by 176.9.209.113 on 09/07/12
For personal use only.

Can. J. Chem. Downloaded from www.nrcresearchpress.com by 176.9.209.113 on 09/07/12
For personal use only.

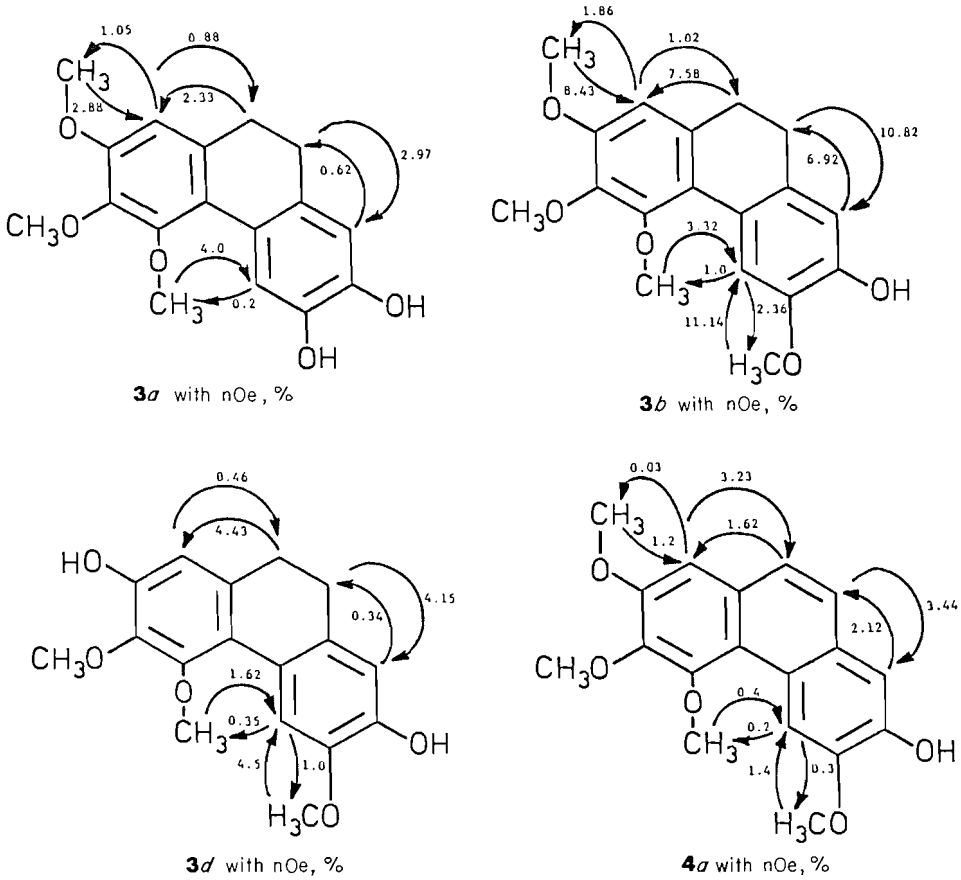

FIG. 1. Summary of nOe and 2D NOESY nmr experiments.

spectrum. Unequivocal proof for the 6,7-dihydroxy orientation was provided by fluoride–hydrogen bonding promoted methylenation of phenol **3***a* with dibromomethane to yield the 6,7-methylene dioxy derivative **6**. Support for the structure of isomer **3***d* was obtained by pyridinium chlorochromate (8) oxidation to the extended quinone **7**. Results of these experiments, combined with the crystal structure determination for the dihydrophenanthrenes **3***b* and **3***c* and subsequent nmr spectral correlations, firmly established the structures of dihydrophenanthrenes **3***a* and **3***d*. Both of these structures had previously been assigned by Letcher (*7a–c*) to *Combretum psidioides* components.

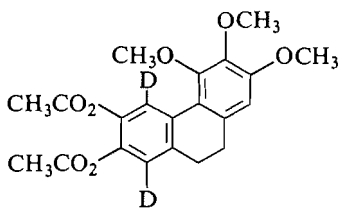

5

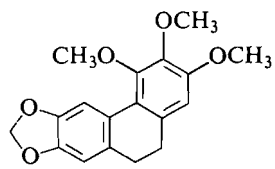

6

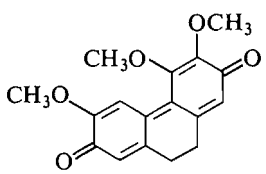

7

Recrystallization of dihydrophenanthrenes **3***b* and **3***c* from hexane–acetone and hexane–2-propanol gave crystalline specimens that yielded to crystal structure determination. Fractional atomic coordinates of both phenols **3***b* and **3***c* are shown in Table 3, with illustrations and atomic numbering given in Figs. 2 and 3 respectively. Relevant molecular parameters are reported in Table 4. Structure **3***b* has been determined much more precisely than structure **3***c*, as evidenced by the standard deviations of the atomic and molecular parameters. Doubtlessly this results from the difference in quality of the crystals. However, we note that the two structures are essentially very similar, with bond lengths and angles of the expected order of magnitude.

Saturation at C(9) and C(10) is clearly apparent from the C(9)—C(10) bond length and the tetrahedral orientation of the angles involving those carbons. The degree of pucker of the C(4a)C(4b)C(10)C(9)C(8a)C(8b) ring is similar in both structures. Consequently, the magnitude of the torsion angles C(4)C(4a)C(8b)C(5), which give a measure of the orientation of the two phenyl rings with respect to each other, are the same. For dihydrophenanthrene **3***b*, O(7)----O(6), measuring 2.665(3) Å within a single molecule, clearly indicates that the hydroxyl hydrogen is involved in intramolecular H-bonding. With the isomer **3***c* there are neither intra- nor inter-molecular close contacts (<3 Å) involving O(2)----O(acceptor); hence we have no evidence for any hydrogen bonding involving the phenolic hydroxyl group of **3***c*.

With the crystal structures of dihydrophenanthrenes **3***b* and **3***c* in hand, the nmr spectral assignments recorded in Tables 1 and 2 were ascertained and confirmed by results of NOEDS

TABLE 3. Fractional atomic coordinates ($\times 10^4$) for non-hydrogen atoms in dihydrophenanthrenes **3***b* and **3***c* and phenanthrene **4***a*

	3*b*			**3***c*			**4***a*		
Atom	*x/a*	*y/b*	*z/c*	*x/a*	*y/b*	*z/c*	*x/a*	*y/b*	*z/c*
C(1)	−635(3)	6969(1)	4485(2)	3891(35)	6973(14)	2567(9)	6187(5)	3463(2)	4253(2)
C(2)	29(4)	6574(1)	3976(2)	2615(36)	6129(13)	2551(9)	5111(6)	3851(2)	3904(2)
C(3)	1037(3)	6797(1)	3423(2)	1617(38)	5664(16)	1956(9)	3746(5)	3606(2)	3514(2)
C(4)	1393(3)	7419(1)	3393(1)	2396(34)	6154(13)	1404(8)	3476(5)	2974(2)	3484(2)
C(4a)	760(3)	7829(1)	3909(1)	3695(34)	6984(14)	1404(8)	4561(5)	2556(2)	3843(2)
C(4b)	−276(3)	7589(1)	4453(1)	4604(37)	7389(13)	1997(8)	5924(5)	2829(2)	4234(2)
C(5)	2473(4)	8772(1)	3592(1)	2848(36)	7378(13)	208(8)	3011(5)	1574(2)	3505(2)
C(6)	2664(4)	9398(1)	3594(1)	3556(37)	7894(14)	−319(8)	2800(6)	950(2)	3583(2)
C(7)	1439(4)	9771(1)	3896(2)	5363(38)	8495(15)	−256(8)	3851(6)	607(2)	4036(2)
C(8)	71(4)	9508(1)	4216(2)	6988(36)	8602(13)	313(7)	5109(6)	899(2)	4392(2)
C(8a)	−138(4)	8878(1)	4233(1)	6258(35)	8094(13)	848(9)	5388(5)	1541(2)	4315(2)
C(8b)	1059(3)	8499(1)	3903(1)	4385(36)	7484(13)	808(8)	4304(5)	1890(2)	3877(2)
C(9)	−1604(4)	8597(1)	4630(2)	7822(35)	8202(13)	1508(8)	6785(6)	1831(2)	4680(2)
C(10)	−1015(4)	8022(1)	5011(2)	6168(34)	8265(13)	2014(8)	7044(6)	2434(2)	4635(2)
O(2)	−192(3)	5952(1)	3973(1)	1999(23)	5691(9)	3103(5)	5215(4)	4477(1)	3892(2)
C(21)	−1231(5)	5695(2)	4519(2)	—	—	—	6574(7)	4762(2)	4276(3)
O(3)	1802(2)	6405(1)	2940(1)	447(23)	4811(9)	1942(5)	2614(4)	4006(1)	3187(1)
C(31)	723(4)	6133(1)	2405(2)	−1822(42)	4889(16)	2071(11)	3046(7)	4142(2)	2489(3)
O(4)	2471(2)	7627(1)	2863(1)	1349(22)	5641(9)	831(5)	2107(4)	2778(1)	3077(1)
C(41)	1841(5)	7650(2)	2146(2)	3096(41)	4949(14)	647(10)	446(6)	2819(2)	3416(3)
O(6)	4004(3)	9711(1)	3304(1)	2166(24)	7839(9)	−929(6)	1590(4)	598(1)	3237(2)
C(61)	5302(4)	9385(2)	2966(2)	245(37)	7158(13)	−1020(9)	374(8)	898(2)	2808(3)
O(7)	1594(3)	10398(1)	3886(1)	5880(26)	8959(9)	−823(6)	3611(4)	−18(1)	4111(2)
C(71)	—	—	—	7814(37)	9637(14)	−800(10)	—	—	—

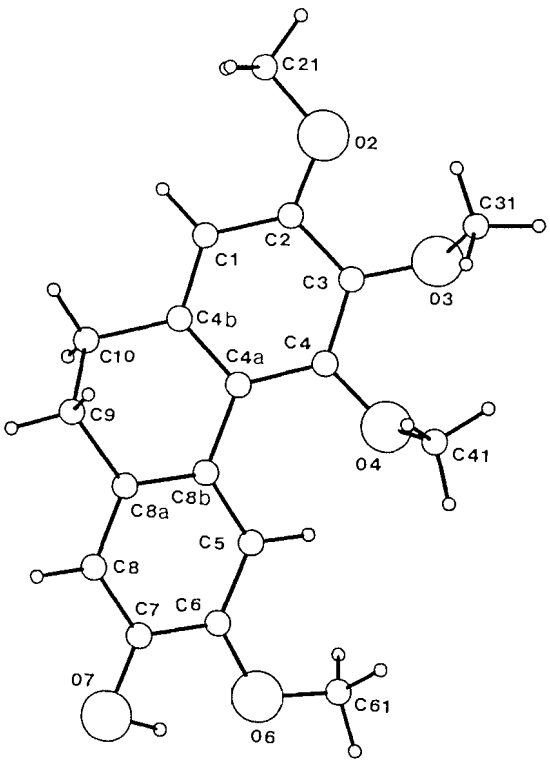

FIG. 2. 7-Hydroxy-2,3,4,6-tetramethoxy-9,10-dihydrophenanthrene (**3***b*).

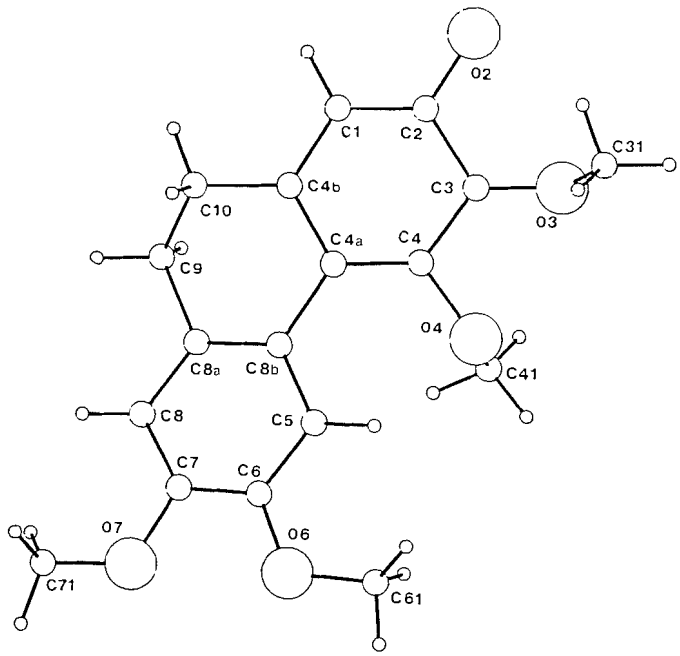

FIG. 3. 2-Hydroxy-3,4,6,7-tetramethoxy-9,10-dihydrophenanthrene (**3***c*).

experiments (cf. Fig. 1). Structure **3***b* has previously been assigned to a component of *Combretum psidioides* by Letcher (ref. 7*c*) but dihydrophenanthrene **3***c* proved to be a completely new structure. In turn, these structural assignments allowed ready access to the structure of phenanthrene **4***a*. The substituent pattern was found analogous to that in dihydrophenanthrene **3***b* and this was further corroborated by NOEDS experiments in deuteriobenzene–deuteriochloroform. The deuteriobenzene-induced shifts in the aromatic region were very useful. Irradiation of the methoxyl groups at δ 4.093 and 4.023 produced enhancement at δ 9.065 corresponding to the C-5 hydrogen. Analogous treatment of the methoxyl group at δ 4.004 attached to the C-2 carbon enhanced the C-1 proton at δ 7.071, thereby allowing assignment of the δ 7.713 chemical

Can. J. Chem. Downloaded from www.nrcresearchpress.com by 176.9.209.113 on 09/07/12
For personal use only.

TABLE 4. Relevant molecular parameters for dihydrophenanthrenes **3***b* and **3***c* and phenanthrene **4***a*

	3*b*	**3***c*	**4***a*
Bond lengths (Å)			
C—C(aryl)	1.367(4)–1.401(3)	1.34(3)–1.45(3)	1.326(6)–1.460(6)
C(aryl)—O	1.373(3)–1.378(3)	1.33(3)–1.42(2)	1.361(5)–1.382(5)
O—C(methyl)	1.403(4)–1.437(4)	1.34(3)–1.45(3)	1.408(7)–1.438(6)
C(4a)—C(8b)	1.486(3)	1.51(3)	Included in C—C(aryl)
C(8a)—C(9)	1.510(4)	1.55(2)	
C(4b)—C(10)	1.517(4)	1.48(3)	
C(9)—C(10)	1.516(4)	1.50(3)	
Bond angles (°)			
C—C—C(aryl)	117.2(2)–121.8(2)	111(2)–127(2)	115.4(4)–125.2(4)
O—C(aryl)–C(aryl)	114.1(2)–125.4(2)	115(2)–125(2)	113.4(4)–126.2(4)
C(methyl)–O—C(aryl)	115.8(2)–119.4(3)	108(1)–120(2)	113.7(3)–118.5(3)
C(4a)—C(8b)—C(8a)	118.1(2)	120(2)	Included in C—C—C(aryl)
C(8b)—C(4a)—C(4b)	118.1(2)	117(2)	
C(8b)—C(8a)—C(9)	119.7(2)	118(2)	
C(4a)—C(4b)—C(10)	118.6(2)	119(2)	
C(8a)—C(9)—C(10)	108.8(3)	107(2)	
C(4b)—C(10)—C(9)	109.0(3)	111(2)	
Torsion angles			
C(4)—C(4a)—C(8b)—C(5)	−27.0(4)	28(3)	5.5(7)
Ring pucker			
C(4a)—C(4b)—C(10)—C(9)—C(8a)—C(8b) total puckering amplitude	0.540(3)	0.52(2)	Not relevant
θ^2	69.3(3)	115(2)	
Planes of rings			
Angles (°) between normals to the ring planes			
C1—C2—C3—C4—C4a—C4b and C5—C6—C7—C8—C8a—C8b	25.80(6)	155.8(6)	7.1
C1—C2—C3—C4—C4a—C4b and C9—C10—C4b—C4a—C8b—C8a	Not relevant		4.5(1)
C5—C6—C7—C8—C8a—C8b and C9—C10—C4b—C4a—C8b—C8a	Not relevant		2.9(1)

shift to the C-8 hydrogen. Furthermore, irradiation of the C-1 proton enhanced the C-10 proton at δ 7.490 and, similarly, irradiation of the C-8 hydrogen at δ 7.713 was felt by the C-9 hydrogens at δ 7.530. A summary of these experiments has been displayed in Fig. 1.

Undebatable evidence for structure **4***a* was achieved by an X-ray crystal structure determination. Fractional atomic coordinates of phenanthrene **4***a* are reported in Table 3, with an illustration and atomic numbering given in Fig. 4. Relevant molecular parameters are given in Table 4. All bond lengths and angles of phenanthrene **4***a* were the expected order of magnitude. The short C(9)—C(10) bond length of 1.326(6) Å confirms the unsaturation of that bond. As expected, all three rings of the structure are planar, with angles between the normals to the ring planes small, giving the molecule some overall degree of planarity. The O(7)....O(6) nonbonded distance of 2.653(5) Å indicates that the hydroxyl hydrogen was most likely involved in intramolecular hydrogen bonding. Phenanthrene **4***a* has been proposed as a component of *Combretum psidioides* (ref. 7*c*).

Presently, investigation of *Combretum caffrum* constituents suggests a biosynthetic pathway proceeding from shikimic acid and tyrosine to the bibenzyl, styrene, dihydrophenanthrene, and phenanthrene systems illustrated by structures **1**, **2**, **3**, and **4**. On the assumption that dihydrophenanthrenes **3***a*, *b*, and *d* and phenanthrene **4***a* owe their PS cell growth inhibitory properties primarily to their phenol substituents, it would appear that the intermediary metabolites (cf. **1** and **2**) possess the most potent biological properties in this plant genus. Pertinent to this point was the recent observation that the 9,10-dihydrophenanthrene juncusol (from *Juncus roemerianus*, Juncaseae), the antimicrobial and cell growth inhibitory (KB, human epidermoid carcinoma of the nasal nasopharynx), may display those biological properties due to its phenolic substituents as indicated by structure/activity relationships (9). Eventually, when sufficient quantities of dihydrophenanthrenes **3***a–d* become available for in vivo antineoplastic and other biological evaluations, their potential will be more clearly ascertained. Regardless of the outcome, the present unequivocal structure elucidations of dihydrophenanthrenes **3***a–d* and phenanthrene **4***a* provide a very secure foundation for solving future structure problems in this area of phenanthrene biosynthetic products.

Can. J. Chem. Downloaded from www.nrcresearchpress.com by 176.9.209.113 on 09/07/12
For personal use only.

Can. J. Chem. Downloaded from www.nrcresearchpress.com by 176.9.209.113 on 09/07/12
For personal use only.

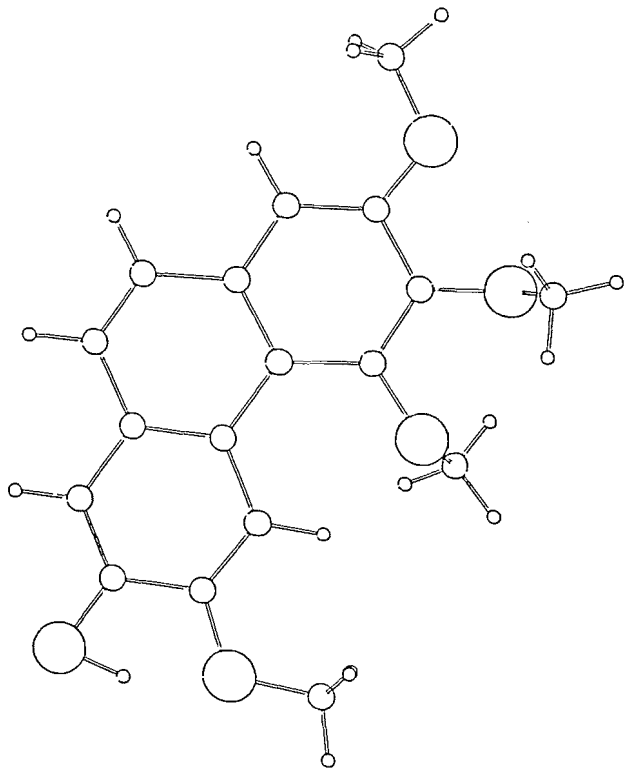

FIG. 4. 7-Hydroxy-2,3,4,6-tetramethoxy-phenanthrene (**4***a*).

Experimental

The general experimental techniques and instruments employed in this study have been summarized in ref. 5. Multiplicities in carbon spectra were determined by SFORD. Nuclear Overhauser effect difference spectroscopy (NOEDS) experiments were conducted by Dr. R. A. Nieman using an 8–12 mmol/L sample size in deuteriochloroform or deuteriobenzene–deuteriochloroform degassed (×6) by the freeze–thaw technique. In each of the nOe experiments measurements were conducted over long time intervals with variable irradiating power, decoupling time, and recovery delay. Since the T_1 for these experiments were not measured, relative enhancements between different irradiations and experiments cannot be compared.

Isolation and characterization procedures

A 77-kg (dry weight) amount of stem-wood from the South African tree *Combretum caffrum* (Eckl. and Zeyh) Kuntze was extracted with methylene chloride – methanol (1:1) and converted to a methylene chloride fraction as briefly summarized in the discussion section of this communication and in detail in our ref. 5. The methylene chloride fraction weighed 827.9 g and was further separated by gel permeation chromatography in methanol on Sephadex LH-20. Two of the fractions (A, 28.6 g, PS ED_{50} 0.36 μg/mL and B, 30.6 g, ED_{50} 0.18 μg/mL) obtained following the removal of the combretastatins (**1** and **2**) were subjected individually to partition chromatography in 3:1:1 hexane–toluene–methanol on columns of Sephadex LH-20. By that method, fraction A provided 0.50 g of *6,7-dihydroxy-2,3,4-trimethoxy-9,10-dihydrophenanthrene* (**3***a*, PS ED_{50} 1.4, 2.2 μg/mL) as a colorless powder from hexane–acetone and broad-shaped crystals from methanol melting at 212–214°C (lit. (7*a*, *b*) mp 207–210°C); R_f 0.405 (silica gel with methylene chloride – methanol–water, 88:12:1), 0.42 (benzene – methylene chloride – methanol–water, 10:80:10:1), 0.38 (methylene chloride – methanol, 9:1), 0.25 (methylene chloride – methanol, 94:6); uv (CH_3OH) λ_{max} (log ε): 227 (4.35), 280 (4.24), 314 (4.14) μm; ir (NaCl) ν_{max}: 3360, 1596, 1512, 1490, 1448, 1405, 1102, and 1075 cm^{-1}; HREIMS, *m/z* (rel. int. %): 302.1154 (100, M^+, calcd. for $C_{17}H_{18}O_5$: 302.1154); 287.0915 (14, M − CH_3, $C_{16}H_{15}O_5$); 269.0812 (11, $C_{16}H_{13}O_4$); 244.0734 (7, $C_{14}H_{12}O_4$). The ^1H nmr and ^{13}C nmr data have been recorded in Tables 1 and 2.

The 1.47-g fraction remaining from the original fraction A, following isolation of dihydrophenanthrene **3***a*, was rechromatographed on Sephadex LH20 employing hexane–toluene–methanol (3:1:1) followed by further separation in hexane – ethyl acetate (4:1) on a column of silica gel to afford 66.9 mg (PS ED_{50} 2.0 μg/mL) of *7-hydroxy-2,3,4,6-tetramethoxyphenanthrene* (**4***a*), which recrystallized from hexane–chloroform as prisms melting at 176–178°C (lit. (7*c*) mp 176–178°C); PS ED_{50} 2.0 μg/mL; R_f 0.40 (1:1 hexane – ethyl acetate); uv (CH_3OH) λ_{max} (log ε): 223 (4.39), 258 (4.86), 281 (4.56), 307 (4.06) μm; ir (NaCl) ν_{max}: 3400, 1504, 1479, 1465, 1421, 1408, 1274, 1233, 1210, 1123, and 1081 cm^{-1}; ^1H nmr and ^{13}C nmr, Tables 1 and 2; HREIMS, *m/z* (rel. int. %): 314.1159 (100, M^+, calcd. for $C_{18}H_{18}O_5$: 314.1154); 300.0987 (30, $C_{17}H_{16}O_5$); 299.0921 (44, $C_{17}H_{15}O_5$); 271.0973 (20, $C_{16}H_{15}O_4$); 256.0738 (30, $C_{15}H_{12}O_4$); 213.0553 (13, $C_{13}H_9O_3$); 185.0600 (13, $C_{12}H_9O_2$).

Parallel separation of fraction B by partition chromatography in 3:1:1 hexane–toluene–methanol on a column of Sephadex LH-20 afforded three fractions containing dihydrophenanthrenes. The first, weighing 1.46 g, was recrystallized from hexane–acetone to yield 50 mg (PS ED_{50} 2.8 μg/mL) of *7-hydroxy-2,3,4,6-tetramethoxy-9,10-dihydrophenanthrene* (**3***b*) melting at 171–172°C (lit. (7*c*) mp 156–158°C) upon recrystallization (needles) from hexane–acetone; R_f 0.69 (47:3 methylene chloride – methanol), 0.57 (1:1 hexane – ethyl acetate); uv (CH_3OH) λ_{max} (log ε): 222 (4.52), 281 (4.26), 303 (4.14), 314 (4.13) μm; ir (NaCl) ν_{max}: 3400, 1592, 1507, 1491, 1456, 1402, 1269, 1124, 1082, 1050, and 1005 cm^{-1}; ^1H nmr and ^{13}C nmr data appear in Tables 1 and 2; HREIMS, *m/z* (rel. int. %): 316.1303 (100%, M^+, calcd. for $C_{18}H_{20}O_5$: 316.1311); 269.0801 (24, $C_{16}H_{13}O_4$). The mother liquors from these recrystallizations were combined and chromatographed in 17:3 hexane – ethyl acetate on a column of silica gel to furnish another 0.50 g of dihydrophenanthrene **3***b*.

The next fraction (2.41 g) obtained from original fraction B was subjected to gradient elution chromatography (×2) in hexane – ethyl acetate on a column of silica gel to provide 10 mg (PS ED_{50} 17 μg/mL) of *2-hydroxy-3,4,6,7-tetramethoxy-9,10-dihydrophenanthrene* (**3***c*) that recrystallized from hexane-2-propanol as colorless needles, mp 177–180°C; R_f 0.56 (1:1 hexane – ethyl acetate); uv (CH_3OH) λ_{max} (log ε): 223 (4.52), 282 (4.32), 313 (4.19) μm; ir (NaCl) ν_{max}: 3420, 1587, 1514, 1482, 1457, 1450, 1437, 1399, 1220, 1116, and 1039 cm^{-1}; ^1H nmr and ^{13}C nmr, see Tables 1 and 2; HREIMS, *m/z* (rel. int.%): 316.1311 (100, M^+, calcd. for $C_{18}H_{20}O_5$: 316.1311); 301.1076 (28, M − CH_3, $C_{17}H_{17}O_5$); 270.0891 (16, M − CH_3 − CH_3O, $C_{16}H_{14}O_4$).

The third fraction (0.57 g) prepared from the initial fraction B was separated by gradient elution in hexane – ethyl acetate on a column of silica gel to afford 86.4 mg (PS ED_{50} 2.6 μg/mL) of *2,7-dihydroxy-3,4,6-trimethoxy-9,10-dihydrophenanthrene* (**3***d*). Recrystallization from hexane–chloroform yielded needles melting at 112–114°C (lit. (7*c*) mp 111–113°C); R_f 0.54 (1:1 hexane – ethyl acetate); uv (CH_3OH) λ_{max} (log ε): 223 (4.57), 281 (4.40), 3.5 (4.26) μm; ir (NaCl) ν_{max}: 3400, 1592, 1509, 1485, 1459, 1446, 1437, 1280, 1272, 1206, and 1114 cm^{-1}; ^1H nmr and ^{13}C nmr, see Tables 1 and 2; HREIMS, *m/z* (rel. int. %): 302.1162 (100, M^+, calcd. for $C_{17}H_{18}O_5$: 302.1154); 287.0928 (17, M^+ − CH_3, $C_{16}H_{15}O_5$).

Acetylation of phenols **3**a, **3**b, **3**d, *and* **4**a

A solution of the phenol (5–25 mg) in pyridine (0.25–0.5 mL) – acetic anhydride (0.5–0.75 mL) was allowed to remain at room temperature for 72 h. After addition of methanol the solvent was evaporated (cyclohexane was added to form an azeotropic mixture) under reduced pressure. The residue in 1:1 hexane – ethyl acetate was chromatographed on a column of silica gel contained in a pipette. The ^1H nmr and ^{13}C nmr data for each of the acetates have been included as part of Tables 1 and 2. The following pure acetyl derivatives were obtained: *6,7-diacetoxy-2,3,4-trimethoxy-9,10-dihydrophenanthrene*

TABLE 5. Crystal data, experimental details of data collections, and refinement parameters for dihydrophenanthrenes **3***b*, **3***c* and phenanthrene **4***a*

Parameter	Compound no. **3***b*	**3***c*	**4***a*
Molecular formula	$C_{18}H_{20}O_5$	$C_{18}H_{20}O_5$	$C_{18}H_{18}O_5$
M_r (g mol^{-1})	316.35	316.35	314.35
Space group	*Pbca*	$P2_1/c$	*Pbca*
a (Å)	7.975(2)	5.641(2)	7.699(4)
b (Å)	21.890(2)	13.541(9)	21.692(6)
c (Å)	18.410(2)	20.95(2)	19.25(1)
β (°)		97.0(2)	
V (Å^3)	3213.9(9)	1588(6)	3215(3)
Z	8	4	8
D_c (mg m^{-3})	1.31	1.32	1.30
Crystal dimensions (mm)	0.23 × 0.25 × 0.38	0.02 × 0.25 × 0.78	0.19 × 0.50 × 0.56
Scan width in ω (°)	(0.63 + 0.35 tan θ)	(0.73 + 0.35 tan θ)	(0.54 + 0.35 tan θ)
Vertical aperture (mm)	4	4	4
Aperture width (mm)	(1.10 + 1.05 tan θ)	(1.94 + 1.05 tan θ)	(1.27 + 1.05 tan θ)
Final acceptance limit	20σ at 20° min^{-1}	20σ at 20° min^{-1}	20σ at 20° min^{-1}
Maximum recording time (s)	40	40	40
Stability of standard reflections (%)	<1	<1	<1.5
Range of reflections (θ)	1–25	1–23	1–25
No. of reflections collected	2495	1382*	2082
No. of reflections observed (with $I_{rel} > 2\sigma I_{rel}$)	1674	569	1330
F(000)	1344	672	1328
μ(MoKα) (cm^{-1})	0.888	0.897	0.885
Number of variables	227	107	226
$R = \Sigma\|\|F_o\| - \|F_c\|\|/\Sigma\|F_o\|$	0.045	0.095	0.047
$Rw = \Sigma w^{1/2}\|\|F_o\| - \|F_c\|\|/\Sigma w^{1/2}\|F_o\|$	0.041	0.083	0.046
w	$(\sigma^2 F)^{-1}$	$(\sigma^2 F)^{-1}$	$(\sigma^2 F)^{-1}$
Maximum Δ/σ in final cycle	0.5	0.4	0.5
Maximum/minimum resid. elec. density and location	0.24/−0.18 smeared near O7	0.51/−0.40 smeared near O2	0.18/−0.18 between C3 and C4

*Few data obtained because of CAD-4 routine, which skips very weak reflections; weakness of reflections arising from poor mosaicity and shape of crystal.

(**3***e*) crystallized as plates from methanol: mp 137.5–139.5°C (lit. (7*a*, *b*) mp 130–133°C); R_f 0.51 (1:1 hexane – ethyl acetate), 0.26 (7:3 hexane – ethyl acetate); ir (NaCl) ν_{max}: 1772, 1598, 1491, 1413, 1371, 1210, 1168, 1114, 1082, and 1045 cm^{-1}; HREIMS, *m/z* (rel. int. %): 386.1363 (23, M$^+$, calcd. for $C_{21}H_{22}O_7$: 386.1366); 344.1254 (39, M$^+$ − CH_2CO, $C_{19}H_{20}O_6$); 302.1150 (100, M$^+$ − 2 × CH_2CO, $C_{17}H_{18}O_5$).

Recrystallization of *7-acetoxy-2,3,4,6-tetramethoxy-phenanthrene* (**4***b*) from methanol gave colorless flakes melting at 137–140°C (lit. (7*c*) mp 138–140°C); R_f 0.52 (1:1 hexane – ethyl acetate), 0.26 (7:3 hexane – ethyl acetate); ir (NaCl) ν_{max}: 1767, 1512, 1505, 1470, 1434, 1254, 1241, 1213, 1198, and 1121 cm^{-1}; HREIMS, *m/z* (rel. int. %): 356.1273 (38, M$^+$, calcd. for $C_{20}H_{20}O_6$: 356.1260); 314.1128 (100, M$^+$ − CH_2CO, $C_{18}H_{18}O_5$); 300.0998 (14, $C_{17}H_{16}O_5$); 299.0934 (41, $C_{17}H_{15}O_5$).

A fine powder was obtained by recrystallization of 7-acetoxy-2,3,4,6-tetramethoxy-9,10-dihydrophenanthrene (**3***f*) from methanol; mp 115–116°C (lit. (7*c*) mp 115–116°C); R_f 0.58 (1:1 hexane – ethyl acetate), 0.34 (7:3 hexane – ethyl acetate); ir (NaCl) ν_{max}: 1765, 1453, 1398, 1240, 1219, 1196, 1144, 1120, 1083, and 1052 cm^{-1}; HREIMS, *m/z* (rel. int. %): 358.1408 (22, M$^+$, calcd. for $C_{20}H_{22}O_6$: 358.1416); 316.1306 (100, M$^+$ − CH_2CO, $C_{18}H_{20}O_5$); 269.0816 (10, $C_{16}H_{13}O_4$).

A specimen of 2,7-diacetoxy-3,4,6-trimethoxy-9,10-dihydrophenanthrene (**3***g*) crystallized from hexane – diethyl ether as an amorphous powder melting at 111–113°C (lit. (7*c*) mp 110–112°C); R_f 0.57 (1:1 hexane – ethyl acetate), 0.30 (7:3 hexane – ethyl acetate); ir (NaCl) ν_{max}: 1765, 1506, 1397, 1242, 1216, 1198, 1068, and 1017 cm^{-1}; HREIMS, *m/z* (rel. int. %): 386.1363 (15, M$^+$, calcd. for $C_{21}H_{22}O_7$: 386.1366); 344.1251 (24, M − CH_2CO, $C_{19}H_{20}O_6$); 302.1144 (100, M − 2 × CH_2CO, $C_{17}H_{18}O_5$).

*Crystal structure determinations for 7-hydroxy-2,3,4,6-tetramethoxy-9,10-dihydrophenanthrene (**3**b), 2-hydroxy-3,4,6,7-tetramethoxy 9,10-dihydrophenanthrene (**3**c), and 7-hydroxy-2,3,4,6-tetramethoxy-phenanthrene (**4**a)*

For each structure the crystal most suitable was selected and irradiated with MoKα (λ = 0.7107 Å) radiation, using an Enraf–Nonius CAD-4 diffractometer. Cell parameters were obtained by least-squares analysis of the setting angles of 24 reflections. During the data collections, intensities of three standard reference reflections were monitored every hour and centering checked every 100 measured reflections. Intensities were corrected by Lorentz and polarization effects but not for absorption.

Each structure was solved by direct methods using a preliminary version of SHELX-S-84[5] and refined using SHELX-76 (11). For phenol **3***c*, the poor quality of the crystal resulted in a paucity of data, which precluded anisotropic treatment, and the non-hydrogen atoms were modelled with isotropic thermal motion. For each structure, aromatic-H and methylene-H atoms were placed in calculated positions with a single temperature factor. All hydrogen atoms in the methyl groups were refined as rigid units, again with a single temperature

[5]G. M. Sheldrick. SHELX-S-84. Direct methods program. Private communication (1983).

Can. J. Chem. Downloaded from www.nrcresearchpress.com by 176.9.209.113 on 09/07/12
For personal use only.

Can. J. Chem. Downloaded from www.nrcresearchpress.com by 176.9.209.113 on 09/07/12
For personal use only.

factor. With phenol **3***b* and phenanthrene **4***a*, the hydroxyl hydrogen was placed as located in the difference map and constrained to ride at 1.00(1) Å from the parent oxygen and at 1.60(1) Å from the adjacent O-(CH_3) group to comply with appropriate H-bonding considerations. In both cases, its final position was acceptable in all respects except for a high isotropic temperature factor. For phenol **3***c* no hydroxyl hydrogen could be located and has therefore been omitted from the structure factor calculation. A weighting scheme, $(\sigma^2 F)^{-1}$ was employed in the final refinements. The program PARST (12) was used for calculations concerning molecular geometry and PLUTO[6] for illustrations. Complex neutral-atom scattering factors were taken from Cromer and Mann (13) for the C and O atoms and from Stewart, Davidson, and Simpson (14) for H, with dispersion corrections from Cromer and Liberman (15). All computations were carried out using a SPERRY 1100 computer. Further details of the data collections, solutions, and refinement of the structures are given in Table 5.[7]

*6,7-Diacetoxy-2,3,4-trimethoxy-5,8-dideuterio-9,10-dihydrophenanthrene (**5**)*

A mixture prepared from deuterium oxide (3 mL), potassium *tert*-butoxide (50 mg), and phenol **3***a* (45.2 mg) was heated at 110°C (sealed tube) for 48 h. After cooling to room temperature and evaporation of the water phase the residue was acetylated with pyridine (1 mL) – acetic anhydride (1 mL) for 1 day at room temperature. The mixture was treated with ice-water, and acetate was extracted with diethyl ether. The ethereal solution was washed successively with water, dilute hydrochloric acid, water, saturated sodium bicarbonate solution, and water. Evaporation of the dry (anhydrous sodium sulfate) solvent and crystallization of the residue from methanol afforded (46 mg) deuterium derivative **5** melting at 135°C. For ^{1}H nmr and ^{13}C nmr data see Tables 1 and 2; HREIMS, *m/z* (rel. int. %): 388.1508 (M^+, 17%, calcd. for $C_{21}H_{20}O_7D_2$: 388.1491); 346.1384 (38, calcd. for $C_{19}H_{18}O_6D_2$: 346.1385); 304.1281 (100, calcd. for $C_{17}H_{16}O_5D_2$: 304.1280).

*6,7-Methylenedioxy-2,3,4-trimethoxy-9,10-dihydrophenanthrene (**6**)*

A solution of phenol **3***a* (5 mg) in dimethylformamide (1 mL) containing cesium fluoride (12.5 mg) (10) was stirred at room temperature under argon for 10 min. At that point dibromomethane (1.15 μL) was added and the mixture heated at 110°C for 3 h (tlc examination indicated completion). Upon cooling to room temperature the residue was triturated with diethyl ether (20 mL) and the ethereal solution was washed with water (20 mL), dried (sodium sulfate), and concentrated. A pure specimen of ether **6** (2 mg) was isolated from the crude product by preparative tlc on silica gel (1:1 hexane – ethyl acetate) and recrystallization from acetone to give a powder melting at 127–129°C; ir (NaCl) ν_{max}: 1595, 1483, 1463, 1454, 1423, 1408, 1243, 1216, 1137, 1102, and 1039 cm^{-1}; HREIMS, *m/z* (rel. int. %): 314.1154 (M^+, 100%, calcd. for $C_{18}H_{18}O_5$: 314.1154).

*3,4,6-Trimethoxy-9,10-dihydrophenanthrene-2,7-quinone (**7**)*

A solution of phenol **3***d* (10 mg, 0.03 mmol) in methylene chloride (1 mL) was added to a solution prepared from pyridinium chlorochromate (ref. 8, 12.9 mg, 0.06 mmol) and sodium acetate (5 mg, 0.06 mmol). After filtering through a pipette column filled with silica gel and elution with methylene chloride, evaporation of solvent yielded a red powder (9.0 mg), mp 131–135°C; uv (CH_3OH) λ_{max} (log ε): 221 (4.37), 282 (4.10), 312 (3.97), 426 (3.38) μm; ir (NaCl) ν_{max}: 1634, 1603, 1576, 1560, 1545, 1437, 1259, 1216, 1178, and 1142 cm^{-1}; ^{1}H nmr and ^{13}C nmr, see Tables 1 and 2; HREIMS, *m/z* (rel. int. %): 300.1004 (M^+, 16, calcd. for $C_{17}H_{16}O_5$: 300.0997).

Acknowledgments

We wish to thank for financial assistance the Arizona Disease Control Research Commission, Eleanor W. Libby, the Waddell Foundation (Donald Ware), the Fannie E. Rippel Foundation, Herbert K. and Dianne Cummings, the Nathan Cummings Foundation, Inc., Mrs. Lotte Flugel, Mrs. Polly J. Trautman, and Grant CA-30311-01A3 awarded by the National Cancer Institute. For other assistance we are pleased to thank Drs. D. L. Doubek and M. I. Suffness and Mr. Phillip J. Daschner. In addition, M.L.N. is grateful for financial support from the Research Grants Committee, UCT, and the CSIR, and we also acknowledge assistance from the NSF Regional Instrumentation Facility in Nebraska (Grant CHE-8211164) and an NSF NMR equipment grant (CHE-8409644).

1. J. S. Ramsdell, G. R. Pettit, and A. H. Tashjian, Jr. J. Biol. Chem. **261**, 17073 (1986).
2. G. R. Pettit, G. M. Cragg, D. L. Herald, J. M. Schmidt, and P. Lohavanijaya. Can. J. Chem. **60**, 1374 (1982).
3. G. R. Pettit, S. B. Singh, and G. M. Cragg. J. Org. Chem. **50**, 3404 (1985).
4. G. R. Pettit, S. B. Singh, and G. M. Cragg. J. Nat. Prod. **50**, 386 (1987).
5. G. R. Pettit, S. B. Singh, M. L. Niven, E. Hamel, and J. M. Schmidt. J. Nat. Prod. **50**, 119 (1987).
6. J. M. Schmidt and G. R. Pettit. Experientia, **34**, 659 (1978).
7. (*a*) R. M. Letcher and L. R. M. Nhamo. J. Chem. Soc. 3071 (1971); (*b*) R. M. Letcher, L. R. M. Nhamo, and I. T. Gumiro. J. Chem. Soc. Perkin Trans. 1, 206 (1972); (*c*) R. M. Letcher and L. R. M. Nhamo. J. Chem. Soc. Perkin Trans. 1, 2941 (1972); (*d*) J. Chem. Soc. Perkin Trans. 1, 1179 (1973).
8. G. Piancatelli, A. Scettri, and M. D'Auria. Synthesis, 245 (1982).
9. D. L. Boger, L. A. Mitscher, M. D. Mullican, S. D. Drake, and P. Kitos. J. Med. Chem. **28**, 1543 (1985).
10. J. H. Clark, H. L. Holland, and J. M. Miller. Tetrahedron Lett. 3361 (1976).
11. G. M. Sheldrick. SHELX-76. *In* Computing in crystallography. *Edited by* H. Schenk, R. Olthof-Hazekamp, H. van Koningsveld, and G. C. Bassi. Delft University Press, Delft, The Netherlands. 1978. pp. 34–42.
12. M. Nardelli. Comput. Chem. **7**, 95 (1983).
13. D. T. Cromer and J. B. Mann. Acta Crystallogr. Sect. A: Cryst. Phys. Diffr. Theor. Gen. Crystallogr. **24**, 321 (1968).
14. R. F. Stewart, E. R. Davidson, and W. T. Simpson. J. Chem. Phys. **42**, 3175 (1965).
15. D. T. Cromer and D. Liberman. J. Chem. Phys. **53**, 1891 (1970).

[6]W. D. S. Motherwell. PLUTO Plotting program. Cambridge University, England. Unpublished.

[7]H atom coordinates, temperature factors, and structure factors may be purchased from the Depository of Unpublished Data, CISTI, National Research Council of Canada, Ottawa, Ont., Canada K1A 0S2.

Anwuweizonic acid and manwuweizic acid, the putative anticancer active principle of *Schisandra propinqua*

JIA-SEN LIU,[1] MEI-FEN HUANG, AND YONG TAO

Shanghai Institute of Materia Medica, Academia Sinica, 319 Yue-Yang Rd., Shanghai 200031, China

Received August 14, 1987

This paper is dedicated to the memory of Professor Karel Wiesner

JIA-SEN LIU, MEI-FEN HUANG, and YONG TAO. Can. J. Chem. **66**, 414 (1988).

The structures of two new triterpenoid acids, anwuweizonic acid (**1**) and manwuweizic acid (**2**), from *Schisandra propinqua* are elucidated by spectroscopic evidence and chemical correlation. Compound **2** shows significant inhibitory activity against Lewis lung cancer, brain tumor-22, and solid hepatoma in mice, and exhibits no cytotoxic action in vitro.

JIA-SEN LIU, MEI-FEN HUANG et YONG TAO. Can. J. Chem. **66**, 414 (1988).

Faisant appel à des données spectroscopiques et à des corrélations chimiques, on a élucidé les structures de deux nouveaux acides, les acides anwuweizonique (**1**) et manwuweizique (**2**), qui ont été isolés du *Schisandra propinqua*. Le composé **2** présente une activité inhibitrice importante vis-à-vis du cancer des poumons de Lewis, du tumeur 22 du cerveau et de l'hépatome solide chez la souris et il ne présente pas d'activité cytotoxique in vitro.

[Traduit par la revue]

Can. J. Chem. Downloaded from www.nrcresearchpress.com by 176.9.209.113 on 09/07/12
For personal use only.

It has been reported that Manshanxiang Complex, a herbal medicine preparation in which the stems and roots of *Schisandra propinqua* (Wall.) Hook. f. et Thoms are a major component, was used for treatment of lung carcinoma in several hospitals of Yunnan Province in China (1), and that the water extract from the stems and roots of *S. propinqua* shows activity against Lewis lung cancer in animal tests (2). To isolate the active principle, we started chemical studies on this plant. Two new triterpenoid acids, anwuweizonic acid (**1**) and manwuweizic acid (**2**), were isolated from its alcoholic extract and the second (**2**) exhibits significant inhibitory activity against Lewis lung cancer, brain tumor-22, and solid hepatoma in mice and shows no cytotoxic action in vitro.[2] Therefore, **2** is probably a major anticancer active principle of the plant under study. In this paper we wish to report the structural elucidation of the two acids.

Anwuweizonic acid (**1**), $C_{30}H_{46}O_3$, gave a monoester on reaction with diazomethane. The ^1H nmr spectrum of **1** reveals the presence of a moiety of the angelic acid terminal (3) (δ 6.10, 1H, t, J = 7, H-24; δ 1.94, 3H, s, H-27), a secondary methyl (δ 0.92, 3H, d, J = 5, H-21), and five tertiary methyls (δ 0.72, 0.90, 1.10, 1.14, 3H, 3H, 6H, 3H each, s), and its ir spectrum shows the characteristics of an α,β-unsaturated acid (1690, 3200–2500 cm^{-1}) and a ketone (1710 cm^{-1}). These features closely resemble those of anwuweizic acid (**3**) (4) except for the ketone group of **1** in place of a hydroxyl in **3**, suggesting that anwuweizonic acid possesses structure **1**. This proposal was verified by reduction of **1** with sodium borohydride in methanol, providing anwuweizic acid (**3**, 8% yield) and its 3β-hydroxyl isomer (85% yield).

Manwuweizic acid (**2**), $C_{30}H_{46}O_4$, furnished a diester on methylation with diazomethane, a feature of a dicarboxylic acid. The ^1H nmr spectrum of **2** shows the presence of an isopropenyl group (δ 4.91, 4.69, 1H each, s, H-28; δ 1.77, 3H, s, H-29) and three tertiary methyls (δ 0.74, 0.94, 0.97, 3H each, s, H-18, H-19, H-30) besides a moiety of the angelic acid terminal (δ 6.09, 1H, dd, J = 6.7/7.1, H-24; δ 1.91, 3H, s, H-27) and a secondary methyl (δ 0.96, 3H, d, J = 4.8, H-21) in the molecule. These facts indicate that manwuweizic acid possesses the 3,4-seco-ring A and a side chain identical to **1**, which led to the proposed structure **2** for manwuweizic acid.

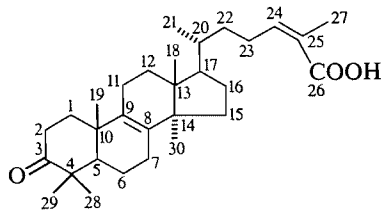

1

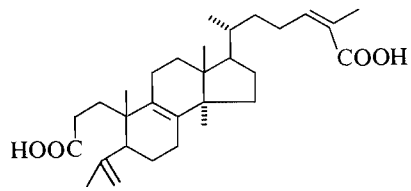

2

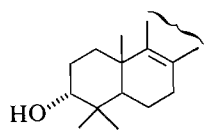

3

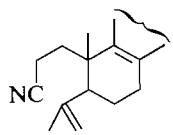

4

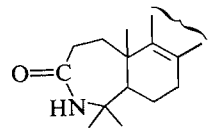

5

The following chemical correlation among anwuweizonic acid (**1**), manwuweizic acid (**2**), and anwuweizic acid (**3**), a known compound (4), further confirmed the proposed structures. Oxidation of **3** in ether with an aqueous solution of sodium dichromate – sulfuric acid provided anwuweizonic acid (**1**, 93% yield), and then oximation of **1** with hydroxylamine hydrochloride in ethanol–pyridine (1:1) afforded an oxime (98% yield). The oxime underwent an abnormal Beckmann rearrangement (5) in anhydrous pyridine and *p*-tosyl chloride at room temperature, giving a nitrile compound (**4**, 25% yield) and a lactam (**5**, 56% yield). Hydrolysis of **4** with 10% ethanolic KOH under reflux for 4 h led to **2** (70% yield), which is identical with natural manwuweizic acid. Therefore, the attribution of structure **1**, 3-oxo-lanosta-8,24*Z*-dien-26-oic acid, to anwu-

[1]Author to whom correspondence may be addressed.

[2]Jin-Long Yang, Department of Pharmacology, Shanghai Institute of Materia Medica, Academia Sinica. Personal communication.

Printed in Canada / Imprimé au Canada

weizonic acid and structure **2**, 3,4-secolanosta-4(28),8,24*Z*-trien-3,26-dioic acid, to manwuweizic acid was fully supported.

Experimental

Melting points were determined on a Kofler hot stage apparatus and are uncorrected. The following instruments were used for the spectra described here: ir, Perkin–Elmer 599B with KBr as the medium; ^{1}H nmr, JEOL PS-100 (100 MHz), Bruker AM-400 (400 MHz); and ^{13}C nmr, Bruker AC-100 (25.18 MHz), with $CDCl_3$ as the solvent, δ in ppm, and J in Hz; ms, Varian MAT-711.

Manwuweizic acid (2)

The crude alcoholic extract of the roots and stems of *Schisandra propinqua* (Wall.) Hook. f. et Thoms, gathered in Yuxi District, Yunnan Province, China, was suspended in water and extracted with ether. Then the ether extract was chromatographed on a silica gel column eluting with petroleum ether/benzene (1:1), benzene, benzene/ethyl acetate (10:1 and 4:1). The fractions eluted with benzene/ethyl acetate (4:1) gave crude crystals of manwuweizic acid (**2**). Its mother liquor was rechromatographed over a silica gel column, again giving **2** (see the isolation of **1**), which was recrystallized from chloroform/petroleum ether as needles (yield 0.04%), mp 191–193°C; $[\alpha]_D^{15}$ +54.3° (*c* 0.291, $CHCl_3$); ir ν_{max}: 3200–2500, 1705, 1695, 1630 cm^{-1}; ^{1}H nmr (400 MHz) δ: 6.09 (1H, dd, J = 6.7/7.1, H-24), 4.91, 4.69 (1H each, s, H-28), 1.91 (3H, s, H-27), 1.77 (3H, s, H-29), 0.74, 0.94, 0.97 (3H each, s, H-18, H-30, H-19), 0.96 (3H, d, J = 4.8, H-21); ^{13}C nmr (25.18 MHz) δ: 179.91 (s, C-3), 172.94 (s, C-26), 147.47 (s, C-4), 146.81 (d, C-24), 139.59, 129.77 (s, C-9, C-8), 126.10 (s, C-25), 113.85 (t, C-28), 51.09, 44.75 (s, C-14, C-13), 50.48 (d, C-17), 47.45 (d, C-5), 40.66 (s, C-10), 36.46 (d, C-20), 36.02, 32.87, 31.46, 31.21, 29.74, 28.12, 26.86, 26.11, 24.37, 22.03 (t each, C-1, C-2, C-6, C-7, C-11, C-12, C-15, C-16, C-22, C-23), 18.74 (q, C-27), 20.40 (q, C-21), 22.29, 23.08, 16.16, 25.30 (q, C-18, C-19, C-29, C-30); ms *m/z*: 470.3402 (M^+, calcd. for $C_{30}H_{46}O_4$: 470.3396), 455.3195 ($M - CH_3$), 397.3078 ($M - CH_2CH_2COOH$), 261.1853 ($C_{17}H_{25}O_2$), 235.1703 ($C_{15}H_{23}O_2$), 233.1560 ($C_{15}H_{21}O_2$).

Anwuweizonic acid (1)

The fractions eluted with benzene/ethyl acetate (10:1) mentioned above and the mother liquor of **2** were combined and rechromatographed on a silica gel column using petroleum ether/acetone (10:1). The late fractions again gave **2** and the early fractions afforded anwuweizonic acid (**1**) (yield 0.012%), crystallized from ether/petroleum ether, mp 126–128°C; $[\alpha]_D^{15}$ +63.8° (*c* 0.273, $CHCl_3$); ir ν_{max}: 3200–2500, 1710, 1690, 1630 cm^{-1}; ^{1}H nmr (100 MHz) δ: 6.10 (1H, t, J = 7, H-24), 1.94 (3H, s, H-27), 0.92 (3H, d, J = 5, H-21), 0.72, 0.90, 1.10, 1.14 (3H, 3H, 6H, 3H each, s, H-18, H-30, H-19, H-28, H-29); ms *m/z*: 454.3445 (M^+, calcd. for $C_{30}H_{46}O_3$: 454.3447), 439.3192 ($M - CH_3$), 271.2082 ($C_{19}H_{27}O$).

Methyl ester of 1

Compound **1** (30 mg) in ether reacted with an ethereal solution of diazomethane affording the methyl ester (30 mg) of anwuweizonic acid, crystallized from methanol, mp 89–90°C; ir ν_{max}: 1720, 1705, 1650 cm^{-1}; ^{1}H nmr (100 MHz) δ: 3.73 (3H, s, $COOCH_3$); ms *m/z*: 468 (M^+), 453 ($M - CH_3$), 421.

Dimethyl ester of 2

The same procedure as described above provided the dimethyl ester of manwuweizic acid, amorphous, ir ν_{max}: 1740, 1720, 1650 cm^{-1}; ^{1}H nmr (100 MHz) δ: 3.60, 3.70 (3H each, s, $COOCH_3 \times 2$); ms *m/z*: 498 (M^+), 483 ($M - CH_3$), 411 ($M - CH_2CH_2COOCH_3$).

Reduction of 1 to 3 and the 3β-hydroxyl isomer of 3

A solution of **1** (100 mg) in methanol (3 mL) with $NaBH_4$ (200 mg) was allowed to stand for 2 h at room temperature. The reaction mixture, after evaporation of the methanol in vacuum, was treated with water (5 mL) and one drop of hydrochloric acid, then extracted with chloroform. The extract was applied to a silica gel column eluting with benzene/ethyl acetate (10:1). The early fractions gave anwuweizic acid (**3**, 8 mg) identical with an authentic sample (4) (mixture mp, ir), and the late fractions afforded the 3β-hydroxyl isomer (85 mg) of **3**, mp 148–149°C, which is distinguished from **3** in the fingerprint region of ir and the H-3α (δ 3.24, 1H, dd, J = 4/9) signal of ^{1}H nmr.

Oxidation of 3 to 1

Compound **3** (45 mg) in ether (5 mL) was oxidized with an aqueous solution (0.6 mL) of sodium dichromate – sulfuric acid (1 g sodium dichromate in 6 mL water mixed with 1 mL 97% sulfuric acid, then diluted to 20 mL with water) under stirring for 5 h at room temperature. The ethereal layer was separated and the water layer was extracted with ether. The combined ethereal solution was washed with a saturated solution of sodium chloride and then concentrated, giving **1** (42 mg) identical to the natural compound (mixture mp and ir).

Oxime of 1

A mixture of **1** (300 mg) in pyridine (3 mL) and hydroxylamine hydrochloride (51 mg) in ethanol (3 mL) was heated on a boiling water bath for 1 h, and then diluted with water (100 mL). The solid product was filtered and crystallized from methanol, giving the oxime (300 mg), mp 184–186°C, ir ν_{max}: 3260, 3200–2500, 1690, 1640 cm^{-1}; ms *m/z*: 469 (M^+), 454 ($M - CH_3$), 436, 418.

Products (4 and 5) of Beckmann rearrangement

To a solution of the oxime (300 mg) in anhydrous pyridine (5 mL) was added *p*-tosyl chloride (300 mg), and the solution was allowed to stand for 24 h at room temperature. After dilution with water (50 mL) and acidification to pH 2 with hydrochloric acid, the reaction mixture was extracted using $CHCl_3$. The extract was chromatographed on a silica gel column eluting with benzene/ethyl acetate (10:1). The early fractions gave the nitrile compound (**4**, 70 mg), amorphous, ir ν_{max}: 3200–2500, 2250, 1690, 1640 cm^{-1}; ^{1}H nmr (100 MHz) δ: 6.10 (1H, t, J = 7, H-24), 4.95, 4.69 (1H each, s, H-28), 1.93 (3H, s, H-27), 1.77 (3H, s, H-29), 0.99, 0.95, 0.75 (3H each, s, H-19, H-30, H-18), 0.94 (3H, d, J = 4, H-21); ms *m/z*: 451 (M^+), 436 ($M - CH_3$), 418, 397.

The late fractions afforded the lactam (**5**, 170 mg), amorphous, ir ν_{max}: 3300, 3210, 3200–2500, 1690, 1640 cm^{-1}; ^{1}H nmr (100 MHz) δ: 5.97 (1H, t, J = 7, H-24), 1.92 (3H, s, H-27), 1.37, 1.31, 1.22, 0.92, 0.74 (3H each, s, H-29, H-28, H-19, H-30, H-18), 0.93 (3H, covered, H-21); ms *m/z*: 470 (M + 1), 469 (M^+), 455, 454, 398, 397, 379, 351.

Manwuweizic acid (2) from hydrolysis of 4

The nitrile compound (**4**) was dissolved in an ethanolic solution of 10% KOH and refluxed for 4 h. After evaporation of ethanol, the reaction mixture was acidified to pH 3 with hydrochloric acid and extracted with $CHCl_3$. The extract was purified on a silica gel column eluting with $CHCl_3$, giving **2** (50 mg) identical to the natural compound (mixture mp, ms, ^{1}H nmr, ir).

Acknowledgements

The authors wish to express their appreciation to the Department of Analytical Chemistry, Shanghai Institute of Materia Medica, Academia Sinica, for all the spectral determinations in this paper, and to the Foundation of the Chinese Academy of Sciences for grant support (R 850922).

1. Report of Treatment for Lung Carcinoma Using Manshanxiang Complex. School of Hygiene, Yuxi District, China. In-house Publication. 1980.
2. G-H. Xu, Z. Yang, G-H. Zhou, and T-H. He. Chin. Tradit. Herb. Drugs, **15**, 432 (1984).
3. J-S. Liu, M-F. Huang, and Y-L. Gao. Huaxue Xuebao, **38**, 361 (1980).
4. J-S. Liu and M-F. Huang. Huaxue Xuebao, **42**, 264 (1984).
5. C. W. Shoppee, N. W. Hughes, R. E. Lack, and J. T. Pinhey. J. Chem. Soc. (C), 1443 (1970).

Can. J. Chem. Downloaded from www.nrcresearchpress.com by 176.9.209.113 on 09/07/12
For personal use only.

^{13}C nuclear magnetic resonance and reactivity of 4*H*-3,1-benzoxazin-4-ones[1]

VALERIE J. ROBINSON AND ROBIN W. SPENCER[2]
Syntex Research (Canada), 2100 Syntex Court, Mississauga, Ont., Canada L5N 3X4

Received June 26, 1987

VALERIE J. ROBINSON and ROBIN W. SPENCER. Can. J. Chem. **66**, 416 (1988).

Complete carbon-13 nuclear magnetic resonance assignments have been made for 22 4*H*-3,1-benzoxazin-4-ones. These compounds are alternate substrate inhibitors of human leukocyte elastase, a serine protease involved in tissue degradation. Correlations between the carbon chemical shifts and rates of alkaline hydrolysis are consistent with hydrolysis via attack at C4, and are also useful in the selection of parameters for structure–activity analysis.

VALERIE J. ROBINSON et ROBIN W. SPENCER. Can. J. Chem. **66**, 416 (1988).

On a fait des attributions complètes des spectres en résonance magnétique nucléaire du ^{13}C de 22 4*H*-benzoxazine-3,1 ones-4. Ces composés sont des inhibiteurs de substrats d'élastase leucocytaire humaine, une protéase de la sérine impliquée dans la dégradation des tissus. Des corrélations entre les déplacements chimiques des carbones et les taux d'hydrolyse alcaline sont en accord avec un mécanisme d'hydrolyse impliquant une attaque en C4; de plus, ces corrélations sont utiles dans la sélection des paramètres nécessaires pour une analyse structure–activité.

[Traduit par la revue]

Can. J. Chem. Downloaded from www.nrcresearchpress.com by 176.9.209.113 on 09/07/12
For personal use only.

Introduction

4*H*-3,1-Benzoxazin-4-ones are potent inhibitors of serine proteases (1–6) with clinical potential in a number of degradative diseases (7). It is well established that benzoxazinones inhibit by acting as alternate substrates, acylating the target protease via attack of serine 195 at C4, and then slowly deacylating (2–6) (Scheme 1).

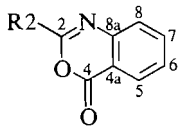

The carbon-13 nmr spectra of 22 benzoxazinones (Table 1) have been examined in detail, to more fully understand the chemistry of this ring system and to develop parameters that may be useful in structure–activity correlations with chemical and biological activity. This approach has been successfully used to correlate ^{13}C chemical shifts with carbonyl reactivity of cephalosporins and penicillins (8). In addition, the benzoxazinones offer an opportunity to investigate the electronic substituent effects on carbon-13 chemical shifts in a complex heterocycle of biochemical interest.

Experimental

Nuclear magnetic resonance spectra were recorded on a Bruker WP 80 spectrometer equipped with a 5-mm dual ^{13}C, ^{1}H probehead. All chemical shifts were determined from 0.3 *M* samples in DMSO-d_6 at 27°C, and more concentrated solutions were used for the ^{13}C coupled and 2D experiments.

J-modulated ^{13}C spectra were recorded using a delay τ of 7.6 ms ($\approx 1/J_{CH}$) and a relaxation delay of 6 s (9). Heteronuclear shift correlation spectra were obtained using the pulse sequence:

$$\text{delay} \rightarrow \pi/2(^1\text{H}) \rightarrow t_1/2 \rightarrow \pi(^{13}\text{C}) \rightarrow t_1/2 \rightarrow \Delta_1 \rightarrow \pi/2(^1\text{H}),$$
$$\pi/2(^{13}\text{C}) \rightarrow \Delta_2 \rightarrow \text{acquisition}$$

with broadband decoupling (10). A 1-s recycle delay was used with delay times $\Delta_1 = 1/(2J) = 1.8$ ms and $\Delta_2 = 1/(4J) = 3.3$ ms. In the f_2 and f_1 domains, 1024 and 256 points were used, respectively. Delays of 50 and 33 ms were used for Δ_1 and Δ_2, respectively, in optimizing for long-range correlations (11).

[1]Contribution number 268 from the Syntex Institute of Bioorganic Chemistry.

[2]Present address: Pfizer Central Research, Groton, CT 06340, U.S.A.

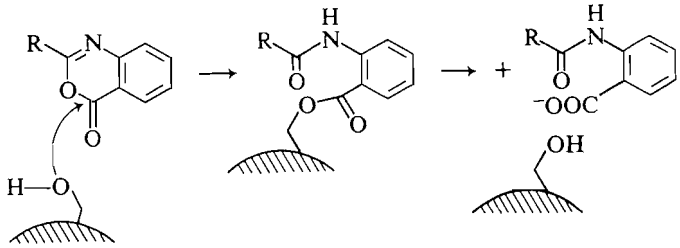

SCHEME 1

Compounds **1–4** and **8–21** have been previously reported (4, 12), as have compounds **7** and **23**[3] (13, 14). Compounds **5**, **6**, and **22** were prepared by Marshall's procedure (13). **5**: mp 65–66°C. *Anal.* calcd. for $C_{11}H_{11}NO_2S$: C 59.71, H 5.01, N 6.33, S 14.49; found: C 59.50, H 4.89, N 6.24, S 14.38. **6**: mp 135–136°C. *Anal.* calcd. for $C_{17}H_{13}NO_2S$: C 61.99, H 4.59, N 4.25, S 9.73; found: C 61.95, H 4.53, N 4.18, S 9.59. **22**: mp 60–61°C. *Anal.* calcd. for $C_{12}H_{13}NO_2S$: C 61.25, H 5.57, N 5.95, S 13.63; found: C 61.33, H 5.46, N 5.94, S 13.50. The ir and ^{1}H nmr spectra were consistent with structural assignments. Further synthetic details will be published separately.

Alkaline hydrolysis rate constants were measured at 25°C by the disappearance of the long wavelength uv chromophore (λ_{max} typically 300–345 nm) (4–6). Human leukocyte elastase (HLE) was obtained and its inhibition assayed as previously described (4–6).

Results and discussion

Assignment of ^{13}C nmr spectra

Very few reports of the carbon nmr of benzoxazinones can be found in the literature (15). All of our assignments were made after confirmation by several different techniques, with the results given in Table 1. The proton nmr spectrum was assigned by comparison to ring-substituted analogues, and the aromatic region of 2-methyl benzoxazinone **14** was then simulated for additional confirmation. All carbon nmr spectra were run using a *J*-modulated spin echo sequence to separate quaternary

[3]3-Methyl isocoumarin **23** is the carbon analog of 2-methyl benzoxazinone **14**

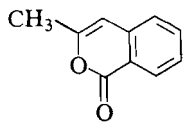

23

TABLE 1. Carbon-13 chemical shifts of the benzoxazinones

No.	Name	δ_{C2}	δ_{C4}	δ_{C4a}	δ_{C5}	δ_{C6}	δ_{C7}	δ_{C8}	δ_{C8a}	$\log(k_{OH^-})^a$	pK_i^b
1	2-CF_3-5-OMe	146.8	152.3	106.3	160.6	113.3	137.9	119.1	145.4	3.54	6.38
2	2-CF_3-5-Me	146.1	155.7	116.6	142.4	133.0	136.2	125.7	144.7	3.14	7.54
3	2-CF_3-6,7-diOMe	145.2	156.1	110.4	107.6	150.8	156.2	109.2	139.4	2.99	
4	2-CF_3	146.2	156.6	118.5	128.4	130.9	137.1	127.6	143.4	3.52	5.00
5	2-EtS-5-Me	162.1	157.2	113.7	141.9	129.6	135.9	123.2	147.4	1.58	9.03
6	2-BnS-6,7-diOMe	160.7	157.7	107.1	107.0	148.6	156.5	107.3	142.5	0.96	5.67
7	2-MeS	163.3	158.0	115.3	128.1	127.4	137.0	125.2	146.0	2.16	7.68
8	2-EtO-5-Me	153.9	158.1	109.6	141.9	128.0	135.8	122.9	149.0	1.31	9.94
9	2,5-diMe	159.8	158.4	114.7	141.6	130.3	135.6	124.0	147.4	0.85	6.00
10	2-MeNH-5-Me	154.5	158.6	111.1	141.6	125.1	135.5	121.9	152.0	0.54	4.51
11	2-Ph	156.3	158.7	116.8	128.5	127.9	136.7	126.8	146.1	1.79	5.02
12	2-Me-6,7-diOMe	159.0	159.0	108.2	106.9	148.9	156.0	107.5	142.2	0.53	3.08
13	2-EtO	154.2	159.0	114.2	128.3	125.8	136.9	124.9	147.7	1.91	8.19
14	2-Me[d]	160.1	159.1	116.3	128.2	127.7	136.7	126.0	146.0	1.69	5.32
15	2-*t*Bu	167.5	159.1	116.3	128.3	127.7	136.6	126.5	145.7	1.38	5.05
16	2-*n*BuNH	154.0	159.4	112.4	127.9	122.5	136.3	123.7	150.7	1.09	6.65
17	2,8-diMe	159.0	159.4	116.1	125.2	127.4	137.2	134.5	144.2	1.18	5.13
18	2-MeNH	154.7	159.5	112.5	128.0	122.8	136.6	123.8	150.6	1.38	5.16
19	2-Me-5-Et	159.8	157.9	114.0	147.7	129.0	136.0	124.2	147.7	0.73	6.92
20	2-*n*BuNH-5-Et	153.9	158.2	110.3	147.8	123.7	135.8	122.1	152.4	0.38	8.38
21	2-EtO-5-Et	154.0	157.7	112.0	148.1	126.8	136.2	123.2	149.4	1.17	10.37
22	2-EtS-5-Et	162.1	156.9	113.2	148.1	128.5	136.4	123.6	147.8	1.37	9.59
23	3-Me-isocoumarin[e]	154.4	161.8	119.1	[c]	[c]	[c]	[c]	137.3	−0.27	<2

[a]Alkaline hydrolysis rates, with k_{OH^-} in $M^{-1}\,s^{-1}$.
[b]Inhibition constants for human leukocyte elastase, with K_i in M.
[c]These resonances were not unambiguously assigned.
[d]Previously reported shifts of 2-methyl benzoxazinone **14** (15*b*) are not in agreement with our results. The published values appear to correspond to those of *N*-acetyl anthranilic acid, a hydrolysis product readily obtained from **14** on standing, even in the solid state (21).
[e]Tabulated data for **23** use benzoxazinone numbering.

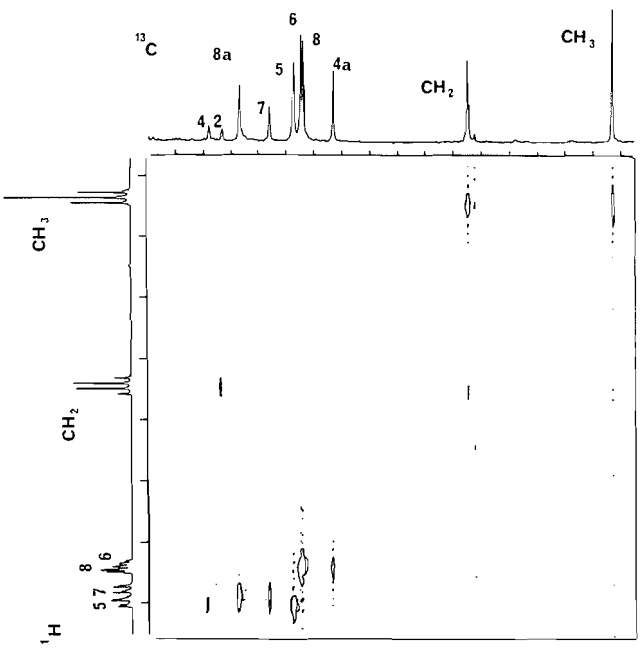

FIG. 1. The 2D heteronuclear shift correlation of 2-ethoxy benzoxazinone **13** is shown with delays optimized for long-range $^{13}C-^{1}H$ couplings.

carbons from those carbons with attached protons. Carbons 5, 6, 7, and 8 were correlated to the proton spectrum via 2D heteronuclear shift correlation for those molecules with ambiguous carbon assignments. Each quaternary carbon was then identified by a further 2D correlation optimized for long-range coupling. An example of this technique is shown in Fig. 1 for 2-ethoxy benzoxazinone **13**.

A clear correlation can be seen from C2 to the methylene of the side chain, distinguishing C2 from C4, which shows a correlation to the proton at 5. In addition, long-range correlations from C8a to H7 and H5, and C4a to H6 and H8 can be seen (noting that $J_{CCC-H} \gg J_{CC-H}$ in aromatic systems, ref. 16). For those molecules with ring substitution, carbon spectra were recorded with the decoupler gated off before the pulse and spectra were interpreted by coupling patterns.

The substituent effects on chemical shift are quite consistent. The effect of methyl substitution at C5 is pronounced, with C5 deshielded by 13.7 ± 0.3 ppm. Substitution of a methyl at C8 produces only an 8.5-ppm downfield shift of C8, which is closer to the 6.2-ppm shift observed in 1-methyl naphthalene (18). In addition, carbon 6 is deshielded by 2.6 ppm by methyl substitution at C5, while carbon 7 is only shifted 0.5 ppm by methyl substitution at C8. By comparison, 1-methyl substitution in naphthalene gives a 0.6 ppm-downfield shift. The *peri* interaction between substituents in 1,8-disubstituted naphthalenes has been shown to cause distortions of up to 3 Å from ring planarity, which are reflected in ^{13}C chemical shifts (18). The anomalous shifts in 5-substituted benzoxazinones would suggest that similar interactions may occur between the carbonyl at C4 and the substituent at C5.

Mechanism of alkaline hydrolysis

In addition to nmr assignments, Table 1 gives the rate constants for aqueous alkaline hydrolysis of the benzoxazinones. Nucleophilic attack by hydroxide could occur at either C2 or C4, and the data of Table 1 provide a unique opportunity to distinguish between these carbons, which is based on a

Can. J. Chem. Downloaded from www.nrcresearchpress.com by 176.9.209.113 on 09/07/12
For personal use only.

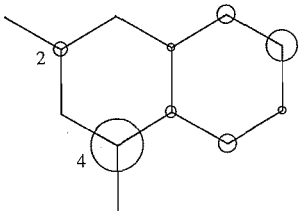

FIG. 2. Multiple regression of log (k_{OH^-}) vs. all $\delta^{13}C$ was carried out for compounds **1**–**22**. The data δ_C of Table 1 were fit to the equation log (k_{OH^-}) = constant + $\beta_2\delta_{C2} + \beta_4\delta_{C4} + \ldots + \beta_{8a}\delta_{C8a}$. The results ($n$ = 22, F = 58.4, r^2 = 0.973, s = 0.20) are shown as circles with areas proportional to the coefficient β obtained for each carbon atom.

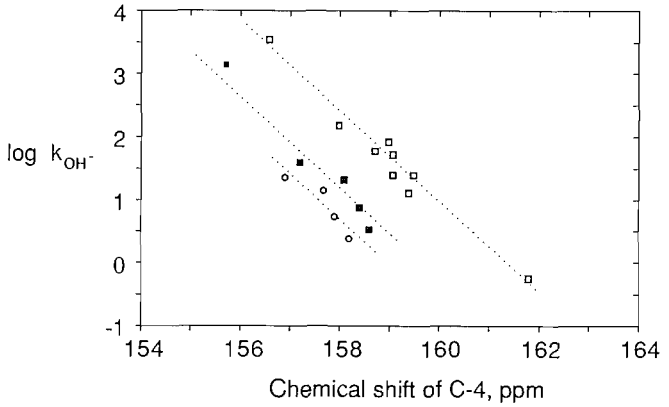

FIG. 3. Alkaline hydrolysis rates are shown vs. the chemical shift of C4 for compounds **2**, **4**, **5**, **7**–**11**, and **13**–**22**. Open squares indicate R5 = H, filled squares indicate R5 = Me, and open circles indicate R5 = Et.

correlation of carbon chemical shifts with observed hydrolytic rates. As shown in Fig. 2, the coefficient of regression of log (k_{OH^-}) with $\delta^{13}C$ is clearly largest at C4, showing that C4 is the most probable site of hydroxide attack. This is in agreement with determinations by the more traditional methods of ^{18}O labelling (19) or inference from substituent effects on reaction rates[4] (20). It is noteworthy that acid and solid-state hydrolyses of benzoxazinones proceed instead by protonation at N1 and water attack at C2 (21).

Examination of log (k_{OH^-}) vs. δ_{C4} alone (Fig. 3) shows that the benzoxazinones must be separated into two classes, those with or those without 5-methyl substitution. Since the electronic effects of 5-substitution should be intrinsically incorporated into δ_{C4}, this observation again suggests a *peri* interaction between R5 and the carbonyl oxygen that affects the rate of hydroxide attack on C4. Regression on the data of Fig. 3 gives the result that log (k_{OH^-}) = 120.6 − (0.75 ± 0.06)δ_{C4} + (1.15 ± 0.12)E_s (n = 18, F = 91.7, r^2 = 0.92, s = 0.27), where E_s is the Taft steric parameter (22) for the substituent at C5.

Thus 5-methyl and 5-ethyl benzoxazinones are $10^{1.15E_s}$ or 27-and 32-fold, respectively, more resistant to alkaline hydrolysis than their C4 chemical shifts would suggest. This shows that when steric (e.g. *peri*) interactions are taken into account, the ^{13}C chemical shift of an electrophilic carbon can be a strong predictor of reactivity. The chemical shifts also suggest that the related molecule 3-methyl isocoumarin **23** displays no enzyme inhibition because its C4 is not electrophilic enough to efficiently acylate serine 195. The chemical shifts also help to estimate the C4 electrophilicity of molecules for which ionization prevents alkaline hydrolysis (e.g. 2-methyl-quinazolin-4-one, with δ_{C4} = 161.9 (15*a*), and which deprotonates at N3 under alkaline conditions).

[4]Regression on 123 benzoxazinones with widely varying 2- and 5-substituents shows that electron withdrawal and donation are the most significant determinants of alkaline hydrolysis rates, supporting a single mechanism, i.e., attack at C4.

TABLE 2. Chemical shift dependence on R2

Carbon	$f + r$	% r
4	−2.5	22
4a	2.1	78
5	0.1	100
6	3.7	53
7	0.6	9
8	1.1	100
8a	−3.3	55

Table 1 also presents the inhibition constants pK_i (= $-\log_{10} K_i$, in M) for HL elastase, which span eight orders of magnitude. There are no significant correlations between these pK_i and the ^{13}C chemical shifts in multiple regression, though limited data sets show a clear correspondence between C4 electrophilicity and pK_i (1, 4). Clearly other factors in enzyme acylation and deacylation, such as specific steric or hydrophobic interactions and hydrogen bonding that are not reflected in ^{13}C spectra, mask any simple correlations with chemical shift.

Assignment of parameters

Structure–activity investigations require that molecular descriptors be carefully chosen. In general, such descriptors should describe the relevant properties of the molecule (e.g. size, hydrophobicity, electrophilicity, potential for hydrogen bonding, pK_a) and be readily available, either as tabulated, calculated, or measured values. Since nucleophilic attack at C4 is involved in both benzoxazinone stability and enzyme inhibition, and since R2 has a unique role in the mechanism of enzyme inhibition (it is electronically coupled to C4 in acylation but not in deacylation: Scheme 1) (4), we have used the effects on $\delta^{13}C$ to choose an appropriate descriptor of electron withdrawal by R2.

The parameters F and R are desirable for their statistical properties and for their field and resonance interpretations (23), and yet they are inadequate as descriptors of R2 for two reasons. First, F and R are tabulated for only a limited set of substituents. Second, a single electronic descriptor is preferable to simplify later regression and interpretation. We therefore investigated δ_{C4} as a function of F and R to guide the selection of one of the more readily available parameters σ_p, σ_m, or σ^*. Multiple regression for compounds **4**, **7**, **11**, **13**, **14**, **15**, and **17** (for which F and R for R2 were available) gave the result:

$$\delta_{C4} = 158.7 - (1.95 \pm 0.58)F - (0.53 \pm 0.16)R$$
$$(n = 7,\ r^2 = 0.85,\ F = 11.5,\ s = 0.47 \text{ ppm})$$

This fit implies 22 ± 8% resonance in the effect of 2-substitution on δ_{C4}, suggeting that σ_m (with 20 ± 2% resonance (23)) is preferable to σ_p (38 ± 3%) or σ^* (13 ± 2%)[5] for further structure–activity correlations.

[5]Determined from regression of tabulated σ^* (24) against F and R (23).

Can. J. Chem. Downloaded from www.nrcresearchpress.com by 176.9.209.113 on 09/07/12
For personal use only.

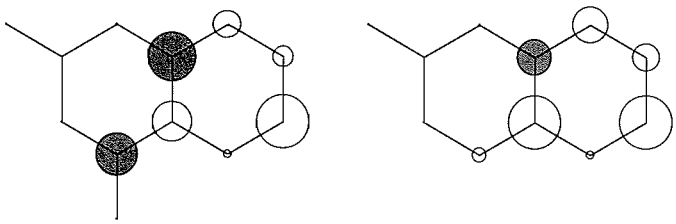

FIG. 4. (a) The data of Table 3 are shown as circles with areas proportionate to $f + r$. Filled circles indicate negative $f + r$. (b) The results for 2-substituted naphthalenes of Kitching *et al.*, Table IVB, ref. 17, are similarly shown as areas proportionate to $\sigma_I + \sigma_R$.

Similar analysis for all assigned $\delta^{13}C$ was carried out using the same set of compounds with the results in Table 2. Here f and r are the coefficients in the regression equation $\delta^{13}C$ = constant + $fF + rR$, and their sum represents the magnitude of the electronic substituent effect of R2 on each $\delta^{13}C$. These magnitudes are also shown in Fig. 4*a*, where the alternating pattern of the effect is clear. Except for the carbonyl carbon, the magnitudes and directions of these effects are very similar to those in 2-substituted naphthalenes (Fig. 4*b*, (17)). Adequate regression could not be obtained for δ_{C2}, because of the overriding local effects on chemical shift at this position.

Conclusions

Carbon 13 assignments have been made for 22 benzoxazinones. The chemical shifts are useful predictors of chemical mechanism and relative reactivities, provide evidence for *peri* interactions, and guide the selection of electronic parameters for structure–activity analysis.

Acknowledgements

We would like to thank Dr. Tim Tam for providing the 2-amino benzoxazinones and 3-methyl isocoumarin, Dr. T. J. Liak for the 2-oxy and 2-thia benzoxazinones, and Drs. Allen Krantz and Roger A. Smith for helpful discussions.

1. T. TESHIMA, J. C. GRIFFIN, and J. C. POWERS. J. Biol. Chem. **257**, 5085 (1982).
2. R. ALAZARD, J.-J. BÉCHET, A. DUPAIX, and J. YON. Biochim. Biophys. Acta, **309**, 379 (1973).
3. L. HEDSTROM, A. R. MOORMAN, J. DOBBS, and R. H. ABELES. Biochemistry, **23**, 1753 (1984).
4. R. W. SPENCER, L. J. COPP, B. BONAVENTURA, T. F. TAM, T. J. LIAK, R. BILLEDEAU, and A. KRANTZ. Biochem. Biophys. Res. Commun. **140**, 928 (1986).
5. A. KRANTZ, L. J. COPP, and R. W. SPENCER. Peptides and proteases: recent advances. *Edited by* A. Barth and R. L. Schowen. Pergamon, Oxford. 1987.
6. A. KRANTZ, R. W. SPENCER, T. F. TAM, E. THOMAS, and L. J. COPP. J. Med. Chem. **30**, 589 (1987).
7. (*a*) H. P. SCHNEBLI. *In* Handbook of inflammation. Vol. 5. *Edited by* I. L. Bonta, M. A. Bray, and M. J. Parnham. Elsevier, New York. 1985. pp. 321–333; (*b*) J. C. POWERS. Am. Rev. Respir. Dis. **127**, S54–S58 (1983).
8. (*a*) A. SCHANCK, B. COENE, J. M. DEREPPE, and M. VAN MEERSSCHE. Bull. Soc. Chim. Belg. **92**, 81 (1983); (*b*) R. MONDELLI and P. VENTURA. J. Chem. Soc. Perkin Trans. 2, 1749 (1977).
9. C. LE COCQ and J. LALLEMAND. J. Chem. Soc. Chem. Commun. 150 (1981).
10. R. FREEMAN and G. A. MORRIS. J. Chem. Soc. Chem. Commun. 684 (1978).
11. W. REYNOLDS, R. ENRIQUEZ, L. I. ESCOBAR, and X. LOZOYA. Can. J. Chem. **62**, 2421 (1984).
12. A. KRANTZ, R. W. SPENCER, T. TAM, and T. J. LIAK. Eur. Pat. Appl. EP 206323 A1, 1986; Chem. Abstr. **106**, 176406h (1986).
13. J. R. MARSHALL. J. Chem. Soc. 938 (1965).
14. R. B. TIRODKAR and R. N. USGAONKAR. J. Indian Chem. Soc. **46**, 935 (1969).
15. (*a*) J. PETRIDOU-FISCHER and E. P. PAPADOPOULOS. J. Heterocycl. Chem. **19**, 123 (1982); (*b*) S. P. SINGH, S. S. PARMAR, V. I. STENBERG, and T. K. AKERS. J. Heterocycl. Chem. **15**, 53 (1987).
16. F. J. WEIGERT and J. D. ROBERTS. J. Am. Chem. Soc. **89**, 2967 (1967).
17. W. KITCHING, M. BULLPITT, D. GARTSHORE, W. ADCOCK, T. C. KHOR, D. DODDRELL, and I. D. RAE. J. Org. Chem. **42**, 2411 (1977).
18. (*a*) J. E. ANDERSON and R. W. FRANCK. Nouv. J. Chim. **7**, 169 (1983); (*b*) D. BRIGHT, I. F. MAXWELL, and J. DE BOER. J. Chem. Soc. Perkin Trans. 2, 2101 (1973); (*c*) J. HANDAL, J. C. WHITE, R. W. FRANCK, Y. H. YUH, and N. L. ALLINGER. J. Am. Chem. Soc. **99**, 3345 (1977).
19. A. WILLIAMS and G. SALVADORI. J. Chem. Soc. (B), 1105 (1971).
20. D. J. CREMIN and A. F. HEGARTY. J. Chem. Soc. Perkin Trans 2, 208 (1978).
21. J. VICENS, M. C. ETTER, and L. A. ERREDE. Tetrahedron Lett. **24**, 723 (1983).
22. C. HANSCH and A. LEO. Substituent constants for correlation analysis in chemistry and biology. Wiley, New York. 1979.
23. C. G. SWAIN, S. H. UNGER, N. R. ROSENQUIST, and M. S. SWAIN. J. Am. Chem. Soc. **105**, 492 (1983).
24. D. D. PERRIN, B. DEMPSEY, and E. P. SERJEANT. pK_a prediction for organic acids and bases. Chapman and Hall, London. 1981.

Can. J. Chem. Downloaded from www.nrcresearchpress.com by 176.9.209.113 on 09/07/12
For personal use only.

Pyrazolo[3,4-*b*]pyridines: Syntheses, reactions, and nuclear magnetic resonance spectra[1]

BRIAN MAURICE LYNCH,[2] MISBAHUL AIN KHAN,[3] HUK CHIA TEO, AND FRANCISCO PEDROTTI[4]

Department of Chemistry, Saint Francis Xavier University, Antigonish, N.S., Canada B2G 1C0 and Secao de Quimica, Instituto Militar de Engenharia, Praia Vermelha, 22290 Rio de Janeiro, Brasil

Received August 10, 1987

BRIAN MAURICE LYNCH, MISBAHUL AIN KHAN, HUK CHIA TEO, and FRANCISCO PEDROTTI. Can. J. Chem. **66**, 420 (1988).

Efficient syntheses of approximately 70 simple substituted representatives of pyrazolo[3,4-*b*]pyridine **1** are reported from the following: (*a*) suitably substituted pyridines onto which a pyrazole ring is annelated, and (*b*) appropriately substituted pyrazoles onto which a pyridine ring is annelated. Selected examples of electrophilic, nucleophilic, and homolytic substitution reactions and group transformations are described, providing regiosynthetic paths to useful intermediate species. Some systematic aspects of substituent chemical shift influences in the ^1H and ^{13}C nuclear magnetic resonance spectra, aiding in structural assignments, are illustrated.

BRIAN MAURICE LYNCH, MISBAHUL AIN KHAN, HUK CHIA TEO et FRANCISCO PEDROTTI. Can. J. Chem. **66**, 420 (1988).

On a développé des synthèses efficaces pour environ 70 pyrazolo[3,4-*b*]pyridines (**1**) substituées simples; ces synthèses impliquent soit l'utilisation de pyridines substituées adéquatement sur lesquelles on referme un cycle pyrazole, soit l'utilisation de pyrazoles substitués adéquatement sur lesquelles on referme un noyau pyridine. On décrit des exemples choisis de réactions de substitutions électrophiles, nucléophiles et homolytiques ainsi que de transformations de groupes qui illustrent des voies régiospécifiques d'obtenir des espèces intermédiaires. On présente des données illustrant quelques aspects systématiques des influences des substituants sur les déplacements chimiques en résonance magnétique nucléaire du ^1H et du ^{13}C qui sont utiles pour faire des attributions de structures.

[Traduit par la revue]

Can. J. Chem. Downloaded from www.nrcresearchpress.com by 176.9.209.113 on 09/07/12
For personal use only.

Introduction

Many polysubstituted derivatives of 1*H*-pyrazolo[3,4-*b*]pyridine **1** have been synthesized as potentially biologically active materials (e.g., refs. 1–25) (for a recent general review of all pyrazolopyridines, see Hardy (26)). Our interest in synthesis and reactivity of the parent compound and its substitution products arises from promise shown as inhibitors of xanthine oxidases (27). A minor portion of our work has been reported in another study of purine analogues (28), and we have also described the synthesis of the parent system by rearrangement accompanying decarboxylation of pyrazolo[1,5-*a*]pyrimidine carboxylic acids (29).

This paper reports efficient syntheses of pyrazolo[3,4-*b*]pyridines from (*a*) suitably substituted pyridines onto which a pyrazole ring is annelated, and (*b*) appropriately substituted pyrazoles onto which a pyridine ring is annelated. We present examples of electrophilic, nucleophilic, and homolytic substitution reactions and group transformations providing regiosynthetic paths to useful intermediate species. Aspects of substituent chemical shift influences in the ^1H and ^{13}C nmr spectra are illustrated.

Syntheses of 1*H*-pyrazolo[3,4-*b*]pyridines[5]

Approach (a), from pyridines

Here, 2-halo-3-substituted pyridines were treated with hydrazines. Nucleophilic displacement of the 2-halogen and cyclizing condensation involving the pyridines' 3-substituents yield the substituted pyrazolo[3,4-*b*]pyridines **1** through **9**. Scheme 1 indicates the typical sequence. The starting materials were obtained from 3-substituted pyridines by successive *N*-oxidation and treatment with phosphorus oxychloride, effecting exclusive cine-substitutive chlorodeoxygenation at the 2-position of the pyridine ring. In principle, cyclocondensation with 2-chloro-3-cyanopyridine might proceed by *two* distinct pathways in *two* stages: initial nucleophilic hydrazinodechlorination, followed by intramolecular attack by the hydrazine component on the electron-deficient carbon of the cyano group, yielding 3-aminopyrazolo[3,4-*b*]pyridines; alternatively, initial reaction may be nucleophilic addition of hydrazines to the cyano function, generating an amidrazone moiety (-C:NH(NH·NH_2)) that then intramolecularly displaces the halogen. Independent studies (30)) show that under the reaction conditions used (excess of hydrazine component), the open-chain species **10** is an intermediate.

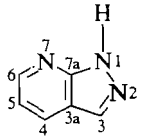

1*H*-pyrazolo[3,4-*b*]pyridine, **1**

2-Chloro-3-formylpyridine (2-chloronicotinaldehyde) was obtained by reduction of 2-chloro-3-cyanopyridine by Raney nickel and formic acid (31); this intermediate is inaccessible by the above *N*-oxidation route (peroxyacid oxidation of 3-formylpyridine yields pyridine-*N*-oxide 3-carboxylic acid). In the synthesis of the parent **1** from 2-chloro-3-formylpyridine, the yield was prejudiced by the formation of the azine species **11**.

Approach (b), from pyrazoles

5-Aminopyrazoles were starting materials in this approach. Grandberg (2) and Hardy and co-workers (5) have shown that highly acidic annelation conditions resembling a Skraup quinoline synthesis furnish pyrazolo[3,4-*b*]pyridines from 5-aminopyrazoles, but yields are poor and work-up tedious. The unsatisfactory results arise from the high reactivity of the 4-carbon of aminopyrazoles towards electrophilic sulfonations, precluding efficient cyclizations.

The main body of our work employed zinc chloride-catalyzed

[1]Previous paper in this series: ref. 50.

[2]Author to whom correspondence may be addressed.

[3]N.S.E.R.C./CNPq Exchange Scientist, 1982–1983. Present address: Department of Chemistry, Islamia University, Bahawalpur, Pakistan.

[4]Secao de Quimica, Instituto Militar de Engenharia.

[5]Characterizing data for all the products obtained are assembled in Table 1 and selected features of ^1H nmr and ^{13}C nmr spectra are summarized in Tables 2 and 3.

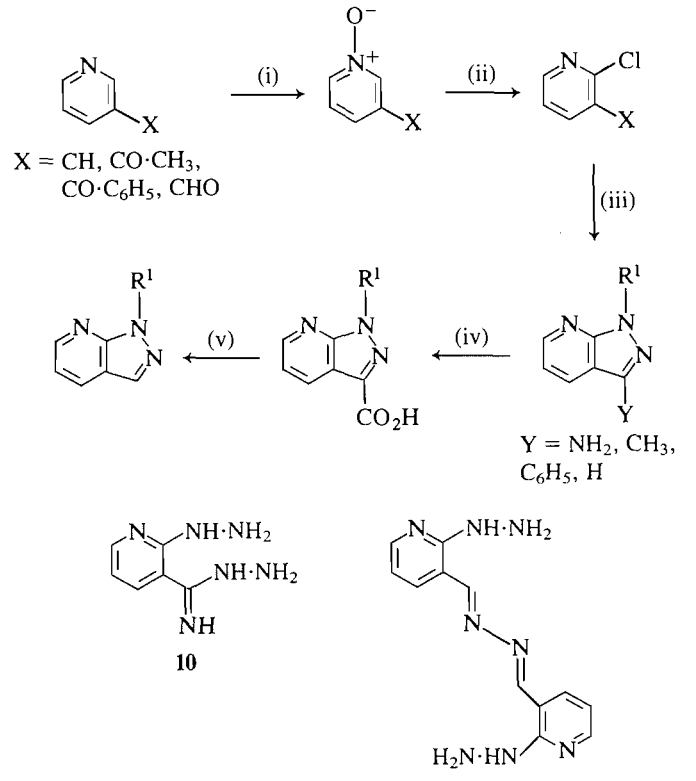

(i) AcO_2H; (ii) $POCl_2$; (iii) $R^1{\cdot}NH{\cdot}NH_2$;
(iv) $KMnO_4$, OH^- (for $R^1 = Y = CH_3$);
(v) $-CO_2$

SCHEME 1

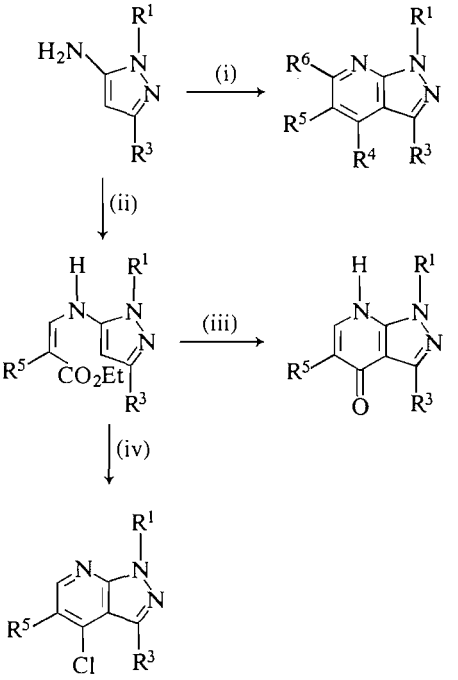

(i) $R^4CO{\cdot}CHR^5{\cdot}COR_6/ZnCl_2//HCl/EtOH$;
(ii) $EtO{\cdot}CH{:}C(CO_2Et)R^5$;
(iii) Ph_2O or Dowtherm A;
(iv) $POCl_3$

SCHEME 2

cyclizations where 1,3-dicarbonyl compounds were reacted with the aminopyrazoles (compare refs. 29, 32, 33). This method (depicted in Scheme 2) proved efficient, yielding the pyrazolo[3,4-*b*]pyridines **2**, **3**, **5**, **12**–**36**. Where unsymmetrical dicarbonyl species were used, the assignments of methyl-group position in the products **26**, **28**–**31**, **33** follow from ^1H nmr spectra: the proton–proton coupling patterns in the pyridine rings are characteristic ($J_{4,5} > J_{5,6}$) and, generally, $\delta(CH_3)$ is approximately 0.20 ppm greater for a 6-methyl than for a 4-methyl substituent (32). Note that this cyclization procedure cannot be applied routinely to 3(5)-aminopyrazoles (with a free NH) since formation of pyrazolo[1,5-*a*]pyrimidines supervenes (see refs. 33, 37). Exceptionally, cyclizations occur preferentially at C-4, not N-1, for reactions using sodium nitromalonaldehyde; these reactions may also be effected under basic conditions.

We also applied the Gould–Jacobs method (34), in which 5-aminopyrazoles reacted with diethyl ethoxymethylenemalonate, ethyl ethoxymethylenecyanoacetate, or ethyl ethoxymethyleneacetoacetate, followed by thermal cyclization in phenyl ether or Dowtherm A to provide the pyrazolo[3,4-*b*]pyrid-4-ones (4-hydroxy pyrazolo[3,4-*b*]pyridines) **37**–**44** (see Scheme 2). The pyrazolopyridones with cyano, ester, or acetyl groups in the 5-position are intermediates for candidate enzyme-inhibitor species (compare Chu and Lynch (27)). The chlorocyclization method developed by Hoehn *et al.* (4) was also applied to some of the pyrazolylaminoacrylates, and the corresponding ring-closed products **45**–**49** were obtained in good yields.

Reactions

The reactivity of the 1*H*-pyrazolo[3,4-*b*]pyridine ring system is of interest since it fuses a pyrazole ring (relatively reactive towards electrophilic substitutions) with a pyridine ring where carbons are unreactive towards many electrophiles; however, the interaction between N-1 and the pyridine ring may resemble that of the reactive 2-aminopyridine. Although a few substitution reactions are recorded (5), detailed information is lacking for "standard" reactions, and no published suggestions exist about the preferred sites of attack. We have effected typical electrophilic nitrations (using "mixed acids") and brominations, where the preferred site of attack is the 3-position: if this position is occupied, then, under more vigorous conditions, the 5-position may be substituted. Also, if N-1 carries an aryl ring, it undergoes preferential mono- or dinitration. Such behavior resembles that of the previously studied *N*-arylpyrazoles (35).

The preferred nitration at the 3-position is in contrast to the behavior of indazole (the corresponding 7-deaza species), where mixed-acid nitrations occur at the 5-position, while brominations of indazole and of 1-substituted pyrazolo[3,4-*b*]-pyridines occur similarly at the 3-position (30, 36). The differences may be interpreted simply in terms of electrostatic deactivation through protonation (or incipient protonation) at the 2-nitrogen of indazole and at the 7-nitrogen of the pyrazolo[3,4-*b*]pyridine, the sites of highest effective π-electron density (and total electron density) in the free bases of these species (see refs. 28, 37, and Figs. 1*a*, 1*b*). The identities of the nitration and the bromination products are defined by their ^1H nmr spectra (disappearance of proton signals at the 3- and (or) 5-positions and the simplification of coupling patterns for the proton signals at positions 4 and 6). Alternatively, the ^{13}C nmr spectra of the 3-substitution products define the structures through proportionalities existing between ipso-substituent chemical shift (scs) effects in the quaternary 3-carbons in the substitution products to those in monosubstituted benzenes (cf. Lynch (38)) (see Fig. 2), while in the

Can. J. Chem. Downloaded from www.nrcresearchpress.com by 176.9.209.113 on 09/07/12
For personal use only.

TABLE 1. 1*H*-Pyrazolo[3,4-*b*]pyridines

Compound no.	R1	R3	R4	R5	R6	Preparation method[a]	Yield (%)	Melting (boiling) range (°C), cryst. solvent[b]
1	H unless otherwise indicated					A	25	97–98,[c] Bz
2	Me					A	50	(78–80/1 Torr)*
						B	50	
						R	65	
						S	90	
3	Me	Ph				A	100	72–74, Bz
						B	71	
						O	45	
4		Me				A	73	158–160, BP
5	Me	Me				A	59	(238–240)
						B	100	
6		Ph				A	88	164–168,[d] EtH
7		NH_2				A		184–185, EtH
8	Me	NH_2				A	46	104–106, Bz
9	Me	NH_2	Me		Me	A	70	90–92, Bz
12	Ph					B	97	53,[e] P
13	Ph		Me		Me	B	82	65–66[f]
14	Me	Ph	Me		Me	B	79	120–121, P
15	Ph	Ph				B	90	96–98, EW
16	Ph	Ph	Me		Me	B	77	112–114[g]
17	Me		Me		Me	B	59	183–184,[h] Eth
18	Me	Me	Me		Me	B	94	234–235,[h] Eth
19	Ph	Me				B	70	50–51,[i] EW
20	Ph	Me	Me		Me	B	85	127–128, EW
21	*p*-$NO_2 \cdot C_6H_4$	Me				B	68	200–202, EW
22	*p*-$NO_2 \cdot C_6H_4$	Me	Me		Me	B	46	225–226, Eth
23	Me	Me		NO_2		B	12	145–146, EW
						E	30	
24	2,4-$(NO_2)_2 \cdot C_6H_3$	Me				B	64	178–180, Eth
						E[j]	82	
						N	25	
25	2,4-$(NO_2)_2 \cdot C_6H_3$	Me		NO_2		B	48	152–156, Eth
						E[k]	91	
26	Ph				Me	B	100	87–88, Eth
27	Me			NO_2		B	11	138–139, Eth
28	Ph	Ph			Me	B	100	123–125, Bzp
29	Me	Ph			Me	B	100	67–68, P
30	*p*-$NO_2 \cdot C_6H_4$	Me			Me	B	75[l]	194–195, Bz
31	*p*-$NO_2 \cdot C_6H_4$	Me	Me			B	15[l]	168–170, Bz
32	Me	Me			Me	B	47	(95/1 Torr)
33	Me				Me	B	62	(90/1 Torr)
34	Ph	Me			Me	B	41	43–46, Bz
35				NO_2		B	85	212–213[m]
36	2,4-$(NO_2)_2 \cdot C_6H_3$	Me	Me		Me	B	100	173–174, Eth
37	Ph		OH	CN		C	32	225–227[m]
38	Me		OH	CN		C	18	>300[m]
39	Me	Me	OH	CN		C	35	>300[m]
40	Me	Ph	OH	CN		C	19	>300[m]
41	Ph		NH_2	CN		C	37	257–260, Eth
42	Me	Me	OH	Ac		C	77	143–144, EW
43	Me	Ph	OH	Ac		C	88	177–178, EW
44	Ph	Me	OH	Ac		C	70	156–157, EW
45	Me	Me	Cl	CO_2Et		D	89	93–94, EW
46	Me	Ph	Cl	CO_2Et		D	73	130–131, EW
47	Ph	Ph	Cl	CO_2Et		D	69	162–163, EW
48	Ph	Me	Cl	CO_2Et		D	80	110, EW
49	Ph	Me	Cl	Ac		D	74	112–113, EW
50	*p*-$NO_2 \cdot C_6H_4$	Me		NO_2		B	25	175, Eth
51		Me		NO_2		E	70	188–190[m]
52		NO_2				E	61	263–264, Eth
53	Me	NO_2				E	90	121–122, EW
54	Me	NO_2		NO_2		E	64	164–165, Eth
55	Me	Br				F	65	81–82, Met
						H	63	

Can. J. Chem. Downloaded from www.nrcresearchpress.com by 176.9.209.113 on 09/07/12
For personal use only.

TABLE 1 (*concluded*)

Compound no.	R1	R3	R4	R5	R6	Preparation method[a]	Yield (%)	Melting (boiling) range (°C), cryst. solvent[b]
56		Br				F	75	165–166, Eth
57	Me	Cl		Cl		G	62	89–90, Eth
58	Me	Br	Me		Me	H	68	115–117, Met
59	Me	Cl				I	58	35–38, Met
60		N_2^+				J	37	178(dec.), EtOAc
61	Me	$NH \cdot NH_2$				K	56	162–164, Met
62		CO_2H				L	16	265–270(dec.), Eth
63	Me	CO_2H				L	44	272–274(dec.), Eth
64	$PhCH_2$(R2)					M	34	142–144, P
65	2,4-$(NO_2)_2 \cdot C_6H_3$					N	35	175–176, Eth
66	2,4-$(NO_2)_2 \cdot C_6H_3$(R2)					N	28	214–215, Met
67	2,4-$(NO_2)_2 \cdot C_6H_3$(R2)Me					N	18	194–196, Eth
68	Me	1-Pyrazolyl				P	76	163–164,[h] Eth
69					$CO \cdot NH_2$	Q	25	290, Eth
70	Ph				$CO \cdot NH_2$	Q	30	207–209, Eth
71	Me			$CO \cdot NH_2$		Q	30	[n]
72	Me				$CO \cdot NH_2$	Q	15	[n]

[a]See text of experimental section.
[b]Abbreviated as follows: Bz = benzene, BP = benzene/pentane; Eth = ethanol; EtOAc = ethyl acetate; EW = ethanol/water; Met = methanol, P = pentane.
[c]Literature (1) mp 98–99°C; also obtained in 82% yield from decarboxylative rearrangement of pyrazolo[1,5-*a*]pyrimidine-3-carboxylic acid (29).
[d]Literature (2) mp 168–169°C.
[e]Literature (2) mp 53.5–54°C.
[f]Literature (3) mp 65°C.
[g]Literature (49) mp 112–115°C.
[h]Picrate derivative.
[i]Literature (2) mp 54°C.
[j]From nitrations of **19** and of **21**.
[k]From nitrations of **24**.
[l]Total yield of mixture. Product mixture was separated by adsorption chromatography on silica gel.
[m]Purified by sublimation.
[n]Unseparated mixture: relative yields established by nmr integration.
*1 Torr = 133.3 Pa.

Can. J. Chem. Downloaded from www.nrcresearchpress.com by 176.9.209.113 on 09/07/12
For personal use only.

substitution products derived from the 1-methylpyrazolo[3,4-*b*]pyridine, **2**, the 1-methyl ^1H shifts are related precisely to the Hammett σ_p constant of the 3-substituent (Fig. 3). In some instances, the identities of the nitration products were also established by independent, direct syntheses. Chlorinations yielded 3,5-dichloro compounds. The results of these substitution reactions are summarized in Scheme 3.

The 3-amino group in 3-aminopyrazolo[3,4-*b*]pyridines behaves as a typical aromatic amine, and provides useful entries to many other 3-substituted species. Hatt and Vass (1) have reported deamination of **7**, providing **1** in unspecified yield via the diazonium species. Aminoazoles (of which **7** is a representative) give very stable internally neutralized diazonium azolides (37) and our attempts at repetition of Hatt and Vass's work provided the compound **60**.

We have accomplished deamination (protodediazoniation) of several 1-alkyl and 1-aryl-3-aminopyrazolo[3,4-*b*]pyridines in excellent yields via aprotic diazotization employing alkyl nitrites in chloroform (39). Similar aprotic procedures (bromodediazoniation using bromoform as solvent/reactant, or chlorodediazoniation using carbon tetrachloride) provided simple, convenient alternatives to the Sandmeyer reaction. The 1-methyl-3-pyrazolo[3,4-*b*]pyridine radical generated in such procedures arylates benzene to 1-methyl-3-phenyl-pyrazolo-[3,4-*b*]pyridine **3**, identical to samples prepared by cyclization routes. The reactions of the 3-amino series are summarized in Scheme 4.

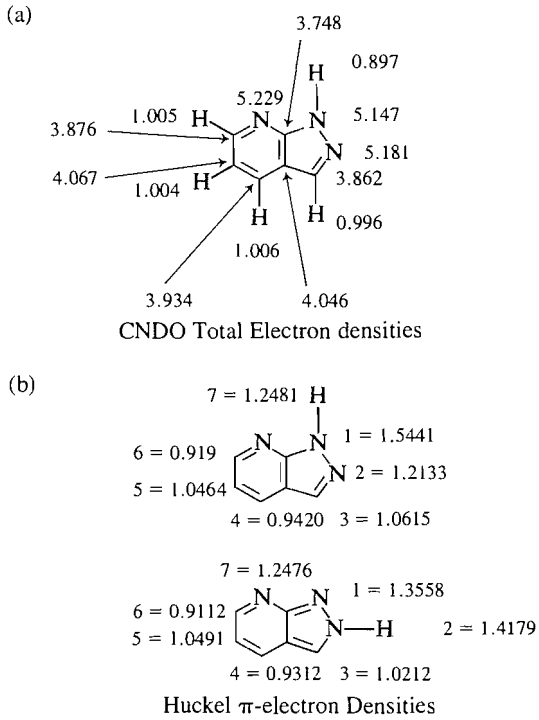

FIG. 1.(*a*) CNDO total electron densities. (*b*) Huckel π-electron densities.

TABLE 2. ^{1}H nuclear magnetic resonance spectra of selected pyrazolo[3,4-*b*]pyridines

Compound no.	R1	R3	R4	R5	R6	H(R)-3	H(R)-4	H(R)-5	H(R)-6	Solvent
1	H unless otherwise indicated					8.78	9.30	7.93	9.28	TFA-*d*
						8.20	8.30	7.23	8.57	DMSO-d_6
						8.15	8.10	7.13	8.65	$CDCl_3$
2	Me					8.73	8.92	7.90	9.15	TFA-*d*(1-Me, 4.47)
						8.01	7.90	6.56	8.56	$CDCl_3$(1-Me, 4.12)
3	Me	Ph				7.25–8.07	8.33	7.13	8.59	$CDCl_3$(1-Me, 4.21)
5	Me	Me				2.55	7.98	7.05	8.56	$CDCl_3$(1-Me, 4.08)
6		Ph				7.57s	8.17	7.53	8.61	DMSO-d_6
7		NH_2				5.63br	8.02	7.00	8.43	DMSO
8	Me	NH_2				5.41br	8.11	6.88	8.35	DMSO
						4.23	7.86	6.91	8.48	$CDCl_3$(1-Me, 3.91)
12	Ph					8.94	8.86	7.92	9.25	TFA(1-Ph, 7.75s)
13	Ph		Me		Me	8.88	2.93	7.55	3.06	TFA(1-Ph, 7.88s)
18	Me	Me	Me		Me	2.50	2.35	5.77	2.40	TFA-*d*(1-Me, 3.75)
23	Me	Me		NO_2		2.88	9.40	—	9.78	TFA-*d*(1-Me, 4.33)
						2.63	8.90	—	9.43	$CDCl_3$(1-Me, 4.15)
26	Ph				Me	8.78	9.00(8)	7.70(8)	2.96	TFA-*d*(1-Ph, 7.70s)
27	Me			NO_2		8.87	9.60	—	9.93	TFA-*d*(1-Me, 4.63)
28	Ph	Ph			Me	7.73s	9.08(8)	7.66(8)	3.03	TFA-*d*(1-Ph, 7.73s)
29	Me	Ph			Me	7.66m	8.96	7.63	3.00	TFA-*d*(1-Me, 4.41)
30	PNP	Me			Me	2.87	7.80(8)	7.69(8)	3.00	TFA-*d*(PNP, 8.72)
31	PNP	Me	Me			2.55	2.85	7.60(6)	8.55(6)	TFA-*d*(PNP, 8.72)
32	Me	Me			Me	2.82	8.81(8)	7.60(8)	3.10	TFA-*d*(1-Me, 4.33)
33	Me				Me	8.60	8.87(8)	7.60(8)	3.07	TFA-*d*(1-Me, 4.40)
35				NO_2		8.45	9.33	—	9.45	TFA-*d*
51		Me		NO_2		2.88	8.76	—	8.64	$CDCl_3$
52		NO_2				—	9.46	8.06	9.16	TFA-*d*
53	Me	NO_2				—	8.64	7.48	8.76	$CDCl_3$(1-Me, 4.32)
54	Me	NO_2		NO_2		—	9.62	—	9.76	TFA-*d*(1-Me, 4.46)
56		Br				—	9.03	7.93	9.15	TFA-*d*
64	CH_2Ph(R-2)					7.88	8.00(8)	7.00(4,8)	8.70(4)	$CDCl_3$ (CH_2Ph, 5.67; -CH_2Ph, 7.35)
Compare literature data (5) for the 1-isomer:										
						7.83	7.80	6.86	8.42	$CDCl_3$ (CH_2Ph, 5.67; -CH_2Ph, 7.10)
65	DNP					8.30	8.00	7.23	8.50	$CDCl_3$
66	DNP(R-2)					8.43	8.37	7.31	8.75	DMSO-d_6
69					$CO{\cdot}NH_2$	8.00	8.14(8)	7.60(8)	—	DMSO
70	Ph				$CO{\cdot}NH_2$	8.78	8.70(8)	8.63(8)	—	TFA-*d*(1-Ph, 7.70s)
71	Me			$CO{\cdot}NH_2$		8.50	—	7.60(5)	8.70(5)	DMSO-d_6 (1-Me, 4.10)
72	Me				$CO{\cdot}NH_2$	8.31	8.34(8)	7.90(8)	—	DMSO-d_6 (1-Me, 4.15)

PNP = *p*-nitrophenyl; DNP = 2,4-dinitrophenyl. Numerical entries in parentheses after chemical shifts are vicinal coupling constants in Hz.

Further exploratory reactions were carried out on the derived products. Thus 3-bromo-1-methylpyrazolo[3,4-*b*]pyridine **5** undergoes smooth nucleophilic hydrazinodebromination yielding 3-hydrazino-1-methylpyrazolo[3,4-*b*]pyridine **61**, converted into 1-methyl-3-(1′-pyrazolyl)pyrazolo[3,4-*b*]pyridine **68** by condensation with 1,1,3,3-tetramethoxypropane. Vigorous oxidation of a 3-methyl group to the 3-carboxylic acids was successful with **4** and **5**, and these oxidations offer alternative routes to pyrazolo[3,4-*b*]pyridines with an unsubstituted 3-position, since the acids are readily decarboxylated. Benzylation of **1** using sodium ethoxide/benzyl chloride yielded 2-benzylpyrazolo[3,4-*b*]pyridine **64** rather than the previously synthesized 1-isomer (5), while *N*-dinitrophenylations of **1** and of **4** via 2,4-dinitro-1-fluorobenzene yielded mixtures of 1- and 2-(2,4-dinitrophenyl)pyrazolo[3,4-*b*]pyridines, readily separable by adsorption chromatography. Differentiation of structure between 2- and 1-substituted pyrazolo[3,4-*b*]pyridines is assisted by the general phenomenon that proton signals in corresponding ring sites in the 2-isomers are downfield from those in the 1-isomers (see Fig. 4, exemplifying 1- and 2-benzyl and 1- and 2-(2,4-dinitrophenyl)pyrazolo[3,4-*b*]pyridines). This is generally consistent with the calculated π-electron density distributions at the 3-, 4-, 5-, and 6-carbon atoms in such species (compare Fig. 1*b*). 2,4-Dinitrophenyl moieties attached to N-1 or N-2 of an azole species are easily displaced by nucleophiles such as methoxide or ethoxide ions (40, 41), and this strategy allows circumvention of the undesirable cyclizations of 5(3)-aminopyrazoles to pyrazolo[1,5-*a*]pyrimidines.

Can. J. Chem. Downloaded from www.nrcresearchpress.com by 176.9.209.113 on 09/07/12
For personal use only.

TABLE 3. ^{13}C nuclear magnetic resonance spectra of selected 1*H*-pyrazolo[3,4-*b*]pyridines

Compound no.	Substituents					Shifts					
	N-1	C3	C4	C5	C6	C3	C3a	C4	C5	C6	C7a
1	H unless otherwise indicated					130.4	114.7	133.2	116.7	148.6	151.7
						(DMSO-d_6)					
2	Me					131.8	115.8	130.0	116.7	148.9	150.7
						(Me, 33.9)					
						($CDCl_3$)					
3	Me	Ph				141.5	112.7	132.9	117.5	149.1	151.2
						(Me, 33.75)					
						($CDCl_3$)					
4		Me				141.2	114.2	129.6	116.1	148.7	152.7
						(Me, 12.1) (DMSO-d_6)					
5	Me	Me				139.6	114.3	129.4	115.6	148.4	150.6
						(1-Me, 32.9, 3-Me, 11.7) (DMSO-d_6)					
						140.5	115.2	129.4	115.8	148.8	151.3
						(1-Me, 33.5, 3-Me, 12.3) ($CDCl_3$)					
6		Ph				144.9	113.7	131.1	117.3	148.8	153.6
						(Ph:ipso 133.5, 2- 127.4, 3- 129.1, 4- 128.7)					
						($CDCl_3$)					
8	Me	NH_2				147.2	106.6	124.7	113.5	148.5	150.8
						(1-Me, 32.4) (DMSO-d_6)					
						145.8	107.0	128.8	114.5	149.4	151.3
						(1-Me, 33.1) ($CDCl_3$)					
12	Ph					134.9	117.1	131.2	118.2	149.5	149.8
						(Ph:ipso 139.5, 2- 120.6, 3- 129.2, 4- 126.0)					
						(DMSO-d_6)					
13	Ph		Me		Me	142.5	129.4	133.5	118.7	158.8	151.0
						(4-Me, 17.8; 6-Me, 24.6; Ph: ipso 139.7, 2- 120.6, 3- 129.2,					
						4- 125.8) ($CDCl_3$)					
19	Ph	Me				129.2	117.6	130.6	120.3	149.5	143.1
						(Ph:ipso 139.5, 2- 120.3, 3- 129.2, 4- 125.5)					
						(3-Me, 12.1) ($CDCl_3$)					
27	Me			NO_2		135.3	113.9	128.0	137.9	144.4	150.7
						(1-Me, 34.0) (DMSO-d_6)					
52		NO_2				147.6	107.9	129.8	121.3	151.2	151.8
55	Me	Br				118.9	116.2	129.5	117.4	150.0	151.1
						(1-Me, 34.2) ($CDCl_3$)					
56		Br				119.3	114.4	128.8	117.7	150.3	151.9
						(DMSO-d_6)					
58	Me	Br	Me		Me	119.3	117.6	142.7	119.3	159.3	152.0
						(1-Me, 34.1, 4-Me, 17.8, 6-Me, 24.7)					
						($CDCl_3$)					

In this way the products **4** and **52** are obtained from the corresponding 1-(2,4-dinitrophenyl) precursors.

A limited study was made of the reactivity of pyrazolo[3,4-*b*]pyridines toward homolytic (free-radical) reagents, employing the nucleophilic carbamoyl radical, which would be expected to attack the pyridine ring preferentially. Carbamoylation using aqueous formamide and hydrogen peroxide in the presence of iron(II) sulfate (following Minisci and Gardini (42)) effected carbamoylation at the 6-position of compounds **1** and **12**, providing **69** and **70**, while **2** gave a mixture of its 4- and 6-carbamoyl derivatives, with the 6-carbamoyl species predominating. The structures again follow from the characteristic proton–proton coupling patterns in the pyridine rings ($J_{4,5} > J_{5,6}$).

Experimental

General

Melting points were determined using a Fisher–Johns block or a Kofler Heizbank and are uncorrected. The ^1H magnetic resonance spectra were acquired for dilute solutions (2% w/v) using a Varian A-60D spectrometer, and ^{13}C magnetic resonance spectra for 10% w/v solutions using a Bruker WP-80 spectrometer operating at 20.12 MHz, a 30° pulse of length 3.00 ms, and 16K data points with sweep width 5000 Hz. Data appearing in Table 3 were acquired using broadband decoupling (3 W), and signal assignments were confirmed using gated decoupling sequences. Signals are in parts per million (δ) from internal tetramethylsilane. Elemental analytical results for the compounds listed in the tables have been deposited with the Depository of Unpublished Data.[6]

Starting materials

The following were prepared according to literature procedures: 5-amino-1-methyl-3-phenylpyrazole (43); 5-amino-1,3-diphenylpyrazole (44); 3(5)-amino-5(3)-phenylpyrazole (45); 5-amino-1,3-dimethylpyrazole (45); 5-amino-3-methyl-1-*p*-nitrophenylpyrazole and 5-amino-3-methyl-1-(2,4-dinitrophenyl)pyrazole (45); 5-amino-4-

[6]These data may be purchased from the Depository of Unpublished Data, CISTI, National Research Council of Canada, Ottawa, Ont., Canada K1A 0S2.

Can. J. Chem. Downloaded from www.nrcresearchpress.com by 176.9.209.113 on 09/07/12
For personal use only.

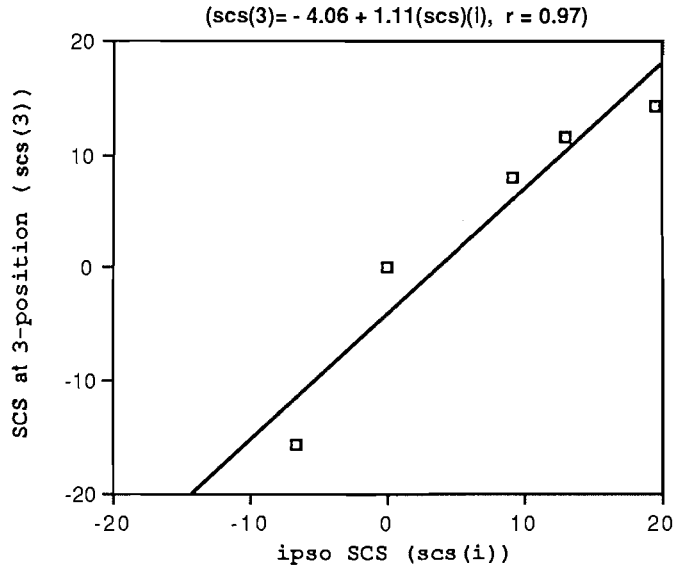

FIG. 2. Plot of 3-SCS (pyrazolo[3,4-*b*]pyridines) vs. ipso SCS.

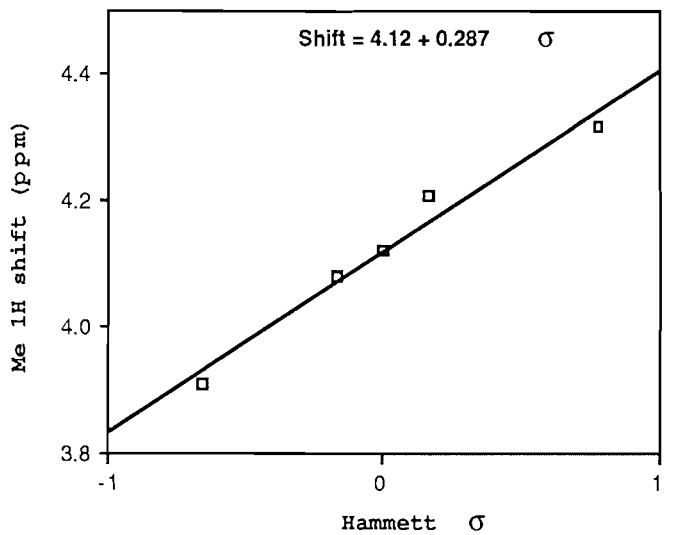

FIG. 3. 1-Me proton shifts vs. σ, for 1-methyl-3-substituted pyrazolo[3,4-*b*]pyridines.

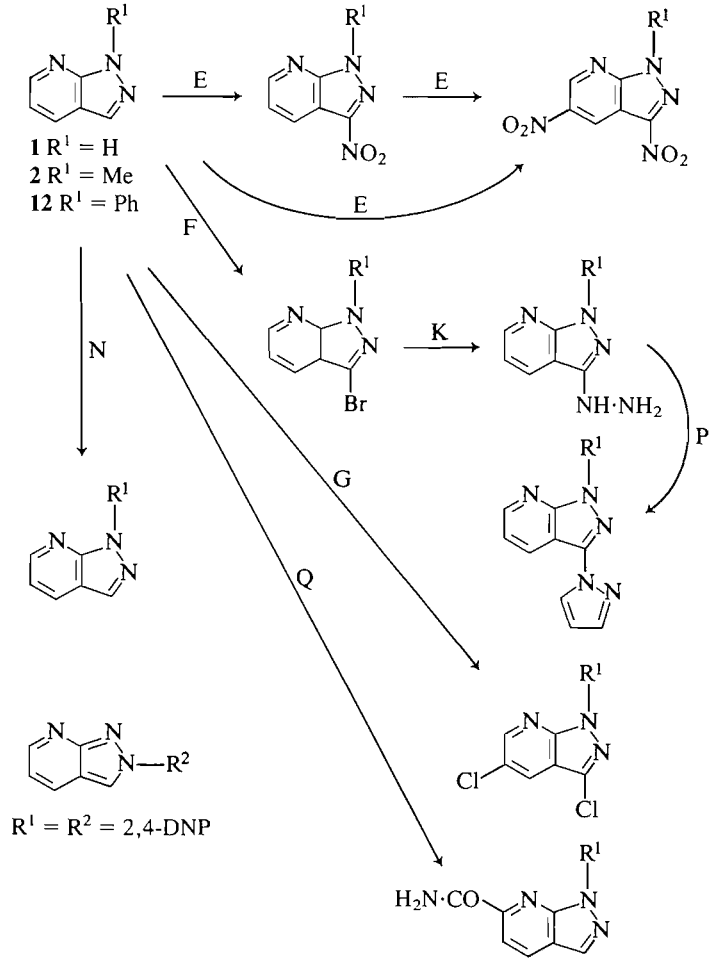

(See text for letter key to methods)

SCHEME 3

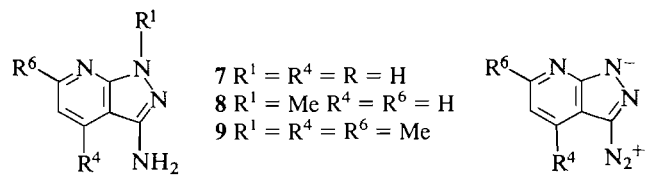

SCHEME 4

cyano-1-methylpyrazole and 5-amino-4-cyano-1-phenylpyrazole (46); 2-chloropyridine-3-aldehyde (from 2-chloro-3-cyanopyridine following ref. 31); ethyl ethoxymethyleneacetoacetate (47). Other reagents and materials were commercial products.

5-Amino-1-methylpyrazole, 5-amino-1-phenylpyrazole

These compounds were prepared by hydrolytic decarboxylation of their corresponding 4-cyano precursors: The pyrazole (30 g) and 85% phosphoric acid (100 mL) were heated at 170–180°C for 20 h. The mixture was poured onto crushed ice, basified with 60% NaOH, and extracted with $CHCl_3$. Evaporation of the extracts afforded 5-amino-1-methylpyrazole, mp 70°C (lit. (48) mp 71–72°C), 5-amino-1-phenylpyrazole, mp 50°C (lit. (49) mp 50°C) in 90% yields.

Pyrazolo[3,4-b]pyridines

The various synthetic methods employed in the syntheses and reactions yielding the compounds **1** through **72** are described below.

Method A. 2-Chloro-3-substituted pyridines with hydrazines

3-Acetylpyridine, 3-benzoylpyridine, and 3-cyanopyridine (0.2 mol) were severally heated for 10 h at 50°C in a mixture of acetic acid (200 mL) and 30% hydrogen peroxide (50 mL). The reaction mixtures were evaporated under reduced pressure and the residues treated with saturated aqueous $NaHCO_3$ and extracted with $CHCl_3$. The *N*-oxides obtained were heated under reflux with phosphorus oxychloride (2 mol) for 6 h. Excess of phosphorus oxychloride was distilled off and the residues were poured onto crushed ice, allowed to stand for 5 h, and extracted with ether, yielding the corresponding 2-chloro-3-substituted pyridines.

A sample of the appropriate 2-chloro-3-substituted pyridine (1 g) was heated under reflux with hydrazine hydrate (10 mL) or methylhydrazine (10 mL) in ethanol (50 mL) for 10 h; the excess of solvent and hydrazine was removed under reduced pressure, and the products were isolated and purified by crystallization or distillation as appropriate (see Table 1).

Reaction with 2-chloropyridine-3-aldehyde was atypical: to a solution of 2-chloropyridine-3-aldehyde (1.0 g) in ethanol (20 mL) was

Can. J. Chem. Downloaded from www.nrcresearchpress.com by 176.9.209.113 on 09/07/12
For personal use only.

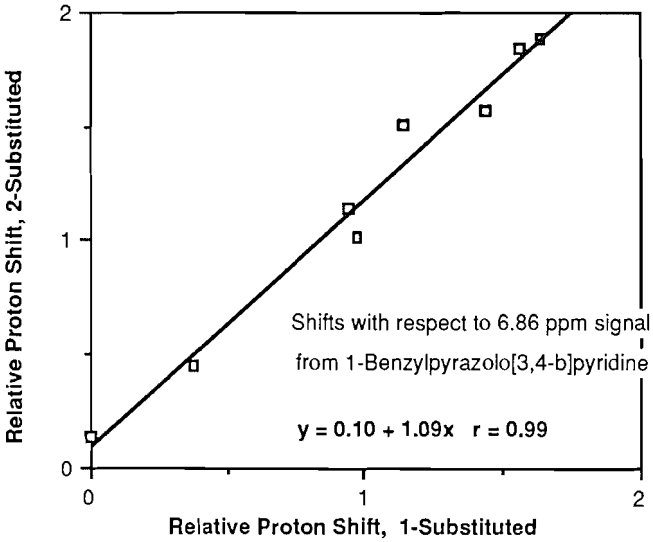

FIG. 4. Relative proton shifts, 2- vs. 1-substituted pyrazolo[3,4-*b*]pyridines.

added hydrazine (2.0 mL), and the mixture was heated under reflux for 24 h. Solvent and excess hydrazine were removed under reduced pressure and the residue was extracted with hot benzene yielding 2-hydrazinopyridine-3-aldehyde azine **11** (yellow needles, from benzene) (1.0 g), mp 191–193°C. *Anal.* calcd. for $C_{12}H_{12}N_8$: C 53.40, H 5.20, N 41.4; found: C 53.60, H 4.94, N 41.6%. The filtrate from the benzene extracts was purified by adsorption chromatography on alumina using benzene as eluent, yielding 1*H*-pyrazolo[3,4-*b*]pyridine **1**, mp 97–98°C (0.23 g), identical with an authentic sample (1, 29).

Method B. Cyclizations of 5-aminopyrazoles with 1,3-dicarbonyl compounds

An appropriate 5-aminopyrazole (0.005 mol) was dissolved in ethanol (10 mL) and 12 M HCl (0.50 mL) was added to the stirred solution, followed by granulated zinc chloride (0.30 g). The mixture was heated to reflux, and to the mixture was added a solution of 0.005 mol of the source of the appropriate 1,3-dicarbonyl compound in ethanol (5 mL), either 4,4-dimethoxy-2-butanone (acetylacetaldehyde dimethylacetal), 1,1,3,3-tetramethoxypropane (malonaldehyde bis(dimethylacetal)), 2,4-pentanedione, or sodium nitromalonaldehyde hydrate. After 1 h the reaction mixture was poured into ice-cold water (15 mL), the resultant solution was made alkaline with concentrated aqueous ammonia, and the product was isolated by suction filtration (for solids) or $CHCl_3$ extraction. The products were isolated and purified by crystallization or distillation as appropriate (see Table 1).

Method C. From 5-aminopyrazoles and ethoxymethylene compounds (see Scheme 2). β-(1-Pyrazol-5-ylaminoacrylates)

Appropriate equimolar mixtures of 5-aminopyrazoles and the ethoxymethylene compounds in ethanol were heated under reflux for 2 h, the reaction mixtures were concentrated and cooled, and the products were collected by suction filtration and crystallized from ethanol. Details of the properties of these compounds, including analytical and spectroscopic data, have been deposited with the Depository of Unpublished Data.[6]

Thermocyclizations of the β-(1-pyrazol-5-ylaminoacrylates) to 4-hydroxypyrazolo[3,4-b]pyridines (see Scheme 2)

The above β-(1-pyrazol-5-ylaminoacrylates) were heated under reflux with a fourfold weight excess of Dowtherm A or phenyl ether for 4 h. Excesses of solvent were removed under reduced pressure and the products isolated by crystallization after dilution with petroleum ether (bp 40–60°C). Details of yields are given in Table 1.

Method D. Chlorocyclization to 4-chloropyrazolo[3,4-b]pyridines (see Scheme 2)

The aminoacrylates used as starting materials for method C were heated under reflux with a fourfold weight excess of phosphorus oxychloride for 4 h. Excesses of solvent were removed under reduced pressure, the residues poured onto crushed ice, and the products crystallized from aqueous ethanol.

The pyrazolo[3,4-*b*]pyrid-4-ones (4-hydroxypyrazolo[3,4-*b*]pyridines) obtained by method C were also convertible into the corresponding 4-chloropyrazolo[3,4-*b*]pyridines by heating under reflux with phosphorus oxychloride.

*Method E. Nitrations (e.g., **1** → **52**; **2** → **53**; **4** → **51**; **5** → **23**; **19** and **21** → **24**; **24** → **25**)*

Mono- and dinitrations of pyrazolo[3,4-*b*]pyridines were carried out using the following typical procedure.

To 1*H*-pyrazolo[3,4-*b*]pyridine (**1**) (0.300 g) in sulfuric acid (d 1.84, 15 mL) was added nitric acid (90%, 0.5 mL) and the reaction mixture was heated at 90°C for 0.5 h, poured onto ice (100 g), and collected and crystallized. Additional amounts of product were recovered by extraction of the filtrates with ethyl acetate, followed by evaporation and crystallization.

*Method F. Brominations (e.g., **1** → **56**; **2** → **55**)*

The substrate pyrazolo[3,4-*b*]pyridine (0.01 mol) was dissolved in $CHCl_3$ (20 mL). Bromine (0.60 mL) was added dropwise over a period of 30 min, the reaction mixture was washed free of acid with aqueous K_2CO_3, and then dried over anhydrous K_2CO_3. The solvent was evaporated and the residue crystallized from an appropriate solvent.

*Method G. Chlorination (e.g., **2** → **57**)*

To 1-methylpyrazolo[3,4-*b*]pyridine **2** (1.3 g) in water (20 mL), acetic acid (0.5 mL) was added, followed by 5% aqueous sodium hypochlorite (15 mL). The mixture was stirred at room temperature for 3 h, neutralized with K_2CO_3, and extracted with $CHCl_3$. Evaporation of the dried extract was followed by crystallization.

*Method H. Bromodediazoniation (e.g., **8** → **55**)*

The substrate 3-aminopyrazolo[3,4-*b*]pyridine (5.0 g) was heated under reflux for 3 h with butyl nitrite (7.0 g) in bromoform (30 mL). Solvent and volatile material were removed under reduced pressure, and the residue was crystallized.

Method I. Chlorodediazoniation

The substrate 3-aminopyrazolo[3,4-*b*]pyridine (1.0 g) was heated under reflux for 3 h with butyl nitrite (1.5 g) in carbon tetrachloride (25 mL). Solvent and volatile material were removed under reduced pressure, and the residue was crystallized.

*Method J. Diazotization (**7** → **60**)*

3-Aminopyrazolo[3,4-*b*]pyridine **7** (2.6 g) in 70% nitric acid (10 mL) was diazotized at 0–5°C by a solution of 30% aqueous sodium nitrite (5 mL), and added to a further 15 mL of 30% aqueous sodium nitrite. Acetic acid (5 mL) was added after 1 h and the mixture was heated at 60–80°C for 30 min, cooled, and filtered, yielding the internal diazonium salt **60**.

*Method K. Hydrazinodebromination (**55** → **61**)*

3-Bromo-1-methylpyrazolo[3,4-*b*]pyridine **55** (1.0 g) was heated under reflux with 95% hydrazine (10 mL) for 24 h. 3-Hydrazino-1-methylpyrazolo[3,4-*b*]pyridine **61** separated from the cooled reaction mixture and was collected by filtration and purified.

Method L. Oxidations

1,3-Dimethylpyrazolo[3,4-*b*]pyridine **5** (1.0 g) was heated under reflux with sodium hydroxide (2.0 g) and potassium permanganate (4.0 g) in water (150 mL) for 2 h. The solid residue was filtered off and the filtrate was acidified with sulfuric acid and extracted with ethyl acetate. The solvent was removed and the residue was crystallized.

*Method M. Benzylation (**1** → **64**)*

1*H*-pyrazolo[3,4-*b*]pyridine **1** (1.2 g) and benzyl chloride (1.6 g) were heated under reflux in 5% ethanolic sodium ethoxide (10 mL) for 90 min. The solvent was evaporated and the residue extracted with $CHCl_3$ and the product was crystallized.

Can. J. Chem. Downloaded from www.nrcresearchpress.com by 176.9.209.113 on 09/07/12
For personal use only.

Can. J. Chem. Downloaded from www.nrcresearchpress.com by 176.9.209.113 on 09/07/12
For personal use only.

Method N. N-(2,4-Dinitrophenylation)

To 1*H*-pyrazolo[3,4-*b*]pyridine **1** (0.30 g) in methyl sulfoxide (5 mL) and triethylamine (0.5 mL) was added 2,4-dinitrofluorobenzene (0.47 g). The solution was stirred for 1 h and poured onto crushed ice. The precipitate was collected, washed with water, and extracted with $CHCl_3$, and the product mixture was separated by adsorption chromatography on silica gel.

Method O. C-Arylation (8 → 3)

3-Amino-1-methylpyrazolo[3,4-*b*]pyridine **8** (0.9 g) was added to butyl nitrite (1.0 g) and benzene (50 mL) and the mixture was heated under reflux for 2 h. Volatile materials were removed and the residue was purified by adsorption chromatography on silica gel, and the product was crystallized.

Method P. Pyrazole synthesis (61 → 68)

A mixture of 3-hydrazino-1-methylpyrazolo[3,4-*b*]pyridine **61** (0.6 g), 1,1,3,3-tetramethoxypropane (0.6 g), 12 M HCl (0.5 mL), and ethanol (20 mL) was heated under reflux for 90 min. The reaction mixture was diluted with water (25 mL), neutralized with aqueous ammonia, and extracted continuously with $CHCl_3$. After removal of solvent from the extract the residue was extracted with pentane and the 1-methyl-3-(1-pyrazolyl)pyrazolo[3,4-*b*]pyridine **68** was crystallized.

Method Q. Carbamoylations

To a solution of pyrazolo[3,4-*b*]pyridine **1** (1.0 g) and sulfuric acid (d 1.84, 0.5 g) in formamide (10 mL) were added, separately and simultaneously, hydrogen peroxide (30%, 3 mL) and powdered iron(II) sulfate heptahydrate (4 g), with efficient cooling (<10–15°C) and stirring over 30 min. The excess of formamide was evaporated under reduced pressure, and the residue Soxhlet-extracted with $CHCl_3$. The carbamoylation product was obtained on evaporation of the extract.

Method R. Protodediazoniation (8 → 2)

3-Amino-1-methylpyrazolo[3,4-*b*]pyridine **8** (1.0 g), $CHCl_3$ (15 mL), and butyl nitrite (1.5 g) were heated under reflux for 1 h. Solvent and volatile material were removed under reduced pressure, and the residue was purified by adsorption chromatography on alumina and crystallized.

Method S. Decarboxylations (63 → 2)

1-Methylpyrazolo[3,4-*b*]pyridine-3-carboxylic acid **63** was heated under reduced pressure in a cold-finger sublimation apparatus until the temperature reached 270°C. The condensate was identical with an authentic sample of 1-methylpyrazolo[3,4-*b*]pyridine **2**.

Acknowledgements

We acknowledge financial support from the Natural Research Councils of Brasil and Canada, the Natural Sciences and Engineering Research Council of Canada, and the National Cancer Institute of Canada, for operating grants and equipment grants funding.

1. T. L. P. Hatt and J. L. R. Vass. Chem. Commun. 293 (1966).
2. I. I. Grandberg. Zh. Obshch. Khim. **31**, 2307 (1961).
3. S. V. Tabak, I. I. Grandberg, and A. N. Kost. Khim. Geterotsikl. Soedin. 116 (1965).
4. H. Hoehn, T. Denzel, and W. Jannsen. J. Heterocycl. Chem. **9**, 235 (1972).
5. R. J. J. Dorgan, J. Parrick, and C. R. Hardy. J. Chem. Soc. Perkin Trans. 1, 938 (1980).
6. E. C. Taylor and A. J. Crovetti. J. Org. Chem. **19**, 1633 (1954).
7. H. Dorn and A. Zubek. Angew. Chem. Int. Ed. Engl. **6**, 958 (1967).
8. G. M. Badger and R. P. Rao. Aust. J. Chem. **18**, 1267 (1965).
9. H. Reimlinger, M. A. Peiren, and R. Merenyi. Chem. Ber. **103**, 3252 (1970).
10. S. Chechi, P. Papini, and M. Ridi. Gazz. Chim. Ital. **85**, 1160 (1955).
11. L. Baiocchi. Ann. Chim. **60**, 403 (1970).
12. H. Dorn and A. Zubek. Chem. Ber. **101**, 3265 (1968).
13. I. A. Korbukh, F. F. Blanko, M. N. Preobrazenskaya, and H. Dorn. J. Org. Chem. U.S.S.R. **7**, 2739 (1971).
14. I. I. Grandberg and S. V. Tabak. Khim. Geterotsikl. Soedin. 112 (1965).
15. R. P. Rao. Rec. Chem. Progr. **29**, 106 (1968).
16. P. Bellani, E. Lauria, and G. Zoni. Farmaco, Ed. Sci. **26**, 872 (1971).
17. J. Haufel and E. Breitmaier. Angew. Chem. Int. Ed. Engl. **12**, 922 (1973).
18. T. Denzel. Arch. Pharm. (Weinheim, Ger.), **307**, 177 (1974).
19. J. L. Imbach, R. Jacquier, and J. L. Vidal. Bull. Soc. Chim. Fr. 1929 (1970).
20. P. Schmidt, K. Meier, and J. Druey. Angew. Chem. **70**, 344 (1958).
21. U. Schmidt and G. Giesselmann. Chem. Ber. **93**, 1590 (1960).
22. L. N. Yakhontov and M. V. Rubtsov. Zh. Obshch. Khim. **30**, 1507 (1960).
23. H. R. Synder. J. Heterocycl. Chem. **12**, 1303 (1975).
24. D. Korbonits, I. K. Szvoboda, and K. Horvath. J. Chem. Soc. Perkin Trans. 1, 759 (1982).
25. H. Hoehn. Z. Chem. **10**, 386 (1970).
26. C. R. Hardy. Adv. Heterocycl. Chem. **36**, 343 (1984).
27. I. Chu and B. M. Lynch. J. Med. Chem. **18**, 161 (1975).
28. B. M. Lynch, A. J. Robertson, and J. G. K. Webb. Can. J. Chem. **47**, 1129 (1969).
29. M. A. Khan and B. M. Lynch. J. Heterocycl. Chem. **7**, 247 (1970).
30. H. C. Teo. M.Sc. thesis, St. Francis Xavier University, Antigonish, N.S. 1971.
31. B. Staskun and O. G. Backebery. J. Chem. Soc. 5880 (1964).
32. L. H. Klemm, C. E. Klopfenstein, R. Zell, D. R. McCoy, and R. A. Klemm. J. Org. Chem. **34**, 347 (1969).
33. B. M. Lynch, M. A. Khan, S. C. Sharma, and H. C. Teo. Can. J. Chem. **53**, 119 (1975).
34. R. G. Gould and W. A. Jacobs. J. Am. Chem. Soc. **61**, 2890 (1939).
35. B. M. Lynch and Y. Hung. Can. J. Chem. **42**, 1650 (1964).
36. L. C. Behr, R. Fusco, and C. H. Jarboe. *In* The chemistry of heterocyclic compounds. Vol. 22. Pyrazoles, pyrazolines, pyrazolidines, indazoles and condensed rings. *Edited by* A. Weissberger. Wiley–Interscience, New York, NY. 1967. p. 305.
37. B. P. Lem. M.Sc. thesis, St. Francis Xavier University, Antigonish, N.S. 1971.
38. B. M. Lynch. Can. J. Chem. **55**, 541 (1977).
39. J. I. G. Cadogan. J. Chem. Soc. C, 1249 (1966).
40. I. L. Finar and R. J. Hurlock. J. Chem. Soc. 3024 (1957).
41. B. M. Lynch and T. Chan. Can. J. Chem. **41**, 274 (1963).
42. F. Minisci and G. P. Gardini. Tetrahedron Lett. 15 (1970).
43. L. G. Tensmeyer and C. Ainsworth. J. Org. Chem. **31**, 1878 (1966).
44. I. I. Grandberg, W. Ting, and A. N. Kost. Zh. Obshch. Khim. **21**, 2311 (1961).
45. E. C. Taylor and K. Hartke. J. Am. Chem. Soc. **81**, 2456 (1959).
46. C. C. Cheng and R. K. Robins. J. Org. Chem. **21**, 1240 (1956).
47. H. Yasuda. Yakugaku Zasshi, **79**, 836 (1959).
48. H. Dorn, G. Hilgetag, and A. Zubek. Angew. Chem. **76**, 920 (1964).
49. P. Schmidt and H. Druey. Helv. Chim. Acta, **41**, 306 (1958).
50. S. C. Sharma and B. M. Lynch. Can. J. Chem. **57**, 3034 (1979).

Cyclopentadienyl–metal bond cleavage and stereospecific bromination. The structure of $(\eta\text{-}C_5H_5)_2Ti(OOCPh)_2$ and its reactions with bromine[1]

C. Robert Lucas

Department of Chemistry, Memorial University of Newfoundland, St. John's, Nfld., Canada A1B 3X7

AND

Eric J. Gabe and Florence L. Lee

Division of Chemistry, National Research Council of Canada, Ottawa, Ont., Canada K1A 0R9

Received August 4, 1987

C. Robert Lucas, Eric J. Gabe, and Florence L. Lee. Can. J. Chem. **66**, 429 (1988).

The ^{13}C and ^1H nmr spectra as well as the X-ray structure determination for $(\eta\text{-}C_5H_5)_2Ti(OOCPh)_2$ are described. The compound crystallizes in space group $P2_12_12_1$ with $a = 7.5135$, $b = 12.5166$, $c = 21.1416$ Å, $Z = 4$, $d_{calcd} = 1.40$ g cm^{-3} (MoKα_1, $\lambda = 0.70932$ Å). The structure was solved with MULTAN using data collected at 115 K and refined to the final $R = 0.059$ for 1500 significant reflections. The molecule has two different carboxylate ligands, one of which has a Ti—O—C angle of 135.4(6)° and longer Ti—O (1.976(5) Å) and O—C (1.300(10) Å) bonds while the other has a Ti—O—C angle of 157.0(7)° with shorter Ti—O (1.913(6) Å) and O—C (1.267(10) Å) bonds. With bromine, ring cleavage occurs giving $C_5H_5Br_3$ or $C_5H_5Br_5$ in which bromination has occurred stereospecifically. The same reaction occurs with chlorine but not with iodine or iodine monochloride. Related reactions have been observed with $(\eta\text{-}C_5H_5)_2MCl_2$ (M = Ti, Zr, and V). A non-radical mechanism is proposed in which the LUMO and HOMO of Br_2 interact simultaneously with one cyclopentadienyl ring and with the metal. This interaction is a consequence of the structure of $(\eta\text{-}C_5H_5)_2M(OOCPh)_2$.

C. Robert Lucas, Eric J. Gabe et Florence L. Lee. Can. J. Chem. **66**, 429 (1988).

On décrit les spectres rmn du ^1H et du ^{13}C ainsi que la détermination de la structure par diffraction des rayons-X du composé $(\eta\text{-}C_5H_5)_2Ti(OOCPh)_2$. Le composé cristallise dans le groupe d'espace $P2_12_12_1$ avec $a = 7{,}5135$, $b = 12{,}5166$ et $c = 21{,}1416$ Å, $Z = 4$ et $d_{calcd} = 1{,}40$ g cm^{-3} (MoKα_1, $\lambda = 0{,}70932$ Å). On a résolu la structure avec MULTAN utilisant les données recueillies à 115 K et on l'a affinée jusqu'à une valeur finale de $R = 0{,}059$ pour 1500 réflexions significatives. La molécule possède deux ligands carboxylates différents, l'un deux forme une angle Ti—O—C de 135,4(6)° et des liaisons Ti—O et O—C plus longues (1,976(5) et 1,300(10) Å respectivement) alors que l'autre forme un angle de 157,0(7)° et des liaisons plus courtes (1,913(6) et 1,267(10) Å). Soumis à l'action du brome, il se produit un clivage de cycle conduisant au $C_5H_5Br_3$ ou au $C_5H_5Br_5$ dans lequel la bromation s'est produite d'une façon stéréospécifique. La même réaction se produit avec le chlore; toutefois, elle ne se produit pas avec l'iode ou avec le chlorure d'iode. On a observé des réactions apparentées avec le $(\eta\text{-}C_5H_5)_2MCl_2$ (M = Ti, Zr et V). On propose un mécanisme radicalaire dans lequel les orbitales moléculaires basse vacante et haute occupée du Br_2 interagissent simultanément avec un cyclopentadiènyle et avec le métal. Cette interaction est la conséquence de la structure du composé $(\eta\text{-}C_5H_5)_2M(OOCPh)_2$.

[Traduit par la revue]

Introduction

It is conventional to regard the pentahapto-cyclopentadienyl group as a non-labile ligand (1). Especially in bent metallocenes, the site of molecular reactivity is not normally the cyclopentadienyl–metal bond and ring replacements are rare. Nevertheless, it has been known for over thirty years that the $\eta^5\text{-}C_5H_5$ group is occasionally transferred between metals (2) or even completely displaced (3*a*) under surprisingly mild conditions e.g. reaction [1] (Cp = $\eta\text{-}C_5H_5$):

$$[1]\quad Cp_2Ti(OEt)_2 + EtOH \xrightarrow{20°C} CpTi(OEt)_3 + \text{other products}$$

Since Cp–metal bond dissociation enthalpies all lie in the range 300–500 kJ/mol (4), the wide variation in Cp–metal bond reactivity must be kinetic in origin. This paper reports structural and synthetic studies which suggest a mechanism for non-radical Cp–metal bond cleavages in early transition metal Cp_2MX_2 species.

Experimental

Reagents were obtained from the Aldrich Chemical Co., Inc., and were used without further purification. Spectroscopic data were obtained using the following instruments: ir, Perkin Elmer Model 283; nmr, Varian EM-360 or Bruker WP80 Fourier-Transform; mass spectra, V.G. Micromass 7070HS. X-ray diffraction data were collected using a Picker FACS-1 four circle diffractometer with local (NRC) automation. Standard Schlenk techniques were used throughout and unless noted, procedures were carried out under an atmosphere of dry nitrogen. Solvents were dried over P_4O_{10}. Analyses were performed by Canadian Microanalytical Service Ltd.

(a) Preparative

$Cp_2Ti(OOCPh)_2$

First reported in the Russian literature (5), $Cp_2Ti(OOCPh)_2$ is more conveniently produced by the alternate method described here. A complete characterization is also presented herein. A suspension of sodium benzoate (1.44 g, 10.0 mmol) and Cp_2TiCl_2 (1.25 g, 5.00 mmol) in CCl_4 (100 mL) was refluxed for 6 h. The orange solution was filtered to remove NaCl, concentrated to 25 mL, and chilled at −20°C overnight to produce orange crystals which were separated by filtration and washed with cold CCl_4 (3 mL). Yield 1.87 g (89%). Mp 183°C (decomp). Mass spectrum: parent ion $m/e = 420$ not seen at 70, 20, 15, or 10 eV ionization potential. Fragments with high abundance have $m/e = 355$, 299, and 105 corresponding to $[CpTi(OOCPh)_2]^+$, $[Cp_2Ti(OOCPh)]^+$, and $PhCO^+$. ^1H nmr (ppm from TMS int. std., CCl_4) 6.55 (s, 10H), 7.31 (m, 6H), 7.87 (m, 4H). ^1H-decoupled ^{13}C nmr (ppm from TMS int. std., $CDCl_3$) 118.7 (Cp), 128.4, 130.1, 132.0, 134.0 (Ph), 172.3 (CO). Ir (Nujol): identical with lit. (5).

$C_5H_5Br_3$

To a solution of $Cp_2Ti(OOCPh)_2$ (4.2 g, 10 mmol) in CCl_4 (300 mL) was added dropwise over 15 min a solution of Br_2 (1.6 g, 0.51 mL,

[1]NRCC No. 28483.

Can. J. Chem. Downloaded from www.nrcresearchpress.com by 176.9.209.113 on 09/07/12
For personal use only.

Can. J. Chem. Downloaded from www.nrcresearchpress.com by 176.9.209.113 on 09/07/12
For personal use only.

20 mmol) in CCl_4 (50 mL). The solvent was distilled under reduced pressure and the sticky residue was fractionally sublimed at 65°C and 0.1 Torr to give colourless cubes of product. Yield 0.64 g (88%). Mp 63.5–64°C. Mass spectrum: parent ion m/e = 308 $[C_5H_5{}^{81}Br_3]^+$, calcd. for $C_5H_5{}^{79}Br^{81}Br_2$, 305.7900; found, 305.7899. ^{1}H nmr (ppm from TMS int. std., d_6-acetone) 4.94 (m, 1H, $J < 0.6$ Hz), 5.33 (m, 2H, $J < 0.6$ Hz), 6.26 (m, 2H, $J < 0.6$ Hz). ^{13}C nmr (ppm from TMS int. std., d_6-acetone) 55.88 (d, $^1J_{CH}$ = 165 Hz), 56.48 (d, $^1J_{CH}$ = 165 Hz), 134.7 (d, $^1J_{CH}$ = 177 Hz). Ir (Nujol): 1690 (w), 1335 (s), 1282 (s), 1250 (s), 1132 (s), 991 (m), 941 (m), 918 (m), 799 (s), 774 (m), 744 (s), 720 (m), 710 (m), 680 (m), and 660 (m). Figure 1 shows the structure of $C_5H_5Br_3$.

$C_5H_5Br_5$

To a solution of $Cp_2Ti(OOCPh)_2$ (1.0 g, 2.38 mmol) in CCl_4 (100 mL) was added a solution of Br_2 (2.3 g, 0.73 mL, 14.4 mmol) in CCl_4 (25 mL). The mixture was sealed and stirred for 4 days, filtered to remove an orange precipitate, and the reddish brown solution was taken to dryness under reduced pressure. The residue was extracted with acetone (3 × 10 mL) to which water (50 mL) was then added. The precipitate was separated by filtration and the filtrate extracted with diethyl ether (3 × 50 mL). The extracts were taken to dryness under reduced pressure and the residue sublimed at 55°C and 0.1 Torr to give colourless crystals of product. Yield 1.65 g (74%). Mp 107–107.5°C. Mass spectrum: parent ion m/e = 466 $[C_5H_5{}^{79}Br_2{}^{81}Br_3]^+$ at 20 eV. ^{1}H nmr (ppm from TMS int. std., CCl_4) 4.63 (m). *Anal.* calcd. for $C_5H_5Br_5$: C 12.92, H 1.08, Br 85.99; found: C 12.47, H 1.55, Br 85.92. Ir (Nujol): 1310 (vs), 1290 (vs), 1280 (w), 1250 (m), 1230 (w), 1215 (s), 1180 (m), 1170 (s), 1155 (vs), 1080 (s), 1045 (m), 970 (w), 795 (s), 782 (m), 760 (s), 740 (s), 595 (vs) cm^{-1}.

$CpTiBr(OOCPh)_2$

To a dilute (~0.04 mol/L) solution of $Cp_2Ti(OOCPh)_2$ in CCl_4 (freshly distilled from P_4O_{10}) a solution of Br_2 (1.0 mol/L) in the same solvent was added until a mole ratio of Br_2:Ti = 2:1 had been reached. The brown–orange solution was filtered to remove a small amount of precipitate and volatiles were removed in vacuum at room temperature. The sticky residue was placed in a sublimer and $C_5H_5Br_3$ removed at 65°C and 0.1 Torr. The brown–orange residue was not purified further and was characterized spectroscopically. ^{1}H nmr ($CDCl_3$, TMS int. std.) 6.52 (s, 5H), 7.3 (m, 6H), 7.9 (m, 4H). Ir (Nujol): 3095 (w), 3070 (w), 1520 (vs), 1410 (vs), 1028 (m), 815 (s), 720 (s), 670 (s) cm^{-1}.

$Br_2Ti(OOCPh)_2$

As described above, a dilute solution of $Cp_2Ti(OOCPh)_2$ was treated with Br_2 to a mole ratio of Br_2:Ti = 4:1. Volatiles were removed in vacuum at room temperature and $C_5H_5Br_3$ was sublimed at 65°C and 0.1 Torr. The orange residue is very sensitive to hydrolysis. ^{1}H nmr ($CDCl_3$, TMS int. std.) 7.4 (m, 3H), 7.8 (m, 2). Mass spectrum: parent ion m/e = 371 $[^{81}BrTi(OOCPh)_2]^+$. Ir (Nujol): 3300 (m, br), 3090 (w), 1692 (m), 1600 (s), 1570 (m), 1495 (vs), 1400 (vs), 1310 (m), 1180 (m), 1162 (w), 1100 (w), 1075 (m), 1030 (m), 1005 (w), 940 (w), 790 (w), 715 (s), 682 (m), 670 (s), 665 (s) cm^{-1}. Satisfactory analyses for $Br_2Ti(OOCPh)_2$ have not been obtained. Results suggest hydrolysis to $Br(OH)Ti(OOCPh)_2$ had occurred in all samples.

(b) X-Ray studies

$Cp_2Ti(OOCPh)_2$ fw = 420.3

Orthorhombic, $P2_12_12_1$, a = 7.5135(14), b = 12.5166(11), c = 21.1416(17) Å, V = 1982.2 Å^3, Z = 4, ρ_c = 1.40 (−158°C: MoKα_1, λ = 0.70932 Å).

The space group was uniquely determined by the occurrence of systematic absences. The diffraction intensities of an approximately 0.3 × 0.2 × 0.1 mm crystal were collected using graphite monochromatized radiation and the $\theta/2\theta$ scan technique with profile analysis (6) to $2\theta_{max}$ = 50° at a scan speed of 4° min. A total of 2026 unique reflections were measured of which 1500 were considered significant with $I_{net} > 2.5\sigma(I_{net})$. Three standards were measured after every 100 reflections and no significant crystal decay was detected. Lorentz and polarization factors were applied but absorption correction was unnecessary (μ = 0.45 mm^{-1}). No evidence for extinction was observed. The cell parameters were obtained by least-squares refinement of the setting angles of 68 reflections with $2\theta > 40°$.

TABLE 1. Positional and thermal parameters for $Cp_2Ti(OOCPh)_2$

Atom	X	Y	Z	B_{iso}[a]
Ti	0.15476(21)	0.47383(11)	0.21344(6)	1.79(6)
O1	0.2793(8)	0.3662(4)	0.16131(23)	2.0(3)
O2	0.1491(9)	0.2086(4)	0.17511(25)	3.3(3)
O3	0.3021(10)	0.5858(5)	0.1811(3)	3.6(3)
O4	0.2952(9)	0.7623(4)	0.1770(3)	3.1(3)
C1	0.2623(12)	0.2643(6)	0.1515(4)	1.9(4)
C2	0.3382(13)	0.6750(6)	0.1558(3)	1.7(4)
C11	0.3967(12)	0.2169(6)	0.1068(3)	1.7(4)
C12	0.5472(13)	0.2730(6)	0.0858(4)	1.9(4)
C13	0.6686(14)	0.2283(6)	0.0437(3)	2.1(4)
C14	0.6430(14)	0.1240(6)	0.0236(3)	2.3(4)
C15	0.4975(13)	0.0661(7)	0.0448(4)	2.6(4)
C16	0.3749(14)	0.1111(6)	0.0862(3)	2.1(4)
C21	0.4555(11)	0.6660(6)	0.0970(3)	1.4(3)
C22	0.5421(12)	0.7544(6)	0.0740(3)	1.8(4)
C23	0.6353(14)	0.7471(7)	0.0176(3)	2.2(4)
C24	0.6373(13)	0.6503(7)	−0.0139(3)	2.4(4)
C25	0.5588(12)	0.5605(6)	0.0095(4)	2.6(4)
C26	0.4664(12)	0.5672(6)	0.0660(4)	2.1(4)
Cp11	−0.0304(14)	0.5298(10)	0.1284(4)	4.1(5)
Cp12	−0.0694(13)	0.4218(8)	0.1393(4)	3.0(5)
Cp13	−0.1342(13)	0.4122(7)	0.2002(4)	2.8(5)
Cp14	−0.1523(13)	0.5152(8)	0.2246(4)	2.9(4)
Cp15	−0.0771(14)	0.5857(8)	0.1820(6)	4.0(6)
Cp21	0.3861(11)	0.4406(7)	0.2852(4)	3.0(5)
Cp22	0.2624(13)	0.3578(6)	0.2929(4)	2.6(4)
Cp23	0.1070(14)	0.4022(7)	0.3155(4)	2.8(5)
Cp24	0.1311(13)	0.5119(8)	0.3217(3)	2.7(4)
Cp25	0.3069(14)	0.5358(8)	0.3048(4)	3.7(5)
H12	0.565	0.355	0.105	3.5
H13	0.787	0.272	0.030	3.3
H14	0.737	0.088	−0.011	3.9
H15	0.476	−0.019	0.031	4.1
H16	0.249	0.069	0.101	3.7
H22	0.538	0.830	0.100	3.5
H23	0.705	0.815	−0.001	3.9
H24	0.710	0.644	−0.060	4.1
H25	0.585	0.482	−0.012	4.4
H26	0.398	0.496	0.086	3.3
Hp11	0.033	0.568	0.084	4.9
Hp12	−0.049	0.360	0.104	4.8
Hp13	−0.172	0.341	0.225	4.5
Hp14	−0.205	0.540	0.269	4.3
Hp15	−0.054	0.674	0.187	5.4
Hp21	0.527	0.426	0.267	4.3
Hp22	0.293	0.275	0.282	4.2
Hp23	−0.015	0.356	0.323	4.4
Hp24	0.032	0.572	0.340	4.1
Hp25	0.379	0.611	0.305	5.3

[a] B_{iso} is the mean of the principal axes of the thermal ellipsoid.

The structure was solved with MULTAN (7) plus a difference Fourier map and refined by full-matrix least squares with counting statistics weights. H-atom positions were calculated but their parameters were not refined. All heavier atoms were refined anisotropically. The final residuals are R_F = 0.059 and R_w = 0.039 for the significant data (R_F = 0.091 and R_w = 0.40 for all data); goodness of fit = 2.977. All calculations were performed with the NRCVAX system of programs (8). Scattering factors were taken from the International tables for X-ray crystallography (9).

The final atomic positional parameters and the equivalent isotropic temperature factors are listed in Table 1 while distances and angles

TABLE 2. Selected distances and angles in $Cp_2Ti(OOCPh)_2$

Bond	Distance (Å)	Bonds	Angle (deg)
Ti—O(1)	1.976(5)	O(1)—Ti—O(3)	91.5(3)
Ti—O(3)	1.913(6)	Ti—O(1)—C(1)	135.4(6)
Ti—Cp(11)	2.379(9)	O(1)—C(1)—O(2)	124.7(8)
Ti—Cp(12)	2.391(9)	O(1)—C(1)—C(11)	114.9(7)
Ti—Cp(13)	2.321(10)	O(2)—C(1)—C(11)	120.4(7)
Ti—Cp(14)	2.376(10)	C(1)—C(11)—C(12)	122.8(7)
Ti—Cp(15)	2.331(10)	C(1)—C(11)—C(16)	119.2(8)
Ti—Cp(21)	2.344(8)	Ti—O(3)—C(2)	157.0(7)
Ti—Cp(22)	2.363(8)	O(3)—C(2)—O(4)	125.1(7)
Ti—Cp(23)	2.364(8)	O(3)—C(2)—C(21)	113.7(7)
Ti—Cp(24)	2.345(8)	O(4)—C(2)—C(21)	121.0(7)
Ti—Cp(25)	2.375(9)	C(2)—C(21)—C(22)	120.2(7)
O(1)—C(1)	1.300(10)	C(2)—C(21)—C(26)	118.7(7)
C(1)—O(2)	1.207(11)	Cp(12)—Cp(11)—Cp(15)	107.5(8)
C(1)—C(11)	1.505(12)	Cp(11)—Cp(12)—Cp(13)	108.1(8)
O(3)—C(2)	1.267(10)	Cp(12)—Cp(13)—Cp(14)	107.3(8)
C(2)—O(4)	1.224(10)	Cp(13)—Cp(14)—Cp(15)	108.1(8)
C(2)—C(21)	1.528(11)	Cp(11)—Cp(15)—Cp(14)	108.4(9)
Cp(11)—Cp(12)	1.403(16)	Cp(22)—Cp(21)—Cp(25)	108.3(8)
Cp(11)—Cp(15)	1.378(16)	Cp(21)—Cp(22)—Cp(23)	107.7(8)
Cp(12)—Cp(13)	1.383(13)	Cp(22)—Cp(23)—Cp(24)	108.7(8)
Cp(13)—Cp(14)	1.395(13)	Cp(23)—Cp(24)—Cp(25)	108.0(9)
Cp(14)—Cp(15)	1.380(15)	Cp(21)—Cp(25)—Cp(24)	107.2(8)
Cp(21)—Cp(22)	1.402(12)		
Cp(21)—Cp(25)	1.395(14)		
Cp(22)—Cp(23)	1.379(14)		
Cp(23)—Cp(24)	1.392(13)		
Cp(24)—Cp(25)	1.401(14)		

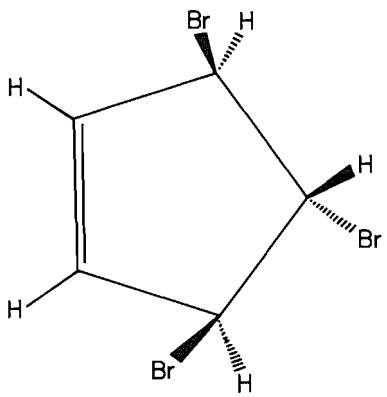

FIG. 1. Structure of $C_5H_5Br_3$.

are in Table 2. Anisotropic thermal parameters and final structure factors are available as suplementary data.[2] Figure 2 shows the atomic numbering scheme and Fig. 3 is a stereo picture of the molecule.

Results and discussion

Early studies of Cp—M cleavage reactions, while synthetically interesting, often left the mechanism of cleavage obscure. For example, reaction [2] has been proposed to occur

[2] $Cp_2Ni + HX + PPh_3 \rightarrow CpNi(PPh_3)X + \frac{1}{2}(CpH)_2$

by two different mechanisms (3*b*). One involves nucleophilic attack by PPh_3 as a first step while the other involves electrophilic attack by HX. The only feature common to both proposed mechanisms is decreased hapticity in the intermediate by the ring which is eventually lost. That Cp rings easily change their steric demands on metals is amply supported by kinetic (10), structural (11), and synthetic (12) observations. In particular, such a process seems to be facile for the early transition metal titanium since $Cp_2Ti(\eta^1\text{-}C_5H_5)_2$ is fluxional at room temperature, its rings undergoing a reversible $\eta^5 \rightarrow \eta^1$ process (13).

We felt that the cyclopentadienyl ligand of reduced hapticity which is likely to be an intermediate in Cp—M cleavages could be captured if the cleavage was carried out using bromine. This electrophilic reagent should be unlikely to attack an electron-poor titanium(IV) center. Furthermore, attack at other than the cyclopentadienyls should be prevented by having groups bound to titanium that do not normally react with bromine at their point of attachment. The reagent of choice was $Cp_2Ti(OOCPh)_2$ which was prepared in 89% yield according to reaction [3] and has an ir spectrum identical to that reported previously (5).

[3] $Cp_2TiCl_2 + 2NaOOCPh \xrightarrow{CCl_4} Cp_2Ti(OOCPh)_2 + 2NaCl$

When $Cp_2Ti(OOCPh)_2$ is treated with bromine in CCl_4, the stoichiometry of the process which occurs is indicated in reaction [4].

[4] $(\eta^5\text{-}C_5H_5)_2Ti(OOCPh)_2 + 6Br_2 \rightarrow 2C_5H_5Br_5 + Br_2Ti(OOCPh)_2$

The simplicity of this equation is, however, deceptive since a change in the stoichiometry also changes the products (reactions [5] and [6]).

[2]A complete set of data may be purchased from the Depository of Unpublished Data, CISTI, National Research Council of Canada, Ottawa, Ont., K1A 0S2.

Can. J. Chem. Downloaded from www.nrcresearchpress.com by 176.9.209.113 on 09/07/12
For personal use only.

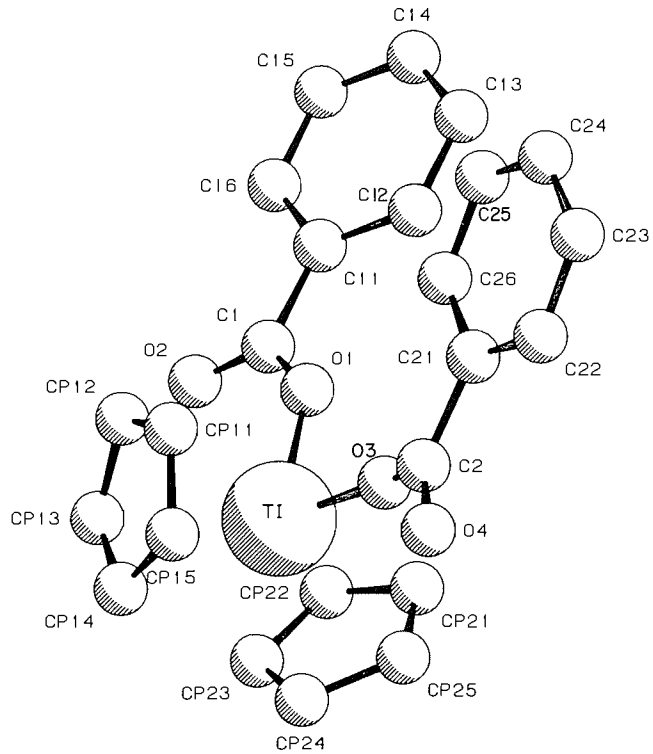

FIG. 2. Atomic numbering scheme for $(\eta\text{-}C_5H_5)_2Ti(OOCPh)_2$.

[5] $(\eta^5\text{-}C_5H_5)_2Ti(OOCPh)_2 + 5Br_2 \rightarrow C_5H_5Br_3 + C_5H_5Br_5 + Br_2Ti(OOCPh)_2$

[6] $(\eta^5\text{-}C_5H_5)_2Ti(OOCPh)_2 + 2Br_2 \rightarrow C_5H_5Br_3 + (\eta^5\text{-}C_5H_5)TiBr(OOCPh)_2$

In all cases, however, at least one ring is removed from the metal and the metal–oxygen bonds remain intact. In fact, the carbonyl stretching vibrations at 1495 and 1400 cm^{-1} in the case of $Br_2Ti(OOCPh)_2$, and at 1520 and 1410 cm^{-1} in the case of $CpTiBr(OOCPh)_2$ suggest bidentate carboxylates (14). Were the Ti—O bonds cleaved by Br_2, benzoyl hypobromite, a known intermediate in Hunsdieker decarboxylation (15) of benzoic acid would be produced leading rapidly to formation of bromobenzene. No bromobenzene was ever detected by glc of the crude reaction solutions.

Although these are synthetically useful reactions, our interest in them lay not so much in their synthetic applications but rather in the nature of $C_5H_5Br_3$, the partially brominated C_5 ring. From spectroscopic data discussed below there is no doubt that the three bromine atoms are on adjacent sp^3-hybridized carbon atoms and that the relative stereochemistry on those three carbon atoms is as shown in Fig. 1. The formula $C_5H_5Br_3$ is confirmed by low and high resolution mass spectroscopy. The presence of the H—C=C—H system is indicated by several spectroscopic properties. There is, for example, no band in the ir spectrum at 1543 cm^{-1} where Br—C=C—Br is reported (16) to absorb but there is a band at 1690 cm^{-1} appropriate for the unsubstituted system. The ^1H nmr spectrum has a signal at 6.26 ppm from TMS, in the range 5.68–6.33 reported (17) for the H—C=C—H system. The ^{13}C nmr spectrum has an absorption due to the olefinic carbons at 134.7 ppm from TMS in the ^1H-decoupled spectrum which appears as a doublet ($^1J_{C—H}$ = 177 Hz) when coupling to hydrogen occurs.

The relative stereochemistry of the sp^3 carbons is revealed by the ^1H nmr spectrum. At first glance, the spectrum appears to consist of three singlets but upon ten-fold expansion these are revealed as multiplets with $J < 0.6$ Hz. To achieve such small coupling constants, the H—C—C—H dihedral angle involving the sp^3 carbons must be close to 110° as would be the case if the bromine substituents are arranged up–down–up with respect to the plane of the ring. Were any other isomer produced, coupling constants of about 8 Hz would be expected. Thus, treatment of $Cp_2Ti(OOCPh)_2$ with bromine not only tends to remove preferentially one cyclopentadienyl ring before the other but it also brominates that ring stereospecifically as it is removed.

To explain these observations, the structure of $Cp_2Ti(OOCPh)_2$ (Figs. 2 and 3) was determined by X-ray methods in the expectation that there would be something odd about one of the C_5 rings or its bonding to the metal. The Cp_2Ti portion of the molecule is, however, unexceptional and has the geometry found commonly in Cp_2MX_2 systems. The rings are planar with normals inclined at ~131°. The Ti—C distances are in the range 2.32–2.39 Å and the C—C distances within the C_5 rings lie in the range 1.38–1.40 Å.

On the other hand, the geometry of the $Ti(OOCPh)_2$ portion of the molecule is pertinent to an understanding of the mechanism of ring cleavage. In solution, both carboxylates appear equivalent by ^{13}C nmr, there being but a single carbonyl carbon resonance at 172.3 ppm from TMS even at −110°C in CH_2Cl_2/SO_2. In the solid state, however, the two monodentate carboxylates are quite different. The most striking difference between them is that one is more sharply bent (135.4(6)°) at the metal-bound oxygen than the other (157.0(7)°). The carboxylate bond lengths are also different with the less

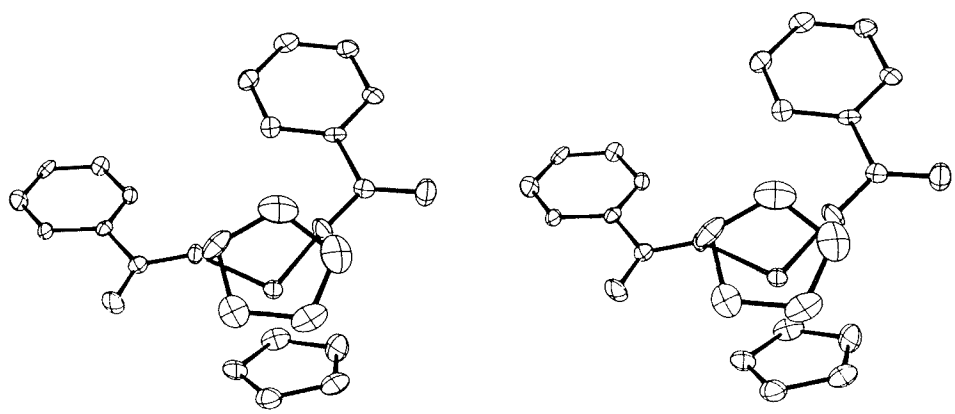

FIG. 3. Stereo picture of $(\eta\text{-}C_5H_5)_2Ti(OOCPh)_2$.

Can. J. Chem. Downloaded from www.nrcresearchpress.com by 176.9.209.113 on 09/07/12
For personal use only.

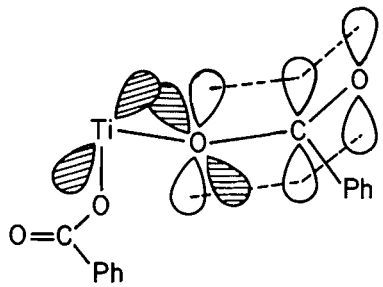

FIG. 4. Bonding in the Ti—O(3)—C(2) carboxylate.

bent Ti—O—C system having shorter Ti—O (1.913(6) vs. 1.976(5) Å) and O—C (1.267(10) vs. 1.300(10) Å) lengths and a longer C=O (1.224(10) vs. 1.207(11) Å).

These dimensions suggest that if the more sharply bent carboxylate is considered "normal" then the less bent may be considered to involve a metal-bound O-atom which is approaching *sp*-hybridization. One of the *p*-orbitals on that oxygen can overlap with a *p*-orbital on the carbonyl-carbon as shown in Fig. 4 which should shorten the O—C and lengthen the C=O bonds compared to the "normal" carboxylate as is observed. The remaining *p*-orbital on oxygen will overlap with the LUMO of the Cp_2Ti fragment which is the molecular orbital originally proposed by Alcock (18) and subsequently confirmed by Green, Green, and Prout (19) as lying in the O—Ti—O plane but outside that angle as shown in Fig. 4. In order to improve its overlap, the *p*-orbital on oxygen should tip towards the Cp_2Ti LUMO which would impart a slight outward bend (23°) to the Ti—O—C system, exactly as observed.

The structural consequences of this mode of bonding are that approach to the titanium atom is hindered on the side of the more bent carboxylate but is virtually unhindered on the side of the less bent. Thus, attack by Br_2 occurs preferentially on one side of the molecule. When a Br_2 molecule is correctly oriented on the metal side of the cyclopentadienyl ligand so that its LUMO (σ^*) can interact with the electron density of the C_5H_5 ring in the usual sense of electrophilic attack, the other end of the Br_2 molecule is correctly positioned for the HOMO (π^*) of Br_2 to interact in a nucleophilic sense with the Alcock–Green LUMO on titanium as illustrated in Fig. 5.

When this stage of the process is complete, there is an η^4-bromocyclopentadiene ligand coordinated to the titanium. All attempts to detect this ligand spectroscopically in the solution which results from mixing $Cp_2Ti(OOCPh)_2$ and Br_2 in a 1:1 molar ratio failed and at all stoichiometric ratios of Br_2:$Cp_2Ti(OOCPh)_2$ up to 2:1, the only observable process was reaction [6]. Although the η^4-bromocyclopentadiene ligand was not detected, presumably because it rapidly reacts further, η^4-diene ligands are well documented in organo-titanium, zirconium, and hafnium chemistry (20, 21). Furthermore, alternative mechanisms, such as ring "slippage" to an η^1- or η^3-structure with subsequent addition of Br_2 across exposed multiple bonds would not lead to the observed stereochemical arrangement of bromine atoms in the organic products.

Further reaction between the η^4-bromocyclopentadiene ligand and Br_2 would be expected to occur by electrophilic attack at the 1 and 4 positions of the diene unit and on the unhindered side of the ring. The resulting η^2-tribromocyclopentene ligand should dissociate readily since η^2-olefin complexes of titanium seem to be unstable, only one (22) ever having been fully characterized. Furthermore, it would have the stereochemical arrangement of bromine atoms that was observed experimentally.

Thus, the preferential cleavage of one ring and its stereospecific bromination are a consequence of preferential attack on one side of the $Cp_2Ti(OOCPh)_2$ molecule. In the case of $Cp_2Ti(OOCPh)_2$ there is an obvious structural reason for preferred attack on one side of the molecule but even in a molecule such as Cp_2TiCl_2 which is not unduly hindered on either side, preferential cleavage of one C_5-ring should still be observed. This follows from the involvement of the Alcock–Green orbital which will direct bromination to only one of the cyclopentadienyl rings at a time.

Several years ago, Gorsich (23) reported that chlorine or bromine will cleave one ring from Cp_2TiCl_2 to form $CpTiCl_3$ or $CpTiCl_2Br$. We have repeated that observation and in addition we find that the organic product of the bromination is identical to that obtained in reaction [6] under similar conditions

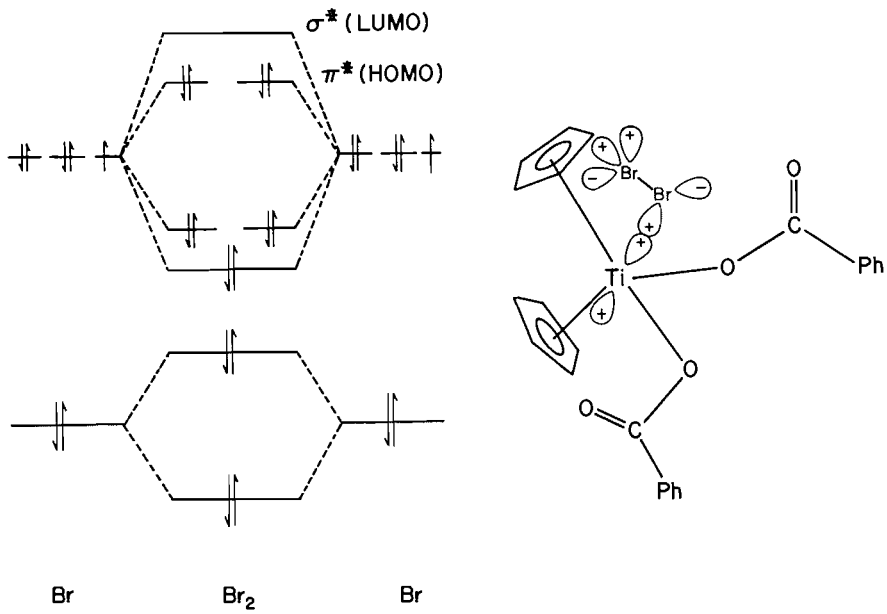

FIG. 5. HOMO–LUMO interactions between Br_2 and $(\eta\text{-}C_5H_5)_2Ti(OOCPh)_2$.

Can. J. Chem. Downloaded from www.nrcresearchpress.com by 176.9.209.113 on 09/07/12
For personal use only.

and stoichiometry while chlorination yields predominantly $C_5H_5Cl_5$. Consistent with the steric requirements of the mechanism, iodine and iodine monochloride (which models show are too large to approach the Cp_2Ti unit in the correct orientation) have been found to be unreactive even over 24 h whereas chlorine and bromine react within minutes.

Other bent Cp_2MX_2 species react similarly, *if no alternate sites for reactivity exist in their molecules*. Thus bis(cyclopentadienyl)metal dialkyls react preferentially at their metal–alkyl bonds but analogous dihalides react at their cyclopentadienyl–metal bonds. Bis(cyclopentadienyl)titanium, zirconium and vanadium dichlorides all give the stereospecifically tribrominated C_5-ring, although in the case of the vanadium compound which has an electron in the Alcock–Green orbital, an oxidation step probably occurs first to empty the orbital and make it available for interaction with the entering halogen molecule. This aspect of the process can be demonstrated by carrying out the reaction using Cp_2MoCl_2 in non-polar solvents in which case, the reaction stops after the oxidation step because the organometallic compound is precipitated as its cation $[Cp_2MoCl_2]^+$.

Although it has been shown by Erker *et al.* (24) that cleavage of a Cp ring from Cp_2ZrCl_2 by Cl_2 in CCl_4 under uv irradiation is a radical chain process, it seems unlikely that a radical mechanism is involved in the reactions discussed above. They have reproducible yields and stereospecificity and they give the same products even when carried out in the dark at reduced (−20°C) temperatures. Furthermore, no reaction occurs with I_2 or ICl (*vide supra*) and when bromination is conducted in the presence of I_2 no incorporation of iodine into the organic product occurs. Therefore, under appropriate experimental conditions, Cp—M cleavage can be achieved by either radical or non-radical processes. Under non-radical conditions, at least for early transition metal bent metallocenes, the Cp group need not behave as a "spectator" ligand providing the Cp—M bond is the molecule's preferred site for attack and providing the steric and electronic requirements of the proposed mechanism for Cp—M cleavage are met.

Acknowledgements

The assistance of Dr. L. K. Thompson with aspects of the X-ray results and of Dr. B. Gregory and Miss M. Baggs with mass spectral data collection is gratefully acknowledged. The Department of Chemistry of Memorial University of Newfoundland is also acknowledged for financial support of this project.

1. J. P. Collman, L. S. Hegedus, J. R. Norton, and R. G. Finke. Principles and applications of organotransition metal chemistry. University Science Books, Mill Valley, CA. 1987. pp. 168, 421.
2. G. Wilkinson, F. A. Cotton, and J. M. Birmingham. J. Inorg. Nucl. Chem. **2**, 95 (1956).
3. A. Z. Rubezhov and S. P. Gubin. Advances in organometallic chemistry. Vol. 10. *Edited by* F. G. A. Stone and R. West. Academic Press, London. 1972. (*a*) p. 385; (*b*) pp. 393, 401.
4. D. B. Jacobsen and B. S. Freiser. J. Am. Chem. Soc. **107**, 7400 (1985).
5. V. N. Vyshinskii, T. I. Ermolaeva, V. N. Latyaeva, A. N. Lineva, and N. E. Lukhton. Dokl. Chem. Engl. Transl. **198**, 487 (1971).
6. D. F. Grant and E. J. Gabe. J. Appl. Crystallogr. **11**, 114 (1978).
7. G. Germain, P. Main, and M. M. Woolfson. Acta Crystallogr. A**27**, 368 (1971).
8. E. J. Gabe, F. L. Lee, and Y. LePage. Crystallographic computing 3. *Edited by* G. Sheldrick, C. Kruger, and R. Goddard. Clarendon Press, Oxford. 1985. p. 167.
9. International tables for X-ray crystallography. Vol. 4. Kynoch Press, Birmingham, England. 1974. p. 99, Table 2.2B.
10. H. G. Schuster-Woldan and F. Basolo. J. Am. Chem. Soc. **88**, 1657 (1966).
11. F. Zingales, A. Chiesa, and F. Basolo. J. Am. Chem. Soc. **88**, 2707 (1966).
12. C. P. Casey and W. D. Jones. J. Am. Chem. Soc. **102**, 6156 (1980).
13. J. L. Calderon, F. A. Cotton, B. G. DeBoer, and J. Takats. J. Am. Chem. Soc. **93**, 3542 (1971).
14. K. Nakamoto. Infrared and Raman spectra of inorganic and coordination compounds. 4th ed. Wiley-Interscience, New York. 1986. p. 231.
15. W. G. Dauben and H. Tilles. J. Am. Chem. Soc. **72**, 3185 (1950).
16. E. T. McBee and K. J. Sienkowski. J. Org. Chem. **38**, 1340 (1973).
17. M. S. Raasch. J. Org. Chem. **45**, 856 (1980).
18. N. W. Alcock. J. Chem. Soc. A, 2225 (1971).
19. J. C. Green, M. L. H. Green, and C. K. Prout. Chem. Commun. 421 (1972).
20. R. Benn and G. Schroth. J. Organomet. Chem. **228**, 71 (1982).
21. G. Erker, K. Berg, C. Kruger, G. Muller, K. Angermund, R. Benn, and G. Schroth. Angew. Chem. Int. Ed. **23**, 455 (1984).
22. S. A. Cohen, P. R. Auburn, and J. E. Bercaw. J. Am. Chem. Soc. **105**, 1136 (1983).
23. R. D. Gorsich. J. Am. Chem. Soc. **82**, 4211 (1960).
24. G. Erker, K. Berg, L. Treschanke, and K. Engel. Inorg. Chem. **21**, 1277 (1982).

Can. J. Chem. Downloaded from www.nrcresearchpress.com by 176.9.209.113 on 09/07/12
For personal use only.

Heat of transport and heat capacity of transport of some aqueous electrolytes

S. K. SANYAL
Department of Agricultural Chemistry and Soil Science, Bidhan Chandra Krishi Viswavidyalaya, Kalyani–741 235, Dt. Nadia, W.B., India

AND

ASHIS K. MUKHERJEE
Department of Chemistry, Presidency College, Calcutta–700 073, India

Received June 11, 1987

S. K. SANYAL and ASHIS K. MUKHERJEE. Can. J. Chem. **66**, 435 (1988).

The thermal diffusion of aqueous solutions of NaCl, KCl, $MgCl_2$, $BaCl_2$, $MgSO_4$, and $CuSO_4$ (0.05 *m*) contained in the pores of a sintered glass diaphragm has been studied. A cell is designed and fabricated for this purpose, and the resulting heat of transport values are compared with those available from the literature and obtained by using independent techniques.

S. K. SANYAL et ASHIS K. MUKHERJEE. Can. J. Chem. **66**, 435 (1988).

On a étudié la diffusion thermique de solutions aqueuses de NaCl, KCl, $MgCl_2$, $BaCl_2$, $MgSO_4$ et $CuSO_4$ (0,05 *m*) contenues dans les pores d'un diaphragme de verre poreux. A cette fin, on a dessiné et construit une cellule spéciale; de plus, on a comparé les valeurs des chaleurs de transport ainsi trouvées avec celles qu'on peut retrouver dans la littérature ou qu'on peut obtenir en faisant appel à des techniques indépendantes.

Can. J. Chem. Downloaded from www.nrcresearchpress.com by 176.9.209.113 on 09/07/12
For personal use only.

Introduction

The results reported for thermal diffusion are predominantly those obtained from the direct or "pure" Soret effect methods (1–5), in which the concentration gradient established in a solution at the steady state is, in general, measured. In such measurements, convection often poses a source of serious error. The present paper describes experiments on thermal diffusion in aqueous electrolyte solutions contained in the pores of a coarse glass (G4) diaphragm with an attempt to minimise the above convective remixing. This method is developed from studying thermal diffusion in thermocells by Agar and Breck (6). More recently, Gaeta and associates (7–9) and Patil (10) have described non-isothermal transport across porous non-selective partitions. The present authors have also described (11) a technique employing G4 glass diaphragm (the technique being different from the present one) which had some similarity with the methods developed earlier (12–14).

Theoretical

A solution-filled pore in a non-isothermal diaphragm may be considered as a microscopic Soret cell in which thermal diffusion proceeds at a moderately fast rate (6, 8). Thus, the relations used for the thermal diffusion studies in a binary system (15) (and for a solvent-fixed reference frame) can be adopted here assuming the chemical potential of component *i* (μ_i) just within the diaphragm at each of its surfaces being the same as that in the adjacent layer of free solution outside the diaphragm (16, 17). The latter holds true for the assumed equilibrium across each surface of the glass disc (G4) used in the present case, and the heat of transport of the solute ($\hat{Q}$) for a solvent-fixed reference frame is given by (2),

$$[1] \quad \hat{Q} = \nu RT^2\sigma\left(1 + \frac{\mathrm{d}\ln\gamma_{\pm}}{\mathrm{d}\ln m}\right)_T$$

where σ is the Soret coefficient, and is given by

$$[2] \quad \sigma = -\left(\frac{\mathrm{d}\ln m}{\mathrm{d}T}\right)_{st} = -\frac{1}{\bar{m}\cdot}\left(\frac{\Delta m}{\Delta T}\right)_{st}$$

$\bar{m}$ being the mean molal concentration, $\gamma_{\pm}$ the mean ionic activity coefficient on molality scale, and T the mean (absolute) temperature. Δm refers to the concentration difference between the cold and warm sides of the diaphragm at steady state, and ν is the total number of ions present in the solution on complete dissociation of one molecule of the electrolyte.

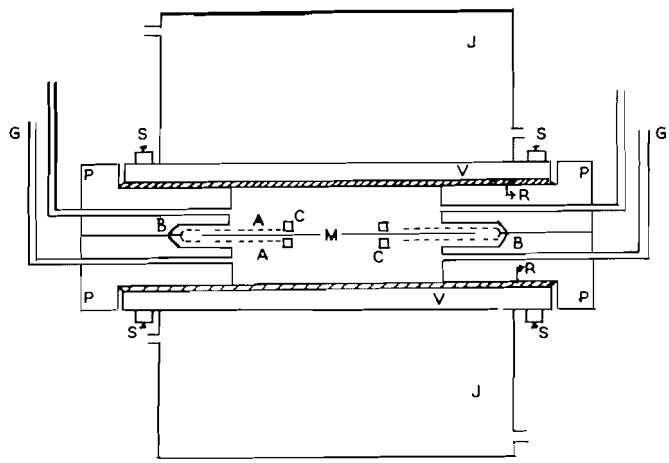

FIG. 1. Schematic diagram of the glass cell. Legend: J, water jacket (diameter 8 cm, height 5.5 cm); S, screw; P, circular perspex block of diameter 10.2 cm; V, brass plate (1 mm thick); B, O-ring; C, thermocouple junction; M, glass diaphragm (1 mm thick); A, diaphragm assembly (of diameter 4.4 cm); R, mylar sheet; G, glass capillary tube of inner diameter 1 mm; diameter of the inlet tubes fixed in grooves of the perspex block is 1.5 mm. Height of each half-cell and the diameter of the cross section of each half-cell are 0.5 cm and 3 cm, respectively.

Experimental

(a) The cell

The thermodiffusive cell (Fig. 1) consists of three parts, the porous G4 glass diaphragm (of thickness 1 mm) forming the central section, being sandwiched in horizontal position between the upper and lower solution chambers through O-ring arrangements to ensure no leakage. Each chamber (or half-cell) is cut into a perspex block in a circular section of diameter 3 cm and depth 0.5 cm. The bottom of each half-cell is closed by a thin mylar sheet (R) kept in position by a brass plate (1 mm thick, V), the outer face of which forms the inside wall of a brass water jacket (J) welded to the former. The plate fits in a well-cut

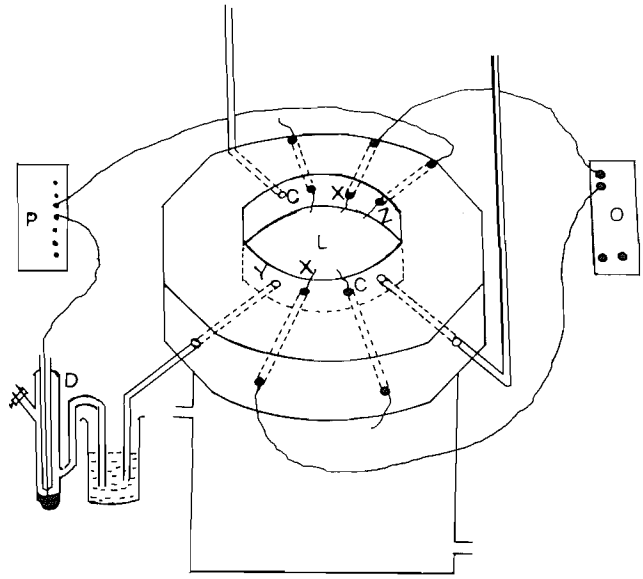

FIG. 2. Conductimetric and potentiometric circuit of lower half of the perspex cell. Legend: X, platinum electrode; Y, salt bridge; Z, Ag/AgCl electrode; C, thermocouple holes; P, potentiometer; O, conductivity meter; D, calomel electrode; L, solution chamber (with height 0.5 cm and diameter 3 cm); G, glass capillary tubes.

groove in the perspex block. The upper and lower water jackets were maintained at different temperatures by way of circulating water from two water thermostats. The entire cell with its three parts is held together by a number of brass nuts and bolts (S) screwed through the outer peripheral parts of the upper and lower brass plates (V). A number of channels (diameter 1.5 mm) ending into each half-cell are cut through the perspex block (Fig. 2). One Ag/AgCl electrode (Z) with a salt bridge (Y), used for the measurement of emf while using chloride solutions, two face-to-face platinum conductivity electrodes (X) for the determination of conductivity of aqueous solutions of electrolytes, two temperature measuring copper–constantan thermocouple junctions (by which the temperature difference across the diaphragm is measured within ± 0.02°C), and two face-to-face 1 mm inside diameter glass capillary tubes (G) (bent at right angles at a distance of 3 mm from the end of the perspex block) for recording any hydrostatic flow through the diaphragm, are held fixed in these channels in each half-cell. The portions of the glass tubes outside the block are covered with glass wool for insulation against the ambient temperature fluctuations.

(b) Materials and methods

The electrolytes used were of high purity grade and their solutions were prepared in doubly distilled (deaerated) water of conductivity 0.5 μmho cm^{-1}. The initial concentration of each solution was 0.05 *m*.

The cell was assembled and filled with the experimental solution by taking care to eliminate the entrapped air bubbles from the whole system. On applying a thermal gradient across the diaphragm, temperatures were measured by thermocouples, and the solution concentrations and their changes with time were periodically monitored by two methods, (*i*) by recording (for chlorides only) the changes of electrode potential of the $Ag/AgCl/Cl^-$ electrode by coupling the latter through a salt bridge with a micro-calomel electrode (Fig. 2), and noting the emf of the cell with a Leeds-Northrup potentiometer capable of recording ± 0.5 μV, and (*ii*) by measuring the conductivity, as a function of time, of the solution in each half-cell. The steady state was indicated by the concentration differences across the diaphragm registering constant values independent of time. The steady-state concentration differences were also checked by determining the latter (between suitable aliquots withdrawn after the steady state was attained) refractometrically, using a Brice Phoonix differential refractometer. The latter was pre-calibrated with a number of standard pairs of solutions of each solute having known concentration differences. The two sets of such values of the steady-state separations agreed within $\pm 1.5\%$ which is considered satisfactory, signifying the absence of any *in situ* concentration gradient in each half-cell.

A number of tests as described below have been applied to the present cell to ensure its satisfactory operation.

(*1*) Initial experiments were run with aqueous solutions of 0.1 *m* $CdSO_4$ at 25°C to check the reliability of the results obtained with the present cell. The Soret coefficient (σ) obtained was within $\pm 1\%$ of the corresponding literature value (18) determined by an independent technique.

(*2*) For a given solution at the mean temperature of 25°C, the apparatus has been operated at ΔT's from 3°C to about 9°C and the same values of σ, within the limits of experimental error, were obtained. The temperatures were monitored throughout a run on the Leeds-Northrup potentiometer capable of recording emf within ± 0.5 μV.

Further, from a detailed consideration of the finite distances between the thermocouple junctions (located in solutions close to the diaphragm surfaces) and the G4 diaphragm surfaces themselves, as well as the thermal conductivities of the solutions and glass used, a correction factor was worked out for arriving at the "true" temperature difference across the G4 disc from the corresponding measured (apparent) value. Thus,

$$\Delta T_{\text{true}} = \frac{\Delta T_{\text{app}}}{1.03}$$

The observed temperature differences were corrected by using the above relation and then used in eq. [2] to obtain σ.

(*3*) The relaxation time (τ) for the present solutions in the given cell was in the range of 400 s (by taking the effective path length of diffusion to be equal to the thickness (0.1 cm) of the disc, i.e., by neglecting any probable internal structure of the porous disc which would otherwise enhance the relaxation time, and by assuming the diffusion coefficient of the given solutes to be of the order of 10^{-5} cm^2 s^{-1}). Thus, for the composition of the solutions to reach within 1% of the final value at the steady state, a time of 5 τ, or about 35 to 40 min must be allowed. The given runs lasted for 50 to 80 min (except for $MgSO_4$ where readings were taken up to 100 min). Trial runs were performed for each solution to find out the time for attainment of the steady-state concentrations in each half-cell, and the former turned out to be well within 80 min in agreement with the requirement of relaxation times as above. Figure 3, showing the plots of separations obtained for various times in different trial runs with the chlorides studied, illustrates the latter.

(*4*) The sintered diaphragm is known to be effective in preventing disturbance of the Soret equilibrium by convection (2) even though for dilute electrolyte solutions (<0.05 *m*), the results may be influenced by ionic adsorption or other surface effects (2). However, the same σ obtained in the present case for different ΔT's applied across a given solution at a particular mean temperature indicates that the convective re-mixing is not appreciable between the solution chambers. The latter should have been more prominent at a higher ΔT leading to a larger separation. The absence of convective remixing was also ensured by a good agreement obtained between concentration differences measured *in situ* and the corresponding values obtained refractometrically (as explained earlier). Indeed the design of the cell is different from those of Saxton, Dougherty, and Drickamer (1954) (12), originally developed for the study of thermal diffusion is binary organic mixtures, and also from our earlier design, developed for the experiments on aqueous non-electrolytes (11), in that the rather small size of the present half-cells did not permit us to have any stirring arrangement. However, the experimental arrangement was such that the colder half-cell was at the bottom. Because the concentration of all the electrolytes studied registered an increase on the colder side of the diaphragm, natural convention was supposed to be constantly operating in each half-cell, thereby destroying any *in situ* concentration gradient developing therein. The degree of such convection for the solutions studied at the

Can. J. Chem. Downloaded from www.nrcresearchpress.com by 176.9.209.113 on 09/07/12
For personal use only.

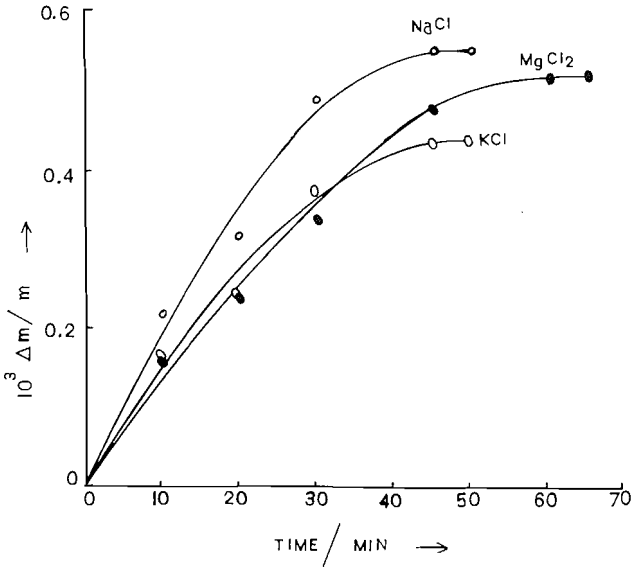

FIG. 3. Plots of the concentration differences (Δm) as noted between the lower and upper half-cells as a function of time for NaCl, KCl, and $MgCl_2$ solutions at a mean concentration of 0.05 $\bar{m}$.

given mean concentration (0.05 m) was quite similar as could be judged from the corresponding Rayleigh numbers R_c and R_T (2).

(5) In the present design, any solvent flow through the G4 diaphragm was ascertained by noting the development of hydrostatic pressure – head difference between the glass capillary tubes (G) attached to the solution chambers. Such solvent flow was found to be negligible after making proper correction for unequal thermal expansions in two halves.[1] In all cases, however, a minute solvent flow was, in fact, observed. The latter caused a small increase in the corrected height (hydrostatic level) in the capillary tubes (G) attached to the upper (warmer) half-cell. Such a volume flow to the warm side was shown (by computation) to contribute not more than 0.1% towards the observed Δm values at the steady state, and the attendant error in ignoring such solvent flow was thus considered negligible. This signifies that the adoption of the solvent – fixed reference frame in the present case is quite satisfactory.

Results and discussion

The results are incorporated in Tables 1 and 2. The errors in the determinations of σ (the mean of three determinations) and heat of transport ($\hat{Q}$) are calculated as the corresponding standard deviations and shown in the parentheses below each of the above values. The values of the thermodynamic factor,

$$1 + \frac{d \ln \gamma_{\pm}}{d \ln m} = B$$

are calculated from the activity or osmotic coefficient data at 25°C and are assumed constant over the experimental temperature range.

The positive heat of transport ($\hat{Q}$) values for the electrolytes (0.05 m) relate to an absorption of heat behind and a liberation ahead in course of diffusional migration in the pores of glass disc which corresponds to the promotion of "local" structure of water adjacent to the ions in dilute solutions. The heat of

[1]By using the known dimensions of perspex block and each half-cell, as well as the thermal expansion coefficients of water and perspex (the latter having it two orders of magnitude lower than that of water), an allowance was made to account for the unequal thermal expansion of water while recording Δh values between the two glass capillary tubes at each mean temperature of study.

TABLE 1. B, σ, and $\hat{Q}$ values of various solutions at different temperatures

Solution (0.05 $\bar{m}$)	T (°C)	B	$10^3\,\sigma_{mean}$ (deg^{-1})	$\hat{Q}$ (J mol^{-1})
NaCl	25.0	0.930	1.64 (±0.01)	2252 (±14.1)
	30.0	0.930	2.03 (±0.03)	2882 (±43.9)
	35.0	0.930	2.33 (±0.03)	3418 (±45.3)
	40.0	0.930	2.97 (±0.04)	4500 (±62.4)
	45.0	0.930	3.59 (±0.04)	5614 (±64.5)
KCl	25.0	0.915	1.24 (±0.01)	1675 (±13.9)
	30	0.915	1.61 (±0.05)	2249 (±71.9)
	35	0.915	2.24 (±0.02)	3233 (±29.8)
	40	0.915	2.74 (±0.07)	4084 (±107.4)
	45	0.915	3.18 (±0.06)	4893 (±95.1)
$MgCl_2$	25	0.830	1.59 (±0.03)	2923 (±56.9)
	30	0.830	2.02 (±0.06)	3839 (±117.4)
	35	0.830	2.38 (±0.04)	4674 (±80.9)
	40	0.830	3.19 (±0.04)	6470 (±83.5)
	45	0.830	3.78 (±0.06)	7913 (±129.4)
$BaCl_2$	25	0.846	3.69 (±0.03)	6914 (±57.9)
	30	0.846	4.22 (±0.05)	8175 (±99.8)
	35	0.846	4.39 (±0.03)	8788 (±61.8)
	40	0.846	4.74 (±0.12)	9799 (±255.5)
	45	0.846	5.30 (±0.05)	11309 (±109.9)
$MgSO_4$	25	0.523	7.78 (±0.03)	6008 (±23.9)
	30	0.523	8.98 (±0.12)	7170 (±98.7)
	35	0.523	10.48 (±0.12)	8646 (±102.0)
	40	0.523	11.48 (±0.05)	9781 (±43.9)
$CuSO_4$	25	0.545	6.71 (±0.02)	5400 (±16.6)
	30	0.545	7.80 (±0.04)	6490 (±34.3)
	35	0.545	9.54 (±0.08)	8201 (±70.9)
	40	0.545	10.39 (±0.10)	9224 (±91.5)

Can. J. Chem. Downloaded from www.nrcresearchpress.com by 176.9.209.113 on 09/07/12
For personal use only.

TABLE 2. $\hat{Q}$, $d\hat{Q}/dt$, and $\hat{C}$ values of various solutions at different temperatures

Solution (0.05 $\tilde{m}$)	T (K)	$\hat{Q}$ (J mol^{-1})	$\frac{d\hat{Q}}{dT}$ (J mol^{-1} deg^{-1})	$\hat{C}$ (J mol^{-1} deg^{-1})	$\hat{Q}_{Lit}$ (J mol^{-1})
NaCl	298	2252	162.3 (±15.0)	154.7	2133[a,b]
KCl	298	1675	161.0 (±6.6)	155.4	1310[a,b]
$MgCl_2$	298	2923	245.3 (±21.7)	235.5	2856[c]
$BaCl_2$	298	6914	202.6 (±16.4)	179.4	6622[c]
$MgSO_4$	298	6008	248.6 (±8.6)	228.4	5670[c]
$CuSO_4$	298	5400	256.3 (±18.0)	238.2	—

[a,b,c]Values of $\hat{Q}$ at the appropriate concentrations are taken from refs. 2, 20, 21 directly, or by interpolation and/or extrapolation of the literature data.

transport values of the simple electrolytes (for example, at 25°C) do not reveal any clear periodic trend even though the same (i.e., $\hat{Q}$) are generally dependent on the valency of the constituent ions (2). The latter arises primarily from the higher ionic potentials of Mg^{2+}, Ba^{2+}, Cu^{2+}, and SO_4^{2-} as compared to those of Na^+, K^+, and Cl^- (in the hydrated state) which promote, through long-range interactions, structure of water in, for instance, the B and C layers of Frank and Wen's concentric zones model (19) of electrolyte solutions, thereby raising $\hat{Q}$.

The $\hat{Q}$ values of electrolytes (at 0.05 m) obtained in the present study are compared with the appropriate literature data, reported by independent techniques (2, 20, 21) (Table 2). The agreement is considered satisfactory, thereby establishing the usefulness of the present technique.

The temperature dependence of $\hat{Q}$ has been expressed in terms of the corresponding heat capacities of transport (at 25°C) of the various electrolytes studied and given in Table 2. For calculating the heat capacities of transport ($\hat{C}$) of the solutions, the slope of the best-fit line of the plot of $\hat{Q}$ vs. T was used in the following equation (2), namely,

$$\hat{C}_T = \left(\frac{d\hat{Q}}{dT}\right) - \frac{\hat{Q}}{T}$$

1. J. N. AGAR. Rev. Pure Appl. Chem. Austr. **8**, 1 (1958).
2. J. N. AGAR. Adv. Electrochem. Electrochem. Eng. **3**, 31 (1963).
3. J. CHANU. Adv. Chem. Phys. **13**, 349 (1967).
4. J. C. R. TURNER and M. J. STORY. Trans. Faraday Soc. **65**, 1810 (1969).
5. C. J. PETIT, J. L. LIN, and K. E. RENNER. J. Solution Chem. **13**, 419 (1984).
6. J. N. AGAR and W. G. BRECK. Trans. Faraday Soc. **53**, 167 (1957); **53**, 179 (1957).
7. F. S. GAETA and D. G. MITA. J. Membrane Sci. **3**, 191 (1978).
8. F. BALLUCCI, E. DRIOLI, F. G. SUMMA, F. S. GAETA, D. G. MITA, and N. PAGLIUCA. J. Chem. Soc. Faraday Trans. II, **75**, 247 (1979).
9. F. BELLUCCI, E. DRIOLI, F. S. GAETA, D. G. MITA, N. PAGLIUCA, and D. TOMADACIS. J. Membrane Sci. **7**, 169 (1980).
10. P. R. PATIL. Reg. J. Energy Heat Mass Transfer, **6**, 189 (1984).
11. A. K. MUKHERJEE and S. K. SANYAL. Can. J. Chem. **64**, 717 (1986).
12. R. L. SAXTON, E. L. DOUGHERTY, and H. G. DRICKAMER. J. Chem. Phys. **22**, 1166 (1954).
13. M. M. RUTHERFORD, E. L. DOUGHERTY, and H. G. DRICKAMER. J. Chem. Phys. **22**, 1289 (1954).
14. D. J. TREVOY and H. G. DRICKAMER. J. Chem. Phys. **17**, 1120 (1949).
15. J. N. AGAR. *In* The structure of electrolyte solutions. *Edited by* W. J. Hamer. Wiley, New York. 1959. Chap. 13. p. 200.
16. A. KATCHALSKY and P. F. CURRAN. Non-equilibrium thermodynamics in biophysics. Harvard Univ. Press. 1965. pp. 112, 185.
17. J. G. KIRKWOOD. *In* Ion transport across membranes. *Edited by* H. T. Clark. Academic Press, New York. 1954. p. 119.
18. L. G. LONGSWORTH. *In* The structure of electrolyte solution. *Edited by* W. J. Hamer. Wiley, New York. 1959. Chap. 12. p. 183.
19. H. S. FRANK and W. Y. WEN. Discuss. Faraday Soc. **24**, 133 (1957).
20. P. N. SNOWDON and J. C. R. TURNER. Trans. Faraday Soc. **56**, 1812 (1960).
21. A. D. PAYTON and J. C. R. TURNER. Trans. Faraday Soc. **58**, 55 (1962).

Can. J. Chem. Downloaded from www.nrcresearchpress.com by 176.9.209.113 on 09/07/12
For personal use only.

Intramolecular Diels–Alder reactions of cyclopentadiene systems: Model studies for the total synthesis of the capnellenes[1,2]

JOCELYNE HELLOU, GERVAIS BÉRUBÉ, MICHAEL J. NEWLANDS, AND ALEX G. FALLIS[3]
Department of Chemistry, Memorial University of Newfoundland, St. John's, Nfld., Canada A1B 3X7

AND

ERIC J. GABE
Division of Chemistry, National Research Council of Canada, Ottawa, Ont., Canada K1A 0R9

Received August 27, 1987

JOCELYNE HELLOU, GERVAIS BÉRUBÉ, MICHAEL J. NEWLANDS, ALEX G. FALLIS, and ERIC J. GABE. Can. J. Chem. **66**, 439 (1988).

Model studies for a general intramolecular Diels–Alder approach to the tricyclo[6.3.0.$0^{2,6}$]undecene skeleton common to the capnellene marine sesquiterpenes are described. Suitably functionalized cyclopentadiene systems **14** and **21** were synthesized and their cycloaddition reactivity examined. Triene **14** cyclized to the tricyclic adducts **15** and **16**. In contrast, the anticipated product **22** from intramolecular cycloaddition of triene **21** was not formed in isolatable yield. Instead the minor adduct (10% yield) possessed an exocyclic double bond and was assigned structure **30** based on its relative stability, as determined by MM2 type calculations, and nuclear magnetic resonance data. X-ray analysis established that the major adduct (40% yield) was a tetracyclic[6.3.1.$0^{1,6}$.$0^{1,10}$]dodecene system corresponding to **32**, and which arose from competitive isomerization of the initial diene and cyclization via an *exo* transition state.

JOCELYNE HELLOU, GERVAIS BÉRUBÉ, MICHAEL J. NEWLANDS, ALEX G. FALLIS, et ERIC J. GABE. Can. J. Chem. **66**, 439 (1988).

On décrit des études modèles effectuées dans le but de déterminer l'utilité des réactions de Diels–Alder intramoléculaires comme méthode générale de synthétiser le squelette du tricyclo[6.3.0.$0^{2,6}$]undécène qui est commun aux sesquiterpènes marins du capnellène. On a synthétisé les systèmes cyclopentadiéniques **14** et **21** substitués d'une façon appropriée et on a examiné leur réactivité vis-à-vis la cycloaddition. Le triène **14** se cyclise pour donner les produits tricycliques **15** et **16**. Par opposition, le produit **22** qui devrait se former par cycloaddition intramoléculaire du triène **21** n'a pu être isolé. Il se forme plutôt un adduit mineur (rendement de 10%) qui possède une double liaison exocyclique et on lui a attribué la structure **30** en se basant sur des données de résonance magnétique nucléaire et sur sa stabilité relative telle que déterminée par des calculs du type MM2. Une étude par diffraction des rayons-X a permis d'établir que le produit principal (rendement de 40%) est un système tétracyclo[6.3.1.$0^{2,6}$,$0^{1,10}$]dodécène correspondant au composé **32** qui se forme par une isomérisation compétitive du diène initial et d'une cyclisation via un état de transition *exo*.

[Traduit par la revue]

Can. J. Chem. Downloaded from www.nrcresearchpress.com by 176.9.209.113 on 09/07/12
For personal use only.

Introduction

The total synthesis of multicyclic, cyclopentanoid natural products is an area of fundamental importance and intense international activity (1, 2). Recent years have witnessed an explosive growth in the development of general methods for the construction of cyclopentanes and diverse strategies for the preparation of fused triquinane sesquiterpenes (3–8). In this regard the tricyclo[6.3.0.$0^{2,6}$]undecene skeleton encountered in the marine natural product $\Delta^{9,12}$capnellene (**1**), and shared with the terrestrial sesquiterpenes hirsutene and coriolin, has served as an attractive target about which to develop new chemistry. This interesting hydrocarbon isolated from the soft coral *Capnella imbricata* (9) has been the object of considerable attention, and several total syntheses have been reported while our studies were in progress. Very briefly these encompass the following: the 1,3-diyl trapping approach of Little *et al.* (10, 11), the Nazarov–Aldol sequence of Paquette and Stevens (12, 13), the alkynone thermolysis procedure of Drieding and co-workers (14), the transannular cyclization and solvolytic rearrangement route of Matsumoto and collaborators (15), iterative application

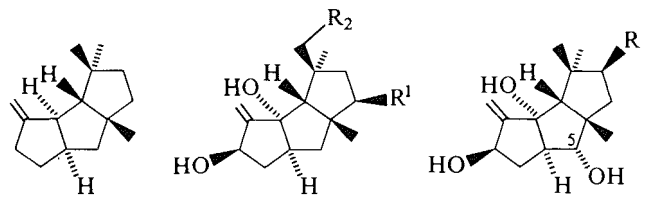

1 | **2** $R^1 = R^2 = H$; **3** $R^1 = OH$, $R^2 = H$; **4** $R^1 = R^2 = OH$ | **5** R = H; **6** R = OH

of the intramolecular magnesium-ene reaction by Oppolzer and Battig (16), a biogenetic approach via epiprecapnelladiene by Birch and Pattenden (17, 18), the palladium-catalyzed carbonylative organostannane coupling sequence of Stille and co-workers (19), an intermolecular Diels–Alder, intramolecular [2 + 2] photoaddition, ring cleavage route developed by Mehta *et al.* (20, 21), a repetitive conjugate addition – methylene cyclopentane annulation sequence utilized by Piers and Karumaratne (7), a combination of [2 + 2] and [4 + 2] cycloaddition reactions used by Liu and Kulkarni (22), a tandem free radical cyclization approach followed by Curran and Chen (23), while the "Tebbe Reagent" with the product of an intramolecular Diels–Alder reaction was employed by Stille and Grubbs (24). In addition to capnellene a variety of more highly oxygenated derivatives **2**–**6** are known (25–28). The diol **2** has

[1]This research constitutes part of the Ph.D. Thesis of J. Hellou, University of British Columbia, 1985, although these studies were conducted at Memorial University of Newfoundland.

[2]Issued as NRCC No. 28259.

[3]Author to whom correspondence may be addressed.

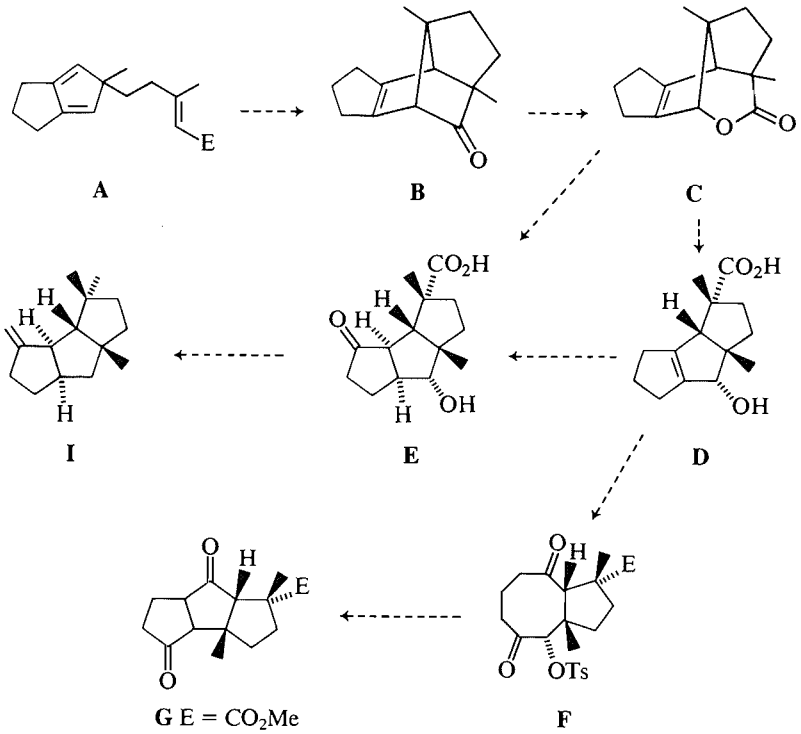

SCHEME 1

been synthesized (29), as has the 8α epimer (30). Recently the triol **3** and tetrol **4** have both been prepared from a common intermediate by Mase and Shibasaki (31). To the best of our knowledge, the C5 hydroxyl systems **5** and the 2β-5α-8β-10α-tetrol **6** (32) have not been totally synthesized. The biological activity of these compounds is not fully delineated but it has been suggested that they are part of the chemical defense mechanism that minimizes algal growth and prevents larval settlement on soft coral (33–35).

In spite of the diverse approaches to these natural products summarized above, most routes are not readily amenable to the preparation of more highly oxygenated derivatives, particularly those bearing a C5 alcohol group. Except in the recent synthesis of Stille and Grubbs (24) and a possible modification of the approach used by Sternbach *et al.* for silphinene (36), the intramolecular Diels–Alder reaction has not figured prominently. Both these routes rely on a cycloaddition sequence analogous to the one we developed earlier for cedrene in which a tricyclo[5.2.1.$0^{1,5}$]decene intermediate played a key role (37). We wish to report the results of our model studies directed toward the capnellene skeleton. These results have provided insight into the behaviour of the ring systems required and will facilitate the extension of this work for use in total synthesis.

Our approach is outlined in general terms in Scheme 1 but, because it involves a bridged intermediate, does not lend itself to simple retrosynthetic analysis. Nevertheless, synthetic strategies that involve intramolecular cycloadditions are frequently used to best advantage, and are most powerful, when the adduct constructed is not directly discernible in the final target. Thus the proposed route depends upon an intramolecular Diels–Alder reaction of a bicyclic cyclopentadiene such as **A** to generate the tetracyclic ketone **B**. It was anticipated that Baeyer–Villiger oxidation would proceed preferentially with migration of the allylic centre to give **C** so that ring opening of the lactone would provide the linear tricyclic skeleton **D** required for conversion to the natural product. The ordering of the steps may be adjusted as required and **E** obtained directly by allylic oxidation and hydrogenation of the lactone. In addition, we were intrigued by the possibility of utilizing the double bond in **D** so that, after ozonolysis and conversion of the secondary alcohol function into a suitable leaving group as illustrated in **F**, base-catalyzed transannular ring closure would provide access to related triquinane systems such as **G** in which the periphery possessed a different substitution pattern. Thus in spite of the results described below, which indicate that a modified strategy is required, the route appeared to possess a high level of stereocontrol and versatility.

Results and discussion

Although several detailed studies of the intramolecular Diels–Alder reaction have been undertaken in recent years, many facets are still imperfectly understood and some cycloadditions fail to proceed as anticipated (38–40). Thus it was considered prudent to examine the initial steps on a model system commencing with 3-methyl-2-cyclopentonone (**9**). The introduction of an α′ substituent in unsaturated ketones is often difficult, particularly the generation of β-keto-esters, but this was accomplished in 71% yield to give **10**, using our recently developed procedure employing diethyl pyrocarbonate and lithium dicyclohexylamide in ether at −78°C (41). It was anticipated that alkylation of this keto-ester with an unsaturated side chain such as **7**, prepared from ethoxy acetylene and 4-chloro-2-butanone followed by acid-catalyzed rearrangement, would provide the necessary conjugated dienophile. Unfortunately, the product was the diester **17** in which the side chain double bond was no longer in conjugation. In a similar manner the reaction of **8** and **10** afforded **18** and neither acidic nor basic conditions were discovered to isomerize the troublesome double bond back into conjugation efficiently to give **12**, although partial reconjugation was achieved with 1,5-diazabicyclo-[5.4.0]undec-5-ene in the case of the bicyclic analogue **26**.

In contrast to the alkylation experiments, Michael addition to

Can. J. Chem. Downloaded from www.nrcresearchpress.com by 176.9.209.113 on 09/07/12
For personal use only.

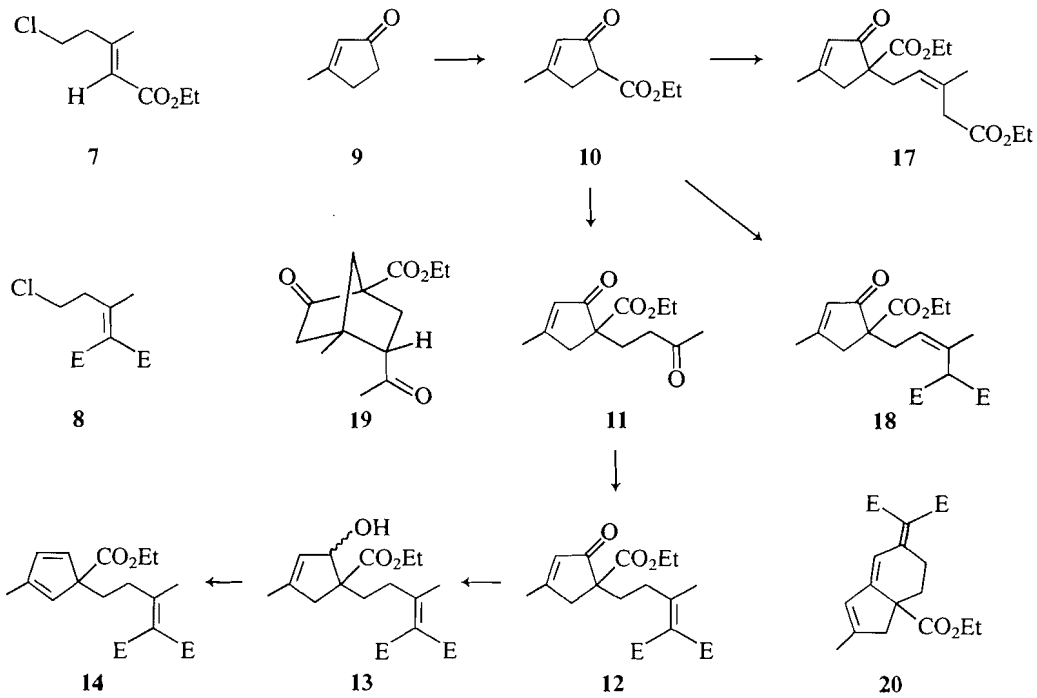

E = CO_2Me

SCHEME 2

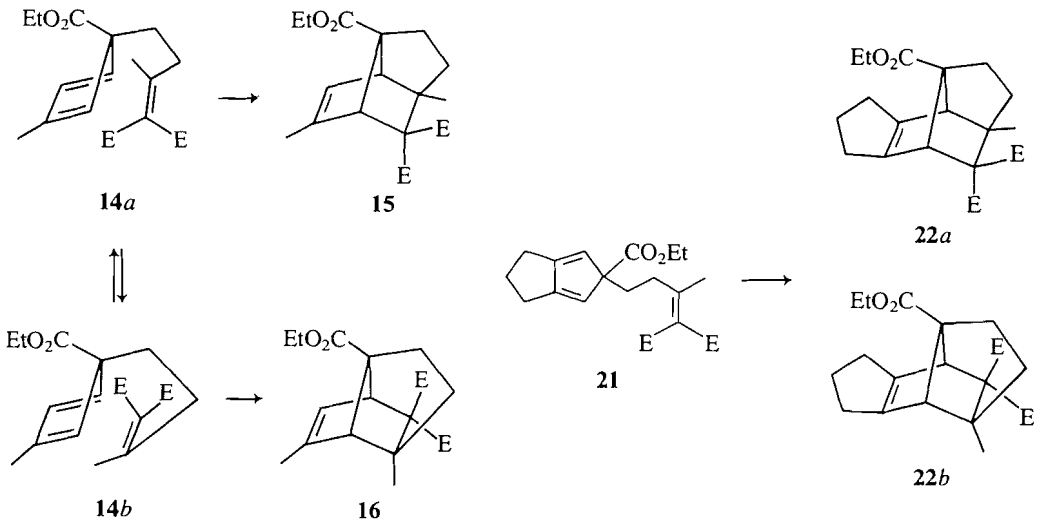

E = CO_2Me

SCHEME 3

methyl vinyl ketone proceeded smoothly to afford **11**. The desired product was accompanied by varying amounts of the bicyclo[2.2.1]heptanone **19** resulting from intramolecular conjugate addition to the cyclopentenone system. The yield of the desired cyclopentenone **11** was raised to 95% and the side product minimized by employing a catalytic amount (1%) of potassium *tert*-butoxide as the base. Attempts to conduct Wittig or Horner–Emmons reactions at the methyl ketone group were disappointing, and there was the same tendency as observed above for the double bond to migrate out of conjugation. Therefore Knoevenagel condensation with titanium tetrachloride and dimethyl malonate was utilized to generate the triester **12** (12%) under nonbasic conditions (42). A low yield (7%) of a second product **20** was obtained due to intramolecular condensation at the cyclopentenone centre. Consistent with the assigned structure, this material displayed two olefinic signals at δ 6.57 and 6.03 in its ^1H nmr spectrum, and its ultraviolet absorption (226 nm, ε = 15 800) was indicative of an extended chromophore. Reduction of the ketone carbonyl in **12** with sodium borohydride containing cerium(III) chloride afforded the alcohol **13** as a 1:1 epimeric mixture that was dehydrated to the triene **14** by *in situ* generation and elimination of its mesylate derivative.

Heating this substituted cyclopentadiene in toluene at 140°C in a sealed tube for 10 h afforded, after chromatography, a 40% yield of an approximately 1:1 mixture of the two tricyclic adducts **15** and **16** (Scheme 3). This is a consequence of the

Can. J. Chem. Downloaded from www.nrcresearchpress.com by 176.9.209.113 on 09/07/12
For personal use only.

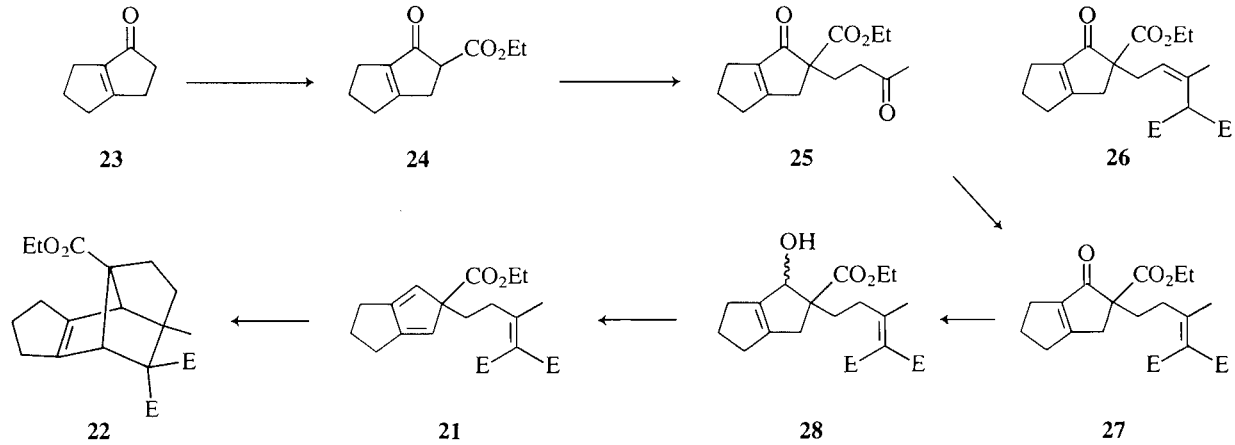

SCHEME 4

facile equilibrium that exists between the two folded triene conformers **14***a* and **14***b*, both of which must possess similar energies. The adducts could not be separated but their presence was clearly indicated by the doubling of the vinyl methyl and vinyl hydrogen signals in the ^{1}H nmr spectrum. Gratified by this result, attention was turned to the bicyclic series in the realization that due to the plane of symmetry in triene **21** the isomer problem would be eliminated. In this instance the anticipated adducts **22***a* and **22***b* are enantiomers and thus chemically equivalent.

The unsaturated bicyclic ketone **23** was prepared from 2-carbomethoxycyclopentanone according to literature precedent (43), although improved yields were realized by modifying the cyclization step using methanesulfonic acid in place of phosphoric acid (44) (Scheme 4). As above, the keto-ester **24** was prepared from the ketone with diethylpyrocarbonate, and alkylation of this material with the chlorodiester **8** gave the nonconjugated system **26** rather than the desired compound **27**. Thus the keto-ester **24** was condensed in the presence of potassium *tert*-butoxide with methyl vinyl ketone as above to give **25**. A parallel series of reactions involving Knoevenagel condensation mediated by titanium tetrachloride, sodium or zinc borohydride reduction, and dehydration via the mesylate afforded **27**, **28**, and the requisite cyclopentadiene system **21** in 18% overall yield from ketone **23**. The ^{1}H nmr spectrum of the unstable triene **21** indicated that the sample was not homogeneous but contained additional diene isomers (δ 5.20, 5.35, 5.73) in which the double bonds were not confined to the same ring.

A toluene solution of the triene **21** heated in a sealed tube in an oil bath at 140°C for 10 h afforded a 50% yield of adducts. Only one *s-cis* diene (i.e., **21**) is possible in the substituted ring, but three additional *s-cis* dienes **31, 33**, and **36** can arise if isomerization into the unsubstituted ring is rapid compared to cycloaddition. It appears from examination of molecular models that all three dienes are theoretically capable of intramolecular cyclization to the tetracyclic structures **32, 34, 37, 38** illustrated (Scheme 5). Unfortunately only a trace of the desired adduct **22** appeared to be present. The nmr spectrum of the reaction mixture indicated that the adducts (4:1 ratio) contained vinyl hydrogens (δ 5.51, 5.26). Hydrolysis of the mixed esters, chromatography, reesterification with ethereal diazomethane, and further chromatography afforded a pure sample of the major adduct. Initially structures of type **29** and **30**, in which the

TABLE 1. ^{13}C nuclear magnetic resonance data for 3,7,7,-tricarbomethoxy-6-methyltetracyclo[6.3.1.0^{1,6}.0^{1,10}]-9-dodecene (**32**)

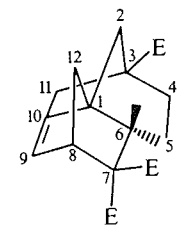

C1	55.1	C8	54.9
C2	35.5	C9	119.8
C3	63.9	C10	158.4
C4	33.4	C11	34.2
C5	31.8	C12	44.3
C6	48.3	C13	19.9
C7	69.2		

double bond had migrated and was no longer confined to the norbornene nucleus, were favoured. Adduct **30** (R = $COOCH_3$) contains four C—H and four CH_2 units and the vinyl hydrogen would be expected to couple with the two methylene protons on the neighbouring carbon and experience further line broadening due to allylic coupling. Similar features are present in the adduct **29**. In contrast, **32** contains two C—H and five CH_2 groups, a feature that was confirmed from the ^{13}C nmr spectrum (Table 1). In addition, in the ^{1}H nmr spectrum the vinyl proton signal at δ 5.51 was coupled (J = 1.5 Hz), as expected for a system with a single bridgehead hydrogen neighbour, and further broadened due to coupling with the allylic methylene hydrogens. These features were most compatible with structure **32**. As illustrated in Fig. 1, this was established unambiguously by X-ray analysis. The structure does not appear particularly distorted, although the C7—C8 sp^3—sp^3 bond (1.587 Å) is significantly longer than normal. In its ^{1}H nmr spectrum the bridgehead methine appears at δ 3.37; the allylic geminal protons form an AB system δ 2.30 (*endo*), δ 2.67 (*exo*), J = 17 Hz; a second AB system arises from the hydrogens in the methylene bridge of the bicyclo[3.2.1]octane unit δ 210, 1.35, J = 9 Hz; and the remaining norbornene methylene forms multiplets at δ 1.58 and 1.95 complicated by long range coupling. As illustrated in Fig. 2, cyclization occurred via an *exo* (with respect to the vinyl methyl) transition state. This allows the bridging cyclohexane ring to adopt a favourable chair conformation compared to the boat-like arrangement required for the competing *endo* pathway, and avoids the severe nonbonded interaction between the methyl group and the transannular allylic hydrogens.

Unfortunately an isomer-free sample of the minor adduct could not be prepared; however, it may be tentatively assigned structure **30** rather than **29** on the following basis. A doublet of

Can. J. Chem. Downloaded from www.nrcresearchpress.com by 176.9.209.113 on 09/07/12
For personal use only.

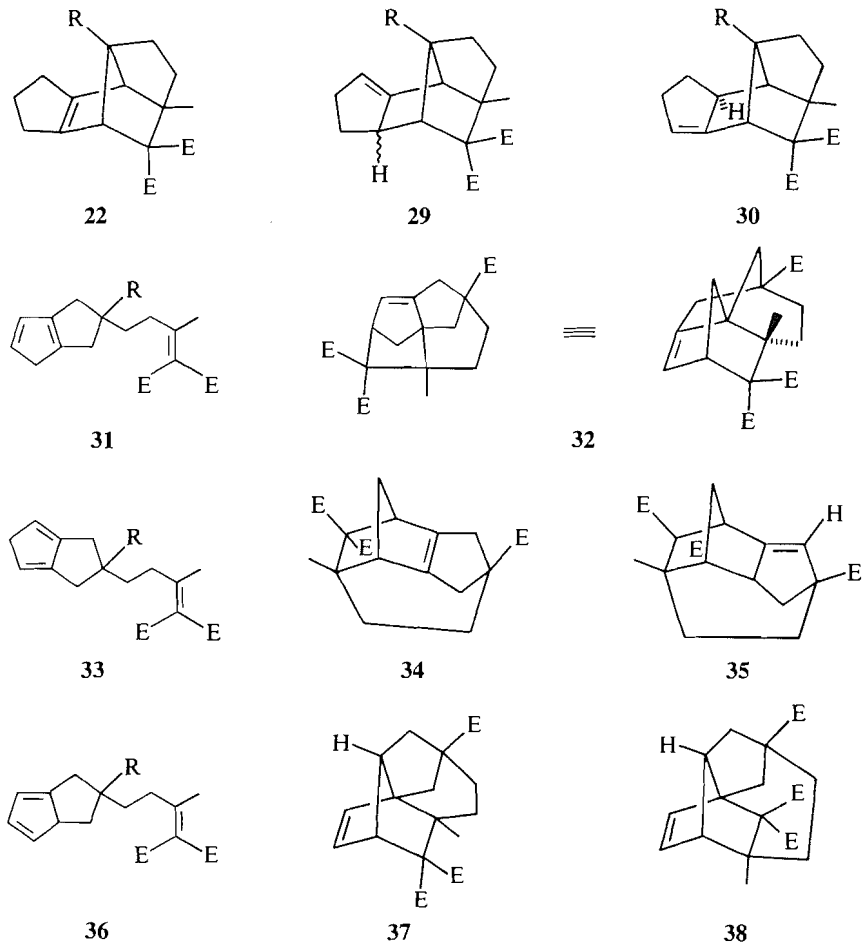

$R = CO_2Et$, $E = CO_2Me$

SCHEME 5

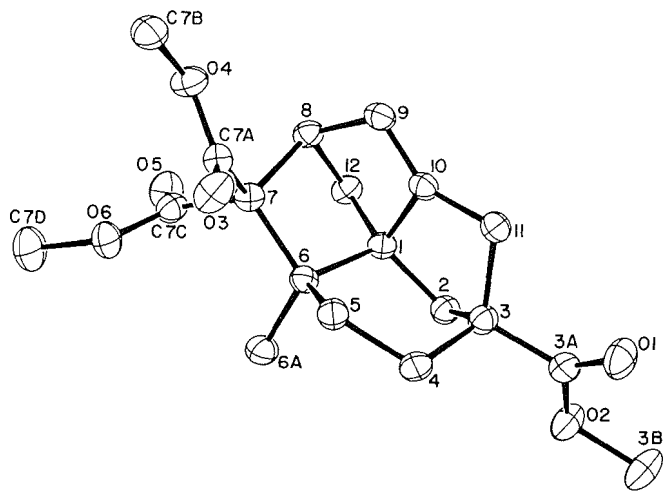

FIG. 1. ORTEP-II projection of 3,7,7-tricarbomethoxy-6-methylte tracyclo[6.3.1.$0^{1,6}$.$0^{1,10}$]-9-dodecene (**32**). H-atoms are omitted for clarity.

doublets (J = 1.5 Hz) with a triplet-like appearance is assigned to the single vinyl hydrogen at δ 5.26 and the *endo* methine proton appears as a multiplet at δ 3.01. Examination of the other structures **34, 35, 37**, and **38** reveals that the anticipated multiplicities for these signals would be different in all cases and thus the data fit **30** best. Additional support was provided by molecular mechanics calculations (MM2 type) on slightly simplified derivatives. These data (Table 2) indicated that structures such as **30***d* and **30***e*, with the fused cyclopentane ring *exo*, were approximately 1.5 kcal more stable than **22***d* and **22***e* and also more stable than adducts of type **29**.[4] Recently, related studies including molecular mechanics calculations have been published on tricyclo[5.2.1.$0^{2,6}$]dec-2(6)-ene (**22***c*) (Table 2) (45). This hydrocarbon was approximately 1.8 and 1.2 kcal more stable than the corresponding *endo* and *exo* isomers **30***f* and **30***c* respectively. Preparation of **22***c* from the related *tertiary* alcohol

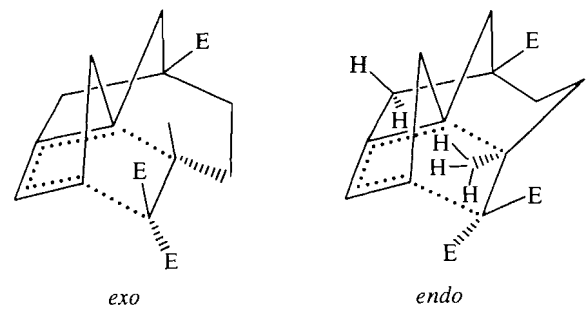

FIG. 2. Approximate transition states for the cyclization of **31**.

[4]We are grateful to C. Bayly and P. Deslongchamps, Université de Sherbrooke, for these calculations.

Can. J. Chem. Downloaded from www.nrcresearchpress.com by 176.9.209.113 on 09/07/12
For personal use only.

TABLE 2. Relative energies of double bond isomers (kcal)

$\Delta^{2,6}$	6-*exo*-$\Delta^{2,3}$	2-*endo*-$\Delta^{5,6}$	6-*endo*-$\Delta^{2,3}$	2-*exo*-$\Delta^{5,6}$
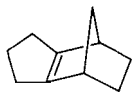			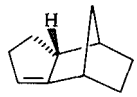	
22*c* 0	**30***c* 1.2		**30***f* 1.8	
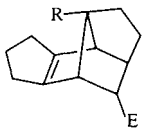	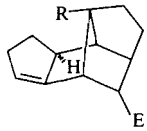	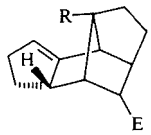	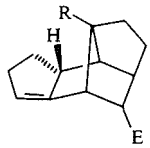	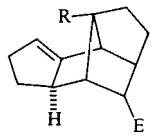
22*d* 1.3 R = CO_2Et **22***e* 1.8 R = E = H	**30***d* 0 R = CO_2Et **30***e* 0 R = E = H	**29***d* 5.7 R = CO_2Et **29***e* 0.8 R = E = H	**30***g* 7.4 R = CO_2Et **30***h* 3.4 R = E = H	**29***g* 7.5 R = CO_2Et **29***h* 4.1 R = E = H

*Isomer energies listed horizontally.

(*endo* ring fusion) by dehydration (*p*-toluenesulfonyl chloride, pyridine, 21°C, 40 h) also afforded 25% of the *endo* olefin **30***f*. The additional bridge in **22***d* and **22***e*, plus the extra substituents, will further increase the strain energy and instability of the tetrasubstituted olefin, thus encouraging the formation of a less strained exocyclic system whenever circumstances permit.

The unexpected results from the cycloaddition of triene **21** indicate that this strategy will not be suitable as a route to linear triquinanes unless blocking groups are employed to prevent double bond migration. Nevertheless the facile preparation of the tetracyclic system represented by **32** has several interesting ramifications and implied synthetic potential. Clearly further study of the migratory tendencies and cycloaddition preferences of other bicyclo[3.3.0]octadiene systems is warranted, to ascertain the preferred pathways that will be followed depending upon the length of the side chain, its point of attachment, and the nature of the dienophile. Molecular models suggest that in many cases one adduct will dominate, leading to tetracyclic adducts with potential utility for a variety of synthetic objectives. Molecular mechanics calculations indicate that for the parent unsubstituted diene hydrocarbons corresponding to **21** and **31** the system with the ring fusion double bond as contained in **31** is approximately 2.9 kcal more stable.[5] Therefore this construction strategy has intriguing possibilities now that the behaviour of these ring systems is more clearly understood and a general method for their preparation has been developed.

Experimental

Melting points were determined in capillary tubes with a Thomas–Hoover Uni-Melt apparatus, or on a Fisher–Johns melting point apparatus, and are uncorrected. Infrared spectra were recorded on a Perkin–Elmer 237B or 451 grating spectrophotometer, and were calibrated with the 2850 and 1601 cm^{-1} bands of polystyrene film. Proton magnetic resonance spectra were measured at 80 MHz with a Bruker WP80 spectrometer employing a chloroform lock or at 60 MHz with a Varian EM 360 spectrometer, or at 300 MHz with a General Electric GN 300 spectrometer, or at 400 MHz (at the University of Alberta) with a Bruker WH 400 spectrometer. Signal positions are reported in ppm downfield from tetramethylsilane (δ scale) as an internal standard; multiplicity, the number of protons, coupling constants, and proton assignments are indicated in parentheses. Mass spectra were determined on a V.G. Micromass 7070 HS instrument using an ionization energy of 70 eV.

Thin-layer chromatographic analyses were carried out on commercial precoated silica gel plates with fluorescent indicator (Eastman Kodak silica gel 13181). Preparative thin-layer chromatography was conducted on 20 × 20 cm glass plates coated with silica gel $PF^{254+366}$ type 60 (E. Merck). Flash chromatography using BDH silica gel Kieselgel 60, 230–400 mesh, was employed for all column chromatography.

Petroleum ether refers to a fraction with boiling range 30–60°C. Anhydrous diethyl ether (ether), tetrahydrofuran (THF), dimethoxyethane (DME), and dioxane were obtained by distillation from lithium aluminium hydride or potassium/benzophenone. Absolute ethanol and methanol were dried by distallation from magnesium. Dry hexamethylphosphoramide (HMPA), dimethylformamide (DMF), dimethyl sulfoxide (DMSO), and diisopropylamine were prepared by distillation from calcium hydride. Solutions in organic solvents were dried over anhydrous magnesium sulfate and stripped of solvent with a Buchi rotary evaporator connected to a water aspirator. Unless otherwise indicated, all reactions were conducted under an atmosphere of dry nitrogen.

*5-Carboethoxy-3-methyl-2-cyclopentenone (**10**)*

3-Methyl-2-cyclopentenone (**9**) (0.480 g, 5 mmol, Aldrich) in ether (10 mL) containing diethylpyrocarbonate (DEPC) (1.2 g, 7.5 mmol) was added rapidly (5 min maximum) to a stirred solution of lithium dicyclohexylamide (prepared from 4.2 mL of *n*-butyllithium (2.5 M, 10.5 mmol, Aldrich) and dicyclohexylamine (2.15 mL, 11 mmol) in ether (15 mL)) at −78°C under nitrogen. After 1 h at −78°C the reaction was quenched with aqueous 10% citric acid (10 mL), allowed to warm to 21°C, extracted with ether, the combined ether extracts washed with brine, dried, filtered, and the solvent removed under reduced pressure. Distillation of the residual diethylpyrocarbonate and the keto-esther (40–60°C/0.1 Torr; 1 Torr = 133.3 Pa) followed by chromatography (15% ether – petroleum ether) gave 5-carboethoxy-3-methyl-2-cyclopentenone (**10**), 0.590 g (71%); ir (neat): 1730 (C=O), 1690 (C=O), 1615 (C=C) cm^{-1}; ^1H nmr (CCl_4) δ: 1.27 (t, 3H, J = 7 Hz, CH_2CH_3), 2.19 (br s, 3H, $C=CCH_3$), 2.80 (m, 2H, CH_2—C=C), 3.31 (m, 1H, CO—CH—CO), 4.12 (q, 2H, J = 7 Hz, OCH_2CH_3), 5.80 (br s, 1H, C=CH). *Exact Mass* calcd. for $C_9H_{12}O_3$: 168.0783; found: 168.0787.

*Ethyl 5-chloro-3-methyl-2-pentenoate (**7**)*

A THF solution (50 mL) of freshly distilled (bp 49–50°C) ethoxy acetylene (18.5 g, 0.26 mmol, Farchan) was added dropwise to methylmagnesium chloride (8.3 mL, 0.24 mol, 2.99 M, Aldrich) dissolved in THF (250 mL) at 21°C, and stirring was continued for a further 0.5 h after addition was complete. Next 4-chloro-2-butanone (14 g, 0.13 mol) in THF (10 mL) was added over 5 min and stirring continued for a further 20 h at 21°C. The reaction was cooled to 0°C and water added dropwise until gas evolution ceased. The mixture was filtered through Celite, the layers separated, and the aqueous layer extracted with ether.

[5]We thank L. Taylor, Biochemistry Department, Memorial University of Newfoundland, for assistance in using the MODEL program of C. Still modified by K. Steliou for these calculations.

Can. J. Chem. Downloaded from www.nrcresearchpress.com by 176.9.209.113 on 09/07/12
For personal use only.

Can. J. Chem. Downloaded from www.nrcresearchpress.com by 176.9.209.113 on 09/07/12
For personal use only.

The combined ether extracts were dried, filtered, and the product purified by chromatography (5% ether/petroleum ether) to provide 4-chloro-2-ethoxyethynyl-2-butanol, 20 g (88%); ir (neat): 3300–3500 (br, OH), 2250 (C≡C) cm^{-1}; ^1H nmr (CCl_4) δ: 4.08 (q, 2H, J = 7Hz, O—CH_2—CH_3), 3.60 (m, 2H, CH_2Cl), 3.04 (s, 1H, OH), 1.96 (m, 2H, CH_2C—O), 1.48 (s, 3H, CH_3C—O), 1.38 (t, 3H, J = 7 Hz, CH_3CH_2) *Exact Mass* calcd. for $C_8H_{13}O_2Cl$: 176.0605; found: 176.0604.

A solution of 4-chloro-2-ethoxyethynyl-2-butanol (20 g, 0.11 mol) in ethanol (20 mL) was added dropwise to 5% sulfuric acid/ethanol (20 mL) maintained at 0°C. After addition was complete, stirring was continued for a further 20 h at 0–10°C. The reaction was diluted with water, extracted with ether, the combined ether extracts washed with 10% aqueous sodium bicarbonate, dried, filtered, and concentrated. The product was purified by chromatograpy (5% ether/petroleum ether) to give the unsaturated ester **7**, 15 g (75%), which was further purified by distillation, bp 65–68°C/0.05 Torr; ir (neat): 1710 (C=O), 1655 (C=C) cm^{-1}; ^1H nmr (CCl_4) δ: 5.70 (br s, 1H, HC=C), 4.10 (q, 2H, J = 7 Hz, O—CH_2—CH_3), 3.63 (t, 2H, J = 7 Hz, CH_2Cl), 3.02, 2.67 (t, t, 2H, J = 7 Hz, 1:1, *E*:*Z*, CH_2—C=C), 2.18, 1.99 (s, s, 3H, 1:1, *E*:*Z*, CH_3C=C), 1.27 (t, 3H, J = 7 Hz, CH_3CH_2).

*4-Chloro-2-methyl-1,1-dicarbomethoxy-1-butene (**8**)*

Titanium tetrachloride (11 mL, 0.10 mol) and carbon tetrachloride (25 mL) were added dropwise over 45 min to a 1-L three-necked flask containing THF (15 mL), maintained at 0°C with an external ice bath and equipped with a mechanical stirrer, condenser, and dropping funnel. After addition was complete, a yellow precipitate had formed and a THF solution (40 mL) containing 4-chlorobutanone (5.3 g, 0.05 mol), and dimethyl malonate (6.6 g, 0.05 mol, Eastman), were added to the stirred reaction mixture over 15 min. This was followed by the dropwise addition of pyridine (16 g, 0.2 mol) in THF (20 mL) over 30 min. The resulting dark orange solution was stirred for a further 24 h at 21°C. The reaction was poured onto ice-water, the organic layer separated, and the aqueous layer extracted with ethyl acetate. The combined extracts were dried, filtered, and concentrated to afford the diester **8**, 6.6 g (60%), which was further purified by distillation, bp 96–98°C/0.3 Torr; ir (neat): 1725 (C=O), 1640 (C=C) cm^{-1}; ^1H nmr ($CDCl_3$) δ: 3.63 (s, 6H, CH_3O), 3.58 (t, 2H, J = 7 Hz, CH_2Cl), 2.76 (t, 2H, J = 7 Hz, CH_2C=C), 1.98 (s, 3H, CH_3C=C). *Exact Mass* calcd. for $C_9H_{13}O_4Cl - CH_3OH$: 188.0237; found: 188.0223.

*Alkylation of keto-esters **10** and **24***

An ether solution (5 mL) of the appropriate keto-ester (5 mmol) was added to a sodium ethoxide solution (prepared from sodium (5 mmol), BDH, and dry ethanol (30 mmol)) in ether (4 mL) at 21°C and resulted in an immediate precipitate. The reaction mixture was lowered into an oil bath (75–80°C), dimethyl sulfoxide (10 mL) was added, followed by the alkyl halide (6 mmol of **7** and 10 mmol of **8**), and stirring continued for 2 h. The solution was then cooled (0°C), acidified (10% HCl), and extracted with ethyl acetate. The combined extracts were washed with brine, dried, filtered, concentrated, and the product purified by chromatography (10% ether – petroleum ether). The diester **17** was isolated in 90% yield; ir (neat): 1740 (C=O), 1710 (C=O), 1630 (C=C) cm^{-1}; 1H nmr ($CDCl_3$) δ: 1.22 (t, 3H, J = 7 Hz, CH_3), 1.26 (t, 3H, J = 7 Hz, CH_3), 1.70 (br s, 3H, C=CCH_3), 2.12 (br s, 3H, COC=CCH_3), 2.86 (m, 4H, CH_2—C=C), 4.02, 4.05 (q, 4H, J = 7 Hz, O—CH_2—CH_3), 5.00 (t, 1H, J = 7Hz, HC=C), 5.72 (m, 1H, HC=CCO); the triester **18** was obtained in 45% yield; ir (neat): 1740 (C=O), 1710 (C=O), 1625 (C=C) cm^{-1}; ^1H nmr ($CDCl_3$) δ: 1.08 (t, 3H, J = 7 Hz, CH_2CH_3), 1.58 (br s, 3H, C=CCH_3), 2.00 (br s, 3H, CH_3C=CCO), 3.62 (s, 3H, OCH_3), 3.67 (s, 3H, OCH_3), 3.73 (s, 1H, $HC(COOCH_3)_2$), 4.06 (q, 2H, J = 7 Hz, OCH_2—CH_3), 5.08 (t, 1H, J = 7 Hz, HC=C), 5.73 (m, 1H, C=CH—CO); the triester **26** was obtained in 65% yield; ir (neat): 1745 (C=O), 1700 (C=O), 1640 (C=C) cm^{-1}; ^1H nmr ($CDCl_3$) δ: 1.27 (t, 3H, J = 7 Hz, CH_3CH_2), 1.78 (br s, 3H, CH_3C=C), 3.70 (s, 6H, CH_3O), 3.93 (s, 1H, $HC(COOCH_3)_2$), 4.14 (q, 2H, J = 7 Hz, OCH_2CH_3), 5.18 (t, 1H, J = 7 Hz, HC=C). *Exact Mass* calcd. for $C_{20}H_{26}O_7$: 378.1671, found: 378.1655.

*5-(3-Oxobutyl)-5-carboethoxy-3-methyl-2-cyclopentenone (**11**)*

A solution of 5-carboethoxy-3-methyl-2-cyclopentenone (5 mmol) in *tert*-butyl alcohol (2 mL) was added dropwise to a stirred potassium *tert*-butoxide solution (prepared from potassium (0.01 mmol) and *tert*-butyl alcohol (4 mL) in ether (2 mL) at 21°C. Stirring was continued for a further 16 h after addition was complete, and the reaction was cooled to 0°C with an external ice bath and acidified with aqueous 1% HCl. The aqueous layer was extracted with ethyl acetate, the combined extracts were washed with brine, dried, filtered, concentrated, and the product purified by chromatography (10% ether – petroleum ether) to give the diketone **11**, 1.20 g (95%); ir (neat): 1730 (C=O), 1700 (C=O), 1625 (C=C) cm^{-1}; ^1H nmr (CCl_4) δ: 5.87 (br s, 1H, HC=C), 4.11 (q, 2H, J = 7 Hz, OCH_2CH_3), 2.19 (br s, 3H, CH_3C=C), 2.10 (s, 3H, CH_3CO), 1.22 (t, 3H, J = 7 Hz, CH_3CH_2).

endo-1-Carboethoxy-4-methyl-5-acetylbicyclo[2.2.1]heptan-2-one (**19**) was also obtained (5–50%) in early experiments when the base concentration was higher, ir (neat): 1765 (C=O strained), 1715 (C=O), 1625 (C=C) cm^{-1}; uv (EtOH): 224 nm, ε = 2000; ^1H nmr (400 MHz) ($CDCl_3$) δ: 4.22 (q, 2H, J = 7 Hz, OCH_2CH_3), 3.02 (ddd, 1H, J = 2, 6, 12 Hz, H-5 *exo*), 2.22 (s, 3H, CH_3CO), 1.45 (s, 3H, CH_3—C—), 1.30 (t, 3H, J = 7 Hz, CH_3CH_2). *Exact Mass* calcd. for $C_{13}H_{18}O_4$: 238.1200; found: 238.1211.

*5-Carboethoxy-5-(dimethyl 3-methyl-3-butenyl-4,4-dicarboxylate)3-methyl-2-cyclopentenone (**12**)*

Titanium tetrachloride (0.22 mL, 2 mmol, BDH) and carbon tetrachloride (1 mL) were added dropwise to a 25-mL three-necked flask containing THF (10 mL), maintained at 0°C with an external ice bath and equipped with a mechanical stirrer, condenser, and dropping funnel. After addition was complete, a yellow precipitate had formed and a THF solution (1 mL) containing diketone **11** (0.230 g, 1 mmol), and dimethyl malonate (0.130 g, 1 mmol, Eastman), were added to the stirred reaction mixture over 10 min. This was followed by the dropwise addition of pyridine (0.315 g, 4 mmol) in THF (1 mL). The resulting dark orange solution was stirred for a further 15 h at 21°C. The reaction was poured onto ice-water, the organic layer separated, and the aqueous layer extracted with ethyl acetate. The combined extracts were dried, filtered, concentrated and purified by chromatography (30% ethyl acetate/*n*-hexane) to afford recovered starting material **11**, 27 mg (12%), and the desired triester **12**, 187 mg (53%); ir (neat): 1750–1700 (C=O), 1630 (C=C) cm^{-1}; ^1H nmr (CCl_4) δ: 5.78 (br s, 1H, HC=C), 4.11 (q, 2H, J = 7 Hz, OCH_2CH_3), 3.72 (s, 6H, CH_3OCO), 2.22 (br s, 3H, CH_3C=CH), 2.03 (s, 3H, CH_3C=C), 1.23 (t, 3H, J = 7 Hz, CH_3CH_2); and 6-carboethoxy-8-methyl-3-(dimethyl methylenedicarboxylate)bicyclo[4.3.0]nona-1,8-diene (**20**) (7%); ir (neat): 1740–1710) (C=O), 1610 (C=C), 1570 (C=C) cm^{-1}; uv (EtOH): 226 nm, ε = 15 800; ^1H nmr (CCl_4) δ: 6.57 (s, 1H, HC=C), 6.03 (br s, 1H, HC=C), 4.07 (q, 2H, J = 7 Hz, OCH_2CH_3), 3.68 (s, 6H, CH_3OCO), 1.91 (br s, 3H, CH_3C=C), 1.23 (t, 3H, J = 7 Hz, CH_3CH_2). *Exact Mass* calcd. for $C_{18}H_{22}O_6$: 334.1414; found 334.1396.

*5-Carboethoxy-5-(dimethyl 3-methyl-3-butenyl-4,4-dicarboxylate)3-methyl-2-cyclopentenol (**13**)*

Sodium borohydride (12 mg, 0.31 mmol, BDH) was added to a stirred methanol solution (10 mL) containing the ketone **12** (100 mg, 0.28 mmol) and cerous chloride ($CeCl_3 \cdot 7H_2O$, 115 mg, 0.31 mmol, BDH). Stirring was continued at 21°C for 1 h after addition was complete. The reaction mixture was then acidified with 5% aqueous HCl, and extracted with ethyl acetate. The combined extracts were washed with brine, dried, filtered, concentrated, and the product purified by chromatography (25% ethyl acetate/*n*-hexane) to afford the alcohol **13**, 65 mg (62%); ir (neat): 3300–3500 (OH), 1725 (C=O), 1625 (C=C) cm^{-1}; ^1H nmr (CCl_4) δ: 5.87 (br s, 1H, HC=C), 5.35, 4.90 (m, 1H, 1:1, CH(OH)), 4.20 (q, 2H, J = 7 Hz, OCH_2CH_3), 3.78 (s, 6H, CH_3OCO), 2.27 (br s, 3H, CH_3C=CH), 2.08 (s, 3H, CH_3C=C), 1.29 (t, 3H, J = 7 Hz, CH_3CH_2).

*1-Carboethoxyl-1-(dimethyl 3-methyl-3-butenyl-4,4-dicarboxylate)4-methylcyclopentadiene (**14**)*

Gaseous sulfur dioxide (Fisher) was bubbled into a dichloromethane

Can. J. Chem. Downloaded from www.nrcresearchpress.com by 176.9.209.113 on 09/07/12
For personal use only.

(1 mL) solution containing methanesulfonyl chloride (0.48 mL, 6 mmol, Aldrich) for 10 min, and added to alcohol **13** (200 mg, 0.6 mmol) dissolved in dichloromethane (3 mL) containing pyridine (0.56 mL, 7.2 mmol) and *N,N*-dimethylaminopyridine (2 mg, Aldrich). The solution was stirred at 20°C for 1 h, cooled at 0°C, and water added. It was then extracted with dichloromethane, and the combined extracts were dried, filtered, concentrated, and purified by chromatography (30% ether/petroleum ether) to afford **14**, 107 mg (53%); ir (neat): 1725 (C=O), 1635 (C=C) cm^{-1}; ^1H nmr ($CDCl_3$) δ: 6.10 (m, 2H, HC=C), 4.80 (m, 1H, HC=C), 4.07, 4.12 (q, q, 2H, 1:1, J = 7 Hz, OCH_2CH_3), 3.65 (s, 6H, CH_3OCO), 2.01 (s, 3H, CH_3C=C), 1.82 (br s, 3H, CH_3C=CH), 1.23, 1.26 (t, t, 3H, 1:1 CH_3CH_2); ms (*m/z*, relative % intensity): 336(3), 304(5) − HOMe, 19(60), 91(100).

*$\Delta^{2,3}$-5-Carboethoxy-9-dicarbomethoxy-2,8-dimethyltricyclo-[4.3.0^{1,5}.0^{4,8}]nonene (**15**) and $\Delta^{2,3}$-5-carboethoxy-9-dicarbomethoxy-3,8-dimethyltricylo[4.3.0^{1,5}.0^{4,8}] (**16**)*

A solution of triene **14** (30 mg, 0.089 mmol) in toluene (1 mL) was placed in a sealed tube and heated in an oil bath at 140°C for 10 h. The solution was then concentrated and purified by chromatography (6% ether/petroleum ether) to afford a 5:4 mixture of **15** and **16**, 14 mg (40%); ir (neat): 1730 (C=O) cm^{-1}; ^1H nmr ($CDCl_3$) δ: 7.10, 6.20 (br s, 1H, HC=C, 5:4), 4.11 (q, 2H, J = 7 Hz, OCH_2CH_3), 3.70 (s, 6H, CH_3OCO), 2.02, 2.04 (br s, 3H, CH_3C=C, 5:4). *Exact Mass* calcd. for $C_{18}H_{24}O_6$: 336.1572; found: 336.1561.

*$\Delta^{1,5}$-Bicyclo[3.3.0]octen-2-one (**23**)*

This compound was prepared from methyl 2-oxocyclopentanecarboxylate by the method of Kulkarni and Dev (43), or preferably by the procedure of Eaton, Carlson, and Lee (44) in which the yield of the final cyclization was improved to 60% using P_2O_5/CH_3SO_3H in place of P_2O_5/H_3PO_4. The largest scale on which this reaction could be performed was 0.11 mol of hydroxy-acid using five equivalents of phosphorus pentoxide and methansulfonic acid, instead of the 10 equivalents recommended in the literature; ir (neat): 1700 (C=O), 1640 (C=C) cm^{-1}; uv (EtOH) 244, ε = 3500; ^1H nmr (CCl_4) δ: 2.2–2.8 (m). *Exact Mass* calcd. for $C_8H_{10}O$: 122.0729; found: 122.0713.

*$\Delta^{1,5}$-3-Carboethoxybicyclo[3.3.0]octen-2-one (**24**)*

An ether solution (10 mL containing $\Delta^{1,5}$-bicyclo[3.3.0]oct-en-2-one (**23**) (0.610 g, 5 mmol) and diethylpyrocarbonate (1.2 g, 7.5 mmol, Aldrich) was added rapidly (5 min maximum) to a stirred solution of lithium dicyclohexylamide (prepared from 4.2 mL of *n*-butyllithium (2.5 M, 10.5 mmol, Aldrich) and dicyclohexylamine (2.15 mL, 11 mmol)) in ether (15 mL) at −78°C under nitrogen. After 1 h at −78°C the reaction was quenched with aqueous 10% citric acid (10 mL), allowed to warm to 21°C, extracted with ether, the combined ether extracts washed with brine, dried, filtered, and the solvent removed under reduced pressure. Distillation of the residual diethylpyrocarbonate and the keto-ester (40–60°C/0.1 Torr) followed by chromatography (15% ether − petroleum ether) gave $\Delta^{1,5}$-3-carboethoxybicyclo[3.3.0]octen-2-one (**24**), 0.760 g (78%); ir (neat); 1735 (C=O), 1700 (C=O), 1640 (C=C) cm^{-1}; uv (EtOH) 245, ε = 4000; ^1H nmr (CCl_4) δ: 1.28 (t, 3H, CH_2CH_3, J = 7 Hz), 2.1–2.9 (m, 8H), 3.61 (br t, 1H, J = 5 Hz, CO—CH—CO), 4.18 (q, 2H, OCH_2CH_3, J = 7 Hz). *Exact Mass* calcd. for $C_{11}H_{14}O_3$: 194.0939; found: 194.0931.

*$\Delta^{1,5}$-3-(3-Oxobutyl)-3-carboethoxybicyclo[3.3.0]octen-2-one (**25**)*

The keto-ester **24** (0.97 g, 5 mmol) in *tert*-butyl alcohol (2 mL) was added to a potassium *tert*-butoxide solution (prepared from potassium (0.01 mmol) and *tert*-butyl alcohol (4 mL) in ether (2 mL)), at 21°C. Methyl vinyl ketone (0.70 g, 10 mmol) in *tert*-butyl alcohol (2 mL) was added dropwise. After stirring for 16 h, the reaction was cooled (0°C) and acidified (1% HCl). After extraction of the aqueous layer with ethyl acetate, the combined extracts were washed with brine, dried, filtered, concentrated, and the product purified by chromatography (5% ether – petroleum ether) to give diketone **25**, 1.25 g, (95%); ir (neat): 1750–1700 (C=O), 1645 (C=C) cm^{-1}; ^1H nmr ($CDCl_3$) δ: 4.11 (q, 2H, J = 7 Hz, OCH_2CH_3), 2.11 (s, 3H, CH_3CO), 1.23 (t, 3H, J = 7 Hz, CH_3CH_2). *Exact Mass* calcd. for $C_{16}H_{22}O_5$: 264.1360; found: 264.1331.

*$\Delta^{1,5}$-3-Carboethoxyl-3-(dimethyl 3-methyl-3-butenyl-4,4-dicarboxylate)bicyclo[3.3.0]octen-2-one (**27**)*

Titanium tetrachloride (5.4 mL, 0.05 mol, BDH) and carbon tetrachloride (18 mL) were added dropwise over 35 min to a three-necked flask containing THF (10 mL) and equipped with a mechanical stirrer, condenser, and dropping funnel. After addition was complete, a yellow precipitate had formed and a THF solution (20 mL) containing $\Delta^{1,5}$-3-(3-oxobutyl)-3-carboethoxybicyclo[3.3.0]octen-2-one (**25**) (6.55 g, 0.025 mol), and dimethyl malonate (3.3 g, 0.025 mol, Eastman), were added to the stirred reaction mixture over 15 min. This was followed by the dropwise addition of pyridine (8 g, 0.1 mol) in THF (10 mL) over 30 min. The resulting dark orange solution was stirred for a further 22 h at 21°C. The reaction was poured onto ice-water, the organic layer separated, and the aqueous layer extracted with ethyl acetate. The combined extracts were dried, filtered concentrated, and purified by chromatography (20–30% ether/*n*-hexane) to afford recovered starting material **24**, 0.79 g (12%), and the desired triester **27**, 5.67 g (60%); ir (neat): 1755–1725 (C=O), 1650 (C=C) cm^{-1}; ^1H nmr (CCl_4) δ: 4.12 (q, 2H, J = 7 Hz, OCH_2CH_3), 3.73, 3.70 (s, s, 6H, 1:1, CH_3OCO), 2.02 (s, 3H, CH_3C=C), 1.24 (t, 3H, J = 7 Hz, CH_3CH_2).

*$\Delta^{1,5}$-3-Carboethoxy-3-(dimethyl-3-methyl-3-butenyl-4,4-dicarboxylate)bicyclo[3.3.0]octen-2-ol (**28**)*

Sodium borohydride (0.38 g, 0.01 mol, BDH) was added to a stirred methanol solution (30 mL) containing the ketone **27** (3.78 g, 0.01 mol) and cerous chloride ($CeCl_3 \cdot 7H_2O$, 3.73 g, 0.01 mol, BDH). Stirring was continued at 21°C for 1 h after addition was complete. The reaction mixture was then acidified with 5% aqueous HCl, and extracted with ethyl acetate. The combined extracts were washed with brine, dried, filtered, concentrated, and the product purified by chromatography (25% ethyl acetate/*n*-hexane) to afford the alcohol **28**, 255 g (67%); ir (neat): 3500 (OH), 1750–1705 (C=O), 1650 (C=C) cm^{-1}; ^1H nmr (CCl_4) δ: 4.60 (br s, 1H, CH(OH)), 4.05 (q, 2H, J = 7 Hz, OCH_2CH_3), 3.64 (s, 6H, CH_3OCO), 1.27 (t, 3H, J = Hz, CH_3CH_2).

In an alternative procedure a zinc borohydride solution (60 mL, 0.16 M in ether, 8.8 mmol) was added to an ether solution (40 mL) containing ketone **27** (3.0 g, 7.9 mmol) at 0°C. After stirring for 30 min at 0°C, and for 30 min at 21°C, a saturated solution of sodium tartrate was added dropwise (1.5 mL) until bubbling ceased. This solution was then dried, filtered, concentrated, and the product purified by chromatography (30% ether – petroleum ether) to afford **28**, 1.6 g (58%).

*3-Carboethoxy-3-(dimethyl-3-methyl-3-butenyl-4,4-dicarboxylate)-bicyclo[3.3.0]octa-1,4-diene (**21**)*

Gaseous sulfur dioxide (Fisher) was bubbled into a dichloromethane (10 mL) solution containing methanesulfonyl chloride (3.8 g, 6.7 mmol, Aldrich) for 10 min at 21°C. This solution was added to the alcohol **28** (2.5 g, 6.7 mmol) dissolved in dichloromethane (10 mL), containing pyridine (2.9 g, 36.8 mmol) and *N,N*-dimethylaminopyridine (5 mg, Aldrich). The resulting solution was stirred at 21°C for 1 h, cooled at 0°C, and water added. The aqueous mixture was then extracted with dichloromethane, and the combined extracts were dried, filtered, concentrated, and purified by chromatography (10% ether/petroleum ether) to afford the cyclopentadiene **21**, 1.45 g (60%); ir (neat): 1730 (C=O), 1635 (C=C) cm^{-1}; ^1H nmr ($CDCl_3$) δ: 5.73, 5.35, 5.20 (br s, br s, br s, 2H, HC=C), 4.10, 4.06 (q, q, 2H, ≃2:1, OCH_2CH_3), 3.72, 3.64 (s, s, 6H, ≃2:1, CH_3OCO), 2.01 (s, 3H CH_3C=C), 1.51, 1.48 (t, t, 3H, ≃2:1, CH_3CH_2); ms (*m/z*, relative % intensity): 362(4), 257(5) − HOMe, COOEt or HCOOEt, OMe, 117(38).

*Cyclization of triene **21**. 3,7,7-Tricarbomethoxy-6-methyltetracyclo-[6.3.1.0^{1,6}.0^{1,10}]-9-dodecene (**32**) and 6-carboethoxy-2-dicarbomethoxy-3-methyltetracyclo-[6.4.0^{1,6}.0^{3,708,12}]-11-dodecene (**30**)*

A toluene solution (1 mL) of **21** (30 mg, 0.081 mmol) was placed in a sealed tube, flushed with nitrogen, and heated in an oil bath at 140°C for 10 h. The solution was concentrated and chromatographed (6% ether/petroleum ether) to afford the adducts, 15 mg (50%); ir (neat): 1735 (C=O) cm^{-1}; ^1H nmr (400 MHz) ($CDCl_3$) δ: 5.51, 5.26 (m, m, 1H, 4:1, J = 1.5 Hz, HC=C), 4.14, 4.15 (q, q, 2H, 4:1, J = 7 Hz, OCH_2CH_3), 3.71, 3.65 and 3.69, 3.66 (s, s, s, s, 6H, 4:4:1:1,

TABLE 3. Atomic coordinates (esd's) and equivalent isotropic B values (B_{iso}, Å^2) for 3,7,7-tricarbomethoxy-6-methyltetracyclo-[6.3.1.0^{1,6}.0^{1,10}]-9-dodecene (**32**) (H atoms omitted)

	x	y	z	B_{iso}
O1	0.39719(22)	0.8701(4)	0.60495(20)	7.32(18)
O2	0.45756(20)	1.1196(4)	0.66723(18)	6.43(15)
O3	0.19623(20)	1.2342(4)	0.19168(18)	6.48(16)
O4	0.06062(17)	1.3885(4)	0.17127(17)	5.59(14)
O5	0.14839(21)	1.7630(4)	0.30149(20)	6.43(17)
O6	0.21873(19)	1.6537(3)	0.21072(18)	5.73(15)
C1	0.23926(23)	1.3653(5)	0.46192(23)	4.12(16)
C2	0.3165(3)	1.3163(5)	0.5491(3)	4.53(17)
C3	0.33889(24)	1.1329(5)	0.52534(24)	4.46(16)
C3A	0.3992(3)	1.0237(6)	0.6025(3)	5.17(20)
C3B	0.5168(5)	1.0262(9)	0.7460(4)	7.5(3)
C4	0.3892(3)	1.1513(6)	0.4555(3)	4.99(20)
C5	0.3267(3)	1.2377(5)	0.3680(3)	4.72(19)
C6	0.27767(23)	1.4027(4)	0.38322(23)	4.15(17)
C6A	0.3491(3)	1.5521(6)	0.4067(3)	5.53(22)
C7	0.18064(23)	1.4542(5)	0.30517(23)	4.18(16)
C7A	0.1504(3)	1.3502(5)	0.21845(24)	4.53(18)
C7B	0.0206(4)	1.3096(8)	0.0840(3)	6.5(3)
C7C	0.1798(3)	1.6419(5)	0.2751(3)	4.88(18)
C7D	0.2181(5)	1.8246(8)	0.1741(5)	7.9(4)
C8	0.10490(25)	1.4325(5)	0.35260(25)	4.64(19)
C9	0.1105(3)	1.2400(6)	0.3694(3)	4.77(20)
C10	0.18234(24)	1.2019(5)	0.43387(24)	4.37(17)
C11	0.2396(3)	1.0518(5)	0.4806(3)	4.87(19)
C12	0.1615(3)	1.4989(6)	0.4476(3)	4.81(19)

CH_3OCO), 3.37, 3.01 (m, m, 1H, 4:1, bridgehead H), 1.25 (t, 3H, J = 7 Hz, CH_3CH_2), 1.17 (s 3H, CH_3—C). *Exact Mass* calcd. for $C_{20}H_{26}O_6$: 362.1727; found: 362.1720.

The adducts **30** (R = COOEt, E = COOMe) and **32** (E(bridgehead) = COOEt, E = COOMe) (20 mg, 0.05 mmol) were added to a solution containing aluminum trichloride (14 mg, 0.11 mmol, Fisher) in ethanethiol (2 mL, Eastman) according to the procedure of Fujita and co-workers (46). Immediately a very viscous precipitate was formed, and stirring was continued at 21°C for 20 h. The reaction mixture was then poured into cold acid (1% aqueous HCl) and extracted with ether and chloroform. The combined extracts were dried, filtered, concentrated, and the product mixture, 17 mg (94%), chromatographed to give 3-carboethoxy-7,7-dicarboxy-6-methyltetracyclo-[6.3.1.0^{1,6}.0^{1,10}]-9-dodecene (5 mg); ir (neat): 3700–2800 (OH), 1725 (C=O) cm^{-1}; ^{1}H nmr (80 MHz) ($CDCl_3$) δ: 8.80 (br s, 2H, COOH), 5.85 (s, 1H, HC=C), 4.08 (q, 2H, J = 7 Hz, CH_2CH_3), 1.25 (t, 3H, J = 7 Hz, CH_3CH_2), 1.23 (s, 3H, CH_3), and 12 mg of fully hydrolyzed material. This was dissolved in methanol (2 mL) and treated with excess ethereal diazomethane, concentrated and chromatographed (20% acetone/*n*-hexane) to give a mixture (3 mg, 5:4) of 3,7-dicarbomethoxy-6-methyltetra-cyclo[6.3.1.0^{1,6}.0^{1,10}]-9-dodecene and 2,6-dicarbomethoxy-3-methyltetracyclo-[6.4.0^{1,6}.0^{3,7}.0^{8,12}]-11-dodecene, ^{1}H nmr ($CDCL_3$) δ: 5.72, 5.21 (m, m, 1H, 5:4, HC=C), 3.70, 3.64, 3.69, 3.62 (s, s, s, s, 3H, CH_3O); followed by the trimethylester **32** (6 mg), ^{1}H nmr ($CDCL_3$) (300 MHz) δ: 5.51 (d, 1H, J = 1.5 Hz, HC=C), 3.71 (s, 3H, CH_3O), 3.70 (s, 3H, CH_3O), 3.65 (s, 3H, CH_3O), 3.37 (br d, 1H, J = 1.5 Hz, bridgehead H), 2.67, 2.30 (AB system, 1H, 1H, J = 17 Hz, *exo* and *endo* allylic CH_2), 2.10, 1.35 (AB system, 1H, 1H, J = 9 Hz, bridge CH_2), 1.95, 1.58 (m, 1H, 1H, bridge CH_2), 1.19 (s, 3H, CH_3C); ^{13}C nmr ($CDCl_3$) δ: 19.9, 31.8, 33.4, 34.2, 35.5, 44.3, 48.3, 51.8, 51.8, 52.4, 54.9, 55.1, 63.9, 69.2, 119.8, 158.4, 170.6, 172.0, 176.1.

Crystallography

3,7,7-Tricarbomethoxy-6-methyltetracyclo[6.3.1.0^{1,6}.0^{1,10}]-9-dodecene (32)

Diffraction intensities from an approximately 0.10 × 0.10 × 0.30 mm crystal were collected with graphite monochromatized CuK$_\alpha$ radiation, using the θ/2θ technique with profile analysis (47) to 2θ$_{max}$ 153° and using an Enraf Nonius CAD4 diffractometer with a PDP-8e computer. A total of 3705 reflections were measured, all of which were unique, and 2112 were considered significant with $I_{net} > 2.5\sigma$ (I_{net}). Lorentz and polarization factors were applied, but absorption corrections were not because of the small size of the crystal and the small value of μ. Cell parameters were obtained by least-squares refinement of the setting angles of 21 reflections within the range 84.00° < 2θ < 92.00°.

TABLE 4. Selected bond lengths (esd's) in Å for 3,7,7-tricarbomethoxy-6-methyltetracyclo[6.3.1.0^{1,6}.0^{1,0}]-9-dodecene (**32**)

Bond	Length (Å)	Bond	Length (Å)
O(1)—C(3A)	1.192(5)	C(3)—C(3A)	1.510(5)
O(2)—C(3A)	1.327(5)	C(3)—C(4)	1.561(5)
O(2)—C(3B)	1.456(6)	C(3)—C(11)	1.550(5)
O(3)—C(7A)	1.193(5)	C(4)—C(5)	1.540(6)
O(4)—C(7A)	1.333(5)	C(5)—C(6)	1.538(5)
O(4)—C(7B)	1.447(5)	C(6)—C(6A)	1.536(5)
O(5)—C(7C)	1.193(5)	C(6)—C(7)	1.607(5)
O(6)—C(7C)	1.356(5)	C(7)—C(7A)	1.529(5)
O(6)—C(7D)	1.447(6)	C(7)—C(7C)	1.530(5)
C(1)—C(2)	1.518(5)	C(7)—C(8)	1.587(5)
C(1)—C(6)	1.585(5)	C(8)—C(9)	1.522(6)
C(1)—C(10)	1.507(5)	C(8)—C(12)	1.546(6)
C(1)—C(12)	1.521(5)	C(9)—C(10)	1.335(5)
C(2)—C(3)	1.539(5)	C(10)—C(11)	1.485(6)

The structure was solved by direct methods using the NRC VAX Crystal Structure programs (48) and refined by full matrix least-square methods to final residuals of R_f and R_w of 0.053 and 0.047 respectively ($R_f = \Sigma(|F_o|-|F_c|)/\Sigma(|F_o|)$; $R_w = \Sigma(w(|F_o|-|F_c|)^2/\Sigma(w|F_o|^2))$. The final difference map had no peaks higher than 0.190 eA^3.

Crystal and other numerical data

$C_{19}H_{24}O_6$ fw = 384.27

Monoclinic, $P2_1/c$, a = 15.094(7), b = 7.750(3), c = 15.985(9) Å, β = 110.50(4)°, (CuKα$_1$, λ = 1.54056 Å, 21 reflections, 84° < 2θ < 92°), V = 1751.48 Å^3, Z = 4, ρ_c = 1.321 mg m^{-3}. Nominal specimen dimensions 0.10 × 0.10 × 0.30 mm; 3705 reflections scanned (2θ$_{max}$ 153°), giving 2112 "observed" ($I_{net} > 2.56\ \sigma I_{net}$). Atomic coordinates are given in Table 3 and selected bond lengths in Table 4. Supplementary data[6] include H-atom coordinates, temperature factors, all bond lengths, and structure factors. Figure 1 is an ORTEP-II projection (49) of the molecular structure.

Acknowledgements

We are grateful to Memorial University of Newfoundland and to the Natural Sciences and Engineering Research Council of Canada for financial support of this research, to B. Gregory for high resolution mass spectra, to C. Jablonski for special nmr experiments, to D. J. Burnell for fruitful discussion, and to R. Andersen (University of British Columbia) for advice and encouragement.

1. L. A. PAQUETTE. Top. Curr. Chem. **119**, 1 (1984).
2. B. M. TROST. Angew. Chem. Int. Ed. Engl. **25**, 1 (1986).
3. M. DEMUTH and K. SCHAFFNER. Angew. Chem. Int. Ed. Engl. **21**, 820 (1982).
4. E. PIERS, J. BANVILLE, C. K. LAU, and I. NAGAKURA. Can. J. Chem. **60**, 2965 (1982).
5. W. A. SMIT, A. S. GYBIN, A. S. SHASHKOV, Y. T. STRYCHKOV,

[6]Tables of supplementary data may be purchased from the Depository of Unpublished Data, CISTI, National Research Council of Canada, Ottawa, Ont., Canada, K1A 0S2.

Can. J. Chem. Downloaded from www.nrcresearchpress.com by 176.9.209.113 on 09/07/12
For personal use only.

L. G. KYZ'MINA, G. S. MIKAELIAN, R. CAPLE, and E. D. SWANSON. Tetrahedron Lett. **27**, 1241 (1986).
6. D. P. CURRAN, M. CHEN, and D. KIM. J. Am. Chem. Soc. **108**, 2489 (1986).
7. E. PIERS and V. KARUNARATRE. Can. J. Chem. **62**, 629 (1984).
8. M. RAMAIAH. Synthesis, 529 (1984).
9. E. AYANOGLU, T. GEBREYESUS, C. M. BEECHAN, C. DJERASSI, and M. KAISIN. Tetrahedron Lett. 1671 (1978).
10. R. D. LITTLE and G. L. CARROLL. Tetrahedron Lett. **22**, 4389 (1981).
11. R. D. LITTLE, G. L. CARROLL, and J. L. PETERSEN. J. Am. Chem. Soc. **105**, 928 (1983).
12. L. A. PAQUETTE and K. E. STEVENS. Tetrahedron Lett. **22**, 4393 (1981).
13. L. A. PAQUETTE and K. E. STEVENS. Can. J. Chem. **62**, 2415 (1984).
14. J. HUGET, M. KARPF, and A. S. DRIEDING. Helv. Chim. Acta, **65**, 2413 (1982).
15. T. FUJITA, T. OHTSUKA, H. SHIRAHAMA, and T. MATSUMOTO. Tetrahedron Lett. **23**, 4091 (1982).
16. W. OPPOLZER AND K. BATTIG. Tetrahedron Lett. **23**, 4669 (1982).
17. A. M. BIRCH and G. PATTENDEN. Tetrahedron Lett. **23**, 991 (1982).
18. A. M. BIRCH and G. PATTENDEN. J. Chem. Soc. Perkin Trans. 1, 1913 (1983).
19. G. T. CRISP, W. J. SCOTT, and J. K. STILLE. J. Am. Chem. Soc. **106**, 7500 (1984).
20. G. MEHTA, D. S. REDDY, and A. N. MURTHY. J. Chem. Soc. Chem. Commun. 824 (1983).
21. G. MEHTA, A. N. MURTHY, D. S. REDDY, and A. V. REDDY. J. Am. Chem. Soc. **108**: 3443 (1986).
22. H. J. LIU and M. G. KULKARNI. Tetrahedron Lett. **26**, 4847 (1985).
23. D. P. CURRAN and M. CHEN. Tetrahedron Lett. **26**, 4991 (1985).
24. J. R. STILLE and R. H. GRUBBS. J. Am. Chem. Soc. **108**, 855 (1986).
25. M. KAISIN, Y. M. SHEIKH, L. J. DURHAM, C. DJERASSI, B. TURSCH, B. DALOZE, J. C. BRAEKMAN, D. LOSMAN, and R. KARLSSON. Tetrahedron Lett. 2239 (1974).
26. Y. M. SHEIKH, G. SINGY, M. KAISIN, H. EGGERT, C. DJERASSI, B. TURSCH, D. DALOZE, and J. C. BRAEKMAN. Tetrahedron, **32**, 1171 (1976).
27. Y. M. SHEIKH, C. DJERASSI, J. C. BRAEKMAN, D. DALOZE, M. KAISIN, B. TURSCH, and R. KARLSSON. Tetrahedron, **33**, 2115 (1977).
28. M. KAISIN, J. C. BRAEKMAN, D. DALOZE, and B. TURSCH. Tetrahedron, **41**, 1067 (1985).
29. M. SHIBASAKI, T. MASE, and S. IKEGAMI. J. Am. Chem. Soc. **108**, 2090 (1986).
30. G. PATTENDEN and S. J. TEAGUE. Tetrahedron Lett. **23**, 5471 (1982).
31. T. MASE and M. SHIBASAKI. Tetrahedron Lett. **27**, 5245 (1986).
32. M. KAISIN and B. TURSCH. Bull. Soc. Chim. Belg. **88**, 253 (1979).
33. L. S. CIERSZKO. Trans. N.Y. Acad. Sci. **24**, 502 (1962).
34. P. R. BURKHOLDER and L. M. BURKHOLDER. Science, **127**, 1174 (1958).
35. B. TURSCH, J. C. BRAEKMAN, D. DALOZE, and M. KAISIN. *In* Marine natural products, chemical and biological perspective. *Edited by* P. J. Scheuer. Academic Press. New York, NY. 1978. Chap. 4.
36. D. D. STERNBACH, J. W. HUGHES, D. F. BURDI, and B. A. BANKS. J. Am. Chem. Soc. **107**, 2149 (1985).
37. E. G. BREITHOLLE and A. G. FALLIS. J. Org. Chem. **42**, 1964 (1978).
38. A. G. FALLIS. Can. J. Chem. **62**, 183 (1984).
39. E. CIGANEK. Org. React. **32**, 1 (1984).
40. D. F. TABER. Intramolecular Diels–Alder reactions and Alder ene reactions. Springer Verlag, Berlin. 1984.
41. J. HELLOU, J. F. KINGSTON, and A. G. FALLIS. Synthesis, 1013 (1984).
42. W. LENHERT. Tetrahedron, **29**, 635 (1973).
43. S. B. KULKARNI and S. DEV. Tetrahedron, **24**, 553 (1968).
44. P. E. EATON, G. R. CARLSON, and J. T. LEE. J. Org. Chem. **38**, 4071 (1973).
45. N. TAKAISHI, H. TAKAHASHI, O. YAMASHITA, and Y. INAMOTO. J. Org. Chem. **51**, 4862 (1986).
46. M. NODE, K. NISHIDE, M. SAI, K. FUJI, and E. FUJITA. J. Org. Chem. **46**, 1991 (1981).
47. D. F. GRANT and E. J. GABE. J. Appl. Crystallogr. **11**, 114 (1978).
48. E. J. GABE, F. L. LEE, and Y. LEPAGE. *In* Crystallographic computing III. *Edited by* G. M. Sheldrick, C. Kruger, and R. Goddard. Clarendon Press, Oxford. 1985. pp. 167.
49. C. K. JOHNSON. ORTEP-II. A Fortran thermal-ellipsoid plot program for crystal structure illustrations, Report 5138. Oak Ridge National Laboratory, Tennessee, U.S.A. 1976.

Can. J. Chem. Downloaded from www.nrcresearchpress.com by 176.9.209.113 on 09/07/12
For personal use only.

Structural studies of a hemicellulose B fraction (B-2) from the cork of *Quercus suber*[1]

AMPARO ASENSIO
Department of Organic Chemistry, University of Valencia, Burjassot, Valencia, Spain

Received August 7, 1987

AMPARO ASENSIO. Can. J. Chem. **66**, 449 (1988).

Polysaccharide B-2 contains xylose, arabinose, glucose, galactose, 4-*O*-methylglucuronic acid, and rhamnose in the molar ratio of 17:12:12:6:4:1. The polysaccharide has a backbone of β(1→4)- and β(1→3)-linked glucopyranosyl, β(1→4)-linked xylopyranosyl, and (1→4)- and (1→6)-linked galactopyranosyl residues. Arabinofuranosyl, rhamnopyranosyl, and some xylopyranosyl and galactopyranosyl groups are present as nonreducing end units. Glucopyranosyluronic acid side chains are attached at O-2 of some xylose residues. The anomeric configurations of the different glycosyl groups were determined by a study of the chromium trioxide oxidation of the acetylated polysaccharide and by nuclear magnetic reasonance spectra of the methylated polysaccharide.

AMPARO ASENSIO. Can. J. Chem. **66**, 449 (1988).

Le polysaccharide B-2 contient du xylose, de l'arabinose, du glucose, du galactose, de l'acide *O*-méthyl-4 glucuronique et du rhamnose dans un rapport molaire de 17:12:12:6:4:1. Le polysaccharide possède un squelette de résidus de glucopyrannosyles liés en β(1→4) et β(1→3), de xylopyrannosyles liés en β(1→4) et de galactopyrannosyles liés en (1→4) et en (1→6). Les groupements arabinofurannosyles, rhamnopyrannosyles et quelques-uns des groupements xylopyrannosyles et galactopyrannosyles sont présents sous la forme d'unités en bout de chaîne qui ne sont pas réductrices. Les chaînes latérales d'acide glucopyrannosyluronique sont attachées en position O-2 de certains résidus de xylose. On a déterminé les configurations anomériques des différents groupements glycosyles en procédant à une oxydation par le trioxyde de chrome du polysaccharide acétylé et à une étude des spectres en résonance magnétique nucléaire du polysaccharide méthylé.

[Traduit par la revue]

Can. J. Chem. Downloaded from www.nrcresearchpress.com by 176.9.209.113 on 09/07/12
For personal use only.

In continuing studies of the polysaccharides from the cork of *Quercus suber*, the structure of the fraction B-2, inferred from the results of complete and partial hydrolysis with acid, methylation analysis, and chromium trioxide oxidation, is now discussed. Hemicelluloses A and B (fraction B-1) have been investigated in detail (1, 2). Both polysaccharides contain (1→4)-linked xylopyranosyl residues in the backbone chains, but different side chains. The polysaccharide B-2 is shown to be highly branched.

The polysaccharide B-2 was isolated as previously described (2), and some impurities of low molecular weight were removed by dialysis. It had a low, positive, optical rotation ($[\alpha]_D$ + 3.96°), indicating that this polymer was structurally different (1, 2) from hemicelluloses A and B-1. It contained xylose, arabinose, glucose, galactose, 4-*O*-methylglucuronic acid, and rhamnose in the molar ratio of 17:12:12:6:4:1. The polysaccharide gave a single peak in chromatography (3) on Sephacryl S-400.

Hakomori methylation (4) of B-2 gave a product with an $[\alpha]_D$ value of +8.3° indicative of α and β linkages, which was confirmed by the nmr spectra (5). A part of the methylated polysaccharide was reduced with lithium aluminium hydride. The two samples were hydrolysed and the sugars were analysed, as the partially methylated alditol acetates, by glc and glc (6) – ms (7). The results are summarized in Table 1.

These results gave an indication of the linkages between the different monosaccharide residues in polysaccharide B-2. The proportions of 2-*O*- and 3-*O*-methylxylose, and 2,3-di-*O*-methylglucose, show that B-2 is highly branched. Identification of 2,3,4-tri-*O*-methylrhamnose, 2,3,5-tri-*O*-methylarabinose, 2,3,4-tri-*O*-methylxylose, 2,3,4,6-tetra-*O*-methyl-glucose and -galactose indicated their derivation from nonreducing end units in the methylated polysaccharide. In the interior part of the polysaccharide, both glucose and xylose are present as (1→4)-linked residues, and the glucose also as (1→3)-linked residues. Galactose is present as (1→4)- and (1→6)-linked residues.

2,3,4-Tri-*O*-methylglucose was detected only in reduced polysaccharide, showing that this sugar was derived from terminal glucopyranosyluronic acid residues. The presence of 2,5-di-*O*-methylarabinose in the hydrolysate of the methylated polysaccharide showed that some arabinosyl groups are joined through (1→3) linkages.

TABLE 1. Products obtained by hydrolysis of the methylated (A); methylated, carboxyl-reduced B-2 (B); and methylated, carboxyl-reduced, degraded polysaccharide B-2 (C)

Sugars[a]	t_R[b]		Mol%		
	a	b	A	B	C
2,3,4-Me_3-Rha	0.43	0.81	4.0	1.9	—
2,3,5-Me_3-Ara	0.51	0.69	15.0	14.6	—
2,3,4-Me_3-Xyl	0.67	0.75	9.6	2.6	0.8
2,5-Me_2-Ara	0.92	0.86	2.5	2.9	—
2,3,4,6-Me_4-Glc	1.00	1.00	tr[c]	1.0	1.1
2,3,4,6-Me_4-Gal	1.25	1.04	6.8	3.4	12.0
2,3-Me_2-Xyl	1.44	0.92	17.1	22.3	2.5
2,4,6-Me_3-Glc	1.87	1.16	3.1	12.2	9.3
2,3,6-Me_3-Gal	2.40	1.17	1.6	3.3	2.2
2,3,6-Me_3-Glc	2.40	1.18	11.0	8.3	24.7
2,3,4-Me_3-Glc	2.40	1.21	—	3.3	1.4
2-Me-Xyl	2.78	1.06	6.5	2.9	—
3-Me-Xyl	2.78	1.08	1.5	5.5	—
2,3,4-Me_3-Gal	3.20	1.19	5.3	3.4	4.8
2,3-Me_2-Glc	4.99	1.35	14.7	11.2	39.8
2,4-Me_2-Gal	5.90	1.41	1.1	1.3	1.3

[a]2,3,4-Me_3-Rha = 2,3,4-tri-*O*-methyl-L-rhamnose, etc.
[b]Retention times of the corresponding alditol acetates, relative to that of 1,5-di-*O*-acetyl-2,3,4,6-tetra-*O*-methyl-D-glucitol on (a) ECNSS-M at 175°C, and (b) OV-1 at 120→ 220°C at 4°/min.
[c]tr = trace.

[1]*Quercus suber* Polysaccharides, Part III. For Part II see ref. 2.

Printed in Canada / Imprimé au Canada

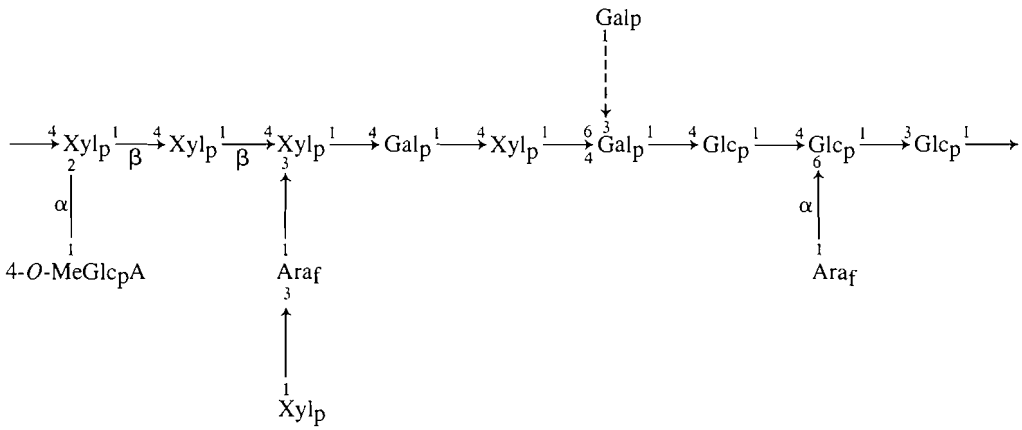

FIG. 1. Average structural features of the B-2 fraction.

The molar percentages of rhamnose, arabinose, xylose, galactose, glucose, and 4-*O*-methylglucuronic acid calculated from the methylation (carboxyl-reduced) analysis, assuming that the molar percentage of rhamnose is the same as in the original polysaccharide, are in close agreement with the sugar composition of the polysaccharide. The ratio of the end groups to branch points (calculated from Table 1) for permethylated polysaccharide is $\simeq$1:1.

As seen from Table 1, some components are not separated by glc on the ECNSS-M column. The alditol acetates derived from 2,3,6- and 2,3,4-tri-*O*-methylglucose and from 2,3,6-tri-*O*-methylgalactose were resolved on a OV-1 column. Both 2- and 3-*O*-methylxylose were also resolved on that column (cf. Fig. 2) and identified by the fragments obtained by glc–ms of their alditol acetates (7, 8). The fragments with *m/z* 43, 87, 129, and 189, characteristic of 3-*O*-methylpentoses, were the same as those of 3-*O*-methyl-D-xylose obtained in previous work (1, 2). Fragments with *m/z* 43, 117, and 261, characteristic of the 2-*O*-methylpentoses, were obtained in the peak with t_R 1.01; and this was identified as the alditol acetate from 2-*O*-methylxylose. The increase of 3-*O*-methylxylose in the methylated carboxyl-reduced polysaccharide (1.5 to 5.5) also suggests that the 4-*O*-methylglucuronic acid is attached at some xylose residues through O-2 (as confirmed below).

The aldobiouronic acid obtained by partial hydrolysis of B-2 was converted into the methyl ester methyl glycoside (9), acetylated, and then subjected to glc–ms (10), which showed it to be 2-*O*-(4-*O*-methyl-α-D-glucopyranosyluronic acid)-D-xylose.

Part of the polysaccharide was subjected to a mild acid hydrolysis, by which arabinosidic linkages should be cleaved. The resulting polymeric material was recovered and subjected to methylation analysis and carboxyl reduction with lithium aluminium hydride. The results, given in Table 1, showed an increase of 2,3,4,6-tetra-*O*-methylgalactose, 2,3,6-tri-*O*-methylglucose, and 2,3-di-*O*-methylglucose. The relatively small proportion of xylose in the degraded polysaccharide suggests that the conditions of hydrolysis were too drastic and that a part of the xylose was hydrolysed off, in addition to the arabinose and rhamnose residues. This was checked by analysis of the neutral monosaccharides from the hydrolysate on paper, and by glc (as their alditol acetates), which revealed arabinose (94%), xylose (4.5%), and galactose (traces).

Oxidation of the peracetylated polysaccharide with chromium trioxide (11) in acetic acid for 2 h resulted in a low recovery of xylose, and high recoveries of rhamnose and arabinose. These results indicated that the xylosyl groups had the β configuration, whereas the rhamnosyl groups had the α configuration. Under the conditions used, most galactose and glucose residues would have been oxidized. Sugar analysis revealed that only a small part of the glucopyranose and galactopyranose residues have been affected. Because acetylated furanoses are nonspecifically oxidized (12) by chromium trioxide, the anomeric configuration of the arabinosyl groups could not be determined by this experiment. In fact, the rate at which arabinose was hydrolysed off with 72% sulfuric acid during 2 h at 30°C indicated that it possibly had the α configuration.

From a consideration of the results of sugar analysis, methylation analysis, oxidation with chromium trioxide, and nmr studies, the average structural features of the B-2 can be tentatively represented as shown in Fig. 1; the sequence of the different branches along the polysaccharide chain is not known. In this structure (Fig. 1), a dotted line indicates a substituent that is not present in all repeating units. The proposed structure is, however, hypothetical, and the present results do not exclude less regular structures. The polysaccharide has a backbone of β(1→4)- and β(1→3)-linked glucopyranosyl, β(1→4)-linked xylopyranosyl, and (1→4)- and (1→6)-linked galactopyranosyl residues. Arabinofuranosyl, rhamnopyranosyl, and some xylopyranosyl and galactopyranosyl groups are present as nonreducing end units. Glucopyranosyluronic acid side chains are attached at O-2 of some xylose residues. For every five xylopyranosyl residues in the main chain there is one uronic acid unit, and for 10 such xylopyranosyl residues there is one 3-*O*-(xylopyranosyl-arabinofuranosyl) group (side chain). For every two glucopyranosyl residues in the main chain there is one arabinofuranosyl unit. For every six galactopyranosyl residues in the main chain there is one galactopyranosyl unit.

Because the hemicellulose has a low, positive rotation, the polymer is likely to contain both α and β anomeric configurations. As the configuration of the 4-*O*-methylglucosyluronic acid groups had already been established as α, and as the arabinofuranosyl groups are likely to have the α configuration (13) (δ 109.21 in the ^{13}C spectrum for C-1), the xylopyranosyl groups are therefore likely to have the β configuration (14) (δ 4.24 in the ^{1}H spectrum for H-1 and δ 102.51 in the ^{13}C spectrum for C-1). The other hemicelluloses

Can. J. Chem. Downloaded from www.nrcresearchpress.com by 176.9.209.113 on 09/07/12
For personal use only.

Can. J. Chem. Downloaded from www.nrcresearchpress.com by 176.9.209.113 on 09/07/12
For personal use only.

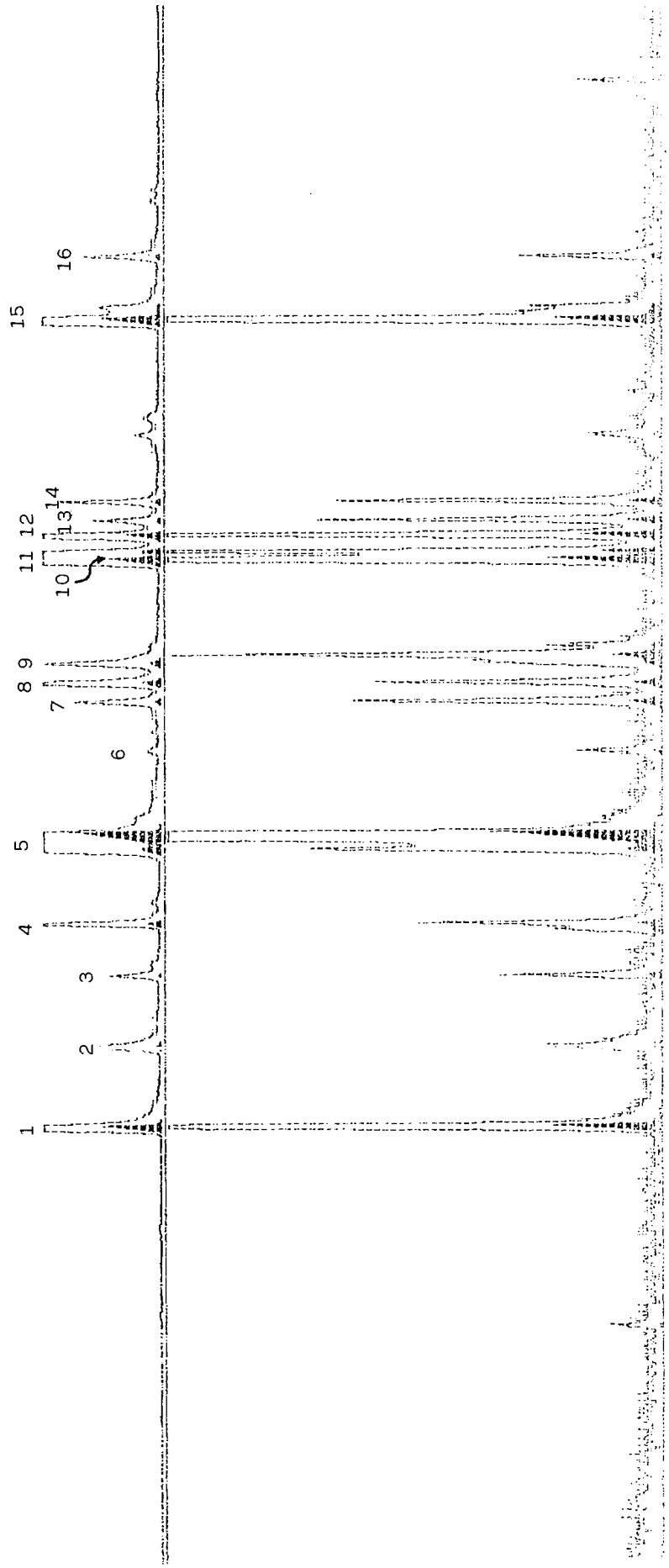

FIG. 2. Gas chromatogram of partially methylated alditol acetates on a capillary column OV-1 at 120→220°C at 4°/min. Peaks: 1 = 2,3,5-Me_3-Ara; 2 = 2,3,4-Me_3-Xyl; 3 = 2,3-Me_2-Rha; 4 = 2,5-Me_2-Ara, 5 = 2,3-Me_2-Xyl; 6 = 2,3,4,6-Me_4-Glc; 7 = 2,3,4,6-Me_4-Gal; 8 = 2-Me-Xyl; 9 = 3-Me-Xyl, 10 = 2,4,6-Me_3-Glc, 11 = 2,3,6-Me_3-Gal; 12 = 2,3,6-Me_3-Glc; 13 = 2,3,4-Me_3-Gal; 14 = 2,3,4-Me_3-Glc; 15 = 2,3-Me_2-Glc; 16 = 2,4-Me_2-Gal. 2,3,5-Me_3-Ara = 1,4-di-*O*-acetyl-2,3,5-tri-*O*-methyl-arabinitol, etc.

(1, 2) of *Quercus suber* contain xylopyranosyl groups in the β configuration. The configuration of glucose and galactose could not be confirmed by this nmr spectroscopic analysis.

Experimental

General methods

Descending paper chromatography (pc) was performed on Whatman Nos. 1 and 3 MM papers using (*A*) ethyl acetate – acetic acid – formic acid – water (18:3:1:4), (*B*) 1-butanol–ethanol–water (2:1:1), and (*C*) 1-butanol–pyridine–water (6:4:3), and detection with diphenylamine aniline (15). Optical rotations were recorded with a Perkin Elmer 141 polarimeter and ir spectra with a Perkin Elmer model 281 spectrophotometer. The ^1H and ^{13}C nmr spectra (internal Me_4Si) were recorded on a Bruker AC-200 (200 MHz) spectrophotometer. Gas–liquid chromatography (glc) was performed with a Hewlett–Packard model 5710A chromatograph fitted with flame-ionization detector and a glass column (200 × 0.6 cm) containing 3% ECNSS-M on Gas Chrom Q (100–200 mesh) at 190°C (alditol acetates) or 175°C (partially methylated alditol acetates). For glc–ms a Hewlett–Packard 5995B instrument, fitted with a capillary column (12 m × 0.2 mm) containing OV-1, was used. Electron impact (EI) mass spectra were recorded at 70 eV with a temperature program of 100→220°C at 4°/min.

Hemicellulose B-2

The extraction of the polysaccharides from the cork of *Quercus suber* and their fractionation into hemicellulose A and B have been reported (2).

To a solution of the hemicellulose B (4 g) in 5% potassium hydroxide (400 mL) was added Fehling's solution until the precipitation was complete. The copper complex was collected by centrifugation. The combined alkaline extracts were dialysed against distilled water for 24 h. The nondiffusable residue was concentrated to a small volume (under reduced pressure) and the polysaccharide was precipitated by addition of ice-cold ethanol (4 vol). After 4 h at 0°C, the precipitated polysaccharide was collected by centrifugation, and then macerated for 1 min with ice-cold ethanol containing 5% of hydrochloric acid. The residue was washed exhaustively with ethanol and then dried over phosphorus pentoxide *in vacuo* to give the polysaccharide (Fraction B-2) (1.8 g), $[\alpha]_D$ +3.96° (*c* 10.4, 1% sodium hydroxide).

The hemicellulose B-1 was isolated from the copper complex as reported (2).

(*a*) *Homogeneity*

Gel-filtration chromatography was performed on a column (46 × 1.6 cm) of Sephacryl S-400 with 0.5 M sodium chloride at 0.5 mL/min. The column was calibrated with dextrans of known molecular weight (Pharmacia). Fractions were monitored by the phenol – sulfuric acid method (3), which showed a single band.

(*b*) *Hydrolysis and sugar analysis*

The polysaccharide B-2 (7 mg) was treated with 72% sulfuric acid (0.2 mL) and kept for 1 h at 30°C. The solution was diluted with water (5 mL) and then heated for 3 h on a boiling-water bath. *myo*-Inositol (2 mg) was added as internal standard, and the hydrolysate was neutralized ($BaCO_3$) and decationized with Amberlite IR-120(H^+) resin. Part of the solution was analysed by pc (solvents *A*–*C*) and sugars were quantified as their alditol acetates by glc (16). The content of glucuronic acid in the hemicellulose B-2 was determined by the carbazole method (17) (using D-glucuronic acid as the standard), and found to be 7.5%.

(*c*) *Characterization of the aldobiouronic acid*

The polysaccharide B-2 (0.5 g) was treated with 0.0125 M sulfuric acid for 90 min at 100°C. The hydrolysate was separated, after neutralization and deionization, into neutral and acidic components (2). Paper chromatography (solvents *A*–*C*) of the acidic sugars revealed an aldobiouronic acid in addition to 4-*O*-methylglucuronic acid. Preparative pc (solvent *A*) gave the aldobiouronic acid, and this was converted into the methyl ester methyl glycosides (methanolic 3% hydrogen chloride (5 mL) for 20 h). This product was acetylated (acetic anhydride – pyridine (1:1)) and then subjected to glc–ms (10), which showed it to be 3,4-di-*O*-acetyl-2-*O*-(methyl 2,3-di-*O*-acetyl-4-*O*-methyl-α-D-glucopyranosyluronate)-α-D-xylopyranoside.

(*d*) *Methylation analysis*

To a stirred solution of sodium methylsulfinylmethanide (prepared under nitrogen from 1 g of sodium hydride and 23 mL of methyl sulfoxide) at room temperature, was added a solution of hemicellulose B-2 (148 mg) in methyl sulfoxide (5 mL). After stirring for 3 h, methyl iodide (4 mL) was added with external cooling. Stirring was continued for 15 h, water (100 mL) was then added, and the mixture was extracted with chloroform. The combined extracts were washed three times with water, dried (Na_2SO_4), and concentrated to a yellow solid, which was dried over phosphorus pentoxide *in vacuo* at 40°C for 2 days. A solution of the product in benzene was diluted with light petroleum (bp 30–60°C) to precipitate the methylated polysaccharide (107 mg), $[\alpha]_D$ +8.32° (*c* 15.7, chloroform), and showed, in its ir spectra, no absorption attributable to OH. A portion (15 mg) of the material was hydrolysed conventionally and the resulting sugars were converted into alditol acetates (18) and analysed by glc and glc (6) – ms (7).

To a solution of another portion (30 mg) in dry tetrahydrofuran (15 mL) was added lithium aluminium hydride (150 mg), and the mixture was boiled under reflux for 24 h. The mixture was worked up in the usual way and the reduced product was extracted into chloroform. The product had ir absorption at 3600 cm^{-1} (OH) but not at 1735 cm^{-1} (ester C=O). The product was hydrolysed as in (*b*) and the methylated sugars were converted into alditol acetates and analysed by glc and glc–ms.

(*e*) *Partially degraded B-2*

The polysaccharide (126 mg) was hydrolysed with 0.0125 M sulfuric acid (12.5 mL) at 100°C for 1 h. The degraded polysaccharide (62.9 mg), which was precipitated by the addition of excess of ethanol, was subjected to Hakomori methylation (4) analysis as in (*d*). Permethylated and reduced material had $[\alpha]_D$ +10.9° (*c* 1.8, chloroform); it was hydrolysed with 72% aqueous sulfuric acid and, after the usual treatment, the partially methylated sugars were converted into their alditol acetates, and these analysed by glc and glc–ms. The results are summarized in Table 1.

The centrifuged partial hydrolysate was neutralised, deionized, and the sugars were converted into alditol acetates, and these analyzed by glc.

(*f*) *Oxidation with chromium trioxide*

Polysaccharide B-2 (25 mg) was mixed with *myo*-inositol (2 mg) as the internal standard, and then dissolved in formamide (5 mL). To this solution was added acetic anhydride (4 mL) and pyridine (5 mL), and the mixture was stirred 22 h at 20°C. The acetylation product was isolated by extraction with chloroform. The peracetylated polysaccharide was oxidized (11) with chromium trioxide (400 mg) in acetic acid (4 mL), with stirring, at 50°C. Aliquots were removed at 0, 1, and 2 h, diluted with water immediately after removal, and the solutions extracted with chloroform. The products were hydrolysed and analysed, as their alditol acetates, by glc (16).

Acknowledgment

The author thanks Dr. D. Manuel Menéndez Gallego (National Institute of Toxicology of Sevilla) for the glc–ms analysis.

1. A. ASENSIO. Carbohydr. Res. **161**, 167 (1987).
2. A. ASENSIO. Carbohydr. Res. **165**, 134 (1987).
3. M. DUBOIS, K. A. GILLES, J. K. HAMILTON, P. A. REBERS, and F. SMITH. Anal. Chem. **28**, 350 (1956).
4. S. HAKOMORI. J. Biochem. (Tokyo), **55**, 205 (1964).
5. J. N. C. WHYTE and J. R. ENGLAR. Can. J. Chem. **49**, 1302 (1971).
6. S. C. CHURMS. Handbook of chromatography. C.R.C. Press, Boca Raton, FL. 1982. pp. 6–10.

Can. J. Chem. Downloaded from www.nrcresearchpress.com by 176.9.209.113 on 09/07/12
For personal use only.

7 H. BJÖRNDAL, B. LINDBERG, and S. SVENSSON. Carbohydr. Res. **5**, 433 (1967).
8. H. BJÖRNDAL, C. G. HELLERQVIST, B. LINDBERG, and S. SVENSSON. Angew. Chem. **82**, 643 (1970).
9. P. C. DAS GUPTA, S. K. SEN, and A. DEY. Carbohydr. Res. **48**, 73 (1976).
10. V. KOVÁCIK, S. BAUER, J. ROSÍK, and P. KOVÁC. Carbohydr. Res. **8**, 282 (1968).
11. J. HOFFMAN, B. LINDBERG, and S. SVENSSON. Acta Chem. Scand. **26**, 661 (1972).
12. S. J. ANGYAL and K. JACKSON. Carbohydr. Res. **12**, 147 (1970).
13. J. D. BLAKE, M. L. CLARKE, and P. E. JANSSON. Carbohydr. Res. **115**, 265 (1983).
14. G. O. ASPINALL and V. PUVANESARAJAH. Can. J. Chem. **61**, 1864 (1983).
15. R. W. BAYLEY and E. J. BOURNE. J. Chromatogr. **4**, 206 (1960).
16. J. S. SAWARDEKER J. H. SLONEKER, and A. JEANES. Anal. Chem. **37**, 1602 (1965).
17. T. BITTER and H. M. MUIR. Anal. Biochem. **4**, 330 (1962).
18. H. BJÖRNDAL, B. LINDBERG, and S. SVENSSON. Acta Chem. Scand. **21**, 1801 (1967).

Can. J. Chem. Downloaded from www.nrcresearchpress.com by 176.9.209.113 on 09/07/12
For personal use only.

^{13}C magnetic resonance studies 133.[1] An examination of the effect of conformation on β-enolization in some bicyclo[3.2.1]octan-2-ones

MICHAEL T. M. CLEMENTS,[2] ROSS E. KLINCK,[3] SRIYAWATHIE PEIRIS, ARTHUR J. RAGAUSKAS,[4] AND J. B. STOTHERS
Department of Chemistry, University of Western Ontario, London, Ont., Canada N6A 5B7

Received September 15, 1987

MICHAEL T. M. CLEMENTS, ROSS E. KLINCK, SRIYAWATHIE PEIRIS, ARTHUR J. RAGAUSKAS, and J. B. STOTHERS. Can. J. Chem. **66**, 454 (1988).

To assess the influence of the conformation of the cyclohexanone moiety in bicyclo[3.2.1]octan-2-ones on the reactivity for β-enolate rearrangement, the behavior of three derivatives under typical homoenolization conditions has been examined for comparison with 3,3-dimethylbicyclo[3.2.1]octan-2-one (**1**), which was known to be smoothly converted to the [3.3.0] isomer **2**. For this purpose, *endo*-3-*tert*-butyl-*exo*-3-methylbicyclo[3.2.1]octan-2-one (**8**), *endo*-9-*tert*-butyl-*exo*-9-methyl-*exo*-tricyclo[5.3.1.$0^{2,6}$]undecan-8-one (**9**), and 9,9-dimethyl-*endo*-tricyclo[5.3.1.$0^{2,6}$]undecan-8-one (**10**) were prepared and treated with *t*-BuO$^-$/*t*-BuOH at ≧185°C for prolonged periods. Each is much less reactive than **1**. The relative orientations of the carbonyl groups with respect to the sites for β-enolization were determined by molecular mechanics (MM2) calculations. $^1H/^2H$ exchange in **9** and **10** was also examined under strongly basic conditions at 185°C.

MICHAEL T. M. CLEMENTS, ROSS E. KLINCK, SRIYAWATHIE PEIRIS, ARTHUR J. RAGAUSKAS et J. B. STOTHERS. Can. J. Chem. **66**, 454 (1988).

Dans le but d'évaluer l'influence de la conformation de la portion cyclohexanone des bicyclo[3.2.1]octanones-2 sur la réactivité conduisant à une transposition β-énolique, on a examiné le comportement de trois dérivés dans des conditions d'homoénolisation pour comparer avec le comportement de la diméthyl-3,3 bicyclo[3.2.1]octanone-2 (**1**) qui se transforme facilement en son isomère [3.3.0] (**2**). À ces fins, on a préparé la *tert*-butyl-3-*endo* méthyl-3-*exo* bicyclo[3.2.1]octanone (**8**), la *tert*-butyl-9-*endo* méthyl-9-*endo* tricyclo[5.3.1.$0^{2,6}$]undécanone-8-*exo* (**9**) et la diméthyl-9,9 tricyclo[5.3.1.$0^{2,6}$]undécanone-8-*endo* (**10**) et on les a traitées avec du *t*-BuO$^-$/*t*-BuOH, à 185°C, pour des périodes prolongées. Chacune de ces cétones est moins réactive que le composé **1**. Les orientations relatives des groupements carbonyles par rapport aux sites de la β-énolisation ont été déterminées par des calculs de mécanique moléculaire (MM2). Utilisant des conditions fortement basiques, à 185°C, on a aussi examiné les échanges $^1H/^2H$ dans les composés **9** et **10**.

[Traduit par la revue]

Introduction

Since the discovery of homoenolization (1) many examples of both acyclic and bicyclic monoketones have been found to undergo proton abstraction from centres other than the α-carbons under strongly basic conditions (2). For most systems, β-enolization is observed, whereby proton abstraction from β-carbons occurs, and the process can lead to skeletal rearrangement and (or) deuterium exchange, if the reaction is carried out in a deuterated medium. The factors governing regioselectivity and the relative reactivity of such proton abstractions are of considerable interest since the rearrangements can provide a means of generating carbon skeletons that are not readily accessible through other routes. Some applications of β-enolization in the syntheses of some naturally occurring carbon skeletons from readily available intermediates have been described (3). The model reaction for the key step in each of these cases was the known, unidirectional conversion of 3,3-dimethylbicyclo[3.2.1]octan-2-one (**1**) to its [3.3.0] isomer **2** (4), as illustrated by the conversion of **3** → **4** (3*c*). A better understanding of both the regioselectivity and stereoselectivity of β-enolization would enhance the scope of potential synthetic applications.

Earlier, we had investigated the behavior of the 7,7-dimethyltricyclo[3.3.1.$0^{2,4}$]nonan-6-ones under typical homoenolization conditions, *t*-BuO$^-$/*t*-BuOH/185°C, and found (5) that the *endo* isomer **5** is stable while its *exo* counterpart **6** readily isomerizes to **7**. This difference in reactivity was attributed to the relative orientation of the carbonyl group and the methano bridge (C-9) in the two isomers, which is governed by the conformation of the six-membered ring. In **1**, **3**, and **6**, this ring will preferentially adopt a chair conformation, but this arrangement is destabilized for **5**, because of the *endo* orientation of C-3, and the cyclohexanone moiety presumably adopts a boat-like conformation. In the latter arrangement the π-system of the carbonyl group is tipped away from C-9, thereby rendering less likely potential overlap with a developing carbanionic site at the methano carbon. To gain further support for this conformational interpretation and to check that the three-membered ring in **5** is not primarily responsible for its deactivation towards β-enolization, we elected to investigate the behavior of other derivatives of **1** for which the cyclohexanone ring cannot exist in a chair arrangement. For this purpose we have prepared *endo*-3-*tert*-butyl-*exo*-3-methylbicyclo[3.2.1]octan-2-one (**8**), its *exo*-trimethylene derivative **9** (*endo*-9-*tert*-butyl-*exo*-9-methyl-*exo*-tricyclo[5.3.1.$0^{2,6}$]undecan-8-one), and 9,9-dimethyl-*endo*-tricyclo[5.3.1.$0^{2,6}$]undecan-8-one (**10**) and examined their behavior in *t*-BuO$^-$/*t*-BuOH at 185 and 200°C for prolonged reaction times. For comparison with our earlier results for **1** (4) and **3** (6), the regioselectivity of proton abstraction in **9** and **10** was established by the requisite H/D exchange experiments. In addition, the molecular geometry of each of the ketones was determined by molecular mechanics (MM2) computations. These results for **8–10** are presented in this paper.

Results and discussion

Syntheses

The preparation of **8** was accomplished by conversion of the

[1]For Part 132 see ref. 18; for Part 131 see ref. 19.

[2]Present address: Chemistry Department, Trinity College, Dublin 2, Ireland.

[3]Permanent address: Adirondack Community College, Glens Falls, New York 12801, U.S.A.

[4]Present address: Division of Biological Sciences, National Research Council of Canada, Ottawa, Ont., Canada K1A 0R6.

Can. J. Chem. Downloaded from www.nrcresearchpress.com by 176.9.209.113 on 09/07/12
For personal use only.

Can. J. Chem. Downloaded from www.nrcresearchpress.com by 176.9.209.113 on 09/07/12
For personal use only.

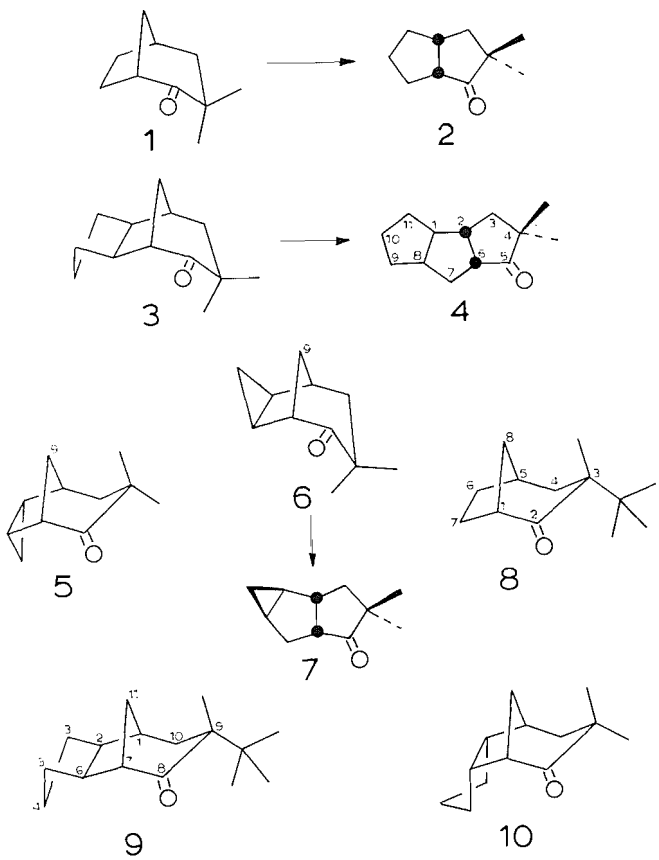

parent ketone **11** to the trimethylsilyl enol ether **12**, which was alkylated with *tert*-butyl chloride/titanium tetrachloride as described by Reetz and Maier (7) to furnish a single 3-*tert*-butyl derivative **13**. The *exo* orientation of the *tert*-butyl group was confirmed by treating **13** with MeO^-/MeOD at room temperature overnight and recovering **13**-d_1 (>95% yield, 0.97 atoms ^2H/molecule) containing no detectable isomer. Similar treatment of *exo*-3-methyl-**11** gave no evidence of epimerization (8). Methylation of **13** with LDA/MeI gave **8** in 43% overall yield from **11**. The analogous sequence with tricyclo[5.3.1.$0^{2,6}$]-undecan-8-one furnished **9** in 35% yield. The structures of **8** and **9** follow from the method of synthesis with subsequent support from their observed reactivities (see below). Alkylation of 3-methyl-**12** with *tert*-butyl chloride/$TiCl_4$ proceeded in very low yields (<10%), but a valuable comparison sample of the *exo-tert*-butyl-*endo*-methyl isomer of **8** was obtained.

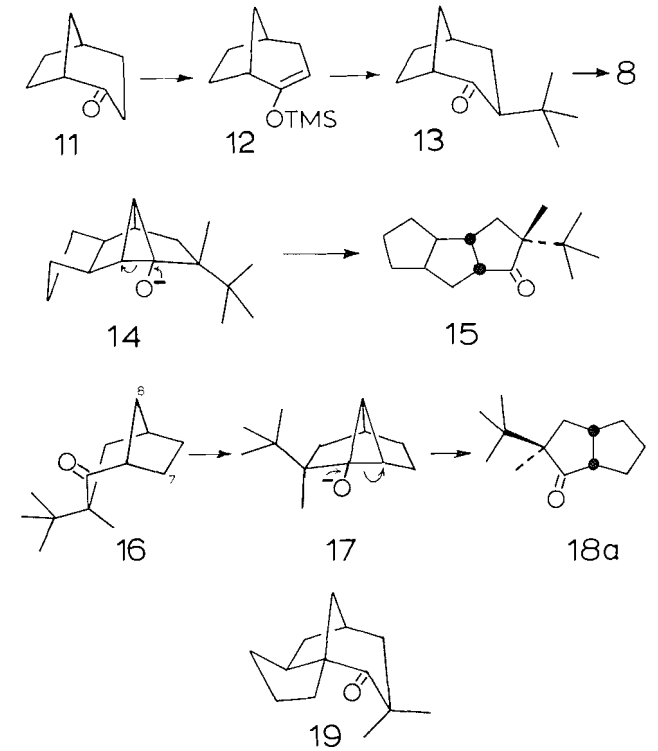

Dimethylation of *endo*-tricyclo[5.3.1.$0^{2,6}$]undecanone-8-one (9) with $NaNH_2$/MeI in anhydrous Et_2O furnished **10** for our experiments.

Homoenolization experiments

The behavior of **10** upon treatment with *t*-BuO^-/*t*-BuOH at 185°C was examined initially following our usual procedures (5). The neutral organic product after 60 and 160 h was recovered in essentially quantitative yield and found to be entirely unchanged starting material by gas–liquid chromatography (glc) and ^{13}Cmr analyses. To ensure that the observed stability of **10** was not because of the inadvertent introduction of traces of water that would significantly decrease the base strength (10), 1:1 mixtures of **3** and **10** were treated with the same stock solution of base at 185°C for >500 h, and glc analysis indicated the neutral product to contain **3** (20%), **4** (30%), and **10** (50%). Since the ratio of **3** and **4** was that expected under these conditions (3*c*), **10** is indeed stable. Samples of **10** were also treated at 200°C and, again, there was no evidence of isomerization after 95 and 200 h; **10** was recovered in >95% yields.

Analogous treatment of **9** at 185°C led to the recovery of starting material in >80% yield after 65 h. However, after 130 h there was evidence of a second component in the neutral product in very low yield (~1%). In an attempt to increase the yield of this new component, we ran a series of experiments at 200°C and, after 240 h, the neutral product, >75% recovery, was found to be a 9:1 mixture of **9** and the new compound. Doubling the reaction time at 200°C did not significantly increase the proportion of the second component, which is isomeric with **9**, having the molecular formula $C_{16}H_{26}O$ by precise mass measurement. It is ketonic, containing a cyclopentanone moiety on the basis of its carbonyl absorption data (1730 cm^{-1}, δ_C 224.1), and could be tentatively assigned structure **15** from its ^{13}C spectrum and comparison thereof with that of **4** and related derivatives (11); the ^{13}C data for **4** and **15** are listed in Table 1. Proton abstraction from C-11 in **9** can lead to β-enolate **14**, or its equivalent, which subsequently opens with protonation at the original C-7 site. This rearrangement is constrained to give the *cis,anti,cis*-tricyclo[6.3.0.$0^{2,6}$]undecane skeleton. To establish that the very slow isomerization of **9** was not due to traces of water in the base solution, a 1:1 mixture of **3** and **9** was treated with the same base solution at 185°C for >500 h. Gas–liquid chromatographic (glc) analysis of the neutral product, >95% yield, showed its composition to be **3** (21%), **4** (29%), **9** (47%), and **15** (3%).

Treatment of **8** in the same manner at 185°C gave a neutral product in >85% yield that, by glc analysis on FFAP, exhibited a single band, but with a Carbowax column glc gave an indication of two very poorly resolved components. The ^{13}C spectra, however, clearly revealed the presence of two components in ratios of 85:15 (favoring **8**) and 50:50 after 40 and 240 h, respectively. The ^{13}C signals for the second component agreed precisely with those exhibited by **16**, the isomer of **8** in

TABLE 1. ^{13}C shieldings[a] for **1–4**, **8–10**, **13**, **15**, **16**, and **18***a*,*b*

Compound	C-1	C-2	C-3	C-4	C-5	C-6	C-7	C-8	C-9	C-10	C-11	Other
4	51.4	46.1	43.8	47.1	224.6	52.0	35.5	44.2	33.7	36.7	34.2	24.9 (*endo*-Me) 25.2 (*exo*-Me)
15	51.3	45.6	39.2	56.4	224.1	52.9	34.6	44.2	(34.1)	26.9	(34.3)	19.2 (*exo*-Me) 26.1 (Me_3) 34.0 (quat C)
2	50.3	224.6	47.6	43.5	36.3	33.6	25.0	29.4				23.1 (*endo*-Me) 25.3 (*exo*-Me)
18*a*	51.9	225.3	56.5	39.1	35.7	33.8	25.1	29.4				19.6 (*endo*-Me) 25.9 (Me_3) 34.2 (quat C)
18*b*	54.8	213.9	52.3	35.8	34.8	28.5	27.8	38.9				21.5 (*exo*-Me) 26.1 (Me_3) 55.6 (quat C)
13	52.8	213.9	52.3	35.8	34.8	28.5	27.8	38.9				27.7 (Me_3) 31.7 (quat C)
16	52.6	220.2	50.5	33.6	35.0	29.6	28.0	40.7				25.8 (*endo*-Me) 26.3 (Me_3) 37.9 (quat C)
1	50.9	218.2	42.1	46.0	35.1	28.7	28.1	35.7				30.6 (*endo*-Me) 31.2 (*exo*-Me)
8	51.0	219.9	49.5	32.3	33.3	31.8	26.2	39.0				26.3 (Me_3) 27.6 (*exo*-Me) 37.1 (quat C)
3	41.3	47.7	33.9	27.9	30.6	46.5	57.1	218.0	42.2	45.4	34.8	30.6 (*endo*-Me) 31.1 (*exo*-Me)
9	39.3	50.9	33.9	26.5	27.8	45.0	57.5	219.2	50.1	(39.2)	(34.1)	26.4 (Me_3) 27.9 (*exo*-Me) 50.1 (quat C)
10	35.7	47.7	29.0	26.6	27.3	46.8	53.0	219.6	40.6	(35.4)	(35.6)	27.9 (*endo*-Me) 34.3 (*exo*-Me)

[a] ^{13}C shieldings in ppm from internal TMS.

Can. J. Chem. Downloaded from www.nrcresearchpress.com by 176.9.209.113 on 09/07/12
For personal use only.

which the orientations of the *tert*-butyl and methyl groups are reversed, and the preparation of which proceeded poorly as noted above. Since we had initially planned to include examination of **16** in this study, its preparation from *exo*-3-methyl-**11** had been attempted, but the very low yields obtained precluded its study separately. However, the generation of **16** from **8** was expected and showed that β-enolization occurs at C-7 in **8** as was found for **1**, for which this is a racemization process. At 185°C there was no evidence of β-enolate rearrangement involving C-8 in **8** (or **16**).

In an effort to equilibrate **8** and **16**, a series of experiments with **8** was carried out at 200°C. After 96 h, a 30:70 mixture of **8** and **16** was formed according to the ^{13}C spectrum but glc did not reveal the presence of significant amounts of other components. However, after 312 h at 200°C, **8** gave a neutral product, ~90% recovery, that gave rise to two well-resolved bands upon glc analysis. These two bands were in a 3:1 ratio and were readily separated by preparative glc. The major band was a 1:4 mixture of **8** and **16** according to its ^{13}C spectrum. The minor band also contained two components in a 3:1 ratio as judged by its ^{13}C spectrum, which also indicated that the two compounds were isomeric. The 1:4 mixture of **8** and **16** was dissolved in fresh base and heated at 200°C for 168 h. The neutral product from this experiment (90% recovery) was found to contain two bands in a 4:1 ratio by glc analysis. The major band was a 1:4 mixture of **8** and **16**, i.e., the equilibrium mixture favoring the *exo*-*tert*-butyl isomer **16**, confirming our structural assignments. The minor band consisted of a 2:1 mixture of the two new components as estimated from the ^{13}C spectra for each of the bands after collection by preparative glc. All attempts to separate the minor components were unsuccessful.

The two-component mixture of minor products from the 200°C experiments exhibited strong carbonyl absorption at 1735 cm^{-1} in the infrared spectrum and at δ_C 225.3 in the ^{13}Cmr spectrum; these values strongly indicate the presence of a cyclopentanone moiety, which would be generated by β-enolization at C-8 in **8** and **16** with protonation at the original C-1 site as shown for **16** → **17** → **18***a*. Precise mass measurements gave the molecular formula $C_{13}H_{22}O$, confirming that these products are isomeric with the starting material. Although only one carbonyl signal was resolved in the ^{13}C spectrum, there were two sets of 10 signals in the high-field region; each set included two quaternary, two methine, four methylene, and two methyl (in a 3:1 ratio) absorptions. By comparison with the ^{13}C shieldings for **2**, these signals can be tentatively assigned to **18***a*, as the major component, and its *exo*-3-methyl-*endo*-3-*tert*-butyl isomer **18***b* as the minor product; these ^{13}C data are collected in Table 1.

These results show clearly that ketones **8–10** are much less reactive than **1** and **3** with respect to β-enolate rearrangement through proton abstraction from the methano bridge carbon. Only in the case of **9** were we able to obtain evidence of the presence of isomerized material at 185°C, and that only in very low yield. This difference in reactivity is exactly analogous to that for **5** and **6** and, therefore, rules out the possibility of a major deactivating effect of the three-membered ring in **5**. However, **5**, **8**, **9**, and **10** share a common feature, which constitutes a major difference from **1**, **3**, and **6** in that the

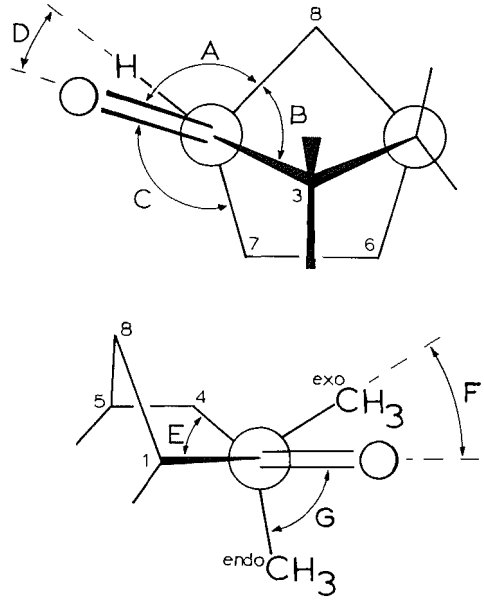

FIG. 1. Dihedral angles A–F (Table 2) defining the orientation of the carbonyl group in **1**.

six-membered ring in each of the former cannot adopt a chair conformation because of nonbonded interactions involving *endo* groups at the α-carbon and the two-carbon bridge in the "3.2.1" system of each. An inspection of molecular models indicates that the dihedral angle between the methano bridge carbon (C-8 in **1** and **8**) and the carbonyl oxygen increases from ca. 120° to ca. 170° upon conformational change of the six-membered ring from a chair to a boat. This change tips the π-system of the carbonyl group away from the site of potential proton abstraction for β-enolization, thereby significantly reducing potential overlap with a developing carbanionic site. This was the explanation offered previously to account for the marked difference in reactivity between **5** and **6** (5).

To obtain better assessments of the geometry of the cyclohexanone moiety in these systems, we carried out molecular mechanics (MM2) calculations (12) for each of the ketones examined. The dihedral angles defining the orientation of the carbonyl group in these systems are shown as A–F in Fig. 1 for **1** and the calculated values are listed in Table 2. These data show that even the introduction of the *exo*-3-*tert*-butyl group in this system, as in **16**, causes some flattening of the six-membered ring relative to its shape in **1** and **3** while the *endo*-α-*tert*-butyl group in **8** and **9** leads to boat-like conformations for the cyclohexanone moiety, which are similar to that found for **10** owing to the *endo* disposition of its trimethylene bridge. It can be seen that angle A relating the carbonyl group and β-enolization site for rearrangement to the "3.3.0" systems is increased by ca. 20° in **8–10** relative to **1** and **3**, the two compounds that undergo this process relatively readily. In **16** this angle is increased by ca. 5° and no rearrangement occurs at 185°C. Perhaps the *exo*-3-*tert*-butyl group sterically hinders the approach of base to the *syn*-8 hydrogen. The *exo*-methyl groups in **8–10** may offer analogous steric hindrance. Although deuterium incorporation was not observed at C-8 in **1** under homoenolization conditions (4), slow exchange occurs at the methano bridge in **3**, **6**, and **9** involving the *syn* proton exclusively (6). For comparison with the latter systems, $^1H/^2H$ exchange was examined in **9** and **10**.

TABLE 2. Dihedral angles[a] illustrating carbonyl orientations in **1**, **3**, **8–10** and **16**, determined by MM2 calculations

Compound	A	B	C	D	E[b]	F	G
1	126.8	52.2	119.6	5.1	25.5	33.0	82.9
3	128.0	51.1	118.4	6.1	23.6	34.8	80.9
16	132.9	48.7	112.8	11.2	19.2	38.4	80.5
8	148.3	30.7	97.4	25.3	−11.8	75.0	43.4
9	148.3	30.7	97.4	25.2	−11.4	74.6	43.5
10	148.9	30.7	97.6	26.7	−7.8	66.2	48.7

[a]As defined for **1** in Fig. 1.
[b]Positive and negative values define the location of C-4 above or below the sp^2 plane of the carbonyl group.

$^1H/^2H$ exchange experiments

Samples of **9** and **10** were heated with *t*-BuO^-/*t*-BuOD at 185°C for 3, 6, 12, 24, 48 and 96 h and the ketones recovered from the neutral fractions by pentane extraction in high yield (80–90%). The ^{13}C spectra of these samples, purified by preparative glc, readily revealed that substantial exchange occurred at the α-bridgehead and *exo*-methyl sites through the appearance of characteristic triplets centred upfield from the normal signals, arising through one-bond $^{13}C-^2H$ coupling and the ^2H-induced isotope shift; absorptions for the neighboring carbons also exhibited the expected isotope shifts (13). In the spectra of the **9**-d_x samples, the α-methyl absorption consisted of a significantly attenuated singlet at δ 27.9 and a triplet, J_{CD} = 19.5 Hz, shielded by 288 ppb (1 ppb = 0.001 ppm), through the one-bond ($^1\Delta$) isotope shift. After 48 and 96 h a quintet, $^1\Delta$ 576 ppb, was also apparent, signifying the presence of species having a dideuteriated methyl group. The bridgehead methine pattern included a weak singlet, δ 57.5, and a triplet, $^1\Delta$ 405 ppb, J_{CD} = 21.6 Hz, indicative of considerable exchange at this site. Two-bond isotope shifts ($^2\Delta$) were also apparent for the C-11 methylene, C-6 methine, and C-9 quaternary absorptions at δ 26.5 (105 ppb), 45.0 (108 ppb), and 50.1 (65 ppb), respectively. The latter pattern also contained prominent components shifted by the presence of deuterium at the α-bridgehead, $^3\Delta$ 26 ppb. Other three-bond isotope shifts were observed in the C-5 and -10 methylene absorptions at δ_C 33.9 (52 ppb) and 39.2 (34 ppb) as well as for the quaternary carbon of the *tert*-butyl group, δ_C 37.2 (16 ppb). Confirmation of the presence of deuterium at only two sites was obtained from the ^2H spectra of these samples, which contained signals at δ 1.16 and 2.35, corresponding to the α-methyl singlet and a broadened doublet in the ^1H spectrum, respectively. The doublet, $J \sim 4.0$ Hz, is undoubtedly due to H-7 exhibiting resolved coupling only with the *anti*-11 proton since its dihedral angular relationship to both the *syn*-11 and -6 protons is ca. 90°. With resolution enhancement, the methyl absorption for the 48- and 96-h samples clearly consisted of three components arising from CH_2D, CHD_2, and CD_3 species (14), establishing that extensive exchange occurred at the α-methyl site. The ^2H-induced isotope effect on the deuteriomethyl shielding is 18 ppb. The total deuterium content in each of these samples was determined by mass spectrometry and the incorporation level at each of the two sites was assessed by integration of the ^2Hmr spectra (Table 3). From the latter data, approximate first-order rate constants were obtained, as is the usual practice (2); these values are given in Fig. 2.

The ^{13}C spectra of the **10**-d_x samples contained prominent triplets with the attenuated signals for the α-bridgehead (δ_C

Can. J. Chem. Downloaded from www.nrcresearchpress.com by 176.9.209.113 on 09/07/12
For personal use only.

TABLE 3. Deuterium incorporation[a] in **9** and **10** at 185°C

	9			**10**			
Time (h)	Total atoms ^2H	C-7	α-Me	Total atoms ^2H	C-6	C-7	*exo*-Me
3	0.91	0.82_5	0.09_5	0.98	—	0.91	0.07
6	1.08	0.86	0.22	1.05	—	0.90	0.15
12	1.26	0.88	0.38	1.25	0.02	0.91	0.32
24	1.50	0.84	0.66	1.40	0.04	0.80	0.56
48	1.90	0.73	1.18	1.90	0.07	0.73	1.09

[a]Total atoms ^2H by mass spectrometry; ^2H assay at individual sites by ^2Hmr, ±0.01.

53.0, $^1\Delta$ 365 ppb, J_{CD} = 21.4 Hz) and one of the methyl carbons (δ_C 34.3, $^1\Delta$ 300 ppb, J_{CD} = 19.5 Hz); the latter absorption can be assigned to the *exo*-methyl group by analogy with the results for several related ketones that exhibit preferential *exo*-methyl exchange (2). Two-bond isotope shifts due to deuterium at C-7 were evident for C-6 (δ_C 47.7, $^2\Delta$ 90 ppb) and C-11 (δ_C 35.6, $^2\Delta$ 100 ppb). The quaternary C-9 pattern (δ_C 40.6) contained components arising from ^2H-7 ($^3\Delta$ 25 ppb) as well as from mono- and dideuteriated methyl groups, $^2\Delta$ 70 ppb/D; these also gave rise to isotope-shifted components in the C-10 absorption, δ_C 35.4 with $^3\Delta$ 30 ppb/D. In addition, however, the methylene and methine signals at δ_C 27.3 and 46.8, respectively, were accompanied by weak isotope shifted components with $^2\Delta$ values of 110 and 100 ppb, respectively. The latter must arise from deuterium exchange at C-6. To confirm this interpretation and to assay the incorporation levels at the various sites undergoing exchange, the ^2Hmr spectra of the **10**-d_x samples were recorded. These spectra exhibited signals at δ 1.18 and 2.65, corresponding to a methyl singlet and a broadened 3-proton multiplet, respectively, in the ^1H spectrum. Upon addition of the shift-reagent Eu(fod)$_3$, a broadened doublet of doublets, J = 3 and 7 Hz, was shifted rapidly out of the 2.65-ppm pattern in the proton spectrum. The remaining two-proton pattern of overlapping multiplets exhibited sensitivity to added Eu(fod)$_3$ comparable to that of a one-proton absorption initially at δ 2.33, attributable to H-1. The overlapping multiplets could be assigned to H-6 and, perhaps, to *endo* H-5. The only other absorption with δ > 2.0 is a doublet, δ 2.20, J = 12 Hz, undoubtedly arising from *syn* H-11. The ^2Hmr spectra of the **10**-d_x samples recorded in the presence of Eu(fod)$_3$ contained three signals since the absorption initially at δ 2.65 was dispersed into a strong and a weak peak, which exhibited sensitivities identical to those found for the components of the original δ 2.65 absorption. Thus, the weak signal was assigned to ^2H-6. As in the case of **9**-d_x, the methyl absorption was found to contain components arising from CH_2D, CHD_2, and CD_3 species upon resolution enhancement, and the two-bond ^2H-induced isotope shift is 20 ppb. These isotope shifts for the methyl deuterons in **9**-d_x and **10**-d_x are the same as the 19-ppb shifts recently reported for fenchone (14), within our experimental error of 3 ppb. From the total deuterium content determined by mass spectrometry and the relative amounts at the three sites found from the ^2Hmr spectra (Table 3), the approximate rates of deuterium incorporation in **10** were extracted and are given in Fig. 2. The corresponding data for the closely related systems **1**, **3**, **5**, **6**, and **19** are included in Fig. 2. It must be noted that a reexamination of the rates of deuterium exchange in **1** has shown that the temperature

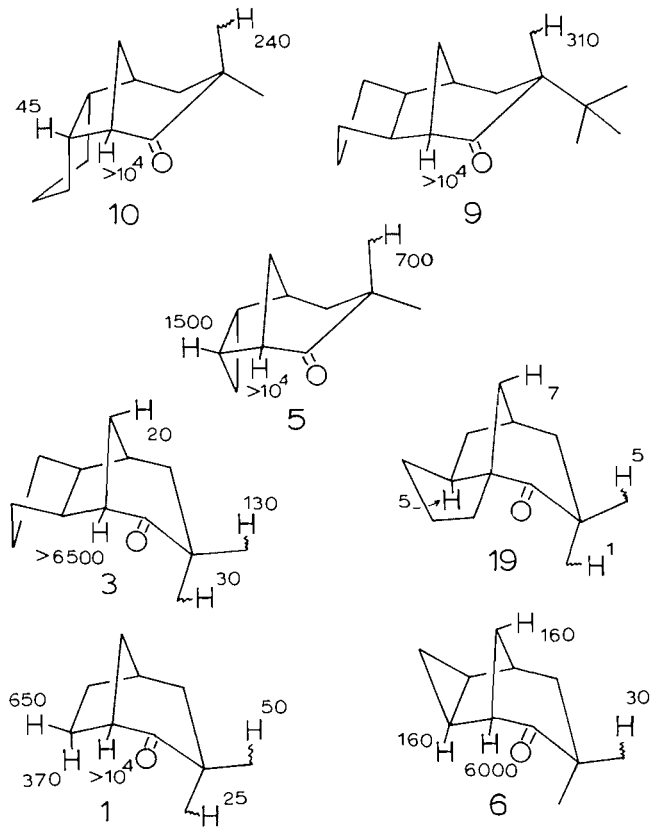

FIG. 2. Deuterium exchange rates ($k \times 10^8$ s^{-1}) at the various sites in **1**, **3**, **5**, **6**, **9**, **10**, and **19** by β-enolization at 185°C in *t*-BuOD.

control for the oven used in the original study (4) was faulty and the rate data have been redetermined using the constant temperature apparatus employed for all of our studies in recent years.

It is apparent from the data in Fig. 2 that the rate of exchange at the *exo*-methyl carbon is distinctly faster in those systems having a non-chair conformation of the cyclohexanone unit (**5**, **9**, and **10**) and no exchange was detectable at the methano carbon in the one-carbon bridge. It may be noted that for those systems that undergo exchange at the methano carbon (**3**, **6**, and **19**) the rate of exchange is significantly slower than the observed rearrangement rate and in each case *syn* exchange is strongly favored. This seems to suggest that exchange and rearrangement involving this site may proceed through different intermediates. The enhanced rate of *exo*-methyl exchange found for the ketones having a non-chair conformation for the

Can. J. Chem. Downloaded from www.nrcresearchpress.com by 176.9.209.113 on 09/07/12
For personal use only.

Can. J. Chem. Downloaded from www.nrcresearchpress.com by 176.9.209.113 on 09/07/12
For personal use only.

cyclohexanone unit may result from the increased dihedral angle relating the methyl and carbonyl groups (ca. 70° vs. ca. 35° for those in which the cyclohexanone unit is a chair). This change could improve overlap of the developing carbanionic centre at the methyl carbon with the π-system of the carbonyl group. In our earlier study of the [3.3.1.$0^{2,4}$] systems (5), it was suggested that the relatively rapid rate of exchange at C-4 is presumably due in part to the increased acidity of this proton because of its bonding to the three-membered ring; the carbonyl group is partly responsible since exchange does not occur at the other cyclopropyl methine position. Exchange at the corresponding β-site in **10**, C-6, was found to be ca. 30-fold slower.

Conclusions

The results of these β-enolization studies of **8**–**10** clearly show that systems in which the cyclohexanone moiety cannot adopt a chair conformation are much less reactive toward "[3.2.1] → [3.3.0]" rearrangement. The decreased reactivity seems strikingly dependent on the relative orientation of the methano bridge carbon and the carbonyl group, but the *exo*-α-alkyl group may also hinder proton abstraction from the bridge carbon. This conformational change, however, enhances the rate of exchange at the *exo*-methyl site but does not lead to ring expansion.

Experimental

Melting points and boiling points are uncorrected. Gas–liquid chromatography (glc) was carried out on Varian 920 and 3700 instruments using columns of 10% Carbowax, 6% FFAP, or 10% SE-30 on Chromosorb W as indicated. Thin-layer chromatography (tlc) was done on Kieselgel 60 F_{254} plates and flash chromatography columns were prepared as described in the literature (15). Tetrahydrofuran and diethyl ether were dried over Na/benzophenone and freshly distilled before use. Diisopropylamine, triethylamine, *tert*-butyl alcohol, and pyridine were distilled from CaH_2 and stored over 4 Å sieves; methyl iodide was dried over 4 Å sieves. Pentane was freshly distilled before use.

Infrared spectra were recorded with a Beckman 4250 instrument and mass spectra were obtained on a Varian MAT-311A system at 70 eV (direct inlet). Routine ^{1}H spectra were recorded with a Varian EM-360 instrument while data for pure samples were collected with Varian XL-200 or -300 systems. The ^{2}H and ^{13}Cmr spectra were obtained at 46.1 and 75.4 MHz, respectively, on the XL-300 system and comparison of the fully decoupled ^{13}C spectra with those obtained with either the APT (16) or DEPT (17) sequences identified the number of hydrogens bonded to each carbon.

endo-*3*-tert-*Butyl*-exo-*3-methylbicyclo[3.2.1]octan-2-one (8)*

Trimethylsilyl enol ether **12** was generated from **11** (0.70 g) according to the literature procedure (9) using LDA (diisopropylamine (1.26 mL), *n*-BuLi (2.5 M in hexane, 3.16 mL), THF (6 mL) at −78°C) with trimethylsilyl chloride (1.29 mL), and Et_3N (0.5 mL) in THF (1 mL) as the quenching solution. The product was recovered in our usual way (9) and purified by Kugelrohr distillation, bp 90–96°C/10 Torr (1 Torr = 133.3 Pa), to give an oil (1.05 g, 94% yield) identical to that reported previously (9).

To a flame-dried, nitrogen-purged flask equipped with a magnetic stirrer and serum cap was added **12** (0.83 g), *tert*-butyl chloride (0.70 mL), and anhydrous methylene chloride (3 mL). After cooling the solution to −47°C, titanium tetrachloride (0.67 mL) was rapidly added by syringe and the reaction mixture was stirred for 5 h before dilution with water (8 mL). The product was extracted with CH_2Cl_2 (4 × 10 mL) and the combined extracts washed with water (2 × 10 mL) before drying over $MgSO_4$. After evaporation of the solvent, glc analysis (FFAP) indicated that the major component constituted approximately 75% of the product mixture. Flash chromatography (Et_2O – petroleum ether, 4:96) furnished **13** (0.53 g, 63%); a sample (>98% pure) was collected by glc for characterization; ir (CCl_4): 1714 cm^{-1}; ^{1}Hmr ($CDCl_3$) δ: 2.65 (bt, $J \sim 5$ Hz, 1H), 2.45 (m, 1H), 2.18 (dd, J = 7.5, 12.2 Hz, 1H), 1.6–2.0 (complex absorption, 7H), 1.50 (ddt, J = 1.3, 3.0, 12.0 Hz, 1H), 0.97 (s, 9H); ^{13}Cmr: see Table 1. *Exact Mass* calcd. for $C_{12}H_{20}O$: 180.1514; found: 180.1518.

A sample of **13** (75 mg) was dissolved in a solution of MeONa/MeOD (2.6 mL, 0.01 M) and, under a N_2 atmosphere, stirred overnight. After the addition of D_2O (4 mL), the product was isolated by pentane extraction to yield **13**-d_1 (70 mg), the ^{13}C spectrum of which indicated essentially complete deuteration at C-3, ms: 3.4% d_0, 96.6% d_1 (total 0.966 ^{2}H/molecule).

To a solution of LDA (diisopropylamine (0.58 mL) and *n*-BuLi (2.50 M in hexane, 1.41 mL) in 5 mL of THF) was added **13** (0.53 g) in THF (2 mL) dropwise. After stirring at −78°C for 0.5 h, the mixture was warmed to room temperature and stirred for an additional 0.5 h before methyl iodide (0.56 mL) was added; stirring was continued overnight. Aqueous 10% NaCl solution (10 mL) was added before the product was isolated by pentane extraction. Evaporation of the solvent gave an oil (0.47 g), which by glc analysis (FFAP) contained **8** (87%) and **13** (4%). Preparative glc furnished pure material for the homoenolization experiments and for characterization; ir (film): 1698 cm^{-1}; ^{1}Hmr ($CDCl_3$) δ: 2.66 (m, 1H), 2.47 (m, 1H), 2.03 (d, J = 12 Hz, 1H), 1.35–1.90 (complex absorption, 7H), 1.16 (s, Me), 0.94 (s, Me_3); ^{13}Cmr: see Table 1. *Exact Mass* calcd. for $C_{13}H_{22}O$: 194.1671; found: 194.1669.

exo-*3*-tert-*Butyl*-endo-*3-methylbicyclo[3.2.1]octan-2-one (16)*

To a stirred solution of LDA, prepared from diisopropylamine (0.73 mL), *n*-BuLi (2.46 M in hexane, 1.86 mL), and THF (1.5 mL) in the usual way, was added *exo*-3-methylbicyclo[3.2.1]octan-2-one (8) (0.45 g). After stirring at −78°C for 45 min, the reaction mixture was quenched with a solution of TMSCl (0.75 mL), THF (0.75 mL), Et_3N (0.27 mL), prepared according to the literature (9). The mixture was then cooled to 0°C and a cold saturated aqueous Na_2CO_3 solution was added by syringe with vigorous stirring. The product was isolated by pentane extraction and Kugelrohr distillation, bp 105–110°C/15 Torr, to yield 0.5 g of the trimethylsilyl enol ether, which glc analysis (FFAP) indicated to be >85% pure. Preparative glc furnished material for characterization; ir (CCl_4): 2980, 1681, 1184, 880 cm^{-1}; ^{13}Cmr ($CDCl_3$) δ_C: 1.1 ($SiMe_3$), 16.0 (CH_3), 30.9, 34.8, 36.6, 40.9 (4 × CH_2), 34.4, 41.7 (2 × CH), 106.2, 149.7 (2 × quat C). *Exact Mass* calcd. for $C_{12}H_{22}Si$: 210.1434; found: 210.1435.

A solution of the silyl enol ether (0.91 g) and *tert*-butyl chloride (0.66 mL) in dry methylene chloride (3.2 mL) was cooled to −47°C and titanium tetrachloride (0.66 mL) was added with stirring. The mixture was stirred at −47°C for 1 h and for 10 h at room temperature. After the mixture was cooled to 0°C, water (8 mL) was added and the product was extracted with CH_2Cl_2 as described for **13**. Evaporation of the solvent furnished an oil (0.70 g), which glc analysis (FFAP) showed to contain ~77% of 3-*exo*-methyl-**11** and ~10% of **16**. Preparative glc afforded a sample (>98% pure) of **16** for characterization; ir ($CHCl_3$): 1698 cm^{-1}; ^{13}Cmr: see Table 1. *Exact Mass* calcd. for $C_{13}H_{22}O$: 194.1671; found: 194.1671.

endo-*9*-tert-*Butyl*-exo-*9-methyl*-exo-*tricyclo[5.3.1.0^{2,6}]undecan-8-one (9)*

8-Trimethylsilyloxy-*exo*-tricyclo[5.3.1.$0^{2,6}$]undec-8-ene (0.73 g), prepared in the course of an earlier study (12), was alkylated with *tert*-butyl chloride/titanium tetrachloride as described above for **13**. Flash chromatography (Et_2O – petroleum ether, 4:96) of the product mixture furnished *exo*-9-*tert*-butyl-*exo*-tricyclo[5.3.1.$0^{2,6}$]undecan-8-one (0.35 g, 51%), which was ca. 95% pure by ^{13}Cmr. A pure sample was obtained by sublimation; mp 69–70°C; ir ($CHCl_3$): 2945, 1706 cm^{-1}: ^{1}Hmr ($CDCl_3$) δ: 0.97 (s, 9H, Me_3), 2.34 (m, 3H), 1.85–2.20 (m, 6H), 1.70 (m, 1H), 1.45 (m, 2H), 1.25 (m, 1H), 0.90–1.15 (m, 2H); ^{13}Cmr ($CDCl_3$) δ_C: 27.7 (Me_3), 27.8, 33.2, 33.9, 34.1, 34.5 (5 × CH_2), 40.4, 46.4, 48.1, 53.2, 58.7 (5 × CH), 31.7 (quat C), 213.8 (CO). *Exact Mass* calcd. for $C_{15}H_{24}O$: 220.1827; found: 220.1823.

Can. J. Chem. Downloaded from www.nrcresearchpress.com by 176.9.209.113 on 09/07/12
For personal use only.

A sample of this α-*tert*-butyl derivative (40 mg) was dissolved in MeONa/MeOD (0.01 M, 1.3 mL) and the solution stirred overnight at room temperature. After quenching with D_2O (2 mL), the product was extracted with pentane and the ketone was recovered (0.35 mg). The ^{13}C spectrum gave no indication of any epimeric material and the signal at δ_C 53.2 was replaced with a weak triplet, J_{CD} = 18.2 Hz at δ_C 52.9 indicating essentially complete exchange of the *endo*-9 proton.

Following the procedure described above for **13**, the α-*tert*-butyl ketone (0.24 g) was added to LDA (diisopropylamine (0.21 mL), THF (2 mL), *n*-BuLi (2.46 M in hexane, 0.53 mL) at −78°C) and, after allowing for formation of the enolate, methyl iodide (0.20 mL) was added. The usual isolation procedure yielded an oil that, by glc analysis (FFAP), was only 70% methylated. Consequently, the product was recycled using the same conditions and was found to be >95% pure **9** after flash chromatography (Et_2O – petroleum ether, 5:95); ir (film): 2960, 1698 cm^{-1}; ^{13}Cmr: see Table 1. *Exact Mass* calcd. for $C_{16}H_{26}O$: 234.1984; found: 234.1981.

9,9-Dimethyl-endo-*tricyclo[5.3.1.0^{2,6}]undecan-8-one (**10**)*

The parent ketone was available from an earlier study (12) and dimethylation of this undecanone (0.42 g) was accomplished using our standard procedure (5) with $NaNH_2$ (0.55 g) in anhydrous Et_2O (16 mL) and four additions of methyl iodide (0.32 mL) after reflux periods of 2, 2, 10, and 4 h. After refluxing for an additional 3 h, the reaction mixture was extracted with pentane to yield **10** (0.33 g, 67%) and a sample (>98% pure) was collected by glc (FFAP); ir (CCl_4): 2962, 1703 cm^{-1}; ^{1}Hmr ($CDCl_3$) δ: 1.03 (s, Me), 1.15 (s, Me), 2.63 (m, 3H), 2.32 (m, 1H), 2.18 (d, *J* = 13 Hz, 1H), 1.27–1.79 (m, 8H), 1.10 (m, 1H); ^{13}Cmr: see Table 1. *Exact Mass* calcd. for $C_{13}H_{20}O$: 192.1514; found: 192.1519.

Homoenolization experiments

Our standard procedure for these reactions in strong base (4) was followed as illustrated for **10**. To a solution of *t*-BuO^-/*t*-BuOH (1.3 M, H_2O content ~60 μg/mL) prepared *in situ* was added **10** to give a solution that was 0.26 M in ketone. A series of 0.5-mL aliquots of this solution were transferred quickly to 5-mL predried, thick-walled glass tubes; the tubes were degassed and sealed before immersion in an oil bath at 185°C. Tubes were removed at various times, cooled before opening, and the contents recovered by washing with water (10 mL). The neutral organic product was isolated by pentane extraction (3 × 15 mL) and the combined extracts back-washed with water (3 × 10 mL). The aqueous washings were reextracted with pentane (2 × 15 mL) and the combined extracts dried over $MgSO_4$. Removal of the solvent by distillation afforded the neutral organic product, in >90% yields from the various tubes, which was analyzed by glc (FFAP, Carbowax, SE-30) and found to contain only starting material; ^{13}Cmr spectra of the products also contained only the signals of **10**. The same result was obtained from experiments at 200°C.

An analogous series of experiments with **9** gave a neutral product (~85% yields) containing a small amount (~1%) of a new component. To obtain somewhat larger amounts of this material, **9** was treated as described above with the temperature raised to 200°C. The new component is ketonic (1730 cm^{-1}) and isomeric with **9**. *Exact Mass* calcd. for $C_{16}H_{26}O$: 234.1984; found: 234.1988. This new ketone was identified as **15** by ^{13}Cmr as described in the text.

A series of experiments similar to those with **9** were carried out with **8** and the results are presented in the text.

To examine the exchange processes, the fate of samples of **9** and **10** using *tert*-butyl alcohol-*O*-d_1 (99% deuterated, D_2O content <200 μg/mL) under these reaction conditions was examined; the results are described in the text.

*Rearrangement products from **8** and **16** (**18**a,b)*

From the runs with **8** and the mixture of **8** and **16** at 200°C (see text), preparative glc (FFAP) furnished samples of the new band tentatively identified as a mixture of **18***a* and *b*; ir (film): 1735 cm^{-1}; ^{1}Hmr ($CDCl_3$) δ: 2.67 (m, 2H), 1.2–1.8 (complex absorption, 8H), 1.08 (s, Me_3, minor), 0.99 (s, Me, minor), 0.95 (s, Me_3, major), 0.91 (s, Me, major); ^{13}Cmr: see Table 1. *Exact Mass* calcd. for $C_{13}H_{22}O$: 194.1671; found: 194.1671.

Acknowledgements

We are grateful for the financial support provided by the Natural Sciences and Engineering Research Council of Canada.

1. A. Nickon and J. L. Lambert. J. Am. Chem. Soc. **84**, 4604 (1962); **88**, 1905 (1966).
2. N. H. Werstiuk. Tetrahedron, **39**, 205 (1983).
3. (*a*) J. L. Jurlina, H. A. Patel, and J. B. Stothers. Can. J. Chem. **62**, 1159 (1984); (*b*) H. A. Patel and J. B. Stothers. Can. J. Chem. **62**, 1926 (1984); (*c*) B. A. Dawson, A. K. Ghosh, J. L. Jurlina, A. J. Ragauskas, and J. B. Stothers. Can. J. Chem. **62**, 2521 (1984).
4. A. L. Johnson, N. O. Petersen, M. B. Rampersad, and J. B. Stothers. Can. J. Chem. **52**, 4143 (1974).
5. A. J. Ragauskas and J. B. Stothers. Can. J. Chem. **63**, 1250 (1985).
6. J. L. Jurlina, H. A. Patel, S. Peiris, and J. B. Stothers. Magn. Reson. Chem. **25**, 109 (1987).
7. M. T. Reetz and W. F. Maier. Angew. Chem. Int. Ed. Engl. **17**, 48 (1978).
8. S. H. Grover, D. H. Marr, J. B. Stothers, and C. T. Tan. Can. J. Chem. **53**, 1351 (1975).
9. V. Patel, A. J. Ragauskas, and J. B. Stothers. Can. J. Chem. **64**, 1440 (1986).
10. D. J. Cram, B. Rickborn, C. A. Kingsbury, and P. Haberfield. J. Am. Chem. Soc. **83**, 3678 (1961).
11. J. L. Jurlina, A. J. Ragauskas, and J. B. Stothers. Magn. Reson. Chem. **23**, 689 (1985).
12. N. L. Allinger. J. Am. Chem. Soc. **99**, 8127 (1977); N. L. Allinger and Y. Y. Yuh. QCPE, 423 (1985).
13. J. L. Jurlina and J. B. Stothers. J. Am. Chem. Soc. **104**, 4677 (1982); Z. Majerski, M. Zvanic, and B. Metelko. J. Am. Chem. Soc. **107**, 1721 (1985); J. R. Wesener, D. Moskau, and H. Gunther. J. Am. Chem. Soc. **107**, 7307 (1985).
14. N. H. Werstiuk, G. Timmins, and B. Sayer. Can. J. Chem. **64**, 1465 (1986).
15. W. C. Still, M. Kahn, and A. Mitra. J. Org. Chem. **43**, 923 (1978).
16. S. L. Patt and J. N. Shoolery. J. Magn. Reson. **46**, 535 (1982).
17. D. M. Doddrell, D. T. Pegg, and M. R. Bendall. J. Magn. Reson. **48**, 323 (1982).
18. D. A. Cuppels, R. D. Stipanovic, A. Stoessl, and J. B. Stothers. Can. J. Chem. **65**, 2126 (1987).
19. G. A. Antoniadis, M. T. M. Clements, S. Peiris, and J. B. Stothers. Can. J. Chem. **65**, 1557 (1987).

Thermodynamics of transfer of glycine, diglycine, and triglycine from water to aqueous solutions of urea, glycerol, and sodium nitrate

HIMANSU TALUKDAR, SIBAPRASAD RUDRA, AND KIRON K. KUNDU[1]
Physical Chemistry Laboratories, Jadavpur University, Calcutta 700 032, India

Received August 18, 1987

HIMANSU TALUKDAR, SIBAPRASAD RUDRA, and KIRON K. KUNDU. Can. J. Chem. **66**, 461 (1988).

Standard free energies (ΔG_t^0) and entropies (ΔS_t^0) of transfer of glycine (G), diglycine (DG), and triglycine (TG), from water to aqueous mixtures of glycerol (GL) and urea (UH) have been determined from solubility measurements at different temperatures. This was also extended to an ionic cosolvent system like aqueous sodium nitrate solutions for G and DG. The observed ΔG_t^0 and $T\Delta S_t^0$–composition profiles, as well as those obtained after correcting for the "cavity effect" as estimated by scaled particle theory (SPT), were examined in the light of various interactions. The corrected ΔG_t^0 and $T\Delta S_t^0$ values show a regular function of the peptide chain length of the amino acids and impart useful information regarding the involved relative structural effects of these ionic and non-ionic cosolvents.

HIMANSU TALUKDAR, SIBAPRASAD RUDRA et KIRON K. KUNDU. Can. J. Chem. **66**, 461 (1988).

En se basant sur des mesures de solubilité effectuées à diverses températures, on a déterminé les énergies libres standards (ΔG_t^0) et les entropies (ΔS_t^0) de transfert de la glycine (G), de la diglycine (DG) et de la triglycine (TG) de l'eau vers des mélanges aqueux de glycérol (GL) et d'urée (UH). Dans le cas de la G ainsi que de la DG, on a aussi étendu cette étude à un système de co-solvants ioniques comme des solutions aqueuses de nitrate de sodium. Les profils observés pour le ΔG_t^0 et le $T\Delta S_t^0$ en fonction de la composition ainsi que ceux obtenus après avoir fait une correction pour l'effet de cavité évalué par la théorie de la particule scalaire (TPS) ont été examinés à la lumière de diverses interactions. Les valeurs corrigées de ΔG_t^0 et de $T\Delta S_t^0$ présentent une fonction régulière de la longueur de la chaîne des acides aminés et fournissent des informations utiles concernant les effets de structure relatifs de ces cosolvants qu'ils soient ioniques ou pas.

[Traduit par la revue]

Can. J. Chem. Downloaded from www.nrcresearchpress.com by 176.9.209.113 on 09/07/12
For personal use only.

Introduction

It is well known that urea (UH) causes unfolding of native conformation of proteins, whereas glycerol (GL) and other polyols cause stabilization of the same. Although several mechanisms of these effects have been proposed from different view points (1–10), a successful explanation seems to be that the opposing effects of urea and polyols on proteins may be predominantly mediated through the changes in solvation properties or alteration of water structure. From the free energy of transfer (ΔG_t^0) studies obtained from solubilities of amino acids and peptides at 25°C in aqueous urea (2*a*), ethylene glycol (EG) (2*b*), and ethanol (EtOH) (2*c*), Nozaki and Tanford concluded that while both non-polar and polar side chains are preferentially solvated in UH + H_2O mixtures, the effect was much reduced in EtOH + H_2O mixtures and less so in EG + H_2O mixtures. Similar experiments by Gekko (10) led him to conclude that polyol can stabilize the protein conformation through hydrophobic interactions. Though their free energy of transfer (ΔG_t^0) data of these solvents are seemingly useful in imparting informations regarding denaturation processes, a more detailed understanding may be possible by evaluating entropies (ΔS_t^0) or enthalpies (ΔH_t^0) of transfer data, since these quantities in general reflect more sensitively the structural (11–13) and interactional parts of the solvent effects. But till recent years relatively little work has been reported regarding these quantities (9, 14–17). Although Gekko has recently reported ΔS_t^0 and ΔH_t^0 of some amino acids including glycine and also of a peptide like diglycine in some low concentrations of polyols including GL (17), such studies on ΔS_t^0 and ΔH_t^0 are still lacking for a series of UH + H_2O mixtures. And since the solubilities of these zwitterions at different temperatures are still unknown in these aquo-organic cosolvents, studies of the same will provide important quantities for evaluation of various thermo-chemical properties at other temperatures as well.

In the present paper we, therefore, report the solubilities of glycine (G), diglycine (DG), and triglycine (TG) in water and in a series of aqueous mixtures of glycerol and urea at five different temperatures and the related transfer energetics, i.e., ΔG_t^0, $T\Delta S_t^0$, and ΔH_t^0 from water to those mixtures. The results have been discussed in terms of the competing effects of solute polarity and the relative solvent structural changes consequent to the introduction of the solutes into those aqueous organic mixtures.

Moreover, since Larson *et al.* (18) and Lilley and co-workers (19) have shown that electrolyte solutions form vital biochemical interests for these studies, the above studies on glycine and diglycine were also extended to 1, 2, and 4 molal sodium nitrate ($NaNO_3$) solutions as these are likely to provide a precursor to suitable model systems of highly complex systems like biofluid. This is to give an idea about the relative stabilization of those amino acids in a typical electrolyte solution with respect to aquo-organic cosolvents as "electrolyte–zwitterion" interactions might play an important role on the conformational structure and stability of proteins.

Experimental

Materials

Glycine (GR grade, E Merck (India)) was recrystallised twice from low conductivity water and was dried at room temperature under vacuum in a desiccator. DG and TG were special reagent grade products from Sigma Chemical Co. and they were used after drying without further purification since their purity was found to be excellent from the solubility data in water and also from the titration of a known solution of each solute in water. Purification of glycerol (B.D.H., AnalR grade) has been described earlier (11). Urea (B.D.H., AnalR grade) was used without further purification. Preparation of solvent mixtures and $NaNO_3$ solution was similar to that described earlier (13, 20). Water employed in these measurements was triply distilled and stored in a CO_2-free atmosphere.

Solubility measurements

Samples in the solvent mixtures were taken in glass tubes fitted with

[1]Author to whom all correspondence should be addressed.

Can. J. Chem. Downloaded from www.nrcresearchpress.com by 176.9.209.113 on 09/07/12
For personal use only.

TABLE 1. Solubilities (g/100 g solvent) of glycine, diglycine, and triglycine in aqueous solutions of urea, glycerol, and $NaNO_3$ at different temperatures

Solvent	Molalities or wt% cosolvent	Glycine					Diglycine					Triglycine				
		15°C	20°C	25°C	30°C	35°C	15°C	20°C	25°C	30°C	35°C	10°C	15°C	20°C	25°C	30°C	35°C
H_2O	0	19.95	22.55	24.99	27.60	30.16	19.79	21.23	22.67	24.26	25.90		4.2	5.5	6.9	8.7	11.0
		20.20[a]	22.52[a]	24.99[a]	27.59[a]	30.32[a]			23.30[b]						6.3[b]		
				25.10[a]					22.75[c]						6.0[c]		
				25.00[d]					22.70[d]						6.06[d]		
Urea	11.52 wt%	18.75	20.70	22.70	24.50	26.31	19.18	20.37	21.58	22.91	24.12	4.9	5.8	7.1	8.3	9.9	—
	20.31 wt%	16.11	18.15	20.05	21.88	23.72	18.44	19.32	20.16	21.18	22.13	5.2	6.1	7.5	9.1	10.6	—
	29.64 wt%	15.60	16.95	18.34	19.70	21.09	17.17	17.95	18.61	19.45	20.21	10.8	11.3	11.6	12.4	12.8	—
	36.83 wt%	12.27	13.35	14.50	15.54	16.81	15.01	15.68	16.69	17.62	18.45	10.2	10.7	11.0	11.7	12.2	—
Glycerol	10 wt%	16.33	18.50	20.56	22.80	25.19	15.90	17.02	18.30	19.45	20.87	—	3.8	4.8	6.2	7.9	9.6
	30 wt%	11.43	12.70	14.13	15.40	16.83	10.57	11.27	11.90	12.82	13.63	—	3.0	4.0	5.1	5.6	6.4
	50 wt%	7.26	8.30	9.25	10.40	11.58	6.66	6.93	7.18	7.53	7.86	—	2.9	3.2	3.3	3.4	3.6
	70 wt%	3.99	4.52	4.95	5.38	5.84	3.17	3.40	3.64	3.72	4.10	—	1.3	1.4	1.5	1.6	1.7
$NaNO_3$	1 *m*	21.14	23.60	25.95	28.70	31.25	23.03	24.05	24.85	25.77	26.50						
	2 *m*	21.76	23.80	25.71	27.85	29.93	24.32	25.76	26.95	28.33	29.58						
	4 *m*	22.81	24.10	25.76	27.70	29.71	25.32	26.36	27.61	29.09	30.24						

[a]Reference 41. [c]Reference 42.
[b]Reference 6. [d]Reference 43.

ground glass stoppers and were shaken for about 24 h. After 2 days, weight amounts of aliquot from the saturated solutions were taken in stoppered conical flasks and the solubility measurements of the amino acid and peptides were made by "formal titration" using the standard NaOH (GR, E Merck) solution and phenolphthalein as indicator. Freshly neutralised formaldehyde solution (GR, E Merck) was used in the method. Equilibrium was found to attain within 3–4 days. At least two sets of measurements were made for all the solutes and the results were found to agree to within 1%.

The measurements were made at five equidistant temperatures ranging from 15 to 35°C. For TG in UH + H_2O mixtures the procedure was repeated from 10 to 30°C.

The purity of our solutes and the general validity of our methods of solubility measurements may be justified by comparing our solubility data with other reported results as shown in Table 1. The difference lying within ±0.6 unit for DG and TG with Nozaki and Tanford's data may be due to the different techniques involved.

Results

The solubilities (S) in g/100 g solvent are summarised in Table 1. As usual (12) the calculated free energies of solution (ΔG_s^0) at different temperatues were fitted by least-squares method to an equation like

$$[1] \quad \Delta G_s^0 = a + bT + cT \ln T$$

where T is the temperature in K. The values of the coefficients a, b, and c are presented in Table 2. These are found to reproduce the experimental data to within ±0.02 kJ. The free energies (ΔG_t^0), entropies (ΔS_t^0), and enthalpies (ΔH_t^0) of transfer of G, DG, and TG from the reference solvent water to the aqueous mixtures were calculated on the mole fraction scale by the equations already described in a previous paper (12). These values were included in Table 2. As in the previous paper (21), the activity coefficients of non-electrolytes ${}_wf_i$ and ${}_sf_i$ (w = water, s = solvent) in the corresponding states of saturated solution in the respective solvents are likely to be more or less equal and hence the activity coefficient factor $RT \ln {}_wf_i/{}_sf_i$ is assumed to be zero. The maximum uncertainties in these quantities are ±0.05 kJ for ΔG_t^0 and ±2.0 J K^{-1} mol^{-1} for ΔS_t^0. Nevertheless, as has been done by Nozaki and Tanford (2*a*,*b*) we have calculated ΔG_t^0 at 25°C by the eq. [2]

$$[2] \quad \Delta G_t^0 = RT \ln \frac{{}_wN_i}{{}_sN_i} + RT \ln \frac{{}_wf_i}{{}_sf_i}$$

in UH + H_2O and GL + H_2O mixtures where the N terms are the mole fractions. Due to the non-availability of activity coefficients of acids in the solvent mixtures, these were assumed to be the same as those in water at the same molality of solute. Since the solute–solute interactions are chiefly electrostatic, we have multiplied $\ln {}_sf_i$ by the ratio of the dielectric constant D_w/D_s (2*b*) where D_w and D_s are the dielectric constants of water and the mixed solvents, respectively (20, 22). The same calculations could not be done for temperatures other than 25°C, since the activity coefficients are not known at other temperatures. This activity corrected ΔG_t^0 values have been shown in Table 3 and when compared with the results obtained by the previous method (Table 2) a maximum differences of 0.2 kJ for UH + H_2O and 0.3 kJ for GL + H_2O mixtures are found, which we feel are fairly tolerable, at least considering the different methods used. The ΔG_t^0 values were then used to calculate the contribution of peptide backbone unit, i.e., the glycyl residue (—CH_2CONH) from water to the solvent mixtures designated by Δg_t^0 by subtracting the corresponding values of G from DG or of DG from TG, assuming additivity of

TABLE 2. Coefficients a, b, and c of eq. [1] and free energies (ΔG_t^0), entropies ($T\Delta S_t^0$), and enthalpies (ΔH_t^0) of transfer (in kJ mol^{-1}) of glycine, diglycine, and triglycine from water to aqueous mixtures of UH, GL, and $NaNO_3$ at 25°C (mole fraction scale)

	Wt.% of molality of cosolvent	mol% cosolvent	a/(kJ mol^{-1})	b/(kJ mol^{-1} K^{-1})	c/(kJ mol^{-1} K^{-1})	ΔG_t^0	$T\Delta S_t^0$	ΔH_t^0
				Glycine				
H_2O	0	0	27.60	−0.3435	0.04229	0	0	0
Urea	11.52 wt%	3.76	76.72	−1.4944	0.21551	0.03	−2.6	−2.6
	20.31 wt%	7.11	32.97	−0.4928	0.06566	0.17	−1.8	−1.6
	29.64 wt%	11.22	35.78	−0.5989	0.08275	0.19	−4.1	−3.9
	36.83 wt%	14.90	24.66	−0.3381	0.04387	0.62	−4.0	−3.4
GL	10 wt%	2.10	49.40	−0.8146	0.11243	0.27	0.6	0.9
	30 wt%	7.73	53.30	−0.9300	0.13094	0.74	−1.5	−0.7
	50 wt%	16.36	37.79	−0.5235	0.06933	1.17	1.0	2.1
	70 wt%	31.34	102.21	−2.0295	0.29665	1.96	−3.2	−1.2
$NaNO_3$	1 *m*	1.77	40.67	−0.6482	0.08800	−0.27	−0.3	−0.6
	2 *m*	3.48	47.94	−0.8632	0.12150	−0.38	−2.9	−3.3
	4 *m*	6.72	−54.94	1.4131	−0.21747	−0.63	−4.5	−5.1
				Diglycine				
H_2O	0		−0.40	0.1942	−0.03465	0	0	0
Urea	11.52 wt%		9.72	−0.0599	0.00408	−0.09	−1.3	−1.4
	20.31 wt%		−9.14	0.3312	−0.05337	−0.09	−3.1	−3.2
	29.64 wt%		0.03	0.1111	−0.02004	−0.08	−3.8	−3.9
	36.83 wt%		12.80	−0.1440	0.01740	0.03	−2.3	−2.3
GL	10 wt%		398.63	−8.6783	1.28800	0.32	4.4	4.7
	30 wt%		−26.02	0.7658	−0.11894	0.91	−1.4	−0.5
	50 wt%		−29.61	0.7879	−0.11998	1.57	−5.4	−3.8
	70 wt%		−23.18	0.7026	−0.10778	2.53	−3.5	−1.0
$NaNO_3$	1 *m*		29.13	−0.5609	0.08038	−0.38	−4.4	−4.8
	2 *m*		22.53	−0.3749	0.05149	−0.73	−2.0	−2.8
	4 *m*		−10.49	0.3578	−0.05770	−1.04	−2.2	−3.2
				Triglycine				
H_2O	0		54.34	−0.5394	−0.06416	0	0	0
Urea	11.52 wt%		−4.58	0.5938	−0.10034	−0.68	−9.2	−9.9
	20.31 wt%		−27.47	1.1401	−0.18284	−1.00	−7.2	−8.2
	29.64 wt%		−27.50	0.7505	−0.11491	−1.98	−26.5	−28.5
	36.83 wt%		−16.92	0.5178	−0.08022	−2.03	−26.2	−28.2
GL	10 wt%		82.38	−1.1670	0.15796	0.08	−0.1	0.1
	30 wt%		845.69	−18.3980	2.73319	0.13	−4.6	−4.5
	50 wt%		−35.08	0.9122	−0.13691	0.57	−30.1	−29.5
	70 wt%		−9.24	0.4004	−0.06113	1.76	−28.0	−26.2

constituent group contributions and these values are shown in Table 4.

Discussion

Free energies of transfer

Figure 1 shows the variation of ΔG_t^0 (activity corrected) of G, DG, and TG with mol% of the cosolvent GL and UH. While the profiles for GL + H_2O mixtures become increasingly positive with the relative order of DG > G > TG those for aqueous UH solutions become increasingly positive for G, less so for DG, and negative for TG with the relative order G > DG > TG. Similar profiles obtained from the data of Gekko (10) in GL + H_2O mixtures and those of Nozaki and Tanford (2*a*) in UH + H_2O mixtures have been found with little differences, as shown in the Fig. 1 (dotted lines) except for TG in high UH-content where the two profiles differ to some extent. Thus the observed increased destabilization of these zwitterionic species ($RH^{\pm}$) in GL + H_2O systems confirms the dictates of mono-ol (EtOH), di-ol (EG), and other polyol systems as shown by Gekko and others (2*b*, 2*c*, 10). Moreover, since the solvation numbers of the amino acids in water are expected to be quite high due to zwitterionic nature of these acids having two solvation sites, the observed destabilization of $RH^{\pm}$ is not only the effect of decreased solvation number of amino acids in the binary mixtures with increase in GL-content in water, but also due to immobilisation of the solvent molecules by solutes due to dipole–dipole, dipole – induced dipole, or dispersion forces etc.

But while the ΔG_t^0 values increase in the order G < DG < TG in the case of aqueous ethanol (2*c*) and ethylene glycol mixtures (2*b*) the order is changed to TG < G < DG in GL + H_2O systems. Two factors may be responsible for this. Firstly, ΔG_t^0 values of G, DG, and TG are becoming less (keeping positive values) in EG than the corresponding values in EtOH and so in GL than that in EG indicating that the probable peptide–peptide hydrogen bonds are stabilized less effectively as the hydroxy methyl chain increases in length (i.e. hydro-

Can. J. Chem. Downloaded from www.nrcresearchpress.com by 176.9.209.113 on 09/07/12
For personal use only.

TABLE 3. Free energies of transfer (ΔG_t^0) (activity corrected) according to eq. [2] from water to aqueous solutions of urea and glycerol at 25°C

	ΔG_t^0 (kJ mol^{-1})							
	Wt% urea				Wt% GL			
	11.52	20.31	29.64	36.83	10	30	50	70
Glycine	−0.03	0.05	0.03	0.40	0.24	0.66	1.01	1.66
Diglycine	−0.16	−0.22	−0.26	−0.21	0.29	0.77	1.26	2.04
Triglycine	−0.65	−0.99	−1.91	−1.99	0.06	0.10	0.40	1.44

TABLE 4. Contributions of glycyl residue to free energy of transfer, Δg_t^0 and Δg_t^0(int) in kJ mol^{-1} from water to aqueous urea, glycerol, and $NaNO_3$ at 25°C

	Wt% or molality (m) of cosolvent	(DG–G)		(TG–DG)	
		Δg_t^0	Δg_t^0(int)	Δg_t^0	Δg_t^0(int)
Urea	11.52 wt%	−0.13	−1.5	−0.49	−3.4
	20.31 wt%	−0.27	−2.9	−0.77	−6.2
	29.64 wt%	−0.29	−4.3	−1.65	−9.9
	36.83 wt%	−0.61	−5.6	−1.78	−12.4
GL	10 wt%	0.05	0.2	−0.23	0.3
	30 wt%	0.11	0.8	−0.67	0.6
	50 wt%	0.25	1.7	−0.86	2.0
	70 wt%	0.38	3.1	−0.60	5.0
$NaNO_3$	1 m	−0.11	2.0	—	—
	2 m	−0.35	3.6	—	—
	4 m	−0.41	6.6	—	—

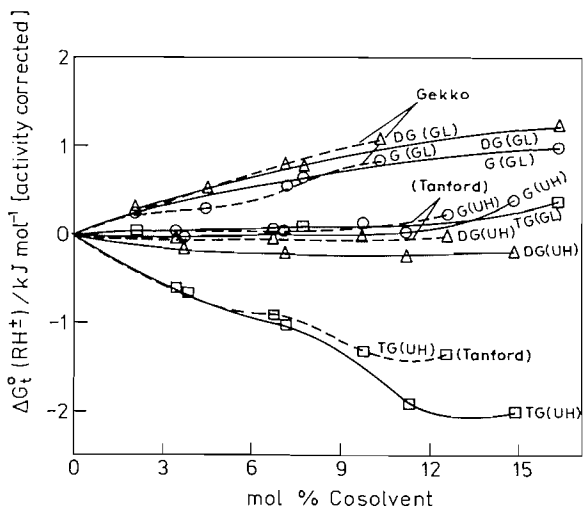

FIG. 1. Variation of ΔG_t^0 of glycine (○), diglycine (△), and triglycine (□) with cosolvent composition in aqueous mixtures of urea (UH) and glycerol (GL) at 25°C.

phobic nature). The other factor may be the involvement of some specific interaction involving hydrophobic interactions and cavity effect that might contribute significantly enough to the total ΔG_t^0 values which have also been accounted for as follows.

It is now well recognised (12, 13, 23–26) that for large-sized species, the true interaction effect, i.e., ΔG_t^0(int) which is ΔG_t^0 but free from any cavity effect, ΔG_t^0(cav) (27), is a better indicator of the true picture of interactions between the solute and solvent molecules. We have therefore calculated ΔG_t^0(cav) by the widely used procedure (12, 13, 24) using the "scaled particle theory (SPT)" (27), taking the diameter of G, DG, and TG as 5.64 (28), 8.0 (29), and 11.5 (29), respectively and those of the cosolvent molecules as given in refs. 12 and 13. Notably, since the radius of equivalent hard sphere of DG and TG will be quite uncertain and also since DG and TG may be best considered according to Cohn *et al.* (29) to be cylindrical of length 8.0 and 11.5 Å, respectively, we have tentatively assumed the excluded volume of diameter of the same magnitudes for the respective species to be equivalent to their hard-sphere model.

Moreover, though the SPT is not applicable for species other than hard spheres and for species having strong and directional interactions with solute molecules (25, 30), the calculations done above might seem to be over exaggerated in the case of DG and TG. Since the diameter of the solute is not that sensitive a parameter as the diameters of cosolvent molecules (25, 27) are, the SPT is now increasingly used in computing thermodynamic quantities of cavity formation of different solutes not only in different organic solvents but also in aqueous mixtures of various ionic and nonionic cosolvents (13, 23–27, 30, 31) assuming tentatively an equivalent hard sphere for each of the solute species. Moreover, while Morel-Desroisers and Morel (30) have used these ΔG_t^0(cav) values as the guiding factor for solvation properties, we have, however, used the same, as some authors did (13, 23–27, 30, 31), for correcting the cavity contribution from the observed transfer free energy ΔG_t^0 to evaluate ΔG_t^0(int) values which are as shown earlier, likely to reflect the true interaction effects.

Thus, the required solvent and solute parameters along with the molar free energies of cavity formation $\bar{G}$(cav), ΔG_t^0(cav), and ΔG_t^0(int) are given in Table 5. From this table and Fig. 2 which shows the ΔG_t^0(int)–composition profiles in GL + H_2O (solid lines) it can be seen that the cavity interaction term contributes negatively in GL + H_2O mixtures. Thus the trends of the profiles in Fig. 1 for the solvation of G, DG, and TG have now become normalised indicating that TG will be more desolvated than DG and G in these systems, as has been observed in EG + H_2O and EtOH + H_2O systems.

Similarly, in the case of UH + H_2O mixtures, the ΔG_t^0(int)–composition profiles (dotted lines) in Fig. 2 for G, DG, and TG become increasingly negative since the cavity effect, i.e., ΔG_t^0(cav) for G, DG, and TG, unlike in GL + H_2O systems, contributes positively in UH + H_2O mixtures as has been seen from Table 5. Thus the observed near invariance of the ΔG_t^0–composition profile of glycine in Fig. 1 is the result of positive contributions of the cavity effect and the negative contributions of the true interaction effect, for glycine is

Can. J. Chem. Downloaded from www.nrcresearchpress.com by 176.9.209.113 on 09/07/12
For personal use only.

TABLE 5. Values of free energy ($\bar{G}$(cav)), enthalpy ($\bar{H}$(cav)) of cavity formation (molar scale), and ΔG_t^0(cav), ΔG_t^0(int), $T\Delta S_t^0$(cav), $T\Delta S_t^0$(int) (mole fraction scale), and the required solvent parameter in aqueous mixtures of different ionic and non-ionic cosolvents at 25°C

Solvent	Wt% or molality (m) of cosolvent	$10^6\alpha/K^{-1}$ [a]	$\bar{G}$(cav)/(kJ mol^{-1})	$\bar{H}$(cav)/(kJ mol^{-1})	ΔG_t^0(cav) (kJ mol^{-1})	ΔG_t^0(int) (kJ mol^{-1})	$T\Delta S_t^0$(cav) (kJ mol^{-1})	$T\Delta S_t^0$(int) (kJ mol^{-1})
				Glycine				
H_2O	0	223	43.6	6.2	—	—	—	—
Urea	11.52 wt%	531	45.3	16.0	1.6	−1.6	8.2	−10.8
	20.31 wt%	435	46.6	14.0	2.8	−2.6	5.0	−6.8
	29.64 wt%	390	48.2	13.5	4.2	−4.0	3.1	−7.2
	36.83 wt%	361	49.6	13.3	5.5	−4.9	1.6	−5.6
GL	10 wt%	345	43.5	9.8	−0.3	0.6	3.9	−3.3
	30 wt%	398	43.2	11.9	−0.9	1.6	6.6	−8.1
	50 wt%	497	42.7	15.6	−1.9	3.1	11.3	−10.3
	70 wt%	478	41.7	15.7	−3.5	5.5	13.0	−16.2
$NaNO_3$	1 m	410	41.2	10.5	−2.4	2.1	6.7	−7.0
	2 m	535	39.2	12.8	−4.5	4.1	11.0	−13.9
	4 m	556	35.7	11.6	−8.0	7.4	13.4	−17.9
				Diglycine				
H_2O	0		81.3	11.8	—	—	—	—
Urea	11.52 wt%		84.4	30.5	3.0	−3.1	15.7	−17.0
	20.31 wt%		86.9	26.7	5.4	−5.5	9.5	−12.6
	29.64 wt%		89.9	25.8	8.2	−8.3	5.8	−9.6
	36.83 wt%		92.3	25.3	10.5	−10.5	3.0	−5.3
GL	10 wt%		81.0	18.7	−0.5	0.8	7.4	−3.0
	30 wt%		80.3	22.6	−1.5	2.4	12.3	−13.7
	50 wt%		79.1	29.7	−3.2	4.8	21.1	−26.5
	70 wt%		76.8	29.8	−6.2	8.6	24.1	−27.6
$NaNO_3$	1 m		76.9	20.0	−4.5	4.1	12.7	−17.1
	2 m		73.0	24.3	−8.4	7.7	20.9	−22.9
	4 m		66.4	22.0	−15.1	14.0	25.2	−27.4
				Triglycine				
H_2O	0		159.0	23.5	—	—	—	—
Urea	11.52 wt%		164.9	59.7	5.8	−6.5	30.4	−39.6
	20.31 wt%		169.9	53.1	10.7	−11.7	18.9	−26.1
	29.64 wt%		175.6	51.3	16.2	−18.2	11.6	−38.1
	36.83 wt%		180.4	50.4	20.9	−22.9	6.0	−32.2
GL	10 wt%		158.2	37.1	−1.0	1.1	14.6	−14.7
	30 wt%		156.6	44.9	−2.9	3.0	24.3	−28.9
	50 wt%		153.8	58.9	−6.2	6.8	41.6	−71.7
	70 wt%		148.8	59.0	−11.8	13.6	47.3	−75.3

[a] $\alpha = -\mathrm{d} \ln d_s/\mathrm{d}T$; d_s = density of cosolvent.

expected to be solvated in these mixtures by dipole–dipole or "zwitterion–zwitterion" type attractive interaction overcoming its hydrophobic effect, as after all both the solvent and solute species possess high dipole moment (μ_{UH} = 4.56 D (32) and μ_G = 15.0 D (33)). In addition, the pronounced solvation of DG and TG is chiefly guided by the pronounced dipole–dipole and amide–amide interactions as also contended by Nozaki and Tanford (2*a*).

Unlike UH + H_2O mixtures, the true interaction profiles of glycine and diglycine in $NaNO_3$ solution (dotted lines, Fig. 3) are fairly different from the observed ΔG_t^0–composition profiles (solid lines, Fig. 3) and in fact contradict the conclusions drawn from the latter. While our observed data including those of Lilley and co-workers (19) and Bhat and Ahluwalia (34) (in NaCl solution) for glycine and diglycine indicate that the zwitterion should be solvated in salt solution through ion–ion interactions localised at the polar heads of the zwitterions, the same is not true when we consider the true interaction effect which shows pronounced salting-out and hydrophobic effects in these salt solutions. Hence the choice of the radius factor for glycine and diglycine might be suspected to cause some doubts as to the relevance of the ΔG_t^0(int) values. But since Kirkwood (28) and Cohn *et al.* (29) have already considered glycine as a spherical solute of radii 2.82 Å (and hence amenable for SPT calculations), the ΔG_t^0(int)–composition profile for glycine should by no means be considered to be an artifact but rather fairly meaningful. Likewise, the same profile for diglycine should also be taken as something real. Evidently, it is not the aforesaid ion–ion type interactions but the effect of significant contributions from the cavity interaction terms (Table 5) which led to the apparent sign and magnitudes of ΔG_t^0 values, especially of large sized species. This often

Can. J. Chem. Downloaded from www.nrcresearchpress.com by 176.9.209.113 on 09/07/12
For personal use only.

Can. J. Chem. Downloaded from www.nrcresearchpress.com by 176.9.209.113 on 09/07/12
For personal use only.

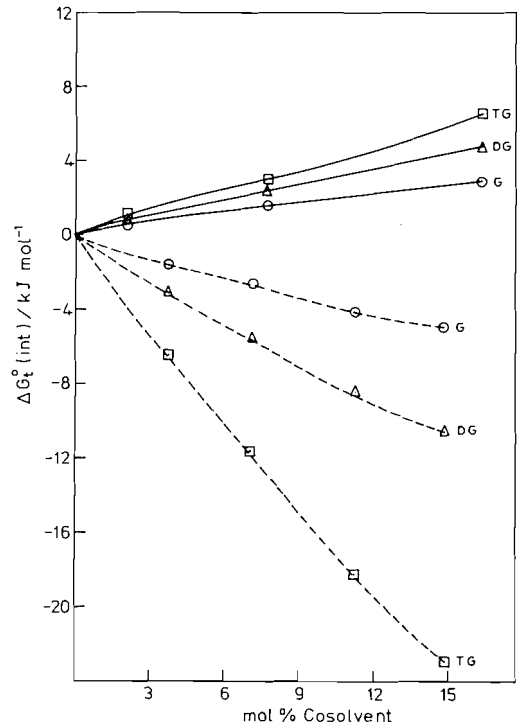

FIG. 2. Variation of ΔG_t^0(int) of glycine (○), DG (△), and TG (□) with cosolvent composition in aqueous mixtures of GL (solid lines) and UH (dotted lines) at 25°C.

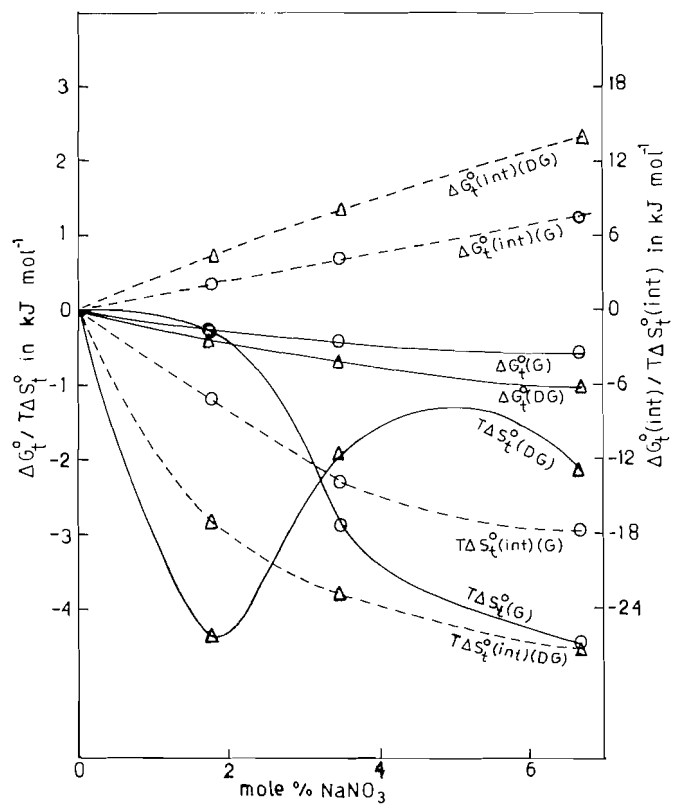

FIG. 3. Variation of ΔG_t^0 and $T\Delta S_t^0$(solid lines) and ΔG_t^0(int) and $T\Delta S_t^0$(int) (dotted lines) of glycine (○) and DG (△) with cosolvent composition in aqueous $NaNO_3$ solution at 25°C.

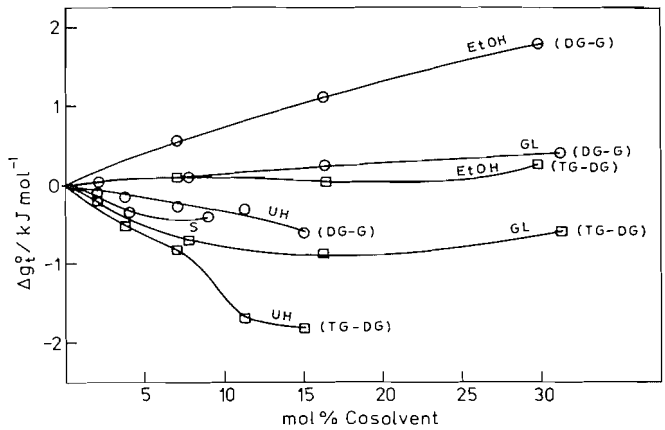

FIG. 4. Variation of Δg_t^0 (= ΔG_t^0(DG) − ΔG_t^0(G)) (○) and Δg_t^0 (= ΔG_t^0(TG) − ΔG_t^0(DG)) (□) with cosolvent composition in aqueous mixtures of EtOH, GL, UH, and $NaNO_3$(s) at 25°C.

obscures the true interaction effect which gets reflected only when one considers the cavity forming contributions. Moreover, afterall these species (G, DG) are typical non-electrolyte (35) organic solutes and might also undergo desolvation in aqueous electrolyte solutions.

Regarding the peptide-backbone unit, it is observed in Table 4 and Fig. 4 that ΔG_t^0–composition profiles of the peptide group i.e., (Δg_t^0 = ΔG_t^0(DG) − ΔG_t^0(G)) are increasingly positive for GL + H_2O and EtOH + H_2O solvents, that are increasingly negative in aqueous urea and $NaNO_3$ solutions. This also confirms the dictates of the observation made by Gekko in GL + H_2O mixtures and by Nozaki and Tanford in UH + H_2O mixtures. The increased negative magnitudes of the same profile in salt solution is still the effect of cavity contribution term which after due modification (which gives Δg_t^0(int)) imparts increasing positive magnitudes as has been seen from Table 4. But when the Δg_t^0 values are obtained from (ΔG_t^0(TG) − ΔG_t^0(DG)) an increasing negative Δg_t^0–composition profile in Fig. 4 was observed (with more or less constant difference between the two profiles) in both GL + H_2O and UH + H_2O mixtures. This is also obtained by Nozaki and Tanford in the latter cosolvent system and also in EtOH + H_2O mixtures (4) as shown in the same figure. This shows that the transfer free energy change for glycyl residue obtained by these two methods is not guided by additive property. This is of course not that unexpected as Nozaki and Tanford also concluded that the large negative values of these Δg_t^0 values obtained from the ΔG_t^0 difference of TG and DG result from the insertion of a glycyl residue into a molecule which already possesses a peptide unit. Moreover, these values when obtained from ΔG_t^0(int) values result in Δg_t^0(int) values (Table 4) which are largely negative in UH + H_2O mixtures and positive in GL + H_2O mixtures as expected from the interactions involved in the processes already discussed.

Entropies of transfer

Figure 5 illustrates $T\Delta S_t^0$–composition profiles of G, DG, and TG for the aqueous mixtures of GL and UH. If we follow the arguments of Spink and Auker (19) proposed in the case of EtOH + H_2O mixtures, the observed maximum for DG in GL + H_2O mixtures appears to suggest that cosolvent GL promotes the 3D structure of water at initial compositions and that DG is a structure breaker in this cosolvent system as is glycine in EtOH

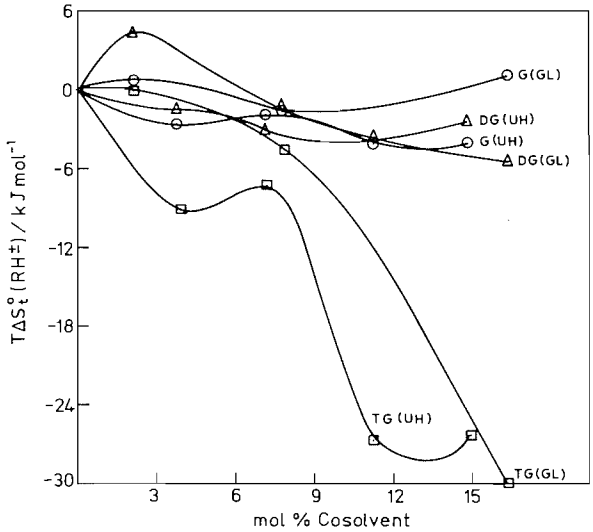

FIG. 5. Variation of $T\Delta S_t^0$ of glycine (○), DG (△), and TG (□) with cosolvent composition in aqueous mixtures of GL and UH at 25°C.

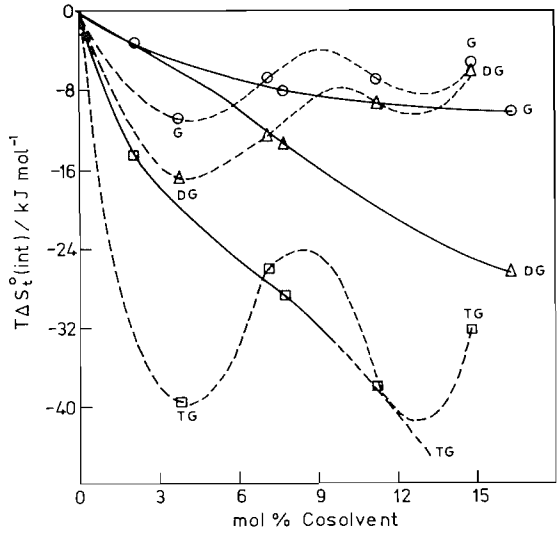

FIG. 6. Variation of $T\Delta S_t^0$(int) of glycine (○), DG (△), and TG (□) with cosolvent composition in aqueous mixtures of GL (solid lines) and UH (dotted lines) at 25°C.

+ H_2O mixtures. On the contrary, the observed downward trends of the profiles for glycine and TG imply that GL induces breakdown of 3D-structure of water. This anomalous behaviour, however, ceases to exist if we analyse the behaviour of true interaction effects on $T\Delta S_t^0$–profiles. We have, therefore, tentatively computed $T\Delta S_t^0$(cav) contributions by evaluating the values of $\overline{H}$(cav), the molar enthalpy of cavity formation, using the SPT formulations given in the previous paper (12). When $T\Delta S_t^0$(cav) values (Table 5) are subtracted from the corresponding experimentally observed $T\Delta S_t^0$ values, the resulting $T\Delta S_t^0$(int) values show a pattern similar to that observed in the cases of other non-electrolytes like benzoic acid (HBz) (12*a*) and *p*-nitroaniline (*p*-NA) (12*b*) in various aquo-organic solvents including these cosolvents. Thus the observed increasing negative $T\Delta S_t^0$(int)–composition profiles (solid lines in Fig. 6) in this solvent system are indicative of the effect of structure breaking propensity of the cosolvent GL conforming to what is contended from various other studies (11*a*, 12) and is expected from structural consideration of this cosolvent.

Similarly, in the case of UH + H_2O mixtures the observed initial downward trend of the $T\Delta S_t^0$(int)–composition profiles (dotted lines in Fig. 6) substantiate the earlier contention that urea is an effective 3D water structure breaker right from the initial composition but induces some structural order due to the possible formation of UH + H_2O aggregates around 4–10 mol% UH as indicated earlier (36). But at high urea-content the observed positive trends in both Figs. 5 and 6 are indicative of some other structural factors such as the possible formation of aggregates of urea (37, 38).

In the case of $NaNO_3$ solutions, the observed $T\Delta S_t^0$–composition profile of G and DG in Fig. 3, though apparently difficult to understand, the normalised $T\Delta S_t^0$(int)–composition profiles (dotted lines in Fig. 3) indicate a regular order conforming to what has been observed earlier in the case of HBz and *p*-NA in KBr solution (12) and lately also in $NaNO_3$ solution (39). Thus, following the arguments adopted earlier in the case of HBz and *p*-NA in aqueous KBr solutions we may conclude that like the salt KBr, $NaNO_3$ is also a 3D water structure breaker, although as per viscosity B-coefficient data (40), it appears to promote overall "electrophilic" order round the ions. Consequently the larger cavity effect is seemingly responsible for the roller-coaster type behaviour of the uncorrected $T\Delta S_t^0$–composition profile of DG as compared to that of G.

Thus, it has been observed that the true interaction effects i.e., ΔG_t^0(int) and $T\Delta S_t^0$(int) rather than ΔG_t^0 and $T\Delta S_t^0$ are more informative and easy to understand the solvation behaviour of G, DG, and TG in these ionic and non-ionic cosolvents and these are also found to be a regular function with the peptide chain length as expected. Hence care should be taken before one derives real implications of the oberved transfer energetics, although the latter undoubtedly reflect the real and overall transfer behaviour of ionic and non-ionic solutes in different aqueous ionic and non-ionic cosolvent systems. Lastly, although the present transfer entropy or enthalpy data have a limited applicability to protein systems but they may represent a basic criterion for the effects of these organics or salt solutions on entropy or enthalpy functions of protein denaturation. Admittedly of course, the magnitudes of cavity effect are somewhat tentative because of various limitations and uncertainties. Yet the conclusions, based on the relative trends of the different propensities are likely to be meaningful.

Acknowledgement

Thanks are due to the University Grants Commission, Government of India, New Delhi, for financial assistance.

1. C. TANFORD and P. K. DE. J. Biol. Chem. **236**, 1711 (1961).
2. Y. NOZAKI and C. TANFORD. J. Biol. Chem. (*a*) **238**, 4074 (1963); (*b*) **240**, 3568 (1965); (*c*) **246**, 2211 (1971).
3. M. L. SCHOLANSKI, F. GASKIN, and C. R. CANTOR. Proc. Natl. Acad. Sci. U.S., **70**, 765 (1973).
4. T. S. LAKSHMI and P. K. NANDI. J. Phys. Chem. **80**, 249 (1976).
5. J. F. BACK, D. DAKENFULL, and M. B. SMITH. Biochemistry, **18**, 5191 (1979).
6. H. UEDAIRA and H. UEDAIRA. Bull. Chem. Soc. Jpn. **53**, 2451 (1980).
7. K. GEKKO and S. N. TIMASHEFF. Biochemistry, (*a*) **20**, 4667 (1980); (*b*) **20**, 4677 (1981).
8. K. GEKKO and T. MORIKAWA. J. Biochem. **90**, 39 (1981).

Can. J. Chem. Downloaded from www.nrcresearchpress.com by 176.9.209.113 on 09/07/12
For personal use only.

9. H. SCHONERT and LEO. STROTH. Biopolymers, **20**, 817 (1981).
10. K. GEKKO. J. Biochem. **90**, 1633 (1981).
11. I. N. BASUMALLICK and K. K. KUNDU. (*a*) Can. J. Chem. **57**, 961 (1979); (*b*) Ind. J. Chem. **18**A, 1 (1979).
12. J. DATTA and K. K. KUNDU. (*a*) J. Phys. Chem. **86**, 4055 (1982); (*b*) Can. J. Chem. **61**, 625 (1983).
13. S. P. RUDRA, H. TALUKDAR, B. P. CHAKRAVARTY, and K. K. KUNDU. Can. J. Chem. (*a*) **64**, 1960 (1986); (*b*) **65**, 2595 (1987).
14. S. H. SPINK and M. AUKER. J. Phys. Chem. **74**, 1742 (1970).
15. G. C. KRESHECK and L. BENJAMIN. J. Phys. Chem. **68**, 2476 (1964).
16. K. P. PRASAD and J. C. AHLUWALIA. Biopolymers, **19**, 273 (1980).
17. K. GEKKO. J. Biochem. **90**, 1643 (1981).
18. J. W. LARSON, W. J. PLYMALE, and A. F. JOSEPH. J. Phys. Chem. **81**, 2074 (1977).
19. (*a*) B. P. KELLEY and T. H. LILLEY. J. Chem. Soc. Faraday Trans. I, **74**, 2771 (1978); **74**, 2779 (1978); (*b*) T. H. LILLEY, P. MOSES, and I. R. TASKER. J. Chem. Soc. Faraday Trans. I, **76**, 906 (1980); (*c*) B. P. KELLEY and T. H. LILLEY. J. Chem. Thermodyn. **11**, 513 (1979); (*d*) T. H. LILLEY and I. R. TASKER. J. Chem. Soc. Faraday Trans. I, **78**, 1 (1982).
20. K. K. KUNDU and K. MAZUMDER. J. Chem. Soc. Faraday Trans. I, **69**, 806 (1973).
21. K. DAS, A. K. DAS, K. BOSE, and K. K. KUNDU. J. Phys. Chem. **82**, 1342 (1978).
22. G. AKERLOF. J. Am. Chem. Soc. **54**, 4125 (1932).
23. M. H. ABRAHAM and A. NASAHZADEH. Can. J. Chem. **57**, 2004 (1979).
24. (*a*) C. TREINER, P. TZIAS, and M. CHEMLA. J. Chem. Soc. Faraday Trans. I, **72**, 2007 (1976); (*b*) C. TREINER. Can. J. Chem. **55**, 682 (1977).
25. N. DESROSIERS and J. E. DESNOYERS. Can. J. Chem. **54**, 3800 (1976).
26. S. P. RUDRA, B. P. CHAKRABORTY, K. K. KUNDU, and I. N. BASUMALLICK. Z. Phys. Chem. **150**, 211 (1986).
27. R. A. PIEROTTI. J. Phys. Chem. **67**, 1840 (1963); **69**, 281 (1965); Chem. Rev. **76**, 717 (1976).
28. J. G. KIRKWOOD. Chem. Rev. **24**, 233 (1939).
29. E. J. COHN, T. L. MCMEEKIN, J. T. EDSALL, and M. H. BLANCHARD. J. Am. Chem. Soc. **56**, 784 (1934).
30. N. MOREL-DESROISERS and J. P. MOREL. Can. J. Chem. **59**, 1 (1981).
31. U. SEN. (*a*) J. Am. Chem. Soc. **101**, 2531 (1979); **102**, 2161 (1960); (*b*) J. Chem. Soc. Faraday Trans. I, **77**, 2883 (1981).
32. R. C. WEAST (*Editor*). Handbook of chemistry and physics. 52nd ed. 1971–1972.
33. E. J. COHN and J. T. EDSALL. Proteins, amino acids and peptides as ions and dipolarions. Reinhold, NY. 1943. p. 275.
34. R. BHAT and J. C. AHLUWALIA. J. Phys. Chem. **89**, 1099 (1985).
35. S. CABANI, G. CONTI, E. METTEOLI, and M. R. TINE. J. Chem. Soc. Faraday Trans. I, **77**, 2377 (1981); **77**, 2385 (1981).
36. A. K. DAS and K. K. KUNDU. J. Phys. Chem. **79**, 2604 (1975) and relevant references therein.
37. R. H. STOKES. Aust. J. Chem. **20**, 2087 (1967).
38. R. L. VOLD, E. S. DANIEL, and S. O. OWEN. J. Am. Chem. Soc. **92**, 6771 (1970).
39. S. P. RUDRA, H. TALUKDAR, and K. K. KUNDU. Can. J. Chem. **66**, 000 (1988).
40. M. KAMINSKI. Discuss. Faraday Soc. **24**, 171 (1957).
41. J. B. DALTON and C. L. A. SCHMIDT. J. Biol. Chem. **103**, 549 (1933).
42. J. P. GREENSTEIN and M. WINITZ. Chemistry of the amino acids. Vol. 1. 1961. p. 547.
43. E. J. COHN, T. L. MCMEEKIN, J. T. EDSALL, and J. H. WEARE. J. Am. Chem. Soc. **56**, 2270 (1934); T. L. MCMEEKIN, E. J. COHN, and J. H. WEARE. J. Am. Chem. Soc. **58**, 2173 (1936).

Can. J. Chem. Downloaded from www.nrcresearchpress.com by 176.9.209.113 on 09/07/12
For personal use only.

Ion–ion–solvent interactions in aqueous ionic cosolvent systems. IV. Transfer energetics of water, *p*-nitroaniline, and benzoic acid from emf/solubility measurements at different temperatures in aqueous sodium nitrate solvent system

SIBAPRASAD RUDRA, HIMANSU TALUKDAR, AND KIRON K. KUNDU[1]
Physical Chemistry Laboratories, Jadavpur University, Calcutta – 700 032, India

Received May 21, 1987

SIBAPRASAD RUDRA, HIMANSU TALUKDAR, and KIRON K. KUNDU. Can. J. Chem. **66**, 469 (1988).

Autoionization constants (K_s) of aqueous mixtures of 1, 2, and 4 *m* sodium nitrate used as an ionic cosolvent system have been determined from emf measurements of the cell: Pt, H_2 (g, 1 atm) / KOH (m_1) KCl (m_2), solvent / AgCl–Ag at five equidistant temperatures ranging from 15–35°C. The standard free energies (ΔG^0) and entropies (ΔS^0) of autoionisation of the solvents were then evaluated from these data. Relative free energies (ΔG^0) and entropies (ΔS^0) of autoionization of the solvents when coupled with the previously determined transfer free energies [$\Delta G_t^0(H^+)$] and entropies [$\Delta S_t^0(H^+)$] of H^+ yielded $\Delta G_t^0(OH)_{app}$ [$= \Delta G_t^0(OH^-) - \Delta G_t^0(H_2O)$], $\Delta S_t^0(OH^-)$, and $\Delta S_t^0(H_2O)$. Values of $\Delta G_t^0(H^+)$ and $\Delta G_t^0(OH^-)$ obtained after correcting for $\Delta G_t^0(H_2O)$, as well as $\Delta G_{t,tr.int}^0(H^+)$ and $\Delta G_{t,tr.int}^0(OH^-)$ obtained after correcting the "cavity effect" and Born-type electrostatic effect suggests that while the "basicity" of the aqueous $NaNO_3$ solutions decreases, the "acidity" more or less increases with $NaNO_3$ concentration. The observed $\Delta S_{t,tr.int}^0(OH^-)$– and $\Delta S_{t,tr.int}^0(H_2O)$–composition profiles were also examined in the light of Kundu *et al.*'s four-step transfer process and the involved order–disorder phenomena, respectively, as proposed earlier.

Standard free energies (ΔG_t^0) and entropies (ΔS_t^0) of transfer of *p*-nitroaniline (*p*NA) and benzoic acid (HBz) for the solvent system have also been determined from solubility measurements at different temperatures. The observed ΔG_t^0– and $\Delta G_{t,tr.int}^0$–composition profiles appear to reflect the salting-out effect of the salt and the ΔS_t^0– and $\Delta S_{t,tr.int}^0$–composition profiles confirm the applicability of either of these quantities rather than $\Delta S_{t,tr.int}^0(HX)$, as a better structural probe both for aquo-ionic and aquo-organic solvents.

SIBAPRASAD RUDRA, HIMANSU TALUKDAR et KIRON K. KUNDU. Can. J. Chem. **66**, 469 (1988).

Utilisant des mesures de f.e.m. de la cellule : Pt, H_2 (g, 1 atm) / KOH (m_1) KCl (m_2) solvant / AgCl–Ag, effectuées à cinq températures équidistantes de 15 à 25°C, on a déterminé les constantes d'auto-ionisation (K_s) de mélanges aqueux de nitrate de sodium 1, 2 et 4 *m* utilisés comme système de cosolvant ionique. On a évalué les énergies libres standard (ΔG^0) et les entropies (ΔS^0) des solvants à partir de ces données. Lorsqu'on a utilisé les énergies libres (ΔG^0) et les entropies (ΔS^0) relatives d'auto-ionisation de concert avec les énergies libres [$\Delta G_t^0(H^+)$] et les entropies [$\Delta S_t^0(H^+)$] de transfert des H^+ qui ont été déterminées antérieurement, on a pu en tirer le $\Delta G_t^0(OH^-)_{app}$ [$\Delta G_t^0(OH^-) - \Delta G_t^0(H_2O)$], le $\Delta S_t^0(OH^-)$ et le $\Delta S_t^0(H_2O)$. On a obtenu les valeurs de $\Delta G_t^0(H^+)$ et de $\Delta G_t^0(OH^-)$ après avoir fait des corrections pour le $\Delta G_t^0(H_2O)$ et on a obtenu les valeurs de $\Delta G_{t,tr.int}^0(H^+)$ et de $\Delta G_{t,tr.int}^0(OH^-)$ après avoir fait des corrections pour l'effet de cavité et pour l'effet électrostatique du type de Born; les valeurs ainsi obtenues suggèrent que pendant que la basicité de solutions aqueuses de $NaNO_3$ diminue, l'acide augmente plus ou moins avec une augmentation de la composition en $NaNO_3$. On a aussi examiné les profils observés pour les valeurs de $\Delta S_{t,tr.int}^0(OH^-)$ et de $\Delta S_{t,tr.int}^0(H_2O)$ en fonction de la composition à la lumière du processus de transfert en quatre étapes et des phénomènes d'ordre et de désordre impliqués qui ont été proposés antiéreurement par Kundu et ses collaborateurs.

En se basant sur des mesures de solubilité à diverses températures, on a aussi déterminé les énergies libres standards (ΔG_t^0) et des entropies (ΔS_t^0) de transfert de la *p*-nitroaniline (*p*NA) et de l'acide benzoïque (HBz) pour le système de solvant. Les profils observés pour le ΔG_t^0 et le $\Delta G_{t,tr.int}^0$ en fonction de la composition semblent refléter un effet de salage du sel et les profils observés pour le ΔS_t^0 et le $\Delta S_{t,tr.int}^0$ en fonction de la composition confirment la possibilité d'utiliser chacune de ces quantités, plutôt que le $\Delta S_{t,tr.int}^0(HX)$, comme une meilleure sonde de structure tant pour les solvants aquo-ioniques qu'aquo-organiques.

[Traduit par la revue]

Introduction

In our previous papers (1–3) we have reported the thermodynamics of HX, X = Cl (1), Br, and I (3), and also the transfer energetics of some electrolytes and the related "ion–ion–solvent" interactions (2) in aqueous solutions of 1, 2, and 4 *m* $NaNO_3$ taking each composition as an individual solvent and taking the infinitely dilute solution of solutes in each solvent as the standard state as in aquo-organic solvent systems.

Since autoionization constants of water in aquo-organic solvents reflect acidity and basicity of the solvents, it would be of particular interest to evaluate the same for this solvent system as well. Moreover, it is now increasingly recognised that thermodynamics of autoionization of water and the transfer energetics of various non-electrolytes including water, provide useful information regarding the three dimensional (3D) "structuredness" of the solvent (4–13). The basis of structural reflections obtainable from entropies of autoionization of water stems from the fact that while the ionization of water accompanying the formation of order-producing H_3O^+ and OH^- ions imparts negative magnitudes to $T\Delta S^0$ (ΔS^0 = entropy of ionization), the required configurational changes including depolymerization of the three dimensional (3D) ice-like structures prior to self-ionization contribute positively to $T\Delta S^0$ (5). Recent studies on $\Delta S_t^0(H_2O)$ as obtained by dissecting from the entropies of autoionization of aqueous mixtures of some aprotic solvents like tetrahydrofuran (THF), dioxane (D), and dimethoxyethane (DME) (5*d*) and quasi-aprotic solvent like 2-methoxy ethanol (5*e*) have offered important reflections about the 3D structuredness of these solvent systems.

Similarly, although there are large number of studies (14–17) on salting-out and salting-in phenomena of various solutes, including benzoic acid (HBz) and *p*-nitroaniline (*p*NA), in various salt solutions and various theories have been proposed to explain the phenomena, so far very few attempts (11, 18, 19)

[1]Author to whom all correspondence should be addressed.

Can. J. Chem. Downloaded from www.nrcresearchpress.com by 176.9.209.113 on 09/07/12
For personal use only.

Can. J. Chem. Downloaded from www.nrcresearchpress.com by 176.9.209.113 on 09/07/12
For personal use only.

have been made to study the temperature effects and the related structural changes of the solvent. However, in a series of papers Kundu and co-workers (8, 9) have recently demonstrated that ΔS_t^0 and particularly $\Delta S_{t,int}^0$ of *p*NA and HBz obtained by subtracting the cavity effect $\Delta S_{t,cav}^0$ (20) from ΔS_t^0 values, throw important suggestions on the structuredness of the aquo-organic solvents, as they are free from the "electrostatic" effect which confuses the structural content of ΔS_t^0 data of HX type of electrolytes (1–3, 8, 9).

Therefore, as a part of our comprehensive studies and to better understand the structural aspects of the aqueous $NaNO_3$ solvent system, we report the transfer energetics (ΔG_t^0 and $T\Delta S_t^0$) of some non-electrolytes like water, *p*NA, and HBz as obtained from autoionization of water from emf measurements and solubility measurements of *p*NA and HBz at different temperatures. This study will help us see the solvent acidity or basicity and the solvent structuredness from a new angle.

As in previous papers (5, 6, 21), the thermodynamics of autoionization in 1, 2, and 4 *m* aqueous $NaNO_3$ solutions have been evaluated from the autoionization constants (K_s) determined by measuring the emf's (E) of cell [A]

[A] Pt, H_2 (g, 1 atm) / KOH (m_1), KCl (m_2), solvent / AgCl–Ag

at five equidistant temperatures ranging from 15–35°C. The transfer energetics of the non-electrolytes *p*NA and HBz have been determined by measuring the solubilities of the solutes at five different temperatures.

Experimental

Sodium nitrate used was of AR quality. The preparation of $NaNO_3$ solutions has been described earlier (1). KCl (Merck, GR) was used after drying at 200°C and cooling in a vacuum desiccator. Stock KOH solutions were prepared by adding carbonate-free KOH (Merck, GR) to weighed amounts of solvent and the molalities were determined by titrations using phenolpthalein as indicator. The preparation of the cell solutions was essentially similar to that described earlier (22). Adequate care was taken to avoid exposing the solutions to atmosphere by using a chamber flushed with N_2. General experimental procedures, including the preparation of the electrodes and measurements of emf, were similar to those described earlier (5, 21, 22). The equilibrium was attained in about 3–4 h. When the emf readings became constant to about ±0.1 mV for 1 h the reaction was considered to be in equilibrium. Readings at 15°C were taken first and then at successively higher temperatures. Readings at lower temperatures, when checked, were found to agree within the experimental error of ±0.3 mV. The alkali concentrations were often checked after the experiments and no significant changes were detected.

The method for measuring the solubility of *p*NA in this solvent system was essentially similar to that described earlier (8*a*). The saturated solutions were diluted with triple distilled water as required. Absorbance values of these solutions were determined at 380 nm using the Perkin Elmer (model 200) spectrophotometer. As before (8*a*), the molar extinction coefficient of *p*NA in the diluted solutions was taken to be equal to that in pure water, viz. 1.28×10^4, as the diluted solutions are practically aqueous bereft of the effect of the "cosolvent" present. Saturation at a given temperature was attained in all the solvents within 3–4 days. The maximum uncertainties in the measured solubilities are about ±1%. HBz (E. Merck, GR) was used after similar pretreatment as described earlier (8*b*). The method adopted for the measurement of the saturated solubility of HBz in all solvents at each temperature was also exactly similar to that described earlier (8*b*). Attainment of saturation usually took 3–4 days in this solvent system. The average uncertainties involved in the measured solubilities for the solute as well are about 1%.

Results

The emf data of the cell [A] (corrected for P_{H_2} = 1 atm) at different temepratures and the corresponding molalities of KOH and KCl for each of the solvent compositions are given in Table 1. The pK_s values (molal scale) in these ionic solvents were obtained by extrapolating the observed linear plots of pK_s' values defined by eq. [1]

$$[1] \quad pK_s' = \frac{F[E^0 - (E_m^0)_{Ag-AgCl}]}{2.303RT} + \log \frac{m_{Cl^-}}{m_{OH^-}}$$

$$= pK_s - \log \frac{a_{H_2O}\gamma_{Cl^-}}{\gamma_{OH^-}} = pK_s + f(\mu)$$

against the "ionic strength" μ to $\mu = 0$. Here a, m, and γ denote the activity, molality, and molal activity coefficient of the species in subscripts. As in aquo-organic solvents (5, 21) and as discussed in our previous paper (1) the standard state in this solvent system is so chosen that at infinite dilution in any composition of $NaNO_3$ $\gamma_{Cl^-} = \gamma_{OH^-} = a_{H_2O} = 1$. Also, the "ionic strength" refers to that caused by the added KOH and KCl only to the respective compositions of $NaNO_3$ solutions. The required values of E_m^0 of the Ag–AgCl electrode in the solvents were obtained from our earlier paper (1). The pK_s values at different temperatures for all the mixed solvents are listed in Table 2. The average standard deviation in pK_s values is of the order of ±0.005.

TABLE 1. Emf values (in V) of cell A at various temperatures for different cell solutions in $NaNO_3$ + water mixtures

m_{KOH}	m_{KCl}	Emf at 15°C	20°C	25°C	30°C	35°C
		1 *m* $NaNO_3$				
0.0034	0.0068	1.0236	1.0233	1.0230	1.0231	1.0230
0.0068	0.0135	1.0242	1.0243	1.0244	1.0243	1.0244
0.0137	0.0271	1.0265	1.0264	1.0262	1.0262	1.0260
0.0206	0.0407	1.0280	1.0282	1.0285	1.0289	1.0294
0.0274	0.0542	1.0285	1.0289	1.0293	1.0296	1.0299
0.0342	0.0677	1.0299	1.0304	1.0312	1.0315	1.0315
		2 *m* $NaNO_3$				
0.0048	0.0053	1.0397	1.0406	1.0414	1.0419	1.0422
0.0096	0.0105	1.0400	1.0411	1.0421	1.0427	1.0431
0.0188	0.0221	1.0394	1.0400	1.0406	1.0411	1.0416
0.0281	0.0330	1.0405	1.0412	1.0419	1.0423	1.0426
0.0382	0.0417	1.0441	1.0447	1.0452	1.0456	1.0460
0.0477	0.0521	1.0447	1.0454	1.0459	1.0462	1.0463
		4 *m* $NaNO_3$				
0.0041	0.0060	1.0317	1.0319	1.0322	1.0324	1.0326
0.0081	0.0120	1.0325	1.0327	1.0329	1.0333	1.0333
0.0162	0.0240	1.0330	1.0336	1.0341	1.0343	1.0344
0.0242	0.0358	1.0388	1.0341	1.0344	1.0346	1.0345
0.0322	0.0476	1.0346	1.0349	1.0352	1.0352	1.0252
0.0403	0.0596	1.0358	1.0360	1.0363	1.0362	1.0357

TABLE 2. pK_s values (molal scale) for the autoionization of $NaNO_3$ + water mixtures at different temperatures

Molality of $NaNO_3$	pK_s values at 15°C	20°C	25°C	30°C	35°C
0.0[a]	14.35	14.17	14.00	13.83	13.68
1.0	13.99	13.78	13.58	13.41	13.23
2.0	14.17	14.01	13.87	13.69	13.51
4.0	14.51	14.33	14.16	13.99	13.83

[a]Reference 35.

TABLE 3. Coefficients in eq. [3] and the values of ΔG^0, $T\Delta S^0$, $\delta(\Delta G^0_N)$, and $T\delta(\Delta S^0_N)$ (mole fraction scale) at 25°C for the auto-ionization of aqueous mixtures of $NaNO_3$

Molality of $NaNO_3$	A/K	B	$C = 10^2/K^{-1}$	ΔG^0_N/kJ	$T\Delta S^0_N$/kJ	$\delta(\Delta G^0_N)$/kJ	$T\delta(\Delta S^0_N)$/kJ
0.0	4615.68	−7.05	1.87	99.86	−43.24	—	—
1.0	6779.19	−20.64	3.85	97.20	−32.95	−2.66	10.29
2.0	−7593.64	74.64	−11.83	98.52	−42.54	−1.34	0.70
4.0	3026.29	3.99	0.007	99.68	−41.84	−0.18	1.40

TABLE 4. Solubilities (S) of pNA and HBz in H_2O and in aqueous $NaNO_3$ solvents at different temperatures

Molality of $NaNO_3$	S for HBz (mol kg^{-1})					S for pNA (mol dm^{-3}) × 10^3				
	15°C	20°C	25°C	30°C	35°C	15°C	20°C	25°C	30°C	35°C
0.0	0.0198[a] 0.0187[b]	0.0237[a] 0.0225[b]	0.0281[a] 0.0268[b]	0.0336[a] 0.0322[b]	0.0388[a] 0.0373[b]	2.88[c]	3.52[c]	4.36[c]	5.42[c]	6.89[c]
1.0	0.0178	0.0204	0.0224	0.0275	0.0316	3.54	4.17	4.77	5.89	7.05
2.0	0.0141	0.0166	0.0186	0.0219	0.0251	3.09	3.80	4.62	5.62	6.80
4.0	0.00832	0.0102	0.0121	0.0141	0.0159	2.98	3.47	3.96	4.90	5.76

[a]Reference 8*b*.
[b]After correcting the degree of dissociation of the acid.
[c]Reference 8*a*.

The pK_s values at different temperatures were as before (5) fitted to the Harned–Robinson expression [2] (23)

[2] $pK_s = A/T + B + CT$

by the method of least squares. The values of the coefficients A, B, and C for the solvents are given in Table 3. The thermodynamic quantities, namely, ΔG^0, ΔS^0, and ΔH^0 accompanying the autoionization of 1 mole of water at each solvent composition, were evaluated at 25°C by using the standard relations (24) comprising the coefficients in eq. [2]. The values of ΔG^0 and ΔS^0 so obtained on molal scale (m) were then converted to mole fraction scale (N) using the usual relations (5, 24) and are listed in Table 3.

The solubilities of HBz in mol kg^{-1} and pNA in molarity in different solvent compositions as well as in pure water (9) are given in Table 4. Just as in aqueous organic solvents (8*b*, 9*b*) and salt solutions (9*b*, 11) of lower dielectric constant than water, the degrees of ionization (α_s) of HBz in these salt solutions are also tentatively taken to be negligibly small as the dielectric constant decreases with increasing salt concentration (1) owing to the well known "dielectric decrement effect" (16, 25). Notably, a tentative estimate of α_s values of HBz at 25°C in the saturated solutions of 1, 2, and 4 m $NaNO_3$, based on simple Born equation (26), leads to a percent error of 2.5, 1.2, and 0.3, respectively. For water, however, the observed solubilities were corrected for the ionization of the acid (24) to give the concentrations of the uncharged acid and are listed in Table 4.

As in previous papers (8, 9), assuming the effect of activity coefficient factor to be negligibly small, the free energies of solutions ΔG^0_s on the molar scale in the case of pNA and on the molal scale in the case of HBz were calculated for each solvent composition using eq. [3]

[3] $\Delta G^0_s = -RT \ln S$

These were then fitted by the method of least squares to an equation of the form [4]

[4] $\Delta G^0_s = a + bT + cT \ln T$

where T is the absolute temperature. The values of the coefficients a, b, and c are listed in Table 5. The standard free energies and entropies of transfer, ΔG^0_t and ΔS^0_t, of both HBz and pNA from water to the mixed solvents were computed at 25°C on mole fraction scale using the formulations described in the previous paper (2). ΔG^0_t and ΔS^0_t values thus computed are given in Table 5. The maximum uncertainties in ΔG^0_t and ΔS^0_t are ±0.03 kJ mol^{-1} and ±2 J K^{-1} mol^{-1}, respectively.

Discussion

Autoionization and transfer free energies

The standard free energy changes accompanying the autoprotolytic reaction in the salt solutions ${}_s\Delta G^0_N$ relative to that in pure water ${}_w\Delta G^0_N$, $\delta(\Delta G^0_N)$ have been computed on the mole fraction scale using the usual relation as described in our previous papers (5*d*, *e*). The values of $\delta(\Delta G^0_N)$ thus obtained are listed in Table 3.

Figure 1 illustrates the variations of $\delta(\Delta G^0_N)$ values with the molality of $NaNO_3$. $\delta(\Delta G^0_N)$ values for this solvent system are found to pass through a minimum around 1.5 m $NaNO_3$ possibly indicating the opposing effects of dielectric constant as well as the acidity and basicity of the salt solutions (5*a*). As indicated in previous papers (5, 22), the quantity of $\delta(\Delta G^0_N)$ is given by

[5] $\delta(\Delta G^0_N) = \Delta G^0_t(H^+) + \Delta G^0_t(OH^-)_{app}$

where $\Delta G^0_t(H^+)$ stands for the transfer free energy of H^+ and gives a thermodynamic measure of the basicity of the salt solutions relative to that of water, and $\Delta G^0_t(OH^-)_{app}$ denotes the transfer free energy change accompanying the process [6]

[6] $OH^-(w) + H_2O(s) \rightleftharpoons OH^-(s) + H_2O(w)$

which gives the corresponding measures for the relative acidity of the salt solutions. Consequently, dissection of $\delta(\Delta G^0_N)$ to $\Delta G^0_t(H^+)$ and $\Delta G^0_t(OH^-)_{app}$ should be useful.

As indicated earlier (5), if the activity of water $(a_{H_2O})^s_w$ be referred to that in pure water $(a_{H_2O})^w_w$ as unity, then $-RT \ln (a_{H_2O})^s_w$ would give a measure of $\Delta G^0_t(H_2O)$ which when added to $\Delta G^0_t(OH^-)_{app}$ gives $\Delta G^0_t(OH^-)$, the standard

Can. J. Chem. Downloaded from www.nrcresearchpress.com by 176.9.209.113 on 09/07/12
For personal use only.

Can. J. Chem. Downloaded from www.nrcresearchpress.com by 176.9.209.113 on 09/07/12
For personal use only.

TABLE 5. Coefficient a, b, c of eq. [7] for HBz and pNA in H_2O and in aqueous $NaNO_3$ solvents and transfer energetics (ΔG_t^0 and $T\Delta S_t^0$) of the solutes from water to aqueous $NaNO_3$ solvents at 25°C (mole fraction scale)

Molality of $NaNO_3$	HBz					pNA				
	a/kJ mol^{-1}	b/kJ mol^{-1} K^{-1}	c/kJ mol^{-1} K^{-1}	ΔG_t^0/kJ	$T\Delta S_t^0$/kJ	a/kJ mol^{-1}	b/kJ mol^{-1} K^{-1}	c/kJ mol^{-1} K^{-1}	ΔG_t^0/kJ	$T\Delta S_t^0$/kJ
0.0	91.2766	−1.5268	0.2195	—	—	−149.1743	4.0091	−0.6079	—	—
1.0	−165.8637	4.1686	−0.6285	0.25	−4.56	−170.5343	4.3646	−0.6579	−0.33	−5.98
2.0	−21.6993	0.9240	−0.1436	0.62	−5.34	0.0494	0.5966	−0.0969	−0.23	−2.69
4.0	208.1457	−4.1856	0.6185	1.38	−3.48	−111.2730	3.0213	−0.4567	0.10	−7.03

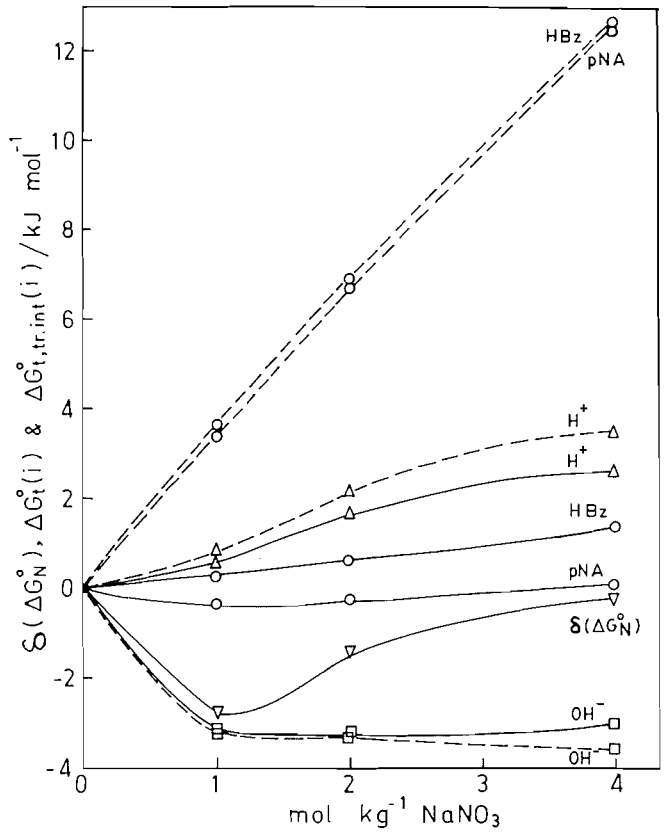

FIG. 1. Variation of $\delta(\Delta G_N^0)$ and ΔG_t^0 of H^+, OH^-, pNA, and HBz (solid lines) and $\Delta G_{t,tr.int}^0$ of H^+, OH^-, pNA, and HBz (dotted lines) in aqueous $NaNO_3$ solvents at 25°C.

free energy change accompanying the transfer of OH^-, alone from water to the mixed solvents.

Utilizing the $\Delta G_t^0(H^+)$ values based on the widely used reference electrolyte assumption (27) but duly modified for the solvent system as reported earlier (2), we have evaluated $\Delta G_t^0(OH^-)_{app}$ and then $\Delta G_t^0(OH^-)$ using $(a_{H_2O})_w^s$ from osmotic coefficient data given in the literature (25) for this solvent system. The values of $\Delta G_t^0(H^+)$ and $\Delta G_t^0(OH^-)_{app}$ and also $\Delta G_t^0(OH^-)$ are given in Table 6. Moreover, as per discussion and formulations given in the preceeding papers (1–3) we have also computed $\Delta G_{t,cav}^0$ and $\Delta G_{t,Born}^0$ for these ions using the scaled particle theory (SPT) (20) and the widely used simple Born equation (26), respectively. These values, when subtracted from $\Delta G_t^0(i)$, values yielded $\Delta G_{t,tr.int}^0(i)$ and are given in Table 6. The values of $\Delta G_t^0(i)$ and $\Delta G_{t,tr.int}^0(i)$ for H^+ and OH^- are plotted against the cosolvent compositions in Fig. 1.

Notably, there are little differences between $\Delta G_t^0(i)$– and $\Delta G_{t,tr.int}^0(i)$–composition profiles of H^+ and OH^- in the solvent system. From Fig. 1 it is observed that while $\Delta G_{t,tr.int}^0(H^+)$ becomes increasingly positive at initial composition, the corresponding values for $\Delta G_{t,tr.int}^0(OH^-)$ are increasingly negative. This implies that the basicity of the salt solutions decreases and the acidity increases with the increased proportion of the cosolvents. The observed decreased basicity or the increased destabilization of H^+ has already been explained in our previous papers (1–3). The increased acidity or the pronounced stabilization of OH^-, as explained earlier in the case of Cl^- (1), is the resultant effect of increasingly larger attractive interaction of OH^- with $(Na^+)_{aq}$ overcoming the weaker repulsive interactions between OH^- and NO_3^-, which are likely to exceed

Can. J. Chem. Downloaded from www.nrcresearchpress.com by 176.9.209.113 on 09/07/12
For personal use only.

TABLE 6. Free energies and enthalpies of cavity formation ($\bar{G}_c$) and ($\bar{H}_c$) and standard free energies of transfer $\Delta G^0_t(i)$, $\Delta G^0_{t,cav}(i)$, $\Delta G^0_{t,Born}(i)$, $\Delta G^0_{t,tr.int}(i)$ and entropies of transfer $T\Delta S^0_t(i)$, $T\Delta S^0_{t,cav}(i)$, $T\Delta S^0_{t,Born}(i)$, and $T\Delta S^0_{t,tr.int}(i)$ (mole fraction scale) in kJ mol^{-1} of H^+, OH^-, H_2O, *p*NA, HBz from water to aqueous $NaNO_3$ solvents at 25°C

Ions/ salts	$\bar{G}_c$[a]		$\bar{H}_c$[a]		$\Delta G^0_t(i)$	$\Delta G^0_{t,cav}(i)$[a]	$\Delta G^0_{t,Born}(i)$[b]	$\Delta G^0_{t,tr.int}(i)$	$T\Delta S^0_t(i)$	$T\Delta S^0_{t,cav}(i)$[a]	$T\Delta S^0_{t,Born}(i)$[b]	$T\Delta S^0_{t,tr.int}(i)$
	Water	Solvent	Water	Solvent								
							1 *m* $NaNO_3$					
H^+	13.5	12.8	1.8	3.1	0.6	−0.7	0.5	0.8	42.3	2.0	−0.6	40.9
OH^-	16.3	15.5	2.2	3.7	−3.3	−0.8	0.8	−3.3	−37.4	2.4	−1.0	−38.8
					−3.2[c]							
H_2O	13.5	12.8	1.8	3.1	−0.1[d]	−0.7	—	—	−5.4	2.0	—	−7.4
*p*NA	67.2	63.5	9.7	16.4	−0.3	−3.7	—	3.4	−6.0	10.4	—	−16.4
HBz	62.2	58.8	9.0	15.2	0.3	−3.4	—	3.7	−4.6	9.6	—	−14.2
							2 *m* $NaNO_3$					
H^+		12.1		3.6	1.7	−1.5	1.0	2.2	20.5	3.3	−1.5	18.7
OH^-		14.7		4.5	−3.2	−1.7	1.7	−3.2	−17.6	4.0	−2.7	−18.9
					−3.1[c]							
H_2O		12.1		3.6	−0.1[d]	−1.5	—	—	2.3	3.3	—	−1.0
*p*NA		60.3		19.9	−0.2	−7.0	—	6.8	−2.7	17.2	—	−19.9
HBz		55.9		18.4	0.6	−6.3	—	6.9	−5.3	15.7	—	−21.0
							4 *m* $NaNO_3$					
H^+		10.7		3.2	2.6	−2.9	2.0	3.5	−0.1	4.3	−7.7	3.3
OH^-		13.5		4.1	−3.0	−2.9	3.5	−3.6	1.0	4.8	−13.6	9.8
					−2.8[c]							
H_2O		10.7		3.2	−0.2[d]	−2.9	—	—	−0.6	4.3	—	−4.9
*p*NA		54.9		18.1	0.1	−12.4	—	12.5	−7.0	20.8	—	−27.8
HBz		50.9		16.7	1.4	−11.3	—	12.7	−3.5	19.0	—	−22.5

[a]The required diameters of the solvent constituents and the values of the scale effect $RT \ln V_w/V_s$ are taken from ref. 1 and $\alpha = -d \ln d_s/dT$ also taken from ref. 1. For the solute species: $b_{H_3O^+} = 0.276$ nm (1), $b_{OH^-} = 0.312$ nm (5*d*, 34), $b_{H_2O} = 0.276$ nm (1), $b_{HBz} = 0.690$ nm (9*b*), $b_{pNA} = 0.720$ nm (9*a*).

[b]The required radii of the ionic species are obtained from the corresponding diameters of the species as indicated in *a* and that of H^+ as equal to 0.276 nm (1).

[c]The values of $\Delta G^0_t(OH^-)_{app}$.

[d]The values of $\Delta G^0_t(H_2O)$ being equated to $-RT \ln ({}^aH_2O)^s_w$ and computed from the relevant osmotic coefficient data (25).

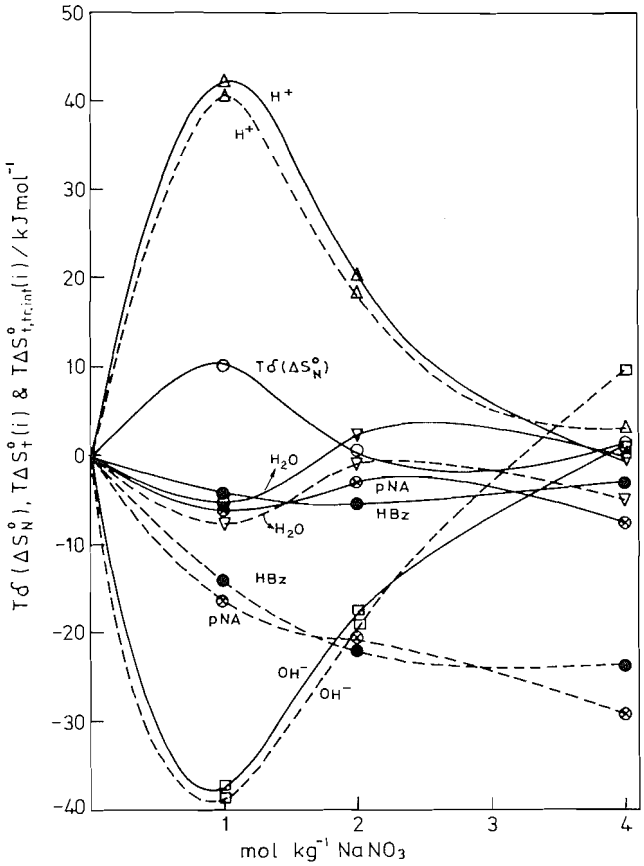

FIG. 2. Variation of $T\delta(\Delta S_N^0)$ and $T\Delta S_t^0$ of H_2O, H^+, OH^-, *p*NA, and HBz (solid lines) and $T\Delta S_{t,tr.int}^0$ of H_2O, H^+, OH^-, *p*NA, and HBz (dotted lines) in aqueous $NaNO_3$ solvents at 25°C.

the OH^-–H_2O interaction in pure water. Notably, the less pronounced destabilization of H^+ and stabilization of OH^- beyond 1.5 *m* $NaNO_3$ indicate the effect of solvent-separated ion pairs $(Na^+)_{aq}NO_3^-$ as obtained from various spectroscopic evidences (28–30).

Figure 1 also shows the variation of ΔG_t^0 and $\Delta G_{t,tr.int}^0$ of *p*NA and HBz with molality of $NaNO_3$. Though the ΔG_t^0–composition profile of HBz is increasingly positive, that of *p*NA passes through a slight minimum. Strikingly enough, the $\Delta G_{t,tr.int}^0$–composition profiles for both *p*NA and HBz are increasingly positive. The observed increased destabilization of *p*NA and HBz with increased proportion of ionic cosolvent $NaNO_3$ seemingly reflects the expected well known "salting-out" effect (14–16). It is also significant that unlike most aquo-organic solvent systems (9), the cavity effects are increasingly negative in this solvent system and thus largely obscures the expected salting-out effect in this solvent system when not duly corrected. Admittedly, however, although there are a number of theories to explain and quantify the salting-out and salting-in phenomena of various solutes including the ones studied here, they only achieve partial success (14–17). Somehow quantification of the "true salt-effect" bereft of the involved cavity effect, being an involved problem, seems difficult at this stage. This should therefore be a matter of particular interest for a future study.

Autoionization and transfer entropies

As in aquo-organic solvents since entropy changes, rather than enthalpy changes, are better indicators of the structural implications (31), analysis of the entropy changes in the present study should be useful. The values of entropy of autoionization on the mole fraction scale, ΔS_N^0, were computed at 25°C using the usual relation given in ref. 24. The variation of $T\Delta S_N^0$ at 25°C relative to that in water $T\delta(\Delta S_N^0)$ ($\equiv T({}_s\Delta S_N^0) - {}_w\Delta S_N^0$) for these solvents are shown in Fig. 2 and the values of $T\Delta S_N^0$ are given in Table 3. Moreover, as indicated in our previous papers (5*d*, *e*), since $\delta(\Delta S_N^0)$ is given by

$$[7]\quad \delta(\Delta S_N^0) = {}_s\Delta S_N^0 - {}_w\Delta S_N^0 = \Delta S_t^0(H^+) + \Delta S_t^0(OH^-) - \Delta S_t^0(H_2O)$$

we have also computed $\Delta S_t^0(H_2O)$ values by subtracting the contribution of $[\Delta S_t^0(H^+) + \Delta S_t^0(OH^-)]$ obtained by plotting the values of $[\Delta S_t^0(H^+) + \Delta S_t^0(X^-)]$ where $X^- = Cl^-$, Br^-, and I^- for those solvent mixtures (1, 3) against $(r_{X^-})^{-1}$ and reading out the values corresponding to $(r_{OH^-})^{-1}$ where r_i is the radius of the corresponding ions (5*d*, *e*). The values of $\Delta S_t^0(H_2O)$ as obtained for the solvent system are given in Table 6 and the variation with cosolvent composition in Fig. 2. $\Delta S_t^0(OH^-)$ values obtained by subtracting the values of $\Delta S_t^0(H^+)$ from $[\Delta S_t^0(H^+) + \Delta S_t^0(OH^-)]$ are presented in Table 6 and illustrated in Fig. 2. Similarly, like the corresponding quantities of free energies of transfer discussed above, the quantities $\Delta S_{t,tr.int}^0(H^+)$ and $\Delta S_{t,tr.int}^0(OH^-)$ were also obtained using the formulations given in the previous papers (1–3) and are listed in Table 6 and illustrated in Fig. 2.

Now as can be observed from Table 6 and Fig. 2, for both H^+ and OH^- the $\Delta S_{t,cav}^0$ and $\Delta S_{t,Born}^0$ contributions more or less compensate each other, and hence the composition profiles of $T\Delta S_t^0$ and $T\Delta S_{t,tr.int}^0$ for both ions hardly differ from each other. Besides, as in the case of other anions, viz. Cl^-, Br^-, and I^- (1–3), $T\Delta S_t^0$– and $T\Delta S_{t,tr.int}^0$–composition profiles of OH^- also exhibit mirror-image behaviour of that of H^+. Thus while both profiles of H^+ pass through a distinct maximum around 1.5 *m* $NaNO_3$ both profiles of OH^- pass through a distinct minimum around that composition. The entropic behaviour of OH^- in this ionic cosolvent system seems to be more or less similar to that of other anions like Cl^-, Br^-, or I^- (1–3) and hence may be accounted for by Kundu *et al.*'s four step transfer process as described in detail in the previous papers (1–3). One may of course argue that unlike halide ions, OH^- is hydrated by three H_2O molecules (32) in pure water and therefore the entropy change in the dehydration step (step 1), ΔS_1^0, of the four step process (1–3, 33) may not be more than that of the halide ions. Since the order produced round the central water molecule in step 2, $-\Delta S_2^0$, is likely to be greater than that round the central OH^-, the value of $\Delta S_1^0 - \Delta S_2^0$ might be negative. This would then augment the negative value of $(\Delta S_3^0 - \Delta S_4^0)$ as OH^- like X^- ions (2, 3) will be interacted upon by $(Na^+)_{aq}$ involved in step 3, i.e. $\Delta S_3^0 \approx 0$ and the entropy change ΔS_4^0 involved in the step 4, accompanying the solvation of OH^- will be more negative in the lower composition of $NaNO_3$. At high composition, however, as in the case of X^- (2, 3), $(\Delta S_3^0 - \Delta S_4^0)$ will be increasingly positive as the interacting species $(Na^+)_{aq}$ will be increasingly replaced by solvent-separated ion pairs $(Na^+)_{aq}NO_3^-$ (28–30).

On the other hand, as in the cases of aqueous dioxane, dimethoxy ethane (5*d*), and 2-methoxy ethanol (5*e*), the observed composition profiles of $T\Delta S_t^0(H_2O)$ as well as $T\Delta S_{t,tr.int}^0(H_2O)$ for $NaNO_3$–water mixtures imply that addition of $NaNO_3$ initially enhances the order of free water molecules around Na^+ and NO_3^- which result from the breakdown of the

Can. J. Chem. Downloaded from www.nrcresearchpress.com by 176.9.209.113 on 09/07/12
For personal use only.

3D water structure induced by the ionic cosolvent $NaNO_3$. But as various spectroscopic evidences (20–30) indicate, after 1.5 *m* $NaNO_3$ the Na^+_{aq} and NO^-_3 are increasingly replaced by "solvent-separated ion pairs" (SSIP), the order around SSIP is likely to diminish as reflected in the observed roller coaster type behaviour of $T\Delta S^0_t(H_2O)$– and $T\Delta S^0_{t,tr.int}(H_2O)$–composition profiles.

Analysis of the observed $T\Delta S^0_t$– and $T\Delta S^0_{t,tr.int}$–composition profiles of *p*NA and HBz for this solvent system (vide Fig. 2) indicates that while the nature of $T\Delta S^0_t$–composition profile of *p*NA is fairly similar to that of H_2O that of HBz is seemingly slightly different. Notably, however, their respective behaviour is also more or less similar to that observed in aqueous LiCl and KBr solutions in the case of HBz (9*b*) and that in aqueous KBr solution in the case of *p*NA (9*a*). Significantly enough, the $T\Delta S^0_{t,tr.int}$–composition profiles also show sharp downward trend both for *p*NA and HBz right from the beginning, as has been observed for these solutes in the respective salt solution referred to above. If one uses the semiquantitative theory of Kundu *et al.*'s four-step transfer process (8, 9) for these solutes as a guide, then the observed sharply downward trend of $T\Delta S^0_{t,tr.int}$–composition profiles in $NaNO_3$ solutions is to be expected as a result of 3D structure breaking propensity of the salt as observed earlier in other salt solutions.

Thus it appears from the above results that just as in aquo-organic solvents (8, 9) $\Delta S^0_{t,tr.int}(i)$ for these non-electrolytes like HBr, *p*NA and particularly H_2O, rather than $\Delta S^0_{t,tr.int}(HX)$ (1) should be a better probe for the 3D structuredness of aqueous mixtures of ionic and non-ionic cosolvents.

Acknowledgement

Thanks are due to the University Grants Commission, Government of India, New Delhi, for the financial assistance.

1. S. P. Rudra, H. Talukdar, B. P. Chakravarty, and K. K. Kundu. Can. J. Chem. **64**, 1960 (1986).
2. S. P. Rudra, H. Talukdar, and K. K. Kundu. Can. J. Chem. **65**, 2595 (1987).
3. S. P. Rudra, H. Talukdar, and K. K. Kundu. Can. J. Chem. **65**, 2843 (1987).
4. S. Rajender and R. Lumry. Biopolymers, **9**, 1125 (1970).
5. (*a*) K. K. Kundu, P. K. Chattopadhyay, D. Jana, and M. N. Das. J. Phys. Chem. **74**, 2635 (1970); (*b*) A. K. Das and K. K. Kundu. J. Phys. Chem. **79**, 2604 (1975); (*c*) I. N. Basu Mullick and K. K. Kundu. Ind. J. Chem. **18**(A), 1 (1979); (*d*) J. Datta and K. K. Kundu. Can. J. Chem. **59**, 3141 (1981); (*e*) P. K. Guha and K. K. Kundu. Can. J. Chem. **63**, 804 (1985).
6. E. M. Wolley, D. G. Hurkot, and L. G. Hepler. J. Phys. Chem. **74**, 3908 (1970).
7. P. Friordiponti, F. Rallo, and F. Rodonte. Z. Phys. Chem. Frankfurt, **88**, 119 (1974).
8. (*a*) K. Bose and K. K. Kundu. Can. J. Chem. **55**, 3981 (1977); (*b*) K. Das, A. K. Das, K. Bose, and K. K. Kundu. J. Phys. Chem. **82**, 1242 (1978).
9. J. Datta and K. K. Kundu. (*a*) Can. J. Chem. **61**, 625 (1982); (*b*) J. Phys. Chem. **68**, 4055 (1962).
10. M. C. Perez-Camino, E. Sanchez, M. Balon, and A. Maestre. J. Chem. Soc. Faraday Trans. I, **81**, 1555 (1985).
11. P. Bhattacharya and I. N. Basu-Mullick. Ind. J. Chem. **25**A, 420 (1986).
12. B. O. Assem and A. A. El-Harakany. Elcctrochim. Acta, **30**, 367 (1985).
13. H. Chebib, C. Jambon, and J. C. Merlin. J. Chim. Phys. Phys-chim. Biol. **80**, 281 (1983).
14. F. A. Long and W. F. McDevit. Chem. Rev. **51**, 119 (1952) and references therein.
15. V. F. Sergeeva. Russ. Chem. Rev. **34**, 309 (1965) and references therein.
16. B. E. Conway. Ionic hydration in chemistry and biophysics. Elsevier Scientific Publishing Company, Amsterdam. 1981. pp. 444–465 and references therein.
17. (*a*) R. F. Cross. J. Phys. Chem. **79**, 1822 (1975); (*b*) R. F. Cross and P. T. McTigue. J. Phys. Chem. **80**, 814 (1976).
18. B. Das and R. Ghosh. J. Chem. Eng. Data, **29**, 137 (1984).
19. S. Suguman. Ind. J. Chem. **22**A, 150 (1983); **23**A, 763 (1984).
20. R. A. Pierotti. J. Phys. Chem. **67**, 1840 (1963); **69**, 281 (1965); Chem. Rev. **76**, 717 (1976).
21. A. K. Das and K. K. Kundu. J. Chem. Soc. Faraday Trans. I, **69**, 730 (1973).
22. K. Bose and K. K. Kundu. Can. J. Chem. **57**, 2470 (1979).
23. H. S. Harned and R. A. Robinson. Trans. Faraday Soc. **38**, 573 (1941).
24. H. S. Harned and B. B. Owen. Physical chemistry of electrolyte solutions. 3rd ed. Reinhold, New York. 1958.
25. R. A. Robinson and R. H. Stokes. Electrolyte solutions. 2nd ed. Butterworths, London. 1959.
26. R. G. Bates. *In* Hydrogen-bonded solvent systems. *Edited by* A. K. Covington and P. Jones. Taylor and Francis, London. 1968. p. 49.
27. B. G. Cox, G. R. Hedwig, A. J. Parker, and D. W. Watts. Aust. J. Chem. **27**, 477 (1974).
28. R. L. Frost and D. W. James. J. Chem. Soc. Faraday Trans. I, **78**, 3223 (1982).
29. D. E. Irish and A. R. Davis. Can. J. Chem. **46**, 943 (1968).
30. M. M. Vollmar. J. Chem. Phys. **39**, 2236 (1963).
31. E. M. Arnett, C. C. Bentrude, J. J. Burke, and Mc. Duggleby. J. Am. Chem. Soc. **87**, 1541 (1965); E. M. Arnett. *In* Physico-chemical process in mixed aqueous solvents. *Edited by* F. Franks. Heinemann, London. 1967. p. 105.
32. (*a*) G. Yagil and M. Anbar. J. Am. Chem. Soc. **85**, 2376 (1963); (*b*) G. Yagil. J. Phys. Chem. **7**, 1034 (1967).
33. (*a*) K. K. Kundu and K. Mazumdar. J. Chem. Soc. Faraday Trans. I, **69**, 806 (1973); (*b*) K. Bose, K. Das, A. K. Das, and K. K. Kundu. J. Chem. Soc. Faraday Trans. I, **74**, 1051 (1978).
34. D. Feakins. *In* Hydrogen-bonded solvent system. *Edited by* A. K. Covington and P. Jones. Taylor and Francis, London. 1966.
35. A. Bhattacharya, A. K. Das, and K. K. Kundu. Can. J. Chem. **59**, 1153 (1981).

Can. J. Chem. Downloaded from www.nrcresearchpress.com by 176.9.209.113 on 09/07/12
For personal use only.

Photochemistry of cyclic α-hydroxy ketones. II. The nature of the photoproducts from 8a-hydroxy-4a-methyl-*trans*- and -*cis*-octahydronaphthalen-1(2*H*)-one and an interpretation of the contrast between the photochemistry of these and of analogous steroidal α-hydroxy ketones[1]

PETER YATES AND SHIRLEY STIVER
Lash Miller Chemical Laboratories, University of Toronto, Toronto, Ont., Canada M5S 1A1

Received October 8, 1987

PETER YATES and SHIRLEY STIVER. Can. J. Chem. **66**, 476 (1988).

Photolysis of either 8a-hydroxy-4a-methyl-*trans*- or -*cis*-octahydro-naphthalen-1(2*H*)-one (**3** or **4**) in benzene gives a 96:4 mixture of the lactones, 5a-methyl-*trans*- and -*cis*-octahydro-1-benzoxepin-2(3*H*)-ones (**7** and **8**). Photolysis of **3** or **4** in ethanol gives identical mixtures of the lactones **7** and **8** and ethyl (2*S**,1*R**)- and (2*R**,1*R**)-2-hydroxy-1-methylcyclohexanebutyrates (**11** and **12**). Photolysis of the 2α-deutero derivatives of **3** or **4** in benzene gives mixtures of the 9a-, 3α-, and 3β-deutero derivatives of lactone **7**. The striking difference between these results and those for photolyses of analogous 5α- and 5β-hydroxy 6-keto steroids, which are stereospecific, is interpreted in terms of the greater flexibility in the cases of **3** and **4** of the acyl side chain in the acyl alkyl diradicals formed by α-cleavage. A further difference—the sole formation of lactones on photolysis of the steroidal α-ketols in ethanol—is interpreted in terms of an analogous increased flexibility in the cases of **3** and **4** of the ketene side chain in the hydroxy ketene intermediates formed from the acyl alkyl diradicals.

PETER YATES et SHIRLEY STIVER. Can. J. Chem. **66**, 476 (1988).

La photolyse effectuée dans le benzène de l'un ou l'autre des isomères *cis* ou *trans* de l'hydroxy-8a méthyl-4a (2*H*)-octahydro-naphtalènone-1 (**3** ou **4**) conduit à un mélange 96:4 des lactones *trans* et *cis* méthyl-5a (3*H*)-octahydro-benzoxépine-1 ones-2 (**7** et **8**). Si l'on effectue la photolyse des composés **3** ou **4** dans l'éthanol, on obtient des mélanges identiques des lactones **7** et **8** et des (2*S**,1*R**) et (2*R**,1*R**) hydroxy-2 méthyl-1 cyclohexanebutyrates d'éthyle (**11** et **12**). La photolyse des composés **3** ou **4** deutérés en position 2α, effectuée dans le benzène, conduit à des mélanges de lactone **7** deutérée en 9a, 3α et 3β. On observe une différence remarquable entre ces résultats et ceux qui ont été observés lors de la photolyse des dérivés analogues hydroxy-5α (ou -5β) céto-6 stéroïdes qui sont stéréospécifiques; on interprète ces différences en fonction d'une plus grande flexibilité, dans le cas des composés **3** et **4**, des diradicaux acyle alkyle qui se forment par le clivage-α. L'autre différence qui est observée, à savoir la formation de seulement des lactones lors de la photolyse des α-cétols dans l'éthanol, est interprétée en fonction d'une augmentation analogue de la flexibilité, dans les cas des composés **3** et **4**, de la chaîne latérale des intermédiaires hydroxy-cétènes qui se forment à partir des diradicaux acyle alkyle.

[Traduit par la revue]

Introduction

In the previous paper in this series (1) we discussed the nature and genesis of the products formed on ultraviolet irradiation of 5-hydroxy 6-keto steroids of types **1** and **2** and of related 6-keto steroids. To compare the photochemical behavior of these with that of their simplest bicyclic analogues, **3** and **4**, we have investigated the nature of the photoproducts from the latter and from their 2α-deutero derivatives, **5** and **6**.[2] We first describe the determination of the structures of these products, and then discuss the origin of the contrasting photochemical behavior of the steroidal and bicyclic α-hydroxy ketones.

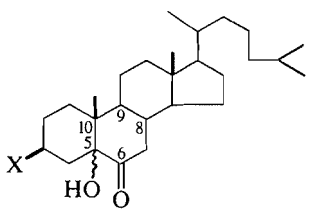

1 α-OH
2 β-OH

X = OAc, H, OBn

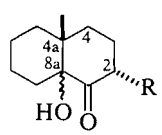

3 R = H, α-OH
4 R = H, β-OH
5 R = D, α-OH
6 R = D, β-OH

[1]For paper 1, see ref. 1; for a preliminary communication concerning part of this work, see ref. 2.

[2]The synthesis of compounds **3–6** is described in ref. 3.

Results

Photochemistry of bicyclic α-ketols

The *trans* and *cis* bicyclic α-ketols **3** and **4** were each photolyzed in benzene and in ethanol. Irradiation of **3** in benzene gave the *trans* lactone **7** as the major photoproduct, isolated in 62% yield (Scheme 1). Gas chromatographic analysis of the photolysate indicated the presence of a very small quantity of the epimeric *cis* lactone **8**. This was not isolated but was identified by the coincidence of its retention time in the gas chromatogram with that measured for an authentic sample (*vide infra*); it was present to the extent of ~4% of the *trans* lactone **7**.

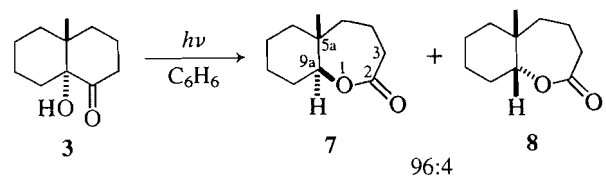

SCHEME 1

The ^{1}H nmr spectrum of the major product shows the C-9a methine proton signal as a doublet of doublets (J = 11, 5 Hz) at δ 4.13 (Table 1). The larger 11-Hz coupling constant, indicative of an axial–axial interaction (4), is consistent with the *trans* ring fusion of **7** assigned to this lactone. However, the 11-Hz coupling constant does not unambiguously establish the nature

Can. J. Chem. Downloaded from www.nrcresearchpress.com by 176.9.209.113 on 09/07/12
For personal use only.

TABLE 1. ^{1}H nuclear magnetic resonance spectral data for the *trans* lactone **7** in deuterochloroform and benzene-d_6

Assignment	δ($CDCl_3$, 400 MHz)	δ(C_6D_6, 200 MHz)	Δδ[a]
CH_3	0.93(s)	0.68(s)	−0.25
C-3α-H	2.48–2.56 (m, width = 29 Hz)	1.83–1.97 (m, width = 29 Hz)	−0.6
C-3β-H	2.60–2.66 (m, width = 21 Hz)	2.35–2.47 (m, width = 21 Hz)	−0.2
C-9a-H	4.13 (dd, J = 11, 5 Hz)	3.46 (dd, J = 11, 5 Hz)	−0.67

[a]Δδ = δ(C_6D_6) − δ($CDCl_3$).

of its ring fusion since an axial–axial interaction would also be present in the steroidlike conformation **8***A* of the *cis* lactone **8** (but not in the nonsteroidal conformer **8***B*).

The definitive structural assignment for the major product as the *trans*-fused lactone **7** relied on the chemical shift of the methyl carbon signal in its ^{13}C nmr spectrum. The axial and equatorial methyl carbons of the equatorial conformer of 1-acetoxy-2,2-dimethylcyclohexane (**9**) resonate in the ^{13}C nmr spectrum at δ 18.6 and 29.0, respectively (5). The former serves as a model for the methyl carbon resonance of the *trans* lactone **7**, and the latter for the methyl carbon in the steroidal conformer of the *cis* lactone **8***A*. The C-5a methyl carbon signal at δ 15.5 in the ^{13}C nmr spectrum of the major photoproduct from **3** dictates the assignment to it of structure **7**. The presence of a γ-interaction between the methyl carbon and C-4 in **7** is considered to account for the shielding of this carbon relative to the model axial-methyl carbon of acetate **9**. The structural assignment for the *trans* lactone **7** was confirmed by an independent synthesis (*vide infra*).

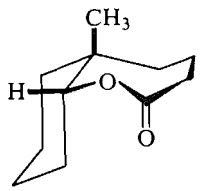

8*A*

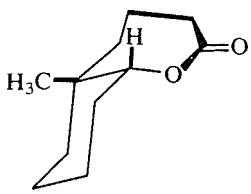

8*B*

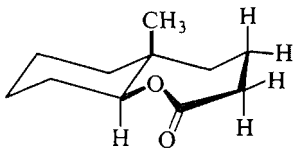

7*A*

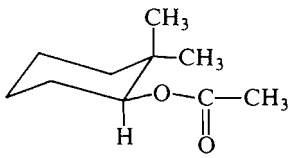

9

Although they partially overlap in the ^{1}H nmr spectrum at 200 MHz in deuterochloroform, the C-3 methylene proton signals of **7** are well resolved from each other in the 200-MHz ^{1}H nmr spectrum in benzene-d_6, where they appear as multiplets at δ 1.83–1.97 (width = 29 Hz) and δ 2.35–2.47 (width = 23 Hz). Coupling constants could not be extracted from either signal.

Models of **7** suggested that there are a number of conformations available to the seven-membered lactone ring, thus making individual assignment of the C-3 methylene proton signals difficult. However, as detailed in the Appendix, a favored conformation, **7***A*, can be assigned, leading to the individual assignments for the C-3 methylene proton signals given in Table 1. These assignments were required for the deuterium labelling studies (*vide infra*).

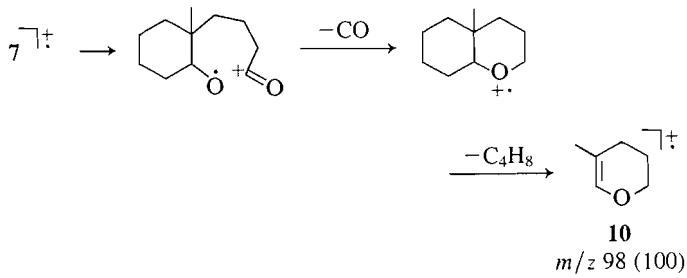

10
m/z 98 (100)

SCHEME 2

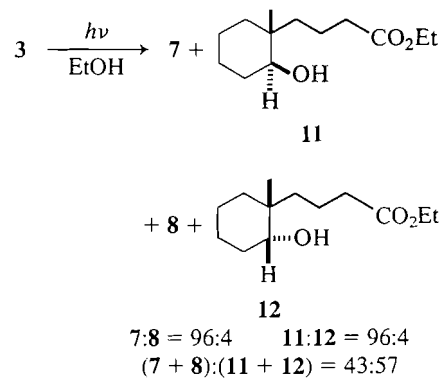

SCHEME 3

The mass spectrum of **7** shows the base peak at *m/z* 98. This is attributed to ion **10**, derived as outlined in Scheme 2 via a fragmentation analogous to that proposed by Ahmad *et al.* (6) for the related steroidal 5α-lactone (1).

Irradiation of the *trans* ketol **3** in ethanol gave a mixture of the *trans* lactone **7** and the stereochemically analogous *trans* hydroxy ester **11** as the major photoproducts (Scheme 3). As determined by gas chromatographic analysis of the total photolysate, the ratio of lactone to ester was 43:57, which corresponds well with isolated yields of 33 and 48%, respectively. Gas chromatography also indicated that each of the major photoproducts, lactone **7** and hydroxy ester **11**, was accompanied by ~4% of their epimeric counterparts, lactone **8** and hydroxy ester **12**. These minor constituents were not isolated, but were identified by comparison of their gas chromatographic retention times with the retention times of authentic samples (*vide infra*).

The 400-MHz ^{1}H nmr spectrum of the major hydroxy ester obtained from photolysis of **3** in ethanol shows a doublet of doublets at δ 3.39 (J = 10, 4 Hz), assigned to the methine proton of the hydroxyl-substituted carbon. The larger, 10-Hz coupling constant is consistent with the existence of the *trans* hydroxy ester **11** in conformation **11***A* (4), in accord with expectation (cf. ref. 7). However, an axial–axial interaction with the methine proton also exists for conformer **12***B* of the

Can. J. Chem. Downloaded from www.nrcresearchpress.com by 176.9.209.113 on 09/07/12
For personal use only.

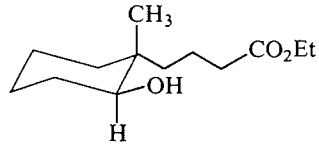

11*A*

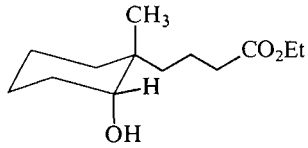

12*A*

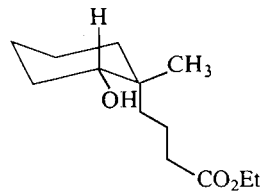

12*B*

epimeric hydroxy ester **12**. But unlike its *trans* epimer, the *cis* hydroxy ester **12** is predicted to exist as a mixture of conformers **12***A* and **12***B* and, as such, this structure would be inconsistent with the observed coupling of the methine proton.

The ^{13}C nmr spectrum of the major ester product confirmed the assignment of structure **11**. Analogous to the assignment for the *trans* lactone **7**, the *trans* structure **11** was indicated by comparison of the methyl carbon resonance observed at δ 17.2 for the photoproduct with the axial and equatorial methyl carbon signals at δ 17.7 and 29.7, respectively, in the equatorial conformer of 2,2-dimethylcyclohexanol **13** (5). Moreover,

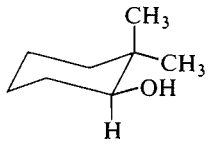

13

ethanolysis of the *trans* lactone **7** to the *trans* hydroxy ester **11**, effected by a strongly acidic Amberlite ion exchange resin, confirmed the like stereochemistry of the two major photoproducts. The structural assignment for **11** was further secured by an independent synthesis (*vide infra*).

Irradiation of the *cis* ketol **4** in benzene and in ethanol gave products identical to those obtained from photolysis of the *trans* ketol **3** (Scheme 4). From the benzene photolysate, a 96:4 mixture of the *trans* and *cis* lactones **7** and **8** was isolated in 55% yield. The total photolysate from irradiation of **4** in ethanol was shown by gas chromatography to comprise lactone and ester photoproducts in a ratio of 43:57. A 97:3 mixture of the epimeric lactones **7** and **8** and a mixture of the same ratio of epimeric hydroxy esters **11** and **12** were isolated in 33 and 41% yield, respectively. Thus not only were the photoproducts from **4** identical with those from **3**, but the product ratios were also effectively identical.

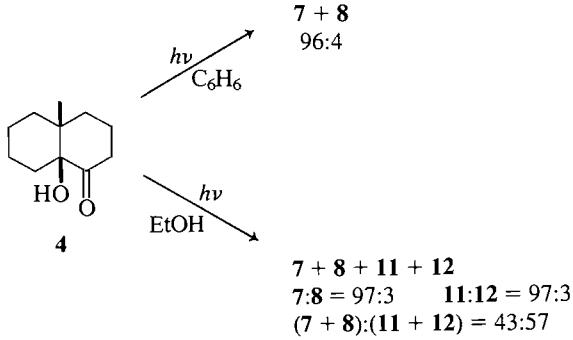

SCHEME 4

The major hydroxy ester **11** isolated from irradiation of **3** and **4** in ethanol was shown to be a primary photoproduct of the reaction and not to be the result of a "dark" ethanolysis of lactone **7**. Evidence of this was obtained by gas chromatography, which showed that the ester was detectable even in the early stages of photolysis, and that the lactone/ester ratio remained constant throughout the course of the photolysis. Furthermore, prolonged irradiation (for 10 times the time required for complete consumption of starting material) of the photolysate in ethanol did not alter this ratio, and there was no evidence for the formation of any of **11** when lactone **7** was irradiated in ethanol for a prolonged time.

The formation of an acid, either a "photo acid" originating from the ethanol used as solvent (8) or a carboxylic acid derived from oxidation of aldehydic photoproducts (*vide infra*), might possibly accompany photolysis of **3** and **4** in ethanol. Since these acids could conceivably catalyze ethanolysis of **7**, the ethanolic photolysis of each ketol was repeated in the presence of a small amount of sodium bicarbonate to test further the conclusion that ester **11** is a primary photoproduct. Filtration and concentration of the resulting photolysates from **3** and **4** gave lactone/ester ratios of 38:62 and 34:66, respectively, eliminating the possibility of acid-catalyzed ethanolysis.

The photolysates of **3** and **4** were each examined after only a portion of the starting ketol had been consumed. The ^1H nmr spectrum of the photolysates from irradiation of **3** in benzene for 0.5 h (10% of the time required for complete consumption of the starting ketol) evidenced methyl singlets attributable to the starting ketol **3** and the *trans* lactone **7**, as well as a singlet coincident with that of the methyl group of the *cis* ketol **4**. In addition, a methyl singlet at δ 1.10 and a multiplet at δ 9.73 were observed, which are ascribed to the keto aldehyde **14**. The

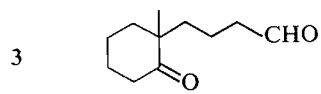

14

ratio of lactone **7** and keto aldehyde **14** formed was determined from the relative intensities of their methyl singlets to be 70:30.

Gas chromatographic monitoring of the photolysis of **3** in benzene indicated that the *cis* ketol **4** was present as a maximum of ~20% of the volatile components of the photolysate. This was observed in the early stages of the photolysis, following which the percentage of **4** in the photolysate decreased, presumably as it underwent photoreaction. The amount of keto aldehyde **14** initially rose to ~20% of the volatile components of the photolysate and declined upon continued irradiation. Although **4** was isolated from a curtailed photolysis of **3**, several attempts to isolate **14** were unsuccessful.

Evidence for the formation of **3** during irradiation of **4** in benzene was more ambiguous. Gas chromatographic monitoring during the course of irradiation evidenced a small peak, corresponding to a maximum of 5% of the volatile components of the photolysate, whose retention time was similar to that of **3**. A neighbouring peak, reaching a maximum of 10%, is attributed to **14** but neither of these attributions was verified by ^1H nmr spectroscopy.

Independent synthesis of the photoproducts

The stereochemistry ascribed to the lactones and hydroxy esters obtained from photolysis of the bicyclic ketols **3** and **4** was confirmed by independent synthesis, as outlined in Scheme 5. Reaction of lithium dimethylcuprate with the enone **15** (3, 9),

Can. J. Chem. Downloaded from www.nrcresearchpress.com by 176.9.209.113 on 09/07/12
For personal use only.

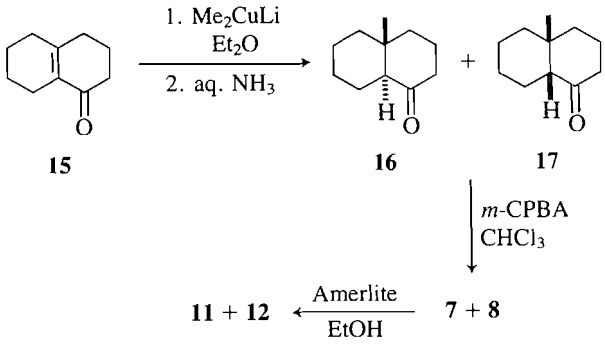

SCHEME 5

according to the procedure of Boeckman and Silver (10), afforded a 40:60 mixture of the *trans* and *cis* 1-decalones **16** and **17**. The ring fusion of **16** and **17** has been previously established (11). Equilibration of a 40:60 mixture of **16** and **17** to a 70:30 mixture of these ketones established that the *trans* isomer is favored thermodynamically (12).

Baeyer–Villiger oxidation of the 40:60 mixture of decalones **16** and **17** with *m*-chloroperoxybenzoic gave a 40:60 mixture of the *trans* and *cis* lactones **7** and **8**. The minor component of this mixture, which corresponds to the major lactone formed in the bicyclic ketol photolyses, can be assigned the *trans* lactone structure **7**, since retention of configuration at the migrating center during Baeyer–Villiger rearrangements is well established (13). Treatment of a nonequilibrium mixture of **16** and **17** with a solution of *m*-chlorobenzoic acid, a stronger acid than its corresponding peroxy acid, gave no evidence of any epimerization. The possibility of equilibration between **16** and **17** prior to Baeyer–Villiger rearrangement is thereby excluded. The excellent yield of the mixture of lactones obtained from the Baeyer–Villiger reaction ensured that no fractionation of epimers had occurred during work-up.

As a further check of the product stereochemistry, a 55:45 mixture of **16** and **17**, obtained by partial epimerization, was oxidized under the same Baeyer–Villiger conditions. This yielded a 55:45 mixture of **7** and **8**. Direct correspondence of the ratio of the starting ketone mixture with the ratio of the lactones derived from Baeyer–Villiger oxidation for two significantly different decalone mixtures established that no crossover had occurred.

In the ^{1}H nmr spectrum of a partially purified sample of the *cis* lactone **8**, a narrow multiplet at δ 4.20 could be discerned for the C-9a methine proton. This signal's narrowness evidenced the preference of this lactone for the nonsteroidal conformation **8***B* (*vide supra*).

Ethanolysis of a 40:60 mixture of the lactones **7** and **8** effected by an Amerlite resin yielded a 40:60 mixture of the hydroxy esters **11** and **12**. The epimeric esters were not separated, but the methyl singlet of the minor component of the mixture, the *trans* hydroxy ester **11**, was coincident with the methyl singlet of the major hydroxy ester isolated from irradiation of the bicyclic ketols.

Photolysis of 2α-deutero bicyclic α-ketols

The 2α-deutero *trans* and *cis* bicyclic ketols **5** and **6** (3), on irradiation in benzene, each gave the same mixture of deuterated lactones **18**, **19**, and **20** (Scheme 6). This mixture of lactones was isolated from the crude photolysate by sublimation and (or) crystallization, since the presence of deuterium label α to the carbonyl group in **19** and **20** precluded purification by chromatography.

TABLE 2. Labeling results for the irradiation of the *trans* and *cis* deutero ketols **5** and **6**

Irradiated ketol	Deuterated site	^{1}H nmr analysis $CDCl_3$ %D[a]	^{1}H nmr analysis C_6D_6 %D[b]	Mass spectral analysis	
trans Ketol **5**	C-9a (**18**)	23	28	d_0	6%
	C-3α (**19**)		62	d_1	92%
		58		d_2	2%
	C-3β (**20**)		13		
	Total D content	81%	103%		
cis Ketol **6**	C-9a (**18**)	22	29	d_0	7%
	C-3α (**19**)		61	d_1	92%
		58		d_2	1%
	C-3β (**20**)		14		
	Total D content	80%	104%		

[a]Calculated relative to the area of the methyl singlet at δ 0.93.
[b]Calculated relative to the area of the multiplet at δ 0.60–1.72.

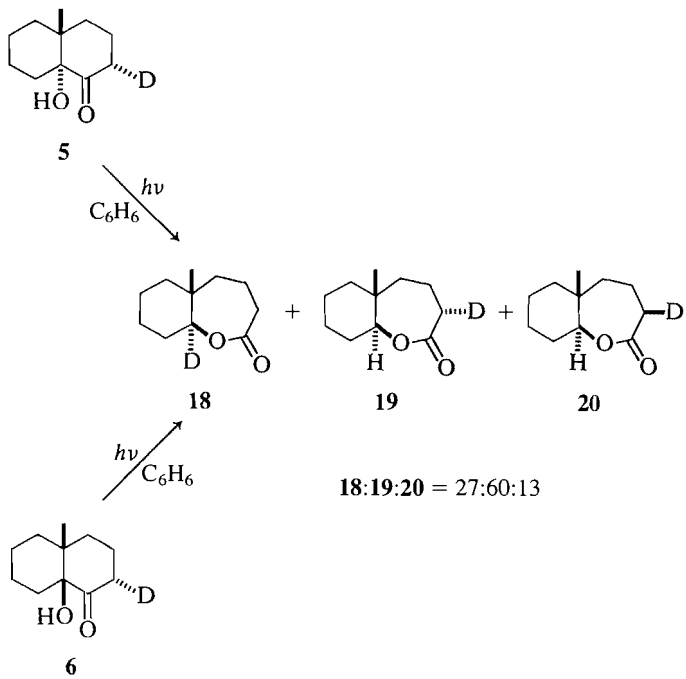

SCHEME 6

As detailed in Table 2, the 200-MHz ^{1}H nmr spectrum of the deuterated lactone mixture in deuterochloroform evidenced deuterium incorporation at the C-9a methine and C-3 methylene sites in the ratio 28:72. The mass spectrum of the deuterated lactone mixture was recorded under carefully monitored conditions, since high source or probe temperatures or high source pressures were found to engender a variable $M + 1$ contribution to the molecular ion, which could have introduced errors into the deuterium content calculations. In view of the errors that could also be associated with the quantitative ^{1}H nmr measurements, the total deuterium content accounted for by the ^{1}H nmr analysis is in reasonable accord with calculations based on the mass spectra.

Examination of the C-3 methylene proton signals in the ^{1}H nmr spectra of the deuterated lactone mixture, recorded in both deuterochloroform and benzene-d_6, revealed that the deuterium at C-3 was preponderantly situated at the α site: in

Can. J. Chem. Downloaded from www.nrcresearchpress.com by 176.9.209.113 on 09/07/12
For personal use only.

Can. J. Chem. Downloaded from www.nrcresearchpress.com by 176.9.209.113 on 09/07/12
For personal use only.

both nmr solvents, the relative area of the multiplet ascribed to the C-3α proton was significantly diminished. A detailed analysis of these spectra (see Appendix) led to the conclusion that the deuterated lactones **18**, **19**, and **20** were present in the ratio 27:60:13 (Table 2).

Discussion

Modes of photoreaction of bicyclic α-ketols

Irradiation of the bicyclic α-ketols **3** and **4** in benzene gives lactones **7** and **8** (Schemes 1 and 4), which are analogous to **21** and **22**, the products formed on photolysis of the steroidal α-ketols **1** and **2** (Scheme 7) (1). The structures of the photoproducts are consistent with exclusive α-cleavage to give alkyl acyl diradicals **23** that are converted to hydroxy ketene intermediates **24** via intramolecular hydrogen transfer (Scheme 8).

When the irradiation of α-ketol **3** in benzene was interrupted at an early stage, the keto aldehyde **14** was detected among the reaction products by vapor phase chromatography, together with the lactones **7** and **8**, unconsumed α-ketol **3**, and its epimer **4**. The failure to detect **14** by vapor phase chromatography after consumption of all of the α-ketols is attributed to its conversion on irradiation to nonvolatile products. The formation of **14** can best be interpreted in terms of intramolecular hydrogen transfer of the hydroxyl hydrogen atom in the diradical **23** (Scheme 9). In the cases of the steroidal α-ketols, the photochemical formation of an analogous keto aldehyde and interconversion of the ketols were not observed. We attribute this dichotomy to differences in the flexibility of the acyl side chain in the diradical intermediates (*vide infra*).

When the bicyclic α-ketols **3** and **4** were irradiated in ethanol, mixtures of lactones and hydroxy esters were formed (Schemes 3 and 4). These are considered to arise from competitive dark reactions of the intermediate hydroxy ketenes **24** involving, respectively, intramolecular reaction and intermolecular reaction with ethanol. This is in clear contrast to the behaviour of the steroidal α-ketols, which on irradiation in ethanol give only intramolecular, lactonic products (Scheme 7). We propose that this difference in behaviour results from differences in the flexibility of the ketene side chain in the hydroxy ketene intermediates (*vide infra*).

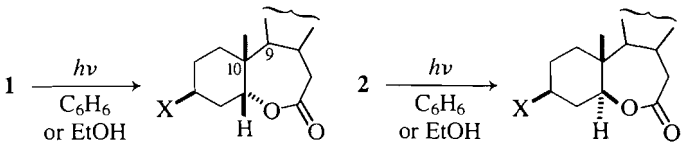

21 22

X = OAc, H, OBn

SCHEME 7

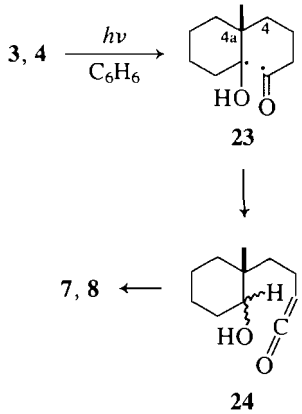

SCHEME 8

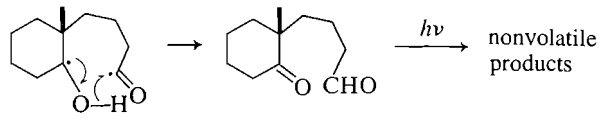

SCHEME 9

Stereochemistry of α-ketol photolyses

The most striking contrast between the photochemical behavior of the bicyclic and steroidal α-ketols pertains to the stereochemistry of the products. The reactions of the steroidal α-ketols are completely stereospecific (Scheme 7), while those of the bicyclic α-ketols, although stereoselective, are not stereospecific, and the same ratios of epimeric products are formed from both α-ketols (Schemes 1, 3, and 4).

In the case of the steroidal α-ketols, we have proposed that the stereospecificity stems from two factors: the geometry of the hydroxy-alkyl radicals, and fast hydrogen transfer in the diradical intermediates (1). The rate of hydrogen transfer was postulated to be fast relative to that of ring inversion and (or) inversion of the radical centre in the diradical intermediate. This fast hydrogen transfer was attributed to the presence of the CD ring system, which restricts rotation of the acyl side chain about the C-9—C-10 bond in the steroidal analogues of the bicyclic diradical **23**, i.e., about the bond corresponding to the C-4—C-4a bond in **23**.

Since it is anticipated that the geometry of the hydroxyalkyl radicals formed from the bicyclic α-ketols will not differ significantly from that of those formed from the steroidal α-ketols, it is concluded that the second factor, the rate of hydrogen transfer, is the crucial source of difference between the bicyclic and steroidal α-ketol photolyses.

In these terms, the nonstereospecific nature of the bicyclic ketol photolyses is attributed to a relatively slow rate of hydrogen abstraction. This in turn is considered to be a consequence of the large degree of rotational flexibility available to the acyl chain in the bicyclic diradicals.[3] Comparison with the steroidal diradicals shows that the bicyclic diradicals are not formed as their favored C-4—C-4a rotamers, and the activation barrier to rotation about the C-4—C-4a bond is lower than that about the analogous C-9—C-10 bond in the steroidal diradicals. We postulate that, following α-cleavage in the photolysis of the bicyclic α-ketols, rotation about the C-4—C-4a bond occurs to relieve an unfavorable *gauche* interaction of the C-3—C-4 bond with the C-4a methyl group and the C-4a—C-8a bond. This removes the hydrogen α to the acyl radical from the vicinity of the alkyl radical center and slows the rate of hydrogen abstraction.

It is proposed that as a consequence of a slow hydrogen abstraction step in the diradical intermediates **25** and **28** first formed from α-cleavage of the *trans* and *cis* bicyclic α-ketols **3** and **4**, respectively, equilibration of the ring conformation and the stereochemistry of the radical center is established prior to hydrogen abstraction (Scheme 10). The preferred diradical that

[3]The term "bicyclic diradicals" is used to connote the diradicals formed from the bicyclic ketols.

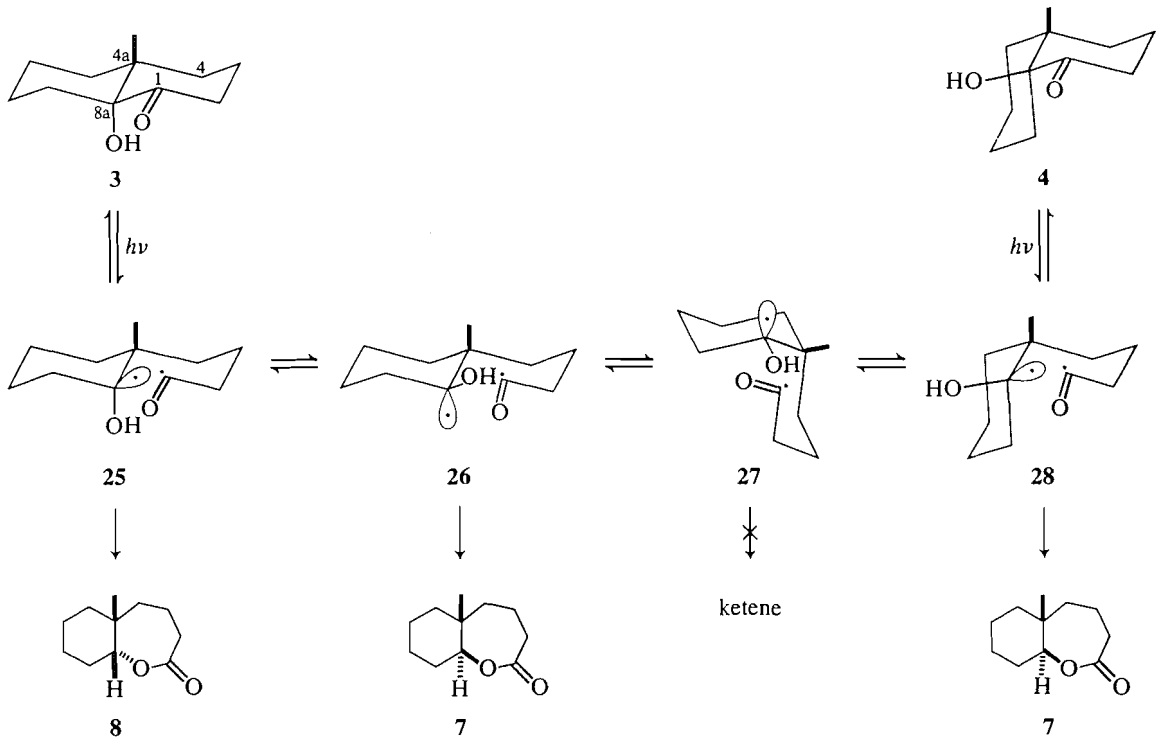

SCHEME 10

emerges from this equilibrium is considered to determine the stereochemistry of the photoproducts.

Evidence that **3** and **4** react via a common diradical is as follows:

(*i*) Both **3** and **4** give the same mixture of photolactones **7** and **8**.

(*ii*) The high degree of stereoselectivity for each of the bicyclic α-ketol photolyses indicates that there is sufficient time for the diradical intermediates to equilibrate. Otherwise a more nearly equal mixture of **7** and **8** would be expected from photolysis of **3**.

(*iii*) Irradiation of the α-deutero labelled *trans* and *cis* ketols **5** and **6** gives an identical mixture of the deuterated lactones **18**, **19**, and **20**.

As outlined in Scheme 10, ring and radical inversions of the diradicals **25** and **28** generate two additional diradicals, **26** and **27**. Of the four diradical intermediates, diradical **26** is considered to be the most stable, since both the acyl side chain and hydroxyl groups are favorably situated in equatorial sites. Hydrogen transfer in this diradical would lead to the *trans* lactone **7**, which is observed experimentally to be by far the preponderant photolactone.

Since the diradical **26** would be expected to close to give the *cis* ketol **4**, the detection of substantial amounts of the latter during the irradiation of **3** is in accord with its intermediacy.[4] Furthermore, the diradical **26** cannot close to the *trans* ketol **3**, and this would explain the lack of evidence for the formation of significant amounts of **3** during the irradiation of **4**.

The only other diradical that might account for the formation of **7** is **28**. However, evidence suggests that the formation of **7** in the photolyses of **3** and **4** derives from hydrogen abstraction in the favored diradical **26** rather than in **28**. The formation of the keto aldehyde **14** shows that abstraction of the hydroxyl hydrogen can occur in the bicyclic ketol systems. This mode of reactivity is compatible with the intermediacy of diradical **26** since the hydroxyl group is oriented equatorially to the ring and is geometrically very accessible for hydrogen abstraction. In contrast, the axial nature of the hydroxyl group in **28** would be expected to preclude formation of **14**.

Further evidence that it is **26** and not **28** that leads to **7** is provided by the results of the irradiations of the α-deutero ketols **5** and **6**. As shown in Scheme 11, transition states **30***A* and **30***B* are available for hydrogen abstraction from the favored diradical **29**, the deuterated analogue of **26**.[5] In these two transition states the C-3—C-4 bond is favorably disposed *anti* to the methyl group. Comparison of their relative energies is difficult. While transition state **30***B* has the acyl radical side chain in an equatorial site, transition state **30***A* permits hydrogen bonding between the hydroxyl group and the acyl group in the favored mode of bonding, between the hydroxyl group and the unpaired *n* electrons of the carbonyl oxygen atom (14). This disposes the unfilled orbital in the bent acyl radical (15, 16) *anti*-periplanar to the C—D bond favoring good orbital overlap during C—D cleavage. Thus a mixture of the deuterated lactones **18** and **19**/**20** is predicted to result if ketene formation in the photolyses of **5** and **6** proceeds via the diradical **29**.

These transition states may be compared with the transition states **32***A* and **32***B* that lead to ketene formation from the diradical **31**, the deuterated analogue of **28** (Scheme 12). These transition states, in addition to being derived from the less favored diradical **31**, incorporate an unfavorable *gauche* interaction of the C-3 methylene group with the methyl group and C-8a. Transition state **32***A* in which the acyl substituent is equatorially disposed is predicted to be favored over transition

[4]The possibility that the photolysis of **3** proceeds via its total rapid conversion to **4** is excluded by the fact that the photolysis of **3** occurs much more rapidly than that of **4**.

[5]In the steroidal systems, a transition state analogous to either **30***A* or **30***B* is not possible for it would place the C-8—C-14 and C-9—C-11 bonds of ring C in a *trans* diaxial orientation.

Can. J. Chem. Downloaded from www.nrcresearchpress.com by 176.9.209.113 on 09/07/12
For personal use only.

Can. J. Chem. Downloaded from www.nrcresearchpress.com by 176.9.209.113 on 09/07/12
For personal use only.

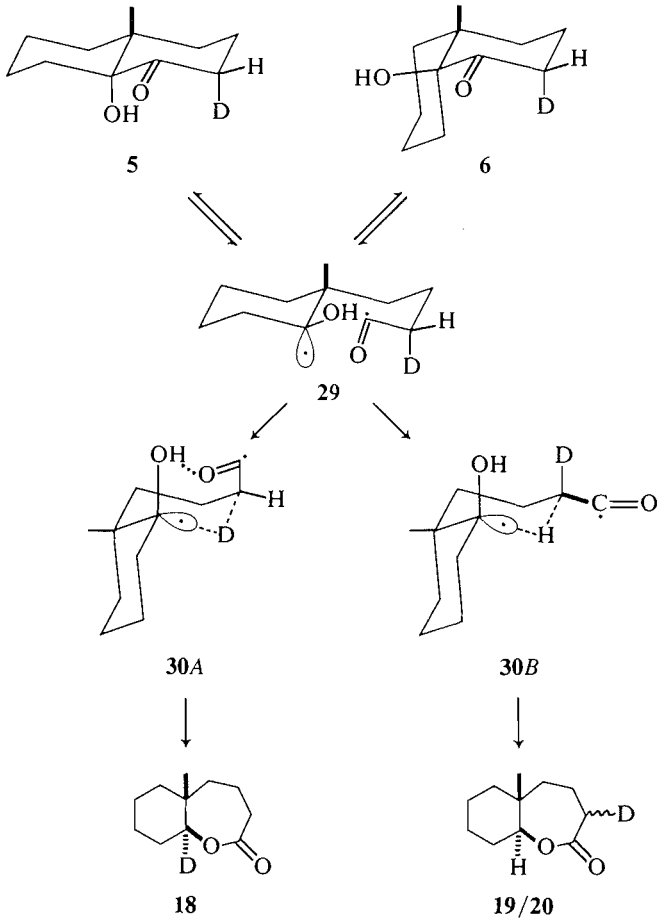

SCHEME 11

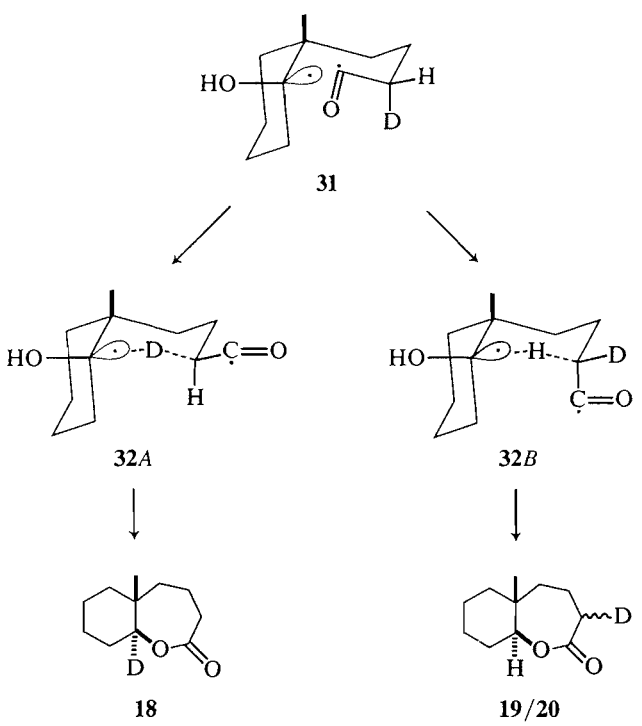

SCHEME 12

TABLE 3. T_1 relaxation parameters for the hydroxy esters **11** and **33**

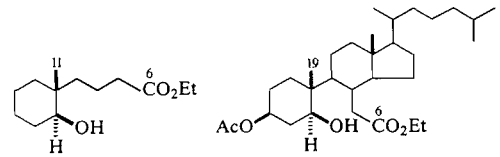

Carbon	**11**[a] T_1 (s)	**33** T_1 (s)
1	1.4[b]	0.26
2	1.1	0.27[c]
3	0.9	0.53
4	1.0	0.28[c]
5	2.6	0.49
6	22.5	5.63
7	1.4[b]	0.27
8	1.4	0.48
9	1.3	0.52
10	15.3	3.92
11[d]	2.8	0.26
OCH_2CH_3	3.8	1.59
OCH_2CH_3	3.2	2.19
12		0.27
13		3.77
14		0.52
15		0.26
16		0.29
17		0.52
18		1.05
19		1.21
20		0.53
21		0.66
22		0.31
23		0.45
24		0.78
25		1.32
26		1.43
27		1.34
$OCOCH_3$		1.25
$OCOCH_3$		7.22
OCH_3		1.37

[a]The numbering convention relates to the steroidal system, and not to I.U.P.A.C. nomenclature.
[b]Carbons 1 and 7 give coincident signals in the ^{13}C nmr spectrum of **11**.
[c]These values are interchangeable.
[d]C-11 in **11** corresponds to C-19 in **33**.

state **32***B*. Thus exclusive deuterium abstraction is anticipated if ketene formation in the photolyses of **5** and **6** were to proceed via diradical **31**.

The mixture of C-9a and C-3 deutero lactones **18** and **19/20** isolated from photolysis of **5** and **6** suggests that ketene formation occurs from the transition states **30***A* and **30***B*. Quantitatively, the 28:72 ratio of **18** to **19/20** represents a combination of the inherent stereoselectivity for 2α- versus 2β-hydrogen abstraction and the deuterium kinetic isotope effect. In the absence of similar studies with the epimeric 2β-deutero ketols, we cannot with certainty separate these effects. However, both Agosta and Wolff (17) and Duthaler and Ganter (18) have observed small deuterium isotope effects for hydrogen abstraction leading to ketene formation in the irradiation of bicyclo[3.2.1]octan-6-ones and bicyclo[3.3.1]nonan-2-ones. Using the deuterium kinetic isotope effect values of

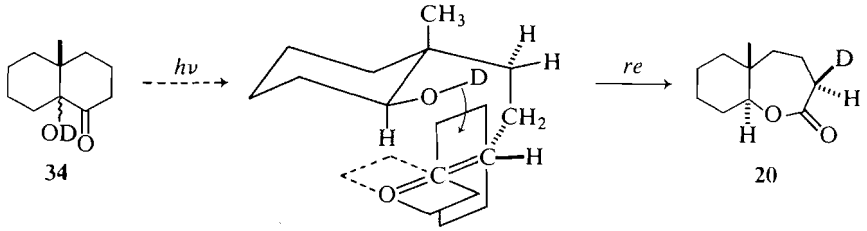

34 35 20

SCHEME 13

1.5–2.1 observed by these workers, we can calculate (18, 19) the inherent stereoselectivity for abstraction of the α- and β-hydrogens α to the acyl radical to be ~40:60. This is in accord with expectation since neither transition state **30***A* or **30***B* is predicted to be strongly favored over the other.

Thus the divergent behavior of the steroidal and bicyclic ketols on photolysis is considered to hinge on the relative flexibilities of the acyl radical side chain formed from each. Evidence for our proposal that the acyl side chains of the bicyclic diradical intermediates have more rotational flexibility than the acyl side chains of the steroidal diradical intermediates can be obtained from T_1 relaxation correlation times. The bicyclic and steroidal esters **11** and **33** (1) serve as models for their diradical counterparts in this study, and the T_1 values for the carbons of these molecules are given in Table 3. The smaller NT_1 values (where N corresponds to the number of protons on the carbon of interest) for the carbons of the acyl chain in the steroidal ester **33** relative to those of the acyl chain of the bicyclic ester **11** indicate that molecular motion in the former is in fact more hindered.

Reactions of the ketene intermediates

Our investigation of the photochemistry of *O*-deuterated steroidal α-ketols **1** and **2** has led us to conclude that the addition of the hydroxyl group to the ketene group in the intermediate hydroxy ketenes is under product development control with the transition states for the additions being formed relatively late on the reaction coordinate (1). Such control was considered to be a consequence of the maintenance of the C-8—C-9—C-10 framework in the hydroxy ketene in an arrangement that approximates the backbone of the preferred conformation of the product lactones.

Although we have not examined the photolysis of the *O*-deuterated bicyclic ketols, our studies of the photolyses of the C-2 deuterated bicyclic ketols (Scheme 6) suggest that in these cases addition to the ketene is under steric approach rather than product development control. The fact that **19** and **20** are formed in a ratio of 82:18 indicates that the β-deutero lactone **20** would be the major product from photolysis of the *O*-deuterated ketols **34**. This is contrary to the stereoselectivity observed in the photolysis of the *O*-deuterated 5β-steroidal ketol. Thus product development control cannot be a significant factor in the mode of addition of the hydroxyl group to the ketene group in the bicyclic systems.

The difference is attributed to the greater flexibility of the ketene side chain in the bicyclic system. In this case the C-4—C-4a bond is relatively free to rotate. The favored rotamer is that which positions the C-3—C-4 bond *anti* to the C-4a—methyl bond. In this rotamer, the *si* face of the ketene system is inaccessible to the hydroxyl group, making the formation of the α-deutero lactone **19** unfavorable. In contrast, a favorable transition state **35** is available for addition to the *re* face of the ketene group (Scheme 13). This addition leads to the formation of the C-3β deutero lactone **20**, with the reaction under steric approach control.

The divergent reactivity of the steroidal and bicyclic ketene intermediates with respect to the incorporation of ethanol, when used as solvent for the α-ketol irradiations, is also attributed to the differences in the relative flexibilities of the ketene side chain in these systems. The presence of ring C in the steroidal ketene intermediate is considered to hold the C-5 hydroxyl group and the ketene system in close proximity, thus leading to exclusive addition to give lactone photoproducts. In contrast, in the bicyclic system the rotational flexibility of the ketene chain removes the ketene group from the vicinity of the hydroxyl group, and addition of ethanol to the ketene group becomes competitive with intramolecular addition, with the result that irradiation of the bicyclic α-ketols in ethanol gives rise to a mixture of lactone and ester photoproducts.

Conclusions

We have shown that the photolyses of the bicyclic α-ketols are highly stereoselective, but not stereospecific as in the case of the steroid α-ketols. This difference is attributed to the greater flexibility of the acyl side chain in the acyl alkyl diradical intermediates, which results in a relatively slow rate of hydrogen transfer leading to ketene formation. As a consequence of this slow hydrogen transfer, equilibration of the conformation of the cyclohexyl ring and the configuration of the radical center in the diradical intermediates first formed from α-cleavage is established prior to hydrogen abstraction. The preferred diradical that emerges from this equilibration is considered to determine the stereoselective formation of the *trans* lactone from the photolyses of the bicyclic α-ketols. Deuterium labeling studies suggest that hydrogen transfer in this diradical leading to ketene formation occurs with a slight preference for abstraction of the β-hydrogen.

In a similar manner, the difference in the relative flexibility of the ketene side chain formed in the bicyclic and steroidal α-ketol photolyses is considered to account for the formation of both hydroxy ester and lactone photoproducts from the former and the exclusive formation of lactones from the latter when the photolyses are carried out in ethanol. Deuterium labelling studies suggest that intramolecular addition to the ketene intermediate in the bicyclic systems is under steric approach control, whereas product development control governs this addition in the steroidal systems.

Thus, the present work confirms our previous conclusion that the stereospecificity of the photolyses of 5-hydroxy 6-keto steroids is not a general attribute of all α-ketol irradiations (1), but results from the particular structural features of the steroidal

Can. J. Chem. Downloaded from www.nrcresearchpress.com by 176.9.209.113 on 09/07/12
For personal use only.

α-ketols. We consider that our observations in the case of the bicyclic α-ketols represent the more general case, where ring and radical inversion motions in the diradical are strongly competitive with hydrogen abstraction, and the relative stabilities of the diradicals that result from these inversions determine the stereochemistry of the photoproducts.

Experimental[6]

*Irradiation of 4a-methyl-8a-hydroxy-*trans*-octahydronaphthalen-1(2*H*)-one (**3**) in benzene. Formation of 5a-methyl-*trans*- and -cis-octahydro-1-benzoxepin-2(3*H*)-one (**7** and **8**)*

A solution (1.5 × 16 cm) of **3** (61 mg, 0.34 mmol) in anhydrous benzene (23 mL) was irradiated under argon, and the photolysis was followed by gas chromatography (3% OV-17 on Chromosorb W; 130°C). After 5 h, starting material was shown to have been completely consumed and the photolysate was concentrated to give a colorless oil (53 mg). Flash chromatography on silica gel (1.5 × 18 cm) with dichloromethane – ethyl acetate (95:5 v/v) as eluent gave a 96:4 mixture of the *trans* and *cis* lactones **7** and **8** (38 mg, 62%) as a colorless oil. Sublimation (80°C/15 Torr; 1 Torr = 133.3 Pa) gave the mixture of lactones as white crystals (*vide infra*).

Irradiation of trans *ketol **3** in ethanol. Formation of* trans *and* cis *lactones **7** and **8** and ethyl (2S*,1R*)- and (2R*,1R*)-2-hydroxy-1-methylcyclohexanebutyrate (**11** and **12**)*

A solution (2.5 × 32 cm) of **3** (264 mg, 1.45 mmol) in anhydrous ethanol (125 mL) was irradiated under argon and the course of the photolysis was monitored by gas chromatography (3% OV-17 on Chromosorb W; 130°C). After 5 h, when the starting material had been completely consumed, the photolysate was concentrated to a colorless oil (308 mg). Flash chromatography on silica gel (2.5 × 17 cm) with dichloromethane – ethyl acetate (98:2 v/v) as eluent gave a 96:4 mixture of *trans* and *cis* lactones **7** and **8** (87 mg, 33%) as a colorless oil. Sublimation (92°C/20 Torr) afforded white needles, mp 85–86°C, which were crystallized from hexanes – diethyl ether to give **7** as a colorless prism, mp 87.5–88.5°C; ir λ_{max}: 5.80, 7.79 (m), 9.00 (m) μm; ^{1}H nmr (200 MHz) δ: 0.93 (s, 3H), 1.07–1.94 (m, 12H), 2.44–2.71 (m, 2H), 4.14 (d, J = 11, 5 Hz, 1H); ^{1}H nmr (400 MHz) δ: 0.93 (s, 3H), 1.14–1.88 (m, 12H), 2.48–2.56 (m, width = 29 Hz, 1H), 2.60–2.66 (m, width = 21 Hz, 1H), 4.13 (dd, J = 11, 5 Hz, 1H); ^{1}H nmr (benzene-d_6, 200 MHz) δ: 0.60–1.72 (m), 0.68 (s), 1.83–1.97 (m, width = 29 Hz, 1H), 2.35–2.47 (m, width = 23 Hz, 1H), 3.46 (dd, J = 11, 5 Hz, 1H); ms m/z: 182 (5), 98 (100). *Exact Mass* calcd. for $C_{11}H_{18}O_2$: 182.1307; found: 182.1340. *Anal.* calcd. for $C_{11}H_{18}O_2$: C 72.49, H 9.96; found: C 72.19, H 9.93.

Further elution with dichloromethane – ethyl acetate (95:5 v/v) gave a 96:4 mixture of the hydroxy esters **11** and **12** (157 mg, 48%) as a colorless liquid. The mixture was molecularly distilled (134°C/20 Torr) to give **11**, containing ~5% of its epimer **12**, as a colorless liquid; ir λ_{max}: 2.88 (sh, w), 2.99 (br, w), 5.78, 7.28 (m) μm; ir λ_{max}(neat): 3.00 (br, m), 5.75, 5.81 (sh), 7.27 (m) μm; ^{1}H nmr δ: 0.90 (s, 3H), 1.23–1.95 (m) and 1.25 (t, J = 7 Hz) and 1.87 (br s, exchanges with deuterium oxide) (16H), 2.13–2.40 (m, 2H), 3.40 (br m, $W_{1/2}$ = 15 Hz, 1H), 4.13 (q, J = 7 Hz, 2H); ^{1}H nmr (400 MHz) δ: 0.88 (s, 3H), 0.94 (weak s, **12** Me), 1.16–1.80 (m) and 1.26 (t, J = 7 Hz) (16H), 2.23–2.35 (m, 2H), 3.39 (dd, J = 10, 4 Hz, 1H), 4.13 (q, J = 7 Hz, 2H); ms m/z: 228 (2), 98 (100). *Exact Mass* calcd. for $C_{13}H_{24}O_3$: 228.1725; found: 228.1714. *Anal.* calcd. for $C_{13}H_{24}O_3$: C 68.38, H 10.59; found: C 67.98, H 10.55.

*Irradiation of 8a-hydroxy-4a-methyl-*cis*-octahydronaphthalen-1(2*H*)-one (**4**) in benzene. Formation of lactones **7** and **8***

A solution (1.5 × 19 cm) of **4** (73 mg, 0.40 mmol) in anhydrous benzene (27 mL) was irradiated as described for its *trans* isomer **3**, and the concentrated photolysate was chromatographed to give a 96:4 mixture of the *trans* and *cis* lactones **7** and **8** (41 mg, 55%) as a white solid.

Irradiation of cis *ketol **4** in ethanol. Formation of lactones **7** and **8** and hydroxy esters **11** and **12***

Ketol **4** (265 mg, 1.46 mmol) was irradiated in anhydrous ethanol (125 mL) for 6 h, as in the case of **3**. The concentrated photolysate (340 mg) was flash chromatographed on silica gel (2.5 × 15 cm) with dichloromethane – ethyl acetate (98:2 v/v) as eluent to give a 97:3 mixture of *trans* and *cis* lactones **7** and **8** (88 mg, 33%) as a white solid. Further elution with the same solvent mixture gave a 97:3 mixture of the hydroxy esters **11** and **12** (135 mg, 41%) as a colorless liquid.

*4a-Methyl-*trans*- and -*cis*-octahydronaphthalen-1(2*H*)-one (**16** and **17**)*

A 40:60 mixture of **16** and **17** was prepared in quantitative yield by the reaction of lithium dimethylcuprate with 3,4,5,6,7,8-hexahydronaphthalen-1(2*H*)-one (**15**) according to the method of Boeckman and Silver (10); ir λ_{max}: 5.86 μm; ^{1}H nmr δ: 0.77 (s, *trans* Me), 1.00 (s, *cis* Me), 1.00–2.57 (m); ms m/z: 166 (32), 111 (100). The *trans*/*cis* ratio was found to be 40:60. On prolonged standing, the ketones had partially equilibrated to a 55:45 *trans*/*cis* mixture.

Equilibration of cis *ketone **17** to* trans *ketone **16***

A 40:60 mixture of **16** and **17** was equilibrated by heating under reflux with sodium carbonate in aqueous methanol for 20 h according to the method of Marshall and Hochstetler (12). This gave a 65:35 mixture of **16** and **17** in 70% yield.

Baeyer–Villiger oxidation of trans *and* cis *ketones **16** and **17**. Formation of lactones **7** and **8***

A stirred suspension of *m*-chloroperoxybenzoic acid (85%; 3.72 g, 18.3 mmol) in chloroform (20 mL) was treated with a solution of a 55:45 mixture of **16** and **17** (1.069 g, 6.44 mmol) in chloroform (20 mL). The resulting solution was protected from light and stirred at room temperature for 41 h. The fine white suspension that formed was poured into stirred aqueous 10% sodium sulfite (150 mL) and, subsequent to a negative starch – potassium iodide test, the layers were separated. The aqueous phase was extracted with chloroform (50 mL, 4 × 25 mL). The combined organic phases were washed with saturated aqueous sodium bicarbonate (2 × 50 mL) and saturated aqueous sodium chloride (3 × 25 mL), dried over anhydrous sodium sulfate, and concentrated to give a 55:45 mixture of **7** and **8** (1.14 g, 97%) as a pale yellow oil; ^{1}H nmr δ: 0.97 (s, major isomer, *trans* lactone Me), 1.03 (s, minor isomer, *cis* lactone Me). Fractional crystallization from pentane gave the *trans* lactone **7** as white needles containing ~5% of the *cis* lactone **8**. The ir and ^{1}H nmr spectra of the *trans* lactone **7** prepared in this manner were identical to those of the lactone isolated from the photolyses of the *trans* and *cis* ketols **3** and **4**. The filtrate, enriched in *cis* lactone **8**, was concentrated to a colorless oil whose ^{1}H nmr spectrum exhibited, in addition to a singlet at δ 1.03, a narrow multiplet at δ 4.20.

Baeyer–Villiger oxidation, in the same manner, of a 40:60 mixture of **16** and **17** gave a 40:60 mixture of **7** and **8** in 97% yield.

Treatment of trans *and* cis *ketones **16** and **17** with* m*-chlorobenzoic acid. Evidence that epimerization does not occur during Baeyer–Villiger oxidation*

A solution of a 40:60 mixture of **16** and **17** (19 mg, 0.11 mmol) and *m*-chlorobenzoic acid (51 mg, 0.33 mmol) in chloroform (2 mL) was stirred at room temperature for 36 h. The solution was added to saturated aqueous sodium bicarbonate (2 mL), and the mixture was extracted with diethyl ether (3 × 10 mL). The combined extracts were washed with saturated aqueous sodium chloride (3 × 5 mL), dried over anhydrous sodium sulfate, and concentrated to give a 40:60 mixture of **16** and **17** in quantitative recovery as a colorless liquid. The ^{1}H nmr spectrum of this mixture was identical to that of the starting material.

In another trial the acid treatment was prolonged to 72 h; gas chromatographic analysis evidenced no epimerization of the ketones.

[6]Photolyses were carried out in Pyrex at 300 nm in a Rayonet photoreactor. For a general description of the experimental procedures used, see ref. 1. Product ratios were determined by gas chromatographic analysis on 5% Carbowax on Chromosorb G at 140°C or 170°C, or from the relative heights of the methyl signals in the ^{1}H nmr spectra.

Can. J. Chem. Downloaded from www.nrcresearchpress.com by 176.9.209.113 on 09/07/12
For personal use only.

Ethanolysis of trans *lactone 7. Formation of hydroxy ester 11*

A solution of **7** (39 mg, 0.21 mmol) in anhydrous ethanol (0.40 mL) was shaken with strongly acidic Amberlite cation exchange resin (IR-120, Rohm and Haas; 17 mg). The progress of the reaction was followed by tlc with dichloromethane–hexanes (4:1 v/v). After 48 h, when the starting material had been completely consumed, the reaction mixture was filtered and concentrated to give **11** (47 mg, 95%) as a colorless liquid. The ir and ^{1}H spectra of **11** obtained by ethanolysis of **7** were identical to those of the hydroxy ester isolated from the photolyses of the *trans* and *cis* ketols **3** and **4**.

Ethanolysis of a mixture of trans *and* cis *lactones 7 and 8. Formation of hydroxy esters 11 and 12*

Ethanolysis of a solution of a 60:40 mixture of **7** and **8** (61 mg, 0.33 mmol) in anhydrous ethanol (0.60 mL) was effected with a strongly acidic Amberlite cation exchange resin (IR-120, Rohm and Haas; 9 mg). The reaction mixture was shaken for 24 h and allowed to sit for 72 h at room temperature. Filtration and concentration of the mixture gave a 60:40 mixture of the hydroxy esters **11** and **12** (67 mg, 88%) as a colorless liquid; ^{1}H nmr δ: 0.87 (s, ester **11** Me, ~60%), 0.93 (s, ester **12** Me, ~40%).

In a similar fashion, a 40:60 mixture of **7** and **8** (33 mg, 0.18 mmol) dissolved in anhydrous ethanol (0.33 mL) was shaken with acid resin (4 mg) for 20 h to give a 40:60 mixture of **11** and **12** (32 mg, 78%) as a pale yellow liquid.

*Irradiation of 2α-deutero-8a-hydroxy-4a-methyl-*trans*-octahydronaphthalen-1(2*H*)-one (5). Formation of 9a-deutero-5a-methyl-*trans*-octahydro-1-benzoxepin-2(3*H*)-one (18) and 3α- and 3β-deutero-5a-methyl-*trans*-octahydro-1-benzoxepin-2(3*H*)-one (19 and 20)*

A solution (1.5 × 14 cm) of **5** (49 mg, 0.27 mmol) in anhydrous benzene (20 mL) was irradiated under argon for 5 h. The colorless photolysate was washed with aqueous 5% sodium bicarbonate (4 mL) and saturated aqueous sodium chloride (3 × 5 mL), dried over anhydrous sodium sulfate, and concentrated. Sublimation (72°C/15 Torr) gave a mixture of the deuterated lactones **18**, **19**, and **20** (26 mg, 53%) as a colorless oil. Crystallization from pentane afforded the mixture as white needles, mp 85.5–86.5°C; ^{1}H nmr (200 MHz) δ: 0.93 (s, 3H), 1.10–1.94 (m, 12H), 2.44–2.69 (m, 1.42H), 4.14 (dd, J = 11, 5 Hz, 0.77H); ^{1}H nmr (benzene-d_6, 200 MHz) δ: 0.60–1.72 (m) and 0.68 (s) (15H), 1.82–1.96 (m, 0.38H), 2.35–2.47 (m, 0.87H), 3.45 (dd, J = 11, 5 Hz, 0.72H); ms m/z: d_0 6%, d_1 92%, d_2 2%.

*Irradiation of 2α-deutero-8a-hydroxy-4a-methyl-*cis*-octahydronaphthalen-1(2*H*)-one (6). Formation of the deuterated lactones 18, 19, and 20*

A solution (1.5 × 13 cm) of **6** (45 mg, 0.25 mmol) in anhydrous benzene (17 mL) was irradiated as for **5**. The colorless photolysate was worked up as before to give a colorless oil (45 mg). The oil was sublimed (72°C/15 Torr) to give a mixture of **18**, **19**, and **20** (28 mg, 63%) as a white, slightly gummy solid, mp 78–83°C; ir λ_{max}: 5.81 μm; ^{1}H nmr (200 MHz) δ: 0.93 (s, 3H), 1.10–1.94 (m, 12H), 2.44–2.69 (m, 1.42H), 4.14 (dd, J = 11, 5 Hz, 0.78H); ^{1}H nmr (benzene-d_6, 200 MHz) δ: 0.60–1.72 (m) and 0.68 (s) (15H), 1.82–1.96 (m, 0.39H), 2.35–2.47 (m, 0.86H), 3.45 (dd, J = 11, 5 Hz, 0.71H); ms m/z: 183 (18), 99 (100); d_0 7%, d_1 92%, d_2 1%.

In another run, crude product was recrystallized from pentane to give a mixture of **18**, **19**, and **20** in 20% yield as white needles, mp 85.0–86.5°C. The 200-MHz ^{1}H nmr spectrum of this mixture was identical to that of the mixture obtained in the earlier run.

Acknowledgments

We thank the Natural Sciences and Engineering Research Council of Canada for financial support of this work and for the award of a postgraduate fellowship to S.S., and Imperial Oil Limited for the award of a Graduate Research Fellowship to S.S.

1. S. Stiver and P. Yates. Can. J. Chem. **66**, 214 (1988).
2. S. Stiver and P. Yates. Tetrahedron Lett. **25**, 3289 (1984); **27**, 2215 (1986).
3. S. Stiver, P. D. Clark, and P. Yates. Can. J. Chem. **66**, 27 (1988).
4. N. S. Bhacca and D. H. Williams. Applications of NMR spectroscopy in organic chemistry. Holden–Day, London. 1964. p. 51.
5. H. Schneider and W. Freitag. Chem. Ber. **112**, 16 (1979).
6. M. S. Ahmad, G. Moinuddin, and I. A. Khan. Org. Mass. Spectrom. **13**, 382 (1978); M. S. Ahmad, M. Mushfiq, M. Asif, and G. A. S. Ansari. J. Prakt. Chem. **317**, 1049 (1975).
7. J. T. Edward, E. Cooke, and T. C. Paradellis. Can. J. Chem. **60**, 2546 (1982).
8. P. Yates. J. Photochem. **5**, 91 (1976); G. Roussi and R. Beugelmans. Tetrahedron Lett. 1333 (1972).
9. I. D. Rae and B. N. Umbrasas. Aust. J. Chem. **28**, 2669 (1975).
10. R. K. Boeckman, Jr. and S. M. Silver. J. Org. Chem. **40**, 1755 (1975).
11. J. W. Blunt, J. M. Coxon, N. B. Lindley, and G. A. Lane. Aust. J. Chem. **29**, 967 (1976); C. Djerassi and D. Marshall. J. Am. Chem. Soc. **80**, 3986 (1958); F. Sondheimer and D. Rosenthal. J. Am. Chem. Soc. **80**, 3995 (1958).
12. J. A. Marshall and A. R. Hochstetler. J. Am. Chem. Soc. **91**, 648 (1969).
13. A. J. Waring. *In* Comprehensive organic chemistry. Vol. 1. *Edited by* J. F. Stoddart. Pergamon, Oxford. 1979. Chap. 5.2. p. 1087.
14. H. S. Aaron. *In* Topics in stereochemistry. Vol. 11. *Edited by* N. L. Allinger and E. L. Eliel. Wiley, New York. 1979. p. 12.
15. A. G. Davies and R. Sutcliffe. J. Chem. Soc. Perkin Trans. 2, 819 (1980).
16. N. J. Turro. Modern molecular photochemistry. Benjamin/Cummings, Menlo Park, CA. 1978. pp. 224–228, 537; N. J. Turro, W. E. Farneth, and A. Devaquet. J. Am. Chem. Soc. **98**, 7425 (1976).
17. W. C. Agosta and S. Wolff. J. Am. Chem. Soc. **99**, 3355 (1977).
18. R. O. Duthaler and C. Ganter. Helv. Chim. Acta, **59**, 415 (1976).
19. D. Y. Curtin and D. B. Kellom. J. Am. Chem. Soc. **75**, 6011 (1953).

Appendix

Assignment of the C-3 proton signals in the ^{1}H nmr spectrum of 7

Dreiding models of each of the various conformations available to the *trans* lactone **7**, considered in relation to the degree of delocalization within the lactone group, the relative stability of the ring, and the spectroscopic properties exhibited by **7**, suggested that its preferred conformation is that depicted in **7***A*. Of the potential conformations available, **7***A* permits the most efficient delocalization within the lactone group.[7] This conformation also has the required geometry for the observed γ-shielding of the C-5a methyl carbon by C-4 in the ^{13}C nmr spectrum of **7** (*vide supra*).

In conformation **7***A* the C-3β proton is pseudoequatorial and the C-3α proton pseudoaxial, leading to assignment of the narrower multiplet at δ 2.35–2.47 to the former and the broader multiplet at δ 1.83–1.97 to the latter (Table 1). The preference of **7** to exist in the conformation **7***A* and these assignments of the C-3 methylene proton signals based on this conformation are corroborated by the differential shieldings in the ^{1}H nmr spectra

[7]Although a boatlike conformation would allow better delocalization in the lactone group, it has several features that are irreconcilable with the ^{1}H and ^{13}C nmr spectra.

Can. J. Chem. Downloaded from www.nrcresearchpress.com by 176.9.209.113 on 09/07/12
For personal use only.

of **7** recorded in deuterochloroform and benzene-d_6, and by an nOe study.

The chemical shifts of the salient signals in the ^{1}H nmr spectra of **7** recorded in deuterochloroform and benzene-d_6 are given in Table 1. These differential shieldings are consistent with the formation of a collision complex between a benzene molecule and the carbonyl group of **7** in the conformation **7***A*. Models indicate that both the C-9a methine proton and C-3α proton are situated in the shielding cone of a benzene molecule so complexed, and, as shown in Table 1, experience a strong shielding in benzene. The C-3β proton is located near the intersection of the shielding and deshielding regions and the C-5a methyl group is remote from any significant influence by the benzene molecule in **7***A*; in accord with this their ^{1}H nmr signals are only slightly shielded in benzene. Thus, the differential ^{1}H nmr shieldings observed support the preference of the lactone for the conformation **7***A*. No other conformation is predicted to give as good a correlation of both the signs and relative magnitudes of the differential proton shifts.

Nuclear Overhauser enhancement studies of the 200-MHz ^{1}H nmr spectrum of **7** in benzene confirmed the above assignments of the C-3 methylene proton signals. Irradiation of the multiplet at δ 1.83–1.97, ascribed to the C-3α proton, induced a 3.5% enhancement in the relative area of the C-9a methine proton signal at δ 3.46. Irradiation of the C-9a methine proton signal resulted in a 6.5% enhancement of the area of the multiplet at δ 1.83–1.97. These observations of an nOe between the C-9a proton and the proton resonating at δ 1.83–1.97 verify the assignment of the latter to the C-3α proton. The smaller magnitude of the nOe observed for the bicyclic lactone **7** compared with that for the corresponding steroidal lactone (1) can be attributed to the larger internuclear distance between the relevant protons (~3 Å, as measured from the Dreiding model).

Can. J. Chem. Downloaded from www.nrcresearchpress.com by 176.9.209.113 on 09/07/12
For personal use only.

Specific interactions between amino acid side chains — a partial molar volume study

MANDAPATI V. R. RAO,[1] MAHALAKSHMI ATREYI, AND MOGANTY R. RAJESWARI[2]
Department of Chemistry, University of Delhi, Delhi-110007, India

Received September 4, 1986[3]

MANDAPATI V. R. RAO, MAHALAKSHMI ATREYI, and MOGANTY R. RAJESWARI. Can. J. Chem. **66**, 487 (1988).

Partial molar volumes of the following mixtures, $\bar{V}^0$(mix) were determined in water at 20°C: (*1*) glutamic acid : glycine; (*2*) arginine:glycine; (*3*) arginine : glutamic acid; (*4*) arginine : aspartic acid; (*5*) lysine : glutamic acid, and (**6**) lysine : aspartic acid. Partial molar volumes of the mixtures calculated using $\bar{V}^0$ of various ionic species of the amino acids agreed with the experimental values for systems *1* and *2*, but were less than the experimental values for systems *3* to *6*. The positive deviations, $\Delta\bar{V}^0$(mix), of the experimental values from the calculated values are discussed in terms of "specific interactions" between ionogenic side chains. The extent of interaction is greater in systems containing aspartic acid and/or arginine.

MANDAPATI V. R. RAO, MAHALAKSHMI ATREYI et MOGANTY R. RAJESWARI. Can. J. Chem. **66**, 487 (1988).

Opérant dans l'eau, à 20°C, on a déterminé les volumes molaires partiels de mélanges, $\bar{V}^0$(mélange), des systèmes suivantes : (*1*) acide glutamique : glycine; (*2*) arginine:glycine; (*3*) arginine : acide glutamique; (*4*) arginine : acide aspartique; (*5*) lysine : acide glutamique et (*5*) lysine : acide aspartique. Les volumes molaires partiels de mélanges calculés en utilisant les valeurs de $\bar{V}^0$ de diverses espèces ioniques des acides aminés sont en bon accord avec les valeurs expérimentales déterminées pour les systèmes (*1*) et (*2*); toutefois, elles sont en moins bond accord pour les autres systèmes. On discute des déviations positives, $\Delta\bar{V}^0$(mélanges), des valeurs expérimentales par rapport aux valeurs calculées en fonction d'interactions spécifiques entres les chaînes latérales ionogènes. L'importance de ces interactions est plus grande dans les systèmes contenant de l'acide aspartique ou de l'arginine.

[Traduit par la revue]

1. Introduction

Analysis of high resolution crystal structure data of proteins has led to a better appreciation of various interactions that stabilise the tertiary and quaternary structure of proteins (1). It is now recognised that electrostatic forces are as important as hydrophobic forces in maintaining the protein structure (1–3). In oxyhaemoglobin, for example, a number of specific inter- and intra-subunit interactions between negatively charged carboxylate groups and positively charged —NH_3^+ or guanidinium groups are observed (1–3). The significance of electrostatic interactions in stabilising the complex structure of tobacco mosaic virus (4) and thermolysin (2, 5) has recently been underscored. Side chain – side chain hydrogen bonds and salt bridges were noticed in crystal structures of amino acid – amino acid salts (6–9). It would be interesting to see whether such interactions exist in solutions of mixtures of two amino acids, one with an acidic and the other with a basic side chain. In the present report, partial molar volumes of mixtures of an acidic amino acid (aspartic acid or glutamic acid) with a basic amino acid (lysine or arginine) and mixtures of glycine and arginine/glutamic acid are presented; positive deviation of the experimental volume data from the calculated volume data indicated specific interaction between the side chains of acidic and basic amino acids.

2. Experimental

Glutamic acid, aspartic acid, glycine, and alanine were from E. Merck. Lysine and arginine were SISCO products. All amino acids were of L-configuration and chromatographically pure. Amino acids, dried overnight at about 50°C under vacuum over P_4O_{10}, were used to make solutions. Deionized water was distilled over alkaline $KMnO_4$, and was boiled and filtered through sintered glass filter C-4 before use.

Density measurements were made with the Precision Density Meter 601 (Anton Paar) which is capable of measuring density with a precision of 1 in 10^6 parts. The instrument constant K was determined daily using dry air and water as standards.

The apparent partial molar volumes of amino acid mixtures were determined (10) using the equation,

$$[1] \quad \bar{V}^0(\text{mix}) = \frac{M}{\rho_0}\left(1 - \frac{\rho - \rho_0}{c}\right)$$

where ρ and ρ_0 are, respectively, the densities of solution and solvent, c is the total concentration of solute in g/mL, and M is the apparent molecular weight given by $M = X_1M_1 + X_2M_2$, where M_1 and M_2 are the molecular weights of amino acid components 1 and 2, and X_1 and X_2 are their mole fractions.

The sum of the concentrations of the two amino acids present in any mixture is quite low ($\simeq 10^{-2}$ M), hence the experimental $\bar{V}$(mix) is taken as $\bar{V}^0$(mix) (10).

pH measurements were made with a Radiometer pHM 26 unit. The temperature of the solution in the cell of density meter was maintained at 20 ± 0.03°C using a circulating thermostatic bath (Hotpack); an Anton Paar digital precision thermometer DT 100-20 was used to measure the solution temperature. It is estimated that the maximum error in partial molar volumes would be ±0.3%.

3. Results and discussion[4]

Glutamic acid : glycine and arginine:glycine mixtures

The partial molar volumes ($\bar{V}^0$(mix)) of mixtures of (*1*) glutamic acid and glycine and (*2*) arginine and glycine were determined. The $\bar{V}^0$ of the mixtures, depicted in Fig. 1, was found to increase with increasing mole fraction of the basic or acidic amino acid. To compare the observed partial molar volume data with calculated values, one has first to take into account the fact that the pH of the mixtures varied as the mole fraction of the acidic (or basic) amino acid was increased (Fig. 1, inset). Consequently, there would be shifts in various ionic equilibria and the concentrations of various ionic species

[1]To whom all correspondence should be addressed.

[2]Present address: Laboratory of Photobiology and Membrane Biophysics, School of Life Sciences, Jawaharlal Nehru University, New Delhi-110 067, India.

[3]Revision received November 24, 1987.

[4]A complete set of data on partial molar volume and pH values of mixtures may be purchased from the Depository of Unpublished Data, CISTI, National Research Council of Canada, Ottawa, Ont., Canada K1A 0S2.

Can. J. Chem. Downloaded from www.nrcresearchpress.com by 176.9.209.113 on 09/07/12
For personal use only.

Can. J. Chem. Downloaded from www.nrcresearchpress.com by 176.9.209.113 on 09/07/12
For personal use only.

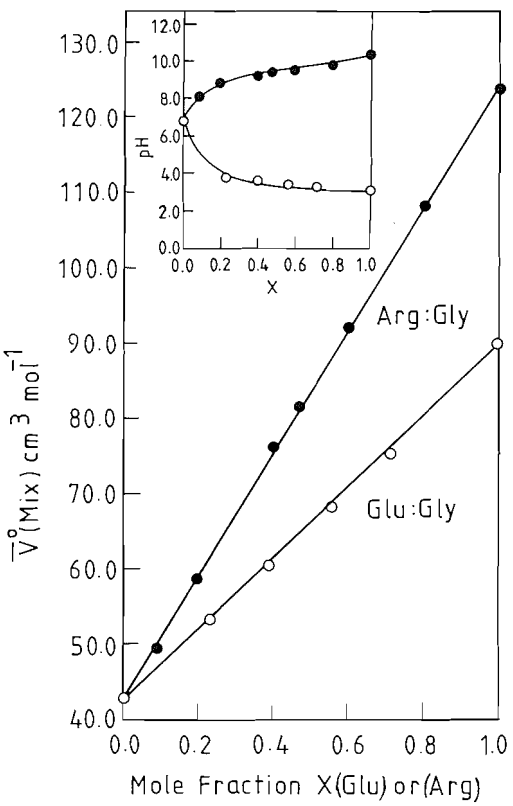

FIG. 1. $\bar{V}^0_{mix}$(expt) vs. mole fraction of Glu:Gly mixtures (○); and Arg:Gly mixtures (●) in water at 20°C. The calculated data are shown as solid lines. pH variations are shown as inset (Glu:Gly, -○-○-; Arg:Gly, -●-●-).

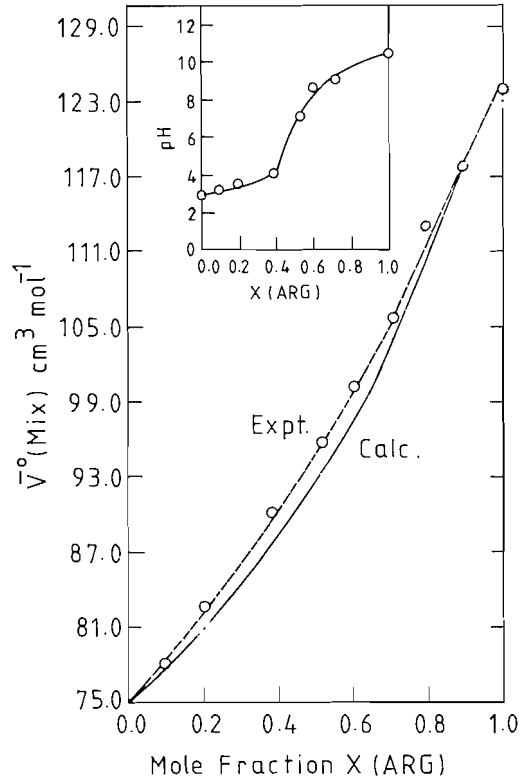

FIG. 2. $\bar{V}^0_{mix}$(expt) vs. mole fraction of arginine for Arg:Asp mixtures (○) in water at 20°C. The calculated data are shown as solid line. pH variations are shown as inset.

in each mixture would have to be evaluated taking into account the different pK's of the amino acids (11).

Glycine can exist as a cation, zwitterion, or anion depending on the pH. However, the other four amino acids under study have an additional charge center on the side chain whose ionisation leads to one more ionic species in addition to the above three. In the case of glutamic acid (also aspartic acid), a cation, a zwitterion, and two anions are possible:

$H_3\overset{+}{N}CH((CH_2)_2COOH)COOH$	$H_3\overset{+}{N}CH((CH_2)_2COOH)COO^-$
Cation	Zwitterion
$H_3\overset{+}{N}CH((CH_2)_2COO^-)COO^-$	$H_2NCH((CH_2)_2COO^-)COO^-$
Anion (i)	Anion (ii)

The side chain ε-NH_2 of lysine and δ-guanidinium (gu) of arginine can readily be charged. This leads to the formation of an additional cationic species. Various species for arginine are as follows:

$H_3\overset{+}{N}CH((CH_2)_3g\overset{+}{u})COOH$	$H_3\overset{+}{N}CH((CH_2)_3g\overset{+}{u})COO^-$
Cation (i)	Cation (ii)
$H_2NCH((CH_2)_3g\overset{+}{u})COO^-$	$H_2NCH((CH_2)_3gu)COO^-$
Zwitterion	Anion

The fractional concentration of all the ionic species can readily be evaluated as a function of pH from the ionisation constants, pK's, (11) of the charged groups. This facilitates the calculation of $\bar{V}^0$ of amino acid mixtures using the partial molar volumes of different ionic species determined for the first time recently in our laboratory (12). In general, the partial molar volumes for an amino-acid – amino-acid mixture, such as Gly:Glu, can be written, assuming the additivity principle for volumes, as:

$$[2]\quad V^0(\text{mix}) = X_{Glu}(f_{11}\bar{V}^0_{11} + f_{21}\bar{V}^0_{21} + f_{31}\bar{V}^0_{31} + f_{41}\bar{V}^0_{41}) + X_{Gly}(f_{12}\bar{V}^0_{12} + f_{22}\bar{V}^0_{22} + f_{32}\bar{V}^0_{32})$$

where X_{Glu} and X_{Gly} are the mole fractions of glutamic acid and glycine; f_{11}, f_{21}, f_{31}, f_{41} are the mole fractions and $\bar{V}^0_{11}$, $\bar{V}^0_{21}$, $\bar{V}^0_{31}$, $\bar{V}^0_{41}$ the partial molar volumes of the cation, zwitterion, anion (i), and anion (ii) of glutamic acid; f_{12}, f_{22}, and f_{32} are the mole fractions and $\bar{V}^0_{12}$, $\bar{V}^0_{22}$, and $\bar{V}^0_{32}$ are $\bar{V}^0$'s of the cation, zwitterion, and anion of glycine.

As a rule, all ionic species of an amino acid do not coexist in a solution at a given pH, and as the pH is changed, some of the terms in the above equation would vanish.

The calculated partial molar volumes for Glu:Gly and Arg:Gly mixtures (using an equation similar to [2]), along with the experimental data are depicted in Fig. 1. The calculated volumes (solid lines) agree very well with the experimental data (circles). This is a very significant observation as it clearly indicates that the partial molar volumes of the ionic species in mixtures of glycine with the acidic amino acid Glu, as well as with the basic amino acid Arg are additive. This point will be discussed further.

Arginine: aspartic acid/glutamic acid; lysine : aspartic acid/glutamic acid mixtures

The partial molar volumes of the following four mixture systems were determined as a function of mole fraction of the basic amino acid:

(3) Arg:Asp; (4) Arg:Glu; (5) Lys:Asp; (6) Lys:Glu

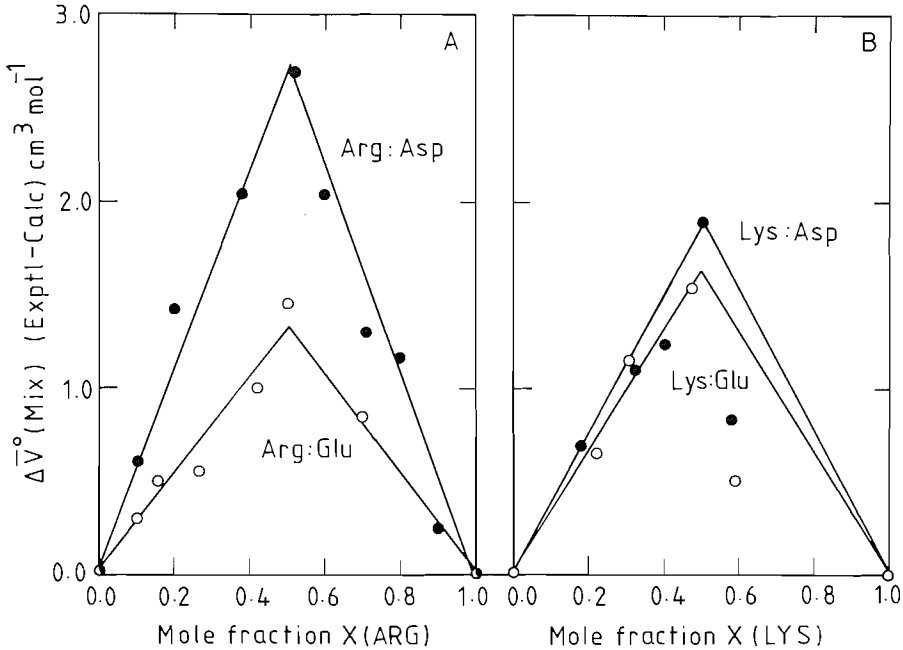

FIG. 3. $\Delta\bar{V}^0_{mix}$, ($\bar{V}^0$(expt) − $\bar{V}^0$(calc)) for mixtures of amino acids: (*A*) Arg:Asp (-●-●-); Arg:Glu (-○-○-) and (*B*) Lys:Asp (-●-●-) and Lys:Glu (-○-○-) in water at 20°C as a function of mole fraction of Arg of Lys.

The sum of the two solute concentrations in all mixtures was about 3×10^{-2} *M*; the variation in the total concentration for different mixtures was only marginal. In the case of Lys:Asp system, for example, the variation in the total concentration was between 3.48 to 3.14×10^{-2} *M*. The pH of systems, as can be expected, varied markedly, when the mole fraction of the basic amino acid was increased (Fig. 2, inset).

The experimental $\bar{V}^0$(mix) data for the basic–acidic amino acid mixtures were significantly different (see Fig. 2 for Arg:Asp systems) from the data calculated in a way similar to that for Arg/Glu:Gly mixtures. The deviation from the calculated value, $\Delta\bar{V}^0$(mix), $\bar{V}^0_{mix}$(expt) − $\bar{V}^0_{mix}$(calcd), for one mole of the mixture is depicted in Fig. 3 as a function of the mole fraction of the basic amino acid. A reference to the figure shows that $\Delta\bar{V}^0$(mix) is always positive and, further, has a maximal value when $X = 0.5$. The positive deviation in systems with asparatic acid is, interestingly, higher than in mixtures containing glutamic acid at corresponding mole fractions (Fig. 3). Again, between the two basic amino acids, arginine caused a higher deviation than lysine; thus deviations of $\bar{V}^0$(mix) from calculated values were highest for Arg:Asp mixtures.

Large volume changes, as high as 10 cm^3 mol^{-1}, were noticed when pure carboxylic acids are mixed with pure amines (13). Such volume changes are obviously due to the formation of strong salt bridges in the mixture of two pure liquids, which are media of rather low dielectric constant. The present studies were, however, made in aqueous medium, which has a high dielectric constant, and at the low concentrations used in the study ($\simeq 10^{-2}$ *M*), ion pair formation due to "non-specific" ionic interactions is more or less obviated. This is clearly seen from the fact that no volume deviations were observed in glutamic acid/arginine : glycine mixtures, even though the former component has another charge center on the side chain, in addition to the zwitterionic charge centers. The significant observation of volume deviation in the basic:acidic amino acid systems therefore suggests the presence of interactions between the positively charged and negatively charged amino acid side chains.

Monte Carlo simulation studies on clusters consisting of aspartate anion (i) or argininium cation (ii) and 250 water molecules carried out by Ranghino and co-workers (14) showed that at least five water molecules are hydrogen bonded to the side chain COO^- in Asp, while six water molecules are associated with the guanidinium group in Arg, and one of these six is simultaneously linked to α-COO^-. The calculations also showed that there are solvation gaps near the hydrophobic side chain region of Arg. Solvation of charged groups causes the well known "electrostriction" in volumes, which in the case of glycine zwitterion is estimated to be 13.0 cm^3 mol^{-1} (15).

In the crystalline state, ordering of oppositely charged groups is expected and observed (16). However, a very interesting feature reported in the crystal structure of the salt arginine glutamate monohydrate (7) is the following: the positively charged gu^+ group forms two intermolecular H-bonds with the side chain γ-COO^- of Glu and, more importantly, also with a water molecule. Nuclear magnetic resonance studies on the peptides Arg-Glu, and Arg-Ala-Gly-Glu indicated that strong interactions between side chains of Arg and Glu exist (17, 18).

The above literature data suggest firstly, that charge centers in amino acid side chains would be "hydrated" in aqueous solution and, secondly, the geometry of side chain groups provides scope for hydrogen bonds and salt bridges between oppositely charged side chains. The positive volume deviations observed in the present studies point out to "specific" side-chain – side-chain interactions which would, in principle, have electrostatic as well as H-bonding contributions.

It is being increasingly realised that specificity in biological interactions is mediated by electrostatic residues along with hydrogen bonding rather than by the latter alone. This is underscored by our observation that there are no volume changes in mixtures of arginine and glutamine; the $CONH_2$ side chain of Glu is polar but neutral (unpublished results).

The net effect of the interactions in the amino acid mixtures is

Can. J. Chem. Downloaded from www.nrcresearchpress.com by 176.9.209.113 on 09/07/12
For personal use only.

to lift, partially, the solvation of the side chain charge centers, which in turn leads to a decreased "electrostriction" and hence the observed positive deviations in the volumes of the mixtures. The deviation in a given system would be expected to have a maximal value at $X = 0.5$, as in these mixtures the concentration of species with change on the side chains (cation ii and anion i) is maximum; but on changing $X > 0.5$ or < 0.5, the mole fraction of such species of either the basic or acidic amino acid decreased.

The existence of specific interaction between acidic and basic amino acids in dilute aqueous solution has been amply substantiated by the present data. It would be rewarding to unequivocally establish the structure of the interacting complex and the strength of the interaction.

The relative strength of interaction in the four systems under study is as follows:

Arg:Asp > Lys:Asp > Arg:Glu > Lys:Glu

This observation may be explained by the intrinsic acidity of the interacting groups; the δ-guanidinium group in Arg is more basic (pK_a 12.52) than ϵ-$\overset{+}{N}H_3$ of lysine (pK_a 10.78) and the β-carboxyl in Asp is a stronger acidic group (pK_a 3.97) than that at the γ-position in Glu (pK_a 4.36) (11).

Acknowledgement

M.R.R. thanks the Council of Scientific and Industrial Research, India, for financial assistance.

1. M. F. Perutz. Science, **201**, 1187 (1978).
2. M. F. Perutz and H. Radit. Nature, **255**, 256 (1975).
3. M. F. Perutz. Br. Med. Bull. **32**, 195 (1976).
4. A. C. Bloomer, J. N. Champnees, G. Bricogne, R. Staden, and A. Klug. Nature, **276**, 362 (1978).
5. G. Beisecker, J. I. Harris, J. C. Thierry, J. E. Walker, and A. J. Wonacott. Nature, **266**, 328 (1977).
6. T. N. Bhat and M. Vijayan. Acta Crystallogr. B**32**, 891 (1976).
7. T. N. Bhat and M. Vijayan. Acta Crystallogr. B**33**, 1754 (1977).
8. D. M. Salunke and M. Vijayan. Acta Crystallogr. B**38**, 1328 (1982).
9. D. M. Salunke and M. Vijayan. Int. J. Peptide Protein Res. **18**, 348 (1981).
10. E. F. Cassasa and H. Eisenberg. Adv. Protein Chem. **19**, 287 (1964).
11. D. D. Perrin. Dissociation constants of organic bases in aqueous solutions. IUPAC, Butterworths, London. 1965.
12. M. V. R. Rao, M. Atreyi, and M. R. Rajeswari. J. Phys. Chem. **88**, 3129 (1984).
13. F. Kohler, R. Gopal, G. Goetze, H. Atrops, M. H. Demris, E. Libermann, E. Willheim, F. Ratkovice, and B. Palagyl. J. Phys. Chem. **85**, 2524 (1981).
14. G. Ranghino, E. Clementi, and S. Romano. Biopolymers, **22**, 1449 (1983).
15. E. J. Cohn and J. T. Edsall. Proteins, amino acids and peptides. Reinhold Publ. New York. 1943. Chap. 7.
16. J. Bose and L. M. Pant. Acta Crystallogr. **18**, 806 (1965).
17. G. Lancelot, R. Mayer, and C. Hélène. J. Am. Chem. Soc. **101**, 1569 (1979).
18. R. Mayer and G. Lancelot. J. Am. Chem. Soc. **103**, 4738 (1981).

Can. J. Chem. Downloaded from www.nrcresearchpress.com by 176.9.209.113 on 09/07/12
For personal use only.

Effect of ring substituents on the fluorescence spectra of substituted diarylcarbenes[1]

J. C. SCAIANO AND D. WEIR
Division of Chemistry, National Research Council of Canada, Ottawa, Ont., Canada K1A 0R6

Received August 19, 1987

J. C. SCAIANO and D. WEIR. Can. J. Chem. **66**, 491 (1988).

The fluorescence spectra of a series of ring-substituted diarylcarbenes have been examined. The solution spectra are generally red shifted by 25–30 nm with respect to the band positions in matrices at 77 K. The difference is believed to reflect emission from non-relaxed conformations at 77 K. Both electron-withdrawing and -donating substituents lead to red shifts in the emission. These shifts are essentially additive, and the carbene emission data show an excellent correlation with free radical fluorescence data for the corresponding diarylmethyl radicals. The temperature dependence of excited carbene lifetimes have been examined for a few representative examples.

J. C. SCAIANO et D. WEIR. Can. J. Chem. **66**, 491 (1988).

On a examiné les spectres de fluorescence d'une série de diarylcarbènes substitués sur le cycle. Par comparaison avec les spectres déterminés dans des matrices à 77 K, les spectres déterminés en solution sont généralement déplacés vers le rouge par 25 à 30 nm. On croit que la différence est le reflet d'une émission provenant de conformations qui ne sont pas soumises à la relaxation à 77 K. Tant les substituants électroaffinitaires que ceux qui sont électrodonneurs conduisent à des déplacements vers le rouge dans l'émission. Essentiellement, ces déplacements sont additifs et les données d'émission des carbènes présentent une excellente corrélation avec les données de fluorescence des radicaux libres diarylméthyles correspondants. Pour quelques exemples représentatifs, on a examiné l'influence de la température sur les temps de vie des carbènes excités.

[Traduit par la revue]

Can. J. Chem. Downloaded from www.nrcresearchpress.com by 176.9.209.113 on 09/07/12
For personal use only.

Introduction

The fluorescence from diphenylcarbene has been the subject of several studies in glasses at low temperature as well as in solution at room temperature (1–8). For example, the lifetime of excited triplet diphenylcarbene is 123 ns in a methylcyclohexane glass at 77 K (5) and 4.2 ns in cyclohexane at 286 K (8). A recent study has compared the chemical reactivity of excited diphenylcarbene and its ground state in glass at low temperature (7); this work confirms an earlier postulate (4) that reactions of the photoexcited carbene may be involved at long exposure times. The luminescence from a few ring-substituted carbenes has also been examined in glasses at 77 K by Trozzolo and Gibbons (6) and by Ono and Ware (5). There are only two reports on the absorption spectra of excited diarylcarbenes (8, 9).

The chemistry and spectroscopy of excited reaction intermediates is a subject of current interest (10, 11). Processes involving excited reaction intermediates can be quite common under conditions of laser excitation. In this paper we report the results of a systematic study of the effects of ring substituents on the triplet–triplet fluorescence spectra from diarylcarbenes, R^1R^2C:. In a few cases we have also determined the lifetimes of the excited carbenes. Dimesitylcarbene is also the subject of a more detailed study of its transient absorption spectroscopy (12), as well as of its excited state lifetime and intermolecular reactivity.

Experimental

Materials

The majority of the diazo precursors were synthesized via the corresponding tosyl hydrazones using the method reported by Smith and Howard for diphenyldiazomethane (13). Dimesityldiazomethane was from a sample prepared by Dr. H. L. Casal following the synthetic procedure of Zimmerman and Paskovick (14), and mesityl-*o*-tolyldiazomethane had been prepared by Dr. A. S. Nazran. All diazo compounds were purified by sublimation with the exception of the dimesityl and mesityl-*o*-tolyl derivatives which were purified by flash chromatography or alumina (80–200 mesh from Fisher) using hexane as the eluent.

Cyclohexane, benzene (Aldrich, Gold Label), and toluene (BDH, Omnisolv) were used as received.

Luminescence spectroscopy

Our laser flash photolysis system and the modifications for two laser experiments have been described elsewhere (15, 16). In these experiments a Lumonics excimer laser delivering 308 nm pulses (~5 ns, ≦25 mJ/pulse) was used to generate the carbene from its diazo precursor, and a Molectron UV-24 nitrogen laser (337.1 nm, ~8 ns, ≦4 mJ/pulse) were used to excite the carbene. Occasionally a PRA LN-1000 nitrogen laser (~600 ps, ≦1 mJ/pulse) were used in place of the Molectron laser to improve the overall time resolution of the system. The system incorporates a Tektronix R-7912 transient digitizer (for kinetic studies) and an EG&G gated intensified optical multichannel analyzer. Throughout this work the gate was fixed at 20 ns and it was timed to coincide with the nitrogen laser pulse. Suitable cut-off filters were employed to eliminate scattered light from the laser.

In order for the diazo solutions to be adequately absorbing at 308 ns, while essentially transparent at 337.1 nm, it is necessary to use very dilute samples (typically $2–5 \times 10^{-5}$ *M*). Under these conditions each 308 nm laser shot causes significant diazo depletion; it was thus necessary to use a flow system to ensure that each pulse irradiated a fresh portion of solution. The cell compartment was constructed of 7×7 mm^2 Suprasil tubing and was connected with Teflon lines to reservoir in which the solutions were deaerated by a stream of nitrogen. The cell temperature was controlled by using an outer quartz jacket and flowing nitrogen at the appropriate temperature around the sample compartment and a pre-equilibration coil.

Results and discussion

The fluorescence spectra for most carbenes were recorded in benzene, where hydrogen abstraction can be ruled out. The general, one- (308 nm) or two-laser (308 followed by 337 nm) excitation led to the same emission spectra, which were readily recorded using the techniques described in the Experimental section. Generation of excited carbenes under conditions of single pulse excitation is not unexpected, since the processes leading to triplet carbene formation (i.e. diazo photodecomposition followed by carbene intersystem crossing) usually occur in

[1]NRCC No. 28372.

Can. J. Chem. Downloaded from www.nrcresearchpress.com by 176.9.209.113 on 09/07/12
For personal use only.

TABLE 1. Fluorescence spectra from diarylcarbenes in solution at room temperature and in matrices at 77 K

Carbene		Room temperature		77 K[a]
R^1	R^2	Solvent	λ_{max} (nm)	$\lambda_{0,0}$ (nm)
C_6H_5	C_6H_5	Benzene	505	483, 480,[b] 482[c]
C_6D_5	C_6D_5	Benzene	504	
4-FC_6H_4	4-FC_6H_4	Benzene	504	
C_6H_5	3-Pyridyl	Benzene	511	
C_6H_5	4-$CH_3C_6H_4$	Benzene	511	486, 487[b]
4-$CH_3C_6H_4$	4-$CH_3C_6H_4$	Benzene	515	492
2-$CH_3C_6H_4$	Mesityl	Benzene	516	482
Mesityl	Mesityl	Benzene	501	486
C_6H_5	4-ClC_6H_4	Benzene	516	492, 488[b]
C_6H_5	4-BrC_6H_4	Benzene	517	491, 487[b]
4-ClC_6H_4	4-ClC_6H_4	Benzene	526	500
C_6H_5	4-$(CO_2CH_3)C_6H_4$	Cyclohexane	527	
C_6H_5	4-CNC_6H_4	Benzene	536	510, 510[c]
4-$CH_3C_6H_4$	4-CNC_6H_4	Cyclohexane	543	516
C_6H_5	2-Naphthyl	Benzene	588	
C_6H_5	4-Biphenyl	Benzene		557
Dibenzosuberyl		Cyclohexane	505	

[a]This work; in a methylcyclohexane glass.
[b]From ref. 6, in a methyltetrahydrofuran glass.
[c]From ref. 5, in a methylcyclohexane glass.

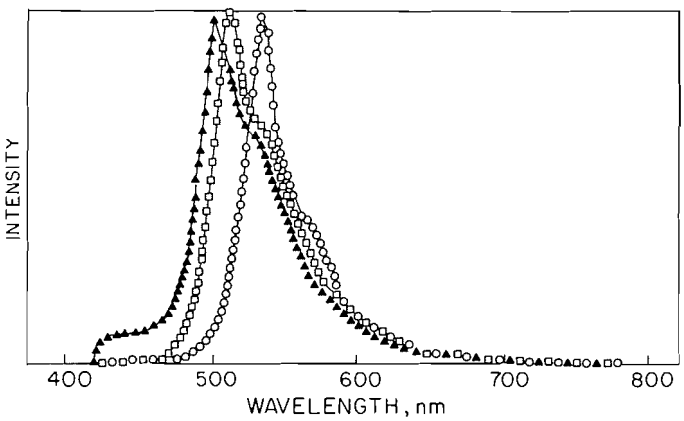

FIG. 1. Room temperature fluorescence spectra from diphenylcarbene (▲), 4-tolylphenylcarbene (□), and 4-cyanophenyl-phenylcarbene (○) in benzene.

the subnanosecond time scale (17). This allows for subsequent carbene excitation within the single (~5 ns) 308 nm laser pulse. Though these processes are not uncommon, they are frequently ignored in laser photolysis studies of carbene reactions.

Table 1 gives the positions of the fluorescence maxima (λ_{max}) for the various carbenes. We note that while we report λ_{max} in most cases the shape of the spectra are such (Fig. 1) that the position of λ_{max} coincides with the 0,0 band ($\lambda_{0,0}$). Whenever possible we have also included values of $\lambda_{0,0}$ for glasses at 77 K. Both electron-withdrawing and -donating substituents lead to red shifts in the emission spectra. This is shown in Fig. 1 where we compare the fluorescence spectra of the methyl and cyano derivatives with that of the parent diphenylcarbene. The situation is similar to that previously encountered in the case of ring-substituted diphenylmethyl radicals (18). Only in the case of dimesitylcarbene do we observe a blue shift in the emission spectrum. This is probably due to geometrical changes induced by steric crowding of the *ortho*-methyl groups.

For carbenes with one substituent per aromatic ring we find the spectral shifts to be essentially additive. For example, for 4-cyano-4-methyldiphenylcarbene, λ_{max} = 543 nm, corresponding to a 38 nm shift with respect to the parent carbene. For comparison the shifts for 4-cyanodiphenylcarbene and 4-methyldiphenylcarbene are 31 and 6 nm, respectively. The same pattern is observed throughout; note for example that each *para*-chloro substituent leads to approximately an 11 nm shift.

For those carbenes where a comparison is possible, we find that the solution fluorescence is red-shifted by about 25–30 nm with respect to the band position at 77 K (5, 6). We attribute these shifts to emission from non-equilibrium conformations at low temperature. Griller *et al.* (19) have used solid state epr methods to demonstrate that dimesitylcarbene can remain in non-equilibrium conformations (presumably with a diazo-like geometry) for extended periods of time, and that the structural relaxation can be achieved by matrix annealing. For example, when an isopentane/ether matrix containing dimesitylcarbene is annealed (by warming from 77 to 188 K) the carbene R^1—C̈—R^2 angle increases towards a more linear equilibrium conformation which is not lost upon re-cooling to 77 K. In this example it is the ground state carbene which retains a non-equilibrium (19) conformation; in the examples in Table 1, it is possible that even if the ground state carbene can relax, it is quite conceivable that in a matrix the excited state retains a ground state like conformation during its short lifetime.

The questions mentioned above were further explored by examining the temperature dependence of the fluorescence lifetimes of these carbenes. The studies were carried out in toluene solutions of ~5×10^{-5} *M* diazo precursor. Figure 2 shows the corresponding Arrhenius plots. Both dimesitylcarbene and *o*-tolylmesitylcarbene show temperature-dependent fluorescent lifetimes. Both plots are curved and approach

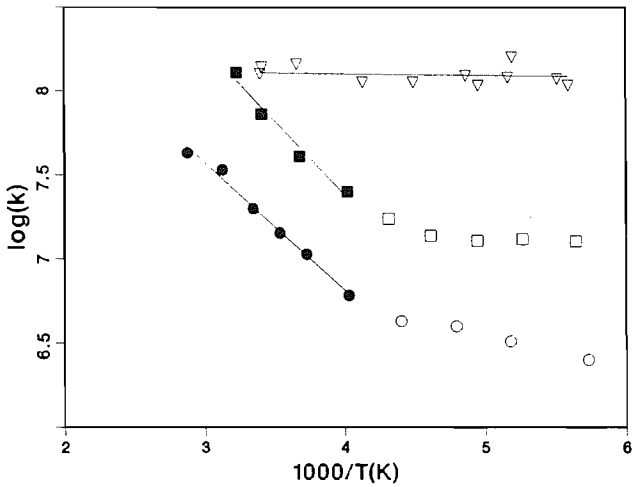

FIG. 2. Arrhenius plots illustrating the temperature dependence of the excited carbene lifetimes for dimesitylcarbene (○, ● from ref. 12), *o*-tolylmesitylcarbene (□, ■) and 4,4′-dimethyldiphenylcarbene (▽). Rate constants in s^{-1}.

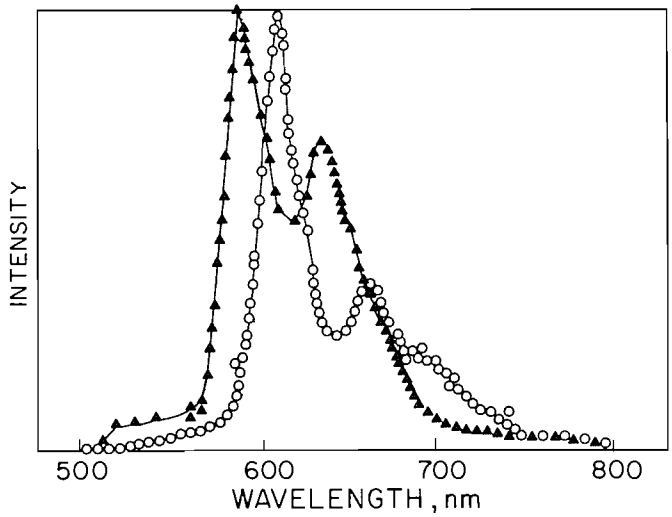

FIG. 3. Room temperature fluorescence spectra for phenyl-2-naphthylcarbene (▲) in benzene, and for the 2-naphthylmethyl radical (○).

plateau regions at low temperature. For example, for *o*-tolylmesitylcarbene the lifetime is ~80 ns at the lowest temperature and seems to extrapolate well to the value of 162 ns determined for the short component (*vide infra*) at 77 K. No temperature dependence was observed for di-*p*-tolylcarbene between 178 and 293 K. Using the high temperature data we determine the activation energies of 3.2 kcal/mol (log (A/s^{-1}) = 9.7) and 3.6 kcal/mol (log (A/s^{-1}) = 10.6) for dimesitylcarbene and *o*-tolylmesitylcarbene, respectively. These activation energies may reflect energy requirements introduced by steric restrictions to excited state relaxation. The emission spectra from phenyl-2-naphthylcarbene (λ_{max} = 588 nm) is not only shifted by 83 nm with respect to diphenylcarbene but also shows well resolved vibrational structure (Fig. 3), a feature that is not present for the other carbenes examined in this work (compare with Fig. 1). Interestingly the carbene fluorescence spectrum is very similar to that from 2-naphthylmethyl radical (20) also included in Fig. 3. This suggests that the carbenic electrons are extensively delocalized on the 2-naphthyl group. The

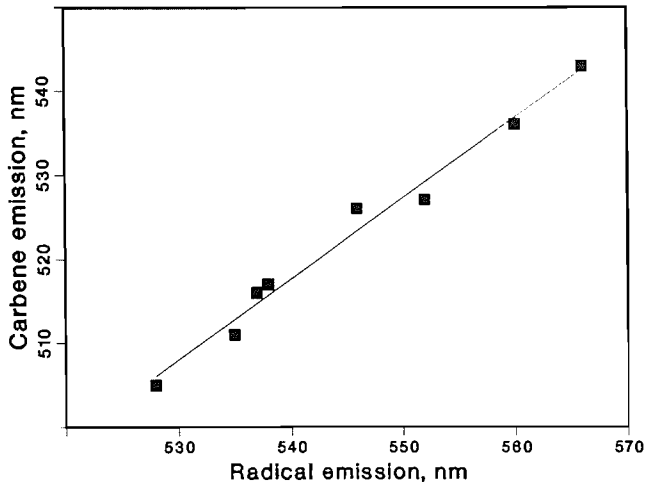

FIG. 4. Correlation between free radical and carbene luminescence spectra (see text).

vibrational separation corresponds to ~1280 cm^{-1} is similar to that in benzylic (21) and diphenylmethyl radicals (22).

It is rather interesting that while there is no correlation with the electron-withdrawing/releasing ability of the substituent, there is a remarkably good correlation between the λ_{max} position for the carbene fluorescence and for the corresponding diarylmethyl radicals which were the subject of a previous study (18). This correlation is shown in Fig. 4. The radical spectra were obtained in cyclohexane following hydrogen abstraction by the photogenerated carbene (18). The plot of Fig. 4 yields:

$$\lambda_{max}(\text{carbene}) = -1.7 \text{ nm} + 0.962\lambda_{0,0}(\text{radical})$$

with a correlation coefficient of 0.991 and λ_{max} and $\lambda_{0,0}$ in nanometers. A similar correlation can be established in terms of frequency (in cm^{-1}, not shown) and yields:

$$\lambda_{max}^{-1}(\text{carbene}) = -102 \text{ cm}^{-1} + 1.049\lambda_{0,0}^{-1}(\text{radical})$$

where λ_{max}^{-1} and $\lambda_{0,0}^{-1}$ are in cm^{-1}.

Figure 4 suggests that the same factors that determine the spectroscopic properties of excited free radicals also determine the properties of excited carbenes. A similar parallel is well established in the case of the absorption spectra of the ground state of diaryl radicals and carbenes (23, 24).

Table 2 shows a summary of the room temperature excited carbene lifetimes, along with low temperature data. In the case of free radicals we have reported an inverse correlation between the excited state lifetimes and the energy separation between the ground state and the first excited state (18). On the basis of the limited data available in Table 2 it would appear that a similar correlation does not apply in the case of carbenes. Note for example that the lifetime is longer for di-*p*-tolylcarbene compared with diphenylcarbene in spite of the red shift observed in the fluorescence spectra.

Finally, a separate study of carbene photophysics in matrices suggests that their decay frequently does not follow single exponential behaviour,[2] even in very dilute diazo solutions ($<10^{-5}$ *M*) where formation of microcrystals is unlikely. For example, for *o*-tolylmesitylcarbene in a methylcyclohexane matrix at 77 K we observe a biexponential decay with 162 and 830 ns lifetimes. It is conceivable that the two may correspond

[2]D. Weir and J. C. Scaiano. Unpublished results.

Can. J. Chem. Downloaded from www.nrcresearchpress.com by 176.9.209.113 on 09/07/12
For personal use only.

TABLE 2. Excited carbon lifetimes

Carbene		Room temperature			77 K[a]
R^1	R^2	Solvent	τ (ns)	Ref.	τ (ns)
C_6H_5	C_6H_5	Benzene	4.2	1	121, 123[b]
		Cyclohexane	4.2	9	
4-$CH_3C_6H_4$	4-$CH_3C_6H_4$	Benzene	7.2	10	109
		Toluene	8.0	[c]	
2-$CH_3C_6H_4$	Mesityl	Benzene	11.6	[c]	830
Mesityl	Mesityl	Benzene	60	13	1600
C_6H_5	4-BrC_6H_4				32
4-BrC_6H_4	4-BrC_6H_4				11[b]
C_6H_5	4-CNC_6H_4				88, 84[b]

[a]D. Weir and J. C. Scaiano, unpublished work unless otherwise indicated. In a methylcyclohexane glass.
[b]From ref. 5.
[c]This work.

to geometrically relaxed and unrelaxed carbenes. The details of these studies will be reported elsewhere.

Conclusion

The T_1–T_0 fluorescence spectra of several diarylcarbenes have been obtained in fluid solution. The carbene fluorescence maxima show an excellent correlation with the position of the D_1–D_0 fluorescence 0,0 bands for the corresponding diaryl radicals. The lifetimes of dimesitylcarbene and *o*-tolylmesitylcarbene show temperature-dependent behaviour which appears to result from hindered aryl motion in the excited state, reflecting the effect of the *ortho*-methyl groups. Relaxation modes involving ring motions (rotation?) may be shut-off at low temperatures, since the lifetimes appear to reach a plateau value and are much longer than those observed in unhindered carbenes. For example, in di-*p*-tolycarbene its lifetime in solution is essentially temperature independent in the 178 to 298 K range.

The fluorescence in matrices is blue shifted with respect to the solution (relaxed) spectra, suggesting that emission in matrices may occur from non-equilibrium conformations.

1. N. J. TURRO, M. AIKAWA, J. A. BUTCHER JR., and G. W. GRIFFIN. J. Am. Chem. Soc. **102**, 5128 (1980).
2. E. V. SITZMANN, Y. WANG, and K. B. EISENTHAL. J. Phys. Chem. **87**, 2283 (1983).
3. E. V. SITZMANN, J. LANGAN, and K. B. EISENTHAL. Chem. Phys. Lett. **102**, 446 (1983).
4. W. A. GIBBONS and A. M. TROZZOLO. J. Am. Chem. Soc. **88**, 172 (1966).
5. Y. ONO and W. R. WARE. J. Phys. Chem. **87**, 4426 (1983).
6. A. M. TROZZOLO and W. A. GIBBONS. J. Phys. Soc. **89**, 239 (1967).
7. E. LEYVA, R. L. BARCUS, and M. S. PLATZ. J. Am. Chem. Soc. **108**, 7786 (1986).
8. K. A. HORN and B. D. ALLISON. Chem. Phys. Lett. **116**, 114 (1985).
9. L. J. JOHNSTON and J. C. SCAIANO. Chem. Phys. Lett. **116**, 109 (1985).
10. J. C. SCAIANO and L. J. JOHNSTON. Pure Appl. Chem. **58**, 1273 (1986).
11. J. C. SCAIANO, L. J. JOHNSTON, W. G. MCGIMPSEY, and D. WEIR. Acc. Chem. Res. In press.
12. J. C. SCAIANO and D. WEIR. Chem. Phys. Lett. **141**, 503 (1987).
13. L. I. SMITH and K. L. HOWARD. Org. Synth. **3**, 351 (1955).
14. H. E. ZIMMERMAN and D. H. PASKOVICH. J. Am. Chem. Soc. **86**, 2149 (1964).
15. J. C. SCAIANO. J. Am. Chem. Soc. **102**, 7747 (1980).
16. J. C. SCAIANO, M. TANNER, and D. WEIR. J. Am. Chem. Soc. **107**, 4396 (1985).
17. C. DUPUY, G. M. KORENOWSKI, M. MCAULIFFE, W. M. HETHERINGTON III, and K. B. EISENTHAL. Chem. Phys. Lett. **77**, 272 (1981).
18. D. WEIR and J. C. SCAIANO. Chem. Phys. Lett. **128**, 156 (1986).
19. A. S. NAZRAN, E. J. GABE, Y. LEPAGE, D. J. NORTHCOTT, J. M. PARK, and D. GRILLER. J. Am. Chem. Soc. **105**, 2912 (1983).
20. L. J. JOHNSTON and J. C. SCAIANO. J. Am. Chem. Soc. **107**, 6368 (1985).
21. A. PELLOIS and J. RIPOCHE. Spectrochim. Acta, **26**A, 1051 (1970).
22. G. FAVARO. Spectrochim. Acta, **26**A, 2327 (1970).
23. G. B. SCHUSTER. Adv. Phys. Org. Chem. In press.
24. A. M. TROZZOLO. Acc. Chem. Res. **1**, 329 (1968).

Can. J. Chem. Downloaded from www.nrcresearchpress.com by 176.9.209.113 on 09/07/12
For personal use only.

Neutron scattering cross sections for methyl groups and tetrahedral molecules

D. W. MATUSCHEK[1] AND A. HÜLLER

Institut für Theoretische Physik I, Universität Erlangen-Nürnberg, Glückstr. 6, 8520 Erlangen, West Germany

Received October 2, 1987

D. W. MATUSCHEK and A. HÜLLER. Can. J. Chem. **66**, 495 (1988).

Neutron scattering intensities for librational excitations of molecules provide valuable information for separating librations from translational lattice modes. We have calculated the intensities for transitions from levels within the ground state multiplet to excited states for XH_3 molecules rotating around their symmetry axis and for XH_4 molecules performing three dimensional rotations. These intensities depend characteristically on the momentum transfer which should allow one to distinguish them from translational modes and from each other. These results may be used to verify assignments of lines which in the past have been based on less reliable criteria.

D. W. MATUSCHEK et A. HÜLLER. Can. J. Chem. **66**, 495 (1988).

Les intensités de la diffusion neutronique des excitations librationnelles des molécules fournissent des informations précieuses pour discerner entre les librations et les modes de translation du réseau. Pour des molécules XH_3 tournant autour de leur axe de symétrie et pour des molécules XH_4 soumises à des rotations en trois dimensions, on a calculé les intensités des transitions à partir de niveaux à l'intérieur du multiplet de l'état fondamental jusqu'aux états excités. Ces intensités dépendent d'une façon caractéristique sur le moment de transfert et cette propriété doit permettre de les distinguer entre eux ainsi que des modes de translation. On suggère d'utiliser ces résultats pour vérifier les attributions des raies qui ont été faites antérieurement sur des bases moins rigoureuses.

[Traduit par la revue]

Can. J. Chem. Downloaded from www.nrcresearchpress.com by 176.9.209.113 on 09/07/12
For personal use only.

1. Introduction

The spectroscopy of single particle rotations (1) in crystals is currently of considerable interest. The combined analysis of tunnelling features in the μeV regime and librational excitations around 10 meV has in some cases permitted a determination of the rotational potential (2–6). The data interpreted are usually experimentally measured frequencies, but intensities also contain valuable information. Calculated structure factors for tunnelling transitions (7) have been successfully used to assign tunnelling lines for physisorbed methane.

The assignment of librations is often a problem because they usually fall into a frequency range where the density of states of the translational modes also has maxima. In this case one may sometimes argue that at low temperatures the librations of hydrogen-containing molecules are the strongest features in the spectrum and that they are rapidly smeared when temperatures increase. In many cases this is not a safe statement. In a few cases several librational peaks have been measured (8) and it would be highly advantageous to uniquely assign the different lines to transitions between rotational states with definite quantum numbers.

Two recent experiments have prompted us to undertake a calculation of the structure factors for librational transitions. One is the Li acetate experiment (5) and its difficulties in assigning observed librational peaks to calculated transition frequencies (9). The second experiment (10) concerns the librational excitations in solid methane. There the ground state tunnelling splitting is 210 μeV or 2.5 K. Above liquid helium temperature the A, T, and E levels in ground state multiplet are all populated, giving rise to allowed transitions to excited librational states. For $T = 0.1$ mK only the A states are occupied and indeed the experiment shows significant changes in the spectrum. Some of the lines disappear whereas other lines show a dramatic increase in intensity. To better interpret these findings we calculated the transition matrix elements between states of definite symmetry within the ground state multiplet to the excited states.

[1]Present address: Physikalisches Institut EP IV, Universität Bayreuth, 8580 Bayreuth, West Germany.

We begin with the XH_3 groups rotating around the threefold symmetry axis. Here the rotational wave functions are well known (Mathieu problem) and the operator causing transitions can be expanded into a Fourier series in the operator for the rotation angle. The calculated results are scattering cross sections for individual transitions valid for all values of the momentum transfer. For XH_4 molecules with three rotational degrees of freedom the eigenstates are approximated by a linear combination of pocket states. With these states we find an expansion of the cross section valid for small values of momentum transfer. We observe marked differences in the intensities of individual transitions. These can be used to interpret temperature scans as in ref. 10. Despite the fact that the calculations are made for the spin-dependent part of the scattering length of the protons there is a pronounced dependence on the momentum transfer $\boldsymbol{Q}$. Angle dependencies are hard to measure. Therefore we have performed powder averages which show a characteristic $|\boldsymbol{Q}|$ dependence. We propose to exploit this $|\boldsymbol{Q}|$ dependence of the scattering cross section for a reliable assignment of the librational lines.

II. Neutron scattering cross section

The spin-dependent part of the double differential cross section for scattering of unpolarized neutrons by a single molecule with N hydrogen atoms is given by

$$[1]\qquad \frac{d^2\sigma}{d\Omega\, dE}(\boldsymbol{Q}) = \frac{8}{3} a_{sd}^2 \frac{k'}{k} \times \sum_{i,f} p_i \sum_{\mu,\mu=\pm 1/2} |\langle \mu' | \langle f | \hat{W} | i \rangle | \mu \rangle|^2 \times \delta(\hbar\omega + E_i - E_f)$$

with the operator $\hat{W}$ for the interaction between a neutron and the molecule

$$[2]\qquad \hat{W} = \sum_{j=1}^{N} \hat{\boldsymbol{S}}\hat{\boldsymbol{I}}(j) \exp\left(i\boldsymbol{Q}\hat{\boldsymbol{R}}(j)\right)$$

where $|\mu\rangle$, $|\mu'\rangle$ are the spin states and k, k' are the moduli of the wave vectors of the neutron before and after scattering, respectively; $|i\rangle$ and $|f\rangle$ are the initial and final states of the

Printed in Canada / Imprimé au Canada

molecule; E_i and E_f are the corresponding energies; p_i denotes the probability for the population of the initial state $|i>$ of the molecule; $\hat{\boldsymbol{S}}$, $\hat{\boldsymbol{I}}(j)$, and $\hat{\boldsymbol{R}}(j)$ are the operators for the neutron spin and the spin and the position of the jth hydrogen atom, respectively; $\hbar\boldsymbol{Q}$ and $\hbar\omega$ denote the momentum and the energy transferred to the molecule. The spin-dependent scattering length a_{sd} is proportional to the difference of the scattering lengths a_+ and a_- for parallel and antiparallel orientation of the spin of the neutron and the proton, respectively:

$$[3] \qquad a_{sd} = (3^{1/2}/4)(a_+ - a_-)$$

To calculate the matrix element in [1], the molecular eigenstates have to be known.

III. Molecular eigenstates

(1) General

A simple model for the description of the molecular motion is a rigid rotator which neglects translations and internal vibrations of the molecule. Molecules in a solid generally do not rotate freely. Hence they can be described by Hamiltonians of the form

$$[4] \qquad \hat{H} = \hat{\boldsymbol{L}}^2/2\theta + \phi(\hat{\alpha})$$

with the operator $\hat{\boldsymbol{L}}$ of the angular momentum and the operator $\phi(\hat{\alpha})$ of an angle-dependent potential ($\hat{\alpha}$ denotes an operator for the rotational angles; θ is the moment of inertia). Furthermore, it is assumed that the only symmetry operations with respect to which the Hamiltonian is invariant are the rotations which map the molecule upon itself.

In this model the molecular eigenstates are elements of the product space $\mathcal{H}^{rot} \otimes \mathcal{H}^{spin}$ which is built from Hilbert spaces for rotational states and spin states. The atoms at the corners of the rotating molecule XH_N are indistinguishable. Therefore the eigenstates have to belong to the irreducible representation A of the group A_N of the even permutations of N particles. Because rotational eigenstates are basis states of the irreducible representation of group A_N, it is useful to classify the spin states according to their relationship to these irreducible representations. Then one can project the products of the symmetrized rotational states and the symmetrized spin states upon the states out of $\mathcal{H}^{rot} \otimes \mathcal{H}^{spin}$ which correspond to the irreducible representation A.

(2) Rotational states

Rotational states are often obtained by inserting an expansion into free rotator states in the Schrödinger equation. Eigenstates for the one dimensional rotator XH_3 and rotational potential $\phi(\alpha) = V\cos(3\alpha)$ are calculated this way.

Another way to obtain at least approximate rotational eigenstates is to use the concept of the pocket states (11). A pocket state is described by a wave function which shows a maximum at an orientation with minimal potential energy and decreases rapidly with deviations from this orientation. Because of the symmetry of the rigid molecule XH_N and its surroundings in our model, there exist $\frac{1}{2}N!$ such minima corresponding to even permutations. For strong potentials certain linear combinations of these pocket states are considered good approximations for the eigenstates (12). To describe different rotational excitations of the molecule one needs various pocket states which correspond to wave functions differing in the number of nodes. The pocket states are denoted by $|\lambda^{(\delta)}>$, where $\lambda = 1, \ldots, N$ counts the energetically equivalent minima, and the index δ denotes the rotational excitation. In the following only the rotational ground states ($\delta = 0$) and the first excited states ($\delta = 1$) are considered. For convenience the index δ is suppressed when it is not important. With one pocket state $|1>$ given, the others follow by rotations:

$$[5] \qquad |\lambda> = \hat{P}_\lambda|1>, \quad \hat{P}_\lambda^+\hat{P}_\lambda = \hat{1}, \quad \lambda = 1, \ldots, \tfrac{1}{2}N!$$

The unitary operators $\hat{P}_\lambda$ describe the symmetry operations of the molecule in its surroundings and hence form the symmetry group A_N of the problem.

The required rotational eigenstates are the basis states of the irreducible representations of the symmetry group. They are built by application of the projectors

$$[6] \qquad \hat{O}_k^\Gamma = \frac{d(\Gamma)}{g}\sum_{\lambda=1}^{g} D_{kk}^\Gamma(\lambda)^*\hat{P}_\lambda, \quad 1 \le k \le d(\Gamma)$$

to the pocket states. $g = \frac{1}{2}N!$ and $d(\Gamma)$ in [6] are the dimensions of the group and of the irreducible representation Γ, respectively. $D_{kk}^\Gamma(\lambda)^*$ is the complex conjugate of the kth diagonal element of the unitary matrix $D^\Gamma(\lambda)$ of the irreducible representation Γ.

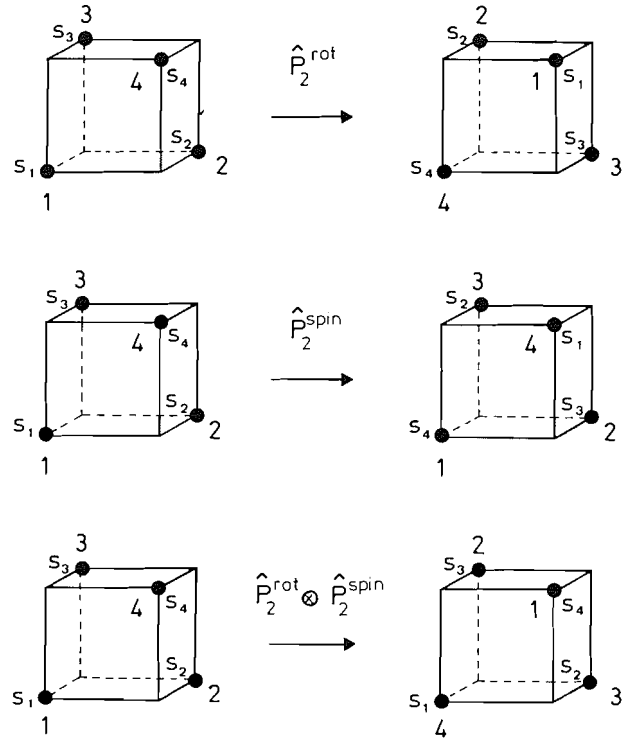

FIG. 1. Example for the action of permutations of the coordinates and the spin values of a tetrahedral molecule. j and S_j denote the number of an atom and the value of the corresponding spin, respectively ($j = 1, 2, 3, 4$).

(3) Spin states

The construction of basis states of the irreducible representations in spin space $\mathcal{H}^{spin}$ is again made by the application of projectors $\hat{O}_k^\Gamma$ from [6] to the product basis of the spin space of the N hydrogen atoms. But now the operators $\hat{P}_\lambda$ on $\mathcal{H}^{spin}$ are interpreted as operators for the permutation of spins similar to $\hat{P}_\lambda$ on $\mathcal{H}^{rot}$ are interpreted as operators for the permutation of the spatial coordinates (cf. Fig. 1).

$$[7] \qquad \hat{P}_\lambda|s_1 \ldots s_N> = |s_{\pi_\lambda(1)} \ldots s_{\pi_\lambda(N)}>$$

for each permutation π_λ of the alternating group A_N ($\lambda = 1, \ldots, \frac{1}{2}N!$).

Can. J. Chem. Downloaded from www.nrcresearchpress.com by 176.9.209.113 on 09/07/12
For personal use only.

(4) Complete states of A *symmetry*

To obtain the required molecular eigenstates one has to project upon the states of irreducible representation A in $\mathcal{H}^{\text{rot}} \otimes \mathcal{H}^{\text{spin}}$. This is done by applying the projector

$$[8] \qquad \hat{O}^A = \frac{1}{g} \sum_{\lambda=1}^{g} \hat{P}_\lambda^{\text{rot}} \otimes \hat{P}_\lambda^{\text{spin}}$$

to the products of symmetrized rotational states and symmetrized spin states and by normalization.

IV. Decomposition of $\hat{W}$

It is useful to factorize operator $\hat{W}$ into parts $\hat{W}_\gamma$ which transform under spatial rotations according to irreducible representations γ of symmetry group A_N:

$$[9] \qquad \hat{W} = \sum_\gamma \hat{W}_\gamma$$

For XH_3 and XH_4, $\hat{W}_\gamma$ is proportional to the product of operator $\hat{G}_\gamma$ involving the position operators and operator $\hat{S}_{\gamma^*}$ which involves the spin operators:

$$[10] \qquad \hat{G}_\gamma = \sum_{j=1}^{N} g_\gamma(j) \exp(i\boldsymbol{Q}\hat{\boldsymbol{R}}(j)), \quad \hat{S}_\gamma = \sum_{j=1}^{N} g_\gamma(j)\hat{\boldsymbol{S}}\hat{\boldsymbol{I}}(j)$$

Under permutations of the spins S_{γ^*} transforms according to the complex conjugate of irreducible representation γ.

The matrix elements of $\hat{W}_\gamma$ corresponding to states with rotational parts of symmetry Γ' and Γ vanish if the product $\Gamma'^* \otimes \gamma \otimes \Gamma$ does not contain the irreducible representation A.

V. Applications

(1) The one-dimensional rotator XH_3

(a) Molecular eigenstates

At low temperatures XH_3 (e.g. a methyl group) rotates around the axis of the bond to the rest of the molecule. Because of the molecular symmetry the angle-dependent potential is invariant under operations of group A_3:

$$[11] \qquad \phi(\alpha + 2\pi/3) = \phi(\alpha)$$

Bloch's theorem (13) dictates that the rotational eigenstates of the Hamiltonian with this periodic potential are characterized by a librational index (the usual band index) $n = 0, 1, 2, \ldots$ and a symmetry label (the usual wave number) $\varkappa = -1, 0, +1$:

$$[12] \qquad <\alpha|n, \varkappa> = \exp(i\varkappa\alpha) u_{n,\varkappa}(\alpha)$$

with a $2\pi/3$ periodic function $u_{n,\varkappa}(\alpha)$.

They are basis states of the irreducible representations A, E^a, and E^b (for $\varkappa = 0, +1, -1$, respectively) of the group A_3. For simplicity the potential will be approximated by the first term $V \cos(3\alpha)$ of the appropriate Fourier series. The potential strength V is measured in units of the rotational constant, $B = \hbar^2/2\theta$, of XH_3. If one writes the periodic function $u_{n,\varkappa}$ as a Fourier series, one obtains a recursion formula for the Fourier coefficients by inserting the Fourier series for $<\alpha|n, \varkappa>$ into the time-independent Schrödinger equation. Consequently the rotational eigenstates are known.

To obtain the eigenstates in $\mathcal{H}^{\text{rot}} \otimes \mathcal{H}^{\text{spin}}$ the rotational states with A, E^a, and E^b symmetry have to be combined with spin states with A, E^b, and E^a symmetry, respectively (see ref. 8). The symmetrized spin states are found in ref. 1. For each librational index there is one level with four states of symmetry A (spin 3/2) and one level with twice two eigenstates of symmetry E (spin 1/2).

To test how well a pocket state approach yields the cross sections the rotational states are approximated by linear combinations of pocket states. To each equivalent orientation of a XH_3 group a pocket state $|1>$, $|2>$, or $|3>$ is assigned. With these pocket states the librational ground states ($\delta = 0$) and the first excited librational states ($\delta = 1$) are constructed as basis states of the irreducible representations A, E^a, and E^b ($\varkappa = 0, +1, -1$, respectively):

$$[13] \qquad |\delta, \varkappa> \cong 3^{-1/2}(|1^{(\delta)}> + \epsilon^{-\varkappa}|2^{(\delta)}> + \epsilon^{\varkappa}|3^{(\delta)}>)$$

$$\epsilon = \exp(i2\pi/3)$$

The corresponding wave functions are chosen to be

$$[14] \qquad <\alpha|1^{(0)}> = (\pi\rho^2)^{-1/4} \exp(-\alpha^2/2\rho^2)$$
$$<\alpha|1^{(1)}> = (\pi\rho^6)^{-1/4}\, \alpha \exp(-\alpha^2/2\rho^2)$$

which are normalized

$$[15] \qquad <1|1> = \int_{-\pi}^{+\pi} |<\alpha|1>|^2 \, d\alpha \cong \int_{-\infty}^{+\infty} |<\alpha|1>|^2 \, d\alpha = 1$$

The other wave functions follow from $<\alpha|1>$ by

$$[16] \qquad <\alpha|2> = <\alpha + 2\pi/3|1>, \quad <\alpha|3> = <\alpha - 2\pi/3|1>$$

The connection between the parameter ρ for the width of the wave functions and the potential strength V is made by the Ritz variational principle.

(b) Fourier series for $\hat{W}$

The interaction operator $\hat{W}$ reads

$$[17] \qquad \hat{W} = \frac{1}{3} \sum_{s=-1}^{+1} \hat{S}_{-s}\hat{G}_s$$

where

$$\hat{S}_s = \hat{\boldsymbol{S}}(\hat{\boldsymbol{I}}(1) + \epsilon^{-s}\hat{\boldsymbol{I}}(2) + \epsilon^{s}\hat{\boldsymbol{I}}(3))$$

$$[18] \qquad \hat{G}_s = \exp(i\boldsymbol{Q}\hat{\boldsymbol{R}}(1)) + \epsilon^{-s} \exp(i\boldsymbol{Q}\hat{\boldsymbol{R}}(2)) + \epsilon^{s} \exp(i\boldsymbol{Q}\hat{\boldsymbol{R}}(3))$$

$$\epsilon = \exp(i2\pi/3)$$

$s = +1, 0, -1$ corresponds to the symmetry E^a, A, E^b, respectively. To obtain a Fourier series for the operator $\hat{G}_s$ it is useful to introduce the following space fixed coordinate system (cf. Fig. 2). The x–y plane is the rotational plane of the XH_3 with the z axis as the rotational axis. q is the projection of $\boldsymbol{Q}$ into the x–y plane; q denotes its modulus. ϕ and θ are azimuthal and polar angles of $\boldsymbol{Q}$.

Now the scalar products are

$$[19] \qquad \boldsymbol{QR}(j) = \boldsymbol{qR}(j) = qr \times \begin{cases} \cos(\alpha - \phi) & j = 1 \\ \cos(\alpha - \phi + 2\pi/3) & \text{if } j = 2 \\ \cos(\alpha - \phi - 2\pi/3) & j = 3 \end{cases}$$

where $r = |\boldsymbol{R}(j)|$ is the radius of the methyl group.

With these expressions the Fourier expansion of the operator $\hat{G}_s$ reads (cf. Appendix A)

$$[20] \qquad \hat{G}_s = 3\sum_{l \in Z} I_{|3l+s|}(iqr) \exp[i(3l + s)(\hat{\alpha} - \phi)]$$

Can. J. Chem. Downloaded from www.nrcresearchpress.com by 176.9.209.113 on 09/07/12
For personal use only.

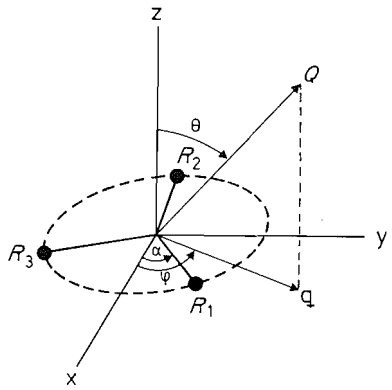

FIG. 2. Space fixed coordinate system for an XH_3 group ($\boldsymbol{R}_j$ denotes the positions of the protons, $j = 1, 2, 3$, ϕ and θ characterize the orientation of the momentum transfer $\boldsymbol{Q}$.

$\hat{\alpha}$ is the operator for the rotational angle, I_m denotes the modified Bessel function of the first kind and of order m; Z is the set of all integers.

(c) Calculation of the matrix elements of $\hat{W}$

The determination of the matrix elements of $\hat{G}_s$ reduces to the calculation of

$$[21] \quad <n',\varkappa'|\exp(i(3l+s)(\hat{\alpha}-\phi))|n,\varkappa>$$

This matrix element equals the integral over all rotational angles:

$$[22] \quad \int_{-\pi}^{+\pi} <n',\varkappa'|\alpha><\alpha|n,\varkappa>\exp(i(3l+s)(\hat{\alpha}-\phi))\mathrm{d}\alpha = 2\pi[\exp(-i(3l+s)\phi)P(n,\varkappa,n',\varkappa',s,l)f(\varkappa,\varkappa',s)$$

with the abbreviations

TABLE 1. Selection rule $f(\varkappa,\varkappa',s)$

		$\varkappa$		
s	$\varkappa'$	-1	0	$+1$
-1		0	1	0
0	-1	1	0	0
$+1$		0	0	1
-1		0	0	1
0	0	0	1	0
$+1$		1	0	0
-1		1	0	0
0	$+1$	0	0	1
$+1$		0	1	0

$$[23] \quad P(n,\varkappa,n',\varkappa',s,l) = \sum_{p\in Z}^{*} a_{n'\varkappa'}(p+l+\eta)a_{n\varkappa}(p)$$
$$\eta = (\varkappa-\varkappa'+s)/3$$

where $a_{n\varkappa}(p)$ denotes the Fourier coefficients in the expansion of $<\alpha|n,\varkappa>$. In the pocket state approach (where $n = 0$ and $n' = 1$) the expression [21] can be calculated by neglecting the overlaps as a Fourier integral and [23] is replaced by

$$[23a] \quad P(n,\varkappa,n',\varkappa',s,l) = i(3l+s)\rho\exp(-(3l+s)^2\rho^2/4)/(2^{3/2}\pi)$$

which is obviously independent of $\varkappa$ and $\varkappa'$.

For fixed $\varkappa$ and $\varkappa'$ the function $f(\varkappa,\varkappa',s)$ equals unity for exactly one value of $s \in \{-1, 0, +1\}$ and vanishes otherwise (cf. Table 1). The squared modulus of the required matrix element of $\hat{G}_s$ is

$$[24] \quad |<n',\varkappa'|\hat{G}_s|n,\varkappa>|^2 = 9\sum_{l,l'\in Z} I_{|3\lambda'+s|}(iqr)^* I_{|3l+s|}(iqr)\exp(i3(l'-l)\phi) \times 4\pi^2 P(n,\varkappa,n',\varkappa',s,l')^* P(n,\varkappa,n',\varkappa',s,l)f(\varkappa,\varkappa',s)$$

So far one would obtain scattering cross sections which depend on the direction of the momentum transfer (characterized by ϕ and $q = Q\sin\theta$) and hence are adapted for scattering by single crystals. For powder samples one needs the squared matrix element [24] averaged over all orientations of $\boldsymbol{Q}$ (cf. Appendix B):

$$[25] \quad g_s(n,\varkappa,n',\varkappa') = (4\pi)^{-1}\int|<n',\varkappa'|\hat{G}_s|n,\varkappa>|^2\mathrm{d}\Omega = (9/2)\sum_{l\in Z}\int_0^{\pi}|I_{|3l+s|}(iQr\sin\theta)|^2\sin\theta\,\mathrm{d}\theta \times 4\pi^2|P(n,\varkappa,n',\varkappa',s,l)|^2 f(\varkappa,\varkappa',s)$$

where

$$[26] \quad \int_0^{\pi}|I_{|3l+s|}(iQr\sin\theta)|^2\sin\theta\,\mathrm{d}\theta = 2(-1)^{l+s}\sum_{p\geq|3l+s|}\frac{(-Q^2r^2)^p}{(2p+1)(p+|3l+s|)!(p-|3l+s|)!}$$

By interchanging the order of the two sums over l and p in [25] the following series results (cf. Appendix C)

$$[27] \quad g_s(n,\varkappa,n',\varkappa') = 9\sum_{p\geq 1}\frac{(-Q^2r^2)^p}{2p+1}\sum_{l=-\mathrm{Int}\left[\frac{p+s}{3}\right]}^{\mathrm{Int}\left[\frac{p-s}{3}\right]}\frac{(-1)^{l+s}}{(p+|3l+s|)!(p-|3l-s|)!} \times 4\pi^2|P(n,\varkappa,n',\varkappa',s,l)|^2 f(\varkappa,\varkappa',s) + 9\delta_{n,n'}\delta_{\varkappa,\varkappa'}$$

where Int ( ) denotes the integer part of a number. The spin-dependent factors

$$[28] \quad F(\varkappa,\varkappa') = (1/9)\sum_{\mu,\mu'=\pm 1/2}\sum_{\varkappa_\varkappa\varkappa'_{\varkappa'}}|<\mu'|<\varkappa'_{\varkappa'}|\hat{S}_{-s}|\varkappa_\varkappa>|\mu>|^2$$

are easily calculated with the knowledge of the spin matrix of XH_3 (14).[2] $|\varkappa_\varkappa>$ and $|\varkappa'_{\varkappa'}>$ are the spin states belonging to the rotational states $|n,\varkappa>$ and $|n',\varkappa'>$, respectively. $|\mu>$ and $|\mu'>$ are spin states of the neutron before and after scattering. The values of $F(\varkappa,\varkappa')$ are given in Table 2.

[2]To get $F(\mathcal{H},\mathcal{H}')$, the values in Table 1 of ref. 14 have to be divided by 3.

Can. J. Chem. Downloaded from www.nrcresearchpress.com by 176.9.209.113 on 09/07/12
For personal use only.

TABLE 2. Spin dependent factors $F(\varkappa,\varkappa')$

	$\varkappa$		
$\varkappa'$	0	+1	−1
0	5/6	1/3	1/3
+1	1/3	1/12	1/3
−1	1/3	1/3	1/12

(d) Results

The scattering cross section for the transition $n\varkappa \rightarrow n'\varkappa'$ is given by

$$[29]\quad \frac{d^2\sigma}{d\Omega dE}(n\varkappa \rightarrow n'\varkappa') = (8k'/3k)a_{sd}^2 p_{n,\varkappa} F(\varkappa,\varkappa') \times g_s(n,\varkappa,n',\varkappa')\delta(\hbar\omega + E_{n\varkappa} - E_{n'\varkappa'})$$

For thermal energies which are high compared to the tunnelling energy and low compared to the energy of the librational excitation, the multiplet of the ground states ($n = 0$) is equally populated whereas all other states are not occupied. The cross sections for the transitions between the energy levels are obtained by addition of the cross sections for the transitions between the adequate states:

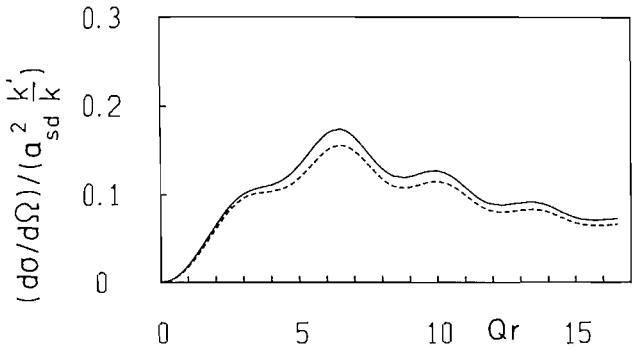

FIG. 3. Cross sections for calculations with exact rotational states (dashed line) and pocket states (solid line) for an XH_3 group and a potential strength of $20B$ (transition $0A \rightarrow 1E$).

$$[30]\quad \frac{d^2\sigma}{d\Omega dE}(0\Gamma \rightarrow n\Gamma', Q) = (k'/3k)a_{sd}^2\delta(\hbar\omega + E_{0\Gamma} - E_{n\Gamma'}) \times \begin{cases} (5/6)g_0(0,0,n,0) & \Gamma = A,\ \Gamma' = A \\ (1/3)[g_{+1}(0,0,n,+1) + g_{-1}(0,0,n,-1)] & \Gamma = A,\ \Gamma' = E \\ (1/3)[g_{-1}(-1,0,n,0) + g_{+1}(0,+1,n,0)] & \text{if}\quad \Gamma = E,\ \Gamma' = A \\ (1/3)[g_{+1}(0,+1,n,-1) + g_{-1}(0,-1,n,+1)] & \\ \quad + (1/12)[g_0(0,+1,n,+1) + g_0(0,-1,n,-1)] & \Gamma = E,\ \Gamma' = E \end{cases}$$

The leading term in Q of the cross section for the transition $0A \rightarrow nA$ is Q^6. Therefore, the cross section for this transition is suppressed for $Qr \lesssim 2$ as seen in Fig. 3 where the cross sections for equal population of the whole librational multiplet are plotted. In Fig. 4 the result of the pocket state approach is compared with the calculation with the exact wave functions. For a potential strength of $20B$ or more, the deviations do not exceed 10% even for large momentum transfers $Qr > 2$. Therefore one can hope that also in the case of XH_4 and for sufficiently strong potentials the rotational states would well be approximated by linear combinations of pocket states. If the potential strength increases, the intensities grow for large momentum transfers and decrease for small momentum transfers.

(2) The three dimensional rotator XH_4

(a) Molecular eigenstates

Here a tetrahedral molecule in surroundings with tetrahedral symmetry is considered. To describe the rotational motion of the molecule, one has to find the eigenstates of the Hamiltonian [4] where the potential energy shows 12 equivalent pockets corresponding to the 12 symmetry operations of the group A_4. The orientation of the molecule with respect to its surroundings is described by a normalized quaternion τ (11).

Hence the potential energy is defined as a function on the unit sphere in four dimensions. In the following it is approximated by the first term $AH_1^{(3)}(\tau)$ of its expansion into cubic rotator functions (11) ($A < 0$ is the parameter of the potential strength). One of its twelve minima is at the position (0 0 0 1) to which the pocket states $|1^{(\delta)}>$ are assigned. The corresponding wave functions with the librational index $\delta = 0$ and $\delta = 1$ are chosen to be (11)

$$[31]\quad <\tau|1^{(0)}> = ((2M_0 + 1)!)^{1/2}(2\pi^2(4M_0 - 1)!!)^{-1/2}2^{M_0}\tau_4^{2M_0}$$

$$<\tau|1^{(1)}> = ((2M_1 + 3)!/(4M_1 + 1)!!)^{1/2}(2\pi^2)^{-1/2}2^{M_1+1}\tau_1\tau_4^{2M_1+1}$$

These wave functions are normalized on the four dimensional unit sphere:

$$[32]\quad <1|1> = \int_{\tau^2=1} |<\tau|1>|^2 d^4\tau = 1$$

where M_0 and M_1 are width parameters connected to the potential strength via the Ritz variational principle. For strong potentials where the overlap of different pocket states is negligible, only the knowledge of these wave functions is necessary to compute the scattering cross section.

With the unitary matrices of the irreducible representations A, E^a, E^b, and T of the group A_4 (compare Table 3) the rotational eigenstates are given by

$$[33]\quad |\eta> = N_\eta \sum_{\lambda=1}^{12} g_{\eta\lambda}|\lambda> \qquad \eta \in \{A, E^a, E^b, T_{xj}, T_{yj}, T_{zj} | j = 1, 2, 3\}$$

with the coefficients $g_{\eta\lambda}$ given in Table 1 of ref. 4 (there, $E1$ and $E2$ correspond to E^a and E^b, respectively).

The normalization constants in the limit of negligibly small overlaps are (4)

$$[34]\quad N_A = N_E = 1/\sqrt{12},\quad N_T = 1/2$$

Can. J. Chem. Downloaded from www.nrcresearchpress.com by 176.9.209.113 on 09/07/12
For personal use only.

TABLE 3. Irreducible representation of symmetry group A_4

λ	Symmetry operation	Permutation π_λ	$D^A(\lambda) = X^A(\lambda)$	$D^{E^a}(\lambda) = X^{E^a}(\lambda)$	$D^{E^b}(\lambda) = X^{E^b}(\lambda)$	$\mathbf{D}^T(\lambda)$	$X^T(\lambda)$
1	E	1234	1	1	1	$\begin{pmatrix} 1 & 0 & 0 \\ 0 & 1 & 0 \\ 0 & 0 & 1 \end{pmatrix}$	3
2	C_{2x}	4321	1	1	1	$\begin{pmatrix} -1 & 0 & 0 \\ 0 & -1 & 0 \\ 0 & 0 & 1 \end{pmatrix}$	−1
3	C_{2y}	3412	1	1	1	$\begin{pmatrix} 1 & 0 & 0 \\ 0 & -1 & 0 \\ 0 & 0 & -1 \end{pmatrix}$	−1
4	C_{2z}	2143	1	1	1	$\begin{pmatrix} -1 & 0 & 0 \\ 0 & 1 & 0 \\ 0 & 0 & -1 \end{pmatrix}$	−1
5	$C_3^-(1\,1\,1)$	3124	1	ϵ	ϵ^*	$\begin{pmatrix} 0 & 0 & -1 \\ -1 & 0 & 0 \\ 0 & 1 & 0 \end{pmatrix}$	0
6	$C_3^+(1\,1\,\bar{1})$	2431	1	ϵ	ϵ^*	$\begin{pmatrix} 0 & 0 & -1 \\ 1 & 0 & 0 \\ 0 & -1 & 0 \end{pmatrix}$	0
7	$C_3^+(\bar{1}\,1\,1)$	1342	1	ϵ	ϵ^*	$\begin{pmatrix} 0 & 0 & 1 \\ -1 & 0 & 0 \\ 0 & -1 & 0 \end{pmatrix}$	0
8	$C_3^+(1\,\bar{1}\,1)$	4213	1	ϵ	ϵ^*	$\begin{pmatrix} 0 & 0 & 1 \\ 1 & 0 & 0 \\ 0 & 1 & 0 \end{pmatrix}$	0
9	$C_3^+(1\,1\,1)$	2314	1	ϵ^*	ϵ	$\begin{pmatrix} 0 & -1 & 0 \\ 0 & 0 & 1 \\ -1 & 0 & 0 \end{pmatrix}$	0
10	$C_3^-(1\,\bar{1}\,1)$	3241	1	ϵ^*	ϵ	$\begin{pmatrix} 0 & 1 & 0 \\ 0 & 0 & 1 \\ 1 & 0 & 0 \end{pmatrix}$	0
11	$C_3^-(1\,1\,\bar{1})$	4132	1	ϵ^*	ϵ	$\begin{pmatrix} 0 & 1 & 0 \\ 0 & 0 & -1 \\ -1 & 0 & 0 \end{pmatrix}$	0
12	$C_3^-(\bar{1}\,1\,1)$	1423	1	ϵ^*	ϵ	$\begin{pmatrix} 0 & -1 & 0 \\ 0 & 0 & -1 \\ 1 & 0 & 0 \end{pmatrix}$	0

Can. J. Chem. Downloaded from www.nrcresearchpress.com by 176.9.209.113 on 09/07/12
For personal use only.

TABLE 4. Table of the molecular eigenstates (I denotes the total nuclear spin)

I	$2I+1$	Normalized molecular eigenstates
2	5	$\|A>\otimes\|A,I_z>$
1	3	$3^{-1/2}(\|T_x1>\otimes\|T_x,I_z>+\|T_x2>\otimes\|T_y,I_z>+\|T_x3>\otimes\|T_z,I_z>)$
1	3	$3^{-1/2}(\|T_y1>\otimes\|T_y,I_z>+\|T_y2>\otimes\|T_z,I_z>+\|T_y3>\otimes\|T_x,I_z>)$
1	3	$3^{-1/2}(\|T_z1>\otimes\|T_z,I_z>+\|T_z2>\otimes\|T_x,I_z>+\|T_z3>\otimes\|T_y,I_z>)$
0	1	$\|E^b>\otimes\|E^a,0>$
0	1	$\|E^a>\otimes\|E^b,0>$

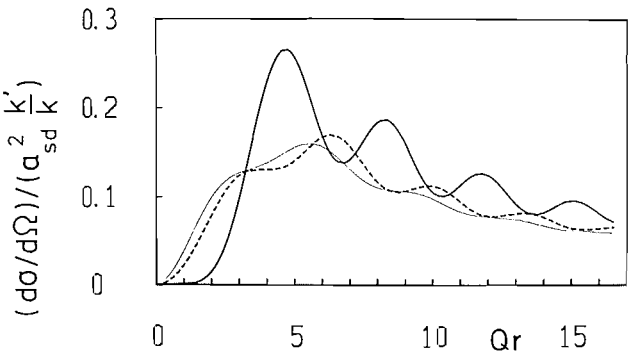

FIG. 4. Cross sections for the transitions $0A \rightarrow 1A$ (bold solid line), $0E \rightarrow 1A$ and $0A \rightarrow 1E$ (bold dashed line), and $0E \rightarrow 1E$ (solid line) for an XH_3 group and the potential strength $10B$.

The levels with E symmetry as well as the levels with T symmetry are degenerated (1).

The symmetrized spin states are found in ref. 15. They are denoted by $|\eta,I_z>$ where η indicates the symmetry and I_z denotes the z component of the total nuclear spin of the four protons. The resulting eigenstates in $\mathcal{H}^{rot}\otimes\mathcal{H}^{spin}$ are listed in Table 4. In another notation, they are also found in ref. 4.

TABLE 5. Factors $g_\gamma(j)$ in the expansion [10] of the symmetrized operator W_γ for XH_4

	j			
γ	1	2	3	4
A	+1	+1	+1	+1
T_x	+1	−1	−1	+1
T_y	+1	−1	+1	−1
T_z	+1	+1	−1	−1
E	0	0	0	0

(b) Approximate calculation of the matrix elements of $\hat{W}$

Operator $\hat{W}$ may be written as

$$[35]\qquad \hat{W}=\frac{1}{4}\sum_{\gamma=A,T_x,T_y,T_z}\hat{S}_\gamma\hat{G}_\gamma$$

(the coefficients $g_\gamma(j)$ in the definitions of $\hat{G}_\gamma$ and $\hat{S}_\gamma$ in [10] are given in Table 5 (1)). To obtain $<1^{(1)}|\hat{G}_\gamma|1^{(0)}>$ the matrix element $<1^{(1)}|e^{i\boldsymbol{QR}}|1^{(0)}>$ will be approximated for small $|\boldsymbol{QR}|$ (cf. Appendix E):

$$[36]\qquad <1^{(1)}|e^{i\boldsymbol{Q}\hat{\boldsymbol{R}}}|1^{(0)}> = F(M_0,M_1)\exp(i\boldsymbol{Q}.\boldsymbol{R}')\boldsymbol{Q}.\mathbf{U}.\boldsymbol{R}'\left\{\frac{i}{M^{1/2}}+\frac{1}{M^{3/2}}\left(2\boldsymbol{Q}.\boldsymbol{R}'-i\left[\frac{9}{8}+\frac{1}{2}(\boldsymbol{Q}\times\boldsymbol{R}')^2\right]\right)\right.$$
$$+\frac{1}{M^{5/2}}\left(i\left[\frac{275}{64}+\frac{37}{16}(\boldsymbol{Q}\times\boldsymbol{R}')^2-3(\boldsymbol{Q}.\boldsymbol{R}')^2+\frac{1}{8}(\boldsymbol{Q}\times\boldsymbol{R}')^4\right]-\frac{3}{2}(\boldsymbol{Q}\times\boldsymbol{R}')^2\boldsymbol{Q}.\boldsymbol{R}'\right)$$
$$+\frac{1}{M^{7/2}}\left(i\left[-\frac{24163}{1152}+\frac{1807}{128}(\boldsymbol{Q}\times\boldsymbol{R}')^2+\frac{135}{8}(\boldsymbol{Q}.\boldsymbol{R}')^2-\frac{1}{48}(\boldsymbol{Q}\times\boldsymbol{R}')^6\right]+\frac{931}{32}\boldsymbol{Q}.\boldsymbol{R}'+\frac{183}{16}(\boldsymbol{Q}\times\boldsymbol{R}')^2\boldsymbol{Q}.\boldsymbol{R}'\right.$$
$$\left.\left.-\frac{77}{64}(\boldsymbol{Q}\times\boldsymbol{R}')^4-4(\boldsymbol{Q}.\boldsymbol{R}')^3+3(\boldsymbol{Q}\times\boldsymbol{R}')^2(\boldsymbol{Q}.\boldsymbol{R}')^2+\frac{1}{2}(\boldsymbol{Q}\times\boldsymbol{R}')^4\boldsymbol{Q}.\boldsymbol{R}'\right)+O\left(\frac{1}{M^{9/2}}\right)\right\}$$

where M denotes the average width parameter $\frac{1}{2}(M_0+M_1)$, the matrix $\boldsymbol{U}$ is defined to be

$$[37]\qquad \boldsymbol{U}=\begin{pmatrix}0&0&0\\0&0&1\\0&-1&0\end{pmatrix}$$

In the range of potential strength considered $30B \le |A| \le 150B$, F varies between 1.04 and 1.02. $<1^{(1)}|\hat{G}_\gamma|1^{(0)}>$ follows from [37] by taking the coordinate vectors $\boldsymbol{R}'_j$ of the four corners of the tetrahedron in an arbitrary coordinate system and summing over j according to the prescription for the operator $\hat{G}_\gamma$, what is done — like the computing of the cross sections — by a computer program.

(c) Results

The scattering cross section for the transition from an energy level 0Γ in the librational ground state multiplet to an energy level $1\Gamma'$ in the first excited librational multiplet reads (in the limit of small overlap)

$$[38]\qquad \frac{d^2\sigma}{d\Omega dE}(0\Gamma\rightarrow 1\Gamma') = (k'/864k)a_{sd}^2 Y(\Gamma,\Gamma')\delta(\hbar\omega+E_{0\Gamma}-E_{1\Gamma'})$$
$$\times\left(a(\Gamma,\Gamma')|<1^{(1)}|\hat{G}_A|1^{(0)}>|^2+t(\Gamma,\Gamma')\sum_{\gamma=T_x,T_y,T_z}|<1^{(1)}|\hat{G}_\gamma|1^{(0)}>|^2\right)$$

Can. J. Chem. Downloaded from www.nrcresearchpress.com by 176.9.209.113 on 09/07/12
For personal use only.

TABLE 6. Dependence of a, t, and Y on Γ and Γ'

Γ	Γ'	a	t	Y_{XH_4}	Y_{XD_4}
A	A	1	0	135	70
A	T	0	1	45	30
T	A				
T	T	3	2	27	42
T	E	0	1	36	36
E	T				
E	E	1	0	0	20

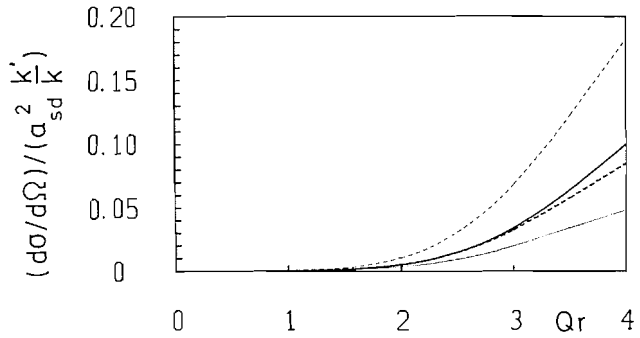

FIG. 5. Cross section for the transition from the level $0A$ into the level $1A$ of XH_4 in different orders of the approximation [36].

The factors $a(\Gamma,\Gamma')$, $t(\Gamma,\Gamma')$, and $Y(\Gamma,\Gamma')$ are listed in Table 6. (For their calculation, compare Appendix E.)

In [38] it is assumed that the sixteen librational ground states are equally populated whereas the excited librational states are not populated. If one considers the case where the temperature is so low that only the lowest energy level is populated and all other states not, one has to multiply the right hand side of expression [38] with 16/5.

The spin matrix elements appear in the factor $Y(\Gamma,\Gamma')$. With the data from ref. 4, the corresponding factors for XD_4 are also available. Because of the 81 states within a librational multiplet, the correction factor 16/81 is necessary. This factor is already taken in consideration in $Y(\Gamma,\Gamma')$ for XD_4. By sole population of the $0A$ level, the additional factor then is 81/15 because of the 15-fold degeneration of the A level.

In Figs. 5 to 7 cross sections for powder samples and a potential strength of $A = -50B$ are plotted. For potential strengths with moduli greater than $50B$, the overlaps of the pocket states are smaller than 1% of the norm of one pocket state and hence are negligible.

To check the reliability of the expansion of the matrix element in expression [36] we plot in Fig. 5 the cross section for the transition $0A \rightarrow 1A$ the different orders of the approximation. The dashed, solid, bold dashed, and bold solid lines are terms up to order $M^{-1/2}$, $M^{-3/2}$, $M^{-5/2}$, and $M^{-7/2}$, respectively. One concludes that the approximation seems to be reliable for $Qr \lesssim 3.5$. For this transition the leading term for small momentum transfers is again $(Qr)^6$. This result is already given in ref. 18. All other cross sections start with the term $(Qr)^2$. Hence, for small transfers $Qr \ll 1$, the transition $0A \rightarrow 1A$ is suppressed with respect to transition $0A \rightarrow 1T$ (there is no transition from the A level into an E level because of the lack of an E symmetric part of the operator $\hat{W}$). The cross sections for the transitions $0E \rightarrow 1E$ for XH_4 and for XD_4 differ only slightly (in the considered units) although for XH_4 there are no

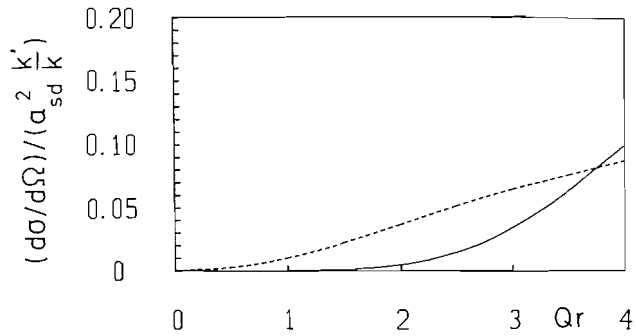

FIG. 6. Cross section for the transition into level $1A$ from the levels $0A$ (solid line) and $0T$ (dashed line) at equal populated librational multiplet 0.

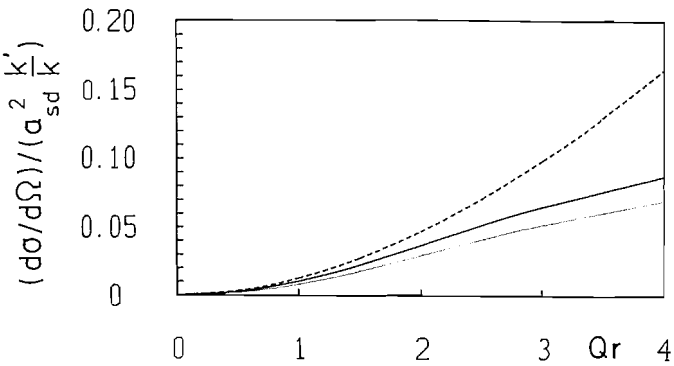

FIG. 7. Cross sections for transitions into level $1T$ from levels $0A$ (bold solid line), $0T$ (bold dashed line), and $0E$ (solid line).

contributions of a transition between E states in contrast to the case of XD_4. The intensities for the transition into the level $1E$ (which equals the intensities for the transition $0E \rightarrow 1T$) is suppressed with respect to the other transitions (Figs. 6 and 7).

VI. Conclusions

In recent years a considerable amount of spectroscopic information on the rotational energy levels of small molecules has been obtained from neutron scattering experiments. Tunnelling transitions are found at energies below 200 μeV, i.e. in a region where no other excitations are expected and therefore the tunnelling lines are easily identified. Except for a few cases (7, 19) line intensities have not been necessary for an interpretation of the spectra. This is completely different for librational excitations of molecules which share the energy range around 10 meV with the translational modes of the lattice. The identification so far has been rather uncertain and it is hoped that our calculations will help to remedy this unsatisfactory situation. To this end we have calculated the line intensities for librational transitions of XH_3 and XH_4 molecules. For protons the overwhelming contribution comes from the spin-dependent scattering amplitude and because of the correlation of the proton spins within one molecule it shows a pronounced dependence on $\boldsymbol{Q}$. The angle dependence is hard to measure and therefore we have averaged the intensities for powder samples. We have obtained characteristic variations with $|\boldsymbol{Q}|$ with marked differences for transitions from the ground state multiplet into excited states of different symmetry. We propose to use the $|\boldsymbol{Q}|$ dependence of the intensities as signatures for the different transitions. Even better discrimination may be achieved by cooling the sample to a temperature where only the A level

Can. J. Chem. Downloaded from www.nrcresearchpress.com by 176.9.209.113 on 09/07/12
For personal use only.

in the ground state multiplet is occupied. Then the observed transitions occur between initial and final states of definite symmetries. For small momentum transfers the intensity for transitions between A states e.g. is proportional to $|\boldsymbol{Q}|^6$. Up to now the $|\boldsymbol{Q}|$ dependence of the librational modes has not been studied systematically, but it would be interesting to check earlier assignments (20–22) of lines in the 10 meV regime to librational modes by determining the $|\boldsymbol{Q}|$ dependence of intensities. The experiment (10) which has prompted this work is hard to interpret. Only the intensity above 4 meV is due to the librations of the ordered molecules and it consists of a few narrow but rather weak features on broad and intense band. The band is probably due to the dispersion of the librational modes whereas the narrow features stem from the van Hove singularities at extrema of the dispersion curves. A much more detailed analysis would be necessary to explain these intensity variations with temperature and momentum transfer.

Our calculations for XH_3 molecules which perform a unidimensional rotation around their symmetry axis is valid for all potential strengths. An experiment to check our predictions for the almost free NH_3 rotators in $Co(NH_3)_6(PF_6)_2$ (23) is in progress (24).

Acknowledgement

This work was supported by the German Ministry for Research and Technology under contract number 03-HU1ERL8.

1. W. Press. Single particle rotations in molecular crystals. Springer tracts in modern physics. Vol. 92. 1981.
2. D. Cavagnat, A. Magerl, C. Vettier, I. S. Anderson, and S. F. Trevino. Phys. Rev. Lett. **54**, 193 (1985).
3. Th. Brückel, W. Prandl, K. Vogt, and C. M. E. Zeyen. J. Phys. C, **17**, 4071 (1984).
4. A. Hüller and W. Press. Phys. Rev. B, **24**, 17 (1981).
5. S. Clough, A. Heidemann, A. H. Horsewill, and M. Paley. Z. Phys. B, **55**, 1 (1984).
6. W. Häusler and A. Hüller. Z. Phys. B, **59**, 177 (1985).
7. M. V. Smalley, A. Hüller, R. K. Thomas, and J. W. White. Mol. Phys. **44**, 533 (1981).
8. Y. Kataoka, W. Press, U. Buchenau, and H. Spitzer. Proceedings of International Symposium of Neutron Scattering, Oct. 1977. Vienna. p. 311.
9. A. Heidemann, J. Eckert, L. Passel, and W. Häusler. Z. Phys. B, **66**, 75 (1987).
10. W. Press, A. Heidemann, H. Lauter, J. A. Morrison, and K. Neumaier. To be published.
11. A. Hüller and D. M. Kroll. J. Chem. Phys. **63**, 4495 (1975).
12. A. Hüller. Phys. Rev. B, **16**, 1844 (1977).
13. N. W. Ashcroft and N. D. Mermin. Solid state physics. 1st ed. Tokyo, Holt-Saunders. 1981. p. 133.
14. S. Clough, A. Heidemann, and M. Paley. J. Phys. C, **13**, 4009 (1980).
15. J. Hama and H. Miyagi. Prog. Theoret. Phys. **50**, 1142 (1973).
16. I. N. Bronstein and K. A. Semendjajew. Taschenbuch der Mathematik, Thun, Frankfurt am Main, H. Deutsch. 1983.
17. R. W. Gerling and A. Hüller. Z. Phys. B, **40**, 209 (1980).
18. Y. Ozaki, Y. Kataoka, and T. Yamamoto. J. Chem. Phys. **73**, 3442 (1980).
19. G. J. Kearley, J. K. Cockcroft, A. N. Fitch, and B. E. F. Fender. J. Chem. Soc. Chem. Commun. 1738 (1968).
20. M. Prager, W. Press, B. Alefeld, and A. Hüller. J. Chem. Phys. **67**, 5126 (1977).
21. S. Clough, A. Heidemann, and H. Kraxenberger. Phys. Rev. Lett. **42**, 1298 (1979).
22. K. J. Tilli and B. Alefeld. Mol. Phys. **36**, 287 (1978).
23. G. J. Kearley, H. Blank, and J. K. Cockcroft. J. Chem. Phys. **86**, 5989 (1987).
24. H. Blank and G. J. Kearley. Private communication.

Appendices

Appendix A: Fourier expansion of the operator $\hat{G}_s$

With the abbreviations

[A1] $$\xi = \alpha - \phi \ , \quad \epsilon = \exp(i2\pi/3)$$

the operator $\hat{G}_s$ reads (compare the definition (18))

[A2] $$\hat{G}_s = \exp[iqr\cos(\xi)] + \epsilon^{-s}\exp[iqr\cos(\xi + 2\pi/3)] + \epsilon^{+s}\exp[iqr\cos[\xi - 2\pi/3)]$$

The Taylor expansion of the exponential function reads (after application of the binomial formula)

[A3] $$\exp[iqr\cos(\xi + x)] = \sum_{N=0}^{\infty}\sum_{k=0}^{N}\frac{1}{k!(N-k)!}\left(\frac{iqr}{2}\right)^N \exp[i(\xi + x)(2k - N)]$$

By insertion in [A2] one gets

[A4] $$\hat{G}_s = \sum_{N=0}^{\infty}\sum_{k=0}^{N}\frac{1}{k!(N-k)!}\left(\frac{iqr}{2}\right)^N \times \{\exp[i\xi(2k - N)]\}L(2k - N - s)$$

where $L(m)$ is defined for integer m by

[A5] $$L(m) = 1 + \epsilon^m + \epsilon^{-m} = 3\sum_{l\in Z}\delta_{m,3l}$$

By interchanging the order of summations and execution of the sum over N, all indices N are replaced by $2k - 3l - s$.

For $N = 2k - 3l - s \geq k$, $k \geq 3l + s$, and hence

[A6] $$\hat{G}_s = \sum_{l\in Z}\exp[i\xi(3l + s)]\sum_{\substack{k\geq 0\\ k\geq 3l+s}}\frac{3}{k!(k - 3l - s)!}\left(\frac{iqr}{2}\right)^{2k-3l-s}$$

For $3l + s \leq 0$, $-3l - s$ equals $|3l + s|$, and the series over k results in (16)

[A7] $$3\left(\frac{iqr}{2}\right)^{|3l+s|}\sum_{k\geq 0}\frac{1}{k!(k + |3l + s|)!}\left(-\frac{q^2r^2}{4}\right)^k = 3I_{|3l+s|}(iqr)$$

For $3l + s > 0$ and the replacement $\tilde{k} = k - 3l - s$ one again gets expression [A7] with the dummy index $\tilde{k}$ instead of k.

Appendix B: Powder averaging of [24]

The integration over the azimuthal angle ϕ leads to the Kronecker delta

[B1] $$\int_0^{2\pi} e^{i3(l'-l)\phi}\,d\phi = 2\pi\delta_{l,l'}$$

and hence to expression [25].

The Bessel function in the integral in [25] is replaced by its Taylor series (16). Because $q = Q\sin\theta$, the following integral appears to hold for a natural number n (16).

[B2] $$\int_0^{\pi}(\sin\theta)^{2n+1}\,d\theta = \frac{\Gamma(n + 1/2)\Gamma(1/2)}{\Gamma(n + 3/2)} = 2\frac{4^n(n!)^2}{(2n + 1)!}$$

The right equation in [B2] is verified by applying the Γ function.

Can. J. Chem. Downloaded from www.nrcresearchpress.com by 176.9.209.113 on 09/07/12
For personal use only.

TABLE 7. Transformation properties of T-symmetric rotational and spin states under tetrahedral rotations: (i) $\pm\beta$ denotes $\pm|T_\beta,I_z>$ for $\beta = x, y, z$; (ii) $\pm j$ denotes $\pm|T_\beta j>$ for $j = 1, 2, 3$ ($\beta = x, y, z$ as in column heading)

	Spin states			Rotational states								
	$\|T_x,I_z>$	$\|T_y,I_z>$	$\|T_z,I_z>$	$\|T_x1>$	$\|T_x2>$	$\|T_x3>$	$\|T_y1>$	$\|T_y2>$	$\|T_y3>$	$\|T_z1>$	$\|T_z2>$	$\|T_z3>$
$\hat{P}_1$	x	y	z	1	2	3	1	2	3	1	2	3
$\hat{P}_2$	x	$-y$	$-z$	1	−2	−3	−1	−2	3	−1	2	−3
$\hat{P}_3$	$-x$	y	$-z$	−1	2	−3	1	−2	−3	−1	−2	3
$\hat{P}_4$	$-x$	$-y$	z	−1	−2	3	−1	2	−3	1	−2	−3
$\hat{P}_5$	y	z	x	2	3	1	2	3	1	2	3	1
$\hat{P}_6$	y	$-z$	$-x$	2	−3	−1	−2	−3	1	−2	3	−1
$\hat{P}_7$	$-y$	z	$-x$	−2	3	−1	2	−3	−1	−2	−3	1
$\hat{P}_8$	$-y$	$-z$	x	−2	−3	1	−2	3	−1	2	−3	−1
$\hat{P}_9$	z	x	y	3	1	2	3	1	2	3	1	2
$\hat{P}_{10}$	z	$-x$	$-y$	3	−1	−2	−3	−1	2	−3	1	−2
$\hat{P}_{11}$	$-z$	x	$-y$	−3	1	−2	3	−1	−2	−3	−1	2
$\hat{P}_{12}$	$-z$	$-x$	y	−3	−1	2	−3	1	−2	3	−1	−2

For the integral in [25] the series reads

$$[B3]\quad 2\sum_{\mu,\mu'\geq 0}(-1)^{\mu+\mu'}\binom{\mu+\mu'+|3l+s|}{\mu}\binom{\mu+\mu'+|3l+s|}{\mu'}\frac{(Q^2r^2)^{\mu+\mu'+|3l+s|}}{[2(\mu+\mu'+|3l+s|)+1]!}$$

Substituting $p = \mu + \mu' + |3l + s| \geq |3l + s|$ one gets for [B3]

$$[B4]\quad 2\sum_{p\geq|3l+s|}\frac{(-Q^2r^2)^p p^{-|3l+s|}}{(2p+1)!}\sum_{\mu=0}^{}\binom{p}{\mu}\binom{p}{\mu+|3l+s|}$$

The inner sum in the expression [B4] can be replaced by the binomial coefficient $\binom{2p}{p+|3l+s|}$. This reflects the normalization of the probabilities

$$[B5]\quad \frac{\binom{p}{p-\mu}\binom{p}{\mu+|3l+s|}}{\binom{2p}{p+|3l+s|}}$$

Appendix C: Determination of the power series [27]

By interchanging the summations over p and l in [25], the following values of l contribute to the coefficient of $(-Q^2r^2)^p$ (i) if $p \geq 1$

for $l > 0$, one has $p \geq +3l + s$, i.e. $l \leq \text{Int}\left(+\frac{p-s}{3}\right)$;

for $l < 0$, one has $p \geq -3l - s$, i.e. $l \geq -\text{Int}\left(\frac{p+s}{3}\right)$.

$l = 0$ gives a contribution, because $p \geq |s|$ and $|s| \leq 1$

(ii) if $p = 0$, then $l = 0$ and $s = 0$.

Because $f(\varkappa,\varkappa',0) = \delta_{\varkappa,\varkappa'}$, one has $\eta = (\varkappa - \varkappa' + s)/3 = 0$ (cf. [24]), and the coefficient of $(-Q^2r^2)^0$ reads

$$4\pi^2|\sum_{r\in Z}a_{n,\varkappa}(r)^*a_{0,\varkappa}(r)|^2\delta_{\varkappa,\varkappa'} = \delta_{n,0}\delta_{\varkappa,\varkappa'}$$

To establish the equal sign, one has to remember that the sum vanishes for $n \neq 0$, because the eigenstates to different eigenvalues are orthogonal. For $n = 0$, the product of 2π and the sum over r equals unity, because the eigenstates are normalized.

Appendix D: Approximation of $<1^{(1)}|e^{i\mathbf{Q}\hat{\mathbf{R}}}|1^{(0)}>$

In refs. 4 and 17, the matrix element is calculated as an integral over the surface of the four dimensional sphere.

$$[D1]\quad <1^{(1)}|e^{i\mathbf{Q}\hat{\mathbf{R}}}|1^{(0)}> = \int_{\tau^2=1}<1^{(1)}|\tau><\tau|1^{(0)}>e^{i\mathbf{Q}\hat{\mathbf{R}}(\tau)}\,d^4\tau$$

with the wave functions [4] and [5], and the identity

$$\boldsymbol{R}(\tau) = (\mathbf{C}(\tau) + \mathbf{1})\boldsymbol{R}'$$

$$[D2]\quad \mathbf{C}(\tau) = 2\begin{pmatrix} -(\tau_2^2+\tau_3^2) & \tau_1\tau_2+\tau_3\tau_4 & \tau_1\tau_3-\tau_2\tau_4 \\ \tau_1\tau_2-\tau_3\tau_4 & -(\tau_1^2+\tau_3^2) & \tau_2\tau_3+\tau_1\tau_4 \\ \tau_1\tau_3+\tau_2\tau_4 & \tau_2\tau_3-\tau_1\tau_4 & -(\tau_1^2+\tau_2^2) \end{pmatrix}$$

$$(\tau_1,\tau_2,\tau_3,\tau_4) = \tau$$

If $\boldsymbol{R}'$ denotes the position of a proton in a molecule fixed system, which is rotated about τ with respect to the space fixed system, then $\boldsymbol{R}(\tau)$ denotes the coordinate vector of the position in the reference system.

To calculate [D1], the exponential function is approximated by the appropriate Taylor polynom of seventh degree. Then only power functions in the quaternions have to be integrated. Those integrals are given in ref. 4.

Can. J. Chem. Downloaded from www.nrcresearchpress.com by 176.9.209.113 on 09/07/12
For personal use only.

TABLE 8. Transformation properties of the symmetrized parts $\hat{G}_\gamma$ and $\hat{S}_\gamma$ under tetrahedral rotations: the sign and the symmetry label γ' of $\pm\hat{X}_{\gamma'} = \hat{P}_\lambda^+ \hat{X}_\gamma \hat{P}_\lambda$ (where X denotes G or S) are listed as a function of γ and λ

	λ											
γ	1	2	3	4	5	6	7	8	9	10	11	12
A	A	A	A	A	A	A	A	A	A	A	A	A
T_x	T_x	T_x	$-T_x$	$-T_x$	$-T_z$	T_z	T_z	$-T_z$	$-T_y$	T_y	$-T_y$	T_y
T_y	$-T_y$	T_y	$-T_y$	$-T_y$	$-T_x$	T_x	T_x	T_x	T_z	$-T_z$	$-T_z$	T_z
T_z	T_z	$-T_z$	$-T_z$	T_z	T_y	$-T_y$	T_y	$-T_y$	$-T_x$	$-T_x$	T_x	T_x

TABLE 9. Spin-dependent factors for XH_4

	A	T_x	T_y	T_z	E^a	E^b
A	15	5	5	5	0	0
T_x	5	3	3	3	2	2
T_y	5	3	3	3	2	2
T_z	5	3	3	3	2	2
E^a	0	2	2	2	0	0
E^b	0	2	2	2	0	0

[D3] $$\int_{\tau^2=1} \tau^{N_1}\tau^{N_2}\tau^{N_3}\tau^{N_4}\,d^4\tau = \begin{cases} 2\pi^2 \prod_{j=1}^{4} (N_j-1)!!/[2^N(1+N)!] & \text{all } N_j \text{ even} \\ 0 & \text{otherwise} \end{cases}$$

with the abbreviation

$$N = \sum_{j=1}^{4} N_j/2$$

(*I*) In analogy to ref. 2, $\boldsymbol{R}'$ is first set to be $\begin{pmatrix}0\\0\\1\end{pmatrix}$. The vector $\mathbf{C}(\tau)\begin{pmatrix}0\\0\\1\end{pmatrix}$ will be named $\begin{pmatrix}x\\y\\z\end{pmatrix}(\tau)$. Because of [D3], only terms with odd powers in y, even powers in x, and arbitrary powers in z provide nonvanishing contributions to the integral [D1].

For integration, all terms in the average width parameter $M = (M_0 + M_1)/2$ are used up to the order $(1/M)^{7/2}$.

(*II*) In the calculation with $\mathbf{C}(\tau)\begin{pmatrix}0\\1\\0\end{pmatrix} = \begin{pmatrix}x'\\y'\\z'\end{pmatrix}$, only terms with odd powers in z', even powers in x', and arbitrary powers in y' contribute. Because of the different signs in the expressions for $x'(\tau)$ and $z'(\tau)$ — compared with those in $x(\tau)$ and $y(\tau)$ — one has to multiply the result of (*I*) with (-1) and to interchange Q_2 and Q_3 to obtain the desired result.

(*III*) No term in the calculation for $\mathbf{C}(\tau)\begin{pmatrix}1\\0\\0\end{pmatrix} = \begin{pmatrix}x''\\y''\\z''\end{pmatrix}$ contributes, because no power in x'', y'', or z'' has a term in which τ_1 and τ_4 appear in odd power and τ_2 and τ_3 appear in even power.

Appendix E: Calculation of the cross sections

For the different transitions, the following sum has to be calculated:

[E1] $$f(\Gamma,\Gamma') = \sum_{0\Gamma\,\text{states}\,|i>} \sum_{i\Gamma'\,\text{states}\,|f>} \sum_{\mu,\mu'=\mp 1/2} |<\mu'|<f|\hat{W}|i>|\mu>|^2$$

The states $|i>$ of the lowest librational multiplet $|f>$ of the first excited librational multiplet are listed in Table 4. The transformation properties of the states and of the operators $\hat{G}_\gamma$ and $\hat{S}_\gamma$ for rotations of the tetrahedron are calculated and listed in Tables 7 and 8. A simple example is the calculation of $f(A,A)$. Here, only the operator $\hat{S}_A\hat{G}_A$ contributes. Because the state $|\tilde{A},I_z>$ is a tensor product in $\mathcal{H}^{\text{rot}} \otimes \mathcal{H}^{\text{spin}}$, the matrix element in [E1] factorizes.

[E2] $$f(A,A) = \frac{1}{16} \sum_{I_z;I_z'=-2}^{2} \sum_{\mu,\mu'=\mp 1/2} |<\mu'|<A,I_z'|\hat{S}_A|A,I_z>|\mu>|^2 |<A^{(1)}|\hat{G}_A|A^{(0)}>|^2$$

For tiny overlaps, the matrix element of $\hat{G}_A$ is diagonal in the pocket states.

[E3] $$<A^{(1)}|\hat{G}_A|A^{(0)}> \cong \frac{1}{12}\sum_{\lambda,\mu=1}^{12} \delta_{\lambda,\mu}<\mu^{(1)}|\hat{G}_A|\lambda^{(0)}> = \frac{1}{12}\sum_{\lambda=1}^{12} <1^{(1)}|\hat{P}_\lambda^+\hat{G}_A P_\lambda|1^{(0)}> = <1^{(1)}|\hat{G}_A|1^{(0)}>$$

The spin-dependent factors formed by the sums over the squared matrix element of $\hat{S}_A$ in [E1] are found in Table 9. The result is

[E4] $$f(A,A) = \frac{1}{16}\frac{135}{9}|<1^{(1)}|\hat{G}_A|1^{(0)}>|^2$$

Multiplication with $1/16$ for the probability of the population and $8/3$ from [1] yields

[E5] $$a(A,A) = 1, \quad t(A,A) = 0, \quad Y(A,A) = 135$$

The abbreviations a, t, and Y are chosen so that [38] holds when a equals 0, 1, or 3.

Can. J. Chem. Downloaded from www.nrcresearchpress.com by 176.9.209.113 on 09/07/12
For personal use only.

Metabolites of *Lachnellula fuscosanguinea* (Rehm). Part 2.[1] The structure of lachnellulone

WILLIAM A. AYER, J. DANIEL FIGUEROA VILLAR, AND BARBARA S. MIGAJ
Department of Chemistry, University of Alberta, Edmonton, Alta., Canada T6G 2G2

Received October 15, 1987

WILLIAM A. AYER, J. DANIEL FIGUEROA VILLAR, and BARBARA S. MIGAJ. Can. J. Chem. **66**, 506 (1988).

Lachnellulone, an antifungal metabolite produced by *Lachnellula fuscosanguinea* (Rehm) Dennis is shown to possess structure **8**. The structure was determined by consideration of the ultraviolet, infrared, ^1H and ^{13}C nuclear magnetic resonance, and mass spectra of **8** and its derivatives and was confirmed by an X-ray crystallographic study of lachnellulone *p*-nitrobenzoate. In solution lachnellulone undergoes facile isomerization to isolachnellulone (**9***a*), which explains the observed mutarotation of **8**. The ^{13}C nuclear magnetic resonance spectra of lachnellulone and the related lachnelluloic acid (**1**) are discussed in some detail. The absolute configuration of lachnellulone has not been determined.

WILLIAM A. AYER, J. DANIEL FIGUEROA VILLAR et BARBARA S. MIGAJ. Can. J. Chem. **66**, 506 (1988).

On a démontré que la lachnellulone, un métabolite fongicide produit par le *lachnellula fuscosanguinea* (Rehm) Dennis, possède la structure **8**. On a déterminé la structure en se basant sur les spectres ultraviolet, infrarouge, résonance magnétique nucléaire du ^1H et du ^{13}C et de masse du produit **8** et on l'a confirmée par des études de diffraction des rayons-X réalisées sur le *p*-nitrobenzoate de la lachnellulone. En solution, la lachnellulone se transforme facilement en isolachnellulone (**9***a*); cette propriété explique la mutarotation observée avec le composé **8**. On discute en détail les spectres en résonance magnétique nucléaire du ^{13}C de la lachnellulone et de l'acide lachnelluloïque (**1**) qui lui est apparenté. On n'a pas déterminé la configuration absolue de lachnellulone.

[Traduit par la revue]

Can. J. Chem. Downloaded from www.nrcresearchpress.com by 176.9.209.113 on 09/07/12
For personal use only.

Lachnellula fuscosanguinea (Rehm) Dennis is a brightly colored fungus of the family Hyaloscyphaceae (Ascomycotina), which is saprophytic on pine and other conifers. It has been shown to be antagonistic to the Dutch elm disease fungus *Ceratocystis ulmi* and to several wood rotting fungi (1). The antifungal activity is due to lachnelluloic acid, shown earlier to possess structure **1**, and to a second and more active component $C_{18}H_{28}O_5$, which we have named lachnellulone (1). In this article we report the structure of lachnellulone.

Lachnellulone, mp 126–127°C, has one oxygen more than lachnelluloic acid (**1**) and has an additional unsaturation. The ultraviolet (uv) spectrum is similar to that of **1** and shows a similar base induced shift. The infrared (ir) spectrum shows concentration independent, hydrogen bonded, hydroxyl absorption (3400 cm^{-1}) and double bond absorption at 1708, 1670, and 1560 cm^{-1}. The compound is optically active, but the specific rotation changes with time, becoming constant after a certain length of time depending on the solvent. Unlike lachnelluloic acid (**1**), lachnellulone does not give a positive ferric chloride test.

The ^1H nuclear magnetic resonance (nmr) spectrum shows the presence of the two isolated spin systems illustrated in Scheme 1. The concentration independent, D_2O exchangeable, H-bonded, proton H_a is spin coupled (3.0 Hz) to a proton (H_b) at δ 4.45. The latter signal is further coupled (6.5 Hz) to a proton (H_c) *geminal* to an ethereal oxygen (δ 4.57). H_c is further coupled to the nonequivalent protons of a methylene group (H_d, $H_{d'}$). The other isolated spin system illustrated in Scheme 1 originates with a somewhat downfield nonequivalent methylene group (H_e, $H_{e'}$, δ 3.76, 3.32, J_{gem} 20 Hz), each hydrogen of which is further coupled to the protons of another nonequivalent methylene pair (H_f, $H_{f'}$, *geminal* coupling 13 Hz). One of these *geminal* protons shows coupling to a hydrogen (H_g) *geminal* to an ethereal oxygen (δ 5.02). This hydrogen is also coupled to the protons of another methylene group (H_h, $H_{h'}$). The ^{13}C nmr spectrum shows sp^2 carbons at

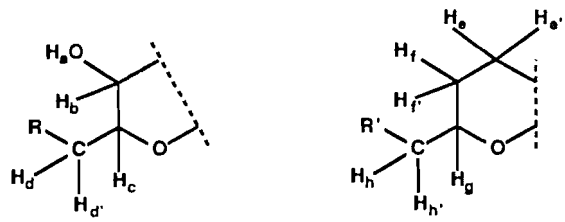

SCHEME 1

δ 191.1, 189.0, 165.3, and 100.2, similar in chemical shift to those in lachnelluloic acid. Oxygenated methine carbons appear at δ 91.4, 77.6, and 71.9 and these are shown by decoupling to be directly bonded to H_g, H_c, and H_b, respectively. In addition, there are signals for nine methylene carbons and two methyl carbons, confirming the presence of two unbranched alkyl chains.

Considering the likely relationship between lachnellulone and lachnelluloic acid (**1**), structures **2** and **3** reasonably explain the evidence presented to this point, with structure **2** favored since it best explains the mutarotation (similar to that observed for carolic acid (**4**), ref. 2), and the strongly H-bonded hydroxyl group.

The base peak in the mass spectrum of lachnellulone appears at *m/z* 211 ($M^+ - C_7H_{13}O$), consistent with the loss of the fragment **5** from the molecular ion as shown in Scheme 2. This serves to locate the five-carbon side chain relative to the hydroxyl group. The *m/z* 211 ($C_{11}H_{15}O_4$) peak may be represented as **6** (one canonical form) on the basis of structure **2**. When the hydroxyl hydrogen is replaced by deuterium, the base peak in the mass spectrum is shifted to *m/z* 212, consistent with the hydrogen transfer depicted in Scheme 2. Acetylation of lachnellulone gave an oily product, which on thin-layer chromatography seems to contain two components. These could not be separated by chromatography, but the ^1H nmr spectrum shows two sets of signals for the hydrogen *geminal* to the acetoxyl group (see below).

Lachnellulone crystallizes as very fine needles, unsuitable for X-ray crystallographic analysis. The *p*-bromobenzoate

[1]For part 1, see ref. 1.

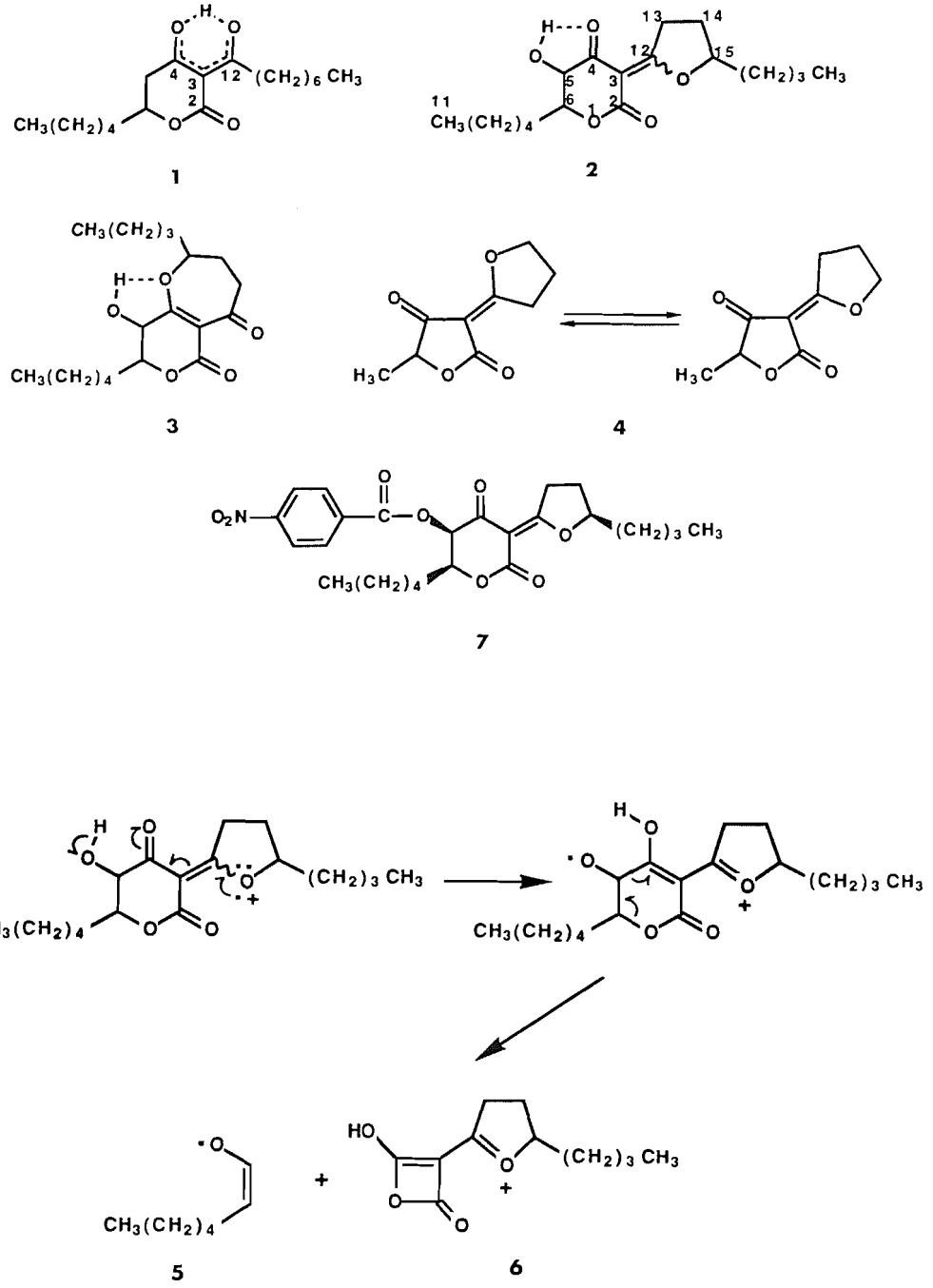

SCHEME 2

behaves similarly. The *p*-nitrobenzoate, which in solution shows two isomers, gives somewhat thicker needles and the crystal structure was determined. Figure 1 is a computer generated perspective drawing of the final X-ray model of lachnellulone *p*-nitrobenzoate.[2] This confirms structure **2** for lachnellulone and defines the relative stereochemistry of the *p*-nitrobenzoate as shown in **7**.

Since the crystalline *p*-nitrobenzoate shows structure **7**, we assign structure **8** to lachnellulone itself. It was noted above that lachnellulone mutarotates. It has also been observed that the ^{1}H nmr spectra of lachnellulone and its derivatives usually reveal the presence of two closely related compounds. For example, the ^{1}H nmr spectrum of freshly dissolved lachnellulone *p*-nitrobenzoate (**7**) in $CDCl_3$ shows a signal at δ 5.80 (J = 4.5 Hz) attributable to the C-5 hydrogen, along with a small signal at δ 5.77 (J = 4.5 Hz). With time the signal at δ 5.77 grows in intensity at the expense of the δ 5.80 signal until the signals are of approximately equal intensity. Similarly, the signals for the protons at C-6, C-15, and especially C-13 become more complicated (overlapping multiplets) with time. We attribute this to the isomerization of **7** to **9** until an equilibrium mixture (approximately 1:1) of the two is obtained. As noted, a similar isomerization has been observed, and studied in detail, in the case of carolic acid (**4**) (2). This

[2]The X-ray crystallographic study was carried out by R. G. Ball, Structure Determination Laboratory, Department of Chemistry, University of Alberta, Edmonton, Alberta, T6G 2G2. Inquiries regarding the crystallographic results should be directed to Dr. Ball at the above address, quoting report number SR:012505-03-85.

Can. J. Chem. Downloaded from www.nrcresearchpress.com by 176.9.209.113 on 09/07/12
For personal use only.

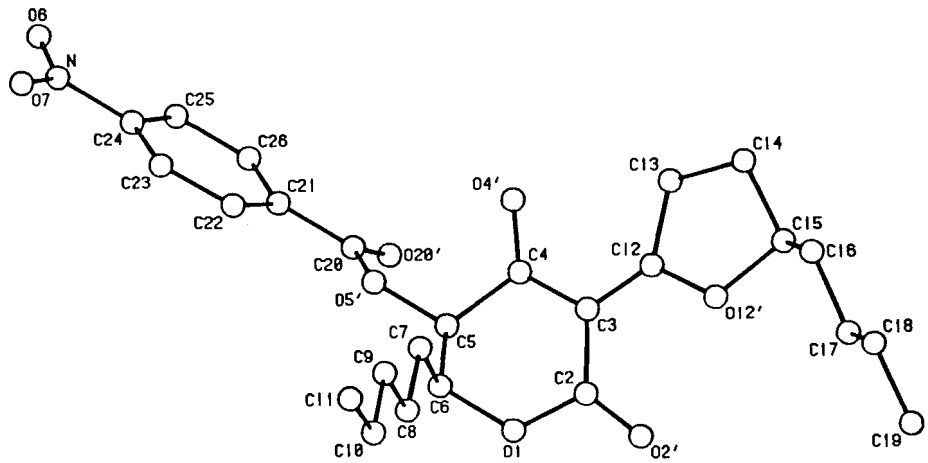

FIG. 1. Computer generated perspective drawing of the X-ray model of lachnellulone *p*-nitrobenzoate.

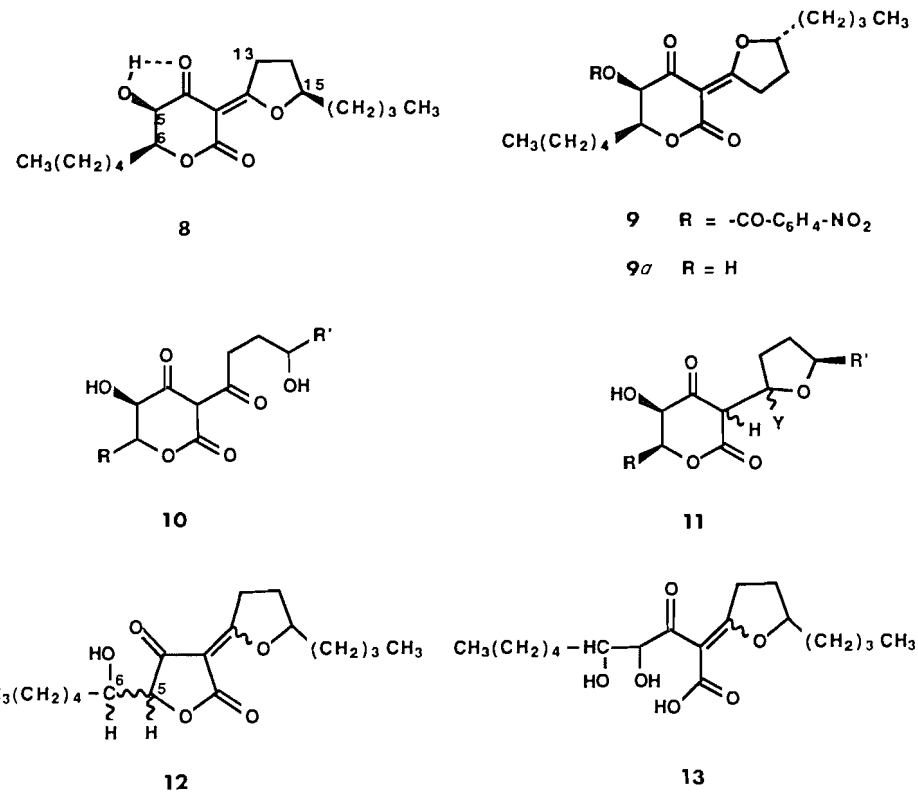

isomerization accounts for the formation of the mixture of acetates, in which case the signals for the two different C-5 protons are observed at δ 5.53 (J = 4.5 Hz) and δ 5.48 (J = 4.5 Hz). The fact that the H-5 coupling constants are the same in both isomers indicates that the change is not due to epimerization at C-5. This isomerization is also detectable in the ^{13}C nmr spectra of lachnellulone and its derivatives.

The isomerization of lachnellulone (**8**) to isolachnellulone (**9***a*) occurs extremely rapidly in methanol, but more slowly in acetonitrile. The change in rotation with time is observed in acetonitrile (+91° to +55° over 24 h). In methanol, no significant change in rotation (+35 ± 2°) is observed. We attribute this to the fact that in methanol equilibrium between **8** and **9***a* is established before the rotation can be measured (~10 min). When the ^1H nmr spectrum of lachnellulone is measured in deuterated methanol, the spectrum immediately shows the presence of approximately equal amounts of the two isomers. When crystalline lachnellulone is dissolved in $CDCl_3$ and the spectrum is recorded immediately, only one set of signals is observed. After the solution has been allowed to stand for several hours a second set of signals (for **9***a*) is apparent. After approximately 24 h (this time period is variable), **8** and **9***a* appear to be present in approximately equal amounts. When either a chloroform solution or a methanol solution of the two isomers is evaporated to dryness, only **8** is present as determined by ^1H nmr spectroscopy (in $CDCl_3$). This suggests that **8** is the least soluble of the two isomers that constitute the natural product.

The coupling between the protons on C-5 and C-6 in the *p*-nitrobenzoate (both isomers) and the other derivatives of lach-

Can. J. Chem. Downloaded from www.nrcresearchpress.com by 176.9.209.113 on 09/07/12
For personal use only.

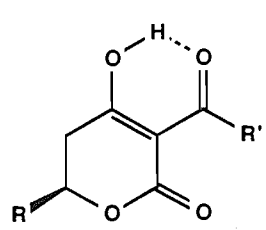

14

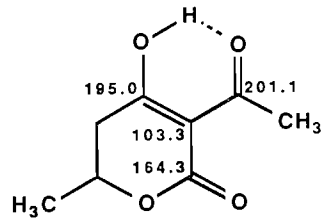

15

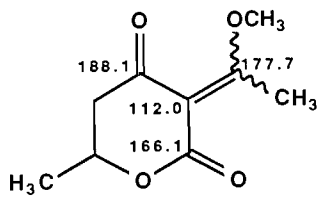

16

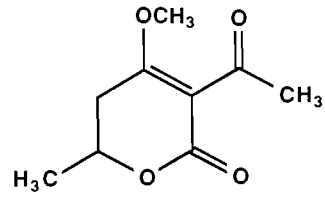

17

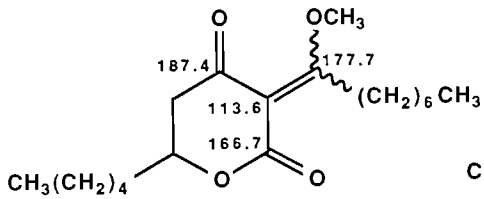

18

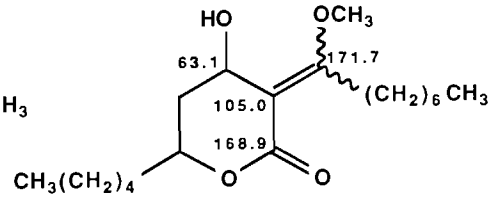

19

nellulone (acetate, 3,5-dinitrobenzoate, α-naphthylurethane) is 4.5–5.0 Hz, consistent with a dihedral angle of approximately 30–40° (3). In lachnellulone itself, this coupling is 6.5 Hz, perhaps reflecting a slight conformational change, with lessening of the dihedral angle, brought about by the strong hydrogen bond between the hydroxyl hydrogen and the oxygen of the C-4 carbonyl group. A nuclear Overhauser effect (nOe) experiment confirmed the proximity of the C-5 hydrogen to the C-6 hydrogen (irradiation of H-5 caused a 12% enhancement of the signal for H-6, irradiation of H-6 caused a 10.5% enhancement of H-5).

The mechanism of isomerization of lachnellulone (**8**) to isolachnellulone (**9***a*) may involve hydrolytic ring opening to give intermediate **10**, followed by ring closure to give either **8** or **9***a*. However, the fact that isomerization occurs in anhydrous solvents (methanol, chloroform, acetonitrile) suggests that an addition–elimination sequence, perhaps catalyzed by traces of acid and proceeding via an intermediate such as **11** (Y = OCH_3, Cl, etc.), is also a possibility. As noted previously, the uv spectrum of lachnellulone in methanol (λ_{max} 275 nm) is similar to that of lachnelluloic acid (λ_{max} 274 nm) and shows a similar base induced shift.

In describing the structure of lachnelluloic acid we originally portrayed a distinct hydrogen bonded enol structure (**14**) although we now feel that it is more meaningful to use the delocalized structure **1**. We have mentioned the similarities of the uv spectra and the ^{13}C nmr spectra of lachnellulone to those of lachnelluloic acid. The sp^2 carbons of lachnellulone absorb at δ 191.1, 189.0, 165.3, and 100.2, those of lachnelluloic acid at δ 204.2 (C-12), 194.9 (C-4), 163.9 (C-2), and 102.9 (C-3). These shift assignments are based on the following considerations. The chemical shifts for the model compound dihydrodehydroacetic acid (**15**) have been assigned as shown in **15** (4). We have prepared **15** labelled with ^{13}C at the sp^2 carbon of the side chain and confirmed that this carbon does give rise to the signal at δ 201.1. Heteronuclear decoupling of the hydrogen at C-6 in lachnelluloic acid causes a sharpening of the signal at δ 194.9; thus it is safe to conclude that the assignments given above are correct for lachnelluloic acid. Attempts to methylate dihydrodehydroacetic acid (**15**) with diazomethane and by treatment with methyl iodide under basic conditions were unsuccessful. However, treatment of **15** with methanolic HCl provides the enol ether **16** in moderate yield. Enol ether **16** shows sp^2 carbon signals at δ 188.1, 177.7, 166.1, and 112.0, assigned as shown in **16**. When the side chain ^{13}C enriched **15** was used to prepare **16**, the signal at 177.7 (which is coupled to the methyl hydrogens at δ 2.21) is increased in intensity. The enol ether is assigned structure **16** rather than **17** since the ketonic carbonyl would not be expected at such a high field (δ 177.7) position. This conclusion is confirmed in the case of lachnelluloic acid methyl ether (**18**), prepared by treating **1** with methanolic HCl. The sp^2 carbons have the chemical shifts shown in **18**. Reduction of **18** with sodium borohydride provides the alcohol **19**, the ^{13}C nmr spectrum of which lacks a signal in the δ 188 region (see **19** for shift assignments). In lachnellulone, heteronuclear decoupling of the C-6 hydrogen causes the carbon signal at δ 191.1 to collapse to a broadened singlet, while the signal at δ 189.0 is very little affected. Since the three-bond coupling is expected to be much larger than that over five bonds (5), the signal at δ 191.1 is assigned to the C-4 carbonyl and the signal at δ 189.0 to the enol ether carbon C-12.

Treatment of lachnellulone with methanolic sodium hydroxide

Can. J. Chem. Downloaded from www.nrcresearchpress.com by 176.9.209.113 on 09/07/12
For personal use only.

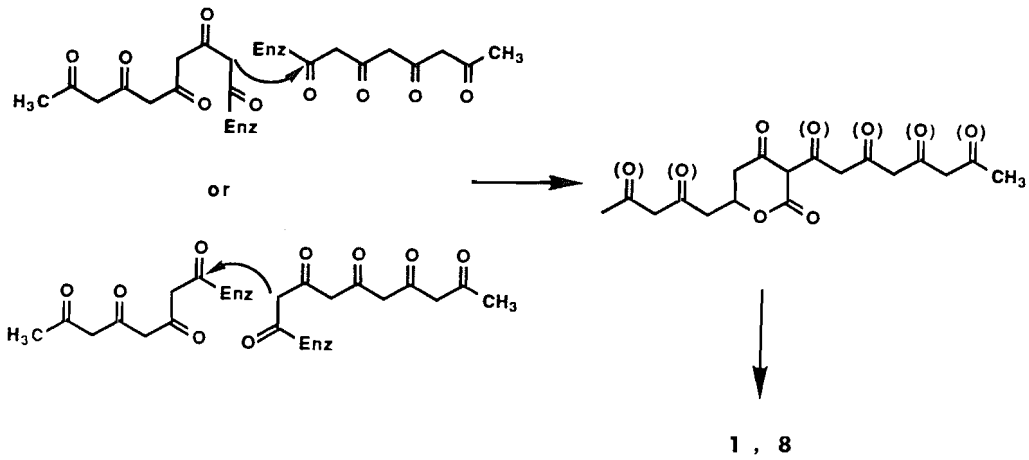

SCHEME 3

followed by acidification gives rise to a mixture of diastereoisomeric products to which we assign structures **12**. This assignment is based on ir (1760, 1695 cm^{-1}), uv (λ_{max} 220, 274 nm), and ^1H nmr spectral evidence. The ir and uv data compare favorably with those quoted for carolic acid (**4**) (6), and the nmr spectrum shows a series of doublets (δ 4.37, 4.39, 4.41, 4.43) coupled to multiplets centered at δ 3.95, which we attribute to the C-5 hydrogens (four diastereoisomers) coupled to the C-6 hydrogens. Compounds **12** arise by opening of the lactone ring in **8** and **9***a* followed by relactonization of hydroxy acid **13** to give the 5-membered ring compounds.

Lachnellulone shows antifungal activity against *Ceratocystis ulmi* (the causative agent of Dutch elm disease), *Hypoxylon mammatum* (which causes canker in poplar) (7), and *Marasmius oreades* (the fairy ring mushroom).[3] It did not show antibacterial activity against the standard test organisms[4] (7).

The biogenesis of lachnellulone and lachnelluloic acid may be rationalized as a condensation of two polyketide chains, a tetraketide and a pentaketide, in either of the two ways illustrated in Scheme 3. As in the case of alternaric acid (4, 8), it is very difficult to distinguish biosynthetically between these alternative routes, and biosynthetic studies have not been pursued.

Experimental

For general experimental details see part 1 (1). In reporting mass spectra, unless diagnostically significant, peaks with intensities less than 20% of the base peak are omitted. Ion formulae reported were determined by high resolution mass spectrometry (hrms).

Isolation of lachnellulone[5]

A 50 mm diameter column was filled with 20 cm of silica gel for flash chromatography and packed using $CHCl_3$. The crude extract of the mycelium of *L. fuscosanguinea* (1.5 g) (1) was applied to the top of the column as a concentrated solution in $CHCl_3$, and eluted with solvent at a rate of 5 cm/min while collecting 50-mL fractions. Fractions 35–40, eluted with 1% CH_3OH in $CHCl_3$, afforded a white crystalline material, which was recrystallized from acetone – Skellysolve B to yield 20 mg of pure lachnellulone, mp 126–127°C; R_f 0.44 ($CHCl_3$): $[\alpha]_D$ +35.0 ± 2° (*c* 1.0, CH_3OH); +91.4° (5 min after dissolution), +55.0° (24 h after dissolution) (*c* 0.77, CH_3CN); λ_{max} (ε) (CH_3OH): 218 (8670), 275 (16 200) nm; λ_{max} (CH_3OH + 0.1 *M* NaOH): 255 nm; λ_{max} (isooctane): 269 (18 200); ir ($CHCl_3$ cast): 3400, 2950, 2925, 2860, 1708, 1670, 1560, 1460, 1380, 1305, 1090, 600 cm^{-1}; ^1H nmr ($CDCl_3$) δ: 5.02 (1H, ddd, *J* = 7.0, 7.0, 7.0 Hz), 4.57 (1H, ddd, *J* = 3.0, 6.5, 10.0 Hz), 4.45 (1H, dd, *J* = 3.0, 6.5 Hz), 3.92 (1H, d, *J* = 3.0 Hz), 3.76 (1H, ddd, *J* = 6.0, 10.0, 20.0 Hz), 3.32 (1H, ddd, *J* = 7.0, 10.0, 20.0 Hz), 2.33 (1H, dddd, *J* = 6.0, 7.0, 10.0, 13.0 Hz), 1.87 (1H, dddd, *J* = 7.0, 7.0, 10.0, 12.0 Hz), 1.71 (2H, m), 1.60 (2H, m), 1.42 (4H, m), 1.30 (6H, m), 0.96 (3H, vt), 0.89 (3H, vt); ^{13}C nmr (CD_2Cl_2) δ: 191.1 (s), 189.0 (s), 165.3 (s), 100.2 (s), 91.4 (d), 77.6 (d), 71.9 (d), 36.4 (t), 34.9 (t), 31.9 (t), 28.7 (t), 27.9 (t), 27.2 (t), 25.9 (t), 22.9 (t), 22.8 (t), 14.1 (q), 14.0 (q); hrms, *m/z*: 324 ($C_{18}H_{28}O_5$, 1.3, M^+), 239 ($C_{13}H_{19}O_4$, 2), 224 ($C_{12}H_{16}O_4$, 10), 211 ($C_{11}H_{15}O_4$, 100), 193 ($C_{11}H_{13}O_3$, 46).

Acetylation of lachnellulone

Lachnellulone (3.0 mg) was dissolved in CH_2Cl_2 (0.5 mL). Acetyl chloride (0.5 mL) was added, with constant stirring, to the lachnellulone solution. After 2 h at room temperature a drop of dry pyridine was added and the solution was stirred overnight. The reaction was worked up by adding water (2 mL) and $CHCl_3$ (1 mL) and vigorously shaking the two-phase system. The organic layer was separated, washed with distilled water, dried over anhydrous Na_2SO_4, filtered, and concentrated to dryness to give lachnellulone acetate (3.0 mg); R_f 0.30 (1% CH_3OH in $CHCl_3$); ir ($CHCl_3$ cast): 1730 cm^{-1}; ^1H nmr ($CDCl_3$), mixture of two isomers, δ: 5.53 and 5.48 (1H, d's, *J* = 4.5 Hz), 4.92 (1H, m), 4.44 (1H, m), 3.65 (1H, m), 3.32 (1H, m), 2.30 (1H, m), 2.21 and 2.19 (3H, s's), 1.89 (1H, m), 1.64 (2H, m), 1.40–1.31 (12H, bm), 0.94 (3H, vt), and 0.90 (3H, vt); hrms, *m/z*: 366 ($C_{20}H_{30}O_6$, 2.5, M^+), 253 ($C_{13}H_{17}O_5$, 51), 211 ($C_{11}H_{15}O_4$, 100), 193 ($C_{11}H_{13}O_3$, 17).

p-Nitrobenzoate of lachnellulone (7)

Lachnellulone (12.0 mg) was dissolved in 10 mL of CH_2Cl_2 under nitrogen. 4-*N*,*N*-Dimethylaminopyridine (7.2 mg) and *p*-nitrobenzoyl chloride (8.4 mg) were added and the reaction mixture was stirred at room temperature. The reaction was monitored by tlc until no lachnellulone was present (about 1.5 h). A small amount of water was then added and the organic solvent was removed. The aqueous residue was extracted with ethyl ether, and the ethereal solution was washed successively with 1 *M* HCl, Na_2CO_3, water, and then dried. The solvent was evaporated and the pale yellow solid residue was crystallized from isopropyl alcohol, mp 138–139°C; R_f 0.65 (5% CH_3OH in $CHCl_3$); λ_{max} (ε): 217 (2460), 274 (21 500); ir ($CHCl_3$ cast): 3075, 2930, 1735, 1680, 1530, 1460, 1265, 1120, 1100, 873 cm^{-1}; ^1H nmr ($CDCl_3$), mixture of two isomers, δ: 8.33 (2H, m), 8.20 (2H, m), 5.80 and 5.77 (1H, d's, *J* = 4.5 Hz), 4.97 (1H, ddd, *J* = 7.0, 7.0, 7.0 Hz), 4.62 (1H, ddd, *J* = 4.5, 7.0, 14.0 Hz), 3.72 and 3.68 (1H, ddd's, *J* = 5.0, 10.0, 20.0 Hz), 3.37 and 3.33 (1H, ddd's, *J* = 7.5, 9.0, 20.0 Hz), 2.34 (1H, dddd, *J* = 2.5, 5.0, 10.0, 20.0 Hz), 1.96 (1H, m), 1.85 (1H, m), 1.74 (1H, ddd, *J* = 3.0, 7.0, 7.0 Hz), 1.56 (1H, m), 1.48 (1H, m), 1.37 (4H, m), 1.33 (6H, m), 0.93

[3]A. Szenthe and P. Craw, private communication.

[4]Difco Bactrol Discs, Set A.

[5]For details on the cultivation of *L. fuscosanguinea*, and the preparation of crude extracts, see ref. 1.

Can. J. Chem. Downloaded from www.nrcresearchpress.com by 176.9.209.113 on 09/07/12
For personal use only.

Can. J. Chem. Downloaded from www.nrcresearchpress.com by 176.9.209.113 on 09/07/12
For personal use only.

(3H, t, J = 6.5 Hz), 0.88 (3H, vt); ^{13}C nmr ($CDCl_3$), mixture of two isomers, δ: 190.0 and 189.8, 187.6, 184.4, 165.3, 163.5, 134.7, 131.2, 123.73 and 123.68, 91.5, 90.8, 75.3, 74.8, 73.2 and 73.0, 36.7 and 36.6, 34.7 and 34.5, 31.5, 30.1 and 29.8, 27.5, 27.2, 25.1, 25.0, 22.5, 22.4, 13.9, 13.8; hrms, m/z: 473 ($C_{25}H_{31}NO_8$, 1.5, M^+), 360 ($C_{18}H_{18}NO_7$, 29), 279 ($C_{17}H_{27}O_3$, 16), 211 ($C_{11}H_{15}O_4$, 67), 193 ($C_{11}H_{13}O_3$, 18), 167 ($C_{10}H_{15}O_2$, 15), 150 ($C_7H_4NO_3$, 100). The crystals for X-ray diffraction studies were grown in a $CHCl_3$/pentane solvent system using the vapour diffusion technique (9).

3,5-Dinitrobenzoate of lachnellulone

Lachnellulone (6.6 mg) was dissolved in 5 mL of CH_2Cl_2 under nitrogen. 4-*N*,*N*-Dimethylaminopyridine (4.4 mg) and 3,5-dinitrobenzoyl chloride (freshly crystallized from CCl_4) (7.0 mg) were added. The reaction was carried out as described for the preparation of the *p*-nitrobenzoate. The product was crystallized from isopropyl alcohol, mp 102–104°C; R_f 0.55 (5% CH_3OH in $CHCl_3$); λ_{max} (ε): 274 (38 800); ir ($CHCl_3$ cast): 3055, 2956, 2930, 1740, 1680, 1547, 1345, 1260, 1162, 728; ^{1}H nmr ($CDCl_3$), mixture of two isomers, δ: 9.38 (1H, ddd, J = 2.0, 2.0, 4.5 Hz), 9.18 (2H, dd, J = 2.0, 4.5 Hz), 5.88 and 5.84 (1H, d's, J = 5.0 Hz), 4.99 (1H, ddd, J = 7.0, 7.0, 7.0 Hz), 4.66 (1H, ddd, J = 5.0, 5.0, 14.0 Hz), 3.74 and 3.68 (1H, ddd's, J = 5.0, 10.0, 20.0 Hz), 3.39 and 3.30 (1H, ddd's, J = 8.0, 10.0, 20.0 Hz), 2.34 (1H, m), 1.85 (1H, m), 1.76 (1H, m), 1.63 (6H, m), 1.47 (1H, m), 1.33 (6H, m), 0.91 (3H, t, J = 7.0 Hz), 0.89 (3H, t, J = 7.0 Hz); hrms, m/z: 518 ($C_{25}H_{30}N_2O_{10}$, 1, M^+), 212 ($C_7H_4N_2O_6$, 12), 211 ($C_{11}H_{15}O_4$, 100), 193 ($C_{11}H_{13}O_3$, 33), 167 ($C_{10}H_{15}O_2$, 30), 149 ($C_7H_3NO_3$, 29).

Base catalyzed rearrangement of lachnellulone

Lachnellulone (8 mg) was dissolved in methanol (1.0 mL), and the solution was adjusted to pH 10 with 1 *M* NaOH. The solution was stirred for 3 h at room temperature. The resulting mixture was acidified to pH 1 with 5% HCl and diluted with water. Extraction of the aqueous solution with ethyl acetate afforded a yellow solid, which was purified by flash chromatography (10 mm diameter column, 2% CH_3OH in $CHCl_3$). Isolachnellulone was obtained as a white solid (4.8 mg); R_f 0.3 in 2% CH_3OH in $CHCl_3$; ir ($CHCl_3$ cast): 3470, 1760, 1695, 1197 cm^{-1}; ^{1}H nmr ($CDCl_3$) δ: 4.94 (1H, m), 4.43 and 4.41 (1/2H, d's, J = 1.0 Hz), 4.39 and 4.37 (1/2H, d's, J = 6.0 Hz), 4.02 (1/2H, bm), 3.86 (1/2H, bm), 3.59 (1H, ddd, J = 4.5, 9.0, 18.0 Hz), 3.26 (1H, 2 ddd, J = 2.0, 9.0, 18.0 Hz), 2.70 (1H, bdd, J = 3.0, 11.5 Hz), 2.37 (1H, m), 1.95 (1H, m), 1.87 (1H, m), 1.75 (1H, m), 1.68 (1H, m), 1.62 (1H, m), 1.50 (1H, m), 1.41 (4H, m), 1.32 (5H, m), 0.94 (3H, vt), 0.90 (3H, vt); ^{13}C nmr ($CDCl_3$), mixture of isomers, δ: 197.5 and 193.7 (s), 186.6 and 185.6 (s), 171.0 and 167.4 (s), 105.0 (s), 92.1 and 91.5 (d), 84.6 and 84.3 (d), 71.0 and 70.9 (d), 34.4 and 34.3 (t), 33.9 and 33.5 (t), 33.6 (t), 31.7 and 31.6 (t), 27.5 and 27.3 (t), 27.1 and 27.0 (t), 25.4 and 25.2 (t), 22.5 (t), 20.4 (t), 13.9 (q), 13.8 (q); hrms, m/z: 324 ($C_{18}H_{28}O_5$, 1), 306 ($C_{18}H_{26}O_4$, 2), 253 ($C_{13}H_{17}O_5$, 2), 224 ($C_{12}H_{16}O_4$, 100), 206 ($C_{12}H_{14}O_3$), 195 ($C_{11}H_{15}O_3$, 3), 195 ($C_{10}H_{11}O_4$, 2), 193 ($C_{11}H_{13}O_3$, 3), 181 ($C_9H_9O_4$, 3), 154 ($C_7H_6O_4$, 12), 142 ($C_6H_6O_4$, 9), 127 ($C_5H_3O_4$, 3).

^{13}C labelled dihydrodehydroacetic acid

^{13}C labelled dihydrodehydroacetic acid was prepared using Tanabe's method (10) for synthesis of 3-acyl-4-hydroxy-2-pyrones. The [1-^{13}C] acetyl chloride used was prepared following the literature procedure (11). [1-^{13}C] acetyl chloride (0.5 mL) in toluene (1 mL) was added to a cool (0°C) solution of 6-methyl-5,6-dihydropyran-2,4-dione (730 mg, 5.7 mmol) and 1,8-diazabicyclo[5.4.0]undec-7-ene (912 mg, 6.0 mmol) in toluene (20 mL). The reaction mixture was stirred for 2 h at 0°C. A saturated aqueous solution of NaCl was added, the layers were separated, and the aqueous layer was extracted with toluene. The combined organic extracts were washed with 5% HCl and saturated sodium chloride solution, and dried over $MgSO_4$. The drying agent was filtered off, 4-*N*,*N*-dimethylaminopyridine (34.1 mg, 0.28 mmol) was added, and the mixture was refluxed for 3 h. The solvent was removed under reduced pressure and the crude reaction mixture was purified by flash chromatography using a $CHCl_3$ – Skellysolve B – acetic acid (100:50:3) solvent system. Crystallization of the crude product from Skellysolve B – acetone gave ^{13}C labelled dihydrodehydroacetic acid (162 mg, 20% yield), identical (ir, tlc) with an authentic sample.

*Dihydrodehydroacetic acid methyl ether (**16**)*

Dihydrodehydroacetic acid (30.0 mg) was dissolved in methanol saturated with hydrogen chloride and stirred at room temperature for 7 days. The HCl was neutralized with sodium methoxide and the reaction mixture filtered and evaporated to dryness. The dry residue was dissolved in ethyl ether, and filtered and purified by preparative tlc using Skellysolve B – ethyl acetate (1:2) as the solvent system. Dihydrodehydroacetic acid methyl ether (9.8 mg, 30% yield) was obtained as an oil; R_f 0.43 (5% CH_3OH in $CHCl_3$); λ_{max} (ε) (CH_3OH): 264 nm (9020); ir ($CHCl_3$ cast): 2970, 1735, 1710, 1675, 1595 cm^{-1}; ^{1}H nmr ($CDCl_3$) δ: 4.58 (1H, qt, J = 6.5, 8.0 Hz), 3.80 (3H, s), 2.49 (2H, d, J = 8.0 Hz), 2.21 (3H, s), 1.47 (3H, d, J = 6.5 Hz); ^{13}C nmr ($CDCl_3$) δ: 188.1 (s), 177.1 (s), 166.1 (s), 112.0 (s), 76.7 (d), 53.0 (q), 43.0 (t), 21.5 (q), 21.1 (q); hrms, m/z: 184 ($C_9H_{12}O_4$, 95, M^+), 153 ($C_8H_9O_3$, 55), 152 ($C_8H_8O_3$, 39), 143 ($C_6H_7O_4$, 100), 127 ($C_5H_3O_4$, 16), 114 ($C_5H_6O_3$, 26), 75 ($C_3H_7O_2$, 48), 69 (C_4H_5O, 26), 59 (C_3H_7O, 32).

*Lachnelluloic acid methyl ether (**18**)*

Lachnelluloic acid (21.8 mg) was dissolved in methanol saturated with HCl (10 mL) and stirred at room temperature for 5 days. The reaction mixture was worked up as described for dihydrodehydroacetic acid methyl ether. The product was purified by ptlc using 0.5% CH_3OH in $CHCl_3$ as the solvent system; R_f 0.55 (0.5% CH_3OH in $CHCl_3$); λ_{max} (ε) (CH_3OH): 266 nm (7700); ir ($CHCl_3$ cast): 2955, 1720, 1680, 1592, 1080 cm^{-1}; ^{1}H nmr ($CDCl_3$) δ: 4.40 (1H, dddd, J = 5.0, 7.5, 8.0, 9.0 Hz), 3.82 (3H, s), 2.49 (4H, m), 1.82 (2H, m), 1.63 (4H, m), 1.30 (12H, m), 0.91 (6H, 2 t, J = 6.5 Hz); ^{13}C nmr ($CDCl_3$) δ: 188.7, 180.2, 166.3, 112.1, 79.3, 52.1, 40.9, 34.2, 33.7, 31.7, 31.4, 29.2, 28.9, 27.0, 24.4, 22.6, 22.5, 14.1, 13.9; hrms, m/z: 324 ($C_{19}H_{32}O_4$, 34, M^+), 293 ($C_{18}H_{29}O_3$, 19), 265 ($C_{17}H_{29}O_2$, 32), 253 ($C_{14}H_{21}O_4$, 31), 250 ($C_{15}H_{22}O_3$, 15), 227 ($C_{12}H_{19}O_4$, 33), 221 ($C_{13}H_{17}O_3$, 46), 198 ($C_{11}H_{18}O_3$, 22), 169 ($C_8H_9O_4$, 15), 142 ($C_6H_6O_4$, 20), 127 ($C_8H_{15}O$, 80), 125 ($C_8H_{13}O$, 77), 57 (C_4H_9, 100).

Reduction of lachnelluloic acid methyl ether

Lachnelluloic acid methyl ether (11.0 mg) was dissolved in methanol (2.7 mL) containing $CeCl_3 \cdot 7H_2O$ (11.6 mg), and sodium borohydride (1.2 mg) was added. The reaction mixture was stirred at room temperature for 15 min and then quenched with saturated aqueous ammonium chloride. The product was extracted with ether and the solution was dried over $MgSO_4$. The crude reaction mixture contained 3 components (tlc). The major product was separated by ptlc, using 2% CH_3OH in CH_2Cl_2 as the solvent system, giving alcohol **19** as an amorphous solid (4.5 mg); R_f 0.45 (2% CH_3OH in CH_2Cl_2); λ_{max} (ε) (CH_3OH): 245 (9040); ir ($CHCl_3$ cast): 3510, 2954, 1716, 1606, 1460, 1087, 1054 cm^{-1}; ^{1}H nmr ($CDCl_3$) δ: 4.68 (1H, dd, J = 8.0, 8.0 Hz), 3.93 (1H, dddd, J = 2.0, 5.0, 10.0, 10.0 Hz), 3.81 (1H, d, J = 2.0 Hz), 3.77 (3H, s), 2.68 (1H, ddd, J = 7.5, 8.0, 13.0 Hz), 2.56 (1H, ddd, J = 7.5, 8.0, 13.0 Hz), 2.17 (1H, ddd, J = 2.5, 7.0, 14.0 Hz), 1.74 (2H, m), 1.56 (3H, m), 1.31 (14H, m), 0.89 (6H, 2 t, J = 6.5 Hz); ^{13}C nmr ($CDCl_3$) δ: 171.7 (s), 168.9 (s), 105.0 (s), 75.5 (d), 63.1 (d), 51.2 (q), 34.9 (t), 34.3 (t), 33.7 (t), 31.8 (t), 31.6 (t), 29.5 (t), 29.1 (t), 27.6 (t), 25.0 (t), 22.7 (t), 22.6 (t), 14.1 (q), 14.0 (q); hrms, m/z: 326 ($C_{19}H_{34}O_4$, 47, M^+), 308 ($C_{19}H_{32}O_3$, 37), 293 ($C_{18}H_{29}O_3$, 25), 267 ($C_{17}H_{31}O_2$, 22), 249 ($C_{17}H_{29}O$, 42), 242 ($C_{13}H_{22}O_4$, 56), 237 ($C_{14}H_{21}O_3$, 100), 201 ($C_{11}H_{21}O_3$, 28), 153 ($C_8H_9O_3$, 38), 144 ($C_6H_8O_4$, 32), 129 ($C_6H_9O_3$, 33), 127 ($C_8H_{15}O$, 57).

Acknowledgements

We acknowledge with thanks the financial support provided by the Natural Sciences and Engineering Research Council of Canada. We also thank the Alberta Heritage Foundation for Medical Research for a studentship (J.D.F.V.) and research

allowance, Dr. T. T. Nakashima for helpful discussion, and Anna Szenthe for technical assistance.

1. W. A. AYER and J. D. FIGUEROA VILLAR. Can. J. Chem. **63**, 1161 (1985).
2. O. SIMONSEN, T. REFFSTRUP, and P. M. BOLL. Tetrahedron, **36**, 795 (1980).
3. M. KARPLUS. J. Am. Chem. Soc. **85**, 2870 (1963).
4. A. STOESSL and J. B. STOTHERS. Can. J. Chem. **62**, 549 (1984).
5. J. L. MARSHALL. Carbon–carbon and carbon–proton NMR couplings. Verlag Chemie, Deerfield Beach, FL. 1983. Chap. 2.
6. L. A. DUNCANSON. J. Chem. Soc. 1207 (1953); A. SVENDSEN and P. M. BOLL. Acta Chem. Scand. Ser. B: **29**, 197 (1975).
7. J. D. FIGUEROA VILLAR. Ph.D. thesis, University of Alberta, Edmonton, Alberta. 1983.
8. W. B. TURNER. Fungal metabolites. Academic Press, London and New York. 1971. p. 136.
9. P. G. JONES. Chem. Br. **17**, 222 (1981).
10. Y. TANABE, M. MIYAKADO, N. OHNO, and H. YOSHIOKA. Chem. Lett. 1543 (1982).
11. J. M. RISLEY and R. L. VAN ETTEN. J. Am. Chem. Soc. **103**, 4389 (1981).

Can. J. Chem. Downloaded from www.nrcresearchpress.com by 176.9.209.113 on 09/07/12
For personal use only.

Ground and excited-state interactions of coumarin and nucleotide base

GRAŻYNA WENSKA AND STEFAN PASZYC
Faculty of Chemistry, A. Mickiewicz University, 70-780 Poznań, Poland

Received April 13, 1987[1]

GRAŻYNA WENSKA and STEFAN PASZYC. Can. J. Chem. **66**, 513 (1988).

Steady-state and time-resolved fluorescence measurements for a series of bichromophoric compounds containing 7-methoxycoumarin and nucleotide base residues have been performed in water and in organic solvents. The data from these studies have been used to calculate the relative proportion of folded and extended conformations of bichromophores. Ground-state stacking interactions of coumarin and nucleotide base have been found to be limited to aqueous solution. The contribution of the dynamic quenching mechanism to the total fluorescence quenching in water has been estimated. The absence of dynamic quenching in organic solvents is explained on the basis of the very short lifetime of the fluorophore in methanol.

GRAŻYNA WENSKA et STEFAN PASZYC. Can. J. Chem. **66**, 513 (1988).

Opérant dans l'eau et dans des solvants organiques, on a mesuré la fluorescence à l'état stationnaire ainsi que celle résolue en fonction du temps d'une série de composés bichromophoriques contenant des résidus méthoxy-7 coumarine et une base nucléotide. On a utilisé les données ainsi obtenues pour calculer les proportions relatives des conformations repliée et étendue des bichromophores. On a trouvé que les interactions d'empilement dans l'état fondamental de la coumarine et de la base nucléotide sont limitées aux solutions aqueuses. On a évalué la contribution du mécanisme de piégeage dynamique au piégeage total de la fluorescence dans l'eau. On explique l'absence de piégeage dynamique dans les solvants organiques par le temps de vie très court du fluorophore dans le méthanol.

[Traduit par la revue]

Introduction

It is well known that heteroaromatic compounds from the psoralen family form noncovalent complexes with nucleic acids (1, 2). The formation of the complex by weak forces, i.e., aromatic ring stacking due to hydrophobic and van der Waals forces, is one of several parameters contributing to the overall photobiological activity of psoralens (furocoumarins). The complexation is usually described in terms of the "intercalation model", which predicts that the psoralen molecule is placed between two adjacent nucleotide base pairs. Both ultraviolet absorption and fluorescence spectroscopy can be used to detect the intercalation complex. Its formation is generally accompanied by the bathochromic shift and hypochromicity of the near ultraviolet (uv) absorption band of the psoralen derivative. The fluorescence properties of psoralens also vary upon intercalation. The ability of nucleic acid bases to form such complexes with psoralen has been tested using model compounds in which both interacting molecules were connected with a hydrocarbon chain. The percentage of stacked or folded conformation, as opposed to extended, was determined by the study of the variation of the hypochromic effect with temperature (3, 4).

Recently we synthesized a series of compounds containing 7-methoxycoumarin and nucleic acid base: adenine, thymine, and uracil, linked together with a polymethylene chain. Intramolecular ring–ring stacking in the compounds was assessed by hypochromism measurement in the ultraviolet [5]. The compounds fluoresce at room temperature, the 7-methoxycoumarin residue being the fluorophore responsible for the observed emission. Our preliminary results indicated that in aqueous solution the emission from a selectively excited 7-methoxycoumarin residue incorporated in the system was efficiently quenched. We have therefore investigated the intramolecular complexing of the units of bichromophoric compounds using fluorescence spectroscopy, and in this paper we would like to present our results.

[1]Revision received November 9, 1987.

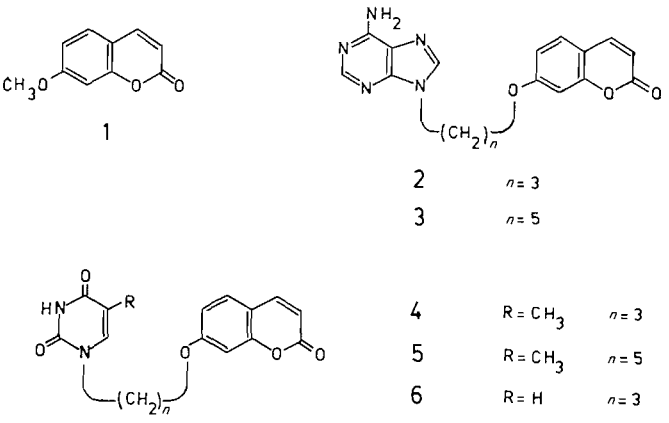

SCHEME 1

TABLE 1. Fluorescence properties of 7-methoxycoumarin

Solvent	Dielectric constant[a]	λ_{fl}^{max} (nm)	φ_{fl}[b]
Benzene	2.28	378	<0.001
Methylene chloride	9.08	380	0.004
Methanol	32.70	385	0.02
Acetonitrile	37.5	385	0.02
Water	80.2	393	0.16

[a]From ref. 9.
[b]Quinine sulfate in 0.1 M H_2SO_4; φ_{fl} = 0.55 (8) was used as a standard. λ_{ex} = 324 nm.

Results and discussion

The fluorescence intensity of 7-methoxycoumarin (**1**, Scheme 1), which was used as a reference compound, is strongly dependent on solvent polarity (Table 1). Fluorescence quantum yield has the highest value in aqueous solution and decreases with decreasing polarity of the solvent. A variation of the fluorescence intensity of 7-methoxycoumarin in methanol–water mixtures was noted previously (6). On the other hand, the

Can. J. Chem. Downloaded from www.nrcresearchpress.com by 176.9.209.113 on 09/07/12
For personal use only.

TABLE 2. Fluorescence properties and intramolecular complexing of bichromophoric compounds **2–6** in aqueous solution

Compound	$\frac{I_{fl}^a}{I_{fl}^0}$	τ (ns)[b]	γ	$(1-\alpha)$ × 100%	$k_q \times 10^{-8}$ (s^{-1})
(**2**) CouO-C_3-Ade	0.12[c]	0.670	0.26 ± 0.02	76 ± 12	8.10
(**3**) CouO-C_5-Ade	0.22[c]	0.832	0.39 ± 0.04	63 ± 10	5.19
(**4**) CouO-C_3-Thy	0.32[c]	0.859	0.54 ± 0.05	46 ± 7	4.81
(**5**) CouO-C_5-Thy	0.85	1.372	0.91 ± 0.09	9 ± 2	0.46
(**6**) CouO-C_3-Ura	0.40	0.922	0.64 ± 0.06	36 ± 6	4.02

[a]Fluorescence intensity of CouO-$(CH_2)_n$-base/CouOMe. λ_{ex} = 324 nm, maximum error ±10%.
[b]Fluorescence lifetime of CouOMe (**1**), τ^0 = 1.465 nm. All fluorescence lifetimes were measured with a precision of ±10 ps.
[c]Data from ref. 5.

location of the emission maximum is only slightly solvent dependent and is red shifted in polar solvents. An explanation of the solvent dependence of the fluorescence of **1** was postulated, based on the variation in energy of excited $^1\pi\pi^*$ and $^3n\pi^*$ levels of coumarin with solvent polarity (6). In nonpolar solvents the $n\pi^*$ singlet and triplet states are just above and just below the S_1 ($\pi\pi^*$) state, respectively. Under these conditions intersystem crossing from the S_1 ($\pi\pi^*$) state to the closely lying $^3n\pi^*$ state is efficient and the fluorescence yield is small. In polar solvents the energy of the S_1 ($\pi\pi^*$) state is lowered below that of the $n\pi^*$ triplet state. As a consequence the efficiency of intersystem crossing decreases and the fluorescence quantum yield increases. However, another explanation is possible. Lai *et al.* (7) have recently studied the photophysical properties of some furocoumarins in different solvents. The authors conclude that the photophysical behaviour of the compounds studied is controlled by the "proximity effect", which is a consequence of vibronic interaction between closely lying $^1\pi\pi^*$ and $^1n\pi^*$ states. In their paper, the strong, coumarin-like solvent dependence of the fluorescence of the furocoumarins was accounted for in terms of the solvent dependent $^1\pi\pi^*$–$^1n\pi^*$ electronic energy gap, which affects the $S_1 \rightsquigarrow S_0$ internal conversion rate.

In compounds **2–6** containing the 7-methoxycoumarin chromophore and nucleotide base the coumarin fluorescence in aqueous solution is much less intense than that of the reference, i.e., 7-methoxycoumarin (**1**) (Table 2, I_{fl}/I_{fl}^0). No new bands are observed in the fluorescence spectra of **2–6** that could be attributed to exciplex emission. The efficiency of the intramolecular quenching process is sensitive to the identity of the attached nucleotide base and to the length of the chain linking the two chromophores.

Quenching of excited states can be achieved either by resonance energy transfer involving large molecular separation or by contact quenching. Since there is no overlap between the emission of coumarin and the absorption spectra of the nucleotide base (5), the observed quenching is not due to energy transfer (10). Two types of contact quenching are known: static and dynamic quenching.[2] Although both types of quenching decrease the emission yield, only the dynamic quenching reduces the emission lifetime. Measurements of the lifetimes allow evaluation of the contribution of the two mechanisms to the total quenching. Static quenching can then be quantitatively related to the proportion of the folded, i.e., intramolecularly complexed, conformations of **2–6**.

[2]Reference 10, pp. 441–443.

The fluorescence emissions of all the compounds **1–6** decay monoexponentially, as shown in Fig. 1. The fluorescence lifetimes of 7-methoxycoumarin (**1**) and bichromophoric compounds **2–6** in water and in methanol are presented in Tables 2 and 3. Monoexponential fluorescence decay of 7-ethoxycoumarin (11) and 7-hydroxycoumarin (12) was reported and it contrasts with that of the furocoumarins. The latter show bi- and triexponential decays in water and in methanol due to the formation of fluorescent complexes with the solvent (12, 13).

A comparison of relative fluorescence intensities and lifetimes in aqueous solution (Table 2) reveals that both quenching processes operate, as illustrated in Scheme 2. Using the approach described previously for the nucleotide base – indole system (14), the fraction γ of light absorbed by the extended form of the bichromophoric compound and the fraction α of unfolded conformations of **2–6** in the ground state can be calculated from eqs. [1] and [2].

$$[1] \quad \gamma = \frac{I_{fl}}{I_{fl}^0} \cdot \frac{\tau^0}{\tau}$$

$$[2] \quad \alpha = \frac{\bar{\varepsilon}}{\varepsilon_0} \cdot \gamma$$

where I_{fl} and τ are the fluorescence intensity and lifetime of **2–6**, I_{fl}^0 and τ^0 the fluorescence intensity and lifetime of **1**, $\bar{\varepsilon}$ is the measured molar extinction coefficient of the bichromophoric compound, and ε_0 the molar extinction coefficient of the extended form of **2–6**, respectively, assumed to be the same as for **1** at λ = 324 nm. The calculated values of $(1-\alpha)$ then represent the fraction of bichromophoric molecules that exist in folded conformation in the ground state; i.e., they correspond to the degree of intramolecular association present in each compound.

The structural preference for ground state interaction of 7-methoxycoumarin with adenine rather than with the pyrimidines (uracil and thymine) is evident from the data obtained (Table 2). The degree of stacking interaction CouO-C_3-Ade > CouO-C_3-Thy ~ CouO-C_3-Ura, obtained here from fluorescence measurements, is in agreement with that obtained from uv absorption (hypochromism) (5). Similar results were obtained for nucleotide base – psoralen pairs. The calculation based on temperature dependence of hypochromism showed that 80% of trimethylene chain linked adenine–psoralen molecules exist in folded conformation at 20°C in H_2O–EtOH (95:5) solution. The preference for interaction of psoralen with adenine rather than with thymine was also observed (4).

Single exponential fluorescence emission decays of **1–6**

Can. J. Chem. Downloaded from www.nrcresearchpress.com by 176.9.209.113 on 09/07/12
For personal use only.

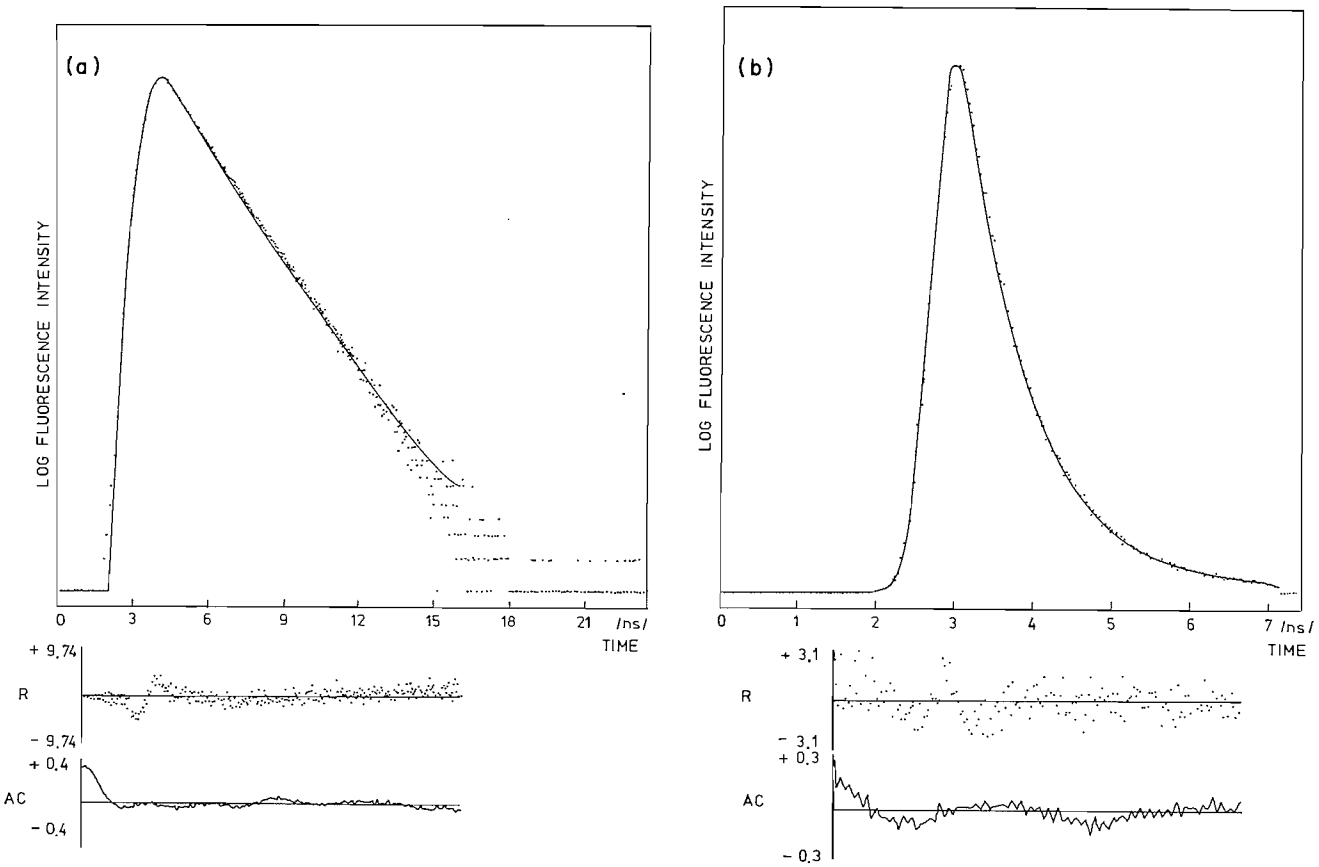

FIG. 1. Logarithmic plots of the fluorescence decay of **1** (a) and **4** (b) in water. The weighted residuals (R) and their autocorrelation function (AC) are also shown.

TABLE 3. Fluorescence properties of bichromophoric compounds in organic solvents

	Methanol		Acetonitrile
Compound	I_{fl}^a / I_{fl}^0	τ (ns)[b]	I_{fl}^a / I_{fl}^0
(**2**) CouO-C_3-Ade	0.81[c]	0.158	0.94
(**4**) CouO-C_3-Thy	1.01[c]	0.189	0.96
(**6**) CouO-C_3-Ura	0.98	0.214	0.95

[a] λ_{ex} = 324 nm.
[b] Fluorescence lifetime of CouOMe (**1**), τ^0 = 0.205 ns in methanol.
[c] Data from ref. 5.

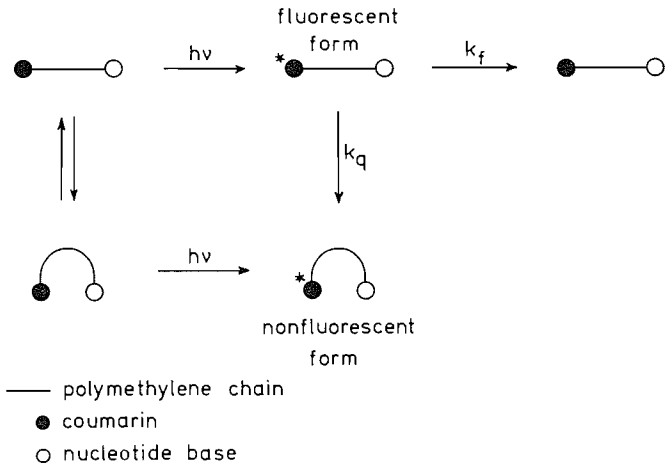

SCHEME 2

allow the calculation of the intramolecular quenching rate constant k_q using eq. [3] (14, 15) (Table 2):

$$[3] \quad k_q = \frac{1}{\tau} - \frac{1}{\tau^0}$$

The differences in the rate constant k_q for all the compounds are evident, and the variation with chain length and structure of nucleic acid base is observed.

In methanol and acetonitrile both the fluorescence quantum yield and fluorescence lifetime of 7-methoxycoumarin are significantly reduced as compared to aqueous solution (Table 1). Possible explanations for this have been discussed above. However, in organic solvents no fluorescence quenching of the 7-methoxycoumarin residue incorporated in the systems **2**–**6** is observed. The relative fluorescence intensities I_{fl}/I_{fl}^0 for **2**, **4**, and **6** presented in Table 3 are close to unity. The compound CouO-C_3-Ade (**2**) is an exception. In this case the fluorescence quenching, inefficient compared to aqueous solution, is, however, only dynamic because the value of I_{fl}/I_{fl}^0 is equal to the value of τ/τ^0 within experimental error. The absence of static quenching indicates that the fraction of folded forms is negligible.

The stacking interaction of 7-methoxycoumarin residue with nucleotide bases is thus limited to aqueous solution. The observation has precedent, lack of any stacking interaction in

Can. J. Chem. Downloaded from www.nrcresearchpress.com by 176.9.209.113 on 09/07/12
For personal use only.

organic solvents having been noted previously for nucleotide base and psoralen (4), indole (14), and quinoline (15) pairs, respectively. The effect of solvents on stacking interaction is not yet completely understood. It is thought, however, that hydrophobic forces play an important role in stabilization of the stacked conformation in aqueous solution (4).

The fluorescence of the 7-methoxycoumarin residue in **4** and **6** is not quenched even through the dynamic quenching mechanism in organic solvents. This fact can be explained by taking into account a very short fluorescence lifetime of 7-methoxycoumarin (0.20 ns in methanol). The intramolecular fluorescence quenching rate is limited by the rate of conformational change around a hydrocarbon chain. The maximum value of the rate constant for changes around a trimethylene bridge was reported to be $10^9\ s^{-1}$ (16); the self-deactivation rate of 7-methoxycoumarin (**1**) was calculated from $1/\tau^0 = 5 \times 10^9\ s^{-1}$ in methanol. It appears that in **4** and **6** the excited state of the fluorophore self-deactivates before the fluorophore and quencher residues in the bichromophoric molecules are brought into close proximity.

Experimental

The synthesis of compounds **2**, **3**, and **4** was reported previously (5). The compounds **5** and **6** were synthesized by alkylation of 7-hydroxycoumarin with 1-(5-bromopentyl)thymine and 1-(3-bromopropyl)uracil, respectively. The purity of all the compounds was checked by ^{1}H nmr and microanalysis, as well as by tlc and gc techniques.

Doubly distilled water, spectroscopic grade methanol (Fisher), and acetonitrile (Merck) were used as solvents. Relative fluorescence intensities were determined by integration and comparison of uncorrected emission spectra of **2**–**6** (I_{fl}) and the reference compound **1** (I_{fl}^0). Solutions of both bichromophoric compound and reference compound had equal absorbance at the exciting wavelength (λ_{exc} = 324 nm). The fluorescence quantum yield for **1** was measured from corrected spectra using quinine sulfate as a standard (0.1 M H_2SO_4, φ_{fl} = 0.55 (8)). Steady-state fluorescence measurements were performed on a Perkin–Elmer MPF-44B spectrofluorimeter. Absorbances of the samples (10-mm cells) for fluorescence studies were all ca. 0.05, i.e., concentrations of the solutions were in the range $(2.2–6.8) \times 10^{-6}$ M. Fluorescence lifetimes were measured with a Spectra-Physics synchronously pumped, cavity-dumped, frequency doubled dye laser system using a time-correlated single photon counting technique. The apparatus, as well as the technique for analyzing the decay curves, has been previously described (17).

Acknowledgments

We thank Dr. M. Szymański from the Institute of Physics, A. Mickiewicz University, Poland, and Dr. A. Siemiarczuk from the Photochemistry Unit, The University of Western Ontario, London, Ontario, Canada, for measuring the fluorescence lifetimes. This work was supported within the project RP.II.13.2.15.

1. B. J. Parsons. Photochem. Photobiol. **32**, 813 (1982), and references cited therein.
2. P. S. Song and K. J. Tapley, Jr. Photochem. Photobiol. **29**, 1177 (1979).
3. J. L. Decout and J. Lhomme. Tetrahedron Lett. **22**, 1247 (1981).
4. J. L. Decout and J. Lhomme. Photochem. Photobiol. **37**, 155 (1983).
5. G. Wenska and S. Paszyc. Can. J. Chem. **62**, 2006 (1984).
6. K. Muthuramu and V. Ramamurthy. J. Photochem. **26**, 57 (1984).
7. T. I. Lai, B. T. Lim, and E. C. Lim. J. Am. Chem. Soc. **104**, 7631 (1982).
8. W. H. Melhuish. J. Phys. Chem. **65**, 229 (1961).
9. S. L. Murrov. Handbook of photochemistry. Dekker, New York. 1973.
10. J. B. Birks. Photophysics of aromatic molecules. Wiley–Interscience, New York. 1970. pp. 567–569.
11. T. Moriya. Bull. Chem. Soc. Jpn. **57**, 1723 (1984).
12. A. Andreou. Chem. Phys. Lett. **114**, 329 (1985).
13. R. V. Bensasson. *In* Primary photo-processes in biology and medicine. *Edited by* R. V. Bensasson, G. Jori, E. J. Land, and T. G. Truscott. Plenum Press, New York. 1985. pp. 243–245.
14. K. Mutai, B. A. Gruber, and N. J. Leonard. J. Am. Chem. Soc. **97**, 4095 (1975).
15. J. Bolte, C. Demuynck, J. Lhomme, M. C. Fournie-Zaluski, and B. P. Roques. Biochemistry, **18**, 4928 (1979), and references cited therein.
16. M. Palmer and H. Morrison. J. Org. Chem. **45**, 798 (1980).
17. A. Maciejewski, R. R. Demmer, D. R. James, A. Safarazadeh-Amiri, R. E. Verall, and R. P. Steer. J. Am. Chem. Soc. **107**, 2831 (1985).

Can. J. Chem. Downloaded from www.nrcresearchpress.com by 176.9.209.113 on 09/07/12
For personal use only.

Synthesis and conformational analysis of 2-amino-1,2,3,4-tetrahydro-1-naphthalenols[1]

ANTONIO DELGADO, JOSÉ MIGUEL GARCIA, DAVID MAULEON,[2] CRISTINA MINGUILLON, AND JOAN RAMON SUBIRATS
Departamento de Farmacología y Química Terapéutica, División de Ciencias de la Salud, Facultad de Farmacia, Laboratorio de Química Farmacéutica, Avda. Diagonal s/n, 08028 Barcelona, Spain

AND

MIGUEL FELIZ, FRANCISCO LOPEZ, AND DOLORES VELASCO
Departamento de Química Orgánica, División Ciencias Experimentales y Matemáticas, Facultad de Química, Martí i Franqués, 1, 08028 Barcelona, Spain

Received March 31, 1987[3]

ANTONIO DELGADO, JOSÉ MIGUEL GARCIA, DAVID MAULEON, CRISTINA MINGUILLON, JOAN RAMON SUBIRATS, MIGUEL FELIZ, FRANCISCO LOPEZ, and DOLORES VELASCO. Can. J. Chem. **66**, 517 (1988).

Synthesis and conformational analysis of several *cis*- and (or) *trans*-2-amino-1,2,3,4-tetrahydro-1-naphthalenols are described. Introduction of the nitrogen atom at the C(2) position of the starting tetralones **3** has been carried out through nitrosation followed by reduction of the intermediate hydroxyimino tetralone and (or) Neber rearrangement of the tosyloxy derivatives **7***a–e*. Stereoselective reduction of the C(1) carbonyl group of acetamidotetralones **5***a–e* or aminotetralones **8***a–e* afforded the corresponding acetamido or aminotetralols, respectively, of OH/N *trans* stereochemistry whereas an opposite stereoselectivity was observed in reduction of C(8)-OCH_3 derivatives **5***f* and **8***f* under the same experimental conditions. Finally, acid hydrolysis of *trans*-acetamidotetralols led to *cis*-aminoalcohols in high yields. Conformational analysis has been carried out by ^1H nuclear magnetic resonance techniques and MM2 theoretical calculations. All *cis* derivatives showed a major conformation in which the C(1)-OH group adopts a pseudoaxial disposition. On the other hand, *trans*-aminoalcohols in $CDCl_3$ showed a major or exclusive OH/N *trans*-dipseudoequatorial conformation in which stabilization by intramolecular OH/N hydrogen bonding is possible. The only exception was found in C(8)-OCH_3 *trans*-aminoalcohols in DMSO-d_6 solution, which showed a major OH/N *trans*-diaxial conformation.

ANTONIO DELGADO, JOSÉ MIGUEL GARCIA, DAVID MAULEON, CRISTINA MINGUILLON, JOAN RAMON SUBIRATS, MIGUEL FELIZ, FRANCISCO LOPEZ et DOLORES VELASCO. Can. J. Chem. **66**, 517 (1988).

On décrit la synthèse et l'analyse conformationnelle de plusieurs amino-2 tétrahydro-1,2,3,4 naphtalénols-1-*cis* et -*trans*. Pour introduire un atome d'azote en position C(2) des tétralones **3** de départ, on a fait appel soit à une nitrosation suivie d'une réduction de l'hydroximino tétralone intermédiaire soit à une transposition de Neber des dérivés tosyloxy **7***a–e*. La réduction stéréosélective du groupement carbonyle en C(1) des acétamidotétralones **5***a–e* ou des aminotétralones **8***a–e* conduit aux acétamido ou aminotétralols correspondants de stéréochimie OH/N *trans*; par ailleurs, on obtient la stéréochimie inverse lorsqu'on réduit les dérivés C(8)-OCH_3, **5***f* et **8***f*, en utilisant les mêmes conditions expérimentales. Enfin, l'hydrolyse acide des acétamidotétralols-*trans* conduit au aminoalcools-*cis*, avec d'excellents rendements. On a réalisé l'analyse conformationnelle à l'aide de la résonance magnétique nucléaire du ^1H et de calculs théoriques MM2. Pour chacun des dérivés *cis*, la conformation prédominante comporte un groupement C(1)-OH dans une position pseudo-axiale. Par ailleurs, en solution dans le $CDCl_3$, les aminoalcools *trans* présentent une conformation majeure, sinon exclusive, OH/N di-pseudo-équatoriale *trans* dans laquelle une stabilisation par liaison OH/N intramoléculaire est possible. On a noté une seule exception; il s'agit des aminoalcools *trans* C(8)-OCH_3 qui, en solution dans le DMSO-d_6, existent dans une conformation OH/N *trans*-diaxiale.

[Traduit par la revue]

As part of our research concerning the synthesis of conformationally restrained arylethanolamines, this paper deals with the synthesis and conformational analysis of several *cis*- and (or) *trans*-2-amino-1,2,3,4-tetrahydro-1-naphthalenols **1***a–i* and **2***a–i* (Scheme 1) as potential adrenergic agents.

In all cases, synthesis started from the corresponding 1-tetralones **3***a–f*, prepared by standard procedures. Introduction of the nitrogen atom at the C(2) position of the 1-tetralone system was carried out according to two alternative procedures (Scheme 2).

First, nitrosation of 1-tetralones **3***a,b,d–f* with butyl- or isoamyl nitrite in the presence of potassium *tert*-butoxide afforded the desired hydroxyiminotetralones **4***a,b,d–f* in 50–80% yield. The comparatively lower yields observed for **4***b*, *d*, and *f* can be explained as a consequence of the concomitant formation of benzoates **9***b,d,f* or **10**, resulting from alkoxide

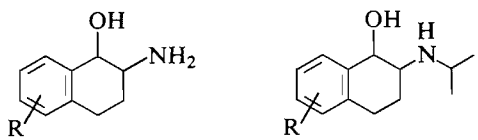

1*a–i* **2***a–i*

	R	OH/N stereochemistry
a	H	*cis* or *trans*
b	5-OCH_3	*cis* or *trans*
c	5-OBzl	*trans*
d	6-OBzl	*trans*
e	7-OBzl	*trans*
f	5,8-$(OCH_3)_2$	*cis* or *trans*
g	5-OH	*trans*
h	6-OH	*trans*
i	7-OH	*trans*

SCHEME 1

[1]This work was presented in a preliminary form at the XX Reunión Bienal de la Real Sociedad Espanola de Química, Castellón, Spain, 1984.

[2]Author to whom correspondence may be addressed.

[3]Revision received November 10, 1987.

Can. J. Chem. Downloaded from www.nrcresearchpress.com by 176.9.209.113 on 09/07/12
For personal use only.

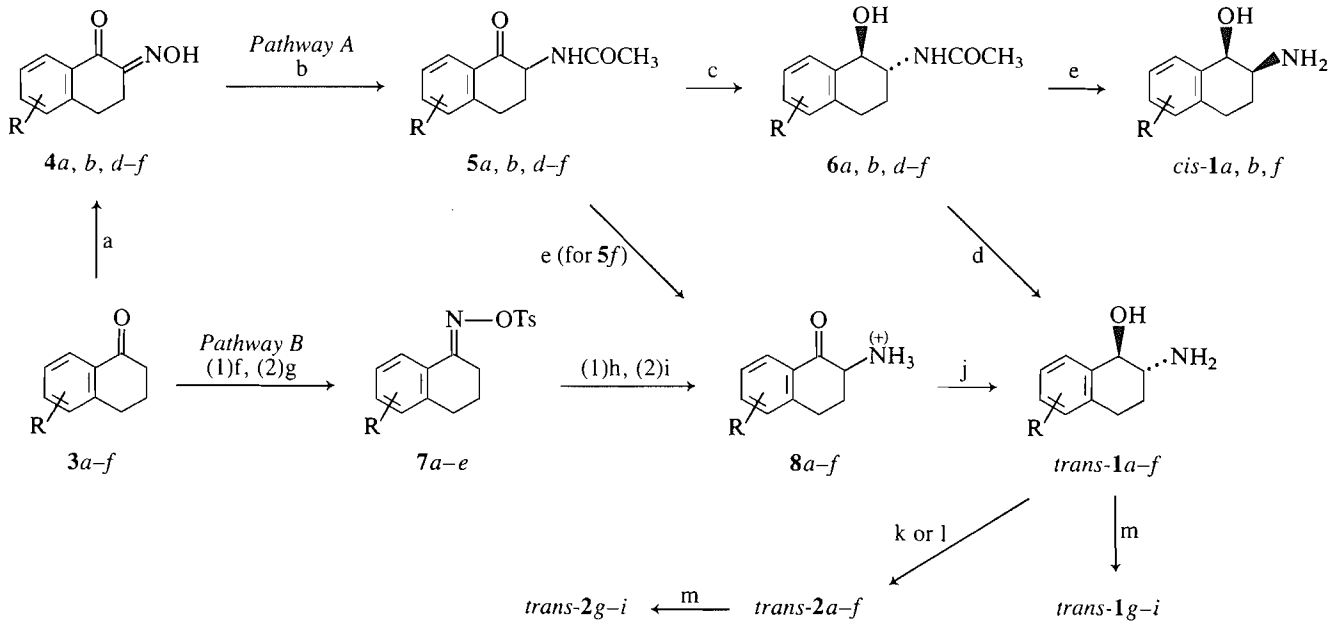

a: BuONO or iso-AmmONO/KO*t*-Bu; b: Zn, Ac_2O, AcOH; c: $NaBH_4$, CH_3OH, H_2O or H_2, PtO_2 (for **5f**); d: KOH, EtOH–H_2O; e: HCl 0.3 M rfx.; f: $NH_2OH \cdot HCl$, pyr.; g: Cl-OTs, pyr.; h: KOEt, benzene, EtOH (Neber rearrangement); i: HCl 5 M; j: $NaBH_4$, CH_3OH–NaOH; k: (1) acetone, benzene, rfx., (2) $NaBH_4$–CH_3OH; l: acetone, CH_3OH, $NaBH_3CN$; m: H_2, Pd/C 5%, 200 psi (from compounds *c*, *d*, and *e*).

SCHEME 2

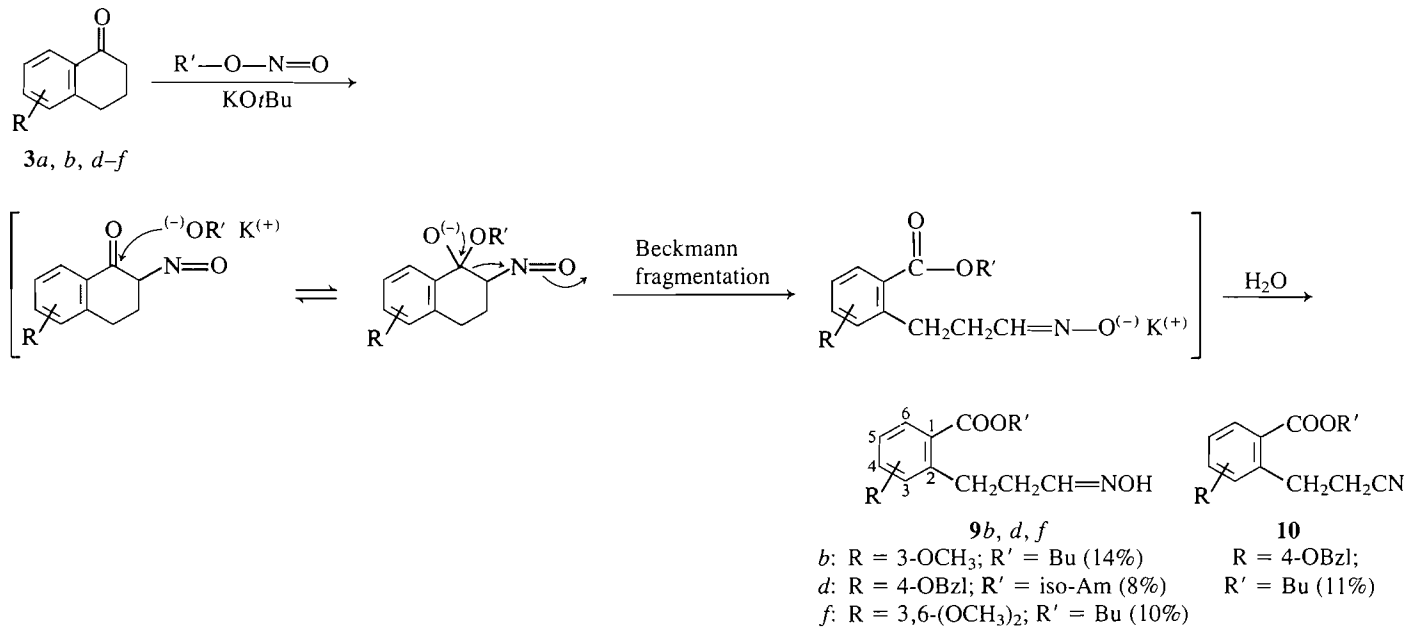

b: R = 3-OCH_3; R′ = Bu (14%)
d: R = 4-OBzl; R′ = iso-Am (8%)
f: R = 3,6-$(OCH_3)_2$; R′ = Bu (10%)

10: R = 4-OBzl; R′ = Bu (11%)

SCHEME 3

attack upon the C(1) position of the initially formed nitroso derivatives and subsequent Beckmann fragmentation (1) (Scheme 3). Nitrile **10** (arising from alkaline cleavage of the oximino ketone) (2) was obtained instead of the oxime, upon nitrosation of **3***d* with butyl nitrite. In general, short reaction times and low temperatures minimize or avoid the formation of the above fragmentation products.

Attempts to elaborate the 2-amino-1-tetralol moiety by direct reduction of hydroxyiminotetralones **4** were unsuccessful. Thus, hydrogenation of **4***d* over palladium–charcoal in acidic medium (3) afforded naphthylamine **11** as the only isolable product (Scheme 4). On the other hand, treatment of both **4***d* and **4***f* with lithium aluminum hydride (4) afforded only trace amounts of a *cis–trans* mixture of aminoalcohols **1***d* and **1***f*, respectively. In consequence, a stepwise reduction of oximino-tetralones **4***a*, *b*, *d–f* was envisaged. Thus, treatment of crude

Can. J. Chem. Downloaded from www.nrcresearchpress.com by 176.9.209.113 on 09/07/12
For personal use only.

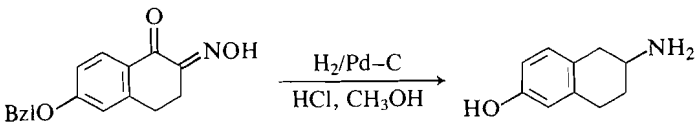

4*d* **11**

SCHEME 4

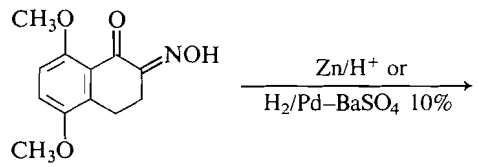

4*f*

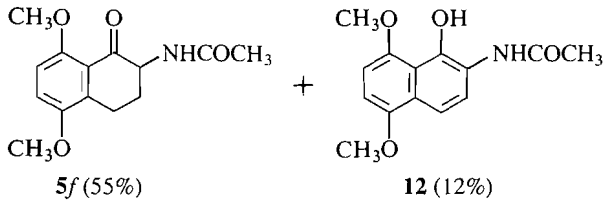

5*f* (55%) **12** (12%)

SCHEME 5

oximinotetralones with zinc dust in acetic acid – acetic anhydride solution (Scheme 2, pathway A), led to 2-acetamido-1-tetralones **5***a,b,d–f* in 55–65% yield. Reduction of **4***f* under the above conditions afforded a 5:1 mixture of **5***f* and naphthol **12** in 77% yield. Formation of **12** can be interpreted as a redox reaction between the hydroxyiminotetralone **4***f* and the initially formed acetamidotetralone **5***f* (Scheme 5). Alternative reduction of **4***f* by hydrogenation over Pd 10%/$BaSO_4$ in AcOH–Ac_2O (5) did not modify the above results.

Neber rearrangement (6) was used as the key step for the second (alternative) pathway to synthesize 2-amino-1-tetralols. The required tosyloxyderivatives **7***a–e* (Scheme 2, pathway B) were routinely obtained in two steps from the corresponding tetralones **3***a–e*. Neber rearrangement was not applied to the preparation of the 5,8-dimethoxylated aminoketone hydrochloride **8***f* since it is known that the steric hindrance exerted by the 8-OCH_3 group precludes formation of **7***f* from **3***f*-oxime (7). However, **8***f* could be obtained by acid hydrolysis of acetamidotetralone **5***f*.

The stereoselective course of the reduction of the carbonyl group in 2-acetamido- and 2-amino-1-tetralones to give the corresponding *trans*-2-acetamido- or *trans*-2-amino-1-tetralols is well documented (5, 8, 9, 10). As expected, sodium borohydride reduction of compounds **5***a,b,d,e* in CH_3OH–H_2O (Scheme 2, pathway A) afforded the corresponding *trans* derivatives **6***a,b,d,e* as the major products (about a 90:10 *trans/cis* ratio based on C(1)H signal integration in the high resolution ^{1}H nmr spectra). The stereochemistry of compounds **6***a,b,d,e* was also confirmed by the $W_{1/2}$ value of about 16 Hz observed for the C(1)H proton, thus indicating a C(1)H–C(2)H pseudoaxial relationship. Alkaline hydrolysis of acetamidotetralols *trans*-**6***a,b,d,e* afforded the desired aminoalcohols *trans*-**1***a,b,d,e* in good yields, whose stereochemistry was confirmed by derivatization into conformationally restrained oxazolidin-2-one derivatives (11) as well as on the basis of the C(1)H chemical shift and coupling constant values (12, 13) of the cycloaliphatic protons (see below). On the other hand, aminoalcohols *trans*-**1***a–e* could be obtained by stereoselective sodium borohydride reduction of 2-amino-1-tetralone hydrochlorides **8***a–e* (again, about a 90:10 *trans/cis* ratio based on C(1)H signal integration was found).

The reverse stereoselectivity observed in the sodium borohydride reduction of the dimethoxylated derivatives **5***f* and **8***f* deserves comment. Thus, treatment under the above experimental conditions afforded in each case a mixture of diastereoisomers in which *cis* derivatives were predominant (about a 65:35 *cis/trans* ratio). Analysis of C(1)H signals in the high resolution ^{1}H nmr spectrum of the crude reaction mixture arising from sodium borohydride reduction of **5***f* revealed a doublet at 4.93 ppm (major isomer) whose coupling constant value (J = 4.3 Hz) was indicative of a *cis*-OH_{axial}/$NHR_{equatorial}$ relationship. Alkaline hydrolysis of this major isomer afforded aminoalcohol *cis*-**1***f*, whose stereochemistry was also confirmed on the basis of ^{1}H nmr data (see below). In the same way, sodium borohydride reduction of hydrochloride **8***f* afforded predominantly aminoalcohol *cis*-**1***f*. These results are opposite to those described by other authors (14), who assigned a *trans* stereochemistry to compound *cis*-**1***f*. The observed reversal of stereoselectivity can be rationalized according to House *et al.* (15, 16), assuming that the geometry of the transition state and that of the final product are similar and adequate to predict the major stereochemical course of borohydride reductions. Thus, the most stable transition state in the reduction of **5***a,b,d,e* and **8***a–e* would lead to a *trans*-OH/NHR diequatorial relationship, whereas the transition state leading to *cis*-**1***f* and *cis*-**6***f* from **5***f* and **8***f*, respectively, would be the most stable one, since steric crowding due to the "*peri*" effect between C(8) and C(1) groups is minimized. This interpretation does not preclude complexation between the 2-acetamido group and borane, which has been postulated in reduction of 2-amino-1-indanones (17).

In contrast to borohydride reductions, hydrogenation over Adams catalyst of 2-acetamidotetralone **5***f* afforded predominantly *trans*-acetamidoalcohol **6***f* (about 80:20 *trans/cis* ratio based on ^{1}H nmr analysis), whose stereochemistry was confirmed by alkaline hydrolysis to aminoalcohol *trans*-**1***f*. The low coupling constant value (J = 4.9 Hz) between C(1)H–C(2)H for *trans*-**6***f* in $CDCl_3$ solution was indicative of the preferred OH/NHR *trans*-diaxial conformation in which *peri* interactions between C(1)H and C(8)OCH_3 groups are avoided. Likewise, the C(1) chemical shift observed for *trans*-**6***f* (see Table 3) is in agreement with the proposed OH-pseudoaxial disposition (18).

In summary, aminoalcohols *trans*-**1***a,b,d,e* could be obtained in comparable yields from the corresponding tetralones **3** by either of the two alternative pathways outlined in Scheme 2 (overall yields: pathway A, 18–20%; pathway B: 12–15%). Finally, hydrogenolysis of aminoalcohols *trans*-**1***c–e* over 5% palladium–charcoal (200 psi; 1 psi = 6.9 kPa) afforded the desired phenolic derivatives *trans*-**1***g–i* in about 50% yield. Attempts to carry out hydrogenolysis under atmospheric pressure gave only starting aminoalcohols whereas hydrogenation under acidic conditions resulted in simultaneous hydrogenolysis of benzyl and 1-hydroxyl groups.

Aminoalcohols *cis*-**1***a*, *b*, and *f* could be readily obtained by acid hydrolysis of acetamidotetralols *trans*-**6***a,b*, and *f*, through a process that is known to proceed via an oxazoline intermediate with inversion of configuration at the C(1) carbon atom (10). Formation of the intermediate oxazoline was found to be very favourable upon acidic treatment of both *cis*- and *trans*-**6***f*. In fact, acidic work-up after sodium borohydride reduction of **5***f* afforded exclusively tetrahydronaphtho[2,1-*d*]oxazol derivative **13** (Scheme 7). Formation of

Can. J. Chem. Downloaded from www.nrcresearchpress.com by 176.9.209.113 on 09/07/12
For personal use only.

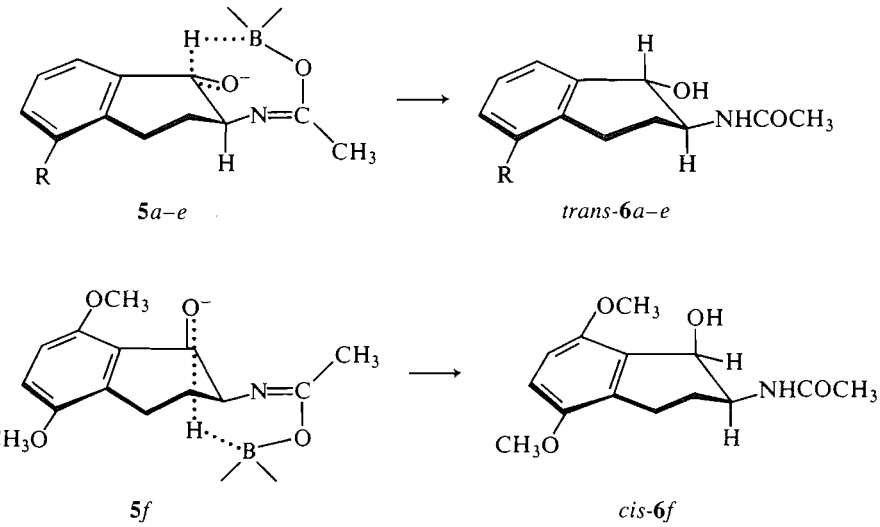

SCHEME 6

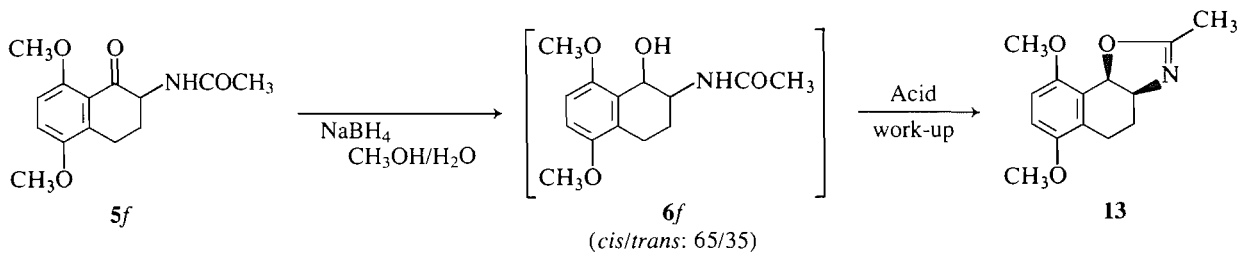

SCHEME 7

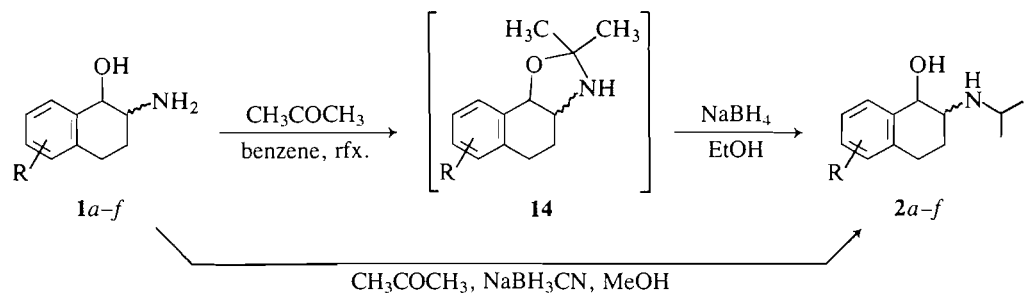

SCHEME 8

13 could be also carried out in an ^{1}H nmr tube. Thus, in the presence of a few drops of TFA, both *cis*- and *trans*-**6***f* in $CDCl_3$ gave an identical product whose ^{1}H nmr signals were superimposable on those of **13** recorded on $CDCl_3$ + TFA. On the other hand, alkaline hydrolysis of **13** afforded aminoalcohol *cis*-**1***f* as the only reaction product. The straightforward formation of **13** from *trans*-**6***f* can be explained in the light of the major *trans*-diaxial OH/NHR conformation of the starting 2-acetamidotetralol (see below).

Isopropyl derivatives **2** were obtained in each case from the corresponding *cis* or *trans* aminoalcohols either by reductive alkylation with excess acetone in benzene followed by sodium borohydride reduction of the intermediate oxazolidine system **14** (19) or in a one-step procedure with acetone – sodium cyanoborohydride in methanol (20) (Scheme 8). As in the amino series, isopropylamino derivatives *trans*-**2***g–i* were obtained by benzyl group hydrogenolysis as described above.

Conformational analysis

Although 2-aminotetrahydro-1-naphthols can be regarded as conformationally restrained analogues of adrenergic arylethanolamines, two limited half-chair conformations are still possible for each compound. Since interpretation of pharmacological data requires the knowledge of the preferred conformation in solution of the molecule under study, we have carried out a conformational analysis of the target aminotetrahydronaphthols by means of nmr data and theoretical calculations.

Assignment of the *cis* or *trans* OH/NHR relationship in amino or isopropylaminotetralols **1** and **2** can usually be carried out by simple inspection of ^{1}H nmr spectra, on the basis of C(1)H chemical shift and coupling constant differences in each diastereomer (12, 13). Thus, whereas compounds *cis*-**1***a,b,f* and *cis*-**2***a,b,f* showed a mean $\delta_{C(1)H}$ ($\pm$SD) of 4.68 ($\pm$0.16) ppm and a mean coupling constant J_{1-2} = 3.7 ($\pm$0.3) Hz, *trans* derivatives **1***a–i* and **2***a–i* (except for *trans*-**1***f* and *trans*-**2***f*, see

Can. J. Chem. Downloaded from www.nrcresearchpress.com by 176.9.209.113 on 09/07/12
For personal use only.

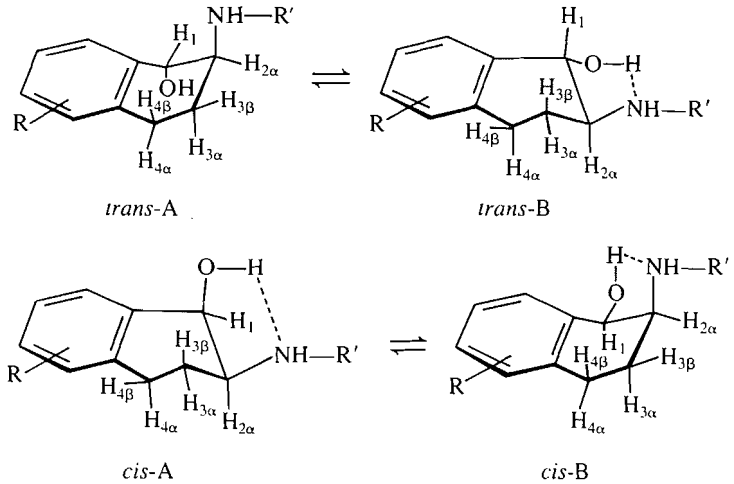

SCHEME 9

TABLE 1. Chemical shifts (ppm) and coupling constants (Hz) for *cis*-**1***b*, *trans*-**1***b*, and *trans*-**1***f* obtained from the LAOCOON/3 analysis*

Protons	*cis*-**1***b*†	*trans*-**1***b*†	*trans*-**1***f*†	*trans*-**1***f*‡
δH_1	4.55	4.30	4.68	4.63
δH_2	3.03	2.92	3.17	3.13
δH_3	1.84	2.00	2.07	2.06
δH_3	1.92	1.68	1.69	1.64
δH_4	2.57	2.79	2.67	2.64
δH_4	2.91	2.83	2.90	2.66
$J(H_1-H_{2\alpha})$	3.2	8.9	7.2	3.6
$J(H_{2\alpha}-H_{3\alpha})$	3.2	3.2	3.2	2.9
$J(H_{2\alpha}-H_{3\beta})$	10.4	11.3	10.8	5.5
$J(H_{3\alpha}-H_{4\alpha})$	6.8	11.9	5.3	7.0
$J(H_{3\alpha}-H_{4\beta})$	4.3	5.6	4.3	9.0
$J(H_{3\beta}-H_{4\alpha})$	10.1	5.9	10.4	4.6
$J(H_{3\beta}-H_{4\beta})$	5.9	3.6	5.3	5.6

*Intensity threshold in all cases was 0.05. The total number of transitions above the intensity threshold was 80, and 60–65 transitions were used in the fitting.
†$CDCl_3$ solution.
‡DMSO-d_6 solution.

below) showed average values of $\delta_{C(1)H} = 4.26$ (±0.13) ppm and $J_{1-2} = 8.6$ (±0.8) Hz. Finally, stereochemistry of 2-amino-1-tetralols has also been confirmed independently by derivatization into the corresponding tricyclic oxazolidin-2-one derivatives (11).

The cycloaliphatic region of the ^1H nmr spectra of *cis* derivatives **1***a*,*b*,*f* and **2***a*,*b*,*f* was almost superimposable. Consequently, we decided to carry out the spin system analysis by means of the LAOCOON-3 program of compound *cis*-**1***b*, which was taken as standard for this purpose (Table 1). Coupling constant values between C(2)H and $C(3)H_\alpha/C(3)H_\beta$ indicate a C(2)H axial disposition and, accordingly, a major or exclusive conformation in which the OH group is pseudoaxial and the NHR group is pseudoequatorial. In this conformation, *peri* interaction between the C(1)OH and C(8) groups (H in *cis*-**1***b*) is avoided and intramolecular OH–NHR hydrogen bonding can be established. Pseudoequatorial C(1)H disposition in *cis* derivatives was confirmed by a nuclear Overhauser effect (nOe) (21) enhancement. Thus, irradiation of the $C(8)OCH_3$ group of *cis*-**1***f* gave rise to a C(1)H nOe enhancement of 13%. On the other hand, a long-range *W* coupling (22) ($J = 0.9$ Hz) was also observed for C(1)H with C(3α)H in *cis*-**1***f* and *cis*-**2***f* derivatives, thus indicating a pseudoequatorial disposition for the above proton.

Theoretical calculations may be used as an independent criterion for performing conformational analysis. By means of the highly reliable Allinger's MM2 force field program (23), energies and geometries of both limited conformers *cis*-A and *cis*-B (Scheme 9) of compounds *cis*-**1***b* and *cis*-**1***f* have been calculated (Table 2). In both cases, *cis*-A conformers turned out to be more stable than the corresponding *cis*-B ones; the observed steric energy differences between them indicate a *cis*-A/*cis*-B relative population of 99:1, which is in agreement with the results of the ^1H nmr study. Moreover, application of the Karplus–Altona equation (24) to the dihedral angles obtained from MM2 analysis afforded a set of coupling constants (Table 2) very similar to those experimentally found (Table 1).

As in the *cis* series, *trans* derivatives **1***a–e* and **2***a–e* showed a nearly superimposable cycloaliphatic region in their ^1H nmr spectra. Spin system analysis of the model compound *trans*-**1***b* (Table 1) indicates a pseudoaxial C(2)H disposition and, consequently, a dipseudoequatorial relationship between amino and hydroxyl groups. This conformation is stabilized by intramolecular hydrogen bonding (broad signal between 3500 and 3000 cm^{-1} in the ir spectra), which overcomes the low *peri* interaction between C(1)OH and C(8)H groups. Accordingly, MM2 calculations for *trans*-A and *trans*-B conformers indicate the higher stability of the diequatorial *trans*-B conformer ($\Delta E =$ 1.21 kcal/mol) as well as a relative population of about 90:10 *trans*-B vs. *trans*-A. Once again, application of the Karplus–Altona equation to the predicted C(2)H coupling constants afforded mean *J* values in agreement with the experimental ones.

Dimethoxylated derivatives *trans*-**1***f* and *trans*-**2***f* were exceptional, since C(1)H protons showed lower J_{1-2} coupling constant and chemical shift values (0.3–0.4 ppm) with respect to C(8) unsubstituted derivatives, such as *trans*-**1***b* (Table 1). This is consistent with an equilibrium between *trans*-A and *trans*-B conformers in which participation of *trans*-A would be important to avoid the strong *peri* interaction between C(1)OH and $C(8)OCH_3$ groups. This situation stands out in DMSO-d_6

Can. J. Chem. Downloaded from www.nrcresearchpress.com by 176.9.209.113 on 09/07/12
For personal use only.

TABLE 2. Selected coupling constants, dihedral angles, and relative energies of *cis*-**1***b*, *trans*-**1***b*, *cis*-**1***f*, and *trans*-**1***f* (from MM2 analysis and the Karplus–Altona equation)

		Conformer A*			Conformer B*					
Compound	Protons	θ	*J* calcd.	Steric energy	θ	*J* calcd.	Steric energy	$\Delta E = E_A - E_B$ (kcal/mol)	% A/B	*J* average
	H_1–$H_{2\alpha}$	−49.08	3.06		45.30	4.69				3.08
cis-**1***b*	$H_{2\alpha}$–$H_{3\alpha}$	65.66	2.88	6.27	−60.25	2.59	8.97	−2.70	99/1	2.89
	$H_{2\alpha}$–$H_{3\beta}$	−174.43	11.82		59.29	3.73				11.73
	H_1–$H_{2\alpha}$	−49.99	2.96		35.75	5.82				2.97
cis-**1***f*	$H_{2\alpha}$–$H_{3\alpha}$	65.90	2.85	9.89	−60.11	2.61	13.51	−3.62	99/1	2.85
	$H_{2\alpha}$–$H_{3\beta}$	−174.02	11.81		59.74	3.66				11.79
	H_1–$H_{2\alpha}$	−74.45	1.96		−168.15	8.63				7.87
trans-**1***b*	$H_{2\alpha}$–$H_{3\alpha}$	−59.57	2.67	7.93	65.92	2.85	6.72	1.21	10/90	2.83
	$H_{2\alpha}$–$H_{3\beta}$	59.85	3.65		−174.07	11.81				10.88
	H_1–$H_{2\alpha}$	−74.00	2.01		−158.41	7.49				2.78
trans-**1***f*	$H_{2\alpha}$–$H_{3\alpha}$	−59.78	2.65	11.57	64.98	2.96	12.64	−1.07	85/15	2.69
	$H_{2\alpha}$–$H_{3\beta}$	59.80	3.66		−174.64	11.82				4.81

*See Scheme 9.

solution (J_{1-2} = 3.5 Hz for *trans*-**1***f*) more than in $CDCl_3$ solution (J_{1-2} = 7.2 Hz for *trans*-**1***f* and 6.2 Hz for *trans*-**2***f*), probably due to the solvating properties of DMSO, which stabilizes the *trans*-A conformation by intermolecular hydrogen bonding. As expected, intramolecular hydrogen bonding is reinforced by protonation of the amino group. Thus, the J_{1-2} value for *trans*-**1***f* in DMSO-d_6 + TFA rises to 6.4 Hz, which is in agreement with a major *trans*-B conformation as in *trans*-**1***a–e* derivatives. The major *trans*-A conformation of *trans*-**1***f* in DMSO-d_6 solution was confirmed by a C(1)H nOe enhancement of 10% on irradiation of the C(8)OCH_3 group. However, although these findings are indicative of conformational equilibrium, no variation of J_{1-2} coupling constants was observed in the temperature range between −60°C ($CDCl_3$) and +60°C (DMSO-d_6).

As above, results of MM2 force field calculations of *trans*-**1***f* (Table 2) were in agreement with ^{1}H nmr experimental data. Thus, the *trans*-A diaxial conformer turned out to be more stable than the *trans*-B (ΔE = 1.07 kcal/mol), and a relative population of about 85% could be estimated for the former. Coupling constant values derived from the Karplus–Altona equation (Table 2) correlate well with those found experimentally in DMSO-d_6 (Table 1). However, spin system analysis of *trans*-**1***f* in $CDCl_3$ afforded a set of coupling constants similar to those found for *trans*-**1***b* by MM2 calculations, which implies the predominance of the diequatorial *trans*-B conformation in nonpolar solvents.

Finally, ^{13}C nmr data (Table 3) are also in good agreement with the above results. Thus, in $CDCl_3$ solution, carbon atom C(1) is observed at 73.2 (±1.4) ppm in *trans* isomers and at 66.5 (±3.2) ppm in *cis* ones. The upfield shift found in *cis* isomers is consistent with the known shielding effect exerted by a pseudoaxial C(1)OH group upon the benzylic carbon atom in a tetralol system (18). On the other hand, carbon atom C(3) is also shielded in some *cis* isomers with respect to *trans* ones, due to a γ-*gauche* effect exerted by the pseudoaxial C(1)OH group. As expected, the C(1) chemical shift of *trans*-**1***f* in DMSO-d_6 solution showed an upfield shift of about 6 ppm, whereas C(3) and C(4) carbon atoms were shielded 3.8 and 2.9 ppm, respectively. Once again, this is consistent with the major *trans*-A diaxial conformation expected for *trans*-**1***f* in this solvent.

Experimental

Melting points were determined in a capillary tube on a Buchi apparatus and are uncorrected. Infrared spectra were recorded on a Perkin–Elmer 1430 spectrophotometer. Proton magnetic resonance spectra were measured at 60 MHz with a Perkin–Elmer R 24B instrument or at 200 MHz with a FT Varian XL-200 spectrometer. Signal positions are reported in ppm downfield from tetramethylsilane (δ scale) as an internal standard, and $CDCl_3$ as a solvent, unless otherwise indicated. The ^{13}C nmr spectra were measured at 50.3 MHz with a Varian XL-200 spectrometer, with internal tetramethylsilane as a reference. Multiplicity of the signal was determined by the ADEPT program (25). Homonuclear chemical shift correlation ^{1}H/^{1}H was determined by the HOMCOR program (26) and heteronuclear chemical shift correlation ^{13}C/^{1}H by the HETCOR program (27). MM2 calculations were performed on an IBM/3083 computer. Mass spectra were recorded on a Hewlett–Packard 5930 A spectrometer. Solutions in organic solvents were dried over anhydrous sodium sulfate and stripped of solvent with a rotary evaporator connected to a water aspirator. Microanalyses were performed by the Departamento de Quimica Organica Biologica (C.S.I.C.), Barcelona.

General synthetic methods

*Benzyl-3,4-dihydro-2*H*-1-naphthalenones (***3***c–e)*

Method A

To a mixture of 0.1 mol of the corresponding hydroxytetralone **3***g* (28), **3***h* (29), or **3***i* (30) and 0.25 mol of anhydrous potassium carbonate, 0.1 mol of benzyl chloride in 150 mL of dry dimethylformamide was added dropwise. The reaction mixture was stirred at 80–100°C for 4 h, poured into ice-water and extracted with ether. The organic extracts were washed with brine, dried, and evaporated to afford **3***c–e*. Compound **3***c* (see also Table 4), ir ($CHCl_3$): 1680 (C=O); ^{1}H nmr (CCl_4): 2.0 (m, 2H, C(3)H_2), 2.4 (m, 2H, C(2)H_2), 2.8 (m, 2H, C(4)H_2), 4.9 (s, 2H, $CH_2C_6H_5$), 6.7–7.5 (m, 3H, ArH), 7.1 (s, 5H, C_6H_5). Compound **3***d* (see also Table 4), ir (KBr): 1660 (C=O), 1600; ^{1}H nmr (CCl_4): 2.0 (m, 2H, C(3)H_2), 2.4 (t, 2H, C(2)H_2), 2.7 (t, 2H, C(4)H_2), 4.8 (s, 2H, $OCH_2C_6H_5$), 6.5 (s, 1H, C(5)H), 6.6 (dd, 1H, C(7)H), 7.1 (s, 5H, C_6H_5), 7.6 (d, 1H, C(8)H). Compound **3***e* (10) (80%).

*2-Hydroxyimino-3,4-dihydro-2*H*-1-naphthalenones (***4***a,b,d–f)*

Method B

An ice-cooled solution of 30 mmol of potassium *tert*-butoxide,

Can. J. Chem. Downloaded from www.nrcresearchpress.com by 176.9.209.113 on 09/07/12
For personal use only.

TABLE 3. ^{13}C nuclear magnetic resonance data (tetrahydronaphthalene carbon atoms) of 2-amino-1,2,3,4-tetrahydro-1-naphthalenols ($CDCl_3$ solution)

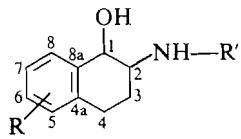

Compound	R	R′	C(1)	C(2)	C(3)	C(4)	C(4a)	C(5)	C(6)	C(7)	C(8)	C(8a)
trans-**1***a*	H	H	74.8	53.8	29.1	27.7	135.6#	126.0*	126.9*	127.0*	128.1*	137.9#
cis-**1***a*	H	H	69.8	50.7	(28.0)	(27.5)	135.9#	126.2*	127.8*	128.6*	130.2*	137.2#
trans-**1***b*	5-OCH_3	H	74.7	53.4	28.5	22.0	124.6	156.5	108.2	126.6	118.8	139.4
cis-**1***b*	5-OCH_3	H	69.7	50.3	25.9	21.6	124.9	156.8	108.8	126.7	122.0	138.5
trans-**1***c*	5-OBzl	H	74.3	53.2	28.7	21.9	124.6	155.0	109.3	126.0	119.8	141.0
trans-**1***d*	6-OBzl	H	74.2	54.1	29.0	27.7	137.4	112.8*	157.0	113.4*	127.8	132.3
trans-**1***e*	7-OBzl	H	74.7	53.9	29.4	26.8	128.3	128.9	113.6*	156.7	113.4*	141.1
trans-**1***f*	5,8-(OCH_3)$_2$	H	72.6	52.6	27.4	21.5	127.2*	151.1#	(107.7)	(108.6)	152.0#	127.3*
cis-**1***f*	5,8-(OCH_3)$_2$	H	63.7	50.9	25.1	23.7	126.1*	151.8#	(108.1)	(109.0)	150.8#	128.8*
trans-**2***a*	H	i-Pr	73.2	57.9	28.3	26.8	138.0#	126.9*	127.0*	128.2*	126.2*	135.5#
cis-**2***a*	H	i-Pr	67.2	54.4	24.4	27.7	136.9#	126.2*	127.7*	128.5*	130.6*	135.9#
trans-**2***b*	5-OCH_3	i-Pr	72.4	56.9	25.3	21.9	124.5	156.4	108.2	126.6	119.1	139.2
cis-**2***b*	5-OCH_3	i-Pr	67.3	53.9	23.7	21.5	125.1	156.8	108.8	126.8	122.5	138.4
trans-**2***c*	5-OBzl	i-Pr	72.9	57.5	23.1	22.7	124.4	155.7	109.7	126.7	119.3	139.6
trans-**2***d*	6-OBzl	i-Pr	72.4	57.8	26.2	28.0	137.1	113.8*	157.7	113.1*	128.6	130.7
trans-**2***e*	7-OBzl	i-Pr	73.2	58.1	(27.5)	(27.1)	127.5	127.7	114.7*	157.4	112.1*	139.2
trans-**2***f*	5,8-(OCH_3)$_2$	i-Pr	69.7	55.6	22.7	21.0	128.4#	151.2*	(107.8)	(108.7)	152.3*	127.5#
cis-**2***f*	5,8-(OCH_3)$_2$	i-Pr	61.6	53.9	(23.4)	(23.6)	127.0#	151.3*	(107.7)	(109.3)	152.6*	127.3#

Parentheses and the superscripts * and # imply that the values may be interchanged.

Can. J. Chem. Downloaded from www.nrcresearchpress.com by 176.9.209.113 on 09/07/12
For personal use only.

in 35 mL of *tert*-butanol and 150 mL of dry ether under a nitrogen atmosphere, was treated with 28 mmol of the appropriate tetralone **3***a*–*f* and 36.5 mmol of freshly distilled butyl nitrite or isoamyl nitrite. After heating at reflux temperature (3 h for tetralones **3***a*, **3***c*, and **3***d*, and 10 min for tetralone **3***e*) or stirring at room temperature for 30 min (tetralones **3***b* and **3***f*) the reaction mixture was quenched with water and washed with ether. The aqueous phase was made acidic with 2 *M* HCl and extracted with dichloromethane to afford hydroxyiminotetralones. Compounds **4***a* (5) (85%), **4***b* (66%), and **4***f* (52%) were used without further purification. Compound **4***b*, ir (KBr): 3300–3100 (OH), 1720 (C=O), 1580 (C=N); ^1H nmr: 2.9 (m, 4H, C(3)H_2 + C(4)H_2), 3.8 (s, 3H, OCH_3), 6.6–7.7 (m, 3H, arom.). Compound **4***d* (*E* isomer) (see also Table 4), ir (KBr): 3500–3000 (OH), 1680 (C=O), 1590 (C=N); ^1H nmr (DMSO-d_6): 2.9 (s, 4H, C(3)H_2 + C(4)H_2), 4.9 (s, 2H, $OCH_2C_6H_5$), 6.6 (s, 1H, C(5)H), 6.7 (dd, J = 8 Hz and J = 2 Hz, 1H, C(7)H), 7.1 (s, 5H, C_6H_5), 7.7 (d, J = 8 Hz, 1H, C(8)H); ms, *m/e* (relative intensity): 281 (0.2), 91 (100). Compound **4***e*, (10) (60%). Compound **4***f*, ir (KBr): 3200 (OH), 1695 (C=O); ^1H nmr: 2.9 (s, 4H, C(3)H_2 + C(4)H_2), 3.7 (s, 3H, OCH_3), 6.7 (s, 2H, arom.), 7.8 (br, 1H, =N—OH).

Evaporation of the ethereal washings from reaction of tetralone **3***d* with isoamyl nitrite afforded a residue, which was chromatographed on silica gel. On elution with benzene – ethyl acetate (95:5), the *Z* isomer of oxime **4***d* was isolated (Table 4); ir ($CHCl_3$): 2900–2800 (OH str), 1600 (N=O); ^1H nmr: 2.9 (s, 4H, C(3)H_2 + C(4)H_2), 4.9 (s, 2H, $OCH_2C_6H_5$), 6.6 (s, 1H, C(5)H), 6.8 (dd, J = 9 Hz and J = 2 Hz, 1H, C(7)H), 7.2 (s, 5H, C_6H_5), 7.8 (d, J = 9 Hz, 1H, C(8)H), 15.2 (s, 1H, =NOH); ms, *m/e* (relative intensity): 281 (0.2), 91 (100). On elution with benzene – ethyl acetate (90:10), a mixture of *E*- and *Z*-4-benzyloxy-2-(2-formylethyl)isopentyl benzoate oximes (**9***d*) was isolated (Table 4); ir (NaCl): 3500–3150 (N—OH), 1710 (C=O), 1610 (C=N); ^1H nmr: 0.9 (d, 6H, CH_3-ipr), 1.5 (m, 3H, CH_2CH), 2.5 (m, 2H, CH_2CH=N), 3.1 (m, 2H, CH_2Ar), 4.1 (m, 2H, $COOCH_2$), 4.9 (s, 2H, $CH_2C_6H_5$), 6.6 (m, 1H, CH=N), 6.6 (s, 1H, C(5)H), 7.2 (s, 5H, C_6H_5), 7.2 (m, 1H, C(7)H), 7.8 (d, 1H, C(8)H), 8.3 (br, 1H, N—OH); ms, *m/e* (relative intensity): 369 (0.05), 91 (100).

Ethereal washings from reaction of tetralone **3***d* with butyl nitrite afforded a residue, which was chromatographed on silica gel. On elution with benzene – ethyl acetate (90:10), butyl 4-benzyloxy-2-(2-cyanoethyl)benzoate **10** (Table 4) was obtained; ir (NaCl): 2240 (CN), 1710 (C=O); ^1H nmr (CCl_4): 0.9 (m, 3H, CH_3), 1.1–1.8 (m, 4H, $CH_2CH_2CH_3$), 2.5 (t, 2H, CH_2CN), 3.1 (t, 2H, CH_2Ar), 4.1 (t, 2H, $COOCH_2$), 4.9 (s, 2H, $OCH_2C_6H_5$), 6.6 (dd, 1H, C(7)H), 6.7 (s, 1H, C(5)H), 7.1 (s, 5H, C_6H_5), 7.7 (d, 1H, C(8)H); ms, *m/e* (relative intensity): 337 (1), 105 (20), 91 (100).

Similarly, ethereal washings from reaction of tetralones **3***b* and **3***f* with butyl nitrite afforded oximes **9***b* and **9***f*, respectively (Table 4). Compound **9***b*, ir (KBr): 3300–3100 (OH), 1720 (C=O), 1580 (C=N); ^1H nmr: 0.8–1.9 (m, 7H, $CH_2CH_2CH_3$), 2.5 (m, 2H, CH_2=CH), 3.1 (m, 2H, $ArCH_2$), 3.7 (s, 3H, OCH_3), 4.2 (m, 2H, $COOCH_2$-), 6.5–7.5 (m, 4H, CH=N + 3H arom.), 8.3 (br, 1H, OH). Compound **9***f*, ir ($CHCl_3$): 3550, 3300, 1725, 1610; ^1H nmr: 0.7–1.9 (m, 7H, $CH_2CH_2CH_3$), 2.2–3.0 (m, 4H, $ArCH_2CH_2$), 3.6 (s, 6H, $2OCH_3$), 4.2 (t, 2H, $COOCH_2$), 6.6 (s, 2H, arom.), 7.2 (m, 1H, CH=N), 8.3–9.3 (br, 1H, =NOH); ms, *m/e* (relative intensity): 309 (13), 236 (24), 218 (50), 193 (100).

*2-Acetamido-3,4-dihydro-2*H*-naphthalenones (***5***a,b,d–f) Method C*

Zinc dust (190 mmol) was added portionwise to an externally cooled solution of 2-hydroxyiminotetralone (65 mmol) in 110 mL of acetic anhydride and 150 mL of acetic acid. After stirring for 1 h at room temperature, solids were removed by filtration and the solution was evaporated *in vacuo*. The residue was made alkaline with 2 *M* sodium hydroxide solution and extracted with dichloromethane. Evaporation of the organic phase afforded crude acetamidotetralones **5**. Acetamidotetralones **5***a* (5) (65%) and **5***b* (31) (62%) afforded analytical data comparable to those described in the literature. Compound **5***d* (see also Table 4), ir (KBr): 3320 (NH amide), 1680 (C=O), 1645–1620 (CONH); ^1H nmr: 1.3–2.0 (m, 1H, C(3)H_e), 2.0 (s, 3H, CH_3), 2.4–3.2 (m, 3H, C(3)H_a + C(4)H_2), 4.2–4.7 (m, 1H, C(2)H), 5.0 (s, 2H, $OCH_2C_6H_5$), 6.4–6.8 (dd, 1H, C(5)H), 6.5 (s, 1H, NHCO), 6.5 (s, 1H, C(7)H), 7.1 (s, 5H, C_6H_5), 7.7 (d, 1H, C(8)H). Compound

Can. J. Chem. Downloaded from www.nrcresearchpress.com by 176.9.209.113 on 09/07/12
For personal use only.

TABLE 4. Elemental analyses and melting points

Compound	Molecular formula	Calculated				Found				Yield (%) (method)	Melting point (°C)	Crystallization solvents
		C	H	N	X*	C	H	N	X*			
cis-**1***a*	$C_{10}H_{13}NO\cdot(C_2H_2O_4)$	56.91	5.97	5.53	—	57.15	6.19	5.71	—	60(J)	163–165 (lit. (35) 213, HCl)	Ethanol
trans-**1***b*	$C_{11}H_{15}NO_2\cdot HCl$	57.52	7.02	6.09	15.43	57.55	7.21	6.02	15.61	45(H)/43(I)	224–226	Ethanol–ether
cis-**1***b*	$C_{11}H_{15}NO_2\cdot HCl$	57.52	7.02	6.09	15.43	57.59	7.30	6.18	15.61	61(J)	238–240	Ethanol–ether
trans-**1***c*	$C_{17}H_{19}NO_2\cdot HCl$	66.77	6.59	4.58	11.59	66.79	6.57	4.61	11.70	91(I)	245–247 (lit. (14) 139–141, base)	Ethanol–ether
trans-**1***d*	$C_{17}H_{19}NO_2\cdot\frac{1}{4}H_2O$	74.56	7.18	5.11	—	74.34	7.35	5.05	—	60(H)/75(I)	97–98 (lit. (32) 210–212, HCl)	Ether–hexane
trans-**1***e*	$C_{17}H_{19}NO_2\cdot\frac{1}{2}H_2O$	73.35	7.24	5.03	—	73.33	7.17	4.88	—	80(H)/90(I)	115–118 (lit. (10) 125–126)	Ether – ethyl acetate
trans-**1***f*	$C_{12}H_{17}NO_3\cdot HCl$	55.49	6.98	5.39	13.65	55.34	6.98	5.36	13.72	80(H)	195–196†	Ethanol–ether
cis-**1***f*	$C_{12}H_{17}NO_3\cdot HCl$	55.49	6.98	5.39	13.65	55.32	6.97	5.38	13.62	57(J)/71(H)	220–221†	Ethanol–ether
trans-**1***g*	$C_{10}H_{13}NO_2\cdot HCl$	55.69	6.54	6.49	16.44	55.68	6.55	6.54	16.21	85(M)	234–236	Ethanol–ether
trans-**1***h*	$C_{10}H_{13}NO_2$	67.02	7.31	7.81	—	67.05	7.40	7.50	—	46(M)	187–189	Methanol
trans-**1***i*	$C_{10}H_{13}NO_2$	67.02	7.31	7.81	—	67.09	7.61	7.77	—	50(M)	183–185 (lit. (10) 196–198)	Ethanol–ether
trans-**2***a*	$C_{15}H_{23}NO_3\cdot HCl$	59.69	8.01	4.64	11.74	59.69	8.11	4.64	11.82	75(L)	217–219	Ethanol–ether
cis-**2***a*	$C_{15}H_{23}NO_3\cdot HCl$	59.69	8.01	4.64	11.74	59.39	8.07	4.60	11.74	68(L)	204–205	Ethanol–ether
trans-**2***b*	$C_{14}H_{21}NO_2\cdot HCl$	61.87	8.16	5.15	13.04	61.59	8.15	5.06	13.21	98(K)	190–193	Ethanol–ether
cis-**2***b*	$C_{14}H_{21}NO_2\cdot HCl$	61.87	8.16	5.15	13.04	61.62	8.05	5.21	13.16	98(K)	255–256	Ethanol–ether
trans-**2***c*	$C_{20}H_{25}NO_2\cdot HCl$	69.05	7.53	4.02	10.19	68.88	7.83	3.90	10.20	91(K)	203–204 (lit. (14) 220–223)	Ethanol–ether
trans-**2***e*	$C_{20}H_{25}NO_2\cdot HCl$	69.05	7.53	4.02	10.19	68.81	7.70	3.97	10.22	85(K)	185–187	Ethanol–ether
trans-**2***f*	$C_{15}H_{23}NO_3\cdot HCl$	59.69	8.01	4.64	11.74	59.79	7.98	4.63	11.61	75(L)	217–219	Ethanol–ether
cis-**2***f*	$C_{15}H_{23}NO_3\cdot HCl$	59.69	8.01	4.64	11.74	59.39	8.07	4.60	11.74	68(L)	203–204	Ethanol–ether
trans-**2***g*	$C_{13}H_{19}NO_2\cdot HCl$	60.57	7.82	5.43	13.75	60.81	8.16	5.71	13.64	85(M)	Oil	(Chromatography)
trans-**2***i*	$C_{13}H_{19}NO_2\cdot HCl$	60.57	7.82	5.43	13.75	60.60	7.90	5.40	13.47	91(M)	195–197	Ethanol–ether
3*d*	$C_{17}H_6O_2$	80.92	6.39	—	—	81.05	6.51	—	—	78(A)	95–96	Hexane
3*e*-oxime	$C_{17}H_{17}NO_2$	73.68	6.41	5.24	—	76.49	6.52	5.26	—	89(E)	103–106	Ether–hexane
E-**4***d*	$C_{17}H_{15}NO_3$	72.58	5.37	4.98	—	72.41	5.33	4.90	—	58(B)	172 (dec.)	Ethyl acetate
Z-**4***d*	$C_{17}H_{15}NO_3$	72.58	5.37	4.98	—	72.35	5.21	4.96	—	3(B)	115–117	Ether
5*d*	$C_{19}H_{19}NO_3$	73.76	6.19	4.52	—	73.77	6.19	4.56	—	65(C)	156–158	Ether
5*f*	$C_{14}H_{17}NO_4$	63.86	6.50	5.32	—	63.59	6.50	5.32	—	55(C)	175–176	Ethyl acetate
trans-**6***d*	$C_{19}H_{21}NO_3$	73.29	6.80	4.50	—	73.29	6.83	4.53	—	70(D)	175–177	Methanol–ether
trans-**6***f*	$C_{14}H_{19}NO_4$	63.38	7.21	5.28	—	63.17	7.23	5.22	—	94	191–192	Ethyl acetate
cis-**6***f*	$C_{14}H_{19}NO_4$	63.38	7.21	5.28	—	63.34	7.47	5.18	—	51	137–138	Ether – ethyl acetate
7*b*	$C_{17}H_{19}NO_4S$	59.10	5.54	4.05	9.28	59.23	5.60	4.02	9.10	77(F)	150–152	Acetone
7*e*	$C_{24}H_{23}NO_4S\cdot\frac{1}{2}H_2O$	66.95	5.61	3.25	7.44	67.07	5.51	3.28	7.21	85(F)	112–115	Ether–acetone
8*b*	$C_{11}H_{13}NO_2\cdot HCl$	58.02	6.19	6.15	15.57	58.17	6.44	5.94	15.63	54(G)	210–212	Ethanol–ether
9*b*	$C_{15}H_{21}NO_4$	64.49	7.57	5.01	—	64.77	7.68	5.16	—	14(B)	84–85	Ether–hexane
9*d*	$C_{22}H_{27}NO_4$	71.52	7.36	3.79	—	71.71	7.44	3.78	—	8(B)	59–61	Ether–hexane
9*f*	$C_{16}H_{23}NO_5$	62.12	7.48	4.52	—	62.04	7.52	4.46	—	10(B)	64–66	Ether–hexane
12	$C_{14}H_{15}NO_4$	64.36	5.78	5.36	—	64.58	5.90	5.32	—	12(C)	130–131	Ether – ethyl acetate
13	$C_{14}H_{17}NO_3$	67.99	6.92	5.66	—	68.12	7.15	5.84	—	70	102–103	Ether–hexane

*Cl or S according to the formula.
†Literature (7) mp 199–202°C, mixture of *cis*-**1***f* and *trans*-**1***f* hydrochlorides.

Can. J. Chem. Downloaded from www.nrcresearchpress.com by 176.9.209.113 on 09/07/12
For personal use only.

5*e* (10) (60%). Compound **5***f* (see also Table 4), ir (KBr): 3300, 3100, 1705, 1670, 1640; ^{1}H nmr: 2.0 (s, 3H, CH_3CO), 2.6–3.3 (m, 4H, C(3)H_2 + C(4)H_2), 3.73 (s, 3H, OCH_3), 3.76 (s, 3H, OCH_3), 4.6 (m, 1H, C(2)H), 6.8 (dd, 3H, C(6)H + C(7)H + NHCO).

Reduction of acetamidotetralone **5***f* also afforded 2-acetamido-5,8-dimethoxy-1-naphthol **12** (Table 4) after chromatography of the crude reaction mixture (elution system: hexane – ethyl acetate 1:1); ir (KBr): 3430, 3340, 2850, 1690, 1530; ^{1}H nmr (200 MHz): 2.23 (s, 3H, CH_3CO), 3.91 (s, 3H, OCH_3), 3.99 (s, 3H, OCH_3), 6.57 (dd, 2H, C(6)H + C(7)H), 7.71 (d, J = 8 Hz, 1H, C(3)H), 7.84 (br, 1H, NHCO), 8.51 (d, J = 8 Hz, 1H, C(4)H), 9.69 (s, 1H, OH); ^{13}C nmr ($CDCl_3$): 28.4 (CH_3), 101.7, 103.7 (C-6 or C-7), 113.6 (C-3), 115.0 (C-4a), 120.1 (C-4), 122.8 (C-8a), 124.2 (C-2), 141.0 (C-1), 149.3, 150.3 (C-5 and C-8), 168.2 (CO).

trans-*2-Acetamido-1,2,3,4-tetrahydro-1-naphthalenols* (trans-**6**a,b,d,e) *Method D*

A solution of 285 mg (75 mmol) of sodium borohydride in 4 mL of water was added dropwise with external cooling to a solution of 15 mmol of the corresponding acetamidotetralone **5** in 15 mL of methanol. After stirring at room temperature until formation of a white precipitate, the resulting solid was washed with water and dried to afford *trans*-**6***a* (5) (80%), *trans*-**6***b* (31) (82%), *trans*-**6***d* (Table 4), and *trans*-**6***e* (10) (95%). Compound *trans*-**6***d*, ir (KBr): 3400–3100 (OH, NHCO), 1630; ^{1}H nmr (DMSO-d_6): 1.7 (s, 3H, CH_3CO), 1.8 (m, 2H, C(3)H_2), 2.7 (m, 2H, C(4)H_2), 3.4–4.0 (m, 2H, C(2)H), 4.3 (m, 1H, C(1)H), 4.9 (s, 2H, $OCH_2C_6H_5$), 6.5 (s, 1H, C(5)H), 6.7 (dd, 1H, C(7)H), 7.2 (d, 1H, C(8)H), 7.3 (s, 5H, C_6H_5), 7.6 (d, 1H, NH).

trans-*2-Acetamido-5,8-dimethoxy-1,2,3,4-tetrahydro-1-naphthalenol* (trans-**6**f)

A solution of 2.0 g (7.6 mmol) of acetamidotetralone **5***f* in 125 mL of methanol was hydrogenated (1 atm, 25°C) over 153 mg (0.78 mmol) of Adams catalyst. After absorption of the theoretical volume, the solution was filtered and the solvent was removed to afford a mixture of diastereomeric acetamidotetralols **6***f* (*trans*/*cis* ratio 9:1, based on ^{1}H nmr). Successive crystallizations afforded pure *trans*-**6***f* (Table 4), ir (KBr): 3350, 2950, 1660, 1540; ^{1}H nmr (200 MHz): 1.80 (m, 1H, C(3)H_a), 1.93 (s, 3H, CH_3CO), 2.16 (m, 1H, C(3)H_a), 2.76 (m, 2H, C(4)H_a + C(4)H_e), 3.78 (s, 3H, OCH_3), 3.82 (s, 3H, OCH_3), 4.20 (m, 1H, C(2)H), 4.84 (d, J = 4.97 Hz, 1H, C(1)H), 6.74 (s, 2H, C(6–7)H); ^{13}C nmr ($CDCl_3$): 20.0 (C-4), 22.7 (CH_3 and C-3), 50.7 (C-2), 66.1 (C-1), 108.6, 109.9 (C-6 and C-7), 126.2, 127.4 (C-4a and C-8a), 151.6, 153.1 (C-5 and C-8), 172.2 (CO).

cis-*2-Acetamido-5,8-dimethoxy-1,2,3,4-tetrahydro-1-naphthalenol* (cis-**6**f)

To an ice-cooled stirred suspension of 2.0 g (7.6 mmol) of 2-acetamidotetralone **5***f* in 20 mL of methanol, a solution of 144 mg (3.8 mmol) of sodium borohydride in 4 mL of water was added dropwise. After 1 h stirring at room temperature the reaction mixture was poured into 100 mL of water, and the methanol was removed *in vacuo*. The aqueous phase was extracted with dichloromethane and the organic extracts afforded a residue, which was chromatographed on silica gel. On elution with ethyl acetate, 1.4 g of a *cis–trans* mixture of acetamidotetralols **6***f* were obtained (*cis*/*trans* ratio, 65:35 based on ^{1}H nmr). Analytically pure *cis*-**6***f* was obtained by crystallization (Table 4); ir (KBr): 3350, 2950, 1640; ^{1}H nmr (200 MHz): 1.9 (m, C(3)H_{a+e}), 2.01 (s, 3H, CH_3CO), 2.58 (m, 1H, C(4)H_a), 2.95 (m, 1H, C(4)H_e), 3.78 (s, 3H, OCH_3), 3.82 (s, 3H, OCH_3), 4.02 (m, 1H, C(2)H), 4.93 (d, J = 4.25 Hz, 1H, C(1)H), 6.74 (m, 2H, C(6–7)H); ^{13}C nmr ($CDCl_3$): 22.7, 23.2 (C-3 and C-4), 23.5 (CH_3), 48.9 (C-2), 63.2 (C-1), 107.7, 109.5 (C-6 and C-7), 126.8, 127.0 (C-4a and C-8a), 151.4, 151.7 (C-5 and C-8), 169.6 (CO).

When the above reaction mixture was poured into 6 *M* hydrochloric acid, and the methanol was removed *in vacuo* on a steam-bath, similar work-up afforded *cis*-2-methyl-6,9-dimethoxy-3a,4,5,9b-tetrahydronaphtho[2,1-*d*]oxazol (**13**) (Table 4); ^{1}H nmr (200 MHz): 1.84 (m, 1H, C(3)H_a), 1.96 (s, 3H, CH_3), 2.10 (m, 1H, C(3)H_e), 2.48 (m, 1H, C(4)H_a), 2.89 (m, 1H, C(4)H_e), 3.84 (s, 3H, OCH_3), 3.91 (s, 3H, OCH_3), 4.48 (m, 1H, C(3)H_a), 5.87 (d, J = 9.7 Hz, 1H, C(9b)H), 6.74 (d, J = 8.9 Hz, 1H, arom.), 6.83 (d, J = 8.9 Hz, 1H, arom.); ms, *m*/*e* (relative intensity): 248 (6), 247 (30), 188 (100), 173 (96); ^{13}C nmr ($CDCl_3$): 14.1 (CH_3), 17.5 (C-5), 27.4 (C-4), 63.2 (C-3a), 73.3 (C-9b), 108.3, 110.0 (C-7 and C-8), 122.4 (C-5a), 130.4 (C-9a), 150.4, 152.8 (C-5 and C-8), 165.7 (C-2).

*3,4-Dihydro-2*H*-1-naphthalenone oximes* (**3**a–e *oximes*) *Method E*

A solution of 50 mmol of tetralone **3***a–e* and 8.0 g (115 mmol) of hydroxylamine hydrochloride in 25 mL of dry pyridine was heated at reflux temperature for 12 h. After pouring into water, the reaction mixture was extracted with dichloromethane and the organic layers were washed with 1 *M* hydrochloric acid and 0.5 *M* sodium bicarbonate. Evaporation of the organic solvent afforded the required oximes; **3***a*-oxime (33) (96%), **3***b*-oxime (34) (84%), **3***c*-oxime (14) (97%), **3***d*-oxime (32) (97%), and **3***e*-oxime (Table 4); ir (KBr): 3340–3000 (OH), 1620 (C=N); ^{1}H nmr: 1.4–1.9 (m, 2H, C(3)H_2), 2.4–2.8 (m, 4H, C(2)H_2 + C(4)H_2), 4.8 (s, 2H, $OCH_2C_6H_5$), 6.6–7.5 (m, C(5) + C(6) + C(8)), 7.2 (s, 5H, C_6H_5), 9.3 (br, 1H, N—OH).

*3,4-Dihydro-2*H*-1-naphthalenone* O*-tosyloximes* (**7**a–e) *Method F*

A solution of 43 g (75 mmol) of *p*-toluenesulfonyl chloride in 80 mL of dry pyridine was added dropwise to an ice-cooled solution of the requisite naphthalenone **6***a–e* oxime (75 mmol) in 80 mL of dry pyridine. After stirring for 16 h at room temperature, the reaction mixture was poured into water and extracted with dichloromethane. The organic layers were washed with 2 *M* hydrochloric acid, 0.5 *M* sodium bicarbonate, and dried. Evaporation afforded crude tosyloximes **7***a* (5) (83%), **7***c* (14) (90%), **7***d* (32) (89%), **7***b*, and **7***e* (Table 4). Compound **7***b*, ir (KBr): 1600, 1575; ^{1}H nmr: 1.5–2.0 (m, 2H, C(3)H_2), 2.4 (s, 3H, CH_3-Ar), 2.5–2.7 (m, 4H, C(2)H_2 + C(4)H_2), 3.7 (s, 3H, OCH_3), 6.6–7.4 (m, 3H, C(6–8)H), 7.2 (d, J = 8 Hz, 2H, C(3′)H + C(5′)H), 7.8 (d, J = 8 Hz, 2H, C(2′)H + C(6′)H). Compound **7***e*, ir (KBr): 1590; ^{1}H nmr: 1.7 (m, 2H, C(3)H_2), 2.3 (s, 3H, CH_3-Ar), 2.6 (m, 4H, C(2)H_2 + C(4)H_2), 4.9 (s, 2H, $OCH_2C_6H_5$), 6.7–7.3 (complex, 3H, C(5–8)H), 7.2 (s, 5H, C_6H_5), 7.4 (dd, 4H, C_6H_4—CH_3).

*2-Amino-3,4-dihydro-2*H*-1-naphthalenone hydrochlorides* (**8**a–e) *Method G*

To a stirred suspension of 16 mmol of tosyloxime **7***a–e* in 15 mL of dry benzene a solution of 16.5 mmol of potassium ethoxide in 10 mL of absolute ethanol was added at 0°C under a nitrogen atmosphere. After 24 h at room temperature, the reaction mixture was filtered and the filtrates were poured into 100 mL of 5 *M* hydrochloric acid. After 15 min stirring at room temperature, the aqueous phase was evaporated *in vacuo* (to afford crude hydrochlorides **8***a*,*b*) or the resulting precipitate was collected and dried (hydrochlorides **8***c–e*). In each case, crystallization from ethanol–ether afforded analytically pure samples. Compound **8***a* (33) (35%), **8***c* (14) (75%), **8***d* (32) (65%), **8***e* (10) (60%). Compound **8***b* (see also Table 4), ir (KBr): 3100, 2800, 1690–1640; ^{1}H nmr (D_2O): 2.1–3.3 (m, 4H, C(3)H_2 + C(4)H_2), 3.7 (s, 3H, OCH_3), 4.3 (dd, 1H, C(2)H), 7.2 (m, 3H, C(6–8)H).

*2-Amino-3,4-dihydro-5,8-dimethoxy-2*H*-1-naphthalenone hydrochloride* (**8**f)

A solution of 250 mg (0.95 mmol) of 2-acetamidotetralone **5***f* in 20 mL of 0.3 *M* hydrochloric acid was heated at reflux temperature. After 5 h, the reaction mixture was evaporated *in vacuo* to afford crude hydrochloride **8***f* (14), which was purified by crystallization from ethanol–ether 1:1 (overall yield, 75%).

trans-*2-Amino-1,2,3,4-tetrahydro-1-naphthalenols* (trans-**1**a–f) *Method H*

Alkaline hydrolysis of *trans*-**6***a*,*b*,*d–f*: To a solution of 7.5 mmol of the requisite acetamidotetralol *trans*-**6***a*,*b*,*d–f* in 80 mL of ethanol, a solution of 6.3 g (110 mg) of potassium hydroxide in 30 mL of water was added dropwise under nitrogen. After 12 h at reflux temperature, the reaction mixture was poured into water, and the ethanol was removed *in vacuo*. The residue was made acidic with 2 *M* hydrochloric acid and washed with ether. The aqueous layer was basified and

Can. J. Chem. Downloaded from www.nrcresearchpress.com by 176.9.209.113 on 09/07/12
For personal use only.

extracted with dichloromethane. The organic extracts were dried and evaporated to afford aminoalcohols *trans*-**1***a–f* (Table 4).

Method I

Sodium borohydride reduction of hydrochlorides **8***a–f*: Hydrochloride **8***a–f* (4 mmol) was added portionwise to an ice-cooled solution of sodium borohydride (200 mmol) in 5 *M* sodium hydroxide (4 mL) and methanol (40 mL). When the addition was complete, the reaction mixture was treated with another 20 mmol of sodium borohydride. After 15 min stirring, 100 mL of water were added, methanol was removed *in vacuo*, and the aqueous phase was extracted with dichloromethane. Evaporation of the aqueous layer afforded crude aminotetralols *trans*-**1***a–f*, which were purified by crystallization of the corresponding hydrochloride.

Compound *trans*-**1***a* (35) (Methods H and I, 45%), *trans*-**1***c* (14) (Method I, 91%), *trans*-**1***d* (32) (Method H, 75%; Method I, 60%). Compound *trans*-**1***b* (Table 4), ir (KBr): 3250, 1610, 1590; ^{1}H nmr (200 MHz, base, see also Table 1): 1.64 (m, 1H, C(3)H$_a$), 2.04 (m, 1H, C(3)H$_e$), 2.60 (m, 1H, C(4)H$_a$), 2.80 (m, 1H, C(4)H$_e$), 2.88 (m, 1H, C(2)H), 3.81 (s, 3H, OCH_3), 4.33 (d, J = 8.6 Hz, 1H, C(1)H), 6.72 (m, 1H, C(6)H), 7.18 (m, 2H, C(7–8)H); ^{13}C nmr: Table 3. Compound *trans*-**1***e* (Table 4), ir (KBr): 3310, 3250, 1610; ^{1}H nmr (200 MHz, base): 1.56–1.82 (m, 1H, C(3)H$_a$), 1.94–2.10 (m, 1H, C(3)H$_e$), 2.76–3.00 (m, 3H, C(4)H$_2$ + C(2)H), 3.10 (3H, exch.), 4.30 (d, J = 8.8 Hz, 1H, C(1)H), 5.06 (s, 2H, $OCH_2C_6H_5$), 6.82 (dd, J_o = 8.43 Hz, J_m = 2.72 Hz, 1H, C(6)H), 6.99 (d, J_o = 8.43 Hz, 1H, C(5)H), 7.19 (d, J_m = 2.72 Hz, 1H, C(8)H), 7.31–7.46 (m, 5H, C_6H_5); ^{13}C nmr: Table 3. Compound *trans*-**1***f* (Table 4), ir (KBr): 3400–3300, 2950, 1610; ^{1}H nmr (200 MHz, base, see also Table 1): 1.64 (m, 1H, C(3)H$_a$), 2.01 (m, 1H, C(3)H$_e$), 2.60 (m, 1H, C(4)H$_a$), 2.84 (m, 1H, C(4)H$_e$), 3.17 (m, 1H, C(2)H), 3.78 (s, 3H, OCH_3), 3.84 (s, 3H, OCH_3), 4.68 (d, J = 7.2 Hz, 1H, C(1)H), 6.70 (s, 2H, C(6–7)H); ^{13}C nmr ($CDCl_3$): Table 3; ^{13}C nmr (DMSO-d_6): 18.6 (C-4), 23.6 (C-3), 50.8 (C-2), 66.8 (C-1), 107.9, 108.6 (C-6 and C-7), 126.3, 127.1 (C-4a and C-8a), 150.5, 152.7 (C-5 and C-8).

cis-*2-Amino-1,2,3,4-tetrahydro-1-naphthalenols* (cis-**1**a,b,f)

Method J

A suspension of 650 mmol of acetamidotetralol *trans*-**6***a,b,f* in 15 mL of 0.3 *M* hydrochloric acid was heated under nitrogen at reflux temperature. After 5 h, the reaction mixture was washed with ether and the aqueous phase was evaporated *in vacuo*. The resulting crude hydrochloride was purified by crystallization from ethanol–ether. Compound *cis*-**1***a* (5) (60%). Compound *cis*-**1***b* (Table 4), ir (KBr): 3300, 1590, 1520; ^{1}H nmr (200 MHz, base, see also Table 1): 1.72–2.06 (m, 2H, C(3)H$_{a+e}$), 2.86 (m, 2H, C(4)H$_{a+e}$), 3.66 (m, 1H, C(2)H), 4.90 (d, J = 3.9 Hz, 1H, C(1)H), 7.30 (m, 5H, arom.); ^{13}C nmr: Table 3. Compound *cis*-**1***f* (Table 4), ir (KBr): 3330, 3280, 1600; ^{1}H nmr (200 MHz, base, see also Table 1): 1.82 (m, 2H, C(3)H$_{a+e}$), 2.50 (m, 1H, C(4)H$_a$), 2.92 (m, 2H, CH-iPr + C(2)H), 3.78 (s, 3H, OCH_3), 3.84 (s, 3H, OCH_3), 4.87 (d, J = 3.9 Hz, 1H, C(1)H), 6.70 (s, 2H, C(6)H + C(7)H); ^{13}C nmr: Table 3.

Alkaline hydrolysis of *cis*-**6***f* (Method H) also afforded aminoalcohol *cis*-**1***f* (Table 4). Alkaline hydrolysis of crude *cis*-**6***f* (*cis*/*trans* ratio 65:35) afforded a mixture of aminoalcohols *cis*-**1***f* and *trans*-**1***f*, which were separated by chromatography on neutral alumina (activity III) on elution with methanol.

2-Isopropylamino-1,2,3,4-tetrahydro-1-naphthalenols (**2**a–f)

Method K

To a suspension of 0.8 mmol of the corresponding 2-amino-1-tetralol in 7 mL of dry benzene, 4.5 mmol of anhydrous acetone was added. After 3 h stirring at reflux temperature, the solvent was removed *in vacuo*, the residue was dissolved in 5 mL of absolute ethanol, and sodium borohydride (2.1 mmol) was added portionwise to the above solution with external cooling. After 2 h stirring at room temperature, the reaction mixture was quenched with 2 *M* hydrochloric acid and the ethanol was removed *in vacuo*. The aqueous phase was washed with ether, made alkaline with 5 *M* sodium hydroxide, and extracted with dichloromethane. The organic extracts were dried and evaporated to afford isopropylamino derivatives *trans*-**2***c* (14) (85%), *trans*-**2***d* (32) (82%), *cis*-**2***b*, *trans*-**2***b*, and *trans*-**2***e* (Table 4). Compound *cis*-**2***b*, ir (KBr): 3250, 2890, 1560; ^{1}H nmr (200 MHz, base): 0.70 (d, 3H, CH_3CH), 1.10 (d, 3H, CH_3CH), 1.70 (m, 1H, C(3)H), 1.92 (m, 1H, C(3)H′), 2.60 (m, 1H, C(4)H$_a$), 2.86 (m, 1H, C(4)H$_e$), 3.04 (m, 2H, C(2)H + $CH(CH_3)_2$), 3.81 (s, 3H, OCH_3), 4.57 (d, J = 4.0 Hz, 1H, C(1)H), 6.76 (d, 1H, C(6)H), 7.08 (d, 1H, C(8)H), 7.18 (d, 1H, C(7)H); ^{13}C nmr: Table 3. Compound *trans*-**2***b*, ir (KBr): 3310, 2990, 1580; ^{1}H nmr (200 MHz, base): 0.98 (d, J = 6.2 Hz, 3H, CH_3CH), 1.05 (d, J = 6.2 Hz, 3H, CH_3CH), 1.46 (m, 2H, C(3)H$_{a+e}$), 2.12 (m, 1H, C(3)H$_a$), 2.68 (m, 3H, C(2)H + C(4)H$_2$), 2.96 (m, 1H, $CH(CH_3)_2$), 3.72 (s, 3H, OCH_3), 4.30 (d, J = 8.9 Hz, 1H, C(1)H), 6.64 (m, 1H, C(6)H), 7.12 (m, 2H, C(7–8)H); ^{13}C nmr: Table 3. Compound *trans*-**2***e*, ir (KBr): 3500–3100 (NH), 3100–2500 (OH); ^{1}H nmr (200 MHz, base): 1.06 (d, J = 6.1 Hz, 3H, CH_3CH), 1.13 (d, J = 6.1 Hz, 3H, CH_3CH), 1.49 (m, 1H, C(3)H$_a$), 1.65 (m, 1H, C(3)H$_e$), 2.20 (m, 1H, C(4)H$_a$), 2.71 (m, 1H, C(2)H), 2.83 (m, 3H, C(4)H$_e$ + exch.), 3.06 (m, 1H, CH—CH_3), 4.32 (d, J = 9.02 Hz, 1H, C(1)H), 5.06 (s, 2H, $OCH_2C_6H_5$), 6.83 (dd, J_o = 8.47 Hz, J_m = 2.79 Hz, 1H, C(6)H), 6.99 (d, J_o = 8.47 Hz, 1H, C(5)H), 7.22 (d, J_m = 2.79 Hz, 1H, C(8)H), 7.46 (m, 5H, C_6H_5); ^{13}C nmr: Table 3.

Method L

To a solution of 2-amino-1-tetralol (0.7 mmol) in 6 mL of methanol under nitrogen, sodium cyanoborohydride (3.5 mmol), acetone (3.5 mmol), and molecular sieve 3Å were added. After 18 h stirring at room temperature, the reaction mixture was poured into water and the methanol was removed *in vacuo*. The aqueous phase was made alkaline with 2 *M* sodium hydroxide and extracted with dichloromethane. The organic extracts were washed with water, dried, and evaporated to afford the corresponding isopropyl derivative (Table 4). Compound *cis*-**2***a*, ^{1}H nmr (200 MHz, base): 1.10 (d, 3H, CH_3CH), 1.14 (d, 3H, CH_3CH), 1.70 (m, 1H, C(3)H), 1.98 (m, 1H, C(3)H′), 2.84 (m, 2H, C(4)H$_2$), 3.06 (m, 2H, CH-iPr + C(2)H), 4.60 (d, J = 4.1 Hz, 1H, C(1)H), 7.30 (m, 5H, arom.); ^{13}C nmr: Table 3. Compound *trans*-**2***a*, ^{1}H nmr (200 MHz, base): 1.07 (d, J = 6.2 Hz, 3H, CH_3CH), 1.13 (d, J = 6.2 Hz, 3H, CH_3CH), 1.58 (m, 2H, C(3)H$_2$), 2.18 (m, 1H, C(4)H$_a$), 2.76 (m, 1H, C(2)H), 2.84 (m, 2H, C(4)H$_e$), 3.0 (m, 1H, CH-iPr), 4.37 (d, J = 9.1 Hz, 1H, C(1)H), 7.14 (m, 4H, C(5–8)H; ^{13}C nmr: Table 3. Compound *cis*-**2***f*, ^{1}H nmr (200 MHz, base): 1.09 (d, 3H, CH_3CH), 1.12 (d, 3H, CH_3CH), 1.74 (m, 2H, C(3)H$_{a+e}$), 2.50 (m, 1H, C(4)H$_a$), 2.84 (m, 1H, C(4)H$_e$), 2.92 (m, 1H, C(2)H), 3.09 (m, 1H, CH-iPr), 3.76 (s, 3H, OCH_3), 3.84 (s, 3H, OCH_3), 4.87 (d, J = 3.9 Hz, 1H, C(1)H), 6.71 (s, 2H, C(6–7)H; ^{13}C nmr: Table 3. Compound *trans*-**2***f*, ^{1}H nmr (200 MHz, base): 1.10 (t, 6H, CH-iPr), 1.61 (m, 1H, C(3)H$_a$), 2.04 (m, 1H, C(3)H$_e$), 2.67 (m, 2H, C(4)H$_{a+e}$), 3.05 (m, 2H, C(2)H + CH-iPr), 3.77 (s, 3H, OCH_3), 3.82 (s, 3H, OCH_3), 4.76 (d, J = 6.2 Hz, 1H, C(1)H), 6.69 (s, 2H, C(6–7)H); ^{13}C nmr: Table 3.

trans-*2-Amino-1,2,3,4-tetrahydronaphthalenediols* (trans-**1**g–i *and* trans-**2**g–i)

Method M

A solution of 3.5 mmol of the corresponding benzyloxy-2-amino-1-tetralol *trans*-**1***c–e* or *trans*-**2***c–e* in 100 mL of absolute methanol was hydrogenated in a Parr apparatus in the presence of 5% palladium on charcoal (350 mg) at 300 psi. After 24 h, the reaction mixture was filtered and the methanol was removed *in vacuo* to afford debenzylated aminotetralols **1***g–i* and **2***g–i* (Table 4). Compound *trans*-**1***g*, ^{1}H nmr (hydrochloride, D_2O, 200 MHz): 1.60 (m, 1H, C(3)H$_a$), 2.05 (m, 1H, C(3)H$_e$), 2.43 (m, 1H, C(4)H$_a$), 2.63 (m, 1H, C(4)H$_e$), 3.13 (m, 1H, C(2)H), 4.50 (d, J = 8.8 Hz, 1H, C(1)H), 6.59 (dd, J = 1.9 Hz, and J = 7.8 Hz, 1H, C(6)H or C(8)H), 6.84 (dd, J = 1.9 Hz, and J = 7.8 Hz, 1H, C(6)H or C(8)H), 6.96 (t, 1H, C(7)H). Compound *trans*-**2***g*, ^{1}H nmr (hydrochloride, D_2O, 200 MHz): 1.37 (d, J = 6.36 Hz, 3H, CH_3-iPr), 1.46 (d, J = 6.46 Hz, 3H, CH_3-iPr), 1.95 (m, 1H, C(3)H$_a$), 2.36 (m, 1H, C(3)H$_e$), 2.71 (m, 1H, C(4)H$_a$), 2.95 (m, 1H, C(4)H$_e$), 3.24 (dd, 1H, C(2)H), 3.58 (m, 1H, CH-iPr), 4.89 (d, J = 9.4 Hz, 1H, C(1)H), 6.73 (dd, 1H, C(7)H), 7.06–7.10 (m, 2H, C(6)H + C(8)H). Compound *trans*-**1***h* (10) (47%). Compound *trans*-**2***h* (32) (85%). Compound *trans*-**1***i*, ^{1}H nmr (base, 200 MHz): 1.65 (m, 1H, C(3)H$_a$), 1.99 (m, 1H, C(3)H$_e$), 2.80 (m, 3H, C(4)H$_2$ + C(2)H), 4.16 (br, 4H, exch.), 4.27 (d, J = 8.87 Hz, 1H, C(1)H), 6.67

(dd, J_o = 8.39 Hz, J_m = 2.57 Hz, 1H, C(6)H), 6.91 (d, J_o = 8.39 Hz, 1H, C(5)H), 6.96 (d, J_m = 2.57, 1H, C(8)H). Compound *trans*-**2***i* (hydrochloride, D_2O, 200 MHz): 1.17 (d, J = 6.5 Hz, 3H, CH_3-iPr), 1.22 (d, J = 6.5 Hz, 3H, CH_3-iPr), 1.28 (m, 1H, C(3)H_a), 1.65 (m, 1H, C(3)H_e), 2.19 (m, 2H, C(4)H_2), 2.72 (m, 1H, C(2)H), 3.03 (m, 1H, CH-iPr), 4.04 (d, J = 11.2 Hz, 1H, C(1)H), 6.64 (dd, J_o = 8.4 Hz, J_m = 2.6 Hz, 1H, C(6)H), 6.8 (d, J_m = 2.6 Hz, 1H, C(8)H), 6.92 (d, J_o = 8.4 Hz, 1H, C(5)H).

*6-Amino-5,6,7,8-tetrahydro-2-naphthalenol (**11**)*

A solution of 1.35 g (4.7 mmol) of hydroxyiminotetralone **4***d* in 50 mL of absolute methanol was hydrogenated (1 atm) in the presence of 5% palladium on charcoal (450 mg) and 9 mL of 2 *M* hydrochloric acid at 30–40°C until hydrogen uptake ceased. Filtration and evaporation of the reaction mixture afforded naphthol **11** (HCl) in quantitative yield (Table 4); ^{1}H nmr (DMSO-d_6): 1.3–3.6 (m, 7H, C(5–8)H), 6.3 (s, 1H, C(1)H), 6.4 (dd, 1H, C(3)H), 6.7 (d, 1H, C(4)H), 8.2 (br, 3H, NH_3^+), 9.0 (br, 1H, OH); ms, *m/e* (relative intensity): 164 (8), 163 (39), 146 (68), 120 (100).

Acknowledgements

We are grateful to the Comisión Asesora de Investigación Científica y Técnica for financial support. We thank Dr. Carlos Jaime for helpful discussions about MM2 calculations.

1. C. A. Grob. Angew. Chem. Int. Ed. Engl. **8**, 535 (1969).
2. D. Mauleon, R. Granados, and C. Minguillon. J. Org. Chem. **48**, 3105 (1983).
3. K. Itoh, H. Sugihara, A. Miyake, N. Tada, and Y. Oka. Chem. Pharm. Bull. **26**, 504 (1978).
4. B. Lal, J. M. Khanna, and N. Anand. J. Med. Chem. **15**, 23 (1972).
5. F. Zymalkowski and H. J. Rimek. Arch. Pharm. **294**, 581 (1961).
6. C. O'Brien. Chem. Rev. **64**, 81 (1964).
7. C. F. Barfknecht, D. E. Nichols, D. B. Rusterholz, J. P. Long, J. A. Engelbrecht, J. M. Beaton, R. J. Bradley, and D. C. Dyer. J. Med. Chem. **16**, 804 (1973).
8. R. I. Thrift. J. Chem. Soc. (C), 288 (1967).
9. K. Itoh, M. Motohashi, H. Kuriki, H. Sugihara, N. Inatomi, M. Nishikawa, and Y. Oka. Chem. Pharm. Bull. **25**, 2917 (1977).
10. T. Chiemprasert, H. J. Rimek, and F. Zymalkowski. Ann. Chem. **685**, 141 (1965).
11. A. Delgado, D. Mauleon, C. Minguillon, M. Feliz, M. Pericas, and A. Riera. Can. J. Chem. **65**, 868 (1987).
12. Y. Oka, M. Motohashi, H. Sugihara, O. Miyashita, K. Itoh, M. Nishikawa, and S. Yurugi. Chem. Pharm. Bull. **25**, 632 (1977).
13. M. Motohashi, E. Mizuta, and M. Nishikawa. Chem. Pharm. Bull. **29**, 1501 (1981).
14. K. Itoh, A. Miyake, N. Tada, M. Hirata, and Y. Oka. Chem. Pharm. Bull. **32**, 130 (1984).
15. H. O. House, R. G. Carlson, H. Muller, A. W. Noltes, and C. D. Slater. J. Am. Chem. Soc. **84**, 2614 (1962).
16. H. O. House, H. Barda, R. B. Toothill, and A. Noltes. J. Org. Chem. **27**, 4141 (1962).
17. D. E. McClure, B. H. Arison, J. H. Jones, and J. J. Baldwin. J. Org. Chem. **46**, 2431 (1981).
18. Y. Senda, J. Ishiyama, S. Imaizumi, and K. Hanaya. J. Chem. Soc. Perkin Trans. I, 217 (1977).
19. J. E. Saavedra. J. Org. Chem. **50**, 2271 (1985).
20. (*a*) R. F. Borch and H. D. Durst. J. Am. Chem. Soc. **91**, 3996 (1969); (*b*) R. F. Borch, M. D. Berustein, and H. D. Durst. J. Am. Chem. Soc. **93**, 2897 (1971).
21. J. H. Noggle and R. E. Schirmer. *In* The nuclear Overhauser effect. Academic Press, New York. 1971.
22. L. M. Jackman and S. Sternhell. *In* Nuclear magnetic resonance spectroscopy in organic chemistry. 2nd ed. Pergamon Press, Oxford. 1969.
23. V. Burkert and N. L. Allinger. Molecular mechanics. A.C.S. Monograph, no. 177. Washington, DC. 1982.
24. (*a*) C. A. G. Haasnot, F. A. A. M. de Leeuw, and C. Altona. Tetrahedron, **36**, 2783 (1980); (*b*) E. Osawa and C. Jaime. QCPE program no. 367 (1984).
25. (*a*) R. Richarg, W. Amman, and T. Wirthlin. Varian Application Note 2-15. Zug, Switzerland. August 1982; (*b*) D. M. Doddell, D. T. Pegg, and M. R. Bendall. Org. Magn. Reson. **8**, 323 (1982).
26. A. Bax, R. Freeman, and G. Morris. J. Magn. Reson. **42**, 169 (1981).
27. A. Bax and G. Morris. J. Magn. Reson. **42**, 501 (1981).
28. K. Nakamura. J. Pharm. Soc. Jpn. **61**, 292 (1941).
29. N. L. Allinger and E. S. Jones. J. Org. Chem. **27**, 70 (1962).
30. V. Vesely and F. Stursa. Collect. Czech. Chem. Commun. **5**, 170 (1933).
31. J. H. Jones, P. S. Anderson, J. J. Baldwin, B. Cineschmidt, D. E. McClure, G. Lundell, W. Randall, G. Martin, M. Williams, H. Hirshfield, G. Smith, and P. Lumma. J. Med. Chem. **27**, 1607 (1984).
32. A. Miyake, K. Itoh, N. Tada, M. Tanabe, M. Hirata, and Y. Oka. Chem. Pharm. Bull. **31**, 2329 (1983).
33. P. W. Neber, A. Bugard, and W. Thier. Ann. Chem. **526**, 77 (1936).
34. E. Hardeger, D. Redlich, and A. Gal. Helv. Chim. Acta, **28**, 628 (1945).
35. F. Zymalkowski, T. Yupraphat, and K. Schmeisser. Arch. Pharm. **301**, 321 (1968).

Can. J. Chem. Downloaded from www.nrcresearchpress.com by 176.9.209.113 on 09/07/12
For personal use only.

COMMUNICATION

Total synthesis of natural quadrone

HSING-JANG LIU AND MONTSE LLINAS-BRUNET
Department of Chemistry, University of Alberta, Edmonton, Alta., Canada T6G 2G2

Received November 2, 1987

This paper is dedicated to Professor Zdenek Valenta on the occasion of his 60th birthday

HSING-JANG LIU and MONTSE LLINAS-BRUNET. Can. J. Chem. **66**, 528 (1988).

Starting from the ammonium salt of (−)-10-camphorsulfonic acid (**4**), an efficient synthesis of quadrone (**1**) in natural form has been accomplished.

HSING-JANG LIU et MONTSE LLINAS-BRUNET. Can. J. Chem. **66**, 528 (1988).

Utilisant le sel d'ammonium de l'acide (−)-camphresulfonique-10 (**4**), on a réalisé une synthèse efficace de la forme naturelle de la quadrone (**1**).

[Traduit par la revue]

(−)-Quadrone (**1**) (1) and (+)-terrecyclic acid A (**2**) (2) are metabolites isolated recently from *Aspergillus terreus*. The interesting cytotoxic properties (1*a*, 2*a*) and the challenging structural features of these novel sesquiterpenes have elicited extensive synthetic activity and, over a rather short period of time, a large number of elegant total syntheses have been achieved (3), including two asymmetric syntheses leading to (+)-quadrone (3*h*) and (−)-terrecyclic acid A (3*i*). Herein we wish to report the first synthesis of natural (−)-quadrone (**1**), providing direct evidence for its absolute configuration.

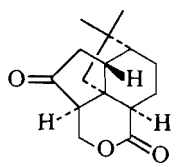

1

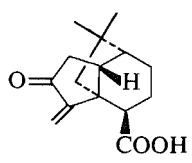

2

In approaches to the synthesis of the target compound **1**, (−)-α-campholenic acid (**3**) presents itself as a highly attractive potential precursor. As can be seen in Scheme 1, this chiral substrate, which is readily accessible from the ammonium salt of (−)-10-camphorsulfonic acid (**4**) by fusion with potassium hydroxide pellets (4), embodies nicely the complete B ring and part of the C ring (boldfaced portion) of compound **1** with the correct chirality. Furthermore, the functionalities of this molecule are adequately situated at the strategic positions facilitating the construction of the required framework.

Reduction of (−)-α-campholenic acid (**3**) with lithium aluminum hydride in ether followed by methylation of the resulting alcohol with dimethyl sulfate in 1,2-dimethoxyethane using sodium hydride as a base gave methyl ether **5** in 85% yield (Scheme 2). Irradiation (tungsten lamp) of a solution of **5** in methylene chloride in the presence of oxygen, acetic anhydride, pyridine, and 4-dimethylaminopyridine (5) using 5,10,15,20-tetraphenyl-21*H*,23*H*-porphine as a photosensitizer gave rise to a 78% yield of enone **6**. The ensuing removal of the methylidene group of enone **6** was initially attempted via a combination of hydration and retro-aldol reaction. In practice, this proved not to be viable. Under none of the conditions applied could the desired ketone **7** be generated. Interestingly, when the 1:1 mixture of the epimeric epoxides, prepared in 90% yield from enone **6** by treatment with hydrogen peroxide and lithium

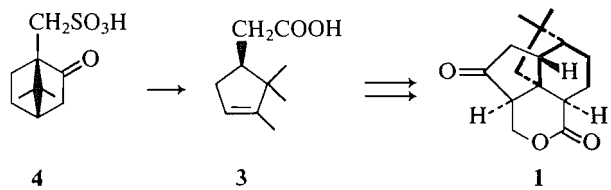

4 **3** **1**

SCHEME 1

hydroxide in methanol, was heated with sodium hydroxide in aqueous methanol at reflux, ketone **7** was produced in 68% yield.

Selective alkylation of ketone **7** with lithium diisopropylamide and diethyl 3-bromo-2-ethoxypropenylphosphonate in tetrahydrofuran (6), followed by acid-catalyzed hydrolysis of the resulting enol ether **8**, afforded diketo phosphonate **9** (48% yield). The intramolecular Horner–Emmons reaction was performed initially using sodium hydride in 1,2-dimethoxyethane (6). Under these conditions, extensive decomposition of the starting material was detected. However, the cyclization proceeded smoothly to give a high yield (85%) of the desired bicyclic enone **10** when carried out in benzene in the presence of 18-crown-6 ether using potassium carbonate as a base (7).

For the formation of ring C, a carbomethoxymethyl group was introduced to the C-1 position of enone **10** as follows. Photocycloaddition of **10** to allene (8) in tetrahydrofuran afforded the desired head-to-head adduct **11** as the chief product along with a small amount of the head-to-tail isomer. Ozonolysis of the mixture in methanol followed by reductive work-up using dimethyl sulfide gave keto ester **12** in 56% yield based on **10**.

Treatment of keto ester **12** with an excess of chlorotrimethylsilane and sodium iodide in acetonitrile (9) at 60°C induced the selective replacement of the ethereal methoxy moiety with an iodine atom. Acid-catalyzed transketalization of the resulting iodo ketone **13** with 2-ethyl-2-methyl-1,3-dioxolane in refluxing benzene gave rise to a 65% yield of the corresponding ketal **14** over two steps. This compound was subjected to cyclization using lithium hexamethyldisilazide in tetrahydrofuran. Subsequent removal of the ketal protecting group via acid-catalyzed transketalization with acetone afforded (−)-keto ester **15** (60% yield from **14**), which was shown to be spectroscopically identical to the corresponding racemic mixture prepared pre-

Can. J. Chem. Downloaded from www.nrcresearchpress.com by 176.9.209.113 on 09/07/12
For personal use only.

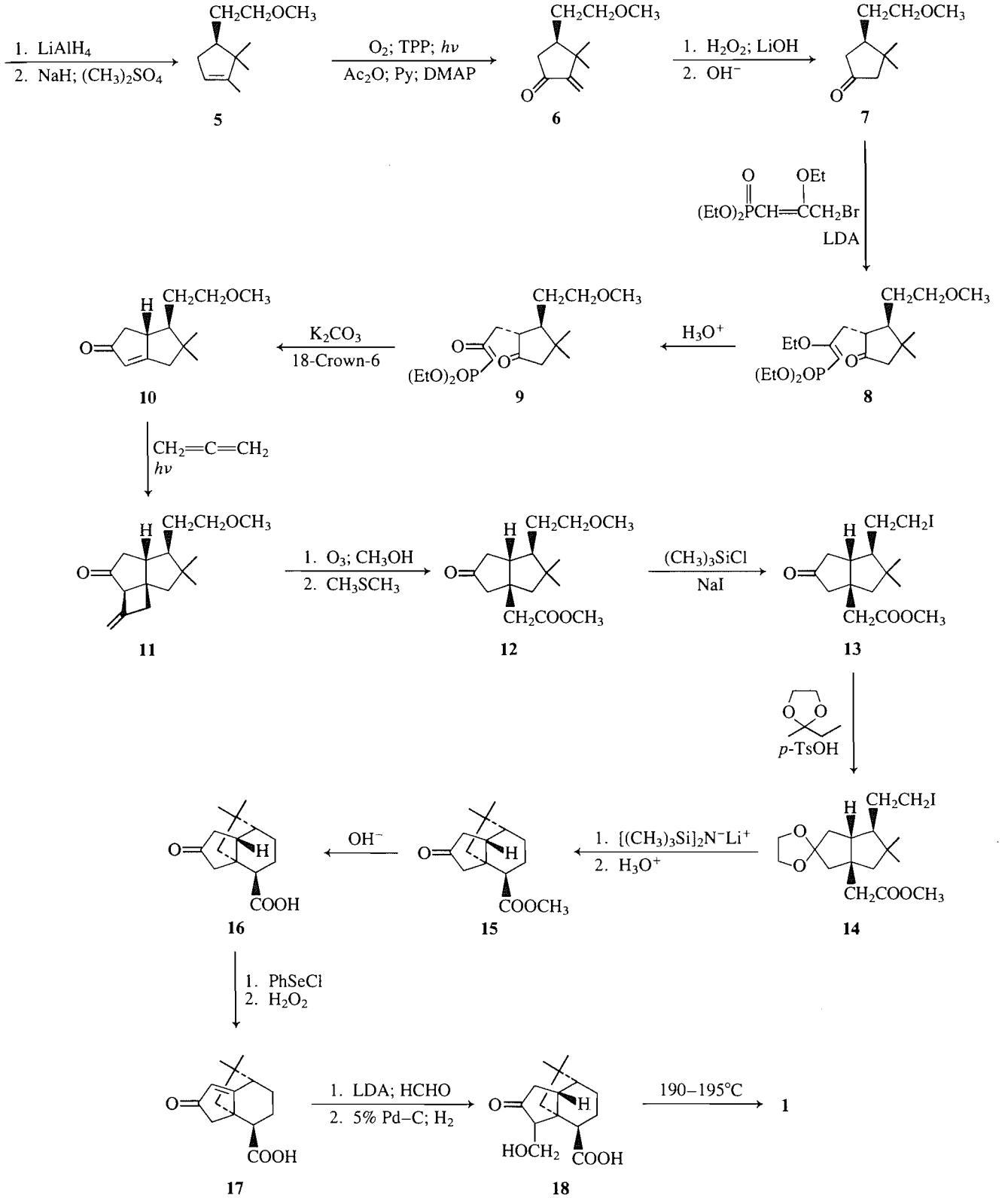

SCHEME 2

viously by Danishefsky and co-workers using a different route (3*a*). These investigators have also succeeded in the transformation of the racemic **15** to (±)-quadrone (3*a*). Application of the reported synthetic sequence to the levorotatory **15** resulted in the total synthesis of the naturally occurring (−)-quadrone (**1**). Alkaline hydrolysis of **15** afforded (−)-acid **16**, which was subjected to selenenylation. Oxidative work-up with hydrogen peroxide resulted in the formation of enone **17**. Treatment of **17** with lithium diisopropylamide and formaldehyde was followed by hydrogenation using 5% palladium on carbon as a catalyst. Pyrolysis of the hydroxy acid **18** thus obtained at 190–195°C resulted in the formation of (−)-quadrone (**1**). The melting point, specific rotation, and spectral data (^{1}H nmr, ir, and mass) of the synthetic material were found

Can. J. Chem. Downloaded from www.nrcresearchpress.com by 176.9.209.113 on 09/07/12
For personal use only.

to be in agreement with those reported for the natural product (1, 2).

Acknowledgements

We are grateful to the Natural Sciences and Engineering Research Council of Canada and the University of Alberta for financial support, and to the Alberta Heritage Foundation for Medical Research for a Studentship to M.L.-B.

1. (*a*) G. J. CALTON, R. L. RANIERI, and M. A. ESPENSHADE. J. Antibiot. **31**, 38 (1978); (*b*) R. L. RANIERI and G. J. CALTON. Tetrahedron Lett. 499 (1978).
2. (*a*) N. NAKAGAWA, A. HIROTA, H. SAKAI, and A. ISOGAI. J. Antibiot. **35**, 778 (1982); (*b*) A. HIROTA, M. NAKAGAWA, H. SAKAI, and A. ISOGAI. J. Antibiot. **35**, 783 (1982).
3. (*a*) S. DANISHEFSKY, K. VAUGHAN, R. C. GADWOOD, and K. TSUZUKI. J. Am. Chem. Soc. **102**, 4262 (1980); **103**, 4136 (1981); (*b*) W. K. BORNOCK, S. S. BAGWAT, J. PONTON, and P. HELQUIST. J. Am. Chem. Soc. **103**, 4647 (1981); (*c*) S. D. BURKE, C. W. MURTIASHAW, J. O. SAUNDERS, and M. S. DIKE. J. Am. Chem. Soc. **104**, 872 (1982); S. D. BURKE, C. W. MURTIASHAW, and J. A. OPLINGER. Tetrahedron Lett. **24**, 2949 (1983); S. D. BURKE, C. W. MURTIASHAW, J. O. SAUNDERS, J. A. OPLINGER, and M. S. DIKE. J. Am. Chem. Soc. **106**, 455 (1984); (*d*) A. S. KENDE, B. ROTH, P. J. SANFILIPPO, a T. J. BLACKLOCK. J. Am. Chem. Soc. **104**, 5808 (1982); (e K. TAKEDA, Y. SHIMONO, and E. YOSHII. J. Am. Chem. Soc **105**, 563 (1983); (*f*) R. H. SCHLESSINGER, J. L. WOOD, A. J. POSS, R. A. NUGENT, and W. H. PARSONS. J. Org. Chem. **48**, 1146 (1983); (*g*) J. M. DEWANCKELE, F. ZUTTERMAND, and M. VANDEWALLE. Tetrahedron, **39**, 3235 (1983); (*h*) A. B SMITH and J. P. KONOPELSKI. J. Org. Chem. **49**, 4094 (1984 (*i*) K. KON, K. ITO, and S. ISOE. Tetrahedron Lett. **25**, 3 (1984); (*j*) E. PIERS and N. MOSS. Tetrahedron Lett. **26**, (1985); (*k*) P. A. WENDER and D. J. WOLANIN. J. Org. C **50**, 4418 (1985); (*l*) R. L. FUNK and M. M. ABELMAN. J. C Chem. **51**, 3248 (1986).
4. H. J. LIU and W. H. CHAN. Can. J. Chem. **60**, 1081 (1982).
5. E. D. MIHELICH and D. J. EICKHOFF. J. Org. Chem. **48**, 4135 (1983).
6. E. PIERS and B. ABEYSEKERA. Can. J. Chem. **60**, 1114 (1982).
7. P. A. ARISTOFF. Synth. Commun. **13**, 145 (1983).
8. R. W. GUTHRIE, A. PHILIPP, Z. VALENTA, and K. WIESNER. Tetrahedron Lett. 2945 (1965).
9. G. A. OLAH, S. C. NARANG, B. G. B. GUPTA, and R. MALHOTRA. J. Org. Chem. **44**, 1247 (1979).

Can. J. Chem. Downloaded from www.nrcresearchpress.com by 176.9.209.113 on 09/07/12
For personal use only.

Excess enthalpies of dibutyl ether + *n*-alkane mixtures at 298.15 K

GEORGE C. BENSON, BEICHEN LUO, AND BENJAMIN C.-Y. LU

Department of Chemical Engineering, University of Ottawa, 770 King Edward Avenue, Ottawa, Ont., Canada K1N 9B4

Received July 2, 1987

This paper is dedicated to Professor J. A. Morrison

GEORGE C. BENSON, BEICHEN LUO, and BENJAMIN C.-Y. LU. Can. J. Chem. **66**, 531 (1988).

Calorimetric measurements of excess enthalpies are reported over the entire composition range for dibutyl ether + *n*-heptane, + *n*-deeane, + *n*-dodecane, and + *n*-hexadecane at 298.15 K. The results are compared with data from the literature, and a correlation of the excess enthalpies of dibutyl ether + *n*-alkane mixtures in terms of the Flory theory is described.

GEORGE C. BENSON, BEICHEN LUO et BENJAMIN C.-Y. LU. Can. J. Chem. **66**, 531 (1988).

Opérant à 298,15 K, on a effectué des mesures calorimétriques d'enthalpies en excès pour l'ensemble des compositions des mélanges d'éther dibutylique + *n*-heptane, + *n*-décane, + *n*-dodécane et + *n*-hexadécane. On compare ces résultats aux données que l'on peut retrouver dans la littérature; de plus, on décrit un corrélation des enthalpies en excès de mélanges d'éther dibutylique + *n*-alcanes en fonction de la théorie de Flory.

[Traduit par la revue]

Can. J. Chem. Downloaded from www.nrcresearchpress.com by 176.9.209.113 on 09/07/12
For personal use only.

The excess thermodynamic properties of *n*-ether + *n*-alkane mixtures have not been investigated sufficiently to provide a good understanding of the molecular interactions in such systems. Some progress has been made in the application of quasi-chemical models in terms of group surface interactions (1), but further experimental studies are needed to adjust the values of the interchange coefficients to include steric and orientational effects (2, 3).

A recent paper (4) from our laboratory reported measurements of the excess enthalpies of the binary mixtures: diethyl ether + *n*-heptane, + *n*-decane, + *n*-dodecane, and + *n*-hexadecane. As an extension of that investigation, we have determined the excess enthalpies of binary mixtures of dibutyl ether with the same set of *n*-alkanes.

Experimental

Component liquids

The dibutyl ether (Gold Label Reagent) and *n*-hexadecane, both with 99 mol% minimum purity, were obtained from the Aldrich Chemical Co. The other *n*-alkanes were Pure Grade Reagents (99 mol% minimum purity) from the Phillips Petroleum Co. The dibutyl ether was kept under dry nitrogen; the *n*-alkanes were stored over Type 4A moelcular sieve beads. The component liquids were used without further purification. Their densities, measured at 298.15 K in an Anton-Paar densimeter, were 763.84, 679.64, 726.26, 745.28, and 770.03 kg cm^{-3} for dibutyl ether, *n*-heptane, *n*-decane, *n*-dodecane, and *n*-hexadecane, respectively.

Calorimetric measurements

Excess enthalpies were determined in an LKB flow microcalorimeter (Model 10700-1) thermostated at 298.15 ± 0.002 K. Details of this equipment and its modification have already been described (5, 6). Over most of the mole fraction range, the errors of the excess molar enthalpy, H_m^E, and the mole fraction, x, are estimated to be less than 0.5% and 5×10^{-4}, respectively.

Results and discussion

The experimental values of H_m^E at 298.15 K for $\{x(C_4H_9)_2O + (1 - x)C_nH_{2n+2}\}$ with $n = 7$, 10, 12, and 16 are summarized in Table 1 and plotted in Fig. 1. Each set of results was fitted with the smoothing function

$$[1] \quad H_m^E/(\mathrm{J\,mol^{-1}}) = x(1 - x)\sum_{j=1}^{m} h_j(1 - 2x)^{j-1}$$

Values of the coefficients h_j, determined by the method of least-squares with all points assigned unit weight, are listed in Table 2 along with the standard deviations s of the representations. Curves calculated from eq. [1] are shown in Fig. 1.

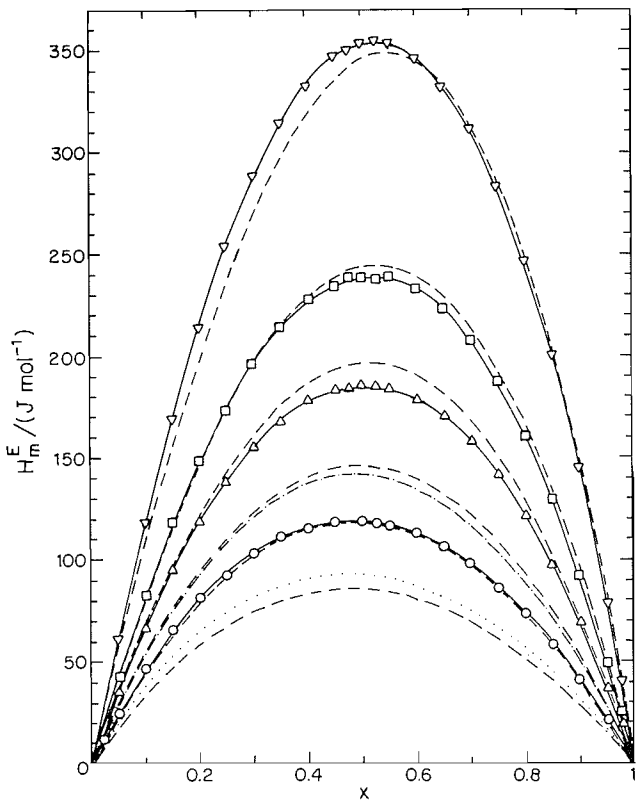

FIG. 1. Excess molar enthalpies H_m^E for $\{x(C_4H_9)_2O + (1 - x)C_nH_{2n+2}\}$ mixtures at 298.15 K. Experimental results: ○, $n = 7$; △, $n = 10$; □, $n = 12$; ▽, $n = 16$. Curves: —, calculated from eq. [1] with coefficients from Table 2; ·····, $n = 6$ taken from ref. 9; - - - -, $n = 8$ taken from ref. 10; ---, calculated from Flory theory with X_{12} from eq. [2].

As far as we are aware, only the system with *n*-heptane has been studied previously (7, 8). The deviation plot in Fig. 2 shows that, over most of the mole fraction range, the results of Villamañan *et al.* (8) are 1.5 to 2.0% higher than the representation of our results by eq. [1]. The results of the earlier investigation (7), for which an error of ±20 J mol^{-1} at $x = 0.5$

TABLE 1. Excess molar enthalpies H_m^E of $\{x(C_4H_9)_2O + (1 - x)C_nH_{2n+2}\}$ mixtures at 298.15 K

x	H_m^E / J mol^{-1}	x	H_m^E / J mol^{-1}	x	H_m^E / J mol^{-1}	x	H_m^E / J mol^{-1}	x	H_m^E / J mol^{-1}
				Dibutyl ether + *n*-heptane					
0.0500	24.7	0.2998	103.4	0.4500	118.8	0.5513	117.1	0.8000	74.0
0.1000	46.6	0.3000	103.3	0.5000	118.8	0.5998	112.7	0.8500	58.5
0.1500	65.5	0.3498	110.9	0.5002	119.5	0.6500	106.4	0.9003	41.1
0.2000	81.5	0.4000	115.3	0.5249	117.9	0.6990	98.8	0.9501	21.6
0.2499	92.6	0.4497	118.2	0.5496	116.4	0.7506	85.5		
				Dibutyl ether + *n*-decane					
0.0500	35.0	0.2998	155.5	0.4499	183.6	0.5501	184.3	0.8000	121.5
0.1000	66.7	0.3498	168.0	0.4751	185.0	0.6002	178.8	0.8500	97.4
0.1000	66.8	0.3500	168.4	0.4999	185.5	0.6501	170.3	0.9000	69.2
0.1500	95.0	0.4001	177.7	0.5251	185.3	0.7001	158.0	0.9500	36.7
0.2004	118.9	0.4498	183.9	0.5497	184.5	0.7503	141.5	0.9751	18.8
0.2501	138.6								
				Dibutyl ether + *n*-dodecane					
0.0499	42.8	0.3001	195.9	0.5000	238.2	0.7001	207.4	0.8999	92.3
0.1000	82.8	0.3498	214.5	0.5252	238.4	0.7501	186.8	0.9500	49.0
0.1501	117.5	0.3997	226.8	0.5501	238.1	0.7503	186.6	0.9500	49.1
0.2001	148.2	0.4500	234.0	0.6001	232.7	0.8000	160.3	0.9752	25.2
0.2500	173.5	0.4750	238.3	0.6502	222.6	0.8500	129.0	0.9752	25.1
				Dibutyl ether + *n*-hexadecane					
0.0500	60.7	0.3000	288.2	0.5001	354.2	0.6501	332.5	0.8501	200.5
0.1000	117.8	0.3501	314.8	0.5003	353.2	0.7000	311.6	0.9000	145.3
0.1501	169.2	0.3997	332.8	0.5257	355.0	0.7500	283.0	0.9500	78.6
0.2000	214.3	0.4501	348.0	0.5500	353.6	0.8001	246.2	0.9754	40.1
0.2500	254.1	0.4754	350.5	0.6000	346.6				

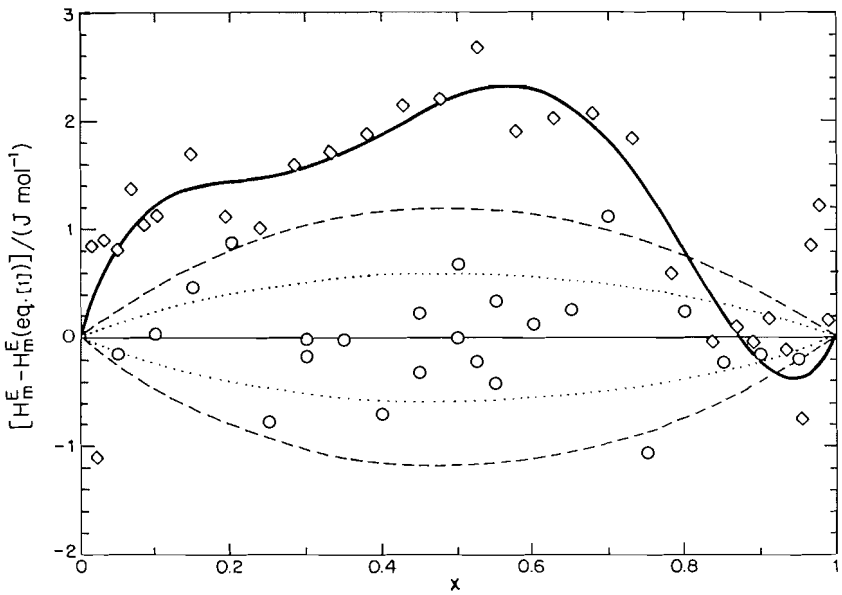

FIG. 2. Comparison of results for $\{x(C_4H_9)_2O + (1 - x)C_7H_{16}\}$ mixtures at 298.15 K. Points and curves represent deviations of excess molar enthalpy H_m^E from eq. [1] with coefficients from Table 2: ○, present work; ◇ and —, Villamañan *et al.* (8); ····, ±0.5% deviation; ---, ±1.0% deviation.

has been estimated (7*a*), are much lower, and fall off the scale of Fig. 2. At $x = 0.5$, the deviation from our value is ~ -10 J mol^{-1} (i.e. −8.5%).[1]

Excess enthalpies at 298.15 K have been reported for dibutyl ether + *n*-hexane (9) and + *n*-octane (10). Smooth representations of these results are included in Fig. 1 for comparison.

It can be seen that H_m^E for dibutyl ether + *n*-alkane mixtures increases fairly regularly with increasing size of the *n*-alkane molecule. The curves are nearly symmetrical about $x = 0.5$, but there is a slight skew of the curves toward $x = 1$ as the size of the *n*-alkane increases.

[1] NOTE ADDED IN PROOF: Since the submission of this paper, another study of dibutyl ether + *n*-heptane at 298.15 K has come to our attention (18). At $x = 0.5$, the deviation from our value is ~ -18 J mol^{-1} (i.e. −15%).

Can. J. Chem. Downloaded from www.nrcresearchpress.com by 176.9.209.113 on 09/07/12
For personal use only.

TABLE 2. Coefficients h_j and standard deviations s for least-squares representations of H_m^E for $\{x(C_4H_9)_2O + (1 - x)C_nH_{2n+2}\}$ mixtures at 298.15 K by eq. [1]

Mixture	h_1	h_2	h_3	h_4	s
Dibutyl ether					
+ *n*-heptane	475.32	35.68	20.31		0.52
+ *n*-decane	742.66	−15.25	20.29		0.21
+ *n*-dodecane	955.57	−66.14	24.40		0.50
+ *n*-hexadecane	1415.09	−127.43	70.05	−100.86	0.51

TABLE 3. Component properties and parameters used in calculations for $\{x(C_4H_9)_2O + (1 - x)C_nH_{2n+2}\}$ at 298.15 K by the Flory theory

Component	V_m / cm³ mol⁻¹	α_p / kK⁻¹	κ_T / TPa⁻¹	p^* / J cm⁻³	V_m^* / cm³ mol⁻¹	T^* / K	s_{12}	X_{12}/J cm⁻³ Fit of H_m^E	X_{12}/J cm⁻³ Eq. [2]
$(C_4H_9)_2O$	170.49	1.126	1207.0	450.7	133.93	4909.8			
C_6H_{14}	131.57	1.387	1703.9	424.2	99.52	4436.1	0.9058	3.319	3.070
C_7H_{16}	147.45	1.256	1460.6	431.9	113.60	4648.1	0.9466	3.692	3.647
C_8H_{18}	163.50	1.164	1302.4	436.8	127.70	4827.0	0.9842	4.129	4.225
$C_{10}H_{22}$	195.94	1.051	1109.6	447.0	155.75	5091.4	1.0516	5.104	5.380
$C_{12}H_{26}$	228.55	0.960	987.6	445.2	184.40	5351.4	1.1125	6.417	6.535
$C_{16}H_{34}$	294.07	0.883	862.0	457.0	240.41	5614.7	1.2153	9.042	8.846

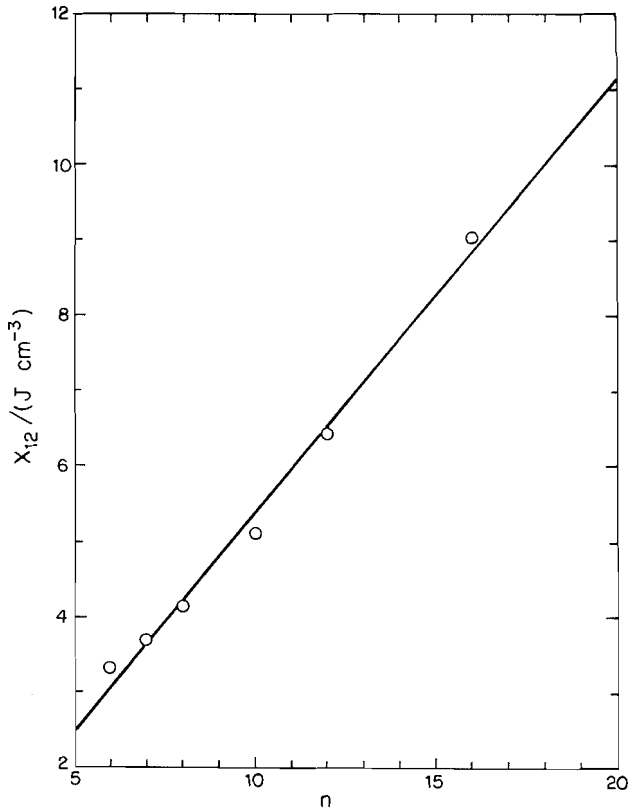

FIG. 3. Flory interchange-energy parameter X_{12} for mixtures of dibutyl ether with *n*-alkanes C_nH_{2n+2} at 298.15 K. Points: ○, from fit of H_m^E (column 9 in Table 3). Line: —, plotted from eq. [2].

In the case of the *n*-decane system, excess enthalpies calculated according to the quasi-chemical model with the interchange parameters given in ref. 1 are in good agreement with the experimental results. However, calculations for the other systems provide further evidence of the need to refine the parameters, since the variations of the excess enthalpies with changes in the length of the *n*-alkane component are underestimated, and the curves for the longer *n*-alkanes are much more skewed toward $x = 1$ than those found experimentally.

Previously (4) we found that the excess enthalpies of diethyl ether + *n*-alkane mixtures could be correlated by the Flory theory (11). The same treatment was applied to the present dibutyl ether mixtures. The calculations used the molar volumes V_m, isobaric thermal expansivities α_p, and isothermal compressibilities κ_T listed for the components in Table 3. In the case of dibutyl ether, α_p was derived from tabulated densities (12), and κ_T was calculated from the thermal pressure coefficient (13). Data for the *n*-alkanes were taken from our previous publications (14–17). The characteristic pressures p^*, molar volumes V_m^*, and temperatures T^*, obtained from the Flory formalism, are also listed in Table 3, together with the ratio s_{12} of (ether/alkane) molecular surface areas of contact per segment and the interchange-energy parameter X_{12} for each mixture. The values of s_{12} are based on the simple assumption that the molecules are spherical. The values of X_{12}, given in the second last column of Table 3, were obtained from least-squares analyses in which the Flory formula for the excess molar enthalpy was fitted to the representations of the experimental results by eq. [1].

As in the case of the diethyl ether mixtures, the values of X_{12} for dibutyl ether + *n*-alkane mixtures increase nearly linearly with the number *n* of carbon atoms in the alkane molecule. This is illustrated in Fig. 3, where the line

$$[2] \quad X_{12} = -0.3961 + 0.5776n$$

corresponding to a correlation coefficient $r = 99.56\%$ is also plotted. Values of X_{12} calculated from eq. [2] are given in the last column of Table 3, and curves obtained from the Flory theory with these values are shown in Fig. 1. The agreement with the experimental curves is reasonable, and suggests that eq. [2] in combination with the Flory theory can provide useful estimates of H_m^E for mixtures of dibutyl ether with other *n*-alkanes.

Can. J. Chem. Downloaded from www.nrcresearchpress.com by 176.9.209.113 on 09/07/12
For personal use only.

Acknowledgement

The continued financial support of the Natural Sciences and Engineering Research Council of Canada (NSERC) is gratefully acknowledged.

1. H. V. KEHIAIAN, J.-P. E. GROLIER, and G. C. BENSON. J. Chim. Phys. **75**, 1031 (1978).
2. H. V. KEHIAIAN. Pure Appl. Chem. **57**, 15 (1985).
3. M. R. TINÉ and H. V. KEHIAIAN. Fluid Phase Equilib. **32**, 211 (1987).
4. B. LUO, G. C. BENSON, and B. C.-Y. LU. J. Chem. Thermodyn. **20**, 267 (1988).
5. R. TANAKA, P. J. D'ARCY, and G. C. BENSON. Thermochim. Acta, **11**, 163 (1975).
6. F. KIMURA, G. C. BENSON, and C. J. HALPIN. Fluid Phase Equilib. **11**, 245 (1983).
7. (*a*) K. SOSNKOWSKA-KEHIAIAN, R. HRYNIEWICZ, and H. KEHIAIAN. Bull. Acad. Polon. Sci. Ser. Sci. Chim. **17**, 185 (1969); (*b*) J. J. CHRISTENSEN, R. W. HANKS, and R. M. IZATT. Handbook of heats of mixing. John Wiley, New York. 1982. p. 795.
8. (*a*) M. A. VILLAMAÑAN, C. CASANOVA, A. H. ROUX, and J.-P. E. GROLIER. J. Chem. Eng. Data, **27**, 89 (1982); (*b*) Int. DATA Ser., Ser. A, 180 (1984).
9. (*a*) K. N. MARSH, J. B. OTT, and M. J. COSTIGAN. J. Chem. Thermodyn. **12**, 857 (1980); (*b*) Int. DATA Ser., Ser. A, 96 (1984).
10. M. KUUS and L. KUDRYAVTSEVA. Int. DATA Ser., Ser. A, 60 (1980).
11. (*a*) P. J. FLORY. J. Am. Chem. Soc. **87**, 1833 (1965); (*b*) A. ABE and P. J. FLORY. J. Am. Chem. Soc. **87**, 1838 (1965).
12. TRC Thermodynamic Tables – Non-Hydrocarbons. Thermodynamics Research Center, Texas A & M University System, College Station, TX. 1986. Table 23-2-1-(1.2115)-a, dated December 31, 1965.
13. G. R. DRIVER and A. G. WILLIAMSON. J. Chem. Eng. Data, **17**, 65 (1972).
14. F. KIMURA and G. C. BENSON. J. Chem. Eng. Data, **28**, 387 (1983).
15. G. C. BENSON and Y. P. HANDA. J. Chem. Thermodyn. **13**, 887 (1981).
16. D. ZHANG, G. C. BENSON, and B. C.-Y. LU. J. Chem. Thermodyn. **18**, 619 (1986).
17. S. E. M. HAMAM, M. K. KUMARAN, and G. C. BENSON. J. Chem. Thermodyn. **16**, 537 (1984).
18. B. MARONGIU, S. DERNINI, L. LEPORI, E. MATTEOLI, and H. V. KEHIAIAN. J. Chem. Eng. Data. In press.

Can. J. Chem. Downloaded from www.nrcresearchpress.com by 176.9.209.113 on 09/07/12
For personal use only.

Reactions of α-carbon- and nitrogen-centered radicals of piperazine with lumiflavin and paranitroacetophenone at pH 7

PARMINDER S. SURDHAR AND DAVID A. ARMSTRONG
Department of Chemistry, University of Calgary, Calgary, Alta., Canada T2N 1N4

Received June 3, 1987

This paper is dedicated to Professor J. A. Morrison

PARMINDER S. SURDHAR and DAVID A. ARMSTRONG. Can. J. Chem. **66**, 535 (1988).

Analysis of data from radiation chemical and photochemical studies shows that the reactions of hydroxyl radicals and flavin triplets (Fl^3) with amines produce aminyl as well as α-amino radicals. This must be taken into account, since the former tend to oxidise $^{\bullet}FlH$ and FlH^-, while the latter are inherently reducing. In the reaction of $^{\bullet}OH$ with piperazine the ratio of aminyl to α-amino radicals at pH 7 is about 60:40. The former undergo complexation to form a $N.^{\bullet}.N^+$ bonded species, which possess a broad absorption peaking at 520 nm and are inert to lumiflavin (Fl) and paranitroacetophenone on a 30 μs time scale. However, they oxidise dihydrolumiflavin anion (FlH^-) to flavin semiquinone radical ($^{\bullet}FlH$). The α-amino radicals of piperazine reduced lumiflavin to $^{\bullet}FlH$ with a rate constant of $3.3 \pm 0.3 \times 10^9\ M^{-1}\ s^{-1}$. This rate constant is similar to that observed for the $CH_3S(CH_2)_2\dot{C}HNH_2$ radical formed from methionine.

The 40:60 mixture of α-amino and $N.^{\bullet}.N^+$ radicals produced in N_2O-saturated piperazine solutions decayed by a second order process with a rate constant of $7.2 \times 10^8\ M^{-1}\ s^{-1}$. Similar mixtures of $^{\bullet}FlH$ and the $N.^{\bullet}.N^+$ species also underwent second order decay ($k = 2.7 \times 10^9\ M^{-1}\ s^{-1}$) with reoxidation of $^{\bullet}FlH$ to Fl as the major process.

PARMINDER S. SURDHAR et DAVID A. ARMSTRONG. Can. J. Chem. **66**, 535 (1988).

Une analyse des données provenant d'études radio- et photochimiques démontre que les réactions des radicaux hydroxyles et des triplets de la flavine (Fl^3) avec des amines conduit à des radicaux aminyles ainsi qu'à des radicaux α-aminés. On doit tenir compte de ces résultats puisque les premiers ont tendance à oxyder les entités $^{\bullet}FlH$ et FlH^- alors que les derniers sont d'une façon inhérente des réducteurs. Lors de la réaction du radical $^{\bullet}OH$ avec la pipérazine, à un pH de 7, le rapport des radicaux aminyles aux radicaux α-aminés est d'environ 60:40. Les premiers subissent une réaction de complexation conduisant à des espèces liées $N.^{\bullet}.N^+$ qui présentent un large maximum d'absorption à 520 nm et qui sont inertes vis-à-vis de la lumiflavine (Fl) et la *p*-nitroacétophénone, à une échelle de temps de 30 μs. Toutefois, ils oxydent l'anion dihydrolumiflavine (FlH^-) en radical flavine semiquinone ($^{\bullet}FlH$). Les radicaux α-aminés de la pipérazine réduisent la lumiflavine en $^{\bullet}FlH$ avec une constante de vitesse de $3{,}3 \pm 0{,}3 \times 10^9\ M^{-1}\ s^{-1}$. Cette constante de vitesse est similaire à celle qui a été observée pour le radical $CH_3S(CH_2)_2\dot{C}HNH_2$ qui se forme à partir de la méthionine.

Le mélange 40:60 des radicaux α-aminés et $N.^{\bullet}.N^+$ qui se forme dans des solutions de pipérazine saturées de N_2O se décompose par un processus du deuxième ordre avec une constante de vitesse de $7{,}2 \times 10^8\ M^{-1}\ s^{-1}$. Des mélanges semblables d'espèces $^{\bullet}FlH$ et $N.^{\bullet}.N^+$ se décomposent aussi par un processus du deuxième ordre ($k = 2{,}7 \times 10^9\ M^{-1}\ s^{-1}$) impliquant une réoxydation de $^{\bullet}FlH$ en Fl comme réaction principale.

[Traduit par la revue]

Introduction

Reactions of flavins with amine radicals are of contemporary interest for a number of reasons. In the first place amine (AH_2) molecules can be used as hydrogen donors to convert flavins (Fl) to their dihydro forms (1–4) through the reaction sequence:

[1] $Fl + h\nu \rightarrow Fl^1 \rightarrow Fl^3$

[2] $AH_2 + Fl^3 \rightarrow {}^{\bullet}AH + {}^{\bullet}FlH$

[3] $^{\bullet}AH + {}^{\bullet}FlH \rightarrow A + FlH_2$

This highly practical photo-initiated reduction has been extensively exploited in recent research on reduced derivatives of flavins. At the same time step [3] in the above mechanism is also a key process in the radical pair mechanism proposed for the action of monoamine oxidase enzymes on normal substrates (3, 5). The formation of stable adducts in the alternative reaction:

[4] $^{\bullet}AH + {}^{\bullet}FlH \rightarrow HA—FlH$

would lead to enzyme inactivation. Studies of these reactions thus have a bearing on our understanding of important biological processes and the pharmacology related to them (4).

An earlier study of the reactions of lumiflavin with amine radicals formed in the sequence [1]–[2], and via reaction [5]

[5] $AH_2 + {}^{\bullet}OH \rightarrow {}^{\bullet}AH + H_2O$

demonstrated that the relative importance of steps [3] and [4] depended on the amine structure (4). It was pointed out in ref. 4 that further progress required a knowledge of the proportions of nitrogen-centered (viz.: $\rangle N^{\bullet+}$) and carbon-centered radicals (viz. —NH—$\dot{C}$H—) formed in reactions [3] and [5] and the separate characterisation of their reactions with flavins.

Since the submission of ref. 4 two studies which are very relevant to the above question have been published. In the first place Mönig *et al.* (6) have shown that deprotonated α-amino acids have a high tendency to form α-carbon-centered radicals, which are strongly reducing. This results from initial attack of the $^{\bullet}OH$ on the nitrogen lone pair and subsequent elimination of CO_2, e.g. for glycine:

[6a] $^{\bullet}OH + \ddot{N}H_2—CH_2—CO_2^- \rightarrow HO.^{\bullet}.NH_2—CH_2—CO_2^-$

[6b] $HO.^{\bullet}.NH_2—CH_2—CO_2^- \rightarrow HO^- + NH_2—\dot{C}H_2 + CO_2$

The second paper is that of Das and von Sonntag (7), who studied the radicals produced from $^{\bullet}OH$ attack on trimethylamine. Their work provided evidence for three radical forms, which were related by the protonation–deprotonation equilibria below:

[7] $(CH_3)_2HN^+CH_2^{\bullet} \underset{+H^+}{\overset{-H^+}{\rightleftharpoons}} (CH_3)_2NCH_2^{\bullet} \underset{-H^+}{\overset{+H^+}{\rightleftharpoons}} (CH_3)_3N^{\bullet+}$

$pK \sim 3.6$ $\qquad$ $pK = 8.0$

Both studies point toward a key role played by the nitrogen.

Can. J. Chem. Downloaded from www.nrcresearchpress.com by 176.9.209.113 on 09/07/12
For personal use only.

When it is deprotonated it appears to represent the main site for •OH attack, except when the carbon chain becomes excessively long. In short chain alkyl amines, the α-carbon-centered radicals are mainly formed via deprotonation as in scheme [7], or, in the case of α-amino acids, via CO_2 elimination (6) as in [6].

This study was designed to utilise the approaches in refs. 6 and 7 to determine the proportions of the two radicals forms and elucidate the nature of their reactions with lumiflavin at neutral pH. The amine chosen was piperazine (Pip). The pKs of this molecule (pK_1 = 5.33) and (pK_2 = 9.73) (8) are such that at pH 7 the monoprotonated form dominates. The structure of this species is shown below:

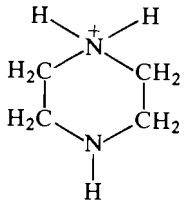

Thus one nitrogen lone pair should be accessible to •OH and other electrophiles. Also one may note that all carbon-centered radicals would be of the α form. As in ref. 4 the •OH radicals were produced by pulse radiolysis of nitrous oxide-saturated solutions containing the amine.

Experimental

Materials

Lumiflavin (Fl), piperazine (Pip), and methionine were purchased from Sigma Chemical Co. The *t*-butyl peroxide and paranitroacetophenone (PNAP) were from Aldrich. All other chemicals were the purest grade available and used as supplied. The water for preparing the solutions was redistilled, first from potassium permanganate and then from acid dichromate (9).

Apparatus and procedures

All experiments were conducted at room temperature (23 ± 2°C) with solutions containing 10 mM phosphate buffer. All solutions were degassed during preparation by prebubbling with nitrous oxide or argon as required. The gases were first passed through a column of "Ridox" (Fisher Scientific Co.) to remove traces of oxygen. Prereduction and oxidation of N_2O-saturated Fl containing 0.1 M Pip was carried out using the technique described in ref. 10.

The pulse radiolysis experiments were performed by utilising 2 μs pulses of electrons with doses of 4–10 Gy/pulse from a 1.5-MeV Van de Graaff generator. Details of the generator and dosimetry have been described earlier (11).

Results and discussion

Formation of —NH—ĊH—

The work of Das and von Sonntag (7) demonstrated that at pHs significantly above the pK of the N-centered radical, the C-centered species dominated and its absorbance spectrum could be obtained separately. The filled circles in Fig. 1*a* show the absorbance of the —NH—ĊH— radical of piperazine at pH 11.2 in the wavelength range of relevance here. Below 300 nm it increases gradually and then rises to a maximum near 260 nm,[1] thus resembling the spectrum for the corresponding radical of trimethylamine in ref. 7. We found that a similar spectrum could be produced at pH 7 by reacting methyl radicals formed via reaction [8] or

[8] $e_{aq}^- + CH_3Cl \rightarrow {}^{\bullet}CH_3 + Cl^-$

[1]P. S. Surdhar and D. A. Armstrong. Unpublished results.

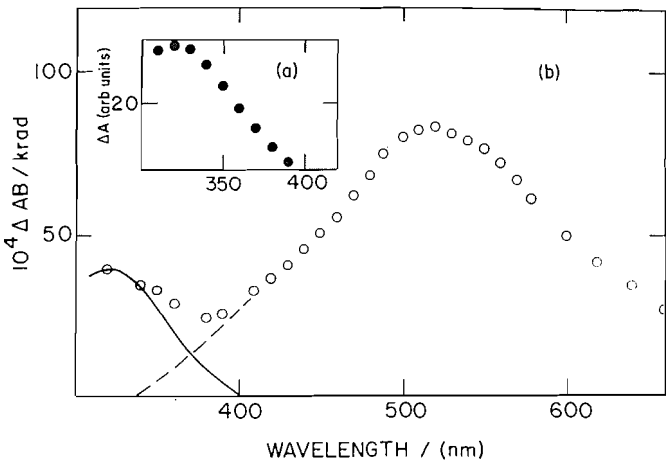

FIG. 1. (*a*) Difference spectrum observed at 20 μs after pulse in N_2O-saturated 0.01 M piperazine at pH 11.2. (*b*) ○○○ Difference spectrum observed at 20 μs after pulse in N_2O-saturated solutions containing 0.1 M piperazine. — Spectrum from (*a*) normalised at 320 nm to ○○○. ---- Spectrum after correcting for the absorption of the —NH—ĊH— radical.

the sequence:

[9a] $e_{aq}^- + t\text{-ButOOt—But} \rightarrow t\text{-ButO}^- + t\text{-ButO}^{\bullet}$

[9b] $t\text{-ButO}^{\bullet} \rightarrow {}^{\bullet}CH_3 + CH_3COCH_3$

Reactions [8] and [9a] proceed at a diffusion-controlled rate (12), while [9b] has a first order rate constant of $1.4 \times 10^6\ s^{-1}$ (13) and would have occurred mostly within our pulse width. Methyl radicals should abstract C—H hydrogens much more rapidly than N—H hydrogens because of the larger N—H bond dissociation energies (14) and data given later confirm this. Residual *t*-ButO• radicals also would have a strong preference for attacking the C—H bonds (14).

Products of •OH + Pip reactions

The spectra of species formed in these reactions was investigated in N_2O-saturated solutions containing 0.001 to 0.1 M Pip. The spectrum observed at 20 μs after pulse in a 0.1 M Pip solution, when the growth was complete, is shown by the circles in Fig. 1*b*. The broad maximum at 520 nm demonstrates that radical species other than —NH—ĊH— are present. The wavelength of maximum absorbance does not correspond to the absorbance of the nitrogen-centered $\rangle N^{\bullet+}$ radical seen by Das and von Sonntag (7), since that species absorbed only below 300 nm. It conforms more closely to the absorbance maxima reported for $N.^{\bullet}.N^+$ species by Alder and co-workers (15, 16). Formation of such a structure would be much more likely with piperazine at pH 7 than with trimethylamine, because of the presence of an unprotonated nitrogen in the former molecule. At Pip concentrations below 0.5 mM other absorption peaks are seen. The dependence of the absorbance on the concentration of Pip, which indicates that it is due to a dimer complex, and its rate of formation will be reported elsewhere, along with other results on the piperazine and related radical systems.[1]

The absorbance of the Pip radicals in the region below 300 nm must be due at least in part to the Pip (—NH—ĊH—) species. We have arbitrarily assumed that at 320 nm the absorbance of the •OH-produced radicals is due *entirely* to the —NH—ĊH— component and have normalised the spectrum from Fig. 1*a* (see solid line in Fig. 1*b*) to the circles at that wavelength. The

Can. J. Chem. Downloaded from www.nrcresearchpress.com by 176.9.209.113 on 09/07/12
For personal use only.

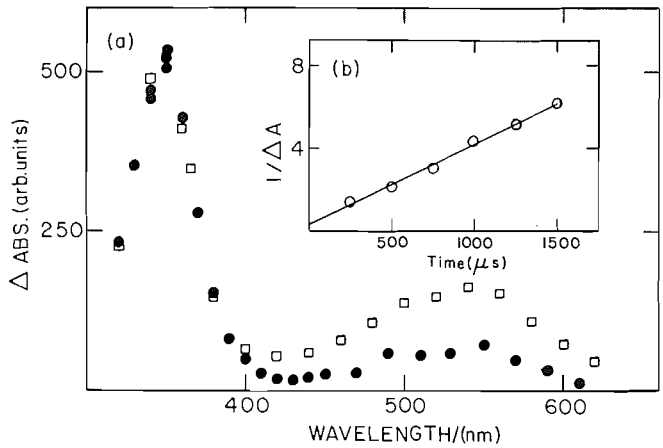

FIG. 2. (*a*) Difference spectra observed in N_2O-saturated solutions. ●●● 50 μ*M* PNAP containing 20 m*M* sodium formate. □□□ 50 μ*M* PNAP containing 40 m*M* piperazine normalised to the former at 340 nm. (*b*) Plot of $1/\Delta A$ versus time at 540 nm.

fact that the normalisation factor was ~0.5 implies that •OH must produce roughly equal proportions of —NH—ĊH— and $\diagdown N^{\bullet\pm}\diagup$ radicals for the conditions of Fig. 2*b*. In order to measure this yield more precisely, the —NH—ĊH— radicals were titrated with PNAP. This compound is known to be reduced by these species but evidently does not react rapidly with $\diagdown N^{\bullet\pm}\diagup$ centered species (6, 7).

The spectrum observed 30 μs after pulsing an N_2O-saturated solution containing 40 m*M* Pip and 50 μM PNAP at pH 7 has been displayed by the squares in Fig. 2*a*. The strong peak at 350 nm is characteristic of $PNAP^{\bullet-}$ (17) and demonstrates that reaction [10]

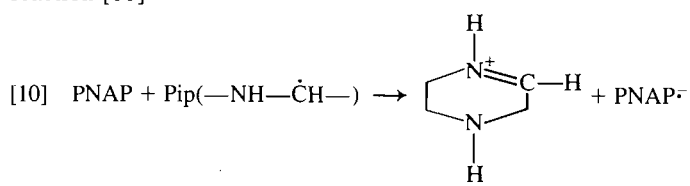

occurred. From the pseudo first order rate constants for the growth of this absorbance a second order rate constant of $3.6 \times 10^9\ M^{-1}\ s^{-1}$ was calculated for k_{10}. This is to be compared with $3.9 \pm 0.4 \times 10^9$ and $4 \times 10^9\ M^{-1}\ s^{-1}$ for the reduction of PNAP by the α-amino radicals of methionine (6) and trimethylamine (7), respectively.

The solid circles in Fig. 2 show the spectrum of $PNAP^{\bullet-}$ obtained in the absence of Pip on reduction by $^{\bullet}CO_2^-$ formed from the reaction of •OH with 20 m*M* of HCO_2^-. Here the yield of $PNAP^{\bullet-}$ should be equal to $g_{\cdot CO_2^-}$ or 6.4 molecules per 100 eV, based on the equation of Schuler *et al.* (18). Assuming that after reaction [10] no species other than $PNAP^{\bullet-}$ contributed to the absorbance at 350 nm, the circles have been normalised to the squares at that wavelength. The value of the normalisation factor (= 0.43) requires that the yield of $PNAP^{\bullet-}$ derived from the Pip (—NH—ĊH—) radicals is $0.43 \times 6.4 = 2.7_4$ molecules per 100 eV. Taking the total yield of Pip radicals also as 6.4, it follows that roughly 43% are able to produce $PNAP^{\bullet-}$ and may be identified as reducing —NH—ĊH— radicals. The remaining 57% of the Pip radicals must be N-centered $\diagdown N^{\bullet\pm}\diagup$ radicals.

Returning to Fig. 1*b*, one may note that subtraction of the solid line from the unfilled circles should give a first approximation to the spectrum of the $N.^{\bullet}.N^+$ species. This is shown by the dashed line. A similar broad absorption is obtained when the contribution of the normalised $PNAP^{\bullet-}$ spectrum produced by $^{\bullet}CO_2^-$ is subtracted from the spectrum formed by Pip radicals obtained from [5] in Fig. 2*a*. This implies that *N*-centered Pip radicals do not react with PNAP on the 30 μs time scale, but form the same species as in its absence. Also interconversion of the $N.^{\bullet}.N^+$ and —NH—ĊH— radical forms of Pip is evidently slower than the time scale of the reaction of —NH—ĊH— with PNAP.

When PNAP was absent the absorption of the Pip radicals at 540 nm decayed by second order kinetics as demonstrated by the reciprocal of Δ*A* plot in Fig. 2*b*. Since mutual reactions of $N.^{\bullet}.N^+$ species would be slow, due to like charges, it seems probable that the main reaction would be between the two different types of radicals, viz.

[11] —NH—ĊH— + $N.^{\bullet}.N^+$ → Products

Thus k_{11} can be estimated from the slope of the line in Fig. 2, divided by the absorbance coefficient of the species at 540 nm for 5 m*M* Pip. This absorbance coefficient was found from Δ*A* at that wavelength and the *g* value for *N*-centered species (= 6.4 × 0.57 = 3.6 molecules per 100 eV) to be 1800 $M^{-1}\ cm^{-1}$. Hence, from the slope in Fig. 2*a*, k_{11} was estimated to be $7.2 \times 10^8\ M^{-1}\ s^{-1}$.

Reactions of —NH—ĊH— radicals with Fl

Three sources of —NH—ĊH— radicals were used: (*a*) $^{\bullet}CH_3$/*t*-ButO• + Pip, (*b*) •OH + methionine, and (*c*) •OH + Pip.

Case (a): The $^{\bullet}CH_3$/*t*-ButO• was formed in reactions [9a] and [9b] and •OH radicals were scavenged by *t*-ButOH. It was shown by pulsing N_2O-saturated *t*-ButOH solutions in the absence of $(t\text{-ButO})_2$ that the radicals from *tert*-butyl alcohol reacted very slowly with Fl and produced only a very weak spectrum. This was also true for methyl radicals from reaction [8] in the absence of Pip. The changes in Δ*A* versus wavelength observed 25 μs after pulsing the argon-saturated system containing $(t\text{-ButO})_2$ have been shown by the squares in Fig. 3*a*. The changes in the absorbance during build up of •FlH for 44 μ*M* Fl took place with $t_{1/2}$ of ~3 μs. The second order rate constant for the reaction:

[12] Pip(—NH—ĊH—) + Fl → Pip(—N=CH—) + •FlH

is therefore about $5 \times 10^9\ M^{-1}\ s^{-1}$.

Case (b): The reactions of •OH with methionine have been investigated by Hiller and Asmus (19). The primary attack is mainly at sulphur, with some abstraction of H from the methyl and —CH_2— groups. The —CH_2• radicals resulting from the former process are expected to be relatively inert to Fl, as are the —CH_2• radicals from *t*-ButOH. Also the combined yield of these and the —C•(H)— radicals is small (19). The reaction of •OH with the S atom leads to elimination of OH^-, interaction of the positive —Ṡ—$^+$ center with the amino group, electron transfer from the carboxylate group and finally elimination of CO_2 to produce the α-amino CH_3—S—CH_2—$CH(NH_2)CH_2$• radical at pH 7. These intramolecular processes all occur on a 0.3 μs time scale. The solid circles in Fig. 3*a* show the changes in absorbance 25 μs after pulsing an N_2O-saturated 10 m*M* solution of methionine in the presence of 54 μ*M* Fl. The spectrum very closely resembles that formed by the Pip(—NH—ĊH—) radical (i.e. the squares). Both spectra can

Can. J. Chem. Downloaded from www.nrcresearchpress.com by 176.9.209.113 on 09/07/12
For personal use only.

Can. J. Chem. Downloaded from www.nrcresearchpress.com by 176.9.209.113 on 09/07/12
For personal use only.

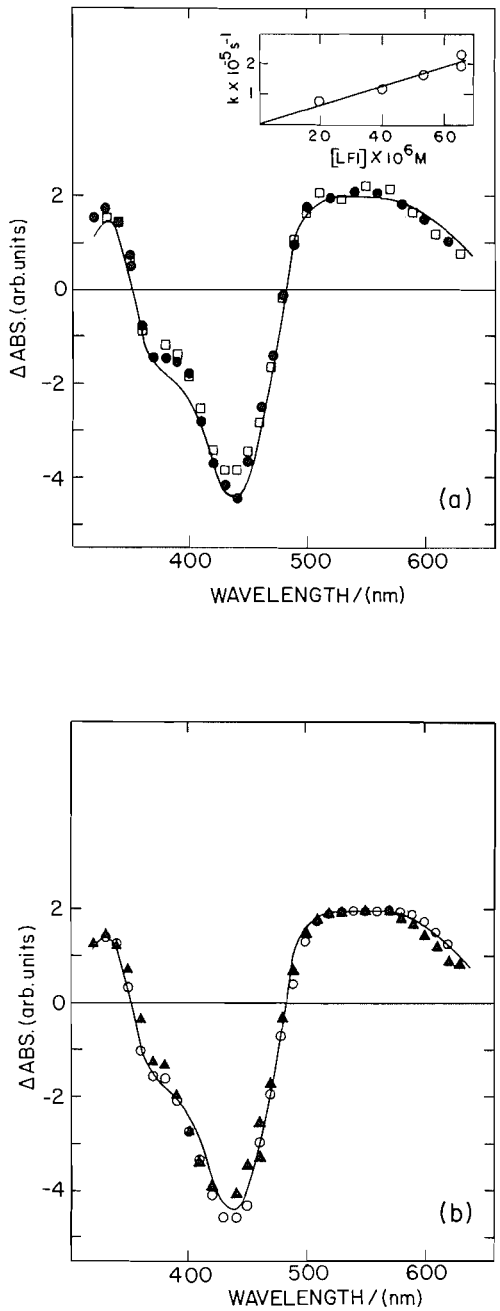

FIG. 3. Difference spectra due to ·FlH formation observed at 20–25 μs after pulse in Fl solutions: (*a*) ●●● 54 μM Fl containing 10 m*M* methionine and N_2O-saturated; □□□ 44 μ*M* Fl containing 5 m*M* *t*-ButOO*t*-But, 2 *M* *t*-ButOH and 0.01 *M* piperazine and argon-saturated. These points and the solid line have been normalized to the methionine points at 540 nm to account for the differences in radical yields; — spectra observed at 20 μs in N_2O or argon-saturated 50 μ*M* Fl solutions containing 20 m*M* sodium formate. Inset: plot of pseudo first order rate constant versus [Fl]. (*b*) ○○○ argon-saturated 40–80 μ*M* Fl solutions containing 0.1 *M* piperazine; ▲▲▲ same conditions as for ○○○ except N_2O-saturated; — as in (*a*).

be compared to the spectrum of ·FlH produced via reaction [13]

[13] $\cdot CO_2^- + Fl\,(+ H^+) \rightarrow CO_2 + \cdot FlH$

in 20 m*M* HCO_2^- solutions saturated with N_2O. The agreement demonstrates that the α-amino radicals produced from Pip via *t*-ButO·/·CH_3 and from methionine via ·OH both produce ·FlH on a 25 μs time scale. The present data do not permit a distinction between H atom transfer, as in [12] above, and electron transfer, followed by protonation, viz.

[12a] $—NH—\dot{C}—H— + Fl \rightarrow —NH^+{=}CH— + \cdot Fl^-$

[12b] $H^+ + \cdot Fl^- \rightarrow \cdot FlH$

However, in the case of methionine the overall reaction rate constant was determined. The inset of Fig. 3*a* presents a plot of the pseudo first order rate constants for the growth of the absorbance at 550 nm as a function of [Fl]. The slope leads to $k_{12} = 3.2 \pm 0.2 \times 10^9\, M^{-1}\, s^{-1}$.

Case (c): As was demonstrated above with PNAP, the α-carbon-centered and *N*-centered radicals of Pip have quite different characteristics. The results under (*a*) above demonstrated that the α-carbon-centered radical species reduced Fl to the ·FlH radical. If the *N*-centered radicals are inert to Fl as they are to PNAP, it follows that the net result of pulsing N_2O-saturated solutions of Pip in the presence of Fl should be to produce a mixture of ·FlH and $N.^{\cdot}.N^+$ radicals. Since the absorbance of the $N.^{\cdot}.N^+$ must correspond closely to that shown by the dashed line in Fig. 1*b*, the spectrum of the ·FlH species can be obtained from the overall changes in ΔA when reaction [12] and or [12a] + [12b] are complete by subtracting the $N.^{\cdot}.N^+$ contribution. The triangles in Fig. 3*b* show the spectrum of ·FlH obtained by this method. The circles show similar data for argon-saturated solutions, where e_{aq}^- reacts with Fl:

[14] $e_{aq}^- + Fl\,(+ H^+) \rightarrow \cdot FlH$

Since the yield of ·OH is about half ($g_{OH} = 2.8$ molecules per 100 eV), the correction for $N.^{\cdot}.N^+$ absorbance is similarly reduced. Again both sets of data are in agreement with the absorbance changes for ·FlH formed via reaction [13] (see solid line). Thus the assumption that nitrogen-centered species are inert to Fl on the 25 μs time scale appears to be justified.

As in the case of the methionine system the build up of the absorbance at 550 nm was followed as a function of [Fl] in N_2O-saturated 0.1 *M* Pip solutions. The slope gave a value of $k_{12} = 3.3 \pm 0.3 \times 10^9\, M^{-1}\, s^{-1}$, which is to be compared with $3.2 \pm 0.2 \times 10^9\, M^{-1}\, s^{-1}$ obtained above for methionine. The value with Pip(—NH—ĊH—) is not however, as reliable, due to the contribution of the $N.^{\cdot}.N^+$ species to the total absorbance at 550 nm. The present rate constants for reduction of lumiflavin are similar to those reported for amine radical reductions of methyl viologen and benzil (20).

The decay of the mixture of $N.^{\cdot}.N^+$ and ·FlH was followed on a 500 μs time scale for a 0.01 *M* Pip solution with 45 μM Fl by observing the combined absorbances at 550 nm. This process was second order and gave a mean rate constant of $2.7 \times 10^9\, M^{-1}\, s^{-1}$, which must be attributed to a combination of reactions between ·FlH + ·FlH, $N.^{\cdot}.N^+$ + ·FlH, and $N.^{\cdot}.N^+ + N.^{\cdot}.N^+$. Due to the like charges, the last process is probably of least importance. The net yield of FlH^- at the end of the decay was negligibly small, showing that the oxidising radicals re-oxidised virtually all ·FlH.

Oxidation of FlH_2 by the nitrogen-centered species

The earlier work in ref. 4 showed that, although the quantum yield was low, Fl could be reduced almost quantitatively to FlH_2 in the presence of Pip on photolysis at 400–480 nm. This must be attributed to a net yield of —NH—ĊH— radicals from reaction [2] (i.e. $\phi(—NH—\dot{C}H—) > \phi(\rangle N^{\cdot\pm})$). Our main

Can. J. Chem. Downloaded from www.nrcresearchpress.com by 176.9.209.113 on 09/07/12
For personal use only.

interest in process [2] here is that photolysis provides a facile method for preparing a solution of FlH^- (pK of FlH_2 = 6.7 (21)) in 0.1 M Pip. When this was effected in a N_2O-saturated solution, subsequent pulsing with electrons would produce the 43% —NH—ĊH— + 57% N-centered radical species of Pip. Since effectively all flavin is now in the reduced form, reaction [12] (or [12a] + [12b]) could not occur. However, a spectrum characteristic of $^{\bullet}FlH$ was still formed, and this must be attributed to reaction [15]:

[15] $N.^{\bullet}.N^+ + FlH^- \rightarrow 2Pip + {}^{\bullet}FlH$

At 20 μM FlH_2 the yield of $^{\bullet}FlH$ estimated from the known $\epsilon(FlH_2)$ at 550 nm (= 4300 M^{-1} cm^{-1}) was similar to the yield of $>N^{\bullet+}$ radicals estimated above by other methods (3.6 per 100 eV). The half life for the growth of $^{\bullet}FlH$ was about 4 μs, showing that the second order reaction must be close to diffusion controlled. The dependence on $[FlH^-]$ was not pursued in sufficient detail to get an accurate value, because it was difficult to ensure complete reduction of Fl at lower concentrations and there is the interference of the absorbance of the Pip radical with $^{\bullet}FlH$ absorbance at 550 nm.

Conclusions

The present study has demonstrated unequivocally the formation of reducing —NH—ĊH— radicals and oxidising nitrogen-centered radicals from reaction [5] with piperazine at pH 7. The fact that the nitrogen-centered radicals form an $N.^{\bullet}.N^+$ complex involving a second piperazine molecule represents a point of difference from the findings on trimethylamine. However, this is not surprising because the piperazine molecule has one unprotonated lone pair on the nitrogen at this pH (8), while trimethylamine is well below its pK for deprotonation. As pointed out above, a more detailed account of the chemistry of the piperazine system per se will be given elsewhere. One point of similarity to the study of Das and von Sonntag is that the yields seen here at low (10 mM) buffer concentration appear to be frozen. That is, there was little evidence of interconversion of the two major radical types on the time scale of their reaction with added substrates. This is not surprising for the $N.^{\bullet}.N^+$ species, because the equilibrium constant for dimerisation is quite large,[1] and relatively little $>N^{\bullet+}$ species should be present. Protonation of the —NH—ĊH— to form $>N^{\bullet+}$ was evidently also slow relative to reaction with PNAP or Fl at our buffer concentrations. However, in the absence of these solutes, when FlH^- was to be oxidised, there was some evidence for a dependence of the $^{\bullet}FlH$ yield on $[FlH^-]$. This suggests that there could have been some slow conversion to $>N^{\bullet+}$ under those circumstances.

As pointed out in the Introduction, studies of amine radical – flavin reactions are of interest because "radical pair intermediates" (i.e. $^{\bullet}AH$ + $^{\bullet}FlH$) have been postulated in one of the mechanisms proposed for monoamine oxidases (5). They are also relevant to an understanding of the quantum yields for photoreduction. From the present observations of the oxidising properties of the N-centered radicals toward $^{\bullet}FlH$ and FlH^- it is evident that the low quantum yields reported for photoreduction by Pip in ref. 4 must mean that high proportions of these species are formed in reaction [2] as well as [5]. As this will also be true for other amines, it means that the reactions of these species with Fl, $^{\bullet}FlH$, $^{\bullet}Fl^-$, and FlH^- will have to be taken into account in interpretations of the photochemical reductions.

Reference 4 was concerned to a large degree with determining whether the products formed by $^{\bullet}AH$ + $^{\bullet}FlH$ radical pairs were recyclable reduced flavins (FlH^-) or inert adducts HA—FlH. Piperazine gave primarily (>90%) the former. Thus evidently the presence of $N.^{\bullet}.N^+$ species does not cause significant addition. It remains to be seen whether some of the large adduct yields seen at pH 7 with diethylamine and ethylamine, where $N.^{\bullet}.N^+$ formation should not occur, were due to reactions of the uncomplexed $>N^{\bullet+}$ radicals or to the β-carbon-centered radicals as assumed in ref. 4.

The involvement of the $>N^{\bullet+}$ centered species in the EDTA system has been recognised for some time (22), and the reaction of EDTA radicals with lumiflavin has been pursued in greater detail in ref. 23. For the case of glycine, the production of FlH^- observed in ref. 4 was >99%. The data of Mönig *et al.* (6) now show that, due to the role of reaction [6], the radicals from reaction of $^{\bullet}OH$ with glycine were not all $NH_2\dot{C}HCO_2^-$, as assumed in ref. 4, but approximately 45% and 60% $NH_2CH_2^{\bullet}$ at pH 7 and 10, respectively. It appears that either one or both of these radicals must react more slowly with lumiflavin at pH 7 than do the Pip or methionine —NH—ĊH radicals, since we observed $k_{10} = 1.8 \pm 0.3 \times 10^9\ M^{-1}\ s^{-1}$ for the combined glycine radicals produced via reaction [5] as opposed to $3 \times 10^9\ M^{-1}\ s^{-1}$ reported here.

Acknowledgement

The authors are indebted to the University of Calgary and to NSERC for financial support. They acknowledge the use of accelerator facilities at the U.S. Department of Energy Radiation Laboratory at the University of Notre Dame, and help from Dr. S. Mezyk, who kindly assisted in those experiments.

1. D. J. Fife and W. M. Moore. Photochem. Photobiol. **29**, 43 (1979).
2. P. F. Heelis. Chem. Soc. Rev. **11**, 15 (1982).
3. J. T. Simpson, A. Krantz, F. D. Lewis, and B. Kokel. J. Am. Chem. Soc. **104**, 7155 (1982).
4. P. S. Surdhar, D. E. Bader, and D. A. Armstrong. Can. J. Chem. **63**, 1357 (1985).
5. R. B. Silverman and S. S. Hoffman. J. Am. Chem. Soc. **102**, 884 (1980).
6. J. Mönig, R. Chapman, and K.-D. Asmus. J. Phys. Chem. **89**, 3139 (1985).
7. S. Das and C. von Sonntag. Z. Naturforsch. **41**b, 505 (1986).
8. H. B. Hetzer, R. A. Robinson, and R. G. Bates. J. Phys. Chem. **72**, 2081 (1968).
9. I. G. Draganić and Z. D. Draganić. The radiation chemistry of water. Academic Press, New York. 1971.
10. P. S. Surdhar and D. A. Armstrong. J. Phys. Chem. **89**, 5514 (1985).
11. A. J. Elliot, F. Wilkinson, and D. A. Armstrong. Int. J. Rad. Biol. **38**, 1 (1980).
12. Selected specific rates of reactions of transients from water in aqueous solution. Hydrated electron. NSRDS-NBS 43. U.S. Government Printing Office: Washington, DC. 1973.
13. M. Erben-Russ, C. Michel, W. Bors, and M. Saran. J. Phys. Chem. **91**, 2362 (1987).
14. A. S. Nazran and D. Griller. J. Am. Chem. Soc. **105**, 1970 (1983).
15. S. F. Nelson, R. W. Alder, R. B. Sessions, K.-D. Asmus, K.-O. Hiller, and M. Göbel. J. Am. Chem. Soc. **102**, 1429 (1980).

16. R. W. ALDER. Acc. Chem. Res. **16**, 321 (1983).
17. G. E. ADAMS and R. L. WILSON. J. Chem. Soc. Faraday Trans. 1, **69**, 719 (1973).
18. R. H. SCHULER, L. K. PATTERSON, and E. JANATA. J. Phys. Chem. **84**, 2088 (1980).
19. K.-O. HILLER and K.-D. ASMUS. J. Phys. Chem. **87**, 3682 (1983).
20. J. C. SCAINO. J. Phys. Chem. **85**, 2851 (1981); N. KIM-THUAN and J. C. SCAINO. Int. J. of Chem. Kinet. **16**, 371 (1984).
21. T. C. BRUICE. Prog. Biorg. Chem. **4**, 1 (1979).
22. J. S. ARMSTRONG, P. HEMMERICH, and R. TRABER. Photochem. Photobiol. **35**, 747 (1982).
23. P. S. SURDHAR, D. A. ARMSTRONG, K. H. SCHMIDT, and W. A. MULAC. Rad. Phys. Chem. In press.

Can. J. Chem. Downloaded from www.nrcresearchpress.com by 176.9.209.113 on 09/07/12
For personal use only.

Brillouin scattering near the α–β phase transitions of N_2 and CO

V. ASKARPOUR, H. KIEFTE, AND M. J. CLOUTER
Physics Department, Memorial University of Newfoundland, St. John's, Nfld., Canada A1B 3X7

Received August 21, 1987

This paper is dedicated to Professor J. A. Morrison

V. ASKARPOUR, H. KIEFTE, and M. J. CLOUTER. Can. J. Chem. **66**, 541 (1988).

The technique of high resolution Brillouin spectroscopy has been used to determine the adiabatic elastic constants of single crystals of β-N_2 and β-CO as a function of temperature, in an effort to study the α–β phase transition. For all elastic constants, there is an increase of approximately 1%/K on cooling and there is no evidence of further mode softening, even within 0.5 K of the phase transition. Three large single crystals of α-CO were grown. The orientations were determined, by Laue X-ray diffraction, and correlated to the orientations of the parent β-crystals. The β-phase hexagonal basal planes appear to transform to planes of the form {1 1 0} in the α-phase cubic structure.

V. ASKARPOUR, H. KIEFTE et M. J. CLOUTER. Can. J. Chem. **66**, 541 (1988).

Dans le but d'étudier la transition de phase α–β, on a utilisé la technique de la spectroscopie de Brillouin à haute résolution pour déterminer les constantes élastiques adiabatiques de cristaux uniques de β-N_2 et β-CO en fonction de la température. Pour toutes les constantes élastiques, on observe une augmentation d'environ 1%/K lorsqu'on refroidit; de plus, on ne détecte pas d'autre assouplissement de mode, même à 0,5 K de la transition de phase. On a fait croître trois gros cristaux uniques d'α-CO. On en a déterminé les orientations par diffraction des rayons-X selon Laue et on a établi un corrélation avec les orientations des cristaux β apparentés. Il semble que les plans hexagonaux de base de la phase β se transforment en plans de la forme {1 1 0} lorsqu'on passe à la structure cubique de la phase α.

[Traduit par la revue]

Can. J. Chem. Downloaded from www.nrcresearchpress.com by 93.93.197.157 on 09/07/12
For personal use only.

Introduction

Brillouin spectroscopy is a very effective technique for probing the dynamical behaviour of phonons in crystals and lattice instability associated with phase transitions. In particular, it allows for accurate determination of elastic constants in single crystals. The present work constitutes an attempt to use Brillouin spectroscopy (and Laue X-ray diffraction) to study very simple phase transitions in diatomic molecular solids, namely, the α–β transitions in solids N_2 and CO. This represents a continuation of previous Brillouin scattering experiments on single crystals of β-N_2 (1) and β-CO (2) very close to their triple points.

The α and β phases of solids N_2 and CO represent systems that undergo orientationally-disordered hexagonal close-packed (hcp) to orientationally-ordered face-centered cubic (fcc) phase transitions. Knowledge of the elastic constants is important in the sense that certain elastic constants may decrease in magnitude as the phase transition temperature is approached. This is caused by softening of acoustic phonon modes in the crystal as mechanical instability increases and molecular binding forces decrease. Eventually the associated frequencies are so low and the associated amplitudes are so high that molecules adopt new sites (3).

CO, while chemically distinct, is similar to N_2 in its condensed phases. The molecules are isoelectronic and have the same size and identical masses. Melting and boiling points and, in fact, the entire low-pressure phase diagrams are very similar and nearest neighbor distances and lattice constants are almost identical (4). In addition to the α and β phases, at very high pressures, N_2 exhibits γ, ε, δ, and ζ phases, whereas CO does not have a γ phase (5), probably because the quadrupole moment of CO is greater than that of N_2 (6). Most of these phases were detected and studied by Raman spectroscopy (see, for example, refs. 4, 7–11). There is a small dipole moment in CO due to its heteronuclear structure. A study of the temperature dependence of molar volume (12) shows that CO and N_2 behave similarly above 70 K and below about 30 K. Between these temperatures, under its own vapour pressure, both solidify to a disordered hcp β phase, the so-called plastic phase, with space group symmetry $P6_3/mmc$ (13–17). At the lower temperatures, they form an ordered cubic α phase where the molecules of N_2 occupy centrosymmetric positions in space group $Pa3$ (18, 19), while CO, because it is heteronuclear, lacks inversion symmetry and packs as $P2_13$ (7). In $Pa3$ the molecular centers are located on fcc lattice points; in $P2_13$ each molecular center is very slightly shifted, from fcc, along the direction of the molecular axis (11, 20). For purposes of the present study, fcc molecular sites may be (as already noted) assumed for α phases of both N_2 and CO.

The vapour–liquid–solid triple points for the β phases are 68.15 K and 63.15 K for CO and N_2, respectively; whereas the α–β phase transition temperatures are 61.55 and 35.6 K, respectively (21). The latter represents the biggest dissimilarity between the two. There are various possible reasons for this: one being that the quadrupolar interaction causes CO to orientationally order more readily (22), the other being that rotation–translation (RT) coupling is stronger for CO because of its physical asymmetry (23). Evidence for RT coupling in these systems is discussed in the last section.

In the present work, the elastic constants of β-N_2 are determined at 47.5 K and those of β-CO at 63.5 and 62.0 K; they are compared to the values previously measured at the respective triple points (1, 2). In addition, the orientations of single crystals of α-CO and β-CO are correlated using Laue X-ray diffraction and a possible phase-transition mechanism is suggested.

Experimental technique

Large single crystals of β-N_2 and β-CO of excellent quality can be grown by slow solidification from the liquid at the triple point, i.e., a modified Bridgman's method (4). Cooling such single van der Waal's crystals is difficult, mainly because of their generally very high coefficient of thermal expansion. On cooling, a crystal prefers to stick to the cell wall rather than to itself and contracts faster than the cell such that it very readily shatters (usually within 2 K of the triple point). In addition to the cooling problem, large single crystals of α-N_2 and α-CO are extremely difficult to produce due to the considerable change

Can. J. Chem. Downloaded from www.nrcresearchpress.com by 93.93.197.157 on 09/07/12
For personal use only.

in molar volume and the consequent highly disruptive nature of the $\alpha-\beta$ transition (as observed by Gannon and Morrison (15) in the birefringence study of α-N_2). Streib *et al.* (13) and Kjems and Dolling (24), however, after many tries, managed to produce one single crystal of α-N_2. Venables (25) has grown a single crystal segment of α-N_2 in a very thin film and studied it by electron microscopy. Aside from the present work, single crystals of α-CO, particularly oriented single crystals, have never been produced.

The crystals were grown in a cylindrical quartz cell, of 3 mm i.d. and 5 mm o.d., which was mounted vertically, in vacuum, in a modified commercial liquid-He cryostat (Janis Research Co., Model 10DT) as shown and discussed in detail in ref. 26. The sample cell was connected to the heat exchanger in the tail section of the cryostat via flexible copper braids and allowed for rotation of the entire cell assembly. One copper braid was fastened with a phosphor-bronze spring clamp to the lower end of the cell, and a miniature GaAs diode was mounted on this clamp close to the quartz tube. The second braid was similarly fastened 1 cm above the lower one and a differential thermocouple was mounted across them. Resistance wires of 50 Ω were wound on each clamp to permit control of the cell temperature. All electrical wires and copper braids were so arranged that the X-rays as well as the light scattered along the direction of the collection optics was not blocked when the cell was rotated through about 120°. The lower end of cell was sealed with a highly polished quartz plug, utilizing epoxy resin cement. This window provided for passage of incident laser light with minimum spurious scattering and provided a cold spot as a nucleation site for formation of the crystal. Because of problems with dust particles settling on the bottom window, a "dust trap" was installed between the cell and the inlet tube.

The cell itself, however, has been changed crucially from that illustrated in ref. 27. A thin optically transparent, electrically conducting coating was deposited (Evaporated Coatings Inc.) on the cell body to allow for melting and hence releasing the crystals from the walls of the cell. The film has a 70% optical transmission coefficient and 10 ohms electrical resistance and covers a height of about 1 cm. Two thin brass clamps, lined inside with indium, were used for electrical contact to the film. Teflon rings electrically isolated these clamps and the film from the rest of the system. The cell arrangement is shown in Fig. 1.

Temperature control was achieved in four stages: (*1*) by automatically adjusting the flow of liquid He into the heat exchanger, using an externally controlled needle valve, (*2*) by automatically and finely adjusting the temperature of the heat exchanger to about 4 K below the cell temperature, using a GaAs sensor and an electric heater in a feedback control system (Lakeshore Cryotronics Inc., Model DTC500), (*3*) by electronically controlling the temperature at the bottom of the cell as in (*2*), and (*4*) by electronically controlling the temperature at the top of the cell, (and therefore the temperature gradient across the cell) utilizing a differential copper-Constantan thermocouple. The absolute calibrated temperature was estimated to be accurate within 0.2 K. The temperature of the cell was controlled to within ± 0.01 K over long periods of time and could be varied automatically at adjustable and set rates.

N_2 gas of 99.9995% purity and CO gas of 99.99% purity (Matheson Gas Products), in each case, was condensed into the cell until it was filled with liquid to a height of about 1 cm. Crystal growth was initiated by maintaining a gradient of about 2.5 K between the top and the bottom of the cell (with the top being warmer) and lowering the temperature by about 0.05–0.1 K per hour until a small (0.5 mm) seed formed on the bottom window. This was annealed for about 1 day and then grown slowly for about 1 day to a height of ~2 mm while the temperature gradient was adjusted to about 1 K/cm. Polaroid transmission Laue X-ray photographs were then taken to determine the quality of the sample and (if possible) the orientation of the crystallographic axes with respect to the laboratory frame of reference. Many crystals were melted at this point either because they were not completely single (even though they might appear perfectly clear or show no birefringence between crossed polaroids) or because of their small range of angle γ. This is the angle between the acoustic wavevector, as

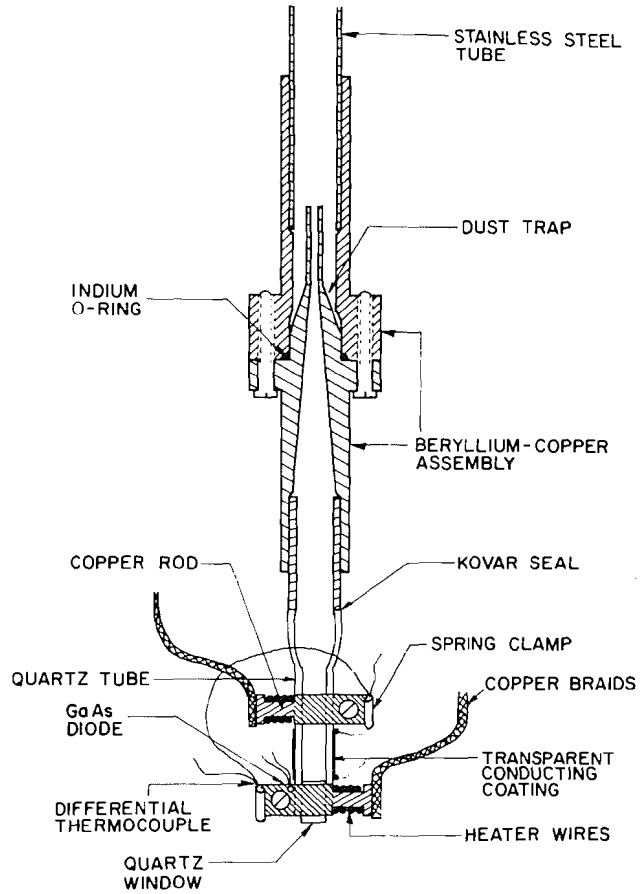

FIG. 1. Detailed diagram of the sample cell and dust trap arrangement.

determined by the geometry of the experimental setup, and the *c* axis of the crystal. A large γ range is necessary to meaningfully determine all five elastic constants.

Appropriate crystals were further grown, for another day, to a height of ~8 mm. The liquid above the crystal was removed completely and the remaining crystal was reduced in size (~6 mm) by pumping very slowly on the cell. Further cooling involved a very delicate combination of heating the walls of the cell and simultaneous pumping on the crystal. The film voltage was raised to 1.6 V in steps of 0.2 V each hour, allowing for continual establishment of equilibrium. The crystal melted at the boundary with the walls of the cell and the resulting liquid was removed by slight and careful pumping. When the crystal was almost completely released (from the walls), having a dome-shaped appearance, it was cooled very quickly, at about 8 K/h, to the desired temperature. For N_2, because of the larger temperature range, this process was carried out three times, whereas for CO once was enough to cool the crystal to just above the $\alpha-\beta$ phase transition temperature. After the cooling process, the pumping was stopped and the gap between the crystal and walls of the cell slowly filled again with solid. The film temperature was then lowered by reducing the voltage to 1.2 V in steps of 0.1 V. Keeping the film temperature fairly high appeared to allow for a more strain-free phase transition. Further cooling through the phase transition was carried out extremely slowly i.e. at about 0.05 K/h. Cooling was stopped periodically, for several hours, to check the crystal and to ensure near-equilibrium conditions.

As noted above, many Laue diffraction photographs were taken throughout these experiments using a Philips (MG 101) X-ray source, a lead collimator, and a Polaroid (XR-7) Land camera, with the film plane perpendicular to the Y axis (see Fig. 2). From the position of spots on the photographs, the crystal orientation with respect to the laboratory frame of reference, as shown in Fig. 2, was determined in terms of Euler angles (θ,ϕ,χ). These were utilized to determine angle

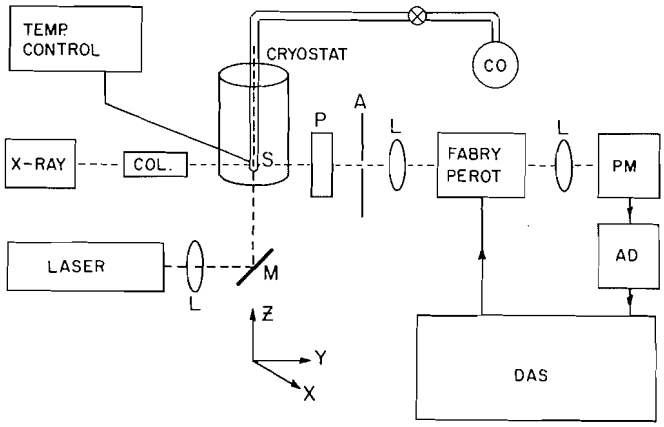

FIG. 2. Experimental layout and scattering geometry. S, sample site; COL, X-ray collimator; P, polaroid X-ray camera; A, aperture; L, lenses; M, mirror; PM, phototube; AD, amplifier discriminator.

γ by the expression: $\cos\gamma = -q_y(\text{lab})\sin\theta\cos\phi + q_z(\text{lab})\cos\theta$, where q_y and q_z are $\pm 1/\sqrt{2}$ and $\mp 1/\sqrt{2}$, respectively, the wavevector direction cosines for 90° scattering. This procedure has been completely computerized in this laboratory and is based on stereographic projection techniques (28). Care was taken to ensure that each and every spot on a photograph was accounted for in the orientation procedure and that Miller indices were assigned, as shown in Fig. 3. It was also important that consistent orientations were obtained as the crystal was rotated, i.e. only the angle ϕ was changed.

The basic experimental layout is shown in Fig. 2 and a more detailed description is given in ref. 26. The incident radiation was produced by a single mode Ar^+ laser (Spectra Physics 165-08) at a wavelength of 514.5 nm. The laser beam, which was limited to 20 mW intensity by neutral density filters and polarized perpendicular to the scattering plane, i.e., polarized along the X axis, was focussed and deflected into the Z direction, along the cell axis. The scattered light was collected at 90°, i.e. along the Y axis, and analyzed with a commercial triple-pass Fabry-Perot interferometer (Burleigh) at a spectral free range of 11.716 GHz. The light was detected by a cooled photomultiplier (ITT FW130) and its output was processed by photon counting techniques using a data acquisition and stabilization system (Burleigh DAS-1). The DAS-1 automatically corrected for frequency and any other drifts in the system as well as optimizing the Fabry-Perot finesse during the course of an experiment. Alphanumeric readout on the DAS-1 display permitted convenient and accurate measurement of the spectra.

Analysis and results

(a) Elastic constants

Brillouin scattering of light is attributed to those inhomogeneities, or fluctuations, in the optical dielectric constant of the scattering medium that are associated with the propagation of thermally excited sound waves. Theory (29, 30) can successfully predict intensity, polarization, and frequency shift of the scattered light with the result that, for a crystal, the spectrum consists of three sets of doublets located symmetrically about the incident laser frequency. The frequency shifts are given by the usual Brillouin equation

$$\nu_\mu(\boldsymbol{q}) = \pm 2\frac{n}{c}\nu_0 v_\mu(\boldsymbol{q})\sin\left(\frac{\alpha}{2}\right)$$

where ν_0 is the frequency of the incident radiation, ν_μ and v_μ are the frequency and phase velocity, respectively, for the μth acoustic mode of wavevector $\boldsymbol{q}$, n is the index of refraction of the medium, c is the velocity of light in vacuum, and α is the (measured) scattering angle.

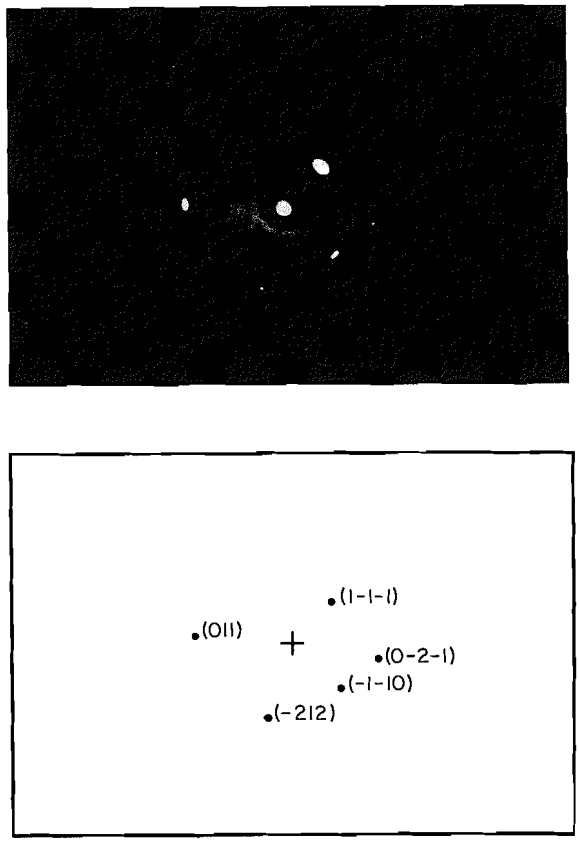

FIG. 3. Transmission Laue photograph of a β-CO crystal. Below it are shown computer-fitted Laue spots labeled by Miller indices of the corresponding reflecting planes as determined by the orientation procedure.

Solution of the eigenvalue equations for the acoustic-wave dynamical matrix yields the relationship between the velocities from the frequency shifts of the Brillouin spectra (as above), density ρ, angle γ, and the five elastic constants c_{11}, c_{12}, c_{13}, c_{33}, and c_{44} for a hexagonal crystal in closed form (1, 31). The three acoustic modes are identified according to their predominant polarization characteristics as the "slow" transverse mode T_1, the "fast" transverse mode T_2, and the longitudinal mode L. The frequency shift data were analyzed to yield the elastic constants by finding solutions to the above equations which best fit the data using a computerized iterative least-squares fit procedure (32).

β-CO: A Brillouin spectrum of β-CO is shown in ref. 2. None of the spectra for the cooled crystals were of as good quality as those taken at the triple point. One of the transverse components T_2 could usually be recognized readily but T_1 appeared infrequently. Generally the longitudinal components were about 150 times weaker than the Rayleigh and about 10 times stronger than the transverse ones. Brillouin spectra were recorded for 15 orientations of one single crystal of CO at 63.5 K and 20 orientations of 5 other single crystals at 62.0 K by rotating the crystals about the cell axis, thereby yielding the frequency shifts for various spectral features at different crystal orientations. The measured frequency shifts are shown on Fig. 4 for different γ angles at 63.5 and 62.0 K, respectively.

A knowledge of density and refractive index is essential in determining the elastic constants. The density for CO crystals at 63.5 and 62.0 K were obtained from molar volume graphs by

Can. J. Chem. Downloaded from www.nrcresearchpress.com by 93.93.197.157 on 09/07/12
For personal use only.

TABLE 1. Elastic constant data for N_2 and CO[a]

Elastic constants (10^9 N/m^2)	β-N_2 63.0 K	β-N_2 47.5 K	β-N_2 37 K (neutron scattering[b])	β-CO 67.7 K	β-CO 63.5 K	β-CO 62.0 K
c_{11}	1.825	2.307 ± 0.007	2.55	1.901 ± 0.004	2.027 ± 0.010	2.021 ± 0.021
c_{12}	1.131	1.454 ± 0.008	—	1.146 ± 0.006	1.234 ± 0.008	1.238 ± 0.023
c_{13}	0.980	1.274 ± 0.007	—	0.951 ± 0.004	1.005 ± 0.007	1.037 ± 0.021
c_{44}	0.320	0.378 ± 0.004	0.43	0.355 ± 0.003	0.380 ± 0.007	0.409 ± 0.015
c_{33}	1.976	2.488 ± 0.008	2.71	2.095 ± 0.006	2.256 ± 0.010	2.222 ± 0.028
c_{13}/c_{44}	3.06	3.37 ± 0.02	—	2.68 ± 0.03	2.64 ± 0.05	2.54 ± 0.11
Adiabatic bulk modulus	1.31	1.68	—	1.33	1.42	1.43

[a]All noted errors are relative as per text. Elastic constants for β-N_2 at 63.0 K are good to within 1% and at 37 K to about 2–3%.
[b]References 24 and 42.

Fukushima *et al.* (12). The values used were: ρ(63.5 K) = 0.920 g/cm^3 and ρ(62.0 K) = 0.921 g/cm^3 with about 1% uncertainty. There was no measured value of the refractive index of solid CO in the literature. However, the refractive index at the triple point has previously been calculated (2) via the Lorentz–Lorenz relation using measured values of liquid refractive index and density. Again the Lorentz–Lorenz relation yields: n(63.5 K) = 1.255 and n(62.0 K) = 1.257 with about 2% uncertainty. The best-fit adiabatic elastic constants and calculated bulk moduli for β-CO at 63.5 and 62 K are given in Table 1. The quoted errors in elastic constants were determined by the quality of the fit and the experimental self consistency corresponding to a single standard deviation. In addition, there was a systematic error of about 4% due to uncertainties in the values of the wavelength, index of refraction, density and the scattering angle.

β-N_2: The spectrum of β-N_2 was very similar to the spectrum of β-CO an example is shown in ref. 1. Both tranverse components were observed more frequently and the shifts were slightly larger than the shifts in β-CO. Longitudinal components were about 100 times weaker than the Rayleigh and about 10 times stronger than the transverse components. Again the spectra of cooled crystals were not of very good quality, in fact, it was not feasible to maintain a good quality crystal for light scattering purposes lower than 47.5 K. Crystals tended to heat up and fracture on exposure to the laser beam. Brillouin spectra were recorded for 35 orientations of four different single crystals of β-N_2 at 47.5 K. The measured frequency shifts are shown in Fig. 5 for different γ angles at 47.5 K.

The density of N_2 at 47.5 K was obtained in a similar manner to that of CO (12) and was ρ = 0.976 g/cm^3 with about 1% uncertainty. The refractive index was also calculated using the density and refractive index at the triple point and Lorentz–Lorenz relation, and was found to be n = 1.244 with less than 1% uncertainty. The best-fit adiabatic elastic constants and calculated bulk moduli for β-N_2 at 47.5 K are given in Table 1. The systematic error for β-N_2 is estimated to be about 2%.

(b) X-ray studies

Several attempts were made to carry out the phase transition in N_2. Close to the phase-transition temperature, pumping (and heating) did not have much affect on freeing and shaping the sample because of the low vapour pressure of N_2. The large temperature range for cooling N_2 required very slow and painstaking progress. It was therefore decided to concentrate on CO because of the much smaller cooling range from the triple point to the phase transition temperature.

Three large single crystals of α-CO were grown out of hcp β-CO single crystals. Just before the phase transition occurred, the β phase underwent some dramatic changes. Tiny spaces and vacancies appeared and the crystal lost transparency and became translucent. After several hours the interface appeared as shown in Fig. 6. Although the interface visually separated the two phases, X-ray diffraction patterns generally indicated traces of the β-phase left in the new α-structure. The complete transition occurred when more cooling was done (0.1 to 0.3 K) and subsequent X-ray patterns indicated pure cubic structure.

By determining the orientation of each crystal relative to the laboratory frame of reference, it was possible to correlate the orientations of the two phases of CO. Any vector $\boldsymbol{X}$ defined in the body frame of reference can be transformed to the lab frame of reference through the relation $\boldsymbol{X}' = \mathbf{A}\boldsymbol{X}$ where $\boldsymbol{X}'$ is the transformed vector and **A** is the Euler angle rotation matrix as defined by Goldstein (33). The components of the c axis of the hcp phase were determined in the laboratory frame using the rotation matrix **A**. These components (of the transformed c axis) were transformed to the body frame of the fcc phase using the inverse of the rotation matrix. Since the c axis is normal to the basal planes in hcp crystals, it was possible to identify those fcc planes to which the hcp basal planes were transformed. The crystal axes for the hcp phase are defined in terms of the usual (body) Cartesian coordinates.

Crystal I: The orientation of the crystal axes of the β-phase crystal relative to the lab frame (for 0° rotation of the cell) was determined to be: (θ, ϕ, χ) = (110.4, 334.4, 104.6). The orientation of the crystal axes of the α-phase crystal (for 0° rotation of the cell) was determined to be: (θ, ϕ, χ) = (110.5, 130.8, 211.4). Using the above procedure, the hcp c axis was found to transform to the [0.64 0.33 −0.68] direction in the fcc crystal which is at an angle of 16° to the $[1\,1\,\bar{1}]$ and 19° to the $[1\,0\,\bar{1}]$ axes. This means that the hcp basal planes transformed to close to the $(1\,0\,\bar{1})$ and $(1\,1\,\bar{1})$ planes of the fcc phase. The transformation was not complete, in that, the Laue pattern of the α crystal showed signs of other crystallites in it. The α phase was melted and regrown again out of the β phase; however, no further improvement was observed for

Can. J. Chem. Downloaded from www.nrcresearchpress.com by 93.93.197.157 on 09/07/12
For personal use only.

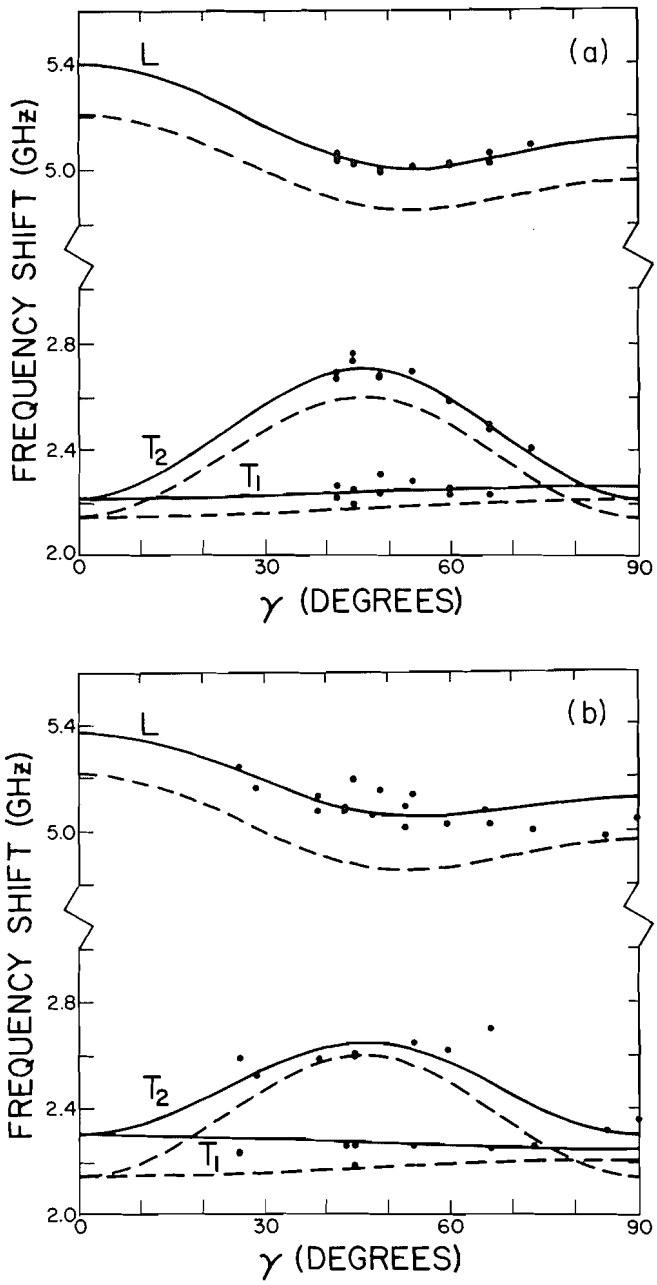

FIG. 4. Measured Brillouin frequency shifts (indicated by the solid dots) and calculated best-fit (solid) curves for β-CO vs. angle γ at (*a*) 63.5 and (*b*) 62.0 K. The dashed curves are calculated from the elastic constants at 67.7 K.

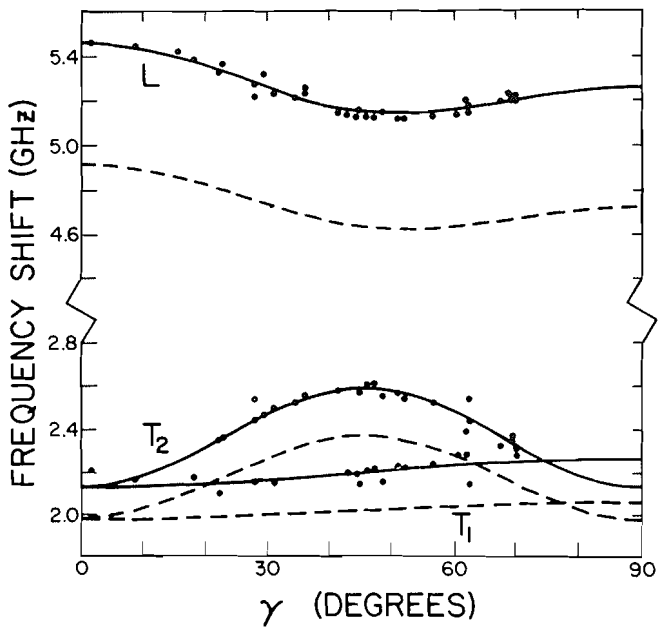

FIG. 5. Measured Brillouin frequency shifts (indicated by the solid dots) and calculated best-fit (solid) curves for β-N_2 vs. angle γ at 47.5 K. The dashed curves are calculated from the elastic constants at 63.0 K.

FIG. 6. Photograph showing sample in the cell. The horizontal line halfway up in the cell is the boundary that visually separates the single-crystal β-phase, at the top, and the single-crystal α-phase, at the bottom.

this particular sample although the orientation was similar to the original α sample.

Crystal II: The orientation of the crystal axes of the β phase relative to the lab frame was determined to be: (θ, ϕ, χ) = (96.0, 128.7, 195.5). The phase transition was carried out leading to a polycrystalline α sample which was melted and the original β phase recovered. This happened because in the cooling process, the crystal was cooled to the extent that half of it was transformed and the other half was still β. A second attempt was made to cool the crystal through the transition temperature. This time the diffraction patterns consisted of more or less well-defined Laue spots. The orientation of the crystal axes of the α phase was found to be: (θ, ϕ, χ) = (94.2, 286.2, 157.2). This phase was regrown twice through the β phase and each time the same orientation was obtained. The corresponding direction for the *c* axis in the fcc structure was found to be [0.29 0.30 −0.90] which is about 30° to both $[0\,1\,\bar{1}]$ and $[1\,1\,\bar{1}]$ and 25° to $[0\,0\,\bar{1}]$. The transition was again somewhat incomplete.

Crystal III: This phase transition was an excellent one, and the diffraction patterns consisted of well defined spots which showed no signs of crystal strain. The orientation of the crystal axes of the β phase relative to the lab frame was determined to be: (θ, ϕ, χ) = (57.7, 32.6, 339.5). The phase transition was carried out and a single crystal of α-CO was obtained. The orientation of the crystal axes of the α phase was (θ, ϕ, χ) = (23.2, 273.9, 339.0). The transformed *c* axis in the fcc structure was [0.48 0.81 0.33] which is within 19° of [1 1 1]. The next day, the crystal had spontaneously changed orientation to: (θ, ϕ, χ) = (34.7, 170.6, 356.4), and remained stable afterwards. This orientation indicated that the *c* axis had transformed to [−0.60 0.70 0.09] which is almost exactly the $[\bar{1}\,1\,0]$ axis of the fcc structure. The spots were well defined and the crystal

Can. J. Chem. Downloaded from www.nrcresearchpress.com by 93.93.197.157 on 09/07/12
For personal use only.

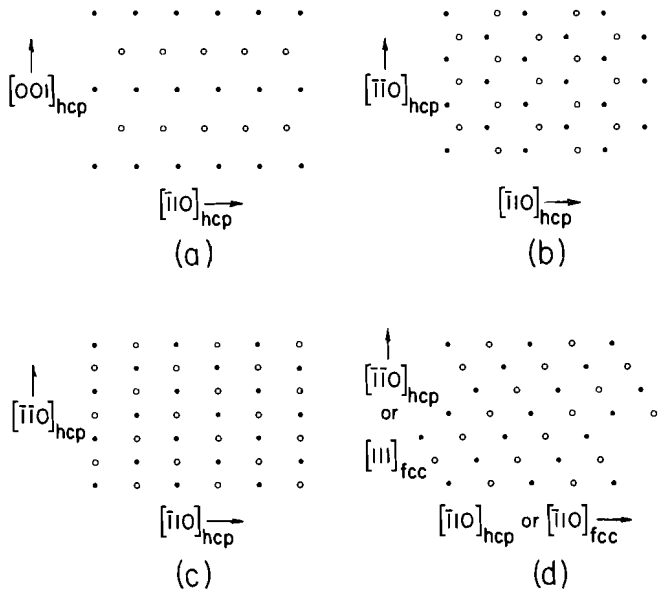

FIG. 7. Configuration of molecular sites as per suggested phase transition mechanism. (*a*) The hcp structure with *c* axis upwards. Solid circles represent one layer (A) and open circles the next layer (B), i.e. ABAB... stacking. (*b*) The hcp structure looking along *c* axis, i.e. into page. (*c*) Same structure with alternate planes moved as per text. (*d*) Basal planes after shearing movement as per text. Note the resulting ABCABC... stacking.

transition appeared to be complete. From crystal III which involves the best transition among the three it is clear that the final stable state for the hcp basal planes were planes of the form {1 1 0} and it did not seem to be happy close to {1 1 1}. This is consistent with crystals I and II where there appears to be competition between {1 1 1} and {1 1 0}. On this basis it is assumed, for purpose of the following discussion, that the basal planes of the hcp structure transform to the planes of the form {1 1 0} in the fcc structure.

There are several ways to imagine the mechanism of this transformation. One possibility is proposed here. Figure 7*a* shows the layering configuration of molecules or lattice sites for an hcp structure. The solid circles represent one layer A and open circles the next layer B, i.e., ABAB... stacking. Looking along the *c* axis the hexagonal nets are seen as in Fig. 7*b*, where the distance between two successive circles (open or solid) is $3a/\sqrt{6}$ in the [$\bar{1}$ 1 0] direction and *a* is the side of the cube in the fcc structure. It is assumed that all the A and B layers then move relative to one another (in the same way) in the [$\bar{1}$ 1 0] direction by $a/\sqrt{6}$ such that the arrangement becomes as shown in Fig. 7*c*. Finally, further relative shearing movement of only $a/2\sqrt{6}$ between successive layers is allowed such that, in seven planes (or layers), the first and last planes remain stationary and the second plane moves to the right by $a/2\sqrt{6}$, the third plane to the right by $a/\sqrt{6}$, the fourth plane to the right by $3a/2\sqrt{6}$, the fifth plane to the left by $a/\sqrt{6}$ (or to the right by $2a/\sqrt{6}$) and the sixth plane to the left by $a/2\sqrt{6}$ relative to the first or last planes in the [$\bar{1}$ 1 0] direction, the result is as shown in Fig. 7*d*. This has the same arrangement as that of the planes of the form {1 1 0} in the fcc structure with the cubic [1 1 1] axis upwards in the plane of the page (note the ABCABC... stacking). In the actual process, the suggested movement described between Fig. 7(*b*) and (*d*) would obviously occur as a single step while the molecules are becoming ordered.

Discussion

(a) Elastic constants

It has long been known that in molecular, especially plastic, crystals there should be a coupling between rotations and translations of molecules. This coupling follows clearly from the distance and orientation dependence of the intermolecular potential. A theoretical approach to RT coupling, for ionic crystals with molecular ions, was first worked out by Michel and Naudts (34). They pointed out the importance of RT coupling near structural phase transitions where ordering and change in lattice structure occur simultaneously. In particular, they obtained good agreement with the measured elastic constants of KCN where c_{44} softens markedly with temperature near the phase transition (35).

Recently, Fracassi and Klein (36) investigated RT coupling and the lattice dynamics of solid CO using several intermolecular potentials. It was concluded that RT coupling leads to an anomaly in the transverse acoustic phonon branch and consequent drastic anomalies in the dispersion curves of α-CO. Signorini *et al.* (23), in their anharmonic lattice dynamics calculations on solid N_2, specifically comment on the much smaller temperature range of existence of β-CO as compared to β-N_2. They point out that this likely denotes the effect of stronger RT coupling in CO, due to the asymmetry of the CO molecule, so that the rotational barrier is easily overcome only when the system is close to melting. This stronger coupling is also reflected in the (above mentioned) anomalous dispersion in α-CO, which is absent in α-N_2.

Also very recently, van der Avoird *et al.* (37) have emphasized the inadequacy of quasi-harmonic approaches to crystal dynamics even in the ordered phases and have developed a new and more general lattice dynamics scheme for handling large amplitude librational motions or hindered rotations, anharmonic translational vibrations, and RT coupling in molecular crystals. This scheme gives very accurate results for the ordered α and γ phases of solid N_2, while it also yields, for the first time, a quantum dynamical description of the molecular motions in the plastic β phase and an accurate α–β transition temperature (37). This theory also suggests that the orientational disorder in β-N_2 is caused by rapid 60° jumps around the *c* axis between localized librational states, and further predicts the correct experimental libron and translational phonon bands at 50 and 25 cm^{-1}, respectively (24, 38).

Experimental evidence for RT coupling, specifically related to the determination of elastic constants in these simple van der Waals systems, was discussed in ref. 26. Rand and Stoicheff (39) identified an anomalously "slow" T_1 mode in the disordered phase of CH_4 and attributed this to RT coupling. On comparison, this effect is not shown in the ordered phase of NH_3 (40). Calculations by Goldman and Klein (41) were found to be in disagreement with β-N_2 transverse-mode data by more than a factor of 2 and they suggested that the anomalously low measured transverse velocities indicated strong RT coupling or, at least, was probably caused by the role of orientational correlations. Elastic constants of single crystals of fcc and hcp argon alloys were determined by Brillouin spectroscopy (26). Slight mode softening was reflected in the dependence of c_{44} on solute concentration as phase instability increased. The Cauchy ratio c_{13}/c_{44} also consistently increased with increasing solute concentration and is relevant in recalling (2) the anomaly in this ratio between β-CO and β-N_2 (see Table 1). It was concluded that RT coupling almost certainly defines the role of diatomic impurities (solute) in stabilizing the hcp Ar structure and that the

Can. J. Chem. Downloaded from www.nrcresearchpress.com by 93.93.197.157 on 09/07/12
For personal use only.

Can. J. Chem. Downloaded from www.nrcresearchpress.com by 93.93.197.157 on 09/07/12
For personal use only.

ratio c_{13}/c_{44} (for hexagonal symmetry) is a sensitive measure of this effect.

From the above, it is clear that RT coupling is an important mechanism in van der Waals solids, especially for phase transitions, and that transverse acoustic modes are very sensitive to this effect (36). It was therefore expected that more clear-cut evidence for strong (and different) RT coupling would exhibit itself in elastic constant determinations in cooled crystals of the β phases of N_2 and CO, especially close to the α–β phase transitions and in the α phases.

The results in Table 1, as reflected in any of the elastic constants, show no clear evidence for mode softening in either β-CO or β-N_2, even within 0.5 K of the phase transition in the case of CO. There is no significant change in the ratio c_{13}/c_{44} on cooling CO crystals, although there appears to be an increase for N_2. All elastic constants tend to show an increase of about 1%/K, or slightly better, on cooling. It is unfortunate that it was not possible to obtain spectra for β-N_2 near the phase transition or for α-CO (of which three single crystals were grown) where mode softening effects would presumably be more evident (especially in the [1 1 1] direction (36)). It should, however, be emphasized that the transverse acoustic modes, i.e., characterized by c_{44}, are already very soft in both β phases. This is particularly evident on comparison with the rare gas solids (2, 26, 30) and the calculations (41) already noted above.

Comparison with other experimental data includes the inelastic neutron work of Kjems and Dolling (24). Three elastic constants, for β-N_2 at 37 K, could be deduced from slopes of their dispersion curves and are shown in Table 1. Agreement is reasonable with the present 47.5 K results when extrapolated at 37 K. Powell *et al.* (42) used this technique to determine three elastic constants c_{11}, c_{33}, and c_{44} for β-N_2, at 55 K and 400 MPa, and they appear to increase dramatically with pressure.

(b) Phase transformation mechanism

The α–β phase transformation in CO appears to be, as has been suggested in the literature, a martensitic transformation. There are several characteristics of these transformations (43) that were observed in the phase transition of CO. The transformation was time independent, i.e., the sample could be left for long times with the interface separating the two phases (as seen in Fig. 6) and only a temperature change would affect the height of the interface. The other aspect of this transformation was its reversibility. The interface between the phases could be lowered and made to vanish by increasing the temperature, the resulting hcp crystal having the same orientation as that of the parent hcp crystal as noted before. Most importantly, there seems to exist a definite relation between the orientations of the original structure and that of the new phase, namely, in the present work, the [0 0 1] and [$\bar{1}\,\bar{1}$ 0] axes of the hcp crystal appears to transform parallel to the [$\bar{1}$ 1 0] and [1 1 1] axes of the fcc crystal, respectively.

Kjems and Dolling (24) obtained a single crystal of α-N_2, surrounded by many small disoriented fragments, by slow cooling of a β-N_2 crystal and apparently were able to correlate the two phases, although not by X-ray analysis. The orientation of the crystal was related to that of the initial β phase crystal: [1 1 1] and [0 $\bar{1}$ 1] cube axes being parallel to the initial [0 0 1] and [1 1 0] hexagonal axes, and is not consistent with the present work. Metallurgists have studied several fcc–hcp phase transitions in metals and alloys. Work on aluminum alloys (44), CuGe alloys (45), cobalt (46), and cobalt alloys (47) all seem to indicate that the *c* axis of the hcp becomes the [1 1 1] direction in the fcc crystal. This may be attributed to the fact that the atomic interaction in metals is much stronger than in molecular crystals although there are also inconsistencies in the metallurgy work. For instance, Christian's study of cobalt (46) suggests that the fcc [1 $\bar{1}$ 0] direction transforms parallel to the hcp [1 1 0] direction, whereas Laird and Aaronson's work on aluminum (44) suggests that it transforms parallel to the hcp [2 $\bar{1}$ 0] direction.

Little other phase-transition work has been done on molecular crystals because of the difficulty in cooling large single crystals and maintaining good quality single crystals during and after phase transitions. The hcp–fcc transition in He has been studied by Frank (48) who concludes that the transition is martensitic. Schuch *et al.* (49) studied the hcp–fcc structure change in H_2 and D_2 using X-ray diffraction techniques. Although solidification occurred as a mass of crystallites, they found that there was always a noticeable preference for the *c* axis to be perpendicular to the cold cell wall. By measuring the intensity of X-ray reflection, they found that no intensity change took place when the hexagonal {0 0 2} reflection became the cubic {1 1 1} reflection. Neutron studies by Yarnell *et al.* (50) showed the hcp–fcc transition in H_2 and D_2 to be martensitic and suggested a substantial density of stacking faults of hexagonal planes evidenced by shifts and widths of the elastic neutron lines in both phases. Hardy *et al.* (51) studied Raman scattering in solid H_2 and D_2 and inferring from the intensity measurements suggested that the hcp–fcc transition takes place by shifting of the hexagonal planes such that the *c* axis becomes the cubic [1 1 1] axis. Silvera (52), however, mentioned that in a H_2 crystal there is a large potential barrier for such a shifting motion and although the energy gained per molecule by orientational ordering is of the order of 3–4 K, the barrier is at least of the order of melting temperature (15–20 K) and hence the thermodynamic probability for such a motion is extremely small. He further suggested that the transition takes place by motion of faults so that the barrier does not have to be crossed. It is interesting to note that Impey and Klein (53), making molecular dynamics computer simulation calculations on different phases of solid ammonia, determined that in the hcp–bcc (body centered cubic) phase transition, the hcp basal planes become bcc {1 1 0} planes and is the least energetic way for the transition.

There were competing factors that contributed to the incomplete phase transition in crystals I and II and to the lack of agreement with some of the above experimental evidence and the usual simple models. In addition, of course, to the orientation of the parent crystal at the top from which the daughter phase is initiated, the walls of the cell are boundary conditions imposing constraints on the transition. The possible presence of a tiny particle or sharp edges at the bottom of the cell could influence the growth of the daughter phase. Perhaps the most important factor is the possibility that the slight $P2_13$ distortion in CO (as noted earlier) is responsible for an inherently different α–β phase-transition mechanism in CO as opposed to N_2 (or some of the other molecular crystals mentioned above). Understanding of the fcc–hcp phase transition in these very simple molecular solids is still clearly not satisfactory.

Acknowledgements

The authors wish to express thanks to S. F. Ahmad for experimental work during the initial stages of this project and to

T. G. White for providing an almost continuous supply of liquid helium. Aside from the authors' desire to contribute to the honouring of J. A. Morrison, they wish also to express gratitude for his willingness to recently have acted as an external examiner for a thesis encompassing the above work.

1. H. KIEFTE and M. J. CLOUTER. J. Chem. Phys. **64**, 1816 (1976).
2. P. H. GAMMON, H. KIEFTE, and M. J. CLOUTER. J. Chem. Phys. **70**, 810 (1979).
3. N. G. PAGE and G. A. SAUNDERS. Nat. Phys. Sci. **237**, 47 (1972).
4. T. A. SCOTT. Phys. Rep. **27**, 89 (1976).
5. R. L. MILLS, B. OLINGER, and D. T. CROMER. J. Chem. Phys. **84**, 2837 (1986).
6. J. C. RAICH and R. L. MILLS. J. Chem. Phys. **55**, 1811 (1971).
7. A. ANDERSON, T. S. SUN, and M. C. A. DUNKERSLOOT. Can. J. Phys. **48**, 2265 (1970).
8. M. M. THIERY, D. FABRE, M. JEAN-LOUIS, and H. VU. J. Chem. Phys. **59**, 4559 (1973).
9. M. M. THIERY and V. CHANDRASEKHARAN. J. Chem. Phys. **67**, 3659 (1977).
10. S. BUCHSBAUM, R. L. MILLS, and D. SCHIFERL. J. Phys. Chem. **88**, 2522 (1984).
11. A. I. KATZ, D. SCHIFERL, and R. L. MILLS. J. Phys. Chem. **88**, 3176 (1984).
12. E. FUKUSHIMA, A. A. V. GIBSON, and T. A. SCOTT. J. Low Temp. Phys. **28**, 157 (1977).
13. W. E. STREIB, T. H. JORDAN, H. W. SMITH, and W. N. LIPSCOMB. J. Chem. Phys. **41**, 756 (1964).
14. A. F. SCHUCH and R. L. MILLS. J. Chem. Phys. **52**, 6000 (1970).
15. D. J. GANNON and J. A. MORRISON. Can. J. Phys. **51**, 1590 (1973).
16. B. C. KOHIN. J. Chem. Phys. **33**, 882 (1960).
17. C. S. BARRETT and L. MEYER. J. Chem. Phys. **43**, 3502 (1965).
18. L. H. BOLZ, M. E. BOYD, F. A. MAUER, and H. B. PEISER. Acta Crystallogr. **12**, 247 (1959).
19. J. A. VENABLES and C. A. ENGLISH. Acta Crystallogr. B, **30**, 929 (1974).
20. B. O. HALL and H. M. JAMES. Phys. Rev. B, **13**, 3590 (1976).
21. J. TIMMERMANS. Physico-chemical constants of pure organic compounds. Elsevier, New York. 1950.
22. V. V. NAUCHITEL' and I. B. GOLOVANOV. Sov. Phys. Cryst. **30**, 27 (1985).
23. G. F. GIGNORINI, P. F. FRACASSI, R. RIGHINI, and R. G. DELLA VALLE. Chem. Phys. **100**, 315 (1985).
24. J. K. KJEMS and G. DOLLING. Phys. Rev. B, **11**, 1639 (1975).
25. J. A. VENABLES. Phil. Magn. **21**, 147 (1970).
26. S. F. AHMAD, H. KIEFTE, M. J. CLOUTER, and M. D. WHITMORE. Phys. Rev. B, **26**, 4239 (1982).
27. S. F. AHMAD, H. KIEFTE, and M. J. CLOUTER. J. Chem. Phys. **75**, 5848 (1981).
28. B. D. CULLITY. X-ray diffraction. Addison-Wesley Publishing Co., MA. 1967.
29. G. B. BENEDEK and K. FRITSCH. Phys. Rev. **149**, 647 (1966).
30. B. P. STOICHEFF. Rare gas solids. Vol. II. *Edited by* M. L. Klein and J. A. Venables. Academic Press, London. 1976.
31. M. J. P. MUSGRAVE. Crystal acoustics. Holden Day, San Francisco. 1970.
32. R. A. MACLAREN, H. KIEFTE, D. LANDHEER, and B. P. STOICHEFF. Phys. Rev. B, **11**, 1705 (1975).
33. H. GOLDSTEIN. Classical mechanics. Addison-Wesley Publishing Co., MA. 1959.
34. K. H. MICHEL and J. NAUDTS. J. Chem. Phys. **67**, 547 (1977); **68**, 216 (1978).
35. S. HAUSSÜHL. Sol. State Commun. **13**, 147 (1973).
36. P. F. FRACASSI and M. L. KLEIN. Chem. Phys. Lett. **108**, 359 (1984).
37. A. P. J. JANSEN, W. J. BRIELS, and A. VAN DER AVOIRD. J. Chem. Phys. **81**, 3648 (1984); A. VAN DER AVOIRD, W. J. BRIELS, and A. P. J. JANSEN. J. Chem. Phys. **81**, 3658 (1984); W. J. BRIELS, A. P. J. JANSEN, and A. VAN DER AVOIRD. J. Chem. Phys. **81**, 4118 (1984).
38. F. D. MEDINA and W. B. DANIELS. J. Chem. Phys. **64**, 150 (1976).
39. S. C. RAND and B. P. STOICHEFF. Can. J. Phys. **60**, 287 (1982).
40. H. KIEFTE, S. W. BRECKON, R. PENNEY, and M. J. CLOUTER. J. Chem. Phys. **83**, 4738 (1985).
41. V. V. GOLDMAN and M. L. KLEIN. J. Chem. Phys. **64**, 5121 (1976).
42. B. M. POWELL, G. DOLLING, and H. F. NIEMAN. J. Chem. Phys. **79**, 982 (1983).
43. J. W. CHRISTIAN. Transformation in metals and alloys. Vol. I. Pergamon Press, Oxford. 1975.
44. C. LAIRD and H. I. AARONSON. Acta Meta. **15**, 73 (1967).
45. J. L. YARNELL, R. L. MILLS, and A. F. SCHUCH. Sov. J. Low Temp. Phys. **1**, 366 (1974).
46. J. W. CHRISTIAN. Proc. R. Soc. London A, **206**, 51 (1951).
47. H. SHOJI. Z. Kryst. **77**, 381 (1931).
48. J. P. FRANCK. Chem. Phys. Lett. **63**, 100 (1979); Phys. Rev. B, **22**, 4315 (1980).
49. A. F. SCHUCH, R. L. MILLS, and D. A. DEPATIE. Phys. Rev. **165**, 1032 (1968).
50. R. L. MILLS, J. L. YARNELL, and A. F. SCHUCH. Proc. Low Temp. Phys. Conf. 13, Boulder. Vol. II. Plenum Press, New York. 1973.
51. W. N. HARDY, I. F. SILVERA, and J. P. MCTAGUE. Phys. Rev. Lett. **26**, 127 (1971).
52. I. F. SILVERA. Rev. Mod. Phys. **52**, 393 (1980).
53. R. W. IMPEY and M. L. KLEIN. Chem. Phys. Lett. **104**, 579 (1984).

Can. J. Chem. Downloaded from www.nrcresearchpress.com by 93.93.197.157 on 09/07/12
For personal use only.

The thermodynamics of the divalent metal fluorides. I. Heat capacity of lead tetrafluorostannate, $PbSnF_4$, from 10.3 to 352 K

JANE E. CALLANAN
Centre for Chemical Engineering, National Bureau of Standards, Boulder, CO 80303, U.S.A.

RON D. WEIR[1]
Department of Chemistry and Chemical Engineering, Royal Military College of Canada, Kingston, Ont., Canada K7K 5L0

AND

EDGAR F. WESTRUM, JR.
Department of Chemistry, University of Michigan, Ann Arbor, MI 48109, U.S.A.

Received August 19, 1987

This paper is dedicated to Professor J. A. Morrison

JANE E. CALLANAN, RON D. WEIR, and EDGAR F. WESTRUM, JR. Can. J. Chem. **66**, 549 (1988).

We have measured the heat capacity of the fast ion conductor $PbSnF_4$ at $10.3 < T < 352$ K by adiabatic calorimetry. Our results show anomalous values in the $C_{p,m}$ in the region $300 < T < 352$ K. These are associated with the $\alpha-\beta$ crystallographic transition reported at 353 K. Because the upper temperature limit of our cryostat is around 354 K, it was impossible to follow the phase transition to completion. A more subtle anomaly in the $C_{p,m}$ was detected between 130 and 160 K. Standard molar thermodynamic functions are presented at selected temperatures from 5 to 350 K.

JANE E. CALLANAN, RON D. WEIR, et EDGAR F. WESTRUM, JR. Can. J. Chem. **66**, 549 (1988).

On a mesuré la chaleur spécifique du conducteur d'ions rapides $PbSnF_4$ par calorimétrie adiabatique sur le domaine de températures entre 10.3 K et 352 K. Les résultats obtenus montrent des anomalies pour les valeurs de $C_{p,m}$ dans la région entre 300 K et 352 K. Celles-ci sont associées à la transition cristallographique $\alpha-\beta$ rapportée à 353 K. Il n'a pas été possible de suivre complètement la transition de phase à cause du cryostat dont la température maximum n'était que de 354 K environ. On a cependant décelé une anomalie plus subtile de la valeur de $C_{p,m}$ entre 130 K et 160 K. Les fonctions standard de thermodynamique molaire sont présentées pour un choix de températures de 5 K à 350 K.

Introduction

The existence of the stable compound $PbSnF_4$ was first revealed by the work of Donaldson and Senior (1), who reported the phase diagram and structural studies of mixtures containing stannous fluoride, SnF_2, and divalent metal fluorides, MF_2. $PbSnF_4$ has been found to possess a high ionic conductivity (2), and is among the best-known anionic conductors. Because of the use of fluoride electrolytes as thin films in galvanic cells, specific electrodes for fluoride ions, or gas detectors (3–6), considerable attention has been directed at experimental work on fluorides with the fluorite-type structure, including the family $MSnF_4$ where M = Pb, Ba, Sr.

Several allotropic forms of $PbSnF_4$ have been shown to exist at temperatures above 273 K by DTA and X-ray diffraction studies (1, 2, 7–10). The normal α-phase at room temperature, which depends upon the method of preparation, has a monoclinic, sometimes called a pseudo-orthorhombic monoclinic, structure with $a = 4.204$, $b = 4.205$, $c = 11.414$ Å, $\gamma = 91°34'$, a space group of $P_{2/n}$ and stability to about 353 K. The β-phase, stable between about 353 and 623 K, possesses a tetragonal structure with a space group of $P_{4/nmm}$ (7–9). When $PbSnF_4$ is prepared via the dry method, the α-phase appears only after annealing (8). The γ-phase, which has a fluorite structure with a space group of F_{m3m}, exists above 623 K to the melting point around 661 K (2, 7–9). Neither Pannetier *et al.* (7) from DTA and DSC studies nor Birchall *et al.* (10) from neutron diffraction work were able to confirm the presence of the monoclinic α-phase. The method of their sample preparation was not described. Whether the same sample was used in each study is not clear.

Within the α-phase of $PbSnF_4$, the cationic framework is made up of layers perpendicular to *c*-axis with a sequence PbPbSnSnPbPb... The F^- sub-lattice is highly disordered and contains a high concentration of F^- vacancies as well as F^- interstitial ions (11). The high ionic conductivity of this crystal is thought to be due to the high defect mobilities in the fluorite structure.

Heat capacity data have not been reported for $PbSnF_4$ and it seemed worthwhile to undertake these measurements by adiabatic calorimetry from very low temperature up to the α-to-β phase transition. All the DTA and structural work reported have been at temperatures above 273 K, although nmr measurements have been done down to 200 K (12), and 125 K (13), and a Mössbauer spectrum has been recorded at 77 K (10).

Experimental

The sample was prepared by a solid state reaction of a 1:1 mixture of PbF_2 and SnF_2. These materials were ground to a fine powder, pressed into pellets within a stainless steel die, and loaded into a copper tube evacuated to 0.133×10^{-5} kPa. Sintering was performed by heating the copper tube in an evacuated silica outer tube for 12 h at 523 K. After sintering, the copper vessel showed no visible signs of reaction with the pellets. An X-ray powder pattern at room temperature confirmed the structure of the sample as α-$PbSnF_4$ in agreement with literature data (8). Once annealed at 523 K for 1 h, the sample was cooled to room temperature where it remained until loading into the calorimeter. It was then cooled to 118 K for heat capacity measurements.

The calorimetric results were determined using the Mark X cryostat, which is an upgraded version of the Mark II cryostat already described (14). A guard shield was incorporated around the adiabatic shield. A capsule-type platinum resistance thermometer (laboratory designation A-5) was used for temperature measurements. The thermometer was calibrated at the U.S. National Bureau of Standards (N.B.S.) against the IPTS-1948 (as revised in 1960) (15) for temperatures above 90 K, against the N.B.S. provisional scale from 10 to 90 K, and by the

[1]To whom correspondence should be addressed.

Can. J. Chem. Downloaded from www.nrcresearchpress.com by 93.93.197.157 on 09/07/12
For personal use only.

Can. J. Chem. Downloaded from www.nrcresearchpress.com by 93.93.197.157 on 09/07/12
For personal use only.

TABLE 1. Experimental molar heat capacity of $PbSnF_4$ (molar mass = 401.8836 g mol^{-1}, R = 8.3145 J K^{-1} mol^{-1})

T/K	$C_{p,m}/R$	T/K	$C_{p,m}/R$
10.33	0.4516	127.08	13.25
10.98	0.4825	133.66	13.55
11.89	0.5760	140.22	13.95
12.96	0.7088	146.81	14.39
14.21	0.8807	153.44	14.51
15.48	1.059	160.07	14.85
16.77	1.252	166.70	15.19
18.09	1.443	173.28	15.33
19.63	1.684	179.95	15.57
21.39	1.944	186.52	15.73
23.16	2.224	193.17	16.00
25.16	2.537	199.85	16.17
27.38	2.881	206.52	16.44
29.47	3.187	213.20	16.63
31.79	3.544	219.89	16.86
34.47	3.950	226.59	16.99
37.44	4.374	233.29	17.18
40.64	4.829	239.98	17.39
44.07	5.303	246.68	17.61
47.74	5.815	253.40	17.50
51.67	6.332	260.10	18.04
55.86	6.865	266.77	18.31
60.32	7.430	273.47	18.58
65.04	8.020	280.16	18.85
69.81	8.536	286.87	18.98
74.63	9.074	293.60	18.92
79.72	9.606	300.30	19.36
85.08	10.18	306.94	19.97
90.34	10.62	313.52	19.97
95.63	11.11	320.19	20.10
101.10	11.51	326.90	20.16
106.59	11.92	333.63	20.18
112.10	12.24	340.36	20.18
117.62	12.64	345.43	19.86
121.53	12.84	348.82	19.28
123.16	12.93	352.25	19.06

technique of McCracken and Chang (16) below 10 K. These calibrations are judged to reproduce thermodynamic temperatures to within 0.03 K between 10 and 90 K and within 0.04 above 90 K (17). Measurements of mass, current, voltage, and time are based upon calibrations done at N.B.S. The heat capacities from about 10 to 352 K were acquired with the assistance of a computer (18, 19), which was programmed for a series of determinations. During the drift periods, both the calorimeter temperature and the first and second derivatives of temperature with respect to time were recorded to establish the equilibrium temperature of the calorimeter before and after the energy input. While the calorimeter heater was on, the heater current and voltage as well as the duration of the heating interval were determined. Also recorded was the apparent heat capacity of the system which included the calorimeter, heater, thermometer, and sample.

A gold-plated copper calorimeter (laboratory designation W-99) without internal vanes, but with a central re-entrant well for the heater and thermometer, was loaded with $PbSnF_4$. After loading, the calorimeter was evacuated and then helium gas was added to the vessel to a pressure of 2.1 kPa at 297 K to facilitate thermal equilibrium. The vessel was then sealed by means of an annealed gold gasket pressed tightly on the 4 mm diameter stainless steel knife edge of the calorimeter top using a screw closure. Buoyancy corrections were calculated on the basis of the crystallographic density of 6.614 g cm^{-3} from the X-ray diffraction studies on the salt (8). The mass of $PbSnF_4$ amounted to 19.14767 g, *i.e.*, 0.04764482 mol based on its molar mass of 401.8836 g mol^{-1}.

TABLE 2. Standard molar thermodynamic functions for $PbSnF_4$ [molar mass: 401.8836 g mol^{-1}; p^0 = 101.325 kPa; R = 8.3145 J K^{-1} mol^{-1}; $\Phi_m^0(T, 0)^{def} = -\Delta_0^T H_m^0(T)/T + \Delta_0^T S_m^0(T)$; $\Delta_0^T X(T) = \{X(T) - X(0)\}$]

T/K	$C_{p,m}/R$	$\Delta_0^T S_m^0(T)/R$	$\Delta_0^T H_m^0(T)/RK$	Φ_m^0/R
5	(0.097)	(0.053)	(0.195)	(0.0142)
10	0.379	0.192	1.29	0.0695
15	0.996	0.455	4.62	0.1466
20	1.735	0.843	11.35	0.2749
25	2.508	1.314	21.95	0.4355
30	3.256	1.837	36.14	0.6329
35	4.013	2.396	54.30	0.8450
40	4.744	2.980	76.19	1.076
45	5.442	3.580	101.7	1.321
50	6.111	4.188	130.5	1.577
55	6.746	4.800	162.7	1.842
60	7.388	5.414	198.0	2.113
65	7.994	6.027	236.2	2.393
70	8.559	6.638	277.6	2.673
75	9.105	7.247	321.7	2.957
80	9.639	7.852	368.6	3.244
85	10.16	8.452	418.1	3.292
90	10.61	9.045	470.0	3.823
95	11.06	9.632	524.2	4.114
100	11.55	10.21	580.6	4.404
105	11.84	10.78	639.0	4.692
110	12.13	11.34	698.9	4.982
120	12.77	12.42	823.4	5.557
130	13.38	13.47	954.3	6.054
140	13.94	14.48	1090.8	6.685
150	14.44	15.46	1232.8	7.236
160	14.88	16.40	1379.4	7.780
170	15.27	17.32	1530.2	8.314
180	15.60	18.20	1684.6	8.839
190	15.89	19.05	1842.0	9.354
200	16.16	19.87	2002.3	9.859
210	16.54	20.67	2165.8	10.35
220	16.86	21.44	2332.8	10.84
230	17.13	22.20	2502.8	11.32
240	17.40	22.94	2675.4	18.79
250	17.70	23.65	2850.9	12.25
260	18.05	24.35	3029.6	12.70
270	18.45	25.04	3212.2	13.15
280	18.85	25.72	3398.7	13.58
290	18.96	26.38	3588.0	14.01
300	19.30	27.03	3778.5	14.44
310	19.98	27.67	3975.9	14.85
320	20.12	28.31	4176.5	15.26
330	20.21	28.93	4378.1	15.67
340	20.10	29.54	4580.0	16.06
350	19.16	30.11	4777.6	16.46
298.15	19.04±0.03	26.91±0.04	3742.9±5.6	14.36±0.02

Results and discussion

The experimental molar heat capacities, $C_{p,m}/R$, of our $PbSnF_4$ sample are presented in Table 1, where the results are given in order of increasing temperature. The measurements were made in two series. The first series extended from 118.7 to 353.9 K without passing completely through the $\alpha-\beta$ transition, and the second extended from 10 to 126 K, thereby overlapping

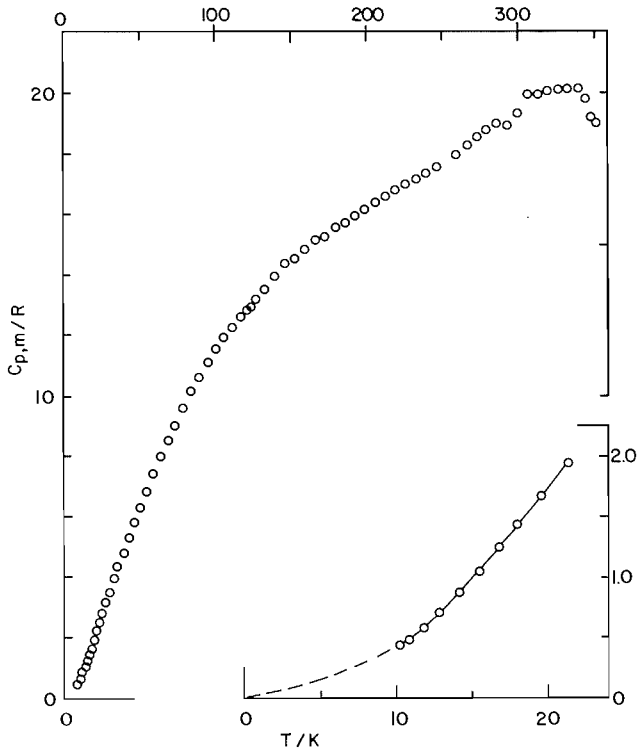

FIG. 1. Molar heat capacity $C_{p,m}/R$ for $PbSnF_4$.

the first series. The probable errors in heat capacity drop from about 1% at 10 K to less than 0.15% at temperatures above 30 K.

Shown in Fig. 1 is the $C_{p,m}/R$ curve for $PbSnF_4$ from 10 to 352 K. Two anomalies occur in the heat capacity. The more obvious region lies above 300 K where the transformation from the monoclinic α-phase to the tetragonal β-phase is in progress. Because the upper temperature limit of our cryostat is around 354 K, it was impossible to follow the phase transition to completion. Neither its enthalpy change nor actual temperature of occurrence could be obtained. The first signs of the transition were detected by us at 300 K. In their DSC and X-ray study, Claudy *et al.* (9) noted the first signs at 320 K for thermal effects and at 340 K for more rapid changes in lattice parameters. Their β-phase was present at 358 K.

The less obvious anomaly is shown in Fig. 2. A smooth curve drawn by using all our experimental points below 280 K shows those between 130 and 160 K to lie consistently above the curve. The deviation plot of the experimental heat capacity minus the smoothed heat capacity resulted in a random difference of less than 0.2% $C_{p,m}$ for $120 > T > 170$. However, for temperatures between 130 and 160 K, the differences are outside the normal deviations. The plot in Fig. 2 shows these deviations approaching 1.2% $C_{p,m}$ in the vicinity of 145 K. The fit of $C_{p,m}$ points from both series of measurements is excellent to the point of being indistinguishable. A critical reevaluation of our experimental conditions and calculations confirms that the tiny anomaly in the heat capacities is real. This rise in experimental $C_{p,m}$ correlates nicely with the nmr work by Chadwick *et al.* (13), whose results show a gentle drop in the ^{19}F spin–lattice relaxation time T_1 for the region $140 < T < 170$ K. Their T_1 then falls rapidly as temperature rises until the α–β transition is reached around 357 K.

Birchall *et al.* (10) found by examining the Mössbauer parameters that the quadrupole splitting increased at 77 K when compared with the values at 298 K. Because the line asymmetry also decreased, they suggest that structural rearrangement may have taken place, which could be consistent with a low temperature phase transformation. The specific temperature for the onset of these effects cannot be determined from their paper, since no parameters are presented between 77 and 298 K. From our heat capacity work, a phase transition can be ruled out for this temperature range, but the anomaly occurring between 130 and 160 K suggests that some rearrangement may be taking place.

The standard molar thermodynamic functions for $PbSnF_4$ are presented at selected temperatures in Table 2. The heat capacities below 10 K were obtained by fitting our experimental values below 20 K to the limiting form of the Debye equation, using a plot of $C_{p,m}/T$ against T^2 and extrapolating to 0 K. A plot of $C_{p,m}/T^3$ against T^2 was not used because our results do not extend to temperatures low enough to pass below the maximum value of $C_{p,m}/T^3$. It is the linear part of the curve below the maximum $C_{p,m}/T^3$ that is required for the extrapolation to 0 K.

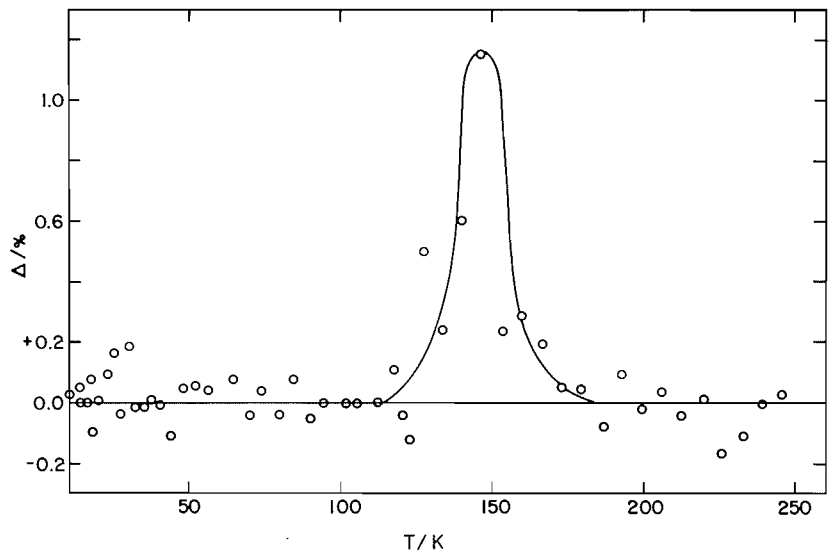

FIG. 2. A comparison of heat capacity results for $PbSnF_4$. $\Delta\% = 100\,[C_{p,m}(\text{exp}) - C_{p,m}(\text{smooth})]/C_{p,m}(\text{exp})$

Can. J. Chem. Downloaded from www.nrcresearchpress.com by 93.93.197.157 on 09/07/12
For personal use only.

Acknowledgements

We should like to thank Dr. A. V. Chadwick for preparing the sample. One of us (R.D.W.) acknowledges the financial support provided by the Department of National Defence of Canada.

1. J. D. DONALDSON and B. J. SENIOR. J. Chem. Soc. A, 1821 (1967).
2. J. M. RÉAU, C. LUCAT, J. PORTIER, P. HAGENMULLER, L. COT, and S. VILMINOT. Mat. Res. Bull. **13**, 877 (1978).
3. J. M. RÉAU and J. PORTIER. Solid electrolytes. *Edited by* P. Hagenmuller and W. Van Gool. Academic Press, New York. 1978. Chap. 19.
4. M. S. FRANT and J. W. ROSS. Science, **154**, 1553 (1966).
5. B. C. LAROY, A. C. LILLY, and C. O. TILLER. J. Electrochem. Soc. **120**, 12 (1973).
6. J. H. KENNEDY and J. C. HUNTER. J. Electrochem. Soc. **123**, 10 (1976).
7. J. PANNETIER, G. DÉNÈS, and J. LUCAT. Mat. Res. Bull. **14**, 627 (1979)
8. G. PEREZ, S. VILMINOT, W. GRANIER, L. COT, C. LUCAT, J. M. RÉAU, J. PORTIER, and P. HAGENMULLER. Mat. Res. Bull. **15**, 587 (1980).
9. P. CLAUDY, J. M. LETOFFE, G. PEREZ, S. VILMINOT, W. GRANIER, and L. COT. J. Fluorine Chem. **17**, 145 (1981).
10. T. BIRCHALL, G. DÉNÈS, K. REUBENBAUER, and J. PANNETIER. Hyperfine Interactions, **29**, 1331 (1986).
11. S. VILMINOT, G. PEREZ, W. GRANIER, and L. COT. Sol. State Ionics, **2**, 87 (1981).
12. G. VILLENEUVE, P. ECHEGUT, C. LUCAT, J. M. RÉAU, and P. HAGENMULLER. Phys. Stat. Sol. B**97**, 295 (1980).
13. A. V. CHADWICK, E. S. HAMMAN, D. VAN DER PUTTEN, and J. H. STRANGE. Proc. 5th Europhys. Soc. Topical Conf. on Lattice Defects in Ionic Crystals, September 1986, Madrid.
14. E. F. WESTRUM, JR., G. T. FURUKAWA, and J. P. MCCULLOUGH. Experimental thermodynamics. Vol. I. *Edited by* J. P. McCullough and D. W. Scott. Butterworths, London. 1968. p. 133.
15. H. F. STIMSON. J. Res. Natl. Bur. Stand. **65**A, 139 (1961)
16. F. L. MCCRACKEN and S. S. CHANG. Rev. Sci. Instrum. **46**, 550 (1975).
17. R. D. CHIRICO and E. F. WESTRUM, JR. J. Chem. Thermodyn. **12**, 311 (1980)
18. E. F. WESTRUM, JR. Proceedings NATO Advanced Study Institute on Thermochemistry at Viana do Castello, Portugal. *Edited by* M. A. V. Ribeiro da Silva. Reidel, New York. 1984. p. 745.
19. J. T. S. ANDREWS, P. A. NORTON, and E. F. WESTRUM, JR. J. Chem. Thermodyn. **10**, 949 (1978).

Can. J. Chem. Downloaded from www.nrcresearchpress.com by 93.93.197.157 on 09/07/12
For personal use only.

On the free energy of nematic wetting layers

DONALD E. SULLIVAN[1]

Department of Physics and Guelph–Waterloo Program for Graduate Work in Physics, University of Guelph, Guelph, Ont., Canada N1G 2W1

AND

REINHARD LIPOWSKY

Institut für Festkörperforschung KFA Jülich, 5170 Jülich, West Germany

Received August 25, 1987

This paper is dedicated to Professor J. A. Morrison

DONALD E. SULLIVAN, and REINHARD LIPOWSKY. Can. J. Chem. **66**, 553 (1988).

The contributions to the free energy of a nematic wetting layer as a function of its thickness l are analyzed. The longest-range contribution is due to distortion of the nematic director across the film, resulting from different preferred molecular orientations at the two interfaces bounding the film. Van der Waals forces as well as the decaying tails of the interfacial order-parameter profiles yield contributions to the free energy of successively shorter range. These effects lead to crossovers between different scaling régimes for variation of the mean wetting-layer thickness with temperature. Experimental implications of the results are described.

DONALD E. SULLIVAN, et REINHARD LIPOWSKY. Can. J. Chem. **66**, 553 (1988).

On a étudié l'influence de l'épaisseur (l) de couches nématiques mouillantes sur l'énergie libre. La contribution qui se fait sentir à la plus grande distance est dûe à une distorsion du directeur nématique à travers le film; cette distorsion résulte elle-même d'orientations moléculaires préférentielles différentes aux deux interfaces qui lient le film. Utilisant les forces de van der Waals ainsi que les profils de l'ordre interfacial/paramètres, on a pu déduire les contributions à l'énergie libre pour des distances de plus en plus courtes. Ces effets conduisent à des croisements entre divers régimes d'échelles pou la variation de l'épaisseur moyenne de la couche mouillante avec la température. On décrit les implications expérimentales de ces résultats.

[Traduit par la revue]

Consider a liquid crystalline material at a temperature T slightly above the transition temperature T_{NI} for the onset of nematic (N) ordering. While the bulk of the material then exists as an isotropic (I) liquid phase with no long-range orientational order, some degree of local nematic order may be spontaneously induced at the interface with another phase α such as a solid substrate or the vapour in coexistence with the liquid. If, on lowering the temperature, the mean thickness $\bar{l}$ of that nematic layer diverges over microscopic length scales as $T \rightarrow T_{NI}$, then we say that the nematic phase *completely wets* the α–I interface. Experimental evidence of this effect has been seen for a number of nematic substances, at both solid–liquid (1–3) and liquid–vapour (3–5) interfaces.[2] Entirely analogous wetting phenomena involving three distinct thermodynamic phases have recently come under extensive study for a variety of physical systems (7).

In this note we draw attention to some novel critical properties characterizing the approach to complete wetting in the case of a nematic layer. In particular, we focus on the asymptotic scaling laws describing the divergence of the mean wetting-layer thickness $\bar{l}$ in the limit that $t \equiv (T - T_{NI})/T_{NI}$ goes to zero. Our approach is similar to ones used successfully to describe wetting in other systems (7–10), based on analysis of the free energy $\sigma(l)$ per unit area of the layer as a function of its thickness l, when the latter is viewed as a thermodynamic order parameter. This approach is meaningful if l is large compared with the characteristic widths $\xi_{\alpha N}$ and ξ_{NI} of the two interfaces bounding the film. We shall discuss later the consequences of a large interfacial width ξ_{NI}, associated with the coherence length for fluctuations in the bulk liquid crystal. In mean-field theory, which neglects *interface* fluctuations, the equilibrium thickness $\bar{l}$ follows from $[\partial\sigma(l)/\partial l]_{l=\bar{l}} = 0$.

The free energy $\sigma(l)$ has the form (7–10)

$$[1] \quad \sigma(l) = Hl + \sigma_{\alpha N} + \sigma_{NI} + V(l)$$

where $\sigma_{\alpha N}$ and σ_{NI} are the equilibrium surface tensions of the α–N and N–I interfaces, respectively, in the limit of infinite separation l and at $T = T_{NI}$. The term Hl describes the increase in free energy due to the presence of a metastable nematic layer when $T > T_{NI}$, where H is the difference in (grand canonical) free energies per unit volume between the bulk nematic and either one of the coexisting α or l phases. For small t, we have

$$[2] \quad H \approx \Lambda t, \; \Lambda \equiv T_{NI}(S_I - S_N)$$

where S_I and S_N are the bulk entropies per unit volume at $T = T_{NI}$. The remaining term $V(l)$ in [1] represents all other contributions to the film free energy when its thickness l is finite rather than infinite. Here we shall *assume* that $V(l)$ has its absolute minimum at infinite l, consistent with the occurrence of complete wetting at N–I coexistence. Whether this indeed occurs or not ultimately depends on the short-range behaviour of $V(l)$, which in turn is related to the nature of microscopic forces in the system (7–10). In contrast, *if* complete wetting does occur, then it is the long-range behaviour of $V(l)$ which determines the critical properties that we shall examine here.

The leading-order contribution to $V(l)$ at large thickness l is due to distortion of the nematic director across the film. This effect arises whenever the separate α–N and N–I interfaces favour different orientations of the molecules, which we argue should be the rule rather than the exception. For example, the director at isolated N–I interfaces is usually observed to be obliquely aligned, with tilt angle Θ_{NI} (relative to the co-ordinate direction z perpendicular to the interface) falling in the range

[1]To whom correspondence should be addressed.

[2]In a recent study (6), near-complete-wetting growth of a *smectic-A* film at a liquid–vapour interface was observed.

Can. J. Chem. Downloaded from www.nrcresearchpress.com by 176.9.209.113 on 09/07/12
For personal use only.

Can. J. Chem. Downloaded from www.nrcresearchpress.com by 176.9.209.113 on 09/07/12
For personal use only.

0.8–1.3 radians (11, 12). This has been found for several different nematic substances, and thus appears to be a universal phenomenon. On the other hand, the alignment at isolated vapour–nematic interfaces is most often found to be homeotropic (4–6, 13), with $\Theta_{VN} = 0$, although one exception is currently provided by the liquid crystal PAA, for which $\Theta_{VN} = \pi/2$ (14). The alignment at a solid substrate is well-known to be highly variable, depending on the specific nature of both the liquid crystal and the substrate surface.

When $\Theta_{\alpha N}$ and Θ_{NI} differ, the director is distorted across the nematic layer if the latter is sufficiently thick. Using standard arguments of the Frank elastic theory (15, 16), in the approximation where one keeps only one elastic constant K,[3] the distortion is described by the tilt-angle variation

$$[3] \quad \Theta(z) = \Theta_{\alpha N} + (\Delta\Theta)z/l, \; \Delta\Theta \equiv \Theta_{NI} - \Theta_{\alpha N},$$

where the α–N and N–I interfaces are located at $z = 0$ and $z = l$, respectively. This yields a contribution (16)

$$[4] \quad V_d(l) \approx \tfrac{1}{2}K(\Delta\Theta)^2/l$$

to the free energy $V(l)$. The power-law dependence $V_d(l) \sim l^{-1}$ is the same,[4] and arises by the same mechanism, as that characterizing distortions of the magnetization vector through domain walls in a Heisenberg ferromagnet. Strain effects in a *solid* wetting layer also produce an l^{-1} contribution to the film free energy, which leads to a thinning of the layer (19). In contrast, $V_d(l)$ as discussed here is positive and thus gives a *repulsive* interaction between the α–N and N–I interfaces, which stabilizes wetting-layer growth at large l.

The mean-field prescription $[\partial\sigma/\partial l]_{l=\bar{l}} = 0$ is valid here, as it is more generally whenever $V(l)$ is dominated by power-law terms in three dimensions (9, 20). The asymptotic behaviour of $\bar{l}$ then follows from [1], [2], and [4] as

$$[5] \quad \bar{l} \approx Bt^{-\psi},$$

where $\psi = 1/2$ and $B = |\Delta\Theta|\sqrt{K/2\Lambda}$. Although the relevance of the distortion energy [4] to nematic wetting was first recognized some time ago (16), we believe that [5] is a new theoretical result.[5] This is the exact leading-order result describing spontaneous growth of a nematic wetting layer as $t \to 0$ in the presence of director distortion. A number of additional asymptotic relations follow from this analysis. For instance, the deviation of the equilibrium α–I surface tension from its value at N–I coexistence, $\Delta\sigma \equiv \sigma(\bar{l}) - (\sigma_{\alpha N} + \sigma_{NI})$, is given by $\Delta\sigma \approx Ct^{2-\alpha_s}$ where $\alpha_s = 3/2$ and $C = (2K\Lambda)^{1/2}|\Delta\Theta|$. This leads to a critical divergence $\sim t^{-\alpha_s}$ in the interfacial specific heat. The parallel correlation length $\xi_{||}$ for interface fluctuations, which is in principle measurable by scattering expeiments with momentum transfer parallel to the interface, follows from standard Ornstein–Zernike arguments (7, 9) to be given by $\xi_{||} = [\sigma_{NI}/V_d''(\bar{l})]^{1/2}$, where the primes denote derivatives with respect to l.[6] Thus one finds $\xi_{||} \approx Dt^{-\nu_{||}}$, with $\nu_{||} = 3/4$ and $D = (|\Delta\Theta|\sigma_{NI})^{1/2}K^{1/4}/(2\Lambda)^{3/4}$.

There is a possible limitation on the above results due to the fact that the tilt angles at the separate α–N and N–I interfaces are not fixed but have finite anchoring energies, $A_{\alpha N}$ and A_{NI}. This leads to l-dependent deviations $\delta\Theta_{\alpha N}(l)$ and $\delta\Theta_{NI}(l)$ of the tilt angles from their equilibrium values at infinite l, and corresponding deviations $\delta\sigma_{\alpha N}(l) \approx A_{\alpha N}(\delta\Theta_{\alpha N})^2$, $\delta\sigma_{NI}(l) \approx A_{NI}(\delta\Theta_{NI})^2$ of the separate surface tensions. Extension of the elastic–theoretic arguments (16) which led to [4] now gives

$$[6] \quad V_d(l) \approx \frac{K}{2l}(\Delta\Theta)^2 \Big/ \left[1 + \frac{K}{2l}\left(\frac{1}{A_{\alpha N}} + \frac{1}{A_{NI}}\right)\right]$$
$$= \frac{K}{2l}(\Delta\Theta)^2 - \left(\frac{K}{2l}\right)^2\left(\frac{1}{A_{\alpha N}} + \frac{1}{A_{NI}}\right)(\Delta\Theta)^2 + O(l^{-3})$$

The linearization in the second line of [6] is valid, hence the asymptotic formula [4] is realizable only for distances $l \gtrsim l_0 \equiv K/A$, where A is the weaker of the two anchoring energies. This is consistent with arguments given in the context of macroscopic nematic films, namely, that director distortion occurs only when l exceeds the "extrapolation length" l_0 (15, 16). Using a typical value for K of 10^{-7} erg/cm and current estimates (11) that $10^{-4} \leq A_{NI} \leq 10^{-2}$ erg/cm^2, we have $10^{-5} \leq l_0 \leq 10^{-3}$ cm. This rather substantial magnitude for l_0 suggests that it would be difficult to observe the power law [5] within the temperature range of current experiments. However, this does not rule out the fact that [5] is what *should* be observed for sufficiently small t. Furthermore, we conjecture that distortion-induced corrections of $O(l^{-2})$ to the leading-order result in [4] may result from other mechanisms besides that based on the anchoring energies of the separate α – N and N–I interfaces. Model calculations, for example, based on a Landau – de Gennes theory allowing for director tilt (22), are needed to elucidate this point.

In the absence of director distortion, the longest-ranged contribution to $V(l)$ is expected to result from van der Waals forces between the molecules. For l on the order of 10–100 nm, this has the form (7–10)

$$[7] \quad V_{vdw}(l) \approx W/l^2$$

where the Hamaker constant W depends on the polarizability densities of the different phases present. Due to anisotropy of the polarizability of liquid crystalline molecules, W has a more complex character than in recent treatments of wetting by ordinary liquids (7–10), but a detailed analysis of this is beyond the scope of the present paper. Here we shall simply make the following observations. For complete nematic wetting to occur, it is necessary (though not sufficient) that $W > 0$. In that case, we obtain the well-known result (8) that the mean thickness $\bar{l}$ obeys [5] with exponent $\psi = 1/3$. This is universally observed at the approach to complete wetting by ordinary liquids (7). In the absence of director distortion, a negative value of W would preempt complete wetting by giving an absolute minimum in $V(l)$ at some finite value of l. It is not clear, however, that this outcome is maintained if the expected crossover to director distortion develops at very large l. Note that the sign of W bears no direct relation to the nature of shorter range intermolecular forces, e.g., due to steric interactions, which can also be important in determining wetting behaviour (7–10).

[3]Generalizations of [3] and [4] to account for anisotropy of the elastic constants are derived in ref. 17. These exhibit a slightly more complex angle-dependence than the present equations.

[4]A repulsion $\sim 1/l$ between two interfaces will also be present for other physical systems, provided the order parameter in the layer breaks a continuous symmetry and the two interfaces bounding the layer prefer different states of the order parameter. This follows quite generally from finite-size scaling (18) when applied to such layers.

[5]The scaling relation [5] with exponent $\psi = 1/2$ also applies to complete wetting in a quite different context, namely for systems containing quenched random impurities (21).

[6]This expression for $\xi_{||}$ holds when only the N–I interface bounding the layer is rough, as in the case where α is a solid. If the α–N interface is also rough, then σ_{NI} is replaced by $\sigma_{NI}\sigma_{\alpha N}/(\sigma_{NI} + \sigma_{\alpha N})$, see ref. 9*b*.

Can. J. Chem. Downloaded from www.nrcresearchpress.com by 176.9.209.113 on 09/07/12
For personal use only.

As remarked earlier, it is important to account for the large magnitude (e.g., up to several hundred Å (11)) of the bulk coherence length ξ_{NI}, which in turn results from the *weakly* first-order nature of the nematic–isotropic transition. The effects of this can be analyzed in the framework of Landau – de Gennes type theories (15, 22, 23) for the spatial variation of orientational order parameters. As also found in Landau theories of wetting by ordinary liquids (7–10, 24), the exponentially decaying tails of the order-parameter profiles yield a contribution to $V(l)$ of the form

$$[8] \quad V_{SR}(l) \approx a\sigma_{NI} \exp -l/\xi_{NI}$$

where $a \sim O(1)$ is a numerical coefficient. Even in the presence of long-range (i.e., van der Waals) forces, the order-parameter profiles will still decay exponentially on intermediate length scales as long as ξ_{NI} is sufficiently large (25). In such a situation, a contribution of the form [8] should be added to the film free energy (26). Neglecting other contributions to $V(l)$, minimization of [1] in the case $a > 0$ now leads to

$$[9] \quad \bar{l} \approx b\xi_{NI} \ln (t_0/t)$$

where $t_0 \equiv a\sigma_{NI}/(\Lambda\xi_{NI})$ and b is a non-universal numerical coefficient which is appended to account for effects of interface fluctuations (9*a*, 27). We therefore envision the possibility for a sequence of crossovers between the behaviours indicated by [9] and [5], with successively $\psi = 1/3$ and 1/2 in the latter, as t approaches zero.

The logarithmic growth of $\bar{l}$ according to [9] agrees with the ellipsometric results of Beaglehole (5) for a nematic wetting layer at the liquid–vapour interface of 5CB, obtained over a reduced temperature range $5 \times 10^{-5} \leq t \leq 10^{-3}$. These results do not rule out the existence of a crossover to power-law behaviour at smaller t. In a more recent experiment, Hsiung *et al.* (28) observed a divergence in the thickness of a *weakly* ordered nematic layer of 5CB at a liquid–solid interface. Their data in the range $4 \times 10^{-4} \leq t \leq 4 \times 10^{-3}$ are well fitted by [5] with $\psi = 1/2$ and $B \approx 7$ Å. This value of the critical amplitude B agrees closely with that predicted by the expression after [5], using values for 5CB of $\Delta\Theta = \Theta_{NI} = 1.1$ (11), $K = 2.1 \times 10^{-7}$ erg/cm, and $\Lambda = 2 \times 10^7$ erg/cm^3 (29). The maximum film thickness measured in this experiment corresponds to about 400 Å, considerably less than current estimates for the length l_0 mentioned earlier. On the other hand, the nematic order parameter (OP) near the substrate, $Q(0)$, was found to be much smaller than the order parameter of the bulk nematic phase. As remarked by Hsiung *et al.* (28), this is difficult to reconcile with present theories of wetting (7, 23). An alternative interpretation of the results in ref. 28 is that they do not describe complete wetting but rather a different surface phenomenon which one might call near-critical adsorption.

If the surface OP $Q(0)$ is positive but close to the value, $Q = 0$, in the bulk isotropic phase, then the Landau – de Gennes theory yields an exponentially decaying OP profile,

$$[10] \quad Q(z) \approx Q(0) \exp -z/\xi_{NI}$$

at large distances from the substrate. In terms of the adsorption Γ, i.e., the integrated value of $Q(z)$, then [10] leads to $\Gamma \sim Q(0)\xi_{NI}$. This is similar to [9], but lacks the logarithmic term associated with complete wetting that arises when $Q(0)$ approaches the bulk nematic OP and the profile $Q(z)$ develops a kink. The above scaling for Γ should hold even beyond the Landau – de Gennes theory as long as $Q(0)$ is small compared to the bulk order parameter of the ordered phase at the transition. A similar effect occurs whenever a *continuous* transition point is approached from the disordered phase in the presence of a wall (30). In such a case, Γ diverges at the bulk transition temperature. Due to the weakly first-order nature of the N–I transition, ξ_{NI} does not actually diverge as $t \to 0$ but presumably obeys $\xi_{NI} \sim (T - T^*)^{-\nu}$, where T^* is slightly less than T_{NI} and ν is an appropriate exponent. At present, there is still some uncertainty (31) about the correct theoretical values for both T^* and ν (in the Landau – de Gennes theory, $\nu = 1/2$), as well as in the analysis of experimental data from different types of measurements in terms of these parameters. Hence the results of ref. 28, i.e., $T^* \approx T_{NI}$ and $\nu = 1/2$, are not inconsistent with an interpretation based on near-critical adsorption. Another factor which could well contribute to the small difference (about 1 K) between the value $T^* \approx T_{NI}$ deduced in ref. 28 and previous estimates (32) of T^* is the presence of impurities.

In conclusion, further experiments on nematic systems which clearly exhibit complete wetting would be useful. In particular, one should try to extend measurements such as those of refs. 5 and 28 to smaller values of t. While on the basis of current theory, the crossover to the distortion régime with $\psi = 1/2$ in [5] may be difficult to observe, it is possible that the correction terms discussed below [6] are sufficiently small to render this régime experimentally accessible. Furthermore, there may exist other possibilities (16) for adsorption of a nematic layer between two phases both of which exhibit large anchoring energies and hence yield a smaller value of l_0, to which the present analysis can be adapted. For example, one could in principle study adsorption of the nematic phase out of the vapour phase in the presence of a solid substrate.

NOTE ADDED IN PROOF

In a subsequent erratum to ref. 28, Hsiung *et al.* (33) report that new measurements on a purer sample of 5CB yield results consistent with partial wetting, with a value of T^* distinctly less than T_{NI}. This finding supports the arguments described here. A short account of these arguments has been given by Lipowsky and Sullivan (34).

Acknowledgement

Donald E. Sullivan wishes to acknowledge the financial support of the Natural Sciences and Engineering Research Council of Canada.

1. K. MIYANO. J. Chem. Phys. **71**, 4108 (1979); J. C. TARCZON and K. MIYANO. J. Chem. Phys. **73**, 1994 (1980).
2. H. A. VAN SPRANG. Mol. Cryst. Liq. Cryst. **97**, 255 (1983); J. Phys. Les Ulis, Fr. **44**, 421 (1983).
3. H. YOKOYAMA, S. KOBAYASHI, and H. KAMEI. Mol. Cryst. Liq. Cryst. **99**, 39 (1983).
4. M. G. J. GANNON and T. E. FABER. Phil. Mag. A**37**, 117 (1978).
5. D. BEAGLEHOLE. Mol. Cryst. Liq. Cryst. **89**, 319 (1982).
6. B. M. OCKO, A. BRASLAU, P. S. PERSHAN, J. ALS-NIELSEN, and M. DEUTSCH. Phys. Rev. Lett. **57**, 94 (1986).
7. D. E. SULLIVAN and M. M. TELO DA GAMA. *In* Fluid interfacial phenomena. *Edited by* C. A. Croxton. Wiley, Chichester. 1986 Chap. 2.
8. P. G. DE GENNES. J. Phys. Lett. **42**, L-377 (1981); Compt. Rend. II, **297**, 9 (1983).
9. (*a*) R. LIPOWSKY. Phys. Rev. Lett. **52**, 1429 (1984); (*b*) Phys. Rev. B, **32**, 1731 (1985).
10. C. EBNER, W. SAAM, and A. K. SEN. Phys. Rev. B**32**, 1558 (1985); M. P. NIGHTINGALE and J. O. INDEKEU. Phys. Rev. B**32**, 3364 (1985); E. H. HAUGE. Phys. Rev. B**33**, 3322 (1986); S. DIETRICH and M. SCHICK. Phys. Rev. B**33**, 4952 (1986).
11. S. FAETTI and V. PALLESCHI. Phys. Rev. A**30**, 3241 (1984).

12. D. LANGEVIN and M-A. BOUCHIAT. Compt. Rend. B **277**, 731 (1973); N. V. MADHUSUDANA and K. R. SUMATHY. Mol. Cryst. Liq. Cryst. **92**, 179 (1983); H. YOKOYAMA, S. KOBAYASHI, and H. KAMEI. Mol. Cryst. Liq. Cryst. **107**, 311 (1984).
13. M. A. BOUCHIAT and D. LANGEVIN. Phys. Lett. **34**A, 331 (1971); P. CHIARELLI, S. FAETTI, and L. FRONZONI. J. Phys. Les Ulis, Fr. **44**, 1061 (1983).
14. P. CHIARELLI, S. FAETTI, and L. FRONZONI. Lett. Nuovo Cimento, **36**, 60 (1983).
15. P. G. DE GENNES. The physics of liquid crystals. Clarendon, Oxford. 1974.
16. E. PEREZ, J. E. PROUST, and L. TER-MINASSIAN-SARAGA. Coll. Poly. Sci. **256**, 784 (1978); J. E. PROUST and L. TER-MINASSIAN-SARAGA. J.Phys. Les Ulis, Fr. **40**, C3-490 (1979).
17. G. BARBERO and R. BARBERI. J. Phys. Les Ulis, Fr. **44**, 609 (1983); G. BARBERO and R. BARTOLINO. Mol. Cryst. Liq. Cryst. **99**, 89 (1983).
18. M. E. FISHER, M. N. BARBER, and D. JASNOW. Phys. Rev. A**8**, 1111 (1973).
19. D. A. HUSE. Phys. Rev. B**29**, 6985 (1984); F. T. GITTES and M. SCHICK. Phys. Rev. B**29**, 209 (1984).
20. R. LIPOWSKY and M. E. FISHER. Phys. Rev. B**36**, 2126 (1987).
21. R. LIPOWSKY and M. E. FISHER. Phys. Rev. Lett. **56**, 472 (1986).
22. A. K. SEN and D. E. SULLIVAN. Phys. Rev. A**35**, 1391 (1987).
23. T. J. SLUCKIN and A. PONIEWIERSKI. *In* Fluid interfacial phenomena. *Edited by* C. A. Croxton. Wiley, Chichester. 1986. Chap. 5; Phys. Rev. Lett. **55**, 2907 (1985).
24. B. WIDOM. J. Chem. Phys. **68**, 3878 (1978).
25. B. Q. LU, R. EVANS, and M. M. TELO DA GAMA. Mol. Phys. **55**, 1319 (1985).
26. R. LIPOWSKY. Z. Phys. B**55**, 335 (1984).
27. D. S. FISHER and D. A. HUSE. Phys. Rev. B**32**, 247 (1985).
28. H. HSIUNG, TH. RASING, and Y. R. SHEN. Phys. Rev. Lett. **57**, 3065 (1986).
29. R. G. HORN AND T. E. FABER. Proc. R. Soc. London A**368**, 199 (1979).
30. M. E. FISHER and P. G. DE GENNES. Compt. Rend. B**287**, 207 (1978).
31. E. F. GRANSBERGEN, L. LONGA, and W. H. DE JEU. Phys. Rep. **135**, 195 (1986).
32. H. J. COLES. Mol. Cryst. Liq. Cryst. **49**, 67 (1978).
33. H. HSIUNG, TH. RASING, and Y. R. SHEN. Phys. Rev. Lett. **59**, 1983 (1987).
34. R. LIPOWSKY and D. E. SULLIVAN. Phys. Rev. Lett. **60**, 242 (1988).

Can. J. Chem. Downloaded from www.nrcresearchpress.com by 176.9.209.113 on 09/07/12
For personal use only.

Neutron inelastic scattering spectra of methane on graphite at the commensurate–incommensurate phase transition

R. P. HUMES AND M. V. SMALLEY
Physical Chemistry Laboratory, Oxford University, South Parks Road, Oxford, OX1 3QZ United Kingdom

T. RAYMENT
Department of Physical Chemistry, Cambridge University, Lensfield Road, Cambridge, CB2 1EP United Kingdom

AND

R. K. THOMAS[1]
Physical Chemistry Laboratory, Oxford University, South Parks Road, Oxford, OX1 3QZ United Kingdom

Received August 5, 1987

This paper is dedicated to Professor J. A. Morrison

R. P. HUMES, M. V. SMALLEY, T. RAYMENT, and R. K. THOMAS. Can. J. Chem. **66**, 557 (1988).

Neutron scattering spectra associated with rotational tunnelling and low frequency vibrations of CH_4 adsorbed on graphite at 4 K and coverages from 0.2 to 1.5 monolayers are reported. Particular consideration is given to the changes which occur across the commensurate–incommensurate phase transition. It is shown that the incommensurate phase has a domain wall structure and is not a floating phase as had previously been proposed from theory.

R. P. HUMES, M. V. SMALLEY, T. RAYMENT et R. K. THOMAS. Can. J. Chem. **66**, 557 (1988).

Opérant à 4 K et à des couvertures allant de 0,2 à 1,5 monocouches, on a déterminé les spectres de diffusion des neutrons associés avec l'effet tunnel de rotation ainsi que les vibrations à basse fréquence du CH_4 adsorbé sur du graphite. On s'est particulièrement intéressé aux changements qui se produisent lors de la transition de phase commensurable–incommensurable. On démontre que la phase incommensurable possède une structure et qu'il ne s'agit pas d'une phase flottante comme il avait été proposé antérieurement en se basant sur la théorie.

[Traduit par la revue]

Introduction

When small molecules such as methane are adsorbed on the basal planes of graphite at sub-monolayer coverages they usually form two types of phase, a $(\sqrt{3} \times \sqrt{3})R30°$ structure, commensurate with the underlying surface, and an incommensurate (I) structure. There are still general features of the C–I transition that need to be understood and little is known experimentally about the transition in the particular system of methane on graphite. For example, it is not known whether the I phase of methane is a domain walled structure or a floating phase. We describe the changes that take place in the rotational tunnelling and vibrational spectra across the C–I transition.

The phase change at low temperatures ($T < 30$ K) has already been followed by neutron diffraction (1–3). Below a coverage of about a monolayer, CH_4 adopts the commensurate structure referred to above with the molecules 4.26 Å apart in a tripod down configuration. As the coverage increases above a monolayer the (10) diffraction peak shifts to higher angles corresponding to a decrease in the mean lattice parameter. This is consistent with the van der Waals diameter of the molecule being less than the $\sqrt{3} \times \sqrt{3}$ separation. Within the resolution of the diffraction experiment the change appears to be a continuous one and there is nothing to suggest that the I phase does not have a uniform spacing. However, for Kr, which has an identical phase diagram to CH_4, higher resolution X-ray studies show satellite peaks from the I phase indicating a domain wall structure (4–6). Phillips has done extensive calculations on the CH_4/graphite system and finds that a transition from the C phase to a freely floating, unwalled, phase preempts the formation of an I phase with domain walls (7, 8).

We have previously used incoherent neutron scattering to investigate rotational tunnelling transitions of CH_4 in its commensurate phase below about 10 K (1, 9). The potential field controlling the reorientation of the molecule is characterized by two barriers, one for rotation about the C—H bond normal to the surface (202 cm^{-1}) and one for rotation about the three equivalent C—H bonds (172 cm^{-1}). Comparison with atom–atom potential calculations indicates that CH_4–CH_4 interactions make a substantial contribution to both barriers, although it is the CH_4–surface interaction which makes the molecule adopt the tripod down configuration (see, for example, ref. 10).

Experimental details

The instruments used were the spectrometers IN4 and IN5 at the Institut Laue-Langevin, Grenoble (11) and the samples were prepared and mounted as described previously (1).

The graphite used was in two forms, Papyex (recompressed, exfoliated graphite) and Vulcan III (2700) (graphitized carbon black) with specific areas of about 20 $m^2\ g^{-1}$ and 71 $m^2\ g^{-1}$, respectively. In comparing results on the two materials it would be an advantage to know the absolute value of the coverage. This cannot be determined accurately because there is no method for doing it. Definition of the coverage with respect to a phase change seems to be the most satisfactory procedure (12). On this basis our absolute accuracy in the coverage measurements is probably about 15% but the relative accuracy is much better, about 2%. The coverages quoted are based on a molecular diameter of 4.26 Å.

Results

Rotational tunnelling spectra of CH_4 on Papyex at various coverages at 4.5 K are shown in Fig. 1. The momentum transfer (κ) here is perpendicular to the surface so the spectrum is expected to be dominated by the two transitions $T \leftrightarrow A$ and $2T \leftrightarrow E$ (9). At low coverage the spectra are those of the commensurate phase, as previously analysed (9). In the figure the intensi-

[1]To whom all correspondence should be addressed.

Can. J. Chem. Downloaded from www.nrcresearchpress.com by 176.9.209.113 on 09/07/12
For personal use only.

Can. J. Chem. Downloaded from www.nrcresearchpress.com by 176.9.209.113 on 09/07/12
For personal use only.

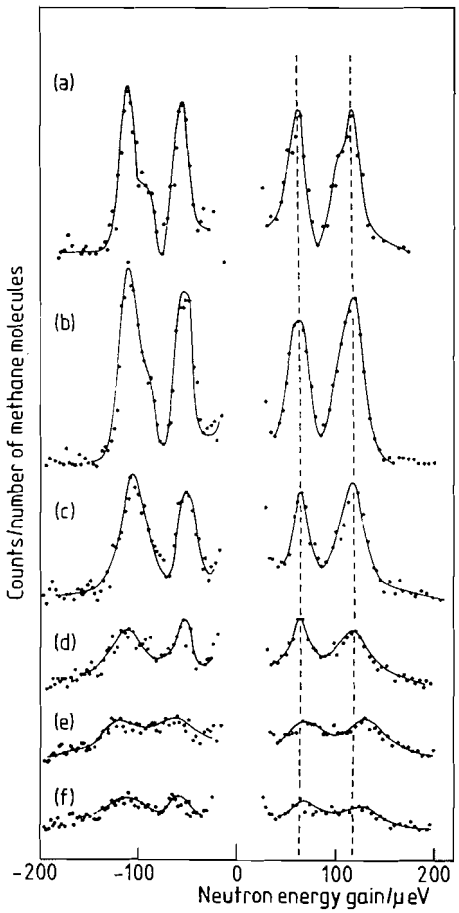

FIG. 1. Rotational tunnelling spectra of CH_4 on Papyex at 4.2 K with κ perpendicular to the surface. Coverages are (*a*) 0.23, (*b*) 0.94, (*c*) 1.03, (*d*) 1.12, (*e*) 1.20, and (*f*) 1.37. The intensities have been ratioed to the coverage.

ties have been divided by the coverage so that they represent the average spectrum per CH_4. From these spectra and others taken with κ parallel to the surface the main features are (*i*) the intensities of the lines per CH_4 molecule for the C phase increase slightly with coverage up to the C–I transition at $\theta = 1.0$; (*ii*) between $\theta = 1.0$ and 1.2 the intensities drop rapidly with increasing coverage but above 1.2 they decrease more slowly; (*iii*) there is a slight increase in the frequency of the transitions on increasing the coverage from 0.2 to 1.0 (only seen in the κ parallel spectra); (*iv*) there is a further small increase in the tunnelling splittings when the coverage changes from 1.0 upwards.

The intensity changes are shown more directly in Fig. 2, both as absolute values and per CH_4 molecule. There is some uncertainty in the exact coverage at the phase transition so the continuous lines in Fig. 2 are only schematic.

Incoherent scattering spectra at higher energies, for CH_4 adsorbed on Vulcan III at 10 K, are shown in Fig 3. Once again they are ratioed to the number of CH_4 molecules present. There are three main features: (*i*) the low coverage spectrum of the C phase has sharper bands than the higher coverage spectrum; (*ii*) across the C—I transition there is a marked change in the spectrum, the most intense peak shifting downwards from about 8.6 to 6 meV; (*iii*) at coverage where bilayer formation must be occurring to a significant extent the spectrum becomes broad and rather featureless.

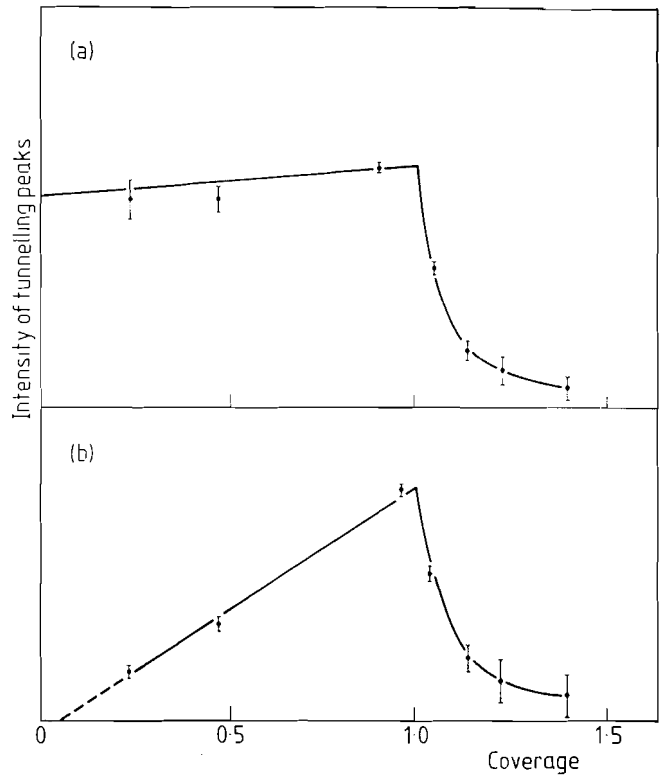

FIG. 2. Intensity of the tunnelling peaks of Fig. 1 against coverage, (*a*) per methane molecule, (*b*) absolute.

Discussion

For barriers to rotation close to those for CH_4 in its C phase the tunnelling spectrum is extremely sensitive to the barrier height. Figure 4 shows the effect of varying the two barrier heights on the tunnelling frequencies. The method of calculation is that of ref. 9. It is difficult to display the variation because the frequencies of all the transitions in the spectrum are changed by alteration of either barrier. Figure 4(*a*) shows the change in the A–$2T$ splitting with unique barrier height, the non-unique barrier being adjusted to keep the T–$2T$ splitting constant. This is approximately equivalent to reducing the barriers between all pocket states while keeping the distortion from a tetrahedrally shaped potential constant. In this case the κ parallel and perpendicular spectra would be related in a similar way to those observed for commensurate CH_4. Figure 4(*b*) and (*c*) show the variation of A–T and T–$2T$ splittings with the value of the non-unique barrier height while the unique barrier is held constant. This would lead to substantial differences between the κ perpendicular and parallel spectra. The conclusions from these calculations are that a small change in the barrier height causes a much larger relative change in the tunnelling splitting and that if the change in one barrier height is more than the other the differences between the κ parallel and perpendicular spectra will be more pronounced than for the C phase.

Molecule–molecule interactions make a significant contribution to the orientational potential of methane on graphite. This may be deduced from atom–atom potential calculations (1) or from the large change which occurs in the tunnelling spectrum of CH_4 when it is surrounded by Kr atoms (13). From the discussion in the previous paragraph it then follows that any change in the intermolecular spacing must lead to a substantial change in the tunnelling spectrum. It may therefore be con-

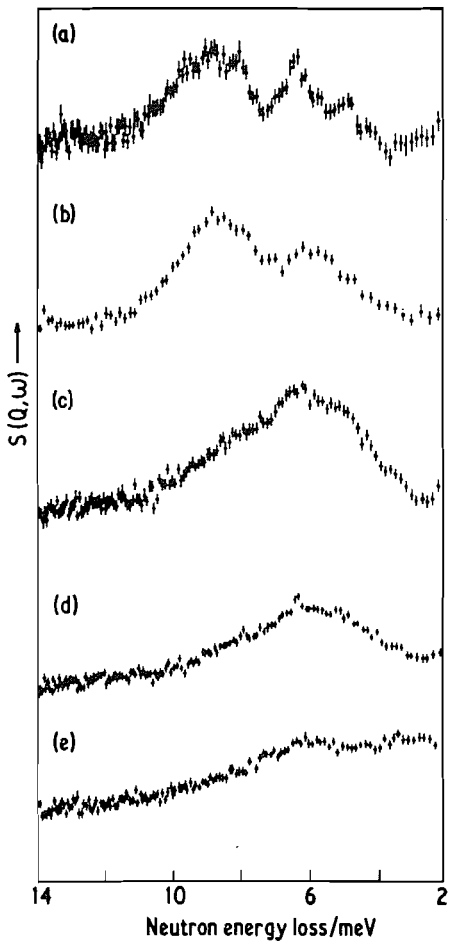

FIG. 3. Incoherent scattering spectra of CH_4 on Vulcan III at 10 K and coverages of (*a*) 0.4, (*b*) 0.8, (*c*) 1.06, (*d*) 1.2, and (*e*) 1.5. The intensities have been ratioed to the coverage to give a spectrum per methane molecule.

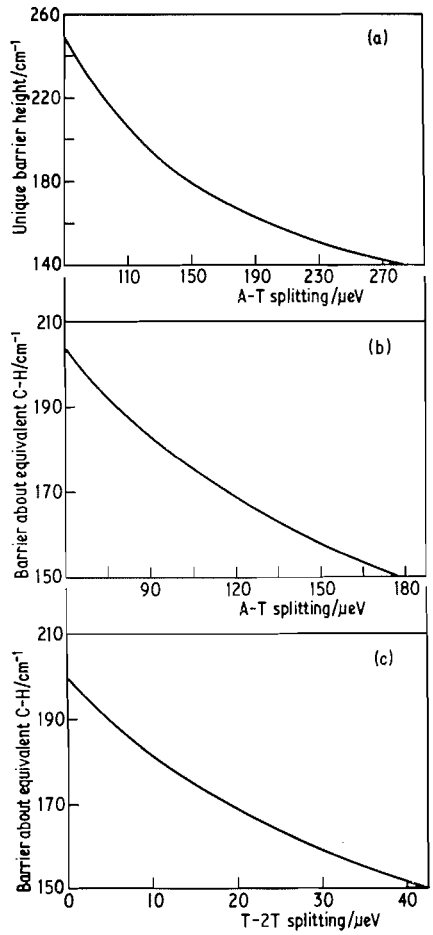

FIG. 4. Predicted variation of tunnelling splittings with barrier heights for CH_4 adsorbed on graphite, (*a*) unique barrier height varying with constant $T-2T$ splitting (18 μeV), (*b*) and (*c*) non-unique barrier varying with unique barrier held constant (200 cm^{-1} = 25 meV).

cluded that the sharp lines observed in the tunnelling spectrum at all the coverages of Fig. 1 must originate from molecules in an orienting potential similar in magnitude and identical in symmetry with that of the C phase. Given the sensitivity of the tunnelling splitting to the potential, this must even be true for the slightly shifted lines in Fig. 1(*f*). Domains of the C phase must therefore be present at coverages above 1.0, i.e. the incommensurate phase contains domains of C phase. The intensity of the lines is a measure of the proportion of molecules in these C domains.

The domains of C phase which are present at coverages above 1 may be of two general types, either part of an intrinsic domain walled structure (regular or irregular, hexagonal or striped, superlattice (14)) or surface domains of different size. The surface of Papyex itself consists of coherent domains of basal plane structure with an average diameter 200–400 Å (12). It is possible that the coverage at which the C–I transition takes place varies with the size of this surface domain. Thus the presence of C domains above a coverage of one could be attributed to surface domains where the C–I transition takes place at a higher coverage. To decide which of the two types of domain produces the sharp tunnelling lines we first discuss the small shifts in the positions of the lines at low and high coverages.

At a coverage of 0.2 the tunnelling frequencies in the κ parallel spectrum are slightly smaller than at 1.0. This corresponds to a change in the unique barrier parameter h_4 from -8 to -8.7 ± 0.3 μeV and no change in the other parameter. Thus the barrier to reorientation about the unique axis decreases slightly as the coverage increases. This can be attributed to the effects of surface domain size. There must be two contributions. One is that the binding energy of CH_4 to the graphite is slightly different according to the size of the surface domain. The second is that the barriers to reorientation depend on the average potential experienced by a molecule and this in turn depends on the amplitude of the zero point motion of the whole layer. Depending on whether molecules at the boundary of the domain are more or less strongly bound, the zero point amplitude of molecules within the domain will be reduced or increased, respectively. The different binding energy in different surface domains will lead to the more energetic being filled preferentially at lower coverage. These will then contain the more tightly bound molecules and therefore those with lower zero point amplitude and a more restricting reorientational potential. This might seem too small an effect to observe. However, tunnelling splittings are extraordinarily sensitive to small changes in the potential. If Vulcan III is used as adsorbent the tunnelling frequencies are observed to be about 3% higher than the weighted average of those observed on Papyex. Since the surface domains on Vulcan are much smaller than on Papyex (3) this suggests that tunnelling frequencies are larger on small surface domains and that the

Can. J. Chem. Downloaded from www.nrcresearchpress.com by 176.9.209.113 on 09/07/12
For personal use only.

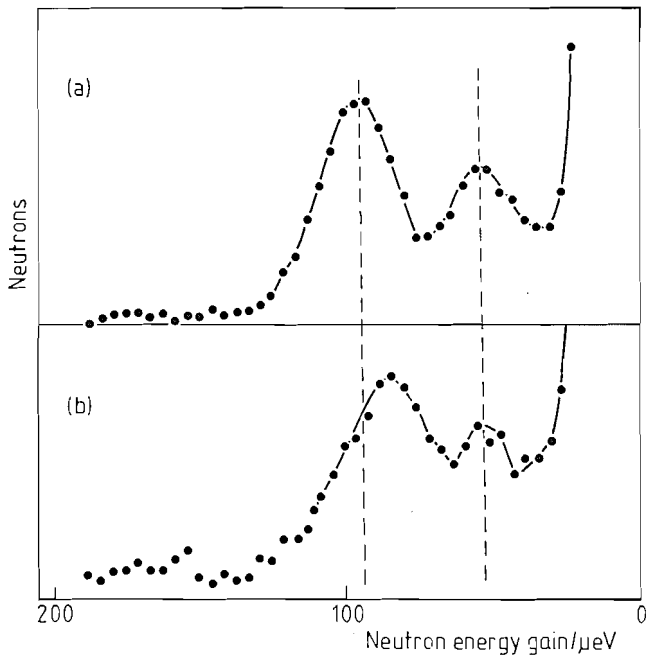

FIG. 5. Rotational tunnelling spectrum of CH_4 on Papyex at 4.2 K in the presence of CD_4. (*a*) CH_4 alone, and (*b*) CH_4 in a 3:1 CD_4/CH_4 mixture. The momentum transfer is parallel to the surface.

larger domains on Papyex are preferentially occupied at low coverage. An example of the effect of zero point energy is given in Fig. 5 where the tunnelling spectrum of CH_4 in a CH_4/CD_4 mixture is shown. The zero point motion in the mixed layer is lowered because the mass of the layer is increased and the tunnelling frequencies show the expected decrease. These correspond to an increase of 8% in the unique barrier and a decrease of 1% in the non-unique one when the layer contains 75% CD_4.

We can use these observations to decide whether CH_4 above one monolayer coverage has an intrinsic domain structure or whether isolated surface domains persist to a higher coverage because of their different size. The tunnelling frequencies at high coverage are greater than in the commensurate phase. The argument of the previous paragraph shows that they must be characteristic of molecules in small domains. If these were surface domains they would be the ones filled up as the coverage approached one monolayer. However, they would produce a greater overall broadening of the lines than observed in the spectrum of Fig. 1(*b*). It can therefore be concluded that the lines in Fig. 1(*d*), (*e*), and (*f*) are not from residual surface domains but from an intrinsic domain walled structure, in which the domains decrease in size as the coverage increases.

In a domain wall structure molecules at the domain walls will be subject to a potential different in both magnitude and symmetry from that at the centre of the domain. This potential will vary with distance from the domain wall in a way that depends on the thickness of the wall. It may also vary within and along a domain wall because the intermolecular spacing may vary and the surface molecule interaction may vary. Molecules in the domain walls will have a range of tunnelling frequencies giving rise to a band of lines, which when combined with the instrument resolution will be similar to a quasielastic spectrum, as observed.

The broad background could also be genuine quasi-elastic broadening, either from molecules in the second layer undergoing diffusive rotational motion or because motion of the molecules in the second layer causes broadening of the tunnelling transitions of molecules in the first layer. It would not be easy to distinguish this broadening mechanism from a domain wall mechanism, although at 4 K the latter is more plausible. Whatever the mechanism it does not affect the conclusion that commensurate domains of CH_4 persist above the C–I transition.

The most intense peak in the low coverage spectra of Fig. 3 (at about 8.7 meV) is associated with librations of the CH_4 molecules in the C phase (1). Although these are cooperative motions of the whole layer, their behaviour at the phase transition can be described qualitatively in terms of a single molecule libration. In contrast to tunnelling splittings, single particle librations are rather insensitive to barriers to reorientation. For example, for a one dimensional rotor in the range of barriers appropriate to CH_4 on graphite, a 10% decrease in the barrier height leads to a 30–40% increase in the tunnelling splitting (see also Fig. 4) but only a 5% decrease in the librational frequency. The large change in the librational peak at the C–I phase change must therefore be associated either with a large reduction in the reorientational potential or with an unusually large damping of the librational phonons. Either of these mechanisms could also give rise to the broad quasi-elastic background observed in the tunnelling spectra. However, librations of the commensurate domains would not necessarily remain unchanged in the vibrational spectrum. The librations are cooperative modes and show significant dispersion (15, 16). These modes would remain cooperative in a domain wall structure and the spectrum would be characteristic of the whole system rather than of the separate domains and walls. In this respect the librational spectrum is totally different in nature from the tunnelling spectrum.

The evolution of the spectra of Fig. 3 with increasing coverage suggests that the librations may be affected both by a reduction in the barriers to rotation and by damping. For example, the change in appearance between Fig. 3(*b*) and (*c*) may require both mechanisms. It seems surprising that the barriers to reorientation should be reduced as the molecules move closer together. However, the tripod down configuration of the C layer is a result of surface molecule interactions dominating the molecule–molecule interactions. A free standing CH_4 layer is predicted to adopt quite a different structure (10). Thus in the heavy walls of the domain structure the competition between the two forces might well act to reduce the reorientational barriers.

A possible mechanism for an increase in damping of the librational modes in the I phase is translation rotation coupling. This is likely to become very strong in the I phase because the barriers to reorientation will be sensitive to the positions of the molecules, both relative to one another and relative to the underlying surface. Tildesley and Lynden-Bell (17) have predicted large translation–rotation coupling effects at the corresponding phase transition in N_2 on graphite.

Unfortunately, neither librational nor tunnelling spectra can be used to characterize the domain wall structure in any detail. It could be argued that because the tunnelling spectra of the C domains retain the features characteristic of trigonal symmetry, so must the domain structure, that is, the domains must be hexagonal. Although it has been shown that what happens at the edges of the domains must influence the barrier, the averaging may be such that the spectrum of any molecule in the domain is not sensitive to the symmetry of the actual domain wall structure. The symmetry of the potential depends on both molecule and environment and where the change in environment is so

Can. J. Chem. Downloaded from www.nrcresearchpress.com by 176.9.209.113 on 09/07/12
For personal use only.

small it may well be that the spectrum is dominated by the molecular symmetry.

Whatever detailed interpretation is correct, the persistence of the C phase tunnelling spectrum at coverages above the phase change shows that there must be some kind of domain wall structure in the I phase of CH_4 at 4.2 K. Although the existence of such domain structures in adsorbed layers has been demonstrated previously by diffraction, it has not been done for CH_4. This may be because only neutron diffraction has been applied to the CH_4 system. The signal to noise and resolution appear to be somewhat lower for neutrons than for X-rays and most of the successful experiments of this kind have been done with X-rays (4, 5, 6, 18).

Phillips and co-workers (7, 8) have predicted that the CH_4 layer will form a floating rather than a domain wall structure. The basic reason for this is that their calculations, in agreement with others, show that the barrier to translation of a methane molecule across the surface is very low, less than about 20 K. This is then predicted to be too weak a periodic substrate potential to induce wall formation. However, although Phillips has included many contributions to the substrate methane interactions, he is not able to include them all. For example, when the barrier is so low, interactions like the coupling of the vibrations of the layer to those of the substrate may have a significant effect. These Phillips has had to neglect. It may also be that in the experimental system the effect of surface domain boundaries may stabilize wall formation at the expense of the floating layer, in which case the existence of the domain wall structure would be in part a consequence of the imperfect structure of the graphite surface.

At temperatures higher than 4.2 K it is expected that the domain wall structure will become unstable with respect to the floating solid. However, the tunnelling spectrum cannot be used to probe the structure to much higher temperatures because the levels are broadened and the consequent broadening of the lines would greatly or totally reduce the sensitivity of the experiment.

Acknowledgement

This work was supported by the Science and Engineering Research Council.

1. G. Bomchil, A. Huller, T. Rayment, S. J. Roser, M. V. Smalley, R. K. Thomas, and J. W. White. Phil. Trans. R. Soc. B**290**, 537 (1980).
2. P. Vora, S. K. Sinha, and R. K. Crawford. Phys. Rev. Lett. **43**, 704 (1979).
3. T. Rayment, R. K. Thomas, G. Bomchil, and J. W. White. Mol. Phys. **43**, 601 (1981).
4. P. W. Stephens, P. Heiney, R. J. Birgeneau, and P. M. Horn. Phys. Rev. Lett. **43**, 47 (1979).
5. R. J. Birgeneau, E. M. Hammond, P. Heiney, and P. W. Stephens. *In* Ordering in two dimensions. *Edited by* S. K. Sinha. North Holland. 1981.
6. D. E. Monckton, P. W. Stephens, R. J. Birgeneau, P. M. Horn, and G. S. Brown. Phys. Rev. Lett. **46**, 1533 (1981).
7. J. M. Phillips. Phys. Rev. B**29**, 4821 (1984).
8. J. M. Phillips and M. D. Hammermacher. Phys. Rev. B**29**, 5865 (1984).
9. M. V. Smalley, A. Huller, R. K. Thomas, and J. W. White. Mol. Phys. **44**, 533 (1981).
10. K. Maki and S. Nose. J. Chem. Phys. **71**, 1392 (1979).
11. Neutron Research Facilities at the ILL High Flux Reactor, ILL, Grenoble. 1986.
12. K. Morishige, C. W. Mowforth, and R. K. Thomas. Surf. Sci. **151**, 289 (1985).
13. M. P. Allen, C. B. Hovenden, R. P. Humes, S. K. Mehta, R. K. Thomas, and M. A. White. Disc **80**, 171 (1985).
14. P. Bak. Rep. Prog. Phys. **45**, 587 (1982).
15. K. Maki and M. L. Klein. J. Chem. Phys. **74**, 1488 (1981).
16. S. J. Roser, M. V. Smalley, T. Rayment, and R. K. Thomas. To be published.
17. D. J. Tildesley and R. M. Lynden-Bell. J. Chem. Soc. Faraday Trans. II, **82**, 1605 (1986).
18. C. W. Mowforth, T. Rayment, and R. K. Thomas. J. Chem. Soc. Faraday Trans. II, **82**, 1621 (1986).

Can. J. Chem. Downloaded from www.nrcresearchpress.com by 176.9.209.113 on 09/07/12
For personal use only.

Solvation of urea and methyl-substituted ureas by water and DMF

J. N. SPENCER AND JAMES W. HOVICK
Department of Chemistry, Franklin and Marshall College, Lancaster, PA 17604, U.S.A.

Received June 23, 1987

This paper is dedicated to Professor J. A. Morrison

J. N. SPENCER and JAMES W. HOVICK. Can. J. Chem. **66**, 562 (1988).

The hydrogen bond enthalpies of urea and methyl-substituted ureas with water and DMF have been determined by the pure-base calorimetric method. Transfer enthalpies between water and DMF have been calculated for dilute solutions of the ureas according to a previously developed model. The first solvation sphere of urea in water consists of five water molecules. Solvation spheres are given for other methyl-substituted ureas in water and DMF.

J. N. SPENCER et JAMES W. HOVICK. Can. J. Chem. **66**, 562 (1988).

Utilisant la méthode calorimétrique des bases pures, on a déterminé les enthalpies des liaisons hydrogènes de l'urée et d'urées portant des groupements méthyles sur les azotes avec de l'eau et du DMF. Faisant appel à un modèle mis au point antérieurement, on a calculé les enthalpies de transfert entre l'eau et le DMF pour des solutions diluées d'urées. Dans l'eau, la première sphère de solvation de l'urée comporte cinq molécules d'eau. On a aussi déterminé les sphéres de solvation d'autres urées substitués dans l'eau et dans le DMF.

[Traduit par la revue]

Can. J. Chem. Downloaded from www.nrcresearchpress.com by 176.9.209.113 on 09/07/12
For personal use only.

Introduction

Due to the ability of urea to act as a strong protein denaturant considerable theoretical and experimental research has been focused on aqueous urea solutions (1–5). In particular, Somsen and co-workers (3–5) have studied the thermodynamic enthalpies of aqueous solutions of urea and methyl-substituted ureas. We have made additional calorimetric measurements on these ureas and have applied a previously developed model (6) to provide more detailed information on the first solvation sphere of dilute solutions of urea in DMF and water.

The enthalpies of hydrogen bond formation by the ureas with *N*,*N*-dimethylformamide (DMF) and water were determined by the pure-base calorimetric method (7) and the transfer enthalpies between DMF and water were calculated by making use of these hydrogen bond enthalpies. These enthalpies are of interest by themselves because DMF has been proposed as a model for the interior of a protein (3). The hydrogen bonding of urea and its methyl analogues will provide insight into the effect of these compounds on the structure of water.

Experimental

The enthalpies of solution were measured with a modified Parr solution calorimeter equipped with a 100 mL reaction vessel and electrical calibration. The experimental procedure and data treatment have been previously reported (8, 9). All enthalpies are at infinite dilution.

An abbreviated system for the naming of the ureas was utilized: urea (U), methylurea (MU), 1,1-dimethylurea (1,1-DMU), 1,3-dimethylurea (1,3-DMU), 1,1,3-trimethylurea (TriMU), and 1,1,3,3-tetramethylurea (TetMU).

MU (Aldrich) was recrystallized from absolute ethanol. Both 1,1-DMU (Aldrich) and 1,3-DMU (Aldrich) were sublimed, and TriMU (Alfa Products) and TMU (Aldrich) were used without further purification. All of the ureas were stored in a desiccator which contained $CaSO_4$. Spectroscopic grade DMF was dried over $CaSO_4$, and chloroform was refluxed over P_2O_5 under a nitrogen atmosphere and fractionally distilled.

Hydrogen bond enthalpies were calculated by the pure-base calorimetric method (7). The pure-base method assumes that when the pure base serves as solvent each acid molecule will be hydrogen bonded to a base molecule. The interactions between the acid and surrounding base molecules are isolated by choosing a model compound as nearly like the acid as possible but without hydrogen bonding capability. The enthalpy of solution of the acid and model is measured in the pure base and a reference solvent. The function of the reference solvent is to account for the differences in the dissociation of the acid and the model. The enthalpy of hydrogen bond formation, ΔH_{HB}, may then be calculated from

$$[1]\quad \Delta H_{HB} = (\Delta H_s^A - \Delta H_s^M)_{base} - (\Delta H_s^A - \Delta H_s^M)_{ref} - (\Delta H_c^A - \Delta H_c^M) - (\Delta H_i^A - \Delta H_i^M) - (\Delta H_c^{M'} - \Delta H_c^{A'}) - (\Delta H_i^{M'} - \Delta H_i^{A'})$$

where ΔH_s^A and ΔH_s^M are the enthalpies of solution of the acid and model compounds; ΔH_c^A and ΔH_c^M are the cavity formation terms for the pure base; $\Delta H_c^{A'}$ and $\Delta H_c^{M'}$ are the cavity terms for the reference solvent; ΔH_i^A and ΔH_i^M are the interaction terms due to dipolar and van der Waals forces for the pure base; and $\Delta H_i^{A'}$ and $\Delta H_i^{M'}$ are the corresponding terms for the reference solvent. A complete discussion of this method has been previously reported (6, 7).

For this study, the model compound was TetMU and the reference solvent was $CHCl_3$. Thus the assumption is made that the weak H-bond formed by $CHCl_3$ with the carbonyls of the model compound and urea of interest have comparable enthalpies.

Methylurea and urea were sufficiently insoluble in the reference solvent $CHCl_3$ that the pure base method had to be modified. The enthalpy of sublimation of urea, 21.0 kcal mol^{-1} (10), and the enthalpy of vaporization of TetMU, 10.9 kcal mol^{-1} (11), were used as reference states for the calculation of hydrogen bond enthalpies for urea in DMF and water so that in eq. [1] the reference term becomes

$$[2]\quad (\Delta H^{sub} - \Delta H^{vap})_{U} \quad _{TetMU}$$

Enthalpies of solution determined in the present work and those previously reported by other investigators are given in Table 1.

Results and discussion

The enthalpies of N—H hydrogen bond formation per mole of compound with water and DMF are given in Table 2. The enthalpies for 1,1- and 1,3-DMU were calculated from direct application of eq. [1] with correction terms taken from ref. 6. The urea enthalpies were calculated using the enthalpy of sublimation for urea and the enthalpy of vaporization for TetMU as the reference state. The N—H hydrogen bond enthalpies for MU were calculated from models and will be discussed later.

The relative correctness of these N—H hydrogen bonds may be checked by comparing experimental transfer enthalpies to

Can. J. Chem. Downloaded from www.nrcresearchpress.com by 176.9.209.113 on 09/07/12
For personal use only.

TABLE 1. Enthalpies of solution (kcal mol^{-1}, 298 K)

Solute	Solvent		
	H_2O	DMF	$CHCl_3$
U	+3.65±0.01[a]	+1.40±0.01[c]	—
MU	+2.67±0.01[b]	+2.73±0.01[b]	—
1,1-DMU	+2.87±0.01[b]	+4.67±0.01[b]	+4.96±0.24
1,3-DMU	+0.25±0.01[b]	+2.67±0.01[b]	+3.90±0.12
TriMU	−0.76±0.03	+3.64±0.04	+2.55±0.08
TetMU	−5.86±0.01[b]	+0.04±0.01[b]	−4.49±0.08

[a]Reference 4.
[b]Reference 5.
[c]Reference 14.

TABLE 2. Enthalpies of N—H hydrogen bond formation

Solvent	ΔH_{HB}(kcal mol^{-1})[c]				
	U	MU	1,1-DMU	1,3-DMU	TriMU
H_2O	−7.0[a]	−4.3[b]	−2.3	−3.9	−2.7
DMF	−11.1[a]	−7.1[b]	−4.4	−5.4	−3.2

[a]Calculated from the enthalpies of sublimation of urea and the enthalpy of vaporization of TetMU by eq. [2].
[b]Calculated by using 1,1-DMU and 1,3-DMU as models, *vide infra*.
[c]The enthalpy changes refer to one mole of the urea. The cavity and interaction terms in $CHCl_3$ are 1.5 and 2.3 kcal mol^{-1}, respectively. Cavity and interaction terms for DMF and H_2O are given in the text.

those calculated according to a model which incorporates these N—H enthalpies. Previous work on the aqueous solvation of amides had allowed the determination of various terms which contribute to the transfer enthalpy of these ureas (6):

$$\underset{(H_2O\rightarrow DMF)}{\Delta H_{tr}} = \underset{CONN}{\Delta H_{tr}} + \underset{C{=}O}{\Delta H_{tr}} + \underset{CH_3}{\Delta H_{tr}} + \underset{N—H}{\Delta H_{tr}}$$

The transfer enthalpy term, $\underset{CONN}{\Delta H_{tr}}$, consists of the dipolar and cavity terms due to the transfer of the

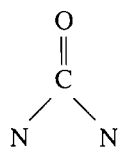

portion of the urea. This transfer had previously determined to be −4.0 kcal mol^{-1} for the *N,N*-dimethylacetamide (DMA) transfer from H_2O to DMF. DMA is taken as the model for the ureas of this work. The increased stability of CONN in DMF is attributed to larger dipole and dispersion interactions in DMF than in water, interactions which outweigh the larger enthalpy required for cavity formation in DMF.

$\underset{C{=}O}{\Delta H_{tr}}$ refers to the enthalpy involved in removing the water molecules hydrogen bonded to the carbonyl of the urea. NMA was chosen as a model for these two bound water molecules and the enthalpy of two molecules bound to the carbonyl previously reported was used (6). Thus

$$\underset{C{=}O}{\Delta H_{tr}} = \underset{DMF}{H_{HB}} - \underset{H_2O}{H_{HB}} = +5.9 \text{ kcal mol}^{-1}$$

of carbonyl group, and was taken to be constant for all ureas.

The transfer enthalpy of a CH_3 group from water to DMF was calculated from parameters determined in earlier work (6).

$$\underset{CH_3}{\Delta H_{tr}} = \underset{DMF}{H_c} - \underset{H_2O}{H_c} - \underset{DMF}{H_i} + \underset{H_2O}{H_i}$$

where H_c and H_i have the meanings previously given. Thus

$$\underset{H_2O\rightarrow DMF}{\underset{CH_3}{\Delta H_{tr}}} = +2.5 - 0.3 + (-3.1) - (-1.9) = +1.0$$

The large interaction enthalpy for water is due to the structuring effect of water molecules about the non-polar methyl group.

The transfer enthalpy of the N—H hydrogen bonds is

$$\underset{N—H}{\Delta H_{tr}} = \underset{DMF}{H'_{HB}} - \underset{H_2O}{H'_{HB}}$$

where H'_{HB} is the N—H hydrogen bond enthalpy in the solvent of interest and is given in Table 2.

Thus the transfer enthalpy of the ureas can be found from

$$\underset{(H_2O\rightarrow DMF)}{\Delta H_{tr}} = -4.0 + 5.9 + 1.0N + \underset{DMF}{H'_{HB}} - \underset{H_2O}{H'_{HB}}$$
$$= +1.9 + N + \underset{DMF}{H'_{HB}} - \underset{H_2O}{H'_{HB}}$$

where N is the number of methyl groups being transferred.

Transfer enthalpies calculated from this model are given in Table 3 along with experimental transfer enthalpies. The agreement is excellent and not only provides clear insight into the origin of these heats but also shows the relative correctness of all terms including the hydrogen bond enthalpies.

An important conclusion which emerges from this analysis is that the methyl groups on the substituted ureas appear to be solvated equally and independently. The differences in transfer enthalpies comes not from differences in solvation of the methyl groups but rather from differences in the way in which the N—H hydrogen bonds are formed.

It is now possible to analyze the solvation spheres of the ureas in more detail. Work by Del Bene (12) has shown that methyl groups in amides are *cis* to the carbonyl group and it has been assumed that the methyl groups of substituted ureas would adopt this conformation. First the N—H···DMF hydrogen bond of TriMU is calculated by the pure-base method to be −3.2 kcal mol^{-1} for the one hydrogen bond that can be formed with DMF. It would be anticipated that two hydrogen bonds would form with 1,1-DMU and that the formation of the second hydrogen bond with the DMF carbonyl would be less energetic than that of the first. Huyskens (13) has shown that electronic changes produced by the formation of the first hydrogen donor weakens the hydrogen bonding capabilities of the second. Thus the enthalpy for the formation of the two hydrogen bonds to 1,1-DMU would be expected not to be twice that of TriMU but rather something between −3.2 and −6.4 kcal mol^{-1}. The H-bond enthalpy calculated is −4.4 kcal per two bonds.

It would be expected that the hydrogen bond enthalpy for the formation of two hydrogen bonds by 1,3-DMU would be twice that of TriMU if the bonds were formed linearly. The N—H protons in 1,3-DMU are considered to be *trans* to the carbonyl. The enthalpy found is −5.4 kcal per two H-bonds. Unless hydrogen bond effects are transmitted from one side of the molecule to the other, it seems clear that the bonds are not the same in TriMU and 1,3-DMU. The most consistent explanation for the discrepancy is that only one DMF molecule binds for

TABLE 3. Enthalpies of transfer from H_2O to DMF

	ΔH_{tr} ($H_2O \rightarrow$ DMF) kcal mol^{-1}					
Origin	U	MU	1,1-DMU	1,3-DMU	TriMU	TetMU
Experimental	−2.25	+0.06	+1.80	+2.42	+4.40	+5.90
Calculated	−2.2	+0.1	+1.8	+2.4	+4.4	+5.9

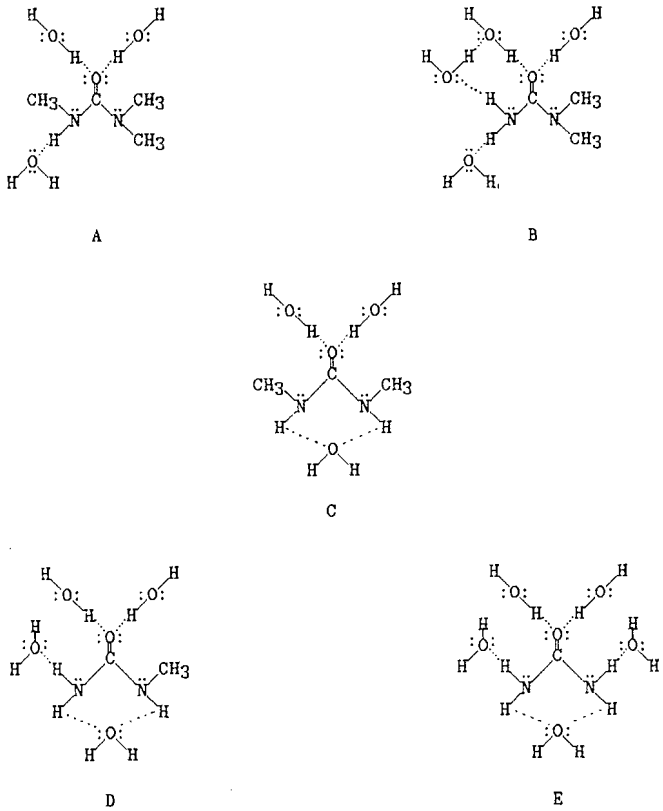

FIG. 1. Possible solvation spheres for urea and substituted ureas in aqueous environment. *A*. Trimethyl urea. *B*. 1,1-DMU. The cyclic structure shown here has been calculated to be less stable than a non-cyclic structure. The solvation sphere of this compound most probably consists of three water molecules, two bound to the carbonyl, one to the nitrogen proton. *C*. 1,3-DMU. The nitrogen protons are considered to be *trans* to the carbonyl group. *D*. Methyl urea. The solvation sphere is assumed to be non-cyclic. *E*. Urea.

each 1,3-DMU molecule which results in a non-linear and, hence, weaker bond. This is consistent with theoretical calculations made on urea and water (2) and seems to be the best rationale in the present case.

The hydrogen bond enthalpy in MU could not be calculated by the pure base method due to the insolubility of MU in $CHCl_3$. This enthalpy was estimated by using the enthalpy for 1,1-DMU and one-half the enthalpy for 1,3-DMU.

Finally the first DMF solvation sphere of urea was taken to consist of three DMF molecules with a combined enthalpy of −11.1 kcal mol^{-1} as calculated by the pure-base method.

Similar means were used to arrive at the enthalpies of N—H···H_2O hydrogen bonds for the ureas in water. Figure 1 shows possible solvation spheres for the ureas. Again the N—H protons have been considered to be *trans* to the carbonyl. For TriMU a single linear N—H hydrogen, −2.7 kcal mol^{-1}, bond is formed with water and two carbonyl to water hydrogen bonds are formed with bond enthalpy of −5.9 kcal mol^{-1} (6). The linear hydrogen bonded structure running from the water molecule bonded to the carbonyl through the water molecule bonded to the *trans* nitrogen proton provides an arrangement which is more stable than the structure which results if the N—H is *cis* to the carbonyl (12).

In amides, a cyclic structure involving a water molecule on the carbonyl oxygen and a water molecule bonded to a nitrogen proton is destabilizing (12). Thus a cyclic structure for 1,1-DMU as shown in Fig. 1*B* may actually be destabilized relative to the formation of a single hydrogen bond to the nitrogen proton. The hydrogen bond enthalpy for 1,1-DMU is less than that for TriMU and it seems likely that only one hydrogen bond is formed.

As with the DMF solvation sphere, the relative hydrogen bond enthalpies of TriMU (−2.7 kcal mol^{-1}) and 1,3-DMU (−3.9 kcal mol^{-1}) suggests one non-linear hydrogen bonded water molecule rather than two separate linear hydrogen bonded water molecules between the nitrogens for 1,3-DMU. The solvation sphere shown in Fig. 1*C* is thus assigned to 1,3-DMU.

Figure 1*D* shows a possible solvation sphere for MU. Comparison of the hydrogen bond enthalpies of MU to 1,3-DMU suggests that a fourth water molecule may be involved in the solvation of MU. Because the transfer enthalpies seem to be correctly calculated using a value of −5.9 kcal mol^{-1} for two water molecules bonded to the carbonyl for all ureas, a value determined from measurements on *N*-methylacetamide, it does not seem likely that a cyclic structure is formed for any urea. If such a cyclic structure were formed the enthalpy of the water molecules bonded to the carbonyl would be expected to be altered from that found for NMA. The solvation sphere of urea, Fig. 1*E*, was assigned by analogous reasoning.

Acknowledgement

Acknowledgement is made to the donors of the Petroleum Research Fund, administered by the American Chemical Society, for support of this research.

1. R. A. KUHARSKI and P. J. ROSSKY. J. Am. Chem. Soc. **106**, 5786 (1984).
2. Y. ORITA and A. PULLMAN. Theoret Chim. Acta. **45**, 257 (1977).
3. M. BLOEMENDAL and G. SOMSEN. J. Am. Chem. Soc. **107**, 3426 (1985).
4. H. PIEKARSKI and G. SOMSEN. Can. J. Chem. **64**, 1721 (1986).
5. A. ROUW and G. SOMSEN. J. Chem. Soc. Faraday Trans 1, **78**, 3397 (1982).
6. J. N. SPENCER, S. K. BERGER, C. R. POWELL, B. D. HENNING, G. S. FURMAN, W. M. LOFFREDO, E. M. RYDBERG, R. A. NEUBART, C. E. SHOOP, and D. N. BLAUCH. J. Phys. Chem. **85**, 1236, (1981).
7. J. N. SPENCER, J. E. GLEIM, C. H. BLEVINS, R. C. GARRETT, and F. J. MAYER. J. Phys. Chem. **83**, 1979 (1979).
8. J. N. SPENCER, J. R. SWEIGART, M. E. BROWN, R. L. BENSING, T. L. HASSINGER, W. KELLY, D. L. HOUSEL, G. W. REISINGER,

Can. J. Chem. Downloaded from www.nrcresearchpress.com by 176.9.209.113 on 09/07/12
For personal use only.

D. S. REIFSNYDER, J. E. GLEIM, and J. C. PEIPER. J. Phys. Chem. **81**, 2237 (1977).
9. J. N. SPENCER, J. E. GLEIM, M. L. HACKMAN, C. H. BLEVINS, and R. C. GARRETT. J. Phys. Chem. **82**, 563 (1978).
10. J. D. COX and G. PILCHER. Thermochemistry of organic and organometallic compounds. Academic Press, New York. 1970.
11. J. A. RIDDICK and W. B. BUNGER. Techniques of chemistry. Vol. II, Organic solvents. 3rd ed. Wiley-Interscience, New York. 1970.
12. J. E. DEL BENE. J. Am. Chem. Soc. **100**, 1387 (1978).
13. P. L. HUYSKENS. J. Am. Chem. Soc. **99**, 2578 (1977).
14. C. DEVISSER, H. J. M. GRUNBAUER, and G. SOMSEN. Z. Physik. Chem. N. F. **97**, 69 (1975).

Can. J. Chem. Downloaded from www.nrcresearchpress.com by 176.9.209.113 on 09/07/12
For personal use only.

Liquid zinc chloride vaporization thermodynamics by modified entrainment

PETER J. GARDNER AND PETER PANG

Chemistry Department, Royal Holloway and Bedford New College, Egham Hill, Egham, Surrey, TW20 0EX, United Kingdom

Received July 31, 1987

This paper is dedicated to Professor J. A. Morrison

PETER J. GARDNER and PETER PANG. Can. J. Chem. **66**, 566 (1988).

The thermodynamics of the vaporization of liquid zinc chloride has been studied in the temperature range 638–978 K by the modified entrainment method. Enthalpy and entropy changes for vaporization have been derived for the monomer and dimer species. These values are unchanged in a melt contaminated with water at a mole ratio of 1%. The proportion of dimer in the saturated vapour is found to decrease with increasing temperature. The vapour pressure equations for monomer and dimer vaporization, $ZnCl_2(l) = ZnCl_2(g)$ and $2ZnCl_2(l) = Zn_2Cl_4(g)$ are $\ln [p_1^0/p^\ominus] = -(15\,300 \pm 60)K/T + (15.39 \pm 0.06)$ and $\ln [p_2^0/p^\ominus] = -(11\,000 \pm 970)K/T + (6.5 \pm 1.3)$ for the temperature range 640–980 K.

PETER J. GARDNER et PETER PANG. Can. J. Chem. **66**, 566 (1988).

Utilisant une méthode d'entrainement modifée et opérant à des températures allant de 638 à 978 K, on a étudié les valeurs thermodynamiques pour la vaporisation du chlorure de zinc liquide. On a déterminé les changements dans les valeurs de l'enthalpie ainsi que de l'entropie de vaporisation des espèces tant monomères que dimères. Ces valeurs ne changent pas dans un mélange fondu contenant de l'eau jusqu'à un rapport molaire de 1%. On a trouvé que, avec une augmentation de la température, la proportion de dimère diminue dans la vapeur saturée. Pour des températures allant de 640 à 980 K, les équations respectives de la tension de vapeur, pour les vaporisations du monomère et du dimère, $ZnCl_2(l) = ZnCl_2(g)$ et $2ZnCl_2(l) = Zn_2Cl_4(g)$, sont les suivantes: $\ln [p_1^0/p^\ominus] = -(15\,300 \pm 60)K/T + (15{,}39 \pm 0{,}06)$ et $\ln [p_2^0/p^\ominus] = -(11\,000 \pm 970)K/T + (6{,}5 \pm 1{,}3)$.

[Traduit par la revue]

Can. J. Chem. Downloaded from www.nrcresearchpress.com by 176.9.209.113 on 09/07/12
For personal use only.

Introduction

There is commercial interest (1) in the use of molten zinc chloride as a hydrocracking solvent. Sulphur in the feedstock causes progressive contamination of the melt with zinc sulphide. Several regeneration procedures have been explored including fluidized-bed combustion (1) in which zinc chloride is vaporized. Although the thermodynamics of vaporization has been studied by several workers (2–7), there remains considerable uncertainty in the published enthalpy and entropy changes. The most contentious aspect of these investigations is the extent of polymerization in the gas phase and the manner in which the extent varies with temperature. Neither vibrational spectra (8–10), both from matrix isolation studies and high temperature gas phase examination, nor mass spectrometry (3, 7, 11) provide unequivocal evidence for the presence of vapour dimers. Most thermodynamic results (from torsion effusion, transpiration, quasistatic vapour phase manometry) are interpreted with the assumption of vapour dimer concentrations of up to 10% between the melting point (591 K) and 1200 K. Furthermore, two independent (3, 5, 6) careful manometric studies predict a quite different variation in dimer concentration with temperature in the vapour in equilibrium with melt. The results of Keneshea and Cubicciotti (3) indicate the pressure fraction of dimer falls with increasing temperature whereas the more recent work of Polyachenok *et al.* (5, 6) suggests the opposite.

The vaporization has been re-examined in the temperature range 638 to 968 K by the modified extrainment method (MEM) in an attempt to resolve this uncertainty in the variation of dimer concentration with temperature.

Experimental

The modified entrainment rig has been described in detail elsewhere (12–14). Briefly, the sample is contained in a spherical quartz capsule approximately 1 cm in diameter and suspended from one arm of a recording microbalance. The capsule orifice is in the form of a vertical capillary (ca. 2 cm long × 1 mm internal diameter); this acts as a diffusive resistance to the ingress of the downward flowing carrier gas (argon, 80 cm^3 min^{-1} at STP) and the egress of the sample vapour. The experimental parameter is the rate of mass loss of the sample ($\dot{\omega}$) at a preset temperature. Improvements to the earlier design include (*i*) the capillary being inset into the capsule by about 2 mm rather than being joined via a short flared section; this permits the capillary resistance (l/r^2: l = length, r = radius) to be measured more precisely, (*ii*) the argon was purified by passage through a rare gas purifier, and (*iii*) carrier gas flows were controlled by mass flow controllers (model AFC 260, Epak Electronics Ltd.). The measuring thermocouple (Pt – 13% Rh/Pt) was calibrated at a commercial calibration laboratory (Harwell Instrument Test Laboratories) to a precision of ±2 K. Two separate capsules were used with capillary resistances 6.090×10^4 m^{-1} and 6.918×10^4 m^{-1}; 192 experimental points in the temperature range 638 ($\dot{\omega} \approx 1.0 \times 10^{-12}$ kg s^{-1}) to 978 K ($\dot{\omega} \approx 8.7 \times 10^{-9}$ kg s^{-1}) were recorded, 32 of these being with a specially doped sample (see Results and discussion).

Materials

Zinc chloride (380 g, AnalaR, BDH Ltd.) was purified and analysed in the laboratories of the Department of Metallurgy and Materials Science, Imperial College. The bulk sample was evacuated to ca. 0.1 Torr and heated slowly over 21 days to about 100 K above its melting point (591 K). All subsequent handling took place in an argon-filled dry box purged to ≤ 10 ppm water. The solid was transferred to a purpose-built purification cell (15), melted under vacuum, and purged with argon. Dry hydrogen chloride followed by dry argon were then bubbled through the melt to remove OH^- and O^{2-}. There followed a pre-electrolysis stage using a stainless steel cathode and a vitreous carbon anode to remove all electroactive species within the zinc chloride potential window. Continuous pumping was maintained during this stage to remove anodic gases and reduce anodic polarization. The base of the cell was fractured remotely permitting the melt to filter through a No. 4 porosity glass frit.

Cyclic voltammetry was used to assay the purity of the resulting melt. Voltammograms were obtained at ramp rates of 50 mV s^{-1} at 636 K using a polished tungsten disc as working electrode, a large Pt flag counter electrode, and an $Ag/AgCl/(ZnCl_2 + NaCl + AgCl)$ (liq) reference electrode. No significant peaks were observed due to electroactive impurities; of the likely impurities (16) (OH^-, O^{2-}, H_2O), O^{2-} should be detected in the anodic sweep and H_2O will appear as a broad diffuse "water wave". Unfortunately the reduction of HO^- is certainly more cathodic than Zn^{2+} reduction so unlikely to be detected directly. However, a polarographic study (17) of NaCl:KCl and LiCl:KCl melts

has shown that treatment with hydrogen chloride and chlorine reduces the OH^- concentration in these melts to negligible levels. The small residual current was ascribed to water impurity and the amount estimated using the Randles-Sevcik equation (18–20) at 0.002 mass%. Considerable care was invested in obtaining a high purity sample as one aspect of this study was to determine the effect of water contamination in the melt on the vaporization thermodynamics.

The carrier gas (argon) was purified by passsage through a commercial rare gas purifier (model RGP-4, BOC Ltd.) which includes a titanium getter operating at 700°C to remove O_2 and N_2, copper oxide at 450°C to remove H_2, hydrocarbons, and CO, and molecular sieves to remove CO_2 and H_2O.

Results and discussion

In the modified entrainment method (12), the partial pressure (p_i^0) of the minority component in a two component system is given by

$$[1] \quad p_i^0 = P[1 - \exp(-\xi_i)]$$

where

$$[2] \quad \xi_i = \dot{\omega}RTl/AM_iP\mathfrak{D}_i$$

Such a system would be the evaporation of zinc in an argon carrier gas. The total pressure is P (commonly close to 1 atm in our experiments), $\dot{\omega}$ is the rate of mass loss, l/A is the ratio of the length to the cross-sectional area of the capillary, M_i is molecular mass of i, and $\mathfrak{D}_i$ is the binary diffusion coefficient of i in the carrier gas. The term, $1 - \exp(-\xi_i)$, may be approximated to ξ_i to an accuracy of 5% if the transport function $\xi_i < 0.1$. In some cases it is necessary to retain a quadratic term in the exponential expansion when the same accuracy is obtainable for $\xi_i < 0.5$. Mass transport in the capillary is via diffusive and convective flow and Cussler (21) has shown that the first of the exponential approximations above is equivalent to the dilute gas approximation where mass transport is assumed to be exclusively diffusive. In systems where more than one component, e.g., monomer and dimer, contribute to the transport this exponential approximation is nearly always invoked (12) because of algebraic tractability. In this work monomeric and dimeric zinc chloride were assumed to be present in the vapour and solving the flux equations for these species, the following expression for $\dot{\omega}$ is obtained ($p^\ominus$ is the standard state pressure, 101 325 N m^{-2}).

$$[3] \quad \dot{\omega} = \frac{AM_1K_1D_1p^\ominus}{RTl}\left\{1 + \frac{2D_2K_2K_1}{D_1}\right\}$$

where M_1 is the molecular mass of the monomer and K_1 and K_2 are the respective equilibrium constants for

$$[4] \quad ZnCl_2(l) = ZnCl_2(g) \qquad K_1, \Delta H_1, \Delta S_1$$

$$[5] \quad 2ZnCl_2(g) = Zn_2Cl_4(g) \qquad K_2, \Delta H_2, \Delta S_2$$

The second term in parentheses in eq. [3] is the contribution made to the mass transport by the dimer. Also, as eq. [3] describes the behaviour of a three component (Ar, $ZnCl_2$, Zn_2Cl_4) system the effects of multicomponent diffusion (22) are included. D_i are the multicomponent diffusion coefficients of the ith component into the mixture; the estimation of $\mathfrak{D}_i$ and D_i is described in the Appendix.

The results from this work were processed by two separate procedures: (*i*) in combination with other published work to establish the compatibility of literature thermodynamic results with ours and (*ii*) independently. By substitution of the equilibrium partial pressures of monomer (p_1^0) and dimer (p_2^0), eq. [3] may be recast as

$$[6] \quad \dot{\omega} = \frac{AM_1}{RTl}\{D_1p_1^0 + 2D_2p_2^0\}$$

This equation may be solved simultaneously with literature equations for total pressure ($P_T = p_1^0 + p_2^0$) to give p_1^0 and p_2^0 separately over the common temperature range and hence ΔH_1, ΔS_1, ΔH_2, and ΔS_2 by regression. Keneshea and Cubicciotti (3) quote

$$[7] \quad \log_{10}(P_T/\text{Torr}) = (9.55 \pm 0.085) - (6\,598 \pm 21)\text{K}/T \qquad 693\text{–}883\ \text{K}$$

and Polyachenok *et al.* (5) give

$$[8] \quad \log_{10}(P_T/\text{Torr}) = (8.866 \pm 0.012) - (6\,032 \pm 11)\text{K}/T \qquad 773\text{–}973\ \text{K}$$

The thermodynamic constants for monomer vaporization and dimerization (equilibria [4] and [5]) obtained by combining eq. [6] with [7] or [8] are collected in Table 1. The results for monomer vaporization have been converted to a common temperature of 800 K using C_p for the liquid and gas quoted by Barin and Knacke (23). The precision of the dimerization results did not warrant correction. Table 1 also includes the thermodynamic constants for equilibria [4] and [5] obtained independently by Keneshea and Cubicciotti (3) and by Polyachenok *et al.* (5, 6).

TABLE 1. Enthalpy and entropy changes[a] for equilibria [4] and [5] at 800 K

ΔH_1 (kJ mol^{-1})	ΔS_1 (J K^{-1} mol^{-1})	ΔH_2 (kJ mol^{-1})	ΔS_2 (J K^{-1} mol^{-1})	Source
128.8±1.5	130.2±1.9	−170±37	−207±47	Eqs. [6] and [7]
101.4±1.0	97.8±1.1	+21±5	+23±6	Eqs. [6] and [8]
128.3±0.4	129.9	−168±17	−203±21	Reference 3
118.1±2.1	117.0±2.1	−84±3	−101±3	Reference 6

[a]The uncertainty intervals quoted are standard deviations from the linear regression of $\ln p_i^0$ vs. T^{-1}.

Although the uncertainty in the results for the dimerization equilibrium is large it is clear that the MEM results are compatible with those of Keneshea and Cubicciotti (3) and not with those of Polyachenok *et al.* (5).

It is readily shown that the temperature derivative of the dimer pressure fraction ($p_2^0/(p_1^0 + p_2^0)$) is proportional to $(\Delta H_1 + \Delta H_2)/T^2$ which is positive when substituting Polyachenok's data (6) but negative using Cubicciotti's results (3). This fact was utilized in the independent processing of the MEM results. The dimer pressure fraction at 900 K is ca. 2% from the results of Keneshea and Cubicciotti (3) and decreasing at higher temperatures. It was assumed therefore that the dimer made negligible contribution to the transport above 900 K and consequently the MEM results above this temperature (58 data points) were processed via the exact equation [1] assuming a two component ($ZnCl_2$ + Ar) system and yielding ΔH_1 and ΔS_1 only. These results when converted to the mid-point of the temperature range of the MEM data points below 900 (102 points) were used with eq. [3] to extract K_2 and hence ΔH_2 and ΔS_2 for a three component system (see Table 2).

It is possible in principle to extract optimum values of ΔH_1, ΔH_2, ΔS_1, and ΔS_2 from the MEM results without making any assumptions about the extent of dimer contribution because there are 160 data points and 4 unknowns. Several minimization routines from the Numerical Algorithms Group (24) were ex-

Can. J. Chem. Downloaded from www.nrcresearchpress.com by 176.9.209.113.on 09/07/12
For personal use only.

TABLE 2. Comparison of the thermodynamic constants[a] for the equilibria $ZnCl_2(l) = ZnCl_2(g)$, ΔH_1, ΔS_1, and $2ZnCl_2(g) = Zn_2Cl_4(g)$, ΔH_2, ΔS_2; all results referenced to 800 K

Source	ΔH_1 (kJ mol^{-1})	ΔS_1 (J K^{-1} mol^{-1})	ΔH_2 (kJ mol^{-1})	ΔS_2 (J K^{-1} mol^{-1})
Reference 3	128.3±0.4	129.9	−168±17	−203±21
Reference 6	118.1±2.1	117.0±2.1	−84±3	−101±3
This work[b]	126.9±0.5	128.0±0.5	−162±8	−202±11
This work (simplex)	128.5(±0.7)	130(±3)	−124(±23)	−220(±56)
This work (doped sample	—	—	−155±3	−180±4

[a]Uncertainty intervals (except for the simplex results) are standard deviations of regression coefficients.
[b]Obtained by separating the results into two temperature ranges and making an assumption about dimer concentration above 900 K (see text).

plored but the results were unsatisfactory in that the convergence criteria were not met or absurd local minima were located. A simplex routine based on Nelder and Mead's (25) algorithm proved more satisfactory in minimizing the sum of the squares of the differences of $\dot{\omega}$ (experimental) and $\dot{\omega}$ (from eq. [3]). Only points at temperatures below 856 K were used for which the transport function, ξ_i, is ≤ 0.1 and points were weighted as recommended by Kohman (26). Some lack of robustness in the algorithm was apparent in that optimum values of ΔH_2 and ΔS_2 varied depending on the choice of the initial simplex but ΔH_1 and ΔS_1 were stable. No uncertainty intervals are obtained from simplex minimization routines as derivitization is not involved and the intervals quoted for the simplex results in Table 2 reflect the range of minima located. It is clear that the MEM results are in satisfactory agreement with those of Keneshea and Cubicciotti (3).

It is of some concern in the industrial exploitation of zinc chloride melts as hydrocracking solvents as to how a steady accumulation of water in the melt will affect the thermodynamic vaporization constants. The water contamination can arise from a damp feedstock or from the reduction of oxygen heteroatoms during cracking. For example, minimal contamination by water has a marked effect (27) on the tranport properties of melts and it has been established that the crystal structure (28) of zinc chloride is profoundly affected by water contamination. A sample of zinc chloride at room temperature was doped *in situ* with water vapour to the extent of 0.3 mass% (2.3% mole ratio). Increasing the temperature to just below the melting point resulted in the loss of about half of the added water. It is assumed that the residue remained in the melt. The fate of this water is uncertain. Zielke (1) reports that molten zinc chloride is resistant to hydrolysis. Water is surprisingly soluble (15) in many melts and, for example, water in 60:40 LiCl:KCl shows Henry's law behaviour up to 5% mole ratio. Hydrolysis via $H_2O + Cl^- = OH^- + HCl$ and $H_2O + 2Cl^- = O^{2-} + 2HCl$ has been detected (29) in other halide melts. Thirty-two data points were recorded for this artificially contaminated melt over the temperature range 640 to 864 K. Predictably, $\ln [\dot{\omega}/\text{kg s}^{-1}]$ correlates well with T^{-1} ($r^2 = 0.998$) and the two linear regression lines, one obtained from the results of the pure sample and the other from the doped sample, were compared by analysis of covariance. This test showed there was no significant difference between the adjusted means or the regression coefficients and consequently it is highly probable that the results derive from the same population. Therefore water doping of $ZnCl_2$ at the 1% molar ratio level has no effect on the thermodynamics of vaporization.

An independent check on ΔS_1 can be obtained by combining McBride's (30) value of $S_{298}(ZnCl_2, c)$ with Cubicciotti and Eding's (31) $C_p(ZnCl_2, l)$, $C_p(ZnCl_2, c)$, and $\Delta S(ZnCl_2, c \rightarrow l)$ to give $S_{800}(ZnCl_2, l) = 208 \pm 2$ J K^{-1} mol^{-1}. Givan and Loewenschuss (9) derive statistical thermodynamic functions for $ZnCl_2(g)$ based on vibrational spectra of matrix isolated zinc chloride; $S_{800}(ZnCl_2, g) = 335.9$ J K^{-1} mol^{-1}. Therefore $\Delta S_1(800) = 128 \pm 2$ J K^{-1} mol^{-1} in good agreement with the MEM results in Table 2. Finally it is obvious from the results collected in Table 2 that the values for ΔH_2 and ΔS_2 from ref. 6 are almost exactly one half of the corresponding values of other workers. This does not appear to be a stoichiometry mistranscription as the authors (6) comment explicitly on their low value of ΔS_2 compared with that of Keneshea and Cubicciotti (3).

Conclusions

The proportion of dimer in the equilibrium vapour above molten zinc chloride decreases with increasing temperature. This is at variance with the most recent examination (5, 6) of this system but supports an earlier study (3). The vapour pressure equations for

[4] $ZnCl_2(l) = ZnCl_2(g)$

[9] $2ZnCl_2(l) = Zn_2Cl_4(g)$

may be derived from the results in Table 2 and are

[10] $\ln [p_1^0/p^{\ominus}] = -(15\,300 \pm 60)\,\text{K}/T + (15.39 \pm 0.06)$ 640–980 K

[11] $\ln [p_2^0/p^{\ominus}] = +(11\,000 \pm 970)\,\text{K}/T + (6.5 \pm 1.3)$ 640–980 K

Acknowledgements

The authors gratefully acknowledge Professor D. Inman, Drs. P. Dudley and S. Duan of the Department of Metallurgy and Materials Science, Imperial College, for assistance with the purification and analysis of zinc chloride. We thank Drs. Holder, Counsell, and Clark (British Petroleum plc) for helpful discussion and B.P. for financial support.

1. R. T. STRUCK and C. W. ZIELKE. Fuel, **60**, 795 (1981); C. W. ZIELKE and W. A. ROSENHOOVER. U.S. Patent 4424111. 1984.
2. H. BLOOM, T. H. SPURLING, and J. WONG. Aust. J. Chem. **23**, 501 (1970).
3. F. J. KENESHEA and D. CUBICCIOTTI. J. Chem. Phys. **40**, 191 (1964).
4. D. W. RICE and N. W. GREGORY. J. Phys. Chem. **72**, 3361 (1968).
5. O. G. POLYACHENOK, O. N. KOMSHILOVA, and G. A. TSIRMAN. Russ. J. Inorg. Chem. **14**, 912 (1969).
6. L. D. POLYACHENOK, K. NAZAROV, and O. G. POLYACHENOK. Russ. J. Phys. Chem. **50**, 1271 (1976).

Can. J. Chem. Downloaded from www.nrcresearchpress.com by 176.9.209.113 on 09/07/12
For personal use only.

Can. J. Chem. Downloaded from www.nrcresearchpress.com by 176.9.209.113 on 09/07/12
For personal use only.

7. K. SKUDLARSKI, J. DUDEK, and J. KAPALA. J. Chem. Thermodyn. **19**, 151 (1987).
8. A. LOEWENSCHUSS, A. RON, and O. SCHNEPP. J. Chem. Phys. **49**, 272 (1968).
9. A. GIVAN and A. LOEWENSCHUSS. J. Chem. Phys. **68**, 2228 (1978).
10. G. N. PAPATHEODOROU. National Bureau of Standards Special Publication 561, October 1979, Proceedings of the 10th Materials Research Symposium on Characterization of High Temperature Vapors and Gases, NBS, Maryland, U.S.A., September 1978.
11. H. SCHAFER and M. BINNEWIES. Z.anorg.allg.Chem. **410**, 251 (1974).
12. D. BATTAT, M. M. FAKTOR, I. GARRETT, and R. H. MOSS. J. Chem. Soc. Faraday I, (*a*) **70**, 2267, (1974); (*b*) **70**, 2280 (1974); (*c*) **70**, 2293 (1974); (*d*) **70**, 2302 (1974).
13. A. FINCH, P. J. GARDNER, E. TARBOX, and S. YARDLEY. J. Chem. Soc. Faraday I, **75**, 545 (1979).
14. B. DE LARGY, A. FINCH, P. J. GARDNER, and N. KELL. J. Chem. Soc. Faraday I, **79**, 383 (1983).
15. S. H. WHITE. *In* Ionic liquids. *Edited by* D. Inman and D. G. Lovering. Plenum Press, 1981. p. 230.
16. R. COMBES. *In* Ionic liquids. *Edited by* D. Inman and D. G. Lovering. Plenum Press. 1981.
17. D. L. MARICLE and D. N. HUME. J. Electrochem. Soc. **107**, 354 (1960).
18. J. E. RANDLES. Trans. Faraday Soc. **44**, 327 (1948).
19. A. SEVCIK. Collect. Czech. Chem. Commun. **13**, 349 (1948).
20. A. J. BARD and L. R. FAULKNER. Electrochemical methods. Wiley. 1980. Chapt. 6.
21. E. L. CUSSLER. Diffusion: mass transfer in fluid systems. C.U.P. 1984. Chapt. 3.
22. E. L. CUSSLER. Multicomponent diffusion. Elsevier. 1976.
23. I. BARIN and O. KNACKE. Thermochemical properties of inorganic substances. Springer-Verlag. 1973.
24. Numerical Algorithms Group Library, NAG Central Office, Oxford, U.K.
25. J. A. NELDER and R. MEAD. Comput. J. **7**, 308 (1965).
26. T. P. KOHMAN. J. Chem. Ed. **47**, 657 (1970).
27. P. CLAES and J. GLIBERT. *In* Ionic liquids. *Edited by* D. Inman and D. G. Lovering. Plenum Press. 1981.
28. J. BRYNESTAD and H. L. YAKEL. Inorganic chemistry. **17**, 1376 (1978); **17**, 3294 (1978).
29. D. G. LOVERING and R. M. OBLATH. *In* Ionic liquids. *Edited by* D. Inman and D. G. Lovering. Plenum Press. 1981. p. 176.
30. J. J. MCBRIDE. Ph.D. Thesis. University of Michigan. 1955. Univ. Microfilms International, P.O. Box 1346, Ann Arbor, MI, U.S.A., ref. no. 5800950.
31. D. CUBICCIOTTI and H. EDING. J. Chem. Phys. **40**, 978 (1964).
32. R. C. REID and T. K. SHERWOOD. The properties of gases and liquids. McGraw-Hill. 1966.
33. T. R. MARRERO and E. A. MASON. J. Phys. Chem. Ref. Data, **1**, 3 (1972).
34. E. A. MASON and B. KRONSTADT. J. Chem. Ed. **44**, 740 (1967).
35. R. A. SVEHLA. NASA Tech. Rept. R-132, Lewis Research Centre, Cleveland, OH, U.S.A. 1962.
36. D. R. STULL and H. PROPHET. JANAF Thermochemical Tables, NSRDS-NBS 37, Catalog No. C13.48:37, U.S. Govt. Printing Office, Washington, DC, 1971 and supplements published in J. Phys. Chem. Ref. Data, **3**, 311 (1974); **4**, 1 (1975); **7**, 793 (1978); **11**, 695 (1982).
37. N. H. CHEN. Ind. Eng. Chem. **51**, 1494 (1959).

Appendix: Diffusion coefficients

There are no literature data for the gaseous diffusion coefficients of zinc chloride monomer or dimer. However, estimation procedures (32) are well-developed and are precise to about 7% if Lennard–Jones potential parameters are available and to ≈12% in their absence. The procedure adopted in this work was to scale results for zinc chloride from a system with structural similarity and for which reliable experimental data exist. The chosen reference system was CO_2–Ar for which (33)

$$[A1] \quad \mathfrak{D}/m^2\,s^{-1} = 1.74 \times 10^{-9} T^{1.646}/\exp(89.1/T) \qquad 296 \text{ to } 1800 \text{ K}$$

Mason and Kronstadt (34) stress that Grahams's Law scaling is a gross oversimplification and a more rigorous scaling expression is

$$[A2] \quad \frac{\mathfrak{D}_{13}}{\mathfrak{D}_{12}} = \left(\frac{M_2}{M_3}\right)^{1/2} \left\{\left(\frac{M_1 + M_3}{M_1 + M_2}\right)^{1/2} \frac{\sigma_{12}^2 \Omega_{12}}{\sigma_{13}^2 \Omega_{13}}\right\}$$

where 1 is Ar, 2 is CO_2, 3 is zinc chloride, M_i are molecular masses, σ_{ij} are Lennard–Jones mixture force constants, and Ω_{ij} is a collision integral, a function of $k_B T/\epsilon_{ij}$ where ϵ_{ij} are Lennard–Jones mixture well-depths. Diffusion coefficients are relatively insensitive to the choice of ϵ_{ij} and, for both the monomer and dimer, ϵ_i were estimated from Svehla's linear correlation (35) of ϵ_i with T_B, the normal boiling point. Hence $(\epsilon/k_B)ZnCl_2 = 1180$ K and $(\epsilon/k_B)Zn_2Cl_4 = 1833$ K. Reid and Sherwood (32) tabulate Lennard–Jones constants for 76 species including 18 diatomic or linear polyatomics. Rejecting data for I_2 and HI, the L–J force constants for the remaining 16 species gave a satisfactory linear correlation ($r^2 = 0.91$) with the square root of the moment of inertia, I/g cm^2.

$$[A3] \quad \sigma/\text{Å} = (3.411 \pm 0.087) + (0.549 \pm 0.047) \times 10^{19}\sqrt{I}$$

Using this correlation, $\sigma(ZnCl_2) = 4.63$ Å and $\sigma(Zn_2Cl_4) = 5.24$ Å. For Zn_2Cl_4, D_{2h} symmetry was assumed, the internal bond angles set to 90°, and the bridging bond lengths set to 1.1 times the terminal bond lengths which were assumed to be 2.05 Å as in $ZnCl_2$. Finally $I(Zn_2Cl_4) = (I_x I_y I_z)^{1/3}$ where I_i are the principal moments. These structural assumptions are common to all M_2Cl_4 species quoted in JANAF tables (36). With the usual combining rules (32) for σ_{ij} and ϵ_{ij} and interpolating Ω_{ij} using Chen's formula (37), diffusion coefficients for zinc chloride monomer and dimer were calculated from eq. [A2] over the temperature range 630 to 980 K and then linearly regressed to a power formula in T.

$$[A4] \quad \mathfrak{D}(ZnCl_2,Ar)/m^2\,s^{-1} = 8.624 \times 10^{-6}(T/273.15)^{1.760}$$

$$[A5] \quad \mathfrak{D}(Zn_2Cl_4,Ar)/m^2\,s^{-1} = 6.793 \times 10^{-6}(T/273.15)^{1.761}$$

Diffusion coefficients in ternary systems will show concentration dependence (22) and a second order treatment (12*c*) of ternary diffusion with one majority component (argon) yields eqs. [A6] to [A10].

$$[A6] \quad D_1 = D(ZnCl_2\text{–}Ar,Zn_2Cl_4) = \mathfrak{D}(ZnCl_2\text{–}Ar)/\gamma_1$$

$$[A7] \quad D_2 = D(Zn_2Cl_4\text{–}Ar,ZnCl_2) = \mathfrak{D}(Zn_2Cl_4\text{–}Ar)/\gamma_2$$

$$[A8] \quad \gamma_1 = 1 + \{[D(3,2)D(1,2)/(\alpha + 1)] - 1\}\xi_1/2$$

$$[A9] \quad \gamma_2 = 1 + \{[D(3,1)D(2,1)\alpha/(\alpha + 1)] - 1\}\xi_2/2$$

$$[A10] \quad D(k, l) = (M_l/M_k)^{1/2} - 1$$

where $\alpha = D_1/(D_2 K_1 K_2)$ and $\xi_i = \omega RTl(\alpha + 1)/[(AM_1 PD_i)(\alpha + 2)]$.

In these equations, 3 is argon and α is a coupling parameter linking the equilibria [3] and [4] and defined as the flux ratio of monomer to dimer. The equations for γ_i contain both α and ξ_i which are themselves functions of the multicomponent diffusion coefficients, D_i. As D_i are evaluated from a knowledge of γ_i, a reiterative procedure is employed with an initial guess of unity and a termination criterion that successive estimates of γ_i differ by less than 1 in 10^4.

Rotational tunneling in a disordered system: nonequilibrium methane CH_4 II

M. PRAGER

Institut für Festkörperforschung der Kernforschungsanlage Jülich, Postfach 1913, D-5170 Jülich, West Germany

Received July 21, 1987

This paper is dedicated to Professor J. A. Morrison

M. PRAGER. Can. J. Chem. **66**, 570 (1988).

A pure methane sample was condensed onto a cold surface (T = 5 K) under conditions used in matrix-isolation spectroscopy. The sample shows a disturbed long range orientational order of CH_4 II. The free rotor and tunneling transitions are considerably broadened. Stacking faults and defects are believed to cause the disorder. The disorder is largely reduced with increasing annealing temperatures T_a but, surprisingly, even at $T_a \simeq 0.7T_m$ the long range order is not fully reestablished.

M. PRAGER. Can. J. Chem. **66**, 570 (1988).

On a condensé un échantillon de méthane pur sur une surface froide (T = 5 K), dans des conditions identiques à celles utilisées en spectroscopie par isolation en matrice. L'échantillon présente un ordre d'orientation à longue distance perturbé de CH_4 II. Les transitions dûes à la rotation libre et à l'effet tunnel sont très élargies. On considère que des failles et des défauts dans l'empilement sont à l'origine du désordre. Le désordre est beaucoup moins important lorsqu'on augmente la température de recuisson, T_a; toutefois, mème lorsque $T_a \simeq 0{,}7T_m$, on observe avec surprise que l'ordre à longue distance n'est pas complètement rétabli.

[Traduit par la revue]

Can. J. Chem. Downloaded from www.nrcresearchpress.com by 176.9.209.113 on 09/07/12
For personal use only.

I. Introduction

Disorder is caused by the partial or complete loss of the three dimensional periodicity of a physical property. In classical glasses the relevant property is the center-of-mass position. In magnetic glassy systems the center of mass structure is still periodic but the magnetic periodicity is removed due to a statistical replacement of magnetic atoms by nonmagnetic ones. Glasses show universal low temperature properties, which are well described by the generally accepted "tunneling model". The physical structure of these tunneling states, however, is probably characteristic for every special system (1).

In molecular solids orientational disorder can be produced if e.g. a part of the anisotropically interacting molecules is replaced by isotropic units (2–4). Usually for low concentrations of the isotropic species (4) and/or weak anisotropic coupling (5), the effects of disorder can be considered as a perturbation of the ordered state. For highly diluted systems (6, 7), however, the long range orientational order can be completely removed, which in some cases is discussed under the aspect of an orientational glass (2) or "frozen-in" orientational disorder (3, 4).

There is the question whether pure molecular systems can be stabilized in an orientationally disordered state also. Long range orientational order can be disturbed if the solid is produced in a nonequilibrium procedure, e.g. by very fast cooling (analogous to glassy metals) or by condensing it from the gas phase onto a cold substrate directly in the solid phase. Such samples are used especially in the matrix-isolation spectroscopy technique to study individual molecules or molecular aggregates. They are known to be composed of small crystallites and to contain defects and stacking faults in rather large concentrations (8). Stacking faults lead to inequivalent molecular sites (fcc and hcp surrounding) and are often used to explain the spectroscopic observations (9). Defects interrupt the long range orientational interaction (as an isotropic impurity) and lead to a relaxed local orientational order. In the present work we tried to get an orientationally disordered sample using a matrix-isolation technique of preparation.

In some materials the effect of disorder can be monitored via its influence on the quantum transitions of a weakly hindered rotor. Rotational tunneling, observable in various molecular solids by incoherent neutron scattering, offers an extremely sensitive probe. Besides solid hydrogen (10), methane is the most intensively studied quantum rotor system (11, 12). In thermal equilibrium methane first crystallizes in an fcc orientationally disordered phase, CH_4 I. Below T_c = 20.4 K the molecules partially order while the center of mass structure is unchanged. The ordering is caused by the octopole–octopole interaction (13). The topology is such that this interaction vanishes at 25% of the sites for symmetry reasons. These sites of 432 symmetry feel only a weak crystalline field and the methane molecules are almost free quantum rotors. The remaining 75% are orientationally ordered at sites of symmetry $\bar{4}2m$ in a relatively strong rotational potential. Due to this potential one observes a tunnel splitting of the librational ground state with transitions at 75 and 140 μeV. Both, free rotors (FR) and tunneling molecules (TM), will be affected by disorder but in different ways. The more sensitive probes certainly are the FR because the relaxation of orientations around a defect removes the compensation of the octopole–octopole interactions. The TM, on the other hand, will feel only a rather weak change of the basic potential.

II. Experiments and results

Inelastic and elastic neutron scattering experiments were performed using light and heavy methane of 99.99% and 99% purity, respectively.

II.1. Sample preparation

Both samples were prepared under similar conditions in the same special inlet system described elsewhere (14), which allows the condensation of large size matrix-isolation samples for neutron scattering experiments. A reference volume of 1 L was filled up to a pressure of 2 bar with CH_4 or CD_4. This volume is connected with the sample holder via a regulation valve. The inlet line is heated to $T \approx 110$ K up to the sample container consisting of Al which was at T = 5 K. During condensation a very slow flux of 10 cm^3/min was maintained. Thus the adsorbed methane had enough time to come close to thermal equilibrium with the cold surface despite the bad thermal conductivity of the matrix. The sample temperature during condensation was always below 15 K (see below).

Can. J. Chem. Downloaded from www.nrcresearchpress.com by 176.9.209.113 on 09/07/12
For personal use only.

II.2 Inelastic spectra

The quantum rotor states of the methane molecules were measured using the high resolution neutron time-of-flight spectrometer IN5 of the Institut Laue-Langevin (ILL) in Grenoble. Two setups with energy resolutions of 34/59 μeV FWHM at incident wavelengths of 8.5/6.0 Å were used. Standard data corrections were performed and the measured spectra transformed into $S(\theta,\omega)$ using the ILL-program package PRIME/CROSSX (15). Figure 1, bottom, shows the spectrum in the energy range up to 1.5 meV (λ_i = 6 Å) as taken immediately after condensation at a sample temperature T = 2 K. Various characteristic changes compared to equilibrium CH_4 II are found: (*i*) The free rotor states at E_{FR} = 1.09 meV are strongly suppressed and asymmetrically broadened to lower energy transfers. (*ii*) The tunneling transitions, shown with better energy resolution in Fig. 2, bottom (λ_i = 8.5 Å), are also strongly asymmetric with the tail to higher energy transfer. (*iii*) The energy region between tunneling and free rotor lines contains a large number of new states. (*iv*) The energy levels are not in thermal equilibrium. A parametrization of the spectrum has been tried by using various lineshapes in potential space (Gaussian, Lorentzian, constant in a range, linear in a range, exponential, power-function, all may be asymmetric) to extract the intensities. The relation between rotational potentials V and quantum transition energy ω_{TM}, ω_{FR} was taken from Hüller and Raich (16) for the TM

$$[1]\quad \hbar\omega_{TM} = 143\ \mu\text{eV}\exp\left(0.0758(37 - V/B)\right)$$

and was just extended phenomenologically to the FR-range as was done in ref. 6

$$[2]\quad \hbar\omega_{FR} = 1.31\ \text{meV}\exp\left(-\frac{(V/B)^2}{400}\right)$$

where B is the rotational constant of a methane molecule.

The solid lines in Figs. 1 and 2 are fits with asymmetric Lorentzians. The distributions of rotational potentials in the freshly prepared sample had widths of $\Gamma_{FR} \approx 8$ B and $\Gamma_{TM} \simeq 6$ B. Gaussians do not reproduce the large intensity between the tunneling and free rotor lines while constant lineshapes overemphasize it. Using the results from the fit with Lorentzians we see that the spin temperature T_s describing the intensities of the FR lines is considerably higher ($T_s \simeq (8 \pm 2)$ K) than the sample temperature T = 2 K. In the tunnel system the population of the E and T states relative to the A states corresponds to a spin temperature around $T_s \simeq 4$ K. The spin temperature approaches somewhat the sample temperature with increasing annealing. However, all these numbers suffer from the problem that it is rather difficult to attribute the intensities of broad distributions unambiguously to FR and TM.

At T = 10 K the described spectra have changed slightly, mainly by broadening. At T = 15 K we observe a broad quasi-elastic line beside the elastic line which is characteristic for rotational diffusion in CH_4 I.

Spectra taken during the condensation of the methane show an intermediate shape. No well-defined inelastic lines can be detected but the broad inelastic intensity is not yet quasi-elastic.

The sample was annealed at temperatures T_a = 30, 50, 70 K for 30 min each. After each annealing, spectra were again measured at a sample temperature T = 2 K. Annealing at T = 30 K did not change the spectra. After heat treatment at T_a = 50 K the tunneling lines are considerably sharpened and the free rotor lines get much more pronounced. The broad intensity between the free rotor and tunneling energies is reduced (Figs. 1 and 2, top). The sharpening of the inelastic features in the spectrum further increases after annealing at T_a = 70 K. Although this temperature is only 22% below the melting point this annealing is not sufficient to produce an equilibrium CH_4 II sample (17).

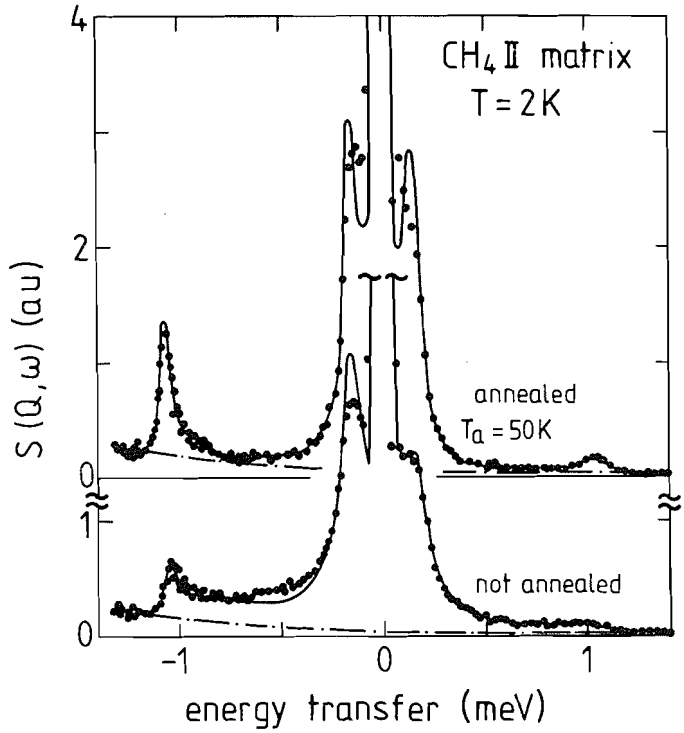

FIG. 1. Inelastic neutron scattering spectra of condensed methane as measured with the high resolution time-of-flight spectrometer IN5 using a wavelength λ_i = 6 Å (energy resolution δE = 59 μeV). Top: annealed at T_a = 50 K for 30 min; bottom: not annealed. The nonzero background is an artefact due to an incomplete empty can subtraction.

II.3 Diffraction experiments

To characterize the structure of our sample neutron powder diffraction patterns were measured using the diffractometer D1a of the ILL, Grenoble, with an incoming wavelength λ_i = 2.98 Å in a range of momentum transfers $1.6 < Q\ (Å^{-1}) < 3.3$. Spectra were taken at three different temperatures T = 7, 15, 25 K from the unannealed sample and after annealing for 30 min at T_a = 60 K. To get pronounced diffraction peaks, the coherent scatterer CD_4 had to be used instead of CH_4. Unfortunately, CD_4 has a phase diagram somewhat different from that of CH_4 (for details see e.g. ref. 18). The pattern at T = 7 (15, 25) K are found, by comparison with earlier unpublished measurements, to be characteristic of phase III (II, I). We only show parts of the diffraction pattern taken at T = 7 K and 25 K before and after annealing (Fig. 3). The essential difference between the two spectra consists in a considerable sharpening of the lines originating from the methane sample. If one assumes that a finite crystal size causes the line broadening $\epsilon_{1/2}$ in the cold condensed sample one estimates a characteristic diameter of the crystallites D ≃ 400 Å from the standard expression (19).

$$[3]\quad D \approx \frac{\lambda_i}{\epsilon_{1/2}\cos\vartheta}\,[\rho]$$

ϑ being the Bragg angle and ρ the vdW-radius of a methane molecule.

Additional Bragg peaks are due to the Al container and to N_2

Can. J. Chem. Downloaded from www.nrcresearchpress.com by 176.9.209.113 on 09/07/12
For personal use only.

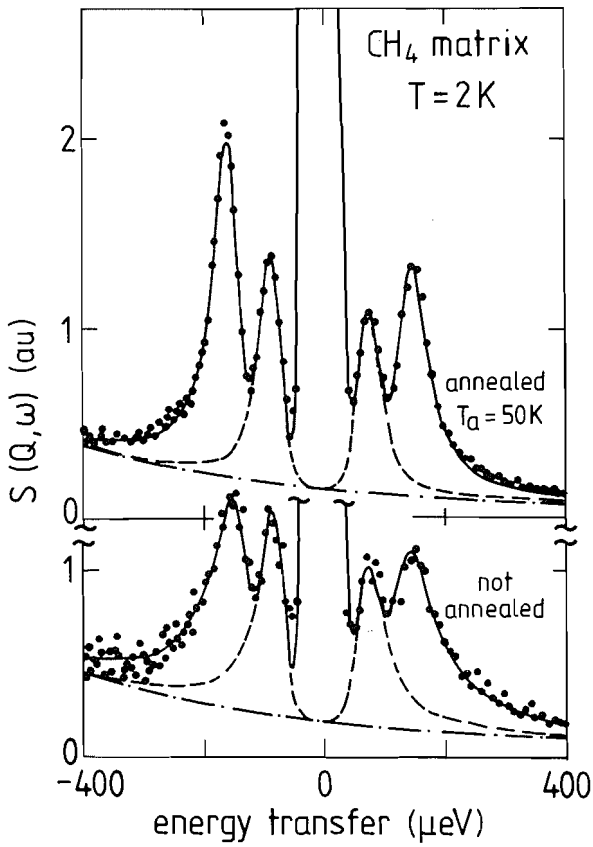

FIG. 2. Inelastic neutron scattering spectra of condensed methane. Spectrometer: IN5. $\lambda_i = 8.5$ Å ($\delta E = 34$ μeV). Top: annealed at $T_a = 50$ K for 30 min; bottom: not annealed. The nonzero background is an artefact due to an incomplete empty can subtraction.

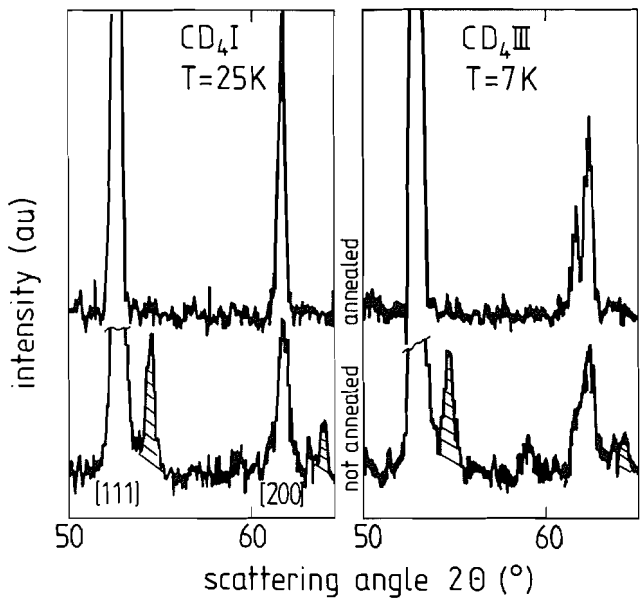

FIG. 3. Neutron diffraction patterns of condensed methane CD_4 in the range of the {111} and {200} reflections as measured with the powder diffractometer D1a of the ILL with a wavelength $\lambda_i = 2.98$ Å. The shaded peaks are due to a N_2 surface contamination. Left: $T = 25$ K, CD_4 I; right: $T = 7$ K, CD_4 III. Top: Sample annealed at $T_a = 60$ K for 30 min; bottom; Sample not annealed.

probably condensed on the outer surface of our sample container.

III. Discussion

The data we have presented on a one-component disordered quantum system would be difficult to obtain by methods other than INS. In particular, we have investigated:

(*i*) *Control of preparation conditions*

To prevent annealing of a matrix during condensation, very low condensation rates are usually used in the matrix production procedure. The temperature in the sample, however, cannot really be measured. In our system this is possible via an internal probe since the tunneling transitions of CH_4 molecules show a characteristic temperature dependence in the range from He temperature to the phase transition temperature T_c (11, 20) above which the molecule is orientationally disordered. Comparing the spectrum taken during condensation with those obtained later under conditions of thermal equilibrium we conclude that the sample temperature during preparation was $T = (12 \pm 2)$ K, even for such large samples as necessary for neutron scattering experiments. Temperature gradients in the sample certainly affect somewhat the accuracy of this statement.

(*ii*) *Perturbed long range orientational order and rotational potentials*

In spite of strong differences, the inelastic spectrum of the unannealed sample is qualitatively similar to spectra from CH_4 II cooled down from the liquid. The crude diffraction patterns are also characteristic for long-range-ordered methane of the phases III, II, I. The finite linewidth of the Bragg peaks can be attributed to finite crystallite sizes. Thus it seems possible that surface effects are influencing the rotational potentials. If one assumes that they are significant in a depth of about 3 molecular diameters below the surface one expects, from the relative volumes, disorder for 5% of the molecules. This is much smaller than the observed value. We note that in particular the free rotor states which in an undisturbed lattice represent already 25% of the molecules are nearly completely suppressed. Thus, the disorder must be of different origin. The matrices used in matrix isolation spectroscopy are known to represent nonequilibrium states, containing stacking faults, dislocations, and so on (8, 9). In methane, rather low concentrations of such statistically distributed defects will remove the compensation of the octopole–octopole interaction at the FR sites and modify the potential strengths at the tunneling sites. The general effects on the spectra thus should be similar to those found in the system CH_4/Kr where the anisotropic octopole–octopole interaction between methane molecules is diluted by some percentages of isotropic Kr atoms (4). Indeed, the spectra resemble each other but there are also differences. In the mixed CH_4/Kr sample the distinction between FR and tunneling states, both weighted according to the probabilities found in the undisturbed lattice, could be maintained up to rather large Kr concentrations ($C_{Kr} \approx 0.1$) while the disorder in the present cold condensed sample strongly suppresses the FR states compared to the TM. The system thus seems to be closer to a fully disordered state.

It is a question whether an orientational "glassy state" can be described by a general distribution function as in the tunneling standard model (STM) of normal glasses (21). There must be some fundamental differences, however. It is a symmetry property of rotational potentials that their minima are equivalent. This means an asymmetry parameter, called Δ is the STM, is always zero. On the other hand, the tunneling parameter λ is

related to the potential strength V since the tunneling frequency depends almost exponentially on V according to [1]. A possible function for molecular system analogous to the STM thus would read simply

[4] $p(V)\,dV = \text{constant}\,dV$

and yields a distribution of tunneling splittings

[5] $p(\omega_t)\alpha \exp(-\beta V)$

In some matrix isolation systems we have indeed found a distribution compatible with [5]. The tunneling states are observed as wings close to the elastic line. The shape of this spectrum remained unchanged if the instrumental resolution was improved (22). In the present case, however, such a distribution function is not able to describe the spectra. Instead rather broad Lorentzians in potential space with cutoffs at the free rotor energy on the one side and at the tunneling energy on the other yield the best fits.

(iii) Influence of disorder on the phase diagram

Due to the presence of disorder the phase diagram of methane is somewhat changed. While the equilibrium sample shows the phase transition to orientationally disordered CH_4 I at $T_c = 20.4$ K, we observe already the quasielastic spectra corresponding to disordered methane at $T = 15$ K. Thus the phase transition temperature T_c is lowered by more than 25% due to disorder, as in the CH_4/Kr mixtures (4). The diffraction patterns reflect the same effect for CD_4. We did not try, however, to get more accurate values of the transition temperatures.

(iv) Effects of annealing

With increasing annealing the inelastic intensity is more and more concentrated into the FR and tunneling lines, which have grown much sharper. But even after annealing at $T_a = 70$ K the spectrum reflects disorder. The inelastic lines still have asymmetric tails and the intensity of the FR transitions is still considerably below the 25% of the inelastic scattering measured for an equilibrium structure of CH_4 II. The remaining defects clearly have to overcome rather large activation barriers. This is in contrast to the assumption that the onset of diffusion fully reconstructs a matrix at annealing temperatures $T_a \simeq 0.4T_m$. With annealing, the size of the methane crystallites has considerably increased, yielding sharp Bragg peaks. All these effects prove that the disorder in our system is not due to surface effects.

(v) Spin conversion

In the unannealed and the annealed matrix the quantum rotor levels, especially the FR, are not in thermal equilibrium with the lattice. While in disordered CH_4/Kr mixtures with rather large Kr concentrations spin conversion is accelerated (23), this seems to be not the case for the matrix system. Thus, it is not the disorder but the presence of Kr atoms that must be responsible for the effect in the CH_4/Kr system. The deviation from the thermal equilibrium, however, is also different to that of quenched CH_4 II (24). In the quenched material E-state molecules do not convert, while in our matrix an increased population of T-states is found. This observation, however, needs a more detailed study.

The interpretation of the present spectra arising from a three-dimensionally-coupled, disordered quantum rotor system must remain incomplete. Theoretical models usually use a molecular field theory to describe the system in a single-particle picture and hence cannot explain the present observations. Here computer simulation seems to be possible and helpful for a deeper understanding of our data.

The single-particle picture is certainly more adapted to single molecular defects in an atomic matrix. Thus, complementary information can be obtained by investigating CH_4 matrix-isolated in rare gases. Such experiments were already performed with limited energy resolution and for equilibrium samples (5). In a cold condensed sample several transitions belonging to inequivalent sites (9, 25) and an additional broad distribution of states is found (25). This is direct evidence for the existence of the defects used to explain the present results.

IV. Conclusions

Methane condensed slowly (10 cm^3/min) onto a cold surface ($T = 5$ K) maintains a long range orientational structure as in CH_4 II but displays orientational disorder, which manifests itself in a significant broadening and weakening of the quantum transitions compared to the undisturbed material. In the disturbed structure the transition temperature into the orientationally ordered phase II is reduced by more than 25%. The disorder shows remarkable differences to that produced by diluting the orientation-dependent interaction with small percentages of rare gases. The free rotor states are strongly suppressed and represent more a broad band of states at energies below that of the free rotor, but no system with random orientations is formed. The disorder, most probably, is caused by stacking faults and defects and is considerably reduced with increasing annealing. Surprisingly even at the highest annealing temperatures $T_a/T_m \approx 0.7$ it could not be completely removed.

Acknowledgements

W. Langel made available his matrix isolation setup. H. Blank and G. Kearly helped with the experiments on IN5. A. Hewat provided measuring time for a short run on D1a. H. Lauter supplied the CH_4. I thank all these colleagues for their collaboration.

1. U. Buchenau, M. Prager, N. Nücker, A. J. Dianoux, N. Ahmad, and W. A. Phillips. Phys. Rev. B **34**, 5665 (1986).
2. A. B. Harris and H. Meyer. Can. J. Phys. **63**, 3 (1985).
3. W. Press, B. Janik, and H. Grimm. Z. Phys. B **49**, 9 (1982).
4. S. Grondey, M. Prager, and W. Press. J. Chem. Phys. **86**, 6465 (1987).
5. Y. Kataoka, W. Press, U. Buchenau, and H. Spitzer. *In* Neutron inelastic scattering 1977. Vol. 1. IAEA, Vienna. 1978. p. 311.
6. S. Grondey, M. Prager, W. Press, and A. Heidemann. J. Chem. Phys. **85**, 2204 (1986).
7. F. de Luca and B. Maraviglia. Phys. Lett. **101**, 300 (1983).
8. S. Cradock and A. J. Hinchcliffe. Matrix isolation. Cambridge University Press, Cambridge, London, New York, Melbourne. 1975.
9. L. H. Jones, S. A. Ekberg, and B. I. Swanson. J. Chem. Phys. **85**, 3203 (1986).
10. I. F. Silvera. Rev. Mod. Phys. **52**, 393 (1980).
11. W. Press. Single particle rotations in molecular crystals. Springer tracts in modern physics. Vol. 92. Springer, Berlin, Heidelberg, New York. 1981.
12. Y. Ozaki, Y. Kataoka, and T. Yamamoto. J. Chem. Phys. **73**, 3442 (1980).
13. H. M. James and T. A. Keenan. J. Chem. Phys. **31**, 12 (1959).
14. W. Langel, H. Kollhoff, and E. Knözinger. J. Phys. E **19**, 86 (1986).
15. R. E. Gosh. ILL Internal Technical Report. 1975.
16. A. Hüller and J. Raich. J. Chem. Phys. **71**, 3851 (1979).

Can. J. Chem. Downloaded from www.nrcresearchpress.com by 176.9.209.113 on 09/07/12
For personal use only.

17. A. HEIDEMANN, W. PRESS, K. J. LUSHINGTON, and J. A. MORRISON. J. Chem. Phys. **75**, 4003 (1981).
18. M. PRAGER, W. PRESS, A. HEIDEMANN, and C. VETTIER. J. Chem. Phys. **77**, 2577 (1982).
19. C. J. BROWN. *In* X-Ray diffraction by polycrystalline materials. *Edited by* H. S. Peiser, H. P. Rooksby, and A. J. C. Wilson. Chapman and Hall, London, New York. 1960.
20. W. PRESS and A. KOLLMAR. Solid State Commun. **17**, 405 (1975).
21. W. HUNKLINGER and M. V. SCHICKFUS. *In* Amorphous solids. *Edited by* W. A. Phillips. Topics in Current Physics, Vol. 24. Springer, Berlin, Heidelberg, New York. 1981.
22. W. LANGEL and M. PRAGER. Unpublished results.
23. P. CALVANI and H. GLÄTTLI. J. Chem. Phys. **83**, 1822 (1985).
24. A. HEIDEMANN, K. J. LUSHINGTON, J. A. MORRISON, K. NEUMAIER, and W. PRESS. J. Chem. Phys. **81**, 5799 (1984).
25. M. PRAGER and W. LANGEL. Unpublished results.

Can. J. Chem. Downloaded from www.nrcresearchpress.com by 176.9.209.113 on 09/07/12
For personal use only.

Rydberg states in adamantanethione, thiofenchone, and thiocamphor

K. J. FALK AND R. P. STEER[1]

Department of Chemistry, University of Saskatchewan, Saskatoon, Sask., Canada S7N 0W0

Received May 15, 1987

This paper is dedicated to Professor J. A. Morrison

K. J. FALK and R. P. STEER. Can. J. Chem. **66**, 575 (1988).

The absorption spectra of adamantanethione (**I**), thiofenchone (**II**), and thiocamphor (**III**) have been measured in the quartz ultraviolet region in both the vapor phase and in perfluoroalkane solutions. Rydberg as well as $\pi \rightarrow \pi^*$ transitions are identified in the gas phase spectra, and are discussed in terms of the known photochemistry of these compounds.

K. J. FALK et R. P. STEER. Can. J. Chem. **66**, 575 (1988).

Opérant dans la région ultaviolette du quartz, tant en phase gazeuse que dans des solutions dans des perfluoroalcanes, on a mesuré les spectres d'absorption de l'adamanthanthione (**I**), de la thiofenchone (**II**) et du thiocamphre (**III**). Dans la phase gazeuse, on a identifié la transition de Rydberg ainsi que la transition $\pi \rightarrow \pi^*$ et on en discute en fonction de la photochimie connue de ces composés.

[Traduit par la revue]

Can. J. Chem. Downloaded from www.nrcresearchpress.com by 176.9.209.113 on 09/07/12
For personal use only.

Introduction

States of $^1(\pi, \pi^*)$ character are known to be involved in the unusual ultraviolet photochemistry and photophysics of molecules containing the thiocarbonyl function (1, 2). The lowest Rydberg states of aliphatic thiones such as adamantanethione (**I**), thiofenchone (**II**), and thiocamphor (**III**) are

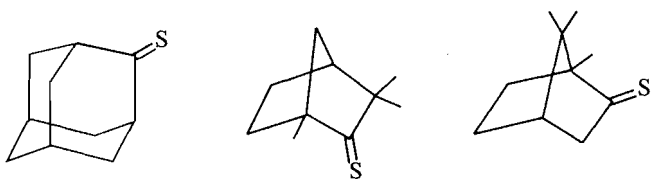

I **II** **III**

therefore of interest because their energies are expected to be similar to those of the $^1(\pi, \pi^*)$ valence states. Early *ab initio* SCF and CI calculations (3, 4) on smaller aliphatic thiocarbonyls placed the $n \rightarrow 4s$ Rydberg transitions at lower energies than the vertical $\pi \rightarrow \pi^*$ transitions. However, substantial bodies of photochemical, photophysical, and spectroscopic evidence have been used to unequivocally establish that the electronic origins of the $\pi \rightarrow \pi^*$ transitions are at least 20–30 kJ mol^{-1} lower than those of the lowest ($n \rightarrow 4s$) Rydbergs (1, 5–7). Subsequent large scale CI calculations (8) have resulted in a downward revision of the calculated $^1(\pi, \pi^*)$ state energy in H_2CS, consistent with this experimental evidence.

The lowest few Rydberg states of several small aliphatic thioketones, including thioacetone, have been identified experimentally (5–7) from their vapor phase absorption spectra. In each of these molecules the electronic transitions to the $^1(n, 4s)$ state ($^1B_2$ in C_{2v} local symmetry) is located between 220 and 230 nm, whereas the onset of the broad $\pi \rightarrow \pi^*$ continuum is near 260 nm. Transitions to the $(n, 4p_y)$, $^1A_1$, and $(n, 4p_z)$, $^1B_2$, states are both found on the short wavelength wing of the $\pi \rightarrow \pi^*$ absorption at $\lambda < 220$ nm. The symmetry forbidden transitions to the $^1(n, 4p_x)$, $^1A_2$, state have not been observed.

The spectrum of thioacetaldehyde (6) suggests that there may be substantial mixing of the $^1(\pi, \pi^*)$ and $^1(n, 4s)$ states (both A' in C_s symmetry) in this molecule. Calculations (8) also suggest that substantial mixing of the valence $^1(\pi, \pi^*)$ and conjugate Rydberg $^1(\pi, 3d)$ configurations may take place in thioformaldehyde. The possible involvement of Rydberg states in the ultraviolet, solution phase photochemistry of larger aliphatic thioketones such as **I**, **II**, and **III** thus has been the subject of some discussion (9, 10). However, the Rydberg states of these larger thiones have never been observed experimentally.

[1]To whom correspondence should be addressed.

Experimental

I, **II**, and **III** were prepared from the corresponding ketones by reaction with P_4S_{10} (11). The crude thiones were purified by column chromatography (silica gel – hexane), sublimed, and stored under vacuum in the dark at −20°C. Cells of 1.0 cm length fitted with suprasil windows were filled with the vapor of the thione at its room temperature vapor pressure (<0.3 Torr). Spectra were taken on a Cary 118C uv–visible spectrophotometer which had been purged with dry N_2 to permit access of $\lambda \sim 190$ nm. An evacuated cell was used as a reference. Spectra in perfluoroalkane solvents ($\lambda > 200$ nm) were also taken in 1 cm cells with the pure perfluoroalkane as a reference. All experiments were performed at 23 ± 2°C.

Results and discussion

The ultraviolet spectra of **I**, **II**, and **III** at their room temperature vapor pressures are shown in Fig. 1. The broad, structureless absorption feature in each spectrum is assignable to the $\tilde{B} \leftarrow \tilde{X}$, $\pi \rightarrow \pi^*$ transition centered on the thiocarbonyl chromophore (1). The gas phase spectra exhibit three additional transitions in the 190–230 nm region. By analogy with thioacetone and other thioketones (5–7), these should be assignable (using notation appropriate for C_{2v} local symmetry) to the $\tilde{C}(^1B_2) \leftarrow \tilde{X}(^1A_1)$, $(^1A_1) \leftarrow \tilde{X}(^1A_1)$, and $(^1B_2) \leftarrow \tilde{X}(^1A_1)$ Rydberg $n \rightarrow 4s$, $n \rightarrow 4p_y$, and $n \rightarrow 4p_z$ transitions, respectively.

The lowest energy Rydberg band system, located at 220–230 nm on the high energy side of the broad $\tilde{B} \leftarrow \tilde{X}$ absorption, is readily assignable to the $n \rightarrow 4s$, $\tilde{C}(^1B_2) \leftarrow \tilde{X}(^1A_1)$ transition in all three molecules. The assignment of the remaining two Rydberg transitions in the 200–210 nm region is less clear. Calculations predict the $^1A_2$ $(n, 4p_x)$, $^1A_1$ $(n, 4p_y)$, and $^1B_2$ $(n, 4p_z)$ states should have almost identical energies in small thiocarbonyls such as thioformaldehyde (8) and thioacetone (3, 4). We rule out an $^1A_2 \leftarrow \tilde{X}(^1A_1)$ assignment for either band system on the grounds that such a transition will be electric dipole forbidden in C_{2v} (local) symmetry.

Whereas the $\tilde{C} \leftarrow \tilde{X}$ transitions are strong in all three molecules, thiofenchone and adamantanethione both have strong $\tilde{D} \leftarrow \tilde{X}$ transitions near 206–209 nm and weaker $\tilde{E} \leftarrow \tilde{X}$ transitions

Can. J. Chem. Downloaded from www.nrcresearchpress.com by 176.9.209.113 on 09/07/12
For personal use only.

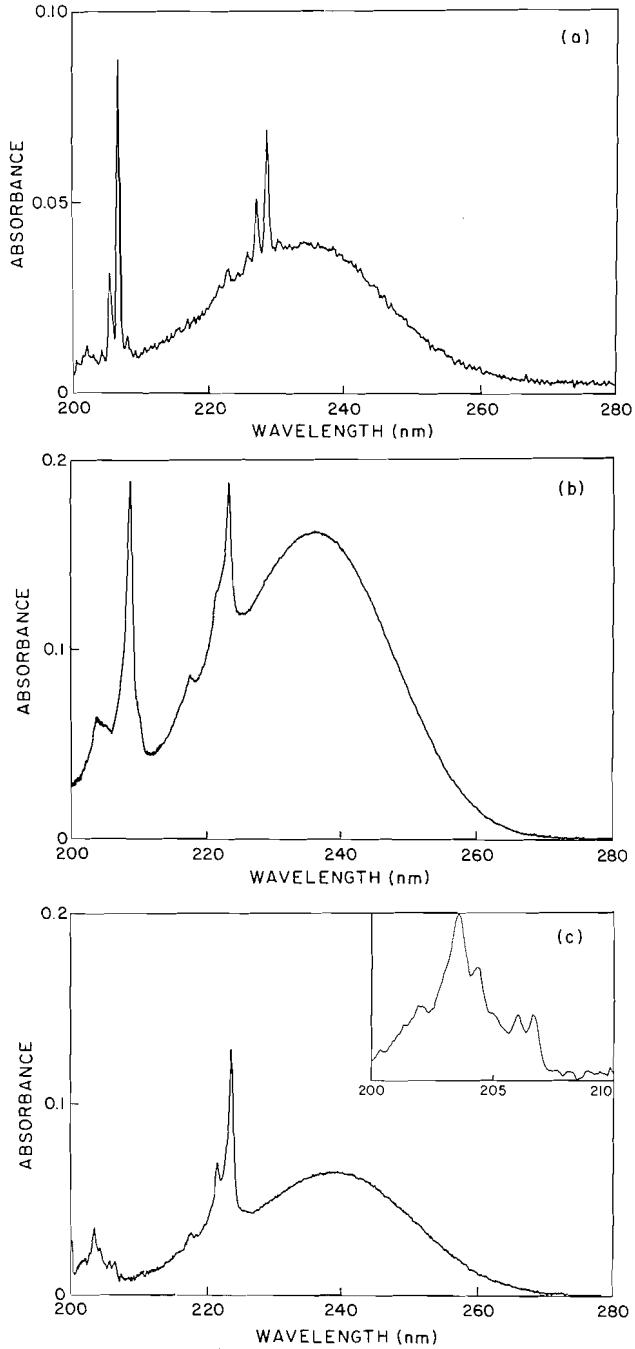

FIG. 1. Ultraviolet absorption spectra of (*a*) adamantanethione, (*b*) thiofenchone, and (*c*) thiocamphor in the gas phase at their room temperature vapor pressures.

near 201–204 nm. In contrast, thiocamphor (see insert, Fig. 1*c*) exhibits a weak $\tilde{D} \leftarrow \tilde{X}$ Rydberg transition at ca. 207 nm and a somewhat stronger $\tilde{E} \leftarrow \tilde{X}$ transition at ca. 204 nm. Their intensity differences notwithstanding, the fact that these two Rydberg transitions occur at almost identical energies in all three molecules (cf. Table 1) leads us to propose that those transitions at similar energies are between states of the same symmetry. Based upon the *ab initio* SCF-CI calculations of Bruna *et al.* (3, 4) on thioacetone, and the absence of contrary evidence, we assign the transitions at ca. 206–209 nm as $\tilde{D}(^1A_1) \leftarrow \tilde{X}(^1A_1)$ and those at ca. 201–204 nm as $\tilde{E}(^1B_2) \leftarrow \tilde{X}(^1A_1)$. The assignments are summarized in Table 1.

The Rydberg transitions of **I** have the most distinct vibrational structure and exhibit Franck–Condon envelopes expected of a rigid molecule. Unlike thioacetaldehyde (6) of C_s symmetry and to a lesser extent 3,3-dimethylbutane-2-thione and 3-methylbutane-2-thione (5), there is little ultraviolet spectral evidence of Rydberg-valence configuration mixing in adamantanethione. The only apparent vibrational progression is one of three members in each of the $\tilde{C} \leftarrow \tilde{X}$ and $\tilde{D} \leftarrow \tilde{X}$ systems. The separation between adjacent bands is 280–300 cm^{-1}, and this is similar to the spacing of the most prominent progression in the corresponding Rydberg transitions in thioacetone (7). In the latter molecule this vibration is attributed to the C—C—C bending mode of a_1 symmetry. No band attributable to the C—S stretching mode is strong enough to be assigned.

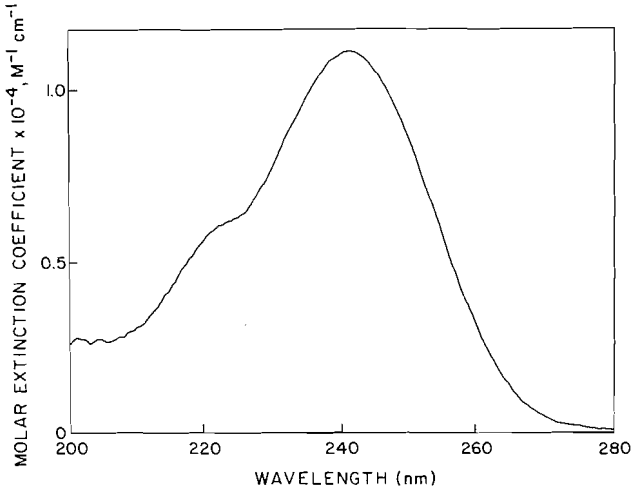

FIG. 2. Ultraviolet absorption spectrum of thiocamphor in perfluorodimethylcyclohexane at a concentration of 2.2×10^{-5} *M*.

The vibrational structure in the Rydberg transitions of thiofenchone and thiocamphor is less well resolved. While this may reflect the greater structual rigidity of tricyclic **I** compared with bicyclic **II** and **III**, the fact that **II** and **III** (but not **I**) are known (9, 10) to exhibit net intramolecular photochemistry when excited to their $\tilde{B}(^1A_1)$ states is an indication of the presence of unbound (with respect to H migration) portions of the potential hypersurface which are accessible at energies lower than those of the lowest Rydberg states. Broadening of the vibrational bands due to shortening of the Rydberg state lifetimes of **II** and **III** is thus possible.

The sharp features ascribed to the Rydberg transitions are missing from the spectra taken in perfluoroalkane solutions. Perfluoroalkanes are very weakly interacting solvents and have been shown (12) to significantly perturb neither the radiative nor the non-radiative electronic transitions of aromatic thiones in their ($^1(\pi, \pi^*)$ states. Sulfur Rydberg orbitals are spatially much larger, however, and, given the exposed location of the S atoms in these molecules, are very susceptible to repulsive solvent perturbation. Thus, as expected on the basis of many other high pressure gas phase and solution studies (13), the Rydberg transitions are obscured even in the perfluoroalkanes. Nevertheless, the solution spectrum of **III** (Fig. 2) exhibits a broad feature consisting of a distortion of the Franck–Condon envelope on the short wavelength side of the strong $\pi \rightarrow \pi^*$ transition. This can be ascribed to the residuum of the $n \rightarrow 4s$ Rydberg transition in solution. Similar, but less distinct features may be seen on close examination of the spectra of **I** and **II** in perfluoroalkane solutions.

Many studies of molecular Rydberg spectra as a function of the pressure of a chemically inert gas reveal that perturbations cause Rydberg bands to broaden asymmetrically to *higher* ener-

TABLE 1. Ultraviolet transition energies (in eV) for **I**, **II**, **III** and other thioketones

State	Excitation	Ultraviolet transition energy					
		$(CH_3)_2CS$[a]	$(CH_3)_3CCSCH_3$[b]	$(CH_3)_2CHCSCH_3$[b]	**I**[c]	**II**[c]	**III**[c]
$\tilde{X}(^1A_1)$	—	0.00	0.00	0.00	0.00	0.00	0.00
$\tilde{B}(^1A_1)$[d]	$\pi \rightarrow \pi^*$	5.6 (4.8)	5.6 (4.7)	5.6 (4.8)	5.29 (4.5)	5.25 (4.5)	5.20 (4.5)
$\tilde{C}(^1B_2)$	$n \rightarrow 4s$	5.49	5.54	5.59	5.43	5.55	5.54
$\tilde{D}(^1B_2)$	$n \rightarrow 4p_z$	6.40[e]	6.21[e]	6.27[e]	6.01	5.94	6.00
$\tilde{E}(^1A_1)$	$n \rightarrow 4p_y$	6.52[e]	6.42[e]	~6.4[e]	6.15	6.08	6.09

[a]Reference 7.
[b]Reference 5. C_{2v} local symmetry used.
[c]Energy of the lowest energy strong vibrational feature.
[d]At λ_{max}. Figures in parentheses are estimates of the approximate origin, determined from the onset of the broad absorption.
[e]Assignments of $\tilde{D}$ and $\tilde{E}$ states may be reversed (6, 7).

gies (13). Thus, in solution, excitation of the three thiones studied to the red of the maxima of their broad uv absorption systems will not involve overlapping Rydberg absorptions. It would therefore appear that de Mayo and coworkers (9, 10) are correct in their conclusion that Rydberg states having symmetries different from that of the $^1(\pi, \pi^*)$ state are not directly involved in the ultraviolet photochemistry of the bicyclic thiones. The existence of partial Rydberg character in the $^1(\pi, \pi^*)$ states is nevertheless still possible through the mixing of Rydberg-valence conjugates, as discussed by Burton *et al.* (8), and Robin (14). Moreover, the lowest Rydberg triplet state, $^3B_2$ of $^3(n, 4s)$ character, might still play a role in the decay dynamics of **I**, **II**, or **III** initially excited to the $^1(\pi, \pi^*)$ state.

Acknowledgment

The authors wish to thank the Natural Sciences and Engineering Research Council of Canada for its continuing financial assistance.

1. R. P. STEER. Rev. Chem. Intermediates, **4**, 1 (1981).
2. V. RAMAMURTHY. *In* Organic photochemistry. Vol. 7. *Edited by* A. Padwa. Marcel Dekker Inc. 1985. Chap. 4.
3. P. J. BRUNA, R. J. BUENKER, and S. D. PEYERIMHOFF. Chem. Phys. **22**, 375 (1977).
4. P. J. BRUNA, S. D. PEYERIMHOFF, R. J. BUENKER, and P. ROSMUS. Chem. Phys. **3**, 35 (1974).
5. A. E. BRUNO, D. J. CLOUTHIER, P. G. MEZEY, and R. P. STEER. Can. J. Chem. **59**, 952 (1981).
6. R. H. JUDGE, D. C. MOULE, A. E. BRUNO, and R. P. STEER. Chem. Phys. Lett. **102**, 385 (1983).
7. S. PAONE, D. C. MOULE, A. E. BRUNO, and R. P. STEER. J. Mol. Spectrosc. **107**, 1 (1984).
8. P. G. BURTON, S. D. PEYERIMHOFF, and R. J. BUENKER. Chem. Phys. **73**, 83 (1982).
9. D. S. L. BLACKWELL, K. H. LEE, P. DE MAYO, G. L. R. PETRASUNIAS, and G. REVERDY. Nou. J. Chim. **3**, 123 (1979).
10. A. COUTURE, J. GOMEZ, and P. DE MAYO. J. Org. Chem. **46**, 2010 (1981).
11. N. RAMNATH, V. RAMESH, and V. RAMAMURTHY. J. Org. Chem. **48**, 214 (1873).
12. A. MACIEJEWSKI, D. R. DEMMER, D. R. JAMES, A. SAFARZADEH-AMIRI, R. E. VERRALL, and R. P. STEER. J. Am. Chem. Soc. **107**, 2831 (1985).
13. M. B. ROBIN. Higher excited states of polyatomic molecules. Vol. I. Academic Press, New York. 1974.
14. M. B. ROBIN. Higher excited states of polyatomic molecules. Vol. III. Academic Press, New York. 1985. p. 269.

Can. J. Chem. Downloaded from www.nrcresearchpress.com by 176.9.209.113 on 09/07/12
For personal use only.

Relative rate constants for abstraction of hydrogen by methyl radicals from ethane and from ethylene

S. I. AHONKHAI[1] AND M. H. BACK

Ottawa-Carleton Institute for Graduate Studies and Research, University of Ottawa Campus, Ottawa, Ont., Canada K1N 6N5

Received June 26, 1987

This paper is dedicated to Professsor J. A. Morrison

S. I. AHONKHAI and M. H. BACK. Can. J. Chem. **66**, 578 (1988).

A method is described for the measurement of relative rate constants for abstraction of hydrogen by methyl radicals from ethane and from ethylene based on the effect of the addition of small quantities of ethane on the rates of formation of products in the thermal reactions of ethylene. The ratio of rate constants for reactions

[3] $CH_3 + C_2H_4 \rightarrow CH_4 + C_2H_3$

[4] $CH_3 + C_2H_6 \rightarrow CH_4 + C_2H_5$

over the temperature range 673–733 K was given by the following expression:

$$\log k_4/k_3 = 0.0 \pm 0.1 + \frac{3500 \pm 500}{2.3RT}$$

($R = 1.987$ cal mol^{-1} deg^{-1}). Using a value of k_4 from the literature the following expression was obtained for k_3, over the same range of temperature:

$$\log k_3 \,(\text{L mol}^{-1}\,\text{s}^{-1}) = 8.8 \pm 0.1 - \frac{15500 \pm 500}{2.3RT}$$

It was concluded that a previous measurement of k_3 in a lower range of temperature was too close to the value of k_4.

S. I. AHONKHAI et M. H. BACK. Can. J. Chem. **66**, 578 (1988).

On décrit une méthode permettant de mesurer les constantes relatives de vitesse pour les réactions d'enlèvement d'hydrogène, par des radicaux méthyles, de l'éthane et de l'éthylène; la méthode est basée sur l'effet de l'addition de faibles quantités d'éthane sur les vitesses de formation des produits dans les réactions thermiques de l'éthylène. Le rapport des constantes de vitesse pour les réactions

[3] $CH_3 + C_2H_4 \rightarrow CH_4 + C_2H_3$

[4] $CH_3 + C_2H_6 \rightarrow CH_4 + C_2H_5$

à des températures allant de 673 à 733 K, peut être exprimée par l'équation suivante:

$$\log k_4/k_3 = 0{,}0 \pm 0{,}1 + \frac{3500 \pm 500}{2.3RT}$$

($R = 1{,}987$ cal mol^{-1} deg^{-1}). En se basant sur une valeur de k_4 tirée de la littérature, on a pu obtenir l'expression suivante pour k_3, aux températures considérées:

$$\log k_3 \,(\text{L mol}^{-1}\,\text{s}^{-1}) = 8{,}8 \pm 0{,}1 - \frac{15500 \pm 500}{2{,}3RT}$$

On en conclut qu'une mesure antérieure de k_3 dans la zone inférieure des températures était trop proche de la valeur de k_4.

[Traduit par la revue]

Introduction

The rates of abstraction or transfer reactions of methyl radicals with various types of hydrocarbons have been throughly studied during the past three decades and the general features of these reactions are well understood (1–3). Although rate constants for the transfer reaction with several olefins have been reported, values of the rate constant for abstraction from ethylene are conspicuously absent. Only two measurements have been reported, one relative to abstraction from acetone (4) and the other relative to acetaldehyde (5). No measurements have been reported above 833 K. Nevertheless this reaction is important in many thermal reactions of hydrocarbons over a wide range of temperatures and a reliable value for the rate constant is crucial in the evaluation of mechanisms through modelling studies. The reaction is also important through its relation to the fundamental properties of the vinyl radical.

Recently a method was developed for measuring the rate of initiation of thermal chain reactions of ethylene in the neighbourhood of 750 K (6, 7). The method was based on the analysis of the effect of small quantities of certain additives on the rate of reaction. The measurement of the ratio of rates of formation of products in the presence and absence of the additive was shown to be directly related to the rates of initiation of the chain reactions in the presence and absence of the additive. The system was a special case of the general effect of additives on the kinetics of the thermal reactions of hydrocarbons analyzed extensively by Professor M. Niclause and his colleagues at the Université de Nancy, France (8–10). Studies of these systems have provided a wealth of information on the mechanism of these reactions and on the values of rate constants for the elementary reactions occurring in these systems.

[1]Present address: Department of Chemistry, University of Benin, Benin City, Nigeria.

Can. J. Chem. Downloaded from www.nrcresearchpress.com by 176.9.209.113 on 09/07/12
For personal use only.

Can. J. Chem. Downloaded from www.nrcresearchpress.com by 176.9.209.113 on 09/07/12
For personal use only.

The effect of small quantities of additives on the rate of a thermal chain reaction usually occurs by two main mechanisms. The additive may enter into chain propagation reactions, particularly if it has a labile hydrogen atom, and as a result the overall rate of the reactions may be either accelerated or inhibited. The additive itself may also undergo dissociation and thus increase the total rate of initiation. This effect increases the overall rate of the reactions. In the analysis of the effects of the additive the basic assumption is made that neither the addition of a new initiation step nor the contribution to the propagation reactions alter significantly the general features of the chain reaction. The dominant chain-carrying radicals and termination steps remain the same. Under these conditions if the additive increases the rate of initiation of radicals the rate of product formation increases but the relative amounts of each product remain unchanged. On the other hand, if the additive enters into the propagation steps and alters the relative rates of these steps, the product distribution may change.

In the studies of the ethylene system (7) both effects of additives were observed but most of the measurements were made where the only effect of the additive was the addition of a new initiation process. Consider as an example the effects of small quantities of ethane on the kinetics of chain reactions of ethylene, the system which will be discussed further in this study. Because ethylene is very reactive toward chain propagation through addition of radicals, small quantities of ethane, whose reactivity toward radical attack is smaller, do not disturb the chain propagation reactions. On the other hand, ethane undergoes bond dissociation more readily than ethylene and small amounts provide a significant increase to the initiation of radicals. In previous studies additions of less than about 2% ethane increased the rate of formation of the main products, methane, propylene, and butene-1 equally, indicating an increased rate of initiation, in other words, an increased concentration of radicals, rather than an alteration to the rates of the various propagation reactions.

In the absence of ethane the main initiation process is the bimolecular formation of radicals,

[1] $2C_2H_4 \rightarrow C_2H_5 + C_2H_3$

while in the presence of ethane the additional process

[E] $C_2H_6 \rightarrow 2CH_3$

occurs. When this is the only effect of ethane the ratio of rates of product formation may be expressed as (7),

$$[2] \quad \frac{(V^0)_a}{V^0} = \left[1 + \frac{k_E[C_2H_6]}{k_1[C_2H_4]^2}\right]^{1/2}$$

where $(V^0)_a$ and V^0 refer to the initial rate of product formation with and without an additive, respectively. This ratio is also an expression of the relative concentration of radicals with and without an additive. Note that although reaction [E] produces methyl radicals the identity of the radical is not important. The methyl radicals rapidly convert to the mix of radicals present in ethylene reacting by itself, since the propagation reactions are not disturbed by the addition of ethane.

With concentrations of ethane greater than about 5% the product distribution changed and the ratio of rates of formation of methane in the presence and absence of ethane was considerably larger than similar ratios for propylene and butene-1. Since methane is formed by abstraction of hydrogen by methyl radicals, while propylene and butene-1 are formed by decomposition of larger radicals, this effect was interpreted to indicate that in addition to the effect on the total initiation, ethane entered into propagation reactions by providing a more easily abstractable hydrogen atom. Ethane did not affect the rate of formation of unsaturated products formed by a sequence of addition and decomposition reactions which did not involve abstraction. The rate of formation of these products increased only when the rate of initiation was significantly increased.

In the presence of ethane, methane was therefore formed by both of the following reactions,

[3] $CH_3 + C_2H_4 \rightarrow CH_4 + C_2H_3$

[4] $CH_3 + C_2H_6 \rightarrow CH_4 + C_2H_5$

The ratio of the initial rate of formation of methane in the presence and absence of ethane, taking into account the change in concentration of radicals given by eq. [2], may be expressed as follows,

$$[5] \quad \frac{(V^0_{CH_4})_a}{V^0_{CH_4}} = \left[1 + \frac{k_E[C_2H_6]}{k_1[C_2H_4]^2}\right]^{1/2}\left[1 + \frac{k_4[C_2H_6]}{k_3[C_2H_4]}\right]$$

Thus to measure k_4/k_3 it is necessary to measure only methane, the product formed by abstraction, and other reactions of the methyl radical need not be considered.

When the additive affects both initiation and propagation, extraction of the ratios of rate constants is subject to some uncertainty, although some systems have been successfully analyzed (11). To exploit the system to obtain ratios of rate constants for abstraction reactions, reaction conditions were sought where the saturated hydrocarbon additive affected only the rates of propagation reactions. These conditions were low temperatures, where the rate of dissociation of the additive becomes negligible compared to the rate of initiation by ethylene itself, and higher concentration of additive where the saturated hydrocarbon may compete with ethylene for abstraction of hydrogen. The present paper describes the results of the addition of ethane to ethylene over the temperature range 673–777 K and illustrates the alteration in the effect of the additive from only new initiation, as observed previously over a higher temperature range, to only new propagation reactions.

Experimental

The experiments were performed in a conventional static pyrolysis system, similar to that described previously (6) but with some modifications. The quartz reaction vessel, with a volume of 210 cm^3 and S/V ratio of 1 cm^{-1}, was housed in a stainless steel cylinder inside a Lindberg cylindrical furnace with three separately-controlled heating zones. The temperature gradient along the length of the vessel was less than one degree and temperatures were reproducible to $\pm 1°$ in a set of experiments. Mixtures of gases were prepared in flasks designed with minimum connecting tubing by admitting first a low pressure of ethane followed by a higher pressure of ethylene. Reactants were thoroughly de-gassed in small quantities before mixing and mixtures were not condensed after preparation. The concentration of ethane in the mixture was analyzed in each experiment.

Products were analyzed by gas chromatography (Hewlett Packard Model 5790). A phenylisocyanate column (3.4 m × 4 mm) gave separation of the four main products, methane, ethane, propylene, and butene-1 from the reactant ethylene, although small yields of propylene and butene-1 were sometimes lost in the tail of the ethylene peak. Analysis centered on these products because they served to describe the effect of an additive on the reaction rate. Ethylene and ethane were research purity gases from Matheson, Whitby, Ont., Canada L1N 5R9. The main impurity in ethylene was ethane. Since ethane was the additive, purification was not pursued. Further purification of ethane also was not required because only small quantities were used.

Can. J. Chem. Downloaded from www.nrcresearchpress.com by 176.9.209.113 on 09/07/12
For personal use only.

The success of the method depends on the accuracy of measurement of the ratio of rates with and without an additive. In previous studies (6, 7) several experiments were performed in pure ethylene for measuring the rates of formation of products, followed by a similar series on the mixtures. The ratios were then obtained from these two averaged rates. In the present study one experiment using pure ethylene was followed immediately by an experiment using a mixture under identical conditions. In this way the measurement of the ratio of rates was emphasized rather than the measurement of separate rates of formation in pure ethylene and in mixtures. The ratios of rates were measured under a variety of conditions of reaction time, composition of the mixtures, and total pressure.

In previous studies (6, 7) measurements in packed vessels with a large increase in S/V ratio had shown that surface reactions are not important in the thermal reactions of ethylene at these temperatures, and such measurements were not repeated in this study.

Results and discussion

The ratios of rates of formation of the main products, methane, propylene, and butene-1 in the presence and absence of ethane were measured over the temperature range 673–764 K at total pressures between 186 and 365 Torr and with ratios of ethane/ethylene between 0.013 and 0.106. The results are summarized in Table 1. In contrast to the results of the previous study, which were well described by eq. [2], the ratios of the rates of formation of methane in the presence and absence of ethane were a linear function of the ratio of ethane/ethylene. For experiments in the lower temperature range the rate of initiation by ethane is negligible compared to the rate of initiation in pure ethylene and the term in the first square brackets in eq. [5] is not significantly greater than one. Two examples are shown in Fig. 1.

The rates of formation of propylene and butene-1 were essentially unchanged by the addition of ethane at temperatures up to 705 K. With further increase in temperature the rates of formation of these products showed a small increase on addition of ethane, the ratio approaching a value of about 1.3 for both products at the highest temperature of 764 K. As discussed in the Introduction this increase in the rates of formation of these products indicates that addition of ethane has increased the total rate of initiation. This effect causes a corresponding increase in the rate of formation of methane. Above 705 K addition of ethane therefore affects the rate of formation of methane in two ways, abstraction from ethane and an increased rate of initiation.

To obtain the increase in rate due only to abstraction, the ratio of rates must be corrected for the effect of the new initiation. From eq. [5] the correction factor is

$$\left[1 + \frac{k_E[C_2H_6]}{k_1[C_2H_4]^2}\right]^{1/2}$$

This factor may be calculated using the value for k_1 measured in the previous study (7) and a value for k_E from the literature (12).

$$k_1 = 11.27 - \frac{64200}{2.3RT} \text{ (L mol}^{-1}\text{ s}^{-1}\text{)}$$

$$k_E = 16.72 - \frac{88850}{2.3RT} \text{ (s}^{-1}\text{)}$$

The factor is also equal to the ratio of rates of formation of propylene or butene-1, on the assumption that these products are not formed by abstraction reactions. Values of k_4/k_3, obtained from the slopes of plots shown in Fig. 1, were corrected using both calculated and experimental factors. The results are given in Table 2. The estimated errors span the values obtained using two methods of correction. The experimental correction is approximate because in many of the experiments the yields of propylene and butene-1 were too small for accurate measurement, appearing as they did on the tail of the large ethylene peak. The average values of k_4/k_3 are shown in an Arrhenius plot in Fig. 2.

TABLE 1. Ratio of initial rates of formation of products in the presence and absence of ethane

T_1 (K)	$p^0_{C_2H_4}$ (Torr)	$\frac{C_2H_6}{C_2H_4}$	$\frac{(V^0)_a}{V^0}$ CH$_4$	$\frac{(V^0)_a}{V^0}$ C$_3$H$_6$	$\frac{(V^0)_a}{V^0}$ C$_4$H$_8$ − 1
673	259	0.0146	1.42	0.85	0.80
	186	0.0293	1.43	—	—
	254	0.106	2.32	—	—
	254	0.106	2.61	—	0.95
	259	0.106	2.63	0.70	—
692	288	0.0135	1.18	1.01	0.97
	219	0.015	1.72	1.0	0.81
	211	0.029	1.87	1.20	1.24
	288	0.045	1.83	0.98	0.96
	211	0.069	2.0	—	—
	221	0.093	2.1	—	—
705	303	0.0135	1.20	0.85	0.87
	221	0.0292	1.38	—	—
	303	0.045	1.60	0.85	0.87
	220	0.0693	1.94	—	—
718	226	0.0130	1.46	1.24	1.21
	222	0.0462	1.69	1.03	1.03
	225	0.0462	1.99	1.14	1.19
	222	0.093	2.59	1.15	1.15
733	224	0.0130	1.36	—	—
	223	0.0130	1.12	—	—
	364	0.0293	1.30	1.13	—
	225	0.0462	1.62		
	356	0.074	2.8	1.46	1.41
	222	0.093	2.85	1.22	1.22
748	225	0.0130	1.45	1.33	1.25
	285	0.0293	1.77	1.5	—
	225	0.0463	1.59	1.13	1.11
	225	0.093	2.84	1.32	1.32
764	201	0.0130	1.31	1.14	1.13
	287	0.0292	1.52	1.35	—
	203	0.0463	1.69	1.03	—
	201	0.093	2.69	1.26	1.32
777*	204	0.0828	2.53	1.6	1.7

*Previous measurement, ref. 7.

Also included in Table 2 and Fig. 2 is the result of a measurement made in the previous study (7) where the ratio of ethane/ethylene was 0.0828 and the ratio of the rate of formation of methane in the presence and absence of ethane was 2.53 compared to 1.6 for the similar ratio for the products propylene and butene-1. In this case the experimental and calculated correction for initiation is the same, since the value of k_1 was obtained from these measurements.

Before analyzing the values of k_4/k_3 in terms of an Arrhenius expression, the applicability of this expression for this ratio in this temperature range should be examined. Reaction [4] has been measured over a wide range of temperature and the results

TABLE 2. Values of k_4/k_3 obtained from eq. [5]

T_1 (K)	k_4/k_3 Uncorrected	k_4/k_3 Corrected, experimental	k_4/k_3 Corrected, calculated	log k_4/k_3	log k_4† (L mol^{-1} s^{-1})	log k_3 (L mol^{-1} s^{-1})
673	14.5±2			1.16±0.06	4.94	3.78
692	16±4			1.20±0.1	5.07	3.87
705	15±2			1.17±0.06	5.16	3.99
718	16.5±2	13	12	1.11±0.06	5.22	4.11
733	18	13	11.5	1.11±0.06	5.31	4.20
748	17.5±2	11	9.6	1.04±0.07	5.40	4.36
764	18±2	11	7.5	0.97±0.10	5.51	4.54
777*		7.0		0.845±0.04	5.61	4.76

*Result from ref. 7.
†Data from Furue and Pacey (15).

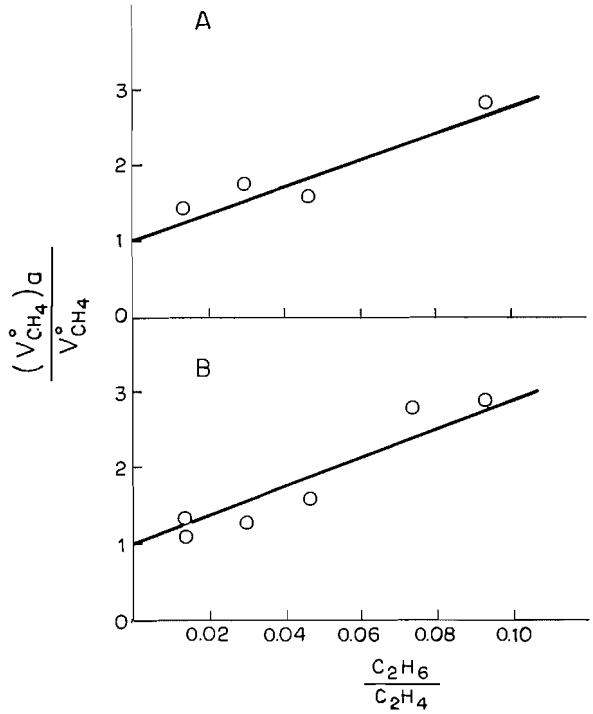

FIG. 1. Plot of the ratio of the initial rate of formation of methane in the presence and absence of ethane as a function of the ratio of the initial concentrations of ethane and of ethylene.

	Temperature, K	Range of pressure of ethylene, Torr
A	748	223–364
B	733	225–285

have been summarized and evaluated by Kerr and Moss (2). They recommend the following expression for k_4,

$$[6] \quad \log k_4\,(\text{L mol}^{-1}\,\text{s}^{-1}) = 8.75 - \frac{11600}{2.3RT}$$

and suggest this may be valid up to 800 K. The non-Arrhenius dependence of the rate constant has been illustrated and analyzed (13–15). Clark and Dove (13) derived an expression for k_4 to describe a continuous curve on an Arrhenius plot and linked values measured in the high and low temperature ranges. Their values are greater than those obtained from eq. [6] by a factor of

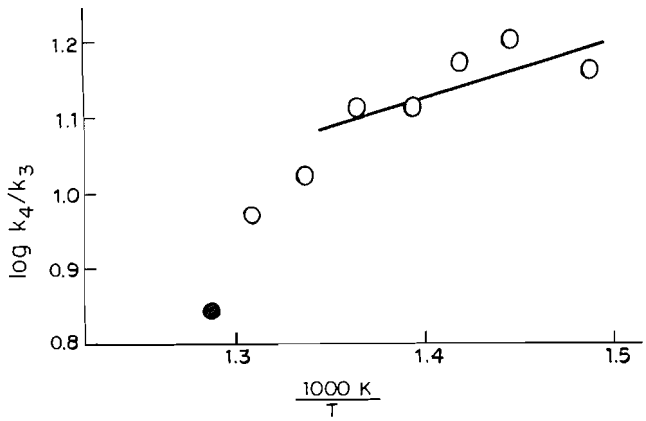

FIG. 2. Average values of k_4/k_3 as a function of $1/T$. ●: ref. 7.

about 2.5 in this temperature range. Furue and Pacey (15) clarified the effects leading to non-Arrhenius behaviour and modified the expression suggested by Clark and Dove. The values obtained from their expression are indistinguishable from those of eq. [6] up to about 730 K. The temperature range of the present experiments is therefore placed just at the beginning of the region where non-Arrhenius effects should become important.

This may be illustrated by an Arrhenius plot of the values for k_3 (Fig. 3) obtained by combining the present measurement of the ratio k_4/k_3 with values of k_4 obtained from the expression proposed by Furue and Pacey and the evaluated Arrhenius expression of Kerr and Moss. It seems clear that non-Arrhenius effects are significant at the three highest temperatures and that Arrhenius parameters should therefore be obtained using only results of the five lowest temperatures. This leads to an average value for k_3 in this region given by

$$[7] \quad \log k_3\,(\text{L mol}^{-1}\,\text{s}^{-1}) = 8.8 \pm 0.1 - \frac{15500 \pm 500}{2.3RT}$$

Similarly, from Fig. 2, the Arrhenius expression for the ratio, k_4/k_3 derived from the five lowest temperatures only, is given as follows:

$$[8] \quad \log k_4/k_3 = 0.0 \pm 0.1 + \frac{3500 \pm 500}{2.3RT}$$

This result suggests that the frequency factors for abstraction from ethane and ethylene are virtually the same, at least in the

Can. J. Chem. Downloaded from www.nrcresearchpress.com by 176.9.209.113 on 09/07/12
For personal use only.

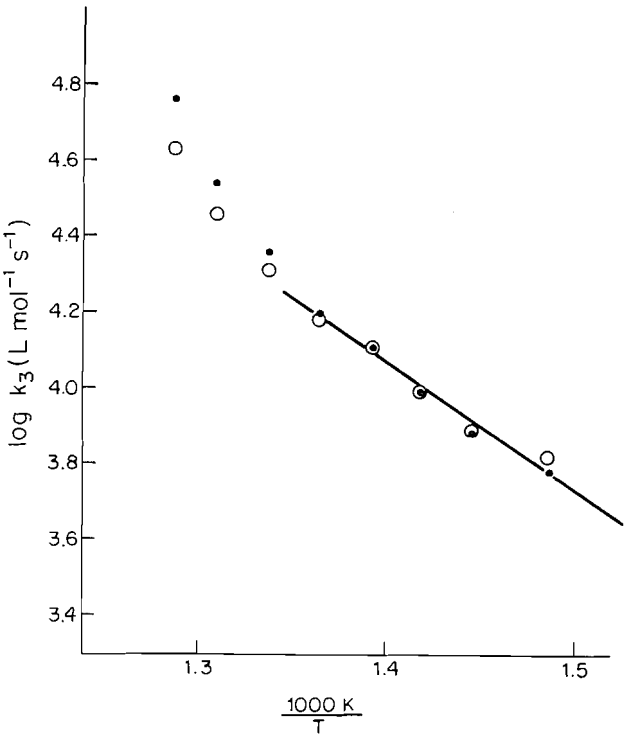

FIG. 3. Arrhenius plot of k_3 obtained using values of k_4 from ●, Furue and Pacey (15) and ○, Kerr and Moss (2).

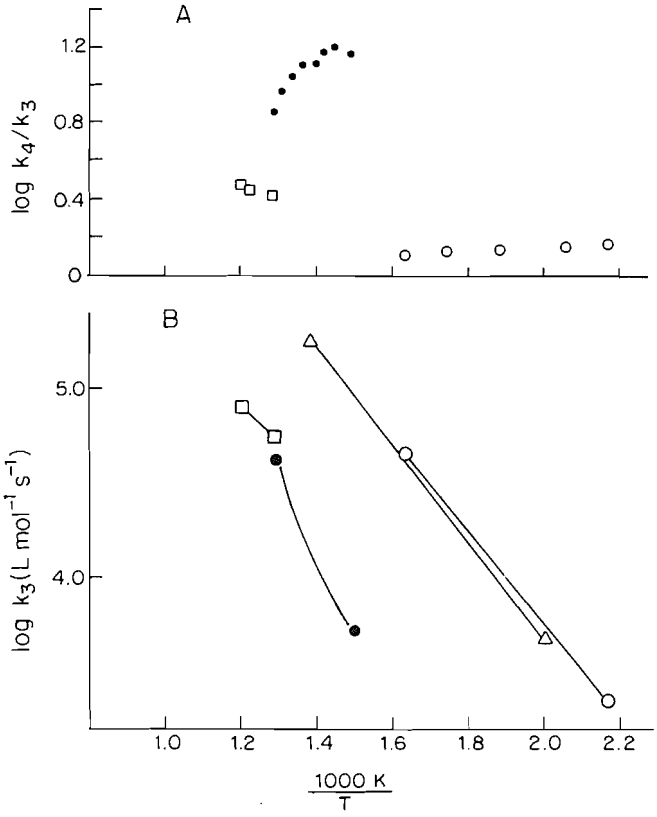

FIG. 4. Comparison of k_3 and the ratio k_4/k_3 with previous measurements, as an Arrhenius plot. ●, Present measurements; ○, Trotman-Dickenson and Steacie (4); □, Rice and Varnerin (5); △, k_4 from Kerr and Moss (2).

region where the rate constant follows an Arrhenius dependence. Most measurements of rates of abstraction from alkanes and from alkenes give frequency factors of approximately the same value. To estimate the difference in activation energies, it seems justified if we neglect the results at the three highest temperatures. It should be noted that the non-Arrhenius behaviour of the ratio at the higher temperatures implies that the curvature in k_3 with increasing temperature is more pronounced than in k_4.

The value for k_3 obtained in the present measurements may be compared with the two previous measurements, both made in rather different systems. The system studied by Trotman-Dickenson and Steacie (4) involved the photolysis of deuterated acetone in the presence of ethylene and the measurements gave the ratios of rate constants for abstraction from ethylene and from acetone.

[9] $CD_3 + C_2H_4 \rightarrow CD_3H + C_2H_3$

[10] $CD_3 + CD_3COCD_3 \rightarrow CD_4 + CD_2COCD_3$

Values of k_9 were obtained using the well-documented values for k_{10} (2). Rice and Varnerin (5) studied the pyrolysis of deuterated acetaldehyde in the presence of ethylene and their measurements gave the ratio of rate constants for abstraction from ethylene and from acetaldehyde.

[9] $CD_3 + C_2H_4 \rightarrow CD_3H + C_2H_3$

[11] $CD_3 + CD_3CDO \rightarrow CD_4 + CD_3CO$

Similarly, values of k_9 were obtained using measured values for k_{11} (2). For the purpose of this comparison k_9 is assumed to be indistinguishable from k_3, since the difference is the result of a secondary isotope effect and well inside the other errors in these measurements.

These values of k_3 are shown in Fig. 4*B*, together with the values for k_4 recommended by Kerr and Moss. In spite of the much lower activation energy for k_3 obtained by Rice and Varnerin the extrapolation of the present measurements of k_3 correlates well with their rate constants. On the other hand, measurements by Trotman-Dickenson and Steacie are more than ten times greater than the present results, and are in fact practically the same as the recommended value for k_4.

These differences are not due to discrepancies in the reference reactions, because the same differences are apparent in the ratio k_4/k_3, Fig. 4*A*, derived from the results reported for both ethane and ethylene in each system. The present results show that abstraction from ethane is considerably faster than from ethylene but the results of Trotman-Dickenson and Steacie indicated that these rates of abstraction were similar, which seems unlikely. Although it is difficult to identify a reason for the apparently fast rate of abstraction from ethylene observed in the experiments of Trotman-Dickenson and Steacie, it seems likely that a small impurity with a labile hydrogen atom could lead to an erroneously fast production of CD_3H.

The present results indicate that the activation energy for abstraction from ethylene is higher than that for abstraction from ethane, in accord with the greater C—H bond dissociation energy in ethylene as compared to ethane. The relation between activation energy and bond dissociation energy for a series of similar reactions has been discussed many times, particularly for hydrogen atom abstraction reactions. Recently a simple correlation has been described for such reactions involving small radicals (16). For the case of methyl radicals, the following relation

Can. J. Chem. Downloaded from www.nrcresearchpress.com by 176.9.209.113 on 09/07/12
For personal use only.

was suggested,

$$E = 0.609D_1 - 0.473D_2$$

for a reaction of the type

$$CH_3 + AH \rightarrow CH_4 + A$$

where E is the activation energy for the reaction and D_1 and D_2 are the C—H bond dissociation energies for AH and CH_4, respectively. For reaction [4], taking $D_1 = 100$ kcal mol^{-1} and $D_2 = 104$ kcal mol^{-1},

$$E = 11.7 \text{ kcal mol}^{-1}$$

in good agreement with the value recommended by Kerr and Moss. For reaction [3], setting $E = 15.5$ kcal mol^{-1} leads to a value of 106 kcal mol^{-1} for D_1. The uncertainty is at least ± 1 kcal mol^{-1}.

It should be pointed out that this value for the dissociation energy in ethylene indicates an activation energy for reaction [1] of 67 kcal mol^{-1} rather than the value of 64.2 kcal mol^{-1} used in the calculation of the correction factor. Since the calculated and experimental correction factors were similar within each uncertainty it seems likely that the value used for k_1 was reasonable. If E_1 is larger the frequency factor may also be larger, leading to a similar value for k_1. The Arrhenius parameters for reaction [1] are not yet firmly established.

Summary

The present results have shown that the rate constant for abstraction of hydrogen by methyl radicals from ethane is between ten and twenty times faster than that for abstraction from ethylene in the temperature range 673–777 K. The difference in activation energy between the two reactions in the low temperature region is 3.5 kcal mol^{-1}. It is concluded that a previous measurement of the rate constant for abstraction from ethylene in the temperature range 461–613 K is too large.

Acknowledgments

The authors thank the NSERC of Canada for financial support of this research. S.I.A. also thanks the NSERC for the award of a CIDA/NSERC Research Associateship, making his visit to Canada possible. Thanks also to Dr. R. A. Back for helpful comments on the manuscript.

1. J. A. Kerr and M. J. Parsonage. Evaluated kinetic data on gas-phase hydrogen transfer reactions of methyl radicals. Butterworths, London. 1976.
2. J. A. Kerr and S. J. Moss. CRC Handbook of bimolecular and termolecular gas reactions. Vol. 1. CRC Press, Boca Raton, U.S.A. 1981.
3. L. Batt. Reactions of methyl radicals. CRC Press, Boca Raton, FL, U.S.A. 1987.
4. A. F. Trotman-Dickenson and E. W. R. Steacie. J. Chem. Phys. **19**, 169 (1951).
5. F. O. Rice and R. E. Varnerin. J. Am. Chem. Soc. **77**, 221 (1955).
6. G. Ayranci and M. H. Back. Int. J. Chem. Kinet. **13**, 897 (1981).
7. G. Ayranci and M. H. Back. Int. J. Chem. Kinet. **15**, 83 (1983).
8. M. Niclause, F. Baronnet, G. Scacchi, J. Muller, and J. Y. Jezequel. Industrial and Laboratory Pyrolysis, ACS Symposium Series 32. 1976. p. 17.
9. R. Martin, M. Niclause, and G. Scacchi. Industrial and laboratory pyrolysis. ACS Symposium Series 32. 1976. p. 37.
10. G. Scacchi, F. Baronnet, and M. Niclause. Can. J. Chem. **60**, 249 (1982); **60**, 257 (1982).
11. C. Richard, A. Boiveaut, and R. Martin. Int. J. Chem. Kinet. **12**, 921 (1980).
12. A. B. Trenwith. J. Chem. Soc. Faraday Trans. I, **75**, 614 (1979).
13. T. C. Clark and J. E. Dove. Can. J. Chem. **51**, 2147 (1973).
14. W. C. Gardiner. Acc. Chem. Res. **10**, 326 (1977).
15. H. Furue and P. D. Pacey. J. Phys. Chem. **90**, 397 (1986).
16. G. Leroy, M. Sana, and A. Tinant. Can. J. Chem. **63**, 1447 (1985).

Can. J. Chem. Downloaded from www.nrcresearchpress.com by 176.9.209.113 on 09/07/12
For personal use only.

Molecular orbital calculations and ^1H nuclear magnetic resonance spectra as indicators of internal rotational potentials in some methyl derivatives of styrene

TED SCHAEFER, RUDY SEBASTIAN, AND GLENN H. PENNER
Department of Chemistry, University of Manitoba, Winnipeg, Man., Canada R3T 2N2

Received June 4, 1987

This paper is dedicated to Professor J. A. Morrison

TED SCHAEFER, RUDY SEBASTIAN, and GLENN H. PENNER. Can. J. Chem. **66**, 584 (1988).

The ^1H nuclear magnetic resonance spectra of the α-methyl, *cis* and *trans*-β-methyl, 4-methyl, and β,β-dimethyl styrenes are analyzed to yield long-range proton–proton coupling constants. With the assumptin that the internal rotational potential for styrene in the gas phase is unaltered in solution, a consistent treatment of over 40 of the long-range coupling constants is given in terms of the known coupling mechanisms. Expectation values of $\sin^2\theta$, where θ is the angle of twist about the exocyclic carbon–carbon bond, are presented for these molecules. These are compared with theoretical potentials at the 6-31G level of molecular orbital theory. The present data indicate rather larger average twist angles than those in the literature. The extrema (at θ = 0° and 90°) in the angle dependent long-range coupling constants appear to be rather smaller in magnitude than are theoretical values obtained from valence bond and molecular orbital approaches.

TED SCHAEFER, RUDY SEBASTIAN et GLENN H. PENNER. Can. J. Chem. **66**, 584 (1988).

On a analysé les spectres en résonance magnétique nucléaire du ^1H des α-méthyl, β-méthyl-*cis* et -*trans*, méthyl-4et β,β-diméthyl styrènes afin d'en tirer les constantes de couplage proton–proton à longue distance. En faisant l'hypothèse que le potential à la barrière interne du styrène est le même en phase gazeuse qu'en solution, on peut traiter d'une façon consistante plus de 40 constantes de couplage à longue distance en fonction des mécanismes connus de couplages. Pour ces molécules, on présente les valeurs attendues pour $\sin^2\theta$, dans lesquelles θ est l'angle torsion autour de la liaison carbone–carbone exocyclique. On les compare aux potentiels calculés par la théorie des orbitales moléculaires au niveau 6-31G. Les données obtenues dans notre travail suggèrent que les angles moyens de torsion sont plus grands que ceux rapportés dans la littérature. Les amplitudes des valeurs extrêmes (à des valeurs de θ de 0° et de 90°) dans les constantes de couplage à longue distance qui dépendent de l'angle semblent être plus faibles que celles que nous laissent prévoir les approches des liaisons de valence et des orbitales.

[Traduit par la revue]

Introduction

The torsional potential (1) about the C(1)—C(α) bond in styrene in the gas phase can be written (2) as eq. [1], where θ is zero

$$[1]\quad V/\text{kJ mol}^{-1} = V_2 \sin^2\theta + V_4 \sin^2 2\theta$$
$$= (12.80 \pm 0.10)\sin^2\theta - (3.29 \pm 0.01)\sin^2 2\theta$$

in the planar form and a sixfold component, V_6, of 0.08 kJ/mol is ignored. Computations, with full geometry optimization, at the 6-31G level of *ab initio* molecular orbital theory give V_2 as 13.19 ± 0.15 kJ/mol and V_4 as −3.18 ± 0.15 kJ/mol (3). Even the 4-31G calculations (2) do not deviate dramatically from eq. [1].

It is not known whether eq. [1] governs the internal motion in solution, although solvent effects might well be small for a hydrocarbon of low polarity. Even for a polar compound like benzyl fluoride the internal rotational potential changes by only 2 kJ/mol as the solvent changes from CS_2 to a polar solvent like acetone (4). In ethyl benzene the internal rotational potential appears to be independent of solvent (5).

Substitution by methyl groups to yield α-methyl- or *cis*-β-methylstyrenes can alter the internal potential drastically. These potentials have not been determined but various angles θ have been deduced by a number of techniques (6–10). A recent variation (6) on the usual (7) interpretation of the photoelectron spectra of these molecules yields some θ values and it is stated (6) that, unfortunately, no accurate data are available on their conformations, knowledge of which is useful for the interpretation of their photochemistry.

It appears that the θ values in the literature, really arc cos $\langle\cos^2\theta\rangle^{1/2}$, are based on an assumed zero for styrene itself, implying that revision is in order.

The success of the molecular orbital calculations on styrene suggests their application to the α- and β-methylstyrenes and such computations are reported here.

In addition, the analyses of the ^1H nmr spectra of the α, *cis*-β, *trans*-β, and 4-methylstyrenes, as well as a partial analysis of the ^1H nmr spectrum of β,β-dimethylstyrene, are performed. A pioneering study of the long-range spin–spin coupling constants between ring and side-chain protons in halostyrene derivatives demonstrates their potential as conformational indicators (11). This study also presents valence bond and molecular orbital formulation of the coupling mechanisms and provides a base for the work described in the present paper.

It turns out that a reasonably consistent treatment of the long-range coupling constants in the methylstyrenes is possible, leading to estimates of $\langle\sin^2\theta\rangle$ somewhat larger than those commonly accepted.

Results and discussion

Molecular orbital calculations

The 6-31G MO computations allowed geometry optimization with the constraint, however, that the benzene carbon framework remain a planar hexagon. Even so, only three values of θ, at 0°, 45°, and 90°, could reasonably be accommodated (the total cpu time was 36.5 h for *trans*-β-methylstyrene on an Amdahl 470). These three values allow a fit to a potential consisting of twofold and fourfold components.

For *trans*-β-methylstyrene, V_2 and V_4 (see eq. [1]) are computed as 11.2 and -3.5_4 kJ/mol, respectively (the total energy at θ = 0° is −346.501 643 au). At 300 K, one has a $\langle\sin^2\theta\rangle$ of 0.203_4.

For *cis*-β-methylstyrene, in which substantial repulsive interactions between the methyl group and the *ortho* ring C—H bond are anticipated, V_2 is calculated as 1.9_7 and V_4 as -7.3_2 kJ/mol, implying $\langle\sin^2\theta\rangle$ as 0.459 at 300 K. The latest value in the literature is 22 ± 6° for θ, but is based on a θ of zero for

Can. J. Chem. Downloaded from www.nrcresearchpress.com by 176.9.209.113 on 09/07/12
For personal use only.

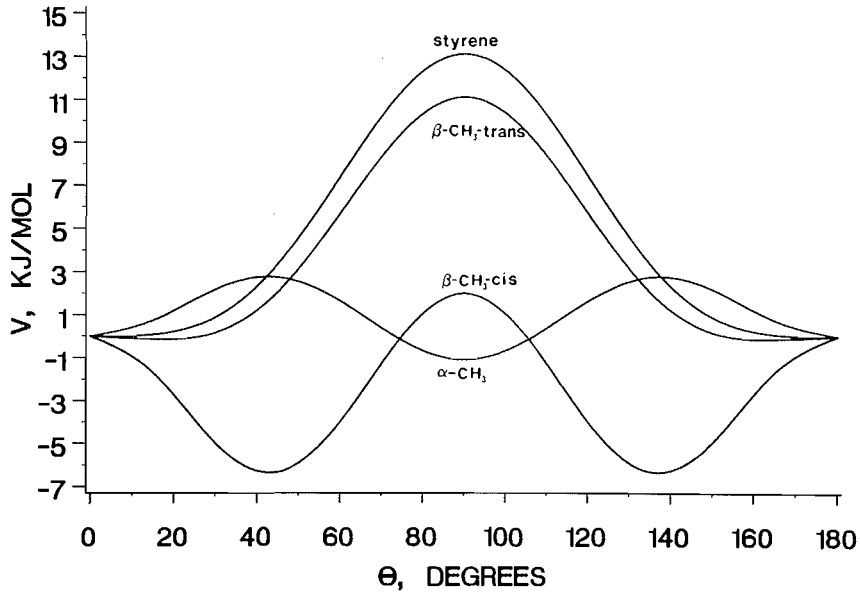

FIG. 1. The 6-31G MO internal rotational potentials about the C(1)—C(α) bond are plotted as a function of the angle θ. The latter is zero for the planar conformation. The potentials contain twofold and fourfold components. That for styrene comes from ref. 3 and has V_2 as 13.19 ± 0.15 kJ/mol and V_4 as −3.18 ± 0.15 kJ/mol. For *trans*-β-methylstyrene, *cis*-β-methylstyrene, and α-methylstyrene, respectively, $V_2(V_4)$ are 11.2 (−3.5), 2.0(−7.3), and −1.1(3.3) kJ/mol. All bond angles and lengths were allowed to vary for these three molecules, but the carbon framework of the phenyl group was constrained to be a regular hexagon and the methyl groups retained threefold symmetry.

styrene (6). At θ = 0°, the total 6-31G energy is −346.495 383 au. The STO 3G MO computations, with geometry optimization at seven values of θ, gave V_2 and V_4 as −1.6 ± 0.2 and −6.1 ± 0.2 kJ/mol, respectively. Hence, at 300 K, $\langle \sin^2 \theta \rangle$ is 0.535. The two calculations agree that V_2 drops markedly from its value of 12.8 kJ/mol in styrene.

For α-methylstyrene, V_2 and V_4 become -1.0_7 and 3.2_7 kJ/mol, respectively, at the 6-31G level of MO theory (the total energy is −346.496 346 au). At 300 K, $\langle \sin^2 \theta \rangle$ is 0.570. V_2 and V_4 have interchanged their signs and the conformation at θ = 90° is now 1.1 kJ more stable than the planar form at θ = 0°.

In Fig. 1 the 6-31G MO potentials are plotted for styrene and the three methylstyrenes. For styrene and its *trans*-β-methyl derivative, these potentials lead to $\langle \sin^2 \theta \rangle$ estimates at 300 K effectively the same as that measured for styrene. For the *cis*-β-methyl derivative, it is anticipated that a strongly nonplanar conformation is caused by large repulsive forces between the methyl group and the *ortho* C—H bond, just as the nonplanarity of styrene itself is plausibly attributable (1) to Pauli overlap of the β and *ortho* C—H bonds. The minimum in the potential curve in Fig. 1 is consistent with this attribution. However, the relatively low energy computed for the perpendicular conformation in this molecule is striking and, at first sight, implies an attractive interaction, perhaps between the methyl group and the aromatic π system, at this θ value. The perpendicular conformation of α-methylstyrene is also unexpectedly stable when viewed from the vantage of conjugative delocalization between the two π electron systems. The following discussion may be of use.

The computed structure of planar α-methylstyrene is shown in Fig. 2. In planar styrene the C(1)C(α)C(β) angle is computed as 127.6° at the same level of MO theory (3), probably so large because of repulsive forces acting between the *ortho* and β C—H bonds. This angle reduces to 124.6° at θ = 90° (3). In the planar α-methylstyrene, this angle is 123.4°. Part of the anticipated increase in the repulsive interaction is relieved by the lengthening of the C(1)C(α) bond from 1.477 to 1.502 Å. The

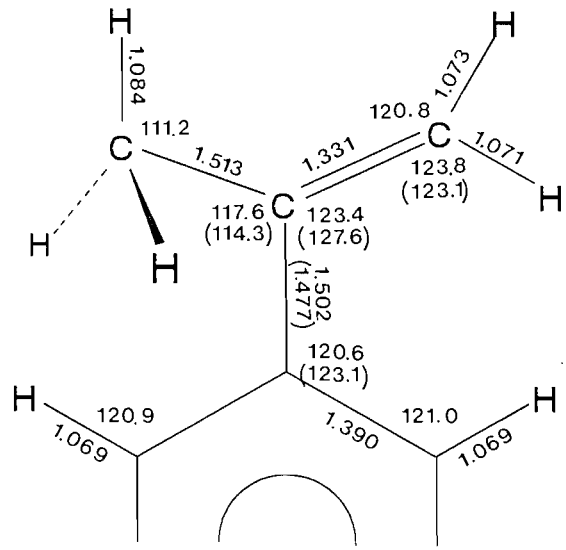

FIG. 2. The 6-31G MO structure of planar α-methylstyrene is shown. Numbers in parentheses are those from another 6-31G computation for planar styrene (3). The present structure assumes threefold symmetry for the methyl group and a regular planar hexagon for the phenyl group. Reference 3 discusses how to adjust the computed bond lengths in styrene to obtain putative experimental lengths. In the computed perpendicular conformer of α-methylstyrene, the C(1)C(α)C(β) angle decreases to 121.5° while the angle C(1)C(α)C(H3) reduces to 115.8°. See the text for similar comparisons for *cis*-β-methylstyrene.

decrease in the C(1)C(α)C(β) angle may arise from the space requirements of the methyl group. The C(1)C(α)C(H3) angle is computed as 117.6°, some 3° larger than the angle C(1)C(α) H in styrene. Note also that the C(2)C(1)C(α) angle in the planar form is 120.6°, some 2.5° less than in planar styrene and consistent with "balancing" steric repulsions at the two *ortho* sites. In the perpendicular conformation, the C(1)C(α)C(H3) angle becomes 115.8°, the C(1)C(α) bond does not change in length, and

Can. J. Chem. Downloaded from www.nrcresearchpress.com by 176.9.209.113 on 09/07/12
For personal use only.

TABLE 1. ^{1}H nuclear magnetic resonance spectral parameters for styrene and some of its methyl derivatives in acetone-d_6 at 300 K, excluding coupling constants between side chain and ring

Parameter	Styrene[a]	4-CH_3[b]	trans-β-CH_3[b]	*cis*-β-CH_3[b]	β,β-diCH_3[c]	α-CH_3[b]
$\nu(CH_3)$[d]	—	690.323(0)[e]	552.906(1)	560.916(1)	562.6,[i] 550.5	640.933(1)
$\nu_2 = \nu_6$	2226	2202.106(1)	2206.833(1)	2192.990(1)	2168.107(5)	2250.156(0)
$\nu_3 = \nu_5$	2189	2143.459(1)	2184.096(1)	2202.559(1)	2191.481(3)	2200.271(1)
ν_4[j]	2167	—	2153.489(1)	2166.109(1)	2151.211(4)	2180.745(1)
$\nu_7(\alpha)$	2016	2012.183(1)	1925.118(1)	1930.868(1)	1883.1	—
$\nu_8(cis)$	1730	1719.205(1)	1884.739(1)	—	—	1616.350(1)
ν_9 (*trans*)	1559	1546.397(1)	—	1734.567(1)	—	1525.209(1)
^2J_g	1.054	1.114(1)	—	—	—	1.634(1)
^3J_c	10.941	10.943(1)	{6.667(1)}[f]	11.641(1)	—	—
^3J_t	17.652	17.657(1)	15.779(1)	{7.197(1)}[f]	—	—
—						
$^4J_c(H,CH_3)$	—	{−0.723(1)}[g]	−1.772(1)	—	—	−1.504(1)
$^4J_t(H,CH_3)$	—	{0.369(0)}[h]	—	−1.876(1)	—	−0.832(1)
$^3J_{23} = {}^3J_{56}$	7.791	7.907(1)	7.807(1)	7.780(1)	7.759(4)	7.905(1)
$^3J_{34} = {}^3J_{45}$	7.445	—	7.432(1)	7.460(1)	7.458(4)	7.429(1)
$^4J_{26}$	1.905	1.997(1)	1.924(1)	1.897(2)	1.871(8)	2.051(2)
$^4J_{24} = {}^4J_{46}$	1.243	—	1.238(1)	1.256(1)	1.256(4)	1.216(1)
$4J_{35}$	1.422	1.956(1)	1.434(1)	1.450(2)	1.480(8)	1.470(2)
$^5J_{25} = {}^5J_{36}$	0.597	0.555(1)	0.604(1)	0.621(1)	0.619(3)	0.594(0)
Calculated trans.	—	2816	2821	2747	134	2800
Assigned trans.	180	1755	1347	1343	64	1631
Observed peaks	—	370	425	483	—	260
Largest diff.	—	0.027	0.031	0.031	0.045	0.025
Root mean square deviation	0.012	0.010	0.011	0.011	0.016	0.009

[a]Chemical shift data were converted to Hz at 300.135 MHz from data at 270 MHz for a 2 mol/L (ca. 16 mol%) solution in acetone-d_6 at 298 K (12). Standard deviations were quoted as 0.002–0.003 Hz (12).
[b]2.5 mol% in acetone-d_6 containing 0.5 mol% of tetramethylsilane (TMS).
[c]5 mol% in acetone-d_6 and internal TMS.
[d]In Hz at 300.135_2 MHz to high frequency of internal TMS.
[e]Numbers in parentheses are standard deviations in the last significant figure.
[f]This is the $^3J(H,CH_3)$ value in the side chain.
[g]This is $^4J_o(H,CH_3)$, the benzylic coupling.
[h]This is $^5J_m(H,CH_3)$.
[i]For β-*cis*-CH_3.
[j]At 300.135 MHz and 300 K, the ν values of the benzene protons are 2198.1_4 Hz for a 16 mol% solution acetone (close to 2 mol/L) and 2205.6_7 Hz for a 2.5 mol% solution in acetone.

the C(i)C(α)C(β) angle reduces to 121.5°, suggesting steric strain involving both *ortho* sites in the planar form. The relatively flat potential curve for α-methylstyrene is then a consequence of a combination of steric destabilization of the planar form, which also reduces π electron conjugation along the C(1)—C(α) bond), followed by partial cancellation of the opposing steric and conjugational energy changes as θ increases. A similar qualitative interpretation of the computed rotational potential for *cis*-β-methylstyrene seems reasonable, altered somewhat by the rather larger destabilizing steric forces in this molecule. Thus, the C(1)C(α)C(β) and C(α)C(β)C(H3) angles are computed as 132.1° and 129.8°, respectively, in the planar form, and decrease by 6.7° and 3.9° in the perpendicular structure. Again, it does appear that conjugational energies may be smaller in this molecule than in styrene. If they were zero, then an attractive interaction of the methyl–π system at θ = 90° would not be present.

^{1}H nuclear magnetic resonance spectral parameters

Tables 1 and 2 contain the ^{1}H nmr spectral parameters for five methylstyrenes. The literature values for styrene (12) are included for comparison. The signs of the long-range coupling constants are based on those determined for styrene (12) and the halostyrenes (11). Signs in brackets are assigned on the basis of the known coupling mechanisms (11).

Theoretical long-range coupling constants

The following discussion refers to the numbering in **1**. The original valence bond calculations (11) predict substantial π electron contributions to *all* coupling constants between ring and olefinic protons, ^nJ (n = 4, 5, 6, or 7 intervening bonds). These contributions have the general form $^nJ/\text{Hz} = A\cos^2\theta + B\sin^2\theta$, where A and B are positive for odd n and are negative for even n. The terms in A arise from π electron delocalization between the conjugated vinyl and phenyl moieties, while those in B come from σ–π interactions.

The INDO MO FPT computations (11) are meant to include also the σ electron components of ^nJ, as well as effects caused by proximity of the bonds containing the coupled nuclei. The details (11) of the numerical results from both types of calculations will not be repeated here.

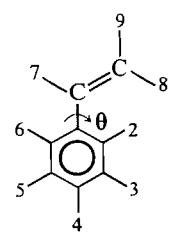

1

Can. J. Chem. Downloaded from www.nrcresearchpress.com by 176.9.209.113 on 09/07/12
For personal use only.

TABLE 2. Inter-ring proton coupling constants for styrene and some of its methyl derivatives[a]

Parameter[b]	Styrene	4-CH_3	*trans*-β-CH_3	*cis*-β-CH_3	β,β-diCH_3	α-CH_3
$^6J_{47}$	−0.227(3)	{(+)0.243(1)}[c]	−0.231(1)	−0.417(1)	0.470(8)	±0.084(1)
$^7J_{49}$	0.281(3)	{(−)0.259(1)}[d]	{(−)0.239(1)}	0.223(1)	—[f]	0.172(1)
$^7J_{48}$	0.237(3)	{(−)0.257(1)}	0.226(1)	{(−)0.153(1)}	—[f]	0.168(1)
$^5J_{37}$	0.368(3)	0.377(1)	0.364(1)	0.356(1)	0.352(6)	{±0.022(0)}
$^6J_{39}$	—	±0.020(1)[e]	{±0.095(0)}	±0.015(1)	—	±0.025(0)
$^6J_{38}$	—	±0.041(1)	±0.033(2)	{±0.030(0)}	—	±0.032(1)
$^4J_{27}$	−0.525(3)	−0.533(1)	−0.529(1)	−0.645(1)	−0.668(9)	{±0.037(0)}
$^5J_{29}$	0.158(3)	0.164(1)	{(−)0.243(1)}	0.280(1)	—	0.166(1)
$^5J_{28}$	—	±0.045(1)	±0.018(1)	±0.185(1)	—	0.000(1)

[a]For the solutions detailed in Table 1.

[b]Note that H-7 is the α proton of the vinyl group, whereas H-8 is the *cis*-β proton.

[c]Numbers in curly brackets involve coupling constants of the methyl protons and therefore refer to a coupling interaction over one more formal bond than is indicated in column 1.

[d]Signs in parentheses are assumed on the basis of the methyl group replacement technique (13), i.e., $^nJ(H,H) \cong -^{n+1}J(H,CH_3)$.

[e]Magnitudes less than 0.035 Hz are probably accurate only to 0.01 Hz, although the presence of these coupling constants is indubitable. Magnitudes of coupling constants below 0.02 Hz are uncertain.

[f]The methyl protons were decoupled, superpositions of quartets from these protons leading to an unanalyzable ring proton spectrum.

Now, it seems quite clear from the pattern of ^nJ in Table 2 that not only the magnitudes of the theoretical contributions to ^nJ but, in some instances, also their very existence is in question (assuming that the conformational preferences of the molecules are not drastically altered in solution).

Consider $^5J_{37}$, for example. According to the valence bond model, $^5J_{37} = 0.39 \cos^2\theta + 1.18 \sin^2\theta$, equivalent to $^5J_{37} = 0.39 + 0.79 \sin^2\theta$. Here 0.39 Hz represents the delocalization term and 1.18 Hz the σ−π term. As $\langle\sin^2\theta\rangle$ increases, therefore, $^5J_{37}$ must increase. Yet $^5J_{37}$ in Table 2 varies hardly at all. Furthermore, in 2,6-dichlorostyrene, $^5J_{37}$ is 0.39 ± 0.04 Hz, equal to the values in Table 2 to within experimental error. According to our STO 3G MO computations for this molecule, $\langle\sin^2\theta\rangle$ is 0.723 at 300 K, as compared to an experimental $\langle\sin^2\theta\rangle$ of 0.175 for styrene and a 6-31G value of 0.167. Furthermore, in α-methylstyrene $^6J_{37} \equiv {}^6J(\text{H-3},CH_3)$ is 0.02 ± 0.01 Hz in magnitude (Table 2). This coupling constant should measure the π electron contribution[1] to $^5J_{37}$. Apparently this contribution is effectively zero. The INDO results have $^5J_{37}$ as 0.75 Hz in the planar form of styrene (average over $\theta = 0°$ and 180°) and as 0.93 Hz at $\theta = 90°$. As for similar calculations for toluene (16), a large stereospecific $^5J_{37}$ is calculated for the all-*trans* arrangement ($\theta = 180°$), mainly a σ electron contribution.[2] However, in toluene, $^5J(H,CH_3)$ appears to obey the relation $C \sin^2\theta + D \sin^2(\theta/2)$, where C represents a σ−π and D a σ component (17, 18). Of course, for an internal rotational potential containing only evenfolded terms, $\langle\sin^2(\theta/2)\rangle$ is 0.5. The data in Table 2 indicate quite strongly that $^5J_{37}$ in styrene depends predominantly on $\sin^2(\theta/2)$ and, therefore, that π and σ−π contributions to $^5J_{37}$ are very small indeed. If this is true, then, intuitively, the theoretical models may well significantly overestimate the π and σ−π components of $^6J_{47}$, a coupling constant presumably dominated by such components.

The valence bond expression (11) for $^6J_{47}$ is $-0.43 \cos^2\theta - 1.25 \sin^2\theta$. That given (11) by INDO is plausibly written as $-0.24 \cos^2\theta - 1.05 \sin^2\theta$ for styrene. Both expressions overestimate the magnitude of $^6J_{47}$ in styrene, which is −0.227(3) Hz (Table 2), assuming that $\langle\sin^2\theta\rangle$ is very near 0.17, as in the gas phase at 300 K. There is no obvious way of assessing the value of $^6J_{47}$ at $\theta = 0°$, that is, of $^5J_0^\pi$, the coefficient of $\cos^2\theta$. An elaborate set of modified INDO MO FPT computations (20) suggests that $^6J_{47}$ be written as $^6J_{47} = {}^6J_0 + {}^6J_{90}\langle\sin^2\theta\rangle$ and that $^6J_0$ is about −0.075 Hz. The following empirical approach to $^6J_{47}$ is designed to reproduce eventually most of the long-range coupling constants in Table 2.

Empirical conformational analysis

Write $^6J_{47} = -0.149 \cos^2\theta - 0.597 \sin^2\theta$. This equation reproduces the $^6J_{47}$ of −0.227(3) Hz in styrene in solution on the assumption that $\langle\sin^2\theta\rangle$ is 0.175 at 300 K, as in the gas phase. In 4-methylstyrene, $^7J(H,CH_3)$ is (+)0.234(1) Hz, as expected if the spin state information about the side-chain proton reaches H-4 via the π electron system of the phenyl group (15, 21). $^6J_{47}$ in *trans*-β-methylstyrene is −0.231(1) Hz, again as expected from intuition and the 6-31G results. For *cis*-β-methylstyrene the $^6J_{47}$ of −0.417(1) Hz then implies a $\langle\sin^2\theta\rangle$ of 0.598, rather higher than the 0.459 implied by 6-31G calculations but nearer the 0.535 obtained from the STO-3G potential. For the β,β-dimethylstyrene $\langle\sin^2\theta\rangle$ becomes 0.716, while the $^6J_{47}$ of −0.53 Hz in 2,6-dichlorostyrene (11) then has $\langle\sin^2\theta\rangle$ as 0.850. Now arc sin $\langle\sin^2\theta\rangle^{1/2}$ is 67° for the latter and for the former it is 58°. The latter number, calculated as is usually done in the literature for styrenes but not to be taken as exact, is rather larger than that of 51° for *cis*-β-methylstyrene. It may well have its origin in the so-called parallel 1:3 interactions between the C—H bond of the two methyl groups. In consequence, a C—H bond of the *cis*-β-methyl group is forced to have a larger repulsive interaction with the *ortho* C—H bond of the ring than in the absence of the second β-methyl group. In the absence of the latter, near-planar conformations are accommodated by a staggering of two C—H bonds about the *ortho* C—H bond.

Now, in α-methylstyrene, $^7J(H,CH_3)$ is (+)0.084(1) Hz and, when multiplied by 0.65/0.75 as required for olefinic systems (22, 23), measures the π electron contribution (as distinct from the σ−π). Hence $\langle\cos^2\theta\rangle$ is 0.073/0.149 or 0.490.

To test this result (the 6-31G value for $\langle\sin^2\theta\rangle$ is 0.43 and the STO-3G value is 0.48), one may examine $^7J_{48}$ and $^7J_{49}$ for the compounds in Table 2. Any σ electron contributions to these coupling constants should be very small (11), yet $^7J_{49}$ is ca. 0.04

[1]The σ−π component does not appear in $^6J(\text{H-3},CH_3)$, in our experience. For example, $^6J(H,CH_3)$ in toluene is a σ−π coupling constant (14–17). In ethylbenzene, $^7J(H,CH_3)$ is undetectable to within 0.02 Hz (5).

[2]The INDO results for toluene have a significant $^5J(H,CH_3)$ at $\theta = 0°$ (16). The experimental evidence suggests a vanishing $^5J(H,CH_3)$ at this angle (18, 19).

Can. J. Chem. Downloaded from www.nrcresearchpress.com by 176.9.209.113 on 09/07/12
For personal use only.

Can. J. Chem. Downloaded from www.nrcresearchpress.com by 176.9.209.113 on 09/07/12
For personal use only.

Hz larger than $^7J_{48}$ in styrene.[3] In 4-methylstyrene, however, the $^8J(H,CH_3)$ values are identical and equal to the mean of $^7J_{49}$ and $^7J_{48}$ in styrene (perhaps there are σ contributions of 0.02 Hz to $^7J_{49}$ and of −0.02 Hz to $^7J_{48}$ in styrene). Take 0.259 Hz as the mainly π electron component, proportional to $\cos^2\theta$, of $^7J_{48}$ and $^7J_{49}$ in styrene, but allow for small σ−π components, proportional to $\sin^2\theta$, as indicated by valence bond and molecular orbital theories. If $^7J_0$ is 0.300 Hz and $^7J_{90}$ is 0.065 Hz, then the $\langle\sin^2\theta\rangle$ values derived from $^6J_{47}$ yield 0.259 Hz for styrene, 0.180 Hz for α-methylstyrene, and 0.100 Hz for 2,6-dichlorostyrene (the observed value is 0.12 ± 0.04 Hz (11)). Approximate numbers for $^9J(CH_3,CH_3)$ in β,β,4-trimethylstyrene are ±0.10 to ±0.15 Hz for the *trans* methyl group and ±0.05 to ±0.10 Hz for the *cis* (24). The $\langle\sin^2\theta\rangle$ of 0.716 above yields 0.132 Hz and the π component should be multiplied by 0.75/0.65 to give 0.14 Hz for $^9J(CH_3,CH_3)$. In β-*cis*-methylstyrene, the estimate above of 0.598 for $\langle\sin^2\theta\rangle$ yields 0.16 Hz for $^7J_{49}$ and $^7J_{48}$. The observed value of $^8J(H,CH_3)$ is (−)0.15 Hz, in reasonable agreement with the predicted $^7J_{48}$, dominated as it is by the π electron term. However, $^7J_{49}$ is 0.23(1) Hz, about 0.06 Hz larger than expected. This disagreement joins that for another coupling constant involving H-9 in this compound (see below).

Turning to $^4J_{27}$, an equation in $^4J_0\cos^2\theta$ and $^4J_{90}\sin^2\theta$ is assumed. The term in $\cos^2\theta$ contains $^4J_0^\pi$ and quite possibly also, as in toluene (25), a σ electron component; that in $\sin^2\theta$ is again σ−π contribution. The numbers for $^4J_{27}$ in styrene and β-*cis*-methylstyrene in Table 2, together with the expectation values of $\langle\sin^2\theta\rangle$ based on $^6J_{47}$, entail $^4J_{90}$ as −0.759 Hz and $^4J_0$ as −0.476 Hz. These parameters imply $^4J_{27}$ as −0.679 Hz in β,β-dimethylstyrene, whereas the experimental value is −0.668(9) Hz.

It is interesting that $^5J(H,CH_3)$ in α-methylstyrene is barely detectable (Table 2). Two explanations are possible. The first notes again that $^5J(H,CH_3)$ measures the π as opposed to the σ−π contribution and that therefore $^4J_0$ is mostly a σ electron term. The second explanation recognizes the possibility of negative through-space or proximate coupling interactions between the methyl and *ortho* ring protons, analogous to those in anisole (26–28). This explanation would need $-0.476\langle\cos^2\theta\rangle$ or about −0.2 Hz for an averaged proximate mechanism if $^4J_0$ is solely a π term, and rather a smaller magnitude were $^4J_0$ to contain a significant σ electron term. In anisole the proximate coupling magnitude for the planar conformation is about −0.3 Hz (note that significant planar populations of α-methylstyrene are implied by the 6-31G potential).

The coupling constants involving the *meta* and β-protons, $^6J_{38}$ and $^6J_{39}$, were not detected in styrene (12), but do appear in 4-methylstyrene. They are very small in magnitude, as they also are in the other methylstyrenes. However, $^7J(H,CH_3)$ in β-*trans*-methylstyrene lies very near 0.1 Hz in magnitude, implying a π electron contribution of (−)0.08 Hz to $^6J_{39}$. The computational results on styrene (11) imply that the σ electron component of $^6J_{39}$ is positive and of opposite sign to the π component. It appears that these components are indeed present and that they effectively cancel each other in styrene. $^6J_{38}$ in the three methylstyrenes in Table 2, and $^7J(H,CH_3)$ in β-*cis*-methylstyrene, all have the same small magnitudes to within experimental error. $^6J_{38}$ is computed as negative and larger in magnitude than $^6J_{39}$ for all angles θ by valence bond and INDO MO methods (11), in line with the data in Table 2. It seems impossible to deduce θ values from these very small coupling constants.

Consider $^5J_{28}$. It is computed and observed as negative at θ = 0°, quite possibly because of a proximate mechanism (11), and is then expected to become positive at angles appreciably removed from zero. The π electron term is positive (11), calculated to depend mainly on $\cos^2\theta$. In styrene and its β-*trans*- and α-methyl derivatives, $^5J_{28}$ is effectively zero and is only ca. 0.05 Hz in 4-methylstyrene. In β-*cis*-methylstyrene, $^6J(H,CH_3)$ is (−)0.185(1) Hz. If this number does not represent a proximate coupling, then it measures the magnitude of the π electron component of $^5J_{28}$ at a $\langle\cos^2\theta\rangle$ of 0.402. If so, then either the π and σ electron mechanisms have opposite signs or $^6J(H,CH_3)$ is a composite of proximate and π electron components. If the former is true, $^5J_{28}$ at θ = 0° is roughly 0.40 Hz. The vanishing $^5J_{28}^\pi$ in α-methylstyrene, at a $\langle\cos^2\theta\rangle$ of 0.49, then implies a composite σ and proximate mechanism of −0.20 Hz. This number appears unlikely. Furthermore, $^6J(H,CH_3)$ in the β-*trans* isomer is (−)0.243(1) Hz, implying the π component of $^5J_{29}$ at 0° as 0.25_5 Hz. The π components of $^5J_{28}$ and $^5J_{29}$ in the present coupling model are required to be equal. A consistent treatment of $^5J_{28}$ is therefore not available at present.

Finally, INDO MO calculations required the average $^5J_{29}$ to be largely independent of θ, as observed for the 4-methyl and α-methyl styrenes in Table 2. However, in the β-*cis* isomer, $^5J_{29}$ is 0.1 Hz larger than in the former molecules. This discrepancy joins that mentioned above for $^7J_{49}$ in the same molecule.

TABLE 3. Values of arc cos $\langle\cos^2\theta\rangle^{1/2}$ in degrees for styrene and some of its methyl derivatives

Molecule	UPS[a]	UVS[b]	6-31G[c]	NMR(*J*)[d]
Styrene	(0)	(0)	24	25[e]
4-Me	11±11	(0)	—	25
trans-β-Me	12±12	(0)	27	25
cis-β-Me	22±6	35	43	51
β,β-di-Me	—[f]	—	—	58
α-Me	29±6	33	49	46

[a]Based on photoelectron spectroscopy (6) and assuming that styrene is planar. An earlier value for α-methylstyrene (7) is 38°. These are effectively arc cos $\langle\cos^2\theta\rangle^{1/2}$ values.

[b]Based on ultraviolet absorption bands, again assuming a planar styrene (8) molecule and yielding arc cos $\langle\cos^2\theta\rangle^{1/2}$. Another value for α-methylstyrene is 30° (29). The Faraday effect gives 32° (10).

[c]These are based on the 6-31G MO internal rotational potentials; arc cos $\langle\cos^2\theta\rangle^{1/2}$ are computed classically at 300 K.

[d]These are arc cos $\langle\cos^2\theta\rangle^{1/2}$ values at 300 K, are derived from the model in this paper, and are based on the experimental gas phase internal potential (1), which yields 25° for arc cos $\langle\cos^2\theta\rangle^{1/2}$ at 300 K.

[e]Note that the larger value for styrene inevitably yields θ values for its derivatives that are larger than those given by UPS and UVS.

[f]An arc cos $\langle\cos^2\theta\rangle^{1/2}$ of 40° was estimated (24) from $^9J(CH_3,CH_3)$ for β,β-trimethylstyrene, assuming planar styrene.

Comparison with other estimates

In Table 3 estimates of the angles arc cos $\langle\cos^2\theta\rangle^{1/2}$ obtained by various methods are given. The early work assumes that styrene is a rigid planar molecule. Consequently these angles, which seem to be essentially values of arc cos$\langle\cos^2\theta\rangle^{1/2}$, are all smaller than those obtained from the MO calculations. Note that at 300 K the value of arc cos$\langle\cos^2\theta\rangle^{1/2}$ is 25° for styrene, based on the experimental (1) gas phase potential. It should again be stressed that the present model assumes the gas phase potential as applicable to solution. The 6-31G computations, when com-

[3]To check this point, the ^{1}H nmr spectrum of 3,5-dibromostyrene for a CS_2 solution was analyzed, confirming the larger magnitude of $^7J_{49}$.

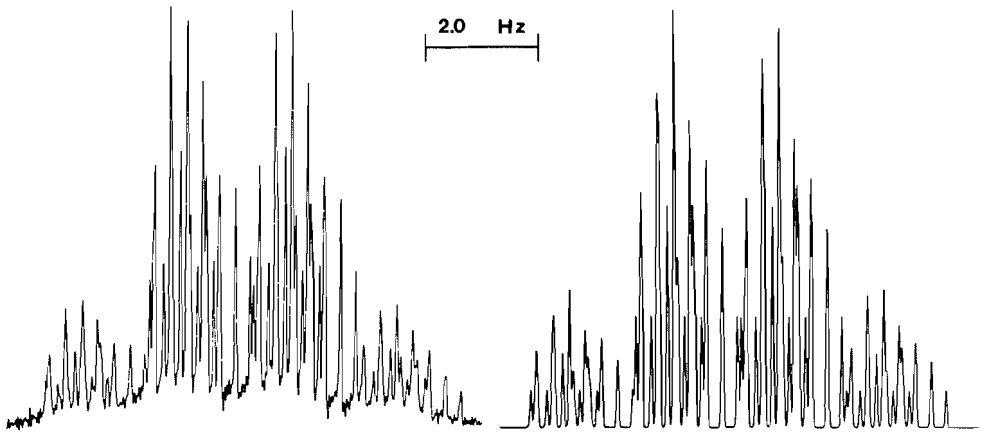

FIG. 3. Half the ^{1}H nmr spectrum of the α proton of *cis*-β-methylstyrene is shown for a 2.5 mol% solution in acetone-d_6, at a probe temperature of 300 K and a spectrometer frequency of 300 MHz. The computed spectrum is also shown and had an assumed linewidth at half-height of 0.04 Hz. Not all the observed peaks are as narrow as this, although some seem to be even narrower. One noticeable discrepancy between the observed and computed spectra occurs at their extreme left.

Can. J. Chem. Downloaded from www.nrcresearchpress.com by 176.9.209.113 on 09/07/12
For personal use only.

pared with the nmr data in Table 3, are in rough agreement with this assumption.

Remarks on the extrema in ^{n}J

The value of −0.6 Hz for $^6J_{47}$ at θ = 90° in the present model is less than 60% of that computed by the INDO MO FPT approach and less than half of the valence bond prediction (11). Similar remarks apply to the majority of the coupling constants in Table 2. Attempts at fitting these data with larger magnitudes of the extrema at θ = 0° and 90° were unsuccessful. Theory does appear also to overestimate the π and σ−π contributions, particularly to the coupling constants for the *meta* protons. For example, $^5J_{37}$ has a π component of 0.39 Hz at 0° and a σ−π component of 1.18 Hz at 90°, according to the valence bond formulation. Yet the numbers in Table 2 are best explained if such components are less than about 0.05 Hz in magnitude.

Of the 45 long-range coupling constants in Table 2, all but two are rationalized by the present discussion. These two involve the β-*trans* olefinic proton. They show that the present model is incomplete. Their interpretation escapes us.

Proton chemical shifts

The ^{13}C chemical shifts of many styrene derivatives, as well as the ^{1}H shifts of their olefinic protons, have been extensively studied and interpreted (29–33), notably by Reynolds and coworkers. Here we note that H-4 in styrene is shielded by 0.10 ppm relative to benzene at the same concentration (footnote in Table 1). This number can be compared to the analogous 0.21 ppm for H-4 in toluene (17), in line with the statement (31) that the vinyl group is almost neutral electronically. The presence of a *trans*-β-methyl group in the side chain coincides with an increase in shielding of H-4 by 0.17 ppm relative to benzene, the molecule having conformational properties very similar to those of styrene. An α-methyl group, however, increases the shielding of H-4 by only 0.08 ppm relative to benzene, less than a vinyl group. The obvious explanation involves the larger twist angle in this compound than in styrene, causing a decreased delocalization or polarization of electron density. Experimentally, $\langle \sin^2 \theta \rangle$ is effectively the same for styrene and its *trans*-β-methyl derivative (see $^6J_{47}$ in Table 2). Consequently it appears from the H-4 chemical shifts that the methyl substituent enhances the π electron donation of the vinyl group.

Experimental

The methylstyrene derivatives, of commercial origin, were diluted to concentrations of 2.5 mol% in acetone-d_6, which contained about 0.5 mol% tetramethylsilane. These solutions were filtered into 5-mm o.d. nmr sample tubes and were degassed by a number of freeze–pump–thaw cycles on a vacuum line. They were then flame sealed to produce symmetrical closed tops. Acetone-d_6 was used as a solvent because the work on styrene used this solvent, but also because narrow peak widths were obtained in acetone-d_6. This was important for satisfactory analyses of the spectra arising from extensively coupled 10-spin systems.

The ^{1}H nmr spectra were accumulated on a Bruker AM300 spectrometer at a probe temperature of 300 K. The procedure has been described in detail previously (17). The ^{1}H nmr spectra were analyzed with the computer program NUMARIT (34), as modified by R.S. Figure 3 displays half of the measured and calculated ^{1}H nmr spectrum of the α proton of *cis*-β-methylstyrene. At least some of the peaks display linewidths at half-height of less than 0.05 Hz. The computed spectrum assumed linewidths of 0.04 Hz.

The molecular orbital computations employed GAUSSIAN 82(35) and an Amdahl 5870 system.

Acknowledgments

We are grateful to the Natural Sciences and Engineering Research Council of Canada for a grant-in-aid.

1. J. M. HOLLAS, H. MUSA, T. RIDLEY, P. H. TURNER, K. H. WEISENBERGER, and V. FAWCETT. J. Mol. Spectrosc. **94**, 437 (1982).
2. T. SCHAEFER and G. H. PENNER. Chem. Phys. Lett. **114**, 526 (1985).
3. C. W. BOCK, M. TRACHTMAN, and P. GEORGE. Chem. Phys. **93**, 431 (1985).
4. T. SCHAEFER, J. PEELING, and R. SEBASTIAN. Can. J. Chem. **63**, 3219 (1985).
5. T. SCHAEFER, G. H. PENNER, and R. SEBASTIAN. Can. J. Chem. **65**, 873 (1987).
6. T. KOBAYASHI, T. ARAI, H. SAKURAGI, K. TOKUMARU, and C. UTSUNOMIJA. Bull. Chem. Soc. Jpn. **54**, 1658 (1981).
7. J. P. MAIER and D. W. TURNER. J. Chem. Soc. Faraday Trans. 2, **69**, 196 (1973).
8. H. SUZUKI. Bull. Chem. Soc. Jpn. **33**, 619 (1960).
9. P. L. BRITTON, C. L. CHENG, R. J. W. LEFÈVRE, L. RADOM, and

G. L. D. RITCHIE. J. Chem. Soc. (B), 2100 (1971), and references therein.
10. P. CASTAN, A. LOPEZ, and R. MARTINO. Tetrahedron, **35**, 1093 (1979).
11. M. BARFIELD, C. J. MACDONALD, I. R. PEAT, and W. F. REYNOLDS. J. Am. Chem. Soc. **93**, 4195 (1971).
12. H. NIES, H. BAUER, K. ROTH, and D. REWICKI. J. Magn. Reson. **39**, 521 (1980).
13. R. A. HOFFMAN. Mol. Phys. **1**, 326 (1958).
14. M. BARFIELD and B. CHAKRABARTI. J. Am. Chem. Soc. **91**, 4346 (1969).
15. C. J. MACDONALD and W. F. REYNOLDS. Can. J. Chem. **48**, 1002 (1970).
16. R. WASYLISHEN and T. SCHAEFER. Can. J. Chem. **50**, 1852 (1972).
17. T. SCHAEFER, R. SEBASTIAN, and G. H. PENNER. Can. J. Chem. **63**, 2597 (1985).
18. T. SCHAEFER and R. LAATIKAINEN. Can. J. Chem. **61**, 2785 (1983).
19. J. PEELING, T. SCHAEFER, and C. M. WONG. Can. J. Chem. **48**, 2839 (1970).
20. R. LAATIKAINEN and E. KOLEHMAINEN. J. Magn. Reson. **65**, 89 (1985).
21. J. B. ROWBOTHAM and T. SCHAEFER. Can. J. Chem. **52**, 496 (1974).
22. M. KARPLUS. J. Chem. Phys. **33** 1842, (1960).
23. P. ALBRIKTSEN, A. V. CUNLIFFE, and R. K. HARRIS. J. Magn. Reson. **2**, 150 (1970).
24. E. R. CURRY and D. J. SARDELLA. J. Am. Chem. Soc. **96**, 1822 (1974).
25. M. BARFIELD, C. J. FALLICK, K. HATA, S. STERNHELL, and P. W. WESTERMAN. J. Am. Chem. Soc. **105**, 2178 (1983).
26. H. A. GAUR, J. VRIEND, and W. G. B. HUYSMANS. Tetrahedron Lett. 1999 (1969).
27. T. SCHAEFER and R. LAATIKAINEN. Can. J. Chem. **61**, 224 (1983).
28. T. SCHAEFER, S. R. SALMAN, T. A. WILDMAN, and G. H. PENNER. Can. J. Chem. **63**, 782 (1985).
29. G. K. HAMER, I. R. PEAT, and W. F. REYNOLDS. Can. J. Chem. **51**, 915 (1973).
30. GURUDATA, J. B. STOTHERS, and J. D. TALMAN. Can. J. Chem. **45**, 731 (1967).
31. G. K. HAMER, I. R. PEAT, and W. F. REYNOLDS. Can. J. Chem. **51**, 897 (1973).
32. W. F. REYNOLDS, A. GOMES, A. MARON, D. W. MACINTYRE, R. G. MAUNDER, A. TANIN, H. E. WONG, G. K. HAMER, and I. R. PEAT. Can. J. Chem. **61**, 2367 (1983).
33. W. F. REYNOLDS, A. GOMES, A. MARON, D. W. MACINTYRE, A. TANIN, G. K. HAMER, and I. R. PEAT. Can. J. Chem. **61**, 2376 (1983).
34. A. R. QUIRT and J. S. MARTIN. J. Magn. Reson. **5**, 318 (1971); J. S. MARTIN, A. R. QUIRT, and K. E. WORVILL. The NMR program library. Daresbury Laboratory, Daresbury, U.K.
35. J. S. BINKLEY, M. J. FRISCH, D. J. DEFREES, K. RAHGAVACHARI, R. A. WHITESIDE, H. B. SCHEGEL, E. M. FLUDER, and J. A. POPLE. GAUSSIAN 82, Dept. of Chemistry, Carnegie–Mellon University, Pittsburgh, PA.

Can. J. Chem. Downloaded from www.nrcresearchpress.com by 176.9.209.113 on 09/07/12
For personal use only.

An investigation of the structures of isomeric ions derived from acetone, diacetone alcohol, and mesityl oxide

RAYMOND EVANS MARCH
Department of Chemistry, Trent University, Peterborough, Ont., Canada K9J 7B8

AND

ALEXANDER BALDWIN YOUNG
Ontario Regional Ion Chemistry Laboratory (ORICL), Department of Chemistry, University of Toronto, Toronto, Ont., Canada, M5S 1A1

Received May 12, 1987

This paper is dedicated to Professor J. A. Morrison

RAYMOND EVANS MARCH and ALEXANDER BALDWIN YOUNG. An investigation of the structures of isomeric ions derived from acetone, diacetone alcohol, and mesityl oxide. Can. J. Chem. **66**, 591 (1988).

An investigation of the structures of isomeric ions formed in ion/molecule reactions occurring in 2-propanone (acetone), 4-hydroxy-4-methyl-2-pentanone (diacetone alcohol), and 4-methyl-3-penten-2-one (mesityl oxide) has been performed using a hybrid mass spectrometer of reversed geometry. Ions of *m/z* 117, which have been observed as products of ion/molecule reactions in acetone and in diacetone alcohol, may have a single structure if an aldol type condensation reaction occurs under acidic conditions in the gas phase; however, high energy collision induced dissociation (CID) results proved the two ions to be isomeric only.

Dehydration of the *m/z* 117 ions produced a species of *m/z* 99 which, in the case of diacetone alcohol, may have the structure of protonated mesityl oxide. That the *m/z* 99 ion formed was unique to each system was demonstrated by high energy CID and kinetic energy release (KER) spectrometry. In the acetone system, CID results suggested that *m/z* 99 was an ion–dipole complex of $C_3H_5^+(CH_3)_2CO$; this hypothesis was tested by clustering $C_3H_5^+$ with $(CD_3)_2CO$ and comparison of its CID results with those obtained above. In the case of *m/z* 99 derived from diacetone alcohol or mesityl oxide, the neutral lost via metastable decomposition in the second field-free region was found to be C_4H_8, presumably 2-methyl propene. While the ion of *m/z* 99 may also eliminate methane to yield a species of *m/z* 83, the dominant metastable elimination from this ion is carbon monoxide rather than ethene as shown by collision induced dissociative ionization (CIDI). The ions of *m/z* 83 observed in the two systems exhibit very similar CID spectra; however, a small variation in the yield of products of *m/z* 41 and 43 suggests two structures for the ion derived from diacetone alcohol, one of which is identical to that seen in mesityl oxide.

RAYMOND EVANS MARCH et ALEXANDER BALDWIN YOUNG. An investigation of the structures of isomeric ions derived from acetone, diacetone alcohol, and mesityl oxide. Can. J. Chem. **66**, 591 (1988).

Utilisant un spectromètre de masse de géométrie inversée, on a étudié les structures des ions isomères qui se forment au cours des réactions moléculaires se produisant dans la propanone-2 (acétone), l'hydroxy-4 méthyl-4 pentanone-2 (diacétone alcool) et la méthyl-4 pentène-3 one-2 (oxyde de mésityle). Il est possible que les ions de *m/z* 117, qui sont observés comme produits dans les réactions ion/molécules de l'acétone et du diacétone alcool, aient une structure unique si une réaction de type aldolique se produit dans des conditions acides, en phase gazeuse; toutefois, il est possible que des résultats de dissociations induites par des collisions à hautes énergies (DIC) prouvent que les produits ne sont que des isomères.

La déshydratation des ions de *m/z* 117 fournit une espèce de *m/z* 99 qui, dans le cas du diacétone alcool, pourrait correspondre à un oxyde de mésityle protoné. Faisant appel à des DIC à hautes énergies et à la spectromètrie d'émission d'énergie cinétique (EEC), on a démontré que l'ion de *m/z* 99 est unique à chaque système. Dans le système de l'acétone, les résultats de DIC suggèrent que l'ion de *m/z* 99 est un complexe ion–dipôle de $C_3H_5^+(CH_3)_2CO$; on a vérifié cette hypothèse en provoquant la formation d'un agrégat entre l'ion $C_3H_5^+$ et le $(CD_3)_2CO$ et en comparant ses résultats de DIC avec ceux obtenus plus haut. Dans le cas de l'ion de *m/z* 99 qui est dérivé du diacétone alcool ou de l'oxyde de mésityle, on a trouvé que l'espèce neutre — qui est perdue par le biais d'une décomposition métastable dans le deuxième champ de la région libre — est du C_4H_8, probablement du méthyl-2 propène. Alors que l'ion de *m/z* 99 peut aussi éliminer du méthane pour fournir une espèce de *m/z* 83, l'ionisation dissociative induite par des collisions (IDIC) permet de démontrer que l'élimination métastable la plus importante qui est observée à partir de cet ion est celle du monoxyde de carbone plutôt que de l'éthène. Les ions de *m/z* 83 qui sont observés dans les deux systèmes présentent des spectres DIC qui sont très semblables; toutefois, une faible variation dans le rendement en produits de *m/z* 41 et 43 suggère qu'il existe deux structures pour l'ion provenant du diacétone alcool et que l'une d'elle est identique à celle provenant de l'oxyde de mésityle.

[Traduit par la revue]

Introduction

Often, the only tractable evidence from gas phase ion/molecule reactions is the variation in intensities of ionic species as a function of reaction time or pressure, thus it is always a temptation to invoke the reaction mechanisms and product structures observed from solution chemistry. A case in point is the well known aldol condensation followed by dehydration reaction:

[1] 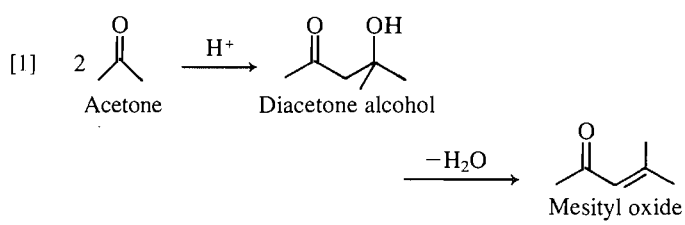

Can. J. Chem. Downloaded from www.nrcresearchpress.com by 176.9.209.113 on 09/07/12
For personal use only.

in the gas phase, the condensation product may be fully covalently bonded;

[2] 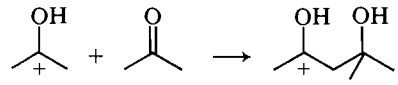

I (m/z 117)

or proton-bound;

[3] 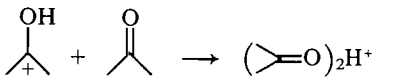

II (m/z 117)

The ionic products of these reactions are indistinguishable by conventional measurements of m/z ratio, necessitating further experiments for their differentiation. The ionic species investigated were derived from 2-propanone (acetone), 4-methyl-4-hydroxy-2-pentanone (diacetone alcohol), and 4-methyl-3-penten-2-one (mesityl oxide), as it had been suggested earlier (1) that the species of m/z 117 formed via self-CI of acetone was identical to protonated diacetone alcohol, and that dehydration of this ion produced m/z 99, tentatively identified as protonated mesityl oxide.

A recent study (2) employed slow infrared multi-photon dissociation (IRMPD) to demonstrate that the species of m/z 117 obtained from acetone differed from protonated diacetone alcohol (reaction [2], structure **I**). Unfortunately, the species of m/z 99 and 83 proved unreactive with slow IRMPD and thus no decision could be made as to common or isomeric structures for these ions generated by different precursors. In an attempt to probe the structures, further experiments were performed with a reversed geometry mass spectrometer. The techniques employed were collision induced decomposition (CID) at high (keV) energy, kinetic energy release (KER) from metastable decomposition in the second field-free region (2ndFFR) and dissociative reionization of fast neutrals produced from metastable decomposition in the 2ndFFR. In addition, the exothermicity of the initial protonation reaction was varied and the effect of the subsequent change in internal energy upon metastable decomposition pathways was investigated.

Experimental

A mass spectrometer of reversed geometry (3) (Vacuum Generators ZAB2F) was employed. Ion/molecule reaction products were formed in the source at an estimated pressure of ca. 13 Pa using a conventional Vacuum Generators' combined electron impact/chemical ionization source. The second field-free region of this instrument is slightly more than a meter in length, and has been fitted with two gas collision cells for the study of bimolecular processes. The upstream collision cell, CC_1, is permanently grounded and the downstream collision cell, CC_2, which is located at the first focal point of the instrument, is electrically isolated so that a variable voltage in the range +5 kV to −5 kV may be applied to it. In the region between the cells, which are separated by some 56 mm, is interposed an ion deflector electrode which may be grounded or to which a variable voltage to +5 kV may be applied so as to prevent ions from entering CC_2. The reversed geometry instrument has the advantage that a particular ion species may be selected by the magnet and any decomposition products formed in the 2ndFFR between the magnet (B) and the electrostatic sector (E) may be mass analyzed employing the well known MIKES technique (4); such decomposition may be either unimolecular or collision induced. The internal energy of the ions formed in the source was varied by employing either isobutane or methane as the chemical ionization reagent. The proton affinities of isobutane and methane are 683 kJ mol^{-1} and 552 kJ mol^{-1}, respectively (5).

CID spectra of mass-selected ion species were obtained by pressurizing the second collision cell (CC_2) with helium to produce a reduction of ca. 30% in the ion signal intensity. The indicated pressure from the ion gauge situated below the cell was 1×10^{-5} Pa. CID spectra were corrected for metastable (unimolecular) decomposition by performing a second experiment in the absence of collision gas, and subtracting the metastable decomposition product intensities from those obtained in the CID experiment. Fast neutrals of several keV of kinetic energy produced through metastable decomposition in the 2ndFFR were examined by collision induced dissociation ionization. In this technique, ions are deflected by means of the deflector electrode situated just prior to CC_2, and only fast neutral fragments may enter the cell. When an appropriate reagent gas is added to CC_2, the neutrals are ionized and dissociated; the charged species produced are subsequently analyzed via the MIKES technique. In the experiments involving m/z 99, O_2 was employed as the reionization gas to reduce the fragmentation of the reionized neutral. He was used for reionization, in the other experiments.

Acetone, diacetone alcohol, mesityl oxide, and 3-bromopropene were supplied by Aldrich Chemical Co. and used without further purification. Perdeutero-acetone was supplied by Merck Sharp and Dohme Isotopes of Montreal, Quebec, Canada.

Results and Discussion

The experiments to be described were concerned with establishing the structures of ions of identical m/z values formed via ion/molecule reactions occurring in either acetone, diacetone alcohol, or mesityl oxide. The ions investigated were, m/z 117 which is common to acetone and diacetone alcohol; m/z 99 which arises from dehydration of m/z 117 and which may have the structure of protonated mesityl oxide (**III**); m/z 83 observed in diacetone alcohol and mesityl oxide, and which is presumably formed by methane elimination from excited m/z 99 (reaction [4]),

[4] 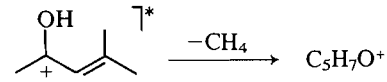

III (m/z 99) m/z 83

where * denotes internal excitation. This ion may also have a common structure from its precursors, m/z 117.

m/z 117

Ions of m/z 117, formed from acetone via isobutane CI in the source, were mass-selected in the magnetic sector and directed into the 2ndFFR. A fraction of metastable ions of m/z 117 fragmented unimolecularly to produce m/z 59 (99%) and m/z 99 (1%). Isobaric metastable ions formed similarly from diacetone alcohol dissociated to form the same fragment ions but with the inverse ratio of products. The internal energy of the m/z 117 ions was then increased by employing methane rather than isobutane as the CI agent; the proton affinity of methane is less than that of isobutane. Enhanced internal energy brought about an additional reaction channel, that is the loss of H_2. m/z 117 from acetone produced m/z 59 (96%), m/z 99 (1%) and m/z 115 (3%), while isobaric ions from diacetone alcohol produced the same fragment ions but with the composition 25%, 73%, and 2%.

m/z 117 ions, again produced by isobutane CI, were subjected to CID using helium as target gas in CC_2. After correction of product ion intensities for unimolecular decomposition, it was found that CID of m/z 117 from acetone produced m/z 41 (1%), m/z 43 (5%), m/z 58 (6%), m/z 59 (86%), and m/z 99 (2%). m/z 117 from diacetone alcohol produced m/z 41 (1%), m/z 43 (18%), m/z 59 (5%), m/z 61 (1%), m/z 83 (2%), and m/z 99 (73%).

Can. J. Chem. Downloaded from www.nrcresearchpress.com by 176.9.209.113 on 09/07/12
For personal use only.

TABLE 1. Fragment ion abundances ($\%I/\Sigma I$) and experimental conditions for mass-selected *m/z* 99 ions derived from acetone, diacetone alcohol, and mesityl oxide

	Metastable decomposition						CID		
	Isobutane CI			Methane CI			Isobutane CI		
Fragment (*m/z*)	Acetone	Diacetone alcohol	Mesityl oxide	Acetone	Diacetone alcohol	Mesityl oxide	Acetone	Diacetone alcohol	Mesityl oxide
27							1	1	1
29							1	1	1
31								1	
39							10	4	6
41	90	6		69	11		61	4	7
43		80	24	4	36	36	8	76	23
53								1	4
55							1	2	6
57			2	7	1	1	2	1	
59	6			4	1	1	9		
69							1		4
71							1		
79									4
81	4	4	68	10	36	58	3	2	14
83		1	2		1	1		4	21
84		2	2		1	1			2
98		7	2	5	12	2	2	2	6

These results demonstrate that the species of *m/z* 117 derived from acetone is an isomer of that produced in diacetone alcohol. The dominant pathway of the former is loss of a neutral fragment of 58 amu, neutral acetone, and this result is consistent with a proton bridged dimer structure **II**. In contrast, the dominant pathway observed in protonated diacetone alcohol is the loss of water, a known reaction of protonated ketones (6, 7). The ion of *m/z* 43 from the CID of this latter ion may be due to loss of a neutral fragment of 74 amu, presumably *t*-butanol, or via losses of acetone and methane or losses of isobutene and water. Protonated acetone, produced by acetone elimination from the ion of *m/z* 117, has been shown to eliminate methane to produce an ion of *m/z* 43 (6).

m/z 99

In Table 1 are shown the corresponding unimolecular fragmentations and CID of *m/z* 99, produced by isobutane CI and methane CI, from acetone, diacetone alcohol, and mesityl oxide. The species produced from mesityl oxide is simply the protonated parent molecule;

[5] 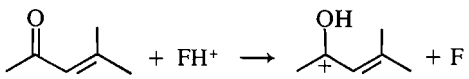 + F

98 **III** (*m/z* 99)

whereas the other species are derived via dehydration of protonated diacetone alcohol;

[6] 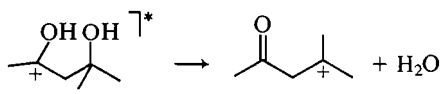 + H_2O

I (*m/z* 117) **IV** (*m/z* 99)

or the proton-bound dimer of acetone;

[7] 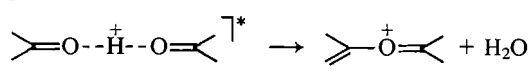 + H_2O

II (*m/z* 117) **V** (*m/z* 99)

Structure **V** has been suggested previously (2).

Inspection of the data in Table 1 shows that the three ion species differ in their metastable decomposition pathways. The species derived from acetone produces predominantly $C_3H_5^+$, *m/z* 41 and as the exothermicity of the initial protonation reaction is increased by changing from isobutane to methane CI, the relative yield of $C_3H_5^+$ is reduced whereas dehydration to *m/z* 81 is increased. In addition, loss of C_3H_4, presumably allene to yield *m/z* 59, is apparently reduced upon methane CI, however, the concomitant appearance of $C_2H_3O^+$, *m/z* 43, may be due to methane elimination from *m/z* 59, protonated acetone. The appearance of the moiety *m/z* 57 is postulated as the loss of a neutral fragment of 42 amu from *m/z* 99. Protonated acetone has been shown not to dehydrogenate readily (6), thus the genesis of *m/z* 57 from *m/z* 59 is thought to be unlikely, hence the neutral lost is suggested as propene or ketene. *m/z* 99 derived from diacetone alcohol primarily eliminates C_4H_8 to produce *m/z* 43 upon isobutane CI. The increase of protonation exothermicity afforded upon methane CI results in an increase in the efficacy of the dehydration pathway, producing *m/z* 81. In addition, minor amounts of *m/z* 57 and 59 are produced. Protonated mesityl oxide, *m/z* 99, exhibits two major fragmentation routes in the absence of collision gas; dehydration to *m/z* 81 and loss of a neutral fragment of 56 amu to produce *m/z* 43. As protonation exothermicity is increased, the dehydration channel is diminished, and the genesis of *m/z* 43 is increased. Minor pathways include methyl radical loss to produce *m/z* 84; methane loss to afford *m/z* 83; allene loss to yield *m/z* 59 and loss of 42 amu to give *m/z* 57.

In Table 1, the CID behaviour of the three ions is depicted, employing helium as the collision gas. Each of the ions exhibited unique behaviour and may be readily distinguished. In acetone, the major fragmentation route produced $C_3H_5^+$, *m/z* 41. The species derived from diacetone alcohol predominantly lost a neutral fragment of 56 amu affording *m/z* 43, whereas the isomeric protonated mesityl oxide exhibited a plethora of products, the three major routes being the production of *m/z* 43, 81, and 83.

Can. J. Chem. Downloaded from www.nrcresearchpress.com by 176.9.209.113 on 09/07/12
For personal use only.

The species of *m/z* 99 derived from acetone is intriguing. Although the enthalpy of formation of the ion of structure **V** is unknown, it is the progenitor of both $C_3H_5^+$ and $(CH_3)_2C^+OH$:

[8] 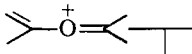 $C_3H_5^+ + (CH_3)_2CO$

$\Delta H = 724 - x$ kJ mol^{-1}

[9] **V**, *m/z* 99 $\longrightarrow$ $(CH_3)_2C^+OH + C_3H_4$

$\Delta H = 682 - x$ kJ mol^{-1}

$\Delta H_f^0 = x$

The observed preponderance of $C_3H_5^+$ indicates that *m/z* 99 dissociates via kinetic control, not thermodynamic, suggesting a loose ion/molecule complex formed between the 2-propenyl cation (or if a 1,2 H shift occurs, the allyl cation) and acetone. The appearance of $C_3H_5^+$ from the postulated structure **V** involves only simple bond cleavage, whereas the reaction producing the protonated ketone, *m/z* 59, involves a proton transfer, hence the former reaction exhibits a more favourable frequency factor than the latter, and predominates despite a greater endothermicity of ca. 40 kJ mol^{-1}.

The structure of **V** was further investigated by reacting 3-bromopropene with acetone-d_6 and mass selecting the $C_3H_5^+$ $(CD_3)_2CO$ species of *m/z* 105. Acetone-d_6 was employed to avoid complications arising from the *m/z* 99 species observed in acetone CI. The CID results obtained with helium in the second collision cell are depicted in Fig. 1, lower trace. For comparison purposes, the upper trace of Fig. 1 shows the CID behaviour of the fully deuterated species of *m/z* 110. This ion was produced via isobutane CI of perdeutero-acetone, the DOH elimination product ion being mass-selected. In the lower trace, the predominant fragmentation pathway is the loss of acetone-d_6 to yield $C_3H_5^+$. The thermodynamically favoured route, producing $(CD_3)_2C^+OH$, *m/z* 65, occurs with approximately equal facility to that shown in Table 1. The ion of *m/z* 46 is CD_3C^+O and is presumed to result through CD_3H elimination from *m/z* 65.

In the upper trace of Fig. 1, the ion of *m/z* 46 may have both the $C_3D_5^+$ and CD_3C^+O structure. The deuteronated d_6-acetone product yield (*m/z* 66) is enhanced in comparison to the lower trace and Table 1, however, due to the isobaric products of *m/z* 46, it is not clear as to whether this enhanced yield is due to a lowered activation energy for deuteron transfer or a diminution of the further fragmentation of *m/z* 66 to yield *m/z* 46. The cluster ion CID behaviour shown in the lower trace of Fig. 1 supports structure **V** for the dehydration product of the proton-bound dimer of acetone, *m/z* 117, although it may be argued that the species of *m/z* 99 observed in acetone is derived by clustering of *m/z* 41 with the neutral acetone, rather than by dehydration. Structures for the isomeric species of *m/z* 99 observed in both diacetone alcohol and mesityl oxide were proposed as **III** and **IV**, respectively:

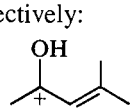

Mesityl oxide, **III**

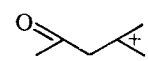

Diacetone alcohol, **IV**

Upon methane CI, the metastable fragmentation spectrum of *m/z* 99 from diacetone alcohol differs significantly from that obtained upon isobutane CI, as shown in Table 1, and approaches the fragmentation spectrum of *m/z* 99 from mesityl oxide. This change in fragmentation patterns may be due to the formation of *m/z* 99 with structures **III** and **IV**. The metastable decomposition of these ions to yield isobutene and *m/z* 43 may be written:

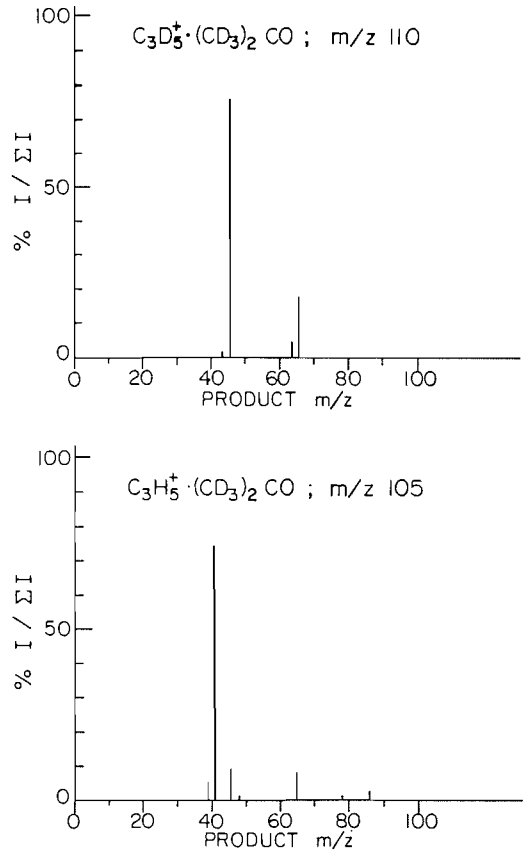

FIG. 1. Percentage ion composition of CID products derived via high energy collisions with helium in CC_2. Metastable decompositions have been subtracted. In the lower trace, the 2-propenyl cation, $C_3H_5^+$, was reacted with perdeutero acetone, and the cluster ion of *m/z* 105 was mass-selected via the magnet for high energy CID. In the upper trace, the fully deuterated analogous species formed in the source from self-CI of perdeutero acetone was mass-selected and collisionally dissociated in CC_2.

[10] 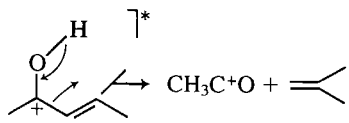 $CH_3C^+O +$

III

[11] 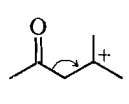 $\longrightarrow$ $CH_3C^+O +$

IV

It is anticipated that reaction [10] which involves a proton transfer should require a greater activation energy than reaction [11]. This difference in endothermicity should be reflected in the metastable peak shapes for the two reactions (8), the peaks are shown in Fig. 2. In each of the traces, the energy spread of the mass-selected *m/z* 99 ion beam was reduced to ca. 0.3 eV which corresponds to approximately 3 eV translational energy. The upper trace was obtained from the metastable decomposition of protonated mesityl oxide (reaction [10]); the lower trace corresponds to reaction [11]. From the measured widths of the ion kinetic energy peaks at half height, corrected for the energy spread inherent in the precursor ion, the translational energy realease, $T_{50\%}$, may be calculated (8). The elimination of C_4H_8

Can. J. Chem. Downloaded from www.nrcresearchpress.com by 176.9.209.113 on 09/07/12
For personal use only.

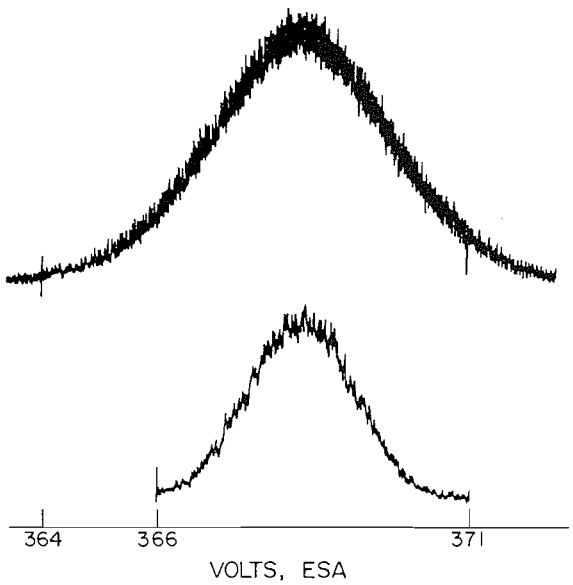

FIG. 2. Ion kinetic energy peaks of the metastable decomposition of *m/z* 99 in the 2ndFFR. The signals correspond to the process $99^+ \rightarrow 43^+ + 56^0$. In the upper trace, *m/z* 99 was generated via isobutane CI of mesityl oxide; in the lower trace, *m/z* 99 was formed via isobutane CI of diacetone alcohol.

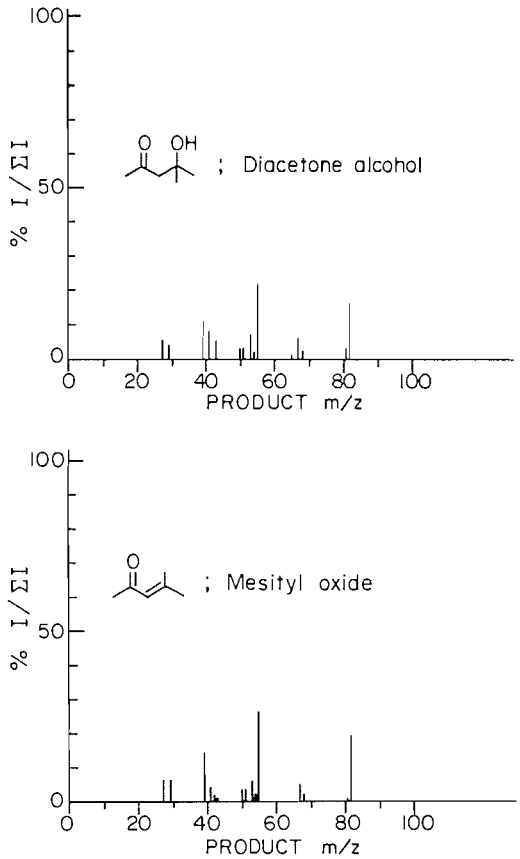

FIG. 3. Percentage ion composition of CID products obtained upon high energy collisions with helium in CC_2. Isobutane CI was employed to generate the *m/z* 83 ions, and contributions to the ion signal intensities due to metastable decompositions have been subtracted.

from protonated mesityl oxide (upper trace) exhibits $T_{50\%} = 32$ meV; the same loss from *m/z* 99 observed in diacetone alcohol has $T_{50\%} = 10$ meV. The larger ion kinetic energy release seen in the upper trace of Fig. 2 is attributed to a greater activation energy for the process. Such an observation is in agreement with reactions [10] and [11].

That the neutral produced in these reactions was C_4H_8 was verified by collision induced dissociative ionization (CIDI) (9). The precursor ion (*m/z* 99) was prepared via isobutane CI, and although the dominant metastable pathway of this ion in the case of mesityl oxide is dehydration, no signals were observed for this H_2O species due to the low collection efficiency for reionized neutrals of low kinetic energy (ca. 1.5 keV for H_2O from *m/z* 99 of 8 keV). Oxygen was employed as collision gas in order to enhance the appearance of the molecular ion (10), and results obtained for the neutral species of reactions [10] and [11] were similar.

m/z 83

The ion of *m/z* 83 was observed only in the diacetone alcohol and mesityl oxide systems and, in the case of the latter, must arise through methane elimination from the protonated molecule. In the diacetone alcohol experiments, *m/z* 83 was observed in minor abundance in the metastable decomposition of *m/z* 99 and in somewhat greater abundance in the high energy CID experiment. This ion was also observed in the high energy CID of protonated diacetone alcohol, although its progenitor may be *m/z* 99.

m/z 83 was generated in the ion source from four separate sets of progenitors, diacetone alcohol and mesityl oxide with each of isobutane and methane as CI agents. The MIKE spectra were virtually indistinguishable for diacetone alcohol and mesityl oxide, and varied only with the CI gas used. With isobutane CI the predominant pathway is the loss of CO (*vide infra*) to produce *m/z* 55. Minor abundances, totalling 7% of the base peak and comprised of *m/z* 43, *m/z* 56, *m/z* 81, and *m/z* 82, were observed with diacetone alcohol. With methane CI, enhanced protonation exothermicity resulted in an enhancement of H$^\bullet$ and H_2 losses at the expense of the pathway producing *m/z* 55, such that the intensities of ion signals due to *m/z* 55 and *m/z* 82 were equal. Approximately 10% of ion abundance was due to *m/z* 81.

In Fig. 3, the CID products of the two ions are depicted. The ions were generated via isobutane CI and the CID experiments were performed at identical reductions (ca. 30%) in precursor ion beam intensities. The major differences between the two spectra lie in the larger signals due to *m/z* 41 and 43 obtained from *m/z* 83 derived from diacetone alcohol, otherwise the spectra are similar.

A possible rationalization of the results may be made by postulating two isomeric ions of *m/z* 83 in the diacetone alcohol experiments, one of which is identical to *m/z* 83 observed in mesityl oxide.

The reaction to produce this ion may be written in the case of mesityl oxide;

[12] 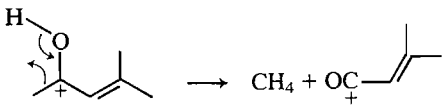

m/z 99, **III** *m/z* 55, **V**

and with *m/z* 99 as the precursor in diacetone alcohol;

[13] 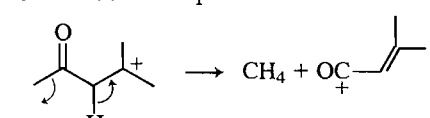

m/z 99, **IV** **V**

Can. J. Chem. Downloaded from www.nrcresearchpress.com by 176.9.209.113 on 09/07/12
For personal use only.

Can. J. Chem. Downloaded from www.nrcresearchpress.com by 176.9.209.113 on 09/07/12
For personal use only.

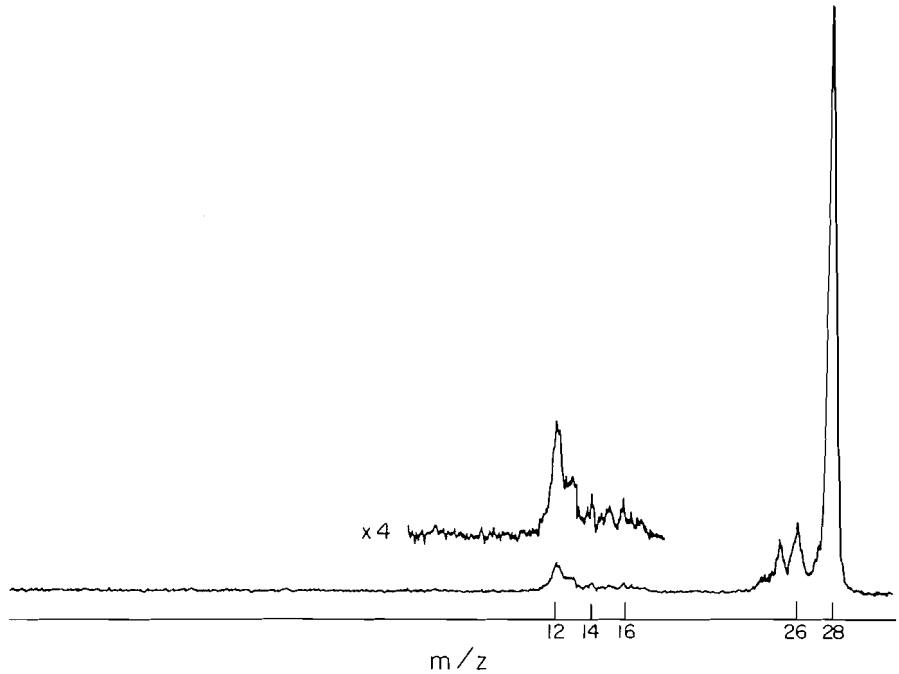

FIG. 4. Collisional reionization spectrum of the neutral fragment formed in the reaction $83^+ \rightarrow 55^+ + 28^0$. Isobutane CI was employed to generate *m/z* 83 from mesityl oxide, and ions were prevented from entering CC_2 by the application of ca. 3 kV to the deflector electrode situated prior to CC_2. Helium was employed as the reionization gas in CC_2; the collision cell was held at a potential of +2.5 kV in order to accelerate the ions formed in CC_2, and thus to enhance the signal intensity (11).

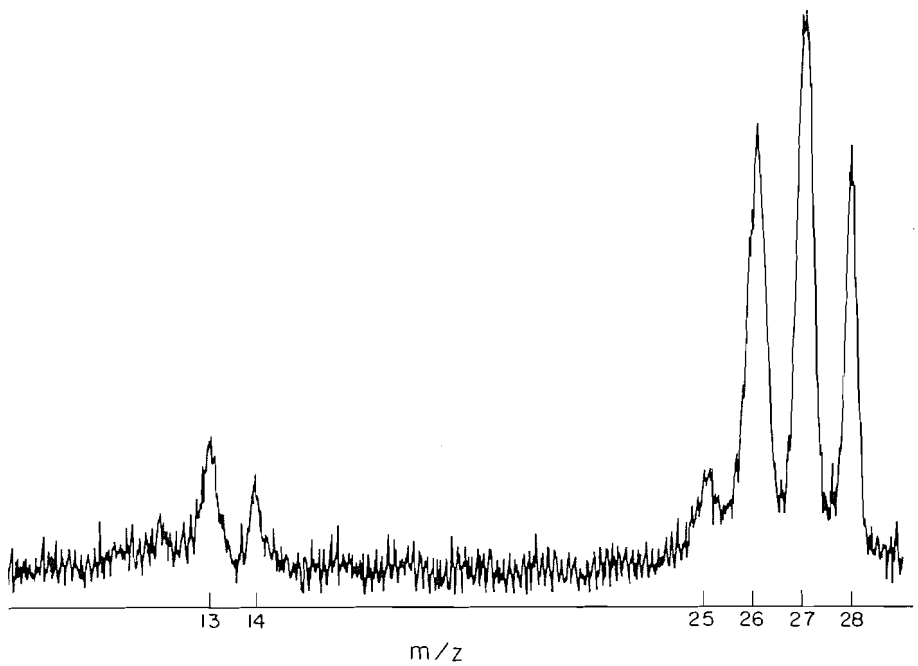

FIG. 5. Collisional reionization spectrum of ethylene obtained via the McLafferty rearrangement of the molecular ion of 2-pentanone. Helium was employed as the reionization gas and CC_2 was biased at +2.5 kV in order to enhance the signal intensities.

The loss of CO may be readily rationalized from structure **V**. An alternative reaction of *m/z* 99 from diacetone alcohol to produce *m/z* 83 may be written:

[14] 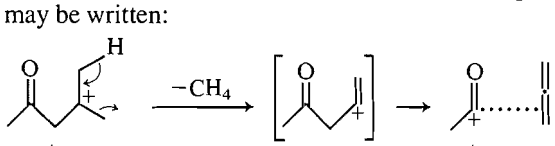

m/z 99 *m/z* 83, **VI**

where **VI** is a mixed associative species which may decompose to CH_3C^+O, *m/z* 43 or via a more endothermic pathway to $C_3H_5^+$, *m/z* 41.

The identity of the neutral produced via metastable decomposition of *m/z* 83 to *m/z* 55 in the 2ndFFR was investigated by CIDI. Briefly, *m/z* 83 was prepared from mesityl oxide via isobutane CI and mass-selected by the magnet. With the deflector electrode potential set at approximately 3 kV and He in CC_2 at an indicated pressure of 1.2×10^{-5} Pa, very little signal was observed due to the poor collection efficiency of $28^{+\cdot}$ at a

translational energy of 2.7 keV (accelerating voltage for *m/z* 83 was 8 kV). To enhance the weak signals, CC_2 was biased at +2.5 kV, hence any positively charged CIDI products received an acceleration from the cell and were more readily detected (11). The results are depicted in Fig. 4, where the dominant peak is *m/z* 28. Although the peaks at *m/z* 12, 13, 14, 15, 25, and 26 might suggest C_2H_4 as the neutral lost, the lack of a peak at *m/z* 27 and the low intensities of *m/z* 26 and *m/z* 25 indicate that C_2H_4 is a minor component only. The CIDI spectrum of C_2H_4 generated via a McLafferty rearrangement from the molecular ion of 2-pentanone (and hence potentially contaminated with some reionized $\cdot CH_3$) is depicted in Fig. 5. The spectrum was obtained under identical conditions to that shown in Fig. 4, and is clearly different, thus the identity of the neutral lost from *m/z* 83 is carbon monoxide.

Summary

Gas phase ion/molecule reactions of acetone lead to the formation of an ion of *m/z* 117 which has the structure of a proton-bound dimer. No evidence was found for an aldol condensation reaction occurring in the gas phase as the ion of *m/z* 117 formed from diacetone alcohol has been shown to be isomeric. The dehydration products of these isomeric ions yielded isomeric ions of *m/z* 99. In the case of acetone, CID studies suggested an ion–dipole complex of acetone and $C_3H^+_5$ as the structure of *m/z* 99. This conclusion was substantiated by clustering $C_3H^+_5$ with perdeutero-acetone and performing the CID experiment. The dehydration product of protonated diacetone alcohol, *m/z* 99, differed from protonated mesityl oxide as revealed by CID experiments and KER measurements. Reionization of the neutral produced in the metastable decomposition of *m/z* 99 from both diacetone alcohol and mesityl oxide revealed that the species lost was C_4H_8. The latter two ions also eliminate methane yielding an ion of *m/z* 83. CID studies of these ions showed nearly identical results; the differences observed were ascribed to two ionic structures present in the ion derived from diacetone alcohol, one of which was identical to that seen in mesityl oxide. Reionization of the neutral produced in the metastable decomposition of these ions showed it to be CO rather than ethylene, C_2H_4.

Acknowledgements

We are indebted to the Natural Sciences and Engineering Research Council of Canada as the operation of the Ontario Regional Ion Chemistry Laboratory (ORICL) is funded, in part, by a grant from NSERC. R. E. March gratefully acknowledges the financial support of NSERC in the form of an Operating Grant and a Research Development grant, and of Trent University. The constructive comments of the referees are much appreciated.

1. M. B. Munson. J. Am. Chem. Soc. **87**, 5313 (1965); J. A. Hunter, C. A. Johnson, J. E. Parker, and G. P. Smith. 14th Meeting of the British Mass Spec. Soc., Heriot-Watt Univ., Edinburgh, U.K., September 18–21, 1984. Abstracts, p. 24.
2. R. E. March, A. Kamar, and A. B. Young. Can. J. Chem. **64**, 1979 (1986).
3. A. G. Harrison, R. S. Mercer, E. J. Reiner, A. B. Young, R. K. Boyd, R. E. March, and C. J. Porter. Int. J. Mass Spectrom. Ion Processes, **74**(1), 13 (1986).
4. R. P. Morgan, J. H. Beynon, R. H. Bateman, and B. N. Green. Int. J. Mass Spectrom. Ion Phys. **28**, 171 (1978); K. Levsen and H. Schwarz. Mass Spectrom. Rev. **2**, 77 (1983).
5. S. G. Lias, J. F. Liebman, and R. D. Levin. J. Phys. Chem. Ref. Data, **13** (3), 695 (1984).
6. A. G. Harrison, T. Gaumann, and D. Stahl. Org. Mass Spectrom. **18**, 517 (1983).
7. M. L. Sigsby, R. J. Day, and R. G. Cooks, Org. Mass Spectrom. **14**, 273 (1979).
8. R. G. Cooks, J. H. Beynon, R. M. Caprioli, and G. R. Lester. *In* Metastable ions. Elsevier, Amsterdam. 1973.
9. P. C. Burgers, J. L. Holmes, A. A. Mommers, and J. K. Terlouw. Chem. Phys. Lett. **102**, 1 (1983); P. C. Burgers, R. Clair, J. L. Holmes, and A. A. Mommers. Org. Mass Spectrom. **20**, 207 (1985).
10. J. L. Holmes. Org. Mass Spectrom. **20**, 169 (1985).
11. R. E. March, and A. B. Young. Int. J. Mass Spectrom. Ion Processes, **76**, 11 (1987).

Can. J. Chem. Downloaded from www.nrcresearchpress.com by 176.9.209.113 on 09/07/12
For personal use only.

Experimental tests for many-body forces in noble gas fluids

P. A. EGELSTAFF
Physics Department, University of Guelph, Guelph, Ont., Canada N1G 2W1

Received July 24, 1987

This paper is dedicated to Professor J. A. Morrison

P. A. EGELSTAFF. Experimental tests for many-body forces in noble gas fluids. Can. J. Chem. **66**, 598 (1988).

Effects due to many-body potentials may be studied by comparing the predictions of precise computer simulations (using a good pair potential) with real experimental data. The differences observed may be of almost any relative magnitude, varying with state parameters and other experimental variables. Results of this kind will be discussed regarding P.V.T. data, transport coefficients, and static and dynamic structure factors of noble gas fluids. They are compared to the predictions of a simple mean field model for each effect, in which pair potential simulation is used as the reference system. The model is used as a tool to determine the information content of each property. Reasonable agreement is found for bulk properties, while the extra sensitivity offered by the microscopic data allows a number of deficiencies in the model to be observed. In contrast, a similar series of tests using a computer model, made from the pair potential and the A–T potential in place of the experimental data, shows significantly better overall agreement with the mean field model. This is believed to be due to the neglect of important short range terms in the A–T model. It is concluded that at least three types of many-body forces are important in discussing dense noble gas fluids.

P. A. EGELSTAFF. Experimental tests for many-body forces in noble gas fluids. Can. J. Chem. **66**, 598 (1988).

Il est possible d'étudier les effets dûs aux potentiels de plusieurs corps en comparant les valeurs expérimentales réelles avec les valeurs que l'on peut prédire par des simulations précises par ordinateur (utilisant une bonne paire de potentiels). L'amplitude des différences que l'on observe est relative et varie avec les paramètres d'état et d'autres variables expérimentales. On discutera de ce type de résultats pour des données de P.V.T., pour des coefficients de transport et pour les facteurs structuraux statiques et dynamiques de gaz nobles fluides. On les compare aux valeurs prédites par un modèle de champ moyen simple pour chacun des effets dans lequel la simulation des potentiels par paire est utilisée comme système de référence. On utilise le modèle comme outil pour déterminer l'information contenue dans chacune des propriétés. On trouve une bonne corrélation pour les propriétés globales; par ailleurs, la sensibilité extrême que présentent les données microscopiques fait que l'on observe un certain nombre de déficiences dans le modèle. Pour fins de comparaison, on a aussi fait une série de tests semblables en faisant appel à un modèle par ordinateur qui a été fait à partir de la paire de potentiels et d'un potentiel A–T à la place des données expérimentales; dans ce cas, l'accord global avec le modèle de champ moyen est bien meilleur. On croit que cette différence est dûe au fait que, dans le modèle A–T, on néglige des termes à courte distance qui sont importants. On en conclut que, pour discuter des gaz nobles fluides denses, au moins trois types de forces entre plusieurs corps sont importants.

[Traduit par la revue]

1. Introduction

The study of dense fluids has now reached the stage where realistic interaction potentials must be considered. Reasonably accurate pair potentials (e.g. Aziz (1)) have been obtained for noble gas atoms, and using these results the properties of a dense fluid (within which there are only pair interactions) may be derived through an extensive computer simulation. The simulation must be extensive to give accurate results, but even so logic demands that these results should not fit the data on the real substance. The reason is simple: in deriving the pair potential it is assumed that atoms are polarizable, while in using the pair theory of fluids it is assumed that they are not. Several effects are related to this discrepancy, but the most obvious are the substantial differences in the critical parameters for the computer pair fluid and the corresponding real experimental fluid. These differences are not well known at present, because of the time taken in this field to extend the data on the Lennard–Jones fluid (2) to model noble gas pair fluids. Nevertheless, differences in T_c and ρ_c of about 10% are expected (3); consequently in the neighbourhood of either critical point there will be infinite differences between numerous corresponding properties of the two fluids. These large differences are caused by many-body forces.

The nature of many-body forces has been discussed in many papers (e.g. Meath and Aziz (4)). From a qualitative point of view there are three effects to be considered. First, there are long range effects which can be discussed through a multipole expansion, and it may be shown that the triple-dipole term is the most important. Secondly, there are medium range effects — say from an atomic diameter to three atomic diameters on a distance scale — which are not well understood even in the case of pair interaction. In the latter case they have been approximated by an ad-hoc formula (1), which may have an incorrect mathematical shape (5). Nevertheless, the pair potential is well known for each noble gas. For many-body potentials some formulae are being proposed (6) which extend into the third scale. Thirdly, there are short range effects observed in many atom collisions and which have been considered in (relatively) complicated theoretical discussions of exchange and correlation effects, etc. More than one effect could be significant here. However, one important effect may be described by a simple physical picture of collisions of deformable atoms. At low density the minimum distance of approach of the nuclei of two flexible atoms, involved in a fast collision, will be less than that for similar rigid atoms involved in a similar collision. This reduced distance appears in the pair potential. In contrast, at high density a given atom might experience many impacts, averaging uniformly over all directions, and thus this reduction in internuclear distance would be less at high density than at low density (see Appendix 1). This implies that the effective atomic diameter should increase as a function of increasing density due to many-body forces.[1] Such an effect might be seen most clearly through changes in the position of the second nearest neighbour peak of the pair correlation function.

[1]B. Nickel, private communication. I am indebted to Dr. Nickel for his comments on this effect.

Can. J. Chem. Downloaded from www.nrcresearchpress.com by 176.9.209.113 on 09/07/12
For personal use only.

Can. J. Chem. Downloaded from www.nrcresearchpress.com by 176.9.209.113 on 09/07/12
For personal use only.

Text books on the theory of liquids usually cover pair theory in great detail and ignore or neglect effects of many-body forces. This has no bearing on the importance of these forces, but is because of the enormous difficulties in producing a tractable many-body theory. Therefore it may be argued that an experimental approach is required to define the principal features in relevant experimental data. This idea is not new although in the past we tended to oversimplify the many-body force question. However, to properly exploit this idea it is necessary to analyse each set of data to determine its information content. After this, information from the different kinds of data may be integrated, and we shall explore such possibilities in this article. Moreover, such analysis can emphasize experiments that test different features and contribute to a new understanding of the significant features of this problem. Thus experimentalists should try to define the contribution of many-body forces to various experimental quantities and suggest physical interpretations of their principal features.

The effect of many-body forces on a property may be defined as the difference between its experimental value for the real substance and its computer simulated value for the artificial fluid composed of atoms interacting with a realistic pair potential only. In this context numerous published papers giving computer results for hard-sphere, Lennard–Jones, or other fluids are inappropriate. Only extensive simulations using the most realistic pair potentials are of value: there are very few, perhaps none, of these. Thus in addition to new experiments, a program of new simulations is also required. As a guide to many-body force effects the difference between two computer simulations can be useful. These are the artificial pair potential fluid and a corresponding artificial fluid for which a many-body force model (e.g. the triple-dipole interaction (7)) has been added. It is difficult to carry out the second simulation as accurately as the first, and hence these differences are not satisfactorily obtained in some cases. This difference technique will also be discussed here.

In the following sections the P.V.T. data, static structure factor, transport coefficients, and dynamic structure factor data will be discussed from the above points of view.

2. A mean-field model for pressure and energy

The third virial coefficient of pressure is the sum of two kinds of terms. The first kind involves pair potential ($u(r)$) only, while the second involves both pair and three-body ($u_3(r, s)$) potential, and is

$$[1] \quad C_2(T) = -\tfrac{1}{3}\int\int \exp -\beta[u(r) + u(s) + u(r-s)]\{\exp[-\beta u_3(r-s)] - 1\}dr\,ds$$

This term is relatively easily measured and has been used to discuss three-body effects for many years. But it is clear from the form of the expression that $C_2(T)$ is relatively insensitive to the details of u_3. Consequently, it would be useful to extend the study of many-body effects to higher density, but this requires one to subtract the total pair terms from experimental data. This in turn means that one must complete extensive computer simulations for many densities along each isotherm to find the total pair terms. This was done for krypton on the 297 K isotherm by Ram and Egelstaff (10) and later by Barker (ref. 8, additional data on xenon are given in ref. 9*a*, and the method is given in ref. 9*b*). These two sets of data are shown in Fig. 1*a* and are in good agreement. The difference between the experimental and simulated pressures is shown in Fig. 1*b*. Ram and Egelstaff (10) commented that if the virial series was truncated at the

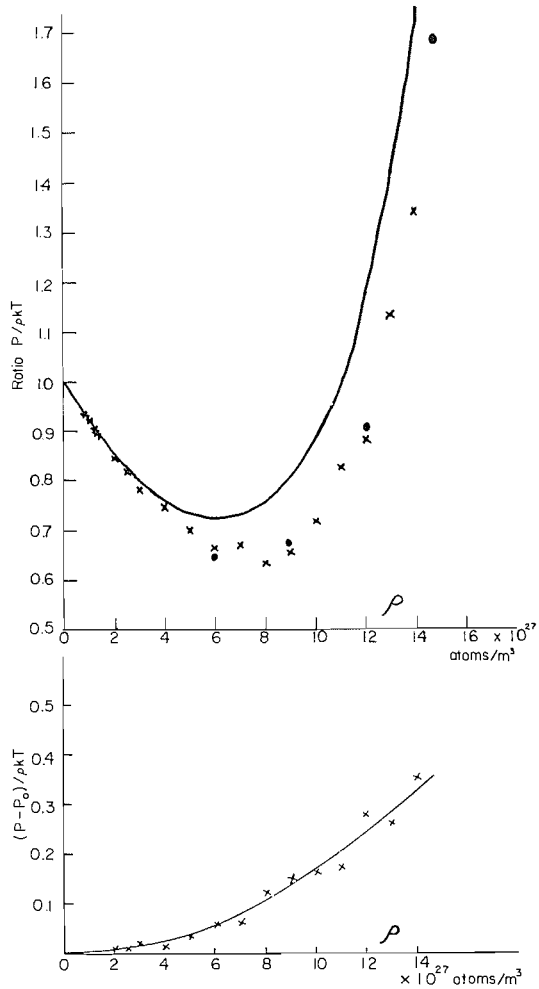

FIG. 1. (*a*) The experimental pressure for krypton on the room temperature isotherm (full line —) compared to the computer simulated pressure using the krypton pair potential (crosses ref. 10, circles ref. 8). (*b*) The difference (10) between the line and the crosses in (*a*) is shown as crosses here. The line is an extrapolation of the many-body force part of the third virial coefficient determined from low density data.

$\rho^3 C_2(T)$ term — eq. [1] — an extrapolation to higher densities would almost fit the difference data in Fig. 1*b*. This is shown by the full line in the figure. Later Egelstaff (11) noted that this result suggested that a mean-field theory of many-body effects might be successful, and proposed a zero order version of such a theory.

Van der Waals theory for the P.V.T. data of a fluid interacting with a pair potential has been reasonably successful, and consequently it might be expected that a generalized version involving the many-body forces could also work. In this case the reference system is the artificial pair theory fluid and the perturbation is a background term due to all the many-body forces taken together. Again the reference system properties can be evaluated only through extensive computer simulations. Thus in Fig. 1*a* the crosses show the simulated pair results having a marked curvature as a function of density, while in Fig. 1*b* the crosses show the total many-body effect with simpler density dependence. It is this greater simplicity, analogous to the simple behaviour proposed by Van der Waals for attractive pair forces, that suggests a mean-field theory might be successful. Also because many-body forces contribute only a maximum of about

30% of the total pressure, small defects in the theory may not have an important influence on the calculated total pressure. Egelstaff (ref. 11*a*, the theory is based on ref. 11*b*) presented a zero-order theory, which could be the starting point for a conventional perturbation expansion, although for the present we are interested in exploiting the zero-order theory.

This theory starts from the thermodynamic relationships used by Widom in his treatment of the Van der Waals model:

$$[2]\quad \rho \left.\frac{\partial \ln (z/z_0)}{\partial \beta}\right|_{\rho} = \rho \left.\frac{\partial (U - U_0)/v}{\partial \rho}\right|_{T} = \left.\frac{\partial \beta (P - P_0)}{\partial \beta}\right|_{\rho} + \frac{U - U_0}{V}$$

and

$$\rho \left.\frac{\partial \ln (z/z_0)}{\partial \rho}\right|_{T} = \left.\frac{\partial \beta (P - P_0)}{\partial \rho}\right|_{T}$$

where P, V, T, ρ, U, and z are the pressure, volume, temperature, density, energy, and fugacity, respectively, of the real fluid, and quantities with subscript zeroes are for the artificial pair fluid. These two fluids are related by the equation:

$$[3]\quad \psi_0 = \psi + c$$

where ψ is the potential seen by a test particle in the real fluid and c is a uniform background potential which "cancels" the effect of many-body forces. In this case it may be shown, following Widom, that:

$$[4]\quad \ln z/z_0 = -\beta c \text{ and } \frac{U - U_0}{V} = -\frac{\rho c}{\alpha}$$

where α is the order of many-body forces (α = 3, 4 etc). Further, we assume, for simplicity, that the background potential is proportional to a single power of density, and if it is also temperature independent it may be shown that this power is $\alpha - 1$. The above equations may then be solved to give:

$$[5]\quad P - P_0 = a\rho^{\alpha}$$
$$\frac{U - U_0}{V} = \frac{a\rho^{\alpha}}{\alpha - 1}$$

where a is a constant. If only weak long-ranged three-body forces are present it may be shown that:

$$[6]\quad a \simeq -\int\int u_3(\boldsymbol{r}\cdot\boldsymbol{s})\mathrm{d}\boldsymbol{r}\mathrm{d}\boldsymbol{s}$$

but, in general, the expression for a would be more complicated. Also while eq. [6] is independent of density and temperature, this may not be so generally. It may be possible to redefine the parameters a and α appearing in eq. [5] so that the density dependence in a (for example) is transferred to α, thus maintaining a as a constant. This question will be examined empirically. The constant a may be eliminated from eq. [5] to give:

$$[7]\quad \alpha = 1 + \frac{(P - P_0)V}{(U - U_0)}$$

and this equation may be used to calculate α from experimental and simulated data. Following the usual Van der Waals picture, we expect this treatment to work best at high temperature or high density.

3. Discussion of pressure and energy

It is useful to compare the above results to a computer simulation model, and the simplest case is to take a realistic pair potential (well depth ϵ at position r_m) and then add the Axilrod–Teller triple-dipole term (or A.T.) where

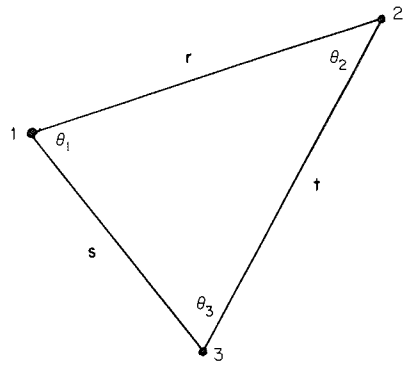

FIG. 2. Diagram showing the definition of angles (θ_1, θ_2, and θ_3) and vectors ($\boldsymbol{r}$, $\boldsymbol{s}$, $\boldsymbol{t}$) appearing in eq. [8].

$$[8]\quad \text{A.T.} = \frac{3C_6P}{4} \cdot \frac{3\cos\theta_1\cos\theta_2\cos\theta_3 + 1}{r^3s^3t^3}$$

The definitions of angular variables for three particles are shown in Fig. 2, and C_6 and P are the two-body r^{-6} coefficient and the atomic polarizability, respectively. The use of the product C_6P in this equation is an approximation, good to about ~4% for krypton and xenon. However, for the work discussed here this error is unimportant, and we point out this form to emphasize the interrelationship between pair potential and higher order potentials. This model of many-body forces is correct only for infinite separation between the particles and has been used widely in the literature for computer simulations and for other calculations. Three errors arise in computer simulations of this kind, statistical errors, errors due to the finite size of the system, and errors due to truncation of the potential model. Many papers do not report adequate details on either the simulation or the errors, and so we shall assume that "reasonable" comparisons will be valid in our context.

We begin by comparing the calculated density dependence of the model pressure of "argon" (at high density) with the predictions of eq. [5]. Loubeyre (6) has made "self consistent harmonic" calculations for solid noble gases using the above potential model. His results for "argon" are shown in Table 1*a*: the errors are not available. The number density is expressed in units of r_m^{-3}, where r_m is the position of the minimum in the pair potential. It can be seen that eq. [5] with α = 4 predicts accurately the variation of pressure with density. Presumably the fact that α = 4 rather than 3, arises because higher order terms are important and they can be incorporated simply into the index α. In other words, the zero-order theory can be extended in a simple way in this case (Apendix 2). To test this idea further we look at the temperature dependence at constant density. The density chosen is that for the triple point liquid or $\rho r_m^3 = 1.10$, and the pressure difference (for this density and $k_BT = 2.09\,\epsilon$) is also predicted in Table 1*a*.

Barker (8) performed the most extensive simulation of the pressure and energy for noble gas fluids using this model. He used a Monte Carlo method with 108 particles but did not give estimates of the errors. An approximate formula was used for pressure and energy and a truncation correction was applied. Levesque *et al* (13) also used this model for one state of xenon. They used a 108-particle system for an M.D. simulation, and corrected their results for truncation of the three-body potential. The range of truncation was the same as Barker's and was

Can. J. Chem. Downloaded from www.nrcresearchpress.com by 176.9.209.113 on 09/07/12
For personal use only.

TABLE 1.
(*a*) Triple dipole pressure of "argon" using A–T model at 300 K (ref. 6)*

Case n	Density ρr_m^3	Pressure difference $(P - P_0)$ kbar	Relative pressure difference P_n/P_1	Predicted change eq. [5] with $\alpha = 4$ $(\rho_n/\rho_1)^4$
1	2.47	7.00	1.00	1.00
2	2.17	4.15	0.593	0.595
3	1.93	2.62	0.374	0.378
4	1.74	1.73	0.247	0.248
5	1.10	0.275†		

*$k_BT/\epsilon = 2.09$; errors on $P - P_0$ are not known.
†Predicted difference for Table 1*b*.

(*b*) Test of temperature independence of eq. [5] for xenon using A–T model*

Quantity	$\frac{k_BT}{\epsilon} = 2.09$ (ref. 6)	$\frac{k_BT}{\epsilon} = 1.48$ (ref. 9)	$\frac{kBT}{\epsilon} = 0.62$ (ref. 13)
$\frac{U - U_0}{N\epsilon}$	—	0.34	0.33
$\frac{(P - P_0)V}{N\epsilon}$	0.96	0.94	0.92
α	4.0	3.8	3.8±0

*Density is $\rho r_m^3 = 1.10$; errors are not known for refs. 6 and 9.

related to box size and so varied with density. They reported errors on pressures and energies. These various features are common to simulations involving a three-body potential. A comparison between these two results is useful as widely different temperatures were used ($k_BT/\epsilon = 1.48$ in refs. 8, 9 and 0.62 in ref. 13), so that the temperature independence of eq. [5] may be tested. To obtain results from Barker's xenon data at the same density used by Levesque *et al.*, a small extrapolation is required. Since Barker's (8, 9) krypton and xenon calculations are for almost the same state (i.e. k_BT/ϵ and $k_BTr_m^9/C_6P$ are almost the same), this was accomplished using the krypton data as a guide because the maximum density exceeded the density required. The results are given in Table 1*b*, for comparisons with those from Table 1*a*. To convert from "argon" to "xenon" the data in Table 1*a* were scaled, following eq. [6], with the coefficient of the A–T potential.

The errors involved may be expected to exceed the temperature-dependent differences in this table, and so temperature independence is observed over a relatively wide range. The data also confirm the independence of a on state parameters, that is, its density and temperature independence are shown by Tables 1*a* and 1*b*, respectively. Moreover, the conversion from "argon" to "xenon" using eq. [6] supports the mean field approximation. Finally for the two "xenon" states the result for α, using eq. [7], is close to 4, in agreement with Table 1*a* and Appendix 2. Consequently, the model satisfies the mean-field approximation at high density provided the parameter α is adjusted. This empirical conclusion should be explored in greater detail with further calculations, including estimates of errors on $P - P_0$ and $U - U_0$.

The behavior of the test model at lower density may be examined using Barker's data (9); this is displayed in Table 2. The values in this table appear to increase with increasing

TABLE 2. Test of density independence of eq. [7] for A–T model

Density ρr_m^3	$(P - P_0)V/(U - U_0)$ Xenon	Krypton
1.15	—	2.7
1.10	2.8*	—
0.96	2.5	2.3
0.77	2.0	2.2
0.58	1.6	1.6

*$k_BT/\epsilon = 0.62$ (13); other cases $k_BT/\epsilon = 1.48$ (8, 9). Errors are not known. For $\rho \to 0$ the ratio listed (11) is $\lesssim 2$.

density. This is probably outside the statistical error (e.g. a 1% error in total energy would contribute an error of 0.3 to 0.4 in this table). Thus if it does not represent a density-dependent systematic error, the mean field is established only at the highest density. In the mean-field theory temperature independence (Table 1*b*) is inconsistent with the trend (with density) in Table 2. Other evidence (on the pair correlation function) suggests the mean-field theory works in principle for the A–T model, and hence it would be desirable to carry out a large scale simulation to reduce systematic errors. For a logical development of this field it is important to compare such simulations and the mean-field predictions accurately.

In order to compare the mean-field predictions with experimental results, we used simulation data which employed the "best" pair potential recommended by Aziz (1). Barker (8, 9) and Levesque *et al.* (13) used 108-particle systems and made truncation corrections, but Barker's errors are not known. Salacuse and Egelstaff (12) used a 256-particle system, made truncation corrections, and quoted statistical errors. Sources of experimental data were given by Barker (9) and Salacuse and Egelstaff (12), but to employ the simulations of Levesque *et al.* (13) we used the experimental results of Street and Sagan (14). All these data are summarized in Table 3. Column 4 shows the pressure change due to many-body effects, and is remarkably constant. Because of the uncertainty in the estimates of α in column 6, we have preferred to divide the data of columns 4 and 5 by $(\rho^*)^n$ (with $n = 2$ or 3), implying from eq. [5] that $\alpha \sim 3$ to 4. Thus the constancy of columns 4 and 5 is a demonstration of the constancy of the parameter a in eq. [5]. The average value in column 6 for α is 3.5. The fluctuations in column 5 are significant, and it is possible that a large part arises from errors in the simulations: the ratio U/U_0 is close to unity in several cases. This view is supported by the fact that the fluctuations in column 4 are less, and that the ratio P/P_0 is normally significantly different from unity. From column 4, one might conclude that $\alpha = 4$ is better than $\alpha = 3$, but clearly simulations of improved quality and known errors are required.

The range of data in Tables 1 and 2 for the model system could be encompassed within the experimental range exhibited in Table 3, after allowance has been made for likely errors. But this means that the model and real fluids behave in the same way to a first approximation (i.e. sufficient for the mean field theory), and more detailed studies are needed to understand how the real system behaves. Thus in an overall way, the mean field approach is supported by existing data on krypton and xenon and on the pair plus A.T. potential model. Only a few parameters are needed to describe the basic behaviour of the equation of state and energy. The order of magnitude of parameter a is given by

Can. J. Chem. Downloaded from www.nrcresearchpress.com by 176.9.209.113 on 09/07/12
For personal use only.

TABLE 3. Summary of experimental cases at high density

1 Element	2 k_BT/ϵ	3 $\rho r_m^3 = \rho^*$	4 $\frac{(P-P_0)V}{N\epsilon(\rho^*)^n}$ $n=3$	4 $n=2$	5 $\frac{U-U_0}{N\epsilon(\rho^*)^n}$ $n=3$	5 $n=2$	6 α eq. [7]	7 Reference for data
Krypton	2.13	1.04	0.66	0.69	0.27	0.28	3.5±0.2	12
Krypton	1.32	1.04	0.67	0.70	0.29	0.30	3.3±0.2	12
Krypton	2.13	0.90	0.69	0.62	0.29	0.26	3.4±0.2	12
Krypton	1.34	0.90	0.71	0.64	0.34	0.31	3.1±0.2	12
Krypton	1.48	1.15	0.69	0.79	0.28	0.32	3.4†	8
Krypton	1.48	0.77	0.71	0.55	0.35	0.27	3.0†	8
Xenon	1.47	0.96	0.70	0.67	0.23	0.22	4.0†	8, 9*a*
Xenon	1.47	0.77	0.68	0.52	0.27	0.21	3.5†	8, 9*a*
Xenon*	0.62	1.10	0.63	0.69	0.21	0.23	3.9±0.2	13, 14

*The simulated state is metastable.
†Error unknown.

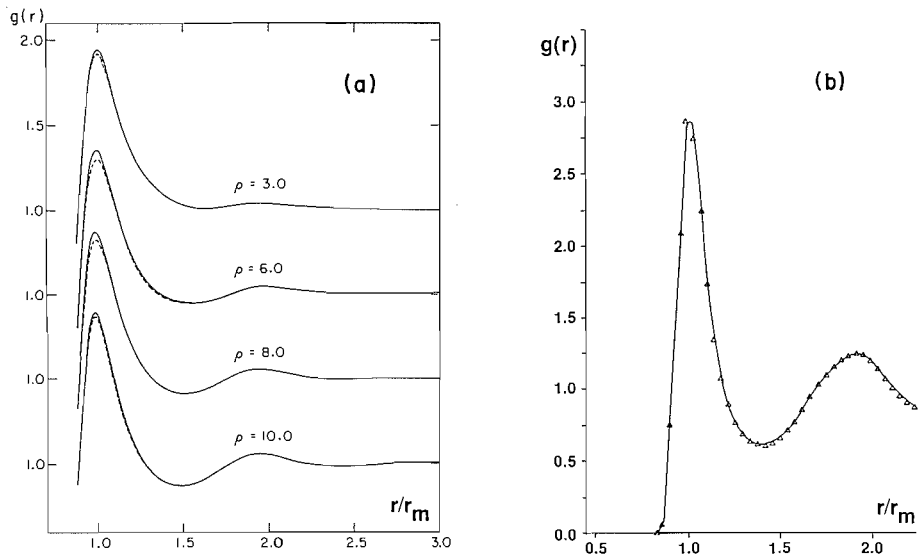

FIG. 3. (*a*) Examples (15) of pair distribution functions using a pair potential for krypton (full line) and those for the addition of eq. [8] to the potential (dashed line). Note the increase in the difference followed by a decrease with increasing density. (*b*) A similar case for the parameters of the triple point of xenon (13). The full line shows the simulation using the pair potential plus eq. [8], and the triangles show the result for the pair potential alone.

the 3rd virial coefficient of pressure, so that the fluids may find it easy to develop mean-field behaviour with increasing density. However, with bulk data of the present quality, exact conclusions cannot be drawn and we turn to microscopic data for more information.

4. The pair correlation function [$g(r)$]

If the mean field is uniform over the whole system, the pair correlation functions will be the same in both real and reference systems. However, if fluctuations in background potential are important, there will be differences on the scale of fluctuations. This may be seen in the low density virial expansion, where the integrand in eq. [1] may be thought of as representing a three-body collision effect. Thus at low density the two pair correlation functions will differ, and as the uniformity of the mean field is established with increasing density this difference should vanish. This matter may be examined through computer simulations involving a pair potential and a model three-body potential. The work of Egelstaff *et al.* (15) is a useful example: they compared simulated $g(r)$'s using the model described by eq. [8] and the krypton pair potential. They modeled krypton for number densities from 3 to 10 atoms/nm^3 (ρr_m^3 from 0.2 to 0.6) and a temperature of 297 K (or 1.48ϵ). Their results are shown in Fig. 3*a*. The principal difference due to adding eq. [8] to the pair potential occurs near the principal maximum in $g(r)$, that is, for atoms in contact. This arises from the strong distance dependence in eq. [8], and indicates that a significant contribution to calculated many-body effects can arise from short distances even when an expression only valid at infinite separations is employed! Thus any results derived from the A–T term have an "illogical aspect" because a significant part arises from a region where this formula is not valid. However, for our purpose eq. [8] may take the status of a "test model" rather than a valid theory. We refer to it as a test model below.

We can see from Fig. 3*a* that the effect at the peak $g(r)$ increases from 3 to 6 atoms/nm^3 and thereafter decreases. This

Can. J. Chem. Downloaded from www.nrcresearchpress.com by 176.9.209.113 on 09/07/12
For personal use only.

Can. J. Chem. Downloaded from www.nrcresearchpress.com by 176.9.209.113 on 09/07/12
For personal use only.

is expected qualitatively as density is increased in a mean-field picture and suggests that for densities of $\rho r_m^3 \sim 0.6$ the mean field works with eq. [8]. This is lower than suggested ($\rho r_m^3 \sim 1$) by the data in Tables 1 and 2, and may indicate that small differences (extended along the r-axis) exist between the two calculations for $0.6 < \rho r_m^3 < 1$. Small extended differences would be difficult to observe in the simulations of $g(r)$, but might be expected to occur at the onset of the mean-field behaviour. Similar calculations near the triple point of the Lennard–Jones fluid were reported by Hoheisel (16) ($\rho r_m^3 \simeq 1.17$ and $k_B T \simeq 0.83\epsilon$), who found no difference between the two $g(r)$'s. Recently Levesque *et al.* (13) have used a realistic potential for xenon near its triple point ($\rho r_m^3 \simeq 1.10$ and $k_B T \simeq 0.62\epsilon$) and again found no change in $g(r)$ when the A–T term is added. These results are shown in Fig. 3*b*, and confirm the deductions from Fig. 3*a*. The errors on simulated data are of the order of 2%, due to the difficulty of calculating the three-body case accurately. Thus, within this limit, the test A–T model behaves as a fluid satisfying the basic requirement of a mean-field system.

Two series of experiments on krypton have been reported in which the static structure factor, $S(Q)$ has been measured carefully for a number of densities at 297 K, where

$$[9] \quad S(Q) = 1 + \rho\int\{g(r) - 1\}(\exp - i\boldsymbol{Q}\cdot\boldsymbol{r})d\boldsymbol{r}$$

Teitsma and Egelstaff (3) measured densities ≤ 6 atoms/nm^3 ($\rho r_m^3 < 0.4$), and Fig. 4 is the summary of some of their data (circles) compared to their computer simulation and virial expansion calculations using a realistic pair potential (crosses). This is the region of densities where the effect in $g(r)$ (Fig. 3) is increasing, and we see that in Fourier space the corresponding effect increases with density. It is concentrated in the low Q region because relatively large distances in real space are needed to accommodate three or more particles. As $Q \rightarrow 0$ the integrated effect over all r in $g(r)$ is observed, and this is found to be approximately equal to that calculated from the A–T term (eq. [8]). Thus in addition to the change in the peak of $g(r)$ (Fig. 3*a*) there will be smaller changes spread along the r-axis, which are not seen in the simulations, but which accumulate in the Fourier space data. For densities ≥ 6 atoms/nm^3 ($\rho r_m^3 > 0.4$), Egelstaff *et al.* (17) report a series of measurements of $S(Q)$ extending to ~14 atoms/nm^3 ($\rho r_m^3 \sim 0.9$). In Fig. 5, some of their data are compared to the simulations given in ref. 15. If the mean-field picture was as successful for the real experimental fluid as for the test model, we would expect the effects shown in Fig. 4 to decrease when ρ increases (this was confirmed in the test model by Ram and Egelstaff (10)). In particular, the range of Q affected should decrease. However, in Fig. 5 some differences extend up to $Q \simeq 1$ Å^{-1} and beyond, and in contrast to the discussion of the previous section there is no indication that they vanish for $\rho r_m^3 \sim 1$.

We shall examine the experimental position of the principal peak in $S(Q)$ compared to the prediction from simulations. It appears to shift to lower Q, especially for $\rho \simeq 14$ atoms/nm^3. This would be in accord with the change in diameter suggested by the collision picture given in the Introduction, and is outside the scope of both the mean-field theory and the test model simulations. A recent paper by Fredrikze (18) on krypton at 200 and 220 K reports larger shifts of the same type. In addition A. Teitsma (unpublished results, 1980) measured four high density states of xenon at 297 K, and his peak positions are shifted relative to the simulations too. It is convenient to plot the peak positions from these three experiments in one figure, compared to the simulated positions. This is done in Fig. 6:

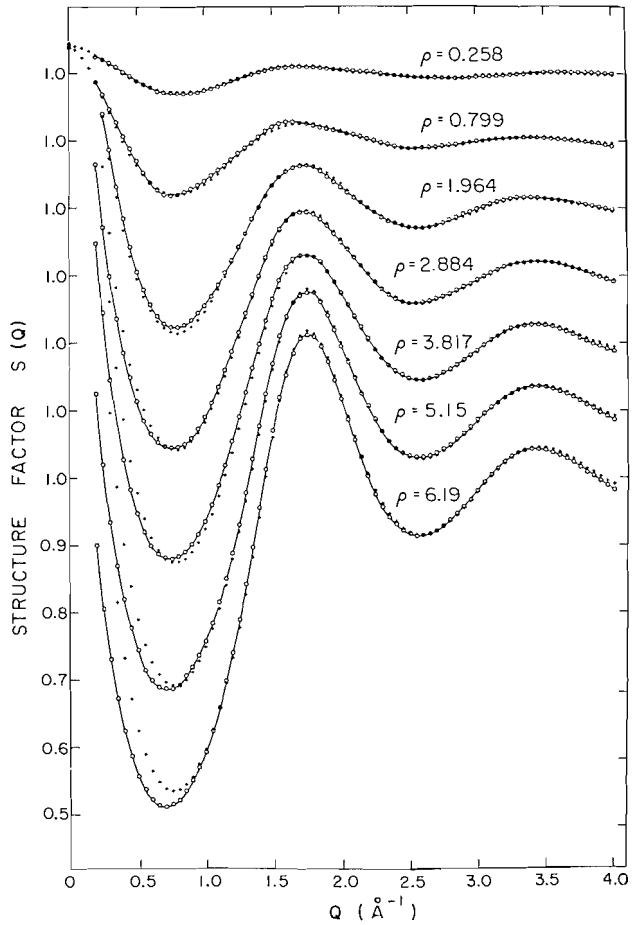

FIG. 4. Experimental structure factors (3) (eq. [9]) at 297 K for several krypton densities (in units of atoms/nm^3) shown by the circles and lines, compared to calculations (15) based on the pair potential alone (crosses).

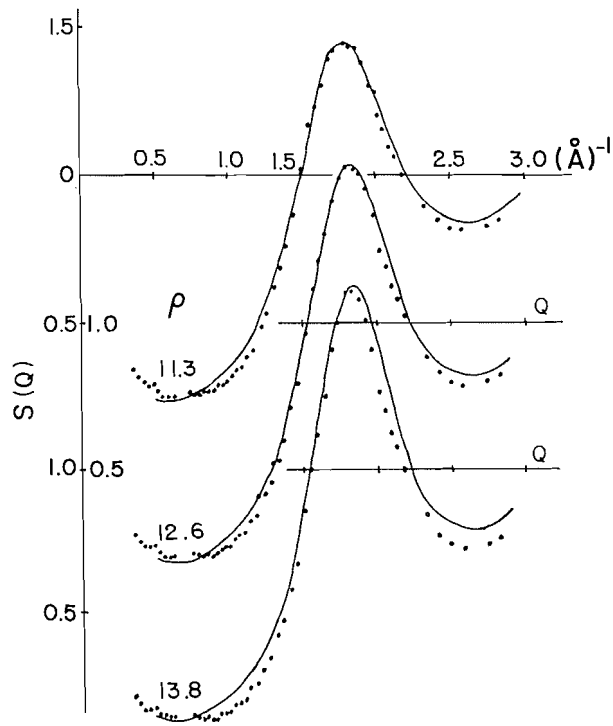

FIG. 5. Experimental structure factors (17) ($S(Q)$-eq. [9]) for krypton on the 297 isotherm, shown by circles, and compared to comptuer simulations (15) shown by the lines.

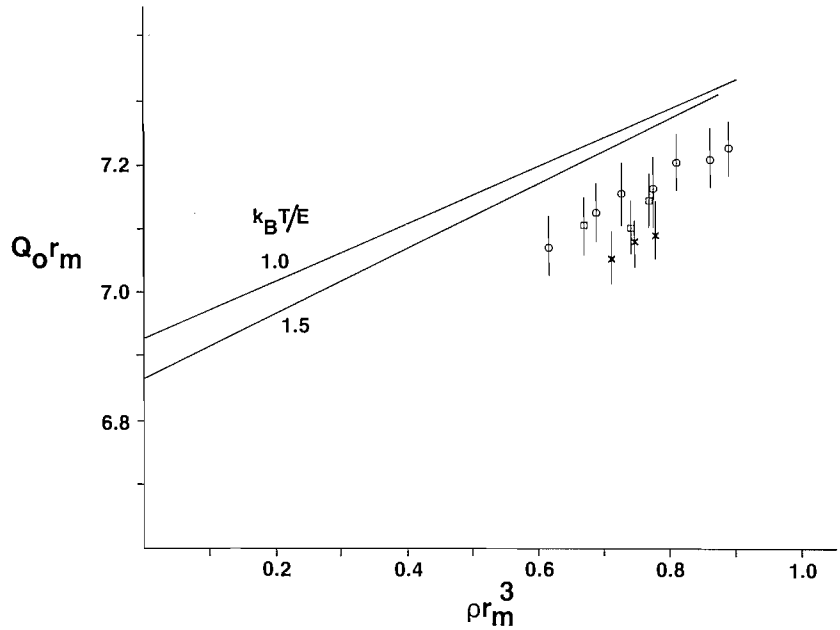

FIG. 6. A summary of the principal peak position, Q_0, in $S(Q)$ as a function of density. The full lines are predictions for $k_BT/\epsilon = 1.0$ and 1.5. The circles, crosses, and squares are experimental results from refs. 17 and 18 and A. Teitsma (1980, unpublished results) for krypton at 297 K, krypton at 200 K, and xenon at 297 K, respectively. Through eq. [9] this peak shift corresponds to a larger diameter in the real fluid than in the model.

where the lines show data from virial coefficient calculations at low ρ and computer simulations using a pair potential at high ρ. Because of the above discussion, the model calculations (10), and computer simulations using the A–T potential model, it is expected that these lines would be unchanged if the A–T potential were added. There is a small shift of the line with temperature ($k_BT/\epsilon = 1.5$ to 1.0), but this is relatively unimportant. All experimental results cluster together at lower peak positions than predicted, thus confirming (through the relationship between $S(Q)$ and $g(r)$) that an effect analogous to a change in effective diameter with increasing density has been observed. If this is due to the collision effect described in the Introduction, it could be modeled by the "shell model" for heavy atoms used in lattice dynamics (Appendix 1). In this event one would expect that the dynamics would be affected also if the appropriate frequencies and wave numbers could be observed. Simulations (19, 20) using the shell model have been made for ionic liquids, and suggest that the effects of the right order of magnitude would be found in noble gas simulations with similar shell constants.

To demonstrate the deviation of the data from the A–T potential test model (eq. [8]) in greater detail, we plot the data from refs. 3 and 17 in the form proposed by Teitsma and Egelstaff (3). Their proposal is to take the difference in direct correlation functions, $c(Q)$, where:

$$[10] \quad c(Q) = \frac{1}{\rho}\left\{1 - \frac{1}{S(Q)}\right\}$$

When considered as a function of density (ρ), the difference between $c(Q)$ for the computer simulation and the experimental result should start from the origin (for $\rho \rightarrow 0$) and initially vary as ρ. The coefficient of ρ may be calculated from the integrand in eq. [1]. In some theoretical papers (e.g. refs. 21, 22) it is noted that on the scale of Fig. 4, the test model will appear to fit the experimental data. However, if the quality of the experimental and simulated data is such as to allow the difference in $c(Q)$'s to be taken, the test model can be examined more severely than by comparing $S(Q)$'s.

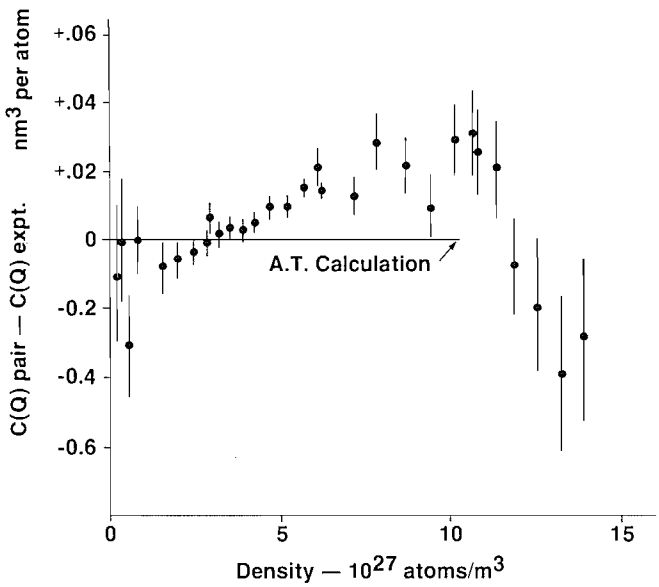

FIG. 7. A difference plot of the kind used in ref. 3. The experimental $c(Q)$ — eq. [10] — and simulated $c(Q)$ are subtracted using the results (3, 17) from Figs. 4 and 5, and plotted as a function of density for $Q = 0.6$ Å^{-1}. The errors increase towards low densities because of the ρ^{-1} factor in eq. [10]. The line shows the prediction (15) using data for the potential at eq. [8] in place of the experimental data.

As an example we show in Fig. 7 the difference in direct correlation functions for $Q = 0.6$ Å^{-1}. At this Q the test model term almost vanishes (i.e. $Q = 0.6$ is a node, if the $c(Q)$ difference is plotted as a function of Q). It can be seen that there is a marked difference between the model result and the experimental result, indicating that the model fails at all densities.

Can. J. Chem. Downloaded from www.nrcresearchpress.com by 176.9.209.113 on 09/07/12
For personal use only.

Also the mean field is seen to be inadequate as the difference data should lie along the $\Delta c(Q) = 0$ axis at higher densities. In addition, this difference is a severe test of the pair potential employed in the simulation. If $u(r)$ is correct in detail, the data should vanish as $\rho \rightarrow 0$ for all Q. It can be seen that this is improbable at $Q = 0.6$ Å^{-1} in Fig. 7. These discrepancies at all Q have been summarized in Fig. 6 of ref. 15 (for the pair potential) and Fig. 8 of ref. 3 (for the three-body potential). The advantages of measuring $S(Q)$ are that there is an internal check on the adequacy of the published pair potentials, and that the test of many-body potential models and of mean field behaviour is both detailed and severe. It is to be expected that the power of this method can be improved using techniques developed in recent years (23).

It thus appears that the test model exhibits good mean-field behaviour and describes bulk data quite well, but that at higher densities the real fluid deviates from both the model and the mean-field picture if examined in appropriate detail. On the other hand, the work of Teitsma and Egelstaff (3) shows that the A–T model (eq. [8]) does yield the right scale for these effects, even though the detail (in Fig. 7 for example) is incorrect. It would appear therefore that two theoretical improvements are required. The first would be an improved three-body potential which would give the correct slopes at low ρ in (for example) Fig. 7. The second would be improved models of the many-body potential short range effects (4) which lie outside the mean field approximation.

5. Non-equilibrium properties

For reasons discussed for the pair correlation function, these properties should be unaltered by the mean field. The transport coefficients for the pair fluid and the test model (eq. 8) have been examined in a number of papers. In the high density work of Hoheisel (16) on an argon model and of Levesque *et al.* (13) on a xenon model, a system of 108 particles near the triple point was examined. Because these systems are small, the time over which valid data may be collected is small. If this time is chosen conservatively to be the time for a sound wave to cross half the width of the box, we obtain $t \leq 1$ ps in Hoheisel's case and $t \leq 1.6$ ps in Levesque *et al.*'s case. In the former example, time integrals extending to more than 2.5 ps were used, and in the latter case time integrals extending to more than 5 ps were used. Levesque *et al.* (13) reported finding no difference in the three collective transport coefficients (shear and bulk viscosity and thermal conductivity) within an error of 5–10%. Their data are listed in Table 4. Hoheisel (16) reported that self-diffusion coefficient was nearly unchanged, but concluded a small difference of ~5% occurred. This arose from parts of the time integral for $t > 1$ ps.

Both papers report data on time correlation functions. Levesque *et al.* (13) show that the stress–stress and energy–energy correlation functions are the same (within error) to 5 ps, while Hoheisel (16) reports the velocity auto-correlation function (VAF) is the same for times < 1 ps, but some differences are seen in the tail beyond 1 ps. For his cases Hoheisel computes the change in the VAF over argon densities of 20–23 atoms/nm^3, and finds smaller changes with increasing ρ. The van Hove space–time correlation function $G(r,t)$ is also discussed in these papers. Again Levesque *et al.* (13) find no effect (within the errors) for $0.31 < Q < 2.43$ Å^{-1} and $t < 5$ ps, when plotting the intermediate scattering function (or space Fourier transform of $G(r,t)$). Hoheisel (16) finds no change in $G(r,t)$ itself for times ~ 1 ps, but a small change for times ~ 2.5 ps. Within the probable limits of these two 108-particle simulations, it may be concluded that the mean-field picture is working satisfactorily. Therefore for all properties, static and dynamic, microscopic or bulk, the test model behaves approximately like a mean-field model at high enough densities.

TABLE 4. Theoretical transport coefficients for xenon at 176 K and 13.2 atoms/nm^3 from ref. 13

Coefficient	Pair potential	Pair + A–T potential
Shear viscosity (m Pa s)	0.40±0.03	0.41±0.03
Bulk viscosity (m Pa s)	0.30±0.03	0.31±0.04
Thermal conductivity (W K^{-1} m^{-1})	0.068±0.004	0.064±0.003

Simulations at lower densities have been carried out by Schommers (22), using the krypton pair potential and the test model (A–T potential). He used densities of 2.9 and 6.2 atoms/nm^3 at 297 K. For the velocity auto-correlation function at 2.9 atoms/nm^3 he found a slower decay for the pair fluid than that for the pair plus A–T potential case. However, this effect virtually disappeared at 6.2 atoms/nm^3. He also studied the force–force correlation function and for the lower density observed a difference near $t \sim 1$ ps, which virtually disappeared at the higher density. If we interpret this as the onset of mean-field behaviour, it has appeared at a similar density in both dynamic and static results. It is likely, however, that for all the above simulations (13, 15, 16, 22) more extensive calculations with larger systems are necessary to improve and confirm the data.

The dynamic structure factor (space and time Fourier transform of $G(r,t)$) has been measured by Egelstaff *et al.* (17), for a number of densities along the room temperature isotherm of krypton. Their highest density was 13.8 atoms/nm^3 or $\rho r_m^3 = 0.9$ (compared to the triple point density of 17 atoms/nm^3 for krypton). For this case Salacuse *et al.* (24) made computer simulations using realistic pair potentials, and compared their results to the experimental ones. Their data at lower values of Q (which are of interest in our case) are shown in Fig. 8, where the dynamic structure factor, $S(Q,\omega)$, is plotted as a function of ω for fixed Q. When $Q \simeq 1.8$ Å^{-1}, which is the maximum of the static structure factor, Fig. 5, there is good agreement. In this case we expect the collisions of two atoms to dominate in $S(Q,\omega)$. However, if Q is decreased from this value, increasing discrepancies between simulation and experiment are observed. For $Q < 1$ Å^{-1}, more than two particles can be seen and the width of $S(Q,\omega)$ is less in the real fluid than in the artificial simulated fluid. This implies that many-body effects slow down the motions at the atomic level. Levesque *et al.* (13) showed that $S(Q,\omega)$ for the A–T potential test model and the pair potential model are the same within simulation errors. Consequently the mean-field approximation is less satisfactory for the real fluid than for the A–T potential test model.

It is interesting that Levesque *et al.* (13) also made test model simulations (of 108 particles) for a system at the same pressure as the pair system (this required a 10% increase in the density). In this case the computed changes in $S(Q,\omega)$ are similar to those seen in Fig. 8, namely, that the atomic motions are slowed down relative to the lower density case and collective modes extend to higher Q. However, in the constant pressure simulation this would appear to be an expected result due to an increase in

Can. J. Chem. Downloaded from www.nrcresearchpress.com by 176.9.209.113 on 09/07/12
For personal use only.

Can. J. Chem. Downloaded from www.nrcresearchpress.com by 176.9.209.113 on 09/07/12
For personal use only.

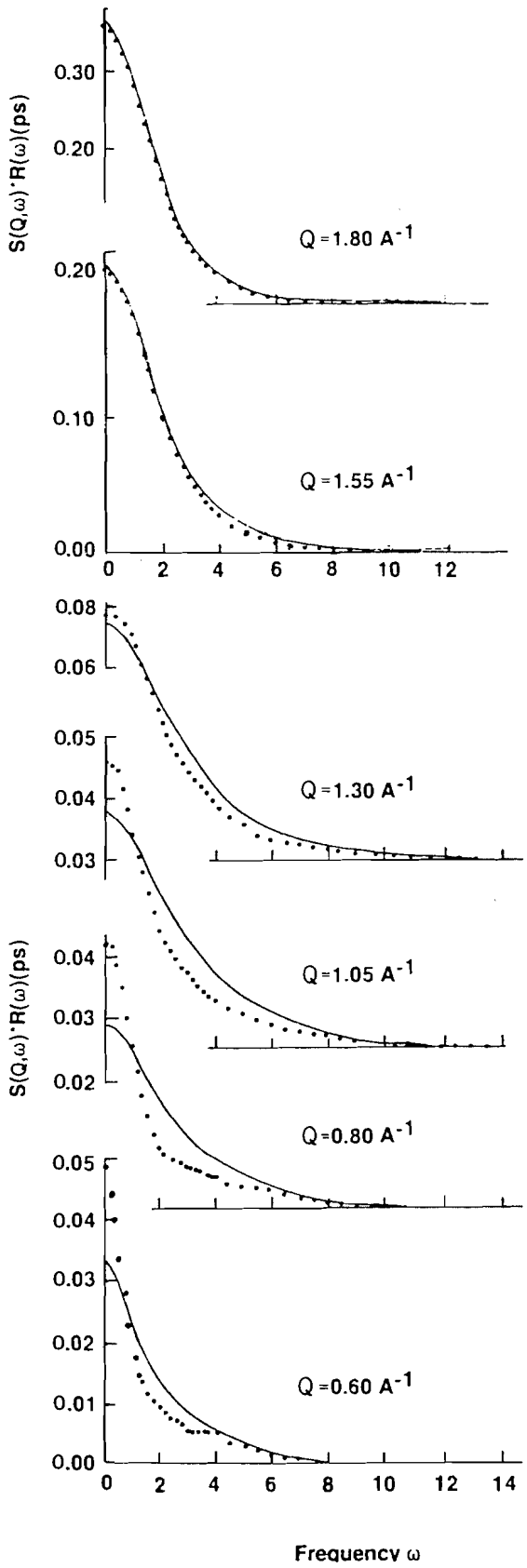

FIG. 8. The dynamic structure factor $S(Q,\omega)$ compared to computer simulated results (24) using the pair potential only. The data are from ref. 17 and $R(\omega)$ is the instrumental resolution function. Circles are the experimental data and the lines are the simulation.

density, whereas in the real substance the many-body forces mimic this higher density effect on a local scale, presumably through an increase in the effective atomic diameter. It is interesting that the same effect would lead to a sharper principal peak in the static structure factor, and this seems to be observed in the data of Fig. 5. These results thus correlate with the position shifts in $g(r)$ and $S(Q)$ which were discussed earlier.

6. Discussion

As pointed out in the Introduction, it is important to consider a range of properties, to understand the information content of each property, and to appreciate the significance of errors in both experimental and simulated data. Otherwise oversimplified conclusions will be reached, as in the case of Barker's conclusions (7–9 using the A–T model where insufficient attention was paid to each of these three issues. Nevertheless, the simple model in which all many-body forces are replaced by the Axilrod–Teller triple-dipole term only gets some of the overall picture right. Thus it alone can establish the scale parameters, i.e. effective distance and well depth parameters, which determine approximate values of integrals such as eqs. [1] or [6]. But on close examination it fails to reproduce much of the detail required from a model (e.g. Figs. 7 and 8) which would also cover the microscopic data. A partial explanation of this phenomenon has been given in various theoretical papers (e.g. ref. 4), but more work is needed to explain it properly especially on the various short range many-body forces.

The predictions of a zero-order mean field model were compared to the published results for the pair potential plus A–T three-body potential model of a fluid, and the index α, representing the order of the many-body forces, was adjusted to fit the data. For high densities it was found that the fluid behaved as a mean-field system with $\alpha = 4$, and that the mean-field behaviour was developed gradually over a range of densities extending up to $\rho r_m^3 = 1$. These empirical observations require further theoretical work to understand their origin properly (Appendix 2).

The picture being presented here is that the minimum number of many-body effects required to explain the data is three: namely, terms arising at large separations and expressed through a multipole expansion, an effect due to deformable outer shells which has been given a simple physical representation as an increase in effective diameter with increasing density and arising from multiple collisions, and a short range exchange effect (6). All three effects are important in the study of the pressure of noble gas fluids and solids. At low pressures the multipole terms give the mean effect because the other two appear to cancel each other approximately. It should be remembered that this cancellation refers to $Q \rightarrow 0$ static properties only (see Figs. 7 and 8), and also that all three effects will contribute to the pair potential. Thus for many-body forces the individual contributions depend in part on the parameters of the pair force (eq. [8] is an example of an approximate relation). The most plausible explanations for any near cancellation of effects might lie either in this connection or in the relationships between all the short range forces.

At intermediate pressures it is possible that all three effects matter. For example, Loubeyre (6) shows that for krypton at 300 K and 27 atoms/nm^3 ($\rho r_m^3 \sim 1.7$), the pair potential alone contributes about 95% of the observed pressure (about 2 GPa), the A–T term adds about 5%, while the exchange term subtracts about 15%. At higher pressures (e.g. 20 GPa) the experimental pressure is only 7% higher than that obtained after the A–T and

Can. J. Chem. Downloaded from www.nrcresearchpress.com by 176.9.209.113 on 09/07/12
For personal use only.

exchange terms have been applied. However, Barker (8, 9) points out that if the core of the Aziz (1) potential is adjusted by a reasonable amount (i.e. P_0 is adjusted), the A–T model (eq. [8]) will fit the experimental pressure difference ($P - P_0$) up to 50 GPa. Both Barker (8, 9) and Loubeyre (6) report calculations at high pressures using this model, and these calculations may be compared to the predictions of the mean-field model using eq. [5] and the data in Table 1*b* for parameter *a*. On the scale of their figures the prediction, for densities up to three times greater than that in Table 1*b*, is in reasonable agreement with their calculations. This confirms the similarity of the A–T model to a mean-field model up to high pressures and that essentially no new information can be obtained from the pressure data alone.

The argument that exchange interactions are important rests partly on the helium data (6) and their scaling to heavier noble gases, partly on other solid state data and partly on theoretical arguments. If the importance of the exchange terms has been established in one experimental regime, it is a matter of calculation to discover their importance in another part of the phase diagram, and hence establish that the known A–T and exchange terms taken together do not fit the bulk data on fluids over the states reviewed here. There is thus room for the "shell-model" contribution suggested by the diffraction experiments, and calculations of its contribution to the pressure (for example) are needed.

Because the mean-field model works reasonably well for the bulk data, such data can be represented by a few parameters involving the scale of these effects. Consequently bulk data are insensitive to the details of many-body potentials, and if the mean-field model was as successful for the microscopic properties, very little could be concluded about the details of many-body forces. Thus it is useful to concentrate on measuring and exploring the detailed effects appearing in microscopic properties, even though the experiments are difficult (23). The structure factor (or pair correlation function) is the most useful and definitive quantity in this field; it can provide clear cut answers to a number of questions. One reason that microscopic properties are more sensitive is because the distance and time parameters may be adjusted to enhance the effect sought.

For studies in $g(r)$ and $S(Q)$ at high pressure where $Q \neq 0$, the change in effective diameter is the dominant effect. Work reviewed here has demonstrated that the multipole effects are unimportant (10) in $S(Q)$, while Reatto[2] has studied the effect of terms similar to those used by Loubeyre (6) and demonstrated that they produce a negligible effect in $S(Q)$. Thus the pair correlation function at high pressure is sensitive to a different effect than the principal ones which influence the pressure. This result demonstrates the importance of analysing the information content of each piece of data. In this article this was achieved partly by comparisons to the mean-field model and partly by comparison to computer simulations. The extension of this approach using other models and other data, particularly data on molecular clusters (25), would be useful.

The reason that the A–T potential test model behaves like a mean-field model in all properties may be seen by examining eq. [1]. A mean field works for long range low amplitude potentials, so why is eq. [8] cut off before the potential reaches a large amplitude at low r? In eq. [1], and all similar equations, the hard core of the pair potential switches off the three-body potential. Except for very low temperatures (where the liquid freezes), this cut-off occurs before the A–T term has a large enough amplitude to destroy its mean field behaviour. Because correlation functions of real systems behave differently (Figs. 6 and 7), it appears that the real many-body potentials have some large amplitude components for distances comparable to or greater than the pair potential cut-off. For $g(r)$ at high pressure these may be represented pictorially as an increase in effective diameter. A more detailed examination of experimental data, more precise experiments, and large scale simulations are required before such effects can be understood properly.

[2]L. Reatto. Private communication. I am indebted to Dr. Reatto for a summary of his results on this effect.

Acknowledgements

This project was supported by a grant from the Natural Sciences and Engineering Research Council of Canada. I am grateful for the hospitality offered by the Laboratoire Leon Brillouin, Saclay, where part of the work was done. I would like to thank Dr. Levesque for a copy of the data of ref. 13 prior to publication.

It is a pleasure to dedicate this article to Jim Morrison, whose multi-faceted career has shown how one individual can produce a joyous many-body interaction among condensed matter scientists.

1. R. A. Aziz. Springer series in chemical physics. Vol. 34. Inert gases. *Edited by* M. L. Klein. Springer-Verlag 1984. p. 5.
2. J. J. Nicolas, K. E. Gubbins, W. B. Street, and D. J. Tildesley, Mol. Phys. **37**, 1429 (1979).
3. A. Teitsma and P. A. Egelstaff. Phys. Rev. A, **21**, 367 (1980).
4. W. J. Meath and R. A. Aziz. Mol. Phys. **52**, 225 (1984).
5. F. Barocchi, M. Zoppi, and P. A. Egelstaff. Phys. Rev. A, **31**, 2732 (1985).
6. P. Loubeyre. Phys. Rev. Lett. **58**, 1857 (1987); Phys. Rev. Lett. To be published.
7. J. A. Barker. Mol. Phys. **57**, 755 (1986).
8. J. A. Barker. Phys. Rev. Lett. **57**, 230 (1986).
9. J. A. Barker. (*a*) Mol. Phys. **60**, 887 (1987); (*b*) Mol. Phys. **21**, 657 (1971).
10. J. Ram and P. A. Egelstaff. Phys. Chem. Liq. **14**, 29 (1984).
11. (*a*) P. A. Egelstaff. Europhys. Letts. **3**, 867 (1987); (*b*) B. Widom. J. Chem. Phys. **39**, 2808 (1963).
12. J. J. Salacuse and P. A. Egelstaff. To be published.
13. D. Levesque, J. Vermesse, and J. J. Weis. Phys. Rev. A. To be published.
14. W. B. Street and L. S. Sagan. J. Chem. Thermodyn. **5**, 5462 (1973).
15. P. A. Egelstaff, A. Teitsma, and S. S. Wang. Phys. Rev. A, **22**, 1702 (1980).
16. C. Hoheisel. Phys. Rev. A, **23**, 1998 (1981).
17. P. A. Egelstaff, W. Gläser, D. Litchinsky, E. Schneider, and J.-B. Suck. Phys. Rev. A, **27**, 1106 (1983).
18. H. Fredrikze. Phys. Rev. A, 36, 2272 (1987).
19. M. J. L. Sangster and M. Dixon. Adv. in Phys. **25**, 247, (1976).
20. G. Jacucci, I. R. McDonald, and A. Rahman. Phys. Rev. A, **13**, 1581, (1976).
21. G. C. Aers and M. W. C. Dharma-Wardana. Phys. Rev. A, **29**, 2734 (1984).
22. W. Schommers. Phys. Rev. A, **22**, 2855 (1980); Phys. Rev. A, **27**, 2241 (1983).
23. P. A. Egelstaff. *In* Neutron scattering. Vol. 2. *Edited by* K. Sköld and D. L. Price. Academic Press. 1987. Chapt. 14.
24. J. J. Salacuse, W. Schommers, and P. A. Egelstaff. Phys. Rev. A, **34**, 1516 (1986).
25. E. E. Polymeropoules, P. Bopp, J. Brickmann, L. Jansen, and R. Block. Phys. Rev. A, **31**, 3565 (1985).

Appendix

1. A simple model to illustrate the change of effective diameter with density in a fluid made of deformable particles

We consider two fluids. One is a simple hard sphere fluid made of spheres of diameter d and mass m. The other consists of deformable particles of mass m; but each particle is made of a massless rigid spherical shell of diameter d and a hard sphere of diameter $d' < d$ located inside the shell and attached to it with springs. Thus under suitable conditions the centre of the shell may be displaced relative to the centre of the interior sphere.

Now we compare the pair potentials for these two fluids. The first case is just the hard sphere potential. The second case differs from this in that the pair potential looks like a soft sphere for distances between d and d'. In fact, if we define an effective diameter d'' by any reasonable formula, we shall find $d' < d'' < d$. The diameter d'' determines the position of the principal peak in $S(Q)$, according to eq. [9]. Thus at low densities the peak positions (Q_{01} and Q_{02}, respectively) of the two fluids differ, with the second fluid having a higher peak position than the first. Roughly we shall have

$$Q_{01}d \approx Q_{02}d''$$

Now consider the situation for a close-packed density, and a temperature such that the normal modes of the springs are not excited. Both fluids will exhibit the pair correlation function for a simple hard sphere fluid of diameter d, because in the second system the shell will not be free to move relative to the inner sphere except for a large scale cooperative motion of the particles. Thus the peaks of the two functions $S(Q)$ will be in the same position for the two fluids (i.e. at Q_{03}).

Now compare the low density case to the high density case for the second fluid using the simple hard sphere fluid as a reference. The usual practice in this field is to begin by scaling the low density results, and then to use the same scaling factor at high density. This would yield the result:

$$Q_{03}d > Q_{03}d''$$

or the peak in $S(Q)$ for the deformable particles will appear to move to lower Q with increasing density relative to a hard sphere system of diameter d''.

It is clear from the above discussion that this effect is a short range *many* body effect. It would be useful to perform computer simulations for this model.

2. Alternative derivation of eqs. [5] and [6], with an alternative interpretation of the index α

Our purpose is to derive eqs. [5] and [6] from the conventional liquid theory expressions for pressure and energy

$$P - P_0 = -\frac{\rho^2}{6}\int r\,\frac{\partial u_2}{\partial r}\,[g_2(r) - g_2^0(r)]\mathbf{dr} - \frac{\rho^3}{6}\int r\,\frac{\partial u_3}{\partial r}\,g_3(\mathbf{r}, \mathbf{s})\mathbf{dsdr}$$

$$\frac{U - U_0}{V} = \frac{\rho^2}{2}\int u_2[g_2(r) - g_2^0(r)]\mathbf{dr} + \frac{\rho^3}{6}\int u_3 g_3(\mathbf{r}, \mathbf{s})\mathbf{dsdr}$$

where $g_2^0(r)$ is the pair correlation function when $u_3 = 0$. We shall assume (*i*) that $g_2(r) \simeq g_2^0(r)$, such that the terms involving u_2 are negligible compared to those in u_3 and (*ii*) that the state dependence of g_3 is unimportant over the range of (**r**, **s**) important to these integrands, and (*iii*) that $u_3 \sim r^{-n}s^{-n}t^{-n}$ over the range important to these integrands. Then we can reduce these equations to the form of eq. [5]. To do this we define a constant a as:

$$a \simeq \frac{n}{6N^{n-2}}\int u_3 V^n g_3(\mathbf{r}, \mathbf{s})\,\frac{\mathbf{dr}}{V}\,\frac{\mathbf{ds}}{V}$$

so we obtain

$$[5'] \quad \frac{U - U_0}{V} \simeq \frac{a\rho^{n+1}}{n} \quad \text{and} \quad P - P_0 \simeq a\rho^{n+1}$$

For a to be a constant we need to work in a regime where the "uniform fluid model" is applicable, so that all distances scale as $V^{1/3}$.

If all the above conditions apply, this model has all the properties of the mean-field model with $\alpha = n + 1$, and n is the inverse power appearing in the model for u_3. For the Axilrod–Teller potential $\alpha = 4$. It is also possible to show that $\alpha = 3$ when $u_3 \sim e^{-\gamma(r+s+t)}$ and $\gamma \to 0$, to give the usual mean-field result.

It would be helpful to examine the four conditions on which [5'] is based, and to calculate how the fluid approaches this limit.

Can. J. Chem. Downloaded from www.nrcresearchpress.com by 176.9.209.113 on 09/07/12
For personal use only.

The infrared multiphoton dissociation of hexafluoroethane

CARL E. BROWN AND DONALD R. SMITH
Department of Chemistry, McMaster University, 1280 Main Street West, Hamilton, Ont., Canada L8S 4K1

Received August 25, 1987

This paper is dedicated to Professor J. A. Morrison

CARL E. BROWN and DONALD R. SMITH. The infrared multiphoton dissociation of hexafluoroethane. Can. J. Chem. **66**, 609 (1988).

The infrared multiphoton dissociation (IRMPD) of "neat" hexafluoroethane has been investigated for the first time. The stable products of photolysis are CF_4, C_2F_4, C_3F_8, and C_4F_{10}. Product analysis involved tunable diode laser (TDL) and fourier transform infrared spectroscopy, as well as gas chromatography where applicable. The high sensitivity and resolution of the TDL allows for measurement of the stable products CF_4 and C_2F_4 after irradiation by a single infrared laser pulse. The yield of $\cdot CF_3$ radicals produced by the IRMPD of C_2F_6 as a function of fluence was measured via the TDL high frequency modulation technique. The role of added H_2, leading to elimination of CF_4 and increase of C_2F_4 as products, is clarified.

CARL E. BROWN et DONALD R. SMITH. The infrared multiphoton dissociation of hexafluoroethane. Can. J. Chem. **66**, 609 (1988).

On a étudié pour la première fois la dissociation multiphotonique infrarouge (DMPIR) de l'hexafluoroéthane à l'état pur. Les produits stables de la photolyse sont le CF_4, le C_2F_4, le C_3F_8 et le C_4F_{10}. Dans les cas où ces techniques pouvaient être appliquées pour l'analyse des produits, on a utilisé un laser à diode ajustable (LDA), la spectroscopie infrarouge par transformation de fourier ainsi que la chromatographie en phase gazeuse. La sensibilité élevée et la grande résolution du LDA permettent de mesurer les produits stables, comme le CF_4 et le C_2F_4, après une irradiation par une seule pulsation du laser infrarouge. On a utilisé la technique de modulation de la haute fréquence du LDA pour mesurer le rendement en radicaux $\cdot CF_3$ produits par DMPIR du C_2F_6, en fonction de la fluidité. On a éclairci le rôle du H_2 ajouté sur l'élimination de CF_4 et l'augmentation du C_2F_4, comme produits de la réaction.

[Traduit par la revue]

Introduction

In earlier work Fisk (1) reported C_2F_4 and CHF_3 as the products of the infrared multiphoton dissociation (IRMPD) of hexafluoroethane in the presence of H_2 or C_6H_{14}. Several years later Arai *et al.* (2) studied the IRMPD of hexafluoroethane in the presence of Br_2, the results of their experiments indicated that the major reaction products were CF_3Br and CF_2Br_2. Our exploratory work on the IRMPD of "neat" hexafluoroethane showed that CF_4 was the major photolysis product, with lesser amounts of C_2F_4, C_3F_8, and C_4F_{10}. Thermodynamically, the most favourable dissociation pathway of C_2F_6 leads to the production of CF_4 and $:CF_2$. However, shock tube studies (3) suggest that this pathway possesses a large energy barrier. The next most favourable pathway is the result of C—C bond scission forming two $\cdot CF_3$ radicals, reaction [2]. Presumably the pre-exponential factor favours reaction [2] as well, since it only involves C—C bond breakage.

[1] $C_2F_6 \rightarrow CF_4 + :CF_2$ $\quad \Delta H_0 = +225.94$ kJ/mol

[2] $\rightarrow 2\cdot CF_3$ $\quad \Delta H_0 = +400.83$ kJ/mol

[3] $\rightarrow \cdot C_2F_5 + \cdot F$ $\quad \Delta H_0 = +512.96$ kJ/mol

[4] $\rightarrow C_2F_4 + F_2$ $\quad \Delta H_0 = +680.32$ kJ/mol

In view of the uncertainty in the dominant reaction channel, and major discrepancy between our work and the literature, we initiated a programme to determine the overall mechanism of IRMPD of hexafluoroethane.

C_2F_6 was subjected to CO_2 laser pulses ≈ 30 cm^{-1} to the low frequency side of its ν_5 absorption band (see Fig. 1). Efficient IRMPD of C_2F_6 was found to occur at relatively low fluences. The major products of photolysis are CF_4, C_2F_4, C_3F_8, and C_4F_{10}. A reaction mechanism involving the production of trifluoromethyl radicals followed by abstraction and radical recombination reactions will be presented. It will be shown that secondary photolysis of $\cdot CF_3$ radicals during the laser pulse is the source of C_2F_4.

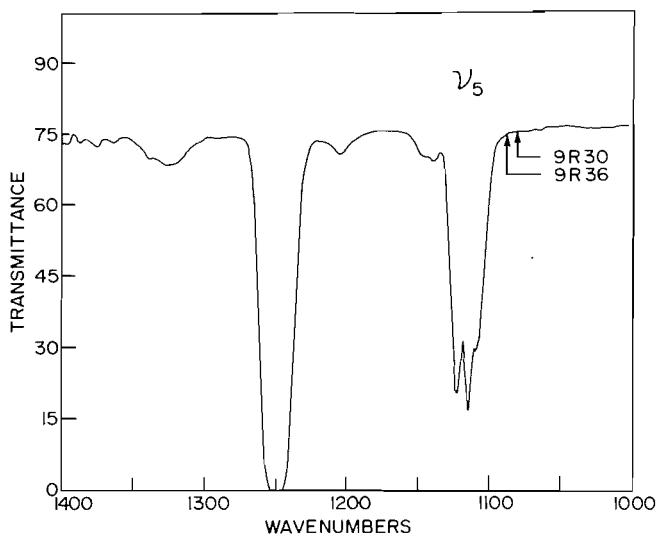

FIG. 1. FTIR spectrum of 2.1 Torr C_2F_6 in a 10 cm long Pyrex cell, 4 cm^{-1} resolution, indicating the CO_2 laser pump lines used in irradiation.

Experimental

Irradiations were performed on 2 Torr samples of C_2F_6 in 10 cm long, 2.5 cm diameter Pyrex or Monel cells equipped with sodium chloride windows, using a Lumonics K-922S pulsed CO_2 laser. The CO_2 laser pulse was focussed with a 25 cm focal length BaF_2 lens. The focal fluence was calculated from the measured focal burn spot area on thermal paper and the pulse energy as measured on a Gentec model ED-500 Joulemeter. The energy of the incident laser pulse was attenuated by a series of polyethylene sheets as necessary, to obtain the desired pulse energy and hence the desired fluence. The stable products

Can. J. Chem. Downloaded from www.nrcresearchpress.com by 176.9.209.113 on 09/07/12
For personal use only.

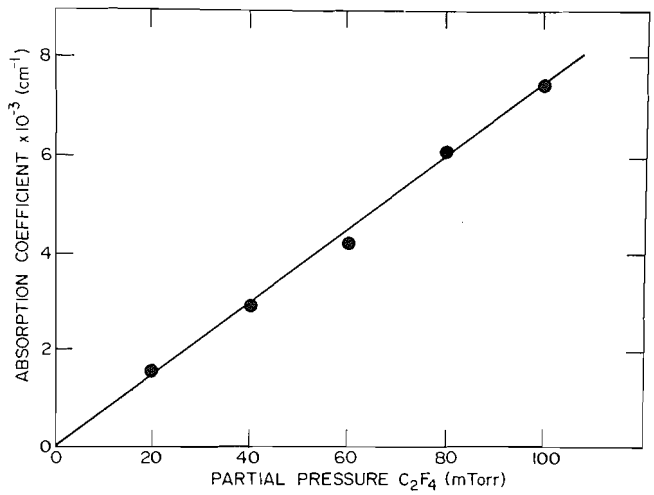

FIG. 2. Line center absorption coefficient (α_0) vs. partial pressure C_2F_4 (mTorr in C_2F_6, 2 Torr total pressure), measured by TDL absorption spectroscopy at 1196.7 cm^{-1}.

were measured following irradiation using a gas chromatograph (GC) and a tunable diode laser (TDL) spectrometer where applicable. The gas chromatograph employed was a Varian Model 3700 equipped with a flame ionization detector, and a 6 foot long Porapak Q 50-80 column. The TDL spectrometer utilises a Spectra Physics Lead-salt diode capable of tuning between 1080 and 1280 cm^{-1}. Both direct absorption and second-harmonic detection of the products are possible. The general concepts and techniques of TDL absorption measurement can be found in ref. 4. For direct measurement of absorbance, Beer's law ($I = I_0 \exp(-\alpha_0 L)$) calibration plots of absorption coefficient vs. partial pressure of the gas were made. In all cases, these plots were linear over the range of partial pressures involved in our studies. For example, Fig. 2 illustrates absorption coefficient versus partial pressure for C_2F_4. Plots involving CF_4 and CHF_3 are also linear over the range studied.

Second harmonic ($2f$) detection is used for high sensitivity work when measurement of less than 1% line centre absorption is required. The TDL frequency is modulated at a few kHz by modulating the diode current. Synchronous detection at twice the modulation frequency, using a lock-in amplifier, achieves a major reduction in background noise. Quantification of the photolysis products was done by comparison of the $2f$ signal strength to that of a standard sample containing a known and comparable amount of the fluorocarbon being measured. CF_4, C_2F_4, and CHF_3 are measured by TDL spectroscopy. C_2F_4, C_3F_8, and C_4F_{10} are measured by gas chromatography. Product identities were verified by Fourier Transform Infrared (FTIR) and quadrupole mass spectrometry in addition to TDL and GC detection.

A description of the apparatus used in the detection of transient species such as trifluoromethyl radicals can be found in ref. 5. Briefly, the precursor C_2F_6 is flowed through a 1 mm diameter 15 cm long waveguide cell and is irradiated by a focussed beam (25 cm focal length lens, ≈0.25 J/pulse) from a Lumonics TEA-801A CO_2 laser. The TDL beam also passes colinearly through the waveguide cell before falling upon a fast (risetime with preamp ≈400 ns) HgCdTe detector. Between the waveguide cell and the detector, a diffraction grating and gas cell are used to separate the intense TEA CO_2 beam from the TDL beam.

To obtain the time-resolved $^{\cdot}CF_3$ absorption spectra the TDL is repeatedly tuned in wavelength back and forth across the expected position of a $^{\cdot}CF_3$ absorption line by modulating the TDL current at 40 kHz. The transient changes in TDL power transmitted by the sample cell are measured by the detector. Successive data sets are collected and averaged on a Tektronics 468 digital oscilloscope and then stored on an IBM-PC microcomputer. The start of each set is synchronized with the CO_2 laser pulse. Background scans of the precursor C_2F_6, obtained with the CO_2 laser beam blocked, can be stored for subtraction of any stable precursor lines. Electrical noise associated with the CO_2 laser pulse prevents the accurate measurement of any absorption signals for approximately 25 μs following the pulse. Elimination of the early noise from the CO_2 laser would allow modulation at frequencies up to 250 kHz and the study of temporal behaviour with a resolution of 2 μs.

C_2F_4, C_4F_{10}, and CF_3I were obtained from SCM Chemicals of Florida, CF_4, CHF_3, and H_2 from Canada Liquid Air Ltd., C_3F_8, $(CF_3)_2CO$, and C_2F_6 from Matheson Gas Products of Canada Ltd. All fluorocarbons were degassed and purified by bulb-to-bulb distillations.

Results and discussion

In our work, irradiation of "neat" hexafluoroethane samples using the 9R(30) and 9R(36) CO_2 laser lines leads to the production of major products CF_4, C_2F_4, C_3F_8, and C_4F_{10}. Typical results are shown in Figs. 3–6. Although these plots illustrate yields after many pulses, it should be noted that TDL absorption measurements of CF_4 and C_2F_4 are possible after a single 13.4 J cm^{-2}, 9R(36) pulse (see Fig. 7). The following trends should be noted: CF_4 is the dominant product at all wavelengths and fluences studied. Conversely, C_4F_{10} is the least abundant product in all cases. At low fluence C_3F_8 is the second most abundant product at both wavelengths. As the fluence is increased the yield of C_2F_4 increases relative to C_3F_8. Separate experiments with C_2F_4 added before irradiation indicate that C_2F_4 is also consumed in the presence of C_2F_6 under similar experimental conditions. Therefore absolute quantitative yields of C_2F_4 after several ir laser pulses are possibly not a true reflection of the overall photochemistry involved.

Previous studies on the IRMPD of hexafluoroethane in the presence of scavengers (1, 2) have suggested that the principal dissociation pathway involves the scission of the C—C bond to produce two $^{\cdot}CF_3$ radicals. These trifluoromethyl radicals were either scavenged by H_2 (1) or Br_2 (2), forming CHF_3 or CF_3Br, or they absorbed more infrared photons and underwent secondary dissociation to difluorocarbene and a fluorine atom. Tetrafluoromethane, octafluoropropane, and decafluorobutane were not mentioned in these reports.

How does one account for the presence of the observed products in the absence of scavengers? It would appear that the primary IRMPD pathway indeed involves scission of the C—C bond to form two $^{\cdot}CF_3$ radicals. We propose that the secondary photolysis of trifluoromethyl radicals (as observed in several cases such as ref. 7) can account for the production of CF_4 and C_2F_4 at high fluence as follows:

$$[5] \quad {}^{\cdot}CF_3 + h\nu \rightarrow :CF_2 + {}^{\cdot}F$$

$$[6] \quad 2\,:CF_2 \rightarrow C_2F_4$$

$$[7] \quad {}^{\cdot}CF_3 + {}^{\cdot}F \rightarrow CF_4$$

Formation of CF_4 and C_2F_4 via disproportionation of two $^{\cdot}CF_3$ radicals has been ruled out in shock-tube studies (3) and in very-low-pressure photolysis experiments (6) and is thus not considered to be the source of these species in the present experiments.

Kato *et al.* (7) have studied the dissociation probability of $^{\cdot}CF_3$ radicals as a function of fluence and found that this probability is greatly reduced at fluences < 2–3 J cm^{-2}. We believe that the C_2F_4 formed in the IRMPD of "neat" hexafluoroethane arises from the recombination of two $:CF_2$ radicals resulting from the secondary dissociation of trifluoromethyl radicals. A lowering of the irradiation fluence should eventually eliminate secondary photolysis and thus the production of C_2F_4. We have irradiated 2 Torr samples of hexafluoroethane at 9R(36) for 4000 pulses at a fluence of about 1 J cm^{-2}. FTIR analysis revealed the presence of CF_4 and C_3F_8, while there was no

Can. J. Chem. Downloaded from www.nrcresearchpress.com by 176.9.209.113 on 09/07/12
For personal use only.

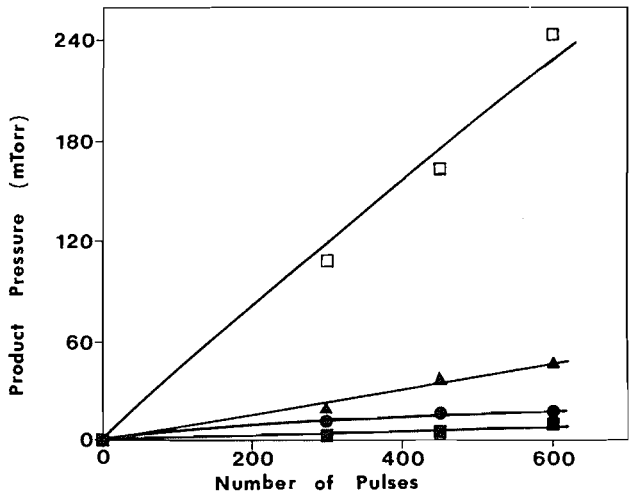

FIG. 3. Yield of products (mTorr) vs. number of pulses, following irradiation of 2 Torr C_2F_6 in a 10 cm long, 2.5 cm diameter Pyrex cell, 25 cm focal length BaF_2 lens, 9R(30) 5.3 J cm^{-2}. ● C_2F_4 GC, ○ C_2F_4 TDL (1196.7 cm^{-1}), □ CF_4 TDL (1269.0 cm^{-1}), ▲ C_3F_8 GC, ■ C_4F_{10} GC. The symbols ● and ○ are always superimposed in this plot.

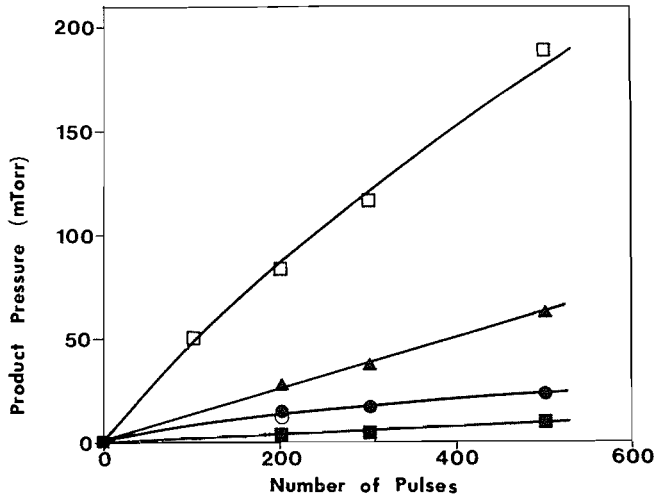

FIG. 5. Yield of products (mTorr) vs. number of pulses, following irradiation of 2 Torr C_2F_6 in a 10 cm long, 2.5 cm diameter Pyrex cell, 25 cm focal length BaF_2 lens, 9R(36) 5.3 J cm^{-2}. ● C_2F_4 GC, ○ C_2F_4 TDL (1196.7 cm^{-1}), □ CF_4 TDL (1269.0 cm^{-1}), ▲ C_3F_8 GC, ■ C_4F_{10} GC. The symbols ● and ○ are sometimes superimposed in this plot.

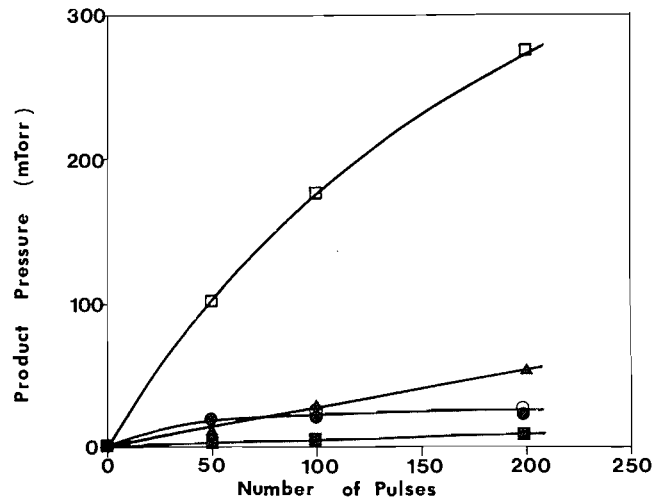

FIG. 4. Yield of products (mTorr) vs. number of pulses, following irradiation of 2 Torr C_2F_6 in a 10 cm long, 2.5 cm diameter Pyrex cell, 25 cm focal length BaF_2 lens, 9R(30) 13.4 J cm^{-2}. ● C_2F_4 GC, ○ C_2F_4 TDL (1196.7 cm^{-1}), □ CF_4 TDL (1269.0 cm^{-1}), ▲ C_3F_8 GC, ■ C_4F_{10} GC. The symbols ● and ○ are sometimes superimposed in this plot.

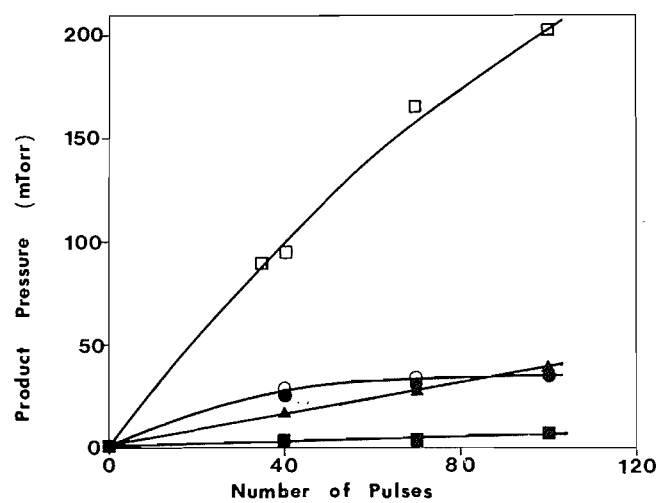

FIG. 6. Yield of products (mTorr) vs. number of pulses, following irradiation of 2 Torr C_2F_6 in a 10 cm long, 2.5 cm diameter Pyrex cell, 25 cm focal length BaF_2 lens, 9R(36) 13.4 J cm^{-2}. ● C_2F_4 GC, ○ C_2F_4 TDL (1196.7 cm^{-1}), □ CF_4 TDL (1269.0 cm^{-1}), ▲ C_3F_8 GC, ■ C_4F_{10} GC. The symbols ● and ○ are sometimes superimposed in this plot.

evidence of C_2F_4 even via second harmonic TDL detection. Thus the secondary dissociation of trifluoromethyl radicals has been suppressed at this fluence. Without ·F atoms present, an additional mechanism for the production of CF_4 is required. Hence we suggest the abstraction of a ·F atom by vibrationally excited $\cdot CF_3^{\dagger}$ from the parent C_2F_6 as follows:

[8] $\cdot CF_3^{\dagger} + C_2F_6 \rightarrow CF_4 + \cdot C_2F_5$

This reaction should be about 17 kJ/mol exothermic. It should be noted that in experiments done using the 9R(30) CO_2 laser pump line, the relative yield of CF_4/C_2F_4 increases as the pressure of C_2F_6 is increased from 1 to 2 Torr. The increase is more evident at low fluence (5.3 J cm^{-2}, 200 pulses) where the relative yield at 2 Torr is 5.8 times that at 1 Torr. At higher fluence (13.4 J cm^{-2}, 200 pulses) the increase in the relative yield at 2 Torr is 2.5 times that at 1 Torr. Reaction [8] therefore becomes more dominant as the pressure of C_2F_6 is increased, especially at low fluence where less secondary photolysis of $\cdot CF_3$ has occurred. Reactions similar to [8] have been proposed in the radiolysis of pentafluoroethyl iodide (8) and trifluoromethyl iodide (9). $\cdot C_2F_5$ may then react with $\cdot CF_3$ to form C_3F_8, reaction [9], or recombine to form decafluorobutane, reaction [10].

[9] $\cdot CF_3 + \cdot C_2F_5 \rightarrow C_3F_8$

[10] $\cdot C_2F_5 + \cdot C_2F_5 \rightarrow C_4F_{10}$

The secondary dissociation of pentafluoroethyl radicals has been observed previously by Hackett *et al.* (10) in the IRMPD of pentafluoroethyl iodide. In our work, the increased yield of C_2F_4 relative to C_3F_8 as the fluence is increased at both 9R(30) and 9R(36) may be due to the secondary photolysis of pentafluoroethyl as well as trifluoromethyl radicals.

[11] $\cdot C_2F_5 + h\nu \rightarrow :CF_2 + \cdot CF_3$

Can. J. Chem. Downloaded from www.nrcresearchpress.com by 176.9.209.113 on 09/07/12
For personal use only.

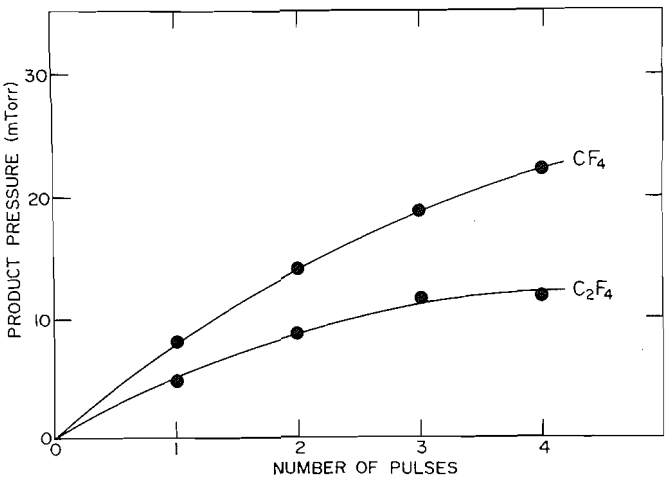

FIG. 7. Yield of CF_4, C_2F_4 vs. number of pulses, following irradiation of 2 Torr C_2F_6, 25 cm focal length BaF_2 lens, 9R(30) 13.4 J cm^{-2}, in a 10 cm long, 2.5 cm diameter Monel cell. The products were measured by second harmonic TDL absorption spectroscopy at 1269.0 and 1196.7 cm^{-1}, respectively. Note that in a Pyrex cell (Fig. 4), the curvature appears to be absent at this low number of pulses.

followed by

[6] $:CF_2 + :CF_2 \rightarrow C_2F_4$

Reactions of $^{\cdot}CF_3$ (11) or $:CF_2$ (12) with C_2F_4 to form heptafluoropropyl radicals or hexafluorocyclopropane are much too slow to be observed under the present experimental conditions.

Detection of trifluoromethyl radicals

The production of $^{\cdot}CF_3$ radicals was monitored immediately following the IRMPD of C_2F_6 via the high frequency modulation technique employing the tunable diode laser (5). Unfortunately there is spectral interference in the region of the $^{\cdot}CF_3$ $^rR_{16}(20)$ line calibrated by Orlando *et al.*,[1] thus a different absorption line was employed for quantification of the $^{\cdot}CF_3$ yield. The absorption line used for quantification of the trifluoromethyl radicals in these experiments has not been identified by Yamada and Hirota (13), however this line is also present immediately following the IRMPD of CF_3I and $(CF_3)_2CO$. To obtain a relative linestrength for the chosen analysis line at $\approx$1264.699 cm^{-1}, the intensity of this line was compared to the measured intensity of the $^rR_{16}(20)$ $^{\cdot}CF_3$ line at 1264.739 cm^{-1}. To accomplish this 600 mTorr of hexafluoroacetone was irradiated at a fluence of $\approx$23 J cm^{-2} using the 10R(14) CO_2 laser pump line. Three sets of 32 laser pulses were averaged for each of the lines, under identical experimental conditions. The ratio of the line intensities (1264.699/1264.739) was found to be 1.47 $\pm$ 0.04. The calibrated linestrength for the chosen $^{\cdot}CF_3$ analysis line at 1264.699 cm^{-1} is therefore $(2.0 \pm 0.5) \times 10^{-20}$ cm $molecule^{-1}$. The $^{\cdot}CF_3$ absorption line at 1264.699 cm^{-1} in the C_2F_6 system exhibits the same temporal growth and decay behaviour as the $^rR_{16}(20)$ line produced in the IRMPD of hexafluoroacetone.[2] In the hexafluoroacetone experiments a measurement of the gas temperature following the absorption of a CO_2 laser pulse was undertaken. A trace of N_2O was added to the photolysis cell, and the time-resolved absorption of N_2O on a temperature-sensitive transition (P(45) at 1243.795 cm^{-1}) was performed. After absorption of a CO_2 laser pulse by the hexafluoroacetone and N_2O mixture, no measurable increase in N_2O absorption (to within 10%) was noted over 20 ms. Thus there was no significant temperature increase. (A 10% increase in N_2O absorption on P(45) would correspond to a temperature change of less than 10K.) Furthermore, from the calculated linestrength, a plot of the reciprocal $^{\cdot}CF_3$ concentration versus time, in C_2F_6 gives a second order recombination rate of $(1.7 \pm 0.4) \times 10^{-12}$ cm^3 $molecule^{-1}$ s^{-1}, which is within the experimental error of the rate as previously determined by us.[2] We are therefore confident that we are indeed measuring the concentration of thermalized $^{\cdot}CF_3$ radicals. From this linestrength, the peak yield of $^{\cdot}CF_3$ produced per laser pulse via IRMPD of 600 mTorr of hexafluoroethane using the 9R(30) CO_2 laser pump line as a function of fluence has been measured. As one can see from Fig. 8, a significant amount of $^{\cdot}CF_3$ is produced by each CO_2 laser pulse (>3% dissociation per pulse at 19.8 J cm^{-2}). The lower limit in Fig. 8 was caused by low TDL power, and is not intended to indicate a threshold for the production of $^{\cdot}CF_3$.

Hydrogen donors

The addition of 2 Torr of a hydrogen-donating species such as H_2 or C_6H_{14} to 2 Torr of C_2F_6, followed by irradiation at the same wavelengths and fluences as above, leads to the elimination of the CF_4 yield. CF_4 is absent whenever the donor is present at pressures $\geq$0.5 Torr. The lack of CF_4 confirms that it is not a primary dissociation product (as predicted), and that reaction [8] is effectively eliminated when H_2 is added. Some of the trifluoromethyl radicals formed in IRMPD may be scavenged by the hydrogen donor as follows:

[12] $^{\cdot}CF_3 + H_2 \rightarrow CHF_3 + {}^{\cdot}H$

and

[13*a*] $^{\cdot}CF_3 + {}^{\cdot}H \rightarrow CHF_3^* \rightarrow :CF_2 + HF$

$\downarrow$ [M]

[13*b*] CHF_3

C_3F_8 and C_4F_{10} are still observable, however they cannot now be produced as previously indicated or CF_4 would also be observed (i.e. reaction [8] does not occur in the presence of a hydrogen donor). Thus we propose that a second dissociation pathway [3] must also be occurring:

[3] $C_2F_6 + h\nu \rightarrow {}^{\cdot}C_2F_5 + {}^{\cdot}F$

as well as

[9] $^{\cdot}CF_3 + {}^{\cdot}C_2F_5 \rightarrow C_3F_8$

and

[10] $^{\cdot}C_2F_5 + {}^{\cdot}C_2F_5 \rightarrow C_4F_{10}$

Fluorine atoms from reaction [3] or from secondary dissociation, reaction [5] will then be efficiently removed by reaction with the hydrogen donor:

[14] $H_2 + {}^{\cdot}F \rightarrow HF + {}^{\cdot}H$

The rate constants for reactions [7] (14) and [14] (15) are roughly equal, ($k_7 = (1.1\text{–}1.7) \times 10^{-11}$ cm^3 $molecule^{-1}$ s^{-1}, k_{14} $= 1.7 \times 10^{-11}$ cm^3 $molecule^{-1}$ s^{-1}), however under the present experimental conditions $[H_2] \gg [^{\cdot}CF_3]$ and reaction [14] should dominate.

[1] J. J. Orlando and D. R. Smith. To be published.

[2] C. E. Brown, J. J. Orlando, J. Reid, and D. R. Smith. To be published.

Can. J. Chem. Downloaded from www.nrcresearchpress.com by 176.9.209.113 on 09/07/12
For personal use only.

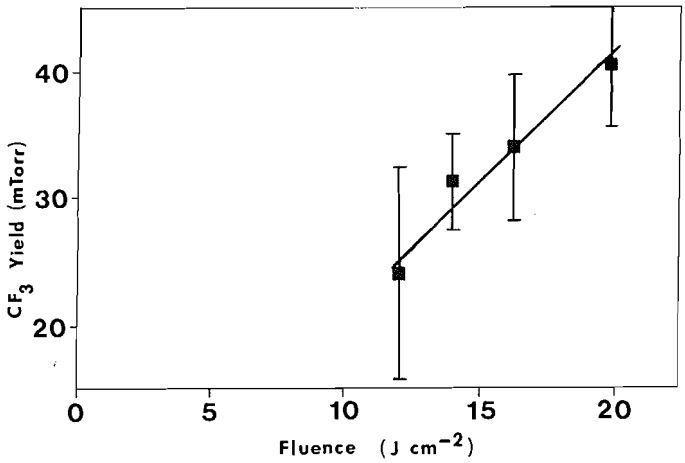

FIG. 8. Peak yield of $^{\cdot}CF_3$ vs. fluence, 50 μs after single pulse irradiation of 600 mTorr C_2F_6, in a 15 cm long, 1 mm diameter quartz waveguide cell, 25 cm focal length BaF_2 lens, 9R(30). The illustrated points are the average of three sets of 32 CO_2 laser pulses.

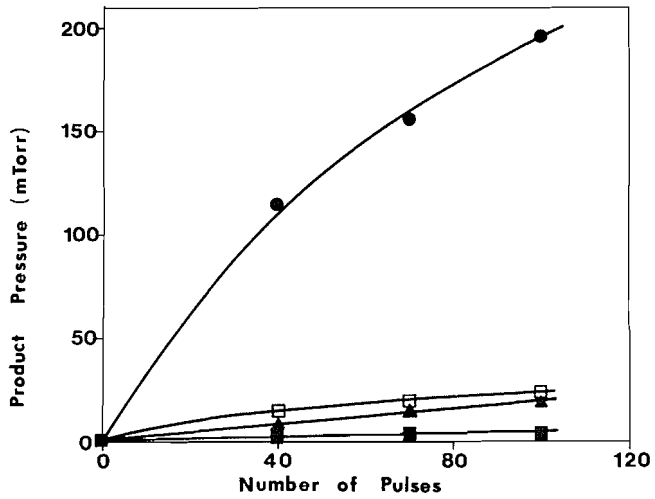

FIG. 9. Yield of products (mTorr) vs. number of pulses, following irradiation of 2 Torr C_2F_6 + 2 Torr H_2, in a 10 cm long, 2.5 cm diameter Pyrex cell, 25 cm focal length BaF_2 lens, 9R(36) 13.4 J cm^{-2}. ● C_2F_4 GC, □ CHF_3 TDL (1162.6 cm^{-1}), ▲ C_3F_8 GC, ■ C_4F_{10} GC.

The major products in the presence of a hydrogen donor are C_3F_8, C_4F_{10}, and CHF_3, as well as greatly increased C_2F_4 yields. Their yields as a function of number of pulses with 2 Torr of H_2 added to 2 Torr C_2F_6 are shown in Figs. 9 and 10.

The question arises as to why the C_2F_4 yield is greatly enhanced in the presence of hydrogen donors. Certainly the secondary dissociation of trifluoromethyl radicals should still occur to some extent, however other sources must contribute to the large increase in yield. To this end we investigated the possibility that the CHF_3 formed in reactions [12] and [13] itself undergoes IRMPD. Samples were prepared containing 20 mTorr of CHF_3 in C_2F_6 at 2 Torr total pressure and then subjected to 100 pulses 9R(36), 5.3 J cm^{-2}. After photolysis TDL measurements showed that 17.2 mTorr of the CHF_3 remained. Thus 14% of the fluoroform was consumed, indicating that it undergoes IRMPD in the presence of hexafluoroethane under the conditions used in the scavenging experiments. Control experiments containing the same known amount of CHF_3 in N_2 show no consumption of CHF_3. It appears that collisional energy transfer between vibrationally excited $C_2F_6^{\dagger}$ and CHF_3 is required to place CHF_3 in the

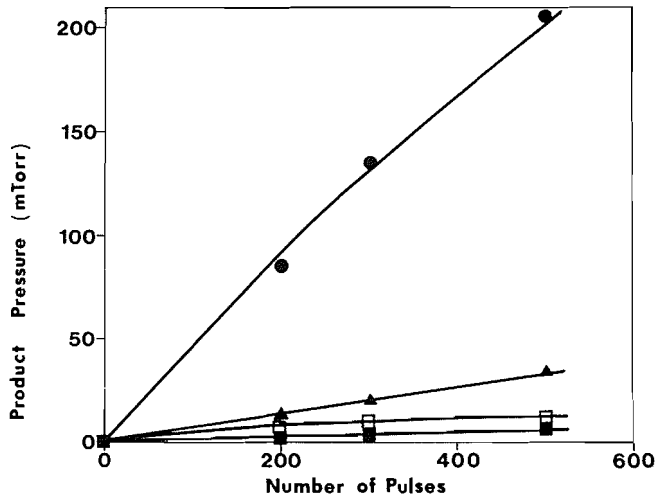

FIG. 10. Yield of products (mTorr) vs. number of pulses, following irradiation of 2 Torr C_2F_6 + 2 Torr H_2, in a 10 cm long, 2.5 cm diameter Pyrex cell, 25 cm focal length BaF_2 lens, 9R(36) 5.3 J cm^{-2}. ● C_2F_4 GC, □ CHF_3 TDL (1162.6 cm^{-1}), ▲ C_3F_8 GC, ■ C_4F_{10} GC.

vibrational quasicontinuum from which it may absorb further photons and dissociate.

[15] $C_2F_6^{\dagger} + CHF_3 \rightarrow C_2F_6 + CHF_3^{\dagger}$

[16] $CHF_3^{\dagger} + h\nu \rightarrow :CF_2 + HF$

The difluorocarbene thus produced would then dimerize to form C_2F_4. In view of the extremely large yield of C_2F_4, it is doubtful that the mechanisms proposed thus far can account for the total C_2F_4 yield. the difference could arise from a reaction between vibrationally excited $C_2F_6^{\dagger}$ and H_2 forming $C_2F_5H^{\dagger}$ which then eliminates HF to form C_2F_4, as proposed by Fisk (1). Alternatively, a more energetically favoured route would be via elimination of HF from excited $CHF_3^{\dagger}$, formed by combination of $^{\cdot}H$ and $^{\cdot}CF_3$, reaction [13*a*], followed by $:CF_2$ combination, reaction [6].

[17] $C_2F_6^{\dagger} + H_2 \rightarrow C_2F_5H^{\dagger} + HF$

[18] $C_2F_5H^{\dagger} \rightarrow C_2F_4 + HF$

In summary, we propose the following reaction mechanism for the IRMPD of "neat" hexafluoroethane:

[2] $C_2F_6 + h\nu \rightarrow 2\ ^{\cdot}CF_3$

[3] $C_2F_6 + h\nu \rightarrow {}^{\cdot}C_2F_5 + {}^{\cdot}F$

[−2] $^{\cdot}CF_3 + {}^{\cdot}CF_3 \rightarrow C_2F_6$

[−3] $^{\cdot}C_2F_5 + {}^{\cdot}F \rightarrow C_2F_6$

[7] $^{\cdot}CF_3 + {}^{\cdot}F \rightarrow CF_4$

[8] $^{\cdot}CF_3^{\dagger} + C_2F_6 \rightarrow CF_4 + {}^{\cdot}C_2F_5$

[9] $^{\cdot}CF_3 + {}^{\cdot}C_2F_5 \rightarrow C_3F_8$

[10] $^{\cdot}C_2F_5 + {}^{\cdot}C_2F_5 \rightarrow C_4F_{10}$

and at higher fluence, in addition to the above:

[5] $^{\cdot}CF_3 + h\nu \rightarrow :CF_2 + {}^{\cdot}F$

[6] $:CF_2 + :CF_2 \rightarrow C_2F_4$

[11] $^{\cdot}C_2F_5 + h\nu \rightarrow :CF_2 + {}^{\cdot}CF_3$

and in the presence of a hydrogen donor the following reactions will replace reactions [7] and [8]:

Can. J. Chem. Downloaded from www.nrcresearchpress.com by 176.9.209.113 on 09/07/12
For personal use only.

[12] $^{\cdot}CF_3 + H_2 \rightarrow CHF_3 + {}^{\cdot}H$

[13a] $^{\cdot}CF_3 + {}^{\cdot}H \rightarrow CHF_3^* \rightarrow :CF_2 + HF$

$\downarrow$ [M]

[13b] CHF_3

[14] $H_2 + {}^{\cdot}F \rightarrow HF + {}^{\cdot}H$

[15] $C_2F_6\dagger + CHF_3 \rightarrow C_2F_6 + CHF_3\dagger$

[16] $CHF_3\dagger + h\nu \rightarrow :CF_2 + HF$

[17] $C_2F_6\dagger + H_2 \rightarrow C_2F_5H\dagger + HF$

[18] $C_2F_5H\dagger \rightarrow C_2F_4 + HF$

Conclusion

The IRMPD of "neat" hexafluoroethane at moderate fluence leads to the formation of CF_4, C_2F_4, C_3F_8, and C_4F_{10}. The major IRMPD dissociation pathway involves the scission of the C—C bond to form two $^{\cdot}CF_3$ radicals. Above several J cm^{-2} fluence, secondary photolysis forms $:CF_2$. Evidence for the participation of a second dissociation pathway, forming a fluorine atom and a pentafluoroethyl radical is also presented. With the addition of a hydrogen donor, the predominant photolysis product CF_4 is eliminated. The elimination of CF_4 is accompanied with an increased yield of C_2F_4, along with the production of a small amount of CHF_3.

Acknowledgments

The authors are grateful to Atomic Energy of Canada Ltd. for the loan of the Lumonics TEA-801A CO_2 laser used in the $^{\cdot}CF_3$ detection experiments. We would also like to thank Dr. J. Reid for his general guidance in the use of tunable diode lasers, and for his help in developing the TDL high frequency modulation technique.

1. G. A. Fisk. Chem. Phys. Lett. **60**, 11 (1978).
2. S. Arai, T. Watanabe, Y. Ishikawa, T. Oyama, O. Hayashi, and T. Ishii. Chem. Phys. Lett. **112**, 224 (1984).
3. A. P. Modica and S. J. Sillers. J. Chem. Phys. **48**, 3283 (1968).
4. P. Beckwith, J. J. Orlando, J. Reid, and D. R. Smith. J. Photochem. **34**, 267 (1986).
5. P. H. Beckwith, C. E. Brown, D. Danagher, J. Reid, and D. R. Smith. App. Opt. **26**, 2643 (1987).
6. M. Rossi and D. M. Golden. Int. J. Chem. Kinet. **11**, 775 (1979).
7. S. Kato, Y. Makide, K. Takeuchi, and T. Tominaga. J. Phys. Chem. **88**, 3977 (1984).
8. T. Hsieh and R. J. Hanrahan. Radiat. Phys. Chem. **12**, 51 (1978).
9. I. McAlpine and H. Sutcliffe. J. Phys. Chem. **73**, 215 (1969).
10. P. A. Hackett, E. Weinberg, M. Gauthier, and C. Willis. Chem. Phys. Lett. **82**, 89 (1981).
11. G. E. Owen Jr., J. M. Pearson, and M. Szwarc. Trans. Faraday Soc. **61**, 1722 (1965).
12. B. Atkinson and D. McKeagan. Chem. Commun. 189 (1966).
13. C. Yamada and E. Hirota. J. Chem. Phys. **78**, 1703 (1983).
14. I. C. Plumb and K. R. Ryan. Plasma Chem. Plasma Process. **6**, 11 (1986).
15. I. B. Goldberg and G. M. Schneider. J. Chem. Phys. **65**, 147 (1976).

Can. J. Chem. Downloaded from www.nrcresearchpress.com by 176.9.209.113 on 09/07/12
For personal use only.

Dipole oscillator strength properties and dispersion energy coefficients for H_2S[1]

R. J. PAZUR, ASHOK KUMAR,[2] R. A. THURAISINGHAM,[3,4] AND WILLIAM J. MEATH[4]
Department of Chemistry, University of Western Ontario, London, Ont., Canada N6A 5B7

Received October 7, 1987

This paper is dedicated to Professor J. A. Morrison[5]

R. J. PAZUR, ASHOK KUMAR, R. A. THURAISINGHAM, and WILLIAM J. MEATH. Can. J. Chem. **66**, 615 (1988).

Globally reliable dipole oscillator strength distributions (DOSDs) have been constructed for the H_2S molecule in its ground state. An adopted DOSD is used to evaluate a variety of dipole oscillator strength sums S_k, logarithmic dipole sums L_k, and mean excitation energies I_k, for H_2S; these dipole properties are important in various physical processes. It is also used to obtain reliable results for the dipole–dipole dispersion energy coefficients C_6 for the interaction of H_2S with itself, and with thirty-nine other atoms and (mostly) molecules, and the triple-dipole dispersion energy coefficient C_9 for $(H_2S)_3$. A pseudo-DOSD for H_2S is presented which facilitates the evaluation of C_6's, and in particular C_9's.

R. J. PAZUR, ASHOK KUMAR, R. A. THURAISINGHAM et WILLIAM J. MEATH. Can. J. Chem. **66**, 615 (1988).

On a développé des distributions globalement fiables de la force d'oscillateurs dipolaires (DFOD) pour la molécule de H_2S dans son état fondamental. Pour le H_2S, on a utilisé une valeur adaptée de DFOD pour évaluer une variété d'oscillateurs dipolaires dont les sommes sont S_k, les sommes dipolaires logarithmiques sont L_k et les énergies d'excitation moyennes sont I_k; ces propriétés dipolaires sont importantes dans divers processus physiques. Elles sont aussi utilisées pour obtenir des résultats fiables concernant les coefficients C_6 d'énergie de dispersion dipôle–dipôle pour l'interaction du H_2S lui-même et pour celle de trente neuf autres atomes et (principalement) molécules ainsi que pour les coefficients C_9 d'énergie de dispersion triple-dipôle du $(H_2S)_3$. Pour le H_2S, on présente un pseudo DFOD qui facilite l'évaluation des coefficients C_6 et en particulier des C_9.
[Traduit par la revue]

Can. J. Chem. Downloaded from www.nrcresearchpress.com by 93.93.197.157 on 09/07/12
For personal use only.

1. Introduction

The main purpose of this paper is to present reliable values for a variety of dipole properties of the ground state H_2S molecule and for the dipole–dipole dispersion energies for the interaction of H_2S with itself and with a variety of other atoms and molecules. The reliable or accurate *ab initio* or direct experimental evaluation of most of the dipole properties we consider, and of dispersion energies for interactions involving molecules of the size of H_2S, is at present not tractable. This can be accomplished (1–6) by combining experimental information on dipole oscillator strengths with theoretical techniques and this is the approach used here.

The construction of the dipole oscillator strength distribution (DOSD) for ground state H_2S, and the evaluation of the dipole properties of this molecule, are discussed in Section 2. Specific results are given for the dipole sums S_k, $k = -12, -10, -8(1)-4, -3(½)0, 1$, and 2, and for the logarithmic dipole sums L_k and mean excitation energies I_k, for $k = -2(1)2$. Section 3 discusses the evaluation of the dipole–dipole and triple-dipole dispersion energy coefficients, C_6 and C_9, respectively, for interactions involving H_2S through the use of pseudo-DOSDs for the interacting species. Specific results are given for C_6 (H_2S,B), for forty species B, and for C_9 for $(H_2S)_3$. The estimated uncertainties and the usefulness of our results, and the methods by which they are obtained, are discussed in Section 4.

[1]This research was supported by a grant from the Natural Sciences and Engineering Research Council of Canada.

[2]Present address: Department of Physics, Meerut University, Meerut, India.

[3]Present address: Department of Chemistry, Mcquarie University, New South Wales, Australia.

[4]Associated with the Centre for Interdisciplinary Studies in Chemical Physics, University of Western Ontario, London, Ont., Canada N6A 3K7.

[5]It is a pleasure to dedicate this paper to Jim Morrison who, throughout his distinguished career, has always dispersed the joy of science.

2. The adopted DOSD and dipole properties for H_2S

The method used to construct DOSDs has been discussed in detail previously (1, 7) and applied to many atoms and molecules (the species analyzed are listed in Table 4). Succinctly the approach uses all available experimental and theoretical data for the dipole oscillator strengths (photoabsorption cross sections) for the species of interest, as a function of photon energy E, and modifies this data, to remove errors inherent in the input data, by use of quantum mechanical constraint procedures. The constraints, in principle, can be furnished by any reliably known dipole properties of the molecule; in practice the Thomas–Reiche–Kuhn sum rule (8), $S_0 = N$ where N is the number of electrons in the molecule, and the experimental molar refractivity as a function of wavelength, $R(\lambda)$ versus λ, are the most often used constraints. The end product is a DOSD which is reliable in a global sense (9) as a function of E, that is, it yields reliable results for a variety of dipole properties which are just integrals, over E, of simple functions of E weighted by the DOSD. It should be emphasized that the dipole properties evaluated in this way, including the dispersion energy constants of Section 3, are rotationally averaged or isotropic results since they are evaluated using rotationally averaged DOSDs for the relevant molecules. The input used to construct the DOSDs consists of isotropic dipole oscillator strength and constraint data; the analogous symmetry analyzed or anisotropic molecular information is in general not available.

Constraints for constructing the DOSD for H_2S are provided by $S_0 = 18$ and by experimental molar refractivity data (10–13). Two molar refractivity values (estimated errors 0.01%) were used as explicit constraints, $R(\lambda_1 = 5729\ \text{Å}) = 9.5747\ \text{cm}^3\ \text{mol}^{-1}$ and $R(\lambda_2 = 4047\ \text{Å}) = 9.9725\ \text{cm}^3\ \text{mol}^{-1}$; both are taken from Huxley and Lowery (12). The adopted DOSD for H_2S yields molar refractivity data that agrees well (disagreement <0.5%) with all the experimental data for 2577 Å $\leq \lambda \leq$ 6564 Å. Disagreements exceeding ~0.1% occur only with the data of Larsen (10) for $\lambda < 2926$ Å and Frivold *et al.* (11) for $\lambda = 6564$

TABLE 1. Integrated dipole oscillator strengths for H_2S*

Energy region (eV)	Values for adopted DOSD	Initial values obtained from experimental data or mixture rules			
5.86–6.57	4.040(−2)(15)	3.804(−2)(15)	3.778(−2)(16)		
6.57–7.76	1.582(−2)(15)	1.560(−2)(15)	1.432(−2)(16)		
7.76–8.14	4.054(−2)(15)	3.997(−2)(15)	2.540(−2)(16)		
8.14–8.78	1.386(−1)(15)	1.342(−1)(15)	1.237(−1)(16)		
8.78–9.14	1.462(−1)(16)	1.135(−1)(15)	1.436(−1)(16)		
9.14–9.87	2.015(−1)(15)	1.978(−1)(15)	1.745(−1)(16)		
9.87–10.34	1.450(−1)(16)	1.337(−1)(15)	1.442(−1)(16)		
10.34–10.69	1.189(−1)(15)	1.186(−1)(15)	1.118(−1)(16)		
10.69–11.11	1.562(−1)(15)	1.560(−1)(15)	1.499(−1)(16)		
11.11–11.5	1.595(−1)(16)		1.596(−1)(16)		
11.5–14.0	1.148 (17)			1.182 (17)	
14.0–16.0	1.100 (17)			1.144 (17)	
16.0–18.0	9.098(−1)(17)			9.369(−1)(17)	
18.0–25.0	1.865 (17)			1.948 (17)	
25.0–70.0	6.924(−1)(M1)	1.197 (M3)	1.898 (M2)	1.084 (17)	6.931(−1)(M1)
70.0–89.0	1.327(−1)(17)		6.397(−1)(M2)	1.326(−1)(17)	2.738(−1)(M1)
89.0–100.0	9.910(−2)(M1)		2.871(−1)(M2)		9.901(−2)(M1)
100.0–164.1	4.467(−1)(M1)				4.453(−1)(M1)
164.1–228.5	1.962 (M1)				1.935 (M1)
228.5–10^3	6.254 (M1)				6.118 (M1)
10^3–2472	5.991(−1)(M1)				5.986(−1)(M1)
2472–10^4	1.510 (M1)				1.507 (M1)
10^4–10^5	1.174(−1)(M1)				1.174(−1)(M1)
10^5–10^{16}	8.247(−4)(S)	8.247(−4)(S)			

*This table contains the adopted integrated dipole oscillator strengths, obtained by applying the constraint procedure outlied briefly in the main text, and the integrated oscillator strengths obtained by using the unmodified experimental or mixture rule DOS data used in constructing the adopted DOSD. The references associated with the adopted DOSD indicate the source of the DOS data for the indicated spectral region. For the mixture rule data, (M1), (M2), and (M3) correspond to eqs. [1], [2], and [3], respectively, and (S) indicates Stobbe formula data. Powers of ten are denoted by $(n) = 10^n$. The absorption edges for H_2S occur at 164.1 eV ($S_{L_{II},L_{III}}$), 228.5 eV (S_{L_I}), and 2472 eV (S_K).

Å. A table comparing our results with experiment can be found in ref. 14.

The sources of experimental dipole oscillator strengths (DOSs) are rather few (15–17) and limited to $E \lesssim 90$ eV with experimental errors of between 10–20%. These data are augmented by DOSs obtained from the following mixture rules:

$$[1]\quad \frac{df}{dE}(H_2S) = \frac{df}{dE}(H_2) + \frac{df}{dE}(SO_2) - \frac{df}{dE}(O_2)$$

$$[2]\quad \frac{df}{dE}(H_2S) = \frac{df}{dE}(H_2O) + \frac{df}{dE}(CS_2) - \frac{df}{dE}(OCS)$$

$$[3]\quad \frac{df}{dE}(H_2S) = \frac{df}{dE}(H_2O) + \frac{1}{2}\frac{df}{dE}(CS_2) - \frac{1}{2}\frac{df}{dE}(CO) - \frac{1}{2}\frac{df}{dE}(O_2)$$

where df/dE is the differential dipole oscillator strength for the appropriate molecule and DOSDs ((df/dE) versus E, refs. 1, 7*b*, 9) for H_2, SO_2, O_2, CS_2, OCS, H_2O, and CO are used to furnish the data for the right hand side of eqs. [1]–[3]. For energies greater than 100 keV the input DOS data were evaluated by using the non-relativistic dipole Stobbe formula (18) following earlier work (1, 7, 19).

The initial DOSD for H_2S was divided into 24 energy intervals as suggested by the structure of the spectra from the individual sources of DOS input data; the integrated DOSs for all the sources for each interval are given in Table 1. The number of different initial DOSDs obtainable by taking various combinations of these data numbers in the millions. This was reduced to 48 initial DOSDs by (*i*) combining energy intervals that correspond to common data sources and (*ii*) recognizing that much of the DOS data from different sources is similar. Each of the resulting initial DOSDs was adjusted using a least squares constraint method (1) to satisfy the imposed constraints. The amount of modification of the initial data that is required to satisfy the constraints can be represented by a standard deviation defined by (3, 7*a*, 7*b*)

$$\mathrm{STD} = \left[\sum_{i=1}^{N} (a_i - \bar{a})^2/N\right]^{1/2}$$

Here the constrained or optimized DOSD, df^c/dE versus E, is related to the initial DOSD, df^0/dE versus E, by a modification factor a_i for each energy interval i, $df^c/dE = (1 + a_i)df^0/dE$, and $\bar{a}$ is the mean value of all the a_i's. This procedure lead to 48 optimized DOSDs with STDs ranging from about 3.4 (least modified) to about 8.8 (most modified). Additional adjustments of the DOS input data based on these modified DOSDs lead to other DOSDs requiring less modification of the initial data. The adopted DOSD for H_2S, corresponding to the adopted values of the integrated oscillator strengths reported in Table 1, has a STD of 2.2 which corresponds favourably to many other DOSDs constructed by this method.

For some molecules integrated dipole oscillator strengths, such as those given here for H_2S, can be used to help assess the reliability of the initial DOS data used to construct the molecular DOSD (1, 7, 9). The analysis for H_2S shows that the limited experimental data for this molecule are consistent with each other, and with the adopted values, if account is taken of the estimated experimental uncertainties (~20%). There are several

Can. J. Chem. Downloaded from www.nrcresearchpress.com by 93.93.197.157 on 09/07/12
For personal use only.

Can. J. Chem. Downloaded from www.nrcresearchpress.com by 93.93.197.157 on 09/07/12
For personal use only.

DOSDs, with STD's ranging from 2.2 to 5, that give similar (agreement to within <1–2%) values for the dipole properties of H_2S and that vary in the initial DOS data used in various of the spectral regions of Table 1.

The adopted DOSD is represented by a set of data points, E_j and $(df/dE)_j$, for $j = 1, \ldots, N_p \gg 24$ where $N_p \sim 335$ for H_2S, and a set of interpolating functions to connect the points. For very high photon energies df/dE is represented by the Born dipole formula (20), $AE^{-3.5}$. The dipole properties are readily evaluated (1) using this representation of the DOSD. The properties of interest here are defined by

$$[4] \quad S_k = \int_{E_0}^{\infty} (df/dE) \left(\frac{E}{2\mathcal{R}}\right)^k dE$$

$$[5] \quad L_k = \int_{E_0}^{\infty} (df/dE) \left(\frac{E}{2\mathcal{R}}\right)^k \ln\left(\frac{E}{2\mathcal{R}}\right) dE$$

$$[6] \quad I_k = 2\mathcal{R} \exp(L_k/S_k)$$

where $\mathcal{R}$ is the Rydberg of energy and E_0 is taken to be the electronic absorption threshold for the molecule. The recommended properties, for various values of k, evaluated using the adopted DOSD for H_2S are given in Table 2.

3. Pseudo-DOSD and dispersion energy coefficients

The dipole–dipole and triple–dipole dispersion energy coefficients, C_6 and C_9, respectively, are conveniently evaluated by using a discrete representation of the adopted DOSDs for the interacting species (21, 22). These pseudo-DOSDs are determined from the known values of the dipole sums S_k by requiring

$$[7] \quad S_k = \sum_{i=1}^{n} \left(\frac{E_i}{2\mathcal{R}}\right)^k f_i \qquad k = 2, 1, 0, -1, \ldots, 3 - 2n$$

and correspond to n pseudo-dipole (excitation energy − oscillator strength) pairs (E_i, f_i). Up to 20 of these pseudo-states have been evaluated for H_2S and the 10 pseudo-state representation of the adopted DOSD for H_2S given in Table 3 is more than adequate for evaluating C_6 and C_9 for interactions involving H_2S to well within the accuracy expected from using the original adopted DOSD for this molecule (21–23).

The dipole–dipole dispersion energy, $-C_6(A,B)R^{-6}$ where R is the intermolecular distance, is the dominant long range interaction energy for the interaction of two rotationally averaged molecules or S state atoms A and B. The pseudo-state expression for C_6 is given by (21)

$$[8] \quad C_6(\mathrm{A,B}) = \frac{3}{2}(2\mathcal{R}a_0^6) \sum_{i=1}^{n_A} \sum_{j=1}^{n_B} \times \frac{f_i(\mathrm{A}) f_j(\mathrm{B})}{E_i(\mathrm{A})E_j(\mathrm{B})[E_i(\mathrm{A}) + E_j(\mathrm{B})]}$$

where a_0 is the Bohr radius. The triple–dipole dispersion energy is the dominant long range non-additive interaction energy for a collection of more than two isotropic molecules and has the form

$$[9] \quad W^{(3)} = [3 \cos\theta_a \cos\theta_b \cos\theta_c + 1] \times C_9(\mathrm{A,B,C}) R_{ab}^{-3} R_{bc}^{-3} R_{ac}^{-3}$$

where R_{ab} is the intermolecular separation between molecules A and B, θ_a is the angle between R_{ab} and R_{ac}, and an expression analogous to [8] is available (22) for C_9. The C_6 coefficients for the interaction of H_2S with itself, and thirty-nine other species, are given in Table 4. Most of the required pseudo-DOSDs are available in the literature (3, 9, 21, 23–25); those for the alkenes and alcohols are available upon request (26). The result for $(H_2S)_3$ is $C_9 = 3897.0$, where the unit for C_9 is $2\mathcal{R}a_0^9$.

TABLE 2. The dipole sums S_k, logarithmic dipole sums L_k, and mean excitation energies I_k, for various k, evaluated using the adopted DOSD for H_2S

Property	Recommended value	Property	Recommended value
S_2	1.791(5)	S_{10}	1.744(5)
S_1	4.614(2)	S_{12}	2.779(6)
S_0	1.800(1)		
$S_{-1/2}$	1.196(1)	L_2	1.398(6)
S_{-1}	1.313(1)	L_1	2.152(3)
$S_{-3/2}$	1.739(1)	L_0	2.873(1)
S_{-2}	2.471(1)	L_{-1}	−5.779
$S_{-5/2}$	3.647(1)	L_{-2}	−1.841(1)
S_{-3}	5.541(1)		
S_{-4}	1.383(2)	I_2 (eV)	6.659(4)
S_{-5}	3.796(2)	I_1 (eV)	2.884(3)
S_{-6}	1.136(3)	I_0 (eV)	1.342(2)
S_{-7}	3.664(3)	I_{-1} (eV)	1.752(1)
S_{-8}	1.262(4)	I_{-2} (eV)	1.292(1)

TABLE 3. The values of the pseudo-DOSD excitation energies (in units of $2\mathcal{R}$) and oscillator strengths for ground state H_2S

E_i	f_i
2.21048(−1)	1.55204(−2)
2.37576(−1)	3.60949(−2)
3.06818(−1)	2.80182(−1)
3.75291(−1)	8.65400(−1)
5.05369(−1)	2.27080(0)
7.17140(−1)	2.68535(0)
1.25686(2)	6.33757(−1)
6.15607(2)	4.14448(0)
2.46216(3)	6.65901(0)
6.53686(4)	4.09403(−1)

4. Discussion

Following procedures developed and used previously (1, 7*b*, 19), error estimates can be provided for the dipole properties of H_2S calculated in this paper. For the properties that depend significantly (2, 27) on the spectral regions which dominate the constraints used in constructing the DOSD for H_2S, namely S_k, L_k, and I_k for $-4 \leq k \leq 1$, the errors are $\lesssim$2% for $k = 1$ and $\lesssim$ 1% for the other values of $k \leq 0$. The errors can increase slowly from ~1% for $k < -4$ and for $k = 2$ are ~3% since they are dominated by uncertainties (2, 27) inherent in the DOS input data used to construct the higher energy portion of the DOSD. The uncertainties in the C_6 coefficients given in Table 4, and in our result for C_9 for $(H_2S)_3$, are $\lesssim$1–2% except in the case of N and O where they could be as high as 5% and 15%, respectively, due to the quality of the input data used to construct the DOSDs for the ground state N and O atoms (1, 28).

The accurate *ab initio* or direct experimental evaluation of most of the properties considered here, for molecules the size of H_2S, is a very difficult problem (1, 29–31) and our results for H_2S are, in most cases, the only available reliable values for

TABLE 4. Recommended values of the dipole–dipole dispersion energy coefficients $C_6(H_2S, B)$ for the interaction of H_2S with various molecules* and atoms (in units of $2\mathcal{R}a_0^6$)

B	$C_6(H_2S, B)$	B	$C_6(H_2S, B)$	B	$C_6(H_2S, B)$
H_2S	216.8	HBr	216.4	CH_4	166.9
H	37.45	SO_2	250.1	C_2H_6	286.4
Li	369.2	CS_2	433.2	C_3H_8	406.2
N	71.62	OCS	295.0	C_4H_{10}	521.9
O	54.80	H_2	51.13	C_5H_{12}	639.4
He	16.70	N_2	123.6	C_6H_{14}	754.2
Ne	33.66	O_2	112.3	C_7H_{16}	869.8
Ar	116.1	NO	120.3	C_8H_{18}	985.0
Kr	166.3	N_2O	197.5	C_2H_4	254.8
Xe	248.5	H_2O	97.60	C_3H_6	378.2
SF_6	337.3	NH_3	138.2	C_4H_8	493.6
HF	61.68	CO	131.1	CH_3OH	217.5
HCl	167.4	CO_2	182.0	C_2H_5OH	337.9
				C_3H_7OH	457.3

*For the organic molecules the results are for normal alkanes, 1-alkenes, and primary alcohols.

these properties and dispersion energy constants. *Ab initio* calculations of the dipole polarizability S_{-2} have been carried out (32, 33). Martin *et al.* (32) obtained values of 23.5 and 23.2 using self consistent field (SCF) and configuration interaction methods respectively; these are ~7% lower than our recommended result of 24.7 which agrees with the experimental result of 24.8 given by Landolt and Bornstein (34) and used by Martin *et al.* to help assess the reliability of their calculation. Ahlström *et al.* (33) report a value of 22.5, at an SCF-level of calculation, which is ~10% smaller than our result. As indicated in Section 3 our values for the molar refractivity of H_2S are generally in excellent agreement with experiment.

The dipole properties for H_2S obtained here, and for the other molecules considered earlier, are important in a variety of research areas (2, 8, 19, 28, 35). Of particular interest are the radiation parameters (I_1,S_1), I_0, and (I_{-1},S_{-1}) which can be used to help evaluate the straggling, the stopping, and the total inelastic scattering cross sections of fast charged particles in molecular matter (19, 35, 36). The various uses and applications of the dipole properties S_k, L_k, and I_k have been reviewed well by Hirschfelder *et al.* (8) and Fano and Cooper (35), see also the more recent discussions of refs. 2, 37, and 38.

Reliable results for the dipole–dipole dispersion energies are useful in many fields. They furnish important input in the construction of interaction potential energies that are valid for all important values of the intermolecular separation R; see for example refs. 39–45, and references therein. Many of the interactions involving H_2S represented in Table 4 should be of considerable interest. For example, recently there have been several investigations (46–48) of dimer potentials involving interactions of H_2S with itself, and with H_2O, HF, and HCl, including a study of stacking interactions (48) for $(H_2S)_2$. The importance of the dispersion energy contribution to the interaction energies has been discussed in these studies and hopefully our reliable results for the relevant dispersion energy coefficients will be of importance in future investigations of potentials of this type.

The pseudo-DOSD for H_2S given in Table 3 is a very useful representation of the original DOSD for this molecule. It can be used to effectively evaluate multiple integrals, over excitation energies, involving the original continuous distribution as has been demonstrated in calculations of the triple-dipole dispersion energy coefficients for a variety of molecules (22, 24). The result given in Section 3 for $C_9(H_2S, H_2S, H_2S)$ can be readily extended to other interactions involving H_2S by using available pseudo-DOSDs for other species (see Section 3). Another use of the pseudo-DOSDs is that they provide part of the information needed to evaluate (1) the (asymptotic) dispersion energy coefficient for the interaction between an adsorbate molecule and a surface and (2) substrate-mediated dispersion energies between adsorbate molecules (49). Also required are the bulk dielectric constant function for the substrate. In this context H_2S is a particularly important molecule since the interaction of H_2S with metallic surfaces, and with other adsorbates, is of importance in studies concerned with sulfur poisoning and hydrodesulfurization processes that occur in heterogeneous catalysis (50).

The method used in this paper is a practical and reliable approach for evaluating a wide variety of rotationally averaged or isotropic molecular dipole properties if sufficient input data are available. It avoids difficulties that occur in other procedures based on less input information (2, 3, 9, 19, 28). The extension to anisotropic dipole properties is not straightforward due to a lack of the required anisotropic oscillator strengths and/or reliable constraints for most species (2, 30). This extension is an important problem since generally the only direct route for the determination of anisotropic properties is through *ab initio* calculations which are reliable only for small atoms and molecules for the wide range of properties of interest in the present context. In some cases, for example, anisotropic dispersion energies, isotropic results, and multiplicative anisotropy parameters are used to generate anisotropic results; this connection is not always rigorous and can involve the use of average energy-like approximations (51).

1. G. D. ZEISS, W. J. MEATH, J. C. F. MACDONALD, and D. J. DAWSON. Can. J. Phys. **55**, 2080 (1977).
2. W. J. MEATH, D. J. MARGOLIASH, B. L. JHANWAR, A. KOIDE, and G. D. ZEISS. *In* Intermolecular forces. *Edited by* B. Pullman. Reidel, Dordrecht. 1981. pp. 101–115.
3. A. KUMAR, G. R. G. FAIRLEY, and W. J. MEATH. J. Chem. Phys. **83**, 70 (1985), and some of the references therein.
4. H. MARGENAU. Phys. Rev. **37**, 1425 (1931); **56**, 1000 (1939).
5. A. DALGARNO and N. LYNN. Proc. Phys. Soc. A**70**, 802 (1957); A. DALGARNO and A. E. KINGSTON. Proc. Phys. Soc. **72**, 1053 (1958); **73**, 455 (1959); **78**, 607 (1961).

Can. J. Chem. Downloaded from www.nrcresearchpress.com by 93.93.197.157 on 09/07/12
For personal use only.

6. P. J. LEONARD and J. A. BARKER. *In* Theoretical chemistry, advances and perspectives. Vol. 1. 1975. p. 117.
7. (*a*) B. L. JHANWAR and W. J. MEATH. Can. J. Chem. **62**, 373 (1984); (*b*) A. KUMAR and W. J. MEATH. Can. J. Phys. **63**, 417 (1985); (*c*) A. KUMAR and W. J. MEATH. Can. J. Chem. **63**, 1616 (1985).
8. J. O. HIRSCHFELDER, W. BYERS BROWN, and S. T. EPSTEIN. Adv. Quant. Chem. **1**, 255 (1964).
9. B. L. JHANWAR and W. J. MEATH. Chem. Phys. **67**, 185 (1982).
10. T. LARSEN. Z. Physik. **111**, 391 (1938).
11. O. F. FRIVOLD, O. HASSEL, and V. S. RUSTAD. Physikal. Z. **38**, 191 (1937).
12. H. HUXLEY and H. LOWERY. Proc. R. Soc. A**182**, 207 (1909).
13. C. CUTHBERTSON and M. CUTHBERTSON. Proc. R. Soc. A**83**, 151 (1909).
14. R. J. PAZUR, B.Sc. (honours) Thesis. University of Western Ontario, London, Ont., Canada. 1986.
15. B. L. CLARK and W. T. SIMPSON. J. Chem. Phys. **43**, 3666 (1965).
16. K. WATANABE and A. S. JURSA. J. Chem. Phys. **41**, 1650 (1964).
17. C. E. BRION, Y. IIDA, and J. P. THOMSON. Chem. Phys. **101**, 449 (1986).
18. M. STOBBE. Ann. Phys. (Leipzig), **69**, 81 (1930).
19. G. D. ZEISS, W. J. MEATH, J. C. F. MACDONALD, and D. J. DAWSON. Radiat. Res. **63**, 64 (1975); **70**, 284 (1977).
20. H. A. BETHE and E. E. SALPETER. Quantum mechanics of one- and two-electron atoms. Academic Press, New York. 1957; R. D. HUDSON. Rev. Geophys. Space. Phys. **9**, 305 (1971).
21. D. J. MARGOLIASH and W. J. MEATH. J. Chem. Phys. **68**, 1426 (1978).
22. D. J. MARGOLIASH, T. R. PROCTOR, G. D. ZEISS, and W. J. MEATH. Mol. Phys. **35**, 747 (1978).
23. B. L. JHANWAR and W. J. MEATH. Mol. Phys. **41**, 1061 (1980).
24. (*a*) A. KUMAR and W. J. MEATH. Mol. Phys. **54**, 823 (1985); (*b*) A. KUMAR and W. J. MEATH. Chem. Phys. **91**, 411 (1984).
25. R. E. JOHNSON, S. T. EPSTEIN, and W. J. MEATH. J. Chem. Phys. **47**, 1271 (1967).
26. B. L. JHANWAR and W. J. MEATH. To be published.
27. B. L. JHANWAR, W. J. MEATH, and J. C. F. MACDONALD. Can. J. Phys. **59**, 185 (1981); G. D. ZEISS, W. J. MEATH, J. C. F. MACDONALD, and D. J. DAWSON. Mol. Phys. **39**, 1055 (1980).
28. G. D. ZEISS and W. J. MEATH. Mol. Phys. **33**, 1155 (1977).
29. G. D. ZEISS, W. R. SCOTT, N. SUZUKI, D. P. CHONG, and S. R. LANGHOFF. Mol. Phys. **37**, 1543 (1979); P. MUKHERJEE, T. MINATO, and D. P. CHONG. Int. J. Quant. Chem. **23**, 447 (1983).
30. F. MULDER, G. F. THOMAS, and W. J. MEATH. Mol. Phys. **41**, 249 (1980); F. MULDER and W. J. MEATH. Mol. Phys. **42**, 629 (1981).
31. H. J. WERNER and W. MEYER. Phys. Rev. A**13**, 13 (1976).
32. R. L. MARTIN, E. R. DAVIDSON, and D. F. EGGERS. Chem. Phys. **38**, 341 (1979).
33. M. AHLSTRÖM, B. JÖNSSON, and G. KARLSTRÖM. Mol. Phys. **38**, 1051 (1979).
34. LANDOLT-BORNSTEIN. Zahlenwerte und Funktionen. 6th ed. II Band, Springer-Verlag, 1971; J. WÜST AND H. REINDEL. Z. PHYSIK. CHEM. B**24**, 155 (1934).
35. U. FANO and J. W. COOPER. Rev. Mod. Phys. **40** , 441 (1968); **41**, 724 (1969).
36. M. INOKUTI, Y.-K. KIM, and R. L. PLATZMANN. Phys. Rev. **164**, 55 (1967).
37. ICRU. Stopping powers for electrons and positrons. Report 37, International Commission on Radiation Units and Measurements, Bethesda, MD. 1984.
38. B. L. JHANWAR, W. J. MEATH, and J. C. F. MACDONALD. Radiat. Res. **106**, 288 (1986).
39. J. T. BROBJER AND J. N. MURRELL. Mol. Phys. **50**, 885 (1983); **51**, 313 (1984).
40. W. R. RODWELL, L. T. SIN FAI LAM, and R. O. WATTS. Mol. Phys. **44**, 225 (1981).
41. C. DOUKETIS, J. M. HUTSON, B. J. ORR, and G. SCOLES. Mol. Phys. **52**, 763 (1984).
42. K. T. TANG and J. P. TOENNIES. J. Chem. Phys. **80**, 3726 (1984).
43. N. CORBIN, W. J. MEATH, and A. R. ALLNATT. Mol. Phys. **53**, 225 (1984).
44. M. S. A. LING and M. RIGBY. Mol. Phys. **51**, 855 (1984).
45. A. VAN DER AVOIRD, P. E. S. WORMER, and A. P. J. JANSEN. J. Chem. Phys. **84**, 1629 (1986).
46. A. LÉS. Theoret. Chim. Acta Berlin, **66**, 375 (1985).
47. M. M. SZIZESNIAK and S. SCHEINER. J. Chem. Phys. **83**, 1778 (1985).
48. P. HOLZA, A. MEHLHORN, P. CÁRSKY, and R. ZAHRADNIK. J. Mol. Spectrosc. **138**, 387 (1986).
49. W.-K. LIU. Phys. Rev. B, **32**, 868 (1985) and references therein.
50. A. STEINBRUNN and C. LATTAUD. Surf. Sci. **155**, 279 (1985); R. J. KOESTNER, M. SALMERON, E. B. KOLLIN, and J. L. GLAND. Chem. Phys. Lett. **125**, 134 (1986).
51. R. T. PACK. J. Chem. Phys. **64**, 1659 (1976); **64**, 2010 (1976); F. MULDER, G. VAN DIJK, and A. VAN DER AVOIRD. Mol. Phys. **39**, 407 (1980).

Can. J. Chem. Downloaded from www.nrcresearchpress.com by 93.93.197.157 on 09/07/12
For personal use only.

Thermochemistry of uranium compounds. XVI. Calorimetric determination of the standard molar enthalpy of formation at 298.15 K, low-temperature heat capacity, and high-temperature enthalpy increments of $UO_2(OH)_2 \cdot H_2O$ (schoepite)[1]

I. R. TASKER, P. A. G. O'HARE,[2] BRETT M. LEWIS,[3] and G. K. JOHNSON
Chemical Technology Division, Argonne National Laboratory, Argonne, IL 60439, U.S.A.

AND

E. H. P. CORDFUNKE
Netherlands Energy Research Foundation ECN, Petten, The Netherlands

Received September 1, 1987

This paper is dedicated to Professor J. A. Morrison

I. R. TASKER, P. A. G. O'HARE, BRETT M. LEWIS, G. K. JOHNSON, and E. H. P. CORDFUNKE. Can. J. Chem. **66**, 620 (1988).

Three precise calorimetric methods, viz., low-temperature adiabatic, high-temperature drop, and solution-reaction, have been used to determine as a function of temperature the key chemical thermodynamic properties of a pure sample of schoepite, $UO_2(OH)_2 \cdot H_2O$. The following results have been obtained at the standard reference temperature $T = 298.15$ K: standard molar enthalpy of formation $\Delta_f H_m^0(T) = -1825.4 \pm 2.1$ kJ mol^{-1}; molar heat capacity $C_{p,m}^0(T) = 172.07 \pm 0.34$ J K^{-1} mol^{-1}; and the standard molar entropy $S_m^0(T) = 188.54 \pm 0.38$ J K^{-1} mol^{-1}. The molar enthalpy increments relative to 298.15 K and the molar heat capacity are given by the polynomials: $\{H_m^0(T) - H_m^0(298.15\ \text{K})\}/(\text{J mol}^{-1}) = -38209.0 + 84.2375(T/\text{K}) + 0.1472958(T/\text{K})^2$ and $C_{p,m}^0(T)/(\text{J K}^{-1}\ \text{mol}^{-1}) = 84.238 + 0.294592(T/\text{K})$, where $298.15\ \text{K} < T < 400$ K. The present result for $\Delta_f H_m^0$ at 298.15 K has been combined with three other closely-agreeing values from the literature to give a recommended weighted mean $\Delta_f H_m^0 = -1826.4 \pm 1.7$ kJ mol^{-1}, from which is calculated the standard Gibbs energy of formation $\Delta_f G_m^0 = -1636.8 \pm 1.7$ kJ mol^{-1} at 298.15 K. Complete thermodynamic properties of schoepite are tabulated from 298.15 to 423.15 K.

I. R. TASKER, P. A. G. O'HARE, BRETT M. LEWIS, G. K. JOHNSON, et E. H. P. CORDFUNKE. Can. J. Chem. **66**, 620 (1988).

On a utilisé trois méthodes calorimétriques précises, adiabatique à basse température, abaissement d'une température élevée et solution-réaction, pour déterminer les propriétés thermodynamiques chimiques clés d'un échantillon pur de schoepite, $UO_2(OH)_2 \cdot H_2O$, en fonction de la température. A la température de référence standard de $T = 298,15$ K, on a obtenu les résultats suivants: enthalpie molaire standard de formation, $\Delta_f H_m^0(T) = -1825,4 \pm 2,1$ kJ mol^{-1}; capacité calorifique molaire, $C_{p,m}^0(T) = 172,07 \pm 0,34$ J K^{-1} mol^{-1} et entropie molaire standard, $S_m^0(T) = 188,54 \pm 0,38$ J K^{-1}. Les incréments à l'enthalpie molaire relative à 298,15 K et la capacité calorifique molaire peuvent être représentés par les polynômes suivants: $\{H_m^0(T) - H_m^0(298,15\ \text{K})\}/(\text{J mol}^{-1}) = -38209,0 + 84,2375(T/\text{K}) + 0,1472958(T/\text{K})^2$ et $C_{p,m}^0(T)/(\text{J K}^{-1}\ \text{mol}^{-1}) = 84,238 + 0,294592(T/\text{K})$, dans lesquels $298,15\ \text{K} < T < 400$ K. On a combiné les résultats obtenus pour $\Delta_f H_m^0$ à 298,15 K avec trois autres valeurs qui lui sont en très bon accord et qui ont été tirées de la littérature pour obtenir une valeur moyenne recommandée du $\Delta_f H_m^0 = -1826,4 \pm 1,7$ kJ mol^{-1} à partir de laquelle on a calculé l'énergie de formation de Gibbs standard à 298,15 K, $\Delta_f G_m^0 = -1636,8 \pm 1,7$ kJ mol^{-1}. On présente une table résumant les propriétés thermodynamiques complètes de la schoepite de 298,15 à 423,15 K.

[Traduit par la revue]

Introduction

Schoepite, $UO_3 \cdot 2H_2O$, is, on the basis of X-ray diffraction and infrared spectroscopic evidence (1), more accurately depicted as $UO_2(OH)_2 \cdot H_2O$. However, the more compact formula will be used for convenience in the present paper. The hydrate has an orthorhombic unit cell (*Pbna*) with $a = 1.3977$ nm, $b = 1.6696$ nm, and $c = 1.4672$ nm, and there are 32 molecules in the cell. Uranium exhibits eight-fold octahedral coordination; the structure is layered with the hydrate water situated between the layers (2).

Our current technical interest in schoepite arises from modelling studies connected with the burial of nuclear waste. Specifically, the question being addressed is the fate of dissolved uranium in contact with concrete at 298.15 K. Under such conditions, and on the basis of existing thermodynamic values, schoepite is calculated to be the phase that limits the uranium activity in solution (3).

The objective of the present research was to obtain by high-precision calorimetry the following molar thermodynamic properties of a single specimen of pure schoepite: the standard enthalpy of formation $\Delta_f H_m^0$ at 298.15 K; the low-temperature heat capacity $C_{p,m}^0$ and, thence, the standard entropy S_m^0; and the enthalpy increments relative to 298.15 K, up to the limit of stability of the material.

Experimental

Schoepite was prepared at ECN by hydration of anhydrous, amorphous UO_3 which had been obtained by thermal decomposition at 625 K of ammonium diuranate $(NH_4)_2U_2O_7$. The UO_3 was hydrated by equilibration with water which was stirred in a round-bottom flask equipped with a reflux condenser. The hydration was performed initially for 5 days at 315 K, and then for 14 days at 345 K, after which the sample was cooled slowly, filtered, washed with water, and dried in the air at room temperature. The X-ray diffraction patterns were identical to those in the literature for schoepite (2). By ignition to U_3O_8, the uranium content of the preparation was determined to be (73.89 ± 0.01) mass%, very close to the theoretical value of 73.91%. The schoepite was boiled with deionized H_2O and the supernatant aqueous extract was analyzed by ion chromatography. Only F^-(aq), NO_3^-(aq), SO_4^{2-}(aq), NH_4^+(aq), and Na^+(aq) were detected, but all were at or below the 1×10^{-6} mass fraction level. All the analytical results, therefore, indicate that our sample of schoepite was very pure.

[1]Work supported by the U.S. Department of Energy, Office of Geological Repositories, Nevada Nuclear Waste Storage Investigations Project, under Contract W-31-109-Eng-38.

[2]To whom correspondence should be addressed.

[3]Participant in Summer 1987 Student Research Program. This program is coordinated by the Department of Educational Programs.

Can. J. Chem. Downloaded from www.nrcresearchpress.com by 176.9.209.113 on 09/07/12
For personal use only.

TABLE 1. Experimental low-temperature molar heat capacities of schoepite ($p^0 = 0.1013$ MPa)

$\langle T \rangle$ / K	$C^0_{p,m}$ / J K^{-1} mol^{-1}	$\langle T \rangle$ / K	$C^0_{p,m}$ / J K^{-1} mol^{-1}	$\langle T \rangle$ / K	$C^0_{p,m}$ / J K^{-1} mol^{-1}	$\langle T \rangle$ / K	$C^0_{p,m}$ / J K^{-1} mol^{-1}
7.59	0.7220	27.24	12.72	87.15	65.33	197.07	131.78
7.68	0.7498	28.00	13.39	89.69	67.62	202.22	134.42
11.68	2.117	29.16	14.34	93.50	70.76	207.06	136.88
12.23	2.362	29.98	15.07	97.21	73.42	212.48	139.60
12.99	2.741	31.65	16.51	102.13	76.82	217.06	142.19
13.66	3.095	34.77	19.23	107.70	81.01	222.73	145.02
14.26	3.424	35.87	20.14	112.21	84.29	227.08	147.02
14.97	3.830	39.43	23.29	118.23	88.64	232.72	149.13
15.30	4.026	41.97	25.55	122.22	91.30	237.10	151.32
15.62	4.231	43.40	26.86	126.82	94.53	242.70	154.44
17.00	5.099	46.21	29.37	128.62	95.62	247.11	155.67
17.21	5.245	47.79	30.76	132.23	97.86	252.68	158.20
17.59	5.501	50.91	33.60	136.91	100.56	257.13	159.55
17.94	5.724	52.65	35.16	142.23	103.78	262.68	161.54
18.30	5.969	55.09	37.34	146.94	106.43	263.44	162.09
19.02	6.467	57.49	39.54	152.24	109.20	266.91	163.24
19.19	6.609	59.74	41.51	156.98	111.59	273.50	165.15
19.92	7.103	63.56	44.85	162.24	114.55	283.59	167.02
21.13	7.950	66.72	47.69	167.03	116.96	293.67	170.65
21.93	8.551	70.45	51.05	172.23	119.55	303.69	174.50
23.41	9.659	73.71	53.86	177.04	121.89	313.23	176.53
23.95	10.08	78.17	57.68	182.26	124.32	323.62	180.57
25.32	11.15	81.62	60.60	187.06	126.56	333.70	183.77
25.99	11.71	86.87	65.07	192.22	129.32	343.88	186.91

For the low-temperature heat-capacity measurements, 7.6699 g of schoepite was loaded into the calorimeter (laboratory designation 6-GS-1) with gentle tamping. The calorimeter was constructed from oxygen-free high-thermal-conductivity copper, had an internal volume of 5.976 cm^3 at 298.15 K, and was sealed by means of a gold gasket. Prior tests had shown, as expected, that intimate contact between copper and schoepite produced no reaction. The calorimeter was cooled to 195 K, evacuated, and 2.317×10^{-5} mol of He was introduced to act as an exchange gas and promote rapid thermal equilibration. For buoyancy and volume corrections, the density of schoepite was taken as 4.65 g cm^{-3} (2). Descriptions of the cryostat, peripheral equipment, the calorimetric procedure, and other relevant details are available in the literature (4).

Our determination of the standard molar enthalpy of formation was based on solution-calorimetric measurements of the enthalpy of the reaction:

[1] $UO_3 \cdot 2H_2O(cr) + 2HF(aq) = UO_2F_2(aq) + 3H_2O(aq)$.

The calorimeter, an LKB-8700 model (LKB Produkter, Bromma, Sweden) was equipped with a stirrer and a 100-cm^3 reaction vessel made of 18-ct gold. Calorimetric specimens of schoepite, each of mass ≈0.56 g, were weighed in air and encapsulated in Teflon as described in an earlier publication (5). The calorimeter was calibrated electrically immediately before and after each enthalpy of reaction measurement, and the arithmetic mean of the values was used for the energy equivalent of the calorimetric system $\langle \epsilon(\text{calor}) \rangle$. The reaction of schoepite with HF(aq), prepared by dilution of reagent-grade acid, was quite rapid and the calorimeter reached equilibrium about 600 s after the sample came into contact with the solution. Temperatures were recorded automatically with a quartz-crystal thermometer (Hewlett-Packard, Model 2804-A) interfaced with a computer which calculated the corrected temperature rise for each experiment and calibration. In order to check the performance of the calorimetric system, we measured the specific enthalpy of protonation in 0.1 mol kg^{-1} HCl(aq) of tris(hydroxymethyl)aminomethane, National Bureau of Standards Reference Material 724a. Our result, $-(246.09 \pm 0.11)$ J g^{-1}, overlapped the certified value of $-(245.76 \pm 0.26)$ J g^{-1}, and indicated that the calorimeter was operating properly.

The drop-calorimetric system (6) used for the enthalpy measurements consisted of a resistance-heated molybdenum-core furnace and a copper-block calorimeter. Furnace-temperature measurements were made with platinum-to-(platinum + mass fraction 0.1 of rhodium) thermocouples. Calorimetric temperatures were determined with a quartz-crystal thermometer (Hewlett-Packard Model 2804-A). The energy equivalent ϵ(calor) of the empty copper-block calorimeter was determined by electrical calibration.

The schoepite (mass 8.7960 g) was loaded into a (platinum + mass fraction 0.1 of rhodium) capsule (mass 19.1948 g and internal volume 6.42 cm^3), which was then welded shut. The capsule also contained 1.85×10^{-4} mol of air. Enthalpy measurements were also conducted on an empty capsule of similar mass and dimensions in order to correct for the enthalpy of the capsule. Experiments were performed at temperatures between 350 and 500 K. However, the enthalpy values at $T \geq 425$ K, when plotted against temperature, lay on a different line than those at lower temperatures. This suggested that the sample had decomposed or undergone a transition. Upon completion of the experiments, the capsule was opened and the schoepite examined. The material was visibly wet and readily lost mass when exposed to the air. It was concluded that the schoepite had undergone decomposition to some form of dehydrated schoepite and water. Hence, only the enthalpy values at approximately 350, 375, and 400 K are valid for pure schoepite.

Results

The molar heat capacities $C^0_{p,m}(T)$ of schoepite given in Table 1 were calculated as the difference, with some minor corrections, between the values obtained with the loaded calorimeter and the results of a prior set of experiments with the empty calorimeter.

Such a correction had to be made to allow for decomposition of the schoepite. There is convincing evidence from the studies of Dawson *et al.* (7), Lindval' and Kuznetsova (8), and Perez-Bustamante *et al.* (9) that schoepite undergoes dehydration upon heating. Thus, in the low-temperature heat-capacity measure-

Can. J. Chem. Downloaded from www.nrcresearchpress.com by 176.9.209.113 on 09/07/12
For personal use only.

Can. J. Chem. Downloaded from www.nrcresearchpress.com by 176.9.209.113 on 09/07/12
For personal use only.

TABLE 2. Standard molar low-temperature thermodynamic properties of schoepite ($p^0 = 0.1013$ MPa)

$\langle T \rangle$ / K	$C^0_{p,m}$ / J K^{-1} mol^{-1}	$S^0_m(T)$ / J K^{-1} mol^{-1}	$H^0_m(T) - H^0_m(0)$ / J mol^{-1}	$-\{G^0_m(T) - H^0_m(0)\}/T$ / J K^{-1} mol^{-1}
10	1.445	0.535	3.97	0.138
20	7.157	3.083	44.0	0.883
30	15.07	7.428	153.8	2.300
40	23.82	12.95	348.0	4.253
50	32.76	19.23	630.8	6.611
60	41.73	25.99	1003	9.272
70	50.62	33.10	1465	12.16
80	59.27	40.42	2015	15.24
90	67.57	47.89	2649	18.45
100	75.45	55.42	3365	21.77
110	82.88	62.96	4157	25.17
120	89.85	70.48	5021	28.63
130	96.36	77.93	5953	32.14
140	102.43	85.30	6947	35.67
150	108.07	92.56	8000	39.23
160	113.36	99.70	9107	42.78
170	118.39	106.73	10266	46.34
180	123.33	113.63	11475	49.88
190	128.23	120.43	12732	53.42
200	133.23	127.14	14039	56.94
210	138.32	133.76	15397	60.44
220	143.42	140.31	16806	63.92
230	148.36	146.80	18265	67.38
240	152.96	153.21	19772	70.83
250	157.09	159.54	21322	74.25
260	160.69	165.77	22912	77.65
270	163.83	171.90	24535	81.03
280	166.73	177.91	26188	84.38
290	169.60	183.81	27869	87.71
300	172.65	189.61	29580	91.01
310	175.92	195.32	31323	94.28
320	179.29	200.96	33099	97.53
330	182.56	206.53	34908	100.74
340	185.68	212.02	36750	103.94
350	188.86	217.45	38622	107.10
360	191.99	222.82	40527	110.24
273.15	164.76±0.33	173.80±0.35	25052±50	82.08±0.16
298.15	172.07±0.34	188.54±0.38	29261±59	90.40±0.18

ments made at $T \geq 273.5$ K, a small part of the electrical energy input contributed to dehydration of the schoepite, and not heating of the sample, as would have occurred in the absence of decomposition. There is, unfortunately, no experimental vapor-pressure equation for the decomposition of schoepite which would enable us to make a precise correction for the thermal effect of dehydration. We have, however, constructed an approximate equation on the basis of our present $\Delta_f H^0_m$ value for schoepite and that for dehydrated schoepite (10) and $H_2O(g)$ (11), along with an estimated standard entropy change for the dehydration. That equation is as follows:

$$[2] \quad \log_{10}(p/p^0) = -2523.8\,(\mathrm{K}/T) + 6.722$$

Because of the vaporization correction, the original (uncorrected) heat-capacity values have been *reduced* in Table 1 by (J K^{-1} mol^{-1}): 0.08 at 273.50 K; 0.15 at 283.59 K; 0.28 at 293.67 K; 0.50 at 303.69 K; 0.81 at 313.23 K; 1.32 at 323.62 K; 2.07 at 333.70 K; and 3.17 at 343.88 K. Thus, above 330 K, the correction exceeds 1% of the calculated heat capacity. Although the uncertainty increases above this temperature, the correction is only 0.25% at 298.15 K and the corresponding errors are not significant here. Other minor corrections were made for differences in the amounts of helium, Apiezon-T grease (Metropolitan-Vickers, U.K.), copper, and gold between the results for the empty and filled calorimeters. A small curvature correction equal to $-(\mathrm{d}^2C_{p,m}/\mathrm{d}T^2)(\Delta T)^2/24$ was applied to each heat-capacity determination.

At 5 K, the heat capacity of the sample was 35% of the total, at 20 K it was 34%, at 100 K it was 19%, and from 200 to 350 K it was about 25%. The values given in Table 1 are estimated to be uncertain by ±5% near 6 K, ±1% near 14 K, and by ±0.2% above 25 K. A plot of $C^0_{p,m}(T)$ against $\langle T \rangle$ showed the normal sigmoidal shape and exhibited no anomalies.

The experimental heat capacities in Table 1 were fitted by means of a weighted least-squares procedure using two polynomials in T, one for the region below 40 K, the other for the region above 20 K. The standard deviations from the fits were ±0.14% and ±0.15%, respectively, with the polynomials merging smoothly at 23.5 K. In the region below the lowest experimental determination, it was assumed that $C^0_{p,m} = AT^3$. At $T = 6$ K, $C^0_{p,m}(T) = 0.3955$ J K^{-1} mol^{-1}, $\{S^0_m(T) - S^0_m(0)\} = 0.1318$ J K^{-1} mol^{-1}, and $\{H^0_m(T) - H^0_m(0)\} = 0.5933$ J mol^{-1}.

TABLE 3. Calorimetric results for the reaction of $UO_3 \cdot 2H_2O$ with HF(aq); $T = 298.15$ K, $p^0 = 0.1013$ MPa[a]

Expt. no.	$\langle\epsilon(\text{calor})\rangle$ / J K^{-1}	$\Delta\theta_c$ / K	$\langle\epsilon(\text{calor})\rangle(-\Delta\theta_c)$ / J	$\Delta_{vap}H$ / J	m / g	$\Delta_r H_m/M$ / J g^{-1}
1	439.30	0.30143	−132.418	−0.052	0.56048	−236.35
2	439.43	0.30211	−132.756	−0.052	0.56299	−235.90
3	439.65	0.30118	−132.414	−0.052	0.56142	−235.95
5	439.51	0.30190	−132.688	−0.052	0.56352	−235.56
6	440.55	0.30471	−134.240	−0.052	0.56191	−238.99
7	439.31	0.30398	−133.541	−0.052	0.56189	−237.76

$\langle\Delta_r H_m/M\rangle = -(236.75 \pm 0.55)$ J g^{-1}[b]

[a]The headings in the table are as follows: $\langle\epsilon(\text{calor})\rangle$, the mean energy equivalent of the calorimetric system; $\Delta\theta_c$, the corrected calorimetric temperature increase; $\Delta_{vap}H$, the correction for saturation of the air in the ampoule with water vapor; m, the mass of schoepite reacted; and $\Delta_r H_m$/M, the specific enthalpy of reaction of schoepite with HF(aq).

[b]Mean and standard deviation of the specific enthalpy of reaction.

TABLE 4. Thermochemical cycle for calculation of standard molar enthalpy of formation of schoepite ($T = 298.15$ K, $p^0 = 0.1013$ MPa)

Reaction	$\Delta_r H_m$ / kJ mol^{-1}
1. $UO_3(cr, \gamma) + 27.540(HF \cdot 115.30H_2O) = UO_2^{2+} \cdot 27.540F^- \cdot 25.540H^+ \cdot 3176.362H_2O$	-106.18 ± 0.38[a]
2. $UO_2^{2+} \cdot 27.540F^- \cdot 25.540H^+ \cdot 3176.362H_2O = UO_3 \cdot 2H_2O(cr) + 27.540(HF \cdot 115.227H_2O)$	76.25 ± 0.35[b]
3. $27.540(HF \cdot 115.227H_2O) + 2H_2O(l) = 27.540(HF \cdot 115.30H_2O)$	0.00[c]
4. $U(cr) + \frac{3}{2}O_2(g) = UO_3(cr, \gamma)$	-1223.8 ± 2.0[d]
5. $2H_2(g) + O_2(g) = 2H_2O(l)$	-571.66 ± 0.08[d]
6. $U(cr) + \frac{5}{2}O_2(g) + 2H_2(g) = UO_3 \cdot 2H_2O(cr)$	-1825.4 ± 2.1[e]

[a]Taken from earlier work (12) at this laboratory.

[b]Based on $\langle\Delta H_r/M\rangle$ from Table 3 and the molar mass of schoepite $M = 322.057$ g mol^{-1}.

[c]Based on a previous study (19) at this laboratory.

[d]CODATA selected value (11).

[e]Standard molar enthalpy of formation $\Delta_f H_m^0$ of schoepite, the sum of reactions 1 through 5. The uncertainty is the square root of the sum of the squares of the uncertainties (standard deviations) of the reactions.

TABLE 5. Drop-calorimetric results for schoepite ($p^0 = 0.1013$ MPa)

T / K	$\Delta\theta_c$ / K	$\epsilon(\text{calor})(-\Delta\theta_c)$ / J	ΔH(capsule) / J	$\Delta H(H_2O)$ / J	ΔH(corr) / J	$H_m^0(T) - H_m^0(298.15\text{ K})$[a] / J mol^{-1}
350.57	0.09174	−401.54	142.25	2.10[b]	0.11	9411.7
376.43	0.13963	−611.14	213.12	5.99[b]	0.22	14344.1
400.55	0.18685	−817.81	279.62	13.96[c]	0.40	19177.4

[a]$\{H_m^0(T) - H_m^0(298.15\text{ K})\} = -\{\epsilon(\text{calor})(-\Delta\theta) + \Delta H(\text{capsule}) + \Delta H(H_2O) + \Delta H(\text{corr})\}/(0.027315\text{ mol})$. The capsule contained 0.027315 mol of $UO_3 \cdot 2H_2O$.

[b]Correction for the vaporization of H_2O is based on eq. [2].

[c]Correction made on the basis of the enthalpy of vaporization of $H_2O(l)$.

Above 6 K, the thermodynamic properties were obtained by appropriate integrations of the two polynomials over their respective temperature ranges, and values at selected temperatures are given in Table 2.

Calorimetric results for the reaction of schoepite wth HF(aq) are given in Table 3 and the column headings are explained in a footnote. The $\Delta_{vap}H$ term was calculated based upon the assumption that the internal volume of each ampoule was 1 cm^3 and the molar enthalpy of vaporization of water was taken as 44016 J mol^{-1} (11). The apparent sample masses were converted to mass based on a density of 4.65 g cm^{-3} for schoepite (2). The thermochemical cycle for the derivation of $\Delta_f H_m^0$ of schoepite is shown in Table 4. The enthalpies of reaction of γ-UO_3 and of schoepite with HF(aq) are taken from an earlier study (12) at this laboratory and from Table 3, respectively. Standard molar enthalpies of formation of γ-UO_3 and $H_2O(l)$ are CODATA-selected values (11).

The drop-calorimetric results are presented in Table 5. The entries in the table have their usual meanings (13). The correction for the water-vapor pressure over the schoepite sample was calculated from eq. [2] except for the experiment at 400.55 K, where the equilibrium vapor pressure was taken to be that of water at the same temperature. These enthalpy values, as well as those between 298.15 and 350 K obtained by low-temperature calorimetry, were fitted by the method of least squares to various polynomials. The following fit was satisfactory:

Can. J. Chem. Downloaded from www.nrcresearchpress.com by 176.9.209.113 on 09/07/12
For personal use only.

TABLE 6. Thermodynamic values for schoepite ($R = 8.31451\ J\ K^{-1}\ mol^{-1}$; $p^0 = 101.325\ kPa$; $T' = 298.15\ K$)

T / K	$C^0_{p,m}/R$	$\Delta^T_{T'}H^0_m/R$ K [a]	Φ^0_m/R [b]	$\Delta^T_0S^0_m/R$ [c]	$\Delta_fH^0_m/R$ kK	$\Delta_fG^0_m/R$ kK
298.15	20.695	0.00	22.676	22.676	−219.66	−196.86
300	20.760	38.49	22.805	22.676	−219.66	−196.73
320	21.470	460.6	24.166	22.728	−219.63	−195.30
340	22.178	897.2	25.489	22.850	−219.58	−193.85
360	22.886	1348	26.777	23.033	−219.51	−192.40
380	23.595	1218	28.034	23.264	−219.44	−190.94
400	24.303	2291	29.262	23.534	−219.34	−189.45
423.15	25.124	2864	23.885	30.652	−219.23	−187.82

[a] $\Delta^T_{T'}H^0_m = H^0_m(T) - H^0_m(T')$.
[b] $\Phi^0_m = -\{G^0_m(T) - H^0_m(T')\}/T$.
[c] $\Delta^T_0S^0_m = S^0_m(T) - S^0_m(0)$.

[3] $\{H^0_m(T) - H^0_m(298.15\ K)\}/(J\ mol^{-1}) = -38209.0 + 84.2375(T/K) + 0.1472958(T/K)^2$ $(298.15\ K < T < 400\ K)$

The fit was constrained to give $\{H^0_m(T) - H^0_m(298.15\ K)\} = 0$ and $C^0_{p,m}(T) = 172.07\ J\ K^{-1}\ mol^{-1}$ at $T = 298.15$ K. The heat capacity of $UO_3{\cdot}2H_2O$ between 298.15 and 400 K is given by the first derivative of eq. [3]:

[4] $C^0_{p,m}(T)/(J\ K^{-1}\ mol^{-1}) = 84.238 + 0.294592(T/K)$

Discussion

There have been no previous determinations of the low-temperature heat capacity or high-temperature enthalpy increments of schoepite. An earlier estimate (14) of the standard entropy at 298.15 K, 176 ± 8 J K^{-1} mol^{-1}, is somewhat lower than the experimental result, 188.5 ± 0.4 J K^{-1} mol^{-1}.

The standard molar enthalpy of formation has previously been reported by Santalova *et al.* (15), Drobnič and Kolar (16), and Cordfunke (17). Santalova *et al.* measured the enthalpy of reaction of schoepite with $HF{\cdot}267H_2O$. In their experiments, the HF was more dilute than ours, and $n(UO_2^{2+})/n(HF)$ was also quite different. It is not surprising, therefore, that the enthalpy of reaction of schoepite given by Santalova *et al.*, −72.7 ± 0.9 kJ mol^{-1}, differs from our value, −76.25 ± 0.35 kJ mol^{-1}. The magnitude of the difference is, perhaps, unexpected. When the Santalova *et al.* result is combined with their enthalpy of hydrolysis of UF_6(cr) and the best modern $\Delta_fH^0_m$ values for UF_6(cr) (18), H_2O(l) (11), F^-(aq) (11), and the enthalpy of dilution of HF(aq) (19), $\Delta_fH^0_m(UO_3{\cdot}2H_2O, cr) = -1831.1 \pm 4.4$ kJ mol^{-1} is obtained, in fair agreement with the present result.

Drobnič and Kolar measured directly the enthalpy of hydration of a highly-reactive specimen of UO_3(am):

[5] $UO_3(am) + 2H_2O(l) = UO_3{\cdot}2H_2O(cr)$

Their corrected results give $\Delta_rH^0_m = -45.9 \pm 0.4$ kJ mol^{-1} for reaction [5]. Combination of this value with selected $\Delta_fH^0_m$ values for UO_3(am) (18) and H_2O(l) (11) yields $\Delta_fH^0_m = -1825.9 \pm 2.0$ kJ mol^{-1} for schoepite, in excellent agreement with the present determination.

Cordfunke has measured the enthalpies of reaction of γ-UO_3 and schoepite with ≈6 mol dm^{-3} HNO_3. His reported values yield $\Delta_rH^0_m = -30.2 \pm 0.3$ kJ mol^{-1} for the reaction:

[6] $UO_3(cr, \gamma) + 2H_2O(aq) = UO_3{\cdot}2H_2O(cr)$

where H_2O(aq) is for a medium of ≈6 mol dm^{-3} HNO_3. We have taken $\Delta_fH_m(H_2O, aq) = -286.44 \pm 0.04$ kJ mol^{-1} (11, 18) and calculate $\Delta_fH^0_m(UO_3{\cdot}2H_2O) = -(1826.9 \pm 2.0)$ kJ mol^{-1}; this result also agrees very well with the present determination.

The weighed mean value of $\Delta_fH^0_m$ from the four studies just discussed yields $\Delta_fH^0_m$ ($UO_3{\cdot}2H_2O$, cr, 298.15 K) = −1826.4 ± 1.7 kJ mol^{-1}, which is our recommended value for the formation reaction:

[7] $U(cr) + 2H_2(g) + \frac{5}{2}O_2(g) = UO_3{\cdot}2H_2O(cr)$

The thermodynamic quantities determined in the present study have been combined with auxiliary quantities from the literature for U (18), H_2 (11), and O_2 (11) to compute the complete set of properties given in Table 6.

It is believed that the thermodynamic properties of schoepite determined and reviewed in the present study may be used with a high degree of confidence in thermodynamic calculations and modelling studies such as those referred to at the beginning of this paper.

Acknowledgement

The authors thank Florence Williams for the ion-chromatographic analyses.

1. E. H. P. CORDFUNKE. The chemistry of uranium. Elsevier, Amsterdam. 1969. pp. 109–112.
2. P. C. DEBETS and B. O. LOOPSTRA. J. Inorg. Nucl. Chem. **25**, 945 (1963).
3. T. J. WOLERY, D. J. ISHERWOOD, K. J. JACKSON, J. M. DELANY, and I. PUIG DOMENECH. Report no. UCRL-91884. 1984.
4. D. W. OSBORNE, F. SCHREINER, H. E. FLOTOW, and J. G. MALM. J. Chem. Phys. **57**, 3401 (1972); E. F. WESTRUM, JR., J. B. HATCHER, and D. W. OSBORNE. J. Chem. Phys. **21**, 419 (1953); G. K. JOHNSON, H. E. FLOTOW, P. A. G. O'HARE, and W. S. WISE. Am. Mineral. **67**, 736 (1982); J. S. PRICE, I. R. TASKER, E. H. APPELMAN, and P. A. G. O'HARE. J. Chem. Thermodyn. **18**, 923 (1986); P. A. G. O'HARE, G. K. JOHNSON, I. R. TASKER, H. E. FLOTOW, and C. W. STRUCK. J. Chem. Thermodyn. **19**, 77 (1987).
5. G. K. JOHNSON, H. E. FLOTOW, P. A. G. O'HARE, and W. S. WISE. Am. Mineral. **68**, 1134 (1983).
6. D. R. FREDRICKSON, R. D. BARNES, M. G. CHASANOV, R. L. NUTTALL, R. KLEB, and W. N. HUBBARD. High Temp. Sci. **1**, 373 (1969).
7. J. K. DAWSON, E. WAIT, K. ALCOCK, and D. R. CHILTON. J. Chem. Soc. 3531 (1956).
8. R. V. LINDVAL' and V. V. KUZNETSOVA. Tr. Kazan. Khim.-Tekhnol. Inst. **54**, 145 (1974).

Can. J. Chem. Downloaded from www.nrcresearchpress.com by 176.9.209.113 on 09/07/12
For personal use only.

9. J. A. PEREZ-BUSTAMANTE, J. B. POLONIO, and R. F. CELLINI. Anal. Real Soc. Españ. Fis. Quim. B**58**, 677 (1962).
10. P. A. G. O'HARE, B. M. LEWIS, and S. NGUYEN. To be published.
11. CODATA recommended key values for thermodynamics, 1977. J. Chem. Thermodyn. **10**, 903 (1978).
12. G. K. JOHNSON and P. A. G. O'HARE. J. Chem. Thermodyn. **10**, 577 (1978).
13. P. A. G. O'HARE, W. N. HUBBARD, G. K. JOHNSON, and H. E. FLOTOW. J. Chem. Thermodyn. **16**, 45 (1984).
14. E. H. P. CORDFUNKE and P. A. G. O'HARE. The chemical thermodynamics of actinide elements and compounds. Part 3. Miscellaneous actinide compounds. International Atomic Energy Agency, Vienna (1978).
15. N. A. SANTALOVA, L. M. VIDAVSKII, K. M. DUNAEVA, and E. A. IPPOLITOVA. Radiokhim. **13**, 592 (1971).
16. M. DROBNIČ and D. KOLAR. J. Inorg. Nucl. Chem. **28**, 2833 (1966).
17. E. H. P. CORDFUNKE. J. Phys. Chem. **68**, 3353 (1964).
18. D. D. WAGMAN, W. H. EVANS, V. B. PARKER, R. H. SCHUMM, I. HALOW, S. M. BAILEY, K. L. CHURNEY, and R. L. NUTTALL. J. Phys. Chem. Ref. Data. **11** (1982), Supplement no. 2.
19. G. K. JOHNSON, P. N. SMITH, and W. N. HUBBARD. J. Chem. Thermodyn. **5**, 793 (1973).

Can. J. Chem. Downloaded from www.nrcresearchpress.com by 176.9.209.113 on 09/07/12
For personal use only.

Heat-of-mixing for the partially miscible system N_2/C_2H_6

JORGE C. G. CALADO, PRAKASH GOPAL, JOHN A. ZOLLWEG,[1] and W. REID THOMPSON
School of Chemical Engineering, Cornell University, Ithaca, NY 14853, U.S.A.

Received September 1, 1987

This paper is dedicated to Professor J. A. Morrison

JORGE C. G. CALADO, PRAKASH GOPAL, JOHN A. ZOLLWEG, and W. REID THOMPSON. Can. J. Chem. **66**, 626 (1988).

Heats-of-mixing for the liquid system nitrogen/ethane have been measured at 92.3 K and 0.6309 MPa using a cryogenic flow calorimeter. The heat-of-mixing versus composition curve shows that the system is only partially miscible; the compositions between which liquid–liquid separation occurs have been estimated.

JORGE C. G. CALADO, PRAKASH GOPAL, JOHN A. ZOLLWEG, et W. REID THOMPSON. Can. J. Chem. **66**, 626 (1988).

Utilisant un calorimètre à flux cryogénique, on a mesuré les chaleurs de mélange du système liquide azote/éthane à 92,3 K et 0,6309 MPa. La courbe de la chaleur de mélange en fonction de la composition démontre que le système n'est que partiellement soluble; on a évalué les compositions entre lesquelles il se produit une séparation liquide–liquide.

[Traduit par la revue]

Can. J. Chem. Downloaded from www.nrcresearchpress.com by 93.93.197.157 on 09/07/12
For personal use only.

Introduction

Enthalpy data for liquid mixtures at low temperatures are scarce compared with thermal property data for low temperature solids. As Lobo and Staveley (1) have pointed out, experimental results have been reported from only four or five laboratories over the last 20 years. The Leiden (2) and Bristol (3) low temperature flow mixing calorimeters as well as the Oxford (4) batch mixing calorimeter have been disassembled. The recently constructed mixing calorimeters at Cornell (5, 6) presently provide capability for making enthalpy measurements on fluid mixtures at low temperatures.

Flow calorimetry is a well-established technique for measurements on fluid mixtures near room temperature, but the extension of this method to measurements at cryogenic temperatures has required some modification, particularly in the method of flow measurement. For measurements on fluids, flow calorimeters have several important advantages over batch calorimeters. Flow calorimeters avoid troublesome vapor space and thus do not require extensive auxiliary information for the reduction of raw experimental data to heat-of-mixing values. In addition, flow calorimeters make it possible, by variation of the flow rates, to eliminate errors caused by heat leaks or incomplete mixing. A drawback of flow calorimeters is that they require large quantities of fluids.

Measurements in a flow calorimeter are effected by first bringing the pure fluid streams to the cryostat bath temperature and then supplying energy to the calorimeter so that the temperature of the fluid mixture at the exit is the same as that of the incoming streams. The heat-of-mixing is then given by

$$[1] \quad H^M = (W + q)/F$$

where W is the electrical power input to the calorimeter heater, q is the heat-leak into the calorimeter, F is the total molar flow rate, and H^M is the the enthalpy of mixing. It must be noted that q can be made small relative to W by operating at high flow rates. Since temperature compensation cannot be perfect, a $C_p\Delta T$ correction would need to be effected, so that (assuming $q \ll W$) the heat-of-mixing can now be determined from the equation:

$$[2] \quad H^M = W/F - C_{p_{mix}}(T_{exit} - T_{in})$$

where $C_{p_{mix}}$ is the heat capacity of the mixture and may be evaluated (for the purpose of this small correction) as the mole fraction weighted sum of the pure component heat capacities, and $(T_{exit} - T_{in})$ is the temperature difference between the fluid at the exit and the inlet of the calorimeter.

Heat-of-mixing measurements are reported here for the nitrogen/ethane system at 92.3 K and 0.6309 MPa. The system and conditions were chosen with Titan — a moon of Saturn — in mind. One of us (7) has shown that for a detailed study of the nature of Titan's surface, clouds, and oceans, it was necessary to obtain phase equilibrium information for the nitrogen/methane/ethane system. L–L–V studies on this ternary system at temperatures between 102 and 116 K by Lu *et al.* (8) showed that liquid–liquid phase separation boundaries existed. Lunine *et al.* (9) and Dermott *et al.* (10) have noted the possibility of liquid–liquid phase separation at conditions prevailing on Titan (about 95 K and 5 bar). It was with the intent of enabling better modeling of the nitrogen/methane/ethane system, such as that attempted by Thompson (7), that we undertook this study. Another use for these results is in testing molecular thermodynamic perturbation theories as applied to molecules with small elongation (11).

Experimental

Measurements were conducted using a computer-interfaced low temperature, high pressure flow calorimeter designed and constructed by Gopal (5). The apparatus was used with only one modification; ethane was preliquefied in an isopropyl alcohol – dry ice bath before being allowed to enter the liquid nitrogen cryostat bath. This helped to conserve the liquid nitrogen in the bath and thus permitted longer experimentation before refilling the cryostat.

The experiment involved three stages. First, the zero of the thermocouple that senses the temperature difference between the exit and the inlet of the mixing calorimeter was measured by passing liquefied nitrogen through both arms of the calorimeter. In the second stage of the experiment, the flow rates of the two components were adjusted and the fluids were allowed to mix in the calorimeter. Finally, the power supply to the calorimeter heater was adjusted so that the thermocouple signal returned approximately to its original value.

The composition was determined as the ratio $f_A/(f_A + f_B)$, where f_A and f_B, the molar flow rates of the components, were measured with Micro Motion™ vibrating tube mass flow meters. The heat-of-mixing was then determined from eq. [2], with the $C_{p_{mix}} \cdot \Delta T$ correction to W/F never accounting for more than 6.0 J/mol.

Results and discussion

Heat-of-mixing measurements for the liquid system nitrogen/ethane at (92.3 ± 0.3) K and (0.6309 ± 0.035) MPa

[1]To whom all correspondence should be addressed.

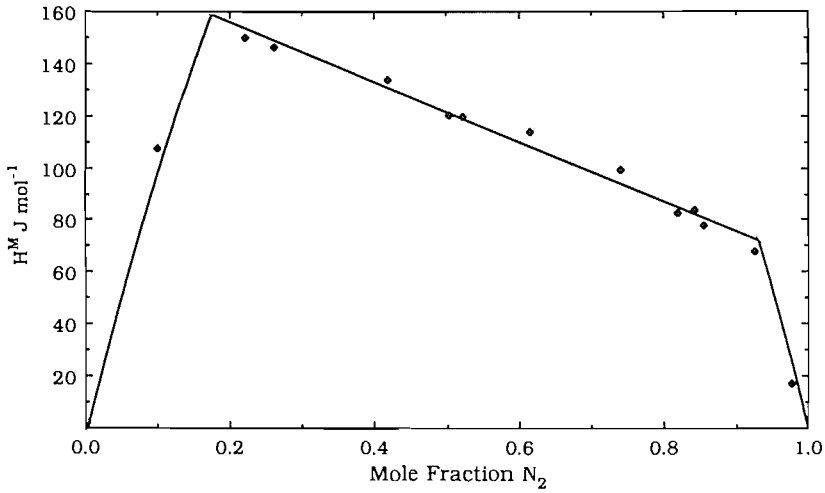

FIG. 1. Heat-of-mixing versus mole fraction for N_2/C_2H_6 at 92.3 K, 0.6309 MPa. The solid line gives a continuous representation of H^M vs. composition.

TABLE 1. Heats-of-mixing for N_2/C_2H_6 at (92.3 ± 0.3) K and (0.6309 ± 0.035) MPa[a]

x_{N_2}	H^M (J/mol)
0.093	107.4
0.215	149.8
0.255	146.6
0.412	134.2
0.497	120.3
0.515	120.0
0.610	114.0
0.735	99.1
0.813	82.4
0.837	83.6
0.850	77.7
0.920	68.1
0.971	17.4

[a] x_{N_2} is the overall mole fraction of nitrogen in the mixture.

are presented in Table 1. The nitrogen used in this work was supplied by Airco and had a certified purity of 99.997%, the main impurities being oxygen and water. Ethane was supplied by MG Industries and had a certified purity of 99.5%; the major impurities were hydrogen and methane.

A linear portion in the H^M–x curve (see Fig. 1) suggests that the nitrogen/ethane system is only partially miscible at 92.3 K and 0.6309 MPa. To the best of our knowledge, this is only the second calorimetric investigation of a partially miscible liquefied gas system, the first one having been performed by Lobo and Staveley (1) on HCl/CF_4. The experimental points in the immiscible-regime fit the equation: $H^M = A + Bx_{N_2}$ with $A = 178.15$ J/mol and $B = -114.71$ J/mol, the standard deviation of the fit being ≈3.4 J/mol. The scatter in the experimental points is attributed to the limited mutual solubility of the two liquids. The standard deviation, while being fairly large, is roughly one-third the standard deviation obtained by Lobo and Staveley (1) for a comparable heat-of-mixing value. (It may be worthwhile mentioning here that flow rates in excess of 6.5 mmol/s had to be employed in the liquid–liquid separation region to ensure that equilibrium had been established, while a flow rate of 5.0 mmol/s was found adequate for compositions where the liquids were miscible.)

The temperature and pressure for different measurements varied over ±0.3 K and ±0.035 MPa, respectively. No effort was made to effect corrections for these variations in experimental conditions. Since the conditions were far removed from the critical temperature of the more volatile component, N_2, it is expected that the corrections would be small compared to the scatter in the data.

From the H^M–x curve shown in Fig. 1, on the ethane-rich side, the nitrogen/ethane mixture is immiscible for nitrogen mole fractions >(0.17 ± 0.03). On the nitrogen-rich side, the liquids are miscible only for nitrogen mole fractions >(0.92 ± 0.03). While heat-of-mixing measurements are no substitute for actual L–L–V experiments, we have demonstrated the usefulness of low temperature calorimetry in identifying compositions at which phase separation may occur.

Acknowledgement

This work was supported by the Gas Research Institute under Contract No. 5086-260-1313.

1. L. Q. LOBO, L. A. K. STAVELEY, V. VENKATASUBRAMANIAN, P. CLANCY, K. E. GUBBINS, C. G. GRAY, and C. G. JOSLIN. Fluid Phase Equilibria, **22**, 89 (1985).
2. M. KNOESTER, K. W. TACONIS, and J. J. M. BEENAKKER. Physica, **33**, 389 (1967).
3. C. J. WORMALD, K. L. LEWIS, and S. E. MOSEDALE. J. Chem. Thermodyn. **9**, 27 (1977).
4. K. L. LEWIS and L. A. K. STAVELEY. J. Chem. Thermodyn. **7**, 855 (1975).
5. P. GOPAL. Ph. D. Thesis. Cornell University, Ithaca, NY. 1987.
6. K. P. WALLIS, P. CLANCY, J. A. ZOLLWEG, and W. B. STREETT. J. Chem. Thermodyn. **16**, 811 (1984).
7. W. R. THOMPSON. Proc. Internat. Workshop, Alpbach, Austria. September 1985. ESA SP-241. 1985.
8. B. C-Y. LU, S-D. CHANG, I. M. ELSHAYAL, P. YU, D. GRAVELLE, and D. P. L. POON. Proc. 1st Internat. Conf. Calorimetry Thermodyn., Warsaw, 1969. p. 755.
9. J. I. LUNINE, D. J. STEVENSON, and Y. L. YUNG. Science, **222**, 1229 (1983).
10. S. F. DERMOTT, P. GIERASCH, J. GRADIE, C. SAGAN, and W. R. THOMPSON. Lunar and planetary science XV, Part 1, Tucson AZ. LPI, 1984. p. 222.
11. M. BOHN, J. FISCHER, and F. KOHLER. Fluid Phase Equilibria, **31**, 233 (1986); K. P. SHUKLA, K. LUCAS, and B. MOSER. Fluid Phase Equilibria, **17**, 19 (1984).

Can. J. Chem. Downloaded from www.nrcresearchpress.com by 93.93.197.157 on 09/07/12
For personal use only.

Local mode assignments for the CD-stretching overtone spectra of deuterated methyl iodide and deuterated methyl cyanide: effects of increased interoscillator coupling on local mode states of C_{3v} symmetry

M. KHALIQUE AHMED[1] AND BRYAN R. HENRY[2]

Department of Chemistry, University of Manitoba, Winnipeg, Man., Canada R3T 2N2

Received June 17, 1987

This paper is dedicated to Professor J. A. Morrison

M. KHALIQUE AHMED and BRYAN R. HENRY. Can. J. Chem. **66**, 628 (1988).

The overtone spectra of CD_3I and CD_3CN are measured at room temperature in the liquid phase in the regions of CD-stretching local mode overtones corresponding to $\Delta v_{CD} = 2–5$. The spectra are analyzed in terms of a harmonically coupled local mode model. The local mode parameters ω, ωx, and $\gamma' v$, the interoscillator coupling between the methyl CD bonds, are determined. A comparison of the spectra of the CH_3Z molecules (Z = Cl, Br, I, CN) to the spectra of CD_3I and CD_3CN reveals the spectral effects of increased interoscillator coupling between the CD bonds.

M. KHALIQUE AHMED et BRYAN R. HENRY. Can. J. Chem. **66**, 628 (1988).

Opérant à la température ambiante et en phase liquide, on a mesuré les spectres d'harmonique du CD_3I et du CD_3CN dans les régions des harmoniques du mode d'élongation CD local correspondant à un $\Delta v_{CD} = 2–5$. On a analysé les spectres en fonction d'un modèle impliquant un couplage harmonique local. On a déterminé les paramètres ω, ωx et $\gamma' \omega$ ainsi que le couplage entre les oscillateurs des liaisons CD du groupement méthyle. Une comparaison entre les spectres des molécules CH_3Z (Z = Cl, Br, I et CN) et ceux du CD_3I et du CD_3CN mettent en évidence les effets spectraux provenant d'une augmentation du couplage entre les oscillateurs des liaisons CD.

[Traduit par la revue]

Introduction

Although the local mode model has been used extensively to interpret and understand the XH-stretching overtone spectra of polyatomic molecules (X = C, O, N, or S) (1–5), comparatively little attention has been paid to the XD-stretching overtone spectra of deuterated molecules. In the local mode model, the XH oscillators are assumed to behave anharmonically but essentially independently (6–8). Zero order vibrational wave functions are constructed as products of functions associated with the individual equivalent XH bonds. High energy overtone spectra ($\Delta v_{XH} \geq 3$) are dominated by transitions to pure local mode states whose components have all of the vibrational energy localized in one of a set of equivalent XH oscillators. The various pure local mode states corresponding to different symmetrized combinations of these components are effectively degenerate for $\Delta v_{XH} \geq 3$ (7–11). Therefore symmetry energy splitting of such states, which arises from coupling between the equivalent XH oscillators, is generally not observed for higher overtones.

Kinetic energy coupling between XD bonds is significantly greater than for XH bonds. This increase of interoscillator coupling on replacement of hydrogen by deuterium can cause a marked change in the local mode overtone spectral pattern. Recently we have observed such changes in a comparison of the overtone spectra of CH_2Z_2 and CD_2Z_2 molecules (Z = Cl, Br, or I) (12). In this paper, we extend our previous work to a study of the effects of increased interoscillator coupling on local mode states of C_{3v} symmetry. We compare the CD-stretching overtone spectra of CD_3I and CD_3CN to the spectra of the CH_3Z molecules (Z = Cl, Br, I, or CN) that we have recently measured (13).

[1]Present address: Department of Chemistry, University of Alberta, Edmonton, Alta., Canada T6G 2G2.

[2]Present address: Department of Chemistry and Biochemistry, University of Guelph, Guelph, Ont., Canada N1G 2W1.

Experimental section

High purity samples (99%) of CD_3I and CD_3CN were obtained from Aldrich Chemical Co. and were used without further purification. Liquid phase overtone spectra in the CD stretching regions of $\Delta v_{CD} = 2–5$ were recorded at room temperature on a Beckman 5270 spectrophotometer with the near ir light source. A 0.1 cm path length cell was used to record the $\Delta v_{CD} = 2$ spectra. The spectra in the regions of $\Delta v_{CD} = 3–5$ were recorded with a 3 cm path length cell. All of the spectra, in a digital format, were transferred to a Nicolet 1280 computer and converted to a linear energy scale. The spectra were plotted in wavenumber units with a Nicolet Zeta 160 plotter.

A single measurement of the $\Delta v_{CD} = 5$ spectra of both CD_3I and CD_3CN gave a very poor signal-to-noise ratio. The signal-to-noise ratio was improved by signal averaging four base line corrected scans on the Nicolet 1280 computer.

The spectra in the region of $\Delta v_{CD} = 2$ of both molecules and of $\Delta v_{CD} = 3$ of CD_3I consist of relatively well resolved peaks. The positions of the peak maxima in these spectra were determined from the digital data with a Nicolet 1280 program which simply identified the wavelength setting at the highest absorbance value in the vicinity of the peak. The spectra in the regions of $\Delta v_{CD} = 3–5$ for CD_3CN and of $\Delta v_{CD} = 4, 5$ for CD_3I were composed of overlapping peaks. These spectra were decomposed with a Fortran 77 curve analysis program, NIRCAP (14), which fitted Lorentzian peaks to the observed bands. The experimental and fitted spectra were plotted and compared to check the quality of the deconvolution fit.

Results and discussion

1. Spectral analysis

The liquid phase overtone spectra of CD_3I and CD_3CN in the regions of $\Delta v_{CD} = 2–5$ are shown in Figs. 1–4. The peak positions for these spectra and for the CD-stretching fundamentals are given in Tables 1, 2, and 3. Two types of peaks are observed. The first type is only associated with CD-stretching and is listed in Table 1. We assign these peaks within the local mode description to symmetrized combinations of Morse oscillator product functions $|v_1,v_2,v_3\rangle$, where v_1, v_2, and v_3 denote the vibrational quanta in each of the three methyl CD

Can. J. Chem. Downloaded from www.nrcresearchpress.com by 176.9.209.113 on 09/07/12
For personal use only.

Can. J. Chem. Downloaded from www.nrcresearchpress.com by 176.9.209.113 on 09/07/12
For personal use only.

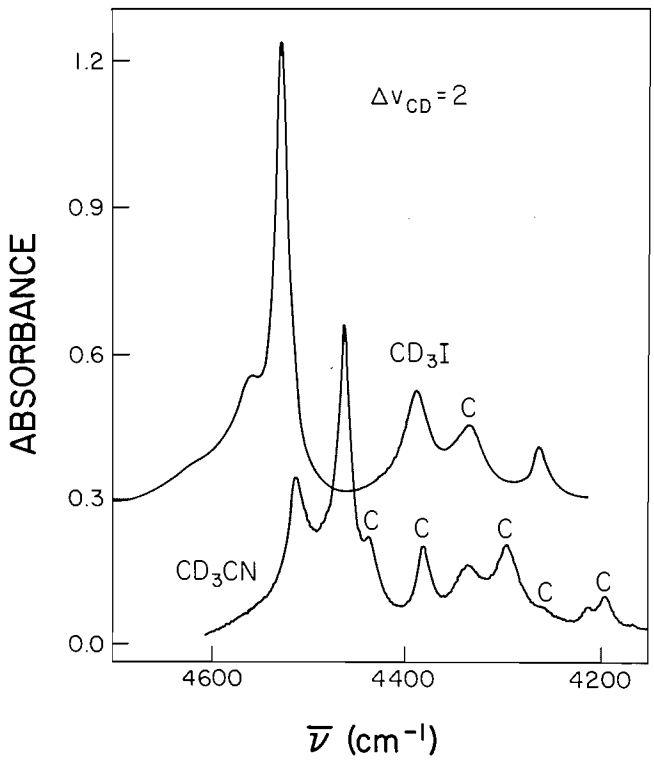

FIG. 1. Liquid phase overtone spectra of CD_3CN and CD_3I in the region of $\Delta v_{CD} = 2$. Spectra were measured at room temperature with a path length of 0.1 cm. The absorbance of CD_3I has been offset by 0.3 absorbance units.

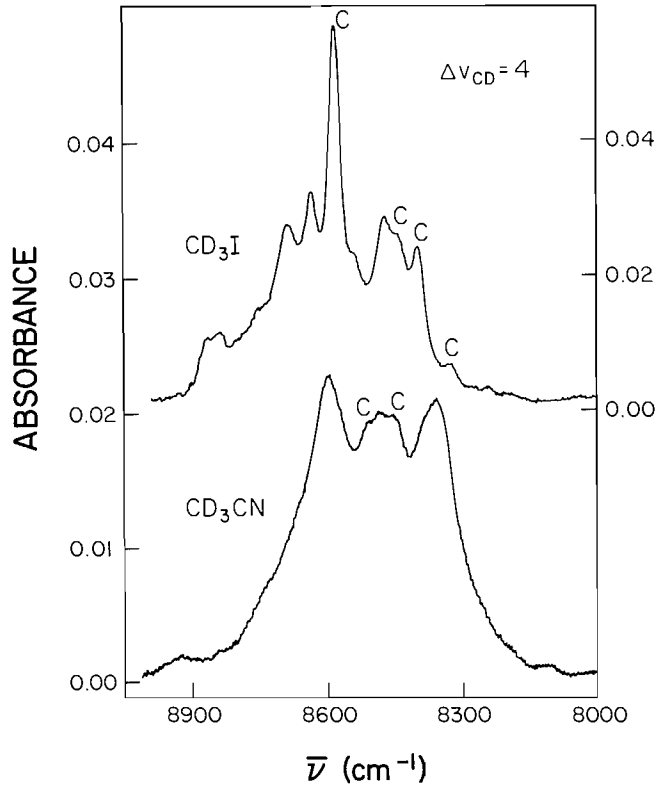

FIG. 3. Liquid phase overtone spectra of CD_3CN and CD_3I in the region of $\Delta v_{CD} = 4$. Spectra were measured at room temperature with a path length of 3.0 cm. The right hand ordinate scale represents the absorbance of CD_3I.

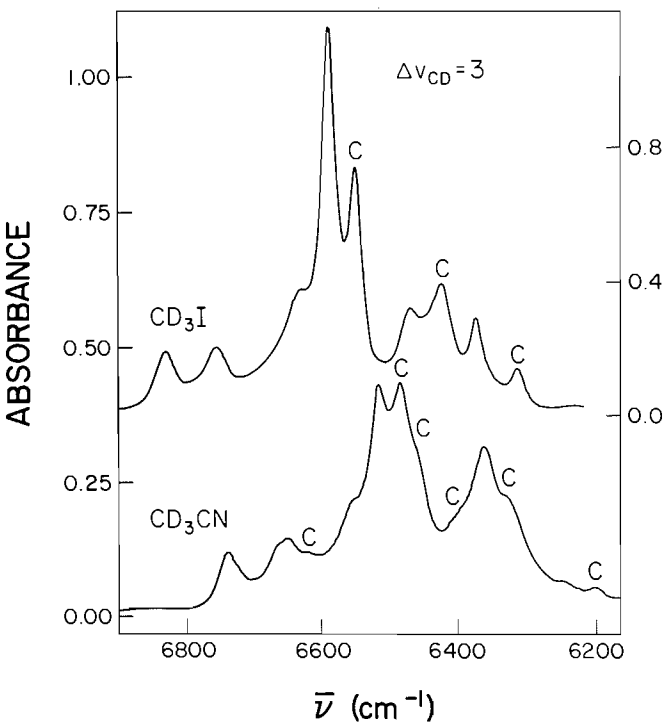

FIG. 2. Liquid phase overtone spectra of CD_3CN and CD_3I in the region of $\Delta v_{CD} = 3$. Spectra were measured at room temperature with a path length of 3.0 cm. The right hand ordinate scale represents the absorbance of CD_3I.

bonds, respectively, and $v_1 + v_2 + v_3 = \Delta v_{CD}$. The second type of peak is marked by a C in Figs. 1–4. In most cases, these local mode – normal mode combination peaks involve two quanta of DCD-bending combined with $v - 1$ quanta of CD-stretching for a given vibrational manifold v.

In assigning the CD-stretching peaks of Table 1, we make use of the harmonically coupled local mode model for an XH_3 system (8, 9, 13, 15) that we have applied previously to the overtone spectra of neopentane (9, 11) and the methyl halides (13). The product functions are symmetrized under the point group C_{3v}. The Hamiltonian is written in the form

$$[1]\quad H = E_0 + (v_1 + v_2 + v_3)\omega - (v_1^2 + v_2^2 + v_3^2 + v_1 + v_2 + v_3)\omega x + (p_1p_2 + p_1p_3 + p_2p_3)\gamma\omega + (q_1q_2 + q_1q_3 + q_2q_3)\phi\omega$$

where E_0 is the wavenumber energy of the ground state, and γ and ϕ characterize the off-diagonal kinetic and potential energy coupling, respectively. These parameters are defined in terms of Wilson **G** and **F** matrix elements ($\gamma = (-\frac{1}{2})G_{ij}/G_{ii}$; $\phi = (\frac{1}{2})F_{ij}/F_{ii}, i, j = 1, 2, 3$). p_i and q_i are normalized momentum and coordinate variables, and are conveniently expressed in terms of creation a^+ and annihilation a operators ($p = a^+ - a$; $q = a^+ + a$).

The details of this model have been described in our previous work (8, 9, 13). The model accounts for all of the anharmonicity that is diagonal in a single CH/CD oscillator. However, coupling between the simple product basis functions is restricted to

Can. J. Chem. Downloaded from www.nrcresearchpress.com by 176.9.209.113 on 09/07/12
For personal use only.

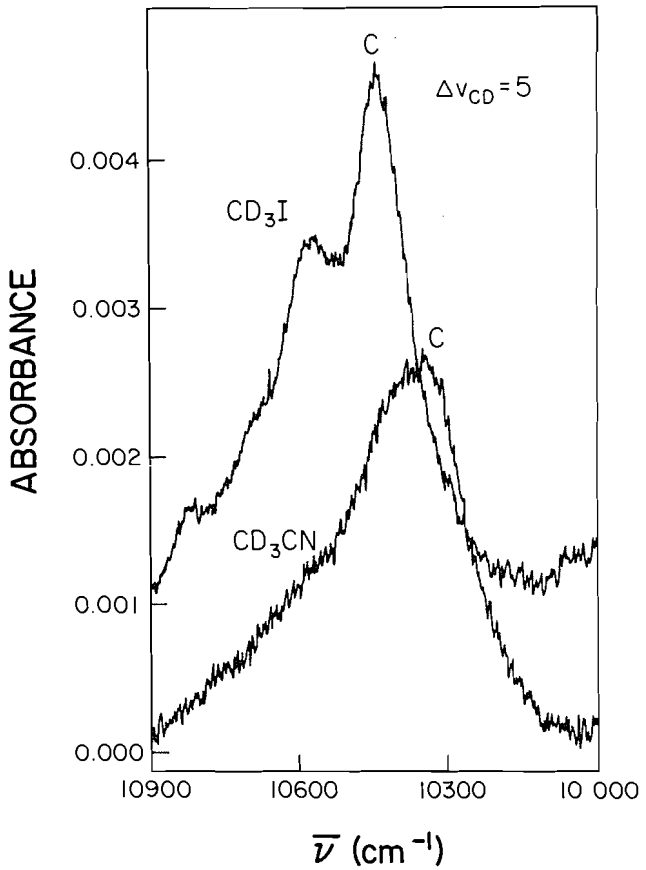

FIG. 4. Liquid phase overtone spectra of CD_3CN and CD_3I in the region of $\Delta v_{CD} = 5$. These spectra are the sum of four base line corrected scans. Individual scans were measured at room temperature with a path length of 3.0 cm. The absorbance of CD_3I has been offset by 0.001 absorbance units.

a given vibrational manifold and to the harmonic limit, i.e., functions couple only when their respective bond excitations differ by a single quantum. A calculation of the CD-stretching vibrational state energies requires the harmonic frequency ω, the anharmonicity constant ωx, and the effective coupling parameter $\gamma'\omega$ ($\gamma' = \gamma - \phi$) which appear in the intramanifold coupling matrices (9, 15, 16) of eq. [1].

As we have noted, in CH-stretching overtones for $\Delta v_{CH} \geq 3$, the spectra are dominated by transitions to pure local mode states whose components have all of the vibrational energy localized in one of a set of equivalent CH bonds. For example, in the methyl halides (13), the dominant peaks correspond to the states $|v,0,0\rangle_{A_1,E}$. Moreover such pure local mode states of different symmetry are effectively degenerate for $\Delta v_{CH} \geq 3$ (7–11). The parameters ω and ωx can be evaluated by fitting the observed energies of these pure local mode peaks to the energy equation of a diatomic Morse oscillator

$$[2] \quad \Delta E(v) = v\omega - (v^2 + v)\,\omega x$$

However, eq. [2] cannot be used to obtain ω and ωx for CD_3I and CD_3CN because extensive interactions between CD stretching states and combination states involving DCD-bending strongly perturb the peak positions. Therefore, in the present work an alternative procedure was used to obtain these local mode parameters.

When deuterium is substituted for hydrogen in a CH oscillator, the change in the harmonic frequency is given by

TABLE 1. Observed and calculated CD-stretching peak positions (cm^{-1}) in the overtone spectra of CD_3I and CD_3CN

	CD_3I		CD_3CN		
Δv_{CD}	Obsd	Calcd	Obsd	Calcd	Assignment
1	2140[a]	2139	2116[b]	2115	$\|100\rangle_{A_1}$
	2289[a]	2288	2263[b]	2263	$\|100\rangle_E$
2	4263	4258	4214	4209	$\|110\rangle_{A_1}$
	4388	4387	4335	4334	$\|200\rangle_E$
	4528	4543	4463	4489	$\|200\rangle_{A_1}$
	4558	4563	4513	4511	$\|110\rangle_E$
3	6371	6354	6243	6277	$\|210\rangle_{A_1}$
	6467	6458	6362	6375	$\|300\rangle_E$
	6588	6594	6516	6509	$\|300\rangle_{A_1}$
	6627	6627	6560	6546	$\|210\rangle_E$
	6752	6784	6656	6701	$\|210\rangle_E$
	—	6810	—	6729	$\|210\rangle_{A_2}$
	6829	6829	6735	6750	$\|111\rangle_{A_1}$
4	8477	8424	8348	8314	$\|310\rangle_{A_1}$
	8536	8500	8391	8381	$\|400\rangle_E$
	8636	8616	8484	8498	$\|400\rangle_{A_1}$
	8689	8667	8597	8555	$\|310\rangle_E$
	8756	8800	8677	8684	$\|310\rangle_E$[c]
	—	8837	—	8722	$\|310\rangle_{A_2}$
	—	8995	8740	8755	$\|211\rangle_{A_1}$
	8850	8864	—	8881	$\|220\rangle_{A_1}$
	—	9004	—	8889	$\|220\rangle_E$
	9057	9064	8926	8955	$\|211\rangle_E$
5	10582	10630[d]	10419	10460[d]	$\|500\rangle$
	10680	—	10569	—	$\|410\rangle$
	10821	—	10758	—	$\|320\rangle$

[a]Reference 17.
[b]Reference 18.
[c]Although the $|2, 2, 0\rangle_E$ coefficient is the highest, both the $|3, 1, 0\rangle_E$ coefficients are almost as high. Thus we designate this state $|3, 1, 0\rangle_E$ in the sense that it has a preponderance of $|3, 1, 0\rangle_E$ character.
[d]Calculated from the Morse oscillator energy equation (eq. [2]).

TABLE 2. Positions (cm^{-1}) and tentative assignments for the local mode – normal mode combination peaks in the overtone spectra of CD_3I

Δv_{CD}	Peak position	Assignment[a]
2	4334	$\|100\rangle_E + 2\delta_E$
3	6312	$\|200\rangle_E + \delta_A + \delta_E$
	6421	$\|200\rangle_E + 2\delta_E$
	6548	$\|200\rangle_{A_1} + 2\delta_E$
4	8319	$\|300\rangle_E + 2\delta_A$
	8399	$\|300\rangle_{A_1} + 2\delta_A$
	8441	$\|300\rangle_E + 2\delta_E$
	8583	$\|300\rangle_{A_1} + 2\delta_E$
5	10438	$\|310\rangle_{A_1} + 2\delta_E$

[a]δ_A = 938 cm^{-1} from ref. 19, δ_E = 1040 cm^{-1} from ref. 17.

$$[3] \quad \omega_D/\omega_H = (m_D/m_H)^{-1/2} = [(12/13)(14/24]^{1/2}$$

where m_D and m_H are the reduced masses for a CD and CH oscillator. ω_D values are obtained from eq. [3] and from ω_H values for CH_3I and CH_3CN which have been taken from our recent work (13) ($\omega_H(CH_3I)$ = 3129 ± 5 cm^{-1}, $\omega_H(CH_3CN)$ =

TABLE 3. Positions (cm^{-1}) and tentative assignments for the local mode – normal mode combination peaks in the overtone spectra of CD_3CN

Δv_{CD}	Peak position	Assignment[a]
2	4196	Combination
	4253	Combination
	4295	$\|100\rangle_{A_1} + 2\delta_A$
	4381	$\|100\rangle_E + \delta_A + \delta_E$
	4438	$\|100\rangle_E + 2\delta_A$
3	6199	Combination
	6322	$\|200\rangle_E + 2\delta_E$
	6397	Combination
	6459	$\|200\rangle_E + \delta_A + \delta_E$
	6484	$\|200\rangle_{A_1} + 2\delta_E$
	6616	$\|200\rangle_{A_1} + 2\delta_A$
4	8447	$\|300\rangle_E + 2\delta_E$
	8516	$\|300\rangle_{A_1} + 2\delta_E$
5	10321	$\|310\rangle_{A_1} + 2\delta_E$

[a] $\delta_A = 1103\ cm^{-1}$, $\delta_E = 1039\ cm^{-1}$ from ref. 18.

$3101 \pm 4\ cm^{-1}$). The resultant values of ω_D are $2296\ cm^{-1}$ and $2275\ cm^{-1}$ for CD_3I and CD_3CN, respectively.

The effective interoscillator coupling parameter $\gamma'\omega$ can be obtained from the observed splitting (17, 18) between the fundamental CD-stretching modes of A_1 and E symmetries (9).

$$[4] \quad 3\gamma'\omega = E(|1,0,0\rangle_E) - E(|1,0,0\rangle_{A_1})$$

Values of $\gamma'\omega$ of 49.7 and 49.0 cm^{-1} are obtained for the CD oscillators of CD_3I and CD_3CN, respectively.

The only parameter left to be determined is the anharmonicity ωx. We determined this parameter by fitting ω, $\gamma'\omega$, and the observed energy of the $|1,0,0\rangle_E$ fundamental (17, 18) to the equation

$$[5] \quad E(|1,0,0\rangle_E) = \omega - 2\omega x + \gamma'\omega$$

Equation [5] expresses the expected energy of the $|1,0,0\rangle_E$ transition on the basis of the harmonic coupling model (9) and yields values of $\omega x = 28.3$ and 30.5 cm^{-1} for CD_3I and CD_3CN, respectively. The anharmonicity could also be extracted from an analogous expression for the energy of the $|1,0,0\rangle_{A_1}$ fundamental. Identical anharmonicity values are obtained on the basis of the observed frequencies (17, 18) of both fundamentals.

Substitution of these local mode parameters into the intramanifold coupling matrices of the Hamiltonian (eq. [1]) followed by diagonalization of these matrices gives the calculated energies of the peaks corresponding to the methyl CD bonds. The calculated and observed energies of these methyl CD-stretching peaks are given in Table 1, along with the peak assignments. The agreement between calculated and observed peak energies is reasonably good. The larger of the discrepancies at $\Delta v_{CD} = 3$ and 4 are generally associated with weak poorly resolved peaks where the experimental uncertainties in peak position are relatively high.

In assigning the spectra, we have identified a given state with the component designation that has the highest coefficient in the eigenvector associated with that particular energy. However, because of the relatively large value of $\gamma'\omega$, these states are often strongly mixed, and so such assignments are not always informative and serve primarily as state labels. In general, state mixing is more pronounced the higher the overtone level.

At $\Delta v_{CD} = 5$, the lowest energy vibrational states are clearly involved in a significant interaction with a close lying combination. The expected energy shift is undoubtedly a factor in the relatively poor agreement between the observed and calculated values in Table 1. At $\Delta v_{CD} = 5$, because the individual states are totally unresolved and because of extensive vibrational mixing, we have only given a calculated value in Table 1 from the simple Morse relation of eq. [2].

We have assigned the highest intensity peak in the spectra in the region of $\Delta v_{CD} = 2$ (Fig. 1) to the transition to the $|2,0,0\rangle_{A_1}$ state. The spectra are well resolved, particularly for CD_3I where there is only a single combination peak, in contrast to the spectra of CD_3CN where many combination peaks appear. From low to high energy, the four CD-stretching peaks correspond to transitions to the states $|1,1,0\rangle_{A_1}$, $|2,0,0\rangle_E$, $|2,0,0\rangle_{A_1}$, and $|1,1,0\rangle_E$. The splitting between the $|2,0,0\rangle_{A_1}$ and $|2,0,0\rangle_E$ peaks is much greater than the corresponding splitting in the spectra of the undeuterated methyl halides (13). This splitting arises from the harmonic coupling of the $|2,0,0\rangle_{A_1,E}$ states with the $|1,1,0\rangle_{A_1,E}$ states of the same symmetry via the γ and ϕ parts of the Hamiltonian (eq. [1]).

In the spectra in the region of $\Delta v_{CD} = 3$ (Fig. 2), the purely CD-stretching peaks again are better resolved in CD_3I than in CD_3CN because of the greater number of combination peaks in the latter spectrum. The splitting between the $|3,0,0\rangle_{A_1}$ and $|3,0,0\rangle_E$ peaks is similar to the corresponding splitting at $\Delta v_{CD} = 2$. The peaks corresponding to the states $|2,1,0\rangle_{A_1,E}$ and $|1,1,1\rangle_{A_1}$ appear with lower intensity than those corresponding to the pure local mode states $|3,0,0\rangle_{A_1,E}$.

The spectra in the region of $\Delta v_{CD} = 4$ (Fig. 3) are congested due to a large number of transitions. Transitions occur to several CD-stretching states of comparable intensity as well as to several combinations. Many of these peaks severely overlap and so the observed peak positions that are listed in Table 1 should be considered only as estimates. The splitting between the $|4,0,0\rangle_{A_1}$ and $|4,0,0\rangle_E$ peaks is reduced from the splittings at the two lower overtones.

"Local mode character" begins to develop at $\Delta v_{CD} = 5$ (Fig. 4). Despite a very strong interaction between the combination state and the two lowest energy CD-stretching vibrational states, it is clear that these latter states are unresolved and that they carry most of the CD-stretching oscillator strength. From diagonalization of the appropriate matrices, we can identify one of these lower energy states as predominantly $|5,0,0\rangle_E$. The other is very highly mixed but it has significant $|5,0,0\rangle_{A_1}$ character. For CD_3CN, the calculated splitting between the $|5,0,0\rangle_E$ state and the state with the greatest amount of $|5,0,0\rangle_{A_1}$ character is 32 cm^{-1}. This splitting is significantly reduced from the splitting at $\Delta v_{CD} = 4$.

Most of the local mode – normal mode combination states denoted "C" in Figs. 1–4 involve transitions to states with $v - 1$ quanta of CD-stretching and two quanta of DCD-bending, i.e., states of the type $|v - 1,0,0\rangle_{A_1,E} + 2\delta_{A_1,E}$. The frequencies of the DCD-bending modes ($\delta_A(CD_3I) = 938\ cm^{-1}$ (19), $\delta_E(CD_3I) = 1040\ cm^{-1}$ (17), $\delta_A(CD_3CN) = 1103\ cm^{-1}$ (18), $\delta_E(CD_3CN) = 1039\ cm^{-1}$ (18)) are approximately one-half of the CD-stretching frequencies. Thus these combination states can effectively interact with the states $|v,0,0\rangle_{A_1,E}$. Such peaks are commonly observed in the overtone spectra of several molecules (8, 13, 20–28).

Tentative assignments of these combination peaks are given in Tables 2 and 3 for the spectra of CD_3I and CD_3CN, respectively. The combinations can steal intensity from the CD-

Can. J. Chem. Downloaded from www.nrcresearchpress.com by 176.9.209.113 on 09/07/12
For personal use only.

stretching peaks through resonant or near resonant interactions. Intensity stealing is particularly pronounced for the $\Delta v_{CD} = 4$ spectra of CD_3I and for the $|3,1,0\rangle_{A_1} + 2\delta_E$ combination in the $\Delta v_{CD} = 5$ spectra of both molecules.

2. Comparison of the spectra of the deuterated and undeuterated methyl halides

The principal differences between the spectra of CD_3Z and CH_3Z molecules can be understood on the basis of the relative values of ωx and $\gamma'\omega$. A similar analysis was possible in the comparison of the spectra of CD_2Z_2 and CH_2Z_2 molecules (12). The parameter $\gamma'\omega$ is determined primarily by kinetic energy coupling, and therefore it increases markedly with the replacement of hydrogens by deuteriums. In the molecules CH_3Z, $\gamma'\omega < \omega x$ (13) ($\omega x/\gamma\omega \sim 2$ for CH_3Cl, CH_3Br, and CH_3I, $\omega x/\gamma'\omega \sim 3$ for CH_3CN). In contrast, for CD_3I and CD_3CN, $\gamma'\omega > \omega x$ ($\omega x/\gamma'\omega \sim 0.6$). This change in the relative values of these local mode parameters affects the energy ordering of the CH/CD-stretching states, the splittings between the symmetrized states $|v_1,v_2,v_3\rangle_{A_1,E}$, and the relative intensities of states $|v_1,v_2,v_3\rangle_{A_1,E}$, where at least two of v_1 and v_2 are non-zero.

In the general local mode pattern, the pure local mode states have the lowest energies among all the CH-stretching states at each overtone level. For example, for the molecules CH_3Z (13), the $|v,0,0\rangle_{A_1}$ states are lowest in energy at each overtone manifold Δv. However, for the molecules CD_3Z, the $|v-1,1,0\rangle_{A_1}$ states are the lowest in energy for $\Delta v_{CD} = 2, 3$, and 4. A primary factor which contributes to a lower energy for these latter states is the subtraction of the term (constant) $\gamma'\omega$ in the diagonal elements of the energy matrices (9, 15, 16) and the increased importance of this term in the CD_3Z molecules.

The energy separation betwen the states $|v,0,0\rangle_{A_1}$ and $|v,0,0\rangle_E$ is much greater in the spectra of CD_3Z molecules than of CH_3Z molecules. As we have noted this splitting increases with an increase in the interoscillator coupling parameter $\gamma'\omega$ because of increased vibrational mixing. Thus the greater splitting in the CD_3Z molecules is not unexpected. The splitting is larger at $\Delta v_{CD} = 2$ and 3 than it is at $\Delta v_{CD} = 4$, and it decreases even more at $\Delta v_{CD} = 5$. Therefore at some higher overtone, the states $|v,0,0\rangle_{A_1}$ and $|v,0,0\rangle_E$ will become degenerate as they are for the molecules CH_3Z at $\Delta v_{CH} \geq 4$.

In the general local mode pattern, as v increases, intensity is increasingly concentrated in transitions to the pure local mode states. For example, in the spectra of the CH_3Z molecules, transitions to the $|v,0,0\rangle_{A_1,E}$ states are the dominant CH-stretching transitions for $\Delta v_{CH} \geq 3$ (13). On the other hand, for the CD_3Z molecules, states whose components have the vibrational energy spread out over more than one methyl bond show considerable intensity at all overtone levels. In fact the local mode combination states $|3,1,0\rangle_{A_1}$, $|3,1,0\rangle_E$, $|2,1,1\rangle_{A_1}$, and $|2,1,1\rangle_E$ carry most of the CD-stetching overtone intensity at $\Delta v_{CD} = 4$. In recent theoretical work on overtone intensities in the spectra of CH_2Cl_2 and CD_2Cl_2 (29, 30), we have suggested that the dominant source of intensity for such local mode combination states is vibrational state mixing of these states with the pure local mode states. As we have noted such vibrational state mixing increases with increasing values of $\gamma'\omega$ and is particularly important for the CD_3Z molecules. Local mode – normal mode combination states "C" are also involved in intensity stealing from the pure local mode states. Their prominence in the overtone spectra of the CD_3Z molecules further perturbs the intensity distribution. The question of individual contributions to overtone band intensity within a given manifold Δv is a complicated one and requires further study.

In summary, the harmonically coupled local mode model can be used to analyze the CD-stretching peak positions in the overtone spectra of the CD_3Z molecules. However, the spectral patterns are not as simple as the familiar local mode patterns exhibited by the spectra of the CH_3Z molecules (13). Moreover, the relative increase in the interoscillator coupling parameter $\gamma'\omega$ causes a greater mixing of the zero order vibrational states in CD_3Z molcules than in CH_3Z molecules and, as a result, the vibrational analysis is not as straightforward.

Acknowledgements

We are grateful to Dr. Allan Tarr and to Mr. Michael Sowa for assistance in the matrix diagonalization procedures. We are also grateful to the Natural Sciences and Engineering Research Council of Canada for financial assistance. B.R.H. is grateful to the Canada Council for a Killam Research Fellowship.

1. B. R. Henry. Acc. Chem. Res. **10**, 207 (1977).
2. B. R. Henry. Vibrational spectra and structure. Vol. 10. *Edited by* J. R. Durig. Elsevier, New York. 1981.
3. M. L. Sage and J. Jortner. Adv. Chem. Phys. **47**, 293 (1981).
4. M. S. Child and L. Halonen. Adv. Chem. Phys. **57**, 1 (1984).
5. M. S. Child. Acc. Chem. Res. **18**, 45 (1985).
6. R. J. Hayward and B. R. Henry. J. Mol. Spectrosc. **57**, 221 (1975).
7. I. A. Watson, B. R. Henry, and I. G. Ross. Spectrochim. Acta A, **37**, 857 (1981).
8. O. S. Mortensen, B. R. Henry, and M. A. Mohammadi. J. Chem. Phys. **75**, 4800 (1981).
9. B. R. Henry, A. W. Tarr, O. S. Mortensen, W. F. Murphy, and D. A. C. Compton. J. Chem. Phys. **79**, 2583 (1983).
10. A. W. Tarr and B. R. Henry. Chem. Phys. Lett. **112**, 295 (1984).
11. A. W. Tarr and B. R. Henry. J. Chem. Phys. **84**, 1355 (1986).
12. M. K. Ahmed and B. R. Henry. J. Phys. Chem. **90**, 1081 (1986).
13. M. K. Ahmed and B. R. Henry. J. Chem. Phys. **87**, 3724 (1987).
14. The Fortran 77 program NIRCAP was written by R. K. Marat and modified by A. W. Tarr.
15. L. Halonen and M. S. Child. J. Chem. Phys. **79**, 4355 (1983).
16. A. W. Tarr. Ph.D. Thesis, The University of Manitoba, Winnipeg, Man., Canada. 1985.
17. M. Avanesoff, H. D. Thang and R. Gauman. Helv. Chim. Acta, **54**, 1013 (1971).
18. J. C. Evans and H. J. Bernstein. Can. J. Chem. **33**, 1746 (1955).
19. F. F. Cleveland and A. G. J. Meister. Chem. Phys. **19**, 1561 (1951).
20. B. R. Henry and W. R. A. Greenlay. J. Chem. Phys. **72**, 5516 (1980).
21. B. R. Henry and M. A. Mohammadi. Chem. Phys. **55**, 385 (1981).
22. H. L. Fang and R. L. Swofford. J. Chem. Phys. **72**, 6382 (1980).
23. H. L. Fang and R. L. Swofford. J. Chem. Phys. **73**, 2607 (1980).
24. B. R. Henry, M. A. Mohammadi, I. Hanazaki, and R. Nakagaki. J. Phys. Chem. **87**, 4827 (1983).
25. H. R. Dubal and M. Quack. J. Chem. Phys. **81**, 3779 (1984).
26. G. A. Voth, R. A. Marcus, and A. H. Zewail. J. Chem. Phys. **81**, 5494 (1984).
27. S. Peyerimhoff, M. Lewerenz, and M. Quack. Chem. Phys. Lett. **109**, 563 (1984).
28. J. W. Perry, D. J. Moll, A. Kuppermann, and A. H. Zewail. J. Chem. Phys. **82**, 1195 (1985).
29. O. S. Mortensen, M. K. Ahmed, B. R. Henry, and A. W. Tarr. J. Chem. Phys. **82**, 3903 (1985).
30. A. W. Tarr, D. J. Swanton, and B. R. Henry. J. Chem. Phys. **85**, 3463 (1986).

Can. J. Chem. Downloaded from www.nrcresearchpress.com by 176.9.209.113 on 09/07/12
For personal use only.

Orientational ordering of ethylene on graphite

J. Z. LARESE and L. PASSELL
Chemistry Department, Brookhaven National Laboratory, Upton, NY 11973, U.S.A.

AND

B. RAVEL
Physics Department, Wesleyan University, Middletown, CT 06457, U.S.A.

Received August 31, 1987

This paper is dedicated to Professor J. A. Morrison

J. Z. LARESE, L. PASSELL, and B. RAVEL. Can. J. Chem. **66**, 633 (1988).

A neutron diffraction study of the low temperature structure and loss of orientational order was performed for the low density phase of ethylene adsorbed on graphite. At temperatures below 30 K the ethylene molecules form a centered-rectangular herringbone structure with their C═C bond parallel to the surface. At $T > 30$ K we observe a gradual loss of orientational order and a simultaneous increase in the near-neighbor spacing. This correlates well with the onset of rotational motions about an axis perpendicular to the C═C bond which remains predominately parallel to the surface plane. We speculate that the transition to this rotator phase is accompanied by a structural change to a triangular lattice.

J. Z. LARESE, L. PASSELL, et B. RAVEL. Can. J. Chem. **66**, 633 (1988).

On a réalisé une étude par diffraction électronique de la structure présente à basse température ainsi que de la perte de l'ordre d'orientation de la phase de basse densité de l'éthylène adsorbé sur du graphite. A des températures inférieures à 30 K, les molécules d'éthylène forment une structure rectangulaire à face centrée, en forme d'arête de poisson, dans laquelle les liaisons C═C sont parallèles à la surface. Lorsque $T > 30$ K, on observe une perte graduelle de l'ordre d'orientation et une augmentation simultanée de l'espacement entre les voisins rapprochés. Ces résultats sont en bonne corrélation avec le début des mouvements de rotation autour de l'axe perpendiculaire à la liaison C═C qui reste d'une façon prédominante parallèle à la surface du plan. On croit que la transition de cette phase de rotation s'accompagne d'un changement de structure conduisant à un réseau triangulaire.
[Traduit par la revue]

Can. J. Chem. Downloaded from www.nrcresearchpress.com by 176.9.209.113 on 09/07/12
For personal use only.

1. Introduction

The structures and dynamics of rare gas and molecular films physisorbed on the basal plane of graphite have been intensively investigated during the past decade. It is by now well established that at sufficiently low temperatures molecules with non-spherical outer electron contours form structures in which the molecular axes retain distinct orientations within the unit cell. The majority of the systems studied to date have been of diatomic or elongated molecules that form herringbone structures which are related to the shape of the adsorbed molecule (1–4).

Here we describe a neutron diffraction study of the structural arrangement of one of the solid phases of ethylene on graphite — the low density (LD) phase — which is of particular interest because it is known to undergo a continuous melting transition (5–7). Ethylene, C_2H_4, is a planar molecule with carbon–carbon distance 1.338 Å, carbon–hydrogen distance 1.093 Å, and hydrogen–carbon–hydrogen angle 117.2°. Both steric arguments and configuration energy calculations suggest that the C═C axes of the molecules in the LD phase are aligned parallel to the substrate surface (8, 9). It is also known from Larese and Rollefson's nmr study of the spin–lattice relaxation time, T_1, that some type of orientational ordering occurs near 37 K, although the structure of the ordered phase could not be identified (10). Additional evidence of ordering is seen in the high resolution heat capacity measurements of Kim *et al.* (11) who find a weak heat capacity signal near 40 K which they conjecture to be associated with orientational ordering. The molecular dynamics (MD) simulations of Nosé and Klein (12) and Moller and Klein (13) on smooth and corrugated graphite substrates respectively also suggest the formation of an orientationally-ordered phase.

Our previous efforts to detect orientational ordering in the LD-solid phase of ethylene on graphite with neutrons had been inconclusive (8). Encouraged by the nmr and heat capacity studies, however, and by the success of the MD simulations in describing the melting behavior of the films, we set out once again to examine this challenging question.

2. Experimental details

The neutron scattering experiments were performed at Brookhaven National Laboratory's High Flux Beam Reactor on the H4M triple axis spectrometer operated in the elastic mode. The incident neutron wave number was set at 2.65 $Å^{-1}$ using a pyrolytic graphite (PG) monochromator. A PG filter was used before the sample to suppress any higher order contamination present in the incident beam. Collimation before and after the sample was 40′. No collimation was used in front of the detector. This resulted in an instrumental resolution of 0.0263 $Å^{-1}$ full width at half maximum (FWHM).

The substrate was a vermicular form of crystalline graphite (Union Carbide GTA grade) which was baked *in vacuo*, recompressed and then loaded in a sample can in a helium-filled glove box. The sample was mounted on the cold tip of a closed-cycle helium refrigerator which was regulated to within 0.1 K of the desired temperature. Deuterated ethylene (C_2D_4) was used in preference to C_2H_4 because it is superior as a coherent scatterer of neutrons.

Diffraction profiles from the ethylene film were obtained as usual by plotting the difference between the scattering with and without adsorbate in the sample cell. The C_2D_4 gas was loaded into the cell at ~140 K and then cooled immediately to 80 K. It was then slowly (~1 K/min) cooled to 50 K where it was annealed for about 3 h. This procedure was followed because previous studies indicated that a slow relaxation process, perhaps due to some type of structural readjustment, occurs between 50 and 60 K.

The ethylene coverage (X) used throughout this study was 0.6 monolayers, where $X = 1.0$ corresponds to a completed $\sqrt{3} \times \sqrt{3}$ monolayer as determined from a nitrogen isotherm. $X = 0.6$ monolayers corresponds to the LD phase as identified in an earlier study (8). It should be pointed out that at all coverages and temperatures the ethylene monolayer is incommensurate with the graphite substrate.

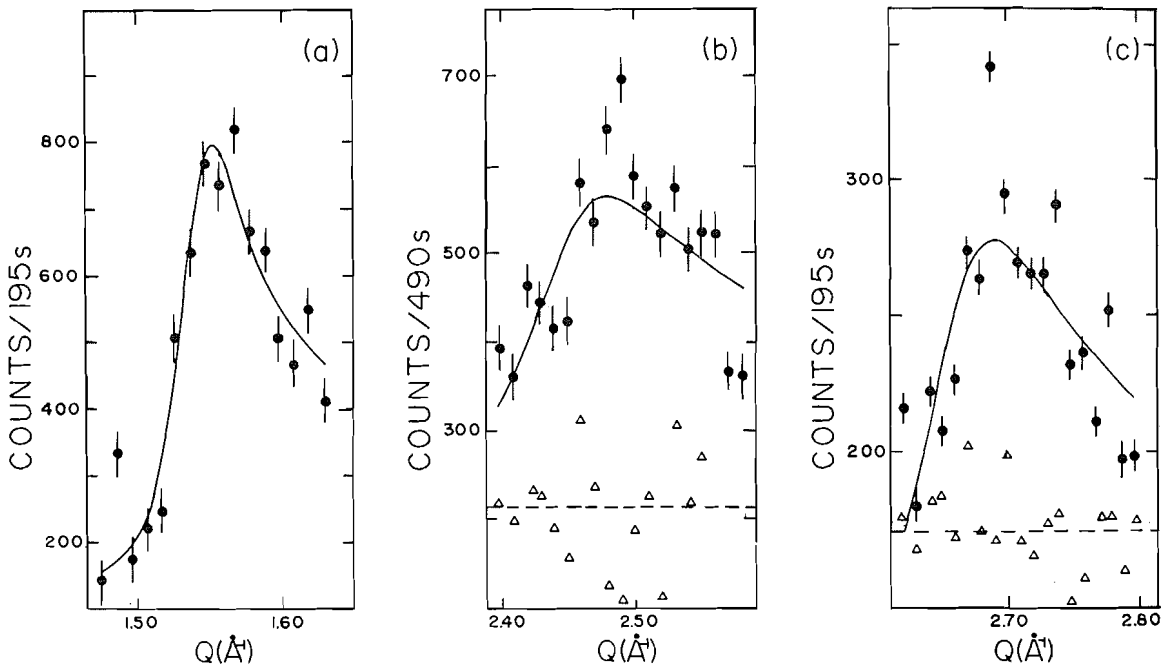

FIG. 1. Diffraction profiles (solid dots) of the (*a*) (1,1), (*b*) (2,0), and (*c*) (2,1) index peaks for a 0.6 monolayer ethylene film at 20 K. The solid lines represent a least-square fit to the experimental data using a powder-averaged Lorentzian lineshape folded with the instrumental resolution. The open triangles in (*b*) and (*c*) are scans made at 50 K. They show clearly that no peaks are present in the difference spectrum at the higher temperature.

Can. J. Chem. Downloaded from www.nrcresearchpress.com by 176.9.209.113 on 09/07/12
For personal use only.

The first experiments were made using a sample can constructed out of aluminum. Unfortunately, the aluminum (111) peak appears at $Q = 2.69$ Å^{-1} which is close to the scattering vector range where the superlattice peaks of the orientationally-ordered phase were predicted to appear. Later measurements were therefore made with a copper can, chosen because its contribution to the background scattering (i.e. the (111) copper Bragg peak) would be outside the range of experimental interest. The amount of graphite loaded into the copper cell was roughly half of that in the aluminum cell. This resulted in a decrease of monolayer gas capacity by the same fraction. Except for a change in the background scattering due to the different sample cans, the results of both runs were the same.

3. Results

Figure 1 shows the results of elastic diffraction scans performed at ~20 K with a C_2D_4 coverage of $X = 0.6$. Three diffracted peaks can clearly be resolved within the q range studied. All have the "sawtooth" profiles characteristic of diffraction from randomly-orientated, two-dimensional crystalline arrays. Using the unit cell constants predicted by Moller and Klein (13), these index respectively as the (1,1) (*a*), (2,0) (*b*), and (2,1) (*c*) peaks of a centered-rectangular lattice. An increase in scattering consistent with the existence of a fourth diffracted peak, the (0,2), is evident near $Q \sim 1.76$ Å^{-1}. Unfortunately, the scan was not extended beyond this point because previous attempts to resolve weak peaks lying in the neighborhood of the intense graphite (002) peak ($Q \sim 1.87$ Å^{-1}) have been unsuccessful. The solid lines in the figure are fits to the experimental data using a powder-averaged Lorentzian lineshape folded with the instrumental resolution.

Figure 2*a* illustrates the temperature dependence of the integrated intensity for the three peaks in Fig. 1. In Fig. 2(*b*) we show how the lowest index peak (which becomes the (1,0) peak in the orientationally disordered LD phase) shifts with temperature. Empty cell scans were taken at 20 and 55 K so that any thermal dependence of the background could be compensated. No evidence of peaks other than that observed at $Q \sim 1.53$ Å^{-1} was detected for $T > 40$ K. In interpreting the total integrated intensities for the ranges 2.65–2.8 Å^{-1} and 2.4–2.55 Å^{-1} in Fig. 2*a* it is important to note that both superlattice peaks sit on the trailing edge of the very intense peak at 1.53 Å^{-1}. Above 40 K all of the intensity can be acounted for as background scattering and scattering from the trailing edge of the $q = 1.53$ Å^{-1} peak: the peaks at 2.49 and 2.69 Å^{-1}, i.e. the superlattice peaks of the fully-ordered structure, have disappeared. Figures 1*b* and 1*c* show difference profiles at $T \sim 50$ K for both peaks which illustrate that no intensity is left in the peaks above the transition. The decrease in integrated intensity in the 1.5–1.59 Å^{-1} range at higher temperatures is due to the Debye–Waller effect. Figure 3 gives the results of a detailed examination of the decrease in integrated intensity for $30 \text{ K} < T < 40$ K. The dotted lines estimate the background level at 40 K.

Figure 2*c* shows the rotational diffusion rates as a function of temperature. These data, derived from a separate incoherent, quasi-elastic neutron scattering study of C_2H_4 (6), demonstrate — as the loss of orientational order implies — that rotational diffusive motions about an axis with an effective proton radius of ~1.5 Å (essentially all of the observed incoherent scattering is produced by the protons) occurs at ~35 K. The reader is reminded that the proton radius for ethylene rotations about an axis normal to the film plane is 1.55 Å.

4. Discussion

Table 1 provides a comparison of the experimental centered-rectangular cell constants with the MD predictions of Moller and Klein (13). The experimental values were determined from the peak positions derived from lineshape analysis. The agreement is very satisfactory. The possibility that the peak near $q \sim 2.65$ Å^{-1} is the superposition of two closely spaced yet unresolved peaks (i.e. the (0,3) and the (2,1)) leads to some systematic uncertainty in our cell constants.

To test the MD orientational parameters a structure factor

Can. J. Chem. Downloaded from www.nrcresearchpress.com by 176.9.209.113 on 09/07/12
For personal use only.

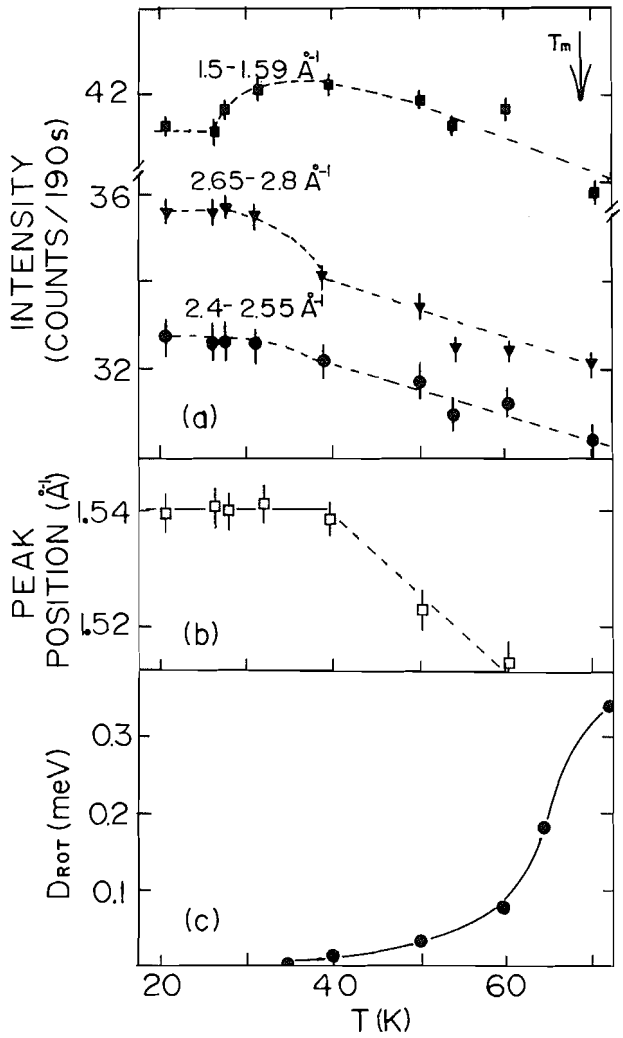

FIG. 2. (*a*) Integrated intensities, for the Q ranges indicated, for a 0.6 monolayer ethylene film on graphite. Shown are the signal plus background intensity. The dashed lines have no theoretical significance. The intensity units are multiples of 1000. T_m indicates where melting occurs. (*b*) Shift in peak position as a function of temperature for the (1,1) centered-rectangular lattic peak $T < 40$ K or the (1,0) triangular lattice peak $T > 40$ K. The solid and dashed lines have no theoretical significance. (*c*) Rotational diffusion rates derived from an incoherent, quasi-elastic neutron scattering study of a 0.6 monolayer ethylene film. The best fit to the rotational diffusion data was obtained with a 1.5 Å radius of rotation. The solid line has no theoretical significance.

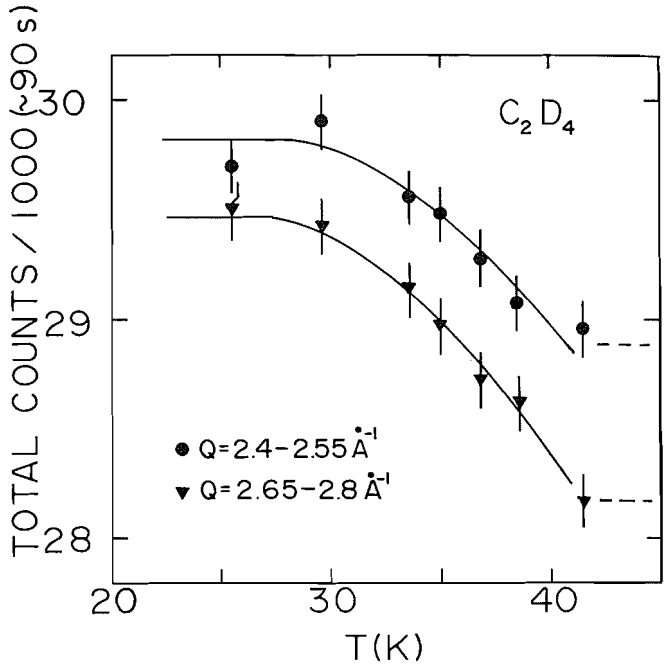

FIG. 3. Detailed measurement of the temperature dependence of integrated intensity over the Q ranges indicated for a 0.6 monolayer ethylene film. The dashed lines are the estimated background intensities. The solid lines have no theoretical significance.

TABLE 1. Ethylene cell constants

Parameter	Value	
	MD	Experimental
a (Å)	4.95	5.03±0.05
b (Å)	7.05	7.05±0.05

calculation was performed using the molecular configurations from the simulation. The relative intensity of the three observed peaks agrees qualitatively with expectations, however, our inability to recover a greater number of reflections limits what we can say about the orientation of the molecules. Past neutron experiments employing a multi-detector array (14) to cover a broad Q range demonstrate that orientational parameters can be obtained for overlayer systems and future experiments incorporating such a device are, in fact, already being planned.

Examining the results shown in Fig. 2 and Fig. 3 suggests the following interpretation. First, the intensities of the (2,0) and the (2,1) peaks decrease steadily between 30–40 K indicating the onset of rotational disorder. Over the same temperature interval the intensity of the (1,1) peak ($q \sim 1.54$ Å^{-1}) grows. This behavior is consistent with loss of orientational order and a redistribution of scattered intensity back into the primary peak of the high-temperature orientationally-disordered phase. Second, we see in Fig. 2*b* that the position of the (1,1) peak remains fixed, apparently until most of the orientational order is destroyed (i.e. $T < 40$ K), at which point it shifts progressively toward lower q. This clearly shows that the 2D lattice expands once the orientational order is lost. The rotational diffusion constants of Fig. 2*c*, indicating the onset of rotational motion about an axis perpndicular to the C=C bond (radius 1.5 Å), are, as we earlier noted, consistent with the loss of the ordered structure.

The above facts seem to point naturally to the following physical picture. Once rotational diffusion about an axis perpendicular to the C=C bond becomes significant, the unit cell expands to minimize the energy associated with the overlap of the outer electron contours of the molecules. Recall that a centered-rectangular cell with sides in the ratio of $1 \times \sqrt{3}$ is a non-primitive unit cell for an equilateral triangular lattice. Therefore, associating the thermal expansion of the ordered solid with a change to a triangular structure can be easily understood. Molecules executing random rotations of the type depicted in Fig. 4*a* project a circular cross-section onto the surface. Combining the experimental results presented above with the fact that the simplest packing of circular discs in two dimensions is triangular, one concludes that a change in symmetry from centered rectangular (unit cell dimensions in the ratio $1 \times \sqrt{2}$) to triangular occurs once the loss of orientational

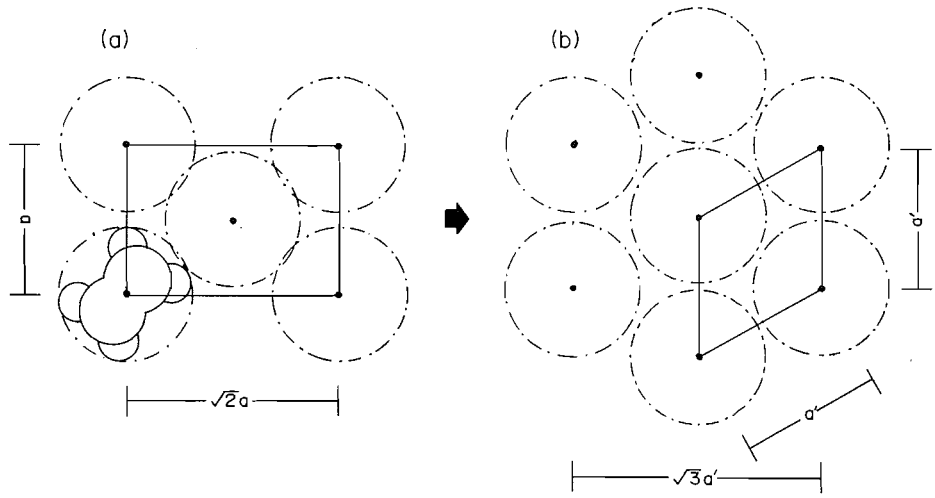

FIG. 4. (a) Schematic view of the centred-rectangular structure with sides of length a and $\sqrt{2}a$. Dash–dotted lines indicate the estimated outer electron contours of ethylene molecules rotating about an axis perpendicular to C=C bond at $T > 40$ K. Notice that some overlap occurs. (*b*) Schematic view of the same molecules on an expanded equilateral triangular lattice with lattice constant a'. Note the analogy with the centered-rectangular structure.

order is complete. Figure 4 shows schematically how this might happen using a simple hard sphere model.

A comment concerning the absence of any higher index peaks for the higher temperature LD triangular phase is necessary. At $q \sim 2.65$ Å^{-1}, for example, the (2,1) index peak would be expected to appear. The only peak observed at $T > 40$ K, however, was the (1,0) peak at ~ 1.53 Å^{-1}. This is because the rapid reorientation of the ethylene molecules above 40 K causes a redistribution of the scattered intensity. Several years ago, Press and Eckert (15) suggested a form factor for ethylene molecules in bulk ethylene which assumes spherical reorientation of the molecules. Examination of this function shows that the intensity of the (2,1) peak would be about 50 times smaller than the (1,0) peak, making it undetectable at our level of sensitivity.

5. Conclusion

Using neutron diffraction we have determined the low temperature unit cell of the orientationally-ordered LD solid phase of ethylene on graphite and observed the loss of orientational order at higher temperatures. The experimental cell constants (5.03 ± 0.05 Å, 7.05 ± 0.05 Å) for the ordered phase agree well with the MD simulations (4.95 Å, 7.05 Å). A definitive determination of the orientational arrangement of the molecules within the unit cell was not possible since an insufficient number of diffracted peaks were observed. Nonetheless, our experimental data strongly suggest a change from rectangular to triangular structure once orientational disorder sets in.

The transition to the orientationally disordered state (as determined by the thermal variation of the integrated intensity) appears to be continuous. This is consistent with the heat capacity results of Kim *et al.* (11). No attempt was made to extract a critical exponent due to the poor statistics associated with the weak diffraction peaks.

6. Acknowledgments

It is a pleasure to acknowledge useful conversations with Moses Chan, Tony Heidemann, Mike Klein, Mike Moller, Dieter Richter and Bill Steele. We thank R. Thomas for his assistance.

This work was supported by the Division of Materials Sciences, U.S. Department of Energy under contract DE-AC02-76CH00016.

1. A. B. HARRIS and A. J. BERLINSKY. Can. J. Phys. **57**, 1852 (1979).
2. R. D. DIEHL, M. F. TONEY, and S. C. FAIN, JR. Phys. Rev. Lett. **48**, 177 (1982); J. ECKERT, W. D. ELLENSON, J. B. HASTINGS, and L. PASSELL. PHYS. REV. LETT. **43**, 1329 (1979).
3. H. YOU and S. C. FAIN. Surf. Sci. **151**, 361 (1985).
4. J. SUZANNE, J. L. SEGUIN, H. TAUB, and J. P. BIBERIAN. Surf. Sci. **125**, 153 (1983).
5. H. K. KIM, Q. M. ZHANG, and M. H. W. CHAN. Phys. Rev. Lett. **56**, 1579 (1986).
6. J. Z. LARESE, L. PASSELL, A. D. HEIDEMANN, D. RICHTER, and J. P. WICKSTED. To be published.
7. M. MOLLER and M. L. KLEIN. To be published.
8. S. K. SATIJA, L. PASSELL, J. ECKERT, W. ELLENSON, and H. PATTERSON. Phys. Rev. Lett. **51**, 411 (1983); B. H. GRIER, L. PASSELL, J. ECKERT, H. PATTERSON, D. RICHTER, and R. J. ROLLEFSON. PHYS. REV. LETT. **53**, 814 (1984).
9. M. SUTTON, S. G. J. MOCHRIE, and R. J. BIRGENEAU. Phys. Rev. Lett. **51**, 407 (1983).
10. J. Z. LARESE and R. J. ROLLEFSON. Surf. Sci. **127**, L172 (1983).
11. H. K. KIM, Y. P. FEND, Q. M. ZHANG, and M. H. W. CHAN. To be published.
12. S. NOSÉ and M. L. KLEIN. Phys. Rev. Lett. **53**, 818 (1984).
13. M. A. MOLLER and M. L. KLEIN. Preprint.
14. H. TAUB. Neutron scattering studies of structure, phase transitions, and dynamics of commensurate, herringbone monolayers, physisorbed on graphite. *In* Time domain in surface and structural dynamics. NATO ASI series. *Edited by* G. J. Lang and F. Grand Jean. Reidel Publ., Dordrecht. 1987.
15. W. PRESS and J. ECKERT. J. Chem. Phys. **65**, 4362 (1976).

Can. J. Chem. Downloaded from www.nrcresearchpress.com by 176.9.209.113 on 09/07/12
For personal use only.

Thermodynamic properties of multicomponent electrolyte solutions in mixed solvents. 5. HCl + NaCl + urea + water at 278.5–318.15 K

DIAN-YUAN MEN, JIA-ZHEN YANG, CHUN-YU LIANG, LI-TIAN ZHANG, HUAN GAO, AND RU-LAN YANG
Department of Chemistry, Liaoning University, Shenyang, People's Republic of China

Received August 4, 1987

This paper is dedicated to Professor James A. Morrison

DIAN-YUAN MEN, JIA-ZHEN YANG, CHUN-YU LIANG, LI-TIAN ZHANG, HUAN GAO, and RU-LAN YANG. Can. J. Chem. **66**, 637 (1988).

This paper reports electromotive force measurements of the cells

$$\text{Pt}|\text{H}_2(\text{g, 101.325 kPa})|\text{HCl}(m_A), x \text{ urea}, (1-x)\text{H}_2\text{O}|\text{AgCl}|\text{Ag} \quad \text{(A)}$$

and

$$\text{Pt}|\text{H}_2(\text{g, 101.325 kPa})|\text{HCl}(m_A), \text{NaCl}(m_B), x \text{ urea}, (1-x)\text{H}_2\text{O}|\text{AgCl}|\text{Ag} \quad \text{(B)}$$

in mixed solvents of urea, mole fraction $x = 0.05$, at five temperatures from 278.15 to 318.15 K. The standard potentials of Ag–AgCl electrode in mixed solvents were obtained from the emf of cell (A) for HCl of molality m_A from 0.02 to 0.11 mol kg^{-1}, both by extrapolation on the basis of an extended Debye–Hückel equation and by a polynomial approach proposed in this paper on the basis of Pitzer's electrolytic solution theory. The standard free energies of transfer for HCl are discussed. The activity coefficients of HCl γ_A in HCl + NaCl + urea + water have also been obtained from the emf of cell (B) at constant total ionic strength $I = 0.5$, 1.0, 1.5, and 2.0 mol kg^{-1}. The experimental results show that HCl obeys Harned's rule and log γ_A is a linear function of absolute temperature T. They also indicate that the relative partial molar enthalpy of HCl obeys a similar Harned's rule.

DIAN-YUAN MEN, JIA-ZHEN YANG, CHUN-YU LIANG, LI-TIAN ZHANG, HUAN GAO et RU-LAN YANG. Can. J. Chem. **66**, 637 (1988).

On a effectué des mesures de force électromotrice sur les cellules

$$\text{Pt}|\text{H}_2(\text{g, 101.325 kPa})|\text{HCl}(m_A), x \text{ urée}, (1-x)\text{H}_2\text{O}|\text{AgCl}|\text{Ag} \quad \text{(A)}$$

et

$$\text{Pt}|\text{H}_2(\text{g, 101.325 kPa})|\text{HCl}(m_A), \text{NaCl}(m_B), x \text{ urée}, (1-x)\text{H}_2\text{O}|\text{AgCl}|\text{Ag} \quad \text{(B)}$$

dans des solvants mixtes, à une fraction molaire d'urée $x = 0{,}05$ et à cinq températures allant de 278,15 à 310,15 K. On a obtenu les potentiels standards pour l'électrode Ag–AgCl dans des solvants mixtes en utilisant les fem de la cellule (A) pour des molalités de HCl m_A allant de 0,08 à 0,11 mol kg^{-1} et en faisant appel soit à une extrapolation sur le base d'une équation de Debye–Hückel étendue soit à l'approche polynomiale proposée dans ce travail sur la base de la théorie des solutions électrolytiques de Pitzer. On discute des énergies libres standard de transfert du HCl. On a déduit les coefficients d'activité du HCl (γ_A) dans le système HCl + NaCl + urée + eau à partir des fem de la cellule (B), à force ionique totale constante de $I = 0{,}5$, 1,0, 1,5 et 2,0 mol kg^{-1}. Les résultats expérimentaux démontrent que le HCl obéit à la loi de Harned et que le log γ_A est une fonction linéaire de la température absolue. Ils indiquent aussi que l'enthalpie molaire partielle relative du HCl obéit à une loi semblable à celle de Harned.
[Traduit par le journal]

Introduction

Thermodynamic properties of mixed electrolytes in aqueous solution have been widely investigated by the emf method, but very rarely in mixed solvents of water with organic solvent. Except for the work of Akerlof *et al.* (1) for HCl + NaCl at a constant ionic strength $I = 1$ mol kg^{-1} in methanol + water and that of Khoo and co-workers (2, 3) for HCl + KCl (or NH_4Cl) in the same mixed solvents at the same ionic strength, the only other reported work of comparable precision appears to be ours (4–6) for HCl + NaCl at $I = 0.1$, 0.5, 1.0, 2.0, and 3.0 mol kg^{-1} in mixed solvents.

In a continuation of previous studies, the present investigation has been carried out by using HCl–NaCl in $x = 0.05$ urea + water mixture. The structure of urea + water is of great importance in understanding protein denaturation in NaCl + urea + water. This paper consists of two parts. In the first, using the emf of cell (A) without liquid junction

$$\text{Pt}|\text{H}_2(\text{g, 101.325 kPa})|\text{HCl}(m_A), x \text{ urea}, (1-x)\text{H}_2\text{O}|\text{AgCl}|\text{Ag} \quad \text{(A)}$$

where m_A is the molality of HCl, the standard electrode potentials of the Ag–AgCl electrode in the mixed solvent at each temperature were determined, both by extrapolation on the basis of the extended Debye–Hückel equation and by a polynomial approach proposed in this paper on the basis of Pitzer's electrolytic solution theory (7, 8); the standard free energies of transfer for HCl are discussed. In the second, using the emf of cell (B)

$$\text{Pt}|\text{H}_2(\text{g, 101.325 kPa})|\text{HCl}(m_A), \text{NaCl}(m_B), x \text{ urea}, (1-x)\text{H}_2\text{O}|\text{AgCl}|\text{Ag} \quad \text{(B)}$$

where m_B is the molality of NaCl, the activity coefficients γ_A of HCl were obtained at total ionic strength $I = 0.50$, 1.00, 1.50, and 2.00 mol kg^{-1} in the mixture at each temperature. The results show that HCl still obeys Harned's rule and indicate the linear relation between log γ_A and absolute temperature T, and that the relative partial molar enthalpy of HCl similarly obeys Harned's rule.

2. Experimental

Urea of A.R. reagent grade was recrystallized twice from 50 mass% alcohol + water and dried *in vacuo* at 303 K.

Hydrochloric acid used in all preparations of the solution was

Can. J. Chem. Downloaded from www.nrcresearchpress.com by 176.9.209.113 on 09/07/12
For personal use only.

TABLE 1. The standard electrode potential of Ag|AgCl in pure water

T(K)	278.15	288.15	298.15	308.15	318.15
E^0_{exp}(V)	0.23412	0.22859	0.22236	0.21558	0.20823
E^0_{lit}(V)	0.23410	0.22857	0.22238	0.21566	0.20836

prepared from G.R. reagent grade by distilling in an all-glass apparatus. Only the middle fraction was collected. The stock solution of HCl was standardized gravimetrically by weighing silver chloride. The average difference among five replicate determinations was less than ±0.02%. The water, which was deionized, was distilled using a quartz still, and its conductance was $(0.9–1.2) \times 10^{-4}\ \Omega^{-1}\ m^{-1}$. NaCl of reagent grade was dried for 3 h before use. All solutions to be measured were freshly prepared by weight with correction for air buoyancy. The concentrations of all solutions were known to within ±0.02%.

The Ag|AgCl electrodes were of the thermal electrolytic type (9) aged in 0.1 mol kg^{-1} HCl, which was deoxygenated by bubbling hydrogen. Three days after preparation, the finished electrodes were compared and had bias potentials of usually less than ±0.05 mV. Standard electrode potentials of Ag|AgCl in pure water were measured by Bates's method (10) and, with the literature data, are listed in Table 1. The hydrogen electrodes were lightly coated with platinum black before each measurement according to the method of Hills and Ives (11). Electrolytically generated hydrogen, purified in the usual manner (11), served as the source of hydrogen.

The cells were of all-glass construction with three isothermal presaturators containing the experimental solution. The cells were thermostated at each temperature with an accuracy of ±0.02 K.

All measurements were made with two Ag–AgCl electrodes and two hydrogen electrodes. Equilibrium was reached about 2–3 h after the initiation of hydrogen bubbling. The potentials of the cells were measured at 298.15, 278.15, 288.15, 298.15, 308.15, 318.15, and 298.15 K by a UJ-25 type potentiometer, which was calibrated against a standard cell. A mirror-type galvanometer was used as a null detector. The criterion for attainment of equilibrium was a steady reading to the nearest 0.05 mV for a period of about 1 h. The standard deviation of readings for four cells was less ±0.1 mV. The emf was measured at 298.15 K at the beginning, in the middle, and at the end of each run. These three readings at 298.15 K agreed within ±0.07 mV. The atmospheric pressure was measured by a barometer and was calibrated for temperature, altitude, and degree of latitude. Observed values of emf were converted to a hydrogen partial pressure of 101.325 kPa.

The densities of solvent mixtures over the range of temperatures involved were determined by the usual pycnometric technique. The dielectric constants of the solvent mixtures were measured by means of a DK-300 type dekemeter.

3. Results and discussion

The emf's of cell (A), which were measured at temperatures from 278.15 to 318.15 K at HCl molalities from 0.02 to 0.11 mol kg^{-1} in mixed solvents of 0.05 mole fraction of urea, are listed in Table 2 where each value of emf is the average of four cells.

1. Standard emf

The most common method used to evaluate the standard potential involves the graphical extrapolation of linear plots of emf of the cell against concentration of HCl on the basis of the extended Debye–Hückel equation, as in the following:

$$[1]\quad E^{0\prime} = E + 2k \log (m_A/m^0_A) - 2kA\sqrt{(m_A\rho)}/[1 + a^0B \times \sqrt{(m_A\rho)}] - 2k \log (1 + 0.002m_AM) = E^0_A - 2bm_A$$

where $m^0_A = 1$ mol kg^{-1}, E^0_A is the standard potential of the cell on the molal scale, E is the observed emf of the cell, ρ is the density of mixed solvent, M is the mean molecular weight of the solvent, $k = RT\ (\ln 10)/F$, R is the gas constant, T is the absolute temperature, F is Faraday's constant, a^0 is the ion-size parameter, chosen as equal to 0.4 nm, and A and B are the Debye–Hückel parameters. When $E^{0\prime}$ was plotted against m_A at each temperature, a good straight line was obtained (see Fig. 1). All linear correlation coefficients r were over 0.99. The intercepts of these straight lines are the standard emf, E^0_M, of cells whose values and standard deviation σ all are listed in Table 2.

Because the ion-size parameter a^0 cannot be measured, the chosen value of a^0 is an arbitrary decision and causes some uncertainty in the extrapolation on the basis of the extended Debye–Hückel equation. However, we here propose a polynomial approach to determine E^0_M on the basis of Pitzer's recent electrolyte solution theory.

The relevant equations for a 1–1 single electrolyte solution derived by Pitzer are

$$[2]\quad \ln \gamma_{MX} = f^\gamma + mB^\gamma_{MX} + m^2C^\gamma_{MX}$$

where each symbol has the same meaning as in Pitzer's article (12, 13). Since the molality of HCl used in the experiment is so dilute, C^γ_{MX} may be recognized as zero. Other quantities in eq. [2] are defined as follows:

$$[3]\quad f^\gamma = -A_\phi x$$

$$[4]\quad x = I^{1/2}(1 + bI^{1/2}) + (2/b)\ln(1 + bI^{1/2})$$

$$[5]\quad B^\gamma_{MX} = 2\beta^{(0)} + 2\beta^{(1)}y$$

$$[6]\quad y = [1 - \exp(-\alpha I^{1/2})(1 + \alpha I^{1/2} - 1/2\alpha^2 I)]/(\alpha^2 I)$$

$$[7]\quad A_\phi = (1/3)(2\pi N_0\rho)^{1/2}(e^2/DkT)^{3/2}$$

where N_0 is Avogadro's constant, D is the dielectric constant, k is Boltzmann's constant, e is the electron charge, and $\beta^{(0)}$ and $\beta^{(1)}$ are parameters characteristic of the electrolyte. According to Khoo's suggestion (12), $\alpha = 2$, $b = 1.2$ in mixed solvents. Then, the Nernst equation reduces to

$$[8]\quad E^{0\prime} = E + 2k' \ln(m/m_0) - 2k'A_\phi x = E^0_M - 2mk'\beta^{(0)} - 2mk'\beta^{(1)}y$$

where $k' = RT/F$ and $m_0 = 1$ mol kg^{-1}. Equation [8] is homologous to the following polynomial:

$$[9]\quad u = a_0f_0 + a_1f_1 + a_2f_2$$

Setting $f_0 = 1$, $f_1 = -2mk'$, $f_2 = -2mk'y$, coefficients of the polynomial were obtained by a polynomial approach program on a computer, where $a_0 = E^0_M$, which were noted as E^0_M(P) and are listed in Table 2. These results show that E^0_M(P) obtained by the polynomial approach nearly agree with those obtained by extrapolation. We also examined other authors' experimental data (13–15) by the method proposed in this paper, and the calculated results are listed in Table 3. From Table 3, the standard emf's of cells obtained by the polynomial approach on the basis of Pitzer's theory agree with traditional extrapolation, within the experimental error.

Can. J. Chem. Downloaded from www.nrcresearchpress.com by 176.9.209.113 on 09/07/12
For personal use only.

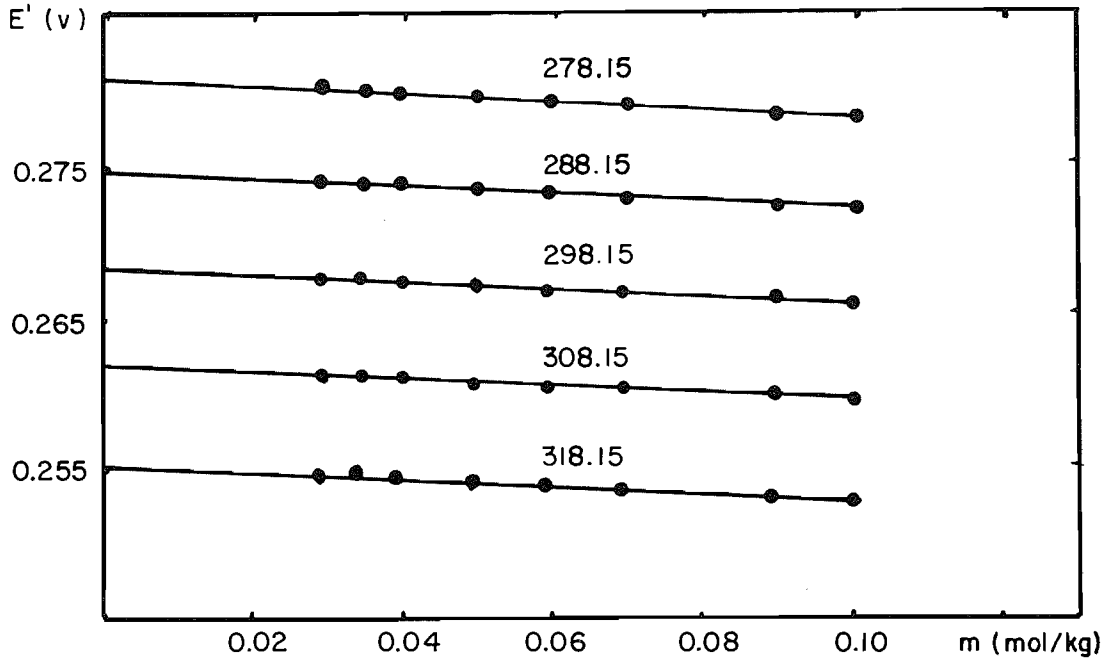

FIG. 1. Plot of $E^{0'}$ against m.

TABLE 2. The values of emf and standard emf of cell (A) at 278.15–318.15 K

$m \times 10^2$ (mol kg^{-1})	T(K)				
	278.15	288.15	298.15	308.15	318.15
2.9184	0.45588	0.45625	0.45623	0.45633	0.45582
3.4778	0.44748	0.44746	0.44772	0.44728	0.44725
3.9425	0.44026	0.44193	0.44143	0.44104	0.44010
4.9709	0.43108	0.43056	0.42997	0.42900	0.42809
5.9475	0.42297	0.42217	0.42127	0.42007	0.41886
6.9359	0.41578	0.41480	0.41369	0.41220	0.41074
8.9755	0.40405	0.40263	0.40110	0.39927	0.39736
10.026	0.39886	0.39732	0.39561	0.39363	0.39157
E^0_M (D–H)	0.28030	0.27418	0.26791	0.26147	0.25477
r	−0.97	−0.96	−0.99	−0.98	−0.94
$\sigma \times 10^4$	1.4	1.6	0.7	1.2	1.9
E^0_M (P)	0.28098	0.27497	0.26837	0.26243	0.25505
R_2	1.3	1.6	0.6	0.8	2.0

r: linear correlation coefficient.

The standard emf on the mole fraction scale E^0_N has been calculated by means of the relationship

[10] $E^0_N = E^0_M - 2k' \ln(1000/M)$

The values of E^0_N could be expressed as a function of temperature in the following form, for pure water:

[11] $${}^{W}E^0_N = 0.14972 + (4.6208 \times 10^{-4})T - (2.9904 \times 10^{-6})T^2$$

and for mixed solvent:

[12] $${}^{S}E^0_N = 0.37426 - (7.4871 \times 10^{-4})T - (9.4296 \times 10^{-7})T^2$$

2. Transfer quantities of HCl

Since solvent effects on the thermodynamic properties of HCl related to the present study will be best reflected in the standard free energy of transfer (ΔG^0_t), the entropy (ΔS^0_t), and the enthalpy (ΔH^0_t) changes accompanying the transfer of a mole of HCl from water (w) to mixed solvent (s), these were evaluated at different temperatures by application of the following relations:

[13] $\Delta G^0_t = -({}^{S}E^0_N - {}^{W}E^0_N)$

[14] $\Delta S^0_t = F(\partial \Delta E^0_N / \partial T)$

[15] $\Delta H^0_t = \Delta G^0_t + T\Delta S^0_t$

The mole fraction scale has been used, because that will eliminate effects arising from concentration changes of HCl accompanying the transfer process and will reflect solvent effects more clearly. The values obtained from eqs. [13]–[15] are listed in Table 4.

As can be seen from the table, all negative ΔG^0_t's suggest that the transfer of HCl from water to the urea–water mixture is favourable. This relative ease of transfer of HCl is of course

Can. J. Chem. Downloaded from www.nrcresearchpress.com by 176.9.209.113 on 09/07/12
For personal use only.

Can. J. Chem. Downloaded from www.nrcresearchpress.com by 176.9.209.113 on 09/07/12
For personal use only.

TABLE 3. The standard emf of different cells

System	Parameter	T(K) 278.15	283.15	288.15	293.15	298.15	303.15	308.15	313.15	318.15	323.15	328.15
Pt|H_2(g)|HCl(m),	E^0_M(V)*	0.19573	0.19038	0.18512	0.17964	0.17429	0.16906	0.16349	0.15765	0.15108	0.14475	0.13863
H_2O, 50% diglyme|	E^0_M(V)	0.19597	0.19057	0.18538	0.17985	0.17451	0.16931	0.16384	0.15806	0.15138	0.14508	0.13898
AgCl|Ag	$\beta^{(0)}$	−0.30699	−0.29837	−0.21040	−0.27470	0.13121	−0.18642	−0.09500	−0.00100	−0.01659	−0.03675	−0.06006
	$\beta^{(1)}$	−0.80343	−0.69062	−0.85391	−0.71986	−0.71074	−0.77687	−0.96295	−1.04534	−0.84641	−0.86805	−0.89151
	$R_2 \times 10^5$	9.16	5.30	6.89	4.94	1.53	5.79	5.35	4.50	6.04	4.58	2.15
	$\sigma \times 10^4$	−2.4	−1.9	−2.6	−2.1	−2.2	−2.5	−3.5	−4.1	−3.1	−3.3	−3.5
Pt|H_2(g)|HBr(m),	E^0_M(V)*	0.06951	0.06492	0.05991	0.05474	0.04952	0.04474	0.03913	0.03350	0.02616	0.02114	0.01467
H_2O, 50% diglyme|	E^0_M(V)	0.06953	0.06490	0.05996	0.05472	0.04953	0.04471	0.03900	0.03350	0.02617	0.02109	0.01457
AgBr|Ag	$\beta^{(0)}$	0.24309	0.25450	0.35942	0.29693	0.33469	0.23708	0.17008	0.33637	−0.54609	0.39689	0.38659
	$\beta^{(1)}$	−2.08832	−1.98284	−2.11718	−1.98026	−2.01334	−1.94580	−1.77445	−2.00550	−2.01367	−1.89220	−1.79808
	$R_2 \times 10^5$	3.77	3.63	4.50	1.54	4.56	2.16	3.19	3.70	1.59	6.14	4.40
	$\sigma \times 10^5$	−2.0	2.0	−5.0	2.0	−1.0	3.0	13	0.0	−1.0	5.0	10
Pt|H_2(g)|HCl(m),	E^0_M(V)*				0.19783	0.19307	0.18820	0.18306	0.17795	0.17259	0.16714	0.16160
H_2O, 50% EC|	E^0_M(V)				0.19793	0.19312	0.18825	0.18316	0.17791	0.17262	0.16714	0.16159
AgCl|Ag	$\beta^{(0)}$				−0.26930	−0.27667	−0.20965	−0.18958	−0.16914	−0.13142	−0.03444	−0.06117
	$\beta^{(1)}$				−0.17582	−0.12989	−0.25984	−0.18791	−0.30807	−0.39828	−0.61916	−0.85880
	$R_2 \times 10^5$				7.19	6.86	6.29	6.26	9.84	1.86	1.37	2.15
	$\sigma \times 10^5$				10	−5.0	−5.0	−10	−4.0	−3.0	0	1.0
Pt|H_2(g)|HBr(m),	E^0_M(V)*	0.07686	0.07511	0.07323	0.07111	0.06888	0.06644	0.06376	0.06094	0.05798	0.05456	0.04935
H_2O, 10% tetrahydrofuran|	E^0_M(V)	0.07657	0.07488	0.7295	0.07075	0.06853	0.06604	0.06332	0.06042	0.05777	0.05428	0.04945
AgBr|Ag	$\beta^{(0)}$	−0.39993	−0.31195	−0.35452	−0.45689	−0.41206	−0.45487	−0.47280	−0.52802	−0.15573	−0.16410	0.47133
	$\beta^{(1)}$	−0.16459	−0.31162	−0.23688	−0.06137	−0.14151	−0.06357	−0.00863	0.12293	−0.48610	−0.34399	−0.03313
	$R_2 \times 10^5$	5.89	6.48	7.32	5.98	5.50	4.43	7.66	9.37	9.05	21.9	13.2
	$\sigma \times 10^4$	2.9	2.3	2.8	3.6	3.5	4.0	4.4	5.2	2.1	2.8	−1.0
Pt|H_2(g)|HBr(m),	E^0_M(V)*	0.07510	0.07230	0.06934	0.06616	0.06241	0.05852	0.05450	0.05019	0.04553	0.04020	0.02930
H_2O, 30% tetrahydrofuran|	E^0_M(V)	0.07501	0.07221	0.06926	0.06568	0.06222	0.05854	0.05449	0.05019	0.04518	0.04031	0.02944
AgBr|Ag	$\beta^{(0)}$	−0.10952	−0.10331	−0.08611	−0.51621	−0.18682	0.09529	0.07953	0.11335	−0.21774	0.29731	0.91540
	$\beta^{(1)}$	−1.08358	−1.09595	−1.12877	−0.38151	−1.00861	−1.40788	−1.36417	1.40346	−0.79532	−1.60670	−1.72293
	$R_2 \times 10^5$	9.11	6.72	12.4	25.5	8.88	5.29	5.75	8.21	10.4	5.86	22.6
	$\sigma \times 10^4$	0.9	0.9	0.8	4.8	1.9	−0.2	0.1	0.0	3.5	−1.1	−1.4
Pt|H_2(g)|HBr(m),	E^0_M(V)*	0.06335	0.05823	0.05308	0.04799	0.04230	0.03669	0.03098	0.02531	0.01934	0.01332	0.00814
H_2O, 50% tetrahydrofuran|	E^0_M(V)	0.07035	0.06529	0.06034	0.05531	0.04987	0.04435	0.03848	0.03325	0.02750	0.02161	0.01692
AgBr|Ag	$\beta^{(0)}$	7.12212	7.07204	7.08920	7.04721	7.15819	7.11978	7.07395	7.13711	7.13864	7.13199	7.32059
	$\beta^{(1)}$	−15.1323	−15.0701	−15.1748	−15.1167	−15.4881	−15.4351	−15.3556	−15.6052	−15.6645	−15.7187	−16.3153
	$R_2 \times 10^3$	2.83	2.91	2.93	2.93	2.93	3.07	3.20	3.25	3.29	3.27	3.51

*Literature.

TABLE 4. Standard free energy, entropy, and enthalpy of transfer of HCl from water to urea + water on the basis of the mole fraction scale

T(K)	278.15	288.15	298.15	308.15	318.15
ΔG_t^0 (kJ mol^{-1})	−4.967	−4.929	−4.943	−4.994	−5.075
ΔS_t^0 (J mol^{-1})	−5.00	−1.11	+2.79	6.69	10.58
ΔH_t^0 (kJ mol^{-1})	−6.359	−5.249	−4.111	−2.934	−1.707

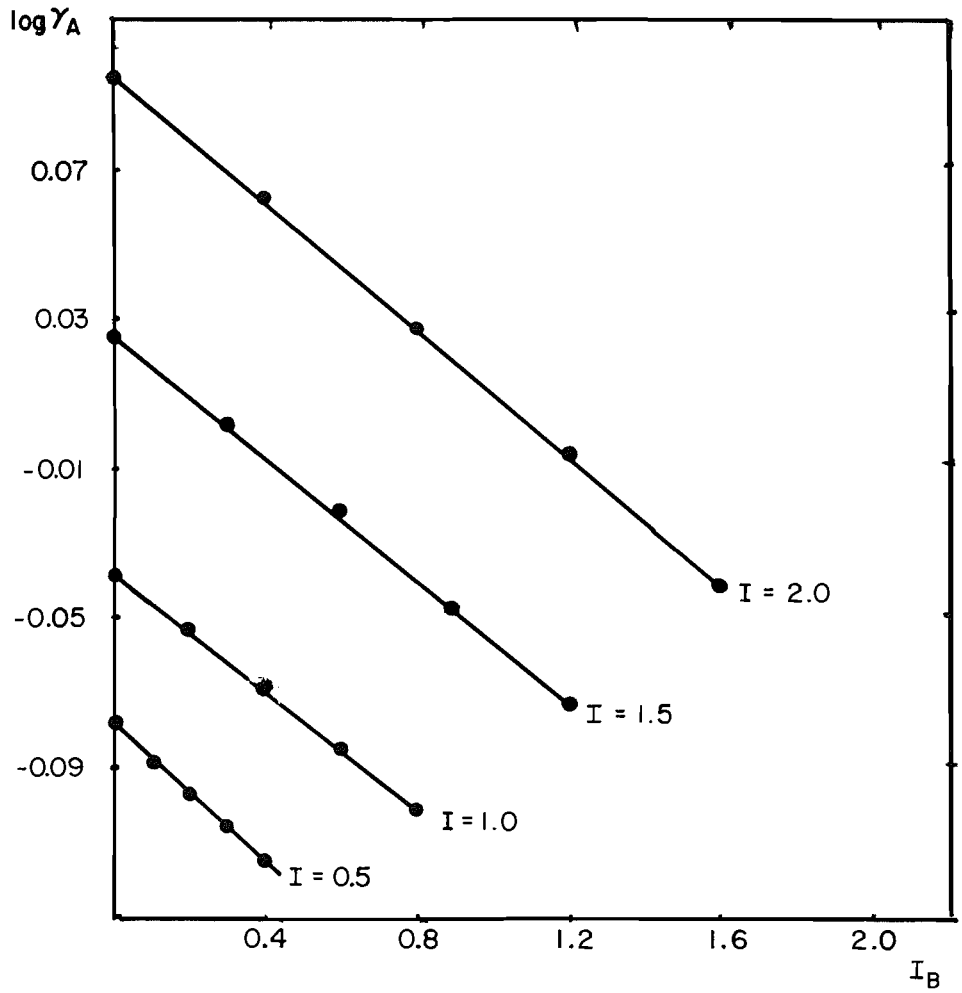

FIG. 2. Plot of log γ_A against I_B at 298.15 K.

partly due to the electrostatic effect arising from a higher dielectric constant of the mixed solvent than of water.

The values of ΔS_t^0 are positive at 298.15, 308.15, and 318.15 K. However, the values are negative at 278.15 and 288.15 K. This suggests more disorder at 298.15–318.15 K in the mixed solvent than in pure water. However, more order at 278.15 and 288.15 K in comparison with pure water is evident.

3. Harned's rule

The emf's of cell (B), which were measured at constant total ionic strength $I = 0.50$, 1.00, 1.50, and 2.00 mol kg^{-1}, ionic strength fraction of NaCl $y_B = 0.00$, 0.20, 0.40, 0.60, and 0.80, at five temperatures from 278.15 to 318.15 K in 0.05 mole fraction urea–water mixed solvent, are summarized in Table 5. The ionic strength fraction y_B of NaCl is given by

[16] $$y_B = m_B/(m_B + m_A) = m_B/I$$

Mean ionic activity coefficients γ_A for HCl in the presence of NaCl were readily calculated from the emf E, the standard emf E_M^0 of cell (B), and y_B by the relationship

[17] $$\log \gamma_A = (E_M^0 - E)/(2k) - 0.5 \log [(1 - y_B)I^2$$

The values of log γ_A calculated from eq. [17] are listed in Table 5.

A good straight line was obtained when log γ_A was plotted against m_B at constant total ionic strength I. All linear correlation coefficients r were over 0.999. These results show that HCl still obeys Harned's rule in these experimental systems,

[18] $$\log \gamma_A = \log \gamma_A^0 - \alpha_A m_B$$

where γ_A^0 is the activity coefficient of HCl in solution containing only the HCl and $m_A = m = I$; α_A is Harned's

Can. J. Chem. Downloaded from www.nrcresearchpress.com by 176.9.209.113 on 09/07/12
For personal use only.

Can. J. Chem. Downloaded from www.nrcresearchpress.com by 176.9.209.113 on 09/07/12
For personal use only.

TABLE 5. The emf of cell (B), coefficients of HCl, and Harned coefficients

		278.15 K		288.15 K		298.15 K		308.15 K		318.15 K		$\log \gamma_A = g + hT$		
I	Y_B	E(V)	$\log \gamma_A$	E(V)	$\log \gamma_A$	E(V)	$\log \gamma_A$	E(V)	$\log \gamma_A$	E(V)	$\log \gamma_A$	h	$g \times 10^3$	r
	0.0000	0.32145	−0.0718	0.31745	−0.0774	0.31324	−0.0823	0.30885	−0.0864	0.30422	−0.0907	0.0578	0.468	−0.998
	0.2000	0.32756	−0.0787	0.32378	−0.0843	0.31977	−0.0889	0.31561	−0.0933	0.31119	−0.0975	0.0504	0.466	−0.998
	0.4000	0.33554	−0.0885	0.33194	−0.0932	0.32819	−0.0976	0.32422	−0.1012	0.32012	−0.1058	0.0298	0.426	−0.999
0.500	0.6000	0.34620	−0.0971	0.34294	−0.1014	0.33952	−0.1053	0.33592	−0.1089	0.33209	−0.1125	0.0092	0.383	−0.999
	0.8000	0.36397	−0.1075	0.36128	−0.1112	0.35848	−0.1150	0.35543	−0.1179	0.35224	−0.1216	0.0106	0.349	−0.999
		$-\alpha = 0.909$	$R = -0.998$	$-\alpha = 0.085$	$R = -0.998$	$-\alpha = 0.082$	$R = -0.988$	$-\alpha = 0.079$	$R = -0.999$	$-\alpha = 0.077$	$R = -0.999$			
	0.0000	0.28238	−0.0188	0.27745	−0.0286	0.27222	−0.0364	0.26686	−0.0441	0.26114	−0.0505	0.1996	0.789	−0.997
	0.2000	0.28958	−0.0356	0.28473	−0.0438	0.27970	−0.0512	0.27445	−0.0577	0.26906	−0.0648	0.1649	0.723	−0.999
	0.4000	0.29835	−0.0526	0.29375	−0.0602	0.28894	−0.0688	0.28395	−0.0729	0.27866	−0.0784	0.1255	0.643	−0.998
1.000	0.6000	0.31012	−0.0712	0.30583	−0.0778	0.30137	−0.0838	0.29670	−0.0891	0.29191	−0.0953	0.0940	0.595	−0.999
	0.8000	0.32880	−0.0899	0.32500	−0.0950	0.32112	−0.11003	0.31703	−0.1049	0.31283	−0.1105	0.0522	0.511	−0.9997
		$-\alpha = 0.089$	$R = -0.9996$	$-\alpha = 0.083$	$R = -0.9996$	$-\alpha = 0.080$	$R = -0.9996$	$-\alpha = 0.077$	$R = -0.9995$	$-\alpha = 0.075$	$R = -0.9993$			
	0.0000	0.25541	0.0494	0.24984	0.0368	0.24410	0.0252	0.23812	0.0149	0.23183	0.0055	0.3534	1.097	−0.998
	0.2000	0.26360	0.0237	0.25821	0.0120	0.25259	0.0019	0.24683	−0.0079	0.24063	−0.0157	0.2971	0.987	−0.998
	0.4000	0.27341	−0.0027	0.26819	−0.0128	0.26275	−0.0216	0.25725	−0.0307	0.25133	−0.0380	0.2427	0.885	−0.999
1.500	0.6000	0.28640	−0.0324	0.28145	−0.0407	0.27628	−0.0479	0.27106	−0.0555	0.26551	−0.0623	0.1747	0.746	−0.999
	0.8000	0.30607	−0.0601	0.30162	−0.0666	0.29703	−0.0727	0.29234	−0.0791	0.28742	−0.0853	0.1148	0.629	−0.9999
		$-\alpha = 0.092$	$R = -0.9997$	$-\alpha = 0.086$	$R = -0.9997$	$-\alpha = 0.082$	$R = -0.9997$	$-\alpha = 0.078$	$R = -0.9999$	$-\alpha = 0.076$	$R = -0.9997$			
	0.0000	0.23316	0.1261	0.22734	0.1086	0.22119	0.0939	0.21475	0.0810	0.20800	0.0694	0.5162	1.410	−0.997
	0.2000	0.24249	0.0900	0.23671	0.0751	0.23062	0.0626	0.22438	0.0507	0.21774	0.0407	0.4305	1.230	−0.997
	0.4000	0.25366	0.0513	0.24802	0.0387	0.24215	0.0276	0.23610	0.0174	0.22976	0.0079	0.3509	1.081	−0.998
2.000	0.6000	0.26758	0.0132	0.26215	0.0032	0.25656	−0.0061	0.25093	−0.0159	0.24510	−0.0255	0.2815	0.965	−0.9999
	0.8000	0.28844	−0.0253	0.28353	−0.0333	0.27847	−0.0408	0.27323	−0.0477	0.26791	−0.0557	0.1836	0.752	−0.9997
		$-\alpha = 0.095$	$R = -0.9999$	$-\alpha = 0.089$	$R = -0.9999$	$-\alpha = 0.085$	$R = -0.9998$	$-\alpha = 0.081$	$R = -0.9999$	$-\alpha = 0.079$	$R = -0.9997$			

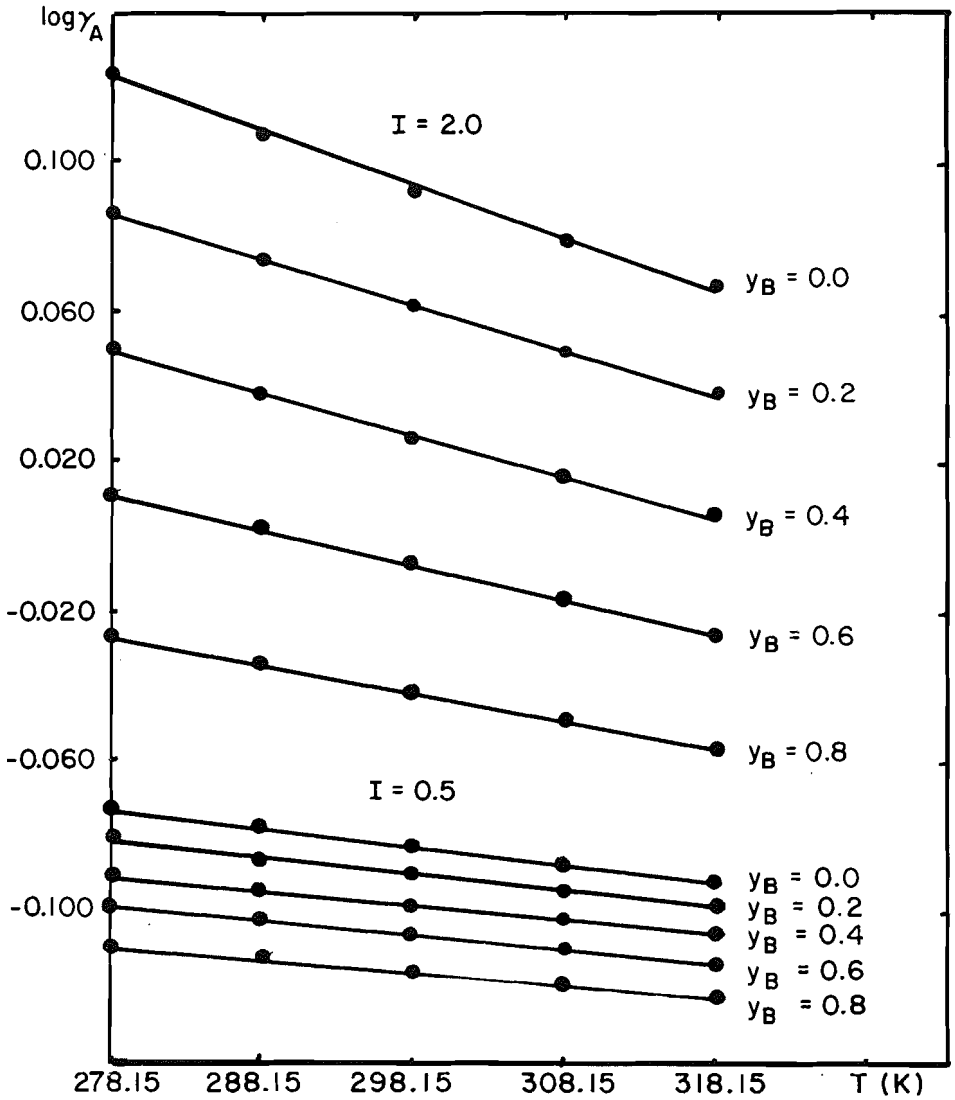

FIG. 3. Plot of log γ_A against T at I = 2.0 and 0.5 mol kg^{-1}

coefficient. The values of α_A, which were obtained from linear regression, are listed in Table 5.

The linear regression of log γ_A against absolute temperature T was carried out; all linear correlation coefficients were over 0.99. The results show that a good straight line may be obtained when log γ_A is plotted against T. The relationship between log γ_A and T may be expressed in the following equation:

$$[19] \quad \log \gamma_A = h + gT$$

where h and g are empirical constants. From eqs. [18] and [19], it can be shown that there is a linear relationship between α_A and T.

The relative partial molar enthalpy of HCl, L_A, may be calculated by the following equation:

$$[20] \quad L_A = 2 \ln (10)\, RT^2\, [\partial \log \gamma_A/\partial T]_{P,M}$$

The values calculated with eq. [20] are summarized in Table 6. The derivative of eq. [18] with respect to T at constant pressure and constant composition of solution was calculated and multiplied by the factor $[-2 \ln (10)RT^2]$, so that the following equation may be used:

$$[21] \quad L_A = L_A^0 + 2 \ln (10)RT^2(\partial\alpha_A/\partial T)_{P,M} I_B$$

where L_A^0 is the relative partial molar enthalpy of HCl in its own solution at the same total ionic strength as the mixture. As above, the $(\partial\alpha_A/\partial T)_{P,M}$ is a constant, then

$$[22] \quad Q = 2 \ln (10)RT^2(\partial\alpha_A/\partial T)_{P,M}$$

Q is also constant at a given temperature. Then

$$[23] \quad L_A = L_A^0 + QI_B$$

Equation [23] shows that the relative partial molar enthalpy L_A is a linear function of NaCl molality. In this sense, eq. [14] is analogous to Harned's rule, so that eq. [23] may be temporarily referred to as the "similar" Harned's rule of relative partial molar enthalpy. When the values of L_A in Table 6 are plotted against I_B at constant ionic strength and against T at constant composition, a good straight line is obtained; all linear correlation coefficients are over 0.999. These agree with results obtained in aqueous solution by Macaskill *et al.* (16).

Can. J. Chem. Downloaded from www.nrcresearchpress.com by 176.9.209.113 on 09/07/12
For personal use only.

TABLE 6. Values of the relative partial molar enthalpy (L_A) of HCl (J mol^{-1})

		L_A					
I	I_B	278.15 K	288.15 K	298.15 K	308.15 K	318.15 K	r
	0.0000	1386	1488	1593	1701	1814	0.999
	0.2000	1576	1691	1811	1934	2062	0.999
0.500	0.4000	1765	1895	2028	2167	2310	0.999
	0.6000	1955	2098	2246	2400	2558	0.999
	0.8000	2145	2302	2464	2632	2806	0.999
	r:	0.9999	0.9999	0.9999	0.999	0.999	
	0.0000	2337	2508	2685	2869	3058	0.999
	0.2000	2539	2724	2917	3116	3321	0.999
1.0	0.4000	2740	2941	3148	3363	3385	0.999
	0.6000	2941	3157	3380	3610	3848	0.999
	0.8000	3143	3373	3611	3857	4112	0.999
	r:	0.9999	0.9999	0.9999	0.9999	0.9999	
	0.0000	3247	3484	3730	3985	4247	0.999
	0.2000	3478	3732	3996	4268	4550	0.999
1.5	0.4000	3709	3980	4261	4552	4852	0.999
	0.6000	3940	4228	4527	4835	5154	0.999
	0.8000	4171	4476	4792	5119	5457	0.999
	r:	0.9999	0.9999	0.9999	0.9999	0.9999	
	0.0000	04177	4482	4799	5126	5464	0.999
	0.2000	4414	4737	5071	5417	5774	0.999
2.0	0.4000	4651	4991	5343	5708	6084	0.999
	0.6000	4888	5245	5616	5999	6394	0.999
	0.8000	5125	5500	5888	6290	6704	0.999
	r:	0.9999	0.9999	0.9999	0.9999	0.9999	

1. G. AKERLOF, J. W. TEARC, and H. TURCH. J. Am. Chem. Soc. **59**, 1916 (1937).
2. C. Y. CHAN, and K. H. KHOO. J. Chem. Soc. Faraday Trans. 1, **70**, 27 (1974).
3. K. H. KHOO, C. Y. CHAN, and T. K. LIM. J. Solution Chem. **7**, 349 (1978).
4. MING-CHEN CHU, JIA-ZHEN YANG, and CHUN-YU LIANG. Acta Phys. Chim. Sin. **1**, 476 (1985).
5. JIA-ZHEN YANG, CHUN-YU LIANG, DENG CAI, and LI-TIAN ZHANG. Huaxue Xuebao, **45**, 220 (1987).
6. DIAN-YUAN MEN, DIAN-ZHEN LU, CHUN-YU LIANG, and JIA-ZHEN YANG. J. Chem. Thermodyn. In press.
7. K. S. PITZER. J. Phys. Chem. **77**, 268 (1973).
8. K. S. PITZER and G. MAYORGA. J. Phys. Chem. **77**, 2300 (1973).
9. R. G. BATES. Determination of pH. John Wiley & Sons Inc., New York. 1964. p. 281.
10. R. G. BATES and R. A. ROBINSON. J. Solution Chem **9**, 00 (1980).
11. G. J. HILL and D. J. G. IVES. *In* Reference electrodes. *Edited by* D. J. G. Ives and G. J. Janz. Academic Press, New York. 1980. p. 107.
12. D. S. P. KOH, K. H. KHOO, and C. Y. CHAN. J. Solution Chem. **14**, 635 (1985).
13. R. N. ROY, B. KENNAN, and S. FASZHOLZ. J. Chem. Thermodyn. **13**, 537 (1981).
14. J. C. HALLE and R. G. BATES. J. Chem. Thermodyn. **7**, 999 (1975).
15. R. N. ROY *et al.* J. Chem. Thermodyn. **7**, 1015 (1975).
16. J. B. MACASKILL, C. A. VEGA, and R. G. BATES. J. Chem. Eng. Data, **23**, 314 (1978).

Can. J. Chem. Downloaded from www.nrcresearchpress.com by 176.9.209.113 on 09/07/12
For personal use only.

Calorimetric studies of the phase transition in iodoform

JULIANA BOERIO-GOATES[1] AND BRIAN F. WOODFIELD
Chemistry Department, Brigham Young University, Provo, UT 84602, U.S.A.

Received August 24, 1987

This paper is dedicated to Professor J. A. Morrison

JULIANA BOERIO-GOATES and BRIAN F. WOODFIELD. Can. J. Chem. **66**, 645 (1988).

The heat capacity of crystalline iodoform prepared by vacuum sublimation has been measured from 50 to 340 K and that of iodoform prepared by recrystallization from acetone measured from 120 to 300 K. Both samples exhibit a phase transition near 260 K. The heat capacity anomaly in the sublimed material shows several small maxima which appear with variable positions and heights depending upon the thermal pretreatment of the sample. The transition, which was undetected by previously-reported spectroscopic measurements, is ascribed to an incomplete ordering of the molecular dipole.

JULIANA BOERIO-GOATES et BRIAN F. WOODFIELD. Can. J. Chem. **66**, 645 (1988).

On à mesuré la capacité calorifique de l'iodoforme cristallin préparé par sublimation sous vide à des températures allant de 50 à 340 K et celle de l'iodoforme préparé par recristallisation de l'acétone de 120 à 300 K. Les deux échantillons présentent une transition de phase près de 260 K. Dans l'échantillon préparé par sublimination, on note une anomalie dans la capacité calorifique qui se traduit par plusieurs petits maxima qui apparaissent à des positions variables et dont les hauteurs dépendent du pré-traitement thermique qu'a subi l'échantillon. C'est à arrangement incomplet du dipôle moléculaire qu'on attribue la transition qui n'avait pas été détectée au cours des mesures spectroscopiques réalisées antérieurement.

[Traduit par la revue]

Can. J. Chem. Downloaded from www.nrcresearchpress.com by 93.93.197.157 on 09/07/12
For personal use only.

Introduction

Halogenated methane derivatives are of interest to theorists and experimentalists probing molecular dynamics in the solid state. These compounds also exhibit an interesting range of crystallographic structures and polymorphic phase transitions at different temperatures. The haloforms, CHX_3 with X = F, Cl, Br, and I, have been widely studied by techniques like X-ray (1, 2) and neutron (3, 4) diffraction, Raman and ir spectroscopy (5–7) and dielectric measurements (8) which probe structural details of the solid-state and characterize phase transitions. However, high-precision heat capacity measurements, frequently used to study phase transitions, have been published only for fluoroform (9); differential scanning calorimetric (DSC) measurements (8) near the solid–liquid and solid–solid phase transitions in bromoform have been made, but no quantitative data were published from this study.

In this paper we report heat capacity measurements of iodoform in order to resolve a discrepancy regarding the existence of a phase transition in this compound. The disagreement arises between spectroscopic (5, 7) studies which show no evidence for a phase transition as the temperature is lowered, and temperature-dependent photoconductivity measurements (10) which exhibit anomalous behavior below 270 K that has been attributed to the onset of a phase transition. The manner of sample preparation differed between two of the investigations: one spectroscopic study (5) used crystals grown from acetone solution while the photo-conductivity measurements (10) were performed on samples of CHI_3 prepared by vacuum sublimation. In order to determine if the two preparation methods yield different types of crystals, one undergoing a transition and the other not, we have made measurements using samples prepared in both fashions.

We present here heat capacity measurements from 50 to 340 K which are in the temperature region of interest with respect to the disputed transition. These measurements are the first to be reported using the automated, adiabatic calorimetric system we have recently assembled; thus, details of its construction and operation will also be given in this paper.

[1]To whom correspondence should be addressed.

TABLE 1. Details of the calorimetric experiments

Parameter	Value for sample type- Sublimed	Recrystallized
Sample mass, g	167.7876	85.9837
Moles of CHI_3	0.42615	0.2184
Free volume in calorimeter, cm^3	32.77	52.47
He exchange gas, Pa at 299 K	4160	4250
Percent contribution to measured heat capacity of empty calorimeter	50 K 16 200 K 25 350 K 25	120 K 33 200 K 19 300 K 21

Experimental

Sample preparation

Iodoform was purchased from Pfaltz and Bauer (11) and purified either by slow vacuum sublimation or recrystallization from reagent-grade acetone under a nitrogen atmosphere, followed by drying for several hours in a vacuum oven at room temperature to remove adsorbed acetone. Both preparations were carried out in the dark to prevent photo-initiated decomposition. The samples prepared by vacuum sublimation have been analyzed by carbon, hydrogen, and iodine analyses and both samples have been analyzed by mass spectrometry. The C,H,I analyses gave the following compositions in mass percent (±0.3% uncertainty): C 3.04 actual, 3.05 theoretical; H 0.28 actual, 0.28 theoretical; and I 96.43 actual, 96.69 theoretical. Analysis by mass spectroscopy indicated that the recrystallized sample was contaminated with an amount of acetone considerably less than one mass percent, but precise quantization of the impurity was not possible. No contaminants were found in the sublimed crystals.

The pertinent information concerning the loading of the samples in the cryostat is summarized in Table 1.

Description of the calorimetric apparatus and measurement system

The calorimetric system incorporates an aneroid cryostat of the Westrum design (12) with modifications of the wiring to allow interchange of thermometers. Electrical leads coming from the heater/thermometer assembly are soldered to gold-plated pins, and the

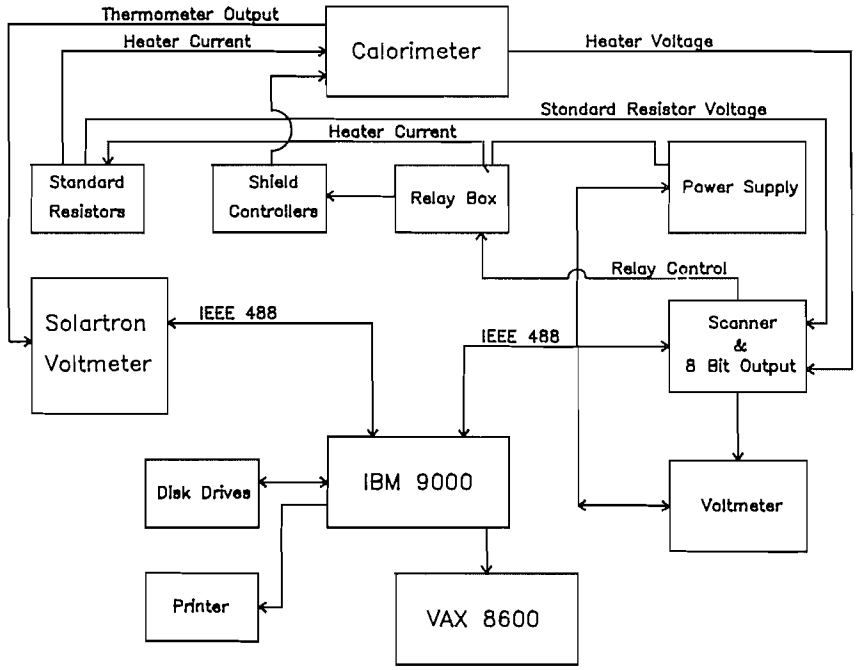

FIG. 1. Block diagram of the instrument control and data acquisition system.

mating connectors and leads are contained in a gold-plated copper block soldered to the bottom of the adiabatic shield.

The gold-plated copper calorimeter vessel used in the experiments is similar in design to that described in ref. 12 for solid samples. It has an internal volume of 73.19 cm^3 and is sealed by pressing a gold gasket onto a knife edge around the mouth of the calorimeter.

Temperatures are measured using a Leeds and Northrup capsule thermometer (# 1624058) first calibrated on the International Practical Temperature Scale of 1948 (IPTS-48). The original thermometer calibration has been converted to yield temperatures on the IPTS-68 scale by applying corrections (13) to the temperature scale supplied by Leeds and Northrup to bring it to the 1968 scale, and fitting the corrected temperature / resistance data within appropriate regions to obtain the necessary coefficients. To check the calibration, the temperatures of the $Na_2SO_4 \cdot 10H_2O$ triple point, ice point, Hg freezing point, and the N_2 boiling point were measured. The maximum deviation from the accepted values was 0.01 K, obtained with the N_2 boiling point.

A Solartron Model 7081 8½ digit voltmeter operating in the true ohms mode is used to measure resistances. This mode is a four-wire resistance measurement using a 1 mA current with corrections for thermal emfs made internally.

Current for the calorimeter heater is provided by an Electronic Development Corporation Model 520A power supply operated with a controlled current output. Energy measurements are made in the conventional manner: voltages across the calorimeter heater and a Guildline 100 Ω standard resistor in series with the calorimeter heater are measured using a Hewlett-Packard Model 3456A 6½ digit voltmeter. A Keithley Model 705 Scanner with a low thermal-voltage card is used to channel the different voltage outputs into the HP DVM. During the equilibration periods, the heater current passes through a 100 Ω dummy resistor; a high-speed, low-thermal mercury relay switches the current to the calorimeter heater during energy inputs.

The temperature of the adiabatic shields surrounding the calorimeter is maintained by home-built controllers in which differential thermocouple voltages are amplified by Ancom amplifiers (14), and the shield heater output is controlled by proportional–integral–derivative circuitry. The thermocouple between the main adiabatic shield and the calorimeter consists a Au(0.07 at% Fe)–Chromel P thermocouple in series with one of Au(0.02 at% Co)–Chromel P. The top and bottom shield heaters are controlled by the output from differential thermocouples referenced to the main shield. These thermocouples consist of two Au(0.07 at% Fe)–Chromel P junctions in series. A fourth control unit maintains the temperature of a tempering ring around which the electrical leads are wound before going to the adiabatic shields; this thermocouple is a double-leg copper–constantan thermocouple. Typical temperature drifts of the calorimeter range from 10^{-4} to 10^{-6} K min^{-1}. Equilibration periods are typically 20 to 30 min from 50 to 350 K. For the iodoform measurements, the equilibration times occasionally increased to about 3 h in the transition region.

Data collection and control

Instrument control and data acquisition have been completely automated using an interface to an IBM Instruments System 9000 computer. The hardware configuration of the various instruments and the computer are depicted in Fig. 1. Communication between the commercial instruments and the System 9000 is done via the IEEE-488 bus; switching relays are interfaced through a parallel port on the Keithley Scanner and controlled through the IEEE-488 bus. All data are printed on rhe System 9000 printer as they are collected and also stored on floppy disk. As the appropriate data become available, the raw heat capacities are calculated and saved on disk. The data are uploaded to a VAX 8600 for further processing upon completion of the experiments, thus freeing the System 9000 for additional data collection.

The controlling program on the System 9000 has been written for maximum flexibility. The number and type of energy input and the type of algorithm to determine the equilibrium temperature can be specified. Two options are available for the type of energy input: a normal heating period or a long heating interval for an enthalpy measurement. Parameters which can be varied in the drift measurements include the time between temperature measurements, the number of points to be included in the drift-termination calculation, and the criterion which establishes equilibrium. One may base the decision of whether equilibrium has been reached by a consistent agreement of either a drift rate or a calculated final temperature for the preceding energy input.

The electrical energy input into the calorimeter is measured by taking periodic voltage measurements across the standard resistor and calorimeter heater for a known length of time. Resulting current and voltage values are multiplied and fit to a cubic polynomial versus time and integrated to obtain the power used during the energy addition. For each energy addition the following two parameters may be specified: duration of energy addition and the desired increase in temperature. The temperature increase may be given as a default increment determined by the temperature, a specified increase, or a value of the current to be set on the power supply.

Can. J. Chem. Downloaded from www.nrcresearchpress.com by 93.93.197.157 on 09/07/12
For personal use only.

The shield controllers must be switched to a higher power setting while energy is added to the calorimeter and then back to the normal setting during the drift. The program allows for this switch at variable times before and after the energy addition to facilitate better shield control.

Performance of the system

Benzoic acid (NBS-Standard Reference Material 39i) was measured in the calorimeter to check the accuracy of the system. The results are consistently high (0.1–0.3%) relative to the data of Furukawa *et al.* (15). The discrepancy is probably sample-related since the work of ref. 15 was performed using the Calorimetry Conference Standard benzoic acid (NBS-SRM 39g) rather than NBS-SRM 39i. Also, the possibility of a systematic error arising from the main adiabatic shield controller is under investigation. Because the conclusions regarding the phase transition of iodoform do not rest on absolute values of heat capacity, nor on derived thermodynamic properties like S°_{298}, the systematic deviation does not pose a significant problem for this research.

The system proved capable of producing very precise results: a smoothed curve could be fit through the experimental points with deviations of about 0.05%.

Results

The results of heat capacity measurements from 50 to 340 K on iodoform crystals prepared by vapor sublimation are given in Table 2. These results are reported in chronological order with the series designation indicating a continuous set of measurements. The size of temperature increment used in the measurements can be inferred from consecutive temperatures within a series.

The heat capacity results obtained from the sublimed crystals are plotted in Fig. 2 along with those obtained on the iodoform crystals grown from acetone solution. The acetone-grown samples exhibited a slightly higher heat capacity over the entire region of measurement than the sublimed crystals and showed a small anomaly near 175 K, which is close to the melting point (177 K) of pure acetone (16). Since acetone has a much higher heat capacity per gram (16) than iodoform, contamination of the iodoform results in a higher heat capacity than would be obtained with pure iodoform. Estimates of the extent of contamination, based upon integration of the excess enthalpy in the acetone fusion region and on the heat capacity difference between the two samples, yield values of about 0.1 mass %, which is consistent with the mass spectrometric measurements. Because we have the results from the uncontaminated, sublimed crystals, we made no efforts to correct the heat capacity from the acetone-grown sample. We include it in Fig. 2 to show the similarity in the region near 260 K with the behavior observed from the sublimed crystals.

Both samples were found to have a region of anomalous heat capacity from 250 to 270 K. When studied with relatively large temperature increments of 5 K (e.g. Series 2 and 4 in Table 2 on the sublimed crystals), both heat capacity curves appear to step up abruptly in this region in a manner suggestive of a glass transition.

The temperature region from 250 to 270 K was studied more extensively with the sublimed crystals using measurements with temperature increments of 1 K (Series 9, 10, 11, and 12) to search for sharp features in the heat capacity more typically associated with phase transitions. Cooling rates, minimum cooling temperatures, and annealing times, factors which can affect the extent of conversion to a low-temperature phase, were varied to ascertain if these had any effects on the heat capacity. The description of the thermal treatment preceding each series in the transition region is given in Table 3.

The results of measurements obtained in the region from 238 to 288 K are displayed in Fig. 3. To show these data with clarity, two curves are presented in Fig. 3. Data from Series 2, 4, 5, 8, 9, and 10 are plotted on curve *a*, while data from Series 11 and 12 are given in curve *b* with the ordinate displaced. Omitted from Fig. 3 are data from Series 2, 4, and 8 in the region from 258 to 270 K which have been obtained with temperature increments larger than 2 K.

As is evident from Fig. 3, neither a long annealing time nor a large degree of undercooling produced significant maxima in the heat capacity curve. Lowering the cooling rate from 0.7 K min^{-1} (Series 5, 8, 9, and 10) to 0.1 K min^{-1} (Series 11 and 12) appeared to have a small but discernible effect on the features observed in the heat capacity. Each series that was cooled at the higher rate exhibited one or more points (e.g. points 9 and 11 of Series 5, points 7 and 8 of Series 8, points 8 and 9 of Series 9, and points 6 and 9 of Series 10) that were about 0.8 to 1.5% above a smooth curve drawn through the remainder of the points of these series. (This smooth curve is given as the solid line in Fig. 3*a* and 3*b*.) A larger positive deviation, 1 to 3.5%, from this same smoothed curve was observed with points from Series 11 and 12, before which the sample had been cooled at the slower rate.

To determine an estimate of the scatter to be expected from measurements made with small increments, a series of 15 points (Series 13), each with ΔT about 1.0 K, was obtained at temperatures well below 250 K. A maximum deviation of −0.4% from the smooth curve generated by the larger-increment data in this region was obtained for a single point while the remainder of the points were well within ±0.2% deviation.

The equilibration times of Series 13 data were comparable to those obtained during the Series 5, 8, 9, and 10 measurements and to some measurements in Series 11 and 12. Therefore, comparable scatter might be expected in these data. Points 3, 4, 5, 6, and 7 of Series 11 and 1, 2, 7, 9, 11, and 13 of Series 12, however, took from 1 to 3 h to equilibrate, with the higher heat capacity points requiring longer equilibration times. The uncertainty associated with these points is consequently larger because of the greater uncertainty in the ΔT measurement.

With these observations in mind, the question then becomes one of determining if the high points arise from one or more sluggish phase transitions, or if long equilibrium times lead to inaccuracies in the temperature measurements which make the points artificially high.

There are several factors which point toward the existence of phase transitions. First, long equilibrium times are frequently associated with phase transitions in molecular crystals. Equilibrium times of several days have been observed in such transitions (17).

The long equilibrium times in the iodoform study appear repeatedly in the temperature region 256 to 270 K, but not once outside it, thus ruling out the possibility of a random system error. Also, the magnitude of the temperature drifts at the end of the long equilibrium periods are consistent with those obtained after runs which come to equilibrium at a faster rate.

Second, calculations have been made to determine the change in heat capacity using the widest range of values of the temperature drift which could conceivably be extracted from the time–temperature data of points with long equilibration times. For point 4 of Series 11, which showed the largest change, the heat capacity could be lowered from 99.09 to 98.67 J K^{-1} mol^{-1}. Such a change still leaves this point about 3% above the smooth curve connecting the non-transition data below 255 and above 270 K shown in Fig. 3*a*. Similar but smaller decreases in

Can. J. Chem. Downloaded from www.nrcresearchpress.com by 93.93.197.157 on 09/07/12
For personal use only.

TABLE 2. Results of heat capacity measurements on sublimed CHI_3

T / K	C_p / $JK^{-1}mol^{-1}$	T / K	C_p / $JK^{-1}mol^{-1}$	T / K	C_p / $JK^{-1}mol^{-1}$	T / K	C_p / $JK^{-1}mol^{-1}$
Series 1		256.11	95.34	Series 8		262.05	97.77
		261.24	97.16			263.09	97.99
159.27	80.77	266.37	98.19	234.55	91.90	264.14	97.41
163.39	81.45	271.50	99.19	239.72	92.67	265.17	96.99
168.55	82.21	276.66	99.88	244.89	93.46	266.20	99.29
173.70	82.99			250.05	94.27	267.24	98.50
178.85	83.78	Series 5		255.21	95.23	268.28	98.22
184.00	84.54			260.34	97.19	269.31	98.87
189.16	85.31	246.39	93.49	263.92	97.94	270.35	98.92
194.31	86.07	248.69	93.87	265.99	97.85	272.42	99.36
199.47	86.83	250.78	94.07			275.53	99.70
204.63	87.60	252.87	94.51	Series 9			
209.79	88.34	254.95	95.00			Series 12	
214.95	89.07	257.03	95.52	256.71	95.27		
220.11	89.84	259.10	95.88	258.97	95.87	256.71	96.46
225.27	90.63	261.16	96.32	260.00	95.92	258.96	97.76
230.43	91.34	263.21	97.13	261.04	95.91	260.00	95.93
235.59	92.08	265.27	97.06	262.06	96.53	261.04	96.78
240.76	92.84	267.31	98.27	263.09	96.74	262.07	96.28
245.94	93.56	269.37	98.53	264.11	96.76	263.09	97.67
		271.43	98.91	265.13	97.45	264.11	98.22
Series 2		273.50	99.31	266.16	98.25	265.14	97.54
		275.57	99.65	267.19	97.41	266.18	98.51
260.48	96.66			268.22	97.66	267.21	97.34
265.18	98.40	Series 6		269.24	98.16	268.24	98.56
270.33	98.95			270.27	98.71	269.26	98.72
275.49	99.74	51.16	56.50	272.33	99.17	270.30	99.58
280.66	100.4	54.49	58.17	275.43	99.65	272.37	99.42
285.83	101.0	59.44	60.28			275.48	99.79
291.00	101.7	64.37	62.12	Series 10			
296.17	102.3	69.34	63.74			Series 13	
301.34	103.0	74.33	65.18	256.73	95.45		
306.50	103.6	79.35	66.50	258.99	95.55	169.07	82.49
		84.38	67.70	260.01	95.65	170.98	82.76
Series 3		89.44	68.81	261.04	96.23	172.02	82.70
		94.51	69.85	262.07	96.12	173.06	82.96
299.38	102.6			263.09	97.19	174.10	82.75
304.58	103.3	Series 7		264.12	96.79	175.13	83.22
309.75	104.0			265.14	97.48	176.17	83.42
314.93	104.6	98.18	70.62	266.17	97.88	177.21	83.52
320.10	105.3	101.87	71.31	267.19	97.52	178.25	83.69
325.26	105.9	106.98	72.24	268.22	98.25	179.29	83.85
330.43	106.6	112.09	73.14	269.25	98.25	180.33	84.05
335.60	107.3	117.20	74.06	270.28	98.27	181.37	84.23
340.76	107.9	122.32	74.89	272.34	99.18	182.40	84.32
		127.44	75.71	275.44	99.70	183.44	84.55
Series 4		132.57	76.57			185.52	84.79
		137.70	77.41	Series 11			
230.83	91.40	142.84	78.22				
235.42	92.07	147.97	79.03	256.72	95.42		
240.59	92.80	153.11	79.90	258.97	95.67		

the other high points can be obtained if one carefully selects the drift values. These hand-picked drifts, however, do not have the consistency of the original computer-determined values, which makes their validity suspect.

The scatter and reproducibility in the data from Series 5 and 8–12 having 2 K increments or less is consistent, then, with that obtained in Series 13, if the high points noted above are rejected from the fit. Inclusion of the high points in an attempt to generate a smooth curve with no maxima causes unreasonably large deviations, even if the lower heat capacity values of the points recalculated using the hand-picked drifts are considered.

Discussion

Iodoform has a structure (4) isomorphous with the α-phase of bromoform (3) in which there is disorder involving the molecular dipole. Figure 4 shows a schematic representation of the unit cell. There are two molecules in the unit cell, with two possible molecular orientations at each of the lattice sites. The

Can. J. Chem. Downloaded from www.nrcresearchpress.com by 93.93.197.157 on 09/07/12
For personal use only.

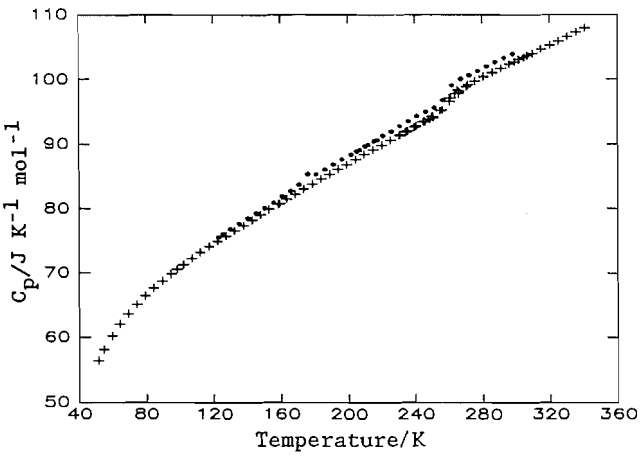

FIG. 2. Results of the heat capacity measurements on iodoform. + curve obtained with sample prepared by vacuum sublimation; ● curve obtained from crystals prepared by recrystallization from acetone. Some data in the transition region of the lower curve have been omitted for clarity.

TABLE 3. Summary of thermal pretreatment in the transition region[a]

Series	Thermal history immediately before measurements
2	Cooled to 150 K; heated up during Series 1; Series 2 continued approximately 6 h after the completion of Series 1
4	Cooled to 230 K; no annealing
5	Cooled to 245 K; no annealing
8	Cooled to 50 K; taken up to 150 K during Series 7; heated approximately 3 K min^{-1} to 230 K; annealed at 230 K for 48 h
9	Cooled to 230 K; no annealing
10	Cooled to 50 K; heated to 230 K; annealed at 230 K for 72 h
11	Cooled to 150 K slowly; heated to 250 K; no annealing
12	Cooled to 100 K slowly; heated to 230 K; annealed at 230 K for 120 h

[a]All cooling with the exception of Series 11 and 12 was performed with the calorimeter in maximum contact with the refrigerant, resulting in a cooling rate of about 0.7 K min^{-1}. For Series 11 and 12, the cooling rate was about 0.1 K min^{-1}.

molecular dipole can be aligned parallel or antiparallel to the c axis of the unit cell. The α-phase of bromoform is known to undergo a phase transition with partial ordering (3) of the molecular dipole to a β-phase 13 degrees below the melting point.

Conflicting evidence has been reported in the literature about the existence of a corresponding phase transition in iodoform. Raman spectroscopic investigations (5, 7) of low-frequency lattice vibrations conclude that no ordering transition occurs down to low temperatures. Temperature-dependent photoconductivity studies (10) of iodoform, however indicated a phase transition near 270 K. In a related study of the drift mobility of photo-generated holes in CHI_3 (18), results indicative of the onset of ferroelectricity in this temperature region were observed. Since the fully-disordered phase is not ferroelectric, the appearance of ferroelectricity means some ordering has taken place.

Despite the lack of a large peak in the heat capacity, we conclude that there is indeed a phase transition in iodoform between 250 and 270 K. There is evidence for at least a small

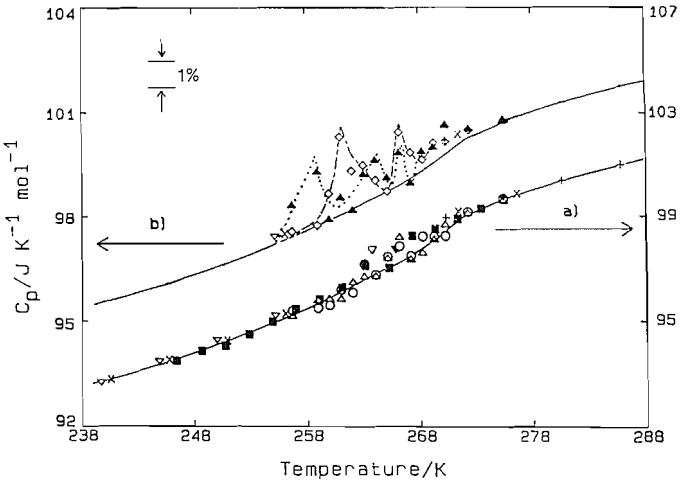

FIG. 3. Details of heat capacity measurements in the transition of vapor-sublimed crystals. Data given by series in Table 2 are identified in the figure by the following symbols: Curve a: Series 2, +; Series 4, ×; Series 5, ■; Series 8, ▽; Series 9, △; and Series 10, ○; curve b: Series 11, ◇; and Series 12, ▲. The solid lines in a and b are the fit of data from Series 2, 4, 5, 8, 9, and 10 and the low points of Series 11 and 12, while the dashed and dotted lines in curve b are estimates of the heat capacity curves generated by Series 11 and 12 data, respectively. Data taken in the transition region with temperature increments larger than 2° have been omitted for clarity.

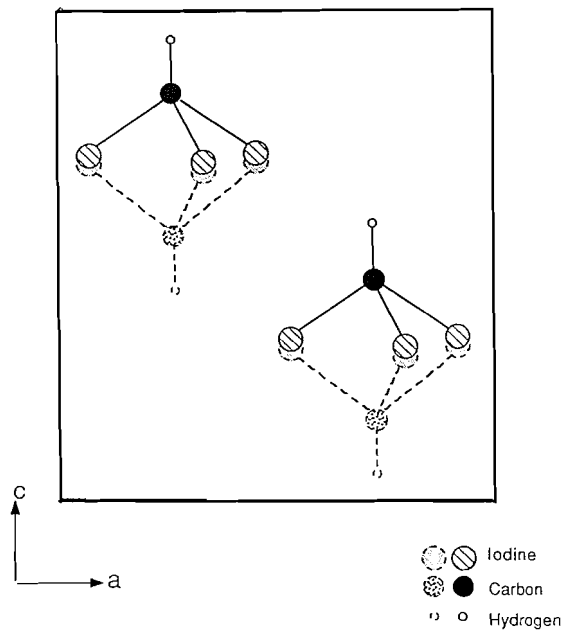

FIG. 4. Schematic representation of the unit cell of iodoform at room temperature illustrating the disorder of the molecular dipole because of the two possible positions of the C—H bond relative to the plane of the iodine atoms.

excess heat capacity, and the long equilibration times and lack of reproducibility of the heat capacity observed in this region are typically associated with sluggish phase transitions in molecular crystals. The temperature region of the heat capacity anomaly as well as its variability are in agreement with the observations of the photoconductivity (10) and drift-mobility (18) work, and show that the same phenomenon is responsible for the effects observed in these studies.

The authors of the neutron diffraction study of iodoform (4)

Can. J. Chem. Downloaded from www.nrcresearchpress.com by 93.93.197.157 on 09/07/12
For personal use only.

depict the crystal structure as being determined by the close-packing of the triangle of iodine atoms with the C—H accommodated non-preferentially on either side. In such a structure, where energetic forces favoring ordering of the dipole are small, and reorientational motion is expected to be hindered (4), extremely slow cooling and/or very long annealing times will be necessary to achieve complete order. The variability in the height of the maxima observed in the heat capacity measurements reflect differences in the extent to which the thermal pretreatment caused ordering to occur.

Since the anomalous C_p behavior was observed on both the solution-grown and vapor-sublimed crystals, the possibility that the two methods of preparation produced different crystal structures can be eliminated.

In view of our inability to obtain a large peak in the heat capacity which would more conclusively identify a phase transition and the overall *S*-shape of the heat capacity generated by large temperature-increment data in this region, one may wish to consider invoking a glassy-crystalline transition rather than an incomplete order–disorder transition to explain our data.

A glassy-crystalline (19) phase is formed when, upon cooling, the reorientational motions of molecules in a solid cease, thereby freezing in some kind of configurational disorder. As the temperature is increased again, the metastable disordered state begins to relax toward an equilibrium state, and the heat capacity curve takes on the appearance of a smoothed step function in this region.

Heat capacity studies of such transitions in RbCN (20) and molecular crystals like thiophene (21) exhibit a common feature missing from our work, however. We did not see the large exothermic drifts observed immediately below the transition temperature in these papers. The positive drifts arise when the metastable disordered state acquires enough thermal energy and spontaneously converts to a more stable state. The lack of such drifts in our iodoform measurements appears to rule out the existence of a glass transition here.

Vibrational spectroscopy studies rely either on changes in the linewidth of the lattice-vibration peaks or the appearance of new peaks to detect a phase transition as the sample temperature is varied. The Raman spectroscopic peaks of iodoform are very broad (5, 7) at room temperature due to anharmonicities of the lattice vibrations as well as the molecular disorder, and the broadness persists even to 20 K. Since the heat capacity measurements indicate that only a partial ordering takes place under typical cooling conditions, the narrowing associated with the transition will be small and probably undetectable in view of the overall width of the peaks. Also, the transition may effect acoustic modes, which are generally undetectable by Raman spectroscopy, more than the optic modes studied in the spectroscopic work. We suspect that these two factors prevented observation of the transition by spectroscopic methods.

Our work provides another example of the importance of investigating phase transitions by a variety of techniques and the utility of using heat capacity measurements to detect subtle phase transitions. Other studies, such as solid-state nmr or dielectric measurements, could determine if changes in molecular motion are associated with the phase transition and would be of interest. A low-temperature neutron diffraction study could provide details of the extent of ordering below 260 K.

Can. J. Chem. Downloaded from www.nrcresearchpress.com by 93.93.197.157 on 09/07/12
For personal use only.

Acknowledgements

We would like to thank Professor E. F. Westrum, Jr. (University of Michigan) for much assistance including provision of the original plans for the cryostat and adiabatic shield controller; Mr. Norman Johnston (University of Michigan) and Mr. Robert Perry (Brigham Young University) for machine work on the cryostat; Mr. Norman Holdaway (Brigham Young University) for construction of the adiabatic shield controllers; and Mr. Larry Sparks (NBS-Boulder) for a gift of the Au(0.02 at% Co) thermocouple wire. Dr. George Furukawa (NBS-Gaithersburg) provided assistance with the IPTS-48 to IPTS-68 temperature conversion. Mrs.Johanne Artman prepared the illustrations. Acknowledgement is also made to the donors of the Petroleum Research Fund, administered by the American Chemical Society, and to the Research Grant Program of the College of Physical and Mathematical Sciences of Brigham Young University for financial support of this research.

1. R. Fourme and M. Renaud. C.R. Acad. Sc. Paris, **263B**, 69 (1966).
2. T. Kawaguchi, K. Takashina, T. Tanaka, and T. Watanabe. Acta Crystallogr. **B28**, 967 (1972).
3. R. Myers, B. H. Torrie, and B. M. Powell. J. Chem. Phys. **79**, 1495 (1983).
4. Y. Iwata and T. Watanabe. Ann. Rep. Res. React. Inst. Kyoto Univ. **7**, 87 (1974).
5. A. Anderson, B. Andrews, and B. H. Torrie. J. Chim. Phys. **82**, 99 (1985).
6. E. Burgos, E. Halac, and H. Bonadeo. J. Chem. Phys. **74**, 1546 (1981).
7. N. V. Sidorov, Y. Krasyukov, E. I. Mukhtarov, and G. N. Zhizhin. Khim. Fiz. **10**, 1320 (1982).
8. A. K. Sharma, V. K. Agarwal, and A Mansingh. Chem. Phys. Lett. **66**, 151 (1979).
9. R. H. Valentine, G. E. Brodale, and W. Giauque. J. Phys. Chem. **66**, 392 (1962).
10. M. Samoc, A. Samoc, and D. F. Williams. Mol. Cryst. Liq. Cryst. **78**, 15 (1981).
11. Pfaltz and Bauer. Research Chemicals Division, Waterbury, Connecticut, 06708, U.S.A.
12. E. F. Westrum, Jr., G. T. Furukawa, and J. P. McCullough. *In* Experimental thermodynamics. Vol. 1. *Edited by* J. P. McCullough and D. W. Scott. Butterworths, London. 1968. Chap. 5.
13. J. L. Riddle, G. T. Furukawa, and H. H. Plumb. Platinum resistance thermometry. U.S. National Bureau of Standards Monograph 126. 1973.
14. Ancom Limited, Devonshire Street, Cheltenham, Gloucestershire, England GL50 3LT.
15. G. T. Furukawa, R. E. McCoskey, and G. J. King. J. Res. Natl. Bur. Stand. **47**, 256 (1951).
16. K. K. Kelley. J. Am. Chem. Soc. **51**, 1145 (1929).
17. R. D. Chirico, I. A. Hossenlopp, A. Nguyen, M. M. Strube, and M. V. Steele. Thermodynamic studies related to the hydrogenation of phenanthrene. National Institute for Petroleum and Energy Research Topical Report No. 247, May 1987, U.S. NTIS Order No. DE87001252.
18. J. Giermanska, A. Samoc, M. Samoc, J. Sworakowski, and Z. Zboinski. Chem. Phys. Lett. **87**, 71 (1982).
19. H. Suga and S. Seki. J. Non-Cryst. Solids, **16**, 171 (1974).
20. T. Shimada, T. Matsuo, H. Suga, and F. Luty. J. Chem. Phys. **85**, 3530 (1986).
21. P. Figuière, H. Szwarc, M. Oguni, and H. Suga. J. Chem. Thermodyn. **17**, 949 (1985).

Standard enthalpies of formation of tris(β-diketonate)manganese(III) complexes: the mean (Mn—O) bond-dissociation enthalpies

MANUEL A. V. RIBEIRO DA SILVA[1] AND M. LUISA C. C. H. FERRÃO

Centro de Investigação em Química, Departamento de Química, Faculdade de Ciências, Universidade do Porto, 4000 Porto, Portugal

Received August 19, 1987

This paper is dedicated to Professor James A. Morrison

MANUEL A. V. RIBEIRO DA SILVA and M. LUISA C. C. H. FERRÃO. Can. J. Chem. **66**, 651 (1988).

The standard molar enthalpies of formation of the crystalline complexes of manganese(III) with 1-phenyl-1,3-butanedione (HBZAC) and 2,2,6,6-tetramethyl-3,5-heptanedione (HDPM) were determined, at 298.15 K, by solution–reaction calorimetry:

$$\Delta_f H_m^0\{Mn(BZAC)_3, cr\} = -1044.9 \pm 8.8 \text{ kJ mol}^{-1}$$

$$\Delta_f H_m^0\{Mn(DPM)_3, cr\} = -1863 \pm 12 \text{ kJ mol}^{-1}$$

The mean molar bond-dissociation enthalpies, $\langle D\rangle$(Mn—O), were derived as 163 ± 10 kJ mol^{-1} and 170 ± 10 kJ mol^{-1}, respectively.

MANUEL A. V. RIBEIRO DA SILVA et M. LUISA C. C. H. FERRÃO. Can. J. Chem. **66**, 651 (1988).

Faisant appel à la calorimétrie par solution–réaction et opérant à 298,15 K, on a mesuré les enthalpies molaires standard de formation des complexes cristallins du manganèse(III) avec la phényl-1 butanedione-1,3 (HBZAC) et la tétraméthyl-2,2,6,6 heptanedione-3,5 (HDPM) qui sont

$$\Delta_f H_m^0(Mn(BZAC)_3, cr) = -1044{,}9 \pm 8{,}8 \text{ kJ mol}^{-1}$$

$$\Delta_f H_m^0(Mn(DPM)_3, cr) = -1863 \pm 12 \text{ kJ mol}^{-1}$$

On en a déduit les enthalpies moyennes des dissociations molaires de liaison, D(Mn—O), qui sont respectivement 163 ± 10 kJ mol^{-1} et 170 ± 10 kJ mol^{-1}.

[Traduit par la revue]

Introduction

The standard molar enthalpies of formation of the crystalline tris(2,4-pentanedionates), $M(ACAC)_3$, of Al(III), Ga(III), Cr(III), Mn(III), and Fe(III) were determined by Irving and co-workers (1–3) using solution–reaction calorimetry. The enthalpies of combustion of $M(ACAC)_3$ (M = Al(III), Ga(III), and In(III)) measured by Cavell and Pilcher (4) confirmed the corresponding results from reaction calorimetry, giving confidence in the reaction calorimetric method.

In this paper, the standard molar enthalpies of formation of two manganese(III) β-diketonates were determined, using the solution–reaction method, to investigate the effect of structural changes in the ligand upon the mean molar manganese–oxygen bond-dissociation enthalpy.

Experimental

The solution calorimeter

The isoperibol LKB 8700 reaction-and-solution precision calorimeter was used. The operation and calculation methods have been described (5). The accuracy of the calorimeter was checked by measuring the molar enthalpy of solution of tris(hydroxymethyl)aminomethane (THAM) in aqueous 0.100 mol dm^{-3} HCl at 298.15 K; $\Delta_{sol}H_m^0 = -29.766 \pm 0.024$ kJ mol^{-1}, in good agreement with the value of Kilday and Prosen (6), $\Delta_{sol}H_m^0 = -29.770 \pm 0.032$ kJ mol^{-1}.

Materials

1-Phenyl-1,3-butanedione: HBZAC (Koch–Light Laboratories Ltd.) was purified by repeated crystallization from ethanol + water. *Anal.* calcd. for $C_{10}H_{10}O_2$: C, 74.06, H 6.22%; found: C 73.89, H 6.25%.

2,2,6,6-Tetramethyl-3,5-heptanedione: HDPM was prepared by Claisen condensation according to the methods of Adams and Hauser (7) and of Kopecky *et al.* (8), was purified by fractional distillation in vacuum, and the purity was assessed as better than 99.9 mol% by glc, using two different columns. The liquid β-diketone was stored under nitrogen in the dark and was freshly distilled prior to use.

Tris(1-phenyl-1,3-butanedionato)maganese(III): $Mn(BZAC)_3$ was prepared as described by Fay and Piper (9), purified by crystallization from acetone + hexane, and dried at 483 K. *Anal.* calcd. for $C_{30}H_{27}O_6Mn$: C 66.92, H 5.05, Mn 10.20%; found: C 66.90, H 5.09, Mn 10.48%.

Tris(2,2,6,6-tetramethyl-3,5-heptanedionato)maganese(III): $Mn(DPM)_3$ was prepared as described by Hammond *et al.* (10) and was purified by vacuum sublimation. *Anal.* calcd. for $C_{33}H_{57}O_6Mn$: C 65.54, H 9.50, Mn 9.08%; found: C 65.28, H 9.43, Mn 9.17%.

Manganese(II) chloride tetrahydrate: Manganese(II) chloride tetrahydrate (AnalaR, BDH) was dried over silica gel; its composition was determined by means of manganese analyses and found to be $MnCl_2 \cdot 4.00H_2O$.

Iron(II) and iron(III) chloride: CERAC samples of $FeCl_2$ and $FeCl_3$ (stated minimum purity 99.99%) were used.

Hydrochloric acid: Concentrated HCl (AnalaR, BDH) was diluted with distilled water. The concentration was determined by titration against $Na_2B_4O_7 \cdot 10H_2O$ and found to be (series of six titrations) 4.590 ± 0.003 mol dm^{-3}, which corresponds (11) to the composition $HCl \cdot 10.98H_2O$.

1,4-Dioxan: 1,4-Dioxan (Carl Erba) was purified as described previously (12).

Carbon and hydrogen analyses were carried out by the Microanalytical Service of the University of Surrey; manganese was analysed by the ethylenediaminetetracetic acid method (13); under the conditions used, the error associated with the manganese analyses is less than 0.02%.

For the hydrolysis and reduction reactions the solvents were

[1]Author to whom correspondence may be addressed.

Can. J. Chem. Downloaded from www.nrcresearchpress.com by 176.9.209.113 on 09/07/12
For personal use only.

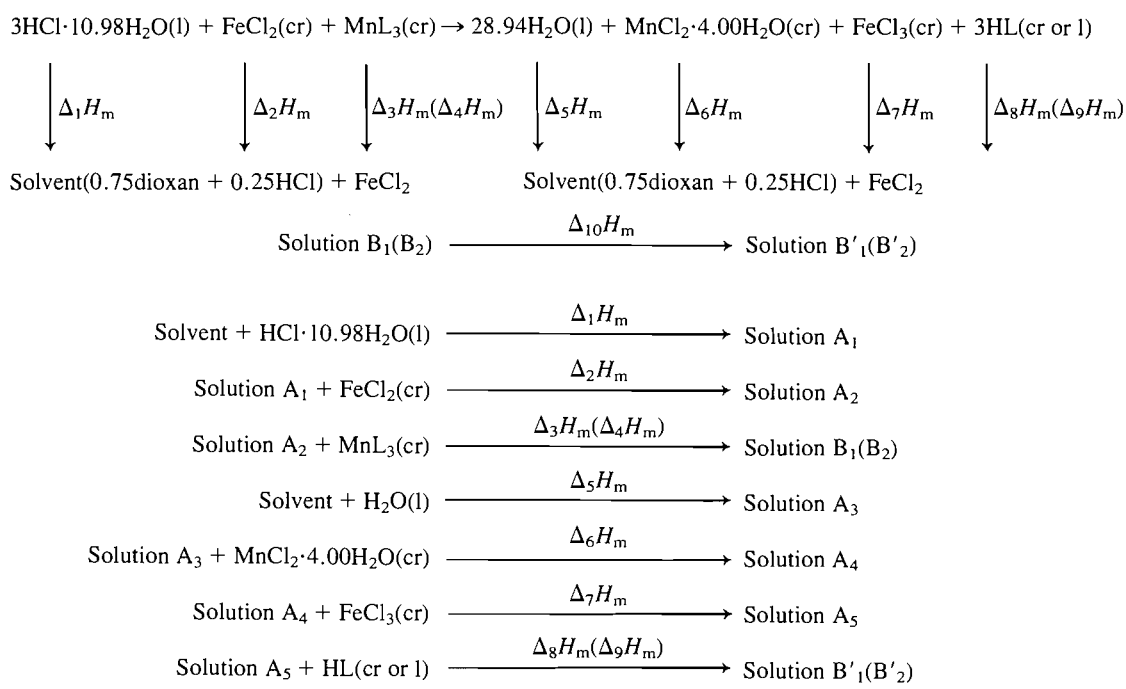

SCHEME 1

degassed and saturated with purified nitrogen prior to each determination.

The relative atomic masses used were those recommended by the IUPAC Commission (14).

All uncertainty intervals given are twice the standard deviation of the mean.

Results and discussion

Preliminary tests showed that the manganese(III) β-diketonates hydrolyse rapidly using 0.75(1,4-dioxan) + 0.25HCl(aq, 4.5 mol dm^{-3}) by volume as the initial calorimetric solvent and, furthermore, that the manganese(III) ion was quantitatively reduced to the manganese(II) ion in the presence of an excess of ferrous salt.

The standard enthalpies of formation of $Mn(BZAC)_3$ and $Mn(DPM)_3$ were determined from the thermochemical reaction

$$MnL_3(cr) + FeCl_2(cr) + 3HCl\cdot 10.98H_2O(l) \rightarrow 28.94H_2O(l) + MnCl_2\cdot 4.00H_2O(cr) + FeCl_3(cr) + 3HL(cr\ or\ l)$$

which was studied in the presence of an excess of $FeCl_2$: to the calorimetric solvent (95.00 cm^3), 5.00 cm^3 of $FeCl_2$, 0.1 mol dm^{-3}, was added. The same batch of solvent was used for both complexes.

The standard enthalpies of the thermochemical reactions ($\Delta_r H_m^0$) were determined by measuring the enthalpies of solution of the reactants and products successively in the initial calorimetric solvent, so that the final solution resulting from the dissolution of all the reactants was of the same composition as that from dissolution of all the products.

The thermochemical cycle and the general procedure for the calorimetric study of the manganese(III) complexes is given in Scheme 1. The quantities of reactants in a particular series of experiments were determined by the amount of $MnL_3(cr)$ (approximately 2.5×10^{-4} mol) in a particular ampoule, so that control of the stoichiometry was maintained for each series.

Thus, the difference between the molar enthalpies of solution of products and reactants, in the correct stoichiometric ratio, gives the enthalpy of the thermochemical reaction ($\Delta_r H_m^0$), provided equilibrium is reached from either side, within the period of the experiment. As a check of the validity of this statement, ampoules of the final solution of reactants were broken, in the calorimeter, into the final solution of products: no heat was detected.

The results are summarized in Table 1, and they lead to

$$\Delta_r H_m^0\{Mn(BZAC)_3\} = 3\Delta_1 H_m + \Delta_2 H_m + \Delta_3 H_m - 28.94\Delta_5 H_m - \Delta_6 H_m - \Delta_7 H_m - 3\Delta_8 H_m$$
$$= -76.9 \pm 1.2\ kJ\ mol^{-1}$$

$$\Delta_r H_m^0\{Mn(DPM)_3\} = 3\Delta_1 H_m + \Delta_2 H_m + \Delta_4 H_m - 28.94\Delta_5 H_m - \Delta_6 H_m - \Delta_7 H_m - 3\Delta_9 H_m$$
$$= -17.0 \pm 1.2\ kJ\ mol^{-1}$$

With the following auxiliary data, $\Delta_f H_m^0$(kJ mol^{-1}): $H_2O(l)$, -285.83 ± 0.04 (15); HCl in $10.98H_2O(l)$, -161.77 ± 0.01 (16); $FeCl_3(cr)$, -399.49 ± 0.29 (16, 17); $FeCl_2(cr)$, -341.79 ± 0.21 (16, 17); $MnCl_2\cdot 4.00H_2O(cr)$, -1687.4 ± 2.1 (16); HBZAC(cr), -335.1 ± 2.8 (18); HDPM(l), -587.7 ± 3.8 (18), the standard molar enthalpies of formation of the crystalline manganese(III) β-diketonates were derived.

$$\Delta_f H_m^0\{Mn(BZAC)_3, cr\} = -1044.9 \pm 8.8\ kJ\ mol^{-1}$$
$$\Delta_f H_m^0\{Mn(DPM)_3, cr\} = -1863 \pm 12\ kJ\ mol^{-1}$$

The values for the sublimation enthalpies of $Mn(BZAC)_3$ and $Mn(DPM)_3$ are not available. Estimates based on their structure, molecular weight, and other known values for similar complexes, using an estimation scheme (19), were used to derive the standard enthalpies of formation of the complexes in the gaseous state. Attempts to measure the enthalpies of sublimation of the Mn(III) β-diketonates, using the "vacuum sublimation" drop-microcalorimetric method (20), were unsuccessful because it was verified that extensive decomposition was associated with the sublimation process. This has also been confirmed by Murray and Hill (21) for the sublimation of $Mn(ACAC)_3$.

Can. J. Chem. Downloaded from www.nrcresearchpress.com by 176.9.209.113 on 09/07/12
For personal use only.

TABLE 1. Molar enthalpies of solution and reaction (kJ mol^{-1}) at 298.15 K

i	Reactant	Solvent	Solution	No. of expts.	$\Delta_i H_m$
1	$HCl \cdot 10.98H_2O$(l)	Initial	A_1	5	−21.00±0.12
2	$FeCl_2$(cr)	A_1	A_2	5	−62.95±0.90
3	$Mn(BZAC)_3$(cr)	A_2	B_1	5	+8.37±0.23
4	$Mn(DPM)_3$(cr)	A_2	B_2	5	+20.22±0.36
5	H_2O(l)	Initial	A_3	5	−0.913±0.003
6	$MnCl_2 \cdot 4.00H_2O$(cr)	A_3	A_4	5	−14.06±0.31
7	$FeCl_3$(cr)	A_4	A_5	5	−82.08±0.49
8	HBZAC(cr)	A_5	B_1'	5	+27.28±0.06
9	HDPM(l)	A_5	B_2'	5	+11.27±0.09
10	Solution B_1	B_1'	$B_1 = B_1'$	5	0.00±0.05
	Solution B_2	B_2'	$B_2 = B_2'$	5	0.00±0.04

TABLE 2. Standard molar enthalpies of formation and sublimation at 298.15 K

Complex	$\Delta_f H_m^0$(cr)/kJ mol^{-1}	$\Delta_{sub} H_m^0$/kJ mol^{-1}	$\Delta_f H_m^0$(g)/kJ mol^{-1}
$Mn(ACAC)_3$	−1379.0±3.7[a]	(120±10)[b]	−1259±11
$Mn(BZAC)_3$	−1044.9±8.8	(195±10)[b]	−850±13
$Mn(DPM)_3$	−1863±12	(140±10)[b]	−1723±16

[a]Reference 3.
[b]Estimated value, ref. 22.

Table 2 lists the estimated enthalpies of sublimation (22) and the standard enthalpies of formation in the crystalline and gaseous states of the Mn(III) β-diketonates studied, together with the corresponding values for the tris(2,4-pentanedionato)manganese(III), recalculated from the value of Hill and Irving (3) using the most recent auxiliary data.

By regarding the six Mn—O bonds in a particular complex as equivalent (23), which is supported by the known X-ray crystal structure of tris(2,4-pentanedionato)manganese(III), where the manganese–oxygen bond lengths are equal (198.5 ± 1.7 pm) (24), the mean manganese–oxygen bond-dissociation enthalpy, $\langle D \rangle$(Mn—O), in MnL_3, may be defined as one sixth of the molar enthalpy of the disruption reaction

$$ML_3(g) \rightarrow Mn(g) + 3L(g)$$

$$\Delta_{disr}H_m^0 = \Delta_f H_m^0(Mn, g) + 3\Delta_f H_m^0(HL, g) - 3\Delta_f H_m^0(H, g) - \Delta_f H_m^0(MnL_3, g) - 3D(O—H, HL, enol)$$

where D(O—H, HL, enol) is the molar enthalpy of dissociation of the enolic hydrogen in the parent ligand

$$HL(g) \rightarrow H(g) + L(g)$$

There are no measured values for this quantity; values have been proposed ranging from 365 to 430 kJ mol^{-1}, and the situation has been recently reviewed (19). In this work, for comparison reasons, the value D(O—H, HL, enol) = 418 ± 20 kJ mol^{-1} (19) is used.

With the auxiliary data, $\Delta_f H_m^0$(kJ mol^{-1}): HACAC(enol, g), −384.4 ± 1.3 (25); HBZAC(enol, g), −251.3 ± 2.9 (18); HDPM(enol, g), −528.4 ± 3.9 (18); H(g), 218.00 ± 0.01 (15); Mn(g), 280.7 ± 4.2 (16), values of $\Delta_{disr}H_m^0$ and $\langle D \rangle$(Mn—O) were derived and are given in Table 3.

The calculated mean manganese–oxygen bond-dissociation enthalpies for the three complexes are almost the same, within the uncertainties associated with them. Inductive or bulky effects due to —C_6H_5 or —$C(CH_3)_3$ substitution in the ligand appear to have no influence, or only a very small one, on the donor properties of the coordinated oxygen atoms. This effect has already been observed for complexes of β-diketones with Be(II) (26), Al(III) (26), Co(II) (27), Cu(II) (28, 29), Cr(III) (30), Fe(III) (31), and Co(III) (32).

TABLE 3. $\langle D \rangle$(Mn—O) at 298.15 K

Complex	$\Delta_{disr}H_m^0$/kJ mol^{-1}	$\langle D \rangle$(Mn—O)/kJ mol^{-1}
$Mn(ACAC)_3$	987±61	164±10
$Mn(BZAC)_3$	977±62	163±10
$Mn(DPM)_3$	1019±61	170±10

Acknowledgements

We thank NATO, Research Grant 1709, for partial support, and the Instituto Nacional de Investigação Científica, Lisboa, for support given to a Research Project (L.5) of the Centro de Investigação em Química, Universidade do Porto. Thanks are also due to the Junta Nacional de Investigação Científica e Tecnológica, Lisboa, for partial support under Research Contract no. 220-80.32.

1. J. O. HILL and R. J. IRVING. J. Chem. Soc. A, 971 (1966).
2. R. J. IRVING and G. W. WALTER. J. Chem. Soc. A, 2690 (1969).
3. J. O. HILL and R. J. IRVING. J. Chem. Soc. A, 1413 (1967).
4. K. J. CAVELL and G. PILCHER. J. Chem. Soc. Faraday Trans. I, **73**, 1590 (1977).
5. M. A. V. RIBEIRO DA SILVA and R. J. IRVING. Bull. Chem. Soc. Jpn. **50**, 734 (1977).
6. M. V. KILDAY and E. J. PROSEN. J. Res. Natl. Bur. Stand. Sect. A: **77**, 581 (1973).
7. J. T. ADAMS and C. R. HAUSER. J. Am. Chem. Soc. **66**, 1220 (1944).
8. K. R. KOPECKY, D. C. NONHEBEL, and G. S. MORRIS. J. Org. Chem. **27**, 1036 (1962).
9. R. C. FAY and T. S. PIPER. J. Am. Chem. Soc. **84**, 2303 (1962).
10. G. S. HAMMOND, D. C. NONHEBEL, and C. S. WU. Inorg. Chem. **2**, 73 (1963).

Can. J. Chem. Downloaded from www.nrcresearchpress.com by 176.9.209.113 on 09/07/12
For personal use only.

11. R. C. WEAST (*Editor*). Handbook of chemistry and physics. 55th ed. The Chemical Rubber Co., Cleveland, OH. 1974.
12. D. D. PERRIN, W. L. ARMAREGO, and R. D. PERRIN. Purification of laboratory chemicals. Pergamon Press, London. 1966.
13. H. A. FLASKA. EDTA titrations. Pergamon Press, London. 1959.
14. Atomic weights of the elements. Pure Appl. Chem. **51** (1979).
15. CODATA. J. Chem. Thermodyn. **10**, 903 (1978).
16. The NBS tables of chemical thermodynamic properties. J. Phys. Chem. Ref. Data, **11**, 1982. Supplement no. 2.
17. M. F. KOEHLER and J. P. COUGHLIN. J. Phys. Chem. **63**, 605 (1959).
18. M. L. C. C. H. FERRÃO, M. A. V. RIBEIRO DA SILVA, S. SURADI, G. PILCHER, and H. A. SKINNER. J. Chem. Thermodyn. **13**, 567 (1981).
19. M. A. V. RIBEIRO DA SILVA (*Editor*). Thermochemistry and its applications to chemical and biochemical systems. NATO ASI Series. Reidel, Dordrecht. 1984. p. 317 ff.
20. F. A. ADEDEJI, D. L. S. BROWN, J. A. CONNOR, M. LEUNG, M. I. PAZ-ANDRADE, and H. A. SKINNER. J. Organomet. Chem. **97**, 221 (1975).
21. J. P. MURRAY and J. O. HILL. Thermochim. Acta, **109**, 383 (1987).
22. M. L. C. C. H. FERRÃO. Ph.D. thesis. University of Porto, Portugal. 1982.
23. E. C. LINGAFELTER and R. L. BRAUN. J. Am. Chem. Soc. **88**, 2951 (1966).
24. J. P. FLACKER and A. AVDEEF. Inorg. Chem. **13**, 1864 (1974).
25. J. M. HACKING and G. PILCHER. J. Chem. Thermodyn. **11**, 1015 (1979).
26. M. A. V. RIBEIRO DA SILVA and A. M. M. V. REIS. J. Chem. Thermodyn. **15**, 957 (1983).
27. M. A. V. RIBEIRO DA SILVA and M. L. C. C. H. FERRÃO. Polyhedron, **7**, 421 (1988).
28. M. A. V. RIBEIRO DA SILVA, M. D. M. C. RIBEIRO DA SILVA, A. P. S. M. CARVALHO, M. J. AKELLO, and G. PILCHER. J. Chem. Thermodyn, **16**, 137 (1984).
29. M. A. V. RIBEIRO DA SILVA and M. L. C. C. H. FERRÃO. J. Chem. Thermodyn. **20**, 359 (1988).
30. M. A. V. RIBEIRO DA SILVA and M. L. C. C. H. FERRÃO. J. Chem. Thermodyn. **19**, 645 (1987).
31. M. A. V. RIBEIRO DA SILVA and M. L. C. C. H. FERRÃO. J. Chem. Thermodyn. **20**, 79 (1988).
32. M. A. V. RIBEIRO DA SILVA and M. L. C. C. H. FERRÃO. Bull. Chem. Soc. Jpn. In press.

Can. J. Chem. Downloaded from www.nrcresearchpress.com by 176.9.209.113 on 09/07/12
For personal use only.

Nitrosodisulphonates and hydroxylamine-*N*,*N*-disulphonates. V. A potassium salt of hydroxylamine-*N*,*N*-disulphonic acid with a displacive superlattice structure

JOHN S. RUTHERFORD
Department of Chemistry, University of Transkei, Private Bag X1001, Umtata, Transkei, Southern Africa
AND
BEVERLY E. ROBERTSON[1] AND RICHARD J. GUTTORMSON[2]
Department of Physics and Astronomy, University of Regina, Regina, Sask., Canada S4S 0A2
AND
DAVID B. RUSSELL
Department of Chemistry, University of Saskatchewan, Saskatoon, Sask., Canada S7N 0W0
Received September 18, 1987
This paper is dedicated to Professor J. A. Morrison[3]

JOHN S. RUTHERFORD, BEVERLY E. ROBERTSON, RICHARD J. GUTTORMSON, and DAVID B. RUSSELL. Nitrosodisulphonates and hydroxylamine-*N*,*N*-disulphonates. V. A potassium salt of hydroxylamine-*N*,*N*-disulphonic acid with a displacive superlattice structure. Can. J. Chem. **66**, 655 (1988).

The structure of the potassium salt of hydroxylamine-*N*,*N*-disulphonate, with the formula $K_5HN_2S_4O_{14}\cdot H_2O$, has been determined by X-ray diffraction. The crystals are triclinic, a = 14.011(6), b = 16.118(9), c = 11.867(6) Å, α = 103.28(6), β = 106.76(3), γ = 86.38(3)°, $P\bar{1}$ with Z = 6. The integrated intensities of 8694 independent reflections were measured on a four-circle diffractometer, 5236 of which were used in the refinement to give a final least-squares weighted residual of 0.107 and a conventional R factor of 0.081.

The structure forms a six-fold derivative lattice, which arises by small displacements (ca. 0.2 Å) of the atom positions from an average structure which is triclinic with Z = 1. This results in three very short H bonds, average length 2.46 Å, which link the three independent anion-dimers, being symmetry-free in this structure. Other bond lengths and angles in the anions are very similar to those in the Rb salt. The K^+ ions show 8, 9, and 10 coordination, in a number of different polyhedral types. The three independent water molecules are each coordinated to three totally distinct K^+ ions, and are linked to the anions by weak H bonds. The structural complexity may be explained in terms of a Lewis acid–base "mismatch" of the cations and anions present.

JOHN S. RUTHERFORD, BEVERLY E. ROBERTSON, RICHARD J. GUTTORMSON et DAVID B. RUSSELL. Nitrosodisulphonates and hydroxylamine-*N*,*N*-disulphonates. V. A potassium salt of hydroxylamine-*N*,*N*-disulphonic acid with a displacive superlattice structure. Can. J. Chem. **66**, 655 (1988).

Faisant appel à la diffraction des rayons-X, on a déterminé la structure du sel de potassium du *N*,*N*-disulfonate de l'hydroxylamine, de formule $K_5HN_2S_4O_{14}\cdot H_2O$. Les cristaux sont tricliniques avec a = 14,011(6), b = 16,118(9) et c = 11,867(6) Å, α = 103,28(6), β = 106,76(3) et γ = 86,38(3)°, Z = 6 et groupe d'espace $P\bar{1}$. On a mesuré les intensités intégrées de 8694 réflexions à l'aide d'un diffractomètre à quatre cercles et on a utilisé 5236 de ces réflexions pour l'affinement jusqu'à des valeurs de R_w = 0,107 et R = 0,081.

La structure forme un réseau sénaire qui provient de petits déplacements (environ 0,2 Å) des positions des atomes par rapport à une structure moyenne qui est triclinique avec Z = 1. Il en résulte qu'il existe trois liaisons hydrogènes qui sont très courtes, longueur moyenne de 2,46 Å, qui relient les trois anions-dimères indépendants et qui sont sans symétrie à l'intérieur de cette structure. Les autres angles et longueurs de liaison des anions sont très semblables à ceux qui ont été observés dans le sel de Rb. Les ions K^+ présentent des coordinations de 8, 9 et 10, dans un certain nombre de types différents de polyèdres. Les trois molécules d'eau indépendantes sont chacune coordonnées à trois ions K^+ totalement différents et elles sont liées aux anions par des liaisons hydrogènes faibles. La complexité de la structure peut être expliquées en fonction d'une mauvaise adaptation acide–base de Lewis des cations et des anions présents.

[Traduit par la revue]

Introduction

Previous articles in this series (1–3) have discussed the preparation and characterisation of a number of alkali metal salts of hydroxylamine-*N*,*N*-disulphonate and related ions, and have examined the epr spectra of these salts when irradiated to compare the spectra obtained with the spectra obtained from Fremy's salt, both as a pure solid, when a triplet state species is observed (2, 4), and as a dilute solid solution in the corresponding potassium hydroxylamine-*N*,*N*-disulphonate, when a free radical species is observed (5). In particular, the triplet state epr spectra obtained from a single crystal of γ-irradiated $Rb_5\{[ON(SO_3)_2]_2H\}\cdot 3H_2O$ could be explained as a consequence of two very distinct centrosymmetric sites for the dimeric ion of the formula $\{[ON(SO_3)_2]_2H\}^{5-}$, where the species formed involves the two NO groups in close proximity, and where, in the unirradiated salt, the two NO groups are linked by a central hydrogen bond N—O...H...O—N (1). The corresponding potassium salt, $K_5\{[ON(SO_3)_2]_2H\}\cdot H_2O$, however, showed a superposition of six very similarly oriented such triplet state spectra[4] and since a preliminary X-ray examination of this salt showed six formula units per triclinic unit cell, it seemed apparent that a more detailed study by X-ray diffraction would be required in order to venture an interpretation of the epr spectrum.

[1]Author to whom correspondence may be addressed.

[2]Current address: Department of Regional Industrial Expansion, Government of Canada, 235 Queen Street, Ottawa, Ont., Canada K1A 0H5.

[3]J.S.R. and B.E.R. were students of his friend and colleague, C. Calvo.

[4]D. B. Russell. Unpublished work.

Can. J. Chem. Downloaded from www.nrcresearchpress.com by 176.9.209.113 on 09/07/12
For personal use only.

Can. J. Chem. Downloaded from www.nrcresearchpress.com by 176.9.209.113 on 09/07/12
For personal use only.

At an early stage of the diffraction study it became clear that the structure of the potassium salt probably contained a six-fold superstructure; i.e., the basic sublattice structure contained only one-half of one formula unit. Some interest has developed regarding group theoretical methods of describing such structures (6) and also regarding relevant phase-determining methods (7–11), since clearly the normal direct method assumptions regarding randomness must break down. We therefore sought to classify this superlattice structure as substitutional or displacive, as commensurate or incommensurate and as to whether it could be considered a modulated structure as described below.

The central hydrogen bonds in the rubidium salt are very short with O...O distances of 2.41(2) and 2.43(2) Å in the two independent dimers. In common with almost all other very short and apparently symmetrical H bonds, as pointed out by Catti and Ferraris (12), these bonds in the rubidium salt are constrained to lie on crystallographic symmetry elements, centres of symmetry in this particular case. Since no such constraint applies to the potassium salt, it would therefore present a rare case of symmetry-free (SF) hydrogen bonds, which should help determine whether such very short H bonds are truly asymmetric.

Experimental

$K_5HN_2S_4O_{14}\cdot H_2O$ Mol. wt. = 599.47

Triclinic, space group $P\bar{1}$, a = 14.011(6), b = 16.118(9), c = 11.867(6) Å, α = 103.28(6), β = 106.76(3), γ = 86.38(3)°, T = 20°C, V = 2497(2) Å^3, Z = 6, D_x = 2.373 g cm^{-3}, μ(MoKα) = 18.9 cm^{-1}, F(000) = 1776, MoKα_1, λ = 0.70926 Å.

The preparation of the crystals was described previously (2). A single crystal too large for X-ray work was ground into a sphere of radius 0.02 cm, and on this measurements were made using a Picker FACS-1 automated diffractometer fitted with graphite monochromator. Lattice parameters and crystal orientation were determined from 20 reflections in the range $32° \leq 2\theta \leq 45°$, and intensities were measured in the 2θ scan mode with a scan rate of 2.0° min^{-1} and a 20 s background count. Of the 8694 unique reflections so measured ($\sin\theta/\lambda \leq 0.639$) 5236 were classified as observed ($I \geq 1.3\sigma(I)$). The data were corrected for Lorentz and polarisation effects but not for absorption.

When the structure was recognised as being based on a superlattice, the diffraction pattern was carefully reexamined in order to confirm the commensurability of the superlattice and the absence of additional features in the diffraction pattern. Also, since the superlattice might arise from a modulating displacement wave (effectively a frozen lattice vibrational mode), the diffraction pattern was examined at various temperatures above room temperature in order to investigate the possible presence of a phase transition to the basic sublattice structure, such as occurs, for instance, in some pyrophosphates (13, 14). No such phase transition was found below 70°C, the decomposition temperature of the crystals.

γ-Irradiated single crystals of the salt $[K_5\{H[ON(SO_3)_2]_2\}\cdot H_2O]$ have a very complicated epr spectrum. The spectrum does, however, show six triplet state spectra with the same splitting parameters but with their principle axes oriented slightly differently in the crystal. This indicates that there are six sites all very similar in environment and close to each other in orientation. This observation led to the detection of a marked subcell, related to the true unit cell by the transformation

$$\begin{pmatrix} 1/6 & -1/3 & 1/6 \\ -1/2 & 0 & -1/2 \\ 1/2 & 0 & -1/2 \end{pmatrix},$$

a subcell where the shortest translation vector (1/6) [1 $\bar{2}$ 1] has length 6.218 Å. The average subcell was solved first, using Patterson methods and the subcell reflections. The subcell showed a centrosymmetric intensity distribution. The subcell Patterson map showed several multiple weight peaks and its was not possible to fit them with a centrosymmetric arrangement of the nine heavy atoms in the subcell. Assuming superposition, a seven atom solution was found which contained the five K atoms and two O atoms. Further electron density calculations revealed the four S atoms. Difference Fourier calculations revealed the remaining non-hydrogen atoms and the subcell was refined by full-matrix least squares to $R = 0.18$. This yielded a complete average subcell structure, in the space group $P\bar{1}$, containing a centrosymmetric anion-dimer similar to those in $Rb_5\{H[ON(SO_3)_2]_2\}\cdot 3H_2O$.

When the reflections are classified according to an index m = [$(h - 2k + l)$ modulo 6], such that the sublattice reflections have $m = 0$, the relative intensity averages for the various classes provide information on the nature of the superstructure. We found

$$\frac{\langle I_{super}\rangle}{\langle I_{sub}\rangle} = \frac{0.13d^{*2}}{1 - 0.65d^{*2}}$$

where the right hand side represents the formula

$$\frac{\frac{4}{3(n-1)}\pi^2 d^{*2}\partial^2}{1 - \frac{4}{3}\pi^2 d^{*2}\partial^2}$$

which is a generalisation of an expression due to Mackay (15) to three dimensions and an n-fold superlattice. This formula applies to a displacive superlattice having a root-mean-square displacement of ∂. In this case ∂ calculates to be 0.22 Å. This test confirms that the superlattice is displacive; i.e., it is based purely on spatial deviations on an identical set of atoms in each subcell, rather than substitutional, where different atomic species (or atoms and voids) occur in different subcells, possibly together with displacements. In the case of a substitutional superlattice the intensity of the superlattice reflections should be significantly non-zero at zero angle. One important type of displacive superlattice is the modulated structure, where the displacements follow a sinusoidal pattern. Superlattice scattering from such a structure should occur predominantly (in the ideal case, exclusively) from the reciprocal lattice vectors corresponding to the modulation wave.

Also, we found the ratios $\langle Im = n\rangle/\langle Im = 0\rangle$ to be 2.2, 0.1, and 0.4 for $n = \pm 1$, ± 2, and 3, respectively. The fact that reflections for which $m = \pm 1$ are the strongest superlattice reflections suggests that the superlattice resembles a modulated structure. The average values of $\langle Im = n\rangle/\langle Im = 0\rangle$ for this model and another were calculated and compared with the observed values of the ratio. The average displacement of the atoms from its average position in each subcell for the two models considered is given in Table 1*a*. The results for $\langle Im = n\rangle/\langle Im = 0\rangle$ are given in Table 1*b*.

Both models are similar in that the displacements are assumed to vary in a regular and predictable way from one subcell to the next, and are identical in the effective "wavelength" of this displacement pattern. In the light of the general agreement of both models, it was decided to choose as a compromise a starting model with displacements 0.9∂, 1.2∂, 0.9∂, -0.9∂, -1.2∂, -0.9∂ in the subcells labelled A to F respectively.

There now remained two problems, one being to assign an origin to the true cell in terms of the co-ordinates used for the subcell, the other of finding values for the ∂_j's, the individual atomic displacements from the average positions. The origin problem arises because in the subcell model, since it conforms to space group $P\bar{1}$, there are eight centres of symmetry (the eight equipoints of order one). In transforming to an n-fold supercell also in space group $P\bar{1}$ only $1/n$ of these centres will be retained. Whether all 8, or 4, 2, or 1 of the subcell equipoint types are represented among the true symmetry centres in the resulting supercell depends on whether the n-fold increase in volume involves a factor of 2 not at all, or in 1, 2, or 3 independent directions. Here, since $n = 6$ involves only one factor of 2, four of the eight subcell equipoint types must be completely eliminated in the transformation. Effectively this means that there is a choice between two possible sets of 4 origins for the supercell, only one of which is correct.

Fortunately in this case the choice is relatively easy, since the three

TABLE 1

(*a*) Average displacement of the atoms in each subcell from their position in the supercell, in Model 1, a *square-wave* displacement model, and Model 2, a *sinusoidal* displacement model

	Average displacement	
Subcell	Model 1	Model 2
A	∂	$\frac{3}{4}\partial$
B	∂	$\frac{3}{2}\partial$
C	∂	$\frac{3}{4}\partial$
D	$-\partial$	$-\frac{3}{4}\partial$
E	$-\partial$	$-\frac{3}{2}\partial$
F	$-\partial$	$-\frac{3}{4}\partial$

(*b*) Observed and predicted values of $\langle Im = n\rangle/\langle Im = 0\rangle$

	Value		
n	Observed	Model 1	Model 2
± 1	2.2	2.37	$2.50m$
± 2	0.1	0	0
3	0.4	0.22	0

occupied equipoints in the subcell structure mentioned previously all belong to one set. It seemed reasonable to pursue the choice of origin which eliminated all symmetry restrictions on atomic positions, rather than the alternative, which placed some atoms in chemically unreasonable environments. This point will be developed further in the discussion. Initial values of ∂_j for each atom were derived from the observed splitting of the atom K(3) in the average structure. Since the electron density corresponding to these atoms, unlike that of any others, was resolved into two peaks of equal weight, it was assumed that one peak position was occupied in three successive subcells and the other in the remaining three. It was further assumed that the environment of these atoms moved in the same direction but to a varying extent in each subcell. These values were then refined by least squares by placing atoms at $+\partial_j$ and $-\partial_j$ in subcells B and E, respectively, and leaving the other subcells empty. This required using only the data $m = 0, \pm 1$, rescaled with $F_0 = F_0/3$ for $m = 0$ and $F_0 = F_0/2$ for $m = \pm 1$. After the ∂_j's were found, all the subcells were filled and refinement proceeded smoothly using all the data.

Anisotropic temperature factors were introduced at an appropriate point, and subsequently the hydrogen atoms, found from a difference map, were introduced and refined with isotropic temperature factors.

The final R factor and R_w factor were 0.081 and 0.107. The weights were assigned as $w^{-1/2} = 2.048 + 0.130\,|F_0| + 0.00005\,|F_0|^2$.

The atomic coordinates and equivalent isotropic thermal parameters are listed in Table 2.[5]

Discussion

The phase-determining procedures used in the solution of the structure are extensions of those previously developed and applied successfully to displacive superlattices by Calvo and co-workers (16–19). In each case an average structure was determined first, using only the sublattice reflections, and subsequently the superlattice reflections were used to derive the small displacements characterising the true structure. There are good reasons to believe[6] that any attempt to phase-determination by a one-step process is likely to fail for these structures which have extremely high non-random variance of the normalised structure factors. Such processes include those direct methods techniques (7–11) which use the renormalisation approach (20).

Figure 1 shows a general view of the structure. Each subcell has associated with it one hydroxylamine anionic moiety and two potassium ions. In addition, the total structure contains three hydrogen atoms, three water molecules, and three further potassium ions, all of which were at centres of symmetry in the averaged supercell structure. The hydrogen atoms join the hydroxylamine moieties in pairs AF, BE, and CD to form the pentavalent dimeric anions which were assumed to exist in the rubidium salt (1). However, the symmetrically bonded hydrogen atoms which join the dimers are readily observed in the potassium salt. The nine atoms which were constrained to be on centres of symmetry in the supercell have been given the labels of subcells A, B, and C.

Average distances and bond angles for the hydroxylamine anion are given in Table 3, with the average of the estimated standard deviations given by least squares and a standard deviation calculated from the variation in the quantities averaged, assuming that their true values are the same. Taylor and Kennard (21) have compared independent determinations of the same structure and concluded that esd's from least squares are underestimated on the average by a factor of approximately 1.5. If we assume such a correction for the average esd in Table 3, the sample standard deviation exceeds the average esd in eleven of 24 cases, and in none of the 24 cases does the sample standard deviation exceed twice the average esd. We conclude that these variations are probably not significant.

Also, the variation among chemically equivalent bond lengths appears not to be significant. However, variation among chemically equivalent bond angles is clearly significant, particularly the N—S—O angles, ranging from 101.0(3, 9) to 109.4(4, 3). These variations in average values reflect features in the packing of the average structure, carried over to the subcells of the superstructure.

The distance O(1)—N(1)—O(1) for the dimers AF, BE, and CD are 2.474(7), 2.446(7), and 2.473(7) Å, respectively. The average, 2.464(16) Å, is larger than in the Rb salt (2.41(2) and 2.43(2) Å).

The dimer configuration is basically the same as in the rubidium salt, with the hydroxylamine moiety in the *trans*-configuration, but, while the central sections of the two independent dimers in the rubidium compound both approximate $2/m$ symmetry, in the potassium compound only one (dimer BE) approaches this symmetry, while the other two dimers (AF and CD) do not. However, in each case they maintain the local pseudo-centre of symmetry at the central H bond intact. The structure is indeed a six-fold displacive superlattice, and the displacements from the average subcell positions are roughly sinusoidal in form, except for atoms K(3A) to K(3F) and the water molecules. If these particular atoms are excluded, the weighted mean of the displacements has the predicted value of 0.22 Å, the values for the individual heavy atoms being K(1A) to K(1C), 0.24 Å; K(2A) to K(2F), 0.17 Å; S(1A) to S(1F), 0.24 Å; and S(2A) to S(2F), 0.25 Å.

All of the oxygen atoms in this structure are co-ordinated to K^+ ions, which, as a result, show irregular eight, nine, or ten co-ordination. The 15 K^+ co-ordination polyhedra in the

[5]Tables of observed and calculated structure factor amplitudes, anisotropic temperature factors, and individual bond lengths and angles may be purchased from the Depository of Unpublished Data, CISTI, National Research Council of Canada, Ottawa, Ont., Canada K1A 0S2.

[6]J. S. Rutherford. Unpublished results.

Can. J. Chem. Downloaded from www.nrcresearchpress.com by 176.9.209.113 on 09/07/12
For personal use only.

TABLE 2. Fractional atomic co-ordinates and isotropic (or equivalent isotropic) temperature factors with estimated standard deviations in parentheses[a]

Atom	Parameter	Value in subcell A	B	C	D	E	F
K(1)	x	91686(14)	74416(14)	57765(21)			
	y	15791(13)	48604(12)	82846(15)			
	z	40343(19)	22147(18)	7227(23)			
	U_{eq}	397(7)[b]	359(6)	664(10)			
K(2)	x	6107(13)	88328(13)	71041(13)	53681(14)	37579(16)	22100(14)
	y	7580(10)	42010(11)	75603(11)	9161(12)	41628(13)	74095(11)
	z	13653(15)	97101(16)	81545(16)	64772(16)	48079(18)	30521(16)
	U_{eq}	268(5)	285(5)	316(5)	316(6)	392(6)	313(5)
K(3)	x	70084(12)	52869(13)	35423(14)	19256(13)	3593(15)	87257(13)
	y	6251(11)	39903(11)	74373(11)	7356(11)	39645(12)	72679(11)
	z	98975(17)	83170(19)	72675(18)	56584(17)	41267(20)	15962(19)
	U_{eq}	282(5)	304(5)	339(6)	299(5)	401(6)	323(5)
S(1)	x	49869(13)	32547(13)	12764(13)	−3846(13)	80647(14)	66782(13)
	y	6508(11)	40104(11)	73687(12)	7178(12)	40282(12)	73210(11)
	z	17558(15)	1009(16)	84179(16)	67462(16)	50395(16)	33696(16)
	U_{eq}	189(5)	214(5)	210(5)	203(5)	227(5)	204(5)
S(2)	x	63800(12)	47489(13)	30238(13)	13472(13)	96106(14)	79804(13)
	y	9580(11)	41600(12)	74048(12)	7681(13)	43488(13)	76937(11)
	z	42094(16)	24562(17)	4743(18)	88187(17)	73292(18)	58641(16)
	U_{eq}	196(5)	226(5)	214(5)	246(6)	268(6)	192(5)
O(1)	x	4506(4)	2890(4)	1242(4)	−435(4)	7777(4)	6105(4)
	y	961(3)	4264(3)	7607(3)	1003(3)	4342(3)	7671(3)
	z	3725(5)	2127(5)	600(5)	8941(5)	7144(5)	5286(5)
	U_{iso}	261(11)	265(11)	256(11)	287(11)	314(12)	307(12)
O(2)	x	4017(4)	2276(4)	279(5)	8598(5)	7006(5)	5707(4)
	y	971(4)	4355(4)	7711(4)	1012(4)	4153(4)	7604(4)
	z	1225(5)	−337(5)	8226(6)	6552(6)	4683(7)	2767(5)
	U_{iso}	359(13)	396(14)	450(15)	491(16)	570(18)	393(13)
O(3)	x	5753(4)	3989(5)	1849(5)	148(5)	8569(5)	7465(5)
	y	938(4)	4306(4)	7697(4)	1078(4)	4479(4)	7612(4)
	z	1334(5)	−351(6)	7806(7)	6127(6)	4471(6)	2999(6)
	U_{iso}	398(14)	473(15)	569(18)	524(17)	494(16)	449(15)
O(4)	x	4977(4)	3213(4)	1257(5)	−350(5)	8310(5)	6692(4)
	y	−261(3)	3097(3)	6455(4)	−197(4)	3150(4)	6413(3)
	z	1668(5)	−54(5)	8214(6)	6548(6)	4930(6)	3321(5)
	U_{iso}	286(11)	321(12)	502(16)	546(17)	517(16)	332(12)
O(5)	x	6372(4)	4836(5)	3307(5)	1662(5)	9726(5)	7941(4)
	y	1617(4)	4750(4)	7891(4)	1327(5)	5021(4)	8370(4)
	z	5278(5)	3595(6)	1683(6)	9985(7)	8422(6)	6885(5)
	U_{iso}	389(13)	522(16)	555(17)	606(19)	527(17)	357(13)
O(6)	x	7137(4)	5474(4)	3598(4)	1901(5)	244(4)	8766(4)
	y	1080(4)	4304(4)	7605(4)	891(4)	4454(4)	7790(4)
	z	3664(5)	1883(6)	9745(5)	8040(6)	6605(5)	5341(5)
	U_{iso}	381(13)	440(15)	403(14)	483(16)	409(14)	372(13)
O(7)	x	6340(4)	4673(5)	2945(5)	1234(5)	9608(5)	7935(4)
	y	114(4)	3292(4)	6501(4)	−93(5)	3526(4)	6866(3)
	z	4397(5)	2540(7)	398(6)	8904(7)	7573(6)	6102(5)
	U_{iso}	396(14)	565(17)	533(17)	599(19)	453(15)	243(13)
O(8)	x	7338(6)		4255(6)		937(6)	
	y	169(5)		6584(5)		3208(6)	
	z	7692(7)		3878(8)		648(8)	
	U_{eq}	452(24)		509(26)		543(28)	
N(1)	x	5253(4)	3616(4)	1841(4)	167(4)	8420(4)	6880(4)
	y	1172(4)	4466(4)	7786(4)	1156(4)	4544(4)	7872(4)
	z	3235(5)	1603(5)	9903(5)	8233(5)	6512(5)	4833(5)
	U_{iso}	223(13)	216(12)	215(12)	235(13)	242(13)	343(13)

Can. J. Chem. Downloaded from www.nrcresearchpress.com by 176.9.209.113 on 09/07/12
For personal use only.

TABLE 2. (*Concluded*)

Atom	Parameter	Value in subcell A	B	C	D	E	F
H(1, 1)	x	411(7)	264(6)	80(7)			
	y	160(6)	484(5)	831(6)			
	z	414(9)	252(8)	84(9)			
	U_{iso}	7(4)	5(3)	8(4)			
H(1, 8)	x	762(11)		559(9)		112(14)	
	y	41(10)		302(8)		369(11)	
	z	748(14)		553(11)		113(18)	
	U_{iso}	10(6)		7(4)		17(9)	
H(2, 8)	x	698(13)		605(15)		34(12)	
	y	−27(12)		384(14)		293(10)	
	z	713(17)		605(20)		74(14)	
	U_{iso}	16(8)		23(10)		13(6)	

[a]The co-ordinates of potassium and sulphur atoms are multiplied by 10^5. Those of oxygen and nitrogen atoms are multiplied by 10^4 and those of hydrogen atoms by 10^3. All temperature factors have been multiplied by 10^4. The subcells are labelled A to F.
[b]Temperature factors are of the form $\exp[-2\pi^2(U_{11}h^2a_1{}^{*2} + \ldots 2U_{12}hka_1{}^*a_2{}^* \ldots)]$ and $U_{eq} = (1/3)\,\Sigma_i \Sigma_j U_{ij}a_i{}^*a_j{}^*\mathbf{a}_i\cdot\mathbf{a}_j$.

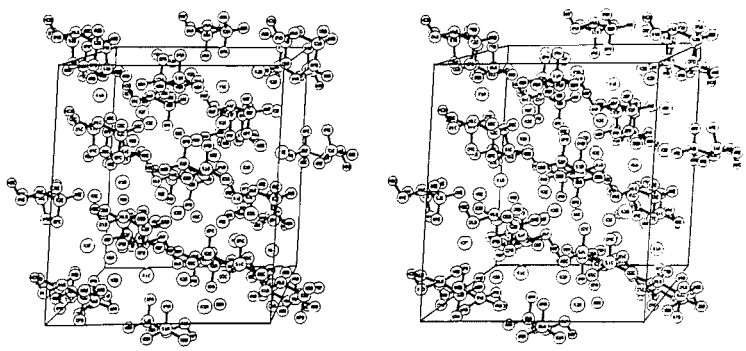

FIG. 1 General stereoscopic view of the structure and atomic labelling. The ***a*** axis is to the right, the ***b*** axis up, and the ***c*** axis is out of the plane of the page.

supercell structure are stereochemically preferred over those forced by the symmetry of the subcell and will be discussed in some detail later.

So irregular are these polyhedra that in some cases the co-ordination number depends on the criterion used to determine it. In what follows a geometric criterion was applied; i.e., is that the co-ordinated oxygen atoms form a significant face, according to the esd's, of the polyhedral domain of the central potassium ion. The convenience of this criterion is that it can be applied using a table of bond lengths and angles without constructing the corresponding figure or its dual, which is the co-ordination polyhedron itself, and without recourse to chemical information such as ionic radii or potential functions. Using this criterion, for atom B to be part of the co-ordination polyhedron of central atom A, requires simply that

$$r_{AB} = \frac{r_{AC}}{\cos < BAC}$$

for all atoms C closer to A than B, for which cos < BAC is positive.

The co-ordination polyhedra so formed were reduced to points on a sphere, and analysed in terms of the interfacial angles by a program described previously (19).

The dimeric anions contain the strong central H bond, which is, however, slightly longer than that in the rubidium salt. The water molecules form H bonds to the anions, but these are relatively weak. The hydrogen bond scheme has been confirmed by neutron diffraction results.

In order to understand the reasons for the formation of this complicated superstructure, bond valence sums were calculated. The parameters collected by Brown (22) were used, except for the N—S bonds, where Brown's values seemed to be inappropriate to the N—S(VI) combination, because they gave bond orders markedly lower than the formal valences required. Instead the value $R_0 = 1.75$ and $B = 0.36$ were chosen as having the same exponent as other similar bonds, and as giving the expected sums at N and S. Since the hydrogen position were not known accurately, they were assumed on the following bases: N—O...H...O—N at the midpoint of the O—O vector, and for water molecules, at a distance of 0.95 Å in the direction from the oxygen atom given by the least-squares refinement. Again following Brown, the N—O group was treated as a

Can. J. Chem. Downloaded from www.nrcresearchpress.com by 176.9.209.113 on 09/07/12
For personal use only.

Can. J. Chem. Downloaded from www.nrcresearchpress.com by 176.9.209.113 on 09/07/12
For personal use only.

TABLE 3. Bond lengths (Å) and angles (deg) for the hydroxylamine anions, averaged over the six subcells[a]

Bond	Length
N(1)—O(1)	1.422(10, 5)
N(1)—S(1)	1.709(6, 16)
N(1)—S(2)	1.726(6, 15)
S(1)—O(2)	1.442(6, 4)
S(1)—O(3)	1.432(8, 12)
S(1)—O(4)	1.440(6, 11)
S(2)—O(5)	1.442(7, 15)
S(2)—O(6)	1.435(8, 9)
S(2)—O(7)	1.438(7, 5)
Bonds	**Angle**
S(1)—N(1)—O(1)	109.2(4, 10)
S(2)—N(1)—O(1)	106.1(4, 7)
S(1)—N(1)—S(1)	116.8(4, 13)
N(1)—S(1)—O(2)	103.8(3, 4)
N(1)—S(1)—O(3)	103.8(3, 2)
N(1)—S(1)—O(4)	109.4(4, 3)
N(2)—S(2)—O(5)	101.0(3, 9)
N(2)—S(2)—O(6)	105.6(3, 6)
N(2)—S(2)—O(7)	108.2(3, 6)
O(2)—S(1)—O(3)	112.6(4, 4)
O(2)—S(1)—O(4)	111.3(4, 7)
O(3)—S(1)—O(4)	114.8(4, 3)
O(5)—S(2)—O(6)	113.4(4, 6)
O(5)—S(2)—O(7)	112.2(4, 5)
O(6)—S(2)—O(7)	115.1(4, 12)

[a]The first number in parentheses after a parameter x is the average estimated standard deviation of the least significant digits of the parameter; i.e. $(1/6)\ \Sigma_{i=1}^{6}\ \sigma_i(x)$. The second number in parentheses is the sample standard deviation for the parameter; i.e. $\{(1/5)\ \Sigma_{i=1}^{6}\ (x_i - \langle x \rangle)^2\}^{1/2}$, $\langle x \rangle = (1/6)\ \Sigma_{i=1}^{6}\ x_i$.

combined negative atom, taking account of the N—O bond order.

In the average subcell structure K^+ ions and the water molecules occur at centres of symmetry. As was mentioned earlier, this restriction is chemically unlikely, and it is instructive to examine what happens to these sites in the true structure. A water molecule cannot hydrogen bond in a centrosymmetric way to surrounding oxygen atoms unless disordered. Also the bond valence balance would also require it to be bonded to three K^+ ions, which again cannot be achieved in a centrosymmetric site. In actuality the water molecules and the K^+ ions of the K(3) type shift in such a way that the water molecule forms part of the co-ordination of one such K^+ ion per subcell, while the other moves away to a distance greater than 4 Å. The co-ordination of each water molecule is then essentially the same, with two potassium ions symmetrically placed above and below the plane of the molecule, a third co-ordinated in the plane on the side opposite the hydrogen atoms, and weak H bonds on the other side.

With regard to possible eight, nine, and ten co-ordinate polyhedra available to the K^+ ions, an analysis in terms of ligand–ligand repulsions, such as that carried out previously by one of us (19), would suggest that a centrosymmetric polyhedron, even when possible, will not be the most stable for that co-ordination number. For eight co-ordination the lowest energy centrosymmetric arrangement is the cube, while the polyhedra normally found are the square antiprism, bisdisphenoid and bicapped trigonal prism.

For nine co-ordination a centrosymmetric arrangement is clearly impossible, and the polyhedra found usually fall in the range intermediate between the monocapped square antiprism (MSAP) and the tricapped trigonal prism (TTP). The co-ordinate normally used to describe this distortion path is the interfacial angle which becomes the diagonal of the square base of the MSAP, labelled δ_a in the previous paper, which is zero for the MSAP and 26.4° for the TTP. Some exceptions to the above rule are found to be derivable from the basic polyhedron by change in the connectivity of the vertices as an interfacial angle other than δ_a becomes negative. (When an interfacial angle is zero, two triangular faces become one quadrilateral one, and a further distortion in the same sense produces two new triangular faces by connection of the opposite diagonal.) For example, such an exceptional polyhedron is found for Nd(3) in $NdOHCO_3$ (23).

For ten co-ordination the two principal polytopes are the bicapped square antiprism (BSAP) and the spenocorona (SC), both of which are far from centrosymmetric. Again intermediate forms correspond to values of the two equivalent interfacial angles δ_m which become the diagonals of the two rectangular faces of the SC. They range from zero for the SC to about 31° for the BASP.

Taking this all into account, we would therefore expect deviations from a centrosymmetric environment for K(1A) to K(1C).

If we examine the polyhedra found, these predictions are borne out. The polyhedron around K(1C) is indeed a slightly distorted cube, the distortion being a trigonal one such that the connectivity of the hexagonal bipyramid results. However, the polyhedra for K(1A) and K(1B) are cubes with one face capped; again a distortion similar to that for K(1C) produces two 6-connected vertices. In contrast the polyhedra for K(2A) to K(3F) comprise one 8 co-ordinate SAP, eight 9 co-ordinate polyhedra (six based on the MSAP—TTP with δ_a ranging from 2.1 to 17.8° and three connected as the $NdOHCO_3$ polyhedron), and three 10 co-ordinate SC with δ_m's ranging from small negative values to +4.8°.

This distinction between K(1A) to K(1C) and K(2A) to K(3F) is also borne out by the bond valence sums. Whereas the sums for the K^+ ions as a whole average to 1.03 ± 0.11 valence units (v.u.), they clearly fall into two classes, for which the averages are 0.85 ± 0.02 v.u. (K(1A) to K(1C) and 1.07 ± 0.08 v.u. (K(2A)...K(3F)), respectively. This supports the view that the distorted cubic environment of the former group is less effective than the other co-ordination polyhedra in allowing the close approach of a large number of ligands to the central atom.

If we apply the same sort of analysis to the K^+ environments in the average structure, we find that K1 is surrounded by a simple distorted cube of oxygens, K2 has a 9 co-ordinate MSAP–TTP polyhedron as might be expected, while K3 shows an extremely elongated and irregular 10 co-ordination, arising from its two types of position in the true structure. When valence sums were calculated for these polyhedra, these yielded values differing markedly from unity, namely 0.70, 1.16, and 1.15 v.u., respectively.

Other results of these sums are as expected. The average sum at the nitrosyl oxygen atom (omitting contribution from the N—O bond) is 0.74 ± 0.02 v.u. in comparison to 0.75 v.u. in $Na_3ON(SO_3)_2 \cdot 3H_2O$. However, the manner in which these

sums are made up differs markedly from one compound to the other, consisting of contributions as follows (average individual contributions in valence units in parentheses): in one case of three Na^+ ions (0.19) and one H bond (0.19), and in the other, the short H bond (0.47) and various combinations of weak H bonds and K^+ ions (0.10). This result supports Brown's contention that the role of water in structures such as these is to mollify the effects of a mismatch in the Lewis acid and base strengths of the cation and anion. In these compounds the average base strength of the nitrosyl oxygen atom (omitting the strong H bond where it occurs) is 0.19 and 0.10 v.u., and of the sulphonate oxygens 0.16 and 0.13 v.u., for the Na and K compounds, respectively. Brown gives the acid strengths of the Na^+ as 0.16 v.u. and K^+ as 0.13 v.u. The obvious conclusion is that the lower Lewis acid strength of K^+ requires the central strong H bond of the dimer to allow a matching to the base strength of the nitrosyl oxygen atom, while in the case of Na^+ the presence of additional water molecules is sufficient. For the Rb compound (Lewis acid strength of Rb^+ is 0.10 v.u.), this mismatch should be greater still. Although a failure to locate the hydrogen atoms makes a complete analysis of the Rb compound impossible, we can observe two effects compatible with the above arguments: shortening of the central H bond and an increase in the hydration compared to the K compound.

Our conclusions regarding $K_5H[ON(SO_3)_2]\cdot H_2O$ run therefore as follows. The presence of the dimeric anion and the extent of hydration are probably determined by the cation/anion matching requirement described above. Since a simple structure with space group $P\bar{1}$, and one formula unit in the unit cell and with this stoichiometry would place the unreasonable restraint of a centrosymmetric environment on certain atoms, instead a superstructure develops which removes these constraints, and which gives a chemically reasonable structure, whether judged in terms of bond lengths and angles, co-ordination polyhedra, or bond valence sums.

So far nothing has been said about the H-atom positions within the three short symmetry-free H bonds in the structure. We felt that this aspect warranted the neutron diffraction study alluded to above, and that discussion of this topic should await the detailed results of that study.

Can. J. Chem. Downloaded from www.nrcresearchpress.com by 176.9.209.113 on 09/07/12
For personal use only.

Acknowledgements

The authors thank the Natural Sciences and Engineering Research Council of Canada for operating grants, and the University of Regina for computer time.

1. R. J. GUTTORMSON, J. S. RUTHERFORD, B. E. ROBERTSON, and D. B. RUSSELL. Inorg. Chem. **13**, 2062 (1974).
2. B. D. PERLSON and D. B. RUSSELL. Inorg. Chem. **14**, 2907 (1975).
3. J. S. RUTHERFORD and B. E. ROBERTSON. Inorg. Chem. **14**, 2537 (1975).
4. B. D. PERLSON and D. B. RUSSELL. J. Chem. Soc. Chem. Commun. 69 (1972).
5. T. E. GANGWER. J. Phys. Chem. **78**, 375 (1974).
6. A. JANNER and T. JANSSEN. Phys. Rev. **B15**, 643 (1977).
7. R. BOHME. Acta Crystallogr. **A38**, 318 (1982).
8. H. F. FAN, J. X. YAO, P. MAIN, and M. M. WOOLFSON. Acta Crystallogr. **A39**, 566 (1983).
9. V. GRAMLICH. Acta Crystallogr. **A40**, 610 (1984).
10. G. CASCARANO, C. GIACOVAZZO, and M. LUIC. Structure and statistics in crystallography. *Edited by* A. J. C. Wilson. Adenine Press, Guilderland, New York. 1985.
11. G. CASCARANO, C. GIACOVAZZO, and M. LUIC. Cryst. **A41**, 544 (1985).
12. M. CATTI and G. FERRARIS. Acta Crystallogr. **B32**, 2754 (1976).
13. R. ROY, E. T. MIDDLESWARTH, and F. A. HUMMEL. Am. Mineral. **33**, 458 (1948).
14. J. G. CHAMBERS, W. R. DATARS, and C. CALVO. J. Chem. Phys. **46**, 806 (1964).
15. A. L. MACKAY. Acta Crystallogr. **6**, 214 (1953).
16. B. E. ROBERTSON and C. CALVO. Acta Crystallogr. **22**, 665 (1967).
17. J. S. STEPHENS and C. CALVO. Can. J. Chem. **47**, 2215 (1969).
18. J. S. RUTHERFORD and C. CALVO. Z. Kristallogr. **128**, 229 (1969).
19. B. E. ROBERTSON and C. CALVO. J. Solid State Chem. **1**, 120 (1970).
20. H. HAUPTMANN and J. KARLE. Acta Crystallogr. **12**, 846 (1959).
21. R. TAYLOR and O. KENNARD. Acta Crystallogr. **B42**, 112 (1986).
22. I. D. BROWN. Structure and bonding in crystals. Vol. III. *Edited by* M. O'Keefe and A. Navrotsky. Academic Press, New York. 1981.
23. A. N. CHRISTENSEN. Acta Chem. Scand. **27**, 2973 (1973).

Excess properties (V^E, ϵ^E, and H^E) of the binary system pyridine (1) + sulfolane (2)

LILIANA JANNELLI[1] AND MICHELE PANSINI

Thermodynamic Section, Department of Materials and Production, Faculty of Engineering, The University of Naples, Piazzale Tecchio, Naples, Italy

Received October 5, 1987

This paper is dedicated to Professor James A. Morrison

LILIANA JANNELLI and MICHELE PANSINI. Can. J. Chem. **66**, 662 (1988).

Volumes of mixing and dielectric constants of the binary system pyridine (1) + sulfolane (2) were measured over the entire composition range, $0 \leq x \leq 1$, at selected temperatures ranging between 293.16 and 323.16 K. Mixing enthalpies were also measured at 303.16 K. Deviations from ideality of the measured properties are consistent with the regular behaviour of sulfolane systems, as evidenced by previous works. Nevertheless the occurrence, in the pyridine-rich region, of a sharp maximum in excess dielectric constants versus composition curves, and of a deep minimum in enthalpies of mixing curves, substantiates the supposition that small dipolar interactions occur between molecules of the components. These steadily decrease in magnitude with increasing temperature and sulfolane content in solution.

LILIANA JANNELLI et MICHELE PANSINI. Can. J. Chem. **66**, 662 (1988).

On a mesuré les volumes de mélange et les constantes diélectriques du système binaire pyridine (1) + sulfolane (2), à toutes les compositions, $0 \leq x \leq 1$, et à des températures sélectionnées entre 293,16 et 323,16 K. On a aussi mesuré les enthalpies de mélange à 303,16 K. Les déviations des propriétés mesurées par rapport à l'idéalité sont en accord avec le comportement régulier des systèmes de sulfolane que l'on a mis en évidence dans nos travaux antérieurs. Toutefois, dans la région riche en pyridine, on observe un maximum net dans les courbes de la constante diélectrique versus la composition aussi que un minimum net dans les courbes des enthalpies de mélange; ce résultat confirme l'hypothèse que des faibles interactions dipolaires se produisent entre les molécules des composants du mélange. Ces interactions diminuent régulièrement avec une augmentation de la température et de la proportion de sulfolane dans la solution.

[Traduit par la revue]

Introduction

As a part of extensive research (1–6) into the behaviour and classification of sulfolane solutions, the binary system pyridine (1) + sulfolane (2) has been selected for investigation. Both components are dipolar substances ($\mu_1 = 2.3$ D; $\mu_2 = 4.8$ D). The mixtures possess fairly high dielectric constants, ranging between 12.4 (pyridine) and 43 (sulfolane) at 25°C. Hence the study of this system may also supply useful data for electrochemical studies. The aromatic character of pyridine and its exposed dipole allow interactions between either like or unlike molecules. On the other hand, the steric hindrance of the sulfolane globular molecule reduces the occurrence of strong interactions of any kind, protonation included, in spite of the fairly high dipole moment of which only the negative end is exposed.

We report herewith volumes of mixing and dielectric constants of these mixtures measured at four selected temperatures (293.16, 303.16, 313.16, 323.16 K), as well as mixing enthalpies measured at 303.16 K in the composition range $0 \leq x \leq 1$.

Experimental

Materials, apparatus, and procedure

Sulfolane, kindly supplied by Shell Italia, was purified and carefully dried as already reported (7); properties of the purified sample strictly agree with the most reliable literature data and with our own previous data (8). Rudy Point Reagent grade pyridine was dried on sodium hydroxide and distilled from barium oxide repeatedly; the middle fraction was stored in dark containers and protected from moisture as far as possible. Properties of the purified sample strictly agree with literature data (9). Solutions were made by weight (reduced to mass), stored in dark containers, and protected from moisture as far as possible.

[1]Author to whom correspondence may be addressed.

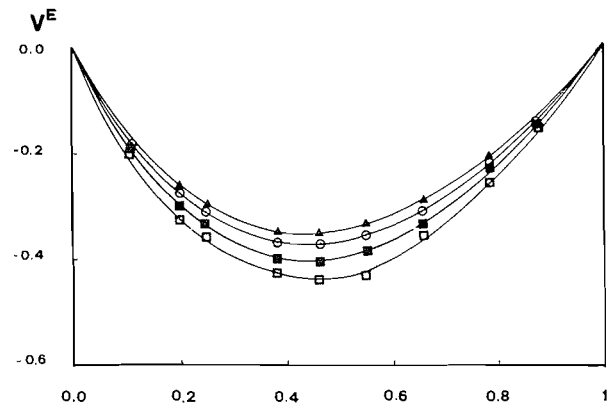

FIG. 1. Excess volumes V^E ($cm^3\ mol^{-1}$) plotted against sulfolane mole fraction x_2, at 293.16 K (full triangles); 303.16 K (open circles); 313.16 K (full squares); 323.16 K (open squares).

Densities were measured at 293.16, 303.16, 313.16, and 323.16 K by an Anton Paar (Austria) vibrating tube densimeter, described elsewhere (10). The maximum error in density did not exceed 1×10^{-5} g cm^{-3}.

Dielectric constants were measured, at 2 MHz, by a W.T.W. dielectric constant measuring apparatus, using the heterodyne beat method. The measuring cell, DFL 2/S type, was thermostatted by water circulation within 0.001 K. The apparatus as well as the calibration procedure have been described elsewhere (11). The maximum error in the dielectric constant was estimated to be 0.01. Mixing enthalpies were determined in an LKB flow microcalorimeter (Model 2107-121) using the auxiliary equipment and operating procedure described in previous works (12). Studies of the test system indicate that the precision of the results is 1% or better over most of the mole fraction range. All measurements were carried out at a temperature of 303.16 ± 0.005 K because at temperatures below 301.61 K

Can. J. Chem. Downloaded from www.nrcresearchpress.com by 176.9.209.113 on 09/07/12
For personal use only.

TABLE 1. Molar volumes of pyridine, V_1^0, and sulfolane, V_2^0, parameters A and B of the smoothing equations, and standard deviations, σ

T (K)	V_1^0 ($cm^3\ mol^{-1}$)	V_2^0 ($cm^3\ mol^{-1}$)	A	B	σ
293.16	80.446	(94.551)*	−1.413	0.3600	0.004
303.16	81.301	95.214	−1.491	0.3912	0.006
313.16	82.127	95.852	−1.593	0.4260	0.007
323.16	83.018	96.550	−1.751	0.3912	0.009

*Value in parentheses is an extrapolated value, because sulfolane is a solid at 293.16 K.

sulfolane is a solid. For the sake of uniformity with previous works sulfolane is indicated as component 2.

Results and discussion

Excess volumes, V^E, of mixing pyridine (1) + sulfolane (2) (volume ratio V_2^0/V_1^0 1.2) at the selected temperatures are shown graphically in Fig. 1. The negative deviations of the systems from ideality never exceed $-0.45\ cm^3\ mol^{-1}$ and only slightly increase with the temperature. The minimum is skewed slightly towards the region rich in the smaller component (pyridine), as expected. The experimental data for V^E, at each temperature, were fitted by a least-squares computer program to smoothing equations of the kind:

$$[1] \quad V^E = x_1x_2\{A + B(x_2 - x_1)\}$$

The parameters A and B of eq. [1] and the standard deviations, σ, are included in Table 1. V^E values, as a function of mole fraction, x_2, of sulfolane, are summarized in Table 2, as well as deviations δV^E from the smoothing equations. The V^E data supply evidence for the supposition that the intermolecular interactions in this system are small. The small volume contractions in this system do not differ in magnitude from those that usually occur on mixing molecules with different geometry.

Deviations from ideality of dielectric constants, $\epsilon_{1,2}^E$, over the entire composition range, at the selected temperatures, are shown graphically in Fig. 2. They are calculated on the basis of a linear dependence of $\epsilon_{1,2}$ values on ideal volume fractions, ϕ_2, in the case of ideal mixtures. The equation:

$$[2] \quad \epsilon_{1,2} = \epsilon_1\phi_1 + \epsilon_2\phi_2 = \epsilon_1^0\phi_1 + \epsilon_2^0\phi_2 + \epsilon_{1,2}^E$$

as well as the symbols have been illustrated elsewhere; $\epsilon_{1,2}$ is the measured dielectric constant of a solution with ideal volume fraction ϕ_i, ϵ_i^0 and ϵ_i are the dielectric constants of the component i, in the pure state and at the mole fraction ϕ_i,

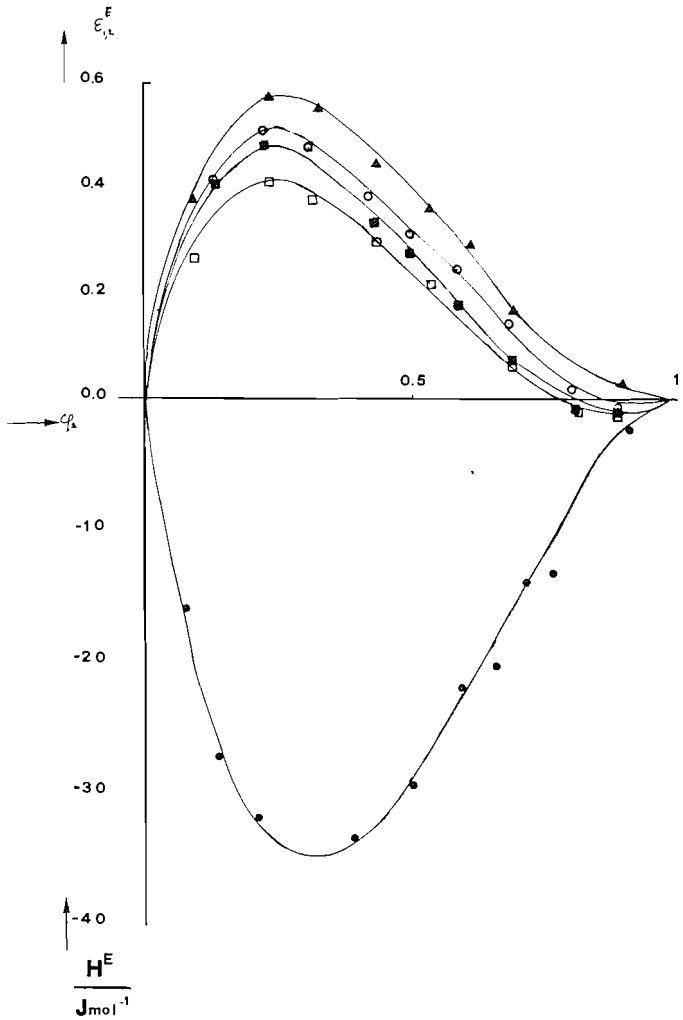

FIG. 2. Dielectric constants, $\epsilon_{1,2}^E$, and enthalpies of mixing, H^E, as a function of ideal volume fraction, ϕ_2.

respectively. The $\epsilon_{1,2}^E$ values were fitted by a least-squares computer program to smoothing equations of the kind:

$$[3] \quad \epsilon_{1,2}^E = x_1x_2\{A' + B'(x_2 - x_1) + \epsilon'(x_2 - x_1)^2 \ldots\ldots\}$$

The parameters A', B', C', ... of eq. [3] and the standard deviations σ are included in Table 3. The $\epsilon_{1,2}^E$ values, as a function of mole fraction ϕ_2 of sulfolane, are summarized in Table 4, as well as $\delta\epsilon^E$ of the smoothing equations. Deviations

TABLE 2. Molar excess volumes, V^E, and deviations, δV^E, from the smoothing equations, at four temperatures

	293.16 K		303.16 K		313.16 K		323.16 K	
x_2	V^E ($cm^3\ mol^{-1}$)	$\delta V^E \times 10^3$ ($cm^3\ mol^{-1}$)	V^E ($cm^3\ mol^{-1}$)	$\delta V^E \times 10^3$ ($cm^3\ mol^{-1}$)	V^E ($cm^3\ mol^{-1}$)	$\delta V^E \times 10^3$ ($cm^3\ mol^{-1}$)	V^E ($cm^3\ mol^{-1}$)	$\delta V^E \times 10^3$ ($cm^3\ mol^{-1}$)
0.11511	—	—	−0.187	−4	−0.196	−1	—	—
0.20062	−0.265	4	−0.277	—	−0.298	−2	−0.326	−8
0.25449	−0.302	0	−0.316	4	−0.337	5	−0.359	9
0.38354	−0.353	1	−0.366	8	−0.396	4	−0.432	4
0.45990	−0.354	4	−0.375	3	−0.409	−5	−0.442	1
0.54918	−0.335	6	−0.359	—	−0.387	−3	−0.436	−12
0.65881	−0.291	0	−0.315	−9	−0.337	−9	−0.355	14
0.78353	−0.209	−4	−0.207	9	−0.219	10	−0.263	−3
0.86926	—	—	−0.141	−4	−0.151	−6	—	0

Can. J. Chem. Downloaded from www.nrcresearchpress.com by 176.9.209.113 on 09/07/12
For personal use only.

TABLE 3. Dielectric constants of pyridine, ϵ_1^0, and sulfolane, ϵ_2^0, parameters A', B', C', ... of the smoothing equations, and standard deviations, σ, at four temperatures

T (K)	ϵ_1^0	ϵ_2^0	A'	B'	C'	D'	E'	F'	σ
293.16	13.66	(44.39)*	1.619	−1.619	0.553	−5.819	0.589	7.080	0.01
303.16	13.07	43.15	1.230	−1.316	1.265	−4.888	−0.401	4.844	0.07
313.16	12.53	41.97	1.040	−1.867	1.244	−3.481	−0.112	4.001	0.02
323.16	12.03	40.81	0.975	−1.656	0.998	−3.180	−1.259	4.946	0.01

*Value in parentheses is an extrapolated value, because sulfolane is a solid at 293.16 K.

TABLE 4. Measured dielectric constants, $\epsilon_{1,2}$, deviations from ideal values, $\epsilon_{1,2}^E$, and deviations from smoothing equations, $\delta\epsilon_{1,2}^E$, at four temperatures

293.16 K				303.16 K			
ϕ_2	$\epsilon_{1,2}$	$\epsilon_{1,2}^E$	$\delta\epsilon_{1,2}^E$	ϕ_2	$\epsilon_{1,2}$	$\epsilon_{1,2}^E$	$\delta\epsilon_{1,2}^E$
0.10150	17.16	0.38	0.00	0.13220	17.47	0.42	0.00
0.24256	21.69	0.58	0.00	0.22715	20.41	0.51	0.01
0.32642	24.24	0.55	0.01	0.28560	22.12	0.46	−0.01
0.43547	27.49	0.45	0.00	0.42151	26.12	0.37	0.01
0.53335	30.42	0.37	−0.01	0.49930	28.40	0.31	0.00
0.61292	32.80	0.30	0.01	0.58791	30.99	0.24	0.00
0.69283	35.12	0.17	0.00	0.69338	34.07	0.14	0.00
0.81177	38.64	0.03	0.00	0.80912	37.43	0.02	0.00
0.90487	41.50	0.03	0.00	0.88619	39.72	−0.01	0.00
313.16 K				323.16 K			
ϕ_2	$\epsilon_{1,2}$	$\epsilon_{1,2}^E$	$\delta\epsilon_{1,2}^E$	ϕ_2	$\epsilon_{1,2}$	$\epsilon_{1,2}^E$	$\delta\epsilon_{1,2}^E$
0.13181	16.82	0.41	0.00	0.10065	15.14	0.22	0.00
0.22655	19.69	0.49	0.00	0.24062	19.38	0.42	0.01
0.42067	25.24	0.33	−0.01	0.32410	21.74	0.38	−0.01
0.49845	27.48	0.28	0.02	0.43288	24.79	0.30	0.00
0.58708	29.97	0.16	−0.02	0.53072	27.53	0.23	−0.01
0.69265	33.00	0.08	0.01	0.69058	31.96	0.06	−0.01
0.80859	36.31	−0.02	0.00	0.81042	35.33	−0.02	0.00
0.88584	38.58	−0.02	0.00	0.90395	38.03	−0.02	0.00

from ideality of the dielectric constants, $\epsilon_{1,2}^E$, are generally positive and never exceed 0.6.

The $\epsilon_{1,2}^E$ vs. ϕ_2 curves (Fig. 2) exhibit a maximum, which steadily decreases in magnitude with temperature, approximately at $0.24\phi_2$, in the region richer in pyridine.

Mixing enthalpies measured at 303.16 K are negative over the composition range $0 \leq x_2 \leq 1$ and never exceed −40 J mol^{-1}. Data are summarized in Table 5; coefficients A'', B'', C'' .... of the smoothing equation:

$$[4] \quad H^E = x_1x_2\{A'' + B''(x_2 - x_1) + C''(x_2 - x_1)^2 \ldots.\}$$

are included in Table 5. H^E values are recorded in Fig. 2 as a function of ϕ_2, the volume fraction of sulfolane, for the sake of comparison with the excess dielectric constant data. A minimum occurs in the H^E vs. ϕ_2 curves at roughly the same composition at which a maximum occurs in the $\epsilon_{1,2}^E$ vs. ϕ_2 curves.

The small positive $\epsilon_{1,2}^E$ values, as well as the small negative H^E values, provide evidence for the supposition of very low intermolecular interactions. Self-association forces should be

TABLE 5. Experimental molar excess enthalpies, H^E, and deviations, δH^E, from the smoothing equation at 303.16 K. Parameters A'', B'', ... of smoothing equation [4]

x_2	H^E (J mol^{-1})	δH^E (J mol^{-1})	
0.0680	−15.774	0.065	
			$A'' = -102.267$
0.1261	−26.264	−0.347	
			$B'' = 115.172$
0.1894	−32.246	0.409	
			$C'' = -127.554$
0.3555	−33.456	0.199	
			$D'' = 33.247$
0.4561	−28.555	−0.429	
			$E'' = 122.44$
0.5544	−22.265	0.260	
0.6290	−18.989	−0.337	
0.6891	−14.719	0.843	
0.7484	−12.751	−0.518	
0.9008	−2.123	0.023	

Can. J. Chem. Downloaded from www.nrcresearchpress.com by 176.9.209.113 on 09/07/12
For personal use only.

limited in the case of pyridine because of the fairly high dielectric constant of the medium, ranging between 12 and 43. Self-association should be nonexistent in the case of sulfolane because of the steric hindrance resulting from its globular structure. Hence the presence of the sharp maximum in the excess dielectric constant curves at $\phi_2 = 0.24$, and of a deep minimum at roughly the same composition in the H^E curve, should be interpreted in terms of a likely complex formation arising from dipole–dipole interactions between unlike molecules. The maximum in the $\epsilon_{1,2}{}^E$ curves decreases with temperature, along with a decrease in complex formation, as expected from the exothermic effect cited above.

Acknowledgment

We are indebted to Lisbo Parrella Luigi for technical assistance.

1. L. JANNELLI and A. SACCO. J. Chem. Thermodyn. **4**, 715 (1972).
2. L. JANNELLI, A. K. RAKSHIT, and A. SACCO. Z. Naturforsch **29**, 355 (1974).
3. L. JANNELLI, A. LOPEZ, R. JALENTI, and L. SILVESTRI. J. Chem. Eng. Data, **27**, 28 (1982).
4. L. JANNELLI, A. LOPEZ, and L. SILVESTRI. J. Chem. Eng. Data, **28**, 166 (1983).
5. A. LOPEZ, M. PANSINI, and L. JANNELLI. J. Chem. Eng. Data, **28**, 173 (1983).
6. M. PANSINI and L. JANNELLI. J. Chem. Eng. Data, **31**, 157 (1986).
7. M. DELLA MONICA, L. JANNELLI, and U. LAMANNA. J. Phys. Chem. **10**, 68 (1968).
8. J. MARTINMAA. *In* The chemistry of non aqueous solvents. Vol. IV. *Edited by* J. J. Lagowski. Academic Press, New York. 1976. Chap. 7, p. 250.
9. A. WEISSBERGER (*Editor*). Technique of organic chemistry. Vol. VII. Interscience, New York. 1955.
10. L. JANNELLI, A. LOPEZ, and S. SAIELLO. J. Chem. Eng. Data, **25**, 259 (1980).
11. O. SCIACOVELLI, L. JANNELLI, and A. DELLA MONICA. Gazz. Chim. Ital. **97**, 1012 (1967).
12. A. LOPEZ, M. PANSINI, and L. JANNELLI. J. Chem. Eng. Data, **28**, 176 (1983).

Can. J. Chem. Downloaded from www.nrcresearchpress.com by 176.9.209.113 on 09/07/12
For personal use only.

Neutron scattering studies of potassium-ammonia layers in graphite

H. ZABEL AND D. A. NEUMANN[1]

Department of Physics and Materials Research Laboratory, University of Illinois at Urbana-Champaign, 1110 W. Green St., Urbana, IL 61801, U.S.A.

Received September 18, 1987

This paper is dedicated to Professor J. A. Morrison

H. ZABEL and D. A. NEUMANN. Neutron scattering studies of potassium-ammonia layers in graphite. Can. J. Chem. **66**, 666 (1988).

Neutron scattering investigations of the structural and dynamical properties of ammonia molecules in the stage 1 compound $KC_{24}(NH_3)_{4.3}$ are discussed. The K–NH_3 intercalate layers represent the two-dimensional analogue of the well-known metal–ammonia solutions. At room temperature the intercalate liquid structure factor can be described by a model in which the K ions are surrounded on the average by four NH_3 molecules, and the remaining molecules are essentially free. Quasi-elastic neutron scattering revealed two independent rotational motions of the NH_3 molecule, one associated with the rotation about the C_3 symmetry axis and the other one about the K ions. Above 200 K translational diffusion also becomes noticeable. The phonon dispersion of the [00q] longitudinal modes show clear signs of a phonon–libron coupling which causes the acoustic branch to split.

H. ZABEL et D. A. NEUMANN. Neutron scattering studies of potassium-ammonia layers in graphite. Can. J. Chem. **66**, 666 (1988).

Utilisant des études de diffusion neutronique on a étudié les propriétés structurales et dynamiques des molécules d'ammoniac dans le composé de stage 1, $KC_{24}(NH_3)_{4.3}$. Les couches intercalées de K–NH_3 représentent l'analogue bi-dimensionnel des solutions bien connues de métal–ammoniac. A température ambiante, on peut décrire le facteur de structure liquide des couches intercalées par un modèle dans lequel les ions de K sont entourés en moyenne par quatre molécules de NH_3 alors que les autres molécules sont essentiellement libres. La diffusion neutronique quasi-élastique permet de mettre en évidence deux mouvements rotationnels indépendants de la molécule de NH_3; un est associé avec la rotation autour de l'axe de symétrie C_3 et l'autre avec la rotation autour des ions de K. Au dessus de 200 K, on commence à noter une diffusion de translation. La dispersion phonique des modes longitudinaux [00q] présente des signes certains d'un couplage phonon–libron qui fait que la branche acoustique se divise.

[Traduit par la revue]

I. Introduction

In this festschrift we would like to provide a short overview of recent neutron scattering studies on potassium–ammonia solutions intercalated in graphite. Although this subject appears highly focused, it nevertheless relates to many other topics of current research interest. Those encompass metal–insulator transitions in two dimensions (2D), the structure of 2D complex molecular liquids, and the translational and rotational excitations of the NH_3 molecules, including coupling of rotational and translational modes.

The layered structure of graphite provides a unique host frame for the investigation of the motions of molecules in spatially confined environments. NH_3 is one example which has attracted intense research activity in recent years. Other examples are the molecules H_2 and HNO_3 which have also recently been studied in much detail by X-ray and neutron scattering experiments. A brief review of the dynamics of these molecules in graphite is presented in ref. 1, and for more general reviews of the structural properties of graphite intercalation compounds (GIC's) we refer to refs. 2–4.

II. Structure

Ammonia molecules are soluble in monatomic layers of potassium which, in turn, are intercalated in graphite, forming a stage 2 (GIC) KC_{24} (5, 6). Here the stage index refers to the number of graphite planes between any consecutive intercalate layers. With increasing ammonia concentration the compound undergoes a staging transformation to a stage 1 compound by filling all galleries between the graphite basal planes with K–NH_3 solution. Saturation is reached at a concentration $x(NH_3/K) = 4.3$, which requires an ammonia gas pressure of about 10 bar at room temperature (6). The ammonia uptake also causes an expansion of the C–I–C (C = graphite basal plane, I = intercalate layer) package thickness from 5.35 Å for a homogeneous potassium intercalate layer to 6.63 Å for the saturated K–NH_3 layer. Figure 1 shows a neutron (00l) scan showing the structural purity and staging fidelity of this stage 1 compound.

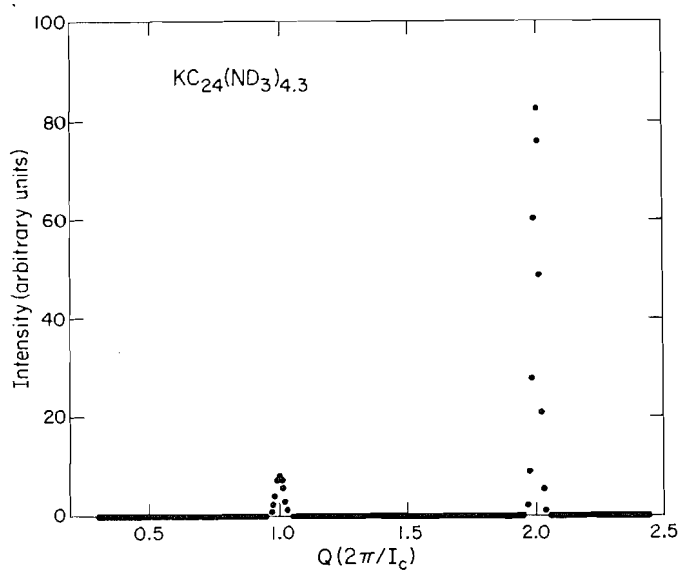

FIG. 1. Neutron elastic (00l) scan of the stage 1 $KC_{24}(ND_3)_{4.3}$ compound (from ref. 14).

Recent X-ray (7) and neutron (8) structural investigations

[1]Present address: Institute for Materials Science and Engineering, National Bureau of Standards, Gaithersburg, MD 20899, U.S.A.

Can. J. Chem. Downloaded from www.nrcresearchpress.com by 176.9.209.113 on 09/07/12
For personal use only.

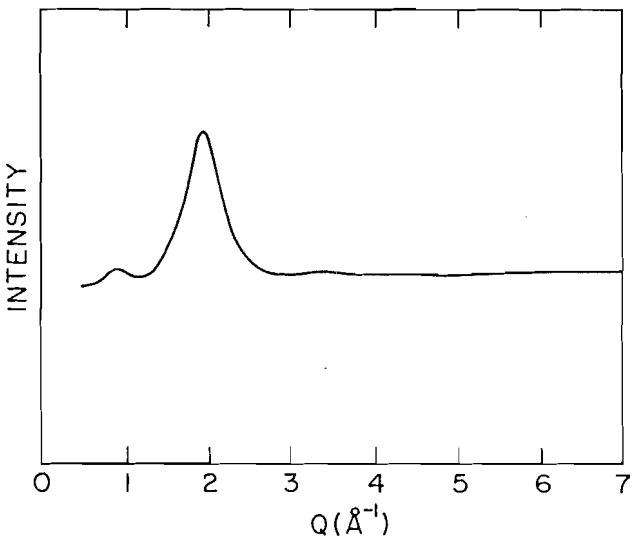

FIG. 2. Elastic neutron (hk0) scan at 300 K showing the liquid structure factor of the K–ND_3 intercalate layer. The graphite (100) (at 2.94 $Å^{-1}$) and (110) at (5.08 $Å^{-1}$) have been removed for clarity (from ref. 8).

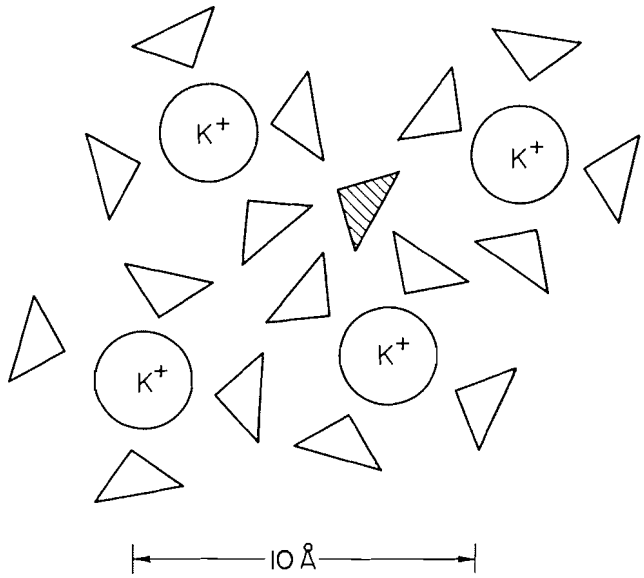

FIG. 3. Schematic diagram of the two-dimensional in-plane structure of the K–ND_3 intercalate liquid in graphite. The circles represent K ions, the open triangles ND_3 molecules which are bonded to the K ions, and the shaded triangle represents a "free" ammonia molecule (from ref. 18).

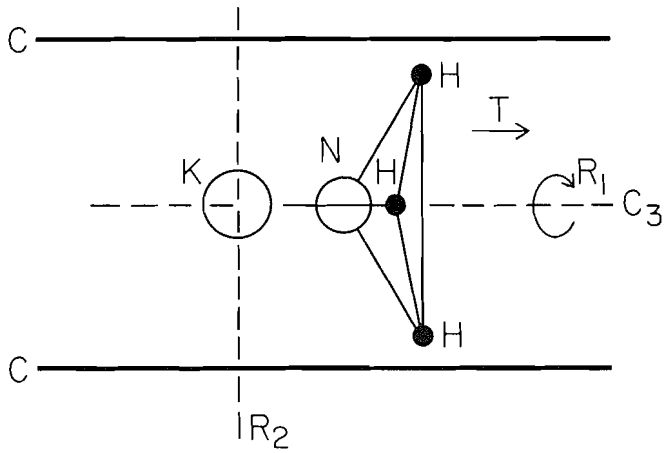

FIG. 4. Schematic diagram of possible motions of NH_3 molecules in $KC_{24}(NH_3)_{4.3}$ (from ref. 14).

have revealed that the K–NH_3 intercalate layer is a 2D liquid at room temperature and that the liquid structure factor can reasonably well be described by a model in which four ammonia molecules are loosely associated with a single K^+ ion and the rest of the ammonia molecules are free. The liquid structure factor of $KC_{24}(ND_3)_{4.3}$ as determined by neutron scattering is shown in Fig. 2. In this scan the scattering vector is pointing parallel to the layers and therefore the structure factor $S(\boldsymbol{Q})$ represents the Fourier transform of six pair correlation functions involving K, N, and D. The (100) and (110) graphite Bragg peaks at 2.94 and 5.08 $Å^{-1}$, respectively, are eliminated for clarity. In spite of the large number of correlation functions the structure factor is surprisingly simple with only one major peak at 1.95 $Å^{-1}$ which is dominated by the ammonia–ammonia pair correlation. The structural model of the 2D liquid is schematically shown in Fig. 3 and is based on a structure factor calculation which assumes that the K–ammonia clusters are four-fold coordinated and that the molecular three-fold axis lies parallel to the graphite and intercalate layers, in agreement with recent nmr results (9).

Neutron scattering scans in which the scattering vector has a component in the c^* direction perpendicular to the planes yield clear evidence that no correlation exists between adjacent intercalate layers, demonstrating the 2D nature of the metal–ammonia layers in these GIC's. Thus the K–ammonia layers form the two-dimensional structural analogue of the well-known three-dimensional metal–ammonia solutions in which the K^+ ion is six-fold coordinated (10, 11). In fact, resistivity anomalies and optical reflectivity measurements (12) as a function of the ammonia concentration have recently provided strong evidence for a metal–insulator transition in two dimensions. In homogeneous stage 1 KC_8 or stage 2 KC_{24} compounds the outer K-4*s* electron is either completely or almost completely donated to the graphite π^*-bands (13). The metal–insulator transition in the K–NH_3 intercalate layer relies crucially on a partial back transfer of electrons from the graphite to the intercalate bands. This back transfer along with the layer expansion implies that the intercalate–graphite interaction is weakened, which should result in a softening of the phonon energies for modes propagating normal to the planes. This effect will be discussed in further detail in part IV of this paper.

While there exists no correlation between the metal–ammonia intercalate layers, the graphite layers maintain the proper A/A/A... stacking sequence typical for stage 1 compounds (8). Here A refers to the graphite basal planes and the slash to the liquid intercalate layer. The graphite stacking order, in addition, indicates that the intercalate layer cannot be described as a simple 2D liquid on a smooth substrate but that it must be, however weakly, modulated by the graphite corrugated substrate potential. This modulation should be observable in a liquid structure factor reflecting the six-fold symmetry of the graphite basal planes. However, corresponding experiments on single crystals have not been carried out yet to verify this conjecture. At 190 K an order–disorder transition takes place, and the low temperature structure presumably represents a discommensuration domain structure. But the structural details of this phase remain to be determined.

Can. J. Chem. Downloaded from www.nrcresearchpress.com by 176.9.209.113 on 09/07/12
For personal use only.

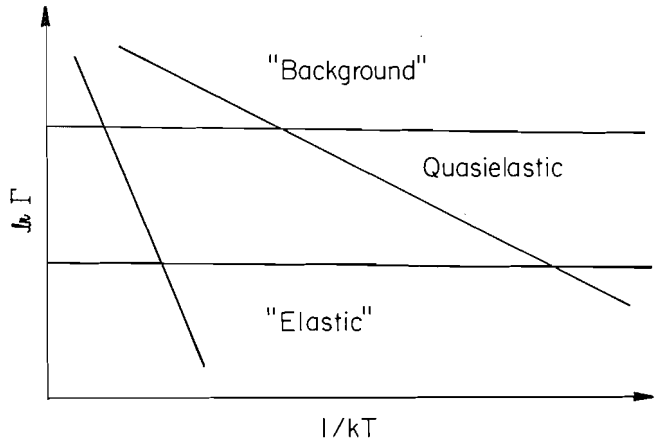

FIG. 5. Schematic Arrhenius plots of two different molecular excitations with different activation energies. Γ is the width of the neutron quasi-elastic line shape which is related to the jump frequency or to the diffusion constant. The "quasielastic" region designates the dynamical range of a neutron spectrometer within which quasi-elastic line shapes can be measured. Any signal outside of this range appears either as an "elastic" peak or contributes to the "background" of the sprectrum.

III. Single molecule dynamics

In the presence of NH_3 molecules several kinds of rigid molecular motions have to be considered, discounting the internal vibrational excitations. The rigid molecular excitations for the bound NH_3 molecules are depicted in Fig. 4, and comprise a rotation of the molecule about its C_3 symmetry axis (R_1), rotation about the enclosed K^+ ion (R_2), translational motion of single molecules of $K(NH_3)$ complexes (T), and finally possible librations or tumbling motions of the molecule. Some of those excitations may be highly coupled. For the free molecules an even more complex picture may be expected which resembles the excitations of molecules in a homogeneous molecular liquid. However, since the number of "free" NH_3 molecules is comparatively small (<10%), we will tentatively neglect their contribution to the excitation spectrum. Recent quasi-elastic neutron scattering (QUENS) work (14) was attempted to unravel these different molecular excitations.

In general, the neutron dynamical scattering function $S(\boldsymbol{Q}, \omega)$ has a Lorentzian line shape for translational diffusion, whereas for re-orientational motions the line shape is composed of a δ-function superimposed on a Lorentzian component (15, 16). The Lorentzian line shape is due to the time-exponential decay of the self correlation function, while the δ-function reflects the fact that the rotating molecule always returns to its original position. The width of the Lorentzian part, $\Gamma(\boldsymbol{Q}, T)$, is related to the diffusion constant or jump frequency of the molecule, and it is therefore very difficult to separate out the different kinds of motion if they appear on similar time scales. A schematic Arrhenius plot for two different excitations is shown in Fig. 5, demonstrating that the energy range over which a particular quasi-elastic broadening is observable depends on the dynamical range of the instrument used to perform the measurement. Quasi-elastic widths which are too narrow to be resolved appear as "elastic" peaks, Lorentzian line shapes that have grown too broad with increasing temperature disappear in the "background" of the spectrum. Thus motions occurring on different time scales can be separated simply by observing them in different temperature regimes or by performing measurements using instruments with different resolution an dynamical ranges.

Rotational and tranlational diffusion can, in addition, be distinguished by their characteristic Q dependence of the dynamical scattering function. Also reorientational jumps versus rotational diffusion and translational jump diffusion versus continuous diffusion are distinguishable in carefully recorded neutron spectra. Space limitation does not allow us to go here in further detail. We simply note that for small scattering vectors $\boldsymbol{Q}$ the Lorentzian width $\Gamma \propto Q^2$ for translational diffusion and $\Gamma =$ constant for rotational diffusion.

In Fig. 6 are shown representative QENS scans from $KC_{24}(NH_3)_{4.3}$ at several temperatures in the ordered as well as in the disordered phase of the K–NH_3 intercalate layer (14). These data were taken at samples containing NH_3 in order to take advantage of the large incoherent cross-section of the H atoms for neutron scattering. In the top panel of Fig. 6 a quasi-elastic scan is shown at 78 K and at $Q_{\parallel} = 2.0$ Å^{-1}, where the subscript $\parallel$ designates the orientation of the scattering vector parallel to the intercalate layers. At this temperature a good fit to the data is obtained using a two component peak, a δ and a Lorentzian component both broadened by the Gaussian instrumental resolution. The two component line shape is indicative of a rotational motion of the NH_3 molecule at this temperature. As the temperature is increased, the width of the broad component increases from 0.79 meV at 78 K to 1.3 meV at 150 K. An Arrhenius plot of the deconvoluted Lorentzian width indicates that this rotation has an activation energy of about 5 meV. Upon further increase of the temperature to 200 K, which is just above the order–disorder temperature, it is found that the scattering due to the first rotational motion has broadened into a flat background, and that a second rotational excitation appears in the spectrum. This spectrum was recorded at a smaller scattering vector than the data below the phase transition, because of the coupling of rotational and diffusion motion which becomes noticeable at higher Q's. At 300 K and at approximately the same Q as the 200 K spectrum, it becomes now aparent that the central peak is broader than the instrumental resolution caused by the translational motion of the ammonia molecules. The translational self-diffusion constant was estimated to be of the order of 10^{-5} cm^2/s at room temperature, and the activation energy of the second rotational excitation was determined to be of the order of 100 meV.

The results described above were obtained with a triple-axis spectrometer at a thermal neutron source. Therefore they do not contain enough spectra at different Q values to allow unique assignments of the observed spectra to certain types of molecular motions. The most reasonable interpretation of the data, however, starts with the fact that at the lowest temperature the quasi-elastic broadening is almost certainly due to rotations of the molecule about the axis with smallest moment of inertia, which is the C_3 symmetry axis. The rotation observed at higher temperatures may then be due to a spin-wheel type motion of the ammonia molecules about the encaged K ions. Finally, the translational diffusion may either involve whole K–NH_3 complexes, diffusion of individual NH_3 molecules between different complexes, diffusion of "free" ammonia molecules, or a combination thereof. Even with more Q values and higher resolution it will be very difficult if not impossible to distinguish between these possibilities. The assignment of the rotational motions is in agreement with recent nmr results (9) which indicate that at room temperature both spinning of the NH_3 molecule about the C_3 axis and precession of the molecular axis about the graphite c axis are present, and that both occur with frequencies greater than 10^5 Hz.

Can. J. Chem. Downloaded from www.nrcresearchpress.com by 176.9.209.113 on 09/07/12
For personal use only.

Can. J. Chem. Downloaded from www.nrcresearchpress.com by 176.9.209.113 on 09/07/12
For personal use only.

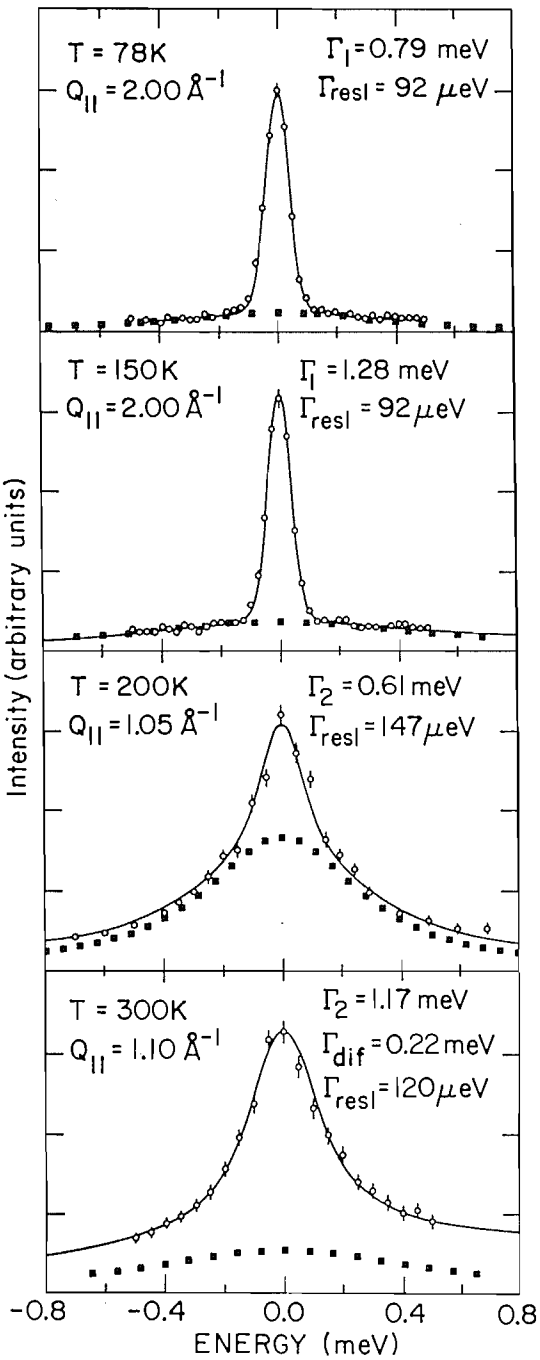

FIG. 6. Quasielastic spectra obtained by inelastic neutron scattering. Open circles represent experimental points, the solid lines are fits to δ functions and Lorentzians, both convoluted with the Gaussian instrumental resolution, and the squares represent the Lorentzian contributions only to the scattering. The data extend to higher positive and negative energy values than shown in the figure. For further details see text (from ref. 14).

Very recent high resolution neutron scattering studies (17) showed a rich tunneling spectrum between 4 and 30 K, which evolves at higher temperatures into the quasi-elastic spectrum discussed above. But since the low temperature intercalate structure is unresolved at the present time, any interpretation of the tunneling spectrum would be premature.

IV Phonon–libron coupling

Additional insight into the dynamics of the K–NH_3 – GIC has also been gained by measuring the phonon dispersion of this system (18). The measured energies of the [00q] longitudinal (L) phonon modes of stage 1 $KC_{24}(ND_3)_{4.3}$ are shown in Fig. 7. These measurements were carried out with deuterated ammonia to reduce the incoherent scattering and enhance the coherent scattering thereby allowing the measurement of the phonon dispersion. Three branches are clearly observed as shown in Fig. 7. However, it is well known that stage 1 compounds typically display only two [00q] L branches because the c axis repeat distance comprises two planes with different areal mass densities (19). Comparison with these homogeneous stage 1 compounds indicates that the lower two branches of $KC_{24}(NH_3)_{4.3}$ belong to the same acoustic branch which has been split by the hybridization of the phonons with an additional excitation at about 7 meV. As will be discussed later, the nature of this mode is not yet certain, but it must be associated with librations of the ammonia molecules. A zone center scan reveals a broad feature centered at 7 meV due to the additional excitation. Thus the librational mode is essentially dispersionless along the c axis, indicating a very weak interaction between ND_3 molecules in adjacent layers. This finding is in accordance with the complete absence of interclate interlayer correlations displayed in the elastic scattering data.

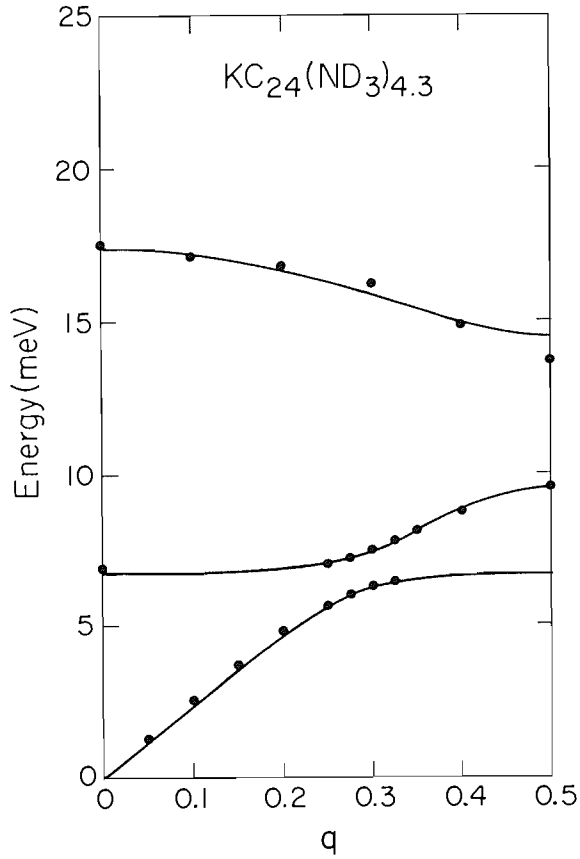

FIG. 7. [00q] longitudinal phonon dispersion of the stage 1 compound $KC_{24}(ND_3)_{4.3}$. The solid lines represent a fit to the data of the one-dimensional Born – von Karman model including phonon–libron coupling term described in the text (from ref. 18).

The observed dispersion relation has been modeled with a 3 × 3 dynamical matrix, **D**, which includes a virtual crystal, one-force constant Born – von Karman model, an Einstein oscillator of energy α representing the libration, and a term containing the coupling constant γ:

$$\mathbf{D} = \begin{bmatrix} \frac{2\phi}{M} & \frac{-\phi}{\sqrt{mM}}(1 + e^{iql_c}) & -\gamma\alpha(1 - e^{i2ql_c}) \\ \frac{-\phi}{\sqrt{mM}}(1 + e^{-iql_c}) & \frac{2\phi}{m} & 0 \\ -\gamma\alpha(1 - e^{-i2ql_c}) & 0 & \alpha^2 \end{bmatrix}$$

Here ϕ is the intercalate-graphite force constant per carbon atom, M is the carbon areal mass density, m is the intercalate areal mass density per carbon atom, and l_c is the c-axis lattice constant. The upper left corner marked by the dotted lines represents the uncoupled phonon dispersion. The best fit parameters corresponding to the dispersion relations displayed as the solid lines in Fig. 7 are $\phi = 2090$ dyn/cm, $\alpha = 6.7$ meV, and $\gamma = 0.70$ meV. The interlayer force constant ϕ is by a factor of two smaller than the value obtained for the binary stage 1 compound KC_8 (19, 20). This decrease is mostly due to the c-axis layer expansion in the ternary compound as compared to the binary compound and partially also to the back transfer of electrons from the graphite π^*-band to the intercalate bands, as alluded to previously.

The actual physical motion corresponding to the observed librational excitation has not been unambiguously determined yet. However, it is possible to make a reasonable speculation. From the quasi-elastic neutron scattering results discussed earlier, it is clear that rotations about the C_3 molecular axis persist to low temperatures. The fact that this component of the quasi-elastic line broadens to an essentially flat background at room temperature, implying almost free rotation, indicates that the libration is certainly not about the C_3 symmetry axis. Thus we are led to consider oscillations of the C_3 axis. A simple model for such excitations is obtained by noting that this is also the axis along which the molecular dipole moment is directed and that the potassium atoms are almost completely ionized. Then if one considers the electrostatic interaction between a point dipole p and a point charge e, both of which are fixed in space, the librational frequency of the dipole is given by $\omega_{lib} = (pe/R^2I)^{1/2}$, where I is the moment of inertia about the librational axis, and R is the dipole-charge separation. For ND_3, $p = 1.3$ Debyes, $I_{cm} = 3 \times 10^{12}$ meV Å$^2/c^2$ (c = speed of light), and the metal–ammonia distance is roughly 3 Å. This gives an energy for librations occurring about the molecular center-of-mass of about 24 meV, far different from the observed value of 7 meV. Thus the barrier is an order of magnitude too large to explain the energy of the observed excitation. However, if the barrier were a factor of 10 smaller, it would then be comparable to the thermal energy and anharmonicity would render the librational excitation, as well as the coupling to the acoustic phonons, unobservable.

The way to resolve these difficulties is to find a mechanism which increases the effective moment of inertia thereby leaving the potential barrier high enough to account for the relatively small degree of anharmonicity. This can be done in two ways. The first is to shift the rotational axis away from the molecular center-of-mass. In order to reduce the librational energy from 25 meV to the observed 7 meV this displacement must be about 1.4 Å, which places the axis of rotation outside of the ND_3 molecule approximately half way between the potassium and ammonia distance. The observed excitation was therefore tentatively named a K–ND_3 "bond-bending" mode (18). It is, however, difficult to picture such a mode since the displacements of the D atoms, which are sterically constrained by the bounding graphite layers, would be large. On the other hand, strong evidence that the librational excitation must have an out-of-plane component is provided by the fact that it couples to the longitudinal phonons propagating normal to the planes, and by nmr results (9) which indiate that the out-of-plane potential is approximately what is required to account for a 7 meV bond-bending mode. There is only one known case in which an in-plane motion leads to a splitting of the [00q]L acoustic branch and this is for alkali-intercalates in stage 2 GIC's (21, 22). Thus, while the bond-bending model explains the observations in a relatively complete fashion, it is not the only model which seems to be capable of doing so. Further experiments are therefore necessary to unambiguously determine, if either, of these models is appropriate for K–ammonia intercalated graphite.

V. Conclusion

We have provided a brief overview of the intriguing structural and dynamical properties of K–ammonia intercalate layers in graphite recently determined by elastic, quasi-elastic, and inelastic neutron scattering experiments. These measurements show that the K–NH_3 layers represent two-dimensional liquids consisting of four-fold coordinated K–ammonia clusters and a small percentage of "free" ammonia molecules. The dynamics of this liquid is very rich, comprising simultaneous rotation of the ammonia molecules about their three-fold symmetry axis, precession of this axis about the encaged K ions, and translational motion of the clusters within the intercalate plane. In addition, a librational excitation of the ammonia molecules couples to longitudinal [00q] phonon modes propagating normal to the graphite and interclate planes. Although the last years have witnessed much progress in unraveling the fascinating properties of two-dimensional metal–ammonia solutions, there are a number of questions which require close attention in future work. Those are the low temperature ordered structure of the K–ammonia layers, the nature of the diffusional motion, the diffusion–rotation coupling, and the origin of the librational excitation.

Acknowledgements

It is our pleasure to acknowledge fruitful collaborations and beneficial discussions with our co-workers who have contributed much to the work described in this paper: S.A. Solin, J.J. Rush, Y.B. Fan, and A. Magerl. This work was supported by the U.S.A. National Science Foundation under grant DMR 86-05565.

1. H. Zabel. Synth. Met. **14**, (1987); Orientational Disorder Cryst. **7**, 2 (1987).
2. S. A. Solin. Adv. Chem. Phys. **49**, 455 (1982).
3. H. Zabel and P. C. Chow. Comments Cond. Mat. Phys. **12**, 255 (1986).
4. M. S. Dresselhaus and G. Dresselhaus. Adv. Phys. **30**, 139 (1986).
5. W. Rüderdorff and E. Schultze. Angew. Chem. **66**, 305 (1954).
6. B. R. York and S. A. Solin. Phys. Rev. B**31**, 8206 (1985).
7. X. W. Qian, D. R. Stump, and S. A. Solin. Phys. Rev. B**33**, 5756 (1986).
8. Y. B. Fan, S. A. Solin, D. A. Neumann, H. Zabel, and J. J. Rush. Phys. Rev. B**36**, 3386 (1987).
9. T. Tsang, R. M. Fronko, H. A. Resing, X. W. Quian, and S. A. Solin. Sol. State. Commun. **63**, 361 (1987).
10. J. L. Dye. Prog. Inorg. Chem. **32**, 327 (1984).
11. J. C. Thompson. Rev. Mod. Phys. **40**, 704 (1986).
12. Y. Y. Huang, Y. B. Fan, S. A. Solin, J. Heremans, G. G.

Can. J. Chem. Downloaded from www.nrcresearchpress.com by 176.9.209.113 on 09/07/12
For personal use only.

TIBBETTS, J. M. ZHANG, and P. C. EKLUND. MRS Proceedings of Symposium K, *Edited by* M. S. Dresselhaus, G. Dresselhaus, and S. A. Solin. Boston, 1986. p. 146.
13. H. KAMIMURA. Ann. Phys. Coll. No. 2, **11**, 39 (1986).
14. D. A. NEUMANN, H. ZABEL, J. J. RUSH, Y. B. FAN, and S. A. SOLIN. J. Phys. **20**, 761 (1987); D. A. Neumann. Thesis, University of Illinois. 1987.
15. T. SPRINGER. Quasielastic neutron scattering for the investigation of diffusive motions in solids and liquids. Springer Tracts in Modern Physics. Vol. 64. Springer Verlag, New York. 1972.
16. H. ZABEL. *In* Nontraditional methods in diffusion. *Edited by* G. E. Murch, H. K. Birnbaum, and J. R. Cost. The Metallurgical Society of AIME, Warrendale, PA. 1984.
17. D. A. NEUMANN, H. ZABEL, S. A. SOLIN, and A. MAGERL. To be published.
18. D. A. NEUMANN, H. ZABEL, Y. B. FAN, S. A. SOLIN, and J. J. RUSH. Phys. Rev. B. In press.
19. H. ZABEL and A. MAGERL. Phys. Rev. B**25**, 2463 (1982).
20. D. A. NEUMANN, H. ZABEL, J. J. RUSH, and N. BERK. Phys. Rev. Lett. **53**, 56 (1984).
21. A. FUNAHASHI, T. KONDOW, and M. IIZUMI. Solid Stat. Commun. **44**, 1515 (1982).
22. A. MAGERL, H. ZABEL, and J. J. RUSH. Synth. Met. **7**, 339 (1983).

Can. J. Chem. Downloaded from www.nrcresearchpress.com by 176.9.209.113 on 09/07/12
For personal use only.

The 9.3547 GHz complex permittivity of water in the temperature interval 0–10°C

T. H. T. VAN KALLEVEEN AND H. A. BUCKMASTER[1]

Department of Physics, The University of Calgary, Calgary, Alta., Canada T2N 1N4

Received August 31, 1987

This paper is dedicated to Professor J. A. Morrison

T. H. T. VAN KALLEVEEN and H. A. BUCKMASTER. Can. J. Chem. **66**, 672 (1988).

This paper reports the results of a high precision study of the 9.3547 GHz complex permittivity of water in the temperature interval from 0–10°C. Measurements were made in ≈0.5°C steps in the interval 0–5°C and ≈1.0°C steps in the interval 5–10°C. The precision for the permittivity and for the dielectric loss was typically ≈0.03% and ≈0.04%, respectively, whereas the accuracy is better than 0.15%. The values of the permittivity $\epsilon'(T)$, the dielectric loss $\epsilon''(T)$, the attenuation per unit length $\alpha(T)$, and the phase shift per unit length $\beta(T)$ have been fitted to the empirical polynomial expressions

$$\epsilon'(T) = 44.68 + 1.318\,T - 0.0253\,T^2 + 0.000378\,T^3 \qquad \sigma(\epsilon') = 0.030$$
$$\epsilon''(T) = 40.54 - 0.0901\,T - 0.0298\,T^2 + 0.000537\,T^3 \qquad \sigma(\epsilon'') = 0.012$$
$$\alpha(T) = 550.3 - 7.08\,T - 0.15\,T^2 + 0.0029\,T^3 \qquad \sigma(\alpha) = 0.17$$
$$\beta(T) = 1416.3 + 15.11\,T - 0.45\,T^2 + 0.0090\,T^3 \qquad \sigma(\beta) = 0.36$$

T. H. T. VAN KALLEVEEN et H. A. BUCKMASTER. Can. J. Chem. **66**, 672 (1988).

Dans ce travail, on a effectué une étude à haute précision du complexe de permittivité de l'eau à 9,3547 GHz, à un intervalle de température de 0 à 10°C. On a effectué les mesures à tous les 0,5°C entre 0 et 5°C et à tous les degrés entre 5 et 10°C. Les précisions sur la permittivité et sur la perte diélectrique sont respectivement de 0,03% et ≈0,04% alors que l'exactitude est mieux que 0,15%. On a ajusté les valeurs de la permittivité $\epsilon'(T)$, de la perte diélectrique $\epsilon''(T)$, de l'atténuation par unité de longueur $\alpha(T)$, et du déplacement de phase par unité de longueur $\beta(T)$ aux expressions polynomiales empiriques suivantes :

$$\epsilon'(T) = 44{,}68 + 1{,}318\,T - 0{,}0253\,T^2 + 0{,}000378\,T^3 \qquad \sigma(\epsilon') = 0{,}030$$
$$\epsilon''(T) = 40{,}54 - 0{,}0901\,T - 0{,}0298\,T^2 + 0{,}000537\,T^3 \qquad \sigma(\epsilon'') = 0{,}012$$
$$\alpha(T) = 550{,}3 - 7{,}08\,T - 0{,}15\,T^2 + 0{,}0029\,T^3 \qquad \sigma(\alpha) = 0{,}17$$
$$\beta(T) = 1416{,}3 + 15{,}11\,T - 0{,}45\,T^2 + 0{,}0090\,T^3 \qquad \sigma(\beta) = 0{,}36$$

[Traduit par la revue]

1. Introduction

The complex permittivity of water has been measured near 9 GHz to a precision of ≈1–2% below 10°C by a number of authors including Collie *et al.* (1), Saxton and Lane (2), Cook (3), Hasted and El Sabeh (4), Buchanan and Grant (5), and at a number of frequencies from 5 to 36 GHz by Pottel (private communication, quoted by Hasted (6)). Kaatze and Uhlendorf (7) have reported a comprehensive synthesis of these and other complex permittivity measurements at microwave frequencies.

Recently, McAvoy and Buckmaster (8) reported the measurement of the 9.346 GHz complex permittivity of water at 20°C and 25°C with a precision of ≈0.06% for the permittivity and ≈0.15% for the dielectric loss. The measurements had been made using a dual channel, double superheterodyne signal processing system and a variable length transmission sample cell described initially by McAvoy and Buckmaster (9). Subsequently, Zaghloul and Buckmaster (10) improved this instrumentation system and reported the measurement of the 9.356 GHz complex permittivity of water in the temperature interval from 10 to 40°C with a typical precision 0.06% for the permittivity and the dielectric loss. It was found that condensation on the sample waveguide windows precluded making measurements below 10°C and that sample temperature inhomogeneity in excess of 0.1°C was the limiting factor above 40°C.

This paper reports the measurement of the 9.3547 GHz complex permittivity of water at temperatures below 10°C using a further improved version of the instrumentation system. The permittivity and dielectric loss have been obtained with a typical precision of 0.03% and 0.04%, respectively.

[1]To whom all correspondence should be addressed.

2. Theory

The complex permittivity ϵ of a dielectric is

$$[1] \quad \epsilon = \epsilon'' - i\epsilon''$$

where the real part ϵ' is the permittivity and the imaginary part ϵ'' is the dielectric loss. The permittivity and dielectric loss can be calculated from the attenuation per unit length α and the phase shift per unit length β using the equations

$$[2a] \quad \epsilon' = (\lambda/2\pi)^2[\beta^2 - \alpha^2] + (\lambda/\lambda_c)^2$$

$$[2b] \quad \epsilon'' = (\lambda/2\pi)^2 2\alpha\beta$$

where λ is the free space wavelength and λ_c is the cutoff wavelength (11). The attenuation and phase per unit length are obtained from the amplitude and the phase of the microwave power which passed through the variable length transmission sample cell. The expressions for α and β are

$$[3a] \quad \alpha = (l/z) \ln [V(z)/V(0)]$$

$$[3b] \quad \beta = (l/z)[\phi(z) - (0)]$$

where $V(z)$ is the signal amplitude and $\phi(z)$ is the signal phase at a sample length z. $V(0)$ is the signal amplitude and $\phi(0)$ is the signal phase at $z = 0$. The cutoff wavelength $\lambda_c = [(m/2a)^2 + (n/2b)^2]^{-1/2}$ (11) and for TE_{mn} mode in the rectangle waveguide of dimensions a and b. It was assumed that only the fundamental mode TE_{10} was excited so $\lambda_c = 2a$.

3. Instrumentation

The instrumentation system used to perform the experiments described in this paper is a modified version of that detailed by Zaghloul and Buckmaster (10). Modifications were only made

Can. J. Chem. Downloaded from www.nrcresearchpress.com by 176.9.209.113 on 09/07/12
For personal use only.

Can. J. Chem. Downloaded from www.nrcresearchpress.com by 176.9.209.113 on 09/07/12
For personal use only.

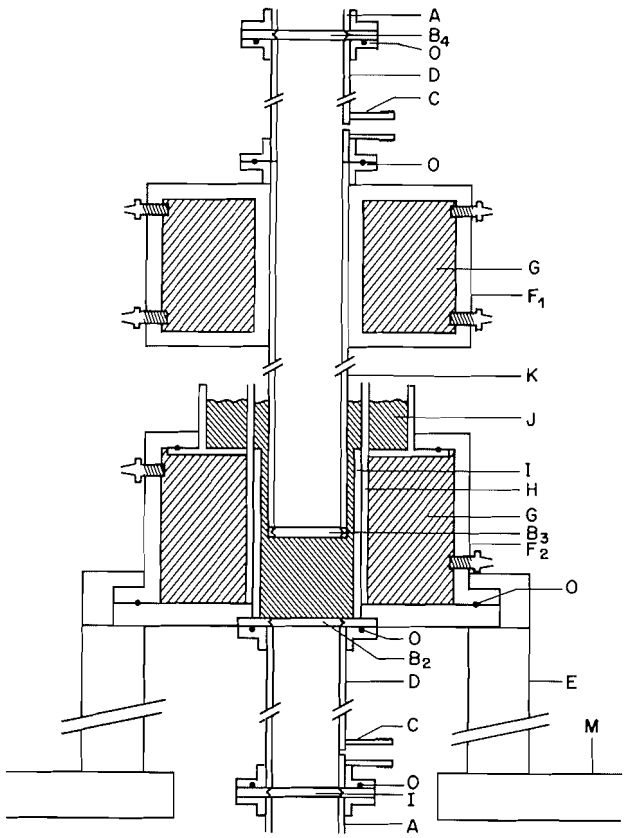

FIG. 1. Schematic diagram of the variable length transmission sample cell: A ≡ Input waveguide, B1, B2, B4 ≡ waveguide windows (MDL-90WF56), B3 ≡ solderable waveguide window (MDL-90WD86), C ≡ evacuation port, D ≡ thin wall stainless steel waveguide, E ≡ Tufnol thermal insulating system support, F1, F2 ≡ upper and lower thermalizing jackets, G ≡ thermalizing fluid, H ≡ temperature measurement tube, I ≡ transmission sample cell outer waveguide (WR102), J ≡ sample fluid, K ≡ transmission sample cell inner waveguide (WR90), M ≡ main system support, O ≡ O-ring.

to the variable length transmission cell. A schematic diagram of the transmission cell is shown in Fig. 1. The upper thermalizing jacket F1 was elongated so that it encased the entire exposed portion of the waveguide K when the transmission sample cell length was zero, i.e., the distance between windows B2 and B3. The stainless steel waveguides D with the evacuation ports C and the waveguide windows (MDL-90WF56) B1 and B4 were added to the system; this permitted the waveguide sections between windows B1 and B2 and between windows B3 and B4 to be evacuated. These features provide greater thermal isolation of the transmission sample cell. A platinum resistance thermometer using a Omega 1Pt100 K2015 Ceramic RTD Element was placed in tube H to measure and to monitor the sample temperature. This thermometer has a resolution of 0.01°C and it was calibrated using a Guideline 9540 Digital Platinum Resistance Thermometer which has an absolute accuracy of 0.01°C and a resolution of 0.001°C. The sample temperature was stable to at least ±0.005°C during the measurement interval of all data sets at a particular temperature.

The measurements were made using a Varian V-153C reflex klystron, a HP-716A klystron power supply, and a Microwave Systems Inc. MOS-1 Microwave Oscillator Synchronizer. This configuration provided ≈ 100 mW of power at 9.3547 GHz with a frequency stability of better than $1:10^8/h$ and spectral purity of ≈ 10 Hz. The frequency stability and spectral purity were transferred to a Gunn diode local oscillator with 60 MHz difference frequency using a Microwave Systems Inc. PLS 2600 Microwave Oscillator Synchronizer.

TABLE 1. The measured values of the attenuation per unit length α, the phase shift per unit length β, and the standard deviations for five typical measurement sequences for water at 9.3547 GHz and at 3.06°C; the calculated values for the permittivity ε′ and the dielectric loss ε″ are also included for the five measurement sequences

Run No.	α ($Np\ m^{-1}$)	σ(α)	β ($deg\ m^{-1}$)	σ(β)	ε′	ε″
1	527.120	0.070	1458.440	0.134	48.489	39.999
2	527.191	0.057	1458.603	0.132	48.499	40.009
3	526.924	0.066	1458.663	0.138	48.511	39.990
4	527.165	0.051	1458.795	0.130	48.514	40.012
5	526.944	0.068	1458.440	0.134	48.493	39.985

The dual channel, double superheterodyne signal processing system was described initially by McAvoy and Buckmaster (9); refinements and improvements to this system were detailed by Zaghloul and Buckmaster (10). This signal processing system enables the amplitude and phase of a microwave signal to be measured to ≈ 0.001 dB and ≈ 0.01° respectively by translating the microwave signal from 9 GHz to 60 MHz and finally to 1 kHz using quasi-synchronous demodulation at each frequency. The amplitude of the 1 kHz signal was measured using a Dana Model 5900 5½ digit Digital Multimeter; the phase of this signal was obtained using a Ithaco 391 Lock-In Analyzer. The amplitude and phase were digitized with 14 bits resolution and stored in a Data Precision 6000 Universal Waveform Analyzer.

4. Experimental Procedure

The measurement procedure is similar to that described by Zaghloul and Buckmaster (10). A measurement was started at a transmission sample cell length of 0.25 in. to eliminate the effects of reflections at the waveguide windows. The transmission sample cell length was incremented in 0.0025 in. steps until the transmission sample cell output power decreased by 20 dB. The microwave power into the transmission sample cell was then increased by 20 dB and the measurement was continued until the transmission sample cell output power had again decreased by 20 dB. After each increment of the cell length, the amplitude and the phase of the transmission sample cell output microwave signal were stored in the Data Precision 6000 memory. At the end of each measurement the amplitude and phase data were transferred from the Data Precision 6000 to a Sun 3/160M workstation for analysis. The total number of increments is dependent on the temperature of the sample and it varied from 133 (≡ transmission sample cell lengths of 0.5825 in.) at 0.04°C to 157 (≡ 0.6425 in.) at 10.09°C.

The attenuation per unit length α and the phase shift per unit length β were calculated from the amplitude and phase data using eqs. [3*a*] and [3*b*]. The permittivity and the dielectric loss were obtained from α and β using eqs. [2*a*] and [2*b*]. All values of ε′ and ε″ reported in this paper are the average of five or six consecutive amplitude and phase measurement data sets. It was found that this number of measurement data sets was sufficient, i.e., an increase in the number of measurement data sets did not appreciably improve the standard deviation of ε′ and ε″.

The complete set of measurements was made without changing the water sample during a period of days because deviations in ε′ and ε″ ≈ 5σ were observed on one occasion although the water was obtained from the same reservoir. If the water is not changed and water is added to the sample to make up for evaporization, measurements made on different days but for the same sample temperature produce average values which are within one standard deviation from each other. Subsequently, it was determined that this deviation probably occurred

TABLE 2. The permittivity ϵ', the dielectric loss ϵ'', the attenuation per unit length α, the phase shift per unit length β, and their standard deviations in the temperature interval 0–10°C at 9.3547 GHz

T (°C)	ϵ'	$\sigma(\epsilon')$	ϵ''	$\sigma(\epsilon'')$	α (Np m^{-1})	$\sigma(\alpha)$	β (deg m^{-1})	$\sigma(\beta)$
0.04	44.726	0.014	40.552	0.016	550.139	0.203	1416.756	0.188
0.39	45.217	0.019	40.510	0.014	547.400	0.144	1422.350	0.252
1.05	46.042	0.010	40.417	0.008	542.603	0.114	1431.634	0.097
1.44	46.512	0.008	40.339	0.014	539.611	0.170	1436.799	0.097
2.01	47.265	0.014	40.251	0.012	535.291	0.091	1445.228	0.216
2.45	47.773	0.011	40.175	0.013	532.212	0.174	1450.835	0.125
3.06	48.501	0.010	39.999	0.010	527.069	0.112	1458.588	0.136
3.51	48.980	0.016	39.900	0.012	523.995	0.137	1463.781	0.197
4.04	49.670	0.006	39.750	0.006	519.310	0.072	1471.150	0.075
4.48	50.112	0.017	39.598	0.013	515.750	0.099	1475.664	0.249
5.07	50.776	0.018	39.380	0.010	510.645	0.124	1482.542	0.270
6.08	51.840	0.010	39.010	0.010	502.072	0.128	1493.345	0.113
7.08	52.838	0.012	38.611	0.008	493.628	0.070	1503.346	0.157
8.04	53.878	0.014	38.184	0.014	484.817	0.105	1513.738	0.146
9.09	54.898	0.011	37.674	0.011	475.245	0.089	1523.621	0.135
10.09	55.776	0.008	37.157	0.012	466.194	0.158	1531.876	0.066

because an air bubble had developed between the Teflon seal and window B2 at the bottom of the transmission sample cell. Care in filling this cell with water has eliminated this effect.

The values of $\epsilon'(T)$, $\epsilon''(T)$, $\alpha(T)$, and $\beta(T)$ were fitted to empirical polynomials with the temperature (°C) as the independent variable using the method of least squares. A computer programme, which is a variation of that described by Bevington (12), calculated the degree of the polynomial for which the goodness of fit to the data is at a minimum.

5. Results and discussion

The values of the attenuation per unit length α, the phase shift per unit length β, and the standard deviations in α and β for water at 3.06°C for a set of five measurement sequences are presented in Table 1. The permittivity ϵ' and the dielectric loss ϵ'' calculated using eqs. [2*a*] and [2*b*], respectively, are also included. The standard deviations $\sigma(\alpha)$ and $\sigma(\beta)$ correspond to the goodness of the fit of the experimental amplitude and phase data to eqs. [3*a*] and [3*b*], respectively. These values are about a factor of 1.5 smaller than those reported by Zaghloul and Buckmaster (10) for a typical measurement sequence. This improvement was achieved by measuring the amplitude of the 1 kHz signal using the Dana Digital Multimeter instead of the Ithaco Lock-In Analyzer. The latter measurement device was used by Zaghloul and Buckmaster (10) to obtain both the phase and the amplitude of the 1 kHz signal. The reason for the improvement became clear when the amplitude data for each measurement sequence was scrutinized to ensure that the incremental changes in the attenuation were constant. This was accomplished by the graphical display of the consecutive differences for the attenuation as a function of the increment number defined as the labelled sequence of the transmission sample cell lengths. This procedure revealed that the consecutive differences varied sinusoidally with the increment number when the amplitude of the 1 kHz signal was measured using the Ithaco Lock-In Analyzer. The technique used by the Lock-In Analyzer to measure the amplitude of an unknown signal involves shifting the phase of the reference input signal by 90° and multiplying the resultant with the unknown signal. The above mentioned sinusoid has been attributed to the reference signal phase shifter in the Lock-In Analyzer. A computer simulation showed that if the phase shift of the reference input signal is not exactly 90°, the consecutive differences of the attenuation will vary sinusoidally with the increment number. The use of the Dana Digital Multimeter for the measurement of the signal amplitude also revealed that the minimum length of the transmission sample cell had to be increased from that used by Zaghloul and Buckmaster (10) by 0.05 in. to 0.25 in. to eliminate the effects of reflections at the waveguide windows.

The values for the permittivity ϵ', the dielectric loss ϵ'', the attenuation per unit length α, the phase shift per unit length β, and their standard deviations in the temperature interval 0–10°C are listed in Table 2. Each value is the average of the values obtained from five or six measurement sequences at each temperature. The values of $\epsilon'(T)$, $\epsilon''(T)$, $\alpha(T)$, and $\beta(T)$ in Table 2 were fitted to empirical polynomials with the temperature (°C) as the independent variable using the method of least squares. The results of this analysis are

$$[4a]\quad \epsilon'(T) = 44.68 + 1.318\,T - 0.0253\,T^2 + 0.000378\,T^3 \qquad \sigma(\epsilon') = 0.030$$

$$[4b]\quad \epsilon''(T) = 40.54 - 0.0901\,T - 0.0298\,T^2 + 0.000537\,T^3 \qquad \sigma(\epsilon'') = 0.012$$

$$[4c]\quad \alpha(T) = 550.3 - 7.08\,T - 0.15\,T^2 + 0.0029\,T^3 \qquad \sigma(\alpha) = 0.17$$

$$[4d]\quad \beta(T) = 1416.3 + 15.11\,T - 0.45\,T^2 + 0.0090\,T^3 \qquad \sigma(\beta) = 0.36$$

Figures 2*a* and *b* depict the permittivity and dielectric loss as a function of the temperature in the interval 0–10°C using the data in Table 2 and eqs. [4*a*] and [4*b*], respectively. These figures show that both quantities vary smoothly with the sample temperature and that no dramatic changes are observed around 4.0°C which corresponds to the temperature at which the absolute density of water goes through a maximum (13). Similarly, no drastic changes are observed below 1°C as the liquid–solid phase transition at 0°C is approached.

The permittivity and dielectric loss of water at 0 and 10°C and at microwave frequencies around 9 GHz as reported in literature and in this paper are summarized in Table 3. The standard

Can. J. Chem. Downloaded from www.nrcresearchpress.com by 176.9.209.113 on 09/07/12
For personal use only.

Can. J. Chem. Downloaded from www.nrcresearchpress.com by 176.9.209.113 on 09/07/12
For personal use only.

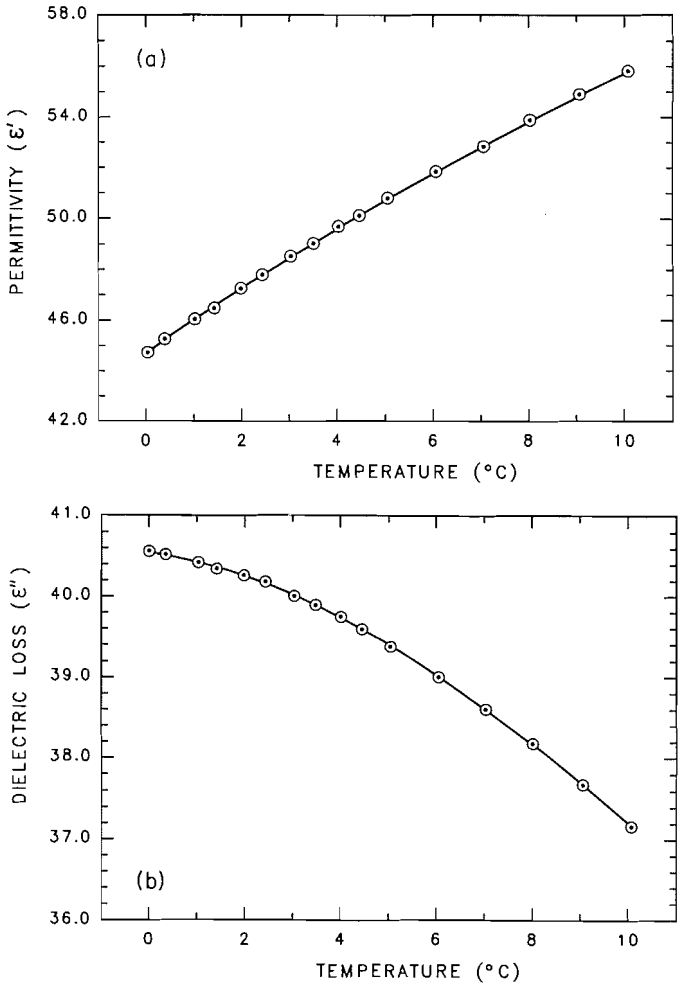

FIG. 2. The permittivity ϵ' (*a*) and the dielectric loss ϵ'' (*b*) as a function of the temperature in the interval 0–10°C at 9.3547 GHz using the data from Table 2 and eqs. [4*a*] and [4*b*], respectively.

deviations of ϵ' and ϵ'' have been included for the values from Zaghloul and Buckmaster (10) and from this work. The standard deviations of the other values are not available, but the precision is reportedly not better than 1–2% (1–5). A comparison of the precision obtained here to that reported by Zaghloul and Buckmaster (10) shows that a much greater degree of precision has been attained in this work. Two factors may have contributed to this. Firstly, Zaghloul and Buckmaster (10) obtained their experimental data using a Ithaco Lock-In Analyzer. A reanalysis of their data revealed that the above mentioned sinusoid was present in all of their attenuation difference graphs. This will affect the value of α to some extent. Secondly, the thermal isolation of the transmission sample cell has been improved greatly and so the sample will have better thermal homogeneity. Also the temperature of the sample can now be measured with greater accuracy.

A comparison of the permittivity at 10°C obtained here to that reported by Zaghloul and Buckmaster (10) shows that the values for ϵ' differ by $\approx$0.5%. However, this difference can be due to the above mentioned improvement in the determination of the sample temperature. An error of $\approx$0.1°C corresponds to $\approx$0.3%. It should be emphasized that measurements made on different days but at the same sample temperature produced average values within one standard deviation from each other.

TABLE 3. The permittivity ϵ' and the dielectric loss ϵ'' of water at 0 and 10°C and microwave frequencies around 9 GHz as reported in this paper and by various authors

T (°C)	ν (GHz)	ϵ'	ϵ''	Reference
0	9.346	44.82	41.64	1
0	9.346	42.63	41.27	2
0	9.39	43.4	41.4	3
0	9.141	46.0	41.0	4
0	9.375	44.0	41.4	5
0.04	9.3547	44.726(14)	40.552(16)	This paper
10	9.346	53.85	37.57	1
10	9.346	54.89	38.06	2
10	9.39	54.4	37.1	3
10	9.141	56.0	37.0	4
10	9.375	54.0	37.8	5
10	9.356	56.052(31)	37.176(28)	10
10.09	9.3547	55.776(8)	37.157(12)	This paper

In summary, this paper reports the first comprehensive, high precision study of the 9.3547 GHz complex permittivity of water in the temperature interval from 0–10°C. Measurements at other frequencies are presently in progress.

Acknowledgements

This research was supported by a NSERC Operating Grant A716 awarded to one of us (H.A.B.) and The University of Calgary. The assistance of Mr. H. Zaghloul and Mr. C. H. Hansen in providing insightful contributions to the improvement of the instrumentation system and the data processing contributions of Mr. P. Milligan are noted with pleasure.

1. C. H. COLLIE, J. B. HASTED, and D. M. RITSON. Proc. Phys. Soc. **60**, 145 (1948).
2. J. A. SAXTON and J. A. LANE. Proc. R. Soc. A**213**, 400 (1952).
3. H. J. COOK. Brit. J. Appl. Phys. **3**, 249 (1952).
4. J. B. HASTED and S. H. M. EL SABETH. Trans. Faraday Soc. **49**, 1003 (1953).
5. T. J. BUCHANAN and E. H. GRANT. Brit. J. Appl. Phys. **6**, 64 (1955).
6. J. B. HASTED. Aqueous dielectrics. Chapman and Hall, London. 1973. p. 45.
7. U. KAATZE and V. UHLENDORF. Z. Phys. Chem. NF**126**, 151 (1981).
8. J. G. MCAVOY and H. A. BUCKMASTER. J. Phys. D: Appl. Phys. **16**, 2519 (1983).
9. J. G. MCAVOY AND H. A. BUCKMASTER. J. Phys. E: Sci. Instrum. **18**, 244 (1985).
10. H. ZAGHLOUL and H. A. BUCKMASTER. J. Phys. D: Appl. Phys. **18**, 2109 (1985).
11. H. FRÖHLICH. Theory of dielectrics. Oxford University Press, London. 1958.
12. P. R. BEVINGTON. Data reduction and error analysis for the physical sciences. McGraw-Hill, New York, NY. 1969. p. 141.
13. CRC Handbook of Chemistry and Physics. The Chemical Rubber Co., Cleveland, OH. 1970. p. F-4.

Temperature variation of nuclear magnetic resonance line shape in solid CHD_3

KENKICHI OKADA
Department of Chemistry, Faculty of General Education, Gifu University, Gifu 501-11, Japan

YOSHIAKI OZAKI
Department of Chemistry, Nagoya Institute of Technology, Nagoya 466, Japan

AND

KAZUO MAKI
Tochigi Research Laboratory, Kao Company, Utsunomiya, Japan

Received September 2, 1987

This paper is dedicated to Professor James A. Morrison

KENKICHI OKADA, YOSHIAKI OZAKI, and KAZUO MAKI. Can. J. Chem. **66**, 676 (1988).

The nuclear magnetic resonance line shape in solid CHD_3 is calculated under the assumption of consecutive interspin modifications conversion. A variable concentration of nuclear spin species can be used to fit the temperature variation of the nuclear magnetic resonance absorption lines as observed at low temperatures with the help of a simple Gaussian line width.

KENKICHI OKADA, YOSHIAKI OZAKI et KAZUO MAKI. Can. J. Chem. **66**, 676 (1988).

Faisant l'hypothèse qu'il se produit une conversion consécutive des modifications de spin, on a calculé la forme des raies en résonance magnétique nucléaire du CHD_3 à l'état solide. On peut utiliser une concentration variable des espèces de divers spins nucléaires pour ajuster la variation, en fonction de la température, des raies d'absorption en résonance magnétique nucléaire qui sont observées à basses températures à l'aide d'une largeur de raie de Gauss simple.

[Traduit par la revue]

Can. J. Chem. Downloaded from www.nrcresearchpress.com by 176.9.209.113 on 09/07/12
For personal use only.

I. Introduction

The observation of nuclear magnetic interactions has given valuable information on the structure and molecular motion in the solid methanes. Among the many investigations in this field one might mention an early systematic T_1 measurement (1), information on tunnel splitting (2), structure determination of phase II (3), and a high pressure study of phase diagrams (4). A recent nmr study at very low temperatures revealed new aspects of the methane problem. Precise measurements of nmr line shapes in solid deuterated methanes by Buchman *et al.* (5–7) show remarkable temperature variation of the line shapes, especially of CHD_3. From their results these authors claim that there is no nuclear spin conversion in CHD_3 at low temperatures. Although they obtained good results for the nmr line shape, their analysis gave a poor fit to the heat capacity data (8) in spite of the employment of many adjustable parameters.

In the present article we shall give an alternative and better explanation of the nmr data for solid CHD_3. Our model of rotational tunneling in solid CHD_3 is the same one already found by one of the present authors to give an excellent fit to the experimental data for the heat capacity of all the isotopic methanes (11). We shall show that the nmr data can also be explained on the basis of the occurrence of spin conversion without introducing many additional parameters.

The theoretical treatment of nmr line shapes in phase III of solid CHD_3 is developed in Sect. II. Comparison of theoretical results with experimental data is given, with some remarks, in Sect. III.

II. Theory of the nuclear magnetic resonance absorption line shape

In the following, we employ a mean field approximation to describe the rotational states of a molecule in solid CHD_3. A rotation–nuclear spin state of a molecule may be classified by means of the molecular symmetry group C_{3v}, whose irreducible representations Γ are A_1, A_2, or E. Each molecule will contribute independently to the total nmr line whether it occupies a C_2 or a C_s site. The effective nuclear spin Hamiltonian for the CHD_3 molecule may be written as:

$$[1] \quad H_N = H_Z + H_Q + H_D$$

where the unperturbed system is governed by the deuteron Zeeman term H_Z:

$$[2] \quad H_Z|\Gamma; I, M\rangle = -\hbar\omega_0 M|\Gamma; I, M\rangle, \qquad \omega_0 = \gamma_D H_0$$

$$I = \begin{cases} 3, 1 & \text{for } \Gamma = A_1 \\ 0 & A_2 \\ 2, 1 & E \end{cases} \qquad (M = I, I-1, \ldots, -I)$$

Here the molecular spin function is constructed from the deuteron spin functions $|\mu\rangle$ ($\mu = 1, 0$, or -1) by means of simple product functions $|\mu, \nu, \lambda\rangle$:

$$[3] \quad |\Gamma; I, M\rangle = \sum_{\mu,\nu} C^{\Gamma I}_{M,\mu,\nu} |\mu, \nu, M - \mu - \nu\rangle$$

The explicit forms of these functions are given in the Appendix. The electric quadrupole interaction term H_Q gives the following first-order perturbations upon the Zeeman levels:

$$\begin{aligned}[4] \quad \langle \Gamma; I, M|H_Q|\Gamma; I, M\rangle = \sum_{\mu,\nu} |C^{\Gamma I}_{M,\mu,\nu}|^2 \{e^2qQ/8I(2I-1)\} \\ \times [\{3\mu^2 - I(I+1)\}(3\cos^2\beta_1 - 1 + \eta\cos 2\alpha_1 \sin^2\beta_1) \\ + \{3\nu^2 - I(I+1)\}(3\cos^2\beta_2 - 1 + \eta\cos 2\alpha_2 \sin^2\beta_2) \\ + \{3(M-\mu-\nu)^2 - I(I+1)\}(3\cos^2\beta_3 - 1 \\ + \eta\cos 2\alpha_3 \sin^2\beta_3)]\end{aligned}$$

Here we denote by (α_i, β_i) the polar angles of the CD direction at the ith deuteron with respect to the frame determined by the static magnetic field H_0 and rf field. In this expression,

$$[5] \quad q = (\partial^2 V/\partial Z^2)_0,$$

$$\eta = \{(\partial^2 V/\partial X^2)_0 - (\partial^2 V/\partial Y^2)_0\}/(\partial^2 V/\partial Z^2)_0$$

TABLE 1. Low-lying rotational energy levels of CHD_3 in phase III (in units of K)

C_2 site sym	K	C_s site sym	K
AA	−0.3335	A	−1.1312
AB	−0.1759	A	0.1202
AA	0.1924	A	0.1731
AB	0.9061	A	0.8092
EB	−0.2620	E	−1.1300
EA	−0.1974	E	0.1257
EB	0.2305	E	0.1782
EA	0.9349	E	0.8402

In the table, the molecular symmetry symbol A occurs in the upper entries and E in the lower ones. The site symmetry symbol A or B follows after the molecular symbol in the case of a C_2 site. See ref. 11 for details.

TABLE 2. Nonvanishing values of $N_{\Gamma,I,M}$

I	M	$N_{A_1,I,M}$
3	±3	−5
	±1	3
	0	4
1	±1	−3
	0	6

The value of $N_{\Gamma,I,M}$ is zero when $\Gamma = A_2$ or E and when $\Gamma = A_1$ with $M = \pm 2$.

are the usual symbols for the field gradient parameter and its anisotropy, respectively.

Since the total wavefunction of a CHD_3 molecule should belong to the irreducible representation A_1 of C_{3v} symmetry, we may take a form of the rotation–deuteron spin part as follows:

[6] A_1 species: $\psi_R(A_1)\psi_D(A_1)$

A_2 species: $\psi_R(A_2)\psi_D(A_2)$

E species: $\sqrt{1/2}\,\{\psi_R(E_1)\psi_D(E_2) + \psi_R(E_2)\psi_D(E_1)\}$

where we denote $\psi_R(\Gamma)$ as a rotational wavefunction and put $\psi_D(\Gamma) = |\Gamma; I, M\rangle$. The rotational eigenfunctions are the same as in ref. 11 and the eigenvalues to which these states belong are given in Table 1. Note that the angular variables to describe the rotational motion of a molecule are referred to the crystal-fixed frame.

The nuclear spin matrix elements [4] may be written as

[4′] $\langle\Gamma; I, M|H_Q|\Gamma; I, M\rangle = N_{\Gamma,I,M}h\tilde{\nu}$

where $\tilde{\nu} = -(e^2qQ/40h)f_{1,2,3'}$

[7] $f_{1,2,3} = 3(\cos^2\beta_1 + \cos^2\beta_2 + \cos^2\beta_3 - 1)$
$+ \eta(\cos 2\alpha_1 \sin^2\beta_1 + \cos 2\alpha_2 \sin^2\beta_2 + \cos 2\alpha_3 \sin^2\beta_3)$

This results from carrying out the summation over μ and ν on the right-hand side of eq. [4]. The nonvanishing values of $N_{\Gamma,I,M}$ are given in Table 2.

Since the transition probability $W^{\Gamma,I}_{M\to M-1}$ between Zeeman levels is proportional to

[8] $|\langle\Gamma; I, M-1|I_-|\Gamma; I, M\rangle|^2 = I(I+1) - M(M-1)$

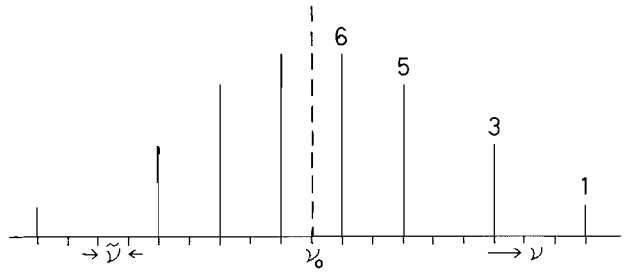

FIG. 1. Calculated pattern of the deuteron nmr absorption spectrum for single crystalline CHD_3. The height of a vertical line is proportional to the line intensity for A_1 species. Numerals are attached to each line to indicate relative heights. The relative heights between A_1 and E species (the latter contributes only to the central peak at the Larmor frequency ν_0, shown as a broken line) depend on temperature. There is no central line at 0 K and the intensity of the nearest wing has one third of the central intensity at high temperature.

the D nmr spectrum associated with CHD_3 molecules in A_1 spin states has the pattern shown in Fig. 1 for a single crystal. The molecules in E spin states contribute only to a central line at the Larmor frequency ν_0 and those in A_2 spin states make a zero contribution. If a powder sample is assumed, any pair of wings in Fig. 1 will deform as shown in ref. 10, for example, into a Pake doublet for the case $\eta = 0$. Further, magnetic dipole–dipole interactions H_D in eq. [11], which come mainly from intramolecular proton–deuteron pairs, broaden every peak in the spectrum. For simplicity, we take these terms into account with the help of a Gaussian convolution having a width σ, for each line and at each temperature.

III. Results and discussion

We agree with the reasoning of Buchman *et al.* (7) that the tunneling is fast compared with e^2qQ/h and gives rise to the A and E spin species. We should, therefore, treat molecular motion with the properly symmetry-adapted wavefunctions given above. Our rotational wavefunctions can reproduce the heat capacity data (8) quite well on the basis of a two-site model in which the molecules occupy both sites of C_2 and C_s symmetries with equal probability.

A temperature variation does not shift peak positions in the present system and therefore does not change the nuclear quadrupole parameters significantly. Without nuclear spin species conversion, one might see essentially the same D nmr spectral pattern over some temperature range. Judging from the observed spectra given in ref. 7, which show that the central peak grows rapidly as temperature increases, it is necessary to increase the E species concentration from 0 at 0 K to the equilibrium value at about 4 K. In Fig. 2, we present typical theoretical line shapes with various abundance ratios of A and E species. For the sake of convenience in comparing with the experimental results, the derivative D nmr spectra are given in Fig. 2. Here we have no intention of giving the "best fit" of theory with experiment but simply wish to demonstrate the comparison between them. Thus, we put $e^2qQ/H = 160$ kHz as experimentally determined (7). We assume the anisotropy factor η is equal to 0 and choose a Gaussian width σ equal to $0.20\,\tilde{\nu}$. Here $\tilde{\nu}$ stands for that in eq. [4′] as averaged over the rotational states $\psi_R(A_1)$. Finite values for η give rise to growth in the central peak for any pair of wings. The temperature indicated beside each spectrum in Fig. 2 refers to the spin species concentrations used in calculating the line shape, these having been determined by Fig. 3 at that temperature. On the

Can. J. Chem. Downloaded from www.nrcresearchpress.com by 176.9.209.113 on 09/07/12
For personal use only.

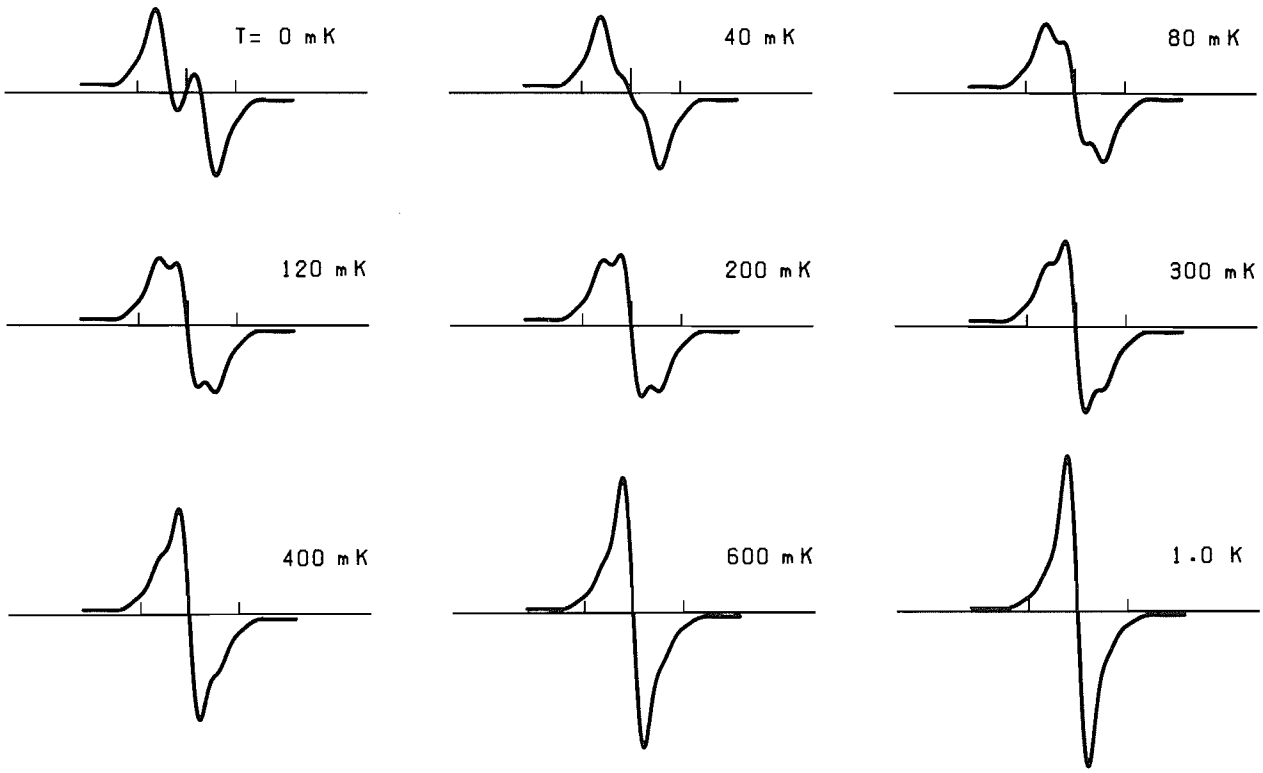

FIG. 2. Calculated deuteron nmr derivative line shapes for polycrystalline CHD_3. The concentrations of A_1 and E molecules at every temperature assigned are taken from those given in Fig. 3 under the assumption of consecutive conversion for molecules at different sites. The abscissa is in units of 30 kHz and the ordinate is in arbitrary units.

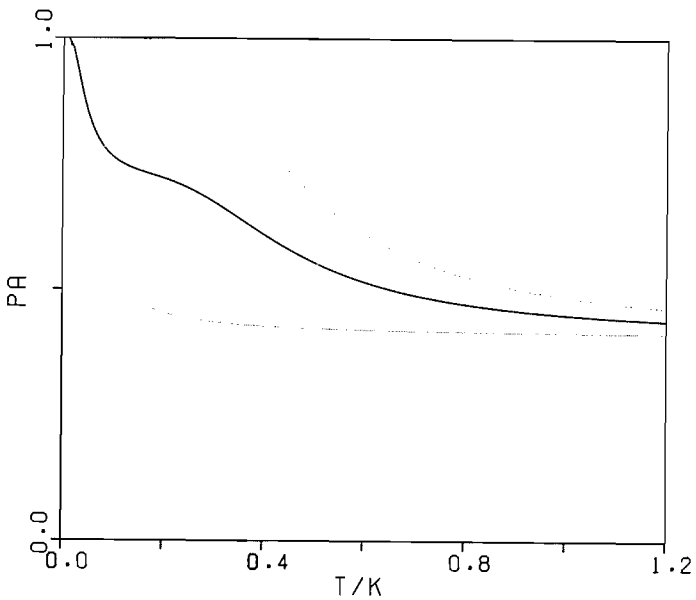

FIG. 3. Assumed temperature variation of concentration of A molecules ($A_1 + A_2$). The solid line gives the total concentration, the light line is for those at the C_2 site, and the dotted line is for those at the C_s site.

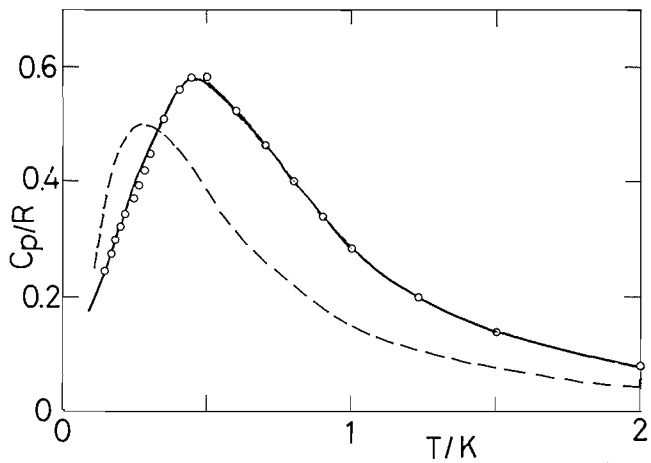

FIG. 4. Temperature variation of the heat capacity of CHD_3. Circles are taken from ref. 8 as smoothed experimental values. The solid line shows the calculated heat capacity based on the 2-site model given in ref. 11. The dashed line shows the calculated heat capacity from the 3-site model, the model 1 given in Fig. 5 of ref. 7.

whole the comparison between the calculated results of Fig. 2 and the experimental results of Buchman *et al.* (7) is quite good.

Buchman *et al.* (7) choose a 3-site model for molecular rotation in phase III of solid CHD_3 instead of our 2-site model (11), to which they failed to refer. In Fig. 4, we present the temperature variation of the theoretical heat capacities of CHD_3 from both models for the sake of comparison with the experimental data. Since heat capacity data are of primary importance to test the model, their model must be modified if it is to reproduce the thermal data. Parameter values obtained from a least-squares fit are not necessarily unique. Generally, different sets of parameter values make equally good fits to the heat capacity data. It is strange to see that their rotational level structures do not contain a difference between the A and E ground state levels (Fig. 4 in ref. 7). We do not as yet, however, know the true crystalline structure of methanes in phase III. Consequently, we had better proceed with the simplest possible model in the present situation. At the very least, it may be premature to assume that there is no spin conversion in CHD_3 at low temperature.

Can. J. Chem. Downloaded from www.nrcresearchpress.com by 176.9.209.113 on 09/07/12
For personal use only.

The order of magnitudes of the nuclear spin conversion time τ differs for molecules at different sites in the solid methanes. We take this fact into account to derive the theoretical spectra of Fig. 2 by making use of the two typical variations of concentration given in Fig. 3. The conversion time for a molecule in the "free" site is about 10 times shorter than in the "hindered" site for the methanes in general. Since a reliable theoretical calculation has not yet been made of the conversion time in solid CHD_3, we have to employ certain tentative assumptions, as in Fig. 3, to analyze the experimental data. As deuteration proceeds from CH_4 to CD_4, τ becomes longer as implied by the intramolecular magnetic dipole–dipole interaction mechanism (9). We believe that this mechanism would yield a τ for CHD_3 that is too long compared with the experimental values at very low temperatures. However, there may be some other mechanisms that might give a smaller value for τ. For example, it may be important to include the effects of certain impurities on the spin conversion rate. Future experiments in equilibration would be desirable.

Acknowledgments

The authors would like to thank the late Professor J. A. Morrison for his kind cooperation and hospitality. They are grateful to Prof. D. Goodings for careful reading of the manuscript and helpful discussions. They also acknowledge the Data Processing Centers of Kyoto and Nagoya University and of the Institute for Molecular Sciences.

1. G. A. DE WIT and M. BLOOM. Can. J. Phys. **47**, 1195 (1969).
2. H. GLÄTTLI, A. SENTZ, and M. EISENKREMER. Phys. Rev. Lett. **28**, 871 (1972).
3. R. F. CODE and J. HIGINBOTHAM. Can. J. Phys. **54**, 1248 (1976).
4. A. J. NIJMAN and N. J. TRAPPENIERS. Physica (Amsterdam), **95B**, 147 (1978); D. VAN DER PUTTEN, N. J. TRAPPENIERS, and K. O. PRINS. Physica (Amsterdam), **124B**, 193 (1984); F. LOSTAK, K. O. PRINS, and N. J. TRAPPENIERS. Physica B + C (Amsterdam), **140B + C**, 272 (1986).
5. S. BUCHMAN, D. CANDELA, W. T. VETTERLING, and R. V. POUND. Phys. Rev. B: Condens. Matter, **26B**, 1459 (1982).
6. S. BUCHMAN, W. T. VETTERLING, D. CANDELA, and R. V. POUND. Phys. Rev. B: Condens. Matter, **26B**, 4826 (1982).
7. S. BUCHMAN, D. CANDELA, W. T. VETTERLING, and R. V. POUND. Phys. Rev. B: Condens. Matter, **28B**, 8 (1983).
8. M. A. WHITE and J. A. MORRISON. J. Chem. Phys. **70**, 5384 (1979).
9. A. J. NIJMAN and A. J. BERLINSKY. Can. J. Phys. **58**, 1049 (1980).
10. M. H. COHEN and F. REIF. Solid State Phys **5**, 321 (1957).
11. K. J. LUSHINGTON, K. MAKI, J. A. MORRISON, A. HEIDEMANN, and W. PRESS. J. Chem. Phys. **75**, 4010 (1981).

Appendix

The C_{3v}-symmetry adapted deuteron spin functions $|\Gamma; I, M\rangle$ from which the molecular rotation – deuteron spin wavefunctions for CHD_3 in eq. [3] are constructed may be written as follows:

$$|A_1; 3, \pm 3\rangle = |\pm 1, \pm 1, \pm 1\rangle$$

$$|A_1; 3, \pm 2\rangle = \sqrt{1/2}\{|0, \pm 1, \pm 1\rangle + |\pm 1, 0, \pm 1\rangle + |\pm 1, \pm 1, 0\rangle\}$$

$$|A_1; 3, \pm 1\rangle = \sqrt{1/15}\{|\mp 1, \pm 1, \pm 1\rangle + |\pm 1, \mp, \pm 1\rangle + |\pm 1, \pm 1, \mp 1\rangle + 2(|\pm 1, 0, 0\rangle + |0, \pm 1, 0\rangle + |0, 0, \pm 1\rangle)\}$$

$$|A_1; 3, 0\rangle = \sqrt{1/10}\{|0, 1, -1\rangle + |0, -1, 1\rangle + |1, 0, -1\rangle + |-1, 0, 1\rangle + |1, -1, 0\rangle + |-1, 1, 0\rangle + 2|0, 0, 0\rangle\}$$

$$|A_1; 1, \pm 1\rangle = \sqrt{1/15}\{|\pm 1, 0, 0\rangle + |0, \pm 1, 0\rangle + |0, 0, \pm 1\rangle - 2(|\mp 1, \pm 1, \pm 1\rangle + |\pm 1, \mp 1, \pm 1\rangle + |\pm 1, \pm 1, \mp 1\rangle)\}$$

$$|A_1; 1, 0\rangle = \sqrt{1/15}\{3|0, 0, 0\rangle - |0, 1, -1\rangle - |0, -1, 1\rangle - |1, 0, -1\rangle - |-1, 0, 1\rangle - |1, -1, 0\rangle - |-1, 1, 0\rangle\}$$

$$|A_2; 0, 0\rangle = \sqrt{1/6}\{|1, -1, 0\rangle - |-1, 1, 0\rangle + |-1, 0, 1\rangle - |1, 0, -1\rangle + |0, 1, -1\rangle - |0, -1, 1\rangle\}$$

$$|E_1; 2, \pm 2\rangle = \sqrt{1/3}\{|0, \pm 1, \pm 1\rangle + \omega^2|\pm 1, 0, \pm 1\rangle + \omega|\pm 1, \pm 1, 0\rangle\}$$

$$|E_1; 2, \pm 1\rangle = \sqrt{1/6}\{|\mp 1, \pm 1, \pm 1\rangle - |\pm 1, 0, 0\rangle + \omega^2(|\pm 1, \mp 1, \pm 1\rangle - |0, \pm 1, 0\rangle) + \omega(|\pm 1, \pm 1, \mp 1\rangle - |0, 0, \pm 1\rangle)\}$$

$$|E_1; 2, 0\rangle = \sqrt{1/6}\{|0, 1, -1\rangle - |0, -1, 1\rangle + \omega^2(|-1, 0, 1\rangle - |1, 0, -1\rangle) + \omega(|1, -1, 0\rangle - |-1, 1, 0\rangle)\}$$

$$|E_1; 1, \pm 1\rangle = \sqrt{1/6}\{|\mp 1, \pm 1, \pm 1\rangle + |\pm 1, 0, 0\rangle + \omega^2(|\pm 1, \mp 1, \pm 1\rangle + |0, \pm 1, 0\rangle) + \omega(|\pm 1, \pm 1, \mp 1\rangle + |0, 0, \pm 1\rangle)\}$$

$$|E_2; I, M\rangle = (|E_1; I, M\rangle)_{\omega \leftrightarrow \omega^2}$$

Here the spin function $|\mu, \nu, \lambda\rangle$ for three deuterons is a simple product of deuteron spin functions $|\mu\rangle$ ($\mu = 1, 0$, or -1). Also $\omega = e^{2\pi i/3}$.

Can. J. Chem. Downloaded from www.nrcresearchpress.com by 176.9.209.113 on 09/07/12
For personal use only.

$CO/N_2/Ar$ orientational glass: magnetic resonance

J. H. WALTON[1]
Department of Physics, Washington University, St. Louis, MO 63130, U.S.A.
MENG-CHOU WU
Department of Physics, College of William and Mary, Williamsburg, VA 23185, U.S.A.
AND
MARK S. CONRADI
Department of Physics, Washington University, St. Louis, MO 63130, U.S.A.
Received September 1, 1987

This paper is dedicated to Professor J. A. Morrison

J. H. WALTON, MENG-CHOU WU, and MARK S. CONRADI. Can. J. Chem. **66**, 680 (1988).

The nmr lineshapes and linewidths of KCN/KBr, N_2/Ar, and $CO/N_2/Ar$ are compared at corresponding states and are found to agree closely. This indicates a similar kind of orientational freezing, despite major differences in the anisotropic molecular interactions. The line narrowing and T_2 data are explicable by two different theories. The one involves an orientation probability function, while the other invokes a broad homogeneous distribution of correlation times. Spin–lattice relaxation measurements indicate that T_1 and dielectric loss are controlled at low temperatures by nearly π flips of CO molecules.

J. H. WALTON, MENG-CHOU WU et MARK S. CONRADI. Can. J. Chem. **66**, 680 (1988).

On a comparé les formes et les largeurs des raies de rmn du KCN/KBr, du N_2/Ar et du $CO/N_2/Ar$ dans des états correspondants et on a trouvé qu'ils sont très semblables. Ce résultat indique que, malgré des différences majeures dans les interactions moléculaires anisotropes, leurs orientations lors de leurs congélations sont semblables. Les données relatives au rétrécissement des bandes et aux valeurs de T_2 peuvent être expliquées par deux théories différentes. La première implique une fonction de probabilité dand l'orientation alors que l'autre fait appel à une distribution homogène large des temps de corrélation. Des mesures de relaxation spin–réseau indiquent que la valeur de T_1 ainsi que la perte diélectrique sont contrôlées, à basse température, par pratiquement π inversions des molécules de CO.

[Traduit par la revue]

I. Introduction

There are three well-studied material systems which form orientational glasses at low temperatures: *ortho*-H_2/*para*-H_2 (1), KCN/KBr (2, 3), and N_2/Ar (4–8). In each of these, non-spherical molecules possessing orientational degrees of freedom (*ortho*-H_2, CN^-, or N_2) are randomly diluted on the crystal lattice by spherical atoms or molecules (*para*-H_2 which is $J = 0$ at low temperatures, Br^-, or Ar). For concentrations x of the non-spherical species which are high enough (typically $x \gtrsim 0.7$) a first-order transition to an orientationally ordered structure occurs as temperature is decreased. For lower concentrations x, no such transition occurs; instead, a continuous freezing is found. Orientational disorder and rapid reorientations at high temperature smoothly change to apparent orientational disorder with static molecular orientations at low temperature. Because of the continuous freezing and the lack of any apparent long-range order, the term orientational *glass* is used to describe the frozen state. Orientational glasses involve random dilution and frustration and are therefore related to spin glasses.

The fundamental physics question surrounding orientational glasses is the exact nature of the continuous freezing. For example, is the freezing a kinetic effect as in window glass or is some kind of order established? Does the system tend towards a unique ground state?

The $CO/N_2/Ar$ system differs from the simpler binary orientational glass former N_2/Ar in that some of the rotors (the CO) are asymmetric head-for-tail. The CO asymmetry was a key aspect of a recent test (9) of a theory of glassy two-level systems (10, 11). It was proposed that the two-level systems responsible for the excess low temperature heat capacity of KCN/KBr orientational glass were head–tail π flips of individual CN^- molecules. In short, the anomalous heat capacity at temperature T is believed due to the small fraction of CN^- that: (*a*) have energy minima within kT of each other, and (*b*) have minima separated by a small enough energy barrier that tunneling can occur within experimental time scales (10, 11). It was remarked (9) that this theory should also describe the physics of $CO/N_2/Ar$, another orientational glass with some asymmetric rotors. Because an energy difference of order kT between the two orientations of a molecule is required to generate a heat capacity at temperature T, the low temperature excess heat capacity would be expected to be due only to π flips of CO and not to π flips of symmetric N_2 molecules. However, it was found experimentally that the excess low temperature specific heat does not depend on CO concentration and has the same value in N_2/Ar. Thus, head–tail flips of asymmetric molecules are not important to the glassy thermal anomalies of $CO/N_2/Ar$, contrary to the expectations from the theory.

However, it remains to be demonstrated that $CO/N_2/Ar$ is an orientational glass like KCN/KBr. The nmr experiments reported here indicate a great deal of similarity between these two systems. We believe this strengthens the previous test of the theory of microscopic origin of the two-level systems.

A further purpose of this work was to experimentally determine whether N_2 and CO are functionally interchangeable in the orientational glass (as has been claimed (12)), except for the dipole moment of CO. The molecules are known to have nearly equal sizes and equal masses and the phase diagrams of pure N_2 and CO are remarkably similar (13). However, the quadrupole moment (14) of CO is 1.7 times that of N_2 and the phase diagrams of CO/Ar and N_2/Ar are very different (15,

[1]On leave of absence from College of William and Mary.

Can. J. Chem. Downloaded from www.nrcresearchpress.com by 176.9.209.113 on 09/07/12
For personal use only.

16). From the experiments reported here, the principal effect of increasing the CO concentration is to slightly increase the temperature of orientational freezing.

Finally, much less is known about the phase diagram and miscibility of $CO/N_2/Ar$ than about the binary solid systems CO/N_2 (17), N_2/Ar (15), and CO/Ar (16). Therefore, the nmr lineshapes have been examined for evidence of phase separation.

II. Experimental

The phase diagram (15) of N_2/Ar shows that N_2 and Ar are miscible in the solid state at low temperatures for all concentrations, but CO/Ar solid solutions segregate below about 50 K (16). Recent work on N_2/Ar indicates that solutions are metastable at low temperatures (18). Our dielectric experiments indicated that $CO/N_2/Ar$ was stable as a uniform solid solution provided the CO concentration was kept below about 30% (12). Unfortunately, there is no other phase information available for this system.

The N_2 and Ar gases were purchased from Matheson and were of greater than 99.99% purity. The CO gas was enriched to 99% in ^{13}C and was purchased from Merck. The gases were mixed in a 75 cm^3 vessel at room temperature and then condensed into the sample cell as a liquid solution at about 60 K. The liquid was allowed to homogenize by being held at this temperature for typically 2 h. The sample was frozen and the temperature reduced to about 6 K in about 5 mins; this was accomplished by turning off the heater on the gas flow dewar.

For most of the samples no evidence of phase separation was found. Specifically, the data taken upon increasing and decreasing temperature agreed and no discontinuities were observed in T_1, lineshape, etc. For the 30/30/40 ($CO/N_2/Ar$) sample, we observed the nmr lineshape to develop a broader component upon briefly warming the sample to 35 K. This broad component had the powder pattern lineshape characteristic of orientationally immobile CO, such as occurs (19) at these temperatures in pure α-CO or in the α phase of CO/N_2. Thus, this solution had partly segregated. We noticed a similar result in a 20/40/40 sample that was cooled from 60 K to 6 K much more rapidly than usual. The same solution showed no sign of phase separation or history dependence provided the initial freezing from 60 K to 6 K was done in the usual ~5 min time. We report here only data from the well-behaved samples.

The sample cell had a volume of about 0.3 cm^3 and was cooled by thermostated, flowing helium gas in a flow dewar. The sample temperature was measured by a calibrated carbon-in-glass thermometer. The temperatures are certain to less than 0.3 K (and probably better than that), much smaller than any feature in the nmr data.

The early nmr experiments were performed at 14.7 MHz and the later ones at 13.3 MHz. The magnetic field was stabilized for long signal averaging. The spectrometer is superheterodyne with quadrature detection. Typical pulse times were 7 μs for $\pi/2$ nutation. A detailed description of the spectrometer, dewar, and temperature control and measurement apparatus is available (20).

III. Results and discussion

In Fig. 1 are presented ^{13}C nmr spectra from $CO/N_2/Ar$ (20/40/40) along with ^{15}N spectra from KCN/KBr (50/50) for comparison (21). In both cases the linewith is dominated by the chemical shift anisotropy of the molecule, a uniaxially symmetric tensor. The chemical shift arises from shielding of the external magnetic field by the electrons of the molecule; this shielding depends on the orientation of the molecule with respect to the external field. For a molecule at fixed angle θ relative to the field, the resonance frequency ω is given by (22)

$$[1] \quad \omega = \omega_0 + \omega_0 \Delta\sigma(\tfrac{3}{2}\cos^2\theta - \tfrac{1}{2})$$

Here ω_0 is the angular average frequency and $\Delta\sigma$ is the anisotropy of chemical shift (about 400 ppm for CO and CN^-).

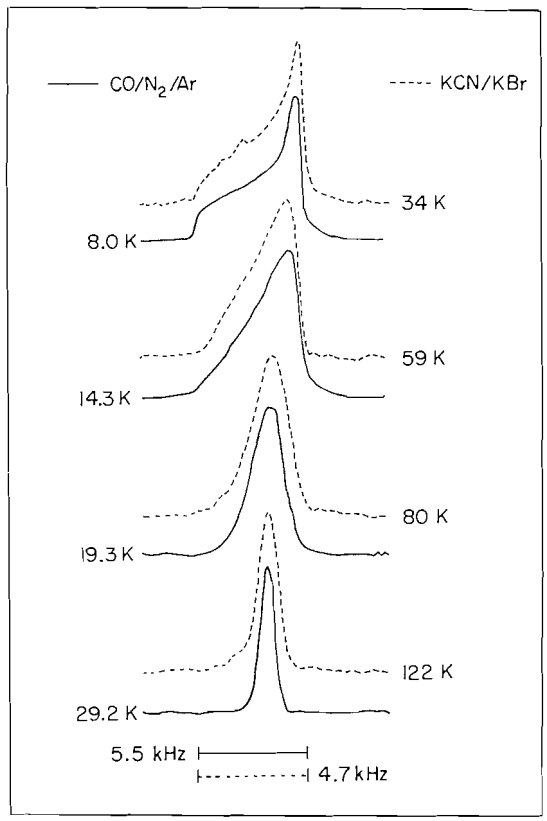

FIG. 1. Temperature evolution of nmr lineshapes in two orientational glass-forming systems: $CO/N_2/Ar$, 20/40/40 (solid curves) and KCN/KBr, 50/50 (dashed curves). The frequency scales are indicated at the bottom and are different because of different resonant frequencies and different anisotropies of chemical shift. Spectra from the two systems are compared for temperatures in the ratio of 4.1:1.

At low temperatures in both systems, the spectra become independent of temperature and display the "powder pattern" lineshape (23). This indicates that at low temperatures the molecules have static and random orientations. As the temperature is increased, the resonance line narrows indicating the onset of rotational motion. However, as discussed below, the motional narrowing is rather different from the traditional discussion of BPP (23–25).

To allow comparison of the $CO/N_2/Ar$ spectra and KCN/KBr spectra, we have scaled the two sets of data. First, the vertical axis in Fig. 1 is absorption intensity and has been scaled trivially to produce spectra of the same height. The shift anisotropies $\Delta\sigma$ and resonance frequencies ω_0 are different for ^{13}CO and $C^{15}N$. Consequently, we have scaled the frequency axes in Fig. 1 to obtain agreement in the low temperature, rigid limit spectra; this scaling is indicated at the bottom of Fig. 1. Finally, the orientational freezing in KCN/KBr occurs at a considerably higher temperature than in $CO/N_2/Ar$, as indicated by the nmr lineshapes. Thus, we compare in Fig. 1 spectra at temperatures in the ratio of 4.1 to 1, an empirically chosen value. This is a kind of corresponding states application. Incidentally, we note that 4.1 is approximately the ratio of orientational ordering transition temperatures T_c for pure KCN (168 K) (2) and pure N_2 (35.6 K (26); our sample has more N_2 than CO). Here we regard the T_c values as crude measures of the anisotropic molecular interaction strengths, which also determine the glassy freezing temperatures in the solid solutions.

There is good general agreement between the two sets of nmr

Can. J. Chem. Downloaded from www.nrcresearchpress.com by 176.9.209.113 on 09/07/12
For personal use only.

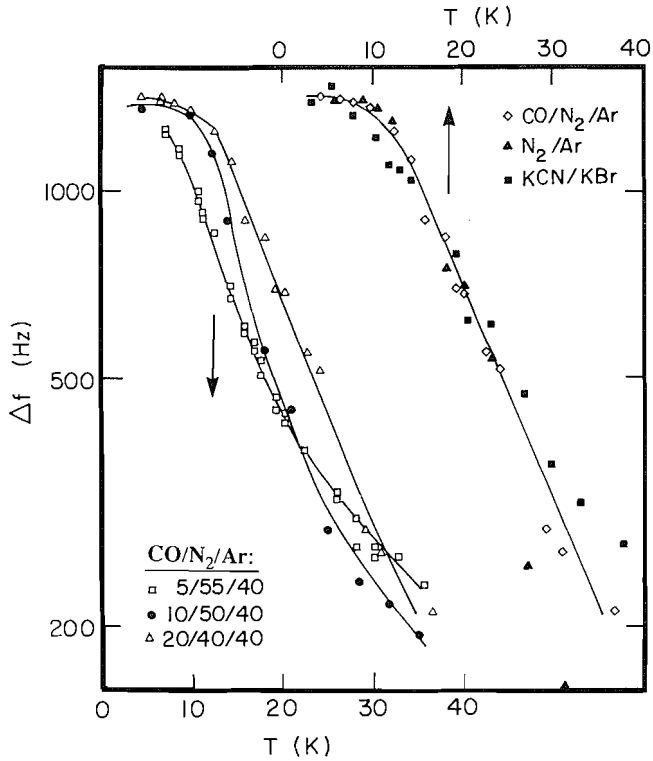

FIG. 2. Comparison of linewidths as functions of temperature for several orientational glasses. The left-hand set of data are from $CO/N_2/Ar$ at three different concentrations. The data demonstrate a weak increase of freezing temperature with increasing CO concentration. The right-hand set of data are offset for clarity and refer to the upper temperature scale. There the data of $CO/N_2/Ar$ (20/40/40), KCN/KBr (50/50), and N_2/Ar (67/33) are compared. The linewidths and temperatures of the KCN/KBr and N_2/Ar data have been scaled as described in the text. The similarity of the linewidth data indicates that a similar orientational freezing occurs in all these materials. The curves fit to the data are eye guides only.

spectra appropriately scaled. The largest differences occur at the highest temperatures where the line narrowing is becoming limited by intermolecular dipolar interactions between the spins. Our scaling arguments refer only to the intramolecular chemical shift anisotropy and should not work in the high temperature regime. The similarities in the KCN/KBr and $CO/N_2/Ar$ spectra suggest that the two systems undergo similar freezings.

The similarities in the line narrowing between KCN/KBr and $CO/N_2/Ar$ are also demonstrated in Fig. 2. The linewidths Δf plotted there are peculiar moments of the resonance absorption spectra $g(f)$. The spectra $g(f)$ were obtained by fourier transformation of spin echoes. We define Δf as

$$[2] \quad \Delta f \equiv \int g(f)|f|df \,/\, \int g(f)df$$

where f is frequency from the center of resonance. The center was always chosen to eliminate the first moment of $g(f)$. The integrals in [2] were performed as discrete sums. The definition of Δf above is experimentally preferable to the more conventional square root of the second moment, because of the sensitivity of second moments to the hard-to-measure tails of the resonance. We stress that the conventionally defined Δf behaves very much like that defined in [2] and shown in Fig. 2.

The N_2/Ar data are not available as published spectra. The data have been fitted as a sum of powder patterns of relative widths σ (4). The σ is generally known as the order parameter and is not related to $\Delta\sigma$ of eq. [1]. Specifically, the distribution of order parameters $P_{(\sigma)}$ has been obtained. As σ is non-negative, the Δf defined in [2] is easily shown to be proportional to $<\sigma>$, the first moment of $P_{(\sigma)}$. Conveniently, the temperature variation of $<\sigma>$ for N_2/Ar has been published recently (27).

The right-hand set of data in Fig. 2 are from $CO/N_2/Ar$ (20/40/40), KCN/KBr (50/50), and N_2/Ar (67/33). For KCN/KBr the linewidths Δf (and for N_2/Ar, the $<\sigma>$ values) were scaled to obtain agreement with $CO/N_2/Ar$ in the low temperature limit. The temperature of the KCN/KBr data was divided by 4.1 (see discussion above) and the N_2/Ar temperatures were multiplied by 1.45. The linewidth data of these three systems agree well, except where the lines are narrow and the linewidths are influenced by dipolar interactions. The scaled linewidths are not expected to be similar at the high temperatures.

The similarities between the $CO/N_2/Ar$, KCN/KBr, and N_2/Ar linewidth results in Figs. 1 and 2 are remarkable. The natures of the continuous orientational freezings appear to be the same, despite very different anisotropic molecular interactions driving the freezings. In KCN/KBr the CN^- interact through lattice distortions. This coupling between phonons and rotations in KCN and KCN/KBr has been studied extensively (28–30). Direct interactions between the CN^- are less important because of the shielding shell of K^+ ions around each anion. In $CO/N_2/Ar$, the dominant anisotropic interactions are the direct electrical quadrupole–quadrupole coupling and the anisotropic part of the Van der Waals potential (26, 31). From Figs. 1 and 2 it appears that orientational glass state formation has a certain universality, extending beyond the details of the physical system.

The left-hand set of data in Fig. 2 refer to $CO/N_2/Ar$ with three different CO concentrations but identical Ar concentrations. An increase in the freezing temperature with increasing CO content is evident. For example, this may be seen by defining the freezing temperature T_F to be the temperature at which the linewidth has decreased to one half of its low temperature limiting value.

The increase of T_F upon substitution of some N_2 by CO is not unexpected — the quadrupole moment of CO is 1.7 times that of N_2 (14). The orientational ordering transition temperature $T_{\alpha\beta}$ of pure N_2 is 35.6 K (26) and of CO is 61.6 K, reflecting the stronger anisotropic interactions in CO. For intermediate concentrations of CO/N_2 the variations of $T_{\alpha\beta}$ is nearly linear (17). Because in a mean field approach $T_{\alpha\beta}$ is a measure of the anisotropic interaction strength, one might expect the ratio of $T_{\alpha\beta}$ of CO/N_2 to T_F of $CO/N_2/Ar$ to be constant for fixed Ar concentration. If this were so, the freezing temperatures T_F would be in the ratio of 1 to 1.05 to 1.17 for samples with 40% Ar and 5, 10, and 20% CO, respectively. Experimentally, with T_F defined by the half narrowing temperature (see above), the T_F values are in the ratio of 1 to 1.1 to 1.3. Thus, the simple notions about mean interaction strengths underestimate the variation of T_F with CO concentration by about a factor of two. However, the important result from the left-hand set of data in Fig. 2 is that replacement of some N_2 by CO serves only to slightly increase the freezing temperature. The character of the freezing appears unchanged.

It should be emphasized that all of the orientational glass forming systems reported in Fig. 2 appear to have no discontinuities in their freezing, as indicated by nmr linewidths. A

Can. J. Chem. Downloaded from www.nrcresearchpress.com by 176.9.209.113 on 09/07/12
For personal use only.

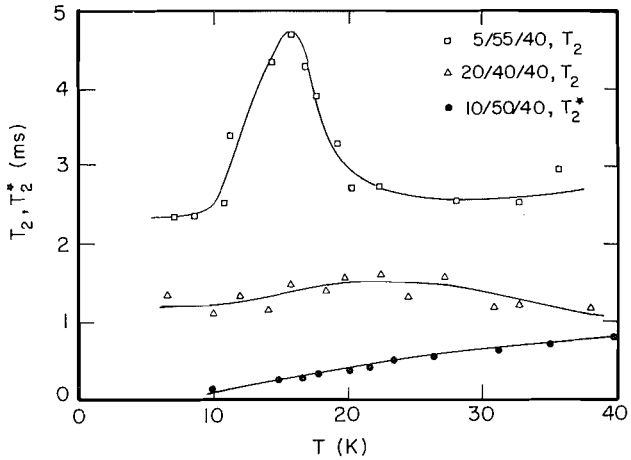

FIG. 3. Relaxation times T_2^* ($1/e$ time of FID) and T_2 (decay time of spin echo envelope) for $CO/N_2/Ar$. The T_2^* data are from the 10/50/40 solution but the other concentrations studied behave similarly, as shown in left-hand part of Fig. 2.

similar conclusion about H_2 orientational glass has been emphasized (32).

The spin–spin relaxation times T_2 reported in Fig. 3 were taken from the envelope of spin echoes. That is, the echo amplitude was plotted as a function of 2τ for the $\pi/2-\tau-\pi-\tau$ echo pulse sequence. The decays were intermediate between gaussian and exponential in shape. The times T_2 were taken as the e^{-1} values of the time 2τ.

For the 20/40/40 sample of $CO/N_2/Ar$, T_2 is essentially independent of temperature. This indicates that intermolecular dipolar interactions between the spins control T_2. The magnitude of T_2 is in fair agreement with the value predicted from a local field calculation (23) and also is in reasonable agreement (19) with the rigid limit T_2 of a solid α-CO sample containing 10% ^{13}C. For the 10/50/40 sample (not shown), T_2 is slightly longer. The 5/55/40 sample displays a maximum of T_2 near 15 K, which we do not understand.

Also plotted in Fig. 3 is the time T_2^*, which is the $1/e$ time of a free induction decay (FID). The time T_2^* was obtained experimentally as the half-width at e^{-1} of maximum of a spin echo. T_2^* is proportional to the reciprocal of the linewidth. The T_2^* data in Fig. 3 refer to the 10/50/40 sample, but the other two samples show similar behavior (i.e., see Fig. 2, left-hand set of data). The interesting observation is that $T_2 \gg T_2^*$, even at temperatures where narrowing occurs. This also occurs in KCN/KBr (21) and in *ortho*-H_2/*para*-H_2 (33, 34).

The formation of any spin echo requires a pulse sequence (here, a π pulse) capable of time-reversing the interaction responsible for the dephasing of the FID (here, the anisotropic chemical shift). Further, the interaction must remain constant or have a static component on the time scale of 2τ. Thus, the observation that $T_2 \gg T_2^*$ indicates that the molecular orientation has a component which is static on the 10^{-3} s time scale.

The theory (BPP) (23–25) most widely used to describe motional narrowing in nmr is incompatible with the observation of $T_2 \gg T_2^*$ in the narrowing regime. In BPP theory, the motion is characterized by a single (exponential) correlation time τ_c. For motional narrowing to occur, τ_c must be $\tau_c \leq T_{2RL}^*$, where T_{2RL}^* describes the decay of the FID in the rigid limit. But since the echo envelope decays at least as slowly as the FID, we have $T_2 \geq T_2^*$. Since the broadest line and shortest FID occur in the rigid limit, $T_2^* \geq T_{2RL}^*$. Together these inequalities imply that $\tau_c \leq T_2$, showing that the motion is *not* static on the time scale of echo formation in the line narrowing regime. The single τ_c model is therefore not appropriate to the orientational glasses.

A model with an inhomogeneous distribution of τ_c is also unsuitable. In such a model, the reorientation of each molecule is described by a single τ_c, but with different τ_c for different molecules. For a very broad distribution of τ_c, the molecules will fall into two classes: $\tau_c \gg T_{2RL}^*$ and $\tau_c \ll T_{2RL}^*$. The former will not experience narrowing at all and the latter will be extremely narrowed. The resulting lineshape, a sharp line superimposed upon a powder pattern line, is completely different than the lineshapes of Fig. 1 or of any orientational glass (1, 4, 21).

One way that motional narrowing can occur with $T_2 \gg T_2^*$ is the favored orientation model (35). Each molecule executes rapid reorientations, but does not spend equal times at all orientations. Thus, each molecule has an orientational probability function $P_{(\Omega)}$ which is nearly spherical at high temperatures, yielding narrow lines. At lower temperatures the anisotropic molecular interactions cause $P_{(\Omega)}$ to become increasingly non-spherical, broadening the line. At very low temperatures, $P_{(\Omega)}$ is sharply peaked and the resulting spectrum is that of a non-rotating collection of molecules: a powder pattern. Since at all temperatures there is a truly static component of molecular orientation due to the non-spherical nature of $P_{(\Omega)}$ and only rapid fluctuations about the average, spin echoes can be formed at long times. In this model, what changes with temperature is not the *rate* of reorientation (as in BPP theory), but the angles to which the orientations are *restricted*. The lineshapes of *ortho*-H_2/*para*-H_2 and N_2/Ar have been well described by the favored orientation model, using the formalism of a distribution of order parameters σ (1, 4, 36).

A second model that can explain the results is a kinetic model with a very broad, *homogeneous* distribution of correlation times τ_c. That is, the orientation of each molecule may be regarded as a linear combination of many "normal coordinates", each of which has a unique τ_c (37). Each molecule shares in the entire distribution of τ_c. Now, provided the distribution is very broad, all the τ_c can be separated into those with $\tau_c \gg T_{2RL}^*$ and those with $\tau_c \ll T_{2RL}^*$. The trivial fraction with $\tau_c \simeq T_{2RL}^*$ is neglected. In this limit, the fast motions can be averaged over and the slow motions can be ignored (they are frozen). As the temperature is decreased, some τ_c values go from the fast to the slow group, broadening the line. The result is identical to the favored orientation model, except that the slow motions are not truly static.

We have observed stimulated (three pulse) echoes at very long times in $CO/N_2/Ar$. At all temperatures below 32 K, stimulated echoes in 5/55/40 have a decay constant longer than 2 s, a factor of 10^5 longer than T_{2RL}^*. Thus, if the homogeneous distribution of τ_c model is correct, the distribution must be exceedingly broad. At 16 K, the decay time is longest (12 s); this is the same temperature as the maximum in T_2 and minimum in T_1 (see below). Stimulated echoes at long times also can be formed in H_2 (33, 38) and in KCN/KBr (21).

Although these experiments cannot distinguish the two models, the models are physically quite distinct and need to be distinguished by some measurement.

The spin–lattice relaxation times T_1 of two $CO/N_2/Ar$ samples are presented in Fig. 4. The data for the intermediate concentration sample falls between the two sets of data in Fig. 4. We focus on the minimum in T_1 near 15 K. The minimum indicates that the rate of some kind of reorientation passes

Can. J. Chem. Downloaded from www.nrcresearchpress.com by 176.9.209.113 on 09/07/12
For personal use only.

Can. J. Chem. Downloaded from www.nrcresearchpress.com by 176.9.209.113 on 09/07/12
For personal use only.

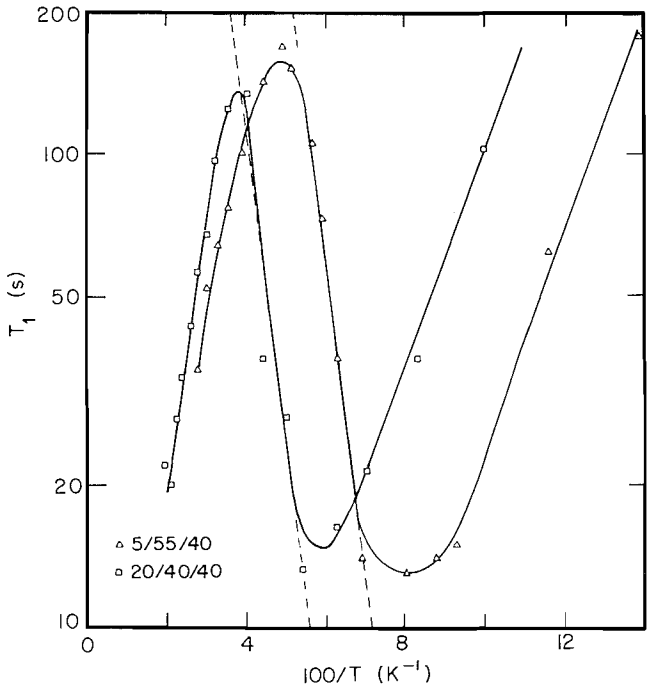

FIG. 4. Spin–lattice relaxation time T_1 in two samples of $CO/N_2/Ar$. The minima in T_1 at temperatures near 15 K indicate that head–tail flips occur at a rate approximately equal to the resonance frequency at that temperature. The solid lines are eye guides. The dashed lines correspond to an activation energy of 150 K. The asymmetric and broad minima are common features in disordered systems.

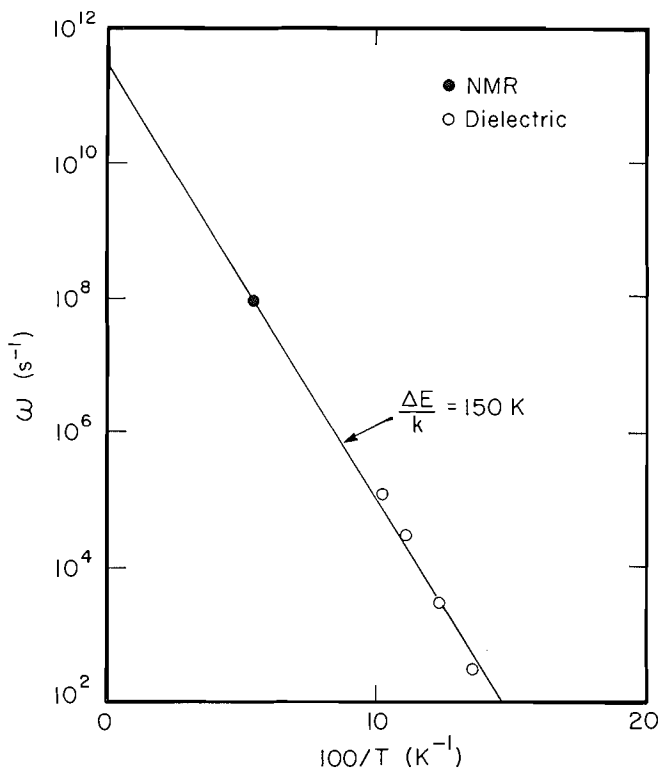

FIG. 5. Relaxation map indicating the frequency and temperature of maxima in the spin–lattice relaxation rate (●) and in the dielectric loss at lower frequencies (○). The reasonable fit to the straight line (slope = 150 K) indicates that the same motion (head–tail flips) is responsible for the spin–lattice relaxation and the dielectric loss.

through the resonance frequency ($2\pi \times 14$ MHz) near 15 K. Figure 5 is a relaxation map showing the temperature–frequency location of the spin–lattice relaxation rate peak as well as dielectric loss maxima at lower frequencies (12), for the 20/40/40 sample (the only one with both kinds of data available). Both kinds of data fit on the straight line describing an activation energy of 150 K. Thus, the same motion is responsible for both the spin–lattice relaxation and the dielectric loss.

In Fig. 4, the dashed lines passing through the data correspond to an activation energy of 150 K. In glassy systems the distribution of motion rates frequently causes an asymmetric T_1 minimum (unequal slopes), as in Fig. 4[2]. The high temperature side is found to have a slope equal to the average activation energy, while the low temperature slope is smaller than the activation energy. This is precisely the case in Fig. 4.

The activation energy of 150 K from Figs. 4 and 5 is somewhat smaller than the 181 K from dielectric data alone (i.e., see Fig. 5). This disagreement may reflect a deviation from simple thermal activation. It is more likely that the disagreement is due to the difficulty in obtaining accurate values from very broad loss peaks (six decades wide or more (12)).

The thermally activated motion responsible for T_1 and the dielectric loss is head–tail (π) flips of CO molecules, as deduced by comparing the nmr line narrowing and the dielectric loss. For comparison, 5 kHz dielectric data are selected because that frequency matches the nmr linewidth in the low temperature limit. The dielectric loss in $CO/N_2/Ar$ (20/40/40) is maximum near 8 K (12). Thus molecules are re-orienting on the 30 μs time scale (= $1/2\ \pi \cdot 5$ kHz). However, the 8 K ^{13}C spectrum of the same material (Fig. 1) is a powder pattern of full width — decreasing the temperature to 4.4 K does not change the line. The nmr seems to imply very little motion at 8 K on the 30 μs time scale. However, the chemical shift and resonance frequency ω are invariant under π flips, which take θ to $\pi-\theta$ in eq. [1]. Thus, the nearly rigid limit nmr spectrum at 8 K can be reconciled with the substantial dielectric loss at 8 K only if the motion is restricted to π (or nearly π) flips.

In pure KCN and in α-CO it has been shown that the molecules flip by $\pi \pm \delta$, where $\delta \ll 1$ (40–43). The deviation from π is due to molecular asymmetry. Because the flips are not by exactly π, a small (undetected) amount of line narrowing occurs. More importantly, the flips can provide a T_1 mechanism (proportional to δ^2), because the flips do slightly modulate the chemical shift (or electric field gradient in $C^{17}O$). In $CO/N_2/Ar$, similar $\pi \pm \delta$ flips should occur and provide a T_1 mechanism.

IV. Conclusions

Because of chemical shift anisotropy, the nmr spectra of $C^{15}N^-$ and ^{13}CO are sensitive to rotational motions. For the orientational glass forming systems KCN/KBr, N_2/Ar, and $CO/N_2/Ar$ the lineshapes and linewidths are in good agreement, after properly scaling the rigid limit linewidths and after scaling the temperatures to account for the different freezing temperatures. It appears that the continuous orientational freezing is similar in KCN/KBr and $CO/N_2/Ar$ (N_2/Ar as well), despite the very different anisotropic molecular interactions driving the freezing.

The lineshapes in the narrowing regime and the observation

[2]Reference 39. The T_1 ρ minimum of their Fig. 4 is a good example of the asymmetry.

that $T_2 \gg T_2^*$ are incompatible with the usual explanations of line narrowing (in which the variation of reorientation rate with temperature drives the line narrowing). One theory that is compatible involves a molecular orientation probability function $P_{(\Omega)}$ which smoothly evolves from spherical at high temperatures to sharply peaked at low temperatures. The other model that is in accord with the nmr results postulates a *homogeneous* distribution of correlation times, with each molecule sharing in the entire distribution. Provided the distribution of correlation times is broad enough, the nmr experiments reported here cannot distinguish between the two models. These remarks apply equally to the H_2 and KCN/KBr systems, which also have $T_2 \gg T_2^*$ in the narrowing regime.

A broad minimum in T_1 near 15 K in $CO/N_2/Ar$ is produced by the same motion responsible for dielectric loss at lower temperatures. By comparing the lack of line narrowing at 8 K and the substantial dielectric loss at the same frequency, it is concluded that the motion is π flips of CO molecules. Thus, as in KCN/KBr (44, 21), the dipolar degrees of orientational freedom (head–tail orientation of CN^- or CO) freeze at a lower temperature than the quadrupolar degrees of freedom.

Acknowledgments

Part of this work was performed at the College of William and Mary. The work was partly supported by the generosity of the donors to the Petroleum Research Fund, administered by the American Chemical Society. The Jeffress Memorial Trust supported part of the research. We appreciate the assistance of S.-B. Liu with the experiments. The magnet system used in this work was a gift of E. I DuPont de Nemours and Co.

1. A. B. Harris and H. Meyer. Can. J. Phys. **63**, 3 (1985).
2. F. Luty. *In* Proceedings of International Conference on Defects in Insulating Crystals, Riga. *Edited by* V. M. Turkevich and K. D. Schwartz. Springer-Verlag, Berlin. 1981. p. 69.
3. K. H. Michel and J. M. Rowe. Phys. Rev. B**22**, 1417 (1980).
4. D. Esteve, N. S. Sullivan, and M. Devoret. J. Phys. Lett. **43**, L793 (1982).
5. W. Press, B. Janik, and H. Grimm. Z. Phys. B**49**, 9 (1982).
6. E. L. Pace, J. H. Smith, and B. E. Jepson. J. Chem. Phys. **50**, 312 (1969).
7. L. G. Ward, A. M. Saleh, and D. G. Haase. Phys. Rev. B**27**, 1832 (1983).
8. A. M. Saleh and D. G. Haase. *In* Proceedings of LT-17. *Edited by* U. Eckern, A. Schmid, W. Weber, and H. Wuhl. Elsevier, New York. 1984.
9. C. I. Nicholls, L. N. Yadon, D. G. Haase, and M. S. Conradi. Phys. Rev. Lett. **59**, 1317 (1987).
10. M. Meissner, W. Knaak, J. P. Sethna, K. S. Chow, J. J. de Yoreo, and R. O. Pohl. Phys. Rev. B**32**, 6091 (1985).
11. J. P. Sethna and K. S. Chow. Phase Transitions, **5**, 317 (1985).
12. S.-B. Liu and M. S. Conradi. Solid State Commun. **49**, 177 (1984).
13. R. L. Mills, B. Olinger, and D. T. Cromer. J. Chem. Phys. **84**, 2837 (1986).
14. D. E. Stogryn and A. P. Stogryn. Mol. Phys. **11**, 371 (1966).
15. C. S. Barrett and L. Meyer. J. Chem. Phys. **42**, 107 (1965).
16. C. S. Barrett and L. Meyer. J. Chem. Phys. **43**, 3502 (1965).
17. M. J. Angwin and J. Wasserman. J. Chem. Phys. **44**, 417 (1966).
18. L. D. Yantsevich, A. I. Prokhvatilov, I. N. Krupskii, and A. S. Barylnik. Sov. J. Low Temp. Phys. **12**, 170 (1986) (Fiz. Nizk. Temp. **12**, 300 (1986).
19. S.-B. Liu and M. S. Conradi. Phys. Rev. B**30**, 24 (1984).
20. Philip L. Kuhns. Ph.D. thesis, College of William and Mary, 1982.
21. M. A. Doverspike, M.-C. Wu, and M. S. Conradi. Phys. Rev. Lett. **56**, 2284 (1986).
22. A. A. V. Gibson, T. A. Scott, and E. Fukushima. J. Magn. Reson. **27**, 29 (1977).
23. A. Abragam. Principles of nuclear magnetism. Clarendon, Oxford. 1961.
24. N. Bloembergen, E. M. Purcell, and R. V. Pound. Phys. Rev. **73**, 679 (1948).
25. C. P. Slichter. Principles of magnetic resonance. Springer, New York. 1980.
26. T. A. Scott. Phys. Rep. **27**, 89 (1976).
27. N. S. Sullivan, C. M. Edwards, and J. R. Brookeman. Mol. Cryst. Liq. Cryst. **139**, 365 (1986).
28. M. L. Klein and I. R. McDonald. Chem. Phys. Lett. **78**, 383 (1981).
29. D. Sahu and S. D. Mahanti. Phys. Rev. B**26**, 2981 (1982).
30. J. Z. Kwiecien, R. C. Leung, and C. W. Garland. Phys, Rev. B**23**, 4419 (1981).
31. B. C. Konin. J. Chem. Phys. **33**, 882 (1960).
32. S. Washburn, R. Schweizer, and H. Meyer. Solid State Commun. **35**, 623 (1980).
33. I. Yu, S. Washburn, and H. Meyer. Solid State Commun. **40**, 693 (1981).
34. D. Esteve and N. S. Sullivan. J. Phys. C: Solid State Phys. **15**, 4881 (1982).
35. M. S. Conradi. Phys. Rev. B**28**, 2848 (1983).
36. D. Esteve, M. Devoret, and N. S. Sullivan. J. Phys. C: Solid State Phys. **15**, 5455 (1982).
37. J. I. Kaplan and A. N. Garroway. J. Magn. Reson. **49**, 464 (1982).
38. N. S. Sullivan, D. Esteve, and M. Devoret. J. Phys. C: Solid State Phys. **15**, 4895 (1982).
39. H. T. Stokes, T. A. Case, D. C. Ailion, and C. H. Wang. J. Chem. Phys. **70**, 3563 (1979).
40. H. T. Stokes, T. A. Case, and D. C. Ailion. Phys. Rev. Lett. **47**, 268 (1981).
41. H. T. Stokes, D. C. Ailion, and T. A. Case. Phys. Rev. B**30**, 4925 (1984).
42. J. Walton, J. Brookeman, and A. Rigamonti. Phys. Rev. B**28**, 4050 (1983).
43. F. Li, J. R. Brookeman, A. Rigamonti, and T. A. Scott. J. Chem. Phys. **74**, 3120 (1981).
44. U. G. Volkmann, R. Bohmer, A. Loidl, K. Knorr, U. T. Hochli, and S. Haussuhl. Phys. Rev. Lett. **56**, 1716 (1986).

Can. J. Chem. Downloaded from www.nrcresearchpress.com by 176.9.209.113 on 09/07/12
For personal use only.

Rotational excitations of A-CH_4 II in the meV range studied by inelastic neutron scattering

W. PRESS
Christian-Albrechts-Universität Kiel, Leibnitzstrasse, D2300 Kiel, Federal Republic of Germany
A. HEIDEMANN AND H. LAUTER
Institut von Laue–Langevin, 156 X, F38042 Grenoble, France
J. A. MORRISON[1]
Department of Chemistry and Institute for Materials Research, McMaster University, Hamilton, Ont., Canada L8S 4M1
AND
K. NEUMAIER
Walter Meissner Institut für Tieftemperaturforschung, Bayerische Akademie der Wissenschaften, D8046 Garching, Federal Republic of Germany
Received August 31, 1987
This paper is dedicated, by his coauthors, to Dr. James A. Morrison in recognition of his service to science

W. PRESS, A. HEIDEMANN, H. LAUTER, J. A. MORRISON, and K. NEUMAIER. Can. J. Chem. **66**, 686 (1988).
The excitation spectrum of solid methane (CH_4) with all molecules converted to the nuclear spin state with A symmetry has been measured with incoherent inelastic neutron scattering. For energies $\hbar\omega \gtrsim 1$ meV, there are no dramatic differences with samples consisting of a mixture of all three spin states A, T, and E. A qualitative understanding of the measurements is achieved by comparison with calculations of Ozaki *et al.*

W. PRESS, A. HEIDEMANN, H. LAUTER, J. A. MORRISON et K. NEUMAIER. Can. J. Chem. **66**, 686 (1988).
Utilisant la diffusion inélastique incohérente de neutrons, on a mesuré le spectre d'excitation du méthane (CH_4) solide dans lequel toutes les molécules ont été transformées à l'état de spin nucléaire de symétrie A. Pour les énergies $\hbar\omega \gtrsim 1$ meV, ce spectre ne présente pas de différences dramatiques avec ceux d'échantillons consistant de mélanges des trois états de spin A, T et E. On arrive à une compréhension qualitative de ces mesures grâce à une comparaison avec les calculs d'Ozaki *et al.*
[Traduit par la revue]

Introduction

For several years solid methane (CH_4) has been used as a model example for the investigation of rotational excitations. At low temperatures CH_4 has a relatively simple structure, with the carbon atoms located on an fcc lattice. There is little doubt that the structure of CH_4 II is the same as that of CD_4 II, with a space group $Fm3c$ and 8 molecules in the unit cell (1, 2): 6 sites (symmetry $\bar{4}2m$) are occupied by orientationally ordered molecules while at 2 sites (symmetry 432) the molecules are orientationally disordered. Early studies employing incoherent inelastic neutron scattering have focused on excitations in the meV range (3–6). Much of the recent progress is due to high-resolution experiments ($\Delta E \simeq 10\ \mu$eV). These experiments have allowed rather precise information on the librational ground states of the ordered molecules ("rotational tunneling") as well as the almost free rotations of the disordered ones (7, 8). For a more complete picture, however, an improved knowledge of the higher energy excitations seemed desirable. This undertaking appears rather simple for the molecules at disordered sites. These excitations have been regarded as single particle excitations possibly without noticeable dispersion of modes if described within the phonon picture. This is clearly not the case for the librational excitations at the ordered sites, except for the ground state splitting where coupling effects complicate the situation (7) but do not lead to dispersion. Due to the anisotropic coupling, mainly octupole–octupole interaction, collective (phonon-like) librations of the ordered molecules occur. At points in reciprocal space with low symmetry there are 18 such modes for each wave vector. Calculations have been made for the collective excitations in both CD_4 II (9) and CH_4 II with all molecules in the A state (10). In the latter case differences with CD_4 II are due to the smaller moment of inertia of the CH_4 molecules and consequently due to more pronounced quantum aspects. Also the disordered molecules are included in the calculation and give rise to additional branches with weaker dispersion. The rather complicated dispersion curves mean that when measuring the incoherent scattering (the scattering of the H atoms dominates by far) one may expect somewhat broad features in the phonon density of states rather than well-defined peaks. More specifically, as the contributions from ordered and disordered molecules cannot be observed separately, one should observe broad features and lines. The situation is complicated further by the fact that there is also a contribution of translational phonon modes. If rotation–translation coupling is neglected, this contribution is about the same above and below the order–disorder phase transition at $T_0 = 20.4$ K. The contribution of the translational phonons should be less intense than that of the rotational excitations, due to a less favourable structure factor. More serious is the fact that it is not only the ground states of the librational states which split up into states with different nuclear spin symmetry, but also the excited ones. Yamamoto *et al.* (11), for example, have pointed out that both the molecular symmetry ($\tilde{\Gamma}$) and the site symmetry (Γ) are needed for completely specifying the rotational states (Fig. 1). For the purposes of the present paper it is sufficient for the description to use the molecular symmetry, which is connected with nuclear spin symmetry via the Pauli principle (A state: $I = 2$; T state: $I = 1$; E state: $I = 0$; here I denotes the total nuclear spin of the CH_4 molecule). Spin incoherent neutron scattering allows transitions between all spin species, except between A and E states. This considerably reduces the applicability of ref. 10 for the present purpose. For this reason we shall mainly use the calculations of Yamamoto *et al.* (11) and, even more specifically for neutron scattering experiments, those of Ozaki *et al.* (12). They,

[1]Deceased.

Can. J. Chem. Downloaded from www.nrcresearchpress.com by 176.9.209.113 on 09/07/12
For personal use only.

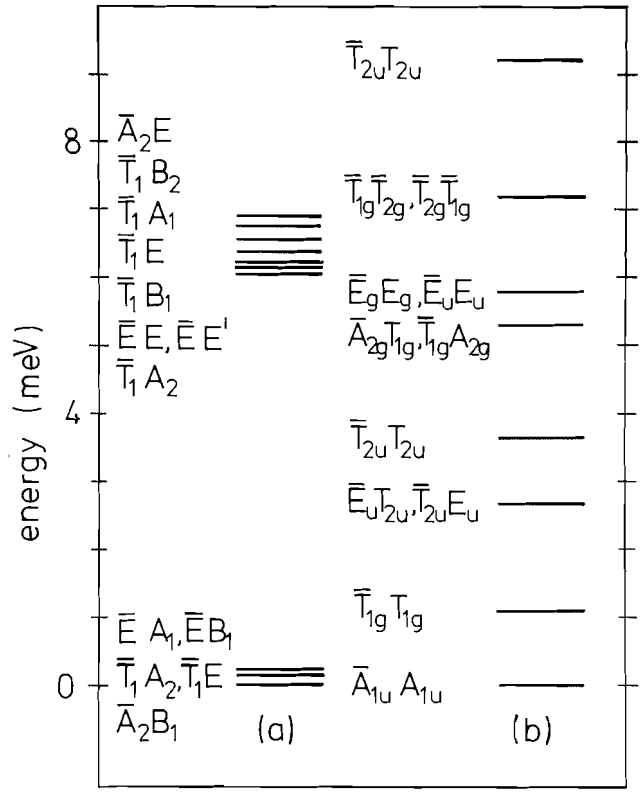

FIG. 1. The figure represents the level scheme of CH_4 molecules on the two sites in CH_4 II (from ref. 11). The complete symmetry labels are given.

however, do not include collective excitations. A level scheme, as obtained with the extended James and Keenan model (that is, octupole–octupole interaction and inclusion of a crystal field term), is shown in Fig. 1 for the two inequivalent CH_4 sites. On the basis of these results, Ozaki *et al.* (12) have calculated the double differential spin-incoherent scattering cross section for CH_4:

$$[1]\quad \left.\frac{d^2\sigma}{d\Omega dE}\right|_{s.d.} = \frac{k_f}{k_i}\exp(-\langle u^2\rangle Q^2)\frac{\sigma^p_{inc}}{4\pi} \times \sum_{i,f} p_i(T) W_{i\to f}\delta(E_i - E_f + \hbar\omega)$$

Here k_i and k_f denote the wave vectors of the incoming and outgoing neutrons, E_i and E_f their respective energies, $\langle u^2\rangle$ the mean-squared amplitude of the molecular centre of mass, σ^p_{inc} = 80 barn (the scattering cross section of a bound proton), $P_i(T)$ the thermal population of the ground state, and $W_{i\to f}$ the square of transition matrix elements from the initial to the final states. The authors group states of the same symmetry together and rather define an "average transition integral" $\bar{W}$ (12) with

$$[2]\quad \bar{W}(\bar{\Gamma}_i \to \bar{\Gamma}_f) = \sum_{J=0}^{\infty}(2J+1) j_J{}^2(Q\rho)\bar{G}_J(\bar{\Gamma}_i \to \bar{\Gamma}_f)$$

The summation index J denotes the rotational quantum number of a free rotor, the $j_J{}^2$ represent spherical Bessel functions of order J, ρ = 1.093 Å is the C—H distance in a molecule, and the $\bar{G}_J$ are tabulated in the paper (12).

By varying the temperature the population $P_i(T)$ can be used as a handle for a more straightforward understanding of measured spectra, e.g., the assignment of peaks.

The population of the A state of ordered molecules, for example, is $P_A(T) = 5/Z$ with

$$[3]\quad Z = 5 + 9\exp(-\Delta_{AT}/k_BT) + 2\exp(-\Delta_{AE}/k_BT)$$

Here Δ_{AT} and Δ_{AE} denote the ground state energy with T and E symmetry (Fig. 1). For a first set of experiments at "high temperatures" (that is, T = 5 K), P_A (5 K) = 0.40, P_T (5 K) = 0.52, and P_E (5 K) = 0.08, are not far from P_A (∞) = 5/16, P_T (∞) = 9/16, and P_E (∞) = 2/16, and indicate the concentration in an "alloy" of spin species. A second set of experiments was done at $T \lesssim 100$ mK with all the molecules converted to the A state (at both sites). To achieve nuclear spin conversion in reasonable times, 0.2% of the paramagnetic molecule O_2 was admixed to the sample. Samples of A-CH_4 II, like pure p-H_2 or o-H_2, mean a considerable simplification because disorder problems, present in equilibrium mixtures at high temperatures, are absent. Previously, high-resolution neutron spectroscopy (7), as well as nmr experiments (13), were performed with A-CH_4. The calculation of the lattice dynamics of A-CH_4 has already been mentioned (10).

Experimental

Samples of solid methane were prepared by condensing CH_4 gas of a quoted purity of 99.995% into a flat aluminium sample container (50 × 30 × 0.35 mm³). After condensation the samples were cooled to low temperatures. The sample cell was mounted at the bottom end of the insert of a dilution refrigerator. Details of this setup have been reported elsewhere (14). Experiments were done both at temperatures T = 5 K and $T \simeq$ 50–100 mK. The cooling from 5 K to 0.1 K was possible in about 3–4 h and then the temperature was stabilized in the stated temperature range for several days. The described procedure was used for pure CH_4 samples, which did not show any measurable conversion during the measurements (≃ 2 days), at least concerning the disordered molecules. A second set of experiments was performed with CH_4 with 0.2% O_2 admixed in the gas phase. In this case complete nuclear spin conversion was achieved. To avoid incomplete conversion of the T-state molecules (7), the samples were cooled down (*i*) several hours before the start of the neutron experiments and (*ii*) the temperature range between 0.3 and 0.7 K was covered much more slowly than was possible with the maximum cooling rate of the dilution cryostat. An alternative method consists in irradiating the sample, thus generating CH_3 radicals and atomic hydrogen, whose Zeeman levels are tuned to resonance with the rotational states by means of strong magnetic fields (13).

The incoherent inelastic neutron scattering experiments were performed on the 3-axis spectrometer IN3 at the high-flux reactor of the Institute Laue–Langevin in Grenoble (15). The combination of a dilution refrigerator and relatively high energy transfer did rule out the use of the time-of-flight spectrometer IN4 with its vertical flight path arrangement. The instrument IN3 was operated with a pyrolytic graphite 002 monochromator and a horizontally curved graphite 002 analyser (15), used for reasons of intensity. The analyser was kept fixed at an energy E_f = 4.06 meV and was used with a cooled Be filter. The measurements were done at constant monitor rates, corresponding to times of about 12 min per setting of the instrument. Apart from effects of higher order neutrons, this procedure renders further corrections of the measured intensities unnecessary.

Results and discussion

The measurements were performed at constant momentum transfer Q = 2.2 Å^{-1}; some additional scans were done at Q = 1.8 Å^{-1}. These values were chosen to maximize the structure factors for the inelastic transitions (eq. [2]). Unfortunately there was not sufficient time to map out the Q dependence from small values to the maximum value (Q = 2.2 Å^{-1}) with satisfactory counting statistics. In Fig. 2*a–c* the results are shown for (*a*) pure methane at $T \lesssim 100$ mK, (*b*) CH_4 with 0.2% O_2 and T =

Can. J. Chem. Downloaded from www.nrcresearchpress.com by 176.9.209.113 on 09/07/12
For personal use only.

Can. J. Chem. Downloaded from www.nrcresearchpress.com by 176.9.209.113 on 09/07/12
For personal use only.

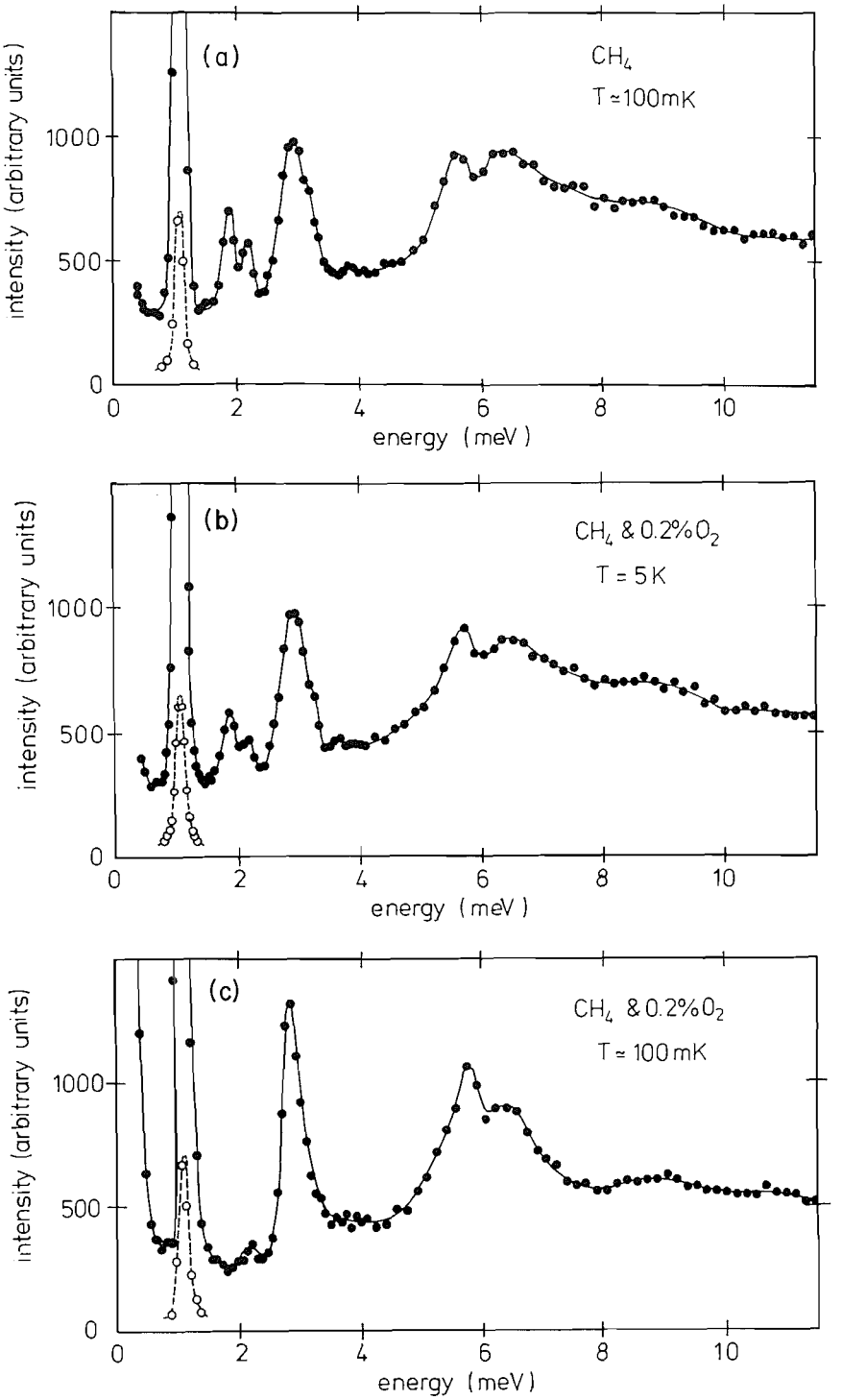

FIG. 2. Neutron scattering intensity from (*a*) pure CH_4 at a temperature of $T \lesssim 100$ mK, and CH_4 doped with 0.2% O_2 at (*b*) $T = 5$ K and (*c*) $T \lesssim 100$ mK. The measurements have been performed at $Q = 2.2$ Å^{-1} with $k_f = 1.4$ Å^{-1}; typical counting times were 12 min per data point. The solid lines are guides to the eye only. The dashed lines mark the 0 to 1 transition with the scale reduced by a factor of 5. The energy scale gives the energy of the excitations.

5 K, and (*c*) CH_4 with 0.2% O_2 at $T \lesssim 100$ mK. All these spectra are measured with neutron energy loss at $Q = 2.2$ Å^{-1}, and for reasons of the geometry of the instrument do not even include the elastic peak nor do they allow the extraction of detailed balance factors. Examples of measurements at $Q = 1.8$ Å^{-1} (CH_4 with 0.2% O_2, $T \lesssim 100$ mK) are shown in Fig. 3. In principle, measurements at $Q = 1.8$ Å^{-1} can be used to determine the position of the elastic peak and the energy resolution at the elastic position. In practice we have done that in an additional measurement at $T = 40$ K, when CH_4 is in its phase *I* and the rotational spectrum is very broad, which also could serve for a background determination including translational phonons in CH_4. The energy resolution was determined to be 0.21 meV ($Q = 1.8$ Å^{-1}) full width at half maximum; due to the horizontally curved analyser this value increases slightly with increasing momentum transfer. The energy resolution and

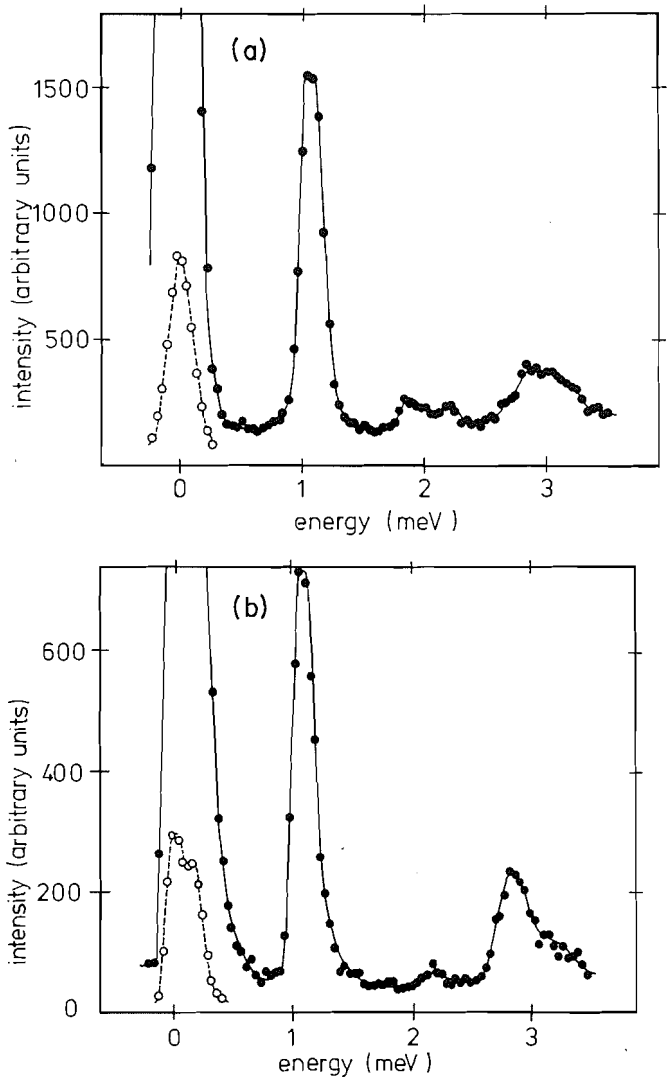

FIG. 3. Neutron scattering intensity from CH_4 doped with 0.2% O_2 measured with a momentum transfer at $Q = 1.8$ Å^{-1}. In (*a*) the temperature is $T = 5$ K; in (*b*) $T \lesssim 100$ mK. For $T = 5$ K and $T \lesssim 100$ mK the counting times were reduced by a factor of two and five, respectively, in comparison with the scans shown in Fig. 2. The scale of the elastic peak (open circles) is reduced by a factor of 10. All lines are guides to the eye only.

TABLE 1. Peak positions $\hbar\omega$ in meV as well as the integrated intensities I observed in the experiments (arbitrary units, normalized to the same monitor rate)

(*a*) $Q = 2.2$ Å^{-1}

$T = 5$ K			$T \simeq 100$ mK		
$\hbar\omega$	I	Assignment	$\hbar\omega$	I	Assignment
1.075	64	0–1	1.082	71	0–1
1.88	9	1–2	—	—	—
2.19	5.5	multi	2.19	7	multi
			2.81	31	
2.98	44	0–2	3.08	18	0–2
5.7	—	f.rot/libr.	5.7	—	f.rot/libr.
6.5	—	libr.	6.5	—	libr.
9.2	—	libr.	9.2	—	libr.

(*b*) $Q = 1.8$ Å^{-1}

$T = 5$ K			$T \simeq 100$ mK		
$\hbar\omega$	I	Assignment	$\hbar\omega$	I	Assignment
1.075	73	0–1	1.092	82	0–1
1.89	6	1–2	—	—	—
2.20	5.5	multi	2.20	6	multi
2.85	15		2.87	32	
3.12	14	0–2	3.16	15	0–2

*"Multi" denotes multiple scattering (2 excitations $J = 0 \rightarrow 1$); uncertainties concerning the assignment are discussed in the text.

thus the quality of the spectra is considerably better than that of earlier measurements. A quick inspection of Fig. 2*a–c* shows that all three spectra look rather similar.

In particular, there are only minor differences between Fig. 2*a* and Fig. 2*b*, which shows that for a similar population of the different spin species the excitation spectra are virtually identical. Differences concern the feature at 1.88 meV. The higher intensity at an energy transfer $\hbar\omega = 1.88$ meV for the sample with pure CH_4 (Fig. 2) indicates that the "rotational temperature" or "nuclear spin temperature" is greater than 5 K. Here we already use the assignment of the peaks given below. The sample with *A*-CH_4 II shows a more pronounced structure and the peak at 1.88 meV is absent.

For an assignment of the peaks, we compare our results with those published by Ozaki *et al.* (12). Obviously the well-defined peaks with energies below about 4 meV are related to the almost free rotations (perturbed by the cubic crystalline field of the neighbouring molecules) of the disordered molecules. Table 1 lists the energies deduced from the three spectra. The peak at about 1.08 meV is the well-known transition from the (perturbed) $J = 0$ to the $J = 1$ state (5, 6), while that at 3.0 meV is the $J = 0$ to $J = 2$ transition. The absence of the peak at 1.88 meV in *A*-CH_4 confirms that this is a transition from an excited state ($J = 1$ to $J = 2$), which disappears upon deexcitation of the $J = 1$ level. The conversion to the ground state also shows up in a 10% increase of the intensity of the $J = 0$ to $J = 1$ transition in *A*-CH_4: this agrees rather well with an increase of the population $P_{J=0}(5\text{ K}) = 0.875$ to $P_{J=0}(0\text{ K}) = 1.0$. The peak at 2.17 meV, which has twice the energy of the $J = 0$ to $J = 1$ transition, obviously is due to double inelastic scattering (intensity about 5% of the single inelastic scattering).

While the peaks do not shift in energy (contrary to the behaviour of the tunneling peaks in a converted sample (7)), all observed peaks are slightly narrower in the sample with *A*-CH_4. This is most pronounced for the structure centred at 3 meV, which becomes considerably narrower. As the larger width is observed both at $T = 5$ K (CH_4 with 0.2% O_2) and at $T \lesssim 100$ mK for pure CH_4, lifetime effects can be ruled out and the distribution of spin species seems to cause the observed width. Even the low temperature data for the oxygen-doped sample at $T \lesssim 100$ mK (Fig. 2*c*) seem to indicate either the presence of a shoulder on the high energy side or, rather, the presence of two peaks. This latter finding is corroborated when inspecting the data measured at $Q = 1.8$ Å^{-1} (with narrower steps in energy transfer); energies of about 2.84 meV and 3.12 meV are found (averaged values), with the first peak strongly temperature dependent and about twice as intense as that at 3.12 meV for *A*-CH_4 II. There seem to be two possible interpretations: (*i*) Either two of the perturbed $J = 2$ states (from three predicted ones (11)) have rather similar energies. This is not in agreement with the predicted separation of almost 1 meV ($E_{0-2A} = 2.65$ meV, $E_{0-2B} = 3.616$ meV (11, 12)). The calculation of

Can. J. Chem. Downloaded from www.nrcresearchpress.com by 176.9.209.113 on 09/07/12
For personal use only.

Can. J. Chem. Downloaded from www.nrcresearchpress.com by 176.9.209.113 on 09/07/12
For personal use only.

transition matrix element yields a $j_2^2(Q\rho)$ dependence (eq. [2]) of the leading term, and an intensity of the second peak that is about 60% of that of the first peak (12). These calculations also explain the absence of a second perturbed $J = 1$ to $J = 2$ transition, which is predicted to have only about 1/4 of the intensity. Nevertheless it remains to be explained why neither peak position is $E_{0-1} + E_{0-2} = 2.97$ meV, which is the mean value of the reported double peak. (*ii*) The other possibility is the presence of dispersion of the perturbed $J = 2$ state. Kobashi *et al.* (10) have included a coupling between ordered and disordered molecules and predict dispersion for modes that dominantly represent rotations of the disordered molecules. As their calculation is restricted to A-CH_4, both concerning ground and excited states, the dispersion reported by them is related to a perturbed $J = 3$ state, which is the lowest-lying excited state with A symmetry. Yet one may speculate that the introduction of a coupling between all neighbouring molecules introduces similar effects concerning the $J = 2$ levels. Then the two peaks may be identified with the density of states originating from the flat portions of a branch with dispersion. At present, however, no calculations are available. It may be noted that the restriction to A-CH_4 for ground and excited states is still very useful for comparison with optical experiments (16–19), which was the intention of the authors (10). For spin-incoherent neutron scattering cross sections, the inclusion of excited states with T symmetry is necessary and desirable. At least one open question remains: the strong increase of the intensity at $\hbar\omega = 2.84$ meV in A-CH_4 cannot simply be understood on the basis of the conversion of the disordered molecules. An assignment to librational excitations of the ordered molecules, however, needs to explain the low energy of the excitations.

For the above reasons we did not attempt to adjust potential parameters of the crystal field as, for example, done in connection with matrix isolated CH_4 molecules (20). As already pointed out by Ozaki *et al.* (12), the inclusion of both energies and Q-dependent intensities is most helpful for such an effort. We believe that a modification of the crystal field parameters has more severe effects on the transition matrix elements, i.e., on the intensities, than on the energy levels. Yet even for the latter there seem to be rather pronounced differences between theory and experiment. The measurement of Q-dependent intensities, therefore, provides the most direct way to the determination of improved eigenfunctions and the related crystal field parameters.

In the present experiment we only have data available for a fairly narrow range of momentum transfers and therefore only intensity ratios can be analysed (e.g., intensities normalized on that of the $J = 0$ to $J = 1$ transition). Here only coarse agreement is found; the $J = 1$ to $J = 2$ transition, e.g., has only about half of the predicted intensity. On the other hand the prediction of one perturbed $J = 0$ to $J = 3$ transition with high intensity may be a useful hint.

A quantitative comparison is even more difficult for excitations with energies larger than 3 meV. While there seems to be almost a "gap" at energies between 3 and 4.5 meV, we observed a broad band of intensity between about 4.5 and 12 meV, essentially in agreement with the results of Harker and Brugger (3). More or less well-defined peaks are observed at energies of about 5.7 and 6.5 meV with a much weaker maximum at 9.0 meV. A clear distinction between ordered and disordered molecules is difficult, and we must also not ignore the presence of translational phonons. We believe, however, that this band is largely due to the librations of the ordered molecules: (*a*) there are three times as many ordered molecules as disordered ones and also (*b*) Ozaki *et al.* (12) predict rather low intensity for transitions to the $J = 3$ and $J = 4$ sates, with the exception of one $J = 0$ to $J = 3$ transition. Within the single particle picture adopted by these authors, all librational excitations fall into the range between 6 and 7 meV (Fig. 1). Dispersion of the modes due to collective aspects clearly extends this range to values compatible with the observed band.

In an equilibrium sample at high temperatures all transitions between states with different spin symmetry contribute, except $A \leftrightarrow E$. The conversion of all molecules to the A state means that only excited A and T states are accessible in a neutron scattering experiment. As the intensity of inelastic A–A transitions is proportional to $j_3^2(Q\rho)$ (for the Q values of the present experiment this is $\sim Q^6$), this contribution is negligible for $Q = 1.8$ Å^{-1} and $Q = 2.2$ Å^{-1} (12, 21),[2] and hence only inelastic A–T transitions are important. This should result in a 30% overall decrease in intensity for the inelastic spectrum of the ordered molecules in A-CH_4 II as compared with a sample at $T = 5$ K. Inspection of the spectra from the doped sample at $T = 5$ K and $T \lesssim 100$ mK indeed yields a decrease of the overall inelastic intensity with the exception of the peak at 5.7 meV. This either could be due to the fact that there is a librational branch with T symmetry whose contribution gets much stronger upon conversion of the ground state to A (due to a favourable structure factor) or the peak at 5.7 meV could be an additional peak in the response of the disordered molecules, superimposed on a librational band. We note the fact that there is a $J = 0$ to $J = 3$ transition with fairly high calculated intensity. Comparison with the calculation of Kobashi *et al.* (11) cannot solve the problem, due to their general restriction to A symmetry. Optical data (16–19) yield peaks in the same energy range, but are restricted to $q = 0$ ($\boldsymbol{q}$ = wave vector in reduced zone-scheme).

When analysing the present data, one also should note that the oxygen impurities needed for enhanced conversion also mean a perturbation of the crystal. It has been suggested (7, 13) that some of the features observed may be due to such perturbations.

Conclusions

While the present experiment indeed provides additional insight into the rotational dynamics of the quantum molecular crystal CH_4, numerous questions remain. One of the ideas was to have a reduced number of transitions by converting all CH_4 molecules into their respective ground state with A symmetry. Here the preparation of A-methane was achieved by cooling an oxygen-doped sample to $T \lesssim 100$ mK. Yet again we found that, contrary to reports in the nmr literature, there is no fast conversion into the ground state for the disordered molecules. During times of the order of 1–2 days, only negligible conversion was observed in a sample with pure CH_4, similar to earlier observation of Kapulla and Gläser (5, 6). It appears that nuclear spin conversion in pure, O_2-doped or diluted samples (solid mixtures of CH_4 and Kr (22) is by no means satisfactorily explained at present (23). Obviously the conversion rate depends very strongly on the energy difference between the two states involved in the conversion process, on local surroundings and magnetic fields, as well as on temperature.[3]

How about the conclusions concerning the rotational states? Here we have to admit that not all assignment problems have been successfully overcome. Perhaps Q-dependent measurements over a wide range in Q could provide the necessary

[2]Also, D. Matuschek and A. Hüller, to be published.

[3]F. Guckelsberger and R. Scherm, unpublished.

solution (12, 21). On the other hand, calculations of the lattice dynamics have to be extended to include (*i*) all the spin states accessible in a neutron scattering experiment as well as (*ii*) the collective aspects due to the orientation–dependent coupling between neighbouring molecules.

As well, an incoherent neutron scattering experiment can only supply a density-of-state like result. Clearly, a direct coherent scattering experiment would yield more detailed information and a more serious test of lattice dynamical calculations. Such an experiment not only requires A-CH_4 II, but in addition a crystal with a sizable polarization with respect to the z-component of the nuclear spin, I_z (8). One could think of "brute force" methods to achieve this polarization (temperatures in the μK range and strong magnetic fields) but also of dynamical polarization (13). The alternative system, deuterated methane (CD_4), (*i*) means a rather dramatic step towards more classical properties and (*ii*) undergoes a phase transition to the more complicated phase III below $T = 22.1$ K. Therefore we suspect that many of the above-mentioned questions will remain open, at least for the near future.

Acknowledgement

The authors would like to thank P. Gerlach and A. Hüller for several helpful discussions.

1. H. M. James and T. A. Keenan. J. Chem. Phys. **31**, 12 (1959).
2. W. Press. J. Chem. Phys. **56**, 2597 (1972).
3. Y. D. Harker and R. M. Brugger. J. Chem. Phys. **46**, 2201 (1967).
4. B. Dorner and H. Stiller. Proc. Symp. Neutron Inelastic Scattering IAEA, 1964. Vol. 2. Bombay, India. 1965. p. 291.
5. H. Kapulla and W. Gläser. Phys. Lett. A, **31**, 158 (1970).
6. H. Kapulla and W. Gläser. Proc. Symp. Neutron Inelastic Scattering IAEA, 1972. Grenoble, France. 1973. p. 841.
7. A. Heidemann, K. J. Lushington, J. A. Morrison, K. Neumaier, and W. Press. J. Chem. Phys. **81**, 5799 (1984), and references therein.
8. W. Press. Single particle rotation in molecular solids. Springer Tracts in Modern Physics. Vol. 92. Springer, Berlin. 1981.
9. A. Hüller. Phys. Rev. B: Solid State, **10**, 4403 (1974).
10. K. Kobashi, R. D. Etters, and T. Yamamoto. J. Phys. C, **17**, 13 (1984).
11. T. Yamamoto, Y. Kataoka, and K. Okada. J. Chem. Phys. **66**, 2701 (1977).
12. Y. Ozaki, Y. Kataoka, and T. Yamamoto. J. Chem. Phys. **73**, 3442 (1980).
13. El Alami Ariba and H. Glätti. J. Phys. **44**, 1351 (1983).
14. K. Neumaier, A. Heidemann, and A. Magerl. Rev. Phys. Appl. **19**, 773 (1984).
15. B. Maier. Neutron research facilities at the ILL high flux reactor. ILL, Grenoble, France. 1986.
16. R. Savoie and R. P. Fournier. Chem. Phys. Lett. **7**, 1 (1970).
17. J. Obriot, F. Fondière, P. Marteau, H. Vu, and K. Kobashi. Chem. Phys. Lett. **60**, 90 (1978).
18. D. Fabre, M. M. Thiéry, and K. Kobashi. J. Chem. Phys. **76**, 4817 (1982).
19. F. D. Medina and W. B. Daniels. J. Chem. Phys. **70**, 242 (1979); **70**, 2688 (1979).
20. Y. Kataoka, W. Press, U. Buchenau, and H. Spitzer. Proc. Symp. Neutron Inelastic Scattering IAEA, 1977. Wien, Austria. 1978. p. 311.
21. D. Matuschek. Diploma thesis, Institute of Theoretical Physics, University of Erlangen, Erlangen, W. Germany. 1987.
22. S. Grondey, M. Prager, W. Press, and A. Heidemann. J. Chem. Phys. **85**, 2204 (1986).
23. A. J. Nijmann and A. J. Berlinsky. Phys. Rev. Lett. **38**, 408 (1977).

Can. J. Chem. Downloaded from www.nrcresearchpress.com by 176.9.209.113 on 09/07/12
For personal use only.

NH_3 reorientation in phases I, II, and III of $Ni(NH_3)_6(NO_3)_2$

GORDON J. KEARLEY AND HERMA BLANK
Institut Max von Laue – Paul Langevin 156X, 38042 Grenoble CEDEX, France
Received September 28, 1987
This paper is dedicated to Professor James A. Morrison

GORDON J. KEARLEY and HERMA BLANK. Can. J. Chem. **66**, 692 (1988).

The inelastic neutron scattering (INS) spectra of rotational tunnelling and librations of NH_3 ligands in phase III of $Ni(NH_3)_6(NO_3)_2$ are not consistent with a rotational hindrance potential containing only cos $(3n\phi)$ terms owing to strong interaction between neighboring cations. This type of interaction, and motion of the whole cation, also influences the classical reorientational motions involving displacement of the H atoms, where the overall radius of rotation is consistently greater than the 0.9 Å expected for isolated NH_3 rotors. Quasielastic neutron scattering (QNS) suggests that in phase III there are two sublattices of cations, one of which becomes completely disordered (with respect to the NH_3 rotors) at the III–II phase transition. Disorder of the second sublattice marks the II–I transformation where only a single type of rotational motion is found.

GORDON J. KEARLEY et HERMA BLANK. Can. J. Chem. **66**, 692 (1988).

Les spectres de diffusion des neutrons inélastiques (DNI) de l'effet tunnel de rotation et des librations des ligands NH_3 dans le $Ni(NH_3)_6(NO_3)_2$ de phase III ne sont pas en accord avec un potentiel d'empêchement à la rotation ne contenant que des termes cos $(3n\phi)$ provenant d'une interaction forte entre les cations voisins. Ce type d'interaction, ainsi que le mouvement du cation dans son ensemble, influencent aussi les mouvements classiques de réorientation impliquant le déplacement des atomes H dans lesquels le rayon global de la rotation est toujours plus grand que le 0,9 Å attendu pour des rotors NH_3 isolés. La diffusion des neutrons quasi-élastiques (DNQ) suggère que, dans la phase III, il existe deux sous-réseaux de cations dont l'un devient complètement désordonné (par rapport aux rotors NH_3) lors de la transition phase III → II. Le désordre du deuxième sous-réseau marque la transformation II → I dans laquelle on ne trouve qu'un seul type de mouvement de rotation.

[Traduit par la revue]

Can. J. Chem. Downloaded from www.nrcresearchpress.com by 93.93.197.157 on 09/07/12
For personal use only.

Introduction

The role played by disorder and reorientations of the ammine ligands in transition-metal hexammine salts has attracted the attention of several groups over the course of a number of years (see ref. 1 and references therein). The overall picture of six ammine groups, which undergo rotational diffusion at high temperature and then freeze into fixed orientations in the lowest-temperature phase transition, is generally accepted, but the details of the NH_3 orientations, particularly in the low-temperature phases, are largely unknown (2–5). In the present study we are concerned with motions not only of the NH_3 groups but also of the entire hexammine ion in three phases of nickel hexammine nitrate.

The sequence of phase transitions has been studied by ir (6), Raman (7), epr (8), and INS (9) spectroscopies, and by specific heat measurements (10, 11). For $Ni(NH_3)_6(NO_3)_2$, the transitions between the phases are usually quoted as (9):

$$\begin{array}{cccccccc} & \sim 180\,K & & 250\,K & & 250\,K & & \sim 90\,K \\ III & \rightarrow & II & \rightarrow & I & \rightarrow & II & \rightarrow & III \end{array}$$

Marked thermal hysteresis of the low-temperature transition is now well established for the nitrates, although it may well have been the source of confusion in the past (10) regarding the presence of an "extra" phase transformation at around 80 K. In the present work all temperature changes were made on heating to avoid ambiguity due to hysteresis. The III–II transition is usually attributed to disorder of the NH_3 ligands (6, 7, 9), while the onset of NO_3^- ion disorder is responsible for the II–I transformation (7).

Recently, neutron scattering spectroscopies have been used to study motions of the NH_3 groups in metal hexammine salts and have given a new insight into the potential energy surface of the NH_3 groups in the lowest-temperature phases (1, 12). Although the situation that emerges is complex, there is qualitative agreement with the idea that all NH_3 groups are essentially identical but that there is a disorder due to at least two energetically equivalent orientations (per cation) available to the ligands (13). The effect of this disorder on the NH_3 rotational potential seems to increase as the cation–cation separation decreases (12). In the present paper, we examine the rotational-tunnelling spectrum of the NH_3 ligands in the nitrate analogue, where the small anion leads to a reduced tunnel splitting and a greater sensitivity to the orientations of NH_3 groups on neighbouring cations compared with the iodide (12) or hexafluorophosphate (1) derivatives.

In many cases the tunnel splitting of the librational ground state can be compared with the energies of the librational modes, to deduce the form of the rotational hindrance potential and the barrier height (1, 12, 14–16). For phase III of $Ni(NH_3)_6(NO_3)_2$, however, the energy of the librational transitions of the NH_3 groups is too high to correlate with the tunnel splitting using a simple cosine potential form. Further, a multiplet of peaks has been reported in the librational region of the INS spectrum (9), which has been tentatively assigned to the presence of rather different barriers to rotation for the various NH_3 groups. This assignment gained support from the results of QNS spectra, which were interpreted as two of the six NH_3 groups on each cation undergoing reorientation on the time scale of this spectroscopy, while the remaining four groups are "stationary" (9). Tunnel splitting varies almost exponentially with the height of the barrier to reorientation, and if the above interpretation were valid, the effects of inequivalent NH_3 groups would be more manifest in the tunnelling spectrum.

In the present study we attempt to clarify the situation by a careful comparison of the tunnelling and librational INS spectra. We then present, and analyse, QNS spectra as a function of temperature in phases I, II, and III, going out to considerably higher momentum transfers than were previously available, to obtain a more accurate description of the reorientational processes.

Experimental

Samples were prepared by dissolving $Ni(H_2O)_6(OH)_2$ in concentrated ammonia solution, forming $Ni(NH_3)_6(OH)_2$. The nitrate ana-

logue was precipitated by the addition of ammonium nitrate solution, filtered, and recrystallized from dilute ammonia solution. The nitrate derivatives in particular lose ammonia rapidly and were handled and dried in an atmosphere with a small partial pressure of ammonia. Deuterated samples were prepared by the use of D_2O and deuterated ammonia solution.

Tunnelling spectra were collected using the IN5 multichopper time-of-flight spectrometer at the Institut Laue–Langevin (ILL), France. An incident neutron wavelength of 16 Å was used, giving an energy resolution (FWHM) of 3.3 μeV with a momentum transfer of 0.64 $Å^{-1}$. For the tunnelling spectrum detectors were grouped together at scattering angles between 90 and 130 degrees, with the final spectrum being obtained from the sum of these detectors. The IN5 spectrometer was also used for the quasielastic scattering experiments, using an incident neutron wavelength of 2.69 Å with detectors grouped to give a useful momentum-transfer range between 0.5 and 4.2 $Å^{-1}$. The resolution lost by the use of such short wavelengths was partly recovered by "squeezing" the neutron pulse length via a careful dephasing of the last two choppers. The measured energy resolution was 410 μeV in place of 700 μeV normally associated with a wavelength of 2.69 Å. Spectra collected at different scattering angles were normalized by comparison with a standard vanadium sample. Individual detector columns containing Bragg peaks were identified by inspection and removed from the data-treatment procedure.

High energy transfer spectra were collected using the IN4 double rotating-crystal time-of-flight spectrometer at the ILL. An incident neutron wavelength of 1.28 Å was used, giving an energy resolution of ca. 2.5 meV. Spectra recorded in all detectors between 100 and 140 degrees were summed together to produce the final spectrum. Standard liquid helium cryostats were used for all experiments, and changes to the sample temperature between quasielastic scattering measurements were made on heating.

Data-treatment routines were written locally using standard neutron-scattering algorithms. The fitting procedures, to extract peak positions and intensities, used a numerical convolution of the experimental resolution function with the calculated scattering functions. The calculated functions were then refined to minimize the difference between the observed and calculated spectra.

Can. J. Chem. Downloaded from www.nrcresearchpress.com by 93.93.197.157 on 09/07/12
For personal use only.

Results

Rotational tunnelling

When the tunnel splitting of rotational ground states is sufficiently large, INS provides a sensitive probe of the environments of the rotors, the subject having been reviewed by Press (17). Probably the most thoroughly studied example is that of methane, in which the spectra of protonated, deuterated, and partially deuterated species have been used to achieve a very complete description of the partially disordered structure of phase II of this compound (18). A similar situation appears to exist for the metal hexammines, and in the present case our concern is to distinguish the effects of disorder from those of crystal-field distortions.

Inspection of the tunnelling spectrum shown in Fig. 1 reveals the presence of at least two peaks in energy loss and in energy gain. These peaks arise from rotational tunnelling of the NH_3 ligands. Their positions provide information about the rotational hindrance potential while, in the simplest case, their intensities reflect the number of NH_3 groups experiencing these potentials, and hence provide a stringent test of the differing barrier heights alluded to above.

Peak positions and intensities, collected in Table 1, were estimated by fitting the spectrum with Gaussian functions convoluted with the instrumental resolution function, with the constraint that the spectrum be symmetric about the elastic peak. The fitted function is represented by the solid line in Fig. 1, with the component peaks below. Peak intensities, relative to the elastic peak, are 0.023 and 0.008 for the peaks at energy transfers of 5.5 and 18.9 μeV, respectively, the low intensities being due to the small momentum transfer, only 0.64 $Å^{-1}$. A comparison of the intensity of the 18.9-μeV peak, at higher momentum transfer, with the tunnelling spectrum of $Ni(NH_3)_6I_2$ (12) reveals that the *total* tunnelling intensity is very similar for the two salts, from which we conclude that for both salts the intensity accounts for essentially all NH_3 ligands.

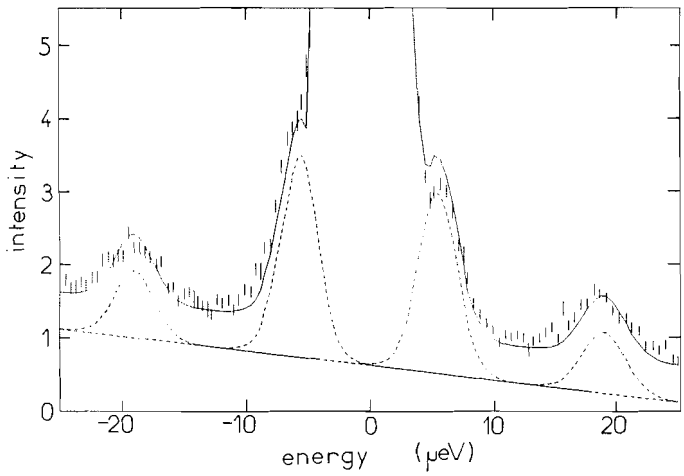

FIG. 1. Tunnelling spectrum of $Ni(NH_3)_6(NO_3)_2$ (1.8 K) obtained using the IN5 spectrometer. The solid line represents the fitted function, while the broken line shows the individual Gaussian components. The sloping background arises from the use of a high neutron pulse rate and was fitted using a single parameter.

TABLE 1. Positions and intensities of the INS peaks in the tunnelling and librational spectra regions. The intensities are quoted relative to the elastic peak intensity being unity

Assignment	Energy transfer	Relative intensity EPP = 1.000)
	(μeV)	
NH_3 tunnelling	5.56	0.008
NH_3 tunnelling	18.94	0.023
	(meV)	
NH_3 librations	20.5–37.9	
ND_3 librations	15.7–32.0	

The intensity ratio of the two tunnelling peaks in the present case, ca. 1:4, is not readily reconciled with crystallographic inequivalences of six NH_3 groups. While it could be argued that there may be a further unresolved peak of unit intensity that is missed due to inaccuracies in our intensity estimates, it is more likely that the observation of more than one peak is due to interaction between ligands, as described for the iodide analogue (12), and that static crystallographic inequivalences play only a minor part. In fact, a comparison of the librational spectrum (below) with the tunnelling spectrum suggests that, as expected, the NH_3–NH_3 interaction is stronger in the nitrate salt than in the iodide, *vide infra*. A study of the temperature dependence of the tunnelling spectrum would help clarify this point.

Librational motions

For $Ni(NH_3)_6(NO_3)_2$ at temperatures below ca. 5 K, the rotational motions are best described by tunnelling and librations rather than by almost free rotation. In principle, we may use the energy transfers of NH_3 tunnelling in this salt (above) to derive the energy transfers of the NH_3 librational modes if we ignore the effects of cation–cation interactions. Assuming that

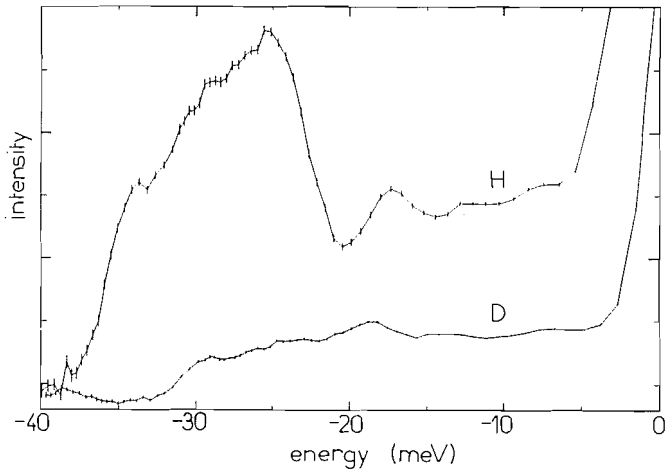

FIG. 2. INS spectra of $Ni(NH_3)_6(NO_3)_2$ and $Ni(ND_3)_6(NO_3)_2$ (5.0 K) in the librational spectral region obtained using the IN4 spectrometer. The low intensity of the peaks in the latter spectrum is due to the small incoherent scattering cross section of deuterium.

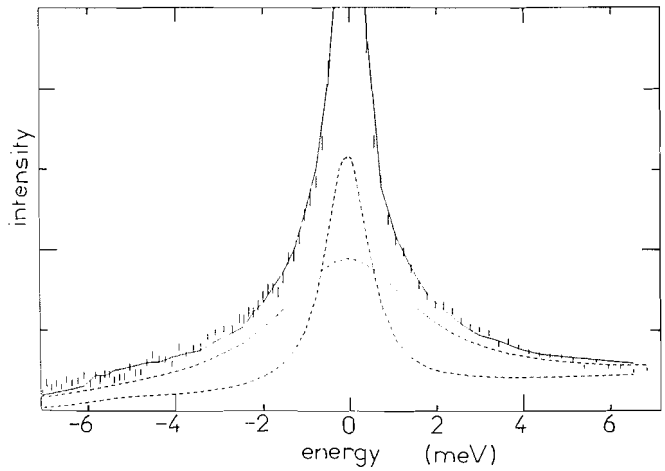

FIG. 3. Example of a QNS spectrum of phase II $Ni(NH_3)_6(NO_3)_2$ recorded at a scattering angle of 82.5 degrees ($Q = 3.1$ Å^{-1}). The solid line represents the calculated function and the broken lines represent the Lorentzian components.

the NH_3 groups retain their molecular C_{3v} symmetry, but occupy a site that has no symmetry on the time scale of the rotation, the hindrance potential, V, has the form cos (3ϕ). This potential can be included in the Schrödinger equation for a one-dimensional rotor:

$$[1] \quad (-\hbar^2 d^2/2I d\phi^2 + V(\phi))\Psi = E\Psi$$

to obtain the eigenvalues.

Attributing the tunnelling energies at 5.5 and 18.9 μeV to $J = 0 \rightarrow J = 1$ transitions gives rotational barrier heights of 38.0 and 27.5 meV, respectively. The corresponding librations ($J = 0 \rightarrow J = 2$) are calculated at 13.7 and 11.2 meV, respectively.

The INS spectra of $Ni(NH_3)_6(NO_3)_2$ and $Ni(ND_3)_6(NO_3)_2$ in the 5–40 meV region are shown in Fig. 2. The large amplitude of the librations, alongside the high scattering cross section of H atoms, strongly suggests that the dominant features, between 20 and 35 meV (Table 1), arise from librational modes, as proposed by ref. 9. This assignment is supported by the approximate $1/\sqrt{2}$ shift of these peaks and loss of intensity in the spectrum of the deuterated analogue. These librational features occur at energies more than twice the values calculated on the basis of a simple cos (3ϕ) potential using the barrier height calculated from the tunnel splitting. Cosine potentials of higher symmetry, cos (3$n\phi$) or combinations of such potentials including phase angles (16, 19), cannot reproduce the large separation between the tunnel-split ground state and the other librational levels. A detailed discussion of the potential form is beyond the scope of the present paper, since we have only two observations on which to base our arguments. We note, however, that the observed separation between the tunnel-split ground state and the librational levels can be produced by the use of a coupled potential (15).

The evidence for a coupled system is quite strong on the basis of both the tunnelling spectrum and the librational spectrum. It is conceivable that in such a coupled system, the multiplet peaks observed in the librational spectral region arise from a group of closely spaced energy levels, since it is clear that they do stem from crystallographically distinct ligands.

Quasielastic neutron scattering

Direct deduction of molecular motions from QNS spectroscopy of powdered samples is rarely feasible for systems of any complexity, but this spectroscopy is particularly useful for investigating the radius of rotational motions and the number density of species performing this rotation. For these purposes the most reliable measured quantity in QNS is the experimental elastic incoherent struture factor (EISF), which is the ratio of the elastic intensity to the elastic plus quasielastic intensity (see review article by Leadbetter and Lechner (20)). For the moment we will consider only the calculated EISF for motion on a circle,

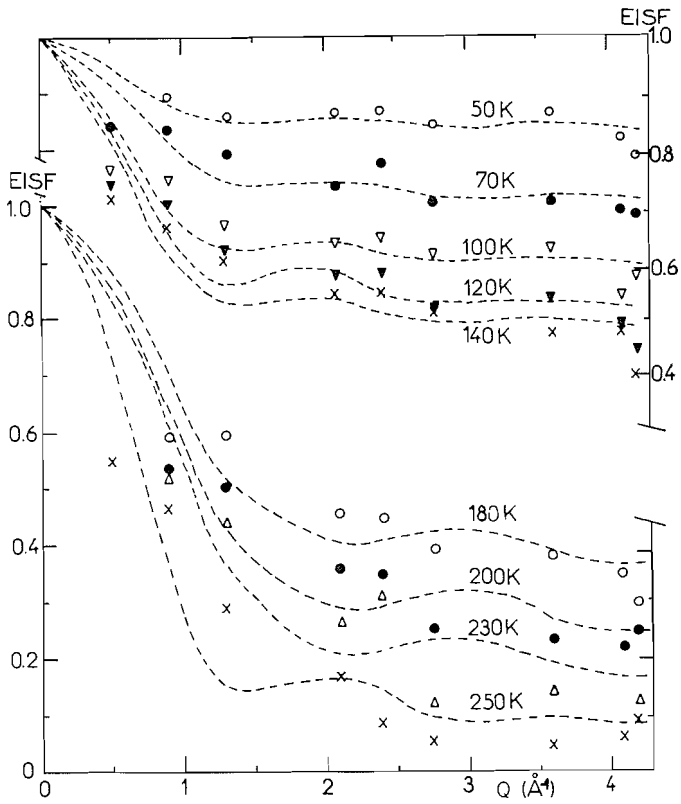

FIG. 4. Total EISFs of $Ni(NH_3)_6(NO_3)_2$ obtained by fitting the QNS spectra with one Lorentzian function (phase I, 250 K: phase III, 50–140 K) and two Lorentzians (phase II, 180–230 K). Broken lines show the best-fit calculated EISF using eq. [2] allowing only the radius, r, and the fraction, F, to refine. The number of sites on the circle, m, was set to 20.

Can. J. Chem. Downloaded from www.nrcresearchpress.com by 93.93.197.157 on 09/07/12
For personal use only.

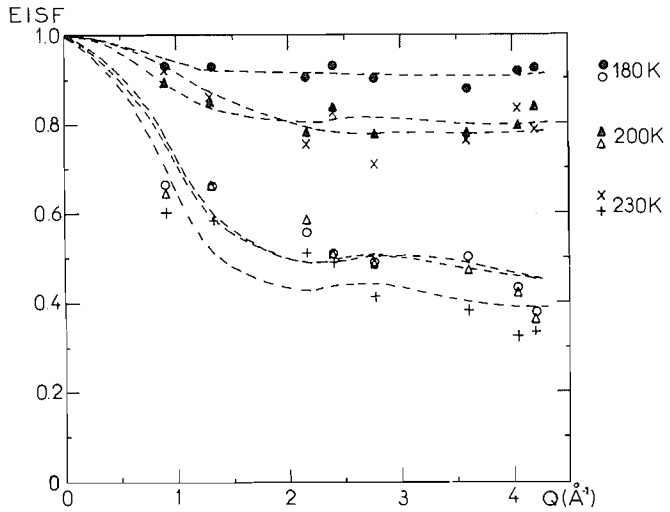

FIG.. 5. Separated EISFs for the two Lorentzians fitted to the quasielastic spectra of phase II $Ni(NH_3)_6(NO_3)_2$. Calculated EISFs were obtained as described for Fig. 2.

which is given by:

$$[2] \quad 1 - F/\pi \sum_{l=1}^{m-1} m^{-1} \sum_{k=1}^{m} j_0(2Qr \sin \pi k/m) \cdot \cos(2\pi lk/m)$$

where j_0 is the zero-order Bessel function, m is the number of sites on the circle of radius, r, and Q is the momentum transfer. F is the fraction of protons in the system undergoing reorientation. If the elastic peak is readily separable from the quasielastic components, the overall experimental EISF is virtually independent of the detailed fitting of the quasielastic components.

In the present case, it transpired that elastic and quasielastic contributions are separable by fitting a single Lorentzian to the quasielastic scattering at sample temperatures below 180 K (phase III), and above 245 K (phase I). Between these temperatures (phase II), two Lorentzian functions were required to fit the data adequately. An example of a single spectrum with two fitted Lorentzian components is illustrated in Fig. 3. To maximize the significance of the fitted parameters, spectra collected at nine different scattering angles were refined simultaneously. Preliminary analyses revealed that the Lorentzian peak widths are Q dependent, from which we conclude that the overall process is of a diffusive nature, rather than jumps between a small number of sites. This conclusion is in good agreement with the mode of NH_3 motion reported for the iodide analogue (3) but in conflict with the instantaneous-jump process reported in previous studies of the nitrate and perchlorate salts (9, 21, 22). The Q dependence of the quasielastic width for diffusion on a circle was taken to be that of the sum of m Lorentzians with widths, τ, proportional to (23):

$$[3] \quad 1/2 \sin^2(\pi l/m)$$

weighted according to eq. [2]. Use of eqs. [2] and [3] with m, the number of sites on the circle, set to 20 gives a very close approximation to rotational diffusion. For motions on a radius of ca. 1 Å the quasielastic width is almost constant below a momentum transfer of 2.5 $Å^{-1}$.

In the event, spectra at nine scattering angles were refined using nine quasielastic intensity factors, an overall scale factor, and two width factors, for each of either one or two quasielastic components. The broken lines in Figs. 4 and 5 represent the best-fit calculated EISFs obtained using eq. [2] with $m = 20$, and allowing only the radius of rotation, r, and the fraction of protons in the system undergoing reorientation, F, to refine. We emphasize that the fitted EISFs are calculated using only rotation on a circle and, clearly, the actual reorientation process is more complicated than this, as evidenced by the systematic misfit of the calculated EISFs at around 1 $Å^{-1}$ (Figs. 4 and 5). We have obtained almost perfect fits to the EISFs by allowing two processes to occur: diffusion on a circle and spherical diffusion, refining the populations and radii of both processes. There is, however, a danger of overinterpretation of the results (the average error on the points of the EISFs (not shown) is about 12%) and we prefer to restrict our discussion to a more approximate overall process using only diffusion on a circle.

Two important results are derived from these EISFs. Firstly, on the timescale of this spectroscopy, the total fraction of

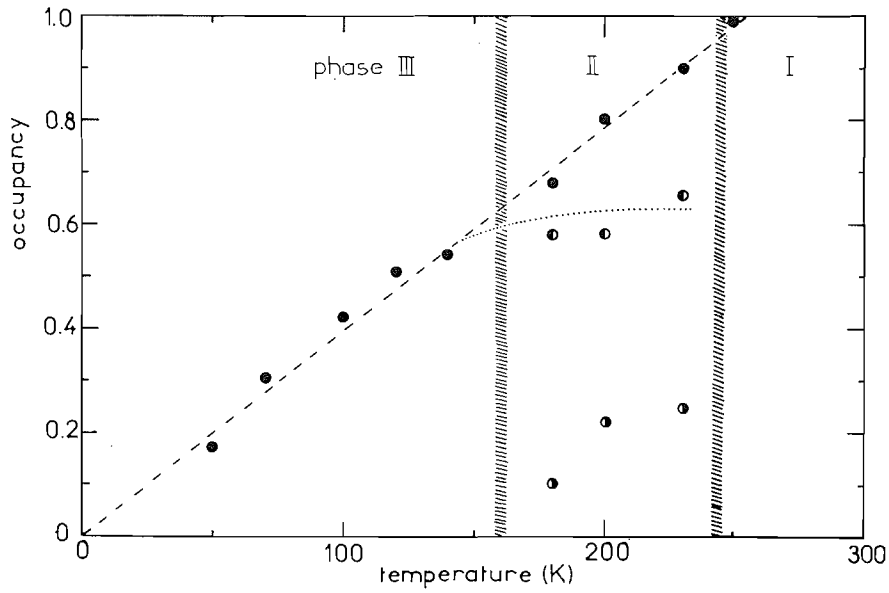

FIG. 6. Variation of the fraction of protons in the system contributing to the EISF with temperature. The filled circles represent the total occupancy; the left-filled and right-filled circles denote occupancies associated with peaks 1 and 2, respectively (Table 2). The dotted line is a guide to the continuity of peak 1 through the III–II phase transition.

Can. J. Chem. Downloaded from www.nrcresearchpress.com by 93.93.197.157 on 09/07/12
For personal use only.

TABLE 2. Radii and fraction of protons involved in motion (occupancy) for the *overall* reorientation processes (on the timescale of the spectroscopy) in $Ni(NH_3)_6(NO_3)_2$ at various temperatures in various phases. These values give the calculated EISFs shown in Figs. 4 and 5

Phase	Temperature (K)	Peak 1		Peak 2	
		Radius (Å)	Occupancy	Radius (Å)	Occupancy
III	50	2.07	0.17		
	70	1.99	0.30		
	100	2.16	0.42		
	120	2.12	0.51		
	140	2.16	0.54		
II	180	1.38	0.58	1.69	0.10
	200	1.44	0.58	1.53	0.22
	230	1.50	0.65	1.07	0.26
I	250	1.96	0.98		

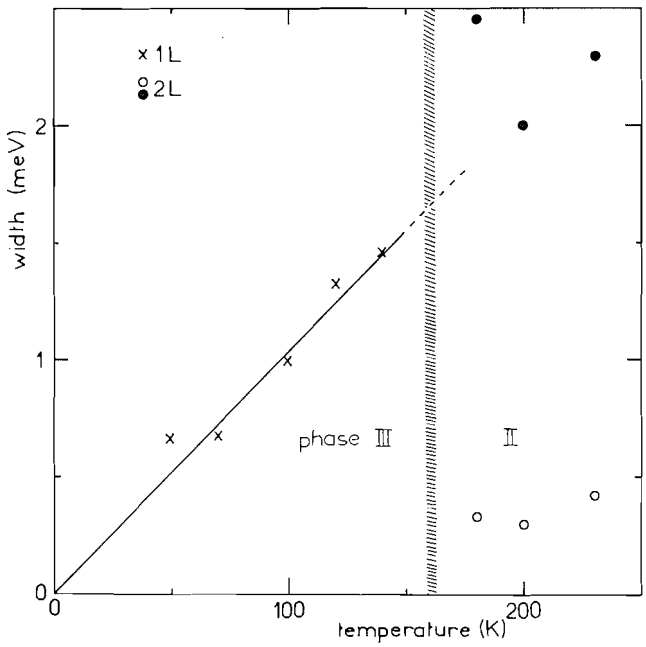

FIG. 7. Variation of peak width (diffusion constant) derived from the quasielastic components. The proportionality between the diffusion constant (HWHM) and temperature is consistent with Einstein behavior.

protons undergoing reorientation increases almost linearly with temperature up to the II–I transition, and is not simply related to crystallographically distinct NH_3 groups. This trend is shown graphically in Fig. 6. Secondly, the radius of rotation at all temperatures, including the two components above 180 K, is >1.0 Å (Table 2). A radius of rotation of ca. 1.5 Å resulted from the refinement of quasielastic peak widths (eq. [3]), and these radii are to be compared with simple NH_3 rotation (radius ca. 0.9 Å). A similar result has been obtained for NH_3 motions in $Ca(NH_3)_6$ (24) for which it was suggested that the NH_3 rotation occurs about a fluctuating axis. Clearly, in the present case there is some motion of the whole cation, but there is no unique interpretation of our results, and we must admit the possibility of tumbling motions, rotations of the octahedral cation around several axes, and simple precession of the Ni–N vectors.

Discussion

The spectra of both tunnelling and librational motions of the NH_3 ligands in this salt support the idea that the rotational potential is very sensitive to the orientation of the NH_3 ligands on the neighboring cation. This effect was predicted by Bates and Stevens (13) on the basis of a simple point-charge model. These authors also calculated that there are two energetically equivalent orientations of the NH_3 ligands on an isolated hexammine cluster, related by 60-degree rotation of all ligands. We denote these orientations A and B. For the isolated hexammine ion, a very low barrier separates the concerted interchange between A and B. The strong interaction between the cations, however, militates against the concerted process, and we are left with a situation in which various arrangements of A and B cations within the lattice must be considered.

It is interesting to note that at the III–II phase transition the population of H atoms involved in the reorientational processes giving the quasielastic scattering is around 50% (see Fig. 6). Further, comparison of the temperature dependence of the diffusion constants (Fig. 7) with the population of H atoms involved reveals that the III–II transition is marked by the onset of a second process rather than any stepwise change in the diffusion constant of the phase III process. This behavior suggests that there are two sublattices of cations (or groups of cations), one of which is ordered in phase III. This behavior could arise from the A and B orientations discussed above, and a crystallographic investigation of phases II and III would be most enlightening.

The trend of the total EISFs shown in Fig. 4 summarizes the nature of the phase transitions rather well. At a sample temperature of 250 K (phase I), the quasielastic scattering was fitted well with a single Lorentzian, as would be expected for the known crystallographic space group, $Fm3m$, of this phase. As with all the EISFs shown in the figures, the falloff with increasing Q is too rapid for simple reorientation of the NH_3 groups. The normal crystallographic description of the NH_3 groups in the cubic phases of these salts is that the three H atoms are disordered between 24 positions (3) (effectively rotational diffusion on a radius of ca. 0.9 Å). More recently, a phenomenological Frenkel model has been applied to describe the X-ray and neutron scattering from the NH_3 groups (25) but the physical meaning of this model is not clear.

Our results suggest that in *all* phases of $Ni(NH_3)_6(NO_3)_2$, NH_3 reorientations between neighboring cations are coupled to each other and to some form of whole-body "cation libration". The involvement of softening of the librational lattice mode in the phase transitions of these salts has already been suggested (5) and certainly merits further investigation.

Can. J. Chem. Downloaded from www.nrcresearchpress.com by 93.93.197.157 on 09/07/12
For personal use only.

Acknowledgments

We are grateful to S. Clarke for his help with the sample preparation and to A. Murani for his assistance with the experiments using the IN4 spectrometer.

1. G. J. KEARLEY, H. BLANK, and J. K. COCKCROFT. J. Chem. Phys. **86**, 5989 (1987).
2. K. ASCH, E. K. SHENDY, J. M. FRIEDT, and J. P. ADLOFF. J. Chem. Phys. **62**, 2335 (1975).
3. J. ECKERT and W. PRESS. J. Chem. Phys. **73**, 451 (1980).
4. T. E. JENKINS and A. R. BATES. J. Phys. C: Solid State Phys. **14**, 817 (1981).
5. A. R. BATES, L. T. H. FERRIS, and T. E. JENKINS. J. Phys. C: Solid State Phys. **12**, 2945 (1979).
6. S. ISOTANI, W. SANO, and J. A. OCHI. J. Phys. Chem. Solids, **36**, 95 (1975).
7. T. E. JENKINS, L. T. H. FERRIS, A. R. BATES, and R. D. GILLARD. J. Phys. C: Solid State Phys. **11**, L77 (1978).
8. L. LARYŚ, J. STANKOWSKI, and M. KRUPSKI. Acta Phys. Pol. A, **50**, 351 (1976).
9. A. BELUSHKIN, J. A. JANÍK, J. M. JANÍK, I. NATKANIEC, W. NAWROCIK, W. OLEJARCZYK, K. OTNES, and T. ZALESKI. Physica, **122B**, 217 (1983).
10. J. BOUSQUET, M. PROST, and M. DIOT. J. Chim. Phys. **6**, 1004 (1972).
11. A. MIGDAŁ-MIKULI, E. MIKULI, M. RACHWALSKA, T. STANEK, J. M. JANÍK, and J. A. JANÍK. Physica, **104B**, 331 (1981).
12. H. BLANK and G. J. KEARLEY. J. Chem. Phys. **87**, 6809 (1987).
13. A. R. BATES and K. W. STEVENS. J. Phys. C: Solid State Phys. **2**, 1573 (1969).
14. B. ALEFELD, A. KOLLMAR, and B. A. DASANNACHARYA. J. Chem. Phys. **63**, 4415 (1975).
15. S. CLOUGH, A. HEIDEMANN, A. H. HORSEWILL, and M. N. J. PALEY. Z. Phys. B: Condens. Matter, **55**, 1 (1984).
16. D. CAVAGNAT, A. MAGERL, C. VETTIER, I. S. ANDERSON, and S. TREVINO. Phys. Rev. Lett. **54**, 193 (1985).
17. W. PRESS. Single-particle rotations in molecular crystals. Springer, Berlin. 1981.
18. K. J. LUSHINGTON, KAZUO MAKI, J. A. MORRISON, A. HEIDEMANN, and W. PRESS. J. Chem. Phys. **7**, 4010 (1981).
19. M. PRAGER, K.-H. DUPRÉE AND W. MÜLLER-WARMUTH. Z. Phys. B: Condens. Matter, **51**, 309 (1983).
20. A. J. LEADBETTER and R. E. LECHNER. The plastically crystalline state. *Edited by* J. N. Sherwood. Wiley, Chichester. 1979.
21. J. A. JANÍK, J. M. JANÍK, K. OTNES, and K. ROSCISZEWSKI. Physica (Utrecht), **B83**, 250 (1976).
22. J. A. JANÍK, J. M. JANÍK, and K. OTNES. Physica (Utrecht), **B90**, 275 (1977).
23. A. J. DIANOUX, F. VOLINO, and H. HERVET. Mol. Phys. **30**, 1181 (1975).
24. F. LECLERCQ, P. DAMAY, and P. CHIEUX. J. Chem. Phys. **88**, 3886 (1984).
25. A. HOSER, W. JOSWIG, W. PRANDL, and K. VOGT. Mol. Phys. **56**, 853 (1985).

Can. J. Chem. Downloaded from www.nrcresearchpress.com by 93.93.197.157 on 09/07/12
For personal use only.

A study of iron–tungsten oxides and iron–chromium–tungsten oxides

THOMAS BIRCHALL,[1] CHRISTOPHER HALLETT, AND ANN VAILLANCOURT
Department of Chemistry and Institute for Materials Research, McMaster University, 1280 Main Street West, Hamilton, Ont., Canada L8S 4M1

AND

KRZYSZTOF RUEBENBAUER
Institute of Nuclear Physics, 31-342 Kraków, ul. Radzikowskiego 152, Poland

Received August 28, 1987

This paper is dedicated to Professor J. A. Morrison

THOMAS BIRCHALL, CHRISTOPHER HALLETT, ANN VAILLANCOURT, and KRZYSZTOF RUEBENBAUER. Can. J. Chem. **66**, 698 (1988).

A ^{57}Fe Moessbauer study of the Fe_2O_3–WO_3 and Fe_2O_3–Cr_2O_3–WO_3 systems has been carried out. Single phase materials could be prepared having the composition $Fe_{2-x}WO_{6-3x/2}$ ($x = 0.28$), the stoichiometric Fe_2WO_6 always contained detectable amounts of α-Fe_2O_3. The iron tungstates are found to be unstable to prolonged heating at 1000°C. The $Cr_{2-y}Fe_yWO_6$ ($0 < y \leq 2$) system was shown to be of the trirutile type when $y \leq 1.7$ but multiphasic when $y > 1.7$, these latter phases have structures based upon the iron and chromium tungstate phases, respectively. The Moessbauer parameters for the $Cr_{2-y}Fe_yWO_6$ compositions do not appear to behave in the same fashion as the related $Fe_{2-x}Cr_xTeO_6$ system.

THOMAS BIRCHALL, CHRISTOPHER HALLETT, ANN VAILLANCOURT, etd KRZYSZTOF RUEBENBAUER. Can. J. Chem. **66**, 698 (1988).

On a réalisé une étude, par effet Moessbauer du ^{57}Fe, des systèmes Fe_2O_3–WO_3 et Fe_2O_3–Cr_2O_3–WO_3. On a pu préparer des produits en phase unique de composition $Fe_{2-x}WO_{6-3x/2}$ ($x = 0,28$) ; le produit de stoechiométrie Fe_2WO_6 contient toujours des quantités détectables d'α-Fe_2O_3. On a trouvé que les tungstates de fer sont instables si on les soumet à un chauffage prolongé à 1000°C. On a démontré que le système $Cr_{2-y}Fe_yWO_6$ ($0 < y \leq 2$) est du type de la trirutile lorsque $y \leq 1,7$, mais qu'il est multiphasique lorsque $y > 1,7$; ces dernières phases possèdent des structures qui sont basées sur des phases de tungstates respectivement de fer et de chrome. Le comportement des paramètres de Moessbauer pour les compositions $Cr_{2-y}Fe_yWO_6$ ne correspond pas à celui de système $Fe_{2-x}Cr_xTeO_6$ apparenté.

[Traduit par la revue]

Introduction

The iron–tungsten–oxygen and the iron–chromium–tungsten oxygen systems have been the subject of considerable interest in recent years (1–8). Senegas and Galy (4) determined the crystal structure of an iron(III) tungstate described as Fe_2WO_6. Subsequently, Leiva *et al.* (5–8) have investigated the properties of iron tungstates prepared as reported by Senegas and Galy (4) and reported that the material is best considered as a solid solution of $FeWO_4$ in Fe_2WO_6 (5, 6). The materials were described by the formula $Fe_{2-2x}W_{1+x}O_6$ (5). Given the sensitivity of Moessbauer spectroscopy (7) to the oxidation state of iron and the uncertainty (4–6) surrounding the oxidation state of iron in "Fe_2WO_6" it seemed surprising that no Moessbauer studies of iron tungstates prepared from Fe_2O_3 and WO_3 have been reported. Hence we have undertaken an iron-57 Moessbauer spectroscopic study of these materials in an attempt to clarify the nature of these materials.

It was also noted that studies of chromium-doped iron tungstates have been recently carried out (7, 8). It was reported that a solid solution series, $Cr_{2-y}Fe_yWO_6$, with the trirutile structure of Cr_2WO_6 could be prepared, although the series did not appear to extend across the composition range $0 \leq y \leq 2$ (7, 8). Given that other mixed metal oxide systems based on iron and chromium have been reported to show magnetic properties which were dependent on x in $Fe_{2-x}Cr_xO_3$ (9) and $Fe_{2-x}Cr_xTeO_6$ (10), and which were sensitive to detection by Moessbauer spectroscopy, the iron–tungsten system has also been examined by this technique.

[1]To whom all correspondence should be addressed.

Experimental

Preparation of materials

Iron tungstates were prepared by the calcination (2 × 30 h) in air of equimolar mixtures of α-Fe_2O_3 and WO_3 at 1000°C. "Iron-deficient" compounds were prepared by analogous methods. Some materials were heated at 1000°C for 3 weeks (see below).

The $Cr_{2-y}Fe_yWO_6$ compounds were prepared in the following manner. A standard solution of ferric nitrate was prepared by dissolving pure iron in concentrated nitric acid. A similar standard solution of Cr^{3+} was prepared by the reaction of $K_2Cr_2O_7$ with 30% H_2O_2 in acid solution. Appropriate quantities of these two solutions, to give the required Fe:Cr ratio, were mixed and aqueous NH_4OH added until complete precipitation of the iron and chromium hydroxides had occurred. The mixture was filtered, the filtrate was tested to ensure that precipitation was in fact complete, and the precipitate thoroughly washed with water and then dried for several hours at 120°C. This was followed by heating at 1000°C for 24 h, grinding the mixture, and reheating at 1000°C for a further period of 24 h. The mixed oxide $Cr_{2-y}Fe_yO_3$ thus formed was thoroughly mixed with the appropriate quantity of WO_3 and heated at 950°C for 24 h. The homogeneity was checked by X-ray powder diffraction. Powder X-ray data were recorded using a Philips horizontal goniometer and copper K_α radiation. Samples were mixed with an internal standard of KCl.

Moessbauer spectroscopy

Moessbauer spectra were recorded on apparatus described elsewhere (11). Samples were cooled to temperatures between 298 and 4.2 K in a "Technology Systems" cryostat while the ^{57}Co/Rh source was maintained at ambient temperature. The sample temperature was monitored by a "Thor" temperature controller. Absorbers were prepared by mixing the finely ground powders with Apiezon grease. The quantity of iron in each absorber (always < 10 mg Fe/cm^2) was calculated according to the method described by Long *et al.* (12) to minimize the effect of

Can. J. Chem. Downloaded from www.nrcresearchpress.com by 93.93.197.157 on 09/07/12
For personal use only.

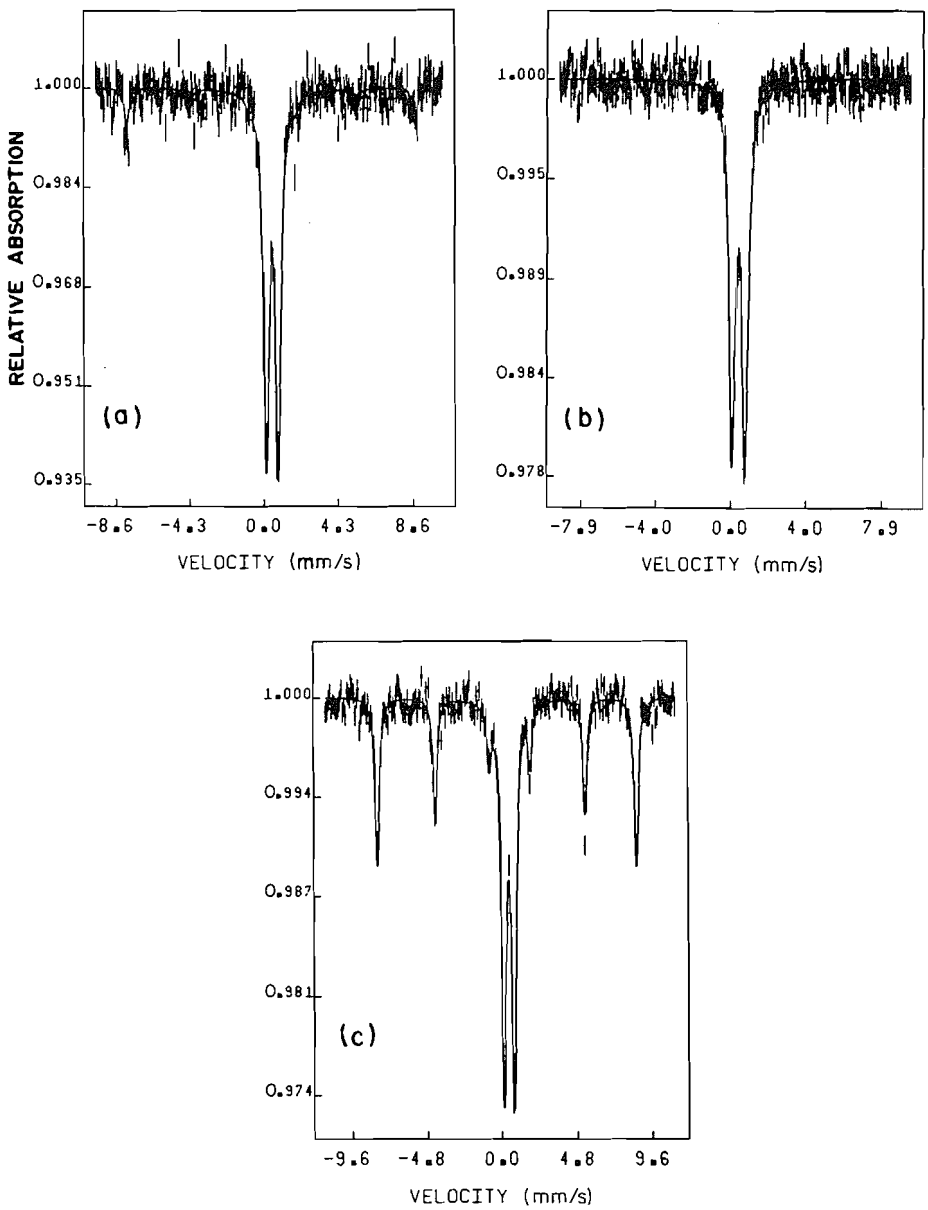

FIG. 1. ^{57}Fe Moessbauer spectra at 298 K of (*a*) Fe_2WO_6 prepared from stoichiometric amounts of Fe_2O_3 and WO_3; (*b*) Fe_2WO_6 with a 6% Fe deficiency; (*c*) Fe_2WO_6 after heating for 3 weeks at 1000°C.

γ-ray scattering by tungsten. The spectra were fitted using a modified version of the program developed by Ruebenbauer and Birchall (13) and all isomer shifts are relative to α-Fe as zero shift.

Results and Discussion

Iron–tungsten oxides

Calcining equimolar mixtures of α-Fe_2O_3 and WO_3 at 1000°C gave dark grey powders which were examined by Moessbauer spectroscopy and powder X-ray diffraction. Whilst PXRD gave little evidence for the presence of an impurity it was obvious from the Moessbauer spectrum that trace quantities of α-Fe_2O_3 were present, Fig. 1(*a*). Since the contribution of the impurity phase is small only the outer peaks of the sextet, which characterizes magnetically ordered α-Fe_2O_3, are visible above the baseline scatter. The Moessbauer data indicate that ca. 10% Fe is located in the haematite phase (Table 1). However, given the uncertainty in the relative recoil-free fractions of iron in Fe_2O_3 and "Fe_2WO_6," and the critical influence of the baseline position places an upper limit of contribution of a minor component at about 5 mol% Fe_2O_3. It is therefore interesting that this datum is consistent with the suggestions made by Leiva *et al.* (5, 6) that equimolar quantities of Fe_2O_3 and WO_3 react to give an iron tungstate together with some α-Fe_2O_3.

In addition Leiva *et al.* (5, 6) reported that iron-deficient mixtures of Fe_2O_3 and WO_3 react to give a monophasic, non-stoichiometric product, although no limits of nonstoichiometry were established. Hence iron-deficient mixtures of Fe_2O_3 and WO_3, with nominal compositions between Fe_2WO_6 and $Fe_{1.56}WO_{5.34}$, were calcined at 1000°C in an attempt to prepare monophasic materials and to investigate the limits of the iron-deficient-type nonstoichiometry. Solids prepared from reactants of nominal compositions from Fe_2WO_6 to $Fe_{1.92}WO_{5.88}$ gave Moessbauer spectra which retained evidence for the presence of α-Fe_2O_3. However, the material with a nominal composition $Fe_{1.88}WO_{5.82}$ gave a Moessbauer spectrum, Fig. 1(*b*), in which the baseline to each side of the doublet, arising from iron

Can. J. Chem. Downloaded from www.nrcresearchpress.com by 93.93.197.157 on 09/07/12
For personal use only.

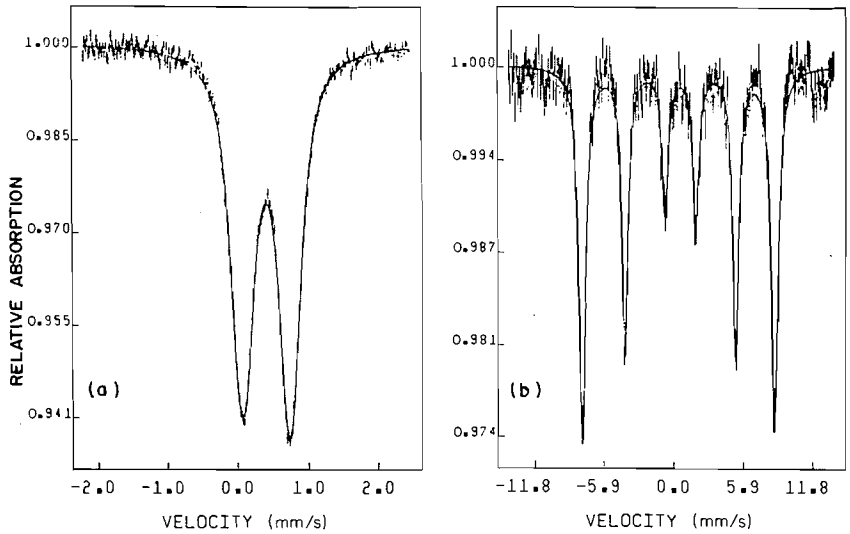

FIG. 2. ^{57}Fe Moessbauer spectra of (*a*) Fe_2WO_6 with a 6% Fe deficiency at 298 K fitted to two iron sites; (*b*) $Fe_{1.68}WO_{5.52}$ at 4.2 K.

tungstate, showed only normal statistical scatter with no evidence for a contribution from α-Fe_2O_3. It is also pertinent to note that materials with nominal composition of $Fe_{1.68}WO_{5.52}$ were found to be pure iron tungstates by both Moessbauer spectroscopy and powder X-ray diffraction. Examination, by powder X-ray diffraction, of solids which were more iron-deficient revealed trace quantities of WO_3. Since 2 mol% WO_3 was found to be readily detectable by X-ray diffraction it seems reasonable to conclude that solids with nominal compositions between $Fe_{1.88}WO_{5.82}$ and $Fe_{1.68}WO_{5.52}$ are monophasic materials which represent the approximate stoichiometry range in this form of iron tungstate. Reduction of the iron content beyond $Fe_{1.68}WO_{5.52}$ to $Fe_{1.64}WO_{5.48}$ reveals X-ray detectable traces of WO_3, whilst increasing the concentration of iron much above $Fe_{1.88}WO_{5.82}$ produces Moessbauer detectable Fe_2O_3.

Although these materials have been discussed in terms of iron and oxygen deficiency it should be noted that this represents the nominal compositions of the reactants. Since the solids were formed by calcination in air, the possible addition or loss of oxygen during the reaction cannot be discounted on the basis of X-ray diffraction or Moessbauer data. The reaction of a mixture of WO_3 and α-Fe_2O_3, which corresponded to a nominal composition of $Fe_{1.72}WO_{5.58}$ was therefore performed *in situ* whilst being monitored by thermal gravimetric analysis. No change in weight occurred during the course of the reaction (24 h). Powder X-ray data recorded from the product showed only lines reported as characteristic of "Fe_2WO_6" (4) with no evidence for WO_3. Taking the powder X-ray, Moessbauer and thermal gravimetric analysis data together, it seems reasonable to describe the iron tungstates prepared in ths work as $Fe_{2-x}WO_{6-3x/2}$.

It also appears worth noting the behaviour of these iron tungstates when subjected to prolonged calcination at 1000°C. The Moessbauer spectrum recorded from the iron tungstate prepared from an equimolar mixture of Fe_2O_3 and WO_3, and which was annealed for 3 weeks at 1000°C, is shown in Fig. 1(*c*). Similar spectra were obtained from an iron tungstate of nominal composition $Fe_{1.68}WO_{5.52}$. The contribution of iron in the form of α-Fe_2O_3 has increased from between 0 and 10% after short-term calcination, to 44% after heating for 3 weeks. Significant weight loss was also noted (ca. 25% of total sample). Hence it appears that iron tungstates decompose on the prolonged calcination at 1000°C with loss of tungsten as a volatile oxide.

Although the formula $Fe_{2-x}WO_{6-3x/2}$ does not require the presence of any Fe^{2+} to maintain charge-balance, the data presented so far have not unequivocally clarified the uncertainty concerning the oxidation states of iron present in iron tungstate (5, 6). It therefore seems pertinent to consider the Moessbauer spectra in more detail.

The Moessbauer spectra recorded for the iron tungstates at room temperature showed a quadrupole doublet, sometimes accompanied by a magnetic contribution from α-Fe_2O_3 (Table 1). While the doublet could be fitted to a model based on a single quadrupole-split resonance from an iron(III) species, the linewidths (0.36 mm s^{-1}) are larger than were observed (0.28 mm s^{-1}) from the room temperature spectra of iron-doped chromium tungstates, and that the fits are not completely satisfactory (Table 1). This would appear to indicate that the iron tungstate spectra reflect the contributions of more than one iron species having slightly different environments. It seems reasonable that these spectra could arise from two iron(III) sites characterized by different quadrupole splittings and similar isomer shifts and this alternate fit (Table 1) is shown in Fig. 2(*a*).

Perhaps a more realistic description would be of a number of slightly different Fe(III) sites and such a model would be consistent with the structure of iron tungstate. The material is composed of "zig-zag" chains of edge-sharing oxygen octahedra with one-third of the chains containing only iron whilst the remainder comprise alternating W- and Fe-centred octahedra (4, 7, 8). Hence it is possible that there might be slight differences between the electric field gradients at the iron nuclei in the two types of chains.

However, Leiva *et al.* (7, 8) suggest the presence of a partially reduced iron species with delocalization of the d^6 electron of the Fe(II) over all iron atoms. If hopping due to this delocalization is slow on the Moessbauer time scale, then a separate Fe^{2+} doublet should be observed. No such doublet was detected. Rapid averaging of electrons between Fe^{2+} and Fe^{3+} environments should result in increased isomer shifts and quadrupole splittings. The data are not abnormal for Fe^{3+} environments so this second possibility is also unlikely. Since magnetic field strengths are very dependent upon oxidation states, spectra were recorded from materials of composition $Fe_{1.84}WO_{5.76}$ and

Can. J. Chem. Downloaded from www.nrcresearchpress.com by 93.93.197.157 on 09/07/12
For personal use only.

TABLE 1. Moessbauer data obtained for iron tungstates at 298 K

Sample	No. of sites	δ^a (mm/s)	ΔE_Q (mm/s)	Γ (mm/s)	ϵ (mm/s)	H^b (T)	Contribution (%)	χ^2/ degree of freedom
Fe_2WO_6	2	0.48	0.68	0.39	—	—	86.2	1.12
		0.38	—	0.30	−0.05	51.7	13.8	
Fe_2WO_6	2	0.45	0.65	0.36			56.1	1.21
annealed		0.42	—		−0.11	51.6	43.9	
$Fe_{1.68}WO_{5.52}$	1	0.41	0.67	0.36	—	—	100	0.93
	2	0.40	0.78	0.31[c]	—	—	48.6	0.78
		0.43	0.56	0.31	—	—	51.4	
$Fe_{1.88}WO_{5.82}$	1	0.41	0.67	0.36	—	—	100	1.73
	2	0.40	0.78	0.32[c]	—	—	49.0	1.17
		0.41	0.56	0.32	—	—	51.0	
$Fe_{1.92}WO_{5.88}$	1	0.41	0.67	0.36	—	—	100	1.71
	2	0.40	0.79	0.32[c]	—	—	48.6	1.12
		0.41	0.55	0.32	—	—	51.4	

[a]Isomer shifts are relative to α-Fe at 298 K with errors of ±0.01 mm/s.
[b]Errors on the magnetic hyperfine fields are ±0.5 T.
[c]Linewidths were constrained to be equal.

TABLE 2. Moessbauer parameters[a] of iron chromium tungstates and iron tungstates at 4.2 and 298 K

Sample	Temperature (K)	δ (±0.01 mm/s)	ΔE_Q (±0.01 mm/s)	ϵ (±0.01 mm/s)	H (T)	e (deg)
$Fe_{1.5}Cr_{0.5}WO_6$	298	0.41	0.27			
	4.2	0.51		−0.07	51.7	35
$Fe_{1.25}Cr_{0.75}WO_6$	298	0.40	0.27			
	4.2	0.51		−0.07	50.7	33
$Fe_{1.0}Cr_{1.0}WO_6$	298	0.40	0.27			
	4.2	0.51		−0.05	51.2	40
$Fe_{0.75}Cr_{1.25}WO_6$	298	0.40	0.24			
	4.2	0.54		−0.05	50.6	36
$Fe_{0.5}Cr_{1.5}WO_6$	298	0.40	0.25			
	4.2	0.51		−0.06	49.2	39
$Fe_{0.25}Cr_{1.75}WO_6$	298	0.40	0.24			
	4.2	0.44		−0.01	45.4	—
$Fe_{1.84}WO_{5.76}$	4.2	0.53		−0.09	50.6	67
$Fe_{1.68}WO_{5.52}$	4.2	0.50		−0.09	51.0	67

[a]Linewidths at room temperature: 0.28 ± 0.01 mm/s; 4.2 K: 0.46 ± 0.02 mm/s.

$Fe_{1.68}WO_{5.52}$ at 4.2 K. The latter, depicted in Fig. 2(*b*) can clearly be described as comprising six well-resolved lines which are expected from a magnetically ordered Fe^{3+} material. It is interesting that the linewidths in the spectrum from $Fe_{1.68}WO_{5.52}$ are larger than those from $Fe_{1.84}WO_{5.76}$. This implies that the higher concentration of iron and oxygen vacancies, which might be expected in the more iron-deficient solid, induces a small magnetic field distribution. Since iron(II) species exhibit much smaller magnetic hyperfine fields than those of iron(III) species, it seems that the Moessbauer data obtained at 4.2 K, and being typical for Fe^{3+} argue against the presence of significant concentrations of reduced iron species in these materials.

Iron–chromium–tungsten oxides

Iron chromium tungstates with nominal compositions of $Cr_{2-y}Fe_yWO_6$ ($0 < y \leq 2$) were prepared, and the products were examined by powder X-ray diffraction. Materials in which $y \leq 1.7$ gave powder X-ray diffraction patterns similar to that reported (14) for Cr_2WO_6 and characteristic of a trirutile-type material. Leiva *et al.* (7, 8) have determined the lattice parameters of similar solids and reported that the materials were solid solutions of iron in chromium tungstate. Materials containing greater concentrations of iron were reportedly multiphasic. Our current data are consistent with those previous reports (7, 8), since powder X-ray diffraction patterns for samples of nominal compositions $1.7 < y < 1.9$ showed evidence for the presence of two phases with structures based on those of chromium tungstate (14) and iron tungstate (4). Although powder X-ray diffraction detected traces of $Fe_{1.95}Cr_{0.05}O_3$ in the solid, when $y = 1.95$, rather than a chromium tungstate-type phase, this does not necessarily imply that solid solution formation of Cr in iron tungstate has occurred. Indeed, given the poor sensitivity of powder X-ray diffraction to minor phases, it would be more reasonable to assume that the concentration of the Cr_2WO_6-type material detected in all other iron-rich solids has merely decreased beyond the detectability limit of the technique.

The Moessbauer data recorded at 298 and 4.2 K of the iron–chromium–tungsten oxides are summarized in Table 2. The chemical isomer shifts, δ, and quadrupole splittings, Δ, recorded at room temperature, are characteristic of iron(III) in

Can. J. Chem. Downloaded from www.nrcresearchpress.com by 93.93.197.157 on 09/07/12
For personal use only.

only slightly distorted octahedral environments. The first order approximation of the quadrupole splittings as defined in ref. 15 was used

$$[1] \quad \epsilon = \frac{e^2qQ}{4} \frac{(3\cos^2\theta - 1)}{2}$$

to determine θ, the angle between V_{ZZ} and the axis of magnetization. The quadrupole interaction (ϵ) was calculated from the line positions (x) in the liquid helium temperature spectra with the help of expression (16)

$$[2] \quad \epsilon = \tfrac{1}{8}[2(x_1 + x_6) - (x_2 + x_3 + x_4 + x_5)]$$

An inspection of the data in Table 2 indicates that both ϵ and θ are generally independent of y in $Cr_{2-y}Fe_yWO_6$ although it is apparent that θ is greater than zero, the value found for Cr_2WO_6 (17). However, it is notable that the quadrupole interaction (ϵ) is larger in the iron tungstates, containing no chromium, than in the series $Cr_{2-y}Fe_yWO_6$ and this is consistent with the room temperature quadrupole splitting data (Table 1). The independence of the Moessbauer parameters, ϵ and θ, from y in the iron–chromium tungstates might seem surprising given that Moessbauer studies of other mixed metal oxide systems, in which chromium may be replaced by iron (1, 10, 18), have revealed novel relationships between relative concentrations of iron and chromium and the Moessbauer parameters, especially ϵ, θ (10, 18), and in some cases T_N, H, and Δ (9). The quadrupole splittings and chemical isomer shifts of the $Cr_{2-y}Fe_yWO_6$ series are also largely independent of the concentrations of iron and chromium, although Δ does appear to undergo a generally decreasing trend with increasing Cr content. This may reflect the decreased lattice distortion as detected by diminishing lattice parameters (7, 8).

It is interesting, however, that an inspection of the data pertaining to the magnitude of the effective magnetic field at the iron nuclei (Table 2) reveals different behaviour. It appears that increasing iron content is accompanied by a concomitant increase in H until the magnitude of the magnetic field strength exceeds that in ternary iron tungstate. However, it should be pointed out that, for values of $2 - y < 0.8$, the ordering temperature might be such that a fully developed hyperfine field is not observed at 4.2 K. Thus the data from iron chromium tungstates contrast markedly with that from the $Fe_{2-x}Cr_xTeO_6$ system in which H is independent of the Fe:Cr ratio while ϵ and θ show strong correlations. The large linewidths observed in the spectra of some of the materials are perhaps not surprising in view of similar data elsewhere (10) and reflect a field distribution induced by imperfect ordering of Fe and Cr.

Acknowledgements

The Natural Sciences and Engineering Research Council of Canada is thanked for financial support. Mr. F. H. Gibbs of the Institute for Materials Research is thanked for carrying out the thermal gravimetric analyses.

1. C. P. M. Barton, N. N. Greenwood, I. J. McColm, and R. J. D. Tilley. J. Solid State Chem. **16**, 265 (1976).
2. H. Pinto, M. Melamud, and H. Shaked. Acta Crystallogr. A**33**, 663 (1977).
3. R. Caruba, A. Baumer, R. Guillen, and J. R. Regnard. Bull. Mineral **105**, 246 (1982).
4. J. Senegas and J. Galy. J. Solid State Chem. **10**, 5 (1974).
5. H. Leiva, K. Dwight, and A. Wold. J. Solid State Chem. **42**, 41 (1982).
6. H. Leiva, K. Sieber, B. Khazai, K. Dwight, and A. Wold. J. Solid State Chem. **44**, 113 (1982).
7. H. Leiva, R. Kershaw, K. Dwight, and A. Wold. J. Solid State Chem. **47**, 293 (1983).
8. K. Sieber, H. Leiva, K. Kourtakis, R. Kershaw, K. Dwight, and A. Wold. J. Solid State Chem. **47**, 361 (1983).
9. T. Birchall and A. F. Reid. J. Solid State Chem. **13**, 351 (1975).
10. F. J. Berry, T. Birchall, C. D. Gibb, C. Frampton, and C. Hallett. Hyperfine Interactions. To be published.
11. T. Birchall, C. Hallett, and D. Hanzel. Hyperfine Interactions **28**, 455 (1986).
12. G. J. Long, T. E. Cranshaw, and G. Longworth. Moessbauer Effect Ref. Data **6**, 42 (1983).
13. K. Ruebenbauer and T. Birchall. Hyperfine Interactions, **7**, 125 (1979).
14. G. Bayes. J. Am. Ceram. Soc. **43**, 495 (1960).
15. T. C. Gibb. Principles of Mössbauer spectroscopy. Chapman and Hall, 1976. p. 161.
16. J. O. Artman, A. J. Muir, Jr., and H. Wiedersich. Phys. Rev. **173**, 337 (1968).
17. W. Kunnmann, S. La Maca, L. M. Corliss, and J. M. Hastings. J. Phys. Chem. Solids, **29**, 1359 (1968).
18. T. Birchall. J. Solid State Chem. **27**, 293 (1979).

Can. J. Chem. Downloaded from www.nrcresearchpress.com by 93.93.197.157 on 09/07/12
For personal use only.

Molar entropies at 80 K of sub-monolayer nitrogen films adsorbed on graphite from heat capacity measurement[1]

AKIRA INABA AND HIDEAKI CHIHARA

Department of Chemistry and Chemical Thermodynamics Laboratory, Faculty of Science, Osaka University, Toyonaka, Osaka 560, Japan

Received August 25, 1987

This paper is dedicated to Professor James A. Morrison

AKIRA INABA and HIDEAKI CHIHARA. Can. J. Chem. **66**, 703 (1988).

The heat capacity of nitrogen adsorbed on an exfoliated graphite (Grafoil GTA) has been measured between 3 and 80 K at surface coverages of $\frac{1}{6}$, $\frac{1}{3}$, $\frac{1}{2}$, $\frac{2}{3}$, and $\frac{5}{6}$ layers. The molar entropies are determined at 80 K. The effect of energetic heterogeneity of the graphite surface seems to be much less than that expected from the measurements of heats of adsorption. The isosteric heat of adsorption at zero coverage $q_{st}(0)$, for a hypothetical homogeneous graphite surface is estimated to be 9.8 kJ mol^{-1} at 80 K, which is in good agreement with that obtained from simulations performed at 75 K, 9.9 kJ mol^{-1}.

AKIRA INABA et HIDEAKI CHIHARA. Can. J. Chem. **66**, 703 (1988).

Opérant entre 3 et 80 K, avec des couvertures de $\frac{1}{6}$, $\frac{1}{3}$, $\frac{1}{2}$, $\frac{2}{3}$ et $\frac{5}{6}$ de couche, on a mesuré la capacité calorifique de l'azote adsorbé sur un graphite exfolié (Grafoil GTA). On a déterminé les entropies molaires à 80 K. Il semble que l'effet de l'hétérogénéite énergétique de la surface de graphite soit beaucoup moindre que celle qu'on pourrait prévoir à partir de mesure des chaleurs d'absorption. À 80 K, on a évalué que la chaleur isostérique d'adsorption à une couverture nulle, $q_{st}(0)$, pour une surface de graphite hypothétique homogène, est égale à 9,8 kJ mol^{-1}; cette valeur est en bon accord avec celle (9,9 kJ mol^{-1}) qui a été obtenue grâce à des simulations effectuées à 75 K.

[Traduit par la revue]

Introduction

Over the past decade, exfoliated graphite has become popular in adsorption studies (1) as one of the most appropriate substrates to meet conflicting requirements: large specific surface area and small extent of surface heterogeneity. The former makes it easy to do a variety of experiments and the latter allows us to distinguish properties intrinsic to adsorption on perfect substrates from those due to substrate heterogeneity. While a number of structural and other investigations have been made of molecular films physically adsorbed on this kind of graphite, much less attention has been paid to the energetics of adsorption prior to recent extensive work by Morrison and co-workers (2–7). They developed an elaborate calorimetric technique to accurately measure differential (isosteric) and integral heats of adsorption, q_{st} and Q, over wide ranges of surface coverage and of temperature.

As a logical extension of their work, we recently developed a calorimeter to directly measure heat capacity of adsorbed films with requisite accuracy. Since a complete analysis of gross thermodynamic properties had been first made on the nitrogen-on-graphite system at 79.3 K (2), where the nitrogen film is in a fluid phase (8), our first investigation was to measure the heat capacity of that system between 3 and 80 K for sub-monolayer coverages. An ac technique developed by Chan and co-workers could resolve the heat capacity with a precision of ±0.2% in their measurements on nitrogen films between 18 and 70 K (9). However, it cannot determine the absolute value of the heat capacity or the molar entropy, as they pointed out.

In this paper we are mainly concerned with the molar entropies and compare those at 80 K determined from our heat capacity measurements with those derived from the measurements of heats of adsorption (2). Our calorimeter vessel and heat capacity data will be fully described elsewhere. It is suggested that such an examination of the thermodynamical consistency would lead us to a better understanding of intrinsic/equilibrium properties of the adsorbed films.

Experimental

The specimen of Grafoil GTA (6.21 g), which is commercially available (Union Carbide Corp.), was taken from the same roll that was used before for measurements of heats of adsorption (2). Its specific surface was determined to be 24 m^2 g^{-1} (2, 6). The sheets were packed tightly into the calorimeter vessel and heated under a vacuum better than 3×10^{-4} Pa at 400°C.

The calorimeter vessel used was constructed of copper, contained graphite adsorbent, and carried platinum and germanium resistance thermometers and a heater. A copper fine-tube attached to the calorimeter vessel was pinched off after introduction of the sample gas through it.

Nitrogen of special grade (minimum 99.9999%) was obtained from Takachiho Kagaku Co., Ltd. and was used without further purification. The amount of the gas to be introduced was determined by using a calibrated bulb (410 cm^3) and a Baratron gage (0–1000 Torr[2] type), both of which were connected to the filling system. The accuracy of the measurement of the amount of gas was better than ±0.2%. The monolayer capacity of the Grafoil for nitrogen as estimated by the B.E.T. method was $n_a = 0.25$ mmol g^{-1} (6).

Heat capacities were measured between 3 and 80 K for surface coverages of $\frac{1}{6}$, $\frac{1}{3}$, $\frac{1}{2}$, $\frac{2}{3}$, and $\frac{5}{6}$ layers. To prevent the films from forming any nonequilibrium/metastable phases prior to the measurements, the adsorbed system was held at 80 K overnight and then cooled down slowly, typically at 1 K min^{-1}. As indications of thermal relaxation or spontaneous release of energy could not be detected throughout the measurements, the films were assumed to be in their equilibrium state at each temperature. Some of the measurements were performed with the reheated graphite specimen to test whether the specimen had collected impurities. However, no significant effect could be seen in the molar entropies obtained. The heat capacity of the adsorbed films was determined from the difference between that of the calorimeter, adsorbent, and gas, and that of the calorimeter and adsorbent only. This difference was very small, for example amounting to 0.2% of the total heat capacity at 80 K in the case of $\frac{1}{6}$ monolayer coverage.

[1]Contribution No. 129 from the Chemical Thermodynamics Laboratory.

[2]1 Torr = 133.322 Pa.

Can. J. Chem. Downloaded from www.nrcresearchpress.com by 176.9.209.113 on 09/07/12
For personal use only.

TABLE 1. Coverage dependence at 80 K of the molar entropies derived from heat capacities of N_2 on Grafoil GTA

n_a/mmol g^{-1}	S_a^C/J K^{-1} mol^{-1}
0.0422	106 ± 3
0.0870	93.6 ± 1.9
0.1261	88.1 ± 0.9
0.1665	81.5 ± 0.8
0.2051	74.5 ± 0.7

Results and discussion

Molar entropy determined from heat capacity measurement

The molar entropy S_a^C at 80 K was obtained from our experimental heat capacities and their extrapolation to below 3 K.

$$[1]\quad S_a^C(80\text{ K}) = \int_{3\text{K}}^{80\text{K}} (C/T)\,dT + S_a^C(3\text{ K})$$

where the heat capacity below 3 K was assumed to be represented by $C \propto T^2$. The results are summarized in Table 1 and plotted in Fig. 1 as a function of the coverage. An indication of the estimated error, which mainly came from the smallness of contribution to the overall heat capacity, is given by the vertical bars attached to specific plotted points. The initial decrease in entropy is usual and has been shown to be mostly due to the change in the configurational entropy S_c with coverage, which is represented by

$$[2]\quad S_c = R\left[-\ln\theta - \frac{1-\theta}{\theta}\ln(1-\theta)\right]$$

where θ is the surface coverage.

Molar entropy derived from heats of adsorption

From a knowledge of the free energy of adsorption (from the isotherm) and the heat of adsorption, the entropy S_a^Q of the adsorbed film can be readily calculated. The S_a^Q for nitrogen on Grafoil was calculated by Piper *et al.* (2) from their experimental data in the following way:

$$[3]\quad S_a^Q = S_g - \frac{Q}{T} - \frac{R}{V}\left(\int_0^V \ln p\,dV - V\ln p\right) - \frac{\alpha}{V}\int_0^V p\,dV$$

The entropy of the ideal gas, S_g, was calculated from the Sackur–Tetrode equation and the small corrections necessary for gaseous imperfection were made. Since their reference temperature of 79.3 K was chosen for convenience and has no particular meaning, the thermodynamic quantities that they obtained were converted to the values at 80 K to permit comparison between the two sets of values; their results at 80 K are also plotted in Fig. 1.

It is worth noting here that there are two factors involved in the evaluation of S_a^Q. One is that approach to equilibrium is a very slow process in adsorption experiments; in fact the slow temperature drift, either exothermic or endothermic, continues for hours, as reported for the ethylene/graphite system (7). The other factor is that if there is a hysteresis effect in the adsorption/desorption isotherm, the measurements of q_{st} would "see" only one branch of the hysteresis loop and would not correspond to the true equilibrium state.

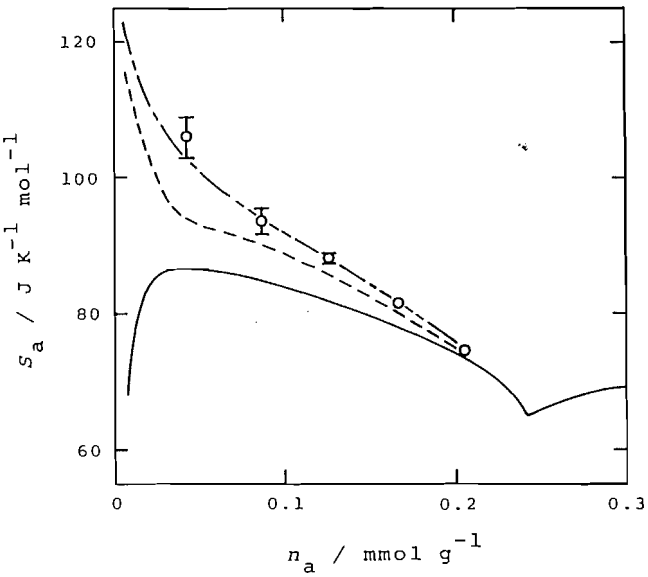

FIG. 1. Molar entropies of N_2 on Grafoil GTA at 80 K. ○, the present results; —, derived from experimental heats of adsorption (2); -------, estimate I; – – –, estimate II. See text for estimates I and II.

Comparison between the calorimetric and the isothermal entropies

It is evident that both the magnitude and the coverage dependence of the entropies S_a^Q of Piper *et al.* (2) are very different from S_a^C obtained from our heat capacity measurements, particularly at low coverages. In the case of bulk specimens, a difference between the calorimetric entropy and the statistical entropy, if any, is usually interpreted as indicating the presence of a zero-point entropy. In the present system, however, such an interpretation in terms of the existence of the zero-point entropy in the adsorbed nitrogen phase should be ruled out because $S_a^C > S_a^Q$.

It is evident from the initial decrease in q_{st} that there is some degree of surface heterogeneity. More active sites on the surface are therefore perferentially occupied by the adsorbed nitrogen, which may or may not be redistributed during the following equilibration process. The rationalization of the difference between the two entropies must be sought in the difference in state for which the entropy was measured and it could lead to better understanding of what is happening on the surface.

Thermodynamic consistency requires that the same value of the entropy should be obtained for the same state of aggregation of the same system. Therefore the fact that S_a^C is different from S_a^Q indicates that either the state or the system (or both) with which we are dealing in the two experiments must be different. With this in mind, there are several possibilities that need to be examined.

1. Surface conditions of graphite

The sample of graphite and its outgassing procedures were the same in both experiments. Furthermore, the results of the present experiment were completely reproducible. Even if there were some strategic impurities in the adsorbate gas that could be adsorbed preferentially on very active sites on the graphite surface, the discrepancy between S_a^C and S_a^Q cannot be explained because such impurities will be more strongly bound by the adsorbent, leading to a smaller heat capacity and therefore smaller S_a^C.

Can. J. Chem. Downloaded from www.nrcresearchpress.com by 176.9.209.113 on 09/07/12
For personal use only.

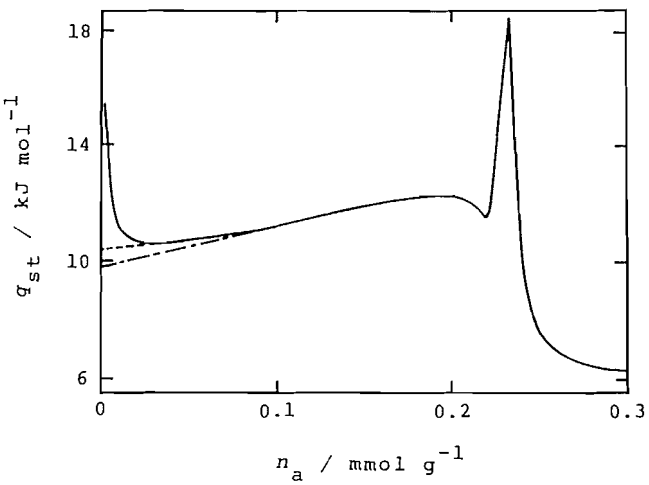

FIG. 2. Isosteric heats of adsorption of N_2 on Grafoil GTA at 80 K. —, experimental heats of adsorption (2); -------, estimate I; – – –, estimate II. See text for estimates I and II.

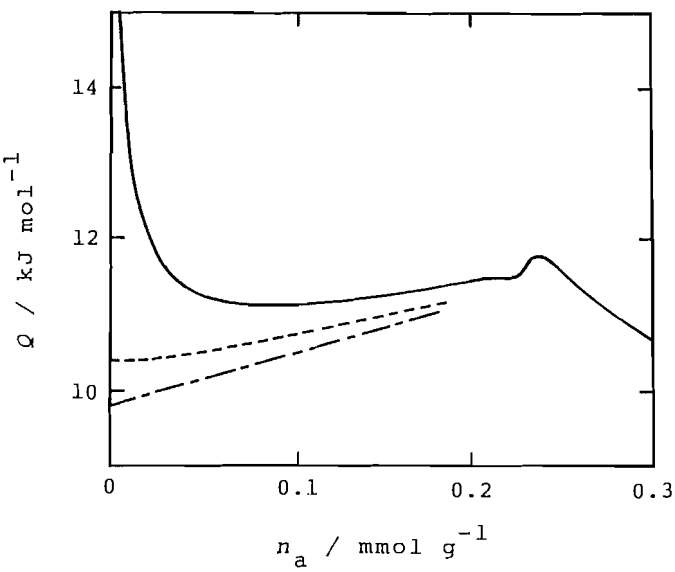

FIG. 3. Integral heats of adsorption of N_2 on Grafoil GTA at 80 K. —, experimental heats of adsorption (2); -------, estimate I; – – –, estimate II. See text for estimates I and II.

2. Lack of equilibrium

In the present experiment, almost all the nitrogen gas in the calorimeter was adsorbed at about 150 K during the cooling process and the calorimeter was aged at 80 K overnight; no appreciable heat effect was observed during the ageing process.

On the other hand, the "isothermal" adsorption at 80 K, as in the q_{st} measurements, is an extremely slow process with drifts of temperature and pressure continuing for hours. If the drift was not measured over a sufficiently long period, and if the exothermic drift was followed by an endothermic effect as was in fact observed in the case of ethylene on graphite, a possibility exists that the measured q_{st} was too large. A kind of ageing also took place in the q_{st} experiment because the calorimeter was cooled down to bring the temperature back to the predefined value. During such cooling the off-equilibrium could have been remedied but no monitoring was done. Lack of equilibrium at low coverages will have a persistent effect on S_a^Q for higher coverages becaue the q_{st} curve is integrated to obtain the integral heat of adsorption Q.

If the above hypothesis applies, it implies that the surface of the graphite has a much smaller degree of heterogeneity than one would assess from the coverage dependence of q_{st} (Fig. 2). We can then examine which q_{st}–coverage curve would reconcile the entropies S_a^C and S_a^Q.

Estimate I

A smooth extrapolation of q_{st}, which is illustrated by the dashed curve in Fig. 2, yields $q_{st}(0) = 10.4$ kJ mol^{-1}. In this estimate, the effect of too large q_{st} is assumed to become negligible beyond a surface coverage of $\frac{1}{6}$ layer. The corresponding integral heat of adsorption Q is plotted in Fig. 3. It should be noted that in the limit where $n_a = 0$, $q_{st}(0)$ and $Q(0)$ must be identical. We see that heats generated at low coverages are so large that their effect on Q makes a significant contribution even at higher coverages. It is evident from Fig. 1 that the S_a is even more sensitive.

Estimate II

Another estimate of $q_{st}(0)$ by a more or less linear extrapolation from higher coverages is possible, as illustrated by the dot-dashed curve in Fig. 2. Here the effect of off-equilibrium is supposed to remain up to $\frac{1}{3}$ layer. This estimate yields $q_{st}(0) = Q(0) = 9.8$ kJ mol^{-1} and reproduces our experimental molar entropies (Fig. 1) very well. As mentioned above, this behavior of the entropy is rather reasonable. Moreover, the estimated $q_{st}(0)$ at 80 K is in good agreement with that from the simulations performed at 75 K, 9.9 kJ mol^{-1} (10). Therefore estimate II gives a consistent overall picture of the properties of adsorbed nitrogen.

Although complete understanding of the behavior of the adsorbate at low coverages is still open to question, we believe that our values of molar entropies determined from the heat capacity measurements are acceptable for the intrinsic/equilibrium state of nitrogen films adsorbed on graphite.

Acknowledgments

This paper is dedicated to Professor James A. Morrison in appreciation of his friendship and of his distinguished contributions to science. We thank Mr. Tatsuya Shirakami for assistance with some of the experiments, and Professor J. A. Morrison and Professor M. L. Klein for helpful comments and guidance. This research was supported by a Grant-in-Aid for Scientific Research administered by the Ministry of Education, Science, and Culture of Japan.

1. J. A. MORRISON. Pure Appl. Chem. **59**, 7 (1987).
2. J. PIPER, J. A. MORRISON, C. PETERS, and Y. OZAKI. J. Chem. Soc. Faraday Trans. 1, **79**, 2863 (1983).
3. J. PIPER and J. A. MORRISON. Chem. Phys. Lett. **103**, 323 (1984).
4. J. PIPER, J. A. MORRISON, and C. PETERS. Mol. Phys. **53**, 1463 (1984).
5. J. PIPER and J. A. MORRISON. Phys. Rev. B, **30**, 3486 (1984).
6. A. INABA, Y. KOGA, and J. A. MORRISON. J. Chem. Soc. Faraday Trans. 2, **82**, 1635 (1986).
7. A. INABA and J. A. MORRISON. Phys. Rev. B, **34**, 3238 (1986).
8. J. K. KJEMS, L. PASSELL, H. TAUB, and J. G. DASH. Phys. Rev. Lett. **32**, 724 (1974).
9. M. H. W. CHAN, A. D. MIGONE, K. D. MINER, and Z. R. LI. Phys. Rev. B, **30**, 2681 (1984).
10. J. TALBOT, D. J. TILDESLEY, and W. A. STEELE. Faraday Discuss. Chem. Soc. **80**, 212 (1985).

Can. J. Chem. Downloaded from www.nrcresearchpress.com by 176.9.209.113 on 09/07/12
For personal use only.

The evolution of membranes

MYER BLOOM

Department of Physics, University of British Columbia, 6224 Agriculture Road, Vancouver, B.C., Canada V6T 2A6

AND

OLE G. MOURITSEN

Department of Structural Properties of Materials, The Technical University of Denmark, Building 307, DK-2800 Lyngby, Denmark

Received September 23, 1987

This paper is dedicated to Professor J. A. Morrison

MYER BLOOM and OLE G. MOURITSEN. Can. J. Chem. **66**, 706 (1988).

Consideration of the influence of cholesterol on the physical properties of biological membranes leads to the conclusion that cholesterol increases the thickness of fluid membrane bilayers without appreciably increasing the microviscosity component of membrane fluidity. At sufficiently high cholesterol concentrations, the gel–liquid crystalline phase transition is completely eliminated in phospholipid–cholesterol mixtures and the system has the properties of a two-dimensional liquid over a wide range of temperatures. It is proposed that with the evolution of cholesterol and related sterols in an oxygen-rich atmosphere, the resulting modification of physical constraints on membrane properties made it possible for new evolutionary driving forces to manifest themselves leading to the peculiar properties of plasma membranes of eucaryotic cells.

MYER BLOOM et OLE G. MOURITSEN. Can. J. Chem. **66**, 706 (1988).

Si on examine l'influence du cholestérol sur les propriétés physiques des membranes biologiques, on est amené à conclure que le cholestérol augmente l'épaisseur des doubles couches des membranes fluides sans augmenter d'une façon appréciable la composante de la microviscosité de la fluidité de la membrane. A des concentrations de cholestérol suffisamment élevées, la transition de la phase cristalline gel–liquide est complètement éliminée des mélanges phospholipide–cholestérol et, pour un grand intervalle de températures, le système possède les propriétés d'une liquide bi-dimensionnel. On est amené à proposer que, avec l'évolution du cholestérol et des stérols apparentés dans un atmosphère riche en oxygène, la modification qui résulte de contraintes physiques sur les propriétés de la membrane fait qu'il est possible pour de nouvelles forces évolutionnaires de se manifester; ceci provoque l'apparition de propriétés particulières pour les membranes plasmatiques des cellules eucaryotices.

[Traduit par la revue]

Introduction

The nature of the three-dimensional structure of integral membrane proteins (1–3), the insights on the molecular evolution of cholesterol provided by Bloch (4–6), and the interpretation of deuterium nuclear magnetic resonance (^{2}H nmr) studies of the interaction between phospholipid molecules and integral membrane proteins (7–11) lead us to propose that the presence of cholesterol, or related sterols where appropriate,[1] modified the physical properties of membranes in a manner which was crucial to the evolution of eucaryotic cells into their present form.

At least two stages of membrane evolution have taken place. The *first stage* accounts for most natural membranes which do not contain cholesterol such as those of procaryotic cells and most organelles of eucaryotic cells. The *second stage* involves the evolution of eucaryotic cells or, at least, the plasma membranes of eucaryotic cells, upon the accumulation of oxygen in the atmosphere (12). The lipid composition of the plasma membranes of eucaryotic cells invariably includes a substantial fraction of cholesterol. Furthermore, Bloch (4, 5) has demonstrated that cholesterol evolved upon the appearance of oxygen in the atmosphere. He has speculated that the biological advantage associated with cholesterol may be due to the "reduced fluidity" or "increased microviscosity" which, it is claimed (13) the addition of cholesterol imparts to the liquid crystalline state of phospholipid bilayer membranes.[2] The discovery of hopanoid, triterpene derivatives in some procaryotic cells and in the form of "molecular fossils" of ancient times has led to the suggestion (14, 15) that these relatively rigid, anaerobically evolved, amphiphilic molecules play a similar "membrane reinforcement" role in some procaryotes to that played by aerobically evolved sterols such as cholesterol in eucaryotes.

In this paper, we propose that the biosynthesis of cholesterol in an aerobic atmosphere removed a bottleneck in the evolution of eucaryotic cells. Our proposal, which concerns a crucial evolutionary role played by the physical properties of membranes, can be related to the broad, phenomenological characterization of the evolution of eucaryotic cells given by Cavalier-Smith (16, 17). He identifies "twenty-two characters universally present in eucaryotes and universally absent from procaryotes" and presents detailed arguments that, of these, the advent of exocytosis (and endocytosis) is the most likely to have provided the driving force for the evolution of eucaryotic cells into their modern form. As described below, we have been led via an unconventional interpretation of measurements of physical properties of membranes to identify a possible physical bottleneck to cytosis which was removed by the appearance of cholesterol. We hypothesize that, in addition to influencing the cohesive strength of membranes, the main role of cholesterol in this evolutionary step was to relax an important constraint on

[1]The word "cholesterol" as used in this paper should sometimes be interpreted as "cholesterol or related sterols". The "related sterols" may be ergosterol in plants or precursors to cholesterol and ergosterol such as lanasterol or cycloartenol (5).

[2]Although we are concerned here with the influence of cholesterol on the physical properties of membranes, it should be noted that cholesterol may play a role in metabolic functions as well (5).

Can. J. Chem. Downloaded from www.nrcresearchpress.com by 93.93.197.157 on 09/07/12
For personal use only.

membrane thickness imposed by the biological necessity of membrane fluidity. In attempting to establish the validity of our hypothesis, we have been confronted with a remarkable lack of relevant information on basic physical properties of membranes. The filling of this information vacuum will lead to a better understanding of membrane properties in addition to checking our hypothesis.

Relationship between membrane evolution and cellular evolution

It is generally agreed that *procaryotic* cells came into existence almost 4×10^9 years = 4 GA ago (1 GA = 10^9 years). Procaryotic cells have only a single membrane and no nucleus. By contrast, most eucaryotic cells which exist today contain many organelles, each encapsulated within its own membrane. Our knowledge of the evolutionary relationship between procaryotic and eucaryotic cells is very fuzzy but it has advanced considerably during the past decade (18). Ten years ago, it was believed (19) that a procaryotic host cell spawned the first eucaryotic cell about 1.5 GA ago, approximately the time at which the earth's hydrosphere is thought to have become oxidizing (20). Cogent arguments have been made that the procaryotic to eucaryotic step occurred via a sub-line of wall-less anerobic procaryotes that gained the capacity for endocytosis (16, 17, 19). It is now known that there exist two distinct kingdoms of procaryotes called "eubacteria" and "archaebacteria" (18). These bacteria have quite different cytological and physiological properties from each other, operate optimally under different environmental conditions and have only distant and uncertain evolutionary linkages (18). If they do have a common ancestor, they parted in the early stages of cellular evolution. Furthermore, from an evolutionary standpoint, eucaryotic cells are as distant from eubacteria and archaebacteria as each of them is to the other.

The impetus to the more quantitative and searching examination of evolutionary connectivity at the cellular level that has taken place in recent years has been supplied by the development of new methods of quantitative analysis of sequences of nucleic acids. In particular, the nucleic acid sequencing of ribosomal RNA (rRNA) has proven to be an effective molecular chronometer over the time scales, of order GA, of importance in bacterial and cellular evolution. In a recent comprehensive review of the subject, Woese (18) predicts that nucleic acid sequencing will stimulate greatly expanded knowledge of cellular evolution in the near future.

A real understanding of the evolution of any biological system requires not only knowledge of changes in genetic characteristics but also insight into the interaction between the biological system and its surroundings. Whether or not a random change in the genes gives rise to a viable biological modification or not is determined by the environmental interactions. Contact between a cell and its surrounding environment is mediated by the plasma membrane, i.e. the outer membrane of the cell. Systematic differences exist between the composition of the plasma membranes of eubacteria, archaebacteria, and eucaryote cells (18, 21). We believe that these differences have an important evolutionary significance. We are now able to attempt an explanation of the relationship between membrane evolution and cellular evolution for eubacteria and eucaryote cells because of improvements in our understanding of the physical properties of biological membranes which have taken place during the past decade. We shall not discuss archaebacteria, partly because the characterization of the physical properties of their membranes has not yet been adequately developed (21). More important, the phospholipid composition of the plasma membranes of eucaryotic cells resembles that of eubacteria but not that of archaebacteria. Thus, if our proposals concerning the importance in the evolution of eucaryotic cells of the modification of the physical properties of their plasma membranes by sterols are confirmed, this would imply a closer evolutionary relationship between eucaryotic cells and eubacteria than archaebacteria.

Relationship between biological activity and membrane fluidity, microviscosity, segmental orientational order, rigidity, and thickness

It is now widely recognized and accepted that biological activity requires that membranes be in their fluid (liquid crystalline) state. When characterizing membrane fluidity, various authors sometimes use terms such as rigidity and microviscosity without adequately defining them, and often they are used in different senses. The confusion in describing the mechanical properties of membranes is caused by the conspicuous anisotropic nature of bimolecular fluid membrane sheet. To avoid ambiguities we shall here clarify the use of these terms and then review the influence of cholesterol on membrane fluidity.

Pure phospholipid bilayer membranes undergo a phase transition upon heating from a solid "gel" phase to a fluid "liquid crystalline" phase. The phase transition is accompanied by two major dramatic changes (7, 22): (*1*) increased conformational freedom and flexibility of the acyl chains leading to decreased segmental orientational order and decreased bilayer thickness, and (*2*) increased lateral diffusivity of the lipid molecules parallel to the plane of the membrane and onset of a more rapid rotational diffusion about the long molecular axis corresponding to decreased microviscosity. The higher *fluidity* of the high temperature phase is therefore caused by changes in two different components, namely orientational order and microviscosity.

In the case of pure phospholipid bilayer model membranes, there is a strong correlation between orientational order and microviscosity but this is not always the case. A prominent example central to our theme is that the introduction of cholesterol into phospholipid bilayer membranes increases the orientational order[3] but does not increase the microviscosity appreciably (24–26). The requirement of fluidity for biological activity should therefore be interpreted in terms of the microviscosity aspect of fluidity.

This interpretation of the influence of cholesterol is different from that given by Dahl *et al.* (13). They found a correlation between the biological viability of various sterols in the cholesterol evolutionary chain and increased "microviscosity". However, this correlation was made on the basis of steady state polarized fluorescence measurements. It is now known that such measurements on an anisotropic system do not actually measure microviscosity but rather a combination of microviscosity and the orientational order of the fluorescent probe (27, 28). A fluorescence depolarization study of membranes containing cholesterol has been carried out recently and the results analysed

[3]The associated decrease in the average membrane surface area per polar head is often called "condensation" in the literature (see, e.g. ref. 23).

Can. J. Chem. Downloaded from www.nrcresearchpress.com by 93.93.197.157 on 09/07/12
For personal use only.

Can. J. Chem. Downloaded from www.nrcresearchpress.com by 93.93.197.157 on 09/07/12
For personal use only.

with the anisotropic orienting potential included (29). In the light of these results, we can now re-interpret the earlier fluorescence measurements as indicating relatively little influence of cholesterol on the microviscosity component of the fluidity while giving a substantial increase in thickness as indicated by the orientational order of the lipid chains.

In some cases the words "increased rigidity" have been used to characterize increased "orientational order" or "microviscosity". It is clear that both cannot always be correct. We would prefer to reserve the word "rigidity" in membranes as a description of the resistance of the bilayer to shear. Since the hydrophobic interior of a fluid membrane is well approximated as an incompressible fluid, small values of "area compressibility" imply small fractional changes in membrane thickness under a given change in stress. Evans and Needham (30) have shown that the addition of cholesterol (CHOL) to a sample of dimyristoylphosphatidylcholine (DMPC) vesicles resulted in a greatly reduced membrane area compressibility. At the same time, the phase transition was eliminated for molar ratios CHOL:(CHOL + DMPC) > 0.125, while the vesicles behaved like liquids with zero surface shear restoring forces even at temperatures well below the phase transition for pure DMPC. The combination of decreased area compressibility and zero surface shear restoring forces is perfectly compatible with the two dimensional character of the membrane fluidity.

A close relationship exists between the average orientational order parameter of the acyl chains and the membrane thickness (7, 10, 31) which makes it possible to estimate the membrane thickness using ^{2}H nmr measurements. Such estimates should be reasonably good whenever the symmetry axis for orientational averaging is normal to the bilayer surface, i.e. they would not be reliable for the gel phase of pure phospholipid bilayers where the chains are tilted with respect to the bilayer normal, but the estimates would be good for the liquid–crystalline phase or for the gel phase close to the melting point for membranes with impurities such as cholesterol present which remove the chain tilt.

The indirect determination of membrane thickness using ^{2}H nmr is potentially very useful since there seems to be no reliable direct means of measuring membrane thickness for either synthetic membranes with impurities or biological membranes. Direct measurements using diffraction methods require that the membrane samples be prepared in the form of good quality smectic liquid crystals having long range order so that several orders of Bragg reflection may be obtained. This has been achieved for pure phospholipid bilayer systems (32, 33) but seems to be difficult for impure systems judging from the absence of good experimental data. Even in the pure systems, some differences of opinion exist on the interpretation of the diffraction data.

A lattice model has been used (31, 34) to derive a relationship between the separation, d, of the first carbon atoms in the acyl chains of the two leaflets, each acyl chain having n C—C bonds, in terms of the maximum separation, $d_{max} = 2.5n$ Å, and the magnitude of the average acyl chain orientational order parameter, $\langle S \rangle$,

$$[1] \quad d = d_{max}\,(0.5 + |\langle S \rangle|)$$

The quantity $|\langle S \rangle|$ is easily obtained from the average ^{2}H splitting of lipids with perdeuterated acyl chains, i.e. from the first moment of the distribution of quadrupolar splittings (35, 36).

Although the lattice model leading to eq. [1] is a simple one, its predictions are in agreement with neutron diffraction studies of ^{2}H-labelled phospholipid acyl chains in model membranes (37). Furthermore, the value of $|\langle S \rangle| = 0.164$ at 50°C for dipalmitoylphosphatidylcholine (DPPC) combined with the value of $d = 26$ Å at 44°C from the X-ray diffraction experiments of Lewis and Engelman (33) would require a value of $d_{max} = 39$ Å corresponding to $n = 39/2.5 = 15.6$, a very reasonable value for an acyl chain of 16 carbons. Reasonable results are also obtained using the measurements of Cornell and Separovic (32) for DPPC.

The most complete measurements of the influence of cholesterol on ^{2}H nmr splittings in a model membrane have been made by Vist (38). His measurements confirm those reported previously by Stockton and Smith (23) and Oldfield (8). For example, the average ^{2}H nmr splitting in DPPC increases by about 60% at 50°C when 25% cholesterol is added (38) so that $|\langle S \rangle|$ changes from about 0.16 to about 0.26. According to eq. [1], this corresponds to a change in d from 26 Å to about 30 Å. Even more striking is the behaviour of erythrocyte membranes where the influence of the large cholesterol concentration was found to give rise to a fluid membrane down to −5°C (39). The average quadrupolar splitting of DPPC in the erythrocyte membranes increased monotonically between 50°C and −5°C to an effective hydrophobic thickness of $d \simeq 35$ Å which is approximately 90% of the maximum value attainable with fully extended acyl chains. Yet, the lipid component of erythrocyte membranes is fluid as indicated by their ^{2}H nmr spectra (39) and measurements of the lateral mobility of lipid probes (25).

In summary, then, we list the effects of physiological concentrations of cholesterol on phospholipid bilayer model membranes.

1. The gel–liquid phase transition is eliminated.
2. No static surface rigidity is observed over a wide temperature range indicating fluid-like macroscopic properties.
3. Translational and rotational diffusion constants are not strongly affected in the high temperature region indicating a fluid-like microviscosity.
4. The area compressibility is greatly reduced leading to greater cohesion and reduced permeability.
5. The orientational order increases indicating greater membrane thickness and "condensation" of the membrane lipids.

Membranes in procaryotic cells – the first stage of membrane evolution

Most biological activity takes place at moderate temperatures and, in particular, not at temperatures well above 37°C. A consequence of this is that biological membranes must operate at moderate temperatures. When combined with the requirement of fluidity, this implies that the thickness of bilayers composed of lipids extracted from membranes which do not contain cholesterol must fall within a narrow range of values. For example, lipid molecules with longer saturated acyl chains lead to thicker bilayers (33) but also higher gel–liquid crystalline phase transition temperatures. Thus, membranes composed mainly of longer lipids would be in the gel phase at moderate temperatures. Shorter lipids would not form stable bilayers. Longer lipids having unsaturated bonds give rise to thinner bilayers than saturated chains of the same length (33) so that the thickness of fluid bilayers of such lipids is not so different at moderate temperatures from that due to shorter saturated chains.

The structure and amino acid sequence of integral membrane proteins indicate that they are predominantly made up of a number of α-helical segments which span the lipid bilayer. On

Can. J. Chem. Downloaded from www.nrcresearchpress.com by 93.93.197.157 on 09/07/12
For personal use only.

the basis of known primary sequences and diffraction studies, it has been demonstrated that the positions of the hydrophilic and hydrophobic parts of integral membrane proteins tend to be correlated with their counterparts in the lipid molecules comprising the membrane bilayer (1–3). In addition, ^{2}H nmr studies on a large number of bacterial and reconstituted membranes (see, e.g. Table 6 of ref. 9) all gave the unanticipated result that $<S>$ of the acyl chains in the fluid phase was unaffected by the presence of physiological concentrations of proteins. These results lead to the following hypothesis which, we suggest, governs some important aspects of the evolution of membranes in procaryotic cells.

Hypothesis 1. Integral membrane proteins operate in an optimum manner in membranes whose natural hydrophobic thickness matches the hydrophobic thickness of the protein.

We have pointed out in a theoretical analysis of the significance of the matching of the hydrophobic regions of lipids and proteins (10) that the ^{2}H nmr experiments were all carried out on lipids and proteins whose hydrophobic thickness were approximately matched. Thus the addition of such proteins would not modify bilayer thickness, and hence $<S>$, providing that Hypothesis 1 was correct. Strong support of Hypothesis 1 also comes from studies of the activity of a variety of membrane enzymes (40, 41) and ion-channels (42) as a function of membrane thickness. By manipulating the bilayer hydropobic thickness either by changing the lipid chain length or by incorporating alkanes and anaesthetics (43, 44) it is invariably found that the activity is optimized at a certain thickness. Perhaps the most striking confirmation of Hypothesis 1 comes from a systematic study of the influence of an integral membrane protein on the phase transition temperatures of phospholipid bilayer model membranes having different acyl chain lengths (45).

The evolutionary driving force which leads to the validity of this hypothesis presumably comes from the superiority of a strain-free membrane, under normal operating conditions, for survival under changes in environmental conditions, e.g. changes in stress, and for the optimum function of protein dynamics in analogy with cytoplasmic proteins (46).

Although we have emphasized that life at moderate temperatures would promote membranes having a relatively narrow range of thickness values, it is well known that some species of procaryotic cells are viable at abnormal temperatures and pressures (see, e.g. ref. 47). Hypothesis 1 also applies to such systems, of course. Lipids capable of being fluid under a certain range of external constraints can provide the basis of cellular membranes providing that appropriate integral membrane proteins can be evolved which match their thickness.

Whatever the cellular system, the capacity of most of the integral membrane proteins to function properly will be severely limited if the stresses on the membrane are extended beyond the range within which the membrane retains its fluid property. We believe that a sensitive parameter in relation to membrane fluidity is membrane thickness. Pure lipids undergo large discontinuous changes in membrane thickness as a result of the gel–liquid crystalline phase transition. Thus, some physical processes which require large excursions in membrane thickness may tend to stimulate a phase transition. This would be true of mixtures of phospholipids with short and long chains because of phase separation effects.

It is striking that, although procaryotic cells were present in an anaerobic atmosphere for more than 10^9 years they did not evolve any cells with organelles and/or compartmentalized nuclear material. Anaerobic molecular evolution did take place in procaryotic cells. We suggest that although the recently discovered triterpene derivatives evolved and are capable of replacing some aspects of cholesterol's influence on membrane properties (14, 15), they lacked the ability possessed by cholesterol to facilitate a crucial stage in the evolution of the type of internal structures associated with eucaryotic cells.

Plasma membranes in eucaryotic cells — the second stage of membrane evolution

In his review of the distinction between the properties of procaryotic and eucaryotic cells, Cavalier-Smith (17) identifies twenty-two universal eucaryotic characteristics which are universally absent from procaryotic cells. It is likely that a small number of these characteristics, possibly a single one, represent the driving force for the evolutionary development of eucaryotic cells as we see them today. We propose here that, with the appearance of large amounts of molecular oxygen in the earth's atmosphere between 2.3 and 1.5 GA ago (20), a bottleneck in the evolution of eucaryotic cells was removed by the resultant incorporation of sterols in the plasma membrane.

In an earlier paper, Cavalier-Smith (16) argued that the advent of exocytosis (and endocytosis) which makes it possible for a cell to export (or import) material at a much faster rate, could provide the "evolutionary driving force" to explain the development of the other universal eucaryotic characteristics. He suggested that cytosis would have been inhibited by the rigid peptidoglycan cell wall present in many procaryotic cells and universally absent in eucaryotic cells (17). This would require the replacement of cell walls by a still strong, but more flexible plasma membrane. We propose here that the development of a plasma membrane having suitable physical properties only became possible with the appearance of molecular oxygen, which gave rise to the evolution of sterols leading to cholesterol and related sterols (4, 5). We propose in a second hypothesis below that the crucial physical property imparted to membranes by cholesterol was its ability, described in an earlier part of this paper, to increase the thickness of fluid membrane bilayers by a large amount without appreciably increasing the microviscosity component of membrane fluidity.

Hypothesis 2. The evolution of eucaryotic cells required the evolution of plasma membranes containing cholesterol or related sterols and thus capable of maintaining their fluidity and integrity as membranes over a wide range of external constraints.

Implicit in this hypothesis is the idea that the process of cytosis requires membrane stretching and/or changes of local membrane curvature which would disrupt the integrity of the membrane in the absence of fluid-like microviscosity. Such fluid-like properties would allow large membrane curvature without abnormal increases in permeability. Presumably, this desirable property would be facilitated by rapid redistribution of molecular species in response to local stresses as discussed recently by Sackmann *et al.* (48).

Eucaryotic cells are on the average one order of magnitude larger in linear extension than procaryotic cells. The mechanical strength required for supporting larger cells could well be provided by cholesterol-containing plasma membranes. In fact, it has recently been demonstrated in model membranes that for a given fluidity, vesicle fusion is facilitated and larger vesicles are stabilized for increased acyl chain orientational order induced by cholesterol (49).

Can. J. Chem. Downloaded from www.nrcresearchpress.com by 93.93.197.157 on 09/07/12
For personal use only.

Experimental considerations

Further support or rejection of the conjectures concerning membrane evolution presented in this paper will require more information on the thermodynamic, mechanical, and dynamic properties of mixtures of lipids, sterols, and proteins as well as natural membranes. Here are a few useful questions and studies which could be approached in the laboratory.

It would be of interest to complement the study of fluorescence depolarization measurements in membranes containing a series of precursors of cholesterol (13) with other measurements of the type discussed earlier in this paper such as ^2H nmr calorimetry, and micromechanics, where possible. If the evolution of sterols in membranes to the biologically optimized forms of cholesterol and ergosterol took place for the type of physical reason we have postulated, it may be possible to identify the crucial physical parameters from a systematic study of model systems. In this respect, some triterpene derivatives such as the hopanoid molecules should be included in the study since these molecules would be expected to be further removed from cholesterol in their crucial physical properties. Some scattered measurements on such properties have been reported, but we make no attempt to review them here since none of them represent complete studies and they have not been focussed in relation to our hypotheses.

It would be highly desirable to carry out a comparative study of the phase diagrams of a mixture of phospholipids with a selected hopanoid and with a selected primitive sterol such as lanosterol. This might explain the observation (50) that, with the exception of tetrahymanol in a ciliate, hopanoids, or similar cyclization products of squalene do not occur as components in membranes of eucaryotic cells.

Experimental studies of the phase diagrams of lipid–cholesterol mixtures have been carried out using a variety of techniques, including ^2H nmr (38, 51), electron spin resonance (52), electron microscopy (53), and micromechanical measurements on individual vesicles (30). In the case of DPPC–cholesterol mixtures, a new fluid phase, sometimes called the "B phase" (51), has been shown to occur at concentrations of cholesterol above about 22%. Between about 8% and 20% cholesterol, the system consists of a mixture of the B phase and either the gel phase for $T < 41°C$ or the liquid crystalline phase for $T > 41°C$. A theoretical analysis of the cholesterol–DPPC system (54) has led to a phase diagram capable of fitting the available experimental observations on the DPPC–cholesterol system (38, 51–53) very well (see Fig. 1). Ipsen *et al.* (54) have characterized the gel phase of the pure lipid as a "solid-ordered phase" (so) and its liquid crystalline phase a "liquid-disordered (ld) phase". The B phase is described as a "liquid ordered (lo) phase" in which the acyl chains are ordered due to the lipid–cholesterol interaction while two dimensional fluidity is retained. This ordering gives a fluid phase of higher cohesive strength (30), presumably because of the increased effectiveness of the van der Waals interactions between neighbouring lipid molecules. The B phase seems, therefore, to have desirable properties for the plasma membranes of eucaryotic cells. The B-phase membranes are fluid over a wide temperature range, corresponding to a large change in membrane thickness, and have great cohesive strength. They have no phase transition corresponding to the gel–liquid crystalline (so–ld) transition which occurs in the absence of sterols.

It is possible that the evolution of sterols in membranes was driven by the advantage of the B phase appearing at the lowest concentration of sterol. This conjecture should be easy to test

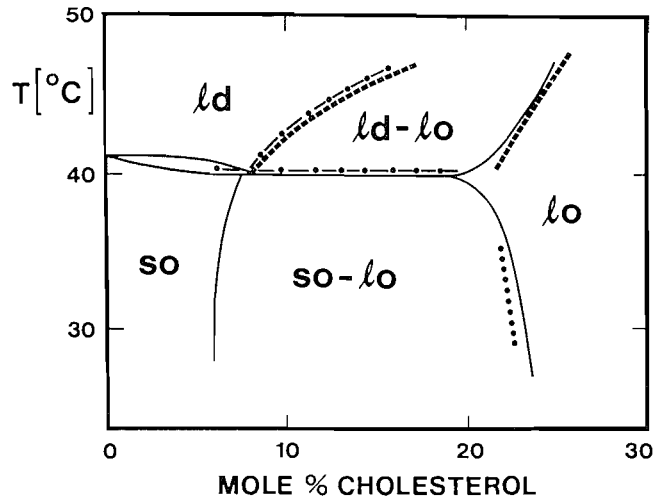

FIG. 1. Phase diagram for DPPC–cholesterol mixtures proposed by Vist (38) and Davis (51) and interpreted theoretically by Ipsen *et al.* (54). This diagram is based on a large number of experiments including several cited in this paper (30, 38, 51–53). The effect of the lipid–cholesterol interaction (54) is to stabilize, at high cholesterol concentrations, a "liquid-ordered" (lo) phase. At low cholesterol concentrations, the usually-discussed "solid-ordered" (so) (i.e. gel) and "liquid-disordered" (ld) (i.e. liquid crystalline) phases are obtained.

experimentally by carrying out careful measurements of the phase diagrams of mixtures of lipids and various sterols found on the evolutionary pathway to cholesterol and ergosterol (4, 5). For example, experiments are underway in the laboratory of one of us (M.B.) to compare the lowest concentration at which the B phase occurs with that of cholesterol in sterol–DPPC mixtures (Fig. 1). An interesting system to study in this way would be α-cholesterol–phospholipid mixtures. Dufourc *et al.* (55) have shown that the α-cholesterol molecule adopts a tilted conformation in phospholipid bilayer model membranes while the β-cholesterol ring structure lies with its plane parallel to the bilayer normal. They have speculated that this is why the β-cholesterol molecule occurs in natural systems while the α-cholesterol molecule does not. We ask here whether the tilt of α-cholesterol is less favourable to the stability of B phase and hence less favourable to the establishment of thermomechanical properties appropriate for plasma membranes of eucaryotic cells.

As described in various references cited in this paper, transient fluorescence depolarization and nmr relaxation measurements offer the possibility of determining the translational and rotational diffusion rates of lipid molecules and/or molecular probes in these same model systems. The relationship between such molecular dynamical properties and thermodynamic and mechanical properties is of great interest.

The methods described above can be applied to study some biological membranes though in some cases it will require the use of molecular probes in membrane extracts. It would be interesting to know whether there are systematic differences between the hydrophobic thickness of plasma membranes of eucaryotic cells and each of the membranes of organelles of the same cells and those of procaryotic cells. In the case of plasma membranes of eucaryotic cells, it would be highly desirable to also study the thickness of membranes formed from their separated lipids. Since plasma membranes have a large amount of polyunsaturated lipids (17), it may well be that the role of

Can. J. Chem. Downloaded from www.nrcresearchpress.com by 93.93.197.157 on 09/07/12
For personal use only.

cholesterol is not to increase the membrane thickness, but rather to restore the thickness to values "normal" for saturated chains while imparting greater cohesive strength without changing the fluidity. Measurements of acyl chain orientational order carried out with perdeuterated fatty acid probes in erythrocytes (56) were in good agreement with those carried out later using perdeuterated phospholipid molecules. Such probes could be used in biological membranes in the experimental program outlined above.

It would also be of value to study cells which are abnormal in their cholesterol content. The cells of cancer tumours are an example (57).

Much insight into the structure of integral membrane proteins and how their geometry relates to membrane geometry is now obtained from the amino acid sequence, when available (1–3). It would be interesting to compare the amino acid sequences of membrane proteins of plasma membranes with those of the organelles of eucaryotic cells to check them as indicators of membrane hydrophobic thickness and/or variability of thickness.

Concluding remarks

As discussed near the beginning of this paper, the three known kingdoms of cells parted company early in the evolutionary history, as perceived via the rRNA molecular chronometer (18). The approximate dates at which eubacteria, archaebacteria, and eucaryotes diverged from each other are not known, however. Up to now, changes in nucleic acid sequences of rRNA have produced reliable information on the time-ordering of evolutionary events, but not on their tempo.

We can say, however, that procaryotic cells (eubacteria and archaebacteria) have existed for more than 3.5 GA, including the first GA in an anerobic atmosphere, without evolving any variants with internal compartments in the manner of what are now called eucaryotic cells. Furthermore, the plasma membranes in *all* eucaryotic cells characterized up to now contain sterols while essentially no procaryotic membranes contain sterols. Though the progenitor of eucaryotic cells may have evolved before the appearance of molecular oxygen in the atmosphere some 2.3 GA ago and the oxidation of the hydrosphere about 1.5 ago (20), the fact that the biosynthesis of sterols requires O_2 (4–6) implies unequivocally that the plasma membranes of eucaryotic cells evolved between 2.3 and 1.5 GA ago.

We have been led, following a detailed reconsideration of the striking effects of cholesterol on the physical properties of phospholipid bilayer model membranes, to postulate that these correlations and anti-correlations are no accident. We argue in this paper that prior to the appearance of cholesterol and related sterols, the available molecular building blocks for biological membranes were incapable of generating physical properties of a plasma membrane compatible with the evolution of modern eucaryotic cells.

The available data on physical properties of membranes are insufficient to test our argument adequately. It is not obvious at this time that molecules such as the cholesterol-resembling hopanoids, which evolved anaerobically in procaryotes and which are capable of replacing cholesterol in living systems under certain experimental conditions, were incapable of providing the physical properties necessary for facilitating special functions such as cytosis which could have provided the evolutionary driving force for eucaryotic cells. The subtle interplay between thermodynamic and micromechanical properties and rates of molecular motion which may be required to promote a process such as cytosis, while still maintaining membrane strength and permeability control, has not yet been examined carefully and exhaustively. When this is done, and it will require a considerable effort, it should be possible to demonstrate whether our hypothesis concerning eucaryotic evolution is correct or not. Whatever the outcome, the required experimental studies will generate considerable understanding concerning the systematics of the physical properties of membranes in relation to their biological function.

A few final words should be added about the relationship of our proposals to the well known and widely accepted symbiosis theory for the evolution of eucaryotic cells. We do not believe that our proposals are in disagreement with the symbiosis theory. On the contrary, it is unreasonable to expect cells to have evolved to the stage of being capable of swallowing an entire bacterium and allowing it to survive in its interior without having previously gone through a pre-bacterium-swallowing evolutionary phase, i.e. cells would first have had to develop and practice the swallowing facility on smaller objects. We have only dealt with this earlier stage in our paper. Whether subsequent internal incorporation of entire, smaller cells would *necessarily* follow such a development, and/or did actually follow it, must be settled by arguments and criteria other than those discussed here.

Acknowledgements

We thank Guy Cox, Ford Doolittle and Evan Evans for helpful discussions. We wish to dedicate this paper to Professor J.A. Morrison whose rigorous use of thermodynamics to characterize the physical and chemical properties of a variety of molecular systems is a model for the study of complex systems such as the biological membranes considered in this paper.

This research was supported by NATO Research Grant No. 392183. The research of M. Bloom was also supported by the Natural Sciences and Engineering Research Council of Canada and that of O.G. Mouritsen by the Danish Natural Science Research Council under Grant J. nr. 5.21.99.72.

1. R. HENDERSON. *In* Membranes and intercellular communications. *Edited by* R. Balian, M. Chabre, and P. F. Devaux. Elsevier/North-Holland, Amsterdam. 1981. pp. 229–249.
2. P. N. T. UNWIN and R. HENDERSON. Sci. Am. **250**, No. 2, 78 (1984).
3. J. DEISENHOFER, O. EPP, K. MIKI, R. HUBER, and H. MICHEL. Nature, **318**, 618 (1985).
4. K. BLOCH. Science, **150**, 19 (1965).
5. K. BLOCH. C.R.C. Crit. Rev. Biochem. **14**, 47 (1983).
6. K. BLOCH. *In* Biochemistry of lipids and membranes. *Edited by* Dennis E. Vance and Jane E. Vance. Benjamin/Cummings Pub. Co. Inc. 1985. pp. 1–24.
7. J. SEELIG and A. SEELIG. Q. Rev. Biophys. **13**, 19 (1980).
8. E. OLDFIELD. *In* Membranes and transport. Vol. 1. *Edited by* E. N. Martinosi. Plenum Press, New York 1982. pp. 115–123.
9. P. F. DEVAUX. *In* Biological magnetic resonance. Vol. 5. *Edited by* L. J. Berliner and J. Reuben. Plenum Press, New York. 1983. pp. 183–299.
10. O. G. MOURITSEN and M. BLOOM. Biophys. J. **46**, 141 (1984).
11. M. BLOOM and I. C. P. SMITH. *In* Progress in protein-lipid interactions. *Edited by* J. J. H. H. M. De Pont and A. Watts. Elsevier, Amsterdam. 1985. pp. 61–88.
12. A. ALBERTS, D. BRAY, J. LEWIS, M. RAFF, K. ROBERTS and J. D. WATSON. Molecular biology of the cell. Garland Publ. Co., New York and London. 1983. Chap. 1.
13. J. DAHL, C. DAHL, and K. BLOCH. Biochemistry, **19**, 1462 (1980).

14. M. ROHMER, P. BOUVIER, and G. OURISSON. Proc. Natl. Acad. Sci. U.S.A. **76**, 847 (1979).
15. G. OURISSON, P. ALBRECHT, and M. ROHMER. Sci. Am. 250, No. 8, 44 (1984).
16. T. CAVALIER-SMITH. Nature, **256**, 463 (1975).
17. T. CAVALIER-SMITH. *In* Molecular and cellular aspects of macrobial evolution. Society for General Microbioligy Ltd., Symposium 32. *Edited by* M. J. Carlile, J. F. Collins, and B. E. B. Moseley. Cambridge University Press. 1981. pp. 33–84.
18. C. R. WOESE. Microbiol. Rev. **51**, 221 (1987).
19. L. MARGULIS. Origin of eucaryotic cells. Yale University Press, New Haven, CT. 1975.
20. J. C. G. WALKER, K. KLEIN, M. SCHIDLEWSKI, J. W. SCHOPF, D. J. STEVENSON, and M. R. WALKER. *In* Earth's earliest biosphere. *Edited by* J. W. Schopf. Princeton University Press, Princeton, NJ. 1983.
21. M. DE ROSA, A. GAMBACORTA, and A. GLIOZZI. Microbiol. Rev. **50**, 70 (1986).
22. J. SEELIG. *In* Membranes and intercellular communications. *Edited by* R. Balian, M. Chabre, and P. F. Devaux. Elsevier/North-Holland, Amsterdam. 1981. pp. 15–78.
23. G. W. STOCKTON and I. C. P. SMITH. Chem. Phys. Lipids, **17**, 251 (1976).
24. G. LINDBLOM, L. B. A. JOHANSSON, and G. ARVIDSON. Biochemistry, **20**, 2204 (1981).
25. N. L. THOMPSON and D. AXELROD. Biochem. Biophys. Acta, **597**, 155 (1980).
26. J. L. R. RUBENSTEIN, B. A. SMITH, and H. M. MCCONNELL. Proc. Natl. Acad. Sci. U.S.A. **76**, 15 (1979).
27. K.KINOSITA, S. KAWATO, and A. IKEGAMI. Biophys. J. **20**, 289 (1977).
28. F. JÄHNIG. Proc. Natl. Acad. Sci. U.S.A. **76**, 6361 (1979).
29. G. VAN GINKEL, L. J. KORSTANJE, H. VAN LANGEN, and Y. K. LEVINE. Faraday Discuss. Chem. Soc. **81**, 49 (1986).
30. E. EVANS and D. NEEDHAM. Faraday Discuss. Chem. Soc. **81**, 267 (1986).
31. J. SEELIG. Q. Rev. Biophys. **10**, 353 (1977).
32. B. A. CORNELL and F. SEPAROVIC. Biochem. Biophys. Acta, **733**, 189 (1983).
33. B. A. LEWIS and D. M. ENGELMAN. J. Mol. Biol. **166**, 211 (1983).
34. H. SCHINDLER and J. SEELIG. Biochemistry, **14**, 2283 (1975).
35. J. H. DAVIS. Biophys. J. **27**, 339 (1979).
36. J. H. DAVIS. Biochim. Biophys. Acta, **737**, 117 (1983).
37. G. ZACCAI, G. BÜLDT, A. SEELIG, and J. SEELIG. J. Mol. Biol. **134**, 693 (1979).
38. M. R. VIST. M.Sc. Thesis. University of Guelph, Guelph, Ont., Canada, 1984.
39. B. MARAVIGLIA, J. H. DAVIS. M. BLOOM, J. WESTERMAN, and K. W. A. WIRTZ. Biochem. Biophys. Acta, **686**, 137 (1982).
40. (*a*) A. JOHANNSSON, C. A. KEIGHTLEY, G. A. SMITH, C. D. RICHARDS, T. R. HESKETH, and J. C. METCALFE. J. Biol. Chem. **256**, 1643 (1981); (*b*) A. JOHANNSSON, G. A. SMITH, and J. C. METCALFE. Biochim. Biophys. Acta, **641**, 416 (1981).
41. C. MONTECUCCO, G. SMITH, DEBBENI-SALA, A. JOHANNSSON, Y. M. GALANTE, and R. BISSON. FEBS Lett. **144**, 145 (1982).
42. J. R. ELLIOT, D. NEEDHAM, J. P. DILGER, and D. A. HAYDON. Biochim. Biophys. Acta, **735**, 95 (1983).
43. D. A. HAYDON, B. M. HENDRY, S. R. LEVINSON, and J. REQUENA. Nature, **268**, 356 (1977).
44. R. G. ASHCROFT, H. G. L. COSTER, and J. R. SMITH. Nature, **269**, 819 (1977).
45. J. RIEGLER and H. MÖHWALD. Biophys. J. **49**, 1111 (1960).
46. M. KARPLUS and J. A. MCCAMMON. Sci. Am. **254**, No. 4, 30 (1986).
47. E. F. DELONG and A. A. YANNANOS. Science, **228**, 1101 (1985).
48. E. SACKMAN, H.-P. DUWE, and H. ENGELHARDT. Faraday Discuss. Chem. Soc. **81**, 353 (1986).
49. R. SAEZ, F. M. GONI, and A. ALONSO. FEBS Lett. **179**, 311 (1985).
50. K. PORALLA. FEMS Microbiol. Lett. **13**, 131 (1982).
51. J. H. DAVIS. Proc. Int. School Phys. "Enrico Fermi" on The Physics of NMR in Biology and Medicine. 1986. *Edited by* B. Maraviglia. In press.
52. D. M. RECHTENWALD and H. M. MCCONNELL. Biochim. Biophys. Acta, **20**, 4505 (1981).
53. B. R. COPELAND and H. M. MCCONNELL. Biochem. Biophys. Acta, **95**, 599 (1980).
54. J. H. IPSEN, G. KARLSTRÖM, O. G. MOURITSEN, H. WENNERSTROM, and M. J. ZUCKERMANN. Biochim. Biophys. Acta. **905**, 162 (1987).
55. E. J. DUFOURC, E. J. PARISH, S. CHITRAKORN, and I. C. P. SMITH. Biochemistry, **23**, 6062 (1984)
56. J. H. DAVIS, B. MARAVIGLIA, G. WEEKS, and D. GODIN. Biochim. Biophys. Acta, **550**, 362 (1979).
57. P. S. COLEMAN and B. B. LAVIETES. C.R.C. Crit. Rev. Biochem. **11**, 341 (1981).

Can. J. Chem. Downloaded from www.nrcresearchpress.com by 93.93.197.157 on 09/07/12
For personal use only.

Molar excess volumes, isentropic compressions, and isobaric heat capacities of methanol – isomeric butanol systems at 298.15 K

TSUKASA OKANO, HIDEO OGAWA, AND SACHIO MURAKAMI[1]

Department of Chemistry, Faculty of Science, Osaka City University, 3-3-138 Sugimoto, Sumiyoshi-ku, Osaka 558, Japan

Received September 10, 1987

This paper is dedicated to Professor James A. Morrison

TSUKASA OKANO, HIDEO OGAWA, and SACHIO MURAKAMI. Can. J. Chem. **66**, 713 (1988).

Molar excess volumes, molar excess isentropic compressions, and molar excess isobaric heat capacities for binary liquid mixtures of methanol with 2-methylpropanol, 2-butanol, and 2-methyl-2-propanol have been determined at 298.15 K. The concentration dependence and magnitude of these thermodynamic functions are quite different from those of the methanol – 1-butanol system, which had been previously determined. Molar excess volumes for two of the present systems are positive over the whole concentration range, except for the 2-methyl-2-propanol system. For the latter system they are negative in the butanol-rich range. Molar excess isentropic compressions of these systems show slightly different concentration dependence from that of the excess volumes, but the order in magnitude resembles that of the excess volumes. Molar excess isobaric heat capacities for all systems are negative and show simple concentration dependence. The minimum values of excess heat capacities are correlated with the magnitude of molar isobaric heat capacities of the pure isomeric butanols. The behavior of these excess functions is discussed with reference to the differences in numbers and strength of hydrogen bonding between the pure liquid and the solution.

TSUKASA OKANO, HIDEO OGAWA et SACHIO MURAKAMI. Can. J. Chem. **66**, 713 (1988).

Opérant à 298,15 K, on a déterminé les volumes molaires en excès, les compressions molaires isentropiques en excès et les capacités calorifiques molaires isobares en excès des mélanges de liquides binaires formés d'une part de méthanol et d'autre part de méthyl-2 propanol, de butanol-2 ou de méthyl-2 propanol-2. La relation avec la concentration ainsi que l'amplitude de ces fonctions thermodynamiques sont très différentes de celles qu'on avait observées avec le système méthanol/butanol-1 qu'on avait étudié antérieurement. Les volumes molaires en excès de deux systèmes, excepté celui du méthyl-2 propanol-2, sont positifs à toutes les concentrations étudiées. Toutefois, avec ce dernier système, ils sont négatifs pour les concentrations riches en butanol. Par comparaison avec les volumes an excès, les compressions molaires isentropiques en excès de ces systèmes présentent des relations avec la concentration qui sont différentes; toutefois, l'ordre de grandeur resemble à celui des volumes en excès. Les capacités calorifiques molaires isobares en excès sont négatives pour tous les systèmes et la relation avec la concentration est simple. Il existe une corrélation entre les valeurs minimales des capacités calorifiques en excès et l'amplitude des capacités calorifiques molaires isobares des butanols isomères purs. On discute des comportements de ces fonctions en excès en fonction des différences dans les nombres et la force des liaisons hydrogènes entre le liquide pur et la solution.

[Traduit par la revue]

Introduction

Many years ago, various thermodynamic properties for mixtures composed of two different alcohols were reported in a series of papers (1–3) by Benson and co-workers. Recently, molar excess volumes, V^E, isentropic compressions, K_s^E, and isobaric heat capacities, C_p^E, for binary mixtures of methanol with ethanol, 1-propanol, and 1-butanol were measured at 298.15 K in our laboratory (4).

To discuss the thermodynamic behavior of mixtures composed of two different alcohols in further detail, the present paper reports the results of similar investigations of the binary liquid mixtures formed by mixing methanol (MeOH) with 2-methylpropanol (*i*-BuOH), 2-butanol (*s*-BuOH), and 2-methyl-2-propanol (*t*-BuOH).

Experimental

Materials

Special grade alcohols from Wako Pure Chemical Industries, Ltd. (Japan) were used as follows. MeOH, *i*-BuOH, and *s*-BuOH were stored over 3Å molecular sieves and fractionally distilled under a stream of N_2 gas. The *s*-BuOH was further vacuum distilled with 3Å molecular sieves. The *t*-BuOH was used without any purification, because no trace of impurities was detected by glc analysis. The water content in the pure samples used in this study was estimated to be less than 0.083 mol% in the same way as described in the previous paper (4).

[1]Author to whom correspondence may be addressed.

Apparatus and procedure

All measurements for systems of MeOH with *i*-BuOH and with *s*-BuOH were carried out at 298.15 K; those with *t*-BuOH were carried out at 299.15 K to avoid solidification of *t*-BuOH in the apparatus.

Excess volumes, V^E, and isentropic compressibilities, κ_s, for these mixtures were estimated from density, ρ, and speed of sound, u, measurements. Densities were measured by using a Picker vibrating densimeter (Sodev 01D, Canada) operated in the static mode. Speeds of sound were determined by means of a "Sing around" technique. All solutions were prepared in a specially devised bottle with same procedure as described previously (5). The error in the concentration of samples is estimated to be less than 3×10^{-5} in the mole fraction. Reproducibilities of ρ and u were better than 3×10^{-6} g cm^{-3} and 0.1 m s^{-1}, respectively.

Excess isobaric heat capacities, C_p^E, were measured by using a flow microcalorimeter constructed in our laboratory (6, 7), which can determine C_p^E accurately by the "direct mixing" method. The isobaric heat capacities C_p of pure component liquids were determined by a "delay loop" method at 298.15 or 299.15 K, in which the purified 1-propanol was used as a standard liquid and Kalinowska's C_p value was adopted at each temperature (8). The errors in C_p and C_p^E are estimated to be less than 0.2 and 0.05 J K^{-1} mol^{-1}, respectively.

The procedures followed in measurements have been described in detail in the previous paper (4). The physical properties of the pure component liquids determined in this study are listed in Table 1, with literature values of thermal expansion coefficients, α, used to calculate excess compressibilities, κ_s^E, of these mixtures.

Results

The experimental results for the present systems are summa-

Can. J. Chem. Downloaded from www.nrcresearchpress.com by 176.9.209.113 on 09/07/12
For personal use only.

Can. J. Chem. Downloaded from www.nrcresearchpress.com by 176.9.209.113 on 09/07/12
For personal use only.

TABLE 1. Densities, ρ, speeds of sound, u, isentropic compressibilities, κ_s, isobaric heat capacities, C_p, and thermal expansion coefficients, α, of component liquids

MeOH 298.15 K	MeOH 299.15 K	*i*-BuOH 298.15 K	*s*-BuOH 298.15 K	*t*-BuOH 299.15 K
		ρ (g cm^{-3})		
0.786564 0.786350[a]	0.785648 0.785407[a]	0.797874 0.79790[b]	0.802487 0.80246[b]	0.779479 0.77940[b]
		u (m s^{-1})		
1102.8 ±0.7	1099.5 ±0.7	1188.5 ±0.6	1212.0 ±0.5	1117.0 ±0.7
		κ_s (TPa^{-1})		
1045.4	1052.8	887.3	848.4	1028.1
		C_p (J K^{-1} mol^{-1})		
80.35	80.54	181.05	198.03	221.88
		$10^3 \times \alpha$ (K^{-1})		
1.201[a]	1.201[a]	0.95[c]	0.91[c]	1.42[c]

[a]Literature (11) or corrected with α.
[b]Literature (1) or corrected with α.
[c]Literature (12).

rized in Tables 2 and 3. The results of u are listed in Table 2, in a form of Δu defined by

$$[1] \quad \Delta u = u - x_1 u_1^* - (1 - x_1) u_2^*$$

where x_i and u_i^* are the mole fraction and u of the pure component i, and subscripts 1 and 2 denote MeOH and isomeric butanol, respectively.

An excess thermodynamic function, X^E(V^E, K_s^E, and C_p^E) is defined by

$$[2] \quad X^E = X - X^{id}$$

where X is any thermodynamic function of solution and X^{id} is the ideal function, which obeys the ideal mixing law. Equations for calculation of these functions should be referred to in the previous paper (4).

Molar excess isothermal compressions, K_T^E, and molar excess isochoric heat capacities, C_V^E, for these mixtures were also calculated by combining the data of κ_s, C_p, V, and α for solution with those of the pure components. In these calculations, excess thermal expansion coefficients, α^E, for these systems were assumed to be zero because of the lack of α^E data, and the α values of solutions were approximated by using the α values of the pure components listed in Table 1. For ideal excess compressibilities, κ_T^{id} or κ_s^{id}, the rigorous definition was adopted, as recommended by Benson and Kiyohara (9) and Douheret *et al.* (10).

The excess functions X^E were fitted to the polynomial

$$[3] \quad X^E = x_1(1 - x_1) \sum_{i=1}^{n} A_i(1 - 2x_1)^{i-1}$$

by the least-squares method. The coefficients A_i are tabulated in Table 4 together with the standard deviations, s. V^E, K_s^E, K_T^E, and C_p^E are shown in Figs. 1–4, respectively. The curves in these figures were calculated from the A_i coefficients in Table 4. The difference in K_T^E calculated from the assumption of $\alpha^E = 0$ and $\alpha^E = -2\alpha^{id}V^E/V$ seems to be a little larger.[2]

The concentration dependence of C_V^E resembles that the C_p^E and the C_V^E value at equimolar concentration is less than the C_p^E value by 0.1 – 0.5 J K^{-1} mol^{-1} in magnitude; the difference in C_V^E from the values assumed for α^E as described above was also small.[3]

Discussion

A few thermodynamic studies of the methanol – isometric butanol systems have been carried out at 298.15 K. Murthy *et al.* (13) reported values of V^E for the *s*-BuOH system that are considerably larger than the present results. French and Criss (14) studied partial molar volumes and heat capacities of the *t*-BuOH system in the region of high dilution of *t*-BuOH, the signs of whose concentration dependence are in agreement with those of the excess partial molar quantities estimated from present results of V^E and C_p^E. However, it is not suitable to compare the magnitude of our results with their results because of a lack of data at high dilution. Our V^E results are in agreement with those of Polák *et al.* (1) within 0.005 cm^3 mol^{-1} at equimolar concentration. Polák *et al.* have determined excess Gibbs energies, G^E, excess enthalpies, H^E, and V^E for the present systems and discussed them in relation to the numbers and strength of intermolecular hydrogen bonding (1). Our V^E, K_T^E, and K_s^E results appear to support their thermodynamic discussion for these systems.

As shown in Figs. 1 and 2, V^E values in the isomeric butanol

[2][$\Delta K = K_T^E(\alpha^E = -2\alpha^{id}V^E/V) - K_T^E(\alpha^E = 0)$]
$\Delta K(x_1 = 0.5)$ is nearly −48 (*n*-BuOH), −68 (*i*-BuOH), −58 (*s*-BuOH), and −68 (*t*-BuOH) cm^3 TPa^{-1} mol^{-1}.

[3][$\Delta C = C_V^E(\alpha^E = -2\alpha^{id}V^E/V) - C_V^E(\alpha^E = 0)$]
$\Delta C(X_1 = 0.5) \simeq 0.1$ J K^{-1} mol^{-1} for all the systems.

Can. J. Chem. Downloaded from www.nrcresearchpress.com by 176.9.209.113 on 09/07/12
For personal use only.

TABLE 2. Densities, ρ, differences in speed of sound, Δu, excess isentropic compressibilities, κ_s^E, molar excess isentropic compressions, K_s^E, and molar excess volumes, V^E, of methanol – isomeric butanol systems

x_1[a]	ρ[b]	Δu[c]	κ_s^E[d]	K_s^E[e]	V^E[f]
		MeOH–*i*-BuOH at 298.15 K			
0.05682	0.797434	2.32	0.03	18	0.0168
0.14234	0.766727	5.32	0.38	69	0.0407
0.20408	0.796189	7.10	0.87	122	0.0559
0.29340	0.795367	9.54	1.17	159	0.0746
0.39494	0.794350	10.82	2.83	290	0.0917
0.50427	0.793160	11.47	4.33	385	0.1029
0.60197	0.791997	11.15	5.57	444	0.1062
0.69917	0.790749	9.60	6.96	491	0.1011
0.79856	0.789390	7.16	7.34	461	0.0846
0.90047	0.787958	3.76	5.73	316	0.0515
0.95062	0.787246	1.84	3.62	186	0.0284
		MeOH–*s*-BuOH at 298.15 K			
0.05214	0.802010	2.04	0.51	55	0.0111
0.14633	0.801057	5.35	1.46	152	0.0329
0.20389	0.800433	7.18	1.91	195	0.0448
0.29746	0.799323	9.51	2.88	278	0.0634
0.40550	0.797916	11.46	3.82	344	0.0796
0.50318	0.796520	12.42	4.41	373	0.0875
0.60608	0.794881	12.33	4.96	387	0.0898
0.70453	0.793156	11.24	4.95	356	0.0826
0.80440	0.791190	8.89	4.33	286	0.0663
0.90221	0.789026	5.15	2.94	175	0.0394
0.95113	0.787834	2.68	1.84	102	0.0215
		MeOH–*t*-BuOH at 299.15 K			
0.06154	0.780427	7.78	−14.13	−1389	−0.0916
0.15546	0.781275	13.32	−23.35	−2174	−0.1491
0.21396	0.781566	14.63	−25.02	−2244	−0.1540
0.29850	0.781793	14.75	−24.10	−2040	−0.1374
0.39457	0.781915	13.38	−20.38	−1605	−0.1025
0.50460	0.782054	11.11	−15.06	−1081	−0.0605
0.59850	0.782266	9.05	−10.65	−698	−0.0305
0.69896	0.782685	6.81	−6.50	−381	−0.0094
0.79800	0.783340	4.65	−3.29	−169	0.0012
0.90022	0.784333	2.43	−1.13	−49	0.0028
0.94699	0.784902	1.44	−0.69	−28	0.0019

[a]Mole fraction of methanol.
[b]Units: g cm^{-3}.
[c]Units: m s^{-1}.
[d]Units: TPa^{-1}.
[e]Units: cm^3 TPa^{-1} mol^{-1}.
[f]Units: cm^3 mol^{-1}.

systems are quite different from each other, and the concentration dependence of K_s^E and the order of the absolute values for these systems resemble those of V^E very well. Strictly speaking, K_T^E can be related to V^E as described previously (4).

Polák suggests that the thermodynamic properties for the *s*-BuOH system, ($H^E < 0$ and $V^E > 0$), are due to the geometrically worse packing of mixed associate species in solution. K_T^E for this system are larger positive values than those of the *i*-BuOH system, as shown in Fig. 3. The positive V^E and K_T^E values suggest loosely packed, easily compressible molecules in solution. This then indicates that by mixing MeOH with *s*-BuOH, there is formation of hydrogen bonds between unlike alcohol molecules ($H^E < 0$) and loosely packed associate spe-

TABLE 3. Molar excess isobaric heat capacities, C_p^E of methanol – isomeric butanol systems

x_1[a]	C_p^E (J K^{-1} mol^{-1})	x_1[a]	C_p^E (J K^{-1} mol^{-1})
	MeOH–*i*-BuOH at 298.15 K		
0.05001	−0.717	0.60003	−2.769
0.10001	−1.311	0.70002	−2.090
0.20002	−2.185	0.80002	−1.457
0.30002	−2.695	0.90001	−0.738
0.40003	−2.915	0.95001	−0.364
0.50003	−2.876		
	MeOH–*s*-BuOH at 298.15 K		
0.05001	−1.88	0.60003	−6.82
0.10001	−3.52	0.70003	−5.50
0.20002	−5.88	0.80002	−3.82
0.30003	−7.30	0.90001	−1.92
0.40003	−7.82	0.95001	−0.93
0.50004	−7.49		
	MeOH–*t*-BuOH at 299.15 K		
0.05000	−3.52	0.59998	−13.58
0.09999	−6.91	0.69998	−11.02
0.19999	−11.66	0.79999	−7.67
0.29998	−14.46	0.89999	−3.83
0.39998	−15.49	0.95000	−1.83
0.49998	−15.08		

[a]Mole fraction of methanol.

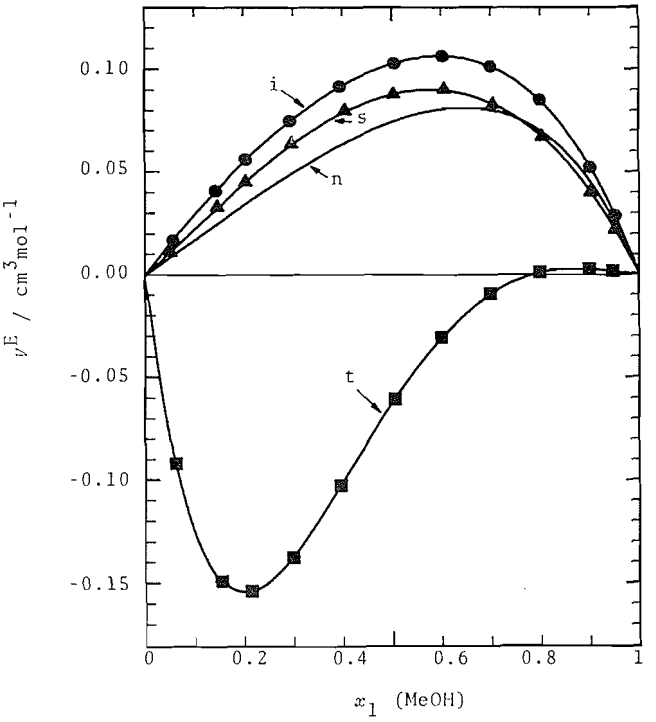

FIG. 1. Molar excess volumes of methanol – isomeric butanol systems. Experimental results: ●, *i*-BuOH at 298.15 K; ▲, *s*-BuOH at 298.15 K; ■, *t*-BuOH at 299.15 K. *n*-BuOH curve from ref. 4; other curves calculated from coefficients in Table 4. The labels *n*, *i*, *s*, and *t* indicate the four isomeric butanols.

TABLE 4. Coefficients, A_i and standard deviations, s of the least-squares fit by eq. [3] of methanol – isomeric butanol systems

Parameter	A_1	A_2	A_3	A_4	A_5	s
			MeOH–*i*-BuOH at 298.15 K			
$\kappa_S^{E\,a}$	16.42	−29.7	25.1	−14.4		0.19
$K_S^{E\,b}$	1496	−1749	774	−257		12
$V^{E\,c}$	0.4111	−0.1459	0.0629	−0.0174		0.0002
$C_p^{E\,d}$	−11.662	−2.89	0.65	−1.94		0.057
			MeOH–*s*-BuOH at 298.15 K			
$\kappa_S^{E\,a}$	17.70	−11.50	6.54	−4.4		0.08
$K_S^{E\,b}$	1502	−456	93	−117		4
$V^{E\,c}$	0.3511	−0.1122	−0.0074	−0.0208		0.0003
$C_p^{E\,d}$	−30.37	−10.48	0.17	−0.86		0.05
			MeOH–*t*-BuOH at 299.15 K			
$\kappa_S^{E\,a}$	−61.46	−97.3	−62.4	−43.5	−30.1	0.13
$K_S^{E\,b}$	−4431	−8905	−7432	−5592	−3407	13
$V^{E\,c}$	−0.2482	−0.7175	−0.6022	−0.2630	−0.105	0.0003
$C_p^{E\,d}$	−60.36	−20.35	−3.62	−0.88	8.9	0.06

[a]Units: TPa^{-1}.
[b]Units: $cm^3\ TPa^{-1}\ mol^{-1}$.
[c]Units: $cm^3\ mol^{-1}$.
[d]Units: $J\ K^{-1}\ mol^{-1}$.

Can. J. Chem. Downloaded from www.nrcresearchpress.com by 176.9.209.113 on 09/07/12
For personal use only.

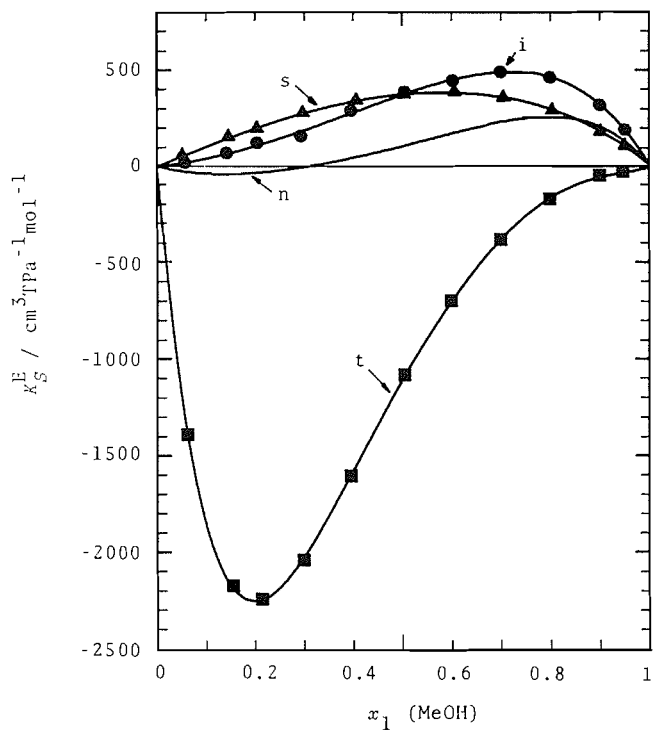

FIG. 2. Molar excess isentropic compressions of methanol – isomeric butanol systems. Experimental results: ●, *i*-BuOH at 298.15 K; ▲, *s*-BuOH at 298.15 K; ■, *t*-BuOH at 299.15 K. *n*-BuOH curve from ref. 4; other curves calculated from coefficients in Table 4. The labels *n*, *i*, *s*, and *t* indicate the four isomeric butanols.

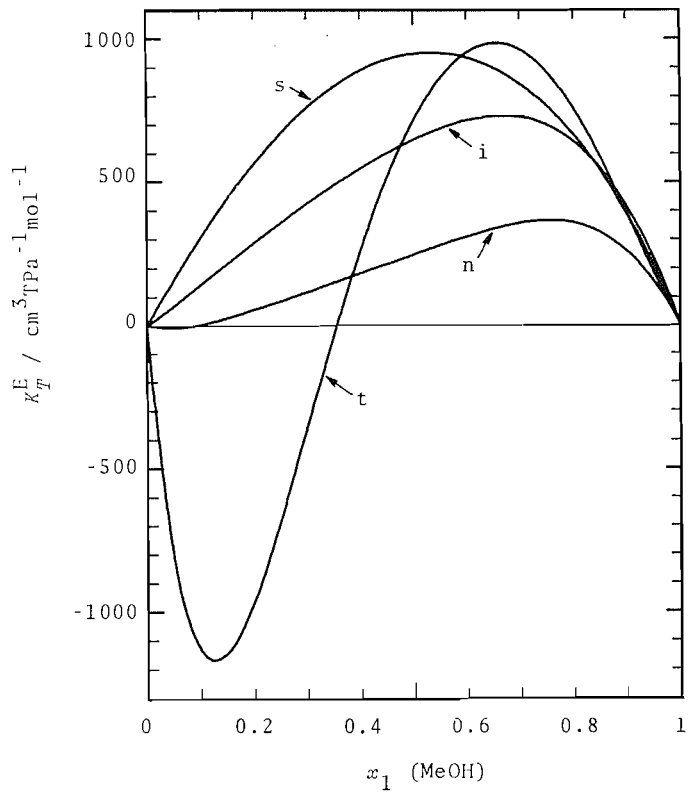

FIG. 3. Molar excess isothermal compressions of methanol – isomeric butanol systems. The labels *n*, *i*, *s*, and *t* indicate the four isomeric butanols; *i*-BuOH and *s*-BuOH at 298.15 K, *t*-BuOH at 299.15 K. *n*-BuOH curve from ref. 4; other curves calculated from coefficients in Table 4.

cies ($V^E > 0$), and a decrease of volume expansion in mixing under higher pressure ($K_T^E > 0$).

A similar situation occurs at the MeOH-rich range of the *t*-BuOH system. When hydrogen bonding between unlike molecules takes place in this region, the bulky *tert*-butyl group in the *t*-BuOH molecule brings about the loose packing of molecules in solution and makes a positive contribution to V^E, as in the *s*-BuOH system. However, this contribution will weaken under higher pressure, resulting in a large positive contribution to K_T^E.

On the other hand, for the range rich in *t*-BuOH in this

Can. J. Chem. Downloaded from www.nrcresearchpress.com by 176.9.209.113 on 09/07/12
For personal use only.

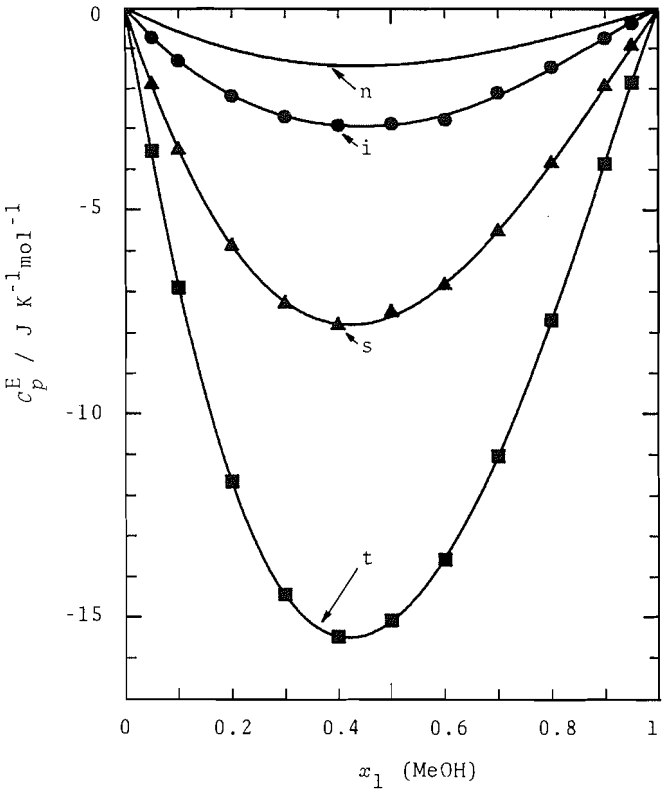

FIG. 4. Molar excess isobaric heat capacities of methanol – isomeric butanol systems. Experimental results: ●, *i*-BuOH at 298.15 K; ▲, *s*-BuOH at 298.15 K; ■, *t*-BuOH at 299.15 K. *n*-BuOH curve from ref. 4; other curves calculated from coefficients in Table 4. The labels *n*, *i*, *s*, and *t* indicate the four isomeric butanols.

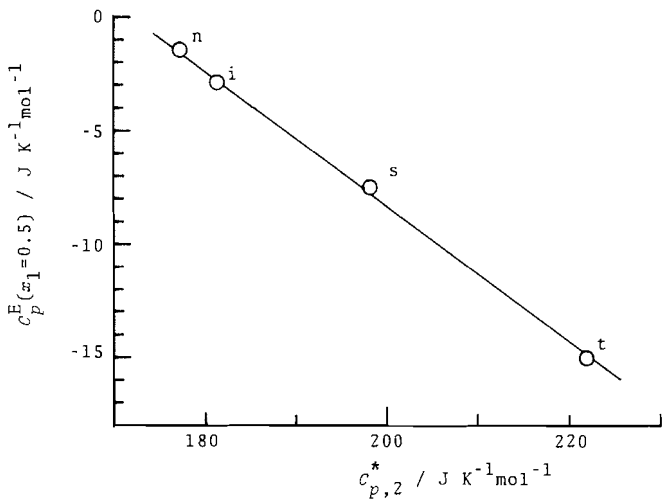

FIG. 5. Correlation of molar excess isobaric heat capacities with molar isobaric heat capacities of pure isomeric butanols. The labels *n*, *i*, *s*, and *t* indicate the four isomeric butanols.

system, the average molecular distance will be decreased on adding MeOH, because the MeOH molecule penetrates into the void space formed by bulky BuOH molecules and the molecules in solution will be closely packed ($V^E < 0$) by the formation of hydrogen bonding between unlike molecules ($H^E < 0$). Consequently, V^E could not decrease significantly with increasing pressure and this gives a large negative contribution to K_T^E.

H^E is positive for the *i*-BuOH system and negative for the *s*-BuOH and *t*-BuOH systems, respectively. On the other hand, the H^E is positive and C_p^E is negative for the MeOH + *n*-alcohol systems (1, 4). C_p^E indicates the temperature dependence of H^E. From these results, it is predicted $C_p^E < 0$ for the *i*-BuOH system ($H^E > 0$) and $C_p^E > 0$ for the *s*-BuOH and *t*-BuOH systems ($H^E < 0$). However, as shown in Fig. 4, C_p^E values for all the systems are negative and show simpler concentration dependence than those of H^E. Absolute magnitude of C_p^E is in the order *t*-BuOH > *s*-BuOH > *i*-BuOH > *n*-BuOH.

C_p^E should not be attributed to the difference in numbers of hydrogen bonds on mixing, but depends rather on the difference in numbers of hydrogen bonds broken, with increase of temperature, between the pure state and the solution state. The order of the absolute magnitude of C_p^E appears to be in agreement with that of the formation of the strong hydrogen bond and to be reciprocal to that of the steric effect, by which unstable associate species are formed in liquid. The more the steric effect exists in the pure alcohol, the more the hydrogen bond is broken down with increase of temperature. On the other hand, relatively more stable mixed associate species are formed in the solution state, resulting in $C_p^E < 0$. This leads to the conclusion that the absolute magnitude of C_p^E at equimolar concentration is closely correlated to the C_p value in the pure isomeric butanols. In Fig. 5, C_p^E at equimolar concentration is plotted against C_p of isomeric butanol. The linear correlation shown in this figure supports the above discussion and is a good source of information about the solution properties.

Summing up, we have presented information about the behavior of the component molecules in mixtures of two different alcohols. We intend to discuss the local concentration fluctuation in the MeOH + *n*-alcohol and isomeric butanol mixtures by use of the Kirkwood–Buff theory in a forthcoming communication.

1. J. POLÁK, S. MURAKAMI, V. T. LAM, H. D. PFLUG, and G. C. BENSON. Can. J. Chem. **48**, 2457 (1970).
2. A. E. POPE, H. D. PFLUG, B. DACRE, and G. C. BENSON. Can. J. Chem. **45**, 2665 (1967).
3. H. D. PFLUG and G. C. BENSON. Can. J. Chem. **46**, 287 (1968).
4. H. OGAWA and S. MURAKAMI. J. Solution Chem. **16**, 315 (1987).
5. M. TAKENAKA, R. TANAKA, and S. MURAKAMI. J. Chem. Thermodyn. **12**, 849 (1980).
6. H. OGAWA and S. MURAKAMI. Thermochim. Acta, **88**, 255 (1985).
7. H. OGAWA and S. MURAKAMI. Thermochim. Acta, **109**, 145 (1986).
8. B. KALINOWSKA, J. JEDLINSKA, W. WOYCICKI, and J. STECKI. J. Chem. Thermodyn. **12**, 891 (1980).
9. G. C. BENSON and O. KIYOHARA. J. Chem. Thermodyn. **11**, 1061 (1979).
10. G. DOUHERET, C. MOREAU, and A. VIALLARD. Fluid Phase Equilib. **22**, 277 (1985).
11. G. C. BENSON and O. KIYOHARA. J. Solution Chem. **9**, 791 (1980).
12. J. A. RIDDICK and W. B. BUNGER. Organic solvents. 3rd ed. Wiley–Interscience, New York. 1970. pp. 152–155.
13. S. MURTHY, R. P. SINGH, and A. P. KUDCHADKAR. Indian Chem. Eng. **20**, 37 (1978).
14. R. N. FRENCH and C. M. CRISS. J. Solution Chem. **10**, 699 (1981).

Thermal expansion and Grüneisen functions of polymer crystal models: 1. Central forces

RUTH MARGARET BARRON,[1] THOMAS HUGH KENNETH BARRON,[2] PAUL MALCOLM MUMMERY,[3] AND MICHAEL SHARKEY

Department of Theoretical Chemistry, University of Bristol, Cantock's Close, Bristol BS8 1TS, England

Received October 28, 1987

This paper is dedicated to Professor James A. Morrison

RUTH MARGARET BARRON, THOMAS HUGH KENNETH BARRON, PAUL MALCOLM MUMMERY, and MICHAEL SHARKEY. Can. J. Chem. **66**, 718 (1988).

With typical pair potentials, a bond is stretched by vibrations along the bond directions, while contraction is caused by the tension set up by vibrations normal to the bond direction. The rôle of these two effects is studied in calculations for parallel linear-chain and zigzag-chain models. For linear chains and rigid zigzag chains, expansion is positive in the plane normal to the chain direction, although it may be strongly anisotropic in this plane. Expansion along the chain direction is negative, and typically an order of magnitude less than that normal to the chain. For a flexible zigzag chain with bond angle 90°, expansion is positive in all directions; the Grüneisen tensor is approximately isotropic, but elastic anisotropy leads to smaller expansion coefficients in the molecular planes. The Reuss-averaged Grüneisen function derived from (6–12) pair potentials is about 3.5 for most of the models; this is higher than observed experimentally in polycrystalline polyethylene, indicating the need for more realistic models of organic polymers.

RUTH MARGARET BARRON, THOMAS HUGH KENNETH BARRON, PAUL MALCOLM MUMMERY et MICHAEL SHARKEY. Can. J. Chem. **66**, 718 (1988).

Avec des paires typiques de potentiel, une liaison est allongée par des vibrations le long des directions de la liaison, alors qu'une contraction résulte d'une tension causée par des vibrations normales à la direction de la liaison. On étudie le rôle de ces deux effets dans des calculs sur des modèles de chaînes parallèles, linéaires ou en zigzag. Pour les chaînes linéaires ou en zigzag rigides, l'expansion est positive dans le plan normal à la direction de la chaîne, même si cette expansion peut être fortement anisotrope dans ce plan. L'expansion le long de la direction de la chaîne est négative et, d'une façon générale, elle est d'un ordre de grandeur plus faible que celle qui est normale à la chaîne. Pour une chaîne en zigzag flexible avec un angle de liaison de 90°, l'expansion est positive dans toutes les directions; le tenseur de Grüneisen est approximativement isotrope, mais l'anisotropie élastique conduit à des coefficients d'expansion qui sont plus faibles dans les plans moléculaires. La fonction de Grüneisen moyenne selon Reuss, obtenue à partir de paires (6–12) de potentiels, est à peu près égale à 3,5 pour la plupart des modèles; cette valeur est plus élevée que celle observée expérimentalement dans le polyéthylène polycristallin et elle indique qu'il est nécessaire d'avoir des modèles plus réalistes pour les polymères organiques.

[Traduit par la revue]

Can. J. Chem. Downloaded from www.nrcresearchpress.com by 93.93.197.157 on 09/07/12
For personal use only.

Introduction

Modelling the thermal expansion of polymeric solids presents formidable difficulties, for two reasons: (*i*) there is usually a strong dependence on morphology and crystal imperfections; (*ii*) the ideal perfect crystals usually have complex structures, in which both the elasticity and the vibrations depend on interatomic forces that are imperfectly understood. In the necessity of providing theories to discuss experimental results, many different ad hoc simplifications, assumptions, and approximations have been employed (see, for example, the brief review of Gibbons (1); also Engeln *et al.* (2), Choy *et al.* (3), and references therein). In an attempt to clear up one area of uncertainty, we have begun at Bristol to make a systematic study of the behaviour of ideal polymer crystals and its dependence both upon structure and upon the nature of the interatomic forces, starting from the simplest models and aiming towards models representing real polymers. In this we have two aims in view: (*i*) to test approximations and so find out under what circumstances they are reliable; (*ii*) to build up a detailed understanding of the underlying mechanism of the behaviour of polymeric crystals.

Theory

Grüneisen parameters and the thermodynamic Grüneisen function

We use the technique of quasi-harmonic lattice dynamics, in which the vibrations are treated as harmonic but with frequencies that depend on strain.[4] The application of this technique to crystals with varying internal strain has been illustrated by Gibbons (4) for tellurium and by Barron and Pasternak (5) for quartz. In lattice dynamics the vibrational modes are labelled by wave vector $\boldsymbol{q}$ and polarization index j. The strain derivatives of the vibrational frequencies $\nu(\boldsymbol{q},j)$ are conveniently described by dimensionless Grüneisen parameters for each mode $\boldsymbol{q},j$:

$$[1] \qquad \gamma_{\alpha\beta}(\mathbf{q},j) = -(\partial \ln \nu(\mathbf{q},j)/\partial \eta_{\alpha\beta})_{\eta'}$$

where $\eta_{\alpha\beta}$ is a component of the strain tensor and the subscript η' denotes that the other components are kept constant during differentiation. For an isotropic material we need consider only the volume dependence:

$$[2] \qquad \gamma(\mathbf{q},j) = -\mathrm{d} \ln \nu(\mathbf{q},j)/\mathrm{d} \ln V$$

These quantities arise in expressions for the thermal stress brought about by an increase of temperature, and the thermal expansion is then determined by the elastic response to this stress.

The thermal stress for an isotropic solid is $-(\partial P/\partial T)_V$. The change in stress is a response to the increase in energy density: $(\partial P/\partial T)_V$ is small at low temperatures, when the heat capacity is small, and varies by orders of magnitude as the temperature is increased. We therefore use the thermodynamic Grüneisen function $\gamma(T,V)$, which gives directly the change in thermal

[1]Now at Merton College, Oxford.

[2]Author to whom correspondence may be addressed.

[3]Now at Department of Metallurgy, Oxford.

[4]Choy *et al.* (3) give "quasiharmonic" a different meaning (see following page).

stress with internal energy density:

$$[3] \quad \gamma(T,V) = [\partial P/\partial(U/V]_V$$

The volumetric thermal expansion is then given by

$$[4] \quad \beta = \gamma C_V \chi_T / V$$

where χ_T is the isothermal compressibility.

For anisotropic solids the thermodynamic Grüneisen function becomes a tensor:

$$[5] \quad \gamma_{\alpha\beta} = -[\partial t_{\alpha\beta}/\partial(U/V)]_\eta$$

where $t_{\alpha\beta}$ is the stress tensor and the subscript η denotes constant strain. The response to the thermal stress is then determined by the elastic constants. In Voigt (single suffix) notation (see, e.g., ref. 6), the thermal expansion coefficients are given by

$$[6] \quad \alpha_\lambda = \sum_\mu s^T_{\lambda\mu}\gamma_\mu C_\eta / V$$

where C_η is the heat capacity at constant strain and the $s^T_{\lambda\mu}$ are elastic compliances. For example, a negative expansion in the z direction, α_3, may arise either from a negative γ_3 (s_{33} is always positive), or from negative cross compliances s_{13} and s_{23} (7).

The rôle of central forces

In quasi-harmonic theory the thermodynamic Grüneisen function is obtained as the average of the mode Grüneisen parameters weighted by the contributions of each mode to C_η:

$$[7] \quad \gamma_{\alpha\beta} = \sum_{\mathbf{q}} \sum_j \gamma_{\alpha\beta}(\mathbf{q}, j)\, c(\mathbf{q}, j; T)/C_\eta$$

Each vibrational mode can thus be considered as contributing separately to the thermal stress and hence to the thermal expansion. Its contribution depends not only on its degree of increased excitation but also on anharmonic terms in the crystal potential. For a pair (central force) interaction, thermal stress can arise in the following two ways (3, 8, 9):

1. *Bond-stretching effect.* When the vibration involves a component of relative motion along the bond, a negative cubic term in the pair potential will give rise to a thermal stress tending to extend the bond length. This effect has also been given the names *compression* (8), *bond anharmonicity* (9), and *intrinsic* (3); the second of these is misleading, since *all* effects in thermal expansion are anharmonic.

2. *Tension effect.* When the vibration involves relative motion perpendicular to the bond, the mean interatomic distance increases, and the resulting increase in bond tension causes a thermal stress tending to contract the bond and so restore the mean interatomic distance to its equilibrium value. This effect has also been given the names *shear* (8) and *quasi-harmonic* (3); the latter is misleading because the bond-stretching effect also is given by quasi-harmonic theory. When the relative motion also has a component along the bond there is an additional tension effect of *rotation* (9): the varying tension in the bond tends to rotate the direction of the bond away from the direction of the relative motion. However, different vibrations cause rotations in different directions: the net effect is identically zero in crystals of cubic symmetry, and is probably small in other crystals. In the present paper we derive only the total tension effect, without attempting to identify the rotation component separately.

The interatomic potentials used in our models are of the form

$$[8] \quad \phi(r) = \phi_0 + \frac{1}{2!}(r-r_0)^2\phi_0'' + \frac{1}{3!}(r-r_0)^3\phi_0'''$$

and are determined by the parameters ϕ_0'' and $r_0\phi_0'''$. The relative strength of the bond-stretching and tension effects is proportional to the ratio $r_0\phi_0'''/\phi_0''$. The Mie/Lennard-Jones 6–12 potential gives this ratio as -21, and not very different values are found for other short-range potentials in common use (10). An isotropic crystal with only one type of interacting pair gives a temperature independent bond-stretching contribution to $\gamma(T,V)$ of $-(r_0\phi'''/\phi_0'')/6$, and hence 3.5 for the 6–12 potential. This can be compared to a maximum contribution at low temperatures of -0.74 for the tension effect in close-packed crystals, decreasing in magnitude to -0.43 at higher temperatures when the vibrations are directed on average more along the bond directions. Tension effects can become larger and even dominant in crystals of open structure, where there are many vibrations polarized well away from any bond directions, and in crystals (such as polymers) where there are interactions of greatly differing magnitudes (1).

These points are conveniently illustrated by the work of Choy *et al.* (3) and Engeln *et al.* (2). To represent the thermal expansion of polymers, Choy *et al.* employed a model of parallel linear chains, in which central forces were supplemented by a bending force constant to keep the chains stiff; the intrachain bonds were stronger than the interchain bonds by about three orders of magnitude. By an appropriate choice of force constants, a fair fit was obtained to the anisotropic expansion of crystalline polyethylene as estimated from experimental data (11). Choy *et al.* concluded that the negative expansion along the chains was due solely to the tension effect; conversely, the positive expansion perpendicular to the chains was due to the bond-stretching effect, with a negligible contribution from the tension effect. This last conclusion is surprising, in view of the appreciable tension contribution to the expansion of close-packed isotropic crystals, and will be investigated further in the present paper.

Engeln *et al.* (2) made independent measurements of the thermal expansion of polyethylene. For a highly crystalline isotropic sample they obtained $\gamma(T,V)$ values of about 2 at low temperatures, falling off at higher temperatures when higher frequency modes were excited. This they compared with a much higher theoretical estimate obtained in the following way. It was assumed that at low temperatures the vibrations were perpendicular to the chain direction, and thus depended on weak intermolecular forces assumed to be derived from a 6–12 potential. An increase in volume was taken to be solely due to the increase in interchain distances, which was therefore given by $\delta r/r = \frac{1}{2}\,\delta V/V$, rather than by the expression $\frac{1}{3}\,\delta V/V$ for interatomic distances in an isotropic solid. $\gamma(T,V)$ was thus derived (from the bond-stretching contribution) as $-(r_0\phi_0'''/\phi_0'')/4 = 5.25$.

This derivation raises several important issues. We note in passing that the experimental value of $\gamma(T,V)$ at low temperatures is uncertain; the results of White and Choy (11) obtained by extrapolation from samples of varying crystallinity suggest a value of about 2.7. The theoretical argument tacitly makes the Reuss approximation (1), which neglects any local stresses that may develop in the material as the anisotropic crystallites expand. It also takes no account of the complex crystal structure of polyethylene, in which the interchain forces are between hydrogen atoms rather than the carbon skeletons, and in which also we have the possibility of changing orientation of the skeletal planes; nor does it consider noncentral forces. Finally, it neglects two effects that can be expected even with central forces between parallel skeletal chains: the tension effect, and the

Can. J. Chem. Downloaded from www.nrcresearchpress.com by 93.93.197.157 on 09/07/12
For personal use only.

effect of interchain interactions that are not perpendicular to the chain direction (thus giving a different value of $\delta r/r$). It is these last two effects we now investigate.

Flexible linear chain polymers

To obtain readily a stable structure, the model was developed from the highly stable face-centered cubic (fcc) lattice. The polymer crystal is obtained by strengthening all the bonds that run in one particular nearest neighbour direction. This destroys the cubic symmetry, and gives a body-centered orthorhombic crystal of parallel flexible chains linked by weaker interchain forces between the other nearest neighbours. With the *c*-axis in the chain direction, and the *b*-axis along an interchain bond perpendicular to the chain direction, the orthorhombic unit cell dimensions for the original fcc geometry are given by

$$[9] \quad a = \sqrt{2}, \qquad b = c = 1$$

where the unit of length is the nearest neighbour distance. Because the force constants no longer have cubic symmetry, thermal expansion will be anisotropic even when the starting configuration is cubic.

Besides the cell dimensions, the other input parameters of the model are the atomic mass, M, and two different sets of the force constants ϕ_0'' and $r_0\phi_0'''$ for the interchain and intrachain bonds. In all the present calculations M was taken to be 50 amu, and the ratio $r_0\phi_0'''/\phi_0''$ to be -21 as given by a 6–12 potential. The interchain force constants were taken to be

$$[10] \quad \phi_0''(\text{interchain}) = 3 \text{ N m}^{-1})$$

and the nearest neighbour distance to be 1 Å. The intrachain forces were varied between 3 N m^{-1} (giving cubic symmetry) and 30 000 N m^{-1} (giving an essentially rigid bond). The results for cubic symmetry gave isotropic behaviour in agreement with earlier work on the fcc lattice (see above). As ϕ_0'' (intrachain) was increased, behaviour became strongly anisotropic. Figure 1 shows the temperature dependence of the Grüneisen functions when ϕ_0'' (intrachain) = 30 000 N m^{-1}. Very large negative values are obtained for γ_3; they are due to the tension effect, the contribution of the bond-stretching terms (~2) being negligible by comparison, in agreement with the conclusion of Choy *et al.* (3). In contrast, γ_1 and γ_2 have increased only slightly from their values in the fcc lattice. As in the fcc lattice, their values are due mainly to the bond-stretching contributions, although the negative contributions of the tension effect remain appreciable. Anisotropy in the *xy* plane is weak.

Two other Grüneisen functions are shown in Fig. 1. γ_{REUSS} is the volumetric Grüneisen function under conditions of isotropic stress, and is an average of the γ_λ weighted by the compressibilities in each direction:

$$[11] \quad \gamma_{reuss} = (\chi_1\gamma_1 + \chi_2\gamma_2 + \chi_3\gamma_3)/(\chi_1+\chi_2+\chi_3)$$

The compressibilities for the model are given in $(TPa)^{-1}$ by

$$[12] \quad \chi_1 = 17.7, \qquad \chi_2 = 11.8, \qquad \chi_3 = 1.18 \times 10^{-3}$$

Despite the high values of γ_3, χ_3 is so small that the term $\chi_3\gamma_3$ is small compared with $\chi_1\gamma_1$ and $\chi_2\gamma_2$. γ_{VOIGT} is the volumetric Grüneisen function under conditions of isotropic strain, and is a simple arithmetic average:

$$[13] \quad \gamma_{VOIGT} = (\gamma_1 + \gamma_2 + \gamma_3)/3$$

It is dominated by γ_3, and hence by the tension effect.

The thermal expansion coefficients are shown in Fig. 2. They are derived by means of eq. [6], using the relevant compliances

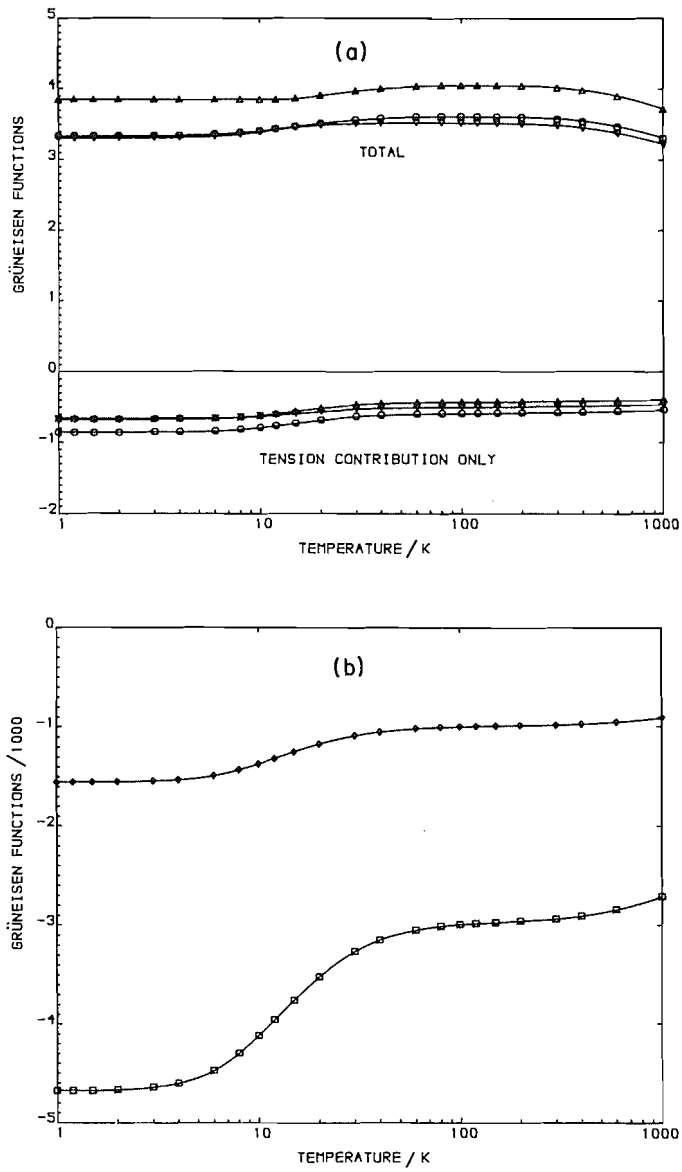

FIG. 1. Grüneisen functions for the linear chain model with cubic geometry and ϕ''(intrachain) = 30 000 N m^{-1}. (a) △, γ_1; △, γ_2; ○, γ_{REUSS}. (b) □, γ_3; ◇, γ_{VOIGT}.

of the static lattice; in Voigt notation, the compliances are given in $(TPa)^{-1}$ by

$$[14] \quad \begin{array}{ll} s_{11} = 29.4 & s_{12} = -11.8 \\ s_{22} = 23.6 & s_{23} = 0 \\ s_{33} = 2.36 \times 10^{-3} & s_{13} = -1.18 \times 10^{-3} \end{array}$$

The negative expansion in the chain direction is due to the tension effect. Despite the virtual incompressibility of the intrachain bonds, its magnitude is typically about 10% that of the expansion perpendicular to the bonds.

The negative values of γ_3 depend upon the magnitude of the tension produced by a given strain in the *c* direction, and hence are approximately proportional to the force constant ϕ_0''(intrachain). Reducing ϕ_0''(intrachain) to 300 N m^{-1}, we find γ_3 varying from about -44 at low temperatures to -26 at 200 K, with a further drop at higher temperatures as the intrachain modes become excited. However, until the intrachain modes are excited the values of γ_1 and γ_2 are very close to those given by ϕ_0''(intrachain) = 30 000 N m^{-1}; in each case the bonds

Can. J. Chem. Downloaded from www.nrcresearchpress.com by 93.93.197.157 on 09/07/12
For personal use only.

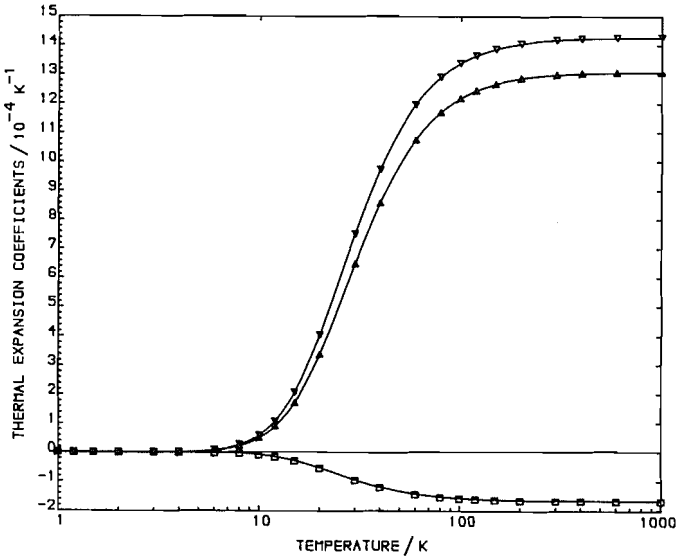

FIG. 2. Thermal expansion coefficients for the model of Fig. 1. ▽, α_1; Δ, α_2; □, α_3.

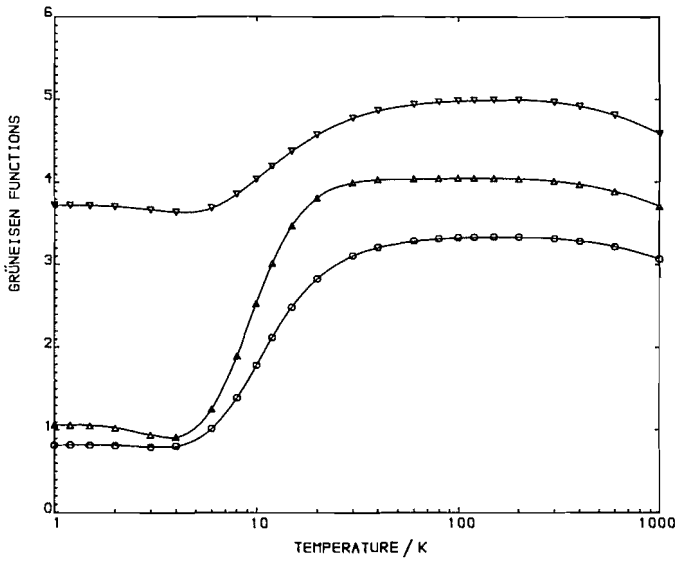

FIG. 3. Grüneisen functions for the linear chain model with the geometry of eqs. [16] and ϕ''(intrachain) = 30 000 N m^{-1}. ▽, γ_1; Δ, γ_2; ○, γ_{REUSS}.

are effectively rigid. We also see little change in the thermal expansion, even in the *c* direction, because although γ_3 is much smaller in magnitude and so gives rise to a lower thermal stress, the compressibility χ_3 is correspondingly larger. Each model corresponds closely to a system of light rigid rods freely jointed at their ends by massive bearings; the thermal motion causes the rods to librate as well as translate, so that the total length in the chain direction decreases.

We can now check whether the approximations used by Engeln *et al.* outlined above are valid for the present model. Since γ_{REUSS} is dominated by γ_1 and γ_2, it is a fair approximation to consider only those strains perpendicular to the polymer chains. But γ_1 and γ_2 are both considerably below the value of 5.25 assumed by Engeln *et al.* The tension effect contributes about −0.5 to the discrepancy. The remainder is chiefly due to the tacit assumption that the interchain interactions are perpendicular to the chain direction; in our model, four out of five bonds are at an angle of 60°, not 90°. A simple calculation shows that these bonds are longer than their interchain distance by a factor of 1/sin 60°, and also are stretched less by a factor sin 60°; allowing for this, the argument quoted by Engeln *et al.* would give a bond-stretching contribution to γ_{REUSS} of

[15] $5.25\,(\frac{4}{5}\sin^2 60° + \frac{1}{5}) = 4.20$

Adding the tension contributions gives an estimate for γ_{REUSS} of about 3.7, close to the computed value of about 3.6. There remains, however, an appreciable discrepancy between this value of 3.6 and experimental polycrystalline values of 2 and 2.7 (2, 11). One possible explanation is that local stresses are not wholly resolved in the experimental material, so that the relevant average of the γ_λ lies between γ_{REUSS} and γ_{VOIGT}.

To test these conclusions further, the geometry of the lattice was altered to make the interchain bonds more closely perpendicular to the chain direction. This was done by taking cell dimensions

[16] $a = 1.658$ Å, $b = 1$ Å, $c = 0.5$ Å

such that the intermolecular bond lengths all remained at 1 Å. Our expectation was that the values of γ_1, γ_2, and γ_{REUSS} would all increase from the values for cubic geometry, with little change in γ_3. In fact, the behaviour is more complicated (Fig. 3). γ_3 is indeed little altered and γ_1 is increased appreciably at high temperatures, and to a lesser extent at low temperatures, but γ_2 falls sharply at low temperatures. There is a large negative contribution from the tension effect to both γ_1 and γ_2 at very low temperatures, and γ_{REUSS} is decreased at all temperatures by appreciable weighting of γ_3 in the Reuss average, where the compressibilities in $(TPa)^{-1}$ differ markedly from those of eq. [12]:

[17] $\chi_1 = 4.11$, $\chi_2 = 8.79$, $\chi_3 = 5.03 \times 10^{-3}$

Admittedly, the model geometry is highly artificial, and possibly close to instability; it is unlikely to be realized by any real crystal. However, the results give warning that behaviour can be strongly dependent on structure, especially at low temperatures.

Parallel zigzag chain polymers

The crystal structure is shown in Fig. 4. The orthorhombic unit cell contains atoms at the points (0, 0, 0), $(ua, 0, \frac{1}{2}c)$, $(\frac{1}{2}a, \frac{1}{2}b, 0)$, $((\frac{1}{2} + u)a, \frac{1}{2}b, \frac{1}{2}c)$, and the geometry becomes face-centered cubic when $a = b = c$ and $u = \frac{1}{2}$. The parameter *u* is not determined by crystal symmetry, and so gives rise to an internal thermal expansion coefficient $\mathcal{A}_u = (\partial u/\partial T)_{\text{zero stress}}$.

In the cubic geometry, each atom has 12 equidistant nearest neighbours; two are in the same polymer chain, and interact strongly; the other 10 are in neighbouring chains. In place of angle forces, the bond angles are stiffened by second neighbour interactions ("struts") along the [001] direction. Calculations were also carried out with two geometries other than cubic, with bond angles of 109.5° (tetrahedral) and 120°, corresponding to ideal sp_3 and sp_2 hybridization in carbon chains. In these models the ratios *a:b:c* have been adjusted so that the interchain nearest neighbour distances remain equal to each other, although no longer equal to the intrachain bond length, which is held at 1.54 Å, a typical C—C bond length. The geometrical parameters of these models are given in Table 1.

In each model the atomic mass, *M*, has been taken to be 14 amu (the mass of a CH_2 group), $r_0\phi_0'''/\phi_0'' = -21$ for all interactions, and ϕ''(interchain) = 1 N m^{-1}. The other two force constants, ϕ''(intrachain) and ϕ''(strut), have been varied widely to give different types of polymeric behaviour. Face-centered

Can. J. Chem. Downloaded from www.nrcresearchpress.com by 93.93.197.157 on 09/07/12
For personal use only.

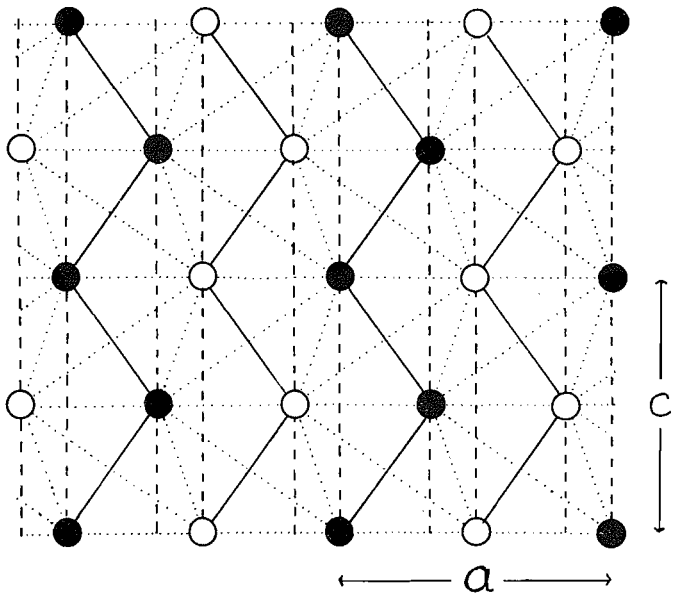

FIG. 4. Projection in the *xz* plane of the crystal structure of the parallel linear chains model. ●, $y = nb$; ○, $y = (n + \frac{1}{2})b$; —, intrachain bond; ---, strut; ·····, interchain bond.

TABLE 1. Geometrical parameters of the zigzag chain models

Bond angle/degrees	u	a/Å	b/Å	c/Å
90.0	$\frac{1}{2}$	2.178	2.178	2.178
109.5	$\frac{1}{3}$	2.515	3.443	2.667
120.0	$\frac{1}{4}$	2.667	4.356	3.080

cubic symmetry is given by cubic geometry with

[18] $\phi''(\text{intrachain}) = 1\ \text{N m}^{-1}, \qquad \phi''(\text{strut}) = 0$

Flexible linear chains

Taking ϕ''(intrachain) = ϕ''(interchain), but making ϕ''(strut) much larger, gives parallel flexible linear chains with a different type of packing from the models of the preceding section. With cubic geometry the symmetry is tetragonal.

Results confirm our previous conclusions. At low and intermediate temperatures, γ_1 and γ_2 remain close to their fcc values, falling off at the highest temperatures when the strut vibrations become excited; γ_3 is strongly negative, due to the tension effect, and rises with temperature. The thermal expansion coefficients perpendicular to the chain, α_1 and α_2, are close to their fcc values at all temperatures down to 20°C, becoming smaller by some 20% at the lowest temperatures; α_3 is negative, in magnitude about 6% (high temperatures) to 15% (low temperatures) of α_1 and α_2.

Flexible zigzag chains

Taking ϕ''(intrachain) much greater than ϕ''(interchain), and ϕ''(strut) = 0, gives a polymeric crystal of flexible zigzag chains. At low temperatures the tension effect produces a large negative thermal stress along each strong bond, tending to decrease the distances between atomic sites along the chain. However, this need not lead to negative values of γ_3 or α_3, because almost all the stress can be relaxed by rearrangement within the unit cell.

Figure 5 shows the Grüneisen functions for a model with

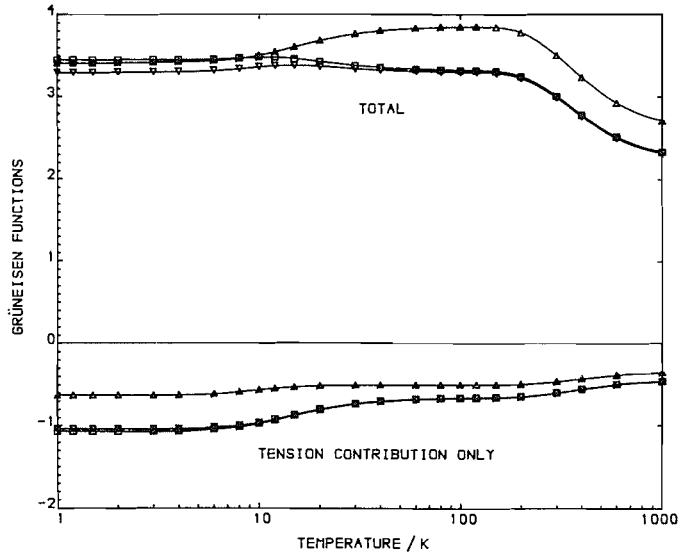

FIG. 5. Grüneisen functions for the flexible zigzag chains model with cubic geometry and ϕ''(intrachain) = 400 N m^{-1}. ▽, γ_1; Δ, γ_2; □, γ_3.

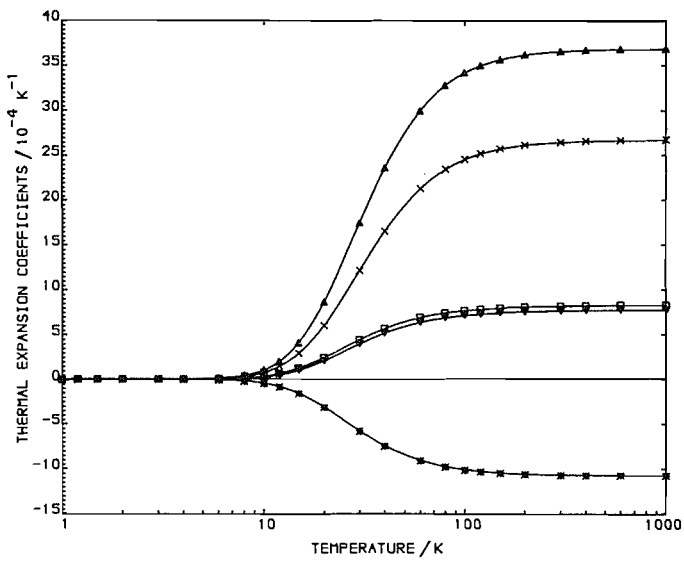

FIG. 6. Thermal expansion coefficients for the model of Fig. 5. ▽, α_1; Δ, α_2; □, α_3; ∗, $\mathcal{A}_u$; ×, α(fcc).

cubic geometry and ϕ''(intrachain) = 400 N m^{-1}. Differences from isotropic behaviour are fairly small; in detail, we note that it is the direction perpendicular to the planes of the molecules which is the odd one out, rather than the direction of the polymer chains. The decrease in the γ_λ at the highest temperatures is due to the excitation of intrachain bond-stretching modes.

Strong departures from isotropy are found for the thermal expansion (Fig. 6), with α_1 and α_3 reduced below fcc values and α_2 enhanced. This behaviour is associated with strong anisotropy in the cross compliances: in (TPa)$^{-1}$

[19] $s_{11} = s_{22} = s_{33} = 136.2$
$s_{23} = s_{12} = -27.3, \qquad s_{13} = -81.6$

Once again, it is the orientation of the molecular planes that appears to matter, and not the chain direction. The macroscopic behaviour would be little altered if the chain direction was taken along the *a*-direction.

The internal expansion coefficient $\mathcal{A}_u$ does, however, reveal

Can. J. Chem. Downloaded from www.nrcresearchpress.com by 93.93.197.157 on 09/07/12
For personal use only.

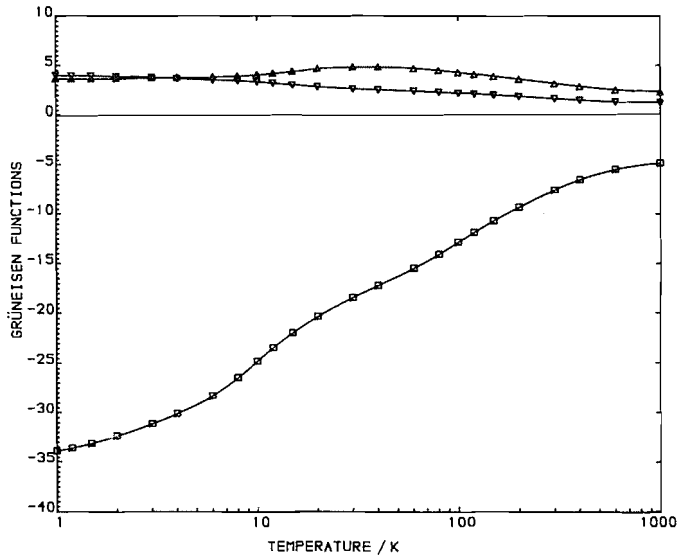

FIG. 7. Grüneisen functions for a stiffened zigzag chains model with tetrahedral bond angles and ϕ''(intrachain) = 400 N m^{-1}, ϕ''(strut) = 100 N m^{-1}. ▽, γ_1; △, γ_2; □, γ_3.

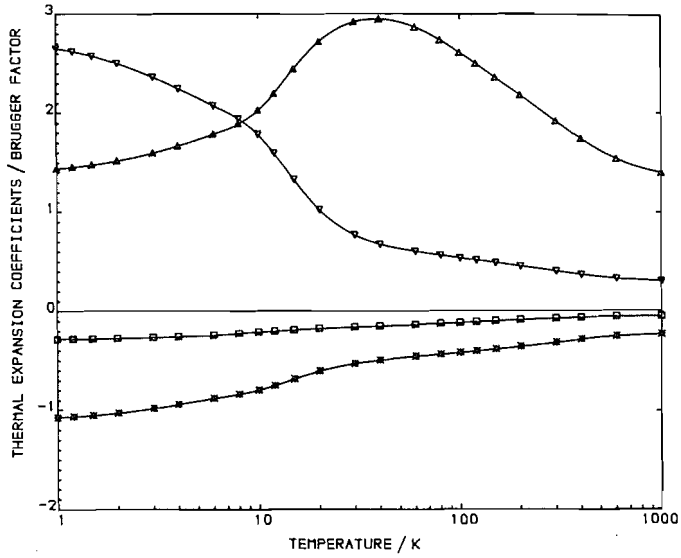

FIG. 8. Thermal expansion coefficients divided by the Brugger factor ($C_V\chi/V$), for the model of Fig. 7. ▽, α_1; △, α_2; □, α_3; ∗, $\mathcal{A}_u$.

dependence on the polymer chain direction. Its strong negative value is evidence of the opening of the angles in the polymer chain and the decrease in the chain width.

Calculations were also made for a model with the same force constants but with tetrahedral bond angles (Table 1). One effect is to enhance the difference between the values of γ_2 and the values of γ_1 and γ_3; at 150 K, $\gamma_1 = 3.2$, $\gamma_2 = 4.5$, $\gamma_3 = 3.0$. The main effect, however, is in the compliances and consequent thermal expansion. The compliances in (TPa)$^{-1}$ are now

$$\begin{array}{llll} & s_{11} = 270.6 & s_{23} = -16.3 \\ [20] & s_{22} = 97.4 & s_{31} = -189.2 \\ & s_{33} = 230.2 & s_{12} = -32.5 \end{array}$$

The balancing of terms of opposite sign in eq. [6] leads now to very small expansion in the chain direction; at 150 K,

$$\begin{aligned} &\alpha_1 = 6.8 \times 10^{-4}\,\mathrm{K}^{-1}, \\ [21]\quad &\alpha_2 = 13.2 \times 10^{-4}\,\mathrm{K}^{-1}, \\ &\alpha_3 = 0.8 \times 10^{-4}\,\mathrm{K}^{-1} \end{aligned}$$

Stiff zigzag chains

Taking both ϕ''(intrachain) and ϕ''(strut) much greater than ϕ''(interchain) gives a model of stiff polymer chains that might be expected to combine features of both the previous models. At low and intermediate temperatures the tension effect now produces negative thermal stresses along both the intrachain bonds and the struts. Stresses along the intrachain bonds can be relaxed as for the flexible chain by internal rearrangement within the unit cell, but those along the struts give rise to large negative values for γ_3.

Figure 7 shows Grüneisen functions for a model with tetrahedral bond angles and

$$\begin{aligned} [22]\quad &\phi''(\text{intrachain}) = 400\ \mathrm{N\ m^{-1}}, \\ &\phi''(\text{strut}) = 100\ \mathrm{N\ m^{-1}} \end{aligned}$$

The behaviour is broadly similar to that of the linear chain models, but with an increased anisotropy in the *ab* plane, due entirely to the bond-stretching contribution.

The elastic compliances are strongly anisotropic: in (TPa)$^{-1}$

$$\begin{array}{llll} & s_{11} = 115.7 & s_{12} = -45.9 \\ [23] & s_{22} = 96.3 & s_{23} = -0.064 \\ & s_{33} = 0.910 & s_{13} = -0.748 \end{array}$$

Combined with the anisotropy in the γ_λ and its variation with temperature, they give rise to a marked anisotropy in the thermal expansion coefficients. These are shown in Fig. 8, divided by the Brugger[5] factor $\chi C_\eta/V$ to reveal details of the low temperature behaviour. The magnitude of the expansion coefficients is markedly lower than for the fcc model.

The internal expansion coefficient $\mathcal{A}_u$ is again negative. At low and intermediate temperatures both the intrachain bond lengths and the strut length decrease with increasing temperature, due to the tension effect; since the bond length is shorter, its relative contraction is greater, so that the bond angle increases with temperature.

Calculations were also undertaken for two other models with the same values for the force constants but with bond angles of 90° (cubic geometry) and 120°. Broadly similar results were obtained, except that the expansion coefficients were lower for the model with the bond angle of 120°, and higher for that with the bond angle of 90°; probably this is because the crystal dimensions increase as the angle increases (Table 1), but the vibrations keep roughly the same amplitudes. The high temperature ratio α_2/α_1 was greatest for the model with bond angle 90°, for which α_2 remained greater than α_1 down to $T = 0$.

The stiffened zigzag chain thus behaves similarly to the flexible linear chain, except that there is greater anisotropy in the plane perpendicular to the chain direction.

Summary and conclusions

With linear chain polymers, and also with rigid zigzag chains, bond stretching causes a positive expansion in the intermolecular bonds; the negative tension effect is appreciable but smaller, so that the Grüneisen functions perpendicular to the chain direction have positive values of about 3.5; this is larger than for isotropic crystals, but considerably smaller than the value of

[5]The ratio $\alpha_\lambda V/\chi C_\eta$ is sometimes called the Brugger Grüneisen function (6, 12).

Can. J. Chem. Downloaded from www.nrcresearchpress.com by 93.93.197.157 on 09/07/12
For personal use only.

5.25 sometimes quoted for a "bundle of tubes" model. Along the chain direction the Grüneisen function is dominated by the tension effect and is large and negative, giving rise to a negative expansion of typically an order of magnitude less than that in the perpendicular directions. This negative expansion persists even when the intramolecular bonding becomes infinitely strong, since it is due not to changes in bond lengths, but to the librations of the rigid bonds. In the present central force models, the tension effect also causes a contraction in the zigzag chain widths and an increase in the bond angle.

The behaviour of a flexible zigzag polymer is radically different, because the tension-induced thermal stresses can be largely relieved by adjusting the bond angle. In the model of Figs. 5 and 6, the Grüneisen tensor is almost isotropic, and the thermal expansion positive in all directions.

The model of Fig. 3 provides a warning against sweeping generalizations, especially when the geometry is unusual. Nevertheless, because central forces play an important rôle in all crystals, the general conclusions outlined above give a valid, if partial, interpretation of observed polymeric behaviour. To go further, we need to take account of noncentral forces, and of internal degrees of freedom due to chain substituents and polymer plane reorientation. A full interpretation will also have to consider the effects of morphology.

1. T. G. GIBBONS. J. Chem. Phys. **60**, 1094 (1974).
2. I. ENGELN, M. MEISSNER, and H. E. PAPE. Polymer, **26**, 364 (1984).
3. C. L. CHOY, S. P. WONG, and K. YOUNG. J. Polym. Sci. **22**, 979 (1984).
4. T. G. GIBBONS. Phys. Rev. B, **7**, 1410 (1973).
5. T. H. K. BARRON and A. PASTERNAK. J. Phys. C: Solid State Phys. **20**, 215 (1987).
6. T. H. K. BARRON, J. G. COLLINS, and G. K. WHITE. Adv. Phys. **29**, 609 (1980).
7. R. W. MUNN. J. Phys. C: Solid State Phys. **5**, 535 (1972).
8. A. BIENENSTOCK and G. BURLEY. J. Phys. Chem. Solids, **24**, 1271 (1963).
9. T. H. K. BARRON and T. G. GIBBONS. J. Phys. C: Solid State Phys. **7**, 3260 (1974).
10. T. H. K. BARRON and M. L. KLEIN. Proc. Phys. Soc. **85**, 533 (1965).
11. G. K. WHITE and C. L. CHOY. J. Polym. Sci. **22**, 835 (1984).
12. K. BRUGGER and T. C. FRITZ. Phys. Rev. **157**, 524 (1967).

Can. J. Chem. Downloaded from www.nrcresearchpress.com by 93.93.197.157 on 09/07/12
For personal use only.

Models of picosecond-scale mobilities in glassy and polycrystalline quinoline

WALTER G. ROTHSCHILD

Physical and Chemical Sciences Laboratories, Ford Motor Co., Dearborn, MI 48121-2053, U.S.A.

Received September 28, 1987

This paper is dedicated to Professor J. A. Morrison

WALTER G. ROTHSCHILD. Can. J. Chem. **66**, 725 (1988).

The observed inhomogeneous band broadening of the 1033-cm^{-1} ir C—H in-plane deformation fundamental of quinoline in a glassy state and a polycrystal at 115 K was related to the theoretical concepts of the underlying vibrational T_2 processes. The motional narrowing model that fits best the spectral data and reflects the particular physical nature of the locally-ordered glass is the recently introduced stretched ("extended", "fractional") exponential $\exp[-(t/\tau)^{\alpha}]$. Extension of the model to shorter time regimes is discussed. The modulation model which simulates the corresponding spectral data and describes the longer-range order of the polycrystal is the damped oscillator $\exp(-t\gamma/2)[\cos\theta t + (\gamma/2\theta)\sin\theta t]$, previously proposed for oscillator – lattice mode coupling.

WALTER G. ROTHSCHILD. Can. J. Chem. **66**, 725 (1988).

La relaxation de phase de la vibration de déformation C—H à 1033 cm^{-1} observée en absorption infrarouge pour la quinoline à l'état vitreux et polycristallin (115 K) est analysée selon les concepts théoriques d'un processus de déphasage vibrationnel. L'exponentielle "étendue" $\exp[-(t/\tau)^{\alpha}]$ que nous avons récemment introduite comme fonction de modulation pour les corps amorphes localement structurés simule bien les données spectrales et rend compte du caractère particulier de l'état vitreux; nous discutons ici son application au régime des temps courts. L'oscillateur amorti $\exp(-t\gamma/2)[\cos\theta t + (\gamma/2\theta)\sin\theta t]$, connu depuis longtemps comme fonction de modulation en présence d'un couplage entre l'oscillateur et les vibrations du reseau, prédit le rétrécissement dynamique du spectre en relation avec l'ordre à longue distance de l'état polycristallin.

Introduction

The inhomogeneous broadening of spontaneous vibrational band contours, the so-called vibrational dephasing or T_2 process, is one of the few mechanisms that can be employed to give quantitative information on the fast dynamics of a "bath" or lattice surrounding a convenient probe oscillator. Briefly, the theory is set up in terms of the equation of motion of the stochastic oscillator amplitude $m(t)$ moving under a perturbation potential $H_1(t)$ that accounts for the elastic interaction between the bath coordinates and the ground and excited vibrational levels of the probe oscillator (1–3). Since phonon depopulation of the excited oscillator level is relatively slow, only the diagonal elements in the bath–oscillator interaction matrix are retained (4). The most convenient approach then resolves, to all practical purposes, to a judicious and problem-related choice of the autocorrelation function of the fluctuation $\Delta V(t)$ of the intermolecular potential $V(t)$ at the oscillator displacement coordinate (3, 5–7). In turn, $\Delta V(t)$ is considered to be proportional to $H_1(t)$ and, hence, to the shift of the stochastic transition frequency $\hbar^{-1}H_1(t) = \omega_1(t)$ (counted from the band center, ω_c, $\omega_1 \equiv \omega - \omega_c$) (8). Consequently, the problem of having to write out the physical model of the particular form of the amplitude autocorrelation

$$[1] \quad C(t) = \langle m(t)m(0)\rangle\langle|m(0)|^2\rangle^{-1}$$

is then reduced to that of formulating a relevant and physically sound correlation function ("modulation function") of $\omega_1(t)$ (2),

$$[2] \quad F(t) = \langle\omega_1(t)\omega_1(0)\rangle\langle|\omega_1(0)|^2\rangle^{-1}$$

with

$$C(t) = \exp\left\{-\langle|\omega_1(0)|^2\rangle\int_0^t dt'(t-t')F(t')\right\}$$

In the following, we shall discuss previously published vibrational dephasing data of the C—H in-plane deformation fundamental of quinoline (a', 1033 cm^{-1}) in a glassy and a polycrystalline phase, using a new model of non-Markovian modulation quite recently introduced by us and a well-known damped-oscillatory modulation function, respectively. It will be seen that the data simulation as well as the expected physics of the static-dynamic properties of the respective systems are considerably better mirrored by these models than by the usual Gauss–Markov mechanism (exponential modulation). Finally, we draw comparisons with other models.

Experimental

The material, the experimental spectral procedures as well as the method of numerical Fourier inversion have been described previously (9, 10). We merely recall that the band of the polycrystal is, as expected, blue-shifted (by 1 cm^{-1}) from that of the glass (quenched liquid, 115 K). The respective (full) halfwidths are 2.5 and 9 cm^{-1}. The oscillator profile of the glass is asymmetric (10); however, the perturbing effect is not serious within the range of the experimental correlation data. Furthermore, the baselines of the profiles are flat and overlap with adjacent bands is minimal or easily corrected (10). Therefore, the correlation data are not disturbed by sinc-type oscillations within the time domain considered here.

The data fit of the theory for the glassy state (see eq. [3]) was performed by using standard integration subroutines and judging the best-fit to the data by eye. The glassy quinoline is in a slow modulation regime; this, as we have discussed previously (11), means that it is not possible to identify a unique set of α, τ but that its most reasonable range must be obtained from considerations of the physics of the system (see also below).

Data fit of the theory for the polycrystal is straightforward; it has been described previously (12).

Results and discussion

Glassy state

The theoretical vibrational amplitude correlation function that is expected to respond well to the complex static and the convoluted dynamics of the vibrational dephasing process of glassy systems is given by (13)

$$[3] \quad C(t) = \exp\{-\langle|\omega_1(0)|^2\rangle(\tau^2/\alpha)[(t/\tau)\gamma(1/\alpha, (t/\tau)^{\alpha}) - \gamma(2/\alpha, (t/\tau)^{\alpha})]\}$$

where $0 < \alpha \leq 1$ is the so-called dispersion or shape parameter

Can. J. Chem. Downloaded from www.nrcresearchpress.com by 176.9.209.113 on 09/07/12
For personal use only.

and τ a time constant, γ denotes the incomplete γ function, and $\langle|\omega_1(0)|^2\rangle$ is the vibrational second spectral moment of the profile $I(\omega)$. Equation [3] is computer-fitted, as described in the previous section, to the experimental $C(t)$ and $\langle|\omega_1(0)|^2\rangle$,

$$[4] \quad C(t) = \text{F.T.}\{I(\omega)\}$$

$$\langle|\omega_1(0)|^2\rangle = \int_{-\infty}^{\infty} d\omega I(\omega)(\omega - \omega_c)^2$$

where F.T. designates Fourier transform and ω_c is set equal to the first moment of the profile.

It is easy to see that setting $\alpha = 1$ in eq. [3] yields the relation (10)

$$[5] \quad C(t) = \exp\{-\langle|\omega_1(0)|^2\rangle[\tau^2(\exp(-t/\tau) - 1) + \tau t]\}$$

that has been so useful to describe vibrational dephasing in nonassociated, mobile liquids (14).

For short t, eq. [3] approximates a Gaussian (leaving the first correction term)

$$[6] \quad C(t) = \exp\{-\langle|\omega_1(0)|^2\rangle t^2[(1/2) - (t/\tau)^\alpha/(\alpha + 2)(\alpha + 1)]\}$$

whereas for long t it approximates an exponential,

$$[7] \quad C(t) = \exp\{-\langle|\omega_1(0)|^2\rangle \tau\Gamma(1 + 1/\alpha)t\}$$

where Γ is the Euler γ function (13).

The modulation function $F(t)$ (see eq. [2]) inherent in eq. [3] is the stretched ("fractional", "extended") exponential

$$[8] \quad F(t) = \exp[-(t/\tau)^\alpha]$$

a formulation that has been shown to describe a wide range of diverse non-Markovian relaxation processes (15). (For a detailed description of its properties within the relaxation scheme of vibrational modes of amorphous systems ref. 13 should be consulted.)

Equation [6] demonstrates that for $t/\tau \equiv t^* \ll 1$, the smaller is α, the shorter is the time domain of pure Gaussian decay. In fact, for times beyond and up to a crossover time, it is easily seen from eq. [6] that $C(t^*, \alpha < 1) > C(t^*, \alpha = 1)$. In other words, for $t^* \lesssim 1$, $C(t^*, \alpha)$ decays the slower the smaller is α, whereas for $t^* \gtrsim 1$, $C(t^*, \alpha)$ decays the faster the smaller is α. The value t_c^* at the crossover point (where all $C(t^*, \alpha)$ intersect) must be calculated from eq. [3]. Comparison of the series development of the latter (13) with that of eq. [5] shows readily that $t_c^* > 1$. Note that the crossover point may not be reached within the experimental range of $C(t)$ if the system is in a slow modulation regime (see below). The crossover point of $F(t^*, \alpha)$ is, of course, at $t_c^* = 1$.

Application of eq. [3] to the spectral profile $I(\omega)$ of the C—H in-plane deformation oscillator of quinoline quenched rapidly from the liquid to 115 K is shown in the left portion of Fig. 1. The system is in a slow modulation regime (13),

$$[9] \quad \sigma = \langle|\omega_1(0)|^2\rangle^{1/2}\Gamma(1 + 1/\alpha)\tau \gtrsim 2$$

with $\langle|\omega_1(0)|^2\rangle = 0.6 \times 10^{24}$ (radian/s)^2.

Therefore, dispersion parameter α and time constant τ cannot be uniquely determined within a desired, narrow range in this system here since, as already mentioned above, the constant factor in the exponent of eq. [3] is so large (τ is so long) that $C(t)$ has dropped below its experimentally known range at a time point still within the condition $t^* \lesssim 1$. (See also Fig. 2 of ref. 11.) In other words, least-squares minimization methods for optimizing the fit of eq. [3] to the data (16) would not converge here to *one* set of α, τ. For instance, the sets α, τ = 1.0, 3 ps; 0.60, 7 ps; and 0.30, 40 ps fit the data about equally well.

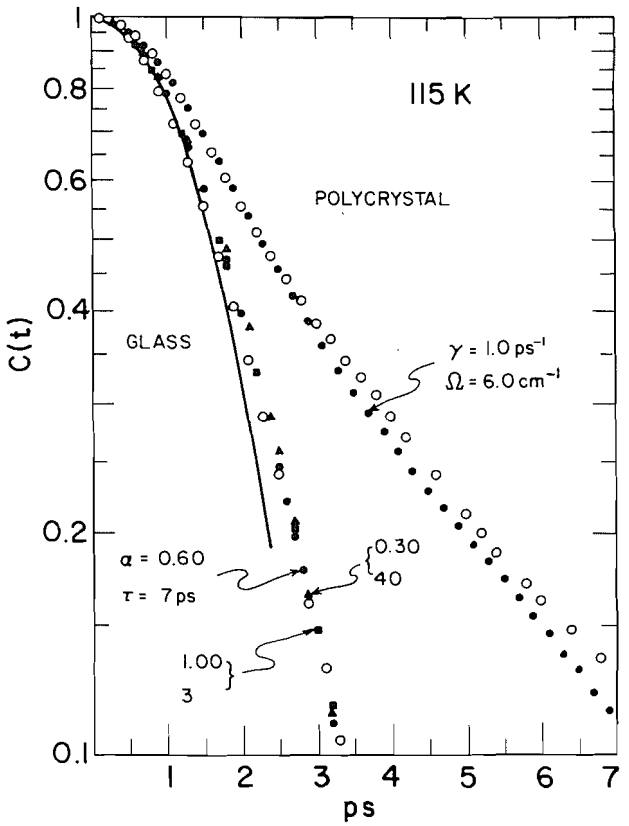

FIG. 1. Vibrational amplitude autocorrelation for the C—H in-plane (a') infrared oscillator of quinoline at 1033 cm^{-1}. The open circles are the data (via eq. [4]), the solid points are calculated with eq. [3] (glass) and eq. [14] (polycrystal).

Yet, it is clear that correlation decay for an assumed static regime ($t \sim 0$), namely the pure Gaussian decay of $C(t)$ (see eq. [6]), is definitely too rapid (see the curve in Fig. 1). Consequently, the particular glassy state of quinoline observed here is not devoid of some type of *relatively rapid* motion which effectively modulates the oscillator frequency. However, we propose that those sets of α associated with longer τ, say $5 < \tau < 40$ ps, render a more plausible picture of the physical dynamical situation in low-temperature glassy quinoline than the shorter τ (at $\alpha \sim 1$). In this respect, consider that modulation time τ for liquid quinoline at 303 K amounts to 0.3 ps (10); using the small, average activation factor of 1 kcal/mol, this would lengthen τ already to ~5 ps at 115 K — all other conditions remaining the same. Notice that $\tau \sim 40$ ps is, in principle, an observable upper limit under optimal accuracy $\Delta\nu = \pm 0.2$ cm^{-1} of a bandwidth measurement.

$$[10] \quad \tau \sim (\pi c \Delta\nu)^{-1} \sim 50 \text{ ps}$$

Values of dispersion parameter α, in the lower ranges of the order of 0.3–0.6, have been established for other relaxation phenomena in amorphous states (17). However, it is difficult to be confident in singling out one of the fundamental physical processes that have been shown to lead to a relaxation function of the type of eq. [8] (15) such as defect diffusion or hierarchically-constrained dynamics. First, it seems that these physical models are only valid for long t, a situation that is not satisfied by

Can. J. Chem. Downloaded from www.nrcresearchpress.com by 176.9.209.113 on 09/07/12
For personal use only.

the observable dynamics of the glassy quinoline system ($\sigma \gg 1$, see eq. [9]). Second, these particular models rest on rather specific boundary conditions (15) such as form of intermolecular potential and dimensionality of the lattice, a situation which has been criticized (18) (it appears rightly) as going against the *universal* experimental applicability of eq. [8] as well as its worthiness at "shorter t". Third, eq. [8] can also result from a model of many, parallel and *independent* relaxation pathways, each of which is governed by pure exponential decay,

$$[11] \quad F(t) = \exp[-(t/\tau)^{\alpha}] = \int_0^{\infty} d\tau p_{\alpha}(\tau) \exp(-t/\tau)$$

where $p_{\alpha}(\tau)$ is the continuous probability density of the τ's (19). The parallel-independent relaxation pathway model has been termed "microscopically arbitrary" (20) as regards $p_{\alpha}(\tau)$ since any reasonable function $F(t)$ should be expressible in terms of its inverse Laplace transform (eq. [11]). Yet, there is no proof against the parallel-independent relaxation model and it has shown its worthiness in many relevant situations (21, 22).

Therefore, under these presently unresolved circumstances, it appears wise to propose a general, less model-dependent basis for the success of eq. [8] in the system investigated here; after all, the ubiquitous pure-exponential modulation model ($\alpha = 1$) is also, fundamentally, an (convenient) assumption. In this frame of mind, it is useful to recall that the age-specific failure rate $h(t)$ associated with $F(t)$ of eq. [8] (23),

$$[12] \quad h(t) = (\alpha/\tau)(t/\tau)^{\alpha-1}$$

decreases hyperbolically with t for $0 < \alpha < 1$. Without attempting to define any *specific* modulation process for a glass, this, at least, gives a useful hint to the effect that the dynamics of the glassy quinoline which lead to a modulation event at the active oscillator site are far removed from a chain of uncorrelated random steps ($\alpha = 1$, $h(t)$ = constant). Equation [12] shows that the later is the time instant of observation, the smaller is the rate $h(t) = f(t)/F(t)$; in other words, the later is t, the smaller is the probability density $f(t)$ that the autocorrelation of the random oscillator frequency $\omega_1(t)$ changes at t relative to the probability $F(t)$ (survivor probability (24))

$$[13] \quad F(t) = \int_t^{\infty} dt\, f(t)$$

that it has *not yet changed* at times $t_i \leq t$. The effect of the sets of α, τ (ps) = 1.00, 3; 0.60, 7; 0.30, 40 on $h(t)$ are shown in Fig. 2, which also contains the (near-identical) associated $F(t)$: the increased drop of $h(t)$ with decreasing α is evident.

We then picture the dynamical events that lead to a modulation step of the oscillator state in the glassy phase of quinoline to arise from motions within large, frozen-in "faults" that suddenly cause a "catastrophic" potential fluctuation in the immediate neighborhood of the probe oscillator *after an initial period of completely randomly-distributed* (Poisson) *modulation events*. Such initial, pure-exponential modulated decay (eq. [5]) has also been observed in other amorphous, locally-structured systems (11, 13, 16). Thus, it appears that the picosecond dynamics of a quenched glassy phase, as they are exhibited here in their effects on motional band narrowing of an internal probe oscillator in quinoline, arise from "liquid-like", completely randomly-occurring fluctuations in the environment of the probe oscillator ($h(t)$ = constant) that are superposed by early, singular (non-Markovian) and more extensive potential excursions ($\alpha < 1$), conceivably due to relaxation of frozen-in structure faults. In this context, it is useful to recall that this particular glassy state was generated by cooling the compound in its absorption cell from its liquid (at 303 K) to 115 K at an approximate cooling rate of 40 deg/min. Also, with respect to the following discussion of the polycrystalline phase, the latter was prepared by gradual cooling to 115 K (mp 258 K).

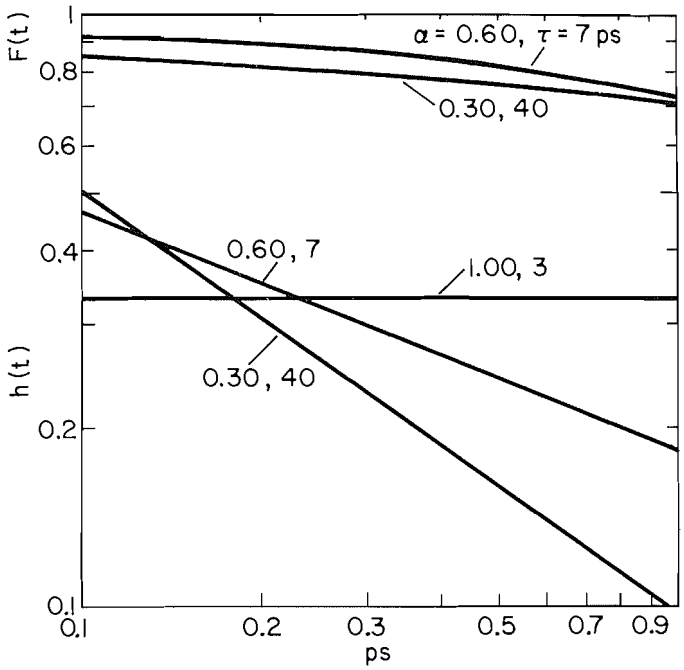

FIG. 2. Survivor functions $F(t)$ (eq. [8]) and age-specific failure rates $h(t)$ (eq. [12]) for the C—H in-plane oscillator of the glassy state of quinoline. For instance, at t = 1 ps, $h \sim 0.1$ for the set α, τ (ps) = 0.30; 40, $h \sim 0.2$ for 0.60; 7, and $h \sim 0.3$ for 1.00; 3 at essentially identical F's.

Polycrystal

The characteristics of the vibrational amplitude correlation of the C—H deformation of quinoline in its polycrystalline phase, shown in the right portion of Fig. 1, are entirely different from those of its glass. First, the vibrational correlation decay of $C(t)$ is slower than in the glass. Second, the experimental $C(t)$ shows a "dip" in the time domain between 2–4 ps, an effect that can be reproduced by the theoretical amplitude correlation function (12, 25)

$$[14] \quad C(t) = \exp(-\langle|\omega_1(0)|^2\rangle\Omega^{-2}[t\gamma + \Omega^{-2}\{(\gamma^2 - \Omega^2) \times [\exp(-t\gamma/2)\cos\theta t - 1] + (\gamma/2\theta)(\gamma^2 - 3\Omega^2)\exp(-t\gamma/2)\sin\theta t\}])$$

where $\theta = (\Omega^2 - \gamma^2/4)^{1/2}$. Equation [14] is based on modulation function

$$[15] \quad F(t) = \exp(-t\gamma/2)[\cos\theta t + (\gamma/2\theta)\sin\theta t]$$

the well-known harmonic librational oscillator, and is proposed to describe coupling of the internal probe oscillator coordinate to lattice phonons of mean frequency Ω (25); γ is here the damping constant of the autocorrelation of the (instantaneously acting) random force of the bath. Notice that eq. [14] has as many adjustable parameters (two) as eq. [3].

The plot of the autocorrelation data and best-fit values of γ and Ω from eq. [14] are displayed in the right-side portion of Fig. 1; Ω corresponds here to a frequency distribution that is

Can. J. Chem. Downloaded from www.nrcresearchpress.com by 176.9.209.113 on 09/07/12
For personal use only.

peaked in the far-infrared. We have not succeeded in finding data on lattice mode distributions of crystalline quinoline which could be used to verify whether $\Omega = 6\ cm^{-1}$ is a reasonable value. On the other hand, such a low frequency would indicate whole-molecule displacements or libratory motion about center-of-mass equilibrium positions (rather than some internal motion). It is also interesting to note that the time scale τ corresponding to $\Omega = 6\ cm^{-1}$ falls near the lower limit of the range of the τ's for the glassy state of quinoline. The motional narrowing effect in the polycrystal is therefore considerably greater than that in the glass. For the latter (eq. [9]), $\sigma = 8$ with the set $\alpha, \tau = 0.6, 7$ ps. For the former, $\sigma = \langle|\omega_1(0)|^2\rangle^{1/2}(\theta + \gamma/2)/\Omega^2 = 0.8$, $\langle|\omega_1(0)|^2\rangle = 11\ cm^{-2}$.

Finally, we note that $F(t)$ of eq. [15] cannot be considered here as proper survivor function (eq. [13]) per se since its derivative (24),

$$[16] \quad -(d/dt)F(t) = f(t) = (\Omega^2/\theta)\exp(-t\gamma/2)\sin\theta t$$

is not a true probability density function ($f(t) < 0$ for $n(\pi/\theta) < t < (n + 1)(\pi/\theta)$, n odd). In fact, $F(t)$ passes first into a negative region at $t = 2.05$ ps. However, $F(t)$ may be artificially truncated to zero for $t > 2$ ps by a step function. The visible perturbation on $C(t)$ by this operation would be small since $C(t)$ becomes essentially exponential (Markovian) for $t \gtrsim 2$ ps.

Comparison with other models

Whereas the inhomogeneous vibrational dephasing process as understood here (that is to say, the scattering of bath excitations by the probe oscillator coordinate without exchange of energy) is by all accepted notions the singly prevalent vibrational relaxation mechanism in amorphous substances, there is no guarantee that this must always be so. There are documented cases of a concurrent, extraordinarily rapid phonon population relaxation by quasi-resonant (intramolecular) energy transfer (26). Yet, it appears that this phenomenon is restricted to C—H valence stretches in near-resonance with a C—H deformation overtone. Therefore, we shall not consider an appropriate two-process vibrational relaxation model, suggested by Guillaume *et al.* (27), since there is no independent data base to verify its contribution to phonon depopulation in the type of systems considered here. Furthermore, the model displays unphysical behavior at $t \rightarrow 0$. Similarly, the two-process relaxation model by Katō and Takenaka (28), which essentially separates the purely static contribution in the exponent of eq. [5], the second-order term, into two portions of which one is factored out into a pure Gaussian ("inhomogeneous" contribution) and the remainder left as leading term of the series in t^* ("homogeneous", rapidly-modulated contribution), is not useful here. It appears futile to establish a countable number of sufficiently different, quasi-static environments in the quenched quinoline without detailed structural information. The modulation function contains an additive, constant term (29): it therefore lacks all finite moments and the corresponding $C(t)$ is unphysical in not attaining exponential decay at long times.

1. A. D. Buckingham. Trans. Faraday Soc. **56**, 753 (1960).
2. P. W. Anderson. J. Phys. Soc. Jpn. **9**, 316 (1954).
3. W. G. Rothschild. Dynamics of molecular liquids. Wiley-Interscience, New York. 1984. p. 221.
4. D. J. Diestler. Chem. Phys. Lett. **39**, 39 (1976).
5. D. W. Oxtoby. J. Chem. Phys. **74**, 1503 (1981).
6. D. W. Oxtoby and S. A. Rice. Chem. Phys. Lett. **42**, 1 (1976).
7. S. F. Fischer and A. Laubereau. Chem. Phys. Lett. **35**, 6 (1975).
8. S. Bratoz, J. Rios, and Y. Guissani. J. Chem. Phys. **52**, 439 (1970).
9. W. G. Rothschild. *In* Molecular motions in liquids. *Edited by* J. Lascombe. D. Reidel Publ. Co, Dordrecht, 1974. p. 247.
10. W. G. Rothschild. J. Chem. Phys. **65**, 455 (1976); see also ref. 3, Fig. 3.12.a.
11. W. G. Rothschild, M. Perrot, and F. Guillaume. Chem. Phys. Lett. **128**, 591 (1986); **131**, 164 (1986) [Erratum].
12. W. G. Rothschild, J. Soussen-Jacob, J. Bessière, and J. Vincent-Geisse. J. Chem. Phys. **79**, 3002 (1983).
13. W. G. Rothschild, M. Perrot, and F. Guillaume. J. Chem. Phys. **87**, 7293 (1987).
14. N. Trisdale and M. Schwartz. Chem. Phys. Lett. **68**, 461 (1979).
15. J. Klafter and M. F. Shlesinger. Proc. Natl. Acad. Sci. USA, **83**, 848 (1986).
16. W. G. Rothschild, R. M. Cavagnat, and M. Perrot. Chem. Phys. **118**, 33 (1987).
17. J. T. Bendler and K. L. Ngai. Macromolecules, **17**, 1174 (1984).
18. R. W. Rendell and K. L. Ngai. *In* Relaxation in complex systems. *Edited by* K. L. Ngai and G. B. Wright. Publ. Natl. Tech. Inform. Serv., US Dept. Commerce, Springfield, VA. 1984. p. 309.
19. E. W. Montroll and J. T. Bendler. J. Statist. Phys. **34**, 129 (1984).
20. R. G. Palmer, D. L. Stein, E. A. Abrahams, and P. W. Anderson. Phys. Rev. Lett. **53**, 958 (1984).
21. T. Doba, K. U. Ingold, and W. Siebrand. Chem. Phys. Lett. **103**, 339 (1984).
22. C. P. Lindsey and G. D. Patterson. J. Chem. Phys. **73**, 3348 (1980).
23. D. R. Cox. Renewal theory. Methuen, London. 1970. p. 21.
24. V. Bury. Statistical models in applied science. Wiley, New York. 1974. p. 30.
25. G. N. Robertson and J. Yarwood. Chem. Phys. **32**, 267 (1978).
26. A. Laubereau and W. Kaiser. *In* Chemical and biological applications of lasers. Vol. 2. Academic Press, New York. 1977. p. 87.
27. F. Guillaume, M. Perrot, and J. Lascombe. J. Chim. Phys. **82**, 949 (1985).
28. T. Katō and T. Takenaka. Mol. Phys. **46**, 257 (1982).
29. T. Katō. J. Chem. Phys. **84**, 3409 (1986).

Can. J. Chem. Downloaded from www.nrcresearchpress.com by 176.9.209.113 on 09/07/12
For personal use only.

The thermodynamics of orientational disorder in a molecular solid: $(CH_3)_3CCHO$

MARY ANNE WHITE[1] AND ALLYSON PERROTT
Department of Chemistry, Dalhousie University, Halifax, N.S., Canada B3H 4J3
Received September 8, 1987

This paper is dedicated to Professor James A. Morrison

MARY ANNE WHITE and ALLYSON PERROTT. Can J. Chem. **66**, 729 (1988)

The heat capacity of *tert*-butylaldehyde, $(CH_3)_3CCHO$, has been measured as a function of temperature from 29 to 298 K, to investigate solid-state polymorphism. There are two solid–solid phase transitions in this material, T_{tr} = 158.5 and 183.9 K, $\Delta S_{tr} = 0.402R$ and $3.153R$ respectively. The thermodynamic parameters for the transitions are consistent with mechanisms proposed on the basis of recent nuclear magnetic resonance investigations of this material.

MARY ANNE WHITE et ALLYSON PERROTT. Can J. Chem. **66**, 729 (1988)

Afin d'étudier le polymorphisme à l'état solide, on a mesuré la capacité calorifique du *tert*-butylaldéhyde, $(CH_3)_3CCHO$, en fonction de la température de 29 à 298 K. Avec ce produit, on a observé deux transitions de phase solide–solide, T_{tr} = 158,5 et 183,9 K, $\Delta S_{tr} = 0{,}402R$ et $3{,}153R$. Les paramètres thermodynamiques pour les transitions sont en accord avec les mécanismes proposés en se basant sur des études récentes en résonance magnétique nucléaire de ce composé.

[Traduit par la revue]

Can. J. Chem. Downloaded from www.nrcresearchpress.com by 93.93.197.157 on 09/07/12
For personal use only.

Introduction

The possibility of relatively free reorientational motion in a solid was first proposed by Pauling in 1930 (1), and the study of orientation disorder in crystals (ODIC) has been fruitful in recent years, both experimentally and theoretically. The archetypal example of restricted rotation or reorientation in the solid phase that exists just below the melting point is, of course, solid methane (2, 3), and the title compound can be considered to be *spiritus paludis ornatum*. $(CH_3)_3CCHO$ (2,2-dimethylpropanal, also known as *tert*-butylaldehyde, pivalaldehyde, pivaldehyde, and trimethylacetaldehyde), like many other substances with roughly spherical molecules, including the *tert*-butylhalides and methyl chloroform, exhibits a solid rotator phase (4–6). This orientationally disordered phase has been confirmed by measurements of dielectric constant and proton magnetic resonance linewidth of $(CH_3)_3CCHO$ (5), and by studies of the ^2H nmr lineshapes for $(CD_3)_3CCHO$ (7).

Since other compounds similar to $(CH_3)_3CCHO$, such as trimethylchlorosilane, 3,3-dimethyl-2-butanone, and 2,2-dimethylpropane nitrile, do not possess solid rotator phases (5), several criteria to predict the presence of rotator phases have been suggested. These criteria include consideration of bond lengths and deviations from spherical symmetry (8); the volume required for dipole rotation (6); the ratio of molecular interaction energies for the dipolar relaxation process and the viscosity process (4). Unfortunately, none of these approaches has proven to be reliable, as can be seen in the compilations of Krishnaji and Mansingh (4) and Segel and Mansingh (5).

Several works (9–11) summarize the observed properties of rotator phases. Although the lattice is crystalline in the rotator phase, rotational freedom of the molecules makes the properties of the rotator phase intermediate between those of the liquid and "normal" solid phases. In some of these properties the rotator phase may actually be closer to the liquid phase. Solids in the rotator phase tend to be soft and waxy, while the non-rotator phases tend to be harder and brittle. Because solids in the rotator phase can be extruded by relatively low pressures, they are often referred to as "plastic" crystals. The X-ray diffraction pattern of a rotator phase is diffuse, with a good deal of background scattering. Although the dielectric constant of an orientationally ordered solid drops dramatically on cooling through the freezing point, the dielectric constant of a substance possessing a solid rotator phase increases slightly on freezing (9, 10).

The heat capacities of two substances possessing solid rotator phases, *tert*-butylchloride (2-chloro-2-methylpropane) and *tert*-butylbromide (2-bromo-2-methylpropane), were investigated by Kushner, Crowe, and Smyth (12). The results showed two solid–solid phase transitions for each compound. For *tert*-butylchloride, the enthalpy and entropy of the lower-temperature transition were found to be substantially lower than those for the higher-temperature transition. It was concluded therefore that most of the rotational freedom does not set in until the higher-temperature transition is reached. For *tert*-butylbromide, the enthalpy and entropy of the lower-temperature transition are greater than those for the higher-temperature transition. In this case, most of the rotational freedom sets in at the lower transition. In both compounds, the entropy of fusion is low ($<0.95R$) indicating that nearly all of the discontinuous increase in entropy taking the ordered solid to the liquid is obtained over the two transitions. This is typical for compounds possessing solid rotator phases, and Timmermans' early criterion (13) for orientational disorder in the solid was based on the value of the entropy of fusion ($<2.5R$).

The aim of the present work was to measure the heat capacity of *tert*-butylaldehyde and determine the enthalpy and entropy of its solid–solid transitions, to clarify the nature of its phase transitions. Discrepancies between the literature values of the melting point of $(CH_3)_3CCHO$ (*vide infra*) and the question of the effect of impurity on the phase transitions led us to measure the heat capacities of both a commercial and a purified (distilled) sample of $(CH_3)_3CCHO$.

Experimental

The heat capacities were measured in an adiabatic heat-pulse calorimeter. The calorimeter, which is described in detail elsewhere (14), is known to have an accuracy of ±0.5% from our measurement of the heat capacity of Calorimetry Conference (NBS-49) benzoic acid. The temperature (resistance of the Pt thermometer) and heat input were measured with a Hewlett–Packard 3456A digital multimeter, interfaced with a Hewlett–Packard HP87A personal computer (14).

As there has been some discrepancy in the literature concerning the purity of *tert*-butylaldehyde (see Results and discussion), two samples were used. The first of these was a commercial sample (Aldrich,

[1]Author to whom correspondence may be addressed.

Can. J. Chem. Downloaded from www.nrcresearchpress.com by 93.93.197.157 on 09/07/12
For personal use only.

TABLE 1. Experimental values of the heat capacity of $(CH_3)_3CCHO$ (undistilled)

T/K	C_p/(J K^{-1} mol^{-1})	T/K	C_p/(J K^{-1} mol^{-1})
29.08	26.31	164.49	155.8
31.96	29.10	164.85	148.5
34.80	30.97	165.31	145.8
35.79	32.28	165.77	144.1
37.17	32.98	166.48	143.7
40.12	38.34	168.52	144.7
44.16	40.10	169.45	143.9
45.05	41.50	170.57	146.0
48.70	44.99	171.53	147.2
53.24	46.19	172.59	149.4
54.98	48.54	173.61	152.5
57.53	50.60	174.59	155.1
62.39	52.38	175.58	158.7
65.04	55.19	177.04	165.9
67.49	56.49	177.94	167.6
72.37	59.98	178.62	169.3
72.41	59.91	179.05	166.8
77.14	63.52	179.45	171.4
81.63	66.77	180.61	179.5
82.29	66.97	181.01	181.1
86.29	70.00	181.41	184.5
86.74	69.94	181.81	186.8
87.14	70.67	182.20	190.2
89.45	72.54	182.57	207.7
90.97	73.15	182.94	246.3
95.11	76.45	183.26	289.1
95.64	76.45	183.57	331.8
97.12	77.70	183.83	422.7
100.31	79.42	184.04	593.7
102.95	81.67	184.19	808.4
104.99	82.70	184.29	1206.
105.14	83.27	184.38	1353.
109.66	86.21	184.44	1570.
110.59	87.18	184.50	1834.
113.19	89.70	184.55	2012.
114.33	90.48	184.60	2163.
118.26	93.85	184.64	2314.
119.02	94.58	184.69	2333.
121.16	96.77	184.73	2518.
125.99	101.6	184.77	2749.
128.95	105.2	184.88	2775.
133.73	110.6	184.92	2614.
136.73	115.1	184.96	2566.
141.48	121.6	185.01	2322.
144.50	127.1	185.06	1807.
146.44	130.7	185.13	1415.
147.14	131.9	185.23	1066.
147.92	133.0	185.39	640.3
148.61	134.7	185.67	287.3
150.48	137.5	186.17	149.7
150.72	138.7	186.71	147.3
152.80	144.3	187.22	148.3
154.83	150.1	187.91	146.1
156.84	156.3	193.52	144.8
158.78	164.6	196.07	144.9
160.68	171.4	202.06	147.3
161.82	179.2	202.36	147.8
162.25	177.8	210.03	148.7
162.50	185.0	210.57	151.1
162.66	179.1	218.14	152.9
163.09	172.1	218.54	154.2
163.51	173.3	226.49	156.8
163.96	149.8	234.49	158.7
164.40	146.8	242.46	163.7
246.58	166.4	266.08	344.4
247.90	166.9	266.27	360.1
249.65	173.0	266.78	383.8
250.84	171.8	267.25	405.1
251.91	176.4	267.70	439.6
253.78	181.4	267.74	444.0
254.10	182.3	267.97	468.6
256.31	187.8	268.20	455.9
256.71	192.0	268.65	494.8
257.63	198.8	269.07	499.5
258.42	202.3	269.11	529.3
259.62	210.8	269.50	526.7
260.46	219.7	269.89	562.8
261.06	223.7	270.30	645.1
262.29	238.0	270.41	629.5
262.46	243.5	270.71	612.7
262.50	248.4	272.23	183.1
262.92	250.7	273.72	185.3
263.52	262.0	276.78	186.0
264.06	287.6	282.12	187.6
264.33	285.9	282.84	190.0
264.66	292.6	290.27	190.3
265.20	305.2	296.81	194.0
265.29	318.8	298.43	192.8
265.76	335.6		

TABLE 1 (*concluded*)

nominally 97%), the same as was used for the protonated-sample measurements in the recent nmr investigations (7). The heat capacity of 2.2969 g of this sample was measured from $T = 28$ to 298 K.

The second sample was prepared from the first by distillation. The fraction collected boiled at 74°C at a pressure of 760.5 Torr (1 Torr = 1.33.3 Pa). The heat capacity of 2.6328 g of this sample was measured from $T = 113$ to 296 K.

Gas chromatographic/mass spectroscopic checks of the two samples revealed that the commercial sample was 95% pure, with nine detectable impurity peaks. The distilled sample was considerably cleaner, 99% pure, with only one detectable impurity. The mass spectrum of the impurity and the infrared spectrum of the distilled sample indicated that the impurity is likely 2,2-dimethylpropanol.

Results and discussion

The experimental values of the molar heat capacity, C_p, of the commercial and distilled samples of *tert*-butylaldehyde are given in Tables 1 and 2, respectively. Neither sample showed any thermal history effects in the heat capacity results, and the relaxation times following heating were relatively short (generally <5 min, but up to 20 min in the region of the higher-temperature solid–solid transition), consistent with rapid attainment of thermal equilibrium.

The only literature value of the heat capacity of $(CH_3)_3CCHO$ available for comparison with the present measurements is one measurement, in the liquid state, at $T = 298$ K (15), and our measurements for the distilled sample are 1.4% higher at this temperature.

The results of the measurements on both samples are illustrated in Fig. 1. The overall features are very similar for both samples, showing the presence of two solid–solid phase transitions prior to melting. At low temperatures, $T < 150$ K, the heat capacity curves merge, but at higher temperatures there are some differences.

TABLE 2. Heat capacity results for $(CH_3)_3CCHO$ (distilled)

T/K	C_p/(J K^{-1} mol^{-1})	T/K	C_p/(J K^{-1} mol^{-1})
112.80	88.28	194.27	146.5
115.59	90.74	197.88	147.9
120.44	95.09	203.25	149.7
125.46	100.1	207.84	151.6
130.25	105.5	209.94	152.5
135.27	112.0	213.16	154.0
139.84	118.5	217.75	156.5
144.86	127.3	217.76	157.7
149.46	136.7	222.97	156.6
151.63	140.9	225.49	156.8
154.07	148.0	227.61	154.8
155.82	154.6	232.87	155.7
156.68	157.2	233.42	156.1
157.55	160.2	237.62	156.6
159.25	163.6	240.31	156.9
160.50	157.2	241.96	157.9
160.96	156.1	242.77	157.6
162.69	146.3	242.84	158.8
163.35	143.9	243.56	157.0
164.46	142.0	244.36	158.6
166.21	143.1	245.16	160.1
166.23	142.4	246.76	158.6
168.00	144.7	247.67	161.6
169.06	146.7	249.09	160.8
169.75	147.9	251.43	164.8
171.49	150.9	252.80	169.6
171.92	152.7	253.71	168.8
173.19	156.1	255.18	173.0
174.77	160.5	255.96	175.2
174.89	160.8	258.16	184.7
176.55	167.0	260.07	198.2
177.58	179.0	260.30	197.2
178.17	185.0	262.39	217.5
179.63	251.9	262.69	242.1
180.16	303.7	263.42	234.3
180.82	335.8	264.32	253.0
181.76	432.9	265.20	276.1
182.36	477.2	266.12	304.5
182.75	546.9	266.93	340.0
183.10	621.4	267.78	368.9
183.42	668.9	268.59	380.5
183.72	719.1	269.31	388.1
184.00	779.5	270.23	429.1
184.25	863.5	270.73	463.9
184.48	939.3	271.84	546.2
184.70	1010.	272.06	553.3
184.91	1047.	272.63	350.3
185.12	987.9	272.99	509.2
185.36	848.3	273.56	358.7
185.71	618.3	273.60	228.9
185.73	475.9	274.40	180.0
187.80	142.6	275.50	180.8
188.38	143.7	275.56	179.6
188.84	142.6	277.50	181.7
189.78	143.7	279.52	182.9
190.71	142.8	282.52	183.6
191.62	144.6	285.58	185.4
192.51	145.2	292.58	188.1
193.40	146.7	295.77	187.8
194.04	146.6		

The earliest report of the synthesis of $(CH_3)_3CCHO$ gave its melting point as 276 K (16). A slightly later synthesis gave $(CH_3)_3CCHO$ with melting point of 279 K (17). We find the melting point of our commercial sample to be 270.3 ± 0.2 K, and that of the distilled sample to be 272.1 ± 0.3 K. If the highest literature value for the melting point, 279 K, is correct, the two present measurements of the melting point as a function of purity must reflect a steep change in melting point at low impurity levels in $(CH_3)_3CCHO$, and a leveling off at slightly higher impurity levels. Our attempts to determine the true melting point of $(CH_3)_3CCHO$ by extrapolation of the plot of the reciprocal of the fraction melted (1 / F) as a function of temperature to F = 1 yielded a value of 277 ± 2 K; the large uncertainty is due to the high curvature of the plot, which indicates that the *tert*-butylaldehyde and its impurity form a solid solution (18). It is interesting to note that the early investigation of the dielectric constant (5) was carried out on a sample with a boiling point that matched that of the literature (17) value, 348 K, but with an exceptionally low melting point, 228 K, yet the dielectric measurements showed clearly the existence of the higher-temperature phase transition.

Two solid–solid phase transitions are seen in the commercial and the distilled sample of $(CH_3)_3CCHO$. A summary of the transition temperatures (determined from the maxima in C_p), enthalpies (determined from the "long heat" method (19)), and entropies is given in Table 3. The transformations overlap somewhat and, for the purpose of assessing the relative contributions of each to the enthalpy and entropy, the solid–solid transitions were partitioned at the minimum between them. Although this division is necessarily arbitrary, it does not affect the total transition entropy or enthalpy. In the distilled sample, 2% of the total entropy occurs within 3.4 K of the lower-temperature maximum in C_p, and 56% of the total transition entropy occurs within 3.8 K of the higher-temperature maximum in C_p, and similar values were obtained for the commercial sample. Therefore, there is no doubt that most of the entropy change is associated with the higher-temperature transformation.

Despite the broadening of the higher-temperature solid–solid transition in the purer sample (see Fig. 1) and its slightly lower transition temperature, the entropy and enthalpy changes of this transition are substantially unchanged with level of purity. The temperature, enthalpy, and entropy of the lower-temperature transformation differ somewhat more between the two samples (Table 3). One curious finding is the slight thermal anomaly at about 220 K in the distilled sample that is absent in the commercial sample. In general, we believe that the purer sample reflects more accurately the true thermodynamic properties of $(CH_3)_3CCHO$, and we will base our further discussion on the results obtained with the sample that was prepared by distillation.

It is useful to compare the transition entropies with those of other *tert*-butyl compounds that also exhibit polymorphism; these values are given in Table 4 for $(CH_3)_3CX$ for X = Cl, Br, SH, CHO. It is striking that each of these compounds has one transition with ΔS_{tr} ca. $3.2R$, and one or more smaller transitions, most often of ΔS_{tr} ca. $0.5R$. The order of these transitions is not the same in each compound; the lowest-temperature transition has the smallest entropy in X = CHO and Cl, while in X = Br and SH it has the highest entropy.

Although these entropy arguments hint that these compounds fall into two categories (CHO and Cl; Br and SH), nmr results show that this view is too simplistic. In particular, ^2H lineshapes

Can. J. Chem. Downloaded from www.nrcresearchpress.com by 93.93.197.157 on 09/07/12
For personal use only.

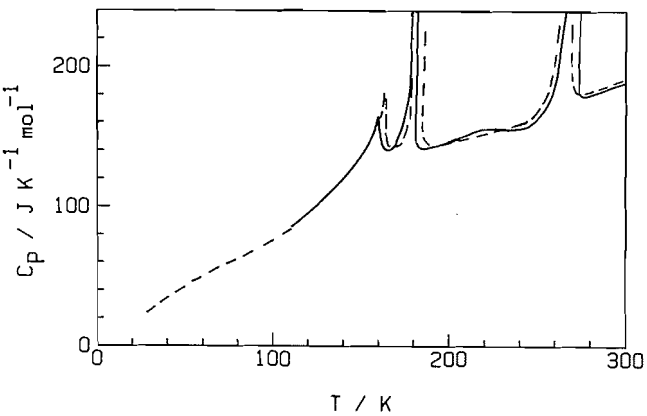

FIG. 1. The experimental molar heat capacity, C_p, of $(CH_3)_3CHO$ as a function of temperature. The dashed line represents the heat capacity of the commercial sample and the solid line represents the heat capacity of the sample that was purified by distillation.

TABLE 3. The thermodynamic parameters for the phase transformations in two samples of $(CH_3)_3CCHO$

Transformation	T/K	ΔH/(J mol^{-1})	ΔS/(J K^{-1} mol^{-1})
Commercial sample (95%)			
Fusion	270.3 ± 0.2	2970 ± 20	11.00 ± 0.07
I→II	184.9 ± 0.1	4868 ± 3	26.40 ± 0.015
II→III	162.5 ± 0.1	675 ± 7	4.41 ± 0.04
Purified sample (99%)			
Fusion	272.1 ± 0.3	2520 ± 30	9.3 ± 0.1
I→II	183.9 ± 0.8	4809 ± 3	26.22 ± 0.015
II→III	158.5 ± 1.9	499 ± 6	3.34 ± 0.04

TABLE 4. The thermodynamic parameters of the phase transformations in $(CH_3)_3CX$

X	T_{tr}/K	$\Delta S_{tr}/R$	Reference
CHO	158.5 ± 1.9	0.402 ± 0.005	This work
	183.9 ± 0.8	3.153 ± 0.002	This work
Cl	183.2	1.2	11
	219.6	3.22	11
Br	208.7	3.3	11
	231.6	0.55	11
SH	151.6	3.23	20
	157.0	0.50	20
	199.4	0.58	20

have shown that the onset of the rotations of the methyl groups (C_3 rotations) and the rotations about the C—X axis (C_3' rotations) is strongly dependent on X, from stepwise onset for *tert*-butylchloride (21) to C_3 and C_3' motions commencing at about the same temperature in *tert*-butylaldehyde (7).

From the nmr study of *tert*-butylaldehyde (7), it is known that the rigid ^2H nmr lineshape for *tert*-butylaldehyde begins its collapse at a temperature of about 100 K, close to the temperature at which the heat capacity begins to rise appreciably from the baseline. It should be emphasized that there is no transition per se at 100 K, but that this serves as a well-documented example of the *initiation* of a phase transition commensurate with changes in the nmr lineshape.

The nmr experiments on *tert*-butylaldehyde have shown that at $T = 153$ K the "fingerprint" of rapid C_3 and C_3' motions, a 12–14 kHz splitting in the ^2H powder spectrum, is observed. Slightly beyond that temperature additional motion sets in, and from the nmr experiments and information known from early dielectric work (5), it has been proposed (7) that rotations about the C_2' axis (the axis passing through the center of mass and parallel to the dipole moment) set in. Although this motion does not give rise to a discontinuity in $^2H(T_1)$, the nmr experiment does show unusual behaviour of the ^2H quadrupole coupling tensor in this temperature region (7). It is now apparent from the calorimetric experiment that C_2' rotations are responsible for the lower-temperature phase transformation. The entropy change associated with this transition can be reconciled with a twofold increase in accessible positions, as $R \ln 2$ ($0.69R$) is quite close to the observed entropy change ($0.53R$), especially considering the error involved in partitioning the total entropy change between the two transitions. It should be noted that this transition has virtually no first-order character.

As the temperature is increased further, the molecular reorientations in *tert*-butylaldehyde become faster, resulting finally in the transformation at $T = 184$ K to the "plastic crystalline" (rotator) phase. This is the transformation that is associated with the larger entropy change, consistent with overall molecular tumbling in the highest-temperature solid phase of *tert*-butylaldehyde. The entropy change is close to that seen in the transformation to the rotator phase in *tert*-butylchloride, which has been attributed to an increase from two orientations in the solid to 40 ($R \ln 40/2 = 3.00R$); the small additional entropy change ($0.22R$ for X = Cl, $0.15R$ for X = CHO) is likely due to slight structural rearrangement of the lattice.

It is interesting to note that replacement of the aldehydic proton of *tert*-butylaldehyde with a methyl group (to give 3,3-dimethyl-2-butanone) apparently prevents the occurrence of an orientationally disordered solid phase (5). Both compounds are predicted to have solid rotator phases on the basis of the Smyth (bond lengths) and the Clemett (dipole–dipole interaction compared to the thermal energy at the freezing point) criteria. It seems likely that the predictive powers of these simple criteria are limited by the assumption of single-particle motions in these solids; reorientational motions in globular molecular solids are more likely to involve intermolecular cooperation.

Finally, we should like to comment that the simplicity of the atomic composition of *tert*-butylaldehyde, and the availability of reliable C,H,O interatomic potentials, make $(CH_3)_3CCHO$ an excellent candidate for Monte Carlo and (or) molecular dynamical simulation calculations.

Acknowledgements

The authors are grateful to Prof. R. E. Wasylishen and Dr. S. Mooibroek for useful discussions, and for making available their results prior to publication. The authors are grateful to the Thermodynamics Research Center for aid in locating original references to the melting point of $(CH_3)_3CCHO$, to Dr. M. J. M. Van Oort for experimental assistance, and to Dr. D. Hooper, M. Snow, and K. Henseleit for analytical help. This work was supported by NSERC through an Undergraduate Research Award (A.P.), and a University Research Fellowship, Operating and Equipment Grants (M.A.W.).

Can. J. Chem. Downloaded from www.nrcresearchpress.com by 93.93.197.157 on 09/07/12
For personal use only.

This paper is dedicated to the memory of the late Professor James A. Morrison, in thanksgiving for his many contributions to science and society.

1. L. PAULING. Phys. Rev. **36**, 430 (1930).
2. M. BLOOM and J. A. MORRISON. *In* Surface and defect properties of solids. Vol. 2. *Edited by* M. W. Roberts and J. M. Thomas. The Chemical Society, London. 1973. p. 140.
3. K. MAKI, Y. KATAOKA, and T. YAMAMOTO. J. Chem. Phys. **70**, 655 (1979).
4. KRISHNAJI and A. MANSINGH. J. Chem. Phys. **44**, 1590 (1966).
5. S. L. SEGEL and A. MANSINGH. J. Chem. Phys. **51**, 4578 (1969).
6. N. E. HILL. Trans. Faraday Soc. **55**, 2000 (1959).
7. S. MOOIBROEK, R. E. WALYLISHEN, J. B. MACDONALD, C. E. RATCLIFFE, and J. A. RIPMEESTER. Can. J. Chem. **66**, 734 (1988).
8. C. P. SMYTH. J. Phys. Chem. Solids, **18**, 40 (1961).
9. N. G. PARSONAGE and L. A. K. STAVELEY. Disorder in crystals. Clarendon Press, Oxford. 1978.
10. J. N. SHERWOOD (*Editor*). The plastically crystalline state. John Wiley and Sons, New York. 1979.
11. C. P. SMYTH. J. Chim. Phys. **63**, 59 (1966).
12. L. M. KUSHNER, R. W. CROWE, and C. P. SMYTH. J. Am. Chem. Soc. **72**, 1091 (1950).
13. J. TIMMERMANS. J. Chim. Phys. **35**, 331 (1938).
14. M. J. M. VAN OORT and M. A. WHITE. Rev. Sci. Instrum. **58**, 1239 (1987).
15. R. FUCHS. Can. J. Chem. **58**, 2305 (1980).
16. L. TISSIER. Ann. Chim. Phys. **29**, 321 (1893).
17. A. RICHARD. Ann. Chim. Phys. **21**, 323 (1910).
18. E. F. WESTRUM, JR. and J. P. MCCULLOUGH. *In* Physics and chemistry of the organic solid state. Vol. 1. *Edited by* D. Fox, M. M. Labes, and A. Weissberger. Interscience, New York. 1963. p. 1.
19. M. J. M. VAN OORT and M. A. WHITE. J. Chem. Soc. Faraday Trans. 1, **81**, 3059 (1985).
20. G. B. GUTHRIE and P. MCCULLOUGH. J. Phys. Chem. Solids, **18**, 53 (1961).
21. J. C. FROST, A. J. LEADBETTER, and R. M. RICHARDSON. Phil. Trans. R. Soc. Lond. B,**290**, 567 (1980).

Can. J. Chem. Downloaded from www.nrcresearchpress.com by 93.93.197.157 on 09/07/12
For personal use only.

A nuclear magnetic resonance study of *tert*-butylaldehyde and *tert*-butyliodide[1]

SANDRA MOOIBROEK,[2] RODERICK E. WASYLISHEN[3], AND J. B. MACDONALD
Department of Chemistry, Dalhousie University, Halifax, N.S., Canada B3H 4J3

AND

CHRISTOPHER I. RATCLIFFE AND JOHN A. RIPMEESTER
Division of Chemistry, National Research Council of Canada, Ottawa, Ont., Canada K1A 0R9

Received September 14, 1987

This paper is dedicated to Professor James A. Morrison

SANDRA MOOIBROEK, RODERICK E. WASYLISHEN, J. B. MACDONALD, CHRISTOPHER I. RATCLIFFE, and JOHN A. RIPMEESTER. Can. J. Chem. **66**, 734 (1988).

Deuterium nuclear magnetic resonance lineshapes for polycrystalline $(CD_3)_3CCHO$ and $(CD_3)_3CI$ have been investigated between 100 K and the melting point of each sample. As in other *tert*-butyl compounds, rotational motion of methyl and *tert*-butyl groups occurs in the lowest temperature phase, while the solid phase just below the melting point is characterized by overall molecular rotations in both *tert*-butylaldehyde and *tert*-butyliodide. The "rotator" phase is observed in *tert*-butyliodide-d_9 between 239 and 212 K only upon cooling; no solid–solid phase transition is observed upon heating. In $(CD_3)_3CCHO$, two solid–solid phase transitions are observed at 165 ± 5 K and 190 ± 2 K. Deuterium nuclear magnetic resonance lineshapes in the solid II phase are consistent with rapid 180° flips about a pseudo-C_2 axis. Deuterium spin-lattice relaxation times were measured in the liquid, solid I, and solid II phases of $(CD_3)_3CCHO$, and in the liquid and rotator phases of $(CD_3)_3CI$ and $(CD_3)_3CCl$. The data for both the chloride and the iodide compounds indicate a discontinuous increase in the rotational correlation time upon melting, similar to that observed in $(CD_3)_3CBr$ and $(CD_3)_3CSH$. However, neither ^2H nor ^{13}C T_1's of the methyls indicate that a discontinuity occurs at the melting point for *tert*-butylaldehyde. Carbon-13 and ^{17}O relaxation times of the aldehyde substituent support this result.

SANDRA MOOIBROEK, RODERICK E. WASYLISHEN, J. B. MACDONALD, CHRISTOPHER I. RATCLIFFE et JOHN A. RIPMEESTER. Can. J. Chem. **66**, 734 (1988).

Opérant entre 100 K et le point de fusion de chaque échantillon, on a étudié les formes des raies en résonance magnétique nucléaire du deutérium du $(CD_3)_3CCHO$ et du $(CD_3)_3CI$ polycristallins. Comme il a été observé avec d'autres composés *tert*-butylés, le mouvement de rotation des groupements méthyles et *tert*-butyles se produisent à la température la plus basse; par ailleurs, la phase solide, juste au-dessous du point de fusion, est caractérisée par des rotations moléculaires globales tant dans le *tert*-butylaldehyde que dans l'iodure de *tert*-butyle. Pour l'iodure de *tert*-butyle-d_9, on n'a pu observer la phase "rotator" que lors du chauffage entre 239 et 212 K. Dans le $(CD_3)_3CCHO$, on a observé les deux phases de transition solide–solide à 165 ± 5 K et à 190 ± 2 K. Les formes des raies en résonance magnétique nucléaire du deutérium de la phase solide II sont en accord avec des inversions rapides de 180° autour du pseudo-axe C_2. On a mesuré les temps de relaxation spin-réseau du deutérium dans les phases liquide, solide I et solide II du $(CD_3)_3CCHO$ et dans les phases liquide et rotator du $(CD_3)_3CI$ et $(CD_3)_3CCl$. Les données tant pour le dérivé chloré que pour le dérivé iodé indiquent qu'il existe une augmentation discontinue du temps de corrélation rotationnel au point de fusion et ce comportement est semblable à celui observé avec le $(CD_3)_3CBr$ et le $(CD_3)_3CSH$. Toutefois, les T_1 des groupements méthyles tant du ^2H que du ^{13}C n'indiquent pas la présence d'une discontinuité au point de fusion du *tert*-butylaldéhyde. Les temps de relaxation du ^{13}C et du ^{17}O du substituant aldéhyde supportent ce résultat.

[Traduit par la revue]

Introduction

tert-Butyl-X compounds (X = CH_3, Cl, Br, SH, etc.) have generated considerable interest over the past few years (1–3) due to their solid–solid phase transitions and characteristic orientational disorder in crystal (ODIC) properties. Typically, these compounds have a "rotator" phase (solid I) just below the melting point, in which the molecules undergo rapid, liquid-like reorientation, and a low temperature phase (solid II or III, etc.) in which reorientation is restricted to rotations or $2\pi/3$ jumps of the methyl groups (C_3) and the *tert*-butyl group (C_3') (4, 5). Other types of reorientation may occur in the intermediate phase(s), but these appear to be highly dependent on the substituent X (6).

Relatively little is known about the X = aldehyde or iodide derivatives in the solid state. Early dielectric measurements on *tert*-butyliodide (7) indicated a phase change at 198 K, while a later study (8) found no evidence for a solid–solid phase change in DTA or X-ray diffraction data, nor any abrupt changes or discontinuities in the temperature dependence of either the dielectric constant or the ^1H nmr second moment below the melting point of 236 K. A smooth decrease in the proton second moment between 115 and 170 K was interpreted as increasingly rapid C_3 and C_3' rotations. However, a more recent ^1H nmr study (9) found a large discontinuity in the temperature dependence of the spin-lattice relaxation time, T_1, at 222 K. A minimum in the lowest temperature phase was attributed to methyl reorientations, while molecular tumbling and translational motions were thought to contribute to T_1 in the 222–236 K interval.

Measurements of the dielectric constant and ^1H nmr linewidth as a function of temperature have also been performed on *tert*-butylaldehyde (pivaldehyde) (10). The dielectric constant abruptly changes from a value of 2–3 below 186 K to ~9 above this temperature, while the ^1H nmr linewidth decreases (*i*) between 90 and 100 K, (*ii*) at 180 K, and (*iii*) again at the melting point. The transition temperature of 180 or 186 K is suspect, however: the melting point of the sample used in the study was 228 K; the literature value is 279 K (11). Again, the large change in the nmr linewidth at 90–100 K is attributed to C_3

[1]NRCC No. 28535.
[2]Holder of an NSERC 1967 Science and Engineering Scholarship.
[3]Author to whom correspondence may be addressed.

Can. J. Chem. Downloaded from www.nrcresearchpress.com by 176.9.209.113 on 09/07/12
For personal use only.

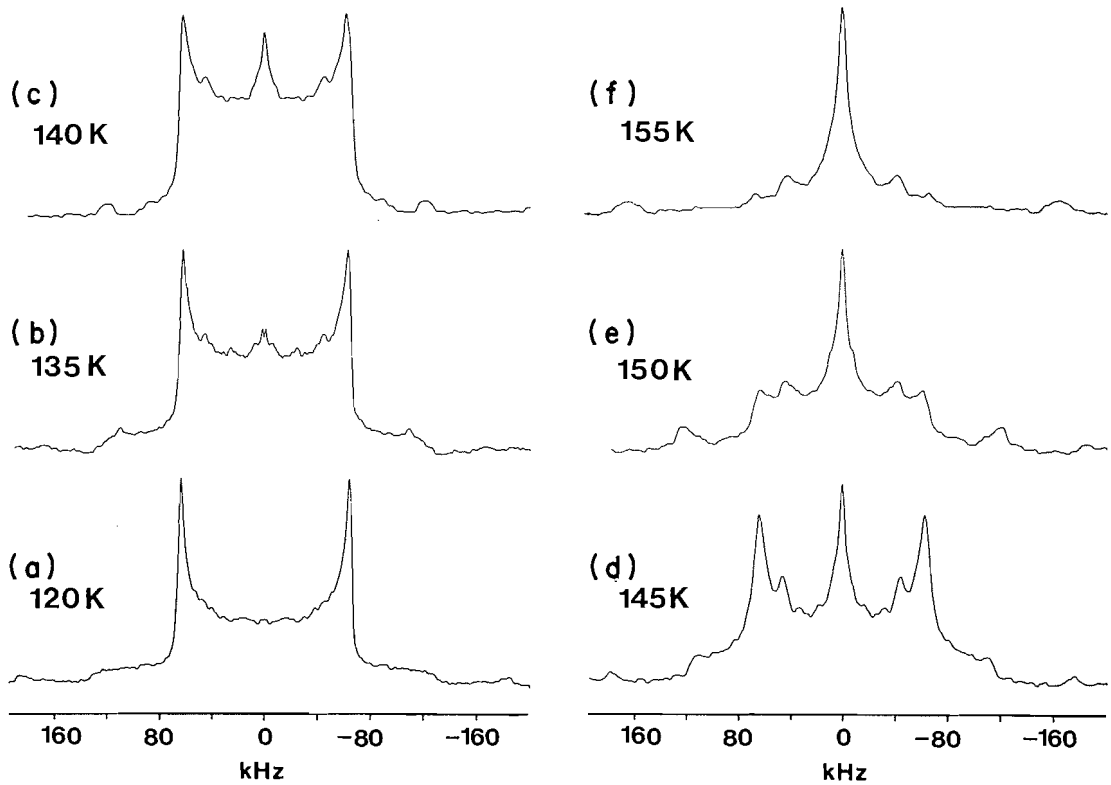

FIG. 1. Deuterium nmr spectra of *tert*-butyliodide-d_9 (solid II): (a) 120 K, (b) 135 K, (c) 140 K, (d) 145 K, (e) 150 K, and (f) 155 K. The quadrupolar splitting in the spectrum recorded at 120 K is 130 ± 2 kHz, corresponding to χ = 174 kHz.

motions, while overall molecular rotations occur in phase I (above 186 K).

The present study of $(CD_3)_3CCHO$ and $(CD_3)_3CI$ was undertaken to determine the type of reorientations present in the solid state, and whether phase transitions similar to those observed in other *tert*-butyl compounds occur here as well. Deuterium nmr has proved to be particularly useful for investigations of this nature (5) since the quadrupolar lineshape of powdered samples can, in favorable cases, distinguish what type of motion is occurring, and ^2H T_1's can provide rotational correlation times free from intermolecular or translational effects over a wide range of reorientational rates. Carbon-13 and ^{17}O spin-lattice relaxation times of the aldehyde group of $(CH_3)_3CCHO$ also provide some insight into the motion of this substituent in the liquid and solid I phases.

In addition, we have reexamined the ^2H T_1's in the liquid and rotator phases of $(CD_3)_3CCl$ (12) in light of the recent results for $(CD_3)_3CSH$ (6) and $(CD_3)_3CBr$ (13), in which small discontinuities were found in T_1 at the melting point.

Experimental

Samples of $(CD_3)_3CCHO$, $(CD_3)_3CI$, and $(CD_3)_3CCl$ were purchased from Merck, Sharp & Dohme Co.; $(CH_3)_3CCHO$ (97%) was obtained from Aldrich Chemical Co. Both labelled and unlabelled *tert*-butylaldehyde had melting points of 270–271 K, and were used without further purification. The samples were transferred to 1-cm cylindrical microcells of 9 mm outer diameter, then degassed using repetitive freeze–pump–thaw cycles before sealing.

All experiments were performed on a Nicolet 360-MHz (^1H) spectrometer, with the following exceptions: ^{17}O T_1 measurements of *tert*-butylaldehyde and ^2H T_1 measurements of $(CD_3)_3CCHO$ in solid II and $(CD_3)_3CI$ in solid I were carried out on a Bruker MSL 200; also low temperature ^2H spectra were obtained on a Bruker CXP 180-MHz instrument.

The probes used for relaxation measurements were calibrated using a copper–constantan thermocouple; temperature regulation is estimated to be within ±2 K. T_1's were obtained with the standard inversion–recovery experiment, typically using 12 values of τ and recycle delays of $\geq 5T_1$. Ninety-degree pulse widths are between 16 and 20 μs for ^{13}C, and 25–35 μs for ^2H on the Nicolet, approximately 18 μs for ^{17}O and 14 μs for ^2H on the MSL high resolution probe, and 7.5–8 μs for ^2H on the MSL broadband probe operating at low power. This latter probe was used to obtain ^2H T_1's of $(CD_3)_3CCHO$ in solid II.

During the ^{13}C T_1 experiments on unlabelled *tert*-butylaldehyde, two-level decoupling was carried out to obtain decoupled spectra with nuclear Overhauser enhancement. To measure the nOe, four (single scan) spectra were collected with the nOe, then four without the enhancement, using recycle delays of >10 T_1. The nOe is calculated from the ratio of the average signal intensity of the first set of four spectra to the average intensity of the second set.

To obtain the low temperature ^2H spectra shown in Figs. 1 and 2, a phase alternated quadrupole echo technique (14) was employed on the Bruker CXP spectrometer. For these spectra, the echo–pulse spacing was ~40 μs with 90-degree pulse widths of 3 μs. Dwell times of 0.5 μs were used to record 512-point quadrupole echoes, which were zero-filled to 4 K before Fourier transformation. The echo sequence was also incorporated into the T_1 experiments on $(CD_3)_3CCHO$ in solid II, in which 1 K points were collected and the echo–pulse spacing was ~30 μs. In this case, similar results were obtained when the echo sequence was not used, since the linewidth is less than 10 kHz.

Results and discussion

A. Lowest temperature phases

In contrast to the process of motional averaging upon warming rigid $(CD_3)_3CCl$ or $(CD_3)_3CBr$, stepwise onset of first C_3', then C_3, motions (5) does not occur in either $(CD_3)_3CI$ or $(CD_3)_3CCHO$. Both of these latter molecules, however, have similar ^2H spectra in the motional averaging temperature range.

When *tert*-butyliodide is warmed above 130 K, some distor-

Can. J. Chem. Downloaded from www.nrcresearchpress.com by 176.9.209.113 on 09/07/12
For personal use only.

Can. J. Chem. Downloaded from www.nrcresearchpress.com by 176.9.209.113 on 09/07/12
For personal use only.

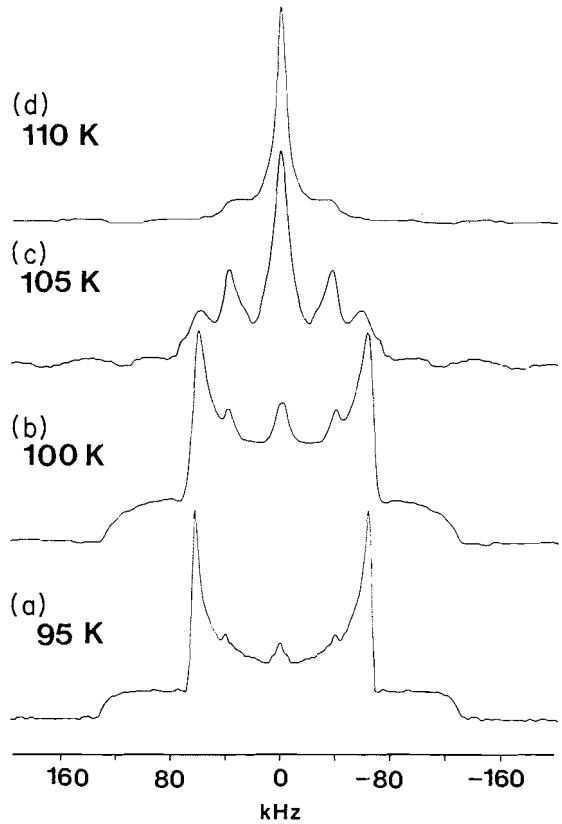

FIG. 2. Low temperature deuterium nmr spectra of *tert*-butylaldehyde-d_9, $(CD_3)_3CCHO$, at (a) 95 K, (b) 100 K, (c) 105 K, and (d) 110 K. The quadrupolar splitting in (a) is 129 ± 2 kHz, corresponding to $\chi = 172$ kHz.

tions occur in the "rigid" lineshape ($\chi = e^2qQ/h = 174$ kHz, $\eta = 0$), with additional peaks, symmetrically placed at + and −45 kHz from the centre of the Pake-like doublet, appearing between 140 and 150 K (Fig. 1). In *tert*-butylaldehyde, a similar rigid lineshape begins to collapse at ~100 K, with a splitting of approximately 80 kHz apparent in the ^2H spectrum (Fig. 2). These spectra are the result of both C_3 and C_3' motions occurring at rates of 10^4–10^6 s^{-1} (15). In *tert*-butyliodide, the persistence of the rigid lineshape singularities up to ~155 K suggests that the rate of C_3' motions is greater than C_3 rotations. The ^2H spectrum at 150 K resembles a simulation of the lineshape with rates of about 10^6 s^{-1} (C_3') and 10^4 s^{-1} (C_3) (15). In *tert*-butylaldehyde, the rapid loss of intensity in the outer wings and relatively high intensity in the central and ±40 kHz peaks suggest that in this case C_3 motions are more rapid than C_3'. The ^2H spectrum of *tert*-butylaldehyde-d_9 at 110 K resembles a C_3' ~10^4 s^{-1}, C_3 ~10^6 s^{-1} lineshape simulation (15). It is of interest to point out that in the gas phase, the barrier to methyl group rotation is approximately three times larger than the barrier for internal rotation about the C—C bond connecting the *tert*-butyl and aldehyde groups (16).

Upon warming *tert*-butyliodide above 150 K, the wings and shoulders of the ^2H spectrum collapse and a featureless lineshape, characteristic of 10^5–10^6 s^{-1} C_3 motion along with 10^5–10^7 s^{-1} C_3' motion (15), is observed. Above 200 K, an axially symmetric 14-kHz Pake doublet becomes apparent and persists up to the melting point of 237 K. The 14-kHz splitting and symmetric lineshape is consistent with rapid ($\geq 10^7$ s^{-1}) C_3 and C_3' motions, as occur in the solid III of *tert*-butylchloride (12, 5) and *tert*-butylbromide (13, 5).

Similarly, the deuterium spectrum of $(CD_3)_3CCHO$ indicates 10^5–10^7 s^{-1} C_3 and C_3' motion at 115 K, and the 12–14 kHz splitting is observed at 153 K (Fig. 3). However, further motional averaging occurs in *tert*-butylaldehyde at temperatures below the transition to the plastic phase, which occurs at 190 ± 2 K. Since rapid C_3 and C_3' motions are already occurring, the additional motion, which narrows the width of the powder spectrum (Fig. 3) to approximately 8 kHz and increases η to ~0.6, must involve whole molecule motion, possibly C_2' flips (*vide infra*).

The observation of whole molecule reorientation in solid II was unexpected, since dielectric data (10) taken at 100 kHz did not indicate any motion of the dipole moment in this phase. The dielectric results might be consistent with the ^2H nmr observations, however, if 2-site exchange is occurring between aldehyde sites oriented such that the molecular dipole moments in each site are approximately parallel. This is not an impossible requirement: the dipole moment of pivaldehyde is oriented about 11° away from the C_2' axis shown in Fig. 4 (16). If this geometry holds for the solid state, the dielectric constant will not be affected significantly by 180° flips about this axis.

The ^2H lineshapes above 167 K are also consistent with a 180° flip motion. Note that if the C—C—C angle in Fig. 4 is tetrahedral, the C_2' axis is oriented approximately 54.7 degrees from the C_3 and C_3' averaged principal axes of the methyl deuterons, and also that the splitting in the 153 K spectrum, approximately 12.5 kHz, corresponds to $\chi \simeq 16.7$ kHz. Numerical simulation of the effect of fast C_2' flips (Fig. 5) shows good agreement with the experimental spectrum at 168 K when χ is assumed to be 15.2 kHz, and the angle between the flip axis and the principal efg axis is taken as 51.5 degrees. The simulation is based on the formalism described by Becker (17), and includes Gaussian linebroadening equivalent to $\frac{1}{10}$ the spectral width.

Onset of motional averaging beyond C_3 and C_3' in the *tert*-butyl-X compounds (e.g., X = Cl, Br, I, SH) is typically accompanied by a phase transition (prior to the plastic phase); thus the observation of whole molecule reorientations in *tert*-butylaldehyde led us to suspect that a phase change occurs in the 152–188 K temperature range. There is no apparent discontinuity in the plots of dielectric constant vs. T (10) or in the plot of ln T_1 (^2H) vs. T^{-1} (Fig. 6) at temperatures *below* the phase transition to the plastic phase; however, the ^2H lineshapes in the 153–188 K range exhibit some very unusual behaviour. Plots of the components of the deuterium quadrupole coupling tensor versus temperature (Fig. 7) indicate that there is an abrupt change at about 165 ± 5 K. From 153 to 165 K the q_{yy} component is almost constant, while the q_{zz} and q_{xx} components decrease rapidly in frequency (i.e., η increases rapidly, Fig. 8), and it is clear that this does not reflect an activated process. From 168 K to temperatures just below the transition to the plastic phase there are only small changes in the frequencies of the ^2H quadrupolar tensor components and, as demonstrated above, the ^2H nmr lineshape can be interpreted in terms of 2-fold flips. The rapid changes occurring in the 153–165 K range might possibly be associated with 2-fold flips between sites having different statistical populations (i.e., an asymmetric double-well potential) (18). Such a model could explain the rapid increase in η between 153 K and 165 K.

The obvious inference from the abrupt changes in the ^2H nmr lineshapes at 165 K (Figs. 7 and 8) is that there is a second solid–solid phase transition, and this has in fact been confirmed from the results of a calorimetric study (19). In the ln T_1(^2H) vs. T^{-1} plot (Fig. 6), 165 K is the temperature at which there appears to be a broad T_1 minimum. Phase transitions without abrupt changes in T_1 are not unknown (20). The minimum in Fig. 6

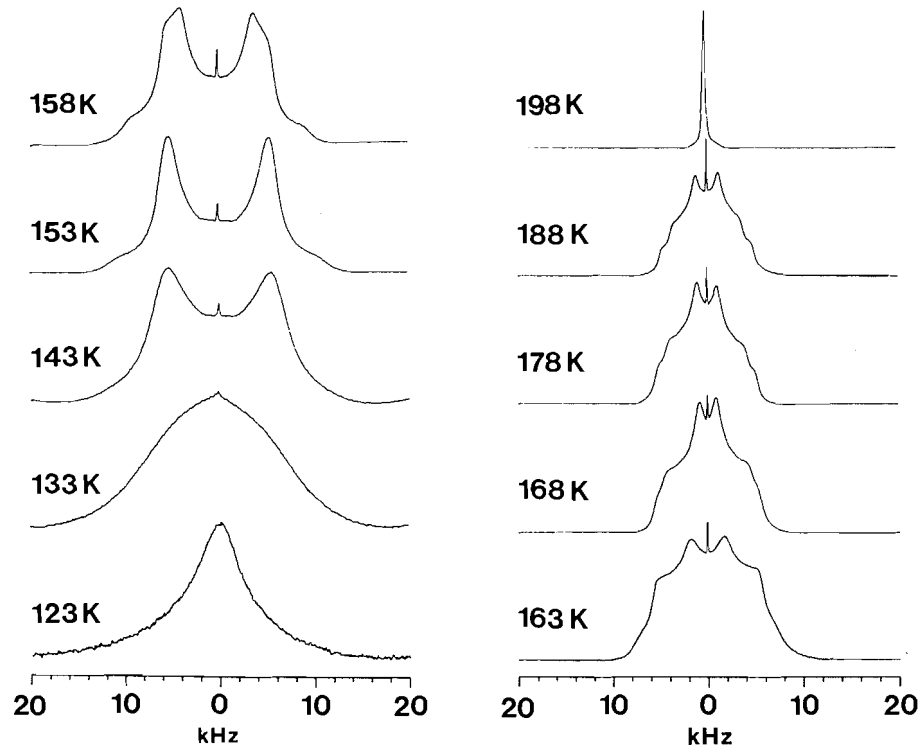

FIG. 3. Deuterium nmr spectra of $(CD_3)_3CCHO$ between 123 and 198 K.

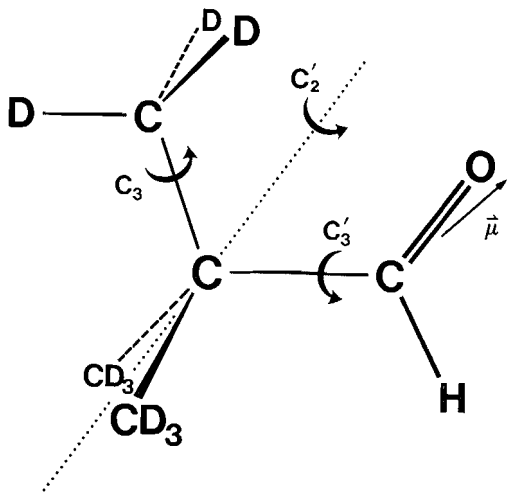

FIG. 4. Illustration of an approximate C_2' axis and the direction of the dipole moment in *tert*-butylaldehyde.

occurs at $T_1 = 2.0$ ms, corresponding to $\tau_{eff} = 0.6158\ \omega_0^{-1} = 3.2 \times 10^{-9}$ s. Assuming that only C_3 and C_3' motions are effective for relaxation near ω_0^{-1}, $T_{1\,min}$ is calculated as 1.7 ms (21) when the rates of both motions are equal and have a value of 8.4×10^7. If the rates of the two motions differ (as expected), the calculated T_1 minimum increases; thus this model can account for the observed value. The E_a from the slope above 165 K is about 15 kJ mol^{-1}.

There is no evidence to suggest that hydrogen bonding plays a role in the reorientational motion of *tert*-butylaldehyde in solid II or solid III. If hydrogen bonding occurred, as in pivalic acid (22), we would expect an activation energy of approximately 50–60 kJ mol^{-1}. By contrast, *tert*-butylaldehyde between 130 and 190 K behaves very much the same as solids II–IV of the thiol analog (6), in which hydrogen bonding does not occur.

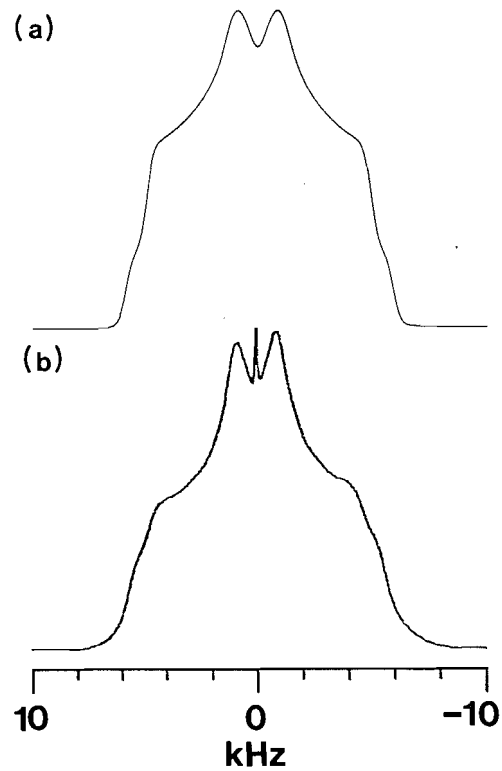

FIG. 5 Experimental ^2H nmr spectrum of $(CD_3)_3CCHO$ at 168 K (bottom) and simulated spectrum (top), assuming fast C_2' flips about an axis oriented 51.5 degrees from the principal axis of the field gradient, a quadrupolar coupling constant of 15.2 kHz, and $\eta = 0$.

B. Rotator phase: Solid I

In a rotator or "plastic" phase, molecular reorientation is rapid enough in all directions to completely average the quadrupolar interaction and only a single line is observed in the ^2H spectrum.

As noted above and by Chihara *et al.* (8), no solid–solid

Can. J. Chem. Downloaded from www.nrcresearchpress.com by 176.9.209.113 on 09/07/12
For personal use only.

Can. J. Chem. Downloaded from www.nrcresearchpress.com by 176.9.209.113 on 09/07/12
For personal use only.

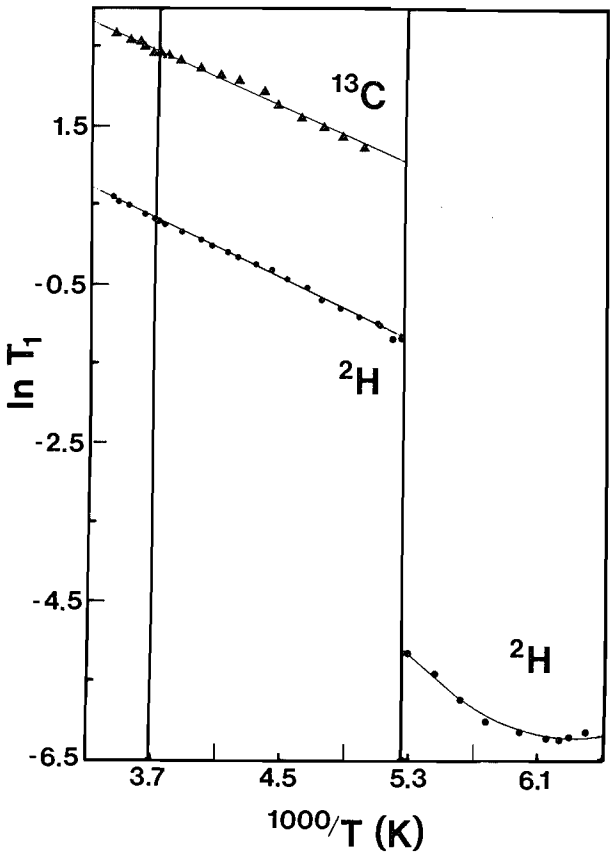

FIG. 6. The temperature dependence of ^{2}H and ^{13}C T_1 values in *tert*-butylaldehyde. The ^{2}H T_1's were obtained for $(CD_3)_3CCHO$ while the methyl ^{13}C T_1 measurements were made on an unlabelled sample of $(CH_3)_3CCHO$. The vertical lines represent the liquid ↔ solid I and solid I ↔ solid II phase transitions.

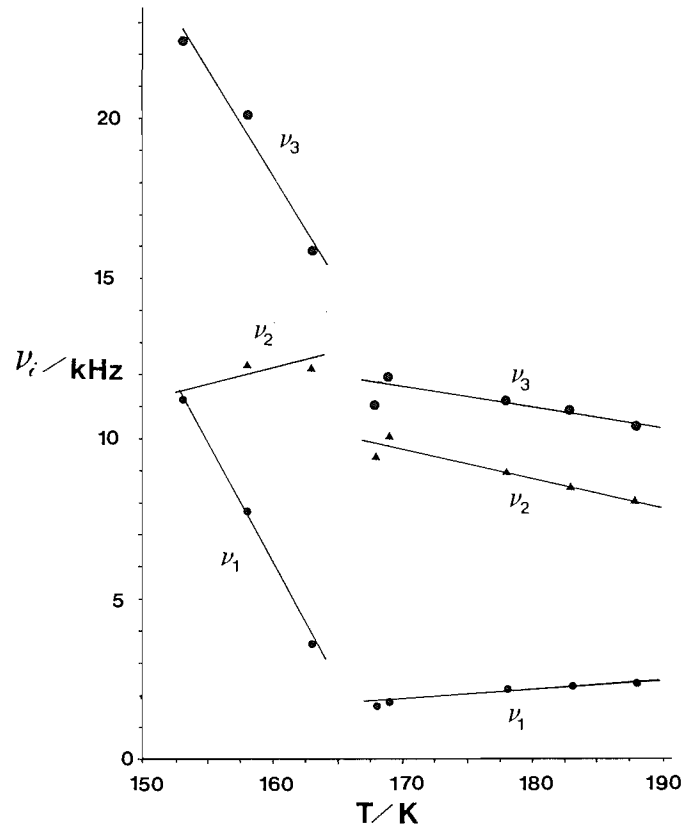

FIG. 7. Plot of the principal components of the quadrupolar coupling tensor vs. temperature for $(CD_3)_3CCHO$ between 150 and 190 K.

phase transitions are observed in *tert*-butyliodide upon warming. However, when the sample is cooled sufficiently slowly, a rotator phase forms at 239 K and is stable down to 212 K where solid II, characterized by the 14 kHz splitting, is observed. Rapid cooling results in formation of solid II at temperatures above the 212 K transition point, hence the transition at 222 K noted by Köksal (9) is not surprising. The equilibrium transition temperature may be even lower than 212 K, which we achieved by cooling at a rate of 2° per hour.

The rotator phase of $(CD_3)_3CI$ can be distinguished from the liquid by both the Arrhenius behaviour and the discontinuity in the ^{2}H T_1 at the freezing point (Fig. 9). The activation energies and effective rotational correlation times obtained from least-square fits of the ln T_1 vs. T^{-1} plots are compared with data from other *tert*-butyl-X compounds in Tables 1 and 2 respectively.

As noted above, spin-lattice relaxation data for the methyl group of *tert*-butylaldehyde are plotted in Fig. 6. Carbon-13 and ^{17}O T_1 measurements were also performed on the aldehyde moiety. The nOe of the methyl carbon is full in both liquid and solid I phases, but the nOe of the aldehyde carbon gradually decreases from the full value of 2.988 at 216 K to 1.95 near the melting point. Both T_1 (observed) and the nOe were thus measured at various temperatures to calculate

$$T_{1dd} = 1.988(T_{1,obs})/(\text{nOe} - 1)$$

and effective rotational correlation times from refs. 23 and 24:

$$[1] \quad (T_{1dd})^{-1} = \left(\frac{\mu_0}{4\pi}\right)^2 n_H \frac{\hbar^2 \gamma_H{}^2 \gamma_C{}^2}{r_{CH}^6} \tau_{eff}$$

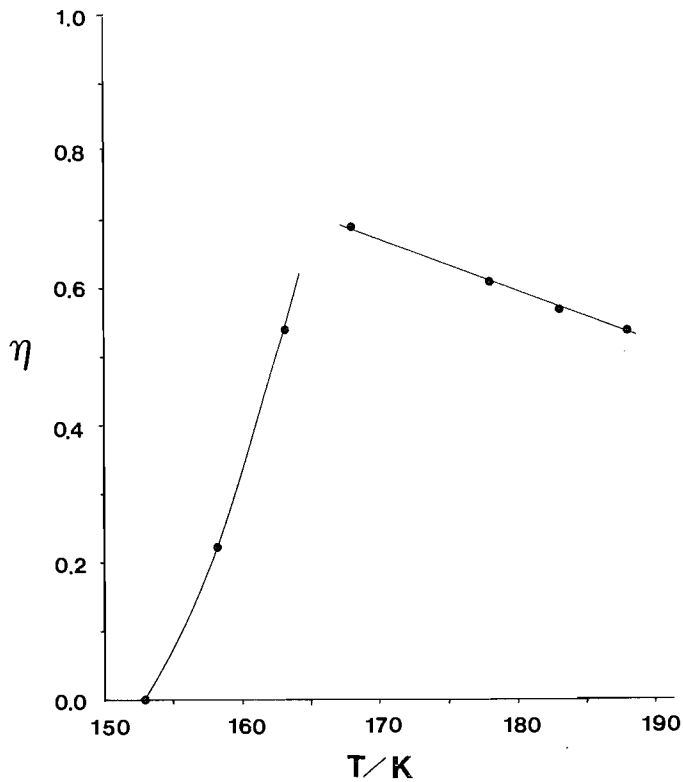

FIG. 8. Plot of the asymmetry parameter, η, vs. temperature for $(CD_3)_3CCHO$ between 150 and 190 K.

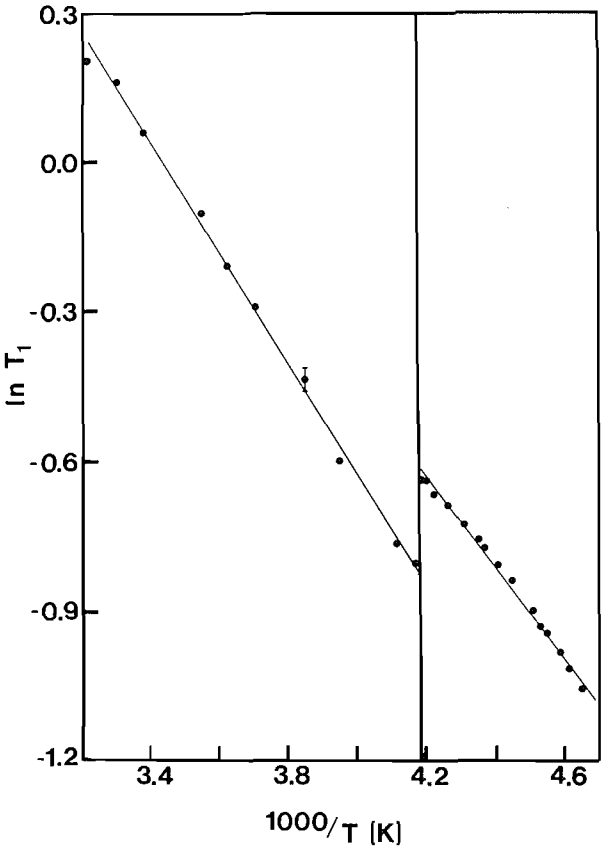

FIG. 9. The temperature dependence of ^2H T_1 values in *tert*-butyliodide. The values obtained in solid II were obtained upon slowly cooling the sample from the liquid.

TABLE 1. Activation energies from the temperature dependence of ^2H T_1's in several *tert*-butyl-X compounds, in kJ mol^{-1}

X	E_a, liquid	E_a, solid I	Reference
CH_3	4.1	4.1	31
Cl	7.0	5.8	Present
SH	7.1	7.1	6
Br	7.9	7.2	13
CHO	7.8	7.8	Present
I	9.1	7.6	Present

Using r = 109 pm for the methyl carbon/hydrogen bond length, and r = 111.4 pm for the C—H of the aldehyde group (as in acetaldehyde (25)), the simple relationships τ_{eff} (methyl) = 15.6 ps/T_{1dd} (in s), and τ_{eff} (aldehyde) = 53.0 ps/T_{1dd}(s) are obtained. The six closest methyl protons (at approximately 272 pm, (25)) contribute less than 3% to T_{1dd} of the aldehyde carbon.

Both ^2H and ^{17}O relax solely by the quadrupolar mechanism, for which (23, 26)

$$[2]\quad (T_1)^{-1} = \frac{3}{10}\,\pi^2\chi^2\,\frac{2I+3}{I^2(2I-1)}\left(1+\frac{\eta^2}{3}\right)\tau_{eff}$$

when $(\tau_{eff}\omega_0)^2 \ll 1$. The quadrupolar coupling constant and asymmetry parameter of ^2H in *tert*-butylaldehyde is 172 ± 2 kHz, η = 0 (see Fig. 2, 95 K), thus $\tau_{eff}(^2H)$ = 2.28 ± 0.05 ps/T_1(s). For the ^{17}O data, χ and η are estimated from the experimental values for formaldehyde (27) and the calculated values for acetaldehyde (28) as 11.8 ± 1 MHz and 0.55 ± 0.1, respectively. Using these values, $\tau_{eff}(^{17}O)$ = 6.8 ± 1.4 ps/T_1 (ms).

TABLE 2. Effective correlation times at the melting point (in ps), determined from ^2H T_1 data of labelled methyl groups in several *tert*-butyl-X compounds

X	τ_{eff}, liquid	τ_{eff}, solid I	Reference
CH_3	0.9	0.9	31
Cl	2.0	1.8	Present
SH	1.5	1.3	6
Br	2.5	2.2	13
CHO	1.6	1.6	Present
I	5.3	4.2	Present

Methyl ^{13}C and ^2H T_1 data for *tert*-butylaldehyde are in good agreement, as shown in Fig. 6. From these data we obtain an activation energy E_a of 7.8 ± 0.5 kJ mol^{-1} for overall molecular tumbling in both solid I and liquid phases. The effective rotational correlation time at the melting point (mp) is 1.5 ± 0.1 ps.

Due to the near-zero slope of T_1 (observed) and errors in the measurements of the nOe, there is considerable scatter in the ln T_{1dd} versus T^{-1} data for the aldehyde carbon. Least-squares fit of the data yields ln T_1/s = $-1.06(10^3)/T + 7.71$, from which E_a is calculated as 9 ± 2 kJ mol^{-1}, and τ_{eff}(mp) = 1.2 ± 0.3 ps. Rapid relaxation and broad lines in the ^{17}O spectrum also result in poor reproducibility of the T_1 data, and make T_1 measurements below 240 K impractical. Despite these difficulties, the least-squares fit of the data over the temperature range 241–292 K, ln T_1/ms = $-1.30(10^3)/T$ + 6.74, yields an E_a for the aldehyde group of 11 ± 2 kJ mol^{-1} and τ_{eff}(mp) = 1.0 ± 0.3 ps, in reasonable agreement with the ^{13}C data. The shorter effective correlation times obtained for the aldehyde substituent relative to that of the methyl groups may indicate independent internal rotation of the aldehyde moiety in solid I, but the uncertainty of the data does not allow us to state this with confidence. Internal rotation would, however, result in differences in the ^{17}O and ^{13}C T_1 data, due to the different orientation of the respective principal axes (28, 17). Microwave data have determined a value of 4.9 kJ mol^{-1} for reorientation of the *tert*-butyl group (V_3) in pivaldehyde (16).

Again, note the striking similarity between pivaldehyde and *tert*-butylthiol; the latter has a melting point of 274 K (29), and an internal barrier V_3 = 7.1 kJ mol^{-1} (30). The correlation times at the melting point of *tert*-butylthiol are 1.5 ± 0.1 ps from the methyl data and 1.1 ± 0.1 ps for the deuterated thiol substituent (6). Overall anisotropic rotational diffusion cannot account for the shorter rotational correlation time of the thiol group.

C. Discontinuity of τ_{eff} at the melting point

In *tert*-butyliodide, an increase in T_1 upon decreasing the temperature from 243 to 241 K (liquid → solid I) indicates a decrease in τ_{eff}, i.e., faster reorientation immediately upon entering solid I. This result has also been observed in *tert*-butylbromide (13), *tert*-butylthiol (6), and, although not previously reported for *tert*-butylchloride (12), more accurate ^2H T_1 data (Fig. 10) confirm that a discontinuous decrease in τ_{eff} upon freezing occurs in this compound as well.

Within experimental error, however, we cannot claim such a discontinuity in the *tert*-butylaldehyde data, although in light of the observation of this result in all other *tert*-butyl-X samples that we have studied, it is somewhat surprising that it is not observed for X = CHO.

Can. J. Chem. Downloaded from www.nrcresearchpress.com by 176.9.209.113 on 09/07/12
For personal use only.

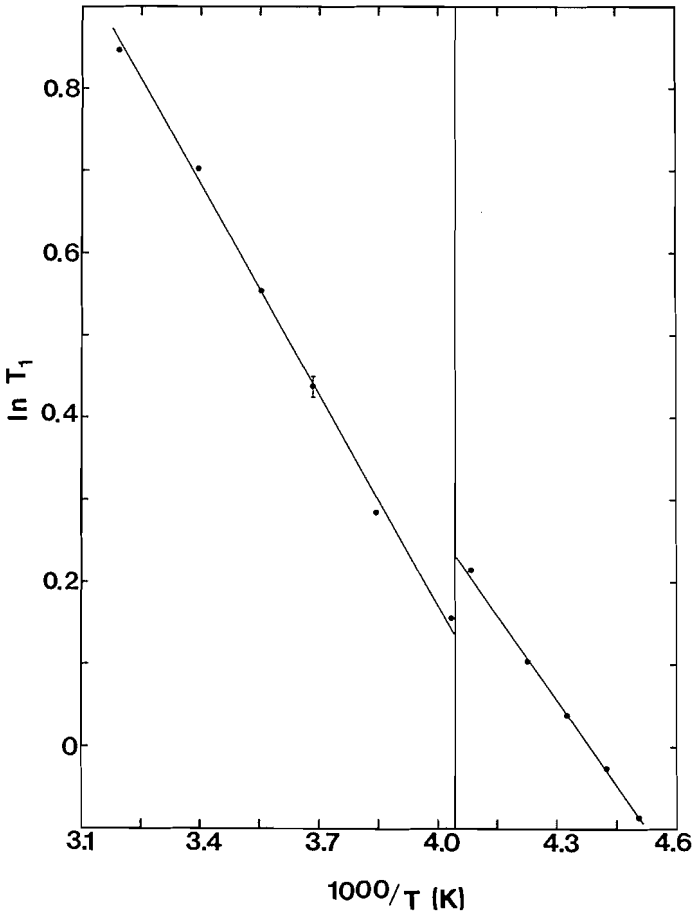

FIG. 10. Deuterium T_1's in the liquid and solid I phases of *tert*-butylchloride.

D. Liquid

The activation energy obtained for $(CD_3)_3CI$ in the liquid phase is 9.1 kJ mol^{-1}, somewhat higher than usual (Table 1). Effective correlation times calculated for *tert*-butyliodide at the melting point, using $\tau_{eff} = 2.23$ ps/T_1 (s), are also 2 to 3 times longer than for the other *tert*-butyl-X compounds. This no doubt reflects the severe departure from tetrahedral symmetry introduced by the large iodine atom, which is likely to be the bulkiest *tert*-butyl substituent for which a plastic phase is observed.

Within experimental error, activation energies calculated for liquid *tert*-butylaldehyde are the same as in solid I. With reference to Table 1, it is interesting to note that the activation energies obtained in solid I of the *tert*-butyl-X compounds are, in all cases, either less than or equal to the activation energies obtained in the liquid.

Acknowledgements

We wish to thank Dr. M. A. White and A. Perrott for their interest in this study and for providing us with calorimetric results prior to publication. We are grateful to NSERC for financial support.

1. N. G. PARSONAGE and L. A. K. STAVELEY. Disorder in crystals. Clarendon Press, Oxford. 1978.
2. J. N. SHERWOOD (*Editor*). The plastically crystalline state. John Wiley and Sons, New York. 1979.
3. S. CALIFANO and R. PICK (*Editors*). Dynamics of molecular crystals. J. Chim. Phys. **82**, 87–328 (1985).
4. J. C. FROST, A. J. LEADBETTER, and R. M. RICHARDSON. Phil. Trans. R. Soc. London B, **290**, 567 (1980).
5. J. A. RIPMEESTER and C. I. RATCLIFFE. J. Chem. Phys. **82**, 1053 (1985).
6. S. MOOIBROEK and R. E. WASYLISHEN. Can. J. Chem. **63**, 2926 (1985).
7. W. O. BAKER and C. P. SMITH. J. Am. Chem. Soc. **61**, 2798 (1936).
8. H. CHIHARA, M. OTSURU, and S. SEKI. Bull. Chem. Soc. Jpn. **39**, 2145 (1966).
9. F. KÖKSAL. J. Chem. Soc. Faraday Trans 2, **76**, 550 (1976).
10. S. L SEGEL and A. MANSINGH. J. Chem. Phys. **51**, 4578 (1969).
11. (*a*) R. C. WEAST (*Editor*). CRC Handbook of Chemistry and Physics. 63rd ed. CRC Press Inc., Cleveland. 1982–1983; (*b*) M. A. RICHARD. Ann. Chim. Phys. **21**, 323 (1910).
12. D. E. O'REILLY, E. M. PETERSON, C. E. SCHEIE, and E. SEYFARTH. J. Chem. Phys. **59**, 3576 (1973).
13. B. A. PETTITT, J. S. LEWIS, R. E. WASYLISHEN, W. DANCHURA, and E. TOMCHUK. J. Magn. Reson. **44**, 508 (1981).
14. J. H. DAVIS, K. R. JEFFREY, M. BLOOM, M. I. VALIC, and T. P. HIGGS. Chem. Phys. Lett. **42**, 390 (1976).
15. A. J. VEGA and Z. LUZ. J. Chem. Phys. **86**, 1803 (1987).
16. A. M. RONN and R. C. WOODS. J. Chem. Phys. **45**, 3831 (1966).
17. H. J. BECKER. Diploma work, Dortmund, 1975; M. MEHRING. High resolution NMR spectroscopy in solids. NMR basic principles and progress. Vol. 11. Springer Verlag, New York. 1976.
18. J. A. RIPMEESTER. J. Chem. Phys. **85**, 747 (1986).
19. M. A. WHITE and A. PERROTT. Can. J. Chem. **66**, 729 (1988).
20. (*a*) R. E. WASYLISHEN, S. PEIRIS, and D. R. ARNOLD. Chem. Phys. Lett. **114**, 31 (1985); (*b*) R. E. WASYLISHEN, O. KNOP, and J. B. MACDONALD. Solid State Commun. **56**, 581 (1985).
21. J. C. PRATT, A. WATTON, and H. E. PETCH. J. Chem. Phys. **73**, 2542 (1980).
22. (*a*) M. J. BIRD, D. A. JACKSON, and J. G. POWLES. Mol. Phys. **25**, 1051 (1973); (*b*) T. HASEBE, N. NAKAMURA, and H. CHIHARA. Bull. Chem. Soc. Jpn. **53**, 896 (1980).
23. R. E. WASYLISHEN. *In* NMR spectroscopy techniques. *Edited by* C. Dybowski and R. L. Lichter. Marcel Dekker Inc., New York. 1987.
24. J. R. LYERLA and G. C. LEVY. *In* Topics in carbon-13 NMR spectroscopy. Vol. 1. *Edited by* G. C. Levy. John Wiley & Sons, New York. 1974.
25. T. IIJIMA and S. TSUCHIYA. J. Mol. Spectrosc. **44**, 88 (1972).
26. A. ABRAGAM. The principles of nuclear magnetism. Clarendon Press, Oxford. 1961.
27. W. H. FLYGARE and J. T. LOWE. J. Chem. Phys. **43**, 3645 (1965).
28. J. E. GREADY. J. Phys. Chem. **88**, 3497 (1984).
29. J. P. MCCULLOUGH, D. W. SCOTT, H. L. FINKE, W. N. HUBBARD, M. GROSS, C. KATZ, R. E. PENNINGTON, J. F. MESSERLY, and G. WADDINGTON. J. Am. Chem. Soc. **75**, 1818 (1953).
30. E. VALENZUELA and R. C. WOODS. J. Chem. Phys. **61**, 4119 (1974).
31. B. A. PETTITT, R. E. WASYLISHEN, R. Y. DONG, and T. P. PITNER. Can. J. Chem. **56**, 2576 (1978).

Can. J. Chem. Downloaded from www.nrcresearchpress.com by 176.9.209.113 on 09/07/12
For personal use only.

Adsorbate spectra of rare-gas atoms on metal surfaces[1]

CONSTANTINE MAVROYANNIS
Laser Chemistry Group, Division of Chemistry, National Research Council of Canada, Ottawa, Ont., Canada K1A 0R6

Received September 2, 1987

This paper is dedicated to Professor J. A. Morrison

CONSTANTINE MAVROYANNIS. Can. J. Chem. **66**, 741 (1988).

The optical excitation spectra of neutral rare-gas atoms physisorbed on metal surfaces have been considered. Emphasis has been given to the dynamic effects of the surface plasmons on the lifetimes of the adsorbed atoms. At low coverage and when the damping of the surface plasmons is much greater than the effective radiative damping, the spectral functions of the symmetric and antisymmetric modes consist of asymmetric Lorentzian lines, whose asymmetry depends on the strength of the surface plasmons. At this limit the relative intensities of the symmetric and antisymmetric modes take positive and negative values describing the physical processes of absorption (attenuation) and stimulated emission (amplification), respectively. Hence, the occasional disappearance of the spectral lines of the optical absorption is due to a cancellation process, which takes place between the frequency profiles arising from two nearby excited states of the adsorbed atom. The red shifted peak of the symmetric mode of the higher excited state and the blue shifted peak of the antisymmetric mode of the lower excited state of the atom cancel each other out provided that their frequency profiles nearly coincide. This may be a possible explanation of the persistence-extinction phenomenon that has been observed for a number of rare-gas substrate systems in the low coverage limit, where it has been proposed that a charge-transfer instability exists. Numerical results indicate that the peaks of excited Xe on Al and excited Kr on Au vanish in the low coverage limit.

CONSTANTINE MAVROYANNIS. Can. J. Chem. **66**, 741 (1988).

On a étudié les spectres d'excitation optique d'atomes de gaz rares neutres adsorbés physiquement sur des surfaces métalliques. On considère principalement les effets dynamiques des plasmons de surface sur les temps de vie des atomes adsorbés. Lorsque la couverture est faible et que le ralentissement des plasmons de surface est beaucoup plus grand que le ralentissement radiatif effectif, les fonctions spectrales des modes symétriques et antisymétriques consistent en des raies asymétriques de Lorentz dont l'asymétrie dépend de la force des plasmons de surface. A cette limite, les intensités relatives des modes symétriques et antisymétriques prennent des valeurs positive et négative en décrivant respectivement les processus physiques d'adsorption (atténuation) et d'émission stimulées (amplification). Il s'en suit que la disparition occasionnelle des lignes du spectre d'absorption optique est due à une processus d'annulation qui prend place entre les profils de fréquence qui proviennent de deux états excités adjacents de l'atome adsorbé. La raie déplacée vers le rouge du mode symétrique de l'état excité le plus élevé de l'atome et la raie déplacée vers le bleu du mode antisymétrique de l'état excité le plus bas de l'atome s'annulent lorsque leurs profils de fréquence coïncident. Ceci est une explication possible du phénomène de persistance–extinction qui a été observé pour un certain nombre de systèmes de substrats de gaz rares à la limite d'une couverture faible et pour lesquels il a été proposé qu'il existe une instabilité de transfert de charge. Les résultats numériques indiquent que les raies dûes au Xe excité sur Al et au Kr excité sur Au disparaissent à la limite d'une couverture faible.

[Traduit par la revue]

Can. J. Chem. Downloaded from www.nrcresearchpress.com by 93.93.197.157 on 09/07/12
For personal use only.

I. Introduction

There has been an accumulation of experimental data concerning the optical spectra of rare-gas atoms physisorbed on metal surfaces. The differential reflectivity experiments were conducted by Flynn and co-workers (1–10) by means of synchrotron radiation. They measured the optical spectra of the adsorbate atoms on metal surfaces as a function of coverage. In the high coverage limit, the observed spectra were found to be similar to comparable excitations in the gas phase and condensed rare gases. Striking changes in the optical spectra have been found (1–4) in the limit of low coverage as should be expected since at this limit, participation of the surface excitations is anticipated to take place. At low coverage the optical spectra disappear on some surfaces but persist on others. For instance, the adsorbed spectra of Xe on Ti, Al and Au and Kr on Au vanish while those of Xe and Ar on Mg, Kr on Al, and Ar on Au persist (1–4).

The dependence of the optical absorption data on the quantity $\phi - I^*$, where ϕ is the metal work function and I^* is the energy required to ionize the rare-gas atom in its lowest excited state, led the authors (3–6) to propose the existence of a "charge-transfer instability" for rare-gas–metal–substrate systems. Briefly, if $I^* > \phi$, the adsorbate level lies well below the Fermi level of the metal substrate, the excited electron cannot enter the metal but is localized on the excited atom; with the result that the final-state adsorbate configuration is neutral. If $\phi > I^*$, the excited state lies above the Fermi level and is unstable against charge-transfer to the metal. The observed spectra led the authors (2, 3, 8) to suggest that the "switch" to blue shifts for $\phi > I^*$ occurs when the excitation causes the rare-gas atom to become ionized. Arguments against the foregoing interpretation of the optical data have been made by Lang and co-workers (11, 12). No theoretical explanation has been developed (11, 13) for the occasional disappearance of the excitonic component of the optical-absorption spectra at low coverage.

Since then, the spectra of the rare-gas adsorbates on metal surfaces have been studied by a number of methods such as Auger electron yield (14), electron-energy-loss spectroscopy (15), and photoemission methods (16). The results derived by these methods differ among themselves and with the optical data obtained by the use of the differential reflectance technique (1–3). Photoemission experiments (12, 16) have suggested adsorbate energy-level configurations, which agree with density-functional calculations (11, 12) but which disagree with the interpretation of the optical data. A recent review on the subject has been written by Flynn (10) to whom we refer for further details and literature. We shall describe here our recent work

[1]NRC No. 28532.

Can. J. Chem. Downloaded from www.nrcresearchpress.com by 93.93.197.157 on 09/07/12
For personal use only.

(17) concerning the optical excitation spectra of neutral rare-gas atoms physisorbed on metal surfaces. The model Hamiltonian, which is used to derive the expressions of the appropriate Green functions of the system is developed in Section II. The excitation spectra of the symmetric and antisymmetric modes of the system have been considered in Sections III and IV, respectively. The computed spectra of Xe, Kr, and Ar on various metal surfaces are graphically presented and discussed. Concluding remarks are presented in Section V.

II. The model Hamiltonian

We take a simple model (17–19), which consists of a plane boundary separating an empty space and a homogeneous isotropic metallic medium having a dielectric function

$$[1] \quad \epsilon(\omega) = 1 - \frac{\omega_p^2}{\omega^2 + i\omega\gamma_{sp}}$$

where ω_p is the plasma frequency of the metallic electrons and γ_{sp} ($\gamma_{sp} \ll \omega$) is the intrinsic damping of surface plasmons due to the decay processes arising from the interactions with electron-hole pairs (20), phonons (21), impurities (22), etc. A neutral atom A is fixed at (0, 0, R) with z-axis taken perpendicular to the plane $z = 0$. The image of the atom A, which is designated by B, will be situated at (0, 0, $-R$) from the plane in the metallic medium described by the dielectric function $\epsilon(\omega)$. Each electron $(x_i, y_i, R - z_i)$ of the atom A with charge e will have an image $(x_i, y_i, R + z_i)$ having a fictitious charge $-e\epsilon_1$, where

$$[2] \quad \epsilon_1 \equiv \epsilon_1(\omega) = \frac{\epsilon(\omega) - 1}{\epsilon(\omega) + 1}$$

The existence of the screening factor $\epsilon_1(\omega)$ is due to boundary conditions at the plane separating the empty space and the homogeneous isotropic metallic medium for distances of the atomic electrons from the plane at which retardation effects can be discarded (18, 19). The limit of either $\omega \to 0$ or $\omega_p \to \infty$ leads to $\epsilon(\omega) \to \infty$ and $\epsilon_1(\omega) = 1$; this limit exists for the so called "perfect conductor", where the medium excludes the field completely.

The atom A is assumed to have nondegenerate electronic states, the ground and excited states denoted by $|0\rangle$ and $|\nu\rangle$ with frequencies E_0 and E_ν, respectively. The electronic transitions $|0\rangle \leftrightarrow |\nu\rangle$ are electric dipole allowed and the transition frequencies are denoted by $E_{\nu 0} = E_\nu - E_0$; units in which $\hbar = 1$ are used throughout. The distance $2R$ between the atom A and its image B is taken such that the inequality $(2RE_{\nu 0}/c) < 1$ is satisfied and retardation effects are unimportant. The distance $2R$ is also taken such that the overlap between the wavefunctions is very small and may be neglected and the interaction between the physisorbed atom A and its image B is of the dipole–dipole type (18); effects associated with the translational motion of the atom A and its image such as recoil, etc., are ignored. The Hamiltonian describing the system consisting of the atom A interacting with its image B at a distance $2R$ apart may be taken to be (17, 19)

$$[3] \quad H = \sum_\nu E_{\nu 0}(b_{A\nu}^\dagger b_{A\nu} + b_{B\nu}^\dagger b_{B\nu}) + \sum_\nu V_{AB}^\nu \bar{b}_{A\nu}\bar{b}_{B\nu} + \sum_{k,\lambda} ck\beta_{k\lambda}^\dagger\beta_{k\lambda} + \frac{\bar{\omega}_p^2}{4}\sum_{k,\lambda}\frac{1}{ck}\bar{\beta}_{k\lambda}^\dagger\bar{\beta}_{k\lambda} + \frac{i\bar{\omega}_p}{2}\sum_{k,\lambda,\nu}\left[f_{0\nu}(\boldsymbol{k},\lambda)\frac{E_{\nu 0}}{ck}\right]^{1/2} \times (e^{-i\boldsymbol{k}\cdot\boldsymbol{R}}\bar{b}_{A\nu} + \epsilon_1 e^{i\boldsymbol{k}\cdot\boldsymbol{R}}\bar{b}_{B\nu})\bar{\beta}_{k\lambda}$$

where $f_{0\nu}(\boldsymbol{k}, \lambda)$ is the oscillator strength of the electronic transition $|0\rangle \leftrightarrow |\nu\rangle$ and $\bar{\omega}_p$ is the plasma frequency of the atomic electrons defined by $\bar{\omega}_p^2 = 4\pi e^2 S/mV$, where S is the number of all optically active electrons of the neutral atom A; and m and V are the electron mass and the volume of the sample container, respectively. The operators $\beta_{k\lambda}^\dagger$ and $\beta_{k\lambda}$ are the boson creation and annihilation operators describing the electromagnetic field with wavevector $\boldsymbol{k}$, frequency ck and transverse polarization $\lambda = 1, 2$, and $\bar{\beta}_{k\lambda} = \beta_{k\lambda} + \beta_{k\lambda}^\dagger$. The atomic excitation operators $b_{A\nu}^\dagger, b_{A\nu}$ and $b_{B\nu}^\dagger, b_{B\nu}$ are defined as

$$[4] \quad b_{A\nu}^\dagger = \alpha_{A\nu}^\dagger\alpha_{A0}, \quad b_{A\nu} = \alpha_{A0}^\dagger\alpha_{A\nu}, \quad b_{B\nu}^\dagger = \alpha_{B\nu}^\dagger\alpha_{B0}, \quad b_{B\nu} = \alpha_{B0}^\dagger\alpha_{B\nu}, \quad \bar{b}_{A\nu} \equiv b_{A\nu} + b_{A\nu}^\dagger, \quad \tilde{b}_{A\nu} \equiv b_{A\nu} - b_{A\nu}^\dagger$$

where $\alpha_{Ai}^\dagger, \alpha_{Bi}^\dagger$ and α_{Ai}, α_{Bi} are the Fermi creation and annihilation operators describing the electron states $i = |0\rangle$ and $i = |\nu\rangle$ of the atom A and image B, respectively; and the corresponding electron number operators are defined as $n_{Ai} = \alpha_{Ai}^\dagger\alpha_{Ai}$ and $n_{Bi} = \alpha_{Bi}^\dagger\alpha_{Bi}$.

The atomic excitation operators $b_{A\nu}^\dagger, b_{A\nu}$ and $b_{B\nu}^\dagger, b_{B\nu}$ satisfy the following commutation relations

$$[5] \quad [b_{A\nu}, b_{A\nu}^\dagger]_- = n_{A0} - n_{A\nu} = 1 - 2n_{A\nu}, \quad [b_{A\nu}^\dagger, b_{B\nu}]_- = [b_{B\nu}^\dagger, b_{A\nu}]_- = 0, \quad [b_{B\nu}, b_{B\nu}^\dagger]_- = n_{B0} - n_{B\nu} = 1 - 2n_{B\nu}, \quad [b_{A\nu}, b_{B\nu}]_- = [b_{A\nu}^\dagger, b_{B\nu}^\dagger]_- = 0$$

where

$$[6] \quad \sum_\nu n_{A\nu} = \sum_\nu n_{B\nu} = 1$$

When the average value of the number operators $n_{A\nu}$ and $n_{B\nu}$ are much smaller than unity, i.e., when

$$\bar{n}_{A\nu} \equiv \langle n_{A\nu}\rangle \ll 1, \quad \bar{n}_{B\nu} \equiv \langle n_{B\nu}\rangle \ll 1,$$

then the excitation operators $b_{A\nu}^\dagger, b_{A\nu}$ and $b_{B\nu}^\dagger, b_{B\nu}$ satisfy approximately Bose statistics.

The first term on the right-hand side (rhs) of eq. [3] represents the free atomic fields while the second term describes the Coulomb interaction between the atom A and its image B; the coupling function $V_{AB}^\nu = \bar{V}\epsilon_1$, where $\bar{V} = \Sigma U_{0\nu}^{AB}(\boldsymbol{R})$ is the Coulomb interaction, which in the dipole–dipole approximation, is the Lennard–Jones energy of interaction (18, 23–25). The third and fourth terms represent the free electromagnetic field and the contribution arising from the square of the vector potential term of the electromagnetic field, respectively. The last term describes the interaction of the electromagnetic field with the electron states of the atoms A and B.

For a perfect conductor $\epsilon(\omega) = \infty$ and $\epsilon_1 = 1$ the Hamiltonian [3] describes the interaction between the atom A and a perfectly conducting plane of distance R apart or the interaction between the atom A and its image B, which is equivalent to that describing the interaction between two identical atoms in the gas phase at a distance $2R$ apart (26–29). All the interactions involved in the Hamiltonian [3] are weak perturbations and, therefore, any time-dependent perturbation method when appropriately chosen is suitable to study the required excitation spectra arising from radiative and nonradiative decay mechanisms. We shall make use of the retarded double-time Green functions whose properties as well as whose use in statistical physics can be found elsewhere (30).

The atom A and its image B interact through their dipole–dipole interactions and radiate to each other as well and, hence, due to the cooperative radiative interaction between the atom A and its image B two new states, the symmetric and antisym-

Can. J. Chem. Downloaded from www.nrcresearchpress.com by 93.93.197.157 on 09/07/12
For personal use only.

metric (with respect to interchange between the atoms), are generated (31). The excitation spectra due to the process $|0\rangle \leftrightarrow |\nu\rangle$ for the symmetric and antisymmetric modes are determined by the imaginary parts of the Green functions $-2\mathrm{Im}G_{AB}^{(\pm)}(\omega)$, where the Green functions $G_{AB}^{(\pm)}(\omega)$ are defined as

$$[7] \quad G_{AB}^{(\pm)}(\omega) = \langle\langle b_{A\nu} \pm b_{B\nu}; b_{A\nu}^{\dagger} \pm b_{B\nu}^{\dagger}\rangle\rangle$$

The plus (+) and (−) signs refer to the symmetric and antisymmetric combination with respect to the interchange between the atom A and its image B. $G_{AB}^{(\pm)}(\omega)$ are Fourier transforms of the corresponding Green functions (30). The expressions for the absorption coefficient describing the transition $|0\rangle \leftrightarrow |\nu\rangle$ for the symmetric and antisymmetric modes of the system consisting of the atom A interacting with its image B are determined by the spectral functions which are obtained from the imaginary parts of the Green functions $G_{AB}^{(\pm)}(\omega)$, namely $-2\mathrm{Im}G_{AB}^{(\pm)}(\omega)$.

Using the Hamiltonian [3] we derive the following equations of motion for the Green functions

$$[8] \quad G_{AB}^{(\pm)}(\omega) = \frac{2(\bar{n}_0 - \bar{n}_\nu)(E_{\nu 0} \pm 2V_{AB}^{\nu})}{\pi(\omega^2 - \omega_{\pm}^2)}$$

where $\bar{n}_0 = \langle\alpha_{A0}^{\dagger}\alpha_{A0}\rangle = \langle\alpha_{B0}^{\dagger}\alpha_{B0}\rangle$ and $\bar{n}_\nu = \langle\alpha_{A\nu}^{\dagger}\alpha_{A\nu}\rangle = \langle\alpha_{B\nu}^{\dagger}\alpha_{B\nu}\rangle$ are the average values of the electron number operators describing the electron population of the states $|0\rangle$ and $|\nu\rangle$ at $t = t'$, respectively. The energies of excitation ω_+ and ω_- are defined as

$$[9] \quad \omega_{\pm}^2 = (E_{\nu 0} \pm 2V_{AB}^{\nu})(E_{\nu 0} \pm \gamma_{\pm})$$

where $\gamma_\pm$ denote scattering functions, which are determined by

$$[10] \quad \gamma_{\pm} \equiv \gamma_{\pm}(\omega) = \tfrac{1}{2}\gamma[1 + \epsilon_1^2(\omega)] \pm \epsilon_1(\omega)\gamma_{AB}$$

with

$$[11] \quad \gamma_{AB} \equiv \gamma_{AB}(\omega) = \bar{\omega}_p^2 \sum_{k,\lambda,\nu} \frac{f_{0\nu}(k,\lambda)E_{\nu 0}}{(\omega^2 - c^2k^2 - \omega_p^2)} \exp 2i(\boldsymbol{k}.\boldsymbol{R})$$

The scattering function $\gamma \equiv \gamma(\omega) \equiv \gamma_{AA}(\omega) \equiv \gamma_{BB}(\omega)$ is derived from the expression $\gamma_{AB}(\omega)$, eq. [11], if the exponential $\exp 2i(\boldsymbol{k}.\boldsymbol{R})$ is replaced by unity. The Green functions $G_{AB}^{(\pm)}(\omega)$ given by eq. [8] will be used to describe the excitation spectrum of the symmetric and antisymmetric modes, which for the sake of convenience, will be discussed separately.

III. Excitation spectra of the symmetric modes

To discuss the excitation spectrum, we consider the case of short distances of separation between the atom and the metal surface, i.e., where the inequality $(2RE_{\nu 0}/c) < 1$ is satisfied and retardation effects are unimportant (17–19, 26–29). In this case, the expressions for $\gamma_\pm(\omega)$ can be calculated from eqs. [10] and [11]; the results of such a calculation are known in the literature (26–29, 32–34). For $(2RE_{\nu 0}/c) < 1$ an expansion in powers of $2RE_{\nu 0}/c$ yields $\mathrm{Re}\gamma_{AB}(\omega) \approx 0$. The imaginary part of $\gamma_{AB}(\omega)$ depends on the distance R through the $\exp 2i(\boldsymbol{k}.\boldsymbol{R})$ in eq. [11]. The dependence of the lifetime of the physisorbed atom on the distance from the surface has been extensively discussed in the literature (35–39) and has been verified experimentally as well (40, 41). In the present study, we confine ourselves only to the case of short distances for which $(2RE_{\nu 0}/c) < 1$, and we are mainly concerned with the effects of surface plasmons on the lifetime of the physisorbed atoms and, hence, variations of the decay process with the distance will be completely ignored. Then the imaginary part of $\gamma_{AB}(\omega)$ is determined by (26–29)

$$[12] \quad \mathrm{Im}\gamma_{AB}(\omega) \approx \mathrm{Im}\gamma(\omega) \approx \gamma_0 = \tfrac{4}{3}(E_{\nu 0}/c)^3|P_{0\nu}|^2$$

and describes the spontaneous emission probability for the transition $|\nu\rangle \rightarrow |0\rangle$, where $\boldsymbol{P}_{0\nu}$ is the matrix element of the transition dipole moment and is assumed to be real. Then from eq. [10], we have

$$[13] \quad \mathrm{Im}\gamma_{\pm} \equiv \mathrm{Im}\gamma_{\pm}(\omega) \approx \tfrac{1}{2}\gamma_0[1 \pm \epsilon_1(\omega)]^2$$

Inspection of eq. [13] reveals that for a perfectly conducting surface for which $\epsilon_1 = 1$, the imaginary part of $\frac{1}{2}\gamma_\pm$ becomes equal to $\frac{1}{2}\mathrm{Im}\gamma_+ \approx \gamma_0$ and $\frac{1}{2}\mathrm{Im}\gamma_- \approx 0$, which coincide with the Dicke result (31, 39) describing the radiative decay of the symmetric and antisymmetric modes arising from the cooperative radiative interaction of two identical atoms in the gas phase, respectively (26–29).

Substituting into eq. [8] the expressions for $\epsilon_1(\omega)$ and $\epsilon(\omega)$ and the Lennard–Jones energy of interaction (17–19, 23) $\boldsymbol{V} = (1/12R^3)\Sigma_\nu|\boldsymbol{P}_{0\nu}|^2$, where only the term proportional for R^{-3} is retained, we derive from eq. [8] the following expression

$$[14] \quad G_{AB}^{(+)}(\omega) = \left(\frac{\bar{n}_0 - \bar{n}_\nu}{\pi}\right) 2E_{\nu 0}[\omega^2 - \omega_{sp}^2(1-\alpha) + i\omega\gamma_{sp}] \times \{(\omega^2 - \omega_{s+}^2)(\omega^2 - \omega_{s-}^2) + i\omega\gamma_{sp}(\omega^2 - E_{\nu 0}^2) + \frac{i\gamma_0}{2}[1 + \epsilon_1(\omega)]^2[\omega^2 - \omega_{sp}^2(1-\alpha) + i\omega\gamma_{sp}]E_{\nu 0}\}^{-1}$$

which describes the Green function of the symmetric modes of the system. The energies of excitation $\omega_{s\pm}$ are determined by

$$[15] \quad \omega_{s\pm}^2 = \tfrac{1}{2}\{E_{\nu 0}^2 + \omega_{sp}^2 \pm [(E_{\nu 0}^2 - \omega_{sp}^2)^2 + 4E_{\nu 0}^2\omega_{sp}^2\alpha]^{1/2}\}$$

where ω_{sp} is the frequency of the surface plasmons defined as $\omega_{sp} = \omega_p/\sqrt{2}$ and the coupling function $\alpha \equiv \alpha(\boldsymbol{R}) = \alpha_s/2R^3$ with α_s being the static polarizability (25) of the atom $\alpha_s = (2/3)\Sigma_\nu|\boldsymbol{P}_{0\nu}|^2/E_{\nu 0}$. The expression [14] describes the Green function of the symmetric modes, where the effects of the damping for the surface plasmons are fully included. Then if energy shifts proportional to $\gamma_0\gamma_{sp}$ are neglected, as being very small, the excitation spectrum of the symmetric modes is determined by

$$[16] \quad J_{AB}^{(+)}(\omega) = -2\mathrm{Im}G_{AB}^{(+)}(\omega) = \frac{(\bar{n}_0 - \bar{n}_\nu)}{\pi}[\bar{I}_s(\omega) + \bar{I}_s(-\omega)]$$

where the spectral functions $\bar{I}_s(\pm\omega)$ are defined as

$$[17] \quad \bar{I}_s(\omega) = \frac{N_s(\omega_{s+})\Gamma_+(\omega_{s+}) - (\omega - \omega_{s+})M_s\gamma_{sp}}{(\omega - \omega_{s+})^2 + \Gamma_+^2(\omega_{s+})} + \frac{N_s(\omega_{s-})\Gamma_+(\omega_{s-}) + (\omega - \omega_{s-})M_s\gamma_{sp}}{(\omega - \omega_{s-})^2 + \Gamma^2(\omega_{s-})}$$

$$[18] \quad N_s(\omega_{s\pm}) = \pm\left(\frac{2E_{\nu 0}}{\omega_{s\pm}}\right)\frac{[\omega_{s\pm}^2 - \omega_{sp}^2(1-\alpha)]}{(\omega_{s+}^2 - \omega_{s-}^2)}, \qquad M_s = \frac{2E_{\nu 0}}{(\omega_{s+}^2 - \omega_{s-}^2)}$$

$$[19] \quad \Gamma_+(\omega_{s\pm}) = \gamma_+(\omega_{s\pm}) + \Gamma_{sp}(\omega_{s\pm})$$

$$[20] \quad \gamma_+(\gamma_{s\pm}) = \frac{\gamma_0}{8}N_s(\omega_{s\pm})[1 + \epsilon_1(\omega_{s\pm})]^2$$

$$[21] \quad \lambda_{sp}(\omega_{s\pm}) = \Gamma_{sp}(\omega_{s\pm})/\gamma_{sp} = \pm\tfrac{1}{2}\frac{(\omega_{s\pm}^2 - E_{\nu 0}^2)}{(\omega_{s+}^2 - \omega_{s-}^2)}$$

Can. J. Chem. Downloaded from www.nrcresearchpress.com by 93.93.197.157 on 09/07/12
For personal use only.

The spectral function $\bar{I}_s(\omega)$ describes asymmetric Lorentzian lines, which are peaked at the frequencies $\omega = \omega_{s\pm}$ having spectral widths of the order of $\Gamma_+(\omega_{s\pm})$; the extent of the asymmetry at $\omega \neq \omega_{s\pm}$ depends on the strength of the damping of the surface plasmons γ_{sp}. Inspection of eq. [15] reveals that one of the energies of excitations is close to the value of the atomic frequency $E_{\nu 0}$ while the other is close to the value of the surface plasmon frequency ω_{sp}. Thus, when $E_{\nu 0}$ is greater than ω_{sp}, $E_{\nu 0} > \omega_{sp}$, then the excitations at $\omega = \omega_{s+}$ ($E_{\nu 0} < \omega_{s+}$) and $\omega = \omega_{s-}$ ($\omega_{sp} > \omega_{s-}$) may be referred to as the atomic and surface plasmon-like excitations, respectively. The reverse is true for $E_{\nu 0} < \omega_{sp}$. The splitting of the excitation spectrum into the frequencies ω_{s+} and ω_{s-} is due to the dipole–dipole interaction between the atom A and its image B. Because of this interaction, $N_s(\omega_{s\pm})$ is given by eq. [18] for $\alpha \neq 0$ while for $\alpha = 0$, which occurs in the limit for $R \rightarrow \infty$, $N_s(E_{\nu 0}) = 2$ and $N_s(\omega_{sp}) = 0$. Hence, for $\alpha \neq 0$, $N_s(\omega_{s\pm})$ takes values less than 2, i.e., $0 < N_s(\omega_{s\pm}) < 2$.

The expressions [16]–[21] imply that the damping of the surface plasmons, which is of a nonradiative nature, contributes in the same way as does that damping arising from radiative decay processes and, hence, should be included for quantitative comparisons with the observed data. The first term in the expression [19] describes the radiative damping, and the second term represents the damping of the surface plasmons, while terms proportional to $\gamma_0\gamma_{sp}$ have been neglected. The expression [20] for $\gamma_+(\omega_{s\pm})$ indicates that the radiative damping at the corresponding frequencies $\omega = \omega_{s\pm}$ is influenced by two effects: firstly, the factor $N_s(\omega_{s\pm})$ describing the effects of the dipole–dipole interaction between the atom and its image for $\alpha \neq 0$ and, secondly, the factor $[1 + \epsilon_1(\omega_{s\pm})]^2$, which describes the cooperative radiative interaction between the atom and its image. For a perfect conductor $\epsilon_1 = 1$ while for a metal surface $\epsilon_1(\omega_{s\pm}) \neq 1$. The deviation of $\epsilon_1(\omega_{s\pm})$ from unity, $\epsilon_1(\omega_{s\pm}) \neq 1$, is due to the screening of the image charge of the atom by the metallic electrons of the surface and describes the dynamic effect arising from the surface plasmons at the frequencies $\omega = \omega_{s\pm}$. For a perfect conductor $\epsilon_1 = 1$ and $N_s \rightarrow 2$ then $\gamma_+ \approx \gamma_0$, which is the Dicke result (31, 36, 39) and which is twice that of the isolated atom. However, in the presence of plasmon damping, since γ_{sp} is always[2] much greater than γ_0, $\gamma_{sp} \gg \gamma_0$ (or the corresponding lifetimes $\tau_0 \gg \tau_{sp}$), the radiative one-atom-image process is erased by the nonradiative process. Hence, the radiative and nonradiative processes compete with each other only when the radiative processes arise from cooperative effects of an assembly of N identical atoms adsorbed on the metal surface. In this case, the effective radiative damping (31, 42) is equal to $N\gamma_0$ for large N and may be in a position to compete with γ_{sp}.

1. Nonradiative excitation spectra

In the case where the surface plasmon mode is heavily damped, namely, when $\gamma_{sp} \gg \gamma_0$, which is always valid, the radiative contributions to the damping can be neglected, and $\Gamma_+(\omega_{s\pm}) \approx \Gamma_{sp}(\omega_{s\pm})$ defined by eq. [21]. In this case nonradiative energy transfer of the excitation energy of the atom to the metal takes place, and in this limit the spectral function [17] is reduced to

$$[22] \quad \gamma_{sp}\bar{I}_s(\omega) = \frac{N_s(\omega_{s+})\lambda_{sp}(\omega_{s+}) - X^{sp}_{s+}M_s}{[X^{sp}_{s+}]^2 + \lambda^2_{sp}(\omega_{s+})} + \frac{N_s(\omega_{s-})\lambda_{sp}(\omega_{s-}) + X^{sp}_{s-}M_s}{[X^{sp}_{s-}]^2 + \lambda^2_{sp}(\omega_{s-})}$$

where

$$[23] \quad X^{sp}_{s\pm} = (\omega - \omega_{s\pm})/\gamma_{sp}$$

defines the reduced frequency. The relative intensity per atom at the frequencies $\omega = \omega_{s\pm}$ in units of γ_{sp} is determined by

$$[24] \quad \gamma_{sp}\bar{I}_s(\omega_{s\pm}) = \frac{N_s(\omega_{s\pm})}{\lambda_{sp}(\omega_{s\pm})}$$

which defines the maximum height of the peak in question. In the absence of interaction between the atom and its image, i.e., when $\alpha \rightarrow 0$ then $\omega_{s+} \rightarrow E_{\nu 0}$, $\omega_{s-} \rightarrow \omega_{sp}$, $\lambda_{sp}(E_{\nu 0}) \rightarrow 0$ while $\lambda_{sp}(\omega_{sp})$ takes its largest value, $\lambda_{sp}(\omega_{sp}) = 0.5$, but in this limit, $N_s(E_{\nu 0}) = 2$ and $N_s(\omega_{sp}) = 0$. On the other hand, at resonance, i.e, when $E_{\nu 0} = \omega_{sp}$ then $\omega^2_{s\pm} = E^2_{\nu 0}(1 \pm \sqrt{\alpha})$, $N_s(\omega_{s\pm}) = (1 \pm \sqrt{\alpha})^{1/2}$ and $\lambda_{sp}(\omega_{s\pm}) = 0.25$, which implies that both modes, the atomic and the surface plasmon-like modes, have equal lifetimes of the order of $4/\gamma_{sp}$.

Using values of α obtained from Table 2 of ref. 25 and eqs. [15], [18], [21], and [23] we derive numerical values for $\omega_{s\pm}$, $N_s(\omega_{s\pm})$, M_s, $\lambda_{sp}(\omega_{s\pm})$, and $\gamma_{sp}\bar{I}_s(\omega_{s\pm})$, respectively. The numerical results are tabulated in Table 1 for the symmetric modes of the excited rare-gas atoms Xe, Kr, and Ar, which are physisorbed on the metal surfaces of Mg, Al, and Au, respectively. For the numerical applications, we have examined two different excited states of Xe, three of Kr, and only one of Ar, respectively. The observed values for the frequencies of the surface plasmons, which have been obtained from ref. 43, have been used for the metals in question. The computed energies of excitation $\omega_{s\pm}$ in eV are shown in the third column of Table 1, which imply that the excitation energies for the atomic-like excitations of the excited rare-gas atoms physisorbed on Mg are blue shifted while those on the metal surfaces of Al and Au are red shifted in comparison with the values of the gas phase excitations of the single isolated atoms in question. Inspection of Table 1 indicates that for the atomic-like excitations, the numerical values of $N_s(\omega_{s\pm})$ are less but near 2, while the corresponding ones for the surface plasmon-like excitations are much less than 1, but the sum $N_s(\omega_{s+}) + N_s(\omega_{s-}) \approx 2$, which is the numerical value for the single isolated atom case for which $\alpha = 0$.

The data in the fifth column of Table 1 for $\lambda_{sp}(\omega_{s\pm})$ indicate that for the surface plasmon-like excitations, $\lambda_{sp}(\omega_{s\pm})$ takes values near but always less than 0.5, while for the atomic-like excitations $\lambda_{sp}(\omega_{s\pm}) \ll 1$. Since $\lambda^{-1}_{sp}(\omega_{s\pm})$ describes the lifetime of the excitations involved in units of γ_{sp}, eq. [21] for values of $\lambda_{sp}(\omega_{s\pm}) \ll 1$ implies that there is a large enhancement of the lifetimes of the atomic-like excitations. Considering that for the atomic-like excitations $N_s(\omega_{s\pm})$ takes values near 2, the expression $\gamma_{sp}\bar{I}_s(\omega_{s\pm})$ given by eq. [24] and the numerical data in the sixth column of Table 1 indicate twice the lifetimes of the excitations in question in units of γ_{sp}.

Using the data from Table 1 the computed spectra from eq. [22] of the atomic-like excitations are illustrated in Figs. 1–4, where the relative intensity per atom $\bar{I}_s(\omega)$ in units of γ_{sp}, $\gamma_{sp}\bar{I}_s(\omega)$, is plotted versus the relative frequency $X^{sp}_{s\pm} = (\omega - \omega_{s\pm})/\gamma_{sp}$ in units of eV/γ_{sp}; the numbering on the abscissa refers to the frequency ω in eV. The data in Table 1 and Figs.

[2]Radiative and nonradiative lifetimes τ_0 and τ_{sp} are of the order of 10^{-7}–10^{-9} s and 10^{-14}–10^{-15} s, respectively; hence, adsorbate excitations on metals are characterized by extremely short nonradiative lifetimes, which are 10^5–10^6 times shorter than the free atom lifetimes (15, 20–22).

TABLE 1. Calculated energies of excitation $\omega_{s\pm}$, probability amplitudes $N_s(\omega_{s\pm})$, spectral widths $\lambda_{sp}(\omega_{s\pm})$ in units of γ_{sp}, relative intensities per atom $\gamma_{sp}\tilde{I}_s(\omega_{s\pm})$ in units of γ_{sp} and asymmetries of M_s in $(eV)^{-1}$ for the *symmetric modes* of excited Xe, Kr, and Ar atoms, which are physisorbed on the metal surfaces of Mg, Al, and Au, respectively; the metallic surfaces have the corresponding surface plasmon frequencies (43) $\omega_{sp} = \omega_p/\sqrt{2} = 7.4953$, 10.8187, and 17.1827 eV

System	E_{v0} (eV)	$\omega_{s\pm}$ (eV)	$N_s(\omega_{s\pm})$	$\lambda_{sp}(\omega_{s\pm})$	$\gamma_{sp}\tilde{I}_s(\omega_{s\pm})$	$M_s(eV)^{-1}$
Xe on Mg	8.437	8.8694	1.5760	0.1247	12.64	0.5624
		6.9759	0.4148	0.3753	1.10	0.5624
	9.570	9.8445	1.1892	0.0578	31.48	0.4155
		7.1309	0.1724	0.4422	0.39	0.4155
Xe on Al	8.437	11.1236	0.2976	0.4435	0.67	0.2848
		8.0307	1.6884	0.0565	29.90	0.2848
	9.570	11.3623	0.5776	0.3784	1.53	0.3861
		8.9178	1.4104	0.1261	11.60	0.3861
Xe on Au	8.437	17.2955	0.0688	0.4916	0.14	0.0728
		8.2032	1.9528	0.0084	232.50	0.0728
	9.570	17.3408	0.0920	0.4873	0.19	0.0892
		9.2805	1.8900	0.0127	148.82	0.0892
Kr on Au	10.03	17.3234	0.0821	0.4881	0.17	0.0982
		9.7851	1.9048	0.0119	160.07	0.0982
	10.56	17.3468	0.0954	0.4855	0.20	0.1083
		10.2882	1.8919	0.0145	130.48	0.1083
	10.60	17.3487	0.0966	0.4852	0.20	0.1091
		10.3260	1.8909	0.0148	127.76	0.1091
Kr on Mg	10.64	10.8000	1.9200	0.0268	71.64	0.3331
		7.2629	0.0733	0.4732	0.15	0.3331
Ar on Mg	11.83	11.9258	1.9644	0.0129	152.28	0.2679
		7.3420	0.0320	0.4871	0.06	0.2679
Ar on Au	11.83	17.3669	0.1112	0.4811	0.23	0.1408
		11.5579	1.8800	0.0189	99.47	0.1408

Can. J. Chem. Downloaded from www.nrcresearchpress.com by 93.93.197.157 on 09/07/12
For personal use only.

1–4 indicate that the relative intensities per atom, $\gamma_{sp}\tilde{I}_s(\omega)$, of the symmetric modes take positive values implying that the physical process of absorption (attenuation) take place at the corresponding frequencies. The height of each peak, $\gamma_{sp}\tilde{I}_s(\omega_{s\pm})$, in Figs. 1–4 determines the total enhancement, which occurs for the atomic-like excitations of the physisorbed excited atoms in question in the limit when the nonradiative lifetimes of the surface plasmons are very much shorter than the corresponding atomic lifetimes, i.e., when $\tau_0 \gg \tau_{sp}$ ($\gamma_{sp} \gg \gamma_0$). It should be emphasized that the spectra in Figs. 1–4 of the atomic-like excitations are due entirely to the interaction of the atom A with its image B, namely, they exist only for values of $\alpha \neq 0$. This implies that the presence of the surface plasmons results in the splitting of their spectrum into surface plasmon-like and atomic-like excitations, whose spectral widths are of the order of magnitude $\lambda_{sp}(\omega_{s-})\gamma_{sp}$ and $\lambda_{sp}(\omega_{s+})\gamma_{sp}$, respectively, and vice versa. Small values of α produce small values of $\lambda_{sp}(\omega_{s\pm})$, which in turn enhance the lifetimes or, equivalently, diminish the damping of the atomic-like excitations. In Figs. 1–4, the spectra have asymmetric Lorentzian lineshapes; they have a sharp cutoff on the high-frequency side and a low-frequency tail; and the extent of the asymmetry depends on the numerical values of M_s. The center of each peak in Figs. 1–4 is depicted at the excitation frequency $\omega = \omega_{s\pm}$ in eV.

IV. Excitation spectra of the antisymmetric modes

Considering the limit of short distances, where $(2RE_{v0}/c) < 1$, we derive from eq. [8] the following expression

$$[25]\quad G^{(-)}_{AB}(\omega) = \frac{(\bar{n}_0 - \bar{n}_v)}{\pi} 2E_{v0}[\omega^2 - \omega_{sp}^2(1+\alpha) + i\omega\gamma_{sp}]\{(\omega^2 - \omega_{a+}^2)(\omega^2 - \omega_{a-}^2) + i\omega\gamma_{sp}(\omega^2 - E_{v0}^2) + \frac{i\gamma_0}{2}[1 - \epsilon_1(\omega)^2][\omega^2 - \omega_{sp}^2(1+\alpha) + i\omega\gamma_{sp}]E_{v0}\}^{-1}$$

which describes the Green function of the antisymmetric modes with the energies of excitation ω_{a+} and ω_{a-} determined by

$$[26]\quad \omega_{a\pm}^2 = \tfrac{1}{2}\{E_{v0}^2 + \omega_{sp}^2 \pm [(E_{v0}^2 - \omega_{sp}^2)^2 - 4E_{v0}^2\omega_{sp}^2\alpha]^{1/2}\}$$

The expressions [25] and [26] can be derived from the corresponding eqs. [14] and [15] if α is replaced everywhere by $-\alpha$ and $[1 + \epsilon_1(\omega)]^2$ in the denominator of [14] is replaced by $[1 - \epsilon_1(\omega)]^2$. Equation [26] implies that the energies of excitation $\omega_{a\pm}$ are real and well separated provided that the inequality

$$[27]\quad (E_{v0}^2 - \omega_{sp}^2)^2 > 4E_{v0}^2\omega_{sp}^2\alpha$$

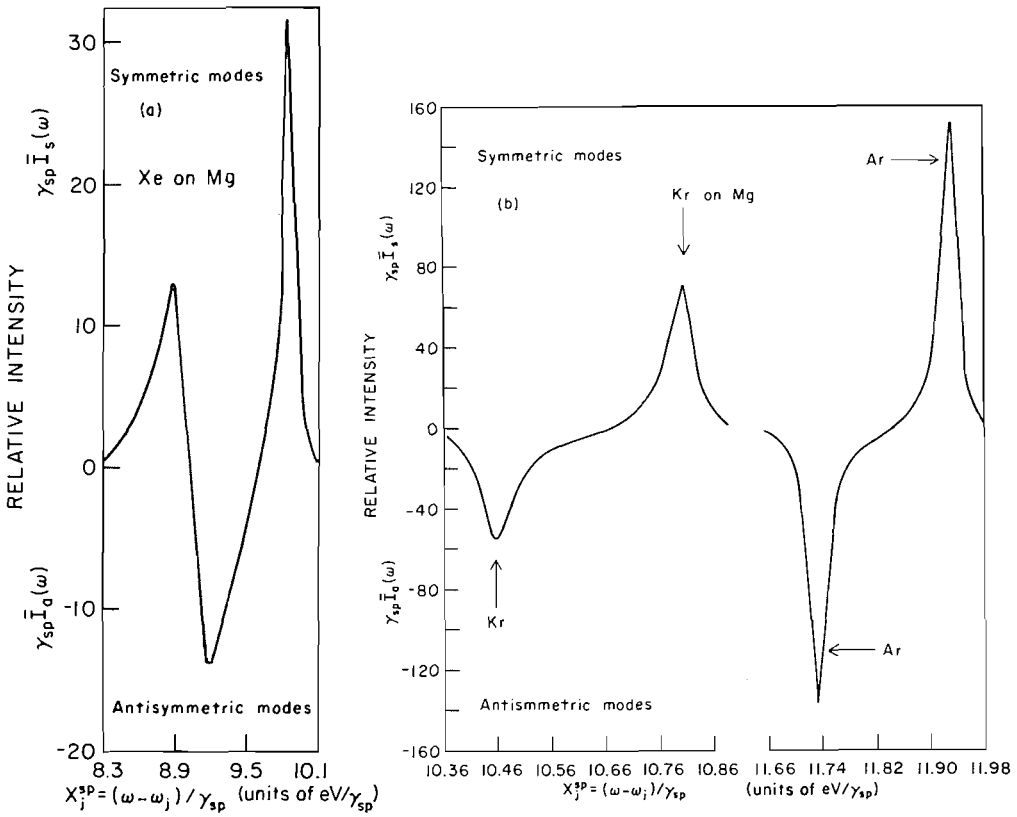

FIG. 1. Spectra of the atomic-like excitations of excited rare-gas atoms physisorbed on the surface of Mg. The relative intensities per atom $\gamma_{sp}\bar{I}_j(\omega)$ in units of γ_{sp} are computed from eqs. [22] and [40], and are plotted versus the relative frequencies $X_j^{sp} = (\omega - \omega_j)/\gamma_{sp}$ in units of eV/γ_{sp}, where $j = s\pm$ and $a\pm$ for the symmetric (positive intensities) and antisymmetric (negative intensities) modes, respectively. The numbering on the abscissa refers to the frequency ω in eV. The center of each asymmetric Lorentzian line is depicted at the excitation frequency $\omega = \omega_j$: (*a*) excited Xe at the frequencies $E_{\nu 0} = 8.437$ and 9.57 eV, respectively; (*b*) excited Kr and Ar at the frequencies $E_{\nu 0} = 10.64$ and 11.83, respectively.

is satisfied. In the opposite limit, i.e., when the inequality

[28] $(E_{\nu 0}^2 - \omega_{sp}^2)^2 < 4E_{\nu 0}^2\omega_{sp}^2\alpha$

is satisfied then eq. [26] becomes

[29] $\omega_{a\pm}^2 = \bar{\omega}_a^2(1 \pm i\gamma_a)$

where

[30] $\bar{\omega}_a^2 = \frac{1}{2}(E_{\nu 0}^2 + \omega_{sp}^2); \quad \gamma_a = \left\{ \frac{E_{\nu 0}^2\omega_{sp}^2(1+\alpha)}{\bar{\omega}_a^4} - 1 \right\}^{1/2}$

The inequality [28] refers to the physical process which occurs whenever the system is close to resonance conditions, where the frequency $E_{\nu 0}$ is very close to the surface plasmon frequency. Hence, when $E_{\nu 0} = \omega_{sp}$, $\gamma_a = \sqrt{\alpha}$ and $\bar{\omega}_a\gamma_a/2$ describes the nonradiative damping of the antisymmetric mode at the frequency $\omega = \bar{\omega}_a$. This situation has been discussed for a number of systems in refs. 24, 25, 44 to which the reader is referred for details. The inequality [28] is satisfied from the data listed in Table 2 for excited Xe at the frequencies $E_{\nu 0} =$ 8.437 and 9.57 eV physisorbed on Mg and Al, respectively; such cases have been discussed elsewhere (17).

In the limiting case where the inequality [27] is satisfied, and energy shifts of the order of $\gamma_0\gamma_{sp}$ are neglected, then following the expansion of the expression [25] about the poles at $\omega^2 = \omega_{a+}^2$ and $\omega^2 = \omega_{a-}^2$, we derive the imaginary part of the Green function as

[31] $\bar{J}_{AB}(\omega) = -2\mathrm{Im}\bar{G}_{AB}(\omega) = \dfrac{(\bar{n}_0 - \bar{n}_\nu)}{\pi}[\bar{I}_a(\omega) + \bar{I}_a(-\omega)]$

where the spectral functions $\bar{I}_a(\pm\omega)$ are defined by

[32] $\bar{I}_a(\omega) = \dfrac{N_a(\omega_{a+})\Gamma_-(\omega_{a+}) - (\omega - \omega_{a+})M_a\gamma_{sp}}{(\omega - \omega_{a+})^2 + \Gamma_-^2(\omega_{a+})} + \dfrac{N_a(\omega_{a-})\Gamma_-(\omega_{a-}) + (\omega - \omega_{a-})M_a\gamma_{sp}}{(\omega - \omega_{a-})^2 + \Gamma_-^2(\omega_{a-})}$

[33] $N_a(\omega_{a\pm}) = \pm\left(\dfrac{2E_{\nu 0}}{\omega_{a\pm}}\right)\dfrac{[\omega_{a\pm}^2 - \omega_{sp}^2(1+\alpha)]}{(\omega_{a+}^2 - \omega_{a-}^2)}$

[34] $M_a = \dfrac{2E_{\nu 0}}{(\omega_{a+}^2 - \omega_{a-}^2)}$

[35] $\Gamma_-(\omega_{a\pm}) = \gamma_-(\omega_{a\pm}) + \Gamma_{sp}(\omega_{a\pm})$

[36] $\gamma_-(\omega_{a\pm}) = \dfrac{\gamma_0}{8}N_a(\omega_{a\pm})[1 - \epsilon_1(\omega_{a\pm})]^2$

[37] $\lambda_{sp}(\omega_{a\pm}) = \Gamma_{sp}(\omega_{a\pm})/\gamma_{sp} = \pm\dfrac{1}{2}\dfrac{(\omega_{a\pm}^2 - E_{\nu 0}^2)}{(\omega_{a+}^2 - \omega_{a-}^2)}$

[38] $\lambda_{sp}(\omega_{a+}) + \lambda_{sp}(\omega_{a-}) = 0.5$

[39] $[1 - \epsilon_1(\omega)]^2 = [1 - \mathrm{Re}\epsilon_1(\omega)]^2 - [\mathrm{Im}\epsilon_1(\omega)]^2$

Can. J. Chem. Downloaded from www.nrcresearchpress.com by 93.93.197.157 on 09/07/12
For personal use only.

Can. J. Chem. Downloaded from www.nrcresearchpress.com by 93.93.197.157 on 09/07/12
For personal use only.

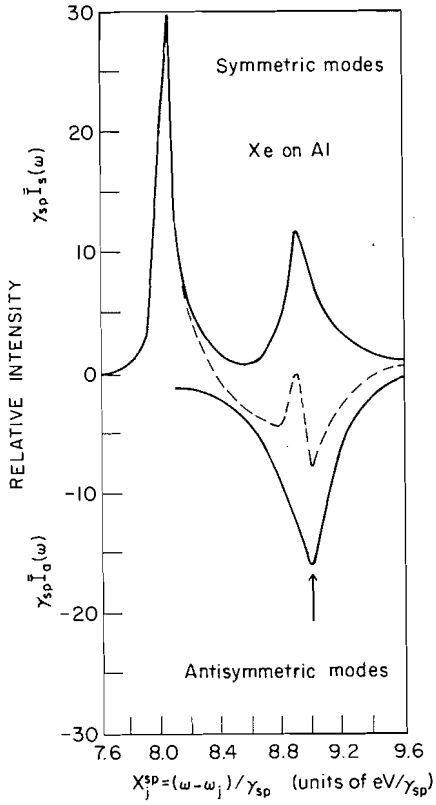

FIG. 2. As in Fig. 1 but on the surface of Al. The dashed line indicates the net lineshape of excited Xe on Al, which results from the combination of the red shifted peak of the symmetric mode at ω_{s-} = 8.9178 eV (atomic excitation 9.57 eV) and the blue shifted peak of the antisymmetric mode at ω_{a-} = 8.9952 eV (atomic excitation 8.437 eV).

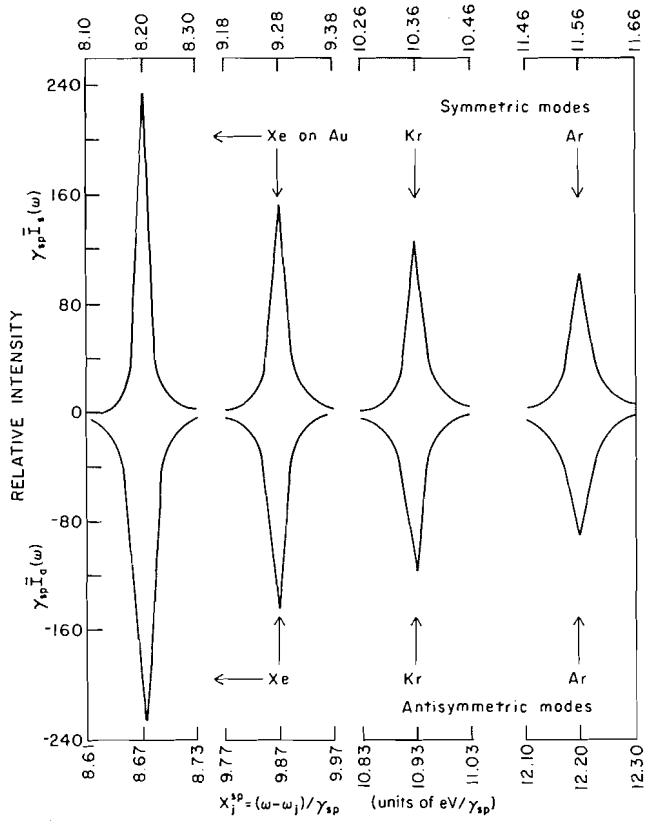

FIG. 3. As in Fig. 1 but on the surface of Au.

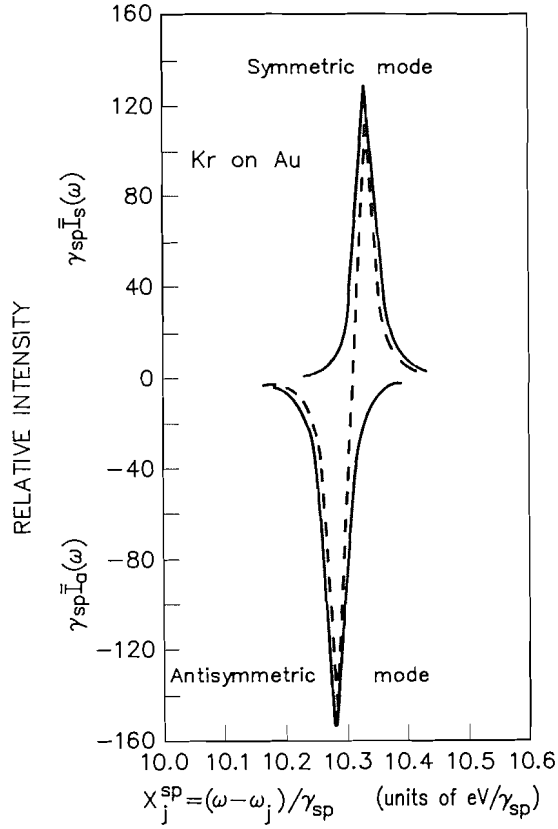

FIG. 4. As in Fig. 1 but for excited Kr at the frequencies E_{v0} = 10.03 and 10.60 eV, respectively, physisorbed on the surface of Au. The dashed line illustrates the net lineshape arising from the combination of the red shifted peak of the symmetric mode at ω_{s-} = 10.326 eV (atomic excitation 10.6 eV) and the blue shifted peak of the antisymmetric mode at ω_{a-} = 10.2815 eV (atomic excitation 10.03 eV).

The expression [31] is analogous to eq. [16] and represents the excitation spectrum of the antisymmetric modes arising from the interaction between the adsorbed atom and its image. Hence, the discussion of the spectrum of the antisymmetric mode is similar to that of the symmetric modes. For a perfect conductor $\epsilon_1(\omega) = 1$, $\omega_a = E_{v0} - \bar{V}$, and $\gamma_-(\omega_a) \rightarrow 0$. This is the Dicke result (29, 31, 39, 45) for the radiative spectra of the antisymmetric modes of two identical atoms in the gas phase, where the photon is trapped between the two atoms. Hence, for perfectly conducting surfaces for which $\epsilon_1(\omega_a) = 1$, the radiative antisymmetric modes describe stationary states, $\gamma_-(\omega_a) = 0$, while for metal and dielectric surfaces where $\epsilon_1(\omega_{a\pm}) \neq 1$, they represent states having radiative lifetimes $1/\gamma_-(\omega_{a\pm})$ arising from radiative decay processes. However, in the presence of the surface plasmon damping, the radiative processes are completely erased since γ_{sp} is always very much larger than γ_0, $\gamma_{sp} \gg \gamma_0$ and, therefore, the nonradiative process dominates.

1. Nonradiative excitation spectra

When $\gamma_{sp} \gg \gamma_0$, which is always applicable, the radiative damping effects are unimportant and can be neglected, and $\Gamma_-(\omega_{a\pm}) \approx \Gamma_{sp}(\omega_{a\pm})$, which is determined by eq. [37]. In this case the spectral function [32] can be written as

$$[40]\quad \gamma_{sp}\bar{I}_a(\omega) = \frac{N_a(\omega_{a+})\lambda_{sp}(\omega_{a+}) - X_{a+}^{sp}M_a}{[X_{a+}^{sp}]^2 + \lambda_{sp}^2(\omega_{a+})} + \frac{N_a(\omega_{a-})\lambda_{sp}(\omega_{a-}) + X_{a-}^{sp}M_a}{[X_{a-}^{sp}]^2 + \lambda_{sp}^2(\omega_{a-})}$$

Can. J. Chem. Downloaded from www.nrcresearchpress.com by 93.93.197.157 on 09/07/12
For personal use only.

TABLE 2. Calculated energies of excitation $\omega_{a\pm}$, probability amplitudes $N_a(\omega_{a\pm})$, spectral widths $\lambda_{sp}(\omega_{a\pm})$ in units of γ_{sp}, relative intensities per atom $\gamma_{sp}\bar{I}_a(\omega_{a\pm})$ in unit of γ_{sp} and asymmetries M_a in $(eV)^{-1}$ for the *antisymmetric modes* of excited Xe, Kr, and Ar atoms, which are physisorbed on the metal surfaces of Mg, Al, and Au, respectively (the numerical values for the surface plasmons of the metals in question are given in Table 1)

System	$E_{\nu 0}$ (eV)	$\omega_{a\pm}$ (eV)	$N_a(\omega_{a\pm})$	$\lambda_{sp}(\omega_{a\pm})$	$\gamma_{sp}\bar{I}_a(\omega_{a\pm})$	M_a $(eV)^{-1}$
Xe on Mg	9.570	9.1484	2.6804	−0.2011	−13.33	0.9754
		8.0044	−0.6728	0.7011	−0.96	0.9754
Xe on Al	8.437	10.3592	−0.9052	0.6843	−1.32	0.6392
		8.9952	2.9284	−0.1843	−15.84	0.6392
Xe on Au	8.437	17.0650	−0.0756	0.5093	−0.15	0.0781
		8.6726	2.0940	−0.0093	−225.16	0.0781
	9.570	17.0141	−0.1068	0.5150	−0.21	0.0996
		9.8667	2.1240	−0.0150	−141.60	0.0996
Kr on Au	10.03	17.0334	−0.0941	0.5138	−0.18	0.1088
		10.2815	2.1070	−0.0138	−152.68	0.1088
	10.56	17.0060	−0.1133	0.5176	−0.22	0.1230
		10.8422	2.1257	−0.0176	−120.78	0.1230
	10.60	17.0037	−0.1150	0.5179	−0.20	0.1242
		10.8848	2.1274	−0.0179	−118.85	0.1242
Kr on Mg	10.64	10.4550	2.1208	−0.0396	−53.56	0.4323
		7.7513	−0.1156	0.5396	−0.21	0.4323
Ar on Mg	11.83	11.7279	2.0436	−0.0152	−134.45	0.2997
		7.6543	−0.0196	0.5152	−0.04	0.2997
Ar on Au	11.83	16.9797	−0.1408	0.5245	−0.27	0.1673
		12.1196	2.1492	−0.0245	−87.72	0.1673

where

[41] $X_{a\pm}^{sp} = (\omega - \omega_{a\pm})/\gamma_{sp}$

is the reduced frequency. The relative intensity per atom at the frequencies $\omega = \omega_{a\pm}$ in units of γ_{sp} is determined by

[42] $$\gamma_{sp}\bar{I}_a(\omega_{a\pm}) = \frac{N_a(\omega_{a\pm})}{\lambda_{sp}(\omega_{a\pm})}$$

which is the maximum height of the peaks in question at the frequencies $\omega = \omega_{a\pm}$. The expressions [40]–[42] are analogous to eqs. [22]–[24] for the symmetric modes. Hence, the discussion of the spectra of the symmetric modes is applicable to the spectra of the antisymmetric modes.

In the limit when the inequality [27] is satisfied the computed data for $\omega_{a\pm}$, $N_a(\omega_{a\pm})$, $\lambda_{sp}(\omega_{a\pm})$, $\gamma_{sp}\bar{I}_a(\omega_{a\pm})$, and M_a, are listed in Table 2 and are analogous to those for the symmetric modes given in Table 1. The computed values for $N_a(\omega_{a\pm})$ and $\lambda_{sp}(\omega_{a\pm})$ listed in Table 2 indicate that when $N_a(\omega_{a\pm})$ takes a positive value the corresponding value for $\lambda_{sp}(\omega_{a\pm})$ is negative and vice versa. This implies that the relative intensities of the peaks always take negative values indicating that the physical process of stimulated emission (amplification) occurs at the corresponding frequencies. The data of the sixth column in Tables 1 and 2 imply that for the atomic-like excitations the relative intensities per atom $\gamma_{sp}\bar{I}_s(\omega_{s\pm})$ of the symmetric modes are slightly larger or smaller in magnitude than the corresponding values of the antisymmetric modes $\gamma_{sp}\bar{I}_a(\omega_{a\pm})$; but they always have opposite signs and, hence, can cancel each other out whenever the corresponding frequencies coincide.

As can be verified from the data in the Tables 1 and 2, when the frequencies of the symmetric modes are *blue* shifted, the corresponding ones of the antisymmetric modes are *red* shifted and vice versa. Therefore, the spectral peaks of the symmetric and antisymmetric modes may cancel each other out either when they belong to the same atomic excitation frequency $E_{\nu 0}$, in which case the energy shift must be extremely small, or when they belong to two different nearby excited states of the atom. The latter case may occur when the atomic-like excitation frequency of the symmetric mode of the higher excited state of the atom is red shifted, while the corresponding one of the antisymmetric mode of the lower excited state of the atom in blue shifted to the extent that the atomic-like excitation frequency of the modes in question nearly coincide. The data in Tables 1 and 2 indicate that such a case has materialized; for instance, for the $P_{1/2}$ excitation (46, 47) of Xe at the frequency $E_{\nu 0} = 9.57$ eV physisorbed on Al, the atomic-like excitation of the symmetric mode at $\omega_{s-} = 8.9178$ eV is red shifted and the relative intensity of the peak is $\bar{I}_s(\omega_{s-}) = 11.60/\gamma_{sp}$. Conversely, for the $P_{3/2}$ excitation (46, 47) of Xe at the frequency $E_{\nu 0} = 8.437$ eV on Al, the atomic-like excitation of the antisymmetric mode at $\omega_{a-} = 8.9952$ eV is blue shifted and the relative intensity of the peak is equal to $\bar{I}_a(\omega_{a-}) = -15.84/\gamma_{sp}$. Hence, the peaks of the symmetric and antisymmetric modes have similar positive and negative profiles, and then may cancel each other out either completely or partially. Because of the large values of $\lambda_{sp}(\omega_{s\pm})$ and $\lambda_{sp}(\omega_{a\pm})$ and the small values of $N_s(\omega_{s\pm})$ and $N_a(\omega_{a\pm})$, the spectra of the surface plasmon-like excitations of the symmetric and antisymmetric modes are broadened to the extent that it is impossible to present them graphically.

Using the data from Table 2, the computed spectra from eq. [40] of the antisymmetric modes are illustrated in Figs. 1–4, where the relative frequency $X_{a\pm}^{sp} = (\omega - \omega_{a\pm})/\gamma_{sp}$ is plotted versus the relative intensity per atom $\gamma_{sp}\bar{I}_a(\omega)$ in units of γ_{sp}. Since the relative intensities $\gamma_{sp}\bar{I}_a(\omega)$ take negative values, the spectra of the antisymmetric modes in Figs. 1–4 occupy the negative axis while the corresponding spectra of the symmetric

modes occupy the positive axis. Peaks having positive and negative intensities describe physical processes, where absorption (attenuation) and stimulated emission (amplification) take place at the corresponding frequencies, respectively. Figures 1*a* and 1*b* indicate that for Xe, Kr, and Ar on Mg, respectively, the peaks of the symmetric modes are blue shifted while the corresponding ones of the antisymmetric modes are red shifted relative to the atomic frequencies $E_{\nu 0}$. The opposite shifts occur for Xe, Kr, and Ar on the surfaces of Al and Au, respectively, where the peaks of the symmetric and antisymmetric modes are red and blue shifted, respectively, as depicted in Figs. 2–4.

Inspection of Figs. 1*a* and 1*b* implies that there is no overlap between the frequencies of the spectral profiles of the symmetric and anti-symmetric modes, which originate either from the same atomic excitation $E_{\nu 0}$ like the case of Kr and Ar or from two different atomic excitations as in the case of Xe. Figure 1*a* illustrates the spectra of the atomic-like excitations of Xe on Mg, where the symmetric modes consist of two blue shifted peaks at $\omega_{s+} = 8.8694$ eV (atomic excitation $E_{\nu 0} = 8.437$ eV) and $\omega_{s+} = 9.8445$ eV (atomic excitation $E_{\nu 0} = 9.57$ eV), while the antisymmetric mode consists only of the red shifted peak at $\omega_{a+} = 9.1484$ eV (atomic excitation $E_{\nu 0} = 9.57$ eV), because, as mentioned previously, the other peak at the atomic excitation $E_{\nu 0} = 8.437$ eV satisfies the inequality [28]. The frequencies of the peaks in question are such that they behave as if they had absorption–amplification and amplification–absorption lineshapes, respectively; however, the frequencies of the peaks are well separated such that there is no cancellation of intensities.

Figure 2 illustrates the spectra of the atomic-like excitations of the symmetric modes of Xe, on Al as well as one peak of the antisymmetric mode for Xe on Al. The dashed line in Fig. 2 indicates the net lineshape of excited Xe on Al, which originates from the combination of two lineshapes: the red shifted peak of the symmetric mode at $\omega_{s-} = 8.9178$ eV (atomic excitation $E_{\nu 0} = 9.57$ eV) and the blue shifted peak of the antisymmetric mode at $\omega_{a-} = 8.9952$ eV (atomic excitation $E_{\nu 0} = 8.437$ eV). These two peaks, whose frequency profiles are nearly overlapping, cancel each other out with the result that the peak at the atomic frequency $E_{\nu 0} = 9.57$ eV vanishes. A peak or a shoulder having a small negative intensity appears on each side of the vanished peak at $\omega_{s-} = 8.9178$ eV as indicated by the dashed line in Fig. 2.

Figure 3 illustrates the spectra of the atomic-like excitations of the symmetric and antisymmetric modes of Xe, Kr, and Ar physisorbed on Au, respectively. Inspection of the spectra in Fig. 3 reveals that the numerical value of the sum of the heights of the peaks $\bar{I}_s(\omega_{s-}) + \bar{I}_a(\omega_{a-})$ for the symmetric and antisymmetric modes occurring at the same atomic excitation $E_{\nu 0}$ takes the lowest value, which is of the order of $7/\gamma_{sp}$ for Xe and Kr adsorbed on Au. However, this cancellation between the positive and negative heights of the peaks never materializes as there is a large frequency shift between the peaks of the modes in question. For instance, in the two excited states of Xe (atomic excitations $E_{\nu 0} = 8.437$ and 9.57 eV) and for Kr (atomic excitation $E_{\nu 0} = 10.64$ eV) on Au, the frequency shifts are equal to $\omega_{a-} - \omega_{s-} = 0.4694$, 0.5862, and 0.5635 eV, respectively. Cancellation between the positive and negative heights of the peaks arising from the symmetric and the antisymmetric modes, respectively, occurs whenever there is an overlap between the frequency profiles of the peaks in question. Hence, there is no cancellation among the two positive peaks of the symmetric modes and the corresponding negative peaks of the antisymmetric modes of Xe on Au, whose lineshapes are shown in Fig. 3. The same argument applies for the peak of

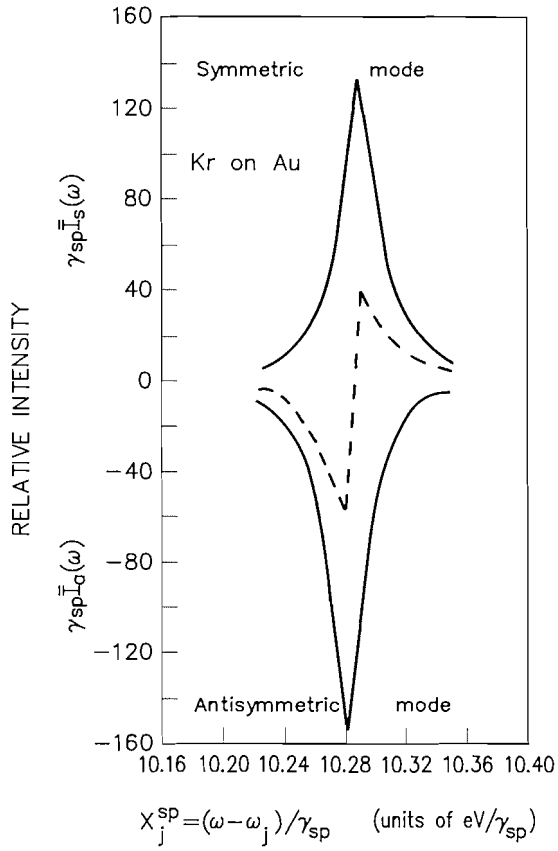

FIG. 5. As in Fig. 4 but for excited Kr at the frequencies $E_{\nu 0} = 10.03$ and 10.56 eV, respectively, physisorbed on the surface of Au. The dashed line illustrates the net lineshape arising from the combination of the red shifted peak of the symmetric mode at $\omega_{s-} = 10.2882$ eV (atomic excitation 10.56 eV) and the blue shifted peak of the antisymmetric mode at $\omega_{a-} = 10.2815$ eV (atomic excitation 10.03 eV).

the symmetric and the corresponding one of the antisymmetric mode of Kr on Au at the atomic frequency $E_{\nu 0} = 10.64$ eV, which are depicted in Fig. 3.

To examine two excited states of Kr adsorbed on Au simultaneously, we consider the two free atom excitations $P_{3/2}$ and $P_{1/2}$ of Kr, which according to Moore's (47) tables occur at the frequencies $E_{\nu 0} = 10.03$ and 10.6 eV, respectively. The computed values for the parameters of the symmetric and antisymmetric modes are listed in Tables 1 and 2, respectively. There are very small differences in the numerical values of the computed parameters when the values of $E_{\nu 0} = 10.60$ and 10.64 eV are used in the calculation. Using the data from Tables 1 and 2, the spectra of Kr on Au are illustrated by solid lines in Fig. 4 for the atomic-like excitations of the two symmetric and two antisymmetric modes, respectively. There is an overlap of the frequency profiles between the red shifted peak at $\omega_{s-} = 10.33$ eV (atomic excitation $E_{\nu 0} = 10.60$ eV) of the symmetric mode and the blue shifted peak at $\omega_{a-} = 10.28$ eV (atomic excitation $E_{\nu 0} = 10.03$ eV) of the antisymmetric mode. The net result of the two lineshapes is illustrated by the dashed line in Fig. 4, which is of the absorption–amplification type, where the system absorbs and amplifies at the frequencies $\omega_{s-} = 10.33$ eV and $\omega_{a-} = 10.28$ eV, respectively.

Inspection of the lineshape of the dashed line in Fig. 4 reveals that the system at this condition is very unstable so that an infinitesimal frequency shift or a very small disturbance in the right direction either on the symmetric or on the antisymmetric mode will stabilize the system, where the positive and negative

Can. J. Chem. Downloaded from www.nrcresearchpress.com by 93.93.197.157 on 09/07/12
For personal use only.

peaks will cancel each other out; the result will be the disappearance of the peak arising at the atomic excitation $E_{\nu 0} = 10.6$ eV. For the remaining peaks at the frequencies $\omega_{s-} = 9.78$ eV and $\omega_{a-} = 10.88$ eV of the symmetric and antisymmetric modes, respectively, other nearby excited states of the atom must be taken into consideration. These nearby states may be vibrationally or rotationally excited, which differ by very small amounts from the pure electronic excited states in question.

Another illuminating example is that of the two excited states of Kr at the frequencies $E_{\nu 0} = 10.03$ and 10.56 eV (47), respectively, which are supposed to be physisorbed on Au. Using the data listed in Tables 1 and 2, the computed spectra of the symmetric and antisymmetric modes are illustrated in Fig. 5. The net result of the two lineshapes is illustrated by the dashed line in Fig. 5, which indicates that the overlap of the frequency profiles between the red shifted peak at $\omega_{s-} = 10.2882$ eV (atomic excitation $E_{\nu 0} = 10.56$ eV) of the symmetric mode and the blue shifted peak at $\omega_{a-} = 10.2815$ eV (atomic excitation $E_{\nu 0} = 10.03$ eV) of the antisymmetric mode is much greater than the corresponding one in Fig. 4. Hence, the net spectrum illustrated in Fig. 5 is much more unstable from that in Fig. 4 and an infinitesimal disturbance in the right direction will stabilize the system by cancelling out the positive and negative components of the symmetric and antisymmetric modes, respectively.

Closing this section, we may conclude that the occasional disappearance of the spectral lines of the optical absorption at low coverages may be attributed to a cancellation process, which occurs between the frequency profiles arising from two nearby excited states of the atom. The red shifted peak of the symmetric mode of the higher excited state and the blue shifted peak of the antisymmetric mode of the lower excited state of the atom cancel each other out provided that their frequency profiles nearly coincide. Thus, in order to perform a thorough investigation, all the closely lying excited states of the free atom must be considered in the calculation.

When there are N excited atoms A physisorbed on the metal surface, the effective lifetime of a system of N excited identical atoms is shortened (31, 42) by a factor proportional to $1/N$ compared with the lifetime of a single isolated atom provided that the excited atoms interact with their common radiation field and decay cooperatively (superradiance). This radiative cooperative effect of the atoms on the metal surface has been considered in ref. 17, where the dipole–dipole interaction between the absorbate atoms on the surface of the metal has been neglected so that the derived results are applicable in the low coverage limit. It is shown (17) that at low coverage the height of the peaks of the spectral lines is proportional to N, while the total spectral function varies as N^2, a fact which is compatible with the experiment (3, 7, 8); the reader is referred to ref. 17 for details.

V. Concluding remarks

We have considered the excitation spectra of neutral rare-gas atoms physisorbed on metal surfaces. It is shown that at low coverage the occasional disappearance of the peaks of the spectral lines is due to the existence of the symmetric and antisymmetric states, whose relative intensities take positive and negative values, respectively. Hence, they may have the opportunity to cancel each other out whenever the frequency profiles on the peaks in question coincide. The relative intensities of the antisymmetric modes become negative only, at least for the cases under investigation, when the damping of the surface plasmons is much greater than the damping due to the radiative decay processes. This implies that the occasional disappearance of the peaks of the spectral lines should be only observed in optical experiments provided that the appropriate conditions are fulfilled; this is compatible with the experimental observations.

The disappearance of the optical spectra of Xe on Al and of Kr on Au is compatible with the observed ones (2, 3, 7, 8). Contrary to the experimental data (1–10), the optical spectrum of Xe on Au failed to disappear because of the existence of large frequency shifts, which occur between the peaks of the symmetric and antisymmetric modes arising from nearby excited states of the free Xe atom. However, the frequency shifts can be reduced through internal or external perturbations (17). We believe that the cancellation of the proper lineshapes between the peaks of the symmetric and antisymmetric modes may be a possible explanation of the persistence-extinction phenomenon that has been observed (1–10) for a number of rare-gas metal substrate systems in the low coverage limit.

It should be mentioned that in deriving the expression for the Green function [8] only linear effects have been taken into consideration and, therefore, the derived spectra of the symmetric and antisymmetric modes are independent of each other. Considering that the experiment yields the overall lineshapes of the spectral lines in question, any improvement of the theory should produce coupling between the symmetric and antisymmetric modes under investigation. The first of such improvements is to consider coupling between nearby excited states of the physisorbed atom. Such couplings are important because, although small, they are of the same order of magnitude as the coupling between the atom and its image.

1. J. E. Cunningham, D. K. Greenlaw, J. L. Erskine, R. P. Layton, and C. P. Flynn. J. Phys. F: Metal Phys. **7**, L281 (1977).
2. J. E. Cunningham, D. K. Greenlaw, and C. P. Flynn. Phys. Rev. Lett. **42**, 328 (1979).
3. J. E. Cunningham, D. K. Greenlaw, and C. P. Flynn. Phys. Rev. B**22**, 717 (1980).
4. J. E. Cunningham, D. Gibbs, T. H. Chiu, and C. P. Flynn. J. Phys. C.: Solid State, **14**, L1113 (1981).
5. C. P. Flynn and Y. C. Chen. Phys. Rev. Lett. **46**, 447 (1981).
6. C. P. Flynn and J. E. Cunningham. J. Phys. C: Solid State, **15**, L1169 (1982).
7. D. Gibbs, J. E. Cunningham, and C. P. Flynn. Phys. Rev. B**29**, 5292 (1984).
8. J. E. Cunningham, D. Gibbs, and C. P. Flynn. Phys. Rev. B**29**, 5304 (1984).
9. Y. C. Chen, J. E. Cunningham, and C. P. Flynn. Phys. Rev. B**30**, 7317 (1984).
10. C. P. Flynn. Surface Sci. **158**, 84 (1985).
11. N. D. Lang, A. R. Williams, F. J. Himpsel, B. Reihl, and D. E. Eastman. Phys. Rev. B**26**, 1728 (1982).
12. N. D. Lang. Phys. Rev. Lett. **46**, 842 (1981).
13. A. Bagchi, R. G. Barrera, and B. B. Dasgupta. Phys. Rev. Lett. **44**, 1475 (1980); A. Bagchi, R. G. Barrera, and R. Fuchs. Phys. Rev. B**25**, 7086 (1982).
14. W. Eberhardt and A. Zangwill. Phys. Rev. B**27**, 5960 (1983).
15. J. E. Demuth, Ph. Avouris, and D. Schmeisser. Phys. Rev. Lett. **50**, 600 (1983); Ph. Avouris and J. E. Demuth. *In* Surface studies with lasers. Proc. Intern. Conf. Mauterndorf, Austria. *Edited by* F. R. Aussenegg, A. Leitner, and M. E. Lippitsch. Springer-Verlag, New York. 1983. p. 24.

Can. J. Chem. Downloaded from www.nrcresearchpress.com by 93.93.197.157 on 09/07/12
For personal use only.

16. F. J. HERBST. Phys. Rev. B**15**, 3720 (1977); K. HORN, M. SCHEFFLER, and A. M. BRADSHAW. Surf. Sci. **80**, 69 (1979); G. KAINDL, T.-C. CHIANG, D. E. EASTMAN, and F. J. HIMPSEL. Phys. Rev. Lett. **45**, 1808 (1980); T.-C. CHIANG, G. KAINDL, and D. E. EASTMAN. Solid State Commun. **41**, 661 (1982).
17. C. MAVROYANNIS. Mol. Phys. In press.
18. C. MAVROYANNIS. Mol. Phys. **6**, 593 (1963).
19. C. MAVROYANNIS and D. A. HUTCHINSON. Solid State Commun. **23**, 463 (1977).
20. J. G. ENDRIZ and W. SPICER. Phys. Rev. B**4**, 4144 (1971).
21. K. SHINJO, S. SUGANO, and T. SASADA. Phys. Rev. B**28**, 5570 (1983).
22. R. FUCHS and K. L. KLIEWER. Phys. Rev. B**3**, 2270 (1971); J. M. ELSON and R. H. RITCHIE. Phys. Rev. B**4**, 4129 (1971); R. H. RITCHIE. Surf. Sci. **34**, 1 (1973).
23. J. E. LENNARD-JONES. Trans. Faraday Soc. **28**, 334 (1932).
24. C. MAVROYANNIS. Chem. Phys. Lett. **56**, 263 (1978).
25. C. MAVROYANNIS. Mol. Phys. **36**, 1565 (1978).
26. M. J. STEPHEN. J. Chem. Phys. **40**, 669 (1964).
27. D. A. HUTCHINSON and H. F. HAMEKA. J. Chem. Phys. **41**, 2006 (1964).
28. A. D. MACLACHLAN. Mol. Phys. **8**, 409 (1964).
29. C. MAVROYANNIS. Phys. Rev. A**18**, 185 (1978).
30. D. N. ZUBAREV. Usp. Fiz. Nauk, **71**, 71 (1960) (Sov. Phys. Usp. **3**, 320 (1960)); Nonequilibrium statistical thermodynamics. Plenum, New York. 1974. Chap. 16; V. L. BONCH-BRUEVICH and S. V. TYABLIKOV. The Green function method in statistical mechanics. North-Holland, Amsterdam. 1962; S. V. TYABLIKOV and V. L. BONCH-BRUEVICH. Adv. Phys. **11**, 317 (1962); S. V. TYABLIKOV. Methods in quantum theory of magnetism. Plenum, New York. 1967. Chap. VIII; C. MAVROYANNIS. The Green function method in physical chemistry. Vol. XIA. *Edited by* E. Eyring, W. Jost, and D. Henderson. Academic, New York. 1975.
31. R. H. DICKE. Phys. Rev. **93**, 99 (1954).
32. H. B. G. CASIMIR and D. POLDER. Phys. Rev. **73**, 360 (1948).
33. C. MAVROYANNIS and M. J. STEPHEN. Mol. Phys. **5**, 629 (1962).
34. R. R. MCLONE and E. A. POWER. Mathematika, **11**, 91 (1964); E. A. POWER. J. Chem. Phys. **46**, 4297 (1967).
35. H. MORAWITZ. Phys. Rev. **187**, 1792 (1969); Phys. Rev. A**7**, 1148 (1973).
36. G. BARTON. Proc. R. Soc. London, A**320**, 251 (1970); J. Phys. B**7**, 2134 (1974); G. D. MAHAN. Phys. Rev. B**5**, 739 (1972); H. MORAWITZ and M. R. PHILPOTT. Phys. Rev. B**10**, 4863 (1974); G. BARTON. Solid State Commun. **27**, 95 (1978).
37. M. R. PHILPOTT. Chem. Phys. Lett. **19**, 435 (1973); J. Chem. Phys. **62**, 1812 (1975); P. MILONI and P. L. KNIGHT. Opt. Commun. **9**, 119 (1973); G. S. AGARWAL. Phys. Rev. Lett. **32**, 703 (1974)
38. (*a*) R. R. CHANCE, A. PROCK, and R. SILBEY. J. Chem. Phys. **60**, 2184 (1974); **60**, 2744 (1974); Phys. Rev. A**12**, 1448 (1975); I. PRIGOGINE and S. A. RICE (*Editors*). Advances in Chemical Physics. Vol. 37. Wiley, New York. 1978. p. 1 and references therein; (*b*) M. MOSKOVITS. Rev. Mod. Phys. **57**, 783 (1985).
39. M. BABIKER and G. BARTON. J. Phys. A**9**, 129 (1976); M. BABIKER. J. Phys. A**9**, 799 (1976).
40. K. H. DREXHANE. Appl. Phys. Lett. **14**, 318 (1969); J. LUMIN. **1–2**, 693 (1970); K. H. DREXHANE. *In* Progress in optics XII. *Edited by* E. Wolf. North-Holland, Amsterdam. 1974.
41. (*a*) H. KUHN. J. Chem. Phys. **53**, 101 (1970); (*b*) H. KUHN, D. MÖBIUS, and H. BÜCHER. *In* Physical methods in chemistry. Part III *B*. *Edited by* A. Weissberger and B. W. Possiter. Wiley, New York. 1972.
42. V. ERNST and P. STEHLE. Phys. Rev. **176**, 1456 (1968); N. E. REHLER and J. H. EBERLY. Phys. Rev. A**3**, 1735 (1971); R. BONIFACIO and H. MORAWITZ. Phys. Rev. Lett. **36**, 1559 (1976).
43. G. G. KLEIMAN and U. LANDMAN. Phys. Rev. B**8**, 5484 (1973).
44. C. MAVROYANNIS. Solid State Commun. **23**, 467 (1977).
45. C. MAVROYANNIS. Opt. Commun. **33**, 42 (1980).
46. W. WILLIAMS, S. TRAJMAR, and A. KUPPERMANN. J. Chem. Phys. **62**, 3031 (1975).
47. C. E. MOORE. Atomic energy levels. Natl. Bur. Stand. U.S. Circ. No. 35, U.S. GPO, Washington, DC. 1971.

Can. J. Chem. Downloaded from www.nrcresearchpress.com by 93.93.197.157 on 09/07/12
For personal use only.

Dynamics of a one-dimensional classical hindered rotor

HIDEO YASUDA
Chemistry Laboratory, College of General Education, Nagoya City University, Mizuho-ku, Nagoya 467, Japan

AND

JOHN C. RAICH
Department of Physics and Laboratory for Condensed Matter Sciences, Colorado State University, Fort Collins, CO 80523, U.S.A.

Received August 28, 1987

This paper is dedicated to Professor J. A. Morrison

HIDEO YASUDA and JOHN C. RAICH. Can. J. Chem. **66**, 752 (1988).

The dynamic susceptibility of a one-dimensional rotor in crystal fields of various symmetry is calculated within the framework of classical mechanics. The contributions from oscillatory and rotary motions are treatable separately. This approach serves to clarify the structure of the spectrum. The nature and magnitude of the quantum effect are investigated and a comparison with earlier quantum mechanical calculations is made.

HIDEO YASUDA et JOHN C. RAICH. Can. J. Chem. **66**, 752 (1988).

Utilisant les principes de la mécanique classique, on a calculé la susceptibilité dynamique d'un rotor unidimensionnel dans des champs cristallins de diverses symétries. Les contributions dûes aux mouvements oscillatoires et rotatoires ont été traités séparément. Cette méthode permet de clarifier la structure du spectre. On a étudié la nature et l'amplitude de l'effet quantique et on a fait une comparaison avec des calculs de mécanique quantique qui ont été effectués antérieurement.

[Traduit par la revue]

Can. J. Chem. Downloaded from www.nrcresearchpress.com by 176.9.209.113 on 09/07/12
For personal use only.

I. Introduction

Molecular crystals and liquid crystals are made up, at least in part, of molecules or molecular ions with angular degrees of freedom. When these molecules are incorporated into a crystal lattice, their angular motions are strongly affected by the presence of neighboring molecules or ions. The environment of the neighboring molecules is represented by an orientational potential (molecular field or crystal field) for a specific molecule. When the temperature is low compared with the barrier height of the orientational potential, molecules are captured in the potential minima and perform small angular oscillations or librations. In addition to these librational modes, quantum mechanical tunnelling between equivalent molecular orientations corresponding to neighboring potential wells can occur. On the other hand, if the temperature is of the order of the orientational potential, the molecule can jump over the barriers and perform continuous rotational diffusion.

An understanding of these different types of rotational excitations is important for the interpretation of experimental observations in terms of intermolecular potentials. To help us understand the spectra of rotational excitations we have studied the susceptibility for single particle excitations quantum mechanically (1). It seems unlikely that one can directly relate the susceptibility of a one-dimensional hindered rotor to experimental observations for three-dimensional crystals. However, we successfully applied a one-dimensional model to describe order–disorder phase transitions in ammonium halide crystals (2) where the susceptibilities for the coupled orientational and translational degrees of freedom were constructed from single particle susceptibilities using mean field treatments (3–5). This limited success provides justification for further study of one-dimensional rotors.

In the present paper we provide a classical calculation of the single-particle orientational susceptibility for a one-dimensional rotor in crystal fields of various symmetry. The desired susceptibility is defined as

$$[1] \qquad \chi_\alpha(\omega) = \phi^q_\alpha(0) + z\int_0^\infty e^{zt}\phi^q_\alpha(t)\,dt \qquad (z = i\omega - \lambda,\ \lambda \to 0_+)$$

with the quasi-relaxational function

$$[2] \qquad \phi^q_\alpha(t) = \beta\langle Q_\alpha(0)Q_\alpha(t)\rangle$$

where $Q_\alpha(t)$ denotes a rotational coordinate at time t.[1]

The main motivation for the present work is to clarify the structure of the spectrum for a one-dimensional hindered rotor and to identify contributions from motions that can be classified as either oscillatory or rotatory. The present calculation can not explain the central peak in the spectrum, which is due to quantum tunnelling. However, one can estimate such quantum effects by comparing the present calculations with previous quantum mechanical results (1). In addition, the present study is expected to provide insight into the theoretical treatment of non-linear rotational modes in molecular crystals.

II. Classical mechanical mode

The hamiltonian for one-dimensional hindered rotor is

$$[3] \qquad H = Bp^2 + V_0 \cos M\phi$$

where B is the rotational constant and $M = 2$, 3, 4, and 6 indicates the symmetry of the crystal field. Considering that the crystal field has potential minima for values of the rotation coordinate $\phi = (2n + V_0/V + 1/2)\pi/M$ with $V = |V_0|$ and $n = 0, 1, 2, \ldots, M - 1$, we make the following variable transformation:

$$[4] \qquad M\phi = (2n + V_0/V + 1/2)\pi + \phi'$$

The new variable is limited to the range $-\pi \leqq \phi' \leqq \pi$. Then the equation of motion is given as

$$[5] \qquad 2MBp = \dot{\phi}', \quad MV \sin\phi' = -\dot{p}$$

This equation suggests that the introduction of dimensionless

[1] The exact definition of the relaxation function is

$$\phi_\alpha(t) = \beta\langle Q_\alpha(0)Q_\alpha(t)\rangle - \beta\langle Q^0_\alpha Q^0_\alpha\rangle$$

where Q^0_α is the invariant part of $Q_\alpha(t)$ with respect to the natural motion (6). One can confirm that the susceptibility [1] remains unchanged when one replaces $\phi^q_\alpha(t)$ with $\phi_\alpha(t)$, that is, one can add an arbitrary constant to $\phi^q_\alpha(t)$ in eq. [1].

time τ defined as

$$[6] \qquad \rho = M(2BV)^{1/2}t$$

simplifies the problem. Let us suppose $\phi' = 0$ and $p = p_0$ at $\tau = 0$; then we have the following solution for ϕ'_τ, which defines ϕ' at time τ:

$$[7] \qquad \sin(\phi'_\tau/2) = \begin{cases} k\,\mathrm{sn}(\mathrm{sign}(p_0)\tau,k) & \text{for } k<1 \\ \mathrm{sn}(\mathrm{sign}(p_0)k_\tau,1/k) & \text{for } k>1 \end{cases}$$

with $k = |p_0|(B/2V)^{1/2}$ and the Jacobi's sn function (7). It follows from eqs. [5], [6], and [7] that the angular momentum p at time τ which is denoted by p_τ, is given as

$$[8] \qquad |p|/(2V/B)^{1/2} = \begin{cases} k\,\mathrm{cn}(\mathrm{sign}(p_0)\tau,k) & \text{for } k<1 \\ k\,\mathrm{dn}(\mathrm{sign}(p_0)k_\tau,1/k) & \text{for } k>1 \end{cases}$$

with Jacobi's cn and dn functions. Equation [8] is essentially same as the well-known solution for a simple pendulum. The expressions for $k < 1$ and $k > 1$ represent oscillatory and rotatory motion, respectively.

In order to treat the quasi-relaxation function defined in eq. [2], we need the solution for eq. [5] which has arbitrary ϕ' and p as the initial condition. This solution is obtained by replacing $\mathrm{sign}(p_0)\tau$ by $u + \mathrm{sign}(p_0)\tau$ in eqs. [7] and [8]. Because of the range of ϕ', we have the limitation $-K(k) \leqq u \leqq K(k)$ for $k<1$ and $-K(1/k) \leqq ku \leqq K(1/k)$ for $k > 1$, where $K(k)$ is the complete elliptic integral of the first kind (7). We also have $\mathrm{sign}(p_0) = \mathrm{sign}(p)$. Then the solution of the equation of motion is rewritten

$$[9] \qquad \sin(\phi'_\tau/2) = \begin{cases} k\,\mathrm{sn}(u + \mathrm{sign}(p)\tau,k) & \text{for } k<1 \\ \mathrm{sn}(ku + \mathrm{sign}(p)k_\tau,1/k) & \text{for } k>1 \end{cases}$$

and

$$[10] \qquad |p|/(2V/B)^{1/2} = \begin{cases} k\,\mathrm{cn}(u + \mathrm{sign}(p)\tau,k) & \text{for } k<1 \\ k\,\mathrm{dn}(ku + \mathrm{sign}(p)k_\tau,1/k) & \text{for } k>1 \end{cases}$$

The variables p and ϕ', which are values of p_τ and ϕ'_τ in eqs. [9] and [10] at $\tau = 0$, appear in the calculation of the average in eq. [2]. Equations [9] and [10] suggest a transformation from the variables p and ϕ' to the set (k,u). Since the Jacobian has the same value $2\,\mathrm{sign}(p)(2V/B)^{1/2}k$ for both $k<1$ and $k>1$, we have

$$[11] \qquad \mathrm{sign}(p)\mathrm{d}p\mathrm{d}\phi' = 2(2V/B)^{1/2}k\mathrm{d}k\mathrm{d}u$$

In terms of the new variables the following hamiltonian results

$$[12] \qquad H = 2Vk^2 - V$$

We choose $Q_C(t) = \cos m\phi_t$ or $Q_S(t) = \sin m\phi_t$ as the rotational variables or coordinates in eq. [2], where ϕ_t indicates a rotational angle ϕ at time t (1, 2). In terms of the dimensionless time τ these rotational coordinates are expressed as

$$[13a] \qquad Q_C(\tau) = [Q_+(\tau) + Q_-(\tau)]/2$$

$$[13b] \qquad Q_S(\tau) = [Q_+(\tau) - Q_-(\tau)]/2i$$

and

$$[14] \qquad Q_\pm(\tau) = \exp\left[\pm i\frac{m}{M}\left(2n + \frac{V_0}{V} + \frac{1}{2}\right)\pi + \phi'_\tau\right]$$

The product $Q_\alpha(0)Q_\alpha(\tau)$, where α = C or S, which is the important quantity appearing in the relaxation function, is a function of the variables m/M, n, V_0/V, k, u, and τ. To illustrate this dependence explicitly we write the product as

$$[15] \qquad Q_\alpha(0)Q_\alpha(\tau) \equiv F_\alpha(m/M,n,V_0/V,k,u,\tau)$$

Next we consider the integral $\int_{-\infty}^{\infty}\mathrm{d}p\int_0^{2\pi}\mathrm{d}\phi f(p,\phi)$ of an arbitrary function $f(p,\phi)$. Using eq. [4], one can reduce this integral to the following form:

$$[16] \qquad \int_{-\infty}^{\infty}\mathrm{d}p\int_0^{2\pi}\mathrm{d}\phi f(p,\phi) = \int_0^{\infty}\mathrm{d}p\int_0^{\pi}\mathrm{d}\phi'\ \frac{1}{M}\sum_{n=0}^{M-1}[f(p,g/M + \phi'/M) + f(p,g/M - \phi'/M) + f(-p,g/M + \phi'/M) + f(-p,g/M - \phi'/M)]$$

with $g = (2n + V_0/V + 1/2)\pi$. Using eqs. [9], [10], and [11], a change of the variables of integration to k and u is easily accomplished.

Applying these methods to the calculation of the quasi-relaxation function [2] at the dimensionless time τ yields

$$[17] \qquad \phi^q_\alpha(\tau) = \beta\int_0^1\mathrm{d}k\int_0^{K(k)}\mathrm{d}u\ kh_\alpha(k,u,\tau)P(k) + \beta\int_1^{\infty}\mathrm{d}k\int_0^{K(1/k)}\mathrm{d}(ku)\ h_\alpha(k,u,\tau)P(k)$$

where

$$[18] \qquad h_\alpha(k,u,\tau) = \frac{1}{M}\sum_{n=0}^{M-1}[F_\alpha(m/M,n,V_0/V,k,u,\tau) + F_\alpha(m/M,n,V_0/V,k,-u,\tau) + F_\alpha(m/M,n,V_0/V,k,u,-\tau) + F_\alpha(m/M,n,V_0/V,k,-u,-\tau)]$$

and

$$[19] \qquad P(k) = 2(2V/B)^{1/2}\exp(-\beta H)/\int_{-\infty}^{\infty}\mathrm{d}p\int_0^{2\pi}\mathrm{d}\phi\exp(-\beta H) = \exp(-2\beta Vk^2)/(Z_1 + Z_2)$$

with

$$[20] \qquad Z_1 = 4\int_0^1\mathrm{d}k\,kK(k)\exp(-2\beta Vk^2)$$

and

$$[21] \qquad Z_2 = 4\int_1^{\infty}\mathrm{d}k\,K(1/k)\exp(-2\beta Vk^2)$$

Using eqs. [13] through [15], expression [18] is straightforwardly reduced to the following:

$$[22] \qquad h_\alpha(k,u,\tau) = \left\{\cos\frac{m}{M}\left(\phi'_\tau - \phi'_0\right) + \cos\frac{m}{M}\left(\phi'_\tau - \phi'_0\right) + \delta(\alpha)f(2m/M,V_0/V) \times\left[\cos\frac{m}{M}\left(\phi'_\tau + \phi'_0\right) + \cos\frac{m}{M}\left(\phi'_\tau + \phi'_0\right)\right]\right\}$$

with

$$[23] \qquad \sin(\phi'_\tau/2) = \begin{cases} k\,\mathrm{sn}(u + \tau,k) & \text{for } k<1 \\ \mathrm{sn}(ku + k_\tau,1/k) & \text{for } k>1 \end{cases}$$

Here the quantities $\delta(\alpha)$ and $f(2m/M,V_0/V)$ denotes

$$[24] \qquad \delta(\mathrm{C}) = 1, \quad \delta(\mathrm{S}) = -1$$

and

$$[25] \qquad f(2m/M,V_0/V) = \begin{cases} 0 & \text{for } 2m/M \neq \text{an integer} \\ (-1)^{m(V_0/V+1)/M} & \text{for } 2m/M = \text{an integer} \end{cases}$$

respectively. Before going to the next step, we must keep in

Can. J. Chem. Downloaded from www.nrcresearchpress.com by 176.9.209.113 on 09/07/12
For personal use only.

mind that ϕ'_τ which appears in eq. [22] and is a function of k, u, and τ is the principal value of the arcsin of the right hand side of eq. [23] for $k < 1$, but not for $k > 1$.

Using eq. [17], one can formally calculate the desired susceptibility [1]. Equation [1] for the case of the present dimensionless time τ can be rewritten as

$$[26] \quad \chi_\alpha(\omega_0) = \phi^q_\alpha(0) + z\int e^{z\tau}\phi^q_\alpha(\tau)d\tau \qquad (z = i\omega_0 - \lambda,\ \lambda \to 0_+)$$

where $\omega_0 = \omega/M(2BV)^{1/2}$. Here, ω is measured in units of $M(2BV)^{1/2}$ with ω_0 a dimensionless frequency.

III. Fourier approximation for the susceptibility

Although the calculation of the rotational susceptibility follows in principle from eq. [26], its calculation in practice is complicated by unknown singularities. This difficulty may be surmounted using a Fourier approximation for expression [22]. Such an approach is reasonable because of the periodic nature of eq. [22].

In the Fourier approximation one expresses eq. [22] as

$$[27] \quad h_\alpha(k,u,\tau) = \sum_{l=0}^{n} A_{\alpha l}(k,u,\tau_0)\cos(2\pi l\tau/\tau_0)$$

where τ_0 is the period of $h_\alpha(k,u,\tau)$ and $n \leqq N$. The meaning of the integer N is explained below. The coefficients $A_{\alpha l}(k,u,\tau_0)$ are determined by the method of least squares as

$$A_{\alpha 0}(k,u,\tau_0) = \frac{1}{2N}\sum_r h_\alpha(k,u,\tau_r)$$

$$[28] \quad A_{\alpha l}(k,u,\tau_0) = \frac{1}{N}\sum_r h_\alpha(k,u,\tau_r)\cos(\pi lr/N) \qquad (l \neq 0,N)$$

$$A_{\alpha N}(k,u,\tau_0) = \frac{1}{2N}\sum_r (-1)^r h_\alpha(k,u,\tau_r)$$

Here $\tau_r = \tau_0 r/2N$ and the summations with respect to r run from $-N + 1$ to N. Equations [22] and [23] imply the period:

$$[29] \quad \begin{aligned} \tau_0 &\equiv \tau_{\mathrm{I}} = 4K(k) && \text{for } k < 1 \\ \tau_0 &\equiv \tau_{\mathrm{II}} = 2MK(1/k)/mk && \text{for } k > 1 \end{aligned}$$

Substituting [19] and [27] in the quasi-relaxation function [17] yields the following expression:

$$[30] \quad \phi^q_\alpha(\tau) = \sum_{l=0}^{n}[\phi_{\mathrm{I}\alpha l}(\tau) + \phi_{\mathrm{II}\alpha l}(\tau)]$$

with

$$[31a] \quad \phi_{\mathrm{I}\alpha l}(\tau) = \beta\int_0^1 dk\, kK(k)A_{\mathrm{I}\alpha l}(k)\cos(2\pi l\tau/\tau_{\mathrm{I}})\,P(k)$$

and

$$[31b] \quad \phi_{\mathrm{II}\alpha l}(\tau) = \beta\int_1^\infty dk\, K(1/k)A_{\mathrm{II}\alpha l}(k)\cos(2\pi l\tau/\tau_{\mathrm{II}})\,P(k)$$

Here the following notation has been employed:

$$[32a] \quad A_{\mathrm{I}\alpha l}(k) = \int_0^1 du\, A_{\alpha l}(k,K(k)u,\tau_{\mathrm{I}})$$

and

$$[32c] \quad A_{\mathrm{II}\alpha l}(k) = \int_0^1 du\, A_{\alpha l}(k,K(1/k)u/k,\tau_{\mathrm{II}})$$

It is apparent from eqs. [30] and [31] that the time-independent part of the quasi-relaxation function, which is just the quantity $\beta\langle Q^0_\alpha Q^0_\alpha\rangle$ on ref. 6 and is denoted by the same symbol, is

$$[33] \quad \beta\langle Q^0_\alpha Q^0_\alpha\rangle = \phi_{\mathrm{I}\alpha 0}(0) + \phi_{\mathrm{II}\alpha 0}(0)$$

Thus we find that the exact relaxation function is given by

$$[34] \quad \phi_\alpha(\tau) = \sum_{l=1}^{n}[\phi_{\mathrm{I}\alpha l}(\tau) + \phi_{\mathrm{II}\alpha l}(\tau)]$$

As pointed out in ref. 6, we may use this relaxation function instead of the quasi-relaxation function $\phi^q_\alpha(\tau)$ in the calculation of the susceptibility [26].

When expressions [34] and [31] are substituted in the susceptibility [26], we obtain

$$[35] \quad \chi_\alpha(\omega_0) = \sum_{l=1}^{n}[\chi_{\mathrm{I}\alpha l}(\omega_0/l) + \chi_{\mathrm{II}\alpha l}(M\omega_0/2ml)]$$

with

$$[36] \quad \chi_{\mathrm{G}\alpha l}(X) = \chi'_{\mathrm{G}\alpha l}(X) + iX''_{\mathrm{G}\alpha l}(X) \quad \mathrm{G} = \mathrm{I}\text{ or }\mathrm{II}$$

where χ' and χ'' represent the real and imaginary parts of χ, respectively. Here

$$[37a] \quad \chi'_{\mathrm{I}\alpha l}(X) = \beta\int_0^1 dk\, kK(k)A_{\mathrm{I}\alpha l}(k)P(k) \times\left[1 - \frac{X}{2}P\left(\frac{1}{X + 2\pi/\tau_{\mathrm{I}}} + \frac{1}{X - 2\pi/\tau_{\mathrm{I}}}\right)\right]$$

$$[37b] \quad \chi'_{\mathrm{II}\alpha l}(X) = \beta\int_1^\infty dk\, K(1/k)A_{\mathrm{II}\alpha l}(k)P(k) \times\left[1 - \frac{X}{2}P\left(\frac{1}{X + M\pi/m\tau_{\mathrm{II}}} + \frac{1}{X - M\pi/m\tau_{\mathrm{II}}}\right)\right]$$

$$[38a] \quad \chi''_{\mathrm{I}\alpha l}(X) = \beta\int_0^1 dk\, kK(k)A_{\mathrm{I}\alpha l}(k)P(k) \times\frac{\pi X}{2}[\delta(X + 2\pi/\tau_{\mathrm{I}}) + \delta(X - 2\pi/\tau_{\mathrm{I}})]$$

$$[38b] \quad \chi''_{\mathrm{II}\alpha l}(X) = \beta\int_1^\infty dk\, K(1/k)A_{\mathrm{II}\alpha l}(k)P(k) \times\frac{\pi X}{2}[\delta(X + M\pi/m\tau_{\mathrm{II}}) + \delta(X - M\pi/m\tau_{\mathrm{II}})]$$

The formula $\lim_{\lambda\to 0_+}(x + i\lambda)^{-1} = P(1/x) - i\pi\delta(x)$ has been used in the above derivations.

We can obtain in principle the analytic functional form for the susceptibility [35] by using eqs. [37] and [38]. Exact calculations are hopelessly difficult in the present form because of the complicated functional forms of τ_{I} and τ_{II} as given by [29]. However, we can derive the following approximations:

$$[39a] \quad 2\pi/\tau_{\mathrm{I}} = \pi/2K(k) \simeq (1 - k^2)^{1/4}$$

$$[39b] \quad M\pi/m\tau_{\mathrm{II}} = \pi k/2K(1/k) \simeq k^{1/2}(k^2 - 1)^{1/4}$$

The derivations of the above approximations are given in the Appendix, where a high precision approximation for the Jacobi sn (u,k) function, utilized in the present work, is also given.

We now adopt the variable transformations $(1 - k^2)^{1/4} = x$ and $k^{1/2}(k^2 - 1)^{1/4} = y$. Then we obtain the relations

$$[40a] \quad kK(k)\,dk = -\pi x^2\,dx$$

$$[40b] \quad K(1/k)\,dk = -\pi y^2(1 + 4y^4)^{-1/2}dy$$

In regard to the approximations [39a] and [39b], the reader is referred to the Appendix which contains a discussion of the adequacy of the present approximations in the vicinity of $k = 1$, where $K(k)$ diverges. Using these approximations we rewrite the imaginary parts of the susceptibilities [38a] and [38b] as

Can. J. Chem. Downloaded from www.nrcresearchpress.com by 176.9.209.113 on 09/07/12
For personal use only.

Can. J. Chem. Downloaded from www.nrcresearchpress.com by 176.9.209.113 on 09/07/12
For personal use only.

follows:

$$[41a]\quad \chi''_{\mathrm{I}\alpha l}(X) = \begin{cases} \beta\pi X^3 A_{\mathrm{I}\alpha l}([1 - X^4]^{1/2}) P_{\mathrm{I}}(X) \\ 0 \qquad \text{for } |X| > 1 \end{cases}$$

for $|X| < 1$

$$[41b]\quad \chi''_{\mathrm{II}\alpha l}(X) = \frac{\beta\pi}{2} X^3 (1 + 4X^4)^{-1/2} \times A_{\mathrm{II}\alpha l}(\{[1 + (1 + 4X^4)^{1/2}]/2\}^{1/2}) P_{\mathrm{II}}(X)$$

Here the quantities $P_{\mathrm{I}}(X)$ and $P_{\mathrm{II}}(X)$ denote

$$[42a]\quad P_{\mathrm{I}}(X) = \exp(2\beta V X^4)/Z_{12}$$

and

$$[42b]\quad P_{\mathrm{II}}(X) = \exp(\beta V[1 - (1 + 4X^4)^{1/2}])/Z_{12}$$

with

$$[43]\quad Z_{12} = 4\int_0^1 dx\, x^2 \exp(2\beta V x^4) + 4\int_0^\infty dy\, y^2 (1 + 4y^4)^{-1/2} \exp(\beta V[1 - (1 + 4y^4)^{1/2}])$$

Here we have used eq. [19] through [21], [38], and the variable transformations.

Using the same approximations as above, we can reduce each component of the real part of the susceptibility [37] to a tractable expression. The Kramers–Kronig relation

$$[44]\quad \chi'_{\mathrm{G}\alpha l}(X) = \frac{1}{\pi} \fint_{-\infty}^{\infty} \frac{\chi''_{\mathrm{G}\alpha l}(\xi)}{\xi - X} d\xi$$

where $\fint$ denotes the principal value of the integral, is satisfied for each component of the susceptibility defined by eq. [36].

The representation [35] together with [41] and [44] is our final result for the susceptibility of a one-dimensional hindered rotor. Numerical calculation for various cases show that the terms with $l = 1$, $\chi \mathrm{G}\alpha 1$, are dominant.[2] This seems to indicate that the function [22] is reasonably well approximated, except for a constant term, by use of only one cos term, that is, $\cos(2\pi l\tau/\tau_0)$.

IV. Spectrum of a classical hindered rotor

In the preceding section, we derived the desired susceptibility in a tractably analytic form. A reasonably accurate approximation to its imaginary part, which consists of two types I (oscillatory motion) and II (rotatory motion) has been obtained. The real part can in principle be evaluated from the Kramers–Kronig relation [44]. However, we discuss only the imaginary part of the susceptibility in the present paper.

It is well known that the imaginary part of the susceptibility is related to the spectral function, which is, in the present case, the spectrum of the spontaneous fluctuations in the $\cos(m\phi)$ or $\sin(m\phi)$ or the Fourier transform of the correlation $\langle Q_\alpha(0) Q_\alpha(t)\rangle$. This quantity can be related to the results of scattering experiments. In our model the spectral function of the dimensionless frequency ω_0 is expressed as

$$[45]\quad S_\alpha(\omega_0) = S_{\mathrm{I}\alpha}(\omega_0) + S_{\mathrm{II}\alpha}(\omega_0)$$

with

$$[46a]\quad S_{\mathrm{I}\alpha}(\omega_0) = f(\omega_0) \sum_{l=1}^{n} \chi''_{\mathrm{I}\alpha l}(\omega_0/l)$$

[2] If $\chi \mathrm{G}\alpha 1$ is zero, the next non-vanishing term $\chi \mathrm{G}\alpha l$ is dominant as discussed in Fig. 5.

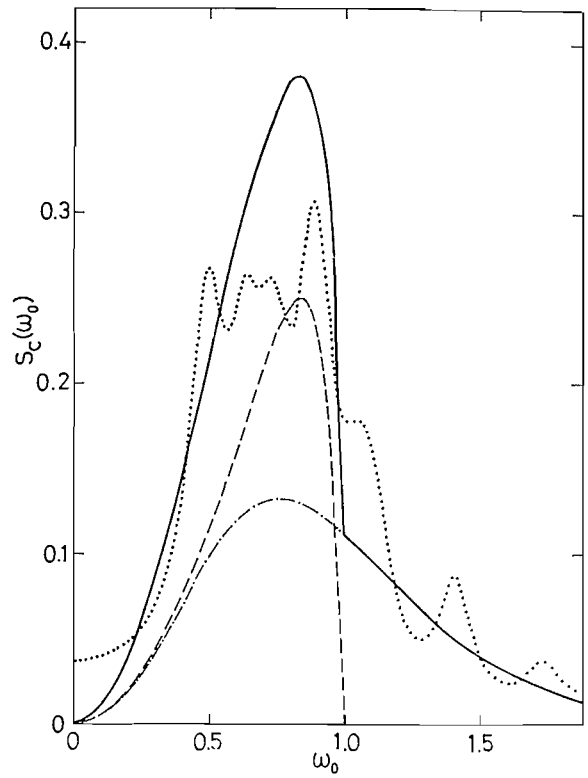

FIG. 1. The spectrum $S_{\mathrm{C}}(\omega_0)$ for the case $m = 1$, $M = 2$, $V_0 = 5B$, and $T = 10B$, where ω_0 is the dimensionless frequency related to frequency ω by $\omega = M(2BV)^{1/2}\omega_0$ as described in the text. Here the index M indicates the symmetry of the crystal field and m is the index for the coordinate in question. The spectrum obtained by the exact quantum mechanical calculation is shown by the dotted curve, where damping constant $\lambda = 0.5$ (in units of B). The oscillatory spectrum $S_{\mathrm{IC}}(\omega_0)$ and the rotatory spectrum $S_{\mathrm{IIC}}(\omega_0)$ calculated classically are given by the dashed and dot–dashed curves, respectively. The solid curve corresponds to the total classical spectrum $S_{\mathrm{C}}(\omega_0)$ $(= S_{\mathrm{IC}}(\omega_0) + S_{\mathrm{IIC}}(\omega_0))$.

and

$$[46b]\quad S_{\mathrm{II}\alpha}(\omega_0) = f(\omega_0) \sum_{l=1}^{n} \chi''_{\mathrm{II}\alpha l}(M\omega_0/2ml)$$

where the factor $f(\omega_0)$ is given by

$$[47]\quad f(\omega_0) = 2/[M(2BV)^{1/2}\beta\omega_0]$$

Equation [47] is obtained from comparison of the definitions of the spectral function and the susceptibility. For a quantum mechanical deviation the factor $f(\omega_0)$ has the form (1, 5)

$$[48]\quad f(\omega_0) = 2/[1 - \exp(-M(2BV)^{1/2}\beta\omega_0)]$$

Because we are considering the classical model we should use eq. [47] for the form of $f(\omega_0)$. When we compare the present results, written in the form of the spectral function, with the previous quantum mechanical results (1) represented in the spectral form we prefer to use eq. [48] rather than eq. [47] for the form of $f(\omega_0)$. The spectral functions derived using the different factors, defined by either eq. [47] or eq. [48], will differ from one another, even if the imaginary parts of the susceptibility are the same. To avoid differentiation just on the basis of the factors, we use eq. [48] for our definition of $f(\omega_0)$ for all calculations. In practice, the difference between [47] and [48] is small when

$$M(2BV)^{1/2}\beta\omega_0 \sim \omega_0 \lesssim 1$$

Can. J. Chem. Downloaded from www.nrcresearchpress.com by 176.9.209.113 on 09/07/12
For personal use only.

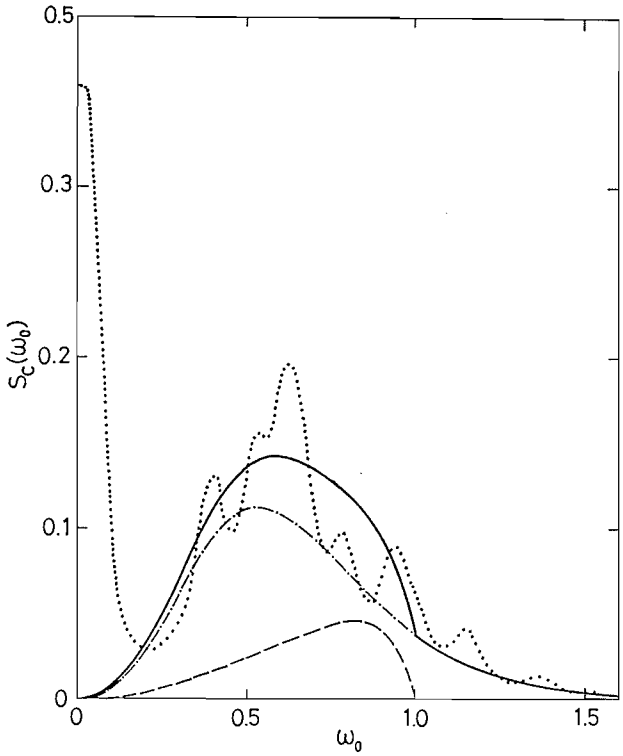

FIG. 2. The spectrum $S_C(\omega_0)$ for the case $m = 1$, $M = 3$, $V_0 = \pm 5B$, and $T = 10B$ ($\lambda = 0.5$). The notation is the same as for Fig. 1.

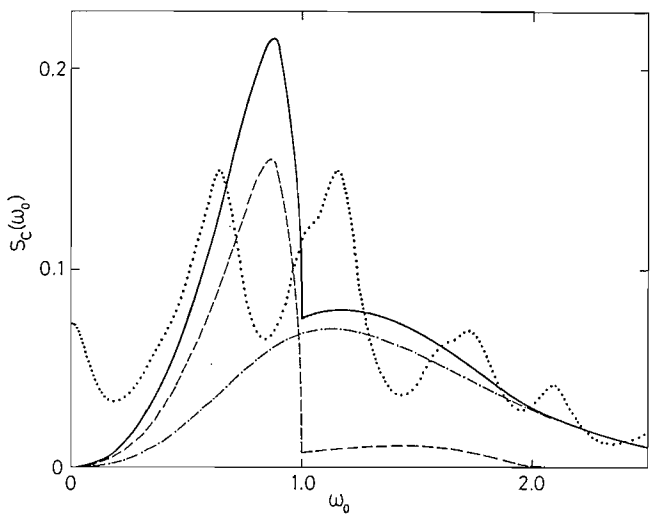

FIG. 3. The spectrum $S_C(\omega_0)$ in the case $m = 2$, $M = 3$, $V_0 = \pm 5B$, and $T = 10B$ ($\lambda = 1.0$). The notation is the same as for Fig. 1.

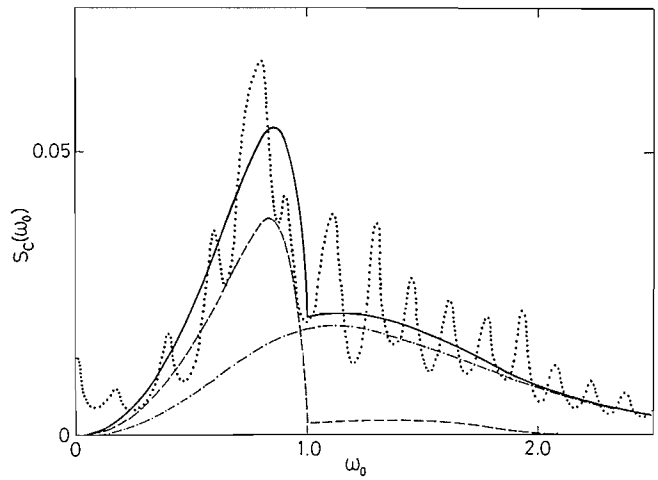

FIG. 4. The spectrum $S_C(\omega_0)$ in the case $m = 2$, $M = 3$, $V_0 = \pm 40B$, and $T = 100B$ ($\lambda = 1.0$). The notation is the same as for Fig. 1.

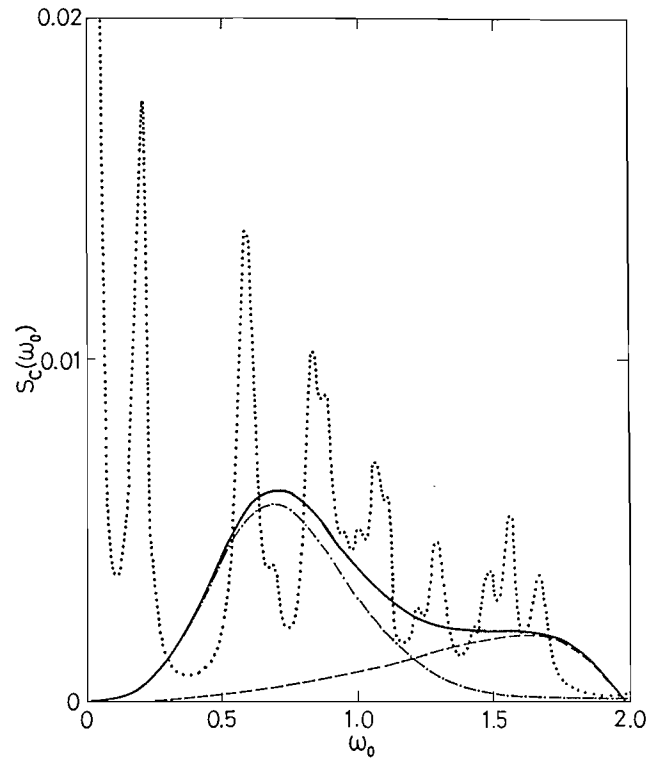

FIG. 5. The spectrum $S_C(\omega_0)$ in the case $m = 2$, $M = 4$, $V_0 = -40B$, and $T = 28B$ ($\lambda = 1.0$). The notation is the same as for Fig. 1.

The methods described above allow us to evaluate the classical spectral functions of the rotational coordinates $\cos m\phi$ and $\sin m\phi$ for a one-dimensional hindered rotor. The spectrum is naturally separated into two parts, those representing the oscillatory and the rotatory motions of the rotor. The imaginary part of the oscillatory susceptibility and that of the rotatory one are easily evaluated using eq. [41*a*] and eq. [41*b*], respectively. Below we describe the numerical calculations of spectral functions for various cases of interest and compare the present classical spectra with previous quantum mechanical results (1).

The value of the integer N defines the number of divisions of the period in the calculation of the coefficients, given by eq. [20], of the Fourier expansion [27]. For the present calculations we choose $N = 20$. The number of terms in the summation over the index in eqs. [46*a*] and [46*b*] is determined by a requirement to include at least 99% of the susceptibility at a given frequency ω_0. One finds that the $l = 1$ term is dominant for those values of ω_0 where the susceptibility is relatively large, the $l = 2$ term is important in the vicinity of $\omega_0 = 0$ and the $l = 4$ term contributes in the region of large ω_0. For the present calculation terms with $l > 5$ are excluded.

First we discuss the spectra for the case where the temperature is of the order of the orientational potential barrier height. The same case has been treated in the previous quantum mechanical paper (1). The results are shown in Figs. 1 through 4 together along with those of the previous quantum mechanical calculation. For Figs. 1 through 3 the relationship between the

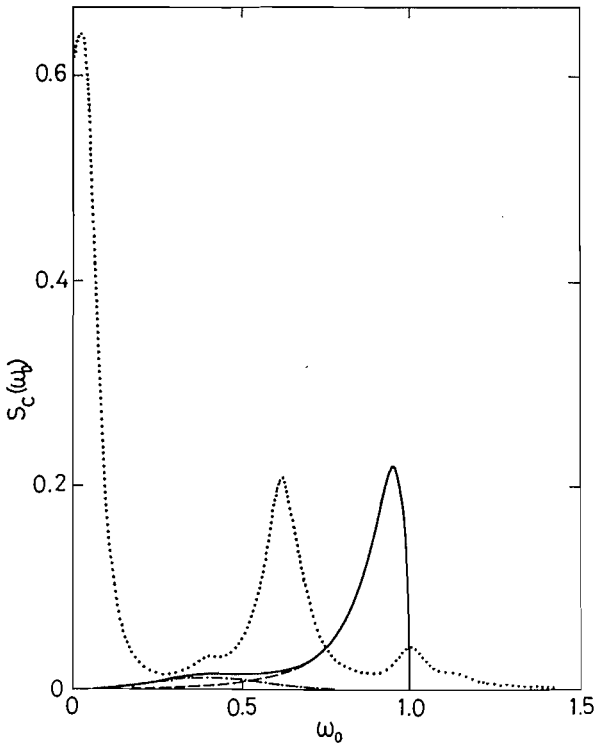

FIG. 6. The spectrum $S_C(\omega_0)$ in the case $m = 1$, $M = 3$, $V_0 = \pm 5B$, and $T = 2B$, where light molecules are postulated ($\lambda = 0.5$). The notation is the same as for Fig. 1.

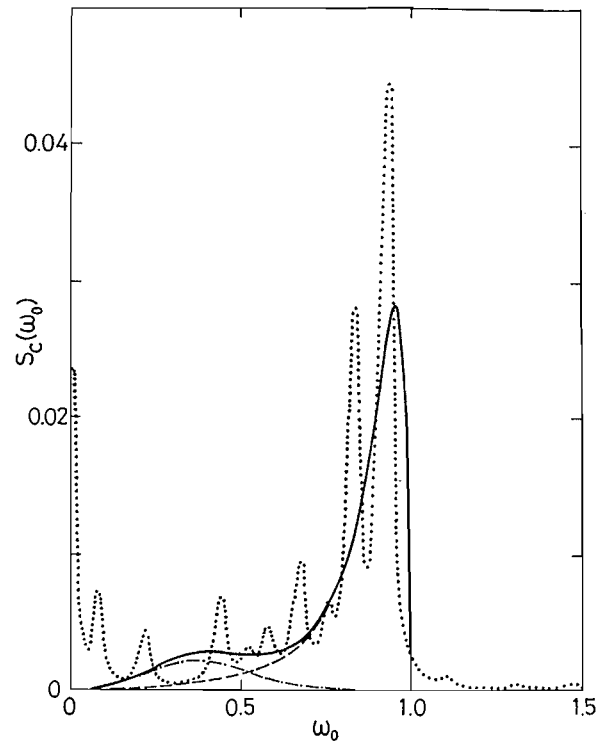

FIG. 7. The spectrum $S_C(\omega_0)$ in the case $m = 1$, $M = 3$, $V_0 = \pm 50B$, and $T = 20B$, where intermediate molecules are postulated ($\lambda = 0.5$). The notation is the same as for Fig. 1.

temperature, T, and the barrier height, V_0 is $V_0 = \pm 2T$; for Fig. 4 the corresponding relation is $V_0 = \pm 0.4T$. We note that the agreement between the quantum mechanical spectra and the classical mechanical one is quite good except in the vicinity of $\omega_0 = 0$. This observation suggests that the spectrum in the vicinity of $\omega_0 = 0$ arises from quantum mechanical tunnelling between equivalent molecular orientations. The figures show that the present classical calculation leads to a significant clarification of the structure of the spectrum. The present calculation allows us to distinguish between the rotational and vibrational contribution to the spectrum. Each of the spectra considered is decomposed into two separate components, one due to periodic angular oscillation and the other due to hindered continuous rotation. These different types of motion correspond to the spectral functions $S_{IC}(\omega_0)$ and $S_{IIC}(\omega_0)$ and are represented by the dashed and dot–dashed curves, respectively, in all figures. For cases when the temperature is comparable to the barrier height one finds roughly equal contributions from rotational and vibrational modes. In cases where the temperature is much less than the barrier height, as discussed below, the vibrational component of the spectrum dominates.

One would expect better agreement between classical and quantum treatments as the mass of the rotor is increased. This is indeed the case, as is evident from a comparison of Figs. 3 and 4 with Figs. 1 and 2.

As another example we consider the case pertinent to an earlier study of phase transitions in ammonium halide crystals (2). For this example the imaginary part of the susceptibility contains only the $l = 2$ term, that is $S_{IC}(\omega_0) = f(\omega_0)\chi''_{IC2}(\omega_0/2)$. The results of the classical and quantum calculations are shown in Fig. 5. In this case there is an appreciable difference between the classical and quantum results.

Finally we examine the spectra for the ordered phase of a molecular or ionic crystal, where molecules are captured in potential minima and perform angular oscillations (about an axis in our model). To illustrate the three cases of interest, we will use $T = 2B$, $V = 5B$ for light rotors (Fig. 6), $T = 20B$, $V = 50B$ for moderately heavy rotors (Fig. 7) and $T = 200B$, $V = 500B$ for massive rotors (Fig. 8) as the relevant relationships between temperature, potential barrier height, and rotational constant. These figures clearly show that the classical and quantum spectra for moderately heavy and heavy molecules (rotors to be exact) are very similar except in the vicinity of zero frequency, where we have central peaks due to quantum tunnelling. As one would expect, in the case of light molecules the agreement between the classical and quantum spectra is poor because of large quantum effects.

One can also observe that the classical calculations for coordinates $\cos m\phi_t$ with $m = 1$ agree better with the quantum results than those with $m = 2$. The effect of temperature in approaching the classical limit is more difficult to discern. The classical spectra of Fig. 3 ($V_0 = \pm 2T$) and Fig. 4 ($V_0 = \pm 0.4T$) are quite similar. The quantum spectrum of Fig. 4, with a higher temperature, has many more oscillations than the spectrum of Fig. 3. At the higher temperatures, the classical spectra appear to average out the oscillations of the quantum spectra.

The previous quantum mechanical treatment which employed methods developed by DeRaedt and DeRaedt (8) evaluated the quantity $\beta\langle Q^0_\alpha Q^0_\alpha\rangle$ in an approximate manner. As we could not calculate this quantity in the classical limit, we replaced it by $\langle Q_\alpha(0)\rangle^2$ under the assumption of ergodicity. At this time we are able to check the validity of this approximation for one dimensional rotational modes. The use of eq. [33] together with eq. [34] allows us to evaluate $\beta\langle Q_\alpha(0)Q_\alpha(0)\rangle$ and $\beta\langle Q^0_\alpha Q^0_\alpha\rangle$ simultaneously. The numerical classical and quantum values for these quantities for the cases corresponding to Figs. 1 through 8 are listed in Table 1.

Can. J. Chem. Downloaded from www.nrcresearchpress.com by 176.9.209.113 on 09/07/12
For personal use only.

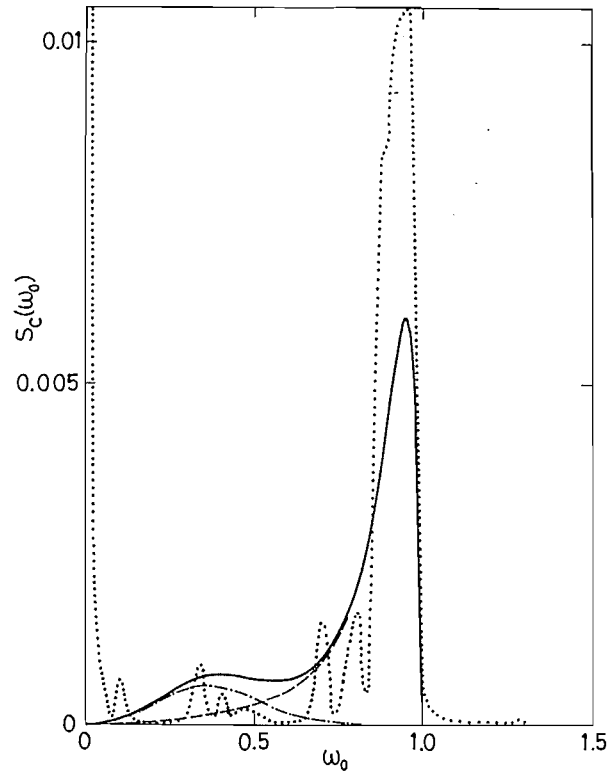

FIG. 8. The spectrum $S_C(\omega_0)$ in the case $m = 1$, $M = 3$, $V_0 = \pm 500B$, and $T = 200B$, where massive molecules are postulated ($\lambda = 0.5$). The notation is the same as for Fig. 1.

TABLE 1. Comparison* of the quantum and classical values for $\beta\langle Q_C(0)Q_C(0)\rangle$ and $\beta\langle Q_C^0 Q_C^0\rangle$

Figure	Case	$\beta\langle Q_C(0)Q_C(0)\rangle$	$\beta\langle Q_C^0 Q_C^0\rangle$	Normalized difference
1	Quantum	0.0376	0.0	0
	Classical	0.0379	0.0	
2	Quantum	0.0492	0.0101	0.358
	Classical	0.0500	0.0280	
3	Quantum	0.0468	0.0070	0.230
	Classical	0.0500	0.0185	
4	Quantum	0.00497	0.00055	0.216
	Classical	0.00500	0.00163	
5	Quantum	0.0272	0.0129	0.496
	Classical	0.0282	0.0269	
6	Quantum	0.233	0.055	0.712
	Classical	0.250	0.233	
7	Quantum	0.0247	0.0194	0.156
	Classical	0.0250	0.0233	
8	Quantum	0.00249	0.00135	0.392
	Classical	0.00250	0.00233	

*The numbers 1 through 8 correspond to the one-dimensional hindered rotors of the figures with the same numbers. The last column represents the difference in $\beta\langle Q_C^0 Q_C^0\rangle$ between the classical and quantum values, divided by $\beta\langle Q_C(0)Q_C(0)\rangle$ in the classical case.

For the examples examined in the present paper, this table shows that the classical values of $\beta\langle Q_\alpha^0 Q_\alpha^0\rangle$ are always larger than the quantum values while the values $\beta\langle Q_C(0)Q_C(0)\rangle$ are almost same in both the classical and quantum cases. This implies that the invariant part of Q_α^0 of the rotational coordinate $Q_\alpha(t)$ with respect to the natural motion decreases by an amount corresponding to quantum tunnelling when one passes from the classical limit to the quantum case. Thus we might expect that the difference between the classical $\beta\langle Q_\alpha^0 Q_\alpha^0\rangle$ and the quantum $\beta\langle Q_\alpha^0 Q_\alpha^0\rangle$ divided by $\beta\langle Q_\alpha(0)Q_\alpha(0)\rangle$ to be a measure for the relative contribution of the central peak to the spectrum. We can confirm this conclusion by a rough comparison of the values in the last column of the table with the corresponding figure.

1. H. YASUDA and J. C. RAICH. Mol. Phys. **47**, 647 (1982).
2. H. YASUDA and J. C. RAICH. Mol. Phys. **51**, 731 (1984).
3. A. HÜLLER and J. C. RAICH. J. Chem. Phys. **77**, 2038 (1982).
4. J. C. RAICH, H. YASUDA, and E. R. BERNSTEIN. J. Chem. Phys. **78**, 6209 (1983).
5. S. W. LOVESEY. Condensed matter physics. Benjamin. 1980.
6. R. KUBO. J. Phys. Soc. Jpn. **12**, 570 (1957).
7. A. ERDELYI (*Editor*). Higher transcendental functions. Vol. II. McGraw-Hill. 1953. Chapt. XIII.
8. H. DERAEDT and B. DERAEDT. Phys. Rev. B, **15**, 5379 (1977).

Appendix

Approximate expressions for the Jacobian elliptic function sn (u,k) and the complete elliptic integral of the first kind (7)

The Jacobian elliptic function sn (u,k) can be expressed in terms of θ functions, with a parameter q which may be computed from

[A1] $$q = \epsilon + 2\epsilon^5 + 15\epsilon^9 + 150\epsilon^{13} (+ \cdots)$$

with

[A2] $$2\epsilon = (1 - k'^{1/2})/(1 + k'^{1/2}), \qquad k' = (1 - k^2)^{1/2}$$

Using θ functions expressed in the form of expansions, we obtain the following approximate expression for sn (u,k):

[A3] $$\mathrm{sn}\,(u,k) = \frac{(1 + 2q + 2q^4)(\sin \pi z - q^2 \sin 3\pi z + q^6 \sin 5\pi z)}{(1 + q^2 + q^6)(1 - 2q \cos 2\pi z + 2q^4 \cos 4\pi z)}$$

with $z = u/2K(k)$, where $K(k)$ is the complete elliptic integral of the first kind. This expression is adequate for our purpose, because, as explained below, there is no need to represent the detailed behaviour of the function sn for k extremely close to 1.

Next we derive the approximations [39*a*] and [39*b*]. As a first approximation we have

[A4] $$\pi/2K(k) \simeq [1 + (1 - k^2)^{1/4}]^2/4$$

For the right hand side of the above, the following is permitted:

[A5] $$[1 - \{1 - (1 - k^2)^{1/4}\}/2]^2 \simeq 1 - \{1 - (1 - k^2)^{1/4}\} = (1 - k^2)^{1/4}$$

Here we have

[A6] $$\pi/2K(k) \simeq (1 - k^2)^{1/4}$$

This appears to be an excellent approximation although it is obtained from two successive rough approximations. Using the same method we can obtain the approximation [39*b*].

We have no problems so long as the approximations [39*a*] and [39*b*] are used for $1/K(k)$ or $1/K(1/k)$. However, when we rewrite them as

[A7] $$2K(k) \simeq \pi(1 - k^2)^{-1/4}$$

and

[A8] $$2K(1/k) \simeq \pi k^{1/2}(k^2 - 1)^{-1/4}$$

we have a problem with respect to the convergence of $K(k)$

Can. J. Chem. Downloaded from www.nrcresearchpress.com by 176.9.209.113 on 09/07/12
For personal use only.

or $K(1/k)$ in the vicinity of $k = 1$. The following limit is well-known:

[A9] $$\lim_{k \to 1-0} 2K(k) = -\ln (1 - k)$$

We then have

[A10] $$\lim_{k \to 1-0} [-\ln (1 - k)]/[\pi(1 - k^2)^{-1/4}] = 0$$

and

[A11] $$\lim_{k \to 1+0} [-\ln (1 - 1/k)]/[\pi k^{1/2}(k^2 - 1)^{-1/4}] = 0$$

Equations [A10] and [A11] indicate that the convergences of the approximate expressions for $K(k)$ and $K(1/k)$, as given by [A7] and [A8], are stronger than the exact ones. The susceptibility is calculated in this paper by use of the approximate expressions. Results such as [41*a*], [41*b*], and [43] show that there is almost no contribution from $k = 1$; $k = 1$ corresponds to $X = 0$ in eq. [41]. Hence, we expect no problems in regard to convergence for the present calculations.

Can. J. Chem. Downloaded from www.nrcresearchpress.com by 176.9.209.113 on 09/07/12
For personal use only.

The critical temperature, the critical pressure, and the dependence of vapour pressure on temperature for dodecafluorocyclohexane and hexafluorobenzene

D. R. DAVIES, M. B. EWING, J. A. HUGILL, AND M. L. MCGLASHAN
Department of Chemistry, University College London, 20 Gordon Street, London WC1H 0AJ, England

Received September 2, 1987

This paper is dedicated to Professor J. A. Morrison

D. R. DAVIES, M. B. EWING, J. A. HUGILL, and M. L. MCGLASHAN. Can. J. Chem. **66**, 760 (1988).

The critical temperature T^c, the critical pressure p^c, and the dependence of the vapour pressure p on the temperature T, have been measured for dodecafluorocyclohexane and hexafluorobenzene. For the first substance, little had previously been known. For the second substance, previous measurements have been confirmed and extended. The results have been analysed by means of Wagner's equation: $\ln(p/p^c) = (T^c/T)(A_2\tau + A_3\tau^{1.5} + A_4\tau^{2.5} + A_5\tau^5)$ where $\tau = (1 - T/T^c)$.

D. R. DAVIES, M. B. EWING, J. A. HUGILL et M. L. MCGLASHAN. Can. J. Chem. **66**, 760 (1988).

Opérant avec du dodécafluorocyclohexane et de l'hexafluorobenzène, on a mesuré la température critique, T^c, la pression critique, p^c, ainsi que la relation qui existe entre ces valeurs et la pression de vapeur p et la température T. Au sujet du premier composé, on connaissait peu de choses. Dans le cas du deuxième produit, on a confirmé et étendu les études qui avaient été réalisées antérieurement. On a analysé les résultats à l'aide de l'équation de Wagner : $\ln(p/p^c) = (T^c/T)(A_2\tau + A_3\tau^{1.5} + A_4\tau^{2.5} + A_5\tau^5)$ dans laquelle $\tau = (1 - T/T^c)$.

[Traduit par la revue]

Introduction

We have taken the opportunity, belatedly, to present the results of measurements of the critical temperature T^c, the critical pressure p^c, and the dependence of vapour pressure p on temperature T, for dodecafluorocyclohexane and hexafluorobenzene. For dodecafluorocyclohexane only two values of the vapour pressure at temperatures above 370 K, and the critical temperature, had previously been measured (1). For hexafluorobenzene both our vapour pressures and our critical temperature and critical pressure confirm previous results (2–8).

Experimental

Dodecafluorocyclohexane and hexafluorobenzene were gifts from the Imperial Smelting Company (now ISC Chemicals plc). The mole-fraction purities determined by glc were 0.94 of c-C_6F_{12} and 0.999 of C_6F_6. The dodecafluorocyclohexane was purified by slow sublimation at atmospheric pressure until its mole-fraction purity was 0.997 of c-C_6F_{12}; we were unable to purify it further. The relative difference $(p^b - p^d)/p^d$ between the bubble pressure p^b and the dew pressure p^d was 0.0017, just a little less than the upper bound allowed by Timmermans (9) for samples intended for accurate physical measurements. The hexafluorobenzene was used without further purification except for drying and degassing; its value for $(p^b - p^d)/p^d$ was 0.0005.

The apparatus and method were the same as those previously described: for dodecafluorocyclohexane and for the earlier measurements on hexafluorobenzene in refs. 10 and 11, and for the later measurements on hexafluorobenzene in ref. 12. Temperatures are all expressed in terms of the IPTS-68 and are denoted by T_{68}.

Results

Our vapour pressures p at temperatures T_{68} are given for dodecafluorocyclohexane in Table 1 and for hexafluorobenzene in Table 2. Our values of the critical constants of each fluid are given and compared with literature values in Table 3. We estimated the critical molar volume V_m^c of c-C_6F_{12} from the dimensions of the tube in which fluid at its critical point was enclosed by mercury and the amount of substance of c-C_6F_{12} in the tube. For hexafluorobenzene the critical pressure obtained by analysing only our own vapour pressures was 3275.2 kPa, by analysing them together with the measurements of Ambrose (2) was 3274.7 kPa, and by analysing all of those together with the measurements of Douslin *et al.* (3) and Counsell *et al.* (4)

TABLE 1. Vapour pressures p of dodecafluorocyclohexane at temperatures T_{68}

T_{68}/K	p/kPa	T_{68}/K	p/kPa	T_{68}/K	p/kPa	T_{68}/K	p/kPa
373.113	423.79	403.117	828.84	433.124	1435.2	456.926	2223.8
383.114	535.61	413.118	1014.3	443.123	1702.1	457.026	2228.3
393.115	669.62	423.120	1208.0	453.126	2076.4[a]	457.126	2230.2

[a]Point excluded from the fit.

TABLE 2. Vapour pressures p of hexafluorobenzene at temperatures T_{68}

T_{68}/K	p/kPa	T_{68}/K	p/kPa	T_{68}/K	p/kPa	T_{68}/K	p/kPa
403.159	402.8	473.191	1634.6	513.209	3104.9	516.411	3259.8
423.164	631.7	493.199	2271.4	516.209	3248.2	516.511	3265.1
448.189	1043.5	503.182	2654.1	516.310	3254.6	516.610	3271.6
433.565	783.6	483.166	1932.2	515.767	3226.9		
462.331	1353.0	503.620	2676.0	516.713	3274.8		

Can. J. Chem. Downloaded from www.nrcresearchpress.com by 176.9.209.113 on 09/07/12
For personal use only.

TABLE 3. Critical constants of dodecafluorocyclohexane c-C_6F_{12} and of hexafluorobenzene C_6F_6

Source	T_{68}^c/K	p^c/kPa	V_m^c/(cm^3 mol^{-1})
	Dodecafluorocyclohexane		
This work	457.29	2242	459
Literature	457.2 (1)	(2400) (1)[a]	—
	Hexafluorobenzene		
This work	516.71	3275	—
Literature	516.73 (3), 516.78 (4), 518 (6), 516.1 (7), 515.9 (8)	3273 (3), 3304 (4), 3292 (5), 3166 (7)	335 (3)

[a]Extrapolated value, using the equation given in the text with the critical temperature reported in ref. 1.

Can. J. Chem. Downloaded from www.nrcresearchpress.com by 176.9.209.113 on 09/07/12
For personal use only.

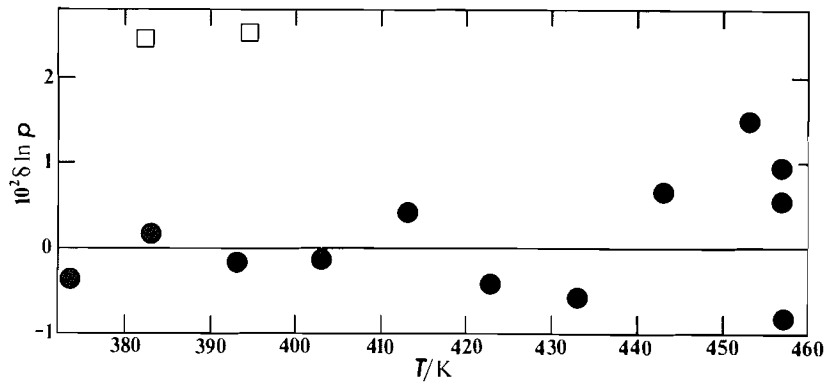

FIG. 1. For dodecafluorocyclohexane, a plot of the deviations $\delta \ln p = \ln(p/p^c) - (T^c/T)(A_2\tau + A_3\tau^{1.5} + A_4\tau^{2.5} + A_5\tau^5)$ from the equation due to Wagner (13) where p denotes the vapour pressure, T the temperature, T^c the critical temperature, and $\tau = (1 - T/T^c)$, with the critical pressure p^c treated as an adjustable parameter, against the temperature T. ●, This work; □, Rowlinson and Thacker (1).

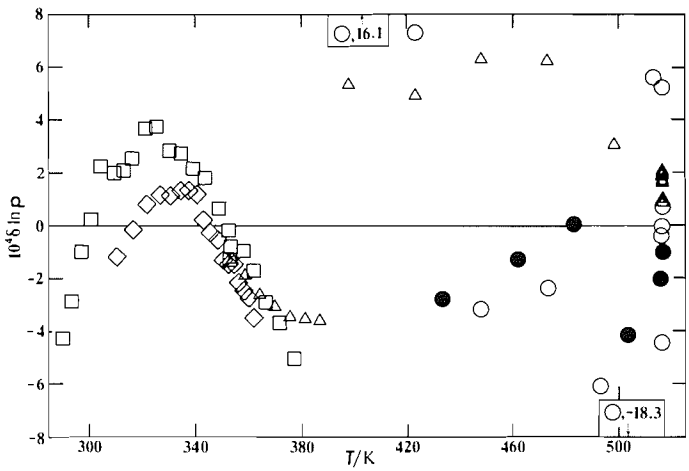

FIG. 2. For hexafluorobenzene, a plot of the deviations $\delta \ln p = \ln(p/p^c) - (T^c/T)(A_2\tau + A_3\tau^{1.5} + A_4\tau^{2.5} + A_5\tau^5)$ from the equation due to Wagner (13) where p denotes the vapour pressure, T the temperature, T^c the critical temperature, and $\tau = (1 - T/T^c)$, with the critical pressure p^c treated as an adjustable parameter, against the temperature T. ●, This work (later measurements); ○, this work (earlier measurements); □, Ambrose (2); △, Douslin *et al.* (3); ◇, Counsell *et al.* (4).

was 3275.0 kPa. To four significant figures all these values are identical.

Discussion

The vapour pressures of each liquid were analysed in terms of the deviations $\delta \ln p$:

$$[1]\quad \delta \ln p = \ln(p/p^c) - (T^c/T)(A_2\tau + A_3\tau^{1.5} + A_4\tau^{2.5} + A_5\tau^5)$$

from the equation of Wagner (13, 14), where $\tau = (1 - T/T^c)$, with the critical pressure p^c treated as an adjustable parameter. For dodecafluorocyclohexane we obtained with $T_{68}^c = 457.290$ K: $p^c = 2241.7$ kPa, $A_2 = -11.82$, $A_3 = 20.10$, $A_4 = -65.2$, and $A_5 = 840$. For hexafluorobenzene we obtained with $T_{68}^c = 516.710$ K: $p^c = 3275.0$ kPa, $A_2 = -8.0657$, $A_3 = 2.0297$, $A_4 = -3.1301$, and $A_5 = -4.080$.

As shown in Fig. 1 for dodecafluorocyclohexane, all our 12 points, except one which was excluded from the regression, give values of $\delta \ln p$ lying within ± 0.01. The two values of Rowlinson and Thacker (1) give values lying a little more than twice as far from zero, both in the same direction. As shown in Fig. 2 for hexafluorobenzene, only two (and those are two of our earlier, and admittedly less accurate, measurements) of the 78 points from this work, and from the work of Ambrose (2), Douslin *et al.* (3), and Counsell *et al.* (4), give values of $\delta \ln p$ lying outside $\pm 8 \times 10^{-4}$. The older measurements, not included in Fig. 2, give deviations $\delta \ln p$ from Wagner's equation [1] ranging for those of Patrick and Prosser (6) from 65×10^{-4} at 312.99 K to -54×10^{-4} at 358.12 K; and for those of Evans and Tiley (7) from 355×10^{-4} at 381.51 K to -254×10^{-4} at 515.61 K.

1. J. S. ROWLINSON and R. THACKER. Trans. Faraday Soc. **53**, 1 (1957).
2. D. AMBROSE. J. Chem. Thermodyn. **13**, 1161 (1981).
3. D. R. DOUSLIN, R. H. HARRISON, and R. T. MOORE. J. Chem.

Thermodyn. **1**, 305 (1969); D. R. DOUSLIN and A. OSBORN. J. Sci. Instrum. **42**, 369 (1965).
4. J. F. COUNSELL, J. H. S. GREEN, J. L. HALES, and J. F. MARTIN. Trans. Faraday Soc. **61**, 212 (1965).
5. D. AMBROSE and C. H. S. SPRAKE. Personal communication.
6. C. R. PATRICK and G. S. PROSSER. Trans. Faraday Soc. **60**, 700 (1964).
7. F. D. EVANS and P. F. TILEY. J. Chem. Soc. B, 134 (1966).
8. D. C.-H. CHENG and J. C. MCCOUBREY. J. Chem. Soc. 4993 (1963).
9. J. TIMMERMANS. Physico-chemical constants of pure organic compounds. Elsevier, New York. 1950. p. 4.
10. D. R. DAVIES and M. L. MCGLASHAN. J. Chem. Thermodyn. **13**, 377 (1981).
11. M. L. MCGLASHAN and I. R. MCKINNON. J. Chem. Thermodyn. **9**, 1205 (1977).
12. J. A. HUGILL and M. L. MCGLASHAN. J. Chem. Thermodyn. **10**, 85 (1978).
13. W. WAGNER. Cryogenics, **13**, 470 (1973).
14. D. AMBROSE. J. Chem. Thermodyn. **18**, 45 (1986).

Can. J. Chem. Downloaded from www.nrcresearchpress.com by 176.9.209.113 on 09/07/12
For personal use only.

Approximations for the inner branch of potential curves of diatomic molecules

Y. P. VARSHNI

Ottawa–Carleton Institute for Physics, University of Ottawa, Ottawa, Ont., Canada K1N 6N5

Received August 17, 1987

This paper is dedicated to Professor James A. Morrison

Y. P. VARSHNI. Can. J. Chem. **66**, 763 (1988).

Three potential energy functions are examined with respect to their ability to reproduce the inner branch of the potential curve for 43 molecular states. Two of the states turn out to be unusual. In the remaining 41 cases, it is found that a potential proposed by the author gives the least error in 28 cases and is close to the least error in another six. The potential curves of NaAr(X) and XeCl(X) are very different from those of the other 41 states considered in this paper. The Born–Mayer potential appears to provide a reasonable representation of the inner branch of the potential curve for XeCl(X).

Y. P. VARSHNI. Can. J. Chem. **66**, 763 (1988).

On a examiné les trois potentiels d'énergie par rapport à leur habilité à reproduire les branches internes de la courbe de potentiel de 43 états moléculaires. Il en ressort que deux de ces états sont inhabituels. Les 41 autres cas se divisent comme suit : pour 28 cas, on a trouvé que le potentiel proposé par l'auteur conduit à une erreur minimale alors que, pour six autres cas, il conduit pratiquement à l'erreur minimale. Les courbes de potentiel du NaAr(X) et du XeCl(X) sont très différentes de celles des 41 autres états considérés dans notre travail. Le potentiel de Born–Mayer semble fournir une représentation raisonnable de la branche interne de la courbe de potentiel du XeCl(X).

[Traduit par la revue]

Can. J. Chem. Downloaded from www.nrcresearchpress.com by 176.9.209.113 on 09/07/12
For personal use only.

Introduction

It is usually difficult to obtain the RKR (Rydberg–Klein–Rees) curves for heavy diatomic molecules. The difficulty stems from the fact that while it may be possible to carry out a reliable vibrational analysis for a particular electronic transition for such a molecule, it is very difficult to achieve a rotational analysis because the spectral lines are so congested. As pointed out by Tellinghuisen and Henderson (1) (TH), in the absence of rotational constants the RKR method can yield only the width of the potential curve, $R_+ - R_-$, as a function of v and G_v. Thus to obtain the potential curve, one must guess the equilibrium internuclear distance and the shape of either the inner or outer branch of the potential curve.

Tellinghuisen and co-workers (2–5) have approximated the unknown repulsive or inner branch (R_-) by a variety of methods, e.g., representing it by an inverse power potential (4) or by a Morse potential (3), then simply adding the RKR width as a function of energy to obtain the outer branch (R_+). TH have tested the approximation of representing the inner branch by a Morse potential (6) approximation on 25 molecular states for which the RKR curves are known. The errors show a whole spectrum of values, from quite small to quite large. The question naturally arises whether better results are possible by the use of other potential functions. There are two other three-parameter functions, the Rydberg potential (7) and a potential proposed by the author (8), which are able to predict $\omega_e x_e$ values better (8, 9) than the Morse curve in many cases. Thus it was of interest to examine the applicability of these two potentials to approximate the inner branch of potential curves. We have considered 18 states in addition to those considered by TH and, also, some of the data that we use are different from those used by TH; in view of these factors we have also included the Morse potential in our investigation. We use the usual symbols for the molecular constants (10).

The three potentials are as follows.

Morse (6):

$$[1] \quad U = D_e[1 - e^{-a(r-r_e)}]^2$$

Rydberg (7):

$$[2] \quad U = D_e[1 + b(r - r_e)]e^{-b(r-r_e)}$$

Varshni III (8, 9):

$$[3] \quad U = D_e\left\{1 - \frac{r_e}{r}\exp\left[-\beta(r^2 - r_e^2)\right]\right\}^2$$

Potential [3] has been found to give quite good results for several molecular properties (11–14). Each of the three potentials has three parameters and these can be readily determined in terms of k_e, r_e, and D_e. The expressions for a, b, and β are as follows:

$$[4] \quad a = (k_e/2D_e)^{1/2}$$

$$[5] \quad b = (k_e/D_e)^{1/2}$$

and

$$[6] \quad \beta = \frac{1}{2r_e^2}[\Delta^{1/2} - 1]$$

where

$$\Delta = k_e r_e^2/2D_e$$

Data

We have considered here a total of 43 states. The data employed by us are shown in Table 1. The 18 states that are in addition to those considered by TH are identified by an asterisk in column 1 of Table 1. The references in column 5 are for RKR curves and for most of the molecular data. Such molecular data that are not from the given references are from TH and from Huber and Herzberg (22). For those states also considered by TH, for the most part our data are the same as those used by TH, except for the following differences.

$K_2(X)$ and $K_2(B)$: Very recently Heinze *et al.* (26) investigated the B–X band system of the K_2 molecule by Doppler-free polarization spectroscopy in a heat-pipe oven. New molecular constants were given as well as the RKR curves for the X and B states. We have used these data. (TH had considered only the $K_2(X)$ state.) Ross *et al.* (38) have also given the RKR curve for the ground state of K_2.

$S_2(X)$: TH used the RKR curve that was calculated by them. We have used the RKR curve from Bradson and Volkmar (31).

$I_2(X)$: Recently Martin *et al.* (33) presented an accurate

Can. J. Chem. Downloaded from www.nrcresearchpress.com by 176.9.209.113 on 09/07/12
For personal use only.

TABLE 1. Molecular data and parameters of the three potentials

State	ω_e (cm^{-1})	r_e (Å)	D_e (cm^{-1})	Ref.	a ($Å^{-1}$)	b ($Å^{-1}$)	β ($Å^{-2}$)
$H_2(X)$	4401.21	0.7414	38300	15	1.9441	2.7494	0.401508
$^6LiH(X)$*	1420.06	1.5956	20287	16	1.1280	1.5953	0.157093
$NaH(X)$*	1176.10	1.8890	16000	17, 18	1.1126	1.5734	0.154368
$KH(X)$*	985.38	2.2400	15000	17, 19	0.9711	1.3734	0.117121
$RbH(X)$*	937.19	2.3673	14500	18, 20	0.9459	1.3377	0.110565
$CsH(X)$*	891.00	2.4938	14805	21–23	0.8919	1.2613	0.098417
$H^{19}F(X)$*	4138.32	0.9168	49380	22	2.2186	3.1376	0.615128
$H^{35}Cl(X)$*	2990.95	1.2746	37255	22	1.8677	2.6414	0.424901
$H^{81}Br(X)$*	2648.97	1.4144	31635	22	1.8095	2.5591	0.389752
$H^{127}I(X)$*	2309.01	1.6092	25790	22	1.7508	2.4761	0.350924
$Li_2(X)$	351.42	2.6733	8620	24	0.8633	1.2209	0.091508
$Li_2(A)$	255.47	3.1082	9450	24	0.5994	0.8477	0.044669
$Na_2(X)$	159.11	3.0786	5990	25	0.8488	1.2004	0.085101
$Na_2(B)$	124.44	3.4132	3120	25	0.9198	1.3008	0.091827
$K_2(X)$	92.40	3.9243	4447	26	0.7448	1.0533	0.062424
$K_2(B)$*	74.89	4.2360	2113	26	0.8757	1.2385	0.075502
$Cs_2(X)$	42.02	4.6499	3550	27	0.7001	0.9902	0.052161
$N_2(X)$	2358.57	1.0977	79890	28	2.6889	3.8026	0.809821
$N_2(A)$	1460.64	1.2866	29690	28	2.7315	3.8630	0.759479
$CO(X)$	2169.81	1.1283	90540	29	2.2994	3.2518	0.626214
$SiO(X)$	1241.56	1.5097	67240	22	1.8601	2.6305	0.396664
$O_2(X)$	1580.19	1.2075	42050	30	2.6538	3.7531	0.755974
$O_2(A)$	799.08	1.5215	6650	30	3.3746	4.7725	0.892997
$O_2(B)$	709.06	1.6043	8120	30	2.7099	3.8324	0.650306
$S_2(X)$	725.65	1.8892	35240	31	1.8821	2.6617	0.358038
$Se_2(X)$	385.30	2.1660	27700	22	1.7821	2.5203	0.304808
$^{19}F_2(X)$*	916.64	1.4119	13380	22	2.9743	4.2063	0.802480
$Cl_2(X)$	559.75	1.9877	20280	32	2.0015	2.8306	0.376922
$^{79}Br_2(X)$*	325.32	2.2811	16060	22	1.9637	2.7771	0.334346
$I_2(X)$	214.52	2.6663	12550	33	1.8576	2.6270	0.278007
$I_2(A)$	94.96	3.0560	1640	4	2.2746	3.2168	0.318623
$I_2(A')$	108.81	3.0600	2510	5	2.1068	2.9795	0.290853
$I_2(B)$	125.67	3.0271	4380	34	1.8420	2.6050	0.249686
$^{35}Cl^{19}F(X)$*	786.15	1.6283	21500	22	2.2908	3.2397	0.514858
$^{79}Br^{19}F(X)$*	670.75	1.7589	20890	22	2.2115	3.1275	0.467036
$^{79}Br^{35}Cl(X)$*	444.28	2.1361	18230	22	1.9725	2.7896	0.352138
$^{127}I^{79}F(X)$*	610.24	1.9098	23530	22	1.9694	2.7851	0.378508
$^{127}I^{35}Cl(X)$*	384.29	2.3209	17560	22	1.8491	2.6150	0.305535
$^{127}I^{79}Br(X)$*	268.64	2.4690	14790	22	1.8765	2.6537	0.297982
$Ar_2(X)$	31.33	3.7590	99.6	35	1.7089	2.4167	0.191920
$Mg_2(X)$	51.08	3.8890	430	36	1.0388	1.4691	0.100500
$NaAr(X)$	13.56	4.9910	40.4	37	0.9923	1.4033	0.079334
$XeCl(X)$	26.22	3.2300	281	3	1.0014	1.4163	0.107097

RKR curve for $^{127}I_2(X)$ from data obtained from an extensive analysis of the $BO_u^+ \rightarrow XO_f^+$ fluorescence spectrum of $^{127}I_2$. We have used this RKR curve.

$I_2(A)$ and $I_2(A')$: We have used the r_e values given in the original references. TH used slightly different values.

$SiO(X)$, $Se_2(X)$, $I_2(B)$, $Mg_2(X)$, and $NaAr(X)$: TH used RKR curves calculated by themselves (unpublished). We have used the RKR curves calculated by us using the program of Tellinghuisen (39).

For all the states marked by an asterisk, except $K_2(B)$, the RKR curves were also calculated by us using the program of Tellinghuisen (39). Where the range of applicability of the $G(v)$ series was not known, the RKR curve was cut off at about 80% of D_e.

Results and discussion

The calculated parameters for the three potentials are shown in the last three columns of Table 1.

For the Morse potential, R_- is calculated from

$$[7] \quad R_- = r_e - \ln [1 + (U/D_e)^{1/2}]/a$$

For the other two potentials an iterative method was used, on a computer.

It is convenient (1) to discuss the results in terms of the dimensionless variables,

$$[8] \quad \delta = \frac{R_-(\text{calcd. from the potential}) - R_-(\text{RKR})}{r_e}$$

and

$$[9] \quad u = U/D_e$$

Generally speaking, for all the three potentials, δ increases with u. A sample illustration is shown in Fig. 1. Sometimes there is a slight reversal of the curvature near the end. The curves for the different potentials do not cross each other. Under the circumstances, for comparison purposes, the maximum

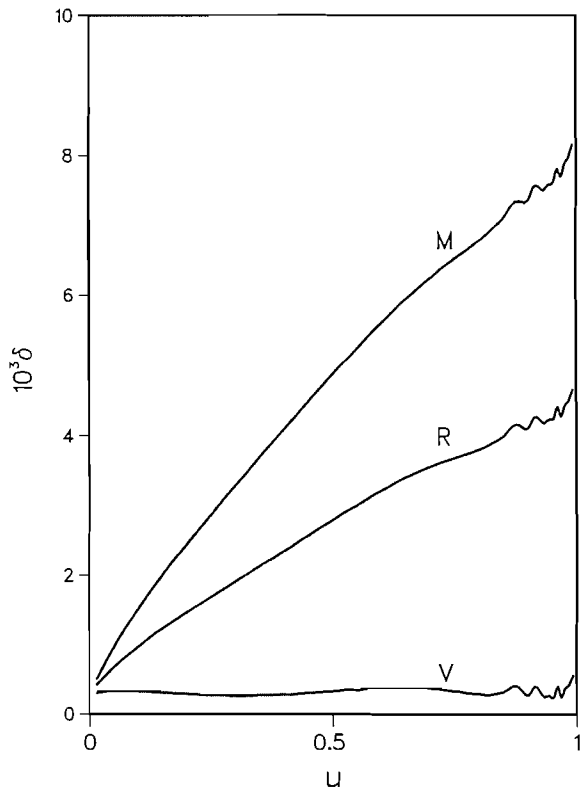

FIG. 1. $10^3\delta$ versus u for $Cl_2(X)$ by the three potentials. M, Morse; R, Rydberg; V, Varshni III. The ripples toward the end are due to slight inaccuracies in the RKR curve.

value of δ is a good measure of the error from the function. In Table 2 we show the δ_{max} values ($\times 10^3$) for the three potentials. The maximum value of u for which the RKR curve was available is also shown.

It will be noticed from Table 2 that the results for NaAr and XeCl are very poor for all three potentials. We shall consider these two molecules later. In the remaining 41 cases, potential [3] gives the best results in 28 cases, the Morse potential in 9, and the Rydberg potential in 4. In the 4 cases for which the results from the Rydberg potential are better than those from [3], the difference is only marginal. A similar remark applies for RbH, where the Morse potential gives the least error, but the difference from the results of eq. [3] is only marginal. For $Ar_2(X)$ the Morse potential gives the smallest error but the results from the other two potentials are pretty close to it.

For all except two of the states that are "common" with TH, there is good agreement between our results and those of TH. The two exceptions are $I_2(A)$ and NaAr(X). In the case of $I_2(A)$ the difference appears to stem from the different r_e values used by us and by TH. As noted earlier we have followed the r_e value given in the quoted reference. For NaAr(X), our value for $10^3\delta_{max}$ is 135.6, while TH give a value of 6. This discrepancy is very large. In the paper by Tellinghuisen *et al.* (37) from which the data were taken, there occurs the following sentence: "However, the initial calculations indicated clearly that a Morse curve rises too rapidly with decreasing R....". Our findings are in agreement with this sentence. Subsequently, in ref. 37, a modified Morse curve was used. It is possible that the value 6 quoted by TH refers to the modified Morse curve and not to the Morse curve. The other two potentials also give large errors for this state. NaAr is a van der Waals molecule and the nature of its potential curve is expected to be much different from most of the other molecules considered in this paper.

TABLE 2. Comparison of δ_{max} for the three potentials

State	u_{max}	$10^3\delta_{max}$ Morse	Rydberg	Equation [3]
$H_2(X)$	0.98	−34.1	−43.7	24.8
^{6}LiH	0.98	−12.2	−19.8	7.3
NaH	0.78	−3.3	−8.5	0.7
KH	0.72	−3.3	−8.3	−2.2
RbH	0.66	0.7	3.9	−1.1
CsH	0.99	−2.5	−8.8	−1.9
$H^{19}F$	0.64	−12.7	−17.7	−8.5
$H^{35}Cl$	0.91	−2.7	−7.7	−5.0
$H^{81}Br$	0.95	−7.5	−12.7	−12.2
$H^{127}I$	0.95	−20.8	−25.6	−27.5
$Li_2(X)$	0.52	11.3	7.6	9.9
$Li_2(A)$	0.58	−7.6	−12.6	1.6
$Na_2(X)$	0.91	24.7	19.8	19.6
$Na_2(B)$	0.91	23.0	18.8	15.5
$K_2(X)$	0.92	30.1	25.6	23.1
$K_2(B)$	0.99	29.6	25.8	21.6
$Cs_2(X)$	0.67	24.5	21.3	18.4
$N_2(X)$	0.55	3.9	0.8	−1.2
$N_2(A)$	0.58	5.0	2.4	−0.5
$CO(X)$	0.57	−3.5	−7.0	−7.4
$SiO(X)$	0.56	−3.8	−7.0	−8.5
$O_2(X)$	0.71	1.3	−2.1	−5.1
$O_2(A)$	0.98	13.3	10.7	7.6
$O_2(B)$	0.90	14.1	11.1	7.5
$S_2(X)$	0.61	4.4	1.8	1.9
$Se_2(X)$	0.39	3.2	1.4	−0.6
$^{19}F_2$	0.79	7.1	4.5	1.5
$Cl_2(X)$	0.99	8.2	4.7	0.6
$^{79}Br_2$	0.78	9.2	6.6	3.4
$I_2(X)$	1.00	9.2	6.4	3.1
$I_2(A)$	0.95	−11.1	−13.0	−14.7
$I_2(A')$	0.83	8.9	7.0	5.2
$I_2(B)$	0.98	7.3	4.8	2.2
$^{39}Cl^{19}F$	0.77	24.4	21.3	17.9
$^{79}Br^{19}F$	0.80	14.0	10.9	7.4
$^{79}Br^{35}Cl$	0.78	8.5	5.7	2.4
$^{127}I^{19}F$	0.79	5.8	2.7	2.3
$^{127}I^{35}Cl$	0.80	10.9	8.2	4.8
$^{127}I^{79}Br$	0.78	11.3	8.8	5.8
$Ar_2(X)$	0.71	1.3	−1.4	−3.0
$Mg_2(X)$	0.99	−7.9	−11.3	−15.4
NaAr(X)	0.98	135.6	132.8	129.5
XeCl(X)	0.95	−76.4	−80.5	−84.2

For molecules for which D_e is poorly known (or not known at all), but $\omega_e x_e$ is known and is positive, D_e can be estimated (9) from

$$[10] \quad D_e = \frac{5Wk_e r_e^2}{2(\omega_e x_e r_e^2 \mu_A - 9W)}$$

where $W = 2.1072 \times 10^{-16}$, and then potential [3] can be applied.

We then consider XeCl(X). The shape of the potential curve for this state is known only approximately, having been obtained through trial and error Franck–Condon calculations (1, 3). The following discussion is subject to this caveat. The nature of the potential curve depends on the nature of the binding. It is reasonable to expect that XeCl binding should have an appreciable ionic component. We have tried the Born–Mayer potential

Can. J. Chem. Downloaded from www.nrcresearchpress.com by 176.9.209.113 on 09/07/12
For personal use only.

$$[11] \quad V = \frac{A}{r} + Be^{-r/\sigma}$$

for this molecule. Using the conditions [8a, b, c] of ref. 8, the three parameters were determined to be: $\sigma = 0.14699$ Å, $A = 950.9\,\text{cm}^{-1}$ Å, and $B = 4.6792 \times 10^{10}\,\text{cm}^{-1}$. A comparison of the resulting curve with the RKR curve showed that the value of $10^3\delta_{max}$ was only -12.0, a considerable improvement on the previous results. We may note here two differences between our application of the Born–Mayer potential and the customary application (40) of this potential to ionic molecules. First, the coefficient of the first term has been taken to be a parameter A, rather than e^2, and second, we have assumed $U(r_e) - U(\infty) = -D_e$, rather than $-D_i$.

The performance of a potential energy function depends on its analytical form and the number of parameters involved in it. For a fixed number of parameters one tries to select the potential that gives the fewest errors. Our aim in this paper has been to focus on such potential functions that can be used when only limited data are available, as in the situation outlined in the opening paragraph. One can obviously expect to improve the agreement with a greater number of parameters. Several potential functions with more than three parameters are available (8, 11, 41–43).

In conclusion we find that for most molecules whose binding is mostly covalent, potential [3] provides a good description of the inner branch of the RKR curve. For XeCl type of molecules, the Born–Mayer potential deserves further exploration.

Acknowledgement

The author is grateful to Dr. J. Tellinghuisen for making available a copy of his computer program.

1. J. Tellinghuisen and S. D. Henderson. Chem. Phys. Lett. **91**, 447 (1982).
2. J. Tellinghuisen, A. Ragone, M. S. Kim, D. J. Auerbach, R. E. Smalley, L. Wharton, and D. H. Levy. J. Chem. Phys. **71**, 1283 (1979).
3. A. Sur, A. K. Hui, and J. Tellinghuisen. J. Mol. Spectrosc. **74**, 465 (1979).
4. K. S. Viswanathan, A. Sur, and J. Tellinghuisen. J. Mol. Spectrosc. **86**, 393 (1981).
5. J. Tellinghuisen. J. Mol. Spectrosc. **94**, 231 (1982).
6. P. M. Morse. Phys. Rev. **34**, 57 (1929).
7. R. Rydberg. Z. Phys. **73**, 376 (1931).
8. Y. P. Varshni. Rev. Mod. Phys. **29**, 664 (1957); **31**, 839 (1959).
9. Y. P. Varshni and R. C. Shukla. J. Chem. Phys. **40**, 250 (1964).
10. G. Herzberg. Spectra of diatomic molecules. Van Nostrand, Princeton, NJ. 1950.
11. I. N. Levine. J. Chem. Phys. **45**, 827 (1966).
12. V. G. Blinkova. Sov. Phys. J. **17**, 1511 (1974).
13. H. B. Schlegel, S. Wolfe, and F. Bernardi. Can. J. Chem. **53**, 3599 (1975).
14. B. J. Laurenzi. J. Chem. Phys. **65**, 217 (1976).
15. T. E. Sharp. At. Data, **2**, 119 (1971).
16. C. R. Vidal and W. C. Stwalley. J. Chem. Phys. **77**, 883 (1982).
17. M. Giroud and D. Nedelec. J. Chem. Phys. **73**, 4151 (1980).
18. S. C. Yang and W. C. Stwalley. ACS Symp. Ser. **179**, 241 (1981).
19. S. C. Yang, D. D. Nelson, Jr., and W. C. Stwalley. J. Chem. Phys. **78**, 4541 (1983).
20. Y. K. Hsieh, S. C. Yang, A. C. Tam, K. K. Verma, and W. C. Stwalley. J. Mol. Spectrosc. **83**, 311 (1980).
21. A. C. Tam and W. Happer. J. Chem. Phys. **64**, 2456 (1976).
22. K. P. Huber and G. Herzberg. Constants of diatomic molecules. Van Nostrand, Princeton, NJ. 1979.
23. S. C. Yang. J. Chem. Phys. **77**, 2884 (1982).
24. P. Kusch and M. M. Hessel. J. Chem. Phys. **67**, 586 (1977).
25. P. Kusch and M. M. Hessel. J. Chem. Phys. **68**, 2591 (1978).
26. J. Heinze, U. Schuhle, F. Engelke, and C. D. Caldwell. J. Chem. Phys. **87**, 45 (1987).
27. G. Honing, M. Czajkowski, M. Stock, and W. Demtroder. J. Chem. Phys. **71**, 2138 (1979).
28. A. Lofthus and P. H. Krupenie. J. Phys. Chem. Ref. Data, **6**, 113 (1977).
29. A. W. Mantz, J. K. G. Watson, K. N. Rao, D. L. Albritton, A. L. Schmeltekopf, and R. N. Zare. J. Mol. Spectrosc. **39**, 180 (1971).
30. P. H. Krupenie. J. Phys. Chem. Ref. Data, **1**, 423 (1972).
31. G. D. Brabson and R. L. Volkmar. J. Chem. Phys. **58**, 3209 (1973).
32. A. E. Douglas and A. R. Hoy. Can. J. Chem. **53**, 1965 (1975).
33. F. Martin, R. Bacis, S. Churassy, and J. Verges. J. Mol. Spectrosc. **116**, 71 (1986).
34. P. Luc. J. Mol. Spectrosc. **80**, 41 (1980).
35. E. A. Colbourn and A. E. Douglas. J. Chem. Phys. **65**, 1741 (1976).
36. C. R. Vidal and H. Scheingraber. J. Mol. Spectrosc. **65**, 46 (1977).
37. J. Tellinghuisen, A. Ragone, M. S. Kim, D. J. Auerbach, R. E. Smalley, L. Wharton, and D. H. Levy. J. Chem. Phys. **71**, 1283 (1979).
38. A. J. Ross, P. Crozet, J. D'Incan, and C. Effantin. J. Phys. B, **19**, L145 (1986).
39. J. Tellinghuisen. J. Mol. Spectrosc. **44**, 194 (1972); Comput. Phys. Commun. **6**, 221 (1974).
40. Y. P. Varshni and R. C. Shukla. J. Chem. Phys. **35**, 582 (1961); J. Mol. Spectrosc. **16**, 63 (1965).
41. J. Goodisman. Diatomic interaction potential theory. Vols. 1 and 2. Academic Press, New York, NY. 1973.
42. J. N. Murrell and K. S. Sorbie. J. Chem. Soc. Faraday Trans. 2, **70**, 1552 (1974).
43. E. S. Kryachko and T. Koga. Adv. Quantum Chem. **17**, 97 (1985).

Can. J. Chem. Downloaded from www.nrcresearchpress.com by 176.9.209.113 on 09/07/12
For personal use only.

Volumes and heat capacities of transfer of ammonium salts from water to aqueous octyldimethylamine oxide at 25°C[1]

DANIEL HÉTU AND JACQUES E. DESNOYERS[2]

Department of Chemistry, University of Sherbrooke, Sherbrooke, P.Q., Canada J1K 2R1 and INRS-Energie, C.P. 1020, Varennes, P.Q., Canada J0L 2P0

Received August 28, 1987

This paper is dedicated to Professor J. A. Morrison

DANIEL HÉTU and JACQUES E. DESNOYERS. Can. J. Chem. **66**, 767 (1988).

The effect of an additive on a water–surfactant system can be studied through thermodynamic functions of transfer of the additive from water to aqueous solutions of the surfactant. These thermodynamic functions often go through extrema in the region of the critical micellar concentration (cmc) of the surfactant. As it can be shown with a simple chemical equilibrium model, the general shape of the transfer functions is primarily related to the pair-wise hydrophobic interactions between the additive and the surfactant monomers, to a shift in the monomer–micelle equilibrium and to the distribution of the additive between the aqueous phase and the micelles. Medium and electrostatic effects are also possible, especially with ionic systems. To separate these effects and identify the salts which distribute themselves in the micelles, the volumes and heat capacities of transfer of hydrophobic ammonium salts from water to aqueous solutions of dimethyloctylamine oxide have been investigated. The short chain salts have only a small effect on monomer–micelle equilibrium by salting out the monomers, whereas the more hydrophobic ones participate also to the micellization process, shifting more strongly the surfactant monomer–micelle equilibrium.

DANIEL HÉTU et JACQUES E. DESNOYERS. Can. J. Chem. **66**, 767 (1988).

L'effet d'un additif sur un système eau–tensioactif peut être étudié par le biais des fonctions de transfert de l'additif de l'eau aux solutions aqueuses du tensioactif. Ces fonctions thermodynamiques passent souvent par un extremum dans la région de la concentration micellaire critique (cmc) du tensioactif. Comme il peut être démontré à l'aide d'un modèle simple d'équilibre chimique, l'allure générale des fonctions de transfert est principalement reliée aux interactions hydrophobes par paires entre les monomères de l'additif et du tensioactif, au déplacement de l'équilibre monomères–micelles du tensioactif, ainsi qu'à la distribution de l'additif entre la phase aqueuse et les micelles. Des effets de milieu ainsi qu'électrostatiques peuvent aussi jouer un rôle important, particulièrement dans le cas de systèmes ioniques. Afin de séparer ces effets et d'identifier les sels qui participent à la micellisation, les volumes et capacités calorifiques de transfert de sels hydrophobes d'ammonium de l'eau aux solutions aqueuses d'oxyde d'octyldiméthylamine ont été investigués. Les sels à courtes chaînes ont seulement un petit effet sur l'équilibre monomères–micelles du tensioactif, dû à un effet de relargage, alors que les sels à plus longues chaînes participent en plus à la micellisation, déplaçant davantage l'équilibre du tensioactif.

Can. J. Chem. Downloaded from www.nrcresearchpress.com by 176.9.209.113 on 09/07/12
For personal use only.

Introduction

Electrolytes have an important effect on the properties of aqueous micellar solutions. Inorganic electrolytes generally lower the critical micellar concentration (cmc) of surfactants by salting out the monomers (1, 2), they modify the shape and size of the micelles (2–4) and they lower the interfacial tension between microemulsions and an aqueous or oil phase (5, 6). As the hydrophobic character of the electrolyte increases, hydrophobic interactions with the surfactant become increasingly important and with long-chain electrolytes, mixed micelles are formed (7). Similar effects are also observed for electrolytes in some hydro-organic mixtures.

One of the best ways of studying the effect of an additive on micellar systems is through thermodynamic functions of transfer of the additive from water to aqueous solutions of surfactants (8). Incidentally, in recent years, the amount of reliable data on such functions has increased remarkably (9–22). At the same time, theoretical models have been developed to simulate the trends in the transfer functions and extract, from the data, fundamental thermodynamic parameters for the mixed micelles (18–27). In this respect, much work has been done to understand the role of alcohols and light oils on micellar systems, but less is known on the transfer of electrolytes to such systems.

The chemical equilibrium model for the formation of mixed micelles introduced by Roux *et al.* (26, 27) assumes that the general trends in the transfer functions of non-electrolytes are mainly due to the pair-wise hydrophobic interactions between the additive and surfactant monomers, to a shift in the monomer–micelle equilibrium of the surfactant induced by the solute and to the distribution of the additive between the aqueous phase and the micelles. With simple electrolytes, no mixed micelles are formed, and the shift in cmc is therefore simply due to the interactions between monomers and to medium effects. In order to verify the importance of each effect and to distinguish between the additives which participate to the micellization from those which simply act on the aqueous medium, a systematic study was made of the functions of transfer of ammonium salts from water to aqueous solutions of a non-ionic surfactant, octyldimethylamine oxide (C_8DAO). Two approaches were adopted. In the first, the transfers of ammonium salts of the homologous series RNH_3Br were investigated. This series starts from an ionic surfactant, octylammonium hydrobromide (OctNH_3Br or OABr), to, decreasing gradually the chain length, finish with a simple salt effect. In the second, the symmetrical quaternary ammonium salts (R_4NBr) were chosen, since the more hydrophobic R_4NBr salts are known to salt in non-electrolytes in water (28).

The two thermodynamic properties that will be reported here are the volumes and the heat capacities. These two properties are easily measured concurrently and the data for the binary system water–C_8DAO are already available (29). Some cmc measurements were also made as a function of the concentration

[1]Paper written in the honour of J. A. Morrison who introduced J. E. Desnoyers to the field of calorimetry and thermodynamics.

[2]Present address: Institut National de la Recherche Scientifique, C.P. 7500, Sainte-Foy, Qué., Canada G1V 4C7.

of electrolytes or alcohols, such data being useful for the interpretation.

Experimental

The flow techniques used for volumes and heat capacities have been well described elsewhere (30–32). The densities and volumetric heat capacities of the ternary system were measured using the binary system (surfactant 2 in water W) as reference liquid, and the apparent molar quantities $V_{\phi,3}$ and $C_{p,\phi,3}$ of the additive 3 were calculated from these measurements (31). Any functions of transfer Y can then be obtained from these data by

$$[1] \quad \Delta Y_3(\mathrm{W} \rightarrow \mathrm{W} + 2) = Y_{\phi,3}(\mathrm{W} + 2) - Y_{\phi,3}(\mathrm{W})$$

This is a good approximation of the standard transfer functions, when the concentration of the additive is sufficiently close to the infinite dilution.

The ternary system solutions were prepared using the corresponding binary solutions of C_8DAO as solvent and the electrolytes added were held at a constant concentration of 0.05 mol kg^{-1} in all cases. This concentration represents a good compromise between a measurable quantity and a good approximation of infinite dilution.

For the cmc measurements, the surfactant solutions were initially prepared and diluted for each measurement using aqueous solutions of the additives as solvent. The data (densities for the added salts and conductivities for the alcohols) were plotted against the surfactant concentration. Assuming a linear behavior of the property studied on both sides of the cmc, the cmc values were taken as the intercept of the two linear sections.

The water used to prepare the solutions and as a reference liquid has been distilled, filtered, deionized, and degassed. Its specific conductivity was always lower than $2 \times 10^{-7}\ \Omega^{-1}$. The alcohols, 2-propanol (2-PrOH), *n*-butanol (BuOH), and *n*-pentanol (PenOH), from Fisher, were of ACS quality. They have been dried over molecular sieves and filtered.

C_8DAO (27) and OABr (33) have been prepared following methods described elsewhere.

Sodium chloride (NaBr), of ACS quality, was purchased from Fisher. It was dried 24 h under vacuum at 200°C and kept, also under vacuum, in the presence of P_2O_5.

With the exception of OABr, the primary ammonium salts of the series RNH_3Br, where R stand for methyl (Me), butyl (Bu), hexyl (Hex), and octyl (Oct), have been prepared and purified following methods described elsewhere (34).

Except for propyl (R = Pr), which comes from Pfaltz & Bauer, all the quaternary symmetric ammonium salts of the series R_4NBr have been purchased from Eastman Kodak. Their purification has been done according to methods described elsewhere (28).

The dibutylammonium bromide (Bu_2NH_2Br) has been synthesized in the same way as OABr, starting with dibutylamine purchased from J. T. Baker Chemical. The purity of the final product was checked by nmr spectroscopy.

The trimethylbutylammonium bromide was prepared by the action of 1-bromobutane, purchased from J. T. Baker Chemical, on trimethylamine provided by Aldrich Chemical in a 25% by weight aqueous solution. For the reaction, the amine was extracted and transferred with dried nitrogen to a solution of 1-bromobutane in benzene, in a reflux apparatus held at 65°C. The solution was stirred. After three recrystallizations in a 5/1 mixture of benzene – absolute ethanol, it was found by nmr spectroscopy that the product contained about 3% of impurities. After five more recrystallizations in the same mixture of solvents and a last one in a mixture of 20% absolute ethanol, 20% diethylether, and 60% acetone, the impurity peak was still present, but at a much smaller level.

Results and discussion

The electrolytes investigated in the present transfer functions to micellar systems vary significantly in nature: they go from simple electrolytes (NaBr) that remain essentially in the aqueous phase, to real surfactants (OABr) which form mixed micelles and bulky hydrophobic electrolytes (Pen_4NBr) which certainly have an affinity for the surfactants, but whose structures are not easily compatible with mixed micellar state. No simple model should therefore account for all of them. The model of Roux *et al.* (26, 27), based on the formation of mixed micelles, will be used as a starting point to see if it is possible through this model to distinguish between solutes that distribute themselves in the micelles and others where other types of interactions are responsible for the observed trends in the transfer functions.

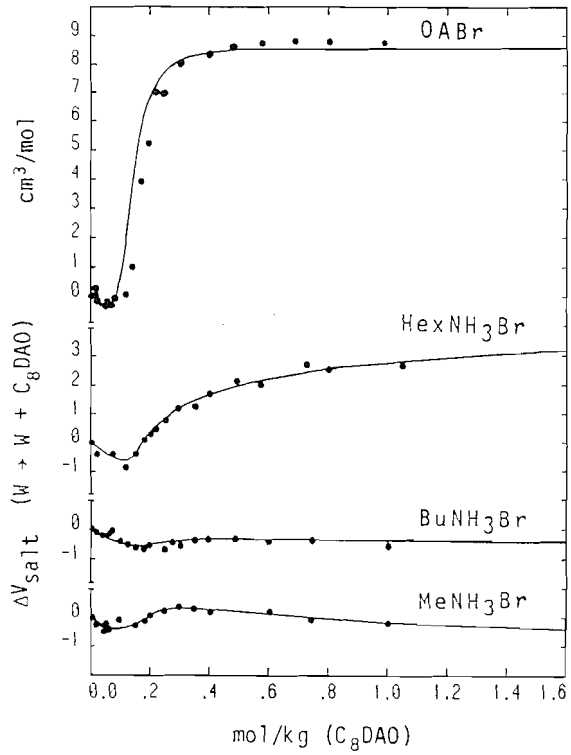

FIG. 1. Volumes of transfer of the salts of the series RNH_3Br from water to aqueous solutions of C_8DAO at 25°C; — simulations.

The original data for all the transfer functions are available elsewhere (38). Only trends will therefore be reported in graphical form and parameters derived from the data will be tabulated.

Homologous series RNH_3Br

The volumes and heat capacities of transfer of the salts of the homologous series RNH_3Br are shown, respectively, in Figs. 1 and 2. The lines represent the simulations using the model of Roux *et al.* (26, 27) with adjustment of K_D, the distribution constant, ΔY_3^M, the change in partial molar quantity Y of the electrolyte between its micellar and aqueous standard states, and $B_{Y,AB}$, the initial slope for pair-wise hydrophobic interactions between the monomers of the solute 2 (A) and those of the electrolyte 3 (B). The values obtained for these parameters are presented in Table 1, where are also given, m_3, the experimental molality of the electrolyte, and ΔH_3^M, the enthalpy change used in the expression of the relaxation term which is responsible for the maximum. The parameters for the binary system water–C_8DAO, for instance m_1 (cmc), n (aggregation number), and the various micellization functions ΔY_2^M, were taken from Desnoyers *et al.* (29).

The functions of transfer of OABr are qualitatively similar to those of alcohols (27) to the same surfactant. In Fig. 1, the

Can. J. Chem. Downloaded from www.nrcresearchpress.com by 176.9.209.113 on 09/07/12
For personal use only.

TABLE 1. Parameters used for the adjusted simulations of the volumes and heat capacities of transfer of the salts of the series RNH_3Br from water to aqueous solutions of C_8DAO at 25°C

Parameters	Value			
	$MeNH_3Br$	$BuNH_3Br$	$HexNH_3Br$	OABr
m_3 (mol kg^{-1})	0.05	0.05	0.05	0.05
ΔV_3^M (cm^3 mol^{-1})	−1.8	−0.75	4.0	8.3
K_D[a]	1.5	1.3	4.2	19.5
$B_{V,AB}$ (cm^3 mol^{-2} kg)	−1.0	−4.6	−5.2	−7.6
$\Delta C_{p,3}^M$ (J K^{-1} mol^{-1})	225	225	5.0	−245
ΔH_3^M (J mol^{-1})	0	0	1000[c]	1975[d]
K_D[b]	1.7	2.4	3.8	18.5
$B_{C,AB}$ (J K^{-1} mol^{-1} kg)	0.0	0.0	0.0	0.0

[a]Value obtained by adjustment of the volumes.
[b]Value obtained by adjustment of heat capacities; K_D is dimensionless but is here defined as the inverse of the molality and must be multiplied by 55.51 to be compared on a mole fraction scale (see ref. 27).
[c]Reference 33.
[d]Reference 35.

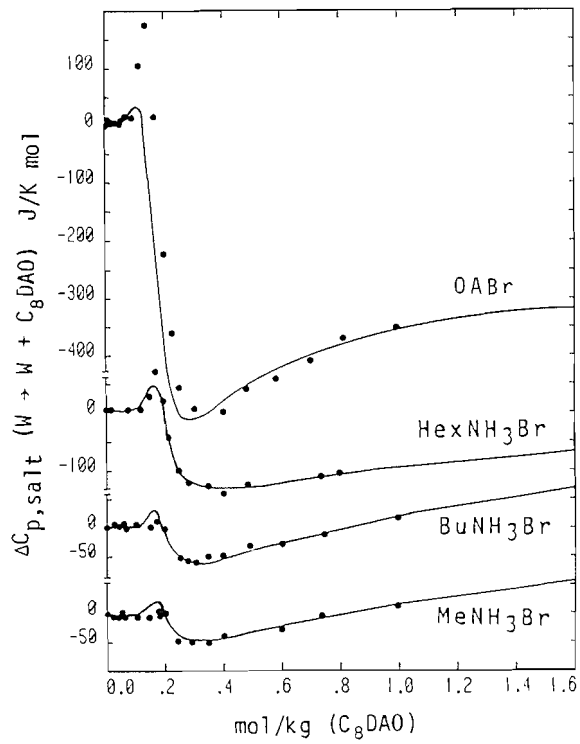

FIG. 2. Heat capacities of transfer of the salts of the series RNH_3Br from water to aqueous solutions of C_8DAO at 25°C; — simulations.

volumes present a small minimum due to the hydrophobic interactions between the monomers of C_8DAO and OABr in the pre-micellar region and a large positive ΔV_3^M which corresponds to the loss of hydrophobic hydration in the post-micellar region. Similarly, a typical large and negative $\Delta C_{p,3}^M$ is observed in Fig. 2. As the chain length of the amine salt decreases, the general trends of the transfer functions remain the same, but the change ΔY_3^M decreases significantly in magnitude. So, if, as expected, OABr participates in the micellization process, such a behaviour does not seem to exist for the two shorter electrolytes of the series.

An analysis of the parameters of Table 1 also leads to interesting conclusions. It is first worth noting that the distribution constants obtained either by the simulation of volumes or heat capacities are generally very close together, as it was the case for the transfer of alcohols (27). In the model of Roux *et al.*, K_D is ideally related to the inverse of the maximum solubility of monomers in water, which is, for a surfactant, given approximately by the cmc. As given by Desnoyers and co-workers (35), the cmc of OABr is 0.22 mol kg^{-1}. This would give a K_D value of 4.5, which is four times lower than the average value in Table 1. This implies that OABr monomers have more affinity for C_8DAO micelles than for their own micelles, which is however not really unexpected, since the electrostatic repulsion between the ionic heads are probably lower in mixed micelles OABr–C_8DAO than in OABr micelles. Also, the volume of transfer of OABr, 8.3 cm^3 mol^{-1}, is of the same magnitude as the volume of micellization of OABr, 8.1 cm^3 mol^{-1} (35). Therefore, the volume occupied by OABr in the micellar and mixed micellar states is the same, which is also expected, since the chain length of the two surfactants involved are the same. On the other hand, the heat capacity of transfer, −245 J K^{-1} mol^{-1}, is less negative than the heat capacity of micellization, −332 J K^{-1} mol^{-1} (35), probably as a result of the difference in the repulsion energies. This difference, which is important for heat capacities but not for the volumes, accounts for the large minimum in the heat capacities of transfer observed with OABr in Fig. 2 and not with the volumes in Fig. 1.

In the case of $HexNH_3Br$, the initial slope for the volumes is less pronounced, which indicates weaker hydrophobic interactions. The K_D and ΔY_3^M values are also smaller in magnitude, which indicates that $HexNH_3Br$ participates to the micellization, but less easily than OABr.

In the case of the two last electrolytes, ΔY_3^M are close to zero or even of opposite sign. This suggests that these electrolytes simply shift the monomer–micelle equilibrium, but do not form mixed micelles. The parameters extracted from the model have therefore little physical meaning in these cases, but it is nevertheless interesting to note that the model can be used to fit the data.

To give an overall view, the parameters obtained with the simulations were plotted, in Fig. 3, as a function of the number of carbon atoms of the hydrophobic chain of the electrolytes transfered. As expected, the initial slopes $B_{V,AB}$ increase in magnitude with the chain length, since the hydrophobic character of the amine salts increases with chain length.

Can. J. Chem. Downloaded from www.nrcresearchpress.com by 176.9.209.113 on 09/07/12
For personal use only.

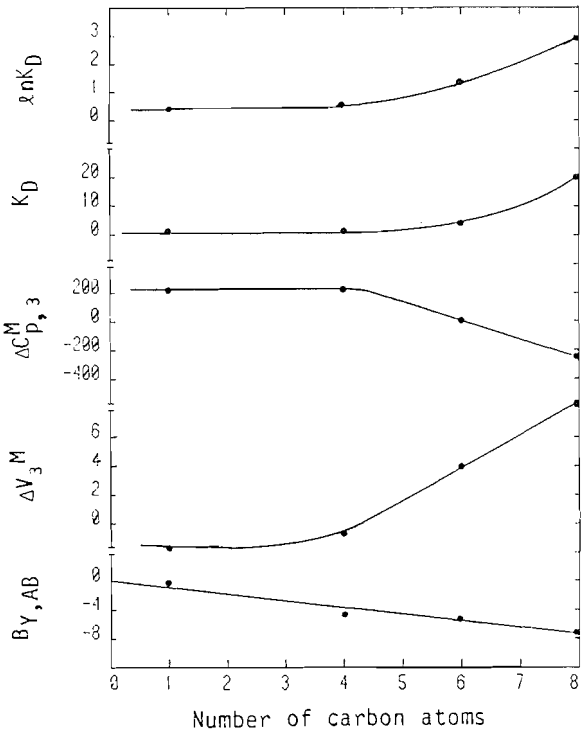

FIG. 3. Parameters obtained with the adjusted simulations of the functions of transfer of the salts of the series RNH_3Br at 25°C.

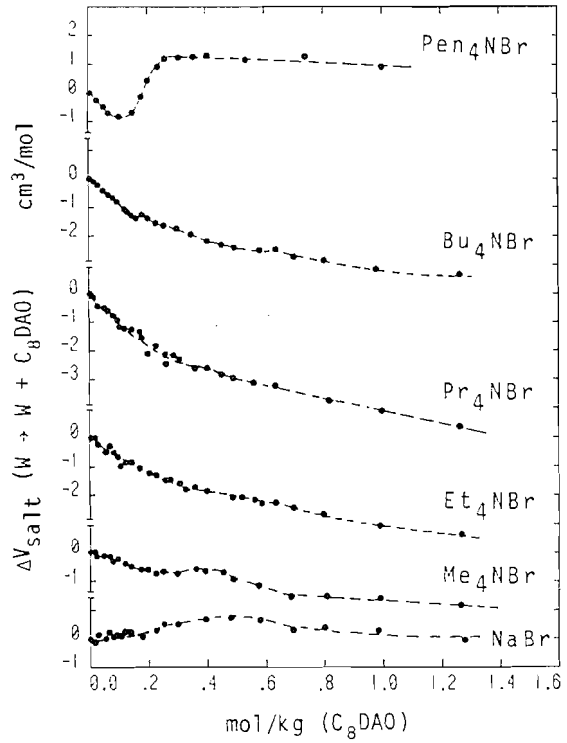

FIG. 4. Volumes of transfer of the salts of the series R_4NBr from water to aqueous solutions of C_8DAO at 25°C.

However, rather than to tend slowly to zero as the chain length decreases, the distribution constant values seem to level off to a small positive value. This is enhanced by the values of ln K_D which should rapidly tend to negative values when K_D tends to zero. This clearly shows that the model cannot be applied significantly to the salts of less than five carbon atoms, the residual value on K_D simply expressing the small electrostatic contributions for the monomer–micelle equilibrium displacement due for example to a salting-out effect. It is also apparent that ΔY_3^M of the short-chain electrolytes is not reflecting any more the change in property of the electrolyte when going from an aqueous medium to a condensed state in mixed micelles.

Symmetric salts R_4NBr

The volumes and heat capacities of transfer of NaBr and of the symmetric tetraalkylammonium salts from water to aqueous C_8DAO are respectively presented in Figs. 4 and 5. No simulation of the data with the mixed micelles model of Roux *et al.* were attempted with this series.

It can be seen that NaBr, which can only have a simple salt effect, behaves greatly like $MeNH_3Br$ in Figs. 1 and 2. The transfer functions simply go through an extremum around the cmc of C_8DAO, essentially due to electrostatic contributions to the monomer–micelle equilibrium displacement, to gradually come back around zero in higher concentration region.

For the ammonium salts, a maximum is also clearly defined in the volumes of Me_4NBr, but for the others, the hydrophobic interactions between R_4N^+ and the surfactant mask nearly completely any contribution due to the shift in monomer–micelle equilibrium. Also, it is only in the case of Pen_4NBr that evidence is seen in the volumes for the formation of mixed micelles. With heat capacities, as seen from the initial slopes close to zero, the contribution of hydrophobic interactions is much smaller. The influence of R_4NBr in shifting the monomer–micelle equilibrium is then more apparent, but as for the volumes, the formation of mixed micelles is strongly

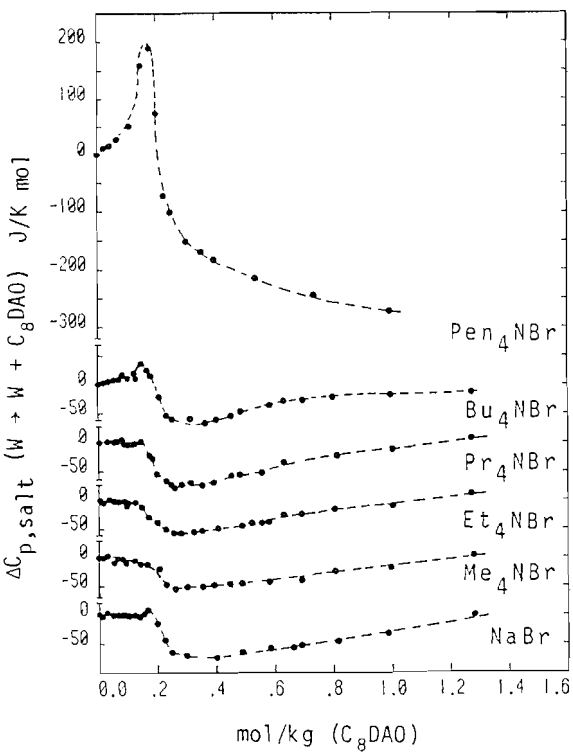

FIG. 5. Heat capacities of transfer of the salts of the series R_4NBr from water to aqueous solutions of C_8DAO at 25°C.

suggested only in the case of Pen_4NBr. It is interesting to note that the shift in equilibrium appears to vary little with hydrophobic character of the electrolytes when no mixed micelles are formed, which tends to confirm that the minimum is essentially due to electrostatic contributions.

In Fig. 6, the transfer volumes of Me_4NBr, Et_4NBr, and

Can. J. Chem. Downloaded from www.nrcresearchpress.com by 176.9.209.113 on 09/07/12
For personal use only.

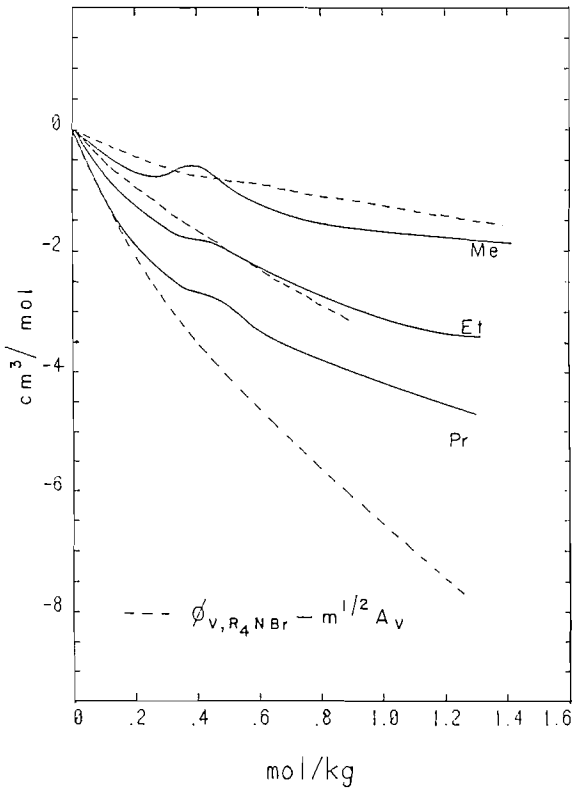

FIG. 6. Comparison of the volumes of transfer of Me_4NBr, Et_4NBr, and Pr_4NBr from water to aqueous C_8DAO with their partial molar volumes in water without Debye–Hückel contributions at 25°C. --- apparent molar volumes, from ref. 40; — volumes of transfer.

Pr_4NBr are compared to their apparent molar volumes in water (40) from which the Debye–Hückel contributions ($m^{1/2}A_V$) were substracted. For Me_4NBr and Et_4NBr, the behaviour in a micellar solution is not much different from the one in water, but it differs in an important way in the case of Pr_4NBr for which the transfer volumes tend to a less negative value than apparent molar volumes. This would mean that Pr_4N^+ is more affected by the presence of C_8DAO micelles than Me_4N^+ and Et_4N^+ and that Pr_4NBr probably participates to a small extent to the micellization process, which was not really apparent in Figs. 4 and 5.

If the extrema are related to the equilibrium displacement, there should be a relationship with the cmc displacements. In order to verify this, the values of d ln cmc/dm_3 of C_8DAO by R_4NBr salts and, for sake of comparison, those of OABr by the alcohols (ROH) were measured. These results are respectively given in Tables 2 and 3. For NaBr and most ammonium salts, there is a nearly constant displacement, which does not seem to exist in the case of alcohols, while with Pen_4NBr, the displacement is large and in the same direction as the effect of alcohols. From these results, we can therefore state that there are two kinds of equilibrium displacements: the first one, which would be very weak in the case of non-ionic polar solute such as alcohols, would be due to a medium or salting effect and the other to the participation of the additive to the micellization process. Also, since the model used for the simulations of the RNH_3Br salts does not take the salting effect explicitly into account, it is not surprising that a clear difference between the short chain salts and the longer ones seems to exist. Incidentally, this was not the case for the transfers of alcohols (27) where the progression of the parameters seemed to be continuous when the chain length was gradually increased.

TABLE 2. cmc displacements of C_8DAO by NaBr and the salts of the series R_4NBr at 25°C

Salt	Radius (Å)	d ln cmc/dm_3	σ
NaBr	1.0[a]	−0.72	0.02
Me_4NBr	2.7[b]	−0.43	0.05
Et_4NBr	3.3[b]	−0.34	0.02
Pr_4NBr	3.7[b]	−0.29	0.02
Bu_4NBr	4.2[b]	−0.81	0.03
Pen_4NBr	4.4[b]	−3.93	0.05

[a]Reference 36.
[b]Reference 37.

An approach similar to the one of Roux *et al.* (26) for mixed micelles can be used to simulate the salting effect on the transfer functions of electrolytes to micellar solutions. This model is based on the mass-action model of Desnoyers *et al.* (29) for the binary systems of non-ionic surfactants, where a one-step process for the micellization is assumed. Then, if α_0 represents the fraction of surfactant molecules A which stay in free monomer form and if m_2 is the molality (mol kg^{-1}) of the surfactant, the concentration of the monomers A is $\alpha_0 m_2$ and that of the micelles M is $(1 - \alpha_0)m_2/n$, n being the aggregation number. The equilibrium constant is therefore given as:

$$[2] \quad K_M = \frac{[M]}{[A]^n} = \frac{(1 - \alpha_0)}{\alpha_0{}^n n m_2{}^{n-1}}$$

where the activity coefficients of species are all neglected. This equation can be expressed in the logarithmic form as:

$$[3] \quad -\frac{1}{n} \ln K_M = \ln \alpha_0 m_2 - \frac{1}{n} \ln [(1 - \alpha_0)m_2/n]$$

When K_M and n are known, this equation can be solved, by a successive approximation method, to find α_0 for any given m_2. The value for K_M is obtained from the inflexion point in α_0 as a function of m_2. This point is defined as $(\partial^2\alpha_0/\partial m_2{}^2)_{m_1} = 0$, which allows to find α_1, α_0 at the inflexion concentration m_1, and to relate α_1 to the aggregation number by the equation:

$$[4] \quad \alpha_1 = \frac{n}{n-1}[1 - (1/2n)^{1/2}]$$

In the mixed micelles model, the equilibrium eq. [3] was modified, to account for the shift in K_M induced by the presence of the additive in the micelles. Similarly, eq. [3] should be modified in the presence of an electrolyte to account for the salting effect on the surfactant monomers. By analogy with the salting effects on alcohols (39), the activity coefficient of the monomers A is related to the concentration of the electrolyte B through a Setchenov constant $B_{G,AB}$ and the final equation for the ternary system has therefore the form:

$$[5] \quad -\frac{1}{n} \ln K_M = \ln \alpha m_2 - \frac{1}{n} \ln [(1 - \alpha)m_2/n] + 2B_{G,AB}m_3$$

where the lack of subscript 0 on α indicates that it is a ternary system. Assuming that K_M is the same as for the binary system, eq. [5] can be solved in the same way as eq. [3]. Because of the last term, the values for α are different from α_0, the difference $(\alpha_0 - \alpha)$ expressing the surfactant monomer-micelles equilibrium displacement.

The expression for the volumes of transfer would now have

Can. J. Chem. Downloaded from www.nrcresearchpress.com by 176.9.209.113 on 09/07/12
For personal use only.

TABLE 3. cmc displacements of OABr by alcohols at 25°C

Alcohol	nb of carbon atoms	d ln cmc/dm_3	σ
2-PrOH	3	−0.12	0.2
PenOH	5	−3.0	0.7
HexOH	6	−6.1	2.0

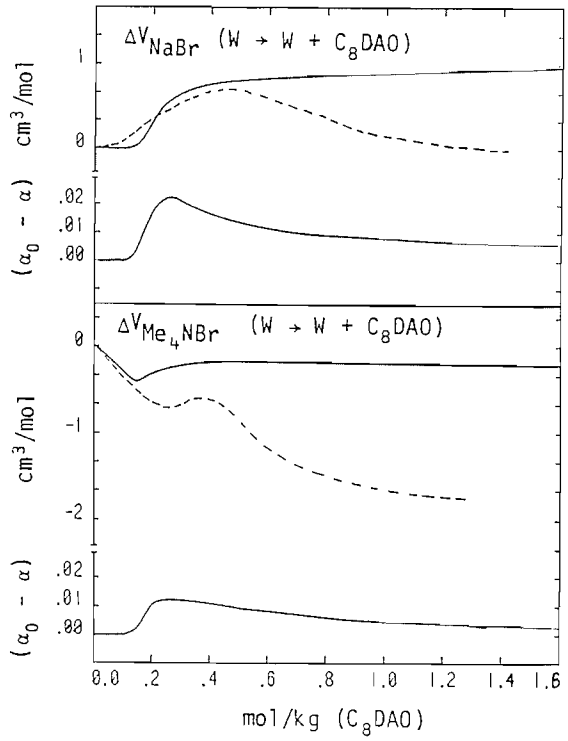

FIG. 7. Simulations of the volumes of transfer of NaBr and Me_4NBr from water to aqueous solutions of C_8DAO at 25°C; --- experimental data; — simulations.

the form:

$$[6]\quad \Delta V_3(\mathrm{W} \rightarrow \mathrm{W}+2) = 2\alpha m_2 B_{V,\mathrm{AB}} + (\alpha_0 - \alpha) m_2 \Delta V_2^M / m_3$$

where $B_{V,\mathrm{AB}}$, the initial slope related to the interactions between the surfactant monomers A and the salt B, is essentially the pressure derivative of $B_{\mathrm{G,AB}}$ and ΔV_2^M, the micellization volume of the surfactant expressing the change between the micellar and aqueous monomer standard states.

The Setchenov constant is directly related to the variation of the cmc with m_3 (25):

$$[7]\quad 2B_{\mathrm{G,AB}} = \mathrm{d}\ln \mathrm{cmc}/\mathrm{d}m_3$$

Therefore, using the experimental values for $B_{\mathrm{G,AB}}$, α can be calculated from eq. [5] and α_0 from eq. [3]. The difference $(\alpha_0 - \alpha)$ and the simulated volumes of transfer of NaBr and Me_4NBr are shown in Fig. 7 and compared with the experimental data. While, as expected, $(\alpha_0 - \alpha)$ goes through a maximum in the micellization region, the simulated volumes of transfer do not go through a maximum, but essentially level off beyond the cmc region. A maximum could of course be generated by introducing an interaction term between the electrolyte and the micelles, but as more adjustable parameters are added the model becomes more empirical. Therefore, although the present simple approach does indicate that the

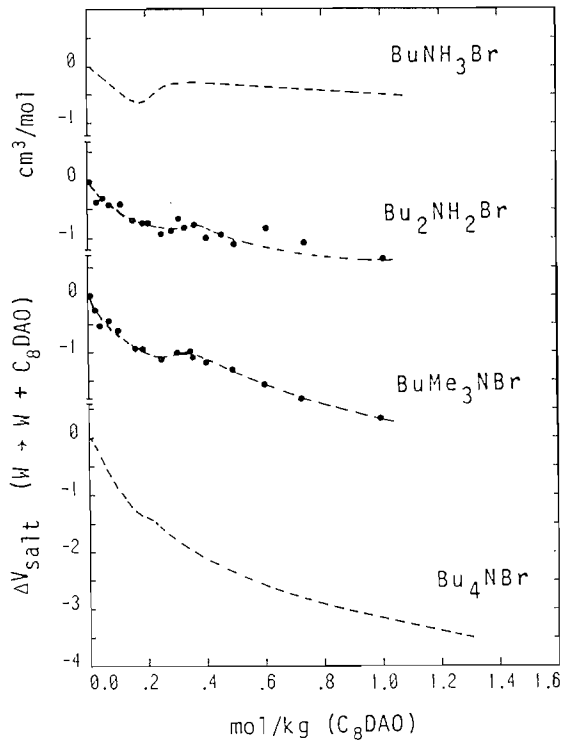

FIG. 8. Volumes of transfer of ammonium salts from water to aqueous solutions of C_8DAO at 25°C.

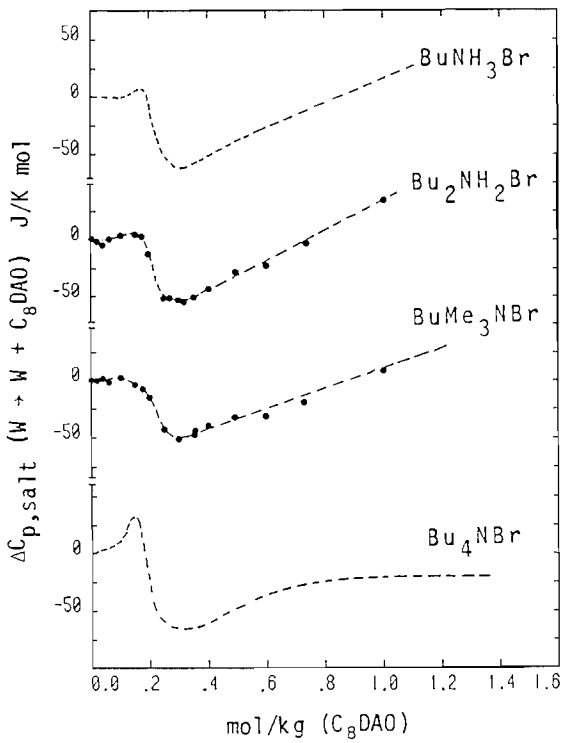

FIG. 9. Heat capacities of transfer of ammonium salts from water to aqueous solutions of C_8DAO at 25°C.

observed trends for the transfer of electrolytes to micellar systems are related to the salting out of surfactant monomers, the theory, at present, is only of qualitative value. It can, however, be mentioned that for the salts which do not form mixed micelles, the change in the micellar region of transfer functions could be interpreted as a modification of the solvent in the presence of the micelles, this contribution being probably

Can. J. Chem. Downloaded from www.nrcresearchpress.com by 176.9.209.113 on 09/07/12
For personal use only.

always present, but masked when mixed micelles are formed. This idea is supported by the constant residual values on ΔY_3^M for the two shorter electrolytes in Fig. 3.

Steric hindrance effect

In Figs. 8 and 9 are shown respectively the volumes and heat capacities of transfer of Bu_2NH_2Br and $BuMe_3NBr$ from water to aqueous C_8DAO. For the sake of comparison, the curves of $BuNH_3Br$ and Bu_4NBr have also been reproduced from previous figures.

The dependance of ΔY_3 ($W \rightarrow W + C_8DAO$) on surfactant concentration are similar for $BuNH_3Br$, Bu_2NH_2Br, and $BuMe_3NBr$ and slightly different for Bu_4NBr in the post-micellar region. On the other hand, Bu_2NH_2Br has the same number of carbon atoms as OABr and half as many as Bu_4NBr. This confirms that symmetry plays a very important role in micelle formation. OABr is a true surfactant which readily forms mixed micelles, Bu_4NBr barely shows tendencies to associate with the micelles and the three other electrolytes in Figs. 8 and 9 primarily have a medium effect on the transfer functions.

Conclusion

The transfer of electrolytes from water to micellar systems fall into three categories. Long-chain ionic surfactants readily form mixed micelles with non-ionic surfactants. The critical chain length for the formation of mixed micelles of course depends on the nature of the non-ionic surfactant, but is of the order of 5 to 6 carbon atoms. Inorganic electrolytes primarily shift the cmc of the micellar system by salting out the monomers. This salting-out effect seems, as a first approximation, to be independent of chain length. Hydrophobic electrolytes, which have chain lengths too short to form mixed micelles or which are bulky, do interact with the surfactant monomers (hydrophobic interactions), but do not show tendencies to associate with the surfactant monomers, until the cations become very hydrophobic (Pen_4N^+). See Denoyers and Arel (34) for a discussion of these effects. Bu_4NBr, and possibly Pr_4NBr, are borderline electrolytes in that they are quite hydrophobic, but show only a small tendency to associate with C_8DAO.

A complete theory for the transfer of organic electrolytes from water to micellar systems would have to include terms for the formation of mixed micelles, for the salting out of monomers by the ionic head, for hydrophobic interactions between the hydrophobic tail of the electrolyte and the surfactant monomers and possibly for the interaction between the electrolyte and the neutral micelles or a change in the solvent in the presence of micelles.

Acknowledgements

The authors are grateful to the Natural Sciences and Engineering Research Council of Canada and to the Quebec Ministry of Education, through its FCAR program, for financial assistance. Grateful acknowledgement is also given to Dr. A. H. Roux of l'université de Clermont, for his suggestions on the treatment of the salts effects.

1. N. NISHIKIDO and R. MATUURA. Bull. Chem. Soc. Jpn. **50**, 1690 (1977).
2. H. SUZUKI. Bull. Chem. Soc. Jpn. **49**, 1470 (1976).
3. D. A. DOUGHTY. J. Phys. Chem. **87**, 5286 (1983).
4. S. OZEKI and S. IKEDA. J. Coll. Interface Sci. **77**, 219 (1980).
5. L. M. PRINCE (*Editor*). Microemulsions: theory and practice. Academic Press, New York. 1977.
6. K. L. MITTAL (*Editor*). Micellization, solubilization and microemulsions. Vols. 1, 2. Plenum, New York. 1977.
7. J. F. SCAMEHORN (*Editor*). Phenomena in mixed surfactant systems. Am. Chem. Soc. Symp. Ser. No. 311 (1986).
8. G. PERRON, R. DELISI, I. DAVIDSON, S. GENEREUX, and J. E. DESNOYERS. J. Coll. Interf. Sci. **79**, 432 (1981).
9. J. LARA, G. PERRON, and J. E. DESNOYERS. J. Phys. Chem. **85**, 1600 (1981).
10. J. LARA, L. AVEDIKIAN, G. PERRON, and J. E. DESNOYERS. J. Solution Chem. **10**, 301 (1981).
11. J. E. DESNOYERS, D. HETU, and G. PERRON. J. Solution Chem. **12**, 427 (1983).
12. R. BURY and C. TREINER. J. Coll. Interf. Sci. **103**, 1 (1985).
13. M. MANABE, S. KIKUCHI, S. KATAYAMA, S. TAKUNAGA, and M. KODA. Bull. Chem. Soc. Jpn. **57**, 2027 (1984).
14. V. MAJER, A. H. ROUX, G. ROUX-DESGRANGES, and A. VIALLARD. Can. J. Chem. **61**, 139 (1983).
15. G. ROUX-DESGRANGES, A. H. ROUX, J.-P. E. GROLIER, and A. VIALLARD. J. Solution Chem. **11**, 357 (1982).
16. F. YAMASHITA, G. PERRON, J. E. DESNOYERS, and J. C. T. KWAK. ref. 7, chap. 6, p. 79.
17. D. HETU, A. H. ROUX, and J. E. DESNOYERS. J. Coll. Interf. Sci. In press.
18. R. DELISI, C. GENOVA, and V. T. LIVERI. J. Coll. Interf. Sci. **95**, 428 (1983).
19. R. DELISI and V. T. LIVERI. Gaz. Chim. Ital. **113**, 371 (1983).
20. R. DELISI, C. GENOVA, R. TESTA, and V. T. LIVERI. J. Solution Chem. **13**, 121 (1984).
21. R. DELISI, V. T. LIVERI, M. CASTAGNOLO, and A. INGLESE. J. Solution Chem. **15**, 23 (1986).
22. R. DELISI, A. LIZZIO, S. MILIOTO, and V. T. LIVERI. J. Solution Chem. **15**, 623 (1986).
23. S. D. CHRISTIAN, E. E. TUCKER, and E. H. LANE. J. Coll. Interf. Sci. **84**, 423 (1981).
24. E. E. TUCKER and S. D. CHRISTIAN. Faraday Symp. Chem. Soc. **17**, 11 (1982).
25. C. TREINER. J. Coll. Interf. Sci. **90**, 444 (1982).
26. A. H. ROUX, D. HÉTU, G. PERRON, and J. E. DESNOYERS. J. Solution Chem. **13**, 1 (1984).
27. D. HÉTU, A. H. ROUX, and J. E. DESNOYERS. J. Solution Chem. **16**, 529 (1987).
28. J. E. DESNOYERS, G. E. PELLETIER, and C. JOLICOEUR. Can. J. Chem. **43**, 3232 (1965).
29. J. E. DESNOYERS, G. CARON, R. DELISI, D. ROBERTS, A. ROUX, and G. PERRON. J. Phys. Chem. **87**, 1397 (1983).
30. P. PICKER, E. TREMBLAY, and C. JOLICOEUR. J. Solution Chem. **3**, 377 (1974).
31. L. AVEDIKIAN, G. PERRON, and J. E. DESNOYERS. J. Solution Chem. **4**, 331 (1975).
32. P. PICKER, P.-A. LEDUC, P. PHILIP, and J. E. DESNOYERS. J. Chem. Thermodyn. **3**, 631 (1971).
33. P.-A. LEDUC, J.-L. FORTIER, and J. E. DESNOYERS. J. Phys. Chem. **78**, 1217 (1974).
34. J. E. DESNOYERS and M. AREL. Can. J. Chem. **45**, 359 (1967).
35. R. DELISI, G. PERRON, and J. E. DESNOYERS. Can. J. Chem. **58**, 959 (1980).
36. T. C. WADDINGTON. Trans. Faraday Soc. **62**, 1482 (1966).
37. N. DESROSIERS and J. E. DESNOYERS. Can. J. Chem. **54**, 3800 (1976).
38. D. HÉTU. Ph.D. Thesis, Sherbrooke. 1986.
39. J. A. DESNOYERS, M. BILLON, S. LEGER, G. PERRON, and J.-P. MOREL. J. Solution Chem. **5**, 681 (1976).
40. W.-Y. WEN and S. SAITO. J. Phys. Chem. **68**, 2639 (1964).

Can. J. Chem. Downloaded from www.nrcresearchpress.com by 176.9.209.113 on 09/07/12
For personal use only.

The low temperature structure of ethylene monolayers physisorbed on the graphite basal plane

MICHAEL A. MOLLER
Department of Chemistry, McMaster University, Hamilton, Ont., Canada L8S 4M1

AND

MICHAEL L. KLEIN
Department of Chemistry, University of Pennsylvania, Philadelphia, PA 19104-6323, U.S.A.

Received August 20, 1987

This paper is dedicated to Professor James A. Morrison

MICHAEL A. MOLLER and MICHAEL L. KLEIN. Can. J. Chem. **66**, 774 (1988).

The low temperature structure of low density ethylene monolayers physisorbed on the graphite basal plane has been examined by molecular dynamics calculations with an intermolecular potential based on atom–atom interactions. The simulations predict that the ethylene molecules are arranged in a herringbone with a centered rectangular unit cell of dimensions 4.95 Å × 7.05 Å. In this structure, the molecular C=C axes are parallel to the surface, and are oriented at 60° angles from each other, while the molecular planes are tilted some 55° from the plane of the surface. The structure was found to be essentially independent of the assumed corrugation of the graphite surface.

MICHAEL A. MOLLER et MICHAEL L. KLEIN. Can. J. Chem. **66**, 774 (1988).

Utilisant des calculs de dynamique moléculaire avec un potentiel intermoléculaire basé sur des interactions atome–atome, on a étudié la structure à basse température de monocouches d'éthylène de faible densité adsorbées physiquement sur le plan de base du graphite. Les simulations prédisent que les molécules d'éthylène seront arrangées sous une forme en arête de poisson possédant une unité cellulaire rectangulaire centrée de dimensions 4,95 × 7,05 Å. Dans cette structure, les axes moléculaires C=C sont parallèles à la surface et sont orientés à des angles de 60° les uns des autres, alors que les plans moléculaires sont déplacés de 55° par rapport au plan de la surface. On a trouvé que la structure est essentiellement indépendante du plissement supposé de la surface du graphite.

[Traduit par la revue]

1. Introduction

There has been a significant amount of effort, both experimental and theoretical, to characterize the phases of simple molecules adsorbed on graphite, and to construct the corresponding phase diagrams. To date a wide variety of structures have been identified. Much of this diversity in structure is due to the shape of the adsorbed molecule, and molecules with similar shapes often produce similar structures and similar phase diagrams. For example, small, aspherical molecules such as N_2 (1), C_2H_4 (2), C_2H_6 (3), C_2N_2 (4), and C_6H_{14} (5) all form herringbone structures on graphite at low coverages. For polar molecules like N_2 and C_2N_2, the herringbone structure arises from the electrostatic quadrupole–quadrupole interactions, whereas for the hydrocarbons it is a consequence of aspherical shape.

Computer simulation molecular dynamics (MD), or Monte Carlo (MC) calculations are particularly suited to the study of physisorbed *molecular* systems. Such simulations can give additional details about the structures of the various phases that are not readily obtainable from diffraction experiments. Molecular dynamics has the added advantage that it can be used to study time-dependent properties such as vibrational frequencies, and hence dynamical properties of adsorbed molecules. In combination with scattering and thermodynamic experiments, MD is thus a powerful technique for the study of physisorbed systems (6).

One molecule, ethylene (C_2H_4), has been the object of considerable interest since the discovery of its incomplete wetting (7) and continuous melting (8) behavior on graphite. Ethylene adsorbed on graphite has been examined by several experimental methods, including both elastic and inelastic neutron scattering (9, 10), synchrotron X-ray diffraction (11, 12), nuclear magnetic resonance (nmr) (13, 14), and calorimetry (8, 15).

These experiments have shown that overlayers of ethylene form two main structural phases at low temperature. If we define a coverage of $n = 1.0$ to be a registered triangular $\sqrt{3} \times \sqrt{3}$ R30° monolayer, then at coverages below $n = 0.8$ ethylene forms the so-called low density (LD) phase. Published diffraction data suggest a triangular lattice for this phase, with a nearest neighbor (n-n) distance of 4.65 Å (9). For $n > 1.05$, ethylene forms the high-density (HD) phase, which is a triangular lattice with n-n distance of 4.22 Å. Calculations suggest that in the HD phase the C=C bonds are aligned perpendicular to the plane of the surface, while in the LD phase the C=C bonds are aligned parallel to the plane of the surface (2). Between $n = 0.8$ and $n = 1.05$ a two-phase (HD + LD) region exists (9, 15). A variety of experiments indicate that both the LD and HD phases have a transition at about 35 K from an ordered herringbone to a phase in which the molecules are rotationally disordered (13–15).

Molecular dynamics has been used previously to probe the behavior of C_2H_4 on graphite (2, 16, 17). These calculations employed atom–atom intermolecular potentials fitted to bulk crystal properties (18), and admolecule–surface interactions (19) fitted to the heat of adsorption (2). The low-temperature structure, the rotator phase, and melting have all been studied (2, 16, 17) with a flat surface model, which ignored the corrugation of the graphite basal plane (19). The calculated low temperature structure was not in agreement with the close-packed triangular lattice deduced for the experimental measurements mentioned above. In particular, the structure was found to be based on a two-molecule centered rectangular cell, approximately $1 \times \sqrt{2}$ rather than $1 \times \sqrt{3}$ characteristic

Can. J. Chem. Downloaded from www.nrcresearchpress.com by 176.9.209.113 on 09/07/12
For personal use only.

Can. J. Chem. Downloaded from www.nrcresearchpress.com by 176.9.209.113 on 09/07/12
For personal use only.

of a triangular lattice. Since these earlier calculations were performed on a flat surface model, the question arises as to whether or not it is the surface corrugation of graphite that causes LD ethylene to adopt triangular $1 \times \sqrt{3}$. We tackle this question with new MD simulations, which explicitly include the corrugation of the graphite surface (19).

2. MD calculations

To examine the effect of the surface corrugation on the low temperature structure, MD simulations were performed on three different models. In most of the simulations, the intermolecular potential was taken as the sum of individual atom–atom exp-6 potentials (8), with the same set of Williams (W) parameters as in the previous study (2). One simulation was performed using a different set of potential parameters, which was taken from the methane potential of Severin and Tildesley (ST) (20). The molecule–surface potentials were also taken as the sum of atom–atom potentials, which were converted to Lennard-Jones (L-J) form and approximated by a Fourier expansion as in the method of Steele (19), keeping the first two terms of the expansion. This procedure gives an analytic form for the *atom*-corrugated surface potential, which contains the two terms $V_0(z)$ and $V_1(x,y,z)$. Here, V_0 is the flat surface approximation for the total potential, and V_1 is a correction term that contains the lateral variation in the potential due to the corrugation. All of the MD calculations were run at 20 K for 20 ps, after a short equilibration period. We have employed the same MD algorithm as in earlier work (2), and a timestep of 2.5 fs, which gave excellent energy conservation.

For the simulations on the flat surface ($V_1 = 0$), we used a system of 96 molecules that was started in a triangular lattice at a coverage of $n = 0.84$. The system was kept at constant spreading pressure, which meant that the sides of the box were allowed to fluctuate with time (21). In this way, the system could relax to its equilibrium structure (2).

The simulations on the corrugated surface ($V_1 \neq 0$) could not be run at constant spreading pressure. Systems with periodic boundary conditions require the potential to be continuous at the boundaries. Therefore MD studies of the corrugated surface model were run at constant area. This was a serious limitation for a simulation that was supposed to allow the system to relax to its equilibrium configuration (*including surface coverage*). So, instead of using a full simulation box, we employed a patch of ethylene molecules placed at the center of a box of fixed area approximately double the size of the patch. The patch contained 108 molecules in a box of dimensions $20 \times 12\sqrt{3}a$, where $a = 4.26$ Å is the unit cell length for the $\sqrt{3} \times \sqrt{3}$ R30° triangular structure. The starting configuration for the molecules in this simulation was the equilibrated structure from the MD calculations on the flat surface.

It has been noted (22) that the Steele method (19) of incorporating the corrugation does not take into account the fact that the carbon atoms in the graphite basal plane are more polarizable within the plane of the surface than normal to it. It was estimated (22) that the actual size of the corrugation is almost double the amount given by the Steele method. Joshi and Tildesley (23) made a thorough study of the melting of N_2 on graphite, and have derived a more realistic form for the corrugated surface potential, which we have employed here.

Finally, we mention that we have made no allowance for the so-called substrate mediated McLachlan interaction, which has been shown to be important for atomic systems (24, 25). In the latter case, these effective 3-body forces weaken the adatom–adatom interactions by about 15%. It remains to adapt the theory to treat molecular as opposed to atomic systems.

3. Results and discussion

The MD results for the different systems are compared with each other and with the experimental results in Table 1. The most important finding is that the corrugation seems to have little effect on the structure. We now discuss each system separately.

3.1 Flat surface

The simulation on the flat surface was essentially a duplication of the previous work (2), but here we present more details. In the present calculations, the system rapidly evolved from a triangular lattice to a rectangular unit cell in a time of 4 ps. We therefore present averages over the last 5-ps segment of the 10-ps MD run. The calculated molecule–surface potential energy E(m-s) is very close to the experimental value of −20.3 kJ/mol (16), corrected to 20 K (see Table 1). Figure 1 shows the radial distribution function $G(R)$ for the centers of mass of the molecules. The inset shows $G(Z)$, the distribution of the carbon atoms of the ethylene in the z-direction, which is normal to the surface. The $G(R)$ has its first three peaks at 4.30, 4.92, and 7.05 Å, which correspond to the three smallest intermolecular distances in the quasi two-dimensional solid. In a triangular lattice, the first two peaks would be degenerate.

Figure 2(a) shows the instantaneous configuration of the system at the end of the simulation at 20 K. The system forms a stable herringbone, with individual molecules exhibiting only a small amount of rotational (librational) motion within the plane of the surface. From this snapshot, and from the $G(R)$ peak positions, we can deduce the following structure for the solid. The ethylene formed a herringbone structure, with a rectangular unit cell of dimensions 4.92 Å × 7.05 Å, corresponding to a coverage of $n = 0.904$, or 0.0577 Å^{-2}.

The C=C bonds of the molecules were aligned parallel to the surface plane, since $G(Z)$ shows only one peak. For the molecule at the corner of the unit cell, the molecular axis makes an angle of 30° with $\boldsymbol{a}$. The molecular axis of the molecule at the center of the cell makes an angle of −30° with $\boldsymbol{a}$. The planes of the molecules do not lie flat (parallel to the surface), but are inclined an average of 62° from the plane of the surface. This compares to a tilt of 35°, found from static calculations (9) that had assumed a triangular lattice at a coverage of $n = 0.85$. The higher tilt is likely a consequence of the higher coverage in our system. In the MD structure, the ethylene molecular axes make an angle of 60° with each other, as opposed to 90° expected for an ideal herringbone that arises from interacting point quadrupoles.

The above structure would produce a strong neutron scattering peak at 1.56 Å^{-1}, and weak ones at 1.78, 2.55, and 2.96 Å^{-1}. The peak position of 1.56 Å^{-1} agrees exactly with the experimental result (9), which was used to index the triangular lattice at a coverage of 0.83. The peak at 1.78 Å^{-1} was not observed. Also, the experiments show only a single peak at 2.70 Å^{-1}, whereas the present simulations at $n = 0.9$ have a double peak, due to the rectangular unit cell.

In summary, these new calculations confirm that the calculated low temperature LD monolayer structure for ethylene on graphite is not triangular.

3.2 Corrugated surface

The MD simulation on the corrugated surface was run for 20 ps. The motivation for this was that we wished to run long

TABLE 1. Molecular dynamics results for ethylene on graphite

Potential	Surface potential	T (K)	E(m-m) (kJ/mol)	E(m-s) (kJ/mol)	Plane tilt (°)	a (Å)	b (Å)	n	Peak position (Å^{-1})
W	Flat	21	−8.01	−20.1	62	4.92	7.05	0.90	1.56, 1.78
W	Corrugated	20	−7.72	−20.6	55	4.90	7.06	0.91	1.56, 1.78
W	Anisotropic	20	−7.69	−20.6	54	4.98	7.03	0.90	1.55, 1.79
ST	Flat	21	−6.80	−20.8	13	5.35	7.35	0.80	1.45, 1.71
Expt[a]		10		−20.3[b]	35	4.65	8.05	0.84	1.57

[a]Data taken from ref. 9.
[b]Data taken from ref. 16 and corrected to 20 K.

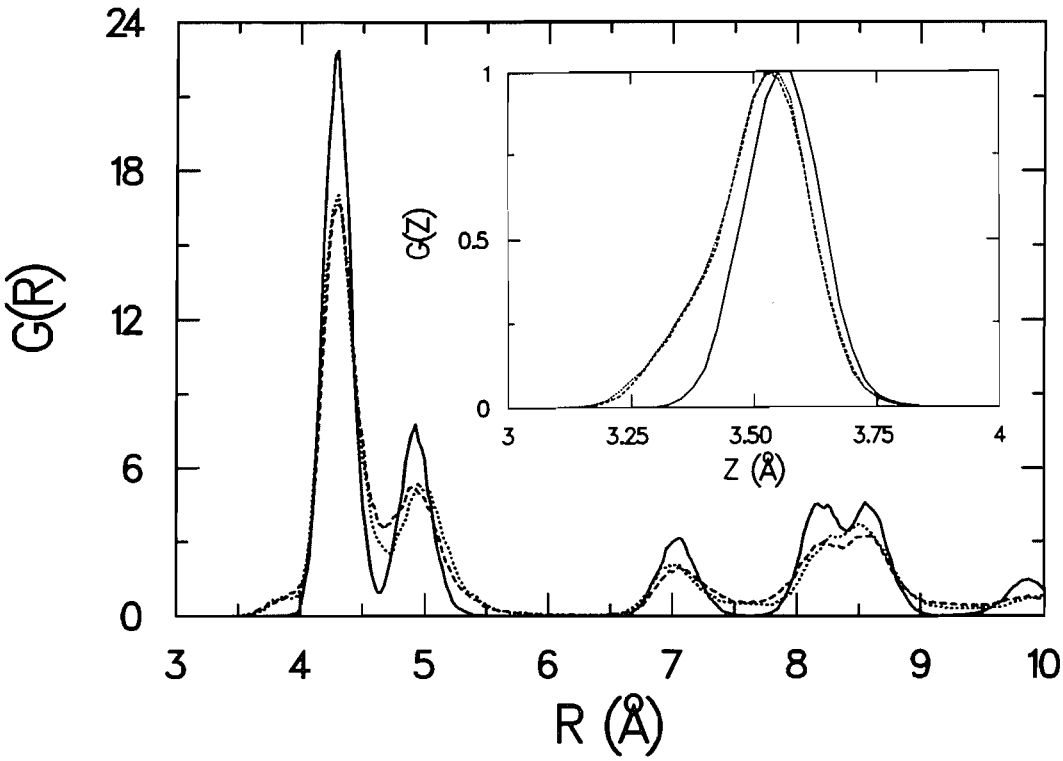

FIG. 1. Pair distribution function $G(R)$ for ethylene overlayers physisorbed on graphite. The inset shows the single particle distribution $G(Z)$ for the carbon atoms of the ethylene molecules in the direction perpendicular to the surface. The solid curve is for the system on a flat surface, the dashed curve is for the patch on a corrugated surface, and the dotted curve is for the patch on a corrugated surface with the anisotropic potential.

enough to allow for local relaxation of molecular orientations, etc. The determination of the true equilibrium structure of a patch would likely require a prohibitively long computation.

The results of the simulation on the corrugated surface are presented in Table 1. Once again, E(m-s) is very close to the experimental value. In this case, by considering only those molecules in the center of the patch, the molecule–molecule potential energy E(m-m) has been adjusted to approximately eliminate the edge effects. Figure 1 shows the $G(R)$ for the centers of mass, and $G(Z)$ for the carbon atoms of the ethylene. Figure 2(b) is a snapshot of the system at the end of the simulation. The $G(R)$ for the corrugated surface is virtually identical to the $G(R)$ for the flat surface. The peaks are somewhat more spread out because of the molecules at the edge of the patch. Unlike the flat surface model, $G(Z)$ is asymmetric and displaced inward, because the ends of the ethylene molecules tend to settle into the centers of the graphite hexagons. Since the ethylene is incommensurate, the effect of the corrugation to some extent is averaged out.

The small shoulder in $G(R)$ at about 3.85 Å deserves mention. This shoulder is due to pairs of canted molecules with their molecular planes and C=C axes aligned parallel to each other. In Fig. 2(b), there are several pairs of molecules arranged in this way. This happens near the edge of the patch, where each molecule has an incomplete set of only a few neighbors.

The $G(R)$ peak positions are at 4.30, 4.90, and 7.06 Å. This corresponds to a centered rectangular unit cell of dimensions 4.90 Å × 7.06 Å, which is a coverage of $n = 0.907$. It is otherwise identical to the unit cell of the flat surface simulations. From the snapshot of the system in Fig. 2(b), it can be seen that the ethylene structure is rotated about 4° with respect to the graphite lattice. This particular structure would produce a strong neutron scattering peak at 1.56 Å^{-1}, and weak ones at 1.78, 2.55, and 2.96 Å^{-1}. Such a pattern is indistinguishable from the pattern deduced from the flat surface simulations.

Because the structures for the flat and corrugated surfaces were so similar, it was natural to consider whether the latter calculation was run for sufficiently long times or if initiating the corrugated surface calculations from the final flat surface structure had prejudiced the calculations. Accordingly, two new

Can. J. Chem. Downloaded from www.nrcresearchpress.com by 176.9.209.113 on 09/07/12
For personal use only.

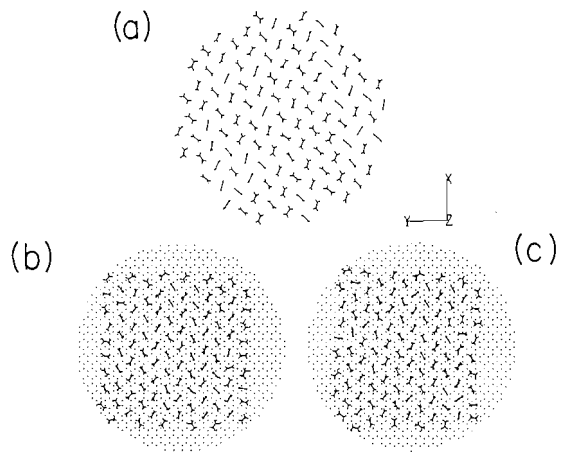

FIG. 2. Top views of the instantaneous configurations for each system at the end of the simulation runs; (a) a section of the system on the flat surface, (b) the patch on the corrugated surface, and (c) the patch on the corrugated surface with the anisotropic potential. The dots represent the positions of the carbon atoms in the first layer of the graphite.

calculations were performed on the corrugated surface starting from structures that were dilated by 2% and 5% in both the x and y directions. In both cases, the MD calculation yielded the same final structure as in Table 1.

3.3 Corrugated surface (anisotropic potential)

The above results show that the surface corrugation had little influence on the low temperature structure of ethylene on graphite. However, recent work has demonstrated the inadequacy of the isotropic form of the atom–surface potential. Both N_2 (23) and C_2H_4 (17), when simulated with the isotropic atom–surface potential, have melting temperatures which are at least 9 degrees below the corresponding experimental values. This observation has been attributed to the fact that the isotropic potential produces a corrugation that is too small. To remedy this, Joshi and Tildesley used the anisotropic potential with two parameters, γ_A and γ_R, which are derived from the polarizability of the graphite atoms (22). The case $\gamma_A = \gamma_R = 0$ corresponds to the isotropic potential. We have taken the values $\gamma_A = 0.4$ and $\gamma_R = -1.05$, which were found to give the correct melting temperature for N_2 on graphite (23). The maximum variation in the ethylene–graphite potential rises from about 50 K to about 95 K when the isotropic form is replaced by the anisotropic form.

The results of the simulation with the anisotropic potential are shown in Table 1. Surprisingly, the enhanced corrugation of this potential seems to have almost no effect on the ethylene structure. The corrugation is not able to produce a triangular lattice. The $G(R)$ and $G(Z)$ for this system are shown in Fig. 1. Figure 2(c) shows a snapshot of the system at the end of the simulation. The peak positions for $G(R)$ are 4.30, 4.98, and 7.03 Å. This corresponds to a centered rectangular unit cell of dimensions 4.98 Å × 7.03 Å, and a coverage of $n = 0.898$. It is otherwise identical to the unit cell for the system on the corrugated surface.

This structure would produce a strong neutron scattering peak at 1.55 $Å^{-1}$, and weaker peaks at 1.79, 2.52, and 2.96 $Å^{-1}$. Again, this is indistinguishable from the results on the other two surfaces.

3.4 A different potential

The agreement between the flat and corrugated surface

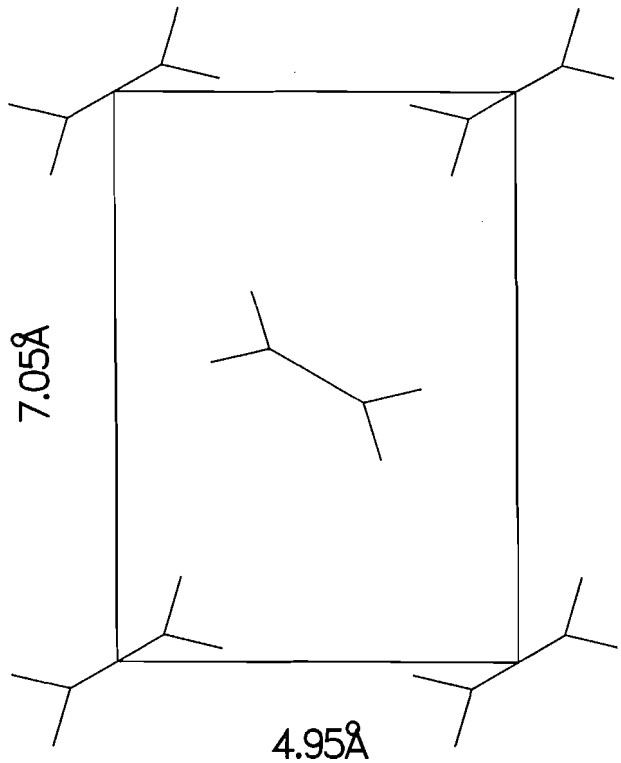

FIG. 3. Unit cell for low temperature ethylene on graphite deduced from the simulations. The molecules are arranged with their C=C axes parallel to the plane of the surface, and rotated 30° with respect to ***a***. The molecular planes are canted 55° away from the plane of the surface.

models suggests that the monolayer structure of ethylene is really not triangular when the coverage is about 0.9. This is a higher surface density than was used in the neutron measurements of ref. 9. The discrepancy between the calculated and measured density for the LD phase may be due to the fact that the Williams intermolecular potential was too attractive. We therefore performed a new simulation with a radically different potential (20). This potential was fitted to experimental properties of *methane* adsorbed on graphite, namely the rotational barrier heights, second virial coefficients, and the isotropic enthalpy at zero coverage (20). In contrast, the parameters used earlier in this study, which were taken from Williams (19), were fitted to the properties of bulk hydrocarbons. On a flat surface, the ST potential produced a herringbone with a unit cell of 5.35 Å × 7.35 Å, which is less dense than both the experimental and earlier simulation results. We conclude that this is not an appropriate potential for ethylene adsorbed on graphite, and unfortunately does not resolve the apparent discrepancy between our model and experiment.

4. Conclusion

We have presented the results of MD simulations of ethylene on graphite, both on a flat surface, and on a corrugated surface. The corrugation appears to have little effect on the low temperature structure, even when the anisotropic surface potential was used. The calculations predicted that ethylene forms the low temperature structure shown in Fig. 3, with a unit cell of 4.95 Å × 7.05 Å, rotated by 4° with respect to the substrate. This would produce diffraction peaks at 1.56, 1.78, 2.52, and 2.96 $Å^{-1}$. To this point, only peaks at 1.56 and 2.70 $Å^{-1}$, which correspond to a triangular lattice, have been seen in the diffraction experiments, at $n = 0.83$. The present

Can. J. Chem. Downloaded from www.nrcresearchpress.com by 176.9.209.113 on 09/07/12
For personal use only.

simulations predict that, at $n = 0.9$, these peaks should be split. If this discrepancy with experiment is confirmed, it could mean that the Williams potential alone is inadequate for surface calculations on substrate supported molecules due to the neglect of substrate mediated interactions.

The fact that the corrugation had such little effect on the structure was quite unexpected, given the large effect it had on the melting temperature (17). Therefore, we will be conducting future investigations into the effect of the corrugation on the dynamical properties of the liquid phase of submonolayer ethylene on graphite.

Acknowledgments

We thank Moses Chan, Toni Heidemann, John Larese, Séamus O'Shea, Larry Passell, Dieter Richter, Bill Steele, and especially Jim Morrison for much helpful discussion and correspondence on this topic.

This work was supported in part by the Natural Sciences and Engineering Research Council of Canada.

1. R. D. Diehl, M. F. Toney, and S. C. Fain, Jr. Phys. Rev. Lett. **48**, 177 (1982).
2. S. Nosé and M. L. Klein. Phys. Rev. Lett. **53**, 818 (1984).
3. J. Suzanne, J. L. Seguin, H. Taub, and J. P. Biberian. Surf. Sci. **125**, 153 (1983).
4. A. Terlain, Y. Larher, F. Angerand, G. Parette, H. Lauter, and I. C. Bassignana. Mol. Phys. **58**, 799 (1986).
5. J. Krim, J. Suzanne, H. Shechter, R. Wang, and H. Taub. Surf. Sci. **162**, 446 (1985).
6. A. D. Migone, H. K. Kim, M. H. W. Chan, J. Talbot, D. J. Tildesley, and W. A. Steele. Phys. Rev. Lett. **51**, 192 (1983).
7. J. Menaucourt, A. Thomy, and X. Duval. J. Phys. (Paris) Colloq. **38**, C4-195 (1977).
8. H. K. Kim, Q. M. Zhang, and M. H. W. Chan. Phys. Rev. Lett. **56**, 1579 (1986).
9. S. K. Satija, L. Passell, J. Eckert, W. Ellenson, and H. Patterson. Phys. Rev. Lett. **51**, 411 (1983).
10. B. H. Grier, L. Passell, J. Eckert, H. Patterson, D. Richter, and R. J. Rollefson. Phys. Rev. Lett. **53**, 814 (1984).
11. M. Sutton, S. G. J. Mochrie, and R. J. Birgeneau. Phys. Rev. Lett. **51**, 407 (1983).
12. S. G. J. Mochrie, M. Sutton, R. J. Birgeneau, D. E. Moncton, and P. M. Horn. Phys. Rev. B: Condens. Matter, **30**, 263 (1984).
13. J. Z. Larese and R. J. Rollefson. Surf. Sci. **127**, L172 (1983).
14. J. Z. Larese and R. J. Rollefson. Phys. Rev. B: Condens. Matter, **31**, 3048 (1985).
15. Q. M. Zhang, Y. P. Feng, H. K. Kim, and M. H. W. Chan. Phys. Rev. Lett. **57**, 1456 (1986); A. Inaba and J. A. Morrison. Phys. Rev. B: Condens. Matter, **34**, 3238 (1986).
16. M. L. Klein and J. A. Morrison. Carbon, **25**, 23 (1987).
17. M. A. Moller and M. L. Klein. Chem. Phys. Lett. In press.
18. D. E. Williams. J. Chem. Phys. **45**, 3770 (1966).
19. W. A. Steele. Surf. Sci. **36**, 317 (1973).
20. E. S. Severin and D. J. Tildesley. Mol. Phys. **41**, 1401 (1980).
21. S. Nosé and M. L. Klein. Phys. Rev. Lett. **50**, 1207 (1983); Mol. Phys. **50**, 1055 (1983).
22. G. Vidali and M. W. Cole. Phys. Rev. B: Condens. Matter, **29**, 6736 (1984).
23. Y. P. Joshi and D. J. Tildesley. Mol. Phys. **55**, 999 (1985).
24. A. D. McLachlan. Mol. Phys. **7**, 381 (1964).
25. S. Rauber, J. R. Klein, M. W. Cole, and L. W. Bruch. Surf. Sci. **123**, 173 (1982); L. W. Bruch and J. M. Phillips. Surf. Sci. **91**, 1 (1980).

Can. J. Chem. Downloaded from www.nrcresearchpress.com by 176.9.209.113 on 09/07/12
For personal use only.

Synthesis of enantiomerically pure β-amino-α-methylene-γ-butyrolactones by way of ozonolysis of aromatic α-amino acids

TORSTEN HVIDT AND WALTER A. SZAREK[1]
Department of Chemistry, Queen's University, Kingston, Ont., Canada K7L 3N6

AND

DAVID B. MACLEAN[1]
Department of Chemistry, McMaster University, Hamilton, Ont., Canada L8S 4M1

Received August 21, 1987

This paper is dedicated to Professor James A. Morrison

TORSTEN HVIDT, WALTER A. SZAREK, and DAVID B. MACLEAN. Can. J. Chem. **66**, 779 (1988).

The (*R*) and (*S*) isomers of β-amino-α-methylene-γ-butyrolactone hydrochloride (4-amino-dihydro-3-methylene-2(3*H*)-furanone hydrochloride) have been synthesized from (*R*)- and (*S*)-tryptophan, respectively. A key step is the ozonolysis of *N*,*O*-diacetyl-2-amino-3-(3′-indolyl)-1-propanol. (*S*)-β-Amino-α-methylene-γ-butyrolactone hydrochloride has been synthesized also by an analogous route starting with (*S*)-phenylalanine.

TORSTEN HVIDT, WALTER A. SZAREK et DAVID B. MACLEAN. Can. J. Chem. **66**, 779 (1988).

Utilisant les (*R*)- et (*S*)-tryptophanes comme produits de départ, on a synthétisé respectivement les isomères (*R*) et (*S*) du chorhydrate de la β-amino α-méthylène γ-butyrolactone (chlorhydrate de l'amino-4 dihydro méthylène-3 (3*H*)-furannone-2). Une étape clé est l'ozonolyse du *N*,*O*-diacétyl amino-2 (indolyl-3′)-3 propanol-1. Utilisant la (*S*)-phénylalanine comme produit de départ, on a synthétisé le chlorhydrate de la (*S*)-β-amino α-méthylène γ-butyrolactone de la même manière.

[Traduit par la revue]

Can. J. Chem. Downloaded from www.nrcresearchpress.com by 176.9.209.113 on 09/07/12
For personal use only.

Introduction

The α-methylene-γ-butyrolactone system, found in many natural products, has stimulated much research because of the interesting biological properties (1–5). Most of the synthetic effort has been directed towards the preparation of lactones substituted with alkyl groups at the β and (or) γ positions. Only a few examples of α-methylene-γ-butyrolactones bearing a heteroatom at the β position are known (6–10); one example is tulipalin B (**1**), which has fungicidal properties (2*a*) and

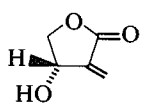

1

cutaneous allergenic activity (2*b*). However, to our knowledge an α-methylene-γ-butyrolactone bearing a nitrogen substituent attached to the ring has not been described. In this article we report the synthesis of enantiomerically pure β-amino-α-methylene-γ-butyrolactone hydrochlorides (4-amino-dihydro-3-methylene-2(3*H*)furanone hydrochlorides) (see **10**) and their *N*-acetyl derivatives (see **11**). In addition to the potential biological activity of **10** and **11**, the varied functionality in the new compounds should make them of interest as intermediates in the synthesis of complex natural products.

Results and discussion

The synthetic route developed for the (*R*) and (*S*) isomers of β-amino-α-methylene-γ-butyrolactone started with (*R*)- and (*S*)-tryptophan, respectively, and involved no chromatographic separations. The conversion of (*S*)-tryptophan (**2**) into the (*S*) isomer **10** is shown in Scheme 1. Treatment of **2** with thionyl chloride in methanol at reflux temperature (11) afforded the ester **3** in quantitative yield. Reduction of **3** using sodium borohydride in aqueous ethanol gave the alcohol **4**, which, on treatment with acetic anhydride and pyridine at room temperature, afforded *N*,*O*-diacetyl-2-amino-3-(3′-indolyl)-1-propanol (**5**) in crystalline form. A solution of **5** in aqueous acetic acid was subjected to a stream of ozone in oxygen for 14 h; oxidative processing, followed by heating of the product in the presence of 2 *N* hydrochloric acid, afforded a syrupy material whose ^{1}H nmr spectrum indicated that it consisted predominantly of the lactone **6**. An analytically pure sample of **6** eventually could be obtained. (The synthesis of **6** was achieved previously (12*a*) by way of reduction of *N*-benzoylasparagine methyl ester using lithium aluminum hydride; also, recently, the carbobenzyloxy derivative of **6** was synthesized (12*b*) by way of the selective reduction of *N*-(carbobenzyloxy)-L-aspartic anhydride.) Treatment of the crude syrupy material with benzophenone imine (13) in dichloromethane gave the imino derivative **7** in crystalline form; this derivative proved to be particularly useful for the subsequent transformations. The conversion of **5** into **7** was achieved in an overall yield of 35%.

The α-methylene function was introduced into **7** in two stages, namely by treatment with sodium hydride and then ethyl formate to give the sodium salt of the α-formyl lactone (**8**), followed by heating a solution of **8** in tetrahydrofuran at reflux temperature in the presence of paraformaldehyde to give the α-methylene lactone **9** in crystalline form. This method of synthesis of α-methylene lactones has been reported by Murray and Reid (14). Hydrolysis of **9** using 1 *N* hydrochloric acid – diethyl ether gave the amine hydrochloride **10**, which, on treatment with acetic anhydride, 4-*N*,*N*-dimethylaminopyridine, and triethylamine in dichloromethane, afforded (*S*)-β-acetamido-α-methylene-γ-butyrolactone (**11**).

The same reaction sequence has been employed for the synthesis of (*R*)-β-acetamido-α-methylene-γ-butyrolactone from (*R*)-tryptophan. Also, (*S*)-phenylalanine has been employed to obtain (*S*)-β-(diphenylmethylene)amino-γ-butyrolactone (**7**) by an analogous route (see Scheme 2). In this case, **7** was obtained in 45% yield (based on *N*,*O*-diacetyl-2-amino-3-phenyl-1-propanol (**14**)), whereas, in the case of the synthesis starting with (*S*)-tryptophan, **7** was obtained in 35% yield (based on **5**).

[1]Authors to whom correspondence may be addressed.

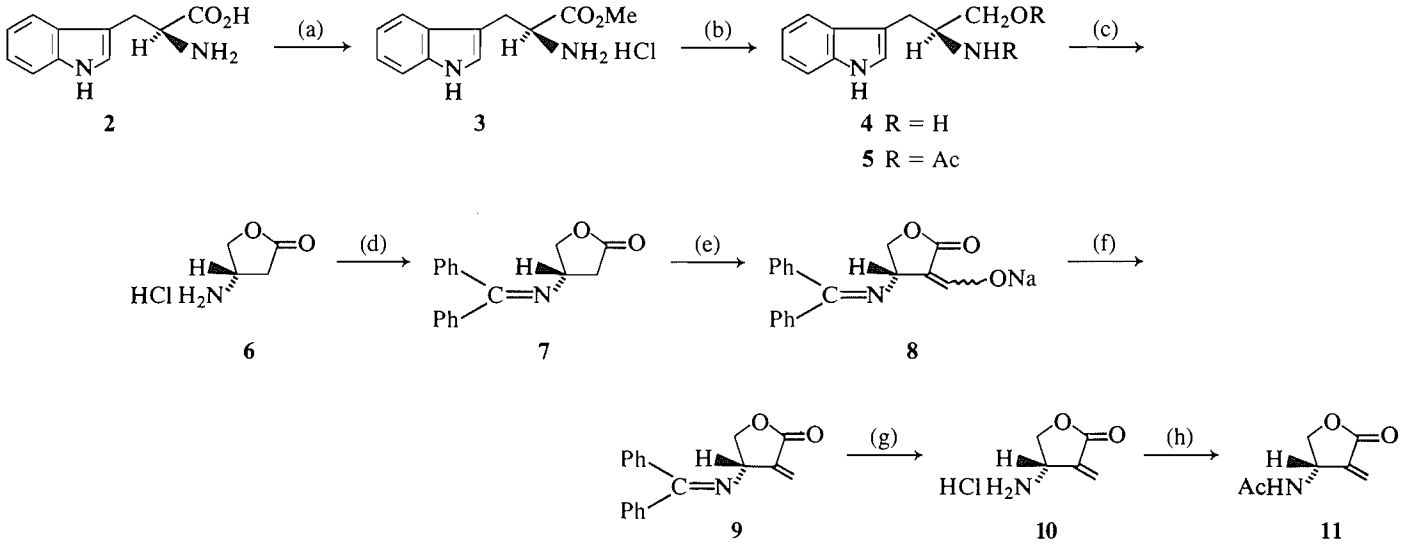

(a) $SOCl_2$, MeOH, reflux temperature; (b) $NaBH_4$, H_2O–EtOH, reflux temperature; Ac_2O, pyridine; (c) O_3, AcOH; H_2O_2; HCl, reflux temperature; (d) $Ph_2C{=}NH$, CH_2Cl_2; (e) NaH, HCO_2Et; (f) paraformaldehyde, tetrahydrofuran, reflux temperature; (g) aqueous HCl/Et_2O; (h) Ac_2O, Et_3N, CH_2Cl_2

SCHEME 1.

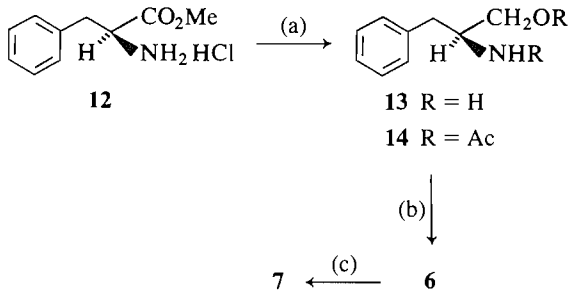

(a) $NaHB_4$, H_2O–EtOH, reflux temperature; Ac_2O, pyridine; (b) O_3, AcOH; H_2O_2; HCl, reflux temperature; (c) $Ph_2C{=}NH$, CH_2Cl_2

SCHEME 2

The work described in this article provides a useful route to the synthesis of α-methylene-γ-butyrolactones bearing a heteroatom at the β position. For example, starting with commercially available (*S*)-2-hydroxy-3-phenylpropanoic acid should afford (*S*)-tulipalin B (**1**). Also, the synthetic utility of **10** is being explored for the synthesis of nitrogen heterocycles.

Experimental

The ^1H nmr spectra were recorded on a Bruker AM400 spectrometer. Tetramethylsilane (TMS) was used as the internal standard for samples examined in organic solvents, and sodium 4,4-dimethyl-4-silapentan-1-sulfonate (DSS) for samples examined in aqueous solution; chemical shifts are reported in ppm (δ) downfield from the signal of TMS. The symbols, s (singlet), d (doublet), t (triplet), q (quartet), m (multiplet), and br (broadened), are used to report the multiplicity and shape of signals. The ^{13}C nmr spectra were recorded on the same instrument at 100.6 MHz. The solvent was used as internal standard when spectra were recorded in $CDCl_3$ (77.00 ppm) or CD_3OD (49.00 ppm); *tert*-butyl alcohol (32.27 ppm) was used as the internal standard for samples examined in aqueous systems. The chemical shifts of all signals are reported relative to TMS; all data were obtained in SEFT experiments. EI mass spectra were recorded on a VG ZAB-E mass spectrometer at an ionizing voltage of 70 eV. Infrared (ir) spectra were recorded on a Bruker IFS 85 FTIR instrument. Optical rotations were measured on a Perkin–Elmer 241 polarimeter in a 1-dm tube at 27 ± 3°C.

Melting points were determined on a Fisher–Johns melting point apparatus and are uncorrected. Silica gel 60 F_{254}, Merck, was used for thin-layer and column chromatography. Elemental analyses were performed by Canadian Microanalytical Services, Ltd., New Westminster, B.C.

(*R*) and (*S*) are used to designate the configuration of chiral centres, which are situated at C-2 for compounds **2**–**5** and **12**–**14**, and at C-3 for compounds **6**–**11**.

Methyl tryptophanate hydrochloride (3)

Tryptophan (25 g, 0.128 mol) was added to a solution of thionyl chloride (11 mL, 0.152 mol) in dry methanol (350 mL) and the resulting mixture heated under reflux for 18 h. The mixture was then evaporated to dryness, affording in quantitative yield a crystalline product that was used without purification in the next step. Recrystallization from methanol – diethyl ether gave an analytical sample; (*R*) isomer: mp 204–205°C; $[\alpha]_D$ −16.7° (*c* 1.5, methanol); (*S*) isomer: mp 203.5–205.0°C; $[\alpha]_D$ +17.1° (*c* 1.2, methanol) (lit. (15) mp 213.5–214.0°; $[\alpha]_D$ +17.1° (*c* 2.0, methanol)); (lit. (16) mp 200–201°C; $[\alpha]_D$ +16.3° (*c* 2.0, methanol)); ^1H nmr (CD_3OD) δ: 3.42 (dd, 1H, *J* = 15.1 and 7.0 Hz, H-3), 3.46 (dd, 1H, *J* = 15.1 and 5.5 Hz, H-3), 3.77 (s, 3H, OMe), 4.32 (apparent t, 1H, *J* = 6.4 Hz, H-2), 7.06 (t, 1H, *J* = 7.5 Hz, H-5′), 7.13 (t, 1H, *J* = 7.5 Hz, H-6′), 7.23 (s, 1H, H-2′), 7.40 (d, 1H, *J* = 8.0 Hz, H-7′), 7.54 (d, 1H, *J* = 8.0 Hz, H-4′); ^{13}C nmr (CD_3OD) δ: 27.5 (C-3), 53.6, 54.6 (C-2, OMe), 107.4 (C-3′), 112.7 (C-7′), 118.8, 120.3, 122.9 (C-4′, C-5′, C-6′), 125.7 (C-2′), 128.2 (C-4a′), 138.2 (C-7a′), 170.8 (C=O).

2-Amino-3-(3′-indolyl)-1-propanol (4)

To a solution of **3** (30 g, 0.178 mol) in a 1:1 (v/v) mixture (350 mL) of water and ethanol was added slowly with stirring a solution of sodium borohydride (23.1 g, 0.612 mol) in 100 mL of the same solvent. When the addition of borohydride was complete the mixture was heated to boiling under reflux for 18 h. The solution was evaporated under reduced pressure to remove ethanol, and the residual aqueous solution treated first with sodium hydroxide to hydrolyze esters of boric acid and then with sodium chloride to saturate the solution before exhaustive extraction with ethyl acetate. The extract was washed with water, dried over anhydrous Na_2SO_4, and evaporated

Can. J. Chem. Downloaded from www.nrcresearchpress.com by 176.9.209.113 on 09/07/12
For personal use only.

Can. J. Chem. Downloaded from www.nrcresearchpress.com by 176.9.209.113 on 09/07/12
For personal use only.

to dryness, affording 16.2 g (72%) of **4** as a glassy solid, which was used without purification in the next step. The product could not be induced to crystallize. (*S*) Isomer: $[\alpha]_D$ −19° (*c* 1.0, methanol) (lit. (17) mp 84–85°C; $[\alpha]_D$ −20.5° (*c* 1.0, methanol)); ^{1}H nmr (CD_3OD) δ: 3.05 (dd, 1H, *J* = 14.5 and 6.5 Hz, H-3), 3.11 (dd, 1H, *J* = 14.5 and *J* = 7.5 Hz, H-3), 3.51 (m, 1H, H-2), 3.59 (dd, 1H, *J* = 11.5 and 6.0 Hz, H-1), 3.75 (dd, 1H, *J* = 11.5 and 3.6 Hz, H-1), 7.04 (dt, 1H, *J* = 7.6 and 1.0 Hz, H-5′), 7.12 (dt, 1H, *J* = 7.6 and 1.0 Hz, H-6′), 7.17 (s, 1H, H-2′), 7.37 (apparent dt, 1H, *J* = 7.6 and ~1.0 Hz, H-7′), 7.58 (apparent dt, 1H, *J* = 7.6 and ~1.0 Hz, H-4′); ^{13}C nmr (CD_3OD) δ: 26.4 (C-3), 55.0 (C-2), 62.1 (C-1), 109.6 (C-3′), 112.5 (C-7′), 119.0, 120.1, 122.7 (C-4′, C-5′, C-6′), 125.0 (C-2′), 128.4 (C-4a′), 138.3 (C-7a′).

N,O-*Diacetyl-2-amino-3-(3′-indolyl)-1-propanol* (***5***)

A solution of **4** (15.5 g, 0.082 mol) in dry pyridine (70 mL) was treated with acetic anhydride (23 mL, 0.245 mol). The resulting solution was kept at room temperature for 14 h; isolation of the product in the usual manner afforded 22.0 g (98%) of **5** as a syrup that slowly crystallized. Recrystallization from ethyl acetate – hexanes gave an analytical sample. (*R*) Isomer: mp 124.5–125.5°C; $[\alpha]_D$ +4.5° (*c* 0.8, methanol); (*S*) isomer: mp 125.5–126.0°C; $[\alpha]_D$ −4.4° (*c* 0.6, methanol); ^{1}H nmr ($CDCl_3$) δ: 1.96 (s, 3H, NAc), 2.10 (s, 3H, OAc), 2.97 (dd, 1H, *J* = 14.5 and 7.2 Hz, H-3), 3.05 (dd, 1H, *J* = 14.5 and 5.4 Hz, H-3), 4.06 (dd, 1H, *J* = 11.2 and 4.8 Hz, H-1), 4.13 (dd, 1H, *J* = 11.2 and 6.0 Hz, H-1), 4.56 (m, 1H, H-2), 5.71 (br d, 1H, *J* = 8.0 Hz, *H*NAc), 7.04 (s, 1H, H-2′), 7.14 (t, 1H, *J* = 8 Hz, H-5′), 7.21 (t, 1H, *J* = 8 Hz, H-6′), 7.37 (d, 1H, *J* = 8 Hz, H-7′), 7.66 (d, 1H, *J* = 8 Hz, H-4′), 8.22 (br s, 1H, NH); ^{13}C nmr (CD_3OD) δ: 20.7 ($NCOCH_3$), 22.7 ($OCOCH_3$), 27.8 (C-3), 50.5 (C-2), 66.3 (C-1), 111.6 (C-3′), 112.2 (C-7′), 119.2, 119.7, 122.3 (C-4′, C-5′, C-6′), 124.1 (C-2′), 128.8 (C-4a′), 138.0 (C-7a′), 172.7 (C=O), 173.0 (C=O). *Anal.* calcd. for $C_{15}H_{18}N_2O_3$: C 65.68, H 6.61, N 10.21; found, (*R*) isomer: C 66.10, H 6.72, N 10.45; found, (*S*) isomer: C 65.63, H 6.58, N 10.10.

β-*Amino-γ-butyrolactone hydrochloride* (***6***)

A stream of ozone in oxygen (0.4 mmol/min of O_3) was passed through a vigorously stirred solution of **5** (4.0 g, 0.015 mol) in 86% acetic acid, at room temperature, for 14 h or until the solution became colorless. Hydrogen peroxide (30 mL, 30%) was then added and the colorless solution allowed to stand at room temperature. After 3 days the excess of peroxide was destroyed by adding a small amount of 10% Pd/C. The peroxide-free mixture was filtered to remove catalyst, and the filtrate was evaporated under vacuum below 40°C. The last traces of acetic acid were removed by adding water to the residue and evaporating again; this process was repeated several times. The residual reddish oil was applied to a column (3 × 28 cm) of Amberlite IR410 ion-exchange resin (OH^- form); the column was washed with water and eluted with 2 *N* hydrochloric acid. The eluate was heated under reflux for 2 h to hydrolyze the acetyl groups. The hot solution was treated with DARCO C, the mixture was filtered, and the filtrate evaporated to dryness. The residue was dried to constant weight over phosphorus pentoxide at 0.2 Torr (1 Torr = 133.3 Pa). The ^{1}H nmr spectrum of the crude product indicated that it consisted mainly of **6**, and the product was used as such in the preparation of **7** described below. An analytical sample of **6** was obtained from a preparation starting with (*S*)-phenylalanine; details of the characterization are given below.

β-*(Diphenylmethylene)amino-γ-butyrolactone* (***7***)

The crude product **6** (2.86 g) prepared above, suspended in dichloromethane (50 mL), was treated with benzophenone imine (13) (4.16 mL, 0.025 mol). The mixture was stirred at room temperature overnight, filtered free of suspended solids, and the filtrate evaporated to dryness. The oily, reddish residue was triturated with diethyl ether and the insoluble matter removed by filtration. The filtrate was washed with a saturated solution of sodium chloride, dried over anhydrous sodium sulfate, and evaporated to dryness. The crystalline residue was recrystallized from diethyl ether – hexanes, affording 1.41 g (35% based on **5**) of **7**; another 0.07 g of **7** was isolated from the mother liquor. (*R*) Isomer: mp 123.0–123.5°C; $[\alpha]_D$ +10.3° (*c* 1.2, chloroform); (*S*) isomer: mp 123.0–123.5°C; $[\alpha]_D$ −10.5° (*c* 1.1, chloroform); ν_{max}(KBr): 1712 (lactone) cm^{-1}; ^{1}H nmr (CD_3OD) δ: 2.52 (dd, 1H, *J* = 17.5 and 3.5 Hz, H-α), 2.77 (dd, 1H, *J* = 17.5 and 7.0 Hz, H-α), 4.29 (m, 2H, H-γ), 4.40 (m, 1H, H-β), 7.16–7.59 (m, 10H, Ph); ^{13}C nmr ($CDCl_3$–CD_3OD, 2:1 (v/v)) δ: 36.3 (C-α), 57.3 (C-β), 73.8 (C-γ), 127.1, 127.9, 128.4, 128.6, 128.8, 130.5, 135.7, 138.4 (Ph), 170.1 (C=N), 176.7 (C=O). *Anal.* calcd. for $C_{17}H_{15}NO_2$: C 76.96, H 5.70, N 5.28; found, (*R*) isomer: C 77.24, H 5.73, N 5.36; found, (*S*) isomer: C 76.90, H 5.73, N 5.27.

β-*(Diphenylmethylene)amino-α-methylene-γ-butyrolactone* (***9***)

A sample of sodium hydride (0.14 g, 5.8 mmol) obtained from a 50% suspension in mineral oil was prepared by washing twice with hexanes. The hydride was suspended in dry diethyl ether (20 mL) and treated successively with absolute ethanol (2 drops), dry ethyl formate (0.45 mL, 5.6 mmol), and **7** (1.4 g, 5.3 mmol); the resulting suspension was stirred for 16 h at room temperature. The suspended solid (crude **8**) was recovered by filtration and washed thoroughly with anhydrous diethyl ether. A ^{1}H nmr spectrum of the crude product indicated that reaction had proceeded in the expected manner; the salt was not further characterized.

The sample of crude **8** prepared above, in dry tetrahydrofuran (20 mL), was treated with paraformaldehyde (0.48 g, 16 mmol). The resulting suspension was heated under reflux for 3 h with the temperature adjusted in a manner that minimized separation of paraformaldehyde on the walls of the condenser. The suspension was cooled and filtered, and the separated solids washed well with dry tetrahydrofuran. The filtrate was evaporated to dryness, affording an oily residue that was adsorbed on a short column of silica gel; elution of the column with 15:1 (v/v) toluene – ethyl acetate gave crystalline **9** (0.758 g, 52% from **7**). Recrystallization from diethyl ether – hexanes gave an analytical sample. (*R*) Isomer: mp 117.5–120.0°C; $[\alpha]_D$ −32.7° (*c* 1.5, chloroform); (*S*) isomer: mp 117.5–120.0°C; $[\alpha]_D$ +33.2° (*c* 1.0, chloroform); ν_{max}(KBr): 1764 (lactone) cm^{-1}; ^{1}H nmr (CD_3OD) δ: 4.27 (dd, 1H, *J* = 9.0 and 5.4 Hz, H-γ), 4.46 (dd, 1H, *J* = 9.0 and 7.8 Hz, H-γ), 4.79 (m, 1H, H-β), 5.69 (d, 1H, *J* = 2.4 Hz, H-β′), 6.28 (d, 1H, *J* = 2.5 Hz, H-β′), 7.25–7.61 (m, 10H, Ph); ^{13}C nmr ($CDCl_3$–CD_3OD, 1:1 (v/v)) δ: 59.8 (C-β), 70.9 (C-γ), 124.0 (C-β′), 127.1, 128.0, 128.5, 128.7, 129.0, 130.7, 135.4, 138.3 (Ph), 137.1 (C-α), 169.9 (C=N), 172.0 (C=O). *Anal.* calcd. for $C_{18}H_{15}NO_2$: C 77.96, H 5.45, N 5.05; found, (*R*) isomer: C 77.99, H 5.48, N 5.06; found, (*S*) isomer: C 78.15, H 5.43, N 5.05.

β-*Amino-α-methylene-γ-butyrolactone hydrochloride* (***10***)

To a solution of **9** (0.32 g, 1.2 mmol) in diethyl ether (15 mL) was added aqueous 1 *N* hydrochloric acid (1.4 mmol). The two-phase system was vigorously stirred until the starting material had disappeared (~4 h); the progress of the reaction was monitored by tlc using 15:1 (v/v) toluene – ethyl acetate. When the reaction was complete, the aqueous phase was separated and washed several times with diethyl ether. Evaporation of the aqueous phase under vacuum, keeping the bath temperature below 40°C, gave a crystalline residue in quantitative yield. (*R*) Isomer: mp > 120°C (dec.); $[\alpha]_D$ +85.7° (*c* 0.5, water); (*S*) isomer: mp > 135°C (dec.); $[\alpha]_D$ −85.2° (*c* 0.6, water); ν_{max}(KBr): 1748 (lactone) cm^{-1}; ^{1}H nmr (CD_3OD) δ: 4.35 (dd, 1H, *J* = 10.7 and 2.8 Hz, H-γ), 4.68 (dd, 1H, *J* = 10.7 and 7.5 Hz, H-γ), 4.77 (m, 1H, H-β), 6.33 (d, 1H, *J* = 1.2 Hz, H-β′), 6.60 (d, 1H, *J* = 1.9 Hz, H-β′); ^{13}C nmr (D_2O) δ: 50.3 (C-β), 71.6 (C-γ), 133.7 (C-α), 134.0 (C-β′), 172.8 (C=O); ms (EI) *m/z* (%): 113 (12), 96 (24), 84 (13), and 67 (100). *Exact Mass* calcd. for $C_5H_7NO_2$: 113.0477; found (hrms): 113.0464.

β-*Acetamido-α-methylene-γ-butyrolactone* (***11***)

A suspension of **10** (0.2 g, 1.33 mmol) in dichloromethane (5 mL) was treated with triethylamine (0.41 mL, 2.9 mmol), acetic anhydride (0.30 mL, 3.2 mmol), and 4-*N*,*N*-dimethylaminopyridine (1 mg). The mixture was stirred for 3 h and then the solution was poured into 3 equivalents of dilute hydrochloric acid. The organic phase was

separated and the aqueous phase, after saturation with sodium chloride, extracted six times with 5-mL portions of ethyl acetate. The combined organic extract was washed with a saturated solution of sodium chloride and dried over anhydrous Na_2SO_4. The organic phase was evaporated to dryness, yielding a crystalline residue (78%) that was further purified by flash chromatography or by recrystallization from ethyl acetate – hexanes. (*R*) Isomer: mp 75–77°C; $[\alpha]_D$ +89.8° (*c* 0.4, chloroform); (*S*) isomer: mp 75–77°C; $[\alpha]_D$ −90.8° (*c* 0.3, chloroform); ν_{max}(KBr): 1764 (lactone) cm^{-1}; ^1H nmr ($CDCl_3$) δ: 2.07 (s, 3H, Ac), 4.10 (dd, 1H, *J* = 10.0 and 4.5 Hz, H-γ), 4.64 (dd, 1H, *J* = 10.0 and 7.5 Hz, H-γ), 5.23 (m, 1H, H-β), 5.96 (d, 1H, *J* = 2.3 Hz, H-β′), 6.35 (br s, 1H, NH), 6.42 (d, 1H, *J* = 2.6 Hz, H-β′); ^{13}C nmr ($CDCl_3$) δ: 22.7 ($NCOCH_3$), 47.6 (C-β), 71.6 (C-γ), 125.9 (C-β′), 135.2 (C-α), 169.2, 170.4 (C=O). *Anal.* calcd. for $C_7H_9NO_3$: C 54.19, H 5.85, N 9.03; found, (*R*) isomer: C 53.87, H 5.85, N 8.83; found, (*S*) isomer: C 53.98, H 5.88, N 8.90.

(S)-Methyl phenylalanate hydrochloride (12)

This compound was prepared from (*S*)-phenylalanine in quantitative yield by the procedure already described for the preparation of **3** from **2**; mp 159–160°C; $[\alpha]_D$ +18.9° (*c* 2.0, methanol) (lit. (18) mp 157–160°C; $[\alpha]_D$ +18.6° (*c* 4.5, methanol)); ^1H nmr (D_2O) δ: 3.24 (dd, 1H, *J* = 14.5 and 7.5 Hz, H-3), 3.36 (dd, 1H, *J* = 14.5 and 5.7 Hz, H-3), 3.84 (s, 3H, OMe), 4.44 (apparent t, 1H, *J* ≃ 6.7 Hz, H-2), 7.28–7.49 (m, 5H, Ph); ^{13}C nmr (D_2O) δ: 38.2 (C-3), 56.2, 56.7 (C-2, OMe), 130.7, 131.8, 131.9, 136.3 (Ph), 172.6 (C=O).

(S)-2-Amino-3-phenyl-1-propanol (13)

This compound was prepared from **12** in 74% yield using the procedure described for the preparation of **4** from **3**; mp 90–91°C; $[\alpha]_D$ −25.3° (*c* 3.1, chloroform) (lit. (19) mp 89–90°C; $[\alpha]_D$ −25.8° (*c* 2.2, chloroform)); ^1H nmr ($CDCl_3$) δ: 2.53 (dd, 1H, *J* = 13.5 and 8.5 Hz, H-3), 2.79 (dd, 1H, *J* = 13.5 and 5.2 Hz, H-3), 3.12 (m, 1H, H-2), 3.38 (dd, 1H, *J* = 10.5 and 7.0 Hz, H-1), 3.63 (dd, 1H, *J* = 10.5 and 4.0 Hz, H-1), 7.19–7.34 (m, 5H, Ph); ^{13}C nmr ($CDCl_3$) δ: 39.6 (C-3), 54.2 (C-2), 64.9 (C-1), 126.4, 128.5, 129.1, 138.0 (Ph).

(S)-N,O-Diacetyl-2-amino-3-phenyl-1-propanol (14)

This compound was prepared from **13** in quantitative yield by the procedure described for the preparation of **5** from **4**; mp 122–123°C; $[\alpha]_D$ −14.1° (*c* 1.5, chloroform); ^1H nmr ($CDCl_3$) δ: 1.97 (s, 3H, NAc), 2.12 (s, 3H, OAc), 2.81 (dd, 1H, *J* = 13.8 and 7.5 Hz, H-3), 2.89 (dd, 1H, *J* = 13.8 and 6.1 Hz, H-3), 4.03 (dd, 1H, *J* = 11.2 and 4.4 Hz, H-1), 4.09 (dd, 1H, *J* = 11.2 and 5.5 Hz, H-1), 4.43 (m, 1H, H-2), 5.59 (br d, 1H, NH), 7.19–7.33 (m, 5H, Ph); ^{13}C nmr ($CDCl_3$) δ: 20.8, 23.2 ($NCOCH_3$, $OCOCH_3$), 37.4 (C-3), 49.4 (C-2), 64.7 (C-1), 126.7, 128.5, 129.1, 136.9 (Ph), 169.6, 170.9 (C=O); ms (EI) *m/z* (%): 236 ($M+1$)$^+$ (6), 235 (M^+) (2), 176 (31), 144 (28), 134 (14), 120 (34), 102 (64), 91 (26), 84 (100). *Exact Mass* calcd. for $C_{13}H_{17}NO_3$: 235.1209; found (hrms): 235.1211.

Preparation of (S)-β-(diphenylmethylene)amino-γ-butyrolactone (7) from 14

Compound **14** was subjected to ozonolysis for 18 h and the ozonolysis product was processed under conditions identical with those used in the ozonolysis of **5**. The crude product **6**, isolated from the ozonolysis mixture, was converted to **7** in the manner described above. The yield of **7** based on **14** was 45%; mp 123–124°C; $[\alpha]_D$ −10.1° (*c* 1.3, chloroform).

Crystalline (S)-β-amino-γ-butyrolactone hydrochloride (6)

In one experiment, in which ozonization of **14** was incomplete, a crystalline product separated spontaneously (after a prolonged period of standing in an open vessel) from the crude syrup obtained on processing of the ozonolysis mixture. The syrupy crystals were triturated with absolute ethanol, and the crystals were recovered by filtration. The crystals were a mixture of **6** and **13**, which was resolved by chromatography on silica gel using *n*-butylalcohol–water – acetic acid (5:1:1 (v/v)) as eluant to afford a sample of crystalline **6**; recrystallization from methanol – diethyl ether gave an analytically pure sample; mp > 180°C (dec.); $[\alpha]_D$ −54.4° (*c* 0.6, water) (lit. (12) mp 185–186°C); ^1H nmr (D_2O) δ: 2.78 (dd, 1H, *J* = 19.0 and 2.5 Hz, H-α), 3.21 (dd, 1H, *J* = 19.0 and 8.5 Hz, H-α), 4.36 (m, 1H, H-β), 4.53 (dd, 1H, *J* = 11.1 and 4.5 Hz, H-γ), 4.72 (dd, 1H, *J* = 11.1 and 6.5 Hz, H-γ); ^{13}C nmr (D_2O) δ: 35.3 (C-α), 49.9 (C-β), 73.9 (C-γ), 180.1 (C=O). *Anal.* calcd. for $C_4H_8NO_2Cl$: C 34.93, H 5.86, N 10.18; found: C 35.08, H 5.89, N 9.94.

Acknowledgements

We thank the Natural Sciences and Engineering Research Council of Canada for financial support of this research in the form of grants to W.A.S. and D.B.M.

1. J. C. Sarma and R. P. Sharma. Heterocycles, **24**, 441 (1986).
2. (*a*) H. M. R. Hoffmann and J. Rabe. Angew. Chem. Int. Ed. Engl. **24**, 94 (1985); (*b*) P. Barbier and C. Benezra. J. Med. Chem. **29**, 868 (1986).
3. S. Kano, S. Shibuya, and T. Ebata. Heterocycles, **14**, 661 (1980).
4. R. B. Gammill, C. A. Wilson, and T. A. Bryson. Synth. Commun. **5**, 245 (1975).
5. P. A. Grieco. Synthesis, 67 (1975).
6. V. Nair and A. K. Sinhababu. J. Org. Chem. **45**, 1893 (1980).
7. E. Fujita and Y. Nagao. Bioorg. Chem. **6**, 287 (1977).
8. P. Barbier and C. Benezra. J. Org. Chem. **48**, 2705 (1983).
9. C. Papageorgiou and C. Benezra. J. Org. Chem. **50**, 157 (1985).
10. A. Bernardi, M. G. Beretta, L. Colombo, C. Gennari, G. Poli, and C. Scolastico. J. Org. Chem. **50**, 4442 (1985).
11. M. Brenner and W. Huber. Helv. Chim. Acta, **36**, 1109 (1953).
12. (*a*) A. C. Chibnall, C. Haselbach, J. L. Mangan, and M. W. Rees. Biochem. J. **68**, 122 (1958); (*b*) G. J. McGarvey, J. M. Williams, R. N. Hiner, Y. Matsubara, and T. Oh. J. Am. Chem. Soc. **108**, 4943 (1986); P. Jolles and C. Fromageot. Bull. Soc. Chim. Fr. **18**, 862 (1951); V. K. Nagai, R. Tanaka, H. Murakami, and A. Sano. Arnzeim.-Forsch. **17**, 1575 (1967).
13. M. J. O'Donnell and R. L. Polt. J. Org. Chem. **47**, 2663 (1982).
14. A. W. Murray and R. G. Reid. J. Chem. Soc. Chem. Commun. 132 (1984).
15. J. A. Maclaren. Aust. J. Chem. **30**, 2045 (1977).
16. H. Peter, M. Brugger, J. Schreiber, and A. Eschenmoser. Helv. Chim. Acta, **46**, 577 (1963).
17. D. B. Repke and W. J. Ferguson. J. Heterocycl. Chem. **13**, 775 (1976).
18. E. P. Kyba, J. M. Timko, L. J. Kaplan, F. De Jong, G. W. Gokel, and D. J. Cram. J. Am. Chem. Soc. **100**, 4555 (1978).
19. G. S. Bates and M. A. Varelas. Can. J. Chem. **58**, 2562 (1980).

Can. J. Chem. Downloaded from www.nrcresearchpress.com by 176.9.209.113 on 09/07/12
For personal use only.

Heats of vaporization and gaseous molar heat capacities of ethanol and the binary mixture of ethanol and benzene

JIN-QUAN DONG, RUI-SEN LIN, AND WEN-HSING YEN[1]
Department of Chemistry, Zhejiang University, Hangzhou, China

Received September 14, 1987

This paper is dedicated to Professor J. A. Morrison

JIN-QUAN DONG, RUI-SEN LIN, and WEN-HSING YEN. Can. J. Chem. **66**, 783 (1988).

A combined system of the Newsham vaporization calorimeter and the Pitzer gaseous heat capacity flow calorimeter were reconstructed with modifications. Both calorimeters were calibrated with benzene, the liquid standard, and were found to be acceptable for measurements, with deviations of 0.4% and 0.9%, respectively. Heats of vaporization of pure ethanol under five pressures and binary mixtures of ethanol and benzene under normal pressure were determined. Gaseous molar heat capacities of pure ethanol under three pressures and of binary mixture of ethanol and benzene at two temperatures were also determined, with anomalies due to association noted. Association of ethanol molecules in the vapor phase was discussed and analyzed, with heats of association and entropy change of association calculated.

JIN-QUAN DONG, RUI-SEN LIN et WEN-HSING YEN. Can. J. Chem. **66**, 783 (1988).

Introduisant des modifications, on a reconstruit un système combinant le calorimètre à vaporisation de Newsham et le calorimètre à écoulement pour capacité calorifique gazeuse de Pitzer. On a calibré chacun de ces calorimètres à l'aide du benzène, le liquide standard, et on les a trouvés acceptables pour effectuer des mesures; les déviations sont respectivement de 0,4 et 0,9%. On a déterminé les chaleurs de vaporisation de l'éthanol pur sous cinq pressions ainsi que d'un mélange binaire d'éthanol et de benzène sous pression normale. On a aussi déterminé les capacités calorifiques molaires gazeuses de l'éthanol à l'état pur sous trois pressions différentes ainsi que d'un mélange binaire d'éthanol et de benzène à deux températures; on a noté des anomalies dues à l'association. On discute et analyse l'association des molécules d'éthanol en phase vapeur et on a calculé les chaleurs d'association ainsi que les changements d'entropie dus à l'association.

[Traduit par la revue]

Can. J. Chem. Downloaded from www.nrcresearchpress.com by 176.9.209.113 on 09/07/12
For personal use only.

Introduction

Among investigations in chemical thermodynamics, liquid–vapor equilibrium research are of great importance in theory as well as in application. Systems involving normal liquids can be treated generally with simple activity corrections, but systems involving associated liquids demand special attention and relevant treatment. Associated liquids, though rather limited in number, constitute many systems important both to natural phenomena and industrial production. Alkanols, ethanol in particular, are liquids most frequently encountered.

Liquid–vapour equilibrium studies are usually undertaken with determinations of constituent concentrations under specific physical conditions, and they were investigated with data reported extensively in literature. However, heat capacities of the liquid phase and the vapor phase, and heats of vaporization of the liquid phase, were only occasionally reported.

A binary system of ethanol and benzene was selected to be studied. Prior to obtaining results on the binary system, pure ethanol and pure benzene were studied for primary data to be used in ultimate comparison and analysis. Pure benzene was employed in the calibration of the Newsham (1) vaporization calorimeter and in the calibration of the Pitzer (2) gaseous heat capacity flow calorimeter with modifications proposed by Hales *et al.* (3). Data for the binary system of cyclohexane and benzene are included for comparison.

Experimental

Apparatus

A schematic drawing for the calorimeters is given in Fig. 1, with the Newsham vaporization calorimeter and the Pitzer gaseous heat capacity flow calorimeter occupying, respectively, the right and left portions of the figure.

The Newsham vaporization calorimeter consists of inner vaporization chamber (I) with heater (H_1), outer vaporization chamber (D), and electric heating envelop (C), with liquids fed by reservoir (B) and feed-back condenser (F). Temperatures of liquids in the inner and the outer vaporization chambers are measured with platinum resistance thermometers (T_v and T_e).

Liquids are heated to boiling in the outer vaporization chamber before entering the inner vaporization chamber through a capillary, with the inner vaporization chamber double-walled, silvered, and under vacuum. The inner vaporization chamber is immersed and protected by the vapor and liquid of the outer vaporization chamber. Nichrome heater of 16 ohms is regulated for steady evaporation.

The Pitzer gaseous heat capacity flow calorimeter consists of a U-tube, through which the gaseous flow is heated with heater (H_2), with the temperatures of vapors measured with platinum resistance thermometers (T_1, T_2, and T_3). The U-tube, enclosed in silvered and evacuated container, is placed in a thermostat, which in turn is enclosed in an electric oven, kept at some 5°C lower than the thermostat. The inlet and outlet vapor temperatures, for which accurate values are not required, are monitored with nickel chromium and nickel silicon thermocouples (TC_1 and TC_2).

Vapors from the Newsham vaporization calorimeter pass through a spiral to be brought to the temperature of the thermostat before entering the U-tube. A nichrome heater of 30 ohms is employed.

Vapor samples of 5–10 g are collected through condenser (G) into receiver (E) for flow measurements.

The platinum resistance thermometers of 46 ohms each were certified with temperature precisions of 0.01°C.

The system is equipped with two external connections: one for evacuation as well as pressure control, and the other for filling-in with air or nitrogen. Glass valves marked 1 to 5 were lubricated with vacuum grease which should not introduce measurable quantities of impurity.

The pressure regulator is shown in Fig. 2, filled with a conducting sulfuric acid solution, acting as a control switch when solution level changes with pressure of the system. Pressure fluctuations were less than 0.5 mm Hg.

Materials

All liquids, ethanol, benzene, and cyclohexane, were purified by fractional distillation from analyzed reagent quality. Normal boiling points and refractive indices were observed and compared with values

[1]Author to whom correspondence may be addressed.

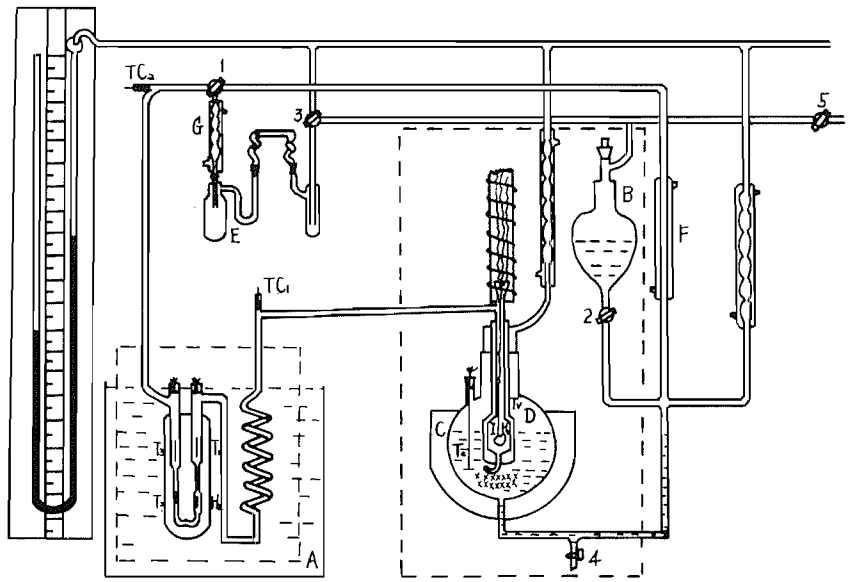

FIG. 1. Schematic drawing of the Newsham vaporization calorimeter and the Pitzer gaseous heat capacity flow calorimeter.

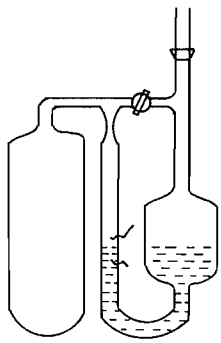

FIG. 2. The pressure regulator.

cited in literature (4). Purities were determined by gas chromatographs. All data are presented in Table 1.

Measurements

All energy inputs and temperature measurements were done electrically with voltage readings on $5\frac{1}{2}$-digit Fluke 8520A voltmeter. The potential difference is measured with a precision of 10^{-6} V. The temperatures on the platinum resistance thermometers were thus given with precisions of 0.005°C, with a working current of 1 mA.

Procedure

The Newsham vaporization calorimeter and the Pitzer heat capacity flow calorimeter constitute one combined system, but measurements may be conducted independently with liquids circulating through the entire system.

Before introducing liquids into the system, the thermostat for the Pitzer heat capacity flow calorimeter, the thermostat for the pressure regulator (kept constant at 25°C), and the entire vapor circuit were brought to the various desired temperatures. The vapor circuit was kept some 5°C above the condensation temperature of the liquids in order to maintain their vapor state. After introducing liquids, the heating rate on the outer vaporization chamber and the pressure regulator were so adjusted to steady boiling. Vapor was brought into circulation when heat was supplied to the inner vaporization chamber. Steady state between the vapor and liquid phases may be reached in 0.5 h for pure liquids and in 1.5 h for mixtures. Different flow rates may be maintained by varying the heating rate in the inner vaporization chamber. Actual operation disclosed that the temperature in the outer vaporization chamber was 0.1°C higher than that in the inner vaporization chamber.

TABLE 1. Physical properties of pure liquids

	T_b (°C)		n_D^{20}		
Liquid	Obsd.	Reference 4	Obsd.	Reference 4	Purity[a]
C_2H_5OH	78.30	78.3	1.3616	1.3616	99.95%
C_6H_6	80.08	80.1	1.5010	1.5011	99.85%
c-C_6H_{12}	80.70	80.7	1.4642	1.4642	99.84%

[a]Determined by gas chromatograph.

TABLE 2. Heats of vaporization of benzene

		ΔH (kJ mol^{-1})		
p (Torr)[a]	T (K)	Obsd.	Reference 5	Reference 6
760.0	353.25	30.625	30.750	30.726
570.0	344.59	31.401	31.272	
380.0	332.31	31.958	31.991	31.922
285.0	324.45	32.436	32.440	32.367
190.0	314.10	33.055	33.017	32.950
144.0	307.40	33.390	33.384	33.326

[a]1 Torr = 133.32 Pa.

Heats of vaporization were measured in duplicates or triplicates at three or more different flow rates in the range of 0.015–0.100 g/s. These apparent heats of vaporization were plotted against reciprocal flow rates to obtain the true heat of vaporization at infinite flow rate with uncalled-for heating effects eliminated.

Heat capacities were measured at three or more different flow rates under each set of pressure and temperature conditions. Platinum resistance thermometers (T_2 and T_3) readings were recorded at steady states both before and during heating. Time for attaining the steady state varied in the range of 10–30 min with different flow rates. Heat inputs were adjusted for an increase of some 3°C in temperature.

Results

Prior to its application for studies on other liquids and binary mixtures, the Newsham vaporization calorimeter was first calibrated with the standard substance, benzene. Its heats of vaporization were determined under six different pressures,

Can. J. Chem. Downloaded from www.nrcresearchpress.com by 176.9.209.113 on 09/07/12
For personal use only.

TABLE 3. Molar heat capacities of benzene (J mol^{-1} K^{-1})

	Molar heat capacities when T in K is							
p (Torr)	323.0	339.4	349.2	361.0	370.0	379.0	395.5	423.0
760.0				105.05	108.89	109.91	114.59	120.44
570.0				104.26	106.76	108.71	114.00	119.74
380.0		97.07	100.97	103.50	105.60	107.73	113.30	119.34
190.0	90.38	96.67	99.89					
144.0	89.66							
0[a]	87.41	96.25	98.82	101.95	102.51	105.51	112.02	118.59

[a]At 0 pressure, $C_p = C_p^0$, molar heat capacity in ideal gas state.

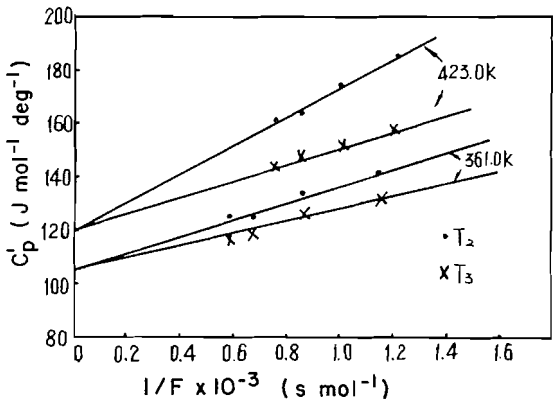

FIG. 3. Inverse flow rate dependence of apparent gaseous molar heat capacities of benzene.

from 760 to 144 Torr. The results are tabulated and compared with values cited in literature (5, 6), as presented in Table 2. Deviations amounted to less than ±0.4%, thus assuring the calorimeter feasibly reliable.

The experimental data were then correlated and represented for use in subsequent analyses by a Thiesen-type equation, as

$$[1] \quad \Delta H = 46.650(1 - T/562.1)^{0.4216}$$

where ΔH, T, and 562.1 are the heat of vaporization, the boiling temperature, and the critical temperature, respectively, of benzene. The corresponding temperatures T for specified pressures are obtained by the Antoine equation (7), because readings on the calorimeter were not as precise enough for calculations.

Similarly, the Pitzer heat capacity flow calorimeter was also calibrated with the standard substance, benzene. Selected molar heat capacities were determined under five different pressures, from 760 to 144 Torr, and at eight different temperatures, from 323.0 to 423.0 K. The results are tabulated in Table 3. These molar heat capacities are not values measured directly, but obtained indirectly through extrapolation of finite flow-rate results taken simultaneously on the two platinum resistance thermometers, T_2 and T_3, to infinite flow-rate, as exemplified in Fig. 3. The introduction of the two thermometers and the graphical extrapolation were directed to the total elimination of energy losses during actual heatings.

In Table 3, molar heat capacities of benzene in the ideal gas state, i.e., at zero pressure, at different temperatures are included. They are deduced individually from equations of the form, as

$$[2] \quad C_p^0(T) = C_p(T) + A(T)_p$$

where $C_p(T)$ and $A(T)$ are molar heat capacity under pressure p and temperature-dependent constant, all at the corresponding temperature T. The molar heat capacities of benzene in the ideal gas state were correlated with the equation,

$$[3] \quad C_p^0 = -78.777 + 0.690T - 5.290 \times 10^{-4}T^2$$

By this equation, interpolated molar heat capacities of benzene in the ideal gas state are compared with values cited in literature (6, 8), as presented in Table 4. Deviations, averaging 0.9%, appeared monotonously smaller than literature values. Intrinsic defects of the flow calorimeter and purity of benzene probably contributed to the systematic errors.

Heats of vaporization of cyclohexane were next determined under four different pressures, from 760 to 190 Torr. The results are tabulated and compared with values cited in literature (9), as presented in Table 5. The experimental data were again represented by a Thiesen-type equation, as

$$[4] \quad \Delta H = 45.057(1 - T/553.4)^{0.4022}$$

Heats of vaporization of ethanol were finally determined under five different pressures, from 760 to 190 Torr. The results are tabulated and compared with values cited in literature (10), as presented in Table 6. The experimental data were again

TABLE 4. Heat capacities of benzene at the ideal gas state

	C_p^0 (J mol^{-1} K^{-1})		
T (K)	Calcd.	Reference 8	Reference 6
333.15	92.25		93.32
341.60	95.05	95.80	
348.15	97.18		97.99
368.15	103.39		103.98
371.20	104.29	104.75	
402.30	113.00	113.91	
403.15	113.23		114.29
436.15	121.32	123.37	
438.15	121.99		123.93

TABLE 5. Heats of vaporization of cyclohexane

		ΔH (kJ mol^{-1})	
p (Torr)	T (K)	Obsd.	Reference 9
760.0	355.80	30.013	30.025
570.0	344.60	30.331	30.565
380.0	332.45	31.060	31.249
190.0	313.85	32.253	32.254

Can. J. Chem. Downloaded from www.nrcresearchpress.com by 176.9.209.113 on 09/07/12
For personal use only.

TABLE 6. Heats of vaporization of ethanol

		ΔH (kJ mol^{-1})	
p (Torr)	T (K)	Obsd.	Reference 10
760.0	351.45	38.778	38.846
570.0	344.35	39.357	39.349
380.0	334.95	40.172	39.993
285.0	328.55	40.374	40.418
190.0	320.05	40.943	40.968

TABLE 7. Molar heat capacities of ethanol (J mol^{-1} K^{-1})

760.00 Torr		506.67 Torr		253.33 Torr	
T (K)	C_p	T (K)	C_p	T (K)	C_p
354.6	108.73	344.4	102.60	330.8	90.44
359.6	101.01	347.3	97.16	339.7	80.07
364.8	92.66	353.6	88.81	347.7	77.17
372.2	86.42	356.4	84.92	358.8	76.12
383.3	84.31	363.2	83.33	375.1	77.06
395.7	84.09	375.6	80.24	385.9	78.81
408.0	84.54	387.6	80.20	401.8	80.30
418.4	85.20	408.6	83.42		
		423.9	85.43		

represented by a Thiesen-type equation, as

[5] $\Delta H = 55.273(1 - T/516.2)^{0.3090}$

Selected molar heat capacities of ethanol were also determined under three different pressures, 760.00, 506.67, and 253.33 Torr, and at relevant temperatures, from 330.8 to 418.4 K. The results are tabulated in Table 7, and graphically presented in Fig. 4.

Molar heat capacities of ethanol under 760 Torr are plotted in Fig. 5, together with corresponding values reported by Sinke and De Vries (11), Strömsöe, Rönne, and Lydersen (12), and Barrow (13), with good agreements. Comparing with the molar heat capacities of benzene under 760 Torr, as shown in Table 3, the behavior of ethanol is anomalous, with values decreasing to a minimum before increasing with increase in temperature, instead of the general trend of values increasing with increase in temperature.

The Newsham vaporization calorimeter is successfully employed in the determination of heats of vaporization of pure liquids, maintaining the liquid and vapor phases at identical temperatures. But, it fails theoretically to give correct heats of vaporization of binary mixtures, because the boiling points (of the liquid phase) and the dew points (of the vapor phase) of mixtures at identical compositions would in no case become identical. However, it may suffice for measurements if the binary components have comparable normal boiling points and comparable heats of vaporization, minimizing and even cancelling out discrepancies.

Benzene, with 353.25 K and 30.625 kJ mol^{-1}, and cyclohexane, with 355.80 K and 30.013 kJ mol^{-1}, was chosen as the exceptional pair for study on the feasibility of the Newsham vaporization calorimeter in the determination of heats of vaporization of binary mixtures. Heats of vaporization of the binary mixture at different mole fraction (x) of benzene were determined under three different pressures, 760, 570, and

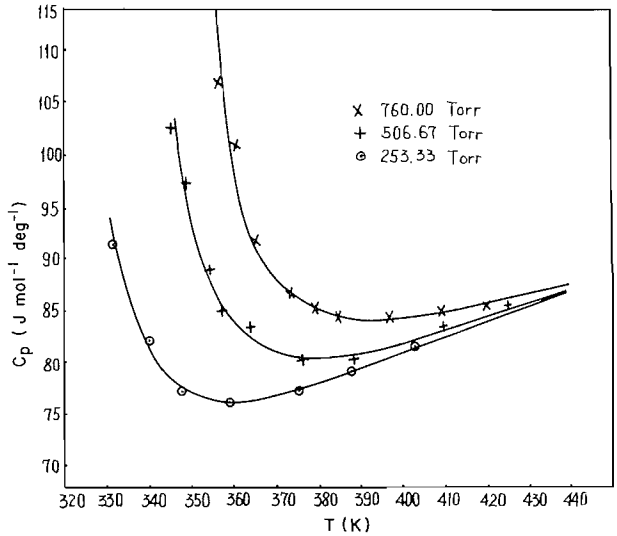

FIG. 4. Temperature dependence of gaseous molar heat capacity of ethanol.

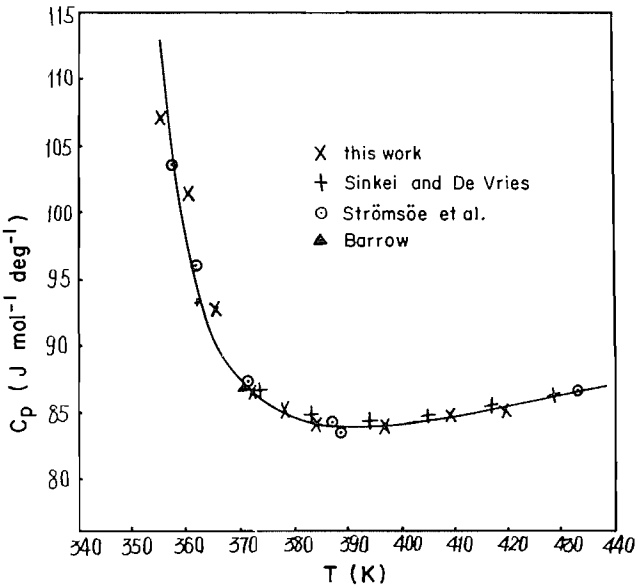

FIG. 5. Comparison of gaseous molar heat capacities of ethanol under 760 Torr.

TABLE 8. Heats of vaporization of benzene and cyclohexane at constant pressure (kJ mol^{-1})

760 Torr		570 Torr		380 Torr	
x	ΔH	x	ΔH	x	ΔH
0.000	30.013	0.000	30.331	0.000	31.066
0.143	29.758	0.180	30.173	0.137	30.778
0.250	29.743	0.243	30.119	0.255	30.578
0.397	29.690	0.354	30.174	0.354	30.606
0.443	29.694	0.440	30.248	0.440	30.798
0.541	29.790	0.544	30.318	0.544	30.817
0.700	30.069	0.634	30.603	0.634	31.263
0.842	30.409	0.792	30.704	0.792	31.433
1.000	30.625	1.000	31.401	1.000	31.958

Can. J. Chem. Downloaded from www.nrcresearchpress.com by 176.9.209.113 on 09/07/12
For personal use only.

TABLE 9. Heats of vaporization of ethanol and benzene at 760 Torr

x	ΔH (kJ mol^{-1})
0.000	30.625
0.071	31.187
0.148	31.606
0.230	32.297
0.328	32.528
0.460	32.922
0.590	33.615
0.690	35.242
0.792	36.517
0.914	37.829
1.000	38.778

TABLE 10. Molar heat capacities of ethanol and benzene at 760 Torr (J mol^{-1} K^{-1})

	Molar heat capacity	
x	365 K	395 K
0.000	105.606	113.578
0.071	102.301	110.682
0.148	100.890	108.517
0.230	97.585	104.452
0.328	95.101	102.479
0.460	91.967	98.261
0.590	89.662	92.897
0.690	89.175	90.292
0.797	88.178	87.629
0.914	88.804	84.246
1.000	92.686	83.540

380 Torr. The results are tabulated in Table 8. (The mole fraction (x) of benzene is determined by the observed refractive index of the recirculating mixture, with the refractive index converted to composition by interpolation on the known refractive index – composition curve.)

Ethanol and benzene, the ultimate study of this work, was finally examined in the Newsham vaporization calorimeter. Heats of vaporization of the binary mixture at different mole fraction (x) of ethanol were determined under the normal pressure of 760 Torr. The results are tabulated in Table 9. (The mole fraction (x) of ethanol is similarly determined with refractive index.)

Ethanol and benzene was the only binary mixture studied in the Pitzer heat capacity flow calorimeter. Molar heat capacities of the binary mixture at different mole fraction (x) of ethanol were determined under the normal pressure of 760 Torr and at two different temperatures, 365 and 395 K. The results are tabulated in Table 10, and graphically presented in Fig. 6.

Discussion

Associated liquids and normal liquids are quite different, exhibiting many divergent properties, some of which are listed in Table 11. Ethanol, an associated liquid, has a boiling point comparable to those of normal liquids, benzene and cyclohexane, but its normal heat of vaporization is not much larger. But the Thiesen-type equation constants (A and B) of ethanol are very much different from the comparable ones of benzene and cyclohexane. These differences denote for ethanol higher

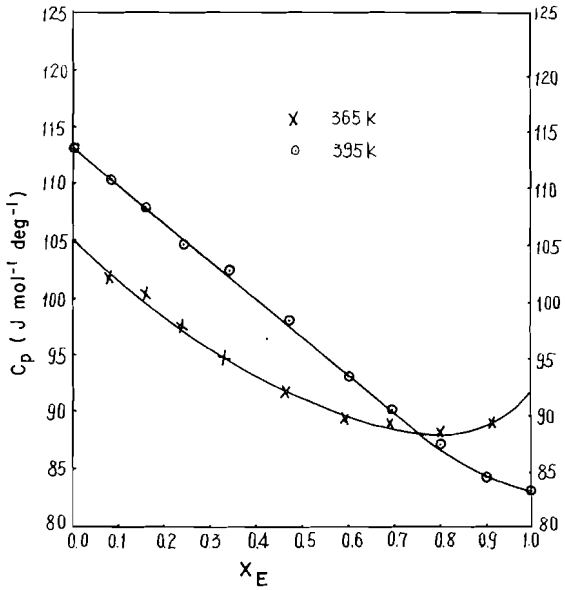

FIG. 6. Variation of gaseous molar heat capacities of mixture of ethanol and benzene with mole fraction at 365 and 395 K.

TABLE 11. Some properties of ethanol, benzene, and cyclohexane

	Value		
Parameter	C_2H_5OH	C_6H_6	c-C_6H_{12}
T_b (K)	351.45	353.25	355.80
ΔH_v (kJ mol^{-1})	38.778	30.625	30.013
T_c (K)	516.2	562.1	553.4
A	55.273	46.650	45.057
B	0.3090	0.4216	0.4022

heats of vaporization at lower temperatures and faster rate of diminution toward a lower critical temperature. These larger heats of vaporization clearly suggest that the excess energy over the normal heats of vaporization is necessary to convert the extensively associated liquid into non-associated liquids composed of free molecules.

The three gaseous molar heat capacity curves of ethanol in Fig. 4 all consist of two sections, one on the left descending steeply with a turn toward the minimum, and another on the right extending almost linearly outward from the minimum. The curves seem to have a tendency to coalesce when extended further to higher temperatures. The molar heat capacities of ethanol at 440 K under the three different pressures all amount to approximately 87 J mol^{-1} K^{-1}, corresponding to 10.5R.

According to the statistical mechanical theories on molecular motions, the gaseous molar heat capacity of non-linear molecules at constant pressure is the sum total of molar heat capacities due to molecular translations, molecular rotations and molecular vibrations (including other vibration-like motions), together with the usual increment of C_p over C_v. With translations and rotations accounted-for classically, the molar heat capacity of ethanol due to vibrations at 440 K amounts to some 6.5R.

A difference of 0.2R can be estimated from the curves between molar heat capacities at 420 K under pressures of 760.00 and 253.33 Torr. This small difference indicates that

Can. J. Chem. Downloaded from www.nrcresearchpress.com by 176.9.209.113 on 09/07/12
For personal use only.

Can. J. Chem. Downloaded from www.nrcresearchpress.com by 176.9.209.113 on 09/07/12
For personal use only.

molecular interactions contribute only slightly in the higher temperature region, but become more important with decrease in temperature.

A value of $11.7R$ is found for the total molar heat capacity at 360 K from the curve under the pressure of 760.00 Torr, and $9.7R$ is found for the molar heat capacity due to molecular motions (including molecular interactions) at 360 K from the linear extension of the high temperature section of the same curve. This difference of $2.0R$ is obviously not of physical origin but of chemical source. Considering liquid ethanol being highly associated, an assumption that gaseous ethanol is composed of free molecules as well as associated molecules in different stages may be reasonable and correct.

With this additional information, vaporization of ethanol should be deemed as a process, by which the associated liquid is converted not just to free molecules, but to free molecules together with associated molecules in different stages with proportions varying with temperature and pressure. Large gaseous molar heat capacities of ethanol at lower temperatures and higher pressures may then be thought of as energy increments due to physical changes in molecular motions and due to chemical changes as manifested by molecular "dissociation".

Weltner and Pitzer (14) measured the gaseous molar heat capacities of methanol, and observed similar anomalies as ethanol. They proposed the existence of duo- and quarto-associated molecules among free molecules in gaseous methanol. Similar proposals were put forward by Barrow (13), McKetta and co-workers (15–19), and Hales *et al.* (3), for other alkanols. Pitzer's assumptions are as follows: (*1*) only two types of association, duo- and quarto-molecules, existing in the gaseous phase; (*2*) all molecules, free and associated, considered to be in the ideal gas state; (*3*) heats of association and entropy change of association assumed to be constant and independent of temperature; (*4*) very few associated molecules coexisting with free molecules, considered to be negligible in comparison.

With these assumptions, chemical equations for the two associations are:

[6] $2A \rightleftharpoons A_2$

[7] $4A \rightleftharpoons A_4$

The respective equilibrium constants, K_2 and K_4, as expressed with partial pressures, are

[8] $K_2 \approx d/p$

[9] $K_4 \approx q/p^3$

where p, d, and q are the total pressure, moles of duo- and quarto-molecules, with moles of single molecules before association taken as 1. The total number of moles n is

[10] $n = 1 - d - 3q$

[11] $n = 1 - K_2p - K_4p^3$

Introducing n into van der Waals equation and neglecting a/v^2,

[12] $pV = n(RT - bp)$

[13] $pV = RT + (b - RTK_2)p - 3RTK_4p^3$

is obtained, where b is the co-volume, with simplification by neglecting second-order terms. Comparing with virial equation,

[14] $v = RT/p + B + Dp^2$

with the p term omitted, and using thermodynamic relationships,

[15] $RT \ln K = -\Delta G$

[16] $\Delta G = \Delta H - T\Delta S$

virial constants in term of ΔH's and ΔS's are given by

[17] $B = b - RT \exp(\Delta S_2/R) \exp(-\Delta H_2/RT)$

[18] $D = -3RT \exp(\Delta S_4/R) \exp(-\Delta H_4/RT)$

From thermodynamic relationships,

[19] $(\partial S/\partial p)_T = -(\partial V/\partial T)_p$

[20] $(\partial S/\partial T)_p = C_p/T$

heat capacity changes with pressure, as

[21] $\partial(C_p/T)/\partial p = -(\partial^2 V/\partial T^2)_p$

Differentiating [14] with B and D substituted, and then integrating [21],

[22] $C_p = C_p^0 + ap + cp^3$

is obtained, where a and c are symbols standing for

[23] $a = (\Delta H_2^2/RT^2) \exp(\Delta S_2/R) \exp(-\Delta H_2/RT)$

[24] $c = (\Delta H_4^2/RT^2) \exp(\Delta S_4/R) \exp(-\Delta H_4/RT)$

Equations [23] and [24] are converted into logarithmic equations, as

[25] $\ln a + \ln(RT^2) = [2 \ln(\Delta H_2) + (\Delta S_2/R)] - (\Delta H_2/RT)$

[26] $\ln c + \ln(RT^2) = [2 \ln(\Delta H_4) + (\Delta S_4/R)] - (\Delta H_4/RT)$

C_p values at given temperatures of gaseous ethanol were read from the three pressure curves in Fig. 4 by interpolation, and they were used in solving [22] to give C_p^0, a and c constants for the relevant temperatures. Logarithmic values of a and c for various given temperatures were plotted according to [25] and [26], respectively, against reciprocal temperatures as linear lines to obtain ΔH's (from slopes) and ΔS's (from intercepts). All solutions were performed through mathematical recursions on computers.

Calculated results are as follows:

for the duo-associations,

$$\Delta H_2 = -15.20 \pm 0.12 \text{ kJ mol}^{-1}$$

$$\Delta S_2 = -70.7 \pm 0.6 \text{ J mol}^{-1} \text{ K}^{-1}$$

for the quarto-associations,

$$\Delta H_4 = -97.2 \pm 0.8 \text{ kJ mol}^{-1}$$

$$\Delta S_4 = -321 \pm 3 \text{ J mol}^{-1} \text{ K}^{-1}$$

These values agree very well with those reported by Barrow (13).

Comparing with hydrogen bond energies of 20–25 kJ mol^{-1}, duo-associations with a smaller energy are obviously weaker, but quarto-associations with energies of four-fold may be thought of as composed of four hydrogen bonds, forming an eight-membered ring of hydrogen and oxygen atoms.

For a binary mixture of mole fraction (x), its vaporization starts from the liquid state at the lower boiling point (T_b), and stops in the gaseous state at the higher dew point (T_d). To specify the temperature for its heat of vaporization, a single intermediate temperature (T_i), other than T_b and T_d, must be assigned.

The vaporization process may be resolved into five steps: (*1*) separating the binary liquid solution into two pure liquids at T_b; (*2*) warming the pure liquids separately from T_b to T_i;

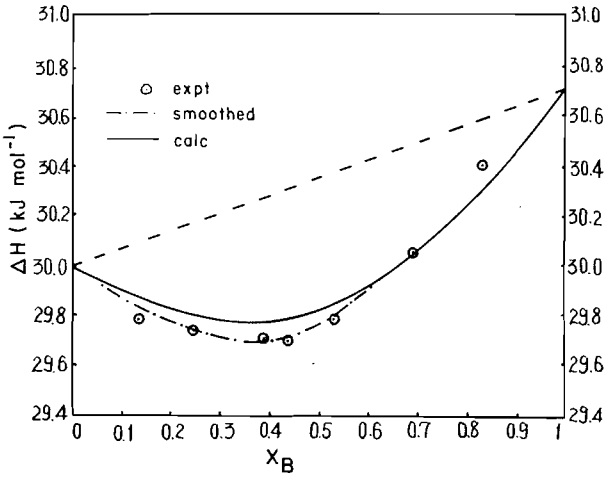

FIG. 7. Variation of heats of vaporization of mixture of benzene and cyclohexane with mole fraction under 760 Torr.

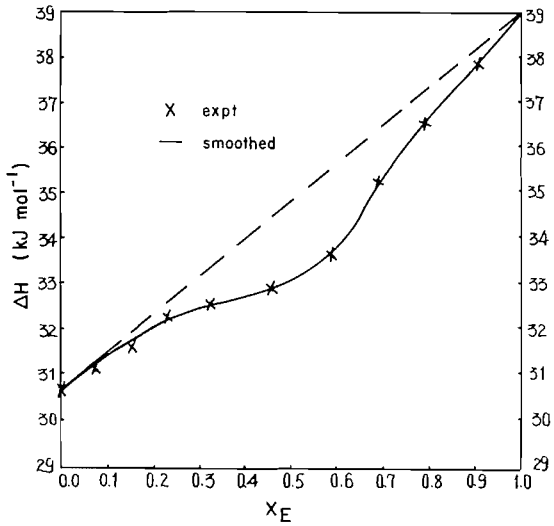

FIG. 8. Variation of heats of vaporization of mixture of ethanol and benzene with mole fraction under 760 Torr.

(*3*) vaporizing the pure liquids into pure gases separately at T_i; (*4*) warming the pure gases separately from T_i to T_d; (*5*) mixing the two pure gases into binary gaseous solution at T_d.

Making use of the relevant data found in literature, heats of vaporization of the binary mixture of benzene and cyclohexane at different mole fraction (x) under a pressure of 760 Torr were theoretically evaluated by adding together the separate calculations undertaken according to the afore-mentioned steps. The results are graphically presented in Fig. 7, as a companion curve to testify the validity of the Newsham vaporization calorimeter to be a reliable instrument for measuring heats of vaporization of liquid mixtures, with experimental results also presented for comparison. Good agreement provides proof of its usefulness. A similar calculation for the system ethanol–benzene has not yet been carried out.

Among the five heat effects in the proposed vaporization process, the heat of vaporization at T_i, $\Sigma x_i \Delta H_{vi}(T_i)$, which is different from $\Sigma x_i \Delta H_{vi}(T_{bi}^0)$, as represented by the dashed line in Fig. 7, constitutes almost the entire heat of vaporization of the binary mixture, $\Delta H_v(T_b - T_d)$. The heat of mixing of liquids at T_b, ΔH_m^L, the negative heat effect of step (1), comes next in magnitude, about 2% of the total, while the heat of mixing of gases at T_d, ΔH_m^G, is very small, if not negligible. The mixings in both phases, in the present case of benzene and cyclohexane, take place endothermically with absorption of heat. The warming-up of the liquid mixture from T_b to T_i and the gaseous mixture from T_i to T_d varies with the composition of the binary mixture, starting from 0 when pure and reaching a maximum at medium compositions, because of the lens-like T_b–T_d intervals between the liquidus and the vaporus curves. The sum total of the heat effects in steps [2] to [4] may be approximately equal to that represented by the dashed line in Fig. 7, and the droop in the experimental heat of vaporization curve should then be due to the evolution of heat in separating the liquids from solution.

Heats of vaporization of the binary mixture of ethanol and benzene at 760 Torr of Table 9 are graphically represented in Fig. 8. Due to pronounced differences in the heats of vaporization of pure ethanol and pure benzene, a side-wise protrusion instead of a droop appears in the experimental heat of vaporization curve of ethanol and benzene. The maximum differences in values on the experimental heats of vaporization curves from those on the dashed lines are very significant, with 1850 J mol^{-1} for ethanol and benzene, and 530 J mol^{-1} for benzene and cyclohexane. Evidently, a simple explanation as that for the binary mixture of benzene and cyclohexane will not suffice. Molecular association of ethanol molecules must be seriously considered. Dissociation of associated liquid ethanol and mixing of the partially dissociated ethanol molecules and benzene molecules both contribute to the heat and mixing of liquid ethanol and liquid benzene, with absorption of heat in larger quantities necessary for dissociation. Dissociation of associated ethanol molecules and mixing of ethanol molecules and benzene molecules also contribute to the heat of mixing of gaseous ethanol and gaseous benzene, with absorption of heat in smaller, though not insignificant, quantities. These considerations may thus explain the slanting lines of deviation from the dashed line at extreme compositions and the bulge at medium compositions.

The gaseous molar heat capacity – composition curves of the binary mixture of ethanol and benzene at 365 and 395 K are strikingly different from each other, as shown in Fig. 6. The curve at 395 K protrudes slightly from the diagonal connecting the heats of vaporization of pure liquids. However, the curve at 365 K droops very strongly from another similar diagonal.

From the gaseous molar heat capacity – temperature curve of ethanol under 760 Torr in Fig. 4, its gaseous molar heat capacity at 395 K is located on the right linear section, while that at 365 K is located on the left descending section. According to afore-mentioned discussions, gaseous ethanol at 395 K consists of free molecules with few or no associated ones, and gaseous ethanol at 365 K consists of free molecules as well as associated ones.

The almost linear gaseous molar heat capacity – composition curve of ethanol and benzene at 395 K denotes that the gaseous mixture is composed of free molecules quite at the ideal gas state, with non-ideality noticeable at increasing ethanol compositions. The drooping curve at 365 K denotes that change in ethanol molecularity plays a significant role in the gaseous molar heat capacity of ethanol and benzene, with changes in molecular motions and "dissociation" of ethanol molecules taking place simultaneously.

1. D. M. T. NEWSHAM and E. J. MENDEZ-LECANDA. J. Chem. Thermodyn. **14**, 291 (1982).
2. K. S. PITZER. J. Am. Chem. Soc. **63**, 2413 (1941).
3. J. L. HALES, J. D. COX, and E. B. LEES. Trans. Faraday Soc. **59**, 1544 (1963).

Can. J. Chem. Downloaded from www.nrcresearchpress.com by 176.9.209.113 on 09/07/12
For personal use only.

4. R. C. WEAST (*Editor*). Handbook of chemistry and physics. 63rd ed. CRC Press, Cleveland. 1982–83.
5. V. MAJER, V. SVOBODA, V. HYNEK, and J. PICK. Collect. Czech. Chem. Commun. **43**, 1313 (1978).
6. S. S. TODD, I. A. HOSSENLOPP, and D. W. SCOTT. J. Chem. Thermodyn. **10**, 641 (1978).
7. R. C. REID, J. M. PRAUSNITZ, and T. K. SHERWOOD. The properties of gases and liquids. 3rd ed. McGraw-Hill, New York. 1977.
8. D. W. SCOTT, G. WADDINGTON, J. C. SMITH, and H. M. HUFFMAN. J. Chem. Phys. **15**, 565 (1947).
9. V. SVODA, F. VESELY, R. HOLUB, and J. PICK. Collect. Czech. Chem. Commun. **38**, 3539 (1972).
10. J. POLAK and G. C. BENSON. J. Chem. Thermodyn. **3**, 235 (1971).
11. G. C. SINKE and T. DE VRIES. J. Am. Chem. Soc. **75**, 1815 (1953).
12. E. STRÖMSÖE, H. G. RÖNNE, and A. L. LYDERSEN. J. Chem. Eng. Data, **15**, 286 (1970).
13. G. M. BARROW. J. Chem. Phys. **20**, 1739 (1952).
14. W. WELTNER, JR. and K. S. PITZER. J. Am. Chem. Soc. **73**, 2606 (1951).
15. J. F. MATHEWS and J. J. MCKETTA. J. Phys. Chem. **65**, 758 (1961).
16. N. S. BERMAN and J. J. MCKETTA. J. Phys. Chem. **66**, 1444 (1962).
17. E. T. BEYNON, JR. and J. J. MCKETTA. J. Phys. Chem. **67**, 2761 (1963).
18. N. S. BERMAN, C. W. LARKAM, and J. J. MCKETTA. J. Chem. Eng. Data, **9**, 218 (1964).
19. N. S. BERMAN. AIChE J. **14**, 497 (1968).

Can. J. Chem. Downloaded from www.nrcresearchpress.com by 176.9.209.113 on 09/07/12
For personal use only.

The derivation of the rotational potential function from atom–atom potentials. III. Borohydride compounds

DAVID SMITH

Pennsylvania State University, Department of Chemistry, Hazleton Campus, Hazleton, PA 18201, U.S.A.

Received August 25, 1987

This paper is dedicated to Professor James A. Morrison

DAVID SMITH. Can. J. Chem. **66**, 791 (1988).

The rotational potential functions for the borohydride ion embedded in potassium and rubidium halides are derived from atom–atom potentials of the Buckingham (exp-6) type. The librational frequencies computed from the potential functions are in good agreement with the observed frequencies. The potential functions for rubidium and potassium borohydrides derived from the atom–atom potentials yield librational frequencies that are about 10% higher than the observed values. Since the entropy of transition for potassium and rubidium borohydrides is less than expected, there is a possibility that there is some ordering of the borohydride ions above the transition temperature. An experimental method is presented for studying the ordering of the borohydride ions based on the difference in the ground level degeneracy of a tetrahedral ion in ordered and disordered states.

DAVID SMITH. Can. J. Chem. **66**, 791 (1988).

Utilisant des potentiels atome–atome du type de Buckingham (exp-6), on a obtenu les fonctions du potentiel de rotation de l'ion borohydrure intercalé dans des halogénures de potassium et de rubidium. Les fréquences de libration calculées à partir des fonctions de potentiel sont en bon accord avec les fréquences expérimentales. Les fonctions de potentiel des borohydrures de rubidium et de potassium qui ont été obtenues à partir des potentiels atome–atome fournissent des fréquences de libration qui sont 10% plus élevées que les valeurs expérimentales. Puisque l'entropie de transition des borohydrures de potassium et de rubidium est plus faible que prévue, il est possible qu'au dessus de la température de transition les borohydrures soient ordonnés. On présente une méthode expérimentale pour étudier la mise en ordre des ions borohydrures; cette méthode est basée sur la différence dans la dégénérescence de l'état fondamental d'un ion tétraédrique dans les états ordonné et désordonné.

[Traduit par la revue]

Can. J. Chem. Downloaded from www.nrcresearchpress.com by 176.9.209.113 on 09/07/12
For personal use only.

I. Introduction

The rotational potential functions have been derived for ammonium chloride compounds (1) and ammonium fluoride compounds (2). The rotational potential functions have been used to compute the hindered rotational energy levels of the ammonium ion in the solids studied. From the energy levels, the librational frequencies, tunneling frequencies, activation energies, rotational heat capacities, and thermal expansions may be determined. In this paper, the rotational potential functions of the borohydride ion embedded in potassium and rubidium halides are derived. The term that makes the greatest contribution to the potential function is the repulsion term. In ammonium compounds, the attractive terms usually make the largest contribution to the potential function.

II. Theory

The rotational potential function has been derived (from atom–atom potentials) by Yasuda for the case of solid methane (3). The interaction between the atoms in a solid with one of the hydrogen atoms of a reference borohydride ion is given by

$$[1]\quad \Phi_{H-X}(R_{ik}) = A_{H-X}\exp(-\alpha_{H-X}R_{ik}) - C_{H-X}/R_{ik}^{6} - q_H q_X/R_{ik}$$

The effective charge on a hydrogen atom of the reference borohydride ion is given by q_H. The value of q_H is set equal to -0.20 electron units (4). The effective charge on an atom X is given by q_X. The interaction between the hydrogen atoms on the reference borohydride ion with other BH_4^- ions considers the other BH_4^- ions as simple spherical ions. In this paper, the parameter C is determined by using the values of C for metal–metal interactions and halide–halide interactions given in ref. 5 and the borohydride–borohydride interaction given in ref. 6. Using the equation

$$[2]\quad C = \sqrt{c_{++}c_{--}}$$

the value of C for the alkali metal ions and halide ions with the borohydride ion can be determined. The value of α in the repulsion term of eq. [1] is set at 1.8 Å, because this value gave the best results. The value of A in the repulsion term is determined by using the equation

$$[3]\quad A_{H-X} = b\exp\{\alpha(r_X + r_{BH_4})\}$$

where $b = 10^3$ and r represents the ionic radius. The values of the ionic radii used in this paper are given in Table 1. The parameters in eq. [1] are also given in Table 1. The values of A_{K-H} and A_{Rb-H} were adjusted to give the best possible match between the observed and computed librational frequencies. The value of A_{K-H} given in Table 1 is essentially the same value that results from using eq. [3], but the value of A_{Rb-H} given in Table 1 is somewhat less than 10% lower than that computed using eq. [3].

III. Analysis of borohydride compounds

The potential function for the motion of the borohydride ion embedded in alkali halides is

$$[4]\quad V(\omega) = \beta B\{\beta_4 V_4(\omega) + \beta_6 V_6(\omega)\}$$
$$\beta_4^2 + \beta_6^2 = 1$$

The rotational constant, B, of the borohydride ion is 3.95 cm^{-1}. Expressions for $V_4(\omega)$ and $V_6(\omega)$ are given in ref. 7. In eq. [4], β is a dimensionless field strength parameter related to the barrier to rotation. Higher terms in the potential function are very small.

In Table 2, the contributions to $\beta_4\beta$ and $\beta_6\beta$ are given for BH_4^- embedded in KCl. The largest contribution to the parameters comes from the repulsion term for the interaction of BH_4^- with the alkali metal ion. The values of the parameters in eq. [4] are given in Table 3. In Table 4, the observed and calculated librational frequencies are compared. The results are favorable for the borohydride ion embedded in alkali halides, but are about 10% high for the alkali borohydrides.

TABLE 1. Parameters in the atom–atom potentials[a]

Interaction	$-C \times 10^{-5}$ ($cm^{-1}/Å^6$)	$A \times 10^{-5}$ (cm^{-1})	r_x (Å)
Cl–H	2.6	8.4	1.81
Br–H	3.6	11.0	1.96
I–H	5.25	16.0	2.16
BH_4–H	2.0	10.0	1.93
K–H	1.3	3.55	1.33
Rb–H	1.8	4.3	1.48

[a]The value of α is 1.8 Å for all the interactions.

TABLE 2. Parameters in the potential function of the borohydride ion embedded in potassium chloride from atom–atom potentials

		$\beta_4\beta$		$\beta_6\beta$	
r^{-1}	H–K	142.8		−11.9	
	H–Cl	20.8		−1.4	
			163.6		−13.3
$\exp(-\alpha r)$	H–K	−677.0		64.3	
	H–Cl	59.9		−26.8	
			−617.1		37.5
r^{-6}	H–K	260.6		−43.7	
	H–Cl	−5.7		3.3	
			254.9		−40.4
			−198.6		−16.2

TABLE 3. Parameters in the potential function of borohydride ion

	T(K)	β	β_4	β_6
$KCl(BH_4^-)$	RT	−199.3	0.997	0.082
$KBr(BH_4^-)$	RT	−170.9	0.999	0.046
$KI(BH_4^-)$	RT	−113.6	0.999	0.037
KBH_4	RT	−162.2	0.999	0.022
$RbCl(BH_4^-)$	77	−233.1	1.000	0.020
$RbBr(BH_4^-)$	77	−192.6	1.000	0.003
	RT	−187.0	1.000	−0.002
$RbI(BH_4^-)$	77	−130.1	1.000	−0.001
$RbBH_4$	RT	−171.2	1.000	−0.015

[a]RT stands for room temperature.

There is a lambda (λ) point transition in the observed heat capacities of all the alkali metal borohydrides (11(*a*) $NaBH_4$; (*b*) KBH_4; (*c*) $RbBH_4$; (*d*) $CsBH_4$). The entropy of the transition is about $R \ln 2$ in $NaBH_4$, but about half that value in the other alkali metal borohydrides (12). The lower entropy of transitions in the heavier alkali metal borohydrides has been attributed to the partial disordering of the borohydride ion, while in $NaBH_4$ the borohydride ion is totally disordered above the transition temperature (13). If the borohydride ion is partially ordered above the transition temperature, a $\beta_3 V_3(\omega)$ term would be introduced into the potential function, eq. [4]. This would further increase the librational frequencies of the borohydride ions in KBH_4 and $RbBH_4$. Why does the rotational potential function derived from atom–atom potentials give values for the librational frequency that are higher than the observed values? In the study of linear molecules in inert gas matrices, a model by Manz and Mirsky that takes into account

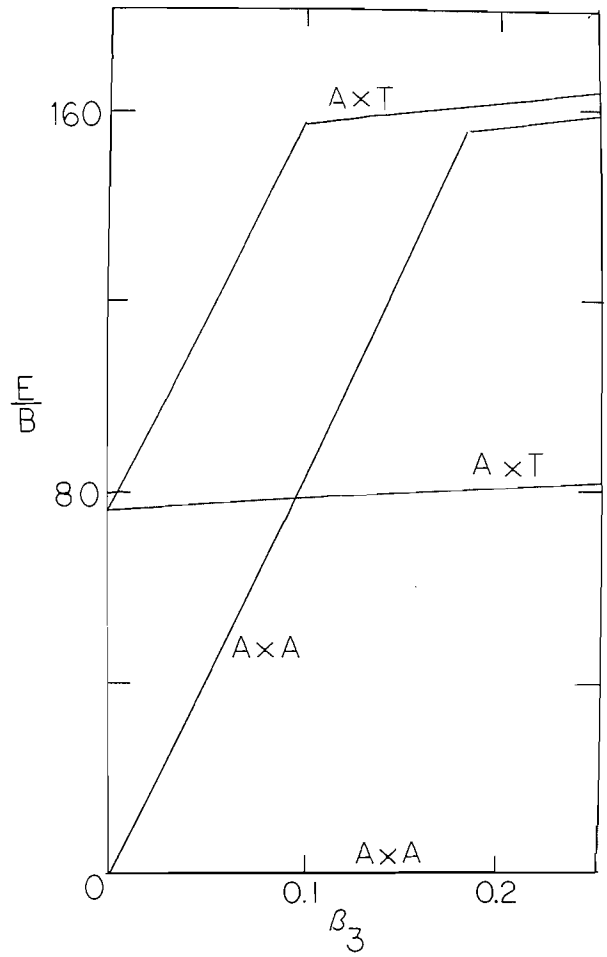

FIG. 1. The effect of β_3 on the lower energy levels with nuclear spin symmetry *A*. The other terms in the potential function are given in Table 3 for $RbBH_4$. The librational frequency varies from 77*B* to 82*B* as β_3 increases from 0 to 0.25.

the relaxation of the lattice near the impurity molecules has been used to interpret the results (14). There would be no purpose in applying such a theory to potassium and rubidium borohydrides, since the degree of order of the borohydride ions above the transition temperature is unknown and therefore the parameters in the rotational potential function are uncertain. The parameters given in Table 3 for KBH_4 and $RbBH_4$ are derived assuming total disorder of the borohydride ions above the transition temperature.

A method of studying the order of tetrahedral ions in solids is based on the difference in the ground level degeneracies of a tetrahedral ion in an ordered and in a disordered state. In a disordered state the ground level comprises five states with a total degeneracy, including nuclear spin, of 32, while in an ordered state there are three states with a total degeneracy of 16. The site symmetry of the tetrahedral ion in the disordered state is O_h, while in the ordered state it is T_d. The difference in the potential function of these two states is that there is a $\beta_3 V_3(\omega)$ in the ordered state. When $\beta_3 = 0$, there are two states with nuclear spin symmetry *A* in the ground level, while if $\beta_3 \neq 0$, there is only one state with *A* symmetry in the ground level. As a small β_3 term is added to a potential such as given in eq. [4], the two states with *A* symmetry will split, as is illustrated in Fig. 1. If the value of β_3 is large enough, the second state with nuclear spin symmetry *A* will eventually

Can. J. Chem. Downloaded from www.nrcresearchpress.com by 176.9.209.113 on 09/07/12
For personal use only.

TABLE 4. Comparison of computed and observed librational frequencies of the borohydride ion[a]

		Librational frequencies	
	T(K)	Computed	Observed
$KCl(BH_4^-)$	RT	363	360[b]
$KBr(BH_4^-)$	RT	323	300[b]
	77	329	350[c]
$KI(BH_4^-)$	RT	257	260[b]
KBH_4	RT	306	280[d]
$RbCl(BH_4^-)$	77	370	367[b]
$RbBr(BH_4^-)$	77	328	324[b]
$RbI(BH_4^-)$	77	265	271[b]
$RbBH_4$	RT	322	273[d]

[a]RT stands for room temperature.
[b]See ref. 8.
[c]See ref. 9.
[d]See ref. 10.

become part of the third librational level; i.e., the total harmonic quantum number will be equal to 2. The effect is illustrated in Fig. 1. However, for small values of β_3, one of the two states with A nuclear spin symmetry will have an energy somewhere between the ground librational level and the third librational level. So it is possible that when β_3 is less than about 0.10, there will be a state with A symmetry that will have an energy less than the librational frequency. There are states with T and E nuclear spin symmetry that will behave in the same manner as the state with A nuclear spin symmetry.

The effect described above may be investigated by a spectroscopic study of $RbBH_4$ at liquid nitrogen temperatures. Since the degree of ordering above the transition temperature is probably small, the value of β_3 will be small. If the effect described above is not observed in the pure substance, addition of RbBr to $RbBH_4$ will weaken the interaction between the borohydride ions and therefore lower the value of β_3. A similar study could be carried out on the ammonium halides below their transition temperature: by adding a rubidium halide to the ammonium halide, the interaction between the ammonium ions will be weakened.

IV. Results

The rotational potential function has been derived for the borohydride compounds using only three parameters, the value of α, the charge on the hydrogen atom of the borohydride ion, and the values of A_{K-H} and A_{Rb-H}. The latter parameters take on values that are close to those computed using eq. [3]. The charge on the hydrogen atoms of the borohydride ion does not have a significant effect on the derived potential function. If q_H is set at -0.15 rather than -0.20 electron units, a small adjustment of the values of A_{K-H} and A_{Rb-H} will yield essentially the same results for the parameters in the potential function.

The electrostatic term makes about the same contribution to the rotational potential function in borohydride compounds as in ammonium compounds. The repulsion term, however, makes a much larger contribution to the rotational potential function in borohydride compounds than in ammonium compounds because of the larger size of the BH_4^- ion. The B—H distance is about 1.26 Å as opposed to about 1.04 Å for N—H.

As with the previous two papers in this series, the question of the transferability of the atom–atom potentials for the major interaction is determined by the fit of the properties computed from the rotational potential functions to experiment (1, 2). Just as in ref. 2, where the results indicated that the transferability of the hydrogen–fluorine interaction is appropriate, so in this paper the good agreement between the computed and observed librational frequencies indicates that the transferability of the alkali metal – hydrogen interaction is appropriate. The use of a constant value of α for all the repulsive interactions in this paper follows the pattern set in ref. 1. All of the repulsive interactions considered in this paper are small, except for the alkali metal – hydrogen interaction, so the values of α for the weak interactions do not make a significant change in the resultant rotational potential function.

V. Acknowledgment

The author thanks M. Giri for his helpful suggestions on this project.

1. D. SMITH. J. Chem. Phys. **82**, 5133 (1985).
2. D. SMITH. J. Chem. Phys. **86**, 4055 (1987).
3. H. YASUDA. Prog. Theor. Phys. **45**, 1361 (1971); J. Chem. Phys. **73**, 3722 (1980); J. Chem. Phys. **74**, 6531 (1981).
4. A. I. BOLDYREV, O. P. CHARKIN, N. G. RAMBIDI, and V. I. AVDEEV. J. Struct. Chem. **19**, 179 (1978).
5. J. SHANKER, G. G. AGRAWAL, and R. P. SINGH. J. Chem. Phys. **69**, 670 (1978).
6. A. P. ALTSHULLER. J. Am. Chem. Soc. **77**, 5455 (1955).
7. D. SMITH. J. Chem. Phys. **74**, 6480 (1982).
8. K. P. BRIERLEY, J. HOWARD, and T. C. WADDINGTON. J. Chem. Soc. Faraday Trans. 2, **77**, 1075 (1981).
9. M. I. MEMOM, W. F. SHERMAN, and G. R. WILKINSON. Spectrochim. Acta, Part A, **37**, 461 (1981).
10. J. TOMKINSON and T. C. WADDINGTON. J. Chem. Soc. Faraday Trans. 2, **72**, 528 (1975).
11. (*a*) H. L. JOHNSTON and N. C. HALLET. J. Am. Chem. Soc. **75**, 1467 (1953); (*b*) G. T. FURUKAWA, M. L. REILLY, and J. H. PICCIRELLY. J. Res. Natl. Bur. Stand. Sect. A, **68**, 651 (1964); (*c*) V. E. GORBUNOV, K. S. GAVRICHEV, and S. I. BAKUM. Russ. J. Phys. Chem. **59**, 1754 (1985); (*d*) V. E. GORBUNOV, K. S. GAVRICHEV, G. A. TOTROVA, and S. I. BAKUM. Russ. J. Phys. Chem. **60**, 296 (1986).
12. V. E. GORBUNOV, K. S. GAVRICHEV, and V. B. LAZAREV. Russ. J. Phys. Chem. **60**, 1240 (1986).
13. D. SMITH. J. Chem. Phys. **60**, 958 (1974).
14. J. MANZ and K. MIRSKY. Chem. Phys. **46**, 457 (1980); V. G. MANZHELII, E. A. KOSOBUTSKAYA, V. V. SUMAROKOV, A. N. ALEKSANDROVSKII, YU. A. FRIEMAN, V. A. POPOV, and V. A. KONSTANTINOV. Sov. J. Low Temp. Phys. **12**, 86 (1986).

Can. J. Chem. Downloaded from www.nrcresearchpress.com by 176.9.209.113 on 09/07/12
For personal use only.

Heat of re-forming a coal liquefaction product from distillate fractions

LEE D. HANSEN, STANISLAW L. RANDZIO,[1] LAURA LEWIS, EDWIN A. LEWIS, AND DELBERT J. EATOUGH
Department of Chemistry, Brigham Young University, Provo, UT 84602, U.S.A.

Received August 25, 1987

This paper is dedicated to Professor James A. Morrison

LEE D. HANSEN, STANISLAW L. RANDZIO, LAURA LEWIS, EDWIN A. LEWIS, and DELBERT J. EATOUGH. Can. J. Chem. **66**, 794 (1988).

Results of calorimetric measurements of the heat of mixing of distillates from distillation of an H-coal liquefaction product are reported. The measurements were made at 373 K with mixing ratios such that the resultant mixture was the same as before distillation. The heat of mixing, which was endothermic in all cases, was found not to be a result of hydrogen bond formation. Intermolecular interactions of aromatic compounds are the probable source of the heats of mixing observed.

LEE D. HANSEN, STANISLAW L. RANDZIO, LAURA LEWIS, EDWIN A. LEWIS et DELBERT J. EATOUGH. Can. J. Chem. **66**, 794 (1988).

On rapporte les résultats de mesures calorimétriques de la chaleur de mélange de distillats obtenus par distillation d'un produit de liquéfaction H-charbon. On a fait les mesures à 373 K, avec des rapports de mélange tels que le produit qui en résulte est le même que celui qui existait avant la distillation. Il ne semble pas que la chaleur de mélange, qui est endothermique dans tous les cas, provienne de la formation d'une liaison hydrogène. Il est probable que la chaleur de mélange observée est due aux interactions intermoléculaires des produits aromatiques.

[Traduit par la revue]

Can. J. Chem. Downloaded from www.nrcresearchpress.com by 176.9.209.113 on 09/07/12
For personal use only.

Introduction

The design and optimization of processes for the liquefaction of coal and the upgrading of coal liquefaction products will require a knowledge of the thermodynamic properties of coal liquid fractions (1). The liquids derived from hydrogenation of coal contain high concentrations of multi-ring aromatic compounds and of polar organic compounds with functional groups capable of forming hydrogen bonds (2–4). As a result of strong intermolecular interactions among these aromatic and polar compounds (5–8), correlation procedures previously developed for petroleum fractions usually cannot be used for estimation of the thermodynamic properties of coal liquid distillates (9). The development of improved correlation procedures requires thermodynamic data for coal liquefaction products at temperatures and pressures relevant to post-liquefaction separation processes such as distillation.

Heat capacities and enthalpies of coal liquids have been collected for distillates covering the whole range of boiling temperatures of liquids obtained from different coals (7–13). The measured enthalpy and specific heat values for coal liquids are larger than those predicted from conventional correlation procedures (9) because of the strong intermolecular interactions mentioned above. Eatough *et al.*[2] have successfully correlated the heat capacity of three different sets of coal distillates with an equation that uses the Watson–Nelson parameter (14) and a parameter describing hydrogen bonding between nitrogen bases and phenols. Allen *et al.*[3] have successfully used group contribution methods to predict the heat capacities of these same coal liquids. The results of these studies demonstrate that data directly related to the formation of hydrogen bonds and other strong intermolecular interactions in coal liquids are needed to predict the physical and thermodynamic properties of the liquids from easily measured parameters.

The distillation of a coal liquid results in changes in the intermolecular interactions, so that the properties of the distillate may be quite different from those predicted from correlations based only on the distillation temperature, the distillate density, and Watson characterization factor, K_W. A case in point is the observation that distillate fractions from coal liquids sometimes have much lower boiling points than distillation temperatures (7). The ΔH values for re-forming the liquid from the several distillates should be useful in identifying and quantifying any strong intermolecular interactions that affect the distillation curve. This paper reports experimental data on the heat of re-forming an H-coal liquid from distillate fractions taken along the distillation curve.

Experimental

Materials

A blend of products from the H-coal liquefaction process was distilled into fractions boiling in 28 K or 42 K increments by Chevron Research Company. Fractions were obtained over the boiling range from 478 to 728 K and also from the start of boiling to 478 K. Samples of distillate cuts were provided to BYU by the Pittsburgh Energy Technology Center (PETC). Selected physical and chemical properties of the 28 K cuts as determined at PETC are listed in Table 1. A more complete description of the samples and the methods used for characterization is given elsewhere.[3] For the purposes of this study, the still bottoms (728 +) were ground to a fine powder with an agate mortar and pestle.

Calorimetric measurements

Measurements of the heat of mixing of the distillates were made in a Setaram C80 calorimeter. The mixing cells supplied with the calorimeter were modified for these experiments as shown in Fig. 1. The total volume of the mixing space was reduced to about 2 cm^3 and the mixing space was centered in the cell. The vapor space never exceeded about 0.5 cm^3. The reduction in the cell volume was necessary because of the small quantities of the distillate cuts that were available. One sample was placed in the holder, 7, and covered with a thick metallic lid, 6. The holder, 7, was then put into the calorimetric cell cylinder, 8, and closed with a Teflon seal, 4, and the bottom screw, 10. The second sample was then placed in the calorimetric cell cylinder directly on the metallic lid, 6, and sealed with a second Teflon seal, 4,

[1]On leave from the Polish Academy of Science, Institute of Physical Chemistry, 01-224 Warsaw, ul. Kasprzaka 44, Poland.

[2]D. J. Eatough, D. T. Allen, M. B. Perry, C. E. Schmidt, and C. M. White. Molecular interactions in and the heat capacity of narrow boiling fractions of an H-coal liquid. 1987. Manuscript in preparation.

[3]D. T. Allen, C. M. White, M. B. Perry, and C. E. Schmidt. Narrow boiling fractions of coal liquids. 1987. Manuscript in preparation.

TABLE 1. Properties and composition of distillate fractions of an H-coal liquid

Fraction[a]	T_b[b] (K)	Density,[c] 289 K (g/mL)	Viscosity,[d] 333 K (Centistokes)	Functional group (mol/kg)[e]				
				Phenol	Tetrahydroquinoline	Pyridine	Quinoline	Aromatic hydrocarbon
728+	—	—	—	—	—	—	—	—
700–728	694	1.070	1080	0.85	0.24	0.00	0.38	2.42
672–700	667	1.046	67	0.71	0.29	0.00	0.20	2.78
644–672	647	1.069	29	0.70	0.31	0.00	0.17	2.46
616–644	623	1.022	11	0.56	0.21	0.00	0.20	2.41
589–616	598	0.990	5.4	0.44	0.17	0.00	0.13	2.13
561–589	567	0.982	3.3	0.43	0.10	0.03	0.07	1.50
533–561	541	0.955	2.3	0.62	0.07	0.11	0.05	0.93
505–533	514	0.950	1.7	0.84	0.06	0.14	0.05	0.60
478–505	494	0.947	1.6	1.75	0.00	0.31	0.07	0.28
478–	473	0.924	1.3	2.11	0.00	0.41	0.03	0.02

[a]The fractions are labeled according to the boiling temperature (K) over which the fraction was collected.
[b]Midpoint of the boiling range of the fraction collected.
[c]From ref. 19.
[d]From ref. 20.
[e]For a description of the methods used to obtain these data, see D. T. Allen, C. M. White, M. B. Perry, and C. E. Schmidt. Narrow boiling fractions of coal liquids. 1987. Manuscript in preparation.

Can. J. Chem. Downloaded from www.nrcresearchpress.com by 176.9.209.113 on 09/07/12
For personal use only.

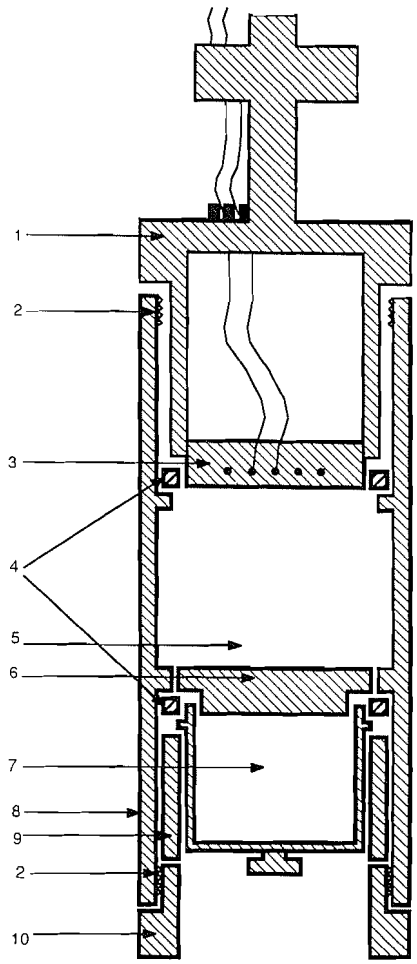

FIG. 1. Schematic diagram of the small volume calorimetric mixing cell. The parts of the cell are (1) upper screw, (2) threaded portion of cell cylinder, (3) calibration heater, (4) Teflon seals, (5) upper sample compartment, (6) lower sample compartment lid, (7) lower sample compartment, (8) cell cylinder, (9) spacer ring, and (10) bottom screw.

and the upper screw, 1. The screw, 1, also contained a miniature calibration heater, 3, made from Omegaclad thermocouple wire. With this design, the calibration heater was in direct thermal contact with the liquid in the cell. This design minimized the dependence of the calorimetric calibration constant on the distribution of the heat produced in the calorimetric cell (15).

The calorimeter output data were digitized at 10-s intervals with a Keithley 195A voltmeter and stored in a Commodore 64 computer. After a calorimetric experiment, the data were transferred to a Vax computer and integrated numerically to obtain the total heat produced in the experiment.

The electrical calibrations were checked by measuring the heat of mixing of *m*-cresol with quinoline. The heat of mixing for these chemicals is known from previous calorimetric measurements (5). The two calibrations disagreed by less than 1%. Since the *m*-cresol/quinoline system contains the most volatile materials used in this study, the vapor space in the mixing cell apparently does not result in any significant error.

The standard Setaram procedure of rotating the calorimeter was used to mix the liquids. Rotation of the calorimeter was repeated several times to insure that chemical equilibrium had been reached. The rotation itself produced negligible thermal effect.

All results reported here were collected at 373 K to decrease the viscosity of the high-boiling distillate fractions. Also, the products of mixing were collected and examined visually to insure that complete mixing had taken place during the experiment. The mixing process was slow compared to the mixing of *m*-cresol and quinoline, as judged by the calorimetric data. Attempts were made to perform measurements at 473 K to further decrease the viscosity of the liquids, but a large exotherm was observed with every rotation of the calorimeter. At 373 K this exotherm was not observed. The design of the mixing cell did not allow for the elimination of oxygen from the mixing space and we believe the exotherm seen at 473 K was due to oxidation of the coal liquid.

In the first series of nine duplicate measurements, we began by mixing the still bottoms (728+) with the highest boiling fraction (686–728) to obtain a mixture designated M686+. The M686+ mixture was mixed with the next higher boiling fraction (644–686) in the second experiment to form a mixture designated M644+. The experiments were continued in this way with successively lower boiling fractions until the final mixing of the M478+ mixture with the lowest boiling fraction, i.e., 478−.

TABLE 2. Heat of re-forming an H-coal liquid from distilled fractions

Experiment		Weight ratio of lower boiling fraction to higher boiling fraction	Heat of mixing[a] (J/(g of mixture))
Series I			
728+	+ 686–728	1.287	0.0
M686+	+ 644–686	0.501	0.0
M644+	+ 616–644	0.697	2.27
M616+	+ 589–616	0.714	2.21
M589+	+ 561–589	0.614	2.42
M561+	+ 533–561	0.361	2.81
M533+	+ 505–533	0.251	2.75
M505+	+ 478–505	0.209	0.10
M478+	+ 478–	0.062	0.08
Series II			
M700+	+ 672–700	1.287	0.0
M672+	+ 644–672	0.492	0.0

[a]All heat of mixing effects are endothermic. Uncertainties are ±0.2 J/g for the zero values and between ±0.1 and ±0.05 J/g for the rest of the values.

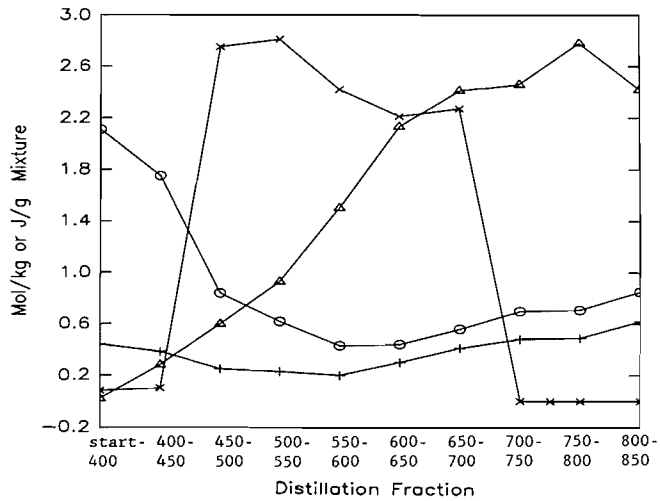

FIG. 2. Heat of re-forming (×) and concentrations (mol/kg) of aromatic hydrocarbons (△), phenols (○), and nitrogen bases (+) as a function of the distillation temperature.

The second series of three duplicate measurements was done in the same way except that 28 K fractions were used and the final mixture was an M700+ mixture. The measurements were performed in such a manner as to re-form the coal liquid as it existed prior to distillation. The mass ratios at which the particular distillate samples were mixed are listed in Table 2. These ratios were calculated from the mass balance of the distillation process determined by Chevron Research Company.

Results

The results of the measurements of the heat of re-forming of the H-coal liquids are given in Table 2. The precision of the calorimetric measurements was limited by the amount of material available for study and also by the very slow evolution of heat during the calorimetric experiments, which was a result of the high viscosity of the samples. The lower limit of detection for the two higher boiling samples where no detectable heat was observed was about 0.2 J/(g mixture). The uncertainty in the other data is about 0.05 to 0.1 J/(g mixture). Most of the data are the mean values of two measurements. A graphical presentation of the heat of mixing data as a function of the midpoint boiling temperature of the lower boiling distillate is given in Fig. 2.

The concentrations of phenols, azaarenes (e.g., pyridine, quinoline, and related compounds), hydrogenated azaarene (e.g., tetrahydroquinoline), and multi-ring aromatic compounds in each of the distillates are given in Table 1 and shown graphically in Fig. 2.

Discussion

To elucidate the factors that determine the heat of mixing values, both specific interactions such as hydrogen bonding and nonspecific intermolecular interactions caused by dispersive forces must be taken into account. The hydrogen bond interactions in a distillate include those resulting from the self-association of the phenols and from association of the phenols with nitrogen bases (5, 6). The effect of these hydrogen bonding interactions on the observed heats of mixing can be predicted by using the thermodynamic quantities for hydrogen bonding in the model system *m*-cresol–tetralin–quinoline–tetrahydroquinoline. The thermodynamic parameters determined for this model system have been used to predict correctly the heat capacity of distillates of coal liquefaction products (see footnote 2), thus showing that the model system provides an accurate portrayal of the thermodynamics of hydrogen bonding in coal liquids. The enthalpy values for the formation of hydrogen bonded complexes between quinoline and *m*-cresol and for the self-association of *m*-cresol are all strongly exothermic (5, 6). However, the heat of mixing of *m*-cresol and quinoline with multi-ring compounds such as tetralin (6) and large polynuclear aromatic compounds (16) is near zero.

If the heat absorbed on mixing the distillate fractions is due to changes in hydrogen bonding, the total hydrogen bonding must decrease as the samples are mixed. Furthermore, data on the model system (5, 6) predict that the change in the hydrogen bonding content must be about 0.1 mol/kg to account for the heat effect. However, calculations based on the free energies of hydrogen bonding reactions in the model system (6) indicate that the changes in hydrogen bond content in the mixing experiments are only about 0.005 mol/kg. Thus, the observed heats of mixing for the various distillate cuts are not controlled by changes in hydrogen bonding during mixing.

The negligible change in the amount of hydrogen bonding is a result of two factors. First, for many of the distillate fractions, the concentrations and ratios of acidic and basic species are approximately constant from fraction to fraction. Second, the heat of self-association of phenols (5, 6) effectively compensates for the decrease in the heat of acid–base interaction for those fractions in which the amount of phenol increases with decreasing boiling point (see Fig. 2). The only conclusion that can be made at the present time is that the heat of mixing is highest for those experiments which have the greatest change in the concentration of multi-ring aromatic hydrocarbons. This suggests that the observed heat of mixing reflects significant changes in non-hydrogen bonded molecular interactions, which occur on mixing the various distillate fractions. This conclusion is in agreement with a previous study (17) of the polarizability of coal liquefaction product distillates which concluded that "van der Waals forces are the dominant intermolecular forces in the H-coal and Wilsonville distillates." Also, data on heats of mixing of pure compounds (18) show that heats of mixing of aliphatic hydrocarbons are generally much smaller than the heat effects observed in this study, but that heats of mixing

Can. J. Chem. Downloaded from www.nrcresearchpress.com by 176.9.209.113 on 09/07/12
For personal use only.

of aromatic compounds are of the same order of magnitude. Thermodynamic data on appropriate model coal liquids are needed to further define the nature of these interactions.

Acknowledgements

This work was supported in part by contract no. DE-FG2 2-83PC60038 from the U.S. Department of Energy.

1. Recon Systems Inc., Fundamental data needs for coal conversion technology. Final Report No. TID-28152, U.S. DOE contract No. EY-76-C-02,4059. January, 1981.
2. C. M. WHITE, F. K. SCHWEIGHARDT, and J. L. SHULTZ. Fuel Process. Technol. **1**, 209 (1978).
3. C. M. WHITE, L. JONES, and N. C. LI. Fuel, **62**, 1397 (1983).
4. M. L. LEE, C. WILLEY, R. M. CASTLE, and C. M. WHITE. Polynuclear aromatic hydrocarbons. Battelle Press, Columbus, OH. 1980. pp. 59–73.
5. E. A. LEWIS, M. S. HOPKIN, D. J. MERRITT, S. L. WOLFLEY, J. J. CHRISTENSEN, L. D. HANSEN, and D. J. EATOUGH. Energy Fuels. Submitted.
6. D. J. EATOUGH, S. L. WOFLEY, L. J. DUNGAN, E. A. LEWIS, and L. D. HANSEN. Energy Fuels, **1**, 94 (1987).
7. J. A. GRAY, C. J. BRADY, J. R. CUNNINGHAM, J. R. FREEMAN, and G. M. WILSON. Ind. Eng. Chem. Process Des. Dev. **22**, 410 (1983).
8. R. SHARMA, V. F. YESAVAGE, and A. J. KIDNAY. AIChE J. **29**, 508 (1983).
9. S. C. MRAW, J. L. HELDMAN, S.-C. HWANG, and C. TSONOPOULOS. Ind. Eng. Chem. Prod. Res. Dev. **23**, 577 (1984).
10. A. J. KIDNAY and V. F. YESAVAGE. Enthalpy measurement of coal-derived liquids. Quarterly Technical Progress Report for the Period June 1975 – March 1979, U.S. DOE Contract No. EX-76-C-0-1-2035. January, 1980.
11. A. J. KIDNAY and V. F. YESAVAGE. Enthalpy measurement of coal-derived liquids. Quarterly Technical Progress Report for the Period October–December 1979 and January–March 1980, U.S. DOE Contract No. ET-13395-3-4. September 15, 1980.
12. A. J. KIDNAY and V. F. YESAVAGE. Enthalpy measurement of coal-derived liquids. Quarterly Technical Progress Report for the Period April–June 1980, U.S. DOE Contract No. ET-13395-5. September 15, 1980.
13. R. SHARMA, A. J. KIDNAY, and V. F. YESAVAGE. Energy Prog. **2**, 9 (1982).
14. K. M. WATSON and E. F. NELSON. Ind. Eng. Chem. **27**, 1 (1933).
15. J.-P. BROSS. Bull. Soc. Chim. Fr. 2582 (1966).
16. K. C. TEWARI and N. C. LI. Adv. Chem. Ser. No. 195 (1982).
17. C. M. WHITE and C. E. SCHMIDT. Fuel, **66**, 1030 (1987).
18. J. J. CHRISTENSEN, R. W. HANKS, and R. M. IZATT. Handbook of heats of mixing. John Wiley & Sons, New York, NY. 1982.
19. C. M. WHITE, M. B. PERRY, C. E. SCHMIDT, and L. J. DOUGLAS. Energy Fuels, **1**, 99 (1987).
20. C. E. SCHMIDT, M. B. PERRY, C. M. WHITE, G. A. GIBBON, and H. L. RETCOFSKY. Structural definition of synthetic fuels: H-coal distillates. DOE/PETC/TR-87-/4. National Technical Information Service, U.S. Department of Commerce, Springfield, VA 22161.

Can. J. Chem. Downloaded from www.nrcresearchpress.com by 176.9.209.113 on 09/07/12
For personal use only.

Computer simulation versus experiment: the structure of orientationally disordered neopentane

WOLFGANG BREYMANN,[1] PHILIPPE DEPONDT, AND ROBERT M. PICK

Département de Recherches Physiques (UA CNRS n° 71), Université Pierre et Marie Curie, Paris, France

Received August 11, 1987

This paper is dedicated to Professor J. A. Morrison

WOLFGANG BREYMANN, PHILIPPE DEPONDT, and ROBERT M. PICK. Can. J. Chem. **66**, 798 (1988).

A method to confront computer simulations to real nature is reported. "Experimental" results calculated from the simulation are analyzed through the same model as the actual experiments. The same terms are thus used to describe the simulated and the real sample; they can then be compared, with some reliability, to one another and also to the corresponding quantities obtained directly from the microscopic information provided by the simulation. The method is applied to neutron diffraction experiments performed on orientationally disordered neopentane ($C(CD_3)_4$) single crystals, a system for which a realistic molecular dynamics simulation has also been performed. Our method turns out to be a severe test both for the simulation and the models used to interpret the experiments.

WOLFGANG BREYMANN, PHILIPPE DEPONDT et ROBERT M. PICK. Can. J. Chem. **66**, 798 (1988).

On expose une méthode pour confronter une simulation par ordinateur à la réalité. Des résultats "expérimentaux" calculés à partir de la simulation sont analysés à l'aide des mêmes modèles que les véritables expériences. On utilise ainsi les mêmes termes pour décrire les échantillons simulés et véritables; ceux-ci peuvent alors être comparés entre eux aussi bien qu'avec les grandeurs correspondantes directement calculées à partir des données microscopiques obtenues dans la simulation. Cette méthode est appliquée à des expériences de diffraction de neutrons sur des monocristaux de néopentane ($C(CD_3)_4$) présentant un désordre d'orientation, système pour lequel une simulation de dynamique moléculaire réaliste a aussi été réalisée. Cette technique s'avère être un test sévère à la fois pour la simulation et pour les modèles utilisés pour l'interprétation des expériences.

I. Introduction

The comparison of information supplied by a molecular dynamics simulation and actual experimental results obtained on the same system may end up being a somewhat difficult task, when no flagrant disagreement between both sets of results occurs, since the two points of view are extremely different. Indeed, once a computer simulation is performed, the successive positions and velocities of each particle of the system are known, so that one may choose to study independently any given aspect of the problem at hand, the only limitations being the size of the sample and the duration of the simulation. The experimental data, on the other hand, are always a mixture of several contributions. Subsequently, they have to be interpreted by using models which are more or less adequate and thus provide information which is more or less reliable. To be specific, the simulation of an orientationally disordered crystal can provide separately, for instance, the orientations of the molecules and the displacements of the molecular centers of mass, while both quantities, among others, will play a role simultaneously, e.g., in a diffraction experiment or in an inelastic neutron scattering experiment performed on the real crystal.

A first step towards this comparison is the use of the microscopic information obtained during the simulation to compute what should have been the experimental result (e.g. Bragg peak intensities, or neutron inelastic spectra), if the experiment had been performed on the simulated system. One may then find out the extent of agreement (or disagreement) between the simulated and the real experiment; this method has been used, for instance, by Klein and co-workers (1) in the case of inelastic neutron spectra obtained in the plastic phase of KCN. Unfortunately, since the experimental data have, generally, no simple, directly understandable physical meaning, such a comparison remains rather qualitative.

A second step may be achieved if one analyses the simulated experiment through the same model(s) as the real one. Then three sets of physical parameters exist to describe the two systems, real and simulated: (*1*) physical parameters obtained by analyzing the experimental data via a given model; (*2*) physical parameters obtained by analyzing the simulated experimental data via the same model; and (*3*) the last set is obtained by computing directly these parameters from the microscopic data of the simulation.

The comparison between (*1*) and (*2*) is a precise test of the extent to which the simulation is realistic. Since it is made in terms with a direct physical meaning, it may also indicate which aspects of the simulation fail to be realistic. The same comparison performed between (*2*) and (*3*) is, conversely, a test of the validity of the model used for analyzing the experiments; any discrepancy between (*2*) and (*3*) means that a similar discrepancy between (*1*) and (*3*) is not a severe test on the validity of the simulation. It gives a measure of the uncertainties existing on the parameters extracted from (*1*).

The present paper illustrates this fairly general method with the example of the orientationally disordered, or plastic, phase of neopentane ($C(CH_3)_4$) in which the molecular centers of mass form a f.c.c. Bravais lattice, while the tetrahedral molecules perform large amplitude rotations. Structural information supplied by a molecular dynamics simulation (2) on the one hand, and by neutron elastic diffraction experiments (3, 4) on the other, have been compared. The simulation shows a situation in which the molecules perform frequent reorientations from one orientational potential well to another equivalent one. The corresponding most probable orientations are D_{2d}, i.e. with one molecular $\bar{4}$ axis parallel to a 4-fold crystal axis and the two other $\bar{4}$ axes parallel to 2-fold crystal axes, giving six equivalent but physically distinct wells. This agrees with the experiment so that one is apt to become interested in more detailed structural aspects.

The structure of the plastic phase is usually described in terms of the orientational probability density function (o.p.d.f.)

[1]Present address: Institut f. Physik, Universität Basel, Klingelbergstr. 82, CH-8056 Basel.

Can. J. Chem. Downloaded from www.nrcresearchpress.com by 176.9.209.113 on 09/07/12
For personal use only.

Can. J. Chem. Downloaded from www.nrcresearchpress.com by 176.9.209.113 on 09/07/12
For personal use only.

$P(\Omega)$, which is the probability that the molecular reference frame can be deduced from the crystal frame through a rotation Ω, where Ω represents the corresponding set of Euler angles. In the case of the computer simulation, $P(\Omega)$ can be evaluated directly since the orientation of each molecule is known independently of other quantities, its center of mass position for instance. On the other hand, the experimental data consist of a set of Bragg peak intensities; they contain a combination of at least orientational and translational effects, assuming one is able to eliminate scattering by the cryostat[2] and the incoherent contribution caused by the remaining hydrogen atoms in $C(CD_3)_4$. As it has been shown in (5), $P(\Omega)$ can be expanded on a set of symmetry adapted functions, and the resulting expansion coefficients, as well as an isotropic Debye–Waller factor related to the molecular center of mass translations, appear in a calculated structure factor, which, in turn, is fitted to the data.

We want to compare in detail an actual orientational probability function supplied by the simulation with the sets of parameters which are provided by the model. We are interested in particular in knowing how well the maxima of $P(\Omega)$ are defined and what is the amount of translational disorder as shown by the Debye–Waller factor. The rest of this paper is devoted to the calculation of the two sets of parameters (*2*) and (*3*) relative to the simulation and to their comparison with set (*1*).

II. Numerical simulation of a neopentane crystal

The simulation is described in detail elsewhere (2) so we will give only a short summary here.

The simulated sample[3] consists of 864 molecules located on a f.c.c. lattice corresponding to a sample of $6 \times 6 \times 6$ unit cells. Each molecule is described by its 17 atoms and considered as rigid. As the molecule of neopentane is electrically neutral and fairly isotropic, the electrostatic forces can be neglected. Therefore, only Buckingham atom–atom potentials between all the atoms of the nearest neighbour molecules have been taken into account (6). The mass and moment of inertia of $C(CH_3)_4$ are quite large, so that quantum effects can be neglected. Three runs have been performed at, respectively, 135 K,[4] 175 K, and 230 K.

The result of such a simulation is a set of positions and orientations of each molecule as a function of time, allowing one to compute any pertinent physical quantity; those of interest are, here, $P(\Omega)$ and the Debye–Waller factor.

III. Computation of Bragg peak intensities

A coherent neutron scattering experiment yields (7):

$$[1] \qquad I(\boldsymbol{Q}) = \int_0^\tau \left| \sum_{n,j} f_j \{\exp i\boldsymbol{Q}(\boldsymbol{R}_n + \boldsymbol{u}_n(t) + \boldsymbol{r}_{nj}(t))\} \right|^2 \mathrm{d}t$$

where $\boldsymbol{R}_n$ is the equilibrium position of the center of mass of molecule n, $\boldsymbol{u}_n(t)$ is the displacement at time t of the center of mass of the same molecule, $\boldsymbol{r}_{nj}(t)$ is the position at time t of atom j relative to the molecular center of mass n, f_j is the coherent scattering length of atom j, $\boldsymbol{Q}$ is the scattering vector, the symbol $\Sigma_{n,j}$ stands for $\Sigma_{n=1}^{N}\Sigma_{j=1}^{\nu}$, N and ν being the number of molecules and atoms in the sample and molecule, and τ is the duration of the experiment.

In eq. [1], the usual thermal average is replaced by an explicit time summation as time appears explicitly in a simulation, but eq. [1] holds as well for the real system as for the simulation.

Equation [1] may be rewritten as

$$[2] \qquad I(\boldsymbol{Q}) = \int_0^\tau \left(\sum_{n,j} f_j \{\exp i\boldsymbol{Q}[\boldsymbol{R}_n + \boldsymbol{u}_n(t) + \boldsymbol{r}_{nj}(t)]\} \sum_{n',j'} f_{j'}^* \{\exp -i\boldsymbol{Q}[\boldsymbol{R}_{n'} + \boldsymbol{u}_{n'}(t) + r_{n'j'}(t)]\} \right) \mathrm{d}t$$

In a Bravais lattice, $\exp i\boldsymbol{Q}\boldsymbol{R}_n$ is equal to 1 if $\boldsymbol{Q}$ belongs to the reciprocal lattice.[5] We see thus that $\boldsymbol{R}_n$ and $\boldsymbol{R}_{n'}$ are, in principle, irrelevant quantities in [2], but since we want to make sure that, in the simulated sample, the f.c.c. extinctions actually do occur, we shall keep these terms.

In a disordered system, correlations between different molecules may exist, but the corresponding correlation lengths are short (approximately 20–30 Å) compared to the macroscopic size of the real sample (at least 1 mm) so that for a given value of n, among the N values of n', only a small number are sensitive to correlation effects. These may then be neglected, which yields:

$$[3] \qquad I(\boldsymbol{Q}) = \int_0^\tau \sum_{n,j} f_j \{\exp i\boldsymbol{Q}[\boldsymbol{R}_n + \boldsymbol{u}_n(t) + \boldsymbol{r}_{nj}(t)]\} \mathrm{d}t \int_0^\tau \sum_{n',j'} f_{j'}^* \{\exp -i\boldsymbol{Q}[\boldsymbol{R}_{n'} + \boldsymbol{u}_{n'}(t) + \boldsymbol{r}_{n'j'}(t)]\} \mathrm{d}t$$

$$= \left| \int_0^\tau \sum_{n,j} f_j \{\exp i\boldsymbol{Q}[\boldsymbol{R}_n + \boldsymbol{u}_n(t) + \boldsymbol{r}_{nj}(t)]\} \mathrm{d}t \right|^2$$

Passing from [1] to [3] is an important step, because neglecting short range correlations, whatever their nature, is possible only because of the large size of the sample. On the other hand, the size of the simulated sample (approx. $(100\ \text{Å})^3$) is not large enough to neglect these correlations, and indeed we have verified their importance in the following manner: the intensity given by eq. [1] should be equal to zero for $\boldsymbol{Q}$ not belonging to the reciprocal lattice of the f.c.c. Bravais lattice. Furthermore, if $\boldsymbol{Q}$ is a reciprocal lattice vector, the existence of centers of symmetry in the f.c.c. lattice implies that in eq. [1], the summation over n and j should not contain an imaginary part. Neither of these tests turned out to be verified with a meaningful accuracy for the simulated sample, which means that [1] cannot be used since we want to compare computed

[2]The experiments were performed between 150 and 253 K.

[3]In order to avoid confusing double meanings, the word "model" will be used only for the models with which the experiments are interpreted, while the simulated model will be called "sample".

[4]Although the real crystal is not in the plastic phase at 135 K, the simulated crystal is, since the constraints of the constant volume simulation prevent orientational ordering.

[5]As we index these vectors in the simple cubic lattice, $\exp i\boldsymbol{Q}\boldsymbol{R}_n$ is in fact equal to 1 only for those reciprocal lattice vectors which satisfy the Miller indices parity rule.

Bragg peak intensities to actual experimental data obtained on large samples for which short range correlations are extremely small. We have thus used eq. [3], in which the correlations have been deliberately eliminated.

As in a simulation we use discrete time steps, we must now transform eq. [3] into:

$$[4]\quad I(\boldsymbol{Q}) = \left| \sum_{n,j} f_j \sum_{k=1}^{\theta} \{\exp i\boldsymbol{Q}[\boldsymbol{R}_n + \boldsymbol{u}_n(k.\delta t) + \boldsymbol{r}_{nj}(k.\delta t)]\}\delta t \right|^2$$

where δt is the time step length in the summation and $\theta = \tau/\delta t$ is the number of time steps.

δt could be chosen to be equal to the simulation step length (1/60 ps) but two successive steps in the simulation are strongly correlated and thus carry almost the same information. Therefore, very little loss of information will occur if δt is chosen to be equal to 1 ps, i.e. a typical correlation time for a single molecule orientation.

Using the composite index $m \equiv k,n$ and writing

$$[5]\quad \rho_{mj} \equiv \boldsymbol{R}_n + \boldsymbol{u}_n(k.\delta t) + \boldsymbol{r}_{nj}(k.\delta t)$$

yields

$$[6]\quad F(\boldsymbol{Q}) = \frac{1}{M} \sum_{m=1}^{M} \sum_{j=1}^{\nu} f_j \exp i\boldsymbol{Q}\cdot\rho_{mj}$$

and

$$[7]\quad I(\boldsymbol{Q}) = M|F(\boldsymbol{Q})|^2\delta t^2$$

with $M = N\cdot\theta = N\tau/\delta t$, and where $F(\boldsymbol{Q})$ is the average single molecule structure factor (SMSF) which is the quantity that appears in most models for diffraction experiments.

Summing up, the procedure leading from eq. [1] to eqs. [6] and [7] means that we have used ergodicity to replace an experiment lasting for τ = 60 ps on a sample with N = 864 molecules by an instantaneous experiment on a much larger sample with M = 51840 molecules. This new sample has now the correct average structure of a real crystal. Indeed, Table 1 shows that the imaginary part of $F(\boldsymbol{Q})$ and the intensity of the forbidden Bragg reflexions are equal to zero with a very good accuracy.

Finally, in order to estimate the standard deviations of our intensity computations, several equivalent reflexions have been taken into account.

IV. Analysis of the Bragg peak intensities

Table 1 exhibits the simulated and experimental Bragg peak intensities. It is clear that a direct comparison is fruitless; thus justifying the procedure described in the Introduction.

(a) Model

In the rigid molecule approximation, the SMSF writes, for molecules on a Bravais lattice:

$$[8]\quad F(\boldsymbol{Q}) = \int P(\boldsymbol{u},\Omega) \sum_{j=1}^{\nu} f_j\{\exp i\boldsymbol{Q}[\boldsymbol{u} + \boldsymbol{r}_j(\Omega)]\}\mathrm{d}\boldsymbol{u}\mathrm{d}\Omega$$

where $P(\boldsymbol{u},\Omega)$ is the probability of finding the molecule with orientation Ω and a center of mass displacement $\boldsymbol{u}$.

Following ref. 9, $P(\boldsymbol{u},\Omega)$ can be expressed as

$$[9]\quad P(\boldsymbol{u},\Omega) = P(\boldsymbol{u})[P(\Omega) + \boldsymbol{P}^{(1)}(\Omega).\boldsymbol{u} + \ldots.]$$

Combining eq. [8] and the first term of eq. [9] provides the zeroth order translational contribution which may be rewritten as (8):

$$[10]\quad \int P(\boldsymbol{u})\mathrm{e}^{i\boldsymbol{Q}.\boldsymbol{u}}\mathrm{d}\boldsymbol{u} = \langle \mathrm{e}^{i\boldsymbol{Q}.\boldsymbol{u}}\rangle = \mathrm{e}^{-(1/2)Q^2\langle u^2\rangle}$$

thus supplying the usual Debye–Waller factor related to the molecular center of mass displacements.

The orientational probability $P(\Omega)$ is expanded on a set of symmetry adapted functions:

$$[11]\quad P(\Omega) = \sum_{l,\lambda,\lambda'} \frac{2l+1}{8\pi^2} A_l^{\lambda\lambda'} \mathcal{R}_l^{\lambda\lambda'}(\Omega)$$

where $\mathcal{R}_l^{\lambda\lambda'}(\Omega)$ is a symmetry adapted function, l is related to the number of nodes of $\mathcal{R}_l^{\lambda\lambda'}(\Omega)$ as in the case of the spherical harmonics $Y_l^m(\theta,\varphi)$, and λ (or λ') labels the irreducible representations of the site (or molecular) symmetry point group (10).

It is easily shown (5) that, when limiting $P(\boldsymbol{u},\Omega)$ to its lowest order term, the SMSF is completely expressed in terms of $\langle u^2\rangle$, $A_l^{\lambda\lambda'}$, and functions depending only on $\boldsymbol{Q}$, f_j, and on the molecular geometry. In the case of a tetrahedral molecule in a cubic lattice, symmetry considerations restrict the $A_l^{\lambda\lambda'}$ coefficients, for the lowest values of l, to A_4^{11}, A_6^{11}, A_8^{11}, and A_{10}^{11} (proper definitions of these coefficients are given in ref. 10). When including the second term of [9], new coefficients related to rotation-translation coupling appear in $F(\boldsymbol{Q})$.

In a plastic crystal, the Bragg peak intensities decrease very rapidly when $|\boldsymbol{Q}|$ increases, due to the large value of $\langle u^2\rangle$, so that the number of independent reflexions which may be used is always small (32 at most for $C(CD_3)_4$) thus limiting the number of fitting parameters. In the analysis of the experimental data, we restricted ourselves to $\langle u^2\rangle$, the four $A_l^{\lambda\lambda'}$ coefficients for $l \leqslant 10$ and to the three lowest translation–rotation coupling coefficients. The latter three parameters have no obvious physical meaning and will consequently not be discussed in the present work.

The Bragg peak intensities obtained from the simulated sample were analyzed following the same procedure.

(b) Direct calculations

The Debye–Waller factor and the expansion coefficients $A_l^{\lambda\lambda'}$ can also be obtained directly from the simulation. The translational term $\langle u^2\rangle$ relative to the molecular centers of mass is:

$$[12]\quad \langle u^2\rangle = \frac{1}{\tau}\int_0^{\tau} \frac{1}{N}\sum_{n=1}^{N} u_{rn}^2(t)\mathrm{d}t$$

where $u_{rn}(t)$ is the projection of $\boldsymbol{u}_n(t)$ on an arbitrary direction $\hat{\boldsymbol{r}}$.

$P(\Omega)$ may be written directly, following the definition of the o.p.d.f.:

$$[13]\quad P(\Omega) = \frac{1}{\tau}\int_0^{\tau} \frac{1}{N}\sum_{n=1}^{N} \delta(\Omega - \Omega_n(t))\mathrm{d}t$$

where $\Omega_n(t)$ is the orientation of molecule n at time t. Applying the orthogonality relation of the symmetry adapted functions to eq. [11] and using eq. [13] yields:

$$A_l^{\lambda\lambda'} = \frac{1}{\tau}\int_0^{\tau} \frac{1}{N}\sum_{n=1}^{N} \mathcal{R}_l^{\lambda\lambda'*}(\Omega_n(t))\mathrm{d}t$$

which can be computed.

Can. J. Chem. Downloaded from www.nrcresearchpress.com by 176.9.209.113 on 09/07/12
For personal use only.

TABLE 1. Experimental and simulated Bragg peak intensities for various peaks*

hkl	$(\mathrm{Re}\ F)^2$	$\sigma_{\mathrm{Re}\,F} \times 100$	$(\mathrm{Im}\ F)^2 \times 10^5$	$\sigma_{\mathrm{Im}\,F} \times 10^5$	F^2_{exp}	$\sigma_{F\,\mathrm{exp}}$
111	22.561	6.3	0.43	0.68	22.561	0.03
200	6.768	1.5	0.40	0.68	5.98	0.02
220	1.78	5.5	32	23	1.95	0.02
311	1.298	3.2	6.7	2.7	2.28	0.03
222	2.943	3.5	14	18	4.05	0.04
400	0.0556	0.29	10	10	0.00	0.05
331	0.688	3	8.6	8.7	1.37	0.04
420	1.188	3	2.7	1.8	2.21	0.04
422	0.563	1.1	6.3	8.9	0.67	0.05
511	0.667	1.6	15	24	0.78	0.04
333	0.3903	0.89	7	11	0.40	0.04
440	0.903	3	18	18	2.04	0.04
531	0.1823	0.34	20	17	0.37	0.06
600	0.326	1.6	47	17	0.63	0.05
442	0.2149	0.66	3.8	4.1	0.50	0.05
620	0.0516	0.67	38	18	0.05	0.05
533	0.0563	0.35	41	27	0.05	0.05
622	0.00064	0.095	10	10	0.00	0.05
444	0.275	1.6	9.5	8.3	0.57	0.07
711	0.0705	0.77	34	34	0.26	0.09
551	0.0053	0.10	4.1	6.1	0.00	0.09
640	0.0080	0.24	54	49	0.03	0.15
642	0.0035	0.13	43	42	0.00	0.15
553	0.073	1	9	11	0.12	0.12
731	0.0063	0.11	16.6	8.8	0.00	0.10
800	0.095	1.3	22	23	0.42	0.06
733	0.0158	0.23	22	27	0.00	0.10
644	0.0512	0.51	21	9.5	0.10	0.06
820	0.0351	0.42	29	37	0.10	0.08
822	0.0155	0.23	13	13	0.05	0.07
660	0.000072	0.0071	6.8	1.7	0.00	0.07
751	0.00393	0.076	33	18	—	—
100	3×10^{-5}	—	1.4	—	—	—
110	3.4×10^{-5}	—	3	—	—	—
210	2×10^{-6}	—	2.4	—	—	—
211	2.14×10^{-4}	—	181	—	—	—

*Column 1: Miller indices of the Bragg peak.

Columns 2 to 5: intensity computed through the simulation at 175 K, with the help of eqs. [6] and [7]; columns 2 and 3: contribution of the real part of the structure factor and standard deviation; columns 4 and 5: contribution of the imaginary part of the structure factor and standard deviation. The five last lines correspond to symmetry-forbidden Bragg peaks.

Columns 6 and 7: experimental intensity measured at 173 K with standard deviations. The numerical values have been multiplied by a constant so that the experimental and simulated intensities of the (111) peak should be equal in order to facilitate comparison.

Can. J. Chem. Downloaded from www.nrcresearchpress.com by 176.9.209.113 on 09/07/12
For personal use only.

V. Results

As mentioned in the Introduction, we now have three sets of parameters which describe the same system in the same terms and can be compared with one another; this comparison leads to interesting results both for the Debye–Waller factor and the o.p.d.f.

(a) Debye–Waller factor

Figure 1 shows the thermal dependence of the three Debye–Waller factors. The two results relative to the simulation coincide almost perfectly, which means that the model used to analyze $I(\boldsymbol{Q})$ is reliable as far as $\langle u^2 \rangle$ is concerned. On the other hand, the experimental values are significantly smaller than the simulated ones. This may be caused by two different effects.

(i) Corrections to the experimental data

No thermal diffuse scattering (TDS) correction has been performed on the experimental data. As the correction increases with the Miller indices, this could lead to an overestimation of the Bragg peak intensities for large momentum transfers, thus to an experimental Debye–Waller factor smaller than the actual one. Nevertheless, the TDS correction is clearly very small for the more intense Bragg peaks, and could be important only for the weak peaks for which the standard deviation is already comparatively large, and have then a small weight in the fitting procedure; the inclusion of the TDS correction is thus not likely to alter significantly the Debye–Waller factor obtained from the experiment.

Similarly, other corrections such as absorption and multiple

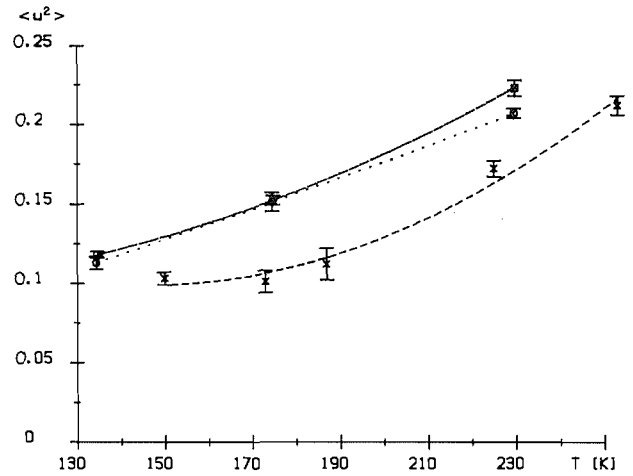

FIG. 1. Thermal dependence of the Debye–Waller factor. Crosses (× ×): experimental data analyzed through the o.p.d.f. expansion model; circles (○○○): simulated data, analyzed with the same model as above; boxes (□□□): calculated directly from the simulation.

scattering were not performed but simply included in the error bars.

(ii) Weakness of the potential

The potentials used in the simulation have been optimized on crystallographic and calorimetric data (6), and then tested on the harmonic dynamics of molecular crystals (11), that is, for usual interatomic distances in crystals. Nevertheless, in ODIC phases, some of these distances will become much shorter (particularly for H–H interactions) during the reorientation processes. The simulation is thus sensitive to a range of distances at which these potentials may be inaccurate. The comparison between the experiment and the simulation suggests strongly that they are, in fact, too weak at short distances.

The general behaviour of the three Debye–Waller factors shown in Fig. 1 is however quite comparable; in particular, one must stress that this factor is much larger than what one expects from the translational phonon contribution (3). There exists, in neopentane, an intrinsic, orientationally induced, contribution to the Debye–Waller factor which dominates it, and which increases with temperature.

(b) Orientational probability distribution functions

Figures 2*a*, *b*, and *c* show the thermal dependence of A_4^{11}, A_6^{11}, and A_8^{11}, respectively. The great accuracy of the coefficients obtained directly, compared to that of the fitted coefficients, may be noticed, along with their linear dependence with temperature. On the other hand, if the differences between the three methods are within error bars for A_4^{11} and A_8^{11} due to their small numerical values, A_6^{11} which has the largest absolute value shows a significant difference between the direct calculation and the fitted values. These results may be discussed from two different view points: (*1*) The fact that A_6^{11} is strongly negative while A_4^{11} is small, both in the direct calculation and in the analysis through the model, is important because this is the signature of an o.p.d.f. with maxima in D_{2d} orientations (3): the model thus provides the correct most probable molecular orientations. (*2*) From a quantitative point of view, the comparison between the two values obtained for A_6^{11} for the same sample on the one hand, as well as that of the respective sizes of the error bars on the other, shows that the analysis of the

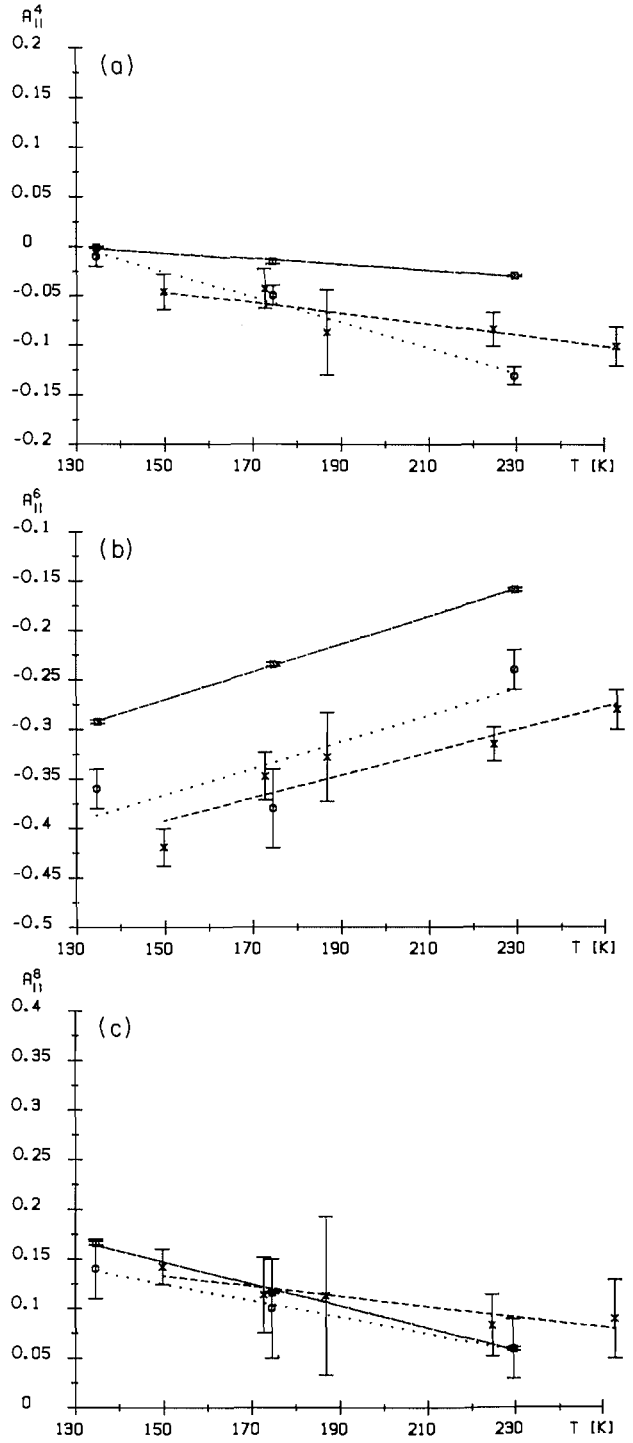

FIG. 2. Thermal dependence of the o.p.d.f. expansion coefficients. Same as above; (*a*) coefficient A_4^{11}; (*b*) coefficient A_6^{11}; (*c*) coefficient A_8^{11}.

data through this model does not describe $P(\Omega)$ properly.[6] The reasons for this inaccuracy lie mainly in two of the assumptions of the model: (*a*) $P(\Omega)$ is a smooth enough function of the

[6]The coefficients A_l^{λ} are quite uncorrelated because the spherical Bessel functions $j_l(kr)$ which enter in the calculation of the SMSF (5) select, for each value of l, different regions of the reciprocal space. There is thus no way of decreasing in a systematic way the differences between the two sets of values.

Can. J. Chem. Downloaded from www.nrcresearchpress.com by 176.9.209.113 on 09/07/12
For personal use only.

orientation so that one may restrict oneself to low values of l; (b) the mean center of mass displacements are small enough for any term in the expansion of the second term of $P(\boldsymbol{u},\Omega)$ beyond the linear one, to be neglected.

It is very likely that none of these assumptions is correct. The large values of $\langle u^2 \rangle$ tend to contradict point (b). Furthermore, the analysis of the experimental data using the TLS model (4) suggests that most of the molecules are in fact much more localized around the D_{2d} orientations than can be described by an expansion of the o.p.d.f. truncated at $l = 10$, thus contradicting point (a). The fitting procedure tends to overcome this difficulty by producing a $P(\Omega)$ which is smoother than in reality, thus making the model somewhat unreliable in this respect.

VI. Conclusion

We have confronted the point of view of Laplace's creature[7] to an actual experiment by performing a simulated "experiment" and then comparing it to real size experimental data. This is, in itself, not unusual (13) but the simulated data were also analyzed through the model which was used to interpret the experiments. This is a demanding test both for the simulation and for the model so that their shortcomings are vividly revealed: (*1*) The expression of the SMSF through a Debye–Waller factor and an expansion of the o.p.d.f. seems to be able to provide reliable information about the translational disorder since one obtains identical values for $\langle u^2 \rangle$ in the simulated sample, whether calculated directly or through the model. The values of the expansion coefficients of the o.p.d.f. in terms of symmetry adapted functions are, however, clearly unreliable in this case contrary to what has been found for adamantane (14) in the case of small Debye–Waller factors. (*2*) The simulation shows at least an excess in translational disorder compared to the real crystal. This discrepancy is very likely related to the short range behaviour of the atom–atom potentials used in the simulation, a conclusion which could not have been reached by simply computing the Bragg peak intensities for the simulated sample and comparing them with the experimental ones.

[7] "Une intelligence qui pour un instant donné connaitrait toutes les forces dont la nature est animée et la situation respective des êtres qui la composent" ("An intelligence which for a given instant would know all the forces by which nature is driven and the respective locations of the beings of which it is composed") (12).

It would have been most desirable to perform a similar comparison between the simulated crystal and the real crystal, making use of the TLS model (4) mentioned in section V. The direct calculation of the pertinent quantities (i.e. $\langle \theta_i^2 \rangle$, where θ_i is a molecular rotation around an axis i) is, however, much more difficult than for the o.p.d.f. expansion coefficients and therefore beyond the scope of this work.

From a more general point of view, two aspects emerge from this specialized study of neopentane: (*1*) The method we have presented here for comparing experimental data with a molecular dynamics simulation allows us to use the complementarity of these two techniques more efficiently than previously: it reveals the weakness of the simulation as well as those of the models used for analysing the experiments.

(*2*) This technique involves the computation of simulated experimental data. The production of such data may imply the use of rather sophisticated techniques because of the inherent differences between the simulated and real samples, such as, in the present case, the size of the sample and the duration of the experiment.

1. I. R. McDonald, D. G. Bounds, and M. L. Klein. J. Phys. C**16**, 3217 (1983).
2. W. Breymann. Thesis, Paris. 1987.
3. B. Denise, Ph. Depondt, M. Debeau, and P. Schweiss. J. Phys. **48**, 615 (1987).
4. Ph. Depondt and M. Debeau. J. Phys. **48**, 1513 (1987).
5. W. Press and A. Hüller. Acta Crystallogr. A**29**, 252 (1973).
6. D. E. Williams. J. Chem. Phys. **47**, 4680 (1967).
7. B. T. M. Willis and A. W. Pryor. Thermal vibrations in crystallography. Cambridge University Press. 1975. p. 175.
8. W. Marshall and S. W. Lovesey. Theory of thermal neutron scattering. Oxford University Press. 1971. p. 62.
9. W. Press, M. Grimm, and A. Hüller. Acta Crystallogr. A**35**, 881 (1979).
10. M. Yvinec and R. M. Pick. J. Phys. **41**, 1045 (1980).
11. R. Righini, S. Califano, and S. H. Walmsley. Chem. Phys. **50**, 113 (1980).
12. P. S. Laplace. Essai philosophique sur les probabilités. Bachelier, Paris. 1825. p. 4.
13. E. R. Cowley, G. Jaccuci, M. L. Klein, and I. R. McDonald. Phys. Rev. B**14**, 1758 (1976).
14. J. P. Amoureux and M. Foulon. Acta Crystallogr. B**43**, 470 (1987).

Can. J. Chem. Downloaded from www.nrcresearchpress.com by 176.9.209.113 on 09/07/12
For personal use only.

Energetics of order/order transitions in nucleic acids[1]

H. H. KLUMP

Department of Biochemistry, Cape Town University, Republic of South Africa

Received September 8, 1987

This paper is dedicated to Professor James A. Morrison

H. H. KLUMP. Can. J. Chem. **66**, 804 (1988).

Besides the temperature induced canonical helix to random coil transition, which serves as a prototype of an order/disorder transition, there is a second group of conformational changes in helical polynucleotides, which will be termed order/order transitions. Depending on the environmental conditions and the sequence of the polynucleotides involved, there are four alternative reaction schemes: (*i*) The inversion of the helical handedness from a right-handed to a left-handed conformation, (*ii*) the disproportionation of a double helix into a single strand and a triple helix, (*iii*) the addition of a single strand to a double helix, and (*iv*) the single/double strand displacement reactions, that is, the displacement of one of the two strands of the helix by a matching single-stranded polynucleotide or the mutual exchange of one strand each between two helical structures. The first three reactions are considered reversible while the last reaction is irreversible; that is, one cannot regain the initial state by inversing the course of the change, here the change in temperature. Both ribo and deoxyribo polynucleotides can undergo these reactions. In the following paper at least one example is given for each of these reactions.

H. H. KLUMP. Can. J. Chem. **66**, 804 (1988).

La température induit une transition de l'hélice canonique en bobine au hasard qui est le prototype d'une transition ordre/désordre; en plus de cette transition, il existe un deuxième groupe de changements conformationnels des polynucléotides hélicoïdaux qu'on appelle transitions ordre/ordre. Suivant les conditions du milieu et la séquence des polynucléotides impliqués, il y a quatre schémas réactionnels possibles : (*i*) l'inversion de la chiralité de l'hélice d'une conformation droite vers la gauche; (*ii*) la dismutation de la double hélice en un brin unique et en une triple hélice; (*iii*) l'addition d'un brin unique à une double hélice et (*iv*) les réactions de déplacements simple/double brins, c'est-à-dire les réactions de déplacements de l'un de deux brins de l'hélice par un polynucléotide approprié à brin unique ou par l'échange mutuel d'un brin de chacune de deux structures hélicoïdales. On considère que les trois premières réactions sont réversibles alors que la dernière serait irréversible, c'est-à-dire qu'on ne pourrait revenir à l'état initial en inversant le changement, dans notre cas, la température. Les ribo- et désoxyribo-polynucléotides peuvent subir ces réactions. Dans ce travail, on décrit au moins un exemple de chacune de ces réactions.

[Traduit par la revue]

Introduction

Three biological reactions of fundamental importance, namely (*i*) the replication and (*ii*) the transcription of the DNA double helix and (*iii*) the crossing over of DNA sequences between two chromosomes are considered to require strand separation prior to the consecutive steps in these processes. The investigation of the helix–coil transition of double-stranded synthetic and (or) native polynucleotides (1) has been taken as an adequate approach to gain insight into the kinetics (2) and the energetics (3) of the opening of the DNA double helix.

However, these model reactions can only serve as a first approximation, for the final state of the DNA under native conditions is always an ordered conformation, mostly a double helix, and sometimes a triple helix. Thus, it is important to develop a set of reaction schemes that is capable of modelling the in vivo reactions. Prerequisite to cope with this task of designing the appropriate model reactions is the evaluation of a sufficiently large body of experimental data such as the transition temperature (T_m) and stoichiometry of helical polynucleotide complexes as functions of the environmental conditions (4). From these data it will be possible to construct a series of phase diagrams. These diagrams will have two useful applications (cf. Fig. 1*a*,*b*). From the diagram, the conformational state of the polynucleotides in the system at any arbitrary set of external conditions (temperature, cation concentration) can be taken simply by inspection. From the behavior of the phase boundaries, the physical effects responsible for the phase transitions can be assessed. The different order/order transitions have different prerequisites (5). In general (24) only strictly alternating purine–pyrimidine sequences are observed from the normal right-handed conformation into a left-handed form (6).

High counterion concentrations of simple monovalent cations and (or) low concentrations of additional transition metal ions are also required. Chemical modifications of the 5′ position in the pyrimidine ring, e.g., by methyl or bromine groups, are capable of facilitating the inversion (7). Addition of organic solvents, which compete for the bound water in the small helix groove, will favour the left-handed helix (8).

The type of order/order reactions favoured is determined only by the thermodynamic stabilities of the final state of products. For example, poly(A)·poly(U) is the stable complex formed in the 1A/1U mixture. At moderately high sodium concentrations (9) (300 mM) this complex rearranges itself at elevated temperatures into poly(A)·2 poly(U), liberating one half of the poly(A) strands. As will be shown in the following, this triple-strand formation can also be brought about by simply adding the extra polypyrimidine as a single strand. Only recently Fresco and co-workers (25) demonstrated a new triple helical complex, consisting of poly(A)·poly(U) and another poly(A) strand of intermediate length. This 2 poly(A)·poly(U) helix is only formed under stringent conditions. It cannot be obtained by thermal disproportionation of the initial poly(A)·poly(U) double helix. Thus we do not include this particular complex in the order/order reactions. This disproportionation reaction occurs also in the poly(I)·poly(C) system (11), but here the competitive formation of the four-stranded poly(I) helix at high counterion concentration will eventually abolish the triple strand altogether. We will discuss this in more detail later in the paper.

[1]NOTE: This paper is being published without benefit of author's correction.

Can. J. Chem. Downloaded from www.nrcresearchpress.com by 176.9.209.113 on 09/07/12
For personal use only.

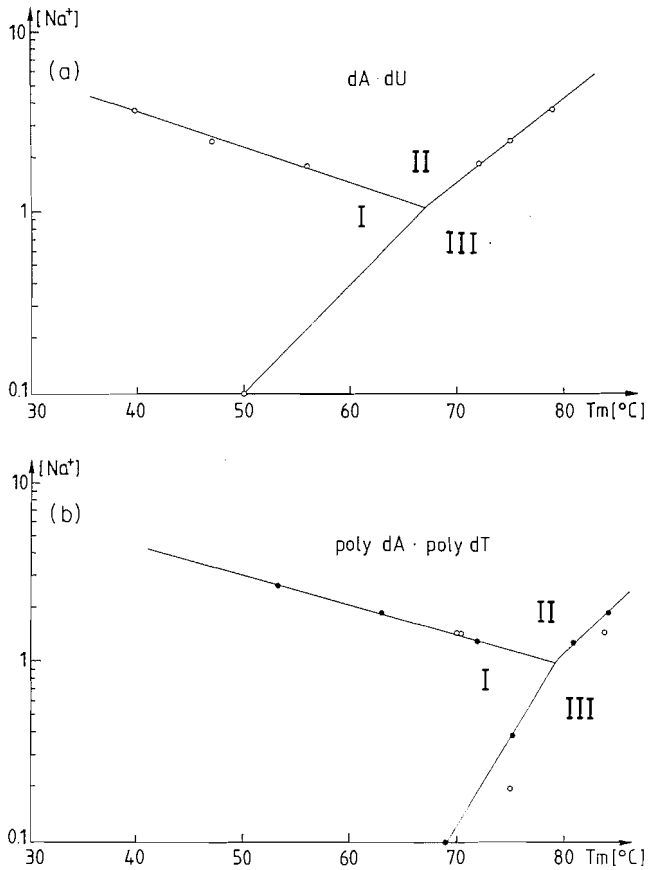

FIG. 1. (a) Phase diagrams of poly(dA)·poly(dU), i.e., transition temperature as a function of cation concentration. Region I represents the stability range of the double helix, region II represents the stability range of the triple helix, and region III is the range of the coiled single strands. (b) Phase diagram constructed from the data of poly(dA)·poly(dT). The assignment of the regions is as in (a).

The evaluation of a complete set of state diagrams for all polynucleotide systems gives an exact overview of the conditions for the preference of any particular double helical polynucleotide complex, and will allow prediction of the potentially irreversible displacement reactions (12).

Another important question to be approached experimentally in this paper is the relative stability of ribo, deoxyribo, and hybrid helices. The data set presented here will allow us to group the different helical complexes according to their thermodynamic stability. The exact enthalpy values per base pair for the different conformational changes are determined by differential scanning calorimetry (13).

Materials and methods

The polynucleotides investigated were purchased from Pharmacia PL-Biochemicals, Freiburg, W. Germany, and used without further purifications. The alternating ribopolymers and poly[d(A-brC)]·poly-[d(G-T)] were furnished by T. Jovin, MPI for Biophysical Chemistry, Göttingen, in the context of cooperative research into alternating ribo and deoxyribo polynucleotides. Some of the results have already been published elsewhere (26). All buffers applied were prepared from double distilled water and the inorganic substances were of analytical reagent grade. The pH of all solutions was set to pH 7.2 by adding the appropriate amount of either HCl or NaOH. Polymer concentrations were calculated from the absorbance at 260 nm, determined with an ultraviolet spectrophotometer, Perkin–Elmer model 124.

Optical melting curves were also measured with the Hitachi–Perkin–Elmer double beam ultraviolet spectrophotometer model 124 and recorded on a Hewlett–Packard model 1800 *xy*-recorder. Temperature signals were taken direct from the solution in the reference cuvette by a resistance thermometer. The voltage of this device was fed into the *x*-axis of the recorder.

Calorimetric measurements were performed with the help of an adiabatic differential scanning calorimeter, type DASM-1, from Mashpriborintorg, Poustshino, Moscow region, USSR. In principle, the instrument plots the difference in heat capacity between solvent and solution. Any transition that is brought about by increasing temperature will absorb heat, causing the apparent heat capacity of the solution to be greater than that of the solvent. The extra energy that has to be put into the solution, to bring the temperature difference between the sample and reference as close to zero as possible, corresponds to the enthalpy change due to the reaction under study. Details of this procedure and of the design of the instrument are given in the literature (13).

Results

Disproportionations

Figures 1*a* and 1*b* give the state diagrams of two polynucleotide systems, the poly(dA)·poly(dT) and the poly(dA)·poly(dU) systems. The transition temperatures are plotted as a function of the sodium concentration. For comparison we show also the reinvestigated, most extensively studied system that undergoes a disproportionation reaction, the poly(A)·poly(U) system (14) (cf. Fig. 2*a*). To obtain the two branches of the state diagram at elevated sodium concentrations the uv absorbance at 280 nm is plotted as a function of temperature. The unanimous observation in all three systems is a drop in absorbance that is shifted to lower temperatures with increasing cation concentration for the first step, and the rise in absorbance that shows the opposite behaviour for the second step. The first transition is due to the disproportionation of two double helices into a triple helix and a partly stacked polypurine single strand. The second transition reflects the thermally driven denaturation of the triple helix into random coils of single-stranded poly(dU) and poly(dA), for example, at elevated temperature. Figure 2*b* gives the corresponding heat capacity scan from the differential microcalorimeter for poly(A) and poly(U). The area under the small peak represents the transition enthalpy ΔH of the order/order transition (disproportionation) and the area under the large peak represents the transition enthalpy for the order/disorder transition (denaturation of triple helix). Both transitions are reversible, i.e., on lowering the temperature below the upper transition the three-stranded helix of polypurine · 2 polypyrimidine is reestablished, and on passing the lower transition temperature the complex rearranges again to form the double helical complexes of polypurine·polypyrimidine.

This also holds for hybrid helices like poly(rA)·poly(dU). For example, Table 1 gives the energetics of the disproportionation reactions, reinvestigated with the help of the advanced instrumentation.

Additions

The triple-strand formation can also be brought about by addition of a matching polypyrimidine single strand to the polypurine–polypyrimidine double helix. The separate polynucleotide species can be mixed at room temperature and at low cation concentration. By raising the cation concentration above a threshold concentration the triple helix formation can be triggered (cf. Fig. 3). The energetics of this reaction can be followed with the help of a differential isothermal scanning

Can. J. Chem. Downloaded from www.nrcresearchpress.com by 176.9.209.113 on 09/07/12
For personal use only.

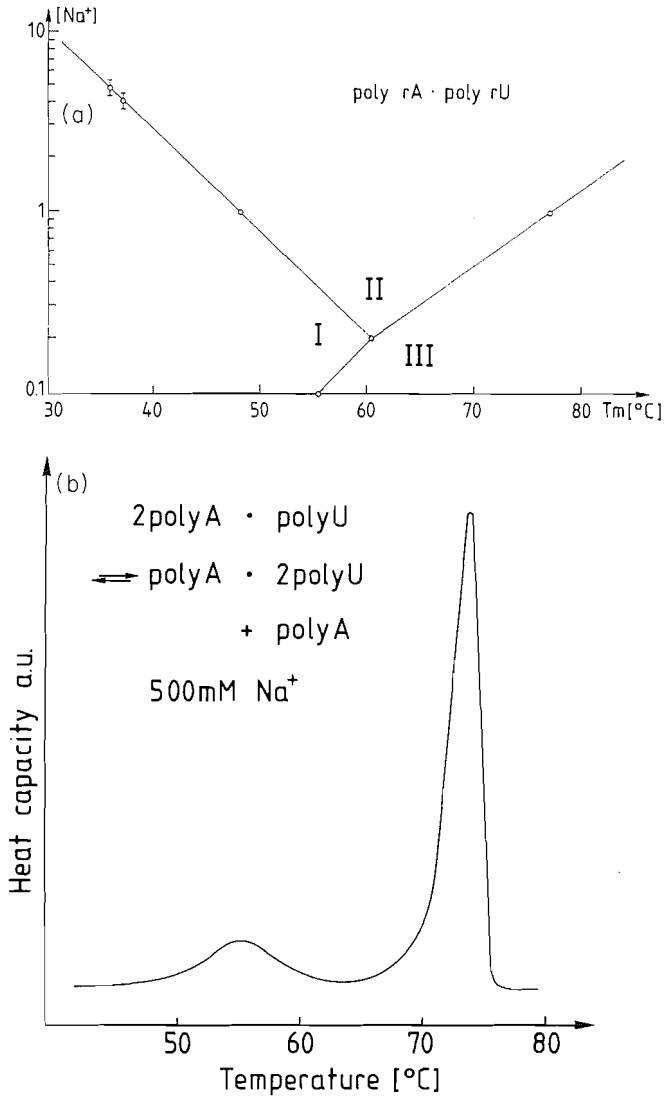

FIG. 2. (a) Phase diagram of poly(A)·poly(U) (assignments as in Fig. 1). (b) Heat capacity of poly(A)·poly(U) at 500 mM Na^+, as a function of temperature. Left peak is due to the disproportionation reaction, right peak represents the enthalpy change accompanying the triple-helix coil transition.

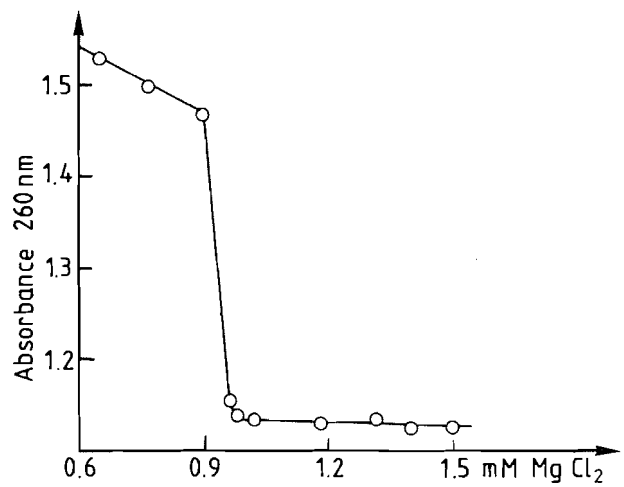

FIG. 3. Triple-strand formation as a function of the Mg^{2+} concentration for poly(U)·poly(A) plus poly(dT).

titration calorimeter to compensate for the heat due to the concentration change of the cations, an effect that is much larger than the heat of adding the third strand to the preexisting double strand (10).

Mixed three-stranded DNA–RNA complexes in which the three strands differ have been reported to occur in vivo, and have been suggested as intermediates in the transfer of information between the nucleic acids (11). The triple-strand formation via addition is included here only for comparison with the other order/order reactions. It does not contain new experimental results.

Coil–helix displacement reactions

Chamberlin and Patterson (11) were the first to study extensively the coil–helix displacement reactions in the poly(I)·poly(C) system. It was demonstrated that the order of thermal stability of the I–C homopolymer pairs could be used to predict relative stabilities of helical complexes, and the displacement reactions were followed spectroscopically at low temperatures. Here we show that the same general scheme also holds for the poly(A)·poly(U) system. Since we were interested in the energetics of these reactions in the first place, the displacement was brought about by raising the temperature just above the thermal transition of the less stable helical complex. At this point the synchronous helix–coil transition of the weaker complex and the helix formation of the more stable complex occurs. The heat capacity change at this temperature is the differential effect of the two reactions. The displacement reaction is facilitated by raising the cation concentration. The reactions observed in the poly(A)·poly(U) system are the following:

$$\text{poly(dA)·poly(rU)} + \text{poly(dU)} \rightarrow \text{poly(dA)·poly(dU)} + \text{poly(rU)}$$

$$\text{poly(dU)·poly(rA)} + \text{poly(rU)} \rightarrow \text{poly(rA)·poly(rU)} + \text{poly(dU)}$$

$$\text{poly(dA)·poly(rU)} + \text{poly(rA)} \rightarrow \text{poly(rA)·poly(rU)} + \text{poly(dA)}$$

$$\text{poly(dU)·poly(rA)} + \text{poly(dA)} \rightarrow \text{poly(dA)·poly(dU)} + \text{poly(rA)}$$

Experimentally the denaturation of the appropriate hybrid helix was forced by raising the temperature continuously through the transition interval while either the change in optical density or in heat capacity was scanned as a function of the temperature. The denaturation of the hybrid helices is a reversible process. In the second run the same polymer solution was mixed with one equivalent of the single-stranded homopolymer in 100 mM NaCl and heated continuously at a constant heating rate of 0.8°/min. Each of the reactions was observed to occur either at 44 or 46°C, the transition temperatures of the hybrid helices.

When two samples that contain one of the alternative hybrids are combined and heated to a temperature just above the transition of the least stable hybrid, concerted replacement reaction takes place. The correct measure of the stability of helical conformations is the free energy ΔG_s of a given state s, and, if all components are in their standard states, the standard free energy ΔG^0_s can be used instead. Whether a given reaction will occur is determined exclusively by the change in the standard free enthalpy (not by the change in enthalpy or by the relative magnitude of T_m) (3). This holds in general but there are exceptions to the rule. If ΔS is constant, then ΔG can be

Can. J. Chem. Downloaded from www.nrcresearchpress.com by 176.9.209.113 on 09/07/12
For personal use only.

TABLE 1. The energetics of the disproportionation reactions

Polynucleotide	T_m (°C)	ΔH_{cal} (kJ·mbp^{-1})	ΔS_{cal} (J·mbp^{-1}·K^{-1})	ΔH_{vH} (kJ·mol^{-1})	m (b)
2[poly(A)·poly(U)]·[poly(A)·2 poly(U)] + poly(A)	45	5.3	16.7	723	136
2[poly(dA)·poly(dT)]·[poly(dA)·2 poly(dT)] + poly(dA)	45	7.4	23.5	789	107
2[poly(dA)·poly(dU)]·[poly(dA)·2 poly(dU)] + poly(dA)	45	7.1	22.5	820	115

Abbrevations: mbp = mol base pairs; b = base; kJ = kilojoule; K = degrees Kelvin; vH = van't Hoff.

TABLE 2. Thermodynamic parameters for B–Z transitions in linear DNAs

Polynucleotide	T (°C)	ΔH_{cal} (kJ·mbp^{-1})	ΔS_{cal} (J·mbp^{-1}·K^{-1})	Lit.
poly[d(G-C)]	38	0	0	[a]
poly[d(G-m5C)]	40	4.2	13.4	17
poly[d(G-m5C)]	42	4.2	13.3	17
poly[d(G-m5C)]	43	2.1	6.7	28
poly[d(A-brC)]·poly[d(G-T)]	48	3.8	12.1	Footnote 2

[a]K. Breslauer and H. H. Klump. Unpublished results.

Can. J. Chem. Downloaded from www.nrcresearchpress.com by 176.9.209.113 on 09/07/12
For personal use only.

replaced by ΔH for the following considerations. For the helix single-strand exchange let us focus on the following reaction:

$$\text{poly(rA)}\cdot\text{poly(dT)} + \text{poly(dA)} \rightleftharpoons \text{poly(dA)}\cdot\text{poly(dT)} + \text{poly(rA)}$$

The scheme presented below represents the different steps of a Born–Harber circular process. The initial state is represented by the three separated single strands. In the first step the formation of the hybrid helix poly(rA)·poly(dT) is considered. The formation enthalpy results in 30.9 kJ per mol of base pairs (mbp). In the second step the poly(rA) strand is displaced by the poly(dA) strand. The displacement enthalpy amounts to 1.5 kJ·mbp^{-1}. In the third step the poly(dA)·poly(dT) double strand is denatured to give back the initial state. The denaturation enthalpy is 32.4 kJ·mbp^{-1}. The sum of the formation enthalpy and the displacement enthalpy equals the denaturation enthalpy of the most stable helical complex in the system. The assumption is that the formation enthalpy and the denaturation enthalpy of a certain double helix are identical.

poly(rA) + poly(dT) + poly(dA)

$\Delta H = 30.9$ kJ·mbp^{-1}
$T_m = 69$°C

poly(rA)·poly(dT) + poly(dA)

$\Delta H = 32.4$ kJ·mbp^{-1}
$T_m = 74$°C

$\Delta H_d = 1.5$ kJ·mbp^{-1} | poly(dA)·poly(dT) + poly(rA)

We can evaluate the free enthalpy change accompanying the displacement (ΔG^0_d) because $T_m = \Delta H^0/\Delta S^0$, and both T_m and ΔH^0 are experimentally accessible quantities. The only assumption that has to be made is that the transition enthalpy ΔH is temperature independent. This assumption seems to be justified because of the almost undetectable small value of ΔC_p. ΔS^0 is also given from the experimental values using the Gibbs–Helmholtz equation (5).

We therefore obtain the standard free enthalpy of formation of poly(rA)·poly(dT) according to the following equation, first applied to nucleic acids by Tinoco (27).

$$\Delta G^0_{dAdT} = \Delta H^0_{rAdT} - T\Delta S^0_{rAdT} = \Delta H^0_{rAdT}(1 - T/T_{m\,rAdT})$$

The exact corresponding equation holds for ΔG^0_{rAdT}. It immediately follows that

$$\Delta G^0_d = \Delta G^0_{dAdT} - \Delta G^0_{rAdT}$$

The quantitative evaluation of the displacement free enthalpy change at 25°C under standard conditions yields $\Delta G^0_d = 0.6$ kJ per base pair in the system given above.

Because ΔH^0 is negative for all known duplex formations, ΔG^0_d is also negative if $T_{m\,dAdT} > T_{m\,rAdT}$, which in fact is correct. The double helix with the higher T_m will be favoured in a helix displacement reaction. The results also demonstrate the general observation that RNA/RNA duplexes are more stable than DNA/DNA duplexes, while the relative stability of RNA/DNA hybrids is less predictable.

Helix/helix displacement reactions

The same approach can be made for a mutual displacement of strands between two metastable hybrid complexes.

To demonstrate this case we will consider the following system:

$$\text{poly(dA)}\cdot\text{poly(rU)} + \text{poly(rA)}\cdot\text{poly(dU)} \rightleftharpoons \text{poly(dA)}\cdot\text{poly(dU)} + \text{poly(rA)}\cdot\text{poly(rU)}$$

In a 100 mM NaCl solution the hybrid helices have a transition temperature of 46°C / 44°C respectively and the poly(rA)·poly(rU) melts at 55.5°C, 5.5° higher than the DNA analogue poly(dA)·poly(dU) ($T_m = 50.0$°C). The corresponding transition enthalpies are 31.6 kJ·mbp^{-1} for poly(dA)·poly(dU), 30.6 kJ·mbp^{-1} for poly(dA)·poly(rU), 28.6 kJ·mbp^{-1} for poly(rA)·poly(dU), and finally 32.2 kJ·mbp^{-1} for poly(rA)·poly(rU). According to

the formalism given above the free enthalpy for the formation of each of the four double helical complexes is calculated. The displacement reaction can be illustrated by the following thermodynamic cycle: The initial state is given by the four separate single strands. In the first step the least stable helix poly(rA)·poly(dU) is formed. In the second step the poly(dA)·poly(rU) helix is formed. An increase of the environmental temperature above the melting temperature of the least stable helix sets one ribo and one desoxyribo strand free. The single ribo strand now displaces the desoxy strand from the second helix and the displaced strand finally reassociates with the residual desoxy strand.

The concerted formation of the final double helical states is equivalent to the independent formation of these species from isolated single strands, as given on the right-hand side of the following scheme. Hence a travel around the circle results in the initial state.

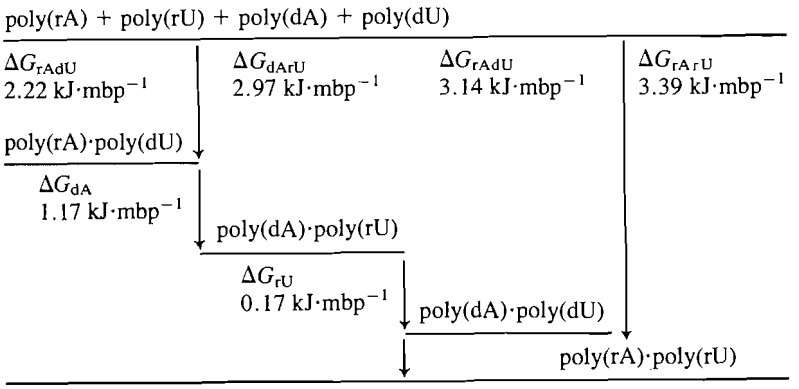

This scheme demonstrates that for the adenine/uridine (poly(A)·poly(U)) system all necessary thermodynamic quantities are known, which enables us to correlate the ΔG^0_d with the T_m parameters. The enthalpy change around the thermodynamic cycle is obviously zero, as the theory requires.

Inversion of handedness in DNAs and RNAs

The left-handed DNA or Z-DNA structure is characterized by a dinucleotide repeat. Thus it is convenient to consider sequences of $2n$ base pairs (bp) as present in the canonical alternating polynucleotides poly[d(G-C)], e.g., to adopt the Z form under certain experimental conditions. This has been demonstrated by crystallographic and solution studies (15). The state with all bp in the B form is taken as the reference state.

A logarithmic dependence of the apparent equilibrium constant K on NaCl concentration was initially observed in the study of poly[d(G-C)] (16). Cooperative transitions were also observed with poly[d(G-C)] undergoing B–Z transitions in the presence of organic solvents either alone or as cosolvents at very low salt concentrations. It is noticeable that the NaCl-induced B–Z transition of poly[d(G-C)] is essentially isoenergetic; i.e., the enthalpy change is less than 0.3 kcal·mbp^{-1} (from calorimetric and from spectroscopic equilibrium-kinetic studies). The reaction has to be entropy driven and is probably dominated by interionic interactions (17). In all other situations, i.e., in mixed solvents or under the influence of bound di- or oligovalent cations and other conformationally selective ligands, the B–Z transition of poly[d(G-C)] can also be induced by temperature variations at constant solvent composition. The latter is also true for DNA sequences methylated at the 5′ position of the cytosine moiety (18). Such substitutions lead to a selective stabilization of the left-handed conformation of the two canonical alternating purine–pyrimidine families, poly[d(G-C)] and poly[d(A-C)]·poly[d(G-T)] (19). With temperature dependent transitions, the apparent spectroscopically determined van't Hoff transition enthalpy change (for an unknown size of the cooperative unit) given by the following equation where n represents the number of strands (27),

$$\Delta H_{vH} = (n + 1)RT_m^2(d\theta/dT)$$

is related to the intrinsic transition enthalpy per base pair (determined by calorimetry). In the case of long polymers described by means of the infinite lengths Ising model

$$\Delta H_{vH} = m\Delta H_{cal}$$

where m is the calculated length of the cooperative unit. The thermodynamic parameters for the temperature dependent B–Z transitions in DNA polymers, obtained from van't Hoff analysis of spectroscopic data and from some directly obtained calorimetric data, are presented in Table 2.

Several conclusions can be drawn from the following information:

(*i*) DNAs with 5′ cytidine substitutions (methyl, halogen) in both sequence families show a similar transition enthalpy ΔH per base pair of ca. 4.2 kJ per mol of base pairs, derived from spectroscopic measurements, which is very close to the directly determined value from adiabatic scanning microcalorimetry (4.2 kJ·mpb^{-1} for poly[d(G-m5C)] (cf. Table 3).

(*ii*) The halogen substituents are more effective than a methyl group in stabilizing the Z form, i.e., it requires less enthalpy to turn the handedness around.

(*iii*) The cooperative lengths, i.e., junctional free energies, vary from one polymer to another, i.e., are DNA-sequence specific as well as a function of environmental conditions. Thus reported values for the cooperative length m for poly[d(G-C)] duplexes range from 25 bp to 100–1000 bp. Three recent estimates for the methylated polymer are 180, 226, and 110 bp.

Energetics of the A–Z RNA transition

Very recently it was successfully demonstrated for the first time that corresponding inversions of helical handedness occur also in double-stranded RNAs (2), contradicting a statement of Drew and Dickerson (19), which in an apodictic way states that it is immediately clear that there is nothing like a Z-RNA

Can. J. Chem. Downloaded from www.nrcresearchpress.com by 176.9.209.113 on 09/07/12
For personal use only.

TABLE 3. Calorimetric measurements of DNAs

Polynucleotide	T_m (°C)	ΔH_{vH} (kJ·mol^{-1})	ΔS (J·K^{-1}·mol^{-1})	ΔH_{cal} (kJ·mbp^{-1})	ΔS_{cal} (J·mbp^{-1}·K^{-1})
poly[r(G-m5C)]	52	1060	3260	4.6	14.2
poly[r(G-C)]	41	1075	3420	4.2	13.2
poly[r(G-br5C)]	46	670	2100	4.4	14.0

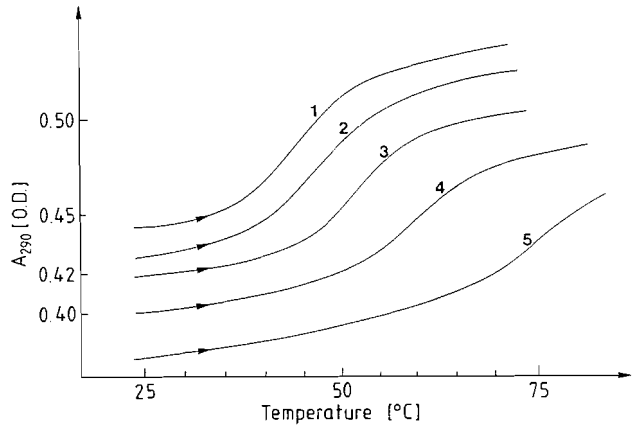

FIG. 4. Inversion curves of poly[r(G-C)] as a function of $NaClO_4$ concentration: 1, 5 *m*; 2, 4.5 *m*; 3, 4 *m*; 4, 3.5 *m*; 5, 3.0 *m*.

because of the 2′-OH group of the ribose ring. This statement seems to be premature in the light of the results presented here for a series of nonmodified poly(G-C) and the methylated and halogenated analogs. The results of the calorimetric measurements are compiled in Table 3. The polymers were obtained from T. Jovin and the details of this investigation have been published as a cooperative paper (26).

The experimental conditions of the calorimetric investigation correspond to the conditions mentioned in the next paragraph.

Ultraviolet spectroscopy

Ultraviolet (uv) spectroscopic studies have shown that poly(G-C) in aqueous solution containing 4 M $NaClO_4$ can be reversibly converted into a left-handed Z-RNA by raising the temperature to 60°C. This conversion temperature will linearly decrease as a function of the logarithmic increase of the perchlorate concentration up to 110°C. The uv melting curves are shown in Fig. 4. Above this temperature the order/order transition merges with the helix–coil transition. The reversibility and cooperativity of the helix/helix conversion facilitates the investigation and the quantitative evaluation of the transition. The van't Hoff enthalpy, which can be derived from the temperature dependence of the degree of transition, i.e., the fraction of polymer strands that populates the left-handed conformational state, is calculated to 820 kJ per mol of the cooperative unit (20). From the ratio of the two enthalpies the size of the cooperative unit (bp) can be determined to amount to about 200 bp. Very similar results are obtained for the poly(G-m5C) and for poly(G-br5C) (cf. Table 3).

Discussion

The fundamental cellular reactions such as replication, transcription, and exchange of genetic material between two chromosomes will be fully explainable with the help of the thermodynamic state functions applied to the base/base interactions in the plane of the complementary Watson–Crick base pairs and (or) along the single strands. The proteins involved are assumed to speed up the reactions but they will not influence the equilibrium between the states of the nucleic acids involved. These proteins are catalysts in the chemical sense. Hence once the activation energy is supplied the reaction has to go spontaneously to the new equilibrium state.

Unfortunately it is impossible to check the hypothesis with native DNA sequences, for the amount of material needed to pick up the physical signals surpasses the limits of biochemical isolation techniques. The difficulties can be avoided by the help of selected model systems. To be able to select the best model system it is advisable to investigate all polynucleotides available. Figures 5*a*–*d* give the four matrices that demonstrate all possible double helical complexes in the poly(A-U), poly(A-T), poly(G-C), and poly(I-C) systems. We have collected all state diagrams either from the literature or from carefully recorded absorbance/temperature scans at different environmental conditions. The details of these measurements will be given elsewhere.[2]

To discuss the unique features of order/order transitions in a given context rather than to review all published data, we will choose the four A-U homopolymer helices and the strictly alternating A-U sequence. The five A-U polymers in solution form stable double helical structures. The degree of hyperchromicity and the sharp melting profile indicate that in the ordered complexes there is a maximum degree of orientation, presumably due to the strict pairing of each adenine residue with a uridine residue. They show, however, marked differences in thermal stability. The occurrence of displacement reactions between randomly coiled polypyrimidines or partly stacked polypurines and the homopolymer helices to form a double helix of even greater thermal stability indicates differences in the thermodynamic properties of the individual double helices. These considerations assume that the final state of all the polynucleotides under study is a randomly coiled conformation, which is reasonable for high temperatures. It is also assumed that the transition entropies (21) are close for all double helix/coil transitions in these systems. As was shown recently by the author, this can safely be assumed. The entropy change per base pair reflects primarily the gain in rotational freedom along the backbone single strands upon the denaturation of the helix. Hence differences in T_m correspond to differences in the transition enthalpy ΔH, and, if we assume that ΔH is temperature independent, to differences in the free enthalpy change. This is a hint that there is some difference in the three-dimensional arrangement of the different helical complexes.[3] A similar situation was found for the I-C homopolymers (11). It is also observed that the thermodynamic stability of the double-stranded RNAs is always bigger than the stability of the corresponding DNAs. The spontaneous course of the helix/helix displacement reaction, such as poly(dA)·poly(rU) +

[2]H. Klump and I. Siepmann, manuscript in preparation.

[3]H. H. Klump and T. Jouin, manuscript in preparation.

Can. J. Chem. Downloaded from www.nrcresearchpress.com by 176.9.209.113 on 09/07/12
For personal use only.

(a)

	rI	rC	dI	dC	dIC	rIC
rI	+ 20	+ 60	(+)	+ 53	–	–
rC	+ 60	–	+ 35	–	–	–
dI	(+)	+ 35	+ 16	+ 45	–	–
dC	+ 53	–	+ 45	–	–	–
dIC	–	–	–	–	+ 36	–
rIC	–	–	–	–	–	+

r(IC) > rIrC > rIdC > dIdC > d(IC) > dIrC (100 mM Na^+)

(b)

	rA	rU	dA	dU	dAU	rAU
rA	+ 75 (H^+)	+ 56	–	+ 44	–	–
rU	+ 56	+ 8	+ 46	–	–	–
dA	–	+ 46	+ (H^+)	+ 50	–	–
dU	+ 44	–	+ 50	+ ca 4	–	–
dAU	–	–	–	–	+ 50	–
rAU	–	–	–	–	–	+ 67

r(AU) > rArU > d(AU) > dArU > rAdU > dAdU (100 mM Na^+)

(c)

	rA	rT	dA	dT	dAT	rAT
rA	+ 75 ($^+$H)	+ 78	–	– 59	–	–
rT	+ 78	+ 30	+ 69	–	–	–
dA	–	+ 69	+ (H^+)	+ 65	–	–
dT	+ 59	–	+ 65	+ ca 18	–	–
dAT	–	–	–	–	+ 54	–
rAT	–	–	–	–	–	+ 76

r(AT) > rArT > dArT > dAdT > rAdT > d(AT) (100 mM Na^+)

(d)

	rG	rC	dG	dC	dGC	rGC
rG	+ 67 (4)	+ 106	– 103	+	–	–
rC	+ 106	–	+ 102	–	–	–
dG	–	+ 102	(+) (4)	+ 82	–	–
dC	+ 103	–	+ 82	–	–	–
dGC	–	–	–	–	+ 96	–
rGC	–	–	–	–	–	+ 109

r(GC) > rGrC > rGdC > dGrC > d(GC) > dGdC (10 mM NaCl)

FIG. 5. Matrix of possible helical complexes of I-C, A-U, A-T, and G-C homonucleotides. (+) represents the observed binary complexes. Numbers given are transition temperatures in °C at neutral pH and at the sodium concentration given in the bottom line (mostly 100 mM with the exception of 10 mM for G-C systems). (+H) refers to acid pH below pH 5, and (4) refers to the four-stranded complexes.

poly(rA)·poly(dU) rearranging to give poly(rA)·poly(rU) + poly(dA)·poly(dU) indicates that the free energy of the mixture of the hybrids is greater than that of the mixture of pure DNA- and RNA-like homopolymer helices.

This is also true for the I-C homopolymers. The displacement of one strand of the hybrid helix by an additional single strand of either type of polynucleotide to yield a homopolymer helix is caused by the same underlying principle. We can conclude that the displacement of the mRNA from the coding strand of the DNA is based on this thermodynamic phenomenon.

The addition of a matching single strand to the homopolymer helix at elevated cation concentrations is thermodynamically driven. The loss in conformational entropy of the single strand upon binding to the double helix is compensated by the gain in stacking and H-bonding energy once the electrostatic repulsion is sufficiently decreased by the shielding of the phosphate groups by cations. Whether the triple-strand formation is possible is also dependent on the tendency of the homopolymer to form ordered secondary structures. Poly(I), for example, has a high tendency to form four-stranded helices at moderate counterion concentration, preventing it from binding as a third strand to poly(I)·poly(C) (cf. Fig. 5). This tendency of self-complementary structure formation is extreme for poly(G). All investigations on structures that contain poly(G) are obscured by this behaviour (22).

The temperature-driven disproportionation reactions are com-

Can. J. Chem. Downloaded from www.nrcresearchpress.com by 176.9.209.113 on 09/07/12
For personal use only.

pletely reversible and also strictly follow the laws of thermodynamics. Whether a disproportionation occurs is governed by the same rules as the addition of a third strand to the double helix. In this case the third strand only originates from the second helix. As is shown for the order/order transitions in general, the disproportionation temperature decreases with increasing cation concentration. This also holds for the inversion of the handedness of the helical complexes formed from a strictly alternating sequence.

For quite a while it was thought that the inversion was only possible for the deoxypolymers. Now we have a growing list of various copolymers that can form the left-handed helix under appropriate conditions, i.e., high counterion concentration and reduction of water activity (8). The energy required for the inversion is surprisingly low (about 4 kJ per mol of base pairs).

The only reason that the polymer is not flipping between the two conformational states is the fact that the inversion is a highly cooperative process. There is only one inversion centre in each double strand, and its formation requires a large activation energy to start (cf. the size of the cooperative unit m).

Summing up the results reported in this paper, it can be stated with confidence that systems presented here are capable of modelling the order/order transitions of nucleic acids proposed for replication, transcription, or chromosomal crossing over.

Acknowledgments

The author acknowledges the constant support throughout these investigations by the Deutsche Forschungsgemeinschaft and Fonds der Chemischen Industrie. The alternating polynucleotides used are the gift of Professor T. Jovin and will be used for further cooperative investigations. The series of melting experiments to set up the four matrices were conducted by J. Siepmann, whose expert technical assistance is gratefully acknowledged.

1. J. WATSON. *In* Molecular biology of the gene. Benjamin Inc., Menlo Park, CA. 1977.
2. D. SOUMPASIS and T. JOVIN. *In* Nucleic acids and molecular biology. *Edited by* F. Eckstein. Springer Verlag, Heidelberg, FRG. 1986.
3. H. KLUMP. *In* Biochemical thermodynamics. *Edited by* M. Jones. Elsevier, Amsterdam. In press.
4. J. MASSOULIE, A. MICHELSON, and F. POCHON. Biochim. Biophys. Acta, **114**, 16 (1966).
5. CH. CANTOR and P. SCHIMMEL. *In* Biophysical chemistry. Vol. 3. Freeman, San Francisco, CA. 1980.
6. A. RICH, G. QUINGLEY, and H. WANG. *In* Biomolecular stereodynamics. *Edited by* R. Sarma. Adenine Press, New York. 1982.
7. T. JOVIN and D. SOUMPASIS. Ann. Rev. Biochem. **38**, 521 (1987).
8. W. SAENGER, W. HUNTER, and O. KENNARD. Nature, **324**, 385 (1986).
9. E. NEUMANN. Doctoral thesis, Münster, FRG. 1969.
10. H. KLUMP. Ber. Bunsenges. Phys. Chem. **82**, 805 (1978).
11. M. CHAMBERLIN and D. PATTERSON. J. Mol. Biol. **12**, 410 (1965).
12. H. KLUMP. *In* Landold–Börnstein: Biophysik. *Edited by* W. Saenger. Springer Verlag, FRG. In press.
13. P. PRIVALOV. FEBS Lett. Suppl. **40**, 140 (1974).
14. H. KRAKAUER and J. STURTEVANT. Biopolymers, **6**, 491 (1968).
15. F. POHL and T. JOVIN. J. Mol. Biol. **67**, 375 (1972).
16. H. KLUMP and R. LOFFLER. Hoppe Seyler Biol. Chem. **366**, 345 (1985).
17. H. KLUMP. FEBS Lett. **196**, 175 (1986).
18. M. BEHE and G. FELSENFELD. Proc. Natl. Acad. Sci. U.S.A. **78**, 1619 (1981).
19. H. DREW and R. DICKERSON. J. Mol. Biol. **152**, 723 (1981).
20. H. KLUMP and T. JOVIN. Biochemistry. In press.
21. H. KLUMP. *In* Structural biochemistry. *Edited by* J. Twardowski. Reidel Publ. Co., Dordrecht, The Netherlands. 1987.
22. H. KLUMP. Biophys. Chem. **5**, 359 (1976).
23. P. BOURTAYRE, J. LIQUIER, L. PIZZORNI, and E. TAILLANDIER. J. Mol. Struct. Dyn. In press.
24. A. WANG, R. GESSNER, G. VAN DER MAREL, J. VAN BOOM, and A. RICH. Proc. Natl. Acad. Sci. U.S.A. **82**, 3611 (1985).
25. S. L. BROITMAN, D. D. IM, and J. FRESCO. Proc. Natl. Acad. Sci. U.S.A. **84**, 5120 (1987).
26. H. H. KLUMP and T. JOVIN. Biochemistry, **26**, 5186 (1987).
27. V. BLOOMFIELD, D. CROTHERS, and I. TINOCO, JR. Physical chemistry of nucleic acids. Harper and Row, New York. 1974.
28. J. CHAIRES and J. STURTEVANT. Proc. Natl. Acad. Sci. U.S.A. **83**, 5479 (1986).

Can. J. Chem. Downloaded from www.nrcresearchpress.com by 176.9.209.113 on 09/07/12
For personal use only.

Molecular to atomic transformation in solid iodine under high pressure

TADEUSZ LUTY
Institute of Organic and Physical Chemistry, Technical University of Wroclaw, Wroclaw, Poland

AND

JOHN C. RAICH
Department of Physics and Condensed Matter Sciences Laboratory, Colorado State University, Fort Collins, CO 80523, U.S.A.

Received October 16, 1987

This paper is dedicated to Professor J. A. Morrison

TADEUSZ LUTY and JOHN C. RAICH. Can. J. Chem. **66**, 812 (1988).

Structural transformations in solid iodine under high pressure are analyzed from the point of view of symmetries of possible charge density distortions coupled to phonons. The transition from the high pressure atomic phase to the low pressure molecular phase is interpreted in terms of phonon softening and formation of molecular bonds and is seen as a condensation of a charge density distortion wave coupled to a phonon mode.

TADEUSZ LUTY et JOHN C. RAICH. Can. J. Chem. **66**, 812 (1988).

Dans le but d'examiner les symétries des distorsions possibles dans les densités de charges couplées aux phonons, on a étudié les transformations structurales de l'iode solide, sous pression. On interprète la transition de la phase atomique à haute pression vers la phase moléculaire à basse pression en fonction d'un ramollissement du phonon et de la formation de liaisons moléculaires et on la considère comme une condensation d'une onde de distorsion de la densité de charge qui est couplée avec un mode phonon.

[Traduit par la revue]

Can. J. Chem. Downloaded from www.nrcresearchpress.com by 176.9.209.113 on 09/07/12
For personal use only.

1. Introduction

Solid iodine has been the subject of many experimental and theoretical studies in part because of its interesting properties under pressure. The dynamical properties of the crystal are of particular interest because they appear to have characteristics intermediate between those of molecular solids and of metals. This intermediate character of solid iodine is evident from experimental studies, which indicate an insulator–metal transition at about 16 GPa (1). According to recent X-ray crystal structure analysis, the insulator–metal transition is followed by a structural phase transition associated with molecular dissociation at 21 GPa (2). It has been known for a long time that there is a chemical bond formation involving $5p$ electrons of nearest iodine molecules in the crystal under atmospheric pressure (3). A common opinion is that the intermolecular bond is of a charge transfer nature, that is, a dative structure involving ionic and covalent bonds between nearest atoms of different molecules is formed. Theoretical studies of the lattice dynamics (4, 5) demonstrated the importance of charge distribution of the intermolecular bond.

Structural studies of iodine under pressure (2) stimulated this theoretical effort to construct a model for charge density distortions and lattice dynamics which gives a phenomenological explanation for the observed structural changes.

The generally accepted viewpoint is that the application of pressure changes the balance between intermolecular charge-transfer interactions and intramolecular covalent bonds, so that the crystal becomes metallic and molecular dissociation follows. Because of the relatively simple crystal structures, it is believed that the pressure-induced transformations in solid iodine can serve as a model to study charge density distortions in molecular crystals caused by applied pressure. The current studies elucidate the transition between the metallic bond and the ionic-covalent bond, so far only weakly suggested by McMillan (6) within the charge density wave concept. The transformation of solid iodine under pressure can be viewed as a solid state chemical reaction ($2N\ I \rightleftharpoons I_2$). Thus, it is believed that concepts needed to understand the transformation in solid iodine will also be useful for an understanding of solid state reactions (dimerization, polymerization) in more complicated systems.

Very recently the description of molecular dissociation of iodine at $p > 21$ GPa became controversial. On the basis of Mössbauer effect measurements (10) it has been argued that "up to 30 GPa the I_2 molecules remain the building blocks of the high pressure structural modifications". The need for assuming a "zig-zag" structure is stressed in ref. 10. We hope that the analysis presented in this paper will provide a compromise (a polymeric structure) between the two interpretations of the transition.

In the present paper we start with a brief description of the iodine crystal structures and phase transitions under pressure. In section 3 we formulate the 16-bond model and determine the possible order parameters for the phase transformations. The next section is devoted to demonstrating that the 16-bond model is equivalent to a 2-bond model in reciprocal space. It is shown that the order parameters can be identified with amplitudes of charge density distortion waves. Finally, we consider the coupling of the charge density distortion waves to phonons.

2. Structures of solid iodine

The low-pressure (LP), molecular phase of iodine is orthorhombic, space group D_{2h}-$Cmca$, with two I_2 molecules per primitive unit cell (7). The iodine molecules form layered structure in the (bc) plane, as shown in Fig. 1. When pressure is applied to the crystal the iodine molecules tilt around the crystallographic a axis in such a way that the angle between the two translationally nonequivalent molecules in the (bc) plane comes closer to $\pi/2$. In the range of stability of the molecular phase ($p < 21$ GPa) no change in the intramolecular bond length has been observed (2) although an insulator–metal transition occurs at about 16 GPa (1). This purely electronic transition is

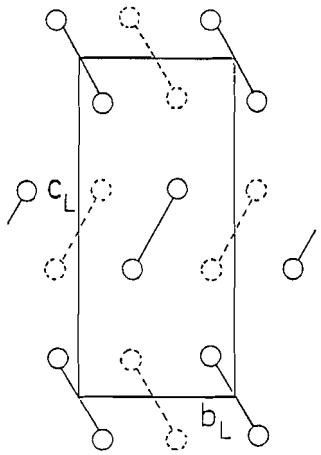

FIG. 1. The (bc) planes of the molecular phase, stable at atmospheric pressure, of solid iodine.

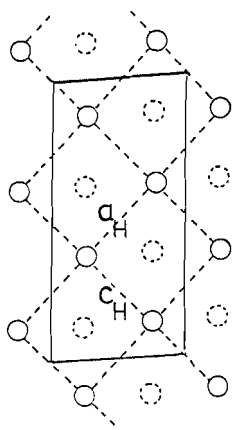

FIG. 2. The iodine atoms on the (ac) plane of the atomic phase at 30 GPa, according to ref. 2.

followed, according to ref. 2, by the first-order structural phase transition at 21 GPa which is essentially molecular dissociation.

The high-pressure (HP), monoatomic phase forms a body-centred orthorhombic lattice, space group D_{2h}-$Immm$, with one iodine atom per primitive unit cell (2). The structure of the phase at 30 GPa according to ref. 2 is shown in Fig. 2. In terms of the basic vectors of the molecular (LP) phase the atomic phase forms a monoclinic structure. If the larger unit cell of the LP phase is considered, the HP monoatomic structure appears as a shear strained LP molecular structure when projected on the (bc) plane. The distortion angle α can be expressed in terms of the strain, $e_{yz} = e_4$, and the basic vectors of the atomic phase, a_H and c_H,

$$[1] \qquad e_4 = \text{ctg}\,\alpha = \frac{c_H^2 - a_H^2}{2a_H c_H}$$

Relationships between crystal axes of the LP phase (a_L, b_L, and c_L) and those of the HP phase (a_H, b_H, and c_H) are:

$$[2] \qquad \begin{aligned} a_L &= b_H \\ b_L &= a_H + c_H \\ c_L &= 2c_H - 2a_H \end{aligned}$$

Recent X-ray diffraction studies of solid iodine have revealed that it undergoes two additional phase transitions, one at about 45 GPa to a face-centred tetragonal structure (11) (space group D_{4h}-$I4/mmm$) and the other at 55 GPa to a face-centred cubic structure (12) (space group O_h-$Fm3m$). The formation of the tetragonal structure (VHP phase) can be seen as decreasing the shear strain defined in eq. [1], when the pressure increases to approximately 45 GPa. In the present paper this very high pressure tetragonal phase is labeled VHP. Electronic band structure calculations have been performed for the tetragonal structure (8).

A comparison of the atomic positions in the LP and HP phases is the basis for a phenomenological model of the LP $\longleftrightarrow$ HP transition (2). The model uses atomic displacements as order parameters without any reference to charge density distortions. The present study also offers a simple phenomenological model for the transition and also combines the charge density distortions and phonon instabilities.

3. 16-Bond model

In the considerations which follow we treat the tetragonal VHP phase as the parent phase. Following arguments of Takemura and co-workers (2) it will be assumed that the dimerization of the iodine atoms occurs primarily in the ($a_H c_H$) or ($b_L c_L$) plane as the applied pressure is decreased. Hence, we believe that a two-dimensional model will be adequate to describe the essential features of the phase transitions. The other basic assumption of the postulated model is that we describe the electronic bonds in solid iodine in a manner similar to the description used by Blinc *et al.* (9) for hydrogen bonding.

Let us consider the VHP tetragonal phase. Each atom has four nearest neighbors in the ($a_H c_H$) plane. In the plane the unit cell is a square and electronic densities (or probabilities) in the four bond directions are equal. This situation is shown schematically in Fig. 3*a*. The HP phase results from the VHP phase by an application of a shear strain resulting in $c_H \neq a_H$ and electronic densities which are different in the orthogonal directions. The schematic of the electron densities for this case is given in Fig. 3*b*. For the diagrams of Fig. 3 the lengths of the lines indicate the strengths of the bonds and not the lengths of the bonds. One would expect an inverse relationship between bond strengths and bond lengths or interatomic distances.

The molecular LP phase has a larger unit cell than the VHP or HP phases with four atoms in the (bc) plane in each unit cell. The strengths of the bonds with nearest neighbors for a typical atom in the molecular phase are shown schematically in Fig. 3*c*.

In order to describe all possible phases of iodine in terms of Brillouin zone center instabilities we consider the unit cell shown in Fig. 4. This unit cell contains eight atoms in the crystal plane, hence is twice as large as needed to describe the molecular phase. The two-dimensional basis is a square lattice. From Fig. 4 it is clear that two choices for unit cells are possible.

In the following we shall consider the 16-bond model as represented in Fig. 4. We assume that the electronic interaction energy for two-particle interactions can be written in the form

$$[3] \qquad U_2 = \frac{1}{2}\sum_{\alpha\beta} a_{\alpha\beta} n_\alpha n_\beta$$

where n_α is the occupation probability for the αth bond in the unit cell. Unit cell indices are neglected in eq. [3] because the chosen cell is the largest one and $a_{\alpha\beta}$ is the interaction parameter summed already over the unit cells. In eq. [3], $\alpha, \beta = 1, 2, \ldots, 16$. The form of the interactions can be justified

Can. J. Chem. Downloaded from www.nrcresearchpress.com by 176.9.209.113 on 09/07/12
For personal use only.

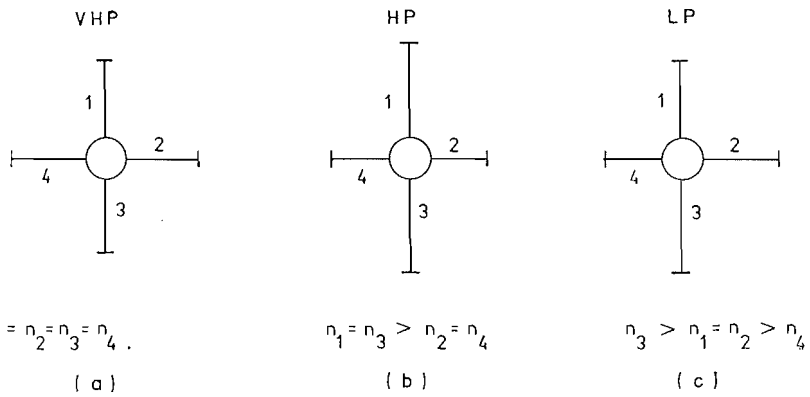

FIG. 3. A schematic representation of electronic densities in four directions around an iodine atom in the (*a*) atomic tetragonal VHP, (*b*) atomic orthorhombic HP, and (*c*) molecular LP phases.

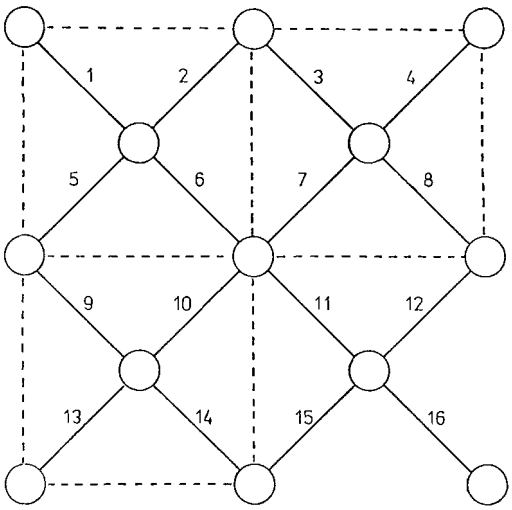

FIG. 4. The 8-atom two-dimensional unit cell with 16 interatomic bonds.

on the basis of Coulomb interactions between bond charge distributions.

We postulate that structural phase transitions in solid iodine are a consequence of changes in occupation probabilities of interatomic bonds. The changes will correspond to eigenvectors of the interaction matrix $\{a_{\alpha\beta}\}$. For the 16-bond model the eigenvectors will transform according to following irreducible representations of the D_{4h} point group: $2A_{1g}$, $2A_{2g}$, $2B_{1g}$, $2B_{2g}$, $4E_u$. The eigenvectors with A_{1g} symmetry correspond to trivial solutions. Hence, all possible changes in the bond occupation probabilities corresponding to the various phases of solid iodine must be linear combinations of eigenvectors with A_{2g}, B_{1g}, B_{2g}, and E_u symmetries. Because we limit ourselves to the two observed phases of solid iodine, an inspection of the schematic representation of HP and LP phases in Figs. 3*b* and 3*c* allows us to reject eigenvectors with A_{2g} and B_{2g} symmetries. None of the distributions shown in these figures is symmetric with respect to the four-fold axis as A_{2g} symmetry requires or with respect to diagonal symmetry planes (σ_d) required by the B_{2g} representation. Therefore, we can conclude that the changes in bond occupation probabilities, which will drive the structural changes to the HP and LP phases must transform according to B_{1g} and E_u representations.

An eigenvector corresponding to B_{1g} symmetry has the form,

$$\begin{aligned}[4]\quad &\delta n_1 = \delta n_3 = \delta n_6 = \delta n_8 = \delta n_9 = \delta n_{11} = \delta n_{14} \\ &\qquad = \delta n_{16} = \delta n \\ &\delta n_2 = \delta n_4 = \delta n_5 = \delta n_7 = \delta n_{10} = \delta n_{12} = \delta n_{13} \\ &\qquad = \delta n_{15} = -\delta n\end{aligned}$$

Here δn denotes a change in the occupation probability n of a particular bond. From the eigenvector [4] an order parameter of B_{1g} symmetry can be constructed as follows:

$$[5]\quad \eta = \{n_1 + n_3 + n_6 + n_8 + n_9 + n_{11} + n_{14} + n_{16} - n_2 - n_4 - n_5 - n_7 - n_{10} - n_{12} - n_{13} - n_{15}\}$$

Now, it is seen that a distortion in the bond probabilities which is of B_{1g} symmetry can be directly assigned to that observed in the HP orthorhombic phase. The corresponding configuration of bonds associated with a given iodine atom for that phase is shown in Fig. 3*b*.

We expect that the LP molecular phase can be described by changes in the bond occupation probabilities from those of the parent phase which transform according to the E_u representation. The eigenvector with this symmetry has the form:

$$\begin{aligned}[6]\quad &\delta n_1 = \delta n_7 = \delta n_9 = \delta n_{15} = \delta l \\ &\delta n_3 = \delta n_5 = \delta n_{11} = \delta n_{13} = \delta n \\ &\delta n_2 = \delta n_4 = \delta n_6 = \delta n_8 = \delta n_{10} = \delta n_{12} = \delta n_{14} \\ &\qquad = \delta n_{16} = \delta m\end{aligned}$$

It follows from the form of the interaction energy, given by eq. [3], that the eigenvalue problem to be solved has the form:

$$[7]\quad \sum_{\beta} (a_{\alpha\beta} - \lambda\delta_{\alpha\beta})\delta n_\beta = 0$$

For example, if interactions between bond charges are limited to nearest neighbors, the eigenvalue problem with eigenvectors [6] can be simplified to:

$$\begin{bmatrix} -\lambda & 2a & 2a \\ a & 2a-\lambda & a \\ 2a & 2a & -\lambda \end{bmatrix} \cdot \begin{bmatrix} \delta l \\ \delta m \\ \delta n \end{bmatrix} = 0$$

where a is the nearest neighbor interaction strength. The solutions for the eigenvalues and eigenvectors for the nearest

Can. J. Chem. Downloaded from www.nrcresearchpress.com by 176.9.209.113 on 09/07/12
For personal use only.

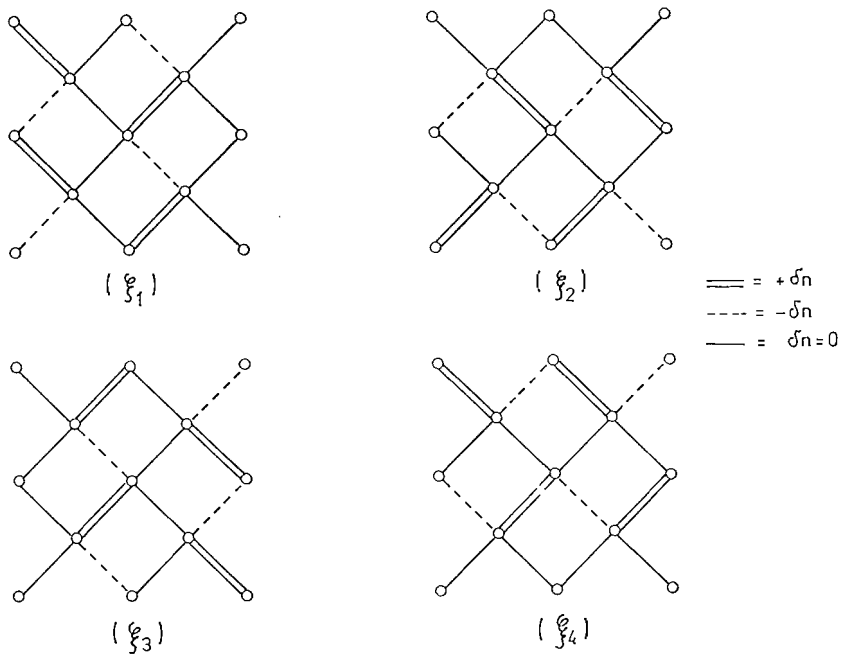

FIG. 5. A representation of the four-component order parameter ξ representing four possible domains of the molecular phase.

neighbor case are:

$$[8a] \quad \lambda = 4a, \qquad \frac{1}{\sqrt{3}}[1, 1, 1]$$

$$[8b] \quad \lambda = -2a, \qquad \frac{1}{\sqrt{2}}[1, 0, -1]$$

$$[8c] \quad \lambda = 0, \qquad \frac{1}{\sqrt{3}}[1, -1, 1]$$

Although the eigenvalues change when further neighbors are considered, the symmetry of the eigenvectors given by eqs. [8a], [8b] and [8c] does not.

The first solution to the eigenvalue problem, eq. [8a], must be rejected because bond-charge conservation condition,

$$\delta l + 2\delta m + \delta n = 0$$

is not fulfilled. For the second solution, eq. [8b], the eigenvector has the form of eq. [6] with $\delta l = -\delta n$, and $\delta m = 0$. For that case the following order parameter of E_u symmetry can be constructed,

$$[9a] \quad \xi_1 = \{n_1 + n_7 + n_9 + n_{15} - n_3 - n_7 - n_{11} - n_{16}\}$$

It is easy to verify that the order parameter ξ_1 is orthogonal to the order parameter η and satisfies the charge conservation condition. As there are four possible choices of equivalent eigenvectors of the form [6], one can construct three additional equivalent order parameters,

$$[9b] \quad \xi_2 = \{n_6 + n_8 + n_{13} + n_{15} - n_5 - n_7 - n_{14} - n_{16}\}$$

$$[9c] \quad \xi_3 = \{n_2 + n_8 + n_{10} + n_{16} - n_4 - n_6 - n_{12} - n_{14}\}$$

$$[9d] \quad \xi_4 = \{n_1 + n_3 + n_{10} + n_{12} - n_2 - n_4 - n_9 - n_{11}\}$$

The distortions in bond occupation probabilities corresponding to E_u symmetry and represented by the four-component order parameter ξ correspond to the distortion shown in Fig. 3c. This figure schematically represents the bonds around an iodine atom in the molecular phase. Four components of the order parameter lead to four equivalent structures which represent distortions with E_u symmetry from the assumed parent phase, the tetragonal VHP phase. The structures are represented in Fig. 5. It is seen that an increase in a bond occupation probability, corresponding to a positive δn, can be identified with a formation of a chemical bond which will cause the dimerization of the atomic phase and the formation of the molecular phase of iodine.

The third solution [8c] of the eigenvalue problem [7] also has E_u symmetry. This distortion in the bond occupation probabilities corresponds to the eigenvector of eq. [6] with $\delta m = -\delta l = -\delta n$. The order parameter which corresponds to this eigenvector is the four component order parameter ξ with the components:

$$[10a] \quad \xi_1 = \{n_1 + n_3 + n_5 + n_7 + n_9 + n_{11} + n_{13} + n_{15} - n_2 - n_4 - n_6 - n_8 - n_{10} - n_{14} - n_{16}\}$$

$$[10b] \quad \xi_2 = \{n_1 + n_2 + n_3 + n_4 + n_9 + n_{10} + n_{11} + n_{12} - n_5 - n_6 - n_7 - n_8 - n_{13} - n_{14} - n_{15} - n_{16}\}$$

$$[10c] \quad \xi_3 = -\xi_1$$

$$[10d] \quad \xi_4 = -\xi_2$$

A graphical representation of the order parameter is shown in Fig. 6. It is seen that the charge density distortions characterized by the order parameter ξ correspond to polymerization of the iodine atoms leading to molecular chains $(I)_n$. Thus, the possibility for polymerization and the formation of a polymerized phase is permitted by the present model. It is quite possible that this is the "zig-zag" chain phase postulated in ref. 10 as an intermediate phase which exists in the pressure range $16 < p < 21$ GPa. One should notice that this postulated "polymeric" phase has the same symmetry as the molecular phase so that the metal–insulator transition at 16 GPa would indeed be iso-structural.

Can. J. Chem. Downloaded from www.nrcresearchpress.com by 176.9.209.113 on 09/07/12
For personal use only.

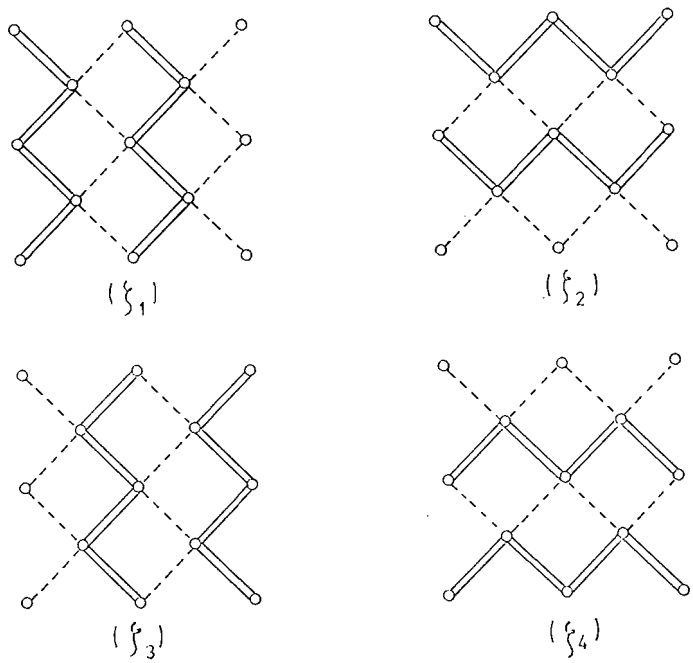

FIG. 6. A representation of the four-component order parameter ξ representing four domains possible of a hypothetical polymerized phase of iodine.

4. Bond charge density distortion waves

The distortions in the bond occupation probabilities discussed for the 16-bond model will now be reinterpreted as bond charge density distortion waves. For this purpose we start with the VHP tetragonal phase and choose the smallest unit cell as the elementary unit. As before, we limit our discussion to a two-dimensional square lattice. The unit cell contains one iodine core and two electron charge densities, $\rho_\alpha(\boldsymbol{l})$. Here $\alpha = x,y$, and $\boldsymbol{l}$ denotes the unit cell vector. Charge densities are assigned to the nearest neighbor interatomic bonds only. Distortions in the charge densities at the wavevector $\boldsymbol{q}$

$$[11] \quad \delta\rho_\alpha(\boldsymbol{q}) = \sum_{\boldsymbol{l}} \delta\rho_\alpha(\boldsymbol{l}) \exp(i\boldsymbol{q}\cdot\boldsymbol{l})$$

will cause a change in the electronic part of the crystal internal energy

$$[12] \quad \delta U = (1/2)\sum_{\alpha\beta}\sum_{\boldsymbol{q}} \delta\rho_\alpha(\boldsymbol{q})\phi_{\alpha\beta}(\boldsymbol{q})\delta\rho_\beta(-\boldsymbol{q})$$

where

$$[13] \quad \phi_{\alpha\beta}(\boldsymbol{q}) = \sum_{\boldsymbol{l},\boldsymbol{l}'} \chi^{-1}_{\alpha\beta}(\boldsymbol{l},\boldsymbol{l}')\exp[i\boldsymbol{q}\cdot(\boldsymbol{l}-\boldsymbol{l}')]$$

and $\chi_{\alpha\beta}(\boldsymbol{l},\boldsymbol{l}')$ is the charge density response in unit cell $\boldsymbol{l}$ to a scalar potential in unit cell $\boldsymbol{l}'$ and χ is a simplified version of an electronic susceptibility $\chi(\boldsymbol{r},\boldsymbol{r}')$.

For our two-dimensional square lattice with one atom in a unit cell, the matrix $\boldsymbol{\phi}(\boldsymbol{q})$ has form

$$[14] \quad \boldsymbol{\phi}(\boldsymbol{q}) = \begin{bmatrix} a(\boldsymbol{q}) & b(\boldsymbol{q}) \\ b(\boldsymbol{q}) & a(\boldsymbol{q}) \end{bmatrix}$$

A condition for the crystal to be stable and to support the charge density distortion described by eq. [11] is that the eigenvalues

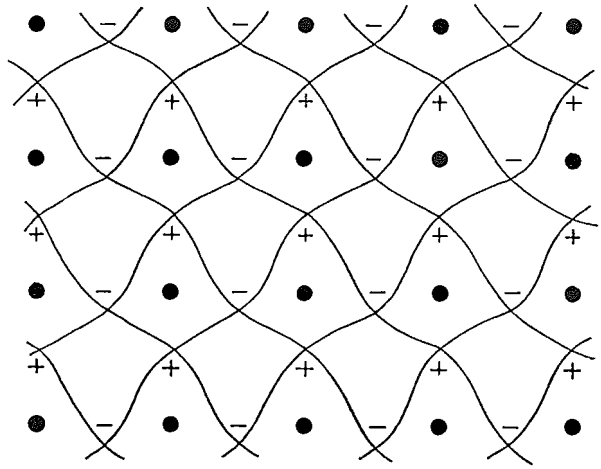

FIG. 7. The bond charge density distortion wave of B_{1g} symmetry in the tetragonal phase of solid iodine.

of the matrix $\boldsymbol{\phi}(\boldsymbol{q})$,

$$[15a] \quad \phi_A(\boldsymbol{q}) = a(\boldsymbol{q}) + b(\boldsymbol{q})$$

$$[15b] \quad \phi_B(\boldsymbol{q}) = a(\boldsymbol{q}) - b(\boldsymbol{q})$$

have to be positive definite. Eigenvectors which correspond to the above eigenvalues are

$$[16a] \quad \delta\rho_A(\boldsymbol{q}) = [\delta\rho(\boldsymbol{q}),\delta\rho(\boldsymbol{q})]$$

$$[16b] \quad \delta\rho_B(\boldsymbol{q}) = [\delta\rho(\boldsymbol{q}),-\delta\rho(\boldsymbol{q})]$$

Because of the charge conservation condition, the totally symmetric eigenvector, $\delta\rho_A(\boldsymbol{q})$ is trivial, $\delta\rho(\boldsymbol{q}) = 0$. Hence, we are only interested in charge density distortions described by the anti-symmetric eigenvector [16*b*]. The distortions corresponding to the wavevector $\boldsymbol{q}$ will transform according to one of the irreducible representation of the corresponding wavevector group $G(\boldsymbol{q})$.

A. Γ-point, $\mathbf{q} = 0$

At the center of the Brillouin zone distortions can be classified according to the D_{4h} point group. The charge density distortion described by the eigenvector [16*b*],

$$[17] \quad \delta\rho_B(\boldsymbol{q} = 0) = [\delta\rho, -\delta\rho]$$

transforms according to the B_{1g} representation and is shown schematically on Fig. 7. It is clearly seen that the distortion corresponds to changes in the bond occupation probabilities of the same symmetry for the 16-bond model. Therefore, the amplitude of the charge density distortion wave, $\delta\rho_B(\boldsymbol{q} = 0)$, can be identified with the order parameter η, introduced in section 3.

B. Δ-direction, $\mathbf{q} = (\pi/2a, \pi/2a, 0)$

The wavevector group for the Δ-direction is isomorphic with the C_{2v} point group. Charge density distortions corresponding to the eigenvector [16*b*] in this direction will transform according to the B_1 representation of the C_{2v} group. The changes in occupation probabilities described by the order parameter ξ will correspond to the charge density distortion wave of B_1 symmetry for the wavevector $\boldsymbol{q}_0 = (\pi/2a, \pi/2a, 0)$. The "bond structures" shown in Fig. 5 and described by the order parameters ξ can now be seen as patterns of the charge density distortion waves for wavevector $\boldsymbol{q}_0$. One of the latter patterns is illustrated in Fig. 8. Thus, the amplitude of the

Can. J. Chem. Downloaded from www.nrcresearchpress.com by 176.9.209.113 on 09/07/12
For personal use only.

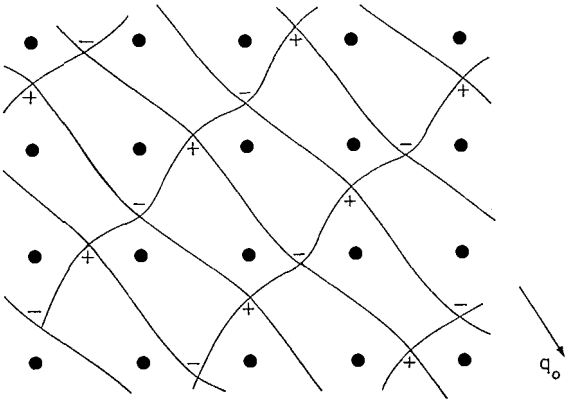

FIG. 8. The bond charge density distortion wave with wavevector $q_0 = (\pi/2a, \pi/2a, 0)$ in the tetragonal phase of iodine.

charge density distortion wave in the Δ-direction can be identified with the order parameter ξ, keeping in mind that $\delta\rho(q_0)$ transforms according to the B_1 irreducible representation of the C_{2v} point group.

The distortions of the bond charge densities described here are coupled to phonons. This coupling leads to indirect interactions between iodine atoms. The indirect interaction produces a softening of certain phonon modes of the tetragonal phase, as described in the next section.

5. Dynamics of the tetragonal phase (two-dimensional model)

Propagating phonon modes are described by quantum numbers (qj), representing the wavevector q and branch index j, with polarization vectors $w(qj)$ and frequency $\omega(qj)$. The frequencies are given by the eigenvalues of the dynamical matrix $\mathbf{D}(q)$, through the solution of the eigenvalue problem

$$[18] \quad m\omega^2(qj)w_\alpha(qj) = \sum_\beta D_{\alpha\beta}(q)w_\beta(qj)$$

In eq. [18], m is the atomic mass and the indices α,β represent the Cartesian components. For the two-dimensional square lattice with one atom per unit cell there are two branches ($j = 1, 2$) for every wavevector.

The force constants which make up the dynamical matrix can be viewed as coming from two separate contributions. The first can be thought of as arising from the forces between "bare" atoms and a second contribution comes from the indirect interaction between the "bare" atoms mediated by charge density distortions. It follows from considerations in the previous section that the amplitudes $\delta\rho_\mu(q)$, $\mu = A,B$, of the bond charge density distortion waves can be chosen as the most natural approximation for the electronic variables. Introducing phenomenological coupling constants $A_{\alpha\mu}(q)$ between the atomic displacement in the α direction and the charge density distortion wave of type μ with wavevector q, the following expression for the dynamical matrix is obtained

$$[19] \quad D_{\alpha\beta}(q) = D^{(0)}_{\alpha\beta}(q) - \sum_\mu A_{\alpha\mu}(q)\phi_\mu^{-1}(q)A_{\beta\mu}(-q)$$

where $\phi_\mu(q)$ are the eigenvalues of the inverse electronic susceptibility, given by eq. [15]. $D^{(0)}_{\alpha\beta}(q)$ is the part of the dynamical matrix which comes from direct interactions between "bare" atoms. The form of eq. [19] is a consequence of the adiabatic approximation: whatever lattice displacement exists at a given time, the charge density distortion amplitudes $\delta\rho_\mu$ instantly adjust themselves to minimize the electronic energy. On introducing the renormalized coupling constants,

$$[20] \quad A_\mu(qj) = \sum_\alpha w_\alpha(qj)A_{\alpha\mu}(q)$$

the expression for the renormalized phonon frequencies is

$$[21] \quad \omega^2(qj) = \omega_0^2(qj) - \frac{1}{m}\sum_\mu A_\mu(qj)\phi_\mu^{-1}(q)A_\mu(-qj)$$

As a consequence of the adiabatic approximation we obtain a useful relation between the amplitudes of the charge density distortion waves, $\delta\rho_\mu(q)$, and the amplitude of the phonon modes, $Q(qj)$,

$$[22] \quad \delta\rho_\mu(q) = -\phi_\mu^{-1}(q)A_\mu(qj)Q(qj)$$

Four acoustic modes the relation reads

$$[23] \quad \delta\rho_\mu(0) = -\phi_\mu^{-1}(q)A_{\mu,\alpha\beta}e_{\alpha\beta}$$

where the components of the strain tensor, $e_{\alpha\beta}$, conveniently describe displacements of atoms due to acoustic phonons

$$[24] \quad e_{\alpha\beta} = \lim_{q\to 0}(Nm)^{-1/2}iq_\beta Q(q_\beta,\alpha)$$

In eq. [24], $Q(q_\beta,\alpha)$ is the acoustic mode amplitude with eigenvector polarized in the α direction and wavevector in the β direction.

Relations [22] and [23] put restrictions on the coupling constants $A_\mu(qj)$. It is clear that only phonon modes or strain components and charge density distortions of the same symmetry can couple bilinearly. We now consider phonons in the two-dimensional tetragonal lattice of solid iodine in the long-wave length limit $q \to 0$ and in the Δ-direction of the Brillouin zone.

A. $\mathbf{q} \to 0$ limit

For a lattice with one atom per unit cell, the dynamical problem in the limit $q \to 0$ reduces to the equations of motion of elasticity theory. The dynamical matrix is expressed in terms of the isothermal elastic constants $c_{\alpha\gamma\beta\delta}$ as

$$[25] \quad D_{\alpha\beta}(q) = \sum_{\gamma\delta} c_{\alpha\gamma\beta\delta}q_\gamma q_\delta$$

For the two-dimensional lattice, the eigenvalues of the elastic constant matrix are

$(1/2)(c_{11} + c_{12})$ with eigenvector $(e_1 + e_2)$ of A_{1g} symmetry,

$(1/2)(c_{11} - c_{12})$ with eigenvector $(e_1 - e_2)$ of B_{1g} symmetry,

$4c_{66}$ with eigenvector (e_6) of B_{2g} symmetry.

Here the Voigt notation for elastic constants and strain components is used.

In the previous section the charge density distortion wave at $q = 0$ is shown to be of B_{1g} symmetry. It follows from eqs. [19] and [25] that the eigenvalue of the effective dynamical matrix can be expressed as

$$[26] \quad (1/2)(c_{11} - c_{12}) = (1/2)(c^0_{11} - c^0_{12}) - \phi_B^{-1}(0)A^2_{B,7}$$

Here $A_{B,7}$ is the coupling constant between the charge density distortion wave and the strain $e_7 = (e_1 - e_2)$. Note that e_7 also has B_{1g} symmetry. c^0_{11} and c^0_{12} are elastic constants of the crystal due to "bare" interatomic interactions only. The relation

$$[27] \quad \delta\rho_B(q = 0) = -\phi_B^{-1}(0)A_{B,7}e_7$$

Can. J. Chem. Downloaded from www.nrcresearchpress.com by 176.9.209.113 on 09/07/12
For personal use only.

Can. J. Chem. Downloaded from www.nrcresearchpress.com by 176.9.209.113 on 09/07/12
For personal use only.

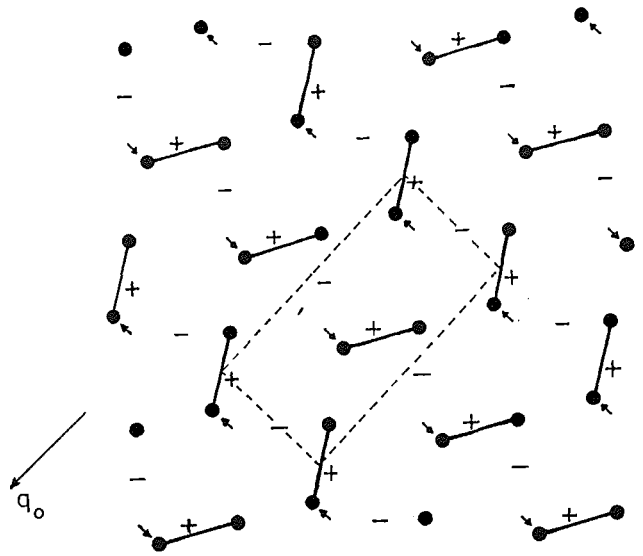

FIG. 9. The formation of the molecular phase of iodine as a result of simultaneous condensation of the bond charge density distortion wave (characterized by increases (+) and decreases (−) in the bond charges) and the transverse phonon mode (characterized by atomic displacements indicated by the arrows), both of B_1 symmetry.

indicates how the amplitude of the charge density distortion wave adjusts to the crystal strain. It is clear from eq. [26] that for sufficiently large coupling constant the eigenvalue $(1/2)(c_{11} - c_{12})$ of the elastic constant matrix vanishes. At that point the crystal is unstable against a homogeneous deformation and will distort continuously to a new structure with symmetry indicated by the e_7 strain. The new structure is orthorhombic and the strain can be used as the primary order parameter to describe the VHP → HP phase transition as the pressure is decreased. Although the strain e_7 is a primary order parameter, the transition is driven by distortions of the electronic charge distributions.

B. Δ-direction

In this direction the two phonon branches of the square lattice of the VHP phase of iodine are classified according to symmetries A_1 and B_1 of the C_{2v} point group. The A_1 phonon corresponds to a longitudinal mode and B_1 represents a transverse mode. It follows from the previous discussion that the frequency of the transverse mode depends on the coupling of the B_1 phonon to the charge density distortion wave of the same B_1 symmetry,

$$[28] \qquad \omega^2_{B_1}(\Delta) = \omega^2_{0,B_1}(\Delta) - \frac{1}{m}|A_B(\Delta)|^2\phi_B^{-1}(\Delta)$$

Again, we expect that the phonon with the wavevector $q_0 = (\pi/2a, \pi/2a, 0)$ will show a tendency to go soft due to indirect interactions mediated by charge density distortion waves of B_1 symmetry. Therefore, we assume that the amplitude of the B_1 phonon at q_0 will be an order parameter for the phase transition to the molecular phase of iodine (iodine dimerization). It has to be stressed that the B_1 phonon at q_0 corresponds to the transverse wave which is used in ref. 2 to explain the HP → LP phase transition. There is, however, an important difference between our approach and that of ref. 2. Here, no additional longitudinal wave with wave vector $q = 2q_0$ is needed to explain the structural changes during the iodine dimerization. The reason is that the transverse bond charge density distortion wave with wave vector q_0 automatically produces simultaneously a longitudinal charge density wave with $q = 2q_0$. Moreover, the dimerization of the iodine atoms in our model is due to the condensation of the phonon mode of B_1 symmetry and, triggered by it, the condensation of the bond charge density distortion wave of the same symmetry. This wave, together with the corresponding atomic displacements, helps to form the chemical bond between iodine atoms. This is visualized schematically in Fig. 9.

The proposed phenomenological model correctly predicts structural changes for transitions VHP → HP and VHP → LP. The model also suggests a possible mechanism which causes the instabilities of the (parent) tetragonal atomic VHP phase leading to the HP and LP phases. The observed sequence of the transformations VHP ⇢ HP ⇢ LP which requires an analysis of thermodynamical properties is not a topic for discussion in this paper.

6. Discussion

On the basis of the present model the phase transformations in solid iodine under high pressure can be explained as follows.

$$\text{Atomic phase} \underset{\text{dissociation}}{\longleftarrow\!\!\!\longrightarrow} \text{molecular phase}$$

can be interpreted in terms of a coupling between a bond charge density distortion wave and a transverse phonon. The driving force for the transformation is the electron–phonon coupling and the instability has a two-dimensional Peierls character. The dimerization results from the condensation of the transverse phonon mode which goes soft as a result of indirect interatomic interactions mediated by charge density distortion waves. The charge density fluctuation coupled to the transverse phonon results in increased electronic charge densities between certain atoms. The displacements corresponding to the soft phonons bring these atoms closer together resulting in chemical bonds between certain iodine atoms and the molecular phase appears.

1. R. W. LYNCH and H. G. DRICKAMER. J. Chem. Phys. **45**, 1020 (1966); N. SAKAI, K. TAKEMURA, and K. TSUJI. J. Phys. Soc. Jpn. **51**, 1811 (1982).
2. O. SHIMOMURA, K. TAKEMURA, Y. FUJII, S. MINOMURA, M. MORI, Y. NODA, and Y. YAMADA. Phys. Rev. B**18**, 715 (1978); K. TAKEMURA, Y. FUJII, S. MINOMURA, and O. SHIMOMURA. Solid State Commun. **30**, 137 (1979); K. TAKEMURA, S. MINOMURA, O. SHIMOMURA, and Y. FUJII. Phys. Rev. Lett. **45**, 1881 (1980); K. TAKEMURA, S. MINOMURA, O. SHIMOMURA, Y. FUJII, and J. D. AXE. Phys. Rev. B**26**, 998 (1982).
3. C. H. TOWNES and D. P. DAILEY. J. Chem. Phys. **20**, 35 (1952).
4. A. PASTERNAK, A. ANDERSON, and J. W. LEECH. J. Phys. C**10**, 3261 (1977).
5. K. KOBASHI and R. D. ETTERS. J. Chem. Phys. **79**, 3018 (1983).
6. W. L. MCMILLAN. Phys. Rev. B**16**, 643 (1977).
7. F. VAN BOLHUIS, P. B. KOSTER, and T. MIGCHELSEN. Acta Crystallogr. **23**, 90 (1967).
8. Y. NATSUME and T. SUZUKI. Solid State Commun. **44**, 1105 (1982).
9. R. BLINC, B. ZEKS, and R. KIND. Phys. Rev. B**17**, 3409 (1978).
10. M. PASTERNAK, J. N. FARRELL, and R. D. TAYLOR. Phys. Rev. Lett. **58**, 575 (1987).
11. Y. FUJII, K. HASE, Y. OHISHI, N. HAMAYA, and A. ONODERA. Solid State Commun. **59**, 85 (1986).
12. Y. FUJII, K. HASE, N. HAMAYA, Y. OHISHI, A. ONODERA, O. SHIMOMURA, and K. TAKEMURA. Phys. Rev. Lett. **58**, 796 (1987).

Polymorphs of rubidium nitrate and their crystallographic relationships

M. SHAMSUZZOHA AND B. W. LUCAS[1]

Department of Physics, University of Queensland, St. Lucia, Brisbane, Queensland, Australia 4067

Received September 4, 1987

This paper is dedicated to Professor J. A. Morrison

M. SHAMSUZZOHA and B. W. LUCAS. Can. J. Chem. **66**, 819 (1988).

The crystal structure relationships between the four thermal polymorphs (IV – 437 K – III – 492 K – II – 564 K – I) of $RbNO_3$ are discussed. Trigonal IV, $a = 10.55(2)$, $c = 7.47(2)$ Å at 298 K, $Z = 9$, and space group $P3_1$ (or its enantiomorph $P3_2$) has Rb atoms arranged on a pseudocubic sublattice defined by $(1/3)[10.\bar{1}]$, $(1/3)[01.\bar{1}]$, $(1/3)[11.1]$ and related segments. The ordered NO_3 groups are enclosed within respective pseudocubes and form close to ideal 8-fold anion–cation coordination with the surrounding Rb atoms. At IV → III, each of the appropriate $(1/3)\langle 10.1\rangle$ and $(1/3)\langle 11.1\rangle$ segments of IV (forming the Rb atom sublattice) transform to a cell edge of an ideal s.c. lattice of Rb atoms, $a = 4.39(1)$ Å, $Z = 1$, and space group $Pm3m$. The orientationally disordered NO_3 groups in III form another close to ideal 8-fold anion–cation coordination with the Rb atoms. At III → II, the s.c. lattice of III changes to form a larger b.c.c. lattice, $a = 8.84(3)$ Å, $Z = 8$, in II. A parallel-axes unit cell relationship, i.e. $\langle 100\rangle_{III} // \langle 100\rangle_{II}$ and $2(a)_{III} = (a)_{II}$, exists between III and II. The NO_3 group in II is postulated to form a close to ideal 8-fold anion–cation coordination with the surrounding Rb atoms. At II → I, II transforms to a f.c.c. lattice, $a = 7.32$ Å, $Z = 4$, and space group $Fm3m$. The NO_3 group in I forms a close to ideal 6-fold anion–cation coordination with the surrounding Rb atoms. It is suggested that $(1/2)[1\bar{1}1]$, $(1/2)[11\bar{1}]$, $(1/2)[\bar{1}11]$ and related segments in II, which form a trigonal Rb atom sublattice, $a = 7.65(3)$ Å and $\alpha = 109.47°$, after II → I, transform to orthogonal cell edges of the cubic lattice of I.

M. SHAMSUZZOHA et B. W. LUCAS. Can. J. Chem. **66**, 819 (1988).

On discute des relations qui existent entre les structures cristallines de quatre polymorphes thermiques (IV – 437 K – III – 492 K – II – 564 K – I) du $RbNO_3$. A 298 K, dans la forme trigonale IV, avec $a = 10{,}55(2)$ et $c = 7{,}47(2)$ Å, $Z = 9$ et groupe d'espace $P3_1$ (ou son énantiomorphe $P3_2$), les atomes de Rb sont arrangés dans un sous-réseau pseudo-cubique défini par $(1/3)[10.\bar{1}]$, $(1/3)[01.\bar{1}]$ et $(1/3)[11.1]$ et des segments apparentés. Les NO_3 ordonnés sont enfermés dans des pseudo-cubes et ils forment, avec les atomes de Rb qui les entourent, une coordination anion–cation octuple pratiquement idéale. Lors de la transition IV → III, chaque segment approprié $(1/3)\langle 10.1\rangle$ et $(1/3)\langle 11.1\rangle$ du composé IV (ils forment le sous-réseau de l'atome de Rb) se transforme en une arête de la cellule d'un réseau idéal cubique simple d'atomes de Rb, avec $a = 4{,}39(1)$ Å, $Z = 1$ et groupe d'espace $Pm3m$. Dans la forme III, les atomes de Rb et les groupements NO_3, qui sont désordonnés du point de vue de l'orientation, forment une autre coordination anion–cation octuple pratiquement idéale. Lors de la transition III → II, le réseau cubique simple de III se transforme en un réseau cubique centré plus grand, avec $a = 8{,}84(3)$ Å, $Z = 8$. Entre les formes III et II, il existe une relation d'unité cellulaire à axes parallèles, c'est-à-dire $\langle 100\rangle_{III} // \langle 100\rangle_{II}$ et $2(a)_{III} = (a)_{II}$. Dans la forme II, on postule que le groupement NO_3 et les atomes de Rb forment une coordination anion–cation octuple pratiquement idéale. Lors de la transition II → I, la forme II se transforme en un réseau cubique à face centrée avec $a = 7{,}32$ Å, $Z = 4$ et groupe d'espace $Fm3m$. Dans I, le groupement NO_3 et l'atome de Rb forment une coordination anion–cation sextuple pratiquement idéale. On suggère que, après la transformation II → I, les segments $(1/2)[1\bar{1}1]$, $(1/2)[11\bar{1}]$, $(1/2)[\bar{1}11]$ et apparentés de la forme II — qui forment un sous-réseau trigonal avec l'atome de Rb avec $a = 7{,}65(3)$ Å et $\alpha = 109{,}47°$ — se transforment en arêtes orthogonales du réseau cubique de I.

[Traduit par la revue]

Introduction

For solids which exhibit phase transitions, information on the crystal structures of the polymorphs is useful in understanding the relationships between them and the mechanisms of the changes. At atmospheric pressure, $RbNO_3$ undergoes the thermal polymorphic phase transitions (1, 2):

$$IV - 437\ K - III - 492\ K - II - 564\ K - I$$

The IV → III transition has been studied (2) by single crystal X-ray diffraction methods, with IV reported to be trigonal, $a = 10.48$, $c = 7.45$ Å, $Z = 9$, and space group $P3_112$ (or its enantiomorph $P3_212$), and III, cubic $a = 4.37$ Å, $Z = 1$. The observation of transformation of the $\langle 00.1\rangle$- and $\langle 10.1\rangle$-axes single crystal diffraction patterns of IV to the corresponding $\langle 111\rangle$- and $\langle 100\rangle$-axes diffraction patterns of III, suggested the unit cell relationships shown in Fig. 1.

Crystallographic studies of the III → II transition were originally made by X-ray powder diffraction methods (3, 4), with III reported to be cubic, $a = 4.37$ Å, and $Z = 1$, and II to be trigonal, $a = 5.48$, $c = 10.71$ Å, and $Z = 3$. Brown and McLaren (2) proposed, from X-ray powder diffraction, II to be tetragonal, $a = 6.19(3)$, $c = 8.74(6)$ Å, and $Z = 6$, and suggested a simple unit cell relationship between III and II, where $\sqrt{2}\,(a)_{phase\ III} = 6.16$ Å $= (a)_{phase\ II}$, $2(a)_{phase\ III} = 8.74$ Å $= (c)_{phase\ II}$. The II → I transition was also studied by X-ray powder diffraction methods (2) with I suggested to have a f.c.c. lattice, $a = 7.32$ Å and $Z = 4$.

The structural relationships between phases III, II, and I have been considered (5–7) and were regarded as a progressive transition conversion from a CsCl-type to a NaCl-type lattice (Fig. 2). The interaxial angle of the trigonal unit cell for II is between 70 and 78°, while the trigonal angles of 90 and 60° correspond to CsCl- and NaCl-type lattice, respectively.

The availability of more recently determined crystal structure details for the various phases of $RbNO_3$ allow further consideration of the structural relationships between the various polymorphs.

Structure of $RbNO_3$ (IV) and its behaviour at the onset of the IV → III transition

The IV crystal system was established as trigonal by early single crystal X-ray diffraction studies (8), although its Laue group remained uncertain long after. Laue photographs taken

[1]Author to whom correspondence may be addressed.

Can. J. Chem. Downloaded from www.nrcresearchpress.com by 176.9.209.113 on 09/07/12
For personal use only.

Can. J. Chem. Downloaded from www.nrcresearchpress.com by 176.9.209.113 on 09/07/12
For personal use only.

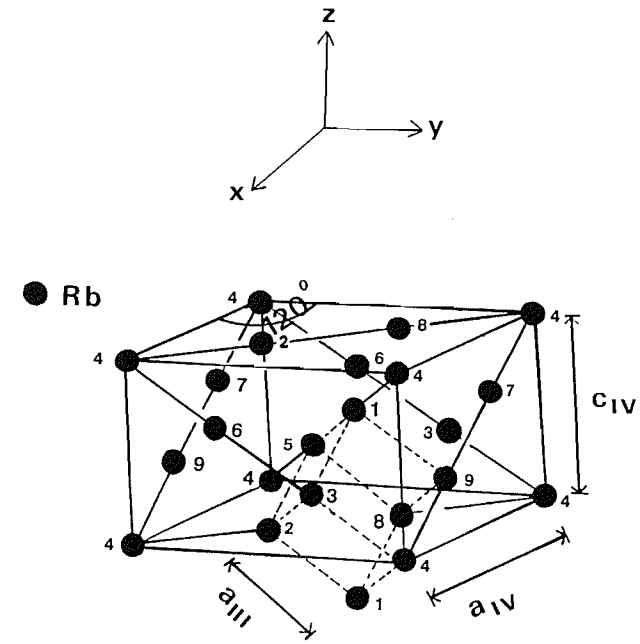

FIG. 1. The relationship between the unit cells of phases IV and III in $RbNO_3$; Rb atoms only are shown (groupings 1,2,3; 4,5,6; 7,8,9 represent symmetry-related atoms, generated by the equivalent positions of the space group $P3_1$) (2,11).

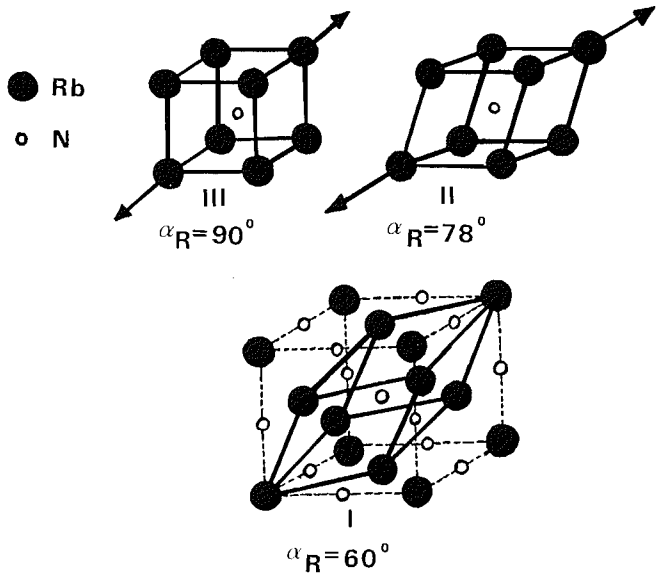

FIG. 2. The structural relationships between III (CsCl-type), II (trigonal), and I (NaCl-type) $RbNO_3$. Large circles represent Rb atoms, small circles, N atoms; the O atoms are not shown. The arrows indicate the direction of the elongation of the trigonal cell, α_R is the trigonal angle (6).

with the X-ray beam along the trigonal axis were reported to exhibit a mirror plane parallel to the 3-fold axis, indicating a Laue group $\bar{3}m$ (2, 8, 9). However, the discovery of optical activity (10) and pyroelectricity along the trigonal axis (9) suggested a point group 3 and Laue group $\bar{3}$. The ambiguity was resolved when the crystal structure, determined by 3-dimensional single crystal neutron diffractometry (11), indicated only an *apparent* mirror plane and the Laue group could be uniquely assigned $\bar{3}$. The structure (Fig. 1) has $a = 10.55(2)$, $c = 7.47(2)$ Å at 298 K, $Z = 9$, space group $P3_1$ (or its

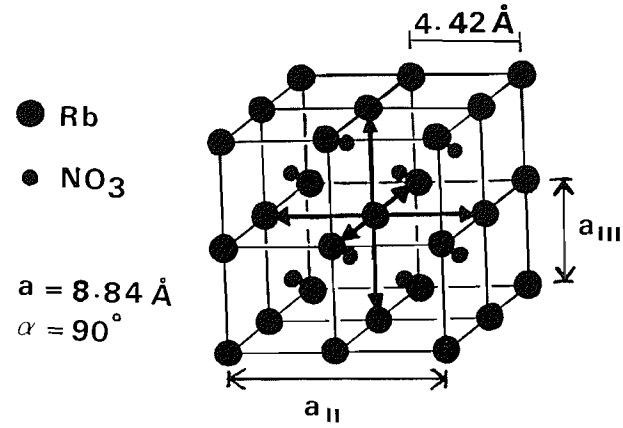

FIG. 3. The unit cell contents of II and its unit cell relationship with III. Large circles represent the Rb atoms, small circle, the NO_3 groups.

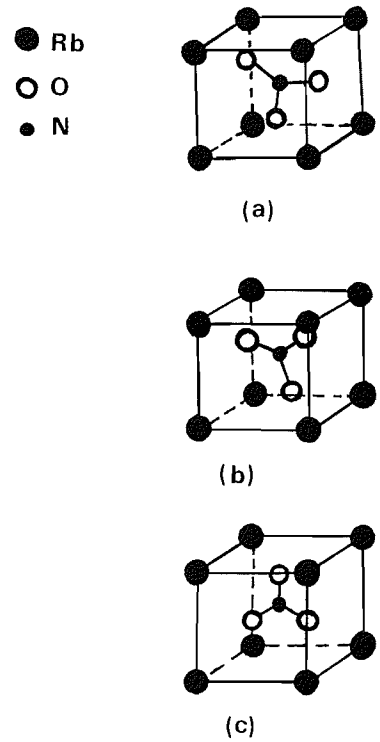

FIG. 4. Three possible orientational models of a planar NO_3 group within a cubic array of Rb atoms in III. The plane of the NO_3 group (*a*) bisects the unit cell edge, (*b*) is normal to the cubic body diagonal, (*c*) is parallel to a face of the surrounding Rb atom cube.

enantiomorph $P3_2$). The Rb atoms form a pseudocubic sublattice with each NO_3 group (of the type shown in Fig. 4(*c*)) in close to ideal 8-fold anion–cation coordination with its surrounding Rb atoms.

From the viewpoint of the IV → III transition, the Rb atom sublattice is significant since its behaviour approaching the IV → III transition temperature is expected to act as a precursor to the forthcoming change and have influence on the resultant lattice of the higher temperature phase. In this respect, the structure of IV determined just below the IV → III transition temperature of 403 K (11) provides useful information on the behaviour of the Rb atom sublattice. The structure, along with that at room temperature, indicates the Rb atom pseudocubic sublattice to have dimension ranging between $a = 4.07(1)$ to 4.62(1) Å and $\alpha = 85.9(2)$ to 95.8(2)° at 298 K and $a = 4.12(1)$

Can. J. Chem. Downloaded from www.nrcresearchpress.com by 176.9.209.113 on 09/07/12
For personal use only.

to 4.53(1) Å and α = 86.9(2) to 93.8(2)° at 403 K (11); the Rb atom sublattice is closer to an ideal cubic lattice at 403 K than at 298 K. This behaviour of the Rb atom sublattice of IV does tend to anticipate its forthcoming change to the cubic symmetry of III (2, 3) at the higher temperature phase.

Structure of $RbNO_3$ (III) and IV → III transition

From early X-ray powder diffraction studies III was reported to have a structure with s.c. cell, a = 4.37 Å and Z = 1, although the NO_3 group orientation was uncertain (3). A single (essentially planar) NO_3 group cannot be fitted into the unit cell for any possible cubic space group; this can only be achieved if orientational disorder is introduced.

The first suggestion incorporating such disorder involved "free rotation" about its centre of mass (3). However, the experimentally observed entropy change at the IV → III transition is 2.15 cal mol^{-1} K^{-1} (5), which is too small to allow such extreme disordering. Strϕmme (12) proposed a III crystal structure with finite equivalent-orientational disorder of the NO_3 group. The structure, with a = 4.37 Å, Z = 1 and space group $Pm3m$, was based on X-ray powder diffraction (13). The Rb atoms were at cell corners, while the NO_3 group was orientationally disordered over mainly aragonite-type (each NO_3 group plane normal to a body diagonal of the surrounding Rb atom cube) and partly calcite-type (each NO_3 group plane bisects a cell edge of the surrounding Rb atom cube) configurations. Recently, powder (14) and single crystal (15) neutron diffraction studies concluded that a 12-fold orientationally disordered model for the NO_3 group (each NO_3 group plane being parallel to a face of the surrounding Rb cube) is preferable to an 8-fold disordered model (pure aragonite-type configuration). This model is compatible with the observed single crystal X-ray diffuse scattering intensity patterns that occur perpendicular to the reciprocal lattice axes (17, 18).

The structure has a = 4.39(1) Å, Z = 1, and space group $Pm3m$, the Rb atom at the corners of a cubic unit cell with a N atom close to its centre. The oxygen atoms of the orientationally disordered NO_3 group lie essentially on a spherical shell of radius equal to the N—O bond length about the cell centre. The NO_3 group in its orientationally disordered state forms close to an ideal 8-fold anion–cation coordination with the Rb atoms.

The lattice relationship between the two phases (11, 15) is shown in Fig. 1. In IV, (1/3)[10.1], (1/3)[01.1], and (1/3)[11.1] and related segments define the pseudocubic sublattice cell, which, at the IV → III transition, transforms to the cell of an ideal s.c. lattice of Rb atoms in III.

Structure of $RbNO_3$(II) and III → II transition

X-ray powder diffraction data of II have been indexed on the basis of *three* different crystal systems, viz trigonal (3, 6, 14), tetragonal (2), and cubic (16). Single crystal diffraction methods to determine the crystal system have not been successful so far, as various reports (2, 19, 20, 21) indicate that single crystals (grown in IV) fragment during the III → II transition, and are unsuitable for single crystal diffraction studies in II. It has been reported, however, that single crystals of $RbNO_3$ grown from the melt can be cooled through the I → II transition to phase II, to give distinct single crystal X-ray diffraction patterns (20, 21). Owing to experimental difficulties in determining various crystallographic axes of such transformed crystals, the resultant single crystal diffraction data have not clearly established the appropriate crystal system of II.

The unit cells of the proposed trigonal, tetragonal, or cubic

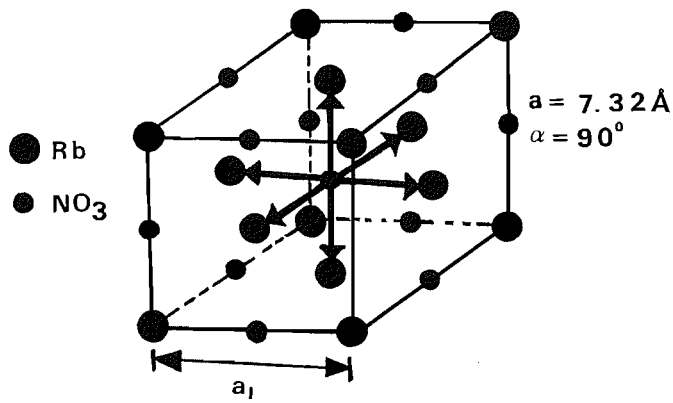

FIG. 5. The unit cell contents of I (14). The large circles represent Rb atoms, small circles the NO_3 groups.

crystal systems are geometrically closely related and this makes difficult discrimination (22) between the fit to the observed X-ray diffraction powder pattern, although as III has been established to have a cubic crystal system (14, 15), a lowering of crystal symmetry to trigonal or tetragonal with higher temperature phase appears unlikely. Antiferroelectricity has been reported for II (23–25), which requires arrangements of antiparallel dipoles within the unit cell. These dipoles would occur as a consequence of the relative displacements between the Rb^+ and NO_3^- units within the unit cell, which is not likely to occur in the crystal structures within the possible space groups $R3$, $R32$, $R3m$, $R3c$, $R\bar{3}m$, $R\bar{3}c$, belonging to the suggested trigonal crystal system. In fact, the determined crystal structure of II by Ahtee and Hewat (14), does not show such antipolar structure; rather, the NO_3 group (in aragonite-type configuration) is disordered over two orientations inside a Rb atom trigonal unit cell with space group $R\bar{3}m$. On the other hand, the cubic crystal system (structure yet to be determined) potentially could have such antiparallel dipoles in the unit cell.

Recent studies suggest that II has a b.c.c. lattice, with Z = 8 and possible space group: $I23$, $I2_13$, $Im3$, $I432$, $I\bar{4}3m$, or $Im3m$ (16). For these space groups, the 8 Rb atoms of the unit cell can only define a b.c.c. lattice if occupying the positions: 0,0,0; $\frac{1}{2},\frac{1}{2},\frac{1}{2}$; $0,\frac{1}{2},\frac{1}{2}$; $\frac{1}{2},0,\frac{1}{2}$; $\frac{1}{2},\frac{1}{2},0$; $\frac{1}{2},0,0$; $0,\frac{1}{2},0$; $0,0,\frac{1}{2}$ in the unit cell. A b.c.c. unit cell of such atomic occupancy may be considered comprised of eight cubic subcells of Rb atoms (Fig. 3) each with a = 4.42(3) Å. If Rb...O distances are kept somewhat greater than the sum of their effective atomic radii 2.88 Å (26), each of the eight planar NO_3 groups of the unit cell can only occupy positions surrounded by one Rb atom cubic subcell. The orientation of the NO_3 group inside the II unit cell according to the observed entropy change of 1.35 cal mol^{-1} K^{-1} (5) at the III → II transition is likely to be disordered. The most probable configuration of the NO_3 groups which could satisfy orientational disordering as well as antiparallel displacements of the NO_3 group in the neighbouring sites of the unit cell are shown in the structural models Fig. 4 (*a*), (*b*), and (*c*). These structural models can be fitted to various space groups suggested for this phase, but only a proper experimental analysis can define the appropriate space group and configuration of the NO_3 group. Since each of these structural models suggests a close to an ideal 8-fold anion–cation coordination, it is reasonable to hypothesize close to an ideal 8-fold anion–cation coordination structure for II.

The lattice of II along with its suggested structure presents an understanding of the Rb lattice rearrangement which takes place

Can. J. Chem. Downloaded from www.nrcresearchpress.com by 176.9.209.113 on 09/07/12
For personal use only.

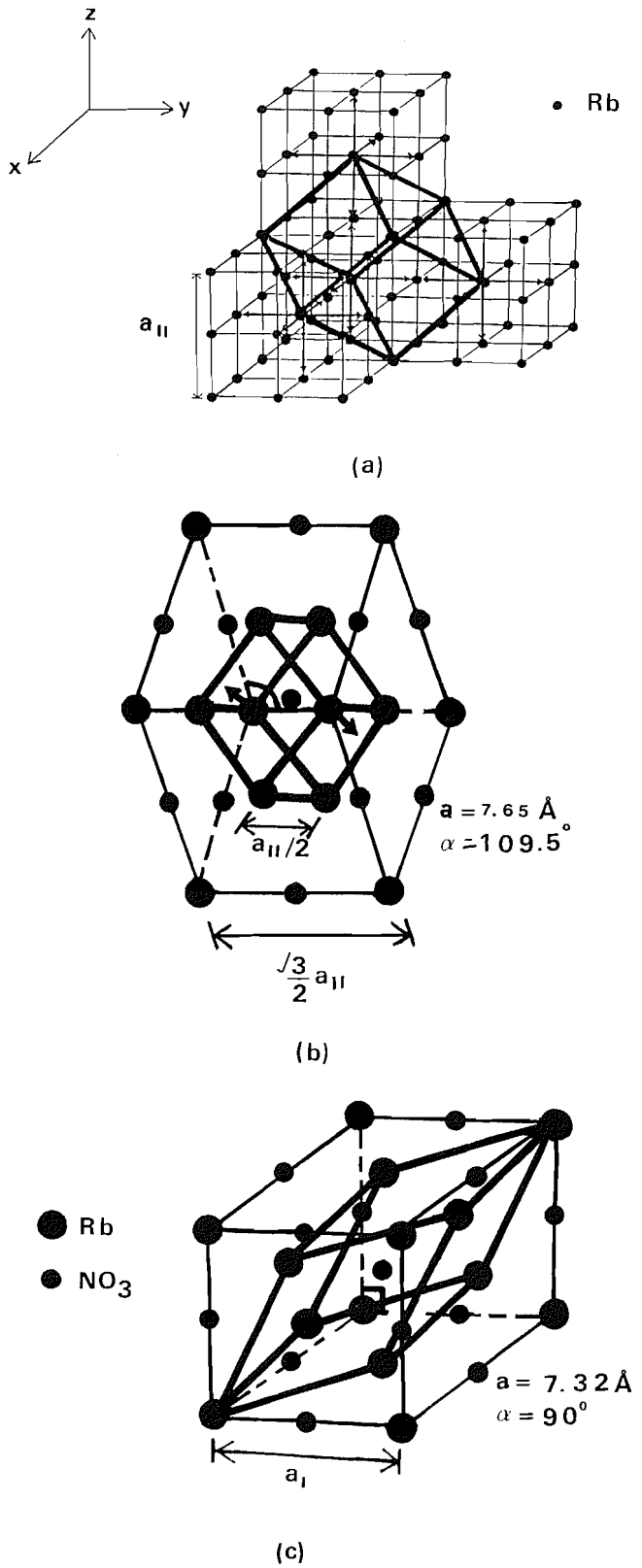

FIG. 6. Lattice transformation processes during the II → I transition. (*a*) (1/2)[1$\bar{1}$1], (1/2)[11$\bar{1}$], (1/2)[$\bar{1}$11] of II form a trigonal subcell (represented by thicker lines). The (101),110), and (011) of II correspond to (100), (010), and (001) of the trigonal subcell. (*b*) The trigonal subcell described in (*a*) is shown separately, with the arrows showing the <111>-direction of elongation. (*c*) Illustrates a NaCl-type cubic unit cell of I.

at the III → II transition (Fig. 3). Eight s.c. unit cells of III combine during the III → II transitions to form a larger b.c.c. unit cell. This results in a parallel-axes unit cell relationship between the two phases, i.e. $<100>_{\text{phase III}} // <100>_{\text{phase II}}$ and $2(a)_{\text{phase III}} = (a)_{\text{phase II}}$.

Structure of $RbNO_3$(I) and II → I transition

Phase 1 has been reported to have a f.c.c. lattice with a = 7.32 Å and Z = 4 (2, 6, 14, 20, 21). Its crystal structure was originally suggested to have the Rb atoms and NO_3 groups forming a NaCl-type cation–anion arrangement. Single crystal X-ray (21) and neutron powder (14) diffraction studies also concluded a similar structure with an aragonite-type configuration of the orientationally disordered NO_3 groups. The structure (14), with a = 7.32(2) Å, Z = 4 and space group $Fm3m$, is shown in Fig. 5; the NO_3 group (small circles) form a close to ideal 6-fold anion–cation coordination with the Rb atoms.

The lattices of II and I and their suggested structures clearly indicate that at the II → I transition, a close to ideal 8-fold anion–cation coordination in II transforms to a close to ideal 6-fold anion–cation coordination in I; a possible lattice conversion mechanism is shown in Fig. 6. For the II lattice, (1/2)[1$\bar{1}$1], (1/2)[11$\bar{1}$], (1/2)[$\bar{1}$11], and related segments (Fig. 6(*a*)) form a trigonal sublattice (Fig. 6(*b*)), with a = 7.65(3) Å, α = 109.47°, Z = 4. The anion–cation coordination in this unit subcell is 8-fold (a NO_3 group represented by small circle within a CsCl-type II $RbNO_3$ cubic subcell of dimension a = 4.41(3) Å, outlined by thick lines in Fig. 6(*b*), is surrounded by eight equidistant Rb atoms). At the transition, the trigonal lattice effectively dilates along the shortest <111>-type direction and transforms to the f.c.c. unit cell (Fig. 6(*c*)) of I. For the b.c.c. unit cell of II, this elongation process is accomplished (*a*) by a homogenous dilation along ±<110> and a simultaneous contraction along ±<100> on the respective {110} planes and (*b*) by a homogenous elongation along the appropriate <111> directions. This results in the transformation of $\{110\}_{\text{phase II}}$ to the corresponding $\{100\}_{\text{phase I}}$.

Discussion

The transitions IV – III – II for $RbNO_3$ are accomplished by very small changes of the Rb atom sublattices from pseudocubic to cubic. The NO_3 groups in these structures change from being orientationally ordered to disordered and have a similar 8-fold anion–cation coordination. The reported tendency for single crystals to fragment at the III → II transition could result from a change of the NO_3 group configuration, rather than the previously suggested Rb atom sublattice.

At the II → I transition, a major Rb atom sublattice rearrangement takes place and no simple unit cell relationship exists between the two phases. The suggested lattice transformation, in accordance with Buerger's (27) proposal, is accomplished by an homogenous dilation along one of the trigonal axes of the CsCl-type phase II structure. The crystals in I are soft and plastic (19, 20), which could account for the sublattice rearrangement at the transition without single-crystal fragmentation.

Acknowledgments

The authors thank the Australian Institute of Nuclear Science and Engineering (AINSE) and the Australian Atomic Energy Commission (AAEC) for assistance from their staff and use of facilities. The work was supported by an AINSE research grant.

1. V. E. PLYUSCHEV, I. B. MARKINA, and L. P. SHKLOVER. Dokl. Akad. Nauk. SSSR, **108**, 645 (1956).
2. R. N. BROWN and A. C. MCLAREN. Acta Crystallogr. **15**, 974 (1962).
3. C. FINBAK and O. HASSEL. Z. Phys. Chem. B**35**, 25 (1937).
4. C. FINBAK, O. HASSEL, and L. C. STRΦMME. Z. Phys. Chem. B**37**, 468 (1937).
5. D. M. NEWNS and L. A. K. STAVELEY. Chem. Rev. **66**, 267 (1966).
6. P. P. SALHOTRA, E. C. SUBBARAO and P. VENKATESWARL. Phys. Status Solidi, **28**, 859 (1969).
7. A. J. IVERSON and S. W. KENNEDY. Acta Crystallogr. B**29**, 1554 (1973).
8. L. PAULING and J. SHERMAN. Z. Krist. **84**, 213 (1933).
9. P. C. BURY and A. C. MCLAREN. Phys. Status Solidi, **31**(2), 799 (1969).
10. S. V. KARPOV and A. A. SHULTIN. Phys. Status Solidi, **39**, 33 (1970).
11. M. SHAMSUZZOHA and B. W. LUCAS. Acta Crystallogr. B**38**, 2353 (1982).
12. K. O. STRΦMME. Acta Chem. Scand. **25**, 211 (1971).
13. U. KORHONEN. Ann. Acad. Sci. Fenn. Ser. A I (No. 102), 35 pages (1951).
14. M. AHTEE and A. W. HEWAT. Phys. Status Solidi, A**58**, 525 (1980).
15. M. SHAMSUZZOHA and B. W. LUCAS. Acta Crystallogr. C**43**, 385 (1987).
16. M. SHAMSUZZOHA and B. W. LUCAS. J. Appl. Cryst. **21**, 74 (1988)
17. Y. SHINNAKA and S. YAMAMOTO. J. Phys. Soc. Jpn. **50**, 2091 (1981).
18. Y. SHINNAKA and S. YAMAMOTO. J. Phys. Soc. Jpn. **52**, 3437 (1983).
19. S. W. KENNEDY. Nature, **210**, 936 (1966).
20. S. W. KENNEDY. Phys. Status Solidi, A**2**, 415 (1970).
21. S. YAMAMOTO, S. SUEMATSU and Y. SHINNAKA. J. Phys. Soc. Jpn. **43**, 1962 (1977).
22. A. C. MCLAREN. Rev. Pure Appl. Chem. **12**, 54 (1962).
23. A. Y. DANSTSIGER and E. G. FESENKO. Sov. Phys. Crystallog. **8**, 717 (1964).
24. A. Y. DANSTSIGER. Sov. Phys. Solid-State, **7**, 1845 (1966).
25. S. FUJIMOTO, N. YASUDA, H. SHIMIZU, S. TSUBOI, K. KAWABE, Y. TAKAGI, and A. M. MIDIRKAWA. J. Phys. Soc. Jpn. **42**, 911 (1977).
26. International tables for X-ray crystallography. Vols. I, III, and IV. Kynoch Press, Birmingham. 1965, 1968, and 1974.
27. (*a*) M. J. BUERGER. *In* Phase transformation in solids. *Edited by* R. Smoluchowski, J. E. Mayer and W. A. Weyl. John Wiley, New York. 1951. pp. 183–211; (*b*) M. J. BUERGER. Fort-Schr. Mineral. **39**, 4 (1961).

Can. J. Chem. Downloaded from www.nrcresearchpress.com by 176.9.209.113 on 09/07/12
For personal use only.

Microcalorimetry and thermochemistry of alloys

JEAN PIERRE BROS

Thermodynamique des systèmes métalliques, Université de Provence, Centre Saint-Charles, Place V. Hugo, 13331 Marseille CEDEX 3, France

Received September 28, 1987

This paper is dedicated to Professor James A. Morrison

JEAN P. BROS. Can. J. Chem. **66**, 824 (1988).

High temperature microcalorimetry is a very fruitful technique for increasing our knowledge of the thermochemistry of multicomponent alloys. As a good example, calorimetric results obtained for the Al + Bi + Ga system have been selected. Using a Calvet microcalorimeter and the indirect drop method, enthalpies of formation were measured over the entire concentration range between 725 and 1170 K and several points of the phase diagram were deduced from these calorimetric results. By means of a computer program, the Al + Bi + Ga equilibrium phase diagram was calculated and thus a thermodynamic description can be predicted. Making use of some simplifying hypotheses, the results indicate a satisfactory agreement between the experimental and the calculated liquid miscibility gap.

JEAN P. BROS. Can. J. Chem. **66**, 824 (1988).

Avec l'énergie libre de Gibbs, la fonction enthalpie de formation, obtenue par calorimétrie directe, joue un rôle important dans l'étude thermodynamique des alliages; pour le système Al + Bi + Ga, les résultats expérimentaux choisis constituent un bon exemple. En effet, par microcalorimétrie haute température, les chaleurs de formation à pression constante ont été mesurées sur tout le domaine de composition à diverses températures ($725\ K < T < 1170\ K$). De plus, dans certaines conditions, ces mesures permettent d'accéder directement aux coordonnées de quelques points du diagramme d'équilibre des phases. À l'aide d'un programme de calcul et de quelques hypothèses simplificatrices, ces résultats ont conduit, avec une précision satisfaisante, à la localisation de la lacune de miscibilité ternaire à l'état liquide de cet alliage.

[Traduit par la revue]

Introduction

The Gibbs free energy of reaction is the most interesting of the thermodynamic functions, but its experimental determination is often difficult. The direct measurement of the heat of reaction at constant pressure plays an important role in the study of reactions between substances in condensed phases, for which the entropy changes are generally small. Enthalpies of reaction are usually obtained by calorimetry. This direct technique, very simple in principle and using several kinds of apparatus, permits determination of the enthalpies of reaction, of dissolution, of phase transition, etc., as well as the molar heat capacities. A detailed description of the different types of calorimeters, a criticism of experimental techniques, and much useful information are contained in the literature, and particularly in Metallurgical thermochemistry, by Kubaschewsky and Alcock (1). Since the publication of this book the number of experimental studies concerning alloys has increased very rapidly. In most cases, enthalpies of formation have been obtained directly by using a high temperature microcalorimeter, the characteristic feature of which is one or two experimental cell(s) completely surrounded by several hundred thermocouples. Groups of researchers using this kind of apparatus are so numerous (for example, Kleppa in Chicago, Collinet in Grenoble, Castanet and Gambino in Marseille, Topor in Moscow, Hertz in Nancy, Hayer and Komarek in Vienna, Predel in Stuttgart) that it is difficult to draw up an exhaustive list.

The main purposes in the determination of the enthalpies of formation of alloys are, on the one hand, to obtain knowledge of the liquid and solid metallic states and, on the other hand, to predict the stability of the metallic phases. Such information can also be used in the study of industrial processes.

To highlight the advantages of microcalorimetric measurements in the field of thermochemistry of alloys, some typical results carried out for binary, or multicomponent, alloys are presented in the second part of this paper. In the following section a description of the calorimeters and the experimental techniques used are reviewed.

Experimental

In general, thermodynamic studies of alloys are performed over a wide temperature range and the choice of the calorimeter depends upon this temperature range of investigation. Between 0 and 1000°C the microcalorimeter described by Calvet and Prat in 1955 (2) is most often employed. Several authors have adapted this apparatus to solve specific problems (for example by changing the cell volume or the number and the nature of thermocouples) but the principle remains the same.

Apparatus

A complete description of the Calvet high temperature microcalorimeter, operable up to 1100°C, has been published by Gaune-Escard (3). The central alumina block (120 mm in diameter) surrounded by two large cylindrical shields in pure alumina is located in a cylindrical furnace heated by four Kanthal resistors (one on the bottom, two on the vertical wall, and one on the cover). Two very similar thermopiles are fixed in the central block. Each thermopile consists of a thin cylindrical alumina tube (16.9 mm in diameter and 80 mm high), closed at the bottom, surrounded by 396 (Pt/Pt + Rh 10 wt.%) thermocouples. About 80% of the external surface of this alumina tube is covered by the junctions of regularly arranged thermocouples.

These two thermopiles are connected differentially to eliminate thermal perturbations due to the furnace. One of the cells is called the "laboratory cell", the other one the "reference cell". The temperature of the calorimeter is regulated or linearly programmed by an electronic device, the sensing element of which is a platinum resistance (100 Ω at 0°C).

The electromotive force (E) of these two piles is recorded versus time (t) by using a millivoltmeter. In the absence of thermal effect in the cells the base line recorded is a straight line parallel to the time axis. When a thermal effect (Q) is developed in one cell a thermogram ($E = f(t)$ curve) is recorded; the area delimited by this curve and the baseline is proportional to the heat effect (Q). Generally the determination of this surface is made either by using a manual planimeter (e.g., an OTT planimeter) or by a trapezoid method. Now automatic data acquisition systems are available. They consist of an amplifier, a scanner, a

Can. J. Chem. Downloaded from www.nrcresearchpress.com by 176.9.209.113 on 09/07/12
For personal use only.

millivoltmeter, and a microcomputer: the emf values measured at constant frequency are entered in the computer; and from these data the area of the thermogram is computed. The integration procedure includes a correction method to take into account the derivation of the baseline.

The nature of the materials and of the thermocouples used to build a microcalorimeter depends on the temperature range investigated. At low temperature a metallic block and shields can be used, as well as other kinds of thermocouples.

Techniques

The experimental techniques worked out in calorimetry for the determination of enthalpies of formation of alloys are numerous. For all of them, the main problem is the elimination of secondary effects arising generally from evaporation of the components, from metal–atmosphere interactions, from solvent– or solute–crucible reactions, from difficulties of mixing, etc. To solve these specific problems various devices have been created.

In ref. 1 the so-called "drop method" has been described by Kubaschewski. This method consists of dropping into the liquid metal (A), or into the liquid alloy (A + C), considered as a solvent and maintained at the experimental temperature T_E, a known amount (m) of the metal B previously stabilized at temperature T_0 (generally the room temperature). This very simple technique has been applied to the Calvet calorimeter. At constant pressure P, the recorded thermal effect ($Q_P = \Delta H$) corresponds to the following relation:

$$Q_P = m/M_B \times \left[\int_{T_0}^{T_{B,fus}} C_{p,Bsol} dT + \Delta H_{B,fus} + \int_{T_{B,fus}}^{T_E} C_{p,Bliq} dT \right] + Q'_P$$

in which M_B, $C_{p,Bsol}$, $C_{p,Bliq}$, $T_{B,fus}$ and $\Delta H_{B,fus}$ are respectively the atomic mass, the molar heat capacity in solid and liquid state, and the temperature and enthalpy of fusion of B. From the experimental value (Q_P), the first, second, and third terms must be subtracted to obtain Q'_P and, accordingly, to calculate the enthalpy of formation (ΔH_M). Unfortunately, for some alloys, the uncertainty in these corrective terms is larger than the value of ΔH_M. Of course the accuracy of these evaluations is not great, particularly when the enthalpy of mixing becomes very small (or tends towards zero).

To reduce these inconveniences (4, 5) we developed the "indirect" drop method that allows us to minimize or to cancel the corrective terms. The added metal (B) is stopped during its drop in the funnel (G) until thermal equilibrium is reached (Fig. 1). The mixing is performed by opening the funnel by means of a magnetic device that lifts the tube (T) up and down. If the funnel and the crucible are at the same temperature the recorded thermal effect corresponds directly to the enthalpy of mixing. A small alumina piece (S) fastened to the magnetic device (Fig. 1-*B*) allows the final liquid alloy to be stirred. This microcalorimetric cell is connected to a vacuum pump (V_1) and to a purified argon circuit (V_2) by a lateral valve (V). For both drop methods, direct and indirect, metallic samples are introduced in the calorimeter by using a special tap (R) and their drop is directed towards the crucible or the funnel by the tube (T). This manual introducer is now replaced by an automatic device, the main parts of which are a vertical disk holding several "nacelles" containing the samples of metal and an electric motor. This apparatus is maintained at constant temperature (room temperature) under a purified argon atmosphere. The partial rotation of the disk, monitored by a microcomputer, brings the nacelle to the top of the drop tube: in this position the nacelle turns around automatically and the sample drops into the experimental crucible. The choice of indirect or direct drop method depends on the intensity and on the sign of the experimental thermal effect.

The break-off ampoule method described earlier by Wittig and Huber (6) has been used to obtain the enthalpy of formation of liquid alloys (Hg + Ga, for example) by microcalorimetry (7). The Pyrex or quartz ampoule has to be thin enough to break with a single soft press. The thermal effect arising from the ampoule breakoff must be very small and reproducible. To measure the enthalpy of formation of Tl + Te alloys (the vapor tension of the second metal is very large) Castanet *et al.* (8) modified this technique: the ampoule containing the more volatile metal and the second metal are enclosed in a gastight syringe. The ampoule is broken by the vertical shift of the piston of the syringe and the mixing process takes place in a small volume. In this method the two components are at the same temperature and the recorded heat effect leads directly to the enthalpy of formation.

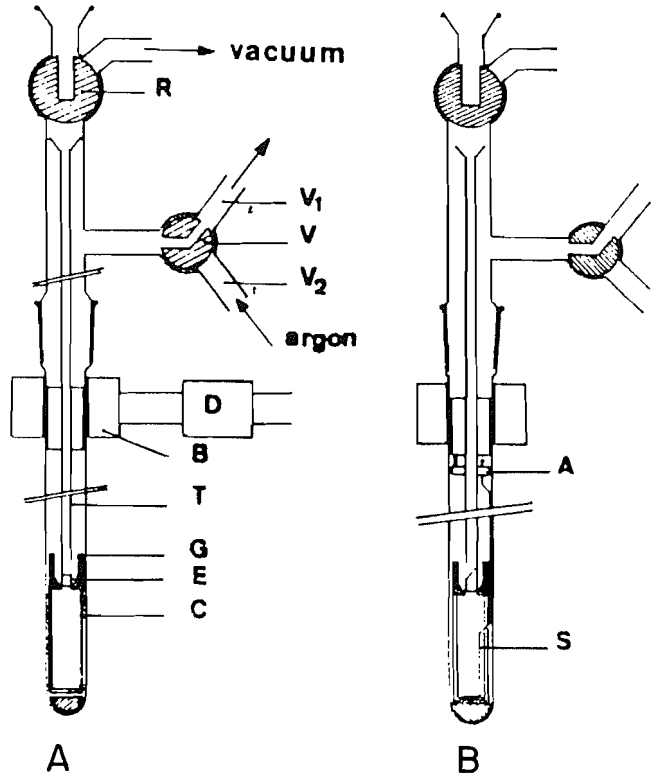

FIG. 1. Calorimetric device used for the indirect drop method; R, introducing tap; V, three-way tap; T, drop tube; G, funnel; C, experimental crucible; B and D, electromagnetic device; S, stirrer (Fig. 1-*A*).

The measurement of the heat of formation of the Ga + In liquid alloys was performed with a simple device. In the calorimetric cell the indium sample is suspended above the bath of gallium by a thin quartz wire. The mixing takes place when the wire comes down. Such a method is used only when vapor tensions of the metals are weak.

Experimental precautions

Careful attention must be paid to obtain reliable results: (*i*) All the experiments are performed under vacuum or under a purified argon atmosphere. Before each experiment the cell, tube, and crucible are degassed. (*ii*) The calorimetric cell is made of quartz; the nature of the crucible (quartz, graphite, alumina) depends on the chemical reactivity of the components of the alloy and on the experimental temperature. (*iii*) The purity of all the metals used during these experiments is about 99.999%.

Calibration

The calorimeter must be calibrated under experimental conditions either by the Joule effect or by drops of alumina or pure metal.

(*a*) By the Joule effect: the lower part of the experimental crucible is surrounded by a small resistance that generates a well-known thermal effect. This calibration, operable up to 900 K, requires precise measurements of time, intensity, and resistance.

(*b*) By drops of alumina or pure metal: at the beginning of each experiment some pieces of metal (A) are added to the liquid bath (A) and thermal effects so released allow calculation of the calibration

Can. J. Chem. Downloaded from www.nrcresearchpress.com by 176.9.209.113 on 09/07/12
For personal use only.

Can. J. Chem. Downloaded from www.nrcresearchpress.com by 176.9.209.113 on 09/07/12
For personal use only.

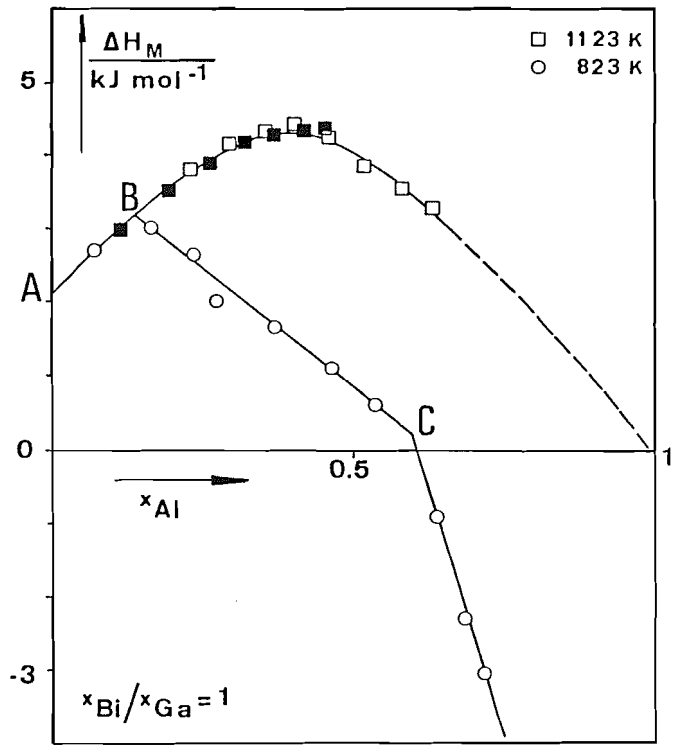

FIG. 2. Enthalpies of formation obtained at 1123 K (□, ■) and 823 K (○) with $x_{Bi}/x_{Ga} = 1/1$.

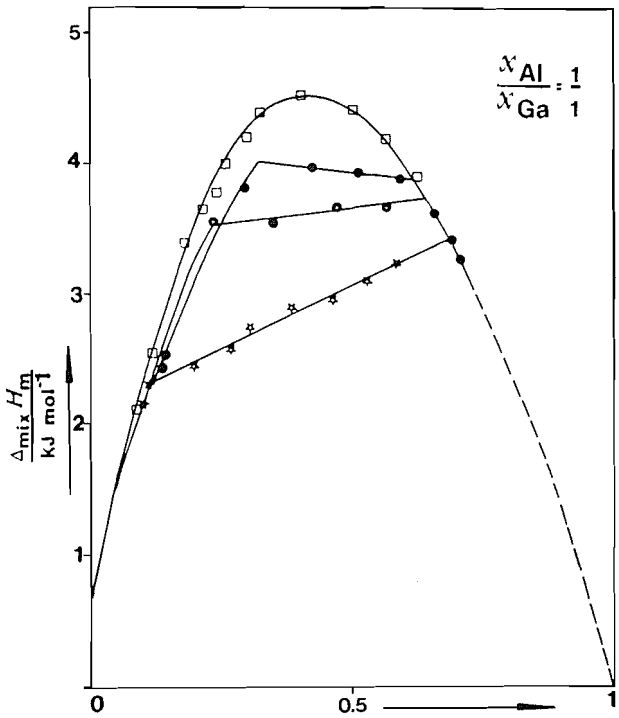

FIG. 3. Enthalpies of formation obtained at 1123 K (□), 981 K (●), 972 K (○), and 823 K (☆) with $x_{Al}/x_{Ga} = 1/1$.

constant. During and at the end of each experiment, drops of NBS alumina crystals permit a second calibration.

Accuracy

A study of the accuracy of calorimetric results (9) leads to the following conclusions: the standard deviation of the calibration experiments is about 1.5% and the uncertainty in the final value for the enthalpies of mixing is estimated to be ±3% at 1000 K.

The experimental temperature is measured at ±0.5°C by using a (Pt/Pt + Rh 10 wt.%) thermocouple located between the two thermopiles in the center of the calorimetric block.

Results

To highlight the interest in calorimetric measurements for the field of thermochemistry of alloys, some results provided by a complete study of ternary Al + Ga + X systems (5) have been assembled. As an example, we have selected the Al + Bi + Ga system; from the equilibrium phase diagram of the three limiting binary systems a large tenary miscibility gap can be predicted.

Al + Bi system

The phase diagram compiled by Hultgren *et al.* (10) shows a large miscibility gap in the liquid state. The coordinates of the eutectic and critical points are respectively $x_{Bi} = 0.9944$ with $T_E = 543$ K and $x_{Bi} = 0.175$ with $T_C = 1323$ K. At the monotectic temperature, $T_M = 940$ K, the limiting molar fractions of the gap are respectively $x_{Bi} = 0.0055$ and 0.84.

Bi + Ga system

Predel (11), from DTA experiments, found a miscibility gap in this system. At the monotectic temperature T_M the limiting molar fractions of the miscibility gap are $x_{Bi} = 0.615$ and 0.085. The coordinates of the critical and eutectic points are respectively $x_{Bi} = 0.30$ with $T_C = 535$ K and $x_{Bi} = 0.0022$ with $T_E = 302.5$ K.

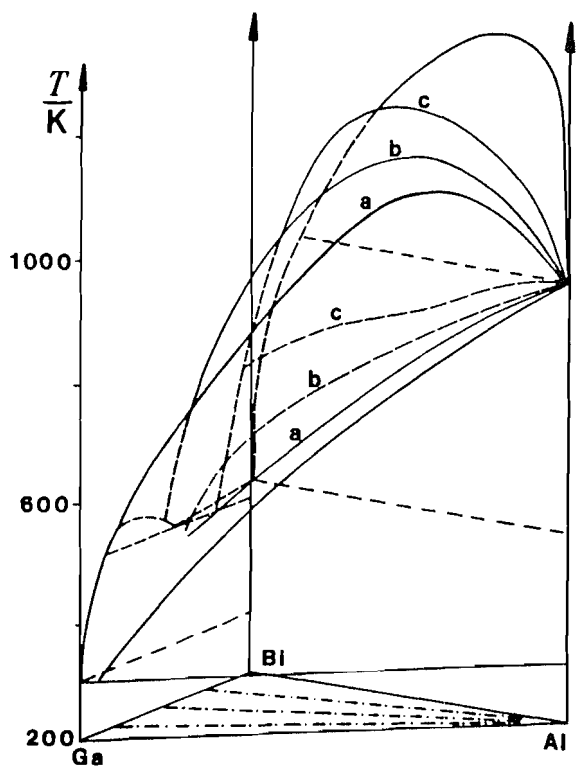

FIG. 4. Experimental equilibrium phase diagram of the Al + Bi + Ga system; a, b, and c correspond to the three sections $x_{Bi}/x_{Ga} = 1/3$, 1/1, and 3/1.

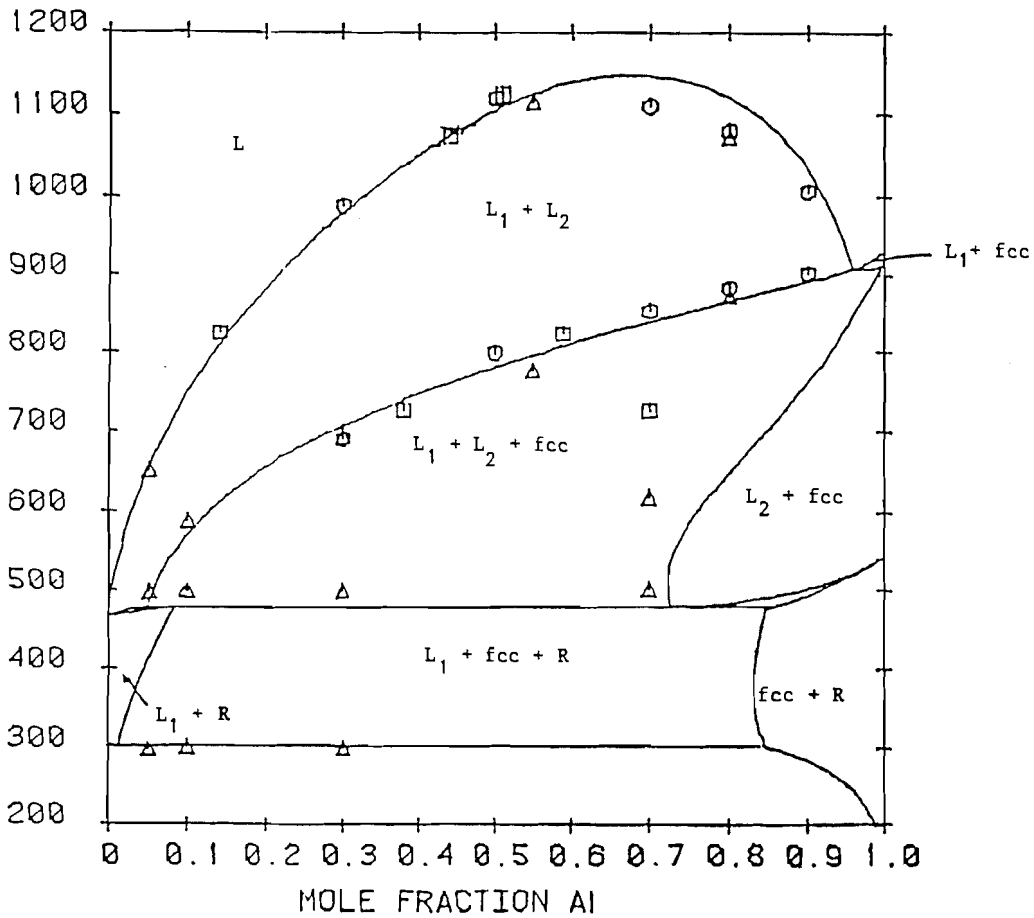

FIG. 5. Vertical section (x_{Ga}/x_{Bi} = 1/1) of the Al + Bi + Ga ternary phase diagram. Continuous lines correspond to the calculated temperatures; experimental points are obtained by microcalorimetry (□), potentiometry (◇), and differential thermal analysis (△).

Al + Ga system

The phase diagram exhibits a eutectic point (T_E = 299.6 K and x_{Ga} = 0.973) very near pure gallium. At the eutectic temperature the solid solubility of gallium in aluminium is about 8.8 at.%. On the other hand the solubility of aluminium in solid gallium is not exactly known (5).

Al + Bi + Ga

The enthalpy and Gibbs free energy of formation of this system are not available and its equilibrium phase diagram is unknown.

Using a high temperature microcalorimeter, enthalpies of formation of binary and ternary liquid alloys have been measured over large concentration ranges and at several temperatures: 725, 817, 823, 948, 972, 981, 985, 1073, 1123, 1136, 1142, and 1170 K (12). Six sections were investigated: three by dropping bismuth pieces in Al + Ga liquid alloys with x_{Al}/x_{Ga} = 1/3, 1/1, and 3/1 and three by adding aluminium samples in Bi + Ga liquid mixtures with x_{Bi}/x_{Ga} = 1/3, 1/1, and 3/1. From these results a complete description of the enthalpy of formation of Al + Bi + Ga liquid alloy can be given on the basis of the Bonnier (12) or Muggianu (14) equations with a ternary term obtained by using the least-squares method. Moreover, these calorimetric measurements allow us to obtain some points on the equilibrium phase diagram. As an example, at 823 K, the change from a one-liquid phase equilibrium to a two-liquid phase equilibrium ($L \longleftrightarrow L_1 + L_2$) is pointed out on the curve $\Delta H_M = f(x)_{x_A/x_C=ct}$ by a break point (B) followed by a straight line (Fig. 2); at the point C, the appearance of a solid phase corresponds, on the $\Delta H_M = f(x)_{x_A/x_C=ct}$ curve, to a straight line running to the enthalpy of fusion of the pure phase. The second curve obtained at 1123 K does not show any discontinuity; it corresponds to the formation of a monophase liquid alloy over the entire concentration range of aluminium. Between A and B no significant temperature variation of the enthalpy of formation of this liquid alloy is observed.

REMARK: when the phase diagram exhibits a definite compound or a solid phase, a sharp discontinuity appears on the enthalpic curve obtained by calorimetry. The triangle (A, B, C) (Fig. 6) corresponds to the precipitation of a solid phase in Al + Ga + Sb liquid alloys at 1185 K.

Calorimetric results obtained at 1123, 981, 972, and 823 K along the section x_{Al}/x_{Ga} = 1/1 are shown in Fig. 3. Linear parts correspond to the crossing of the ternary miscibility gap. All the coordinates of the break points obtained by calorimetry are collected in Table 1.

Several equilibrium temperatures were obtained from experiments performed with a Calvet microcalorimeter transformed into a differential enthalpic analyzer (DEA). For this purpose the electronic regulator was replaced by a linear temperature programmer; so modified, this apparatus becomes a very sensitive differential enthalpic analyser. Its very slow heating rate (about 12 K min^{-1}) permits a clear separation of the thermal effects.

Can. J. Chem. Downloaded from www.nrcresearchpress.com by 176.9.209.113 on 09/07/12
For personal use only.

Can. J. Chem. Downloaded from www.nrcresearchpress.com by 176.9.209.113 on 09/07/12
For personal use only.

TABLE 1. Coordinates of the break points obtained by calorimetry

x_{Al}/x_{Ga}	T/K	x_{Bi}
		0.11
	823	
		0.69
		0.25
1/1	972	
		0.65
		0.32
	981	
		0.62
1/3	823	0.34

x_{Bi}/x_{Ga}	T/K	x_{Al}
	1073	0.30
3/1	1143	0.35
	1170	0.51
		0.70
	725	
		0.38
		0.14
1/1	823	
		0.59
	1073	0.44
	1123	0.51
	817	0.27
1/3	948	0.42
	985	0.45

TABLE 2. Equilibrium temperatures of the Al + Bi + Ga ternary alloys obtained by DEA

x_{Bi}/x_{Ga}	x_{Al}	T/K		
3/1	0.10	296	497	
	0.20	297	505	
	0.43	501	830	
1/1	0.05	295	497	649
	0.10	298	496	587
	0.30	298	498	692
	0.55	777	1115	
	0.70	500	617	
	0.80	871	1073	
1/3	0.05	296	498	617
	0.10	297	497	682
	0.20	297	498	549
	0.285	297	498	597
	0.50	296	498	724

We studied 16 alloys selected on the ternary sections (x_{Bi}/x_{Ga} = 1/3, 1/1, and 3/1). When the temperature was increasing, two endothermic peaks were recorded: the first one between 295 and 298 K and the second one, sometimes split in two parts, between 494 and 508 K. All these temperatures were obtained with a mean accuracy of ±3K.

Results collected in Table 2 show the presence of two invariant horizontal planes corresponding to the coexisting phases: (*i*) liquid + Bi(sol) + Ga(sol) + aluminium-rich solid solution at about 297 K; (*ii*) liquid 1 + liquid 2 + Bi(sol) + aluminium-rich solid solution at about 497 K.

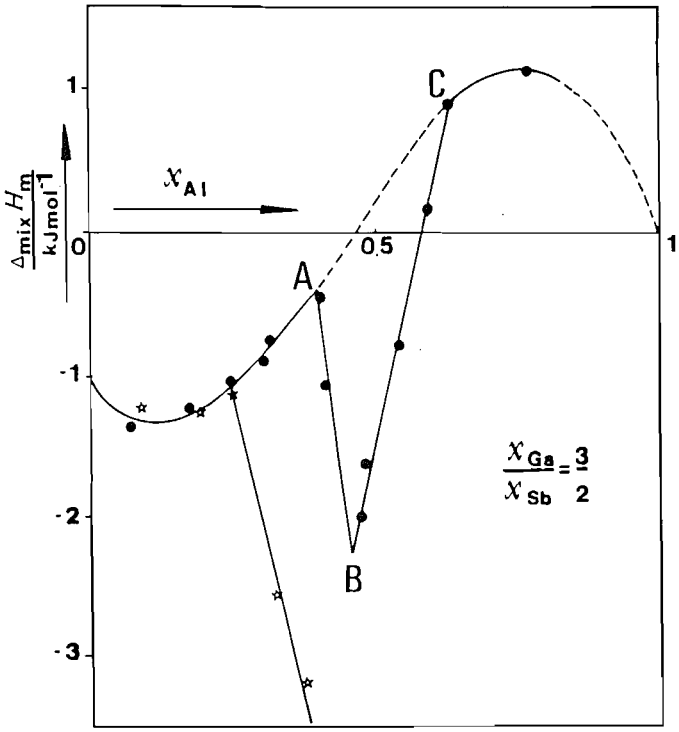

FIG. 6. Enthalpies of formation of the Al + Ga + Sb system along the section x_{Ga}/x_{Sb} = 3/2, obtained respectively at 1143 K (☆) and 1185 (●).

From all the thermodynamic data (13, 14) the equilibrium phase diagram was calculated (Fig. 4) by means of a computer program developed by Jansson (15). On the vertical section (x_{Bi}/x_{Ga} = 1/1), experimental temperatures have been reported and a good agreement was found with calculated values as represented by the continuous line (Fig. 5), except in the solid-rich aluminium region.

Conclusion

To improve our knowledge of the thermodynamic properties of multicomponent alloys, high temperature calorimetry is a very fruitful method. For ternary alloys (Al + Bi + Ga, Al + Ga + In, Al + Ga + Sn, Bi + Ga + Zn, etc.) this technique permits us to determine, from the same set of data, the enthalpies of formation on the one hand and several points of the equilibrium phase diagram on the other hand. Moreover, the temperatures of the phase transitions of these alloys have been obtained with the same calorimeter transformed into a differential enthalpic analyzer. Using a special computer program the complete set of the thermodynamic properties of formation can be predicted and the equilibrium ternary phase diagram deduced.

1. O. KUBASCHEWSKI and C. B. ALCOCK. Metallurgical thermochemistry. 5th ed. Pergamon Press, Oxford, New York. 1979.
2. E. CALVET et H. PRAT. Microcalorimétrie. Masson, Paris. 1955.
3. M. GAUNE-ESCARD. Thèse Doctorat d'Etat, Sc. Phys. Marseille, France, 1972.
4. M. GAMBINO. Thèse Doctorat d'Etat, Sc. Phys. Marseille, France, 1976.
5. C. GIRARD. Thèse Doctorat d'Etat, Sc. Phys. Marseille, France, 1985.
6. F. E. WITTIG and F. HUBER. Z. Electrochem. **60**, 1181 (1956).
7. M. GAUNE-ESCARD and J. P. BROS. Thermochim. Acta, **31**, 323 (1979).

8. R. CASTANET, J. P. BROS, and M. LAFFITTE. J. Chim. Phys. **65**, 1536 (1968).
9. G. HATEM. J. Chim. Phys. **83**, 197 (1986).
10. R. HULTGREN, P. D. DESAI, D. T. HAWKINS, M. GLEISER, and K. K. KELLEY. Selected values of the thermodynamic properties of binary alloys. Am. Soc. Metals, Metals Park, OH. 1973.
11. B. PREDEL. Z. Phys. Chem. **24**, 206 (1960).
12. C. GIRARD, R. BARET, J. M. MIANE, and J. P. BROS. J. Chem. Thermodyn. **17**, 1187 (1985).
13. C. GIRARD, R. BARET, J. M. MIANE, J. RIOU, and J. P. BROS. Fluid Phase Equilib. **20**, 331 (1985).
14. C. GIRARD, J. P. BROS, J. AGREN, and L. KAUFMAN. CALPHAD: Comput. Coupling Phase Diagrams Thermochem. **9**, 129 (1985).
15. B. JANSSON. Internal Report D 19, R. Inst. Technol. S-10044, Stockholm, Sweden. 1979.

Can. J. Chem. Downloaded from www.nrcresearchpress.com by 176.9.209.113 on 09/07/12
For personal use only.

Ionic conductivity of pure and doped sodium chloride crystals

IRENE E. HOOTON AND P. W. M. JACOBS
Department of Chemistry, The University of Western Ontario, London, Ont., Canada N6A 5B7

Received September 24, 1987

This paper is dedicated to Professor J. A. Morrison

IRENE E. HOOTON and P. W. M. JACOBS. Can. J. Chem. **66**, 830 (1988).

New measurements are reported for the ionic conductivity of well-annealed crystals of pure NaCl, NaCl doped with Sr^{2+} ions, and NaCl doped with S^{2-} ions. Analysis of these data leads to the conclusions (*i*) that the Schottky defect model is entirely adequate for NaCl (in contrast to KCl); and (*ii*) that the activation energy for the migration of anion vacancies is 0.74 eV. This last result is in agreement with values derived from the analysis of conductivity and diffusion data for pure NaCl and NaCl doped with Sr^{2+}, and with theoretically-calculated values, but at variance with results from recent measurements on quenched sulphide-doped crystals.

IRENE E. HOOTON et P. W. M. JACOBS. Can. J. Chem. **66**, 830 (1988).

On a effectué de nouvelles mesures de conductivité ionique de cristaux bien recuits de NaCl pur, de NaCl dopé avec des ions Sr^{2+} et de NaCl dopé avec des ions S^{2-}. Une analyse de ces données permet de conclure (*i*) que le modèle de défaut de Schottky est entièrement satisfaisant pour le NaCl (et ceci est en opposition avec ce qui est observé avec le KCl) et (*ii*) que l'énergie d'activation pour la migration des lacunes des anions est de 0,74 eV. Ce dernier résultat est un bon accord avec les valeurs qu'on peut obtenir à partir d'une analyse des données de conductivité et de diffusion du NaCl pur et du NaCl dopé par du Sr^{2+} ainsi qu'avec les valeurs calculées sur une base théorique; toutefois, elles diffèrent des résultats qui dérivent de mesures récentes effectuées sur des cristaux trempés, dopés au sulfure.

[Traduit par la revue]

Introduction

The experimental study of the transport properties of ionic crystals is the principal source of data from which both the mechanisms of ion transport and numerical values of the thermodynamic properties of the crystal defects can be deduced. Doping with aliovalent ions alters the relative contributions of different species to the transport process and so is a considerable aid in data analysis. Since the early work of Koch and Wagner (1) cation doping of alkali and silver halides has been employed to accentuate the contribution of cation vacancies to the transport process. Indeed, since even nominally pure alkali halide crystals invariably contain divalent cation impurities, a rough upper bound to the cation vacancy migration energy can be obtained from measurements of the ionic conductivity, σ, by plotting the data in the Arrhenius form, $\log \sigma T$ against T^{-1} with T the thermodynamic temperature, and determining the slope of the curve in the extrinsic region. While salts like $CaCl_2$ are quite soluble in the alkali chlorides to the extent of several hundred parts per million (ppm), the corresponding situation with respect to divalent anion doping is far less satisfactory. Nevertheless, Chandra and Rolfe (2–5) have successfully doped KCl, KBr, KI, and RbI with CO_3^{2-}. Bénière, Bénière, and Chemla (6) found the maximum solubility of SO_4^{2-} in KCl to be only 36.4 ppm but even so SO_4^{2-}-doped crystals were employed in detailed studies of KCl both by themselves (7) and by Acuña and Jacobs (8, 9). Unfortunately, the solubility of SO_4^{2-} in NaCl is less than 2 ppm so similar procedures are not possible. However, Na_2S is soluble in NaCl (Baba, Ikeda, and Yoshida (10, 11), and Cook and Dryden (12, 13)) and so NaCl:S^{2-} crystals have been used in this work in an attempt to increase the anion transport number at high temperatures. The relatively low and roughly temperature-independent anion transport number in pure NaCl are major difficulties in the successful computer analysis of ionic conductivity data for pure NaCl (14, 15). Indeed, even after a very careful and detailed analysis of conductivity data for pure NaCl and NaCl:Sr^{2+}, Allnatt, Pantelis, and Sime (14) decided that no useful conclusions about the anion vacancy (av) parameters could be drawn from their work. Computer analysis of data for two pure crystals (14) yielded enthalpies of anion vacancy migration of 1.43 eV and 1.75 ± 0.18 eV, but the Arrhenius plot of the anion diffusion coefficient calculated from their defect parameters had much too high a slope, although it was intersected at about 1000 K by a plot of Laurance's experimental data. In marked contrast, they were able to fix the cation vacancy (cv) migration energy at 0.65 ± 0.01 eV and their calculated Na^+ diffusion was in excellent agreement with the experimental measurements of Nelson and Friauf (17).

In their analysis of conductivity and diffusion data for KCl, Acuña and Jacobs (8, 9) were able to determine a set of defect parameters that fitted consistently eight different sets of transport measurements, namely the conductivity of pure, Sr^{2+}-doped and SO_4^{2-}-doped KCl; cation diffusion in pure KCl and KCl:Sr^{2+}; anion diffusion in pure and Sr^{2+}-doped KCl; and SO_4^{2-}-diffusion in KCl:SO_4^{2-}, but only by a model that included small concentrations of cation and anion interstitials in addition to the conventional Schottky-defect model. One of the objects of this work was to determine if Frenkel defects also occur in NaCl. The other objective was to determine from conductivity measurements the energy and entropy for anion vacancy migration. This had not proved to be practicable from measurements on NaCl and NaCl:Sr^{2+} alone (14) and our intention therefore was to utilize measurements on NaCl:S^{2-} as well.

The anion migration problem in NaCl

It is true that information about the anion vacancy defect parameters can be determined from measurements of anion diffusion and this has been done for NaCl. The earliest measurements used the sectioning technique and were made by Chemla (18) over a limited temperature range. Laurent and Bernard (19) made similar measurements over an extended range and found an Arrhenius energy E_1 of 2.23 eV. A quite different method that involved measuring the rate of exchange of chlorine between the crystal and a circulating gas was developed by Morrison and associates (20–24). Among the advantages of this method are the fact that measurements can be

Can. J. Chem. Downloaded from www.nrcresearchpress.com by 176.9.209.113 on 09/07/12
For personal use only.

Can. J. Chem. Downloaded from www.nrcresearchpress.com by 176.9.209.113 on 09/07/12
For personal use only.

carried out to much lower temperatures than with the sectioning technique and that measurements at a number of different temperatures can be made with the same specimen. Patterson, Rose, and Morrison (20) found an Arrhenius energy E_2 of 1.67 eV in the low-temperature regime; later Harrison, Morrison, and Rudham (21) found the Arrhenius plot of log D against T^{-1} to comprise two parts, with a "knee" at about 500°C and energies of $E_1 = 2.29 \pm 0.03$ eV at high T and $E_2 = 1.61 \pm 0.04$ eV at low T. Lidiard (25) pointed out that E_2 could not correspond to diffusion by single vacancies since at low temperatures the naturally-occurring divalent cation impurity would depress the concentration of single anion vacancies. He suggested that the species responsible for Cl^- transport at low temperatures was the vacancy pair (vp) and that this might be confirmed by diffusion experiments on crystals doped with divalent cations. Soon afterwards, Morrison and Rudham (22) found Cl^- diffusion in KCl to be insensitive to divalent-cation doping, thus providing the first experimental evidence that anion transport at low temperatures was indeed due to vacancy pairs. Laurance (16), using the sectioning technique, found Arrhenius energies of 2.12 eV for pure NaCl and 2.49 eV for Ca^{2+}-doped NaCl (in the intrinsic region) thus confirming that pairs contribute to anion transport in NaCl.

The fact that anion diffusion in NaCl must be partitioned between that due to pairs and to single vacancies, complicates data analysis, but Barr, Morrison, and Schroeder (24) were able to separate the contributions from pairs and singles and found that in the intrinsic region, the Arrhenius energy for the motion of single anion vacancies (av) was $E_{av} = 1.92$ eV while $E_{ap} = 2.37$ eV. Despite minor differences in actual numbers, a pattern of consistency had now emerged in the diffusion measurements, but E_{av} must still be separated into $\frac{1}{2}h_S + \Delta h_{av}$ where h_S is the enthalpy of Schottky defect formation and Δh_{av} the enthalpy of migration of an anion vacancy. Barr, Morrison, and Schroeder (24) used the then-determined experimental value of 2.02 eV for h_S by Etzel and Maurer (26), which gave $\Delta h_{av} = 0.91$ eV. This value of h_S is too low by current standards, so that 0.91 eV would be an upper bound.

The most complete analysis of the transport properties of NaCl is that of Bénière, Chemla, and Bénière (7) using measurements of anion and cation diffusion (obtained using the sectioning technique) and of the ionic conductivity of pure NaCl and NaCl:Sr^{2+}. Their self-consistent set of defect parameters included $\Delta h_{av} = 0.77$ eV. And if we use their value for h_S, 2.44 eV, with the Arrhenius energy $E_{av} = 1.92$ eV determined by the exchange-gas method (24) we find $\Delta h_{av} = 0.70$ eV, essentially in agreement both with the value of Bénière *et al.* (7) and the value of 0.71–0.72 eV for the energy of anion vacancy migration Δu_{av} (at 0 K) calculated by lattice simulation techniques (27), which represents a lower bound to Δh_{av}. (For an explanation of why an experimental enthalpy determined over a range of temperatures of ~800–1000 K may be compared with a theoretical energy at 0 K, see, for example, refs. 28 and 29.)

The situation with respect to the anion vacancy migration energy was therefore beginning to look fairly satisfactory by 1976, but three years later Cook and Dryden (12, 13) reported a migration enthalpy for anion vacancies in NaCl of 1.24 ± 0.05 eV, determined from impedance measurements on quenched crystals of NaCl:S^{2-}. The model used to analyze their data is that the separated S^{2-} ions and anion vacancies present at high temperatures reform complexes at lower T by the diffusion of anion vacancies to immobile S^{2-} ions. This model leads to second-order kinetics for the isothermal decay of conductivity, in agreement with experiment. Quenching to different final temperatures provides sufficient data to determine the anion migration enthalpy. The temperature dependence of the conductivity of freshly quenched material was also measured over a rather narrow range (~345–385 K) limited at the upper end by the requirement that no significant time-dependence occur during the time required to make the measurement and at the lower end by the sensitivity of the electrical measurement. Essentially the same value for Δh_{av} was obtained from these measurements as from their data on the kinetics of the decay of conductivity.

In this paper we also report measurements of the ionic conductivity of NaCl:S^{2-}, but these were made on well-annealed rather than quenched crystals.

Experimental technique

The ionic conductivity of NaCl crystals was measured using a quartz conductivity cell similar to that described by Acuña and Jacobs (8, 30). The only materials in the high temperature zone of the furnace, apart from the sample, are alumina, mica, quartz, Pt, and Pt–Rh. The electrical conductivity of the cell was measured using one of three bridges: a Wayne-Kerr B905, a General Radio 1621, or a General Radio 1689, according to the desired frequency range or the resistance of the specimen. Most measurements were made with the B905 at 1.02 and 10.2 kHz, with frequent checks to confirm that polarization resistance was negligible at the higher frequency. Temperature control was effected by a Trirect MK2 controller with a Pt resistance thermometer sensor. The temperature at each face of the crystal was measured by Pt/Pt–Rh thermocouples. The lead resistance was measured but these corrections proved to be negligible, even at the highest temperatures. Crystal dimensions were measured with a Mitutoyo Profile Projector Type PJ-250 before and after a run to confirm the absence of crystal deformation. The general technique including thorough annealing of the crystals followed closely that described previously (8, 31). The data were processed initially on a DEC 11/24 computer and plotted on an HP 7225B plotter. Non-linear least-squares analysis of the final data in the form of log σT as a function of T was carried out on a mainframe computer (Cyber 825).

Large crystals of pure NaCl containing about 1 ppm of residual divalent cation impurity were purchased from the Harshaw Chemical Co. Doping of these with Sr^{2+} or S^{2-} was effected by diffusion of $SrCl_2$ or Na_2S into small crystals (cleaved from the original blocks of pure NaCl) in graphite boats in a slow stream of argon at 750°C for periods of 2 weeks. The boats were machined from reactor-grade graphite (Ultra-carbon UF-4S) and then soaked twice in concentrated nitric acid to dissolve any metal fragments from machining. They were then soaked several times in distilled water and finally heated overnight in a stream of argon in the furnace tube used for the diffusion anneals. The particular boat used for the diffusion anneals had been used at least 15 times for growing NaCl crystals from ultra-pure NaCl powder of at least 4N7 purity so that any residual NaCl-soluble impurities would have been leached out of the graphite by the molten salt. Na_2S solutions were prepared in a glove bag under argon, the appropriate amount placed on the crystals in the glove bag, and the crystals then transferred rapidly to the furnace tube which was being flushed with argon. The crystal containing 7.1 ppm S^{2-} was kindly given to us by Dr. J. S. Dryden. This had been grown from molten NaCl containing Na_2S (12).

Results

Arrhenius plots of the ionic conductivity of undoped (Harshaw) NaCl in the form log σT against T^{-1} display the typical segmented form characteristic of alkali halides with the "knee" at about 480°C. A typical example is illustrated in Fig. 1. However. the intrinsic region is remarkably straight with no evidence (to the eye) of the curvature so characteristic of KCl (8, 33), indicating either that the cation transport number is

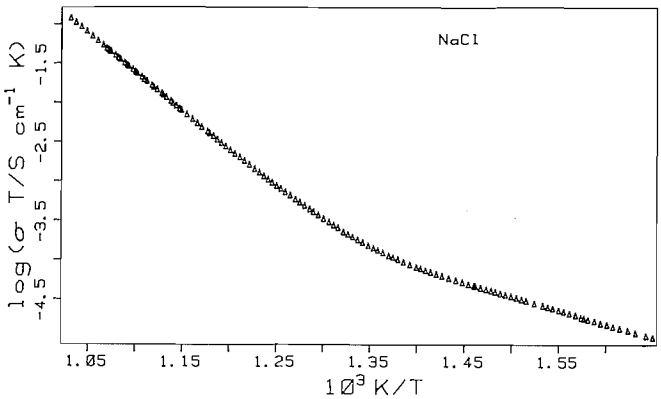

FIG. 1. Arrhenius plot of the ionic conductivity of undoped NaCl.

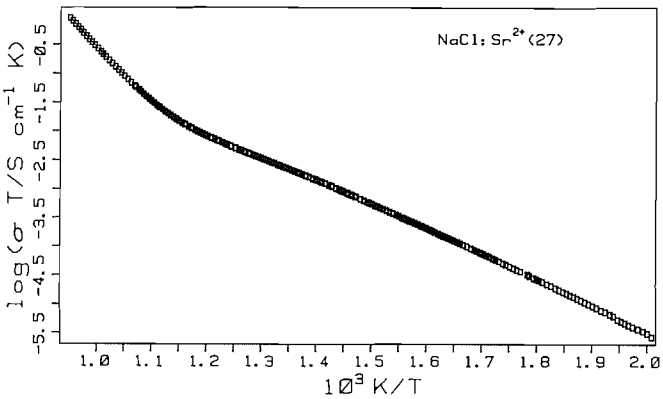

FIG. 2. Arrhenius plots of the ionic conductivity of NaCl containing 27 ppm of Sr^{2+} ion.

much greater than that of the anion, or that the Gibbs energies of migration of cation and anion vacancies must be very similar. The extrinsic part of the conductivity curve is also rather straight because of the low level of divalent cation impurity (~1 ppm) and the limited temperature range before the conductivity became too low to measure accurately.

Figure 2 shows the Arrhenius conductivity plot for NaCl doped with 27 ppm of Sr^{2+}. The extrinsic conductivity has been increased so that the knee is now centred at ~615°C. Curvature of the conductivity plot in the extrinsic region is clearly evident, due to association between Sr^{2+} and cation vacancies (cv). The high density of data is typical of this investigation. At several points the temperature was held constant for 8 h to test for precipitation, which finally occurred to a small extent at 515 K. The curve contains data determined both with T decreasing and T increasing and the excellent reproducibility verifies that the data refer to a crystal in thermal equilibrium.

A plot of log σT against T^{-1} for an NaCl:S^{2-} crystal containing 8.6 ppm of S^{2-} is shown in Fig. 3, along with the corresponding plot of a pure NaCl Harshaw crystal. The conductivity of these two crystals was measured in a double cell so that the two crystals were at the same temperature during each measurement. We note immediately that the conductivity of the pure crystal is decreased in the intrinsic region by doping with S^{2-}. Because the product of the concentrations of anion and cation vacancies is constant at constant T, doping with S^{2-} will have the effect of replacing some cv by av. The consequent lowering in σ tells us the mobility of the av is slightly lower than that of the cv. Because the concentration of dopant is only 8.6 ppm this effect decreases as T increases, and when $\exp(-g_S/2kT)$, where g_S is the Gibbs energy of formation of

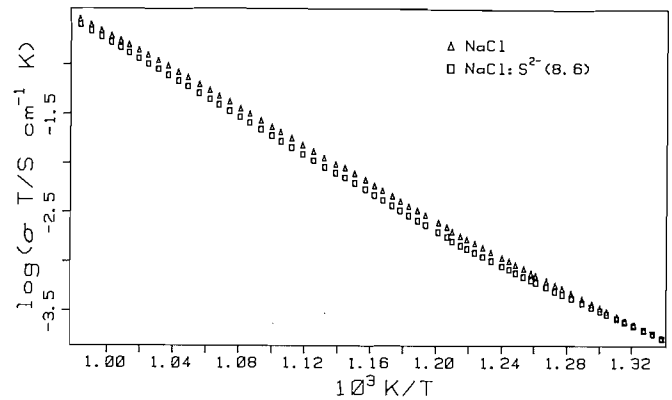

FIG. 3. Arrhenius plots of the ionic conductivity of NaCl and of NaCl containing 8.6 ppm of S^{2-} ion, measured in a double cell.

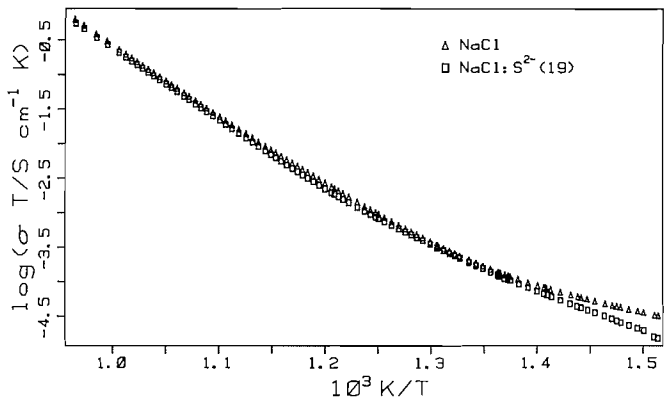

FIG. 4. Arrhenius plots of NaCl and of NaCl containing 19 ppm of S^{2-} ion (double cell).

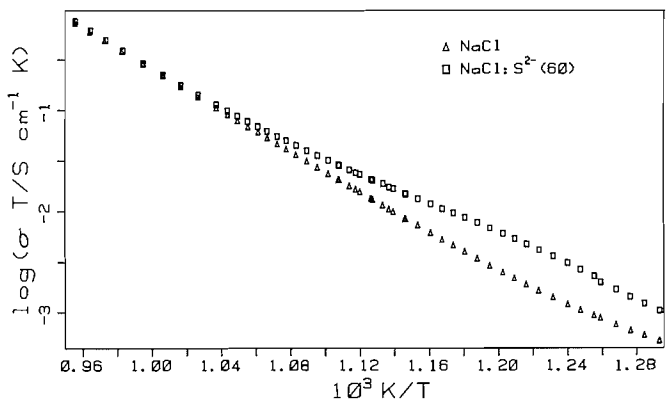

FIG. 5. Arrhenius plots of NaCl and of NaCl containing 60 ppm of S^{2-} ion (double cell).

a Schottky defect, becomes comparable with the concentration of S^{2-}, the curves converge. As $c_{S^{2-}} > c_{M^{2+}}$, where M^{2+} denotes the residual divalent cation impurity in the Harshaw NaCl (almost certainly largely Ca^{2+}) the two conductivity curves converge also as T decreases, as is to be expected because of the slightly higher knee-temperature for NaCl:S^{2-}.

At higher S^{2-} concentrations, the lowering of the intrinsic conductivity should lessen, until eventually the enhanced concentration of anion vacancies more than compensates for their lower mobility and the conductivity curve for NaCl:S^{2-} lies above that for pure NaCl. These effects are illustrated in Figs. 4 and 5. Figure 4 shows the conductivity curves for pure Harshaw NaCl and for NaCl:S^{2-} containing 19 ppm of the

Can. J. Chem. Downloaded from www.nrcresearchpress.com by 176.9.209.113 on 09/07/12
For personal use only.

Can. J. Chem. Downloaded from www.nrcresearchpress.com by 176.9.209.113 on 09/07/12
For personal use only.

dopant. We note the same lowering of conductivity as in Fig. 3 but the effect is less pronounced, as is to be expected. The knee for the doped crystal occurs at some 20 K higher than that for pure NaCl and the initial extrinsic slope is greater for the anion-doped crystal than for pure NaCl. These initial slopes correspond to Arrhenius energies of 1.03 eV and 0.67 eV, respectively,and represent rough upper bounds for the migration enthalpies Δh_{av} and Δh_{cv}. However, the absence of an upwards curvature in the intrinsic conductivity curve for pure NaCl shows that the cv and av mobilities do not differ by several tenths of an eV (cf. KCl, ref. 8) so that we conclude that in NaCl:S^{2-} av and S^{2-} ions are strongly associated, as was also true for SO_4^{2-} ions in KCl (8, 9).

Figure 5 shows the conductivity plots for pure NaCl and NaCl:S^{2-} containing 60 ppm of the divalent impurity. We observe the raised knee temperature and enhanced extrinsic conductivity so typical of doped crystals. The extrinsic region for NaCl:S^{2-} has a negative curvature, which might be taken as indicating a temperature-dependent association of S^{2-} and av. However, as there is already considerable association between S^{2-} and av at $c_{S^{2-}} = 19$ ppm and the initial slope of the extrinsic curve in Fig. 5 is greater than the corresponding slope in Fig. 4, it is possible that the marked downward curvature below 830 K is already indicating some precipitation of Na_2S. At 795 K the conductivity of NaCl:S^{2-} dips sharply, due to precipitation of some of the Na_2S. (The lower curve for pure NaCl is smoothly continuous confirming that this effect is characteristic of the doped crystal and not due to some error in temperature measurement, which would affect both curves equally.)

Data analysis

Non-linear least-squares analysis of the conductivity data were carried out on the basis of two models. The first one tried, and the one finally favoured, supposes that: (*i*) a perfectly pure crystal would contain Schottky defects; (*ii*) that Harshaw NaCl contains a residual divalent cation impurity (which is probably Ca^{2+}); (*iii*) that divalent cations and cv may associate to form complexes; (*iv*) that in NaCl:S^{2-}, the divalent S^{2-} ions associate with av to form complexes. The anion-doped crystals were assumed to contain the same level of divalent cation impurity as the undoped Harshaw crystals, namely 1.2 ppm. One might expect pairing of M^{2+} and S^{2-} ions on nn sites, but as long as the resultant complexes do not have a temperature-dependent degree of association, this has no effect on the analysis. The S^{2-} concentrations quoted would simply be reduced by 1.2 ppm.

Data points taken at temperatures lower than those at which precipitation was first observed in the conductivity plot were removed in the initial analysis. After preliminary fitting, a pronounced increase in the residuals at temperatures just above a precipitation discontinuity were interpreted as indicating the onset of precipitation (even though this might not be evident in the Arrhenius plot) so these points were removed and the analyses repeated. For example, this procedure led to the lower limit of data accepted for least squares analyses for the data plotted in Fig. 5 being set at 842.5 K, slightly above where the detectable increase in curvature commences and well above the obvious precipitation at 795 K. Early precipitation during runs carried out with decreasing T is a problem in anion-doped crystals because of the lower solubility of S^{2-} and we erred on the side of caution in ensuring that the $c_{S^{2-}}$ parameter really could be regarded as constant.

By substituting the conservation conditions in the equilibrium equations (30) the number of unknown defect concentrations can be reduced to one, and the resulting fourth-order algebraic equation solved for initially chosen values of the parameters (enthalpies, entropies, and dopant concentrations). The conductivity is calculated and the parameters are then varied systematically so as to minimize RSS, the weighted residual sum of squares, where

$$[2] \quad \mathrm{RSS} = \sum_i [\{\sigma_i(\text{calcd.}) - \sigma_i(\text{expt.})\}/\sigma_i(\text{expt})]^2$$

and σ_i means $\sigma(T_i)$. For pure or cation-doped crystals, the variable in the fourth-order equation was chosen to be c_{cv} and for anion-doped crystals, c_{av}. Because of the large number of parameters (14) in this model, the fitting of the conductivity was performing in the following cycle. First, the pure-crystal data was fitted, with only the Schottky defect formation parameters and the impurity concentration variable, the other parameters being fixed. Next the data for cation-doped crystals was analyzed with only the cv migration and association parameters and the impurity concentration variable. Finally, the data for anion-doped crystals was analyzed with only the av migration and association parameters and the impurity concentration variable. This sequence was repeated until no further decrease in RSS occurred. The fixed parameters were then released and the fitting cycles continued until a final set of parameters was obtained for each crystal. These parameters, together with their average values, are given in Table 1.

In Model 2, the perfectly pure crystal was supposed to contain Frenkel defects on the cation sublattice, in addition to Schottky defects. The fitting of the data to this model was no more satisfactory than achieved with Model 1 — sometimes the s.d. was a little better and sometimes it was worse. One would expect cation interstitials to be most important in crystals doped with a divalent anion impurity and the fact that no significant improvement could be achieved makes it plain that the case for a significant concentration of cation interstitials in NaCl is "not proven", at least for these data. A modification of Model 2 which included both anion and cation interstitials gave worse fittings than the Schottky defect model.

Discussion

Mechanism of ion-transport

The first conclusion to be drawn from the computer analysis of these conductivity data is that the Schottky defect model is adequate for NaCl. The existence of cation Frenkel defects had been tentatively suggested previously (33), as a possible means of accounting for the unsatisfactory fitting of the conductivity of NaCl to the Schottky model, but later it was realized that this was due to the use of a steepest-descent algorithm which has unsatisfactorily slow convergence. Our results do not prove that Frenkel defects do not form in NaCl, but they do show that it is not necessary to include cation and/or anion Frenkel defects in fitting the conductivity. This is in marked contrast to KCl where the inclusion of Frenkel defects on both sub-lattices was shown to be essential in order to account for the transport data. A definitive experiment would be the measurement of the anion diffusion coefficient as a function of the concentration of added Sr^{2+}, analogous to that performed by Fuller (34) for KCl. An increase in D_{Cl^-} at high Sr^{2+} concentrations would be a clear indication of the presence of anion interstitials (8). The analogous experiment for D_{Na^+} seems not to be possible at present because of the low concentration of divalent anions that can be dissolved in NaCl.

TABLE 1. Defect parameters for NaCl, derived from non-linear least-squares analysis of ionic conductivity data[a]

Parameter	Value										Average value
	NaCl		$NaCl:Sr^{2+}$			$NaCl:S^{2-}$					
	A	B	A	B	C	A	B	C	D	E	
$c_{M^{2+}}$/ppm	1.6	1.5	370	190	27	(1.2)	(1.2)	(1.2)	(1.2)	(1.2)	
$c_{S^{2-}}$/ppm	0	0	0	0	0	60	32	19	8.6	7.1	
h_S/eV	2.388	2.397	2.420	2.521	2.478	2.347	2.285	2.429	2.305	2.533	2.410
s_S/k	8.816	8.936	9.086	10.217	9.778	7.931	7.404	9.221	7.179	10.391	8.896
Δh_{cv}/eV	0.654	0.632	0.635	0.619	0.621	0.621	0.619	0.620	0.620	0.621	0.626
Δs_{cv}/k	1.257	1.010	1.022	1.029	1.079	1.047	1.050	1.052	1.055	1.053	1.065
Δh_{av}/eV	0.750	0.741	(0.741)	(0.741)	(0.741)	0.718	0.756	0.768	0.743	0.734	0.744
Δs_{av}/k	2.271	2.242	(2.242)	(2.242)	(2.242)	2.367	2.251	2.282	2.184	2.310	2.272
$-\Delta h_{ck}$/eV	0.609	0.614	0.639	0.644	0.647	(0.644)	(0.644)	(0.644)	(0.644)	(0.644)	0.643[b] 0.612[c]
$-\Delta s_{ck}$/k	2.680	2.337	2.523	2.274	2.181	(2.224)	(2.224)	(2.224)	(2.224)	(2.224)	2.326[b] 2.508[c]
$-\Delta h_{ak}$/eV	—	—	—	—	—	0.750	0.716	0.775	0.782	0.733	0.751
$-\Delta s_{ak}$/k	—	—	—	—	—	1.339	1.619	1.086	1.616	1.429	1.418
RSS × 10^4	0.817	1.464	1.877	0.518	0.465	5.429	2.496	5.712	1.232	0.856	
T range/K											
upper	1031.1	1004.6	869.8	1022.9	1026.1	964.8	998.2	1036.6	1021.8	979.7	
lower	629.9	608.8	667.7	699.5	536.4	842.5	801.7	683.8	757.5	750.2	

[a]The following symbols for defect thermodynamic quantities are used; k denotes the Boltzmann constant. h_S, enthalpy of formation of a Schottky defect; s_S, entropy of formation of a Schottky defect; Δh_{cv}, enthalpy of migration of a cation vacancy; Δs_{cv}, entropy of migration of a cation vacancy; Δh_{av}, enthalpy of migration of an anion vacancy; Δs_{av}, entropy of migration of an anion vacancy; h_{ck}, enthalpy of association between an M^{2+} cation and a cation vacancy; s_{ck}, entropy of association between an M^{2+} cation and a cation vacancy; h_{ak}, enthalpy of association between an S^{2-} anion and an anion vacancy; s_{ak}, entropy of association between an S^{2-} anion and an anion vacancy; c_M, site fraction of divalent cation impurity in ppm; c_X, site fraction of divalent anion impurity in ppm. The temperature range refers to the data actually used in the least squares analysis and may be slightly smaller than the temperature range covered by the experimental data, for reasons that are explained in the text. Numbers in parentheses indicate that the parameter was held constant at that value.

[b]Association parameters for Sr^{2+}.

[c]Association parameters for naturally-occurring impurity, almost certainly Ca^{2+}.

Vacancy migration parameters

The cation vacancy migration enthalpy Δh_{cv} is 0.626 eV, in satisfactory agreement with the previous experimental values of 0.65 ± 0.01 eV (14) and 0.69 eV (7) and the calculated values of 0.66–0.67 eV (35) and 0.66 eV (36). The anion vacancy migration enthalpy is 0.744 eV, well below the upperbound of 1.03 eV set by the slope of the conductivity curve for doped NaCl in Fig. 4 and in excellent agreement with the value of 0.77 eV obtained by Bénière *et al.* by fitting conductivity, cation diffusion and anion diffusion, but in disagreement with Cook and Dryden's (12, 13) value of 1.24 eV derived from conductivity measurements on $NaCl:S^{2-}$. Their value was obtained by measuring the conductivity of quenched crystals at fixed temperatures. Such crystals are supersaturated with Na_2S and the danger exists that precipitation may occur during the run and remain undetected. If $c_{S^{2-}}$ is not constant, the value of Δh_{av} from the slope of the conductivity plot will be too high by an unknown amount. Also, the av association parameters h_{ak}, s_{ak} in Table 1 indicate a considerable degree of association p (for example, p = 0.515–0.637 for $c_{S^{2-}}$ = 60 ppm in the range 960–845 K) and this will also raise the slope of the conductivity plot. Cook and Dryden (12) also measured the rate of isothermal decay of conductivity in quenched crystals and found second-order kinetics, as expected for the association of av with free S^{2-} ions. Such measurements could also in principle be affected by precipitation, but this would upset the second-order kinetics which were well-obeyed over about three half-lives. The order of a reaction is notoriously difficult to determine and requires measurements of the fractional change in concentration α covering at least 90% of the extent of reaction, and this range of α was practically realized in the measurements referred to. We have no clear explanation, then, of why Cook and Dryden's experiments on the decay of conductivity (12) yield a much higher migration enthalpy than do our measurements on well-annealed crystals, but we note the difficulties in ensuring that precipitation is not occurring during measurements, and the relatively few temperatures at which the decay in conductivity could be followed, and the need to separate the polarization and conductance losses.

The small difference between the migration enthalpies of cv and av obtained in this work (0.18 eV) is consistent with the extreme linearity of the intrinsic conductivity plots which display no visible upward curvature (Fig. 1), in marked contrast to KCl (8, 9, 32). Finally, if we calculate from our parameters the Arrhenius energy expected for single av diffusion, we find $\frac{1}{2}h_s + \Delta h_{av}$ = 1.95 eV, in good agreement with the single-vacancy value of 1.92 eV derived by Barr, Morrison, and Schroeder (24).

Acknowledgements

This research was supported by the Natural Sciences and Engineering Research Council of Canada. I.E.H. thanks this Council and the Province of Ontario for the award of scholarships.

1. E. KOCH and C. WAGNER. Z. Physik. Chem. B, **38**, 295 (1937).
2. S. CHANDRA and J. ROLFE. Can. J. Phys. **48**, 397 (1970).
3. S. CHANDRA and J. ROLFE. Can. J. Phys. **48**, 412 (1970).

Can. J. Chem. Downloaded from www.nrcresearchpress.com by 176.9.209.113 on 09/07/12
For personal use only.

4. S. CHANDRA and J. ROLFE. Can. J. Phys. **49**, 2098 (1970).
5. S. CHANDRA and J. ROLFE. Can. J. Phys. **51**, 236 (1973).
6. M. BÉNIÈRE, F. BÉNIÈRE, and M. CHEMLA. Solid State Commun. **13**, 1339 (1973).
7. M. BÉNIÈRE, M. CHEMLA, and F. BÉNIÈRE. J. Phys. Chem. Solids, **37**, 525 (1976).
8. L. ACUÑA and P. W. M. JACOBS. J. Phys. Paris, **41**, C6-72 (1980).
9. L. ACUÑA and P. W. M. JACOBS. J. Phys. Chem. Solids, **41**, 595 (1980).
10. M. BABA, T. IKEDA, and S. YOSHIDA. Jpn. J. Appl. Phys. **14**, 1273 (1975).
11. M. BABA, T. IKEDA, and S. YOSHIDA. Jpn. J. Appl. Phys. **15**, 231 (1976).
12. J. S. COOK and J. S. DRYDEN. J. Phys. C, **12**, 4207 (1979).
13. J. S. COOK and J. S. DRYDEN. J. Phys. Paris, **14**, C6-425 (1980).
14. A. R. ALLNATT, P. PANTELIS, and S. J. SIME. J. Phys. C, **4**, 1778 (1971).
15. F. BÉNIÈRE, M. BÉNIÈRE, and M. CHEMLA. J. Phys. Chem. Solids, **31**, 1205 (1970).
16. N. LAURANCE. Phys. Rev. **120**, 57 (1960).
17. V. C. NELSON and R. J. FRIAUF. J. Phys. Chem. Solids, **31**, 825 (1970).
18. M. CHEMLA. C.R. Acad. Sci. Paris, **234**, 2601 (1952).
19. J. F. LAURENT and J. BENARD. J. Phys. Chem. Solids, **7**, 218 (1958).
20. D. PATTERSON, G. S. ROSE, and J. A. MORRISON. Phil. Mag. **1**, 393 (1956).
21. L. G. HARRISON, J. A. MORRISON, and R. RUDHAM. Trans. Faraday Soc. **54**, 106 (1958).
22. J. A. MORRISON and R. RUDHAM. J. Phys. Chem. Solids, **6**, 402 (1958).
23. L. W. BARR, I. M. HOODLESS, J. A. MORRISON, and R. RUDHAM. Trans. Faraday Soc. **56**, 697 (1960).
24. L. W. BARR, J. A. MORRISON, and P. A. SCHROEDER. J. Appl. Phys. **36**, 624 (1965).
25. A. B. LIDIARD. J. Phys. Chem. Solids, **6**, 298 (1958).
26. H. W. ETZEL and R. J. MAURER. J. Chem. Phys. **18**, 1003 (1950).
27. C. R. A. CATLOW, J. CORISH, K. M. DILLER, P. W. M. JACOBS, and M. J. NORGETT. J. Phys. Paris, **37**, C7-253 (1976).
28. M. J. GILLAN. Phil. Mag. A, **43**, 301 (1981).
29. P. W. M. JACOBS, J. CORISH, and B. A. DEVLIN. Photogr. Sci. Eng. **26**, 50 (1982).
30. P. W. M. JACOBS. *In* Mass transport in solids. *Edited by* F. Bénière and C. R. A. Catlow. Plenum Press, New York. 1983. pp. 81–106.
31. P. W. M. JACOBS and P. PANTELIS. Phys. Rev. B, 3757 (1971).
32. A. R. ALLNATT and P. W. M. JACOBS. Trans. Faraday Soc. **58**, 116 (1962).
33. A. R. ALLNATT and P. PANTELIS. Solid State Commun. **6**, 309 (1968).
34. R. G. FULLER. Phys. Rev. **142**, 524 (1966).
35. C. R. A. CATLOW, J. CORISH, K. M. DILLER, P. W. M. JACOBS, and M. J. NORGETT. J. Phys. C, **12**, 451 (1979).
36. I. E. HOOTON and P. W. M. JACOBS. Unpublished work.

Can. J. Chem. Downloaded from www.nrcresearchpress.com by 176.9.209.113 on 09/07/12
For personal use only.

Differential effect of tetramethylammonium chloride and sodium chloride on duplex melting temperatures of deoxyoligonucleotides: resolution of a salt effect into specific and non-specific components[1]

LUIS A. MARKY, KENNETH S. BLUMENFELD, AND KENNETH J. BRESLAUER
Department of Chemistry, Rutgers, The State University of New Jersey, New Brunswick, NJ 08903, U.S.A.

Received September 8, 1987

This paper is dedicated to Professor J. A. Morrison

LUIS A. MARKY, KENNETH S. BLUMENFELD, and KENNETH J. BRESLAUER. Can. J. Chem. **66**, 836 (1988).

Temperature-dependent uv spectroscopy has been used to determine the differential salt effect of tetramethylammonium chloride (Me_4NCl) and sodium chloride (NaCl) on the thermal stabilities of a series of deoxyoligonucleotide duplexes that systematically differ in base composition and sequence. This approach has allowed us to resolve the AT-specific effect of Me_4N^+ from the more general, non-specific cation effects of Me_4N^+ versus Na^+. Our results reveal that in the absence of AT-specific effects, Me_4N^+ (relative to Na^+) significantly reduces the thermal stability of duplex structures. We offer an interpretation of this differential salt effect in terms of the influence of the condensed cation on water structure at the surface of the duplex. We also observe an AT-specific effect of Me_4N^+ which results in an increased thermal stability for AT-containing duplexes in Me_4NCl relative to NaCl. This specific effect which is governed by mass action is found to be uninfluenced by base sequence and to be a linear function of the percent AT base pairs in the duplex.

LUIS A. MARKY, KENNETH S. BLUMENFELD et KENNETH J. BRESLAUER. Can. J. Chem. **66**, 836 (1988).

On a utilisé la spectroscopie uv à température variable pour déterminer l'effet différentiel de sel des chlorures de tétraméthylammonium (Me_4NCl) et de sodium (NaCl) sur les stabilités thermiques d'une série de duplex de désoxyoligonucléotides qui diffèrent d'une façon systématique dans la composition de la base ainsi que dans la séquence. Cette approche nous a permis de différencier entre l'effet spécifique au AT du cation Me_4N^+ des effets cationiques plus général mais non spécifiques du Me_4N^+ vs Na^+. Nos résultats révèlent que, en l'absence d'effets spécifiques au AT, le Me_4N^+ (par rapport au Na^+) réduit d'une façon importante la stabilité thermique des structures des duplex. On offre une interprétation de cet effet différentiel de sel en fonction de l'influence du cation condensé sur la structure de l'eau à la surface du duplex. On a aussi observé un effet du Me_4N^+ qui est spécifique au AT et qui provient d'une augmentation, dans le Me_4NCl par rapport au NaCL, de la stabilité thermique des duplex contenant du AT. On a trouvé que ces effet spécifique, qui est soumis à la loi d'action de masse, n'est pas influencé par la séquence de la base et qu'il est une fonction linéaire du pourcentage des paires de bases AT dans le duplex.

[Traduit par la revue]

Introduction

The effect of added salt on the stability of helical polynucleotides is well documented and generally depends on the nature of the cationic species (1–4). Cations can exert their stabilizing or destabilizing influences through specific and/or non-specific interactions with the polymer. Examples of non-specific interactions include general electrostatic effects (e.g. cation condensation and screening) as well as the resulting perturbation of local water structure surrounding the polymer. Essentially all cations in aqueous solution manifest such non-specific effects to varying degrees. By contrast, a specific salt effect involves a direct interaction in which the cation influences helix stability by actually "binding" to a specific site of the helical structure. Not all cations are capable of interacting in this manner. Such specific and non-specific salt effects on polymer transitions have been the subject of previous investigations with particular attention given to salts that are capable of eliminating the usual dependence of melting temperature on base composition (5–9).

In this paper we report the first resolution of an overall salt effect accompanying an oligonucleotide transition into its specific and non-specific components. The details of both interactions are discussed in terms of current theories. In addition, the oligomeric salt effects are compared with polymer data.

Our approach involves comparing the effect of two different cations on the thermal stability of a series of deoxyoligonucleotide duplex structures that systematically differ in base composition and sequence.

Experimental

Materials

All measurements reported in this paper were carried out in pH 7 phosphate buffer solutions containing either NaCl (0.1 or 1.0 *M*) or Me_4NCl (0.1 or 1.0 *M*).

Each of the self-complementary deoxyoligomers was characterized spectroscopically (nmr and uv) and chromatographically. The purities were verified by hplc. The hexamer d(ATGAT) was synthesized by a modified diester method as previously described (12). The hexamer d(GCGCGC) and octamer d(GGAATTCC) were synthesized by Collaborative Research Waltham, MA and were kind gifts from Drs. Douglas Turner and Dinshaw Patel, respectively. The dodecamer d(CGCGAATTCGCG) was synthesized by Dr. K. Itakura at the City of Hope using a modified triester method and was provided by Dr. Dinshaw Patel. The poly (dA-dT) was obtained from PL Biochemicals, Inc., purified by dialysis against distilled water, and obtained in dry form by lyophilization.

All the oligomers were desalted by chromatography on Sephadex G-10 and dialyzed exhaustively against water. Membranes having a molecular weight cutoff of 1000 daltons were used for the dialysis.

Me_4NCl obtained from Fisher (reagent grade) was purified by recrystalizing the salt twice from distilled water and then drying approximately 24 h at 100°C. The dry solid was washed twice with purified diethyl ether and the ether removed by drying for 24 h in a vacuum desiccator (13, 14). One of these cations, tetramethylammonium ion (Me_4N^+) can interact both specifically (with AT base pairs) and non-specifically (5–10) while the other, sodium ion (Na^+) only interacts in a non-specific manner (1, 11). Thus, by examining the differential effect of these two cations on the thermal stabilities of a series of oligomer duplexes of varying AT-content we have been able to isolate the contributions from the specific and non-specific interactions.

Can. J. Chem. Downloaded from www.nrcresearchpress.com by 176.9.209.113 on 09/07/12
For personal use only.

TABLE 1. Duplex melting temperatures (°C) in Me_4NCl and NaCl

		t_m				Δt_m(Me_4NCl − NaCl)	
		Me_4NCl		NaCl			
Oligonucleotide	% AT	0.1 *M*	1.0 *M*	0.1 *M*	1.0 *M*	0.1 *M*	1.0 *M*
d(GCGCGC)	0	47.4	49.3	52.2	54.4	−4.8	−5.1
d(CGCGAATTCGCG)	33	50.0	62.8	52.4	64.5	−2.4	−1.7
d(GGAATTCC)	50	24.7	34.7	25.8	34.2	−1.1	0.5
d(ATGCAT)	67	16.8	23.6	16.6	21.7	0.2	1.9
poly d(AT)	100	63.1	80.6	61.8	74.9	1.3	5.7

Methods

Ultraviolet spectroscopy

The absorbance vs. temperature profiles were measured at 260 nm by using a temperature-programmable, thermoelectrically controlled Perkin-Elmer 575 spectrophotometer interfaced to a Tektronix 4051 computer for data acquisition and analysis. The temperature was increased continuously from 5 to 95°C at a rate of 0.5°C/min. Repetitive runs revealed the melting temperature, t_m, to be reproducible to better than ±0.5°C. Since the melting temperatures, t_m's, for these oligomers are concentration dependent, precautions for this effect were taken into account as follows: Aqueous stock solutions of equal concentrations were prepared for all oligomers. Aliquots of each oligomer stock solution were diluted with the appropriate buffers to yield solutions of equal concentrations (~0.1 m*M* in phosphate). In this way comparisons between t_m values for a given oligomer in NaCl versus Me_4NCl were not influenced by concentration effects.

Results and discussion

The four self-complementary deoxyoligomers examined in this investigation are (in order of increasing AT content): d(GCGCGC); d(CGCGAATTCGCG); d(GGAATTCC); d(ATGCAT) as well as the self-complementary polymer poly d(AT).

Temperature-dependent uv profiles were determined for each of these duplex structures at 0.1 and 1.0 *M* concentrations of Me_4NCl and NaCl. Typical uv melting curves are shown in Fig. 1. The resulting melting temperature data, t_m, are listed in Table 1. The final column gives the differential effect on t_m of the two salts at both concentrations investigated. The trends in these data are most clearly seen by examination of Fig. 2 in which Δt_m (t_m in Me_4NCl − t_m in NaCl) is plotted against the % AT base pairs present in each duplex structure.

Several significant features should be noted: (*1*) Δt_m is a linear function of the % AT present in the duplex. (*2*) Δt_m values are negative for oligomers with less than about 50% AT base pairs. (*3*) The 0.1 and 1.0 M salt data have different slopes in Fig. 1 but converge to a common point at zero percent AT base pairs. (*4*) Within experimental error, the polymer data fall on the lines extrapolated from the oligomer results.

In the sections that follow, we elaborate on each of these observations.

Non-specific effect

The specific Me_4N^+ effect depends on the presence of AT base pairs (5–7). Thus, we can selectively eliminate this specific interaction and thereby compare the non-specific effects of the two cations by examining an oligomer that forms a duplex void of AT base pairs; namely, the self-complementary hexamer d(GCGCGC). Inspection of Table 1 reveals that the Δt_m for this oligomer is about −5°C at both salt concentrations. Thus, based solely on non-specific effects, Me_4N^+ causes a significantly larger destabilization of helical structure than Na^+. At this point one should be reminded that our operational definition of non-specific salt effects is intentionally very broad for the purposes of the desired resolution. The definition includes all differential salt effects except those associated exclusively with

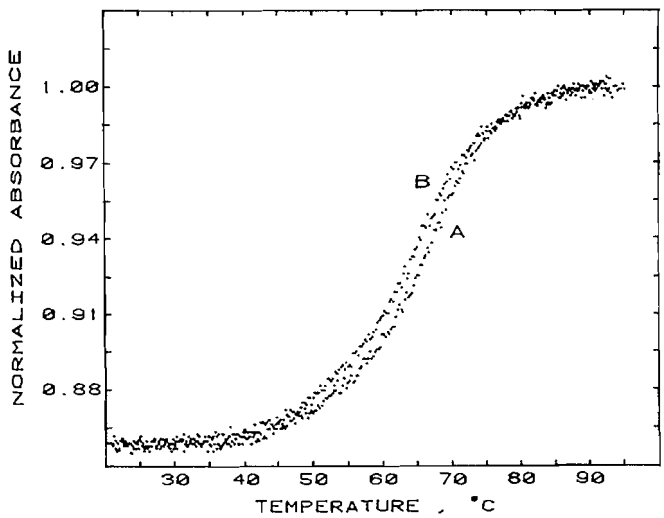

FIG. 1. Typical absorbance vs. temperature profiles for d(CGCGAATTCGCG) in 1 *M* NaCl (A) and 1 *M* Me_4NCl (B).

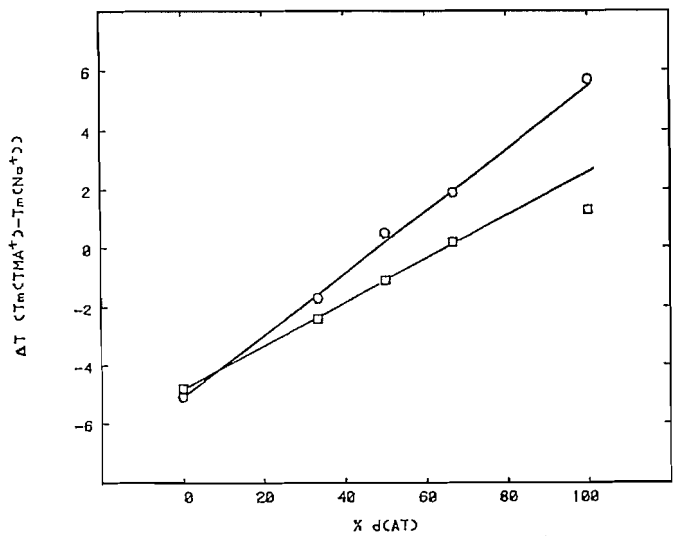

FIG. 2. Differences in the t_m values of the oligomer duplexes in Me_4NCl and NaCl solutions (□, 0.1*M*; ○, 1.0 *M*) plotted against the percent AT base pairs in the duplex structure $\Delta t = t_m$ (Me_4NCl) − t_m (NaCl).

Can. J. Chem. Downloaded from www.nrcresearchpress.com by 176.9.209.113 on 09/07/12
For personal use only.

TABLE 2. Differences in duplex melting temperatures in Me_4NCl and NaCl as a function of the AT content in each duplex

Oligonucleotide	% AT	$\Delta\Delta t_m$(Me_4NCl − NaCl) 0.1 *M*	1.0 *M*
d(GCGCGC)	0	0	0
d(CGCGAATTCGCG)	33	+2.4	+3.4
d(GGAATTCC)	50	+3.7	+5.6
d(ATGCAT)	67	+5.0	+7.0
poly d(AT)	100	+6.1	+10.8

the specific interaction of AT base pairs with Me_4N^+. With these definitions, we can isolate and define the AT-specific effect of Me_4N^+ without also attempting to resolve the many contributions to the non-specific, differential salt effect.

Due to the complexity and multiplicity of possible non-specific interactions, a unique molecular interpretation for the observed differential salt effect is quite difficult. Therefore, we simply present below one possible "explanation" as a basis for further discussion.

Consider that the diffuse hydration sphere surrounding a nucleic acid can act as a destabilizer of helical structure by providing local water molecules which compete with base pairing for hydrogen bonding. When a cation is added to an aqueous, polyion solution, the cation will condense onto the polyion surface to produce an effective local cation concentration in excess of one molar (1, 11). This high local cation concentration is independent of the concentration of the cation in solution (1). Such a high local cation concentration will significantly effect the water structure near the vicinity of the polyion surface which in turn will effect the stability of the polyion structure.

Specifically, when Na^+ ions condense with DNA double helices, they tie-up significant amounts of water molecules (as waters of hydration) in the vicinity of the duplex structure. By contrast, Me_4N^+ ions are not significantly hydrated. Consequently, when Me_4N^+ ions condense with DNA duplexes, they do not "tie up" (electrostriction) water molecules in the vicinity of the double helix. Thus, in Me_4N^+ solutions (in contrast to Na^+ solutions) water molecules close to the surface of the duplex are available to compete with interstrand base pairing thereby resulting in lower duplex melting temperatures in Me_4N^+ solutions compared with Na^+ solutions. We recognize that this "explanation" is rather simplistic and present it only as a basis for further discussion. Clearly, additional data are required before a more sophisticated explanation of non-specific, differential salt effects can be proposed.

Specific effect

To isolate and define the AT-specific stabilizing effect of Me_4N^+ versus N^+, we investigated the differential salt effect on a series of oligomers containing various AT/GC ratios. Inspection of the data in Table 1 and Fig. 2 reveals that the Me_4N^+-induced specific effect serves to stabilize the AT-containing helices. This contrasts with the non-specific Me_4N^+ effect described above which we showed results in lower t_m values relative to Na^+. Thus, the nearly zero values observed for Δt_m at about 50% AT base pairs results simply from a balancing of the opposing specific and non-specific effects of Me_4N^+ relative to Na^+. A similar effect previously has been observed with DNA polymers (7–9).

The specific effect can be more clearly seen if we isolate it by subtracting the constant background of −5°C contributed by the non-specific interaction. The data derived in this fashion are shown in Table 2. From these "corrected" data, we calculate a specific, Me_4N^+-induced stabilization relative to Na^+ of 0.1°C per % AT base pair at 1 M salt concentration.

It should be noted that the linear relationship between Δt_m and % AT base pairs holds despite considerable heterogeneity of base sequence in the oligomers studied. This strongly suggests that the specific interaction between the Me_4N^+ cation and the AT base pair is a highly local phenomenon that is not influenced by either nearest neighbor effects or the location of the AT base pair (terminal vs. interior).

Inspection of Fig. 1 further reveals that the 0.1 and 1.0 *M* lines are of different slope. This is consistent with a picture in which the specific binding of Me_4N^+ to AT base pairs is governed by mass action. In contrast, the non-specific salt effect associated with cation condensation should show no mass action behavior at these overall concentrations (1, 11). This prediction is supported by the observation that for d(GCGCGC), where no specific effects are possible, the Δt_m data are identical for 0.1 and 1.0 *M* salt concentrations.

Finally, one should note that the Δt_m data for poly d(AT) fall on the same lines as the oligomer results. Thus, we can conclude that for these two cations the polymer and oligomer salt effects are comparable. This suggests that the base composition of an oligomer or polymer can be determined by measuring the difference in t_m values in Me_4NCl and NaCl. However, more systems need to be investigated before such an approach can be used with confidence.

Acknowledgments

The authors are grateful to their colleague Dr. G. Manning for helpful discussions. This work was supported by the National Institutes of Health Grant GM23509, the Research Corporation, and the Charles and Johanna Busch Memorial Fund.

1. G. S. MANNING. Q. Rev. Biophys. **11**, 179 (1978).
2. M. T. RECORD, C. F. ANDERSON, and T. M. LOHMAN. Q. Rev. Biophys. **11**, 103 (1978).
3. E. PALECEK. Prog. Nucl. Acids Res. **18**, 151 (1976).
4. L. A. MARKY, D. PATEL, and K. J. BRESLAUER. Biochemistry, **20**, 1427 (1981).
5. J. T. SHAPIRO, B. S. STANNARD, and G. FELSENFELD. Biochemistry, **8**, 3233 (1969).
6. A. WANG and N. KALLENBACH. J. Mol. Biol. **62**, 591 (1971).
7. W. B. MELCHIOR and P. H. VON HIPPEL. Proc. Natl. Acad. Sci. USA, **70**, 298 (1973).
8. G. DEMURCIA, B. WILHELM, F. X. WILHELM, and M. P. DAUNE. Biophys. Chem. **8**, 377 (1978).
9. T. GOLAS, M. MILLER, and D. SHUGAR. Chem. Biol. Interactions, **30**, 209 (1980).
10. J. REUBEN, M. SHPORER, and E. J. GABBAY. Proc. Natl. Acad. Sci. USA, **72**, 245 (1975).
11. G. S. MANNING. Acct. Chem. Res. **12**, 443 (1979).
12. L. A. MARKY, L. CANUEL, R. A. JONES, and K. J. BRESLAUER. Biophys. Chem. **13**, 141 (1981).
13. I. BENCOWITZ and R. R. RENSHAW. J. Am. Chem. Soc. **48**, 2146 (1926).
14. L. W. JONES and H. F. WHALEN. J. Am. Chem. Soc. **47**, 1343 (1925).

Can. J. Chem. Downloaded from www.nrcresearchpress.com by 176.9.209.113 on 09/07/12
For personal use only.

Kinetically cooperative models: boundary movement in optical resolution, phase transitions, and biological morphogenesis

LIONEL G. HARRISON
Department of Chemistry, University of British Columbia, Vancouver, B.C., Canada V6T 1Y6

AND

BEVERLEY R. GREEN
Department of Botany, University of British Columbia, Vancouver, B.C., Canada V6T 1Y6

Received August 27, 1987

This paper is dedicated to Professor James A. Morrison

LIONEL G. HARRISON and BEVERLEY R. GREEN. Can. J. Chem. **66**, 839 (1988).

Computer simulations are described for simple models of kinetically cooperative competition between two or more a priori equally matched antagonists. These might be optically enantiomeric molecules, crystal defects in two phases, differentiation states of biological cells, etc. The models give a perspective on the relationship between the reaction–diffusion theory of pattern formation, homeogenetic induction between biological cells, and the currently popular "cellular automaton" computer programmes. The models express self-activation without inhibition. Therefore, they do not have all that is needed for indefinitely long stabilization of pattern by reaction–diffusion, as first established in the Turing activator–inhibitor model and used later in most reaction–diffusion models. But by the same token, boundaries between disparate regions do not reach stable positions, but must move until they finally reach the edges of the system and disappear. Therefore, these models are convenient for studying aspects of boundary movement in the régime of small-number statistics. To see this without artefacts from array geometry, we use hexagonal arrays in place of the more popular square ones.

We conclude that the behaviour of these models in one respect contrasts with and in another resembles the expected deterministic behaviour in large-number statistics. Regions totally surrounded by an antagonist often grow, while deterministically they must shrink. On the other hand, boundaries tend to straighten, as they would deterministically. In a system of overall rectangular habit, with or without periodic edge conditions making it a cylinder or a torus, boundaries tend to align with the shorter dimension, making a pattern of "square stripes".

LIONEL G. HARRISON et BEVERLEY R. GREEN. Can. J. Chem. **66**, 839 (1988).

On décrit des similations par ordinateur de modèles simples de compétitions, coopératives d'un point de vue cinétique, entre deux ou plusieurs antagonistes qui sont a priori équilibrés. Ces antagonistes peuvent être des molécules optiquement énantiomères, des défauts cristallins dans deux phases, des états de différentiation de cellules biologiques, etc. Les modèles donnent une perspective sur la relation qui existe entre la théorie de réaction–diffusion des motifs de formation, l'induction homéogénétique entre les cellules biologiques et les programmes d'ordinateurs «automatons cellulaires» qui sont actuellement très populaires. Les modèles expriment l'auto-activation sans inhibition. Ils n'ont donc pas tout ce qu'il faut pour la stabilisation à long terme du motif de réaction–diffusion, tel qu'il a été établi originalement dans le modèle activant–inhibiteur de Turing et qui a été utilisé ultérieurement dans la plupart des modèles de réaction–diffusion. En conséquence, les frontières disparaissent entre les régions disparates qui n'atteignent pas des positions stables mais qui doivent toutefois se déplacer jusqu'à ce qu'elles atteignent enfin les bords et qu'elles disparaissent. Ces modèles sont donc utiles pour étudier des aspects du mouvement aux frontières dans un régime de statistiques des petits nombres. Afin de voir ceci sans artefacts provenant de la géométrie matricielle, on utilise une matrice hexagonale plutôt ques les matrices carrées qui sont plus populaires.

On en conclut que le comportement de ces modèles contraste par certains points avec le, et par d'autres points ressemble au, comportement déterministe qu'on peut attendre dans les statistiques des grands nombres. Des régions qui sont totalement entourées par un antagoniste croissent souvent, alors que d'un point de vue déterministe elles devraient retrécir. Par ailleurs, les frontières tendent à devenir droites, comme on pourrait s'y attendre sur une base déterministe. Dans un système d'habitude globalement rectangulaire, avec ou sans conditions de bord periodique les transformant en cylindre ou en tore, les frontières tendent à s'aligner sur la dimension la plus courte et à former un motif de «bandes carrées».

[Traduit par la revue]

Can. J. Chem. Downloaded from www.nrcresearchpress.com by 176.9.209.113 on 09/07/12
For personal use only.

Kinetic cooperativity

Fifty-five years ago, when James James Morrison Morrison was probably thinking about going down to the end of the town (1), Mills (2) published a proposed kinetic mechanism for spontaneous optical resolution. In essence, this was the production of chiral substances by stereospecific autocatalysis of higher kinetic order than the first in product concentration. The simplest illustration is second-order autocatalysis, whereby, if the ratio of enantiomers is at one moment 2:1, the ratio of rates of formation is 4:1, so that kinetic effects are taking the system away from racemic equilibrium and towards resolution. Essentially identifying autocatalysis with the growth of a living tissue, Mills concluded that "the optical activity of living matter is an inevitable consequence of its property of growth".

This concept was elaborated, and in more than one instance independently rediscovered, by a number of workers (2–11). At least two such accounts, Frank (3) and Harrison (7), mentioned the possibility of patterns of oppositely resolved regions as an intermediate stage on the way to resolution. Frank pointed out that a boundary between two such regions would advance in the direction towards which it was concave (Fig. 1). If one thinks of a boundary in the form of a closed loop, this behaviour has paradoxically contrasted aspects. First, on a flat surface (Fig. 1*a*), there will be progress towards resolution by "mopping-up" of surrounded areas. Second, if a boundary is closed by going right around the curved surface of a cylinder, it will tend to straighten out (Fig. 1*b*). This process tends to slow down its movement along the cylinder and impede resolution.

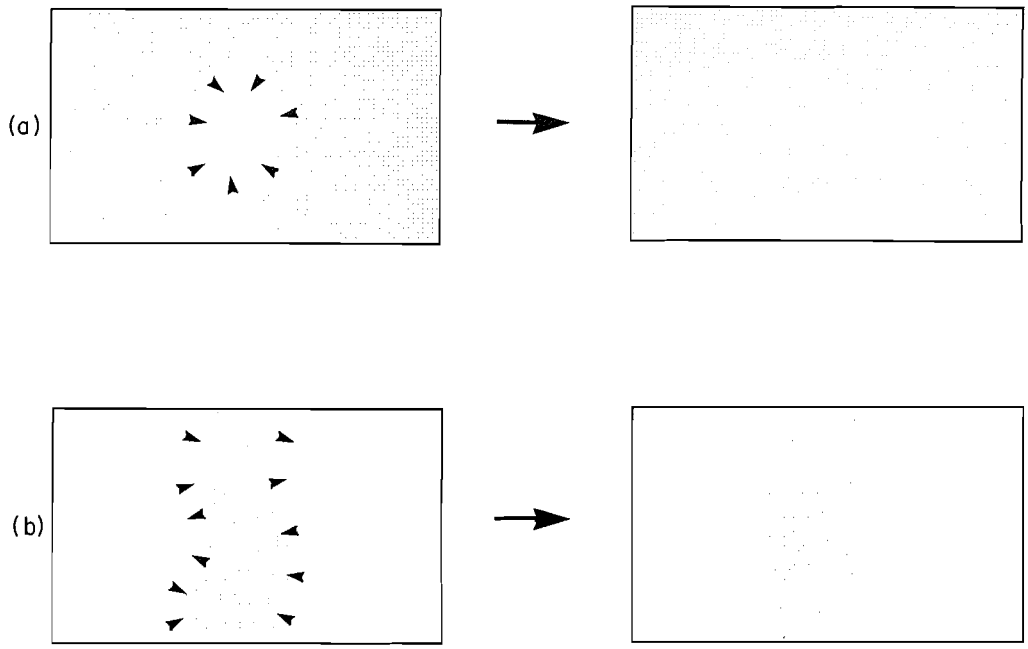

FIG. 1. Sketch to illustrate deterministic movement of boundaries in a kinetically cooperative model for optical resolution, the movement being always into the concavity of the boundary, so that (a) surrounded regions vanish; (b) boundaries running into edges of the region (or right around a cylinder, if periodic boundary conditions are applied to top and bottom edges) tend to straighten.

Can. J. Chem. Downloaded from www.nrcresearchpress.com by 176.9.209.113 on 09/07/12
For personal use only.

The difference between the two cases, topologically, is that in the first the integrated concavity *in the surface* is a full turn, while in the second, the integrated concavity is zero, the turn to close the loop being made *by the surface itself*. Anyone interested in phase transitions will also notice that the first kind of behaviour is just the opposite of nucleation.

The Mills mechanism, for a diffusible substance, can give rise to transient pattern. But, especially in relation to the morphogenesis of living organisms, there is much interest in putative mechanisms for formation of stable pattern. For generality of perspective on all possible mechanisms, the word "stable" must here be understood as an indication of chronological persistence without a priori implications as to whether the system is in a thermodynamic equilibrium or whether it is being kinetically maintained out of equilibrium. For the latter possibility, hypothetical patterning mechanisms are generally discussed under two headings: "reaction–diffusion theory" and "dissipative structure". The former term specifies a field with a 35-year history, starting from Turing's equations (12). The latter term is that of the Prigogine school (13, 14) for a more general category. One of us (15) has suggested that "kinetically maintained structures" is a clearer term.

Reaction–diffusion theory has been extensively discussed in relation to biological morphogenesis (16–22) but is still far from being generally accepted by experimental biologists; see recent review by one of us (23). Equations of the reaction–diffusion type have also appeared in the theory of kinetics of phase transitions (24–26). Most reaction–diffusion equations have nonlinearities in the reaction-kinetic terms that correspond, mechanistically, to some kind of kinetic cooperativity. Quite often, the most important nonlinearity takes the form of a squared concentration, being the simplest form to assume in instances where anything above the first power of concentration would do the job, just as in Mills' suggestion for optical resolution. For instance, the Gierer–Meinhardt equations, which are the form of reaction–diffusion theory so far most closely applied to specific instances of biological development, contain terms for rates of formation, destruction,and diffusive transport of an activator A and an inhibitor H. The rate of formation of A is dominated by a term proportional to A^2/H. Likewise, the Brusselator mechanism of the Prigogine school includes the step:

[1] $Y + 2X \rightarrow 3X$

which again has kinetics second order in the autocatalyst X.

The Turing equations appear at first glance an exception. For an activator X and an inhibitor Y, they contain only linear terms in the variables U and V that represent departures from a spatially uniform steady state X_0, Y_0, i.e.,

[2] $U = X - X_0$ and $V = Y - Y_0$

The equations are

[3a] $\partial U/\partial t = k_1U + k_2V + D_X\nabla^2U$

[3b] $\partial V/\partial t = k_3U + k_4V + D_Y\nabla^2V$

where D_X and D_Y are diffusivities of the species X and Y. Terms such as k_1U, however, representing an equal tendency for X to depart from X_0 either upwards or downwards, need for their simplest explanation a mechanism containing kinetic cooperativity. Thus if X is fomed by second-order autocatalysis and destroyed by first-order decay:

[4] $dX/dt = k_fX^2 - k_dX$

there is an unstable steady state:

[5] $X_0 = k_d/k_f$

and the rate of departure from it in either direction is

[6] $dU/dt = k_dU + k_fU^2$

At small U, the linear term is dominant, but only because the other term contains a squared concentration.

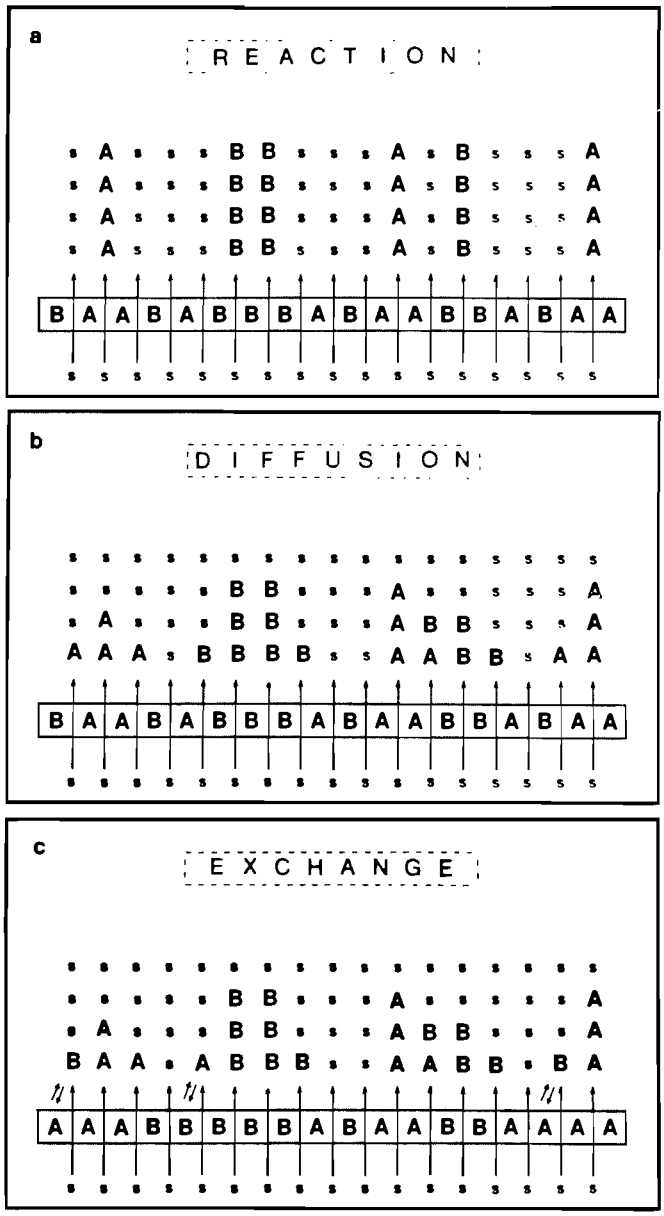

FIG. 2. Excerpts from a simulation (15) of the optical resolution model in one dimension. The row of 18 boxes is a catalyst bed. Reactant "s" flows upwards in solution. Each arrow is a potential catalytic site, activated only if it has the same enantiomer (A or B) adsorbed in boxes on both sides of it, for stereospecific catalysis of production of the same enantiomer. Product in solution diffuses sideways and exchanges back onto the catalyst bed. This simulation leads to increasingly long patches of A's and B's and was continued until there were 9 B's on the left and 9 A's on the right.

If A and B are optical enantiomers, the Mills mechanism for spontaneous resolution may be written formally in terms of the optical asymmetry

[7] $$X = A - B$$

[8] $$dX/dt = dA/dt - dB/dt = k_f(A^2 - B^2) = k_f(A + B)X$$

Circumstances are easily envisaged in which the asymmetry X can change rapidly while the total concentration $(A + B)$ remains constant, or almost so. In that kind of situation, complete nonlinear equations may be quite complicated, but the dominant behaviour as the system starts to depart from the racemic state is the linear relation of rate of departure of X from zero in either direction as shown in eq. [8] if $(A + B)$ is regarded as constant.

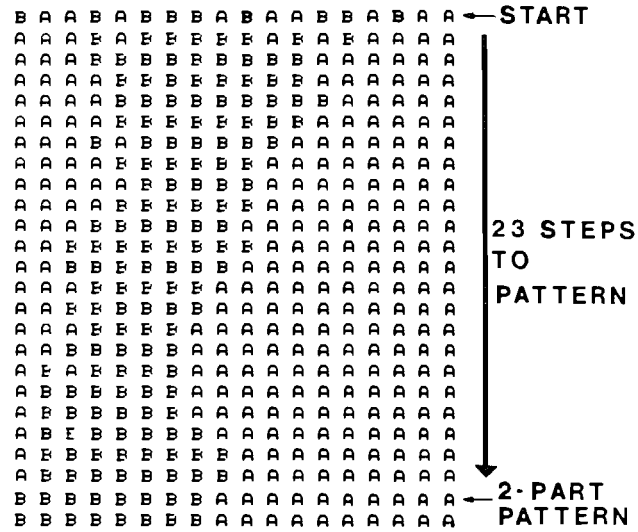

FIG. 3. Results from a computer programme (Appendix A) for one-dimensional optical resolution. In repeated runs, a patch of B's on the left and A's on the right almost invariably forms, but their relative sizes are not reproducible. Each row shows the composition of the adsorbed layer on the catalyst bed (Fig. 2) after one sequence of the operations shown in Fig. 2.

"Automata", boundaries, and the stochastic regime

One of us (15) published a very simple reaction–diffusion simulation in one dimension, in which a row of 18 objects, 9 A's and 9 B's, initially chaotically arranged, developed into an orderly two-part pattern. It was indicated that the dynamic rules of the model could be followed not only without mathematical knowledge but even without knowledge of how to read or write, beyond the ability to put down half a dozen symbols on paper. The simulation was done in half an hour with pencil and paper, and converted by manual draughtsmanship into about 50 frames for an animated film. This procedure, without use of a digital computer, makes it particularly obvious to the person doing it that no numerical calculation whatever has been done. Figure 2 shows a few stages from the sequence.

This model, which is essentially the Mills model for optical resolution, is quite easily programmed for a microcomputer (Appendix A). From a starting row of A's and B's set up either by a random number generator or in whatever initial pattern the operator wishes to choose, the computer examines a pair of adjacent sites. If both are occupied by A, a position one or two places to the left or right, at random, and with a probability distribution for one or two places representing a diffusivity, is converted to A (if it was not A already); similarly for the B's. The readout displays the appearance of the row as this operation is carried out repeatedly (Fig. 3).

Such computation lacks the expository power of the kind of graphic presentation shown in Fig. 2 for showing the chemical–mechanistic nature of the model. But the use of a computer lets one see very quickly two features of the dynamics that were mentioned but not illustrated in the earlier account (15): (*i*) The symmetrical two-part pattern is not always achieved, but something approximating it usually arises if the same input is used repeatedly. This is because the dynamics of the model pick up long-range biases in the input. For the specific example of an

Can. J. Chem. Downloaded from www.nrcresearchpress.com by 176.9.209.113 on 09/07/12
For personal use only.

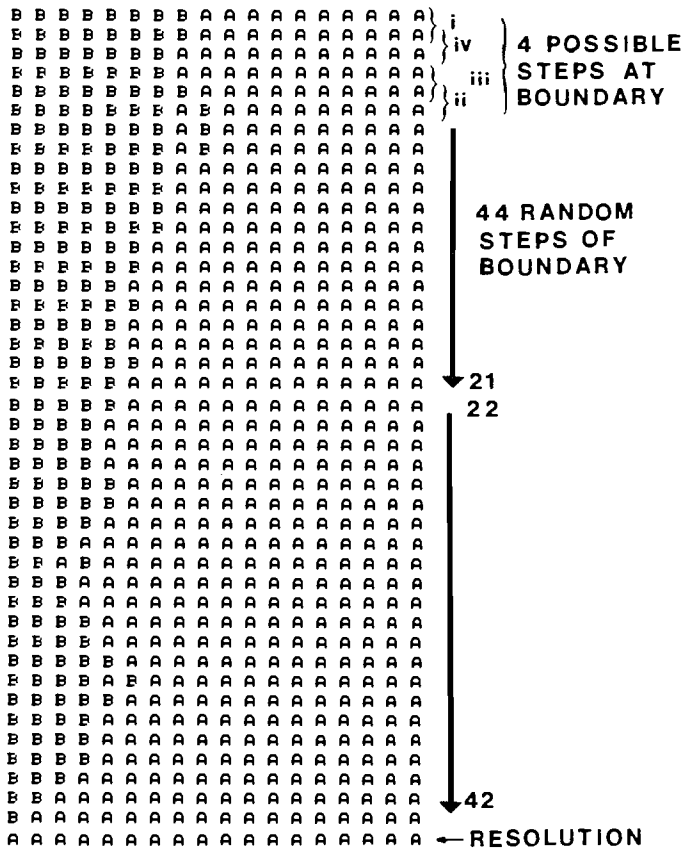

FIG. 4. Continuation of the simulation in Fig. 3. The boundary between *A*-resolved and *B*-resolved regions occasionally becomes "fuzzy" for a short time (possible step ii) but essentially becomes a diffusible entity executing a random walk by unit jumps left (iv) or right (iii), leading to eventual resolution.

input (Figs. 2 and 3), this initial arrangement happened to have 5 *B*'s and 4 *A*'s in the left-hand half, and the reverse in the right-hand half. The developing output always amplifies this bias, but not always to precisely the same extent. (*ii*) When a two-part pattern has been established, the boundary between the two parts starts to execute a random walk, whereby it must eventually reach either the left- or right-hand end of the row. The system has then achieved resolution as all *A*'s or all *B*'s. Figure 4 shows one such random walk, in which resolution took somewhat less than the expectation value of 64 steps.

The main purpose of this paper is to establish that it is useful to regard a boundary between disparate regions as an entity in its own right with significant properties. Some of these are seen only if the region has at least two spatial dimensions, as discussed in the next section, because the boundary then has a shape and such properties as the curvature that governs the deterministic behaviour discussed above in relation to Fig. 1.

In small-number statistics, the above one-dimensional case has led to the concept of a boundary as a randomly walking or diffusible entity. This study can be extended to two dimensions with quite unsophisticated computations to show that, with array sizes rather similar to those of arrays of cells in developing biological organisms, boundary movement displays a peculiar mixture of stochastic and deterministic aspects.

This behaviour is related not only to array size directly, but also to concentration profile, which depends both upon array size and upon the nonlinearities in the kinetic model. Most discussion in deterministic terms of pattern-forming models such as those of Turing, Gierer and Meinhardt, and the Prigogine school (and Frank's suggestion illustrated in Fig. 1) take concentrations of chemical species to be continuous functions of position. If, for instance, a concentration X varies sinusoidally with position so that its departure U from the uniform steady-state X_0 is

$$[9] \quad U = U_0 \sin (2\pi s/\lambda - \delta)$$

where s is the position and λ the wavelength, then

$$[10] \quad \partial^2 U/\partial s^2 = (4\pi^2/\lambda^2)U$$

The implication of this rather well-known formula for the present purpose is that if at any point along the distribution one knows the value of both U and its second derivative, one knows the wavelength. Thus every small region of a self-organizing system in a certain sense "knows" what its wavelength is; and if there is a condition such as no-flux across the ends of the system, so that the ends must be antinodes of the chemical waveform, regions within the system likewise in a certain sense know how far they are from the ends. Thus movement of the pattern in relation to the ends of the system is not random, but deterministic. In a Mills-type optical resolution model, with a diffusible chiral product turning the mechanism into reaction–diffusion, long-wave components will grow in amplitude faster than short-wave components (15), so that, even in one dimension, short regions will tend to be systematically eliminated. A central boundary ($U = 0$, separating a U-positive from a U-negative region), once displaced from the centre, will tend to continue to move in the same direction rather than executing a random walk.

All the above discussion is quite inapplicable to a square-wave pattern of oppositely resolved regions, with constant concentration in each and sharp boundaries between them. In that case, no small region of the pattern knows where it is in relation to the ends of the system. Nor are there differing finite values of wavelength to distinguish one region from another. In the sense of eq. [10], wavelength is everywhere infinite. Thus if internal boundaries move at all, they must move randomly, because they totally lack spatial information.

The model used in Figs. 2, 3, and 4 is strongly nonlinear, as discussed in ref. 18, especially section 2.3 containing equation 12 of that paper. The nonlinearities tend to lead to square-wave (i.e., patch-resolved) patterns, and do so particularly quickly if a rather small number of points are used in a simulation, so that the simulation has very limited ability to represent concentrations as anything like continuous variables.

The optical resolution model as presented here clearly resembles the kind of algorithm known as a "cellular automaton", in which elements of a one- or two-dimensional array change according to the values of neighbouring elements. Such algorithms, some of them having remarkable pattern-forming ability, have been designed for computers large and small. They have been discussed in popular language, for recreational purposes (27, 28), and also for scientific purposes, sometimes with minimal mathematics (29) and sometimes in mathematical language that might overwhelm the biological experimentalist, even when the problems addressed are in developmental biology (30). (From a rapidly growing literature, the references cited here are those which are most accessible to such an experimentalist, or which directly address problems related to theories of biological development.) One popular application, which is essentially an optical resolution model, is the "voting game" (29, 33). In this, array elements are adherents of political parties trying to persuade neighbours to change their allegiance. Simulations usually lead to the one-party state.

Can. J. Chem. Downloaded from www.nrcresearchpress.com by 176.9.209.113 on 09/07/12
For personal use only.

Can. J. Chem. Downloaded from www.nrcresearchpress.com by 176.9.209.113 on 09/07/12
For personal use only.

Wolfram (29) states that simple cellular automaton rules can capture the essential features of the usual partial differential equations of nonlinear chemical reaction–diffusion systems, citing Greenberg, Hassard, and Hastings (31) and Madore and Freedman (32). To a biochemically minded biologist who would like to interpret the model as a simulation of chemical processes at the molecular level, the correspondence may not be at all obvious, for the good reason that it is not there in most of the automaton models. An automaton model usually consists of an array of rectangular boxes, each labelled with one of a limited number of letters, numbers, or colours. In relation to a biological system, does each box represent a cell or a molecule? When a box induces a neighbour to change to the same label as itself, is this autocatalysis, diffusion, or homeogenetic induction, in which living cells cause neighbours to differentiate like themselves?

Two diagnostic tests are straightforward. First, if the programme nowhere uses a random number generator and the output shows no hint of stochastic behaviour, diffusion has not been simulated at the molecular scale. Second, if boxes that have not yet changed can be in one of two states, inducible (excitable) or refractory (quiescent), the state being time dependent, then the boxes represent not merely a biological cell, but a special kind of cell: the excitable cell, such as a neuron. Both of Wolfram's references to automaton models for reaction–diffusion systems are to this kind of model.

Such models are more promising for moving patterns of excitation in neuronal networks (brainwaves) than for most of the pattern-forming phenomena of development. Both papers also describe modelling of the moving spiral patterns of the Belousov–Zhabotinskii reaction when it is carried out in a Petri dish. This is a solution system without gross cellular compartmentalization. But its mechanism is a complex one. The Oregonator model of Field and Noyes (34–36) shows this complexity. It is a three-morphogen model; most reaction–diffusion models have only two morphogens. Such models as the Oregonator express the most kinetically significant steps in a reaction mechanism. Automaton models are at a farther remove: their cell-to-cell interactions are not unit steps in the chemical mechanism.

Nonstochastic automata for less specialized cell types (without refractory behaviour) may be relevant to homeogenetic induction, in which, for example, a false nervous system is propagated from a neural plate transplant (37–39) and, in plants, a new cambium ring forms by differentiation of wound-response callus tissue (40). But even in such cases, automata may give an overoptimistic impression of the ability of induction, unaided by long-range controls, to direct the spatial orientation of elongated or dendritic extensions of a tissue. In the automaton simulations, these directions are determined with zero error limits, and are strongly dependent on the configuration of the starting cluster. Any realistic introduction of random disturbances could lead to serious dead-reckoning errors in the navigation of the path of induction across the tissue.

At the *molecular* level, stochastic behaviour so dominates that it, in a sense, reverses its nature. Instead of being a nuisance as a disturber of order, it provides the means of communication that permits long-range control of order, across the full spatial scale of the system. The simulations described in this paper are designed to illustrate this in the simplest possible way, and to clarify how automaton-like rules with a little randomness abbreviate a reaction–diffusion mechanism at the molecular level when the mechanism is rudimentary and very little abbreviation has to be done.

Boundary movement in two dimensions

A boundary in two dimensions is not just a point. It has a shape, and hence has much more interesting properties. Its movement, in simulations, may be compared with the curvature-dominated deterministic behaviour in Fig. 1. Much biological pattern formation is in fact essentially two-dimensional, in single layers of cells or on the surfaces of individual cells. But what one learns from two dimensions is likely also to have some relevance in the three-dimensional world of phase transitions.

Using essentially a two-dimensional Mills model (but sometimes with more than two a priori equally matched antagonists), we conclude principally that small patches tend to grow or shrink stochastically, but that boundaries tend to straighten once they extend right across the system. Also, they tend to align with the shorter dimension of the system.

Such computations are within the scope of "computer recreations" for the microcomputer. Thus besides giving conclusions, as is usual in a research paper, we may invite readers to repeat the experiments. Actual running of such a programme gives a clearer indication of its kinetics than a few excerpts from the output can convey. Because of this, and also because of the very interdisciplinary nature of our topic, we find that we cannot clearly separate a pedagogic objective from the usual objective of presenting research results, in writing this paper.

In two dimensions, as previously in one dimension, we are using a model of such mechanistic simplicity that it lacks the power to stabilize a pattern of disparate parts indefinitely long or with a precisely reproducible geometry from repeated uses of the same disorderly input. When, however, the pattern has been reduced to a small number of parts with long boundaries between them, further progress towards uniformity is usually very slow. To stabilize pattern indefinitely long needs additional features in the kinetics of the model, but, in a sense, their task of stopping boundary movement altogether is not onerous.

These additional features are, of course, the presence of an inhibitor, and its diffusion at a faster rate than the self-enhancing activators, as first proposed by Turing and put into most later elaborations of reaction–diffusion theory for pattern formation (12–18). This sort of kinetic feature is likely to be necessary not only for theories of stable pattern, but also (Koga, personal communication) for further progress in the understanding of nucleation kinetics in phase transitions, for which the present level of knowledge is expressed in refs. 24–26 . For some computer programmes relevant to formation of stable pattern, see Meinhardt (17).

The kinetic principles of the model used here are the same as those used in one dimension. But the entire plane of the output must now show the array at one time-step, i.e., the whole picture is analogous to a single row in Fig. 3 or Fig. 4. For correspondence to Fig. 2, the flow direction of reactant "s" and products in solution is the third dimension, out of the plane of the diagram.

In two dimensions, the array can be quite large, and one may want to see output for time-steps shorter than that required for one systematic survey of the whole array for pairs. To show how the entire array is developing on a shorter time-scale, and to improve the correspondence to events on a molecular scale, it is best to visit points of the array in a random sequence in the computation procedure.

Most cellular automaton models use a square array, in which the neighbours of one square are considered to be either the four squares sharing sides with it (von Neumann neighbourhood, Fig. 5*a*) or those together with the four diagonal neighbours (Moore neighbourhood, Fig. 5*b*). For the present purpose, we

Can. J. Chem. Downloaded from www.nrcresearchpress.com by 176.9.209.113 on 09/07/12
For personal use only.

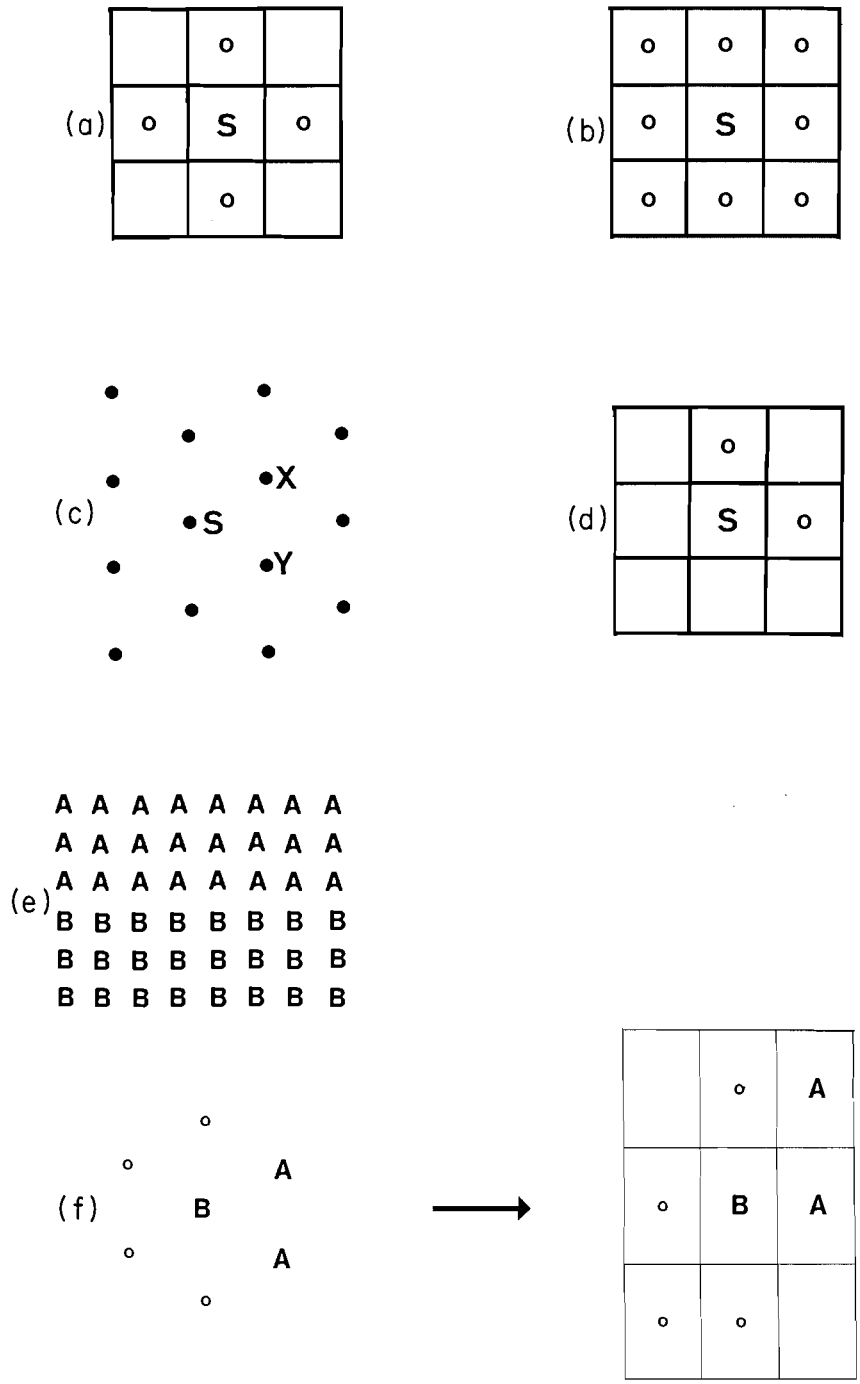

FIG. 5. Local geometries in cellular automaton calculations, relevant to two-dimensional models with bimolecular kinetic cooperativity. (a) von Neumann neighbourhood of a site S, marked by four o's; (b) Moore neighbourhood of site S; (c) close-packed hexagonal array, in which X and Y are two nearest neighbours of site S and are also nearest neighbours of each other; (d) the "two-nearest-neighbours" catalyst in a square array; (e) the artificial restriction of boundary movement in the square array; this boundary cannot move, because no letter has a diagonal pair of neighbours that are both the other letter; (f) the hexagonal array, which is free from this artificial restriction, nonconformally mapped into a rectangular array for ease of display on a microcomputer.

have found it more convenient to programme for a close-packed hexagonal layer (Fig. 5*c*). This change is not at all trivial in regard to movement of the boundaries, as explained below. Each site in the array has six nearest neighbours, and adjacent nearest neighbours are also nearest neighbours of each other, in contrast to the square array. In the programme, a site S is chosen at random, one of its nearest neighbours is chosen, also at random, and the next neighbour clockwise around the hexagon is checked for whether it has the same label as the first neighbour. If so, the site S is given the same label as that pair. This is a back-to-front way of representing an adjacent pair acting as an autocatalyst, and the product of the catalysis diffusing away a short distance in either direction from the centre of the catalytic pair. There is just sufficient random choice in this programme for a proper representation of reaction–diffusion with a fairly low diffusivity, or a high

Can. J. Chem. Downloaded from www.nrcresearchpress.com by 176.9.209.113 on 09/07/12
For personal use only.

reaction rate. If, for instance, each catalyst pair processes molecules at a typical rate for enzyme catalysis, $100–1000\,s^{-1}$, and the nearest neighbour separation is 5 Å, then the diffusion distance of one nearest neighbour spacing per processing time of one molecule would correspond to a diffusivity of $10^{-13}–10^{-12}\,cm^2\,s^{-1}$.

The hexagonal array avoids all ambiguities about what arrangements should be regarded as neighbours, and thereby avoids a pitfall in certain obvious choices in the square array. Suppose, for instance, that one chose a site S in the square array and changed it to the same label as two of the von Neumann neighbours touching each other cornerwise (Fig. 5*d*). If, at any stage in the computation, a boundary between regions of two different labels has become linear, it can never change (Fig. 5*e*). This might be a good model for some aspects of crystal growth, in which flat surfaces will not grow and persistent steps are necessary catalysts for growth. But it is probably not a good model for the biological growth situations of morphogenesis. In the hexagonal array, this trap is simply not there to fall into. Computations with our programme will show boundaries repeatedly straightening out and then breaking up again into disorderly configurations.

A hexagonal array with a few thousand sites corresponds rather closely to a living system of great current importance in developmental biology: the *Drosophila* egg after nuclear division 13. The egg should then contain, ideally, 8096 nuclei. About 6000 of these, arranged in a single ellipsoidal layer close to the surface of the egg, are involved in a striped segmentation pattern, which can be revealed at this stage by selective fluorescent staining of particular gene products related to well-known mutations (41, 42). The pattern of the nuclei is roughly close-packed hexagonal. Various interesting problems of a physicochemical nature arise in this patterning process. It is not yet clear to what extent reaction–diffusion on a molecular scale may be involved, and on the other hand to what extent the particles of the system can be thought of in terms of small-number statistics as the 6000 nuclei, communicating by homeogenetic induction (43, 44). Within a 1-h period, at constant number of nuclei, the system changes, by formation of cell membranes, from a single cell with thousands of nuclei all in the same continuous cytoplasm to thousands of cells, each with one nucleus. The striped pattern arises before cellularization, while some patterns within the stripes arise immediately after cellularization. One might expect the cellularization to lead to a switch from large-number to small-number statistics, and hence possibly from deterministic to stochastic regimes of behaviour. But the actual behaviour observed is remarkably precisely deterministic throughout.

Clearly, a full explanation of the observed phenomena will involve a complex set of activator–inhibitor interactions, and the formation of stripes requires particular kinds of nonlinearity in the dynamics. But the striped pattern can be made visible at early stages because of alternating character (gene-off, gene-on) in the stripes for certain genes known as the "pair rule" genes, e.g., the gene associated with the *fushi tarazu* ("not enough segments") mutation. If the "off" and "on" states are approached by rather similar kinetics, in terms of quantitative values of rate constants, as seems to be implied in the inductive scheme of Meinhardt (43), then the dynamics of establishment of the alternating stripes may contain much that is kinetically isomorphous with the Mills mechanism for optical resolution. Computer simulations of this very rudimentary model may throw some light on certain limited but important aspects of the processes, especially in regard to the formation, positional stabilization, and straightness of boundaries between disparate regions.

Here, we present a programme for such simulations (Appendix B), some results (Fig. 6), and the suggestion that anyone interested in this topic (as well as many other instances of sharp and potentially mobile boundaries between disparate regions in living organisms or inanimate condensed systems) may gain a certain perspective on such processes by setting up microcomputer programmes of this kind and doing a few computer experiments with them. For a programme to be fairly quickly executed by a microcomputer, we have not tried to show the hexagonal array undistorted in the output. Instead, we have mapped it on to a rectangular array. In the mapping, the six neighbours of a site become the four von Neumann neighbours and two of the diagonals of the Moore neighbourhood (Fig. 5*f*). This is a nonconformal mapping in which one diameter of the hexagons has been arranged at 45° across the diagram, and a stretch of a factor of $3^{1/2}$ made in this direction, if the rectangles are squares. The ones in our display (Fig. 6) are not squares, but have diagonals at about 60° to the horizontal. It may occur to the reader that, because of this special shape of the rectangles, we could have represented a hexagonal array alternatively, without distortion, by using only alternate rectangles, i.e., one colour only of a chequerboard pattern. The centres of these rectangles would be a hexagonal array, but the rectangles themselves would still misrepresent which relative positions are nearest neighbour and which are not.

In this mapping, a region with boundaries following no special directions and therefore tending to become circular should appear as an ellipse with major axis inclined at 60° to the right. We have usually imposed boundary conditions as vertical and horizontal lines *in the map*. Thus, a change from undirected regions to regions responding to boundary conditions should appear as a change from inclined boundaries to vertical or horizontal ones.

Simple computer experiments, and some results

The programme suggested here (Appendix B) will produce an output of at most $23 \times 79 = 1817$ coloured rectangular patches on an IBM PC screen. The initial distribution need not have only two colours, suggesting two enantiomers. Up to 14 colours can be used, to represent morphogenetic substances, differentiation states of cells, allegiance to political parties, and so forth. Figure 6*a* has only 4 initial colours, for clarity in halftone. Numbers of cells of the order of this array size are common in developing sheets of cells. Expansion by a factor of two in both directions gives, roughly, the number of nuclei in *Drosophila* at the developmental stage mentioned above. But if the rectangle is regarded as representing the prolate ellipsoidal *Drosophila* blastoderm opened out, it should be noted that the *long* dimension (horizontal) represents the circumference on the short-axis radius, while the *short* dimension represents the long-axis length. The segmentation pattern would be a set of horizontal stripes, and this model will not produce such a pattern. If this model generates anything resembling stripes, they will be more or less square, with vertically oriented boundaries traversing the short dimension of the field (Fig. 6*a*).

The main interest in these simple computations is to gain some impression of the balance between deterministic and stochastic aspects of the shapes and movements of boundaries between disparate regions, for small-number statistics relevant to assemblies of biological cells and perhaps to aspects of the

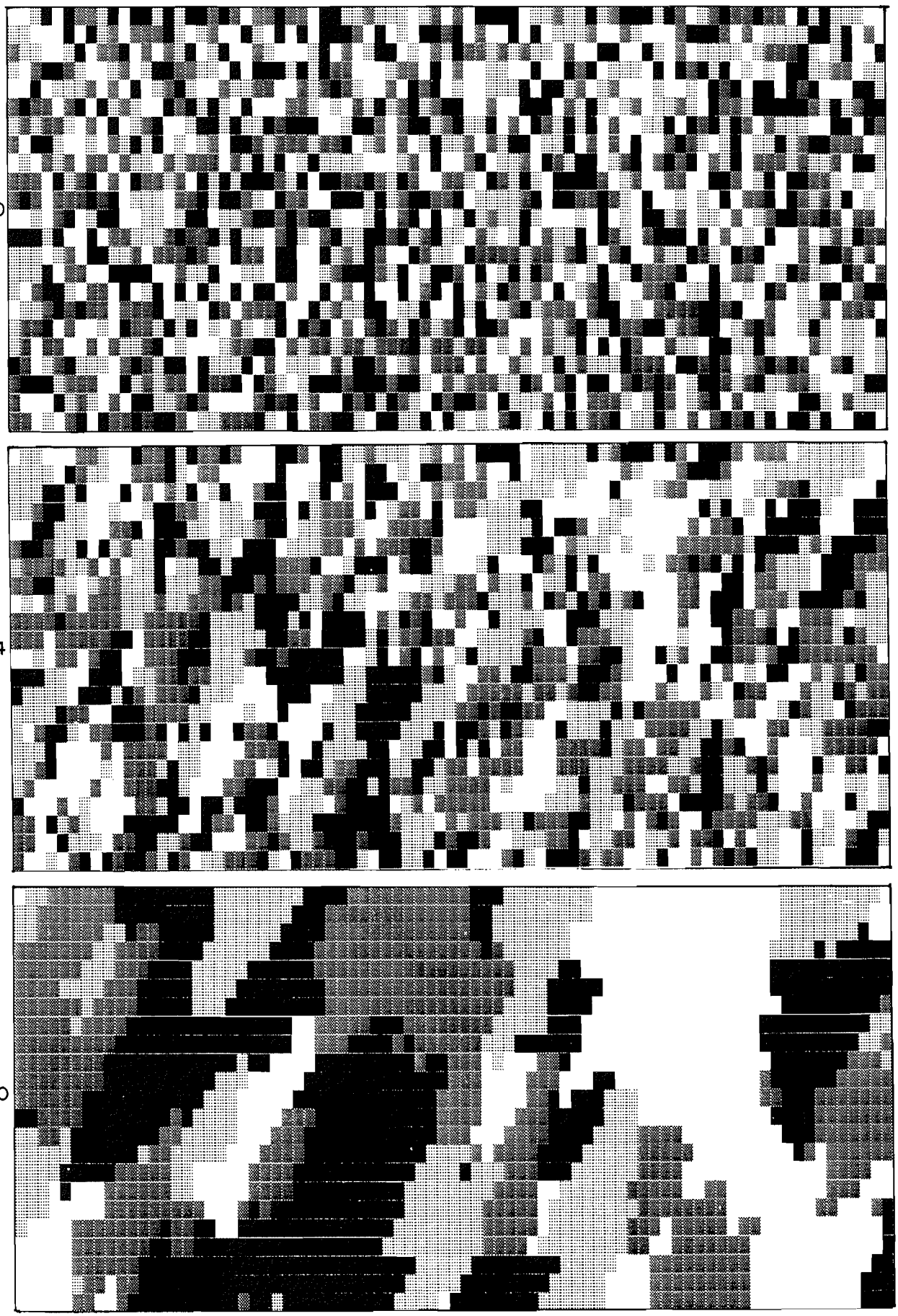

FIG. 6. Two-dimensional analogue of Figs. 3 and 4 but with four starting colours. Each rectangular diagram represents the adsorbed layer on the catalyst surface at one time, corresponding to one row in Fig. 3 or 4. Numbers are approximate total running times of the programme in an IBM PC microcomputer, in minutes.

Can. J. Chem. Downloaded from www.nrcresearchpress.com by 176.9.209.113 on 09/07/12
For personal use only.

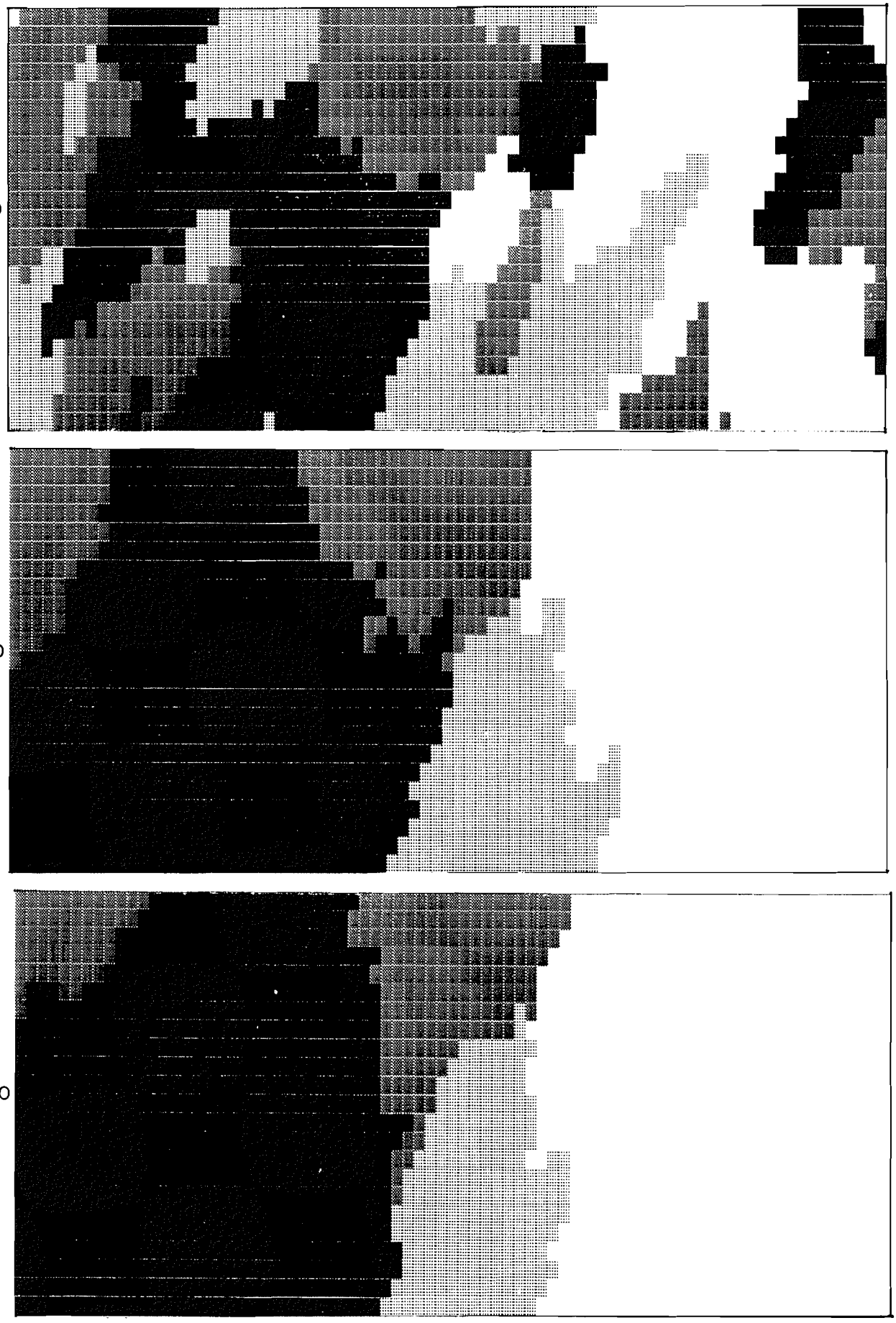

FIG. 6 (*concluded*)

Can. J. Chem. Downloaded from www.nrcresearchpress.com by 176.9.209.113 on 09/07/12
For personal use only.

kinetics of phase transitions. Our principal conclusions may be given as a contrast and comparison to the two kinds of large-number deterministic behaviour shown in Fig. 1 for two different topologies of boundaries: (*a*) Small regions with a boundary loop closed in the surface with a full-turn concavity behave stochastically: they are as likely to grow larger as to diminish. (*b*) Boundaries running right across the region from one edge to the opposite one, or forming a closed loop around the curved surface of a cylinder, if periodic boundary conditions have been used at opposite edges to wrap the rectangle into a cylinder, have a strong tendency to straighten (but "prominences" will repeatedly erupt from them, usually to disappear fairly quickly). (*c*) From a 14-colour start, several colours are eliminated quite quickly. But, although the ultimate destiny of the whole field is to become uniform in colour, the movement of boundaries becomes extremely slow by the stage at which there are only two colours left and boundaries run right across the system. In general, the model behaves substantially more deterministically than one might intuitively expect. Some of the experiments that one may carry out on such a model are as follows:

1. *Run the programme several times with the same input*

Response to imbalances in numbers of labels in various regions is usually more striking in two dimensions than in one. Some regions very reproducibly block out with the same label every time, though the shape of the block will not be exactly reproducible. The effect remains quite remarkable with up to 14 different colours used for the labels.

2. *Run the programme with both no-flux boundaries and wrap-around (periodic, cyclic) boundary conditions*

The latter, applied at top and bottom and sides, effectively convert the array into a torus (doughnut). Usually, in the early stages of a simulation, there is a strong suggestion of sloping lines as regional boundaries, indicating that there are no preferred directions. As the simulation continues, the regions tend to straighten out their boundaries into directions parallel to the boundaries of the whole array. This tendency is, however, no less with wrap-around boundary conditions than with no-flux boundaries. Thus, the directions to which the patterns respond are those in which the overall length or width of the array is specified.

3. *The worm that turns*

Make an array much wider than it is high—a horizontal "worm". Start, not with a random arrangement, but with an orderly pattern of two or more longitudinal stripes. As the simulation proceeds, these will break up into smaller blocks and gradually reorganize into vertical stripes. Murray (22) showed that nonlinear two-morphogen models for pattern formation tend to respond in this way to the dimensions of the pattern-forming area, accounting for the common occurrence of striped tails in mammals. This model shows the same response quite clearly, though with less regularity to the patterns formed, even though the model is so much cruder than a two-morphogen one.

Acknowledgements

We wish to thank Dr. T. C. Lacalli for stimulating comments and criticism, and NSERC Canada for financial support.

In this account, we honour James A. Morrison by showing that concepts from the fields of physical chemistry, which he long encouraged, have wider application to other experimental fields, such as developmental biology. One of us (L.G.H.) wishes to thank Dr. Morrison for such meticulous instruction, many years ago, in the writing of papers, that Dr. Morrison would hardly permit anything to be written except when he was present and participating in the task. This led to the following commentary (45):

> James James Morrison Morrison
> Works at the N.R.C.
> He takes great care with his papers
> Great care with his papers takes he.
> James James Morrison Morrison
> Says to his Fellows, says he:
> "You must never write down
> A verb or a noun
> Unless you do it with me."

1. A. A. MILNE. When we were very young. 10th ed. Methuen, London. 1925.
2. W. H. MILLS. Chem. Ind. 750 (1932).
3. F. C. FRANK. Biochim. Biophys. Acta, **11**, 459 (1953).
4. F. F. SEELIG. J. Theor. Biol. **31**, 355 (1971).
5. F. F. SEELIG. J. Theor. Biol. **32**, 93 (1971).
6. F. F. SEELIG. J. Theor. Biol. **34**, 197 (1972).
7. L. G. HARRISON. J. Theor. Biol. **39**, 333 (1973).
8. P. DECKER. J. Mol. Evol. **4**, 49 (1974).
9. L. G. HARRISON. J. Mol. Evol. **4**, 99 (1974).
10. L. G. HARRISON. *In* Origins of optical activity in nature. Symp. Chem. Inst. Canada. *Edited by* D. C. Walker. Elsevier, Amsterdam. 1979. p. 125.
11. P. DECKER. *In* Origins of optical activity in nature. Symp. Chem. Inst. Canada. *Edited by* D. C. Walker. Elsevier, Amsterdam. 1979. p. 109.
12. A. M. TURING. Philos. Trans. R. Soc. London, B: **237**, 37 (1952).
13. I. PRIGOGINE. *In* Fast reactions and primary processes in chemical kinetics. *Edited by* S. Claesson. Almqvist and Wiksell, Stockholm; Interscience, New York. 1967. p. 371.
14. G. NICOLIS and I. PRIGOGINE. Self-organization in nonequilibrium systems. Wiley, New York. 1977.
15. L. G. HARRISON. *In* Developmental order: its origin and regulation. *Edited by* S. Subtelny and P. B. Green. Alan R. Liss, New York. 1982. p. 3.
16. A. GIERER and H. MEINHARDT. Kybernetik, **12**, 30 (1972).
17. H. MEINHARDT. Models of biological pattern formation. Academic Press, London. 1982.
18. L. G. HARRISON and T. C. LACALLI. Proc. R. Soc. London, B: **202**, 361 (1978).
19. T. C. LACALLI and L. G. HARRISON. J. Theor. Biol. **76**, 419 (1979).
20. T. C. LACALLI. Philos. Trans. R. Soc. London, B: **294**, 547 (1981).
21. J. D. MURRAY. Lectures on nonlinear-differential-equation models in biology. Clarendon Press, Oxford. 1977.
22. J. D. MURRAY. Philos. Trans. R. Soc. London, B: **295**, 473 (1981).
23. L. G. HARRISON. J. Theor. Biol. **125**, 369 (1987).
24. H. METIU, K. KITIHARA, and J. ROSS. J. Chem. Phys. **64**, 292 (1976).
25. Y. KOGA. J. Cryst. Growth, **66**, 35 (1984).
26. Y. KOGA. Physica B. In press.
27. B. HAYES. Sci. Am. **250**(3), 12 (1984).
28. M. GARDNER. Wheels, life and other mathematical amusements. Freeman, San Francisco, CA. 1983.
29. S. WOLFRAM. Nature, **311**, 419 (1984).
30. A. LINDENMAYER and G. ROZENBERG. Automata, languages, development. North-Holland, Amsterdam. 1976.
31. J. M. GREENBERG, B. D. HASSARD, and S. P. HASTINGS. Bull. Am. Math. Soc. **84**, 1296 (1978).

Can. J. Chem. Downloaded from www.nrcresearchpress.com by 176.9.209.113 on 09/07/12
For personal use only.

32. B. F. MADORE and W. L. FREEDMAN. Science, **222**, 615 (1983).
33. A. K. DEWDNEY. Sci. Am. **252**(4), 18 (1985).
34. R. J. FIELD and R. M. NOYES. Faraday Symp. Chem. Soc. **9**, 21 (1974).
35. J. D. MURRAY. J. Theor. Biol. **56**, 329 (1976).
36. L. G. HARRISON. Chem. Soc. Rev. **10**, 491 (1981).
37. H. SPEMANN and O. MANGOLD. Arch. Microsk. Anat. Entwicklungsmech. **100**, 599 (1924).
38. O. MANGOLD. Naturwissenschaften, **21**, 761 (1933).
39. J. M. W. SLACK. From egg to embryo. Cambridge University Press, Cambridge. 1983.
40. J. WARREN WILSON and P. M. WARREN WILSON. *In* Positional controls in plant development. Cambridge University Press, Cambridge. 1984. Chap. 9.
41. S. B. CARROLL and M. P. SCOTT. Cell, **43**, 47 (1985).
42. S. DINARDO, J. M. KUNER, J. THEIS, and P. H. O'FARRELL. Cell, **43**, 59 (1985).
43. H. MEINHARDT. J. Cell Sci. Suppl. **4**, 357 (1986).
44. L. G. HARRISON and K. Y. TAN. BioEssays. In press.
45. L. G. HARRISON. *In* Applied poetry: an anthology. *Strongly suspected of being edited by* James A. Morrison. Applied Poetry Section, Division of Pure Chemistry, N.R.C., Ottawa. 1960. p. 23.

Appendix A: one-dimensional programme

This programme is for the type of simulation shown in Figs. 3 and 4, but is not restricted to only two competing letters (see example below programme). Diffusivity may be changed by altering the threshold values of P. The programme is in BASIC and was used on an IBM PC computer.

The following example shows three quite different results obtained in three separate runs, all starting from the same input, which uses six different letters (a, b, c, x, y, z).

```
10 CLS:WIDTH 80:COLOR 2,0
20 PRINT "                                   A's and B's"
90 DIM X$(80),Y$(80),Z$(80)
100 PRINT "Enter the letters for the initial sequence without any spaces between
 them."
110 PRINT "Hit Enter only when finished.":INPUT F$
120 IF LEN(F$)>79 THEN PRINT "Too long, try again":GOTO 100
130 IF LEN(F$)<1 THEN GOTO 100
140 N=LEN(F$)
150 FOR J=1 TO N
160     X$(J)=MID$(F$,J,1)
170     Y$(J)=X$(J):Z$(J)=X$(J)
180 NEXT J
190 PRINT "Initial pattern is:"
200 FOR J=1 TO N
210 PRINT X$(J);
220 NEXT J
230 LPRINT "Initial pattern is:";CHR$(13)
240 FOR J=1 TO N
250 LPRINT X$(J);
260 NEXT J
270 LPRINT CHR$(13)
280 PRINT:PRINT "Ready to go? Hit any key to start."
290 PRINT:PRINT "      (While program is running, hit Escape to stop.)"
300 LPRINT "Resulting patterns are:";CHR$(13)
310 W$=INKEY$: IF W$="" THEN GOTO 310
320 A=0
330 RANDOMIZE TIMER       'diffn+exchange
340 IF X$(1)<>X$(2) GOTO 370
350 P=RND(1)
360 IF P<=.2 THEN Y$(3)=X$(1)
370     FOR I=2 TO N-2
380     IF X$(I)<>X$(I+1) THEN GOTO 420
390     P=RND(1)
400     IF P>=.8 THEN Y$(I-1)=X$(I)
410     IF P<=.2 THEN Y$(I+2)=X$(I)
420     NEXT I
430 IF X$(N-1)<>X$(N) GOTO 460
440 P=RND(1)
450 IF P>=.8 THEN Y$(N-2)=X$(N-1)
460 PRINT
470 REM                   'swap y and x
480 FOR I=1 TO N
490     IF Y$(I)<>X$(I) THEN X$(I)=Y$(I)
500 NEXT I
510 FOR I=1 TO N
520 PRINT X$(I);
530 NEXT I
540 REM                   'Next Round
550 A=A+1
560 W$=INKEY$:IF W$=CHR$(27) THEN GOTO 570 ELSE GOTO 330
570 CRINT :PRINT "Program stopped after ";A;" rounds of reaction-diffusion."
580 FOR I=1 TO N
590 LPRINT X$(I);
600 NEXT I
610 LPRINT:LPRINT "                                  ";A;" rounds of reaction-diffusion
."
620 PRINT:INPUT "Another game with same pattern(Y/N)";ANS$
630 IF ANS$="Y" OR ANS$="y" GOTO 650
640 PRINT:PRINT "END": LPRINT:LPRINT "REALLY THE END": LPRINT CHR$(13);CHR$(13);
END
650 PRINT:PRINT "Original sequence was:"
660 FOR J=1 TO N
670     X$(J)=Z$(J):Y$(J)=Z$(J)
680     PRINT X$(J);
690 NEXT J
700 A=0
710 PRINT:PRINT:PRINT "Running........"
720 GOTO 330
```

Can. J. Chem. Downloaded from www.nrcresearchpress.com by 176.9.209.113 on 09/07/12
For personal use only.

```
Initial pattern is:

aaaaxxbyycczzzzxxbbccccccaaaxyyyyxxaaabbbcccxyzzzzxaaabbcabxzzycbbaaayyxxzzzbbcc

Resulting patterns are:

zzzzzzzzzzzzzzzzzzzzzzzzzzaaaaaaaaaaaaaaaaaaaaaaazzzzzzzzzzzzzzzzzzzzzzzzzzzzzzzzzzzzzzzz
                                   166  rounds of reaction-diffusion.
aaaaaaaaaaaaaaaaaaaaaaaaaaaabbbbbbbbbbbbbbbbbbbbbbbabaaaaaaaaaaaaaaaaaaaaaaaaaaaaaa
                                   155  rounds of reaction-diffusion.
yyyyyyyyyyyyyyyyyyyyyyyyyyyyyyyzzzzzzzzzzzzzzzzzzzzzzzzzzzzzzzzzzzzzzzzzzzzzzzzzzzzzz
                                   782  rounds of reaction-diffusion.
```

Appendix B: two-dimensional programme

This programme was used to generate output like Fig. 6. By using the fact that colours are numbered in BASIC, it is possible to generate patterns with up to 14 colours, using the COLOR command without any characters. The programme is called MONDRIAN because of the resemblance of some of its output to the style of that designer. A compiled version is available on request from the authors.

```
10 REM
20 REM
30 REM
40 REM
50 REM
60 REM
70 REM ************************************************************
80 REM            *********  Initialization  *********
90 SCREEN 0,1: COLOR 0,6,6
100 WIDTH 80:KEY OFF:CLS
110 DEFINT A-C,I-K,M,N,P-T,W-Z
120 DEFSNG F
130 DEF FNMUD(FULLSTEPS,Z)=FULLSTEPS-(INT(FULLSTEPS/Z)*Z)
140 DIM A(30,80),B(30,80),TALLY1(6),TALLY2(6),LS(3)
150 ON ERROR GOTO 3220
200 PRINT "  ***************   CHECKER3   ***************"
210 PRINT:PRINT "      THE BLACK AND WHITE VERSION OF MONDRIAN"
220 PRINT :PRINT"Patterns can be generated with up to 5 different shades of"
230 PRINT"white to black. Pattern can be printed at any time during game"
240 PRINT                  "by doing a screen dump (PrtSc)."
250 PRINT:PRINT "ARRAY MENU":PRINT
260 PRINT "This menu allows you to select the initial array and edit it"
270 PRINT "                  to your taste.":PRINT
280 PRINT "1. New array: random number generator."
290 PRINT "2. New array: enter each element individually."
300 PRINT "3. Re-use the starting array if it ie etill in RAM."
310 PRINT: INPUT "Your choice";M
320 IF M=<0 OR M>3 THEN PRINT "Try again.":GOTO 280
330 IF M=3 GOTO 390
340 PRINT "The pattern is X columns by Y rows.":PRINT
350 INPUT "Enter number of columns (X), up to max. of 79";X
360 IF X<1 OR X>79 GOTO 350
370 PRINT: INPUT "Enter number of rows (Y), up to max. of 24";Y
380 IF Y<1 OR Y>24 GOTO 370
390 ON M GOSUB 830,1030,1300                    'generate array
400 REM
410 REM   ************  Tally Initial Distribution ******
420 PRINT "Just a minute, please.."
430 FOR K=0 TO W:TALLY1(K)=0:NEXT K
440 FOR I=0 TO Y-1
450     FOR J=0 TO X-1
460     PARTY=A(I,J)
470     TALLY1(PARTY)=TALLY1(PARTY)+1
480     NEXT J
490 NEXT I
500 PRINT:PRINT "Initial distribution:"
510 FOR K=0 TO W
520 PRINT "There are";TALLY1(K);" ";K;"'s"
530 NEXT K
540 FOR K=0 TO W:TALLY2(K)=TALLY1(K):NEXT K
590 REM  ************************************************************
600 REM           ************     MAIN MENU     ************
605 REM  ************************************************************
610 PRINT :PRINT "MAIN MENU"
620 PRINT "In each round an element is randomly selected. One of its six"
630 PRINT "hexagonal neighbours is then selected and compared to the next"
640 PRINT "neigbour in a clockwise direction. If they are identical, the"
650 PRINT "first element is changed to agree with them."
660 PRINT "  1.No bounderies (i.e. it wraps)."
670 PRINT "  2.With bounderies."
680 PRINT "  3.Return to array menu

690 PRINT "  4.End program
700 PRINT:PRINT "While game in progress,hit Esc for Bulletin/Menu."
710 PRINT :INPUT "Your choice";N
720 IF N<1 OR N>4 THEN PRINT "Try again":GOTO 620  'N outside range
730 IF N=3 THEN RTCOUNT=0:FULLSTEPS=0: GOTO 250     'Back to array menu
740 IF N=4 THEN GOTO 3040                              'To quit routine
750 PRINT :PRINT "To speed up game, screen will be updated every Z steps."
760 INPUT "Enter Z";Z
770 FULLSTEPS=0:GOSUB 1830                             'Print array
780 ON N GOTO 2010,2510,250,3200
790 REM   ************************************************
800 REM         1.Random Number-Generated Array
810 REM  '************************************************
820 PRINT "Random Number Generated Array"
830 PRINT: PRINT "How many different kinds of elements would you like"
840 INPUT "in this pattern (1 to 5)";NUMEL
850 W=NUMEL-1
860 RANDOMIZE TIMER:PRINT "Working....."
870 FOR I=0 TO Y-1
880     FOR J=0 TO X-1
890     A(I,J)=INT(RND*(NUMEL))
900     B(I,J)=A(I,J)
910     NEXT J
920 NEXT I
930 GOSUB 1830                    'Print pattern on screen
940 PRINT
950 INPUT "Would you like to make changes to the array (Y/N)";ANS$
960 IF ANS$="Y" OR ANS$="y" THEN GOSUB 1500
970 RETURN

1000 REM************************************************************
1010 REM        2.ARRAY ELEMENTS ENTERED A ROW AT A TIME
1020 REM ************************************************************
1030 CLS:PRINT "*** Routine for entering elements individually ***":PRINT
1040 PRINT "Five shades between white and black are available, with numbers"
1050 PRINT "  0 = white"
1060 PRINT "  1 = black"
1070 PRINT "  2 = pale grey dots"
1080 PRINT "  3 = dark grey herringbone"
1090 PRINT "  4 = square dot on white"
1100 W=0
1110 FOR I=0 TO Y-1
1120 PRINT "Type the numbers for row";I+1;"without any spaces between them."
1130 PRINT "Hit Enter at the end of the line.":INPUT F$
1140 LNGTH=LEN(F$):IF LNGTH>X THEN PRINT "Too long,try again":GOTO 1120
1150    FOR J=0 TO X-1
1160    A(I,J)=VAL(MID$(F$,J+1,1))
1170    B(I,J)=A(I,J)
1180    IF W<A(I,J) THEN W=A(I,J)
1185    IF W>4 THEN PRINT "No colour assigned to numbers over 4."
1190    NEXT J
1200    PRINT "The";LNGTH;"numbers you have entered are:"
1210    FOR J=0 TO X-1: PRINT A(I,J);: NEXT J
1220    PRINT:INPUT "Would you like to re-enter them (Y/N)";ANS$
1230    IF ANS$="Y" OR ANS$="y" GOTO 1120
1240    PRINT
1250 NEXT I
1260 GOSUB 1830                          'Print array
1270 PRINT :INPUT "Would you like to make any changes (Y/N)";ANS$
1280 IF ANS$="Y" OR ANS$="y" THEN GOSUB 1500
1290 RETURN
1300 REM ************************************************************
1310 REM       3.RE-USE THE STARTING ARRAY FROM SAME SESSION
1320 REM ************************************************************
1330 FOR I=0 TO Y-1
1340    FOR J=0 TO X-1
1350    A(I,J)=B(I,J)
1360    NEXT J
1370 NEXT I
1380 FULLSTEPS=0: RTCOUNT=0
1390 LOCATE 24,1
1400 PRINT "THE STORED ARRAY IS.......":FOR K=1 TO 2000: NEXT K
1410 GOSUB 1830                          'Print array
1420 PRINT:INPUT "Would you like to make any changes (Y/N)";ANS$
1430 IF ANS$="Y" OR ANS$="y" THEN GOSUB 1500
1440 RETURN
1500 REM ************************************************************
1510 REM                      EDIT THE ARRAY
1520 REM ************************************************************
1530 PRINT:PRINT "The shades of white to black correspond to numbers 0-4"
1540 PRINT "  0 = white"
1550 PRINT "  1 = black"
1560 PRINT "  2 = pale grey dots"
1570 PRINT "  3 = dark grey herringbone"
1580 PRINT "  4 = square dot in white"
1600 INPUT "Which row would you like to change";Q
1610 IF Q>Y THEN PRINT "This pattern has";Y;"rows. Try again":GOTO 1600
1620 PRINT "This row is:"
1630 FOR J=0 TO X-1: PRINT A(Q-1,J);: NEXT J
1640 PRINT :PRINT "Enter the corrected row":INPUT F$
1650 IF LEN(F$)>X THEN PRINT "Too long. Try again.": GOTO 1640
1660 FOR J=0 TO X-1
1670    A(Q-1,J)=VAL(MID$(F$,J+1,1))
1680    B(Q-1,J)=A(Q-1,J)
1690    IF W<A(Q-1,J) THEN W=A(Q-1,J)
1700 NEXT J
1710 GOSUB 1830
1720 PRINT :INPUT "Any more changes (Y/N)";ANS$
1730 IF ANS$="Y" OR ANS$="y" GOTO 1530
1740 RETURN
1800 REM ************************************************************
1810 REM                      PRINT THE ARRAY
1820 REM ************************************************************
1830 CLS                              'Print Array
1840 LOCATE 1,1
1850 FOR I=0 TO Y-1
1860    COLOR 0,7,6:PRINT
1870    FOR J=0 TO X-1
1880    IF A(I,J)=0 THEN PRINT CHR$(32);       'white (blank)
1890    IF A(I,J)=1 THEN PRINT CHR$(219);      'black
1900    IF A(I,J)=2 THEN PRINT CHR$(176);      'pale grey dot pattern
1910    IF A(I,J)=3 THEN PRINT CHR$(178);      'dark grey herringbone
1920    IF A(I,J)=>4 THEN PRINT CHR$(249);     'square dot in white
1930    NEXT J
1940 NEXT I
1950 COLOR 0,7,6
1960 RETURN
2000 REM  ************************************************************
2010 REM       *****  OPTION #1: WRAPPED VERSION  *********
2020 REM  ************************************************************
2030 RTCOUNT=0:FULLSTEPS=0: TIME$="00"
```

Can. J. Chem. Downloaded from www.nrcresearchpress.com by 176.9.209.113 on 09/07/12
For personal use only.

```
2040 RANDOMIZE TIMER: RTCOUNT=RTCOUNT+1     'Change counter
2050 I=INT(RND*Y)
2060 J=INT(RND*X)
2070 REM
2080 NBR1=INT(RND*6)
2090 FULLSTEPS=FULLSTEPS+1
2100 REM                                Find 1st neighbour's coordinates
2110 IF NBR1=5 THEN R=I:C=J-1
2120 IF NBR1=0 THEN R=I-1:C=J
2130 IF NBR1=1 THEN R=I-1:C=J+1
2140 IF NBR1=2 THEN R=I:  C=J+1
2150 IF NBR1=3 THEN R=I+1:C=J
2160 IF NBR1=4 THEN R=I+1:C=J-1
2170 REM                                 Wrap
2180 IF R<0 THEN R=Y-1
2190 IF R=Y THEN R=0
2200 IF C<0 THEN C=X-1
2210 IF C=X THEN C=0
2220 NBR2=NBR1+1                         'Find 2nd neighbour's coordinates
2230 IF NBR2=5 THEN S=I:D=J-1
2240 IF NBR2=6 THEN S=I-1:D=J
2250 IF NBR2=1 THEN S=I-1:D=J+1
2260 IF NBR2=2 THEN S=I:  D=J+1
2270 IF NBR2=3 THEN S=I+1:D=J
2280 IF NBR2=4 THEN S=I+1:D=J-1
2290 REM                                 Wrap for 2nd neighbour
2300 IF S<0 THEN S=Y-1
2310 IF S=Y THEN S=0
2320 IF D<0 THEN D=X-1
2330 IF D=X THEN D=0
2340 W$=INKEY$:IF W$=CHR$(27) THEN GOSUB 2900   'Interrupt for bulletin,etc
2350 IF FNMUD(FULLSTEPS,Z)=0 THEN GOSUB 1840
2360 IF A(S,D)<>A(R,C) GOTO 2050            'Neighbours not identical
2370 IF A(I,J)=A(R,C) GOTO 2050             'Cell,neighbour already same
2380 IF A(I,J)<>A(R,C) THEN TALLY2(A(I,J))=(TALLY2(A(I,J)))-1
2390 A(I,J)=A(R,C)
2400 TALLY2(A(I,J))=TALLY2(A(I,J))+1
2410 IF TALLY2(A(I,J))=X*Y  THEN GOTO 3100
2420 GOTO 2040                           'back through randomize
2500 REM  ************************************************************
2510 REM     ******* OPTION 2:  BOUNDARIES *******
2520 REM  ************************************************************
2530 RTCOUNT=0:FULLSTEPS=0:TIME$="00"
2540 RANDOMIZE TIMER: RTCOUNT=RTCOUNT+1
2550 I=INT(RND*Y)                        'Pick the cell
2560 J=INT(RND*X)
2570 REM
2580 NBR1=INT(RND*6)
2590 REM                                 Find neighbour's coordinates
2600 IF NBR1=5 THEN R=I:C=J-1
2610 IF NBR1=0 THEN R=I-1:C=J
2620 IF NBR1=1 THEN R=I-1:C=J+1
2630 IF NBR1=2 THEN R=I:  C=J+1
2640 IF NBR1=3 THEN R=I+1:C=J
2650 IF NBR1=4 THEN R=I+1:C=J-1
2660 REM                                  Get rid of non-existent neighbours
2670 IF R<0 OR R=Y THEN GOTO 2550
2680 IF C<0 OR C=X GOTO 2550
2690 NBR2=NBR1+1                         'Find neighbour #2
2700 IF NBR2=5 THEN S=I:D=J-1
2710 IF NBR2=6 THEN S=I-1:D=J
2720 IF NBR2=1 THEN S=I-1:D=J+1
2730 IF NBR2=2 THEN S=I:  D=J+1
2740 IF NBR2=3 THEN S=I+1:D=J
2750 IF NBR2=4 THEN S=I+1:D=J-1
2760 REM                                      Get rid of non-existent neighbours
2770 IF S<0 OR S=Y THEN GOTO 2550
2780 IF D<0 OR D=X GOTO 2550
2790 W$=INKEY$:IF W$=CHR$(27) THEN GOSUB 2900   'To pause
2800 FULLSTEPS=FULLSTEPS+1                      'Step counter
2810 IF FNMUD(FULLSTEPS,Z)=0 THEN GOSUB 1840
2820 IF A(S,D)<>A(R,C) GOTO 2550        'neighbour pair not identical
2830 IF A(I,J)=A(R,C) GOTO 2550         'cell and neighbour already same
2840 IF A(I,J)<>A(R,C) THEN TALLY2(A(I,J))=TALLY2(A(I,J))-1
2850 A(I,J)=A(R,C)
2860 TALLY2(A(I,J))=TALLY2(A(I,J)) +1
2870 IF TALLY2(A(I,J))=X*Y THEN GOTO 3100
2880 GOTO 2540              'back through randomize, counter for changes
2900 REM ************************************************************
2910 REM               ..... BULLETIN........
2920 REM ************************************************************
2930 GOSUB 1840
2940 LOCATE 20,1
2950 PRINT "BULLETIN! (Rules #";N;") Time=";TIME$;"  No.elements=";X*Y
2960 PRINT "No. steps=";FULLSTEPS;" No. changes=";RTCOUNT
2970 FOR K=0 TO W
2980 PRINT "The ";K;"'s have";TALLY2(K);", changed from ";TALLY1(K)
2990 NEXT K
3000 LOCATE 25,1:INPUT "Enter: 1=continue, 2=menu, 3=quit";WHICH
3010 IF WHICH=1 THEN GOSUB 1830:RETURN
3020 IF WHICH=2 THEN CLS: RETURN 610
3030 IF WHICH<1 OR WHICH>3 THEN LOCATE 24,1:PRINT "Try again":GOTO 3000
3040 CLS:LOCATE 10,10
3050 PRINT "   END OF GAME "
3060 PRINT :INPUT "Are you sure (Y/N)";ANS$
3070 IF ANS$<>"Y" AND ANS$<>"y" GOTO 3080 ELSE END
3080 CLS:WIDTH 80:COLOR 0,6,6:RETURN 250
3090 REM ************************************************************
3100 REM                    END OF GAME
3110 REM ************************************************************
3120 GOSUB 1840
3130 LOCATE 20,1:PRINT "END OF GAME!    (RULES #";N;")":BEEP
3140 FOR K=0 TO W
3150 PRINT "The ";K;"'s have";TALLY2(K);",changed from ";TALLY1(K)
3160 NEXT K
3170 PRINT "Number of Elements=";X*Y
3180 PRINT "Number of changes=";RTCOUNT;"Number of rounds=";FULLSTEPS
3190 PRINT "Elapsed time=";TIME$
3200 PRINT: INPUT "Would you like to play another game (Y/N)";ANS$
3210 IF ANS$="Y" OR ANS$="y" THEN GOTO 250 ELSE END
3220 REM************************************************************
3230 REM              ERROR-TRAPPING ROUTINE
3240 REM ************************************************************
3250 ERRNO=ERR:ELINE=ERL
3260 PRINT "The program has trapped error #";ERRNO;" in line #";ELINE
3270 STOP
```

Can. J. Chem. Downloaded from www.nrcresearchpress.com by 176.9.209.113 on 09/07/12
For personal use only.

Lattice and molecular dynamics

ALEC R. JANZEN[1] AND JOHN W. LEECH
Guelph–Waterloo Program for Graduate Work in Physics, Waterloo Campus, Waterloo, Ont., Canada N2L 3G1

Received September 2, 1987

This paper is dedicated to Professor J. A. Morrison

ALEC R. JANZEN, and JOHN W. LEECH. Can. J. Chem. **66**, 852 (1988).

A frequency analysis is made of a molecular dynamical (MD) simulation of crystalline CS_2. At 20 K the peak MD frequencies agree with those calculated using lattice dynamics (LD). However, they are not as dominant as might be expected. At 150 K the peak frequencies are generally not the LD ones. Experience with the Fermi–Pasta–Ulam linear chain problem suggests the reason may be obscuring of fundamental by combination frequencies in highly anharmonic situations.

ALEC R. JANZEN, et JOHN W. LEECH. Can. J. Chem. **66**, 852 (1988).

Utilisant une simulation de dynamique moléculaire (DM), on a efectué une analyse des fréquences du CS_2 cristallin. A 20 K, les fréquences principales en DM correspondant bien avec celles qui ont été calculées en utilisant la dynamique des réseaux (DR). Toutefois, elles ne sont pas aussi dominantes qu'ont aurait pu l'espérer. A 150 K, les fréquences principales ne sont généralement pas celles prévues par la DR. Une expérience avec le problème de la chaîne linéaire de Fermi–Pasta–Ulam suggère que ce résultat est peut être dû à l'obscurcissement de la fréquence fondamentale par des fréquences de combinaison dans des situations hautement inharmoniques.

[Traduit par la revue]

Can. J. Chem. Downloaded from www.nrcresearchpress.com by 176.9.209.113 on 09/07/12
For personal use only.

Introduction

Lattice and molecular dynamical investigations of crystalline solids both attempt to determine details of the vibrational behaviour of mathematical models of those solids. The two methods differ in approach and are limited in different ways. Most notably lattice dynamics (LD) cannot, except with great computational effort, deal with anharmonic details of the motion, and molecular dynamics (MD) can only take into consideration samples of extremely small size. Wisdom suggests treating them as complementary methods in which case it seems important to check their degree of overlap by determining what predictions are common to both. Surprisingly little effort seems to have been devoted to this task. The primary aim of the present investigation was to answer the question "do lattice and molecular dynamical methods predict the same basic frequencies of vibration?"

Crystalline CS_2 was chosen as the substance whose model properties were to be investigated. This is because satisfactory highly equilibrated LD models were available from previous work (1, 2). Specifically model VIII of ref. 1 was selected. This is a simple Lennard–Jones 12–6 model whose details are given in Table 2. As far as harmonic LD is concerned this model behaves essentially the same as a number of others assuming different Lennard–Jones potentials (e.g. IV, V, and VII of ref. 1). However, since our investigation began, model VIII of ref. 1 has been investigated by Impey and Klein (4) together with another model (I of ref. 1 but taken from work by Tildesley and Madden (5)) using the "new" molecular dynamics (NMD). Their finding was that model VIII was unstable and developed, in the course of an MD run, into a lattice of much lower symmetry. Their other model, indistinguishable from model VIII in its LD and conventional MD behaviour, persisted in the same lattice form but changed its lattice parameters by appreciable amounts. Our MD method was the conventional one and was unable to identify these properties since the sample was constrained as to lattice type and specific dimensions though the inclinations of the molecules with respect to the crystal axes were free to change.

[1]Present address: Physics Department, Brock University, St. Catharines, Ont., Canada L2S 3A1.

The MD model

CS_2 forms a face-centred orthorhombic crystal with two molecules per unit cell. The non-primitive orthorhombic cell containing 4 molecules is shown in Fig. 1 and its parameters appropriate to 0 and 150 K are given in Table 1. The melting point at atmospheric pressure is variously quoted as 161.7 (6) and 173 K (7). The parameters of the Lennard-Jones type potential functions taken from ref. 1 and used here are given in Table 2.

The simulated crystal consisted of 108 molecules in $3 \times 3 \times 3$ non-primitive unit cells. The use of periodic boundary conditions confined the wave vectors employed to those shown in Fig. 2. When evaluating the interaction of a given molecule i with its neighbour j only the periodic image closest to i is considered. This limits the range of interaction to a maximum of one half the smallest dimension of the simulated crystal. In our work the potential cut off was 7 Å.

In the MD simulations molecule positions were specified in terms of the cartesian coordinates of their centres of mass together with quaternion parameters representing orientation.

The numerical method employed was a Störmer-based one in which positions, velocities, and accelerations at the various steps are related by:

$$[1a] \quad x_{l+1} = x_l + hv_l + (h^2/12)(7a_l - a_{l-1})$$

$$[1b] \quad a_{l+1} = a[x_{l+1}, (l+1)h]$$

$$[1c] \quad v_{l+1} = v_l + (h/12)(5a_{l+1} + 8a_l - a_{l-1})$$

The time step length h was 2×10^{-14} s corresponding to 1/14 of the period of the highest expected frequency (3.65 THz).

The initial configuration of the molecules in the 20 K simulation was that of static equilibrium of the crystal except that (for reasons concerning equilibrium and discussed in ref. 1) the molecular orientation to the crystal y-axis was 45.6° and not the experimentally measured 48.2°. In ref. 1 a number of LD models were investigated and a general tendency to equilibrate at the new 45.6° inclination was discovered.

The molecules were assigned computer-generated random values of linear and angular momentum. These were constrained to (*a*) zero total linear momentum for the whole

Can. J. Chem. Downloaded from www.nrcresearchpress.com by 176.9.209.113 on 09/07/12
For personal use only.

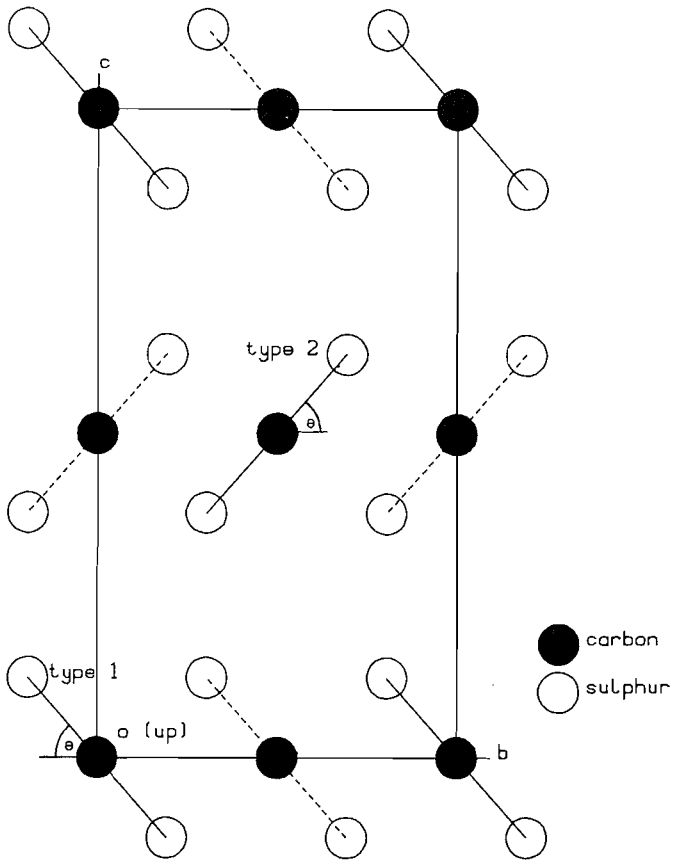

FIG. 1. Non-primitive orthorhombic unit cell for CS_2 containing 4 molecules. Solid molecules lie in yz plane, dashed ones at $\pm a/2$.

TABLE 1. Experimental data for CS_2 (ref. 3)

Parameter		Value 0 K	Value 150 K
Lattice parameters (Å)	a	6.086	6.4141
	b	5.286	5.5787
	c	9.463	8.8928
C—S bond length (Å)		1.546	1.529
Molecular orientation	θ	48.2°	43.2°

crystal,(b) zero angular momentum of the crystal about its centre of mass, (c) zero total spin angular momentum for each of the four types of molecule in the non-primitive unit cell, and (d) a total KE for each component of motion calculated to produce a temperature of approximately 20 K (it was actually found to be 18.6 K on equilibriation). The initial conditions represent a specialized state not conforming to a Boltzmann distribution.

The 150 K simulation configuration was that determined experimentally (3) and shown in Table 1.

Results for 20 K

An immediate consequence of the small size of the simulated crystal is the restriction of the normal modes of vibration to those corresponding to just 54 different wave vectors. Of these 16 form the irreducible set corresponding to distinct wave vectors. If LD and MD treatments overlap in the way expected the frequencies predicted by LD (approx. 16 × 10 in number)

TABLE 2. Potential parameters for CS_2 (ref. 1)

$$\phi_{XY} = A_{XY}r^{-12} - C_{XY}r^{-6} = \epsilon_{XY}\left[\left(\frac{\sigma_{XY}}{r}\right)^{12} - 2\left(\frac{\sigma_{XY}}{r}\right)^{6}\right]$$

XY	A_{XY} (kJ (gmol)$^{-1}$ Å^{12})	B_{XY} (kJ (gmol)$^{-1}$ Å^{6})	ϵ_{XY} (K)	σ_{XY} (Å)
CC	4.677×10^7	2.910×10^4	544	3.841
CS	1.122×10^7	1.040×10^4	290	3.595
SS	1.633×10^7	0.265×10^4	13	4.806

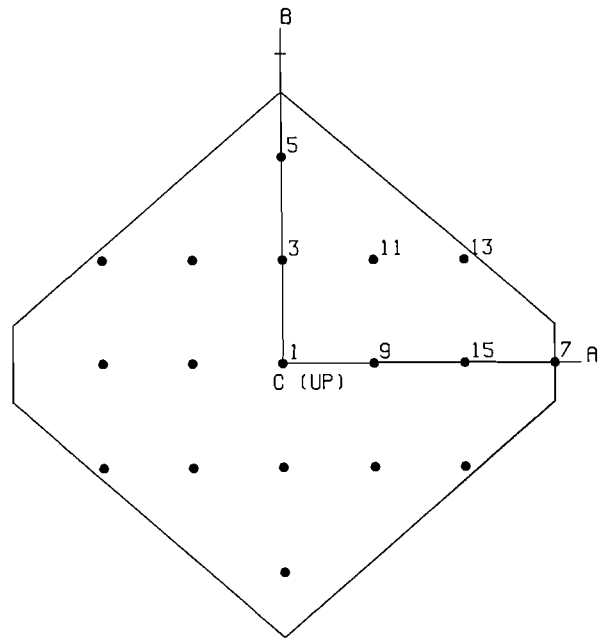

FIG. 2. Intersection of first Brillouin zone for CS_2 with xy plane. Solid dots are $\boldsymbol{k}$ vectors accessible to the simulation. Numbered dots are those belonging to the irreducible set. Further sets of 18 accessible points lie in the planes at $\pm c/3$.

should be the dominant ones present in the motions calculated by MD.

A selection of spectra obtained by discrete fourier transformation (DFT) of our MD results (8) corresponding to a temperature of approximately 20 K is shown in Fig. 3. The spectra represent the space–time DFT's of the x component of linear momentum. (Momentum was chosen as the quantity of interest, rather than the customary displacement, because linear momentum can be compared directly with angular momentum. In contrast it is difficult to identify an "angular displacement vector" to compare with its linear counterpart.) Superimposed are vertical lines representing the predicted LD frequencies (1). The correspondence between these vertical lines and principal features of the spectra is seen to be generally good though identification of the LD frequencies from the MD curves alone is sometimes difficult owing to the existence of other principal maxima. Higher frequency peaks are systematically somewhat greater than the corresponding LD frequencies according to the relation (9):

$$[2] \quad \omega' = (2/h)\sin^{-1}(h\omega/2)$$

between the actual frequency of a vibration (ω) and the value

Can. J. Chem. Downloaded from www.nrcresearchpress.com by 176.9.209.113 on 09/07/12
For personal use only.

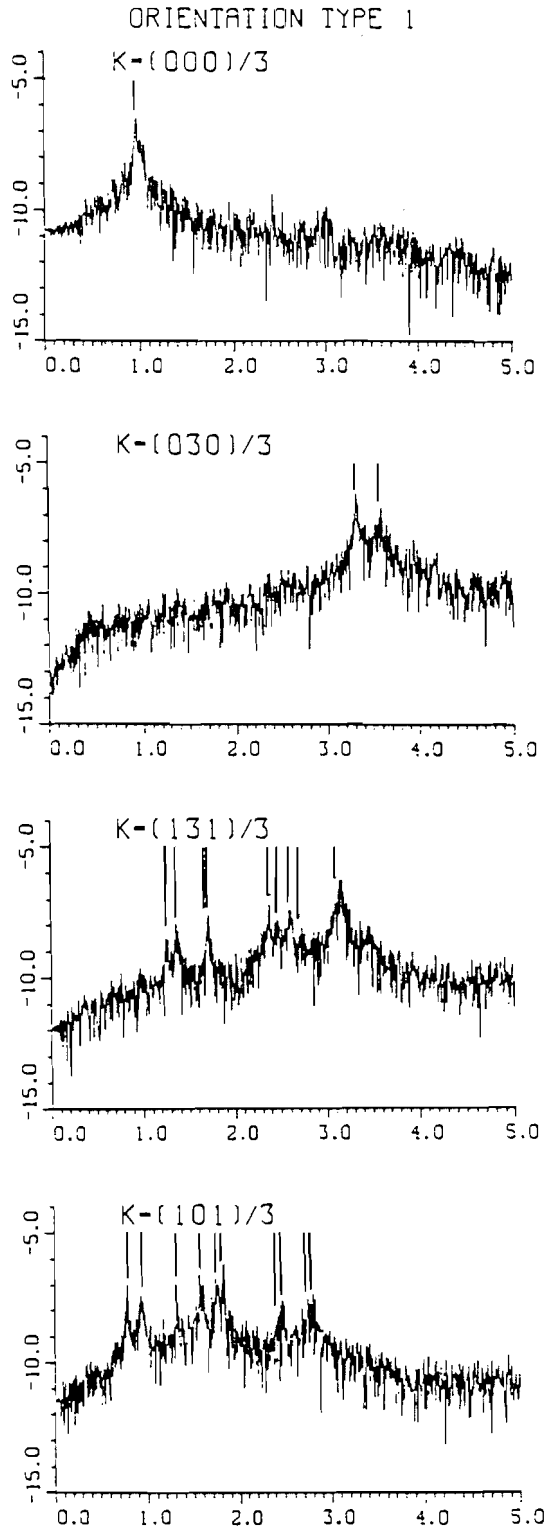

FIG. 3. Sample spectra for CS_2 at 20 K showing log (intensity) vs. frequency in THz for x component of linear momentum.

(ω') determined using a Störmer based-numerical method employing a calculational step length h. In the present case an actual frequency 3.46 THz would be determined as 3.50 THz.

A further correspondence with LD findings is that the CS_2 molecules appear to equilibriate at $45.7 \pm 2.1°$ with the crystal y axis in agreement with the LD values of 45.6°.

The MD spectra are perhaps surprising in that they do not show the LD frequencies dominating the other features as might be expected from the normal view that 20 K is a low temperature.

As a preliminary to the present investigation a simpler 1-D problem was considered. This is reported in ref. 9. The model there was a 16-particle Fermi–Pasta–Ulam (FPU) ring of identical particles interacting anharmonically through a potential function containing quadratic and cubic terms of the form:

$$[3] \quad E = \sum_{n=1}^{16} \dot{x}_n^2/2 + y_n^2/2 + y_n^3/3$$

where $y_n \equiv x_{n+1} - x_n$ and $x_{n+16} \equiv x_n$. The initial conditions consisted of a displacement only of the 16th particle. The amplitude of this displacement determined the degree of anharmonicity.

Spectra of the motion using space–time DFT's were obtained for each of 4 degrees of anharmonicity including zero. They each consisted of a principle maximum, only minutely different from the corresponding harmonic frequency, together with combination frequencies whose amplitudes increase with the degree of anharmonicity. Figure 4 (taken from Fig. 6 of ref. 9) shows a selection of spectra corresponding to the greatest degree of anharmonicity considered ($x_n(0) = 0.5 \times \delta_{16,n}$). The anharmonic structure is complex but it was shown that each feature corresponds to a distinct combination frequency and that the motion is reversible to 1 part in 10^{11} after 8 000 steps of calculation. This extreme reversibility can be traced to the use of what is essentially the Feynman algorithm in the calculation of velocities and displacements. Its consequence is that details of the motion are dependent upon initial conditions as well as upon details of the interaction potential.

The 3D MD runs simulating CS_2 are *not* reversible. There are two reasons for this: (*a*) the calculational algorithm used to determine the velocities is not reversible although that for the displacements is, (*b*) the use of quaternions in the simulation of the angular part of the motion involves a normalisation procedure at each step which also destroys reversibility. It follows that the motion is not strictly determinate as is that of the FPU ring though properties such as the interpretation of subsidiary structure of the spectra as combination frequency amplitudes must still be approximately valid.

Evidence for irreversibility lies in a slow decay with time of the energy of the assembly. This decay is almost entirely in the KE which reduces by 15 parts in 18 800 (i.e. ~0.1%) over 13 000 calculational steps.

The use of MD in simulating the properties of a thermodynamic system implies the hope that some form of irreversibility is present to the extent that thermal equilibrium is simulated though the commonly observed secular decay is unwelcome. It would thus be inappropriate to employ a completely reversible method but the identification of a suitable irreversible one is not obvious.

A measure of the approach to thermal equilibrium is through consideration of fluctuations. Using an obvious generalisation of the result obtained in ref. 10, the KE fluctuations in an "MD ensemble" in thermal equilibrium are given by:

$$[4] \quad (\delta K/K)^2 = 2/\nu N - k/C_V$$

where N is the number of particles each with ν degrees of freedom. For our ensemble assuming a harmonic solid the prediction is that $(\delta K/K)^2 = 1/540$. The observed value is 1/518. The difference could be explained by a C_V value of 574 K instead of the harmonic solid value of 540 K. However, this runs counter to the usual finding that anharmonicity lowers the value of the specific heat. An alternative explanation is that

Can. J. Chem. Downloaded from www.nrcresearchpress.com by 176.9.209.113 on 09/07/12
For personal use only.

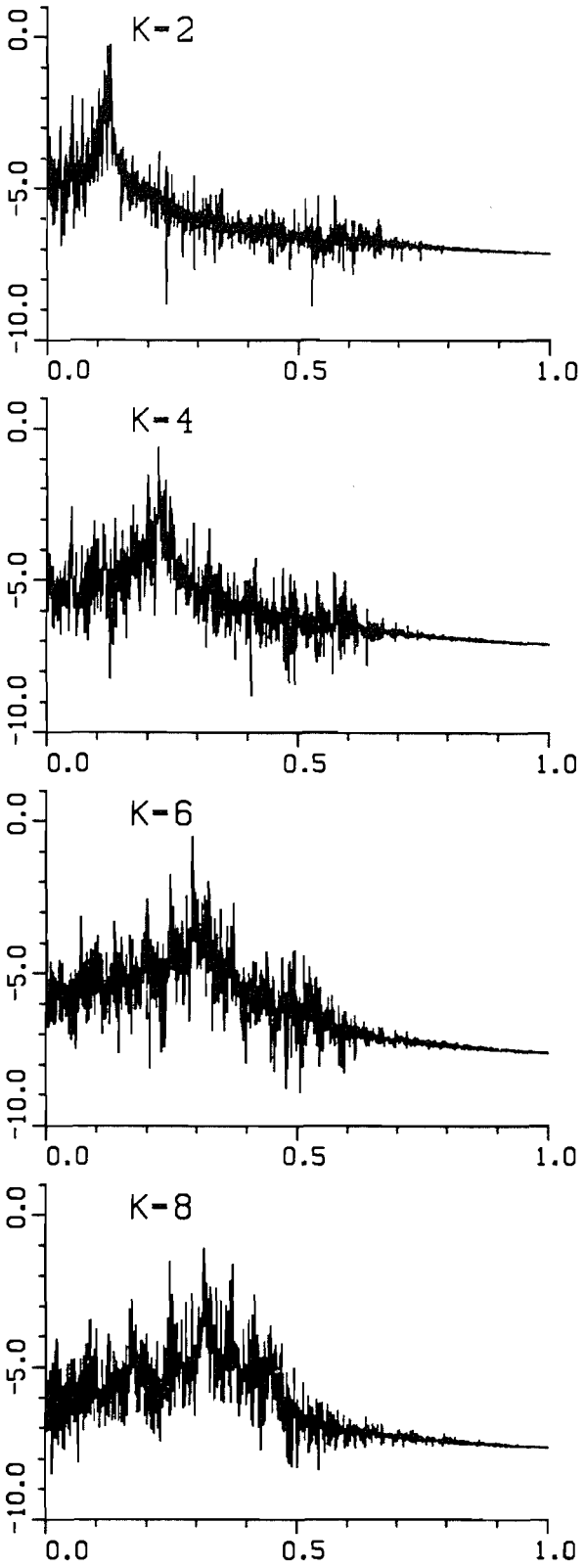

FIG. 4. Sample spectra for FPU linear chain with 16 members, showing log (intensity) vs. frequency for displacement.

fewer than 540 degrees of freedom are operative. This suggests that thermal equilibrium has not been completely attained.

A statistical analysis was made also of the KE fluctuations associated with various components of motion of individual molecules of the ensemble. Several averages over 1000 time steps of the KE associated with the T_x and R_x components of molecules numbers 1, 26, 51, and 76 were calculated. These averages each confirm the 18.8 K "temperature" of the ensemble. However, the individual values of $(\delta K/K)$ lie outside the 95% confidence limits of the value $\sqrt{2/1000}$ predicted by supposing thermal equilibrium in 25 of 40 cases. This may correspond with the motion being a correlated one approximating to a deterministic one consisting of normal modes together with the various possible sum and difference frequencies as was found with the FPU problem.

The conclusion concerning the 20 K simulation is that the motion is a complex correlated one in which the LD normal modes are observable but not dominant, and that it does not correspond to complete thermal equilibrium.

Results for 150 K

Figure 5 shows a selection of spectra relating to an MD run with mean KE corresponding to approximately 150 K. The curves have obvious broad maxima but only in a few cases, for instance $\boldsymbol{k} = (0, 0, 0)$, was there any obvious correlation with calculated LD frequencies.

As at 20 K the 150 K calculations were found not to be reversible even after as few as 20 calculational steps. A secular decrease of some 0.5% over 13 000 steps was found in the KE. Fluctuations in the KE were determined as at 20 K. The findings were that, for the whole sample, $(\delta K/K)^2 = 1/564$ consistent with all 540 degrees of freedom being operational and C_V being less than the harmonic value (by about 4%) as would be expected with anharmonic motion. Determination of the fluctuations for individual degrees of freedom over 1000 steps showed 17 cases of 40 investigated exceeding the 95% confidence limit again suggesting the existence of correlated motions.

The general conclusion concerning the 150 K MD calculations is that, except in two particulars, they are consistent with the behaviour of a simulated CS_2 crystalline sample in thermal equilibrium. The exceptions are the secular decay of amplitudes and the general lack of agreement between the broad but reasonably well defined peaks of the MD frequency curves for various wave numbers and the corresponding LD frequencies

The secular decay is an undesirable feature commonly met with in MD simulations. Since algorithm [1] is known to be drift-free when applied to a single anharmonic oscillator (11), we attribute this decay to quaternion normalisation. Normalisation introduces an irreversible error of the order of the truncation error ($O(h^4)$ in the case of algorithm [1]) at each step. This is many orders of magnitude above the level of double-precision roundoff, which might otherwise be blamed for the energy decay.

The frequency disagreement is not found in the single case of $\boldsymbol{k} = (0, 0, 0)$. Here the calculated LD and MD frequencies (at approximately 1.0, 2.0, and 2.3 THz) are in agreement. The 2.0 THz value is confirmed by neutron and optical methods (12, 13). The effects of anharmonicity are sometimes discussed in terms of frequency shifts and it is conceivable that the predicted LD frequencies are not good indications of those to be observed under the highly anharmonic conditions present at 150 K. There is, however, no obvious pattern to the shifts other than that the MD maxima are at larger frequencies than what appears to be their LD counterparts. There is also no universal correspondence between the numbers of MD maxima and the numbers of LD frequencies.

Further experimental observations using neutron diffraction and/or optical techniques could be helpful in deciding between the 2 sets of predictions but are unlikely to be made at the rather specialized wave-vectors in question. Incomplete neutron dif-

Can. J. Chem. Downloaded from www.nrcresearchpress.com by 176.9.209.113 on 09/07/12
For personal use only.

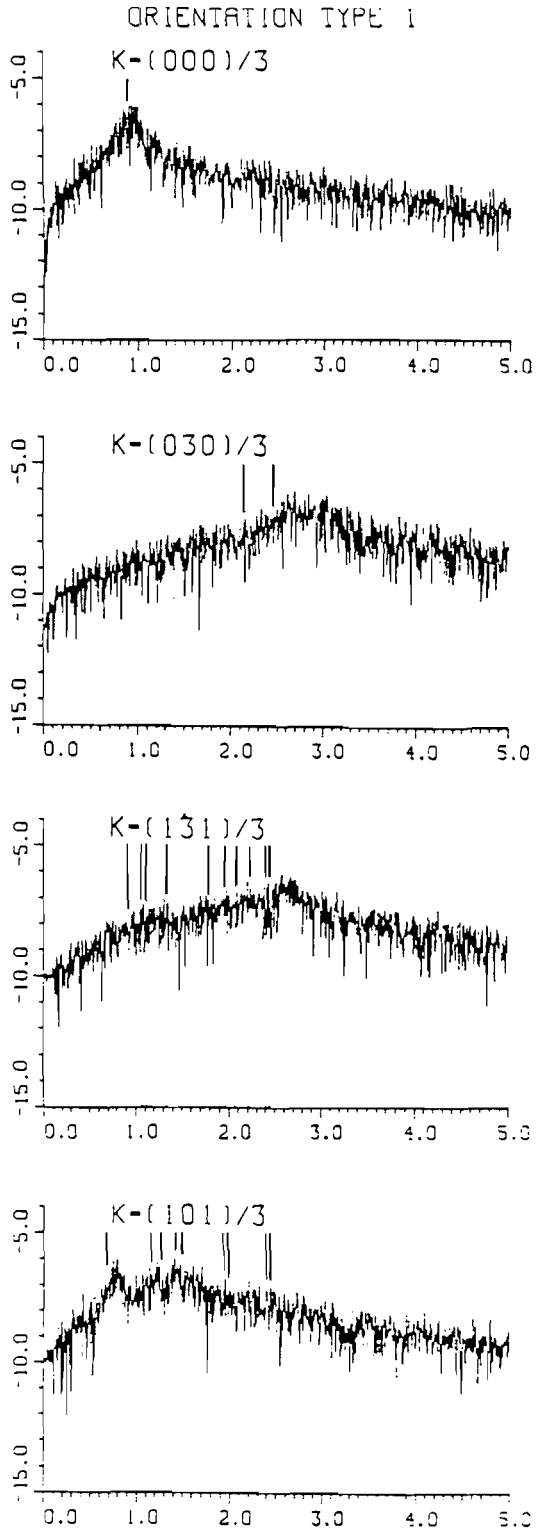

FIG. 5. Sample spectra for CS_2 at 150 K showing log (intensity) vs. frequency in THz for x component of linear momentum.

fraction evidence (12) concerning the point $k = (0, 1, 0)$ seems to favour the LD rather than the MD predictions.

Analogy with the FPU problem findings suggests regarding all the detailed structure of the 3D CS_2 frequency curves as combination frequency amplitudes. The observed growth of structure in the FPU case indicates this may ultimately dominate the normal modes thus giving rise to effectively shifted frequencies. In this way the dominant details of the spectra would be determined by incidental (anharmonic) features of potential functions designed merely to reproduce the original normal mode frequencies and disagreement with observable spectra would not be surprising.

Conclusion

Investigation of an MD model for crystalline CS_2 at 20 K shows good agreement with LD investigation of the same model though some degrees of freedom appear to be inoperative and the LD frequencies do not seem as dominant as might be expected.

The same model at 150 K agrees with LD predictions at $k = (0, 0, 0)$. Predicted broad maximum frequencies for other points in k-space are in disagreement with LD ones but little experimental evidence is available as a check. Previous investigation of the FPU linear chain suggests that combination frequency amplitudes have increased to the extent that they dominate the harmonic ones. The net effect is an apparent shifting of the harmonic frequencies. Since, however, the degree of apparent shift depends upon the anharmonic details of potential functions which are designed merely to reproduce the low temperature harmonic frequencies there is no guarantee that the predicted shifts are correct. The meager evidence available suggests otherwise.

Acknowledgements

The financial support of the Natural Sciences and Engineering Research Council of Canada is gratefully acknowledged.

One of us (J.W.L.) wishes to confess to a long term feeling of respect and gratitude for past help and inspiration from discussion with the one to whom this special issue is dedicated. He's a braw lad is our Jim!

1. P. J. GROUT and J. W. LEECH. Mol. Phys. **45**, 51 (1982).
2. P. J. GROUT and J. W. LEECH. J. Phys. C: Solid State Phys. **15**, L 1083 (1982).
3. B. M. POWELL, G. DOLLING, and B. H. TORRIE. Acta Crystallogr. B**38**, 28 (1982).
4. R. W. IMPEY and M. L. KLEIN. Chem. Phys. Lett. **103**, 143 (1983).
5. D. J. TILDESLEY and P. J. MADDEN. Mol. Phys. **42**, 1137 (1981).
6. R. C. WEAST (*Editor*). CRC handbook of chemistry and physics. 66th ed. CRC Press. 1985. p. C-196.
7. C. E. WEIR, G. J. PIERMARINI, and S. BLOCK. J. Chem. Phys. **50**, 2089 (1969).
8. A. R. JANZEN. Ph.D. Thesis, University of Waterloo, Waterloo, Ont., Canada. 1986.
9. J. W. LEECH and A. R. JANZEN. Can. J. Phys. **65**, 492 (1987).
10. J. L. LEBOWITZ, J. K. PERCUS, and L. VERLET. Phys. Rev. **153**, 250 (1967).
11. A. R. JANZEN and J. W. LEECH. Comput. Phys. Commun. **32**, 349 (1984).
12. B. M. POWELL, G. DOLLING, B. H. TORRIE, and G. S. PAWLEY. J. Phys. C: Solid State Phys. **15**, 4265 (1982).
13. A. ANDERSON, P. J. GROUT, J. W. LEECH, and T. S. SUN. Chem. Phys. Lett. **21**, 9 (1973).

Infrared multiphoton absorption and decomposition of ethanol vapour[1]

R. A. BACK

Photochemistry Section, Division of Chemistry, National Research Council of Canada, 100 Sussex Drive, Ottawa, Ont., Canada K1A 0R6

AND

D. K. EVANS, ROBERT D. MCALPINE, E. M. VERPOORTE,[2] MIKE IVANCO, J. W. GOODALE, AND H. M. ADAMS[3]

Atomic Energy of Canada Limited, Physical Chemistry Branch, Chalk River Nuclear Laboratories, Chalk River, Ont., Canada K0J 1P0

Received September 23, 1987

This paper is dedicated to Professor James A. Morrison

R. A. BACK, D. K. EVANS, ROBERT D. MCALPINE, E. M. VERPOORTE, MIKE IVANCO, J. W. GOODALE, and H. M. ADAMS. Can. J. Chem. **66**, 857 (1988).

Multiphoton absorption (MPA) by ethanol has been studied using pulsed HF and CO_2 lasers. For the same laser fluence, a CO_2 laser excites the ethanol molecule to a much higher energy than an HF laser. The multiphoton decomposition (MPD) of methanol has been studied using the $9P(16)$ CO_2 laser line for pulse widths of 10 and 60 ns. The major decomposition channel produces C_2H_4 and H_2O. However, other decomposition channels, resulting in the products CH_3CHO, C_2H_6, CH_4, and C_2H_2, are also studied and the channel ratios are found to vary with laser pulse width and with pressure. The mechanistic implications of these results are discussed.

R. A. BACK, D. K. EVANS, ROBERT D. MCALPINE, E. M. VERPOORTE, MIKE IVANCO, J. W. GOODALE et H. M. ADAMS. Can. J. Chem. **66**, 857 (1988).

Utilisant des lasers pulsés au HF et au CO_2, on a étudié l'absorption multiphotonique (AMP) de l'éthanol. Pour un même flux de laser, un laser au CO_2 excite la molécule d'éthanol à un plus haut niveau d'énergie qu'un laser au HF. Utilisant la raie $9(P)16$ du laser au CO_2 avec des largeurs de pulsation de 10 et de 60 ns, on a étudié la décomposition multiphotonique (DMP) du méthanol. Le chemin principal de décomposition conduit principalement à du C_2H_4 et à du H_2O. Toutefois, on a aussi étudié d'autres voies de décomposition conduisant au CH_3CHO, au C_2H_6, au CH_4 et au C_2H_2 et on a trouvé que les rapports des diverses voies varient avec la longeur de la pulsation du laser et avec la pression. On discute des implications mécanistiques de ces résultats.

[Traduit par la revue]

1. Introduction

A series of molecules, ROH, has proven to be very useful for studying Multiphoton Absorption (MPA) and Decomposition (MPD) (1, 2). The highly anharmonic -OH stretch mode can be pumped by an HF laser, and the weakly anharmonic -CO stretch mode by a CO_2 laser. For methanol, pumping into the -CO stretch mode rather than the -OH mode reduces the fluence needed to achieve MPD by about a factor of 100. The anharmonicity bottlenecking for pumping of the -OH stretch mode by an HF laser can be reduced in two ways: (*a*) R can be chosen to have a large density of states. For example, the fluence required to achieve collisionless HF laser-induced MPD of methanol (R = CH_3) is about 30 000 J/cm^2 compared to 800 J/cm^2 for ethanol (R = CH_3CH_2). (*b*) Collisions dramatically reduce the fluence required to achieve MPD. Effect (*a*) is greatest for molecules such as methanol having relatively low densities of states. Consequently, comparison studies of MPA and MPD of methanol and ethanol provide insight into the MPD process. Previously, we studied the MPA and MPD of methanol. Here we report a comprehensive study of the MPA and MPD of ethanol.

The first part of the present paper reports MPA results for ethanol with both HF and CO_2 lasers. The MPD of ethanol vapour was first studied by Selwyn, Back, and Willis (1) in 1978, using a pulsed HF laser at a wavelength of 2.744 μm. Danen (2), in a brief study with a pulsed CO_2 laser, showed by experiments with ethanol–propanol mixtures that the decomposition at pressures less than 0.13 kPa was selective, and thus involved unimolecular decomposition of isolated molecules, while more detailed experiments by Gandini and Back (3) with a CO_2 laser showed some significant differences from the earlier HF laser study. Interest in the system has continued, with results reported from China (4), Japan (5), Brazil (6), USSR (7, 8), and England (9),[4] mostly using pulsed CO_2 lasers, but with two further HF laser studies (8, 9).[4]

Previous studies have discussed the pyrolysis and the MPD of ethanol in terms of the following primary processes:

[1] $CH_3CH_2OH \rightarrow CH_2CH_2 + H_2O$

[2] $\rightarrow CH_3 + CH_2OH$

[3] $\rightarrow CH_3CHO + H_2$

[4] $\rightarrow CH_4 + CH_2O$

[5] $\rightarrow CH_3CH_2 + OH$

There is no direct evidence about the energy barriers for any of these reactions. However, barriers for [1], [3], and [4] are expected to be sizeable, while those for [2] and [5] will be close to the strength of the bond that is broken. For all of the MPD studies previously performed, and also for those to be reported here, the major reaction under all conditions is dehydration, reaction [1]. However, at high fluences or high pressures of ethanol, reactions [3] and [5], and several other processes, also

[1]NRCC No. 28374 and AECL No. 9710.

[2]Present address: Department of Chemistry, University of Alberta, Edmonton, Alberta.

[3]Present address: Surface Science Western, University of Western Ontario, London, Ontario.

[4]Also, G. Oldershaw, private communication.

Can. J. Chem. Downloaded from www.nrcresearchpress.com by 176.9.209.113 on 09/07/12
For personal use only.

Can. J. Chem. Downloaded from www.nrcresearchpress.com by 176.9.209.113 on 09/07/12
For personal use only.

occur. The results of the MPD studies differ from those of the pyrolysis studies in that channel [1] is the predominant primary channel for MPD but free radical chain mechanisms yielding CH_3CHO and H_2 (11) dominate for thermal decomposition. Unimolecular dehydration has been observed in the pyrolysis of several alcohols (10), but not in ethanol. Danen (2) estimates E_1 = 297 kJ/mol, while Tsang (12) estimated Arrhenius parameters $A_1 = 10^{14}\ s^{-1}$ and E_1 = 320 kJ/mol, based on an analogy between the alcohols and alkyl chlorides. In a recent *ab initio* calculation, Yamabe *et al.* (13) concluded that reaction [1] was the lowest energy path for the decomposition of ethanol, with $A_1 = 1.7 \times 10^{14}\ s^{-1}$ and E_1 = 298 kJ/mol. There is less information about reaction [3], with only the calculations of ref. 13, which yielded values of $A_3 = 3.1 \times 10^{14}\ s^{-1}$ and E_3 = 469 kJ/mol. There is no information at all about reaction [4]. Three chemical activation studies produced C_2H_5OH in vibrationally excited states and the subsequent decomposition of these provides insight into the decomposition channels of ethanol. The first of these studies involves the insertion of $O(^1D)$ atoms into a C—H bond of C_2H_6 to give C_2H_5OH with excess vibrational energy of about 607 kJ/mol, and studies in several laboratories (14, 15) found products that could be entirely accounted for by the reactions of free radicals resulting from channels [2] and [5]. Tsang (12) compared these results with theoretical calculations that predicted rate constants for reactions [1], [2], and [5] of 2.5×10^9, 55×10^9, and $26 \times 10^9\ s^{-1}$ respectively for molecules of this energy. With "strong collision" deactivation, decomposition of partially relaxed ethanol molecules of reduced energy would have been minimal; the expected occurrence of 3% of reaction [1] would not have been easily detected, especially as C_2H_4 could also be formed by disproportionation of ethyl radicals from reaction [5]. Thus chemically activated ethanol created by reaction of $O(^1D)$ with C_2H_6 is not well suited to give information about reaction [4] (or other molecular dissociations), which cannot compete with reactions [2] and [5] because of the much lower frequency factors of the molecular channels. The second chemical activation system, the reaction of $CH_2(^1A_1)$ with CH_3OH, is complicated by insertion of CH_2 into both C—H and O—H bonds, with the latter yielding predominantly CH_3OCH_3 (16, 17).[5] The C_2H_5OH formed by insertion in the C—H bond had an excess vibrational energy of 418 kJ/mol, but at the lowest pressure employed (0.17 kPa) was apparently completely stabilized; no C_2H_4 formation was reported. Studies at lower pressures would be desirable, as the relatively low energy would favour observation of reaction [1], but this may present some experimental difficulties. Finally, the third system, which was actually not interpreted as involving chemical activation, may offer some evidence for the occurrence of reactions [1], [3], and [4]. The reaction of H atoms with C_2H_5OH in a flow-discharge system at pressures of 0.27–2.0 kPa gives C_2H_4, H_2O, CH_3CHO, CH_4, and C_2H_6 as important products (18). While these were explained by the authors by a sequence of abstraction reactions, it seems possible that the sequence:

[6] $H + C_2H_5OH \rightarrow C_2H_4OH + H_2$

[7] $H + C_2H_4OH \rightarrow C_2H_5OH^* \rightarrow$ Products

could account for the products observed, especially the C_2H_4, although the authors argued against it (18). This chemical activation system merits further exploration, especially as the low-energy channel, reaction [1], would be favoured and also perhaps reactions [3] and [4] would be favoured relative to reactions [2] and [5], for which the energy of $C_2H_5OH^*$ would be close to threshold.

The dependence of the relative rates of these primary processes on pressure and fluence is not yet fully understood, nor is the difference between the results with HF and CO_2 lasers. The present measurements of absorption and decomposition using a short-pulse (10 and 60 ns) CO_2 laser, in which there are effectively no collisions during the pulse, were undertaken to explore the pressure and fluence dependence under these conditions, to separate the effects of collisions on the absorption and the decomposition, and to distinguish between the effects of fluence and intensity.

2. Experimental

The ethanol used was prepared as follows. A 15-g sample of 4A molecular sieve was activated by heating at 550°C for 1 h. After the molecular sieve was cooled to room temperature, 50 mL of anhydrous alcohol was added slowly. This sample was stored in a sealed vessel for several weeks and the water content was determined by a Karl–Fischer titration to be less than 0.05% by weight. Small aliquots were transferred on a glass vacuum line equipped with greaseless stopcocks for use in MPA experiments. The samples were regularly degassed by repeatedly freezing in liquid nitrogen and pumping.

Both the HF and CO_2 lasers have been described elsewhere (19, 21). MPA photoacoustic results and the corresponding calibrations by transmission were recorded on a microcomputer-based data acquisition system (22). In the transmission experiments cells of 31.9, 88.9, and 300.2 cm length equipped with NaCl windows were used for the HF laser experiments and the 88.9-cm cell was used with the CO_2 laser. The results were analyzed as previously described (22). Cells used for the MPD experiments were made from 22 mm inside diameter Pyrex tubing, 10 cm long. NaCl windows were fitted to the ends at about a 5 degree angle (to prevent reflections back into the lasers). The laser beam was focussed at the centre of the cells using BaF_2 lenses of focal lengths 50 or 100 cm with the fluence at each pulse length adjusted using calibrated CaF_2 filters. Analysis of products and ethanol depletion was done on a Hewlett–Packard 5700A gas chromatograph with flame ionization detection. The Poropak T-18 column, 3 mm diameter × 2.44 m length stainless steel, was held at 60°C for 4 min and then heated at 16 degrees per minute to 140°C and held at that temperature. Calibrations of peak areas were obtained from authentic samples and checked frequently.

3. Results and discussion

3.1 HF laser MPA of ethanol

The results of both the transmission measurements and the calibrated photoacoustic measurements with HF laser irradiation are summarized in Table 1. The uncertainties quoted are for 95% confidence intervals for the linear least-squares fits. These indicate the precision of the measurements but, for the photoacoustic results, uncertainties in the calibration give an accuracy of about a factor of 2 in reported excitation. For HF laser measurements, the fluence available for transmission measurements is low and these results do not overlap with the photoacoustic results. A sample measurement at 400 Pa is shown in Fig. 1. At higher pressures the gap between transmission and photoacoustic results decreases, while it increases at lower pressures.

The HF laser $P_1(7)$ photons at 3644.16 cm^{-1} are absorbed by the OH stretching mode, a rather weak absorption feature in the infrared spectrum of ethanol (23). The excitation, given as $\langle n \rangle$, the average number of photons absorbed per molecule, showed no measurable dependence on the pressure of ethanol. Measurements of other molecules such as CDF_3 (24, 25), CH_3OH (26), and cyclobutanone (27) showed a first-order relaxation as $P\tau$,

[5] Also, H. M. Frey, private communication.

TABLE 1. Absorption of HF and CO_2 laser radiation by C_2H_5OH. The observations have been fitted to the form $\log \langle n \rangle = a + b \log \phi$. The fluence, ϕ, is the fluence at beam center (24)

(a) HF laser, $P_1(7)$ line

	Pressure (kPa)	a	b
(i) Transmission	0.027	−1.19 ±0.13	0.769 ±0.053
	0.167	−0.85 ±0.04	0.972 ±0.015
	0.400	−0.938±0.03	0.9316±0.014
	0.667	−0.836±0.41	0.979 ±0.017
	1.000	−0.841±0.02	0.984 ±0.009
	1.333	−0.862±0.02	0.977 ±0.007
	2.000	−0.920±0.04	0.955 ±0.016
	2.667	−0.819±0.03	0.983 ±0.011
	5.333	−0.831±0.01	0.992 ±0.006
(ii) Photoacoustic	0.027	−0.989±0.13	1.018 ±0.102
	0.167	−0.710±0.01	0.052 ±0.011
	0.400	−0.729±0.01	0.048 ±0.007
	0.667	−0.724±0.01	0.037 ±0.009
	1.000	−0.743±0.01	0.055 ±0.009
	1.333	−0.792±0.02	0.997 ±0.016
	2.000	−0.773±0.01	1.029 ±0.008
	2.667	−0.698±0.01	1.051 ±0.006
	5.333	−0.747±0.007	1.048 ±0.007

(b) CO_2 laser, $9P(16)$ line

	Pressure (kPa)	Pulse length (ns)	Fluence range (J/cm^2)	a	b
(i) Transmission	0.027	10		−0.095±0.41	0.767±0.281
	0.67	10		−0.104±0.04	0.775±0.025
	0.133	10		−0.149±0.03	0.888±0.021
	0.027	60		−0.212±0.08	0.714±0.041
	0.67	60		−0.139±0.01	0.827±0.008
	0.133	60		−0.280±0.01	0.862±0.003
(ii) Photoacoustic	0.027	10	<4	−0.106±0.03	0.944±0.100
			>4	−0.395±0.03	0.501±0.022
	0.067	10	<4	−0.123±0.02	0.737±0.067
			>4	−0.397±0.02	0.496±0.014
	0.133	10	<4	−0.329±0.01	1.003±0.026
			>4	−0.605±0.02	0.512±0.012
	0.027	60	<4	−0.106±0.01	0.955±0.020
			>4	−0.344±0.06	0.549±0.051
	0.067	60	<4	−0.204±0.02	0.792±0.056
			>4	−0.453±0.02	0.464±0.015
	0.133	60	<4	−0.336±0.03	0.947±0.076
			>4	−0.628±0.03	0.473±0.024

the product of pressure and laser pulse duration, increased. This was interpreted as rotational relaxation giving access to a larger fraction of the molecules. For the experiments reported here, the smallest $P\tau$ product was 8000 Pa ns whereas the other systems mentioned were seen to be essentially fully relaxed at a $P\tau$ of 4000–8000 Pa ns. Presumably, if it had been possible to use lower pressures than 27 Pa, a pattern similar to that of the other molecules might have been observed. In section 3.2, a test of this hypothesis for a different excitation mode using the shorter CO_2 laser pulses is reported.

Previous work (28) on the MPA of HF laser photons by ethanol was not calibrated by transmission; the response of the microphone was taken to be the same for all the alcohols studied and calibrations were performed only with methanol. The present experiments show that the microphone response varies less with pressure in ethanol than in methanol. The pressure dependence previously reported is not seen when separate calibration experiments with ethanol are done; however, the behaviour with changing fluence is the same. For fluences above about 1 J/cm^2, the slope of $\log \langle n \rangle$ against log fluence is greater than one, indicating that molecules, once excited, are excited further more easily than in the ground state.

Can. J. Chem. Downloaded from www.nrcresearchpress.com by 176.9.209.113 on 09/07/12
For personal use only.

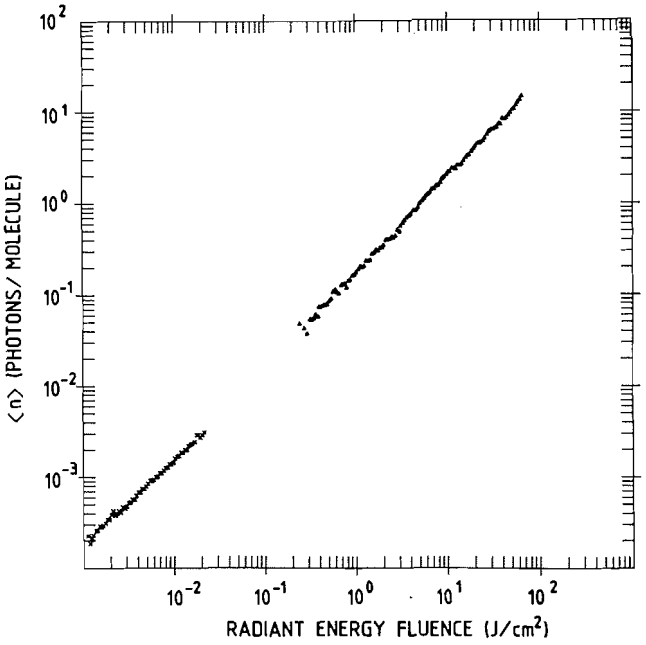

FIG. 1. The MPA of the HF laser $P_1(7)$ line by 0.4 kPa ethanol using a pulse of width 300 ns. The transmission results (×) are extrapolated from the low fluence range to the higher fluences of the photoacoustic results (△) and are used for calibration of the latter.

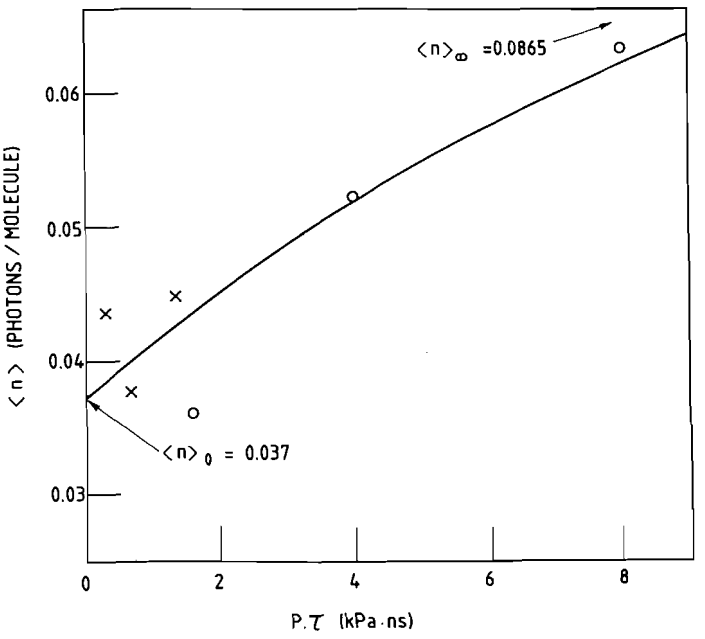

FIG. 2. The dependence of $\langle n\rangle(\phi)$ on $P\tau$ (where P is ethanol pressure and τ is laser pulse duration) for MPA of the CO_2 9P(16) laser line by ethanol. (×) τ = 10 ns, (○) τ = 60 ns. The fluence, ϕ, is the fluence at beam centre (24).

3.2 CO_2 laser MPA of ethanol

Measurements with smooth CO_2 laser pulses of 10 and 60 ns FWHM were made at low pressures to investigate the region of pressure pulse width below 8000 Pa ns, the lowest accessible with the present HF laser. The results are summarized in Table 1. An increase in excitation with increasing $P\tau$ was observed for the region studied. The results at each value of $P\tau$, for a fluence at beam centre of 0.02 J/cm^2, were fitted to eq. [8] characteristic of the relaxation model used with other molecules (24, 27)

$$[8]\quad \langle n\rangle(P\tau) = \langle n\rangle_\infty + (\langle n\rangle_0 - \langle n\rangle_\infty)\exp[-kP\tau]$$

Values of $\langle n\rangle_0$, $\langle n\rangle_\infty$, and k were found to be 0.037, 0.0865, and 8.9 × 10^{-5} Pa^{-1} ns^{-1}, respectively. Figure 2 shows the results at 0.02 J/cm^2 and the curve for the relaxation model. For CO_2 laser excitation, rotational relaxation of ethanol occurs at a rate comparable to other molecules. At 8000 Pa ns, the excitation has reached over 75% of its asymptotic value. The lack of pressure dependence with HF laser irradiation is consistent with this relaxation time.

For each pressure and pulse width, the CO_2 laser excitation of ethanol showed a bend in the plot of log $\langle n\rangle$ vs. log fluence at about 4 J/cm^2. At these fluences, a pressure rise was observed in the microphone cell, which was attributed to decomposition of the ethanol. The ethanol was replaced frequently to ensure the concentration did not change. Separate decomposition experiments showed measurable decomposition at these fluences. Thus we cannot determine from these experiments whether the observed bend is caused by some bottleneck to further absorption or whether some of the absorbed energy is being used for chemistry and therefore is not contributing to the pressure pulse measured by the microphone.

3.3 Comparison of HF and CO_2 laser excitation

For this comparison, we cannot simply look at $\langle n\rangle$, since the HF photons used are 3.5 times as energetic as the CO_2 photons. Thus we have multiplied $\langle n\rangle$ for the HF laser by 3.5 to compare the average energy of excitation of the ethanol molecules by each laser. Figure 3 shows such a comparison for the photoacoustic measurements at 27 Pa using the HF laser, with data for the CO_2 laser at two pulse lengths. The CO_2 laser results are independent of laser pulse length indicating no dependence on intensity or bandwidth. (The relative bandwidths of the CO_2 laser pulses has been determined by measuring the collisionless MPA of SF_6. This is described elsewhere (29).) The average level of excitation of an ethanol molecule is about an order of magnitude lower for an HF laser than for a CO_2 laser at the same fluence. At fluences high enough for decomposition to occur, the difference in the photoacoustic signal is not so large, but this might be a consequence of the type of measurement and not a true difference in the behaviour of the molecule. Any effect of the larger $P\tau$ for the HF laser would decrease the difference in excitation.

The lowest pressure used for the HF laser, 27 Pa, is still sufficiently high to allow access to most of the molecules by rotational hole filling. The complementary measurements with the CO_2 laser support this interpretation. At low pressures, we found that excitation of ethanol is at least a factor of 3 easier using a CO_2 laser than with an HF laser. Even though 3.5 times as many photons must be absorbed, the larger cross section at the CO_2 laser frequency more than compensates. The cross section at 3644 cm^{-1} increases slightly with the level of excitation, as determined in earlier work. Ethanol is an example of a large molecule with several vibrational modes that can be excited, and it is probably the strength of the absorption, rather than the magnitude of the vibrational quanta, that determines the easiest way to excite the molecule.

3.4 MPD studies

3.4.1 Reaction products

As in previous MPD studies, the major product under all conditions was C_2H_4 (54–99%), presumably accompanied by

Can. J. Chem. Downloaded from www.nrcresearchpress.com by 176.9.209.113 on 09/07/12
For personal use only.

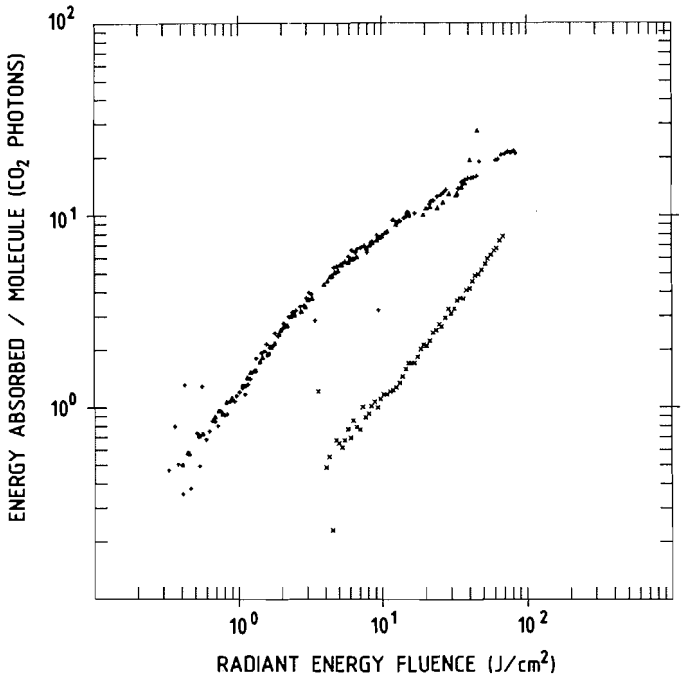

FIG. 3. A comparison of the excitation levels reached pumping ethanol with either an HF or a CO_2 laser. To compare energies of excitation, $\langle n \rangle$ for the HF laser has been multiplied by 3.5 and is still lower than the CO_2 laser excitation of the same fluence. CO_2 laser; (△) τ = 10 ns, (+) τ = 60 ns. HF laser: (×) τ = 300 ns.

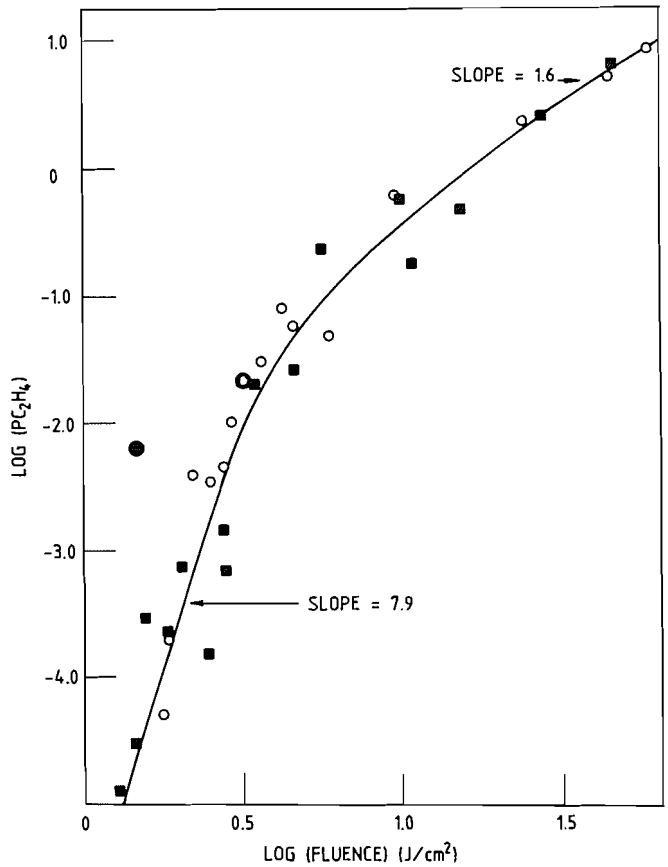

FIG. 4. The probability of decomposition of C_2H_5OH to form C_2H_4 versus laser fluence for the CO_2 laser, $9P(16)$ line. (■) τ = 60 ns, (○) τ = 10 ns and (●) is an average for 6 experiments.

H_2O, which was not measured. Minor products in approximately diminishing order of importance were CH_3CHO, C_2H_6, CH_4, C_2H_2, and C_3H_6, while even smaller yields of ethylene oxide, propane, and several other C_3 and C_4 hydrocarbons were detected but were not measured systematically. Product yields, expressed as partial pressures generated per pulse in the reaction vessel, are given in Table 2 for a variety of experimental conditions. Also given are the ratios of the minor products to C_2H_4, and values of $P_{C_2H_4}$, the probability of decomposition to form C_2H_4 in a single pulse for a molecule of C_2H_5OH in the reaction zone. The latter was taken to be the central cylindrical portion of the focussed beam with dimensions given by radius = $0.5f\theta$, and length = 2(radius × f)/R, where f = focal length of lens, θ = divergence in radians, and R = radius of unfocussed beam. Reaction volumes thus obtained were 0.331 and 0.021 cm^3 for f = 100 and 50 cm respectively. Values of $P_{C_2H_4}$ were approximately corrected for depletion of C_2H_5OH in the reaction vessel over the course of multipulse experiments, taking C_2H_4 formation as a rough measure of depletion (ignoring other products). No correction was made for depletion in the reaction zone during a single pulse, and complete renewal between pulses of the reagent in the reaction zone from the bulk of the reaction vessel was assumed.

3.4.2 Dependence on fluence and intensity

Figure 4 shows the dependence of $P_{C_2H_4}$ on fluence at constant pressure of 0.13 kPa for two pulse lengths, 10 and 60 ns, for the CO_2 laser $9P(16)$ line. A strong dependence is seen at low fluence, with the slope of the log–log plot about 8. The dependence becomes less at high fluence as $P_{C_2H_4}$ approaches unity, corresponding to decomposition of all the molecules in the reaction zone in a single pulse. At the highest fluence, above about 20 J/cm^2, values of $P_{C_2H_4}$ exceed unity, indicating decomposition outside the central cylindrical zone; this is confirmed by the final slope of 1.6, close to the value of 1.5 expected for this situation (30). Within the experimental scatter, values of $P_{C_2H_4}$ appear to be independent of pulse duration, and hence, at a given fluence, independent of intensity or bandwidth.

Figure 5 shows how the four minor products, CH_3CHO, C_2H_6, CH_4, and C_2H_2, expressed as ratios to C_2H_4, varied with fluence. Only the smoothed curves are shown here to minimize congestion. All the individual data points are given in Table 2. In each case a marked increase of the ratio with increasing fluence was observed, with a definite dependence on pulse length, and hence, at a given fluence, on intensity; values of product ratios are significantly higher for the 10-ns pulse.

3.4.3 Dependence on pressure

The pressure dependence of $P_{C_2H_4}$ at 9(±1) J/cm^2 shows a downward trend at higher pressures, which can probably be accounted for by attenuation of the laser radiation in the central reaction zone by the absorption in the converging beam between the front window and the reaction zone. There is again no significant difference between the 10-ns and 60-ns pulses. A series of experiments at a higher fluence of about 50 (±8) J/cm^2 showed no trend of $P_{C_2H_4}$ with pressure.

The ratios CH_4/C_2H_4, C_2H_2/C_2H_4, and CH_3CHO/C_2H_4 all show an upward trend with pressure for irradiation at both 9 and 50 J/cm^2, and all four product ratios show a significant dependence on pulse length.

3.4.4 Primary processes

As in previous MPD studies, reaction [1] is always the most important, ranging from ~99% of the decomposition at the lowest fluence to ~54% at the highest fluence and pressure. In

Can. J. Chem. Downloaded from www.nrcresearchpress.com by 176.9.209.113 on 09/07/12
For personal use only.

TABLE 2. (*a*) Product yields for the MPD of ethanol induced by the $9P(16)$ line of the CO_2 laser. P_N is the ethanol pressure after N laser pulses

P_O (Pa)	ϕ_{max} (J/cm^2)	$N \times 10^{-2}$	Cell volume (cm^3)	P_N (Pa)	Product partial pressures (Pa)						$P_{C_2H_4}$
					CH_4	C_2H_4	C_2H_6	C_2H_2	C_3H_6	CH_3CHO	
					τ = 10 ns						
26.6	9.0	15	202	17	0.028	2.05	0.29	—	—	—	0.52
26.6	4.4	2	202	12	0.099	2.27	0.49	0.071	0.047	0.16	4.34
26.6	5.2	1	202	—	0.079	1.72	—	0.047	—	0.89	6.51
53.3	8.2	10	202	42.7	0.073	2.33	0.31	0.024	0.017	0.23	0.47
80.0	8.7	10	204	60.0	0.20	3.73	0.49	0.036	0.026	0.40	0.47
107	9.0	10	194	98.7	0.21	5.73	0.72	0.067	0.078	0.53	0.52
133	1.8	40	57.5	137	—	0.16	—	—	—	—	5.2×10^{-5}
133	1.8	40	51.2	137	—	0.73	0.22	—	—	—	2.1×10^{-4}
133	2.2	30	194	133	—	0.17	—	—	—	—	3.9×10^{-3}
133	2.5	45	194	129	—	0.23	—	—	—	—	2.5×10^{-3}
134	2.8	30	57.5	116	0.21	21.9	0.57	—	0.072	0.17	1.0×10^{-3}
133	2.9	30	57.5	79.3	0.11	22.0	0.29	—	—	0.48	1.0×10^{-2}
133	3.0	19.3	51.2	117	0.16	23.1	1.09	—	0.10	0.20	1.5×10^{-2}
133	3.0	9.7	57.5	115	0.093	15.6	0.45	—	0.029	0.21	2.2×10^{-2}
134	3.1	12.7	57.5	121	0.072	11.6	0.37	—	0.033	0.19	1.2×10^{-2}
133	2.7	20	57.5	104	0.024	6.93	—	—	—	0.13	4.6×10^{-3}
133	3.2	23.24	57.5	108	0.21	32.0	1.24	—	0.16	0.35	2.1×10^{-2}
133	3.3	29.4	51.2	87.3	0.33	62.7	2.11	—	0.036	0.33	3.3×10^{-2}
133	3.3	14.7	57.5	115	0.20	23.3	1.08	—	0.073	0.26	2.3×10^{-2}
133	3.6	30	51.2	76.7	0.51	60.7	3.11	0.029	0.364	0.56	3.1×10^{-2}
134	4.2	30	204	127	0.027	3.20	0.11	—	—	0.077	8.0×10^{-2}
134	4.6	25	57.5	61.3	1.22	76.0	5.01	0.10	—	1.29	5.8×10^{-2}
133	5.9	8.78	57.5	104	0.53	28.0	1.93	0.067	0.42	0.80	4.7×10^{-2}
133	24	3	202	113	0.57	9.73	1.63	0.33	0.15	0.81	2.5
133	44	2	204	103	1.05	14.0	2.93	0.73	0.36	1.33	5.5
133	57	1	204	—	0.95	12.0	2.67	0.64	—	1.28	9.3
333	8.9	10	202	293	0.83	11.9	1.92	0.20	0.21	1.31	0.35
667	8.7	10	204	587	1.28	13.6	1.88	0.28	0.22	2.31	0.20
667	58	1	194	520	7.93	39.2	5.60	4.80	0.96	9.33	5.7
					τ = 60 ns						
13.3	8.0	30	194	—	—	0.83	0.052	—	—	—	0.20
23.2	4.4	32.8	50.1	25.3	—	4.27	—	—	—	—	9.4×10^{-3}
23.2	5.8	8.8	57.5	32.0	—	3.33	—	—	—	—	3.0×10^{-2}
23.2	10.7	5.06	57.5	13.3	—	9.73	0.70	—	0.040	—	0.19
26.7	9.4	10	204	20.0	0.00093	1.43	0.11	—	—	0.017	0.54
40.0	7.7	20.1	204	25.3	0.023	3.07	0.14	—	—	0.093	0.39
53.3	8.5	20	202	41.3	0.063	4.67	0.33	—	0.019	0.13	0.45
80.0	8.8	10	202	72.0	0.085	3.87	0.19	0.0093	0.0077	0.20	0.48
133	1.4	40	51.2	133	—	0.10	—	—	—	0.093	2.9×10^{-5}
133	1.6	40	51.2	121	—	1.04	—	—	—	—	3.0×10^{-4}
133	1.3	40	57.5	133	—	0.040	—	—	—	—	1.3×10^{-5}
133	1.8	40	57.5	115	—	0.68	—	0.28	—	—	2.2×10^{-4}
133	2.0	20	57.5	128	0.20	1.20	—	—	0.41	0.55	7.9×10^{-4}
133	2.5	28.95	50.1	133	—	0.40	—	—	—	—	1.6×10^{-4}
133	2.7	29.81	50.1	133	—	3.87	—	—	—	—	1.5×10^{-3}
133	2.7	29.84	57.5	133	—	1.60	—	—	—	—	7.1×10^{-4}
134	3.3	13	57.5	121	0.12	19.6	0.41	0.031	0.056	0.24	2.1×10^{-2}
133	4.5	17.07	57.5	113	0.13	30.7	1.49	—	0.10	0.13	2.7×10^{-2}
134	5.5	8	51.2	86.7	1.01	45.3	2.63	—	0.42	1.23	0.24
133	9.8	10	194	129	0.13	8.40	0.64	0.028	0.074	0.18	0.61
133	0.6	5.08	57.5	72.0	1.47	62.1	4.48	0.27	1.24	1.87	0.18
133	15	5	202	128	0.096	3.33	0.24	0.011	0.11	0.23	0.50
133	27	5	204	120	0.60	16.9	2.24	0.44	0.33	0.88	2.67
133	45	1	194	128	0.60	8.0	1.24	0.37	0.16	0.55	6.60
333	8.4	10	194	307	0.37	10.5	0.99	0.037	0.097	0.072	0.30
667	5.0	10	202	627	0.84	13.7	1.39	0.071	0.17	1.96	0.20

Can. J. Chem. Downloaded from www.nrcresearchpress.com by 176.9.209.113 on 09/07/12
For personal use only.

TABLE 2 (*concluded*)

(*b*) The effect of added oxygen for a fixed ethanol pressure of 133 Pa for the $9P(16)$ CO_2 laser line and $\tau = 10$ ns

ϕ_{max} (J/cm^2)	P_{O_2} (added) (Pa)	$N \times 10^{-2}$	Cell volume (cm^3)	P_N (Pa)	Product partial pressures (Pa)						$P_{C_2H_4}$
					CH_4	C_2H_4	C_2H_6	C_2H_2	C_3H_6	CH_3CHO	
3.4	417	16.76	57.5	92.0	0.53	25.1	—	—	—	1.87	2.2×10^{-2}
3.6	313	16.72	51.2	100	0.40	30.9	—	—	—	1.87	2.5×10^{-2}
3.7	70.7	20	57.5	100	0.31	31.5	—	—	0.012	1.67	2.3×10^{-2}
3.8	160	17	51.2	32.0	0.36	17.5	—	—	—	—	1.3×10^{-2}
3.8	141	17.74	57.5	108	0.27	20.0	—	—	0.016	1.60	1.6×10^{-2}
3.4	417	16.76	57.5	92.0	0.53	25.1	—	—	—	1.87	2.2×10^{-2}
3.6	313	16.72	51.2	100	0.40	30.9	—	—	—	1.87	2.5×10^{-2}
3.7	70.7	20	57.5	100	0.31	31.5	—	—	0.012	1.67	2.3×10^{-2}
3.8	160	17	51.2	32.0	0.36	17.5	—	—	—	—	1.3×10^{-2}
3.8	141	17.74	57.5	108	0.27	20.0	—	—	0.016	1.60	1.6×10^{-2}

these experiments and previous work (3, 6), yields of C_2H_4 were unaffected by the addition of O_2, an efficient radical scavenger; hence it is most probably formed in a simple unimolecular dehydration. Reaction [3] is generally the third most important, varying from about 1 to 24% of reaction [1]. In the present experiments it was followed by measuring the acetaldehyde. In previous work (3), only H_2 was measured; neither H_2 nor CH_3CHO was affected by the addition of O_2, so again a simple unimolecular elimination is suggested. Reaction [4], similarly, is postulated as before (3), because yields of CH_4 were unaffected by O_2. Reaction [2] is suggested as a source of CH_3 radicals that form C_2H_6 by combination. Their removal by reaction with O_2 accounts for the observed suppression of C_2H_6 formation. From the yield of ethane, and recognizing that perhaps half of the CH_3 radicals combined with CH_2OH, the extent of reaction [2] may be taken as 4 times the yield of ethane, making reaction [2] the second most important primary process, rising to as much as 80% of reaction [1] at the highest fluence. Reaction [5] probably occurs to a minor extent, accounting for the small yields of propane and butane observed, formed by recombination reactions of C_2H_5 and CH_3. Evidence for reaction [5] also comes from the direct observation of OH in the system at high fluence (7).

3.4.5 Secondary processes

Propylene is always a very minor product (<3% of C_2H_4); the source is not clear, but several secondary reactions involving C_2H_4 or CH_3CHO can be suggested.

Acetylene, also a minor product, shows a strong dependence on fluence. Its yield does not depend on conversion, but it could be formed by secondary decomposition of C_2H_4 during a single pulse, perhaps by multiphoton absorption by vibrationally excited C_2H_4 product.

The yield of CH_3CHO relative to C_2H_4 declines with increasing extent of reaction; this could be due to direct decomposition by absorption of laser radiation, or perhaps by secondary attack by CH_3 or other radicals, and is probably responsible for the CO reported as a product in some studies (5, 6, 9). Carbon monoxide was not a significant product in a previous investigation of the system (3), and no analysis was made for it in the present experiments. The possibility that CH_3 radicals were formed by the decomposition of CH_3CHO is not supported by the fluence dependence of C_2H_6 formation, and the primary dissociation, reaction [2], remains the most probable source of CH_3.

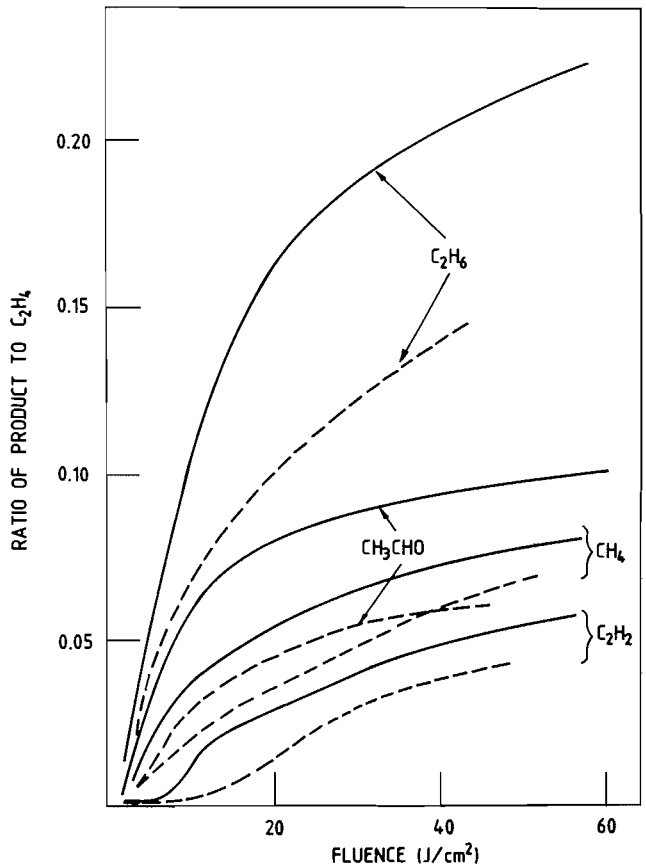

FIG. 5. The product ratios for C_2H_6, CH_3CHO, CH_4, and C_2H_2 compared to C_2H_4. For each product the solid line is a smooth curve of results using a 10-ns pulse and the dashed line is for a 60-ns pulse.

3.4.6 Energies and relative rates of primary processes

The energetics of reactions [1]–[4] are summarized in Fig. 6. There is no direct experimental information about the energy barriers for any of these reactions.

The present data, notably the dependence of product ratios on fluence and pulse length, and all previous MPD studies support the conclusion that reaction [1] is the lowest-energy channel, in accord with empirical (12) and theoretical (13) predictions. The relative rates of reactions [3] and [2], however, do not support the relatively high barrier of 469 kJ/mol suggested for the

Can. J. Chem. Downloaded from www.nrcresearchpress.com by 176.9.209.113 on 09/07/12
For personal use only.

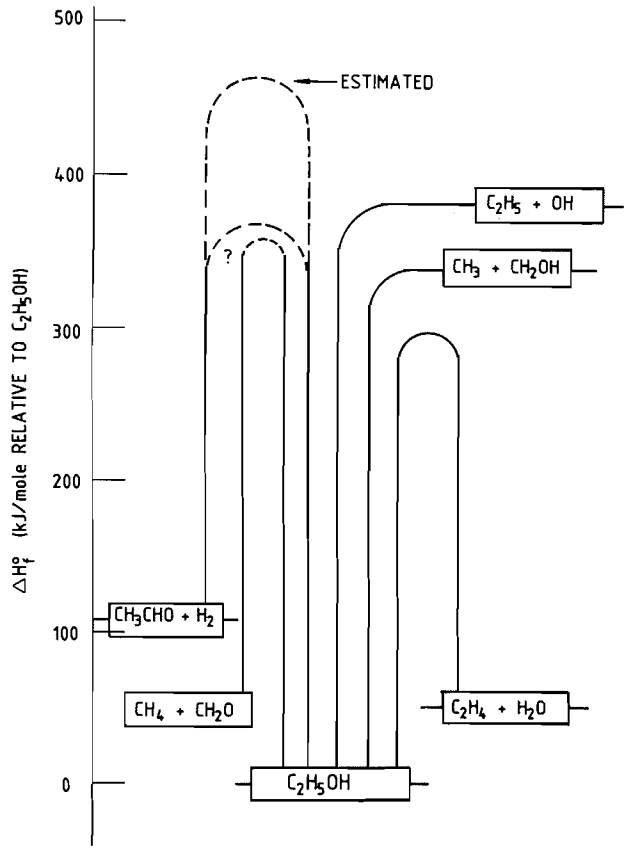

FIG. 6. The energetics of reactions [1]–[4]. Dashed lines indicate uncertainty in the activation energies of the channels.

former (13); the similar fluence dependence of reactions [3] and [4] to that of reaction [2] in fact points to similar activation energies for all three. The activation energy for reaction [2] must be close to its endothermicity (343 kJ/mol), while a frequency factor of $A_2 = 10^{16.4}$ s^{-1} has been estimated by Tsang (12).

Independent confirmation of the occurrence of reactions [1]–[5], and estimates of their relative rates, is obviously desirable. Reaction [1] appears well established, with Arrhenius parameters probably close to those estimated by Danen (2) and Tsang (12), and there seems little doubt about reactions [2] and [5]. Reactions [3] and [4] are more suspect, with high barriers predicted for both (13). Evidence for their occurrence as simple unimolecular processes relies heavily on the lack of effect of O_2 on H_2, CH_4, and CH_3CHO production, and it is just possible that free-radical reactions occurring with vibrationally hot species in the reaction zone, unsusceptible to scavenging by O_2, might account for these products.

3.5 Mechanism of the MPD decomposition

The lack of dependence of $P_{C_2H_4}$ on pulse duration suggests that little or no collisional deactivation took place during the pulse, not unexpected at these pressures and pulse lengths. Hence, to a first approximation the total energy deposited during the pulse, rather than its rate of deposition, determined the number of molecules pumped to levels capable of decomposition by reaction [1]. The enhancement of the higher-energy channels described by reactions [2]–[4], relative to reaction [1], with the 10-ns pulse (Fig. 5) shows, however, that the *energy* of the decomposing molecules does depend on intensity as well as fluence. This implies that there was appreciable decomposition via reaction [1] during the pulse in competition with up-pumping by the laser radiation, so that at higher intensity, higher energy levels were attained before decomposition. One might therefore expect some decrease in $P_{C_2H_4}$ as reactions [2]–[4] became significant; the extent of the latter reactions, however, was only a small fraction of that of reaction [1], except at the highest fluence, and the corresponding decrease in $P_{C_2H_4}$ would hardly have been noticed in Fig. 4; there may also have been a small countervailing enhancement of reaction [1] itself at the higher intensity.

The dependence of $P_{C_2H_4}$ and the product ratios on pressure is more complex. The decomposition can be considered the sum of two processes, the first a collision-free decomposition of excited molecules during and shortly after the pulse, the second a decomposition of molecules whose energy content and distribution have been modified by collisions, largely after the pulse. The first must be independent of pressure; the second will be affected by pressure and will merge at long times and high pressures into a bulk thermal decomposition. The ratio of the first process to the second will decrease with increasing pressure. The factors affecting the relative efficiencies of the collision-free and collision-modified processes are manifold and complex, involving the energy distributions of the decomposing molecules in each, the radiation intensity, the pulse length, and the mechanism and rate of cooling after the pulse, the last factor depending in turn on the dimensions of the reaction zone. In two previous studies (3, 6), the overall probability of decomposition clearly declined with increasing pressure, indicating a lesser efficiency for collision-modified processes; in the present experiments there is little change in $P_{C_2H_4}$ with pressure, as noted earlier, which combined with the increasing product ratios leads to a modest *increase* in the overall decomposition probability. This is in agreement with the MPA observations shown in Fig. 2 where more energy is absorbed per molecule in the laser beam. The increase in energy absorbed does not just get collisionally spread and degraded to heat but is used to cause chemical reaction. What is clear, however, from this and all previous studies, is that reactions [2]–[4] increase with respect to reaction [1] with increasing pressure. This would appear to indicate a higher average energy for the molecules decomposing in collision-modified reactions compared with collision-free decomposition.

1. L. SELWYN, R. A. BACK, and C. WILLIS. Chem. Phys. **32**, 323 (1978).
2. W. C. DANEN. J. Am. Chem. Soc. **101**, 1187 (1979).
3. A. GANDINI and R. A. BACK. J. Photochem. **18**, 241 (1982).
4. W.-S. ZHU, Z.-B. ZHANG, P.-R. ZHU, Y.-Y. ZHAO, L.-M. ZHANG, T.-Y. REN, A.-Z. ZHANG, and W.-Z. JIN. Jiguang, **9**, 199 (1982); Chem. Abstr. **98**, 98660 (1983); Z.-B. ZHANG, W.-S. ZHU, P.-R. ZHU, Y.-Y. ZHAO, J.-R. XU, C. ZHU, and Z.-Q. WU. Wuli, **11**, 151 (1982); Chem. Abstr. **97**, 205648 (1982).
5. T. MAJIMA, S. ARAI, T. YAMAUCHI, and T. ISHII. Reza Kagaku Kenkyu, **6**, 67 (1984); Chem. Abstr. **102**, 176309 (1985).
6. S. R. DE A. LEITE, P. C. ISOLANI, and J. M. RIVEROS. Can. J. Chem. **62**, 1380 (1984).
7. V. N. BAGRATASHVILI, M. V. KUZMIN, R. R. OSMANOV, F. N. PUTILIN, and L. N. VERESHCHAGINA. Chem. Phys. Lett. **120**, 211 (1985).
8. G. P. ZHITNEVA and S. YA. Pshezhetskii. Khim. Vys. Energ. **18**, 176 (1985).
9. R. B. BHATNAGAR. Ph.D. thesis, University of Hull, England. 1979; C. J. SHAW. Ph.D. thesis, University of Hull, England. 1984.

Can. J. Chem. Downloaded from www.nrcresearchpress.com by 176.9.209.113 on 09/07/12
For personal use only.

10. W. TSANG. Int. J. Chem. Kinet. **8**, 173 (1976).
11. J. A. BARNARD and H. W. D. HUGHES. Trans. Faraday Soc. **56**, 55 (1960).
12. W. TSANG. Int. J. Chem. Kinet. **8**, 193 (1976).
13. T. YAMABE, M. KOIZUMI, K. YAMASHITA, and A. TACHIBANA. J. Am. Chem. Soc. **106**, 2255 (1984).
14. K. J. MINTZ and R. J. CVETANOVIC. Can. J. Chem. **51**, 3386 (1973).
15. C. L. LIN and W. B. DEMORE. J. Phys. Chem. **77**, 863 (1973).
16. D. DICKENS. Ph.D. thesis, University of Reading, England. 1969.
17. S.-Y. HO and H. B. LIN. J. Chin. Chem. Soc. (Taipei), **20**, 27 (1973); Chem. Abstr. **78**, 142370 (1973).
18. W.-K. ADERS and H. GG. WAGNER. Ber. Bunsenges. Phys. Chem. **77**, 712 (1973).
19. D. K. EVANS, R. D. MCALPINE, and F. K. MCCLUSKY. Chem. Phys. **32**, 81 (1978).
20. R. D. MCALPINE, D. K. EVANS, and F. K. MCCLUSKY. Chem. Phys. **39**, 263 (1979).
21. A. W. PASTERNAK, D. J. JAMES, J. A. NILSON, D. K. EVANS, R. D. MCALPINE, H. M. ADAMS, and E. B. SELKIRK. Appl. Opt. **20**, 3849 (1981).
22. H. M. ADAMS, E. B. SELKIRK, J. W. GOODALE, D. K. EVANS, and R. D. MCALPINE. Rev. Sci. Instrum. **55**, 1298 (1984).
23. I. MOTAYAMA and C. H. JARBOE. J. Phys. Chem. **70**, 3226 (1966).
24. D. K. EVANS, R. D. MCALPINE, and H. M. ADAMS. J. Chem. Phys. **77**, 355 (1982).
25. R. D. MCALPINE, D. K. EVANS, and H. M. ADAMS. J. Chem. Phys. **78**, 5990 (1983).
26. D. K. EVANS, R. D. MCALPINE, and H. M. ADAMS. Israel J. Chem. **24**, 187 (1984).
27. R. A. BACK, D. K. EVANS, and H. M. ADAMS. Can. J. Chem. **62**, 1525 (1984).
28. R. D. MCALPINE, D. K. EVANS, and F. K. MCCLUSKY. J. Chem. Phys. **73**, 1153 (1980).
29. R. D. MCALPINE, D. K. EVANS, J. W. GOODALE, and M. I. IVANCO. To be published.
30. S. SPEISER and J. JORTNER. Chem. Phys. Lett. **44**, 399 (1976).

Can. J. Chem. Downloaded from www.nrcresearchpress.com by 176.9.209.113 on 09/07/12
For personal use only.

Simulations of O_2 adsorbed on graphite at 45 K: the monolayer to bilayer transition

VENKAT BHETHANABOTLA AND WILLIAM STEELE

Department of Chemistry, The Pennsylvania State University, 152 Davey Laboratory, University Park, PA 16802, U.S.A.

Received September 1, 1987

This paper is dedicated to Professor J. A. Morrison

VENKAT BHETHANABOTLA and WILLIAM STEELE. Can. J. Chem. **66**, 866 (1988).

Molecular dynamics computer simulations are reported for O_2 physisorbed on the graphite basal plane at 45 K. Surface coverages ranged from the low density monolayer through the compressed monolayer up to roughly two layers. Thermodynamic properties, orientational distribution functions, and two-dimensional structure factors are presented. The time-dependent translational motion is characterized both by computer-generated trajectory plots and by evaluation of the mean square in-plane displacements as a function of time. It is concluded that the O_2 orientations shift from predominantly surface-parallel to surface-perpendicular as the first layer density increases, in agreement with deductions from experiment. The structure factors indicate that some translational ordering is present in the fluid phases and that the bilayer is a composite made up of a solid monolayer plus a fluid overlayer; these observations are in agreement with recent experimental studies of this system.

VENKAT BHETHANABOTLA et WILLIAM STEELE. Can. J. Chem. **66**, 866 (1988).

On rapporte les résultats de simulations par ordinateur de la dynamique moléculaire du O_2 physiquement adsorbé sur du graphite basal plan, à 45 K. Les taux de surface qui sont couverts vont de la monocouche à faible densité à pratiquement des doubles couches, en passant par la monocouche comprimée. On présente les propriétés thermodynamiques, les fonctions de distribution d'orientation ainsi que les facteurs de la structure bidimensionnelle. On a caractérisé le mouvement de translation qui varie avec le temps par le biais de diagrammes de trajectoires obtenus à l'aide d'un ordinateur ainsi que par une évaluation des valeurs quadratiques moyennes des déplacements dans le plan en fonction du temps. On en conclut que, au fur et à mesure qu'on augmente la densité de la première couche et conformément aux déductions qui ont été faites en se basant sur les expériences, les orientations du O_2 passent d'une position principalement parallèle à la surface à une position perpendiculaire à la surface. Les facteurs de structure indiquent qu'il existe un certain ordre de translation dans les phases fluides et que la double couche est une composite formée d'une monocouche solide et d'une couche superficielle liquide; ces observations sont en accord avec les études expérimentales récentes effectuées dans ce système.

[Traduit par la revue]

1. Introduction

The structures and transitions of the low temperature solid and liquid phases in monolayer O_2 adsorbed on the graphite basal plane are currently a subject of considerable interest (1–9). Experimental studies reveal considerable differences between oxygen and the analogous N_2 monolayer/graphite system (1). We have undertaken molecular dynamics computer simulations of both materials adsorbed on a model graphite substrate in an attempt to better understand the reasons for the contrasting behavior. It appears that simple models of the intermolecular interactions can be found for these systems which produce simulated thermodynamic and dynamic properties in reasonably good agreement with experimental data. In these models, the sizes and shapes of N_2 and O_2 are similar, but the electrostatic quadrupole moments, which are known from independent measurements, are quite different. This difference seems to be capable of accounting for much of the contrasting monolayer phase behavior. In previous work, molecular dynamics simulations of O_2 layers were undertaken at fixed density but temperatures varying from 15–60 K (2). One such scan was done for a solid layer that filled only half the surface at low temperature. The structure of this film was found to be an orientationally ordered centered-rectangular lattice at low temperature, in agreement with X-ray and L.E.E.D. measurements. As temperature increased, the solid expanded slightly, melted to a two-dimensional liquid and eventually, vaporized to a two-dimensional gas. Furthermore, the model potential used for the O_2/solid interaction produced a strong preference for orientation parallel to the surface at temperatures up to ~60 K. A similar temperature scan at a larger areal density showed the same low temperature ordering but different phase behavior at higher temperature due in part to the fact that the adsorbed monolayer is being studied essentially at constant density whereas the patches (actually infinitely long strips after periodic boundary conditions are imposed) are not restricted in this way. It is not surprising to find that melting of the filled-surface monolayer occurs at a higher temperature than the patch and is no longer a first order phase change. Of greater interest is the fact that molecular orientation is affected by the increase in density — melting is here accompanied by an increase in the number of molecules with a significant tilt angle relative to the surface. Inasmuch as experiments indicate the presence of several slightly different phases of surface-tilted molecules at high monolayer densities, we have carried out a simulation scan of density at a fixed temperature in order to learn more about the properties of the high density monolayer and the bilayer of O_2 adsorbed on graphite. This paper reports the results obtained for such a scan taken at 45 K with areal densities taken in the region of the θ phase observed in L.E.E.D. experiments (5) (more precisely, in the region of liquid – θ-phase coexistence). It has been suggested that this phase is ordered but incommensurate. These simulations confirm the existence of unusual behavior in this part of the phase diagram and help elucidate the properties of the θ-phase by providing information concerning both the distribution of molecular orientation relative to the surface and the translational dynamics of the monolayer.

2. Details of the simulation

The work reported here is an extension of the previous simulation study of this system (2). Thus, the intermolecular interactions and the simulation algorithm were kept the same in

Can. J. Chem. Downloaded from www.nrcresearchpress.com by 176.9.209.113 on 09/07/12
For personal use only.

TABLE 1. Parameters of the site–site interactions

Parameter	Value
ϵ_{OO}/k	52.1 K
ϵ_{OC}/k	38.2 K
σ_{OO}	2.99 Å
σ_{OC}	3.195 Å

TABLE 2. Simulation data

ρ (Å^{-2})	Fraction in layer 1	Timesteps to equilibrium	Timesteps after equilibrium
0.0735	1.000	4 000	15 000
0.0763	1.000	3 000	10 250
0.0954	1.000	4 000	20 000
0.1145	1.000	4 000	20 000
0.1908	0.699	9 000	9 750

order to allow comparisons between the two sets of results. The O_2–O_2 and the O_2–graphite energies were modelled as pairwise sums of Lennard–Jones site–site interactions. Values of the well-depth and size parameters used are listed in Table 1. The molecular dynamics was based on a predictor-corrector algorithm, with molecular orientations specified by quaternions and with periodic boundary conditions in the x,y directions parallel to the surface. No molecules were observed to leave the adsorbed phase under the conditions of these simulations. Coverages studied and numbers of timesteps during equilibration and during computation are listed in Table 2. A timestep of 0.0049 ps was used throughout, so that the durations of the computational parts of the simulations were from 48 to 98 ps. Reduced units are used so that distances are reduced by 2.46 Å, the lattice spacing for the graphite basal plane, and energies are reduced by the ϵ_{gs}, the site–site well-depth for the C—O site interaction. Note that the densities listed in Table 2 can be converted to multiples of the registered lattice density by dividing by 0.0636 Å^{-2}. In these simulations, the number of O_2 molecules was 192 for the most part (208 were taken in the run at ρ = 0.0735 Å^{-2}); coverages were varied by changing the size of the simulation cell. In all but the highest density, the molecules were initially placed in an orientationally ordered monolayer. During the equilibration period, in-plane disordering was essentially complete and the out-of-plane orientational ordering, while not lost, changed significantly from the initial surface-parallel configuration. The initial configuration for the highest coverage studied was set with 120 molecules in layer 1 and 72 in layer 2, both in an ordered configuration (consequently, layer 2 was initially a patch that covered ~2/3 of the surface). As time went on, layer 2 spread out into a fluid phase distributed over the entire surface (detailed evidence for this will be presented below) and seven molecules changed from layer 1 to layer 2. Because layer changes produce large temperature jumps in a small number of molecules running in a constant energy simulation, a constant temperature algorithm due to Evans *et al.* (10) was employed. As it turned out, no molecules changed layers during the computational parts of the simulations (all layer changes observed were actually during the equilibration stage in the high-coverage system). To ensure thermodynamic equilibrium, it would have been desirable to run long enough for such interchanges to occur in the bilayer film but the temperature chosen was apparently somewhat too low and the duration of the simulation not long enough for this to happen. The fact that molecules were squeezed out of the first layer during equilibration indicates that the configurations observed are at least close to equilibrium.

Equilibrium properties evaluated in these simulations included a number of average potential energies, the structure factor $S(\boldsymbol{k})$, and the distributions of in-plane and out-of-plane orientation angle. In particular, the total potential energy of an

TABLE 3. Average O_2–O_2 interactions per molecule (divided by ϵ_{gs})

	Average number		
ρ (Å^{-2})	Layer 1	Layer 2	Between layers 1 and 2
0.0735	−9.39	—	—
0.0954	−13.35	—	—
0.1145	−15.04	—	—
0.1908	−15.17	−10.51	−5.66

adsorbed O_2 molecule was divided into the average molecule–solid energy $\langle u^*_{gs}\rangle$, and the average molecule–molecule energy $\langle u^*_{mm}\rangle$. For the bilayer system, u_{mm} was further subdivided by evaluating the interaction of a molecule in the nth layer with its neighbors in the same layer ((11) or (22)) and with its neighbors in a different layer (12). Results of this calculation are given in Table 3.

The structure factor is defined the usual way for a two-dimensional phase:

$$S(\boldsymbol{k}) = \langle \exp i\boldsymbol{k}\cdot\boldsymbol{\tau}_{12}\rangle$$

where $\boldsymbol{\tau}_{12}$ is the center-of-mass separation of a pair of molecules (both in the same layer) and the two-dimensional wave vector $\boldsymbol{k}$ is restricted to fit into the simulation box. (That is, $\exp(i\boldsymbol{k}\cdot\boldsymbol{r})$ must be the same function in each member of the infinite array of box images produced by the periodic boundary conditions.)

Two orientational distribution functions were simulated: the distribution of in-plane angle and the distribution of cos β where β is the angle between a molecular axis and the normal to the surface. Of these, only $P(\cos\beta)$ indicated significant ordering and thus, plots shown here are limited to that function. Note that $P(\cos\beta)$ for the bilayer system was evaluated separately for first and for second layer molecules.

3. Results

Considerable insight into the properties of these simulated films can be gained by viewing the trajectories of the center-of-mass (c.o.m.) motions of the O_2 molecule, projected onto the surface. These are shown for time intervals of 50 ps in Fig. 1a for three of the monolayer systems. However, one must also view the distribution of the orientation of the molecular axes relative to the surface to understand the changes in film structure with density. Appropriate plots are shown in Fig. 2. Taken together with Fig. 1a, we see that the O_2 layer at ρ = 0.076 Å^{-1} is characterized by relatively random c.o.m. motion with most of the molecules parallel to the surface. As density increases to 0.0954, the c.o.m. motion becomes much more solid-like, with

Can. J. Chem. Downloaded from www.nrcresearchpress.com by 176.9.209.113 on 09/07/12
For personal use only.

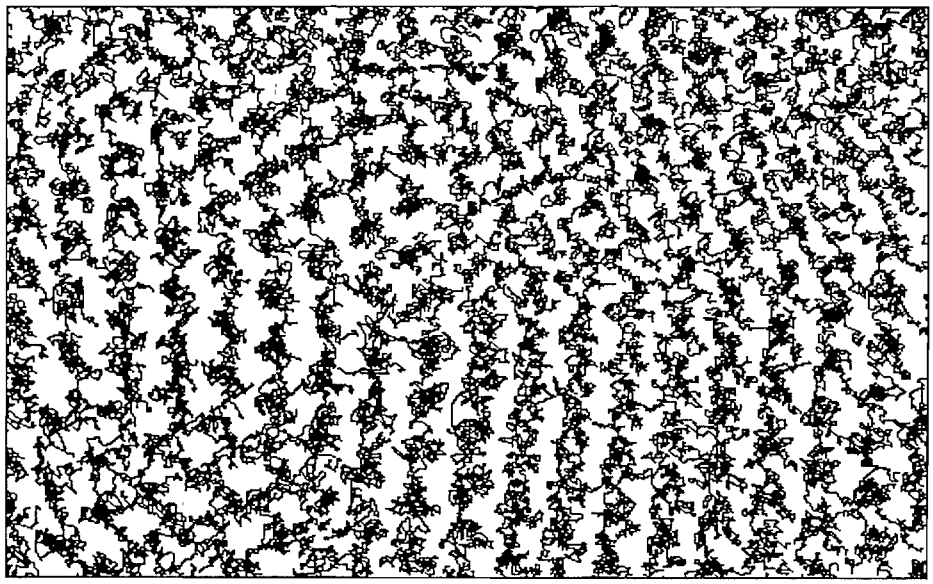

0.0763

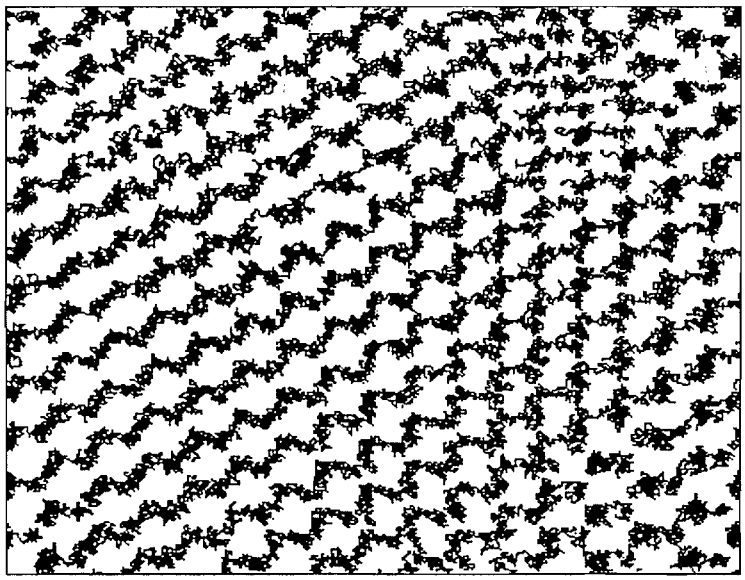

0.0954

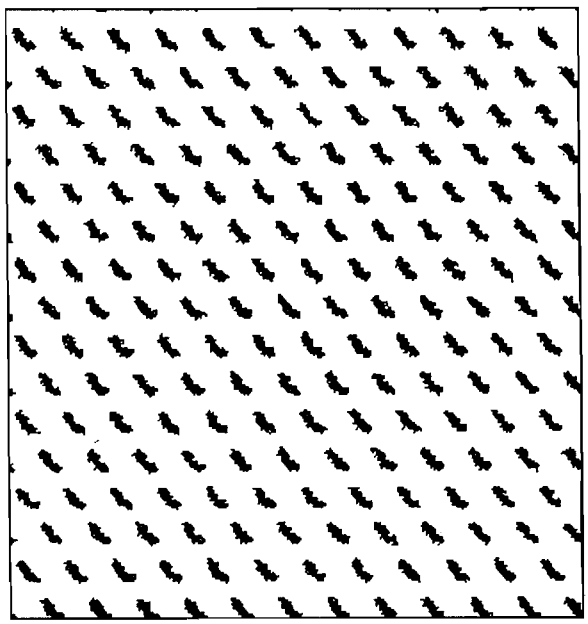

0.1145

FIG. 1a

Can. J. Chem. Downloaded from www.nrcresearchpress.com by 176.9.209.113 on 09/07/12
For personal use only.

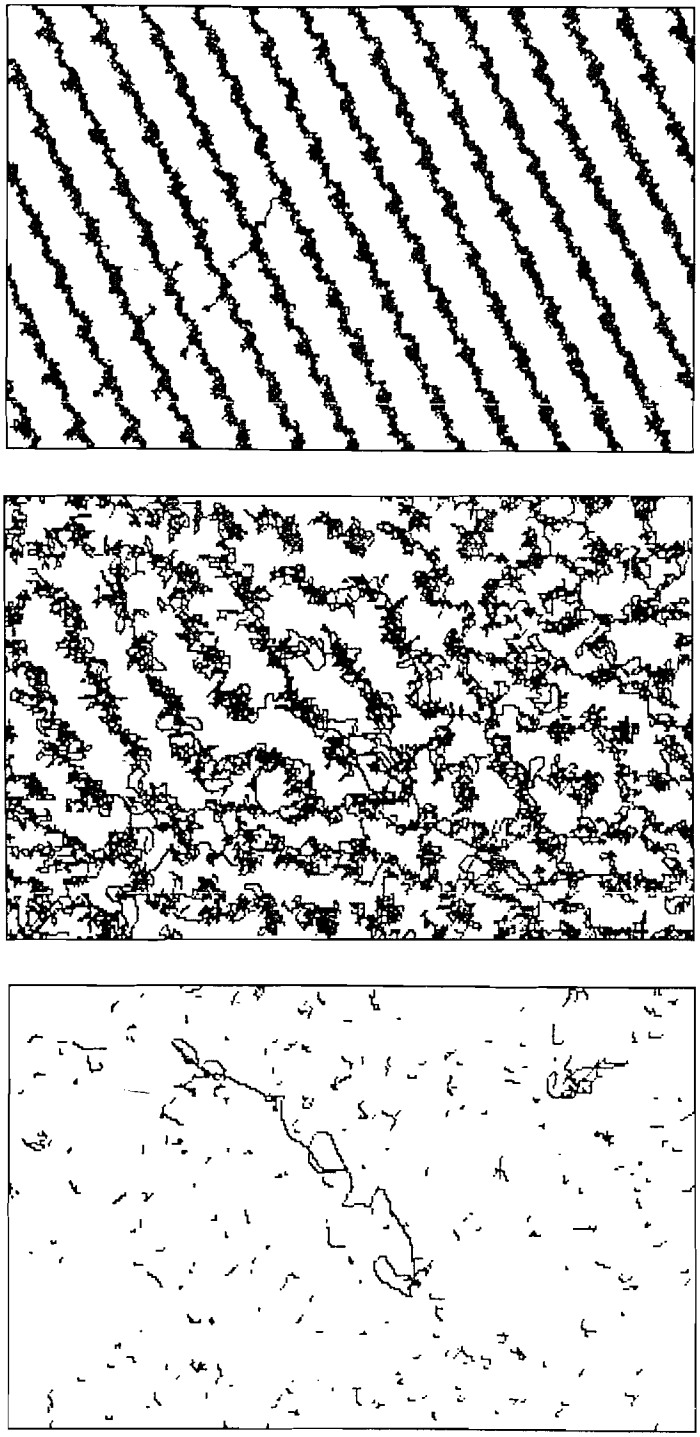

FIG. 1. Projections in the plane of the computer-generated trajectories of the O_2 molecules are shown here for four of the surface coverages studied. Part (*b*) shows results for the highest density ($\rho = 0.1908$ Å^2). At the highest density, molecules may be found in three layers, and trajectories are shown for each layer separately in part (*b*). The fully solidified layers "float" slowly across the surface — an artifact of the simulation model which provides no mechanism for pinning the solids in place.

some "skating" motion of the entire solid. (This is a physically unrealizable consequence of the perfectly periodic surface — in reality, pinning at a defect will certainly occur.) Note, however, the change in orientational distribution to one where a significant fraction of the molecules are standing on end. At a density of 0.01145, the change to a hexagonal solid-like layer of molecules oriented nearly perpendicular to the surface is complete. The average potential energies of the molecules in the first layer that are shown as a function of density in Fig. 3 are readily understood in terms of this picture. The reduced gas–solid energy drops from the "patch" value of −32.8 to −23.7 as the molecules are forced to reorient from mainly parallel to mainly perpendicular with increasing density (6). At the same time, the O_2–O_2 interaction becomes more attractive because the well-depth for pairs of molecules parallel to each other (but perpendicular to the surface) at optimum separation

Can. J. Chem. Downloaded from www.nrcresearchpress.com by 176.9.209.113 on 09/07/12
For personal use only.

Can. J. Chem. Downloaded from www.nrcresearchpress.com by 176.9.209.113 on 09/07/12
For personal use only.

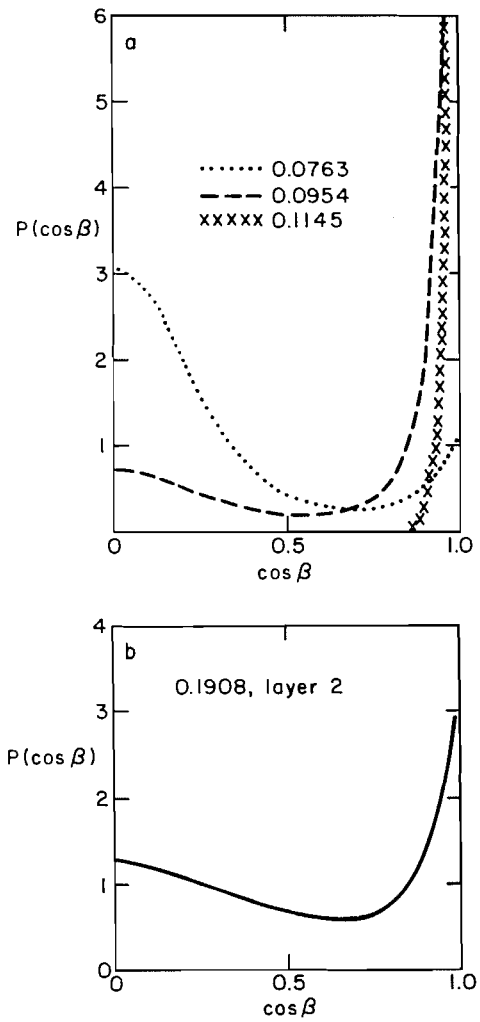

FIG. 2. Distributions of the cosine molecular orientation angle relative to the surface normal are shown here for the first layer molecules at four of the densities simulated. The distributions become extremely sharp at cos β = 1.0 for the two highest densities considered and actually go off-scale for ρ = 0.0954, 0.1145, and 0.1908 Å^{-2} (first layer). Part (*b*) shows the orientational distribution for the second layer molecules in the 0.1908 system.

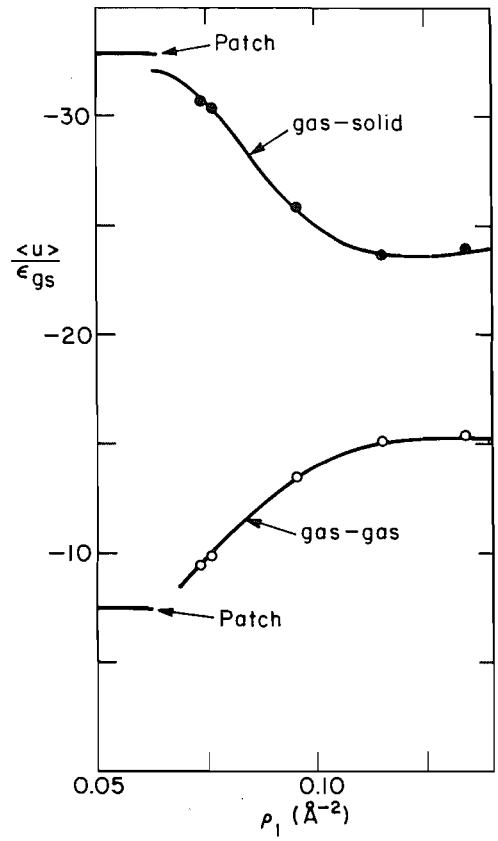

FIG. 3. Average potential energies per first layer particle are plotted here as a function of the first layer density. Circles show the simulation data and curves are drawn as an aid to the eye. At densities lower than ~0.07 Å^{-2}, patches of adsorbed molecules form with indicated energies obtained in a previous study (2).

distance is deeper than for pairs of molecules randomly oriented in the plane of the surface.

At the highest surface coverage considered (ρ = 0.1908 Å^2), the first layer is somewhat compressed (see Table 2), but considerable second and even some third layer adsorption occurs, as shown by the trajectory plots in Fig. 1b. The first layer is a well-organized solid of molecules perpendicular to the surface. Figure 3 indicates that both the O_2–solid and the O_2–O_2 interaction in this layer are little changed in going from ρ_1 = 0.1145 to ρ_1 = 0.135. (Presumably the alterations in energy with changing orientation and distance are balanced to give a negligible net change in energy in this range.)

According to the L.E.E.D. data, most of these simulations were carried out in a region in the phase diagram corresponding to two-phase equilibrium between fluid and θ-phase, where the θ-phase is an incommensurate phase exhibiting weak six-fold diffraction peaks. Thus, we have evaluated structure factors for these films in an effort to see whether the model system reproduces the observations. The three-dimensional views of $S(\boldsymbol{k})$ shown in Fig. 4 indicate that this is the case. The first picture shows the weak ring observed for a true two-dimensional fluid at 65 K. At the lower temperature of the systems studied here, peaks are observed with six-fold symmetry even at the low densities. These peaks sharpen considerably and move outwards as the first layer density increases. Specifically, the k^* values for the maxima in $S(\boldsymbol{k})$ occur at 0.705, 0.74, 0.84, and 0.91 for ρ = 0.0735, 0.0765, 0.0954, and 0.1145, respectively. For the highest coverage, the maximum in $S(k)$ for the first layer occurs at 0.90. The difference between this value and that for ρ* = 0.1145 is probably not significant. It could well be produced by a small mis-match of the lattice with the cell dimensions.

These structure factors are more-or-less equivalent to a mapping of the simulated L.E.E.D. patterns. The peaks sharpen considerably when a solid is formed but do appear to confirm the θ-phase suggested by Fain and co-workers (5).

Figure 5 shows the surface-averaged two-dimensional c.o.m. density ρ*(z*) for four of the densities considered. These plots confirm the description suggested by the energies and orientational distributions. The surface-parallel molecules at

FIG. 4. Pictures of the two-dimensional structure factors $S(\boldsymbol{k})$ for these systems are shown here, together with a reference diagram obtained for the two-dimensional fluid at 65 K (near the two-dimensional critical point). Part (*b*) shows the separate structure factors for the first and second layer molecules present at ρ = 0.1908 Å^2.

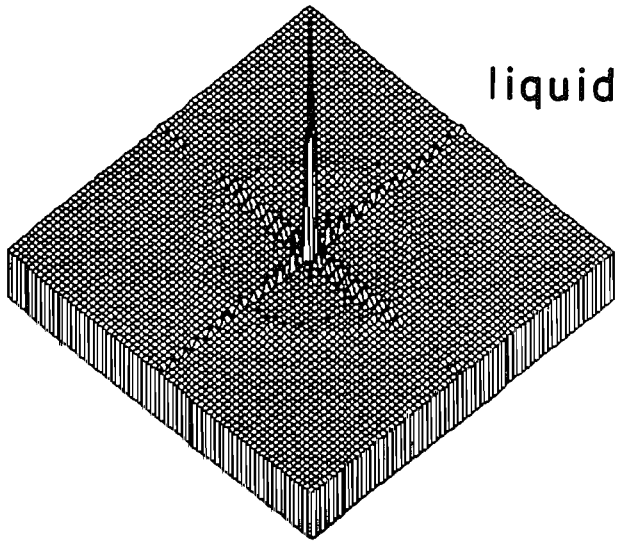

FIG. 4a

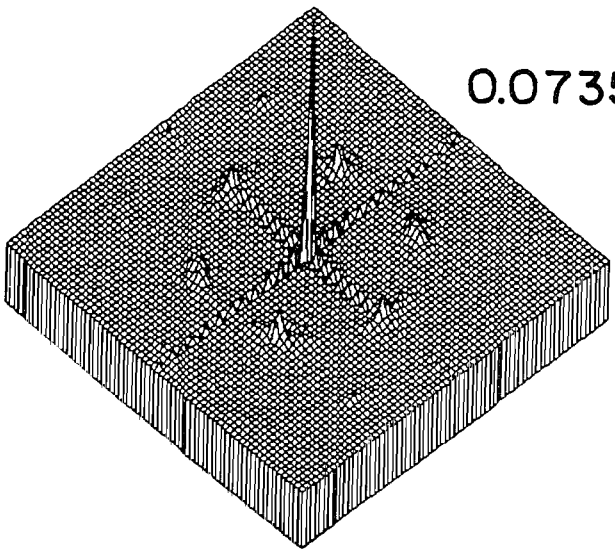

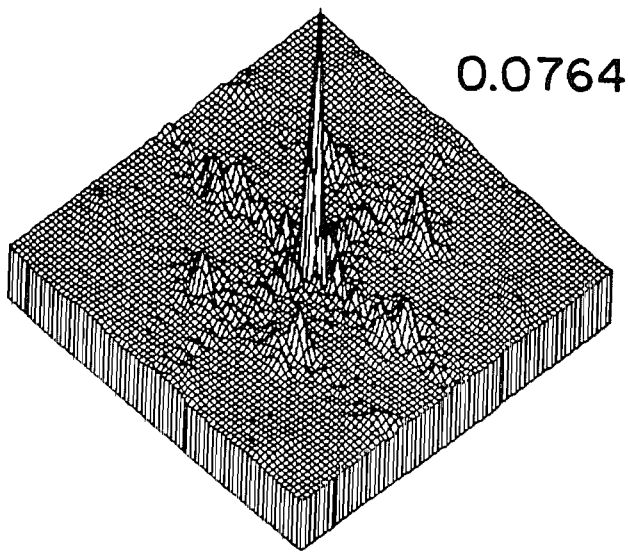

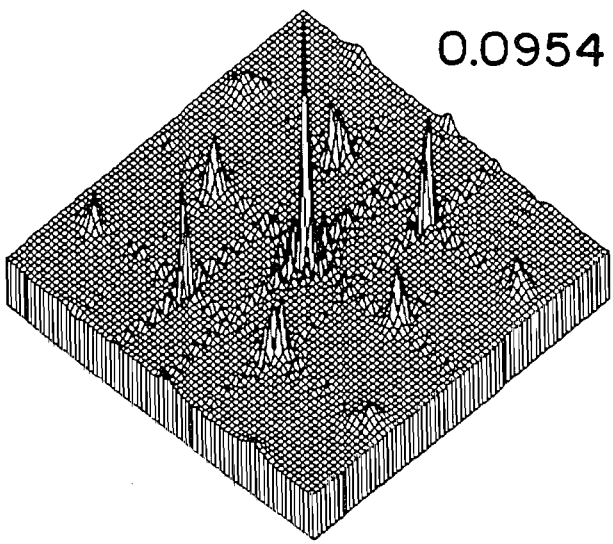

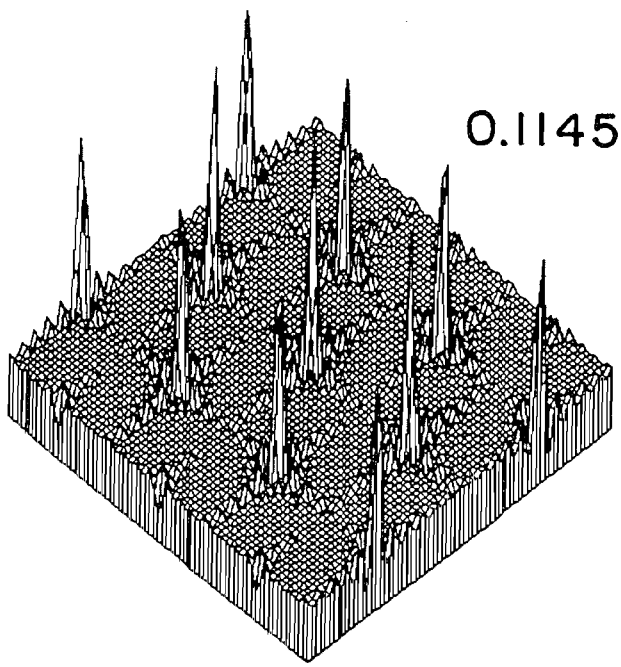

Can. J. Chem. Downloaded from www.nrcresearchpress.com by 176.9.209.113 on 09/07/12
For personal use only.

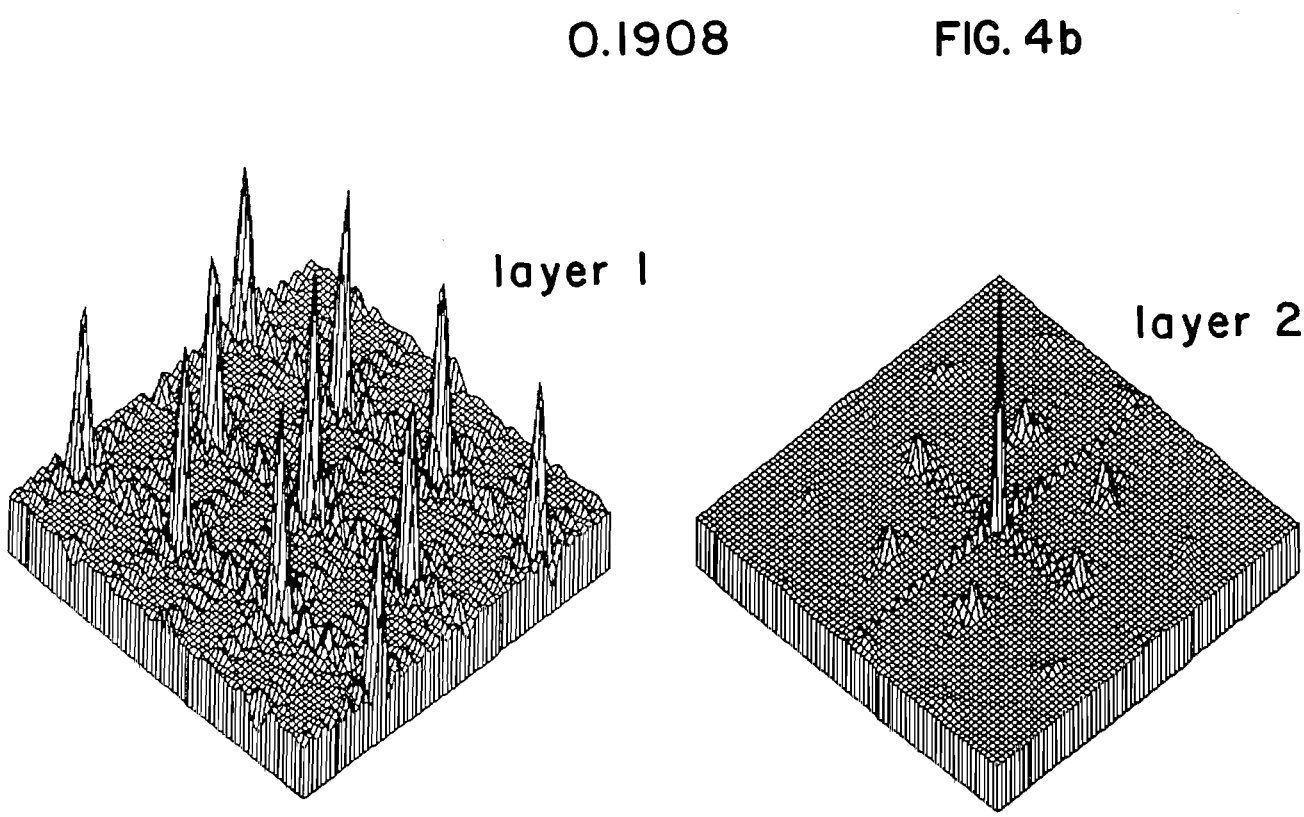

Can. J. Chem. Downloaded from www.nrcresearchpress.com by 176.9.209.113 on 09/07/12
For personal use only.

$\rho = 0.076$ Å^{-2} form a reasonably compact layer at $z^* = 1.3$, with a shoulder in $\rho^*(z^*)$ at ~ 1.55. As the surface coverage increases, the first layer molecules split into two groups which can be characterized as surface-parallel and surface-perpendicular. For instance, the areas under the peaks for $\rho = 0.0954$ Å^{-2} indicate $\sim 3/4$ perpendicular, whereas the first-layer molecules are essentially all perpendicular at the two highest densities. Note that the shift in layer center-of-mass position z^* as orientation changes should be (and is) equal to half the reduced molecular length of 0.48.

The results shown so far indicate a possible two-phase equilibrium made up of molecules predominantly perpendicular to the surface (up) and parallel (down). However, if these molecules segregate into separate phases, one would expect to find a predominance of up–up and down–down pairs and few up–down pairs (which would occur only along the edges of each phase). This can be studied by determining the center-of-mass pair correlation functions $g(\tau)$ for the three types of molecular pair. We have simulated this function by defining an "up" molecule to have orientation angle less than 45° and "down" to be those with angle greater than 45°. For a random distribution of such molecules, one expects that $g(\tau)$ or, more precisely, the areas under the peaks in this function will be identical for all three cases, whereas phase separation would give $g(\tau)$ nearly equal to zero for the up–down correlation (no neighbors of the other kind). The plots in Fig. 6 show clearly that the number of up–down nearest neighbors is far from zero and in fact, the nearest neighbor peaks have nearly the same areas, indicating a random distribution in the surface layer. The shapes of the peaks change slightly, with the widths and positions of $g(\tau)$ for up–up pairs indicating well-ordered hexagonal array. The peaks are broadened and move out slightly when one or both molecules in the pair lies down. This is not surprising, since rotation in the plane of the surface is relatively free and would give an effective molecular size which is somewhat larger and less well-defined than for a molecule standing on end.

We have also investigated whether or not these phases are fluid by determining the nature of the translation parallel to the surface. The time-dependence of the mean square displacements are shown in Fig. 7. The first layer molecules at the two highest coverages show the characteristic behavior of a solid-like layer (consistent with the trajectory plots of Fig. 1), whereas linear increases with time that indicate diffusional motion are observed at the smaller two coverages.

4. Discussion

Evidently, these simulations indicate the presence of an unusual monolayer phase at densities between ~ 0.07 and ~ 0.11 Å^{-2}. Above 0.11 Å^{-2}, a solid hexagonal phase forms with the molecules orientationally perpendicular to the surface. At densities less than 0.07 Å^{-2}, a fluid phase forms with the molecules orientationally ordered parallel to the surface. In the intermediate regime (θ-phase), the structure factors indicate weak but distinct hexagonal ordering relative to the graphite substrate, in agreement with the L.E.E.D. experiments. However, the mean square displacements are those expected for a fluid phase, not a solid. It is legitimate to suggest that the order observed might be a residual effect of the initial conditions of the simulation which would disappear in a sufficiently long run. Although this hypothesis cannot be strictly proven incorrect, there are several counter-arguments. For instance, the initial configuration is a centered rectangular lattice with all molecules parallel to the surface. Both the symmetry and the orientations change during the equilibration period. Support for the presence

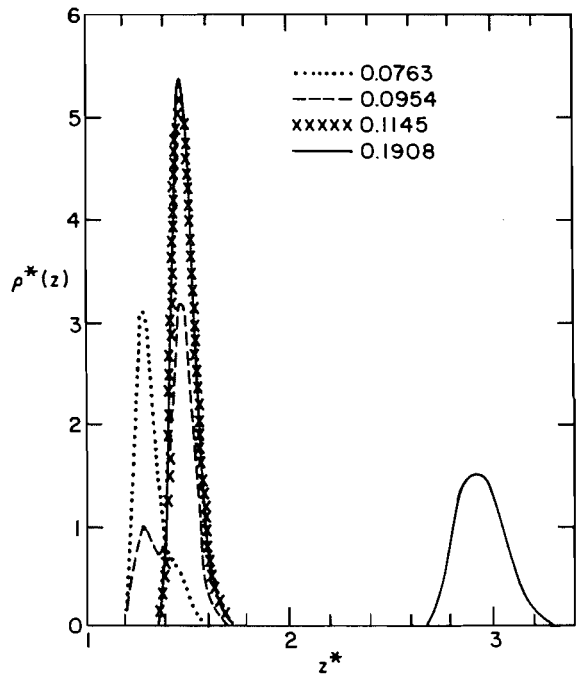

FIG. 5. Center-of-mass two-dimensional densities for four surface coverages are shown as a function of reduced distance from the surface z^*. Reduced density $\rho^*(z^*) = \rho(z)a^2$, with $a = 2.46$ Å.

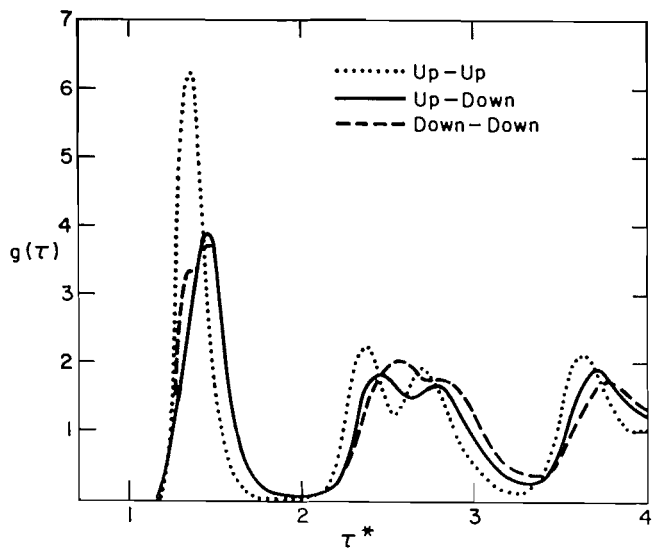

FIG. 6. Pair correlation functions for the orientationally distinct molecules in the layer with $\rho = 0.0954$ Å^{-2} are plotted here as a function of the reduced center-of-mass separation distance in the plane of the surface. A molecule in a hexagonal array has 6 neighbors at the nearest neighbor distance τ_{nn}, 6 at $\sqrt{3}\tau_{nn}$, 6 more at $2\tau_{nn}$, etc. For the up–up function, $\tau_{nn}^* = 1.35$; a second peak occurs at 2.35 (expected value = 2.34) and a third at 2.71 (expected = 2.70). Areas under the peaks in $\pi g(\tau)\tau$ are roughly constant.

of an equilibrium layer also comes from the mean square displacements. If one extrapolates the curve in Fig. 7*a* for 0.0954 Å^{-2} to a time interval of 50 ps, one finds a root mean displacement of ~2 Å, which should be sufficiently large to remove all memory of the initial configuration. (For $\rho =$ 0.0763 Å^{-2}, the r.m.s. displacement is ~6 Å after 50 ps.) In fact, the most significant disagreement with experiment is not a lack of structure, but too much structure, especially at the

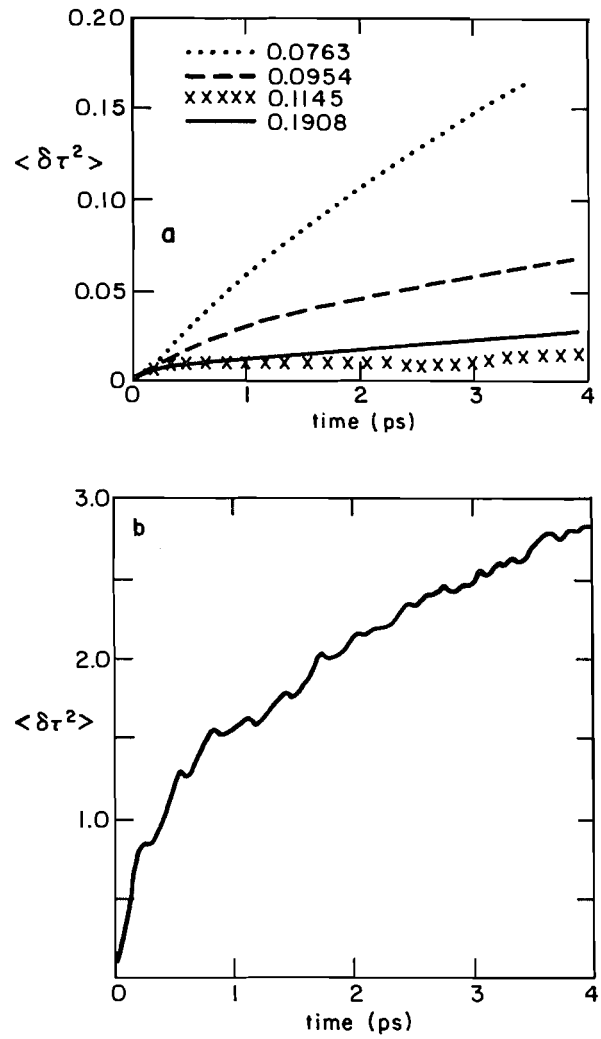

FIG. 7. Mean square displacements (in reduced units) in the plane of the surface are shown for first layer molecules at several coverages (part (*a*)) and for the second layer molecules at the highest coverage (part (*b*)). The oscillations in the curve of part (*b*) are probably of no physical significance. The slow upward drifts of the two lowest plots in part (*a*) reflect the floating of these solid layers across the surface (see Fig. 1).

lowest density. One should remember that O_2–O_2 interaction was not perfectly modelled in this study — in particular, there are indications that the well-depths of the site–site potential used here is ~20% too deep (11). If so, this is equivalent to simulating the real O_2 at a temperature ~20% less than the nominal 45 K used, which should be characterized by more ordering than that observed experimentally at 45 K.

Although we have not yet made an exhaustive study of the bilayer system, the results obtained so far appear to indicate a fluid second layer coexisting with the solid monolayer. Weak orientational ordering in the second layer fluid is observed together with orientational distribution showing some evidence of a mixture of parallel and perpendicular molecules. Indeed, the second layer at this coverage behaves as a poorly defined θ-phase. Additional simulations of thick O_2 films are being carried out at various temperatures in an attempt to characterize the melting and possibly the wetting behavior of these systems.

Acknowledgments

This work was supported by NSF grant DMR-84-19261-A02.

Can. J. Chem. Downloaded from www.nrcresearchpress.com by 176.9.209.113 on 09/07/12
For personal use only.

Many helpful conversations with Professors S. Fain and M. Chan are gratefully acknowledged.

1. S. C. FAIN, JR., M. F. TONEY, and R. D. DEIHL. *In* Proceedings of the Ninth International Vacuum Conference and Fifth International Conference on Solid Surfaces. *Edited by* J. L. de Segovia. Imprenta Moderna, Madrid. 1983.
2. V. BHETHANABOTLA and W. A. STEELE. Langmuir. **3**, 581 (1987).
3. S. TANG, S. D. MAHANTI, and R. K. KALIA. Phys. Rev. Lett. **56**, 484 (1986); R. D. ETTERS and O. DUPARC. J. Chem. Phys. **82**, 1020 (1987).
4. K. FLURCHICK and R. K. ETTERS. J. Chem. Phys. **84**, 4657 (1986); Y. P. JOSHI and D. J. TILDESLEY. Surf. Sci. **166**, 169 (1986); R. D. ETTERS, R.-P. PAN, and V. CHANDRASEKHARAN. Phys. Rev. Lett. **45**, 645 (1980); R. P. PAN, R. D. ETTERS, K. KOBASHI, and V. CHANDRASEKHARAN. J. Chem. Phys. **77**, 1035 (1982); R. D. ETTERS and K. KOBASHI. J. Chem. Phys. **81**, 6249 (1984).
5. H. YOU and S. FAIN. Phys. Rev. B**33**, 5886 (1986); M. F. TONEY and S. F. FAIN. Phys. Rev. B. **36**, 1248 (1987).
6. S. G. J. MOCHRIE, M. SUTTON, J. AKIMITSU, R. J. BIRGENAU, P. M. HORN, P. DIMON, and D. E. MONCTON. Surf. Sci. **138**, 599 (1984); P. A. HEINEY, P. W. STEPHENS, S. G. J. MOCHRIE, J. AKIMITSU, R. J. BIRGENAU, and P. M. HORN. Surf. Sci. **125**, 539 (1983); P. W. STEPHENS, P. A. HEINEY, R. J. BIRGENAU, P. M. HORN, J. STOLTENBERG, and O. E. VILCHES. Phys. Rev. Lett. **45**, 1959 (1980).
7. J. KRIM, J. P. COULOMB, and J. BOUZIDI. Phys. Rev. Lett. **58**, 583 (1987).
8. R. MARX and B. CHRISTOFFER. J. Phys. C, **18**, 2849 (1985); Phys. Rev. B. To be published.
9. J. DERICBOURG. Surf. Sci. **59**, 554 (1976).
10. D. J. EVANS and G. P. MORRIS. Computer Phys. Rpts. **1**, 297 (1984); Chem. Phys. **87**, 451 (1984); S. NOSÉ. J. Chem. Phys. **81**, 511 (1984).
11. M. J. BOJAN and W. A. STEELE. Langmuir. **3**, 116 (1987).

Can. J. Chem. Downloaded from www.nrcresearchpress.com by 176.9.209.113 on 09/07/12
For personal use only.

Intermolecular hydrogen tunneling in solids. Comparison between diabatic and adiabatic rate expressions[1]

PHILIP D. PACEY[2]
Department of Chemistry, Dalhousie University, Halifax, N.S., Canada B3H 4J3

AND

WILLEM SIEBRAND
Division of Chemistry, National Research Council of Canada, Ottawa, Ont., Canada K1A 0R6

Received October 6, 1987

This paper is dedicated to Professor J. A. Morrison

PHILIP D. PACEY and WILLEM SIEBRAND. Can. J. Chem. **66**, 875 (1988).

Rate expressions are derived for hydrogen transfer between two molecules in a solid, typical examples being hydrogen abstraction by methyl radicals in solid methane and in glassy methanol. These expressions are based on two-dimensional potential-energy surfaces describing the motion of the hydrogen atom along with that of the atoms between which it is transferred. A diabatic rate expression, based on the Golden Rule, is compared with an adiabatic rate expression, based on transition-state theory with a tunneling correction. In both cases, the two degrees of freedom must be treated quantum-mechanically rather than classically. For the adiabatic case, this leads to a new expression in which the barrier permeability is averaged over the wavefunction of the slow motion. The result differs from the Golden-Rule expression but yields similar rate constants. Numerical estimates are presented to illustrate the temperature and isotope dependence of these rate constants. The concept of a tunneling path is shown to break down at low temperature, so that the conventional one-dimensional tunneling approach becomes invalid.

PHILIP D. PACEY et WILLEM SIEBRAND. Can. J. Chem. **66**, 875 (1988).

On a dérivé des équations représentant la vitesse du transfert d'hydrogène entre deux molécules dans un solide; l'enlèvement d'hydrogène par des radicaux méthyles dans du méthane solide et dans du méthanol vitreux en sont des exemples typiques. Ces équations sont basées sur des surfaces d'énergie potentielle en deux dimensions qui décrivent le mouvement de l'atome d'hydrogène ainsi que ceux des atomes entre lesquels le transfert se produit. On compare une équation de vitesse diabatique qui est basée sur la «règle d'or» avec une équation de vitesse adiabatique qui est basée sur la théorie des états de transition avec une correction pour l'effet tunnel. Dans les deux cas, on doit faire appel à la mécanique quantique plutôt qu'à la mécanique classique pour traiter des deux degrés de liberté. Dans le cas adiabatique, ceci conduit à une nouvelle expression dans laquelle on fait une moyenne de la barrière à la perméabilité sur toute la fonction d'onde du mouvement lent. Le résultat est différent de celui obtenu à l'aide de l'expression dérivée de la «règle d'or»; toutefois, on obtient des constantes de vitesse qui sont semblables. On présente des évaluations numériques pour illustrer l'influence de la température et des isotopes sur ces constantes de vitesse. On montre que le concept de trajet de tunnel ne tient pas à basse température; il en résulte que l'approche conventionnelle par effet tunnel à une dimension devient invalide.

[Traduit par la revue]

I. Introduction

In this contribution we consider transfer of a hydrogen atom between two molecules in a solid at low temperatures. A typical example would be hydrogen exchange between a methane molecule and a trapped methyl radical in solid methane. Theoretically more complicated but experimentally more accessible is the equivalent reaction of methyl and methanol (1–14). In both cases hydrogen transfer is opposed by a high potential-energy barrier which reduces the rate of transfer over its top to negligible values at the low temperatures where these materials are solid. However, hydrogen is light enough to transfer by quantum-mechanical tunneling, a process that can take place even at 0 K.

The general characteristics of this tunneling process are well known (15). Its rate depends on the mass and energy of the tunneling particle and on the width and height of the barrier. However, in practice, it is not so simple to relate the barrier parameters to the known structural and energetic parameters of the system. While it is often possible to find a one-dimensional barrier that reproduces a set of observed tunneling rate constants, measured at different temperatures and perhaps for different hydrogen isotopes, in most cases the physical significance of the corresponding barrier height and width remains obscure. Instead of explaining the observed tunneling rates, such an analysis only presents the data in a different form.

Classically, the barrier represents the potential energy of the tunneling particle along the reaction coordinate. For intermolecular transfer, this coordinate always involves at least two degrees of freedom, namely one that describes the motion of the hydrogen atom relative to the heavier atoms between which it is exchanged and another that describes the motions of these heavier atoms relative to each other (16–19). At low temperatures these motions behave quantum-mechanically so that the concept of a reaction coordinate becomes irrelevant: the constraints imposed by the uncertainty principle will dominate those imposed by classical turning points. The two (or more) degrees of freedom governing the tunneling must then be treated separately.

If the tunneling is slow, the interaction causing the transfer is weak and can be treated simply as a perturbation. The rate of tunneling can then be expressed in terms of the Golden Rule (16, 18, 19). This makes it easy to include an arbitrary number of degrees of freedom, provided they are adiabatically separable. It has been shown that a two-dimensional Golden-Rule treatment can account satisfactorily for the rates of many hydrogen-tunneling reactions (18), including those of hydrogen abstraction by methyl radicals in glassy methanol (1). In this

[1]NRCC No. 28591.
[2]NRCC Visiting Scientist 1987.

Can. J. Chem. Downloaded from www.nrcresearchpress.com by 176.9.209.113 on 09/07/12
For personal use only.

Can. J. Chem. Downloaded from www.nrcresearchpress.com by 176.9.209.113 on 09/07/12
For personal use only.

approach the barrier does not enter directly; instead the transfer is described as a transition between reactant and product eigenstates which are derived from spectroscopic data. In principle, the coupling driving the transfer can be calculated quantum-chemically (20). However, this calculation requires a diabatic basis set, leading to crossing potentials. Standard quantum-mechanical methods are based on adiabatic basis sets, leading to avoided crossings. The problem is aggravated if the coupling is not weak so that higher-order terms must be included. In most Golden-Rule treatments of tunneling available to date, the coupling is parametrized rather than calculated.

Hence it remains worthwhile to pursue the alternative method based on transition-state theory (15, 21) which allows the use of standard quantum-chemical potentials. However, its usual form is based on classical approximations which fail at low temperature (22). For our purpose we need an adaptation suitable to describe tunneling in low-temperature solids. To this end, the motion of the hydrogen atom is described in terms of a two-dimensional potential-energy surface, derived from quantum-chemical calculations (20) in conjunction with spectroscopic and thermochemical data (1). The two degrees of freedom determining this surface are assumed to be adiabatically separable and treated quantum-mechanically. The results are compared with the Golden-Rule expression previously fitted to experimental data (1, 3).

II. Model system

We consider reactions of the type

[1] $$CH_3^{\bullet} + CH_3X \rightarrow CH_4 + {}^{\bullet}CH_2X$$

where X = H or OH. We also consider these reactions with H replaced by D. For simplicity, we restrict our calculations to symmetrical potentials (i.e., to X = H) for which quantum-chemical computations are available (20). These computations refer to the system $H_3C....H....CH_3$ and determine the structure of the transition state but not the complete surface. Their results are therefore combined with parameters derived from experimental data. The harmonic CH-stretch frequency and CH-bond dissociation energy are readily available from spectroscopic and thermochemical measurements (23). For the CC-stretching mode, we use the parameters derived previously (1) for the methyl–methanol system. Starting from these parameter values, we use the method of ref. 22 to construct a potential-energy surface. A typical result is illustrated in Fig. 1.

Actually, this construction involves some compromise, since the CC interaction used is valid only for small amplitudes. To obtain a realistic potential in the transition-state region, we would have to include a steep repulsion term. Since such a term is missing from the simplified approach of ref. 22, the resulting barrier is considerably lower than quantum chemical calculations indicate. However, this does not affect the final results significantly, since the transition-state region hardly contributes to the low-temperature transfer rate.

To compensate to some extent for the absence of a repulsive term, Fig. 1 is calculated with an electronic coupling term that does not depend on the CC distance. It has been shown previously that this does not affect the form of the result but only rescales some parameters (19). It follows that the potential surface in Fig. 1 is of limited accuracy in regions where high accuracy is not necessary for our purpose. The skewed-axes plot illustrates the motion of a spherical atom along this surface. However, the actual motion of the hydrogen atom will be shown to be quite different.

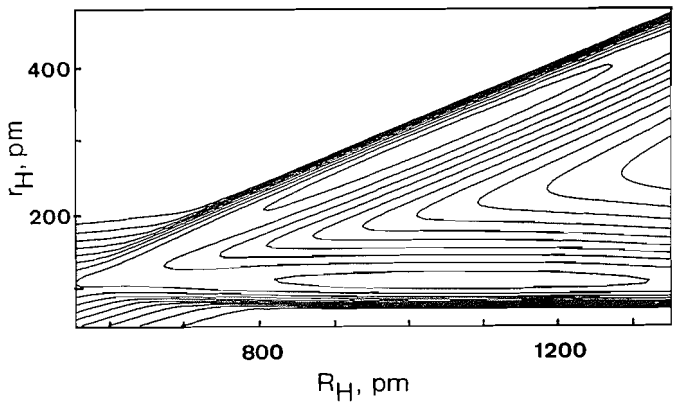

FIG. 1. Skewed and mass-weighted contour diagram of a potential-energy surface for transfer of H from CH_4 to $CH_3^{\bullet}$. The axes are scaled for an effective mass equal to the hydrogen mass. The elongated oval contours have the lowest energy, 20.5 kJ/mol above the minima, and represent the loci of classical turning points of the two-oscillator system with zero-point energy. Successive contours are mutually separated by 41 kJ/mol. The surface, calculated by the method of ref. 22, is based on the following parameter values: D_{CH} = 472.4 kJ/mol, $\bar{r}_A = \bar{r}_B$ = 108 pm, $\bar{R}$ = 395 pm, m = 1.008 g/mol, M = 15.04 g/mol, $\bar{J}$ = 34 kJ/mol, ω = 3289 cm^{-1}, Ω = 130 cm^{-1}.

To calculate hydrogen transfer rate constants, we do not use this potential surface directly, but start from the original parameters from which the surface is deduced. Where appropriate, we shall use analytical approximations to the potentials, so as to obtain simple expressions for the rate constants. In this way we can demonstrate the qualitative features of the method without having to rely on detailed numerical calculations. For the same reason, we restrict ourselves to resonant transitions in which the quantum numbers v and V of the CH and CC oscillators do not change. Since we consider only low-temperature transitions, we set $v = 0$, so that the temperature dependence of the transfer will be governed by the rate constants and Boltzmann populations of the levels $V = 0, 1, 2, \ldots$.

Given the strong dependence of the tunneling rate on the transfer distance (1), it is likely that transfer will only take place when the C...H...C system is collinear or nearly so. In principle, the tunneling rate will thus depend on the rotational and librational states of the molecules in the lattice. For simplicity, we assume that, on the timescale of the transfer, the methyl radicals and groups and/or the methane molecules are "freely" rotating and tumbling. Then the rotational degrees of freedom will introduce only temperature-independent statistical factors, compensated in part by the statistical factors representing the number of nearest-neighbor molecules of each radical. All of these factors we shall ignore for the present purpose.

III. Golden-Rule approach

The model allows a simplified version of the Golden-Rule treatment of refs. 1 and 18. The probability per second of a transition from an initial state $|i\rangle$ to a final state $|f\rangle$ is given by the diabatic rate constant

[2] $$k_{fi}^{d} = (2\pi/\hbar)|U_{fi}|^2\delta(\epsilon_f - \epsilon_i)$$

where U_{fi} is the matrix element coupling the states and the δ function signifies energy conservation. States $|i\rangle$ and $|f\rangle$ are represented by products of two harmonic oscillator wavefunctions

Can. J. Chem. Downloaded from www.nrcresearchpress.com by 176.9.209.113 on 09/07/12
For personal use only.

[3] $|i\rangle = \chi_v(r - \bar{r}_A)\chi_V(R - \bar{R})$

$|f\rangle = \chi_w(r - \bar{r}_B)\chi_W(R - \bar{R})$

characterized by frequencies ω and Ω. For the present model, the vibrational quantum numbers are $v = w = 0$ and $V = W$. R is the instantaneous CC distance with an equilibrium value $\bar{R}$, r is the instantaneous hydrogen position and $\bar{r}_A$ and $\bar{r}_B$ are the hydrogen equilibrium positions before and after transfer, respectively. Since the CH and CC coordinates r and R are collinear, we have $\bar{r}_B - \bar{r}_A = R - 2\xi$, where ξ is the equilibrium CH distance. We have assumed that the two vibrations are adiabatically separable; we further assume that the coupling operator J, representing the interaction between the donor (A) and acceptor (B) carbon atoms, does not depend on r. Then we obtain

[4] $U_{fi}(V) = \langle\chi_V(R - \bar{R})|J(R)S_{00}(R)|\chi_V(R - \bar{R})\rangle$

$S_{00}(R) = \langle\chi_0(r - \bar{r}_B)|\chi_0(r - \bar{r}_A)\rangle$

$= \exp\{-[\frac{1}{2}q(R - 2\xi)]^2\}$

where $q = (m\omega/\hbar)^{1/2}$. Taking

[5] $J = \bar{J}\exp[-z(R - \bar{R})]$

where z is the characteristic orbital radius expressed in units of the Bohr radius, we can solve the integral analytically (19)

[6] $U_{fi}(V) = \bar{J}\exp[2z(\bar{R} - 2\xi) + 2z^2/q^2]\int|\chi_V|^2\exp[-\frac{1}{4}q^2(R - 2\xi + 2z/q^2)^2]dR$

$= \bar{J}(1 - g)^{1/2}\exp[-\gamma^2 + 2z(\bar{R} - 2\xi) + 2z^2/q^2]\sum_{K=0}^{V}\frac{V!}{K![(V - K)!]^2}(g/2)^{V-K}H_{2(V-K)}(\gamma)$

where

[7] $g = q^2/(q^2 + 4Q^2)$

$\gamma = [qQ/(q^2 + 4Q^2)^{1/2}](\bar{R} - 2\xi + 2z/q^2)$

$Q = (M\Omega/\hbar)^{1/2}$

and $H_{2(V-K)}(\gamma)$ are Hermite polynomials. As usual, we replace the δ function in eq. [2] by a density of states, ρ_0. We then obtain

[8a] $k^d(V) =$

$$k^d(0)\left\{\sum_{K=0}^{V}\frac{V!}{K![(V - K)!]^2}(g/2)^{V-K}H_{2(V-K)}(\gamma)\right\}^2$$

[8b] $k^d(0) =$

$$(2\pi/\hbar)\bar{J}^2\rho_0(1 - g)\exp[-2\gamma^2 + 4z(\bar{R} - 2\xi + z/q^2)]$$

In this form, the treatment is suitable for qualitative purposes only. A more accurate form of these equations has been explored elsewhere (1, 3).

IV. Semi-classical approach

Semi-classically, the adiabatic rate constant of transfer through a one-dimensional barrier $U(r)$ is given by the frequency with which the hydrogen atom impinges on the barrier multiplied by the barrier permeability (15, 24, 25)

[9] $k^a(E) = (\omega/2\pi)P(E)$

$P(E) = \exp\{(-2/\hbar)\int_s(2m)^{1/2}[E - U(r)]^{1/2}dr\}$

where E is the energy of the atom and s is its path inside the barrier. This formulation has been the starting point for some very elaborate treatments (26–28) presumed to be capable of producing accurate numerical results. However, for our purpose we prefer to use a more traditional approach adapted so as to produce analytical results of the same type as those of the simplified Golden-Rule approach. This will allow a direct comparison of the two methods in a physically transparent form. To this end we identify ω in eq. [9] with the CH-stretch frequency and replace the actual barrier, depicted in Fig. 1, by a symmetrical Eckart barrier (15, 29)

[10] $U(r) = U_0/\cosh^2(\pi r/\lambda)$

which allows us to express the permeability in analytical form (15, 29):

[11] $P(E) = \dfrac{\sinh^2 b}{\sinh^2 b + \cosh^2 a}$

where

[12] $a = [(\lambda/\hbar)^2 2mU_0 - 4\pi^2]^{1/2} \simeq (\lambda/\hbar)(2mU_0)^{1/2}$

$b = (\lambda/\hbar)(2mE)^{1/2}$

To relate the Eckart barrier to our potential, we set $E = E_0 = \frac{1}{2}\hbar\omega$ and take the barrier width for $U(r) = \epsilon_0$ equal to the tunneling distance $R - 2\xi$. The barrier height $U_0(R)$ is taken from quantum-chemical calculations (20). The barrier width parameter $\lambda(R)$ is then given by

[13] $\lambda(R) = \frac{1}{2}\pi(R - 2\xi)/\text{arc cosh}\,[2U_0(R)/\hbar\omega]^{1/2}$

$\simeq \pi(R - 2\xi)/\ln[8U_0(R)/\hbar\omega]$

where the last step is valid if $2U_0(R) \gg \hbar\omega$. Substitution in eq. [12] yields

[14] $a(R) = \pi(R - 2\xi)qL/2\ln(2L)$

$b(R) = \pi(R - 2\xi)q/2\ln(2L)$

$L = [2U_0(R)/\hbar\omega]^{1/2}$

from which we obtain an expression for the rate constant as a function of ϵ_0 and R.

So far our treatment is basically standard. Conventionally one now proceeds by choosing a representative value of R, for instance the value corresponding to the classical turning point (15, 21). However, in the present case this would be improper since the oscillators are in low quantum states so that we are far from the classical region. Instead, we calculate the probability that a given R is realized by standard quantum mechanics, viz.

[15] $p_V(R) = |\chi_V(R - \bar{R})|^2$

The tunneling rate constant for an energy $\epsilon_0 = \frac{1}{2}\hbar\omega$ and a vibrational quantum number V is thus

$$[16]\quad k^a(\epsilon_0;V) = \int p_V(R)k^a(\epsilon_0,R)\mathrm{d}R = (\omega/2\pi)\int|\chi_V|^2P(\epsilon_0,R)\mathrm{d}R$$

$$P(\epsilon_0,R) = \frac{\sinh^2[\pi q(R-2\xi)/2\ln(2L)]}{\sinh^2[\pi q(R-2\xi)/2\ln(2L)] + \cosh^2[\pi qL(R-2\xi)/2\ln(2L)]}$$

To evaluate this integral, we need an expression for $L(R)$ and thus for $U_0(R)$. In our model, this potential ridge varies between $U_0(R_0)$, where R_0 is the transition state value, and $U_0(\infty) = D_{CH}$, the CH bond dissociation energy. For R near R_0, we use quantum-chemical results to obtain $U_0(R_0)$ as well as the harmonic frequency ω_0. To extrapolate to $R \rightarrow \infty$, we use a Morse potential:

$$[17]\quad U_0(R) = U_0(R_0) + \Delta U\{1 - \exp[-(M\omega_0^2/2\Delta U)^{1/2}(R - R_0)]\}^2$$

where $\Delta U = D_{CH} - U_0(R_0)$. After substitution into eq. [16], the resulting integral can be evaluated numerically.

However, in our case we can obtain a simple analytical approximation. For realistic R values, we have

$$[18]\quad a(R) \gg b(R) \gg 1$$

so that the hyperbolic functions in eq. [16] can be approximated by exponentials:

$$[19]\quad P(\epsilon_0,R) \simeq \exp\{2[b(R) - a(R)]\} = \exp[-\pi q\eta(R - 2\xi)]$$

where

$$[20]\quad \eta = [L(R) - 1]/\ln[2L(R)]$$

Within the range of R values for which significant transfer takes place, L is a number in the range 2.5–4.5, so that $\eta = 1.3 \pm 0.3$. Since η varies slowly with R, we shall approximate it by a constant, implying that $P(\epsilon_0,R)$ is approximated by an exponential function of R. We thus obtain

$$[21]\quad k^a(\epsilon_0;V) = (\omega/2\pi)\int_{-\infty}^{\infty}|\chi_V|^2\exp[-\pi q\eta(R - 2\xi)]\mathrm{d}R$$

which can be integrated analytically to yield

$$[22]\quad k^a(\epsilon_0;V) = k^a(\epsilon_0;0)\sum_{K=0}^{V}\frac{V!\sigma^{2(V-K)}}{2^{V-K}K![(V-K)!]^2}$$

$$k^a(\epsilon_0;0) = (\omega/2\pi)\exp[-\sigma Q(\bar{R} - 2\xi - \sigma/4Q)]$$

where

$$[23]\quad \sigma = \pi\eta q/Q \simeq 4q/Q$$

In practice, it may be advisable to apply this result only as a semi-empirical equation in which η is an adjustable parameter close to unity. In this form, it can be used to obtain relative rate constants as a function of temperature and isotopic species.

V. Comparison

Resonant hydrogen tunneling leads to splitting of the corresponding energy levels. In terms of the Golden-Rule approach this splitting is given by

$$[24]\quad \Delta\epsilon^d = 2|U_{fi}|$$

Semi-classically, the splitting can be represented by (30)

$$[25]\quad \Delta\epsilon^a = (\hbar\omega/\pi)P^{1/2}$$

Since

$$[26]\quad |U_{fi}| = (2\hbar k/\pi\rho)^{1/2}$$

and

$$[27]\quad P^{1/2} = (2\pi k/\omega)^{1/2}$$

these formulas are equivalent (31) for one-dimensional tunneling with $\rho = 1/\hbar\omega$.

For two-dimensional tunneling of the type considered, we obtain from eq. [24]

$$[28]\quad \Delta\epsilon_V^d = 2|\langle V|J(R)S_{00}(R)|V\rangle|$$

and from eq. [25]

$$[29]\quad \Delta\epsilon_V^d = (\hbar\omega/\pi)|\langle V|P(\epsilon_0,R)|V\rangle|^{1/2}$$

These results are no longer equivalent, since the integration over $\chi_V(R - \bar{R})$ enters in a different manner. The integral $\langle V|P|V\rangle$ represents an averaging procedure and should not be interpreted as a transition matrix element. Thus for an asymmetric barrier corresponding to a transition from χ_V to χ_W, the integral $\langle V|JS_{00}|V\rangle$ in [28] becomes $\langle W|JS_{00}|V\rangle$, but the integral $\langle V|P|V\rangle$ in [29] becomes $\frac{1}{2}|\langle V|P|V\rangle + \langle W|P|W\rangle|$. Although standard transition-state theory does not consider the final state explicitly, this averaging is imposed by the principle of microscopic reversibility.

The same differences are observed between the diabatic and adiabatic rate constant expressions [8] and [22]. Clearly the R coordinate is treated differently in the two approaches. In the Golden-Rule approach, it is treated on the same footing as the r coordinate. In the transition-state approach, the two coordinates are treated differently, such that r is the reaction coordinate and R modifies the barrier. This is thus an "oscillating barrier" treatment. Both treatments are approximate, but they involve different approximations so that their results will not be identical.

VI. Quantitative aspects

In our adiabatic approach, the tunneling rate constant $k^a(\epsilon_0;V)$ is expressed as an integral over all tunneling paths, each characterized by a single-path rate constant $k^a(\epsilon_0,R;V)$, which in turn is expressed as the product of a probability $\chi_V^2(R - \bar{R})$ and a permeability $P(\epsilon_0,R)$:

$$[30]\quad k^a(\epsilon_0;V) = \int_{-\infty}^{\infty}k^a(\epsilon_0,R;V)\mathrm{d}R$$

$$k^a(\epsilon_0,R;V) = (\omega/2\pi)P(\epsilon_0,R)|\chi_V(R - \bar{R})|^2$$

All of these quantities are plotted in Fig. 2. The permeability $P(\epsilon_0,R)$ is a nearly exponential function of R for relevant R values, so that eq. [19] with constant η should be a satisfactory approximation for our model. The single-path rate constants $k^a(\epsilon_0,R;V)$ peak well outside the classical region delimited by the inner turning points shown in Fig. 2. The effective R value denoted by $\tilde{R}$ and defined by

$$[31]\quad k^a(\epsilon_0,V) = (\omega/2\pi)\int_{-\infty}^{\infty}P(\epsilon_0,R)\delta(R - \tilde{R})\mathrm{d}R/\tilde{R} = (\omega/2\pi)P(\epsilon_0,\tilde{R})$$

Can. J. Chem. Downloaded from www.nrcresearchpress.com by 176.9.209.113 on 09/07/12
For personal use only.

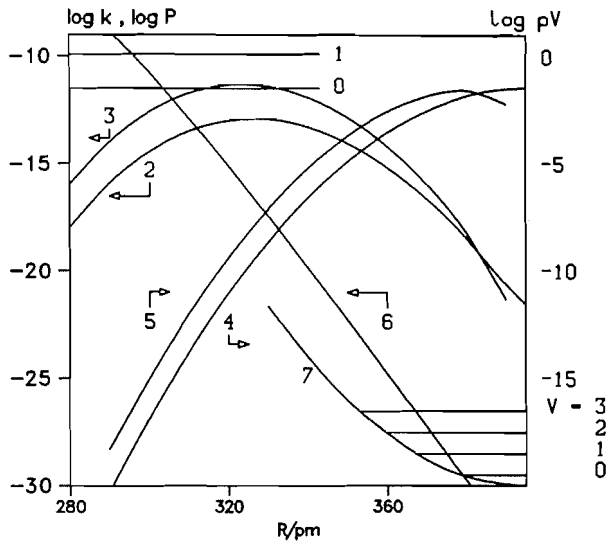

FIG. 2. Adiabatic rate constants of hydrogen transfer from CH_4 to $CH_3^{\bullet}$ and their components plotted as a function of R, the instantaneous CC distance. The rate constants $k^a(\epsilon_0;0)$ and $k^a(\epsilon_0;1)$, calculated from eq. [16], are labeled 0 and 1, respectively. Their R-dependent components $k^a(\epsilon_0,R;0)$ and $k^a(\epsilon_0,R;1)$, defined by eq. [30], are labeled 2 and 3, respectively. The curves labeled 4 and 5 depict the squared harmonic wavefunctions $\chi_0^2(R-\bar{R})$ and $\chi_1^2(R-\bar{R})$, respectively. Curve 6 depicts $P(\epsilon_0,R)$ defined by eq. [16], and curve 7 depicts the harmonic CC stretch potential, showing the classical turning points associated with vibrational quantum numbers $V = 0$–3. Parameter values are taken from ref. 1, except that the exothermicity ΔE has been taken equal to zero, and, from ref. 2 for the transition-state region: $\omega/2\pi = 1.41 \times 10^{13}\,s^{-1}$, $R_0 = 267$ pm, $U_0(R_0) = 357$ kJ/mol, $\Delta U = 98$ kJ/mol, $\bar{R} = 395$ pm, $\xi = 1.08$ pm, $(M\omega_0^2/2\Delta U)^{1/2} = 0.0123\,pm^{-1}$, $q = 0.0899\,pm^{-1}$, $Q = 0.0626\,pm^{-1}$.

is found to be about 9 pm smaller than the inner turning points for $V = 0$ and 1. If $\bar{R}$ is replaced by the turning point value, the resulting rate constants would be too small by about 10^5. Hence turning points do not provide a useful definition of the barrier for low quantum numbers.

The rate constants $k^a(\epsilon_0;0) = 3.2 \times 10^{-12}\,s^{-1}$ and $k^a(\epsilon_0;1) = 1.2 \times 10^{-10}\,s^{-1}$ depicted by horizontal lines at the top of Fig. 2 are obtained by numerical integration of eq. [16]. The corresponding approximate results, obtained from eq. [22] are $k^a(\epsilon_0;0) \simeq 2.2 \times 10^{-12}\,s^{-1}$ and $k^a(\epsilon_0;1) \simeq 4.0 \times 10^{-11}\,s^{-1}$, for $\eta = 1.3$. These results are about six orders of magnitude smaller than the rate constants observed at 5 K for the methyl–methanol system (1) and would be too small to be measured by conventional methods. This discrepancy is thought to be mostly due to the assumption of zero exothermicity, a conclusion supported by Golden-Rule results obtained earlier (1, 8). Since the exothermicity ΔE for the methyl–methanol system is about 26 kJ/mol (32), resonant transitions $vV \rightarrow wW$ with $w - v = 1$ or $W - V = 10$–20 would be expected. It is clear that these would have much higher rates than the $w - v = W - V = 0$ transitions calculated here. Hence our calculations predict that hydrogen exchange between methyl radicals and methane molecules in solid methane, where ΔE vanishes by symmetry, will be extremely slow and probably unobservable. This prediction does not depend on the details of the potential. It should be realized, however, that for quantitative calculations of rate constants, very accurate potentials are required. The formulas presented here should be used only for qualitative purposes.

Qualitatively, the present expressions for the temperature and isotope dependence of the adiabatic rate constants are compatible with the diabatic results obtained earlier (1, 3) and hence with the experimental data to which they were fitted. Thus $k^a(T)$ assumes a constant value in the limit $T \rightarrow 0$ and increases nonexponentially with temperature due to the gradual population of the low-frequency oscillator levels. Since the experimental data show a good deal of scatter at low temperatures, we compare the predictions of eq. [16] with those of the Golden-Rule *calculations* of ref. 1. In both cases the temperature dependence of $k(T)$ is negligible for $T < 25$ K. The ratio $k(50\text{ K})/k(25\text{ K})$ is given as 2.4 by eq. [16] and as 3.2 by ref. 1. The ratio of the rate constants for hydrogen and deuterium transfer $k_H(50\text{ K})/k_D(50\text{ K})$ is given as 1.2×10^5 by eq. [16] and 1.5×10^4 by ref. 1. While the agreement is not quantitative, it is satisfactory if the difference between the potentials is taken into account.

VII. One-dimensional tunneling

Conventionally hydrogen transfer is treated as a one-dimensional tunneling problem (15). It is therefore of interest to inquire whether our two-dimensional treatment can be reduced to one dimension by the introduction of suitable approximations. In terms of our formalism, the one-dimensional rate constant for fixed $R = \bar{R}$ would be given by eq. [31] with ϵ_0 replaced by $E = \epsilon_0 + (V + \frac{1}{2})\hbar\Omega$. For a high barrier, eq. [19] can be rewritten in the generalized form

$$[32] \quad P(E;\bar{R}) \simeq \exp\,[-\pi q\tilde{\eta}(E)(\bar{R} - 2\xi)]$$

where

$$[33] \quad \tilde{\eta}(E) = 2[(U_0/E)^{1/2} - 1]/\ln(4U_0/E)$$

is a generalization of eq. [20]. We now set this one-dimensional rate constant equal to the corresponding two-dimensional rate constant for $V = 0$ and 1. Using eqs. [21]–[24], we obtain

$$[34a] \quad \tilde{\eta}(0) = \eta(\bar{R} - 2\xi - \pi q\eta/4Q^2)/(\bar{R} - 2\xi)$$

$$[34b] \quad \tilde{\eta}(1) \simeq \tilde{\eta}(0) - \frac{4\ln[\pi q\eta(\bar{R} - 2\xi)]}{\pi q(\bar{R} - 2\xi)}$$

where $\tilde{\eta}(0) = \tilde{\eta}(\frac{1}{2}\hbar\omega + \frac{1}{2}\hbar\Omega)$ and $\tilde{\eta}(1) = \tilde{\eta}(\frac{1}{2}\hbar\omega + \frac{3}{2}\hbar\Omega)$. If $\tilde{\eta}(E)$ varies slowly with E, i.e., if $E \ll U_0$ we can set

$$[35] \quad \tilde{\eta}(0) \simeq \tilde{\eta}(1) \simeq \eta$$

yielding

$$[36] \quad \bar{R} = \bar{R} - \pi q\eta/4Q^2$$

However, this makes $\bar{R}$ and thus the barrier width isotope dependent since q varies as $m^{1/4}$. Moreover, it would imply that the second term at the right-hand side of eq. [34*b*] is small. This is not generally true, however; for our model parameters it is about 0.3 and thus not negligible compared to $\tilde{\eta}(0)$ which is of order unity. The same argument is readily extended to $\tilde{\eta}(2)$, $\tilde{\eta}(3)$, etc. Hence eqs. [34] and [35] are not mutually consistent; specifically [34] contradicts the assumption $E \ll U_0$ and requires a strongly curved $\ln P$ against R plot instead of the nearly linear plot of Fig. 2. Thus to fit the temperature dependence of the transfer rate constant with a one-dimensional barrier, this barrier must be equated with a cut through the adiabatic surface that does not pass through the top (i.e., the quantum-chemical transition state). Since the position of the cut cannot be identified in the one-dimensional picture, the corresponding barrier height remains an empirical quantity.

Can. J. Chem. Downloaded from www.nrcresearchpress.com by 176.9.209.113 on 09/07/12
For personal use only.

Can. J. Chem. Downloaded from www.nrcresearchpress.com by 176.9.209.113 on 09/07/12
For personal use only.

Moreover there is no guarantee that it is the same for hydrogen and deuterium: for our system, the hydrogen barrier yields a deuterium transfer rate constant that is much too small compared to the hydrogen rate constant, due to the isotope dependence of $\bar{R}$. Comparison of the Golden-Rule barriers of refs. 1 and 22 with reported one-dimensional barriers for the same reactions (9) confirms these conclusions.

As a further illustration, we compare the rate constants $k^a(\frac{1}{2}\hbar\omega;1)$ and $k^a(\frac{1}{2}\hbar\omega + \hbar\Omega;0)$, which differ in the way the thermal energy quantum $\hbar\Omega$ is distributed over the two degrees of freedom. In a one-dimensional treatment, they are thus indistinguishable. However, application of eq. [16] or eq. [24] readily shows that $k^a(\frac{1}{2}\hbar\omega;1) \gg k^a(\frac{1}{2}\hbar\omega + \hbar\Omega;0)$ for our model.

We therefore conclude that a two-dimensional analysis of hydrogen transfer data is much more informative and meaningful than the conventional one-dimensional analysis. If high accuracy is not required, the extra effort involved in including the second dimension is minimal, as the present calculations show.

VIII. Discussion

We have shown that conventional transition-state theory, corrected for tunneling, can be used to calculate the rate of hydrogen transfer between molecules in low-temperature solids, provided at least two relevant degrees of freedom are included and treated quantum-mechanically rather than classically. In the proper limit this method is a convenient alternative to the Golden-Rule approach. The physical pictures associated with the two methods are different. In the Golden-Rule method the transfer is described as a transition between two zeroth-order diabatic eigenstates mediated by a coupling. This is basically a time-dependent perturbation method. In transition-state theory, the transfer is described as tunneling through an adiabatic potential-energy barrier. This is basically a time-independent approach, the permeability being derived from a time-independent Schrödinger equation (29). To turn this into a time-dependent description, one needs to localize the system at a given initial time at one side of the barrier: this requires a "classical" assumption. However, the actual treatment of the degrees of freedom involved in the tunneling must be quantum-mechanical rather than classical in order to produce valid results in the low-temperature region.

This implies that the classical notion of a distinct tunneling path is lost at low temperatures, since many different paths contribute. Alternatively, one can say that the path taken is fuzzy as befits a quantum particle. Of course, the concept of a tunneling path is alien to the Golden-Rule treatment. Here the transfer rate is limited by vibrational overlaps, i.e., by the Franck–Condon principle. Transfer occurs during those statistically rare events where the amplitudes of all relevant degrees of freedom are large and in phase, such that the instantaneous hydrogen position could have arisen from either the reactant or product state with comparable probability. In this picture the proton transfers because quantum mechanics allows it to stray occasionally very far from its origin.

Of course, these are elementary pictures which tend to get blurred in more sophisticated treatments. It is possible to overcome the apparent handicaps of the two theories and get accurate results but this requires elaborate computations and extensive numerical testing. This is impractical in the case of complex systems or limited data sets, for which the traditional one-dimensional tunneling method remains the most popular approach. We hope that the present contribution offers some insight into the merits and limitations of that approach and the available alternatives.

1. T. Doba, K. U. Ingold, W. Siebrand, and T. A. Wildman. Faraday Discuss. Chem. Soc. **78**, 175 (1984).
2. T. Doba, K. U. Ingold, and W. Siebrand. Chem. Phys. Lett. **103**, 339 (1984).
3. T. Doba, K. U. Ingold, W. Siebrand, and T. A. Wildman. J. Phys. Chem. **88**, 3165 (1984).
4. S. P. J. Sullivan and W. S. Koski. J. Am. Chem. Soc. **85**, 384 (1963).
5. A. Campion and F. Williams. J. Am. Chem. Soc. **94**, 7633 (1972).
6. M. C. R. Symons and G. W. Eastland. J. Chem. Res. (S)254, M(2901) (1977).
7. R. L. Hudson, M. Shiotani, and F. Williams. Chem. Phys. Lett. **48**, 193 (1977).
8. K. Toriyama and M. Iwasaki. J. Am. Chem. Soc. **101**, 2516 (1979).
9. R. J. Le Roy, H. Murai, and F. Williams. J. Am. Chem. Soc. **102**, 2325 (1980).
10. A. A. Stepanov, V. A. Tkatchenko, B. V. Bol'shakov, and V. A. Tolkatchev. Int. J. Chem. Kinet. **10**, 637 (1978).
11. B. V. Bol'shakov, A. A. Stepanov, and V. A. Tolkatchev. Int. J. Chem. Kinet. **12**, 271 (1980).
12. B. V. Bol'shakov and V. A. Tolkatchev. Chem. Phys. Lett. **40**, 468 (1976).
13. V. L. Vyazovkin, B. V. Bol'shakov, and V. A. Tolkatchev. Chem. Phys. **75**, 11 (1983); **95**, 93 (1985).
14. E. D. Sprague. J. Phys. Chem. **77**, 2066 (1973); **81**, 516 (1977); **83**, 849 (1979).
15. R. P. Bell. The tunnel effect in chemistry. Chapman and Hall, London. 1980.
16. V. A. Benderskii, V. I. Goldanskii, and A. A. Ovchinnikov. Chem. Phys. Lett. **73**, 492 (1980).
17. M. M. Kreevoy, D. Ostovic, D. G. Truhlar, and B. C. Garrett. J. Phys. Chem. **90**, 3766 (1986).
18. W. Siebrand, T. A. Wildman, and M. Z. Zgierski. J. Am. Chem. Soc. **106**, 4083 (1984); **106**, 4089 (1984).
19. W. Siebrand, T. A. Wildman, and M. Z. Zgierski. Chem. Phys. Lett. **103**, 339 (1984).
20. T. A. Wildman. Chem. Phys. Lett. **126**, 325 (1986).
21. D. G. Truhlar, W. L. Hase, and J. T. Hynes. J. Phys. Chem. **87**, 2664 (1983).
22. P. D. Pacey, W. Siebrand, and T. A. Wildman. Tunneling. *Edited by* J. Jortner and B. Pullman. Reidel, Dordrecht. 1986. p. 117.
23. R. J. Hayward and B. R. Henry. J. Mol. Spectrosc. **50**, 58 (1974).
24. E. C. Kemble. Phys. Rev. **48**, 549 (1935).
25. B. Jeffreys. Proc. Cambridge Phil. Soc. **38**, 401 (1942).
26. D. G. Truhlar and B. C. Garrett. Ann. Rev. Phys. Chem. **35**, 159 (1984).
27. B. C. Garrett, N. Abusalbi, D. J. Kouri, and D. G. Truhlar. J. Chem. Phys. **83**, 2252 (1985).
28. J. G. Lauderdale and D. G. Truhlar. J. Chem. Phys. **84**, 1843 (1986).
29. C. Eckart. Phys. Rev. **35**, 1303 (1930).
30. D. M. Dennison and G. E. Uhlenbeck. Phys. Rev. **41**, 313 (1932).
31. P. Senn and K. Dressler. J. Chem. Phys. **87**, 1205 (1987).
32. F. Bernardi, H. B. Schlegel, and S. Wolfe. J. Mol. Struct. **35**, 149 (1976).

Thermodynamics of aqueous EDTA systems: Apparent and partial molar heat capacities and volumes of aqueous $EDTA^{4-}$, $HEDTA^{3-}$, H_2EDTA^{2-}, $NaEDTA^{3-}$, and $KEDTA^{3-}$ at 25°C. Relaxation effects in mixed aqueous electrolyte solutions and calculations of temperature dependent equilibrium constants[1]

JAMEY K. HOVEY AND LOREN G. HEPLER
Department of Chemistry, University of Alberta, Edmonton, Alberta, Canada T6G 2G2

AND

PETER R. TREMAINE
Alberta Research Council, Oil Sands Research Department, P.O. Box 8330, Station F, Edmonton, Alberta, Canada T6H 5X2

Received October 5, 1987

This paper is dedicated to Professor James A. Morrison

JAMEY K. HOVEY, LOREN G. HEPLER, and PETER R. TREMAINE. Can. J. Chem. **66**, 881 (1988).

Calorimetric and densimetric measurements have led to apparent molar heat capacities and volumes for aqueous solutions of the mixed electrolytes $[(CH_3)_4N]_4EDTA + (CH_3)_4NOH$, $Na_4EDTA + NaOH$, and $K_4EDTA + KOH$, and single electrolytes Na_2H_2EDTA and $[(CH_3)_4N]_3[HEDTA]$ at 25°C. We have analyzed these results in terms of Young's rule and Pitzer's ion interaction model to obtain standard state partial molar heat capacities and volumes of $EDTA^{4-}(aq)$, $HEDTA^{3-}(aq)$, $H_2EDTA^{2-}(aq)$, $NaEDTA^{3-}(aq)$, and $KEDTA^{3-}(aq)$ at 25°C. For these calculations it was also necessary to evaluate the "relaxation" contribution to the measured heat capacities of some solutions. The partial molar heat capacities obtained here have been used with enthalpies from previous investigations for calculations of several equilibrium constants over wide ranges of temperature; volumes can be used for similar calculations of the effects of pressure.

JAMEY K. HOVEY, LOREN G. HEPLER et PETER R. TREMAINE. Can. J. Chem. **66**, 881 (1988).

Des mesures calorimétriques et de densités ont permis d'obtenir les capacités et les volumes molaires apparents de solutions aqueuses des électrolytes mixtes $[(CH_3)_4N]_4EDTA + (CH_3)_4NOH$, $Na_4EDTA + NaOH$ et $K_4EDTA + KOH$ ainsi que des électrolytes simples Na_2H_2EDTA et $[(CH_3)_4N]_3[HEDTA]$, à 25°C. Dans le but d'obtenir les capacités calorifiques et les volumes molaires partiels dans l'état standard des ions $EDTA^{4-}(aq)$, $HEDTA^{3-}(aq)$, $H_2EDTA^{2-}(aq)$, $NaEDTA^{3-}(aq)$ et $KEDTA^{3-}(aq)$, à 25°C, on a analysé ces résultats en fonction de la règle de Young et du modèle de Pitzer pour les interactions ioniques. Pour faire ces calculs, il est nécessaire d'évaluer la contribution de la «relaxation» aux capacités calorifiques de quelques-unes de ces solutions. On a utilisé les capacités molaires partielles ainsi obtenues en conjonction avec des enthalpies obtenues au cours d'études antérieures pour calculer plusieurs constantes d'équilibre, sur un large éventail de températures; les volumes peuvent aussi être utilisés pour faire des calculs semblables relativement aux effets de la pression.

[Traduit par la revue]

Introduction

Aqueous solutions of EDTA (ethylenediaminetetraacetic acid and its salts) have found use in many applications, as discussed previously (1, 2). As a result of our own and other investigations we now have reasonably complete thermodynamic data for aqueous complexes of EDTA with several cations. On the other hand, we are missing potentially valuable thermodynamic data for complexes of EDTA with some other important cations and for the acid dissociation species $HEDTA^{3-}(aq)$, and $EDTA^{4-}(aq)$. In this latter connection, the speciation (3) of EDTA solutions at 25°C as a function of pH at 0.1 molar ionic strength is illustrated in Fig. 1.

Thermodynamic measurements carried out with constant ionic strength media of alkali metal salts are complicated by the formation of alkali metal ion – EDTA complexes (4, 5). Similarly, investigations with the highly alkaline solutions that are required to obtain most of the EDTA as the $HEDTA^{3-}(aq)$ and $EDTA^{4-}(aq)$ anions are also complicated by the formation of EDTA complexes with the cations that inevitably accompany hydroxide ions.

Several investigations of equilibrium constants and enthalpies of reaction involving solutions of EDTA have been carried out over a limited temperature range near 25°C, thereby permitting calculations of ΔC_p^0 values by way of

$$[1] \qquad (\partial \ln K/\partial T)_p = \Delta H^0/RT^2$$

and

$$[2] \qquad (\partial \Delta H^0/\partial T)_p = \Delta C_p^0$$

Accurate values of ΔC_p^0 would allow both ΔH^0 and $\ln K$ to be extrapolated to temperatures beyond the range of the original measurements. Unfortunately, the magnification of errors and uncertainties associated with differentiation, and also the complications mentioned above, cause many ΔC_p^0 values from eq. [2] to have very large uncertainties. We have therefore carried out the calorimetric measurements of heat capacities that are described in this paper. We have also measured densities that lead to new apparent and partial molar volumes. Analysis of our experimental data to obtain the desired standard state partial molar properties of specified ions is complicated because all of the solutions investigated have contained at least one cationic species and two anionic species.

Experimental

Water to be used for all experiments was filtered through activated charcoal and then passed through a Milli-RO4/Milli-Q reagent grade mixed bed ion exchange and activated carbon system to yield water with resistivity greater than 18 MΩ cm.

Solutions of NaCl (Fisher certified, ACS) were prepared by mass

[1]Alberta Research Council contribution no. 1571.

Can. J. Chem. Downloaded from www.nrcresearchpress.com by 176.9.209.113 on 09/07/12
For personal use only.

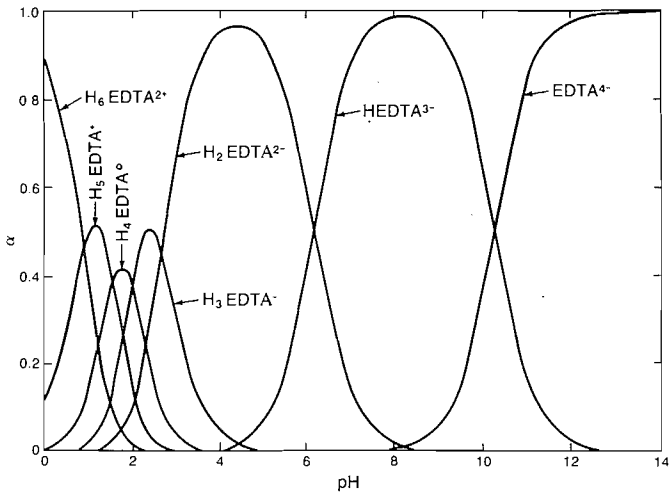

FIG. 1. Speciation of aqueous EDTA at 25°C and $I = 0.10$ molar.

after drying the salt at 110°C for several hours. Crystalline H_4EDTA (Fisher certified, ACS) was dried at 140°C for several hours to yield material that has been described (6) as a primary standard. Aqueous solutions of NaOH (50%) and KOH (1 molar) were obtained from Fisher (certified, ACS). Aqueous solutions of $(CH_3)_4NOH$ (25%) were obtained from both Fisher (certified) and Alfa (certified purity 99.9999%). The solution from Alfa was used without further purification, but the sample from Fisher was purified by passing it through an anion exchange column with resin in the hydroxide form to remove chloride and other anionic impurities. All hydroxide solutions were standardized by titration against potassium hydrogen phthalate. A solution of Na_2H_2EDTA was prepared by dissolving the salt (Fisher certified, ACS) in pure water and then standardized by titration against standard solutions of zinc chloride (6). A solution of $[(CH_3)_4N]_3[HEDTA]$ was prepared by adding a weighed amount of $(CH_3)_4NOH$ (Alfa) solution to a weighed amount of H_4EDTA, followed by adjustment to pH = 8.30 with a very dilute solution of $(CH_3)_4NOH$. Further solutions were prepared by dilution of this solution with very dilute $(CH_3)_4NOH$. Stock solutions of known stoichiometric compositions of $[(CH_3)_4N]_4EDTA + (CH_3)_4NOH$ (Alfa and Fisher), $Na_4EDTA + NaOH$, and $K_4EDTA + KOH$ were prepared by adding weighed amounts of standardized hydroxide solutions to weighed amounts of dried H_4EDTA. Further solutions were prepared by dilution with standardized hydroxide solutions. All of these alkaline solutions were prepared under nitrogen and then stored in nitrogen filled desiccators containing silica gel and Ascarite pellets to minimize carbonate contamination.

Densities were measured relative to water at 25.00 ± 0.01°C with a Sodev 03D vibrating tube densimeter (7), which was calibrated with pure water and a standard solution of NaCl. Heat capacities were measured relative to water with a Sodev CP-C Picker flow microcalorimeter (8). Temperatures were controlled (constant to ±0.001°C) with a Sodev CT-L circulating bath and monitored with calibrated thermistors. For the density and specific heat capacity of water at 25°C we used the values (9, 10) 0.997047 g cm^{-3} and 4.1793 J K^{-1} g^{-1}, respectively. Daily evaluation of the calorimetric heat loss correction factor (11) by way of measurements on standard solutions of NaCl led to $f = 1.006 \pm 0.002$.

Results and calculations

$[(CH_3)_4]_4NEDTA$

The Picker vibrating tube densimeter and calorimeter measure $[(c_p d/c_{p,1}^0 d_1^0) - 1]$ and $(d - d_1^0)$, in which c_p and $c_{p,1}^0$ are the specific heats of solution and of pure water, and d and d_1^0 are the densities of solution and of pure water, respectively. It is most useful to express our experimental results for mixed electrolyte solutions of $[(CH_3)_4N]_4EDTA + (CH_3)_4NOH$ as "experimental" apparent molar properties (${}^\Phi V_\Sigma^{exp}$, ${}^\Phi C_{p,\Sigma}^{exp}$) that are defined by

$$[3] \qquad {}^\Phi Y_\Sigma^{exp} = (Y_{sol} - n_1 Y_1^0)/(n_2 + n_3)$$

Here, Y_{sol} is the extensive property (volume or heat capacity) of a specified quantity of solution, Y_1^0 is the property (volume or heat capacity) of one mole of pure solvent (water), and n_1, n_2, and n_3 are the amounts (moles) of water and of solutes 2 (M_4EDTA) and 3 (MOH) in the specified quantity of solution.

For solutions containing molalities of solutes represented by m_2 and m_3, the equations that define ${}^\Phi V_\Sigma^{exp}$ and ${}^\Phi C_{p,\Sigma}^{exp}$ are given by

$$[4] \qquad {}^\Phi V_\Sigma^{exp} = [(1 + m_2 M_2 + m_3 M_3)/d_{sol} - 1/d_1^0]/(m_2 + m_3)$$

and

$$[5] \qquad {}^\Phi C_{p,\Sigma}^{exp} = [c_{p,sol}(1 + m_2 M_2 + m_3 M_3) - c_{p,1}^0]/(m_2 + m_3)$$

where M_2 and M_3 are the molar masses of the solutes. These experimental results are listed in Table 1.

At high pH values nearly all of the dissolved EDTA is in the $EDTA^{4-}(aq)$ form, as shown in Fig. 1. There is evidence (3), however, that $EDTA^{4-}(aq)$ at high concentrations of $(CH_3)_4NOH$ (>0.1 molal) forms complexes or ion pairs (small stability constant) with $(CH_3)_4N^+(aq)$. We have calculated the speciation of our solutions with the assumption that the rather uncertain equilibrium constant is exactly correct and have found that the amount of complex present in our solutions is so small as to have negligible effect upon the results we have obtained by extrapolation to infinite dilution. Consequently, we describe here only the simpler calculations based on neglect of ion pair or complex formation of $(CH_3)_4N^+(aq)$ with $EDTA^{4-}(aq)$.

Because the high pH solutions in which most of the dissolved EDTA is in the form of $EDTA^{4-}(aq)$ contain two anionic species (the $EDTA^{4-}(aq)$ of present interest and also $OH^-(aq)$), it is necessary to make use of some model for the excess thermodynamic properties of mixed electrolyte solutions to permit extraction of the desired properties of $EDTA^{4-}(aq)$ from the experimental quantities defined by eq. [3]. Because our solutions contained relatively large amounts of "extra" electrolyte and also because the electrolytes are of different charge types, we have used two methods of carrying out these calculations. One method is based on Young's rule and the other is based on Pitzer's ion interaction model.

Young's rule (12) expresses the apparent molar properties of a mixture of electrolytes in terms of properties (at an ionic strength equal to the total ionic strength of the solution) of the solute components of the mixture. Young's rule can be expressed as

$$[6] \qquad {}^\Phi Y_\Sigma = \Sigma(m_i/\Sigma m_i){}^\Phi Y_i + \delta$$

where m_i is the molality of the ith solute, ${}^\Phi Y_i$ is the corresponding apparent molar property, and δ is an excess mixing term. For solutions containing two solutes whose molalities are denoted by m_2 and m_3, δ has the form

$$[7] \qquad \delta = k_{23}[m_2 m_3/(m_2 + m_3)^2]I = k_{23} F_2 F_3 I$$

in which k_{23} is a binary interaction coefficient, $F_i = m_i/\Sigma m_i$, and I is the total molal ionic strength. Equations [6] and [7] can also be applied to systems in which one of the solutes dissociates or complexes to form other species. In such cases m_i refers to

Can. J. Chem. Downloaded from www.nrcresearchpress.com by 176.9.209.113 on 09/07/12
For personal use only.

Can. J. Chem. Downloaded from www.nrcresearchpress.com by 176.9.209.113 on 09/07/12
For personal use only.

TABLE 1. Compositions of solutions and results of calorimetric and densimetric measurements*

m_2 (mol kg^{-1})	m_3 (mol kg^{-1})	$^{\phi}V^{exp}$ (cm^3 mol^{-1})	$^{\phi}C_p^{exp}$ † (J K^{-1} mol^{-1})
	$[(CH_3)_4N]_4EDTA$ + $(CH_3)_4NOH$ (Fisher)		
0.1132	0.00170	489.78	803.7
0.09151	0.02149	417.26	668.0
0.06943	0.04161	341.99	536.3
0.04734	0.06174	263.60	391.7
0.02509	0.08200	181.29	257.2
0.01413	0.09199	139.68	183.7
0.1166	0.08247	326.11	518.3
0.1277	0.1715	260.78	407.5
0.04269	0.1289	187.62	273.1
0.04042	0.4014	123.10	169.7
	$[(CH_3)_4N]_4EDTA$ + $(CH_3)_4NOH$ (Alfa)		
0.1086	0.1126	288.24	467.7
0.09517	0.1133	274.02	442.4
0.08173	0.1139	258.11	412.3
0.06871	0.1145	240.40	376.9
0.06223	0.1148	230.82	359.8
0.05146	0.1153	213.09	325.5
0.04180	0.1158	195.23	293.9
0.02934	0.1164	168.84	246.7
0.02174	0.1167	150.65	215.3
0.01195	0.1172	123.91	171.1
	Na_3[NaEDTA] + NaOH		
0.2057	0.1609	85.84	162.3
0.1744	0.1566	80.04	139.8
0.1552	0.1539	75.77	123.5
0.1321	0.1507	69.89	103.2
0.1168	0.1486	65.43	88.7
0.09857	0.1461	59.28	69.8
0.07562	0.1429	49.91	42.3
0.05594	0.1402	40.18	17.1
0.03969	0.1380	30.38	−5.82
0.02053	0.1353	15.86	−39.9
	K_3[KEDTA] + KOH		
0.2049	0.1763	106.23	37.0
0.1456	0.1669	91.88	2.03
0.1237	0.1635	85.02	−13.2
0.08943	0.1580	71.55	−37.5
0.05980	0.1533	56.54	−61.2
0.03655	0.1497	40.80	−82.7
0.01932	0.1469	26.31	−99.4
0.1740	0.2763	75.34	−9.87
0.1641	0.3423	67.12	−5.96
0.01746	0.2302	18.71	−98.3
0.01577	0.3046	15.09	−98.0
	$[(CH_3)_4N]_3$[HEDTA]		
0.2194		423.29	705.3
0.1710		423.32	694.2
0.1299		423.31	694.0
0.1299		423.17	
0.1078		423.12	687.4
0.08617		423.08	683.2
0.06433		422.72	679.4
0.03648		422.56	673.1
0.01649		422.22	665.5
	Na_2[H_2EDTA]		
0.2588		160.38	285.1
0.1631		158.81	261.0
0.1251		158.14	248.0
0.1015		157.67	243.4
0.06069		156.49	225.0
0.03530		155.48	211.2
0.02597		155.03	207.4

TABLE 1 (*concluded*)

*m_2 is the stoichiometric (total) molality of EDTA from all species and m_3 is the stoichiometric molality of base.

†$^{\phi}Y^{exp}$ used in the heading represents $^{\phi}Y_{\Sigma}^{exp}$ for solutions containing $[(CH_3)_4N]_4$EDTA, Na_3[NaEDTA], and K_3[KEDTA].

the molality of each species rather than to the stoichiometric molality of each component.

Apparent molar properties of strong electrolytes can be represented to moderate concentrations by Debye–Hückel equations of the type

$$[8] \qquad {}^{\phi}Y = \bar{Y}_2^0 + A_Y\omega I^{1/2} + B_Y I + C_Y I^{3/2} + \ldots$$

in which $\bar{Y}_2^0$ is the value of $^{\phi}Y$ at infinite dilution, A_Y is derived from the Deybe–Hückel theory (13, 14), and B_Y and C_Y are adjustable parameters. The ionic strength I and the "valence factor" ω are defined and related by

$$[9] \qquad I = \omega m = 0.5\Sigma m_i z_i^2$$

We have made calorimetric and densimetric measurements leading to apparent molar heat capacities and volumes of solutions of $(CH_3)_4NOH$ prepared with material from Alfa and from Fisher and have reported (15) the results obtained for the solutions from Alfa. Apparent molar volumes for the solutions from Fisher are in good agreement with those for the solutions from Alfa, with both of the infinite dilution values showing good agreement with the value calculated from properties of $(CH_3)_4NCl$, NaCl, and NaOH. The apparent molar heat capacity at infinite dilution derived from the measurements on solutions from Alfa is also in good agreement with the value that can be calculated from heat capacities for the other electrolytes mentioned above. The result from the Fisher salt differs from this value by 11 J K^{-1} mol^{-1}. As a result, we have weighted the data obtained from measurements on solutions from Alfa more heavily than those obtained from solutions from Fisher.

In Table 2 we report the results of least-squares fits of eq. [8] to heat capacities and volumes of solutions of $(CH_3)_4NOH$ and other "auxiliary" electrolytes to be considered later. We have used the parameters in Table 2 with our experimental results (Table 1) in fitting eqs. [6]–[8] to obtain the desired standard state properties of $EDTA^{4-}$(aq) and other parameters as listed in Table 3. Results of different fits (different parameters set equal to zero) are mostly in good agreement. Uncertainties in the desired values of $\bar{C}_p^0$ are larger than for most of our other investigations because the solutions contained relatively large amounts of the auxiliary electrolyte and also because of the uncertainty in the product ωA_J for highly charged electrolytes such as $[(CH_3)_4N]_4$EDTA. We have plotted in Figs. 2 and 3 the results of our fits with Young's rule as presented in this section, and with the Pitzer model which follows. These plots illustrate some of the model dependency of the fitted results as well as some of the uncertainties in our data. We have estimated that *total* uncertainties (chemical, our measurements, Debye–Hückel slopes, and fitting model) in $\bar{V}^0$ and $\bar{C}_p^0$ for $EDTA^{4-}$(aq) are ±2 cm^3 mol^{-1} and ±25 J K^{-1} mol^{-1}, respectively.

Can. J. Chem. Downloaded from www.nrcresearchpress.com by 176.9.209.113 on 09/07/12
For personal use only.

TABLE 2. Extended Debye–Hückel parameters for aqueous hydroxides and chorides according to eq. [8]*

Solute	$\bar{V}^0$ ($cm^3\ mol^{-1}$)	A_V ($cm^3\ kg^{1/2}\ mol^{-3/2}$)	B_V ($cm^3\ kg\ mol^{-2}$)	C_V ($cm^3\ kg^{3/2}\ mol^{-5/2}$)	D_V ($cm^3\ kg^2\ mol^{-3}$)
$(CH_3)_4NOH$ (Fisher)	85.01 ± 0.04	1.8743	−1.483		
$(CH_3)_4NOH$ (Alfa)	85.54 ± 0.03	1.8743	−1.609		
NaOH	−5.259 ± 0.019	1.865	1.492	−0.3846	0.03241
KOH	4.917 ± 0.011	1.865	1.224	−0.3033	0.01976
$(CH_3)_4NCl$	107.27 ± 0.03	1.865	−1.33		
NaCl	16.616 ± 0.005	1.865	−0.178	0.179	
KCl	26.89 ± 0.01	1.865	0.0476		

Solute	$\bar{C}_p^0$ ($J\ K^{-1}\ mol^{-1}$)	A_J ($J\ K^{-1}\ kg^{1/2}\ mol^{-3/2}$)	B_J ($J\ K^{-1}\ kg\ mol^{-2}$)	C_J ($J\ K^{-1}\ kg^{3/2}\ mol^{-5/2}$)	D_J ($J\ K^{-1}\ kg^2\ mol^{-3}$)	E_J ($J\ K^{-1}\ kg^{5/2}\ mol^{-7/2}$)
$(CH_3)_4NOH$ (Fisher)	80.9 ± 0.5	32.783	4.897			
$(CH_3)_4NOH$ (Alfa)	92.1 ± 0.5	32.783	−1.098			
NaOH	−97.40 ± 0.30	28.95	45.92	−17.78	1.879	
KOH	−130.52 ± 0.22	28.95	32.93	−16.57	3.470	
$(CH_3)_4NCl$	107.7 ± 0.2	28.945	−5.0			−0.2882
NaCl	−84.4 ± 0.2	28.945	15.6			
KCl	−114.2 ± 0.2	28.945	8.2			

*The values in this table came directly from refs. 11 and 15–19 except for volumetric values for NaCl and KCl that were refitted to the data in refs. 7 and 19.

Na_3[NaEDTA] and K_3[KEDTA]

We have listed results of our measurements on solutions labelled Na_3[NaEDTA] and K_3[KEDTA] in Table 1, with experimental quantities and compositions defined as previously specified. Analysis of these results to obtain the desired standard state properties of $NaEDTA^{3-}$(aq) and $KEDTA^{3-}$(aq) requires consideration of mixed electrolyte effects as in the previous section. It is also necessary to consider detailed speciation and contributions of "chemical relaxation" to the measured heat capacities. Calculations with the stability constants from Daniele *et al.* (3) show that complexes of type $MEDTA^{3-}$(aq) are the principal species, but concentrations of $EDTA^{4-}$(aq) are too large to be ignored.

Concentrations of the various species have been obtained with equilibrium constants from Daniele *et al.* (3) by way of calculations based on eq. [10] as follows:

$$[10]\qquad \underset{(1-\alpha)m_2}{MEDTA^{3-}(aq)} = \underset{(3+\alpha)m_2 + m_3}{M^+(aq)} + \underset{\alpha m_2}{EDTA^{4-}(aq)}$$

The equilibrium properties of EDTA species have usually been based on a standard state having an ionic strength equal to 0.1 molar rather than the usual infinite dilution reference state. We denote the 0.1 molar reference state by the superscript † instead of ^{0} for the infinite dilution state.

Results obtained by Daniele *et al.* (3) for ionic strengths from 0.02 to 1.0 molar have been summarized by the equation

$$[11]\qquad \log K(I) = \log K^\dagger - z\{I^{1/2}/(2 + 3I^{1/2}) - (0.1)^{1/2}/[2 + 3(0.1)^{1/2}]\} + C(I - 0.1) + D[I^{3/2} - (0.1)^{3/2}]$$

We have listed values of $\log K^\dagger$, z, C, and D in Table 4 to allow easy calculation of the equilibrium constants and note that the small numerical differences between molality and molarity are less than the uncertainties in $K(I)$. Results of these speciation calculations are summarized in Table 5. We have corrected our measured apparent molar heat capacities for relaxation contributions to these functions as detailed in Appendices I and II. We subsequently have fitted expressions of type [6] and [8], using data from Roux *et al.* (16) for NaOH and KOH, and our calculated values for the hypothetical Na_4EDTA and K_4EDTA as listed in Table 3 for $[(CH_3)_4N]_4EDTA$. These calculations have also made use of auxiliary data for $(CH_3)_4NCl$, NaCl, and KCl (7, 11, 17–19) listed in Table 2, along with eq. [7] extended to three electrolytes as in

$$[12]\qquad \delta = k_{23}F_2F_3I + k_{24}F_2F_4I + k_{34}F_3F_4I$$

to obtain standard state and other parameters. The relative concentrations of the species in the solutions containing $NaEDTA^{3-}$(aq) allow us to ignore interactions of the uncomplexed $EDTA^{4-}$(aq) anion, which simplifies eq. [12] to eq. [7] in this case. On the other hand, analysis of the experimental data for solutions in which $KEDTA^{3-}$(aq) was an important anion is more complicated because of the larger number of non-negligible parameters to be included in the fit. Results of all of these calculations for solutions containing $NaEDTA^{3-}$(aq) and $KEDTA^{3-}$(aq) are given in Table 6. We have plotted our data and the resultant fits for these solutions in Figs. 3 and 4. Again these plots show our fits to Young's rule as described here and as calculated from the Pitzer ion interaction model, which follows directly below.

The basic equation in the Pitzer treatment that we now use considers the excess free energy to result from long-range electrostatic interactions (given by Debye–Hückel theory) and

TABLE 3. Conventional standard state (infinite dilution) partial molar volumes, heat capacities, B_Y, C_Y, and k_{23} parameters for solutions of $[(CH_3)_4N]_4EDTA + (CH_3)_4NOH$ derived using Young's rule approach* †

Solute	$\bar{V}^0$ ($cm^3\ mol^{-1}$)	B_V ($cm^3\ kg\ mol^{-2}$)	C_V ($cm^3\ kg^{3/2}\ mol^{-5/2}$)	k_{23}^V ($cm^3\ kg\ mol^{-2}$)
Fisher	485.4 ± 0.5	−8.544		1.295
	§485.5 ± 0.7	−8.332		
Alfa	490.2 ± 0.9	−7.108		−6.6
	§488.8 ± 0.3	−9.380		
	490.2 ± 0.8	−14.72	3.9	

Solute	$\bar{C}_p^0$ ($J\ K^{-1}\ mol^{-1}$)	B_J ($J\ K^{-1}\ kg\ mol^{-2}$)	C_J ($J\ K^{-1}\ kg^{3/2}\ mol^{-5/2}$)	k_{23}^J ($J\ K^{-1}\ kg\ mol^{-2}$)
Fisher	§ 604 ± 5	−122		−43.2
	605 ± 14	−133		
Alpha	631 ± 5	−118.2		(−43.2)‡
	§ 622 ± 6	−133.1		
	657 ± 18	−275	104	

*The ± values correspond to the statistical estimates of the uncertainties from our least-squares fits.

†Values of the important parameters $\bar{V}^0$ and $\bar{C}_p^0$ depend on the fitting equation that is used. We have adopted the values marked §. Based on the differences between fits and other factors discussed in the text, we assign total uncertainties to be ±2 $cm^3\ mol^{-1}$ and ±25 $J\ K^{-1}\ mol^{-1}$ for $\bar{V}^0$ and $\bar{C}_p^0$.

‡We have assumed that k_{23}^J is the same as that for the Fisher solutions, which had a wider variation in m_2 and m_3.

short-range binary and ternary interactions. The model yields the following general equation for a mixture of any number of electrolytes (48–50)

$$[13]\quad \frac{G^{EX}}{RT} = f(I) + 2\sum_c\sum_a m_c m_a(B_{ca} + EC_{ca}) + \sum_c\sum_{c'} m_c m_{c'}(\theta_{cc'} + \sum m_a\psi_{cc'a}/2) + \sum_a\sum_{a'} m_a m_{a'}(\theta_{aa'} + \sum m_c\psi_{caa'}/2)$$

Here c and a refer to individual cationic and anionic species, $f(I)$ is the Pitzer form of the extended Debye–Hückel equation

$$[14]\quad f(I) = -A_\phi(4I/1.2)\ln(1 + 1.2I^{1/2})$$

and E is given by

$$[15]\quad E = \sum m_c z_c$$

Combination and rearrangement of our equations for the experimental apparent molar properties and appropriate derivatives of eq. [13] leads to the "Pitzer expressions" that we apply to our results for solutions of $[(CH_3)_4N]_4EDTA + (CH_3)_4NOH$:

$$[16]\quad {}^\phi V_\Sigma = [1/(m_2 + m_3)][(A_V I/1.2)\ln(1 + 1.2I^{1/2}) + m_2\bar{V}_2^0 + m_3\bar{V}_3^0 + 2RT(m_c m_2 B_2^V + m_c^2 m_2 C_2^V + m_c m_3 B_3^V + m_c^2 m_3 C_3^V + m_2 m_3\theta_{23}^V)]$$

$$[17]\quad {}^\phi C_{p,\Sigma} = [1/(m_2 + m_3)][(A_J I/1.2)\ln(1 + 1.2I^{1/2}) + m_2\bar{C}_{p,2}^0 + m_3\bar{C}_{p,3}^0 - 2RT^2(m_c m_2 B_2^J + m_c^2 m_2 C_2^J + m_c m_3 B_3^J + m_c^2 m_3 C_3^J + m_2 m_3\theta_{23}^J)]$$

In these equations m_c refers to the molality of the common cation, given by $m_c = 4m_2 + m_3$. The contributions of non-ideal ternary interactions to the excess properties have been neglected because previous experience has suggested that such interactions are unimportant in the relatively dilute solutions under consideration.

Similar more complicated expressions that are applicable to solutions of M_3[MEDTA] + MOH are as follows:

$$[18]\quad {}^\phi V_\Sigma = [1/(m_2 + m_3)][(A_V I/1.2)\ln(1 + 1.2I^{1/2}) + m_2\bar{V}_2^0 + m_3\bar{V}_3^0 + m_4\bar{V}_4^0 + 2RT(m_c m_2 B_2^V + m_c^2 m_2 C_2^V + m_c m_3 B_3^V + m_c^2 m_3 C_3^V + m_c m_4 B_4^V + m_c^2 m_4 C_4^V + m_2 m_3\theta_{23}^V + m_2 m_4\theta_{24}^V + m_3 m_4\theta_{34}^V)]$$

$$[19]\quad {}^\phi C_{p,\Sigma} = [1/(m_2 + m_3)][(A_J I/1.2)\ln(1 + 1.2I^{1/2}) + m_2\bar{C}_{p,2}^0 + m_3\bar{C}_{p,3}^0 + m_4\bar{C}_{p,4}^0 - 2RT^2(m_c m_2 B_2^J + m_c^2 m_2 C_2^J + m_c m_3 B_3^J + m_c^2 m_3 C_3^J + m_c m_4 B_4^J + m_c^2 m_4 C_4^J + m_2 m_3\theta_{23}^J + m_2 m_4\theta_{24}^J + m_3 m_4\theta_{34}^J)]$$

Again for systems in which one of the solute components dissociates, m_2, m_3, and m_4 refer to the molality of different species rather than to the molality of the stoichiometric component, as is the case elsewhere in this paper.

This application of the Pitzer model to solutions of a single electrolyte $M_{\nu_M}X_{\nu_X}$ leads (51) to

$$[20]\quad {}^\phi V = \bar{V}^0 + \nu|z_M z_X|(A_V/2b)\ln(1 + bI^{1/2}) + 2\nu_M\nu_X RT[mB^V + m^2(\nu_M z_M)C^V]$$

and

$$[21]\quad {}^\phi C_p = \bar{C}_p^0 + \nu|z_M z_X|(A_J/2b)\ln(1 + bI^{1/2}) - 2\nu_M\nu_X RT^2[mB^J - m^2(\nu_M z_M)C^J]$$

in which $\nu = \nu_M + \nu_X$, $b = 1.2$, C^Y is an adjustable parameter, and B^Y is a function of ionic strength that has the form

$$[22]\quad B^Y = \beta^{(0)Y} + 2\beta^{(1)Y}[1 - (1 + \alpha I^{1/2})\exp(-\alpha I^{1/2})]/\alpha^2 I$$

Here $\beta^{(0)Y}$ and $\beta^{(1)Y}$ are adjustable parameters and $\alpha = 2$.

We have fitted equations of type [16]–[22] to our experimental data for mixed electrolytes as listed in Table 1 (with auxiliary data from Tables 5 and 7) to obtain the desired

Can. J. Chem. Downloaded from www.nrcresearchpress.com by 176.9.209.113 on 09/07/12
For personal use only.

Can. J. Chem. Downloaded from www.nrcresearchpress.com by 176.9.209.113 on 09/07/12
For personal use only.

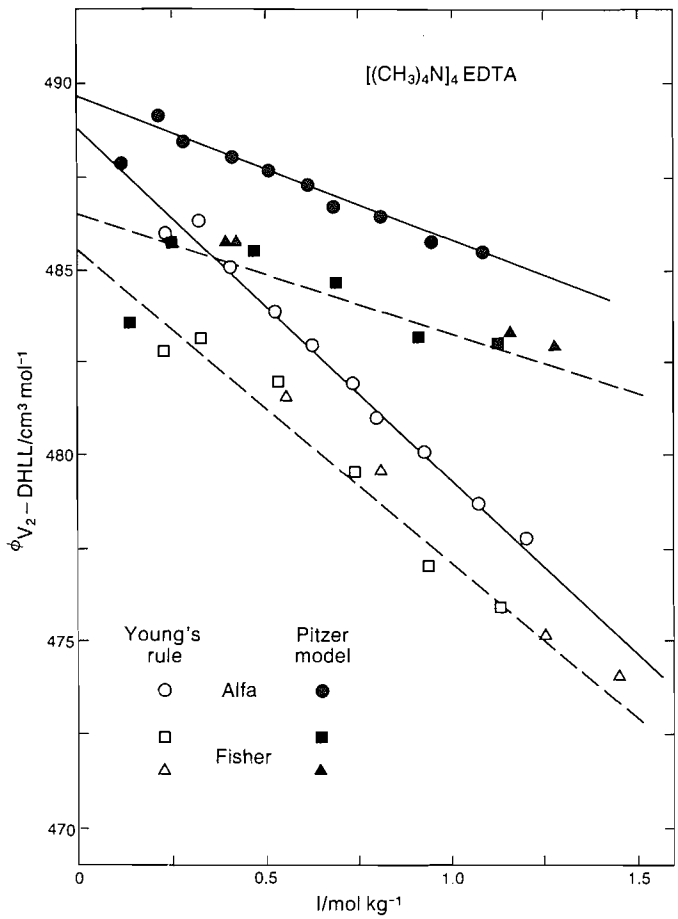

FIG. 2. Apparent molar volumes for $[(CH_3)_4N]_4EDTA$ minus the Debye–Hückel limiting law (DHLL) contribution against ionic strength (I) as calculated from both Young's rule and the Pitzer model. Our selected fits to the Pitzer model were mathematically manipulated to produce linear fits with ionic strength and subsequently do not represent true ionic strength values but rather ωm_2, but do show the desired "goodness" of fit.

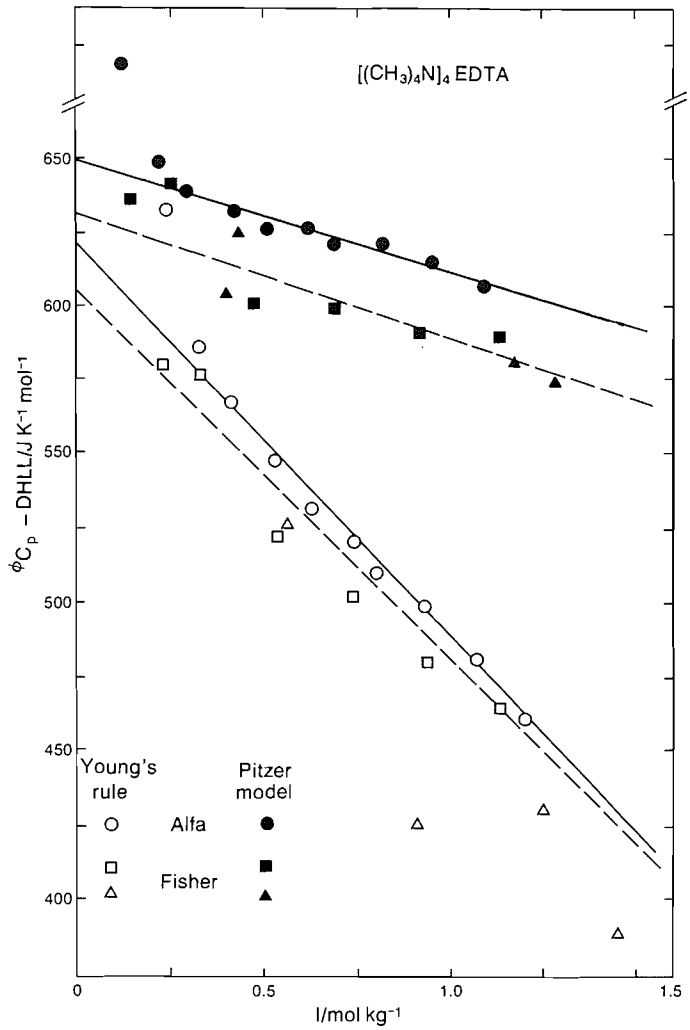

FIG. 3. Apparent molar heat capacities for $[(CH_3)_4N]_4EDTA$ minus the Debye–Hückel limiting law (DHLL) contribution against ionic strength (I) as calculated from both Young's rule and the Pitzer model. The plotted ionic strength values from the two models are different (see Fig. 2 caption).

parameters that are listed in Table 8. Plots of our fits to these data are given in Figs. 2–5.

$[(CH_3)_4N]_3HEDTA$ and Na_2H_2EDTA

We express our experimental results for solutions of Na_2H_2EDTA and $[(CH_3)_4N]_3HEDTA$ as experimental apparent molar properties ($^{\phi}V^{exp}$, $^{\phi}C_p^{exp}$) defined by

$$[23] \qquad {}^{\phi}Y^{exp} = (Y_{sol} - n_1 Y_1^0)/n_2$$

in which meanings of symbols have been specified previously. These experimental results are listed in Table 1.

The important equilibria in solutions of $[(CH_3)_4N]_3HEDTA$ are

$$[24] \qquad \underset{(1-\alpha-\beta)m_2}{HEDTA^{3-}(aq)} + H_2O(l) = \underset{\alpha m_2}{H_2EDTA^{2-}(aq)} + \underset{(\alpha-\beta)m_2}{OH^-(aq)}$$

and

$$[25] \qquad \underset{(1-\alpha-\beta)m_2}{HEDTA^{3-}(aq)} + \underset{(\alpha-\beta)m_2}{OH^-(aq)} = \underset{\beta m_2}{EDTA^{4-}(aq)} + H_2O(l)$$

The experimental apparent molar heat capacities and volumes contain contributions from the $H_2EDTA^{2-}(aq)$ and $EDTA^{4-}(aq)$ anions as well as the $HEDTA^{3-}(aq)$ anion that is the principal species of interest here. The experimental apparent molar heat capacities also contain relaxation contributions associated with the equilibria described by eqs. [24] and [25]. Evaluations of the relaxation contributions are presented in Appendices I and II.

TABLE 4. Equilibrium constant data for $Na^+(aq)$ and $K^+(aq)$ complexation with $EDTA^{4-}(aq)$, from Daniele *et al.* (3) for use in eq. [11]

	$M^+ + EDTA^{4-} = MEDTA^{3-}$		$nH^+ + EDTA^{4-} = H_nHEDTA^{n-4}$		
Property	Na^+	K^+	n = 1	n = 2	n = 3
log $K^{\dagger}$	1.81	0.80	10.39	16.58	19.26
z	8	8	8	14	18
C	1.84	1.84	1.84	3.27	4.3
D	−0.96	−0.96	−0.96	−1.68	−2.2

Concentrations of all species in solutions in which $HEDTA^{3-}(aq)$ was the principal anion have been calculated by way of eqs. [24] and [25] in combination with equilibrium constants from Daniele *et al.* (3) for EDTA equilibria and for the ionization of water from Sweeton *et al.* (52), with results that are summarized in Table 9.

TABLE 5. Concentrations of species in solutions containing Na_3[NaEDTA] + NaOH and K_3[KEDTA] + KOH*

m_2 (mol kg^{-1})	m_3 (mol kg^{-1})	α	$(1-\alpha)m_2$ (mol kg^{-1})	αm_2 (mol kg^{-1})	I (mol kg^{-1})	${}^{\phi}C_{p,\Sigma}^{rel}$ (J K^{-1} mol^{-1})	${}^{\phi}C_{p,\Sigma}$ (J K^{-1} mol^{-1})
			Na_3[NaEDTA] + NaOH				
0.2057	0.1609	0.01884	0.2018	0.00387	1.4106	0.89	161.4
0.1744	0.1566	0.02106	0.1707	0.00367	1.2176	0.94	138.3
0.1552	0.1516	0.02317	0.1539	0.00360	1.0993	0.98	122.5
0.1321	0.1507	0.02671	0.1286	0.00353	0.9577	1.05	102.2
0.1168	0.1486	0.02989	0.1133	0.00349	0.8636	1.10	87.58
0.09857	0.1461	0.03482	0.09513	0.00343	0.7512	1.16	68.65
0.07562	0.1429	0.04348	0.07233	0.00329	0.6098	1.24	41.01
0.05594	0.1402	0.05403	0.05291	0.00302	0.4879	1.25	15.88
0.03969	0.1380	0.06578	0.03708	0.00261	0.3865	1.18	−7.00
0.02053	0.1353	0.08411	0.01880	0.00173	0.2654	0.87	−40.76
			K_3[KEDTA] + KOH				
0.2049	0.1763	0.1713	0.1698	0.03510	1.5460		37.04
0.1456	0.1669	0.2031	0.1160	0.02957	1.1587		2.027
0.1237	0.1635	0.2255	0.09581	0.02790	1.0173		−13.20
0.08943	0.1580	0.2778	0.06459	0.02484	0.7940		−37.47
0.05981	0.1533	0.3460	0.03911	0.02070	0.5950		−61.2
0.03655	0.1497	0.4194	0.02122	0.01533	0.4303		−82.7
0.01932	0.1469	0.4846	0.00996	0.00936	0.3003		−99.4
0.1740	0.2763	0.1667	0.1450	0.02901	1.4365		−9.87
0.1641	0.3423	0.1611	0.1377	0.02645	1.4329		−5.96
0.01746	0.2302	0.4098	0.01302	0.00715	0.3636		−98.3
0.01577	0.3046	0.3574	0.01013	0.00563	0.4218		−98.0

*m_2 is the stoichiometric molality of M_3[MEDTA] and ${}^{\phi}C_{p,\Sigma} = {}^{\phi}C_{p,\Sigma}^{exp} - {}^{\phi}C_{p,\Sigma}^{rel}$.

TABLE 6. Conventional standard state (infinite dilution) partial molar volumes, heat capacities, B_Y, C_Y, and k_{23} parameters for solutions of Na_3[NaEDTA] + NaOH and K_3[KEDTA] + KOH from Young's rule* †

Solute	$\bar{V}^0$ (cm^3 mol^{-1})	B_V (cm^3 kg mol^{-2})	C_V (cm^3 kg$^{3/2}$ mol$^{-5/2}$)	k_{23}^V (cm^3 kg mol^{-2})
Na_3[NaEDTA]	§142.6±0.1	−1.061		
	141.8±0.6	−2.191		3.88
K_3[KEDTA]‡	176.1±0.4	0.916		

Solute	$\bar{C}_p^0$ (J K^{-1} mol^{-1})	B_J (J K^{-1} kg mol^{-2})	C_J (J K^{-1} kg$^{3/2}$ mol$^{-5/2}$)	k_{23}^J (J K^{-1} kg mol^{-2})
Na_3[NaEDTA]	79.4±2	−3.06		
	90.3±5	−41.2	26.3	
	§ 98.9±8	22.8		−88.5
K_3[KEDTA]‡	−79.8±4	−10.35		

*The ± values correspond to the statistical estimates of the uncertainties from our least-squares fits.

†Values of the important parameters $\bar{V}^0$ and $\bar{C}_p^0$ depend on the fitting equation that is used. We have adopted the values marked §. Based on the differences between fits and other factors discussed in the text, we assign total uncertainties to be ±2 cm^3 mol^{-1} and ±25 J K^{-1} mol^{-1} for $\bar{V}^0$ and $\bar{C}_p^0$.

‡In obtaining the values listed, we have not used data for solutions with a KOH concentration greater than 0.2 molal.

The experimental apparent molar properties of these solutions can be expressed as the sum of the apparent molar properties of the individual species present weighted according to concentrations present (same basic assumption as in Young's rule)

$$[26]\quad {}^{\phi}Y^{exp} = (1-\alpha-\beta){}^{\phi}Y[3(CH_3)_4N^+ + HEDTA^{3-}] + \alpha{}^{\phi}Y[2(CH_3)_4N^+ + H_2EDTA^{2-}] + \beta{}^{\phi}Y[4(CH_3)_4N^+ + EDTA^{4-}] + (\alpha-\beta){}^{\phi}Y[(CH_3)_4NOH] - (\alpha-\beta)Y^0(H_2O)$$

We have used the standard state volume and heat capacity for water listed in Table 10, along with data for $[2(CH_3)_4N^+ + H_2EDTA^{2-}]$ calculated from our previously reported properties (1) for Na_2H_2EDTA and properties of the auxiliary electrolytes $(CH_3)_4NCl$ and NaCl as listed in Table 2. We have fitted equations of types [8] and [26] to obtain the desired information about the apparent molar properties of $[3(CH_3)_4N^+ + HEDTA^{3-}]$ as listed in Table 11. We show plots of our fitted eq. [8] to the experimental results in Figs. 6 and 7.

The principal equilibria in solutions containing H_2EDTA^{2-}(aq) as the principal anion are

Can. J. Chem. Downloaded from www.nrcresearchpress.com by 176.9.209.113 on 09/07/12
For personal use only.

TABLE 7. Values of parameters from the Pitzer model for aqueous hydroxides and chlorides*

Solute	$\bar{V}^0$ ($cm^3\ mol^{-1}$)	$\beta^{(0)V} \times 10^4$ ($kg\ cm^3\ J^{-1}\ mol^{-1}$)	$\beta^{(1)V} \times 10^4$ ($kg\ cm^3\ J^{-1}\ mol^{-1}$)	$C^V \times 10^5$ ($kg^2\ cm^3\ J^{-1}\ mol^{-2}$)
$(CH_3)_4NOH$ (Fisher)	85.16 ± 0.06	−2.000		
$(CH_3)_4NOH$ (Alfa)	85.64 ± 0.03	−2.179		
NaOH	−5.47 ± 0.06	2.235	6.433	−0.597
KOH	4.77 ± 0.03	1.908	5.806	−0.518
$(CH_3)_4NCl$	107.27 ± 0.01	−1.861	1.578	
NaCl	16.63 ± 0.01	1.155	0.387	
KCl	26.91 ± 0.01	1.288	0.316	

Solute	$\bar{C}_p^0$ ($J\ K^{-1}\ mol^{-1}$)	$\beta^{(0)J} \times 10^5$ ($kg\ mol^{-1}\ K^{-2}$)	$\beta^{(1)J} \times 10^4$ ($kg\ mol^{-1}\ K^{-2}$)	$C^J \times 10^6$ ($kg^2\ mol^{-2}\ K^{-2}$)
$(CH_3)_4NOH$ (Fisher)	80.2 ± 1	−0.684	−0.154	
$(CH_3)_4NOH$ (Alfa)	94.0 ± 1	−0.984	0.120	
NaOH	−101.0 ± 1	−1.307	−0.528	0.630
KOH	−133.5 ± 0.9	−0.806	−0.440	0.248
$(CH_3)_4NCl$	107.2 ± 0.1	−0.1409	−0.02144	
NaCl	−84.9 ± 0.1	−1.544	−0.0174	
KCl	−114.7 ± 0.1	−1.024	−0.0237	

*The ± values listed here correspond to statistical estimates of the standard deviations of the intercepts. The values in this table were obtained from refitting the experimental data or fitted equations from refs. 7, 11, 15–19.

TABLE 8. Values of parameters from the Pitzer model applied to solutions of $[(CH_3)_4N]_4EDTA + (CH_3)_4NOH$, $Na_3[NaEDTA] + NaOH$, and $K_3[KEDTA] + KOH$* †

Solute	$\bar{V}_2^0$ ($cm^3\ mol^{-1}$)	$\beta_2^{(0)V} \times 10^4$ ($kg\ cm^3\ J^{-1}\ mol^{-1}$)	$\beta_2^{(1)V} \times 10^4$ ($kg\ cm^3\ J^{-1}\ mol^{-1}$)	$\theta_{23}^V \times 10^5$ ($kg^2\ cm^3\ J^{-1}\ mol^{-2}$)
$[(CH_3)_4N]_4EDTA$ (Fisher)	486.5 ± 0.5	−16.09		7.51
$[(CH_3)_4N]_4EDTA$ (Alfa)	489.7 ± 0.3	−19.63		
$Na_3[NaEDTA]$	§145.2 ± 0.1	5.748		
	146.2 ± 0.1	8.239	−1.997	
$K_3[KEDTA]$‡	180.6 ± 0.4	12.90		

Solute	$\bar{C}_{p,2}^0$ ($J\ K^{-1}\ mol^{-1}$)	$\beta_2^{(0)J} \times 10^5$ ($kg\ mol^{-1}\ K^{-2}$)	$\beta_2^{(1)J} \times 10^4$ ($kg\ mol^{-1}\ K^{-2}$)	$\theta_{23}^J \times 10^6$ ($kg^2\ mol^{-2}\ K^{-2}$)
$[(CH_3)_4N]_4EDTA$ (Fisher)	§632. ± 8	7.070		
	631. ± 8	6.632		0.275
$[(CH_3)_4N]_4EDTA$ (Alfa)	649. ± 4	6.309		
$Na_3[NaEDTA]$	§109.1 ± 1.9	−6.524		
	124.5 ± 13	−7.935	1.108	
$K_3[KEDTA]$‡	−22.8 ± 6	−4.565		

*The ± values listed correspond to the statistical estimates of the uncertainties from our least-squares fits.

†Values of the important parameters $\bar{V}^0$ and $\bar{C}_p^0$ depend on the fitting equation that is used. We have adopted the values marked §. Based on the differences between fits and other factors discussed in the text, we assign total uncertainties to be ±2 $cm^3\ mol^{-1}$ and ±25 $J\ K^{-1}\ mol^{-1}$ for $\bar{V}^0$ and $\bar{C}_p^0$.

‡In obtaining the values listed, we have not used data for solutions with a KOH concentration greater than 0.2 molal.

[27] $H_2EDTA^{2-}(aq) = H^+(aq) + HEDTA^{3-}(aq)$
$(1 - \alpha - \beta)m_2 \quad (\alpha - \beta)m_2 \quad \alpha m_2$

and

[28] $H_2EDTA^{2-}(aq) + H^+(aq) = H_3EDTA^-(aq)$
$(1 - \alpha - \beta)m_2 \quad (\alpha - \beta)m_2 \quad \beta m_2$

The experimental apparent molar heat capacities and volumes contain contributions from the $HEDTA^{3-}(aq)$ and $H_3EDTA^-(aq)$ anions as well as $H_2EDTA^{2-}(aq)$, which is of principal interest here, and the apparent molar heat capacities also contain relaxation contributions associated with the equilibria represented by eqs. [27] and [28]. Appendices I and II describe evaluation of these relaxation contributions from equilibrium constants and enthalpies of reaction.

Concentrations of all species in these solutions have been calculated from equilibrium constants given by Daniele *et al.* (3) and Sweeton *et al.* (52) in combination with our eqs. [27] and [28], with results summarized in Table 9.

The experimental apparent molar properties are expressed as appropriate sums as done previously in eq. [26]:

Can. J. Chem. Downloaded from www.nrcresearchpress.com by 176.9.209.113 on 09/07/12
For personal use only.

Can. J. Chem. Downloaded from www.nrcresearchpress.com by 176.9.209.113 on 09/07/12
For personal use only.

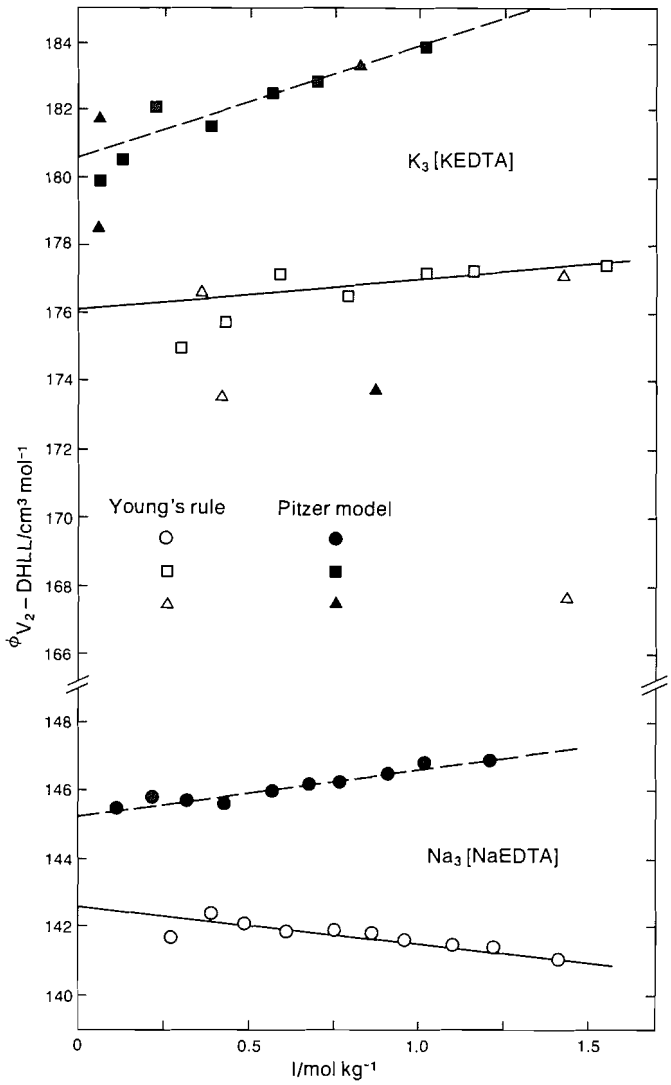

FIG. 4. Apparent molar volumes for Na_3[NaEDTA] and K_3[KEDTA] minus the Debye–Hückel limiting law (DHLL) contribution against ionic strength (I) as calculated from both Young's rule and the Pitzer model. The plotted ionic strengths from the two models are different (see Fig. 2 caption). △ represent higher $OH^-/KEDTA^{3-}$ ratios.

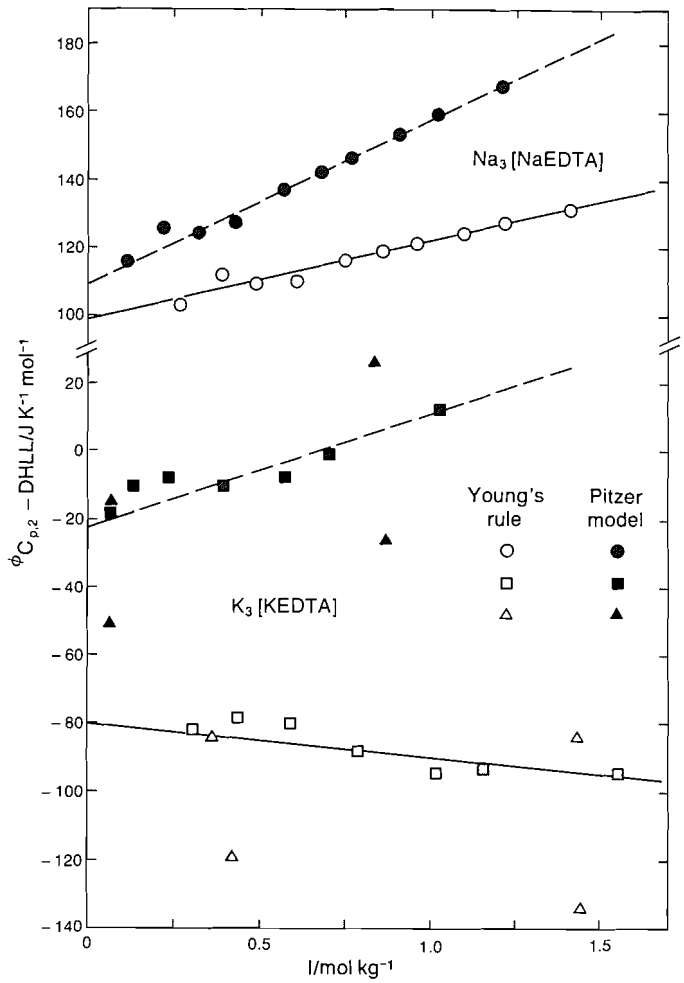

FIG. 5. Apparent molar heat capacities for Na_3[NaEDTA] and K_3[KEDTA] minus the Debye–Hückel limiting law (DHLL) contribution against ionic strength (I) as calculated from both Young's rule and the Pitzer model. The plotted ionic strengths from the two models are different (see Fig. 2 caption). △ represent higher $OH^-/KEDTA^{3-}$ ratios.

[29] $$^{\phi}Y^{exp} = (1 - \alpha - \beta)^{\phi}Y(2Na^+ + H_2EDTA^{2-}) + \alpha^{\phi}Y(3Na^+ + HEDTA^{3-}) + \beta^{\phi}Y(H_3EDTA^-) + (2\beta - \alpha)^{\phi}Y(Na^+) + (\alpha - \beta)^{\phi}Y(H^+)$$

To make use of eq. [29] we have used the standard state heat capacity and volume of Na^+(aq) as listed in Table 10. Properties of $3Na^+$(aq) + $HEDTA^{3-}$(aq) have come from our measurements and calculations based on eq. [26]. There are two indirect routes to the required properties of H_3EDTA^-(aq). In our previous work (1) we combined $d\Delta H/dT$ results (cited in Appendix II) for the ionization of H_2EDTA^{2-}(aq) with our measured heat capacities for H_2EDTA^{2-}(aq) to obtain a value (large uncertainty) for the heat capacity of H_3EDTA^-(aq). Another route is to estimate the desired standard state properties for H_3EDTA^-(aq) on the basis of the now reliably known properties for other EDTA species and trends observed for a few other systems. In this latter way (see Fig. 8) we have estimated $\bar{V}^0 = 159\ cm^3\ mol^{-1}$ and $\bar{C}_p^0 = 210\ J\ K^{-1}\ mol^{-1}$ for H_3EDTA^-(aq). Fortunately, because β values used in eq. [29]

TABLE 9. Speciation of solutions of $[(CH_3)_4N]_3HEDTA$ and Na_2H_2EDTA

m_2 (mol kg^{-1})	$\alpha \times 10^2$	$\beta \times 10^2$	$^{\phi}C_p^{rel}$ (J K^{-1} mol^{-1})	$^{\phi}C_p^{exp}$ (J K^{-1} mol^{-1})
		$[(CH_3)_4N]_3HEDTA$		
0.2194	0.8406	0.8389		705.3
0.1710	0.8286	0.8264		694.2
0.1299	0.8242	0.8214		694.0
0.1078	0.8226	0.8193		687.4
0.08617	0.8220	0.8181		683.2
0.06433	0.8206	0.8157		679.4
0.03648	0.8122	0.8039		673.1
0.01649	0.7908	0.7714		665.5
		Na_2H_2EDTA		
0.2588	1.755	1.741	7.07	278.0
0.1631	1.776	1.752	7.15	253.9
0.1251	1.780	1.748	7.15	240.9
0.1015	1.780	1.740	7.15	233.2
0.06069	1.773	1.708	7.09	214.8
0.03530	1.754	1.652	6.96	201.0
0.02597	1.743	1.614	6.89	197.3

TABLE 10. Selected conventional partial molar properties* for ions at $I = 0$ (superscript ^{0}) and $I = 0.1$ molal (superscript †)*

Ion	$\bar{C}^0_{p,2}$ ($J\,K^{-1}\,mol^{-1}$)	$\bar{C}^\dagger_{p,2}$ ($J\,K^{-1}\,mol^{-1}$)	$\bar{V}^0_2$ ($cm^3\,mol^{-1}$)	$\bar{V}^\dagger_2$ ($cm^3\,mol^{-1}$)
$H^+(aq)$	0	0	0	0
$Na^+(aq)$	42.8	46.2	−1.21	−1.08
$K^+(aq)$	13.0	14.9	9.00	9.23
$(CH_3)_4N^+(aq)$	234.9	234.1	89.38	89.34
$Cl^-(aq)$	−127.2	−113.7	17.89	18.55
$ClO_4^-(aq)$	−25.5	−9.9	43.99	44.64
$OH^-(aq)$	−140.2	−122.0	−4.05	−3.03
$H_2O(l)$	75.291		18.068	
$H_2EDTA^{2-}(aq)$	81.0	129.3	156.3	159.2
$HEDTA^{3-}(aq)$	−82.0	−25.2	151.2	154.8
$EDTA^{4-}(aq)$	−310	−186	131	138
$H_3EDTA^-(aq)$	(210)	(284)	(159)	(162)
$NaEDTA^{3-}(aq)$	−24	58	148	151
$KEDTA^{3-}(aq)$	−90	−33	151	154

*The values for the EDTA species were derived from this work. Values for the other ions were derived from results of Table 2, except for $Cl^-(aq)$ from ref. 53 and $ClO_4^-(aq)$ from ref. 15. Values for $H_2O(l)$ were taken from ref. 54. Values in parentheses represent estimates, see text.

TABLE 11. Standard state (infinite dilution) partial molar heat capacities, volumes, and B_Y parameters at 25.0°C*

Solute	$\bar{C}^0_{p,2}$ ($J\,K^{-1}\,mol^{-2}$)	B_J ($J\,K^{-1}\,kg\,mol^{-1}$)	C_J ($J\,K^{-1}\,kg^{3/2}\,mol^{-5/2}$)	$\bar{V}^0_2$ ($cm^3\,mol^{-1}$)	B_V ($cm^3\,kg\,mol^{-2}$)	C_V ($cm^3\,kg^{3/2}\,mol^{-5/2}$)
Na_2H_2EDTA	166.6 ± 0.7	42.19		153.87 ± 0.11	2.347	
$[(CH_3)_4N]_3HEDTA$	622.7 ± 1.6	−238.9	112.2	419.3 ± 0.2	−10.69	3.511

*The ± values listed correspond to the statistical estimates of the uncertainties from our least-squares fits.

are small, the uncertainties in these estimated values do not cause much uncertainty in the desired properties of $2Na^+(aq) + H_2EDTA^{2-}(aq)$. Finally, using auxiliary results mentioned here, we have fitted eqs. [8] and [29] to our experimental apparent molar properties listed in Table 1 to obtain the desired properties of $2Na^+(aq) + H_2EDTA^{2-}(aq)$ that are listed in Table 11. Figs. 6 and 7 show plots of our fits of eq. [8] to our experimental data.

Selections of ionic properties

For calculation of the temperature and pressure dependence of thermodynamic quantities (such as standard equilibrium constants) we use partial molar heat capacities and volumes (identical to the corresponding apparent molar properties at infinite dilution). It is most convenient to tabulate these standard state quantities as the conventional ionic properties, based on $\bar{Y}^0(H^+, aq) \equiv 0$.

Our selections of values for these conventional standard state quantities for $HEDTA^{3-}(aq)$ and for $H_2EDTA^{2-}(aq)$ are straightforward, based on our results in Table 11 in combination with properties listed in Table 10 for $Na^+(aq)$ and $(CH_3)_4N^+(aq)$. Results of these calculations are listed in the bottom half of Table 10.

Our applications of Young's rule and the Pitzer model to extraction of standard state properties of $[(CH_3)_4N]_4EDTA$ from experimental results for solutions of $[(CH_3)_4N]_4EDTA + (CH_3)_4NOH$ have led (Tables 3 and 8) to a small difference between the desired $\bar{V}^0$ values and to a substantial difference between the two $\bar{C}^0_p$ values that "should" be identical. In addition to this difference that comes from the two methods of data analysis, there are also different results from the two stock solutions that we have used. Because there is no clear reason for selecting any one value of $\bar{C}^0_p$ or $\bar{V}^0$ as best, we have decided to use a weighted average of the various results, with appropriate consideration of the uncertainties. In this way we have selected $\bar{V}^0 = 488 \pm 2\ cm^3\ mol^{-1}$ and $\bar{C}^0_p = 630 \pm 20\ J\ K^{-1}\ mol^{-1}$ as the best available values of these thermodynamic properties for $[(CH_3)_4N]_4EDTA(aq)$. These selected values then lead in straightforward fashion to the conventional ionic properties listed in Table 10 for $EDTA^{4-}(aq)$.

As can be seen in Tables 6 and 8, the two different methods of data analysis lead to somewhat different values for the properties of $Na_3[NaEDTA](aq)$ and $K_3[KEDTA](aq)$ at infinite dilution. These differences are due mostly to the differences in the properties of $[(CH_3)_4N]_4EDTA$ derived from the two methods of data analysis. Here we have used the average values to obtain $\bar{V}^0 = 143.9 \pm 1\ cm^3\ mol^{-1}$ and $\bar{C}^0_p = 104 \pm 15\ J\ K^{-1}\ mol^{-1}$ for $Na_3[NaEDTA](aq)$ and $\bar{V}^0 = 178 \pm 2\ cm^3\ mol^{-1}$ and $\bar{C}^0_p = -51 \pm 25\ J\ K^{-1}\ mol^{-1}$ for $K_3[KEDTA](aq)$. These values lead to the conventional ionic standard state properties for $NaEDTA^{3-}(aq)$ and $KEDTA^{3-}(aq)$ that are listed in Table 10.

Many of the published thermodynamic results (equilibrium constants and enthalpies) for aqueous EDTA systems refer to solutions having constant ionic strength (mostly 0.1 molar), rather than to the infinite dilution condition that is appropriate to the selected ionic properties cited earlier in this section. We have therefore used our results to obtain partial molar heat

Can. J. Chem. Downloaded from www.nrcresearchpress.com by 176.9.209.113 on 09/07/12
For personal use only.

Can. J. Chem. Downloaded from www.nrcresearchpress.com by 176.9.209.113 on 09/07/12
For personal use only.

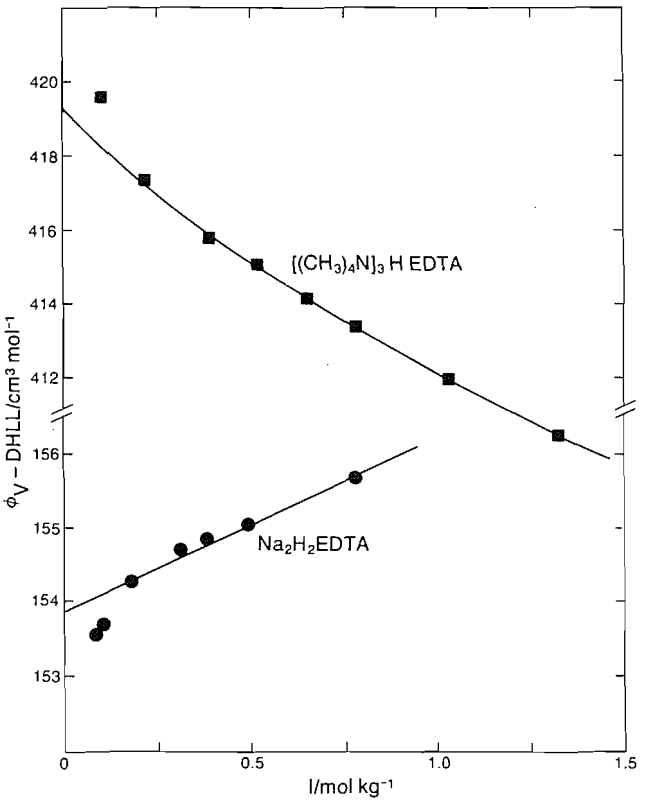

FIG. 6. Apparent molar volumes for Na_2H_2EDTA and $[(CH_3)_4N]_3$-HEDTA minus the Debye–Hückel limiting law (DHLL) contribution against ionic strength (I).

TABLE 12. Partial molar properties at $I = 0.10$ molal at 25°C from fits based on Young's rule

Species	$\bar{V}^\dagger$ (cm³ mol⁻¹)	$\bar{C}_p^\dagger$ (J K⁻¹ mol⁻¹)
$[(CH_3)_4N]_4EDTA$	496	754
Na_3[NaEDTA]	148	197
K_3[KEDTA]	182	11
$[(CH_3)_4N]_3$HEDTA	422.8	677.1
Na_2H_2EDTA	157.0	221.7

capacities and volumes applicable to 0.1 M solutions by way of

[30] $\quad \bar{Y} = {}^{\Phi}Y + I(\partial {}^{\Phi}Y/\partial I)$

Results of these calculations are listed in Table 12, and related conventional properties of ionic species are listed in Table 10.

The only previous direct calorimetric investigation of heat capacities of EDTA solutions pertinent to our present work was our investigation (1) of solutions of H_2EDTA^{2-}(aq). We note, however, that Vasil'ev *et al.* (46, 55–59) have measured enthalpies of several reactions involving EDTA in moderately concentrated solutions over narrow (mostly 20°) ranges of temperature, with results that lead with eq. [2] to ΔC_p values for these same reactions. These ΔC_p values can be combined with results of our previous direct heat capacity measurements (1, 2) to provide estimates for the $\bar{C}_p^0$ of $EDTA^{4-}$(aq). We have used and will use some of these ΔH values in thermodynamic calculations, but we do not use their ΔC_p values for reasons that follow. Vasil'ev *et al.* have estimated that uncertainties in their derived ΔC_p values are about ± 50 J K⁻¹ mol⁻¹. We believe that this estimate of uncertainties is optimistic because of

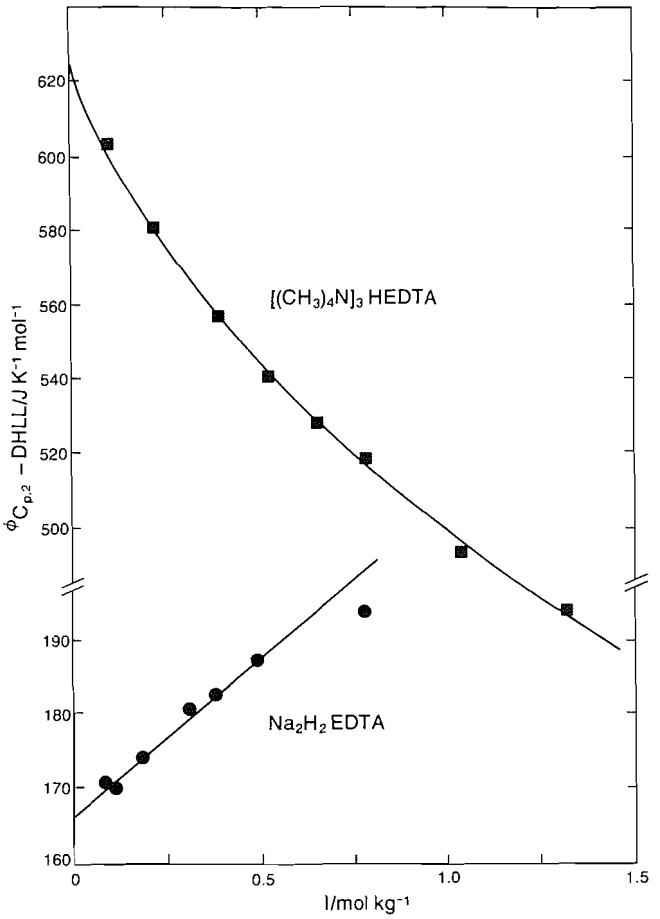

FIG. 7. Apparent molar heat capacities for Na_2H_2EDTA and $[(CH_3)_4N]_3$HEDTA minus the Debye–Hückel limiting law (DHLL) contribution against ionic strength (I).

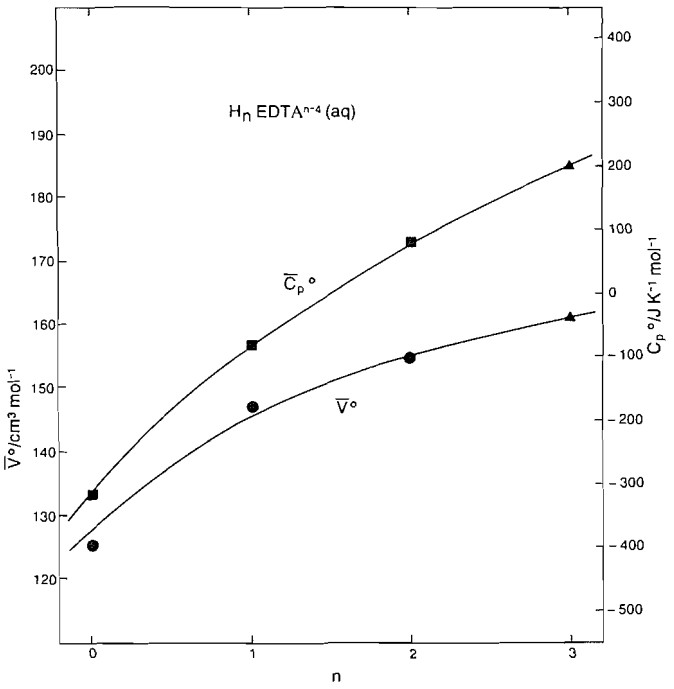

FIG. 8. Hydrogen ligand number dependence of the limiting partial molar volumes and heat capacities for EDTA ions with 1–3 protons.

TABLE 13. Thermodynamic parameters for the ionization of EDTA and complexation by $EDTA^{4-}(aq)$ at 0.1 molal or molar and 25°C*

n	M^+	$\log K^\dagger$	$\Delta H^\dagger$ (kJ mol^{-1})	$\Delta S^\dagger$ (J K^{-1} mol^{-1})	$\Delta C_p^\dagger$ (J K^{-1} mol^{-1})	$\Delta V^\dagger$ (cm^3 mol^{-1})
			$H_{4-n}EDTA^{-n}(aq) = H_{3-n}EDTA^{-(n+1)}(aq) + H^+(aq)$			
−2		(−1.20)	(4.5)	(14.3)	(−152)	(−1.9)
−1		−1.51	−2.63	−37.7	(−152)	(−2.0)
0		−1.96	−1.32	−42.0	(−153)	(−2.2)
1		−2.68	−5.5	−69.8	−155 [−183 ± 50]	−2.8
2		−6.19	18.2	−57.5	−155 [−147 ± 50]	−4.4
3		−10.39	23.0	−122	−161 [−98 ± 50]	−16.8
			$H_6EDTA^{2+}(aq) = 6H^+(aq) + EDTA^{4-}(aq)$			
		(−23.93)	36.3	−336	(−928)	(−30.1)
					(−853)† [−490 ± 60]†	(−29.7)†
			$M^+(aq) + EDTA^{4-}(aq) = MEDTA^{3-}(aq)$			
	Na^+	1.84	−8.45	6.9	198	14.1
	K^+	0.80	0.0	15.3	138	6.8
			$H_2O(l) + H^+(aq) + OH^-(aq)$			
		−13.78	56.62	−73.93	−197	−21.1

*Values in parentheses represent our estimates of these values and square-bracketed values represent $\partial\Delta H/\partial T$ results that were calculated previously (1) from the results of Vasil'ev *et al.* (34–39).

†These values are estimates at the infinite dilution reference state.

inadequate allowance for the magnification of uncertainties associated with differentiation and also because of additional uncertainties in extrapolating their results to the standard states of present interest (infinite dilution or 0.1 molar or 0.1 molal). The only previous investigation of volumes of $H_2EDTA^{2-}(aq)$ was our work (1).

Thermodynamics of ionization reactions of EDTA

One of the principal purposes of this work has been to obtain partial molar heat capacities and volumes of species of EDTA, with a view toward using these results in thermodynamic calculations as described in the next section. Here (and in Appendix II) we are concerned with selecting the values of various thermodynamic properties (K, ΔH, etc.) associated with the following ionization reactions of aqueous EDTA:

[31] $H_6EDTA^{2+}(aq) = H^+(aq) + H_5EDTA^+(aq)$

[32] $H_5EDTA^+(aq) = H^+(aq) + H_4EDTA(aq)$

[33] $H_4EDTA(aq) = H^+(aq) + H_3EDTA^-(aq)$

[34] $H_3EDTA^-(aq) = H^+(aq) + H_2EDTA^{2-}(aq)$

[35] $H_2EDTA^{2-}(aq) = H^+(aq) + HEDTA^{3-}(aq)$

[36] $HEDTA^{3-}(aq) = H^+(aq) + EDTA^{4-}(aq)$

[37] $H_6EDTA^{2+}(aq) = 6H^+(aq) + EDTA^{4-}(aq)$

Equilibrium constants (K) and enthalpies (ΔH) for each of these reactions [31]–[37] have been selected as summarized in Appendix II. Our experimental results lead to accurate values of ΔC_p and ΔV for reactions [35] and [36] and to less accurate values of ΔC_p and ΔV for reaction [34], as discussed earlier. We regard these ΔC_p values as more reliable than those that can be obtained by way of application of $d\Delta H/dT$ to the enthalpy of reaction data of Vasil'ev *et al.* (26, 34–39). The only experimental route that we have to ΔC_p for reaction [37] is by application of $d\Delta H/dT$ to the enthalpies of reaction measured in concentrated solution by Vasil'ev *et al.* (38). Finally, we have used the ΔC_p values mentioned above in constructing plots of ΔC_p against n (or alternatively against $\log K$, which yields a reasonably linear relationship) for ionization of $H_nEDTA^{n-3}(aq)$ and have thereby *estimated* the "missing" ΔC_p values for reactions [31]–[33]. We have made similar plots for ΔV values against $\log K$ for the ionization reactions [34]–[36] to *estimate* values for eqs. [31]–[33]. All of the selected (based on experimental and estimated results) thermodynamic quantities ($K^\dagger$, $\Delta H^\dagger$, $\Delta C_p^\dagger$, and $\Delta V^\dagger$) for reactions [31]–[37] are collected in Table 13. We have also listed selected values for complexation of $Na^+(aq)$ and $K^+(aq)$ with $EDTA^{4-}(aq)$ in Table 13.

Extrapolations of equilibrium constants to higher temperatures

Equilibrium constants vary with temperature according to the van't Hoff equation [1] and the Kirchhoff equation [2] and vary with pressure according to

[38] $$(\partial \ln K/\partial p)_T = -\Delta V^0/RT$$

We begin by combining eqs. [1] and [2] with the specification that ΔC_p is (approximately) independent of temperature to obtain

[39] $$\ln K_T^\dagger = \ln K_{298}^\dagger + \Delta H_{298}^\dagger[(1/298.15) - (1/T)]/R + \Delta C_p^\dagger[\ln (T/298.15) - 1 + (298.15/T)]/R$$

Here we have written this equation in terms of the 0.1 molar reference state that is commonly used for EDTA studies. Experience has shown that eq. [39] provides a more accurate representation of the temperature dependence of equilibrium constants over wide ranges of temperature than does the simpler equation based on integration of [1] with the pretence that ΔH is independent of temperature ($\Delta C_p = 0$).

In obtaining eq. [39] we have specified that $\Delta C_p^\dagger$ is (approximately) independent of temperature because we have no direct evidence about the possible temperature dependence of this quantity for the reactions of present interest. Experience (23,

Can. J. Chem. Downloaded from www.nrcresearchpress.com by 176.9.209.113 on 09/07/12
For personal use only.

TABLE 14. Calculated equilibrium constants for some ionization reactions of H_4EDTA*

	log $K^\dagger$						
t (°C)	$H_{4-n}EDTA^{-n}(aq) = H_{3-n}EDTA^{-(n+1)}(aq) + H^+(aq)$ $n=-2$	$n=-1$	$n=0$	$n=1$	$n=2$	$n=3$	Na^+/K^+ exchange eq. [34]
0	−1.3	−1.50	−1.98	−2.64	−6.53	−10.80	1.19
20	−1.2	−1.50	−1.98	−2.68	−6.26	−10.48	1.07
25	−1.2	−1.51	−1.96	−2.68	−6.19	−10.39	1.04
37	−1.2	−1.53	−2.00	−2.75	−6.10	−10.27	0.99
50	−1.2	−1.57	−2.01	−2.79	−5.97	−10.11	0.94
75	−1.2	−1.67	−2.08	−2.91	−5.82	−9.90	0.86
100	−1.2	−1.79	−2.17	−3.04	−5.71	−9.75	0.82
125	−1.3	−1.93	−2.27	−3.18	−5.65	−9.65	0.79
150	−1.4	−2.08	−2.38	−3.33	−5.61	−9.58	0.77
175	−1.5	−2.24	−2.51	−3.48	−5.60	−9.54	0.77
200	−1.6	−2.41	−2.66	−3.66	−5.63	−9.55	0.78
250	−1.9	−2.76	−2.97	−4.02	−5.74	−9.62	0.81

*The uncertainties in these values depend on the uncertainties in the values of log $K^\dagger$ at 25°C and in our extrapolation. Experience has shown that errors in log K due to the extrapolations increase to about ±0.5 at 250°C.

60, 61) has shown that ΔC_p values for "isocoulombic" reactions (symmetric with respect to number and charges of ions) are much more nearly independent of temperature than for electrically asymmetric reactions. We therefore focus our attention on reactions [31], [32], and the following reactions that are related to [33]–[36], all of which are either isocoulombic or pseudo-isocoulombic:

[40] $EDTA^{4-}(aq) + H_2O(l) = HEDTA^{3-}(aq) + OH^-(aq)$

[41] $HEDTA^{3-}(aq) + H_2O(l) = H_2EDTA^{2-}(aq) + OH^-(aq)$

[42] $H_2EDTA^{2-}(aq) + H_2O(l) = H_3EDTA^-(aq) + OH^-(aq)$

[43] $H_3EDTA^-(aq) + H_2O(l) = H_4EDTA(aq) + OH^-(aq)$

Equilibrium constants, $\Delta H^\dagger$, and $\Delta C_p^\dagger$ values for reactions [40]–[43] are related to corresponding values for reactions [33]–[36] by $K^\dagger$, $\Delta H^\dagger$, and $\Delta C_p^\dagger$ for the ionization of water; we take $K^\dagger$ and $\Delta H^\dagger$ values from earlier investigations (45, 62), and have used the values in Table 10 to calculate $\Delta C_p^\dagger$. We have used all of these quantities and applied eq. [39] to all of the ionization reactions of EDTA, and have reported the results in Table 14.

Integration of eq. [38] leads to

[44] $$\ln K_p^\dagger = \ln K_1^\dagger - (p-1)(\Delta V^\dagger/RT)$$

where $\ln K_1^\dagger$ represents the value of the logarithm of $K^\dagger$ at 1 bar (100 kPa), and $\ln K_p^\dagger$ the value at a pressure p. Although the effect of pressure on equilibrium constants is small at pressures up to the saturation pressure of water at 200°C, we have included this effect in the values listed in Table 14, calculated using saturation pressures of water from Haar *et al.* (24).

Results of similar calculations for the isocoulombic exchange reaction involving $NaEDTA^{3-}(aq)$ and $KEDTA^{3-}(aq)$ given by

[45] $K^+(aq) + NaEDTA^{3-}(aq) = KEDTA^{3-}(aq) + Na^+(aq)$

are listed along with the ionization constants in Table 14.

Acknowledgments

We thank the Natural Sciences and Engineering Research Council, the Alberta Oil Sands Technology and Research Authority, and the Alberta Research Council for support of this work. J.K.H. is grateful to the Natural Sciences and Engineering Research Council for a postgraduate scholarship.

1. J. K. HOVEY and P. R. TREMAINE. J. Phys. Chem. **86**, 5541 (1985).
2. J. K. HOVEY, L. G. HEPLER, and P. R. TREMAINE. J. Solution Chem. **15**, 977 (1986).
3. P. G. DANIELE, C. RIGANO, and S. SAMMARTANO. Anal. Chem. **57**, 2956 (1985).
4. A. E. MARTELL and R. M. SMITH. Critical stability constants. Vol. I: amino acids. Plenum Press, New York. 1974.
5. G. ANDEREGG. Critical survey of stability constants of EDTA complexes. Pergamon Press, Oxford. 1977: IUPAC Chemical Data Series No. 14.
6. D. A. SKOOG and D. M. WEST. Fundamentals of analytical chemistry. Holt, Rinehart and Winston, New York. 1976. p. 272.
7. P. PICKER, E. TREMBLAY, and C. JOLICOEUR. J. Solution Chem. **3**, 377 (1974).
8. P. PICKER, P. A. LEDUC, P. R. PHILIPS, and J. E. DESNOYERS. J. Chem. Thermodyn. **3**, 631 (1971).
9. G. S. KELL. J. Chem. Eng. Data, **12**, 66 (1967).
10. G. S. KELL. *In* Water—a comprehensive treatise. *Edited by* F. Franks. Plenum Press, New York. 1972.
11. J. E. DESNOYERS, C. DE VISSER, G. PERRON, and P. PICKER. J. Solution Chem. **5**, 605 (1976).
12. T. F. YOUNG and M. B. SMITH. J. Phys. Chem. **58**, 716 (1954).
13. D. J. BRADLEY and K. S. PITZER. J. Phys. Chem. **83**, 1599 (1979).
14. J. ANANTHASWAMY and G. ATKINSON. J. Chem. Eng. Data, **29**, 81 (1984).
15. J. K. HOVEY, L. G. HEPLER, and P. R. TREMAINE. Thermochim. Acta. **126**, 245 (1988).
16. A. H. ROUX, G. PERRON, and J. E. DESNOYERS. Can. J. Chem. **62**, 878 (1984).
17. G. PERRON and J. E. DESNOYERS. J. Chem. Eng. Data, **17**, 136 (1972).
18. G. PERRON, N. DESROSIERS, and J. E. DESNOYERS. Can. J. Chem. **54**, 2163 (1976).
19. J.-L. FORTIER, P.-A. LEDUC, and J. E. DESNOYERS. J. Solution Chem. **3**, 323 (1974).
20. E. M. WOOLLEY and L. G. HEPLER. Can. J. Chem. **55**, 158 (1977).
21. G. J. MAINS, J. W. LARSON, and L. G. HEPLER. J. Phys. Chem. **88**, 1257 (1984).

Can. J. Chem. Downloaded from www.nrcresearchpress.com by 176.9.209.113 on 09/07/12
For personal use only.

22. J. W. LARSON, K. G. ZEEB, and L. G. HEPLER. Can. J. Chem. **60**, 2141 (1982).
23. J. A. BARBERO, L. G. HEPLER, K. G. MCCURDY, and P. R. TREMAINE. Can. J. Chem. **61**, 2509 (1983).
24. L. HAAR, J. S. GALLAGHER, and G. S. KELL. NBS/NRC steam tables, thermodynamic and transport properties and computer programs for vapor and liquid states of water in SI units. Hemisphere, Washington, DC. 1984.
25. C. JOLICOEUR, L.-L. LEMELIN, and R. LAPALME. J. Phys. Chem. **83**, 2806 (1979).
26. V. P. VASIL'EV, L. A. KOCHERGINA, and T. D. ORLOVA. J. Gen. Chem. USSR (Engl. Transl.), **49**, 1649 (1979).
27. G. SCHWARZENBACH and H. ACKERMANN. Helv. Chim. Acta, **30**, 1798 (1947).
28. J. J. WATTERS and O. E. SCHUPP. J. Inorg. Nucl. Chem. **30**, 3359 (1968).
29. V. PALATY. Can. J. Chem. **41**, 18 (1963).
30. J. BOTTS, A. CHASHIN, and H. L. YOUNG. Biochemistry, **4**, 1788 (1965).
31. J. D. CARR and D. G. SWARTZFAGER. J. Am. Chem. Soc. **95**, 3569 (1973).
32. G. ANDEREGG. Helv. Chim. Acta, **50**, 2333 (1967).
33. J. J. CHRISTENSEN, D. J. EATOUGH, and R. M. IZAAT. Handbook of metal ligand heats. 2nd ed. Marcel Dekker, New York. 1975.
34. V. P. VASIL'EV, L. A. KOCHERGINA, and T. D. ORLOVA. J. Gen. Chem. USSR (Engl. Transl.), **46**, 2109 (1976).
35. V. P. VASIL'EV, L. A. KOCHERGINA, and T. D. ORLOVA. J. Gen. Chem. USSR (Engl. Transl.), **48**, 2511 (1978).
36. V. P. VASIL'EV, L. A. KOCHERGINA, and T. D. YASTREBOVA. J. Gen. Chem. USSR (Engl. Transl.), **43**, 971 (1973).
37. V. P. VASIL'EV, L. A. KOCHERGINA, and T. D. YASTREBOVA. J. Gen. Chem. USSR (Engl. Transl.), **44**, 1371 (1974).
38. V. P. VASIL'EV, V. P. LYMAR, and A. I. LYTKIN. Russ. J. Phys. Chem. (Engl. Transl.) **22**, 1440 (1977).
39. V. P. VASIL'EV, V. P. LYMAR, and A. I. LYTKIN. Russ. J. Phys. Chem. (Engl. Transl.) **22**, 1357 (1977).
40. J. J. CHRISTENSEN, R. M. IZAAT, D. P. WRATHALL, and L. D. HANSEN. J. Chem. Soc. (A), 1212 (1969).
41. G. C. KUGLER and G. H. CAREY. Talanta, **17**, 907 (1970).
42. M. J. L. TILLOTSON and L. A. K. STAVELEY. J. Chem. Soc. 3613 (1958).
43. G. ANDEREGG. Helv. Chim. Acta, **46**, 1833 (1963).
44. G. ANDEREGG. Z. Naturforsch. B: Anorg. Chem. Org. Chem. **31**, 786 (1976).
45. R. G. CHARLES. J. Am. Chem. Soc. **76**, 5854 (1954).
46. V. P. VASIL'EV and A. K. BELONOGOVA. Russ. J. Phys. Chem. (Engl. Transl.) **21**, 350 (1976).
47. L. G. HEPLER. Thermochim. Acta, **50**, 69 (1981).
48. K. S. PITZER. *In* Activity coefficients in electrolyte solutions. *Edited by* M. R. Pytkowicz. CRC Press, Boca Raton, FL. 1979. Chap. 7.
49. K. S. PITZER. J. Chem. Soc. Faraday Trans. 1, **80**, 3451 (1984).
50. R. C. PHUTELA and K. S. PITZER. J. Solution Chem. **15**, 649 (1986).
51. K. S. PITZER, J. C. PEIPER, and R. H. BUSEY. J. Phys. Chem. Ref. Data, **13**, 1 (1984).
52. F. H. SWEETON, R. E. MESMER, and C. F. BAES, JR. J. Solution Chem. **3**, 191 (1974).
53. G. C. ALLRED and E. M. WOOLLEY. J. Chem. Thermodyn. **13**, 147 (1981).
54. D. D. WAGMAN, W. H. EVANS, V. B. PARKER, R. H. SCHUMM, I. HALOW, S. M. BAILEY, K. L. CHURNEY, and R. L. NUTTAL. J. Phys. Chem. Ref. Data, **11**, Supplement 2 (1982).
55. V. P. VASIL'EV and A. K. BELONOGOVA. Russ. J. Inorg. Chem. (Engl. Transl.) **21**, 31 (1976).
56. V. P. VASIL'EV and A. K. BELONOGOVA. Russ. J. Inorg. Chem. (Engl. Transl.) **20**, 16 (1975).
57. V. P. VASIL'EV and A. K. BELONOGOVA. Russ. J. Inorg. Chem. (Engl. Transl.) **21**, 1646 (1976).
58. V. P. VASIL'EV and A. K. BELONOGOVA. Russ. J. Inorg. Chem. (Engl. Transl.) **22**, 1303 (1977).
59. V. P. VASIL'EV, A. K. BELONOGOVA, and T. V. KOROLEVA. Russ. J. Inorg. Chem. (Engl. Transl.) **28**, 647 (1983).
60. W. T. LINDSAY, JR. Proc. 41st International Water Conf. Eng. Soc. Western Penn., Pittsburgh, PA. 1980. pp. 284–294.
61. R. C. MURRAY and J. W. COBBLE. Proc. 41st International Water Conf. Eng. Soc. Western Penn., Pittsburgh, PA. 1980. pp. 295–310.
62. G. OLOFFSON and L. G. HEPLER. J. Solution Chem. **4**, 127 (1975).

Appendix I

Relaxation contributions to heat capacities of mixed electrolyte solutions

There have been several accounts (20–23, 25)[2] of the contributions of chemical relaxation to heat capacities of aqueous solutions of electrolytes, but none has dealt with the kinds of mixed electrolyte effects encountered here. We therefore provide the following treatment.

The total enthalpy of a system containing k components can be expressed (21) by

$$[I\text{-}1] \qquad H = \sum_k n_k H_k$$

in which n_k and H_k represent the number of moles and the partial molar enthalpy of the kth component. Differentiation with respect to temperature leads to

$$[I\text{-}2] \qquad C_p = (\partial H/\partial T)_p = \Sigma n_k (\partial H_k/\partial T)_p + \Sigma H_k (\partial n_k/\partial T)_p$$

In this equation the first summation term represents the "compositional" or "species" contribution to the heat capacity and the second summation term represents the contribution to the heat capacity due to the change in distribution (chemical relaxation) of species induced by the change of temperature that is necessary for heat capacity measurements. The last term (relaxation contribution to the heat capacity) must be subtracted from the measured heat capacity to obtain the compositional contribution of the chemical species of interest.

Evaluation of the relaxation contribution for mixed aqueous electrolyte solutions of present interest can begin along the lines of an earlier investigation (20) by expressing the heat capacity C_p of a solution (containing 1 kg of water) as a sum of compositional or species and relaxation contributions denoted by superscripts sp and rel as in

$$[I\text{-}3] \qquad C_p(\text{sol}) = (\partial H/\partial T)_p^{\text{sp}} + (\partial H/\partial T)_p^{\text{rel}}$$

Combination of this equation with our defining eq. [3] gives (see ref. 20)

$$[I\text{-}4] \qquad {}^{\Phi}C_{p,\Sigma}^{\text{exp}} = [(\partial H/\partial T)_p^{\text{sp}} - C_p(\text{H}_2\text{O})]/(m_2 + m_3) + (\partial H/\partial T)_p^{\text{rel}}/(m_2 + m_3)$$

A start on the evaluation of the relaxation term in [I-4] is provided (20) by

$$[I\text{-}5] \qquad (\partial H/\partial T)_p^{\text{rel}} = [\partial H/\partial(\alpha m_2)]_p [\partial(\alpha m_2)/\partial T]_{p,m} = m_2 \Delta H (\partial\alpha/\partial T)_{p,m}$$

in which α is the fractional extent of the reaction, m_2 is the stoichiometric molality of the reacting electrolyte, and ΔH is the molar enthalpy of the reaction. Now we write

$$[I\text{-}6] \qquad {}^{\Phi}C_{p,\Sigma}^{\text{rel}} = [m_2/(m_2 + m_3)]\Delta H (\partial\alpha/\partial T)_{p,m}$$

[2]Also J. K. Hovey and L. G. Hepler, in preparation.

Can. J. Chem. Downloaded from www.nrcresearchpress.com by 176.9.209.113 on 09/07/12
For personal use only.

TABLE A1. Relaxation contributions to heat capacities of solutions of Na_3[NaEDTA] + NaOH

m_2 (mol kg^{-1})	$\alpha \times 10^2$	$-(\partial\alpha/\partial T)_m \times 10^4$ (K^{-1})	${}^{\Phi}C_p^{rel}$ (J K^{-1} mol^{-1})	${}^{\Phi}C_{p,\Sigma}^{rel}$ (J K^{-1} mol^{-1})	${}^{\Phi}C_{p,\Sigma}^{exp}$ (J K^{-1} mol^{-1})	${}^{\Phi}C_{p,\Sigma}$ (J K^{-1} mol^{-1})
0.2057	1.88	1.99	1.59	0.89	162.3	161.4
0.1744	2.10	2.22	1.78	0.94	139.8	138.4
0.1552	2.32	2.44	1.95	0.98	123.5	122.5
0.1321	2.67	2.80	2.24	1.05	103.2	102.2
0.1168	2.99	3.12	2.49	1.10	88.67	87.58
0.09857	3.48	3.61	2.89	1.16	69.81	68.65
0.07562	4.35	4.46	3.57	1.24	42.28	41.04
0.05594	5.40	5.48	4.39	1.25	17.13	15.88
0.03969	6.58	6.59	5.27	1.18	−5.82	−6.998
0.02053	8.41	8.27	6.62	0.87	−39.89	−40.76

TABLE A2. Relaxation contributions to heat capacities of solutions of Na_2H_2EDTA

m_2 (mol kg^{-1})	$\alpha \times 10^2$	$\beta \times 10^2$	$(\partial\alpha/\partial T)_m \times 10^4$ (K^{-1})	$(\partial\beta/\partial T)_m \times 10^4$ (K^{-1})	${}^{\Phi}C_{p,\alpha}^{rel}$ (J K^{-1} mol^{-1})	${}^{\Phi}C_{p,\beta}^{rel}$ (J K^{-1} mol^{-1})	${}^{\Phi}C_p^{exp}$ (J K^{-1} mol^{-1})	${}^{\Phi}C_p^{exp} - {}^{\Phi}C_{p,tot}^{rel}$ (J K^{-1} mol^{-1})
0.2588	1.76	1.74	2.84	2.83	5.54	1.53	285.1	278.0
0.1631	1.78	1.75	2.88	2.85	5.60	1.55	261.0	253.9
0.1251	1.78	1.75	2.88	2.85	5.61	1.54	248.0	240.9
0.1015	1.78	1.74	2.88	2.84	5.61	1.54	240.4	233.2
0.06069	1.77	1.71	2.86	2.80	5.57	1.52	221.9	214.8
0.03530	1.75	1.65	2.82	2.72	5.49	1.47	208.0	201.0
0.02597	1.74	1.61	2.79	2.67	5.44	1.45	204.1	197.3

for the contribution of chemical relaxation to the apparent molar heat capacities that come directly from our calorimetric measurements. Evaluation of $(\partial\alpha/\partial T)_{p,m}$ is done in terms of the equilibrium constant K, the temperature dependence of K as in eq. [1], activity coefficients, and the temperature dependence of the activity coefficients. Because of limitations imposed by the available data, we have ignored the distinction between ΔH and ΔH^0 (related to the temperature dependence of activity coefficients) and have used K values that refer to specified concentrations and that have been expressed in terms of concentrations of various species.

Solutions of Na_3[NaEDTA] and K_3[KEDTA]

The equilibrium reaction to be considered in connection with these solutions was represented by eq. [10] in the main text. Mathematical manipulation of K for reaction [10] expressed in terms of α in combination with eq. [1] leads to

[I-7] $$(\partial\alpha/\partial T)_m = K\Delta H(1-\alpha)/[RT^2(3m_2 + 2\alpha m_2 + m_3 + K)]$$

We have used K values (given as a function of ionic strength) from Daniele *et al.* (3) as listed in Table 4, and $\Delta H = -8.5$ kJ mol^{-1} (Appendix II) to evaluate the relaxation contributions to the heat capacities of solutions of Na_3[NaEDTA] + NaOH as listed in Table A1. Because $\Delta H \simeq 0$ for the corresponding reaction involving K^+(aq), the relaxation contribution for these solutions is nearly zero.

Solutions containing $HEDTA^{3-}$(aq) and H_2EDTA^{2-}(aq)

The relaxation components of the experimental apparent molar heat capacities of solutions containing $HEDTA^{3-}$(aq) and H_2EDTA^{2-}(aq) are given by the usual expressions for coupled reactions (α and β defined in terms of eqs. [24], [25], and [27], [28]):

[I-10] $${}^{\Phi}C_{p,\alpha}^{rel} = \Delta H_\alpha(\partial\alpha/\partial T)_m$$

[I-11] $${}^{\Phi}C_{p,\beta}^{rel} = \Delta H_\beta(\partial\beta/\partial T)_m$$

Mathematical manipulations with equilibrium constants for two coupled equilibria in combination with eq. [1] lead to complicated expressions for $(\partial\alpha/\partial T)_m$ and $(\partial\beta/\partial T)_m$ that are similar in principle to those for other systems of coupled equilibria (21).[2] We have selected values of ΔH (Appendix II) to be used in eqs. [I-8], [I-9] to find that the relaxation components of the heat capacities are negligibly small for solutions in which $HEDTA^{3-}$(aq) is the principal species of interest, and have also obtained the non-negligible relaxation contributions to the heat capacities of solutions of H_2EDTA^{2-}(aq) as listed in Table A2.

Appendix II

Selections of thermodynamic data

Previous selections (1) of "best" equilibrium constants from Anderegg (5) for the ionization reactions of H_4EDTA(aq) at 25°C and 0.1 molar ionic strength have been extended by accepting the equilibrium constants reported by Daniele *et al.* (3). The equilibrium constant data for the two protonation reactions of H_4EDTA(aq) are much less certain than the other values. We have chosen the value listed by Anderegg (5) for the first protonation of H_4EDTA and have considered the recommendations of Anderegg (5) and Vasil'ev *et al.* (26) in estimating $\log K^{\dagger} = -1.2 \pm 0.6$ for protonation of H_5EDTA^+(aq), by considering the trends in all of the other equilibrium constants of H_4EDTA(aq) at 0.1 molar.

Several investigations (3, 5, 27–32) have led to values of the equilibrium constant for association of Na^+(aq) with $EDTA^{4-}$(aq); we have used the results of Daniele *et al.* (3). The chosen equilibrium constants for association of K^+(aq)

Can. J. Chem. Downloaded from www.nrcresearchpress.com by 176.9.209.113 on 09/07/12
For personal use only.

with $EDTA^{4-}(aq)$ reported by Daniele *et al.* (3) are in good agreement with results from others (28, 30, 31).

We have revised some previous (1) choices for $\Delta H^{\dagger}$ values for the ionization of $H_4EDTA(aq)$. We have averaged selected direct calorimetric values (many cited by Christensen *et al.* (33)) obtained usually at 0.1 molar (some values were corrected to 0.1 molar from equations given by the respective authors) and 25°C (Vasil'ev *et al.* (26, 34–39), Christensen *et al.* (40), and Kugler and Carey (41)) and also values at 20°C (Tillotson and Staveley (42) and Anderegg (43)) corrected to 25°C using our $\Delta C_p^{\dagger}$ values listed in Table 13. Values reported by Christensen *et al.* (40) seemed inconsistent with other results and were not included in the averages.

For association of $Na^+(aq)$ with $EDTA^{4-}(aq)$ we have several reported (33, 44–46) $\Delta H^{\dagger}$ values and have chosen to use the value from Vasil'ev *et al.* (46) to which we have assigned an uncertainty of about ± 2 kJ mol^{-1}. For association of $K^+(aq)$ with $EDTA^{4-}(aq)$ we have $\Delta H^{\dagger} \simeq 4$ kJ mol^{-1} (after correcting for the effect of temperature on the molarity (42) in the van't Hoff eq. [1]) (large uncertainty) from equilibrium constants at several temperatures (3) and $\Delta H^{\dagger} = 0 \pm 2$ kJ mol^{-1} from calorimetric measurements by Vasil'ev *et al.* (46); we have chosen to use this latter value, which leads to a negligible relaxation contribution to the heat capacity. All of these $\Delta H^{\dagger}$ values used in our calculations are listed in Table 13.

Can. J. Chem. Downloaded from www.nrcresearchpress.com by 176.9.209.113 on 09/07/12
For personal use only.

The structures and dynamics of SF_6: new insights

B. M. POWELL AND G. DOLLING

Atomic Energy of Canada Research Company, Chalk River Nuclear Laboratories, Chalk River, Ont., Canada K0J 1J0

Received August 24, 1987

This paper is dedicated to Professor J. A. Morrison

B. M. POWELL and G. DOLLING. Can. J. Chem. **66**, 897 (1988).

The structural and dynamical properties of the orientationally disordered solid SF_6 have been studied. The present understanding of this state is discussed in terms of the microscopic nature of the orientational disorder, the influence of steric repulsion, and the concept of orientational frustration. A possible mechanism is considered for the phase transition to an ordered structure.

B. M. POWELL et G. DOLLING. Can. J. Chem. **66**, 897 (1988).

On a étudié les propriétés structurales et dynamiques du SF_6 solide et dont l'orientation est désordonnée. On discute de la compréhension actuelle de cet état en fonction de la nature microscopique du désordre de l'orientation, de l'influence de la répulsion stérique et du concept de la frustration de l'orientation.

[Traduit par la revue]

Can. J. Chem. Downloaded from www.nrcresearchpress.com by 176.9.209.113 on 09/07/12
For personal use only.

I. Introductory review

In addition to the two well-established states of condensed matter, solid and liquid, there exist several other states or phases which are intermediate between these extremes. They exhibit particular characteristics which can be said to derive from *both* the solid and liquid states. One such intermediate state is that of an orientationally disordered solid (OD). This state may exist in solids containing charged ions such as CN^-, SO_4^{2-}, but also exists in solids composed of rather small, often globular and electrically neutral molecules, coupled by intermolecular potentials that are weakly anisotropic. In such molecular solids there are extra orientational degrees of freedom in addition to the usual three translational degrees of freedom. As the molecular liquid is cooled, the translational and orientational degrees of freedom do not necessarily condense out at the same temperature. If the translational degrees condense first and the anisotropic part of the intermolecular potential is too weak to impose orientational order at that temperature, then the resulting solid may have the molecular centres of mass ordered on a crystal lattice, as in a true crystalline solid, but the molecular orientations may remain disordered, as in a liquid. This state of condensed matter is called an orientationally disordered solid.

The existence of a class of molecular solids whose properties might be due to orientational disorder has been known for a long time (1). These solids were originally termed "plastic crystals" by Timmermans and their characteristics have been reviewed more recently (2). However, it is only during the last decade or so that the microscopic nature of the disorder has been studied and elucidated in detail.

In this Introduction we review the present understanding of the OD phase for a particular molecular solid, sulphur hexafluoride (SF_6). New results are discussed in Section II and some conclusions concerning our understanding of this phase are drawn in Section III.

The existence of a phase transition at 96 K in solid SF_6 was first observed in calorimetric measurements (3) and subsequently confirmed by nmr observations (4). From the temperature dependence of the nmr lineshape it was determined that the molecules were undergoing reorientational motion in the high temperature phase. The crystal structure of this phase was shown by X-ray diffraction to be body-centred cubic (4). Later detailed nmr measurements (5) confirmed the reorientational motion of the high temperature phase, but also indicated a second phase transition at $\approx$45 K. The data showed that two inequivalent sites must exist in the low temperature phase and that reorientation of at least some molecules sets in between 45 K and the transition at 96 K. The conclusion from these studies was that the high temperature phase of SF_6 was probably orientationally disordered, but the detailed nature of the disorder remained obscure.

a. Crystal structure and orientational disorder

The high-temperature phase extends from 96 K to the sublimation point at 223 K, an exceptionally large temperature range. Its detailed crystal structure was elucidated by neutron powder diffraction methods (6, 7). Well-defined Debye–Scherrer peaks were observed whose positions could be indexed on the basis of a bcc unit cell. The intensities were analyzed by writing the structure amplitude as the product of a term due to the molecular centre of mass (including a translational Debye–Waller factor) and a term due to a rotational form factor. The latter term was then expanded in a series of symmetry adapted functions. Since SF_6 is cubic (point group symmetry O_h) the appropriate functions are the Kubic Harmonics. These particular functions were introduced into crystal structure analysis by Seymour and Pryor (8) and independently employed by Press and Hüller in their detailed analysis of methane (9). For the octahedral symmetry of SF_6 the four lowest order terms are the zeroth, fourth, sixth, and eighth harmonics. Analysis of the neutron diffraction data in terms of these functions showed that the fourth order harmonic was dominant. Dolling *et al.* (7) showed that the probability distribution describing the orientation of the molecule is determined directly by the coefficients of the expansion in symmetry-adapted functions. This "orientational distribution function" for SF_6, determined from the neutron diffraction data, is shown in Fig. 1.

The distribution function has a maximum along the cubic axes, i.e. the S—F bonds are preferentially aligned along these directions. However, the function has significant values as much as 20° away from these axes. The reason for this can be understood from the unit cell and molecular dimensions. If the S—F bonds are aligned precisely along the cube axes then the closest F atoms in molecules adjacent along these directions will overlap. Such perfect alignment will thus be prevented by steric repulsion. No other maxima in the orientational distribution were found and hence the molecular and site symmetries are the same. High temperature measurements on SF_6 (at 200 K) showed the same qualitative features as those near the transition but extensive diffuse scattering was also observed (7). Analysis

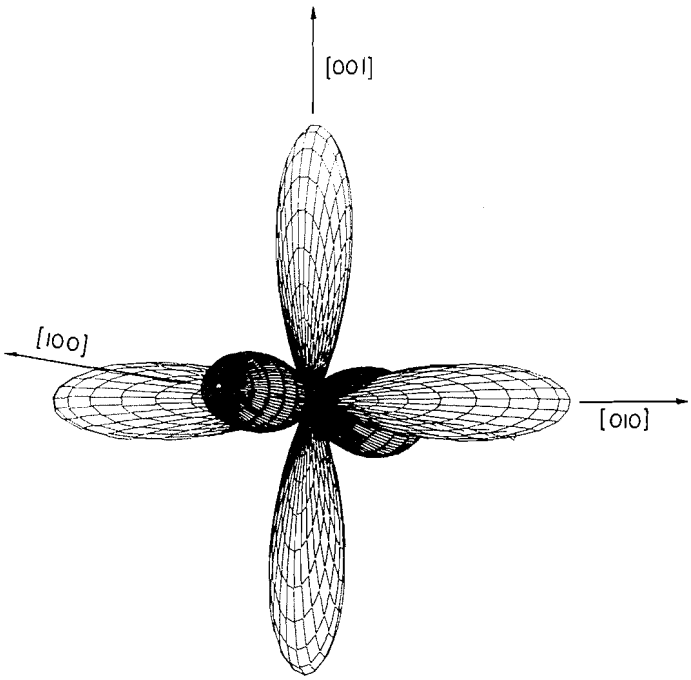

FIG. 1. Orientational distribution function of S—F bonds in SF_6 at 100 K.

of this scattering in terms of randomly oriented SF_6 molecules showed significant discrepancies with the neutron data. These were interpreted as evidence for orientational correlations. Thus the picture of the SF_6 crystal structure emerging from these measurements is one in which the molecular centres of mass lie on an ordered bcc lattice; steric repulsion prevents orientational ordering of the molecules and the preferential cubic axis alignment indicated by the orientational distribution function is merely the time-averaged molecular orientation. The reorientation is not "free", however, and orientational correlations exist between neighbouring molecules.

This experimentally determined picture of SF_6 has been augmented by extensive molecular dynamics simulation (MDS) calculations. The calculations for SF_6 were carried out on an ICL Distributed Array Processor at the University of Edinburgh with a large simulation sample (4096 molecules). The intermolecular potential was written as a summation over pairwise F–F interactions between F atoms in the origin molecule and those in the nearest and next nearest neighbour molecules of the bcc lattice. The F–F interaction is represented by a Lennard–Jones potential. The model is thus as simple as possible while retaining enough essential features to resemble the real SF_6 crystal. The calculations (10, 11) confirmed the experimental orientational distribution function and showed that the molecules were undergoing rotational diffusion. There did not appear to be any well-defined collective librational excitations. Particularly revealing were calculations of the intermolecular potential as a function of separation between pairs of SF_6 molecules with different relative orientations. These showed that when the molecules are aligned parallel to the cube axes the force between the molecule at the origin and its nearest neighbour (the body centred molecule) is attractive, while the force between the origin molecule and its next-nearest neighbour (along the cubic axis) is repulsive (the steric repulsion mentioned previously). The intermolecular potentials are shown in Fig. 2. Thus nearest neighbour interactions favour orientational ordering while next-nearest neighbour interactions oppose this. The competition between these interactions means that the origin molecule does not feel a well-defined orientational potential. Dove and Pawley (11) called this competition "orientational frustration", and suggested that it was the origin of the orientational disorder. At high temperatures the orientational frustration is resolved dynamically, producing an average crystal lattice of high symmetry. The concept of orientational frustration enables a classification of OD crystals into two categories. For orientationally frustrated solids the competing interactions prevent neighbouring molecules from ordering simultaneously, whereas in other OD solids each molecule is either randomly oriented, e.g. CD_4 (9), β-N_2 (12), or resides in one of a finite number of symmetry-related orientations, e.g. CBr_4 (7), adamantane (13).

b. Collective excitations

It is evident that the particular nature of the OD phase will have a significant effect on the character of the intermolecular collective excitations. For a normal molecular solid the intermolecular modes will generally be of mixed translational–librational character. If the solid has high symmetry, then pure translational or pure librational modes may exist for particular directions of propagation. The intermolecular mode dispersion relations can be measured by inelastic neutron scattering techniques and the measurements for HMT (14) show results typical of a normal, high symmetry molecular solid. In an OD phase, however, the absence of long-range orientational order means that well-defined, purely librational modes cannot propagate through the crystal; they will always be rapidly damped out. This intuitive picture has been confirmed by the failure of inelastic neutron scattering measurements to observe well-defined librational modes in OD crystals: it has also been confirmed, in the case of SF_6, by the MDS calculations (11).

Since long range positional order does exist in the OD phase, it would be expected that pure translational modes and mixed modes with predominantly translational character will be largely unaffected by the orientational disorder. Consequently measurements of the long wavelength acoustic modes would be expected to yield well-defined excitations, becoming broadened perhaps as they acquire increasing librational character.

In order to investigate the excitation spectrum for SF_6, inelastic neutron scattering measurements were made on a single crystal at 200 K (15). The experiment concentrated on observing the translational acoustic modes and measurements were made along three high-symmetry directions. Typical results are shown in Fig. 3. Although there is some evidence of discrete structure in the distributions, the dominant feature is the intense, generally featureless scattering at low frequencies. The qualitative characteristics of the experimental distributions are largely independent of momentum transfer and measurements at 100 K showed few differences from those at 200 K. The distributions resemble those expected from overdamped modes and imply very strong rotational–translational coupling. They are in contrast to analogous measurements on other OD solids (12, 13, 16, 17), which generally show well-defined acoustic modes, even when superimposed on a background due to an overdamped librational mode.

These results were completely unexpected, for SF_6 was considered one of the more normal or "more crystalline" of the OD crystals. The only theory of excitations in an orientationally disordered phase is that of Michel and Naudts (18). It was developed originally for the alkali cyanides (18), but has been successfully applied to CBr_4 (17) and β-N_2 (12). It is essentially

Can. J. Chem. Downloaded from www.nrcresearchpress.com by 176.9.209.113 on 09/07/12
For personal use only.

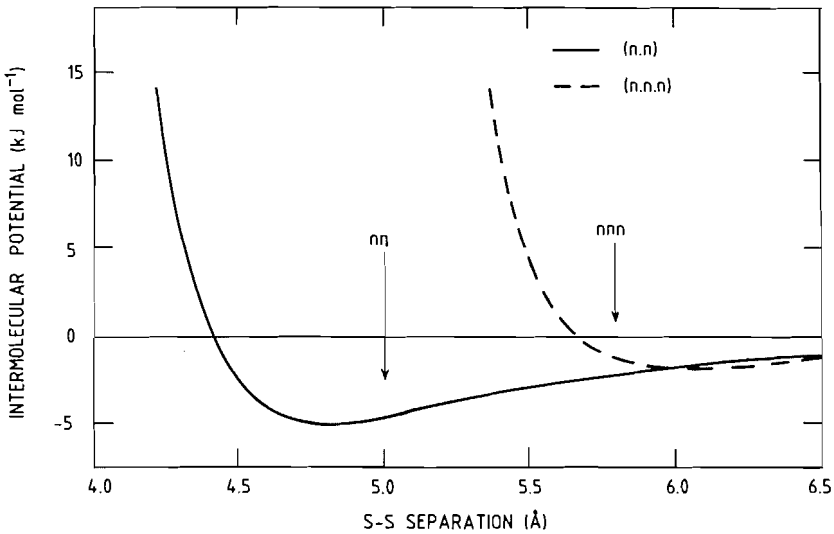

FIG. 2. Intermolecular potential curves for nearest and next-nearest neighbour molecules (see ref. 10).

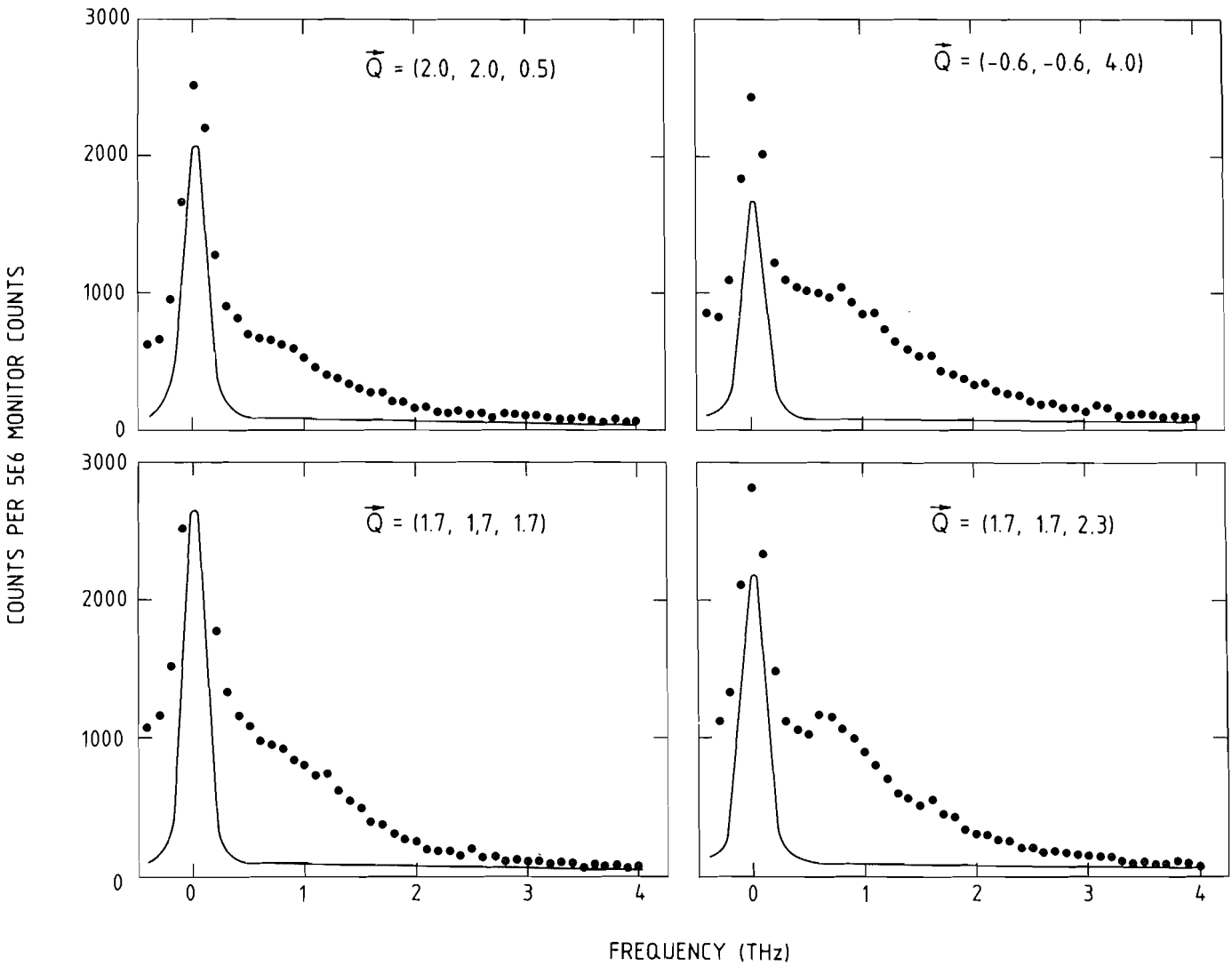

FIG. 3. Inelastically scattered neutron distributions from SF_6 at 200 K. The line shows the background from the container.

Can. J. Chem. Downloaded from www.nrcresearchpress.com by 176.9.209.113 on 09/07/12
For personal use only.

a mean field theory, and since steric repulsion is clearly of crucial importance in the concept of orientational frustration, its applicability to SF_6 is uncertain. In view of this uncertainty, the neutron scattering data were analyzed by means of MDS calculations (15). The same simulation sample used to investigate the static properties of SF_6 (10, 11) was utilised and the simulation was allowed to run for a total of 16 000 time steps (80 ps). From this, the dynamical structure factor $S(\boldsymbol{Q}, \omega)$ was calculated for the same momentum transfers, $\boldsymbol{Q}$, used in the neutron measurements. After convoluting the calculated $S(\boldsymbol{Q}, \omega)$ with the experimental resolution, the calculated lineshapes could be directly compared with those measured experimentally. The comparison is shown in Fig. 4. Although there are quantitative discrepancies, the overall qualitative agreement is very good, evidence that the concept of orientational frustration is a valid interpretation of the orientational disorder in SF_6.

c. Orientational ordering and the phase transition

The phase transitions to the low temperature phase of OD crystals are usually first order and the low temperature crystal structures are usually of low symmetry. Consequently a critical test of our understanding of the behaviour of these solids is the ability to explain how (or indeed if!) the ordered low temperature phase arises from the disordered high temperature phase as the temperature is lowered. An essential requirement for this is a knowledge of the low temperature crystal structure, which, in the case of SF_6, was until very recently quite uncertain and a matter of some dispute.

Neutron powder diffraction data (19) indicated the structure to be of low symmetry and showed that it must be very similar at 20 K and 75 K. However, all efforts to find unit cell parameters to index these diffraction data failed. This failure implied that the symmetry of the low temperature phase could be no higher than triclinic. However, electron diffraction data (20) obtained between 45 K and 96 K could be analyzed in terms of a hexagonal cell containing three molecules. These measurements also indicated that at lower temperatures the hexagonal cell distorted to one of monoclinic or lower symmetry. The apparent conflict between the neutron and electron diffraction data immediately below the transition remained unresolved for several years. The two crystal structures observed by electron diffraction could, however, be reproduced by MDS calculations (21). While these suggested that the crystal structure at the lowest temperatures was triclinic, space group $P\bar{1}$, with three ordered molecules in the unit cell, at temperatures just below the transition a trigonal structure was found in which only two-thirds of the molecules are ordered. These two structures are shown in Fig. 5, which is taken from ref. 21. However, subsequent attempts to use this information in the analysis of the neutron diffraction data proved unsuccessful.

II. New results and speculations

The lineshape calculations referred to in Section I(*b*) and shown in Fig. 4 suggest a more complex structure for the excitation spectrum in SF_6. For wave-vectors smaller than those investigated by the neutron scattering experiments, the indications are that well-defined, long wavelength, acoustic modes do indeed exist. In a recent high-resolution inelastic neutron scattering experiment on a single crystal of SF_6, these well-defined modes were observed. Some results are shown in Fig. 6. These data are at present being analyzed (22), following Dove and Lynden-Bell (23), to give information about both the rotational–translational coupling and the correlation functions in SF_6.

The uncertainty concerning the low temperature structure of SF_6 referred to in Section I(*c*) has been resolved recently with the development of a new procedure to index diffraction data, starting from trial structures suggested by molecular packing considerations (24). When applied to the neutron data from SF_6, it succeeded in indexing the pattern in terms of a triclinic unit cell (25). The analysis determined the unit cell parameters with sufficient accuracy that a complete refinement was possible. The detailed crystal structure of SF_6 at 23 K and 85 K has recently been determined from new neutron diffraction data (26). At both temperatures the structure was found to be triclinic, space group $P\bar{1}$, with three ordered molecules in the unit cell, in agreement with the MDS calculations (21). But no evidence for a hexagonal phase below 96 K could be found. It is possible that the intermediate hexagonal phase observed by electron diffraction is restricted to the very thin surface layers that are probed by the electron beam. We believe that it does not exist in bulk SF_6 at any temperature.

The phase transition thus involves a dramatic lowering of symmetry, from cubic to triclinic. However, the triclinic structure can be derived from the cubic by distortions in two stages accompanying the onset of orientational order. First the bcc cell transforms to a hexagonal cell with the hexagonal axis along a cubic <111> direction. This stage involves a significant molecular displacement and a contraction along this direction (26). The MDS calculations (21) show that below 96 K the molecules order along <111> directions, the ordering direction in the cubic OD phase. But since the contraction along this direction causes a closer approach of next nearest neighbour molecules (the "disordering" interaction in the OD phase), not all molecules are able to order. The calculations show that two adjacent rows along <111> can order, but in the next row the molecules remain orientationally disordered. Thus, of the three molecules in the hexagonal cell, two will be ordered and one will remain disordered. The second state of the transition then involves a shear of the hexagonal cell to form the triclinic cell. The shear is perpendicular to the basal plane and appears to involve tilting the hexagonal axis towards the $[1\bar{1}0]$ direction. Since the triclinic structure is fully ordered, this second stage must be associated with the orientational ordering of the remaining third of the molecules. The relation between the cubic, hexagonal and triclinic cells is shown in Fig. 7. Since the hexagonal phase is not observed by the neutron diffraction experiments it appears that in bulk samples of SF_6 both ordering effects occur together at the transition at 96 K; the separation of the two stages seen by electron diffraction may be a purely surface phenomenon.

III. Concluding remarks

The last decade has seen very substantial advances in our understanding of the orientationally disordered state of condensed matter. This is particularly true for the case of SF_6. It has been brought about to a large extent by the application of neutron scattering techniques to the problem and by the increasing availability of large scale molecular dynamics simulation calculations to interpret experimental data. As a result we now know the microscopic nature of the orientational disorder in some detail. Its origin is neither statistical in nature nor large-amplitude thermal fluctuations, but is determined by steric repulsion effects, and may be understood in terms of the concept of orientational frustration. Its character thus differs markedly from the disorder in many other OD crystals.

MDS calculations allow many of the single molecule prop-

Can. J. Chem. Downloaded from www.nrcresearchpress.com by 176.9.209.113 on 09/07/12
For personal use only.

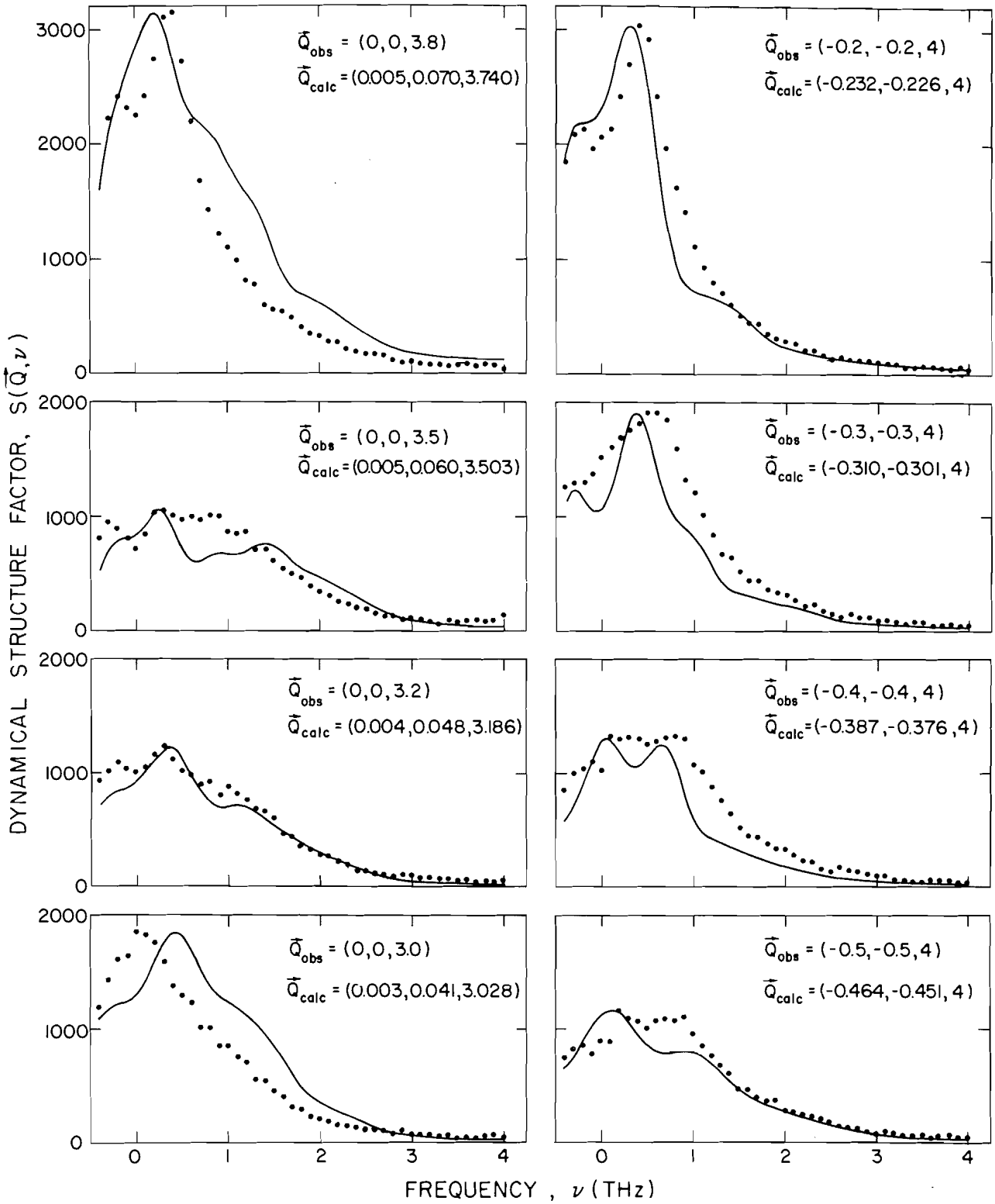

FIG. 4. Comparison of dynamical structure factors measured by inelastic neutron scattering with those obtained from MDS calculations. The points are observed and the line is the calculation.

erties (e.g. the autocorrelation functions, orientational distribution function, near neighbour correlations) to be understood, as well as the overdamped collective excitations observed by neutron scattering. The crystal structure of the low temperature phase is now known in detail and the transition can be understood, qualitatively at least, in terms of orientational ordering. For a quantitative understanding of the characteristics of the OD phase, however, more work is required.

Elucidation of the details of the collective excitation spectrum is a particularly difficult problem. The prediction of well-defined collective excitations at smaller wave-vectors and their subsequent observation show that the collective excitation spec-

Can. J. Chem. Downloaded from www.nrcresearchpress.com by 176.9.209.113 on 09/07/12
For personal use only.

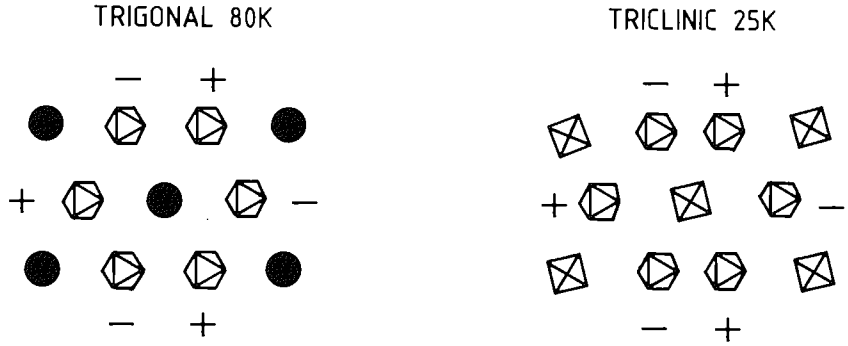

FIG. 5. The ordering in SF_6 at 25 K and 80 K suggested by the simulation calculations (21). The filled circles indicate orientationally disordered molecules. The structures are viewed along the [111] direction of the high temperature cubic phase. The structure of the latter would be similar to that shown at 80 K, but *all* molecules would be disordered.

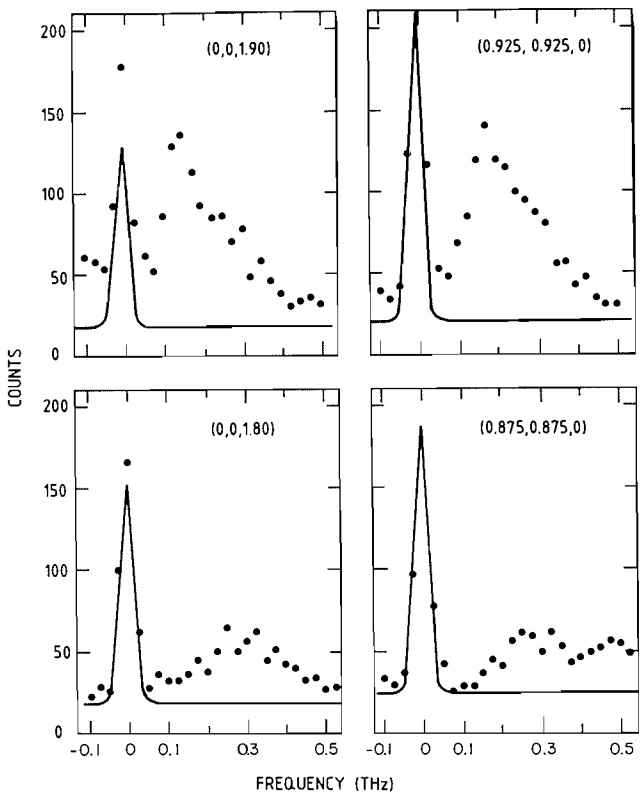

FIG. 6. High-resolution neutron scattering results from SF_6 at small propagation vectors. The line is the background from the container.

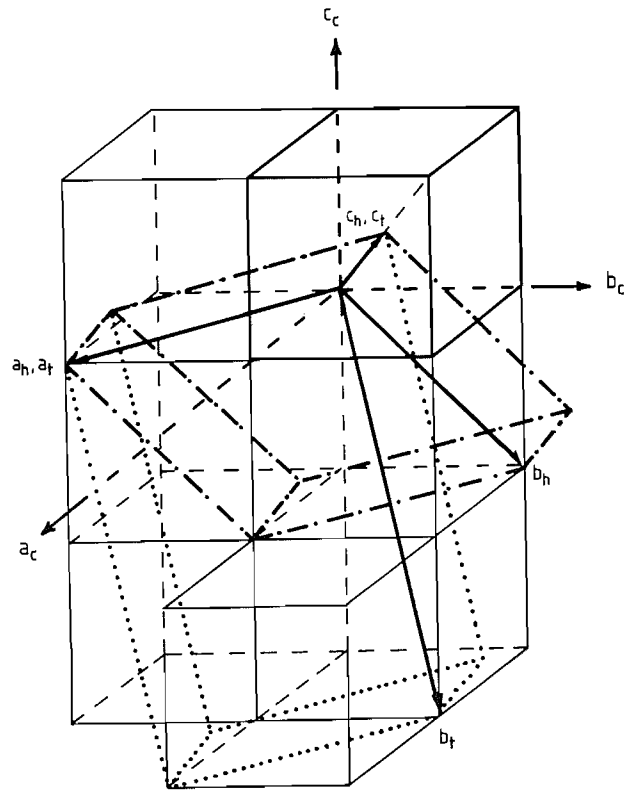

FIG. 7. The relationship between the cubic, hexagonal and triclinic cells suggested by the simulation calculations (21, 26). The subscripts c, h, t refer to cubic, hexagonal, and triclinic, respectively. The axes specifying the unit cells are shown by the bold vectors. The cubic, hexagonal, and triclinic cells are outlined by solid, dot–dash, and dotted lines, respectively, and the original cubic lattice is shown by faint lines.

trum is quite complex. It appears to be determined by the relative magnitudes of two effects: (*i*) the strength of the rotational–translational coupling and (*ii*) the separation between the relaxational frequencies of the translational and orientational correlation functions. The rotational–translational coupling parameter has recently been calculated for SF_6 by MDS (27). For the centro-symmetric SF_6 molecule it is a maximum at the zone centre and decreases to zero at the zone boundary. It is found to be rather independent of temperature and of the specific translational and rotational displacements considered. Relaxational frequencies have also been calculated recently (28). The translational relaxational frequency ("undamped" phonon) is zero at the zone centre and increases to values comparable with the orientational frequencies near the zone boundary. The interplay of these two effects means that there are several regimes of behaviour for the collective excitations as a function of propagation vector (28).

The relationship between orientational ordering and the phase transition lacks a quantitative basis at present and the conditions under which either the hexagonal or the triclinic phases are formed are not entirely clear. Finally, the applicability of the concept of orientational frustration to other OD crystals and other rotational–translational coupled systems remains to be explored. In many respects our increased insight into the nature of the orientationally disordered state has merely served to reveal further complexities in this intermediate phase of condensed matter.

1. J. TIMMERMANS. J. Chim. Phys. **35**, 331 (1938); J. Phys. Chem. Solids, **18**, 1 (1961).

Can. J. Chem. Downloaded from www.nrcresearchpress.com by 176.9.209.113 on 09/07/12
For personal use only.

2. N. G. PARSONAGE and L. A. K. STAVELY. *In* Disorder in crystals. Clarendon Press, Oxford. 1978; J. N. Sherwood (*Editor*). The plastically crystalline state. John Wiley and Sons, New York. 1979.
3. A. EUCKEN and E. SCHRÖDER. Z. Physik. Chem. B**41**, 307 (1938).
4. J. MICHEL, M. DRIFFORD, and P. RIGNY. J. Chim. Phys. **67**, 31 (1970).
5. S. K. GARG. J. Chem. Phys. **66**, 2517 (1977).
6. J. C. TAYLOR and A. B. WAUGH. J. Solid State Chem. **18**, 241 (1976).
7. G. DOLLING, B. M. POWELL, and V. F. SEARS. Mol. Phys. **37**, 1859 (1979); B. M. POWELL, V. F. SEARS, and G. DOLLING. *In* Neutron scattering — 1981. *Edited by* J. Faber Jr. AIP #89, New York. 1982. p. 221.
8. R. S. SEYMOUR and A. W. PRYOR. Acta Crystallogr. B**26**, 1487 (1970).
9. W. PRESS and A. HÜLLER. Acta Crystallogr. A**29**, 252 (1973); W. PRESS, Acta Crystallogr. A**29**, 257 (1973).
10. M. T. DOVE and G. S. PAWLEY. J. Phys. C (Solid State), **16**, 5969 (1983).
11. M. T. DOVE and G. S. PAWLEY. J. Phys. C (Solid State), **17**, 6581 (1984).
12. B. M. POWELL, G. DOLLING, and H. F. NIEMAN. J. Chem. Phys. **79**, 982 (1983).
13. J. C. DAMIEN, J. LEFEBVRE, M. MORE, B. HENNION, R. CURRAT, and R. FOURET. J. Phys. C (Solid State), **11**, 4323 (1978); C. G. WINDSOR, D. M. SAUNDERSON, J. N. SHERWOOD, D. TAYLOR, and G. S. PAWLEY. J. Phys. C (Solid State), **11**, 1741 (1978).
14. G. DOLLING and B. M. POWELL. Proc. R. Soc. London A**319**, 209 (1970); G. DOLLING, G. S. PAWLEY, and B. M. POWELL. Proc. R. Soc. London, A**333**, 363 (1973).
15. M. T. DOVE, G. S. PAWLEY, G. DOLLING, and B. M. POWELL. Mol. Phys. **57**, 865 (1986).
16. W. G. STIRLING, W. PRESS, and H. STILLER. J. Phys. C (Solid State), **10**, 3959 (1977).
17. M. MORE and R. FOURET. Faraday Discuss. **69**, 75 (1980).
18. K. H. MICHEL and J. NAUDTS. J. Chem. Phys. **68**, 216 (1978).
19. B. M. POWELL, G. DOLLING, J. C. EVANS, and H. F. NIEMAN. AECL Report No. 7055, unpublished data (1980).
20. G. RAYMOND, G. J. TATLOCK, and J. A. VENABLES. Acta Crystallogr. B**38**, 1896 (1980).
21. G. S. PAWLEY and G. W. THOMAS. Phys. Rev. Lett. **48**, 410 (1982); G. S. PAWLEY and M. T. DOVE. Chem. Phys. Lett. **99**, 45 (1983).
22. M. T. DOVE and B. M. POWELL. To be published.
23. M. T. DOVE. J. Phys. C (Solid State), **19**, 3325 (1986); M. T. DOVE and R. M. LYNDEN-BELL. J. Phys. C (Solid State), **19**, 3343 (1986).
24. J. C. CAILLAT and L. S. BARTELL. Quantum Chemistry Program Exchange program no. 520, Indiana University, Bloomington, IN. 47405 (1986).
25. L. S. BARTELL, J. C. CAILLAT, and B. M. POWELL. Science, **236**, 1463 (1987).
26. B. M. POWELL, M. T. DOVE, G. S. PAWLEY, and L. S. BARTELL. Mol. Phys. **62**, 1127 (1987).
27. M. T. DOVE and R. M. LYNDEN-BELL. *In* Dynamics of molecular crystals. *Edited by* J. Lascombe. Elsevier, Amsterdam. 1987. p. 705.
28. M. T. DOVE. ODIC Newsletter. Vol. 6. *Edited by* R. Weir. 1987. p. 6.

Can. J. Chem. Downloaded from www.nrcresearchpress.com by 176.9.209.113 on 09/07/12
For personal use only.

Enthalpies of mixing of ternary alkane mixtures with branched chain components

WEI-GUO SHEN AND ARTHUR G. WILLIAMSON[1]

Department of Chemical and Process Engineering, University of Canterbury, Christchurch, New Zealand

Received September 10, 1987

This paper is dedicated to Professor James A. Morrison

WEI-GUO SHEN and ARTHUR G. WILLIAMSON. Can. J. Chem. **66**, 904 (1988).

Measurements at 25°C are reported for the enthalpies of mixing of 2-methyl pentane with *n*-dodecane and with each of three pseudo *n*-dodecanes prepared from equimolar mixtures of *n*-undecane + *n*-tridecane, *n*-decane + *n*-tetradecane, and *n*-octane + *n*-hexadecane respectively. Measurements for mixtures of the equimolar decane + tetradecane mixture with each of the other three branched hexane isomers are also reported. The results are compared with the work of Benson and co-workers for binary mixtures of *n*-dodecane with the same hexanes. The deviations of 1–2% from the principle of congruence are similar to those reported previously for the ternary *n*-alkane mixtures.

WEI-GUO SHEN et ARTHUR G. WILLIAMSON. Can. J. Chem. **66**, 904 (1988).

Opérant à 25°C, on a mesuré les enthalpies de mélange du méthyl-2 pentane avec le *n*-dodécane ainsi qu'avec chacun des trois pseudo *n*-dodécanes qui ont été préparés respectivement à partir de mélanges équimolaires de *n*-undécane + *n*-tridécane, *n*-décane + *n*-tétradécane et *n*-octane + *n*-hexadécane. On rapporte aussi les résultats des mesures effectuées à l'aide du mélange équimolaire de décane + tétradécane avec chacun des trois autres isomères ramifiés de l'hexane. On compare ces résultats avec ceux obtenus par Benson et ses collaborateurs pour des mélanges binaires du *n*-dodécane avec les mêmes hexanes. On a observé des déviations de 1 à 2% du principe de la congruence et ces déviations sont semblables à celles rapportées antérieurement pour des mélanges tertiaires de *n*-alcanes.

[Traduit par la revue]

Introduction

The principle of congruence (1) has been applied to many binary systems and a few multicomponent systems (2, 3) of *n*-alkanes and the experimental results are in excellent agreement with the values predicted from the principle. The study has been extended to excess volumes of ternary mixtures obtained by mixing a pseudo *n*-dodecane with hexane isomers (4). This work reports the excess molar enthalpies of pseudo *n*-dodecane (10:14) [0.500 *n*-decane + 0.500 *n*-tetradecane] + 2-methyl pentane (2-MP), + 3-methyl pentane (3-MP), + 2,3-dimethyl butane (2,3-DMB), + 2,2-dimethyl butane (2,2-DMB), of pseudo *n*-dodecane (11:13) [0.500 *n*-decane + 0.500 *n*-tridecane], and of pseudo *n*-dodecane (8:16) [0.500 *n*-octane + 0.500 hexadecane] + 2-MP.

Experimental

Excess molar enthalpies were measured with an isothermal dilution calorimeter of the type described by Costigan *et al.* (5). The volume of the glass calorimeter vessel was 59.41 (±0.06) cm^3 and the volume of mercury displaced from the vessel into the pipette was 32.59 (±0.015) cm^3. The pipette level was adjusted so that there was always a positive pressure on the calorimeter vessel of 2–3 kPa above atmospheric pressure. Injections were made with a motorized burette with an estimated uncertainty of ±0.01 cm^3 per injection. The difference between the cumulative volume of the injections and the volume of displaced mercury was always less than 0.15 cm^3 and the corresponding error in mole fraction for a binary mixture was less than ±0.001. The water bath temperature was maintained at a constant temperature (±0.0004 K) and monitored with a thermistor and a bridge arrangement similar to that used in the calorimeter. The temperature was measured with a platinum resistance thermometer (Rosemount Model WS104) and a Rosemount ac bridge (Type VLF 51A).

Branched hexanes were "Aldrich" materials with quoted purities better than 98% for 2,2-DMB, 97% for 2,3-DMB, and 99% for 2-MP and 3-MP. *n*-Alkanes were Koch-Light, "puriss" grade (99% minimum purity). All chemicals were taken from freshly opened bottles without further purification. Gas–liquid chromatographic analysis of the materials with chain length less than C_{10} suggested that the actual purities were significantly better than the quoted minimum purities. Our past experience has been that despite the quoted minimum purities of the alkanes from these sources being only 98 or 99%, the consistency of measurements made with the materials as supplied indicates that such impurities as are present have a negligible effect on enthalpies of mixing and volumes of mixing with other alkanes. The densities of all these chemicals were measured with a Mettler DMA60/DMA602 vibrating tube densimeter and are compared with literature values in Table 1. Pseudo *n*-dodecanes were prepared by weighing the *n*-alkanes into stoppered flasks. The density of each batch of newly prepared pseudo *n*-dodecane was measured before it was used to prepare ternary mixtures, as is listed in Table 2. The differences in the densities of four preparations of pseudo *n*-dodecane (10:14) were less than $\pm 3 \times 10^{-5}$ g cm^{-3}, which corresponds to a maximum error of ±0.001 in mole fraction. The measured densities of pseudo *n*-dodecane (8:16) indicated no significant change in composition between runs (Nos. 6 and 7 in Table 2). The discrepancies in the excess enthalpies in the composition-overlap region were less than 1 J mol^{-1}. The equipment and method were checked by measurements of the system x *n*-dodecane + $(1 - x)$ 2-MP, which were compared with the previous published results of Benson and co-workers (6).

Results and discussion

The measured excess molar enthalpies of (x *n*-dodecane + $(1 - x)$ 2-MP) and six ternary systems are listed in Table 3. The results for (x *n*-dodecane + $(1 - x)$ 2-MP) shown in Fig. 1 agree with those of Benson and co-workers (6) within 0.5 J mol^{-1} at $x = 0.5$. Although Benson's measurements are significantly smoother than ours, we believe that the agreement justifies direct comparison of our measurements with the corresponding binary data from Benson within ±0.5 J mol^{-1}.

An equation of the type:

$$[1] \quad H^E/(\text{J mol}^{-1}) = x(1-x)\sum_{j=1}^{m} A_j(1-2x)^{j-1}$$

where x is the mole fraction of *n*-dodecane or pseudo *n*-dodecane, was fitted to each set of results by the method of least squares with all points weighted equally.

The parameters for these representations and their standard

[1]Author to whom correspondence should be addressed.

Can. J. Chem. Downloaded from www.nrcresearchpress.com by 93.93.197.157 on 09/07/12
For personal use only.

TABLE 1. Densities (g cm^{-3}) of chemicals used in this work at 298.15 K

Compound	Source					
	This work	Ref. 7	Ref. 8	Ref. 9	Ref. 10	Ref. 11
Octane	0.69854	0.69876	0.69866		0.69849	0.69862
Decane	0.72600	0.72622	0.72609	0.72588	0.72625	0.72635
Undecane	0.73629	0.73652				0.7365
Dodecane	0.74510			0.74519	0.74516	0.74518
Tridecane	0.75341	0.75315				0.75271
Tetradecane	0.75905			0.75906		0.75920
Hexadecane	0.77069			0.77006		0.76994
2-MP	0.64853				0.64852	
3-MP	0.65960				0.65976	
2,3-DMB	0.65677				0.65702	
2,2-DMB	0.64431				0.64446	

TABLE 2. Densities of pseudo *n*-alkanes at 298.15 K

n-Alkanes	Batch	Density (g cm^{-3})
n-C_{10} + n-C_{14}	1	0.74508
	2	0.74505
	3	0.74508
	4	0.74508
n-C_{11} + n-C_{13}	5	0.74532
n-C_8 + n-C_{16}	6	0.74631
	7	0.74633

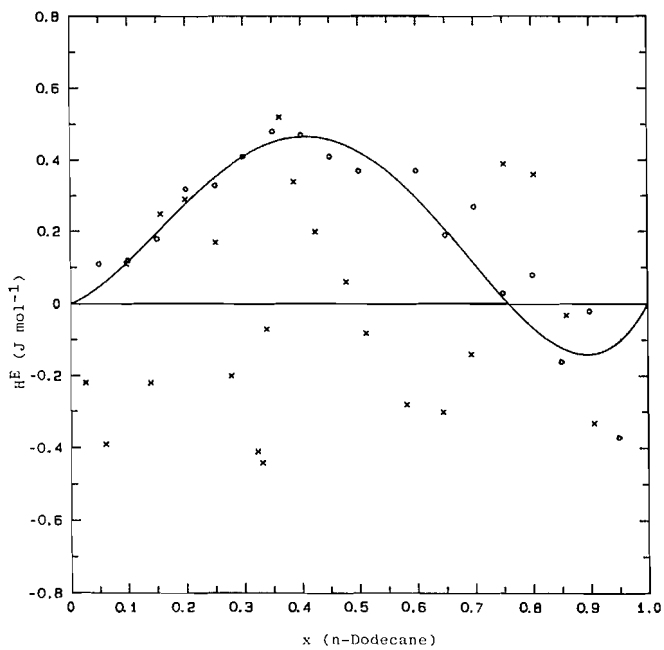

FIG. 1. Deviations of enthalpies for *n*-dodecane and 2-MP: (—) H^E calculated with eq. [1] (Benson) − H^E calculated with eq. [1] (this work); (x) H^E Exp. (this work) − H^E calculated with eq. [1] (this work); (○) H^E Exp. (Benson) − H^E calculated with eq. [1] (this work).

deviations:

$$[2] \quad R = [\Sigma r/(n-m)]^{1/2}$$

where $r = H^E$ (eq. [1]) − H^E experimental, and n = the number of experimental points, are listed in Table 4.

The excess molar enthalpies of mixtures of pseudo *n*-

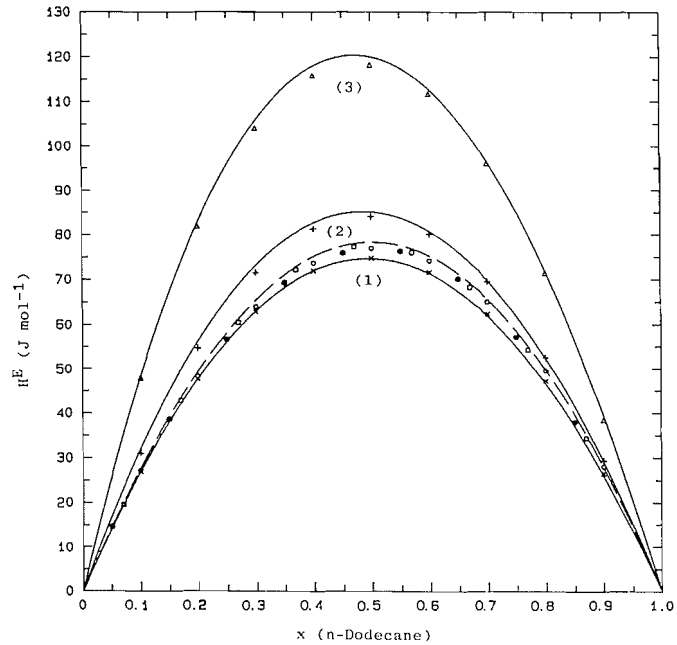

FIG. 2. Excess enthalpies for *n*-dodecane and isomers of hexane. (------) Equation [1] with parameters from Table 4, system 2, for *n*-dodecane + 2-MP. (———) Equation [1] with parameters from Table 4 for (1) *n*-dodecane + 3-MP (system 6), (2) *n*-dodecane + 2,3-DMB (system 8), (3) *n*-dodecane + 2,2-DMB (system 10). Experimental results: (○) pseudo *n*-dodecane (10:14) + 2-MP; (×) pseudo *n*-dodecane (10:14) + 3-MP; (+) pseudo *n*-dodecane (10:14) + 2,3-DMB; (△) pseudo *n*-dodecane (10:14) + 2,2-DMB; (*) pseudo *n*-dodecane (11:13) + 2-MP; (□) pseudo *n*-dodecane (8:16) + 2-MP.

dodecane and of *n*-dodecane with hexane isomers are compared in Fig. 2. The curves are from values calculated by eq. [1] with the parameters optimized from this work for *n*-dodecane + 2-MP (dotted curve), and from Benson for *n*-dodecane + the other three hexane isomers (solid curves). The points are the experimental values for the ternary mixtures.

The magnitudes of the excess molar enthalpies for pseudo *n*-dodecane + hexane isomers decrease in the order: 2,2-DMB > 2,3-DMB > 2-MP > 3-MP, just as Benson and co-workers (6) observed from their measurements for *n*-dodecane + hexane isomers.

The results of this study are very similar to those previously obtained for ternary *n*-alkane mixtures, namely, that the behaviour of multicomponent mixtures is almost the same as that

Can. J. Chem. Downloaded from www.nrcresearchpress.com by 93.93.197.157 on 09/07/12
For personal use only.

Can. J. Chem. Downloaded from www.nrcresearchpress.com by 93.93.197.157 on 09/07/12
For personal use only.

TABLE 3. Excess molar enthalpies H^E of (x n-C_{12} + (1 − x) C_6) at 298.15 K

x	H^E (J mol^{-1})	r (J mol^{-1})	x	H^E (J mol^{-1})	r (J mol^{-1})
		n-Dodecane + 2-MP			
0.026	7.55	0.22	0.387	74.42	−0.34
0.060	16.78	0.39	0.424	76.60	−0.20
0.097	26.94	−0.11	0.478	78.20	−0.06
0.138	36.28	0.22	0.512	78.22	0.08
0.156	40.75	−0.25	0.581	76.03	0.28
0.199	49.45	−0.29	0.645	71.44	0.30
0.251	58.50	−0.17	0.694	66.29	0.14
0.278	62.06	0.20	0.752	58.68	−0.39
0.331	68.59	0.44	0.804	49.48	−0.36
0.363	72.67	−0.52	0.859	37.53	0.03
0.323	67.66	0.41	0.906	25.90	0.33
0.339	69.72	0.07			
		[0.500 n-Undecane + 0.500 n-tridecane] + 2-MP			
0.054	15.24	0.43	0.391	73.29	−0.61
0.101	27.43	0.13	0.428	75.22	−0.29
0.145	37.67	−0.02	0.490	77.55	−0.74
0.154	39.86	−0.45	0.537	77.18	−0.58
0.204	49.28	−0.27	0.586	75.18	−0.36
0.247	56.33	−0.00	0.645	70.37	0.23
0.280	61.16	−0.14	0.685	65.89	0.43
0.345	68.01	0.69	0.736	58.92	0.43
0.358	69.38	0.62	0.788	50.58	−0.03
0.394	72.72	0.20	0.825	43.22	0.12
0.416	73.53	0.75	0.894	28.29	−0.50
0.322	65.92	0.34	0.941	15.93	−0.09
0.351	69.53	−0.19			
		[0.500 n-Octane + 0.500 n-hexadecane] + 2-MP			
0.025	7.18	0.10	0.358	71.04	−0.02
0.058	16.12	0.16	0.384	73.09	0.14
0.104	28.37	−0.24	0.417	75.31	0.00
0.145	37.79	−0.25	0.490	77.58	−0.02
0.168	42.90	−0.38	0.551	77.02	−0.25
0.209	50.76	−0.32	0.601	74.63	−0.28
0.253	58.09	−0.17	0.653	70.55	−0.49
0.284	62.70	−0.14	0.695	65.88	−0.49
0.330	67.95	0.23	0.747	57.99	0.08
0.364	71.05	0.47	0.799	49.15	−0.02
0.395	73.48	0.54	0.839	40.75	0.30
0.322	66.75	0.54	0.899	29.43	0.41
			0.891	16.14	0.54
		[0.500 n-Decane + 0.500 n-tetradecane] + 2-MP			
0.027	7.83	0.09	0.417	74.69	−0.26
0.063	17.57	0.02	0.472	76.43	0.07
0.107	28.72	−0.16	0.508	77.22	−0.37
0.156	39.78	−0.27	0.573	75.36	0.05
0.200	48.74	−0.41	0.644	70.90	−0.08
0.245	56.19	−0.10	0.724	61.87	−0.09
0.278	60.55	0.34	0.779	53.58	−0.31
0.337	67.39	0.67	0.827	44.04	0.17
0.361	69.61	0.83	0.908	25.73	0.20
0.329	67.38	−0.14	0.954	12.96	0.50
0.379	72.32	−0.39			
		[0.500 n-Decane + 0.500 n-tetradecane] + 3-MP			
0.042	12.10	−0.16	0.446	74.02	−0.23
0.091	24.60	−0.05	0.533	74.17	0.06
0.148	37.77	−0.18	0.597	71.79	−0.18
0.199	47.84	−0.35	0.650	67.97	−0.42
0.253	56.55	−0.12	0.669	65.95	−0.22
0.312	63.93	0.21	0.736	57.55	−0.10
0.355	68.04	0.35	0.784	49.94	0.08
0.405	71.59	0.39	0.828	41.81	0.07
0.352	68.04	0.10	0.898	26.65	0.26
0.401	71.58	0.18	0.949	13.55	0.57
		[0.500 n-Decane + 0.500 n-tetradecane] + 2,3-DMB			
0.030	9.68	0.34	0.475	83.84	0.07
0.053	16.82	0.40	0.514	84.07	−0.24
0.084	26.12	0.17	0.563	82.40	−0.11
0.138	41.07	−0.33	0.611	79.26	−0.08
0.194	53.86	−0.38	0.652	75.50	−0.16
0.249	64.12	−0.47	0.697	70.14	−0.23
0.309	72.32	0.22	0.748	62.53	−0.39
0.351	77.18	−0.01	0.796	52.83	0.50
0.403	80.86	0.43	0.846	42.35	0.12
0.356	77.65	0.04	0.891	31.50	0.16
0.386	79.92	0.27	0.950	15.25	−0.02
0.420	81.98	0.25			
		[0.500 n-Decane + 0.500 n-tetradecane] + 2,2-DMB			
0.015	7.70	0.52	0.393	114.52	0.40
0.051	25.99	0.27	0.441	117.32	0.20
0.077	37.77	0.23	0.493	118.15	−0.17
0.111	52.28	−0.11	0.553	116.01	−0.47
0.147	65.17	0.02	0.600	111.70	−0.35
0.184	77.33	−0.32	0.652	104.61	−0.16
0.245	93.56	−0.50	0.694	96.97	0.05
0.270	98.51	−0.32	0.746	85.31	0.35
0.343	110.18	−0.26	0.793	72.64	0.45
0.368	112.44	0.26	0.847	56.29	0.18
0.323	106.88	0.40	0.893	41.50	−0.59
0.353	110.68	0.47	0.951	19.12	−0.07

TABLE 4. Parameters and standard deviations (J mol^{-1}) for representation of H^E for (n-C_{12} + C_6 isomers) with eq. [1] at 298.15 K

System[a]	A_1	A_2	A_3	A_4	A_5	R
1	315.03	−0.43	−11.88			0.10
2	313.33	−2.19	−8.98			0.31
3	307.38	−6.45	−4.69			0.36
4	307.54	−8.51	−14.84	24.53		0.45
5	310.41	−0.82	−14.27			0.34
6	298.54	5.92	−9.38			0.10
7	298.39	2.74	−5.81			0.28
8	340.56	19.57	−2.85			0.11
9	335.91	11.45	−3.75			0.30
10	480.10	52.54	8.90	12.13		0.11
11	471.47	40.63	28.55	38.79	−31.54	0.38

[a]Systems are as follows: 1: n-dodecane + 2-MP (from ref. 6; 2: n-dodecane + 2-MP (this work); 3: [0.500 n-decane + 0.500 n-tetradecane] + 2-MP; 4: [0.500 n-undecane + 0.500 n-tridecane] + 2-MP; 5: [0.500 n-octane + 0.500 n-hexadecane + 2-MP; 6: n-dodecane + 3-MP (from ref. 6; 7: [0.500 n-decane + 0.500 n-tetradecane] + 3-MP; 8: n-dodecane + 2,3-DMB (from ref. 6; 9: [0.500 n-decane + 0.500 n-tetradecane] + 2,3-DMB; 10: n-dodecane + 2,2-DMB (from ref. 6; 11: [0.500 n-decane + 0.500 n-tetradecane] + 2,2-DMB.

of the congruent binary mixtures, but that the excess enthalpies of the multicomponent mixtures are usually lower than those of the binaries by an amount only marginally greater than the experimental accuracy of the measurements. The excess volumes of the same ternary mixtures at 25°C (4) showed no significant deviation from those of congruent binaries.

We had hoped that the excesss thermodynamic properties of mixing of ternary mixtures of the branched system with binary *n*-alkane mixtures might reveal larger deviations from congruence than those of the congruent binary *n*-alkane plus branched chain systems. This was expected to arise from the different experimental behaviours of the long and short alkanes with the branched chains compared with that of the congruent intermediate chain length system. As can be seen by comparison of the current results with the *n*-alkane results, this is not so. As yet we have not been able to find systems in which major deviations from simple congruence occur.

Acknowledgements

This work has been supported by grants from Lanzhou University, People's Republic of China, and the New Zealand University Grants Committee.

1. S. P. KHO and A. G. WILLIAMSON. Chem. Eng. J. **19**, 85 (1980).
2. C. J. LOOI, C. J. MAYHEW, and A. G. WILLIAMSON. J. Chem. Thermodyn. **6**, 1171 (1974).
3. C. B. LIM and A. G. WILLIAMSON. J. Chem. Thermodyn. **12**, 65 (1980).
4. W. G. SHEN and A. G. WILLIAMSON. 9th IUPAC Conf. on Chem. Thermodyn. Lisbon, 14–18 July, 1986.
5. J. M. COSTIGAN *et al.* Aust. J. Chem. **33**, 2103 (1980).
6. S. M. HAMAM, M. K. KUMARAN, and G. C. BENSON. J. Chem. Thermodyn. **16**, 537 (1984).
7. R. S. HUTCHINGS and W. A. VAN HOOK. Fluid Phase Equilib. **21**, 165 (1985).
8. J. R. GOATES, J. B. OTT, and R. B. GRIGG. J. Chem. Thermodyn. **13**, 907 (1981).
9. A. M. AWWAD and E. I. ALLOS. Fluid Phase Equilib. **22**, 353, (1985).
10. J. A. RIDDICK and W. B. BUNGER. *In* Techniques in chemistry. Vol. 2. Organic solvents. 3rd ed. *Edited by* Arnold Weissberger. Wiley–Interscience, New York. 1977.
11. TRC thermodynamic tables — hydrocarbons. Vol. 1. Thermodynamics Research Center, The Texas A & M University System, College Station, TX. 1985.

Can. J. Chem. Downloaded from www.nrcresearchpress.com by 93.93.197.157 on 09/07/12
For personal use only.

Orientational order–disorder transitions in solid hydrogen

N. S. SULLIVAN
Department of Physics, University of Florida, Gainesville, FL 32611, U.S.A.

Received August 17, 1987

This paper is dedicated to Professor J. A. Morrison

N. S. SULLIVAN. Can. J. Chem. **66**, 908 (1988).

We discuss the orientational ordering in solid ortho–para hydrogen mixtures. Following a brief sketch of the properties of the ortho and para hydrogen modifications and the long-range ordering of an assembly of $J = 1$ quantum rotors (ortho-H_2), we consider the nature of the purely local ordering seen in random dilute ortho–para mixtures. Measurements of the quasi-static glass order parameter and the mean correlation time for the molecular alignments are interpreted in terms of a rapid but continuous freezing of the orientational fluctuations.

N. S. SULLIVAN. Can. J. Chem. **66**, 908 (1988).

On discute de la mise en ordre de l'orientation qui s'établit dans des mélanges solides d'hydrogènes ortho et para. Après avoir présenté une brève ébauche des propriétés des formes ortho et para de l'hydrogène et de la mise en ordre d'un groupe de $J = 1$ rotors quantiques (H_2 ortho), on considère la nature de la mise en ordre purement locale qui est observée dans des mélanges ortho–para dilués au hasard. On interprète les résultats des mesures du paramètre d'ordre vitreux quasi-statique et du temps moyen de corrélation des alignements moléculaires en fonction d'un gel rapide mais continu des fluctuations des orientations.
[Traduit par la revue]

Can. J. Chem. Downloaded from www.nrcresearchpress.com by 176.9.209.113 on 09/07/12
For personal use only.

I. Introduction

Solid hydrogen is the simplest molecular solid that exists in nature and the search for a detailed understanding of the many-body properties at low temperatures has held the interest of researchers in both theory and experiment for many years (for a review of the properties of solid hydrogen, see ref. 1). The reason for this is that the ordering of the rotational degrees of freedom of the molecules can be understood from first principles considerations. The interaction Hamiltonians are believed to be well-known and studies of the ordering of the molecular orientations provide a rich testing ground for interesting new regimes of collective behavior. This has been seen in recent nmr studies (2, 3) which have led to the observation of a new phase — the "quadrupolar glass" phase for dilute samples of ortho hydrogen. This regime of purely local ordering is believed to result from the combined effects of frustration and disorder which are thought to be universal features of the magnetic spin glasses. In this sense the dilute ortho mixtures resemble a quantum rotor spin-glass at low temperatures.

In this paper, we will give a short description of the long range periodic orientational ordering for samples rich in ortho molecular species and then discuss the outstanding problems concerning the nature of the purely local ordering in random dilute ortho–para H_2 mixtures. We will present recent measurements of the quasi-static glass order parameter and of the quadrupolar correlation time (inferred from nmr relaxation) which show that the molecules go through a rapid but continuous freezing of their orientational fluctuations on cooling into the glass regime. The transition appears to be that of a dynamic gel and not a thermodynamic phase transition.

II. Fundamentals

There are two distinct molecular species of hydrogen (ortho and para) that arise from the two ways that the total wave function can be antisymmetrised (as required by the exclusion principle). For *ortho hydrogen* the nuclear wave function is symmetric ($I_{total} = i_1 + i_2 = 1$), and for *para hydrogen* the nuclear wave function is antisymmetric ($I_{total} = 0$), the corresponding orbital wave functions are antisymmetric (orbital angular momentum J odd) and symmetric (J even), respectively (see Table 1). The different J states are widely separated in energy. The rotational kinetic energy $E_J = B_J J(J+1)$ with $B_J = 85.6$ K, and the $J = 1$ and $J = 2$ rotational states are 171 K and 510 K above the $J = 0$ ground state, respectively. We therefore only need to consider the lowest rotational states, $J = 1$ and $J = 0$ in the solid. Furthermore, the anisotropic interactions between the molecules which can mix the different J states are very weak ($V_{aniso} \sim 1$ K), J is therefore a good quantum number and we may consider the ortho–para solids as mixtures of quantum rotors. The order/disorder transitions seen at low temperatures are those of an interacting array of $J = 1$ rotors, and thus a problem of fundamental interest in solid state physics.

TABLE 1. Symmetries of nuclear and orbital wave functions of ortho and para species

Parameter	Value	
	ortho-H_2	para-H_2
$\chi_{nuclear}$	Even, $I = 1$	Odd, $I = 0$
ϕ_{orb}	Odd, $J = 1, 3, 5 \ldots$	Even, $J = 0, 2, 4 \ldots$

The conversion of ortho molecules to the para ground state ($J = 0$) is very slow because it is doubly forbidden; two symmetries need to be broken simultaneously, the symmetry of the nuclear wave function and that of the orbital wave function, in order to convert an ortho molecule into a para molecule. In the pure solid this conversion is induced by the intermolecular magnetic interactions which lead to a bimolecular rate constant of 1.9% per hour. This rate is sufficiently slow that we may consider the ortho species as stable on the time scale of ordinary experiments. On the other hand, over a few weeks or months, the experimenter may explore a wide range of ortho concentrations continuously by simply allowing a sample to age at constant low temperature.

The $J = 1$ molecules are not spherically symmetric; they have end-on symmetry and hence no permanent electric dipole moment, but they do have a small electric quadrupole moment. There is therefore a weak electrostatic quadrupole–quadrupole (EQQ) interaction between ortho molecules which depends on

Can. J. Chem. Downloaded from www.nrcresearchpress.com by 176.9.209.113 on 09/07/12
For personal use only.

their relative orientations (4). At high temperatures the molecules are free to rotate about fixed sites, but at low temperatures the ortho molecules adopt mutual orientations to minimize their EQQ interactions. The resulting states lead to a rich phase diagram of oriented structures as a function of ortho concentration.

For high ortho concentrations one observes first-order phase transitions to a periodic ordering of the quadrupolar alignments in a Pa_3 configuration. As the ortho molecules are replaced by inert para molecules, there is a small perturbation of the orientations in the neighbourhood of the para molecule for small dilutions, but at a critical concentration of approximately 55% for hydrogen, the long range periodic ordering is lost. At low concentrations one finds a random ordering of the molecular axes and of the degree of ordering from site to site. This has been referred to as a "quadrupolar glass" (5). The experimentally established phase diagram is illustrated in Fig. 1. In the following we will try to understand the underlying physics of these two different types of ordering in terms of the properties of the quadrupolar interactions which drive the transitions.

The intermolecular electrostatic interactions between two rigid molecules can be written down easily using a standard multipolar expansion, the quadrupole–quadrupole term is the first in the expansion for symmetric diatomic molecules and is given by (4)

$$[1]\quad V_{12}^{QQ} = \frac{20\pi}{9}(70\pi)^{1/2}\Gamma_{12} \times \sum_{m_1 m_2} C^{224}_{m_1 m_2 m} Y_2^{m_1}(\Omega_1) Y_2^{m_2}(\Omega_2) Y_4^{m}(\Omega_{12})^*$$

Ω_1 and Ω_2 designate the polar angles ($\Omega_1 = \alpha_1, \beta_1$) specifying the orientation of the molecules with respect to some arbitrary reference frame. Ω_{12} specifies the orientation of the intermolecular vector $\boldsymbol{R}_{12}$ (connecting the centers of mass). $C^{224}_{m_1 m_2 m}$ is a Clebsch–Gordon coefficient and the strength of the interaction is measured by

$$[2]\quad \Gamma_{12} = \frac{6e^2Q^2}{25R_{12}^5} \simeq 0.85\ \text{K}$$

Q is the electric quadrupole moment of the molecule. The next highest-order interaction is the hexadecapole–quadrupole interaction, $V^{QH} \simeq 0.02\, V^{QQ}$, at the nearest neighbour separation (6).

Since J is a good quantum number for solid hydrogen we can replace the spherical harmonics Y_1^m by their irreducible operator equivalents O_1^m in the manifold $J = 1$, using

$$[3]\quad \langle JM|Y_l^m|JM\rangle = \alpha_{(J=1)}\langle JM|O_l^M|JM\rangle$$

with

$$[4]\quad \alpha = -\tfrac{2}{5}$$

and

$$O_i^0 = \frac{1}{\sqrt{6}}(3J_Z^2 - 2)$$

$$O_i^{\pm 1} = \mp\tfrac{1}{2}(J_Z J_\pm + J_\pm J_Z)$$

$$O_i^{\pm 2} = \tfrac{1}{2}(J_\pm)^2$$

i labels the lattice sites. The operators O_l^m are formulated in the local molecular reference frame, and are related to the laboratory frame by

$$(O_2^m)^1 = \sum_n D^2_{mn}(\chi_i) O_2^n(i)$$

where the $D^2_{mn}(\chi_i)$ are the rotation matrices specifying a rotation through the Eulerian angles $\chi_i = (\alpha_i, \beta_i)$ for molecule i.

The quadrupole–quadrupole interaction can therefore be written in the simple form

$$V_{ij}^{QQ} = \sum_{m,n} \zeta_{ij}^{mn} O_i^m O_j^n$$

where the lattice constants and interaction strength are collected in the factor

$$[5]\quad \zeta_{ij}^{mn} = \frac{(70\pi)^{1/2}}{3}\Gamma_{ij} \times \sum_{m'n'} C^{224}_{m'n'} [Y_4^{m',+n'}(\Omega_{ij})]^* D^{(2)}_{mm'}(\chi_i) D^{(2)}_{n'n}(\chi_j)$$

χ_i *and* χ_j are the Eulerian angles specifying the orientation of the local symmetry axes of the molecules (i and j) with respect to the laboratory frame (which will be fixed relative to the crystal axes).

Anisotropic forces other than the quadrupole–quadrupole and quadrupole–hexadecapole interactions do occur. These include the anisotropic components of Van der Waals and valence forces (8), but theoretical estimates place their strengths well below the EQQ interaction. Indirect interactions (4) mediated by phonons are also believed to be very weak but they are long-ranged (R^{-3}) and are expected to dominate the short-range interactions at very low concentrations ($x < 1\%$). In the following treatment of the long-range ordering we will neglect all but the quadrupolar interaction.

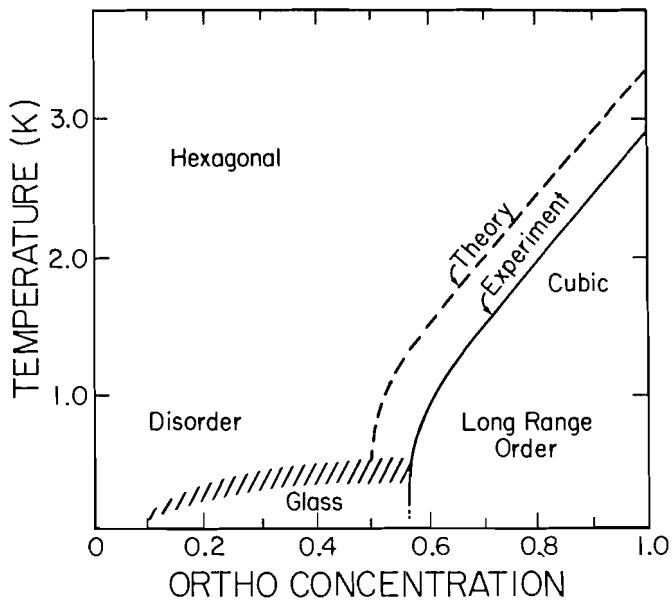

FIG. 1. Phase diagram for the orientational ordering seen in solid ortho–para hydrogen mixtures. The hatched region designates the continuous growth of local ordering on cooling into the glass phase.

III. Orientational ordering for high ortho concentrations

We are interested here in the nature of the order/disorder transition on a fixed lattice. The ground-state configuration has been shown (9) to be a Pa_3 configuration in which the fcc lattice is divided into four interpenetrating simple cubic sublattices: in each sublattice the molecules are aligned parallel to a body-

Can. J. Chem. Downloaded from www.nrcresearchpress.com by 176.9.209.113.on 09/07/12
For personal use only.

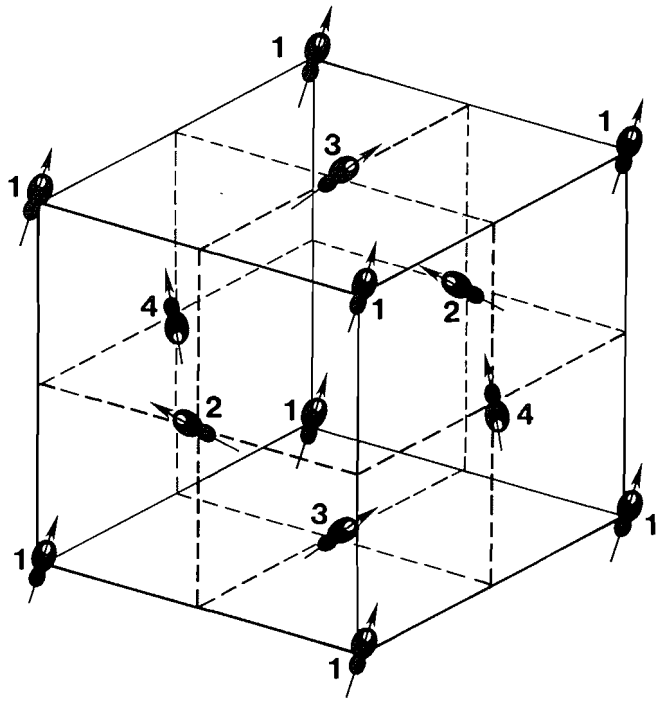

FIG. 2. The Pa_3 configuration showing the four interpenetrating simple cubic sublattices.

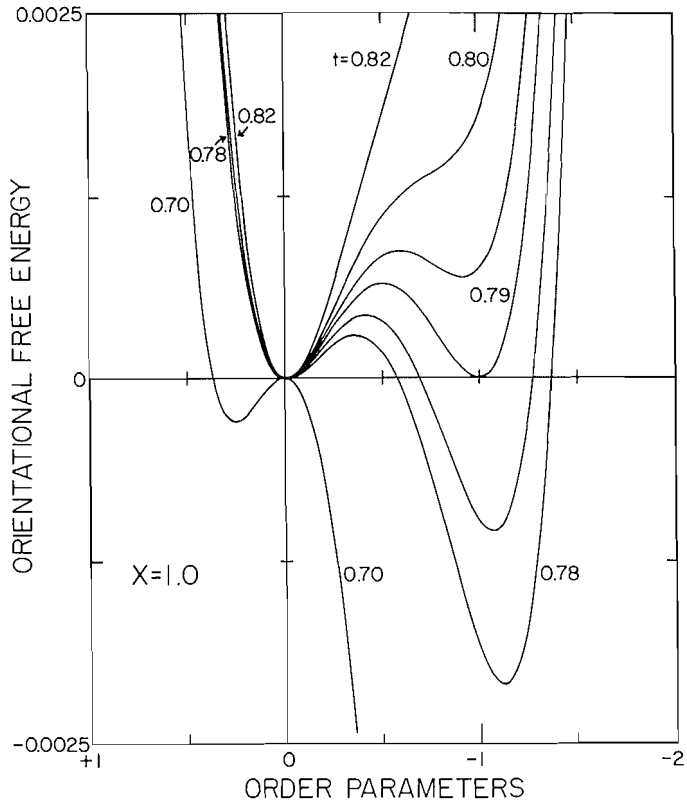

FIG. 3. Calculated orientational free energies $F(S)$ as functions of the order parameter for several temperatures near the transition temperature. The ortho concentration $X = 1.0$. The reduced temperatures $t = T/T_b$ where $T_b = 19\Gamma_{12}/4 \ln 2$ is the mean field transition temperature. A first order transition occurs at $t_c = 0.79$.

diagonal of the fcc lattice, a different body-diagonal being associated with each sublattice (Fig. 2). This structure has been well verified experimentally (10) and in the following we will develop the theory of the ordering, taking the axes of the Pa_3 system as fixed local reference frames, and treat the quantum mechanical alignment $S_i = \langle 3J_j^2 - 2\rangle_i$ (evaluated with respect to the local axes Z_i) as the relevant thermodynamic variable. The parameter S_i is an appropriate measure of the local orientational order at site i. $S_i(T) \rightarrow 0$ if all states in the manifold $J = 1$ are equally populated and $S_i \rightarrow -2$ at low temperatures if the ground state corresponds to $J_{z_i} = 0$.

In order to calculate the variation of S as a function of the temperature we will use Kirkwood's method of restricted traces (11) which will give the mean-field approximation as a zeroth-order approximation. The virtue of the method is that, treated to higher orders of approximation, it includes the contribution of correlations arising from "flip–flop" terms such as $\langle O_i^n O_j^n\rangle_{m,n\neq 0}$ which are important for an assembly of quantum rotors.

In the method of restricted traces one calculates the partition function $Z = \text{tr}\,[\exp(-\beta H)]$ assuming a fixed value of S, i.e. we write

$$[6] \quad Z = \sum_{\{S\}} \text{tr}_S'(e^{-\beta H})$$

where tr′ refers to the trace calculated subject to the constraint that S is fixed. The sum $\sum_{\{S\}}$ over the range of S will be sharply peaked at the value of S (say S_0), which minimizes the free energy, and Kirkwood's approximation consists of neglecting all terms in the sum except for $S = S_0$. The calculations can be simplified by noting that

$$[7] \quad \log Z = \log \langle e^{-\beta H}\rangle_S + \log W(S)$$

where $\langle\ \rangle_S$ denotes the expectation value subject to the constraint $S = 1/N\Sigma_i\langle 3J_{Z_i}^2 - 2\rangle$, and $W(S)$ is the number of configurations with fixed S.

$$[8] \quad \log W(S) = \frac{1}{3N}\{-(2+S)\log(2+S) - (1-S)\log(1-S) + (2+S)\log 2 + 3\log 3\}$$

The temperature-dependent term of $\log Z$ is calculated using the high temperature expansion

$$\log\langle e^{-\beta H}\rangle = \sum_{n=1}^{\infty} (-\beta)^n M_n/n!$$

where the first two cumulants are $M_1 = \langle H\rangle$ and $M_2 = \langle H^2\rangle - \langle H\rangle^2$. Since $\zeta_{ij} \propto R_{ij}^{-5}$, we restrict i and j to nearest neighbours; i and j must therefore belong to distinct sublattices and we can vary $\langle O_i\rangle$ and $\langle O_j\rangle$ independently in the calculation of $\langle H\rangle$. We find $M_1 = 6x\gamma S^2$ where N is the number of lattice sites, Z is the co-ordination number, and $\gamma = 19\Gamma/72$ for the Pa_3 structure.

In the mean-field approximation we limit the expansion to the first cumulant. The orientational free energy per particle is given by

$$[9] \quad F(S) = \tfrac{1}{3}k_B T[(2+S)\log(2+S) + (1-S)\log(1-S) - S\log 2] + 6X\gamma S^2$$

This is minimised as a function of S when

$$[10] \quad 36\beta|\gamma|S = \log\left(\frac{2+S}{2-2S}\right)$$

At large β (low temperature), the solution is given by $S_0 = -2$,

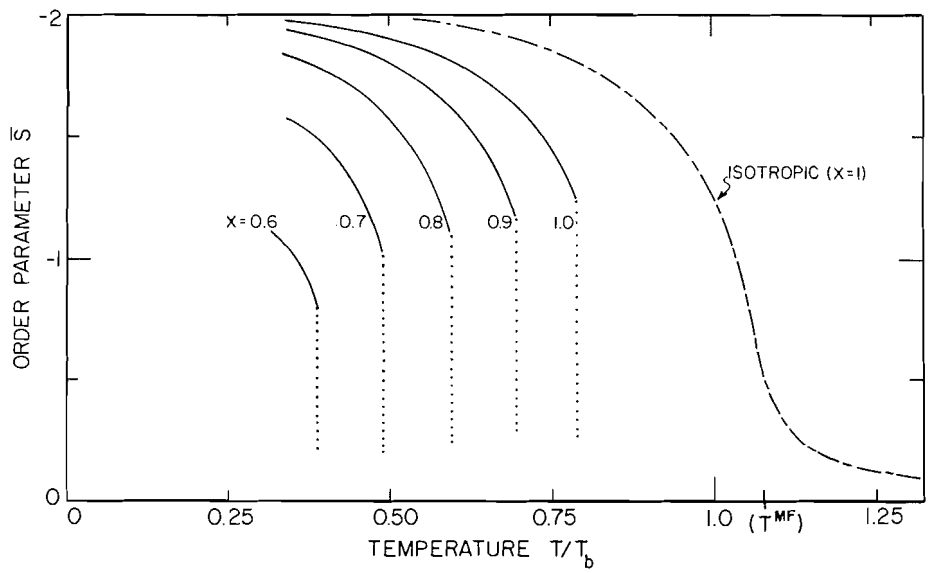

FIG. 4. Temperature dependence of the equilibrium values of the order parameter obtained from the free energy minima (such as those seen in Fig. 3) for several ortho concentrations. The broken vertical lines indicate first-order phase transitions. The dashed line gives the variation calculated for an isotropic quadrupolar interaction for $X = 1.0$.

and as β is reduced (rising temperature), S_0 increases toward -1 where there is a discontinuous jump to the value $S = 0$ at the critical temperature

$$[11] \quad k_B T_c = \left(\frac{19\Gamma}{4 \ln 2}\right) X$$

This is a factor of two higher than the experimental values at high ortho concentrations and there is no evidence for the critical behaviour near $X_c = 0.55$.

The inclusion of higher-order correlations in the evaluation of the free energy modifies the predicted phase diagram for periodic ordering quite drastically. The reason for this is that the critical concentration for propaging the 4-sublattice structure is much higher than the simple site percolation concentration (12). The importance of the correlations can be seen by extending the above calculations to include the second cumulant M_2. If we consider, at first, only the isotropic terms of the Hamiltonian, i.e.

$$H = \frac{1}{2} \sum_{(ij)} \zeta_{ij}^{00} O_i^0 O_j^0$$

then

$$M_2^{iso} = \frac{1}{4} \sum_{\{ijkl\}} \zeta_{ij}^{00} \zeta_{kl}^{00} \{\langle O_i^0 O_j^0 O_k^0 O_l^0 \rangle - \langle O_i^0 O_j^0 \rangle \langle O_k^0 O_l^0 \rangle\}$$

Summing over three types of terms: (*i*) 4-particle terms with all indices different $(ij) \neq (kl)$, (*ii*) 3-particle terms with one comon index $i = k, j \neq l$, and (*iii*) 2-particle terms $i = k$ and $j = l$; one finds (13)

$$[12] \quad M_2^{iso} = 6Nx^2\gamma^2(2 - S - S^2)[2 - S - (2x - 1)S^2]$$

It should be noted that the sign of the correlation term (in square brackets) changes sign at $X = 50\%$. This is a major contribution to the critical behavior at X_c in this approximation. The anisotropic terms in M_2 have also been calculated (13).

$$M_2^{aniso} = 27Nx^2\gamma^2 S(0.88 - 1.51S)$$

The free energy functionals $F(S)$ (per particle) for different temperatures calculated as a function of S using the above values for M_2 are illustrated in Fig. 3. One observes a first-order transition with a jump in the equilibrium value of the order parameter S_0 at the critical temperature $T = T_c$. Below T_c, S_0 approaches -2 as $T \rightarrow 0$ for large X. One finds only second-order transitions if the anisotropic interactions are neglected.

Explicit calculations of $F(S)$ for several values of ortho concentration lead to the temperature dependence of S_0 shown in Fig. 4. The corresponding variation of the critical temperatures with ortho concentration is given in Fig. 5. While the calculated phase diagram for the transitions to the periodically ordered structures is in reasonably good qualitative agreement with the experimental observations, the results should be taken with caution. The inclusion of second-order approximations has a very significant influence on the phase diagram, and it is important to check that third-order corrections make only a small correction.

IV. Quadrupolar glass regime

The low temperature – low concentration region of the phase diagram has been referred to as a quadrupole glass regime in analogy to the spin glasses such as $Eu_xSr_{1-x}S$ (14). No true phase transition to the glass region has been detected and most of the current research effort is devoted towards understanding the nature of the onset of local ordering on cooling from the high temperature disordered para-orientational phase. The crystal lattice remains hcp (15) in the glass-like region and this is to be contrasted with the behaviour for high ortho concentrations. (For $X > 55\%$, the onset of orientational ordering triggers a crystal transformation from the hcp phase to the fcc phase, but subsequent small thermal cycles leaves the cubic phase stable and the order/disorder transitions to the Pa_3 structure can be considered to occur on an fcc lattice.)

One of the key concepts underlying the physics of the quadrupolar glass phase, and the spin glasses in general, is the inherent frustration in the system, and in our case the interacting quadrupoles. The minimum energy configuration for a pair of quadrupoles is a "Tee" configuration with the molecular axes mutually perpendicular. While this can be satisfied for a square

Can. J. Chem. Downloaded from www.nrcresearchpress.com by 176.9.209.113 on 09/07/12
For personal use only.

Can. J. Chem. Downloaded from www.nrcresearchpress.com by 176.9.209.113 on 09/07/12
For personal use only.

array, it is impossible to arrive at a configuration with all quadrupoles mutually perpendicular in any other lattice. The quadrupolar interaction is topologically incompatible with the symmetry of the supporting lattice. It is the introduction of disorder, by the replacement of quadrupole-bearing ortho molecules by para molecules in the frustrated system, that leads to the glass phase. As stressed by Klenin (16), the frustration is especially severe for quadrupoles on an hcp lattice because the ground state is a Pc_{21} structure (17) with some molecules almost parallel to their neighbors (i.e. highly frustrated) while others are almost perpendicular (i.e. negligible frustration). In contrast to the cubic structure, the frustration is now highly inhomogeneous. This inhomogeneity imposes additional constraints and this renders the nucleation of long-range periodic ordering especially difficult. Even if they can be nucleated, possible clusters of periodic orientational ordering will be fragile with respect to random site dilution, and it is not surprising that only local ordering is achieved below the critical concentration.

There is another important feature of the hexagonal structure. For the non-cubic structure, the random occupation of lattice sites by the quadrupoles leads to the existence of local electric field gradients, the field conjugate to the local order parameter. The ordering of a random dilute hcp lattice is therefore analogous to that of the local dipolar ordering in spin glasses in the presence of random internal magnetic fields. These fields may not only smear out a transition, but even exclude any meaningful transition on cooling from the para-orientational phase.

Fictitious model

Some limited insight into the collective nature of the local freezing in the glass phase can be obtained from a fictitious model (18, 19) which assumes a Gaussian distribution of interaction strengths for the quadrupoles. This is of course not the situation in solid hydrogen but it is useful in that it does lead to a glass-like ordering for the quadrupoles. If we consider the truncated Hamiltonian

$$H = \frac{1}{2}\sum_{(ij)} \zeta_{ij} O_i^0 O_j^0$$

with a Gaussian probability distribution

$$[13] \quad P(\zeta_{ij}) = \left(\frac{1}{2\pi\tilde{\zeta}^2}\right)^{1/2} [\exp - (\zeta_{ij} - \zeta_0)^2/2\tilde{\zeta}^2]$$

for the ζ_{ij} where ζ_0 is the mean value and $\tilde{\zeta}^2$ the variance, then the free energy can be evaluated in terms of an average over an ensemble of n replicas, following the technique of Edwards and Anderson (20).

$$\tilde{F} - -k_B T \lim_{n\to 0} \frac{1}{n} (\overline{Z^n} - 1)$$

is calculated in terms of the quadrupolar glass order parameter

$$Q = \overline{6\langle (O_i^0)_\mu (O_i^0)_\nu \rangle}$$

where μ and ν label different replicas of the random array and the bar designates a configurational average. The average local molecular alignment is $S = \sqrt{6}\,\langle O_i^0 \rangle$.

Minimising F with respect to S and Q we find

$$S = \left(\frac{1}{2\pi}\right)^{1/2} \int e^{1/2y^2} F(\eta)\, dy$$

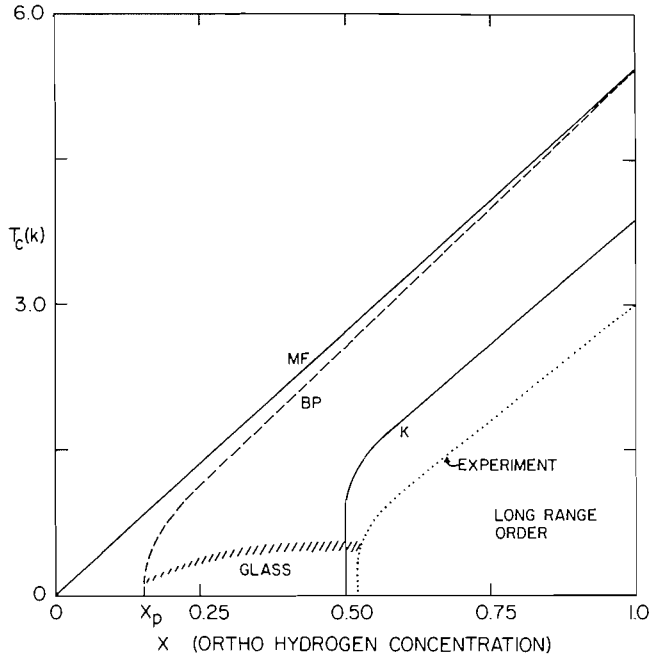

FIG. 5. Comparison of the observed concentration dependence of the critical temperatures with various theoretical treatments. MF, molecular field approximation; BP, first order Bethe–Peierl's approximation; K. Kirkwood's method of restricted traces.

where

$$F(x) = \frac{2e^x - 2e^{-2x}}{2e^x + e^{-2x}} \quad \text{and} \quad \eta = \beta[\tilde{\zeta}(ZQ)^{1/2} y + \zeta_0 ZS]$$

and

$$Q = (2 - S) - \left(\frac{1}{2\pi}\right)^{1/2} \int e^{-1/2y^2} F'(\eta)\, dy$$

$$[F'(x) = \partial/\partial_x F(x)]$$

For the case $\tilde{\zeta} = 0$ (i.e. fixed interactions) we find $Q = 2 - S$, as it should, and at the transition $\eta = \eta_0 = \beta\tilde{\zeta}_0 ZS$ with $S = F(\eta_0)$ or $36\beta_c\zeta_0 S = \ln (2 + S)/(2 - 2S)$ which is just the molecular field result obtained in section II above.

In the opposite limit of very broad distributions ($\tilde{\zeta} \gg \zeta_0$), we find at low temperature that

$$Q = \frac{5}{2} - \frac{27}{2} e^{B^2} \operatorname{efrc}(B)$$

where $B = 3\beta\tilde{\zeta}(ZQ/2)^{1/2}$ and erfc (t) is the complementary error function. Expanding the error function one finds that there is no solution except the trivial solution for

$$k_B T > k_B T_g = \frac{5}{27}\sqrt{\frac{5\pi}{3}}\, Z\tilde{\zeta} \simeq 0.4 Z^{1/2}\tilde{\zeta}$$

A rough estimate of the magnitude of $\tilde{\zeta}$ for a system similar to solid hydrogen can be made by averaging the angle dependent interaction constants of the EQQ potential over all possible orientations for an hcp lattice. This gives $k_B T_g \simeq 0.7X^{1/2}$ K. The glass transition temperatures $T_g(X)$ for this fictitious model are shown in Fig. 4 and they correspond to the temperature region for which one observes a rapid but continuous growth of local orientational order. The inclusion of a distribution of random crystal fields in the model would smear out any transition and

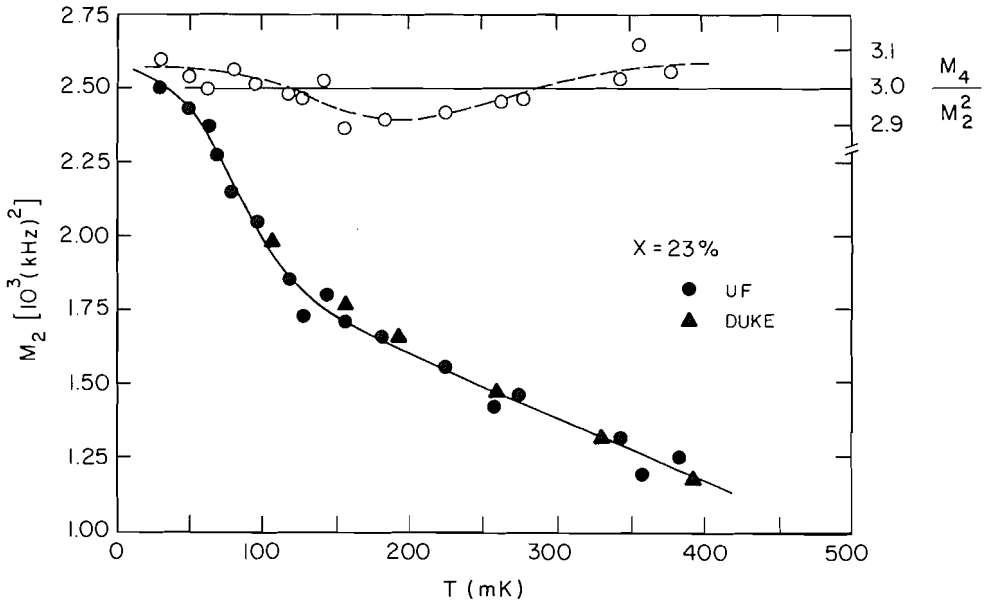

FIG. 6. Temperature dependence of the intramolecular second moment M_2 of the nmr spectra for ortho concentration $X = 23\%$. M_2 is directly proportional to the Edwards–Anderson glass order parameter.

this would give a first approximation to the behavior in solid hydrogen.

The value of S obtained at low temperatures for a broad distribution of ζ_{ij} is small, $|S| \simeq 0.5$, and this is in qualitative agreement with the experimental values. Experimentally one observes a broad distribution of local molecular alignments and S is the mean value.

Monte Carlo simulations of the ordering of classical quadrupoles have been carried out (21, 22) and they are also consistent with a continuous random freezing of the quadrupole fluctuations.

Goldbart and Scherrington (23) have considered the Parisi replica-symmetry breaking scheme for a set of m-dimensional uniaxial quadrupoles. They find that for three dimensions there is a phase transition to an *isotropic glass* at a critical temperature, $T_{\text{crit}} \sim \langle\zeta^2\rangle^{1/2}$, but there is a *further* transition at very low temperatures to a canted long-range ordered phase.

V. Nuclear magnetic resonance measurements and discussion

The local order parameters can be observed directly by nmr techniques. The reason for this is that the intramolecular nuclear dipole–dipole interaction between the protons of an ortho-H_2 molecule does not average to zero if the molecule has a preferred alignment. Each molecule contributes a doublet to the nmr spectrum with a frequency splitting

$$\Delta\nu_i = \pm D[\tfrac{1}{2}S_i P_2(\cos\theta_i) + \tfrac{3}{4}\eta_i \sin^2\theta_i \cos 2\phi_i]$$

where θ_i, ϕ_i) are the polar angles defining the orientation of the applied magnetic field with respect to the local symmetry axes of molecule i. S_i is the *alignment* and $\eta_i = \langle J_{x_i}^2 - J_{y_i}^2\rangle$ the eccentricity. For axial symmetry (as is usually assumed) $\eta_i = 0$. ($D = 173.1$ kHz.)

In the long-range ordered phase the order parameters S_i have the same value S_0 at each site and the resulting nmr lineshape is the well known Pake doublet (24) with two cusps separated by $(1/2)\,DS_0$. The temperature dependent S_0 exhibits a jump at the critical temperatures indicated in Fig. 1 for $x > 55\%$. In the glass regime one observes a completely different nmr spectrum which has been interpreted as a superposition of Pake doublets due to a broad distribution of local order parameters S_i (2, 3).

While there has been agreement on the existence of a broad distribution of S_i in the quadrupolar glass regime, there has been a serious controversy concerning the temperature dependence of the onset of the glass-like ordering. The first observations at Saclay (5) reported sharp transitions while subsequent studies at Duke (2) showed only a continuous evolution with temperature. It was suggested that the difference was related to sample preparation techniques; the Saclay group using powdered specimens while the Duke group grew single crystals. The results presented here from a new series of experiments in Florida agree with the conclusions of the Duke group. Furthermore, we have extended the temperature range explored down to 34 mK well below the limits of all of the previous studies (typically 100 mK).

We have measured the Edwards–Anderson glass order parameter defined by

$$Q_{\text{EA}}(T) = [\langle 3J_Z^2 - J^2\rangle_i^2]_c$$

for the quadrupolar system. This is determined directly from the nmr data because Q_{EA} is given by the second moment of the order parameter distribution function and hence proportional to the intramolecular component of the dipolar second moment of the nmr line shape

$$M_2^{\text{intra}} = \tfrac{9}{20} D^2 Q_{\text{EA}}(T)$$

Typical results for the variation of M_2 are shown in Fig. 6. The temperature dependence is featureless with no hint of either a thermodynamic phase transition or a dynamical transition down to the lowest temperatures attained (~34 mK).

The molecular dynamics in the glass-like regime has been explored by studies of nuclear spin–lattice relaxation T_1 which measures the spectral densities of the molecular motion. The results show that T_1 has a strong spectral inhomogeneity (25) across the nmr spectrum, and this has been interpreted in terms of collective excitations, or *para-librons* (25, 26), in large clusters of well-defined short-range order. The characteristic quadrupolar fluctuation rates τ_Q^{-1} estimated from the T_1

Can. J. Chem. Downloaded from www.nrcresearchpress.com by 176.9.209.113 on 09/07/12
For personal use only.

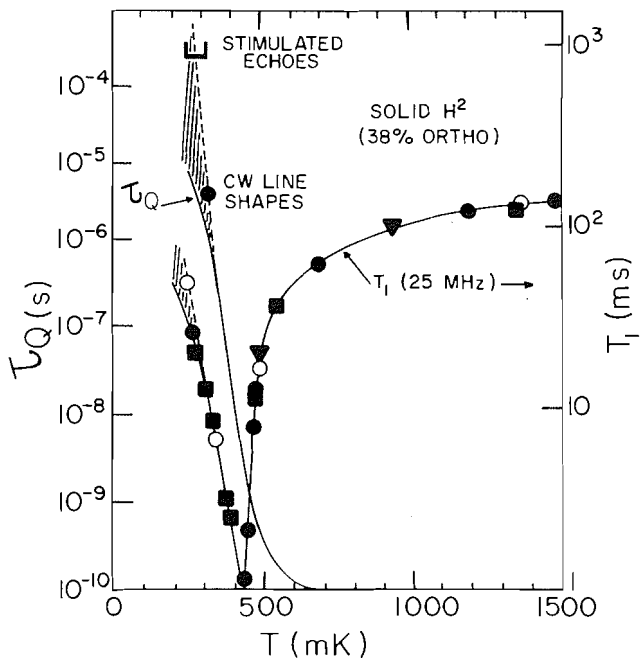

FIG. 7. Rapid dynamical freezing in the quadrupolar glass phase. The characteristic quadrupole fluctuation rates τ_Q^{-1} are deduced from the nuclear spin–lattice relaxation times T_1.

measurements are shown in Fig. 7. The rates decrease very rapidly, but smoothly, on cooling into the glass-regime.

As a result of the new measurements discussed above there is now a consensus concerning the nature of the onset of local ordering in the glass phase. The rapid quenching of the molecular reorientation rates and the continuous growth of the Edwards–Anderson glass parameter show that there is a collective dynamic gel of the molecular reorientation rates as the temperature is lowered. The qualitative picture of a glass-like phase (5) at low temperatures with both the local symmetry axes *and* the degree of local alignment S_i varying from site to site is basically correct.

Acknowledgement

This work has been supported by the National Science Foundation — Low Temperature Physics program — DMR 8611620.

1. I. F. SILVERA. Rev. Mod. Phys. **52**, 393 (1980); J. VAN KRANENDONK. Solid hydrogen. Plenum, New York, 1983.
2. A. B. HARRIS and H. MEYER. Can. J. Phys. **63**, 3 (1985).
3. N. S. SULLIVAN, C. M. EDWARDS, Y. LIN, and D. ZHOU. Can. J. Phys. To be published.
4. A. B. HARRIS. Phys. Rev. B**1**, 1881 (1970).
5. N. S. SULLIVAN, M. DEVORET, B. P. COWAN, and C. URBINA. Phys. Rev. B**17**, 5016 (1978).
6. P. N. GIBBS, C. G. GRAY, J. L. HUNT, P. S. REDDI, R. H. TIPPING, and K. S. CHANG. Phys. Rev. Lett. **33**, 256 (1974).
7. J. C. RAICH and R. D. ETTERS. Phys. Rev. **168**, 425 (1968).
8. T. NAKAMURA. Prog. Theoret. Phys. **14**, 135 (1955).
9. H. M. JAMES and J. C. RAICH. Phys. Rev. **162**, 649 (1957).
10. W. N. HARDY, I. F. SILVERA, and J. P. MCTAGUE. Phys. Rev. Lett. **26**, 127 (1971); **22**, 297 (1969).
11. J. G. KIRKWOOD. J. Chem. Phys. **6**, 70 (1938).
12. M. DEVORET. J. Phys. C. (Solid State), **13**, 2257 (1980).
13. N. S. SULLIVAN. J. Phys. Paris, **37**, 981 (1976).
14. H. MALETTA and W. FELSCH. Phys. Rev. B**20**, 1245 (1979).
15. J. V. GATES, P. R. GANFORS, B. A. FRAAS, and R. O. SIMMONS. Phys. Rev. B**19**, 3667 (1979).
16. M. A. KLENIN. Phys. Rev. B**28**, 5199 (1983).
17. R. J. LEE and J. C. RAICH. Phys. Rev. B**5**, 1591 (1972).
18. N. S. SULLIVAN and M. DEVORET. Proceedings Int. Quantum Crystals Conference, Colorado State Univ., Fort Collins, CO. Aug. 1977.
19. V. B. KOKSHENEV. Solid State Commun. **44**, 1593 (1982).
20. S. F. EDWARDS and P. W. ANDERSON. J. Phys. F. (Metals), **5**, 965 (1975).
21. M. A. KLENIN. Proc. Quantum Fluids and Solids Conf. Sanibel Island, Fl, April 1983; A.I.P. Conf. Proc. **103**, 121 (1983); Phys. Rev. B**28**, 5199 (1983).
22. M. DEVORET and D. ESTEVE. J. Phys. C. (Solid State), **16**, 1827 (1983).
23. P. M. GOLDBART and D. SHERRINGTON. J. Phys. C**18**, 1923 (1985).
24. F. REIF and E. M. PURCELL. Phys. Rev. **111**, 188 (1958).
25. S. WASHBURN, M. CALKINS, H. MEYER, and A. B. HARRIS, J. Low Temp. Phys. **53**, 585 (1983).
26. Y. LIN and N. S. SULLIVAN. J. Low Temp. Phys. **65**, 1 (1986).

Can. J. Chem. Downloaded from www.nrcresearchpress.com by 176.9.209.113 on 09/07/12
For personal use only.

A light scattering and calorimetric study of micelle formation by a polystyrene -*b*-hydrogenated polyisoprene block copolymer in a binary solvent (pentane–cyclopentane)

KAREL PROCHÁZKA
Department of Physical Chemistry, Charles University, Prague, Czechoslovakia

AND

HÉLÈNE DELCROS AND GENEVIÈVE DELMAS
Département de Chimie, Université du Québec à Montréal, Montréal, Case Postale 8888, Succ. A (Qué.), Canada H3C 3P8

Received October 16, 1987

This paper is dedicated to Professor J. A. Morrison

KAREL PROCHÁZKA, HÉLÈNE DELCROS and GENEVIÈVE DELMAS. Can. J. Chem. **66**, 915 (1988).

A light scattering and calorimetric study was made of micelle formation by a polystyrene-*b*-hydrogenated polyisoprene in a binary mixture. The polymer 0.42 weight percent PS, is unassociated in cyclopentane (*c*-C5) but forms micelles with a PS core in *n*-pentane, a non-solvent for PS. Light scattering measurements and heats of mixing, obtained over the binary composition range at a polymer concentration higher than the c.m.c., show that the solution changes from the unassociated to the micellar state for solutions richer in pentane than 0.4 volume fraction. Using heats of mixing of the corresponding homopolymers, the heat of micellization is found to be $-5.1 + 0.3$ J g^{-1}, a value which supports the model of an enthalpy driven process of micellization.

KAREL PROCHÁZKA, HÉLÈNE DELCROS et GENEVIÈVE DELMAS. Can. J. Chem. **66**, 915 (1988).

Utilisant la calorimétrie et la diffraction de la lumière, on a étudié la formation de micelles par un polystyrène-*b*/polyisoprène hydrogéné, dans un mélange binaire. Dans le cyclopentane (*c*-C5), le polymère contenant 0,42 pourcent en poids de PS n'est pas associé; toutefois, dans le *n*-pentane qui n'est pas un solvant pour le PS, il forme des micelles avec un coeur de PS. Des mesures de diffraction de la lumière et de chaleurs de mélanges, réalisées sur un éventail de concentrations de la région binaire et à des concentrations en polymère plus grandes que la c.m.c., ont permis de montrer que, dans le pentane contenant une fraction molaire supérieure à 0,4, la solution passe d'un état qui n'est pas associé à un état micellaire. Utilisant les chaleurs de mélange des homopolymères correspondants, on a trouvé que la chaleur de micellisation est de $-5,1 \pm 0,3$ J g^{-1}; cette valeur est en accord avec le modèle d'un processus de micellisation d'origine enthalpique.

[Traduit par la revue]

Introduction

Block copolymers when dissolved in a solvent which is good for one of the corresponding homopolymer and a nonsolvent for the other, associate reversibly and form spherical micelles (1). As predicted by the "closed association" mechanism (2), the micelles are in equilibrium with the molecularly dissolved copolymer (unimer). The mass, size, structure, size distribution, and micellization equilibrium of block copolymer micelles have been studied by different techniques such as viscosimetry, osmometry, sedimentation velocity analysis, size exclusion chromatography (SEC) (3, 4), elastic light scattering, and electron microscopy (see ref. 1). New techniques such as neutron scattering (5, 6) and light scattering photon correlation spectroscopy (7, 8) have also been applied successfully to block copolymer micellar systems. From these studies, the micelles are found to be quite uniform in weight, size, and composition while the micellar mass and micelle-to-unimer ratio depends on the copolymer composition, the thermodynamic quality of the solvent, and the temperature.

With simplifying assumptions, the thermodynamic parameters associated with the micellization, namely, the free energy and enthalpy of micelle formation have their usual expressions:

$$\Delta G_m = RT \ln (\text{c.m.c.})$$

$$\Delta H_m = -RT^2 \, \mathrm{d} \ln (\text{c.m.c.})/\mathrm{d}T$$

The study of the temperature dependence (9*a*) of the c.m.c. of polystyrene-*b*-polyisoprene block copolymer in *n*-hexadecane lead to a value of ΔH_m in good agreement with that determined calorimetrically (9*b*). The aim of the present paper was to study the formation of micelles in a similar copolymer, polystyrene-*b*-hydrogenated polyisoprene (PS-*b*-h·PIP) by light scattering in a mixture of two solvents having each a different quality for PS and to measure directly ΔH_m in the same system.

Experimental

Materials

Polymers

The polystyrene-*b*-hydrogenated polyisoprene two-block copolymer (G 1701 Shell Chemical Co., U.S.A.) was characterized by nmr, light scattering analysis in benzene, and size exclusion chromatography (SEC) in tetrahydrofuran. From these measurements, the copolymer is found to have a M_w of 105 000, an average weight fraction of polystyrene $w = 0.42$ and a narrow molar mass distribution as indicated by SEC analysis.

The homopolymer polystyrene a standard from Pressure Chemical Co., Pittsburgh, U.S.A., with $M_w = 2100$ and $M_w/M_n = 1.1$ was studied in the present work and through heats of dilution in ref. 10. The results for polypropylene (PP) were obtained previously (11) on an atactic sample obtained by solvent extraction from a partially crystalline PP followed by purification (12).

Using DSC, the T_g of the PS standard was found around 75°C but that of the copolymer was not clearly defined. However, the heat of transition from the glass to the liquid $\Delta H_{\text{glass–liquid}}$ of the PS part of the copolymer must be similar in magnitude to that of the homopolymer.

Solvents

Pentane and benzene (99% pure, from Aldrich Co., Milwaukee), cyclopentane (spectrograde, from BDH, Toronto) were used without purification.

Can. J. Chem. Downloaded from www.nrcresearchpress.com by 176.9.209.113 on 09/07/12
For personal use only.

Can. J. Chem. Downloaded from www.nrcresearchpress.com by 176.9.209.113 on 09/07/12
For personal use only.

Apparatus

Light scattering

A KMX-6 Low Angle Light Scattering Photometer, with a low power helium laser (Chromatix, U.S.A.) was used. No extrapolation to zero angle of the light scattering $G(\theta)$ was made since the scattering angle is low (3–4°). If G_0 is the signal of the primary beam transmitted through the sample, the scattered factor R_0 is

$$R_0 = \text{constant } G(\theta)/G_0$$

The constant is obtained from a compound whose Rayleigh factor is known. The molar mass can be calculated from the standard equation:

$$[1] \quad Kc/R_0 = 1/M_w + 2A_2c$$

c is the polymer concentration, K and A_2 have their usual definition. In the case of micellar solutions, M_w is the micelle molecular mass usually written as M_w^{app}. The solutions were clarified by filtration via Fluoropore filters (0.2 m, Millipore Corp., Bedford, U.S.A.) and their concentrations ranged from 0.1 to 5×10^{-3} g cm^{-3}.

Calorimetry

The heats of dissolution were measured with a differential tilting Tian-Calvet calorimeter (Setaram, France) with cells similar to those described earlier (12). The polymer is placed on a support and immersed under mercury. The rest of the cell is filled with the solvent. Polymer and solvent are brought into contact after equilibrium by rotating the calorimeter. Due to its specific features (size of the heat-sink block, differential setting, good temperature regulation), the calorimeter has an excellent stability in time. Teflon plugs assure a good vapor-tightness even with volatile solvents. The concentrations were between 0.3 and 0.5%. The heat evolved per run was between 20 and 400 mJ.

Choice of the solvent

Cyclopentane is a good solvent for PP which may be taken as a model for hydrogenated polyisoprene and a medium quality solvent for PS. *N*-Pentane, a non-solvent for PS and a good solvent for PP, dissolves the copolymer but favors micelles with a PS core. The presence of micelles in the pentane solutions is revealed by the bluish color of dilute solutions of the copolymer. When cyclopentane is added to the solution, the color vanishes, indicating a change in the structure of the solution. The dissolution of the polymer even in *n*-pentane is achieved in less than 3 h for concentrations around 0.5%. A longer time of dissolution found, for instance, with methyl ethyl ketone (which gives micelles with a hydrogenated polyisoprene core) will lead to important errors in the evaluation of the heats since the heat flow due to the dissolution and micelle formation is small.

Results and discussion

Light scattering

Figure 1 shows the values of Kc/R_0 versus the copolymer concentration, the different curves corresponding to different solvent compositions. In pure cyclopentane ($\varphi_{c\text{-}C5} = 1.0$) and cyclopentane-rich solvents ($\varphi_{c\text{-}C5} = 0.8$), the curves are typical of a monomolecular solution with a positive virial coefficient. They extrapolate to the inverse of the value of the molecular weight found in benzene, M_w. For intermediate solvent compositions ($\varphi_{c\text{-}C5} = 0.45$ and 0.50), the concentration dependence of Kc/R_0 is typical of a closed association, the c.m.c. being estimated, respectively, at 0.5 and 2.9×10^{-3} g cm^{-3}. In the pentane-rich solutions and in pure pentane Kc/R_0 does not vary with concentration down to $c < 10^{-4}$ g cm^{-3}. In more concentrated polymer concentration M_w^{app} can be evaluated from the plateau of Kc/R_0. The curve in Fig. 2 corresponds to M_w^{app} at $c = 4 \times 10^{-3}$ g cm^{-3} chosen as such because it is similar to the concentration used for the heats of dissolution experiments (0.3–0.5% or $3–5 \times 10^{-3}$ g cm^{-3}). By extrapolating the curve, one finds that at that polymer concentration, the micelles start to form in solutions with $\varphi_{c\text{-}C5} < 0.60$. For $\varphi_{c\text{-}C5} = 0.5$, where

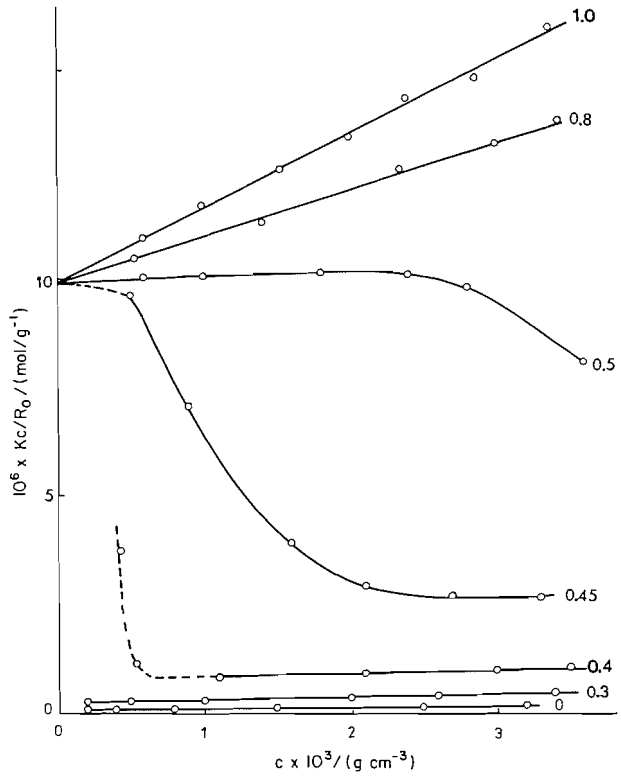

FIG. 1. A plot of Kc/R_0 against concentration for the polystyrene-*b*-h-polyisoprene copolymer in a series of cyclopentane/pentane mixtures at 25°C. The values of $\varphi_{c\text{-}C5}$ are indicated on each curve. For four concentrations $0.45 < \varphi_{c\text{-}C5} < 1.00$, the extrapolation at $c = 0$ gives the molar mass of the unassociated polymer (105 000). In solutions richer in pentane, the higher molar mass is indicative of a micellar solution. The dotted lines correspond to measurements in very dilute solutions where the state of aggregation of the molecules is changing with concentration.

Kc/R_0 is not independent of c, M_w^{app} has been estimated by extrapolating two points at lower concentrations. For two concentrations 0.45 and 0.50, the values of M_w^{app}, cannot be read accurately on Fig. 2 but correspond, respectively, to 365 000 and 150 000.

As the solvent refractive indices differ by less than 0.05, the possible preferential adsorption which could occur in the mixed solvent should not change significantly the value of the refractive index increment dn/dc (included in K of eq. [1]). Consequently, the value of (dn/dc) at constant solvent compostion has been used instead of that at constant chemical potential of low molecular mass components.

Calorimetry

The heat of micellization, ΔH_{micel} can be obtained directly by measuring, ΔH_{diss}, the heat of dissolution of the sample at increasing polymer concentration. A rapid change of heat is expected when the c.m.c. is reached. Alternatively, in a mixed solvent such as *c*-C5 and *n*-C5, ΔH_{diss} may be obtained at different solvent compositions using always the same polymer concentration. Micellization in solution should be marked by a noticeable change in ΔH_{diss} with $\varphi_{c\text{-}C5}$. Since the very small c.m.c. would not allow precise determination of the heat of micellization, the second method has been chosen, using a polymer concentration above the c.m.c.

In Fig. 3, the different ΔH_{diss} in J g^{-1} are plotted against $\varphi_{c\text{-}C5}$. Curve 1 is that obtained for the copolymer. It is to be noted that

Can. J. Chem. Downloaded from www.nrcresearchpress.com by 176.9.209.113 on 09/07/12
For personal use only.

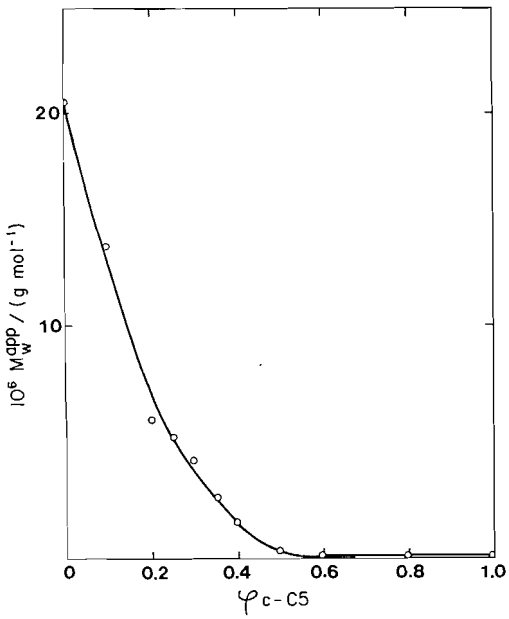

FIG. 2. Apparent molar mass of the polystyrene-*b*-h·polyisoprene versus $\varphi_{c\text{-}C5}$ obtained from light scattering data at $c = 4 \times 10^{-3}$ g cm^{-3}. M_w^{app} is already higher than M_w at $\varphi_{c\text{-}C5} = 0.50$ (150 000) and 0.45 (365 000).

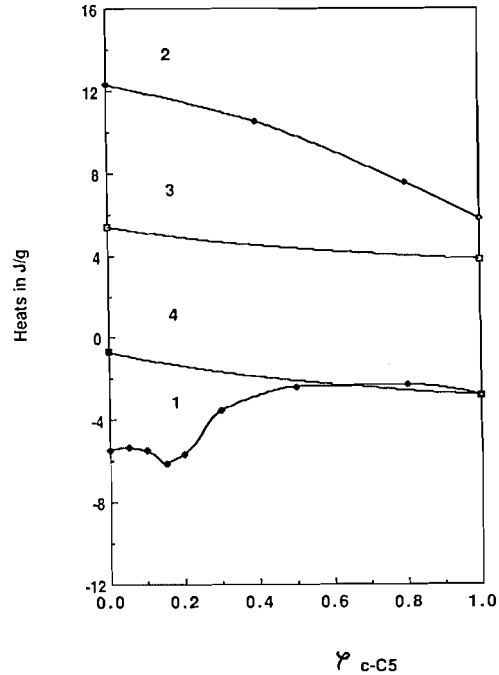

FIG. 3. Heats of dissolution of PS and the copolymer versus $\varphi_{c\text{-}C5}$. *Curve* 1: ΔH_{diss} of the copolymer; *curve* 2: ΔH_{diss} for a standard PS (molar mass = 2100). The corresponding curve for pure PP has not been put on the graph but would run as a straight line between −2.3 J g^{-1} for *c*-C5 and −4.0 J g^{-1} for *n*-C5; *curve* 3: ΔH_1diss of the copolymer as calculated with eq. [5] from the experimental heats of PP (ref. 12) and PS (curve 1); *curve* 4: identical to curve 2 but displaced by $\Delta H_{glass\text{-}liquid}$ (−6.1 J g^{-1}). ΔH_{micel} is taken s the maximum difference, in the region of the micellar structure, between curves 1 and 4, namely −5.1 J g^{-1}.

the change of heat starts at the same $\varphi_{c\text{-}C5}$ as that found in Fig. 2 for the increase of M_w^{app} by light scattering. The ΔH_{micel} is associated with the difference between the value in cyclopentane-rich solutions (−2 J g^{-1}) and the values in the micellar solutions (about −6 J g^{-1}) so that ΔH_{micel} has a value of −4 J per g of micelle by simple reading of the experimental ΔH_{diss}. However, to have a more refined data, one has to evaluate the ΔH_{diss} of the polymer in the hypothetical case where no micelle would form. The other calorimetric measurements have been made with that aim and are detailed below.

The ΔH_{diss} for an homopolymer come chiefly from the contribution, $\Delta H_{contact\text{-}interchange}$ which has its origin in the replacement of solvent–solvent contacts and polymer–polymer contacts by solvent–polymer contacts. A second contribution which is exothermic, $\Delta H_{glass\text{–}liquid}$ is to be counted if the polymer is a glass and a third ΔH_{micel} when association occcurs. Assuming that these contributions are additive, one can write:
Homopolymer:

[2] $\Delta H_{diss} = \Delta H_{contact\text{-}interchange}$

Homopolymer (glass):

[3] $\Delta H_{diss} = \Delta H_{contact\text{-}interchange} + \Delta H_{glass\text{–}liquid}$

Copolymer (glass) forming micelles:

[4] $\Delta H_{diss} = \Delta H_{contact\text{-}interchange}(w) + \Delta H_{glass\text{–}liquid} + \Delta H_{micel}$

In eq. [4], $\Delta H_{contact\text{-}interchange}$ (w) can be obtained as an approximation by making a weight average of the values for the two corresponding homopolymers. If *w* is the weight fraction of PS in the copolymer one has:

[5] $\Delta H_{contact\text{-}interchange}(w) = w\Delta H_{contact\text{-}interchange,\ PS} + (1 - w)\Delta H_{contact\text{-}interchange,\ h.PIP}$

In the range of $\varphi_{c\text{-}C5}$ where the molecules asociate, $0.00 < \varphi_{c\text{-}C5} < 0.60$, all the terms of eq. [4] contribute while for $0.6 < \varphi_{cC5} < 1.0$, the last term is absent. ΔH_{micel} is expected to be negative since non-favorable polymer–solvent contacts are replaced by good polymer–polymer contacts in the core of the micelle and solvent–solvent contacts outside.

Heats of dissolution of PS, PP, and copolymer in cyclopentane, $\Delta H_{glass\text{-}liquid}$ for PS

In curve 2 of Fig. 3, one sees that ΔH_{diss} of PS varies between 5.7 and 12.3 J g^{-1} over the whole concentration range. In order to separate the two terms of eq. [3], we can use the heat of dilution of PS in cyclopentane which has been measured over the concentration range of polymer φ_p such as $0 < \varphi_p < 0.7$. The heat $\Delta H_{contact\text{-}interchange,\ PS}$ is calculated to be 11.0 J g^{-1}. Considering that from the contact-interchange energy point of view, the hydrogenated part of PIP is similar to PP (or a random ethylene–propylene copolymer rich in PP), one can use here, the heat $\Delta H_{contact\text{-}interchange,\ PP}$ found to be −2.3 J g^{-1} (11). Using eq. [5], the calculation for the copolymer in cyclopentane gives:

[5a] $\Delta H_{contact\text{-}interchange}(w)$ (J g^{-1}) $= 0.58(-2.3) + 0.42 \times (11.0) = 3.3$

The difference between 3.3 and the experimental value (−2.8) is due to $\Delta H_{glass\text{–}liquid}$ which can be calculated to be $-(3.3 - (-2.8)) = -6.1$ J.

Heats of dissolution of PS, PP, and copolymer in n*-pentane*

To obtain $\Delta H_{contact\text{-}interchange,\ PS,\ n\text{-}C5}$ from the experimental heat of dissolution of PS in pentane (12.3 J), one should add 6.1 J. One obtains 18.4 J g^{-1}. $\Delta H_{contact\text{-}interchange,\ PP,\ n\text{-}C5}$ has been

estimated to two ways either by extrapolating from the values in higher alkanes (11) and also from comparison from the result in *n*-C5 of atactic polybutene-1 (12). The two methods give very similar results averaged to $-4.0\ J\ g^{-1}$. Using again eq. [5], one finds for the copolymer in pentane:

[5b] $$\Delta H_{\text{contact-interchange}}(w) = 0.58 \times (-4.0) + 0.42 \times (18.4) = 5.40$$

The values in [5*a*] and [5*b*] make the pure solvent points of curve 3. Since the difference of heats is small enough a linear interpolation between these points is used for the copolymer in the mixed solvent.

In order to compare to the experimental values, one has to add to curve 3, $\Delta H_{\text{glass-liquid}}$ ($-6.1\ J\ g^{-1}$), which gives curve 4.

The exothermic heats found for PP and the EP copolymers and used in the above equation include the free-volume term which comes from the difference in expansion coefficients of the polymer and solvent (13, 14). This negative term may become dominant when the free volume term is large (volatile solvents) and when $\Delta H_{\text{contact-interchange}}$ is small (mixture of a non-polar polymer with a non-polar chemically similar solvent). In order to simplify the terminology in eqs. [2]–[5], only the interactional term $\Delta H_{\text{contact-interchange}}$ and not the free volume term has been listed.

It is reasonable to assume that averaging ΔH_{diss} of the two polymers will take care also of the free volume contribution.

The different contributions to the heats in *c*-C5 and *n*-C5 can be seen qualitatively in the trace of the heat versus time during the dissolution. Although the total heats become more and more negative in the pentane-rich concentrations as seen in Fig. 3, the heat starts endothermic for these solutions at the beginning of the dissolution and changes to exothermic at a fraction (10–15%) of the dissolution time. In *c*-C5-rich solutions, the heat is always exothermic due mainly to the dominance of $\Delta H_{\text{glass-liquid}}$.

ΔH_{micel}, which is the difference between the experimental curve for the copolymer (curve 1) and that found for the copolymer without micellization (curve 4) in the pentane-rich solvent, is found to be $-5.1\ J\ g^{-1}$ at its maximum (-4.8 in pure pentane). The incertitude on this value has different origins: the error in the experimental ΔH_{diss} may be at most 0.15 J in the pentane-rich region due to the slower speed of dissolution. The error in assuming a linear relationship betwen ΔH_{diss} and the solvent composition (curve 4) can be estimated from previous work on homopolymers in mixed solvents (15). In the case of random mixing, the deviation from linearity is calculated to depend on the magnitude of the heat of mixing of the two solvents but is found experimentally smaller than calculated when the polymers have a large surface to volume ratio as is the case for PS. It is then reasonable to asssume that the errors coming from this simplification and those implicit in eq. [5] do not exceed 0.15 J so that $\Delta H_{\text{micel}} = -5.1 \pm 0.3\ J\ g^{-1}$. This result is higher than that found directly from the change of ΔH_{diss} (curve 1) versus concentration because in the first evaluation, account was not taken of the increase of ΔH_{diss} when the bad solvent *n*-pentane is added.

When expressed by gram of PS, ΔH_{micel} increases to 12.1 J per g of PS (5.1/0.42). This is to be compared to the value found in *n*-hexadecane for polystyrene-*b*-polyisoprene whose PS chain has a molecular weight of 7 000 (9*b*), namely, $44\ kJ/7 \times 10^3 = 6.7$ J. The larger value found in the present system is due both to the worse quality of *n*-pentane than *n*-hexadecane for the PS sequence and to the high molar mass of PS in the present sample (42,000 instead of 7,000). The smaller value of the c.m.c. for the system PS-*b*-hydrogenated PIP + (*n*-C5 + *c*-C5) compared to that for the system PS-*b*-PIP + *n*-hexadecane is in line with its larger ΔH_{micel}. Forming a micelle corresponds in reverse to dissolving a polymer in a bad solvent. The heat of dissolution of a polymer (atactic, liquid) in a θ solvent gives a good model for the heat one should recover when the micelle is formed. For instance ΔH_{diss} of PIB in benzene at 25°C near phase separation has been found to be $19\ J\ g^{-1}$ (15*a*) which is higher but of the same order of magnitude that ΔH_{micel} found presently. The sign and the value of ΔH_{micel} for this PS-*b*-h·PIP confirm the previous conclusion of the importance of the enthalpic origin of the stability of these block-copolymer micelles.

Acknowledgementss

We would like to thank the CRSNG of Canada and the Université du Québec for general support of this research. We are grateful to Dr. D. Gray of Paprican in Montreal for use of the Chromatrix and to the Shell Company in Canada for providing the copolymer samples.

1. Z. Tuzar and P. Kratochvíl. Adv. Colloid Interface Sci. **6**, 201 (1976).
2. H. G. Elias and R. Bareiss. Chimia, **21**, 53 (1967).
3. C. Price. Pure Appl. Chem. **55**, 1563 (1983).
4. K. Procházka, G. Glöckner, M. Hoff, and Z. Tuzar. Makromol. Chem. **185**, 1198 (1984).
5. (*a*) P. Marie, R. Duplessix, Y. Gallot, and C. Picot. Macromolecules, **12**, 1180 (1979); C. M. Duval and C. Picot. Polymer, **28**, 793 (1987); **28**, 798 (1987).
6. Ch. J. Edwards, R. W. Richards, and R. F. T. Stepto. Polymer, **27**, 643 (1986).
7. C. Price, J. D. G. Adams, T. P. Lally, and D. Woods. Polymer, **15**, 228 (1974).
8. Z. Tuzar, P. Štěpaněk, C. Koňak, and P. Kratochvíl. J. Colloid Interface, **105**, 327 (1985).
9. (*a*) C. Price, E. K. Chan, R. H. Mobbs, and R. B. Stubbersfield. Eur. Polymer. J. **221**, 355 (1985); (*b*) C. Price, E. K. M. Chan, G. Pilcher, and R. B. Stubbersfield. Eur. Polymer. J. **221**, 627 (1985).
10. D. Gaeckle. Ph.D. Thesis. McGill University, Montreal. 1972.
11. H. Phuong-Nguyen and G. Delmas. Macromolecules, (*a*) **12**, 746 (1979); (*b*) **12**, 740 (1979).
12. G. Delmas and P. Tancrède. Eur. Polym. J. **9**, 199 (1973).
13. G. Delmas, T. Somcynski, and D. Patterson. J. Polym. Sci. **57**, 79 (1962)
14. D. Patterson, G. Delmas, and T. Somcynski. J. Polym. Sci. **8**, 503 (1966).
15. (*a*) G. Delmas, D. Patterson, and S. N. Battacharyya. J. Phys. Chem. **68**, 1468 (1964); (*b*) D. Pouchly and D. Patterson. Macromolecules, **68**, 1468 (1964).

Can. J. Chem. Downloaded from www.nrcresearchpress.com by 176.9.209.113 on 09/07/12
For personal use only.

Energies of the phases of ice at low temperature and pressure relative to ice Ih[1]

Y. Paul Handa, D. D. Klug, and Edward Whalley
Division of Chemistry, National Research Council of Canada, Ottawa, Ont., Canada K1A 0R6

Received November 18, 1987

This paper is dedicated to Professor J. A. Morrison

Y. Paul Handa, D. D. Klug, and Edward Whalley. Can. J. Chem. **66**, 919 (1988).

The enthalpy of transformation to ice Ic of ice II, IX, V, VI, and VIII that have been recovered at 77 K and ambient pressure, and of the transformation of ice Ic to Ih, has been measured in a heat-flow calorimeter. The enthalpy of transformation of ice Ic to Ih depends on the high-pressure phase used to make the ice Ic. The thermodynamics of the transformation of ice IX, which was made by cooling ice III at 0.3–0.7 K s^{-1}, to ice III shows that the ice IX was fully orientationally ordered to the precision of the experiments.

Y. Paul Handa, D. D. Klug, et Edward Whalley. Can. J. Chem. **66**, 919 (1988).

Utilisant un calorimètre à écoulement de chaleur, on a mesuré les enthalpies de transformation en glace Ic des glaces II, IX, V, VI et VIII, récupérées à 77 K et à pression ambiante, ainsi que de la transformation de la glace Ic en glace Ih. L'enthalpie de transformation de la glace Ic en glace Ih dépend de la nature de la phase à haute pression qui a été utilisée pour faire la glace Ic. Les propriétés thermodynamiques associées à la transformation de la glace IX, préparée par refroidissement de la glace III à 0,3–0,7 K s^{-1}, en glace III démontre que, à la précision des expériences, la glace IX est complètement ordonnée d'un point de vue de l'orientation.

[Traduit par la revue]

Can. J. Chem. Downloaded from www.nrcresearchpress.com by 176.9.209.113 on 09/07/12
For personal use only.

1. Introduction

Ice forms a wide range of crystalline (1–13) and amorphous (4, 14, 15) phases. The energies of these phases at zero temperature and pressure are excellent tests of proposed intermolecular potentials of water (ref. 16 and references quoted there). They have been estimated in the past from the enthalpies of the spontaneous transformation of the high-pressure phases, as recovered at low temperatures and pressures, to ice Ic (17, 18), and from the equilibrium pressures, temperatures, and volume changes as extrapolated to zero temperature (ref. 16).[2] When measuring the enthalpies of some order–disorder transformations of the various phases of ice at ambient pressure, the enthalpies of transformation of several crystalline phases to ice Ic and of ice Ic to Ih were measured; a preliminary account of some of the measurements of ice V and VI has been published (19). The enthalpy of the transformations at ambient pressure is, of course, the difference of energy between the phases at the temperature of the transformation, and so the energy of transformation from the high-pressure phase to ice Ih can be obtained. These enthalpies of transformation are reported in this paper.

As the energy of ice Ih at zero pressure relative to the vapor is well known throughout its range of stability, the energies of the high-pressure phases relative to the vapor can be obtained. The principal immediate use of these energies will be to test and adjust intermolecular potentials of water, both two-body and multi-body potentials, and to adjust the phase boundaries to more accurate locations.

2. Experimental methods

Ice II, IX, V, VI, and VIII were made by placing 1.5–2.7 g of degassed water in an indium cup, which was then capped with indium, and the ice and the indium were pressurized in a piston-cylinder apparatus having an inside diameter of 12.5 mm. The course of the compression was followed by measuring the displacement of the piston relative to the cylinder to 2 μm by a dial gauge. Samples of ice II were made by compressing ice Ih to 3.5 kbar at about 200 K and were identified by the pressure and change of volume at the transformation from ice Ih. Samples of ice III, V, and VI were made in similar ways by compressing ice Ih to 4, 6, and 9 kbar respectively at 240 K, and samples of ice VII were made at 22 kbar and 280 K. All samples were cooled under pressure in about 5 min by immersing them in liquid nitrogen, when ice IX, V, and VI, each having an uncertain degree of order, and ice VIII were formed. They were stored in liquid nitrogen.

The calorimetric measurements were made at ambient pressure by placing the experimental sample in its indium cup in the sample cell of an automated Setaram model-BT Tian-Calvet heat-flow calorimeter (20) that had been cooled to 77 K. A reference cup whose mass was identical to that of the sample cup to ±10 mg, except that it was empty, was placed in the reference cell of the calorimeter, and the two cells were flushed with helium. The calorimeter was operated in the scanning mode using a scan rate of 10 K h^{-1}. The water in the sample cup was weighed at the end of each run. The details of the calorimeter, the operational technique, and the methods used to analyze the raw data are described elsewhere (20). The temperature was measured with a platinum thermometer located just outside the measurement cell, and represents the sample temperature except during a thermal event, when the sample temperature is slightly different.

3. Results

Representative scans of ice II, IX, V, VI, and VIII are plotted in Figs. 1–5, in which endothermic and exothermic peaks point upwards and downwards, respectively. Each has at least two transformations, one being the transformation from the high-pressure phase to ice Ic, which occurs in the range 120–160 K, and the other the transformation of ice Ic to Ih, which occurs near 200 K, as is marked on the figures.

All samples of ice II and VIII have weak exothermic transformations at about 105 K, which is outside the range of the curves in Figs. 1 and 5, and ice V and VI have moderate endothermic transformations at about 125 and 140 K, respectively. The exotherms are probably caused by irreversible transformations from a partly orientationally disordered state that was frozen in during the cooling. This was confirmed by recooling the samples to 80 K and reheating to 105 K; the exotherms were not observed. The endotherms of ice V and VI have already been reported briefly (19) and they and the two exo-

[1]NRCC No. 28593.

[2]In ref. 16 the lattice energy of ice VIII in Table VII should be −60.70 kJ mol^{-1} instead of −62.4 kJ mol^{-1}, and the last sentence should be omitted.

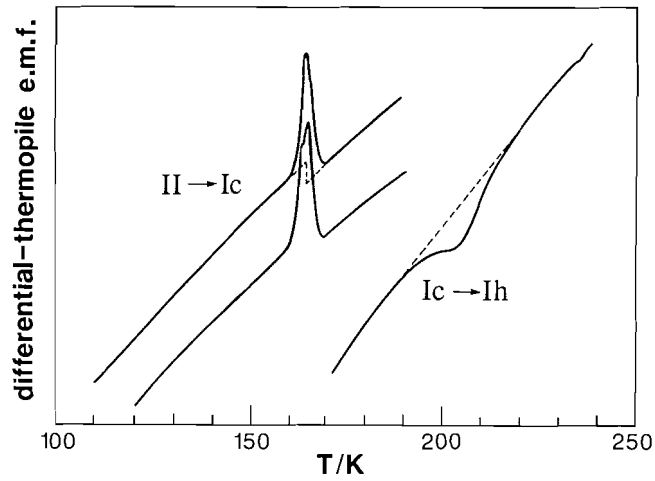

FIG. 1. Thermal e.m.f. of the differential thermopile during the transformation of ice II to ice Ic and then to ice Ih, plotted against temperature, for two experiments in order to show the different shapes of the endotherms at the transformations of ice II to Ih. The dashed lines are the assumed base lines of the transformations.

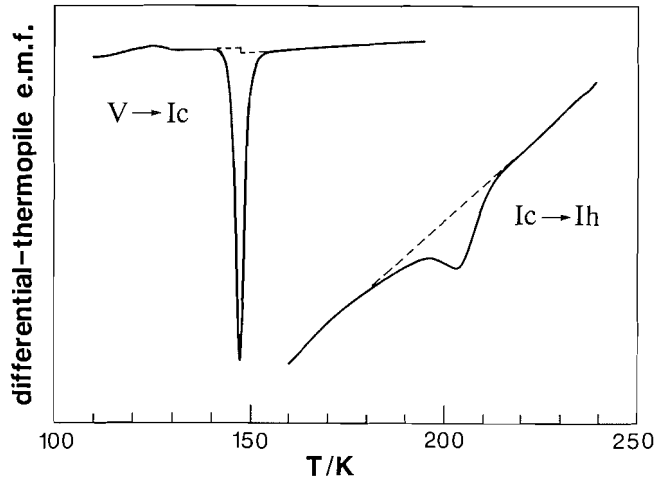

FIG. 3. Thermal e.m.f. generated between the sample cell and the reference cell when ice V transforms to ice Ic and then to ice Ih, plotted against temperature. Part of the transformation of ice VI to Ic is drawn on an enlarged ordinate in order to show clearly the disordering transformation near 135 K.

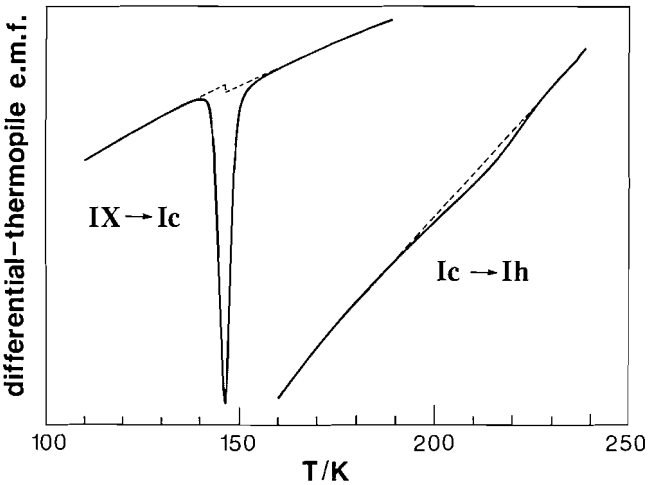

FIG. 2. Thermal e.m.f. generated between the sample cell and the reference cell when ice IX transforms to ice Ic and then to ice Ih, plotted against temperature.

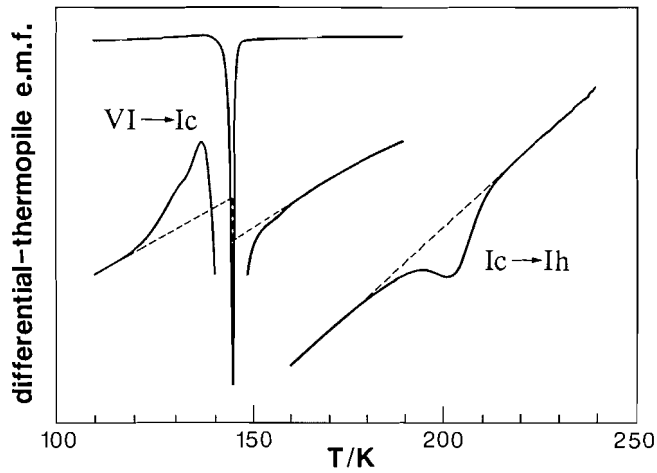

FIG. 4. Thermal e.m.f. generated between the sample cell and the reference cell when ice VI transforms to ice Ic and then to Ih, plotted against temperature.

therms will be reported in detail in later papers. Five samples of ice II, two of ice IX, four of ice V, two of ice VI, and two of ice VIII were measured. The enthalpy of the transformations to ice Ic and of ice Ic to Ih are summarized in Tables 1 and 2, respectively.

The transformation of ice II to Ic sometimes produced a symmetric peak in the calorimeter scans, and sometimes produced peaks with small irregularities, as is illustrated in one of the scans in Fig. 1. The cause of the irregularities is not known, but they seem to have no significant influence on the enthalpies of transformation. The enthalpies of transformation seem to fall into two reasonably well defined groups, the first three samples averaging 57.4 ± 1 J mol^{-1} and the last two samples having the value 48.1 J mol^{-1}. All five are consistent with the average value of 54 ± 5 J mol^{-1}, and the two groups are tentatively considered to differ insignificantly.

Two measurements of the enthalpy of transformation of ice IX to Ic were made, and the average value is -340 ± 3 J mol^{-1}, which agrees well with the earlier and less accurate value (17). Ice IX is partly ordered (9, 17, 21–25) but the degree of order of our samples is not known *a priori*. The endothermic contribution from the disordering transformation is included in the observed enthalpy of transformation. Yamamuro and others (26) have recently described making ice IX by applying 2.5 kbar of helium pressure to either the liquid or the ice I at about 250 K. They cooled the samples to 77 K and released the helium. When the samples were heated, an endothermic transformation occurred. In the present experiments, ice II transformed to ice Ic endothermically but ice IX transformed to ice Ic exothermically, which agrees with the earlier data (17). It seems likely that Yamamuro and others (26) made not ice IX, but ice II, as Rabideau and co-workers showed (27) when helium was the pressurizing fluid.

The endothermic transformations of both ice V and VI in the range 106–132 K and 120–141 K, respectively, are probably due to disordering of the molecular orientations. The endotherm in ice V depended upon the conditions and had a maximum value (19) of 229 ± 10 J mol^{-1} and seems to be quite well separated from the exotherm of the transformation of ice V to Ic, whose enthalpy change is -915 ± 45 J mol^{-1}, as is clear in Fig.

Can. J. Chem. Downloaded from www.nrcresearchpress.com by 176.9.209.113 on 09/07/12
For personal use only.

TABLE 1. Enthalpy of the irreversible transformation ΔH of the high-pressure phases of ice to ice Ic

Phase of ice	Sample no.	T_i^a / K	T_t^a / K	T_f^a / K	ΔH / J mol^{-1} Measured	Average	Reference (17, 18)
II	1	157.0	161.6	172.8	56.3		
	2	155.4	160.6	176.2	57.4		
	3	159.6	162.3	174.4	58.5	54±5	0±40 at ~170 K
	4	158.2	162.7	172.4	48.1		
	5	157.0	162.1	173.2	48.1		
IX	1	125.0	142.8	171.6	−337.7	−340±3	−300 at ~150 K
	2	125.3	143.1	174.4	−342.3		
V	1	141.4	145.3	154.6	−914.8		
	2	140.8	144.4	155.1	−910.8	−915±4	−830 at ~150 K
	3	141.0	145.0	156.0	−912.7		
	4	136.5	144.1	160.1	−919.7		
VI	1	141.4	142.7	152.8	−1422	−1404±20	−1200 at ~ 150 K
	2	140.7	142.8	153.4	−1385		
VIII	1	117.5	124.4	174.7	−2685	−2667±25	−2340 at ~125 K
	2	117.6	123.0	176.3	−2649		

[a]Approximately, T_i and T_f are, respectively, the temperatures at which the thermal effect appeared to start and end and T_t is the apparent transformation temperature, all as defined in ref. 39.

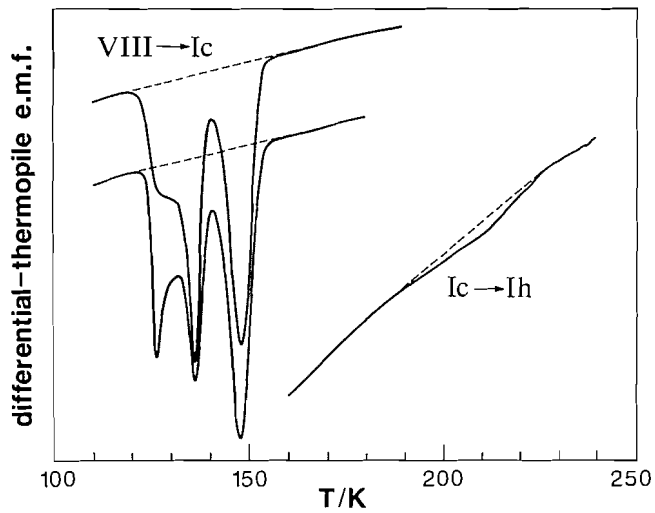

FIG. 5. Thermal e.m.f. generated between the sample cell and the reference cell when ice VIII transforms to ice Ic and then to Ih, plotted against temperature. Two scans are plotted in order to illustrate the difference in the shape of the exotherm of the transformation of ice VIII to Ic.

3. It seems likely that ice V is fully disordered before its transformation to ice Ic.

The endotherm of ice VI clearly overlaps the exotherm caused by the transformation of the partly ordered ice VI to Ic, as is shown in Fig. 4, and could not be properly separated from it in these experiments. The endotherm and exotherm occur with an average apparent enthalpy change of 115 ± 2 and −1404 ± 20 J mol^{-1}, but the endotherm is probably more positive and the exotherm more negative than they seem to be because of the overlap. What we know about the true value of the exotherm is discussed in Section 4.4.

The transformation of ice VIII to ice Ic that is drawn in the lower curve of Fig. 5 has three distinct exotherms, which can be approximately separated into peaks whose areas are listed in Table 3. In the transformation represented by the upper curve of Fig. 5, the peak at the lowest temperature seems to have broadened to become only a shoulder of the center peak, but the areas of the three features are consistent with the areas under the curve in the lower part of the figure. The average area under all the features is −2667 ± 25 J mol^{-1}. All the enthalpies of transformation are consistent with the less accurate values that were measured in a simple apparatus over 20 years ago (17, 18).

The enthalpy of transformation of ice Ic to Ih depends on the phase that the ice Ic was made from. It was about −35 ± 5 J mol^{-1} when either ice II, ice VIII, or the low-density amorph was the source of the ice Ic, was about −13 ± 4 J mol^{-1} when ice IX was the source, and was about −50 ± 5 J mol^{-1} when either ice V or VI was the source. The differences between the enthalpy changes are so great that they are well outside the experimental uncertainties.

Four possible causes of the differences are the formation of ice Ic with a substantial fraction of stacking faults, the formation of regular stacking variants that are intermediate between ice Ih and Ic, a transformation of ice Ic to Ih that releases some of its heat too slowly to detect, and formation of ice Ic having grains that are small enough to have an energy of some tens of joules per mole. Stacking variants are known in the closely related system ammonium fluoride (28), phase I of which is isomorphous with ice Ih, but have never been reported in the phases of ice. Stacking faults are known to occur in ice Ih (29) but seem not to have been identified in the numbers needed to explain differences in energy of transformation of as much as 40 J mol^{-1}. Stacking faults in ice Ic have not yet been reported but probably exist in small numbers. The formation of small grains is certainly possible, so that the interfacial energy accounts for

Can. J. Chem. Downloaded from www.nrcresearchpress.com by 176.9.209.113 on 09/07/12
For personal use only.

TABLE 2. Enthalpy of transformation ΔH of ice Ic, which was made from various high-pressure phases of ice, to ice Ih

Origin of ice Ic	Sample no.	T_i^a / K	T_f^a / K	ΔH/J mol^{-1} Measured	ΔH/J mol^{-1} Average
Ice II	1	190.7	225.5	−33.4	
	2	—	—	—	
	3	178.0	230.3	−42.7	−36.2±4
	4	187.6	224.8	−32.6	
	5	188.3	225.4	−36.1	
Ice IX	1	183.4	232.8	−13.3	
	2	178.2	232.0	−17.4	−13.2±4
	3[b]	175.0	225.0	−8.8	
Ice V[c]	2	180.8	218.3	−49.9	
	3	177.9	217.3	−51.9	−50.7±1
	4	178.1	216.7	−50.4	
Ice VI[c]	1	177.6	217.1	−47.2	−50.2± ~3
	2	176.5	216.7	−53.1	
Ice VIII	1	186.7	228.0	−33.9	−34.5± ~1
	2	186.0	228.0	−35.1	
Low-density amorphous ice[d,e]	1			−38.4	
	2			−30.6	−35±4
	3			−35.5	

[a] T_i and T_f are defined in Table 1.
[b] The transformation of sample 3 of ice IX to ice Ic was not measured, and so the sample is not included in Table 1. It was annealed in the calorimeter at 146–150 K for 1 h in order to eliminate any perturbation of the initial baseline for the transformation of ice IX to Ic.
[c] These values have already been reported briefly in ref. 40 and are listed here for comparison.
[d] The low-density amorphous ice was made by heating high-density amorphous ice that had itself been made by compressing ice Ih at 77 K to about 13 kbar (14).
[e] These values have already been reported (39) and are listed here for comparison.

the difference in the energies of transformation of ice Ic to Ih. But then a correlation between the volume and heat changes at the transformation to ice Ic might be expected, but none is apparent. As the ice Ih forms at temperatures as high as 220 K, it seems likely that the grains are quite large and so have only a small interfacial energy. If the average interfacial energy between the grains of ice Ic were about 10 nJ mm^{-2} and the average grain had dimensions of about 100 nm, which varied from sample to sample depending on the origin, then the difference in the transformation energies of ice Ic to Ih could be explained.

It will be assumed tentatively that this explanation is correct, and that the ice Ih that is made (at about 225 K) has a large enough grain size that the interfacial energy is small. Then, the enthalpies of transformation of the high-pressure phases to ice Ih can be obtained accurately. The values so obtained are summarized in Table 4. They agree reasonably well with the changes of enthalpy at zero temperature as obtained from the phase relations and from simple thermal measurements (16–18).

4. Discussion

4.1 Transformation of ice II to Ih

The difference of internal energy U on the equilibrium line II–Ih, U_{Ih}–U_{II} (3), changes linearly with the temperature from −68.6 J mol^{-1} at 238.2 K to −53.5 J mol^{-1} at 198.2 K. If the line is extrapolated linearly to 162 K, the change of energy is −40 J mol^{-1}. The difference between this value and the 18 J mol^{-1} that is reported in Table 4 is, presumably, accounted for by the effect of temperature and pressure on the internal energy, but the existing data for this and other equilibrium lines are insufficient to evaluate the effect.

The enthalpy of transformation of ice II to ice Ih is 18 ± 5 J mol^{-1} at 162 K. Its sign disfavors the transformation, so the transformation must be driven by an increase in the entropy. Because ice II is orientationally ordered and ice Ih is not (30–32), the change of configurational entropy at the transformation is approximately (R) ln (3/2), where R is the gas constant and 3/2 is approximately the number of orientational configurations per molecule (33), i.e. 3.37 J K^{-1} mol^{-1}. The change of Gibbs function G at the transformation at ~200 K is

$$[1] \quad G_{Ih} - G_{II} = H_{Ih} - H_{II} - T(S_{Ih} - S_{II}) = -656 \pm \sim 16 \text{ J mol}^{-1}$$

so the transformation is predicted to go in the observed direction.

The pressure p_e at which ice II and Ih are at equilibrium is described by the equation

$$[2] \quad p_e = -\Delta_e A/\Delta_e V$$

where A is the Helmholtz function and subscript e means at thermodynamic equilibrium. At zero temperature, eq. [2] becomes

$$[3] \quad p_e = -\Delta_e U/\Delta_e V$$

Because the difference of enthalpy is 18 ± 5 J mol^{-1} at 162 K and ambient pressure, and because the heat capacity of ice II,

Can. J. Chem. Downloaded from www.nrcresearchpress.com by 176.9.209.113 on 09/07/12
For personal use only.

TABLE 3. Enthalpy of transformation ΔH of ice VIII to ice Ic at zero pressure, and approximate enthalpies of transformation of the three peaks.

Sample no.	Total ΔH J mol^{-1}	Peak 1 T_p[a] K	Peak 1 ΔH[b] J mol^{-1}	Peak 2 T_p[a] K	Peak 2 ΔH[b] J mol^{-1}	Peak 3 T_p[a] K	Peak 3 ΔH[b] J mol^{-1}
1	−2685	126	−620	136	−810	147	−1250
2	−2649	128	−520	136	−880	148	−1250

[a] T_p is the temperature at which the e.m.f. of the thermopile reached a maximum.
[b] The enthalpies of the peaks were obtained by resolving the peaks graphically.

TABLE 4. Enthalpies of transformation ΔH of the high-pressure phases of ice to ice Ih

Phase of ice	T[a] K	ΔH J mol^{-1}
Ice II	162	18±5
Ice IX	143	−353±6
Ice V	144	−966±6
Ice VI	143	−1454±20
Ice VIII	124	−2702±25

[a] T is the average of the temperatures T_t reported in Table 1, rounded to the nearest integer.

which has not yet been measured, is probably greater than that of ice I, the difference of energy of ice II and ice Ih at zero temperature is greater than 18 ± 5 J mol^{-1}. The volume of ice II is less than that of ice I by 3.5 cm^3 mol^{-1} at about 100 K and ambient pressure (30–32). If the unknown difference of thermal expansivity of ice Ih and II is neglected, the equilibrium pressure at zero temperature is −51 ± ~20 bar, and so ice II is the most stable phase of ice at zero temperature and pressure. Bridgman (3) pointed out 75 years ago that the equilibrium line between ice II and Ih extrapolated to about zero temperature and pressure, and Whalley (16) estimated from Bridgman's measurements that the intercept of the line on the pressure axis was 0.14 ± 0.2 kbar, which agrees with the present, more accurate, result.

The equilibrium temperature T_e is defined by the equation

[4] $$T_e = \Delta_e H/\Delta_e S$$

The value of the enthalpy change at zero pressure can be taken as that at 162 K without a great uncertainty, and is about 18 J mol^{-1}. From this, the entropy change, which has already been discussed, and eq. [4], the equilibrium temperature at zero pressure is about 5 K.

Some years ago it was pointed out (34) that if ice II were the stable phase of ice at zero temperature and pressure, and if ice Ih and II had the same configurational entropy, our world would be vastly different from what it is and, in particular, that life as we know it could not exist. We are indeed fortunate that ice Ih is disordered and ice II is not.

4.2 Transformation of ice IX to Ih

The difference of enthalpy between ice IX and Ih at ambient pressure, is, according to Table 4,

[5] $$H_{Ih} - H_{IX} = -353 \pm 7 \text{ J mol}^{-1} \text{ at } 143 \text{ K}$$

The difference of enthalpy between ice III and Ih can be obtained from the position and slope of the equilibrium line and the difference of volume between ice III and Ih. Then the thermodynamics of the transformation of ice III to ice IX can be determined, in order to determine the configurational entropy of ice IX.

An estimate of the enthalpy of transformation of ice Ih to ice III can be obtained from the slope of the ice Ih–III equilibrium line and the volume change across it, according to the Clausius–Clapeyron equation

[6] $$H_{III} - H_{Ih} = T\left(\frac{\partial p}{\partial T}\right)(V_{III} - V_{Ih})$$

The slope of the equilibrium line is (35) −2.58 ± 0.02 bar K^{-1}, which replaces Bridgman's (3) value, whose line is much too strongly curved.

The change of volume on the equilibrium line at 238 K and 2120 bar is

[7] $$V_{III} - V_{Ih} = -3.53 \pm \sim 0.02 \text{ cm}^3 \text{ mol}^{-1}$$

which is the average of Bridgman's (3) and Gagnon's (36) values. It follows that

[8] $$H_{III} - H_{Ih} = 217 \pm \sim 3 \text{ J mol}^{-1} \quad \text{at} \quad 238 \text{ K} \quad \text{and} \quad 2120 \text{ bar}$$

This value can be reduced to zero pressure by the equation

[9] $$\left(\frac{\partial \Delta H}{\partial p}\right)_T = \Delta V - T\left(\frac{\partial \Delta V}{\partial T}\right)_p$$

The first term on the right-hand side of eq. [9] can be integrated, assuming a difference of compressibility of 3 ± ~1 Mbar^{-1}, to

[10] $$(H_{III} - H_{Ih})(p = 0) - (H_{III} - H_{Ih})(p = 2120 \text{ bar}) = 751 \pm \sim 6 \text{ J mol}^{-1} \quad \text{at} \quad 238 \text{ K}$$

The second term of eq. [9] is of the magnitude of 1 J mol^{-1} if the difference of thermal expansions of ice Ih and III is a third of the thermal expansion of ice Ih, and can be neglected. Then, from eqs. [8] and [10]

[11] $$(H_{III} - H_{Ih})(p = 0) = 968 \pm 7 \text{ J K}^{-1} \text{ mol}^{-1} \quad \text{at} \quad 238 \text{ K}$$

This value can be reduced to 143 K by means of the equation

$$\left(\frac{\partial \Delta H}{\partial T}\right)_p = \Delta C_p$$

where ΔC_p is the difference of heat capacities at constant pressure. The difference of heat capacities can be estimated approximately from the peak infrared frequency of the librations of ice Ih and III or IX, i.e. 840 (37) and 812 cm^{-1} (38), respectively, ignoring the translational vibrations because their frequencies are not known well enough. If the librations are approximated by a single frequency then at ambient pressure

Can. J. Chem. Downloaded from www.nrcresearchpress.com by 176.9.209.113 on 09/07/12
For personal use only.

[12] $(H_{III} - H_{Ih})(238\ K) - (H_{III} - H_{Ih})(143\ K) = 25 \pm \sim 10\ J\ mol^{-1}$

It follows from eqs. [11] and [12] that at ambient pressure

[13] $H_{III} - H_{Ih} = 943 \pm \sim 12\ J\ mol^{-1}$ at 143 K

It further follows from eq. [13] and the difference of enthalpy between ice Ih and IX of $-353 \pm 6\ J\ mol^{-1}$ that

[14] $H_{III} - H_{IX} = 590 \pm \sim 13\ J\ mol^{-1}$ at 143 K and ambient pressure

The enthalpy of the transformation of ice III to ice IX, as measured in a high-pressure differential scanning calorimeter (21) that was cooled at the rate 0.01–0.04 K s^{-1}, was $-230 \pm \sim 50\ J\ mol^{-1}$, which is less than half the value that is determined in this work. The cause of the discrepancy is not immediately obvious.

If W_{III} and W_{IX} are the numbers of configurations per molecule in ice III and IX respectively, then

[15] $RT \ln W_{III}/W_{IX} = 590 \pm \sim 13\ J\ mol^{-1}$

If the transformation temperature T is taken as about 173 K (9, 21) which is where a major part of the transformation occurs, although the transformation occurs over the range 200–165 K, then

[16] $W_{III}/W_{IX} = 1.51 \pm 0.02$

which is, within the experimental precision, equal to the value for fully disordered ice III and fully ordered ice IX within the ice rules. The ice IX made in this work seems, therefore, to be fully ordered.

4.3. Transformation of ice V to ice Ih

The transformation of fully disordered ice V to ice Ih occurs at 144 K with an enthalpy change of $-966 \pm 6\ J\ mol^{-1}$.

4.4 Transformation of ice VI to ice Ih

If ice VI had no orientational disorder, the maximum enthalpy change at the disordering transformation would be RT ln (3/2) or 470 J mol^{-1} at 140 K. The enthalpy of transformation is at least 115 J mol^{-1}. If ice VI were fully ordered, then about -355 J mol^{-1} should be added to the enthalpy of the transformation of ice VI to Ic. The enthalpy of transformation of ice VI, as made in this work, to Ic could, then, be as high as about 1760 J mol^{-1} and as low as 1405 J mol^{-1}.

4.5. Transformation of ice VIII to ice Ih

The transformation of fully ordered ice VIII to Ic occurred in three distinct exothermic peaks in one sample, and in the second sample the lowest-temperature peak seems to have broadened to form a shoulder on the low-temperature side of the center peak. The characteristic temperatures and the enthalpy changes in each peak are summarized for the two samples in Table 3.

The cause of the three features is not known; the principal possibilities are samples that are reproducibly inhomogeneous, and samples that sequentially transform from ice VIII to two other phases and finally to ice Ic. Reproducible inhomogeneity seems unlikely, and a sample of ice VIII that was held at 125 K for 21 h and then had its X-ray powder pattern taken at about 90 K was about half ice VIII and half ice Ic, and there was no evidence of intermediate phases (18).

1. G. TAMMANN. Ann. Phys. **2**, 1 (1900).
2. J. DEWAR. Chem. News, **91**, 216 (1905).
3. P. W. BRIDGMAN. Proc. Am. Acad. Arts Sci. **47**, 441 (1912).
4. E. F. BURTON and W. F. OLIVER. Proc. R. Soc. London, A**153**, 166 (1935).
5. P. W. BRIDGMAN. J. Chem. Phys. **3**, 597 (1935).
6. P. W. BRIDGMAN. Proc. Am. Acad. Arts Sci. **72**, 45 (1937).
7. H. KÖNIG. Z. Krist. **105**, 279 (1943).
8. E. WHALLEY, D. W. DAVIDSON, and J. B. R. HEATH. J. Chem. Phys. **45**, 3976 (1966).
9. E. WHALLEY, J. B. R. HEATH, and D. W. DAVIDSON. J. Chem. Phys. **48**, 2362 (1968).
10. B. KAMB, A. PRAKASH, and C. KNOBLER. Acta Crystallogr. **22**, 706 (1967).
11. Y. TAJIMA, T. MATSUO, and H. SUGA. J. Phys. Chem. Solids, **45**, 1135 (1984).
12. K. R. HIRSCH and W. B. HOLZAPFEL. Phys. Lett. **101**A, 142 (1984).
13. T. MATSUO and H. SUGA. J. Phys. Coll. Cl. Supp. No. 3, **48**, 477 (1987).
14. O. MISHIMA, L. D. CALVERT, and E. WHALLEY. Nature, **310**, 393 (1984).
15. O. MISHIMA, L. D. CALVERT, and E. WHALLEY. Nature, **314**, 76 (1985).
16. E. WHALLEY. J. Chem. Phys. **81**, 4087 (1984).
17. J. E. BERTIE and E. WHALLEY. J. Chem. Phys. **38**, 840 (1963).
18. J. E. BERTIE and E. WHALLEY. Can. J. Chem. **42**, 1373 (1964).
19. Y. P. HANDA, D. D. KLUG, and E. WHALLEY. J. Phys. Coll. Cl. Supp. No. 3, **48**, 435 (1987).
20. Y. P. HANDA, R. E. HAWKINS, and J. J. MURRAY. J. Chem. Thermodyn. **16**, 623 (1984).
21. K. NISHIBATA and E. WHALLEY. J. Chem. Phys. **60**, 3189 (1974).
22. W. C. HAMILTON, B. KAMB, S. J. LAPLACA, and A. PRAKASH. *In* Physics of ice. *Edited by* N. Riehl, B. Bullemer, and H. Engelhardt. Plenum, New York. 1969. p. 44.
23. S. W. RABIDEAU, E. D. FINCH, G. P. ARNOLD, and A. L. BOWMAN. J. Chem. Phys. **49**, 2514 (1968).
24. B. KAMB and A. PRAKASH. Acta Crystallogr. B**24**, 1317 (1968).
25. S. J. LAPLACA, W. C. HAMILTON, B. KAMB, and A. PRAKASH. J. Chem. Phys. **58**, 567 (1973).
26. O. YAMAMURO, M. OGUNI, T. MATSUO, and H. SUGA. J. Phys. Chem. Solids, **48**, 935 (1987).
27. G. P. ARNOLD, R. G. WENZEL, S. W. RABIDEAU, N. G. NERESON, and A. L. BOWMAN. J. Chem. Phys. **55**, 589 (1971).
28. M. A. NABAR, L. D. CALVERT, and E. WHALLEY. J. Chem. Phys. **51**, 1353 (1969).
29. M. OGURO and A. HIGASHI. *In* Physics and chemistry of ice. *Edited by* E. Whalley, S. J. Jones, and L. W. Gold. Royal Society of Canada, Ottawa, 1973. p. 338.
30. B. KAMB. Acta Crystallogr. **17**, 1437 (1964).
31. E. D. FINCH, S. W. RABIDEAU, R. G. WENZEL, and N. G. NERESON. J. Chem. Phys. **49**, 4361 (1968).
32. B. KAMB, W. C. HAMILTON, S. J. LAPLACA, and A. PRAKASH. J. Chem. Phys. **55**, 1934 (1971).
33. L. PAULING. J. Am. Chem. Soc. **57**, 2680 (1935).
34. E. WHALLEY. Structure problems of ice. *In* Physics of ice. *Edited by* N. Riehl, B. Bullemer, and H. Engelhardt. Plenum, New York. 1969. p. 19.
35. G. S. KELL and E. WHALLEY. J. Chem. Phys. **48**, 2359 (1968).
36. R. GAGNON, H. KIEFTE, M. J. CLOUTER, and E. WHALLEY. Acoustic velocities in ice Ih, II, III, V, and VI by Brillouin spectroscopy and their densities. To be published.
37. J. E. BERTIE and E. WHALLEY. J. Chem. Phys. **40**, 1636 (1964).
38. J. E. BERTIE and E. WHALLEY. J. Chem. Phys. **40**, 1646 (1964).
39. Y. P. HANDA, O. MISHIMA, and E. WHALLEY. J. Chem. Phys. **84**, 2766 (1986).
40. Y. P. HANDA, D. D. KLUG, and E. WHALLEY. J. Chem. Phys. **84**, 7009 (1986).

Can. J. Chem. Downloaded from www.nrcresearchpress.com by 176.9.209.113 on 09/07/12
For personal use only.

A new method for calculating the rotational tunnelling splitting for three-dimensional rotors

GÜNTER VOLL AND ALFRED HÜLLER

Department of Theoretical Physics, University of Erlangen, 8520 Erlangen, Glückstraße 6, West Germany

Received September 15, 1987

This paper is dedicated to Professor James A. Morrison

GÜNTER VOLL and ALFRED HÜLLER. Can. J. Chem. **66**, 925 (1988).

We present a recursion method for calculating the rotational part of the wave function and the rotational tunnelling splitting ω for three-dimensional rotors. This Pocket Recursion Method (PRM) is designed to include the case of splittings that are smaller than 10^{-2} μeV. The PRM combines two advantages: fast convergence and accuracy. Applications to the various $(NX_4)_2SnCl_6$ model potentials are shown (X = H, D). For the Smith potential, the calculated isotope shift agrees well with the recent experimental results. Applications to other rotational tunnelling systems are straightforward.

GÜNTER VOLL et ALFRED HÜLLER. Can. J. Chem. **66**, 925 (1988).

On présente une méthode récursive permettant de calculer, pour des rotors tridimensionnels, la portion rotationnelle de la fonction d'onde et la levée de la dégénerescence (ω) dûe à l'effet tunnel rotationnel. On a développé cette méthode récursive de poche (MRP) de façon à inclure les cas où les séparations entre les niveaux sont plus petits que 10^{-2} μeV. La MRP présente deux avantages : une convergence rapide et une bonne précision. On présente des applications à divers potentiels modèles du $(NX_4)_2SnCl_4$ (X = H, D). Dans le cas du potentiel de Smith, le déplacement isotopique qui a été calculé est en bon accord avec les données expérimentales rapportées récemment. Des applications à d'autres systèmes présentant une levée de la dégénerescence dûe à l'effet tunnel rotationnel sont immédiates.

[Traduit par la revue]

Can. J. Chem. Downloaded from www.nrcresearchpress.com by 176.9.209.113 on 09/07/12
For personal use only.

1. Introduction

1.1 A qualitative picture of rotational tunnelling

A molecule in a solid experiences an angle-dependent potential (1–3). The moment of inertia J of the rotor determines the natural energy unit, termed "rotational constant", $B = \hbar^2/(2J)$, where $\hbar$ denotes Planck's constant; Table 1 gives the values of B for some molecules.

In this section we develop a qualitative picture of rotational tunnelling at zero temperature, using as an example a tetrahedral molecule, like CH_4 or NH_4, in a tetrahedral crystal field (Fig. 1). For tetrahedral molecules the orientational potential can be divided into at least 12 disjointed identically shaped regions, according to the invariance of the rotor with respect to the 12 rotations that are the symmetry operations of the tetrahedral symmetry group T. We call the regions "potential pockets" (4). For a tetrahedral crystal field there are just 12 pockets and the symmetry within a pocket is high (4): the rotations around the three twofold symmetry axes of the molecule are energetically equivalent; the same is true for the rotations around the four threefold symmetry axes.

For high (in units of B) and broad potential barriers the orientational probability distribution of the quantum rotor is sharply peaked at the potential minima. A real valued ("ansatz") wave function, which is peaked in a single pocket, is called a "pocket state" (4). We take 12 pocket states, denoted by $|1\rangle$, $|2\rangle$, ..., $|12\rangle$, of identical shape, each centered in one of the 12 pockets (Figs. 2–4). The rotations of the tetrahedral group transform the pocket states into each other. The pocket states are neither eigenstates of the Hamiltonian, nor orthogonal to each other.

The orientations that differ by one of the molecule's symmetry operations are indistinguishable. Consequently, approximate eigenstates of the Hamiltonian can be constructed as linear combinations of the 12 pocket states. The eigenstates are classified according to the irreducible representations A, T, and E of the tetrahedral group; there are two E-symmetric functions, nine T-functions, and one A-function (4). Functions of the same symmetry type are energetically degenerate. As an example, we give one (unnormalized) eigenstate of each symmetry approximated by the appropriate linear combination of pocket states (4) (Fig. 4):

TABLE 1. The order of magnitude of some rotational constants $B = \hbar^2/(2J)$. J denotes the moment of inertia of the rotor; $\hbar$ is Planck's constant; k_B is Boltzmann's constant

Molecule	B
$-CH_3$, NH_4^+, CH_4	$8Kk_B$: 0.7 meV
$-CD_3$, ND_4^+, CD_4	$4Kk_B$: 0.3 meV
H_2	$85Kk_B$: 7.3 meV
D_2	$43Kk_B$: 3.7 meV

$$|A\rangle \approx \sum_{i=1}^{12} |i\rangle$$

[1] $$|T_x\rangle \approx |1\rangle - |2\rangle - |3\rangle + |4\rangle$$

$$|E^-\rangle \approx |1\rangle + |2\rangle + |3\rangle + |4\rangle - |6\rangle - |8\rangle - |10\rangle - |12\rangle$$

We choose $\langle i|i\rangle = 1$ to simplify the notation; for the diagonal matrix element of the Hamiltonian H we write $e_i = \langle i|H|i\rangle$. By construction of the set of pocket states, all e_i are equal and are denoted e. Because of the tetrahedral crystal field, there are only two types of overlaps and off-diagonal elements of the Hamiltonian (4): the matrix elements linking pocket states that differ by a 120° rotation around the respective symmetry axis of the molecule (e.g., the pair ($|4\rangle$, $|5\rangle$)); Fig. 4) are all equal and are denoted by $b = \langle 4|5\rangle$ and $h = \langle 4|H|5\rangle$; analogously, the matrix elements between 180° adjacent pocket states are all equal and we write $\bar{b} = \langle 4|1\rangle$ and $\bar{h} = \langle 4|H|1\rangle$. The eigenenergies are approximated in terms of these matrix elements as follows (the upper index "ps" stands for "calculated

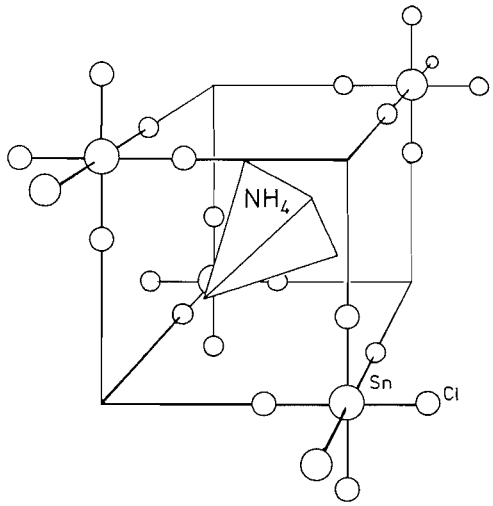

FIG. 1. $(NH_4)_2SnCl_6$. The NH_4 rotor sits in a crystal field of tetrahedral symmetry.

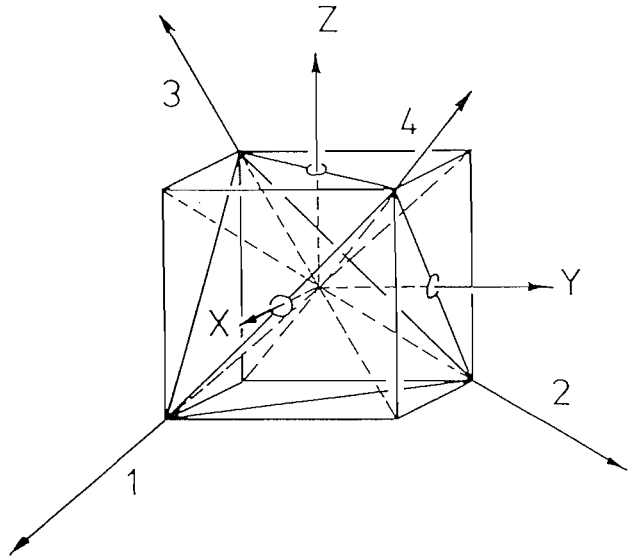

FIG. 2. The choice of the space-fixed coordinate system (XYZ) relative to the standard orientation of the tetrahedral rotor. In its standard orientation the rotor has minimal potential energy in a H_{11}^3-type potential (Fig. 5).

with pocket states"):

$$E_E = \frac{\langle E^-|H|E^-\rangle}{\langle E^-|E^-\rangle} \approx \frac{e - 4h + 3\tilde{h}}{1 - 4b + 3\tilde{b}} = E_E^{ps}$$

[2] $$E_T = \frac{\langle T_x|H|T_x\rangle}{\langle T_x|T_x\rangle} \approx \frac{e - \tilde{h}}{1 - \tilde{b}} = E_T^{ps}$$

$$E_A = \frac{\langle A|H|A\rangle}{\langle A|A\rangle} \approx \frac{e + 8h + 3\tilde{h}}{1 + 8b + 3\tilde{b}} = E_A^{ps}$$

The energy differences $\omega(TA) = E_T - E_A$ and $\omega(ET) = E_E - E_T$ characterize the fine structure of the librational ground state multiplet; they are called tunnelling energies or "tunnelling splittings", if the splittings are smaller than roughly 10^{-1} B (Table 1). We note several important aspects: The degeneracy between A, T, and E states is lifted by the overlap matrix elements (h, $\tilde{h}$, b, and $\tilde{b}$) of adjacent pocket states. The tunnelling splittings decrease with increasing potential barrier height. For high potential barriers, the 180° terms contribute far less to the tunnelling energy than the 120° terms (Fig. 5) and we can neglect the former: $1 \gg b \gg \tilde{b}$ and $|d| \gg |\tilde{d}|$ with $\tilde{d} = \tilde{h} - e\cdot\tilde{b}$ and $d = h - e\cdot b$ characterizing[1] the respective contributions to the splitting; this is the case in which we are interested:[2]

[3] $$E_E \approx e + 4|d|$$
$$E_T \approx e \qquad \text{for} \quad |d| \gg |\tilde{d}|$$
$$E_A \approx e - 8|d|$$

So far we have not explicitly stated the assumption used above, eq. [1]: A priori, we need three different sets of pocket states, one for each symmetry label. In eq. [1] we used instead only one common set. In the case of a high potential barrier, eq. [3], we therefore obtain a ratio $R = \omega(TA)/\omega(ET)$ equal to 2. The experimental results for tiny tunnelling splittings show that the value of R is close to 2 (1.96; ref. 5). Variational calculations, using free rotor states as a basis, also support the assumption made, as they show that R approaches quickly the value 2 (Sect. 3) with increasing potential barrier height.[3]

1.2 Bonding interpretation

The energy values E_A^{ps}, E_T^{ps}, and E_E^{ps} are obtained by inserting the linear combination, eq. [1], of the pocket states into the definition, eq. [2], of the eigenenergies E_A, E_T, and E_E, but can also be understood in more detailed terms by what we call a "bonding interpretation" of the (real valued) wave functions: In each of the linear combinations (eq. [1]) the pockets are either occupied with positive or negative amplitude ($s_i = \pm 1$) or they are empty ($s_i = 0$); the s_i are simply the coefficients in the linear combinations. The bond between two different pockets i and j is said to be "symmetric" if $s_i s_j = +1$, or to be "antisymmetric" if $s_i s_j = -1$, or to be open if $s_i s_j = 0$. Antisymmetric bonds correspond to nodes of the wave function in the potential barrier region leading to a stronger localization of the rotor and consequently to an increase of the energy of the state relative, instead, to a state with an open bond. Symmetric bonds correspond to a doubling of the amplitude of the wave function under the barrier, thus leading to a relative decrease of the energy. Both the increase and the decrease of the energy have the same absolute value. This simple counting scheme leads to the following structure of the energy formulas (eq. [2]):

[4] $$E^{ps} = \frac{\Sigma_{i,j} s_i s_j \langle i|H|j\rangle}{\Sigma_{i,j} s_i s_j \langle i|j\rangle} \qquad \text{with} \quad i,j = 1, \ldots, 12$$

We assume pocket no. 4 (Fig. 4) to be occupied ($s_4 = +1$). For each of the eigenstates, all occupied ($s_i \neq 0$) pockets can be treated equivalently (Sect. 1.1). Therefore, the corresponding pocket states $\langle i|$ in eq. [4] may be replaced by $\langle 4|$, s_i by $s_4 = +1$, and the summation over i yields the same factor both in the numerator and in the denominator and drops out. We obtain:

[1]Note the invariance of d (and $\tilde{d}$) with respect to energy shifts $H \rightarrow H + \Delta$: $e \rightarrow e + \Delta$, $h \rightarrow h + b\cdot\Delta$, $b \rightarrow b$ and therefore $d \rightarrow d$.

[2]The ground state needs to be A-symmetric, therefore $d \leq 0$.

[3]Th. Brückel, private communication.

Can. J. Chem. Downloaded from www.nrcresearchpress.com by 176.9.209.113 on 09/07/12
For personal use only.

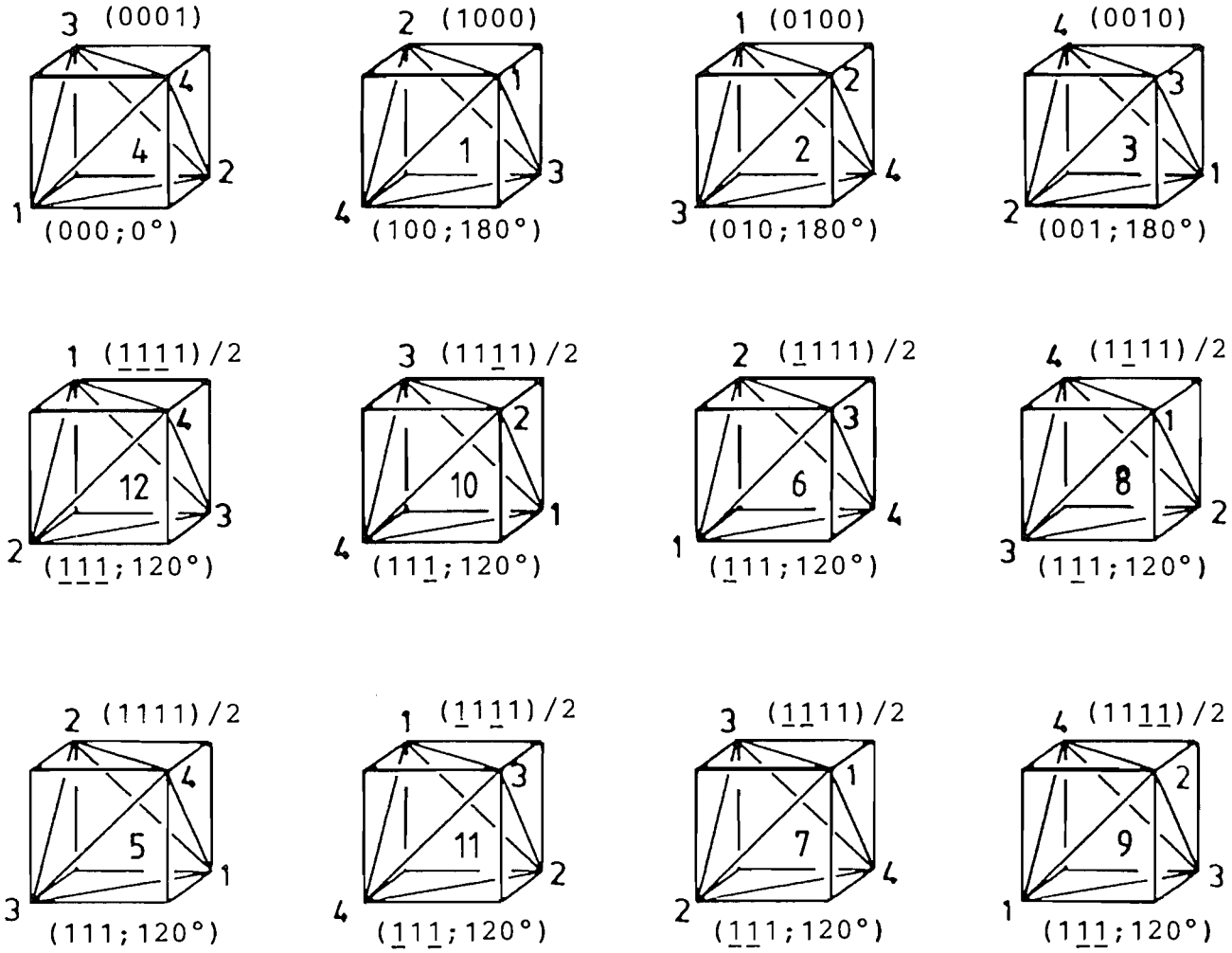

FIG. 3. There are always 12 energetically equivalent orientations of a tetrahedral rotor. The orientations of minimal potential energy in a H_{11}^3-type potential are given both in quaternions $q = (q_1,q_2,q_3,q_4)$ and in the form (rot. axis; rot. angle), referring to the standard orientation (0, 0, 0, 1), respectively (000;0°). The enumeration of the orientations follows Fig. 4.

$$[5] \qquad E^{ps} = \frac{\Sigma_j s_j \langle 4|H|j\rangle}{\Sigma_j s_j \langle 4|j\rangle} \qquad \text{with} \qquad j = 1, \ldots, 12$$

Inserting for the s_j the coefficients of the linear combinations, eq. [1], and specializing for the case of tetrahedral crystal symmetry (Sect. 1.1), we obtain the energy formulas (eq. [2]).

The bonding interpretation will be useful for the construction of so-called *artificial states* (Sect. 1.4).

1.3 Earlier methods and their drawbacks

Various attempts have been made to calculate the tiny tunnelling splittings ω/B. All of them are variational calculations. Two main methods exist, reflecting the two limiting cases of vanishing and infinitely high potential barriers. In the first case, free rotor functions (6), and in the second, pocket functions are used as a basis (4). The obvious choice of a pocket function is to take eigenfunctions of the harmonic oscillator (7). Power law functions have also been tried for some technical advantages (8).

All theoretical methods are confronted with the basic problem that two complementary aspects are involved in the lower part of the experimentally interesting and accessible range from $\omega \approx 100$ μeV (n-scattering (9)) down to $\omega \approx 30$ neV (nmr (10)), namely accuracy vs. fast convergence. Even for the highly symmetric tetrahedral crystal field, at a potential barrier height of about $100B$ (at the saddle; Fig. 5), the Free Rotor Method (FRM) needs functions up to an angular momentum l of at least $l_{max} = 16$ to yield satisfying convergence of the calculated energies $E(l_{max})$ on the scale of the tunnelling splitting (6). The FRM would need considerably more functions for the case of a nonsymmetric crystal field and (or) a stronger potential.

The Pocket State Method (PSM) suffers from the fact that all variational parameters are used to approximate the eigenfunction in the region of the potential minimum, whereas one also needs a good approximation in the saddle point region (Fig. 5) of the potential. The PSM is unreliable. This can be seen by inspecting the local fulfillment $A(q;\phi,E)$ of the stationary Schrödinger equation (SSE), which is defined by

$$[6] \qquad A(q;\phi,E) = \frac{(H\phi)(q) - E\cdot\phi(q)}{B\cdot\phi(q)}$$

For an eigenfunction ψ of the Hamiltonian H with eigenvalue E_ψ, the SSE $(H\psi)(q) = E_\psi\psi(q)$ is satisfied for any orientation q of the rotor, that is, $A(q;\psi,E_\psi) = 0$ for all q. Figure 6 shows $A(q;\phi,E_\phi)$ for rotations leading directly from an orientation

Can. J. Chem. Downloaded from www.nrcresearchpress.com by 176.9.209.113 on 09/07/12
For personal use only.

Can. J. Chem. Downloaded from www.nrcresearchpress.com by 176.9.209.113 on 09/07/12
For personal use only.

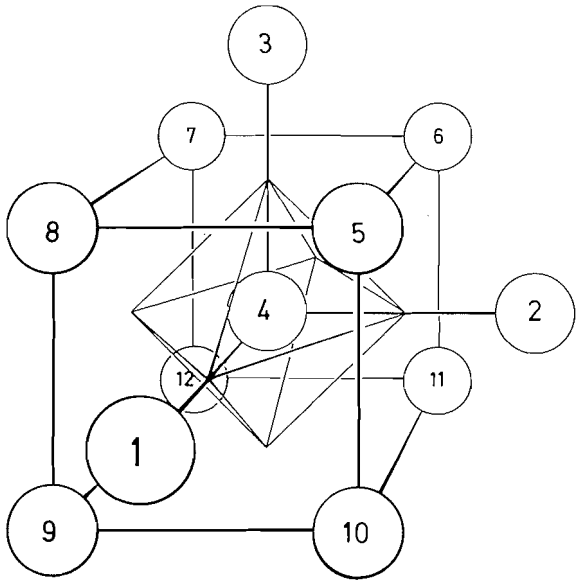

FIG. 4. The enumeration of the 12 pockets and pocket functions is shown in the configuration space (CS). Any point in CS corresponds to an orientation of the (rigid) rotor in real space (RS). The origin of the coordinate system in CS lies in the center of pocket no. 4 and corresponds to the standard orientation of the rotor (Fig. 3). The CS coordinate axes (100), (010), and (001) are chosen through the centers of the pockets no. 1, no. 2, and no. 3. The (space-fixed) axis of rotation (xyz) in RS (Fig. 2) corresponds to the direction xyz in CS, while the rotation angle in RS is represented by a certain distance along the xyz direction in CS. Note that the drawing shows the correct topology of CS, but the same rotation angle in RS leads to different distances in the drawing, depending on the axis of rotation. The boundary of the central pocket is shown as an octahedron.

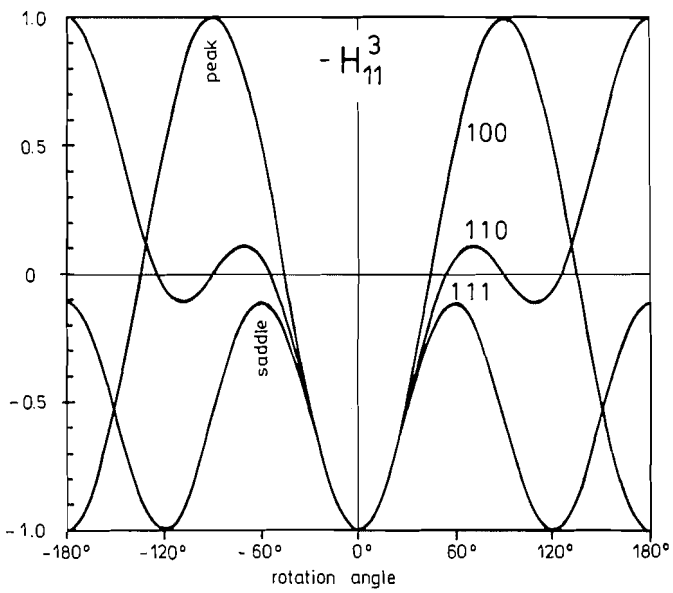

FIG. 5. The first nontrivial cubic rotator function of tetrahedral symmetry is $H_{11}^3(q)$ (eq. [11]). The shape of $-H_{11}^3$ is plotted for three axes of rotation, (100), (110), and (111), starting from the center (at 0°) of pocket no. 4 (Fig. 4); e.g., the rotation around the (111) axis leads through the centers of the pockets no. 5 (at 120°) and no. 12 (at −120°). From a (space-fixed) axis of rotation (xyz) (with $x^2 + y^2 + z^2 = 1$) and the rotation angle Θ, we get $\rho = \sin(\Theta/2)$ and the quaternion $q = (\rho x, \rho y, \rho z, \sqrt{1-\rho^2})$.

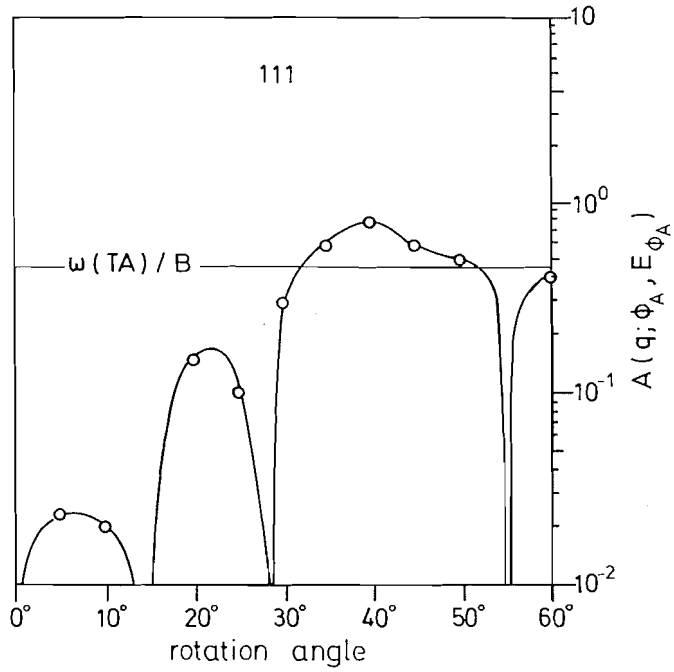

FIG. 6. The local fulfillment $A(q;\phi_A,E_{\phi_A})$ (eq. [6]) of the stationary Schrödinger equation is shown for rotations around the (111) axis; ϕ_A is an optimized variational wave function, using a combination of pocket and free rotor functions ($l_{max} = 6$) (Sect. 1.3); $E_A = \langle\phi_A|H|\phi_A\rangle/\langle\phi_A|\phi_A\rangle$ where H is the Hamiltonian. The potential is of the simple H_{11}^3 type. The potential strength in this example is quite low ($A_{11}^3 = -30B$), but nevertheless the calculated tunnelling splitting $\omega(TA)/B$ is not reliable: the fluctuations $(|\phi_A|^2 \cdot A)(q)$ around E_{ϕ_A}/B reach 20% of $\omega(TA)/B$ at rotation angles of only 20°. Consequently, we cannot consider ϕ_A to be a good approximation to the A eigenfunction in the saddle point region of the potential (around (111;60°)), which is decisive for the value of the tunnelling splitting.

of minimal potential energy across the potential saddle to a neighbouring minimum; $E_\phi = \langle\phi|H|\phi\rangle/\langle\phi|\phi\rangle$ is the energy associated with the optimized variational wave function ϕ, resulting from a sophisticated ansatz that combines pocket states and free rotor states.[4] The pocket states are used to approximate the sharp peaks of the eigenfunction around the potential minimum, with the effect that the difference to the eigenfunction ought to be a slowly varying function. The difference was thought to be accurately representable by only a few free rotor functions ($l_{max} = 6$). The result is disappointing, as can be seen from the figure: for rotation angles Θ of only 20°, $A(q;\phi,E_\phi)$ already reaches the order of magnitude of the tunnelling splitting ω/B. Now the amplitude of the (real valued) wave function at $\Theta = 20°$ amounts to 60% of its maximal value; consequently the local fluctuations $|\phi^2 \cdot A|$ around the mean value E_ϕ are large on the scale of the tunnelling energy. The calculated ω value is not reliable even for the small potential barrier height of only $30B$!

The drawbacks of the variational methods pose the problem of designing a fast converging, but nevertheless accurate, method to be able to make reliable theoretical predictions for the very interesting situations of low crystal field symmetry (e.g., CH_4 adsorbed on graphite surfaces) and for the experimentally measured tunnelling splittings close to the neV range.

[4]M. V. Smalley, private communication.

Can. J. Chem. Downloaded from www.nrcresearchpress.com by 176.9.209.113 on 09/07/12
For personal use only.

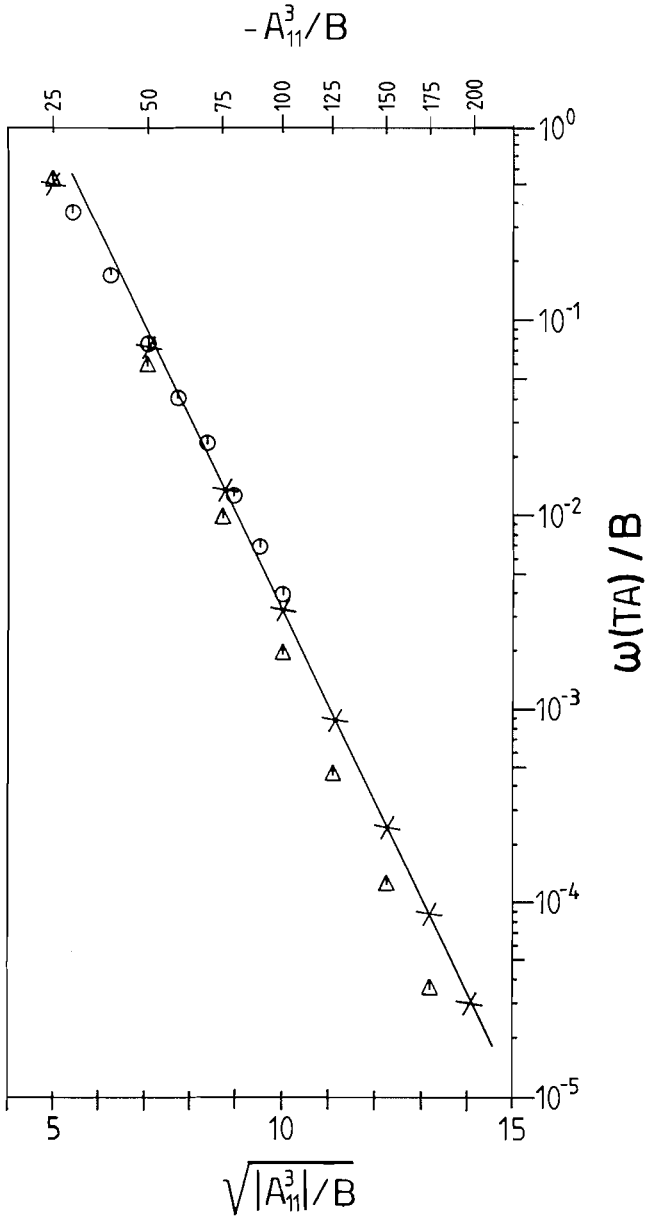

FIG. 7. Asymptotically, the tunnelling splitting ω decreases exponentially with increasing square root of the potential strength. This behaviour can be expected by considering simple one-dimensional examples. By our calculations the expected behaviour is confirmed to hold for the three-dimensional case, too, if the potential strength is larger than about $50B$. The plot compares the results of several methods. The PRM results for $\omega(TA)$ ($l_{max} = 10$) are shown by the crosses; the straight line is fitted only to results for the interval $50B < -A_{11}^3 \leq 150B$. The splittings for $-A_{11}^3 > 150B$ should lie exactly on the straight line, but are distributed a little bit around it. This is not surprising, as the PRM with $l_{max} \leq 10$ is not able to deal with potential strengths of more than about $150B$ (Fig. 11). The triangles show the results of Hüller and Kroll (13); the circles show the values which Smalley (see footnote 4, Sect. 1.3) obtained. Surprisingly (Fig. 8), the available results of Hüller and Raich (7) coincide with the PRM values.

1.4 Asymptotic behavior and extrapolation

With growing potential strength all methods run into similar difficulty in achieving the desired relative accuracy for an increasingly small tunnelling splitting. In the FRM (3, 6, 11, 12) a rising number of basis states (up to $l_{max} = 32$) has to be used to comply with the demands. The Pocket Recursion Method (PRM; Sect. 2) gives reliable results up to $V_0 \approx 150B$ using only very few terms in the ansatz of the recursion wave function (Sect. 3). By V_0 we denote the difference between the values of rotational potential at the saddle point and the center of the pocket (Fig. 5). See Fig. 7 for a one-parameter model and Fig. 13 for several three-parameter potentials, for which $V_0 = -8A_{11}^3/9 - 40A_{11}^4/27 - 140A_{11}^6/243$. For $V_0 = 150B$ the tunnelling splitting is several times $10^{-4}B$, yet we want to go further down to at least $10^{-5}B$. Luckily, there exists an additional aspect: explicit calculations for simple one-dimensional problems reveal the asymptotic behavior of the tunnelling splitting ω with increasing potential strength V_0.

$$[7] \quad \ln(\omega/B) \sim \alpha\sqrt{V_0/B} + \beta \qquad \alpha < 0$$

Our pocket recursion calculations verify eq. [7] for the three-dimensional case, where the linear dependence begins at potential strengths of about $50B$ (Fig. 7). Therefore we have the broad range of potential strengths from $50B$ to $150B$ to calculate accurately the parameters α and β for a given potential function, a fact that allows the extrapolation of the tunnelling energy for very high potential barriers (Figs. 7 and 13).

2. Pocket Recursion Method (PRM)

2.1 Program

The partition of the potential into fully equivalent pocket regions implies calculating the spectrum of the Hamiltonian in a single pocket. This can be done by finding just that part of each eigenfunction which is in the pocket chosen. To reach that goal we need exact constraints, termed "continuation conditions", characterizing the eigenfunctions of the Hamiltonian. The constraints ought to be as close as possible to the pocket center. There are two types of constraints, corresponding to symmetric and antisymmetric bonds (Sect. 1.2): for short we term them "sb condition" and "asb or node condition". Their locations are found from symmetry considerations (Sect. 2.3) of the eigenfunctions of the Hamiltonian.

Now we imagine a wave function (eq. [1]) to be expanded around a pocket center:

$$[8] \quad \psi(q_1,q_2,q_3,\rho) = \sum_{l=0}^{\infty} \sum_{m=-l}^{l} f_{lm}(\rho) K_{lm}(q_1,q_2,q_3)$$

The excursion from the center is denoted by $\rho = \sin(\Theta/2)$, where Θ is the rotation angle; (q_1,q_2,q_3) with $q_1^2 + q_2^2 + q_3^2 = \rho^2$ denotes the space-fixed axis of rotation. These coordinates are intimately related to the quarternions: any quaternion on the sphere $S^3 = \{q \in \mathcal{R}^4 | \Sigma_{i=1}^4 q_i^2 = 1\}$ corresponds to an orientation of the rotor relative to a standard orientation $q^s = (0,0,0,1)$ (Fig. 2); note $q_4 = \cos(\Theta/2)$; henceforth we abbreviate the quadrupel (q_1,q_2,q_3,ρ) by $r(q)$. The K_{lm} are the cubic harmonics (see Appendix 1) and the $f_{lm}(\rho)$ are polynomials in ρ:

$$[9] \quad f_{lm}(\rho) = \sum_{n=0}^{\infty} g_n^{(lm)} \rho^n$$

We now calculate the function $(H\psi)(r(q))$, where H is the Hamiltonian, and insert it into the stationary Schrödinger equation (SSE) $(H\psi) - E\psi = 0$, which then appears as a vanishing linear combination

$$[10] \quad \sum_{l=0}^{\infty} \sum_{m=-l}^{l} \sum_{n=0}^{\infty} \Lambda_n^{(lm)} \rho^n K_{lm}(q_1,q_2,q_3) = 0$$

Can. J. Chem. Downloaded from www.nrcresearchpress.com by 176.9.209.113 on 09/07/12
For personal use only.

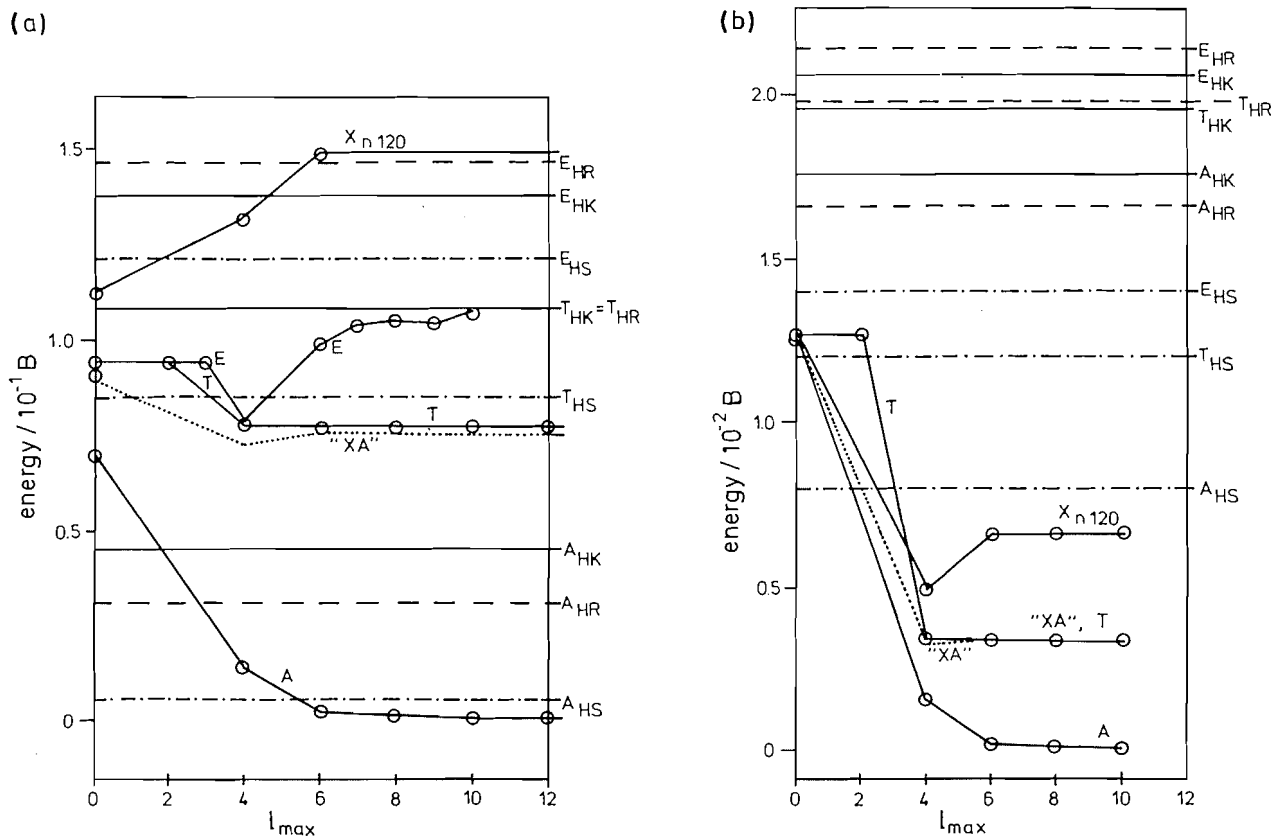

FIG. 8. The convergence of the PRM energies with increasing number of terms in the PRM ansatz for both $A^3_{11} = -50B$ and $-100B$. Also marked are results of earlier pocket state calculations (indices: K, Kroll; R, Raich; S, Smalley; H, Hüller). For $A^3_{11} = -100B$ the earlier results differ by more than the value of the splitting from the correct results. (a) $A^3_{11} = -50B$: The energy of the E recursion function does not converge on the scale of the tunnelling splitting (Sect. 3), but can be substituted by $E_A + (3/4)(E_{X_{n120}} - E_A)$, eq. [18], for the case of very strong potentials. To test the validity of that substitution, we check whether eq. [19] is satisfied (dotted "XA" line) by the X_{n120} energy value. The visible (relative to $\omega(TA)$) difference between the XA and T results indicates that $A^3_{11} = -50B$ cannot be considered to be a very strong potential. (b) $A^3_{11} = -100B$: XA and T values become indistinguishable on the scale of the tunnelling splitting. The fast convergence is remarkable.

with coefficients $\Lambda_n^{(lm)}$ that are functions of the yet unspecified energy E and the starting coefficients $g_0^{(lm)}$ of the polynomials $f_{lm}(\rho)$, eq. [9]. Only the $f_{lm}(\rho)$ for symmetry-allowed K_{lm} are nonvanishing. To let the linear combination, eq. [10], vanish for any rotation axis and angle, it is necessary to set the coefficients $\Lambda_n^{(lm)}$ to nil. Recursion relations for the $g_n^{(lm)}$ follow (Sect. 2.2). The choice $g_0^{(00)} = 1$ uses the freedom of normalization.

The "set of recursion parameters" $(E, \{g_0^{(lm)}\}_{l=1,\ldots,\infty}^{m=-l,\ldots,l})$, for which the recursion wave function satisfies the continuation condition of an eigenstate, contains the corresponding eigenvalue E. If we use only a finite number l_{max} of terms in the ansatz [8], the continuation condition cannot be fulfilled exactly; consequently E is not an exact eigenvalue. But we find the function $E(l_{max})$ (Fig. 8) to be rapidly convergent, except for the E-symmetric case (Sect. 3). The parameter n_{max}, at which the summation in [9] is broken off, is easy to handle and is chosen large enough not to influence the results; typically $n_{max} \geq 60$ and ≥ 150 for potential strengths of $50B$ and $100B$, respectively (Sect. 4).

2.2 An example of a recursion relation

To illustrate the details of our program outlined above, we now derive the recursion relation for an isotropic ansatz function ($l_{max} = 0$ in eq. [8]) used in the specific example of a tetrahedral molecule in the simplest tetrahedral potential, an H^3_{11}-potential function (Fig. 5):

$$[11]\quad H^3_{11}(q) = 16\sum_{i=1}^{4} q_i^6 - 20\sum_{i=1}^{4} q_i^4 + 5 \quad \text{with} \quad q \in S^3$$

The potential then reads $V(q) = A^3_{11} \cdot H^3_{11}(q)$. With $A^3_{11} \leq 0$, one of the 12 potential minima lies at $q^s = (0,0,0,1)$, which corresponds to the standard orientation of the rotor (Fig. 2). The potential can be expressed in the form of expansion [8]:

$$[12]\quad H^3_{11}(q_1,q_2,q_3,\rho) = V_{00}(\rho)K_{00}(q_1,q_2,q_3) + V_{41}(\rho)K_{41}(q_1,q_2,q_3) + V_{61}(\rho)K_{61}(q_1,q_2,q_3)$$

with $V_{00}(\rho) = 1 - 8\rho^2 + 16\rho^4 - \frac{64}{7}\rho^6$; $V_{41}(\rho) = -20(1 - \frac{12}{11}\rho^2)/N_{41}$; $V_{61}(\rho) = 48/N_{61}$; $N_{41} = 5\sqrt{21}/4$, $N_{61} = 231\sqrt{26}/8$; note $K_{00} \equiv 1$. The potential is invariant with respect to the change $\rho \rightarrow -\rho$, which means that clockwise and counterclockwise rotations around any axis are energetically equivalent. Therefore all odd expansion terms vanish in the ansatz [8] of the recursion function:

$$[13]\quad \phi_0 = f_{00}(\rho)\cdot K_{00}(q_1,q_2,q_3) = f_{00}(\rho) = \sum_{n=0}^{n_{max}} g_{2n}^{(00)}\rho^{2n}$$

The operator $\hat{T}$ of the kinetic energy (see A.2) applied to the isotropic ansatz reads

$$[14]\quad \hat{T}\phi_0 = \frac{B}{4}\left(\left(\rho^2\frac{\partial^2}{\partial\rho^2} + 3\rho\frac{\partial}{\partial\rho}\right) - \left(\frac{\partial^2}{\partial\rho^2} + \frac{2}{\rho}\frac{\partial}{\partial\rho}\right)\right)f_{00}(\rho)$$

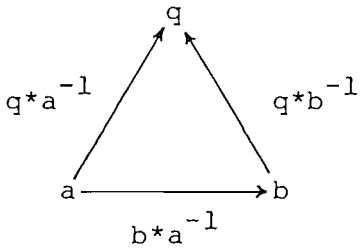

FIG. 9. The orientation q is said to lie on the middle between the orientations a and b, if the rotation angles from a to q and from b to q are equal. A necessary condition for equal rotation angles is $(q*a^{-1})_4 = (q*b^{-1})_4$, where a, b, and q are the respective quaternions, * denotes the quaternionic multiplication (14).

Inserting the isotropic ansatz ϕ_0 into the SSE therefore yields for the coefficients $\Lambda^{(00)}_{2n}$ (eq. [10]):

$$\Lambda^{(00)}_{2(n-1)} = \left\{ \left(n(n-1)g^{(00)}_{2(n-1)} - n\left(n+\frac{1}{2}\right)g^{(00)}_{2n} \right) \right.$$

$$[15] \quad + \frac{A^3_{11}}{B}\left(g^{(00)}_{2(n-1)} - 8g^{(00)}_{2(n-2)} + 16g^{(00)}_{2(n-3)} - \frac{64}{7}g^{(00)}_{2(n-4)} \right)$$

$$\left. - \frac{E}{B}g^{(00)}_{2(n-1)} \right\} \rho^{2n-2} \quad \text{with} \quad g^{(00)}_m = 0 \quad \text{for} \quad m < 0$$

Setting the coefficients $\Lambda^{(00)}_{2(n-1)}$ of $\rho^{2n-2}\cdot K_{00}$ to nil yields $g^{(00)}_{2n}$ in terms of the $g^{(00)}_{2n'}$ of lower order ($n' < n$), thus establishing a recursion relation for $g^{(00)}_{2n}$.

2.3 Continuation conditions

All orientations $q \in S^3$, which are the same rotation angle apart from two given orientations $a, b \in S^3$, satisfy the condition (Fig. 9)

$$[16] \quad \sum_{i=1}^{4} q_i(a_i - b_i) = 0$$

and are said to lie on the "middle" $M_{a,b}$ of (a,b): $M_{a,b} = \{q \in S^3 | \sum_{i=1}^4 q_i(a_i - b_i) = 0\}$. Let a and b be the centers of different pockets, and φ_a and φ_b the respective pocket functions. As we have already pointed out (Sect. 1.1), φ_a and φ_b are identically shaped, but centered at different orientations. Therefore $\varphi_a + \varphi_b$ satisfies the sb condition (Sect. 2.1), whereas $\varphi_a - \varphi_b$ has nodes in all points of $M_{a,b}$. In this way we consider all pairs of contributing pocket functions for a given eigenfunction, sorting out (e.g., below) the type (node or sb condition) and locality of the exact continuation conditions. They are listed in Table 2 for a tetrahedral molecule in a tetrahedral crystal field and are easy to adapt for other symmetries of the surrounding.

As an example for the procedure described above, we derive the continuation conditions for the E-symmetric state $|E^-\rangle$, eq. [1]: The pocket function centered in pocket i is denoted $\varphi_i(r(q)) = \langle r(q)|i\rangle$ with $r(q)$ ($q \in S^3$) describing the orientation of the rotor (Sect. 2.1). From the list of linear combinations [1] and the numbering convention given by Fig. 4, we easily get a very useful illustration (Fig. 10a) of the E-state.

Applying any symmetry operation of the tetrahedral group to the E-state shown (Fig. 10a) would only rotate the E-state, but would not fundamentally change the picture, because all pocket functions φ_i have the same shape (Sect. 1.1). Therefore, all we need to discuss is which are the continuation conditions between the central pocket function φ_4 and all its neighbours φ_i ($i \neq 4$), and whether or not the continuation condition for any pair (φ_4, φ_i) ($i \neq 4$) is disturbed by any other φ_j ($j \neq i$).

In our case of a tetrahedral rotor in a tetrahedral crystal field, the discussion is once again simplified, because many axes of rotation are equivalent (Sect. 1.1). For the three pairs $(\varphi_4, \varphi_i)_{i=1,2,3}$ we obviously have the sb condition on the respective middles $M_{4,i}$ (the faces of the cube in Fig. 10a), and the presence of the other pocket functions φ_j ($j \neq 1, 2, 3, 4$) does not conflict with that finding, because each of them is symmetric with respect to each $M_{4,i}$ ($i = 1, 2, 3$). For the four pairs $(\varphi_4, \varphi_k)_{k=6,8,10,12}$ we find the asb condition to hold on the respective middles $M_{4,k}$. Note that, e.g., the functions $\varphi_1 - \varphi_8$, $\varphi_2 - \varphi_6$, and $\varphi_3 - \varphi_{12}$ are antisymmetric with respect to $M_{4,10}$ and therefore they do not spoil the asb condition on $M_{4,10}$; the same holds for any $M_{4,k}$ ($k = 6, 8, 10, 12$). Figure 10b summarizes our discussion; it shows the locations of the continuation conditions for the E-state (eq. [1]).

2.4 Artificial states

The PRM offers a unique opportunity: we can perform our program for any continuation condition we want; and there is a meaningful choice on the basis of the bonding interpretation (Sect. 1.2). As an example we choose the amplitude in one pocket to be positive nonvanishing ($s_4 = +1$), as usual (Sect. 1.2), and assume antisymmetric bonds to each 120° adjacent pocket (Fig. 4); the bonding interpretation then predicts the energy

$$[17] \quad E_{X_{n120}} \approx e + 8|d| \qquad \text{for} \qquad |d| \gg |\tilde{d}|$$

for the artificial wavefunction X_{n120} in the case of high potential barriers, that is, if the 180° overlaps are negligible compared to the 120° terms (eq. [3]). The artificial function X_{n120} cannot be extended to the full sphere S^3 without violating either the SSE or the natural boundary conditions of 2π periodicity for the threefold rotation axes. Therefore X_{n120} cannot appear in the FRM and PSM calculations (Sect. 1.3). But it can be used successfully in the PRM, because the PRM does not work on the whole sphere S^3. The interesting aspect is that the energy $E_{X_{n120}}$ has a fixed relation to the eigenvalues sought:

$$[18] \quad \omega(XA) = E_{X_{n120}} - E_A \approx \frac{4}{3}(E_E - E_A)$$

$$\text{for} \qquad |d| \gg |\tilde{d}|$$

The PRM calculations of the energy $E_{X_{n120}}$ of the artificial function show (Fig. 8) that $E_{X_{n120}}$ converges very quickly with increasing order $l_{\max}$ in the ansatz [8]. The ansatz itself is the same as for an A-symmetric function, because we merely substitute the symmetric 120° bonds of the A-state (Table 2) by antisymmetric bonds and because of the irrelevance of the 180° bonds with respect to the tunnelling energy in our case of strong potentials. The importance of the artificial function X_{n120} for the PRM is illustrated by the discussion in Sect. 3.

3. Test of the Pocket Recursion Method

In this section we discuss the features and the quality of the PRM results in detail, using again the simple H^3_{11}-potential function (Fig. 5). The PRM results for the energy $E_S(l_{\max})$ (with $S = A, T, E$) are presented in Fig. 8 for a medium potential strength of $A^3_{11} = -50B$. Obviously, $E_E(l_{\max})$ does not converge on the scale of the tunnelling splitting. The reason is simple: the ansatz of the recursion function does not contain enough terms ($l_{\max} \leq 8$; Sect. 2.1) to satisfy the E-symmetric continuation conditions. To understand that, consider a 120°

Can. J. Chem. Downloaded from www.nrcresearchpress.com by 176.9.209.113 on 09/07/12
For personal use only.

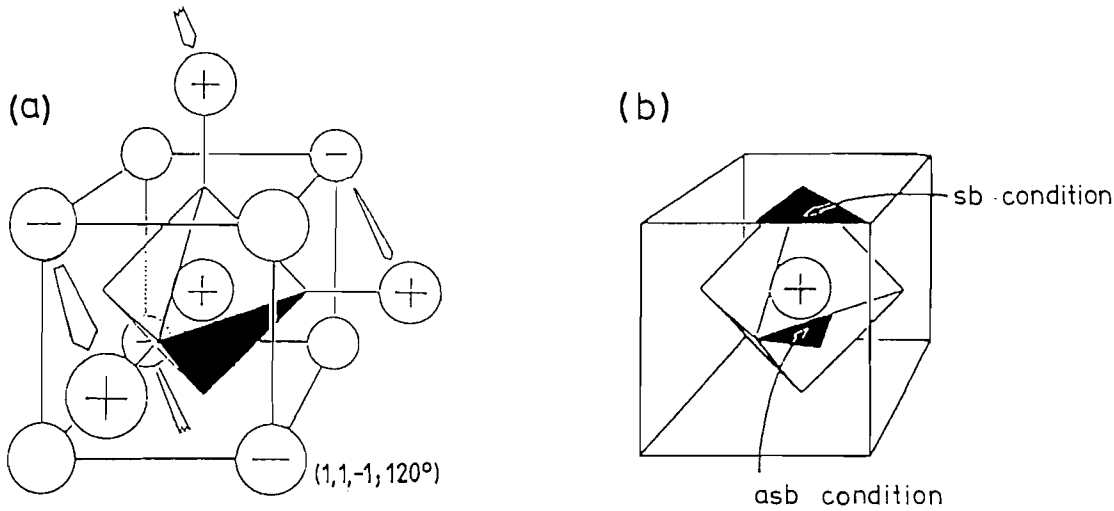

FIG. 10. (a) The E-state used in the PRM calculations (Fig. 8) is shown. The middle between the central and the $(1,1,-1;120°)$ pocket is also the middle between the pairs of pockets connected in the drawing. (b) The irreducible regions where sb and asb conditions have to be imposed on the recursion wave function for the case of a crystal field of tetrahedral symmetry. For a less symmetric crystal field, the irreducible regions would be larger.

TABLE 2. The continuation conditions given here for the $X_{n_{120}}$ recursion function and those of A, T, and E symmetry have to be rotated, using the operations of the tetrahedral symmetry group T, to obtain the full restrictions. Notation: In $M_{c,i}$ (Sect. 2.3) i stands for the quaternion coordinate of the center of pocket no. i (e.g., $i = 2 \Leftrightarrow (0,1,0,0)$; Fig. 3) and $c = (0,0,0,1)$ is taken to emphasize the central pocket (no. 4). Because of the 2:1 homomorphism (15) between SU_2 and SO_3, the two quaternions of opposite sign correspond to exactly the same physical orientation of a rigid body, but in calculations one has to be careful; therefore "$-c$" appears

Symmetry	Continuation condition
A	sbc on $M_{c,5} \cup M_{-c,5}$
$X_{n_{120}}$	asbc on $M_{c,5} \cup M_{-c,5}$
T	asbc on $(M_{c,1} \cup M_{-c,1}) \cap M_{3,2}$
	sbc on $M_{c,3} \cup M_{-c,3}$
E	asbc on $M_{c,10} \cup M_{-c,10}$
	sbc on $M_{c,3} \cup M_{-c,3}$

neighbouring (relative to pocket no. 4; Fig. 4) pocket P_{120}, in which the E-symmetric eigenstate ψ_E [1] has one of its maxima (e.g., no. 6; Fig. 4). We recall (Sect. 2.3) that the center of P_{120} lies on the middle $M_{4,i}$ of each pair $(\varphi_4,\varphi_i)_{i=1,2,3}$ of 180° adjacent pocket functions. To fulfill the sb condition in P_{120} for a recursion parameter that is equal or close to the eigenvalue of the E-state ψ_E, it is necessary for the recursion function to have maximal amplitude in P_{120}. With $l_{max} = 8$ we reach only 60% of the required amplitude. In the case of E symmetry, larger values of l_{max} would contradict the requirement for a fast converging method, because too many (more than 9) cubic harmonic functions K_{lm} would be symmetry allowed and would therefore be needed in the ansatz [8] of the recursion function. Consequently the number of adjustable parameters would become larger than we consider to be reasonable. From eq. [18] and Fig. 8 it is clear that we can overcome the difficulty by calculating $E_{X_{n120}}$.

Except for $E_E(l_{max})$, all PRM results converge quickly (Fig. 8), but this is not a sufficient condition for identifying the PRM energies with the eigenvalues sought. How reliable are the PRM energies? To answer this question, let us compare the PRM results with the FRM results[3,5] for $l_{max} = 21$ (Table 3), which are surely very good approximations (upper bounds) for the exact eigenenergies at medium potential strengths of about $50B$. The FRM results ($l_{max} = 21$) for a potential strength of $1400\,Kk_B$ (with $B = 8.381\,Kk_B$ we get $|A^3_{11}| \approx 50B$) were made available to us.[3] After all, the PRM results for E_A and E_T for $10 \leq l_{max} \leq 12$, $l_{max} = 8$, respectively agree very well with the FRM output for $l_{max} = 21$ (Table 3). The $E_{XA}(l_{max})$ values in Table 3 are obtained from

$$[19] \quad E_{XA} = \frac{E_{X_{n120}} + E_A}{2} \approx E_T \qquad \text{for} \qquad |d| \gg |\tilde{d}|$$

and ought to be (eqs. [3], [17]) equal to E_T, if the 180° overlap $\tilde{d}$ is negligible relative to the 120° overlap d. For $A^3_{11} \approx -50B$, the FRM shows that the ratio R (Sect. 1.1) is about 1.97, which means that $\tilde{d}$ cannot be neglected with respect to d; therefore we expect and see E_{XA} to deviate visibly from E_T in Fig. 8a. For stronger potentials, like $A^3_{11} = -100B$ (Fig. 8b), $E_{XA}(l_{max} = 10)$ and $E_T(l_{max} = 8)$ are equal within less than 1% of the tunnelling splitting. The fast convergence is remarkable (Fig. 11): for $E_T(l_{max} = 6)$, the $\omega(XA)$ value, eq. [18], deviates only 3% from its value for $l_{max} = 10$. This allows a reasonable approximation of the tunnelling energy with only three functions K_{lm}, namely K_{00}, K_{41}, and K_{61}, in the ansatz [8] of the recursion function, which means that only three recursion parameters (Sect. 2.1) are needed.

The local fulfillment $A(q;\phi,E_\phi)$ of the SSE by the optimal recursion functions also looks very promising. As can be seen by comparing Figs. 6 and 12, even the isotropic ansatz is as good as the sophisticated ansatz of Hüller and Smalley (Sect. 1.3); $A(q;\phi,E_\phi)$ hardly depends on the potential strength but strongly on l_{max} (Fig. 12). Table 4 gives a brief survey

[5]The different normalization of the potential functions in ref. 6 and in this work leads to the factor $\sqrt{(2l+1)/(8\pi^2)}$ in the calculation of A^l_{mn} from their potential strength.

Can. J. Chem. Downloaded from www.nrcresearchpress.com by 176.9.209.113 on 09/07/12
For personal use only.

TABLE 3. A comparison between the results of the PRM (Sect. 2) and the FRM (Sect. 1.3) at equal potential strength of $1400Kk_B$ (that is $A^3_{11} \approx -50B$; Sect. 3) reveals the fast convergence and high reliability of the PRM. The energy E_{XA} is defined in eq. [19]

Source	l_{max}	E_A/B	E_{XA}/B	E_T/B	E_E/B	$E_{X_{n120}}/B$
	0	−22.46956	−22.44622	−22.44101		−22.42287
	2			−22.44088		
	4	−22.52454	−22.46353	−22.45795		−22.40252
PRM	6	−22.53505	−22.45991	−22.45809		−22.38476
	8	−22.53632	−22.46050	−22.45827		−22.38467
	10	−22.53670	−22.46075			−22.38480
	12	−22.53676	−22.46078			−22.38479
FRM	21	−22.53668		−22.45824	−22.41845	

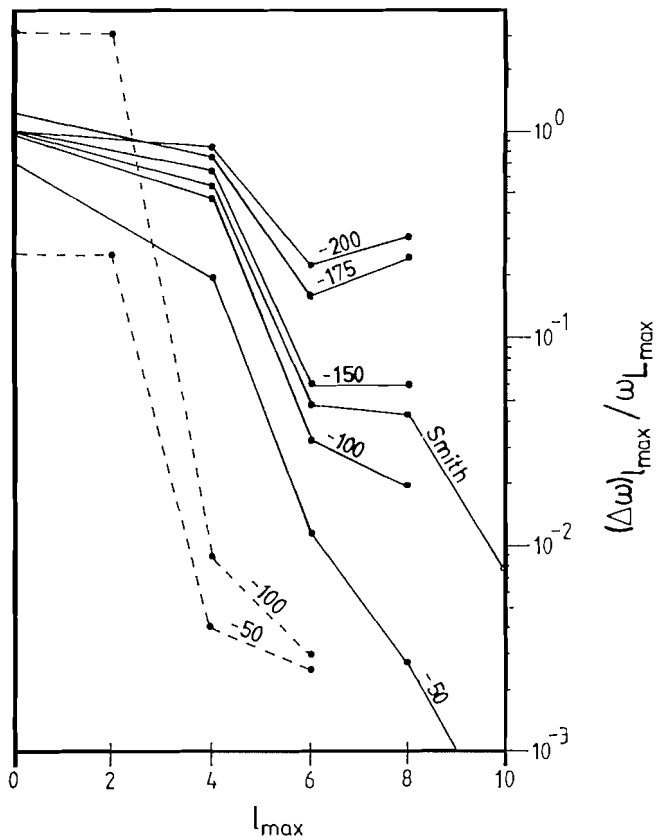

FIG. 11. The convergence of the tunnelling splitting $\omega_{l_{max}}$ towards the value $\omega_{L_{max}}$ obtained in the highest order L_{max} that we used (L_{max} = 10 and 12, respectively) in the PRM (Sect. 2.1); $(\Delta\omega)_{l_{max}} = \omega_{L_{max}} - \omega_{l_{max}}$. The respective potentials are indicated by the A^3_{11}/B values for the case of a simple H^3_{11} potential; "Smith" stands for the potential given in Table 5. The dashed lines show the convergence of $\omega_{l_{max}}$ using the PRM for T- and A-symmetric wave functions, whereas the solid lines connect the values obtained by using the artificial state X_{n120} (Sect. 2.4) instead of the T-state.

of the local fluctuations around the recursion parameter E_{ϕ_A} (Sect. 1.3), using the optimal A recursion function ϕ_A for $A^3_{11} = -50B$: The main fluctuations around $E_{\phi_A}(l_{max} = 10)$ occur in the saddle point region of the potential and they are very small on the scale of the tunnelling energy (Fig. 8a). Therefore we regard $E_{\phi_A}(l_{max} = 10)$, resulting from the PRM, to be reliable; the same holds for the energies of the optimized recursion functions ϕ_T and $\phi_{X_{n120}}$ and consequently it also holds for the tunnelling energies calculated by the PRM.

4. Application to $(NH_4)_2SnCl_6$ model potentials

We examine three different sets (Table 5) of potential parameters for ammonium hexachlorostannate ($(NH_4)_2SnCl_6$). The potentials are given as linear combinations of cubic rotor functions H^l_{mn} (see A.4):

[20] $$V(q) = A^3_{11}\cdot H^3_{11}(q) + A^4_{11}\cdot H^4_{11}(q) + A^6_{11}\cdot H^6_{11}(q)$$

Using the PRM, we calculate (Table 6; Fig. 13) the tunnelling splitting $\omega(TA)/B$ as a function of the potential strength V_0/B (Table 5) for each model potential; V_0 denotes the height of the potential saddle point relative to the potential at the center of the pocket. The numerical values of the tunnelling splitting for protonated and deuterated rotors are given in Table 6. The values are obtained as follows: In the first step, we calculate the tunnelling splittings $\omega(TA)$ for at least three potentials of the type $a\cdot V(q)$, which differ only in the value of the factor a. The calculations for $a = 1$ are shown by S, M, and V in Fig. 13. Secondly, we use the χ^2 method to find an optimal straight line through the points $(V_0, \omega(TA))$ obtained for each potential. The splittings calculated for $V_0 \leq 50B$ were not included in the χ^2 procedure; they indicate the lower limit of the potential strengths for which the asymptotic behaviour, eq. [7], is valid. The parameters α and β of eq. [7], which are obtained from the χ^2 algorithm, are given in Table 6 and allow extrapolation of the tunnelling splittings for potential barriers that are even higher than those for which the PRM (with $l_{max} \leq 10$) still yields reliable results. If we assume that deuteration of the rotor does not change the rotational potential function, then only the rotational constant B is affected: $B_d = B_p/2$. Consequently one can read, from Fig. 13, the tunnelling splitting of the deuterated rotor at an effective potential strength V_0/B_d, which has twice the value of the protonated case. The predicted values of the tunnelling splitting are shown in Fig. 13, again in units of B_d.

A recent nmr experiment (19) reveals a tunnelling splitting of $2\pi\hbar(7.5 \pm 0.5)$ MHz for the deuterated rotor in a $(ND_4)_2SnCl_6$ single crystal. The PRM results for the Smith potential agree fairly well with the experimental values of the tunnelling splitting for both protonated and deuterated rotors.

5. Comparison of the model potentials

For a comparison of the different model potentials (Table 5), we scale their strengths such that the theoretically predicted value of the tunnelling splitting for the protonated rotor equals the experimentally measured value (Table 6). For the scaled potentials, we derive from eq. [7] the predicted values of the splitting for the deuterated rotor (Table 7). The isotope shift can be characterized by the parameter β (eq. [7]), or by $\sigma(\beta)$

Can. J. Chem. Downloaded from www.nrcresearchpress.com by 176.9.209.113 on 09/07/12
For personal use only.

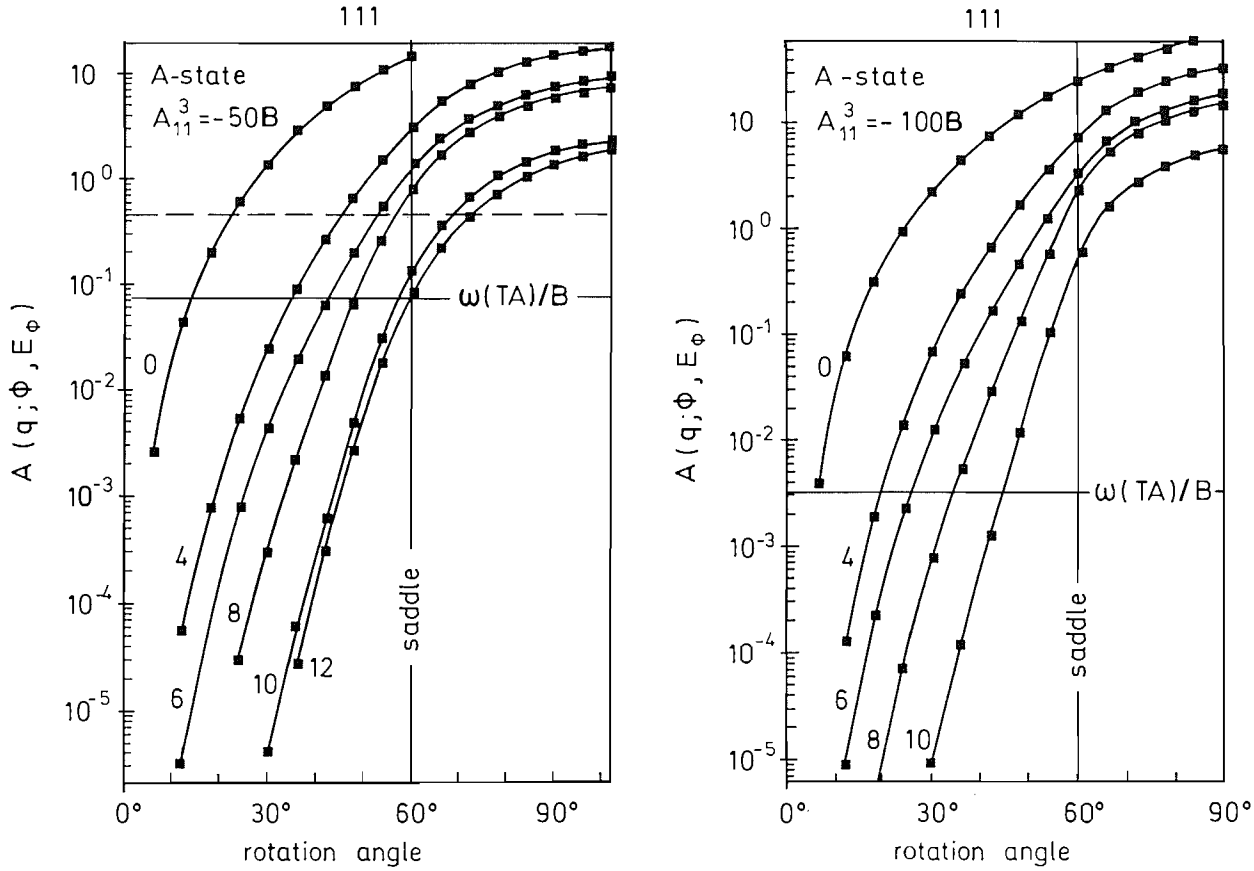

FIG. 12. The deviation $B \cdot A(q;\phi,E_\phi)$ (Sect. 1.3) of the local energy $(H\phi)(q)/\phi(q)$ (H = Hamiltonian) from the recursion parameter E_ϕ for an optimized A-symmetric wave function $\phi(q)$ is given for two potential strengths A_{11}^3 and different orders l_{max} of the PRM. The deviation depends strongly on l_{max} and weakly on the potential strength. The final results of the PRM tunnelling splitting calculations are also shown. The splitting for $A_{11}^3 = -30B$ is indicated by the dashed line. By comparison with Fig. 6 we see that even the isotropic ($l_{max} = 0$) recursion wave function yields results that are as good as the sophisticated ansatz ($l_{max} = 6$) of Hüller and Smalley (Sect. 1.3).

TABLE 4. The deviation $(\phi^2 A)(q)$ (eq. [6]) of the local energy from the recursion parameter E_ϕ for an optimized (real-valued) A-symmetric recursion function $\phi(q)$ ($l_{max} = 10$) at a potential strength of $A_{11} = -50B$. The maximal amplitude of the function ϕ is set to unity. The ϕ amplitude is maximal at the center (0°) of the central pocket. The biggest fluctuations occur around (111;60°), which is the locus of the saddle point of the potential (Fig. 5)

Rot. angle	20°	30°	40°	60°	90°
Rot. axis	All	All	All	111	100
$\phi(q)$	0.6	0.3	0.1	0.04	10^{-3}
$A(q;\phi,E_\phi)$	10^{-11}	10^{-7}	10^{-5}	4×10^{-3}	1
$(\phi^2 A)(q)$	10^{-11}	10^{-8}	10^{-7}	10^{-5}	10^{-6}

TABLE 5. $(NH_4)_2SnCl_6$ model potentials (8, 16, 17). V_0 is chosen to be the height of the potential saddle point relative to the center of the central pocket. Recently Smith (18) proposed a further potential. We have not performed a calculation for this set of parameters

		Smith	Müller	Vogt
Potential parameters	A_{11}^3/B	−132.84	−95.60	−49.70
	A_{11}^4/B	0	−27.90	−61.47
	A_{11}^6/B	42.70	46.80	55.24
Potential strength	V_0/B	92.5903	99.3481	103.4189

defined as follows:

$$[21] \quad \frac{\omega_d}{B_d} = \sigma \cdot \left(\frac{\omega_p}{B_p}\right)^{\sqrt{2}} \quad \text{with} \quad \sigma = e^{\beta(1-\sqrt{2})}$$

Only the scaled Smith potential yields an isotope shift that agrees with the experimentally observed one. But the results for the other model potentials are not far off, despite the fact that their parameters (Table 5) are quite different.

If we express the potential in the form

$$[22] \quad V(q) = A_{11}^3 \cdot (H_{11}^3(q) + C_{11}^4 \cdot H_{11}^4(q) + C_{11}^6 \cdot H_{11}^6(q)) \quad \text{with} \quad C_{11}^4 = A_{11}^4/A_{11}^3,\ C_{11}^6 = A_{11}^6/A_{11}^3$$

there are clearly lines of constant isotope shift in the (C_{11}^4, C_{11}^6)-parameter space. The model potentials of Smith, Müller, and Vogt type (Table 5) are lying almost on a straight line in the (C_{11}^4, C_{11}^6) plane. If we assume a linear dependence of the parameter σ of the isotope shift on C_{11}^4 and C_{11}^6

$$[23] \quad \sigma(C_{11}^4, C_{11}^6) = s_0 + s_1 \cdot C_{11}^4 + s_2 \cdot C_{11}^6$$

inside the narrow band in (C_{11}^4, C_{11}^6) space that is determined by the Smith-, Müller-, and Vogt-type potentials, we find $s_0 = 0.0246$, $s_1 = -0.3591$, and $s_2 = -0.5376$. For the experimental value of the isotope shift (Table 7) we then get the straight line $C_{11}^6 = -0.33 - 0.67 C_{11}^4$. The point (0,0) characterizes the H_{11}^3-type potentials and is far outside the band. The value derived above for s_0 gives the isotope shift for the H_{11}^3-type potentials ($\sigma = 0.025$), which is only one fourth of

Can. J. Chem. Downloaded from www.nrcresearchpress.com by 176.9.209.113 on 09/07/12
For personal use only.

TABLE 6. The PRM results for the model potentials of Table 5 compared to the experimental values (5, 19). The value of the rotational constant B of the NH_4 rotor is taken to be 8.381 Kk_B (6). For the deuterated rotor, we assume B to be equal to 8.381 $Kk_B/2$. The asymptotic behaviour (eq. [7]) for the H^3_{11}-type potentials is given as well

		PRM results				Experimental results
		Smith	Müller	Vogt	H^3_{11}	
Asymptotic behaviour	α	−0.9827	−0.9489	−0.8620	−1.133	
	β	3.9170	4.1002	4.1671	5.645	
$\omega(TA)/B$						
protonated rotor		3.93×10^{-3}	4.71×10^{-3}	10.07×10^{-3}		$(4.1\pm0.5)\times10^{-3}$
deuterated rotor		7.82×10^{-5}	9.37×10^{-5}	26.7×10^{-5}		$(8.6\pm0.6)\times10^{-5}$

TABLE 7. The results for the scaled model potentials. The scaling is such that the PRM value of the tunnelling splitting for the protonated rotor equals the experimentally measured one ($4.1\times10^{-3}B$). The predicted values (eq. [7]) (Table 6) of the tunnelling splitting for the deuterated rotor are compared to the experimental results. The values of the rotational constants are taken from Table 6. The values of the shift parameter σ (eq. [21]) are determined from the β values given in Table 6

		Theoretical results				Experimental results
		Smith	Müller	Vogt	H^3_{11}	
Scaled strength	$\tilde{V}_0$	91.7192	102.2367	125.6228		
$\omega(TA)/B$ deuterated rotor		8.33×10^{-5}	7.72×10^{-5}	7.51×10^{-5}		$(8.6\pm0.6)\times10^{-5}$
Shift parameter	σ	0.1974	0.1830	0.1780	0.096	0.2037

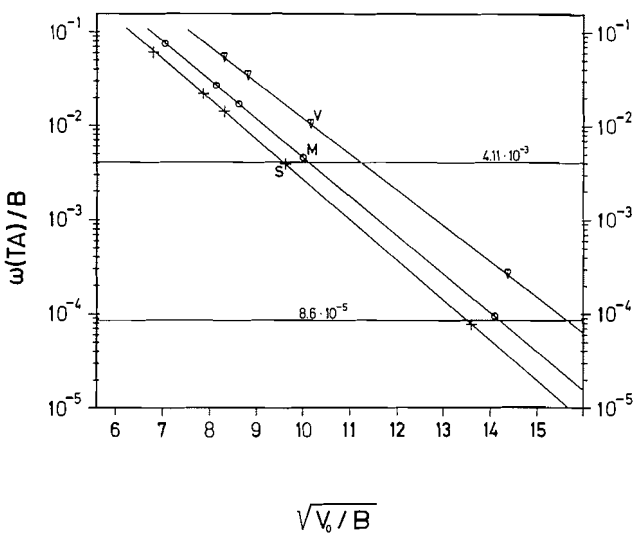

FIG. 13. The dependence of the logarithm of the tunnelling splitting $\omega(TA)$ on the square root of the potential strength V_0 turns out to be linear above $V_0 = 50B$ (Fig. 7). Therefore we can predict the splitting for a deuterated rotor in a given potential. The PRM predictions of the splittings for the three potentials of Table 5 (S, Smith; M, Müller; V, Vogt) are compared with the experimental values for the protonated ($4.1\times10^{-3}B_p$ (5)) and deuterated rotor ($8.6\times10^{-5}B_d$ (19)). The Smith potential is obviously the best choice. Notation: $V_0 = V$(potential saddle) − V(center of the pocket).

the value calculated directly (Table 7). This indicates that the function $\sigma(C^4_{11},C^6_{11})$ rises, going from any of the model potentials of Table 5 towards the H_{11}-type potentials.

The simultaneous analysis (8) of the librational frequency and the tunnelling splitting for the protonated rotor yields the straight line $C^6_{11} = -0.30 - 0.62C^4_{11}$. Unfortunately, it is almost parallel to the straight line derived above from the value of the measured isotope shift. Thus the isotope shift and the librational frequency do not lead to an independent determination of the potential parameters. However, it is satisfying to observe the consistency: the two straight lines are very close together.

Further useful information on the rotational potential might be drawn from an experimental determination of the librational frequencies in the deuterated sample. Unfortunately, due to the much smaller neutron scattering cross section of deuterium, the librational excitations are less intense and it has not been possible to separate them from the other lattice modes.[6]

Acknowledgments

This work was supported by the Bundesministerium für Forschung und Technologie under contract no. 03HU1ERL8. Thanks are due to Martin Smalley, Thomas Brückel, and Hajo Leschke for contributing valuable information and for stimulating discussions.

[6]M. Prager, private communication.

Can. J. Chem. Downloaded from www.nrcresearchpress.com by 176.9.209.113 on 09/07/12
For personal use only.

1. J. H. COLWELL, E. K. GILL, and J. A. MORRISON. J. Chem. Phys. **39**, 635 (1963).
2. W. PRESS. Single-particle rotations in molecular crystals. Springer Tracts Mod. Phys. **92** (1981).
3. Y. OZAKI, K. MAKI, K. OKADA, and J. A. MORRISON. J. Phys. Soc. Jpn. **54**, 2595 (1985).
4. A. HÜLLER. Phys. Rev. B: Solid State, **16**, 1844 (1977).
5. M. PRAGER, W. PRESS, B. ALEFELD, and A. HÜLLER. J. Chem. Phys. **67**, 5126 (1977).
6. TH. BRÜCKEL, W. PRANDL, K. VOGT, and C. M. E. ZEYEN. J. Phys. C: **17**, 4071 (1984).
7. A. HÜLLER and J. RAICH. J. Chem. Phys. **71**, 3851 (1979).
8. W. MÜLLER and A. HÜLLER. J. Phys. C: **15**, 7295 (1982).
9. W. PRESS and A. KOLMAR. Solid State Commun. **17**, 405 (1975).
10. M. PUNKKINEN, E. E. YLINEN, and L. P. INGMAN. Magnetic resonance and related phenomena. Proc. XXth Congress Ampère, Tallinn, UDSSR. 1978.
11. D. SMITH. J. Chem. Phys. **74**, 6480 (1981).
12. D. SMITH. J. Chem. Phys. **68**, 619 (1978).
13. A. HÜLLER and D. M. KROLL. J. Chem. Phys. **63**, 4495 (1975).
14. S. FLÜGGE. Mathematische Methoden der Physik. Vols. 1, 2. Hochschultext, Springer-Verlag, Berlin, Heidelberg, New York. 1980.
15. R. D. RICHTMYER. Principles of advanced mathematical physics. Vols. 1, 2. Texts and Monographs in Physics, Springer-Verlag, Berlin, Heidelberg. 1978.
16. D. S. SMITH. Chem. Phys. Lett. **66**, 84 (1979).
17. K. VOGT and W. PRANDL. J. Phys. C: **16**, 4753 (1983).
18. D. SMITH. J. Chem. Phys. **82**, 5133 (1985).
19. L. P. INGMAN, E. KOIVULA, Z. T. LALOWICZ, M. PUNKKINEN, and E. E. YLINEN. Z. Phys. Condens. Matter, **66**, 363 (1987).
20. F. C. VON DER LAGE and H. A. BETHE. Phys. Rev. **71**, 612 (1947).
21. A. HÜLLER and J. W. KANE. J. Chem. Phys. **61**, 3599 (1974).
22. C. J. BRADLEY and A. P. CRACKNELL. The mathematical theory of symmetry in solids. Clarendon Press, Oxford. 1972.
23. J. MORET-BAILLY, L. GAUTIER, and J. MONTAGUTELLI. J. Mol. Spectrosc. **15**, 355 (1965).
24. I. S. GRADSHTEYN and I. M. RYSHIK. Table of integrals, series and products. Academic Press, New York. 1965.
25. F. HUND. Z. Phys. **51**, 1 (1928).

Can. J. Chem. Downloaded from www.nrcresearchpress.com by 176.9.209.113 on 09/07/12
For personal use only.

Appendix

A.1 *Cubic harmonics*

The cubic harmonics (CH) $K_{lm}(q_1,q_2,q_3)$ (note: $\Sigma_{i=1}^{3} q^2 = \rho^2$; $l = 0, 1, 2, \ldots$, and $-l \leq m \leq l$, with $m \in \mathfrak{Z}$) form a complete orthogonal basis for the continuous functions defined on the sphere $S^2(\rho)$ with radius ρ. The CH are symmetry adapted to the cubic symmetry (20). To allow easy comparison of the explicit expressions used here and those listed elsewhere (20–23) we give K_{00}, K_{41}, and K_{61} explicitly:

$$K_{00}(q_1,q_2,q_3) = 1$$

$$K_{41}(q_1,q_2,q_3) = N_{41}\cdot\left(\sum_{i=1}^{3} q_i^4 - \frac{3}{5}\rho^4\right)$$

[24] $$\text{with} \quad N_{41} = \frac{5\sqrt{21}}{4}$$

$$K_{61}(q_1,q_2,q_3) = N_{61}\cdot\left(q_1^2q_2^2q_3^2 + \frac{1}{22N_{41}}K_{41}\cdot\rho^2 - \frac{1}{105}\rho^6\right)$$

$$\text{with} \quad N_{61} = \frac{231\sqrt{26}}{8}$$

With the abbreviation $\partial_i = \partial/\partial q_i$ and the use of the summation convention ($i = 1, 2, 3$), we summarize several important facts about the CH:

1. "harmonic" means: $\partial_i\partial_i K_{lm}(q_1,q_2,q_3) = 0$

2. K_{lm} is homogeneous of degree l: $K_{lm}(\lambda q_1,\lambda q_2,\lambda q_3) = \lambda^l\cdot K_{lm}(q_1,q_2,q_3)$. It follows that $q_i\partial_i K_{lm}(q_1,q_2,q_3) = l\cdot K_{lm}(q_1,q_2,q_3)$.

3. Using properties 1 and 2, and the product rule, one can easily see that K_{lm} is an eigenfunction of the angular part of the three-dimensional Laplacian (A.3) with the eigenvalue $-l(l+1)\cdot\rho^{-2}$. This property, together with symmetry considerations, provides a simple method of generating the K_{lm} as polynomials in q_1, q_2, and q_3 (degree l).

4. The K_{lm} are orthogonal in the sense:

[25] $$\frac{1}{4\pi}\oint_{S^2(\rho)} dq_1dq_2dq_3K_{lm}K_{jn} = \delta_{lj}\delta_{mn}\cdot\rho^{l+j+3}$$

5. A very useful formula (24):

[26] $$\frac{1}{4\pi}\oint_{S^2(\rho)} dq_1dq_2dq_3q_1^{2a}q_1^{2a}q_3^{2c} = \frac{(2a-1)!!(2b-1)!!(2c-1)!!}{(2a+2b+2c+1)!!}\cdot\rho^{2a+2b+2c+3}$$

where $a,b,c \in \mathcal{N}$. The integral would be zero if at least one exponent were odd.

6. The CH can be expressed as linear combinations of the spherical harmonics. These linear combinations are listed in ref. 22 up to $l_{max} = 12$ and in ref. 23 up to 21.

A.2 *The kinetic energy operator*

The mathematical description of the orientation of a rigid body obviously involves the rotation group SO_3. Instead, we can use the (unitary) group SU_2, because of the isomorphism between SO_3 and the quotient group $SU_2/\{\iota,-\iota\}$.[7] The SU_2 group manifold is the sphere S^3 ($\subset \mathfrak{R}^4$); antipodes of S^3 correspond to the same physical orientation of the body.

It follows that the physical rotation of a (rigid) body is equivalent to the motion of a mass point confined to S^3. This illustrates that the operator $\hat{T}$ of the kinetic energy (abandoning the translational degrees of freedom) is proportional to the angular part of the four-dimensional Laplacian (A.3). The explicit expression [25] for $\hat{T}$ is highly symmetric if it is written[8] in the Cartesian coordinates of the S^3 points ($q_iq_i = 1$):

[27] $$\hat{T} = -\frac{B}{4}(\partial_i\partial_i - 3q_i\partial_i - q_iq_j\partial_i\partial_j) \quad \text{with} \quad i,j = 1,2,3,4$$

The Cartesian coordinates of the S^3 points constitute the so-called elements of the (real) quaternion $q = (q_1,q_2,q_3,q_4)$.

Another set of coordinates $(q_1,q_2,q_3,\rho) = r(q)$ with $\rho = \sqrt{1-q_4^2}$ ($\Sigma_{i=1}^{3} q_i^2 = \rho^2$ follows) is more appropriate to be used in expansions around the standard orientation $q^s = (0,0,0,1)$, $r(q^s) = (0,0,0,0)$, respectively. By means of the chain rule, one can easily apply $\hat{T}$ to functions of the new coordinates. We give a very useful formula:

[28] $$\hat{T}f(\rho)K_{lm}(q_1,q_2,q_3) = \frac{B}{4}K_{lm}(q_1,q_2,q_3)\hat{U}_lf(\rho)$$

[7] The identity element of SU_2 is denoted ι and is written $(0,0,0,1)$ in the quaternionic representation; $-\iota \Leftrightarrow (0,0,0,-1)$.

[8] We use the summation convention; ∂_i denotes the partial derivative with respect to q_i.

where the operator $\hat{U}_l$ is defined as follows:

$$[29]\quad \hat{U}_l = (\rho^2 - 1)\frac{\partial^2}{\partial\rho^2} + \left((2l+3)\rho - 2\frac{l+1}{\rho}\right)\frac{\partial}{\partial\rho} + l(l+2)$$

The proof of eq. [28] is based on the properties no. 2 and no. 3 (A.1) of the cubic harmonics K_{lm}.

A.3 *Angular part of the* d*-dimensional Laplacian*

Let $x_1, \ldots, x_d$ be the Cartesian coordinates in $\mathcal{R}^d$ and denote the partial differentiation with respect to x_i by ∂_i; we use the summation convention. The d-dimensional Laplacian then reads $\partial_i\partial_i$. Its radial part (15) is given by

$$[30]\quad R_{(d)} = \frac{1}{r^{d-1}}\frac{\partial}{\partial r}\left(r^{d-1}\frac{\partial}{\partial r}\right)$$

where $r^2 = x_i x_i$. Applying the chain rule, we obtain $R_{(d)}$ expressed in Cartesian coordinates:

$$[31]\quad R_{(d)} = \frac{1}{r^2}\cdot((d-1)x_i\partial_i + x_i x_j \partial_i\partial_j)$$

The difference $\partial_i\partial_i - R_{(d)}$ constitutes the angular part of the d-dimensional Laplacian.

A.4. *The cubic rotor functions* H^3_{l1}, H^4_{l1}, *and* H^6_{l1}

The $(NH_4)_2SnCl_6$ model potentials (Table 5) are given as linear combinations of the following cubic rotor functions (21):

$$H^3_{11}(q) = 2^4\sum q_i^6 - 2^2\cdot 5\sum q_i^4 + 5$$

$$H^4_{11}(q) = \frac{2^4\cdot 5}{3}\sum q_i^8 - \frac{2^4\cdot 5\cdot 7}{3^2}\sum q_i^6 + \frac{2^2\cdot 5\cdot 7}{3}\sum q_i^4 + \frac{2^6\cdot 5\cdot 7}{3}q_1^2q_2^2q_3^2q_4^2 - \frac{91}{3^2}$$

$$[32]\quad H^6_{11}(q) = \frac{2^5\cdot 7\cdot 11}{3}\sum q_i^{12} + \frac{2^6\cdot 7\cdot 11}{3}[q_1^6(q_2^6+q_3^6+q_4^6) + q_2^6(q_3^6+q_4^6) + q_3^6q_4^6] - 2^5\cdot 7\cdot 11\sum q_i^{10} + 2^3\cdot 3^2\cdot 5\cdot 7\sum q_i^8 - 2^5\cdot 3\cdot 5\cdot 7\cdot q_1^2q_2^2q_3^2q_4^2 - \frac{2^6\cdot 5\cdot 7}{3}\sum q_i^6 - 2\cdot 3\cdot 5\cdot 7\sum q_i^4 + \frac{241}{3}$$

Notation: Σ abbreviates $\Sigma_{i=1}^4$.

Can. J. Chem. Downloaded from www.nrcresearchpress.com by 176.9.209.113 on 09/07/12
For personal use only.

Phase transitions in the organic semiconductor dipropylamine tetracyanoquinodimethane: DPA $TCNQ_2$

ANDRÉ D. BANDRAUK, KIM D. TRUONG, AND MARCEL AUBIN
Groupe de Recherche sur les Semiconducteurs et Diélectriques, Faculté des Sciences, Université de Sherbrooke, Sherbrooke (Qué.), Canada J1K 2R1

Received September 29, 1987

This paper is dedicated to Professor J. A. Morrison

ANDRÉ D. BANDRAUK, KIM D. TRUONG, and MARCEL AUBIN. Can. J. Chem. **66**, 938 (1988).

Dipropylamine tetracyanoquinodimethane, DPA $TCNQ_2$, is by stoichiometry a 1:2 organic salt giving rise to a $\frac{1}{4}$ filled band quasi one dimensional electronic system. Conductivity measurements indicate the presence of at least three phase transitions. A dominant transition at 215 K shows simultaneous large discontinuities in both electric and magnetic properties. Infrared measurements suggest a structural change at 215 K related to conduction electron–molecular vibration interactions in view of the appearance of A_g TCNQ modes in the infrared spectrum. Deuteration of the donor $\overset{+}{N}$—H bond lowers the main transition temperature by 5 K but maintains the same physical properties as in the nondeuterated compound.

ANDRÉ D. BANDRAUK, KIM D. TRUONG, et MARCEL AUBIN. Can. J. Chem. **66**, 938 (1988).

Le dipropylamine tétracyanoquinodiméthane (DPA $TCNQ_2$) est un sel organique de stoechiométrie 1:2 qui donne lieu à un système électronique quasi-unidimensionnel comportant une bande qui n'est remplie qu'au $\frac{1}{4}$. Des mesures de conductivité suggèrent la présence d'au moins trois transitions de phases. Une transition dominante à 215 K présente des discontinuités simultanées importantes tant dans les propriétés électriques que magnétiques. Des mesures infrarouges permettent de voir apparaître les modes A_g du TCNQ et suggèrent qu'il se produit un changement de structure à 215 qui est relié à des interactions de vibration de conduction électron–molécule. La deutération de la liaison donneur N—H diminue par 5 K la température d'apparition de la transition principale; toutefois, on retrouve les mêmes propriétés physiques que celles du produit non-deutéré.
[Traduit par la revue]

Introduction

Investigation of organic charge transfer salt has proven to be very useful for an adequate understanding of the physical properties of low dimensional electronic systems. In particular the organic salts of the strong acceptor TCNQ give rise to varied stoichiometries and hence unusual fillings of the quasi one dimensional electronic bands arising from the segregated stacking of the acceptor molecules face-to-face in the crystal. This geometry produces quasi one dimensional π-electron networks, and thus gives rise to highly anisotropic electric and magnetic properties of these systems (1).

Of current interest is the influence of the counterions, i.e., donors in the case of TCNQ salts, on these properties. As an example, we have been able to show via Resonance Raman Spectroscopy of crystals of the ternary system TMAITCNQ (trimethylammonium iodide TCNQ) that a semimetal–semiconductor phase transition occurring in this system involves coupling of a chain of I_3 counterions to the conducting $TCNQ^-_{2/3}$ stacks (2). In other examples, we have found hydrogen-bonding to be a determining factor for the occurrence of parallel or non-parallel stacking of acceptors in the crystal (3–5).

In the present case we investigate the electric and magnetic properties of a 1:2 organic charge transfer salt of dipropylamine (DPA) with TCNQ. One expects as a result of the stoichiometry that each TCNQ will acquire a ¼ electric charge and crystallize in one dimensional arrays of $TCNQ^{-\frac{1}{2}}$ ions separated by the donor, as occcurs in the well studied TEA (triethylamine) (6) and MEM (methylethylmorpholinium) $TCNQ_2$ systems (7, 8). In the limit of weak electronic correlations ($U \rightarrow 0$, where U is the on-site electronic repulsion in the Hubbard model (9)), such systems have $\frac{1}{4}$ filled electronic bands and are expected to undergo an electronic instability, called the electronic Peierls transition leading to a phase transition between a metallic and a semiconducting state. The metallic state is characterized by a nearly temperature-independent conductivity whereas the semiconducting state has an activated conductivity. In the lower temperature semiconducting state one expects tetramerization ($2k_F$ periodicity, where k_F is the metallic state Fermi level) of the uniform metallic stacks, with two electrons per tetrameter. Large electron–electron repulsion (U) will suppress this tendency to form tetramers with the end result that a dimerized structure ($4k_F$) will be preferred. This has been observed in MEM $TCNQ_2$ at high temperatures. Of note is that the magnetic susceptibility remains unaffected in the above compound at the $4k_F$ or metal–dimer phase transition, although a large conductivity change is observed, and the electronic spin system behaves as an antiferromagnetic system in the dimerized phase (hopping of alternating spins between the dimers). This antiferromagnetic behaviour of dimerized chains with one charge per dimer is also well documented in the TMTSF (tetramethylselenofulvalene) salts where the now positive organic chains can give rise to superconductivity at low temperatures (10). Common to all these systems is the appearance of a magnetic phase transition at much lower temperatures than the first transition described above. At these low temperatures, one finds a disappearance of the magnetic susceptibility accompanied by a slight tetramerization. This is called a spin–Peierls transition ($2k_F$), since it is clear that it is the magnetic (spin energies) which drive the quasi one-dimensional electronic system to this new instability.

Theoretical studies of finite rings of degenerate electronic systems show that the electronic repulsion U regulates the temperature of the $4k_F$ and $2k_F$ phase transitions (11). At large U, one expects the $4k_F$ electronic transition to occur at high temperatures, whereas the $2k_F$ magnetic transition should occur at very low temperatures. This is the case of MEM $TCNQ_2$ (7–9, 11). Our studies on the DPA $TCNQ_2$ system, reported below, indicate an important phase transition at 215 K. Of note is that we found both electric and magnetic properties to change simultaneously at that temperature, contrary to the MEM

Can. J. Chem. Downloaded from www.nrcresearchpress.com by 176.9.209.113 on 09/07/12
For personal use only.

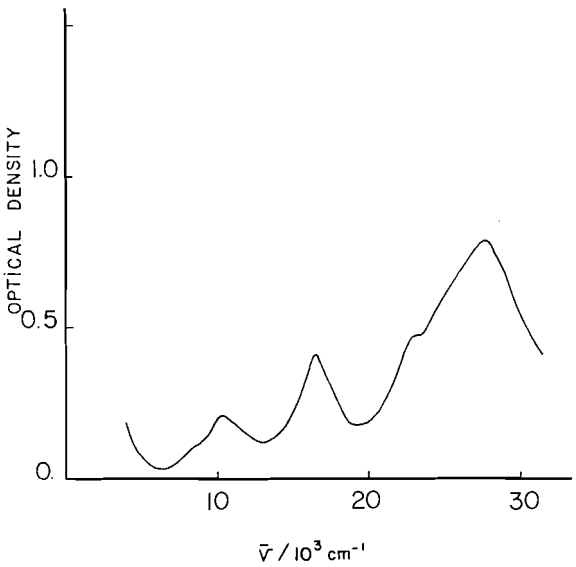

FIG. 1. Electronic absorption spectrum of DPA $TCNQ_2$ crystals in KBr pellets at room temperature.

$TCNQ_2$ case where the sharp electronic conductivity variation occurs at 335 K and the magnetic susceptibility essentially vanishes at 19 K. We report in the remainder of this paper the details of this finding on the DPA compound.

Experimental results

(i) Preparation

DPA $TCNQ_2$ was synthesized from the monoiodide of dipropylamine mixed with recrystallized TCNQ in distilled acetonitrile. The resulting reaction

[1] $H_2(CH_3—CH_2—CH_2)_2\overset{+}{N}I^- + 2TCNQ \rightarrow H_2(CH_3CH_2CH_2)_2\overset{+}{N}[TCNQ_2]^- + \frac{1}{3}I_3^-$

gave in solution black needles. Chemical analysis of the recrystallized needles confirmed the 1:2 stoichiometry between the dipropylamine (DPA) donor and the TCNQ acceptor (theoretical % value in parentheses):

C = 70.51 (70.59; H = 4.86 (4.70); N = 24.78 (24.70)

Deuteration of the nitrogen in DPA was achieved by preparing the monoiodide with DI acid, giving DPAd $TCNQ_2$.

(ii) Spectra

Ultraviolet, visible, and ir spectra were obtained from pressed KBr pellets of the compound, following the procedures in our previous work (3). In Fig. 1 we illustrate the electronic spectrum. The strong bands at 27800 cm^{-1} and 16500 cm^{-1} are usually attributed to TCNQ localised electronic excitations. The lower bands at 10200 cm^{-1} and ~3000 cm^{-1} are attributed to charge transfer bands between the TCNQ ions (12). The low energy electronic band at 3000 cm^{-1} is typical of mixed valence systems, and presages nonnegligible conductivities.

In Fig. 2 we illustrate the infrared spectra at room temperature and at 150 K, i.e., below the phase transition. A noticeable sharpening and splitting is observed below the transition temperature. Prominent vibrations appear at 150 K at frequencies 2170, 1560, 1410 cm^{-1}. These are usually attributed to TCNQ A_g modes, which are activated by conduction – electron vibration couplings (13, 14). These and other vibrations are tabulated in Table 1.

TABLE 1. $TCNQ^{-1/2}$ vibrations in DPA $TCNQ_2$ at 298 K and 150 K

298 K	150 K*	Assignment (ref. 3)
2190	2204	
2160	2195	
	2170 (s)	C≡N (A_g, ω_2)
	2165	
1550	1582, 1580	
1500	1570	
	1560 (s)	C=C(A_g, ω_3)
	1545, 1538	
	1510, 1502	
	1475, 1445	
1360	*1410* (s)	C—H (A_g, ω_4)
1340	1370	
1300	1320	
1180	1190, 1180	
1100	1150	
950	960, 950	
860	860, 840	
830	830	
750	760, 740	
690	700	

*(s) = strong.

(iii) Electrical properties

The electrical resistivity was measured on single crystals along the needle axis using standard four probe silver contacts (4).

The resistivity of DPA $TCNQ_2$ was found at room temperature to be 0.07 Ωm, increasing gradually upon lowering the temperature. Such behaviour is characteristic of a semiconductor, possessing an electronic energy gap E_g, for which we can write

[2] $$\ln \rho = \ln A + \frac{E_g}{2kT}$$

In Fig. 3 we present a graph of ln ρ vs. $10^3/T$. Three transitions are readily identified at 215, 245, and 302 K. The gap energies can be determined from eq. [2] as:

$$E_g\,(T \geq 302\text{ K}) = 0.14\text{ eV}$$

$$E_g\,(280\text{–}302\text{ K}) = 0.81\text{ eV}$$

$$E_g\,(215\text{–}245\text{ K}) = 0.33\text{ eV}$$

$$E_g\,(T \leq 215\text{ K}) = 0.3\text{ eV}$$

The largest resistivity change occurs at T_c = 215 K, with an increase of 6.1 Ωm at 214 K to 31.5 Ωm at 216 K.

Measurements were also performed, Fig. 4, on single crystals of the deuterated compound DPAd $TCNQ_2$, where deuteration of the $\overset{+}{N}$—H bond is expected to occur following the preparation described above. Room temperature conductivity is similar to the nondeuterated compound, 0.09 vs. 0.07 Ωm. The largest conductivity change is similar, 7.7 Ωm at 209 K and 39.3 Ωm at 212 K. The corresponding phase transition now occurs at T_c = 210 K as opposed to 215 K for the nondeuterated compound.

Changes in slope for ρ (eq. [2]), are observed also at 255 K and 295 K. The corresponding activation energies for the deuterated compound are:

Can. J. Chem. Downloaded from www.nrcresearchpress.com by 176.9.209.113 on 09/07/12
For personal use only.

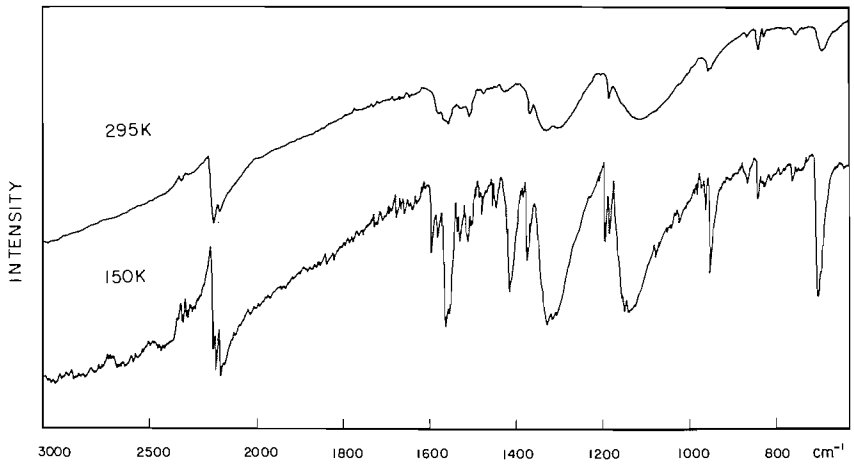

FIG. 2. Infrared spectra of DPA $TCNQ_2$ in KBr pellets at 295 and 150 K.

$$E_g\,(T \geq 295\text{ K}) = 0.2\text{ eV}$$
$$E_g\,(260\text{–}290\text{ K}) = 0.7\text{ eV}$$
$$E_g\,(210\text{–}250\text{ K}) = 0.17\text{ eV}$$
$$E_g\,(T \leq 210\text{ K}) = 0.15\text{ eV}$$

When compared to the nondeuterated compound, we note that the transition temperatures are now lowered by about 5 K in the deuterated compound. In particular, the low temperature E_g is about *half* of that observed in the nondeuterated compound.

(*iv*) *Electron spin resonance*

Integrated intensities are reported in Figs. 5 and 6 for the nondeuterated and deuterated compounds respectively. Measurements were performed on fine powders of the sample as a function of temperature between 140 and 360 K, with a temperature precision of ±5 K. A strong signal is observed at room temperature with a g factor of 2.0021 and there was no evidence of fine structure. The integrated intensity of the signal decreases monotonically from 295 to 220 K. Between 210 and 200 K an abrupt decrease in intensity is observed. At lower temperatures, the temperature variation becomes regular again. The esr spectrum actually consists of two lines below the transition temperature T_c = 215 K, which gradually merge into one line at the transition. This suggests that in the low temperature phase one is observing inequivalent TCNQ's.

The sharp variation of the esr line and intensity around the same temperature where a sharp decrease in conductivity occurs, i.e., at T_c = 215 K is indicative of an abrupt change in magnetic activation energy. We shall assume an activated form for the esr intensity, which is characteristic of linear chains of spins with antiferromagnetic alternating interactions (15, 16),

$$[3] \quad I = (C/T)\exp -(J/kT)$$

where J is the exchange energy between neighbouring spins. Alternatively one could have chosen the exact expression for the magnetic susceptibility of a localized singlet–triplet system (9),

$$[4] \quad \chi_{ST} = \frac{C}{T}\,[3 + \exp(2J/kT)]^{-1}$$

For large J or low T, this expression also describes an activated behaviour, as in the antiferromagnetic expression [3]. Fitting eq. [3] to Fig. 5 above and below the transition temperature, T_c

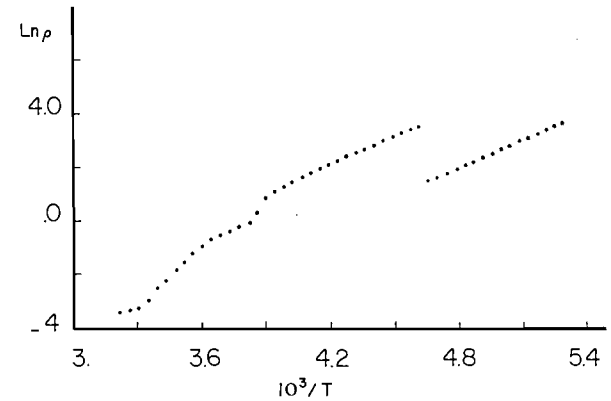

FIG. 3. Temperature dependence of resistivity ρ (Ωm) for DPA $TCNQ_2$.

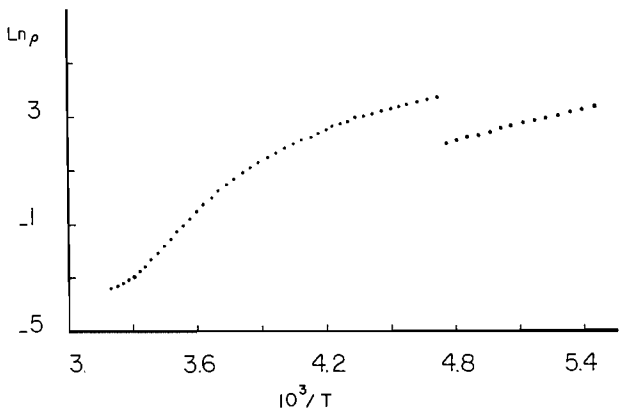

FIG. 4. Temperature dependence of resistivity ρ (Ωm) for deuterated DPAd $TCNQ_2$.

= 215 K we obtain for DPA $TCNQ_2$:

$$J(T \geq T_c) = 0.018\text{ eV}; \qquad J(T \leq T_c) = 0.044\text{ eV}$$

and for DPAd $TCNQ_2$, T_c = 210 K (Fig. 6),

$$J(T \geq T_c) = 0.013\text{ eV}; \qquad J(T \leq T_c) = 0.044\text{ eV}$$

Clearly, in both nondeuterated and deuterated compounds the magnetic excitation energies J are similar, and the low temperature phase exhibits a larger exchange energy.

Can. J. Chem. Downloaded from www.nrcresearchpress.com by 176.9.209.113 on 09/07/12
For personal use only.

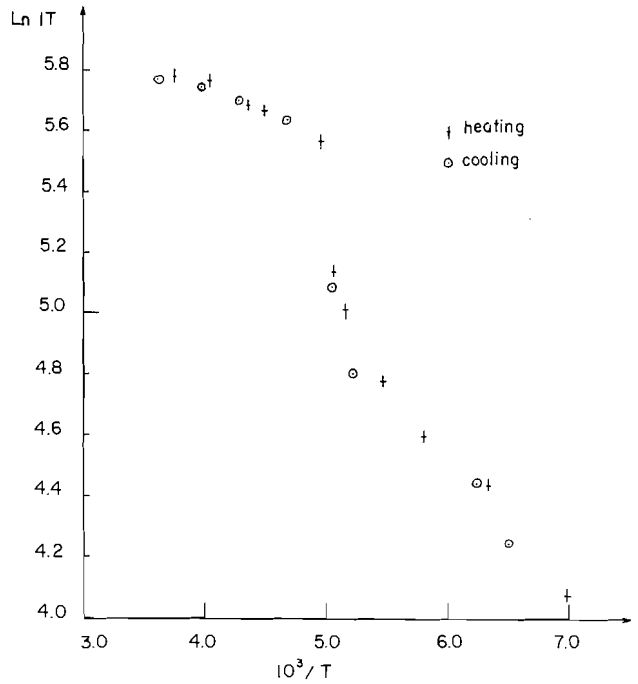

FIG. 5. Temperature dependence of integrated esr intensity $I \times T$ for DPA $TCNQ_2$.

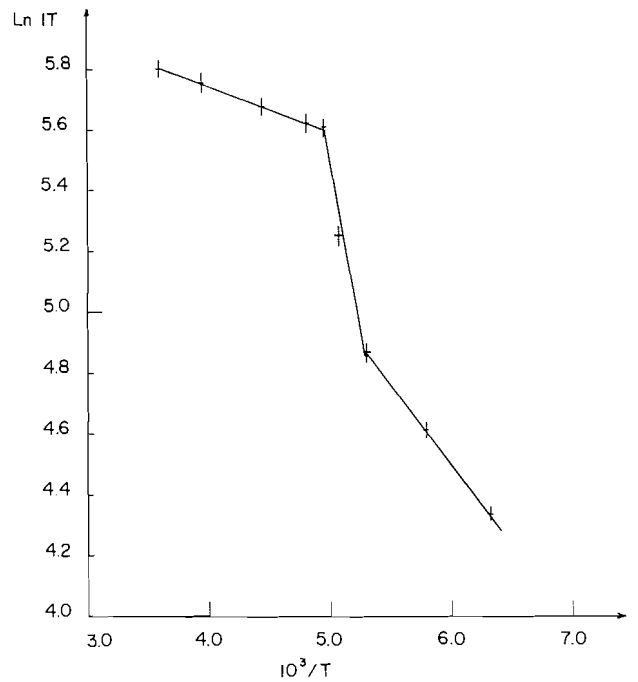

FIG. 6. Temperature dependence of integrated esr intensity $I \times T$ for deuterated DPAd $TCNQ_2$.

Discussion

The conductivities of both the deuterated and nondeuterated compounds indicate three distinct regions of electronic behaviour: a high temperature semiconducting phase above 300 K with small activation energy, an intermediate phase between 300 and 250 K with a large anomalous activation energy and a low temperature semiconducting phase below 215 K with moderate activation energy. It is only in this low temperature phase that the conduction activation energies of the deuterated and nondeuterated compounds differ by a factor of 2, suggesting the importance of hydrogen bonding between donor and acceptor chains at low temperatures.

It is also only the lower temperature phase transition T_c (210, 215 K) which shows simultaneous discontinuities in electric and magnetic properties. We emphasize that both electronic conductivities and esr signals change abruptly when crossing below T_c, indicating that these are sharp transitions. The other two transitions occurring at higher temperatures are less well defined, and may probably be continuous transitions due to the gradual onset of order in the donor chain, as in the case of MEM $TCNQ_2$ (7, 8). These may be second-order transitions, for which the quoted activation energies may not be physical. Further clarification of this region is required.

Preliminary X-ray studies of our compound indicate that the TCNQ chains are slightly dimerized and that the donor DPA molecules are indeed disordered at room temperature (17). Thus our treatment in the previous section of the room temperature phase as an antiferromagnet with electrons exchanging dimer sites concurs with the stoichiometry of the system and the X-ray data, leading to a low exchange energy. At the lower temperature, a tripled exchange energy is observed, suggesting stronger interactions, as a result of increased overlap between adjacent molecules in a contracting lattice. The onset of sharp A_g modes in the infrared spectrum below T_c and the complication of the spectrum is further suggestive of a structural transition whereby the electrons are more localized (13, 14).

Our compound behaves in many respects like another 1:2 TCNQ salt, DMM (dimethylmorpholinium) $TCNQ_2$ in its monoclinic phase (18). This compound exists at room temperature in the form of dimerized TCNQ chains (19). At high temperatures (475 K), a transition is observed suggestive of a $4k_F$ transition to uniform chains as in MEM $TCNQ_2$. Below T_c = 260 K, the chains are tetramerized, indicative of a spin–Peierls or $2k_F$ transition (20). At temperatures below T_c, two lines are observed in the esr spectrum which gradually merge at T_c. We have observed this same phenomenon in DPA $TCNQ_2$ which suggests the appearance of inequivalent TCNQ's at the lower temperatures.

However, contrary to the present DPA compound, DMM $TCNQ_2$ does *not* show a discontinuity in its esr intensity at T_c, i.e., the spin–Peierls transition does not seem to be observed in the temperature dependence of the magnetic susceptibility in the latter. This is explained as due to weak coulomb correlations U or large hopping (transfer), t, of electrons between adjacent sites (18), i.e., the system behaves like an antiferromagnet. Following this argument, we would conclude that DPA $TCNQ_2$ is a large U and small t system, as in MEM $TCNQ_2$. If such were the case, one would have expected conductivity and magnetic susceptibilities anomalies to occur at much different temperatures. Thus DPA $TCNQ_2$ does not follow this simple rule which distinguishes $4k_F$ and $2k_F$ transitions.

In conclusion, we emphasize that DPA $TCNQ_2$, a semiconductor, exhibits simultaneous discontinuities in its electrical and magnetic properties at T_c = 210 K. This is indicative of simultaneous electronic and spin–Peierls transitions. A similar phenomena has been observed recently in the compound $(BEDT\text{–}TTF)_3(ClO_4)_2$ (BEDT–TTF = bis(ethylenedithiols)-tetrafulvalene) which undergoes a metal–insulator phase transition at 171 K with simultaneous sharp drops in conductivity and magnetic susceptibilities (21). The origin of this phase transition is not known. Both compounds above, indicate from their magnetic data a strong localisation of the spins at low temperatures. The dynamics of the accomanying structural transition

Can. J. Chem. Downloaded from www.nrcresearchpress.com by 176.9.209.113 on 09/07/12
For personal use only.

which induces a simultaneous large change in the conductivity and magnetic susceptibility needs to be further explored by careful temperature dependent X-ray and nmr studies of the present and analogous systems.

Acknowledgments

This research was partly financed by the Research and Development Branch of the Department of National Defence (DND) under Contract 8SD85-00313.

We wish to particularly thank Dr. J. Morrison for his precious advice and continuing support of GRSD in his role as scientific consultant to DND.

1. H. MEIER. Organic conductors. Verlag Chemie, Berlin. 1974.
2. A. D. BANDRAUK, K. D. TRUONG, C. CARLONE, and S. JANDL. Chem. Phys. Lett. **95**, 78 (1983); J. Phys. **44**(C-3), 1473 (1983).
3. A. D. BANDRAUK, K. D. TRUONG, C. CARLONE, S. JANDL, and K. ISHII. J. Phys. Chem. **89**, 434 (1985).
4. A. D. BANDRAUK, K. ISHII, K. D. TRUONG, M. AUBIN, and A. W. HANSON. J. Phys. Chem. **89**, 1478 (1985).
5. A. D. BANDRAUK, K. D. TRUONG, C. CARLONE, and A. W. HANSON. J. Phys. Chem. **91**, 2063 (1987).
6. A. FILHOL and M. THOMAS. Acta Crystallogr. B**40**, 44 (1984).
7. B. V. BODEGOM and A. BOSCH. Acta Crystallogr. B**37**, 833 (1981).
8. R. J. VISSER, S. OOSTRA, C. VETTIER, and J. VOIRON. Phys. Rev. B**28**, 2074 (1983).
9. J. S. PEDERSEN and K. CARNEIRO. Rep. Prog. Phys. **50**, 995 (1987).
10. C. BOURBONNAIS. *In* Low-dimensional conductors and superconductors. *Edited by* D. Jerome and L. G. Caron. NATO ASI vol. B155. Plenum Press, NY. 1987. pp. 155–184.
11. J. KOMMANDEUR. *In* Low-dimensional conductors and superconductors. *Edited by* D. Jerome and L. G. Caron. NATO ASI vol. B155. Plenum Press, NY. 1987. pp. 87–94.
12. J. B. TORRANCE. Acc. Chem. Res. **12**, 79 (1979).
13. M. J. RICE, V. M. YARTSEV, and C. S. JACOBSEN. Phys. Rev. B**21**, 3437 (1980).
14. A. D. BANDRAUK. *In* Low-dimensional conductors and superconductors. *Edited by* D. Jerome and L. G. Caron. NATO ASI vol. B155, Plenum Press, NY. 1987. pp. 295–306.
15. J. TANAKA, M. INOUE, M. MIZUNO, and K. HORAI. Bull. Chem. Soc. Jpn. **43**, 1998 (1970).
16. L. N. BULAEVSKII. Solid State (Soviet Phys.) **11**, 921 (1969).
17. A. W. HANSON. To be published.
18. C. F. SCHWERDTFEGER, S. OOSTRA, R. J. VISSER, and G. A. SAWATZKY. Solid State Commun. **39**, 1133 (1981).
19. P. KAMINGA and B. VANBOGEDOM. Acta Crystallogr. B**37**, 114 (1981).
20. J. A. M. MIDDELDORP, R. J. J. VISSER, and J. L. DE BOER. Acta Crystallogr. B**41**, 369 (1985).
21. S. S. PARKIN, M. MILJAK, and J. R. COOPER. Phys. Rev. B**34**, 1485 (1986).

Can. J. Chem. Downloaded from www.nrcresearchpress.com by 176.9.209.113 on 09/07/12
For personal use only.

Static and dynamic properties of hydrogen sulphide in hydroquinone clathrates

HARUTOSHI UKEGAWA,[1] TAKASUKE MATSUO, AND HIROSHI SUGA
Department of Chemistry and Chemical Thermodynamics Laboratory, Faculty of Science, Osaka University, Toyonaka, Osaka 560, Japan

ALAN J. LEADBETTER[2] AND RICHARD C. WARD
Rutherford Appleton Laboratory, Chilton, Didcot, OX11 0QX, England

AND

JON W. CLARK[3]
University of Exeter, Exeter, EX4 4QD, England

Received August 26, 1987

This paper is dedicated to Professor James A. Morrison

HARUTOSHI UKEGAWA, TAKASUKE MATSUO, HIROSHI SUGA, ALAN J. LEADBETTER, RICHARD C. WARD, and JON W. CLARK. Can. J. Chem. **66**, 943 (1988).

A variety of investigations has been undertaken on hydrogen sulphide hydroquinone clathrates, with the aim of achieving a better understanding of the motions of the guest molecules and of the phase transition near 8 K. Measurements have been made, over a wide temperature range including the phase transition, of heat capacities on H_2S, D_2S, and HDS clathrates, dielectric constants perpendicular and parallel to the trigonal axis of single crystal specimens, incoherent quasi-elastic neutron scattering, and neutron diffraction. All of the data are consistent with the H_2S molecular dipole being able to rotate rather easily about an axis parallel to the trigonal crystal *c* axis. Rotations about the other axes are much more difficult. The rotation about the trigonal axis is almost free at high temperatures but there is evidence for three preferred orientations at temperatures just above the phase transition. No discrete energy states are observed at any temperature due to strong guest–cage and guest–guest interactions. The experiments provide direct evidence that the phase transition is associated with a cooperative freezing out of the dipole reorientations.

HARUTOSHI UKEGAWA, TAKASUKE MATSUO, HIROSHI SUGA, ALAN J. LEADBETTER, RICHARD C. WARD et JON W. CLARK. Can. J. Chem. **66**, 943 (1988).

Afin de parvenir à une meilleure compréhension des mouvements des molécules hôtes ainsi que de la phase de transition autour de 8 K, on a entrepris une série d'études sur les clathrates du sulfure d'hydrogène/hydroquinone. Opérant sur un large éventail de températures, y compris celle de la transition de phase, on a fait des mesures relatives aux capacités calorifiques des clathrates du H_2S, du D_2S ainsi que du HDS, aux constantes diélectriques perpendiculaire ainsi que parallèle à l'axe trigonal d'échantillons de cristaux uniques, à la dispersion neutronique quasi-élastique incohérente ainsi qu'à la diffraction des neutrons. Toutes les données sont en accord avec le fait que le dipôle moléculaire du H_2S pourrait effectuer des rotations faciles autour d'un axe parallèle à l'axe trigonal-*c* du cristal. Les rotations autour des autres axes sont beaucoup plus difficiles. À des températures plus élevées, la rotation autour de l'axe trigonal est pratiquement libre; toutefois, juste au-dessus de la transition de phase, il semble exister trois orientations préférées. À cause des fortes interactions qui existent soit entre l'hôte et la cage ou entre l'hôte et l'hôte, aucun état d'énergie défini n'a pu être observé sur tout l'éventail de températures étudiées. Les expériences fournissent toutefois des preuves directes à l'effet que la transition de phase est associée avec une élimination coopérative des réorientations des dipôles.

[Traduit par la revue]

Introduction

In the hydroquinone clathrate compounds, various kinds of small molecules are encaged in nearly spherical cavities of free diameter ca. 0.4 nm (1). The cavity wall, formed by six benzene rings on the side and two six-membered rings of hydrogen-bonded oxygen atoms top and bottom, is rather rigid and retains otherwise volatile guest molecules firmly in the cavities. The rigidity of the cavity wall is demonstrated by the formation of non-stoichiometric clathrate solutions Q_3G_x (where Q is the hydroquinone and G the guest molecule) of the same structure over a wide range of values of x, and also by the constancy of the unit cell size for guest molecules smaller than methanol (2). The translational vibrations of the guest molecule in such a cavity are highly anharmonic and may be described as a rattling motion. For diatomic and polyatomic guest molecules, their rotational vibration is also anharmonic, approaching free rotation in the low-barrier limit. These properties, which depend on the interaction of a guest molecule with a host cavity, have been studied calorimetrically and spectroscopically (3–5).

Occurrence of phase transitions in the hydroquinone clathrate compounds was first reported for the methanol and hydrogen cyanide compounds (6, 7). The role played by the guest–guest interaction was stressed there. In these compounds, the guest–host interactions are also important, as the appreciable dielectric loss indicates the presence of a barrier to rotation whose origin is primarily the guest–host interaction. Various aspects of the guest–host and guest–guest interactions and their connection to the molecular motion have been reviewed in refs. 8 and 9.

The rigidity of the host lattice gives rise to the possibility of studying the properties of an assembly of small molecules in an unusual situation: the guest molecules are quasi-free to move and rotate in the cavity but they can also interact with each other through angle-dependent potentials without coming in direct contact with each other (10). In the present paper, we report calorimetric, dielectric, and neutron scattering studies of the hydroquinone clathrates of H_2S, D_2S, and HDS guest mole-

[1]Present address: Sumitomo Electric Industry Limited, Konohana-ku, Osaka, Japan.

[2]Author to whom correspondence may be addressed.

[3]Present address: Duracell Batteries Limited, Mallory House, Gatwick Road, Crawley, West Sussex, RH10 2PA, England.

Can. J. Chem. Downloaded from www.nrcresearchpress.com by 176.9.209.113 on 09/07/12
For personal use only.

cules. These were undertaken with a view to reaching a better understanding of the behaviour of the enclathrated molecules and of the phase transitions that occur when the guest molecules are polar (11). Some of the experimental results on the H_2S compound have been published elsewhere (10).

Experimental

Sample preparation

All the samples were prepared according to the method described in ref. 2. For the D_2S clathrate $[C_6H_4(OD)_2]_3\cdot(D_2S)_x$, the hydroxyl group of hydroquinone was deuterated by repeated recrystallization from D_2O. D_2S was prepared from Al_2S_3 according to the reaction :

$$Al_2S_3 + 6D_2O \rightarrow 2Al(OD)_3 + 3D_2S$$

The D_2S clathrate was then prepared in the same way as for the normal compound with care being taken to avoid contamination from atmospheric moisture. The half-deuterated clathrate $[C_6H_4(OH)(OD)]_3\cdot(HDS)_x$ was also prepared, using an equimolar mixture of the normal and hydroxyl-deuterated hydroquinone and half-deuterated hydrogen sulphide. The latter was prepared from Al_2S_3 and an H_2O–D_2O mixture. The half-deuterated clathrate thus prepared had H_2S, HDS, and D_2S as the guest molecules with the statistical ratio 1:2:1.

The heat capacity measurement showed the presence of water occluded in the sample crystal. The amount of water impurity determined from the heat capacity peak due to its melting was 0.23 mass percent for the hydrogenous compound and 0.13 mass percent for the deuterated compound, and these were taken into account in the heat capacity reduction.

The extent of deuteration was examined by Raman spectroscopy. The Raman active ν_1 occurred at 2588 cm^{-1} for the H_2S and at 1875 cm^{-1} for the D_2S clathrate. For the half-deuterated clathrate, the guest spectra also occurred at 2588 and 1875 cm^{-1} with nearly the same intensities, but both were broader than the spectrum of the single component clathrate. From the absence of the H–SD stretching frequency in the clathrate of the D_2S clathrate, the deuteration was estimated to be better than 96%.

For the neutron diffraction experiment, a completely deuterated specimen $[C_6D_4(OD)_2]_3\cdot(D_2S)_x$ was also prepared. The ring protons were exchanged with deuterons in a refluxing deuteroxide solution acidified with deuterated sulphuric acid. Ten grams of hydroquinone was deuterated twice, each time using 100 cm^3 of 99.8% D_2O and 1–2 cm^3 of concentrated D_2SO_4. The proton nmr on the hydroquinone sample dissolved in deuterated acetone showed that the deuteration level was 92%. The deuteration of the hydroxyl group and the preparation of D_2S were carried out as described above. A partially deuterated clathrate sample $\{[C_6D_4(OH)_2]_3\cdot(H_2S)_x\}$ for the incoherent quasi-elastic neutron scattering experiment was prepared using ring deuterated hydroquinone kindly supplied by Professor G. W. Gray, Hull University.

The occupancies x of the cavities were determined from elemental analysis for C, H (D), and S.

Single crystals of the H_2S clathrate for the anisotropic dielectric measurement were grown from pressurized aqueous solutions cooled from 80 to 20°C in 2 weeks. Crystals ~8 × 8 × 8 mm^3 with no particular anisotropic growth were obtained.

Calorimetric and dielectric measurements

The two calorimeters used in the present work have been described elsewhere (12, 13). The rhodium–iron thermometer was calibrated on the temperature scale EPT-76 and the platinum thermometer on IPTS-68.

The dielectric constant was measured using a General Radio 1620 transformer bridge. Since the sample was free from dielectric loss at all temperatures, it was measured at 1 kHz only. The samples cut parallel and perpendicular to the crystallographic c axis were placed in a doubly thermostated cryostat cooled with liquid helium. Gold foils attached to the crystal faces with Apiezon grease were used as electrodes.

Neutron diffraction and quasi-elastic scattering

The neutron diffraction measurements were made using a freshly powdered sample of material with the aromatic hydrogens approximately 92% deuterated and the remaining hydrogens better than 95% deuterated. The cage occupancy was 96 ± 2%. The high resolution powder diffractometer (14) at the spallation neutron source ISIS was used for the measurements; the sample-detector distance was 1 m, giving a resolution $\Delta d/d \sim 10^{-3}$. Measurements were made at 3.8, 6.5, 12, 30, and 150 K.

Incoherent neutron quasi-elastic scattering measurements were made on two separate samples; both were slab-shaped samples scattering 10% of the incident neutrons. One was completely hydrogenous, with a cage occupancy of 80%, and was investigated using the 1N6 spectrometer at the Institute Laue–Langevin, Grenoble. The other sample had the aromatic hydrogen deuterated to better than 95% with an H_2S cage occupancy of 90% and the measurements were made using the IN5 spectrometer. The energy resolution of the two instruments was determined using the scattering from a vanadium plate. For IN5 the incident wavelength was 7.0 Å giving a maximum elastic scattering vector Q_{el} = 1.60 $Å^{-1}$ with a resolution of 20 μeV (FWHM); measurements were made at 5, 10, and 15 K. For IN6 the wavelength was 5.1 Å with a resolution varying from 75 μeV (FWHM) at Q_{el} = 0.4 $Å^{-1}$ to 140 μeV (FWHM) at Q_{el} = 2.1 $Å^{-1}$; measurements were made at 5, 10, 15, 87, and 180 K.

Results and discussion

Heat capacity

The heat capacity data are given in the Appendix; Tables A1–A4, H_2S clathrate $T \leq 20$ K; Table A5, HDS clathrate, $T \leq 15$ K; Table A6, D_2S clathrate $T \leq 30$ K; Table A7, H_2S clathrate $T \leq 300$ K; Table A8, D_2S clathrate $T \leq 300$ K. The heat capacities have been normalized to three moles of hydroquinone. They therefore represent different amounts of the guest species, depending on the stoichiometry.

The heat capacities of the H_2S and D_2S clathrates are shown in Fig. 1 for the higher temperature region. They are free from anomalies at temperatures above 10 K. The heat capacity of the D_2S clathrate is larger than that of the H_2S clathrate because of the mass effect. The heat capacities of the H_2S clathrates for $T \leq 20$ K have been given graphically in ref. 10. They have peaks between 7 and 8 K for occupancies x larger than 0.9. The regions of the heat capacity peaks are shown in Fig. 2 on an enlarged scale for the H_2S, D_2S, and HDS clathrates. The heat capacity peaks occur at 7.61, 7.80, and 7.72 K for the H_2S, D_2S, and HDS compounds, respectively. On the assumption that the transition temperature depends linearly on the occupancy, the transition temperatures of the fully occupied clathrate are calculated to be 8.01, 8.48, and 8.04 K for the H_2S, D_2S, and HDS. The isotope effect on the transition temperature is quite small. The transition temperatures are summarized in Table 1 together with the previous data on the other clathrates (10).

Dielectric constant

The dielectric constants were measured on single crystals of the H_2S clathrate with x = 0.95. They are very anisotropic, as shown in Fig. 3. The orientational polarization characterized by the strong temperature dependence contributes only to $\varepsilon_\perp$, where the polarization perpendicular to the c axis is measured. The largest value ($\varepsilon_\perp$ = 7.82) is found at 14.2 K. $\varepsilon_\parallel$ changes very little with temperature, always being between 3.4 and 3.8. The maximum temperature for $\varepsilon_\perp$ is much higher than the temperature of the heat capacity peak, 7.61 K. However, the strong increase of $\varepsilon_\perp$ around this temperature must be associated with the phase transition. The $\varepsilon_\perp$ value is significantly larger

Can. J. Chem. Downloaded from www.nrcresearchpress.com by 176.9.209.113 on 09/07/12
For personal use only.

Can. J. Chem. Downloaded from www.nrcresearchpress.com by 176.9.209.113 on 09/07/12
For personal use only.

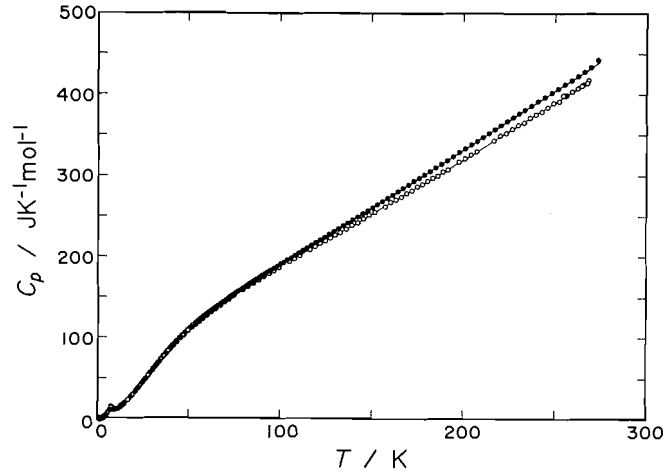

FIG. 1. Heat capacities of $[C_6H_4(OH)_2]_3{\cdot}(H_2S)_{0.95}$ (—○—) and $[C_6H_4(OD)_2]_3{\cdot}(D_2S)_{0.92}$ (—●—).

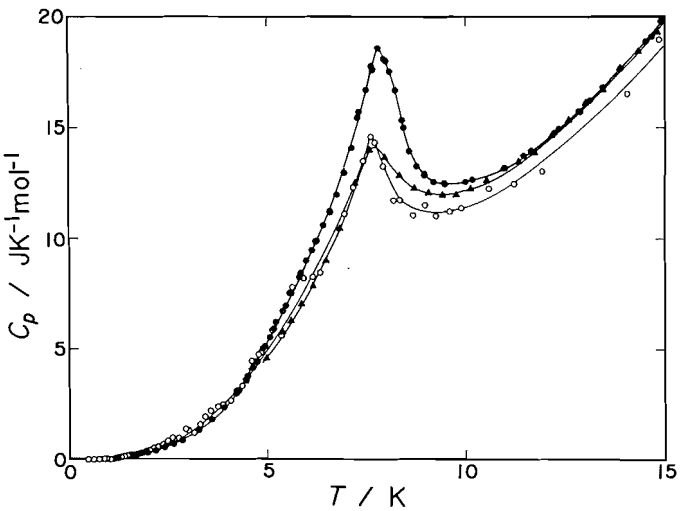

FIG. 2. Heat capacities of $[C_6H_4(OH)_2]_3{\cdot}(H_2S)_{0.95}$ (—○—), $[C_6H_4(OD)_2]_3{\cdot}(D_2S)_{0.92}$ (—●—), and $[C_6H_4(OD)(OH)]_3{\cdot}(HDS)_{0.96}$ (—▲—).

TABLE 1. Transition temperatures of H_2S, D_2S, and HDS clathrate compounds

Cavity occupancy x		Transition temperature (K)
H_2S	0.85	6.75±1.0
	0.92	7.56±0.09
	0.95	7.61±0.05
	0.96	7.65±0.07
D_2S	0.92	7.80±0.05
HDS	0.96	7.72±0.06

than $\varepsilon_{\parallel}$ at 4.2 K, which shows that a part of the dipolar polarization responds to the applied field even at this low temperature.

The strong anisotropy of the dielectric constant indicates that the guest dipoles have a strong preferential orientation perpendicular to the trigonal c axis, which is normal to the plane containing the hydroxyl rings. The dipole reorientation is thus essentially confined within the *ab* plane although no details are determined about the motion in this plane nor concerning

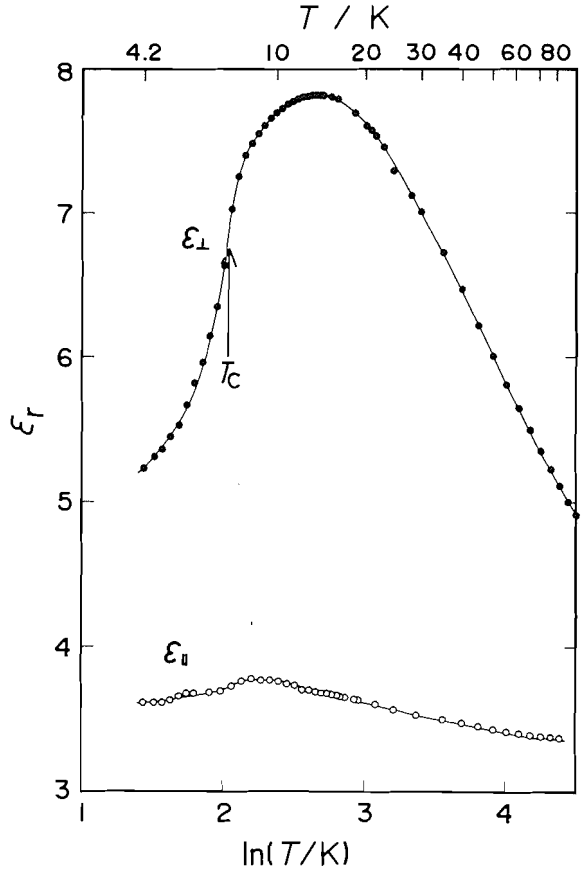

FIG. 3. Dielectric constants of single crystals of $[C_6H_4)OH)_2]_3{\cdot}(H_2S)_{0.95}$ measured perpendicular ($\varepsilon_\perp$) and parallel ($\varepsilon_\parallel$) to the c axis.

molecular orientation about the dipolar axis. The dielectric result is consistent with the nonpolar structure found at 295 K (15).

The different temperatures of the ε and heat capacity maxima have also been found in the HCl clathrate compound,[4] for which the maximum occurred at 20 K, and the heat capacity peak at 12.3 K. This may be related to the anisotropic structure of the clathrates in which the nearest neighbour guests form a chain that runs along the c axis.

Rotational heat capacity and entropy

The experimental heat capacity is the sum of the guest and host contributions. By making the assumption that these are additive, subtraction of the known host heat capacity (17) from the total gives the guest heat capacity shown in Fig. 4. At high temperatures, the curve was reproduced well by the following equation:

$$[1] \quad C = 3C_E(\theta = 104.5\,K) + 2C_E(\theta = 249.8\,K) + \tfrac{1}{2}R$$

The first Einstein term represents the rattling motion in the close space limit, the second term describes two of the three rotational degrees of freedom, and the last the third rotational degree of freedom. This very anisotropic rotational motion is indicated by a calculation of the rotational barrier (see below) and by the dielectric results. At lower temperatures, the heat capacity expression [1] fails to apply for two reasons: the clas-

[4]H. Ukegawa, T. Matsuo, and H. Suga. To be published.

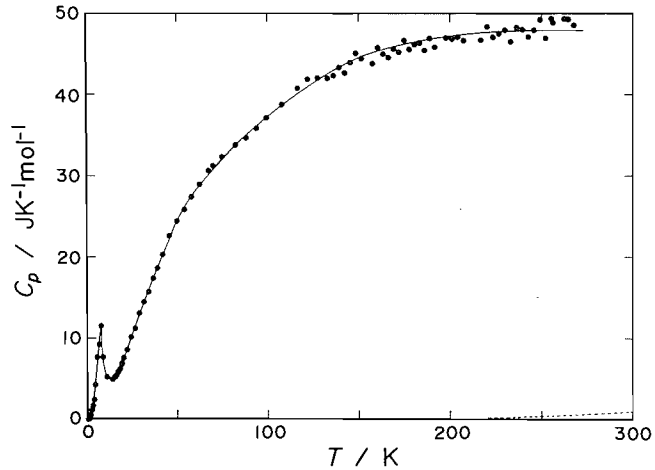

FIG. 4. Molar heat capacity of H_2S enclathrated in $[C_6H_4(OH)_2]_3\cdot(H_2S)_{0.95}$.

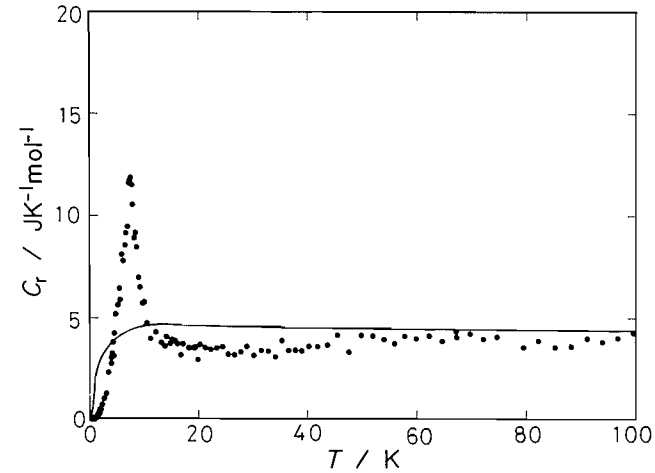

FIG. 5. Rotational heat capacity of H_2S enclathrated in $[C_6H_4(OH)_2]_3\cdot(H_2S)_{0.95}$ about the c axis. Experimental (. . .) and uniaxial free rotation (———).

sical value $\frac{1}{2}R$ of the rotational heat capacity cannot be used, and the guest–guest interaction becomes significant compared to the thermal energy. The rotational heat capacity calculated by subtracting the first two terms of eq. [1] from the guest heat capacity given in Fig. 4 is drawn in Fig. 5, where the one-dimensional rotator heat capacity is also plotted for the sake of comparison. The moment of inertia used in the calculation was 1.25×10^{-46} kg m^2. This value assumes that the guest molecule rotates in the cavity about the point of the lowest guest–host potential energy (see below). The discrepancy between the experimental and calculated heat capacities is of course caused by the phase transition arising from the guest–guest interaction that is not taken into account in the theoretical curve.

The entropy due to the orientational disordering was calculated from the rotational (or orientational) heat capacity plotted in Fig. 5. Figure 6 shows the entropy curves for the different occupancies normalized to 1 mole of H_2S. The entropy value at 15 K, where the main part of the heat capacity anomaly has finished, is 9.5 J K^{-1}mol^{-1}. The number of states occupied at this temperature is equal to exp (9.5/8.3144) = 3.13. In the free rotation model, the uniaxial rotation of H_2S occupies one of the three states: $m = 0$ and $m = \pm 1$ where m is the rotational quantum number. However, in the neutron scattering experiment no discrete excitations were observed at any temperature but only broad quasi-elastic wings above the transition, which indicates that the rotational states are extremely broadened. In terms of a classical order–disorder picture, the number of states 3.13 indicates that the guest H_2S has three equivalent orientations in the high temperature phase. The rhombohedral symmetry ($R\bar{3}$) of the crystal certainly appears consistent with this interpretation.

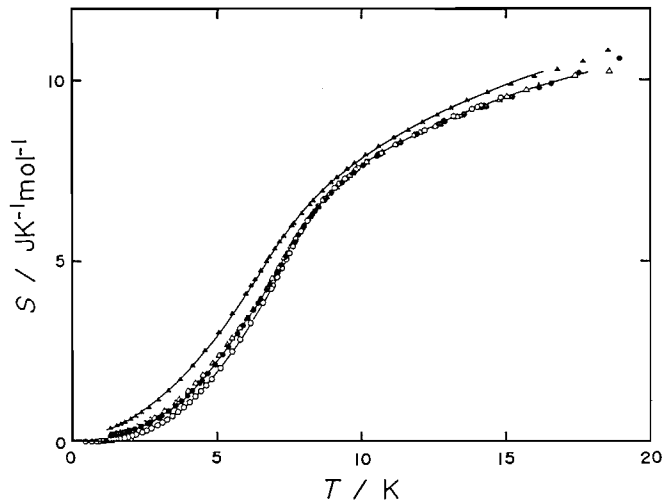

FIG. 6. Molar entropies of enclathrated H_2S in $[C_6H_4(OH)_2]_3\cdot(H_2S)_x$. —▲— $x = 0.85$; —△— $x = 0.92$; —○— $x = 0.95$; —●— $x = 0.96$.

Isotope effect

The general behaviour of the H_2S, D_2S, and HDS clathrates is very similar. In particular, the transition temperatures are essentially the same, in view of the probable variation of the occupancies. There would potentially be two aspects of the isotope substitution. One is that the rotational energy levels are closer together for D_2S than for H_2S. The other is that all the free rotational energy levels are available to HDS molecules whereas there is a restriction for H_2S and D_2S due to the symmetry requirement of the states. The experimental observation that there is no significant isotope effect shows that neither of these effects operates in the actual situation. From the first, one can argue that the moment of inertia of the guest molecule in the cavity may be larger than the free-rotator value because the host–guest interaction forces the guest molecule to rotate about a centre away from the molecular centre of mass. This causes the mass of the sulphur to dominate the rotational properties of the three isotopic species, thus diminishing the possible isotope effect. From the second, the absence of an isotope effect indicates that the rotational motion that exchanges H and D does not take place. The dielectric measurement alone could not exclude this possibility of the rotation of the H_2S molecule about its bisector axis, but the neutron scattering results described below also support the conclusion that it does not occur.

Incoherent neutron quasi-elastic scattering

Typical results for the higher Q-values are shown in Fig. 7 for temperatures of 5 and 10 K. All the results are dominated by the scattering from the protons and for both samples most of the protons are static and thus contribute only elastic scattering. Hence, for the fully hydrogenous sample only approximately 10% of the observed scattering carries useful information, and by deuteration of the aromatic hydrogens this could only be increased to 25%.

Can. J. Chem. Downloaded from www.nrcresearchpress.com by 176.9.209.113 on 09/07/12
For personal use only.

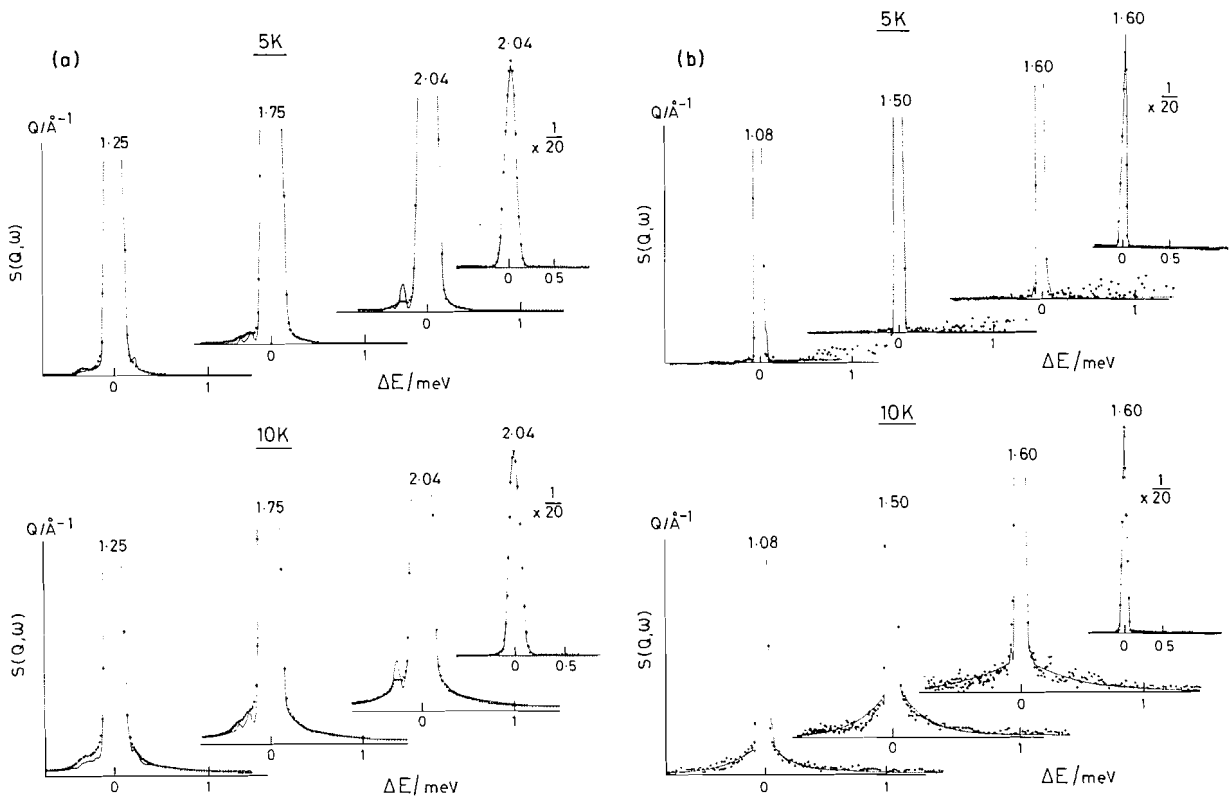

FIG. 7. Quasi-elastic neutron scattering results on H_2S enclathrated in (a) $[C_6H_4(OH)_2]_3 \cdot (H_2S)_{0.8}$ and measured on IN6 at ILL. The energy loss peaks are scattering from the cryostat. (b) $[C_6D_4(OH)_2]_3 \cdot (H_2S)_{0.9}$ measured on IN5 at ILL.

Nevertheless, the results very clearly show a distinct quasi-elastic broadening above the transition, which completely disappears below it, and no discrete inelastic peaks are seen at any temperature. At 5 K and also at 87 and 180 K the data were indistinguishable from the measured resolution function. For the low temperature this means that there are no excitations in the meV range and no stochastic motions faster than approximately 10^9 s^{-1}. For the higher temperatures the result means that the rotational/rattling motions of the H_2S molecules are fast enough to give a very broad quasi-elastic component indistinguishable from the background. The free rotational energy levels of H_2S extend from 1.7 meV upwards and the fact that no such excitations were observed, but only quasi-elastic broadening, shows that the rotational states are completely smeared out by collisional broadening through guest–host interactions and by the strongly fluctuating potential resulting from guest–guest interactions, which are comparable with thermal energies at temperatures just above the transition.

Unfortunately, because the signal from the H_2S protons is relatively weak, and also because for the higher-resolution IN5 experiment technical problems restricted the data collection time, neither the elastic incoherent structure factor nor the temperature dependence of the quasi-elastic broadening could be reliably determined. Nevertheless, the scattering is certainly consistent with rotation of the H_2S molecules about a single axis with a radius of ca. 1 Å. The correlation time τ_1 determined from a fit of a model of uniaxial rotation (18) is 2.0 ± 0.3 ps so that the rotation of the molecules is very rapid even at 10 K.

The INQES results therefore confirm unequivocally that the phase transition is associated with the freezing-out of the H_2S dipole reorientational motion. In the disordered phase the strong interactions of the guest molecules with other guests, and with the cage, make the motions essentially stochastic, although the geometrical details are not directly determined. Finally, because the freezing-out of the dipole motions does not of itself affect possible reorientational motion about the dipole axis, then the fact that no such motion is observed below the transition implies that these rotations are very much slower than the dipole reorientation itself, at least at low temperatures. This is in agreement with the results of model calculations presented below.

Neutron diffraction

A portion of the time-of-flight diffraction pattern at four temperatures is shown in Fig. 8. A full analysis of these results will be published later and at this stage only a brief discussion is given. The data at 150 K are completely in agreement with the X-ray structure (15, 19) except for the contribution of the sulphur hydrogens, which should be located by the neutron data. With decreasing temperature the lattice contracts anisotropically, the contraction from ambient temperature to 12 K being about 1% along *a* and 3% along *c*, which accounts for the observed splitting of some of the diffraction peaks at 12 K. This is consistent with a rapid rotation of the H_2S dipole in the *ab* plane and with a strong decrease in the amplitude of the rattling motion along *c* as the temperature decreases. At the transition, the freezing-out of the dipole motions causes a distortion of the lattice in the *ab* plane but very little change in the *c*-direction. This is shown by the splitting of most of the diffraction peaks from the high temperature phase into two or three components at low temperatures. Apart from these splittings, however, no new reflections appear, showing that the structural change associated with the ordering of the H_2S molecules does not involve an increase in the unit cell size but is confined to distortions of the high temperature unit cell amounting to 2 or 3 parts in 10^3.

Can. J. Chem. Downloaded from www.nrcresearchpress.com by 176.9.209.113 on 09/07/12
For personal use only.

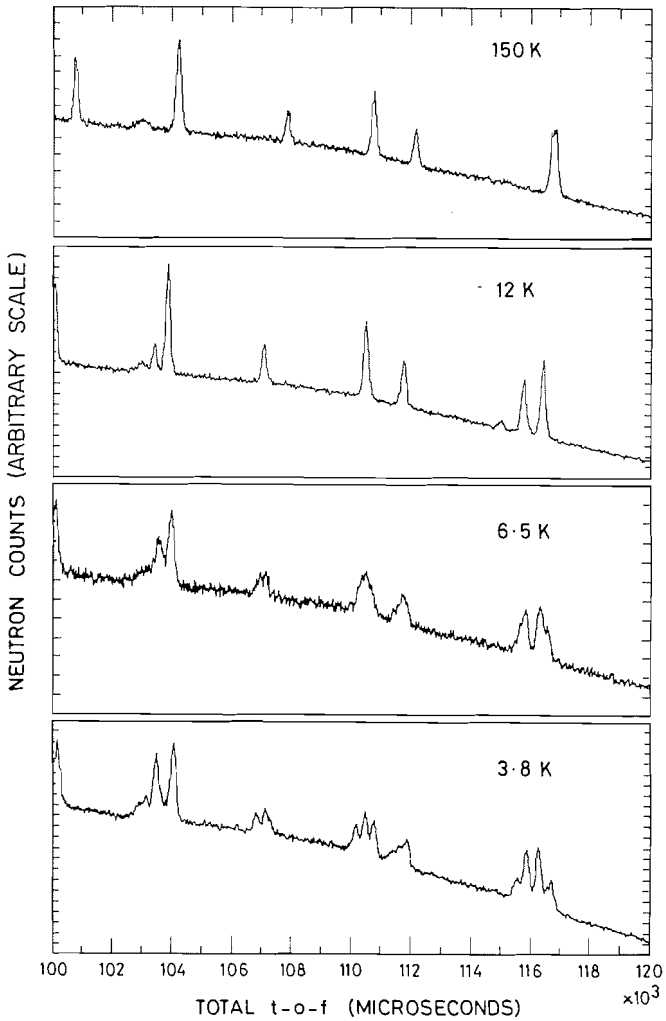

FIG. 8. Time-of-flight diffraction patterns from $[C_6D_4(OD)_2]_3 \cdot (D_2S)_{0.96}$ obtained using the high resolution powder diffractometer at ISIS; (d/A = (t/ms)/48.3).

TABLE 2. Numerical values of coefficients of the potential function

Atom pair	A/kJ mol^{-1} nm^D	B/nm^{-1}	C/kJ nm^6 mol^{-1}	D
H–H	27 600	40.80	205.9 × 10^{-6}	0
C–H	0.1874	20.40	523.0 × 10^{-6}	6
O–H	0.1757	20.40	552.2 × 10^{-6}	6
H–S	169 500	38.51	1110 × 10^{-6}	0
C–S	1.069	18.11	2862 × 10^{-6}	6
O–S	1.001	18.11	2994 × 10^{-6}	6

Calculation of the guest–host interaction energy

It was stated in the introduction that the rigid host lattice provides a restricted space in which the guest molecule may rotate. In this section we present a simple calculation of the guest–host potential energy as a function of the rotation angles. The interaction energy was calculated as the sum of atom–atom potentials for which the following form was assumed (20):

$$V(r) = \frac{A \exp[-Br]}{r^D} - \frac{C}{r6}$$

where r is the interatomic distance and the parameters A, B, C, and D are given in Table 2.

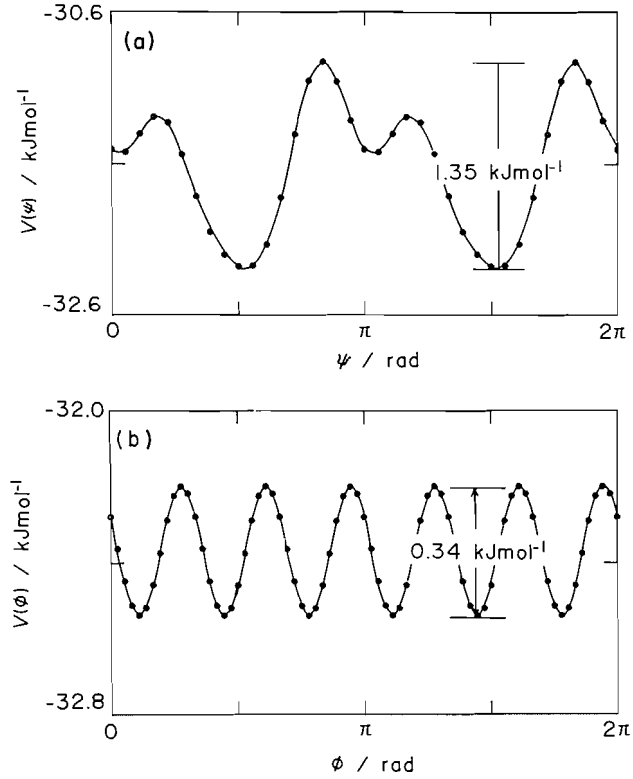

FIG. 9. (a) Potential energy of H_2S as a function of the rotation angle ψ (see text). The axis of rotation is the molecular bisector axis and is perpendicular to the c axis (i.e., $\theta = \pi/2$). $\psi = 0$ corresponds to the molecular plane being parallel to c. (b) Potential energy of H_2S as a function of the rotation angle ϕ (see text). The molecule lies flat in the ab plane and rotates about the c axis.

The sum was taken for all the pairs made by each of the three atoms of the guest H_2S and each of the atoms of the six benzene rings and the two six-membered rings of the hydrogen-bonded oxygen atoms that form the cage. Two of the potential curves are shown in Fig. 9.

First the guest molecule was moved translationally along the crystallographic a axis (as defined in ref. 19), keeping the dipolar axis parallel to the a axis and the proton–proton vector parallel to the c axis. The lowest energy was found at the position where the S atom was 0.045 nm away from the centre of the cavity. The rotational barrier was then calculated around this position. For the calculation, the molecular orientation was specified by the polar and azimuthal angles (θ, ϕ) of the dipolar axis, measured from the c and a axes, respectively, and the rotation angle ψ about the dipolar axis. The zero of the ψ angle was taken at the position where the proton–proton vector lies in the ac plane.

The potential energy calculated as a function of ψ for $\theta = \pi/2$ and $\phi = 0$ is plotted in Fig. 9(a). Two equivalent minima occur at $\psi \sim \pi/2$ and $3\pi/2$. The barrier height is 1.35 kJ mol^{-1}. The minima correspond to the molecule lying approximately flat in the ab plane. Rotation of the dipolar axis from $\theta = 0$ to π, keeping $\phi = 0$ and $\psi = \pi/2$, also gave a minimum near $\theta = \pi/2$ with a barrier height of approximately 1.35 kJ mol^{-1}. The potential energy as a function of ϕ for $\theta = \pi/2$ and $\psi = \pi/2$ is plotted in Fig. 9(b). This represents the rotation of the molecule lying flat in the ab plane about the c axis. This calculation gives six potential minima with a barrier height of 0.34 kJ mol^{-1} and an average energy of −32.37 kJ mol^{-1}. The similar rotation of the molecular dipole about the c axis but with the molecular

Can. J. Chem. Downloaded from www.nrcresearchpress.com by 176.9.209.113 on 09/07/12
For personal use only.

plane perpendicular to the *ab* plane (i.e., $\theta = \pi/2$, $\psi = 0$) gave an average potential energy of -31.50 kJ mol^{-1} and a very small barrier, 0.014 kJ mol^{-1}.

These calculations show first that the barriers to rotation are smaller than those in ordinary molecular crystals by a factor of about $\frac{1}{10}$ to $\frac{1}{1000}$. This is a reasonable result in view of the special nature of the clathrate compound where the guest molecules rotate in the space secured by the host lattice. The second conclusion is that even though the rotational potential surface is very flat it does have minima and maxima differing by about 1 kJ mol^{-1}. The difference will be significant at low temperatures (<100 K) where the molecules will preferentially occupy the low energy orientations, which implies that the plane of the molecule and hence the dipole axis tends to be located in the *ab* plane. This explains the anisotropic dielectric response found experimentally at low temperatures.

Anisotropic potentials have also been obtained by explicit calculations of the energy using the Lennard–Jones (8) and electric multipole (16) interactions for N_2, O_2, and other larger guest molecules.

These potential barriers, calculated here, represent lower limits because of the neglect of the possible formation of hydrogen bonds and of dipole–dipole interactions with other guest molecules. However, the calculation clearly demonstrates the anisotropy of the rotational motions. Furthermore, estimates of the reorientation frequency about the bisector axes based on this potential show that while the correlation time will be about 1 ps at 100 K, it has increased to more than 1 ns below 20 K and would not be seen in the neutron scattering data, as was the case in practice.

Conclusions

All of the results presented are consistent with strongly anisotropic rotational motions of the H_2S molecules in the clathrate cages at temperatures above the 8 K phase transition. The guest dipoles are located in the crystallographic *ab* plane and rotate very rapidly ($\omega \sim 5 \times 10^{11}$ s^{-1} at 10 K) about an axis parallel to *c*. Rotations about the other axes are much more difficult. The heat capacity analysis shows that this motion is nearly free rotation at high temperatures, but the transition entropy implies that there are three distinguishable states just above the transition although the potential calculations suggest six. It would in fact not be surprising to find some such localization of the molecular orientations at low temperatures in the disordered phase and it is interesting to note that the existence of three orientations (but not six) would remove the centre of symmetry, giving space group $R3$, as for the HCl clathrate, rather than $R\bar{3}$.

The neutron scattering results confirm that the phase transition is associated with the freezing-out of the H_2S dipole reorientations and show that the molecular motions immediately above the transition are essentially stochastic in nature, in accord with the expected strong interactions with the cage and with other guest molecule dipoles.

What remains now to be determined are the precise locations of the H_2S molecules through the transition, which will provide the essential structural information required to model the phase transition. Analysis of the high resolution powder diffraction data currently in progress is expected to provide this information.

Acknowledgements

This work was supported partly by a Grant-in-Aid for the Special Project Research 58118007, partly by the Japan Society for Promotion of Science via the UK–Japan Co-operation Research Project, and partly by the Science and Engineering Research Council.

1. D. E. PALIN and H. M. POWELL. J. Chem. Soc. 208 (1947).
2. D. PALIN and H. M. POWELL. J. Chem. Soc. 815 (1948).
3. N. G. PARSONAGE and L. A. K. STAVELEY. Mol. Phys. **3**, 59 (1960).
4. G. L. STEPAKOFF and L. V. COULTER. J. Phys. Chem. Solids, **24**, 1435 (1963).
5. J. C. BURGIEL, H. MEYER, and P. L. RICHARDS. J. Chem. Phys. **43**, 4291 (1965).
6. T. MATSUO, H. SUGA, and S. SEKI. J. Phys. Soc. Japan. **30**, 785 (1971).
7. T. MATSUO. J. Phys. Soc. Jpn. **30**, 794 (1971).
8. P. SIXOU and P. DANSAS. Ber. Bunsen-Ges. Phys. Chem. **80**, 364 (1976).
9. D. W. DAVIDSON and J. A. RIPMEESTER. *In* Inclusion compounds. Vol. 3. *Edited by* J. L. Atwood, J. D. Davies, and D. D. MacNicol. Academic Press, New York. 1984. p. 69.
10. H. UKEGAWA, T. MATSUO, and H. SUGA. J. Inclusion Phenom. **3**, 261 (1985)
11. T. MATSUO and H. SUGA. J. Inclusion Phenom. **2**, 49 (1984).
12. N. ARAI, M. SORAI, H. SUGA, and S. SEKI. Bull Chem. Soc. Jpn. **50**, 1702 (1977).
13. T. MATSUO and H. SUGA. Thermochim. Acta, **88**, 149 (1985).
14. M. W. JOHNSON and W. I. F. DAVID. RAL-85-112, Rutherford Appleton Laboratory Report (1985).
15. T. C. W. MAK, J. S. TSE, C. S. LEE, and Y. H. CHONG. J. Chem. Soc. Perkin Trans. I2, 1169 (1976).
16. S. HIROKAWA. Mol. Phys. **36**, 31 (1978).
17. N. G. PARSONAGE and L. A. K. STAVELEY. Mol. Phys. **2**, 212 (1959).
18. J. D. BARNES. J. Chem. Phys. **58**, 5193 (1973).
19. W. C. Ho and T. C. W. MAK. Z. Kristallogr. **161**, 87 (1982).
20. E. GIGLIO. Nature, **222**, 339 (1969).

Can. J. Chem. Downloaded from www.nrcresearchpress.com by 176.9.209.113 on 09/07/12
For personal use only.

Appendix

TABLE A1. Molar heat capacity of hydroquinone hydrogen sulfide clathrate $[C_6H_4(OH)_2]_3 \cdot (H_2S)_{0.85}$

T/K	C_p/J K^{-1} mol^{-1}	T/K	C_p/J K^{-1} mol^{-1}	T/K	C_p/J K^{-1} mol^{-1}	T/K	C_p/J K^{-1} mol^{-1}
1.341	0.316	4.598	4.122	12.831	14.30	6.298	7.490
1.403	0.343	4.836	4.607	13.321	15.76	6.501	8.579
1.533	0.507	5.062	5.049	13.883	15.89	6.714	8.453
1.595	0.454	5.282	5.423	14.550	17.69	7.004	8.555
1.666	0.501	5.520	5.977	15.339	18.83	7.322	8.711
1.743	0.549	5.757	6.362	16.200	21.14	7.632	9.127
1.837	0.615	6.290	6.990	17.057	23.78	7.961	9.059
1.940	0.681	6.507	8.091	18.081	24.06	8.339	9.360
2.033	0.799	6.751	8.641			8.752	10.14
2.121	0.839	7.008	8.490	6.161	7.413	9.165	9.920
2.212	0.909	7.288	8.638	6.333	7.756	9.623	10.15
2.305	0.998	7.599	8.891	6.501	7.624		
2.411	1.091	7.905	9.008	6.661	8.299	10.089	10.71
2.533	1.212	8.227	9.281	6.812	8.489	10.616	11.35
2.667	1.373	8.587	9.315	6.969	8.339	11.131	11.67
2.820	1.542	8.962	9.669	7.174	8.441	11.637	12.82
2.992	1.729	9.370	10.12	7.419	8.483	12.133	13.87
3.163	1.923	9.773	10.29	7.660	9.088	12.641	14.12
3.337	2.149	10.163	10.76	7.940	9.029	13.127	16.18
3.538	2.427	10.527	11.22	8.262	9.259	13.679	16.22
3.740	2.701	10.908	11.10	8.659	9.762	14.368	17.15
3.947	3.046	11.366	11.84	9.089	9.888	15.181	18.69
4.170	3.388	11.869	13.09	9.505	10.35	15.973	19.80
4.379	3.745	12.338	14.04	6.047	7.185	16.754	21.39

TABLE A2. Molar heat capacity of hydroquinone hydrogen sulfide clathrate $[C_6H_4(OH)_2]_3 \cdot (H_2S)_{0.92}$

T/K	C_p/J K^{-1} mol^{-1}	T/K	C_p/J K^{-1} mol^{-1}	T/K	C_p/J K^{-1} mol^{-1}	T/K	C_p/J K^{-1} mol^{-1}
1.337	0.181	8.513	10.98	2.598	1.003	11.850	12.62
1.405	0.204	5.361	5.715	2.874	1.295	12.580	13.28
1.522	0.251	6.356	8.005	3.210	1.711	13.358	15.03
1.673	0.322	7.129	10.62	3.581	2.269	14.145	17.84
1.901	0.451	7.671	11.53	3.891	2.762	14.809	18.54
2.220	0.669	8.161	11.41	4.193	3.326	15.706	19.37
2.538	0.933	8.701	10.92	4.535	4.105		
2.823	1.212	9.155	10.84	4.868	4.788	1.363	0.186
3.107	1.578	9.613	11.08	5.176	5.451	1.460	0.227
3.406	2.004	9.724	11.13	5.519	6.002	1.643	0.310
3.712	2.478	10.207	11.42	5.916	6.740	1.939	0.475
4.025	3.032	10.753	11.99	5.585	6.086	2.327	0.756
4.356	3.672	11.370	12.61	6.026	7.025	2.732	1.148
4.675	4.381	12.769	13.34	6.467	8.425	3.665	2.325
4.991	5.114	13.525	15.20	6.914	10.27	4.283	3.465
5.358	5.764	14.277	16.07	7.337	11.58	5.078	5.186
5.779	6.304	15.060	17.78	7.734	11.90	6.109	7.288
6.238	7.500	16.123	19.64	8.243	11.42	6.942	9.517
6.712	9.066	17.353	21.46	8.813	11.24	7.402	10.72
7.144	10.88	18.549	21.60			7.847	11.11
7.564	11.68			10.609	11.42		
8.013	11.30	2.274	0.716	11.185	12.50		

Can. J. Chem. Downloaded from www.nrcresearchpress.com by 176.9.209.113 on 09/07/12
For personal use only.

TABLE A3. Molar heat capacity of hydroquinone hydrogen sulfide clathrate $[C_6H_4(OH)_2]_3 \cdot (H_2S)_{0.95}$

T/K	C_p/J K^{-1} mol^{-1}	T/K	C_p/J K^{-1} mol^{-1}	T/K	C_p/J K^{-1} mol^{-1}	T/K	C_p/J K^{-1} mol^{-1}
1.046	0.015	5.360	5.628	2.724	1.083	7.423	13.50
1.090	0.022	5.686	6.174	2.852	1.167	7.641	13.68
1.132	0.033	5.976	8.456	2.968	1.267	7.923	13.26
1.179	0.066	6.310	7.678	3.101	1.393	8.267	11.68
1.237	0.075	6.695	8.903	3.245	1.640	8.650	11.33
1.304	0.092	7.053	10.71	3.398	1.869	9.096	11.25
1.380	0.119			3.557	2.217	9.597	11.23
1.478	0.129	4.829	4.490	3.756	2.474	10.158	11.69
1.576	0.167	5.103	3.974	3.993	2.344		
1.669	0.240	5.288	5.723	4.210	3.132	0.518	0.001
1.756	0.239	5.523	6.605	4.404	3.724		
1.841	0.310	5.795	7.569	4.611	4.481	0.694	0.015
1.940	0.380	6.080	7.987	4.825	5.131	0.863	0.030
2.026	0.417	6.343	8.473	5.080	5.980	0.893	0.028
2.100	0.450	6.608	9.342	5.357	6.833	0.932	0.037
2.198	0.489	6.885	10.30	5.629	7.811	0.993	0.051
2.334	0.662	7.164	12.33	5.920	8.223	1.062	0.059
2.459	0.665	7.440	13.31	6.242	8.352	1.119	0.074
2.607	0.985	7.693	14.42	6.595	9.376		
2.764	0.976	7.984	12.86	6.948	11.13	0.481	0.001
2.940	1.384	8.342	11.75	7.275	12.86	0.551	0.005
3.146	1.393	8.723	11.21	7.524	14.14	0.622	0.007
3.339	1.661	9.089	11.06	7.716	14.32	0.691	0.009
3.541	2.039	9.440	11.18	7.910	13.28	0.756	0.021
3.745	2.403	9.821	11.06	8.110	12.55	0.823	0.024
3.950	2.885	10.217	11.35	8.313	11.99	0.891	0.033
4.141	2.243	10.594	11.46	8.514	12.28	0.957	0.045
		10.941	12.37	8.712	11.91	1.008	0.050
1.398	0.133	11.291	11.99	8.977	11.53	1.059	0.064
1.474	0.171	11.607	14.05	9.345	11.02	1.136	0.076
1.551	0.211	11.922	13.04	9.895	11.39	1.217	0.097
1.648	0.239	12.215	14.04	10.585	12.26	1.313	0.126
1.758	0.314	12.493	16.24	11.213	12.47	1.407	0.161
1.877	0.366	12.867	15.72	11.863	13.01	1.484	0.189
2.006	0.437	13.402	15.42	12.771	14.72	1.556	0.215
2.127	0.518	14.049	16.53	13.852	16.68		
2.231	0.579	14.717	17.54	14.845	18.96	3.009	1.322
2.337	0.684	1.029	0.250	15.747	21.13	3.206	1.562
2.450	0.737	1.096	0.050	16.789	22.93	3.424	1.941
2.583	1.007	1.160	0.077	17.982	25.39	3.665	2.258
2.725	1.025	1.229	0.126	19.016	29.92	3.873	2.493
2.862	1.120	1.315	0.096	19.954	30.85	4.072	2.964
2.995	1.334	1.385	0.119			4.274	3.268
3.147	1.216	1.467	0.146	4.350	3.350	4.462	3.599
3.298	1.593	1.567	0.176	4.553	3.713	4.642	4.188
3.481	2.019	1.704	0.239	4.717	4.620	4.852	4.884
3.669	2.187	1.837	0.289	4.888	5.157	7.612	14.58
3.858	2.290	1.950	0.463	5.127	5.876	7.854	13.60
4.068	2.681	2.074	0.474	5.537	7.208	8.184	11.73
4.233	3.173	2.222	0.619	6.157	8.282	8.680	11.07
4.529	3.094	2.364	0.690	6.755	10.08	9.254	11.04
4.785	4.781	2.486	0.847	7.108	11.97	9.872	11.44
4.948	2.272	2.599	0.959	7.268	12.98		

Can. J. Chem. Downloaded from www.nrcresearchpress.com by 176.9.209.113 on 09/07/12
For personal use only.

Can. J. Chem. Downloaded from www.nrcresearchpress.com by 176.9.209.113 on 09/07/12
For personal use only.

TABLE A4. Molar heat capacity of hydroquinone hydrogen sulfide clathrate $[C_6H_4(OH)_2]_3 \cdot (H_2S)_{0.96}$

T/K	C_p/J K^{-1} mol^{-1}	T/K	C_p/J K^{-1} mol^{-1}	T/K	C_p/J K^{-1} mol^{-1}	T/K	C_p/J K^{-1} mol^{-1}
1.381	0.184	15.344	19.34	6.740	9.72	4.256	3.494
1.439	0.181	16.537	22.54	7.095	11.36	4.499	4.105
1.518	0.218	18.365	25.66	7.459	12.66	4.761	4.741
1.610	0.248			7.816	12.27	5.189	5.960
1.699	0.302			8.179	11.75	5.696	6.959
1.812	0.364	5.978	7.468	8.576	11.44	6.112	7.819
1.943	0.431	6.407	8.410	8.968	11.29	6.509	8.860
2.144	0.570	6.838	9.773	9.353	11.25	6.823	10.40
2.405	0.783	7.229	11.69	9.750	11.11	7.151	11.96
2.644	1.000	7.652	12.82	10.173	11.40	7.511	12.73
2.878	1.250			10.705	12.18	7.867	12.60
3.116	1.538						
3.353	1.871	1.422	0.187				
3.602	2.256	1.471	0.201	11.609	13.19	6.355	8.103
3.879	2.724	1.547	0.235	12.699	14.61	6.711	9.463
4.159	3.341	1.635	0.272	13.542	15.57	7.071	11.03
4.422	3.916	1.724	0.306	14.339	17.52	7.413	12.21
4.681	4.502	1.840	0.417	15.235	19.60	7.768	12.66
4.940	5.204	2.006	0.420	16.136	20.85	8.143	11.82
5.210	5.957	2.284	0.664	17.257	22.12	8.523	11.21
5.525	6.751	2.623	0.971	18.900	26.73	9.338	11.14
5.887	7.370	2.993	1.392			9.899	11.28
6.255	8.018	3.480	2.075			10.560	11.77
6.608	9.089	4.004	2.983	1.417	0.173	11.233	12.77
6.956	10.67	4.408	3.886	1.475	0.196	11.953	13.76
7.299	12.23	4.691	4.627	1.559	0.233	12.723	14.07
7.658	12.62	5.038	5.510	1.662	0.281	13.583	15.71
8.025	11.95	5.386	6.329	1.770	0.336	14.802	19.04
8.402	11.46	5.698	7.047	1.885	0.397	16.213	21.41
8.772	11.27	6.057	7.491	2.008	0.468	17.483	24.60
9.147	11.32	6.419	8.419	2.186	0.599		
10.080	11.46	6.754	9.744	2.443	0.809		
10.669	11.86	7.075	11.16	2.717	1.077	10.773	12.22
11.369	12.43	7.405	12.23	3.017	1.425	11.846	13.33
12.138	13.39	7.725	12.85	3.327	1.837	12.867	14.74
12.911	14.68	8.070	11.86	3.591	2.253	14.370	17.41
13.716	15.62	8.456	11.44	3.782	2.570	16.339	21.11
14.556	14.04	8.885	11.25	3.989	2.963	18.178	25.12

TABLE A5. Molar heat capacity of hydroquinone deuterium sulfide clathrate $[C_6H_4(OH)(OD)]_3 \cdot (HDS)_{0.96}$

T/K	C_p/J K^{-1} mol^{-1}	T/K	C_p/J K^{-1} mol^{-1}	T/K	C_p/J K^{-1} mol^{-1}	T/K	C_p/J K^{-1} mol^{-1}
4.28	3.992	7.59	13.98	11.74	13.89	4.42	3.667
4.45	3.721	7.97	13.65	12.16	14.65	4.66	4.169
4.62	4.195	8.34	12.86	12.58	15.34	4.98	4.847
4.80	4.442	8.72	12.31	13.00	16.12	5.19	5.293
4.99	4.610	9.08	12.09	13.44	16.70	5.70	6.527
5.39	5.807	9.42	11.99	13.88	17.69	6.20	7.932
5.60	6.299	9.77	12.00	14.32	18.43	6.68	9.728
5.86	7.066	10.13	12.25	14.80	19.29	7.15	12.10
6.16	7.886	10.53	12.64	3.96	3.274	7.59	14.07
6.49	9.026	10.94	13.15	4.05	3.223	7.93	13.72
6.83	10.47	11.33	13.48	4.28	3.434	8.22	13.01
7.21	12.51						

TABLE A6. Molar heat capacity of hydroquinone hydrogen sulfide clathrate $[C_6H_4(OD)_2]_3 \cdot (D_2S)_{0.92}$

T/K	C_p/J K^{-1} mol^{-1}	T/K	C_p/J K^{-1} mol^{-1}	T/K	C_p/J K^{-1} mol^{-1}	T/K	C_p/J K^{-1} mol^{-1}
4.64	4.190	4.51	3.793	8.57	13.95	24.63	45.94
5.07	5.561	4.73	4.471	8.76	13.28	25.69	49.36
5.47	6.990	4.95	5.157	8.96	12.94	26.77	52.59
5.85	8.471	5.17	5.942	9.20	12.59	27.86	56.16
6.22	9.890	5.39	6.747	9.47	12.53	28.98	59.80
6.58	11.26	5.60	7.544	10.17	12.67		
6.93	13.00	5.80	8.283	10.99	13.21	1.62	0.207
7.28	15.47	5.98	9.022	11.46	13.75	1.79	0.275
7.62	17.77	6.13	9.494	12.34	14.95	1.97	0.321
7.99	17.99	6.25	9.918	13.11	16.23	2.18	0.413
8.44	15.00	6.42	10.62	13.88	17.66	2.40	0.567
8.96	12.88	6.58	11.21	14.66	19.10	2.64	0.713
9.48	12.49	6.75	12.01	15.43	20.88	2.85	0.875
10.00	12.59	6.94	12.99	16.20	22.66	3.13	1.374
10.52	13.13	7.13	14.09	16.97	24.71	3.27	1.341
11.64	13.98	7.32	15.72	17.72	26.48	3.59	1.829
12.23	14.77	7.49	16.71	18.47	28.35	3.90	2.371
12.83	15.74	7.65	17.58	19.23	30.38	4.23	3.079
13.43	16.82	7.79	18.56	20.00	32.75	4.56	5.092
14.51	18.88	7.93	18.08	20.80	34.67	4.89	5.044
14.89	19.79	8.08	17.53	21.68	37.15	5.22	6.251
		8.23	16.68	22.61	39.97	5.56	7.557
4.28	3.157	8.39	15.33	23.60	43.02		

TABLE A7. Molar heat capacity of hydroquinone hydrogen sulfide clathrate $[C_6H_4(OH)_2]_3 \cdot (H_2S)_{0.95}$ (13 ~ 300 K)

T/K	C_p/J K^{-1} mol^{-1}	T/K	C_p/J K^{-1} mol^{-1}	T/K	C_p/J K^{-1} mol^{-1}	T/K	C_p/J K^{-1} mol^{-1}
294.18	471.8	153.03	266.4	273.30	444.3	44.13	99.72
296.76	475.3	153.03	266.4	277.29	489.8	45.18	102.0
299.33	478.8	155.86	270.4	281.28	453.6	46.20	104.1
301.90	482.3	158.67	274.2			47.27	106.3
		161.47	278.2	14.01	25.06	48.41	108.5
82.92	168.2	164.24	282.2	14.51	25.94	49.51	110.7
84.35	170.4	167.11	286.4	15.33	27.06	50.58	112.7
85.77	172.6	170.07	290.7	16.43	29.06	51.62	114.7
88.50	176.4	173.01	295.2	17.42	31.07	52.64	116.7
89.79	178.4	175.93	299.0	18.37	33.51	53.64	118.5
91.07	180.0	178.84	303.1	19.31	36.02	54.61	120.2
92.35	182.3	181.83	307.5	20.17	38.42	55.64	121.9
93.62	183.8	184.91	312.4	20.98	40.55	56.71	123.8
94.98	185.5	187.97	316.7	21.83	42.45	58.26	126.4
96.59	187.7	191.17	321.3	22.72	44.89	60.26	129.6
98.36	190.1	194.51	326.0	23.56	47.20	62.19	132.5
100.10	192.9	197.82	330.9	24.36	49.42	64.04	135.3
101.83	194.9	201.13	335.7	25.17	51.57	65.83	138.0
103.81	197.9	204.41	340.6	25.97	53.76	67.58	140.6
106.03	200.6	207.68	345.0	26.76	55.96	69.39	143.1
108.22	203.6	210.94	349.6	27.54	58.07	71.27	145.8
110.39	206.7	214.19	354.5	28.40	60.37	73.10	148.6
112.53	209.9	217.42	359.2	29.22	62.45	74.89	151.0
114.78	213.0	220.64	364.0	29.75	63.96	76.64	153.4
117.18	216.4	223.84	368.5	30.27	65.44	78.38	156.3
119.59	219.8	227.04	373.2	30.86	67.06	80.11	158.2
121.98	223.0	230.23	378.0	31.68	69.38	81.81	160.4
124.35	226.2	233.41	382.4	32.64	71.99	83.49	162.7
126.83	229.8	236.84	387.6	33.57	74.48	85.14	164.9
129.40	233.4	240.52	392.9	34.45	76.87	86.76	166.9
131.95	236.8	244.19	398.0	35.31	79.22	88.41	168.9
134.48	240.5	247.85	403.3	36.14	81.33	90.06	171.1
136.99	243.8	251.49	408.7	37.09	83.77	91.70	173.2
139.60	247.7	255.11	414.0	38.27	86.67	93.42	175.3
142.30	251.4	258.73	418.9	39.53	89.73	95.24	177.8
144.98	255.4	262.33	424.4	40.75	92.41	97.47	180.8
147.65	258.9	265.92	429.9	41.92	94.97	100.09	184.1
150.29	262.7	269.49	435.4	43.05	97.42		

Can. J. Chem. Downloaded from www.nrcresearchpress.com by 176.9.209.113 on 09/07/12
For personal use only.

TABLE A8. Molar heat capacity of hydroquinone deuterium sulfide clathrate $[C_6H_4(OD)_2]_3 \cdot (D_2S)_{0.92}$ (13 ~ 300 K)

T/K	C_p/J K^{-1} mol^{-1}	T/K	C_p/J K^{-1} mol^{-1}	T/K	C_p/J K^{-1} mol^{-1}	T/K	C_p/J K^{-1} mol^{-1}
13.22	15.54	49.83	109.8	132.96	230.2	233.20	365.1
14.16	17.77	51.95	113.1	136.23	234.5	236.41	371.1
15.17	19.86	53.97	116.9	139.32	239.2	239.59	375.2
16.16	21.96	55.91	120.4	142.38	242.4	242.75	378.7
17.19	24.43	57.79	124.2	145.41	247.3	245.89	383.8
18.23	26.87	59.91	128.0	148.43	252.1	249.02	389.3
19.22	29.44	62.27	132.2	151.47	255.2	252.12	391.5
19.43	30.02	67.17	140.6	157.46	262.1	255.21	398.1
20.29	32.48	67.27	140.5	160.42	267.7	261.45	413.7
21.23	34.91	69.75	144.7	163.36	270.6	264.45	410.9
22.25	37.68	72.17	148.2	166.27	273.9	267.47	414.4
23.33	40.80	74.66	152.1	169.16	278.6	270.45	429.1
24.43	44.00	79.48	158.7	172.03	281.9	273.21	553.6
25.53	46.82	82.23	163.0	174.89	287.0	275.96	439.1
26.64	49.98	85.23	166.9	177.72	289.6	278.14	455.1
27.78	53.35	91.06	175.3	180.53	293.8	280.32	434.6
28.96	56.67	93.89	178.9	183.32	297.7		
30.21	60.07	96.67	182.8	186.10	300.5	256.13	398.9
31.54	63.98	99.47	186.7	188.86	305.5	259.17	403.9
32.87	67.60	102.30	190.9	191.67	308.2	262.18	407.8
34.16	70.80	105.09	194.2	197.78	317.5	265.19	412.4
35.37	74.76	107.93	198.0	201.03	321.8	268.17	418.1
36.59	77.46	110.84	201.6	204.25	326.3	271.05	462.7
37.82	80.60	113.71	205.9	207.44	330.2	273.86	482.5
38.99	83.49	116.54	209.3	213.56	338.8	276.70	431.2
40.30	86.92	119.34	213.2	216.89	343.1	279.62	433.8
41.89	90.70	122.11	217.0	220.19	349.2	282.52	439.8
43.69	94.96	124.85	220.0	223.48	352.4	285.41	443.2
45.56	99.64	127.56	223.7	226.74	357.3	291.13	455.0
47.61	103.3	130.25	227.4	229.98	362.1		

Can. J. Chem. Downloaded from www.nrcresearchpress.com by 176.9.209.113 on 09/07/12
For personal use only.

Monte Carlo simulation of chlorine adsorbed on graphite

SOONG-HYUCK SUH AND SEAMUS F. O'SHEA
Department of Chemistry, University of Lethbridge, Lethbridge, Alta., Canada T1K 3M4
Received November 17, 1987
This paper is dedicated to Professor J. A. Morrison

SOONG-HYUCK SUH and SEAMUS F. O'SHEA. Can. J. Chem. **66**, 955 (1988).

Monte Carlo calculations are reported for patches of molecular chlorine adsorbed on the basal plane of graphite. A variety of combinations of intermolecular and molecule–surface potentials have been tested, and the resulting structural predictions cover a wide range of behaviour. None of the combinations employed here can explain the recent experimental observations, but it is clear that at least some could be adjusted to do so. However, the lack of thermodynamic data concerning the interaction between the molecules and the surface presents a major obstacle. Further experiments which give information about the energetics of the system are needed before a definitive account of the structure and dynamics can be given.

SOONG-HYUCK SUH et SEAMUS F. O'SHEA. Can. J. Chem. **66**, 955 (1988).

On a effectué des calculs de Monte Carlo sur des plaques de chlore moléculaire adsorbées sur le plan basal du graphite. On a évalué un grand nombre de combinaisons des potentiels intermoléculaires et molécule/surface; les prédictions relatives à la structure qui en résultent couvrent un large éventail de comportements. Aucune des combinaisons utilisées dans ce travail ne peut expliquer les résultats expérimentaux observés récemment; mais il est évident que quelques-unes pourraient être ajustées pour le faire. Toutefois, le manque de données thermodynamiques concernant l'interaction entre les molécules et la surface présente un obstacle important. De nouvelles expériences qui pourraient donner des informations concernant les énergies du système sont nécessaires avant qu'une explication définitive de la structure et de la dynamique puissent être données.

[Traduit par la revue]

Can. J. Chem. Downloaded from www.nrcresearchpress.com by 176.9.209.113 on 09/07/12
For personal use only.

Introduction

James A. Morrison and his collaborators were among the pioneers in high precision surface calorimetry, including the study of the heats of adsorption of linear molecules of various surfaces (1–6). Physisorption of simple molecules on well characterized surfaces continues to be of interest, and recent papers include a number on the adsorption of linear molecules on the basal plane of graphite (5–24). While most of this work has dealt with molecular nitrogen (5, 7–15), oxygen (17–24), and with carbon monoxide (6, 16), a recent paper (25) describing an experimental study of the adsorption of molecular chlorine provides the opportunity to address a new system which may display some novel and interesting features. The basis for this expectation lies in the history of the study of solid three-dimensional (3-D) chlorine.

Because of the apparent simplicity of the structures of the homonuclear diatomic molecules, and of the solids composed of them, theorists have devoted a considerable amount of effort to constructing intermolecular potentials capable of accounting for the observed solid structures, thermodynamics, and dynamics. The ideas used for other systems are based heavily on experience gained in the study of nitrogen and Scott (26) gives a good account of early work in this area. In spite of some early successes, the general picture is fairly gloomy: at present there is not a single diatomic system for which we have an intermolecular potential of the quality of those available for the interaction of spherical systems, such as pairs of rare gas atoms.

Nonetheless, there are many approximate potentials which are effective in accounting for a restricted range of phenomena for a given element. The present work concerns a particularly interesting case, that of molecular chlorine. In early studies of the solid the site–site model, particularly in the form of two "atoms" interacting by means of Lennard–Jones interactions (2LJ), proved both popular and, to a limited extent, successful (27–31). 2LJ may be augmented by electrostatic interactions, written as the interaction of simple point multiples (26, 30), of "many-point-charges" (32), or of "distributed-multipole" arrangements (33). The simplest problem should be that of finding a model which would yield a structure of the solid consistent with the one observed experimentally. For the halogens, including chlorine, this proved to be substantially more difficult (27–31) than, e.g., for nitrogen (26). Indeed, the difficulties encountered in the case of chlorine have led to innovative suggestions (34, 35) concerning methods of representing the potential. Almost simultaneously two groups proposed to solve the problem of the structure of solid chlorine by using an atom–atom model which consists of anisotropic atoms. Burgos *et al.* (34) used the conventional LJ model for the atom–atom interactions but scaled the resulting value by a function combining the usual isotropic part with angular terms of some chosen multipole interaction, such as quadrupole–quadrupole. The resulting potential gives the correct structure and lattice frequencies for the crystal. Price and Stone (35) combined a detailed distributed-multipole model of the electrostatics with an anisotropic exponential repulsion and the best available estimates of the (isotropic) dispersion coefficients to give a more complicated model potential which also provides the correct stable structure. No further refinements have been introduced since, but Price (36) has recently published a very interesting analysis of the anisotropic atom model; she follows the method of English and Venables (30) in examining the relationship of atom–atom potentials to crystal structure.

The recently reported (25) X-ray study of the structure of chlorine adsorbed on graphite seems to indicate that 2-D solid chlorine will prove every bit as intriguing as has the 3-D one. The relevant results of that study are as follows: the solid is incommensurate; it is almost rectangular with a unit-cell angle of (97.54 ± 0.16°) and unit cell spacings of a = (4.033 ± 0.009) Å and b = (3.548 ± 0.008) Å; the lattice spacings are very insensitive to both temperature and coverage; the layer is so dense that the molecules must be standing with their bond axes close to the normal to the surface; above monolayer coverage, and certainly above about one and one third monolayers, formation of the second layer competes with bulk crystalliza-

tion; the 2-D critical and triple temperatures are believed to be higher than those in 3-D, in contrast to the usual case of the 2-D values being about 50% of the 3-D ones. The authors also show the close similarity between 2-D and 3-D solids. A setting of the 2-D unit cell similar to that used for layers in the 3-D cell yields lattice constants only slightly different from the 3-D values and a cell area which is almost identical. These are the essential features for which explanations are sought.

It is correct to say that any system consisting of adsorbent plus adsorbate constitutes a mixture, and therefore poses particularly difficult problems for anyone attempting a detailed explanation of its structures and dynamics. The source of the difficulty is that one must not only provide an accurate representation of the interactions among the adsorbate molecules but also a balanced account of the adsorbate–adsorbent interactions. In the present case little enough is known about the interactions among chlorine molecules, but essentiatlly nothing is known about the chlorine–graphite interaction. The work described here is a first attempt at explaining the structure and dynamics of the system, undertaken more to identify the features which need continued further study than in any hope of providing immediate answers. The treatment of the molecule-surface interaction is the simplest possible, using a sum of atom–atom Lennard–Jones interactions. This approach works well for rare gases on graphite (37). Even at this level of simplicity the lack of data, experimental and theoretical, prevents us from determining the two necessary parameters for chlorine on graphite.

Three versions of the intermolecular interaction were used together with two simple models of the molecule–surface interaction to investigate various aspects of the system. The temperatures and coverages studied are fairly restricted, but serve to highlight important aspects of the phase behaviour related to the experimental results. The models are introduced in the next section, and the calculations are described in the following one. The paper concludes with a discussion and suggestions for future work.

Interaction potentials

In their systematic study of the (classical) structures of diatomic solids English and Venables (30) used the two centre Lennard–Jones (2LJ) model

$$[1]\quad V_{\text{mol-mol}} = 4\epsilon \sum_i^2 \sum_j^2 \left[\left(\frac{\sigma}{R_{ij}}\right)^{12} - \left(\frac{\sigma}{R_{ij}}\right)^{6} \right]$$

R_{ij} is the distance between site i in one molecule and site j in the other; the sites either coincide with the atomic positions or are very close to them. English and Venables used a ratio of bondlength (d) to atomic diameter (σ) of $d/\sigma = 0.63$, and the well depth for atomic interactions was $\epsilon/k = 282$K. Singer and co-workers (38) used a similar value of d/σ, but with a range of ϵ values, the smallest being $\epsilon/k = 178.3$ K. We have used one of the Singer potentials which has $d/\sigma = 0.632$ and a well depth of $\epsilon/k = 256.6$ K.

The second intermolecular potential (PS) is that due Price and Stone (35), and it is also based on an atom–atom model, but the atoms are now anisotropic. The general form of the non-coulombic part of the interatomic potential is

$$[2]\quad V_{\text{a-a}} = c \exp\{-\alpha(\Omega)[R_{ij} - \rho(\Omega)]\} - \frac{A}{R_{ij}^6}$$

The angle dependence of the repulsive parameters is given by

TABLE 1. Potential parameters

(*a*) Lennard–Jones atom–atom potential for Cl_2–Cl_2

$\sigma = 3.198$ Å $\quad \epsilon/k = 256.6$ K $\quad d = 2.020$ Å

(*b*) Price and Stone atom–atom potential for Cl_2–Cl_2

$\rho_0 = 3.4829$ Å $\quad \rho_1 = 0.0424$ Å $\quad \rho_2 = 0.1498$ Å

$\alpha_0 = 3.51$ Å^{-1} $\quad \alpha_1 = -0.4966$ Å^{-1} $\quad c = 4.184$ J/mol

$d = 1.9814$ Å $\quad A = 8182.5$ kJ/(mol Å^6)

(*c*) Electrostatics of the PS and 2LJPC models
Molecular moments referred to the centre of mass:

$Q_2 = 2.688\, ea_0^2$, $Q_4 = 84.35\, ea_0^4$, $Q_6 = 872.2\, ea_0^6$, $Q_8 = 6193\, ea_0^8$

Point charges (positrons) and positions (Å) relative to the centre of mass:

1.2506	−2.2322	1.9632	−2.2322	1.2506
−1.4566	−1.0100	0.0	1.0100	1.4566

Moments of the PC model referred to the centre of mass:

$Q_2 = 2.688\, ea_0^2$ $Q_4 = 84.35\, ea_0^4$ $Q_6 = 872.2\, ea_0^6$ $Q_8 = 7457\, ea_0^8$

(*d*) Lennard–Jones atom–atom potential for Cl_2–graphite interaction

LB: $\sigma = 3.299$ Å $\quad \epsilon/k = 84.76$ K
FH: $\sigma = 3.299$ Å $\quad \epsilon/k = 50.49$ K

$$\alpha(\Omega) = \alpha_0 + \alpha_1[S_{202} + S_{022}]$$

$$[3]\quad \rho(\Omega) = \rho_0 + \rho_1[S_{303} + S_{033}] + \rho_2 S_{110}$$

The S functions are the angle-dependent terms appearing in expansions of pair properties of linear molecules in terms of the orientation angles of the bond vectors. In the convention followed here the relevant S functions are

$$S_{101} = z_1 \cdot \hat{\boldsymbol{R}}$$

$$S_{011} = z_2 \cdot \hat{\boldsymbol{R}}$$

$$S_{110} = z_1 \cdot z_2$$

$$[4]\quad S_{202} = (3S_{101}^2 - 1)/2$$

$$S_{022} = (3S_{011}^2 - 1)/2$$

$$S_{303} = (5S_{101}S_{202} - 2S_{101})/3$$

$$S_{033} = (5S_{011}S_{022} - 2S_{011})/3$$

$\hat{\boldsymbol{R}}$ is a unit vector pointing from site 1 to site 2 and z_1 and z_2 give the directions of the molecular bonds. It is very important to note that the convention used by Price and Stone (35) for the unit vectors along the bond is opposite to that commonly used; they use z_i to represent a vector pointing *from* the site *towards* the molecular centre. The electrostatic component of the intermolecular potential is also represented by an atomic model, but the atoms each carry a series of multipoles, from dipole to hexadecapole, so that the resulting series for each site–site interaction is formidable. The requisite values of the parameters are given in Table 1.

The third model (2LJPC) combines Price–Stone electrostatics with the 2LJ model, giving a potential which has simple isotropic atom–atom interactions and very detailed electrostatics. To simplify the evaluation of the potential and reduce the long computation times encountered with the PS model, we

Can. J. Chem. Downloaded from www.nrcresearchpress.com by 176.9.209.113 on 09/07/12
For personal use only.

Can. J. Chem. Downloaded from www.nrcresearchpress.com by 176.9.209.113 on 09/07/12
For personal use only.

constructed a "5-q" type (32) equivalent of the PS electrostatics. Point charges were placed on the atoms (q_1 at $\pm d/2$), symmetrically outside the atoms (q_2 at $\pm z$), and at the molecular centre ($-2q_1 - 2q_2$). The 5-q model was calibrated to fit the first three moments of the molecular charge distribution measured with respect to the centre of symmetry. These were obtained by transferring the moments of the "ATOM" model of Price and Stone (35) to the centre; an ambiguity in sign relating to the coordinate system was resolved by requiring that the molecular quadrupole moment have the value given in their "MOL" model. The fourth moment of the distribution is well reproduced by our point charges; see Table 1 for details. We calculated the charge model for the slightly larger bondlength value used with the Singer potential (38). Figure 1 shows some typical curves of the intermolecular potential as a function of intermolecular separation at fixed orientation for four models: 2LJ, PS, 2LJ + PS electrostatics (method of moments), and 2LJPC; the last two are plotted together in Fig. 1 and it is clear that the differences between them are not physically significant.

The interaction of the molecules with the surface is also written as a sum of atom–atom terms. Individual chlorine atoms interact with the carbon atoms of the graphite substrate by means of a Lennard–Jones potential. We used two models which differ only in the well depth parameters. The σ values for the molecule–surface interaction ($\sigma_{Cl—C}$) are found from those for the pure elements by means of the Lorentz combining rule (39)

$$[5] \quad \sigma_{Cl—C} = \frac{\sigma_{Cl—Cl} + \sigma_{C—C}}{2}$$

The value used for carbon is $\sigma_{C—C}$ = 3.4 Å. The well depth parameter can be found from the Bertholet rule (39)

$$[6] \quad \epsilon_{Cl—C} = \sqrt{\epsilon_{Cl—Cl}\epsilon_{C—C}}$$

The well depth may also be estimated by the Fender–Halsey rule (39, 40)

$$[7] \quad \epsilon_{Cl—C} = \frac{2\epsilon_{Cl—Cl}\epsilon_{C—C}}{\epsilon_{Cl—Cl} + \epsilon_{C—C}}$$

This approach gives values of $\epsilon_{Cl—C}$ which are closer to the lesser of the ϵ's for the pure systems, $\epsilon_{C—C}$ = 28 K; here it results in a drop of almost exactly 40% in $\epsilon_{Cl—C}$, from 84.76 to 50.49 K. Evidence concerning the usefulness of alternatives to the Bertholet rule is mixed. In 3-D fluid mixtures this rule has proved more effective than the geometric mean rule when the disparity between the well depths of the pure systems is large (39). However, the possibility of using combining rules other than Lorentz–Bertholet was discussed and rejected by Steele (37) in his work on the adsorption of rare gases on graphite.

The gas–surface interaction energy was calculated by means of the Fourier method introduced by Steele (41, 42), and, as usual, only the leading two terms of the series are used; the first represents the laterally averaged (flat) part of the potential, and the second term gives the dominant part of the corrugation. We used the Euler–MacLaurin representation give by Steele (37) for the flat part, and constructed an accurate analytical approximation to the z-dependence of the corrugation amplitude. In many calculations the second term was omitted, so that the surface was treated as being atomically flat. In any event, for the graphite substrate the corrugation term is very much smaller than the flat part, being about 1.5% in the region of the minimum; the maximum barrier to translation is a few tens of degrees.

Calculations

The calculations were implemented using the conventional Metropolis algorithm (43) for Monte Carlo simulation of the (N, V, T) ensemble, and production calculations were done on the CYBER 205 supercomputer at the University of Calgary. Typical calculations involved 5–10 $\times$ 10^5 steps of equilibration followed by 5–20 $\times$ 10^5 steps of accumulating data to form thermal averages of thermodynamic and structural quantities. Because the equilibration "times" are long at low temperatures most of the results reported here are for runs of 2 $\times$ 10^6 steps; the results of the first and second halves of the run were juxtaposed to ensure that the data are stable. Calculations were made for temperatures of 100, 160, 200, and 240 K. For each intermolecular potential a series of calculations was made using the Lorentz–Bertholet (LB) model and subsequent calculations incorporated the Fender–Halsey (FH) model. Most calculations were made on finite patches of 127 molecules, started from hexagonal configurations. A few calculations were done at a coverage of 0.5 monolayers (based on the $\sqrt{3} \times \sqrt{3}R30°$ structure), using 126 molecules with periodic boundary conditions. The cutoff for the intermolecular potential is 14.2 Å in the case of periodic systems, but many calculations were made without a potential cutoff for the finite patches. No systematic differences are evident between the patches with and without a cutoff.

Results

The pair energy curves of Fig. 1 are very useful for interpreting the results of the simulations. The cross (both molecules perpendicular to the intermolecular axis and to one another) configuration is the most stable for each of the three potentials. The optimum binding energy for 2LJ and 2LJPC interactions is noticeably greater (by $\approx$200 K) than for PS, and it is generally true that the binding energies are smaller for PS than for the others for the important configurations. Another important difference is that the parallel configuration (both molecules perpendicular to the intermolecular axis and parallel to one another) is more stable in 2LJ and 2LJPC than many other configurations, but this is not the case for PS. In fact, an even more stable configuration for 2LJ and 2LJPC is one in which the molecules are parallel but make an angle of about 70° to the intermolecular axis; at the minimum in the pair energy curve for these configurations the intermolecular separation is relatively small, about 3.5 Å. The T configuration is relatively favourable for all models, and this is the interaction which stabilizes the herringbone structure of solid nitrogen on graphite. Finally, the colinear arrangement is very unfavourable for the PS model and less so for the other two. These pair interactions compete with one another and with the molecule surface energy to determine the structure of the overlayer. For an isolated molecule the optimum structure is lying flat on the surface. The extra energy needed to make a molecule stand up must come either from the random thermal energy or from enhanced pair interactions in the upright position.

At 100 K the 2LJ–LB combination produces a compact but non-uniform solid structure. Many molecules stand up, but many also lie flat on the surface (Fig. 2) in a defective version of the herringbone structure. Here, at least in isolated patches, only some molecules can achieve the dense upright configurations, while the remaining molecules surround them with the

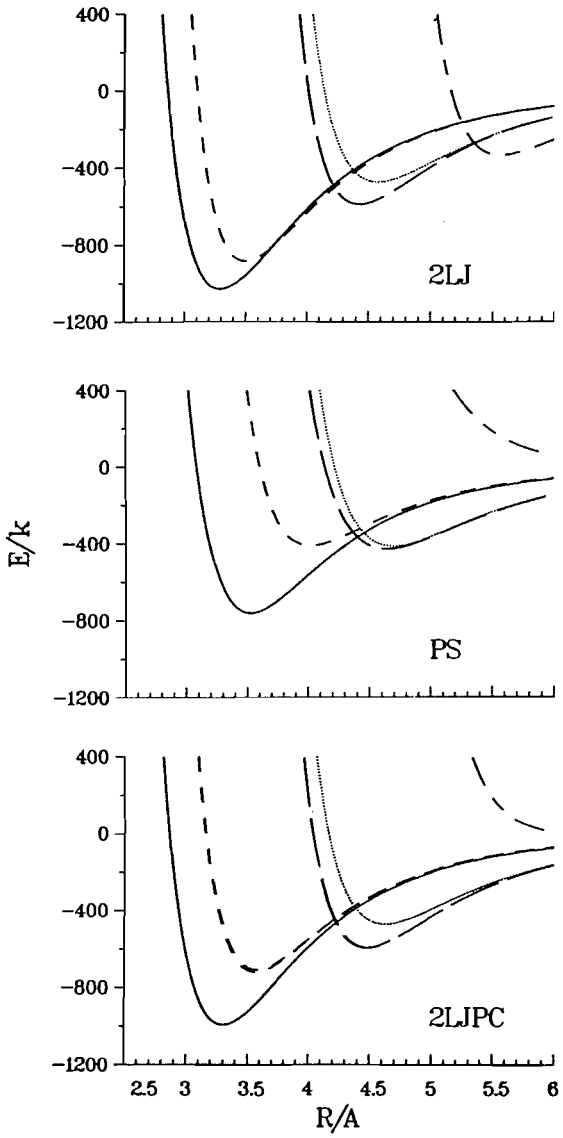

FIG. 1. The intermolecular pair potential as a function of the separation of the centres of mass at fixed orientation. For each model the solid line represents the cross configuration, the small dashes the parallel configuration, the large dashes the canted (45°) parallel configuration, the dots the T configuration, and the alternating dashes the linear configuration, respectively. In the case of 2LJPC two sets of results are plotted, one calculated with the method of moments and the other with the point charge representation; for most curves the results are indistinguishable. See the text for details.

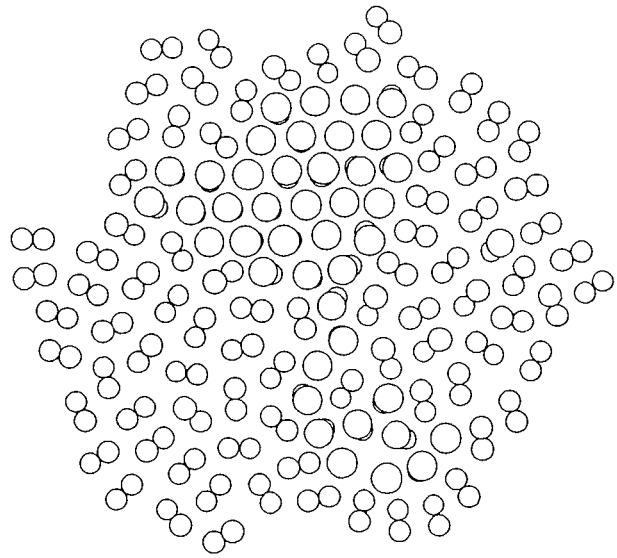

FIG. 2. The final configuration of the calculation for the 2LJ–LB model at 100 K. The radius of the atom increases with its height above the surface.

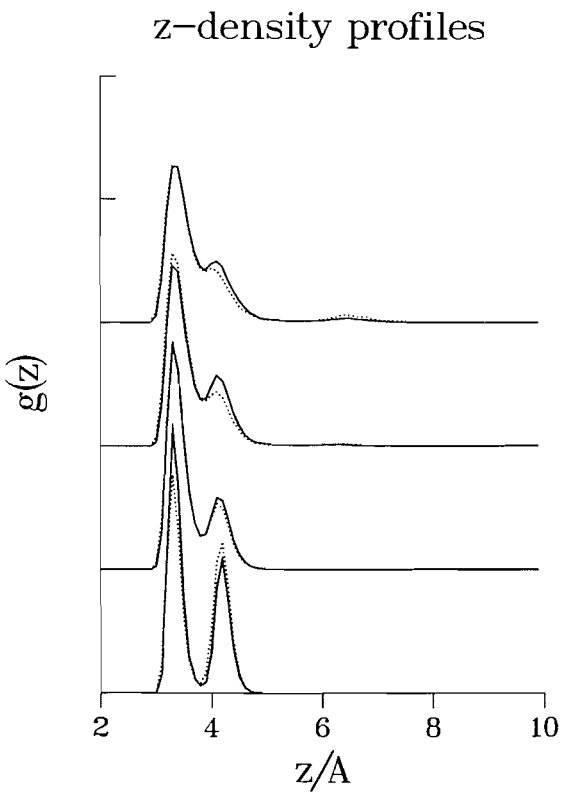

FIG. 3. The density profile as a function of the height of the centres of mass of the chlorine molecules above the graphite basal plane. The solid lines were calculated using the flat LB surface, and the dotted lines using the corrugated LB surface, both in combination with the 2LJ intermolecular potential. From bottom to top the data refer to temperatures of 100, 160, 200, and 240 K, respectively.

lower density flat structure; at lower temperatures one might expect the fraction of upright molecules to increase to some limiting value, unless another structure intervenes in the low temperature limit. The periodically replicated system at a coverage of 0.5 gives very similar results, showing that coverage is unimportant, at least for these parameters and conditions. When the system is heated to 160 and 200 K, the structure melts but remains compact. The thermal agitation destroys the dense upright rafts and, although a few of the molecules do stand up, the dominant structure is flat, as can be seen from the z-profile of the molecular centres of mass (Fig. 3). At 100 K there is a double peak, with one at the height (3–3.3 Å) appropriate to a layer flat on the surface and the other on the high-z side (≈4 Å) where one would expect to find the centres of mass of molecules which are standing up. At 160 and 200 K the second peak is much smaller. At 240 K a very small peak also appears at the bilayer position, $z \approx 6$–7 Å.

Raising the temperature to relatively high values produces two paradoxical kinds of behaviour: the spreading of the patch

Can. J. Chem. Downloaded from www.nrcresearchpress.com by 176.9.209.113 on 09/07/12
For personal use only.

Can. J. Chem. Downloaded from www.nrcresearchpress.com by 176.9.209.113 on 09/07/12
For personal use only.

to form a 2-D vapour, and promotion of molecules to form a partial bilayer in the patch. Ultimately every patch must evaporate because in the absence of an equilibrium vapour, both 2-D and 3-D, a patch can at best be metastable. Here, because of the limited calculations we can perform, we can detect only a massive and rapid evaporation of the patch which shows that the system has become completely unstable. The strong surface potential here favours 2-D evaporation. For 2LJ–LB this does not appear to happen up to 240 K, but there are indications that it is starting to happen at 240 K. Once it begins it probably happens rapidly, because the loss of coherence of the patch reduces the potential which prevents spreading. As the molecules spread they are largely parallel to the surface, reflecting the greater stability of this orientation for an isolated molecule. The existence of the corrugation term has relatively little effect on any of the dominant aspects of the behaviour of the patch, except that the density appears to be slightly larger for the flat case at low temperature; for obvious reasons it is impossible to determine the density of a finite patch precisely. The energies are entirely consistent with the observed structural behaviour; at low temperature the molecule–molecule energy favours the dense upright rafts at the expense of surface energy, and the collapse of the rafts at high temperature results in a net gain in surface energy and a greater loss of molecule–molecule energy. The formation of a partial bilayer, which can be detected in Fig. 3, provides a mechanism whereby the evaporation of a molecule to the 3-D vapour can occur in stages, each of which has a lower energy cost. For the strong LB surface potential a staged mechanism is probably necessary at the temperatures studied here.

No evidence of molecules standing up in any systematic way was found when the PS model was used to represent the intermolecular interactions. There are some important differences between PS and 2LJ in relative stabilities of different configurations, but the reduction in overall binding energy is probably the most important point here. The surface potential is strong enough to tip the balance in favour of T configurations, easily achieved in herringbone-like structures, rather than the parallel structures employed by a molecules in a layer which is predominantly standing up. The PS–LB (flat) system appears to be solid at 160 K, although there are some structural defects including occasional attempts to promote molecules to the second layer. The corrugated equivalent appears to be melted, but is still very compact. At 200 K there are clear signs that the system has become dilated and highly disordered, but it has not yet evaporated; at 240 K the system is even more dilated and shows weak indications of second layer molecules. Further calculation may well show that one or both of these systems would evaporate. In general, this model shows little tendency to have the molecules standing upright at any temperature studied here.

The 2LJPC–LB combination produces a result closer to PS–LB than to 2LJ–LB. Some molecules stand upright, but they are relatively few, and the effect of raising the temperature is to reduce the number upright (Fig. 4). By 160 K the structure is so defective that it almost certainly liquid. At 200 K the system is less dense but still compact, and at 240 K it shows evidence of fragmenting. The number of molecules standing up is slightly increased, but the separate peaks indicating two local minima have broadened to give a single peak with a pronounced shoulder on the high-z side. There is less evidence of promotion here than in the case of 2LJ–LB, probably because the intermolecular interactions in 2LJ favour upright molecules

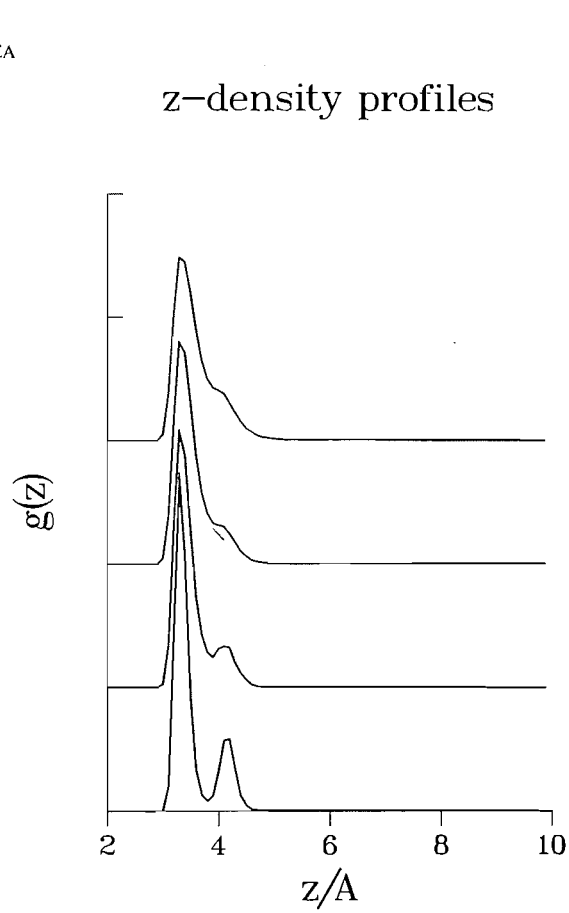

FIG. 4. The z-density profile for the 2LJPC–LB combination, following the conventions of Fig. 3.

more, and these are both precursors to and stabilizers of promotion.

It was at this stage that we introduce the FH model. As one might expect on the basis of the reduced well depth for the molecule–surface interaction, the influence of the surface is substantially reduced. At 100 K a patch of 2LJ molecules is very compact, with most of the molecules in the centre of the patch standing almost vertical, although many of those immediately at the edge are lying down. As the temperature is raised the system again becomes more disordered, but now the molecules continue to stand up, and the tendency to promote to the second layer is substantially greater (Fig. 5) than for any of the LB models. At 240 K the system is best described as a droplet sitting on the surface, and many of the molecules in the droplet are almost vertical, particularly those in the upper layer. Clearly, reducing the net binding to the surface tips the behaviour towards that found in layers of the 3-D solid (30), or what might be expected in 3-D droplets.

In this regime of reduced surface binding the PS model continues to predict flat herringbone structures (Fig. 6). The z-profile for the centre of mass positions shows virtually no molecules standing upright at 100 K, and heating the system to 160 K melts it, but produces only a slow growth in the number of upright molecules. The shape of the peak shows that the upright position is not a well defined local minimum, probably because the upright molecules are isolated from one another in a disordered environment. There are indications of molecules being promoted at higher temperatures, and of the patch evaporating laterally (2-D). By 240 K it has also started to evaporate off the surface.

The 2LJPC–FH combination yields results closely resem-

Can. J. Chem. Downloaded from www.nrcresearchpress.com by 176.9.209.113 on 09/07/12
For personal use only.

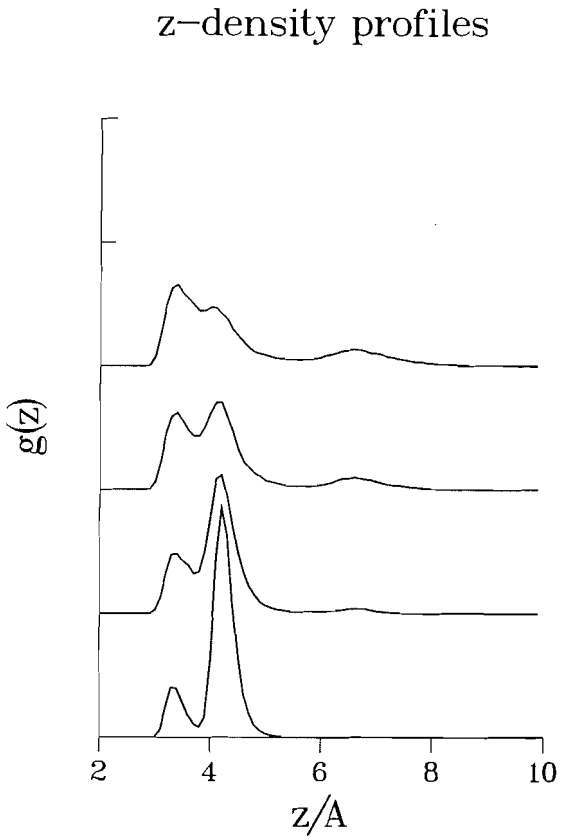

FIG. 5. The z-density profile for the 2LJ–FH combination, following the conventions of Fig. 3.

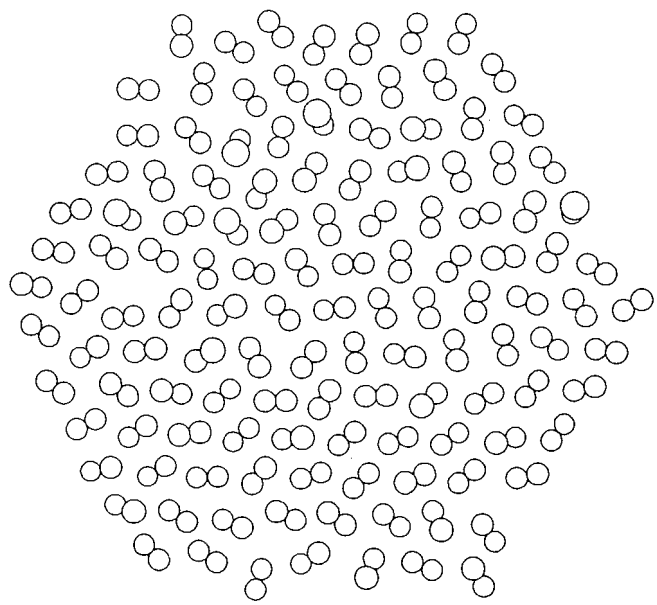

FIG. 6. The final configuration of the calculation for the PS–FH model at 100 K.

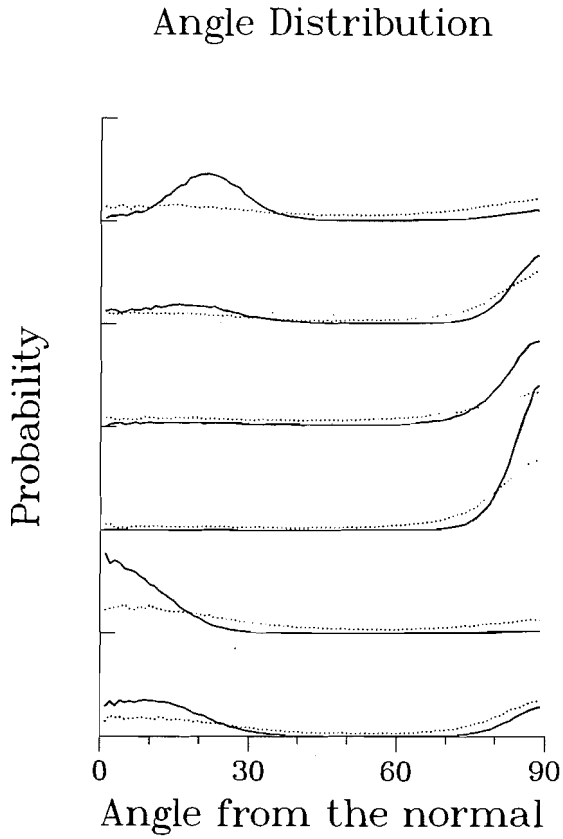

FIG. 7. The probability density for the angle of orientation of the bond axis measured from the normal to the surface. From bottom to top the data are for the 2LJ–LB, 2LJ–FH, PS–LB, PS–FH, 2LJPC–LB, and 2LJPC–FH, respectively. The solid lines were calculated for T = 100 K, and the dotted ones for 200 K.

bling those of 2LJ–FH. The low temperature structure is dominated by molecules standing upright in a dense mesh. One point of interest here is that the upright molecules are now canted at an angle of about 20° to the normal, a characteristic of the 2LJPC model which can also be seen in the 2LJPC–LB case (Fig. 7). Heating it to 160 K melts the system, and reduces the number of molecules standing up; some molecules are promoted to the second layer, where they tend to stand up. At 200 K the system forms a dense droplet (Fig. 8) having a lower layer which is mainly lying down and a top layer which has a significant number of upright molecules. At 240 K the droplet is still surprisingly compact, with only a few molecules separating from the main body.

Discussion

The main point which emerges from this survey of interaction potentials is that within this range of choices it is possible to produce a considerable variation in behaviour. The structures due to the 2LJ and PS models are sharply different whatever the surface potential, and 2LJPC lies somewhere between, closer to 2LJ in the FH case and to PS in the LB case. The balance between 2LJ-like and PS-like behaviour in 2LJPC is determined by the surface potential. A strong surface potential gives flat herringbone configurations which are PS-like in their behaviour, and a weaker surface permits some molecules to stand up and use the 2LJ-like parallel configurations (Fig. 1). The fact that 2LJPC is sometimes more like 2LJ than PS shows that the anisotropy due to the electrostatic interaction is important but not dominant, a result that is consistent with the work of Price and Stone on the 3-D solid (35). PS has a smaller well depth for configurations in which the molecules are parallel and nearly normal to the intermolecular vector, and this militates against the formation of rafts of upright molecules. As far as surface potentials are concerned, the weakening of the interaction with

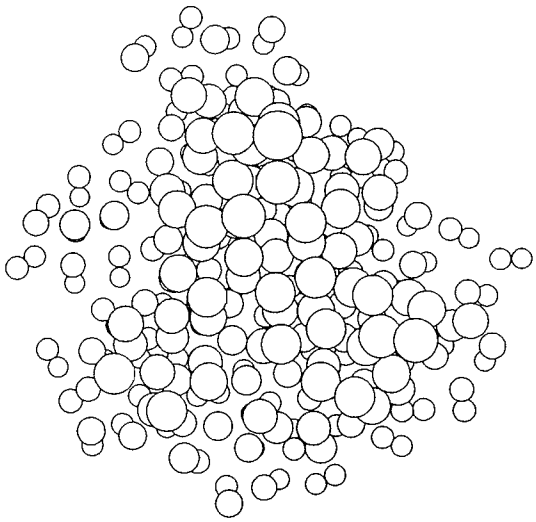

FIG. 8. The final configuration of the calculation for the 2LJPC–FH model at 200 K.

the surface in going from LB to FH results in a shift from a situation which is clearly more favourable to wetting, towards one in which wetting is probably incomplete.

The observed behaviour can almost certainly be rationalized by some combination of the molecule–molecule and molecule–surface interactions studied here. The 2LJ and 2LJPC models both predict upright rafts of molecules, as observed experimentally (25). However, in the 2LJ case the molecules stand vertical, leading inevitably to a regular triangular structure of the kind obtained for rare gases on graphite (41). 2LJPC leaves the molecules standing with a polar angle of 20° and a spacing of about 3.6 Å, in general agreement with the observed data. This canted structure seems more likely to yield a non-triangular lattice. We have not pursued this point, feeling that the uncertainties in the surface potential are so large that refining the models at this stage would be futile. The 2LJPC–FH combination apparently gives non-wetting behaviour (Fig. 8) when the temperature is high enough to melt the system, but appears to wet, at least incompletely, at low temperatures. The question of wetting behaviour is complex and difficult (44), and must also await further refinement of the molecule–surface interactions.

One important aspect neglected in the present paper is the role of surface mediation (45, 46) in modifying interactions among the molecules. The effects of surface mediation on the structure can be predicted, at least qualitatively. It reduces the attractive interactions between atoms at equal heights above the surface, by as much as 16–20% for atoms near the optimum height, while increasing the attraction between atoms more or less vertically above one another. The dominant effect that can be expected is a reduction in the effective well depth for intermolecular interaction, and a consequent increase in the relative importance of molecule–surface interactions. The second aspect deals with the competition between different overlayer structures. Inspection of the pair geometries of important configurations shows that this effect, although reducing attraction forces between molecules, does so differentially, favouring configurations in the following order: upright pairs, one upright plus one flat, flat and parallel, flat T, and, least of all, flat linear; bilayer configurations are actively favoured. Thus, surface mediation of interactions is likely to promote wetting by increasing the relative importance of molecule–surface interactions, to favour upright structures in the monolayer, and to favour bilayer formation over bulk condensation (because of the rapid decay of this mechanism with height above the surface).

The fact that the range of models treated here appears to be able to support a rich variety of phase behaviour is a mixed blessing. It is clear that progress towards a reliable explanation of the observations cannot be made until further experimental information becomes available. Of particular interest is the heat of adsorption, especially the limiting isosteric heat. This can be obtained from the analysis of isotherms in the Henry's Law region. We have calculated Henry's Law coefficients K_H for both molecule–surface models used here, and obtained the isosteric heat from the slope of ln (K_H) vs. $1/T$ (47). The resulting values for the low temperature, low coverage limit are 2970 K for LB and 1730 K for FH (24.7 and 14.4 kJ/mol, respectively). The experimental precision is such that it should be relatively easy to determine which is the more appropriate value; in fact, these values probably set limits to the true isosteric heat. While the isosteric heat would be useful, a detailed thermodynamic investigation of the kind done for nitrogen on graphite (5, 12) would be even more helpful in unravelling the details of this complex system.

Acknowledgements

This work reflects the continuing interest on the part of S.F.O. in subjects to which he was introduced by Jim Morrison and Mike Klein, a right pair of troublemakers. Jim also introduced S.F.O. to Laphraoig, a great benefit.

Let no one carp
If you bag the biggest harp.
May the cloud on which you sit
Fit. (after Kuno Meyer)

This work was supported by a grant from the Natural Sciences and Engineering Research Council of Canada. Computer resources were supplied by the University of Lethbridge, and by SuperComputing Service of the University of Calgary under an agreement with the Province of Alberta. We gratefully acknowledge this support.

1. J. A. MORRISON and G. J. SZASZ. J. Chem. Phys. **16**, 280 (1948).
2. J. A. MORRISON and J. M. LOS. Discuss. Faraday Soc. **8**, 321 (1950).
3. J. A. MORRISON, L. E. DRAIN, and J. S. DUGDALE. Can. J. Chem. **30**, 890 (1952).
4. L. E. DRAIN and J. A. MORRISON. Trans. Faraday Soc. **49**, 654 (1953).
5. J. PIPER, J. A. MORRISON, C. PETERS, and Y. OZAKI. J. Chem. Soc. Faraday Trans. I, **79**, 2863 (1983).
6. J. PIPER, J. A. MORRISON, and C. PETERS. Mol. Phys. **53**, 1463 (1984).
7. T. T. CHUNG and J. G. DASH. Surf. Sci. **66**, 559 (1977).
8. W. A. STEELE. J. Phys. (Paris), **38**, C4-61 (1977).
9. J. ECKERT, W. B. ELLERSON, J. B. HASTINGS, and L. PASSELL. Phys. Rev. Lett. **51**, 192 (1979).
10. S. F. O'SHEA and M. L. KLEIN. Chem. Phys. Lett. **66**, 381 (1979).
11. R. D. DIEHL, M. F. TONEY, and S. C. FAIN. Phys. Rev. Lett. **48**, 177 (1982); R. D. DIEHL and S. C. FAIN. Surf. Sci. **125**, 116 (1983).
12. A. D. MIGONE, H. K. KIM, M. H. W. CHAN, J. TALBOT, D. J. TILDESLEY, and W. A. STEELE, Phys. Rev. Lett. **51**, 192 (1983);

Can. J. Chem. Downloaded from www.nrcresearchpress.com by 176.9.209.113 on 09/07/12
For personal use only.

M. H. W. CHAN, A. D. MIGONE, K. D. MINER, and Z. R. LI. Phys. Rev. B**30**, 2681 (1984).
13. J. TALBOT, D. J. TILDESLEY, and W. A. STEELE. Mol. Phys. **51**, 1331 (1984); Faraday Discuss. **80**, 91 (1985); Surf. Sci. **169**, 71 (1986).
14. G. CARDINI and S. F. O'SHEA. Surf. Sci. **154**, 231 (1985).
15. D. J. TILDESLEY and R. M. LYNDEN-BELL. J. Chem. Soc. Faraday Trans. II **82**, 1605 (1986).
16. S. C. FAIN. Ber. Bun. Ges. **90**, 211 (1986).
17. B. GILQUIN. Thesis, University of Nancy, 1979 (unpublished); B. GILQUIN and Y. LARHER. Surf. Sci. **75**, 703 (1978).
18. M. BIENFAIT, J. L. SEGUIN, J. SUZANNE, E. LERMER, J. KRIM, and J. G. DASH. Phys. Rev. B**29**, 983 (1984).
19. D. D. AWSCHALOM, G. N. LEWIS, and S. GREGORY. Phys. Rev. Lett. **51**, 586 (1983).
20. C. E. BARTOSCH and S. GREGORY. Phys. Rev. Lett. **54**, 2513 (1985).
21. S. G. J. MOCHRIE *et al.* Surf. Sci. **138**, 599 (1984); P. A. HEINEY *et al.* Surf. Sci. **125**, 539 (1983); P. A. STEPHENS *et al.* Phys. Rev. Lett. **45**, 1959 (1980).
22. J. A. VENABLES, J. L. SEQUIN, J. SUZANNE, and M. BIENFAIT. Surf. Sci. **145**, 345 (1984).
23. M. DRIR and G. B. HESS. Phys. Rev. B**33**, 4758 (1986).
24. M. F. TONEY and S. C. FAIN. Phys. Rev. B**36**, 1248 (1987).
25. H. KLEE, K. KNORR, and H. WIECHERT. Surf. Sci. **171**, 103 (1986).
26. T. A. SCOTT. Phys. Rep. **27C**, 89 (1976), and *op cit.*
27. K. YAMASAKI. J. Phys. Soc. Jpn. **17**, 1264 (1962).
28. S. C. NYBURG. J. Chem. Phys. **40**, 2493 (1964); **48**, 4890 (1968).
29. I. H. HILLIER and S. A. RICE. J. Chem. Phys. **46**, 3881 (1967).
30. C. A. ENGLISH and J. A. VENABLES. Proc. R. Soc. A**340**, 57 (1974).
31. S. C. NYBURG and W. WONG-NG. Proc. R. Soc. A**367**, 29 (1979).
32. C. S. MURTHY, S. F. O'SHEA, and I. R. MCDONALD. Mol. Phys. **50**, 531 (1983).
33. A. J. STONE. Chem. Phys. Lett. **83**, 223 (1981).
34. E. BURGOS, C. S. MURTHY, and R. RIGHINI. Mol. Phys. **47**, 1391 (1982).
35. S. L. PRICE and A. J. STONE. Mol. Phys. **47**, 1457 (1982).
36. S. L. PRICE. Mol. Phys. **62**, 45 (1987).
37. W. A. STEELE. J. Phys. Chem. **82**, 817 (1978).
38. K. SINGER, A. TAYLOR, and J. V. L. SINGER. Mol. Phys. **33**, 1757 (1977).
39. G. C. MAITLAND, M. RIGBY, E. B. SMITH, and W. A. WAKEHAM. Intermolecular forces. Oxford University Press, Oxford. 1981.
40. B. E. F. FENDER and G. D. HALSEY, JR. J. Chem. Phys. **36**, 1881 (1962).
41. W. A. STEELE. Surf. Sci. **36**, 317 (1973).
42. W. A. STEELE. The interaction of gases with solid surfaces. Pergamon Press, Oxford. 1974.
43. N. METROPOLIS, A. W. ROSENBLUTH, M. N. ROSENBLUTH, A. H. TELLER, and E. TELLER. J. Chem. Phys. **21**, 1087 (1953).
44. R. J. MUIRHEAD, J. G. DASH, and J. KRIM. Phys. Rev. B**29**, 5074 (1984).
45. O. SINANOGLU and K. S. PITZER. J. Chem. Phys. **32**, 1279 (1960).
46. A. D. MCLACHLAN. Mol. Phys. **7**, 381 (1964).
47. M. J. BOJAN and W. A. STEELE. Langmuir. **3**, 116 (1987).

Can. J. Chem. Downloaded from www.nrcresearchpress.com by 176.9.209.113 on 09/07/12
For personal use only.

Structural, spectroscopic, and electron paramagnetic resonance studies on two solid phases of bis-dipropylammonium tetrachlorocuprate(II) (DPACC)

MARCUS R. BOND,[1] TIMOTHY J. JOHNSON, AND ROGER D. WILLETT
Chemical Physics Program, Washington State University, Pullman, WA 99163-4620, U.S.A.

Received September 17, 1987

This paper is dedicated to Professor James A. Morrison

MARCUS R. BOND, TIMOTHY J. JOHNSON, and ROGER D. WILLETT. Can. J. Chem. **66**, 963 (1988).

Bis-dipropylammonium tetrachlorocuprate(II) exists in two known crystalline phases. Below 330 K (β phase) the crystal is orthorhombic *Pbca* with cell constants (at 293(1) K) a = 13.029(2) Å, b = 15.252(3) Å, c = 20.997(2) Å, V = 4175.5(9) Å^3. The crystal undergoes a phase transition at 330 K to the α phase, which is monoclinic $P2_1/n$ with cell constants (at 342(1) K) a = 13.277(4) Å, b = 10.280(3) Å, c = 16.362(13) Å, β = 104.31(5)°, V = 2164(2) Å^3. The β phase consists of discrete, distorted tetrahedral $CuCl_4^{2-}$ anions, which are surrounded by dipropylammonium cations. Hydrogen bonding between the anions and cations results in a two-dimensional network of linked anions coplanar with the c-glide plane of the unit cell. The terminal carbon of one of the dipropylammonium chains assumes the higher energy *gauche* conformation while all other carbon and nitrogen atoms are found in the *anti* conformation. The local geometry of the α phase is very similar to that of the β phase. Powder electron paramagnetic resonance measurements in both phases confirm the persistence of the β phase anion geometry in the α phase. The disorder and increased thermal motion of the alkyl groups of the cation account for observed differences between the crystal structures of the two phases. This phase transition is similar to those found in long chain monoalkylammonium metal halide layer compounds that involve "melting" of the alkyl chain. Near infrared – visible spectra at 77 and 295 K show two distinct peaks at 12 700 and 9800 cm^{-1} in the first case and a very broad band maximizing at 11 200 cm^{-1} in the latter case. The highest-energy d–d transition correlates well with those of other $CuCl_4^{2-}$ anions of varying tetragonal distortion from tetrahedral geometry. The present data are used in conjunction with earlier data to develop the correlation between the highest-energy d–d transition and the distortion from tetrahedral symmetry.

MARCUS R. BOND, TIMOTHY J. JOHNSON et ROGER D. WILLETT. Can. J. Chem. **66**, 963 (1988).

Le tétrachlorocuprate(II) de bis-dipropylammonium existe sous deux phases cristallines connues. En-dessous de 300 K (phase β), le cristal est orthorhombique, groupe d'espace *Pbca* avec (à 293(1) K) a = 13,029(2), b = 15,252(3) et c = 20,997(2) A et V = 4175,5(9) Å^3. Le cristal subit une transition de phase à 330 K qui le transforme en phase α, monoclinique, groupe d'espace $P2_1/n$ avec (à 342(1) K) a = 13,277(4), b = 10,280(3) et c = 16,362(13) Å, β = 104,31(5)° et V = 2164(2) Å^3. La phase β comprend des anion tétraèdres déformés de $CuCl_4^{2-}$ qui sont entourés de cations dipropylammonium. Les liaisons hydrogènes entre les anions et les cations conduisent à la formation d'un réseau bidimensionnel d'anions coplanaires liés au plan de glissement c de la cellule unitaire. Le carbone terminal d'une des chaînes du groupement dipropylammonium se trouve dans une conformation *gauche* d'énergie élevée; tous les autres atomes de carbone et d'azote se retrouvent dans une conformation *anti*. La géométrie locale de la phase α est trés semblable à celle de la phase β. Des mesures de resonance paramagnétique électronique effectuées sur des poudres confirment que la géométrie de l'anion de la phase β persiste dans la phase α. Le désordre ainsi qu'une augmentation du mouvement thermique des groupements alkyles du cation expliquent les différences qui sont observées entre les structures cristallines des deux phases. Cette transition de phase est semblable à celle qui est observée dans les couches d'halogénures de monoalkylammonium métalliques à longues chaînes impliquant la «fonte» de la chaîne alkyle. Les spectres proche-infrarouge – visible, déterminés à 77 et 295 K, présentent deux bandes distinctes à 12 700 et 9800 cm^{-1} dans le premier cas et une bande très large avec maximum à 11 200 cm^{-1} dans le deuxième cas. Il existe une bonne corrélation entre la transition d–d de haute énergie et celles d'autres anions du $CuCl_4^{2-}$ présentant des distorsions variées par rapport à la géométrie tétraédrique. On utilise ces données de concert avec d'autres obtenues antérieurement pour développer une corrélation entre la transition d–d de haute énergie et la distorsion par rapport à la symétrie tétraédrique.

[Traduit par la revue]

Introduction

Compounds of the A_2CuX_4 (A = monopositive cation, X = halide) system have been found to exhibit a number of interesting phase transitions. The $(RNH_3)_2CuX_4$ systems are known to crystallize as layers of corner-sharing CuX_6^{4-} octahedra with the alkylammonium cations sandwiched between the layers (1). The long chain alkylammonium compounds, in particular, undergo phase transitions involving the "melting" of the alkyl groups while leaving the copper halide layers rigid (1, 2). When bulkier cations are used, these systems are known to crystallize as isolated CuX_4^{2-} ions surrounded by the cations. A number of these compounds exhibit thermochromic phase transitions (e.g., the diethylammonium and *N*-methylphenethylammonium salts) in which the coordination geometry of the copper(II) ion changes (3). The $[(CH_3)_4N]_2CuX_4$ systems exhibit commensurate–incommensurate phase transitions that involve rotation of the CuX_4^{2-} tetrahedra (4).

White and co-workers (5) recently studied the thermal properties of the $[(C_nH_{2n+1})_2NH_2]_2CuCl_4$ salts (n = 2–6) by differential scanning calorimetry and found that the title compound undergoes a solid–solid phase transition at 330 K with ΔH_{trans} = 4.26 kJ mol^{-1}. This transition has also been observed by Tomovic *et al.* (6). There has also been continued interest in correlating the d–d transition energies of tetrahedrally coordinated Cu(II) ions with varying degrees of tetragonal distortion (7, 8). The purpose of this paper is to report the crystal structures and spectroscopic properties of two solid phases of bis-dipropylammonium tetrachlorocuprate(II) (DPACC) (the α phase existing between the transition temperature at 330 K and the melting point at 353 K, the β phase existing below 330 K), and to correlate the maximum d–d transition energy of the room

[1]Author to whom correspondence may be addressed.

Can. J. Chem. Downloaded from www.nrcresearchpress.com by 176.9.209.113 on 09/07/12
For personal use only.

temperature phase with that of other distorted tetrahedral $CuCl_4^{2-}$ ions.

Experimental

Synthesis

Crystals of DPACC were grown by slow evaporation of an ethanolic solution containing stoichiometric amounts of dipropylammonium chloride and anhydrous copper(II) chloride. The dipropylammonium chloride was prepared by neutralizing dipropylamine (Aldrich, 99%) with concentrated HCl, recrystallizing the product from water, and washing with acetone. The light green crystals, which often grow as large (~1 cm^3) plates, exhibit a gradual thermochromism (green to yellow with increasing temperature). Samples for immediate use may be quickly prepared by fusing together stoichiometric quantities of the reagents at ~100°C with stirring. The sample for spectroscopic study was prepared in this manner.

Crystal data, β phase

$C_{12}H_{32}Cl_4CuN_2$ fw = 395.75

Orthorhombic, *Pbca*(no. 61) (systematic absences: $0kl$, $k = 2n + 1$; $h0l$, $l = 2n + 1$; $hk0$, $h = 2n + 1$; $h00$, $h = 2n + 1$; $0k0$, $k = 2n + 1$; $00l$, $l = 2n + 1$); at 293 K: $a = 13.029(2)$ Å, $b = 15.252(3)$ Å, $c = 20.997(2)$ Å, $V = 4175.5(9)$ Å^3 (from 25 reflections in the range $29° < 2\theta < 30°$) (ref. 9); $Z = 8$, $\rho_{calc} = 1.30$ g/cm^3, $F(000) = 1720$ e.

Structure determination, β phase

Radiation, Mo $K\alpha_1$, $\lambda = 0.70926$ Å (graphite monochromator); light-green, block-shaped crystal, 0.35 mm × 0.35 mm × 0.43 mm, glued to a glass fiber. Reflections (Nicolet R3m/E four-circle diffractometer, 0.85° ω scans, scan speed: 4.88–29.3°/min): total (to $2\theta = 45°$; $0 \le h \le 14$; $0 \le k \le 16$; $0 \le l \le 22$) 3095, 6 rejected as asymmetric; total unique, 2718; total used ($|F_o| \ge 3\sigma(|F_o|)$), 1858. Check reflections ($\bar{2}\,\bar{4}\,5$, $\bar{6}\,0\,4$, $\bar{7}\,1\,6$) collected every 100 reflections, variations within counting statistics. Lorenz polarization corrections and crystal decay correction based on a curve fitted to the intensities of the standard reflections were applied. Empirical absorption correction assuming ellipsoidal crystal shape ($\mu = 15.6$ cm^{-1}; limits of transmission, 0.38–0.42; $R_{merge} = 0.0176$ (before), 0.0095 (after)). Isotropic extinction correlation made; $F = F_{calc}/[1.0 + 0.002 \times X \times F^2/\sin(2\theta)]^{0.25}$, X refined to 0.00013. Weighting scheme: $w^{-1} = \sigma^2(F_o) + g|F_o|^2$, g refined to 0.0. Temperature factor: $T = \exp[-2\pi^2(h^2a^{*2}U_{11} + k^2b^{*2}U_{22} + l^2c^{*2}U_{33} + 2klb^*c^*U_{23} + 2hla^*c^*U_{13} + 2hkab^*U_{12})]$.

Structure solution and refinement were achieved using the SHELXTL package of programs provided by Nicolet (10) (scattering factors from ref. 11). The structure was solved using direct methods and refined using a blocked cascade least-squares method. Copper and chlorine atom positions were identified from the E-map produced from direct methods, while positions of the remaining non-hydrogen atoms were identified from subsequent electron density difference maps. The hydrogen atoms were also located on the electron density difference map and were included in the refinement but constrained to a C—H distance of 0.096 Å, an N—H distance of 1.034 Å, and an idealized geometry. Anisotropic thermal parameters are refined for all non-hydrogen atoms and a common isotropic thermal parameter was refined for the hydrogen atoms. Final refinement with 186 least-squares parameters gave $R = 0.0512$ and $R_w = 0.0318$ (0.0825 and 0.0343, respectively, for all data). Goodness of fit = 1.429, $|\Delta/\sigma|_{mean} = 0.005$, $|\Delta/\sigma|_{max} = 0.023$. The excursions on the final electron density difference map ranged from −0.338 to 0.366 e/Å^3.

Positions and equivalent isotropic thermal parameters for non-hydrogen atoms are listed in Table 1, anisotropic thermal parameters in Table 2, and interatomic distances and angles in Table 3. An ORTEP plot of the formula unit with atom labels is shown in Fig. 1, while a stereographic diagram of the structure is shown in Fig. 2. Tables of observed and calculated structure factors and hydrogen atom positions are included in the supplementary material.[2]

[2]Copies of these tables and figures may be purchased from the Depository of Unpublished Data, CISTI, National Research Council of Canada, Ottawa, Ont., Canada K1A 0S2.

TABLE 1. Atomic coordinates (×10^4) and isotropic thermal parameters (Å^2 × 10^3) for the β (I) and α (II) phases of DPACC

I

Atom	x	y	z	U
Cu	5641(1)	2961(1)	1241(1)	46(1)*
Cl(1)	6295(1)	2813(1)	2225(1)	74(1)*
Cl(2)	7172(1)	3279(1)	794(1)	59(1)*
Cl(3)	4126(1)	3506(1)	1575(1)	58(1)*
Cl(4)	4996(1)	2301(1)	370(1)	66(1)*
N(1)	2534(3)	2886(3)	454(2)	50(2)*
C(1)	1984(4)	2345(4)	941(3)	57(3)*
C(2)	2473(5)	1463(4)	1023(3)	67(3)*
C(3)	1868(5)	888(4)	1477(3)	82(3)*
C(4)	2127(4)	3797(4)	396(3)	67(3)*
C(5)	2585(6)	4285(4)	−167(3)	86(3)*
C(6)	3726(5)	4476(4)	−106(3)	99(4)*
N(2)	8864(3)	2988(4)	1939(2)	52(2)*
C(7)	9451(4)	3657(4)	1584(3)	62(3)*
C(8)	9079(5)	4562(4)	1726(3)	81(3)*
C(9)	9680(6)	5234(5)	1362(4)	143(5)*
C(10)	9153(4)	2071(4)	1771(3)	63(3)*
C(11)	8631(5)	1418(5)	2167(3)	93(4)*
C(12)	8883(5)	479(4)	1998(3)	96(4)*

II

Atom	x	y	z	U
Cu	86(1)	6702(1)	2745(1)	68(1)*
Cl(1)	719(2)	8613(2)	2449(2)	110(1)*
Cl(2)	1665(1)	5771(2)	3162(2)	87(1)*
Cl(3)	−1263(2)	7562(2)	3172(2)	90(1)*
Cl(4)	−748(2)	4857(2)	2249(2)	103(1)*
N(1)	1838(5)	9488(7)	7427(6)	87(4)*
C(1)	1272(8)	8712(11)	6688(8)	119(7)*
C(2)	1610(9)	8861(11)	5957(9)	150(7)*
C(3)	972(8)	8081(13)	5190(7)	186(8)*
C(4)	1523(7)	9280(10)	8208(8)	115(6)*
C(5)	1963(11)	10066(12)	8946(9)	166(8)*
C(6)	1500(14)	9906(18)	9643(9)	227(12)*
C(6A)	3115(12)	10087(61)	9208(22)	134(39)
N(2)	1801(4)	2936(6)	2369(4)	77(3)*
C(7)	1060(6)	2710(8)	1541(5)	97(5)*
C(8)	1295(7)	3527(10)	868(6)	122(5)*
C(9)	543(8)	3287(11)	20(7)	177(7)*
C(10)	1583(6)	2180(8)	3062(5)	93(5)*
C(11)	2413(7)	2271(9)	3846(6)	120(6)*
C(12)	2156(7)	1587(10)	4569(6)	156(6)*

*The equivalent isotropic U is defined as one third of the trace of the orthogonalized U_{ij} tensor.

Crystal data, α phase

Monoclinic, $P2_1/n$(no. 14, cell choice 2) (systematic absences: $h0l$, $h + l = 2n + 1$; $h00$, $h = 2n + 1$; $0k0$, $k = 2n + 1$; $00l$, $l = 2n + 1$); at 342 ± 1 K: $a = 13.277(4)$ Å, $b = 10.280(3)$ Å, $c = 16.362(13)$ Å, $\beta = 104.31(5)°$, $V = 2164(2)$ Å^3 (from 25 reflections in the range $25° < 2\theta < 27°$) (ref. 9); $Z = 4$, $\rho_c = 1.26$ g/cm^3, $F(000) = 860$ e.

Structure determination, α phase

Radiation, Mo $K\alpha_1$, $\lambda = 0.70926$ Å (graphite monochromator); crystal of dimensions 0.33 mm × 0.33 mm × 0.25 mm glued to a glass fiber, coated with epoxy glue, and heated to 345(1) K. High crystal temperature was attained via a stream of heated air directed along the ϕ-axis of the diffractometer. The temperature control circuit was connected to a chromel–alumel thermocouple placed at the outlet nozzle of the air heater. The temperature at the center of the diffractometer circle

Can. J. Chem. Downloaded from www.nrcresearchpress.com by 176.9.209.113 on 09/07/12
For personal use only.

TABLE 2. Anisotropic thermal parameters ($Å^2 \times 10^3$) for the β (I) and α (II) phases of DPACC

I

Cu	42(1)	53(1)	43(1)	2(1)	1(1)	5(1)
Cl(1)	55(1)	121(2)	45(1)	19(1)	0(1)	21(1)
Cl(2)	50(1)	83(1)	45(1)	−3(1)	5(1)	−12(1)
Cl(3)	48(1)	78(1)	49(1)	−10(1)	−3(1)	17(1)
Cl(4)	51(1)	82(1)	64(1)	−25(1)	2(1)	0(1)
N(1)	43(3)	64(4)	44(3)	−8(3)	−3(3)	−6(3)
C(1)	47(4)	74(5)	51(4)	−13(4)	3(4)	−2(4)
C(2)	76(5)	63(5)	63(4)	−4(4)	10(4)	−5(4)
C(3)	95(6)	73(5)	77(5)	−9(4)	11(5)	−16(5)
C(4)	59(5)	53(5)	89(5)	−18(4)	−20(4)	10(4)
C(5)	114(7)	53(5)	90(6)	10(4)	− 34(6)	−11(5)
C(6)	109(7)	93(6)	95(6)	21(5)	2(5)	−16(6)
N(2)	47(3)	54(4)	55(3)	−2(3)	−10(3)	−0(3)
C(7)	49(4)	71(5)	67(4)	20(4)	−7(4)	−11(4)
C(8)	91(6)	58(5)	94(5)	12(5)	−20(5)	−14(5)
C(9)	155(9)	107(7)	167(9)	58(7)	−55(8)	−40(7)
C(10)	51(4)	72(5)	67(4)	5(4)	−0(3)	13(5)
C(11)	81(6)	85(6)	113(7)	15(5)	19(5)	11(5)
C(12)	95(6)	77(6)	116(6)	11(5)	−7(6)	12(5)

II

Cu	55(1)	53(1)	96(1)	−2(1)	20(1)	4(1)
Cl(1)	72(2)	60(2)	204(3)	29(2)	45(2)	9(1)
Cl(2)	59(1)	62(2)	133(2)	9(1)	12(1)	7(1)
Cl(3)	73(2)	70(2)	135(2)	−15(2)	44(1)	5(1)
Cl(4)	71(2)	74(2)	165(3)	−38(2)	31(2)	−6(1)
N(1)	69(5)	75(6)	111(7)	−18(6)	11(5)	4(4)
C(1)	113(9)	124(10)	133(12)	17(9)	54(9)	7(8)
C(2)	151(11)	147(12)	146(13)	−22(10)	25(10)	−25(9)
C(3)	161(11)	241(16)	146(11)	−52(12)	17(9)	−16(11)
C(4)	126(9)	118(10)	133(11)	58(9)	96(9)	58(8)
C(5)	178(13)	136(11)	146(14)	−58(12)	−30(11)	64(10)
C(6)	377(25)	253(20)	75(12)	−11(12)	100(14)	81(18)
N(2)	61(4)	65(5)	110(6)	−8(5)	33(4)	3(4)
C(7)	68(6)	94(8)	125(9)	−16(6)	16(6)	−0(6)
C(8)	106(8)	136(9)	120(9)	16(8)	19(7)	22(8)
C(9)	193(12)	185(13)	128(11)	11(11)	−6(10)	52(11)
C(10)	106(7)	61(6)	129(9)	7(6)	60(6)	−7(5)
C(11)	147(9)	100(8)	114(9)	21(7)	37(8)	−2(7)
C(12)	212(11)	132(10)	142(10)	17(8)	78(9)	4(9)

was measured with an iron–constantan thermocouple prior to mounting the crystal. Fluctuations of a few tenths of a degree Kelvin in the temperature were observed while driving the diffractometer angles. Reflections (Syntex $P2_1$ four-circle diffractometer upgraded to Nicolet P3F specifications, 1.0° ω scans, scan speed: 3.91–29.3°/min): total (to $2\theta = 40°$; $0 \leq h \leq 12$; $0 \leq k \leq 9$; $-15 \leq l \leq 15$) 2300, 3 rejected as asymmetric, 1 rejected due to background imbalance; total unique, 2018; total used ($|F_o| \geq 3\sigma(|F_o|)$), 1431. After measuring 1080 reflections the crystal was found to have moved slightly (due, presumably, to a small amount of surface melting). The temperature was then lowered to 342(1) K and data collection resumed on the same crystal. Reflection intensities are assumed to be relatively unchanged by the temperature drop since the intensities of the standard reflections were the same, within counting statistics, immediately before and after the temperature change. Check reflections ($\bar{5}\ \bar{3}\ 0$, $\bar{1}\ 2\ \bar{5}$) were collected every 45 reflections with an approximate 17% decrease in intensity over the course of the data collection. The rate of intensity loss was unaffected by the above mentioned temperature drop. A crystal decay correction based on a curve fitted to the intensities of the check reflections over time was applied as were Lorenz polarization corrections. Empirical absorption correction assuming ellipsoidal shape ($\mu = 15.0\ cm^{-1}$; limits of transmission, 0.70–0.84; $R_{merge} = 0.0359$ (before), 0.0133 (after)). Intensities of equivalent reflections were averaged ($R_{merge} = 0.0158$). Weighting scheme: $w^{-1} = \sigma^2(F_o) + g|F_o|^2$, $g = 0.00006$. Temperature factor: $T = \exp[-2\pi^2(h^2a^{*2}U_{11} + k^2b^{*2}U_{22} + l^2c^{*2}U_{33} + 2klb^*c^*U_{23} + 2hla^*c^*U_{13} + 2hka^*b^*U_{12})]$.

Structure solution and refinement were achieved using the SHELXTL package of programs provided by Nicolet (12) (scattering factors from ref. 11). The structure was solved using direct methods and refined using a blocked cascade least-squares method. Copper and chlorine atom positions were identified from the *E*-map produced following direct methods. Positions of the remaining non-hydrogen atoms were identified from subsequent electron density difference maps. An unusually large thermal parameter on C(6) suggested disorder of the atom. The disordered atom (C(6a)) was refined with the following constraints: C(5)—C(6a) distance ~1.49 Å; C(4)—C(6a), C(6)—C(6a) distance ~2.43 Å; S.O.F.(C(6a)) + S.O.F.(C(6)) = 1(S.O.F. = site occupation factor, S.O.F. C(6) refined to 0.86(2)). The hydrogen atoms were not visible on the electron density difference map but reasonable positions were calculated, with the exception of the hydrogen atoms bonded to C(6) or C(6a), constraining the atoms to a C—H distance of 0.96 Å, an N—H distance of 1.034 Å, and an idealized geometry. Anisotropic thermal parameters were refined for all non-hydrogen atoms, except C(6a), and the hydrogen atom thermal parameters were fixed at 1.2 times the equivalent isotropic thermal parameter of the carbon or nitrogen atom to which the hydrogen atoms

Can. J. Chem. Downloaded from www.nrcresearchpress.com by 176.9.209.113 on 09/07/12
For personal use only.

TABLE 3. Interatomic distances (Å) and angles (°) for the β (I) and α (II) phases of DPACC

I

Atoms	Distance (Å)	Atoms	Angle (°)
Cu—Cl(1)	2.246(2)	Cl(1)—Cu—Cl(2)	94.0(1)
Cu—Cl(2)	2.257(2)	Cl(1)—Cu—Cl(3)	94.7(1)
Cu—Cl(3)	2.255(2)	Cl(2)—Cu—Cl(3)	145.5(1)
Cu—Cl(4)	2.249(2)	Cl(1)—Cu—Cl(4)	147.6(1)
N(1)—C(1)	1.497(7)	Cl(2)—Cu—Cl(4)	95.1(1)
N(1)—C(4)	1.493(8)	Cl(3)—Cu—Cl(4)	95.2(1)
C(1)—C(2)	1.498(9)	C(1)—N(1)—C(4)	113.5(4)
C(2)—C(3)	1.517(9)	N(1)—C(1)—C(2)	111.7(5)
C(4)—C(5)	1.518(9)	C(1)—C(2)—C(3)	111.7(5)
C(5)—C(6)	1.519(10)	N(1)—C(4)—C(5)	112.3(5)
N(2)—C(7)	1.477(8)	C(4)—C(5)—C(6)	114.4(6)
N(2)—C(10)	1.491(9)	C(7)—N(2)—C(10)	113.4(4)
C(7)—C(8)	1.494(9)	N(2)—C(7)—C(8)	111.6(5)
C(8)—C(9)	1.499(10)	C(7)—C(8)—C(9)	111.2(6)
C(10)—C(11)	1.464(9)	N(2)—C(10)—C(11)	112.8(5)
C(11)—C(12)	1.511(10)	C(10)—C(11)—C(12)	114.3(6)

II

Atoms	Distance (Å)	Atoms	Angle (°)
Cu—Cl(1)	2.236(3)	Cl(1)—Cu—Cl(2)	93.9(1)
Cu—Cl(2)	2.252(3)	Cl(1)—Cu—Cl(3)	95.3(1)
Cu—Cl(3)	2.258(3)	Cl(2)—Cu—Cl(3)	145.4(1)
Cu—Cl(4)	2.244(3)	Cl(1)—Cu—Cl(4)	147.4(1)
N(1)—C(1)	1.488(14)	Cl(2)—Cu—Cl(4)	95.2(1)
N(1)—C(4)	1.455(16)	Cl(3)—Cu—Cl(4)	94.8(1)
C(1)—C(2)	1.387(20)	C(1)—N(1)—C(4)	115.9(8)
C(2)—C(3)	1.552.(16)	N(1)—C(1)—C(2)	115.8(9)
C(4)—C(5)	1.450(17)	C(1)—C(2)—C(3)	114.3(10)
C(5)—C(6)	1.434(24)	N(1)—C(4)—C(5)	120.3(10)
C(5)—C(6A)	1.483(21)	C(4)—C(5)—C(6)	115.8(12)
N(2)—C(7)	1.482(10)	C(4)—C(5)—C(6A)	115.1(22)
N(2)—C(10)	1.461(12)	C(6)—C(5)—C(6A)	112.6(18)
C(7)—C(8)	1.479(14)	C(7)—N(2)—C(10)	114.3(6)
C(8)—C(9)	1.515(13)	N(2)—C(7)—C(8)	112.2(7)
C(10)—C(11)	1.472(11)	C(7)—C(8)—C(9)	112.1(8)
C(11)—C(12)	1.487(14)	N(2)—C(10)—C(11)	113.2(7)
		C(10)—C(11)—C(12)	113.2(8)

are bonded. Final refinement with 177 least-squares parameters gave $R = 0.0557$ and $R_w = 0.0413$ (0.0823 and 0.0430, respectively for all data). Goodness of fit = 1.661, $|\Delta/\sigma|_{mean} = 0.006$, $|\Delta/\sigma|_{max} = 0.022$. The excursions on the final electron density difference map ranged from −0.304 to 0.358 e/Å^3.

Positional and equivalent isotropic thermal parameters for non-hydrogen atoms are listed in Table 1, anisotroic thermal parameters in Table 2, and interatomic distances and angles in Table 3. An ORTEP plot of the formula unit with atom labels is shown in Fig. 3, while a stereographic diagram of the structure is shown in Fig. 4. Tables of observed and calculated structure factors and hydrogen atom positions are included in the supplementary material.[2]

Electron paramagnetic resonance spectroscopy

Electron paramagnetic resonance (epr) spectra were measured on a Varian E-3 X-band spectrometer. The finely powdered samples were packed in a 1 mm diameter glass tube. Temperature control was attained via circulation of heated Dow–Corning 200 Fluid around the sample tube. The sample tube was contained in a larger, vacuum-jacketed quartz tube, which was connected by rubber tubing to a reservoir in which returning fluid was collected and heated. Circulation of the fluid was achieved with a centrifugal pump. Sample temperature was measured by an iron–constantan thermocouple placed in the fluid ~8 cm upstream from the sample. Variations in thermocouple voltage indicated that temperature fluctuation was within ±1 K of the desired temperature.

Optical spectroscopy

Ultraviolet–visible – near infrared spectra were recorded using a Cary Model 14 spectrophotometer. The DPACC samples were melted to thin films held between two quartz plates. A specially constructed device was used to record both high and low temperature spectra; a chromel–alumel thermocouple served to measure the temperature.

Results

Crystal structure of the β phase

The structure of the β phase of DPACC consists of discrete $CuCl_4^{2-}$ anions and dipropylammonium cations. Since all atoms sit on general positions in the unit cell, there is no inherent symmetry within the individual ions. The geometry of the $CuCl_4^{2-}$ ion can be described as a tetragonally distorted tetrahedron with idealized D_{2d} point symmetry, i.e., a tetrahedron compressed along one of its S_4 axes. The anion geometry is

Can. J. Chem. Downloaded from www.nrcresearchpress.com by 176.9.209.113 on 09/07/12
For personal use only.

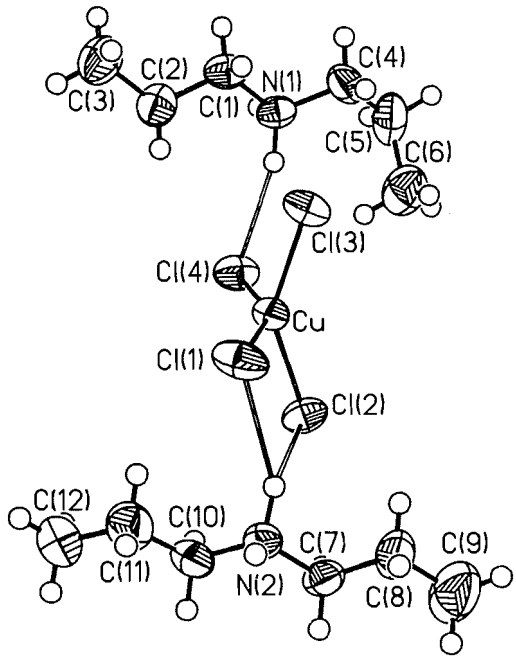

FIG. 1. View of a formula unit in the β phase of DPACC. Open bonds are hydrogen bonds.

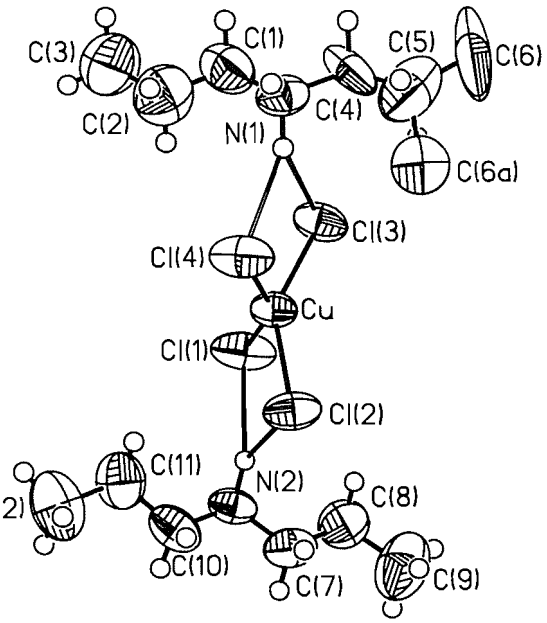

FIG. 3. View of the formula unit in the α phase of DPACC. Open bonds represent hydrogen bonds. C(6) was refined in two positions with C(6a) having an isotropic thermal parameter and a refined occupancy of 14(2)%.

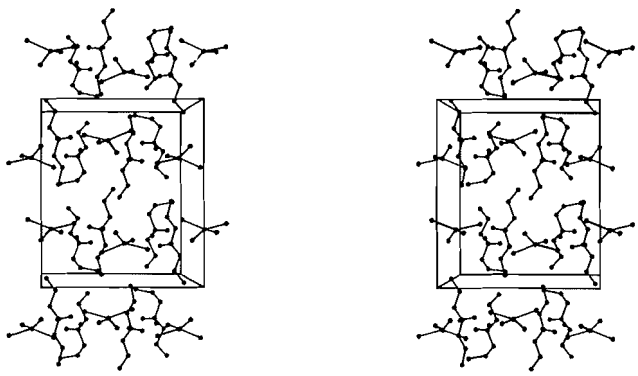

FIG. 2. Stereoview of the β phase of DPACC with the *b*-axis vertical, the *a*-axis horizontal, and the *c*-axis out of the plane of the paper. The box represents the boundaries of the unit cell. Only half of the unit cell along the *c*-axis is depicted. Chain 1 (N(1)) is the chain with a *gauche* configuration, and makes an angle with the normal to the *xz* plane of 29°. Only amino protons are shown for clarity.

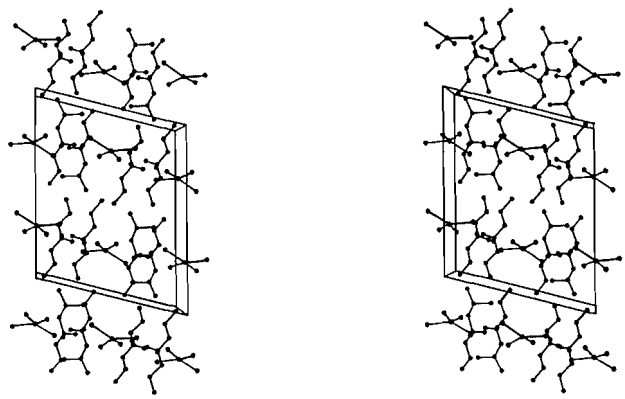

FIG. 4. Stereoview of the α phase of DPACC with the *c*-axis vertical, the *a*-axis horizontal, and the *b*-axis into the plane of the paper. The box represents the boundaries of the unit cell. Chain 1 appears with a disordered terminal carbon and makes an angle of 17° with the normal to the *xy* plane. Only amino protons are shown for clarity.

fairly regular with an average Cu—Cl bond distance of 2.252(5) Å, an average *trans* Cl—Cu—Cl bond angle of 146.6(15)°, and an average *cis* Cl—Cu—Cl bond angle of 94.8(5)°. The dihedral angle of 46.0° between planes Cl(1)—Cu—Cl(3) and Cl(2)—Cu—Cl(4) indicates a geometry halfway between tetrahedral and square planar. Slight distortions of chloride atom pairs related by a twofold rotation about the distortion axis, i.e., Cl(1) and Cl(4), and Cl(2) and Cl(3), are found, which destroy rigorous D_{2d} symmetry. The Cu—Cl bond length in each pair is the same within error while the difference in average bond length between the pairs is on the order of 0.01 Å. Due to electronic repulsion, the pair with the shorter average bond length (Cl(1) and Cl(4)) possesses the larger *trans* Cl—Cu—Cl bond angle. Distortions from C_{2v} symmetry are indicated by the *cis* Cl—Cu—Cl angles. The smallest *cis* angle, Cl(1)—Cu—Cl(2), results from the symmetric, bifurcated hydrogen bond (*vide infra*) to both chloride ions causing the angle to close relative to the Cl(3)—Cu—Cl(4) angle (see Table 3). The bifurcated hydrogen bond to Cl(3) and Cl(4) is asymmetric (with a difference of 0.23 Å between the bond lengths), making the C_{2v} symmetry description only approximate. The dipropylammonium cations all exist in a staggered conformation with the carbon and nitrogen atoms *anti* (dihedral angle ~180°), with the exception of C(6), which is *gauche* with respect to N(1) (dihedral angle = 66.8°) (cf. Fig. 2).

Hydrogen bonding between the dipropylammonium cations and the tetrachlorocuprate anions creates a two-dimensional network of linked anions parallel to the *xz* plane and coplanar with the *c*-glide plane with adjacent layers related by inversion. This hydrogen bonding network is shown in Fig. 5 with hydrogen bond lengths and angles given in Table 4. The anions do not lie on the plane; rather, the copper ions are displaced ~0.7 Å from either side of the plane such that the least-squares plane of the copper ions defines the layer plane. The cations are situated

Can. J. Chem. Downloaded from www.nrcresearchpress.com by 176.9.209.113 on 09/07/12
For personal use only.

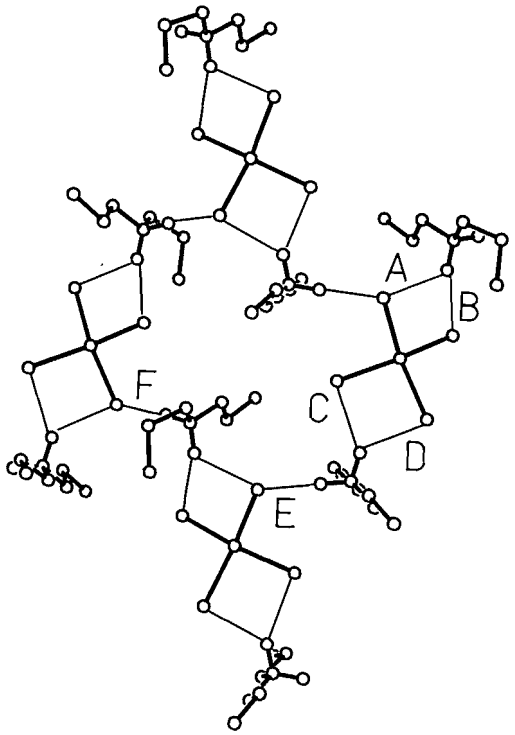

FIG. 5. View of the hydrogen bonding in a layer of the β phase of DPACC. The letters correspond to the letters in the far left column of Table 4, I.

such that one of the hydrogen atoms bonded to nitrogen forms a bifurcated hydrogen bond with two chloride ions while the other amino hydrogen atom forms a single hydrogen bond to a chloride ion of a different $CuCl_4^{2-}$ group. The pair of chloride ions with extra hydrogen bonds (Cl(2) and Cl(3)) are the pair with the longer average Cu—Cl bond length. The anions in a layer are further arranged in columns parallel to the *c*-axis of the crystal. Neighboring ions in the column are related by a *c*-glide such that the orientation of a particular anion is the mirror image of its neighbors in the column while the next nearest neighbors in the column are related by a lattice translation along the *c*-axis.

Crystal structure of the α phase

While the gross features of the α phase structure are similar to those of the β phase, there are distinct differences, the most conspicuous of which is the change in lattice parameters. (Cell constants will henceforth be subscripted with an α or a β to distinguish between the two phases.) The b_α-axis corresponds to approximately one-half the c_β-axis, thus doubling the number of lattice translations. However, the b_α-axis is actually slightly *less* than one-half the length of the c_β-axis, indicating a macroscopic *contraction* along the c_β-axis of the crystal in passing into the high temperature phase. The γ_β angle increases from 90° to 104.31(5)°, the result of the layers moving parallel to the *a*-axis. The $b_\beta(c_\alpha)$-axis shows the largest increase above the phase transition and indicates an increased interlayer separation.

As a result of the halving of the c_β-axis, anions related by a *c*-glide in the β phase are related by a unit cell translation along the *b*-axis in the α phase. This causes the orientations of the anions in a given column to be the same, in contrast to the β phase where nearest neighbors in the column have mirror symmetry. Adjacent columns are related by the 2_1-axis parallel to *b* such that the orientations of anions in adjacent columns differ by a 180° rotation. If the anion is considered to possess D_{2d} symmetry, it is found for both phases that all of the anions are oriented such that the S_4-axis of the anion lies almost perpendicular to the layer plane, although there are minor deviations of the axis from this orientation that affect the epr spectra (*vide infra*). If the S_4-axis of a particular anion in the β phase is arbitrarily given a direction, it is then found that in the β phase the directions of the principal axes of its neighbors in the column point in the opposite direction due to the mirror symmetry. Thus, in the β phase the principal axes of one-half of the anions point in one direction while the axes of the other half point in the opposite direction. In the α phase the principal axes of the anions in a given column all point in the same direction; however, the axes of neighbouring columns in the layer point in the opposite direction, since they are related by a 180° rotation to the anions in the first column. Although the *total* number of anions found with a particular direction of their S_4 axes does not change between the two phases, the directions of the S_4 axes are reversed for one-half of the anions in going from the β to the α phase.

To understand the development of the monoclinic angle it is profitable to consider the relationship between the two layers found in a unit cell. As stated previously, the two layers in a unit cell are related by inversion in the β phase. Nearest neighbor columns in adjacent layers of the same unit cell are also related

TABLE 4. Hydrogen bond lengths and angles for the β phase (I) and the α phase (II) of DPACC

I

	Atoms	Length (Å)	Atoms	Angle (°)
A	H(N1a)—Cl(3)	2.61	N(1)—H(N1a)—Cl(3)	122
	N(1)—Cl(3)	3.28		
B	H(N1a)—Cl(4)	2.38	N(1)—H(N1a)—Cl(4)	153
	N(1)—Cl(4)	3.33		
C	H(N2b)—Cl(2)	2.50	N(2)—H(N2b)—Cl(2)	134
	N(2)—Cl(2)	3.29		
D	H(N2b)—Cl(1)	2.55	N(2)—H(N2b)—Cl(1)	141
	N(2)—Cl(1)	3.41		
E	H(N2a)—Cl(3′)	2.24	N(2)—H(N2a)—Cl(3′)	163
	N(2)—Cl(3′)	3.23		
F	H(N1b)—Cl(2″)	2.17	N(1)—H(N1b)—Cl(2″)	173
	N(1)—Cl(2″)	3.20		

Symmetry key: ′: $1/2 + x, y, 1/2 - z$; ″: $-1/2 + x, 1/2 - y, -z$.

II

	Atoms	Length (Å)	Atoms	Angle (°)
A	H(N2b)—Cl(2)	2.46	N(2)—H(N2b)—Cl(2)	135
	N(2)—Cl(2)	3.28		
B	H(N2b)—Cl(1)	2.44	N(2)—H(N2b)—Cl(1)	141
	N(2)—Cl(1)	3.31		
C	H(N1b)—Cl(4)	2.50	N(1)—H(N1b)—Cl(4)	140
	N(1)—Cl(4)	3.36		
D	H(N1b)—Cl(3)	2.46	N(1)—H(N1b)—Cl(3)	136
	N(1)—Cl(3)	3.28		
E	H(N1a)—Cl(3′)	2.20	N(1)—H(N1a)—Cl(3′)	171
	N(1)—Cl(3′)	3.22		
F	H(N2a)—Cl(2″)	2.21	N(2)—H(N2a)—Cl(2″)	164
	N(2)—Cl(2″)	3.21		

Symmetry key: ′: $-1/2 - x, -1/2 + y, 1/2 - z$; ″: $1/2 - x, 1/2 + y, 1/2 - z$.

Can. J. Chem. Downloaded from www.nrcresearchpress.com by 176.9.209.113 on 09/07/12
For personal use only.

Can. J. Chem. Downloaded from www.nrcresearchpress.com by 176.9.209.113 on 09/07/12
For personal use only.

by a center of inversion. For example, the nearest neighbor in the adjacent layer of a column whose axis passes through $x = 0.5641$ and $y = 0.2500$ is the column whose axis passes through $x = 0.4359$ and $y = 0.7500$, and the two are related by the inversion center at $x = 0.5000$, $y = 0.5000$, and $z = 0.5000$. The plane defined by these two column axes makes an angle of 102.4° with respect to the xz plane, which is very close to the value of the monoclinic angle, β_α. By symmetry these interlayer planes for all such pairs of columns are parallel; however, since lattice translations along the b_β-axis are perpendicular to the xz plane, none are coplanar. To achieve the c_α-axis translational symmetry, pairs of layers, other than the pair in the origin unit cell, must move in the x-direction until these interlayer planes are approximately coplanar. Referring to Fig. 2, the pair of layers that lie one positive b_β-axis translation from the origin unit cell layers must shift by 3.8 Å in the negative x direction, while the pair of layers that lie one negative b-axis translation away must shift 3.8 Å in the positive x direction. This produces a structure that has the approximate unit cell parameters of the α phase with the columns staggered about planes parallel to the yz-plane of that phase. The paired layers also shift by ~0.5 Å in the x direction relative to each other such that the plane defined by the pair of columns related by inversion makes a larger angle with the x-axis.

The molecular geometry of the α phase is very similar to that of the β phase. The $CuCl_4^{2-}$ ion exhibits pseudo D_{2d} symmetry (average Cu—Cl bond length = 2.248(10) Å, average *trans* Cl—Cu—Cl angle = 146.4(14)°, average *cis* Cl—Cu—Cl angle = 94.8(6)°). The *trans* chloride ion pairs have bond lengths that are equal within error while the difference between the average bond lengths of the pairs is 0.015 Å. Both of the bifurcated hydrogen bonds are symmetric in this phase, resulting in smaller *cis* angles between pairs of chlorides bonding to the same hydrogen atom than for the other pairs. For unknown reasons, the Cl(1)—Cu—Cl(2) angle is significantly smaller than the Cl(3)—Cu—Cl(4) angle. Hydrogen bonding links individual anions together in a manner analogous to that of the β phase to create a layer structure coplanar with the xy plane. Hydrogen bond lengths and angles for the α phase are listed in Table 4 with a view of the hydrogen bonding in Fig. 6. Adjacent layers are related by inversion, as in the β phase; however, the structure of the layers is somewhat different. Both dipropylammonium chains assume an *anti* configuration; however, C(6) is *gauche* relative to N(1) 14(2)% of the time (dihedral angle = 53.8°).

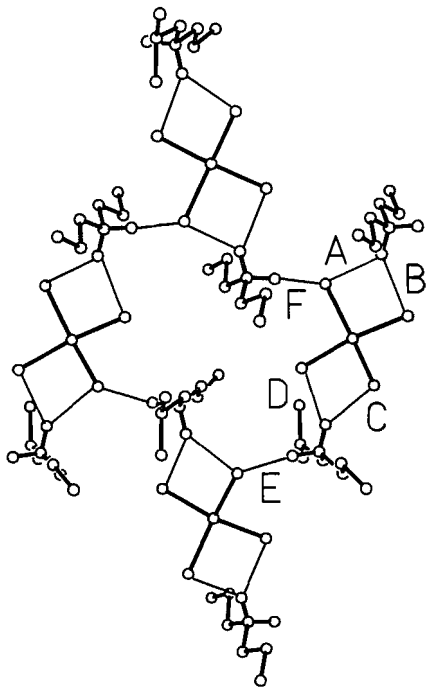

FIG. 6. View of the hydrogen bonding in a layer of the α phase of DPACC. The letters correspond to the letters in the far left column of Table 4, II.

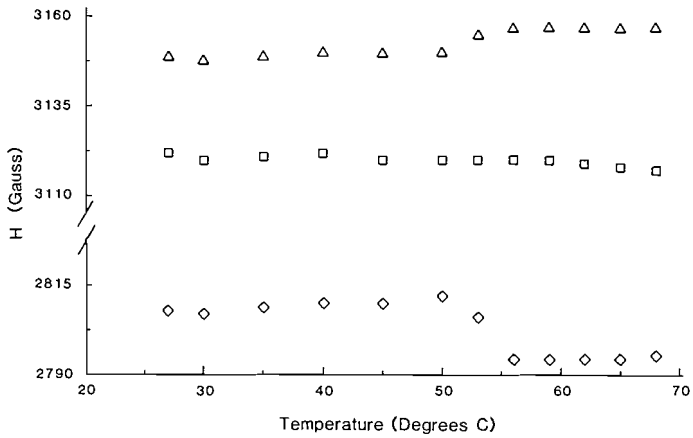

FIG. 7. $H_\parallel$ (◇), $H_{\perp,\min}$ (□), and $H_{\perp,\max}$ (△) (in gauss) versus temperature (in °C).

Electron paramagnetic resonance spectroscopy

Powder epr spectra were taken at temperatures between 27 and 68° C. Typical axial spectra were obtained for both phases with no indication of hyperfine interactions in the spectra. Two features were always found in the spectra corresponding to $g_\parallel$ (low field) and $g_\perp$ (high field), while the high temperature spectra often developed structure at intermediate fields resulting from a preferred orientation of the crystallites. Single crystal spectra exhibited only a single absorption line. This, coupled with the lack of hyperfine lines, indicates that sufficient exchange coupling exists between magnetically inequivalent anions to produce an exchange-averaged spectrum. Thus, the crystal g values represent geometric averages of the individual molecular g tensors. A plot of $H_\parallel$, $H_{\perp\min}$, and $H_{\perp\max}$ versus T is shown in Fig. 7, where $H_{\perp\min}$ is defined as the minimum in the derivative spectrum of the high field line. As the two figures show, there is very little difference between the spectra in the two phases. The most significant changes start at 56° C where $H_\parallel$ decreases by ~15 G while $H_\perp$ increases by ~5 G and broadens slightly. Although it is difficult to tell from the powder spectra, it appears that the width of the $g_\parallel$ peak does not change significantly. Since the copper chloride geometry is virtually identical in the two phases the similarity of the spectra in the two phases is not unexpected. The peak shift at the phase transition is easily explained by the change in anion (and, hence, g tensor) orientation between the two phases. Assuming D_{2d} symmetry for the anions, it is found in both phases that the S_4 axes of the anions are approximately perpendicular to the layer plane (*vide supra*); however, in both phases the anions are rotated by a small amount about an axis parallel to the a-axis (the S_4 axis corresponds to a principal axis of the g tensor of the anion). In the β phase the principal axis of an anion (assumed to be the normal to the least-squares plane calculated for the atoms of the anion)

Can. J. Chem. Downloaded from www.nrcresearchpress.com by 176.9.209.113 on 09/07/12
For personal use only.

forms an angle of 11° with respect to the normal to the layer plane, while in the α phase it forms an angle of 4° with respect to the normal. The anions on the eight general positions in the β phase and the four general positions in the α phase are oriented such that half of the principal axes are rotated in one direction while the other half are rotated an equal amount in the opposite sense. Due to exchange averaging the $g_{\|}$ value of the crystal is less than the $g_{\|}$ value for a single D_{2d} anion. Since the principal axes of the anions are more closely aligned in the α phase than in the β phase, an increase in the value of $g_{\|}$ (crystal) and a decrease in the value of $g_{\perp}$ (crystal) going from the β to the α phase is expected. It should also be noted that the orientations of the anions with respect to rotations about their principal axes differ from site to site; however, the anion g tensors have pseudo-axial symmetry (from the quasi-D_{2d} symmetry of the anion) and such differences should be of little consequence in the epr spectrum. No spectrum was observable in the melt due to extreme broadening of the line.

Optical spectroscopy

Visible – near infrared spectra of DPACC were studied as a function of temperature. At room temperature, in addition to charge-transfer bands at 26 100 and 29 200 cm^{-1}, one very broad peak was observed in the near infrared – visible region. At 25°C this highly asymmetric peak maximized at 895 nm (11 200 cm^{-1}), having a slight shoulder near 800 nm (12 500 cm^{-1}) and displaying a long red tail into the ir region. Lowering the temperature to 78 K removed much of this tail and resolved at least two bands within the room temperature envelope, one fairly sharp band at 790 nm (12 700 cm^{-1}) and a broader less intense band maximizing near 1020 nm (9800 cm^{-1}).

Attempts to record absorption spectra at higher temperatures resulted in either thermal- or photo-decomposition. If the sample remains in the beam the higher energy band decreases in intensity more quickly (resulting in an apparent red shift), and if left in the beam at higher temperatures for any length of time, both bands eventually extinguish. Reported peak positions are from spectra recorded from freshly prepared samples.

Discussion

Within the dipropylammonium chain the *gauche* conformation has a higher potential energy than the *anti* conformation; therefore, in the β phase the assumption of a *gauche* conformation by one of the chains must entail a lowering of the crystal packing energy. To understand the difference between the conformation of the two dipropylammonium chains in the β phase it is necessary to consider their positions in the structure and the manner in which this affects the energy of the crystal. Both chains lie with their lengths approximately perpendicular to the xz plane; however, the axis of chain 1 (N(1)) lies at an angle of 29(2)° with respect to the normal to the xz plane while the axis of chain 2(N(2)) lies at an angle of 13.0(4)°. (The angle for chain 1 was calculated by averaging the angles between the normal to the xz plane and the vectors between atoms in the sets {N1, C2, C5} and {C1, C3, C4}; the chain 2 angle was calculated in a similar manner.) The length of the projection of an ideal dipropylammonium chain (bond lengths = 1.5 Å, bond angles = 109.5° excluding hydrogen atoms) with an *anti* conformation onto its chain axis is 7.35 Å, while for a chain with one terminal carbon in a *gauche* conformation the corresponding length is only 6.12 Å (the bond to the *gauche* carbon is perpendicular to the chain axis). Since the interlayer spacing in the structure is 7.63 Å and the chains are offset by 0.6–0.8 Å from the center of the layer, chains with axes perpendicular to the layer are forced to extend into the neighboring layer. This is the case for chain 2, which, even though it is canted from the normal to the layer plane, has a length in the y direction of 7.25 Å ($b \times [y(C(9)) - y(C(12))]$). Chain 1, however, is canted at a much larger angle and has one terminal carbon *gauche*, resulting in a much smaller length in the y direction ($b \times [y(C(6)) - y(C(3))] = 5.47$ Å, well within the interlayer distance). Thus, assumption of the *gauche* conformation by C(6) allows the layers to be closer than would an *anti* conformation, lowering the crystal packing energy through increased van der Waals interactions between the layers.

In the α phase the dipropylammonium chains occur primarily in the *anti* conformation. Although disorder was refined only for C(6), the magnitude of the thermal parameters suggests that disorder is also possible for other carbon atoms. Assumption of the lower energy *anti* conformation and the increased entropy resulting from disorder of the alkyl chains appear to be the driving force behind the β → α phase transition. Preliminary nmr studies do show some resonance line shifting and motional narrowing with temperature; however, a more careful nmr study of the phase transition is necessary to quantify these results and determine the amount of cationic disorder at the phase transition. The following discussion will demonstrate that the structural changes accompanying the phase transition occur to accommodate the increased motion of the alkyl chains.

The increase in interlayer spacing from 7.63 to 7.93 Å allows greater freedom of movement for the alkyl groups, particularly for chain 1 of the β phase, which is now free to assume a completely *anti* configuration. This also allows the angle between the β phase, chain 1 axis, and the normal to the layer plane (the xz plane in the β phase) to decrease, i.e., chain 1 may now extend into the adjacent layers. Comparison of the stereoviews of the two phases in Figs. 2 and 4 illustrates the dramatic decrease in angle from 29° for chain 1 in the β phase to the smaller angles in the α phase (17(2)° for chain 1 and 14(1)° for chain 2). (It should be noted that due to the change in symmetry there is not a one-to-one correspondence between the numbered cation chains of the two phases.) Structurally, the decrease in chain angle causes a decrease in the component of the chain length in the z_{β} direction, which accounts for the previously mentioned macroscopic contraction of the crystal on passing into the α phase.

The development of the monoclinic angle can best be understood by considering the two phases individually. In the β phase chain 1 is contained within the layer while chain 2 (with the completely *anti* conformation) extends into both neighboring layers. From Fig. 2 it should be noticed that chain 2 lies on a line between two $CuCl_4^{2-}$ anions (the anions are related by a b_{β} translation) such that a *trans* chloride ion pair and a copper ion of a particular anion form the cap of a cavity into which a methyl group fits. Since each anion caps only two cavities, the terminal carbons of chain 2 occupy all of the possible cavities in the β phase. In the α phase both chains are *anti*, make approximately the same angle with the xy plane, and, therefore, extend into neighboring layers. The interlayer distance is quite a bit larger in the α phase, which does relieve crowding; however, the cations are staggered about the layer plane (just as in the β phase) such that one end extends further into a neighboring layer than the other. Shifting the pairs of planes in adjacent unit cells moves the β phase cavities into a position such that the more extended methyl groups of each chain fit into a cavity, as can be seen by comparison of Figs. 2 and 4.

TABLE 5. Comparison of the highest-energy d–d transition and geometrical parameters for complexes containing the $CuCl_4^{2-}$ anion

Compound	d–d band energy (cm^{-1})	Θ (°)	Mean Cu—Cl distance (Å)	Reference
Cs_2CuCl_4	9 050	129.2	2.230	13, 14, 16, 17
$[(C_6H_5)CH_2N(CH_3)_3]_2CuCl_4$	8 850	132.5	2.256	14, 18, 19
$[(C_2H_5)_3NH]_2CuCl_4$	9 390	134.8	2.241	14, 15
$[(CH_3)_2NH_2]_3Cl{\cdot}CuCl_4$	9 520	135.8	2.230	22, 27
(d-mampH)$_2CuCl_4$*†	10 200	138.3	2.238	27
$[2NH_25PicH]_2CuCl_4$*	9 900	139.9	2.240	23, 24
(NPhpipzH_2)$CuCl_4$*	10 750	142.0	2.250	20
$[(C_2H_5)_4P]_2Cu_2Cl_6$	11 250	143.5	2.248	25–27
$[(C_6H_5)_4As]_2Cu_2Cl_6$	11 500	144.9	2.263	21, 25
(cinH_2)$_2CuCl_4{\cdot}3H_2O$*†	11 100	145.2	2.250	8
$[(C_3H_7)_2NH_2]_2CuCl_4$	11 200	146.6	2.252	This work
$[Pt(en)_2Cl_2]CuCl_4{\cdot}H_2O$	12 990	154.1	2.258	20, 28
(metH)$_2CuCl_4{\cdot}H_2O$*	15 700	180.0	2.268	29
$[(C_6H_5)(CH_2)_2NH_2CH_3]_2CuCl_4$	16 100	180.0	2.265	7, 27

*For the cations, the following abbreviations have been used: (d-mampH)$^+$ = bis-[(+)-*N*,α-dimethylphenethylammonium]; $2NH_25PicH^+$ = 2-amino-5-picolinium (or 5-methyl-2-aminopyridinium); (NPhpipzH_2)$^{2+}$ = *N*-phenylpiperazinium; (cinH_2)$^{2+}$ = $(C_{19}H_{24}N_2O)^{2+}$ (cinchoninium); (metH)$^+$ = 1-methyl-4-oxo-3,3-diphenylhexyldimethylammonium (methadonium).

†For both the (cinH_2) and (d-mampH) salts the crystal structures have shown the $CuCl_4^{2-}$ anion to exist in two distinct conformations. The crystallographic data are taken as the average of the two.

Optical spectroscopy

The absorption bands observed at 26 100 and 29 200 cm^{-1} are of a greater relative intensity than those observed in the near-infrared region and are presumably due to chloride – copper ligand – metal charge transfer transitions (LMCT). However, our attention is focussed on the broad band in the near infrared maximizing at 11 200 cm^{-1}, not an atypical value for the d–d transitions of the $CuCl_4^{2-}$ ion. The Jahn–Teller theorem precludes a tetrahedral (T_d) geometry for the d^9 $CuCl_4^{2-}$ ion, and only in a few instances are the Cl–Cl steric repulsions overcome for the ion to assume a ligand field stabilizing square-planar (D_{4h}) geometry (27, 29). In most instances the ion assumes the intermediate geometry of a tetrahedron compressed along one of its S_4 axes having (approximate) D_{2d} symmetry. This has been observed here for the DPA salt, the anion geometry being essentially identical in both phases. The degree of distortion is conveniently measured by taking the average of the two Cl—Cu—Cl angles larger than 109.47°: an angle of 109.47° corresponds to tetrahedral gometry, 180.0° to a square-planar system. Typical values for $CuCl_4^{2-}$ fall in the range of 130–145°. The value obtained for the room temperature salt in this system is 146.6°.

Early work in this laboratory and by Lamotte-Brasseur recognized that the position of the highest-energy d–d band measured at room temperature correlated well with the distortion of $CuCl_4^{2-}$ from tetrahedral geometry: the greater the distortion from tetrahedral geometry, the further blue-shifted is the highest-energy (and indeed all of the) d–d transition(s) (14, 30). Such an empirical relation has subsequently been used in several different contexts (7, 20, 31). With several new $CuCl_4^{2-}$ structures now available, we wish to extend this analysis to include a great deal more data, and make available a convenient reference for other workers as to the probable geometry of the anion in systems containing $CuCl_4^{2-}$.

The criteria used in selecting data are three: First, the geometry about the copper must be four-coordinate. Care has been taken to exclude all systems having a contact interaction with a fifth or sixth ligand, such as in a 4 + 2 coordination geometry. Although we have included two $Cu_2Cl_6^{2-}$ dimers in the data, this is not a problem since most of the geometries are determined, at least in part, by chloride interaction with some neighboring cation, usually a proton. Thus, while the dimer interaction strongly affects the magnetic properties, it has little effect on the positions of the d–d bands. Second, both the crystal structure and the optical data should have been collected at room temperature. In many instances the geometry of the anion changes with temperature, shifting the positions of the absorption bands (thermochromism) (27, 30). Third, we use only the peak position of the highest-energy d–d band obtained from unpolarized room temperature absorption or diffuse reflectance data. Although the room temperature peak is normally an envelope of several vibronic peaks, and possibly two or more d–d peaks (as in this case), the data are this way internally consistent. Furthermore, this makes it more convenient, for example, for other workers considering whether an unusual geometry might be present, warranting a crystal structure.

The data used in the study are summarized in Table 5 along with the appropriate references. To measure the distortion, the average of the two largest Cl—Cu—Cl angles within the anion, Θ, was used. Other choices are possible, such as half this angle or the dihedral angle, but this is the most convenient. Figure 8 presents a plot of this empirical correlation. Considering the width of some of the d–d bands and the number of data included, the fit is very satisfactory. The data are fit by a least-squares line with slope 143 ± 6 cm^{-1} deg^{-1} and intercept −9600 ± 600 cm^{-1}. This corresponds to the highest-energy d–d transition having a value of approximately 6000 cm^{-1} for a tetrahedral geometry, a plausible value (7, 16, 36).

The low temperature spectrum resolves the broad room temperature d–d envelope into two peaks at 12 700 cm^{-1} and 9800 cm^{-1}. The dearth of optically resolved spectra for $CuCl_4^{2-}$ ions at large distortion angles (but not the square-planar limit) makes definitive assignment of the states difficult. That is, there exist only a few studies of $CuCl_4^{2-}$ using either polarized or cryogenic spectroscopic methods (17, 19). For the square-planar (D_{4h}) limit, however, a very detailed theoretical analysis

Can. J. Chem. Downloaded from www.nrcresearchpress.com by 176.9.209.113.on 09/07/12
For personal use only.

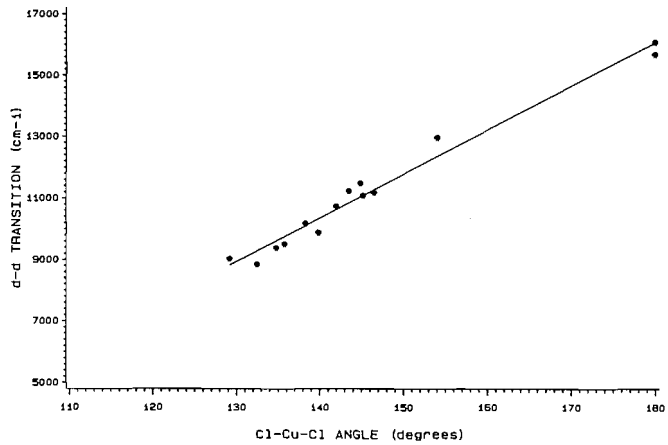

FIG. 8. A plot of the highest-energy d–d transition energy from the room temperature spectra versus the average of the two larger Cl—Cu—Cl angles in the $CuCl_4^{2-}$ anion. Data are from Table 5.

(32) and an extensive spectroscopic investigation including the thermal dependence and vibrational fine structure of the d–d transitions have been undertaken (33). In the distorted tetrahedral case, however, the energy level ordering is not as well understood. The early spectroscopic work of Ferguson on Cs_2CuCl_4 (17) and Furlani *et al.* (19) on $[(C_6H_5)CH_2N(CH_3)_3]CuCl_4$ has shown that the ordering of the term energies (ignoring spin-orbit coupling) in these systems is $^2B_2(xy) << {}^2E(xz, yz) < {}^2B_1(x^2 - y^2) < {}^2A_1(z^2)$, corresponding to a $^2B_2(xy)$ ground state. In the D_{2d} point group, the $^2B_2 \rightarrow {}^2E$ and $^2B_2 \rightarrow {}^2A_1$ transitions are dipole allowed and have been assigned as the lowest and highest-energy d–d bands, respectively, in these systems, while the forbidden $^2B_2 \rightarrow {}^2B_1$ was assigned as a weak band in the Cs_2CuCl_4 case only, assuming contribution from spin-orbit coupling effects and site group symmetry lowering. However, reference to Table 5 shows that both of these studies correspond to relatively small distortions from tetrahedral symmetry, whereas the DPACC system has a large distortion value ($\Theta = 146.6°$). Several theoretical studies have shown that the ordering of the ^2E and $^2B_1$ terms shifts near large θ values (8, 31, 32, 34, 35). Thus, we may assign the 12 700 cm^{-1} band as due to the $^2B_2 \rightarrow {}^2A_1$ transition, but may not definitively assign the 9800 cm^{-1} band. It is presumably due to the $^2B_2 \rightarrow {}^2E$ transition, but a combination of greater distortion from D_{2d} symmetry at low temperatures and differing enhancement mechanisms adding intensity to the $^2B_2 \rightarrow {}^2B_1$ excitation makes difficult the correct assignment of the transition.

Conclusions

The thermochromic phase transitions in several copper(II) chloride salts studied previously have involved a phase transition in which the coordination geometry of the copper(II) chromophore changed (3, 37). In each case, the driving force has been identified as the onset of thermal disorder of the organic counterion. In DPACC, virtually no change occurs in the coordination geometry about the copper. Rather, it exhibits a gradual thermochromism caused by a shifting of the d–d absorption bands that tail into the visible region. The phase transition in DPACC is much more similar to the melting transitions in monoalkylammonium metal chloride salts. These latter salts consist of an exclusively inorganic layer (corner-sharing MCl_6^{4-} octahedra), which is unaltered through the phase transition, and an organic layer sandwiched between inorganic layers. The amino groups of the alkylammonium chains are hydrogen bonded to the chloride ions in the layer while the alkyl groups extend away from the layer and are ordered below the transition temperature while extremely disordered above the transition temperature. DPACC is structurally similar in that there is a well-defined layer structure, although in this case the amino groups are intimately associated with the bonding in the layer, the alkyl groups extending away from the layer on both sides. The epr spectra show that if there is any fluctuation or dynamic disorder of the anion, it is occurring on a time scale much larger than the time scale of the epr experiment; thus the layers appear to be fairly rigid in both phases. Below the transition temperature the alkyl chains are well ordered while above the transition temperature the chains show a great deal of thermal motion and some disorder. This disorder is indicated by the large amount of thermal motion in the α phase of the terminal carbon atoms as compared to the nitrogen atoms (cf. Table 2). Since the alkyl chains in this compound have only three carbon atoms, compared to nine or more in other layer compounds exhibiting melting transitions, it could provide a clearer view of the motion of the alkyl chains in the different phases of this class.

Acknowledgments

We are grateful to Mark Pressprich for constructing the high temperature device for the X-ray diffractometer. We would also like to acknowledge the support of NSF Grant CHE-8408407 and of The Boeing Company for establishment of the X-ray diffraction facility. M.R.B. wishes to thank Washington State University for a summer assistantship. This work was supported by PRF grant 16525-AC3, 7.

1. M. VACATELLO. Ann. Chim. (Rome), **64,** 19 (1974).
2. G. F. NEEDHAM, R. D. WILLETT, and H. F. FRANZEN. J. Phys. Chem. **88**, 145 (1985).
3. D. R. BLOOMQUIST and R. D. WILLETT. Coord. Chem. Rev. **47**, 125 (1982).
4. J. SUGIYAMA, M. WADA, A. SAWADA, and Y. ISHIBASHI. J. Phys. Soc. Jpn. **49**, 1405 (1980).
5. M. J. M. VAN OORT, G. NESHVAD, and M. A. WHITE. J. Solid State Chem. **69**, 145 (1987).
6. J. TOMOVIC, Z. BIELA, and J. GAZO. Chem. Zvesti, **38**, 75 (1984).
7. R. L. HARLOW, W. J. WELLS III, G. W. WATT, and S. H. SIMONSEN. Inorg. Chem. **14**, 1768 (1975).
8. K. DRYEK, J. GOSLAR, S. A. HODOROWICZ, S. K. HOFFMANN, B. J. OLEKSYN, and A. WESELUCHA-BIRCZYŃSKA. INORG. CHEM. **26**, 1481 (1987).
9. C. F. CAMPANA, D. F. SHEPHERD, and W. N. LITCHMAN. Inorg. Chem. **20**, 4039 (1981).
10. G. M. SHELDRICK. SHELXTL Version 4.1 Users Manual. Nicolet Instrument Corp., Madison, WI. 1984.
11. International Tables for X-ray Crystallography. Vol. IV. The Kynoch Press, Birmingham, England. 1974. (Present distributor D. Reidel, Dordrecht.)
12. G. M. SHELDRICK. SHELXTL Version 5.1 Users Manual. Nicolet Instrument Corp., Madison, WI. 1986.
13. J. A. MCGINNETY. J. Am. Chem. Soc. **94**, 8406 (1972).
14. J. LAMOTTE-BRASSEUR. Acta Crystallogr. Sect. A: Found. Crystallogr. **A30**, 487 (1974).
15. J. LAMOTTE-BRASSEUR, L. DUPONT, and O. DIDEBERG. Acta Crystallogr. Sect. B: Struct. Crystallogr. Cryst. Chem. **B29**, 241 (1973).
16. W. E. HATFIELD and T. S. PIPER. Inorg. Chem. **3**, 841 (1964).
17. J. FERGUSON. J. Chem. Phys. **40**, 3406 (1964).
18. M. BONAMICO, G. DESSY, and A. VACIAGO. Theor. Chim. Acta, **7**, 367 (1967).

Can. J. Chem. Downloaded from www.nrcresearchpress.com by 176.9.209.113 on 09/07/12
For personal use only.

19. C. FURLANI, E. CERVONE, F. CALZONA, and B. BALDANZA. Theor. Chim. Acta, **7**, 375 (1967).
20. L. P. BATTAGLIA, A. BONAMARTINI CORRADI, G. MARCOTRIGIANO, L. MENABUE, and G. C. PELLACANI. Inorg. Chem. **18**, 148 (1979).
21. R. D. WILLETT and C. CHOW. Acta Crystallogr. Sect. B: Struct. Crystallogr. Cryst. Chem. **B30**, 207 (1974).
22. R. D. WILLETT and M. L. LARSEN. Inorg. Chim. Acta, **5**, 175 (1971).
23. H. PLACE and R. D. WILLETT. Acta Crystallogr. Sect. C: Cryst. Struct. Commun. **C43**, 1050 (1987).
24. R. M. GAURA, P. STEIN, R. D. WILLETT, and D. X. WEST. Inorg. Chim. Acta, **60**, 213 (1982).
25. W. LUDWIG and M. TEXTOR. Helv. Chim. Acta, **54**, 1143 (1971).
26. M. TEXTOR, E. DUBLER, and H. R. OSWALD. Inorg. Chem. **13**, 1361 (1974).
27. R. L. HARLOW, W. J. WELLS III, G. W. WATT, and S. H. SIMONSEN. Inorg. Chem. **13**, 2106 (1974).
28. K. P. LARSEN, R. GRØNBÆK HAZELL, H. TOFTLUND, P. R. ANDERSEN, P. BISGÅRD, K. EDLUND, M. ELIASEN, C. HERSKIND, T. LAURSEN, and P. M. PEDERSEN. Acta Chem. Scand. Ser. A: **29**, 499 (1975).
29. H. C. NELSON, S. H. SIMONSEN, and G. W. WATT. J. Chem. Soc. Chem. Commun. 632 (1979).
30. R. D. WILLETT, J. A. HAUGEN, J. LEBSACK, and J. MORREY. Inorg. Chem. **13**, 2510 (1974).
31. E. I. SOLOMON, J. W. HARE, D. M. DOOLEY, J. H. DAWSON, P. J. STEPHENS, and H. B. GRAY. J. Am. Chem. Soc. **102**, 168 (1980).
32. J. DEMUYNCK, A. VEILLARD, and U. WAHLGREN. J. Am. Chem. Soc. **95**, 5563 (1973).
33. R. G. MCDONALD, and M. A. HITCHMAN. Inorg. Chem. **25**, 3273 (1986).
34. D. W. SMITH. J. Chem. Soc. A, 2529 (1969).
35. D. W. SMITH. J. Chem. Soc. A, 2900 (1970).
36. G. FELSENFELD. Proc. R. Soc. (London), A: **236**, 506 (1956).
37. M. PRESSPRICH, D. R. BLOOMQUIST, and R. D. WILLETT. Inorg. Chem. Submitted.

Can. J. Chem. Downloaded from www.nrcresearchpress.com by 176.9.209.113 on 09/07/12
For personal use only.

Thermal effects in polyelectrolyte ion exchange reactions: the Jahn–Teller effect

KANG SUN[1] AND GEORGE E. BOYD
Department of Chemistry, University of Georgia, Athens, GA 30602, U.S.A.

Received September 10, 1987

This paper is dedicated to Professor J. A. Morrison

KANG SUN and GEORGE E. BOYD. Can. J. Chem. **66**, 974 (1988).

Microcalorimetric determinations were made of the thermal effects accompanying the exchange of the divalent cations of Mn, Fe, Co, Ni, Cu, and Zn in dilute aqueous perchlorate solutions with Mg^{2+} ion initially bound in a crosslinked polyelectrolyte gel. The calorimetric measurements, together with microchemical equilibrium distribution determinations with the same cations, were employed to estimate the standard state Gibbs energy, enthalpy, and entropy changes associated with their ion exchange reactions.

All the transition elements were selectively absorbed relative to Mg^{2+} with the sequence being: Mn < Fe < Co < Ni > Cu > Zn, showing divalent Ni(II) cation to possess the greatest affinity for the polyelectrolyte phase. The sequence of standard state reaction enthalpy change, ΔH^0, revealed that Ni^{2+} also was the most exothermic of all 3*d* transition element cations. However, the ΔH^0 values became more negative in the order: Mn < Fe < Co < Ni > Cu < Zn, showing that Cu^{2+} ion behaved anomalously in being less negative than expected. This behavior (and that in the ΔS^0 values also) suggested that a destabilization of the octahedrally coordinated Cu^{2+} in aqueous solutions must occur, possibly because of Jahn–Teller effects on its d^9 electronic configuration when the cation is placed in an environment of cubic symmetry. Because of a thermodynamic compensation of the magnitudes of ΔH^0 and ΔS^0, the position of Cu^{2+} in the ΔG^0 value sequence was regular.

KANG SUN et GEORGE E. BOYD. Can. J. Chem. **66**, 974 (1988).

On a effectué des déterminations calorimétriques des effets thermiques qui accompagnent l'échange des cations divalents du Mn, du Fe, du Co, du Ni, du Cu et du Zn présents dans des solutions aqueuses diluées de perchlorate avec l'ion Mg^{2+} qui est lié initialement à un gel réticulé de polyélectrolyte. Afin d'évaluer les ΔG^0, ΔH^0 et ΔS^0 associés aux réactions d'échange de leurs ions, on a utilisé les mesures calorimétriques de concert avec des déterminations de la distribution de l'équilibre microchimique des mêmes cations.

Par rapport au Mg^{2+}, tous les éléments de transition sont absorbés sélectivement et la séquence observée Mn < Fe < Co < Ni > Zn démontre que le cation divalent Ni(II) possède l'affinité la plus grande pour la phase polyélectrolyte. La séquence des ΔH^0 révéle aussi que le Ni^{2+} est le plus exothermique des cations des éléments de transition 3*d*. Toutefois, les valeurs deviennent de plus négatives dans la séquence Mn < Fe < Co < Ni > Cu < Zn; ces résultats démontrent que le comportement du Cu^{2+} est anormal puisqu'il est moins négatif que prévu. Co comportement (ainsi que les valeurs de ΔS^0) suggérent que, dans des solutions aqueuses, il se produit une déstabilisation de l'ion Cu^{2+} qui est coordonné d'une façon octaédrique; cette déstabilisation est peut-être provoquée par les effets de Jahn-Teller sur sa configuration electronique d^9 lorsque le cation est placé dans un environnement de symétrie cubique. A cause d'une compensation thermodynamique des amplitudes des ΔH^0 et ΔS^0, la position du Cu^{2+} dans la séquence des valeurs de ΔG^0 est régulière.

[Traduit par la revue]

Introduction

Investigation into the causes of ion exchange equilibrium selectivity shown by ionogenic, high molecular weight organic polymers towards mobile cations or anions have produced much useful information since synthetic ion exchangers were first produced more than forty years ago. Quite frequently the preferential uptake of ions observed seems to be largely a reflection of the tendency for the electrostatic free energy of the system to be lowered. Electrostatic interactions between unlike charged ions and between like-charged ions in either or both the polyelectrolyte ion exchanger and in the external equilibrium mixed ion solution are usually the most evident. However, ion – polar solvent interactions in the exchanger and in the external solution may be of comparable importance particularly in aqueous systems. For example, the short-range structure of water is believed to be modified by the hydrophobic interaction of non-polar molecular ions leading to a strong preferential uptake of these species by ion exchangers.

There is some evidence also that the electronic configurations of ions such as in the tervalent rare earth cations may interact with their environment leading to small differences in relative ion exchange selectivity. The divalent cations of the 3*d* transition elements appeared to offer attractive possibilities for investigation in this connection. It is known that the d^9 configuration of Cu(II) makes its coordination symmetry subject to Jahn–Teller distortions when this species is placed in an environment of cubic symmetry. The unique properties of Cu(II) complexes appear to result from such a distortion (1). If Jahn–Teller distortions affect the character of the hydration of Cu(II), this might be mirrored in the thermodynamic property changes which accompany its ion exchange reactions.

Accordingly, an experimental program was undertaken to estimate the standard state Gibbs energy, enthalpy and entropy changes at 298 K which occur in the reactions of the divalent cations of Mn(II), Fe(II), Co(II), Ni(II), Cu(II), and Zn(II) with Mg^{2+} ion. Measurements of the enthalpy changes with a microcalorimeter proved particularly revealing with Cu(II), and this was ascribed to a Jahn–Teller distortion of the octahedral symmetry of hydrated Cu(II) ion. Enthalpy change values for the series were combined with Gibbs energy changes derived from equilibrium constant measurements to obtain ion exchange reaction entropy changes. A larger than expected (i.e. more positive) ΔS^0 value for Cu(II) was observed. In contrast, the magnitude of the ΔG^0 value for Cu(II) was not anomalous relative to the other 3*d* divalent cations. This study has appeared to confirm that calorimetric measurements, as well as X-ray crystallographic and spectroscopic observations can provide a sensitive probe for Jahn–Teller effects in ion exchange reactions.

[1]Current address: R&D Department, Arkwright Inc., Main Street, Fiskeville, Rhode Island 02823, U.S.A.

Can. J. Chem. Downloaded from www.nrcresearchpress.com by 176.9.209.113 on 09/07/12
For personal use only.

Can. J. Chem. Downloaded from www.nrcresearchpress.com by 176.9.209.113 on 09/07/12
For personal use only.

Experimental

General remarks

The experiments were designed to yield measurements for use in the evaluation of the thermodynamic property changes occurring in the ion exchange reactions of the divalent cations, M^{2+}, of 3*d* transition elements between a polyelectrolyte gel and aqueous electrolyte mixtures at room temperature. Reactions involving the selective uptake of M^{2+} by the ion exchanger with Mg^{2+} as a "reference ion" in equilibrium constant and calorimetric determinations were studied systematically. Magnesium ion was chosen because of its relatively low affinity for the exchanger, because of its "rare gas" electronic structure, and because of its octahedral coordination in aqueous solutions. Purified perchlorate salts and dilute solutions (0.01 m) were used throughout to minimize the magnitudes of the corrections for aqueous phase nonideality. A moderately highly cross-linked polyelectrolyte gel was employed so as to enhance the selectivity differences between the M^{2+} cations, and to effectively eliminate absorption of ClO_4^{2-} ion by the gel. Thus, the normality of the aqueous phase remained strictly constant at $N = 0.02$ equiv. L^{-1} in all experiments. Care was exercised in the preparation of the electrolyte solutions, and homo-ionic salt-forms, MR_2 and MgR_2, of the exchanger, and in handling these in experiments and analysis. Details are described more fully elsewhere (2).

Chemicals and reagents

Stock solutions of the transition metal and magnesium perchlorates were made to approximately 1 *N* concentration with reagent grade $M(ClO_4)_2.6H_2O$ and pure water ($\kappa = 10^{-6}$ mho cm^{-1}). The pH of these solutions was adjusted to 3.0–3.5. The ferrous perchlorate solution was prepared specially, involving the addition of small amounts of ascorbic acid to reduce Fe(III) impurity and the stabilization of ferrous ion with ultra-pure iron wire.

Analytical grade cross-linked poly(styrene sulfonate), Dowex AG 50W-X8, was employed. Its exchange capacity was determined as 4.88 mequiv./g dry HR. The homo-ionic salt-forms, MnR_2, CoR_2, NiR_2, CuR_2, ZnR_2, and MgR_2, were prepared by treating the acid-form of the exchanger, HR, with 1 *N* MCl_2 solutions, respectively. Special measures were taken to prepare the FeR_2 form (2).

Chemical analyses were conducted to confirm that the conversion of MR_2 and MgR_2 from HR was at least 99.5% complete. Direct titrations of the MR_2 and MgR_2 preparations to determine their metal contents were carried out with standard 0.1000 *M* EDTA at pH = 10 using Eriochrome Black T or Murexide as indicators. The FeR_2 form was titrated with standard 0.1000 *N* $K_2Cr_2O_7$ using diphenylamine sulfonate as an indicator. The preparations were used in a partially hydrated, or "wet", state for convenience in handling. This conversion was accomplished by placing the salt-form in a humidistat, and bringing them to water vapor equilibrium with a saturated $Ca(NO_3)_2{\cdot}6H_2O$ solution.

Equilibrium distribution measurements

Mass law concentration-product quotients, K'_c for the transition metal – magnesium ion equilibria were determined with an ion exchange column technique. A cylindrical bed of approximately 1.5 g HR was formed in a glass column, and 10–15 "bed volumes" of 0.02 *N* $[(M^{2+} + Mg^{2+})ClO_4]_2$ mixtures with pre-determined M^{2+}/Mg^{2+} mole ratios of 0.25, 0.50, and 0.75 were passed through the bed. Equilibrium was assumed to have been reached when the pH of the influent and effluent solutions became identical. The metal ion mole ratio in the exchanger was determined by quantitative elution with 4 *N* H_2SO_4 followed by analysis of the eluate plus wash solution for its M^{2+} and Mg^{2+} contents separately. Numerical values of K'_c were computed from its definition:

$$[1] \quad K'_c = N_M M_{Mg}/N_{Mg} M_M$$

where *N* is the ion equivalent fraction in the exchanger and *M* is the ion molality in the aqueous mixture.

Calorimeter system and measurements

Design and other details on the solution microcalorimeter and its associated circuitry have been presented elsewhere (2, 3). Three features, however, may be of possible interest: (*a*) the response of the calorimeter was increased by reducing its thermal mass by using a specially constructed silvered-glass Dewar vessel with an inner wall of minimal (0.6 mm) thickness; (*b*) a reduction in the heat leak from the calorimeter to its surroundings was effected by leaving the top-most inch of the Dewar unsilvered; (*c*) the rate of the ion exchange reaction was increased significantly by using exchanger preparations consisting of small (i.e. 50–100 micron) spherical particles.

Measurement of ion exchange reaction thermal effects at 25.00 ± 0.05°C were conducted by filling the calorimeter with 500 mL of 0.02 *N* $M(ClO_4)_2$ or $Mg(ClO_4)_2$ solution weighed to ±0.1 g, and placing exactly determined weights of analyzed MgR_2 or MR_2 in sealed 3 mL cylindrical glass pipettes mounted on a suitable holder in the solution. When a steady-state temperature drift in the stirred solution was reached the pipette was opened. The thermal effect accompanying the mixing of the exchanger with the solution was complete within five minutes. Electric energy calibrations were made on the final state of the system with a precision of ±0.05%. Measurements of the heat of solution of NBS standard tris(hydroxylmethyl)aminomethane in 0.100 *N* HCl were conducted periodically to check on the overall performance of the calorimeter system.

The ion exchanger was recovered from the calorimeter and was subjected to chemical analysis to determine its ionic composition. Exhaustive elution with 4 *N* H_2SO_4 solution was used to release the M^{2+} and Mg^{2+} ions from the reacted exchanger. The concentrations of transition metal and magnesium ion in the various solutions and eluates from the calorimeter were estimated by titration with standardized 0.1000 *M* EDTA at pH = 10 using reagent Eriochrome Black T, Murexide and diphenylamine sulfonate as indicators. The equilibrium compositions of the exchanger, the final mixed aqueous electrolyte solution, and the number of milliequivalents of ion exchange reaction were computed from the analyses (2). Heats of partial exchange for the uptake of the preferred ion, M^{2+}, expressed in defined Joules equivalent^{-1}, Q^M_{Mg}, were calculated from the measured thermal effect and the estimated milliequivalents of reaction.

TABLE 1. Mass law concentration product quotient, K'_c, and heat of partial ion exchange, Q^M_{Mg}, for ion exchange reaction: $MgR_2 + M(ClO_4)_2 = MR_2 + Mg(ClO_4)_2$

	K'_c for $[M^{2+}]/[Mg^{2+}]$ =			
M(II)	0.25*	0.50	0.75	Q^M_{Mg} (J equiv.$^{-1}$)
Mn	1.094	1.111	1.111	770
Fe	1.157	1.156	1.154	−42
Co	1.220	—	1.216	−301
Ni	1.330	—	1.327	−485
Cu	1.237	—	1.240	−109
Zn	1.126	—	1.132	−134

*M^{2+}/Mg^{2+} mole ratio in $[M^{2+} + Mg^{2+})ClO_4]_2$ mixtures.

Treatment of experimental data

Mass law concentration product quotients, $K'_c = K^M_{Mg}$, derived for the ion-exchange reaction which occurred in the calorimeter, and the corresponding heats of partial ion exchange, Q^M_{Mg}, are listed in Table 1. The magnitudes (Table 2) of the standard state Gibbs energy, enthalpy, and entropy changes, ΔG^0, ΔH^0, and ΔS^0 for the ion-exchange reactions at equilibrium at 298 K when the products and reactants are in their defined standard states may be derived from K'_c and Q^M_{Mg}. This hypothetical but defined magnesium-first transition series divalent cation equilibrium exchange reaction may be written as:

$$[2] \quad MgR_2{\cdot}nH_2O(a = 1, \text{equilibrium with } 0.02\,N\,Mg(ClO_4)_2) + M(ClO_4)_2(a = 1, aq) = MR_2{\cdot}mH_2O \; (a = 1, \text{equilibrium with } 0.02\,N\,M(ClO_4)_2) + Mg(ClO_4)_2\,(a = 1, aq) + (m - n)H_2O$$

TABLE 2. Thermodynamic property changes in the reaction at 298.0 K: $MgR_2 + M(ClO_4)_2 = MR_2 + Mg(ClO_4)_2$

M(II)	$-\Delta G^0$(J equiv.$^{-1}$)	ΔH^0(J equiv.$^{-1}$)	ΔS^0(J equiv. deg^{-1})	$T\Delta S^0$(J equiv.$^{-1}$)	K_a
Mn	27	757	2.6	784	1.044
Fe	72	−44	0.1	28	1.124
Co	116	−234	−0.4	−118	1.205
Ni	175	−452	−0.9	−277	1.327
Cu	148	−69	0.3	79	1.269
Zn	104	−125	−0.1	−21	1.182

The standard states of the hydrated exchanger salt forms, $MR_2 \cdot mH_2O$ and $MgR_2 \cdot nH_2O$, are defined when they are in vapor phase equilibrium with 0.02 N $M(ClO_4)_2$ and 0.02 N $Mg(ClO_4)_2$ solutions, respectively. The standard states for the mixed electrolyte solution phase are chosen as the usual ones which make ion activities approach corresponding molalities as the solute content of the solution becomes vanishingly small. The reference states for the solvent are chosen so that the activity of water, a_w, in each phase is the same and $a_w = 1$ for the pure solvent. It will be assumed that the anion, ClO_4^-, in the equilibrium electrolyte mixture was present in the gel phase of the exchanger to a negligible extent or, what is the same, that the total normality of the external electrolyte mixture remained constant during the ion exchange reactions. However, allowance is made for changes in the hydration of the exchanger.

The thermodynamic equilibrium constant, K_a, for reaction [2] may be estimated with the relation:

$$[3] \quad K_a = N_M f_M M_{Mg} \gamma_{Mg} / N_{Mg} f_{Mg} M_M \gamma_M$$

where f_M and f_{Mg} are the activity coefficients of the components MR_2 and MgR_2 in the ion exchanger, and γ_M and γ_{Mg} are the molal ionic activity coefficients in the equilibrium aqueous mixture. All of the quantities appearing on the right-hand side of eq. [3], except f_M and f_{Mg}, may be derived from experiment. Values of the activity coefficients for the ion components in the ion exchanger phase may be derived by application of Gibbs–Duhem equation to the three-component system. Substitution into eq. [3] leads to a result, eq. [4], for the standard state Gibbs energy change, ΔG^0, as derived by Gaines and Thomas (4)

$$[4] \quad \Delta G^0 = (-1/Z_{Mg}Z_M)RT(Z_{Mg} - Z_M) - (RT/Z_{Mg} - Z_M) \int_0^1 \ln K_c dN_{Mg} - RT \int_{a_w(M)}^{a_w(Mg)} n_w d \ln a_w$$

where Z_i is the cation charge, and K_c is defined by the equation:

$$[5] \quad K_c = K_c'(\gamma_{Mg}/\gamma_M) = K_c'[\gamma_\pm(Mg)/\gamma_\pm(M)]^6$$

The quantity, K_c, is a function only of the ionic composition of the ion exchanger (as are f_M and f_{Mg}), and is determined by K_c' which is known from chemical analysis, and by $\gamma_\pm(Mg)$ and $\gamma_\pm(M)$ which are the experimentally known mean molal activity coefficients for the salts $Mg(ClO_4)_2$ and $M(ClO_4)_2$ in the aqueous phase. The evaluation of the activity coefficient ratio in eq. [5] is described elsewhere (2), where it is shown also that the last term on the right-hand side of eq. [4] effectively vanishes.

A plot of K_c against N_M showed that K_c was a constant independent of the composition of the exchanger, so that eq. [4] further simplified to:

$$[6] \quad \Delta G^0 = -(1/Z_{Mg}Z_M)RT \ln K_c$$

The standard state enthalpy change, ΔH^0, for eq. [2] will be given by

$$[7] \quad \Delta H^0 = \Delta H + \Delta\phi_L + \Delta H_m$$

where ΔH is the integral or total enthalpy for the conversion of one equivalent of ion exchanger from MgR_2 to the first transition series metal salt form, MR_2, ΔH_m is the enthalpy of mixing in the aqueous phase, and $\Delta\phi_L$ is the relative apparent molal heat content difference (i.e., heat of dilution difference), $\phi_L[Mg(ClO_4)_2] - \phi_L[M(ClO_4)_2]$, for the magnesium and first transition series perchlorate solutions in their mixtures at 0.02 N. These concentrations are sufficiently low that the prediction, $\Delta\phi_L = 0$, from Debye–Hückel limiting law is a fair approximation. Relative apparent molal heat content values, ϕ_L, for $M(ClO_4)_2$ solutions at 0.02 N ($m = 0.01$) have been reported by Vanderzee (5–8) as 391, 389, 387, 387, 385, and 387 J equiv.$^{-1}$ for Mn, Fe, Co, Ni, Cu, and Zn perchlorates, respectively. The value for $Mg(ClO_4)_2$ is 387 J equiv.$^{-1}$ which was estimated by using an extended Debye–Hückel equation (9). Computations using these values confirm the approximation, $\Delta\phi_L = 0$, to be satisfactory within ±5 J equiv.$^{-1}$ which is about the same order as the error in the values of ϕ_L themselves. The enthalpy of mixing of $Mg(ClO_4)_2$ and $M(ClO_4)_2$ at $m = 0.01$ concentration was 4 mJ, which is negligible.

The magnitude of ΔH in eq. [7] is given by the area under the differential heat of exchange, $\overline{\Delta H}$, vs. composition curve:

$$[8] \quad \Delta H = \int_0^1 \overline{\Delta H} dN_M = \int_0^1 (dQ/dN_M) dN_M$$

where Q is the heat of partial ion exchange measured in the calorimeter experiments, and N_M is the equivalent fraction of M in the exchanger.

The quantity ΔH^0, eq. [7], is defined as the standard enthalpy change which accompanies the complete conversion of the homoionic exchanger MgR_2 in an ion exchange reaction to MR_2, each exchanger being in its respective standard state.

The entropy change, ΔS^0, for the standard state ion exchange reaction may be derived from the enthalpy and Gibbs energy change with the Gibbs–Helmholtz relation.

Results and discussion

Ion exchange equilibrium coefficients, K_c, for the first transition series divalent cations, M, initially in 0.02 N aqueous perchlorate solution with magnesium ion initially in the exchanger, are plotted in Fig. 1 against the atomic number, Z_M. Instead of a monotonically increasing value of K_c with Z_M, as for the exchange reactions of the alkali metal cations with Li^+ ion, or, for the alkaline earth cations with Mg^{2+}, the relative affinities (as measured by K_c) pass through a maximum for Ni^{2+} ion, and the sequence of "affinities" is Mn < Fe < Co < Ni > Cu > Zn. This atypical behavior of some of the 3d divalent

Can. J. Chem. Downloaded from www.nrcresearchpress.com by 176.9.209.113 on 09/07/12
For personal use only.

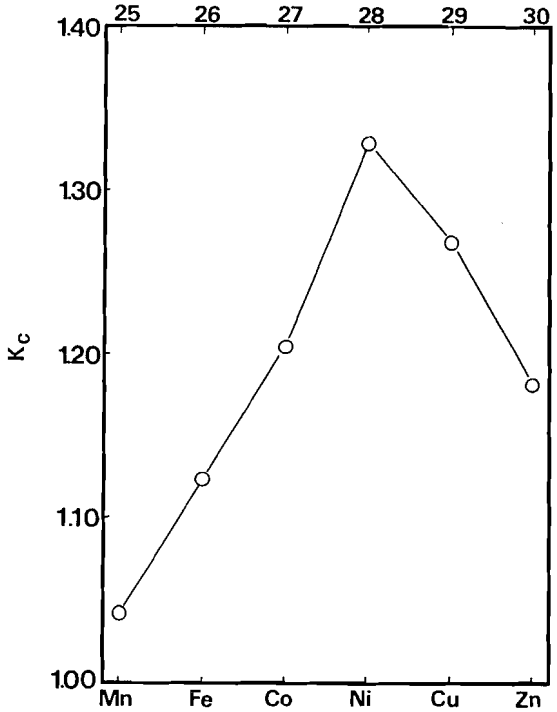

FIG. 1. Ion exchange equilibrium constants: $MgR_2 + M(ClO_4)_2 = MR_2 + Mg(ClO_4)_2$.

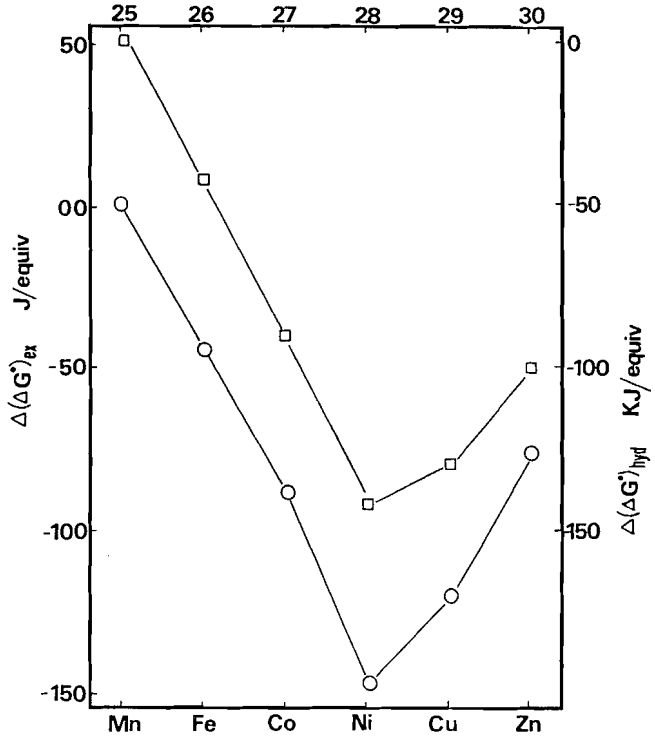

FIG. 2. ○ Standard Gibbs energy changes in ion exchange reactions, and □ Gibbs energy changes of hydration of divalent cations (the value of ΔG^0_{hyd} for Mn^{2+} was arbitrarily taken as zero).

cations had been noted earlier in this laboratory in unpublished studies with Co, Ni, Cu, and Zn ions in slightly more concentrated (0.03 *N*) perchlorate solutions using a virtually identical cation exchanger.[2] The sequence was Co < Ni > Cu > Zn. Sensitive thermometric titrations with EDTA using a Tronac 1200 isothermal solution microcalorimeter were employed in the K_c determinations. A small, linear dependence of K_c on N_{NiR_2} and N_{CuR_2} was observed in contrast with this research.

A plot (Fig. 2) of the standard state Gibbs energy change, ΔG^0, for the reactions of the transition element cations reveals a relatively large negative value for Ni^{2+} ion consistent with its strong preferential uptake by MgR_2. A comparison of the variations in ΔG^0, and the standard Gibbs energy change of ion hydration, ΔG^0_{hyd}, with atomic number (the value of ΔG^0_{hyd} for Mn^{2+} was arbitrarily taken as zero) may be made in Fig. 2. The qualitatively close correspondence may be understood on the basis of the crystal-field stabilization energies (CFSE) for 3*d* elements; Ni(II) ion should be stabilized more than any other ion in a weak octahedral field because it has greatest CFSE (12 *Dq*). The d^6, d^7, and d^9 ions have somewhat less stabilization energy, and the d^5 and d^{10} species have $Dq = 0$. Interestingly, there is no indication of the consequences of partially filled *d*-shell, or, of the effects of *d*-orbital splitting, in the values of ΔG^0.

By reason of the Gibbs–Helmholtz relation the sign and magnitude of ΔG^0 is determined by the signs and magnitudes of the standard enthalpy, ΔH^0, and entropy, $T\Delta S^0$, changes. Values of ΔH^0 from calorimetric measurements and values of $T\Delta S^0$ from ΔG^0 and ΔH^0 when plotted, Fig. 3, against Z_M also show unexpected features. The general trend of these quantities for the M(II) cations in their exchange reactions with Mg^{2+}

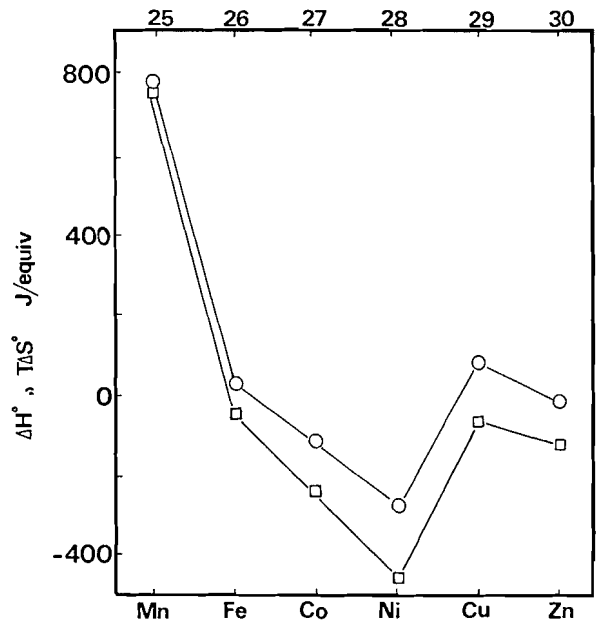

FIG. 3. □ Standard enthalpy changes and ○ standard entropy changes in ion exchange reactions.

seems normal up to Ni(II) ion, beyond which new interactions appear to set in which make ΔH^0 less negative and ΔS^0 more positive. Conceivably, changes in ion-solvent interaction may occur, in spite of the fact that the hydration enthalpies for the M(II) cations are large indicating strong ion–water forces (10). The exchange reaction of Cu(II) ion differed notably from the other 3*d* cations in that its preferential uptake was accompanied by an entropy increase, while the enthalpy change was negative.

[2]D. P. Wilson and G. E. Boyd. Unpublished researches. University of Georgia, Athens, GA. 1976. The ion exchanger employed was Dowex AG50W X-8 (Bio-Rad Control No. 6736), 5.16 mequiv./g dry HR.

Can. J. Chem. Downloaded from www.nrcresearchpress.com by 176.9.209.113 on 09/07/12
For personal use only.

Further, the positive ΔS^0 of reaction contributed significantly to the selective uptake.

The unique behavior of copper among the transition elements may possibly arise because its *d* electron configuration makes its hydrated ion subject to Jahn–Teller distortion. The existence of a well-defined, distorted $Cu(H_2O)_{4,eq}\cdot(H_2O)_{2,ax}$ octahedron in copper perchlorate solutions has been indicated by the X-ray diffraction researches of Magini (11). The Jahn–Teller theorem does not predict the details of the distortion, however. An elongation along one 4-fold axis occurs to produce a planar array of four short Cu—H_2O bonds and two long *trans*-bonds according to the X-ray results.

In dilute aqueous perchlorate solutions only water molecules are expected to enter the inner coordination spheres of 3*d* transition element cations. Although direct proof is lacking, it is likely that these ions also retain their primary hydration spheres when they are present inside the cation exchanger. The water contents of the MR_2 and MgR_2 salt-forms are certainly more than sufficient. Their environment, however, would be unlikely to possess cubic symmetry so that Jahn–Teller distortions are not expected. The structure of the cation exchanger gel phase is surely complex, and is very poorly understood. It has been likened to that of a concentrated aqueous electrolyte solution.

This research may be of general interest because it appears to demonstrate the feasibility of microcalorimetric methods in searching for Jahn–Teller and possibly other electronic effects in ion exchange reactions with organic polyelectrolytes. Thermal effects caused by *d*-orbital splitting are expected to be small, but existing microcalorimeters seem to be sensitive enough to detect and measure them quantitatively.

1. A. F. WELLS. Structural inorganic chemistry. 4th ed. Clarendon Press, Oxford. 1975.
2. K. SUN. M.S. thesis, University of Georgia, Athens, GA. 1983.
3. G. E. BOYD. Ion exchange in the process industries. Society of Chemical Industry, London. 1970.
4. G. L. GAINES and H. C. THOMAS. J. Chem. Phys. **24**, 714 (1953).
5. L. J. GIER and C. E. VANDERZEE. J. Chem. Eng. Data, **19**, 315 (1974).
6. L. J. GIER and C. E. VANDERZEE. J. Chem. Eng. Data, **19**, 323 (1974).
7. R. L. BERG and C. E. VANDERZEE. J. Chem. Thermodyn. **7**, 219 (1975).
8. L. J. GIER and C. E. VANDERZEE. J. Chem. Eng. Data, **20**, 259 (1975).
9. H. S. JONGENBURGER and R. M. WOOD. J. Phys. Chem. **69**, 4231 (1965).
10. H. F. HALLIWELL and S. C. NYBERG. Trans. Faraday Soc. **59**, 1126 (1963).
11. M. MAGINI. Inorg. Chem. **21**, 1535 (1982).

Can. J. Chem. Downloaded from www.nrcresearchpress.com by 176.9.209.113 on 09/07/12
For personal use only.

An efficient algorithm for estimating dimensionalities[1]

R. L. SOMORJAI[2]
Division of Chemistry, National Research Council of Canada, Ottawa, Ont., Canada K1A 0R6
AND
M. K. ALI
Department of Physics, University of Lethbridge, Alberta, Lethbridge, Alta., Canada T1K 3M4
Received August 11, 1987
This paper is dedicated to Professor James A. Morrison

R. L. SOMORJAI and M. K. ALI. Can. J. Chem. **66**, 979 (1988).

We present an algorithm for estimating dimensionality. It is based on a multivariate k nearest neighbor (k-NN) density estimator and shows explicitly that the dependence of k-NN distances on k does not follow pure power law behavior. We achieve very high efficiency ($\leq$2000 points for up to 20 dimensions) by abandoning the distribution free feature of our algorithm; it is *calibrated* for two distributions and tested on a number of strange attractors, the discretized Mackay–Glass system, and trajectories of 3, 10, and 20 coupled harmonic oscillators. The danger of embedding in higher dimensional spaces is demonstrated.

R. L. SOMORJAI et M. K. ALI. Can. J. Chem. **66**, 979 (1988).

On présente un algorithme permettant d'évaluer la dimensionnalité. Il est basé sur un évaluateur de densité à plusieurs variables sur k voisins les plus proches (k-VP) et il démontre explicitement que la dépendance des distances k-VP sur k ne suit pas une loi des puissances pure. On a réalisé une très grande efficacité ($\leq$2000 points jusqu'à 20 dimensions) lorsqu'on a abandonné la caractéristique non paramétrique de notre algorithme; celui-ci est *calibré* pour deux distributions et on l'a évalué sur un certain nombre d'attracteurs étranges, sur le système de Mackay–Glass discrétisé ainsi que sur les trajectoires de 3, 10 et 20 oscillateurs harmoniques couplés. On démontre les dangers qui découlent du plongement dans des espaces de dimensionnalité plus élevée.

[Traduit par le journal]

Can. J. Chem. Downloaded from www.nrcresearchpress.com by 176.9.209.113 on 09/07/12
For personal use only.

In recent years the characterization of strange attractors has received much attention (1–8). Of special interest is the fractal dimensionality d. It is now recognized that for practical purposes the Balatoni–Rényi generalized dimension (9) d_q, $q \geq 0$, subsumes, for different q's, all currently used definitions of d (see, however, ref. 10).

Consider a strange attractor, embedded in d_E-dimensional Euclidean space, and let $\{x_i\}_{i=1}^n$ be n d_E-dimensional points of a time series on the attractor. We want to estimate from $\{x_i\}$ its dimensionality $d \neq d_E$. Box-counting methods are inefficient (11) for $d \geq 3$. All other published algorithms are based on some form of neighbor–distance relationship and, although more efficient, were tested mostly on systems with $d \leq 3$.

To devise a classification scheme for trajectories of both integrable and nonintegrable Hamiltonian systems of high dimension, we adopted an algorithm (12) that was developed for estimating the "intrinsic dimensionality" of a set of patterns typically encountered in discrimination analysis, pattern recognition, etc. (13–15), and improved its efficiency such that even for $d = 20$, 2000 points of $\{x_i\}$ give high accuracy. We sketch the derivation of the algorithm to make contact with current dimensionality estimators.

Consider our set $\{x_i\}$, $i = 1, 2, \ldots, n$ in Euclidean d_E-space. The x_i are sampled from an *unknown* distribution $p(x)$. The simplest estimator of $p(x)$, $\hat{p}(x)$ is (16)

$$[1] \quad \hat{p}(x) = (k/n)/V, \ \lim_{n\to\infty} (k/n) = 0$$

where k is the number of nearest neighbors (NN's) of x within a hypersphere of radius R_k about x. The volume is $V = V_d R_k^d$, where $V_d = \pi^{d/2}/\Gamma(d/2 + 1)$ is the volume of a unit d-dimensional hypersphere. Substituting into eq. [1] and taking logarithms (12) gives

$$[2] \quad \log R_k = (1/d)\{\log k - \log n - \log [V_d \hat{p}(x)]\}$$

Equation [2] cannot be used directly to estimate d because $\hat{p}(x)$ is not independent of k. Let $r_k(x)$ be the distance from x to its kth NN. If $p(x)$ is continuous and nonzero at x, then the density function for $r_k(x)$ for sufficiently large n and small $r > 0$ is (12) $f_{k,x}(r) = (d/r\Gamma(k))C^k \exp(-C)$, $C = np(x)r^d V_d$. The expected value of $r_k(x)$ is $E(r_k(x)) = [k/np(x)V_d]^{1/d}/G_{k,d}$, where $G_{k,d} = k^{1/d}\Gamma(k)/\Gamma(k + 1/d)$. If $\bar{r}_k$ is the sample-averaged distance to the kth NN over the set of points, $\bar{r}_k = (1/n)\sum_{i=1}^n r_k(x_i)$, then the expected value of this average is

$$[3] \quad E(\bar{r}_k) = (1/n)\sum_{i=1}^{n} E(r_k(x_i)) = G_{k,d}^{-1} k^{1/d} S_n$$

where S_n is independent of k. Taking logarithms of eq. [3] gives

$$[4] \quad \log G_{k,d} + \log E(\bar{r}_k) = (1/d)\log k + \log S_n$$

The term $\log G_{k,d}$ is in the range $0 \leq \log G_{k,d} \leq 0.12$ for all k and d, the maximum occurring for $k = 1$ and $d \simeq 2.17$ (12). The algorithm consists of replacing $E(\bar{r}_k)$ by $\bar{r}_k$ in eq. [4]. Using this observed value gives an estimator $\hat{d}$ of d:

$$[5] \quad \log G_{k\hat{d}} + \log \bar{r}_k = (1/\hat{d}) \log k + \log S_n$$

Plotting $\log \bar{r}_k$ vs. $\log k$ for $k = 1, 2, \ldots, k_{max}$ will give a least-squares fitted straight line with slope $1/\hat{d}$. One has to solve for $\hat{d}$ iteratively; the initial estimator $\hat{d}_0$ is obtained by setting $\log G_{k\hat{d}}$ to zero (12). Typically 4–5 iterations are sufficient for $\hat{d}$ to converge within 0.003. Note that $\hat{d}_0$ is frequently quite inaccurate.

The algorithm (and its other variants in the literature) is based on statistical methods for estimating probability densities via

[1]NRCC No. 28616.
[2]Author to whom correspondence may be addressed.

TABLE 1. Dimensionalities d_{Sm}, m = 2,6 with 2000 points for the *surface* of d_E-spheres. The fitted values are d^f_{Sm}

d_E	d_{S2}	d^f_{S2}	d_{S6}	d^f_{S6}
1	1.000±0.000	1.001	0.999±0.001	1.034
2	2.001±0.002	1.987	1.997±0.005	1.991
3	2.981±0.004	3.003	2.992±0.005	2.994
4	3.916±0.003	4.025	3.955±0.004	4.013
5	4.789±0.007	5.030	4.855±0.010	5.009
6	5.620±0.007	6.041	5.728±0.009	6.024
7	6.385±0.007	7.021	6.592±0.015	6.999
8	7.232±0.013	8.018	7.300±0.015	7.982
9	7.822±0.014	9.022	8.064±0.019	9.007
10	8.464±0.010	9.993	8.740±0.018	9.961
11	9.103±0.011	11.016	9.444±0.015	11.003
12	9.656±0.012	11.954	10.066±0.014	11.974
13	10.209±0.011	12.947	10.668±0.012	12.963
14	10.732±0.010	13.940	11.251±0.017	13.969
15	11.233±0.021	14.950	11.800±0.028	14.969
16	11.716±0.009	15.982	12.354±0.022	16.035
17	12.161±0.016	16.996	12.858±0.024	17.058
18	12.563±0.013	17.970	13.274±0.026	17.948
19	12.976±0.024	19.022	13.748±0.037	19.012

TABLE 2. Dimensionalities d_{Vm} with 2000 points for the *interior* of d_E-spheres. The fitted values are d^f_{Vm}

d_E	d_{V2}	d^f_{V2}	d_{V6}	d^f_{V6}
2	1.937±0.003	2.008	1.960±0.004	2.011
3	2.822±0.003	2.996	2.862±0.005	2.994
4	3.679±0.006	4.000	3.740±0.006	3.993
5	4.494±0.007	5.005	4.596±0.008	5.010
6	5.263±0.008	5.998	5.391±0.010	5.996
7	6.000±0.012	6.999	6.164±0.017	6.998
8	6.794±0.007	8.002	6.907±0.013	8.001
9	7.373±0.012	9.001	7.609±0.016	8.990
10	8.023±0.012	10.021	8.316±0.018	10.018
11	8.614±0.010	10.995	8.934±0.018	10.975
12	9.210±0.013	12.025	9.596±0.019	12.031
13	9.741±0.006	12.987	10.176±0.008	12.995
14	10.272±0.011	13.994	10.760±0.017	14.004
15	10.760±0.013	14.967	11.300±0.022	14.977
16	11.257±0.018	16.003	11.849±0.025	16.004
17	11.720±0.011	17.018	12.389±0.024	17.056
18	12.149±0.015	18.002	12.871±0.020	18.037
19	12.549±0.013	18.962	13.271±0.028	18.881
20	12.970±0.023	20.021	13.781±0.039	19.994

multivariate k-NN estimators (17, 18). An important feature of the latter is that they are *nonparametric*, i.e., distribution free. This means in general that the efficiency of the algorithms is much less than optimal.

Since practical considerations limit the number of points n, it is essential to determine the optimum rate of convergence of $\hat{d}(n,k)$ to d with n and k. One necessary condition is $\lim_{n\to\infty}(k/n) = 0$. Another is that $k = k(n)$ be a sequence of positive integers such that $k \to \infty$ as $n \to \infty$. Then (17) the fastest rate at which the local mean square error of the estimated density decreases is $\sim n^{-\beta}$ if $k \sim n^{\beta}$, $\beta = 4/(4 + d)$. Furthermore, the *variance* of the estimated density is $0(1/k)$ and its *bias* is $0((k/n)^{2/d} + 1/k)$.

We tested the accuracy of the algorithm based on eq. [5] by applying it to various distributions of *known* dimensionality. In particular, uniformly distributed random points were generated from the interior of the unit d_E-sphere as well as from its surface, and from the unit d_E-torus, using the fast algorithms in ref. 12. Typically, for each dimension d_E, 10 samples of n = 250, 500, 1000, and 2000 points each were drawn and their apparent dimensionality determined via eq. [5]. The averages and their standard deviations were computed, each for $k = [m\sqrt{n}/4]$ $m = 9 - l$, l = 2(1)7 NN's ([ ] denotes the integer part). In Table 1 the results from the *surface* are recorded under d_{S2} and d_{S6}, for n = 2000 and m = 2, 6. Table 2 contains comparable data from the *interior* of the hyperspheres, d_{V2} and d_{V6}. Results for the d_E-torus are quite close to d_{V2} and d_{V6}.

A crude error analysis suggests that $(1/d)$ could be expanded in inverse powers of $\hat{d}$. In fact, the fitted values d^f in the tables were obtained by writing $1/d^2_E = \Sigma^3_{i=0}\, a_i/\hat{d}^i$ and determining by least-squares fitting the best a_i. The fitting errors are ± 0.24% over the four sets. Note that $a_i = a_i(n, k)$. For fixed n, low degree polynomials in k give excellent fits and, for fixed k, equally good fits with such polynomials in $1/n$ can be obtained. Thus reasonable interpolation is possible in the k–$1/n$ plane.

As expected (17), the variances of the estimated dimensions increase with d_E and decrease with both k and n. Furthermore, $\hat{d}$ increases only sublinearly with increasing d_E, rendering $\hat{d}$ less and less reliable. Thus the majority of dimensionality estimators in the literature would underestimate the true dimension of higher dimensional attractors. For fixed n, the larger the k, the slower the convergence of $\hat{d}(k, n)$ to d. The larger the n, the closer is $\hat{d}(k, n)$ to d.

In Table 3 we collect the results of applying our algorithm, both directly and after calibration, to a set of strange attractors.[3] These include the logistic map, with parameter = 4 (LOG4), Zaslawskii's map (ZASL), Henon's map (HENON), Rössler's equations (19) (RÖSS), and the Lorenz equations (20) (LOR). All of these are low ($d \leq 3$) dimensional attractors and the difference between $\hat{d}$ and d^f is small. The recorded results are averages over N subsets of 2000 points each of the appropriate time series of length $2000N$, where $3 \leq N \leq 50$, depending on the system. Our results compare quite favorably with data quoted in the literature (1, 3, 6–8): LOG4: 1.000 (exact); HENON: 1.21–1.28; RÖSS: 1.81; LOR: 2.05–2.10; ZASL: 1.22–1.80. The latter is particularly difficult to characterize in terms of its dimensionality, because of two distinct power law behaviors for small and large n (6). The latest study (7) gives d = 1.56. Note that most current methods require $10^4 \leq n \leq 10^6$ points on the attractor.

Inspection of Table 3 reveals the penalty one has to pay for efficiency: the fitted dimensionalities depend on the nature of the distribution. Fortunately, this dependence appears to be quite weak.

To further test this distribution dependence, we generated long trajectories for 3, 10, and 20 coupled harmonic oscillators on constant total energy surfaces. Thus the trajectories evolve in 6-, 20-, and 40-dimensional phase space, but because of integrability they are confined to the surface of at most 3-, 10-, and 20-dimensional tori, respectively. These are then the *maximum dimensionalities possible*. The results under HO-3, HO-10, and HO-20 indicate that the fitted dimensionalities are within 10% of the true ones. Furthermore, the d^f_S values are better than d^f_V fits for HO-3, and worse for HO-10 and HO-20. (It should be pointed out that it is increasingly more difficult to create *finite* trajectories in phase space that cover reasonably

[3]See ref. 4 for appropriate references for the strange attractors.

Can. J. Chem. Downloaded from www.nrcresearchpress.com by 176.9.209.113 on 09/07/12
For personal use only.

TABLE 3. Dimensionalities for 10 dynamical systems; 2000 points and 2 sets (m = 2,6) of NN's were used. The fitted values to the two distributions are denoted by S and V. The embedding dimension is d_{EMB}. For details consult the text

System	$d_{m=2}$	d^f_{S2}	d^f_{V2}	$d_{m=6}$	d^f_{S6}	d^f_{V6}	d_{EMB}
LOG4	1.00	1.00	1.01	1.00	1.00	1.01	1
	1.00	1.00	1.01	1.00	1.00	1.01	2
ZASL	1.73	1.73	1.78	1.75	1.76	1.78	2
	3.53	3.59	3.83	3.60	3.62	3.83	8
HENON	1.27	1.26	1.30	1.31	1.28	1.33	2
	1.21	1.20	1.23	1.22	1.20	1.24	4
	1.21	1.20	1.23	1.22	1.20	1.24	6
RÖSS	1.79	1.78	1.84	1.83	1.83	1.86	3
LOR	2.06	2.06	2.13	2.06	2.07	2.11	3
HO–3	3.02	3.04	3.23	3.29	3.31	3.48	6
HO–10	7.68	8.80	9.47	8.38	9.46	10.09	20
HO–20	12.81	18.57	19.60	13.31	18.08	19.08	40
MG23	2.25	2.26	2.35	2.33	2.33	2.39	3
	2.35	2.36	2.45	2.43	2.43	2.50	4
	2.35	2.36	2.46	2.44	2.45	2.52	5
MG100	5.06	5.32	5.73	5.20	5.39	5.76	10
	5.90	6.36	6.86	6.02	6.37	6.82	12
	6.64	7.34	7.91	6.74	7.27	7.78	14
	7.37	8.34	8.99	7.39	8.12	8.69	16
	8.85	10.60	11.39	8.78	10.06	10.77	20

densely and uniformly the surface of the d_E-torus as d_E increases, even with incommensurate relative frequencies, e.g., $1:\sqrt{2}:\sqrt{3}:\ldots\sqrt{p_i}$, p_i the ith prime. This may explain the underestimates.)

Finally, we applied the algorithm and the fitting scheme to the Mackey–Glass delay-differential equation (21) for τ = 23 and 100. Following ref. 4 we transformed the equation into a set of 1200 difference equations and embedded members of the time series produced into d_{EMB}-dimensional spaces. The results for τ = 23, denoted by MG23, are to be compared with (2.38, 2.43, 2.44) (ref. 4), 2.65(d_{EMB} = 10) (ref. 6), while for τ = 100 (MG100), with (5.8, 6.6, 7.2, 7.5) (ref. 4) and 12.6(d_{EMB} = 30) (ref. 6). Note that the d_V estimates give consistently higher dimensionalities than the d_S values, more in line with the results of ref. 4 for τ = 23. However, for τ = 100 the calibrated d^f increase linearly with d_{EMB} even for d_{EMB} = 20, thus displaying no sign of saturation (4).

The last column of Table 3 contains d_{EMB}, the dimension of Euclidean space in which the time series was embedded. For the HO systems this is $2f$, where f is the number of degrees of freedom. The infinite dimensional MG systems may have low dimensional attractors. Thus one increases d_{EMB} until d saturates. The d_{EMB}-dimensional points are $X_i = \{x(t_i), x(t_i + \tau), \ldots, x(t_i + (d_{EMB} - 1)\tau)\}$. The practical rationale for embedding is (22) that one has access only to a few components of a multidimensional time series. d_{EMB}-dimensional vectors X_i would then be formed and X-space would be used instead of x-space. τ is a judiciously chosen interval such that reasonable correlation exists amongst the components. The examples for LOG4 (2),[4] ZASL (8), and HENON (4, 6) show what may happen. ZASL (8) gives d's which are approximately twice as large as for ZASL (2); HENON (4, 6) are both smaller than HENON (2)! (Our simple construction uses d_{EMB} consecutive x_j's to form a d_{EMB}-dimensional vector, but the n vectors chosen are not necessarily consecutive.) Our principal conclusion is that embedding is a delicate process that requires more care than commonly believed. In particular, $\hat{d}$ as a function of d_{EMB} does not always behave predictably.

Our algorithm behaved erratically for the logistic map for $a = a_\infty = 3.5699\ldots$. The theoretical value for $d_2 = \sigma = 0.517$ (4). We found, with 2000 points ($d_{m=2}$, $d_{m=6}$) = (0.48, 0.45) for d_{EMB} = 1 (average of 25 sets), (0.40, 0.33; 2/12), (0.48, 0.44; 3/8), and (0.50, 0.47; 5/5). Inspection of individual $\hat{d}$ values that made up these averages reveals that for d_{EMB} = 1 the components cluster around 0.55, 0.50, 034, 0.21, 0.16.

The erratic behavior may be due to excessive fluctuations in the k–NN distances, which sample-averaging failed to smooth out. Rejection of outliers may then be beneficial and could be simply implemented by using the L_1 norm (instead of the L_∞ norm) for the distance calculations, as well as determining the best slope of log $\bar{r}_k$ vs. log k via L_1 fitting, using linear programming. This is robust against outliers, although computationally less efficient.

Both the construction and implementation of our algorithm argue for a probability measure dimension, σ in fact (5). This "information dimension" has recently been shown (10) to be invariant under "reasonable" changes of variables, a desirable property for a "dimension" to have. It was shown elsewhere (23) how to generalize the algorithm to obtain *moments* of the probability density. This will provide a measure of the nonuniformity of the distribution.

Other possible algorithms than the one based on eq. [5] follow from the theory. Thus assume that $(1/n)\,\Sigma_i\, p(x_i)^{-1/d}$ is very weakly dependent on n. Write $r(n,k,d) \equiv E(r_k)$. Then $T_1 \equiv r(n,k,d)/r(n',k,d) = (n'/n)^{1/d}$ for large n,n', $T_2 \equiv r(n,k,d)/r(n,k',d) = \Gamma(k')\Gamma(k + 1/d)/\Gamma(k)\Gamma(k' + 1/d)$. If $k' = k + 1$, $T_2 = k/(k + 1/d)$. Thus log T_1 vs. log (n'/n) is a straight line with slope $1/d$, and T_2 vs. $1/k$ has slope $-1/d$ for $kd \gg 1$. These alternatives were not tested.

In summary, we have presented explicit evidence that all the standard dimensionality algorithms that use variants of log r_k vs. log k depend on the distribution of the sample points and do not follow exact power laws. We demonstrated with examples the efficacy and need of *calibrating* dimensionality algorithms against *known* distributions of *known* dimensionality d, especially for d large, and used this calibration to show that embedding into higher dimensional spaces is a delicate process fraught with dangers.

[4]Numbers in parentheses denote the embedding dimension.

1. P. GRASSBERG and I. PROCACCIA. Phys. Rev. Lett. **50**, 346 (1983).
2. J. GUCKENHEIMER and G. BUZYNA. Phys. Rev. Lett. **51**, 1438 (1983).
3. R. BADIIA and A. POLITI. Phys. Rev. Lett. **52**, 1661 (1984).
4. P. GRASSBERGER and I. PROCACCIA. Physica D: **9D**, 189 (1983).
5. H. G. E. HENTSCHEL and I. PROCACCIA. Physica D: **8D**, 435 (1983).
6. Y. TERMONIA and Z. ALEXANDROWICZ. Phys. Rev. Lett. **51**, 1265 (1983).
7. P. GRASSBERGER and I. PROCACCIA. Physica D: **13D**, 34 (1984).
8. P. GRASSBERGER. Phys. Lett. A, **97A**, 224, 227 (1983).
9. J. BALATONI and A. RÉNYI. Publ. Math. Inst. Hung. Acad. Sci. **1**, 9 (1956).
10. E. OTT, W. D. WITHERS, and J. A. YORKE. J. Stat. Phys. **36**, 687 (1984).

Can. J. Chem. Downloaded from www.nrcresearchpress.com by 176.9.209.113 on 09/07/12
For personal use only.

11. D. A. RUSSELL, J. D. HANSON, and E. OTT. Phys. Rev. Lett. **45**, 1175 (1980).
12. K. W. PETTIS, TH. A. BAILEY, A. K. JAIN, and R. D. DUBES. IEEE Trans. Pattern Anal. Machine Intell. PAMI-1, 25 (1979).
13. N. WYSE, R. DUBES, and A. K. JAIN. *In* Pattern recognition in practice. *Edited by* E. S. Gelsema and L. N. Kanal. North Holland Publ. Co., Amsterdam 1980. p. 415.
14. K. FUKUNAGA. *In* Handbook of statistics. Vol. 2. *Edited by* P. R. Krishaiah and L. N. Kanal. North Holland Publ. Co., Amsterdam. 1982. p. 347.
15. L. DEVROYE and J. J. WAGNER. *In* Handbook of statistics. Vol. 2. *Edited by* P. R. Krishaiah and L. N. Kanal. North Holland Publ. Co., Amsterdam. 1982. p. 193.
16. R. O. DUDA and P. E. HART. Pattern classification and scene analysis. Wiley, New York. 1973. p. 87.
17. Y. P. MACK and M. ROSENBLATT. J. Multivar. Anal. **9**, 1 (1979).
18. M. ROSENBLATT. *In* Smoothing techniques for curve estimation. *Edited by* Th. Gasser and M. Rosenblatt. Lecture notes in Math. No. 757, Springer, Berlin. 1979.
19. O. E. RÖSSLER. Z. Naturforsch. A: Phys. Phys. Chem. Kosmophys. **31**A,. 1168 (1976).
20. E. N. LORENZ. J. Atmos. Sci. **20**, 130 (1963).
21. M. C. MACKEY and L. GLASS. Science, **197**, 287 (1977).
22. F. TAKENS. *In* Proc. Warwick Symp. 1980. *Edited by* D. Rand and B. S. Young. Lecture Notes in Math. No. 898, Springer, Berlin. 1981.
23. R. L. SOMORJAI. *In* Dimensions and entropies in chaotic systems, *Edited by* G. Mayer-Kress. Springer Verlag, Berlin. 1986. pp. 137–147.

Can. J. Chem. Downloaded from www.nrcresearchpress.com by 176.9.209.113 on 09/07/12
For personal use only.

Infrared spectroscopic characterization of the interaction of ascorbyl palmitate with phospholipid bilayers[1]

U. KÖHLER, H. H. MANTSCH, AND H. L. CASAL
Division of Chemistry, National Research Council of Canada, Ottawa, Ont., Canada. K1A 0R6

Received July 31, 1987

This paper is dedicated to Professor James A. Morrison

U. KÖHLER, H. H. MANTSCH, and H. L. CASAL. Can. J. Chem. **66**, 983 (1988).

The interaction of ascorbyl palmitate (AP) with phospholipid bilayers of 1,2-dipalmitoyl-*sn*-glycero-3-phosphocholine (DPPC), 1,2-dimyristoyl-*sn*-glycero-3-phosphoethanolamine (DMPE), and 1,2-dipalmitoyl-*sn*-glycero-3-phosphoethanolamine (DPPE) has been studied by variable temperature infrared spectroscopy. The incorporation of AP into these lipid bilayers induces a considerable increase in the gel to liquid-crystal phase transition temperature of the lipid. The increase in this temperature is dependent on the nature of the lipid head group, on the relative concentration of AP, and on its degree of ionization; i.e., smaller temperature increases are observed when AP is ionized, forming salts with cations (NH_4^+, Li^+, K^+, and Ca^{2+}). The stabilizing effect of the long chains in the bilayers plays an important role in inducing temperature increases. However, in the case of AP the present data also demonstrate that specific interactions at the polar head group serve to further stabilize the incorporation of AP into lipid bilayers. The infrared spectra demonstrate that in the case of DPPC:AP mixtures there are changes compatible with the formation of hydrogen bonds between the OH group at position 3 in AP and the ester carbonyl group at the *sn*-2 chain in DPPC. In the case of PE:AP mixtures the spectra are compatible with AP intercalated between PE head groups acting as a hydrogen bond bridge linking the phosphate and ammonium groups of two different PE molecules.

U. KÖHLER, H. H. MANTSCH et H. L. CASAL. Can. J. Chem. **66**, 983 (1988).

Utilisant la spectroscopie infrarouge à température variable, on a étudié les interactions entre le palmitate d'ascorbyle (PA) et des doubles couches de phospholipides de dipalmitoyl-1,2 *sn*-glycéro phosphocholine-3 (DPPC), de dimyristoyl-1,2 *sn*-glycéro phosphoéthanolamine-3 (DMPE) et de dipalmitoyl-1,2 *sn*-glycéro phosphoéthanolamine-3 (DPPE). L'introduction de PA dans ces doubles couches de lipides induit une augmentation considérable de la température de transition au cours du changement de phase gel – cristal liquide du lipide. L'augmentation de cette température dépend de la nature de la partie polaire du lipide, de la concentration relative de PA et de son degré d'ionisation; on observe des augmentations plus faibles de la température lorsque le PA est ionisé et qu'il forme des sels avec les cations (NH_4^+, Li^+, K^+ et Ca^{2+}). L'effet stabilisant des longues chaînes des doubles couches joue un rôle important en induisant des augmentations de température. Toutefois, dans le cas du PA, les données que nous avons obtenues démontrent que les interactions spécifiques des groupements polaires stabilisent aussi l'incorporation du PA dans les doubles couches de lipides. Les spectres infrarouges démontrent que, dans le cas des mélanges DPPC:PA, il se produit des changements qui sont compatibles avec la formation de liaisons hydrogènes entre le groupement OH en position 3 du PA et le groupement ester en position *sn*-2 de la chaîne du DPPC. Dans le cas des mélanges PE:PA, les spectres sont compatibles avec la présence d'un PA intercalé entre deux molécules de PE; le PA sert comme pont hydrogène reliant les groupements phosphate et ammonium de deux molécules différentes de PE.

[Traduit par la revue]

Introduction

The interaction of specific chemicals (often referred to as guest molecules) with biological membranes continues to be an active area of research with the general aim of understanding membrane-associated phenomena as well as characterizing the structures of these mesomorphic phases. In particular, the interaction of long-chain fatty acids and alcohols with phospholipids has received considerable attention (1–8). Generally, the presence of additives in lipid bilayers lowers the gel to liquid-crystal phase transition temperature (T_m) of the lipid. However, when fatty acids are mixed with lipid bilayers the modification of the thermal phase behaviour is dependent on the fatty acid chain length. In the case of long-chain fatty acids there is a marked increase of the gel to liquid-crystal phase transition temperature; on the other hand, short-chain compounds induce a decrease of T_m. These results are rationalized in terms of hydrogen bonding between the polar phospholipid head group and the carboxylate group of the guest fatty acid (cf. 9 and refs. therein). The different effects induced by fatty acids of different chain length emphasize the subtle balance of forces that regulate the phase behaviour of phospholipid bilayers: on the one hand, polar interactions (such as hydrogen bonding) at the head group may serve to stabilize the bilayer, thus inducing a higher T_m; on the other hand, when these polar interactions involve a concomitant bilayer disordering (such as that brought about by the presence of short chains), T_m decreases. Accordingly, "bulkier" guests also induce decreases in T_m (10).

In this report we describe the thermal phase behaviour of phospholipid bilayers of phosphatidylcholine (PC) and phosphatidylethanolamine (PE) mixed with ascorbyl palmitate (AP), a lipophilic derivative of vitamin C. AP provides an excellent model for the study of both polar interactions with the lipid head group and nonpolar interchain interactions with the lipid hydrocarbon core. The rationale behind the selection of the two classes of lipids used in this study, PC and PE, is their different hydrogen bonding capabilities. While both lipid head groups have the capability to serve as hydrogen bond acceptors (through the phosphate and the ester carbonyl groups), only PE has the additional capability of serving as hydrogen bond donor (via the NH_3^+ group). An investigation of these interactions at the molecular level is of particular interest, given the resemblance of AP to the important class of glycolipids (11). Furthermore, AP, which is a potent antioxidant by itself, also enhances the antioxidant potency of vitamin E, especially when mixed with lecithins (12–15).

[1]Issued as NRCC No. 28617.

Can. J. Chem. Downloaded from www.nrcresearchpress.com by 93.93.197.157 on 09/07/12
For personal use only.

Can. J. Chem. Downloaded from www.nrcresearchpress.com by 93.93.197.157 on 09/07/12
For personal use only.

Experimental

Materials and sample preparation

1,2-Dipalmitoyl-*sn*-glycero-3-phosphocholine (DPPC), 1,2-dipalmitoyl-*sn*-glycero-3-phosphoethanolamine (DPPE), and 1,2-dimyristoyl-*sn*-glycero-3-phosphoethanolamine (DMPE) were purchased from Sigma Chemical Co. (St. Louis, MO); 1,2-perdeuteriopalmitoyl-*sn*-glycero-3-phosphocholine (DPPC-d_{62}) was from Avanti Polar Lipids (Birmingham, AL), ascorbic acid (AA) from BDH Chemicals (Toronto, Canada), and ascorbyl palmitate (AP) from Aldrich Chemical Co. (Milwaukee, WI). The AP salts with different cations were prepared at pH 7 using standard procedures (16). Samples for infrared spectroscopy were prepared from the appropriate amounts of solid AA, AP or its salts, and DPPC, DMPE, or DPPE. The mixtures were hydrated by adding H_2O or D_2O (80% by weight) and warming to ca. 10°C above the corresponding T_m, vortexing while warm, and allowing to cool to room temperature; this procedure was repeated three times. Identical results were obtained with samples prepared by mixing the components as solutions in chloroform/methanol, followed by solvent evaporation and hydration.

Spectra and data processing

Infrared spectra at 2 cm^{-1} resolution were recorded with a Digilab FTS-15 FT-IR spectrometer. The samples (12 μm thickness) were held between ZnSe windows. Procedures for data collection and analysis have been described previously (17). Fourier self-deconvolution procedures were used to resolve broad band contours into their constituent bands (18, 19).

Results and discussion

The principal effect of the addition of AP into bilayers of either PC or PE is a pronounced elevation of the gel to liquid-crystal phase transition temperature. The changes in the lipid thermotropic phase behaviour were studied by variable-temperature infrared spectroscopy. At the same time, the infrared spectra reveal subtle changes at the molecular level. Therefore, we separate the presentation and discussion of our results into two main areas: the thermal phase behaviour of AP:lipid mixtures and the interpretation of spectral changes observed at the level of different functional groups.

Thermotropic phase behaviour of lipid:AP mixtures

The thermal phase behaviour of mixtures of AP with lipids was followed by measuring the temperature dependence of the wavenumber of the symmetric stretching mode, $\nu_s(CH_2)$ of the methylene groups of the fatty acyl chains (17). In these lipid:AP mixtures both the lipid and AP molecules contain fatty acyl chains that give rise to $\nu_s(CH_2)$ bands. It is well established that the wavenumber of the $\nu_s(CH_2)$ mode undergoes a shift of 2–3 cm^{-1} when bilayer lipid assemblies change from the gel phase to the liquid-crystalline phase (17). Similarly, in the case of AP the $\nu_s(CH_2)$ wavenumber increases when hydrated assemblies change from the coagel to the micellar state at 63°C.[2] Figure 1 shows typical plots illustrating the temperature dependence of the $\nu_s(CH_2)$ wavenumber of the following samples: (*i*) AP mixed with DPPC (1:1 molar ratio); (*ii*) AP mixed with DPPE (1:1 molar ratio); and (*iii*) the potassium salt of AP (APK) mixed with DPPC (1:1 molar ratio). The transition temperatures in Table 1 were determined by monitoring spectral changes of the vibrational modes of the fatty acyl chains. The same transition temperatures were found when monitoring the temperature dependence of vibrational modes in the polar head group region of both the lipid and AP molecules, indicating that the transition occurs concomitantly in the hydrocarbon core of the membrane and in the polar regions. The increase in T_m is dependent on the concentration of AP (Table 1); thus, T_m is 51°C for a 1:1 mixture of AP and DPPC and 46°C for a 1:5 mixture. We did not study samples with excess AP, and the possibility of compound (complex) formation with a specific stoichiometry was not investigated. Fatty acids are known to form 2:1 complexes with lipids such as PC (9, 10).

Since, as noted above, both the lipid and AP fatty acyl chains give rise to $\nu_s(CH_2)$ bands at the same wavenumber, the temperature dependence of this mode in lipid:AP mixtures contains information from both components. However, by using deuterated DPPC it is possible to separate spectroscopically the thermal events of the individual components of the mixture. Figure 2A shows the temperature dependence of the $\nu_s(CD_2)$ mode from the fully deuterated fatty acyl chains of DPPC-d_{62} in a 1:1 mixture with AP. The transition occurs at 47.5°C in the DPPC-d_{62}:AP mixture, while it is at 37°C for pure DPPC-d_{62} (21). The same transition temperature is obtained when monitoring the behaviour of the $\nu_s(CH_2)$ modes of the AP acyl chain in the same

[2]Unpublished results from this laboratory.

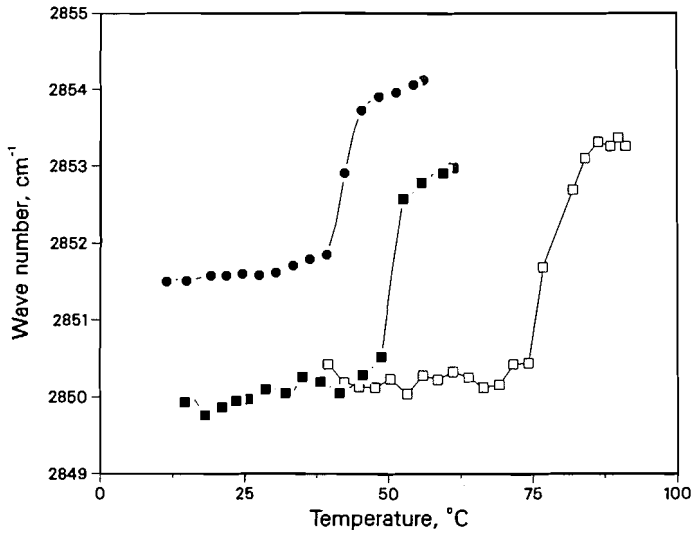

FIG. 1. Temperature dependence of the $\nu_s(CH_2)$ wavenumber in the infrared spectra of DPPC:KAP (1:1) (●), DPPC:AP (1:1) (■), and DPPE:AP (1:1) (□).

TABLE 1. Transition temperatures (T_m and T_p) of mixtures of ascorbyl palmitate (AP) with different lipids[a]

Sample	Molar ratio	T_p/°C	T_m/°C
DPPC	—	35	41.5
DPPC:AP	1:1	34	51
DPPC:AP	5:1	34	46
DPPC-d_{62}	—	—	37
DPPC-d_{62}:AP	1:1	—	47.5
DPPC:LiAP	1:1	33	44
DPPC:KAP	1:1	35	44
DPPC:NH_4AP	1:1	35	40
DPPC:$CaAP_2$	1:1	—	49
DPPC:AA	1:1	34	40
DPPE	—	—	63
DPPE:AP	1:1	—	80
DMPE	—	—	49
DMPE:AP	1:1	—	65

[a]Determined from the temperature dependence of the $\nu_s(CH_2)$ wavenumber in the case of T_m and from the temperature dependence of the $\delta(CH_2)$ mode in the case of T_p.

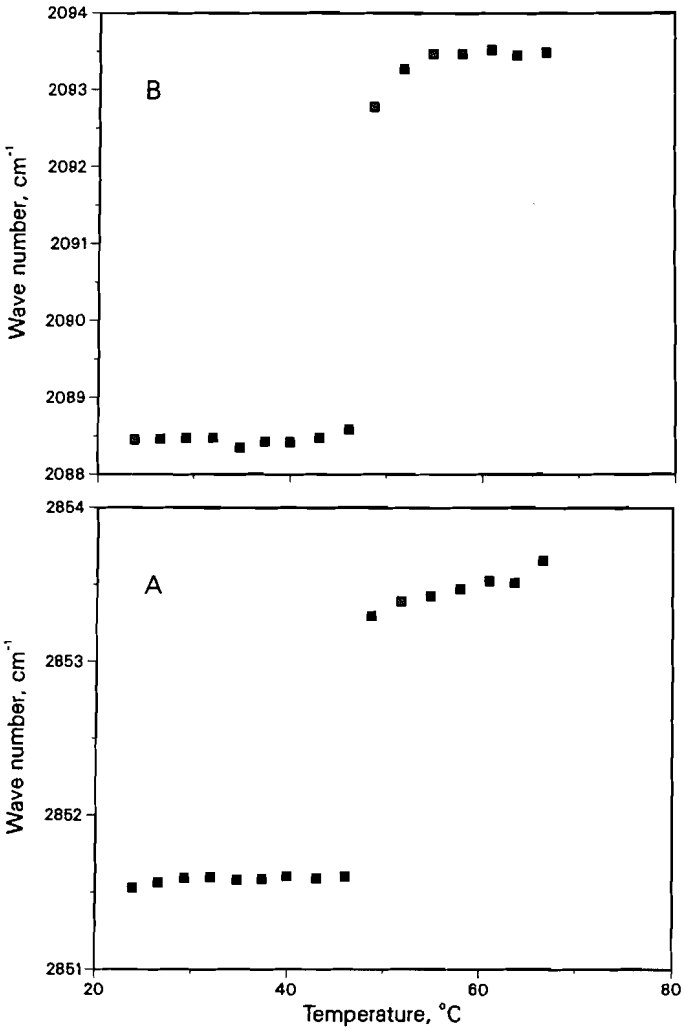

FIG. 2. Temperature dependence of the $\nu_s(CH_2)$ (A) and $\nu_s(CD_2)$ (B) wavenumbers in the infrared spectra of a DPPC-d_{62}:AP (1:1) mixture.

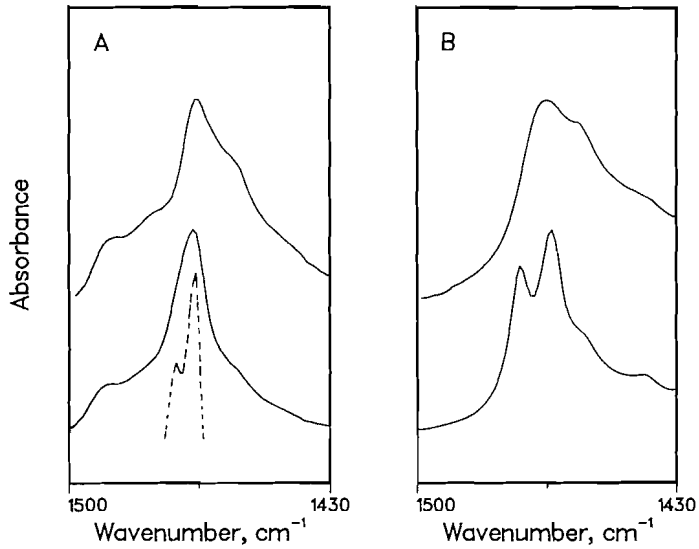

FIG. 3. A. The 1500–1430 cm^{-1} region of the infrared spectrum of a DPPC:AP mixture (1:1) at 20 and 60°C. The broken curve is the result of deconvolution with a Lorentzian line of 5 cm^{-1} full width at half height using a resolution enhancement factor of 1.8. B. The 1500–1430 cm^{-1} region of the infrared spectrum of a DMPE:AP mixture (1:1) at 20 and 70°C.

spectra (Fig. 2B). These data demonstrate that the conformational melting of DPPC and AP occurs at the same temperature; it is therefore concluded that DPPC mixes well with AP and that there is no phase separation. The increment of T_m in DPPC-d_{62} induced by AP is the same (approximately 10°C) as that induced by AP with nondeuterated DPPC, which indicates that the effects that lead to this increase of T_m must be primarily associated with interactions at the head group of the lipid molecules.

So far, the data indicate that the temperatures of the main phase transitions of PC and PE increase considerably due to the presence of AP. No "new" transitions are observed, suggesting that no phase separation occurs. This elevation of T_m has some features in common with the situation of fatty acids mixed with lipids. For example, fatty acids induce increases in T_m but their salts have a negligible effect; similarly, AP salts induce a smaller increase (Table 1). In contrast, palmitic acid (2:1 mixture) increases the T_m of DPPC by 20°C (to 61.5°C) (22) but has no effect on DPPE (9). On the other hand, AP increases the T_m of DPPE by 17°C (to 80°C, see Table 1) and that of DPPC by only 10°C. Thus, the interaction of AP with PCs and PEs is different from that of fatty acids and also different for these two classes of lipids.

Given that AP interacts differently with PC and PE, it is plausible to suggest that the differences between the head groups of PC and PE are responsible for the different interactions. This point is addressed in the next section.

The long palmitoyl chain of AP must be inserting within the hydrocarbon core of PC and PE bilayers, possibly causing changes in the packing of the fatty acyl chains. The pretransition of PCs at T_p is very sensitive to changes in the packing pattern of the fatty acyl chains as it involves primarily a change in packing from orthorhombic (below T_p) to hexagonal (above T_p). Infrared spectra, in particular the CH_2 scissoring vibrations $\delta(CH_2)$ of the acyl chains, are especially sensitive to the packing of polymethylene chains. This mode can be used to ascertain the packing pattern and therefore to determine the temperature of the pretransition (23). In the spectra of mixtures of DPPC with AP we find that the temperature dependence of the $\delta(CH_2)$ mode is the same as that of pure DPPC. From this temperature dependence we find that the pretransition temperatures of DPPC mixed with AP are all approximately 34°C. These temperatures are also given in Table 1.

Figure 3 shows the region 1500–1430 cm^{-1} of the spectra of a DPPC:AP mixture (1:1 molar ratio) and a DMPE:AP mixture (1:1 molar ratio). In the spectra of DPPC:AP at temperatures below T_p there are two bands at 1471 and 1468 cm^{-1} as in the spectrum of pure DPPC (see Fig. 4 of ref. 17 for comparison). The two bands collapse to one at 1468 cm^{-1} above T_p. The appearance of two bands for the $\delta(CH_2)$ mode is a consequence of correlation field splitting and demonstrates that there is interchain vibrational coupling of the fatty acyl chains, compatible with the acyl chains being packed in an orthorhombic-like subcell (23). In the spectrum of DPPC:AP in Fig. 3A the two component bands are separated by 3 cm^{-1} (1471 and 1468 cm^{-1}), whereas in spectra of pure DPPC recorded at the same temperature (20°C) the separation between the two component bands is larger (6 cm^{-1}; cf. Fig. 4 of ref. 17). As the separation between the component bands is related to the magnitude of the interchain potential, a smaller frequency separation indicates that this potential is weaker in the DPPC:AP mixture than in pure DPPC. The most ready explanation for a weaker coupling

Can. J. Chem. Downloaded from www.nrcresearchpress.com by 93.93.197.157 on 09/07/12
For personal use only.

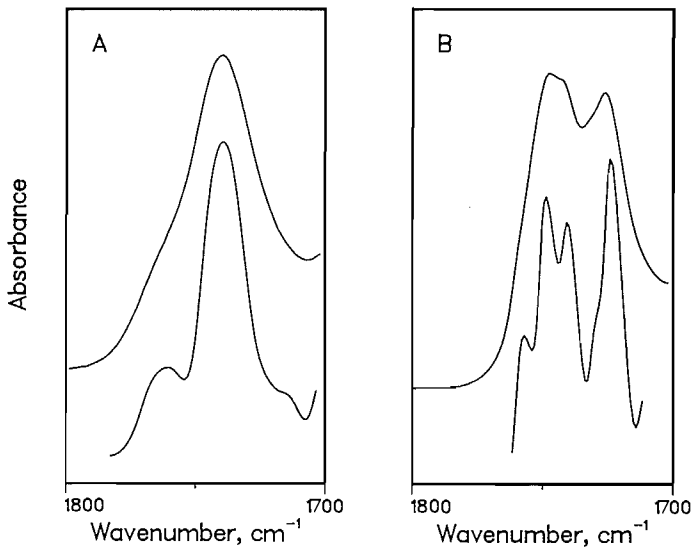

FIG. 4. A. The 1800–1700 cm^{-1} region of the infrared spectrum of a DPPC:AP mixture (1:1) at 20°C. B. The 1800–1700 cm^{-1} region of the infrared spectrum of a DMPE:AP mixture (1:1) at 20°C. In both cases, the bottom traces are the result of deconvolutions with a Lorentzian line of 18 cm^{-1} full width at half height using a resolution enhancement factor of 2.

is that in DPPC:AP the interchain distances are larger and therefore the packing of the fatty acyl chains is somewhat "looser" compared to that of pure DPPC, but that the pretransition is still present at approximately the same temperature. The fact that the incorporation of the AP acyl chains into the DPPC hydrocarbon core does not induce a large change in interchain interaction, but that the main transition temperature is increased by 10°C, suggests that interaction at other moieties must play an important role.

PEs show no pretransition comparable to that of PCs, and in the spectra of hydrated PEs the $\delta(CH_2)$ mode is split[3] at all temperatures below T_m. The frequency separation between the components of $\delta(CH_2)$ in PEs is 2–3 cm^{-1} (25). However, a much larger separation (8 cm^{-1}) is found in the spectra of the DMPE:AP mixture at 20°C where the bands are at 1472 and 1464 cm^{-1} (Fig 3B, bottom). Thus, in contrast to the case of DPPC the packing of the fatty acyl chains of PE is markedly affected by the presence of AP molecules. In the case of PEs the acyl chains are more closely packed in the presence than in the absence of AP; the opposite was found for PC:AP.

From the spectral characteristics of the fatty acyl chains (the CH_2 stretching and CH_2 scissoring modes) the thermal phase behaviour of AP mixed with PC and PE can be summarized as follows: The introduction of AP into DPPC bilayers increases the gel to liquid-crystal phase transition temperature by 10°C, does not affect the temperature of the pretransition, and modifies slightly the packing of the fatty acyl chains by inducing larger interchain interactions. The introduction of AP into PE bilayers increases the transition temperature by 16 to 17°C and induces a much tighter packing of the fatty acyl chains.

Molecular-level interactions

We now turn to the question of the molecular-level interactions giving rise to the thermal effects just described. Previous studies have established that a large increase of T_m in lipids is observed when there exists the possibility of intermolecular hydrogen bonding between the guest and lipid molecules (9, 10). It is with this in mind that we search for hydrogen bonding between PC and PE with AP.

A note on the possible states of ionization of the molecules involved is worth mentioning here since the thermal phase behaviour of lipids is affected by their state of ionization (26). All our experiments were carried out in nonbuffered dispersions prepared with D_2O; the pH of these preparations is between 6 and 7. The pK_a of AP must be the same as that of ascorbic acid (4.26) while the pK_a of DPPC is between 2 and 3 (9, 27). Therefore, AP cannot protonate DPPC. At the same time, the spectrum of ionized AP is completely different from that of AP and thus characteristic of the state of the sample. In particular, the C═O and C═C stretching bands of AP are diagnostic of the ionization state because changes in the charge density at position 3 are transmitted to these bonds.

It has been proposed that guests that are hydrogen bond donors (fatty acids, alcohols, amines) interact with lipids by forming hydrogen bonds to the lipid phosphate group (9, 10, and refs. therein). In the spectra of DPPC mixed with AP and AP salts the bands due to phosphate vibrations are the same as those in the spectra of pure DPPC. In particular, the antisymmetric O═P═O stretching band appears at 1220 cm^{-1} at all temperatures in spectra of DPPC, DPPC:AP, and mixtures of DPPC with salts of AP. The value of this wavenumber is characteristic of hydrated phosphate groups in lipids (28) and the fact that it is the same with and without AP suggests that here are no dramatic changes in the hydrogen bonding scheme of the phosphate group. Evidence for hydrogen bonding between AP and DPPC is found in the ester C═O stretching bands.

Figure 4A shows the 1800–1700 cm^{-1} region of the spectrum of DPPC:AP (1:1 molar ratio) at 20°C (i.e., gel phase). This spectrum of DPPC:AP is not a simple superposition of the spectra of DPPC and AP. For comparison, we recall the spectrum of pure DPPC; the ester C═O groups give two bands at 1740 and 1728 cm^{-1}, assigned to the C═O groups in the *sn*-1 and *sn*-2 chains respectively (29, 30). The difference in the two groups arises from the conformational nonequivalence of the two chains in the C2—C3 bonds. These two bands are observed in both the gel and liquid-crystal phases of DPPC at approximately the same frequencies. Meanwhile, the spectrum of pure AP shows three C═O stretching bands, at 1762 cm^{-1} (ascorbate C═O) and at 1747 and 1732 cm^{-1} (palmitate C═O). The spectrum of the 1:1 DPPC:AP mixture in the gel phase (Fig. 4A) shows three bands in this region, at 1764, 1739, and 1714 cm^{-1}. The band at 1764 cm^{-1} in the spectrum of the mixture results from the AP ascorbate moiety, while the bands at 1739 and 1714 cm^{-1} result from the palmitate groups of DPPC and AP.

The fact that the spectrum of the mixture is not a simple superposition of the spectra of DPPC and AP reveals that the lipid carbonyl groups are in a different environment when the molecules are mixed. In particular, the two DPPC C═O stretching bands at 1742 and 1728 cm^{-1} have merged into one band at 1739 cm^{-1}. The most likely explanation for this observation is that the conformational nonequivalence of the C2—C3 segments of the DPPC chains has been removed. Apparently, in the DPPC:AP mixture the two DPPC ester bonds have become equivalent. However, as discussed above, this has not brought about important changes in the packing characteristics of the fatty acyl chains.

In the spectrum of the DPPC:AP gel phase (Fig. 4A) there appears a third C═O stretching band at 1714 cm^{-1}. Extensive

[3]Different nonhydrated phases of PEs show different patterns for the $\delta(CH_2)$ mode (24). However, all our PE samples were well hydrated.

Can. J. Chem. Downloaded from www.nrcresearchpress.com by 93.93.197.157 on 09/07/12
For personal use only.

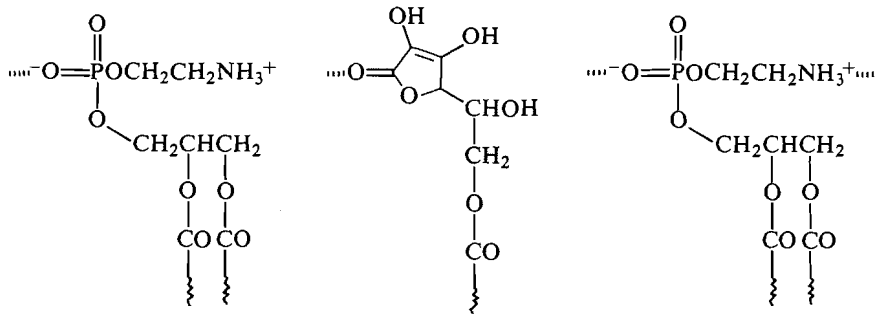

SCHEME 1

studies by Levin and co-workers (29, 30) established that C=O stretching bands below 1720 cm^{-1} occur when these C=O groups participate in strong hydrogen bonding. Thus, the appearance of this band at 1714 cm^{-1} strongly suggests that one (or two) of the DPPC ester C=O groups becomes hydrogen bonded in the presence of AP. AP has several OH groups that could serve as donors for this type of hydrogen bonding. In the spectra of DPPC mixed with AP salts, where the OH group at position 3 is ionized, the band at 1714 cm^{-1} does not appear and the DPPC C=O stretching bands are the same as in the spectra of pure DPPC. From this, it is possible to conclude that the OH group at position 3 of AP engages in hydrogen bonding to at least one of the DPPC ester carbonyl groups. Apparently, the formation of this hydrogen bond also induces a change in the conformation of the *sn*-2 chain in the C2—C3 segment. We emphasize that AP is not ionized; the spectral characteristics of ionized AP are not observed in these spectra of DPPC:AP mixtures; the AP OH bending modes (1400–1200 cm^{-1}) are observed and in a pattern that indeed suggests hydrogen bonding and not ionization. The C=C stretching band of AP is at 1677 cm^{-1}, again indicating hydrogen bonding and not ionization; this band appears at 1598 cm^{-1} in the spectra of ionized AP.

Thus, when the DPPC:AP mixture is in the gel phase below T_m there is hydrogen bonding between the OH group at position 3 of AP (donor) and at least one of the DPPC ester C=O groups (acceptor). The lack of change in the bands due to the phosphate group of DPPC cannot be taken as definitive evidence of lack of hydrogen bonding to this group. In the liquid-crystal phase of the DPPC:AP mixture the situation changes. The band at 1714 cm^{-1} (from the hydrogen-bonded C=O group) disappears and at the same time the AP C=C stretching band shifts from 1677 to 1682 cm^{-1}; these changes are compatible with the hydrogen bond between the AP 3-OH group and the ester C=O groups disappearing. Also, the DPPC C=O bands become the same as in pure DPPC and two bands are now observed at 1740 and 1728 cm^{-1}; the removal of the hydrogen bond is accompanied by the reestablishment of the conformational nonequivalence of the two DPPC ester carbonyl groups.

The C=O stretching bands observed in the spectra of the DMPE:AP mixture are completely different from those of the DPPC:AP mixture (compare Figs. 4A and 4B). Surprisingly, the C=O stretching bands of DMPE appear at almost the same wavenumbers as those in the spectra of pure DMPE. It appears that while AP induces a large increase in T_m of DPPE and DMPE, it does not lead to conformation changes in the C=O ester groups nor does it introduce new hydrogen bonds. At the same time, the $\delta(CH_2)$ bands in the spectra of DMPE:AP (Fig. 3B) demonstrate that in this mixture the fatty acyl chains are packed very tightly. Also, the bands due to the phosphate group are very similar in the spectra of the DMPE:AP mixture and in pure DMPE; thus in both cases the O=P=O asymmetric stretching bands are at 1220 cm^{-1}, characteristic of hydrated PE. The OH deformation bands of the ascorbyl moiety of AP are very different in the spectrum of the DMPE:AP mixture compared to those in pure AP, which is compatible with the fact that these groups are engaged in hydrogen bonding to PE. The C=O stretching band of AP in the DMPE:AP spectrum is at 1756 cm^{-1}, compared to 1768 cm^{-1} in pure AP, suggesting hydrogen bonding; the characteristics of the AP spectrum indicate that AP is not ionized. From these spectral characteristics we propose that in this case the AP C=O group serves as an acceptor while the NH_3^+ group of PE acts as the donor. At the same time, the OH group at position 3 of AP may serve as donor for a hydrogen bond to the phosphate group of PE. Scheme 1 shows a tentative model for these hydrogen bonds between PE and AP based on the spectral characteristics alone. In this model the AP molecule serves as a hydrogen-bond bridge between two PE molecules; moreover it implies that the insertion of this bridge in the already rigid network of PE hydrogen bonds serves to strengthen it further, which is reflected in a higher T_m of the DMPE:AP mixture (see Table 1). We also note that at the phase transition of these PE:AP mixtures large changes are observed in the position of the AP C=C stretching and ascorbate C=O stretching modes; the former shifts from 1670 to 1684 cm^{-1} while the latter shifts from 1756 to 1768 cm^{-1}, suggesting that the hydrogen bonding does not exist (or is much weaker) in the liquid-crystal phase.

Finally, a control experiment was carried out with a mixture of ascorbic acid (AA) and DPPC, also at a 1:1 molar ratio. The transition temperature of this mixture is 40°C, somewhat lower than that of pure DPPC (see Table 1). The spectra of the DPPC component of this mixture are very similar to those of DPPC and DPPC:AP in the liquid-crystal phase, but there are subtle changes in the bands due to AA, suggestive of a weak interaction between AA and DPPC. The lower T_m of the DPPC:AA mixture suggests that the weak interaction with AA leads to a spreading of the fatty acyl chains of DPPC, particularly since similar effects have been observed in mixtures of DPPC with carbohydrates (20). These results emphasize the importance of the insertion of the acyl chain of AP in the hydrocarbon core of lipid bilayers to yield a complex with altered thermotropic behaviour.

Conclusions

The incorporation of ascorbyl palmitate (AP) into bilayers of PC and PE induces a large increase of the gel to liquid-crystal phase transition temperature of the lipids. The nature of the phase transition in the lipid:AP mixtures is the same as in pure

Can. J. Chem. Downloaded from www.nrcresearchpress.com by 93.93.197.157 on 09/07/12
For personal use only.

lipds and involves the conformational melting of both the lipid fatty acyl chains and the palmitoyl chains of AP. AP mixes with the lipid bilayers and there is no AP-induced phase separation. In the case of PC:AP mixtures the pretransition of the lipid bilayer is also preserved; since the pretransition involves primarily a change in acyl chain packing, we conclude that the insertion of AP molecules into the PC hydrocarbon core does not induce important changes in the packing of the lipid fatty acyl chains. In contrast to the increase in the temperature of the gel to liquid-crystal transition there is no increase in the temperature of the pretransition, suggesting that this event is controlled by interchain interactions alone. In the case of the PC:AP mixtures the spectra also reveal a much looser packing of the fatty acyl chains than in pure PC bilayers or in the PE:AP mixtures in the gel phase.

The results obtained with mixtures of AP salts and DPPC demonstrate that the acidic enol group at position 3 of the ascorbate moiety plays a dominant role in determining the interaction at the polar group of DPPC. The ester C=O stretching bands of DPPC reveal that there is a major conformational change involving these groups and there is evidence for the formation of hydrogen bonds between the enolic OH group of AP and the DPPC C=O groups. No such hydrogen bonds are formed between AP and PE. On the contrary, there is evidence that in the PE:AP mixtures the AP C=O moiety acts as the acceptor group while the PE NH_3^+ moiety acts as the proton donor; thus, the spectra of DMPE:AP are compatible with the ascorbate moiety of AP serving as a hydrogen-bond bridge between the NH_3^+ and PO_4^- groups of two PE molecules.

The thermotropic effects observed by incorporation of AP into PC and PE bilayers are similar to those observed when mixing long-chain fatty acids with PC. However, fatty acids induce only a small increment of T_m (1–2°C) when mixed with PE, in contrast with the 16–17°C increment observed with AP. Thus, different mechanisms of interaction at the molecular level are operational for the interaction of fatty acids and AP. When AP is ionized there are only small changes in the thermal phase behaviour of the lipids, similar to the effect of fatty acid salts. As a general point, the present data demonstrate that AP mixes well with PC and PE, and, that since the AP molecules are protected from ions in solution, the mixing of this lipophilic vitamin C with lipids may serve as a means of transport across membranes of this potent antioxidant. At the same time, incorporation of AP into bilayers containing PE may serve as a means of creating more rigid structures.

Acknowledgements

U.K. thanks the Alexander von Humboldt Foundation for a F. Lynen fellowship.

1. S. E. SCHULLERY, T. A. SEDER, D. A. WEINSTEIN, and D. A. BRYANT. Biochemistry, **20**, 6818 (1981).
2. J. M. BOGGS, G. RANGARAJ, and K. M. KOSHY. Chem. Phys. Lipids, **40**, 23 (1986).
3. A. W. ELIASZ, D. CHAPMAN, and D. F. EWING. Biochim. Biophys. Acta, **448**, 220 (1976).
4. F. K. HUI and P. G. BARTON. Biochim. Biophys. Acta, **296**, 510 (1973).
5. A. B. KOHN and S. E. SCHULLERY. Chem. Phys. Lipids, **37**, 143 (1985).
6. K. P. PAULS, A. L. MCKAY, and M. BLOOM. Biochemistry, **22**, 6101 (1983).
7. D. M. MARSH and J. M. SEDDON. Biochim. Biophys. Acta, **690**, 117 (1982).
8. E. K. ROONEY, J. M. EAST, O. T. JONES, J. MCWIRTHER, A. C. SIMMONDS, and A. G. LEE. Biochim. Biophys. Acta, **728**, 159 (1983).
9. J. M. BOGGS. *In* Biomembranes. Vol. 12. *Edited by* M. Kates and L. A. Manson. Plenum Press, New York. 1984.
10. J. M. BOGGS. Biochim. Biophys. Acta, **908**, 353 (1987).
11. G. A. JEFFREY. Acc. Chem. Res. **19**, 168 (1986).
12. D. SWERN, A. J. STIRTON, J. TURNER, and P. A. WELLS. Oil Soap, **20**, 224 (1943).
13. J. DELGA and R. BOULU. Ann. Pharm. Fr. **15**, 691 (1957).
14. G. PONGREZ. Int. J. Vitam. Nutr. Res. **43**, 517 (1977).
15. J. E. PACKER, T. F. SLATER, and R. L. WILSON. Nature, **278**, 737 (1979).
16. H. SAPPER, D. G. CAMERON, and H. H. MANTSCH. Can. J. Chem. **59**, 2543 (1981).
17. H. L. CASAL and H. H. MANTSCH. Biochim. Biophys. Acta, **779**, 381 (1984).
18. J. K. KAUPPINEN, D. J. MOFFATT, H. H. MANTSCH, and D. G. CAMERON. Appl. Spectrosc. **35**, 271 (1981).
19. H. H. MANTSCH, H. L. CASAL, and R. N. JONES. *In* Spectroscopy of biological systems. *Edited by* R. J. H. Clark and R. E. Hester. John Wiley & Sons, Chichester. 1986.
20. L. M. CROWE, J. H. CROWE, and D. CHAPMAN. Arch. Biochem. Biophys. **236**, 289 (1985).
21. S. SUNDER, D. G. CAMERON, H. H. MANTSCH, and H. J. BERNSTEIN. Can. J. Chem. **56**, 2121 (1978).
22. S. MABREY and J. M. STURTEVANT. Biochim. Biophys. Acta, **486**, 444 (1977).
23. D. G. CAMERON, H. L. CASAL, and H. H. MANTSCH. Biochemistry, **19**, 3665 (1980).
24. H. H. MANTSCH, S. C. HSI, K. W. BUTLER, and D. G. CAMERON. Biochim. Biophys. Acta, **728**, 325 (1983).
25. H. L. CASAL and H. H. MANTSCH. Biochim. Biophys. Acta, **735**, 387 (1983).
26. H. EIBL. Angew. Chem. Int. Ed. Engl. **23**, 257 (1984).
27. D. PAPAHADJOPOULOS. Biochim. Biophys. Acta, **163**, 240 (1968).
28. H. L. CASAL, H. H. MANTSCH, and H. HAUSER. Biochemistry, **26**, 4408 (1987).
29. S. F. BUSH, H. LEVIN, and I. W. LEVIN. Chem. Phys. Lipids, **27**, 101 (1980).
30. I. W. LEVIN. *In* Advances in infrared and Raman spectroscopy. Vol. 11. *Edited by* R. J. H. Clark and R. E. Hester. Wiley–Heyden, London. 1984. pp. 1–48.

Can. J. Chem. Downloaded from www.nrcresearchpress.com by 93.93.197.157 on 09/07/12
For personal use only.

Steric effects on the self-association of branched and cyclic alcohols in inert solvents. Apparent heat capacities of secondary and tertiary alcohols in hydrocarbons

MERCEDES CÁCERES-ALONSO
Departamento de Química Física, Facultad de Ciencias Químicas, Universidad Complutense, Madrid 28040, Spain

MIGUEL COSTAS
Departamento de Física y Química Teórica, División de Ciencias Básicas, Facultad de Química, Universidad Nacional Autónoma de México, México D.F. 04510, México

AND

LINA ANDREOLI-BALL AND DONALD PATTERSON[1]
Department of Chemistry, McGill University, 801 Sherbrooke St. West, Montreal, P.Q., Canada H3A 2K6

Received December 14, 1987

This paper is dedicated to Professor J. A. Morrison

Can. J. Chem. Downloaded from www.nrcresearchpress.com by 176.9.209.113 on 09/07/12
For personal use only.

MERCEDES CÁCERES-ALONSO, MIGUEL COSTAS, LINA ANDREOLI-BALL, and DONALD PATTERSON. Can. J. Chem. **66**, 989 (1988).

Apparent heat capacities have been measured for fifteen branched and cyclic alcohols in dilute *n*-decane solution at 25°C. The alcohols were 2-methyl-2-propanol, cyclohexanol, 3-methyl-3-pentanol, *trans*-, *cis*-, and mixed isomer 2-methylcyclohexanol, 1-methylcyclohexanol, 3-ethyl-3-pentanol, cyclooctanol, 3,7-dimethyl-1-octanol, 5-decanol, 4-propyl-4-heptanol, cyclododecanol, 5-butyl-5-nonanol, and 8-hexadecanol (in *n*-hexane). Excess heat capacities C_p^E throughout the concentration range were measured at 25°C for: 1-hexanol + *n*-hexadecane (*n*-C_{16}) and + 2,2,4,4,6,8,8-heptamethylnonane (br-C_{16}), 4-propyl-4-heptanol, and 1-decanol + *n*-decane, 3-methyl-3-pentanol + *n*-C_{16} and + br-C_{16} and at 27°C for cyclohexanol + *n*-C_{16} and + br-C_{16}. Also, for 3-methyl-3-pentanol + *n*-decane C_p^E was measured at 10, 25, 40, and 50°C. For a series of isomeric alcohols, the apparent molar heat capacities show a maximum against concentration which decreases and moves to higher alcohol concentration as the hydroxyl group on the alcohol becomes increasingly hindered, effectively reducing the alcohol self-association capabilities. This situation is also reflected by the heat capacities of the pure alcohols which increase strongly in magnitude in going from a linear 1-alcohol to an isomeric alcohol which has its hydroxyl group on a quaternary carbon atom. C_p^E of the mixtures are negative at low alcohol concentrations turning positive at increasingly higher alcohol concentrations as the steric hindrance on the hydroxyl group increases. Throughout most of the concentration range C_p^E for the branched or cyclic alcohols is considerably more positive than for the corresponding isomeric 1-alcohol. For the highly hindered 3-methyl-3-pentanol $C_p^E(T)$ passes through a maximum. All of the above behaviour is explained by the Treszczanowicz–Kehiaian model for self-associated liquids + inert solvents which has been applied to the present data. Equilibrium constants have been obtained for alcohol association and are sensitive to alcohol structure. At low alcohol concentrations, while for the linear 1-alcohols tetramers are the predominant species and dimer are almost absent, for the corresponding isomeric alcohols the concentration of tetramers is severely reduced and the lower species, i.e. trimers and dimers, are more important. For the highly hindered alcohols, monomers are the predominant species in dilute solution reflecting the decrease in self-association ability that steric hindrance of the hydroxyl group imposes on them.

MERCEDES CÁCERES-ALONSO, MIGUEL COSTAS, LINA ANDREOLI-BALL et DONALD PATTERSON. Can. J. Chem. **66**, 989 (1988).

Opérant à 25°C, on a mesuré les capacités calorifiques apparentes de quinze alcools ramifiés et cycliques en solutions diluées dans le *n*-décane. Il s'agit des alcools suivants : méthyl-2 propanol-2, cyclohexanol, méthyl-3 pentanol-3, les isomères *cis*- et *trans*- du méthyl-2 cyclohexanol, méthyl-1 cyclohexanol, éthyl-3 pentanol-3, cyclooctanol, diméthyl-3,7 octanol-1, décanol-5, propyl-4 heptanol-4, cyclododécanol, butyl-5 nonanol-5 et hexadécanol-8 (dans le *n*-hexane). Opérant à 25°C, on a mesuré les capacités calorifiques en excès, C_p^E, à toutes les concentrations pour les mélanges : hexanol-1 + *n*-hexadécane (*n*-C_{16}) et heptaméthyl-2,2,4,4,6,8,8 nonane (C_{16}-ram), propyl-4 heptanol-4 et décanol-1 + *n*-décane, méthyl-3 pentanol-3 + *n*-C_{16} et + C_{16}-ram; les mêmes valeurs ont été mesurées à 27°C pour les mélanges : cyclohexanol + *n*-C_{16} et C_{16}-ram. Pour le mélange méthyl-3 pentanol-3 + *n*-décane, on a mesuré les C_p^E à 10, 25, 40 et 50°C. Pour une série d'alcools isomères, la courbes des capacités calorifiques molaires apparentes en fonction de la concentration présente un maximum qui diminue et qui se déplace vers des concentrations d'alcool plus élevées au fur et à mesure que le groupement hydroxyle de l'alcool devient plus encombré et qu'il réduit effectivement les possibilités d'auto-association de l'alcool. Cette situation se reflète aussi dans le fait que les capacités calorifiques des alcools purs qui augmentent fortement lorsqu'on passe des alcools primaire linéaires vers des alcools isomères tertiaires. A de faibles concentrations en alcool, les C_p^E des mélanges sont négatives; elles deviennent positives lorsque les concentrations d'alcool augmentent et que l'empêchement stérique du groupement hydroxyle augmente. Sur l'ensemble des concentrations, les valeurs de C_p^E des alcools cycliques ou ramifiés sont beaucoup plus positives que celles des alcools primaire correspondants. Dans le cas du méthyl-3 pentanol-3 qui est hautement empêchée, la valeur de $C_p^E(T)$ passe par un maximum. Tous ces comportements peuvent être expliqués par le modèle de Treszczanowicz–Kehiaian qui a été développé pour les liquides auto-associés + les solvants inertes et que nous avons appliqué aux données obtenues. On a déterminé les constantes d'équilibre pour les associations d'alcools et on a mis en évidence qu'elle sont sensibles à la structure des alcools. A des concentrations faibles en alcools, les tétramères des alcools primaires sont les espèces prédominantes et les dimères sont pratiquement absents;

[1]A complete set of data may be purchased from the Depository of Unpublished Data, CISTI, National Research Council of Canada, Ottawa, Ont., Canada K1A 0S2.

par ailleurs, pour les alcools isomères correspondants, la concentration des tétramères est sévèrement réduite et les trimères et les dimères deviennent importants. Dans les cas des alcools fortement empêchés, les monomères sont les espèces prédominantes en solution diluée; cette situation est le reflet du fait que la possibilité d'auto-association est diminuée par l'empêchement stérique qui est imposé à ces groupements hydroxyles.

[Traduit par la revue]

Introduction

Amongst different thermodynamic quantities, the heat capacity is unique in that it is a very sensitive indicator of structure in pure liquids and solutions (1). In particular, heat capacity measurements for 1-alcohol + inert solvent mixtures have proven to be very useful in understanding the self-association of alcohol molecules in solution (1, 2). It has been found that, with the exceptions of methanol and ethanol, the associational part of the apparent molar heat capacity ϕ_C(assoc) of all linear alcohols is independent of both alcohol and alkane chain length. As a consequence, values of ϕ_C(assoc) for different systems follow a single corresponding states curve when plotted against a new concentration variable, ψ_1, essentially the hydroxyl concentration in solution (3). This remarkable result is predicted by the Treszczanowicz–Kehiaian (TK) theory (4) for self-associated liquids + inert solvents with a unique equilibrium constant for H-bond formation. Tetramers were found to be the predominant species with trimers and dimers being almost absent. The adherence of all primary alcohols + inert alkane mixtures to a corresponding states ϕ_C(assoc) vs. ψ_1 curve implies that for these alcohols self-association is only governed by the concentration of hydroxyl groups in solution, i.e. for linear alcohols the availability of the hydroxyl group to form H-bonds with neighbouring alcohol molecules is the same and independent of the size of the linear hydrocarbon tail attached to it. It appeared then interesting to study the effect that the introduction of various degrees of steric hindrance of the hydroxyl group has on the self-association ability of an alcohol. The present work reports heat capacity data for a series of branched and cyclic, secondary and tertiary alcohols mixed with an inert hydrocarbon solvent.

The TK model for self-associated liquids + inert solvents

In the TK model each molecule is capable of two energy levels corresponding to the associated state and the dissociated monomer as indicated by Fig. 1. For a pure alcohol, at very low temperature the associational energy U(assoc) will be low because all the alcohol molecules will be associated through H-bonds; as the temperature is raised the energy will rise corresponding to dissociation of the H-bonds. In Fig. 1, room temperature (T') will correspond to a temperature where most of the alcohol molecules will still be associated forming H-bonds. For a highly concentrated mixture of an alcohol with an inert solvent (I in Fig. 1), it will be slightly easier to break up the H-bonds; there is now a greater entropic driving force towards the randomly dispersed alcohol molecules. Going to lower concentrations in the inert solvent, the driving force towards dissociation becomes greater giving curves II and III in Fig. 1. Taking the slope of the energy curves, i.e. $dU(\text{assoc})/dT$, the association heat capacity of the alcohol, ϕ_C(assoc), is obtained at the different concentrations as a function of T; this is indicated in the lower part of Fig. 1 where ϕ_C(assoc) curves have the form of "Schottky peaks" (5). ϕ_C(assoc) is given explicitly by the model (1) as

$$[1]\quad \phi_C(\text{assoc}) = \frac{\left(\frac{\Delta H^0}{T}\right)^2 \frac{1}{R}\left[\sum_{i=2} \frac{i-1}{i} K_i^{\varphi} \frac{{\varphi_A}^i}{\varphi_1}\left(i - 1 + \sum_{j\neq i}(i-j)K_j^{\varphi}{\varphi_A}^{j-1}\right)\right]}{\left[1 + \sum_{i=2} iK_i^{\varphi}{\varphi_A}^{i-1}\right]}$$

where ΔH^0 is the enthalpy change for the formation of a H-bond, φ_1 the alcohol volume fraction and K_i^{φ} the volumetric equilibrium constant for species i. Equation [1] assumes that the i-mers are linear, i.e. that they involve $i - 1$ H-bonds. In the event that the i-mers are cyclic, i.e. involve i H-bonds, $i - 1$ becomes i and eq. [1] and the $i \neq j$ summation drops out. The fraction of monomers φ_A in eq. [1] is the closest root to zero of the equation

$$[2]\quad \sum_{i=2} K_i^{\varphi}{\varphi_A}^i + \varphi_A - \varphi_1 = 0$$

which can be easily found using a numerical method. The TK model can predict the excess heat capacity ${C_p}^E$ starting from

$$[3]\quad {C_p}^E = x_{OH}(\phi_C - {C_p}^0)$$

with ϕ_C being the apparent heat capacity of the alcohol in solution and ${C_p}^0$ the value for the pure state. In using this equation we need only be concerned with that part of the heat capacity which is due to association since the internal C_p of the alcohol is eliminated and other inter-molecular contributions will be small. In eq. [3] ${C_p}^0$(assoc) is obtained using eq. [1] with $\varphi_1 = 1$ and $\varphi_A = {\varphi_A}^0$.

Parameters of the theory, i.e. ΔH^0 and K_i^{φ}, can be fitted in the least square sense to experimental $\phi_C(\text{assoc}) = \phi_C - \lim \phi_C(x_{OH} \rightarrow 0)$ where the infinite dilution apparent molar heat capacity represents the contribution to the heat capacity of the alcohol in the absence of any association, each alcohol molecule being isolated in an inert solvent. For linear alcohols (1, 3) tetramers turned out to be the predominant species; the K_4^{φ} were found to change rapidly with the 1-alcohol studied reflecting the inter-alcohol rather than inter-hydroxyl character of these volumetric equilibrium constants. However, these K_4^{φ} can be translated into a single equilibrium constant for H-bond formation in tetramers, K_4. In contrast, for the branched and cyclic alcohols reported in this work the K_i^{φ} values fitted to the experimental ϕ_C(assoc) using eq. [1] indicate that, compared to linear alcohols, the concentration of tetramers is severely reduced and the lower species, i.e. trimers and dimers, are more important. Furthermore, the K_i^{φ} no longer lead to common values of K_i for H-bonding in the multimers. Thus the present

Can. J. Chem. Downloaded from www.nrcresearchpress.com by 176.9.209.113 on 09/07/12
For personal use only.

Can. J. Chem. Downloaded from www.nrcresearchpress.com by 176.9.209.113 on 09/07/12
For personal use only.

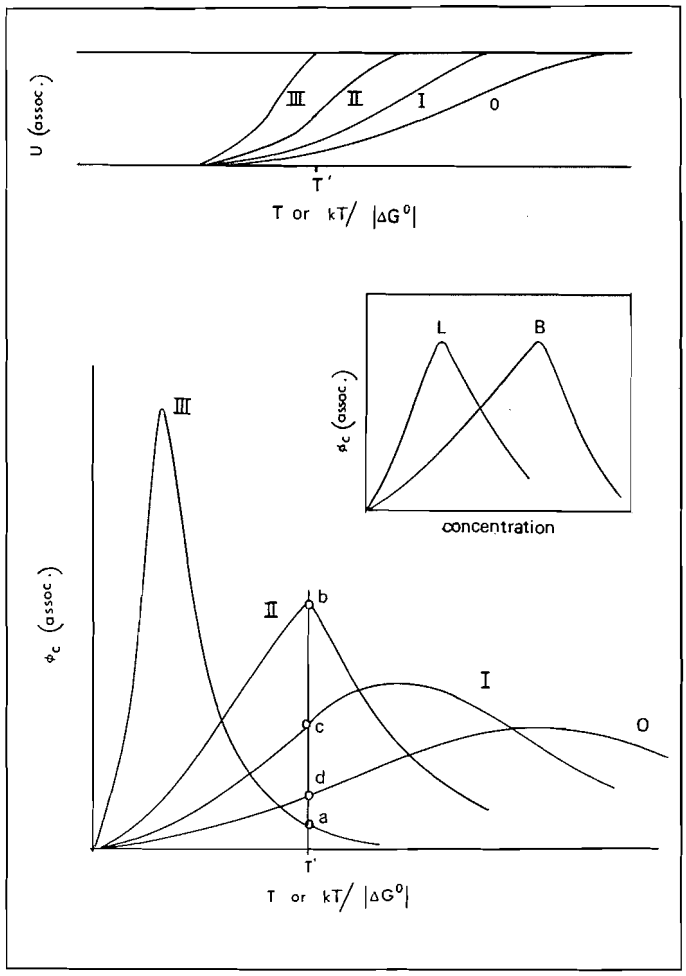

FIG. 1. Schematic representation of energy (upper diagram) and heat capacity (lower diagram) against $kT/|\Delta G^0|$ for an alcohol in the pure state (0) and at increasing dilution in an inert solvent (I, II, III). T' represents the experimental temperature.

systems deviate from the corresponding states scheme followed by the 1-alcohols where there is one dominant species. Different degrees of deviation are found to be related to the steric hindrance of the hydroxyl group which effectively decreases the alcohol self-association ability.

Experimental

Values for the apparent molar heat capacity ϕ_C of a series of branched and cyclic alcohols mixed with *n*-decane in the concentration range 0.1–10wt.% were determined at 25°C (*n*-hexane was used as solvent for 8-hexadecanol). Table 1 lists these alcohols together with their molar volumes, heat capacities, and ϕ_C at infinite dilution. Excess heat capacities C_p^E throughout the concentration range were measured for the following systems at 25°C: 1-hexanol + *n*-hexadecane (*n*-C_{16}) and + 2,2,4,4,6,8,8-heptamethylnonane (br-C_{16}), 4-propyl-4-heptanol and 1-decanol + *n*-decane, 3-methyl-3-pentanol + *n*-C_{16} and + br-C_{16}. At 27°C C_p^E was obtained for cyclohexanol + *n*-C_{16} and br-C_{16}. Also, for 3-methyl-3-pentanol + *n*-decane C_p^E was determined at 10, 25, 40, and 50°C. Heat capacity data both throughout the concentration range and in the dilute alcohol region may be purchased from the Depository of Unpublished Data.

All materials used in this work were obtained from either Aldrich Chem. Co. or Wiley Organics. Their stated purities range between 98 and 99.9%. Volumetric heat capacities were measured using a Picker Flow Microcalorimeter (Sodev, Sherbrooke, Quebec, Canada) and were transformed to a molar basis through solution densities obtained using a vibrating-cell densimeter (Sodev). The instrumentation and procedures have been described in the literature (7). The volumetric heat capacity of the liquid flowing through the working cell is measured against that of the reference cell. Solutions were prepared by weight and extreme care was taken during their preparation and handling in order to minimize evaporation losses. In the extremely dilute concentration range the heat capacity of each solution was determined using the pure solvent as reference. Heat capacity data for pure *n*-decane and *n*-hexane was taken from ref. 8. In the less diluted concentration range, where the heat capacity of the solutions differ greatly from that of the pure solvent, each solution acted as reference for the next as discussed in ref. 7. Heat capacities for pure alcohols were measured using as reference either 2-methyl-2-propanol or 1-decanol as indicated in Table 1; the heat capacity for pure 1-decanol was taken from ref. 1 and that for 2-methyl-2-propanol measured against *n*-decane. Heat capacities for pure *n*-C_{16} and br-C_{16} were taken from refs. 8 and 9, respectively, while those for *n*-decane at 10, 40, and 50°C were measured using benzene as reference; heat capacity data for benzene was taken from ref. 10. Through repetition of the present systems the precision appears to be ± 4 J K^{-1} mol^{-1} for ϕ_C in the dilute region, ± 5 to 6 J K^{-1} mol^{-1} for ϕ_C at infinite dilution and ± 0.1 J K^{-1} mol^{-1} for C_p^E.

Results and discussion

The Schottky peaks indicated in Fig. 1 can explain both the concentration and temperature dependences of ϕ_C(assoc). At T' = 25°C ϕ_C(assoc) is small for very low concentration (point *a* on curve III) because there is no structure in the solution, almost all the alcohol being dissociated; as the concentration increases (point *b* on curve II) ϕ_C(assoc) increases corresponding to increased structure due to the coming together of alcohol molecules into multimers over long distances. With further increases in concentration (point *c* in curve I) ϕ_C(assoc) decreases. Structure has decreased since although almost all alcohol molecules are associated into multimers they have come together over smaller distances. According to Fig. 1 then ϕ_C(assoc) must go through a maximum when plotted against concentration at constant temperature as indicated by the inset in Fig. 1. In Fig. 1 the maximum in ϕ_C against concentration at T' occurs at concentration II (point *b*). Compared to primary alcohols, secondary and tertiary alcohols form weaker H-bonds reflecting the fact that the hydroxyl group on the alcohol becomes increasingly hindered, effectively reducing the alcohol self-association capabilities. For secondary and tertiary alcohols the free energy of association ΔG^0 is less negative than for primary alcohols. In Fig. 1, the abscissa is more properly taken to be $kT/|\Delta G^0|$ rather than T itself, representing the ratio of the thermal energy to the H-bonding free energy. With this change the experimental temperature T' for a secondary or tertiary alcohol will correspond to a higher value of the $kT/|\Delta G^0|$ ratio in Fig. 1 than for a primary alcohol, and will act like a primary alcohol at $T > T'$. Figure 1 predicts then that for a secondary or tertiary alcohol ϕ_C(assoc) will have a maximum which will occur at higher alcohol concentration than for the corresponding isomeric primary alcohol. Then, in the inset in Fig. 1 curve L would correspond to ϕ_C(assoc) for a linear alcohol while curve B would be for a branched or cyclic alcohol. Figure 2 illustrates this situation through the experimental ϕ_C(assoc) at 25°C for 1-decanol and three of its isomers: another primary alcohol (3,7-dimethyl-1-octanol), a secondary alcohol (5-decanol) and a tertiary (4-propyl-4-heptanol). The introduction of two methyl groups along the hydrocarbon chain does not significantly affect the self-association ability of the primary alcohol. However, for the secondary and tertiary alcohols the maximum is progressively

TABLE 1. Molar volumes, heat capacities, and limiting apparent molar heat capacities at 25°C

Alcohol	$\bar{V}$ ($cm^3\ mol^{-1}$)	C_p^0 ($J\ K^{-1}\ mol^{-1}$)	$\lim_{x_{OH} \to 0} \phi_C$ ($J\ K^{-1}\ mol^{-1}$)
2-Methyl-2-propanol	94.89	215.37[a]	165
Cyclopentanol[b]	91.36	181.57	152
2-Methyl-2-butanol[b]	109.61	248.86	189
Cyclohexanol	105.89	209.99[a]	150
3-Methyl-3-pentanol	122.04 (10°C)	277.33[c] (10°C)	—
	123.93 (25°C)	302.25[a] (25°C)	200
	126.06 (40°C)	320.25[c] (40°C)	—
	127.57 (50°C)	332.75[c] (50°C)	—
trans-2-Methylcyclohexanol	124.10	262.98[a]	205
2-Methylcyclohexanol (mixed isomers)	123.28	267.44[a]	205
cis-2-Methylcyclohexanol	122.45	268.95[a]	205
1-Methylcyclohexanol	136.45	279.05[a]	150
3-Ethyl-3-pentanol	138.41	353.91[d]	227
Cyclooctanol	133.35	—	215
3,7-Dimethyl-1-octanol	192.11	367.21[a]	315
5-Decanol	192.88	405.77[a]	320
4-Propyl-4-heptanol	191.10	446.60[d]	315
Cyclododecanol	174.93[e]	—	330
5-Butyl-5-nonanol	239.97	548.63[d]	387
8-Hexadecanol	292.36[e]	—	515

[a]Measured using 1-decanol as reference.
[b]From ref. 6.
[c]Obtained as discussed in ref. 7 in the C_p^E experiment with *n*-decane.
[d]Measured using 2-methyl-2-propanol as reference.
[e]Estimated from the partial molar volume at infinite dilution.

displaced towards higher alcohol concentrations, i.e. ϕ_C(assoc) for these two alcohols correspond to ϕ_C(assoc) for 1-decanol at $T > 25$°C (as shown in Fig. 5 in ref. 1).

The excess heat capacities for 1-decanol and its three isomers mixed with *n*-decane at low alcohol concentration are shown in Fig. 3; C_p^E is negative at low alcohol concentrations becoming positive at increasingly higher alcohol concentrations as the steric hindrance of the hydroxyl group increases. C_p^E turns positive at $x_{OH} \sim 0.01$ (~1.1wt.%) for 5-decanol and at $x_{OH} \sim 0.03$ (~3.3wt.%) for 4-propyl-4-heptanol. According to eq. [3] C_p^E corresponds to the difference between two Schottky curves, one for the alcohol in solution and the other in the pure state. At very low alcohol concentration (curve III in Fig. 1) ϕ_C(assoc) < C_p^0(assoc) and hence $C_p^E < 0$; furthermore, as the difference between points *a* and *d* in Fig. 1 increases as $kT/|\Delta G^0|$ increases, C_p^E must become more negative as ΔG^0 is decreased through the substitution of a primary alcohol by a secondary or tertiary at constant temperature. This is illustrated by the results shown in Fig. 3. The negative C_p^E corresponds to a net breaking of H-bonds on passing from the pure alcohol to the solution which is so dilute as to contain only monomeric alcohol, this behaviour being completely general for all alcohol + inert mixtures. As the alcohol concentration is increased, the solution Schottky peak moves to higher $kT/|\Delta G^0|$ (curve II in Fig. 1) and here at T' ϕ_C(assoc) > C_p^0(assoc) producing $C_p^E > 0$. Since the difference between points *b* and *d* decrease as $kT/|\Delta G^0|$ increases in this concentration region C_p^E for a secondary or tertiary alcohol + an inert will be less positive than for the corresponding primary isomeric alcohol. This prediction has been corroborated by the experimental C_p^E results displayed in Fig. 4 for 4-propyl-4-heptanol and 1-decanol + *n*-decane and 3-methyl-3-pentanol and 1-hexanol + n-C_{16} at 25°C. The positive C_p^E indicates that the solution is extremely structured, corresponding to a localization of monomers into multimers, i.e. a process of order creation in solution through the formation of H-bonds. Finally, at higher alcohol concentration (curve I in Fig. 1) $C_p^E > 0$ but now since the difference between points *c* and *d* increases as $kT/|\Delta G^0|$ increases, C_p^E for a secondary or tertiary alcohol + an inert will be more positive than for the primary isomeric alcohol as indicated in Fig. 4, where the branched alcohols are seen to have a much larger C_p^E than for the corresponding linear isomers. In Fig. 1 it is also possible to move to the right along the $kT/|\Delta G^0|$ axis by increasing the temperature for any given alcohol + inert mixture; hence, three concentration regions also appear with the following characteristics: (*i*) $C_p^E < 0$ with $dC_p^E/dT < 0$ at very dilute, (*ii*) $C_p^E > 0$ with $dC_p^E/dT < 0$ at slightly higher concentrations, and (*iii*) $C_p^E > 0$ with $dC_p^E/dT > 0$ at higher alcohol concentration. These changes have been experimentally observed for 1-decanol + *n*-decane and are displayed in Figs. 8 and 9 in ref. 1. The above description of C_p^E behaviour in the three concentration regions, obtained either by changing T for a given alcohol + inert mixture or by changing the primary alcohol to a hindered alcohol at constant T, should be completely general for any alcohol mixed with an inert solvent.

The temperature dependence of C_p^E for branched or cyclic alcohols also follows from the Schottky curves in Fig. 1. Figure 5*a* shows Schottky peaks for a pure associated component and for a given concentration (say equimolar) in an inert solvent, while Fig. 5*b* shows C_p^E obtained through eq. [3] by the

Can. J. Chem. Downloaded from www.nrcresearchpress.com by 176.9.209.113 on 09/07/12
For personal use only.

Can. J. Chem. Downloaded from www.nrcresearchpress.com by 176.9.209.113 on 09/07/12
For personal use only.

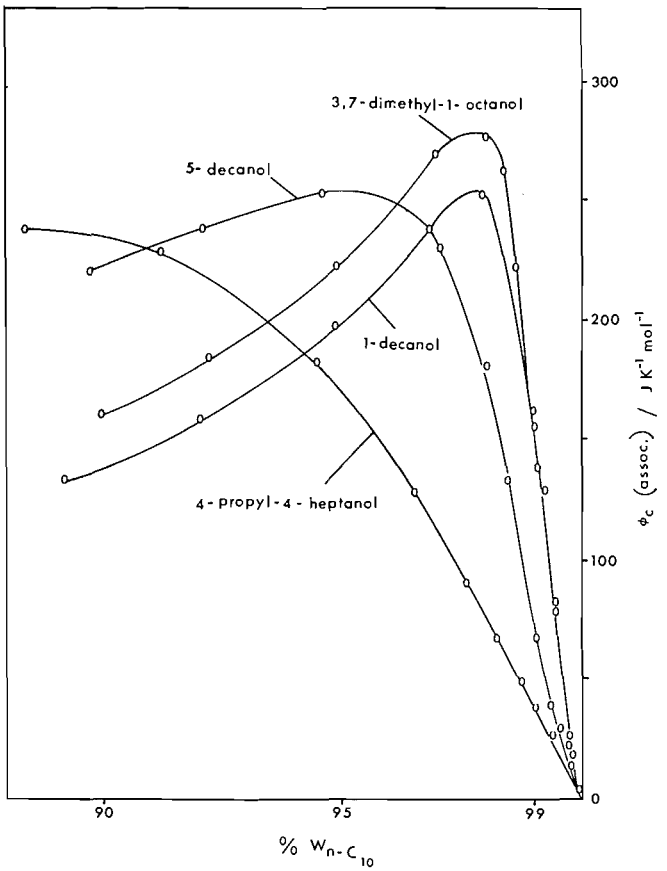

FIG. 2. Associational part of the apparent molar heat capacity for 1-decanol (from ref. 3), 3.7-dimethyl-1-octanol, 5-decanol, and 4-propyl-4-heptanol + *n*-decane at 25°C.

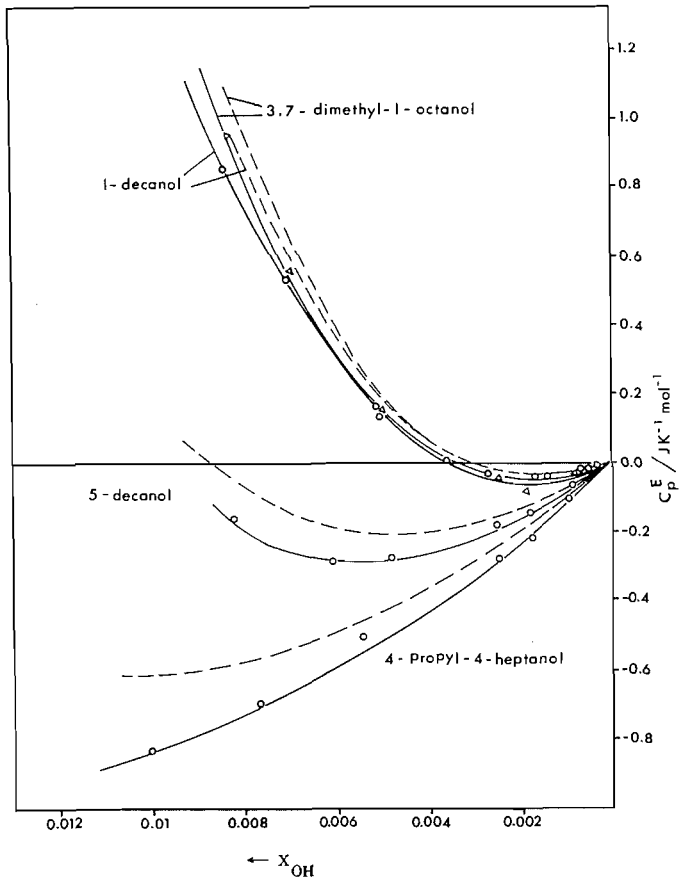

FIG. 3. Excess heat capacity for 1-decanol (from ref. 3), 3,7-dimethyl-1-octanol, 5-decanol, and 4-propyl-4-heptanol + *n*-decane at 25°C. Dashed lines are TK model calculations.

subtraction of the two curves in Fig. 5*a*. At constant temperature, it is possible to move from left to right along the horizontal axes in Fig. 5*a* or 5*b* by decreasing ΔG^0, i.e. by making the association weaker. For linear alcohols, where ΔG^0 is large, $C_p^E > 0$ and $dC_p^E/dT > 0$ but for secondary and tertiary alcohols where ΔG^0 is lower $C_p^E > 0$ and dC_p^E/dT changes from positive to negative as indicated by the shadowed area in Fig. 5*b*. The C_p^E data for the tertiary alcohol 3-methyl-3-pentanol + *n*-decane shown in Fig. 5*c* are an example of such behaviour; here, ΔG^0 has been reduced from that corresponding to the isomeric primary alcohol due to the steric hindrance of the hydroxyl group and hence the ratio $kT/|\Delta G^0|$ is increased for the usual temperature range. C_p^E is very large and dC_p^E/dT now changes sign from positive to negative within the temperature range studied, 10 to 50°C. The negative C_p^E region at low alcohol concentration is also visible. It is clear then that Fig. 1 provides a general framework for understanding heat capacity data for all alcohols.

The above qualitative arguments for ϕ_C(assoc) and C_p^E can be made quantitative through the use of the TK model whose parameters, i.e. the enthalpy change for the formation of a H-bond ΔH^0 and the volumetric equilibrium constants K_i^φ for each species i (i = 2, 3, and 4), were fitted to dilute ϕ_C(assoc) data using eq. [1] and are displayed in Table 2. Figures 3, 4, and 5*d* show C_p^E calculations using these parameters and eqs. [1] to [3]; note that although the TK model parameters were fitted to dilute alcohol concentration data, good predictions throughout the concentration range are obtained. In Fig. 5*d*, the theory is seen to give a semi-quantitative representation of C_p^E over a wide range of temperature. The reduction in self-association capabilities in going from the primary alcohol to the secondary or tertiary alcohols can also be observed in their pure component heat capacities. Table 2 reports values of the associational part of pure alcohol C_p, C_p^0(assoc) found by subtracting columns three and four in Table 1. Table 2 also gives theoretical C_p^0(assoc) values from eq. [1]. For a given carbon number C_p^0(assoc) increases strongly in magnitude in going from a linear 1-alcohol (C_p^0 and C_p^0(assoc) for 1-alcohols are given in ref. 3) to an isomeric alcohol which has its hydroxyl group in a quaternary carbon atom. For instance, C_p^0(assoc) for 1-decanol is 35 J K^{-1} mol^{-1} (3) whereas for 4-propyl-4-heptanol the corresponding value is 132 J K^{-1} mol^{-1}. This remarkable sensitivity of C_p^0(assoc) to steric hindrance corresponds to weaker H-bonding and a shift to higher $kT/|\Delta G^0|$ values along curve 0 in Fig. 1. The weaker H-bonding is also seen in higher thermal expansion coefficients for these alcohols. Theoretical C_p^0(assoc) values in Table 2 reproduce successfully the experimental trend but they are only qualitatively correct due to the fact that the TK parameters were fitted to dilute alcohol concentration data.

The evaluation of the volumetric equilibrium constant for every species allows the calculation of the volume fractions for each i ($\varphi_{A_i} = K_i^\varphi \varphi_A{}^i$). One of the most interesting results of applying the TK model to the experimental data for linear alcohols (1, 3) is that tetramers turned out to be the predominant species, dimers being almost absent even at very low alcohol concentration. For 1-decanol and 4-propyl-4-heptanol + *n*-

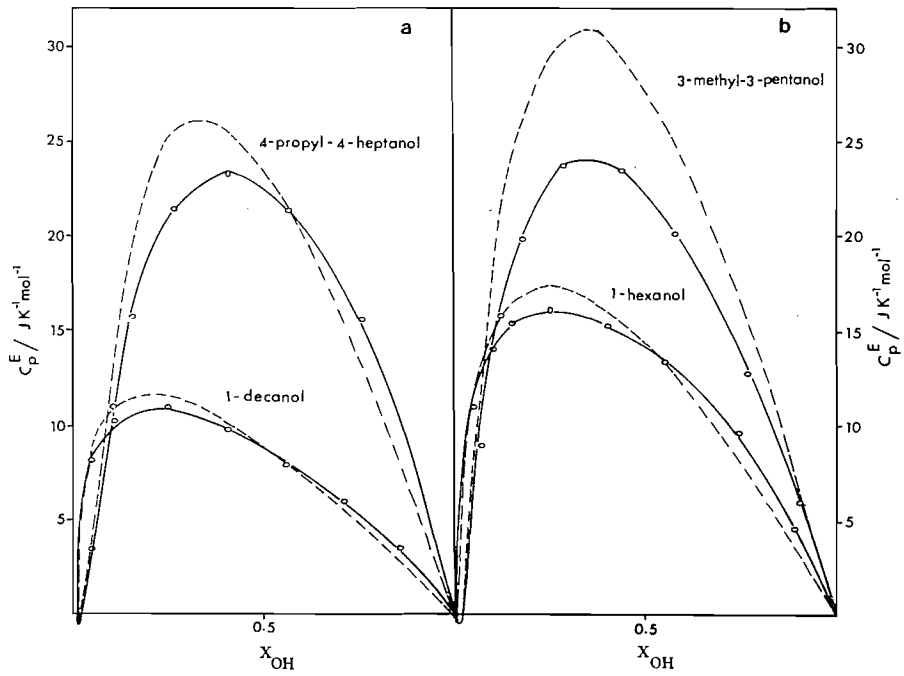

FIG. 4. Excess heat capacity at 25°C for (*a*) 1-decanol and 4-propyl-4-heptanol + *n*-decane and (*b*) 1-hexanol and 3-methyl-3-pentanol + *n*-hexadecane. Negative C_p^E values at very low alcohol concentration have been omitted due to crowding. Dashed lines are TK model calculations.

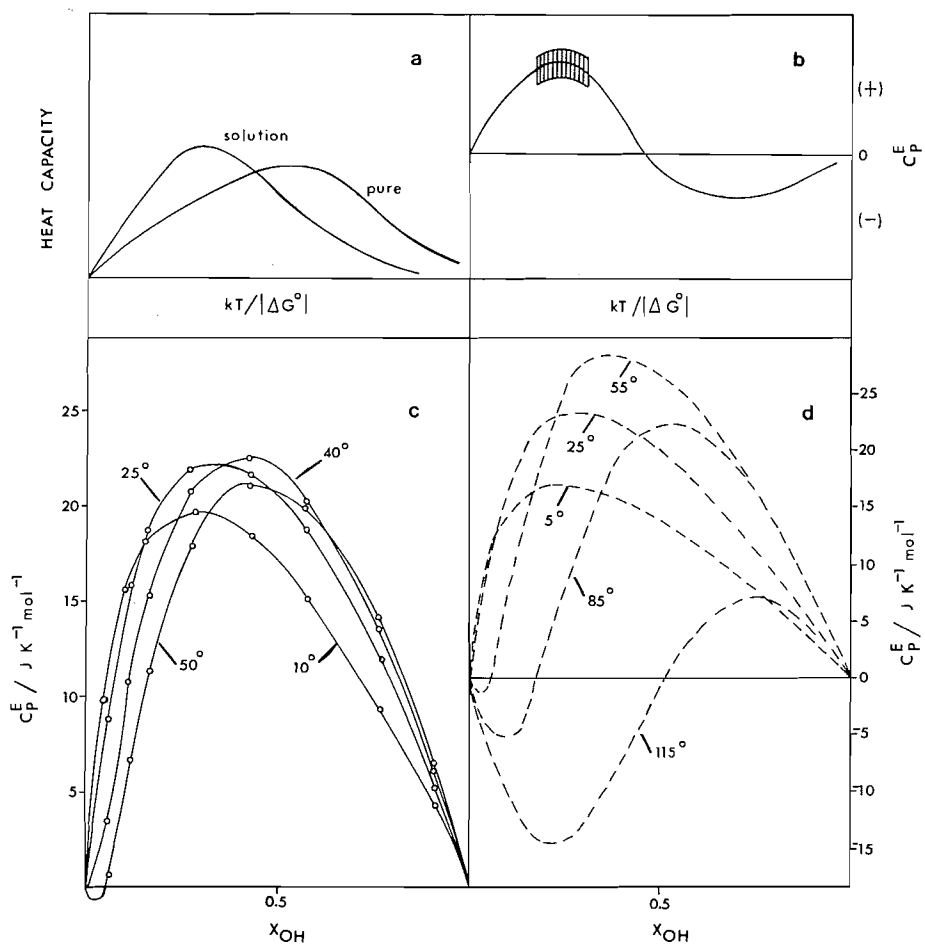

FIG. 5. (*a*) Schematic representation of the heat capacity for a pure associated liquid and a solution in an inert solvent against $kT|\Delta G^0|$; (*b*) variation of the excess heat capacity C_p^E against $kT|\Delta G^0|$ (shadowed area represents $C_p^E(T)$ for alcohols where there is steric hindrance of the hydroxyl group); (*c*) C_p^E for 3-methyl-3-pentanol + *n*-decane at 10, 25, 40, and 50°C, and (*d*) TK model calculations.

Can. J. Chem. Downloaded from www.nrcresearchpress.com by 176.9.209.113 on 09/07/12
For personal use only.

TABLE 2. Volumetric equilibrium constants K_i^{φ}, ΔH^0, and experimental and calculated C_p^0(assoc) at 25°C for branched and cyclic alcohols + inert solvent[a]

Alcohol	$-\Delta H^0$ (kJ mol^{-1})	$(K_i^{\varphi})^{1/(i-1)}\bar{V}^b$ (cm^3 mol^{-1})			C_p^0(assoc) (J K^{-1} mol^{-1})	
		$i = 2$	$i = 3$	$i = 4$	Exp	Calc
1. 2-Methyl-2-propanol	30.4	80	5986	7052	51	29
2. Cyclopentanol[c]	28.5	0	0	8376	30	21
3. 2-Methyl-2-butanol[c]	32.1	0	3733	1929	60	61
4. Cyclohexanol	30.6	4	5441	8697	60	27
5. 3-Methyl-3-pentanol	28.6	1822	422	4284	100	86
6. *trans*-2-Methylcyclohexanol	28.0	757	3198	5853	58	35
7. 2-Methylcyclohexanol (mixed isomers)	26.6	523	3057	4913	62	35
8. *cis*-2-Methylcyclohexanol	25.8	490	2663	3203	64	42
9. 1-Methylcyclohexanol	31.0	0	4609	2910	129	57
10. 3-Ethyl-3-pentanol	30.0	730	1584	1563	127	94
11. Cyclooctanol	31.3	100	7481	6011	—	42
12. 3,7-Dimethyl-1-octanol	29.7	1291	3506	11686	52	32
13. 5-Decanol	30.4	588	4256	4581	86	71
14. 4-Propyl-4-heptanol	30.5	1536	799	2583	132	102
15. Cyclododecanol	31.0	3138	2896	9866	—	40
16. 5-Butyl-5-nonanol	31.2	2232	981	2836	162	117
17. 8-Hexadecanol	28.6	0	4145	5068	—	65
18. Cholesterol[d]	24.0	8	3468	6180	—	—

[a]Solvent was *n*-decane with the exceptions of 8-hexadecanol and cholesterol where the solvents used were *n*-hexane and CCl_4, respectively.
[b]$\bar{V}$ is the molar volume of the alcohol from Table 1.
[c]From ref. 6 where *n*-heptane was used as solvent.
[d]From ref. 14 (for this alcohol $\bar{V}$ = 359.58 cm^3 mol^{-1} estimated from the partial molar volume at infinite dilution).

Can. J. Chem. Downloaded from www.nrcresearchpress.com by 176.9.209.113 on 09/07/12
For personal use only.

decane, Fig. 6 shows the distribution of tetramers, dimers, and monomers of the total alcohol present in solution, as a function of the weight percent of the solvent. At each concentration φ_1, the real volume fraction of alcohol in solution, represents 100%. The percentage for dimers for 1-decanol + *n*-decane is not shown since its values are extremely small. In contrast to the predominance of tetramers in the linear alcohol case, for the highly hindered tertiary alcohol monomers are the predominant species in this concentration range reflecting the decrese in self-association ability imposed by the steric hindrance of the hydroxyl group. At 2wt.% alcohol in Fig. 6, which corresponds to the highest concentration in Fig. 3, the solution contains ca. 93% of monomers and 7% dimers; the negative C_p^E in Fig. 3 in then due to the breaking of structure on passing from the pure alcohol to the solution which contains many monomers and just a few dimers. For this tertiary alcohol, the order-creation process in solution is delayed to higher concentrations where finally enough stucture, i.e. higher species like tetramers, has been created and C_p^E becomes positive.

Deviations from the predominance of one species (tetramers) found for all 1-alcohols (3) are seen for all the branched and cyclic alcohols listed in Table 2. In ref. 3, the experimentally determined volumetric equilibrium constants K_i^{φ} were found to be related to the more fundamental equilibrium constant for H-bond formation for linear *i*-mers $K_{i,L}$ through

$$[4] \quad (K_i^{\varphi})^{1/(i-1)}\bar{V} = i^{1/(i-1)}K_{i,L}(v\sigma\omega^2/z)$$

where $\bar{V}$ is the molar volume of the alcohol, z is the lattice coordination number, v is the molar volume of a segment in the lattice, σ the symmetry number, and ω a parameter which characterizes the flexibility of the chain. From eq. [4]

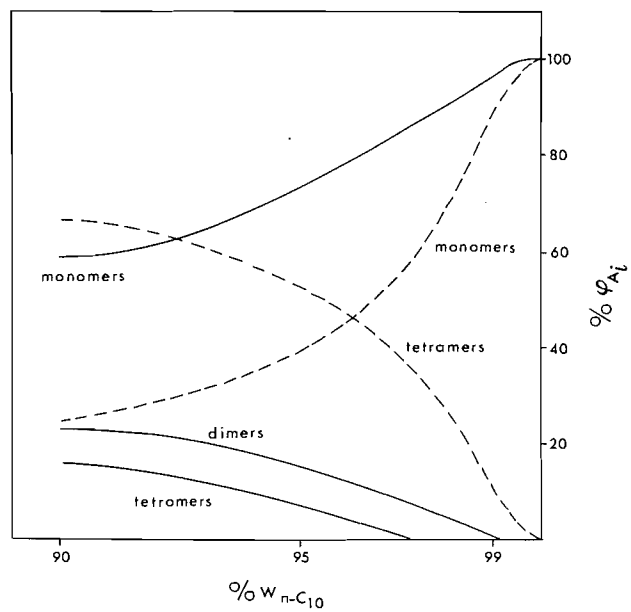

FIG. 6. Distribution in *i*-mers of the total alcohol present in solution for 4-propyl-4-heptanol + *n*-decane (full lines) and 1-decanol + *n*-decane (dashed lines) at 25°C.

$$[5] \quad \Delta G_i^+/RT = \Delta G_i^0/RT - \ln(v\sigma\omega^2/z)$$
$$= (\ln i)/(i-1) - \ln[(K_i^{\varphi})^{1/(i-1)}V]$$

where ΔG_i^0 is the free energy of association for species *i*. Calculation of ΔG_i^0 is, however, hampered by the difficulty in

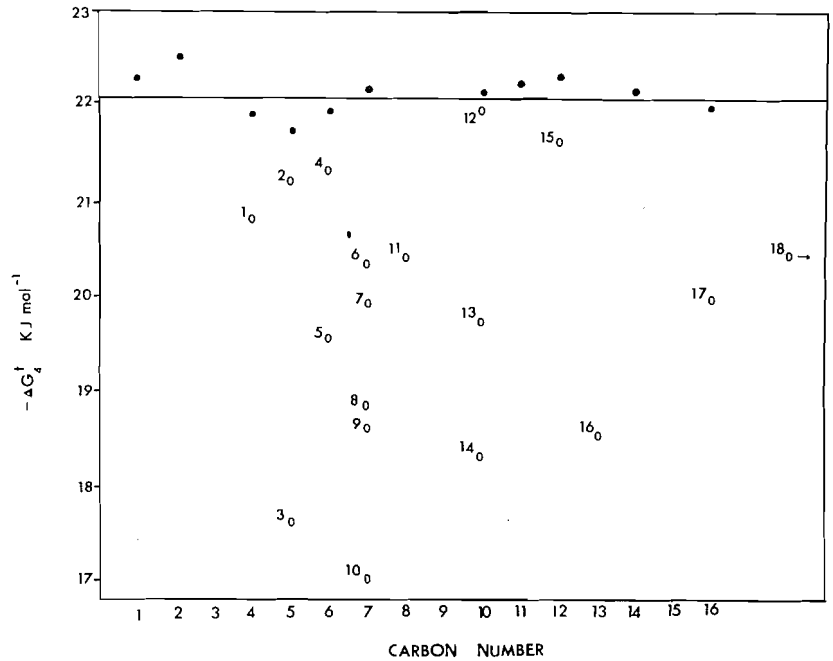

FIG. 7. $-\Delta G_4^+$ from eq. [5] against carbon number for linear alcohols (●) from ref. 3 and for branched and cyclic alcohols (○). Code is that indicated in Table 2. For alcohol number 18, i.e. cholesterol, the carbon number is 27.

choosing values for the quantities v, σ, ω, and z; nevertheless, to within the constant ln $(v\sigma\omega^2/z)$, comparison between different alcohols is possible through the calculation of ΔG_i^+ from eq. [5]. Figure 7 shows ΔG_4^+ values for 1-alcohols (3) and for all the branched and cyclic alcohols studied in this work. In this figure, all 1-alcohols are seen to have essentially the same ΔG_4^+ while secondary and tertiary alcohols depart from this behaviour. For a given carbon number $|\Delta G_4^+|$ decreases in going from the primary to the tertiary alcohol. As the steric hindrance of the hydroxyl group increases ΔG_4^+ becomes less negative reflecting the increasing difficulty for tetramer formation. In Table 2 almost all alcohols have $|\Delta H^0|$ values which are higher than the average $|\Delta H^0|$ for linear alcohols (28.9 kJ mol^{-1}) found in ref. 3 under the assumption of linear tetramers. The assumption of cyclic tetramers and no other i-mers gave $|\Delta H^0| = 3/4\ (28.9) = 21.7$ kJ mol^{-1}. In the present case we believe that due to steric hindrance cyclization of the i-mers should be less pronounced than in the case of the linear alcohols and hence $|\Delta H^0|$ must remain higher for the branched and cyclic alcohols than for the linear. The weakness of the H-bonds formed by cyclic and branched alcohols as compared to those present in linear alcohols emerges then from a larger negative entropy change which reduces $|\Delta G_4^+|$ below the value for the corresponding isomeric linear alcohol. It was unexpected that going from a linear to branched alcohol should entail changes of opposite sign in $|\Delta H^0|$ and $|\Delta S^0|$ and particularly that $|\Delta H^0|$ should be increased. However, we do not believe this result to be an artefact of the TK fitting. The maximum of the ϕ_C(assoc) vs. x_1 curve has essentially the same height for branched and linear alcohols (see for instance Fig. 2). This height is proportional to $(\Delta H^0/RT)^2$, where the proportionality constant increases with the size of the multimer (i). Linear alcohols are characterized by a predominance of tetramers with negligible dimers and trimers while the branched species, as seen in Table 2 and Fig. 6, shift substantially to dimers and trimers. Thus the same height of the ϕ_C(assoc) maximum for branched and linear alcohols means that $|\Delta H^0|$ must be higher for the branched species to compensate for the relatively larger dimer and trimer populations.

2-Methyl-2-propanol and n-butanol are amongst the most studied branched and linear alcohols. The alkyl inductive effect which is stronger for 2-methyl-2-propanol than for n-butanol indicates that the oxygen atom for 2-methyl-2-propanol should be more negative than for n-butanol while the hydrogen should be less positive. This is in agreement with the Kamlet–Taft parameters α (hydrogen bonding donor ability) and β (hydrogen bonding acceptor ability) which are (11) for 2-methyl-2-propanol $(\alpha, \beta) = (0.68, 1.01)$ and for n-butanol (0.79, 0.88). Thus the more basic oxygen of 2-methyl-2-propanol should increase $|\Delta H^0|$ and the less acidic hydrogen should produce the opposite effect making it difficult to decide on this basis the sign of the change in $|\Delta H^0|$. The majority of the reported values for $|\Delta H^0|$ have been obtained through nmr or ir measurements in CCl_4 (12). However, CCl_4 is not a truly inert solvent. For instance, C_p measurements in this laboratory for alcohols in CCl_4 give apparent $|\Delta H^0|$ values which are much lower than found with alkane solvents. An ir determination of $|\Delta H^0|$ for 2-methyl-2-propanol compared with methanol in hexadecane gives $|\Delta H^0|$ larger for 2-methyl-2-propanol (13*a*); however, the situation is reversed for 2-methyl-2-propanol compared with n-butanol in heptane (13*b*). The assertion that $|\Delta H^0|$ is higher is neither confirmed or denied by the literature. If indeed $|\Delta H^0|$ is larger for the branched alcohols then it implies that the H-bond itself is strengthened but steric hindrance between the branched alkyl groups increases $|\Delta S^0|$ sufficiently to produce a net decrease in $|\Delta G^0|$.

In Fig. 7, comparison between ΔG_4^+ values for cycloalkanols and other secondary alcohols such as 5-decanol and 8-hexadecanol indicate that cycloalkanols are able to form tetramers more easily. Comparison between different cycloalkanols also indicate that the size of the cyclic ring attached to the hydroxyl group does not seem to have a significant influence in the formation of tetramers. While in 5-decanol and 8-hexadecanol the hydroxyl group is attached to a carbon atom in the middle of a long hydrocarbon chain, in the cyclohexanols the more exposed hydroxyl group produces a more favourable molecular shape for the formation of higher H-bonded species like tetramers. It appears that as far as the hydroxyl group is not surrounded by bulky groups the alcohol is able to self-associate

Can. J. Chem. Downloaded from www.nrcresearchpress.com by 176.9.209.113 on 09/07/12
For personal use only.

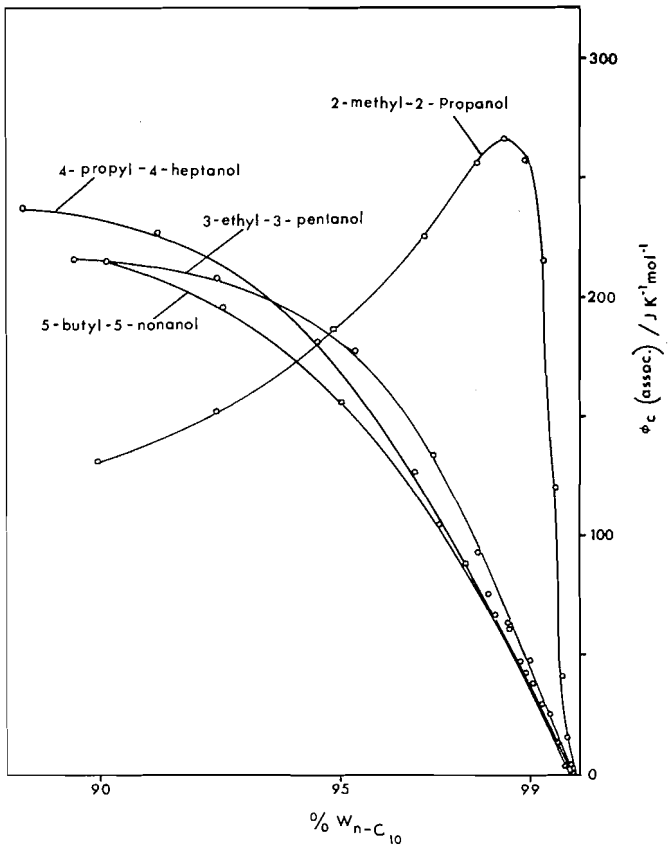

FIG. 8. Associational part of the apparent heat capacity for 2-methyl-2-propanol, 3-methyl-3-pentanol, 4-propyl-4-heptanol, and 5-butyl-5-nonanol + *n*-decane at 25°C.

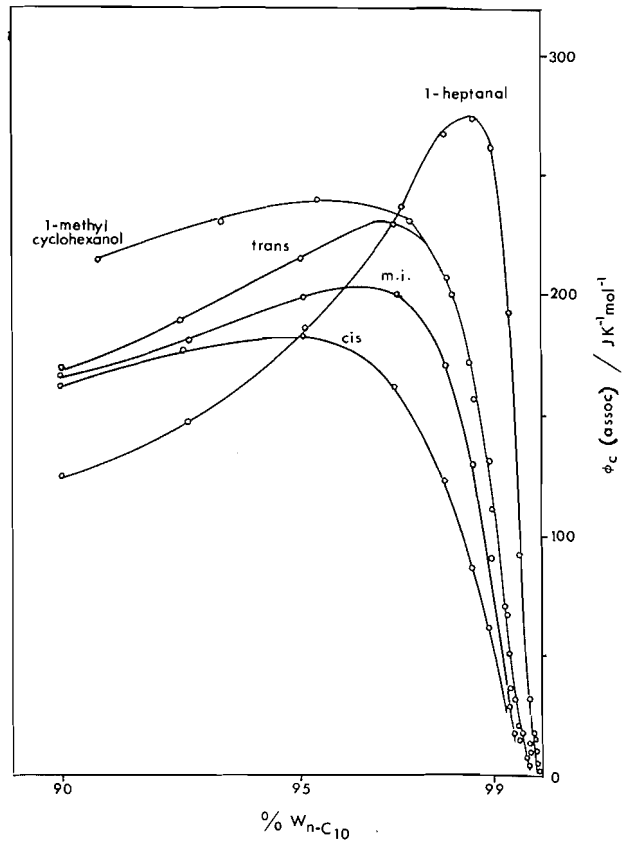

FIG. 9. Association part of the apparent heat capacity for 1-heptanol (from ref. 3), 1-methylcyclohexanol, *trans*-, *cis*-, and mixed isomers (m.i.) 2-methylcyclohexanol + *n*-decane at 25°C.

in dilute solution forming species higher than dimers; another example of this is given by cholesterol which, as indicated in Fig. 7, has a tetramer forming ability (14) comparable to that of cyclooctanol. Since more self-association has been observed (15) in using a hydrocarbon as solvent than when CCl_4 is used, the lower $|\Delta H^0|$ for cholesterol in Table 2 is a reflection of the solvent selection.

Amongst the tertiary alcohols in Fig. 7 and Table 2 the series 2-methyl-2-propanol, 3-methyl-3-pentanol, 4-methyl-4-heptanol, and 5-butyl-5-nonanol illustrates the effect of changing the molecular shape while keeping the same "degree of crowding" of the hydroxyl group. Starting with 2-methyl-2-propanol, the addition of CH_2 groups on the three hydrocarbon tails attached to the carbon where the hydroxyl is linked, changes the molecular shape from being spherical to a T-like shape. The ϕ_C(assoc) for these tertiary alcohols is shown in Fig. 8 where a substantial change on the self-association behaviour is observed when the spherical 2-methyl-2-propanol is substituted by either one of the three "tail extended *t*-butanols." This situation is reflected on the K_i^{φ} values in Table 2 which indicate that while for *t*-butanol tetramers are predominant and dimers almost absent, for the other three alcohols the formation of *i*-mers in this concentration region is almost totally hindered and monomers are by far the predominant species (see Fig. 6). In Fig. 8 there is no continuous progression of ϕ_C(assoc) curves in going from 2-methyl-2-propanol to 5-butyl-5-nonanol but it appears that the change in self-association is rather abrupt, indicating that the formation of higher species such as tetramers depend critically on the alcohol molecular shape being geometrically favourable.

The sensitivity with which the heat capacity responds to slight changes on the molecular shape and the steric hindrance of the hydroxyl group prompted the measurement of ϕ_C(assoc) for a series of isomeric methylcyclohexanols. These results are shown in Fig. 9 together with those for the corresponding linear alcohol (1-heptanol) from ref. 3. As expected, the methylcyclohexanols show a self-association behaviour which corresponds to that of 1-heptanol at $T > 25$°C. A ^{13}C nmr spectroscopy study (16) on the conformational equilibria in isomeric methylcyclohexanols has concluded that the dominating species are those where the CH_3 group is in the equatorial position. It appears then that the dominating species for *cis*- and *trans*-2-methylcyclohexanol are the ae and ee conformers, respectively (the first letter of each pair refers to the orientation of the hydroxyl group). Molecular models show quite readily that amongst these two alcohols the hydroxyl group is less hindered and hence more available for H-bond formation when it is in the equatorial position, i.e. that the *trans* isomer should have a better self-association ability than the *cis* isomer. This is confirmed by the results in Fig. 9 where ϕ_C(assoc) for the *trans* isomer show a higher maximum which occurs at lower alcohol concentration. This situation is also reflected in Table 2 where the *trans* isomer is seen to have a better ability for tetramer formation and in Fig. 7 where ΔG_4^+ is considerably more negative than for the *cis* isomer. Figure 9 also shows the results for a mixture of the *trans*- and *cis*-2-methylcyclohexanol ϕ_C(assoc) being, as expected, intermediate between those for each separate isomer. For 1-methylcyclohexanol ref. 16 indicates that the dominating species is the ae conformer; in this case the steric hindrance of the hydroxyl group is not only due to its axial position but also to the fact that the CH_3 is attached to the same carbon atom in the ring structure. Accordingly, in Fig. 9 ϕ_C(assoc) for this alcohol

Can. J. Chem. Downloaded from www.nrcresearchpress.com by 176.9.209.113 on 09/07/12
For personal use only.

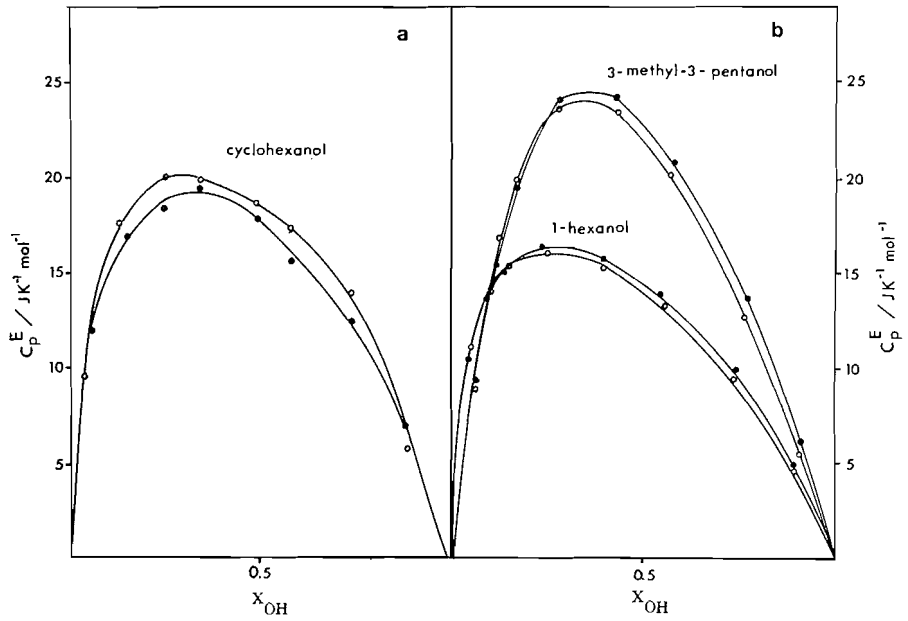

FIG. 10. Excess heat capacity for n-C_{16} (○) and br-C_{16} (●) mixed with (*a*) cyclohexanol at 27°C and (*b*) 3-methyl-3-pentanol and 1-hexanol at 25°C.

shows only a shallow maximum, its weak tetramer formation ability producing the least negative ΔG_4^+ of all the methylcyclohexanols studied.

Much thermodynamic work has been done studying the correlation of molecular orientation (CMO) in long chain n-alkanes (2). Changes in the thermodynamic functions X due to the presence of CMO are small and difficult to isolate, but they manifest themselves in the mixing (ΔX) or excess (X^E) functions. Furthermore, it has been found that increasing degrees of chain branching reduce the ability of the alkane to order in the pure or solution states, essentially eliminating the order contribution to ΔX or X^E for highly branched alkanes such as br-C_{16}. Amongst many different thermodynamic functions X, C_p^E has proven to be a good CMO-destruction indicator. The presence of CMO in the pure n-alkane increases the heat capacity of the pure liquid and, upon mixing with a spherical molecule, gives a negative contribution to C_p^E: at equimolar concentration C_p^E for n-C_{16} + cyclohexane is -6.7 J K^{-1} mol^{-1} while for br-C_{16} + cyclohexane it is only -0.5 J K^{-1} mol^{-1}. Since in studying alcohol + inert solvent mixtures the solvent used is often a hydrocarbon, it appeared interesting to assess the effect that the presence of CMO could have on the alcohol self-association. C_p^E was then measured for n-C_{16} and br-C_{16} mixed with 1-hexanol, 3-methyl-3-pentanol, and cyclohexanol the results being shown in Fig. 10. Surprisingly, it appears that for each alcohol C_p^E for the n-C_{16} mixtures is very close to that for the br-C_{16} mixtures, i.e. the alcohol does not appear to destroy the CMO between n-C_{16} molecules. On the other hand, results in Fig. 10 give support to an underlying assumption in this work and that with 1-alcohols (1, 3), namely, that the so-called physical contribution to the heat capacity for alcohol + inert hydrocarbon mixtures can be neglected. The use of the TK model in the form presented here for the analysis of heat capacity data is then fully justified.

Acknowledgments

We are grateful to the Natural Sciences and Engineering Research Council of Canada, the Ministère de l'Education du Québec, the Consejo Nacional de Ciencia y Tecnología de México, and the Ministerio de Educación y Ciencia de España for financial support.

1. M. COSTAS and D. PATTERSON. J. Chem. Soc. Faraday Trans. I, **81**, 635 (1985).
2. M. COSTAS and D. PATTERSON. Thermochim. Acta. **120**, 161 (1987).
3. L. ANDREOLI-BALL, D. PATTERSON, M. COSTAS, and M. CÁCERES-ALONSO. J. Chem. Soc. Faraday Trans. I. To be published.
4. H. KEHIAIAN and A. J. TRESZCZANOWICZ. Bull. Acad. Chim. Fr. **5**, 1561 (1969).
5. I. PRIGOGINE and R. DEFAY. Chemical thermodynamics. Longmans, London. 1962. pp. 298, 299.
6. G. C. BENZON and P. J. D'ARCY. J. Chem. Thermodyn. **18**, 493 (1986).
7. (*a*) P. PICKER, P. A. LEDUC, P. R. PHILIP, and J. E. DESNOYERS. J. Chem. Thermodyn. **3**, 631 (1971); (*b*) J. L. FORTIER and G. C. BENSON. J. Chem. Thermodyn. **8**, 411 (1976).
8. G. TARDAJOS, E. AICART, M. COSTAS, and D. PATTERSON. J. Chem. Soc. Faraday Trans. I, **82**, 2977 (1986).
9. M. COSTAS, H. V. TRA, D. PATTERSON, G. TARDAJOS, M. CÁCERES-ALONSO, and E. AICART. J. Chem. Soc. Faraday Trans. I. In press.
10. J. A. RIDDICK and W. B. BUNYER. Organic solvents, physical properties, and methods of purification. Wiley Interscience, New York. 3rd. ed. 1970.
11. M. J. KAMLET, J. L. M. ABBOUD, M. H. ABRAHAM, and R. W. TAFT. J. Org. Chem. **48**, 2877 (1983).
12. A. S. N. MURTHY and C. N. R. RAO. Appl. Spectrosc. Rev. **2**, 69 (1968).
13. (*a*) E. E. TUCKER and E. D. BECKER. J. Phys. Chem. **77**, 1783 (1973); (*b*) G. GEISLER, J. FRUWERT, and H. SEIDEL. Spectrochim. Acta, **27A**, 1893 (1971).
14. M. COSTAS and D. PATTERSON. J. Chem. Soc. Faraday Trans. I, **81**, 655 (1985).
15. A. N. FLETCHER and C. A. HELLER. J. Phys. Chem. **71**, 3742 (1967).
16. O. A. SUBBOTIN, N. M. SERGEYEV, V. N. CHLOPKOV, N. G. NIKISHOVA, and Y. G. BUNDEL. Org. Magn. Reson. **13**, 259 (1980).

Can. J. Chem. Downloaded from www.nrcresearchpress.com by 176.9.209.113 on 09/07/12
For personal use only.

Calorimetric determination of the deviation between the International Practical Temperature Scale 1968 and the Thermodynamic Temperature Scale

GÜNTER ERNST,[1] GÜNTER BRÄUNING, AND JOON-FEN LAI

Institut für Technische Thermodynamik, Fakultät für Maschinenbau, Universität Karlsruhe, Kaiserstr. 12, 7500 Karlsruhe 1, Federal Republic of Germany

Received August 28, 1987

This paper is dedicated to Professor James A. Morrison

GÜNTER ERNST, GÜNTER BRÄUNING, and JOON-FEN LAI. Can. J. Chem. **66**, 999 (1988).

A flow calorimeter was constructed to measure the isobaric heat capacity c_p for dilute fluids for pressure $p \leqq 1500$ kPa and for temperature $-20 \leqq t$ (°C) $\leqq +200$. The special design features of the calorimeter facilitate measurements at extremely high accuracy. In this paper the measurements have been used to explore the metrology of the temperature. Measured values of c_p were compared with corresponding theoretical values calculated via statistical mechanics. From the comparison, the deviation between the International Practical Temperature Scale of 1968 and the (theoretical) Thermodynamic Temperature Scale has been obtained. The results of this metrology are in good agreement with those obtained with the PVT gas thermometer and those obtained by radiometry. The comparison establishes the accuracy of the calorimeter and, more important, the feasibility of c_p metrology, especially for probing local stretching or contraction of the International Practical Temperature Scale. The integration of this distortion, starting from the triple point of water, yields the deviation between the scales. It is, e.g., between 30 mK and 40 mK at the boiling point of water, according to our results.

GÜNTER ERNST, GÜNTER BRÄUNING et JOON-FEN LAI. Can. J. Chem. **66**, 999 (1988).

On a construit un calorimètre à écoulement dans le but de mesure la capacité calorifique isobare, c_p, de fluides dilués, à des pressions, p, allant jusqu'à 1500 kPa et à des températures allant de -20 à $+200$°C. Les caractéristiques spéciales du calorimètre permettent d'effectuer des mesures avec une très grande précision. Dans ce travail, on a utilisé les mesures pour examiner la métrologie de la température. On a comparé les valeurs de c_p mesurées avec les valeurs théoriques correspondantes calculées à l'aide de la mécanique statistique. Pour fins de comparaison, on a aussi déterminé la déviation entre l'échelle internationale de température pratique (1968) et l'échelle thermodynamique de température (théorique). Les résultats de cette métrologie sont en bon accord avec ceux obtenus soit avec le thermomètre à gaz PVT ou par radiométrie. Cette comparaison permet d'établir la précision du calorimètre et, encore plus important, la possibilité d'utiliser la métrologie c_p pour étudier des élongations ou des contractions locales de l'échelle internationale de température pratique. L'intégration de cette distorsion, commençant avec le point triple de l'eau, permet d'établir la déviation entre les échelles. Au point d'ébullition de l'eau, nos résultats suggèrent que cette déviation est de 30 à 40 mK.

[Traduit par la revue]

1. Introduction

The PVT (Pressure–Volume–Temperature) gas thermometry of Guildner and Edsinger (1) and the radiometric thermometry of Quinn and Martin (2) established that differences exist between the International Practical Temperature Scale 1968 (IPTS-68) and the Thermodynamic Temperature Scale (TTS) that are much larger than were previously estimated to be the maximum possible errors in IPTS-68. It was demonstrated by Haar (3) that differences between the two temperature scales could be derived from corresponding differences between accurate values of the isobaric heat capacity c_p referred to each of these scales. (The c_p difference is proportional to the temperature derivative of the difference between the scales, so that a calorimetric method offers the potential for probing the local stretching and contraction of IPTS-68.) In this paper we explore differences between the temperature scales using this "new" metrology based on calorimetry.

We designed a state of the art flow calorimeter to measure c_p for dilute vapor states; the range includes values of pressure $\leq$1500 kPa and values of temperature $-20 \leq t$ (°C) ≤ 200. Measured values of c_p, which refer to the IPTS-68, are to be compared with corresponding theoretical values based on statistical mechanics. These theoretical values refer *ipso facto* to the TTS. If, as found by Guildner, the difference between values of temperature on the two scales amounts to several hundredths of a kelvin at the boiling point of water, then, for our metrology to be meaningful, the combined errors in the measured and theoretical values of c_p would have to be not larger than a few hundredths of a percent. An analysis of possible errors suggests that the calorimeter is capable of achieving results at this level of accuracy.

Xenon was selected to be the working fluid. Over the experimental range, the specific heat capacity of xenon for the ideal gas state is constant. The principal error source for the value of this constant is the possible error in the molecular gas constant and in the value used for the molecular mass of xenon.

Results based on the new metrology are consistent with those reported for conventional thermometry, and for radiometric thermometry.

This report includes six sections: The theoretical basis is described in Sect. 2; Sect. 3 contains a description of the calorimeter and the experimental procedure; estimates of possible error are given in Sect. 4; Sect. 5 includes experimental results; short conclusions are contained in Sect. 6.

2. Theoretical basis

We will consider numerical values of the temperature and of the ideal gas state heat capacity to explain the basic theory. The symbol T designates a numerical value of temperature on the IPTS-68 for a fluid in a particular thermodynamic state. The symbol θ designates the corresponding numerical value of temperature for the same state on the TTS. Thermodynamic quantities that are represented as a function of θ are to be determined via statistical mechanics. We define, for the

[1]Author to whom correspondence may be addressed.

Can. J. Chem. Downloaded from www.nrcresearchpress.com by 176.9.209.113 on 09/07/12
For personal use only.

particular thermodynamic state, the quantity μ as the deviation between the numerical values of the temperature on the TTS and on the IPTS-68:

$$[1] \quad \mu \equiv \theta - T$$

The specific enthalpy for the ideal gas state ($p = 0$) at a particular temperature is apparently independent of the temperature scale used:

$$[2] \quad \hat{h}^0(\theta) \equiv h^0(T)$$

The symbol ˆ is used to distinguish between the different mathematical dependencies on the generally different variables θ and T. (This difference between θ and T results from the transition to the numerical values of the temperature.) Differentiation of eq. [2] at constant pressure ($p = 0$) yields, for the numerical values of the ideal gas state, the specific heat capacity

$$[3] \quad \hat{c}_p^0(\theta) \cdot \frac{d\theta}{dT} = c_p^0(T)$$

The $dT/d\theta$ is the local stretching or contraction of the IPTS-68. Differentiation of eq. [1] yields

$$[4] \quad \frac{d\theta}{dT} = 1 + \frac{d\mu}{dT}$$

Equations [3] and [4] yield

$$[5] \quad \hat{c}_p^0(\theta) \cdot \frac{d\mu}{dT} = c_p^0(T) - \hat{c}_p^0(\theta)$$

Integration of eq. [5] yields

$$[6] \quad \mu(T_a) - \mu(273.16) = \int_{273.16}^{T_a} \frac{c_p^0(T) - \hat{c}_p^0(\theta)}{\hat{c}_p^0(\theta)} \cdot dT$$

where by definition of IPTS-68, $\mu(273.16) \equiv 0$.

If $\hat{c}_p^0(\theta)$ varies with θ, we can obtain it as a function of the integration variable T by means of a Taylor series expansion

$$[7] \quad \hat{c}_p^0(\theta) = \hat{c}_p^0(T) + \mu \cdot \frac{d\hat{c}_p^0}{d\theta}(T) + \ldots.$$

With the noble gas xenon as the working fluid, the ideal gas state specific heat capacity can be taken as constant. Thus eq. [6] is evaluated easily

$$[8] \quad \mu(T_a) = \frac{\overline{c_p^0}(T_a) - c_p^0}{c_p^0} \cdot (T_a - 273.16)$$

with c_p^0, used for $\hat{c}_p^0(\theta)$, as the numerical value of $(5/2) \cdot R \cdot M^{-1}$ (R = molecular gas constant; M = molecular mass) and $\overline{c_p^0}(T_a)$ from the extrapolation of the mean values determined experimentally with a temperature rise in the calorimeter from T_a to 273.16 or from 273.16 to T_a:

$$[9] \quad \overline{c_p^0}(T_a) = \frac{1}{T_a - 273.16} \int_{273.16}^{T_a} c_p^0(T) \cdot dT$$

3. Experimental

Detailed descriptions of the equipment and the experimental procedure have been reported (4–6).

Calorimeter

The calorimeter is a U-shaped tube, isolated by vacuum and a radiation shield (Fig. 1). The tube is made of stainless steel with 8 mm outer diameter and 0.15 mm wall thickness.

The gas is heated electrically. Its temperature is measured in front of and behind the heater. Mass flow rate m (≈ 0.2 g s^{-1}), heating power P (≈ 1 W), and temperature rise Δt (≈ 6 K) yield as a first approximation

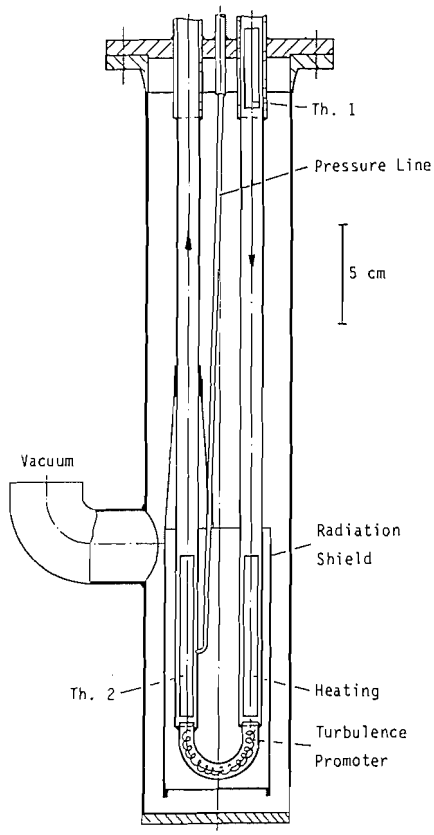

FIG. 1. Cross section of the calorimeter.

$$[10] \quad c_p = P \cdot m^{-1} \cdot \Delta t^{-1}$$

The coiled heating wire is connected with two leads at each end to the current circuit and to a digital voltmeter. The current is measured at a standard resistor in the circuit.

The resistance thermometers are platinum wires of 20 Ω at 0°C, wound strainfree and bifilar on Al_2O_3 crosses. The wires are in direct contact with the flowing gas. The resistance of the thermometers is measured with an A7 ac bridge from ASL, Leighton Buzzard, U.K.

The two thermometers were calibrated with water triple-point cells and with a platinum resistance thermometer from Leeds and Northrup Co., North Wales, PA, U.S.A. calibrated twice at the National Bureau of Standards, Gaithersburg, MD, U.S.A., in 1973, and once at the Physikalisch-Technische Bundesanstalt, Braunschweig, F.R.G. Several recalibrations at our institute, the last in November 1985, showed agreement within about 0.5 mK among the thermometers and between the termometers and the water triple-point cells.

The thermometers can be mounted and removed easily. This is convenient for recalibrating and exchanging. They are positioned in the tube at points where the temperature gradients in the tube and in the electrical leads are very small (Fig. 2). Therefore heat loss by conduction out of the control area is reduced. The radiation shield surrounding the heated part of the control area is fixed on the tube behind the end of the control area and is heated by the outflowing gas. Thus the shield is very close in temperature to the heated gas, so that the heat loss caused by radiation is further reduced.

The influence of the heat loss decreases with increasing mass flow rate m of the gas. If both m and the heating power P are increased so that the temperature rise Δt is unchanged, the heat loss is constant as a first approximation, but the ratio between heat loss and heating power decreases. More strictly, the heat loss decreases with increasing m even with unchanged Δt because the temperature profile in the tube and the electrical leads is modified by the gas flow and the temperature

Can. J. Chem. Downloaded from www.nrcresearchpress.com by 176.9.209.113 on 09/07/12
For personal use only.

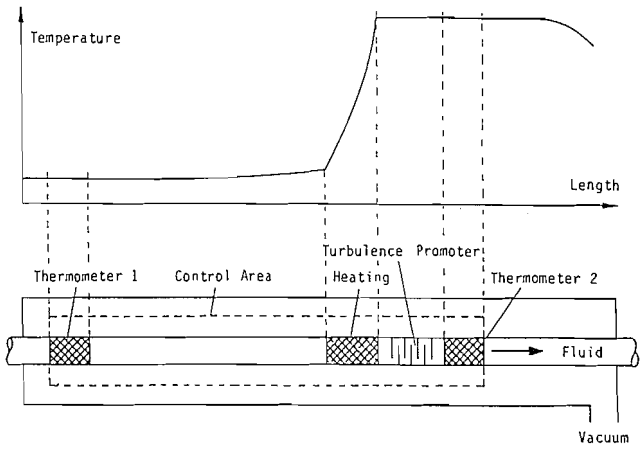

FIG. 2. Temperature profile along the tube of the calorimeter (simplified). Thermometers at points of low temperature gradient.

gradients at the thermometers decrease with increasing m (Fig. 2). If m is increased at constant p, Δt and, with it, the heat loss decrease. Results presented in Table 1 show no systematic influence of the mass flow rate m and, therefore, of the heat loss on the measured values of c_p. The scatter is within ±0.02%. For xenon with its low c_p, the temperature rise and, therefore, the heat loss relative to the heating power would be large without appropriate means for its reduction.

Flow system

The gas flow is produced at constant pressure by evaporating the liquid from a thermostated two-phase container (Fig. 3). The mass flow and the pressure in the calorimeter are adjusted with two needle valves, one before and one behind the calorimeter. The gas is condensed behind the second needle valve, alternatively in one of two condensers cooled with liquid air. A filled condenser is heated to push the liquid back into the two-phase container. Thus the apparatus can be used continuously. The mass flow rate m is measured by weighing the condensate in a small detachable condenser and measuring the collecting time.

Experimental procedure

Each c_p value is given by the difference between a main experiment and a blank experiment (Fig. 4). The main experiment is made with heating, an the blank experiment without. The heating power causes the temperature difference from 2b to 2m at the second thermometer Th2. The c_p, therefore, is assigned to the pressure p_2 measured at the second thermometer Th2 and to the mean temperature of the second thermometer.

$$[11] \quad \bar{t} = (t_{2b} + t_{2m})/2$$

This assignment is independent of the specific profiles of temperature and pressure along the tube of the calorimeter (Fig. 2)!

The experimental c_p is calculated from the difference of the temperature differences

$$[12] \quad \overline{c_p}(p_2, \bar{t}) = P \cdot m^{-1} \cdot ((t_2 - t_1)_m - (t_2 - t_1)_b)^{-1}$$

It is obvious that the first thermometer Th1 only checks the constancy of the temperature of the thermostat and yields the correction for slight changes between the blank and the main experiment (mK).

The difference $(t_2 - t_1)_b$ in the blank experiment for the most part includes the effects of Joule–Thomson cooling (and also changes in potential and kinetic energy). Thus subtracting the blank measurement largely eliminates this major limitation to the accuracy of flow calorimetry and yields the assignment of c_p to the constant pressure p_2. (With very large temperature rises (up to 200 K), the difference of the kinetic energy at Th2 between the blank and the main experiment causes a temperature difference at Th2 of about −15 ppm of $(t_2 - t_1)_m$, calculated with the recovery factor.)

The heating power in the leads to the heater in the calorimeter is not negligible. It is eliminated because it is also contained in the blank experiment: the same current as in the main experiment flows in the blank experiment through the current lead and the potential lead of one end of the heating wire. This potential lead has the same properties as the current lead at the other end of the heating wire. The heating power in the leads, therefore, is the same in the main experiment as in the blank experiment and the difference between the main and the blank experiment is the measured heating power delivered to the calorimeter from the heating wire.

TABLE 1. Specific heat capacity c_p of xenon[a]

1[b]		2[c]	
m (g s^{-1})	c_p (J g^{-1}K^{-1})	m (g s^{-1})	c_p (J g^{-1}K^{-1})
0.21182	0.16144	0.21081	0.15897
0.19979	0.16140	0.20976	0.15900
0.14718	0.16143	0.19798	0.15902
0.14220	0.16142	0.18723	0.15898
0.13951	0.16140	0.17315	0.15899
0.13494	0.16141	0.16523	0.15899
0.13266	0.16142	0.15010	0.15901
0.13183	0.16144	0.14898	0.15899
0.12815	0.16140	0.13116	0.15901
0.11019	0.16141	0.12769	0.15900
0.10859	0.16139	0.10477	0.15902
0.10814	0.16143	0.10235	0.15896

[a]Experimental results for different mass flow rates m show no influence of heat loss.
[b]1: $\Delta t \approx 6$ K at $t = -20$°C and $p = 100$ kPa.
[c]2: Δt from 0°C to 175°C at $p = 60$ kPa.

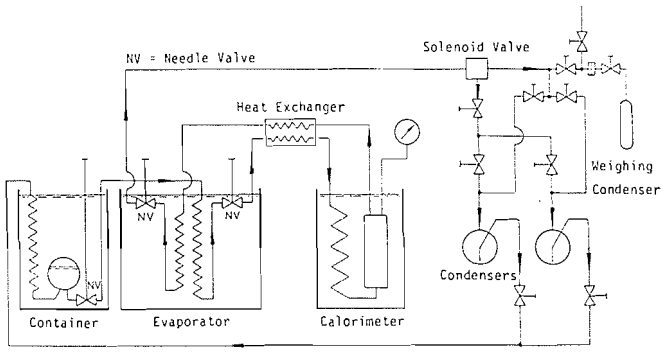

FIG. 3. Scheme of the flow apparatus.

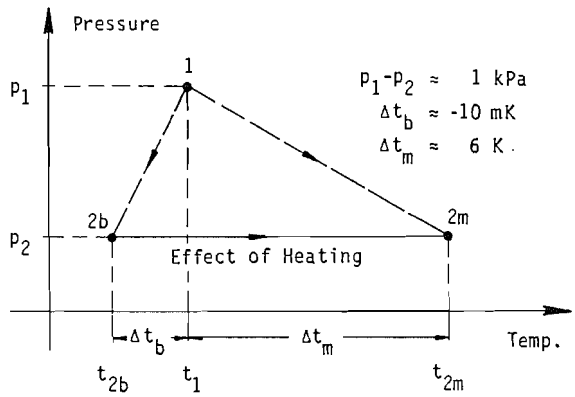

FIG. 4. Evaluation of c_p from blank experiment (1 → 2b) without heating and main experiment (1 → 2m) with heating.

Can. J. Chem. Downloaded from www.nrcresearchpress.com by 176.9.209.113 on 09/07/12
For personal use only.

Can. J. Chem. Downloaded from www.nrcresearchpress.com by 176.9.209.113 on 09/07/12
For personal use only.

TABLE 2. Direct experimental results for the mean specific heat capacity of xenon $\overline{c_p}$ (J g^{-1} K^{-1}): mean values for the "high temperature rise" in the calorimeter from t_a to 0°C or from 0°C to t_a

	t_a (°C)									
p (kPa)	−20	−10	30	50	80	100	125	150	175	200
60		0.15976					0.15910		0.15899	
65	0.16002			0.15948		0.15922		0.15912		0.15901
70			0.15972		0.15939					
80	0.16042	0.16028	0.15993	0.15977	0.15956	0.15945	0.15937	0.15931	0.15923	0.15919
100	0.16097	0.16078	0.16035	0.16016	0.15989	0.15974	0.15965	0.15957	0.15948	0.15941
150	0.16233	0.16206	0.16139	0.16111	0.16070	0.16049	0.16035	0.16023	0.16009	0.16000
200	0.16369	0.16333	0.16243	0.16207	0.16152	0.16123	0.16105	0.16089	0.16065	0.16056

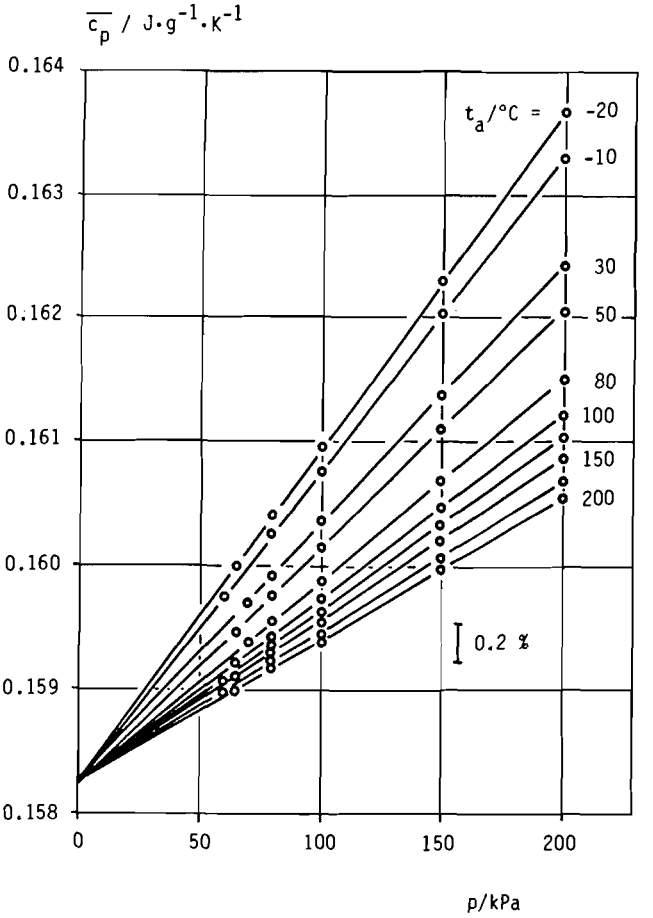

FIG. 5. Experimental results for the mean specific heat capacity of xenon; mean values for the "high temperature rise" in the calorimeter from t_a to 0°C or from 0°C to t_a.

4. Error analysis

Measurements

The possible error in the measurement of the heating power P is smaller than ±0.005%. The possible error in the measurement of the mass flow rate m is smaller than about ±0.005%. The temperature difference in eq. [12] can be written as

$$[13] \quad \Delta t = (t_{2m} - t_{2b}) - (t_{1m} - t_{1b})$$

It is apparent that many of the systematic errors in the individual temperature measurements cancel out. For the measurements with small temperature difference $\Delta t \approx 6$ K, this cancellation is nearly total, so that the possible error of Δt is estimated to be ±0.001 K, ±0.02% of Δt. The cancellation decreases with the size of the interval, so that for $\Delta t \approx 200$ K the possible error is approximately ±0.003 K, but as a percentage of Δt it is $< \pm 0.002\%$. This reduction of the relative uncertainty is the principal reason for basing the metrology on the measurements made at large temperature intervals.

The possible error in assigning c_p to p_2 and $\bar{t}$ is negligible over the pressure and temperature range of the measurements.

The direct experimental results for $\overline{c_p}$ (Table 2, Fig. 5) were calculated for each state as mean values from at least three measurements. They were fitted to linear isotherms for the extrapolation to $p = 0$. Their absolute distance from the isotherms is, on the average, 20 ppm of $\overline{c_p}$ with two extreme values of 80 and 120 ppm. The possible error constituted by the extrapolation to $p = 0$ at a 95% confidence level (following

TABLE 3. Deviation μ between the values of the temperature on the TTS and on the IPTS-68 (unit: K)

Temperature t_a (°C)	Mean value[a] $\overline{c_p^0}$	$d \times 10^{6b}$	$\mu \times 10^{3c}$
−20	0.158247	−392	+8
−10	0.158235	−467	+5
30	0.158255	−341	−10
50	0.158234	−474	−24
80	0.158247	−392	−31
100	0.158250	−373	−37
125	0.158251	−366	−46
150	0.158259	−316	−47
175	0.158274	−221	−39
200	0.158260	−310	−62

[a]Experimental mean value for the temperature rise in the calorimeter from t_a to ≈0°C or from ≈0°C to t_a: $\overline{c_p^0}$. Theoretical value: $c_p^0 = 0.158309\ (J\,g^{-1}\,K^{-1})$.
[b]Relative difference $d \equiv (\overline{c_p^0}(T_a) - c_p^0) \cdot c_p^{0-1}$ (eq. [8]).
[c]Deviation at t_a (=(T_a − 273.15)°C): μ = θ − T (eq. [1]).

Student's statistical test) is about ±50 ppm, or ±0.005%. The influence of uncertainties other than fitting with linear isotherms appears to be the major contributor to this source of possible error of $\overline{c_p^0}$.

The change in the kinetic energy at the thermometer 2 was found to be very small. It increases with increasing temperature difference in the calorimeter. The correction is 15 ppm for the largest temperature difference, $\Delta t = 200$ K. The possible error from this correction is negligible.

Another error results from the impurities in the xenon. According to the supplier, Deutsche L'Air Liquide, Düsseldorf, the sum of the impurities is below 30 mol-ppm. The principal impurity constituents are Ar, Kr, H_2, O_2, N_2, and H_2O. Their highest possible concentration would cause the $\overline{c_p^0}$, obtained from the experiments, to be too large by nearly 30 ppm. The values of c_p^0, therefore, were reduced by 15 ppm and ±15 ppm is the possible error we assign to impurities.

Measurements repeated after long time intervals confirmed that the xenon was not noticeably contaminated during the experiments. The average of the difference between the mean values and results taken at the different time intervals is 0.01%; the maximum difference (an outlier) is 0.035%. We conclude that there is no influence of time on the purity of the xenon or on the apparatus.

Uncertainty of $\hat{c}_p^0(\theta)$

Because xenon is a noble gas, $\hat{c}_p^0(\theta)$ is nearly constant $(=c_p^0)$; statistical mechanics yields $(5/2)\cdot R\cdot M^{-1}$ to within ±0.001% over the experimental range. The molecular gas constant is 8.3144 J mol^{-1} K^{-1} ± 30 ppm (7), so that the possible error in c_p^0 from this source is ±0.003%. The molecular gas constant, determined by Moldover *et al.* is about 8 ppm higher.[2] With this value, the deviation between the temperature scales at the normal boiling point of water would be about 1 mK higher (−38 mK; cf. Table 3).

The molecular mass of xenon was taken as 131.300 g mol^{-1} calculated with information from the supplier for the isotopic composition of naturally occurring xenon:

^{124}Xe: 0.096 mol%, 123.9061 g/mol
^{126}Xe: 0.090 mol%, 125.9042 g/mol
^{128}Xe: 1.920 mol%, 127.9035 g/mol
^{129}Xe: 26.440 mol%, 128.9048 g/mol
^{130}Xe: 4.080 mol%, 129.9035 g/mol
^{131}Xe: 21.180 mol%, 130.9051 g/mol
^{132}Xe: 26.890 mol%, 131.9042 g/mol
^{134}Xe: 10.440 mol%, 133.9054 g/mol
^{136}Xe: 8.870 mol%, 135.9072 g/mol

The uncertainty in the value for the molecular mass is ±15 ppm (8), so that the possible error in c_p^0 from this uncertainty is less than ±0.002%.

5. Experimental results and comparison of temperature scales

Table 4 lists the c_p values for xenon, which were determined in the measurements with a low temperature rise of about Δt = 6 K in the calorimeter. Summing up the uncertainties of the heating power P, the mass flow rate m, and the temperature difference Δt, one gets a maximum uncertainty for the c_p values of about ±0.05%.

The direct experimental values of the $\overline{c_p}$ for the intervals of the high temperature rises are contained in Table 2 and plotted in Fig. 5. These results were used for comparing the temperature scales. Their uncertainty from the uncertainties of P, m, and Δt, assuming a Gaussian law of errors, is about ±125 ppm at Δt = 10 K and about ±75 ppm at Δt = 200 K. As already mentioned, each value contained in Tables 1, 2, and 4 is based on at least 3 measurements.

Table 3 and Fig. 6 contain the results of the comparison for the temperature scales. The values of c_p^0 in Table 3 were determined by extrapolating the direct experimental results (Table 2). They were corrected for the possible influence of the impurities in the xenon used and for the influence of the kinetic energy change at Th2. The highest correction for both influences (at Δt = 200 K) is about one-half unit of the last digit of the numbers contained in Table 2 for the direct experimental results. The values of c_p^0 listed in Table 3 have one more digit than the values of $\overline{c_p}$ in Table 2.

The difference between $\overline{c_p^0}$ and c_p^0 is a small difference between two large numbers. Small relative uncertainties of these numbers, therefore, cause a high relative uncertainty in the small difference. The possible error of the relative difference between $\overline{c_p^0}$ and c_p^0 (eqs. [6], [8]; Table 3) and, therefore, of the deviation between the values of the temperature on the TTS and on the IPTS-68 is about ±30%. It was determined assuming a Gaussian law of errors for the following uncertainties:

from the direct experimental results: ±(75–125) ppm
from the extrapolation to p = 0: ±50 ppm
from the impurities: ±15 ppm
from the molecular gas constant: ±30 ppm
from the molecular mass of the xenon used: ±15 ppm

The hatched area in Fig. 6 represents the possible error of ±30% in the deviation between the temperature scales.

6. Conclusions

The results presented are in satisfactory agreement with results from the gas thermometric work of Guildner and

[2]M. R. Moldover, J. P. M. Trusler, T. J. Edwards, J. B. Mehl, and R. S. Davis. Measurement of the universal gas constant R using a spherical acoustic resonator. Personal communication, October 1987.

Can. J. Chem. Downloaded from www.nrcresearchpress.com by 176.9.209.113 on 09/07/12
For personal use only.

TABLE 4. Experimental results for the specific heat capacity of xenon c_p (J g^{-1} K^{-1}); mean values for the "low temperature rise" in the calorimeter $\Delta t \approx 6$ K; maximum uncertainty: ±0.05%

	t (°C)							
p (kPa)	−20	−10	−5	0	15	40	75	100
60	0.16016			0.15982				
65	0.16032	0.16008				0.15934	0.15911	
70			0.16009		0.15970			0.15905
80	0.16077	0.16048	0.16034		0.15990	0.15957	0.15929	0.15915
90	0.16111							
100	0.16140	0.16103	0.16085	0.16080	0.16030	0.15989	0.15954	0.15937
150	0.16294	0.16239	0.16214	0.16210	0.16131	0.16070	0.16017	0.15991
200	0.16449	0.16376	0.16343	0.16340	0.16232	0.16149	0.16079	0.16046
300				0.16612				
400				0.16896				

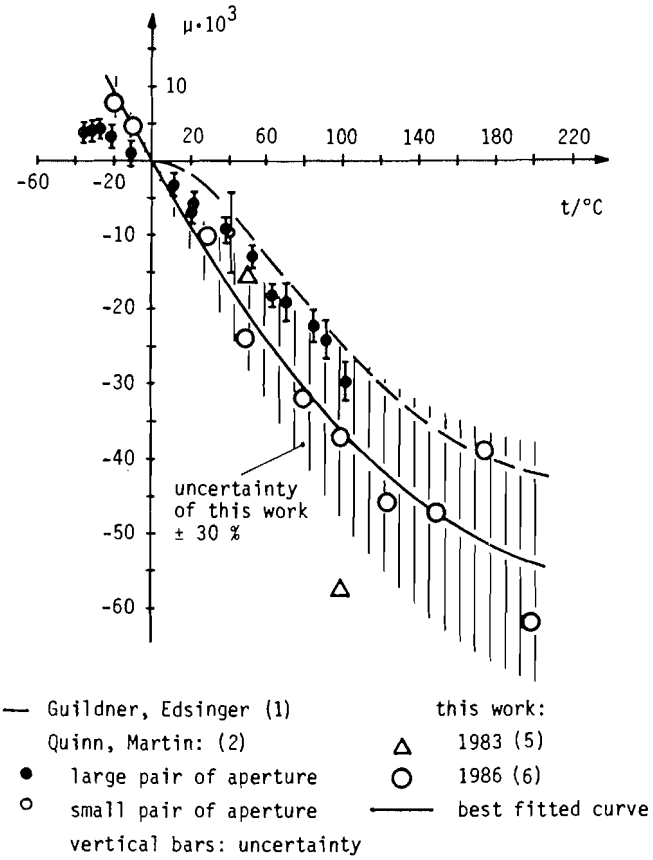

FIG. 6. Deviation μ between the values of the temperature on the Thermodynamic Temperature Scale and on the International Practical Temperature Scale 1968 (unit: K).

Edsinger (1) and the radiometric work of Quinn and Martin (2). The agreement is everywhere within the combined tolerances. This result is of particular importance, since this is a new method (PVT gas thermometry has been used for over a century). The differences between the numbers on the TTS and on the IPTS-68 are sufficiently large that they may be important for experimental work of the highest accuracy.

Acknowledgements:

We thank G. T. Furukawa and J. L. Riddle from the National Bureau of Standards, Gaithersburg, MD, U.S.A., and W. Thomas and co-workers from the Physikalisch-Technische Bundesanstalt, Braunschweig, F.R.G., for the extremely careful calibrations of our standard thermometer. We especially want to thank L. Haar from the National Bureau of Standards, Gaithersburg, for his very careful revising and partial rewriting of this article. Financial support from the Deutsche Forschungsgemeinschaft is gratefully acknowledged.

1. L. A. GUILDNER and R. E. EDSINGER. J. Res. Natl. Bur. Stand. (U.S.), Sect. A: **80**A, 703 (1976).
2. T. J. QUINN and J. E. MARTIN. Phil. Trans. R. Soc. London, **316**, 85 (1985).
3. L. HAAR. Am. Assoc. Adv. Sci. **176**, 1293 (1972).
4. G. ERNST. Chem. Ing. Tech. **41**, 554 (1969).
5. G. BRÄUNING. Fortschr.-Ber. VDI-Z. Reihe 6: Nr. **138** (1983).
6. J.-F. LAI. Fortschr.-Ber. VDI-Z. Reihe 19: Nr. **1** (1986).
7. Recommended consistent values of the fundamental physical constants, 1973. International Council of Scientific Unions, Committee on Data for Science and Technology. CODATA 11, Bulletin (1973).
8. A. O. NIER. Z. Elektrochem. **58**, No. 8 (1954).

Can. J. Chem. Downloaded from www.nrcresearchpress.com by 176.9.209.113 on 09/07/12
For personal use only.

An examination of the shell structure of atoms and ions as revealed by the one-electron potential, $\nabla^2\sqrt{\bar{\rho}(r)}/2\sqrt{\bar{\rho}(r)}$

ROBIN P. SAGAR, ANDREW C. T. KU, AND VEDENE H. SMITH, JR.
Department of Chemistry, Queen's University, Kingston, Ont., Canada, K7L 3N6
AND
ALFREDO M. SIMAS
Departamento de Quimica Fundamental, Universidade Federal de Pernambuco 50000 – Recife, PE, Brasil
Received November 23, 1987
This paper is dedicated to Professor J. A. Morrison

ROBIN P. SAGAR, ANDREW C. T. KU, VEDENE H. SMITH, JR., and ALFREDO M. SIMAS. Can. J. Chem. **66**, 1005 (1988).

The one-electron potential, $\nabla^2\sqrt{\bar{\rho}(r)}/2\sqrt{\bar{\rho}(r)}$, appearing in the Schrödinger equation for the charge density is calculated for the neutral atoms from hydrogen to uranium, and the singly positive ions, from helium to barium and lutetium to radium. These computations, utilizing the nonrelativistic SCF wavefunctions of Clementi and Roetti and McLean and McLean, were performed in order to investigate the concept of shell structure as defined by this potential. $\nabla^2\sqrt{\bar{\rho}(r)}/2\sqrt{\bar{\rho}(r)}$ exhibits a number of zeros and extrema corresponding to classically allowed and forbidden regions, with its topology being very similar in nature to that of $\nabla^2\bar{\rho}(r)$. The significant difference is that $\nabla^2\sqrt{\bar{\rho}(r)}/2\sqrt{\bar{\rho}(r)}$ displays all seven shells in the heavier elements of the periodic table, whereas $\nabla^2\bar{\rho}(r)$ displays only five shells; i.e. compared with $\nabla^2\bar{\rho}(r)$, $\nabla^2\sqrt{\bar{\rho}(r)}/2\sqrt{\bar{\rho}(r)}$ has additional zeros and extrema at large distances corresponding to the two outer shells. The positions of these additional zeros and extrema, when plotted against atomic number Z, exhibit large deviations from the Bohr model of the hydrogen atom. The outermost zero-extremum is not displayed in the transition elements; i.e. where d-orbital filling is present. The model of classically allowed and forbidden regions is shown to provide an alternative definition of shell structure to that of the simple Bohr–Schrödinger theory of an atom. The odd-numbered zeros in $\nabla^2\sqrt{\bar{\rho}(r)}/2\sqrt{\bar{\rho}(r)}$ provide a topological feature capable of representing all shells. Furthermore, these zeros appear at precisely the atomic number as the corresponding shell predicted by the aufbau principle.

ROBIN P. SAGAR, ANDREW C. T. KU, VEDENE H. SMITH, JR. et ALFREDO M. SIMAS. Can. J. Chem. **66**, 1005 (1988).

Le potentiel d'un électron, $\nabla^2\sqrt{\bar{\rho}(r)}/2\sqrt{\bar{\rho}(r)}$, qui apparaît dans l'équation de Schrodinger pour la densité de charge, a été calculé pour les atomes neutres de l'hydrogène à l'uranium ainsi que pour les ions portant une seule charge positive, de l'hélium au baryum et du lutécium au radium. On a effectué ces calculs, qui utilisent les fonctions d'onde des champs auto-cohérents non-relativistes de Clementi et Roetti ainsi que de McLean et McLean, dans le but d'étudier la structure de couche définie par ce potentiel. Le potentiel $\nabla^2\sqrt{\bar{\rho}(r)}/2\sqrt{\bar{\rho}(r)}$ présente un certain nombre de zéros et d'extremums qui correspondent aux régions qui sont d'un point de vue classique permises et défendues et sa topologie est très semblable en nature à celle de la fonction $\nabla^2\bar{\rho}(r)$. La différence importante provient du fait que le potentiel $\nabla^2\sqrt{\bar{\rho}(r)}/2\sqrt{\bar{\rho}(r)}$ représente les sept couches des éléments lourds du tableau périodique alors que $\nabla^2\bar{\rho}(r)$ ne représente que cinq de ces couches; par exemple, si on compare $\nabla^2\bar{\rho}(r)$. avec le potentiel $\nabla^2\sqrt{\bar{\rho}(r)}/2\sqrt{\bar{\rho}(r)}$, ce dernier possède plus de zéros et d'extremums aux grandes distances qui correspondent aux deux couches extérieures. Lorsqu'on trace une courbe des positions de ces zéros et de ces extremums en fonction du numéro atomique Z, on observe de grandes déviations par rapport au modèle de Bohr pour l'atome d'hydrogène. Les zéros et les extremums extérieurs ne sont pas représentés dans les éléments de transition, c'est-à-dire lorsqu'on remplit les orbitales d. On démontre que, par rapport à la théorie simple de Bohr–Schrödinger d'un atome, le modèle classique impliquant des régions permises et défendues fournit une alternative à la définition de la structure des couches. Les zéros impairs du potentiel $\nabla^2\sqrt{\bar{\rho}(r)}/2\sqrt{\bar{\rho}(r)}$ fournissent une caractéristique topologique capable de représenter toutes les couches. De plus, ces zéros apparaissent précisément au numéro atomique de la couche correspondante prédite par le principe de aufbau.
[Traduit par la revue]

Introduction

Density functional theory (1) offers the possibility of reducing the N-electron problem into a more viable one-electron one. However, there are difficulties that are encountered such as N-representability, i.e. to guarantee that a computed density is representative of an ensemble of N fermions (2). In the case of the wavefunction, this N-representability is achieved by making the wavefunction antisymmetric with respect to exchange of coordinates of any two of the N indistinguishable fermions.

The Schrödinger equation for the electron density as proposed by Hunter (3) is of interest since this equation is an "exact dynamical model of the motion of a single electron in a many-electron system" (3). Thus, this particular Schrödinger equation is useful for the interpretation of molecular and atomic structure based on the potential,[1] $\{U(\boldsymbol{r}) - E\} = \nabla^2\sqrt{\rho(\boldsymbol{r})}/2\sqrt{\rho(\boldsymbol{r})}$, within which any one electron moves.

[1]This potential is defined in eq. [6].

The shell structure of atoms and ions has been previously discussed with regard to $D(r)$, the radial distribution function (5–8), $I(p)$, the radial momentum density (9), and more recently in conjunction with $\nabla^2\bar{\rho}(r)$, the Laplacian of the spherically averaged charge density (10). The topological features most indicative of a shell were the maxima in $D(r)$ and $I(p)$, and the odd-numbered zeros in $\nabla^2\bar{\rho}(r)$ (8–10). For the purposes of those studies a shell was defined within the independent particle model as the set of those orbitals having the same principal quantum number. Based on these criteria, the authors noted (8) that five shells at most were apparent in $D(r)$ and likewise, $\nabla^2\bar{\rho}(r)$ also exhibited five shells at most (10). It was also shown that all shells do not have expression in $D(r)$ and $\nabla^2\bar{\rho}(r)$, for all the studied atomic and ionic cases (8, 10). In fact, these authors noted that it was in particular the outer shells which were not expressed in $D(r)$ and $\nabla^2\sqrt{\bar{\rho}(\boldsymbol{r})}$ for all the studied atomic and ionic cases.

The potential $\{U(\boldsymbol{r}) - E\}$ which governs the motion of one

Can. J. Chem. Downloaded from www.nrcresearchpress.com by 176.9.209.113 on 09/07/12
For personal use only.

Can. J. Chem. Downloaded from www.nrcresearchpress.com by 176.9.209.113 on 09/07/12
For personal use only.

electron is related to $\nabla^2\rho(\boldsymbol{r})$ but differs by the additional term $-|\nabla\rho(\boldsymbol{r})|^2/[2\rho(\boldsymbol{r})]$ and division by $4\rho(\boldsymbol{r})$. Since this additional term makes a negative contribution to the potential $\{U(\boldsymbol{r}) - E\}$, Hunter has argued that the allowed regions of space would be increased and perhaps make the outer regions, and hence the outer shells, visible[2] (3).

In the present study we shall examine the nature of $\nabla^2\sqrt{\rho(\boldsymbol{r})}/2\sqrt{\rho(\boldsymbol{r})}$ in order to examine the concept of shell structure as defined within this potential for atoms and ions. Due to the nature of the square root operator, i.e. a nonlinear operator, the technique of examining the contributions from the various shells to the total, previously used in shell structure studies cannot be utilized (9, 10).

It was previously shown (8, 10) that the topological features (zeros and extrema) of $D(r)$ and $\nabla^2\bar{\rho}(r)$ (as functions of the nuclear charge Z) correlate very well with the functional dependence on Z predicted by the Bohr–Schrödinger model of the hydrogenic atom. Thus, this correlation with the hydrogenic atom shall also be investigated for $\nabla^2\sqrt{\rho(\boldsymbol{r})}/2\sqrt{\rho(\boldsymbol{r})}$.

Theoretical considerations

We adopt the notation of Hunter (3) and denote the electronic wavefunction for a particular stationary state k, by $\psi^k(\boldsymbol{r}', s', \boldsymbol{r}, s|\boldsymbol{R})$ where s and $\boldsymbol{r}$ are the spin and spatial coordinates respectively of a particular electron, $\boldsymbol{R}$ are the coordinates of the nuclei, and s' and $\boldsymbol{r}'$ are the spin and spatial coordinates of the remaining electrons. Since we are considering only the ground states of atomic systems, we shall suppress the index k and the nuclear vector $\boldsymbol{R}$. Thus we write $\rho(\boldsymbol{r})$ instead of $\rho^k(\boldsymbol{r}|\boldsymbol{R})$, etc.

The wavefunction can be factorised into

$$[1] \quad \psi(\boldsymbol{r}', s', \boldsymbol{r}, s) = \theta(\boldsymbol{r})\chi(\boldsymbol{r}', s', s|\boldsymbol{r})$$

and substituted into the N-electron Schrödinger equation, $\mathbf{H}\psi = E\psi$, premultiplied by $\chi(\boldsymbol{r}', s', s|\boldsymbol{r})$, and then integrated with respect to $\boldsymbol{r}'$, s', s in the manner described in ref. 4 to yield

$$[2] \quad \left\{-\frac{1}{2}\nabla^2 + U(\boldsymbol{r})\right\}\theta(\boldsymbol{r}) = E\theta(\boldsymbol{r})$$

where

$$[3] \quad U(\boldsymbol{r}) = \int\chi(\boldsymbol{r}', s', s|\boldsymbol{r})\mathbf{H}\chi(\boldsymbol{r}', s', s|\boldsymbol{r})\mathrm{d}\boldsymbol{r}'\mathrm{d}s'\mathrm{d}s$$

$\mathbf{H}$ refers to the N-electron Hamiltonian and Hartree atomic units are used here and throughout this paper.

By utilizing the relationship between the one-electron wavefunction $\theta(\boldsymbol{r})$, and the charge density $\rho(\boldsymbol{r})$,

$$[4] \quad \rho(\boldsymbol{r}) = N|\theta(\boldsymbol{r})|^2$$

Equation [2] can be changed (3) into an equation for the charge density

$$[5] \quad \left\{\frac{\nabla^2\rho(\boldsymbol{r})}{4} - \frac{|\nabla\rho(\boldsymbol{r})|^2}{[8\rho(\boldsymbol{r})]}\right\} + U(\boldsymbol{r})\rho(\boldsymbol{r}) = E\rho(\boldsymbol{r})$$

As noted by Hunter (3), this equation has the same potential energy function, $U(\boldsymbol{r})$, as eq. [2] for the charge density amplitude $\theta(\boldsymbol{r})$ but the kinetic energy has a different form.

[2]The statement by Hunter (3) "Thus, the attractive classically allowed regions computed from eq. [15] (eq. [6] of the present paper) are always larger than those predicted by $\nabla^2\bar{\rho}(r)$" is not strictly correct, because negative regions of $\nabla^2\bar{\rho}(r)$ are interpreted as regions of charge accumulation (11) rather than as classically allowed regions of space; i.e. the negative regions of $\{U(r) - E\}$ are larger than those of $\nabla^2\bar{\rho}(r)$, but their respective interpretations are different.

Equation [5] may be rearranged into

$$[6] \quad \{U(\boldsymbol{r}) - E\} = \left\{\frac{[\nabla^2\rho(\boldsymbol{r})]}{4\rho(\boldsymbol{r})} - \frac{|\nabla\rho(\boldsymbol{r})|^2}{[8\rho(\boldsymbol{r})^2]}\right\} = \frac{\nabla^2\sqrt{\rho(\boldsymbol{r})}}{2\sqrt{\rho(\boldsymbol{r})}}$$

The potential $\{U(\boldsymbol{r}) - E)\}$ governs the motion of a single electron. The region where this potential is negative is a classically allowed region of space and where it is positive is a classically forbidden region of space. As a result it provides a map of alternating allowed and forbidden regions. Hunter (3) has speculated that the number of these regions corresponds to the shell structure of an atom or an ion.

The physically meaningful charge density for atomic systems is spherical because an ensemble average must be taken over degenerate states. As a result we shall focus our attention on $\bar{\rho}(r)$ and $\nabla^2\sqrt{\bar{\rho}(r)}/2\sqrt{\bar{\rho}(r)}$. The latter will be computed from eq. [6]. The wavefunctions used for the computation of $\nabla^2\bar{\rho}(r)$, $\nabla\bar{\rho}(r)$ and $\bar{\rho}(r)$ were the non-relativistic self-consistent field wavefunctions of Clementi and Roetti (12) and of McLean and McLean (13). Published wavefunctions for the singly positive ions with open f-shells could not be found.

As discussed elsewhere (9), the Laplacian operator for the spherically averaged charge density expressed in spherical polar coordinates (10) is,

$$[7] \quad \nabla^2\bar{\rho}(r) = \frac{\partial^2}{\partial r^2}\bar{\rho}(r) + \frac{2}{r}\frac{\partial}{\partial r}\bar{\rho}(r)$$

The expression for the gradient of $\rho(\boldsymbol{r})$ in spherical polar coordinates is,

$$[8] \quad \nabla\rho(\boldsymbol{r}) = \frac{\partial}{\partial r}\rho(\boldsymbol{r})\hat{r} + \frac{1}{r}\frac{\partial}{\partial\theta_r}\rho(\boldsymbol{r})\theta_r + \frac{1}{r\sin\theta_r}\frac{\partial}{\partial\phi}\rho(\boldsymbol{r})\hat{\phi}_r,$$

which reduces to

$$[9] \quad \nabla\bar{\rho}(r) = \frac{\partial}{\partial r}\bar{\rho}(r)\hat{r}$$

for a spherically averaged charge density. Substitution of eqs. [7] and [9] into eq. [6] yields

$$[10] \quad \{U(r) - E\} = \frac{\nabla^2\sqrt{\bar{\rho}(r)}}{2\sqrt{\bar{\rho}(r)}} = \frac{1}{8\bar{\rho}(r)^2}\left\{2\bar{\rho}(r)\frac{\partial^2}{\partial r^2}\bar{\rho}(r) + \frac{4}{r}\bar{\rho}(r)\frac{\partial}{\partial r}\bar{\rho}(r) + \left(\frac{\partial}{\partial r}\bar{\rho}(r)\right)^2\right\}$$

The potential can thus be seen to be related to the various curvatures of $\bar{\rho}(r)$, the spherically averaged charge density, which has been the topic of a recent study (8).

Results and discussion

In Figs. 1 and 2 plots of the potential $\nabla^2\sqrt{\bar{\rho}(r)}/2\sqrt{\bar{\rho}(r)}$ for the neutral atoms Zn ($Z = 30$), Ga ($Z = 31$) and the singly positive ion Cl^+ ($Z = 17$) are presented. From eq. [10] and the MacLaurin expansion of $\bar{\rho}(r)$

$$[11] \quad \bar{\rho}(r) = \bar{\rho}(0)[1 - 2ZC_{en}r] + 0(r^2)$$

where C_{en} is the electron–nuclear cusp ratio (14)

$$[12] \quad C_{en} = -\lim_{r\to 0}\frac{\bar{\rho}'(r)}{2Z\bar{\rho}(r)}$$

we observe that if C_{en} is non-zero, the potential rises from negative infinity as r increases. C_{en} has the value one for the exact electron density as well as the exact Hartree–Fock $\bar{\rho}(r)$. For the present functions, C_{en} is approximately one (14). The

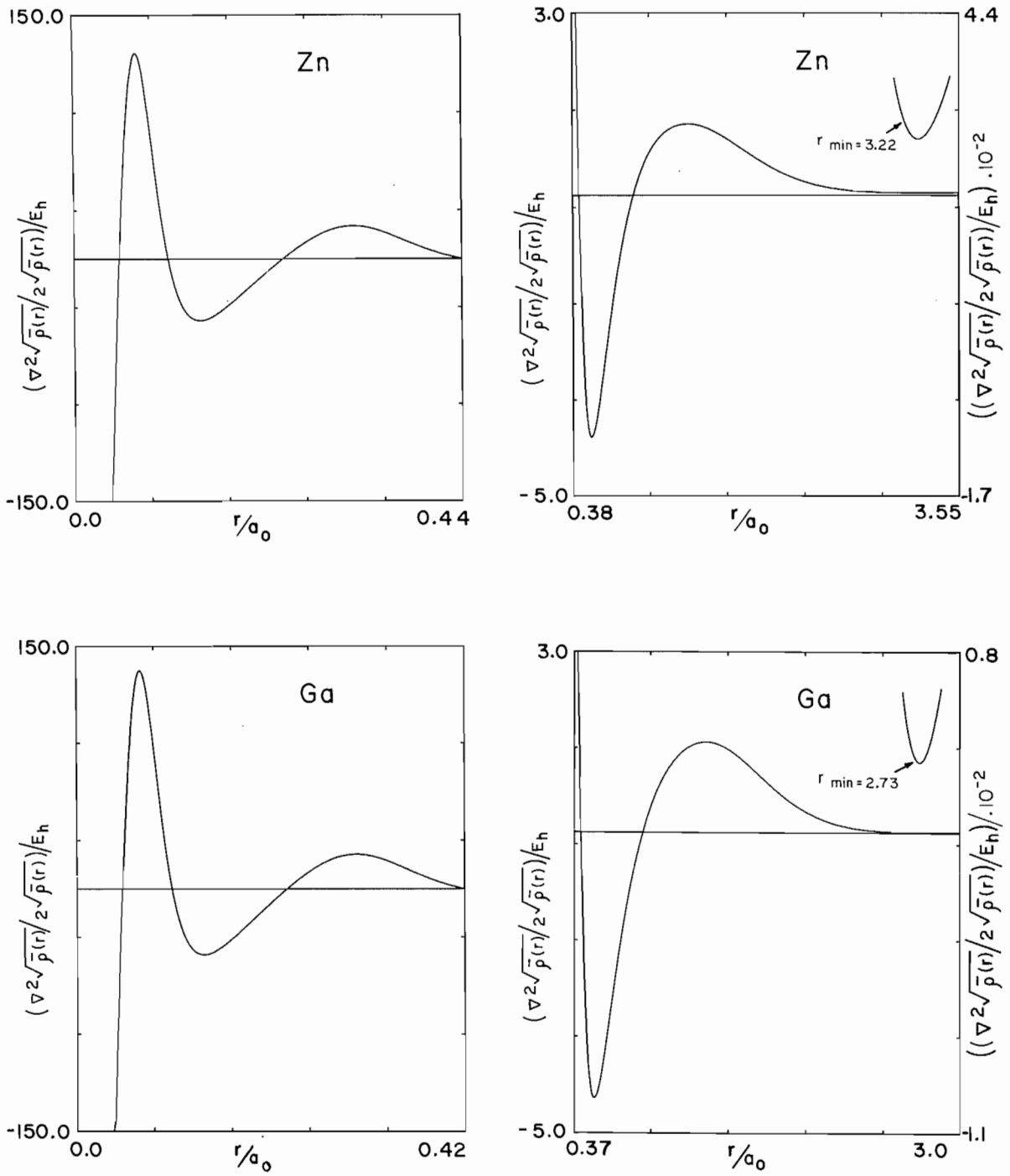

FIG. 1. The one-electron potential, $\nabla^2\sqrt{\bar{\rho}}(r)/2\sqrt{\bar{\rho}}(r)$, for the neutral atoms zinc ($Z = 30$) and gallium ($Z = 31$).

potential exhibits a number of zeros, maxima and minima, with the absolute value of the function becoming smaller at each successive extremal point. As $r \rightarrow \infty$, the potential $\{U(r) - E\}$ has the ionization potential of the system as its asymptotic value (3).

The topology of this potential greatly resembles that of $\nabla^2\bar{\rho}(r)$ (10), but differs in that the relative magnitudes of $\nabla^2\sqrt{\bar{\rho}}(r)/2\sqrt{\bar{\rho}}(r)$ from a particular maxima to a successive minima are not as great as that displayed by $\nabla^2\bar{\rho}(r)$.

The positions of the extrema in $\nabla^2\sqrt{\bar{\rho}}(r)/2\sqrt{\bar{\rho}}(r)$ are plotted against atomic number Z, for the atoms in Fig. 3 and the ions in Fig. 4. The extrema arbitrarily assigned to a particular shell have been joined in order to guide the eye, with the thicker lines corresponding to the maxima and the thinner ones to the minima. The first maximum shall be arbitrarily denoted as the K shell, with successive maxima denoted as L, M, N, etc. the minima located between two maxima will be denoted by the two letters corresponding to the two maxima between which the particular minimum is situated. These minima shall be arbitrarily considered to be reflections of regions between the shells, i.e. an intershell region.

As was previously demonstrated (8, 10) plots of this nature should yield roughtly first order hyperbolae according to the simple hydrogenic model (i.e. Bohr theory of an atom) which

Can. J. Chem. Downloaded from www.nrcresearchpress.com by 176.9.209.113 on 09/07/12
For personal use only.

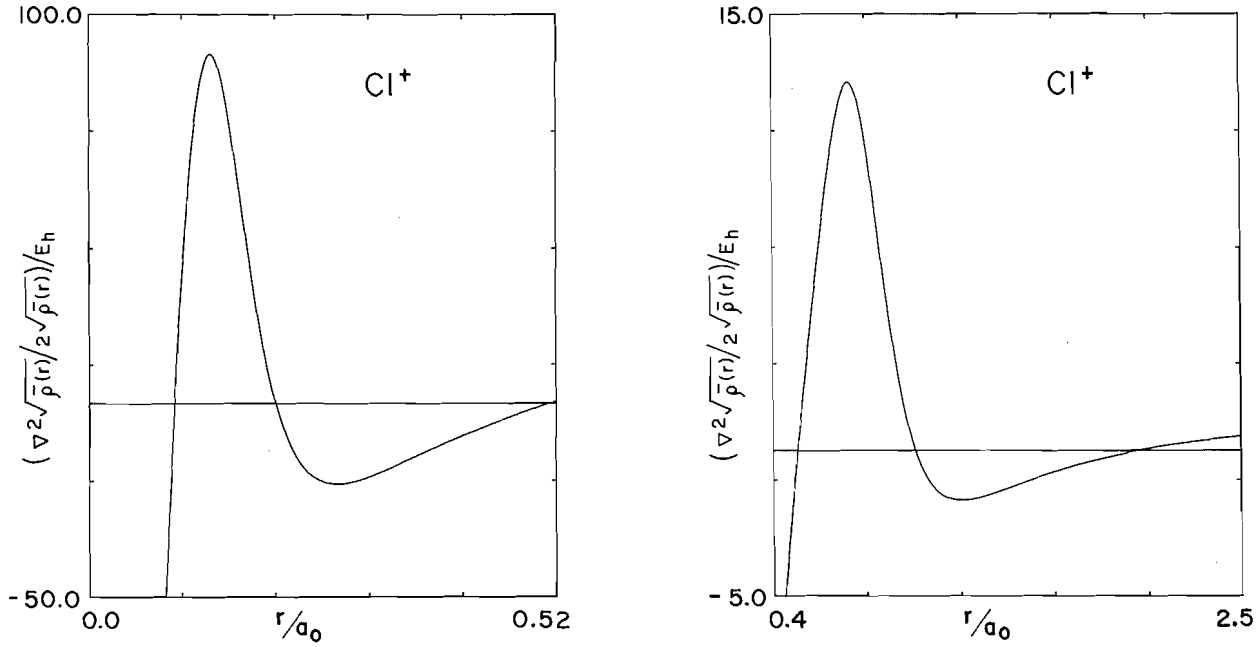

FIG. 2. The one-electron potential, $\nabla^2\sqrt{\bar{\rho}}(r)/2\sqrt{\bar{\rho}}(r)$, for the singly positive ion Cl^+ ($Z = 17$).

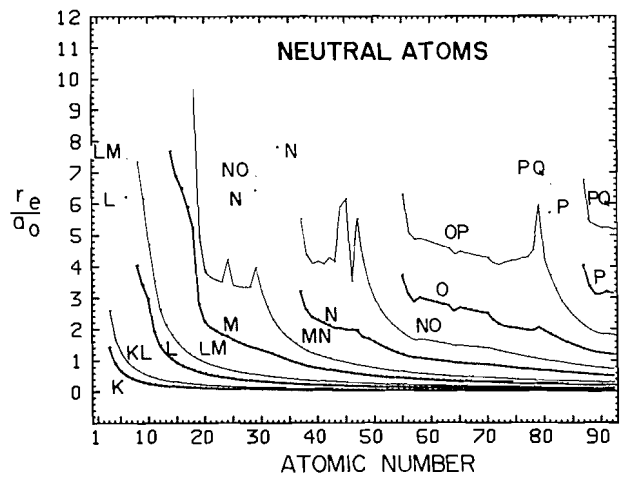

FIG. 3. The positions of the extrema of the one-electron potential $\nabla^2\sqrt{\bar{\rho}}(r)/2\sqrt{\bar{\rho}}(r)$, as a function of atomic number Z, for the neutral atoms. Those values belonging to a particular extremum (i.e. 1st, 2nd, 3rd) have been connected. The thicker lines connect those r-values for the maxima which have been arbitrarily classified acording to each shell (e.g. K, L, M, ---) while the thinner ones connect the minima that have been arbitrarily classified according to an intershell region (e.g. KL, LM, MN, etc.). Note that in this and the following figures the lines joining the points have no physical significance and are merely meant to guide the eye.

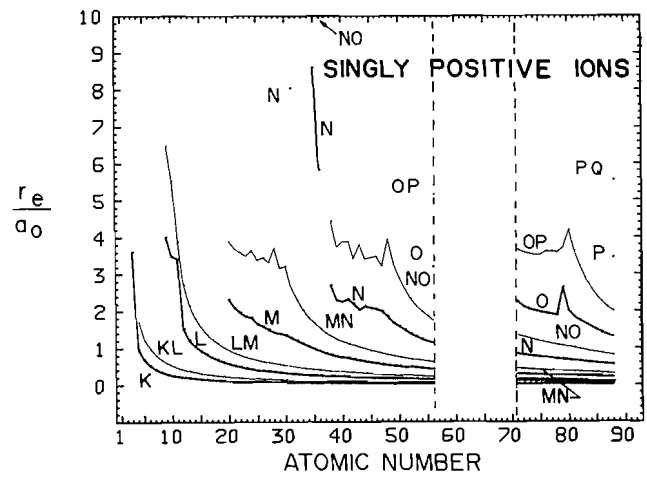

FIG. 4. The positions of the extrema of the one-electron potential $\nabla^2\sqrt{\bar{\rho}}(r)/2\sqrt{\bar{\rho}}(r)$, as a function of the atomic number Z, for the singly positive ions. Those values belonging to a particular extremum (i.e. 1st, 2nd, 3rd) have been connected. The thicker lines connect those r-values for the maxima which have been arbitrarily classified according to each shell (e.g. K, L, M, ---) while the thinner ones connect the minima that have been arbitrarily classified according to an intershell region (e.g. KL, LM, MN, etc.). Note that the gap $57 \leqq Z \leqq 70$ is due to the unavailability of published wavefunctions for ions with open f-shells.

specifies shells with radii equal to

$$[14] \quad \left(\frac{n^2}{Z}\right)\left(\frac{\hbar^2}{m_e e^2}\right)$$

where $\hbar$, m_e, e are the Planck–Dirac constant, mass and charge of the electron, respectively. However, it may be seen in Figs. 3 and 4 that there are significant deviations from a hyperbolic form, with the deviations becoming larger in the case of the outermost minima.

An examination of Fig. 3 also indicates that the L shell and the LM intershell region appear at the carbon atom ($Z = 6$) and are present for all atoms in the range ($6 \leqq Z \leqq 92$) with the only exception being the nitrogen atom. The N shell and the NO intershell regions are present for the range ($29 \leqq Z \leqq 92$) with breaks occurring at ($29 < Z < 33$) and ($33 < Z < 37$). The P shell and PQ intershell regions are present in the range ($81 \leqq Z \leqq 92$) with the only break occurring in the interval ($81 < Z < 87$). The remainder of the shell and intershell regions display no breaks, i.e. once a particular shell or intershell region is present at some value of the atomic number Z, it will remain present for all other

Can. J. Chem. Downloaded from www.nrcresearchpress.com by 176.9.209.113 on 09/07/12
For personal use only.

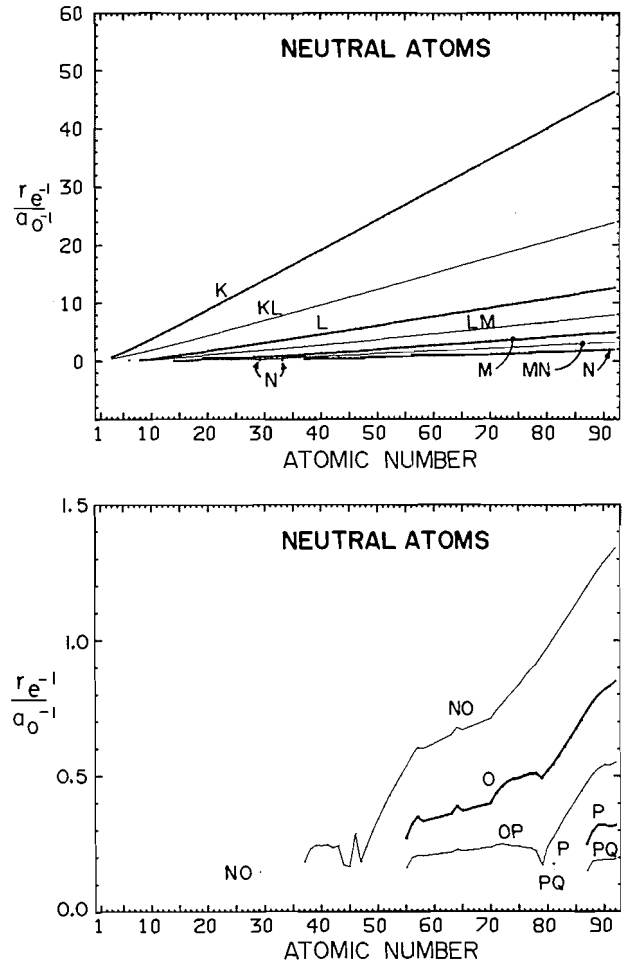

FIG. 5. Inverses of the positions of the extrema of the one-electron potential, $\nabla^2\sqrt{\bar{\rho}}(r)/2\sqrt{\bar{\rho}}(r)$, as a function of the atomic number Z, for the neutral atoms. Those values belonging to a particular extremum (i.e. 1st, 2nd, 3rd, etc.) have been connected. The thicker lines connect those r-values for the maxima which have been arbitrarily classified according to each shell (e.g. K, L, M, ---) while the thinner ones connect the minima that have been arbitrarily classified according to an intershell region (e.g. KL, LM, MN, etc.).

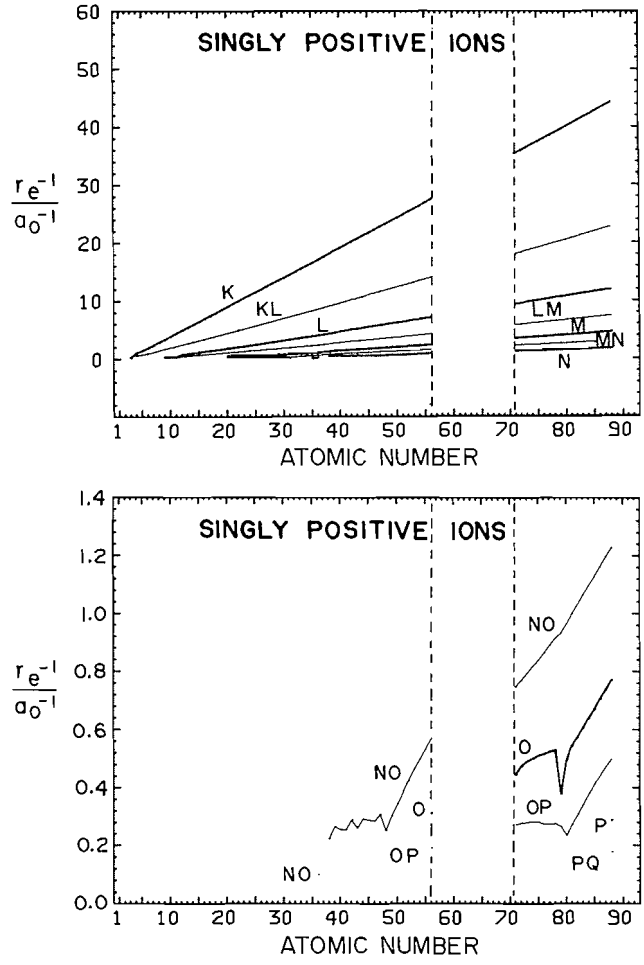

FIG. 6. Inverses of the positions of the extrema of the one-electron potential, $\nabla^2\sqrt{\bar{\rho}}(r)/2\sqrt{\bar{\rho}}(r)$, as a function of the atomic number Z, for the singly positive ions. Those values belonging to a particular extremum (i.e. 1st, 2nd, 3rd, etc.) have been connected. The thicker lines connect those r-values for the maxima which have been arbitrarily classified acording to each shell (e.g. K, L, M, ---) while the thinner ones connect the minima that have been arbitrarily classified according to each intershell region (e.g. KL, LM, MN, etc.). Note that the gap $57 \leqq Z \leqq 70$ is due to the unavailability of published wavefunctions for ions with open f-shells.

values of atomic number $Z' > Z$. It should be noted from Fig. 3 that there are at most twelve extrema displayed by $\nabla^2\sqrt{\bar{\rho}}(r)/2\sqrt{\bar{\rho}}(r)$ while a previous study on $\nabla^2\bar{\rho}(r)$ reported nine extrema at most (10).

For the ions, inspection of Fig. 4 indicates that the N shell is present in the interval ($31 \leqq Z \leqq 90$) for the ions studied, with a break occurring at ($31 < Z < 35$) and at ($35 < Z < 38$). The NO intershell region is present in the interval ($36 \leqq Z \leqq 90$) with the only break occurring at $Z = 37$. The O shell and the OP intershell region appear simultaneously in the interval ($51 \leqq Z \leqq 90$) with the assumption that these features are present in the interval ($51 < Z < 71$) where no data is available.

Figures 5 and 6 are plots of the inverses of the curves in Figs. 3 and 4 for the atoms and the ions, respectively. The large deviations from linearity in Figs. 5(b) and 6(b) where these curves correspond to the outermost extrema, i.e. at large r, is indicative of the failure of the Bohr theory at large r. Electronic shielding, previously explored (8) with regard to $D(r)$, can be used to explain why the curves in Figs. 5(a) and 6(a) exhibit marked linearity even though the curves in Figs. 3 and 4 show deviations from hyperbolae. Equation [14] indicates that if shielding were present, i.e. $Z = Z - s$, where s is a shielding parameter, then the intercepts and not the slopes would be affected. A least-squares fit was performed on the data points in Figs. 5(a) and (b) and figs. 6(a) and (b) for the atoms and the ions with the determined parameters tabulated in Tables 1 and 2 for the atoms and the ions, respectively. The values which are close to unity for R^2, the square of the correlation coefficient, for the extrema closer to the nucleus is supportive of the graphical evidence in Figs. 5(a) and 6(a) for the atoms and the ions. The comparatively large deviation from unity in R^2 for the curves in Figs. 5(b) and 6(b) supports the observation that the outer extrema are not directly related to the Bohr theory of an atom.

A similar analysis to that performed on the extrema was done for the zeros of $\nabla^2\sqrt{\bar{\rho}}(r)/2\sqrt{\bar{\rho}}(r)$. These results are presented in Figs. 7–10 for the neutral atoms and the ions. Inspection of Fig. 7 shows that there are at most thirteen zeros present for an atom in comparison with the maximum number of nine zeros previously reported for $\nabla^2\bar{\rho}(r)$ (10). These plots have been labelled according to the arbitrarily selected convention that the

Can. J. Chem. Downloaded from www.nrcresearchpress.com by 176.9.209.113 on 09/07/12
For personal use only.

TABLE 1. Data[a] from a linear least-squares fitting of the data points in the curves of Figs. 5(*a*) and (*b*) for the neutral atoms

Extrema of $\nabla^2\sqrt{\bar{\rho}}(r)/2\sqrt{\bar{\rho}}(r)$	A	B	R^2	Y	S_{yx}
1st	0.517	−1.43	1.00	23.1	0.133
2nd	0.267	−0.909	1.00	11.8	0.135
3rd	0.149	−1.22	0.999	6.14	0.0859
4th	0.0930	−0.850	0.998	3.75	0.101
5th	0.0629	−1.05	0.994	2.28	0.115
6th	0.0438	−0.862	0.994	1.55	0.0755
7th	0.0285	−0.755	0.991	1.05	0.0462
8th	0.0204	−0.634	0.966	0.667	0.0653
9th	0.0141	−0.534	0.911	0.504	0.0497
10th	0.00876	−0.355	0.686	0.289	0.0668
11th	0.0143	−0.976	0.899	0.285	0.0190
12th	0.00446	−0.216	0.669	0.178	0.0125

[a]The following definitions have been used: slope, A; y-intercept, B; square of the correlation coefficient, R^2; average y-value, $\bar{Y}$; standard deviation, S_{yx}.

TABLE 2. Data[a] from a linear least-squares fitting of the data points in the curves of Figs. 6(*a*) and (*b*) for the singly positive ions[b]

Extrema of $\nabla^2\sqrt{\bar{\rho}}(r)/2\sqrt{\bar{\rho}}(r)$	A	B	R^2	Y	S_{yx}
1st	0.513	−1.33	1.00	14.9	0.0996
2nd	0.263	−0.805	0.999	7.67	0.117
3rd	0.148	−1.22	1.00	3.92	0.0549
4th	0.0897	−0.769	0.998	2.36	0.0605
5th	0.0597	−0.975	0.988	1.45	0.0930
6th	0.0420	−0.806	0.982	0.897	0.0802
7th	0.0278	−0.740	0.972	0.605	0.0534
8th	0.0173	−0.474	0.943	0.388	0.0455
9th	0.00991	−0.245	0.981	0.429	0.0134
10th	0.00524	−0.0998	0.999	0.256	0.00142

[a]The same definitions have been used as in Table 1.
[b]Note that no fitting was performed for the 11th and 12th extrema since these are only present for Ra^+ ($Z = 88$) in the cases studied.

odd-numbered zeros (i.e. 1st, 3rd, etc.) be denoted as the shells and the even numbered zeros (i.e. 2nd, 4th, etc.) be denoted as an intershell region. The intershell regions have been labelled with two letters, with the first corresponding to the shell indicative of the $(n-1)$ zero and the second letter corresponding to the shell indicative of the $(n+1)$ zero, where n is the even-numbered zero being labelled. Figure 7 illustrates that while there are no breaks in the curves for the K, L, M shells and the KL, LM intershell regions, the MN intershell region and the N shell are present in the period ($19 \leqq Z \leqq 92$) but are not present in the intervals ($23 < Z < 25$) and ($25 < Z < 32$). The NO intershell region and the O shell are present in the period ($37 \leqq Z \leqq 92$) with a large break occurring in the interval ($39 < Z < 50$). The OP intershell region and the P shell are present in the period ($55 \leqq Z \leqq 92$) with a break occurring at ($72 < Z < 83$). As was previously noted for the case of the outer extrema, deviations from a hyperbolic form are also more evident for the outer zeros, i.e. as the distance from the nucleus increases. This further validates the notion that the topology of the potential $\nabla^2\sqrt{\bar{\rho}}(r)/2\sqrt{\bar{\rho}}(r)$ is dependent upon the extent of electronic shielding in a particular atom or ion. Most interestingly, these breaks are seen to occur in regions where the *d*-orbitals of the next innermost shell are being filled. Hence, the outermost shell is not visible.

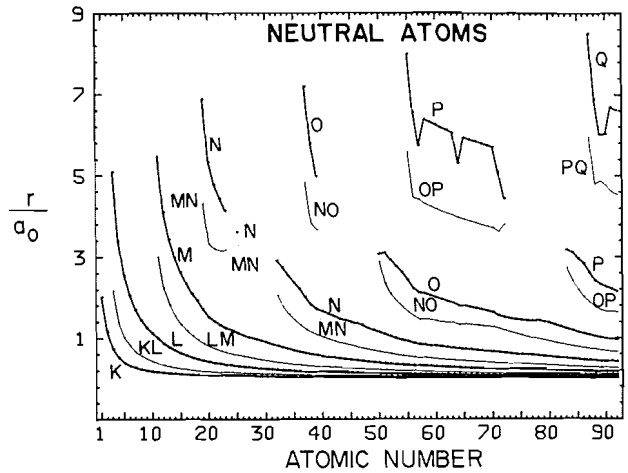

FIG. 7. The positions of the zeros in the one-electron potential, $\nabla^2\sqrt{\bar{\rho}}(r)/2\sqrt{\bar{\rho}}(r)$, as a function of the atomic number Z, for the neutral atoms. Those values belonging to a particular zero (i.e. 1st, 2nd, 3rd) have been connected. The thicker lines connect those r-values for the odd numbered zeros (1st, 3rd, etc.) which have been arbitrarily classified according to each shell (e.g. K, L, M, ---) while the thinner ones connect the even numbered zeros (2nd, 4th, etc.) that have been arbitrarily classified according to each intershell region (e.g. KL, LM, MN, etc.).

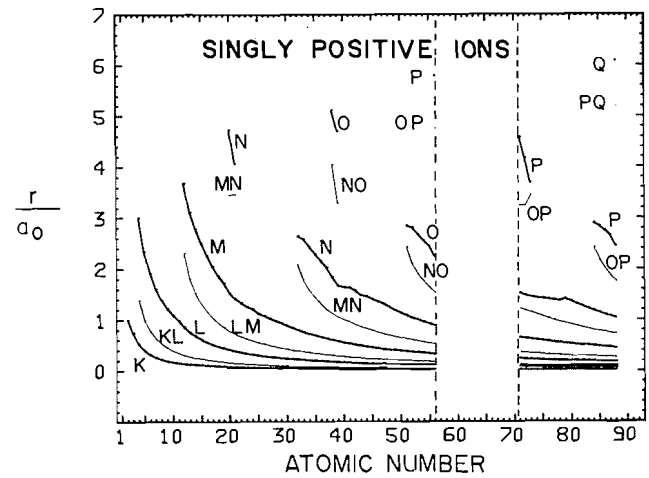

FIG. 8. The positions of the zeros of the one-electron potential $\nabla^2\sqrt{\bar{\rho}}(r)/2\sqrt{\bar{\rho}}(r)$, as a function of atomic number Z for the singly positive ions. Those values belonging to a particular zero (i.e. 1st, 2nd, 3rd) have been connected. The thicker lines connect those r-values for the odd numbered zeros (1st, 3rd, etc.) which have been arbitrarily classified according to each shell (e.g. K, L, M, ---) while the thinner ones connect the even numbered zeros (2nd, 4th, etc.) and have been arbitrarily classified according to each intershell region (e.g. KL, LM, MN, etc.). Note that the gap $57 \leqq Z \leqq 70$ is due to the unavailability of wavefunctions with open *f*-shells.

Figure 8 for the singly positive ions indicates that there are at most thirteen zeros present for the studied cases in comparison to the nine reported for $\nabla^2\bar{\rho}(r)$. The MN intershell region and the N shell are present in the period ($20 \leqq Z \leqq 90$) with a break occurring in the interval ($21 < Z < 32$). The NO intershell region and the O shell are present in the period ($38 \leqq Z \leqq 90$) with a break occurring at ($39 < Z < 51$). Consequently the OP intershell region and the P shell are present in the period ($56 \leqq Z \leqq 90$) with a break occurring at ($73 < Z < 84$). Figures 9 and 10 are the inverses of the curves presented in Figs. 7 and 8

Can. J. Chem. Downloaded from www.nrcresearchpress.com by 176.9.209.113 on 09/07/12
For personal use only.

Can. J. Chem. Downloaded from www.nrcresearchpress.com by 176.9.209.113 on 09/07/12
For personal use only.

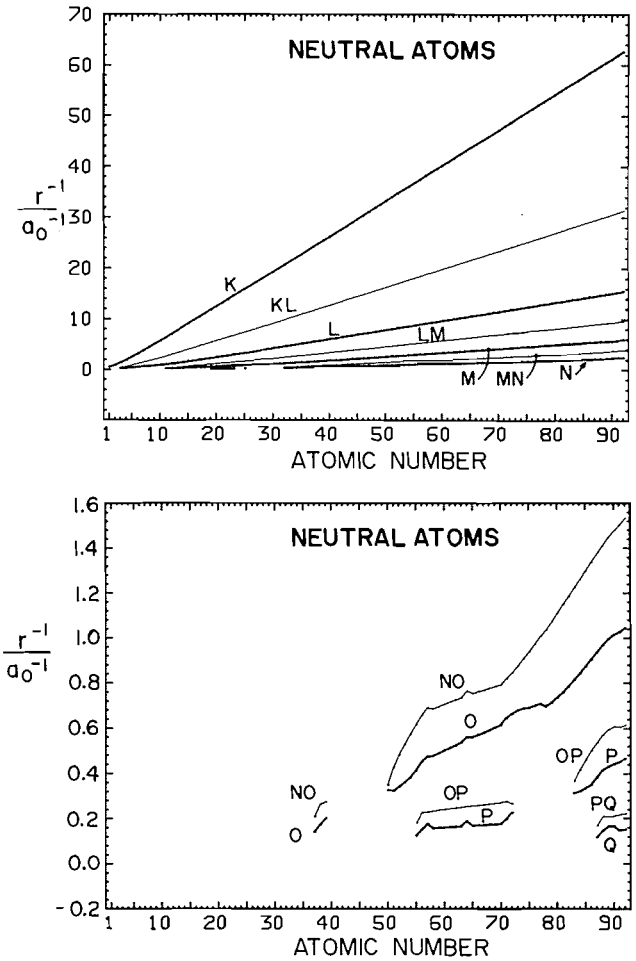

FIG. 9. The inverses of the positions of the zeros of the one-electron potential, $\nabla^2\sqrt{\bar{\rho}}(r)/2\sqrt{\bar{\rho}}(r)$, as a function of atomic number Z for the neutral atoms. Those values belonging to a particular zero (1st, 2nd, 3rd, etc.) have been connected. The thicker lines connect those r-values for the odd numbered zeros (1st, 3rd, etc.) which have been arbitrarily classified according to each shell (e.g. K, L, M, ---) while the thinner ones connect the even numbered zeros (2nd, 4th, etc.) that have been classified according to each intershell region (e.g. KL, LM, MN, etc.).

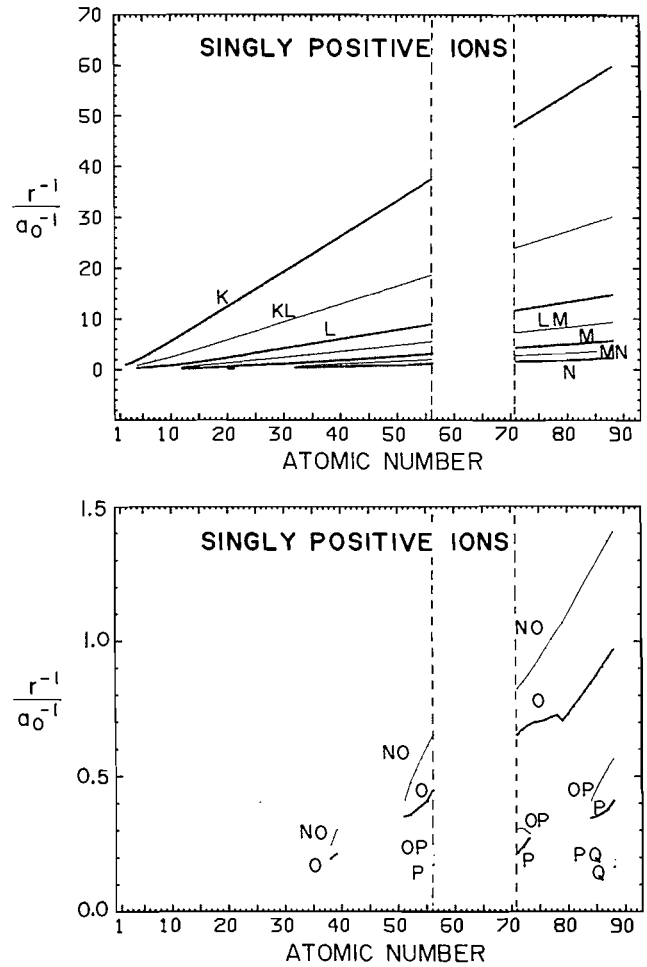

FIG. 10. The inverses of the positions of the zeros of the one-electron potential, $\nabla^2\sqrt{\bar{\rho}}(r)/2\sqrt{\bar{\rho}}(r)$, as a function of atomic number Z for the singly positive ions. The values belonging to a particular zero (1st, 2nd, 3rd, etc.) have been connected. The thicker lines connect those r-values for the odd numbered zeros (1st, 3rd, etc.) which have been arbitrarily classified according to each shell (e.g. K, L, M, ---) while the thinner ones connect the even numbered zeros (2nd, 4th, etc.) that have been arbitrarily classified according to each intershell region (e.g. KL, LM, MN, etc.). Note that the gap $57 \leqq Z \leqq 70$ is due to the unavailability of wavefunctions with open f-shells.

for the neutral atoms and the singly positive ions, respectively. Examination of Figs. 9(a) and 10(a) shows that there is marked linearity for the zeros closer to the nucleus, but the results in Figs. 9(b) and 10(b) are indicative that the Bohr theory of an atom fails more drastically at larger distances from the nucleus than at closer distances. Tables 3 and 4 contain the parameters from a least-squares linear regression analysis of the data points in Figs. 9(a) and (b) and Figs. 10(a) and (b), respectively. The values of close to unity for the square of the correlation coefficient for the inner zeros are supportive of the observed linearity, while the deviations from unity of the outer zeros further compliments the evidence of large deviations from the Bohr theory of an atom at larger values of r.

The classically allowed and forbidden regions model suggests that a shell may be defined as an interval where $\nabla^2\sqrt{\bar{\rho}}(r)/2\sqrt{\bar{\rho}}(r)$ is correspondingly negative and positive. Thus, the topological features present in this interval may be indicative of shell structure. Figures 7 and 8 show that all shells are present when the odd-numbered zeros are chosen as the topological feature indicative of a shell. Furthermore, these zeros appear at

TABLE 3. Data[a] from a linear least-squares fitting procedure of the data points in the curves of Figs. 9(a) and (b) for the neutral atoms

Zeros of $\nabla^2\sqrt{\bar{\rho}}(r)/2\sqrt{\bar{\rho}}(r)$	A	B	R^2	Y	S_{yx}
1st	0.692	−1.26	1.00	30.9	0.202
2nd	0.353	−1.18	1.00	15.6	0.136
3rd	0.178	−0.989	0.999	7.47	0.155
4th	0.117	−1.16	0.999	4.89	0.0803
5th	0.0733	−0.959	0.994	2.81	0.136
6th	0.0527	−1.06	0.993	2.02	0.0905
7th	0.0317	−0.635	0.987	1.21	0.0745
8th	0.0233	−0.721	0.959	0.880	0.0714
9th	0.0155	−0.445	0.979	0.622	0.0336
10th	0.0111	−0.451	0.901	0.348	0.0470
11th	0.00871	−0.378	0.919	0.250	0.0331
12th	0.00836	−0.543	0.676	0.205	0.0121
13th	0.00509	−0.307	0.286	0.149	0.0168

[a]The same definitions have been used as in Table 1.

TABLE 4. Data[a] from a linear least-squares fitting of the data points in the curves of Figs. 10(*a*) and 10(*b*) for the singly positive ions

Zeros of $\nabla^2\sqrt{\bar{\rho}}(r)/2\sqrt{\bar{\rho}}(r)$	A	B	R^2	Y	$S_{y,x}$
1st	0.686	−1.15	1.00	20.3	0.168
2nd	0.349	−1.09	1.00	10.2	0.116
3rd	0.174	−0.896	0.997	4.72	0.158
4th	0.114	−1.06	0.998	3.09	0.0737
5th	0.0671	−0.767	0.988	1.67	0.120
6th	0.0506	−1.005	0.983	1.29	0.0855
7th	0.0284	−0.518	0.975	0.768	0.0589
8th	0.0175	−0.398	0.962	0.579	0.0440
9th	0.0143	−0.365	0.992	0.432	0.0165
10th	0.00562	−0.103	0.918	0.280	0.0165
11th	0.00464	−0.0901	0.806	0.226	0.0224

[a]The same definitions have been used as in Table 1.
[b]Note that no fitting was performed for the 12th and 13th zeros since these are only present for Ra^+ ($Z = 88$) in the studied cases.

precisely the atomic number predicted by the aufbau principle. In this manner the zeros of $\nabla^2\sqrt{\bar{\rho}}(r)/2\sqrt{\bar{\rho}}(r)$ would seem to be an indicative feature of shell structure within this framework.

Conclusions

The number of topological features (zeros, extrema) exhibited by the potential $\nabla^2\sqrt{\bar{\rho}}(r)/2\sqrt{\bar{\rho}}(r)$ are greater than the number displayed in $\nabla^2\bar{\rho}(r)$ and $D(r)$ for the larger atoms and ions. This means that a comparatively larger number of shells are visible in the potential. These features are seen to show significant deviations from the Bohr–Schrödinger theory which become greater for the outer extrema and zeros, i.e. as the distance from the nucleus increases. There are also breaks present in the curves of the positions of a particular zero or extremum plotted against atomic numbers. These breaks correspond to a particular topological feature being present at some atomic number Z, but then not being present at some higher atomic number Z'. They are seen to coincide with the filling of the d-orbitals corresponding to the next innermost shell. $\nabla^2\bar{\rho}(r)$ was shown to exhibit no breaks in the curves pertaining to the zeros, however breaks were observed in the curves of the extrema (9).

The fact that the computed potential $\nabla^2\sqrt{\bar{\rho}}(r)/2\sqrt{\bar{\rho}}(r)$ involves the use of a non-linear operator makes it difficult to perform a shell by shell analysis of this potential. This reasoning casts doubts on its ability to reveal the shell structure of an atom or an ion, if a shell is defined within the independent particle model as the set of those orbitals possessing the same principal quantum number. However, within the framework of classically allowed and forbidden regions, $\nabla^2\sqrt{\bar{\rho}}(r)/2\sqrt{\bar{\rho}}(r)$ is shown to correctly represent all shells, at the precise value of the atomic number predicted by the aufbau principle, when the odd-numbered zeros are used as the feature indicative of a shell.

Acknowledgements

This research was supported in part by the Natural Sciences and Engineering Research Council of Canada (NSERCC) and also by the Conselho Nacional de Desenvolvimento Cientifico e Technologico (CNPq – Brasil). The helpful comments of the referees are gratefully acknowledged.

1. R. G. PARR. Ann. Rev. Phys. Chem. **34**, 631 (1983).
2. A. J. COLEMAN. Rev. Mod. Phys. **35**, 668 (1963); J. E. HARRIMEN. *In* Density matrices and density functionals. *Edited by* R. Erdahl and V. H. Smith, Jr. Reidel, Dordecht. 1987. pp. 359–373.
3. G. HUNTER. Int. J. Quantum Chem. **29**, 197 (1986); *In* Density matrices and density functionals. *Edited by* R. Erdahl and V. H. Smith, Jr. Reidel, Dordrecht, 1987. pp. 583–596; E. N. LASSETTRE. J. Chem. Phys. **83**, 1709 (1985); M. LEVY, J. P. PERDEW, and V. SAHNI. Phys. Rev. A **30**, 2745 (1984); N. H. MARCH. Int. J. Quantum Chem. Quantum Biol. Symp. **13**, 3 (1986).
4. G. HUNTER. Int. J. Quantum Chem. **9**, 237 (1975).
5. H. WEINSTEIN, P. POLITZER, and S. SREBENIK. Theoret. Chim. Acta, (Berlin), **38**, 159 (1975).
6. J. T. WABER and D. T. CROMER. J. Chem. Phys. **42**, 4116 (1965).
7. R. J. BOYD. J. Phys. B, **9**, L69 (1976).
8. A. M. SIMAS, R. P. SAGAR, A. C. T. KU, and V. H. SMITH, JR. Can. J. Chem. In press.
9. A. M. SIMAS, W. M. WESTGATE, and V. H. SMITH, JR. J. Chem. Phys. **80**, 2636 (1984).
10. R. P. SAGAR, A. C. T. KU, V. H. SMITH, JR., and A. M. SIMAS. J. Chem. Phys. In press.
11. R. F. W. BADER and H. ESSEN. J. Chem. Phys. **80**, 1943 (1984).
12. E. CLEMENTI and C. ROETTI. Atom. Data Nucl. Data Tables, **14**, 177 (1974).
13. A. D. MCLEAN and R. S. MCLEAN. Atom. Data Nucl. Data Tables, **26**, 197 (1981).
14. W. M. WESTGATE, A. D. BYRNE, V. H. SMITH, JR., and A. M. SIMAS. Can. J. Phys. **64**, 1351 (1986) and references therein.

Can. J. Chem. Downloaded from www.nrcresearchpress.com by 176.9.209.113 on 09/07/12
For personal use only.

Calorimetric study of the acidity of Y-zeolites treated with silicon tetrachloride

ZHI CHENG SHI
Research Institute of Petroleum Processing, P.O. Box 914, Beijing, China

AND

ALINE AUROUX[1] AND YOUNES BEN TAARIT
Institut de recherches sur la catalyse, Centre national de la recherche scientifique, 2, Avenue A. Einstein, 69626 Villeurbanne CEDEX, France

Received September 3, 1987

This paper is dedicated to Professor James A. Morrison

ZHI CHENG SHI, ALINE AUROUX, and YOUNES BEN TAARIT. Can. J. Chem. **66**, 1013 (1988).

The acidity of synthetic HY samples dealuminated with silicon tetrachloride vapour at various temperatures is investigated using microcalorimetry. The work covers sample preparation, characterization, and acidic properties. The differential heats of ammonia adsorption versus coverage and the acidity spectra are described. The catalytic performance is measured in the hydrogen transfer reaction.

ZHI CHENG SHI, ALINE AUROUX et YOUNES BEN TAARIT. Can. J. Chem. **66**, 1013 (1988).

L'acidité d'échantillons de zéolithes HY désaluminées par traitement par $SiCl_4$ vapeur à différentes températures est déterminée essentiellement par microcalorimétrie. Ce travail recouvre la préparation, les caractéristiques et les propriétés acides de ces échantillons. Les chaleurs différentielles d'adsorption d'ammoniac en fonction du recouvrement ainsi que les spectres d'acidité sont présentés. Les performances catalytiques sont mesurées à partir d'une réaction de transfert d'hydrogène.

Can. J. Chem. Downloaded from www.nrcresearchpress.com by 176.9.209.113 on 09/07/12
For personal use only.

Introduction

Faujasite is one of the most open-structured zeolites. This important class of materials has been widely used in commercial chemical processes as well as in the petroleum industry. However, it is difficult to synthesize Y-type faujasite with a Si/Al ratio greater than 3. In the last few years the aluminium-deficient zeolites have been found to have increased chemical and thermal stability. To prepare and study aluminium-deficient zeolites, several techniques are now proposed for their preparation by dealumination of the low Si/Al analogs.

Recently Scherzer reviewed the important processes used in this field (1). Among them, dealumination by silicon tetrachloride vapour has become more and more popular because of its simplicity as a laboratory procedure. Furthermore, it has been reported that dealumination by $SiCl_4$ effects the removal of structural aluminium from any cationic form of Y-zeolite without excessive loss of crystallinity (2, 3).

The present work will deal in detail with dealuminated Y-zeolite with Si/Al ratios up to 60. The work covers sample preparation, characterization, and acidic properties.

Experimental

Sample preparation

The parent zeolite used is Na-Y-zeolite from the Linde Division of Union Carbide Corporation, with a unit cell formula $Na_{56}(AlO_2)_{56}(SiO_2)_{136}$ and a Si/Al ratio of about 2.4. The NaY samples were calcinated at 400°C under a stream of dry nitrogen to ensure thorough dehydration and possibly dehydroxylation of residual silanol groups.

The dealumination procedure used in our study follows that proposed by Beyer and Belenykaja (3): the dehydrated samples were heated in the flow of a $SiCl_4 + N_2$ mixture obtained by bubbling dry N_2 through a saturator containing liquid $SiCl_4$ maintained at 0°C. The extent of dealumination was controlled by monitoring the temperature of the substitution reaction, which can be written as:

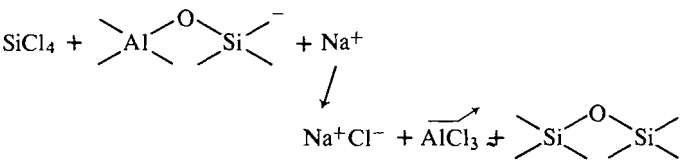

The reaction was allowed to continue for 1 h and the sample was then flushed for an additional 2-h period at the same temperature to remove excess reagent and possibly volatile reaction products. The substitution reaction temperature was varied between 250 and 450°C. At this latter temperature, total dealumination was eventually achieved.

The samples were subsequently cooled down to room temperature and divided into two parts. One part was washed by deionized water. The other part was boiled in an acidic (HCl) solution at a pH of 2 for 30 min (4). The operation was repeated 3 times. The samples washed only by deionized water were further subjected to ion exchange with NH_4Cl.

Structural characterization

Beyer reported (3) that during the dealumination reaction using $SiCl_4$, only part of the aluminium that leaves the framework positions escapes in the form of volatile aluminium chloride. $Na(AlCl_4)$, which is not volatile under the reaction conditions and is formed by melting NaCl with $AlCl_3$, remains in the zeolite cavity. Thus, in most cases, at least part of the extra-framework aluminium will be found with the dealuminated zeolite (5, 6).

Since these two kinds of aluminium have different properties, it is essential to know the distribution between the framework and the extra-framework aluminium.

Recent advances in ^{29}Si solid-state and ^{27}Al solid-state nmr have made possible the accurate determination of the framework aluminium content in faujasite-type zeolites (7). In the absence of solid-state nmr facilities, it is desirable to have other methods of estimating the framework aluminium. Fortunately, it has long been recognized that for a faujasite-type zeolite the unit cell size decreases with increasing Si/Al ratio (8).

Applications of infrared spectroscopy to zeolite structural problems have also been reviewed (9). The frequency shift of infrared stretching-mode bands with variation of the Si/Al ratio is known. A nearly linear decrease is shown for the position of the main asymmetric stretch band near 980–1100 cm^{-1}. Since the masses of Al and Si atoms are nearly the

[1]Author to whom correspondence may be addressed.

TABLE 1. Structural analysis of zeolite samples

Sample	Preparation temperature (°C)	Acid leaching	Unit cell constant a_0(Å)	Infrared frequency (cm^{-1})	Framework Al per unit cell			Si/Al ratio			Extra-framework Al
					n.Al, X-ray	*n*.Al, ir	*n*.Al, nmr	nmr	X-ray	Infrared	
S-200	200	No	24.54	1047	32	30	37	4.25	4.94	5.3	No
S-250	250	No	24.48	1053	26	26	30	5.45	6.41	6.4	No
S-300	300	No	24.46	1059	24	21	27	6.36	7.06	8.1	No
S-350	350	No	24.43	1065	20	17	20	9.49	8.32	10.6	No
S-375	375	No		1080		5	7			36.6	No
S-450	450	No		1083	2	3	5	37.1			No
SH-200	200	Yes	24.36	1058	13	22	29	5.72	13.6	7.7	Yes
SH-250	250	Yes	24.44	1056	22	24	28	5.89	7.8	7.2	Yes
SH-300	300	Yes	24.42	1061	20	20	24	7.25	8.8	8.7	Yes
SH-350	350	Yes	24.35	1067	12	15	21	9.02	15	11.7	Yes
SH-375	375	Yes		1080							Yes
SH-450	450	Yes	24.27	1083	3	3	3	59.9	55.4	66.8	Yes

same, the decrease in frequency with increasing Al concentration appears to be related to the variation in bond length and bond order. The increased length of Al—O bonds and decreased electronegativity of Al atoms result in a decrease in the force constant.

Correlations between the Si/Al ratio and ir absorptions and unit cell dimensions, using nmr data as the primary means, have been provided (10).

In our study ^{29}Si and ^{27}Al solid-state nmr were employed to determine the framework Si/Al ratio and we also utilized X-ray powder diffraction and ir to monitor the Si/Al ratios of the samples. For the ir structural analysis the zeolite wafer was prepared in a metallurgical die. The total wafer weighed 0.3 g, mixed with KBr. The percentage of the zeolite in a wafer was 0.1%. Before analysis by X-ray diffraction the zeolite sample was saturated with water at room temperature for 24 h.

Surface acid characterization

Many methods have been evolved for measuring the nature and the number of acid sites. Methods have been developed that distinguish between Brönsted and Lewis sites (11, 12) while others measure the total amount and distribution of various acid sites present.

Microcalorimetric measurements, associated with spectroscopic methods, appear to be the most reliable method to date to fully characterize the acidity of solid materials both qualitatively (nature, strength) and quantitatively (number, strength distribution, etc.). Strong bases such as piperidine, pyridine, ammonia, and butylamine have been used to determine the adsorption heats on zeolite HY (13–15).

In this study, microcalorimetry was employed to measure the acid sites quantitatively and also to determine their distribution. Dry ammonia was used as the molecular basic probe. Ammonia was adsorbed at 150°C to prevent physisorption. The zeolite sample in powder form, approximately 60 mg in weight, was pretreated in a quartz cell, first with oxygen by heating at 2°C per minute and holding at 350°C for about 4 h and then under vacuum (1.33 mPa) at the desired temperature (350°C or 600°C) for about 2 h. The pretreated sample was transferred to a SETARAM Tian–Calvet microcalorimeter of the twin conduction type maintained at constant temperature (150°C). The gaseous probe was then admitted to the zeolite sample in successive small doses of ~0.04 cm^3, the gas pressure before expansion and at equilibrium being measured for every dose by a Datametrics Barocel gauge of maximum pressure 200 Pa. Both the gas pressure and the thermogram were monitored graphically for every dose to determine the sorption equilibrium. The sorption process was followed both volumetrically and calorimetrically (with facilities for automation and computer processing) up to a final pressure of ca. 150 Pa.

Catalytic reaction

The hydrogen transfer reaction was selected as a catalytic test reaction, cyclohexene being employed as the reaction agent. We used a flowing type reactor with hydrogen as flowing gas.

Since the samples deactivate very quickly, after every 20 s of reaction time, the reaction was stopped by passing only the flowing gas through the reactor without the cyclohexene. The sample weighed about 50 mg. The gas flow was 3 L per hour, and the reaction temperature was 250°C. The reaction proceeded until the sample became stable. The products were analysed by chromatography.

Results and discussion

Structural analysis

Table 1 gives the results of structural analysis. The numbers in the first column (S-200, etc.) express the temperature of the dealumination reaction and thus represent degree of dealumination.

The results of the X-ray powder diffraction analysis show that all samples maintain good crystallinity, and that with increase of the Si/Al ratio the unit cell constant decreases.

The results of the ir spectra in the structural region also show the dependence of the ir wavenumber on the Si/Al ratio. With the increase of ir frequency, the Si/Al ratio increases. These results are in good agreement with those of the nmr analysis. Samples shown in the upper part of Table 1 were washed only by deionized water after the dealumination reaction; those shown in the lower part were subjected to acid leaching. It is interesting to note that ^{27}Al solid-state nmr shows that there is almost no extra-framework aluminium in samples washed by deionized water, in contrast to the samples leached with acid in which some extra-framework aluminium continues to be present.

Originally we hoped that acid leaching would remove the extra-framework aluminium formed during the dealumination process from the zeolite cavity without influencing the framework aluminium. In fact the acid leaching further removed the structural aluminium. The aluminium produced during acid leaching becomes the extra-framework aluminium remaining in the zeolite cavities. Probably these extra-framework aluminium atoms are retained in small cavities, so that they are difficult to remove.

Surface acid characterization

Figure 1 presents the curves of differential heats of NH_3 adsorption versus the adsorbed ammonia volume for the samples washed with deionized water, pretreated at 350°C before adsorption at 150°C. When the Si/Al ratio increases to a certain degree the initial differential heat increases. This means that more strong acid sites are formed. This is the case for S-200–S-375, which show initial heat increasing from 170 to 215 kJ

Can. J. Chem. Downloaded from www.nrcresearchpress.com by 176.9.209.113 on 09/07/12
For personal use only.

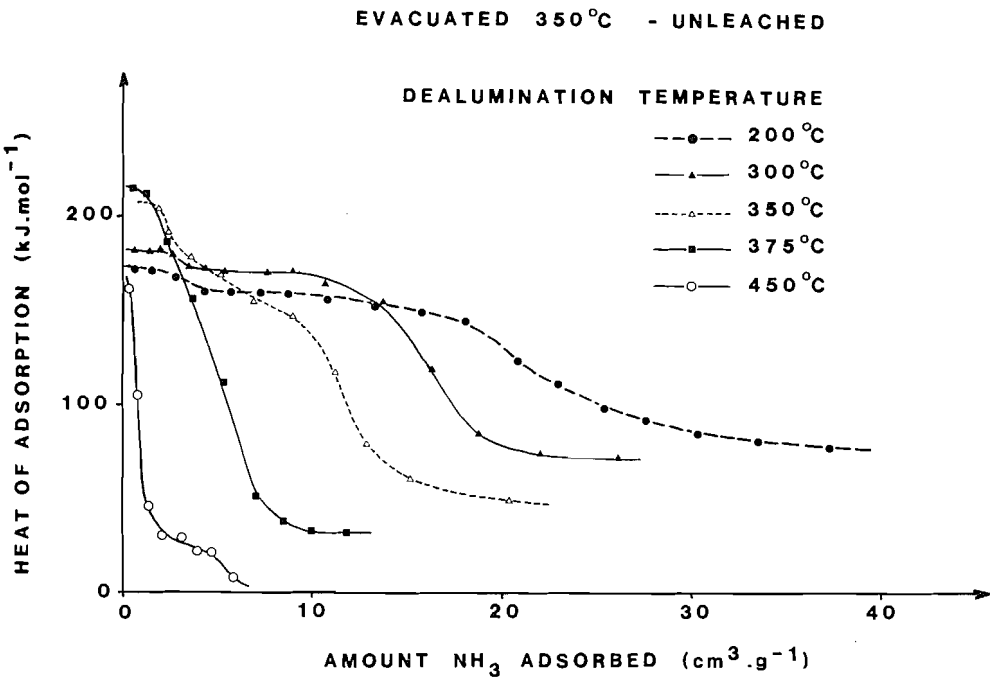

FIG. 1. Differential heats of adsorption of NH_3 versus coverage on dealuminated and unleached Y-zeolites. The temperatures indicated represent the temperature of dealumination.

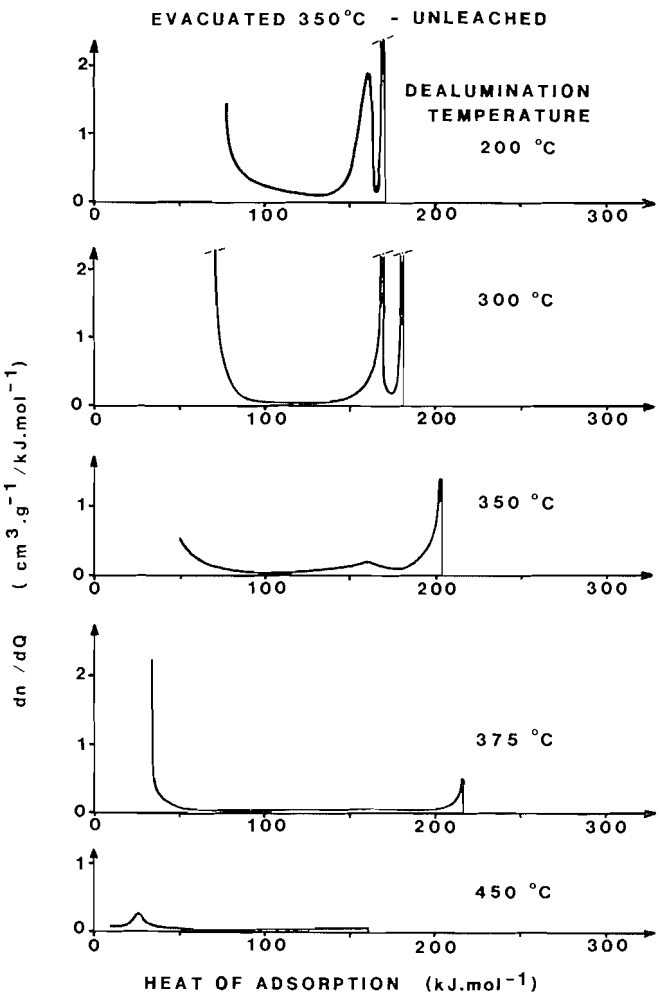

FIG. 2. Acidity spectra of dealuminated and unleached H-Y samples.

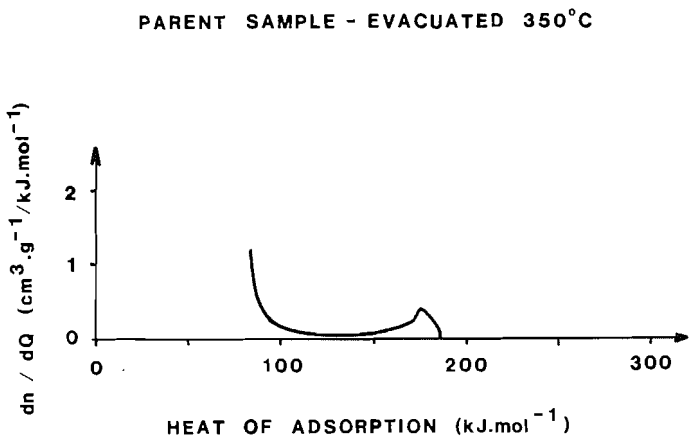

FIG. 3. Acidity spectrum of parent H-Y sample.

mol^{-1}. But for S-450 the initial differential heat decreases due to the excess dealumination. One should also notice that plain samples exhibited, for a given sample, essentially constant differential heats over a wide range of coverage with ammonia.

For a better appreciation of the acid strength scatter, Fig. 2 shows dn/dQ as a function of Q for the same samples. The vertical and horizontal coordinates stand for the numbers and the strengths of acid sites, respectively. It is found that after treatment at 350°C all samples except S-375 (and evidently S-450) show two peaks between 150 and 210 kJ mol^{-1}.

This behaviour is quite different from that of the parent sample, which has only one peak in the same range (see Fig. 3). Table 2 gives the positions of the two peaks (a) and (b). With increasing Si/Al ratio, the primary peak (a) first shifts to the right and then to the left. For sample S-350 this peak is rather flat. The second peak (b) always moves to the right with increasing Si/Al ratio. Referring to another study in ir spectroscopy, of the adsorption/desorption of pyridine onto the same samples (to

Can. J. Chem. Downloaded from www.nrcresearchpress.com by 176.9.209.113 on 09/07/12
For personal use only.

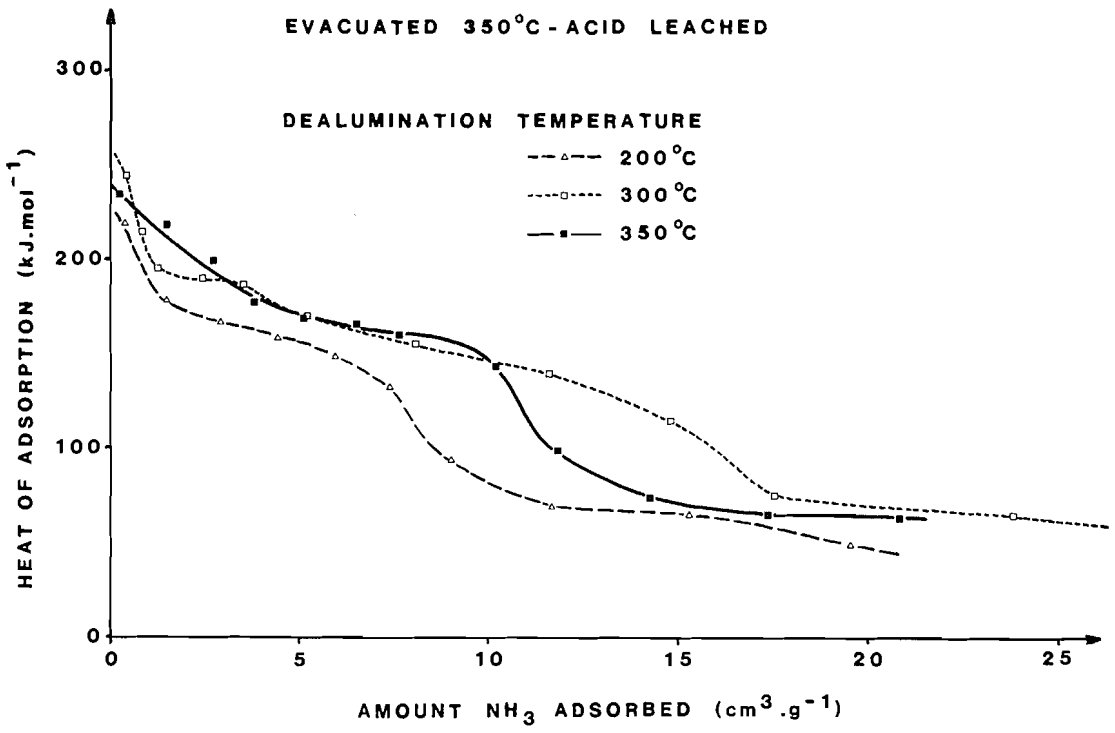

FIG. 4. Differential heats of adsorption of NH_3 versus coverage on dealuminated and acid leached Y-zeolites. The temperatures indicated represent the temperature of dealumination.

TABLE 2. Distribution of acid sites for samples without acid leaching, pretreated at 350°C

	Sample					
	S-200	S-300	S-350	S-375	S-450	Parent zeolite
Si/Al (nmr)	4.26	6.36	9.49	36.6	37.1	2.43
Peak (a) position (kJ mol^{-1})	160	169	160*	—	—	—
Peak (b) position (kJ mol^{-1})	170	181	203	215	—	176

*The peak is not very prominent.

TABLE 3. Distribution of acid sites for acid-leached samples, pretreated at 350°C

	Sample			
	SH-200	SH-300	SH-350	Parent zeolite
Si/Al (nmr)	5.72	7.25	9.02	2.43
Peak (a) position (kJ mol^{-1})	160	158	160	—
Peak (b) position (kJ mol^{-1})	—	188	—	176

be published), it is suggested that the primary peak and the secondary peak should be attributed to 3640 cm^{-1} and 3540 cm^{-1} hydroxyl stretch modes, respectively.

Samples that have been acid leached (Fig. 4) show an additional feature in the histogram: the initial heats of NH_3 adsorption are essentially higher than usual for Brönsted-type acidity. Samples SH-200–SH-300 show initial heat between 220 and 240 kJ mol^{-1}. Moreover, the differential heats for a given sample decrease steadily until the value of the plateau characteristic of the unleached analogue is reached. It again seems reasonable to ascribe this behaviour to the presence of a pure zeolitic phase coexisting with an extra-framework aluminium phase having Lewis-type acidity characteristics. The corresponding acidity spectra of these acid-leached samples are given in Fig. 5 and the energy of the observed peaks is given in Table 3.

Catalytic reaction

The catalytic activity of samples was determined with respect to the cyclohexene transformation at 250°C. Under these conditions the cyclohexene reacts as follows:

Hydrogen transfer reaction:

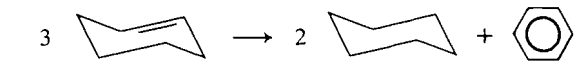

Isomerization:

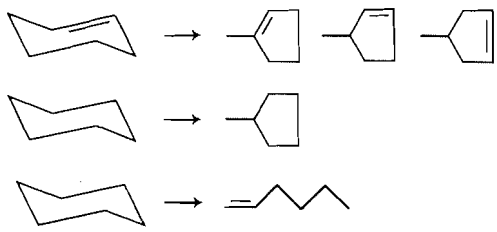

Can. J. Chem. Downloaded from www.nrcresearchpress.com by 176.9.209.113 on 09/07/12
For personal use only.

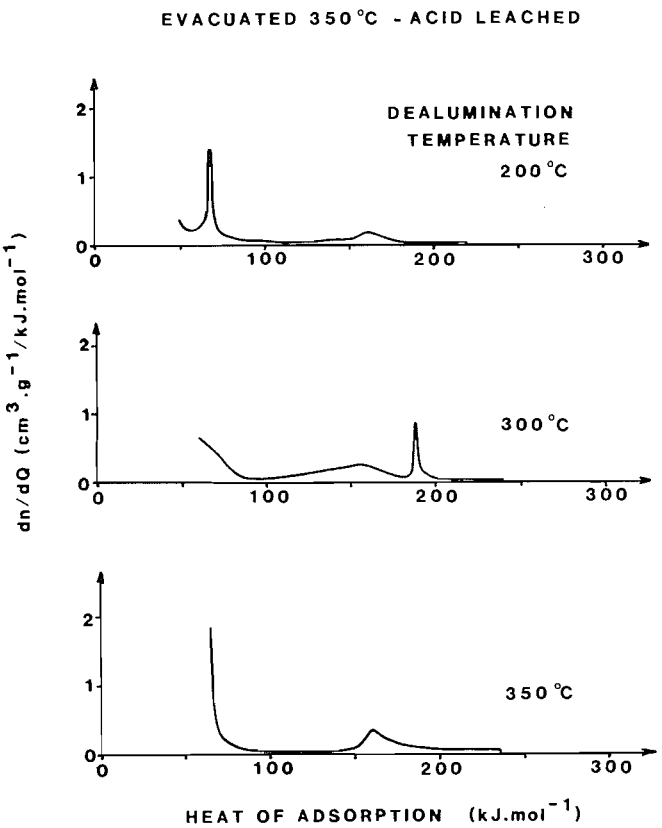

FIG. 5. Acidity spectra of dealuminated and acid leached H-Y samples.

All the compounds mentioned above are found in the product stream. From the reaction mechanism we can distinguish between intramolecular hydrogen transfer and intermolecular hydrogen transfer. Cyclohexane is considered as the product from intermolecular reaction and methylcyclopentene as that from intramolecular reaction. Methylcyclopentane and hexene can result from both intermolecular and intramolecular reaction. Table 4 shows the variation of selectivity at a conversion level of 23% for samples with different lattice aluminium content. The selectivity of the intermolecular reaction decreases and the selectivity of intramolecular reaction increases with decrease of lattice aluminium because the lower acid site density favors the intramolecular reaction.

Conclusions

1. Dealumination by $SiCl_4$ at moderate temperatures produces Y-zeolite having increased Si/Al ratio with good crystallinity and without having significant extra-framework aluminium.

2. The zeolite is always sensitive to acid. Acid leaching will probably remove framework aluminium.

3. Catalytic reaction of cyclohexene shows that the selectivity of both intermolecular and intramolecular hydrogen transfer reactions depends on the composition of the samples.

4. During dealumination, the type, number, and acidity of the OH groups varies. The total acidity for a certain zeolite depends on the nature, the strength, and the number of the acid sites. There is a maximum value of total acidity; microcalorimetric measurements show that it occurs at a Si/Al ratio of about 7 (sample S-300).

TABLE 4. Variation of selectivity on dealumination at isoconversion (conversion level 23%)

	Sample				
	S-200	S-350	SH-350	S-375	S-450
n lattice Al (nmr)	37	20	21	7	5
Selectivity, intermolecular	89	75	75	57	53
Selectivity, intramolecular	10	25	25	43	47

1. J. SCHERZER. J. Catal. **54**, 285 (1978).
2. V. BOSACEK *et al.* J. Catal. **61**, 435 (1980).
3. H. K. BEYER and I. BELENYKAJA. *In* Catalysis by zeolites. *Edited by* B. Imelik *et al.* Elsevier, Amsterdam. 1980. pp. 5, 203.
4. C. Y. LI and L. V. C. REES. Zeolites, **6**, 51 (1986).
5. C. V. MCDANIEL and P. K. Maher. *In* Molecular sieves. Soc. Chem. Ind., London. 1968. p. 186.
6. P. FEJES, I. HANNUS, and I. KIRICSI. Zeolites, **4**, 73 (1984).
7. J. HARTMAN. J. Chem. Soc. Faraday Trans. **78**, 1025 (1982).
8. V. ANDERA *et al.* Zeolites, **5**, 67 (1985).
9. E. M. FLANIGEN. A.C.S. Monogr. **179**, 85 (1984).
10. J. R. SOHN, S. J. DECANIO, J. H. LUNSFORD, and D. J. O'DONNELL. Zeolites, **6**, 255 (1986).
11. J. WARD. A.C.S. Monogr. **171**, 118 (1976).
12. M. W. ANDERSON and J. KLINOWSKI. Zeolites, **6**, 455 (1986).
13. Y. MITANI, K. TSUTSUMI, and H. TAKAHASHI. Bull. Chem. Soc. Jpn. **56**, 1917 (1983).
14. A. L. KLYACHKO, T. R. BRUEVA, I. V. MISHIN, G. I. KAPUSTIN, and A. M. RUBINSTEIN. Acta Phys. Chem. **24**, 183 (1978).
15. R. D. SHANNON, K. H. GARDNER, R. H. STALEY, G. BERGERET, P. GALLEZOT, and A. AUROUX. J. Phys. Chem. **89**, 4778 (1985).

Can. J. Chem. Downloaded from www.nrcresearchpress.com by 176.9.209.113 on 09/07/12
For personal use only.

Molecular dynamics simulation of the phase transition in adamantane

A. S. TREW AND G. S. PAWLEY
Department of Physics, University of Edinburgh, King's Buildings, Edinburgh EH9 3JZ, U.K.

Received November 2, 1987

This paper is dedicated to Professor J. A. Morrison

A. S. TREW and G. S. PAWLEY. Can. J. Chem. **66**, 1018 (1988).

Phase changes in adamantane have been studied by MD simulation on the DAP computers, using a zero-pressure technique to simulate clusters of 128 and 256 molecules where each member interacts with all others via the rigid molecule model and the 6-exp atom–atom potential. The form of the potential has been modified to permit the use of the 16 hydrogen sites only, giving a 65% saving in the calculation times. This model is shown to give lattice dynamics of adamantane closely similar to results with potentials which are generally accepted.

Using this potential the system equilibrates into the correct low temperature phase ($P\bar{4}2_1c$) and on heating, a transition is observed at 210 ± 10 K to an $Fm3m$ phase where the molecules lie preferentially in the T_d orientations, as expected. Further heating beyond 240 ± 15 K removes all apparent orientational order, though the underlying lattice is still fcc. On recooling the cluster from 300 to 100 K the orientational distribution function developed a significant degree of order as determined through the calculation of a correlation function designed to show any local order. This order is consistent with the lowest phase structure, but would in itself be insufficient to suggest a particular crystal structure.

A. S. TREW et G. S. PAWLEY. Can. J. Chem. **66**, 1018 (1988).

Dans le but d'étudier les changements de phase de l'adamantane, on a fait appel à une simulation MD sur des ordinateurs DAP et on a utiliser une technique à pression zéro pour simuler des agrégats de 128 et 256 molécules dans lesquels chaque membre interagit avec tous les autres par le biais d'une molécule modèle et par le potentiel atome–atome au 6-exp. On a modifié la forme du potentiel pour permettre l'utilisation de seulement 16 sites d'hydrogène et on a ainsi sauvé 65% du temps de calcul. On démontre que ce modèle fournit des dynamiques du réseau de l'adamantane qui sont très semblables aux résultats obtenus avec des potentiels qui sont généralement acceptés.

Lorsqu'on utilise ce potentiel, le système s'équilibre et, à basse température, il atteint la bonne phase ($P\bar{4}2_1c$) par chauffage, on observe une transition à 210 ± 10 K qui conduit à une phase $Fm3m$ dans laquelle les molécules se trouvent préférentiellement, tel qu'attendu, dans les orientations T_d. Si on continue le chauffage au-delà de 240 ± 15 K, tout ordre apparent d'orientation est éliminé même si le réseau sous-jacent est encore fcc. En refroidissant l'agrégat de 300 à 100 K, la fonction de distribution de l'orientation présente un degré important d'ordre qui a été déterminé par le biais de calculs de la fonction de corrélation développée pour mettre en évidence l'ordre local. Cet ordre est en accord avec la structure de la phase la plus basse; toutefois, cet ordre serait insuffisant pour suggérer une structure cristalline particulière.

[Traduit par la revue]

Can. J. Chem. Downloaded from www.nrcresearchpress.com by 176.9.209.113 on 09/07/12
For personal use only.

Introduction

There has been considerable interest for some time in the study of plastic crystals and their phase changes. Experimental measurements of deuterated adamantane using neutron coherent inelastic scattering when compared with model lattice dynamics calculations (1) suggested that simple atom–atom potentials would be appropriate for modelling. The use of these potential functions for molecular dynamics (MD) was then suggested as the obvious way to model the plastic phase. The computing power available at the time of these experiments was not sufficient for a serious attempt at a MD simulation, but now that very cost-effective computation can be done with parallel computers the problem becomes viable. In this paper we present the results of a MD investigation of the phase transition of adamantane in its deuterated form ($C_{10}D_{16}$) using the ICL Distributed Array Processor (DAP) (2).

A somewhat simpler problem was chosen to test the MD method for the modelling of plastic to crystalline phase transitions before embarking on adamantane. SF_6 was chosen because of its smaller size, and a simulation of a sample of 4096 molecules was done on the DAP. It was obvious at the outset that the conditions required of such phase transition studies included the control of the pressure of the system. A zero pressure simulation soon yielded a transition to a crystalline phase (3) which has now been shown to be found in nature (4). Another necessary condition for a physically acceptable simulation is that the behaviour of the sample should not be determined by the boundary conditions, whatever these conditions may be. For SF_6 these were cyclic conditions, and there was clearly no finite-size artefact as the crystal phase developed as a mass of crystallites. A similar study of the phase transition in *n*-butane (5) using the stress-free algorithm of Parrinello and Rahman (6) and recent unpublished work on adamantane both failed to give lower crystal phases, and another method is now sought to avoid any sample constraints resulting from cyclic conditions.

Adamantane, or tricyclo-(3,3,1,1)-decane is one of the best known of plastic crystals. It has been extensively studied experimentally (1, 7) and computationally (1, 8). It is a globular molecule displaying tetrahedral symmetry T_d consisting of an octahedron formed by six methylene groups from which four methine groups extend. X-Ray diffraction studies (9, 10) show that at low temperatures the crystal has a $P\bar{4}2_1c$ space group with $a = b = 6.60$ A, $c = 8.81$ Å, while above 208.6 K it transforms to a plastic phase with space group $Fm3m$, $a = 9.45$ Å. In the low temperature phase the molecules are oriented at an angle of 9° relative to the *a* or *b* axes (9) while in the plastic phase they are randomly distributed between the two T_d orientations (10). This is a rotationally frustrated state and so individual molecules will alternate dynamically between the two orientations. In addition, an ordered structure with space group $F43m$ has been reported at room temperature (11) but this is somewhat controversial and is thought to be due to the unusual annealing conditions for the crystals studied (10). The triple point of adamantane is 543 K but it sublimes easily even at room temperature as we find with our simulations.

We have chosen to perform MD calculations on a free cluster

Can. J. Chem. Downloaded from www.nrcresearchpress.com by 176.9.209.113 on 09/07/12
For personal use only.

in order to remove as much as possible the constrictions of boundaries. The simulation is therefore stress-free; the gain in avoiding self-image boundary condition artefacts is off-set to some extent by having a large fraction of the sample molecules involved with the cluster surface. Nevertheless we expect that our experience with SF_6 clusters containing similar numbers of molecules will be reflected in the adamantane simulations (12). For a sample of 128 SF_6 molecules a phase change was clearly observed on cooling, this transition being exactly as observed in the cyclic boundary 4096 molecule simulation and was achieved in a fraction of the computer time. Diffraction patterns from larger cluster simulations of SF_6 have been compared with electron diffraction results using similar sized clusters, and give excellent agreement (13). These results lead us to conclude that there is a good proportion of molecules in orientations as found in the bulk, and that cluster simulations are well suited to the search for the solid state phase transitions we wish to study.

Earlier experiments had failed to find non-crystallographic structures from this molecular system (14), in contrast to the results from atomic clusters (15). Simulations have been done in search of icosahedral structures in very small molecular (16, 17) and atomic (16, 18) systems, on 2-dimensional (19) and 3-dimensional (20) atomic liquid clusters, and on water (21) using the model of Stillinger and Rahman (22).

Thus although the simulation of clusters is now new, their use in the search for bulk properties in the solid has been neglected. Although the quantity of bulk material is reduced in free clusters, the method gives the possibility of studying other phenomena. Surface effects are an obvious area of study, but any defect in the bulk can now be studied, from vacancies and interstitials to twinning and grain boundaries. The technique is surprisingly efficient on the DAP. Nevertheless, it is a computationally intensive method for very large systems when all possible interactions are calculated, and this usually limits the size of the cluster to a few hundred molecules. Algorithms giving more efficiency for the very large systems will require more computer storage than is currently readily available; storage will certainly increase in future machines and the method will become more generally feasible.

The simulations

The calculations were performed on the two ICL DAPs at Edinburgh University. These machines are SIMD arrays of 64 × 64 interconnected processing elements and are very well suited to problems which involve the calculation of many-body interactions. The present problem runs with about 90% efficiency. The DAP has a speed of 20 Mflops but as such figures are always misleading we prefer to state that in this type of work the DAP is roughly 30% more powerful than a Cray-1 running an appropriate algorithm (D. Tildesley, private communication).

To form the cluster, a spherical sample of molecules is created in the required initial crystalline state. Molecules are given translational and orientational order but with random linear and angular velocities obeying a gaussian distribution for the prescribed temperature. The interaction between each pair of atoms belonging to different molecules is then calculated and hence the resultant forces and torques on each molecule. These may then be used to predict the next configuration. Time integration is accomplished by use of the Beeman algorithm (23). This method is well known and extensively used and gives good energy stability in our calculations, provided that the time-step chosen is not too large. For all of this work, except immediately after initialisation of a new cluster, we have used a time-step of 0.015 ps. The systematic energy fluctuation is then typically at most 1 part in 10^6 per time-step. This is close to the precision expected from arithmetic round-off in performing the calculations.

Restrictions on the amount of computer time available effectively determine the number of molecules in the system. Clusters with 128 adamantane molecules were chosen as the largest practicable for general investigations on the ICL DAP. However, we have also performed a number of simulations with 256 molecules and find that there is no qualitative difference in the results from these and the smaller systems. This is in agreement with previous investigations of SF_6 (12) by the cluster method which showed that the phases and transitions produced were independent of the number of molecules but that transition temperatures increased with cluster size.

A brief description of how the DAP is used to perform these calculations will help in understanding the applicability of SIMD computers to these problems. For our 128 molecule problem let us think of the molecule information arranged as 128 component vectors both along and top and down the side of a 128 × 128 matrix. The components of this matrix can be used to contain the interaction between the row and column molecules, and the total force and torque on a particular molecule can then be found by summing the interactions by rows (or indeed by columns). Row summation is particularly easy on the DAP, as also is the row and column broadcasting needed before calculating the interactions at the various matrix elements. The matrix elements are the processing elements (PEs) of the DAP, and as the DAP has only 64 × 64 PEs (32 × 32 in the AMT DAP 510), the mapping just described has to be done in stages, but this gives us the opportunity of avoiding most of the double calculation implicit in the description above. In fact it is easy to avoid all double calculation except for the case where the number of molecules is N for a $N \times N$ DAP. For other mapping strategies the reader is referred to a paper devoted to SIMD mapping (24).

Let us now return to the adamantane simulations. As with previous investigations (1, 8) we assume a rigid molecule interacting via the 6-exp pairwise additive potential

$$[1] \quad V(i,j) = -A_{ab} r_{ij}^{-6} + B_{ab} \exp(-C_{ab} r^{ij})$$

where a and b indicate the species of the atoms at sites i and j, and r_{ij} is the distance between two atoms belonging to different molecules. Several studies have been undertaken to measure the A, B, and C parameters for the H—H, C—H, and C—C interactions, most notably by Williams (25) and Kitaigorodskii (26), both of which give similar lattice dynamics (cf. Figs. 1 and 2). In these calculations the deuterated form of the molecule is used but the standard H—H potential is assumed for D—D. Because of the large amount of computation necessary for a complex molecule such as adamantane we have derived a modified H—H potential which when used on its own for adamantane gives the lattice dynamics of Fig. 3. The corresponding modes are easily identified, and the frequencies for the "reduced" potential are nicely bracketed by those of Williams and Kitaigorodskii. The rationale behind the simplification of the potential is that the molecule trajectories are principally determined by the interactions between the deuteriums, and the interactions involving the carbon atoms, being somewhat screened by the deuteriums, do not contribute significantly to the motion. The immediate consequence of this modification is that it permits the use of a "reduced molecule" of 16 atoms thus diminishing the amount of computation by a factor of $(26/16)^2$. The smaller cluster there-

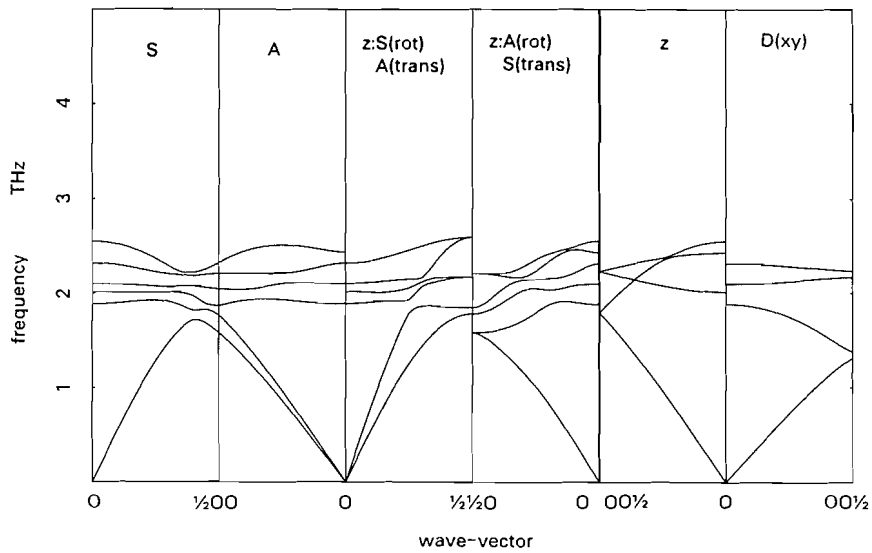

FIG. 1. Lattice dynamics calculations for the $P\bar{4}_1c$ phase of deuterated adamantane using the Williams (24) potential. The first four sections show the modes with wave-vectors in the ***a*–*b*** plane, the last two sections show modes with wave-vectors along the ***c*** axis. For (ξ00) modes S and A mean, respectively, symmetric and antisymmetric with respect to the diad axis perpendicular to ***c***. The representations for the (ξξ0) modes are distinguished by the *z* rotational and translational eigenvector components; when the former are symmetric, *S*(rot), then the latter are antisymmetric, *A*(*trans*), and vice versa. At (1/2, 1/2, 0) there are two representations, both doubly degenerate, in which *z* rotation and translation only occur in the two branches which are continuous over this boundary. For (00ξ), *z* denotes modes with eigenvectors along the ***c*** axis, *D*(*xy*) means a double degeneracy with eigenvectors in the ***a*–*b*** plane.

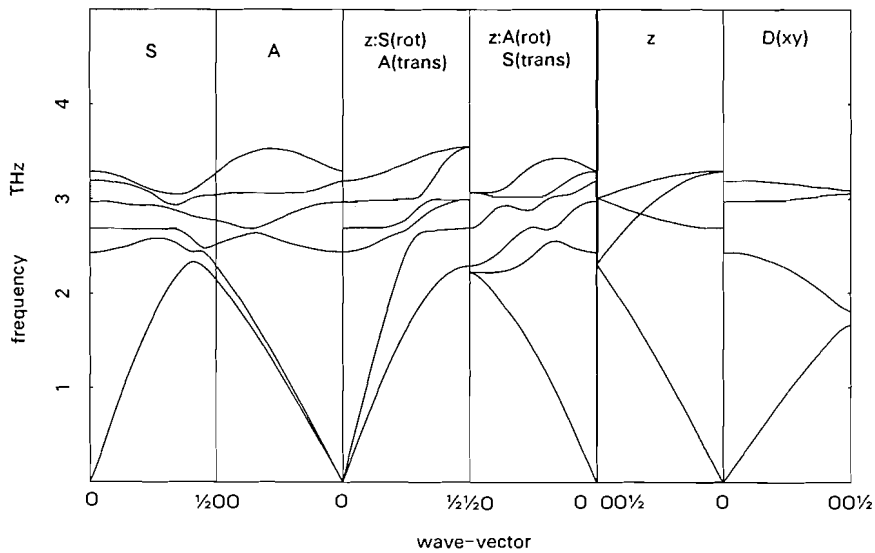

FIG 2. Lattice dynamics calculations for the $P\bar{4}_1c$ phase of deuterated adamantane using the Kitaigorodskii (25) potential. The representations correspond to Fig. 1.

fore necessitates the calculation of $16^2 \times 128^2/2$ (about 2.2 million) forces per time-step and takes approximately 7 s on the DAP.

The modified potential has parameters $A_{HH} = 128.25$ kcal mol^{-1} Å^{-6}; $B_{HH} = 94500.0$ kcal mol^{-1}; $C_{HH} = 4.86$ Å^{-1}.

On initialisation, or after a temperature change, it is necessary to let the cluster equilibrate. This is done in effect by placing the system in a heat bath at the desired temperature and allowing it to gain or lose energy as necessary for temperature equalisation. This is achieved by the usual velocity/angular-velocity scaling. Given that the system may have to undergo a phase change, equilibration is deemed to have occurred when the potential energy stabilises. This usually takes from 5 to 10 ps, i.e. 1 250 to 2 500 time-steps.

Analysis

We have used two basic techniques for analysing the clusters, an orientational and a structural analysis. These have been the working tools for understanding the simulations, and demonstrate the importance of graphics beyond that of result presentation.

(i) Orientational analysis

As the molecules have T_d symmetry it is possible to project four vectors from the centre of the molecule through the tetrahedral vertices and onto the surface of a sphere, marking the points of intersection by a dot. Groups of molecules with similar orientations will then produce clustering of dots on the sphere. In fact because of the symmetry of the structures found, all

Can. J. Chem. Downloaded from www.nrcresearchpress.com by 176.9.209.113 on 09/07/12
For personal use only.

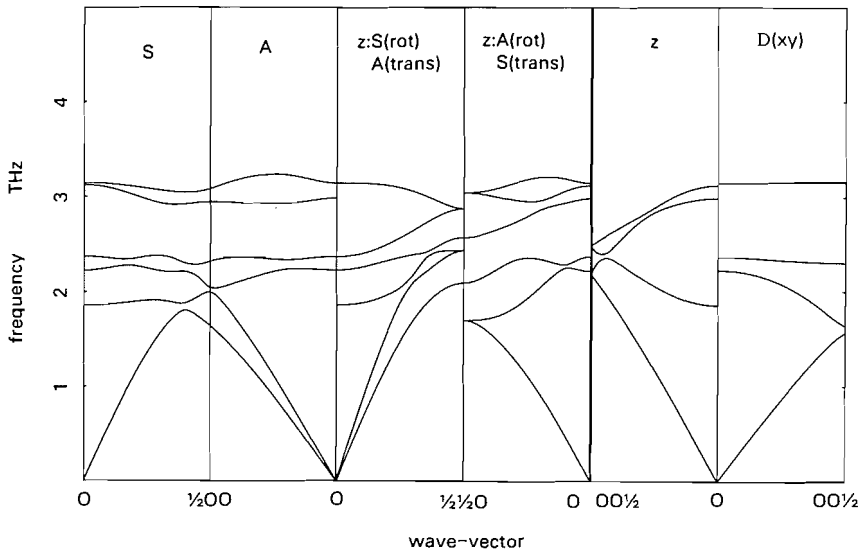

FIG. 3. Lattice dynamics for the $P\bar{4}_1c$ phase of the reduced molecule using the modified H—H potential. The representations correspond to Fig. 1.

necessary information is contained within one hemisphere and we can thus confine attention to this. On average each molecule will give two dots, though producing one or three is also possible. For representation in two dimensions the distance from the pole to each dot on the hemisphere is calculated and used as the radius for that dot on a plane, positioned at the same azimuthal angle. This gives an "equal-area" presentation, so that the density of dots on the plot corresponds exactly to the solid angle density of the orientational distribution function.

(ii) Structural analysis

Although the dot-plots give a good overall impression of the orientational state of the molecules in the cluster they contain no information about the translational structure. While powder diffraction patterns could be produced to investigate this, the calculations are computationally intensive and the small size of our cluster (radius ~20 Å) means that any features in the Fourier transform are rather broad. It is consequently difficult to measure lattice spacings accurately, and we therefore use the molecule radial distribution function both to derive lattice spacings and to show any translational order. This works well, giving a typical peak of about 0.2 Å full width at half maximum, and we are thus confident of the derived lattice spacings to about 0.1 Å.

Results

The $P\bar{4}2_1c$ to $Fm3m$ phase transition involves a change in the definition of the ***a*** and ***b*** lattice vectors by a 45° rotation about ***c***. In order to avoid confusion about the directions of ***a*** and ***b*** we prefer to fix these parallel to those in the cubic system. This has the effect of increasing the quoted tetragonal lattice parameters by a factor of $\sqrt{2}$ (6.60 → 9.33 Å). However, this convention has an added bonus later when we attempt to determine the direction of the local ***c*** axis.

Starting with an initial configuration at 100 K in the observed low-temperature phase, both the 128 and 256 molecule clusters equilibrated into the $P\bar{4}2_1c$ state within 5–10 ps but with a unit cell $a = b = 9.6$ Å, $c = 9.1$ A. This is approximately 3% larger than determined by X-ray diffraction studies of real crystals (9) — a discrepancy which is significant at the 1σ level. However, lattice statics investigations of the low temperature phase using the modified potential also show a similar increase in the crystallographic cell. We are therefore confident that this is not a consequence of the free-boundary condition technique used, or the small size of the sample. Figure 4 shows the dot plot representations and radial distribution functions of the cluster in the tetragonal phase after equilibration at 100 K. Examination of the orientational dot plot shows that the 9° orientation of the molecules relative to the tetragonal axes is reduced to 4 ± 1°. This may be correlated with the slight increase in cell size.

On heating to 220 K it was found that a phase change took place, as evident from Fig. 5. The new lattice has an fcc structure with $a = 9.9$ Å. This is a 6% increase on the experimental value, and the dot plot shows that the molecules have lost their orientation with respect to the tetragonal ***a, b*** axes. The molecules are therefore adopting the expected tetrahedral orientations. Inspection of individual molecules shows jumps between the two T_d orientations, but because of lack of computer time the statistics of reorientations are poor. We are, however, confident that both the observed low and high temperature phases have been simulated.

Determination of transition temperatures in these simulations is difficult to achieve precisely. One method for improving the accuracy is to overlay dot plots generated by the addition of configurations for different times at the same temperature. Unfortunately, calculation of sufficient data requires prohibitive amounts of computer time. Our best estimate of the transition temperature is 210 ± 10 K. It is not clear, given the uncertainty in this value and the interpretation difficulties on cooling, to determine whether there is hysteresis present on cooling.

Further heating of the fcc phase beyond 240 ± 15 K gave a second change. Although the new structure maintained its fcc lattice with the same lattice parameter the molecular orientations became disordered, c.f. Fig. 6. The increased random component in the radial distribution function is due to surface relaxation.

Recooling this phase to 100 K produced a structure with the same fcc lattice, $a = 9.9$ Å, but with a non-random orientational distribution — c.f. Fig. 7. A possible explanation is that the cluster has undergone the phase change back to the low temperature phase but is no longer a single crystal, rather a collection of crystallites distinguishable by the direction of their c axes.

Can. J. Chem. Downloaded from www.nrcresearchpress.com by 176.9.209.113 on 09/07/12
For personal use only.

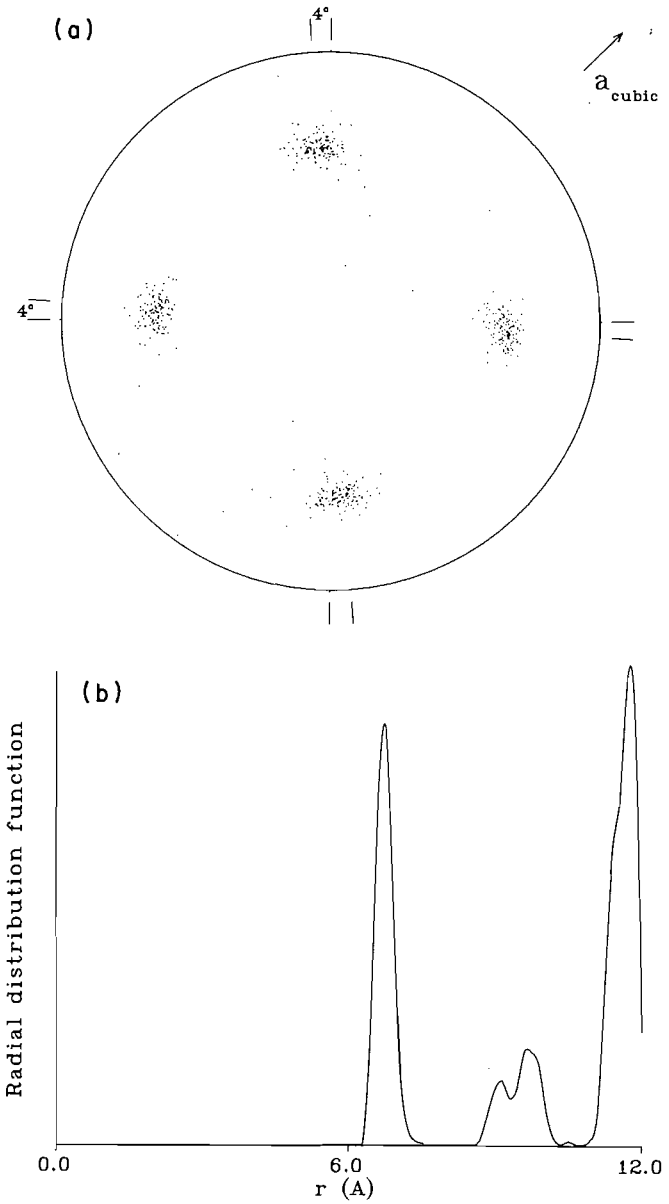

FIG. 4 (*a*) Dot plot representation of the $P\bar{4}_1c$ phase at 100 K for the 256 molecule cluster. The lines indicating the two molecular orientations with respect to the tetragonal axes are also shown. (*b*) Radial distribution function for the 256 molecule cluster at 100 K.

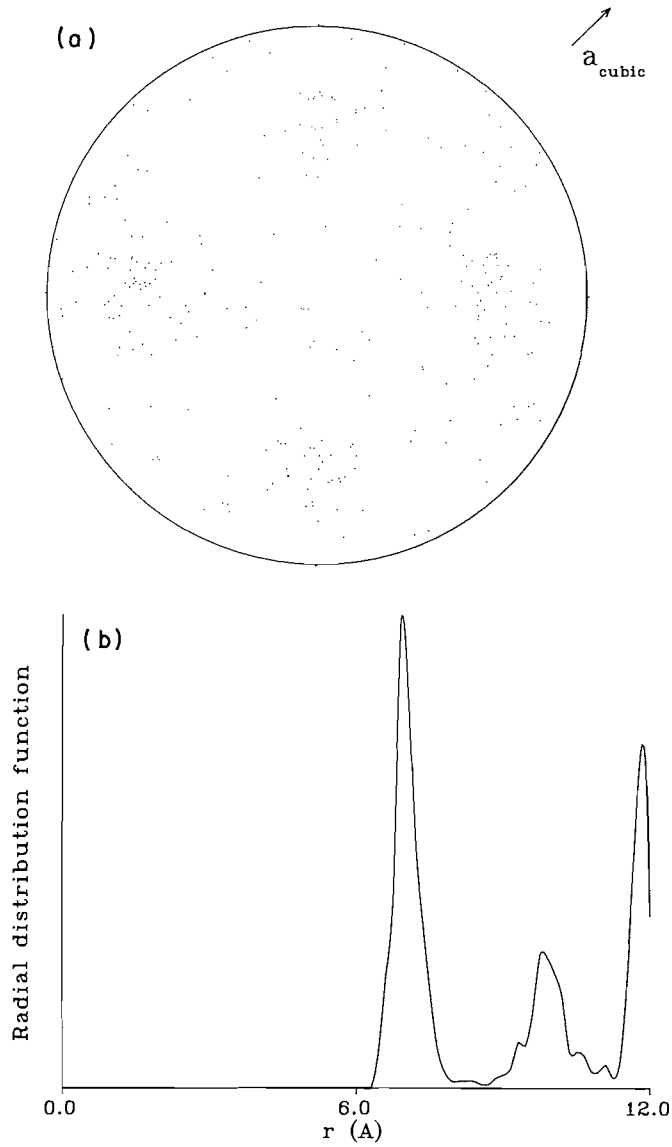

FIG. 5. (*a*) Dot plot of the $Fm3m$ phase after heating to 220 K for the 128 molecule cluster. (*b*) Radial distribution function for the 128 molecule cluster at 220 K.

In order to investigate any short range order in the ***c***-axis direction we consider each molecule site in turn and calculate the local lattice parameters by measuring the centre-to-centre distances to the next molecule along the cubic cell directions. Since the ***c*** axis is the shortest of the three axes for the tetragonal phase (in the cubic axial system) we may identify the smallest measured distance as defining the local ***c***-axis direction, provided that it is less than some limit, c_{max}, and that the data for the site are complete (i.e. all three local cell parameters can be found). Comparison of the state (***c***-axis direction) of a site with that of its nearest neighbours, next nearest neighbours etc. can then be used to form correlation functions on a variety of length scales.

It is simple to predict the expected number of agreements between sites on the basis of a random distribution of states. Let us suppose that we have a number of sites, some fraction, f, of which are assigned a state drawn randomly from k posssible states; in our case $k = 3$. If N comparisons are made, then, taking care not to double count, the expected number of agreements is

$$[2] \quad L = Nf^2/k$$

and hence the correlation function has a mean value, w, which is simply

$$[3] \quad w = L/N = f^2/k$$

with a standard deviation given by the binomial distribution of

$$[4] \quad \sigma = \{f^2(1 - f^2/k\}^{1/2}$$

A value of unity for the correlation function can occur only for a bulk sample because f is reduced by the virtue of the cluster surface. Figure 8 shows the observed correlation functions for the nearest and next nearest neighbours respectively. The curves are for configurations at 100 K (before heating, upper curve), 300 and 100 K (after cooling) together with those expected from random crystallite orientations, denoted r 300 K and r 100 K for the 300 K and 100 K (after cooling) configurations, respectively. These random curves are calculated from eq. [3] using the value of f determined for that particular cluster and value of

Can. J. Chem. Downloaded from www.nrcresearchpress.com by 176.9.209.113 on 09/07/12
For personal use only.

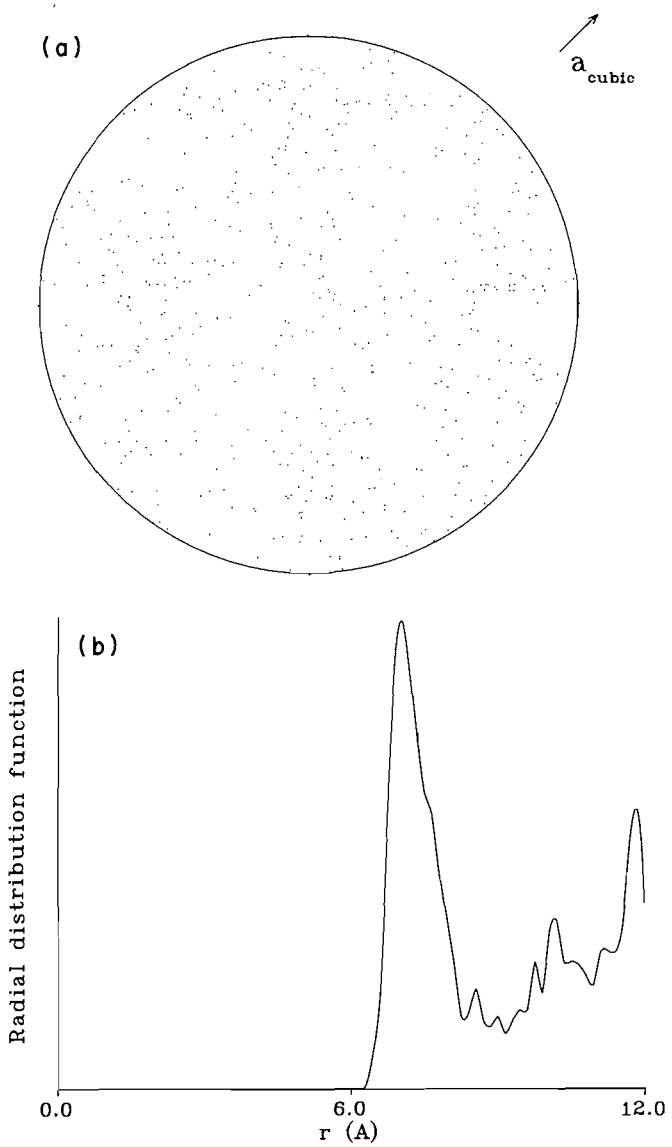

FIG. 6. (*a*) Dot plot of the plastic phase after heating to 300 K for the 256 molecule cluster. (*b*) Radial distribution function for the 256 molecule cluster at 300 K.

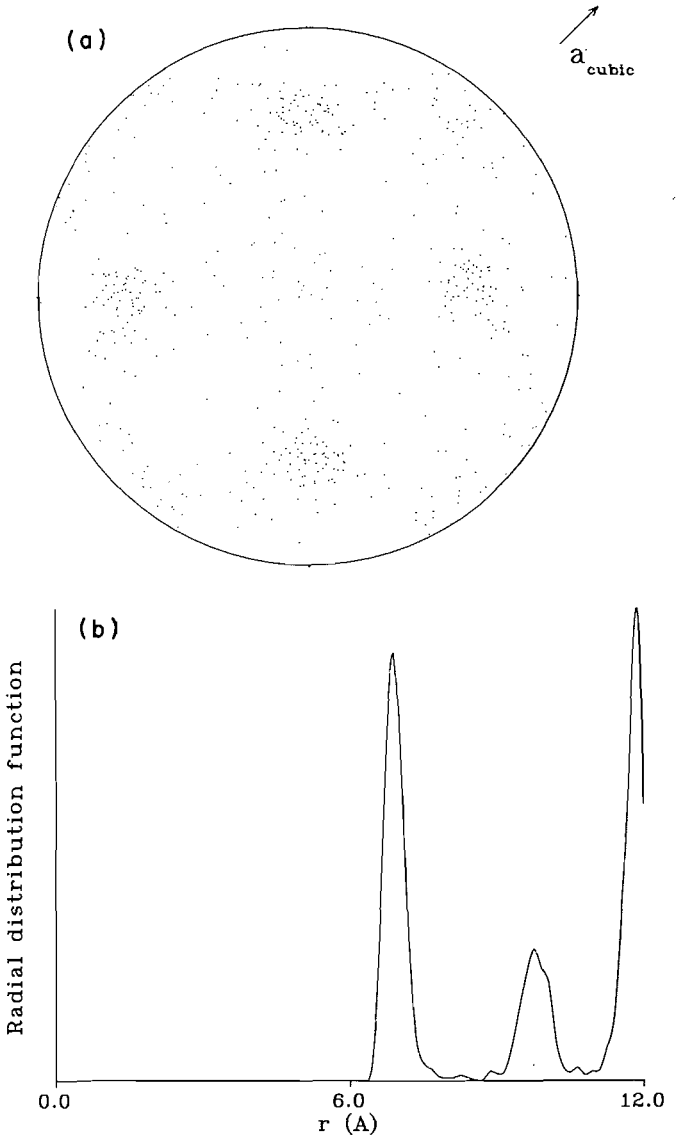

FIG. 7. (*a*) Dot plot of the $P\bar{4}_1c$ phase after cooling to 100 K from 300 K for the 256 molecule cluster. (*b*) Radial distribution function for the 256 molecule cluster cooled to 100 K.

c_{max}. Differences between random curves therefore reflect variations in the fraction of sites which are assigned *a* state. Both diagrams display the same general features. The error bars are $\pm\sigma$; those on the observed curves are calculated from observed temporal fluctuations, while those on the random curves are a combination of these errors with those calculated from eq. [4].

Examination of these figures shows the high degree of order in the structure before heating. Also clear are the relative displacements along the abscissa of the correlation functions after heating to those before heating. This is caused by the lattice expansion already noted.

A comparison of the correlation functions at 300 K with the random curves shows that the simulation curves remain above the levels expected, although this is not statistically significant at the 2σ ($P < 5\%$) level. This may be indicative of some slight local correlation but a direct search for crystallites in the fcc structure proved unsuccessful. On cooling, the level of correlation rises to become statistically significant at the 2σ level and a number of possible "crystallites" can be identified in the larger cluster, though these are small and contain only a few molecules each. While the correlation functions have not reproduced the original degree of order, this would not be expected even from a polycrystalline system when compared with a single crystal, because of the disorder at crystallite boundaries. It may be supposed that these boundaries also contribute to the larger potential energy of the recooled cluster which, at 100 K is 23% more than at the same temperature before heating. Unfortunately, the system is so small that examination of the spatial distribution of the molecule potential energies does not show localised minima corresponding to the crystallites.

Conclusions

A comprehensive MD study has been made of phase changes in adamantane using approximately 100 h of calculation time on the ICL DAPs at the University of Edinburgh. We have employed a H—H potential modified so that when used on its own with deuterated adamantane it gives lattice dynamics similar to those of Williams (25) or Kitaigorodskii (26) in both high and low temperature phases. This enables the use of a reduced molecule of 16 atoms with a consequent reduction in the necessary calculation by 65%.

Can. J. Chem. Downloaded from www.nrcresearchpress.com by 176.9.209.113 on 09/07/12
For personal use only.

Can. J. Chem. Downloaded from www.nrcresearchpress.com by 176.9.209.113 on 09/07/12
For personal use only.

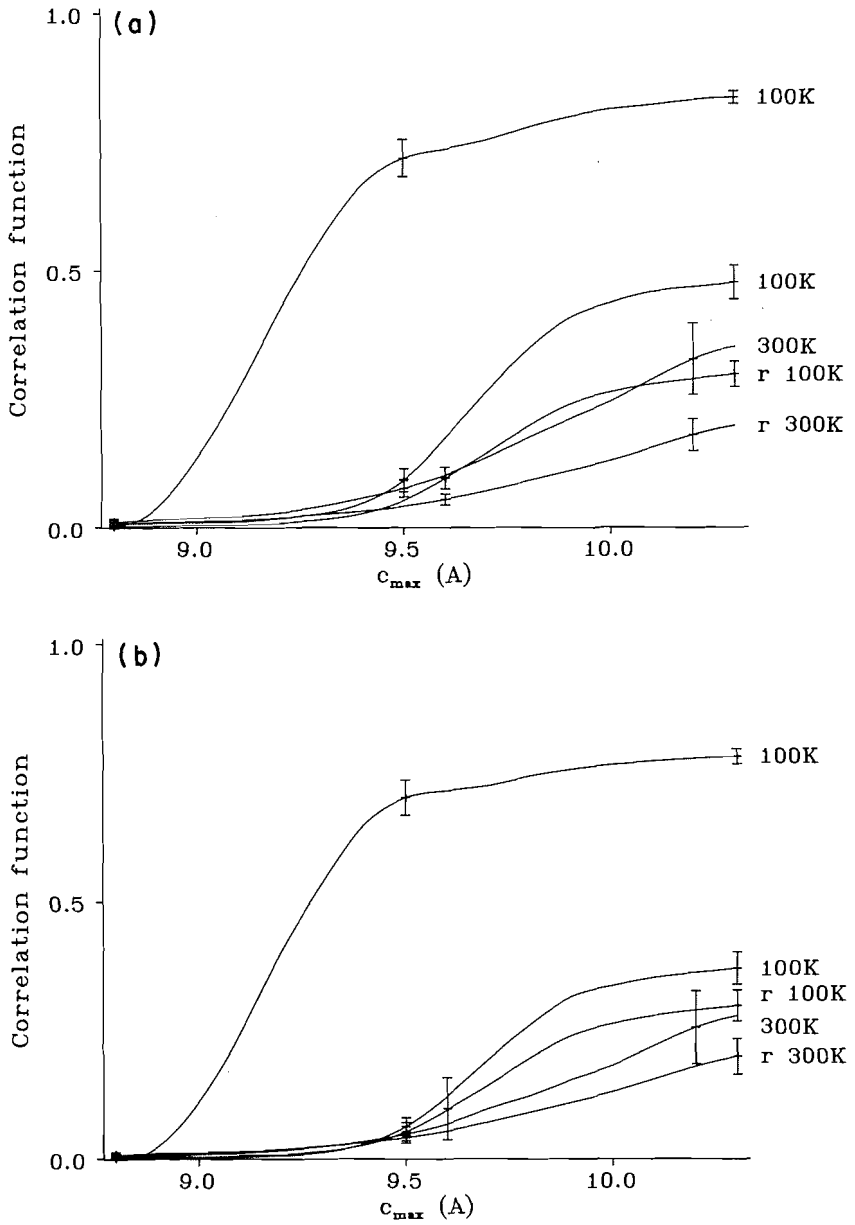

FIG. 8. (*a*) Correlation functions for the nearest neighbours plotted as a function of the minimum acceptable value of c, c_{max}. (*b*) Correlation functions for the next nearest neighbours plotted as a function of c_{max}.

Using this potential we observe the system to equilibrate into the correct low temperature phase ($P\bar{4}2_1c$) with lattice parameters only slightly larger than expected from lattice dynamics. This non-trivial achievement demonstrates that the modified potential and the reduced rigid molecule give a good model.

On heating the system a phase transition is observed at 210 ± 10 K (experimental value 208.6 K) to a rotationally frustrated phase on a fcc lattice. Further heating removed the orientational order though the translational structure was preserved until sublimation took place.

Recooling the cluster to 100 K gave regions which could be identified as a collection of crystallites rather than a single crystal. This is not surprising since the cubic phase is not uniaxial and therefore there are three possible directions for the new local *c*-axis. We suppose that given sufficient time for annealing at an optimum temperature, or equivalently a very much slower cooling rate through the transition, larger crystallites could have been formed. Unfortunately, this would require much more computer time than is currently practicable, though with the rapid improvements in computer technology will soon render such simulations feasible.

Future work will involve the search for local transient ordering in the plastic phase and a study of reorientations in both the rotationally frustrated and orientionally disordered structures. Furthermore it is hoped that future simulations will help in the interpretation of the inelastic neutron scattering experiments which initiated this work (1, 7).

1. C. G. WINDSOR, D. H. SAUNDERSON, J. N. SHERWOOD, D. TAYLOR, and G. S. PAWLEY. J. Phys. C, **11**, 1741 (1978).
2. R. W. HOCKNEY and C. R. JESSHOPE. Parallel computers. Adam Hilger, Bristol. 1981.
3. G. S. PAWLEY and G. W. THOMAS. Phys. Rev. Lett. **48**, 410 (1982).
4. B. M. POWELL, G. DOLLING, G. S. PAWLEY, and L. S. BARTELL. Mol. Phys. In press.

5. K. Refson and G. S. Pawley. Mol. Phys. **61**, 669 (1987); **61**, 693 (1987).
6. M. Parrinello and A. Rahman. Phys. Rev. Lett. **45**, 1196 (1980).
7. J. C. Damien, J. Lefebvre, M. More, B. Hennion, R. Currat, and R. Fouret. J. Phys. C, **11**, 4323 (1978); C. G. Windsor, J. C. Damien, J. Lefebvre, and R. M. Richardson. J. Phys. C, **14**, 1555 (1981); M. Bee, J. P. Amoureux, and R. E. Lechner. Mol. Phys. **40**, 617 (1980).
8. M. Meyer and G. Ciccotti. Mol. Phys. **56**, 1235 (1985); M. Meyer, C. Marhic, and G. Ciccotti. Mol. Phys. **58**, 723 (1986); G. Ciccotti, M. Ferrario, E. Memeo, and M. Meyer. Phys. Rev. Lett. **59**, 2574 (1987).
9. C. E. Nordman and D. L. Schmitkons. Acta Crystallogr. **18**, 764 (1965).
10. J. P. Amoureux, M. Bee, and J. C. Damien. Acta Crystallogr. B**36**, 2633 (1980).
11. P. A. Reynolds. Acta Crystallogr. A**34**, 242 (1978).
12. A. H. Fuchs and G. S. Pawley. J. Phys. In press.
13. J. Farges, M. F. de Feraudy, B. Raoult, G. Torchet, A. Fuchs, and G. S. Pawley. In preparation.
14. J. Farges, M. F. de Feraudy, B. Raoult, and G. Torchet. J. Chem. Phys. **78**, 5067 (1983).
15. J. J. Burton. J. Chem. Soc. Faraday Trans. 2, **69**, 540 (1973); M. R. Hoare and P. Pal. J. Cryst. Growth, **17**, 77 (1972).
16. B. W. van de Waal. J. Chem. Phys. **79**, 3948 (1983).
17. R. D. Etters, K. Flurchick, R. P. Pan, and V. Chandrasekharan. J. Chem. Phys. **75**, 929 (1981).
18. L. B. Spornick, R. L. Danilowicz, A. A. Helmy, and R. D. Etters. J. Chem. Phys. **84**, 2310 (1986).
19. F. H. Stillinger and T. A. Weber. Phys. Rev. A**25**, 978 (1982).
20. S. M. Thompson, K. E. Gubbins, J. P. R. B. Walton, R. A. R. Chantry, and J. S. Rowlinson. J. Chem. Phys. **81**, 530 (1984).
21. F. H. Stillinger and T. A. Weber. J. Phys. Chem. **87**, 2833 (1983).
22. F. H. Stillinger and A. Rahman. J. Chem. Phys. **60**, 1545 (1974).
23. D. Beeman. J. Comp. Phys. **20**, 130 (1976).
24. G. S. Pawley and G. W. Thomas. J. Comp. Phys. **47**, 165 (1982).
25. D. E. Williams. J. Chem. Phys. **47**, 4680 (1967).
26. A. I. Kitaigorodskii. J. Chim. Phys. **63**, 6 (1966).

Can. J. Chem. Downloaded from www.nrcresearchpress.com by 176.9.209.113 on 09/07/12
For personal use only.

Photocycloaddition of cytosine to 5-methoxyuracil in dinucleotide model compound

BOHDAN SKALSKI, GRAZYNA WENSKA, STEFAN PASZYC,[1] AND ZDZISLAW STEFANIAK
Faculty of Chemistry, A. Mickiewicz University, 60-780 Poznan, Poland

Received February 12, 1987[2]

BODHAN SKALSKI, GRAZYNA WENSKA, STEFAN PASZYC, and ZDZISLAW STEFANIAK. Can. J. Chem. **66**, 1027 (1988).

The intramolecular photocycloaddition of cytosine (Cyt) to 5-methoxyuracil (mo^5U) in Cyt-$(CH_2)_3$-mo^5Ura, a dinucleotide model compound, occurs upon irradiation with near ultraviolet light ($\lambda > 300$ nm) with the formation of an unstable cyclobutane dimer. The dimer undergoes spontaneous dark deamination with a rate constant $k = 9.0 \times 10^{-5}\ s^{-1}$ and $t_{1/2} = 128$ min, to give a related uracil derivative.

BODHAN SKALSKI, GRAZYNA WENSKA, STEFAN PASZYC et ZDZISLAW STEFANIAK. Can. J. Chem. **66**, 1027 (1988).

La photocycloaddition intramoléculaire de la cytosine (Cyt) sur le méthoxy-5 uracile (mo^5U) conduisant à la Cyt-$(CH_2)_3$-mo^5Ura, un composé modèle des dinucléotides, se produit par irradiation avec de la lumière pratiquement ultraviolet ($\lambda > 300$ nm) et avec la formation d'un cyclobutane dimère instable. Le dimère subit une désamination spontanée à l'abri de la lumière; la constante de vitesse $k = 9{,}0 \times 10^{-5}\ s^{-1}$, $t_{1/2} = 128$ min et la réaction conduit à un dérivé uracile apparenté.

[Traduit par la revue]

Introduction

It has been found recently that complexes of certain tRNAs with *Escherichia coli* or yeast ribosomes could be cross-linked upon irradiation with near uv light ($\lambda > 300$ nm) (1–5). This cross-linking results in covalent bond formation between the tRNA 5′-anticodon base 5-methoxy or (5-carboxymethoxy) uracil and cytosine-1400 of the rRNA (5). Based on the photoreversal of the cross-link by 254-nm light, the cyclobutane-type dimer was proposed as the structure of the photoproduct (2).

Since the available information on the photocycloaddition of cytosine to uracils, and on the stability of the resulting photodimers, is still limited (6), we decided to investigate this reaction using a model compound in which cytosine and 5-methoxyuracil are connected by a trimethylene chain.

Results and discussion

The Cyt-$(CH_2)_3$-mo^5Ura **6** was synthesized by a multistep synthesis (Scheme 1) in which the triazole derivative **5** was a key intermediate. In the first step the 1-(3-bromopropyl)uracil **1** (7) was transformed into pyridinium salt **2** by reacting with 4-chlorophenylphosphorodichloridate ($4ClPhOPOCl_2$) in the presence of pyridine (8). The synthetic procedure, identical to that applied previously for synthesis of other nucleobase-derived pyridinium salts (8, 9), led to the concentrated aqueous solution of pure **2**. The presence of a pyridinium cation in **2** was confirmed by ^1H nmr spectroscopy (see Experimental). Treatment of the aqueous solution of **2** with 1,2,4-triazole (3 equiv.), at room temperature for 48 h, gave crystalline 1-(3-chloropropyl)-4-(1,2,4-triazol-1-yl)uracil **3** in which the bromine of the bromopropyl chain was quantitatively replaced by chlorine, as revealed by ms analysis of the product. As we found, this replacement takes place during the phosphorylation reaction of **1** and does not occur when reaction is carried out in the presence of an excess (6 equiv.) of pyridine hydrobromide. In the next step the triazole derivative **3** was reacted with 5-methoxyuracil (10) in dry dimethylformamide in the presence of anhydrous K_2CO_3, to give a mixture of three products. The desired product, 1-[3-(5-methoxyurac-1-yl)propyl]-4-(1,2,4-triazol-1-yl)uracil **5**, was isolated by means of preparative tlc with a 30% yield.

The 4-(azol-1-yl) derivatives of uracils can be transformed into the related cytosine derivatives, or reversed to the parent heteroaromatic bases, depending upon the conditions applied (11). Thus, the triazole derivative **5** was converted into both Cyt-$(CH_2)_3$-mo^5Ura **6** by treatment with aqueous ammonia and into Ura-$(CH_2)_3$-mo^5Ura **7** using mild alkaline hydrolysis.

In the proton-coupled ^{13}C nmr spectrum of **7** the C(6) carbon of the 5-methoxyuracil residue (δ_C 126.9 ppm) is coupled with the protons of the trimethylene chain ($^3J_{C(6),H} = 3.6 \pm 06$, $^1J_{C(6),H} = 180.6 \pm 0.6$ Hz), indicating that in **7** and thus in its precursor **5** the mo^5Ura is alkylated at position N(1).

Irradiation of a deoxygenated, aqueous solution of **6** ($c = 1.3 \times 10^{-4}$), at room temperature with near uv light ($\lambda > 300$ nm), resulted in the loss of uv absorption at $\lambda = 270$ nm, characteristic of the 5,6 double bond in pyrimidine residues (Fig. 1). Simultaneous tlc and hplc analyses of the irradiated solution revealed the presence of only one photoproduct (74% conversion). This product appeared to be reversible to the parent compound **6** upon irradiation with short wavelength uv light ($\lambda = 254$ nm) (see curve 3 in Fig. 1).

The lack of uv absorption and photoreversal to the starting monomer, characteristic for cyclobutane dimerization of pyrimidine bases (6), pointed to the cyclobutane dimer as the structure of the photoproduct.

Unfortunately, the isolation and direct identification of the photoproduct in the pure state was not possible. The tlc and hplc analyses of the solution, within 6 h after irradiation, showed the gradual decay of the photoproduct with concomitant formation of a new compound. This dark transformation was followed by a further decrease in the uv absorption of the solution (curve 4 in Fig. 1).

Irradiation of the solution in which the dark transformation was completed with $\lambda = 254$ nm light resulted in the appearance of a new absorption band with the maximum blue-shifted ca. 5 nm compared to that for **6** (curve 5 in Fig. 1). A new product, identical chromatographically with the previously synthesized Ura-$(CH_2)_3$-mo^5Ura **7** (see Scheme 1) was detected in the solution.

Based on these observations, the following reaction pathway (Scheme 2) is proposed: **6** undergoes an intramolecular cycloaddition to form the cytosine cyclobutane dimer **8**, followed by the dark deamination process to give the uracil derivative **9**. It must be pointed out that spontaneous deamination is a general property of 5,6 saturated cytosine derivatives (6, 12).

To prove the proposed reaction scheme, the preparative scale irradiation of **6** ($c = 3 \times 10^{-4}$ *M*, 1 L) was performed. The

[1]Author to whom correspondence may be addressed.
[2]Revision received November 20, 1987.

Can. J. Chem. Downloaded from www.nrcresearchpress.com by 93.93.197.157 on 09/07/12
For personal use only.

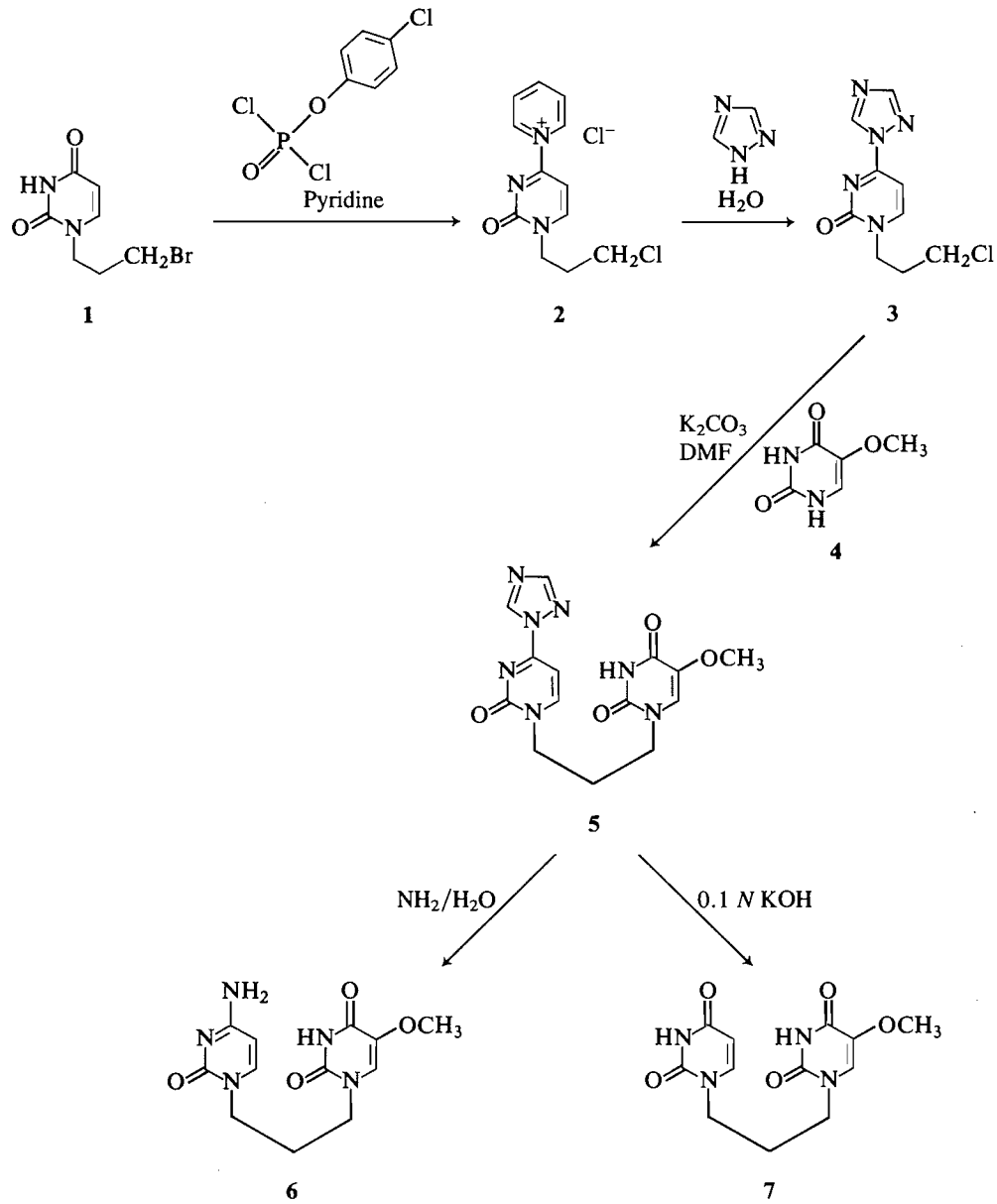

SCHEME 1

transformation product obtained from the primary photoproduct of Scheme 2 was isolated and identified (nmr, ms, uv, elemental analysis) as the Ura-$(CH_2)_3$-mo^{5}Ura cyclobutane dimer **9**. The structure of **9** was also confirmed by splitting the dimer by irradiating with $\lambda = 254$ nm light (see Scheme 2 and Fig. 2) and comparing the resulting monomer with an authentic sample of **7** obtained from **5** (Scheme 1). Analogously, **7** was converted into **9** by irradiation with $\lambda > 300$ nm light.

The dark deamination process **8** → **9** was studied by means of quantitative hplc analysis. It was found that the reaction proceeds according to first-order kinetics (Fig. 3) with a rate constant $k = 9.0 \times 10^{-5}$ s^{-1} and a half-life $t_{1/2} = 128$ min at room temperature.

The results of this work support the proposed mechanism for tRNA and rRNA photo cross-linking in view of possible cyclobutane dimer formation between cytosine and 5-methoxyuracil residues (1–5). It might be surprising that no deamination of the photoproduct was observed in cross-linked tRNA–rRNA complexes except for the very recent report on photo cross-linking of *E. coli* acetylvalyl tRNA and *Artemia salina* ribosomes, in which some conversion of cytosine into uracil was detected (13). However, it must be noted that most of the previous studies (1–5, 13) involved RNAs containing the carboxy analog of mo^{5}U, namely, cmo^{5}U. It is very likely that the nearby negative charge due to the carboxyl group and (or) the steric effects of the environment of the polynucleotide have inhibited the deamination reaction.

Experimental

Spectra were measured on a Carl Zeiss Jena uv–vis spectrophotometer, a JEOL 90 FX Fourier transform nmr instrument, and a JEOL MS-D-100 mass spectrometer. TMS and dioxane were used for δ_H chemical shift measurements. All δ_H values (ppm) are given relative to TMS. Melting points were taken on a Boetius apparatus and are uncorrected. Elemental analyses were made on a Perkin Elmer 240 analyser.

Thin-layer chromatography was performed on precoated silica gel $60F_{254}$ (Merck) plates in the following solvent systems: (a) isopro-

Can. J. Chem. Downloaded from www.nrcresearchpress.com by 93.93.197.157 on 09/07/12
For personal use only.

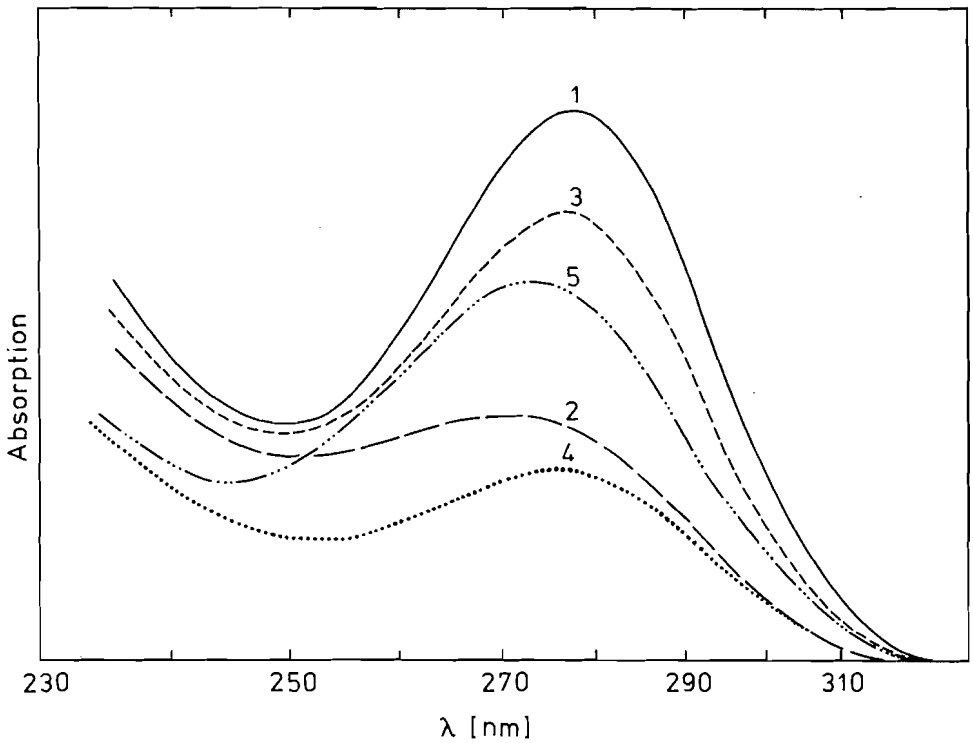

FIG. 1. Absorption spectra of aqueous solutions of Cyt-$(CH_2)_3$-mo^{5}Ura: (1) before irradiation; (2) after irradiation with $\lambda > 290$ nm; (3) solution 2 after reirradiation with $\lambda = 254$ nm; (4) solution 2 after being stored for 24 h in dark, at room temperature; and (5) solution 4 reirradiated with $\lambda = 254$ nm.

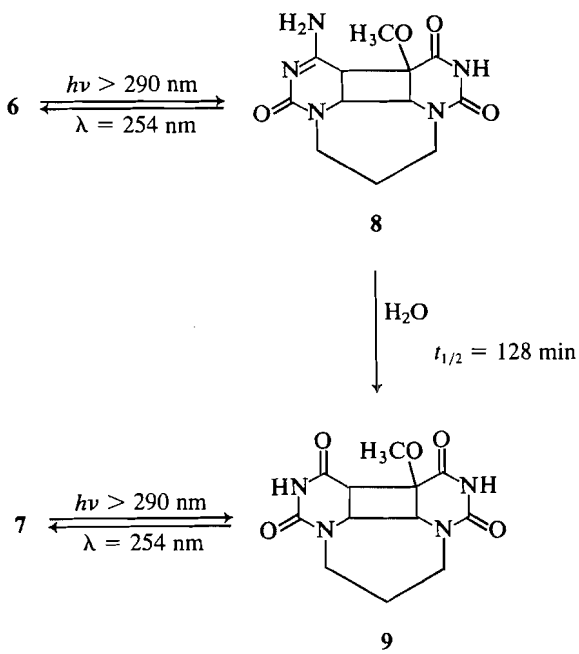

SCHEME 2

panol/H_2O/NH_4OH (8:2:1); (b) $CHCl_3$/CH_3OH (5:1); (c) ethyl acetate/CH_3OH (5:1). Quantitative hplc analyses were performed on a silica gel column eluted with a mixture of ethanol and 1 M aqueous ammonium acetate (5:1) at a flow rate of 0.35 mL/min. The hplc instrument was equipped with an uv–vis absorption detection system.

Materials

5-Methoxyuracil **4** (10) and 1-(3-bromopropyl)uracil **1** (7) have been described previously and were synthesized in this work according to the reported procedures.

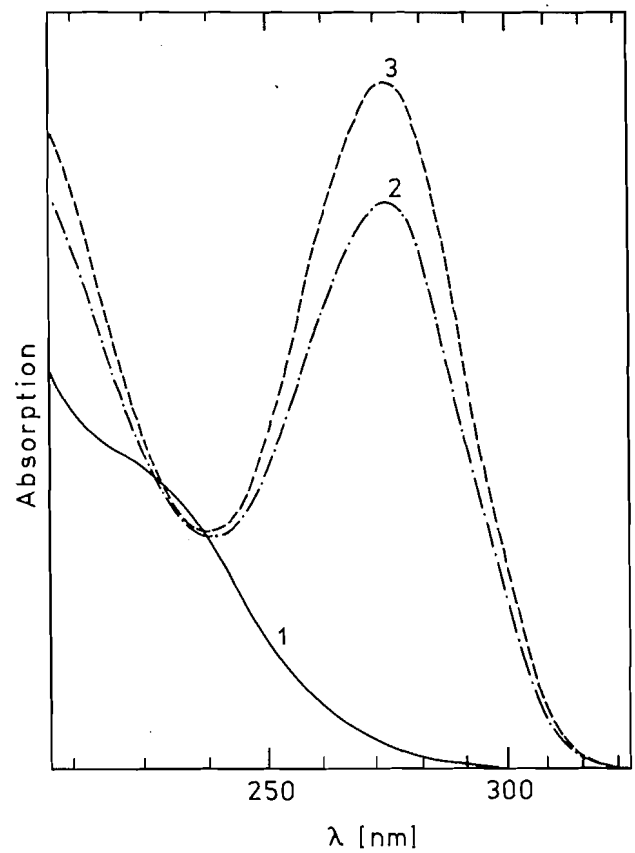

FIG. 2. Ultraviolet absorption spectra in water: (1) the cyclobutane dimer **9** isolated from irradiated water solution of **6**; (2) the reversal of the dimer **9** upon irradiation with $\lambda = 254$ nm; and (3) Ura-$(CH_2)_3$-mo^{5}Ura **7**.

Can. J. Chem. Downloaded from www.nrcresearchpress.com by 93.93.197.157 on 09/07/12
For personal use only.

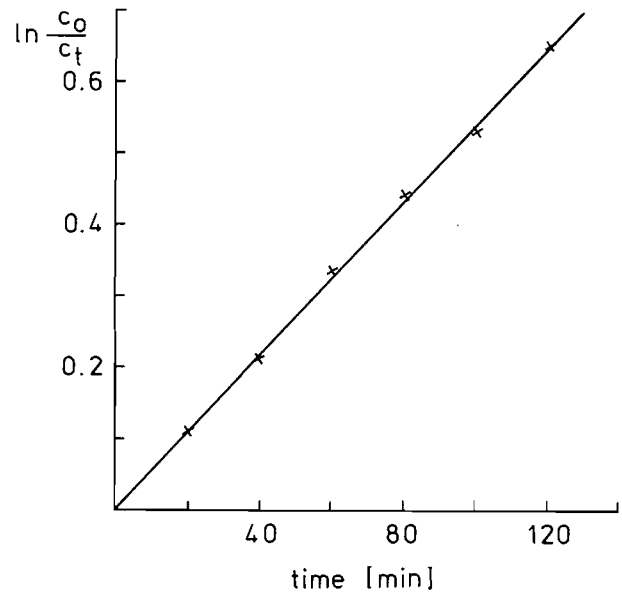

FIG. 3. The first-order plot for deamination of **8** (**8** → **9**).

N-*[1-(3-Chloropropyl)pyrimidin-2(1*H*)-one-4-yl)pyridinium chloride, 2*

Dry 1-(3-bromopropyl)uracil **1** (3.5 g, 15 mmol) was dissolved in pyridine (50 mL) and treated with 4-chlorophenylphosphorodichloridate (5.6 mL, 30 mmol). The reaction mixture was left at room temperature for 12 h. The white precipitate containing pyridinium salt **2** and cocrystallizing pyridine hydrochloride was filtered off, washed with pyridine, and dissolved in water (50 mL). The aqueous solution was treated with charcoal, filtered, and neutralized with Dowex 1 resin (HCO_3^-) to pH 6.5. The resin was filtered off, and the solution concentrated under vacuum to one third of the initial volume and tested for the presence of the pyridinium salt by means of uv and ^{1}H nmr spectroscopy: uv (H_2O): 266 and 333 nm (max), 259 and 296 nm (min); δ_H (D_2O): 9.55 (m, $Py^{+\alpha}$-H), 8.89 (m, $Py^{+\gamma}$-H), 8.77 (d, ura 6-H), 8.39 (m, $Py^{+\beta}$-H), 7.37 (d, ura 5-H, J = 5 Hz), 4.30 (t, N-CH_2, J = 4.5 Hz), 3.74 (t, —CH_2Cl), 2.38 (m, —CH_2—).

*1-(3-Chloropropyl)-4-(1,2,4-triazol-1-yl)pyrimidin-2(1*H*)-one, 3*

Obtained as above, the concentrated aqueous solution of **2** was diluted with water to V = 50 mL, treated with 1,2,4-triazole (2.06 g, 30 mmol), and left overnight at room temperature. The reaction mixture was filtered to yield ca. 1.1 g of crude product. The filtrate was extracted with chloroform (3 × 30 mL). The solvent was evaporated and the residue combined with a crude solid and purified by chromatography on a silica gel column ($CHCl_3$/CH_3OH 10:1) to give 1.79 g of pure **3**, 50% yield estimated relative to the 1-(3-bromopropyl)uracil used; mp 171°C; uv (H_2O): 246 nm (12 400), 311 nm (8200): δ_H ($CDCL_3$): 9.24 and 8.12 (2s, triazole 3-H and 5-H), 7.94 (d, Ura 6-H, J = 7 Hz), 7.05 (d, Ura 5-H), 4.18 (t, N-CH_2, J = 6 Hz), 3.61 (t, —CH_2Cl, J = 6 Hz), 2.34 (m, —CH_2—); ms m/e (rel. int.): 239 (18), 204 (69), 190 (13), 177 (100), 176 (9), 163 (6), 162 (4), 149 (16), 148 (11). *Anal.* calcd. for $C_9H_{10}N_5OCl$: C 45.09, H 4.17, N 29.22; found: C 44.98, H 4.14, N 28.81.

*1-[3-(5-Methoxyurac-1-yl)propyl]-4-(1,2,4-triazol-1-yl)pyrimidin-2(1*H*)-one, 5*

5-Methoxyuracil (0.171 g, 5 mmol), 1-(3-chloropropyl)-4-(1,2,4-triazol-1-yl)uracil **3** (1.19 g, 5 mmol), anhydrous K_2CO_3 (1.4 g, 10 mmol), and dimethylformamide (100 mL) were stirred together, with the exclusion of moisture, at room temperature. After 24 h, the reaction mixture was filtered and concentrated to a small volume. The major product (R_f = 0.35 in system b and 0.19 in system c) was isolated by means of preparative tlc and recrystallized from 50% aqueous ethanol to give 0.52 g of **5**. Yield 30%; mp 239–241°C; uv (H_2O) 236 nm (11 600), 247 nm (13 700), 270 nm (8000), 291 nm (10 100); δ_H ($(CD_3)_2SO$): 9.42 (s, triazole 5-H), 8.49 (d, triazoloura 5-H), 8.38 (s, triazole 3-H), 7.36 (s, mo^5Ura 6-H), 6.95 (d, triazoloura 6-H), 3.95 (t, triazoloura N-CH_2), 3.72 (t, mo^5Ura N-CH_2), 3.58 (s, O-CH_3), 2.05 (m, —CH_2—); ms m/e (rel. int.): 345 (2), 204 (25), 203 (100), 190 (3), 177 (21), 176 (7), 169 (3), 167 (5), 164 (3), 149 (8), 148 (12), 135 (3), 126 (2), 121 (4), 112 (3), 110 (4), 109 (4), 108 (6), 96 (7). *Anal.* calcd. for $C_{14}H_{15}N_7O_4$: C 48.69, H 4.35, *N* 28.41; found: C 48.36, H 4.22, N, 28.19.

1-[3(Cytos-1-yl)propyl]-5-methoxyuracil, 6

Compound **5** (0.150 g, 0.43 mmol) was treated with aqueous ammonia (0.5 M, 150 mL) at room temperature. After 6 h the reaction mixture was concentrated under reduced pressure and the residue recrystallized from aqueous ethanol to give 0.11 g of **6**. Yield 87%; mp 283–286°C; uv (H_2O): 277 nm (14 800); δ_H (CF_3COOD): 7.62 (d, Cyt 6-H, J = 8 Hz), 7.06 (s, mo^5Ura 6-H), 6.20 (d, Cyt 5-H, J = 8 Hz), 3.93 (m, Cyt N-CH_2 and mo^5Ura N-CH_2), 3.76 (s, OCH_3), 2.54 (m, —CH_2—); ms m/e (rel. int.); 293 (18), 182 (9), 155 (3), 152 (8), 151 (13), 138 (33), 137 (5), 125 (16), 124 (36), 110 (43). *Anal.* calcd. for $C_{12}H_{15}N_5O_4$: C 49.15, H 5.12, N 23.89; found: C 48.66, H 5.04, N 23.80.

1-[3-(Urac-1-yl)propyl]-5-methoxyuracil, 7

Compound **5** (0.150 g, 0.43 mmol) was treated with a 0.1 M aqueous solution of sodium hydroxide (150 mL) at room temperature. After 6 h, the reaction mixture was neutralized to pH 7.2, concentrated under reduced pressure to ca. 1/3 of the initial volume, and filtered off. The white precipitate was recrystallized from aqueous ethanol (60%) to give 0.108 g of **7**. Yield 85%; mp 278–281°C; uv (H_2O): 272 nm (14 100); δ_H (CF_3COOD): 7.18 (d, Ura 6-H), 6.84 (s, mo^5Ura 6-H), 5.94 (d, Ura 5-H, J = 8 Hz), 3.64 (s and m, mo^5Ura N-CH_2, Ura N-CH_2, and OCH_3), 2.02 (m —CH_2—); δ_C (CF_3COOD): 169.26 (C═O), 154.03 (C═O), 152.35 (C═O), 149.54 (Ura 6-C), 139.24 (C═O), 126.94 (mo^5Ura 6-C), 103.81 (Ura 5-C), 122.55 (mo^5Ura 5-C), 58.62 (O-CH_3), 48.54 (N-CH_2), 29.14 (—CH_2—); ms m/e (rel. int.): 294 (48), 182 (13), 169 (15), 153 (100), 149 (16), 141 (5), 139 (9), 126 (20), 125 (17), 110 (16). *Anal.* calcd. for $C_{12}H_{14}N_4O_5$: C 48.98, H 4.76, N 19.04; found: C 48.32, H 4.37, N 18.68.

Irradiation of 6

The preparative scale photochemical reaction of **6** was carried out in a cylindrical Pyrex glass reactor using an immersed, water-cooled high-pressure mercury lamp TQ 150 (Original Hanau) equipped with a Pyrex cutoff filter (λ > 300 nm).

Compound **6** (90 mg, 0.3 mmol) was dissolved in water (1 L, c = 3 × 10^{-4} M). The solution was deoxygenated prior to the irradiation by purging with nitrogen, and then irradiated portionwise (130 mL) under a continuous flow of nitrogen. The reaction was monitored by taking the uv spectra of the samples of irradiated solution and was continued until no further decrease in absorption at 260 nm occurred (ca. 74% conversion after 30 min of irradiation). The irradiated portions were combined and left for 12 h at room temperature (pH 6.7) to allow for complete dark transformation of the primary photoproduct into compound **9**. Chromatography on silica gel (system b) followed by recrystallization of the isolated product from aqueous ethanol gave 0.054 g of photodimer **9**. Yield 59%; mp 307–312°C; δ_H (CF_3COOD): 4.31 (m, Ura N-CH and mo^5Ura N-CH), 4.05 (m, Ura 5-H, Ura 6-H, and mo^5Ura 6-H), 3.41 (s, OCH_3), 2.66 (m, —CH_2—), 1.98 and 1.47 (2 m, Ura N-CH and mo^5Ura N-CH); ms m/e (rel. int.): 294 (36), 182 (15), 169 (15), 153 (100), 152 (29), 149 (8), 139 (9), 126 (19), 125 (14), 110 (14). *Anal.* calcd. for $C_{12}H_{14}N_4O_5$: C 48.98, H, 4.76, N 19.04; found: C 48.52, H 4.43, N 18.98.

Irradiation of 7

The irradiation of **7** (60 mg, 0.2 mmol in 500 mL of water) and isolation of the photoproduct was performed in the same manner as for **6** (except for dark reaction step) to give 41 mg of the compound identical in all respects with photodimer **9** described above, 68% yield.

Can. J. Chem. Downloaded from www.nrcresearchpress.com by 93.93.197.157 on 09/07/12
For personal use only.

Acknowledgments

This work was supported by the Polish Ministry of Education, project RP. II.13.2.15. The authors wish to thank Ms. Z. Gdaniec for measuring the nmr spectra.

1. J. B. PRINCE, B. H. TAYLOR, D. L. THURLOW, J. OFENGAND, and R. A. ZIMMERMANN. Proc. Natl. Acad. Sci. U.S.A. **79**, 5450 (1982).
2. J. OFENGAND and R. LIOU. Biochemistry, **19**, 4814 (1980).
3. J. OFENGAND, P. GORNICKI, K. CHAKRABURTTY, and K. NURSE. Proc. Natl. Acad. Sci. U.S.A. **79**, 2817 (1982).
4. C. EHRESMANN, B. EHRESMANN, R. MILLON, J. P. EBEL, K. NURSE, and J. OFENGAND. Biochemistry, **23**, 429 (1984).
5. C. EHRESMANN and J. OFENGAND. Biochemistry, **23**, 438 (1984).
6. G. J. FISHER and H. E. JOHNS. *In* Photochemistry and photobiology nucleic acids. Vol. I. *Edited by* S. Y. Wang. Academic Press, New York. 1976.
7. D. T. BROWN, J. EISINGER, and N. J. LEONARD. J. Am. Chem. Soc. **90**, 7302 (1968).
8. R. W. ADAMIAK, E. BIALA, and B. SKALSKI. Nucleic Acids Res. **13**, 2989 (1986).
9. R. W. ADAMIAK, E. BIALA, Z. GDANIEC, S. MIELEWCZYK, and B. SKALSKI. Chem. Scr. **26**, 3 (1986); **26**, 7 (1986).
10. J. H. CHESTERFIELD, J. F. W. MCOMIE, and M. S. TUTE. J. Chem. Soc. 4590 (1960).
11. W. L. SUNG. Nucleic Acids Res. **9**, 6139 (1981).
12. A. J. VARGHESE. Photochem. Photobiol. **13**, 365 (1971); Biochemistry, **10**, 2194 (1971); Photochem. Photobiol. **15**, 113 (1972).
13. J. CIESIOLKA, K. NURSE, J. KLEIN, and J. OFENGAND. Biochemistry, **24**, 3233 (1985).

Can. J. Chem. Downloaded from www.nrcresearchpress.com by 93.93.197.157 on 09/07/12
For personal use only.

L'azote, site basique des amides encombrées ?

GEORGES GUIHENEUF,[1] JOSÉ-LUIS M. ABBOUD[2] ET ABDELJALIL LACHKAR
Laboratoire de chimie physique organique, Université Cadi Ayyad, BP S 15, Marrakech, Maroc

Reçu le 16 avril 1987[3]

GEORGES GUIHENEUF, JOSÉ-LUIS M. ABBOUD et ABDELJALIL LACHKAR. Can. J. Chem. **66**, 1032 (1988).

L'augmentation de la taille des substituants R des amides $R'CONR_2$ entraîne une élévation des constantes de complexation avec la molécule d'iode si R = CH_3. À l'inverse, lorsque R est un groupe alkyle différent de CH_3, les constantes diminuent jusqu'à un seuil critique d'encombrement de R et R'. Au-delà de cette limite les valeurs des constantes augmentent brutalement dans des proportions importantes. Ce comportement s'explique par un changement du site de fixation de l'iode. Alors que généralement le site basique des amides *N,N*-disubstituées est l'atome d'oxygène du carbonyle, les contraintes stériques en diminuant la conjugaison des groupes CO et NR_2 réduisent la basicité de l'oxygène et au-delà d'un seuil critique confèrent à l'atome d'azote un caractère basique proche de celui des amines. Cette interprétation est confirmée par la position de la bande de transfert de charge et par la comparaison avec les constantes de formation des complexes iode–amines et iode – composés carbonylés α-aminés.

GEORGES GUIHENEUF, JOSÉ-LUIS M. ABBOUD, and ABDELJALIL LACHKAR. Can. J. Chem. **66**, 1032 (1988).

If R = CH_3, an increase in the bulk of the R groups of the amides $R'CONR_2$ provokes an increase in the complexation constants with iodine. Conversely, if R is an alkyl group (but not a CH_3), the constants decrease up to a critical size for the bulkiness of R and R'. Above these limits, an abrupt increase of the constants is observed. This behaviour is rationalized in terms of a change in the point of fixation of the iodine. While the basic site of the *N,N*-disubstituted amides is the oxygen of the carbonyl, steric hindrance reduces the conjugation of the CO and NR_2 groups and hence the basicity of the oxygen; above the critical size and due to steric hindrance, the basicity of the nitrogen atom becomes similar to that of amines. This explanation is confirmed by the position of the charge transfer band and by a comparison with the formation constants of the complexes iodine–amines and iodine – α-amino carbonyl compounds.

[Journal translation]

Can. J. Chem. Downloaded from www.nrcresearchpress.com by 93.93.197.157 on 09/07/12
For personal use only.

Introduction

Les pivalamides *N,N*-disubstituées $(CH_3)_3CCONR_2$ sont moins basiques que les acétamides disubstituées CH_3CONR_2 correspondantes (1). Les effets électroniques des groupes méthyle et *tert*-butyle étant équivalents (2), la diminution des constantes d'association avec un acide de Lewis donné ne peut résulter que des contraintes stériques induites par les groupes $(CH_3)_3C$ et NR_2. Nous avons, dans un travail précédent (1), comparé les effets stériques des substituants $N(CH_3)_2$ et $N(C_2H_5)_2$ à l'aide de la différence des enthalpies libres de complexation des amides CH_3CONR_2 et $(CH_3)_3CCONR_2$ avec l'iode. En élargissant la gamme des substituants R à d'autres groupes plus encombrants, tel le cyclohexyle, nous avons observé que les constantes d'association des pivalamides avec l'iode deviennent très grandes. L'étude de divers substituants R nous a permis de déterminer l'origine de cette particularité.

Partie expérimentale

Les valeurs des constantes et des enthalpies libres de formation des complexes amides–iode, à 25°C en solution dans l'heptane, sont réunies dans le tableau 1. La similitude des conditions expérimentales autorise une comparaison directe avec nos résultats antérieurs (1, 3).

Lorsque les constantes sont inférieures à 1000 L mol^{-1}, nous utilisons la méthode décrite précédemment (3). Dans tous les cas où la valeur est supérieure à 1000 L mol^{-1}, la détermination est faite par des mesures spectrophotométriques sur la bande de transfert de charge (274 nm) dont le coefficient d'extinction molaire supérieur à 2×10^4 L mol^{-1} cm^{-1} autorise l'emploi de solutions très diluées. Pour éviter la formation des ions I_3^- il est nécessaire que la concentration en iode soit de l'ordre de 10^{-5} mol L^{-1} et que la concentration en donneur ne dépasse pas 5×10^{-4} mol L^{-1}; ces limites sont le résultat des nombreux essais auxquels nous avons procédé. Ces contraintes nous ont conduit à retenir la méthode proposée par Bellon (4). La solution d'iode est placée dans une cellule de 10 cm d'épaisseur et le spectre est enregistré, puis la solution de donneur est ajoutée par fraction de 0,1 cm^3, le volume total ajouté étant de 2 à 3 cm^3. Après chaque addition le spectre est enregistré. Les concentrations en iode et en donneur sont calculées en supposant les volumes additifs, ce qui, en raison de l'extrême dilution des solutions, ne peut entraîner d'erreur significative.[4] La valeur de la constante est ensuite déterminée par la procédure de Rose et Drago (5).

Mesures spectrophotométriques

Tous les spectres dans le domaine uv–visible ont été enregistrés sur un spectrophotomètre Cary 219. La température est maintenue constante par une circulation d'eau à partir d'un cryostat Lauda K2R.

Synthèse des produits

Les amides ont été préparées par action des amines convenables sur les chlorures d'acide correspondants; le composé $(C_6H_{11})_2NCH_2COOC_2H_5$ a été obtenu en faisant agir la dicyclohexylamine sur le chloroacétate d'éthyle. Tous les produits ont été purifiés par distillation, recristallisation ou sublimation.

Résultats et discussion

1. Influence du substituant R dans la série CH_3CONR_2

L'examen du tableau 1 met immédiatement en évidence l'augmentation des valeurs K_c ou $\Delta G°$ avec la taille du substituant NR_2: K_c est multipliée par deux en passant du groupe $N(CH_3)_2$ à $N(C_6H_{11})_2$. Nous trouvons ici une variation analogue à celle observée pour la basicité des alcools aliphatiques (6) pour lesquels la basicité augmente avec la longueur de la chaîne du substituant. Or la somme des effets inductif et de

1. Adresse pour toute correspondance: Institut universitaire de technologie, B.P. 420, 44606 Saint-Nazaire CEDEX, France.

2. Adresse actuelle: Instituto de Quimica Fisica « Rocasolano », C.S.I.C. Serrano, 119, 28006 Madrid, Espagne.

3. Révision reçue le 20 novembre 1987.

4. On peut acheter les tableaux des valeurs expérimentales des concentrations en iode, en amides et des absorbances correspondantes, utilisées pour la detérmination des constantes de complexation I_2–amides, en s'adressant au Dépôt des données non publiées, ICIST, Conseil national de recherches du Canada, Ottawa (Ontario), Canada K1A 0S2.

TABLEAU 1. Constantes et enthalpies libres de formation des complexes avec l'iode[a]

Composés	$K_c \pm \delta K_c$ (L mol^{-1})	$\Delta G° \pm \delta\Delta G°$ (kJ mol^{-1})
$CH_3CON(CH_3)_2$[b]	15 ± 1	−6,7 ± 0,4
$CH_3CON(C_2H_5)_2$[b]	18,8 ± 0,5	−7,3 ± 0,4
$(CH_3)_3CCON(CH_3)_2$[c]	6,7 ± 0,4	−4,7 ± 0,2
$(CH_3)_3CCON(C_2H_5)_2$[c]	6,7 ± 0,9	−4,7 ± 0.4
$CH_3CON[CH(CH_3)_2]_2$	27 ± 4	−8,15 ± 0,4
$CH_3CON[CH_2CH(CH_3)_2]_2$	21,5 ± 3	−7,75 ± 0,4
$CH_3CON(C_6H_{11})_2$	31 ± 4	−8,6 ± 0.4
$C_2H_5CON(C_6H_{11})_2$	15 ± 1	−6,7 ± 0,4
$(CH_3)_2CHCON(C_6H_{11})_2$	1350 ± 200	−18,0 ± 0,4
$(CH_3)_3CCON(C_6H_{11})_2$	4300 ± 600	−21,0 ± 0.3
$(CH_3)_3CCON[CH(CH_3)_2]_2$	350 ± 150	−14,6 ± 1,7
$(CH_3)_3CCON[CH_2CH(CH_3)_2]_2$	250 ± 50	−13,8 ± 0,6
$C_2H_5OCOCH_2N(C_6H_{11})_2$	3800 ± 320	−20,5 ± 0,3

[a]À 25°C, en solution dans l'heptane, reproductibilité pour un degré de confiance de 95%.
[b]Valeur extraite de la référence 3.
[c]Valeur extraite de la référence 1.

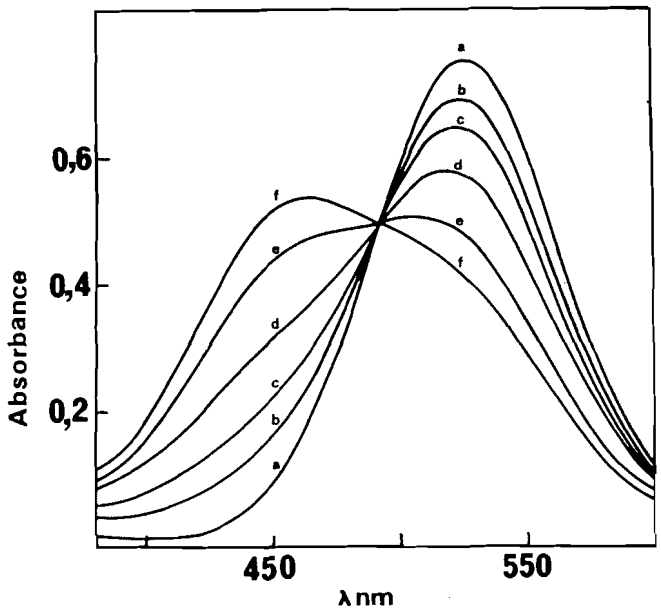

FIG. 1. Absorption de l'iode dans les mélanges iode–*N*,*N*-dicyclohexylacétamide (T = 298 K; solvant : heptane). $[I_2] = 8{,}3 \times 10^{-4}$ mol L^{-1}; $[CH_3CON(C_6H_{11})_2] \times 10^{-3}$ mol L^{-1} : (a) = 0; (b) = 2,8; (c) = 5,1; (d) = 9,6; (e) = 17,3; (f) = 23,7.

résonance demeure pratiquement constante alors que la polarisabilité augmente avec le nombre de groupes CH_2 (7). Il semble donc que l'augmentation de la basicité des amides *N*,*N*-disubstituées soit liée à la polarisabilité croissante du substituant NR_2.

Ces résultats confirment également l'absence de contrainte stérique notable entre les groupes NR_2 et CH_3, ceci indépendamment de la taiHe des groupes alkyles R; cette supposition, base de notre estimation des interactions stériques (1), trouve ainsi une justification supplémentaire.

Pour tous les composés de la série CH_3CONR_2, les spectres des solutions mixtes iode–amides, dans l'heptane, sont analogues. La figure 1 illustre ces spectres pour le complexe iode–*N*,*N*-dicyclohexylacétamide. Nous relevons les présences

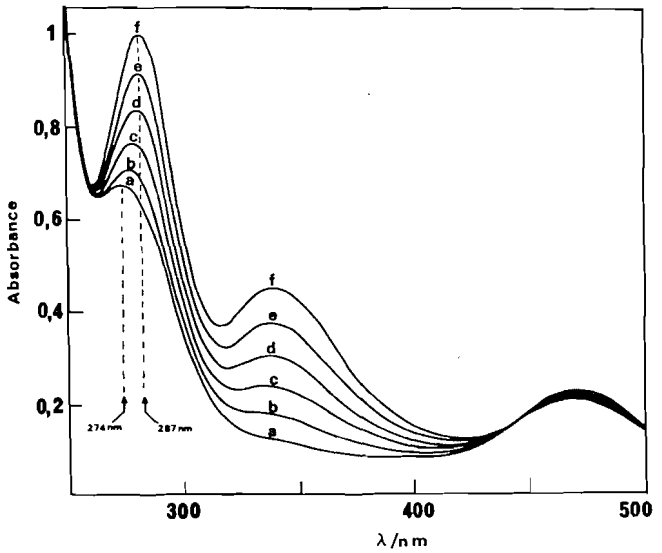

FIG. 2. Evolution de l'absorption d'un mélange iode–*N*,*N*-dicyclohexylpivalamide au cours du temps (T = 298 K; solvant : heptane). $[I_2] = 1{,}2 \times 10^{-5}$ mol L^{-1}; $[(CH_3)_3CCON(C_6H_{11})_2] = 10^{-4}$ mol L^{-1}. Temps : (a) = 0; (b) = 30 min; (c) = 60 min; (d) = 90 min; (e) = 120 min; (f) = 150 min.

de la bande de l'iode libre (520 nm) et de la bande de l'iode complexé (maximum au voisinage de 470 nm) dont l'intensité augmente avec la concentration en amide (la concentration en iode est maintenue constante). Hormis ces deux bandes il n'existe pas d'autre absorption caractéristique; en particulier il est impossible de mettre en évidence, dans le domaine de longueur d'onde accessible ($\lambda > 200$ nm), une absorption de transfert de charge.

2. Association I_2–$(CH_3)_3CCON(C_6H_{11})_2$

En choisissant des domaines de concentrations, pour l'iode et l'amide, identiques à ceux retenus précédemment (I_2, 10^{-3} mol L^{-1}; amide, 10^{-2} mol L^{-1}) les spectres enregistrés présentent des différences appréciables.

(a) La bande de l'iode complexé (470 nm) n'apparaît pas, quelle que soit la concentration en iode et en amide. De même, le point isobestique, présent sur le spectre de la figure 1, est absent.

(b) Une absorption intense se manifeste au voisinage de 350 nm dont l'intensité croît plus rapidement que la concentration en amide. Il ne peut donc s'agir d'une bande de transfert de charge, puisque dans cette hypothèse, les variations d'absorbance seraient inférieures à celles résultant de la relation de Beer–Lambert.

(c) Il n'existe pas de relation entre les variations d'absorbance aux différentes longueur d'onde et aucun résultat significatif ne peut être calculé pour les constantes K_c.

(d) Les spectres évoluent très rapidement dans le temps et nous avons remarqué la formation d'un précipité, même aux faibles concentrations.

Par ailleurs, et parallèlement à l'absorption située à 350 nm, une bande apparaît entre 280 et 300 nm. Ces deux bandes sont semblables aux bandes des ions I_3^- (8). Nous pouvons donc penser que des ions I_3^- se forment très rapidement dans le cas du complexe I_2–$(CH_3)_3CCON(C_6H_{11})_2$, même en solution dans l'heptane, qui ne favorise pas la formation de ces ions, et pour des solutions très diluées en iode et en donneur. C'est la première fois qu'un tel comportement des complexes iode – composés carbonylés est observé.

Can. J. Chem. Downloaded from www.nrcresearchpress.com by 93.93.197.157 on 09/07/12
For personal use only.

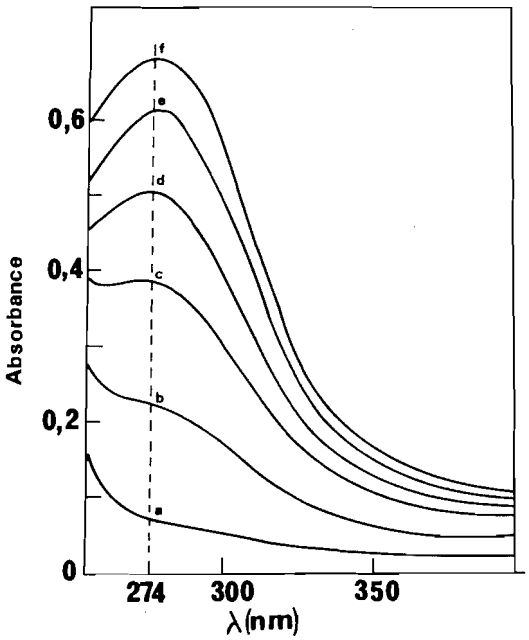

FIG. 3. Absorption des mélanges I_2–$(CH_3)_2CHCON(C_6H_{11})_2$ (T = 298 K; solvant : heptane). $[I_2] \times 10^5$ mol L^{-1} : (a) = 1,67; (b) = 1,65; (c) = 1,63; (d) = 1,615; (e) = 1,60; (f) = 1,58. $[(CH_3)_2CHCON(C_6H_{11})_2] \times 10^5$ mol L^{-1} (a) = 0; (b) = 2,88; (c) = 6,42; (d) = 9,70; (e) = 13,5; (f) = 16,1.

L'enregistrement des spectres en fonction du temps permet de préciser la suite des réactions (figure 2). Initialement, un choix convenable des concentrations ($I_2 = 1{,}2 \times 10^{-5}$ mol L^{-1}; amide = 10^{-4} mol L^{-1}) élimine la présence de la bande à 350 nm; en revanche, nous notons une absorption très intense à 274 nm. Au cours du temps, l'intensité de cette dernière bande diminue pendant qu'apparaissent les bandes à 350 nm et 287 nm. Ensuite, en laissant une durée suffisante d'évolution, les bandes à 350 et 287 nm disparaissent.

La bande située à 274 nm qui n'appartient ni à l'iode ni à l'amide doit être attribuée au complexe. L'existence d'une bande de transfert de charge dans ce domaine de longueur d'onde est tout à fait remarquable; en général il est impossible d'observer les transitions de transfert de charge des complexes iode – composés carbonylés.

L'évolution des spectres dans le temps conduit à proposer le processus suivant : dans un premier stade, il y a formation du complexe par transfert de charge identifié par la bande à 274 nm. Ensuite ce complexe évolue vers un complexe ionique avec apparition des ions I_3^- (bande à 290 et 350 nm). À ce jour, une évolution de ce type n'avait pas été observée pour les complexes CO..I_2 alors que des phénomènes semblables sont fréquents avec les complexes amines–iode (9); si nous prenons l'exemple du complexe iode–triéthylamine, la bande de transfert de charge, à 278 nm, présente au moment de la mise en solution disparaît ensuite progressivement. Nous remarquons la similitude des positions des bandes de transfert de charge pour les deux types de complexes iode–amine (278 nm) et iode–*N*,*N*-dicyclohexylpivalamide (274 nm).

Nous avons ensuite procédé à la recherche des conditions expérimentales et des concentrations permettant une détermination de la constante de formation du complexe initial. Ceci nous a conduit à modifier la méthode utilisée habituellement (cf. Partie expérimentale). En choisissant une concentration en iode très faible (10^{-5} mol L^{-1}) et en faisant varier la concentration en amide de 10^{-5} mol L^{-1} à environ 5×10^{-4} mol L^{-1} il est possible d'avoir des solutions qui n'évoluent pas significativement pendant le temps de l'expérience (1–2 h). Un exemple de spectre et donné sur la figure 3.

En exploitant la mesure de l'absorbance au maximum de la bande de transfert de charge, la valeur calculée de K_c est égale à 4300 L mol^{-1} ($\Delta G° = -21$ kJ mol^{-1}). Cette valeur est très supérieure à celle habituellement obtenues pour les complexes iode – composés carbonylés et est totalement incompatible avec la valeur K_c du complexe I_2–$CH_3CON(C_6H_{11})_2$: en raison de la contrainte stérique entre les groupes $(CH_3)_3C$ et $N(C_6H_{11})_2$, la constante devrait être inférieure à 30 L mol^{-1} pour le complexe I_2–*N*,*N*-dicyclohexylpivalamide.

Ces anomalies et l'analogie remarquée à plusieurs reprises avec les propriétés des complexes iode–amines, permettent de conclure à une complexation au niveau de l'atome d'azote de la *N*,*N*-dicyclohexylpivalamide.

Le site basique des amides *N*,*N*-disubstituées est toujours l'atome d'oxygène, aussi bien pour les complexes par transfert de charge (10, 11) que par liaison hydrogène (3). Il s'agit donc du premier exemple de fixation d'un acide de Lewis sur l'atome d'azote d'une amide acyclique. Cette particularité peut s'expliquer par l'effet stérique très grand du groupe $N(C_6H_{11})_2$. Pour les substituants $N(CH_3)_2$ et $N(C_2H_5)_2$, la substitution du groupe CH_3 par le groupe $(CH_3)_3C$ entraîne une diminution importante de K_c et de la stabilité du complexe. Cet abaissement est plus marqué avec $N(C_2H_5)_2$ en raison de l'effet stérique plus important du groupe éthyle. La contrainte stérique est levée soit par une ouverture de l'angle C—CO—N soit par une rotation du substituant NR_2 autour de la liaison C—N. Il en résulte une diminution de l'effet mésomère donneur du groupe NR_2 et un abaissement de la basicité du groupe carbonyle. Lorsque la contraite stérique devient très forte comme c'est le cas avec le substituant $N(C_6H_{11})_2$, l'angle de rotation peut devenir tel que la conjugaison entre les groupes CO et NR_2 est pratiquement absente. Le site le plus basique devient alors l'atome d'azote qui possède une basicité analogue à celle de l'azote d'une amine porteur d'un substituant attracteur par effet inductif et sans effet mésomère.

3. *Influence de l'encombrement stérique du substituant R′ de R′CON(C_6H_{11})$_2$*

Afin de confirmer l'interprétation proposée, nous avons fait varier l'encombrement du substituant noté R′ et avons déterminé les K_c de formation des complexes avec l'iode pour la série R′ = CH_3, CH_2CH_3, $CH(CH_3)_2$ et $C(CH_3)$. La substitution progressive des atomes d'hydrogène par des groupes méthyles s'accompagne d'abord d'une diminution de K_c, similaire à celle qui se produit en passant de $CH_3CON(CH_3)_2$ à $C_2H_5CON(CH_3)_2$. Puis une brutale inversion est provoquée par le groupe isopropyle, la constante K_c devient égale à 1350 L mol^{-1} et la bande de transfert de charge à 274 nm apparaît alors qu'elle était absente avec les composés précédents. La substitution par le groupe isopropyle donne un composé dont les propriétés de basicité sont les mêmes que celles de la *N*,*N*-dicyclohexylpivalamide. La valeur K_c moins élevée s'explique par une contrainte stérique moins forte qu'avec le *tert*-butyle et une conjugaison résiduelle entre les groupes CO et NR_2. Conformément aux prévisions faites à partir du modèle proposé, la basicité commence par diminuer, puis augmente au-delà d'un encombrement stérique « critique » des substituants. En fait, la basicité de l'oxygène continue à diminuer puisque la conjugaison s'affaiblit, mais la détermination expérimentale de sa valeur est impossible.

Can. J. Chem. Downloaded from www.nrcresearchpress.com by 93.93.197.157 on 09/07/12
For personal use only.

4. Substitutions sur l'atome d'azote

La substitution des groupes alkyle de l'atome d'azote exerce également une influence sur la nature de l'association avec l'iode. Ainsi, pour les composés $(CH_3)_3CCON[CH(CH_3)_2]_2$ et $(CH_3)_3CCON[CH_2CH(CH_3)_2)]_2$, apparaît également une bande de transfert de charge vers 275 nm, mais pour avoir une intensité d'absorption significative il est nécessaire d'accroître les concentrations en iode et en amide. Dans ces conditions, la formation des ions I_3^- et l'évolution des solutions sont très rapides. Les constantes de formation des complexes ont été déterminées à partir de l'absorption de l'iode à 520 nm en nous assurant que les ions I_3^- ne perturbaient pas les mesures. Pour cela, nous avons été contraints de nous placer dans des domaines de concentrations où la proportion d'iode complexé est faible; la reproductibilité est alors moins satisfaisante que pour les autres valeurs de constantes. Toutefois, en raison des différences importantes entre les constantes, les écarts sont significatifs. Pour les deux composés, les constantes sont comprises entre 250 et 350 L mol^{-1}, le site basique est donc à nouveau l'atome d'azote, mais en raison de la conjugaison résiduelle, sa basicité et plus faible que celle de la *N,N*-dicyclohexylpivalamide. L'augmentation progressive des constantes avec l'encombrement stérique des substituants est parfaitement en accord avec une complexation sur l'azote provoquée par les contraintes stériques.

5. Comparaison avec les amines et les composés carbonylés α-aminés

La constante déterminée pour le complexe iodo–dicyclohexylpivalamide est compatible avec celles relevées dans la littérature pour les complexes iode – amines tertiaires. Dans l'heptane, à 20°C, ces valeurs sont, par exemple, de 13 804 L mol^{-1} pour le complexe I_2–$(CH_3)_2N(C_6H_{11})$ et de 2 344 L mol^{-1} pour I_2–$CH_3N(C_6H_{11})_2$ (12).

Pour confirmer cet accord, nous avons étudié le complexe I_2–$C_2H_5OCOCH_2N(C_6H_{11})_2$. L'encombrement autour de l'azote est proche de celui existant dans la *N,N*-dicyclohexylpivalamide et le groupe CH_2 élimine la conjugaison entre le carbonyle et l'azote. L'atome d'azote doit donc posséder des propriétés basiques proches de celles de l'azote de la *N,N*-dicyclohexylpivalamide. La bande de transfert de charge du complexe est située à 280 nm; les solutions évoluent également dans le temps avec disparition de la bande de transfert de charge et formation des ions I_3^- caractérisés par les bandes à 350 et 287 nm. La constante de complexation déterminée à partir de l'absorption de transfert de charge est se 3 800 L mol^{-1}, comparable à la valeur 4300 obtenue pour le complexe iode–*N,N*-dicyclohexylpivalamide.

L'ensemble des données spectrales, thermodynamiques et d'effets structuraux sur ces grandeurs vont dans le sens d'un changement du site basique dans les amides encombrées. Il faut remarquer que cette conclusion s'applique au cas de l'iode, acide mou dans la classification de Pearson (13, 14); elle ne peut pas être étendue, sans vérification expérimentale préalable, à des acides durs tels que les donneurs de liaison hydrogène.

1. G. Guiheneuf, J. L. M. Abboud et C. Rafik. J. Org. Chem. **48**, 4761 (1983).
2. R. W. Taft et C. A. Grob. J. Am. Chem. Soc. **95**, 1236 (1974).
3. C. Laurence, G. Guiheneuf et B. Wojkowiak. J. Am. Chem. Soc. **101**, 4793 (1979).
4. L. Bellon. Thèse de doctorat, Bordeaux (1960).
5. N. J. Rose et R. S. Drago. J. Am. Chem. Soc. **81**, 6138 (1959).
6. J. L. M. Abboud, K. Sraidi, G. Guiheneuf, M. J. Kamlet et R. W. Taft. J. Org. Chem. **50**, 2870 (1985).
7. W. J. Hehre, C. F. Pau, A. D. Headley et R. W. Taft. J. Am. Chem. Soc. **108**, 1711 (1986).
8. R. E. Buckles, J. P. Yuk et A. I. Popov. J. Am. Chem. Soc. **74**, 4379 (1952).
9. H. D. Bist et W. B. Person. J. Phys. Chem. **73**, 482 (1969).
10. E. Augdahl et P. Klaboe. Acta Chem. Scand. **19**, 1637 (1962).
11. C. D. Schmulbach et R. S. Drago. J. Am. Chem. Soc. **82**, 1637 (1960).
12. C. Takayama, T. Fujita et M. Nakajima. J. Org. Chem. **44**, 2871 (1979).
13. R. G. Pearson. J. Am. Chem. Soc. **85**: 3533 (1963).
14. W. B. Jensen. Chem. Rev. **78**, 1 (1978).

Can. J. Chem. Downloaded from www.nrcresearchpress.com by 93.93.197.157 on 09/07/12
For personal use only.

Convolutive voltammetry with microelectrodes

A. R. HARMAN AND A. S. BARANSKI
Department of Chemistry, University of Saskatchewan, Saskatoon, Sask., Canada S7N 0W0

Received September 9, 1987

A. R. HARMAN and A. S. BARANSKI. Can. J. Chem. **66**, 1036 (1988).

Hemispherical microelectrodes prepared by electroplating of mercury on platinum microelectrodes were used in studies of fast charge transfer processes under convolutive voltammetry conditions. The algorithm used in the convolutive transformation was modified to account for spherical symmetry of diffusion. The sweep rate was varied from 0.1 to 220 V/s. Low sweep rate experiments were used to test the symmetry of the mass transport. It was found that the mass transport to (and inside) the electrodes can be described with good accuracy by the spherical symmetry diffusion. It was shown that the spherical convolution can be used to determine from cyclic voltammetric data the diffusion coefficient of a depolarizer and the number of electrons transfered to (or from) the depolarizer molecule in the electrode process.

At high sweep rates the technique was found useful in studies of fast electrode reactions. The technique was tested in the determination of kinetic parameters for Cd^{2+} reduction in aqueous solutions and *p*-dicyanobenzene reduction in DMF solutions. In both cases good agreement with values reported in literature was found. Properties of Hg/Pt microelectrodes were also studied using the ac impedance techniques. The ac impedance measurements were carried out at various frequencies (0.1 Hz to 100 kHz) in solutions containing 0.1 to 10^{-5} *M* of the supporting electrolyte.

A. R. HARMAN et A. S. BARANSKI. Can. J. Chem. **66**, 1036 (1988).

On a préparé des micro-électrodes hémisphériques en faisant de l'électrodéposition de mercure sur des micro-électrodes de plantine et on les a utilisées pour étudier les processus rapides de transfert de charge dans des conditions de voltampérométrie de convolution. On a modifié l'algorithme utilisé dans la transformation de convolution pour tenir compte de la symétrie sphérique de la diffusion. On a fait varier la vitesse de balayage de 0,1 à 220 V/s. On a utilisé les expériences aux basses vitesses de balayage pour vérifier la symétrie de la masse de transport. On a trouvé que la masse de transport vers les (et à l'intérieur des) électrodes peut être décrite avec une bonne précision en utilisant la diffusion de symétrie sphérique. On a démontré qu'on peut utiliser la convolution sphérique pour déterminer, à partir des données de la voltampérométrie cyclique, le coefficient de diffusion d'un dépolarisant ainsi que le nombre d'électrons qui sont transférés vers (ou de) la molécule dépolarisante dans le processus de l'électrode.

A des vitesses de balayage élevées, on a trouvé que la technique est utile dans des études de réactions à l'électrode qui sont rapides. On a vérifié la technique dans la détermination des paramètres cinétiques de la réduction du Cd^{2+} en solutions aqueuses ainsi que de la réduction du *p*-dicyanobenzène dans des solutions de DMF. Dans chacun des cas, on a trouvé une bonne corrélation avec les valeurs rapportées dans la littérature. Utilisant des techniques d'impédance en ca, on a aussi étudié les propriétés de micro-électrodes Hg/Pt. On a effectué des mesures d'impédance en ca à diverses fréquences (0,1 Hz à 100 kHz), dans des solutions contenant de 0,1 à 10^{-5} *M* d'électrolyte de support.

[Traduit par la revue]

Introduction

In most electrochemical measurements the rate of the process can be calculated directly from the value of the current flowing through the circuit. However, the determination of rate constants is more complicated because it requires knowledge of the concentration of reactants at the reaction site. The convolution method introduced by Oldham (1, 2) and independently by Saveant and co-workers (3–5) allows simple determination of the surface concentration of a depolarizer from the current–time dependence measured during an electrochemical experiment. Originally this method was based on semi-integration of current with respect to time and it was applicable to processes involving semi-infinite linear diffusion of reactants. Recently the method was extended to include spherical symmetry of diffusion (6). The spherical symmetry convolution can be easily applied to analysis of cyclic voltammetry curves obtained with spherical or hemispherical microelectrodes. Such electrodes can be readily produced by electroplating of mercury on platinum disk microelectrodes (7, 8). Cyclic voltammetry with microelectrodes (microvoltammetry) has several advantages. The solution resistance (R_s) of a hemispherical electrode can be described as:

$$[1] \quad R_s = 1/2\pi\kappa r$$

where κ is the electrical conductivity of the solution and r is the radius of the electrode.

The electrical capacitance of the electrode is proportional to its surface area:

$$[2] \quad C = 2\pi C_d r^2$$

where C_d is the specific capacitance of the metal–solution interface.

Consequently, the time constant of the electrode is

$$[3] \quad \tau = R_s C = C_d r/\kappa$$

In some cases it is possible to construct a cell with time constant lower than 10 ns. This, of course, means that very high sweep rates can be used in cyclic voltammetry experiments and, as a result, kinetics of very fast electrode reactions can be studied (9, 10).

Another important aspect of microvoltammetry is a significant reduction of the resistance polarization. This is apparent particularly at high sweep rates, when mass transport to a microelectrode resembles that to a conventional size electrode. In such a case the current is proportional to the surface area of the electrode. Since the solution resistance is inversely proportional to the radius, the resistance polarization of the electrode decreases with its radius. Recently it has been shown that microelectrodes can be successfully employed in electroanalysis in solvents of low dielectric constant (9), organic solvents without supporting electrolyte (11), organic glasses (11), and even in the gas phase (12).

Can. J. Chem. Downloaded from www.nrcresearchpress.com by 93.93.197.157 on 09/07/12
For personal use only.

Can. J. Chem. Downloaded from www.nrcresearchpress.com by 93.93.197.157 on 09/07/12
For personal use only.

Advantages of using microelectrodes in the study of the heterogeneous electron transfer kinetics are obvious. Since the mass transport becomes faster, and the solution resistance per surface area becomes smaller with a decrease in the size of an electrode, the activation resistance of the electrode reaction (connected in series with mass transport impedance and solution resistance) can be more precisely determined on small rather than on large electrodes. It was demonstrated that with microelectrodes the rate constants of fast electron transfer reactions ($k_s > 1$ cm/s) can be measured under both: steady-state conditions (i.e. slow sweep rates) (13, 14), and fast perturbation conditions (i.e. fast sweep rates) (9, 15).

The measurements reported in literature were done exclusively with solid microelectrodes: disk (9), ring (13, 14), and hemicyclindrical (15).

In this work the usefulness of mercury microelectrodes in studies of heterogeneous mass transfer processes is demonstrated. In addition a large part of these studies was dedicated to the evaluation of the quality of microelectrodes by ac impedance techniques.

Experimental

Reagents

Analytical grade chemicals and Millipore water were used to prepare aqueous solutions. *N*,*N*-Dimethylformamide (DMF) was dried with calcium hydride then it was distilled at reduced pressure under argon atmosphere. Tetrabutylammonium perchlorate (TBAP) was recrystallized from distilled water and dried *in vacuo* over P_2O_5 at 50°C. *p*-Dicyanobenzene (Aldrich) was used without additional purification.

Electrodes

Platinum microelectrodes were prepared by sealing a platinum wire (25 μm in diameter, Goodfellow Metals) in Pyrex glass. Before use the glass tube containing the wire was cut perpendicularly to its length and the surface of the electrode was polished with an extra fine carborundum sandpaper followed by polishing with 0.3 μm alumina.

A hemispherical mercury microelectrode was prepared by the electrodeposition of an exact amount of mercury on the Pt microelectrode. The process was carried out under controlled current conditions from a saturated aqueous solution of KBr containing 0.1 *M* $HgBr_2$ (high concentration of Br^- ions was necessary to ensure direct reduction of $HgBr_4^{2-}$ complex to Hg without formation of Hg_2Br_2). After the deposition the electrode was cycled several times in 0.1 *M* $NaClO_4$ between 0 and −1.0 V in order to spread the Hg over the platinum disk. Each Hg/Pt microelectrode before its use was carefully examined with an optical microscope in order to eliminate electrodes improperly sealed into glass or incompletely covered with mercury. For convenience and reproducibility the deposition process was totally controlled by microcomputer. The effective radius of the microelectrode, as determined from a low sweep rate voltammetric experiment, varied no more than ±7% for electrodes deposited under identical conditions.

Electrochemical measurements

In all electrochemical measurements the reference electrode was an aqueous calomel electrode containing a saturated solution of NaCl.

In non-aqueous media the reference electrode was separated from the analyzed solutions by a sintered glass junction and an intermediate solution containing 0.1 *M* TBAP in DMF. Prior to all electrochemical experiments the solutions were deaerated for 10 min with argon.

Microvoltammetric measurements were done without a potentiostat in a two electrode cell. The electronic system consisted of an Apple IIe microcomputer equipped with an 3.6 MHz accelerator card and a 12-bit A/D converter (both from Applied Engineering) as well as an AdaLab card (Interactive Structures) containing 12-bit D/A convertor and four 16-bit timers. The current passing through the system was monitored by a Current Preamplifier EG&G-PAR Model 181 with a sensitivity 10^{-3} A/V to 10^{-9} A/V and a bandwidth of 100 kHz at 10^{-6} A/V. The output of the preamplifier was connected to the A/D convertor through a low pass filter. The low pass filter was made of a 1 kΩ resistor and interchangeable capacitors.

A machine language program written in this laboratory enabled cyclic voltammetry experiments at sweep rates up to 220 V/s. A potential ramp used in these experiments was numerically generated and had the form of a staircase function with the step height dependent on the sweep rate. For sweep rates lower than 55 V/s the step height was always 2 mV, for sweep rates between 55 and 110 V/s the step height was 4 mV, and finally for sweep rates greater than 110 V/s it was 8 mV. However, due to the action of the low pass filter at the current preamplifier output the results obtained with this experimental setup closely resembled ones obtained under standard linear sweep voltammetry conditions. The significance of using the low pass filter will be discussed later.

The double layer capacitance measurements at microelectrodes were carried out using a EG&G-PAR Model 273 Potentiostat/Galvanostat and a EG&G-PAR Model 5301EC Lock-In amplifier.

Convolution programs were created in this laboratory using the Zbasic compiler. All computations were carried out on a Macintosh Plus microcomputer.

Results and discussion

Data analysis

As it was shown by Myland *et al.* (6) in the case of spherical diffusion the concentration of the depolarizer at the surface of the electrode can be obtained from the convolution of current which for species present in the electrolytic solution (diffusion outside the sphere) can be expressed as:

$$[4] \quad C_O^S = C_O^0 - \frac{I_{out}}{3nFV}$$

$$[5] \quad C_R^S = C_R^0 + \frac{I_{out}}{3nFV}$$

In eqs. [4] and [5] C_O^S and C_R^S are the surface concentrations of the oxidized and reduced forms of a depolarizer respectively, C_O^0 and C_R^0 are the initial, bulk concentration of the oxidized and reduced forms of a depolarizer, V is the volume of the electrode, and other symbols have their usual meaning. I_{out} is the convoluted current which can be calculated as:

$$[6] \quad I_{out} = \int_0^t i(t)\sigma_{out}(t-\tau)d\tau$$

where $i(t)$ is the faradaic current passing through the electrode and $\sigma_{out}(t-\tau)$ is the mass transport symmetry function for the diffusion outside a sphere given by:

$$[7] \quad \sigma_{out}(z) = \left(\pi \frac{Dz}{r^2}\right)^{-1/2} - \exp\left(\frac{Dz}{r^2}\right) \operatorname{erfc} \sqrt{\frac{Dz}{r^2}}$$

In this equation D is the diffusion coefficient of the reduced or oxidized form of a depolarizer and r is the radius of the electrode. Note that in order to calculate the surface concentration of the oxidized form of a depolarizer from eq. [4], the diffusion coefficient of the oxidized form must be used in eq. [7], and vice versa. In many cases, however, the diffusion coefficients of reduced and oxidized forms of a depolarizer are practically identical (in this work such an assumption was made in the case of *p*-DCB).

For the diffusion inside the sphere (metals dissolved in mercury) the corresponding equations have the form:

$$[8] \quad C_M^S = C_M^0 + \frac{I_{in}}{3nFV}$$

Can. J. Chem. Downloaded from www.nrcresearchpress.com by 93.93.197.157 on 09/07/12
For personal use only.

$$[9] \quad I_{in} = \int_0^t i(t)\sigma_{in}(t-\tau)d\tau$$

and

$$[10] \quad \sigma_{in}(z) = 3 + 2\sum_j^{\infty} \exp\left(\frac{-y_j D_M z}{r^2}\right)$$

where C_M^S and C_M^0 are the surface concentration and the initial, bulk concentration of the amalgam, respectively, D_M is the diffusion coefficient of the depolarizer in amalgam, I_{in} and $\sigma_{in}(z)$ are the convoluted current function and the mass transport symmetry function for the diffusion inside a sphere, y_j is the jth positive root of the equation $y = \tan(y)$ and other symbols have the same meaning as in eqs. [4], [6], and [7].

The numerical method used in computations of integrals [6] and [9] was similar to one described by Myland *et al.* (6).

In computer-controlled voltammetric experiments applying the potential in a form of a staircase function, directly from a D/A convertor, is always simpler than interfacing the computer with an analog linear sweep generator. In addition, charging currents under staircase voltammetry conditions are usually smaller than under linear sweep voltammetry conditions (16). However, the interpretation of data obtained under staircase voltammetry conditions is more complex. In order to compute correct values of the I_{in} and I_{out} functions, $i(t)$ in eqs. [6] and [9] must represent the average faradaic current passing through the circuit during a given sampling period. It was shown (17) that the current–potential function in staircase voltammetry changes significantly depending on the sampling parameter:

$$[11] \quad s = 1 - t_s/t_0$$

where t_0 is the width of the step and t_s is time at which current is sampled (counted from the beginning of the step). Stefani and Seeber (18) show the excitation potential in staircase voltammetry can be represented as a sum of the linear ramp and a sawtooth function; consequently the current response of the electrode can be expressed as a current expected for the linear sweep voltammetry (linear sweep component) and a periodic current created by the sawtooth polarization (ac component). The ac component reaches zero for a certain value of the sampling parameter s_0. It was calculated that for a totally reversible process $s_0 = 0.7$. Unfortunately, for quasi-reversible processes the value of s_0 varies, depending on the electrode potential and kinetic parameters of the studied system. In the case of microelectrodes the situation is complicated even more due to the non-linear symmetry of mass transport. To avoid problems with the interpretation of the data, the sampling parameter was always equal to 0.5 and the voltage output of the current preamplifier was smoothed by passing it through a low pass filter. The time constant of the filter (T_f) was exactly known and it was always within the range:

$$[12] \quad 3W_E < T_f < 6W_E$$

where W_E is the width of the step in the applied potential program.

While the filter removed the ac component of the current sufficiently, it also caused some distortion of the linear sweep component. This distortion can be described by:

$$[13] \quad V_2(t) = V_1(t) + T_f(dV_2/dt)$$

where V_1 and V_2 are voltages at the output of the current-to-voltage convertor and the output of the filter, respectively.

Equation [13] was actually used to correct the linear sweep component of the current for the distortion caused by the filter.

Under the experimental conditions used in this work the charging current was practically the same as it would be under linear sweep voltammetry conditions. Charging currents were subtracted from the *CV* curves using the procedure suggested by Nadjo *et al.* (4).

Double layer capacitance studies

Since the electron transfer kinetics is affected by the nature of electrode surface, it was necessary to establish whether the interfacial properties of Hg/Pt microelectrodes are the same as traditional mercury electrodes. This was accomplished by carrying out detailed ac impedance studies of hemispherical Hg/Pt microelectrodes in aqueous solutions of $NaClO_4$. The first group of experiments involved double layer capacitance measurements over a large range of frequencies. Measurements at high frequencies 100 kHz to 10 Hz were done using a lock-in amplifier, while at low frequencies the Fast Fourier Transform (FFT) technique was employed. In both cases ac impedance software from EG&G was used; however, in order to increase the sensitivity of the measurements a Model 181 current preamplifier was used as a current-to-voltage convertor. In Fig. 1 a typical frequency dependence of the apparent capacitance (C_d) of the hemispherical Hg/Pt microelectrode (25 μm in diameter) and the in-phase impedance of the cell, Z_{in}, is shown. The measurements were taken in 0.1 *M* aqueous solution of $NaClO_4$ at −1.0 V vs. SCE. The apparent capacitance was calculated as:

$$[14] \quad C_d = (2\pi Z_{out}\omega r^2)^{-1}$$

where Z_{out} is the out-of-phase impedance of the cell, ω is the angular frequency, and r is the radius of the working electrode.

At high frequencies Z_{in} approaches 2800 Ω which is the sum of the actual solution resistance retained by the working microelectrode, R_s, and the resistance of a junction between the analyzed solution and the reference electrode (all measurements were carried out in a two electrode system). At frequencies lower than 1 kHz, Z_{in} increases rapidly with a decrease in frequency. This may be caused by a systematic error in the measurements. At low frequencies the flow of current is limited mostly by the impedance associated with the double layer capacitance, the phase angle of the current approaches 90°, and consequently, the in-phase component of the current and the in-phase impedance of the circuit can no longer be determined exactly. The apparent double layer capacitance is remarkably stable over a large range of frequencies; it was found equal to 112 pF (11.4 μF cm^{-2}) at 64 kHz and 129 pF (13.1 μF cm^{-2}) at 100 Hz. C_d increases significantly only at frequencies lower than 10 Hz. It is obvious that the quality of Hg/Pt microelectrodes is much higher than microelectrodes made of carbon fiber sealed into polyethylene (19). First of all, the determined value of C_d is in reasonably good agreement with one expected for the Hg/0.1 *M* $NaClO_4$ interface (about 15 μF/cm^2); the small discrepancy may be caused by an error in the determination of the surface area of the electrode or, less likely, by contamination of the electrode with surfactants. The frequency dispersion of the capacitance observed at low frequencies may be explained by the presence of a narrow pore, filled with the electrolyte, between the metal and the insulator. The impedance of porous electrodes was discussed in detail by DeLevie (20). Porous behavior may also be emulated by a residual ionic conductivity

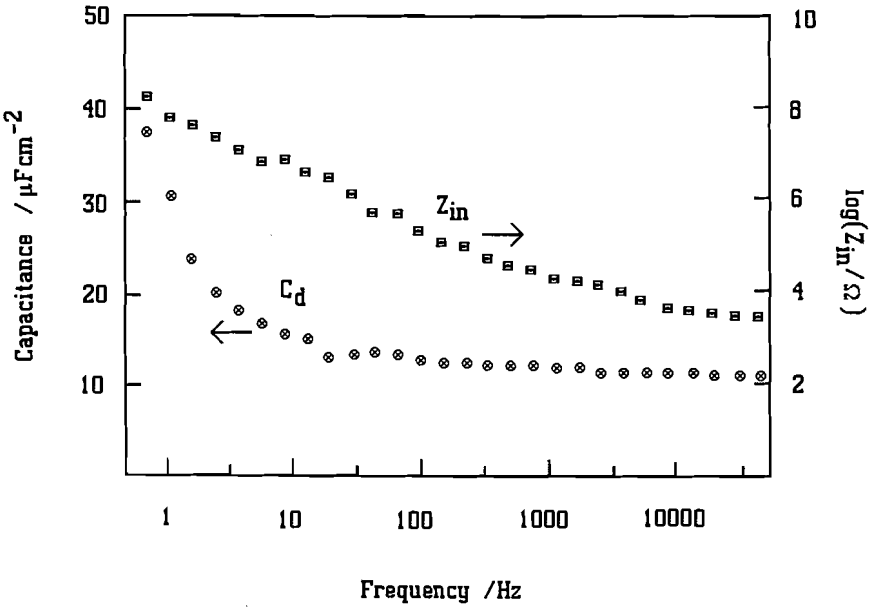

FIG. 1. Frequency dependence of the apparent differential capacitance, C_d, and the in-phase impedance, Z_{in}, of a hemispherical Hg/Pt electrode (12.5 μm in radius) in 0.1 *M* aqueous $NaClO_4$ at −1.0 V vs. SCE.

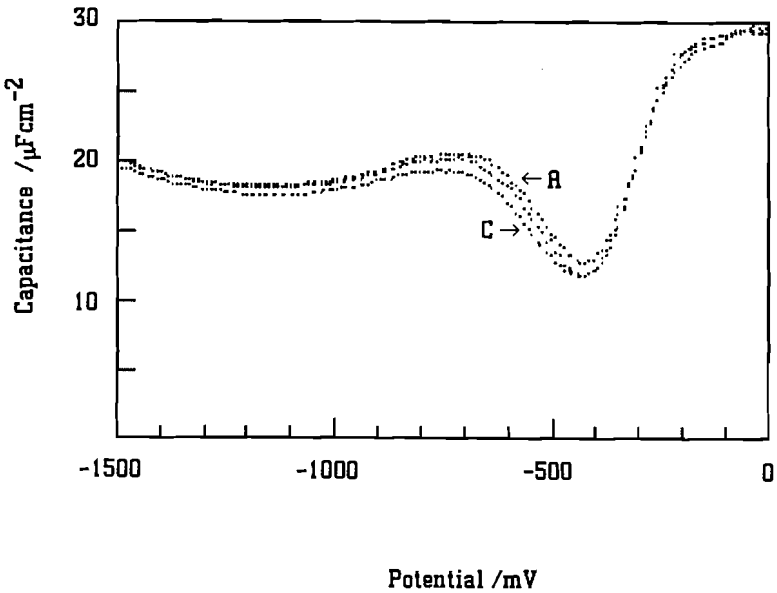

FIG. 2. Apparent differential capacitance of a hemispherical Hg/Pt electrode (12.5 μm in radius) in 10^{-3} *M* aqueous $NaClO_4$ measured at 1020 Hz. *A*: recorded immediately after immersing the electrode into the solution; *B*: 15 min after (*A*); *C*: 30 min. after (*A*).

of glass surrounding the microelectrode. Finally, residual faradaic processes occurring at the electrode may produce an apparent increase in C_d and R_s parameters. This is possible because current flow caused by irreversible faradaic processes becomes more significant at low frequencies when the impedance associated with the double layer capacitance becomes large. In any case the frequency dispersion of the double layer capacitance is much smaller at Hg/Pt electrodes than at carbon fiber or Pt electrodes (19), perhaps because mercury creeps onto the walls of the platinum wire (between the wire and the insulator) sealing all existing pores or, more likely, because the surface of mercury is much cleaner than the surface of most solid electrodes and consequently currents associated with residual faradaic processes are much smaller on mercury than on solid electrodes.

In another series of experiments the differential capacitance of Hg/Pt microelectrodes was measured as a function of potential in aqueous solutions containing 0.1 to 10^{-5} *M* $NaClO_4$. At low concentration of the supporting electrolyte the differential capacitance curves show a characteristic minimum indicating the zero charge potential, PZC (Fig. 2). It was interesting to find that on some Hg/Pt microelectrodes the PZC shifts with time in the direction of positive potentials. Time scale and range of the PZC shift varied considerably from

Can. J. Chem. Downloaded from www.nrcresearchpress.com by 93.93.197.157 on 09/07/12
For personal use only.

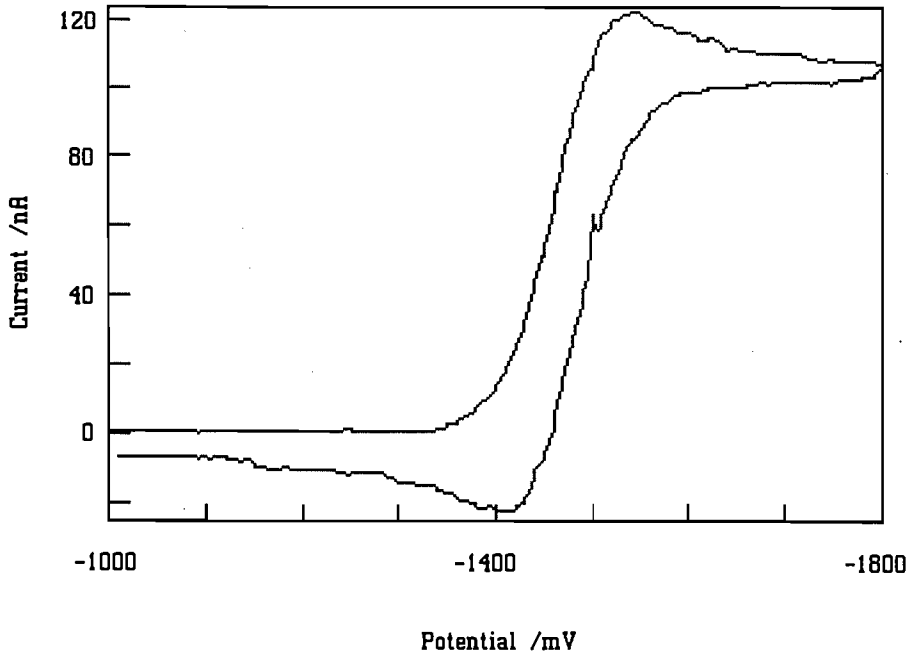

FIG. 3. Current–voltage curve obtained for 10^{-2} *M p*-DCB in 0.1 *M* TBAP in DMF. A hemispherical Hg/Pt electrode (12.5 μm in radius) was used. The sweep rate was 0.1 V/s.

experiment to experiment; in some cases a shift of up to 250 mV was observed in 16 min, in other cases the shift did not occur at all in a 1 h time period.

It was thought that this phenomenon can be caused by slow dissolution of platinum in mercury. In order to verify this hypothesis a saturated platinum amalgam was prepared and its PZC was determined using the streaming electrode technique. It was found, however, that the zero charge potentials of mercury saturated with Pt and pure mercury are the same within an experimental error of ±2 mV. Thus, other possible causes must be considered. The PZC may change if, in some areas of the electrode, the mercury layer is lost and the solid background material is uncovered. This process may be triggered by a drift of the electrode potential in the positive direction due to corrosion by traces of oxygen during a period between experiments. Since the surface energy of both the mercury and the base material (Pt or solid Pt–Hg compounds) depends on the electrode potential, the change in the electrode potential may cause a change in the spreading coefficient of mercury on the solid phase. It is worth mentioning that a significant potential dependence of the spreading of Hg on Ni and Fe was in fact observed (21, 22). Consistent with this hypothesis the drift of PZC was never observed if the electrode was kept at a potential of −1.5 V between the measurements. Another phenomenon often observed in this series of experiments was a slight broadening of the PZC minimum with time, as shown in Fig. 2. These last changes are most likely caused by the adsorption of impurities present at trace level in the studied solutions. Due to fast mass transport, contamination of microelectrodes with surfactants occurs much faster than in the case of standard size electrodes. Contamination of microelectrodes causes some problems in studies of electron transfer kinetics and it will be discussed later.

Determination of diffusion coefficients

In order to calculate the convolution for the spherical symmetry of mass transport the dimensionless diffusion coefficient of the oxidized form of depolarizer, $\mathcal{D}_O = D_O\Delta t/r^2$, must be known. Of course, the $\mathcal{D}_O$ can be determined from an independent experiment e.g. chronoamperometry; this, however, complicates the experimental procedure. Our primary interest was to examine the possibilities of determining the dimensionless diffusion coefficient using cyclic voltammetry alone. Two electrochemical systems were studied: *p*-DCB in DMF; in this case both reduced and oxidized forms of the depolarizer were in solution and they had a common symmetry of mass transport (semi-infinite, spherical), and Cd^{2+} in water; in this case the reduced form was dissolved in mercury and its mass transport was governed by a finite-volume, spherical symmetry.

In Fig. 3 a cyclic voltammetry curve recorded during the reduction of 0.01 *M* DCB in a DMF solution of 0.1 *M* TBAP is shown. In this experiment a hemispherical Hg/Pt electrode of radius 12.5 μm was used. The sweep rate was 0.1 V/s. Due to a large contribution from non-linear diffusion, the *CV* curve has a characteristic step-like shape with superimposed small anodic and cathodic peaks. The potential dependence of the convolution integral calculated for the linear symmetry of diffusion ($I_{plane} = \lim_{r\to\infty}(I_{out}\sqrt{D_O}/r)$) is shown in Fig. 4. Soon after the cathodic peak is reached concentration of the depolarizer at the surface of the electrode drops to zero; this should produce a time-independent value of integral I_{plane}. In Fig. 4, however, I_{plane} does not reach a plateau but rather increases constantly with time. This is caused by the time-independent flux resulting from non-linear mass transport to the electrode. It is obvious that in the case of microvoltammetry at low sweep rates, the linear diffusion convolution does not allow determination of surface concentration of a depolarizer. It should be noted, however, that the slope of the plot in the region between two current peaks carries information about the dimensionless diffusion coefficient. A direct determination of the diffusion coefficient from the shape of the curve in this region is very difficult, however, because the shape of the curve is affected in a complex way by the electron transfer kinetics, *IR* drops etc.

Can. J. Chem. Downloaded from www.nrcresearchpress.com by 93.93.197.157 on 09/07/12
For personal use only.

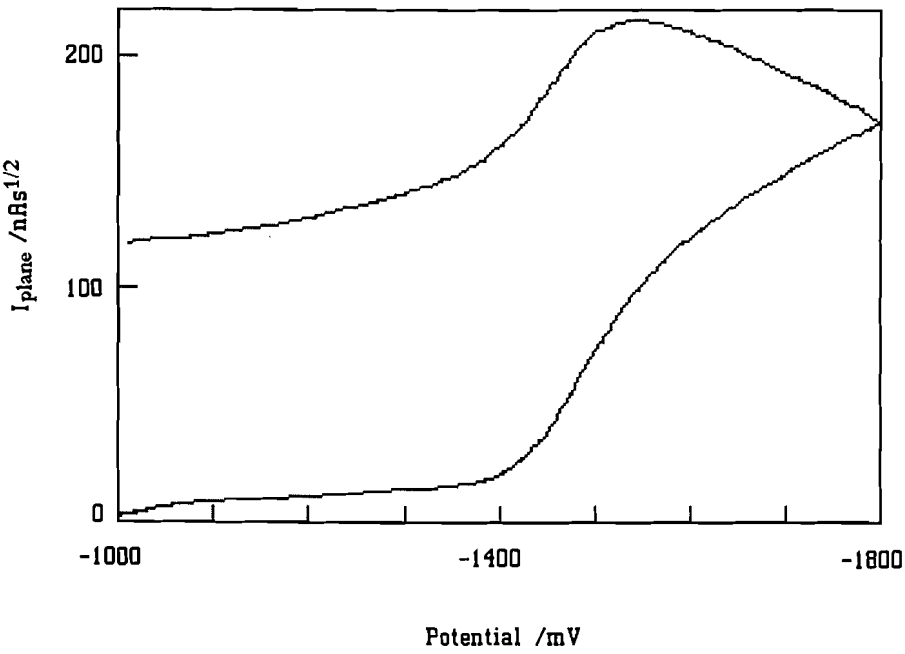

FIG. 4. Potential dependence of the plane convolution of current, I_{plane}, obtained by the semi-integration of the curve shown in Fig. 3.

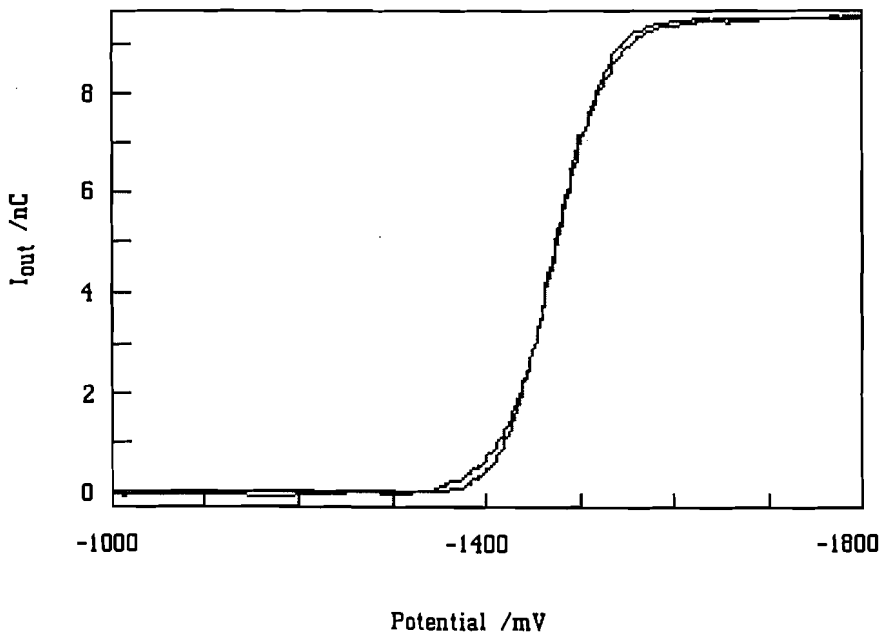

FIG. 5. Potential dependence of the spherical convolution of current, I_{out}, obtained by the successive approximation method for the curve shown in Fig. 3.

Instead, $\mathcal{D}_O = D_O\Delta t/r^2$ was determined by a successive approximation method:

[15] $(\mathcal{D}_O)_{n+1} = (\mathcal{D}_O)_n(1 + S_n/H_n)$

where $(\mathcal{D}_O)_n$ and $(\mathcal{D}_O)_{n+1}$ are the old and new values of the dimensionless diffusion coefficient, H_n is the average value of the convoluted current, and S_n is the average slope of the convoluted current (dI_{out}/dt) in the potential region: $E_c + 5RT/nF$ to E_v (where E_c is the cathodic peak potential and E_v is the vertex potential).

At first the convolution was performed assuming an arbitrarily chosen value of $(\mathcal{D}_O)_{n=0}$ (usually 10^{-5} cm^2 s$^{-1} \times \Delta t/r^2$) in order to find $S_{n=0}$ and $H_{n=0}$ parameters, then the first approximation of the dimensionless diffusion coefficient, $(\mathcal{D}_O)_{n=1}$, was calculated from eq. [15]. The result was used to calculate a new table of the mass transport symmetry function, $\sigma_{out}(z)$, then the convolution was repeated and the next approximation of S, H, and $\mathcal{D}_O$ parameters was obtained. This procedure was continued until the relative slope, S_n/H_n, was close enough to zero (in this work the condition $S_n/H_n < 0.02$ was used to exit the loop). It was assumed that the last approximation of H and $\mathcal{D}_O$ parameters represents the true values. The potential dependence of the convoluted current obtained by this method is shown in Fig. 5. The convolution was performed on the *CV* curve from the previously described experiment (Figs. 3 and 4). According to eq. [4] the height of the step in Fig. 5 is

Can. J. Chem. Downloaded from www.nrcresearchpress.com by 93.93.197.157 on 09/07/12
For personal use only.

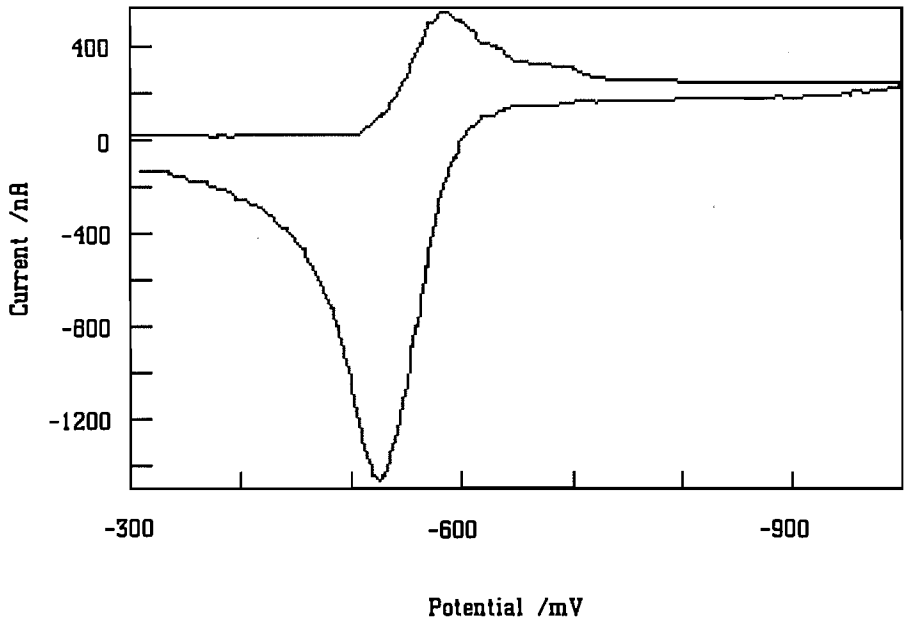

FIG. 6. Current–voltage curve obtained for 10^{-2} *M* Cd^{2+} in aqueous 0.5 *M* $NaClO_4$ with a hemispherical Hg/Pt electrode (12.5 μm in radius). The sweep rate was 10 V/s.

TABLE 1. Diffusion coefficient and number of electrons obtained by the successive approximation method from cyclic voltammetry experiments with a hemispherical Hg/Pt microelectrode (25 μm in diameter)

Solution	Sweep rate V/s	D_O 10^{-5} cm^2/s	D_M 10^{-5} cm^2/s	*n*
10^{-2} *M* DCB in 0.1 *M* TBAP/DMF	0.1	L: 1.46		0.65
		H: 2.16		0.42
	0.5	L: 1.08		1.04
		H: 1.20		0.95
	1	L: 1.06		1.10
		H: 1.24		0.97
	5	L: 1.11		1.14
		H: 1.26		1.04
	10	L: 1.22		1.09
		H: 1.36		1.02
	50	L: 1.61		0.96
		H: 1.96		0.86
10^{-2} *M* Cd^{2+} in 0.5 *M* $NaSO_4/H_2O$	10	L: 0.87	1.31	1.85
		H: 1.00	1.44	1.70
	25	L: 0.88	1.10	1.60
		H: 0.98	1.22	1.80

[16] $H = 3nFVC_O^0$

Since $\mathcal{Q}_O = D_O\Delta t/r^2$ is also known, then, in theory, any two experimental parameters (*n*, *r*, D_O, or C_O^0) can be determined, if two others are known. For example, when radius of the electrode and the depolarizer concentration are known the diffusion coefficient and the number of electrons involved in the elemental process can be calculated. This can be useful in studies of complex electron transfer reactions. However, since this is an absolute method it is, in general, less reliable than the relative one described in our previous publication (23). This method fails when the concentration of a depolarizer is lower than about 2×10^{-3} *M* (due to errors introduced by the charging current correction) and when the sweep rate is too high or too low. The last limitation arises from the fact that the parameter *S* in eq. [15] becomes independent of $\mathcal{Q}_O$, when r^2/D_O is much larger or much smaller than the time window of the experiment.

Values of *n* and D_O calculated from *CV* curves obtained at various sweep rates for reduction of DCB in DMF and Cd^{2+} in water are shown in Table 1. For each experiment two sets of parameters are reported; values marked by "L:" were obtained when the initial value of the dimensionless diffusion coefficient, $(\mathcal{Q}_O)_{n=0}$, in eq. [15] was set to 5×10^{-6} cm^2 $s^{-1} \times (\Delta t/r^2)$, "H:" corresponds to $(\mathcal{Q}_O)_{n=0} = 3 \times 10^{-5}$ cm^2 $s^{-1} \times (\Delta t/r^2)$. For sweep rates lower than 0.5 V/s and higher than 10 V/s the difference between the low and the high values of D_O increases indicating diminished precision of the method. The diffusion coefficient of DCB obtained for the intermediate sweep rates (0.5–10 V/s) is in good agreement with a value determined by the polarographic method (1.17×10^{-5} (24)), the *n* oscillates around 1 indicating that the calculations are internally consistent.

The diffusion coefficient of Cd in mercury, in Table 1, was obtained by analyzing the oxidation portions of corresponding *CV* curves. An example of such a curve obtained with a hemispherical Hg/Pt (25 μm in diameter) in aqueous 0.5 *M* solution of Na_2SO_4 contining 0.01 *M* Cd^{2+} at the sweep rate of 10 V/s is shown in Fig. 6. The anodic peak in this voltammogram is narrower and much larger than the corresponding cathodic peak due to preconcentration of cadmium in a small volume of mercury. It should be noted that the finite volume effect is very strong at 10 V/s, although it decreases with an increase in the sweep rates, it cannot be neglected even at 200 V/s. Shape of the current–time curve after the anodic peak is very strongly affected by the value of the $\mathcal{Q}_M = D_M\Delta t/r^2$ parameter. If a correct value of this parameter is used in the convolution transformation the I_{in} function is time independent and equal to zero soon after the anodic peak is reached. If the diffusion coefficient used to calculate the mass transport symmetry function is too small or too large the slope of I_{in} function after the anodic peak is positive or negative, respectively (as it is shown in the upper left corner of Fig. 7). Therefore this slope can be used as a feed-back parameter in the determination of $\mathcal{Q}_M$ by the previously described successive

Can. J. Chem. Downloaded from www.nrcresearchpress.com by 93.93.197.157 on 09/07/12
For personal use only.

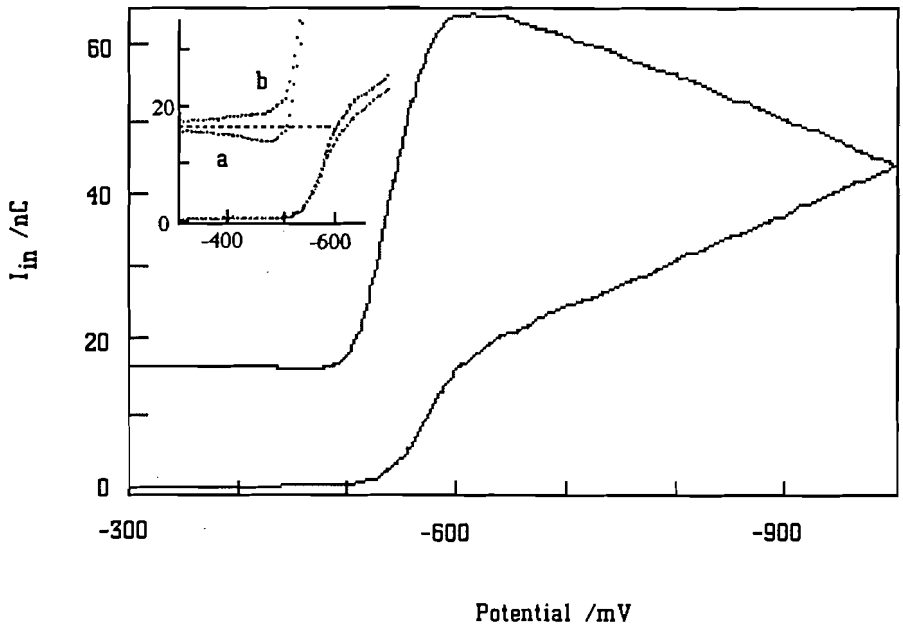

FIG. 7. Potential dependence of the spherical convolution of current, I_{in}, calculated for the curve shown in Fig. 6 using the successive approximation method. In the upper left corner: (*a*) I_{in} function obtained for $D_M = 1.2 \times 10^{-5}$ cm^2/s, (*b*) I_{in} function obtained for $D_M = 1.9 \times 10^{-5}$ cm^2/s.

approximation method. When this method was applied to the *CV* curve shown in Fig. 6 the slope equal to zero was obtained for $D_M = 1.4 \times 10^{-5}$ cm^2/s, which is in an excellent agreement with the literature value (1.48×10^{-5} cm^2/s (25)). However, I_{in} after the anodic peak was not equal to zero (Fig. 7); obviously not all cadmium was oxidized in the anodic cycle. Cadmium may form intermetallic compounds with platinum which are insoluble in mercury; similar compounds between Zn and platinum group metals are well known (22). However, in the case of the Pt–Hg–Cd system the reaction seems to occur only if fresh platinum electrodes are used, and if the amount of Cd introduced to mercury is relatively small (26). It is possible that Cd–Pt compound blocks the Pt–Hg interface and considerably slows down further reaction between Pt and Cd. It is also possible that cadmium reacts with impurities present in platinum rather than platinum itself, since according to manufacturer specifications the Pt wire used in this experiment contains about 75 ppm of Au and other metals. In any case the chemical reaction of Cd on Hg/Pt electrodes can be minimized by cycling the electrode several times in a solution containing Cd^{2+} before an experiment.

It can be shown that in the absence of following chemical reactions the successive approximation method gives not only a correct value of the diffusion coefficient of metals in mercury but also, after the oxidation peak, the zero slope of the I_{in} function coincides with the zero value of that function. Such a relationship was observed for lead (Fig. 8).

In the case of both cadmium and lead the I_{in} function increases with time in the region between the cathodic and anodic peaks; this is an expected behavior caused by the preconcentration of metals in a finite volume of mercury (6).

Determination of the electron transfer rate constant parameters

Properly calculated I_{out} and I_{in} functions allow the determination of the surface concentration of reduced and oxidized forms of a depolarizer using eqs. [4] and [5] or [4] and [8] depending on the studied system. Then the rate constant of the electron transfer process can be calculated using the Butler–Volmer expression:

$$[17] \quad i_f(t) = nFAk_f(E)\{C_O^S - C_R^S \exp[(E - E^0)nF/RT]\}$$

where $k_f(E)$ is the potential-dependent rate constant of the forward reactions, A is the surface area of the electrode, E^0 is the formal potential of a studied redox couple, and other symbols have their usual meaning.

The formal potential used in eq. [17] can be determined from the potential at which the current in the reverse cycle reaches zero (zero crossing potential) following the procedure described by Saveant and Tessier (5):

$$[18] \quad E^0 = E_{i=0} - (RT/nF) \ln [C_O^S(i = 0)/C_R^S(i = 0)]$$

where $E_{i=0}$ is the zero crossing potential, $C_O^S(i = 0)$ and $C_R^S(i = 0)$ are the surface concentrations of the oxidized and reduced form of the depolarizer at $E_{i=0}$.

In order to obtain meaningful kinetic parameters the sweep rate in a cyclic voltammetry experiment must be high enough to ensure irreversibility of the electrode reaction. In both studied cases (*p*-DCB in DMF and Cd^{2+} in H_2O) a significant departure from the Nernstian behavior is observed at sweep rates greater than 100 V/s. The potential dependence of the convoluted current at the sweep rate 200 V/s for the electrode process involving 2×10^{-3} *M* *p*-DCB in a DMF solution of 0.1 *M* TBAP is shown in Fig. 9. The potential dependence of the electron transfer rate constant obtained from this experiment is shown in Fig. 10. The apparent standard rate constant was 0.18 ± 0.05 cm/s and the apparent electron transfer coefficient, α, was 0.51 ± 0.03. Both are in excellent agreement with values previously determined using ac admittance techniques (27). It should be emphasized that these results were obtained without any correction for ohmic drop by software or hardware; in fact no potentiostat was used in these experiments. If a similar experiment (without *IR* compensation) is run using HMDE the ohmic drop causes a major systematic error and the calculated rate constant is about 0.02 cm/s.

Can. J. Chem. Downloaded from www.nrcresearchpress.com by 93.93.197.157 on 09/07/12
For personal use only.

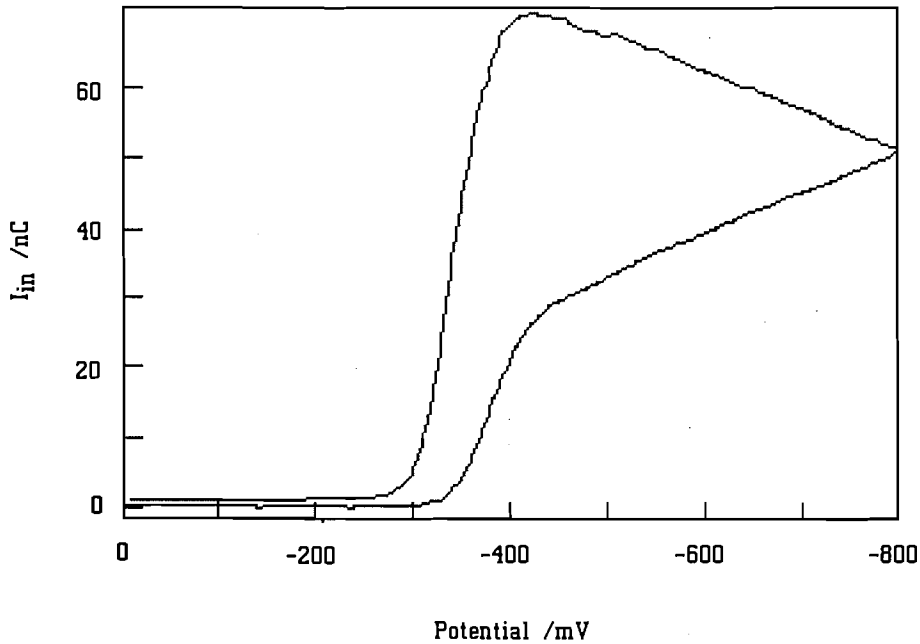

FIG. 8. Potential dependence of the spherical convolution of current, I_{in}, obtained for the reduction–oxidation process of 10^{-2} *M* Pb^{2+} in 0.5 *M* in aqueous $NaClO_4$. A hemispherical Hg/Pt electrode (12.5 μm in radius) was used. The sweep rate was 10 V/s.

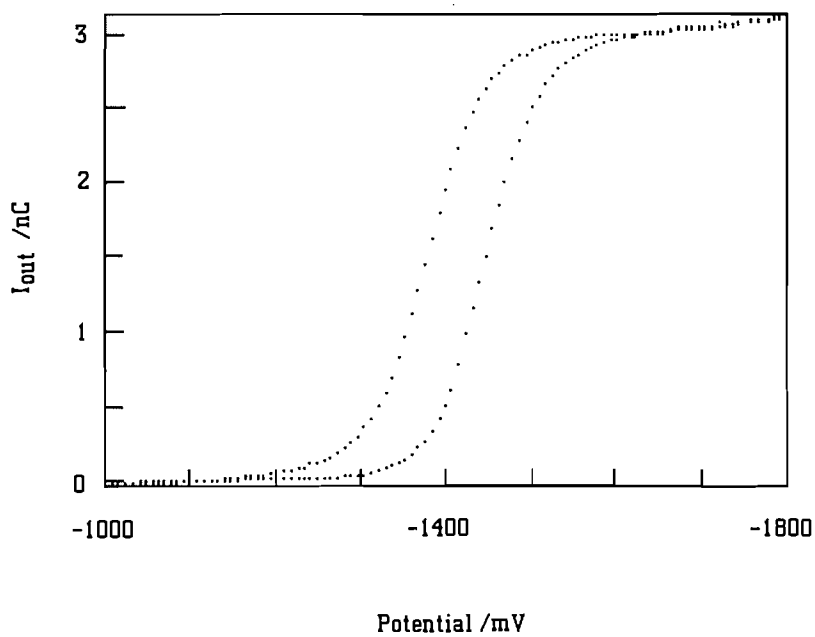

FIG. 9. Potential dependence of the spherical convolution of current, I_{out}, obtained for the reduction–oxidation process of 2×10^{-3} *M* *p*-DCB in 0.1 *M* TBAP in DMF. A hemispherical Hg/Pt electrode (12.5 μm in radius) was used. The sweep rate was 200 V/s.

The kinetic parameters determined for reduction of Cd^{2+} in aqueous solutions of 0.5 *M* Na_2SO_4 at the sweep rate 200 V/s were $k_s = 0.2 \pm 0.05$ cm/s and $\alpha n_\alpha = 1.05 \pm 0.05$ (an average of four measurements at different microelectrodes). This again is in good agreement with literature data, $k_s = 0.24$ cm/s (28).

Microelectrodes can be an important tool in studies of fast electron transfer processes, particularly in poorly conductive media; however, particular care should be taken to keep solutions extremely clean and to avoid unnecessarily long exposure of electrodes to studied solutions. Microelectrodes are very susceptible to contamination by adsorption of impurities. Fast diffusional transport of surfactants and the small surface area of microelectrodes result in 50 to 100 times faster contamination compared to standard size electrodes. Blocking of the electrode is more severe in aqueous than in non-aqueous media. This finding may seem surprising since water can usually be purified much more effectively than organic solvents. On the other hand, however, the adsorption of large molecules at the Hg–solution interface is expected to be much stronger in the case of aqueous solutions than non-aqueous ones. This happens because breaking of the water structure causes a substantial increase in the free energy of large molecules in the bulk of aqueous media. In fact, adsorption of neutral molecules at Hg/organic solvents interface is rarely observed. We believe

Can. J. Chem. Downloaded from www.nrcresearchpress.com by 93.93.197.157 on 09/07/12
For personal use only.

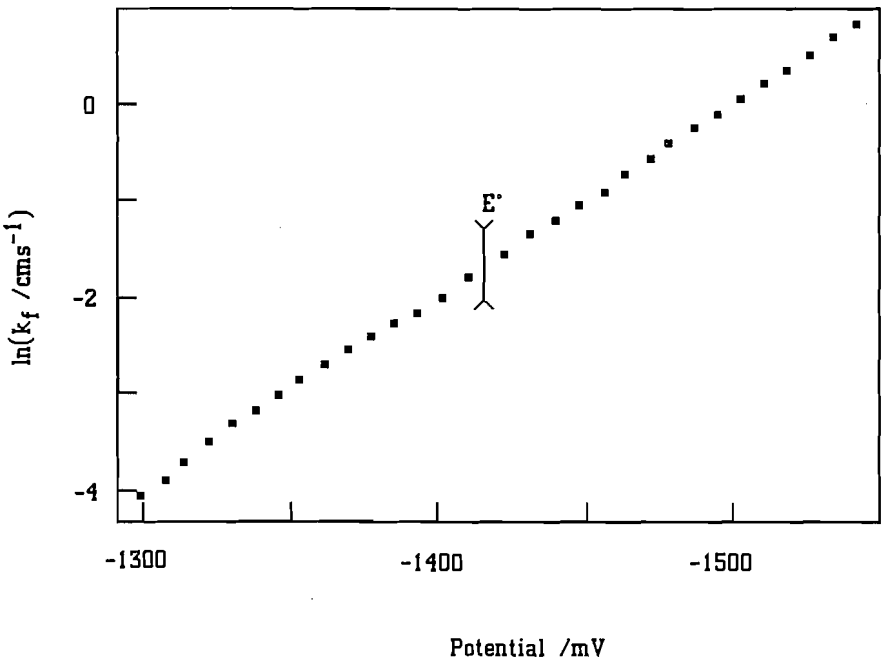

FIG. 10. Potential dependence of the forward rate constant of the electron transfer process calculated from the curve shown in Fig. 9.

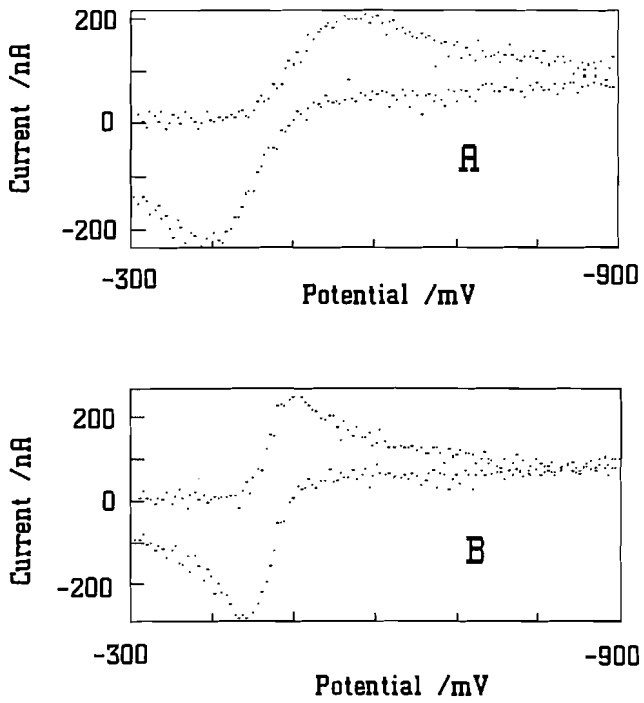

FIG. 11. Cyclic voltammetric curves obtained for 2×10^{-3} *M* Cd^{2+} in aqueous 0.5 *M* Na_2SO_4 with a hemispherical Hg/Pt electrode (12.5 μm in radius). The sweep rate was 100 V/s. *A*: microelectrode was left in the solution for about 15 min; *B*: the same electrode after being washed with concentrated H_2SO_4.

that in these studies the main sources of contamination were salts used as supporting electrolytes and the laboratory air to which solutions were exposed during their preparation.

A voltammogram shown in Fig. 11*A* was obtained in an aqueous solution of 0.5 *M* Na_2SO_4 containing 2×10^{-3} *M* Cd^{2+}; a Hg/Pt microelectrode was left in the solution for 15 min prior to recording the curve. The difference between the cathodic and anodic peak potentials at sweep rate 100 V/s was about 200 mV. This potential difference corresponds to a standard rate constant of about 1.2×10^{-2} cm/s, which is about 20 times less than the correct value. It is obvious that the electrode reaction was inhibited by the adsorption of some kind of surfactants present in solution. Fortunately, it was discovered that a contaminated mercury microelectrode can be cleaned by immersing it for a few seconds into concentrated (98%) sulfuric acid followed by an extensive washing with double distilled water. A *CV* curve shown in Fig. 11*B* was obtained in exactly the same conditions as in Fig. 11*A*, also the same electrode was used but the electrode was cleaned with H_2SO_4 using the procedure described above. The peak separation in this last case was about 60 mV and the standard rate constant determined by the convolution method was 0.27 cm/s.

Conclusion

Mercury microelectrodes were found to be very useful in studies of the kinetics of electron transfer processes. AC impedance studies have shown that Hg/Pt microelectrodes (25 μm in diameter) can be as ideal as standard size HMDE (i.e. they exhibit a correct value of the double layer capacitance and the zero charge potential as well as very small frequency dispersion of the capacitance). It is possible to prepare an almost ideal hemisphere by electrodeposition of Hg on Pt; as it was shown the mass transport to (and inside) such an electrode is governed by the spherical symmetry diffusion. Although preparation of microelectrodes is fast and simple, their stability is rather poor. Microelectrodes are very vulnerable to contamination by surfactants. In the case of Hg/Pt microelectrodes additional problems are caused by poor adhesion of Hg to Pt or solid Pt–Hg phases; under some experimental conditions the Hg coverage of the electrode may be partially lost. One method of improvement would be to replace Pt with a metal which is more easily wetted by Hg. Some brief experiments were done with Ag microelectrodes sealed into a heat shrinkable TFE/FEP Teflon tubing. However, mercury deposited on such electrodes sinks

Can. J. Chem. Downloaded from www.nrcresearchpress.com by 93.93.197.157 on 09/07/12
For personal use only.

relatively fast into an Ag (probably by creeping along walls of the silver wire), as a result the shape of the electrode and its surface area changes with time. Clearly, a satisfactory base metal for preparation of Hg microelectrodes is still to be found. Some recent works indicate that such a metal can be iridium (29, 30). Unfortunately a sufficiently thin iridium wire is not yet available commercially.

Application of the convolution method to analysis of microvoltammetric curves does not present any problems. Convolutive microvoltammetry seems to be particularly promising in studies of kinetics of fast electron transfer processes in poorly conductive media. In this work correct values of the standard rate constants for relatively fast processes were obtained without any correction for *IR* drops. In the case of standard size electrodes three methods of *IR* correction are widely used: positive feed back compensation, current interrupt technique and the convolutive analysis which allows *IR* compensation after the experiment on the software level. If necessary, any of these methods can be applied to microvoltammetry; however, the third one requires particular attention. Although it was not demonstrated in this work due to hardware limitations, the use of microelectrodes allows cyclic voltammetry experiments at very high sweep rates (up to 100 000 V/s) (9). At this speed, an electronic *IR* compensation is not available due to slow response of existing potentiostats. Of course, microvoltammetric experiments can be carried out without a potentiostat (10); in such a case the convolutive analysis is the only method of *IR* compensation. Rough estimates indicate that convolutive microvoltammetry can be used to measure standard rate constants smaller than 1 cm/s in solutions of specific conductivity greater than $10^{-5}\ \Omega^{-1}\ cm^{-1}$. This opens a possibility of studying fast electron transfer reactions at very low temperatures. Such studies of the reduction of η6-(substituted arene)-η5-cyclopentadienyliron complexes are under way in this laboratory.

Another interesting conclusion arising from this work is that microelectrodes enable measurements of the double layer capacitance in poorly conductive media. In the ac impedance technique the capacitance of an electrode can be determined precisely only if the capacitance reactance accounts for at least few percent of the total impedance of the electrodes. It follows that such measurements cannot be done correctly if the solution resistance is too large. Since solution resistance is inversely proportional to the radius of an electrode and capacitive reactance is inversley proportional to the surface area of the electrode, the ratio of the capacitive reactance to the solution resistance is more favorable for small than for large electrodes. According to our experience the double layer capacitance of 25 μm electrodes can be measured without problems in aqueous solutions containing supporting electrolyte at concentration 10^{-5} *M* or higher. Some attempts were made to measure double layer capacitance in distilled water without any supporting electrolyte. At this stage, however, such measurements are not reliable. In order to make the capacitive reactance large enough, the measurements must be carried out at low frequencies (5 Hz or lower); consequently, the results are noisy and data acquisition takes a long time. This together with poor stability of microelectrodes and their non-ideal behavior at low frequencies makes interpretation of results very difficult.

Can. J. Chem. Downloaded from www.nrcresearchpress.com by 93.93.197.157 on 09/07/12
For personal use only.

Acknowledgment

The financial support of the Natural Sciences and Engineering Research Council of Canada (NSERC), through an operating grant, is gratefully acknowledged.

1. K. B. Oldham. Anal. Chem. **44**, 196 (1972).
2. M. Grenness and K. B. Oldham. Anal. Chem. **44**, 1121 (1972).
3. J. C. Imbeaux and J. M. Saveant. J. Electroanal. Chem. **44**, 169 (1973).
4. L. Nadjo, J. M. Saveant, and D. Tessier. J. Electroanal. Chem. **52**, 403 (1974).
5. J. M. Saveant and D. Tessier. J. Electroanal. Chem. **65**, 57 (1975).
6. J. C. Myland, K. B. Oldham, and C. G. Zoski. J. Electroanal. Chem. **195**, 3 (1985).
7. K. R. Wehmeyer and R. M. Wightman. Anal. Chem. **57**, 1989 (1985).
8. B. Scharifker and J. G. Hills. J. Electroanal. Chem. **130**, 81 (1981).
9. J. O. Howell and R. M. Wightman. Anal. Chem. **56**, 524 (1984).
10. A. Fitch and D. H. Evens. J. Electroanal. Chem. **202**, 83 (1986).
11. A. M. Bond, M. Fleishchmann, and J. Robinson. J. Electroanal. Chem. **180**, 257 (1984).
12. J. Ghoroghchian, F. Sarfarazi, T. Dibble, J. Cassidy, J. Smith, A. Rassel, G. Dunmore, M. Fleischmann, and S. Pons. Anal. Chem. **58**, 2278 (1986).
13. M. Fleischmann, S. Bandyopadhyay, and S. Pons. J. Phys. Chem. **89**, 5537 (1985).
14. A. Rassel, K. Repka, T. Dibble, J. Ghoroghchian, J. J. Smith, M. Fleischmann, C. H. Pitt, and S. Pons. Anal. Chem. **58**, 2961 (1986).
15. C. A. Amatore, B. Fosset, M. R. Deakin, and R. M. Wightman. J. Electroanal. Chem. **225**, 33 (1987).
16. G. C. Barker. *In* Advances in polarography. *Edited by* I. S. Longmuir. Pergamon Press, New York. 1960. p. 144.
17. L. L. Miaw, P. A. Boudreau, M. A. Pichler, and S. P. Perone. Anal. Chem. **50**, 1988 (1978).
18. S. Stefani and R. Seeber. Anal. Chem. **54**, 2524 (1982).
19. A. S. Baranski. J. Electrochem. Soc. **133**, 93 (1986).
20. R. DeLevie. *In* Advances in electrochemistry and electrochemical engineering. Vol. 6. *Edited by* P. Delahay and C. W. Tobias. Wiley-Interscience, New York. 1967.
21. A. S. Baranski. Ph.D. Thesis, University of Warsaw. 1974.
22. Z. Galus. CRC Crit. Rev. Anal. Chem. **4**, 359 (1974).
23. A. S. Baranski, W. R. Fawcett, and C. M. Gilbert. Anal. Chem. **57**, 166 (1985).
24. A. S. Baranski and W. R. Fawcett. Unpublished results.
25. A. Baranski, S. Fitak, and Z. Galus. J. Electroanal. Chem. **60**, 175 (1975).
26. A. S. Baranski. Anal. Chem. **59**, 662 (1987).
27. A. S. Baranski and W. R. Fawcett. J. Electroanal. Chem. **100**, 185 (1979).
28. R. S. Nicholson. Anal. Chem. **37**, 1351 (1965).
29. S. P. Kounaves and J. Buffle. J. Electroanal. Chem. **216**, 53 (1987).
30. Z. Galus, J. Golas, and J. Osteryoung. Electrochim. Acta, **32**, 669 (1987).

Quelles procédures utiliser en polarisation diélectrique pour mettre en évidence, avec certitude, les interactions entre des dérivés chlorés et bromés de l'éthane et la *N*,*N*-diméthylacétamide

M. GUÉRIN ET L. BENAZIZ

Laboratoire de chimie minérale et laboratoire de physico-chimie des diélectriques, Université de Poitiers, Bât G.O.N., 40 avenue du Recteur Pineau, 86022 Poitiers CEDEX, France

Reçu le 22 septembre 1987

M. GUÉRIN et L. BENAZIZ. Can. J. Chem. **66**, 1047 (1988).

De nombreux travaux ont montré l'efficacité particulièrement grande des méthodes diélectriques, dans la mise en évidence, en solution, des interactions moléculaires spécifiques de faible énergie. Leurs applications exigent au préalable, d'évaluer les interactions non spécifiques entre espèces en solution (interactions désignées ici par effet «normal» du solvant). Or précisément, dans le cas des dérivés halogénés de l'éthane, qui peuvent présenter en solution, simultanément, plusieurs conformères de polarités parfois très différentes, nous ne disposions pas encore de cette possibilité. Dans ces conditions, l'objectif principal de notre travail a été de rechercher toutes procédures acceptables d'évaluation de cet effet de solvant.

M. GUÉRIN and L. BENAZIZ. Can. J. Chem. **66**, 1047 (1988).

Numerous studies have shown the particular usefulness of dielectric methods for observing low energy specific molecular interactions in solution. Before applying these methods, it is necessary to evaluate the non-specific interactions between species in solution (in this paper, these interactions are termed the "normal" effect of the solvent). However, in the particular case of halogenated derivatives of ethane, which can exist in solution as several conformers of different polarities, this possibility was not available. The object of our work has been to study all the procedures that might be acceptable in evaluating this solvent effect.

[Journal translation]

Can. J. Chem. Downloaded from www.nrcresearchpress.com by 93.93.197.157 on 09/07/12
For personal use only.

Introduction

L'étude de la polarisation diélectrique de solutions diluées, binaires et ternaires de composés A et B dissous dans un solvant inerte permet d'évaluer la polarisation totale P_{AB} et la constante de formation K_{AB} d'un complexe AB formé. En fait, pour obtenir avec une bonne précision des grandeurs exploitables il faut tenir compte des effets dus aux interactions non spécifiques de type van der Waals désignées parfois par le terme effet «normal» de solvant (1, 2).

Récemment en procédant ainsi Dumas *et al.* (3) ont pu mettre en évidence le rôle joué par l'halogène dans les interactions entre des dérivés chlorés et bromés du méthane (représentants d'anesthésiques généraux) et deux amines tertiaires (modèle de constituants de la membrane des cellules nerveuses). Une étude peut aussi être envisagée pour une autre catégorie importante d'anesthésiques volatils, les dérivés halogénés de l'éthane. Or ces espèces diffèrent considérablement du point de vue diélectrique, de celles étudiées par Dumas (3), en particulier parce que certaines d'entre elles peuvent présenter en solution simultanément plusieurs conformères de polarités parfois très différentes.

Dans ces conditions, pour pouvoir exploiter avec plus de certitude les résultats expérimentaux, obtenus avec les dérivés halogénés de l'éthane, il convient d'aborder alors le problème suivant: (*i*) les procédures (concernant essentiellement l'effet de solvant) adoptées jusqu'à présent, pour analyser tout mélange binaire et ternaire, sont-elles encore acceptables et suffisantes? et (*ii*) éventuellement quelles modifications y apporter, lorsque le soluté, présent dans ces mélanges, est susceptible d'avoir différents conformères en équilibre?

Des réponses à cette question permettraient alors de traiter, sans exception, tous les anesthésiques volatils et constitueraient ainsi l'outil de base indispensable à l'étude diélectrique des interactions spécifiques, entre tout dérivé halogéné du carbone et les espèces considérées comme modèles simples des constituants de la membrane.

Techniques expérimentales

Les mesures diélectriques ont été effectuées à l'aide d'un dipôlemètre de type DM.01 de «Wissenshaftlich Technische Werkstatten» équipé d'une cellule-DFL1 (capacité 20 cm^3) ou DFL2 (capacité 8 cm^3) thermorégulée à 25,0 ± 0,1°C.

Les masses volumiques des corps purs et des solutions ont été mesurées à l'aide d'un densimètre digital DMA 45 de A. Paar thermorégulé.

Les indices de réfraction des corps purs ont été mesurés à l'aide d'un réfractomètre d'Abbe équipé d'une lampe à vapeur de sodium.

Les solvants (cyclohexane, *n*-heptane, *n*-dodécane, diméthyl-2,2 butane et tétrachlorométhane) produits de qualité spectroscopique, utilisés sans traitement préalable, ont été conservés sur tamis moléculaire. Ces solvants très purs ont permis l'étalonnage des appareils utilisés.

Tous les autres produits (dérivés halogénés de l'éthane, et *N*,*N*-diméthyl acétamide) ont été distillés sous pression réduite d'azote sec, puis conservés sur tamis moléculaire généralement à l'abri de la lumière.

Dans la suite de ce travail, nous avons séparé en deux groupes l'ensemble des dérivés de l'éthane étudiés:

Le groupe G1: espèces polaires ne présentant pas de conformère: trichloro-1,1,1 éthane; pentachloroéthane; trichloro-1,1,1 trifluoro-2,2,2 éthane; dichloro-1,1 éthane; *le groupe G2*: espèces polaires pouvant exister en solution sous plusieurs formes «isomères» de conformation: dichloro-1,2 éthane; dibromo-1,2 éthane; tétrachloro-1,1,2,2 éthane; tétrabromo-1,1,2,2 éthane; bromo-1 chloro-2 éthane; trichloro-1,1,2 éthane.

Méthodes d'exploitation des résultats

1. Exploitation des mesures expérimentales

(a) Mélanges binaires

La détermination du moment dipolaire d'un soluté A dans un solvant apolaire S a été effectuée dans le cadre de la théorie de Debye (4) appliquée à un grand nombre de solutions diluées:

$$[1] \qquad \mu_{A/S} = \sqrt{\frac{9k}{4\pi N}} \cdot \sqrt{(P_{A\infty/S} - R_{M.D})T}$$

Printed in Canada / Imprimé au Canada

Can. J. Chem. Downloaded from www.nrcresearchpress.com by 93.93.197.157 on 09/07/12
For personal use only.

où la constante $\sqrt{9k/4\pi N}$ a pour valeur 0,012813 lorsque μ est exprimé en Debye (D); $P_{A\infty/S}$: polarisation molaire à dilution infinie de A dans S en $cm^3\ mol^{-1}$, évaluée à l'aide de la méthode de Halverstadt et Kumler (5); $R_{M.D}$: réfraction molaire de A pour la raie D du sodium en $cm^3\ mol^{-1}$; T: température de l'expérience en K.

(b) Mélanges ternaires

Pour mettre en évidence quantitativement les interactions spécifiques au sein d'un mélange ternaire A/B/S, les conclusions d'une étude comparée de plusieurs méthodes physico-chimiques (6) nous ont incités à retenir pour cette étude, la méthode diélectrique de Cleverdon, Collins et Smith (7). Cette méthode consiste à déterminer la polarisation molaire à dilution infinie du soluté A lorsqu'il est mis en solution dans le solvant S et dans divers solvants mixtes BS. Les auteurs attribuent alors la totalité des écarts entre $P_{A\infty/BS}$ et $P_{A\infty/S}$ à la formation du complexe (AB) supposé de stoechiométrie 1–1 :

$$[2] \quad \frac{1}{P_{A\infty/BS} - P_{A\infty/S}} = \frac{1}{K_{AB} \cdot \Delta P} \cdot \frac{M_B \cdot V_{BS}}{W_B} + \frac{1}{\Delta P}$$

où ΔP, l'incrément de polarisation du complexe AB est défini par la relation : $P_{AB} = P_A + P_B + \Delta P$; M_B : masse molaire de B; w_B : fraction du soluté B dans le solvant mixte BS de volume massique V_{BS}.

Remarque : En l'absence de toute interaction spécifique ($K_{AB} = 0$ et $\Delta P_{AB} = 0$), l'expression précédente montre que les polarisations $P_{A\infty/BS}$ et $P_{A\infty/S}$ devraient être égales. Une telle identité ne peut pas se vérifier, si l'on admet l'existence générale d'un effet normal de solvant, lorsque le soluté A passe du solvant S au solvant mixte BS (voir ci-dessous). En toute rigueur il convient alors d'effectuer une correction convenable du terme $P_{A\infty/S}$ dans la relation de Cleverdon, Collins et Smith.

2. Procédures d'évaluation de l'effet normal de solvant applicables aux mélanges binaires et (ou) ternaires

(a) Soluté du groupe G1

Il a été montré (2, 8) qu'en l'absence de toute interaction spécifique, l'expression de Barclay–Le Fèvre (9) en particulier permet, pour un soluté donné, de relier les moments dipolaires dans le solvant apolaire S et en phase gazeuse :

$$[3] \quad \mu_S^2/\mu_g^2 = 1 + \left(e^{x^2} - \frac{\epsilon_{\infty S}}{\epsilon_\infty}\right)\frac{\epsilon_S - 1}{\epsilon_S + 2}$$

ϵ_S : permittivité diélectrique du solvant S; $\epsilon_{\infty S}$, ϵ_∞ : permittivités diélectriques à fréquence infinie du solvant et du soluté; e^{x^2} : paramètre associé à la forme de la molécule de soluté, est défini par les dimensions de celle-ci, a (suivant la direction du moment dipolaire), b et c (dans deux directions perpendiculaires à celle du moment) :

$$x^2 = \frac{c^2 - a^2}{a^2} \text{ si } a > b > c; x^2 = \frac{c^2 - a^2}{b^2} \text{ si } b > a > c \text{ et}$$

$$x^2 = \frac{c^2 - a^2}{c^2} \text{ si } b > c > a$$

À partir de cette relation fondamentale [3] peuvent être établies plusieurs autres expressions en termes de polarisation (ou de moment dipolaire) permettant d'évaluer l'effet normal de solvant subi par le soluté polaire lorsqu'il est considéré successivement dans un solvant S puis un solvant différent S'. Leurs formulations ainsi que les conditions de leur utilisation ont déjà été présentées dans la littérature (cf. par ex. les références 3 et 10).

TABLEAU 1. Paramètres physico-chimiques nécessaires à l'évaluation de l'effet de solvant

(*a*)

Solutés	e^{x^2}	ϵ_∞^*
Pentachloroéthane	0,902	2,4504
Dichloro-1,1 éthane	0,926	2,0964
Trichloro-1,1,1 éthane	1,209	2,1717
Trichloro-1,1,1 trifluoro-2,2,2 éthane	1,040	2,0507

*Valeurs calculées selon la méthode de Boyer–Donzelot (11–13).

(*b*)

Solvants	$\epsilon_S = \epsilon_{\infty S}$
Cyclohexane	2,0170
n-Heptane	1,9170
Tétrachlorométhane	2,2275
n-Dodécane	2,0090
Diméthyl-2,2 butane	1,8628

(b) Soluté du groupe G2

Pour rendre compte de l'effet de solvant correspondant, s'il existe, et qui vient s'additionner à celui déjà cité ci-dessus, toujours présent, il convient de mettre en œuvre l'expression proposée par Abraham *et al.* (14–17). En effet, cette dernière, déjà utilisée dans un contexte moins favorable (18), semble, tant par sa nature même que par les nombreuses validations dont elle a été l'objet, tout à fait convenir à cette étude.

Supposons un soluté A du groupe G2 en solution dans un solvant S; A existe sous deux formes limites («isomères» de rotation très différents), les conformères *gauche* et *trans*.

Ces deux derniers, de moments dipolaires respectifs $\mu_{gh/S}$ et $\mu_{tr/S}$ sont considérés en équilibre suivant l'équation de réaction : $A_{gh} \rightleftarrows A_{tr}$. En désignant par $x_{gh/S}$ la fraction molaire de A_{gh} et par $x_{tr/S}$ celle de A_{tr} nous pouvons obtenir les relations suivantes :

$$[4] \quad \bar{\mu}_S^2 = x_{gh/S}\mu_{gh/S}^2 + x_{tr/S}\mu_{tr/S}^2$$

où $\bar{\mu}_S$: moment dipolaire expérimental,

$$[5] \quad \frac{x_{tr/S}}{x_{gh/S}} = K \exp\left(-\frac{\Delta G^S}{RT}\right)$$

K : facteur de poids statistique; $\Delta G^S = G_{tr}^S - G_{gh}^S$ représente la différence d'énergie libre entre les deux conformères A_{gh} et A_{tr} dans le solvant S.

L'expression de Abraham *et al.* (14–17) permet de connaître ΔG^S ou plus précisément ΔE^S, la différence d'énergie de solvatation entre les conformères *gauche* et *trans*, ces auteurs ayant indiqué clairement les raisons qui justifient cette approximation :

$$[6] \quad \Delta E^S - \Delta E^g = \frac{(k_{gh} - k_{tr})X}{1 - lX} - \frac{3(h_{gh} - h_{tr})X}{5 - X} - \left[b_{ghf}\left(1 - \exp\left[\frac{-b_{ghf}}{16RT}\right]\right) - b_{trf}\left(1 - \exp\left[\frac{-b_{trf}}{16RT}\right]\right)\right]$$

$$[7a] \quad X = \frac{\epsilon_S - 1}{2\epsilon_S + 1}$$

Can. J. Chem. Downloaded from www.nrcresearchpress.com by 93.93.197.157 on 09/07/12
For personal use only.

$$[7b] \quad l = \frac{2(n_D^2 - 1)}{n_D^2 + 2}$$

$$[7c] \quad f = \left| \frac{(\epsilon_S - 2)(\epsilon_S + 1)}{\epsilon_S} \right|^{1/2} \quad f = 0 \quad \text{si} \quad \epsilon_S < 2$$

$$[8a] \quad k_i = \frac{\mu_i^2}{a^3}$$

$(i = gh, tr)$

$$[8b] \quad h_i = \frac{3q_i}{2a^5}$$

$$[8c] \quad b_i = 4{,}35\left(\frac{T}{300}\right)^{1/2} \frac{a^{3/2}}{r^3}\left(k_i + h_i \frac{a^2}{r^2}\right)^{1/2}$$

μ_i, q_i: moments dipolaire et quadripolaire du conformère i; a: rayon de la cavité sphérique de Onsager (19),

$$\left(\frac{4}{3}\pi N a^3 = \frac{M}{\rho}\right)$$

occupée par la molécule étudiée, de masse molaire M et de masse volumique ρ; r = distance soluté solvant; ΔE^g: différence d'énergie entre les deux conformères A_{gh}, A_{tr} en phase gazeuse.

La détermination des paramètres h_i et k_i nécessite la connaissance de la géométrie et des moments dipolaires de liaison, en particulier celui de la liaison carbone halogène (C—Hal), du soluté A. De plus pour calculer h, il est nécessaire de connaître aussi le centre de gravité du volume occupé par A. Ce dernier est déterminé selon Abraham *et al.* (16, 20) en affectant à chaque atome j (constituant la molécule du soluté) de coordonnées x_j, y_j et z_j (dans un repère orthonormé ox, oy, oz) un coefficient égal à son volume v_j de van der Waals. Les coordonnées du centre de gravité du volume sont alors (v_j étant calculé à partir du rayon de van der Waals de l'atome j):

$$[9a] \quad x = \frac{\Sigma x_j v_j}{\Sigma v_j}$$

$$[9b] \quad y = \frac{\Sigma y_j v_j}{\Sigma v_j}$$

$$[9c] \quad z = \frac{\Sigma z_j v_j}{\Sigma v_j}$$

L'évaluation de l'effet de solvant (c'est-à-dire le calcul du passage de $\bar{\mu}_S$ à $\bar{\mu}_g$) d'un soluté du groupe G2 est donc abordée ici en combinant les expressions de Barclay–Le Fèvre et de Abraham.

Un premier programme de calcul, correspondant au cas $\mu_{A\,tr} = 0$ (ou $\mu_{A\,tr} \simeq 0$) principalement étudié, permet d'exploiter les expériences réalisées sur les solutions binaires AS.

Dans le cas des systèmes ternaires, un autre programme de calcul reposant sur les mêmes relations [3]–[9c] permet d'accéder aux polarisations $P_{A\infty/BS}$ calc.

Les représentations des conformères *gauche* et *trans* de chaque soluté sont présentées figure 1, les valeurs des principales données décrivant ces formes constituent le tableau 2.

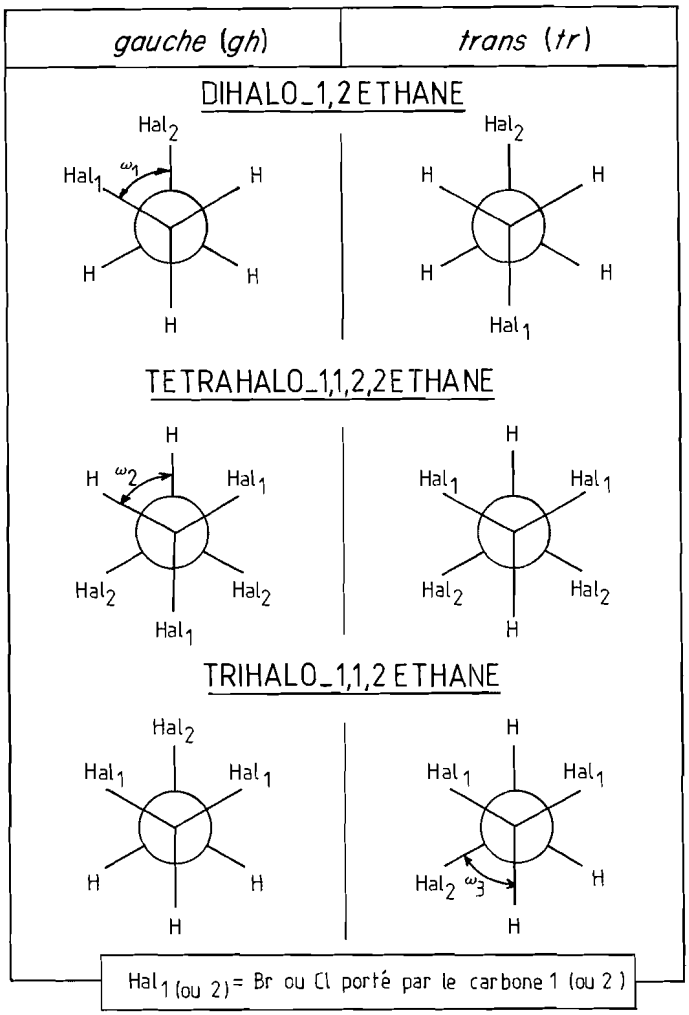

FIG. 1. Géométrie standard des solutés.

TABLEAU 2. Données relatives à la géométrie standard des solutés (indiquée figure 1) (16, 21)

1. Rayons de Van der Waals (en Å) : C (1,60); H (1,20); Cl (1,80); Br (1,95)

2. Longueurs de liaisons (en Å) : C—C (1,53); C—Br (1,93); C—Cl (1,77); C—H (1,09)

3. Angles de liaisons et angles des dièdres (en°) : C—C—H (109,47); H—C—H (109,47); C—C—Hal (111,00); Hal—C—Hal (111,00); ω_1(70); ω_2 (66); ω_3 (50)

Résultats et interprétations

1. Les mélanges binaires

(a) Solutés du groupe G1

Dans le tableau 4 figurent, pour chaque système soluté–solvant, la valeur expérimentale, μ_S, et celle calculée à l'aide de la relation de Barclay–Le Fèvre, μ_g. Pour quelques systèmes, des valeurs de μ_S sont signalées dans la littérature diélectrique classique (les tables de McClellan par exemple). Celles que nous présentons ci-dessous tableau 4 sont généralement en accord avec ces résultats déjà publiés.

L'examen de ces résultats et tout particulièrement la comparaison des valeurs de μ_g calc. à celles de μ_g exp. (qui peuvent être relevées dans la littérature) en tenant compte bien sûr des incertitudes correspondantes, nous amène à constater qu'il y a généralement un bon accord entre ces grandeurs.

Avec ces exemples et par référence aux travaux de Colnay *et al.* (2), il semble bien que l'expression de Barclay–Le Fèvre

TABLEAU 3. Valeurs des différents paramètres utilisés pour l'évaluation de l'effet de solvant

Paramètre	Soluté				
	CH_2ClCH_2Cl	CH_2BrCH_2Br	$CHCl_2CHCl_2$	$CHBr_2CHBr_2$	CH_2BrCH_2Cl
ϵ_∞	2,1986	2,5583	2,4171	3,0641	2,3769
e^2_{gh}	0,840	0,833	1,534	1,934	0,837
a (Å)	3,16	3,25	3,47	3,59	3,21
k^*_{gh}	13,7±0,4	$10,6\pm0,2_5$	4,0±0,1	2,98±0,06	$12,9_5\pm0,3$
k^*_{tr}	0	0	0	0	0
h^*_{gh}	7,5±0,2	$6,0\pm0,1_5$	$2,3_0\pm0,05$	1,61±0,01	7,2±0,1
h^*_{tr}	24,2±0,8	$19,8\pm0,4_5$	6,3±0,2	5,37±0,03	$23,5_5\pm0,5$
ΔE^{g*}	5,02	6,85	0	0,84	6,10

*En kJ mol^{-1}.

TABLEAU 4. Valeurs de μ_g calc. obtenues à l'aide de l'expression de Barclay et Le Fèvre appliquée aux valeurs expérimentales μ_S (t = 25°C)

Soluté	Solvant	μ_S (D)	μ_g calc. (D)	$\Delta\mu_S$ exp. ou $\Delta\mu_g$ calc. (D)	μ_g exp. ± $\Delta\mu_g$ exp. (D)
Dichloro-1,1 éthane					2,06±0.05
	C_6H_{12}	1,98	2,00	0,02	
	nC_7H_{16}	2,00	2,01	0,02	
	CCl_4	1,95	2,00	0,02	
	$nC_{12}H_{26}$	1,98	1,99	0,02	
	DM-2,2 B	2,04	2,03	0,02	
Trichloro-1,1,1 éthane					1,78±0,03
	C_6H_{12}	1,84	1,79	0,02	
	nC_7H_{16}	1,83	1,77	0,02	
	CCl_4	1,81	1,76	0,02	
	$nC_{12}H_{26}$	1,82	1,77	0,02	
	DM-2,2 B	1,83	1,79	0,02	
Pentachloroéthane					0,92±0,05
	C_6H_{12}	1,00	0,98	0,02	
	nC_7H_{16}	1,01	0,99	0,02	
	CCl_4	1,00	1,00	0,02	
	$nC_{12}H_{26}$	0,98	0,97	0,02	
	DM-2,2 B	1,02	1,00	0,02	
Trichloro-1,1,1 trifluoro-2,2,2 éthane					(—)
	C_6H_{12}	0,79	0,80	0,02	
	nC_7H_{16}	0,78	0,78	0,02	
	CCl_4	0,82	0,83	0,02	

permette de relier de façon satisfaisante μ_S exp. et μ_g exp. Pourtant ces deux grandeurs correspondent à des états de la matière pour lesquels les forces d'interactions entre les dipôles des différentes molécules sont notablement différentes.

(b) Solutés du groupe G2

Dans le tableau 5 figurent les résultats obtenus après avoir utilisé la méthode de calcul proposée ci-dessus.

Ainsi pour chaque système soluté–solvant, face à la valeur expérimentale $\bar{\mu}_S$ nous avons indiqué, avec quelques grandeurs caractéristiques des espèces, la valeur de $\bar{\mu}_g$ calc. obtenue en combinant les expressions d'effet de solvant de Abraham et de Barclay–Le Fèvre, à comparer à celle correspondante de μ_g exp. (donnée de la littérature) incertitudes expérimentales comprises.

L'examen des résultats portés dans le tableau 5 nous montre que pour tous les solutés étudiés, il existe un bon accord entre les valeurs de $\bar{\mu}_g$ calculées et celle observée expérimentalement. Cette constatation semble donc prouver que la correction introduite est satisfaisante.

Cas du trichloro-1,1,2 éthane:

Comme tout soluté du groupe G2, le trichloro-1,1,2 éthane existe dans le solvant S sous la forme de deux isomères de rotation. Dans ce cas, par contre, le moment dipolaire du conformère *trans* (non nul) n'est plus négligeable comme dans celui du bromo-1 chloro-2 éthane. Cette seule différence, avec les cas examinés ci-dessus, correspond en fait à l'introduction dans tous nos calculs de l'inconnue supplémentaire μ_{tr}.

Pour pouvoir évaluer l'effet de solvant, subi par ce soluté, nous avons donc dû modifier en conséquence certaines parties du programme de calcul précédemment utilisé. Dans ce nouveau mode de calcul nous accèdons uniquement à $\bar{\mu}_S$ calc. La qualité de cette détermination nous est indiquée en comparant la valeur calculée à celle déterminée expérimentalement, incertitudes comprises (tableau 6).

Can. J. Chem. Downloaded from www.nrcresearchpress.com by 93.93.197.157 on 09/07/12
For personal use only.

TABLEAU 5. Valeurs de $\bar{\mu}_g$ calc. obtenues à l'aide des expressions d'Abraham et de Barclay–Le Fèvre appliquées aux valeurs expérimentales $\bar{\mu}_S$ (t = 25°C)

Soluté	Solvant	$\bar{\mu}_S$ (D)	ΔE^S (kJ/mol)	$x_{gh/S}$	$\mu_{gh/S}$ (D)	$\mu_{gh/g}$ (D)	$\bar{\mu}_g$ calc. (D)	$\Delta\mu_S$ ou $\Delta\mu_g$ calc.	$\bar{\mu}_g$ exp. ± $\Delta\mu_g$ exp. (D)
	C_6H_{12}	1,40	4,036	0,2814	$2,63_5$	2,68	1,22	0,02	1,22±0,02
	CCl_4	1,44	3,850	0,3000	2,66	2,71	1,24	0,02	
CH_2ClCH_2Cl	nC_7H_{16}	1,37	4,135	0,2733	2,62	2,65	1,21	0,02	
	$nC_{12}H_{26}$	1,39	4,051	0,2801	$2,62_5$	2,67	1,22	0,02	
	DM-2,2 B	1,37	4,172	0,2704	$2,63_5$	2,65	1,21	0,02	
	C_6H_{12}	1,55	−0,765	0,7315	1,81	$1,68_5$	1,37	0,02	1,36±0,02
	CCl_4	1,56	−0,828	0,7366	1,82	1,68	1,37	0,02	
$CHCl_2CHCl_2$	nC_7H_{16}	1,51	−0,715	0,7275	1,77	$1,64_5$	1,35	0,02	
	$nC_{12}H_{26}$	1,54	−0,758	0,7309	1,80	$1,67_5$	1,36	0,02	
	DM-2,2 B	1,55	−0,719	0,7278	1,82	1,69	1,38	0,02	
	C_6H_{12}	0,92	6,147	0,1430	$2,44_5$	2,46	0,82	0,02	0,88±0,05
CH_2BrCH_2Br	CCl_4	0,96	6,001	0,1504	2,47	2,49	0,83	0,02	
	nC_7H_{16}	0,90	6,240	0,1385	2,42	2,44	0,81	0,02	
	C_6H_{12}	1,35	0,583	0,6124	$1,72_5$	$1,51_5$	1,16	0,02	
$CHBr_2CHBr_2$	CCl_4	1,38	0,537	0,6169	1,76	1,52	1,16	0,02	
	nC_7H_{16}	1,33	0,607	0,6101	1,71	1,51	1,16	0,02	
CH_2BrCH_2Cl*	C_6H_{12}	1,19	5,188	0,1977	2,68	2,69	1,02	0,02	1,03±0,03
	nC_7H_{16}	1,15	5,297	0,1908	2,63	2,64	1,01	0,02	

*Nous avons considéré le bromo-1 chloro-2 éthane comme un dihalo-1,2 éthane symétrique, reprenant en cela, l'approximation déjà admise par Abraham *et al.* (20).

TABLEAU 6. Valeurs de $\bar{\mu}_S$ calc. obtenues à l'aide des expressions d'Abraham et de Barclay–Le Fèvre dans le cas du trichloro-1,1,2 éthane à 25°C

	Solvant		
Paramètre	Cyclohexane	Diméthyl-2,2 butane	Tétrachlorométhane
$\mu_{gh/S}$ (D)	2,88	2,85	2,90
$\mu_{tr/S}$ (D)	1,36	1,34	1,36
ΔE^S (kJ/mol)	6,857	7,034	6,565
$x_{gh/S}$ (D)	0,0304	0,0283	0,0340
$\bar{\mu}_S$ calc. (D)	1,43 (±0,02)	1,41 (±0,02)	1,44 (±0,02)
$\bar{\mu}_S$ (D)	$1,46_5$ (±0,02)	1,43 (±0,02)	1,47 (±0,02)

NOTA: Valeur des principaux paramètres utilisés: ϵ_∞ = 2,3018; $e^{x^2}_{gh}$ = 1,655; $e^{x^2}_{tr}$ = 1,500; a (Å) = 3,33; k_{gh} (kJ mol^{-1}) = 11,4; k_{tr} (kJ mol^{-1}) = 2,61; h_{gh} (kJ mol^{-1}) = 2,42; h_{tr} (kJ mol^{-1}) = 10,1 et ΔE^g (kJ mol^{-1}) = 7,94; $\mu_{gh/g}$ = 2,65 D; $\mu_{tr/g}$ = 1,27 D.

2. Les mélanges ternaires

L'étude des systèmes ternaires A/B/S repose sur l'utilisation de l'expression de Cleverdon, Collins et Smith (7) où le terme $P_{A\infty/S}$ (pour tenir compte de l'effet normal de solvant) est remplacé par $P_{A\infty/BS}$ calc. Cette polarisation est calculée à partir de la formule de Barclay–Le Fèvre dans le cas d'un soluté A du groupe G1, et en combinant les expressions d'Abraham et de Barclay–Le Fèvre pour tout soluté A du groupe G2. Toutefois, avant d'aborder (sur la base que nous venons de définir) l'exploitation des expériences réalisées, nous devons nous assurer que pour tout mélange ternaire reconnu sans interaction il y a bien identité entre polarisations calculées et mesurées $P_{A\infty/BS}$.

Nous avons donc examiné le comportement d'un grand nombre de systèmes témoins. C'est pourquoi nous avons déterminé la polarisation diélectrique de solutions diluées d'un soluté A introduit dans un solvant mixte, par ex. soluté B/solvant cyclohexane de concentration variable en B, A et B étant choisis de façon à ne pas mettre en jeu d'interactions spécifiques.

Nous avons retenu par exemple: A: dérivés halogénés du méthane ou de l'éthane (G1 ou G2); B: dérivés halogénés du méthane ou de l'éthane (G1). De plus, si le soluté A est toujours suffisamment polaire ($\mu > 2$ D), le soluté B par contre peut avoir une polarité très variable.

Deux cas se dégagent très nettement:

1. Le solvant mixte est apolaire, ou contient un soluté B assez peu polaire ($\mu \simeq 1$ D) à une concentration réduite ($w_B < 3\%$). Les polarisations expérimentales et calculées peuvent être considérées comme identiques puisqu'elles ne diffèrent pas de plus de 1%. Elles correspondent toujours à des faibles valeurs de ϵ_{BS} (voisines de celle de ϵ_S). Avec de tels solvants mixtes il est alors possible d'exploiter des systèmes ternaires à l'aide de l'expression de Cleverdon, Collins et Smith proposée ci-dessus.

2. Le soluté B est assez polaire ($\mu > 2$ D) et le solvant mixte

Can. J. Chem. Downloaded from www.nrcresearchpress.com by 93.93.197.157 on 09/07/12
For personal use only.

TABLEAU 7. Valeurs de l'incrément de polarisation P_{AB} ($cm^3\ mol^{-1}$) et de la constante de formation K_{AB} ($L\ mol^{-1}$) du complexe AB déterminées dans le cyclohexane à 25°C (B = *N*,*N*-diméthylacétamide)

A	ΔP_{AB}	K_{AB}
Solutés du groupe G1		
Trichloro-1,1,1 éthane	200±20	0,2±0,1
Trichloro-1,1,1 trifluoro-2,2,2 éthane	50±3	0,6±0,1
Dichloro-1,1 éthane	133±7	0,6±0,1
Pentachloroéthane	163±8	2,1±0,3
Solutés du groupe G2		
Dichloro-1,2 éthane	82±4	1,6±0,2
Dibromo-1,2 éthane	40±2	1,9±0,2
Tétrachloro-1,1,2,2 éthane	317±15	2,6±0,3
Tétrabromo-1,1,2,2 éthane	190±20	4,3±0,9

NOTA : La très faible auto-association de la *N*,*N*-diméthylacétamide (23) ne perturbe pas les résultats indiqués ci-dessus.

préparé présente une valeur de ϵ_{BS} assez différente de ϵ_S même pour des concentrations très petites de l'espèce B.

Assez systématiquement nous observons P exp. $< P$ calc. et l'écart entre ces deux polarisations devient de plus en plus grand (jusqu'à 10%) quand ϵ_{BS} augmente de façon sensible. S'agissant de systèmes exempts d'interaction, quelles peuvent donc être les causes de tels écarts entre P exp. et P calc. ? Nous pouvons supposer que l'utilisation des expressions d'effet normal de solvant, non adaptées aux systèmes ternaires dans le cas de solvant polaire B_S, nous conduise ainsi à des valeurs erronées de P calc. En fait, en se référant aux travaux d'Abraham et de Barclay–Le Fèvre, plusieurs considérations nous permettent de rejeter cette proposition. En conséquence, il apparait alors que cette anomalie ne peut que provenir de l'adoption de la méthode d'extrapolation à dilution infinie de Halverstadt et Kumler utilisée pour déterminer la valeur de $P_{A\infty/BS}$.

$$[10]\quad P_{A\infty/BS} = P_S + \lim_{w_A\to 0}\left(\frac{\partial P_{ABS}}{\partial w_A}\right) - \lim_{w_A\to 0}\left(\frac{\partial P_{BS}}{\partial w_A}\right)$$

Smith (22) considère que le dernier terme de [10] est négligeable quand le solvant utilisé est apolaire et w_A petit. Aussi ce terme est traditionnellement négligé, certainement par suite de la grande difficulté de l'évaluer avec précision pour des systèmes semblables à ceux que nous considérons dans cette étude.

Or dans le cas d'un solvant mixte composé d'un soluté polaire dilué dans un solvant apolaire l'introduction du terme

$$\lim_{w_A\to 0}\left(\frac{\partial P_{BS}}{\partial w_A}\right)$$

dans l'équation de Halverstadt et Kumler utilisée s'impose (5). Ce qui vient d'être indiqué au sujet de l'expression proposée par Halverstadt et Kumler, peut s'appliquer aussi à plusieurs autres formules d'extrapolation à dilution infinie disponibles dans la littérature. Nos expériences précises sur les systèmes témoins nous ont permis alors d'évaluer ce terme, et de calculer correctement $P_{A\infty/BS}$ à introduire dans l'expression de Cleverdon, Collins et Smith.

Compte-tenu des remarques précédentes nous sommes parvenus aux résultats suivants (tableau 7).

Nous disposons d'assez peu de données pour vérifier totalement la qualité des valeurs de K_{AB} que nous indiquons tableau 7. Pour les systèmes dichloro-1,1 éthane/*N*,*N*-diméthylacétamide/cyclohexane et pentachloroéthane/*N*,*N*-diméthylacétamide/cyclohexane étudiés par calorimétrie (M. Lakraïmi, résultats non publiés) nous avons respectivement :

$$K_{AB} = 0{,}7 \pm 0{,}2\ L\ mol^{-1}, \qquad -\Delta H = 17 \pm 2\ kJ\ mol^{-1}$$

et

$$K_{AB} = 3{,}0 \pm 0{,}3\ L\ mol^{-1}, \qquad -\Delta H = 14 \pm 2\ kJ\ mol^{-1}$$

Nous avons noté, toutefois, une très grande analogie entre nos propres résultats et ceux publiés par Dumas *et al.* (3) concernant les systèmes voisins (dérivés halogénés du méthane/*N*,*N*-diméthylacétamide/cyclohexane). Ces arguments nous suffisent déjà pour considérer ces résultats comme satisfaisants. En effet nous avons pu constater sur de nombreux exemples publiés que la prise en compte de termes correctifs (tels ceux indiqués ci-dessus) dans l'expression de Cleverdon, Collins et Smith permettait d'exploiter avec plus de certitude les données expérimentales ... au point de trouver des valeurs de K_{AB} identiques à celles obtenues par d'autres techniques physico-chimiques.

Conclusion

Disposant de procédures d'évaluation de l'effet normal de solvant acceptables, il est maintenant possible d'entreprendre en polarisation diélectrique toute étude structurale et thermodynamique des interactions entre les dérivés halogénés de l'éthane et les amides (ou toute autre espèce de caractère basique).

1. J. M. DUMAS, M. GOMEL et M. GUÉRIN. *Dans* The chemistry of functional groups. Supp. D. Part 2. *Éditeur*: S. Pataï et Z. Rappoport. John Wiley, New York. 1983. pp. 985–1020.
2. M. E. COLNAY, A. VASSEUR et M. GUÉRIN. J. Chem. Res (S), 220 (1983); (M) 2050 (1983).
3. J. M. DUMAS, C. GÉRON, A. R. KRIBII et M. LAKRAIMI. Can. J. Chem. **62**, 2634 (1984).
4. P. DEBYE. Polar molecules. Dover Publications, New York. 1929.
5. I. F. HALVERSTADT et W. D. KUMLER. J. Am. Chem. Soc. **64**, 2988 (1942).
6. B. CASTAGNA. Thèse de Doctorat d'État, Poitiers, France. 1975.
7. D. CLEVERDON, G. B. COLLINS et J. W. SMITH. J. Chem. Soc. 4499 (1956).
8. M. GUÉRIN. Thèse de Doctorat d'État, Poitiers, France. 1975.
9. G. A. BARCLAY et R. J. W. LE FEVRE. J. Chem. Soc. 556 (1950).
10. J. M. DUMAS, C. GÉRON, H. PEURICHARD et M. GOMEL. Bull. Soc. Chim. Fr. 720 (1976).
11. M. BOYER-DONZELOT. Bull. Soc. Chim. Fr. 425 (1970).
12. M. BOYER-DONZELOT. C.R. Acad. Sci. Fr. Ser. C, **270**, 1481 (1970).
13. M. BOYER-DONZELOT et P. BOYER. Bull. Soc. Chim. Fr. 1172 (1971).
14. R. J. ABRAHAM et Z. L. ROSSETTI. J. Chem. Soc. Perkin Trans. 2, 582 (1973).
15. M. H. ABRAHAM et R. J. ABRAHAM. J. Chem. Soc. Perkin Trans. 2, 47 (1974).
16. R. J. ABRAHAM et R. BRETSCHNEIDER. *Dans* Internal rotation in molecules. *Éditeur*: W. J. Orville-Thomas. Wiley, Londres. 1974. pp. 481–584.
17. M. H. ABRAHAM et R. J. ABRAHAM. J. Chem. Soc. Perkin Trans. 2, 1677 (1975).
18. J. MONTEAU, H. HUSER, M. GUÉRIN et M. GOMEL. J. Chem. Res. (S) 256 (1978); (M) 3217 (1978).
19. L. ONSAGER. J. Am. Chem. Soc. **58**, 1486 (1936).
20. R. J. ABRAHAM, L. CAVALI et K. G. R. PACHLER. Mol. Phys. **11**, 471 (1966).
21. R. J. ABRAHAM et K. PARRY. J. Chem. Soc. B, 539 (1970).
22. J. W. SMITH. Electric dipole moments. Butterworths Scientific Publications, Londres. 1955.
23. J. M. DUMAS, M. GUÉRIN et A. KRIBII. J. Chim. Phys. **81**, 333 (1984).

Can. J. Chem. Downloaded from www.nrcresearchpress.com by 93.93.197.157 on 09/07/12
For personal use only.

Retardation of Cd^{2+} and Zn^{2+} discharge at the dropping mercury electrode by adsorbed phenyl substituted phosphonium cations

A. ANASTOPOULOS, A. CHRISTODOULOU, AND I. MOUMTZIS

Laboratory of Physical Chemistry, Chemistry Department, Aristotelian University of Thessaloniki, 54006 Thessaloniki, Greece

Received April 1, 1987[1]

A. ANASTOPOULOS, A. CHRISTODOULOU, and I. MOUMTZIS. Can. J. Chem. **66**, 1053 (1988).

The effect of adsorbed propargyltriphenyl- and vinyltriphenylphosphonium cations on the discharge of Cd^{2+} and Zn^{2+} at dropping mercury electrode is studied by direct current polarographic measurements. Adsorption characteristics are determined by capacitance measurements. The size parameters of the activated complex and the surfactant particles are derived and an elucidation of the mechanism of the inhibited reaction is attempted.

A. ANASTOPOULOS, A. CHRISTODOULOU et I. MOUMTZIS. Can. J. Chem. **66**, 1053 (1988).

Utilisant des mesures polarographiques à cd, on à étudié l'effet des cations adsorbés de propargyltriphényl- et de vinyltriphénylphosphonium sur la décharge du Cd^{2+} et le Zn^{2+} au dme. On a déterminé les caractéristiques d'adsorption à l'aide de mesures de capacitance. On à dérivé les paramètres de taille du complexe activé et des particules d'agent de surface et on a essayé d'élucider le mécanisme de la réaction inhibée.

[Traduit par la revue]

Can. J. Chem. Downloaded from www.nrcresearchpress.com by 93.93.197.157 on 09/07/12
For personal use only.

Introduction

The study of the inhibitory action of surface active substances undergoing interfacial transformations on simple electrode reactions can be used as a means for testing the extent of applicability of the existing theories and equations (1, 2).

Although the above theories are developed assuming no irregularities during film formation, systems exhibiting interfacial rearrangements (3–5) are found to be in noticeable agreement to the relevant equations. However, we encountered difficulties in correlation of the size parameters. These difficulties can be resolved (3) when the structure of the activated complex and the reaction paths followed are properly determined.

In these frames, the study of phosphonium cations, which in aqueous solutions are known to present irregular development of the adsorption film, would be of interest for the elucidation of the reaction mechanism at high coverages with ionic surfactants. Earlier publications remained qualitative (6) or reached a quantitative level (7, 8) concerning the inhibitory action of the phosphonium cations.

In the present work we attempt a systematic examination of the influence of propargyltriphenylphosphonium bromide ($PgPh_3PBr$) and vinyltriphenylphosphonium bromide (VPh_3PBr) on the Cd^{2+} and Zn^{2+} deposition at the dropping mercury electrode (dme). Here, the size ratio, $r\neq/r_i$, obtained at $0.80 < \theta$ is correlated to an independently determined number of solvent molecules replaced at the interface by each activated complex, $r\neq$, and surfactant particle, r_i, with respect to recent theories (3) on the structure of the activated complex.

Experimental

Direct current polarographic measurements of current against potential and time at the dme, were performed by Radiometer PO-4 and Metrohm Polarecord E-504 systems. The later was also used for phase selective capacitance measurements performed with a 10 mV p.p. signal at a frequency of 75 Hz and a voltage scan rate of 2 mV s^{-1}. A Houston Instrument Omnigraphic 2000 X-Y recorder was used for recording the i–t curves. The dme had a flow rate of 2.12 mg s^{-1} at a reservoir height of 40 cm and an open circuit drop time of 5 s, restricted to 3 s during the i–E and C–E measurements.

The out-of-phase capacitance current vs. potential curves of aqueous 0.2 M KNO_3 were calibrated against Payne's data (9). The reproducibility of the differential capacitance values at the potential region from −1.60 V(SCE) was always better than 1% deteriorating to 1.5–2% at the positive and negative extremes of the potential scale. The reproducibility of the i–E measurements was of the order of 0.5%, while some problems in locating current zero of i–t curves led to a reproducibility of the order of 1–1.5%. All solutions were bubbled by a stream of nitrogen saturated with vapours of the supporting electrolyte solution. All potentials were measured against a large area calomel electrode saturated with KCl. Temperature was kept constant at 25 ± 0.05°C.

Water and mercury were used after double distillation. KNO_3 (Merck, puriss p.a.) and $PgPh_3PBr$ (Fluka, purum) were used without further purification. VPh_3PBr (Fluka, pract. >95%) was twice recrystallized from water–ethanol solutions, and dried at 140°C under reduced pressure.

Results and discussion

Adsorption characteristics of $(PgPh_3P)^+$ and $(VPh_3P)^+$ cations

The adsorption of $PgPh_3PBr$ and VPh_3PBr from 0.2 M KNO_3 aqueous solutions at the dme was studied by means of capacitance measurements for surfactant concentrations ranging from 0.065 to 0.5 mM. The differential capacitance vs. potential curves of aqueous 0.2 M KNO_3 in the presence of VPh_3PBr and $PgPh_3PBr$ additions are given in Figs. 1 and 2, respectively.

As it is seen from Figs. 1 and 2, at concentrations higher than 0.10 mM and for a wide potential range, the capacitance values are practically independent of concentration, indicating the attainment of full coverage of the electrode surface. The irregular shape of the C vs. E curves reveals the occurrence of interfacial rearrangements during film formation, which in the case of Fig. 2 are usually identified with association or condensation of the adsorbed particles. The irregularities during film formation are also reflected to the i–t polarographic curves obtained at the potential region −0.8 to −1.5 V(SCE). Two sets of such curves are provided in Fig. 3.

Curves of this type are known to represent surface coverages controlled by adsorption rate. This may be due (10) to a reduced rate of transfer of the surface active particles from the dissolved into the adsorbed state or to slow association or condensation reaction of the particles in the adsorbed state. The very good linearity (Table 1) of the relation between the time t_s required for saturation coverage and the inverse square of the surfactant

[1]Revision received January 7, 1988.

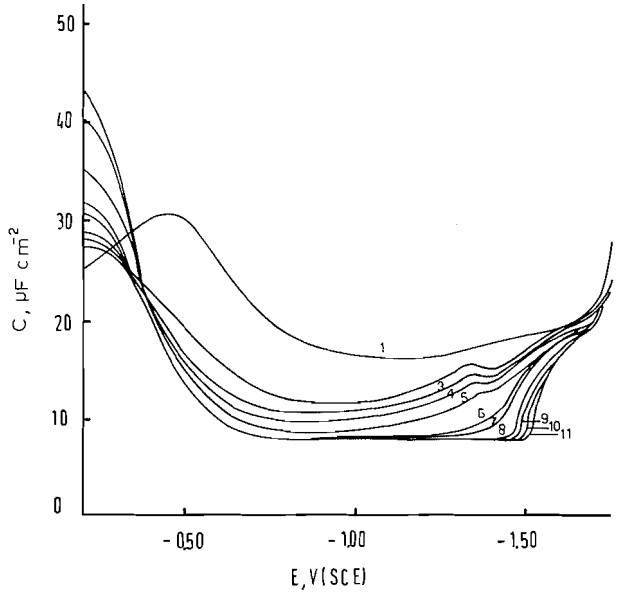

FIG. 1. Dependence of the differential capacitance of the dme against the electrode potential for the following additions of VPh_3PBr in m*M*: (*1*) 0.0, (*2*) 0.065, (*3*) 0.08, (*4*) 0.09, (*5*) 0.10, (*6*) 0.125, (*7*) 0.15, (*8*) 0.20, (*9*) 0.30, (*10*) 0.40, and (*11*) 0.50. Base solution: aqueous 0.2 *M* KNO_3.

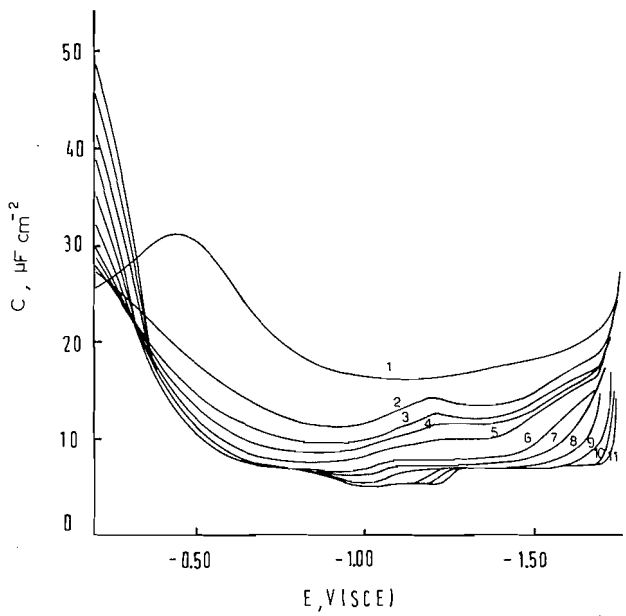

FIG. 2. Dependence of the differential capacitance of the dme against the electrode potential for the following additions of $PgPh_3PBr$ in m*M*: (*1*) 0.0, (*2*) 0.065, (*3*) 0.08, (*4*) 0.09, (*5*) 0.10, (*6*) 0.125, (*7*) 0.15, (*8*) 0.20, (*9*) 0.30, (*10*) 0.40, and (*11*) 0.50. Base solution: aqueous 0.2 *M* KNO_3.

bulk concentration c, according to the relation:

$$[1] \quad t_s = 1.82 \times 10^6 \frac{\Gamma_s^2}{Dc^2}$$

implies that the transfer of the surfactant particles from the dissolved to the adsorbed state is diffusion controlled. Diffusion step is thus presumed to be followed by a time-dependent variation of the electrode coverage, produced by slowly progressing structural changes in the adsorbed film.

The form of the *i–t* curves of Fig. 3 shows that, except for

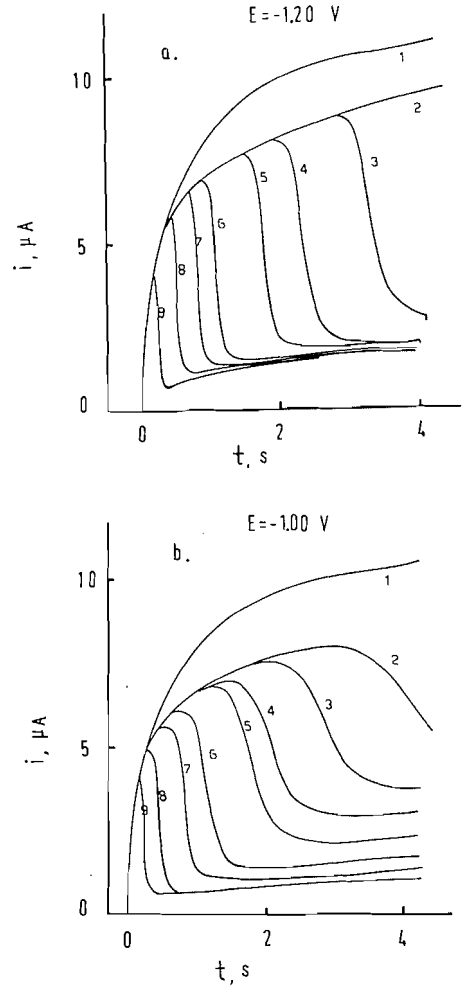

FIG. 3. Polarographic current–time curves for the Cd^{2+} reduction in the presence of the following additions of (*a*) $PgPh_3PBr$ and (*b*) VPh_3PBr in m*M*: (*1*) 0.0, (*2*) 0.065, (*3*) 0.08, (*4*) 0.09, (*5*) 0.10, (*6*) 0.125, (*7*) 0.15, (*8*) 0.20, and (*9*) 0.30. Base solution: aqeuous 0.2 *M* KNO_3. Potentials shown by the figures.

very dilute solutions ($c < 0.1$ m*M*), within the 3 s of the controlled drop time used for *i–E* and *C–E* measurements, the current reaches to a steady state value which can be identified with the weakly time dependent values following its initial increase and the subsequent sudden decrease.

Although full thermodynamic equilibrium is eventually not attained, it can be assumed that the steady state values represent some sort of quasi equilibrium state of the surface coverage under the given conditions of polarization, concentration, temperature, etc.

Figure 3 also shows that in the case of $PgPh_3PBr$ for $c \geq 0.125$ m*M* and $t \gtrsim 1.2$ s, and in the case of VPh_3PBr for $c \geq 0.15$ m*M* and $t \gtrsim 1.0$ s, *i–t* curves almost coincide, thus revealing the fulfillment of the condition $\theta \simeq 1$.

The application of eq. [1] permits the determination of Γ_s, the surface concentration at saturation, which is provided in Table 1. For this calculation, the value of the diffusion coefficient, D, of both organic surfactants equals $(5 \pm 0.2) \times 10^{-6}$ cm^2 s^{-1}, derived polarographically, is used.

The test of our adsorption data against the Frumkin isotherm:

$$[2] \quad \ln \frac{\theta}{(1-\theta)c} = \ln \beta + 2\alpha\theta$$

Can. J. Chem. Downloaded from www.nrcresearchpress.com by 93.93.197.157 on 09/07/12
For personal use only.

TABLE 1. Values of the saturation surface concentration of $(PgPh_3P)^+$ and $(VPh_3P)^+$ cations and correlation coefficient, R^2, from the test of linearity of eq. [1]

E(V/SCE)	Γ_s $(PgPh_3P)^+$ $\times 10^{10}$ mol cm^{-2}	R^2 $c_i > 8 \times 10^{-5}$ M	Γ_s $(VPh_3P)^+$ $\times 10^{10}$ mol cm^{-2}	R^2 $c_i > 8 \times 10^{-5}$ M
−0.80	2.4_5	0.989	2.6_8	0.997
−1.00	2.5_0	0.981	2.4_9	0.998
−1.20	2.4_9	0.982	2.5_0	0.999
−1.40	2.8_4	0.965	3.2_4	0.968

TABLE 2. Test results on Frumkin and Flory–Huggins isotherms

		Frumkin isotherm			Flory–Huggins isotherm			
Surfactant	E V(SCE)	$\beta \times 10^{-3}$	α	R^2	$\beta \times 10^{-3}$	α	r_i	R^2
$PgPh_3PBr$	−0.90	2.6_2	1.6_8	0.986	Limited agreement			0.894
	−1.00	2.7_6	1.5_9	0.988	Limited agreement			0.846
	−1.10	2.8_0	1.4_5	0.989	2.7_2	1.4_5	1.0_4	0.952
	−1.20	2.0_5	1.6_1	0.992	1.7_7	1.5_8	1.2_7	0.993
VPh_3PBr	−0.90	1.3_0	2.2_9	0.943	No agreement			<0.80
	−1.00	2.0_2	1.9_4	0.966	Limited agreement			0.880
	−1.10	2.6_7	1.6_6	0.972	Limited agreement			0.865
	−1.20	2.5_3	1.6_2	0.974	No agreement			<0.80

has revealed a very satisfactory agreement as it is evident from the values of the correlation coefficient, R^2, of the linear regression method employed.

The coverage values used in eq. [2] — and hereafter — are determined, in the potential region from −0.90 to −1.30 V, by means of the known (11) relation:

$$[3] \quad \theta_{app} = (c_0 - c)/(c_0 - c_s)$$

and they evidently are of apparent character.

In eq. [2] and Table 2, β is the adsorption equilibrium constant and α is the interaction parameter. The Frumkin isotherm is valid for values of the interaction parameter greater than 1. The values of the interaction parameter must not be correlated to attractive adsorbate–adsorbate interactions, but to positive deviations of the interfacial solvent–adsorbate system from Raoult's law (12).

On the other hand, Flory–Huggins isotherm:

$$[4] \quad \ln \frac{\theta}{c} = \ln \beta + r_i \ln (1 - \theta) + 2\alpha r_i \theta$$

was used for the independent determination of the number, r_i, of water molecules replaced by one adsorbate particle. As it is seen from Table 2, Flory–Huggins isotherm generally fails to describe the adsorption of VPh_3PBr as it is evident from the values of the correlation coefficient, R^2, of the multi-linear regression method used for the fit of eq. [4]. However, good agreement is obtained between the adsorption data of $PgPh_3PBr$ and eq. [4] for $r_i \simeq 1$, which is the case of Frumkin isotherm.

As far as the adsorption equilibrium constant, β, is a measure of the adsorbability of each adsorbate, the maximum value attained at $E = -1.1$ V(SCE) (Table 2) indicates that this potential may be approximately related to the point of maximum adsorption. However, this criterion allows only a rough determination of the potential of maximum adsorption, which can be more accurately defined by means of charge-potential curves (11). Nevertheless, due to the lack of such curves, we confined our discussion only to adsorption data obtained at the potential range: $-1.0 \leq E \leq -1.2$ V(SCE), i.e. at the neighbourhood of maximum adsorption, where relation [3] is applicable (11). In these frames, the values of Γ_s obtained are for both substances equal (Table 1) to about 2.5×10^{-10} mol cm^{-2}, equivalent to a value of an area per adsorbate particle of 66 Å^2. This value is in reasonable agreement with $S_{(PgPh_3P)^+} \simeq 70$ Å^2 and $S_{(VPh_3P)^+} \simeq 64$ Å^2, estimated by space filling models, when an orientation of the adsorbed phosphonium cations with the two phenyl groups and the alhyl residue towards the electrode surface is adopted. This orientation must be favoured at cathodic polarizations as far as the alternative orientation with the three phenyl groups in contact to the electrode, leading to an area of 77 Å^2, is more likely not to be favoured at potentials negative to −1.00 V(SCE). The experimental value of 66 Å^2, when correlated to the area per adsorbed water (13) molecule, $S_{H_2O} = 12.3$ Å^2, gives $r_i \simeq 5$.

The validity of the Frumkin isotherm for both adsorbates examined enables one to claim that each phosphonium cation replaces at the interface a cluster of 5 water molecules. However, the replacement at the interface of solvent associates by adsorbate particles (14) has been critically discussed (15, 16) and for this reason the above results are reported with some caution.

Inhibition characteristics of $PgPh_3PBr$ and VPh_3PBr

Figures 4 and 5 give the maximum instantaneous polarographic current against potential curves of Cd^{2+} and Zn^{2+} discharge, respectively, in the presence of VPh_3PBr and $PgPh_3PBr$. These polarographic curves show the strong inhibitory effect of even small additions of both surfactants on the reduction of Cd^{2+} and Zn^{2+}. The increase of adsorbate concentration does not seem to lead to a remarkable coincidence of the i–E curves at high negative potentials. This means that at these potentials (negative to −1.2 V/SCE) the rate of the electrode reactions is concentration-dependent, even at poten-

Can. J. Chem. Downloaded from www.nrcresearchpress.com by 93.93.197.157 on 09/07/12
For personal use only.

Can. J. Chem. Downloaded from www.nrcresearchpress.com by 93.93.197.157 on 09/07/12
For personal use only.

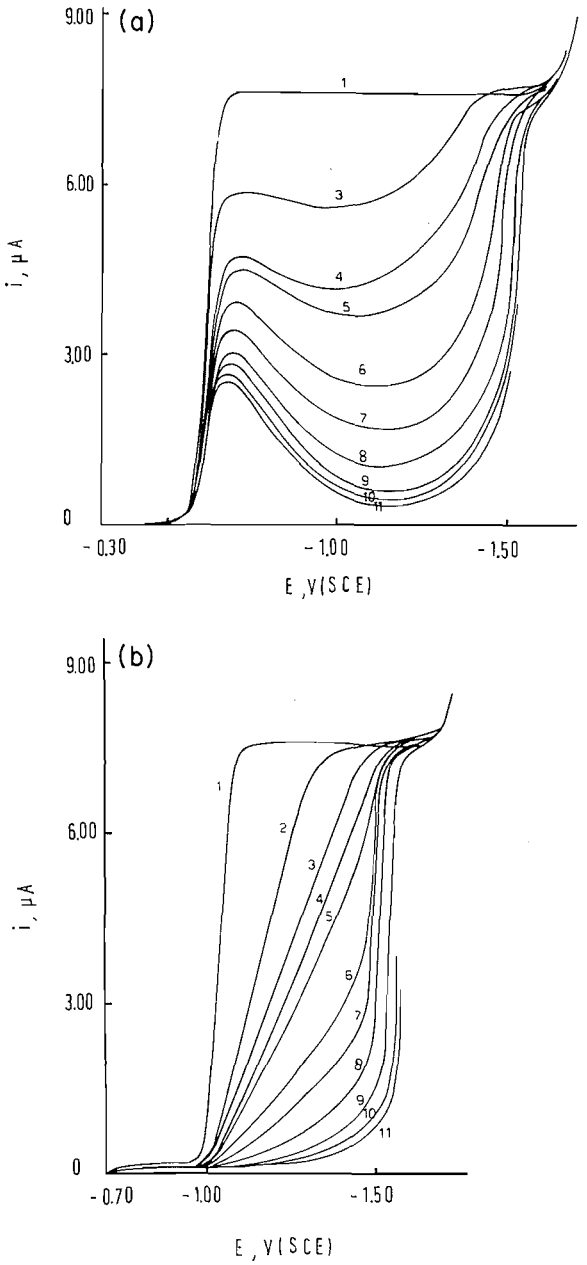

FIG. 4. Direct current polarographic curves of the Cd^{2+} (*a*) and Zn^{2+} (*b*) reduction in the presence of the following VPh_3PBr additions in m*M*: (*1*) 0.0, (*2*) 0.065, (*3*) 0.08, (*4*) 0.09, (*5*) 0.10, (*6*) 0.125, (*7*) 0.15, (*8*) 0.20, (*9*) 0.30, (*10*) 0.40, and (*11*) 0.50. Base solution: aqueous 0.2 *M* KNO_3.

tials and concentrations at full coverage as evidenced from the *C–E* curves of Figs. 1 and 2.

Minima are observed in the curves of Figs. 4*a* and 5*a*, which at higher concentrations approximately mark the position of the adsorption maximum ($\simeq -1.15$ V/SCE for VPh_3PBr and $\simeq -1.05$ V/SCE for $PgPh_3PBr$). The form of the curves of Fig. 5*a* is more composite than those of Fig. 4*a*, evidently because of the interfacial rearrangements observed during the development of the adsorption film of $(PgPh_3P)^+$ cations. These rearrangements are not reflected in the form of the curves of Fig. 4*b*.

The curves of Fig. 4*a* are similar to those reported for $C_5H_{11}(C_2H_5)_2PO$, $C_6H_{13}(C_2H_5)_2PO$ (3), and $C_8H_{17}(CH_3)_2PO$ (4), while the curves of Fig. 5*a* look much like those of $[(C_6H_5)_3CH_3P]ClO_4$ (8). The formal rate constants of Cd^{2+} and Zn^{2+} discharge were determined from the *i–E* curves by the

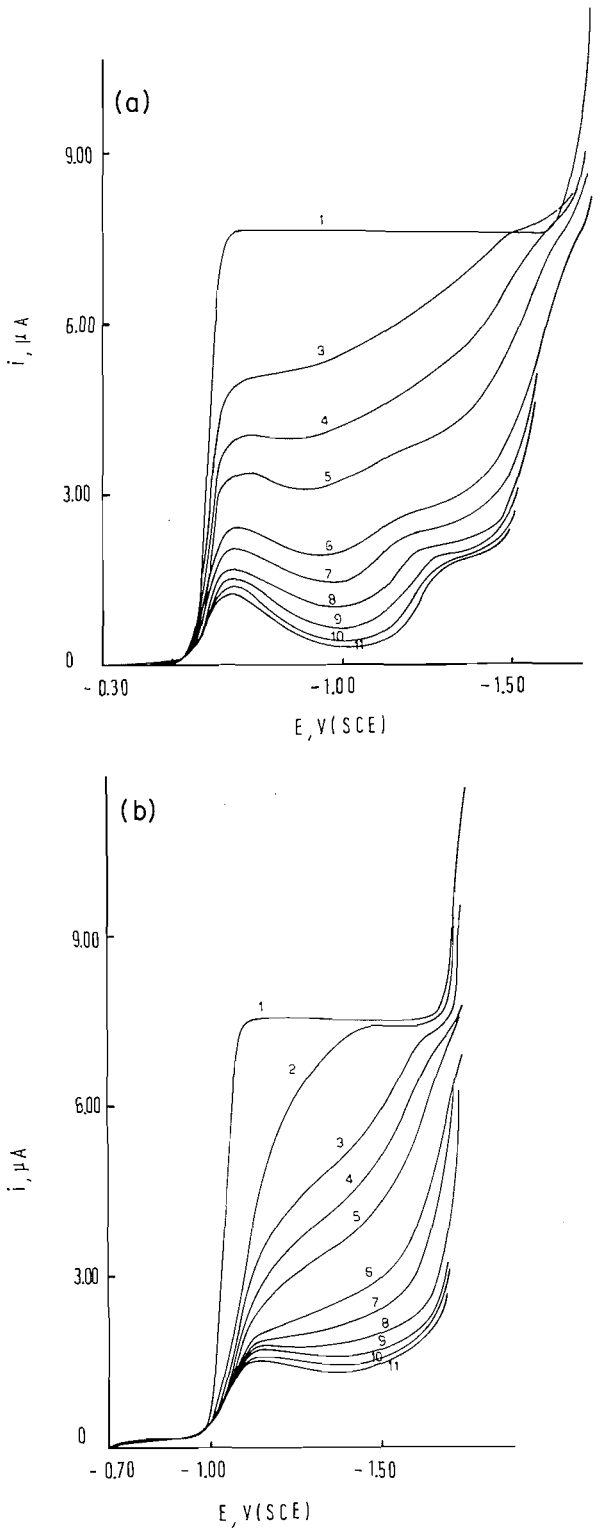

FIG. 5. Direct current polarographic curves of the Cd^{2+} (*a*) and Zn^{2+} (*b*) reduction in the presence of the following $PgPh_3PBr$ additions in m*M*: (*1*) 0.0, (*2*) 0.065, (*3*) 0.08, (*4*) 0.09 (*5*) 0.10, (*6*) 0.125, (*7*) 0.15, (*8*) 0.20, (*9*) 0.30, (*10*) 0.40, and (*11*) 0.50. Base solution:

standard Koutecký procedure (17) at the potential range from -0.8 to -1.2 V(SCE) for Cd^{2+} and -1.1 to -1.3 V(SCE) for Zn^{2+}. The cathodic limits of our study were selected to avoid any complications introduced from the discharge of the phosphonium cations which occur in the vicinity of -1.7 V(SCE).

The rate constants were used for the determination of the size ratio $r\neq/r_i$ by means of the known (1) equation:

TABLE 3. Experimental values of the size ratio $r\neq/r_i$ calculated with eq. [5]

E (V/SCE)	$r^{\neq}/r_i$ ($PgPh_3PBr$)	$r^{\neq}/r_i$ (VPh_3PBr)
$Cd^{2+} + 2e \rightarrow Cd(Hg)$		
−0.80	1.85±0.25	1.41±0.08
−1.00	1.93±0.29	1.77±0.15
−1.20	1.87±0.30	2.27±0.12
$Zn^{2+} + 2e \rightarrow Zn(Hg)$		
−1.10	1.05±0.25	1.99±0.09
−1.20	1.08±0.27	2.22±0.10
−1.30	1.18±0.27	2.34±0.16

$$[5] \quad \ln k_F = -\left(\frac{r\neq}{r_i}\right) \ln c_i + \text{constant}$$

at surfactant concentrations, c_i, greater than 0.1 mM in order to assure coverage values greater than 0.8. The values of the diffusion coefficients of Cd^{2+} and Zn^{2+} employed were found polarographically equal to 6.9×10^{-6} and 6.3×10^{-6} $cm^2 s^{-1}$, respectively, with the reproducibility reported in the experimental part for the polarographic measurements. The results of these calculations are provided in Table 3.

Table 3 shows that the values of $r\neq/r_i$ are always greater than 1.00 and usually greater than 1.50, showing a tendency to increase with increasing negative potentials. Better fit of experimental results to eq. [5] is obtained in the presence of VPh_3PBr, where the correlation coefficient of the linear regression fit is always better than 0.96 for concentrations greater than 0.1 mM and in the potential range $-0.80 < E < -1.3$. Within the above concentration and potential range in the presence of $PgPh_3PB_r$ the correlation coefficient of the linear regression fit to eq. [5] ranges from 0.86 to 0.95. In both cases the fit deteriorates with increasing cathodic potentials.

A discussion about the effect of the presence of $(PgPh_3P)^+$ and $(VPh_3P)^+$ cations on the Cd^{2+} and Zn^{2+} reduction can be carried out by determining the structure of the activated complex through the estimation of its cross-sectional area, $S_{\neq}$. This can be achieved either by deriving the $r\neq = S_{\neq}/S_{H_2O}$ values at $0 < \theta < 1$ by means of the equations (1, 2, 18–20):

$$[6] \quad \log k_F = \log k_0 + r\neq \log (1 - \theta)$$

or

$$[7] \quad \log k_F = \log k_0 + r\neq \log (1 - \theta) - \frac{A_{\neq,i}}{2.3}\theta$$

or by correlating the $r\neq/r_i$ values of Table 3 obtained at $\theta \rightarrow 1$ to the areas occupied by each adsorbate and water molecule viz. $S_{org.}$ and S_{H_2O}, respectively. To start with the former we applied eqs. [6] and [7] to coverage data obtained by eq. [3] from capacitance measurements at the potential range $-1.00 < E < -1.20$ V(SCE), where the potential of maximum adsorption is found to exist. The results of these calculations are collected in Table 4.

To apply eq. [7] a multilinear regression procedure was followed, using $r\neq$ and the interaction parameter $A_{\neq,i}$ as adjustable parameters. This method was used instead of that proposed by Afanas'ev (20) because for the latter the graphical determination of the term $d \ln (k_\theta/k_0)/d\theta$ was found to produce important errors.

However, regardless of the good fit of our data to eqs. [6] and [7], as deduced from the values of R^2 provided in Table 4, the values of $r^{\neq} = S_{\neq}/S_{H_2O}$ lead to $S_{\neq} < S_{H_2O}$, which can hardly be regarded as representing the cross-sectional area of a fully or even a partially hydrated reactant particle. Following the alternative procedure we combined the $r\neq/r_i$ values of Table 3 with the values $S_{H_2O} = 12.3$ Å^2 and $S_{(VPh_3P)^+} \simeq S_{(PgPh_3P)^+} \simeq 66$ Å^2. The resulting $S_{\neq}$ values are collected in Table 5.

The values of $S_{\neq}$ in Table 5 when correlated to the values of $S_{(PgPh_3P)^+}$, $S_{(VPh_3P)^+}$, and S_{H_2O} cannot be viewed as values for hydrated reactant particles. At first sight, they seem to correspond to a reactant–surfactant complex which incorporates a number of 4–5 water molecules. However, the latter case presents some notable weakness. At $\theta \simeq 1$, where the values of $r^{\neq}/r_i$ were determined, the water concentration is very low and therefore the availability of such a number of water molecules cannot be justified. In addition, the positive charges of both reactant and surfactant do not favour the formation of such a complex. On the other hand, there are no indications for concentration independence of the k_F values leading to $r^{\neq}/r_i \simeq 0$, which is the criterion (3) for the occurrence of a surface association reaction between reactant and surfactant preceding the discharge step. The discharge of a fully or partially hydrated reactant ion possibly occurs at low coverages. However, the $S_{\neq}$ values obtained from eqs. [6] and [7] for a wide range of coverage values, $0 < \theta < 1$, are generally smaller than the cross-sectional area of 12.3 Å^2 corresponding to a single H_2O molecule. On the other hand, the i–t curves of Fig. 2 show that the reduction of Cd^{2+} and Zn^{2+} is taking place even at a fully covered electrode surface and also that the polarographic current increases with time even at concentrations where $\theta \simeq 1$.

At low coverages the electrode surface is almost saturated with water molecules, while at high coverages the reactant ions are separated from the electrode surface by a layer saturated with $(VPh_3P)^+$ or $(PgPh_3P)^+$ cations. Therefore, in passing from low to high coverage a change in the reaction mechanism can be reasonably suggested. To the extent that neither the

TABLE 4. Inhibition parameters of $PgPh_3PBr$ and VPh_3PBr on the discharge reaction of Cd^{2+} and Zn^{2+} at the dme and correlation coefficients, R^2, from the fit of eqs. [6] and [7]

	$PgPh_3PBr$							VPh_3PBr						
E(V/SCE)	$r^{\neq}$ eq. [6]	$S_{\neq}$ (Å^2)	R^2	$r^{\neq}$ eq. [7]	$S_{\neq}$ (Å^2)	R^2	$A_{\neq,i}$	$r^{\neq}$ eq. [6]	$S_{\neq}$ (Å^2)	R^2	$r^{\neq}$ eq. [7]	$S_{\neq}$ (Å^2)	R^2	$A_{\neq,i}$
$Cd^{2+} + 2e \rightarrow Cd(Hg)$														
−1.00	1.6_6	$20._4$	0.95	—	—	—	—	0.39	4.8	0.97	0.32	3.9	0.99	0.63
−1.20	1.1_7	$14._4$	0.99	0.92	11.3	0.99	0.88	0.44	5.4	0.95	0.36	4.4	0.96	1.39
$Zn^{2+} + 2e \rightarrow Zn(Hg)$														
−1.10	0.67	8.2	0.88	0.34	4.2	0.88	0.98	0.42	5.2	0.96	0.39	4.8	0.96	0.47
−1.20	0.77	9.5	0.97	0.37	4.5	0.99	1.00	0.45	5.5	0.96	0.39	4.8	0.97	0.74

Can. J. Chem. Downloaded from www.nrcresearchpress.com by 93.93.197.157 on 09/07/12
For personal use only.

TABLE 5. Cross-sectional areas of the activated complex derived from $r\neq/r_i$ data of Table 3

E V(SCE)	$S_{\neq}$ (Å^2) $PgPh_3PBr$	VPh_3PBr
$Cd^{2+} + 2e \rightarrow Cd(Hg)$		
−1.00	119	109
−1.20	115	140
$Zn^{2+} + 2e \rightarrow Zn(Hg)$		
−1.10	65	122
−1.20	66	137

polarographic i–E curves of Figs. 4 and 5 nor the C–E curves of Figs. 1 and 2 gave some of the known (5) indications of micelle formation, within the concentration range examined, we have to look for some other reaction channel at $\theta \simeq 1$.

In analogy to the views of Jehring (21) and the data reported by Kůta *et al.* (22), we can suppose that a condensation reaction of the adsorbed phosphonium cations might lead to the creation of dense and diluted parts in the adsorption layer. Through these holes the Cd^{2+} and Zn^{2+} discharge takes place at rates gradually decreasing with increasing adsorbate concentrations. However, to the extent that our ac and dc polarographic measurements do not offer a quantitative basis for the safe determination of the inhibited reaction mechanism, which would be possibly enabled by admittance measurements, this assumption remains to a phenomenological level.

1. J. LIPKOWSKI and Z. GALLUS. J. Electroanal. Chem. **61**, 11 (1975).
2. B. B. DAMASKIN and B. N. AFANAS'EV. Elektrokhimiya, **13**, 1099 (1977).
3. E. MÜLLER, H. EMONS, H.-D. DÖRFLER, and J. LIPKOWSKI. J. Electroanal. Chem. **142**, 39 (1982).
4. E. MÜLLER, H. EMONS, J. LIPKOWSKI, and H.-D. DÖRFLER. J. Electroanal. Chem. **160**, 261 (1984).
5. H.-D. DÖRFLER, H. EMONS, M. HEINZE, and E. MÜLLER. Z. Phys. Chem. Leipzig, **267**, 985 (1986).
6. A. ANASTOPOULOS, A. CHRISTODOULOU, and D. JANNAKOUDAKIS. Z. Phys. Chem. N.F. **137**, 231 (1983).
7. H.-D. DÖRFLER and E. MÜLLER. J. Electroanal. Chem. **121**, 153 (1981).
8. E. MÜLLER, K. MÜLLER, S. VOIGT, and H.-D. DÖRFLER. Z. Phys. Chem. Leipzig, **262**, 785 (1981).
9. R. PAYNE. J. Electrochem. Soc. **113**, 999 (1966).
10. C. REILLEY and W. STUMM. *In* Progress in polarography. Vol. 1. *Edited by* P. Zuman and I. Kolthoff. Interscience Publishers. 1962. p. 81.
11. B. B. DAMASKIN, O. PETRII, and V. BATRAKOV. *In* Adsorption of organic compounds on electrodes, Plenum Press, New York. 1971.
12. F. PULIDORY, G. BORGHESANI, R. PEDRIALI, A. DE BATTISTI, and S. TRASSATI. J. Chem. Soc. Faraday I, **74**, 79 (1978).
13. J. LAWRENCE and R. PARSONS. J. Phys. Chem. **73**, 3577 (1969).
14. H. P. DHAR, B. E. CONWAY, and K. M. JOSHI. Electrochim. Acta, **18**, 789 (1973).
15. P. NIKITAS. J. Chem. Soc. Faraday Trans. 1, **80**, 3315 (1984).
16. P. NIKITAS. J. Chem. Soc. Faraday Trans. 1, **82**, 977 (1986).
17. J. HEYROVSKÝ and J. KŮTA. *In* Principles of polarography. Academic Press, New York. 1966.
18. J. LIPKOWSKI and Z. GALLUS. J. Electroanal. Chem. **98**, 91 (1979).
19. R. GUIDELLI, M. L. FORESTI, and M. R. MONCELLI. J. Electroanal. Chem. **113**, 171 (1980).
20. B. N. AFANAS'EV, G. I. ANILOVA, and N. A. BORISOVA. Elektrokhimiya, **14**, 310 (1978).
21. H. JEHRING, V. RETTER, and E. HORN. J. Electroanal. Chem. **149**, 153 (1983).
22. J. KŮTA, L. POSPISIL, and I. SMOLER. J. Electroanal. Chem. **75**, 407 (1977).

Can. J. Chem. Downloaded from www.nrcresearchpress.com by 93.93.197.157 on 09/07/12
For personal use only.

Approaches towards the synthesis of a 2,9,16,23-tetrasubstituted phthalocyanine as a pure isomer

SHAFRIRA GREENBERG, A. B. P. LEVER, AND CLIFFORD C. LEZNOFF[1]
Department of Chemistry, York University, North York (Toronto), Ont., Canada M3J 1P3

Received June 26, 1987

SHAFRIRA GREENBERG, A. B. P. LEVER, and CLIFFORD C. LEZNOFF. Can. J. Chem. **66**, 1059 (1988).

Treatment of 4-neopentoxyphthalonitrile with hydrogen sulfide gas yielded 1-imino-6-neopentoxy-3-thioisoindoline and 1-imino-5-neopentoxy-3-thioisoindoline, which on alkylation with iodomethane gave 1-imino-3-methylthio-6-neopentoxyisoindolenine and 1-imino-3-methylthio-5-neopentoxyisoindolenine. The methylthioisoindolenines readily condensed at room temperature to a mixture of tetrasubstituted phthalocyanines and a series of linear open-chained purple compounds characteristic of isoindigos, while condensation at −20°C in the presence of zinc acetate gave, in at least one experiment, 2,9,16,23-tetraneopentoxyphthalocyanine as a pure isomer. The low temperature formation of phthalocyanines is remarkable and the syntheses described herein provide guidelines for the synthesis of pure isomers of 2,9,16,23-tetrasubstituted phthalocyanines. The purple and red compounds are shown to have isoindigo structures rather than a ring-opened phthalocyanine structure as previously reported.

SHAFRIRA GREENBERG, A. B. P. LEVER et CLIFFORD C. LEZNOFF. Can. J. Chem. **66**, 1059 (1988).

La réaction du néopentoxy-4 phtalonitrile et du sulfure d'hydrogène gazeux conduit à l'imino-1 néopentoxy-6 thio-3 isoindoline et à l'imino-1 néopentoxy-5 thio-3 isoindoline qui, par alkylation avec l'iodométhane, conduisent à l'imino-1 méthylthio-3 néopentoxy-6 isoindoline et à l'imino-1 méthylthio-3 néopentoxy-5 isoindoline. À la température ambiante, les méthylthioisoindolines se condensent facilement pour donner un mélange de phtalocyanines tétrasubstituées et une série de composés linéaires pourpres caractéristiques des isoindigos; par ailleurs, une condensation à −20°C, en présence d'acétate de zinc, a conduit—au moins dans une expérience—à la tétranéopentoxy-2,9,16,23 phtalocyanine sous la forme d'un isomère pur. La formation de phtalocyanines à basse température est remarquable et les synthèses décrites dans ce travail fournissent des indications sur les méthodes de synthèse des isomères purs des phtalocyanines substituées en 2,9,16,23. On a démontré que les composés pourpre et rouge possèdent des structures reliées à celle de l'isoindigo plutôt que des structures reliées à celle de la phtalocyanine qui avaient été suggérées antérieurement.

[Traduit par la revue]

Tetrasubstituted phthalocyanines having one substituent on each of the four benzo rings of phthalocyanine have been known for some time (1) but have received more attention recently due to their importance in electrocatalytic studies (2, 3). Most tetrasubstituted phthalocyanines are prepared by self-condensation of a suitable 3 or 4-substituted phthalonitrile or derivative (4, 5). For example, the isoindoline of 4-neopentoxyphthalonitrile will, upon condensation, give not only 2,9,16,23-tetraneopentoxyphthalocyanine (**1**) but also the 2,10,16,24-, 2,9,17,24-, and 2,9,16,24-tetraneopentoxyphthalocyanine isomers (6, 7). Indeed, we have shown that the 2,9,16,23-tetraneopentoxyphthalocyanine zinc(II) (**2**) derivative exhibited peaks in its ^{1}H nmr spectrum, indicating the presence of seven of the possible eight environments collectively present in the four isomers (7). A full discussion of this phenomenon was also recently demonstrated for some quaternized tetra-2,3-pyridinoporphyrazines (8). In this latter example, it was suggested that steric considerations favoured the symmetrical isomer, having C_{4h} symmetry, but that the other isomers were present in lesser amounts. Virtually all tetrasubstituted phthalocyanines known in the literature (1) exist as a mixture of the four possible isomers, and in the case of substituents at the 2 position are usually referred to as the 2,9,16,23-tetrasubstituted isomer. On the other hand, in a very recent paper, Gaspard and Maillard (9) have succeeded in preparing the pure isomer 2,9,17,24-tetra-*tert*-butylphthalocyanine zinc(II), using metallic zinc as the condensing agent.

In connection with our studies on multinuclear phthalocyanine (6, 7, 10) and with the possibility of obtaining one pure isomer of a binuclear phthalocyanine for X-ray diffraction studies, we were interested in exploring synthetic methods of phthalocyanine formation that could give rise exclusively to the 2,9,16,23-tetrasubstituted phthalocyanines as one isomer. In a previous paper we showed that dithioamides do form phthalocyanines with diiminoisoindolines at modest temperatures (11). We envisioned that a 5-substituted iminothioamide should self-condense in one direction to form exclusively a 2,9,16,23-tetrasubstituted phthalocyanine as one isomer, because the imino group on one side of the molecule should displace selectively the methythio group on the other side of a second molecule. It turns out that treatment of phthalonitrile (**3**) with hydrogen sulfide gas gives 1-imino-3-isoindoline (**4**) directly, as reported by Baguley and Elvidge (12), but **4** does not readily condense to phthalocyanine under normal conditions (4, 5). Despite the fact that we were unable to successfully *S*-alkylate dithioamides (11) under a variety of conditions, we found that the iminothioamide **4** is readily alkylated to a separable mixture of *N*-methyl-2,3-dihydro-3-thioxo-1*H*-isoindol-1-one (**5**) and 1-imino-3-methylthioisoindolenine (**6**). The *S*-alkyl derivative **6** readily condenses to phthalocyanine (**7**) under the usual conditions but *at room temperature* instead of 150°C (Scheme 1).

This encouraging result led us to examine the possibility of using a *substituted* 1-imino-3-methylthioisoindolenine in the *exclusive* formation of 2,9,16,23-tetrasubstituted phthalocyanines as one isomer. Treatment of 4-neopentoxyphthalonitrile (**8**) with hydrogen sulfide (12) gave a mixture of 1-imino-6-neopentoxy-3-thioisoindoline (**9**) and 1-imino-5-neopentoxy-3-thioisoindoline (**10**), separable by flash chromatography (13). In separate experiments pure **9** and **10** were treated with iodomethane to give 1-imino-3-methylthio-6-neopentoxyisoindolenine (**11**) and 1-imino-3-methylthio-5-neopentoxyisoindolenine (**12**) respectively. In separate experiments, compounds **11** and **12** self-condensed spontaneously *at room temperature* to 2,9,16,23-tetraneopentoxyphthalocyanine (**1**), *as a mixture*

[1]Author to whom correspondence may be addressed.

Can. J. Chem. Downloaded from www.nrcresearchpress.com by 93.93.197.157 on 09/07/12
For personal use only.

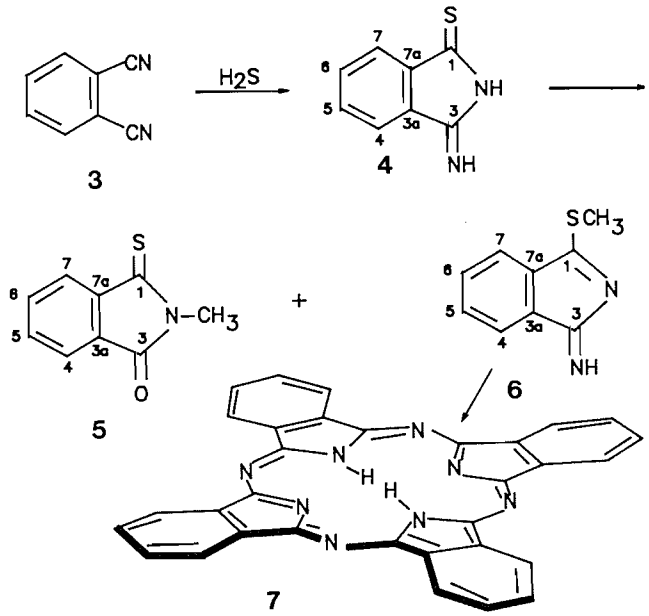

SCHEME 1

of isomers as analyzed previously by ^{1}H nmr spectroscopy (7). In addition a mixture of purple coloured compounds (**13–16**) could be recovered by flash chromatography. The assignments of the structures of compounds **13–16** remain tentative and are based on mass spectroscopy, high resolution mass spectroscopy, nmr, and uv/vis spectroscopy. Mass spectroscopy of this mixture of purple compounds could be accounted for by a mixture of compounds (**13–16**) exhibiting parent ions for all of the compounds. Further purification gave small quantities of pure **13** and **14**, whose structures are consistent with their exact high resolution mass spectra (see Experimental). Interestingly, the ^{1}H nmr spectra of **13** and **14** were consistent with the assigned structures but the absorptions for the neopentoxy substituents indicated that **13** and **14** were formed as one isomer each and that mixtures of isomers in which the position of the neopentoxy groups was different in each benzo ring were not obtained. Alternatively, the absorptions of the different positional isomers of **13** and **14** could have been coincident but this possibility is unlikely.

We were interested in characterizing the precursors **4–6** and **9–11** by ^{13}C nmr spectroscopy but found that it was necessary to obtain ^{13}C nmr spectra of pure 1,3-diimino-5-neopentoxyisoindoline (**17**) (see Experimental) and monoiminophthalimide (**18**) (14) (Fig. 1). Using the ^{13}C nmr of **17** and **18** it was possible to assign the absorptions of **4–6** and **9–11** (Table 1). In addition, the uv spectra of **4–6**, **9–11**, and **17** are recorded in Table 2.

It is well known that aromatic thioamides undergo condensation to isoindigo dyes (12), so that the formation of **13–16** is not too surprising. The presence of the neopentoxy substituents of **13–16** solubilized these normally poorly soluble compounds and allowed us to effect a separation to isolate pure **13** and **14**. The uv/vis spectra of **13** and **14** are unique and neither resembles phthalocyanines nor isoindigos. In a recent paper Fujiki *et al.* (15) describe the preparation of a hydroxygermanium(IV) α,β,γ-triazabenzcorrole formed by a ring contraction of dichlorogermanium phthalocyanine. Illumination of this corrole derivative is reported (15) to give a red compound whose uv/vis is identical to **13** and **14**. These authors propose three structures **19–21** for their red compound, none of which would be consistent with the carbon–carbon double bond structure of **13** and **14**. In light of our results a possible structure for their red compound could be illustrated below.

A representation of their red compound by the structure **22** in Fig. 2 would be likely and would not involve cleavage of a carbon–carbon double bond. Repetition of the work of Fujiki *et al.* (15) using neopentoxy-substituted phthalocyanines would give soluble derivatives of their red compound that could be purified and adequately characterized.

Condensation of **11** or **12** at −20°C in dimethylformamide (DMF) and using $Zn(OAc)_2$ as a template for macrocycle formation gave **2** directly and a mixture of purple compounds, likely **13–16**. In two experiments, condensation of **11** or **12** led to 2,9,16,23-tetraneopentoxyphthalocyanine **2** as mainly one isomer when examined by ^{1}H nmr spectroscopy (Table 3), but larger scale preparations of this reaction again led to **2**, but only as a mixture of isomers. Of course, both 2,9,16,23-tetraneopentoxyphthalocyanine (**1**) and 2,10,16,24-tetraneopentoxyphthalocynanine should exhibit only one peak for the *tert*-butyl groups and the method of synthesis should favour **1**, but the formation of the latter isomer cannot be entirely excluded. It should be pointed out that the mixture of isomers thus obtained was not identical to the statistical distribution of isomers of **2** previously reported (7) (Table 3).

In summary, we have demonstrated the remarkable low temperature formation of phthalocyanines from iminomethylthioisoindolenines, have aided in the characterization of the coloured by-products formed in these as similar reactions, and have initiated experiments directed towards the isolation of pure isomers of tetrasubstituted phthalocyanines.

Experimental

Matheson high purity argon was used to maintain inert atmosphere conditions. Infrared (ir) spectra were recorded on a Pye Unicam SP1000 infrared spectrophotometer using KBr discs for solids or as neat films between NaCl discs. Nuclear magnetic resonance (nmr) spectra for carbons and protons were recorded on a Bruker AM300 nmr spectrometer using deuterochloroform as a solvent and tetramethylsilane as the internal standard unless otherwise stated. The positions of the signals are reported in δ units. (The splittings of the signals are described as singlets (s), doublets (d), triplets (t), quartets (q), or multiplets (m).)

The visible–ultraviolet spectra (uv) were recorded on a Hewlett Packard HP8451A Diode Array spectrophotometer. Mass spectra (ms) were recorded at 70 eV on a VG Micromass 16F mass spectrometer in the EI mode.

Melting points (mp) were determined using a Kofler hot stage melting point apparatus and are uncorrected. Thin-layer chromatography (tlc) was performed using silica gel G as the adsorbent. Flash chromatography was performed using silica gel of particle size 20–45 μm. All reactions were stirred with a magnetic stirrer. All solvents were freshly distilled before use. Microanalyses were performed by Guelph Chemical Laboratories Ltd., Guelph, Ont.

Purification of 5-neopentoxy-1,3-diiminoisoindoline (17)

The crude 5-neopentoxy-1,3-diiminoisoindoline obtained from 134 mg of 4-neopentoxyphthalonitrile (0.63 mmol) by standard procedure (6) was dissolved in ethyl acetate, washed with water, and dried over anhydrous magnesium sulfate. Evaporation of the ethyl acetate and recrystallization from ethyl acetate/hexanes gave in 68% yield 98 mg of pure 5-neopentoxy-1,3-diiminoisoindoline as white crystals, mp 200–203°C; ir (cm^{-1}): 3260 (NH), 3200 (NH), 1695, 1650, 1620–1600, 1540, 1450, 1440, 1315, 1240, 1140, 1065, 1020, 885, 820; ^{1}H nmr δ: 7.59 (d, J = 8.4, 1H), 7.24 (br, 1H), 7.12 (dd, J = 8.4, 2.1, 1H), 3.70 (s, 2H, CH_2O), 1.06 (s, 9H, $(CH_3)_3C$); ms m/z: 231 (M^+, 25), 161 (M^+ − 70, 80), 71 (38), 57 (47), 43 (100). *Anal.* calcd. for $C_{13}H_{17}N_3O$: C 67.51. H 7.41, N 18.17; found: C 68.01, H 7.74, N 18.05.

Can. J. Chem. Downloaded from www.nrcresearchpress.com by 93.93.197.157 on 09/07/12
For personal use only.

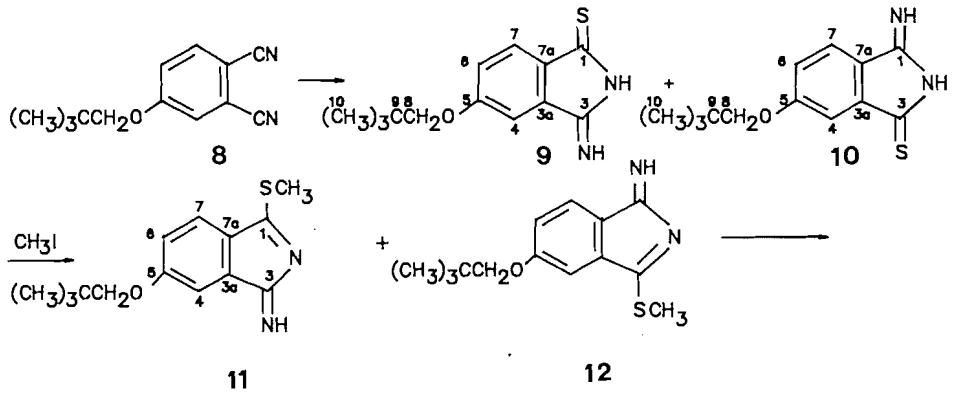

8 9 10

11 12

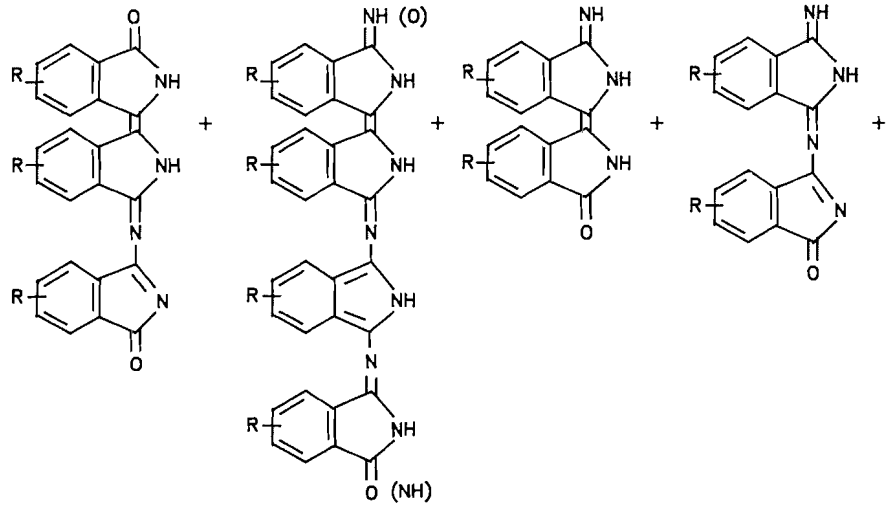

13 R = $OCH_2C(CH_3)_3$ 14 R = $OCH_2C(CH_3)_3$ 15 R = $OCH_2C(CH_3)_3$ 16 R = $OCH_2C(CH_3)_3$

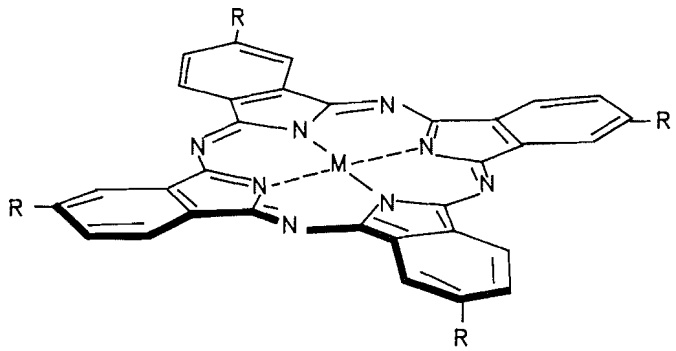

1 R = $OCH_2C(CH_3)_3$, M = H_2

2 R = $OCH_2C(CH_3)_3$, M = Zn

7 R = H , M = H_2

SCHEME 2

1-Imino-3-thioisoindoline (4)

The 1-imino-3-thioisoindoline was prepared from phthalonitrile and sodium hydrogen sulfide according to the procedure of Baguley and Elvidge (12), mp 220°C (dec.) (lit. (12) mp 218°C); ir (cm^{-1}): 3160 (NH), 1665, 1465, 1390, 1290, 1270, 1240, 1080, 910, 765, 675; ^1H nmr (DMSO-d_6) δ: 10.88 (vbr. 2H, NH), 7.99 (d, J = 7.3, 1H), 7.81–7.67 (m, 3H); ms m/z: 162 (M^+, 100), 146 (20), 135 (30), 129 (92), 76 (47).

1-Imino-3-methylthioisoindolenine (6) and N-methylmonothiophthalimide (5)

A solution of 101 mg of 1-imino-3-thioisoindoline (0.63 mmol) in 1 mL ethanol was methylated with dimethyl sulfate according to the procedure of Baguley and Elvidge (12). The crude product was precipitated from water, filtered, and washed with water to give in 65% yield, 71 mg of **6**. An attempt to recrystallize **6** resulted in decomposition, accompanied by phthalocyanine formation, mp 86–90°C (dec.)

Can. J. Chem. Downloaded from www.nrcresearchpress.com by 93.93.197.157 on 09/07/12
For personal use only.

TABLE 1. ^{13}C nuclear magnetic resonance chemical shifts (in ppm (δ), in $CDCl_3$) of some imino and thioanalogs of phthalimide

Compound	Carbon												
	1	3	3a	4	5	6	7	7a	8	9	10	N—CH_3	S—CH_3
4[a]	199.92[b]	164.97[b]	134.00	121.72	132.54[c]	132.34[c]	123.02	137.80	—	—	—	—	—
5	197.36	169.79	127.38	123.64	134.02	133.08	122.69	137.06	—	—	—	27.54	—
6	182.37	171.52	140.45	122.75	131.12[c]	130.97[c]	119.86	136.64	—	—	—	—	13.25
9[a]	197.85	163.31[d]	131.67	106.91	163.27	118.83	124.90	130.69	77.99	31.59	26.24	—	—
10[a]	165.26[b]	200.23[b]	140.25	107.67	162.53	118.98	123.32	122.01	77.78	31.54	26.22	—	—
11	n.o.[e]	n.o.	n.o.	108.12	162.13	117.54	121.27	n.o.	77.83	31.58	26.24	—	12.92
17[a]	169.17	169.17	138.80	106.89	161.56	116.70	122.21	128.51	77.76	31.60	26.30	—	—
18[a,f]	172.9[b]	164.5[b]	134.2[b]	122.0	132.9	132.3	122.5	133.1	—	—	—	—	—

[a]Taken in DMSO-d_6.
[b]Broadened.
[c]These values may be interchanged.
[d]Signal overlap with C5.
[e]n.o.: not observed due to low concentration. Sample should not be heated to dissolve.
[f]Data taken from ref. 14.

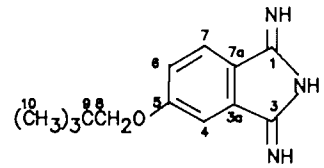

17

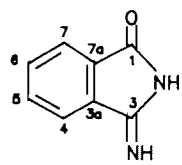

18

FIG. 1. Compounds used in aiding assignments of ^{13}C nmr spectra (Table 1).

TABLE 2. Ultraviolet spectra of iminothioisoindolines and related compounds in $CHCl_3$ at 24°C

Compound	λ_{max}(nm) (log ε)
4[a]	234(4.29), 310(4.13), 345(3.90)
5	242(3.75), 300(4.16), 332(4.01)
6[a]	285(3.98), 436(2.72)
9	258(4.24), 340(4.23)
10	256(4.40), 326(4.28)
11[b]	254(4.36), 298(4.18), 366(3.42)
17	244(4.24), 266(4.24), 312(sh) (4.12)

[a]Data taken from ref. 12.
[b]This compound is not very stable.

(lit. (12) mp 98–100°C); ir (cm^{-1}): 3180 (NH), 1655, 1480, 1360, 1265, 1240, 1040, 960, 770, 760, 685; ^1H nmr δ: 9.49 (br, 1H), 7.93 (br, 1H), 7.55–7.43 (m, 3H), 2.74 (s, 3H, S—CH_3); ms *m/z*: 176 (M^+, 35), 129 (100).

When left overnight the filtrate deposited orange needles, which were filtered off to give in 9% yield 10 mg of *N*-methylmonothiophthalimide, mp 97–98°C (lit. (16) mp 97°C, 86–87°C); ir (cm^{-1}): 1740 (C═O), 1470, 1375, 1340, 1325, 1075, 990, 770, 700; ^1H nmr δ: 7.96 (m, 1H), 7.77 (m, 1H), 7.69 (m, 2H), 3.48 (s, 3H, N—CH_3); ms *m/z*: 177 (M^+, 100), 117 (80).

1-Imino-6-neopentoxy-3-thioisoindoline (9) and 1-imino-5-neopentoxy-3-thioisoindoline (10)

A suspension of 15.1 g of sodium sulfide nonahydrate (62.9 mmol) in 5 mL of water was saturated with a slow stream of hydrogen sulfide gas for 1 h. The suspension became cloudy and the stream of H_2S was increased for a further 45 min. The grey solution was then added to a solution of 4.2 g of 4-neopentoxyphthalonitrile (6) (19.6 mmol) in 11 mL of 95% ethanol and the mixture was stirred at room temperature for 48 h. The reaction mixture was diluted with 200 mL of water and the precipitate was filtered and washed with water to yield 3.9 g of crude product. Further purification was done by flash chromatography (13) on silica gel, using ether/petroleum ether (3:2) as eluant. The first 100 mL consisted of dark impurities and a trace of 5-neopentoxydithiophthalimide (11). Continued elution gave a yellow moving band consisting of 1-imino-6-neopentoxy-3-thioisoindoline. Evaporation of the eluant gave in 17% yield 0.84 g of pure **9** as very light brown crystals, mp 126–130°C (dec.); ir (cm^{-1}): 3280–3180 (NH), 1660, 1610, 1490, 1480–1460, 1365, 1255, 1105, 830; ^1H nmr (acetone-d_6) δ: 7.83 (d, J = 8.4, 1H), 7.53 (br, 1H), 7.26 (dd, J = 8.4, 2.3, 1H), 3.82 (s, 2H, CH_2O), 1.06 (s, 9H, $(CH_3)_3C$); ms *m/z*: 248 (M^+, 100), 178 (82), 71 (27), 43 (28). *Anal.* calcd. for $C_{13}H_{16}N_2OS$: C 62.87, H 6.49, N 11.28; found: C 62.95, H 6.70, N 11.42.

Continued elution of the silica gel gave a second yellow moving band consisting of 1-imino-5-neopentoxy-3-thioisoindoline. Evaporation of the eluant gave in 20% yield 0.97 g of pure **10** as golden crystals, mp 189–191°C (dec.); ir (cm^{-1}): 3250 (NH), 1660, 1610, 1495, 1380, 1365, 1325, 1280, 1200, 1050, 1020, 865, 830, 820, 730; ^1H nmr (acetone-d_6) δ: 7.88 (d, J = 8.5, 1H), 7.37 (d, J = 2.2, 1H), 7.32 (dd, J = 8.5, 2.2, 1H), 3.83 (s, 2H, CH_2O), 1.07 (s, 9H, $(CH_3)_3C$); ms *m/z*: 248 (M^+, 42), 178 (80), 71 (52), 43 (100). *Anal.* calcd. for $C_{13}H_{16}N_2OS$: C 62.87, H 6.49, N 11.28; found: C 63.09, H 6.75, N 11.22.

1-Imino-3-methylthio-6-neopentoxyisoindolenine (11) and 1-imino-3-methylthio-5-neopentoxyisoindolenine (12)

A solution of 64.4 mg of 1-imino-6-neopentoxy-3-thioisoindoline (0.26 mmol), 1 mL ethanol, and 0.22 mL of 1.25 *N* sodium hydroxide (0.28 mmol) was diluted with 1 mL of water and stirred while 0.02 mL of methyl iodide (0.32 mmol) was added dropwise at room temperature. After 45–60 min, ice-cold water was added and the product was filtered and washed with water to give in 82% yield 56 mg of 1-imino-3-methylthio-6-neopentoxyisoindolenine as brown crystals. Compound **11** was used directly in the next step, mp 115–117°C (turned green); ir (cm^{-1}): 3260–3180 (NH), 1660, 1605, 1480–1460, 1360, 1250, 1100, 825; ^1H nmr δ: 9.34 (br, 1H), 7.46 (br, 1H), 7.35 (d, J = 8.2, 1H), 7.00 (d, J = 8.2, 1H), 3.69 (s, 2H, CH_2O), 2.72 (s, 3H, SCH_3), 1.05 (s, 9H, $(CH_3)_3C$); ms *m/z*: 262 (M^+, 10), 192 (23), 71 (65), 57 (48), 43 (100). *Anal.* calcd. for $C_{14}H_{18}N_2OS$: C 64.09, H 6.92, N 10.68; found: C 64.06, H 7.02, N 11.05.

Similarly a solution of 101 mg of 1-imino-5-neopentoxy-3-thioisoindoline was methylated with methyl iodide at 0°C for 3 min to give a dark oily product. The crude product was extracted with ether and the organic layer was washed thoroughly with water. After drying over anhydrous magnesium sulfate, the solvent was evaporated to give in 75% yield 80 mg of a very dark oil. Compound **12** is very unstable and therefore it is used directly in the next step. An attempt to purify **12** by flash chromatography caused decomposition, hydrolysis of the

Can. J. Chem. Downloaded from www.nrcresearchpress.com by 93.93.197.157 on 09/07/12
For personal use only.

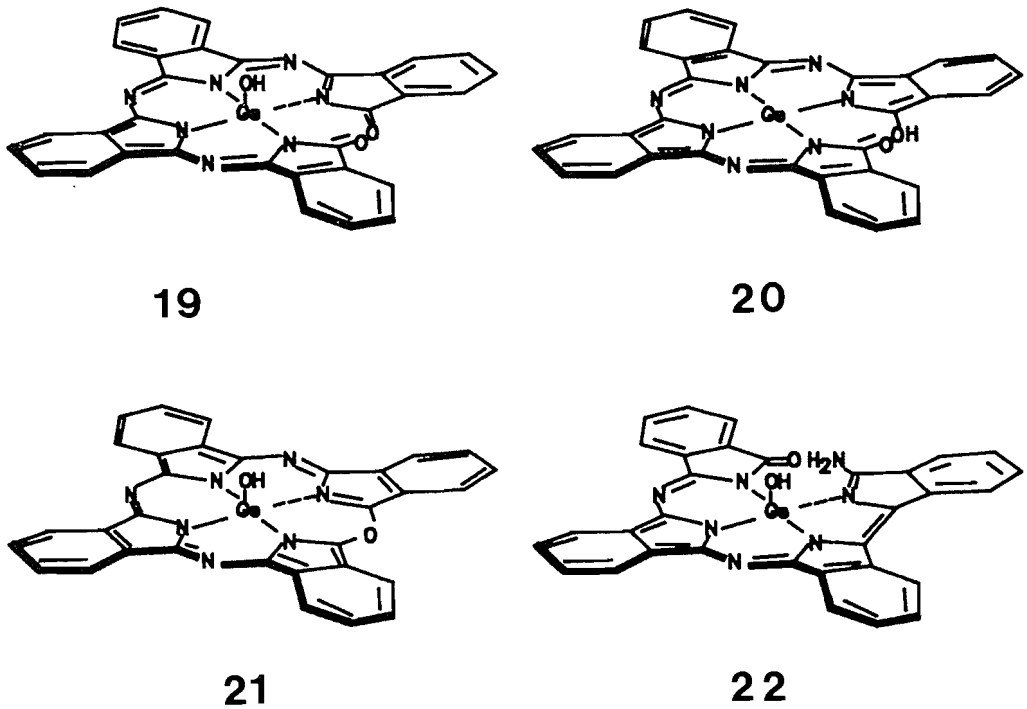

FIG. 2. Reported and new suggested structures for the red compound.

TABLE 3. ^{1}H nuclear magnetic resonance chemical shifts (in ppm (δ), of 2,9,16,23-tetraneopentoxyphthalocyanine (**1**) and its Zn derivative (**2**) for different methods of preparation

Phthalocyanine	Precursor	Reaction conditions	$(CH_3)_3C$	NH
1	**17**	160°C, DMAE[a]	1.27, 1.26, 1.25, 1.232, 1.226	−4.94, −5.12, −5.21, −5.64
1	**11**	60°C, DMAE	1.29, 1.26, 1.25, 1.24, 1.23	−2.62, −4.98, −5.14, −5.27
1	**11**	24°C, DMAE	1.28, 1.27, 1.222, 1.218	−2.30, −2.48
1	**12**	24°C, DMAE	1.30, 1.28, 1.27, 1.24, 1.23	−2.73, −3.27
2	**1** via **17**	100°C, $Zn(OAc)_2$	1.27, 1.26, 1.25, 1.22, 1.21	—
2	**11**	−18°C, $Zn(OAc)_2$	1.26, 1.20	—
2	**12**	−20°C, $Zn(OAc)_2$	1.26	—

[a]*N*,*N*-Dimethylaminoethanol.

imino group, and phthalocyanine formation; ^{1}H nmr δ: 7.64 (d, J = 9, 1H), 7.44 (d, J = 3, 1H), 6.97 (dd, J = 9, 3, 1H), 3.73 (s, 2H, CH_2O), 2.81 (s, 3H, SCH_3), 1.06 (s, 9H, $(CH_3)_3C$); ms m/z: 262 (M^+, 31), 247 (M^+ − 15, 9), 215 (M^+ − SCH_3, 40), 192 (M^+ − 70, 14), 145 (95), 71 (98), 43 (100).

Phthalocyanine formation from 11

Compound **11** obtained from 100 mg of **9** (0.40 mmol) in 1–2 mL of *N*,*N*-dimethylaminoethanol underwent self-condensation under argon at room temperature for 60 h. The crude reaction product was purified as previously described (6) to give, after flash chromatography, in 5–18% yield, 2,9,16,23-tetraneopentoxyphthalocyanine (**1**) as a mixture of isomers. From the ^{1}H nmr it seemed that some isomers were more selectively formed than others, but complete selectivity was not obtained. If during the self-condensation the argon is bubbling directly inside the reaction mixture, to remove the ammonia that is formed during the reaction, the desired phthalocyanine is not formed at room temperature. Raising the temperature to 60°C (oil bath) increased the yield but reduced the selectivity of the formation of isomers. Phthalocyanine formation was observed to take place when a solution of **11** in ether was left at room temperature overnight or when a sample of **11** was left partially dissolved in DMSO-d_6 inside an nmr tube. In both cases no selectivity towards the formation of one isomer was detected by ^{1}H nmr. During the purification of **1** by flash column chromatography it was observed that some purple material was left on the top of the column. At room temperature the purple colour became very intense. Therefore, after all of **1** was eluted with toluene, the solvent system was changed to 2-methoxyethanol/toluene (1:50). Several fractions were collected and, after evaporation of the solvent, it was found that some fractions contained mixtures of only **13** and **14**. The spectral data of this mixture is given as follows: ir (cm^{-1}): 3400 (NH), 2940, 1765, 1730, 1610, 1490, 1365, 1230, 1045, 1010, 745; uv (ether): 582, 542, 510, 346 nm; ^{1}H nmr δ: 7.75 (d, J = 8.3 Hz), 7.32 (d, J = 2.0 Hz), 7.20 (dd, J = 8.2 and 2.0 Hz), 3.71 (s, CH_2O), 1.06 (s, $(CH_3)_3C$); ^{13}C nmr δ: 168.00, 167.93, 164.83, 135.24, 125.18, 124.27, 120.66, 108.57, 78.80, 31.88, 29.66, 26.44. Further purification on a few mg was achieved by preparative tlc using the same eluting solvent as above to give **13** and **14** in estimated yields of 5% and 7% respectively; ms (high resolution) m/z, calcd. for $C_{39}H_{44}N_4O_5$, **13**, (M^+): 648.35404; found: 648.3555; calcd. for $C_{52}H_{61}N_7O_5$, **14**, (M^+): 863.47337; found: 863.4696.

Compounds of related structure were discussed by Fujiki *et al.* (15).

Can. J. Chem. Downloaded from www.nrcresearchpress.com by 93.93.197.157 on 09/07/12
For personal use only.

Phthalocyanine formation from ***12***

Compound **12** obtained from 116 mg of **10** (0.47 mmol) in 1–2 mL of *N*,*N*-dimethylaminoethanol underwent self-condensation under argon at room temperature for 18 h. The crude reaction product was purified as previously described (6) to give, after flash chromatography, in 8% yield, 8 mg of 2,9,16,23-tetraneopentoxyphthalocyanine as a mixture of isomers; some isomers were more selectively formed than others, in comparison with the isomers formed from the self-condensation of 5-neopentoxy-1,3-diiminoisoindoline (**17**) at 150°C. Further elution of the column with 2-methoxyethanol/toluene (1:50) gave purple/red material consisting of **13–16** as analyzed by mass spectroscopy. The physical and spectral data of **1** (except for the ^{1}H nmr) were identical to the ones previously reported (6).

2,9,16,23-Tetraneopentoxyphthalocyanine zinc(II) (2)

A mixure of 20 mg of **11** (0.076 mmol) and 5.7 mg (0.031 mmol) of zinc acetate was cooled in the freezer to −15°C. Cold DMF (−15°C) was added (1 mL); the mixture turned green and was left in the freezer for 1 week. The crude product was purified by flash column chromatography in a cold room (3°C). The column was packed a day in advance and was left in the cold room overnight. The crude product was applied to the column as is, and was eluted with cold toluene at 3°C to give 1 mg of **2** (5% yield); ^{1}H nmr (C_6D_6) δ: 1.26, 1.20; ms *m*/*z*: 922 (M^+, 100), 851 ($M^+ - 71$, 40), 460 ($M^{+2} - 1$, 65). Similarly a mixture of **12** derived from 102 mg of **10** (0.41 mmol) underwent self-condensation in the presence of zinc acetate in DMF at −15 – −18°C. Purification as above gave a mixture of **2** contaminated by **13** and **14**. Further purification by preparative tlc using 2-methoxyethanol/toluene (1:50) as eluting solvent followed by flash column chromatography gave 10.8 mg of **2** in 11% yield uncontaminated by **13** and **14**; ^{1}H nmr (C_6D_6) δ: a major peak at 1.26 and 2 small peaks at 1.23 and 1.21 ppm. This experiment was repeated at −40°C and gradually the temperature was raised to +5°C. Purification as above gave a trace of the desired product as indicated by a faint blue spot on tlc; ^{1}H nmr (C_6D_6) δ: 1.26 ppm. A control experiment using **11** in 2-*N*,*N*-dimethylaminoethanol showed that metal-free phthalocyanine formation did not take place at temperatures below 10°C.

Acknowledgements

We are grateful to the Natural Sciences and Engineering Research Council of Canada for financial support of this research. This work was also partially funded by the Office of Naval Research (Washington) and by the Midwest Center for Mass Spectrometry, a National Science Foundation Regional Instrumentation Facility (Grant No. CHE 8211164).

1. F. H. Moser and A. L. Thomas. Phthalocyanine compounds. Van Nostrand – Reinhold, Princeton, NJ. 1963; A. B. P. Lever. Adv. Inorg. Chem. Radiochem. **7**, 27 (1965); F. H. Moser and A. L. Thomas. The phthalocyanines, Vols. 1 and 2. CRC Press Inc., Boca Raton, FL. 1983.
2. A. B. P. Lever, M. R. Hempstead, C. C. Leznoff, W. Liu, M. Melnik, W. A. Nevin, and P. Seymour. Pure Appl. Chem. **58**, 1467 (1986).
3. D. Dolphin, B. R. James, A. J. Murray, and J. R. Thornback. Can. J. Chem. **58**, 1125 (1980); B. Simic-Glavaski, S. Zecevic, and E. J. Yeager. J. Electroanal. Chem. Interfacial Electrochem. **150**, 469 (1983); N. Kobayashi and Y. Nishiyama. J. Phys. Chem. **89**, 1167 (1985); W. A. Nevin, M. R. Hempstead, W. Liu, C. C. Leznoff, and A. B. P. Lever. Inorg. Chem. **26**, 570 (1987).
4. P. J. Brach, S. J. Grammatica, O. A. Ossanna, and L. Weinberger. J. Heterocycl. Chem. **7**, 1403 (1970).
5. G. Pawlowski and M. Hanack. Synthesis, 287 (1980).
6. C. C. Leznoff, S. M. Marcuccio, S. Greenberg, A. B. P. Lever, and K. B. Tomer. Can. J. Chem. **63**, 623 (1985).
7. S. M. Marcuccio, P. I. Svirskaya, S. Greenberg, A. B. P. Lever, C. C. Leznoff, and K. B. Tomer. Can. J. Chem. **63**, 3057 (1985).
8. D. Wohrle, J. Gitzel, I. Okura, and S. Aono. J. Chem. Soc. Perkin Trans. 2, 1171 (1985).
9. S. Gaspard and Ph. Maillard. Tetrahedron, **43**, 1083. (1987).
10. S. Greenberg, S. M. Marcuccio, C. C. Leznoff, and K. B. Tomer. Synthesis, 406 (1986); W. A. Nevin, W. Liu, S. Greenberg, M. R. Hempstead, S. M. Marcuccio, M. Melnik, C. C. Leznoff, and A. B. P. Lever. Inorg. Chem. **26**, 891 (1987); C. C. Leznoff, H. Lam, S. M. Marcuccio, W. A. Nevin, P. Janda, N. Kobayashi, and A. B. P. Lever. J. Chem. Soc. Chem. Commun. 699 (1987).
11. C. C. Leznoff, S. Greenberg, B. Khouw, and A. B. P. Lever. Can. J. Chem. **65**, 1705 (1987).
12. M. E. Baguley and J. A. Elvidge. J. Chem. Soc. 709 (1957).
13. W. C. Still, M. Kahn, and A. Mitra. J. Org. Chem. **43**, 2923 (1978).
14. L. I. Spiessens, and M. J. O. Anteunis. Bull. Soc. Chim. Belg. **92**, 965 (1983).
15. M. Fujiki, H. Tabei, and K. Isa. J. Am. Chem. Soc. **108**, 1532 (1986).
16. W. Köhler, M. Bubner, and G. Ulbricht. Chem. Ber. **100**, 1073 (1967); M. Machida, K. Oda, E. Yoshida, and Y. Kanaoka. J. Org. Chem. **50**, 1681 (1985).

Can. J. Chem. Downloaded from www.nrcresearchpress.com by 93.93.197.157 on 09/07/12
For personal use only.

Mechanism of electrodeposition of cadmium selenide from $SeSO_3^{2-}$ solution

JEFFREY P. SZABO AND MICHAEL COCIVERA

The Guelph–Waterloo Centre for Graduate Work in Chemistry, University of Guelph, Guelph, Ont., Canada N1G 2W1

Received August 17, 1987

JEFFREY P. SZABO and MICHAEL COCIVERA. Can. J. Chem. **66**, 1065 (1988).

The mechanism of the electrodeposition of CdSe from selenosulfite and cadmium–NTA complex has been studied by analysis of the Tafel regions of linear sweep voltammograms. The Tafel plots were linear for up to 20% of the peak height, and were used to calculate the dependence of the reduction rate on the concentration of each of the reactants. The electron transfer process was found to be first order with respect to $SeSO_3^{2-}$ and zero order with respect to each of the other reactants. These results are consistent with a two-step reduction of $SeSO_3^{2-}$ to Se^{2-}, followed by precipitation of CdSe. The reduction of $Cd(NTA)^-$ to cadmium metal appears to be blocked or inhibited in the presence of $SeSO_3^{2-}$, resulting in CdSe films of nearly perfect stoichiometry to be deposited.

JEFFREY P. SZABO et MICHAEL COCIVERA. Can. J. Chem. **66**, 1065 (1988).

Faisant appel à une analyse des régions de Tafel des voltampérogrammes à balayage linéaire, on a étudié le mécanisme de l'électrodéposition du CdSe à partir du sélénosulfite et du complexe cadmium–NTA. Les courbes de Tafel sont linéaires jusqu'à 20% de la hauteur du pic et on les a utilisées pour calculer la relation entre la vitesse de réduction et la concentration de chacun des réactifs. On a trouvé que le processus de transfert d'électron est du premier ordre par rapport au $SeSO_3^{2-}$ et d'ordre zéro par rapport à chacun des autres réactifs. Ces résultats sont en accord avec un mécanisme de réduction du $SeSO_3^{2-}$ en Se^{2-} qui impliquerait deux étapes et qui serait suivi d'une précipitation du CdSe. La réduction du $Cd(NTA)^-$ en cadmium métallique semble être bloquée ou inhibée par la présence du $SeSO_3^{2-}$ et il en résulte que ce sont des films de CdSe de stoechiométrie pratiquement parfaite qui se déposent.

[Traduit par la revue]

Introduction

The mechanism of electrodeposition of cadmium selenide from solutions containing selenosulfite ($SeSO_3^{2-}$) and the ethylene diamine tetracetate (EDTA) complex of cadmium is simplified by the fact that the cadmium–EDTA complex is not reducible in the range where reduciton of $SeSO_3^{2-}$ to Se^{2-} occurs (1). If nitrilotriacetate ion (NTA) is used as a ligand in place of EDTA, the resulting CdSe film exhibits sustantially higher light-to-electric power conversion efficiencies (1, 2). Furthermore, the NTA process is very reproducible, providing high quality (high efficiency) films consistently (2). When NTA is used, reduction of cadmium metal occurs at potentials more positive than that for reduction of $SeSO_3^{2-}$, leading to speculation in earlier studies that the formation of CdSe might somehow involve cadmium in the reduction step (2). The aim of the present study is to elucidate the mechanism of the electrodeposition process by determining the reaction order with respect to each of the reactants. After the first few monolayers, the electrochemical process occurs at the CdSe/solution interface. Consequently, during almost all of the film growth, it is the electrochemistry at this interface that is important and is reported in this paper.

Experimental

Preparation of stock solutions

All stock solutions were made from water purified by the Millipore Milli-Q Water System. Selenosulfite stock solutions were prepared by stirring anhydrous Na_2SO_3 and elemental Se together for a few hours, and then slowly adding water. Typically, 2 g of Se and 50 g of Na_2SO_3 were dissolved in 500 mL water. Sodium sulfite stock solution contained 50 g Na_2SO_3 in 500 mL water. NTA (NTA^{3-} = nitrilotriacetate ion) stock solution contained 7.09 g trisodium nitrilotriacetate monohydrate $[N(CH_2CO_2Na)_3 \cdot H_2O]$ in 250 mL. The pH of the NTA stock solution was adjusted with HCl to 9.7, which was the measured pH of the stock selenosulfite solution. Stock solutions of $Cd(NTA)^-$ complex were stable for only a few hours and so were prepared immediately before each set of experiments. Typically, 0.24 g of anhydrous $CdCl_2$ was dissolved in 15 mL of stock NTA solution. The following concentrations will be referred to as "standard": 0.595 *M* Na_2SO_3, 0.0380 *M* Se, 0.0258 *M* $Na_3NTA \cdot H_2O$, and 0.0218 *M* $CdCl_2$. A solution which contains all four species will be referred to as a "deposition solution", or "standard deposition solution" if the concentrations are standard. This standard deposition solution appeared more stable than the $Cd(NTA)^-$ solution and could be used for several days without evidence of chemical precipitation.

Unless stated otherwise $[Na_2SO_3]$ = 15.6 × total selenium and $[Na_3NTA \cdot H_2O]$ = 1.12 × total cadmium. In all cases, concentrations refer to *total* concentrations of a given species, i.e. $[SeSO_3^{2-}]$ = total selenium, $[Cd(NTA)^-]$ = total $CdCl_2$, $[NTA^{3-}]$ = total $Na_3NTA \cdot H_2O$, and $[SO_3^{2-}]$ = total Na_2SO_3. (The former two identities are valid under conditions used here, since the concentrations of unbound selenium and cadmium are extremely low.)

Preparation of CdSe working electrode

Titanium wire 0.81 mm in diameter was etched in 10% HF and rinsed well prior to electrodeposition. CdSe was electrodeposited on the Ti wire according to a previously described method (2). Typically, CdSe films were deposited at −1.000 V vs. SCE for 5–10 min from a standard deposition solution. The electrode area (~50 mm^2) was kept constant for a series of experiments by insulating the top portion with black sealing wax. Figures showing more than one set of data correspond to a single electrode area, unless stated otherwise. Just prior to use of the electrode for cyclic voltammetry (CV), the potential was cycled between −400 and −1300 mV vs. SCE in selenosulfite solution for a few minutes at 100 mV/s. Cycling was done to improve the reproducibility of the CV's. No other post deposition treatments were done.

Cyclic voltammetry

Cyclic voltammograms were done in quiet solutions using a CdSe working electrode, a platinum counter electrode, and a standard calomel reference electrode (SCE). All potentials were reported with respect to SCE. An in-house potentiostat was used for all CV's. The voltage ramp was supplied by the D/A converter of a Tecmar PC Mate Lab Master board installed in an IBM PC computer. The current and potential were recorded using the A/D converters of the Tecmar board. The sweep rates used in this study ranged from 10 to 500 mV/s, and 5 mV/point was the typical resolution used for data collection.

Can. J. Chem. Downloaded from www.nrcresearchpress.com by 93.93.197.157 on 09/07/12
For personal use only.

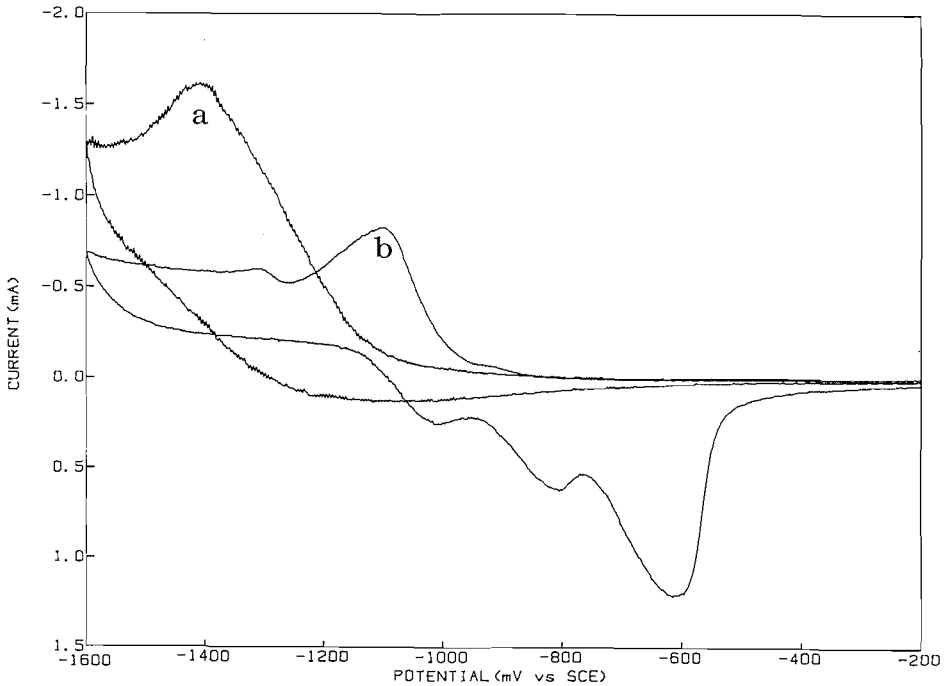

FIG. 1. Cyclic voltammogram at CdSe electrode of solutions which contained (*a*) $SeSO_3^{2-}$ and SO_3^{2-}, (*b*) $Cd(NTA)^-$ and NTA^{3-}. The sweep rate was 20 mV/s and the concentrations of all reagents were standard (see Experimental).

TABLE 1. Concentrations of stock solutions employed for kinetic order determinations

Species	Solution number	Concentrations (M)[a]			
		$[SeSO_3^{2-}]$	$[Cd(NTA)^-]$	$[NTA^{3-}]$	$[SO_3^{2-}]$
$SeSO_3^{2-}$	1	0.04470	0.01087	0.01213	0.7001
	2	—	0.01087	0.01213	0.7001
NTA^{3-}	3	0.03800	0.002328	0.002514	0.7000
$Cd(NTA)^-$	4	0.01948	—	—	1.282
	5	0.01948	0.02681	0.03172	1.282
SO_3^{2-}	6	0.01858	0.004529	0.005090	0.2907

[a]In all cases concentrations refer to *total* concentrations. For instance, $[NTA^{3-}] = [Cd(NTA)^-] + [NTA^{3-}]_f$, where the latter term corresponds to the uncomplexed ligand.

Order of the reaction

The order of the reaction was found with respect to each of the reactants by measuring the relative rate (see Results) for various concentrations of each species. Table 1 illustrates the way in which the concentrations were changed in a controlled manner. The concentration of $SeSO_3^{2-}$ was varied by mixing various aliquots of two stock solutions (#1 and #2, Table 1): one which contained $SeSO_3^{2-}$ and one which did not. Both solutions contained identical concentrations of $Cd(NTA)^-$, NTA^{3-}, and SO_3^{2-}. The concentration of Cd^{2+} could not be varied by adding $CdCl_2$ directly to the deposition solution due to the precipitation of $Cd(OH)_2$ and/or CdSe. The concentration of Cd was varied in two ways. First, the concentration of unbound Cd^{2+} was varied (solution #3, Table 1) by more than 3 orders of magnitude by the addition of NTA^{3-} (in the form of $Na_3NTA \cdot H_2O$), which binds to Cd^{2+} very strongly ($K = 10^{9.8}$, ref. 3). Second, the concentration of bound Cd^{2+} was varied by mixing aliquots of a solution which contained both Cd^{2+} and NTA^{3-} (solution #5), and one which contained neither (solution #4). Both solutions contained equal concentrations of $SeSO_3^{2-}$ and SO_3^{2-}. The concentration of unbound Cd^{2+} was kept constant for this set of experiments by maintaining a constant ratio of $[Na_3NTA \cdot H_2O]:[CdCl_2]$. This precaution proved later to be unnecessary as the ratio was found to have no effect on the reaction rate, so long as $[NTA^{3-}] > [CdCl_2]$. The concentration of SO_3^{2-} was modified by adding Na_2SO_3 to the deposition solution (solution #6). The reaction rate was unaffected by the addition of Na_2SO_3 up to 1.6 M, which changed the ionic strength from 0.93 M to 5.7 M.

Results

Cyclic voltammetry

The reduction wave of $SeSO_3^{2-}$ at the CdSe electrode *in the absence* of $Cd(NTA)^-$ was characterized by a broad irreversible wave with a peak at ~ -1400 mv vs. SCE (Fig. 1(*a*)) and with very small current in the potential range -700 to -900 mV, which was the range employed in this study for kinetic analysis. When subsequent scans were done, the peak current was observed to decrease with each cycle and a reddish-orange species accumulated in the vicinity of the working electrode, although the electrode itself remained unaltered in colour and texture. If the electrode was rinsed and the solution was stirred after each scan, then a plot of the logarithm of the peak height versus the logarithm of the sweep rate was linear with a slope of 0.55 (Fig. 2(*a*)). The CV of $Cd(NTA)^-$, Fig. 1(*b*), was characterized by a sharp reduction peak at ~ -1080 mV and a broad anodic stripping wave. In the absence of $SeSO_3^{2-}$, cadmium metal deposition was significant in the potential range usually used for CdSe deposition, -950 to -1200 mV.

Figure 3 shows a CV for several scan rates of the deposition solution, which contained $SeSO_3^{2-}$ and $Cd(NTA)^-$ in the ratio 1.7:1. There were two irreversible reduction waves, the first of which will be referred to as the "deposition peak", since it occurred in the region where depositions are usually carried out (-1000 to -1200 mV). If the cathodic limit of the CV was quite negative (< -1300 mV) then both peaks were observed to decrease with repetitive scans and the electrode became dark red. If the scan reversal was more positive than -1200 mV, then each cycle produced identical CV's, and the electrode remained

Can. J. Chem. Downloaded from www.nrcresearchpress.com by 93.93.197.157 on 09/07/12
For personal use only.

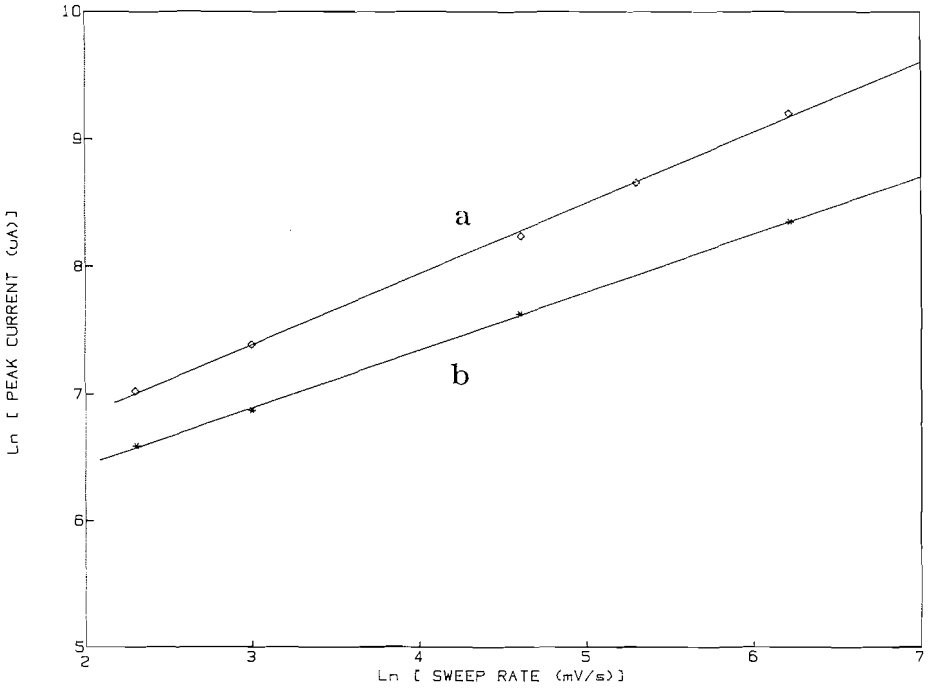

FIG. 2. Plot of logarithm of the peak current versus logarithm of the sweep rate for (*a*) selenosulfite solution, (*b*) deposition peak. Selenosulfite solution contained $SeSO_3^{2-}$ and SO_3^{2-}; the deposition solution contained standard concentrations of all reagents. The deposition peak height used here was corrected for overlap of the second peak (see Results).

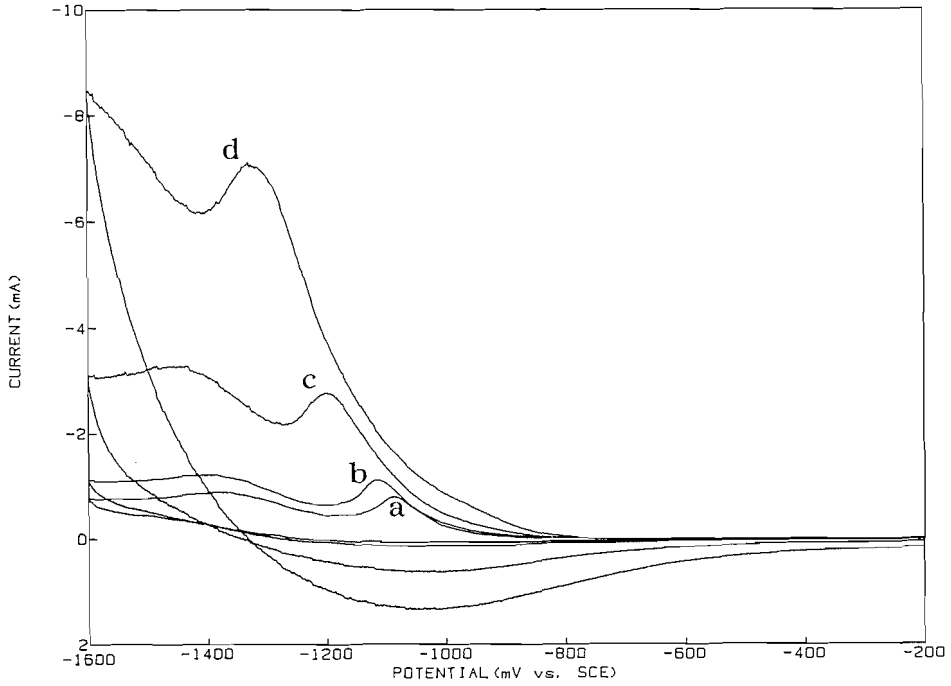

FIG. 3. Cyclic voltammograms of a standard deposition solution at various sweep rates: (*a*) 10 mV/s, (*b*) 20 mV/s, (*c*) 100 mV/s, and (*d*) 500 mV/s. The electrode was rinsed between cycles.

grey. The deposition peak increased and moved negative with increasing scan rate.

The second, more negative peak of the deposition solution had the same broad shape and occurred at the same potential as that for $SeSO_3^{2-}$ reduction in the absence of $Cd(NTA)^-$ (Fig. 1). Since the two waves overlapped, the deposition peak height was estimated by subtracting the cathodic current for $SeSO_3^{2-}$ reduction (Fig. 1) from the deposition solution current (Fig. 3). If the electrode was rinsed and the solution stirred after each scan, then a plot of the logarithm of the corrected peak height versus the logarithm of the sweep rate was linear with a slope of 0.45 (Fig. 2(*b*)). The deposition peak increased and moved *negative* with increasing $Cd(NTA)^-$ concentration (Figs. 4 and 5); the peak increased and moved *positive* with increasing $SeSO_3^{2-}$ concentration. The peak at −1400 mV increased with increasing $[SeSO_3^{2-}]$, but *decreased* with increasing

Can. J. Chem. Downloaded from www.nrcresearchpress.com by 93.93.197.157 on 09/07/12
For personal use only.

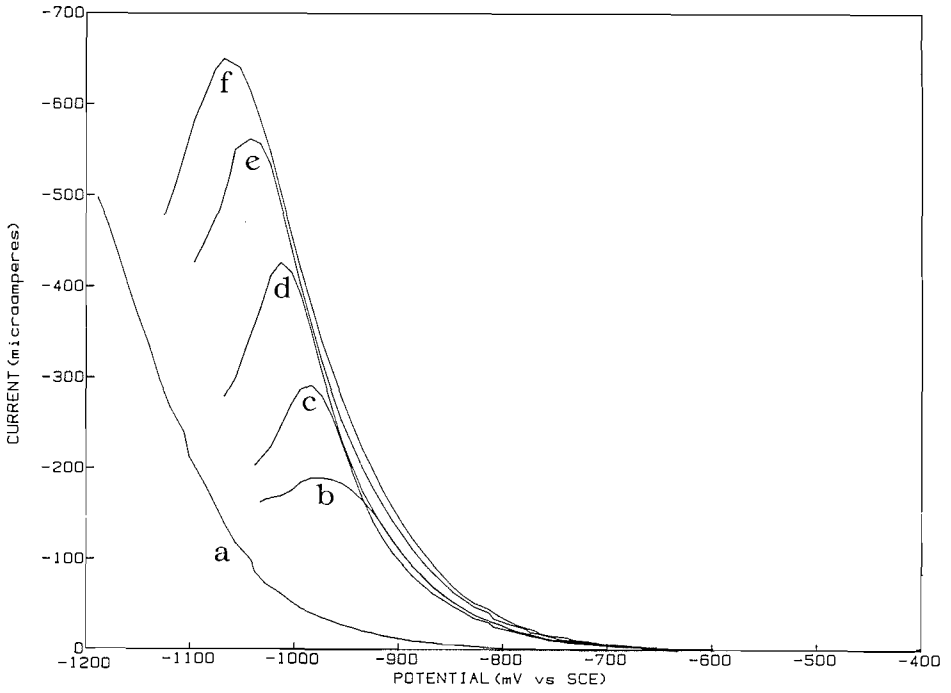

FIG. 4. Linear sweep voltammogramms (i.e. only cathodic half of a cycle) of a deposition solution for various concentrations of $Cd(NTA)^-$: (*a*) 0, (*b*) 1.68×10^{-3} *M*, (*c*) 3.16×10^{-3} *M*, (*d*) 6.71×10^{-3} *M*, (*e*) 1.14×10^{-2} *M*, (*f*) 1.46×10^{-2} *M*. The concentrations of the other species were as follows: $[SeSO_3^{2-}] = 0.01948$ *M*, $[SO_3^{2-}] = 0.3052$ *M*, and $[NTA^{3-}] = 1.12 \times [Cd(NTA)^-]$. Sweep rate was 20 mV/s.

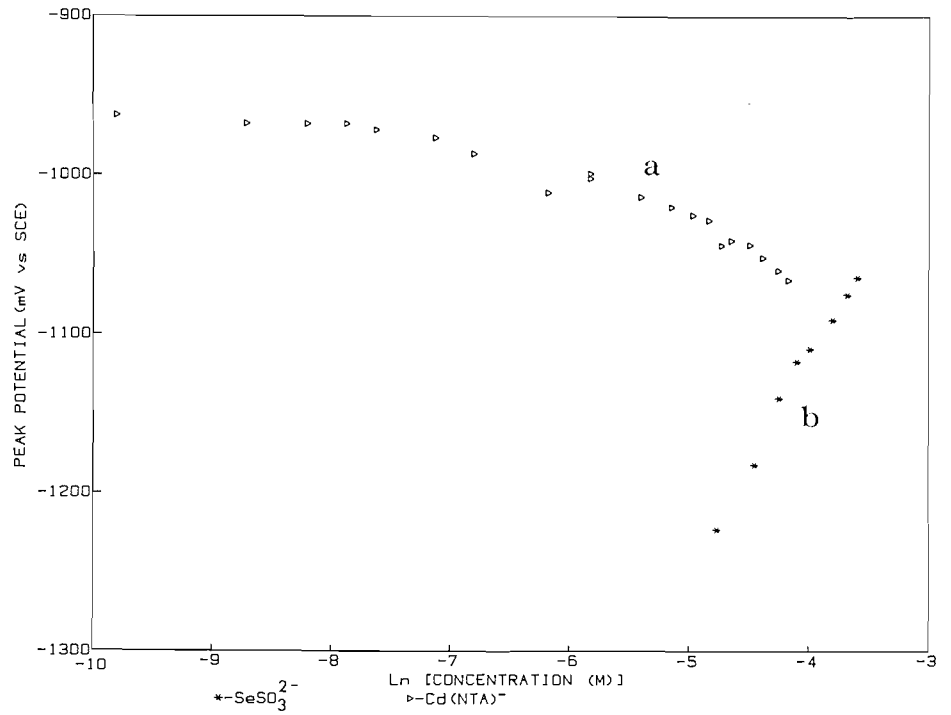

FIG. 5. Peak potential versus logarithm of (*a*) $[Cd(NTA)^-]$ and (*b*) $[SeSO_3^{2-}]$. The concentration of the other reactant was standard.

$[Cd(NTA)^-]$. No anodic stripping wave was observed for the deposition solution if $[SeSO_3^{2-}] > [Cd(NTA)^-]$. For solutions in which the concentration of $Cd(NTA)^-$ was greater than that of $SeSO_3^{2-}$, an anodic stripping wave was observed on the reverse scan.

Composition

A detailed study of the effect of reagent concentrations, thickness, and deposition potential on the composition of the CdSe film has been previously reported (2) and is summarized below. Typically, films have no excess cadmium and are made from solutions in which the ratio $[SeSO_3^{2-}]$: $[Cd(NTA)^-] = 1.7$. For these films, the Cd:Se ratio was found to be close to 0.95 and to be independent of NTA concentration, deposition potential in the range -950 to -1200 mV, and thickness. For depositions made from solutions in which $[Cd(NTA)^-] > [SeSO_3^{2-}]$, the Cd:Se ratio was significantly above 1, indicating metallic cadmium was present along with CdSe.

Can. J. Chem. Downloaded from www.nrcresearchpress.com by 93.93.197.157 on 09/07/12
For personal use only.

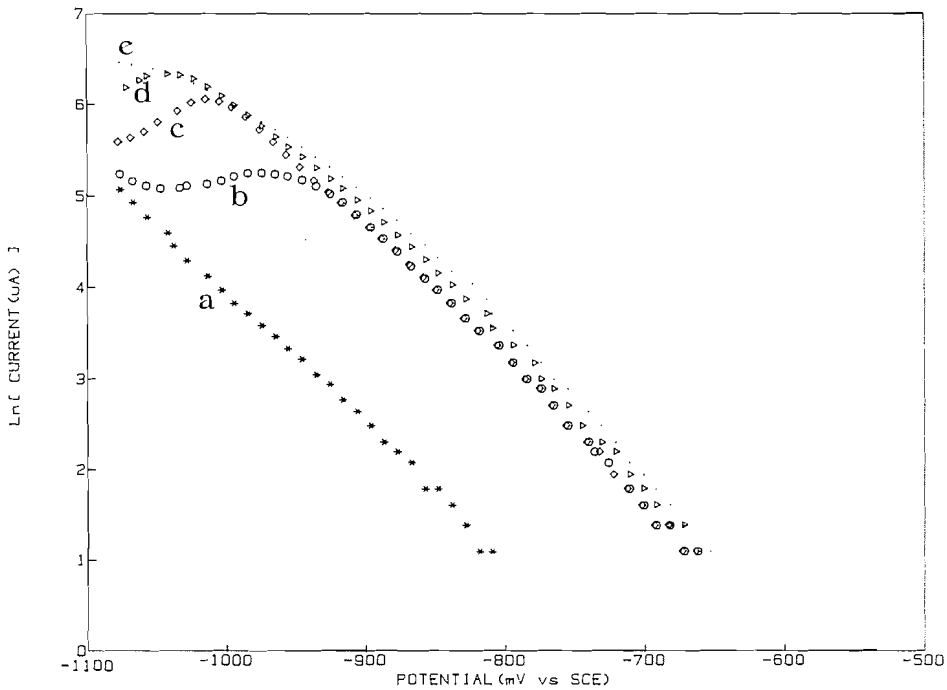

FIG. 6. Tafel plots for various concentrations of $Cd(NTA)^-$: (*a*) 0, (*b*) 1.68×10^{-3} *M*, (*c*) 6.71×10^{-3} *M*, (*d*) 1.14×10^{-2} *M*, (*e*) 1.92×10^{-2} *M*. Other concentrations as in Fig. 4. Sweep rate was 20 mV/s.

Tafel plots

The Butler–Volmer equation describes the current (i) – potential (E) relationship well in the absence of mass transfer effects, i.e. when there is no significant concentration gradient near the electrode surface. The latter may be achieved by stirring the solution or by keeping the current less than 10% of the limiting diffusion current (ref. 4, Chap. 3). Consider the cathodic term of the Butler–Volmer equation (ref. 4, Chap. 3 ref. 5) for which the reactants have concentrations c_1, c_2, ... and reaction orders p_1, p_2, ... :

$$[1] \quad i = nFAk^0 c_1^{p_1} c_2^{p_2} \ldots \exp[-\alpha nF(E - E^0)/RT]$$

In the above equation the anodic term has been neglected because no significant anodic current could be detected during the reverse scan. Most likely the overpotential is large for oxidation of CdSe. In eq. [1], n is the number of electrons (1 in this case), A is the electrode area, α is the charge transfer coefficient, and k^0 is the heterogeneous rate constant at the standard electrode potential E^0. Faraday's constant, the gas constant, and absolute temperature are denoted by F, R, and T, respectively. Taking the natural logarithm of [1] gives

$$[2] \quad \ln i = \ln nFAk + \Sigma_j p_j \ln c_j - [\alpha nF(E - E^0)/RT]$$

In this study, the current/potential data were obtained from the CV's for currents less than 20% of the peak current. This method assured reproducibility because the peak current and potential could be monitored. If the second scan did not reproduce the previous scan, the data were rejected. Tafel plots were constructed from CV's by plotting the natural logarithm of the current for cathodic sweeps versus the potential.

As shown in Fig. 6, these plots were linear for currents less than 10 to 20% of the peak current, which usually corresponded to a potential range from −700 to −900 mV. The value of α determined from the slope ($-\alpha nF/RT$) was fairly constant for a given electrode and set of solutions, e.g. $\alpha = 0.36 \pm 0.02$, assuming transfer of one electron in the rate determining step. For a number of electrodes and solutions, an overall average of $\alpha = 0.3 \pm 0.1$ was found. The Tafel plot for the deposition wave (Fig. 7(*b*)–(*e*)) had the same slope as that for $SeSO_3^{2-}$ reduction in the absence of $Cd(NTA)^-$ (Fig. 6(*a*)). The initial effect of adding small amounts of $Cd(NTA)^-$ (as little as 10^{-5} *M*) to a solution of $SeSO_3^{2-}$ was to shift the Tafel plot 160 mV positive, but additional $Cd(NTA)^-$ produced no further shift in the *foot* of the wave. (As mentioned above, the *peak* moved negative and increased with increasing $Cd(NTA)^-$ concentration.) The Tafel plot for $Cd(NTA)^-$ reduction (Fig. 7(*a*)) differs markedly from the deposition Tafel plots. The $Cd(NTA)^-$ Tafel plot has a much steeper slope and is not linear for small currents. It is possible that cadmium metal deposition on the CdSe electrode is controlled by nucleative growth rate rather than electron transfer rate in the "Tafel region" of the wave. The effect of adding more $SeSO_3^{2-}$ to the deposition solution was to shift the Tafel plot positive (Fig. 7(*b*)–(*g*)). There was no effect on the Tafel plots when extra NTA^{3-} or SO_3^{2-} was added.

Concentration dependence

For $SeSO_3^{2-}$, NTA^{3-}, $Cd(NTA)^-$, and SO_3^{2-}, the kinetic order was determined from Tafel plots generated for solutions in which the concentration of one species was varied, while those for the other three were held constant (see Experimental for details). This process yielded families of Tafel plots (Figs. 6 and 7). From eq. [2], it can be seen that at a given potential, the slope of a plot of ln i vs. ln c_j should be equal to the order of the species j:

$$[3] \quad \frac{\partial \ln i}{\partial \ln c_j} = p_j$$

Figure 8 shows sample order plots for $Cd(NTA)^-$ and $SeSO_3^{2-}$. Table 2 gives the average order found for each species, and the concentration range over which the order is valid (usually 1–2 orders of magnitude). Table 2 also gives the number of trials, n, and the standard error $s/n^{1/2}$ (where s is the standard deviation). As Table 2 shows, the electrodeposition rate is first order with respect to $SeSO_3^{2-}$ but essentially zero order for all other species. Note that the order with respect to $Cd(NTA)^-$ is zero order only for low concentrations. As Fig. 8(*a*) shows, for concentrations

Can. J. Chem. Downloaded from www.nrcresearchpress.com by 93.93.197.157 on 09/07/12
For personal use only.

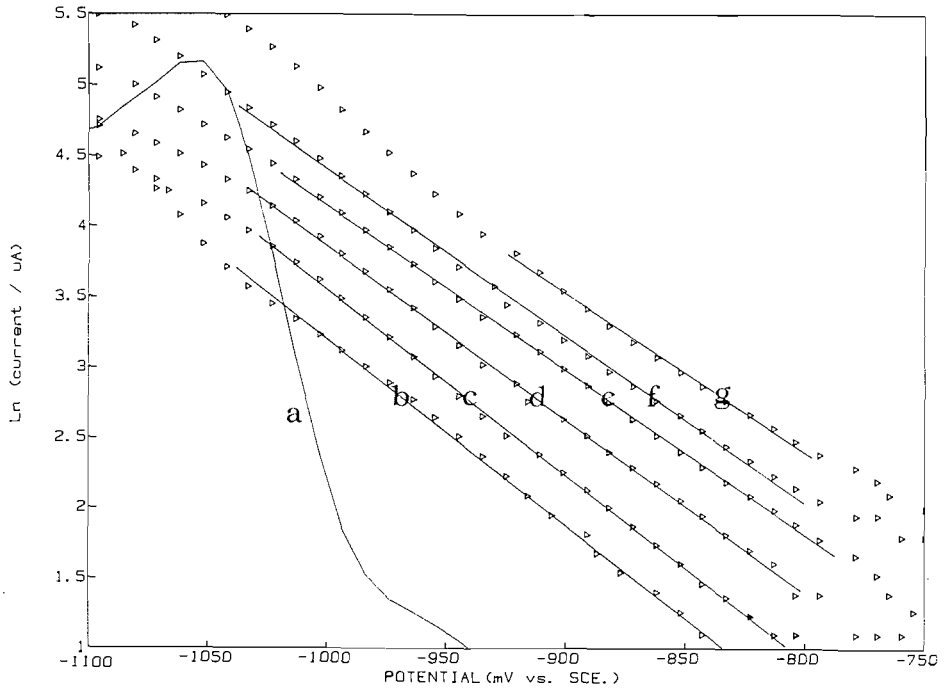

FIG. 7. Tafel plots for various concentrations of $SeSO_3^{2-}$: (*a*) 0, (*b*) 4.71×10^{-3} *M*, (*c*) 8.52×10^{-3} *M*, (*d*) 1.17×10^{-2} *M*, (*e*) 1.43×10^{-2} *M*, (*f*) 1.84×10^{-2} *M*, (*g*) 2.75×10^{-2} *M*. The concentrations of the other species were as follows: $[Cd(NTA)^-] = 0.0100$ *M*, $[SO_3^{2-}] = 0.700$ *M*, and $[NTA^{3-}] = 0.0121$ *M*. Sweep rate was 20 mV/s.

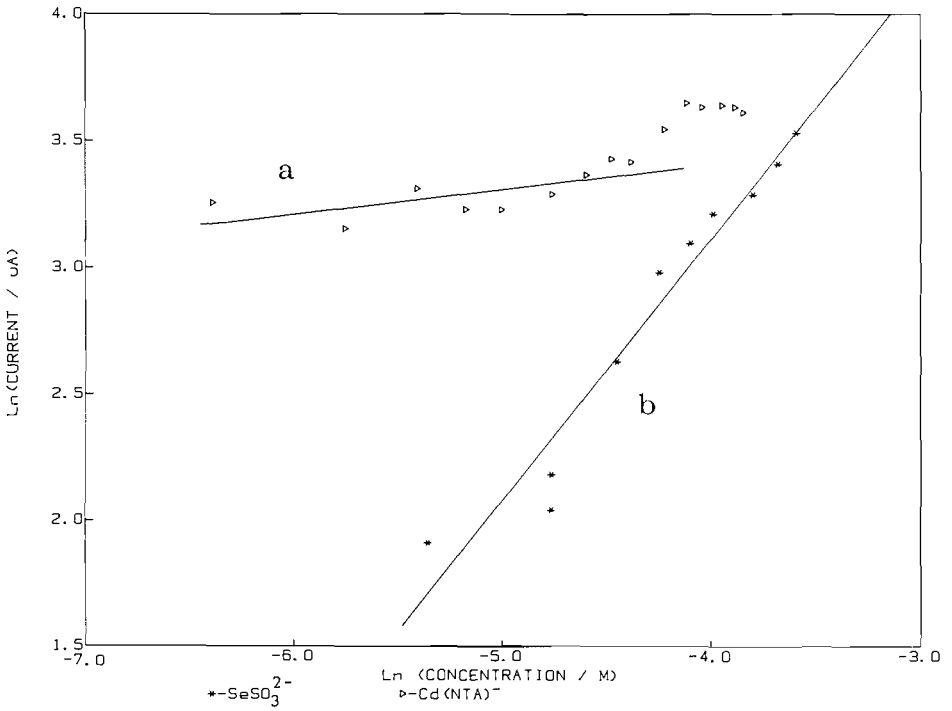

FIG. 8. Effect of $[Cd(NTA)^-]$ and $[SeSO_3^{2-}]$ on reaction rate using data shown in Figs. 6 and 7, respectively. Logarithm of current versus logarithm of concentration for (*a*) $Cd(NTA)^-$ at −800 mV and (*b*) $SeSO_3^{2-}$ at −900 mV. The electrode areas were not the same for (*a*) and (*b*).

of $Cd(NTA)^-$ greater than 4×10^{-3} *M*, the rate rises through a maximum and then falls off with increasing $Cd(NTA)^-$ concentration. The region of the maximum occurs when [Cd] ≈ [Se], and under these conditions a small anodic stripping wave is observed in the cyclic voltammogram. In comparison to the data scatter found at lower $Cd(NTA)^-$ concentration, this maximum observed at higher $Cd(NTA)^-$ is too large to attribute to data scatter. Furthermore, this feature is observed consistently in repeated trials. Probably it indicates the onset of cadmium metal deposition to give nonstoichiometric CdSe films because an anodic stripping current becomes observable in this concentration range.

Discussion

Based on the observed reaction orders, the rate of charge transfer at a particular potential in the Tafel region for solutions in which $[SeSO_3^{2-}] > [Cd(NTA)^-]$ may be written as

$$\text{Rate} = i/nFA = k[SeSO_3^{2-}]$$

Can. J. Chem. Downloaded from www.nrcresearchpress.com by 93.93.197.157 on 09/07/12
For personal use only.

TABLE 2. Average kinetic order determined for pertinent species

Species	No. of trials	Average order	$s/n^{1/2}$	Concentration range (M)
SO_3^{2-}	3	−0.162	0.031	6.1×10^{-2} to 1.7
NTA^{3-}	4	0.076	0.110	2.2×10^{-3} to 2.0×10^{-1}
$SeSO_3^{2-}$	2	1.023	0.011	4.8×10^{-3} to 2.7×10^{-2}
$Cd(NTA)^-$	4	0.044	0.037	4.5×10^{-5} to 4.1×10^{-3}

where k is the heterogeneous rate constant. The simplest mechanism that is consistent with the rate law involves a slow one electron reduction of $SeSO_3^{2-}$ followed by rapid transfer of the second electron and a rapid equilibrium:

$$SeSO_3^{2-} + e \xrightarrow{\text{slow}} Se^- + SO_3^{2-} \qquad E_{rev}$$

$$Se^- + e \xrightarrow{\text{fast}} Se^{2-}$$

[A] $$Cd^{2+} + Se^{2-} \rightleftarrows CdSe$$

Overall: $$SeSO_3^{2-} + Cd^{2+} + 2e \rightarrow CdSe + SO_3^{2-} \qquad E_1$$

This process is ascribed to the reduction wave occurring in the region of −1100 mV for the deposition solution. The second wave at −1400 mV (Fig. 3) for this solution occurs at the same reduction potential observed for the $SeSO_3^{2-}$ solution in the absence of $Cd(NTA)^-$ (Fig. 1). In both cases, scans to this potential region result in what appears to be the same reddish-orange precipitate. As a result, we suggest that the same process applies in these two cases. The absence of any oxidation wave indicates removal of the reduced species by a rapid chemical reaction. Composition data (2) show that depositions carried out at potentials more negative than −1250 mV result in formation of deposits that have up to twice as much selenium as cadmium. Consequently we suggest the reaction of selenide ion with selenosulfite ion to produce di- and polyselenide species, which may precipitate with a metal ion subsequently.

$$SeSO_3^{2-} + e \rightarrow Se^- + SO_3^{2-} \qquad E_{rev}$$

$$Se^- + e \xrightarrow{\text{fast}} Se^{2-}$$

[B] $$Se^{2-} + SeSO_3^{2-} \rightarrow Se_2^{2-} + SO_3^{2-}$$

Overall: $$2SeSO_3^{2-} + 2e \rightarrow Se_2^{2-} + 2SO_3^{2-} \qquad E_2$$

Weak adsorption of the product resulting in this first reduction (Se^-) or second reduction step (Se^{2-}) in mechanisms [A] and [B] can be neither confirmed nor precluded by the scan rate information. Weak adsorption is not expected to alter the dependence of the reduction peak current on the square root of the scan rate (ref. 4, pp. 530, 531). Furthermore, although weak adsorption is expected to move the peak potential in the positive direction as the scan rate is increased (ref. 4, pp. 530, 531), this effect may be obscured by the larger negative shift (Fig. 3) due to the irreversible nature of the reduction. Support for adsorption comes from inhibition of Cd(II) reduction (discussed below).

The reversible reduction of $SeSO_3^{2-}$ to Se^{2-} occurring at E_{rev} is not observed because of the succeeding chemical reaction. The effect of the chemical reaction is to cause a positive shift of the reduction potential of $SeSO_3^{2-}$ from E_{rev} to E_2 (6). Mechanism [B] occurs in the absence of $Cd(NTA)^-$ and also in the presence of $Cd(NTA)^-$ when $[SeSO_3^{2-}] > [Cd(NTA)^-]$ as illustrated in Figs. 1 and 3, respectively. For the latter conditions, mechanism [A] occurs also (wave in the region −1100 mV), i.e. reduction of $SeSO_3^{2-}$ occurs at an even more positive equilibrium potential, E_1. This description is consistent with identical values of the charge transfer coefficient, $\alpha = 0.36$, for the selenosulfite solution (Fig. 6(*a*)) and the deposition solution (Fig. 6(*b*)–(*e*)). Consequently, in the deposition solution the wave around −1100 mV depends on diffusion of $Cd(NTA)^-$ to interface (for chemical reaction), while the one near −1400 mV depends on diffusion of $SeSO_3^{2-}$. Both waves are observed when the flux of $SeSO_3^{2-}$ is greater than that of $Cd(NTA)^-$.

An approximation of the maximum value of the positive shift, $\Delta E = E_1 - E_{rev}$, may be calculated from the solubility product of CdSe in water, $K_{sp} = 7 \times 10^{-36}$ (7):

$$\Delta E = -(RT/nF) \ln (K_{sp}/[Cd^{2+}])$$

If a value of $[Cd^{2+}] \cong 10^{-10}$ M is used (the association constant for Cd^{2+} and NTA^{3-} is $10^{9.8}$ (ref. 3)), then $E_1 - E_{rev} = +770$ mV. Consequently, the observed shifts are well within this maximum value, indicating that the proposed model is not unreasonable. An analogous positive shift has been observed in the electrodeposition of CdSe from $SeCN^-$ and $Cd(EDTA)^{2-}$ complex, and was ascribed to the low solubility of the CdSe deposit (8). In this case, the $SeCN^-$ reduction peak potential was shifted 320 mV positive in the presence of $Cd(EDTA)^{2-}$.

The initial effect of small amounts of $Cd(NTA)^-$ is to shift the Tafel plot positive by ~ 160 mV, but there is no further shift in the Tafel plot for a wide concentration range (Table 2). There was also no effect with additional NTA^{3-}. The concentration of $Cd(NTA)^-$ did, however, affect the peak height and peak position (Fig. 4). It seems unlikely that this negative shift in peak potential is due to IR drop because a positive shift occurs when $[SeSO_3^{2-}]$ is increased (the increase in peak current is comparable to that found for $[Cd(NTA)^-]$ increase). An explanation consistent with this result is that at the peak potential, the current is controlled by the subsequent chemical reaction, i.e. is limited by diffusion of $Cd(NTA)^-$ to the electrode. On the other hand, in the Tafel region, the current is limited by the slow electron transfer to $SeSO_3^{2-}$. These results also appear to preclude other mechanisms involving the adsorption of either $Cd(NTA)^-$ or $SeSO_3^{2-}$.

It appears that $SeSO_3^{2-}$ has an inhibiting effect on the reduction of $Cd(NTA)^-$ to Cd metal. The voltammogram of $Cd(NTA)^-$ exhibits a sharp rise in the reduction current at ~ −1000 mV, so one might expect that a mixture of Cd and CdSe would be deposited at potentials more negative than −1000 mV. However, the onset of Cd deposition on CdSe does not occur until $[Cd(NTA)^-] \geq [SeSO_3^{2-}]$ as indicated by the occurrence of a small stripping wave on the anodic scan. For a solution in which $[SeSO_3^{2-}] = 2[Cd(NTA)^-]$, the total charge passed on the anodic half of the cyclic potential scan is less than 2% of the charge passed during the cathodic scan. These results are consistent with composition studies (2), which indicate that stoichiometric films are grown under these conditions. The inhibition of Cd metal deposition may be explained by the adsorption of Se^- or Se^{2-} following the reduction of $SeSO_3^{2-}$. As mentioned above, the results of the scan rate study do not preclude this possibility. An analogous mechanism was used to explain the electrodeposition of CdS from diethylene glycol solutions (9). Finally, an examination of the Tafel plots (Fig. 7) shows that the slope for $Cd(NTA)^-$ reduction is much larger than the one for $SeSO_3^{2-}$ reduction. The fact that there is no change in the slope of the deposition Tafel plots from −800 to −1100 mV is additional evidence that $SeSO_3^{2-}$ reduction dominates in this potential range when $SeSO_3^{2-}$ is present in the

Can. J. Chem. Downloaded from www.nrcresearchpress.com by 93.93.197.157 on 09/07/12
For personal use only.

concentration range employed. Nevertheless, the deviation from zero order for $Cd(NTA)^-$ exhibited in Fig. 8 is an indication that $Cd(NTA)^-$ reduction becomes more important as $[Cd(NTA)^-]$ becomes greater than $[SeSO_3^{2-}]$, i.e. the magnitude of the Tafel slope is expected to increase relative to that for Fig. 7(*g*) as $[SeSO_3^{2-}]$ is decreased further.

Conclusion

The electrodeposition of cadmium selenide from selenosulfite solution occurs via a two-step reduction of $SeSO_3^{2-}$ to Se^{2-} followed by precipitation with Cd^{2+}. Under electron transfer limiting conditions, the rate of reduction depends only on $[SeSO_3^{2-}]$, but at potentials for which mass transfer is limiting, the rate also depends on $[Cd(NTA)^-]$ because the current is controlled by the subsequent chemical reaction. In the presence of $Cd(NTA)^-$, the Tafel plot for $SeSO_3^{2-}$ reduction is shifted 160 mV positive due to the effect of the succeeding reaction with Cd^{2+}.

Acknowledgements

We are pleased to acknowledge the very helpful discussions and suggestions of Professor J. Lipkowski. This work is supported in part by a grant (M.C.) from the Natural Sciences and Engineering Research Council of Canada.

1. M. S. KAZACOS and B. MILLER. J. Electrochem. Soc. **127**, 2378 (1980).
2. J. SZABO and M. COCIVERA. J. Electrochem. Soc. **133**, 1247 (1986).
3. T. S. WEST. Complexometry with EDTA and related reagents. 3rd ed. BDH Chemicals Ltd., Poole. 1969. p. 221.
4. A. J. BARD and L. R. FAULKNER. Electrochemical methods. John Wiley and Sons. 1980. Chap. 3.
5. J. O'M. BOCKRIS. Modern electrochemistry. Vol. 2. Plenum Press. 1970. Chap. 8.
6. R. S. NICHOLSON and I. SHAIN. Anal. Chem. **36**, 706 (1964).
7. F. A. KROGER. J. Electrochem. Soc. **125**, 2028 (1978).
8. M. SKYLLAS-KAZACOS. J. Electroanal. Chem. **148**, 233 (1983).
9. A. S. BARANSKI and W. R. FAWCETT. J. Electrochem. Soc. **131**, 2509 (1984).

Can. J. Chem. Downloaded from www.nrcresearchpress.com by 93.93.197.157 on 09/07/12
For personal use only.

Mononuclear Rh, Ir, Pd, and Pt complexes of the tripod ligand $(Ph_2P)_3CH$. The molecular structure of bis[1,1,1-tris(diphenylphosphino)methane]platinum(II) tetrafluoroborate

KENNETH J. BECKETT AND STEPHEN J. LOEB[1]

Department of Chemistry, University of Winnipeg, Winnipeg, Man., Canada R3B 2E9

Received September 14, 1987

KENNETH J. BECKETT and STEPHEN J. LOEB. Can. J. Chem. **66**, 1073 (1988).

The mononuclear complexes $[Rh(\eta^2\text{-}(Ph_2P)_3CH)_2]X$, $[Ir(CO)(\eta^2\text{-}(Ph_2P)_3CH)_2]X$, $[Pd(\eta^2\text{-}(Ph_2P)_3CH)_2]X_2$, and $[Pt(\eta^2\text{-}(Ph_2P)_3CH)_2]X_2$ ($X = Cl^-$, BF_4^-, BPh_4^-, ClO_4^-) are synthesized and fully characterized by $^{31}P\{^1H\}$ nmr and infrared spectroscopy. The complex $[Pt(\eta^2\text{-}(Ph_2P)_3CH)_2][BF_4]_2$ was further characterized by a single crystal X-ray diffraction study. Crystals are triclinic, $a = 12.514(6)$ Å, $b = 13.289(7)$ Å, $c = 12.609(9)$ Å, $\alpha = 120.63(4)°$, $\beta = 104.51(5)°$, $\gamma = 99.45(4)°$, $Z = 1$, space group $P\bar{1}$. The structure was solved by conventional heavy atom methods and refined by full-matrix least-squares procedures to $R(\%) = 6.87$ and $R_w(\%) = 7.28$ for 2995 reflections with $F_o^2 > 3\sigma F_o^2$. The Rh, Pd, and Pt complexes are square planar and shown by $^{31}P\{^1H\}$ nmr to exist in solution as a mixture of *syn* and *anti* isomers. The structure of $[Pt(\eta^2\text{-}(Ph_2P)_3CH)_2][BF_4]_2$ shows the *anti* isomer exists in the solid state for this complex. Both the *syn* and *anti* isomers of the complex $[Rh(\eta^2\text{-}(Ph_2P)_3CH)_2][BF_4]$ react with HX (X = Cl, Br) to give a single octahedral Rh(III) product *trans*-$[RhX(H)(\eta^2\text{-}(Ph_2P)_3CH)_2)][BF_4]$ characterized by $^{31}P\{^1H\}$ and ^1H nmr.

KENNETH J. BECKETT et STEPHEN J. LOEB. Can. J. Chem. **66**, 1073 (1988).

On a synthétisé les complexes mononucléaires $[Rh(\eta^2\text{-}(Ph_2P)_3CH)_2]X$, $[Ir(CO)(\eta^2\text{-}(Ph_2P)_3CH)_2]X$, $[Pd(\eta^2\text{-}(Ph_2P)_3CH)_2]X_2$ et $[Pt(\eta^2\text{-}(Ph_2P)_3CH)_2]X_2$ ($X = Cl^-$, BF_4^-, BPh_4^-, ClO_4^-) et on les a complètement caractérisés par spectroscopies rmn $^{31}P\{^1H\}$ et infrarouge. De plus, on a aussi caractérisé le complexe $[Pt(\eta^2\text{-}(Ph_2P)_3CH)_2][BF_4]_2$ à l'aide de la diffraction des rayons-X. Les cristaux sont tricliniques, groupe d'espace $P\bar{1}$, avec $a = 12{,}514(6)$, $b = 13{,}289(7)$ et $c = 12{,}609(9)$ Å, $\alpha = 120{,}63(4)$, $\beta = 104{,}51$ et $\gamma = 99{,}45(4)°$ et $Z = 1$. On a résolu la structure par les méthodes conventionnelles aux atomes lourds et on l'a affinée par la méthode des moindres carrés (matrice entière) jusqu'à des valeurs de $R(\%) = 6{,}87$ et $R_w(\%) = 7{,}28$ pour 2995 réflexions avec $F_o^2 > 3\sigma F_o^2$. Les complexes du Rh, du Pd et du Pt sont plans carrés et, à l'aide de la rmn du $^{31}P\{^1H\}$, on a démontré que, en solution, ils existent sous la forme d'un mélange des isomères *syn* et *anti*. La structure qui a été déterminée pour le complexe $[Pt(\eta^2\text{-}(Ph_2P)_3CH)_2][BF_4]_2$ démontre que, à l'état solide, il existe sous la forme de l'isomère *anti*. Les isomères *syn* ainsi que *anti* du complexe $[Rh(\eta^2\text{-}(Ph_2P)_3CH)_2][BF_4]_2$ réagissent avec les HX (X = Cl et Br) pour conduire à un seul type de produit Rh(III) octaédrique, les *trans*-$[RhX(H)(\eta^2\text{-}(Ph_2P)_3CH)_2)][BF_4]$, qui ont été caractérisés par rmn du $^{31}P\{^1H\}$ et du ^1H.

[Traduit par la revue]

Introduction

The tridentate phosphorus ligand 1,1,1-tris(diphenylphosphino)methane, $(Ph_2P)_3CH$, exhibits a variety of coordination modes. Complexes in which $(Ph_2P)_3CH$ acts as an $\eta^3\text{–}\mu_3$ bridging ligand (1–7), an $\eta^3\text{–}\mu_2$ bridging-chelating ligand (8, 9), an η^2 or η^3 chelating ligand (9, 10) and an η^1 monodentate ligand (9) have been characterized. As is the case for the small bite-angle, bidentate phosphorus ligand bis(diphenylphosphino)methane, dppm, the bridging modes of coordination are favoured over the chelating modes since the latter requires the formation of a strained four-membered chelate ring (11). Indeed, the tripod ligand, $(Ph_2P)_3CH$, is ideally suited for the complexation of a triangular array of metal atoms and this $\eta^3\text{–}\mu_3$ coordination mode has been well demonstrated by the binding to a triangular metal face in the tetranuclear carbonyl cluster compounds $[M_4(CO)_9((Ph_2P)_3CH)]$, M = Co, Rh, Ir (1, 3–7).

It should also be possible, however, to convert a mononuclear chelated complex to a bi- or trinuclear bridged complex via a chelate ring opening reaction and further metal incorporation. This type of synthetic approach has been successful in the preparation of heterobinuclear complexes bridged by dppm (12–15). As part of our initial studies into the potential use of tripod ligands such as $(Ph_2P)_3CH$ for "building" trinuclear metal complexes, we have prepared some mononuclear chelated complexes of Rh, Ir, Pd, and Pt. We report herein, the synthesis and characterization of complexes of the general formula $[M(\eta^2\text{-}(Ph_2P)_3CH)_2]^{n+}X_n$ and the X-ray structural determination of the complex $[Pt(\eta^2\text{-}(Ph_2P)_3CH)_2][BF_4]_2$.

[1]Author to whom correspondence should be addressed.

Experimental

trans-$[RhCl(CO)(PPh_3)_2]$ (16), *trans*-$[IrCl(CO)(PPh_3)_2]$ (17), and 1,1,1-tris(diphenylphosphino)methane (1, 18) were prepared by literature methods. K_2PtCl_4, K_2PdCl_4, $IrCl_3\cdot 3H_2O$, $RhCl_3\cdot 3H_2O$ (Strem), *n*-BuLi, $NaBF_4$, $NaClO_4$, $NaBPh_4$, PPh_3, and bis(diphenylphosphino)methane (Aldrich) were purchased and used as received. Unless otherwise stated, all synthetic procedures were conducted under a dry, dinitrogen atmosphere using dry, deoxygenated solvents and standard Schlenk techniques.

$^{31}P\{^1H\}$ and ^1H nmr spectra were obtained at 121.5 and 300.1 MHz, respectively, on a Brüker AM300 spectrometer using deuterated solvents as lock. Phosphorus chemical shifts were measured relative to external 85% H_3PO_4 with positive shifts downfield. Infrared spectra were recorded on a Perkin Elmer 781 grating spectrometer. Elemental analyses were performed by Canadian Microanalytical Service Ltd., New Westminster, British Columbia.

[Rh(η²-(Ph₂P)₃CH)₂]Cl, *1*a

trans-$[RhCl(CO)(PPh_3)_2]$ (0.50 g, 0.72 mmol) and $(Ph_2P)_3CH$ (0.82 g, 1.44 mmol) were dissolved in benzene (15 mL). The dark orange solution rapidly lightened and produced an orange precipitate after ~5 min. This suspension was stirred for a further 4 h at room temperature. The solid was allowed to settle and the benzene solution removed via syringe. The resulting orange product was washed with benzene (2 × 5 mL) and dried *in vacuo*. The yield was 0.80 g (88%). The complex was recrystallized from CH_2Cl_2/diethyl ether. *Anal.* calcd. for $C_{74}H_{62}ClP_6Rh$: C 69.68, H 4.91; found: C 67.44, H 4.90.

Can. J. Chem. Downloaded from www.nrcresearchpress.com by 93.93.197.157 on 09/07/12
For personal use only.

Can. J. Chem. Downloaded from www.nrcresearchpress.com by 93.93.197.157 on 09/07/12
For personal use only.

[Rh(η²-(Ph₂P)₃CH)₂]BF₄, **1**b

[Rh(η²-(Ph₂P)₃CH)₂]Cl, **1***a*, (0.25 g, 0.20 mmol) was dissolved in CH_2Cl_2 (15 mL) and $NaBF_4$ (0.033 g, 0.30 mmol) added with stirring. This mixture was stirred for 12 h, the solution filtered over Celite and the solvent removed *in vacuo*. The orange product was recrystallized from CH_2Cl_2/diethyl ether. The yield was 0.25 g (94%). *Anal.* calcd. for $C_{74}H_{62}BF_4P_6Rh$: C 66.98, H 4.72; found: C 65.54, H 4.65. The BPh_4^-, **1***c*, and ClO_4^-, **1***d*, complexes were prepared similarly using appropriate sodium salts. Orange crystals of **1***b*, **1***c*, or **1***d* were easily obtained by slow diffusion of diethyl ether into an acetonitrile or dichloromethane solution of the complex.

[Ir(CO)(η²-(Ph₂P)₃CH)₂]Cl, **2**a

trans-[IrCl(CO)(PPh₃)₂] (0.50 g, 0.64 mmol) and $(Ph_2P)_3CH$ (0.73 g, 1.28 mmol) were dissolved in benzene (15 mL). The solution was stirred for 18 h at room temperature during which time a fine pale yellow precipitate formed. The solid was allowed to settle and the benzene solution removed via syringe. The resulting pale yellow solid was washed with benzene (2 × 5 mL) and dried *in vacuo*. The yield was 0.65 g (73%). The complex was recrystallized from CH_2Cl_2/diethyl ether. *Anal.* calcd. for $C_{75}H_{62}ClIrOP_6$: C 64.67, H 4.50; found: C 62.61, H 4.60; ir: ν(CO), (CH_2Cl_2) 1958 cm^{-1}, (Nujol) 1938 cm^{-1}.

[Ir(CO)(η²-(Ph₂P)₃CH)₂]BF₄, **2**b

This complex was prepared from **2***a* in a procedure identical to that used for **1***b*. The yellow product was recrystallized from CH_2Cl_2/diethyl ether. The yield was 98%. *Anal.* calcd. for $C_{75}H_{62}BF_4IrOP_6 \cdot CH_2Cl_2$: C 59.69, H 4.23; found: C 58.63, H 4.37. Infrared: ν(CO), (CH_2Cl_2) 1958 cm^{-1}, (Nujol) 1950 cm^{-1}. The BPh_4^-, **2***c*, and ClO_4^-, **2***d*, complexes were similarly prepared using the appropriate sodium salts. Yellow crystals of **2***b*, **2***c*, or **2***d*, as the CH_2Cl_2 solvate, were easily prepared by slow diffusion of diethyl ether into a CH_2Cl_2 solution of the complex.

[Pd(η²-(Ph₂P)₃CH)₂]Cl₂, **3**a

K_2PdCl_4 (0.10 g, 0.31 mmol) was dissolved in distilled water (3 mL) and this solution added dropwise to a solution of $(Ph_2P)_3CH$ (0.35 g, 0.62 mmol) in ethanol (20 mL) at ~45°C. The mixture was stirred at this temperature for 2 h during which time an orange precipitate formed. The suspension was then stirred for a further 12 h at room temperature. Solvents were removed, the product washed with distilled water (2 × 10 mL), toluene (2 × 10 mL), and CH_2Cl_2 (2 × 10 mL) and dried *in vacuo*. This product was insufficiently soluble for recrystallization or solution studies but this preparative method provided analytically pure material. The yield was 0.12 g (30%). *Anal.* calcd. for $C_{74}H_{62}Cl_2P_6Pd \cdot CH_2Cl_2$: C 64.37, H 4.62; found: C 63.43, H 4.79.

[Pd(η²-(Ph₂P)₃CH)₂][BF₄]₂, **3**b

[Pd(η²-(Ph₂P)₃CH)₂]Cl₂, **3***a*, (0.10 g, 0.076 mmol) and $NaBF_4$ (0.024 g, 0.22 mmol) were suspended in CH_2Cl_2 (25 mL) and the mixture stirred for 18 h. During this time the solids dissolved to produce a yellow solution and a fine colourless residue. The solution was filtered over Celite, the solvent removed *in vacuo* and the resulting pale yellow solid recrystallized from CH_2Cl_2/diethyl ether. The yield was 0.084 g (84%). *Anal.* calcd. for $C_{74}H_{62}B_2F_8P_6Pd \cdot CH_2Cl_2$: C 59.96, H 4.30; found: C 59.69, H 4.25.

[Pt(η²-(Ph₂P)₃CH)₂]Cl₂, **4**a

This complex was prepared from K_2PtCl_4 in a procedure identical to that used for **3***a*. The product was an extremely insoluble, off-white solid. The yield was 61%. *Anal.* calcd. for $C_{74}H_{62}Cl_2P_6Pt$: C 63.34, H 4.46; found: C 63.32, H 4.53.

[Pt(η²-(Ph₂P)₃CH)₂][BF₄]₂, **4**b

This complex was prepared from **4***a* in a procedure identical to that used for **3***b*. The yield was 98%. Slow diffusion of diethyl ether into an acetonitrile solution of the complex produced single crystals suitable for X-ray diffraction studies.

[RhCl(H)(η²-(Ph₂P)₃CH)₂]BF₄, **5**a

[Rh(η²-(Ph₂P)₃CH)₂]BF_4, **1***b*, (0.10 g, 0.075 mmol) was dissolved in CH_2Cl_2 (10 mL) and HCl(g) introduced in place of the N_2(g) atmosphere. The orange solution immediately turned pale yellow. After stirring this solution for 1 h, with no further change, the excess HCl(g) was purged from the flask and the N_2(g) atmosphere returned. This produced no visible change in the solution. The solution was then taken to dryness and the product washed with diethyl ether (2 × 10 mL). The pale yellow product was air stable. The yield was effectively quantitative. *Anal.* calcd. for $C_{74}H_{63}BClF_4P_6Rh$: C 65.19, H 4.67; found: C 63.22, H 4.89. Infrared: ν(RhH), (CH_2Cl_2) 2095 cm^{-1}. ^{1}H nmr: (CD_2Cl_2) δ(hydride) −11.80 ppm(dq), $^2J_{PH}$ = 12.8 Hz, $^1J_{RhH}$ = 17.5 Hz.

[RhBr(H)(η²-(Ph₂P)₃CH)₂]BF₄, **5**b

The complex was prepared using HBr(g) in a procedure identical to that used for **5***a*. Satisfactory elemental analysis could not be obtained for this compound; however, spectroscopic data are consistent with the formulation and compare well with those found for **5***a*. Infrared: ν(RhH), (CH_2Cl_2) 2093 cm^{-1}. ^{1}H nmr: (CD_2Cl_2) δ(hydride) −10.61 ppm(dq), $^2J_{PH}$ = 12.4 Hz, $^1J_{RhH}$ = 18.4 Hz.

X-ray crystallographic analysis of bis[1,1,1-tris(diphenylphosphino)-methane] platinum(II) tetrafluoroborate, **4**b

Colourless crystals were obtained by vapour diffusion of diethyl ether into an acetonitrile solution of **4***b*. Diffraction experiments were performed on a four-circle Syntex $P2_1$ diffractometer with graphite monochromatized MoKα radiation. The initial orientation matrix was obtained from 15 machine-centred reflections selected from rotation photographs. Partial rotation photographs around each axis were consistent with a triclinic crystal system. Ultimately, 63 high-angle reflections ($11° < 2\theta < 37°$) were used to obtain the final lattice parameters and orientation matrix. Machine parameters, crystal data, and data collection parameters are summarized in Table 1. The observed diffraction symmetry was consistent with space groups $P1$ and $P\bar{1}$. $P\bar{1}$ was confirmed by a successful structure refinement. Intensity data ($\pm h, \pm k, +l$) were collected in one shell ($4.5° < 2\theta < 40.0°$). The intensities of three standard reflections ($\bar{2}\,3\,3$, $\bar{3}\,6\,6$, $\bar{7}\,0\,3$) were collected every 197 reflections and showed no statistically

TABLE 1. Summary of crystal data, intensity collection, and structure refinement for [Pt(η²-(Ph₂P)₃CH)₂][BF₄]₂, **4***b*

Formula	$C_{74}H_{62}B_2F_8P_6Pt$
Crystal colour, form	Colourless, blocks
a (Å)	12.514(6)
b (Å)	13.289(7)
c (Å)	12.609(9)
α (deg)	120.63(4)
β (deg)	104.51(5)
γ (deg)	99.45(4)
Crystal system	Triclinic
Space group	$P\bar{1}$ (C_i^1, No. 2)
Volume (Å³)	1636(2)
Density (g cm^{-3}), calcd.	1.087
Z	1
Crystal dimension (mm)	0.26 × 0.41 × 0.39
Absorption coefficient, μ (cm^{-1})	22.4
Transmission coefficients	max. 0.992; min. 0.967
Radiation, λ (Å)	MoKα, 0.71069
Temperature (°C)	24
Scan Speed (deg min^{-1})	2.0–5.0 (θ/2θ scan)
Scan range (deg)	1.0 below $K\alpha_1$; 1.1 above $K\alpha_2$
Background/scan time ratio	0.5
Data collected	3238; 2θ of 4.5 to 40° ($\pm h, \pm k, +l$)
Number of unique data $F_o^2 > 3\sigma(F_o^2)$	2995
Number of variables	160
R (%)	6.87
R_w (%)	7.28

TABLE 2. Selected bond distances and bond angles

Bond	Distance (Å)	Bond	Distance (Å)
Pt—P1	2.305(3)	P3—C51	1.796(9)
Pt—P2	2.299(3)	P3—C61	1.816(10)
P1—C1	1.891(11)		
P2—C1	1.878(10)	B—F1	1.34(1)
P3—C1	1.830(12)	B—F2	1.33(1)
P1—C11	1.778(8)	B—F3	1.26(1)
P1—C21	1.774(7)	B—F4	1.37(1)
P2—C31	1.776(8)		
P2—C41	1.755(8)		

Bonds	Angle (deg)	Bonds	Angle (deg)
Pt—Pt—P2	72.2(1)	C1—P2—C31	112.4(4)
Pt—P1—C1	93.3(3)	C1—P2—C41	109.8(5)
Pt—P2—C1	93.8(4)	C31—P2—C41	106.5(4)
P1—C1—P2	92.1(5)	C1—P3—C51	102.3(5)
P1—C1—P3	120.1(7)	C1—P3—C61	102.7(5)
P2—C1—P3	120.0(6)	C51—P3—C61	99.1(5)
Pt—P1—C11	121.4(3)		
Pt—P1—C21	114.0(2)	F1—B—F2	107.2(10)
C1—P1—C11	110.4(4)	F1—B—F3	116.6(10)
C1—P1—C21	112.0(5)	F1—B—F4	108.8(10)
C11—P1—C21	105.5(4)	F2—B—F3	110.8(12)
Pt—P2—C31	117.0(3)	F2—B—F4	102.7(11)
Pt—P2—C41	116.9(2)	F3—B—F4	109.9(12)

significant changes over the duration of the data collection. The data were absorption corrected (μ = 22.4 cm^{-1}) empirically by interpolation in 2θ and ϕ between Ψ-scans of reflections $\bar{2}$ 3 3, $\bar{3}$ 6 6, and 1 3 2. The data were processed by using the SHELX-76 program package on the computing facilities shared with the University of Manitoba. A total of 3238 reflections were collected and 2995 with $F_o^2 > 3\sigma(F_o^2)$ were used in the refinement.

The Pt atom was positioned at (0,0,0) with half-occupancy and the remaining unique non-hydrogen atoms were located from successive difference Fourier map calculations. Refinement was carried out using full-matrix least-squares techniques on F minimizing the function $\Sigma w(|F_o| - |F_c|)^2$, where $w = 4F_o^2/\sigma^2(F_o^2)$ and F_o and F_c are the observed and calculated structure factors. Atomic scattering factors (19) and anomalous dispersion terms (20, 21) were taken from the usual sources. In the first cycles of least-squares refinement, all non-hydrogen atoms, with the exception of the phenyl C atoms, were assigned anisotropic thermal parameters. The phenyl rings were constrained to an idealized C_{6h} symmetry with C—C distances of 1.39 Å and assigned isotropic thermal parameters. Fixed H atom contributions were included with C—H distances of 0.95 Å and thermal parameters equal to 1.1 times the isotropic thermal parameter of the bonded C atoms. No H atoms were refined, but all values were updated as refinement continued. This resulted in $R = \Sigma||F_o| - |F_c||/\Sigma|F_o| = 0.0687$ and $R_w = (\Sigma w(|F_o| - |F_c|)^2/\Sigma w|F_o|^2)^{1/2} = 0.0728$ at final convergence.

The Δ/σ values for any parameters in the final cycles were less than 0.004. A final difference Fourier map calculation showed no peaks of chemical significance; the largest was 2.1 e/Å^3 associated with the Pt atom. Selected bond lengths and angles are summarized in Table 2 and atomic positional and thermal parameters in Table 3. Anisotropic thermal parameters (Table S-1), hydrogen atom parameters (Table S-2), and values of $10|F_o|$ and $10|F_c|$ (Table S-3) are deposited as supplementary material.[2]

[2]Supplementary Tables S-1, S-2, and S-3 may be purchased from the Depository of Unpublished Data, CISTI, National Research Council of Canada, Ottawa, Ont., Canada K1A 0S2.

TABLE 3. Positional parameters[a]

Atom	x	y	z
Pt	0	0	0
P1	1015(3)	2078(3)	1725(3)
P2	1902(3)	467(3)	134(3)
P3	3697(3)	3301(3)	2226(3)
C1	2199(10)	2191(9)	1066(12)
C11	380(7)	3238(7)	1945(6)
C12	389(7)	4107(8)	3194(6)
C13	−145(7)	4987(8)	3339(6)
C14	−687(7)	4998(8)	2236(6)
C15	−695(7)	4129(8)	988(6)
C16	−162(7)	3249(8)	842(6)
C21	1592(6)	2368(6)	3329(6)
C22	1001(6)	1489(6)	3475(6)
C23	1336(6)	1688(6)	4728(6)
C24	2260(6)	2764(6)	5834(6)
C25	2851(6)	3643(6)	5688(6)
C26	2517(6)	3444(6)	4436(6)
C31	2092(8)	−163(6)	−1403(8)
C32	2047(8)	406(6)	−2078(8)
C33	1968(8)	−256(6)	−3396(8)
C34	1933(8)	−1488(6)	−4040(8)
C35	1977(8)	−2058(6)	−3365(8)
C36	2057(8)	−1395(6)	−2047(8)
C41	2899(7)	173(8)	1101(8)
C42	4044(7)	342(8)	1147(8)
C43	4826(7)	85(8)	1897(8)
C44	4464(7)	−342(8)	2601(8)
C45	3319(7)	−511(8)	2555(8)
C46	2537(7)	−254(8)	1805(8)
C51	3511(8)	4777(8)	2781(8)
C52	4311(8)	5752(8)	4076(8)
C53	4304(8)	6963(8)	4619(8)
C54	3496(8)	7200(8)	3868(8)
C55	2696(8)	6225(8)	2573(8)
C56	2703(8)	5013(8)	2030(8)
C61	4407(6)	3206(9)	1102(9)
C62	3980(6)	3371(9)	89(9)
C63	4657(6)	3417(9)	−623(9)
C64	5760(6)	3297(9)	−322(9)
C65	6186(6)	3131(9)	690(9)
C66	5510(6)	3086(9)	1402(9)
B1	9889(16)	7891(18)	2232(18)
F1	84(8)	1391(8)	−1777(8)
F2	1159(13)	3023(13)	−1483(16)
F3	−705(12)	2546(15)	−2273(17)
F4	152(16)	1454(16)	−3473(14)

[a]Multiplied by 10^4.

Results and discussion

Synthesis and characterization of the complexes

The bright orange complex [Rh(η^2-$(Ph_2P)_3CH)_2$]Cl, **1***a*, is easily prepared by reacting a benzene solution of *trans*-[RhCl(CO)$(PPh_3)_2$] with 2 equivalents of $(Ph_2P)_3CH$ according to reaction [1].

[1] *trans*-[RhCl(CO)$(PPh_3)_2$] + 2$(Ph_2P)_3CH$ $\xrightarrow[\text{R.T.}]{\text{benzene}}$ [Rh(η^2-$(Ph_2P)_3CH)_2$]Cl + 2PPh_3 + CO

The product precipitates from solution, in high yield, as the Cl^- salt. Treatment of **1***a* with an excess of NaX (X = BF_4^-, BPh_4^-, ClO_4^-) in CH_2Cl_2 yields the corresponding X^- salts. The infrared spectra of complexes **1***a*–**1***d* show no absorptions in the

Can. J. Chem. Downloaded from www.nrcresearchpress.com by 93.93.197.157 on 09/07/12
For personal use only.

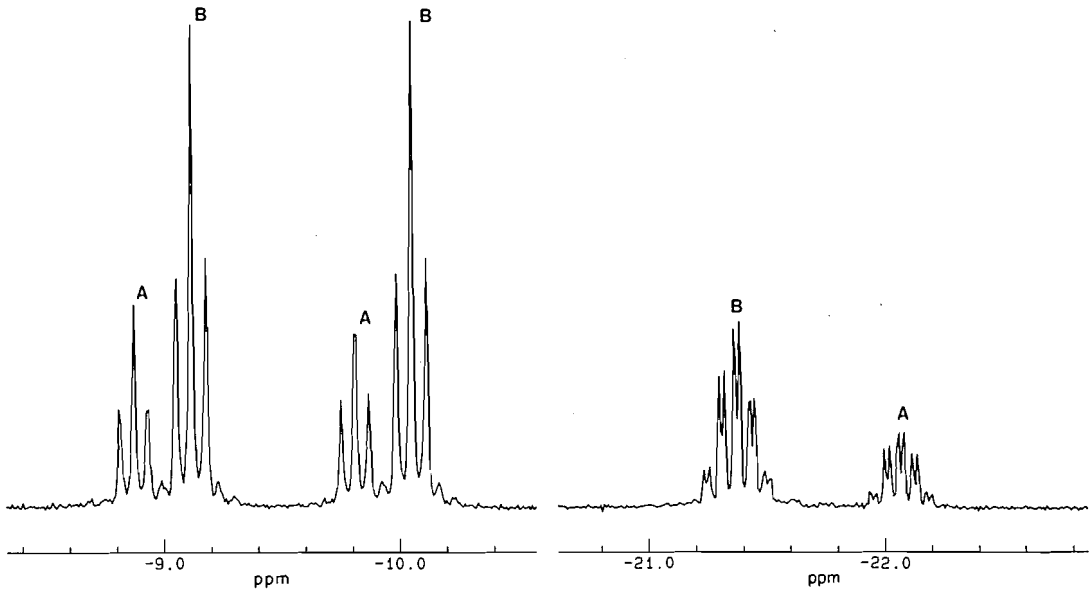

FIG. 1. The $^{31}P\{^1H\}$ nmr spectrum of $[Rh(\eta^2\text{-}(Ph_2P)_3CH)_2][BF_4]$, **1***b* in CD_2Cl_2 at 220 K, showing the major (B) and minor (A) isomers present in solution.

TABLE 4. $^{31}P\{^1H\}$ nmr spectral data[a]

Compound	δ(M),[b] ppm	δ(u),[c] ppm	$^2J_{PP}$, Hz	$^1J_{MP}$, Hz	$^3J_{MP}$, Hz
1*b*, major isomer	−9.6(dt)[d]	−21.4(dq)	7.8	113.5	2.7
1*b*, minor isomer	−9.3(dt)	−22.1(dq)	7.3	114.0	2.8
2*b*	−45.8(t)	−15.1(q)	10.3	—	—
3*b*, major isomer	−14.9(t)	−17.3(q)	9.1	—	—
3*b*, minor isomer	−20.0(t)	−20.7(q)	11.3	—	—
4*b*, major isomer	−22.8(tt)	−15.7(tq)	11.1	2013.1	111.8
4*b*, minor isomer	−25.6(tt)	−19.4(tq)	9.5	1998.9	97.5
5*a*	5.6(dt)	−17.5(q)	9.2	83.7	—
5*b*	4.9(dt)	−16.0(q)	8.7	83.5	—

[a]Recorded in CH_2Cl_2/CD_2Cl_2 (75:25) solution.
[b]M = appropriate metal: coordinated PPh_2 groups.
[c]u = uncoordinated PPh_2 groups.
[d]d = doublet, t = triplet, q = quintet.

ν(CO) region and the complexes are formulated as the four-coordinate species $[Rh(\eta^2\text{-}(Ph_2P)_3CH)_2]X$. The $^{31}P\{^1H\}$ nmr spectra of **1***a*–**1***d* are identical and also consistent with the formulation of these complexes as salts of the square planar cation $[Rh(\eta^2\text{-}(Ph_2P)_3CH)_2]^+$. Each shows two sets of resonances at room temperature, a broad singlet of intensity 1 at ca. −20 ppm and a broad doublet of intensity 2 at ca. −7 ppm. As the temperature is lowered these resonances sharpen and separate to produce the limiting spectrum at 220 K (Fig. 1). At this temperature there are four separate sets of resonances, two doublets of triplets (δ = −9.6, $^1J_{RhP}$ = 113.5 Hz, $^2J_{PP}$ = 7.8 Hz; and δ = −9.3, $^1J_{RhP}$ = 114.0 Hz, $^2J_{PP}$ = 7.3 Hz) and two doublets of quintets (δ = −21.4, $^3J_{RhP}$ = 2.7 Hz and δ = −22.1, $^3J_{RhP}$ = 2.8 Hz).

This can be explained by the presence of two geometrical isomers of the $[Rh(\eta^2\text{-}(Ph_2P)_3CH)_2]^+$ cation. One isomer, (A), will have uncoordinated PPh_2 groups oriented on the same side of the Rh(P—P)$_2$ coordination plane, and the other isomer, (B), will have uncoordinated PPh_2 groups oriented on opposite sides of the Rh(P—P)$_2$ coordination plane. These isomers are referred to as the *syn*, (A), and *anti*, (B), isomers (Fig. 1). Each isomer shows two sets of resonances due to coordinated PPh_2 groups with appropriate $^1J_{RhP}$ and $^2J_{PP}$ and uncoordinated PPh_2 groups with appropriate $^3J_{RhP}$ and $^2J_{PP}$, in a 2:1 intensity ratio (Table 4). It should also be noted that the relative ratio of these two isomers in solution is approximately 3:1. Although it is impossible to unambiguously determine which isomer is the major component, molecular models indicate that the *anti*-form is the least sterically crowded in terms of intramolecular contacts. Although we have not observed the high temperature averaged spectra, the temperature dependence of the nmr spectra presumably reflects an intramolecular exchange process which interchanges coordinated and uncoordinated PPh_2 groups at the coordinatively unsaturated Rh(I) centre. A mechanism that involved deprotonation of the ligand and inversion at the apical carbon, C(1), is also possible but unlikely under these experimental conditions.

A similar reaction to reaction [1] employing *trans*-$[IrCl(CO)(PPh_3)_2]$ as the starting material gives the pale yellow complex $[Ir(CO)(\eta^2\text{-}(Ph_2P)_3CH)_2]Cl$, **2***a*, and the X^- salts, **2***b*–**2***d*, are readily prepared from treatment with excess NaX in CH_2Cl_2, as for **1***b*–**1***d*. The infrared spectra of **2***a*–**2***d*, in CH_2Cl_2 solution, exhibit a single absorption in the ν(CO) region illustrating that for the iridium complexes the CO group is not lost upon

Can. J. Chem. Downloaded from www.nrcresearchpress.com by 93.93.197.157 on 09/07/12
For personal use only.

Can. J. Chem. Downloaded from www.nrcresearchpress.com by 93.93.197.157 on 09/07/12
For personal use only.

complex formation as is the case for **1***a*. The $^{31}P\{^1H\}$ nmr spectra of **2***a*–**2***d* are identical but show no temperature dependence. The spectra show only two sets of resonances, a triplet of intensity 2 ($\delta = -45.8$, $^2J_{PP} = 10.3$ Hz) and a quintet of intensity 1 ($\delta = -15.1$). This results in a formulation of complexes **2***a*–**2***d* as salts of the 5-coordinate, coordinatively saturated cation $[Ir(CO)(\eta^2\text{-}(Ph_2P)_3CH)_2]^+$. Since the $^{31}P\{^1H\}$ nmr spectra show only two types of PPh_2 groups, this cation must necessarily have either a square pyramidal structure with a *syn* orientation of the PPh_2 groups or a rapidly fluxional trigonal bipyramidal structure. The square pyramidal geometry is known to be favoured over trigonal bipyramidal geometry for small bite-angle chelate ligands with strongly bound ligands, such as CO, occupying the apical position (22). The observation of only one isomeric form for $[Ir(CO)(\eta^2\text{-}(Ph_2P)_3CH)_2]^+$ is presumably due to large energy differences between the possible ligand arrangements. The presence of the apical CO ligand above the square coordination plane likely stabilizes the *syn* isomer of the complex with the uncoordinated PPh_2 groups oriented away from the CO ligand in order to avoid steric interactions between the $(Ph_2P)_3CH$ ligands and the CO group. The absence of any exchange process enhances this view but could also be the result of coordinative saturation at the Ir(I) centre which would eliminate any associative exchange mechanism necessarily requiring a 6-coordinate, 20-electron intermediate. Any attempt, thermally, photochemically, or chemically to remove CO from complexes **2***a*–**2***d*, to produce the analogs of **1***a*–**1***d*, failed. These reactions resulted in either no reaction or decomposition of the $(Ph_2P)_3CH$ ligand.

It should be noted that others (9, 22) have reported attempts to prepare rhodium complexes of $(Ph_2P)_3CH$ via the complexes $[RhCl(COE)_2]_2$ (COE = cyclooctene) and $[RhCl(CO)_2]_2$. In each case, only uncharacterized dimeric species (9) or ill-defined products were isolated (22). This is interesting since in the course of this study we reacted $[RhCl(COD)]_2$ (COD = 1,5-cyclooctadiene) with two equivalents of $(Ph_2P)_3CH$ in CH_2Cl_2 at room temperature under a CO atmosphere. We found that the only product from this reaction is $[Rh(\eta^2\text{-}(Ph_2P)_3CH)_2][Rh(CO)_2Cl_2]$. The $^{31}P\{^1H\}$ nmr shows a spectrum identical to that of **1***a*–**1***d* and the infrared spectrum shows an extra ν(CO) absorption at 2066 cm^{-1} due to the complex anion. The same reaction with $[IrCl(COE)_2]_2$ produces $[Ir(CO)(\eta^2\text{-}(Ph_2P)_3CH)_2][Ir(CO)_2Cl_2]$ also identified by comparison of $^{31}P\{^1H\}$ nmr and infrared spectroscopy with those of **2***a*–**2***d*. Since the exact reaction conditions of these attempts are not published we can only assume that some type of thermal decomposition was occurring in these other studies.

The Pd(II) and Pt(II), square planar complexes analogous to **1***a* are readily prepared by the reaction of an aqueous solution of K_2MCl_4 (M = Pd, Pt), with $(Ph_2P)_3CH$ in warm ethanol according to reaction [2].

$$[2]\quad K_2MCl_4 + 2(Ph_2P)_3CH \xrightarrow[R.T.]{H_2O/EtOH} [M(\eta^2\text{-}(Ph_2P)_3CH)_2]Cl_2 + 2KCl \qquad M = Pd, Pt$$

The pale yellow Pd, **3***a*, and cream Pt, **4***a*, complexes precipitate from solution. Although very insoluble, both complexes are isolated in moderate yield as analytically pure samples by washing with H_2O, toluene, and CH_2Cl_2 to remove impurities. The BF_4^- salts **3***b* and **4***b* were prepared, as before, from the treatment with an excess of $NaBF_4$ in CH_2Cl_2. Both

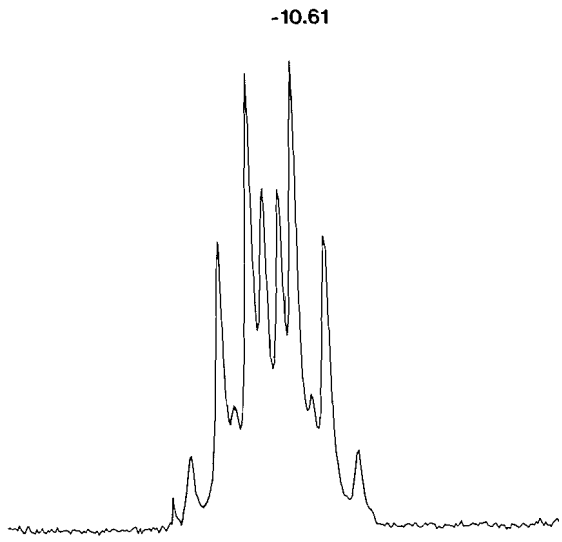

FIG. 2. The ^1H nmr spectrum of *trans*-$[RhBr(H)(\eta^2\text{-}(Ph_2P)_3CH)_2][BF_4]$, **5***a* in CD_2Cl_2 at 300 K showing the hydride resonance only.

complexes are formulated as the square planar dications $[M(\eta^2\text{-}(Ph_2P)_3CH)_2]^{2+}$, (M = Pd, Pt). As was the case for the Rh(I) complexes, the $^{31}P\{^1H\}$ nmr spectra show the presence of two separate *syn* and *anti* isomers in solution for **3***b* and **4***b* (Table 4). However, the exchange process is much slower and a static spectrum is observed near room temperature for both the Pd(II) and Pt(II) complexes. Also, the ratio of major to minor isomer is much larger, approximately 10:1 for both complexes. As noted previously for the Rh(I) complexes, it is impossible to determine which isomer is the major species in solution; however, it appears that one is much more favourable for the Group 10 metals. A detailed X-ray crystallographic analysis of **4***b* shows that in the solid state the only form present is the *anti* isomer (Fig. 3). This evidence makes it likely that the *anti* isomer is also favoured in solution, but such extrapolations are purely speculative.

Since the unreactivity of the $[Rh(\eta^2\text{-}(Ph_2P)_3CH)_2]X$ complexes towards CO did not allow the direct comparison of the Rh(I) and Ir(I) complexes, it was of interest to investigate briefly, the reaction of the coordinatively unsaturated $[Rh(\eta^2\text{-}(Ph_2P)_3CH)_2]^+$ cation (**1***b*, X = BF_4^- was used) towards the oxidative addition of HX (X = Cl, Br).

Reaction of **1***b* with HCl(g) yields the Rh(III) hydride complex *trans*-$[RhCl(H)(\eta^2\text{-}(Ph_2P)_3CH)_2]BF_4$, **5***a*. The same reaction with HBr(g) yields *trans*-$[RhBr(H)(\eta^2\text{-}(Ph_2P)_3CH)_2]BF_4$, **5***b*. Both reactions are clean and produce a pale yellow solid which can be recrystallized from CH_2Cl_2/diethyl ether. Infrared spectra show a characteristically weak ν(RhH) absorption at 2095 and 2093 cm^{-1} for **5***a* and **5***b*, respectively. $^{31}P\{^1H\}$ and ^1H nmr for both reactions are consistent with the formation of a single metal complex with no evidence of isomers. The $^{31}P\{^1H\}$ nmr spectra showed two sets of resonances for each complex, a doublet of triplets of intensity 2 and a quintet of intensity 1 (Table 4). The ^1H nmr spectra showed only one hydride resonance for each complex which appeared as an overlapping doublet of quintets (**5***a*: $\delta = -11.80$, $^1J_{RhH} = 17.5$ Hz, $^2J_{PH} = 12.8$ Hz; and **5***b*; $\delta = -10.61$, $^1J_{RhH} = 18.4$ Hz, $^2J_{PH} = 12.4$ Hz) (Fig. 2). From this evidence, the Rh(III) complexes must be octahedral with a *trans* disposition of the HX addenda and a *syn* arrangement of the $(Ph_2P)_3CH$

Can. J. Chem. Downloaded from www.nrcresearchpress.com by 93.93.197.157 on 09/07/12
For personal use only.

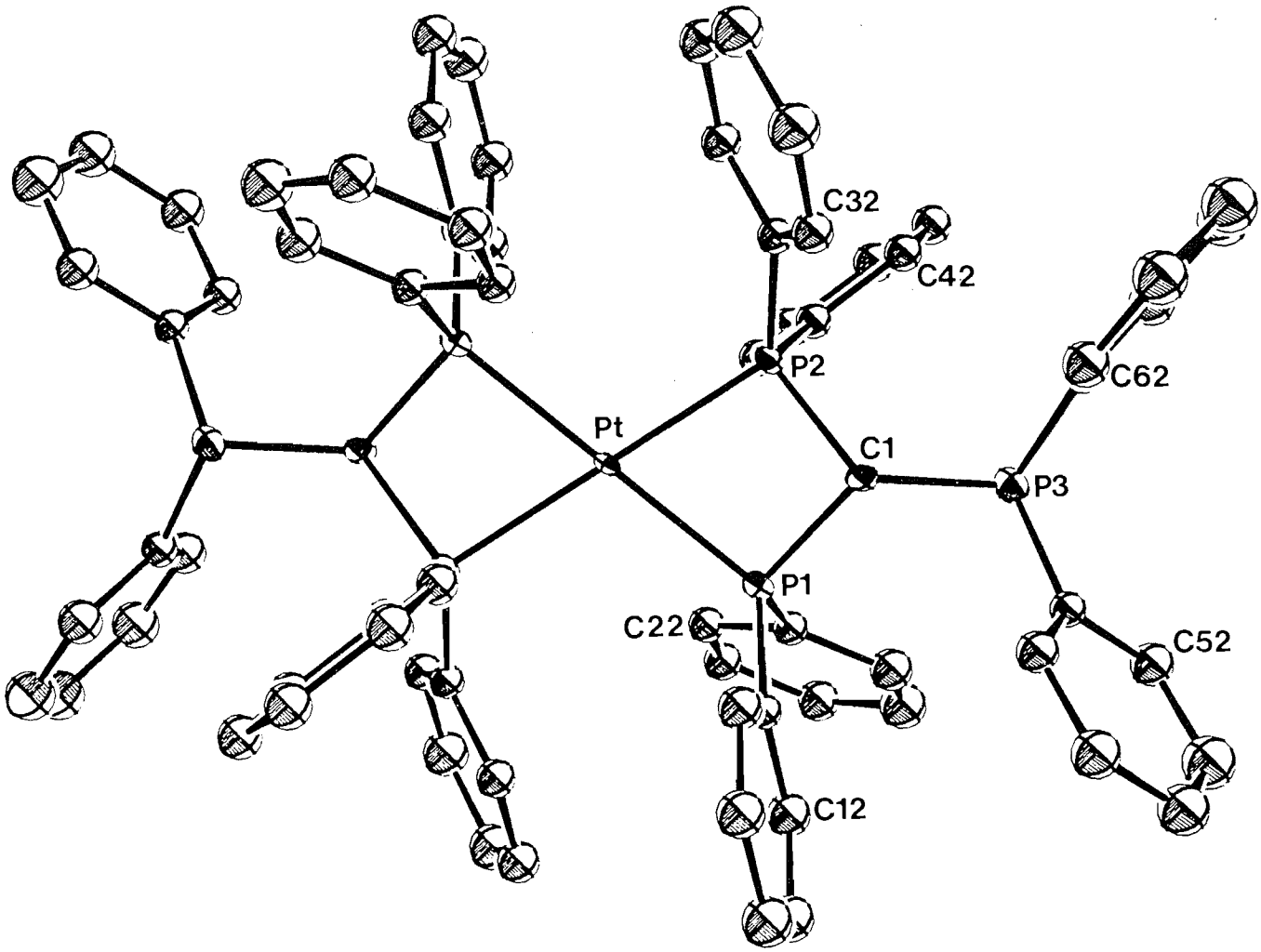

FIG. 3. Perspective ORTEP drawing of the $[Pt(\eta^2\text{-}(Ph_2P)_3CH)_2]^{2+}$ cation of **4***b* showing the numbering scheme. The numbering of phenyl ring carbon atoms starts at the atom bound to phosphorus; 20% thermal ellipsoids are shown.

ligands, likely with the uncoordinated PPh_2 groups oriented towards the smaller hydride ligand.

Structure description of $[Pt(\eta^2\text{-}(Ph_2P)_3CH)_2][BF_4]_2$

A perspective view of **4***a* giving the atom-numbering scheme is shown in Fig. 3, and a representation of the inner coordination sphere of the molecule is shown, with some relevant parameters, in Fig. 4. The unit cell contains one discrete complex dication and two BF_4^- anions. The closest intermolecular non-bonded contact between cations is 2.53 Å between H55 and H15′. The closest intramolecular cation to anion approach is 2.15 Å between F1 and H16 and the closest Pt to anion distance is 3.57 Å to F1. Complete listings of interatomic distances and angles may be found in Table 2.

The complex cation exhibits square planar coordination geometry at the Pt(II) centre and the $(Ph_2P)_3CH$ ligands are arranged in an *anti* conformation with the uncoordinated PPh_2 groups oriented on opposite sides of the coordination plane. The four-membered chelate ring shows considerable distortion as evidenced by a P1—Pt—P2, chelate bite-angle of 72.2(1)° and a P1—C1—P2 angle of 92.1(5)° compared to normal bond angles of 90° and 109°, respectively. The bite-angle is comparable to those found for complexes containing chelated dppm, where the P—M—P angles range from 67–74° (11). The

TABLE 5. Least-squares plane, deviations from the plane, and torsion angles for the chelate ring Pt—P1—P2—C1 in **4***b*[a]

(*a*) Deviations from the plane

Atom	Deviation (Å)
Pt	−0.1579(2)
P1	0.1945(5)
P2	0.1967(5)
C1	−0.233(1)

(*b*) Torsion angles

Bond	Angle (deg)
Pt—P1—C1—P2	−23.91
P1—C1—P2—Pt	23.98
C1—P2—Pt—P1	−20.49
P2—Pt—P1—C1	20.33

[a]Equation of least-squares plane $0.4273X - 0.2711Y + 0.8625Z - 0.1579 = 0$, where X, Y, and Z are the orthogonal coordinates (Å) with X along the a axis, Y in the $(a\text{–}b)$ plane, and Z along the c^* axis.

Can. J. Chem. Downloaded from www.nrcresearchpress.com by 93.93.197.157 on 09/07/12
For personal use only.

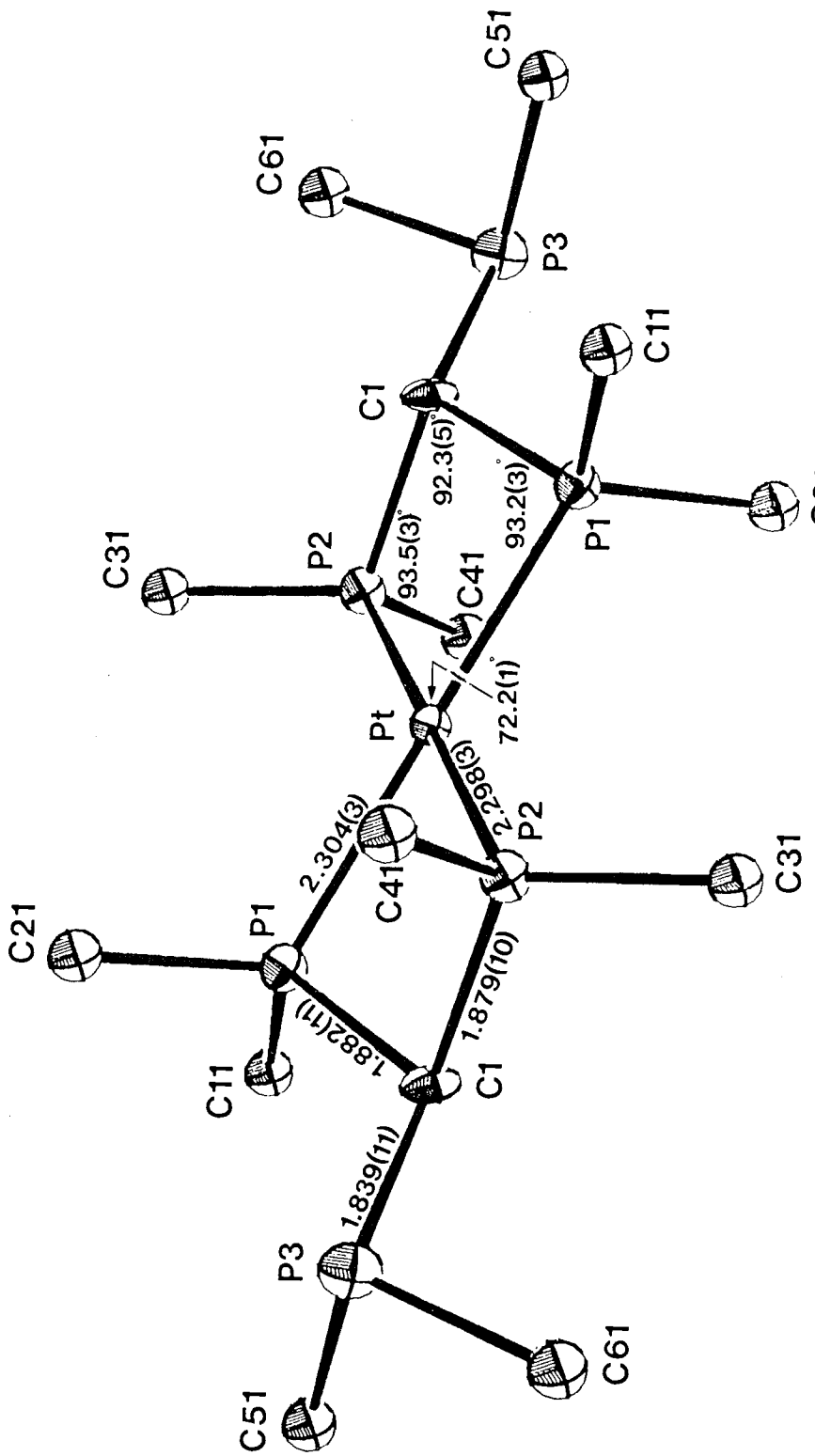

FIG. 4. Perspective ORTEP drawing of the $[Pt(\eta^2\text{-}(Ph_2P)_3CH)_2]^{2+}$ cation of **4***b*, with only the first carbon atom in each phenyl ring and showing some relevant bonding parameters.

P1—C1—P2 angle falls in the range of 91–97° found for dppm complexes (11, 23–26) and between the values of 88° and 103° found for η^3-$(Ph_2P)_3CH$ (9) and η^3,μ^3-$(Ph_2P)_3CH$ (1–7), respectively. These distortions result in a dihedral angle of 30.4° between the planes defined by P1—Pt—P2 and P1—C1—P2. Least-squares plane calculations and torsional angles are summarized in Table 5. This puckering of the chelate ring is slightly greater in **4***a* than in complexes of chelated dppm in which the dihedral angle varies from 16–24° (23–26). This is probably due to the steric requirements of the uncoordinated PPh_2 group in $(Ph_2P)_3CH$ which must be oriented away from the coordination sphere to eliminate intramolecular interactions between phenyl rings.

The phenyl rings are oriented approximately face-to-edge around the metal centre. This also occurs for the complex *trans*-$[RhCl(H)(dppm)_2][BPh_4]$ (23) and other complexes (see, for example, ref. 27) in which four PPh_2 groups occupy a square planar arrangement. All other bond distances and bond angles in the dication and anion are as expected.

Acknowledgements

This work was supported by a grant from the Natural Sciences and Engineering Research Council of Canada. We thank the University of Manitoba for use of their nmr facilities and D. W. Stephan, University of Windsor, for collecting the X-ray data.

1. A. A. Bahsoun, J. A. Osborn, C. Voelker, J. J. Bonnet, and G. Lavigne. Organometallics, **1**, 1114 (1982).
2. J. A. Osborn and G. G. Stanley. Angew. Chem. Int. Ed. Engl. **19**, 1024 (1980).
3. A. A. Bahsoun, J. A. Osborn, J.-P. Kintzinger, P. H. Bird, and U. Siriwardane. Nouv. J. Chem. **8**, 125 (1984).
4. J. A. Clucas, M. M. Harding, B. S. Nicholls, and A. K. Smith. J. Chem. Soc. Chem. Commun. 319 (1984).
5. D. J. Darensbourg, D. J. Zalewski, and T. Delford. Organometallics, **3**, 1210 (1984).
6. D. J. Darensbourg and D. J. Zalewski. Organometallics, **4**, 92 (1985).
7. D. J. Darensbourg, D. J. Zalewski, A. L. Rheingold, and R. L. Durney. Inorg. Chem. **25**, 3281 (1986).
8. A. A. Bahsoun, J. A. Osborn, P. H. Bird, D. Nucciarone, and A. V. Peters. J. Chem. Soc. Chem. Commun. 72 (1984).
9. J. T. Mague and S. E. Dessens. J. Organomet. Chem. **262**, 347 (1986).
10. J. D. Goodrich and J. P. Selegue. Organometallics, **4**, 798 (1985).
11. R. J. Puddephatt. Chem. Soc. Rev. 99 (1983), and references therein.
12. D. M. McEwan, P. G. Pringle, and B. L. Shaw. J. Chem. Soc. Chem. Commun. 2509 (1983).
13. A. T. Hutton, P. G. Pringle, and B. L. Shaw. Organometallics, **2**, 1889 (1983).
14. C. R. Langrick, D. M. McEwan, P. G. Pringle, and B. L. Shaw. J. Chem. Soc. Dalton Trans. 2509 (1983).
15. A. Blagg, G. R. Cooper, P. G. Pringle, R. Robson, and B. L. Shaw. J. Chem. Soc. Chem. Commun. 933 (1984).
16. D. Evans, J. A. Osborn, and G. Wilkinson. Inorg. Synth. **11**, 99 (1968).
17. J. P. Collman, C. T. Sears Jr., and M. Kubota. Inorg. Synth. **11**, 101 (1968).
18. K. Issleib and H. P. Abricht. J. Prakt. Chem. **312**, 456 (1970).
19. D. T. Cromer and J. T. Waber. International tables for crystallography. Vol. IV. Kynoch Press, Birmingham, England. 1974.
20. D. T. Cromer and J. B. Mann. Acta Crystallogr. Sect. A: Cryst. Phys. Diffr. Theor. Gen. Crystallogr. A**24**, 321 (1968).
21. D. T. Cromer and J. B. Mann. Acta Crystallogr. Sect. A: Cryst. Phys. Diffr. Theor. Gen. Crystallogr. A**24**, 390 (1968).
22. A. F. M. J. Van der Ploeg and G. Van Koten. Inorg. Chim. Acta, **51**, 225 (1981).
23. M. Cowie and S. K. Dwight. Inorg. Chem. **18**, 1209 (1979).
24. F. A. Cotton, K. I. Hardcastle, and G. A. Rusholme. J. Coord. Chem. **2**, 217 (1973).
25. W. L. Steffen and G. J. Palenik. Inorg. Chem. **15**, 2432 (1976).
26. K. K. Cheung, T. F. Lai, and K. S. Mok. J. Chem. Soc. A, 1644 (1971).
27. M. C. Hall, B. T. Kilbourn, and K. A. Taylor. J. Chem. Soc. A, 2539 (1970); J. S. Miller, C. G. Young, S. J. Rettig, and B. R. James. Can. J. Chem. **64**, 51 (1986).

Can. J. Chem. Downloaded from www.nrcresearchpress.com by 93.93.197.157 on 09/07/12
For personal use only.

On the crossed-aldol reaction of cyclohexane-1,2-dione with acetone, and the preparation of pyrroline derivatives from the product

GEORGE M. STRUNZ AND CHAO-MEI YU

Canadian Forestry Service – Maritimes, P.O. Box 4000, Fredericton, N.B., Canada E3B 5P7

Received October 13, 1987

This paper is dedicated to the memory of Professor Karel Wiesner

GEORGE M. STRUNZ and CHAO-MEI YU. Can. J. Chem. **66**, 1081 (1988).

Acetone reacts with cyclohexane-1,2-dione, on refluxing in the presence of potassium carbonate, to give the crossed-aldol product, 2-hydroxy-2-acetonylcyclohexanone, **2** (R = CH_3). Other methyl ketones react similarly with cyclohexane-1,2-dione. This is believed to be a consequence of unfavorable dipole interaction in the 1,2-dione. The product, on reaction with liquid ammonia, afforded the 5-amino-4-hydroxy-1-pyrroline derivative, **5**, which was reduced with lithium aluminum hydride to the 3-hydroxy-1-pyrroline, **7**.

GEORGE M. STRUNZ et CHAO-MEI YU. Can. J. Chem. **66**, 1081 (1988).

En faisant réagir la cyclohexane dione-1,2 avec l'acétone sous ébullition en présence du carbonate de potasse, on obtient un produit d'aldolisation croisée, soit l'hydroxy-2 acétonyl-2 cyclohexanone, **2** (R = CH_3). D'autres cétones méthyliques réagissent de la même façon avec la cyclohexane dione-1,2. Il s'agit d'un interaction dipolaire entre les groupes carbonyles voisins de la cyclohexane dione-1,2. En faisant réagir ce produit avec l'ammoniac liquide, on a obtenu le dérivé **5**, c.à d. l'amino-5 pyrroline hydroxy-4, qui est réduit en hydroxy-3 pyrroline-1 (**7**) par le tétrahydridoaluminate de lithium.

Can. J. Chem. Downloaded from www.nrcresearchpress.com by 93.93.197.157 on 09/07/12
For personal use only.

Reaction of cyclohexane-1,2-dione with methyl iodide and potassium carbonate in acetone was reported by Gibson (1) to give the expected 2-methoxycyclohex-2-enone in only 11% yield. By-products isolated from the reaction were an oil that was not characterized, and a crystalline compound, $C_{13}H_{18}O_4$ (6.5%), tentatively identified as 3-(1-hydroxy-2-oxocyclohexyl)-2-methoxycyclohex-2-enone, **1**. The benzyl enol ether was prepared from cyclohexane-1,2-dione in 35% yield (1).

During the *O*-alkylation of cyclohexane-1,2-dione with methyl bromoacetate, effected in 60% yield under similar conditions,[1] we also observed that the desired product was accompanied by an oily by-product. The major component of this material was identified, on the basis of its spectra, as the crossed aldol 2-hydroxy-2-acetonylcyclohexanone, **2** (R = CH_3), formed from cyclohexane-1,2-dione in some 5% yield. When cyclohexane-1,2-dione was refluxed in acetone solution with potassium carbonate in the absence of an alkylating agent, **2** (R = CH_3) was produced in 65% yield.[2] Several minor products, which were more polar, were not readily separable.

Structurally diagnostic signals in the ^1H nmr spectrum of **2** (R = CH_3) and their assignments are indicated in Fig. 1, and key mass spectral fragmentations are depicted in Fig. 2 (see also experimental section). The infrared spectrum (chloroform solution) shows carbonyl absorptions at 1710 and 1700 (sh) cm^{-1}, and the hydroxyl group is manifested as a band at 3460 cm^{-1}. The characteristics of the hydroxyl absorption, measured at several concentrations, indicate intramolecular hydrogen bonding (2). Inspection of models suggests that the most favorable partner for such bonding is the side-chain carbonyl oxygen.

Four different aldols might, in principle, be formed from a mixture of acetone and cyclohexane-1,2-dione. Aldol condensation involving bond formation at C-3 of cyclohexane-1,2-dione is not, however, a favorable process. This stems from the fact, revealed by Hückel molecular orbital calculations (3), that C-3 of the monoanion (enolate) of the 1,2-dione carries a partial positive charge. In effect, enone-type resonance overcomes electron release from enolate oxygen (3). Furthermore, it is well known that in the base-catalysed self-condensation of acetone, the equilibrium does not favor the aldol, diacetone alcohol (2).

Among the factors that contribute to the accumulation of the crossed aldol **2** (R = CH_3) observed in the present study, the unfavorable dipole interaction of the two adjacent carbonyl groups in cyclohexane-1,2-dione appears to be of central importance. The flexibility of the six-membered ring allows some relief from this energetically unfavorable interaction. It is further alleviated by enolization and, in the absence of solvent, cyclohexane-1,2-dione at 25°C exists as a tautomeric mixture containing about 40% of the enol form (4). The reaction of one carbonyl group of the dione with a suitable nucleophile, for the case in point the acetone enolate, clearly provides an alternative means to remove the unfavorable interaction, and is energetically favorable.

Treatment of cyclohexane-1,2-dione with 2-butanone under similar conditions afforded the aldol **2** (R = C_2H_5) in 33% yield (not optimized), and reaction with acetophenone gave **2** (R = Ph) (75%).

If the dipole interaction of the 1,2-dione provides a driving force for the formation of aldols **2**, it might be predicted that cyclopentane-1,2-diones, which are almost completely enolized (4), should have a lower propensity to undergo comparable condensations. This expectation was borne out when 3-methylcyclopentane-1,2-dione failed to give significant amounts of aldol products when subjected to identical treatment with potassium carbonate in acetone. (Longer reaction time resulted in the formation of a mixture from which a product, tentatively identified as **3**, was isolated in less than 1% yield.)

As a 1,4-diketone, **2** may be considered, *inter alia*, to be a potential precursor of heterocycles. Treatment of 2-monoalkyl- or 2,2-dialkyl-1,4-diketones with ammonia has been reported to yield hydroxypyrrolines, via a Paal–Knorr type

[1]C.-M. Yu: unpublished results.

[2]Although the "saturated ketonic impurity" contaminating his methylation product may have been **2** (R = CH_3), the work-up procedure employed by Gibson (1), in experiments otherwise similar to those described herein, could be expected to remove most of the aldol. We observed that shaking an ether solution of **2** (R = CH_3) with 2 N aqueous potassium hydroxide solution (cf. ref. 1) quite rapidly regenerates cyclohexane-1,2-dione (alkali soluble) by a retro-aldol process.

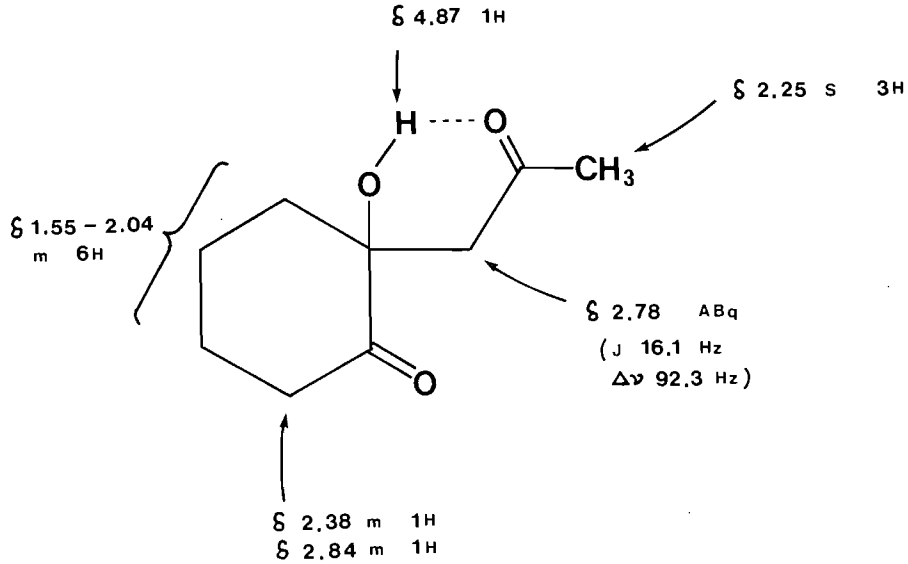

FIG. 1. Signals in the ^1H nmr spectrum of **2** (R = CH_3) and their assignments.

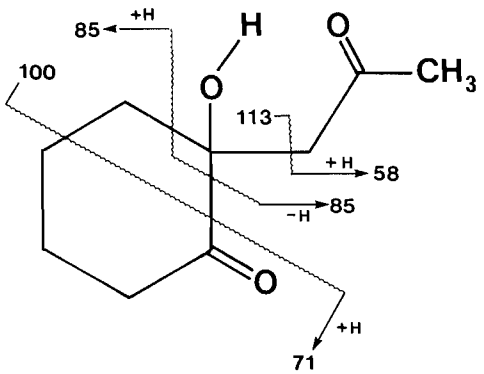

FIG. 2. Key mass spectral fragmentations of **2**.

process (5), and the related products from 2-acyl-2-alkyl-1,4-diketones are intermediates in an interesting rearrangement (6). Reaction of **2** (R = CH_3) with an excess of liquid ammonia (cf. ref. 5) afforded a crystalline product whose formula, $C_9H_{16}N_2O$, suggested one of the isomeric structures **4**–**6**. The formulation **4** was excluded by the ^{13}C nmr spectrum, which revealed only one sp^2 hybridized carbon (δ 173.08, s). Of the remaining possibilities, **5** was favored by the ^1H nmr spectrum, which showed a singlet at δ 2.02 ppm for the methyl protons, and an AB quartet, ($|J_{AB}|$ 17.1 Hz; $\Delta\nu$ 24.2 Hz) at δ 2.57 for the methylene protons in the five-membered ring. (No other signals for non-exchangeable protons were evident below δ 2.00.)

The production of **5** from **2** (R = CH_3) contrasts with the behavior of the 2,2-dialkyl-1,4-diketones investigated previously (5). The latter, under similar conditions, reacted with only one equivalent of ammonia, and the products cyclized to hydroxypyrrolines. The different behavior, which is associated with the presence of the 2-hydroxyl function, may be a consequence of the ability of that group to participate in hydrogen-bonded association with ammonia molecules. Treatment of **5** with lithium aluminum hydride afforded the pyrroline **7** in high yield. The reaction occurs presumably by initial reduction of the imino function of **5**, followed by elimination of ammonia, probably during the work-up procedure. The structure and functionality of pyrroline **7** are reminiscent of an oxidation product, **8**, obtained from tetrahydrocarbazole (7). The latter

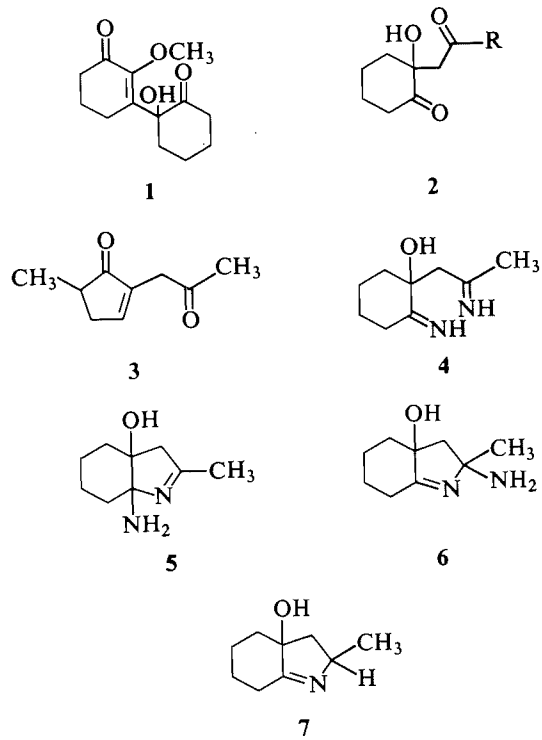

readily undergoes rearrangement to the spiro derivative **9**, under the action of acid, alkali, or heat (7). The driving force for this rearrangement was considered to be derived from resonance stabilization of the vinylogous lactam system present in **9**. In consonance with this view, **7**, which would not form a conjugated spiro product, was unchanged (tlc) under conditions that result in rearrangement of **8**.

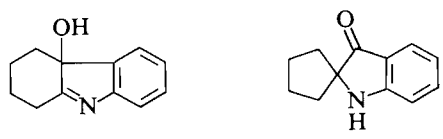

Can. J. Chem. Downloaded from www.nrcresearchpress.com by 93.93.197.157 on 09/07/12
For personal use only.

Can. J. Chem. Downloaded from www.nrcresearchpress.com by 93.93.197.157 on 09/07/12
For personal use only.

Experimental

Melting points were determined on a hot-stage apparatus and are uncorrected. Infrared spectra were recorded on a Philips Pye Unicam PU9516 infrared spectrophotometer. Nuclear magnetic resonance spectra were run on a Varian XL-200 instrument. Accurate mass measurements were provided by Dr. A. Hogg, University of Alberta. Microanalysis was performed by Spang Microanalytical Laboratory, Eagle Harbor, MI.

Aldol condensation of cyclohexane-1,2-dione with acetone

A mixture of 1,2-cyclohexanedione (1.0 g), acetone (100 mL), and potassium carbonate (1.4 g) was heated under reflux for 5 h, in a flask protected from atmospheric moisture by a calcium chloride drying tube. When cold, the mixture was filtered, and the filtrate evaporated to dryness on a rotary vacuum evaporator. The residue was chromatographed on a column of silica gel using a gradient of chloroform and ether. Elution with chloroform–ether (9:1) afforded pure **2** (R = CH_3) as an almost colorless oil (0.98 g; 65%); ir ($CHCl_3$): 3460, 1710, and 1700 (sh) cm^{-1}; ^1H nmr ($CDCl_3$, 200 MHz) δ: 1.55–2.04 (6H, m), 2.25 (3H, s), 2.38 (1H, m), 2.78 (2H, ABq, J_{AB} = 16.1 Hz, $\Delta\nu$ = 92.3 Hz), 2.84 (1H, m), 4.87 (1H, exch.); mass spectrum (*inter alia*), *m/z* (relative intensity) (ion): 170.0945 (10.8) ($M^{\ddagger}$) (calcd. for $C_9H_{14}O_3$: 170.0943), 152.0839 (7.5) ($C_9H_{12}O_2$; M − H_2O)‡, 113.0603 (28.7) ($C_6H_9O_2$; M − C_3H_5O)$^+$, 100.0524 (100) ($C_5H_8O_2$)‡, 85.0655 (22.9) (C_5H_9O)$^+$, 85.0293 (41.4) ($C_4H_5O_2$)$^+$, 71.0498 (10.3) (C_4H_7O)$^+$, 58.0440 (29.3) (C_3H_6O)‡, 55.0202 (53.4) (C_3H_3O)$^+$.

Aldol condensation of cyclohexane-1,2-dione with 2-butanone

A mixture of 1,2-cyclohexanedione (0.54 g), 2-butanone (30 mL), and potassium carbonate (0.80 g) was heated under reflux for 10 h. The product, after work-up, was chromatographed on a column of silica gel using a gradient mixture of chloroform, ether, and hexane. Elution with chloroform–ether–hexane (7.5:1.5:1) afforded **2** (R = C_2H_5), which was further purified on silica gel preparative layer plates (solvent system, hexane – ethyl acetate (7:3)). The product **2** (R = C_2H_5) was obtained as an almost colorless oil (0.29 g, 33%); ir ($CHCl_3$): 3460, 1710, and 1700 (sh) cm^{-1}; ^1H nmr ($CDCl_3$, 200 MHz) δ: 1.05 (3H, t, *J* = 7.3 Hz), 1.56–2.06 (6H, m), 2.26–3.02 (4H, m), 2.77 (2H, ABq, J_{AB} = 15.9 Hz, $\Delta\nu$ = 91.7 Hz), 4.92 (1H, s); mass spectrum (*inter alia*), *m/z* (relative intensity) (ion): 184.1099 (27.0) ($M^{\ddagger}$) (calcd. for $C_{10}H_{16}O_3$: 184.1099), 166.0995 (4.5) ($C_{10}H_{14}O_2$; M − H_2O)‡, 156.1152 (4.6) ($C_9H_{16}O_2$; M − CO)‡, 127.0761 (42.0) ($C_7H_{11}O_2$; M − C_3H_5O)$^+$, 114.0682 (76.3) ($C_6H_{10}O_2$; M − C_4H_6O)‡, 99.0447 (26.7) ($C_5H_7O_2$)$^+$, 85.0656 (23.7) (C_5H_9O)$^+$, 72.0578 (21.1) (C_4H_8O)‡, 57.0362 (100.0) (C_3H_5O)$^+$.

Aldol condensation of cyclohexane-1,2-dione with acetophenone

A mixture of 1,2-cyclohexanedione (0.53 g), acetophenone (10.0 mL), and potassium carbonate (0.80 g) was heated at 90°C with stirring for 5 h. The product, after work-up, was chromatographed on a column of silica gel, and elution with chloroform–ether–hexane (7:1:2) gave crude **2** (R = Ph) as a pale yellow oil (0.82 g, 75%). A sample was purified by chromatography on silica gel preparative layer plates (solvent system, chloroform–ether–hexane (7:1:2)); ir ($CHCl_3$): 3470, 1715, 1670 cm^{-1}; ^1H nmr ($CDCl_3$, 200 MHz) δ: 1.64–2.09 (6H, m), 2.47 (1H, m), 2.91 (1H, m), 3.38 (2H, ABq, J_{AB} = 16.7 Hz, $\Delta\nu$ = 79.7 Hz), 4.94 (1H, s, $W_{1/2} \sim 6$ Hz), 7.43–7.65 (3H, m), 7.94–7.99 (2H, m); mass spectrum (*inter alia*), *m/z* (relative intensity) (ion): 232.1102 (10.2) ($M^{\ddagger}$) (calcd. for $C_{14}H_{16}O_3$: 232.1099), 214.0998 (1.5) ($C_{14}H_{14}O_2$; M − H_2O)‡, 204.1148 (15.1) ($C_{13}H_{16}O_2$; M − CO)‡, 162.0678 (58.0) ($C_{10}H_{10}O_2$; M − C_4H_6O)‡, 147.0446 (28.9) ($C_9H_7O_2$)$^+$, 120.0577 (23.0) (C_8H_8O)‡, 105.0343 (100.0) (C_7H_5O)$^+$, 77.0393 (44.4) (C_6H_5)$^+$.

Attempted aldol condensation of 3-methylcyclopentane-1,2-dione with acetone

When a mixture of 3-methylcyclopentane-1,2-dione (0.50 g), acetone (50 mL), and potassium carbonate (0.70 g) was heated under reflux for 5 h, little evidence of any reaction was observed. Increasing the reaction time to 36 h afforded a mixture from which a product, tentatively identified as **3**, was isolated by chromatography, in less than 1% yield; ir ($CHCl_3$): 1720 (sh), 1700, and 1635 cm^{-1}; ^1H nmr ($CDCl_3$, 200 MHz) δ: 1.20 (3H, d, *J* = 7.5 Hz), 1.65–2.99 (3H, m), 2.21 (3H, s), 3.34 (2H, s), 7.50 (1H, m, $W_{1/2}$ = 7 Hz).

Preparation of aminopyrroline, 5

Hydroxydiketone **2** (R = CH_3) (1.39 g) was stirred under reflux with anhydrous liquid ammonia (ca. 30 mL) for 5 h. The Dry Ice condenser was then removed and the ammonia was allowed to evaporate. Removal of the last traces of ammonia was effected on a rotary volume evaporator. The residue was crystallized twice from ether, affording colorless crystals of **5** (0.61 g, 45%), mp 98–100°C; ir ($CHCl_3$): 3500–3100, 1640 cm^{-1}; ^1H nmr ($CDCl_3$, 200 MHz) δ: 1.21–1.94 (10H, m), 2.02 (3H, s), 2.57 (2H, ABq, J_{AB} = 17.1 Hz, $\Delta\nu$ = 24.2 Hz), 3.47 (1H, m); ^{13}C nmr ($CDCl_3$) δ: 20.93 (q), 21.16 (t), 22.80 (t), 33.94 (t), 37.68 (t), 49.84 (t), 78.82 (s), 85.00 (s), 173.08 (s); mass spectrum (*inter alia*), *m/z* (relative intensity) (ion): 168.1264 (16.8) ($M^{\ddagger}$) (calcd. for $C_9H_{16}N_2O$: 168.1263), 151.0999 (16.3) ($C_9H_{13}NO$; M − NH_3)‡, 127.0999 (100) ($C_7H_{13}NO$; M − C_2H_3N)‡, 98.0615 (50.2) (C_5H_8NO)$^+$, 57.0600 (50.0) (C_3H_7N)‡.

Reduction of aminopyrroline 5 to pyrroline 7

A solution of **5** (200 mg, 1.19 mmol) in anhydrous tetrahydrofuran (20 mL) was heated under reflux with lithium aluminum hydride (87 mg, 2.29 mmol), in an atmosphere of dry nitrogen, for 3 h. Excess reagent was decomposed by cautious addition of wet ether, and the resulting mixture was filtered. The filtrate was dried over magnesium sulfate, filtered, and evaporated to dryness *in vacuo*. Purification of the product by preparative thin-layer chromatography (silica gel; hexane–acetone, 7:3), and crystallization from ether, gave colorless crystals of pyrroline **7** (155 mg, 85%). A sample, sublimed at 0.1 Torr (1 Torr = 133.3 Pa), melted at 75–77°C. Crystallized **7** displayed ir absorption ($CHCl_3$) at 3600 (sharp), 3500–3100, 1650 cm^{-1}; ^1H nmr ($CDCl_3$, 200 MHz) δ: 1.27 (3H, d, *J* = 6.9 Hz), 1.35–2.07 (6H, m), 2.13–2.29 (2H, m), 2.44–2.55 (2H, m), 3.55 (1H, br, exch.), 4.05 (1H, m); mass spectrum (*inter alia*), *m/z* (relative intensity) (ion): 153.1154 (100) ($M^{\ddagger}$) (calcd. for $C_9H_{15}NO$: 153.1154), 138.0922 (21.8) ($C_8H_{12}NO$; M − CH_3)$^+$, 125.1206 (83.4) ($C_8H_{15}N$; M − CO)‡, 110.0970 (65.9) ($C_7H_{12}N$; M − CO and CH_3)$^+$, 97.0892 (38.3) ($C_6H_{11}N$)‡, 82.0664 (55.8) (C_5H_8N)$^+$, 71.0501 (61.1) (C_4H_7O)$^+$. *Anal.* calcd. for $C_9H_{15}NO$: C 70.55, H 9.87, N 9.14%; found: C 70.61, H 9.94, N 9.12%.

Acknowledgments

The authors are indebted to Ms. Carla Mersereau and Mr. Larry Calhoun, University of New Brunswick, for providing the nmr spectral data. A useful discussion with Dr. J. A. Findlay, University of New Brunswick, is acknowledged.

1. M. S. Gibson. J. Chem. Soc. 681 (1962).
2. J. March. Advanced organic chemistry. 3rd ed. J. Wiley and Sons, New York. 1985.
3. A. S. Kende and R. G. Eilerman. Tetrahedron Lett. 697 (1973).
4. E. S. Gould. Mechanism and structure in organic chemistry. Holt, Rinehart and Winston, New York. 1959.
5. P. K. Chiu, K. H. Lui, P. N. Maini, and M. P. Sammes. J. Chem. Soc. Chem. Commun. 109 (1987).
6. M. P. Sammes, P. N. Maini, and A. R. Katritzky. J. Chem. Soc. Chem. Commun. 354 (1984).
7. B. Witkop and J. B. Patrick. J. Am. Chem. Soc. **73**, 2188 (1951).

The structure, stereochemistry, and biosynthetic origin of a diterpenoid fungal metabolite, traversianal, established by ^{1}H, ^{2}H, and ^{13}C magnetic resonance[1,2]

ALBERT STOESSL AND G. L. ROCK
Agriculture Canada, London Research Centre, London, Ont., Canada N6A 5B7
J. B. STOTHERS
Chemistry Department, University of Western Ontario, London, Ont., Canada N6A 5B7
AND
R. C. ZIMMER
Agriculture Canada, Research Station, P.O. Box 3001, Morden, Man., Canada R0G 1T0

Received October 22, 1987

ALBERT STOESSL, G. L. ROCK, J. B. STOTHERS, and R. C. ZIMMER. Can. J. Chem. **66**, 1084 (1988).

The structure of traversianal, a tricyclic diterpenoid fungal metabolite of *Cercospora traversiana*, has been elucidated through detailed ^{1}H and ^{13}C magnetic resonance studies, including homo- and heteronuclear correlation spectra of the natural product and examination of ^{13}C-labelled material obtained by [1,2-$^{13}C_2$]acetate incorporation experiments. Its stereochemistry was established from a series of nuclear Overhauser effect difference spectra. The tricyclic carbon skeleton of traversianal is that of the fusicoccin /cotylenin and ophiobolane terpenes although the oxygenation pattern closely resembles the latter. Incorporation experiments with [2,2,2-$^{2}H_3$, 1-$^{13}C_1$]acetate revealed that traversianal arises by a sequence that differs substantially from that established for the fusicoccanes but rather resembles that previously shown for the ophiobolanes, in the retention of hydride at C-2, -10, and -14. However, the opposite configuration of the methyl group at C-3 suggests that the route to traversianal involves a terminal *trans*-geranylgeranyl unit instead of the *cis* unit implicated in ophiobolin generation.

ALBERT STOESSL, G. L. ROCK, J. B. STOTHERS et R. C. ZIMMER. Can. J. Chem. **66**, 1084 (1988).

Le traversianal est un métabolite fongique de la série des diterpénoïdes tricycliques qui est isolé du *Cercospora traversiana*; on en a déterminé la structure grâce à des études détaillées par résonance magnétique nucléaire du ^{1}H et du ^{13}C, y compris des corrélations spectrales homo- et hétéronucléaires du produit naturel, et par un examen du produit marqué au ^{13}C obtenu par des expériences d'incorporations d'unités acétates [$^{13}C_2$-1,2]. On a établi sa stéréochimie à partir d'une série de spectres différentiels de l'effet Overhauser nucléaire. Le squelette carboné tricyclique du traversianal correspond à celui des terpènes fusicoccine/cotylénine et ophibolane, même si la distribution des oxygèns ressemble plus à celle de ces derniers. Les expériences d'incorporation d'acétate [$^{2}H_3$-2,2,2 $^{13}C_1$-1] révèlent que le traversianal provient d'une séquence qui diffère beaucoup de celle établie pour les fusicoccanes, mais qui ressemble plutôt à celle qui a été mise en évidence pour les ophiobolanes et qui comporte une rétention de l'hydrure dans les positions C-2, C-10 et C-14. Toutefois, la configuration inverse du groupement méthyle en C-3 suggère que la voie menant au traversianal implique une unité *trans*-géranylgéranyle terminale plutôt que l'unité *cis* impliquée dans la génération de l'ophioboline.

[Traduit par la revue]

Introduction

In the course of a program on myco- and microbial phytotoxins, we recently isolated a novel diterpenoid aldehyde **1** (1) from a fungus that had been found to infect a field of fenugreek and identified as *Cercospora traversiana* (2). The present paper gives the full experimental evidence that led to the structural and stereochemical assignments. It also describes additional biosynthetic studies, utilizing acetate doubly labelled with ^{2}H and ^{13}C, which throw light on the relationship between this *C. traversiana* aldehyde, which we have named traversianal, and other natural products having the same tricyclic carbon skeleton. Not all of these are of fungal origin; those that are comprise the fusicoccins and cotylenins (3, 4), the classical ophiobolins A–F (3–5), the 6-epiophiobolins (5, 6), ophiobolins G and H (5, 7), and two recently reported 21-dihydroophiobolins (8). Several of these compounds are important as much-studied phytotoxins (3–7) and at least one, ophiobolin H, has been identified as a mycotoxin (5–7). Rather surprisingly, therefore, in tests that will be reported elsewhere, traversianal was found to be essentially inactive as a wilt or necrosis toxin towards a range of plants, although it does cause the efflux of betacyanins from beetroot slices. It is very active in the brine shrimp (*Artemia salina*) bioassay and is strongly molluscicidal. There is, therefore, room for concern about its potential as a mycotoxin.

Results and discussion

Structure

Traversianal crystallized readily on concentration of EtOAc or C_6H_6 extracts of potato-dextrose agar cultures of the fungus, and additional amounts were obtained by chromatography of the mother liquors over silica leading to overall yields of ca. 36 mg/L after 15 days' growth. Recrystallization from C_6H_6 furnished material that melted sharply at 234–235°C and had an optical rotation of $[\alpha]_D^{24}$ −248°. From its empirical constitution of $C_{20}H_{28}O_3$, established by microanalysis and precise mass measurement, the compound appeared to be a diterpene. Its ir spectrum contained hydroxyl absorption (3530 cm^{-1}) and carbonyl bands indicative of a cyclopentanoid ketone (1740 cm^{-1}) and an α,β-unsaturated aldehyde (1678, 2720, 2850 cm^{-1}); the latter chromophore exhibited uv absorption at 234 nm (ε 13 000). The ^{1}Hmr spectrum in CD_2Cl_2 solution showed that the formyl group (δ 9.09) was bonded to a trisubstituted double bond (δ 7.15, dd, J = 8.6, 8.8 Hz, 1H). In addition there was absorption characteristic of an isopropenyl group (δ 1.71 (dd, J = 0.7, 1.3 Hz, 3H), 4.72 (ddq, J = 0.7, 0.7, 2.5 Hz, 1H), and 4.81 (dq, J = 1.3, 2.5 Hz, 1H)), secondary and

[1]Part 135 of ^{13}Cmr studies; for Part 133 see ref. 25, for Part 134 see ref. 26.

[2]Contribution No.1053 from the Research Centre, London, Ont.

Can. J. Chem. Downloaded from www.nrcresearchpress.com by 93.93.197.157 on 09/07/12
For personal use only.

Can. J. Chem. Downloaded from www.nrcresearchpress.com by 93.93.197.157 on 09/07/12
For personal use only.

tertiary methyl groups (δ 0.78 (d, J = 7.6 Hz) and 1.16 (s)), and one exchangeable hydroxyl proton. These features confirmed the diterpenoid nature of the metabolite. The ^{13}Cmr spectrum exhibited carbonyl signals at δ_C 220.7 and 193.6, attributable to a cyclopentanone and a conjugated aldehyde, respectively, with sp^2 absorption at δ_C 113.8 and 148.3 for the isopropenyl group and at δ_C 146.2 and 167.1, arising from the conjugated double bond. A quaternary carbon signal at δ_C 79.1 indicated the presence of a tertiary alcohol while the higher field sp^3 region contained signals for a quaternary carbon, four methine, five methylene, and three methyl carbons.

The product from the first experiment was examined by ^{1}Hmr in C_6D_6 but the limited solubility of subsequent crops of purer material led to their examination as CD_2Cl_2 solutions. Differences in the relative shieldings of the proton multiplets in the two solvents provided complementary data, which aided detailed interpretation of the proton spectra. However, in the following discussion the CD_2Cl_2 solution data are presented in detail but the ^{1}H results for C_6D_6 solution have been tabulated. ^{1}H–^{1}H and ^{13}C–^{1}H correlation spectra were recorded; the heteronuclear correlation permitted ready identification of the origins of the individual proton multiplets as methylene and methine patterns.

A methylene proton pattern at δ 3.32 and 2.27 was found to be coupled to the olefinic absorption at δ 7.15 and a methine pattern at δ 1.84 that was also coupled to a methine pattern centred at δ 3.03. The latter pattern exhibited strong coupling with methylene protons absorbing near 1.7 ppm and weak coupling to one of the isopropenyl olefinic protons (δ 4.72). The methylene absorption at δ 1.7 was also coupled to methylene protons centred at δ 1.45. These results led to part structure **A**, with which are included the ^{13}C shieldings for the protonated carbons. The proton spectrum, in conjunction with the ^{13}C–^{1}H correlation spectrum, led also to the identification of a second major fragment **B**. Methylene proton absorption at δ 2.52 and 2.59 with J_{gem} = 19.6 Hz was found to be coupled to a methine pattern at δ 2.29, which, in turn, exhibited coupling to the secondary methyl group (δ 0.78) and a methine pattern at δ 2.61. The latter pattern was coupled to two methylene protons (J_{gem} = 14.6 Hz) at δ 1.34 and 1.70.

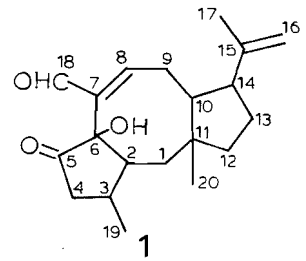

1

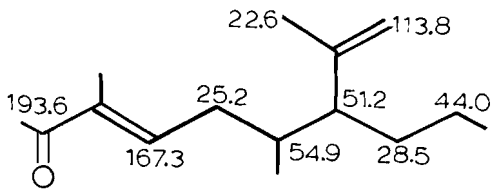

A

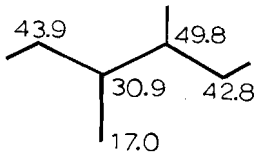

B

TABLE 1. ^{1}H and ^{13}Cmr data[a] for traversianal

Position	^{1}H In C_6D_6	^{1}H In CD_2Cl_2	^{13}C In CD_2Cl_2
1α	1.00(14.2,12.3)	1.33_7(14.6,12.3)	42.8
β	1.35(14.2,3.9)	1.69_6(14.6,3.6)	
2	2.40(12.3,8.4,3.9)	2.61_0(12.3,7.8,3.6)	49.8
3	1.80(m)	2.28_7(8.0,7.8,7.6,2.8)	30.9
4α	2.66(19.6,1.4)	2.52_1(19.6,2.8)	43.9
β	2.33(19.6,8.8)	2.59_1(19.6,8.0)	
5	—	—	220.7
6	—	—	79.1
7	—	—	146.2
8	6.22(9.1,8.4)	7.15_2(8.8,8.6)	167.1
9α	1.96(11.9,9.1)	2.27_0(11.9,8.6,1.0)	25.2
β	3.20(11.9,8.4,8.4)	3.32_0(11.9,8.8,8.6)	
10	1.32(m)	1.84(m)	54.9
11	—	—	44.4
12	~1.26(m)	1.45(m)	44.0
13α	1.65(m)	~1.7	28.5
β	1.75(m)		
14	2.83(11.5,9.1,9.1)	3.03_4(11.6,9.0,9.0,0.7)	51.2
15	—	—	148.3
16	4.80(2.5,0.7)	4.80_6(2.5,1.3)	113.8
	4.86(2.5,1.4)	4.72_3(2.5,0.7,0.7)	
17	1.64(1.4,0.7)	1.71_0(1.3,0.7)	22.6
18	8.74	9.09	193.6
19	0.68(7.6)	0.78_2(7.6)	17.0
20	1.13	1.16_2	18.5

[a]Shieldings in ppm from internal TMS; ^{1}H–^{1}H couplings in Hz listed in parentheses.

These part structures **A** and **B** together with a cyclopentanoid carbonyl, a tertiary carbinyl carbon, and the quaternary carbon bearing the tertiary methyl group account for the 20 carbons and for four sites of unsaturation. Thus, traversianal is tricyclic including one cyclopentanoid unit and, with the assumption that no carbon–carbon rearrangements occur during its generation from geranylgeranyl pyrophosphate, can be most plausibly assigned structure **1**. The ^{1}H and ^{13}Cmr data are presented in Table 1.

To confirm the proposed structure, traversianal was isolated from cultures of the fungus grown on liquid potato-dextrose medium supplemented with [1,2-$^{13}C_2$]acetate with the addition of 10 mL of a 0.04 M solution to each 100 mL of culture on days 10 and 13. The ^{13}Cmr spectrum of $1^{-13}C_x$ isolated on day 16 showed that all carbons were labelled (4.4% specific incorporation) in the pattern **2**, precisely in accord with our expectations. The heavy bonds in **2** represent intact acetate units for which the observed J_{CC} values in Hz are indicated, while the dark circles indicate the carbons arising from C-2 of the four mevalonate units. The relatively high enrichment level signals the formation of multilabelled species, the presence of which will increase the probability of ^{13}C incorporation at contiguous carbons in **1** that arise from different acetate units. Thus, additional information on the carbon connectivities was sought through two-dimensional ^{13}C–^{13}C correlation (COSY) and double quantum coherence (2D-INADEQUATE) spectra (9). From the ^{13}C

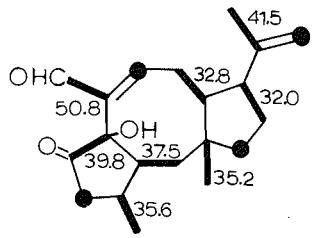

2

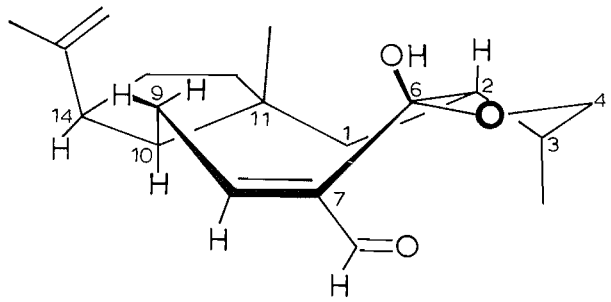

3

COSY experiment, contour plots of which are shown in Fig. 1, the immediate neighbors of each of the sp^2 carbons and of the carbinyl carbon were readily established (Fig. 1*a*). The connectivities of all of the sp^3 carbons were also revealed (Fig. 1*b*) with the exception of the C-1, -11, -12 linkages, which undoubtedly involve signals at δ_C 42.9, 44.4, and 44.0, respectively. It may be noted that weak, off-diagonal elements confirming the C-10, -14 bonding become observable in plots at higher intensity levels. The 2D-INADEQUATE experiment provided corroboration of these results. Thus the structure of **1** in planar projection was established.

Stereochemistry

To determine the stereochemistry of **1** the intramolecular proton nuclear Overhauser effects were examined by nOe difference spectra. Saturation of the angular methyl protons at δ 1.16 enhanced the methine absorption at δ 2.61 (H-2) and the methylene pattern at δ 3.32 (H-9), which is vicinally coupled to H-10 at δ 1.84, J = 8.6 Hz. Irradiation at δ 3.32 only enhanced the pattern for its methylene partner at δ 2.27, which was also affected by irradiation of the olefinic proton at δ 7.15. It may be noted that the vicinal coupling between the 9-proton at δ 2.27 and H-10 is small, J = 1.0 Hz. Enhancement of the H-10 pattern (δ 1.84) was observed upon saturation of the multiplet at δ 3.03 (H-14) and of that at δ 1.34 (H-1), which is strongly coupled to H-2, J = 12.3 Hz, indicative of an antiperiplanar interaction. The H-1 pattern (δ 1.34) was enhanced by saturation of the secondary methyl protons (0.78) that also affected the multiplets for H-3 (δ 2.29) and the 4-methylene proton at δ 2.52. The latter two protons exhibited vicinal coupling of 2.8 Hz. Saturation of the olefinic methyl protons (δ 1.71) indicated that the olefinic pattern at δ 4.81 arises from the *cis* proton. These results lead to the relative stereochemistry illustrated in **3** with the angular methyl, the isopropenyl group, H-2, and the 6-OH group in β configurations while the secondary methyl group, H-10, and H-14 are α-oriented. Although the orientation of the hydroxyl group was not established, an examination of Dreiding models indicates that a *cis* junction of the cyclopentanoid ring at C-2 and -6 is more favorable than a *trans* ring junction with a 6α-hydroxyl group.

Biosynthesis

The tricyclic carbon skeleton of **1** is the same as that in other diterpenes, namely the fusicoccanes and cotylenins from *Fusicoccum amygdali* (10) and a *Cladosporium* (11), respectively, as represented by fusicoccin A (**4**), the fusicoplagins (12) and anadensin (13) from liverworts, as represented by fusicoplagin A (**5**), and several compounds such as roseanolone (**6**) and roseadione (**7**) from the higher plant *Hypoestes rosea* (14). The same tricyclic skeleton having an extended side chain is also found in the sesterterpenoid ophiobolins such as ophiobolin A (**8**) and 6-epiophiobolin A from *Cochliobolus* (*Helminthosporium*) and *Cephalosporium* spp (6, 15), ophiobolin G (**9**) from *Aspergillus ustus* (5, 7); as well as ceroplastol (**10**) and related compounds from the scale insect *Ceroplastes albolineatus* (16).

Detailed biosynthetic studies of the fusicoccins (17) have established the sequence in Scheme 1 involving successive hydride shifts from C-14 to C-15, from C-6 to C-7, and from C-2 to C-6 with proton loss from C-10 and C-1. Similar detailed studies of the ophiobolin biosynthesis (18) have shown that these protons do not migrate although there is a remarkable "1,5-hydride shift" from C-8 to C-15 (Scheme 2). It was of interest, therefore, to examine the genesis of **1** in more detail than that provided by the [1,2-$^{13}C_2$]acetate incorporation experiments described above to obtain evidence regarding hydride shifts. Two incorporation experiments were carried out for this purpose. In the first, the culture medium was supplemented with [2,2,2-$^2H_3$, 2-$^{13}C_1$]acetate, using the same experimental procedures as those employed in the earlier biosynthetic experiment. The ^{13}Cmr spectrum of **1**-^2H_x,$^{13}C_y$ isolated from

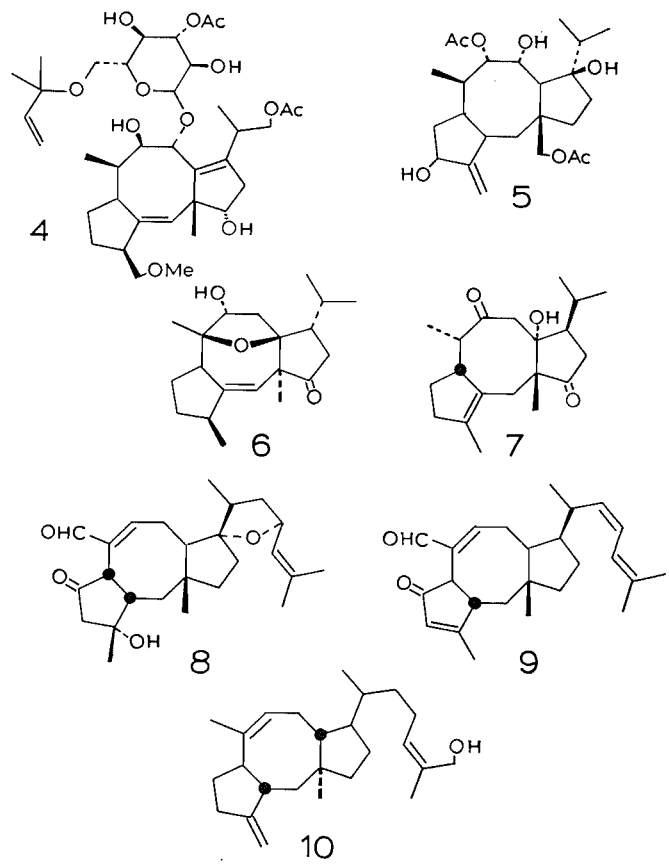

Can. J. Chem. Downloaded from www.nrcresearchpress.com by 93.93.197.157 on 09/07/12
For personal use only.

Can. J. Chem. Downloaded from www.nrcresearchpress.com by 93.93.197.157 on 09/07/12
For personal use only.

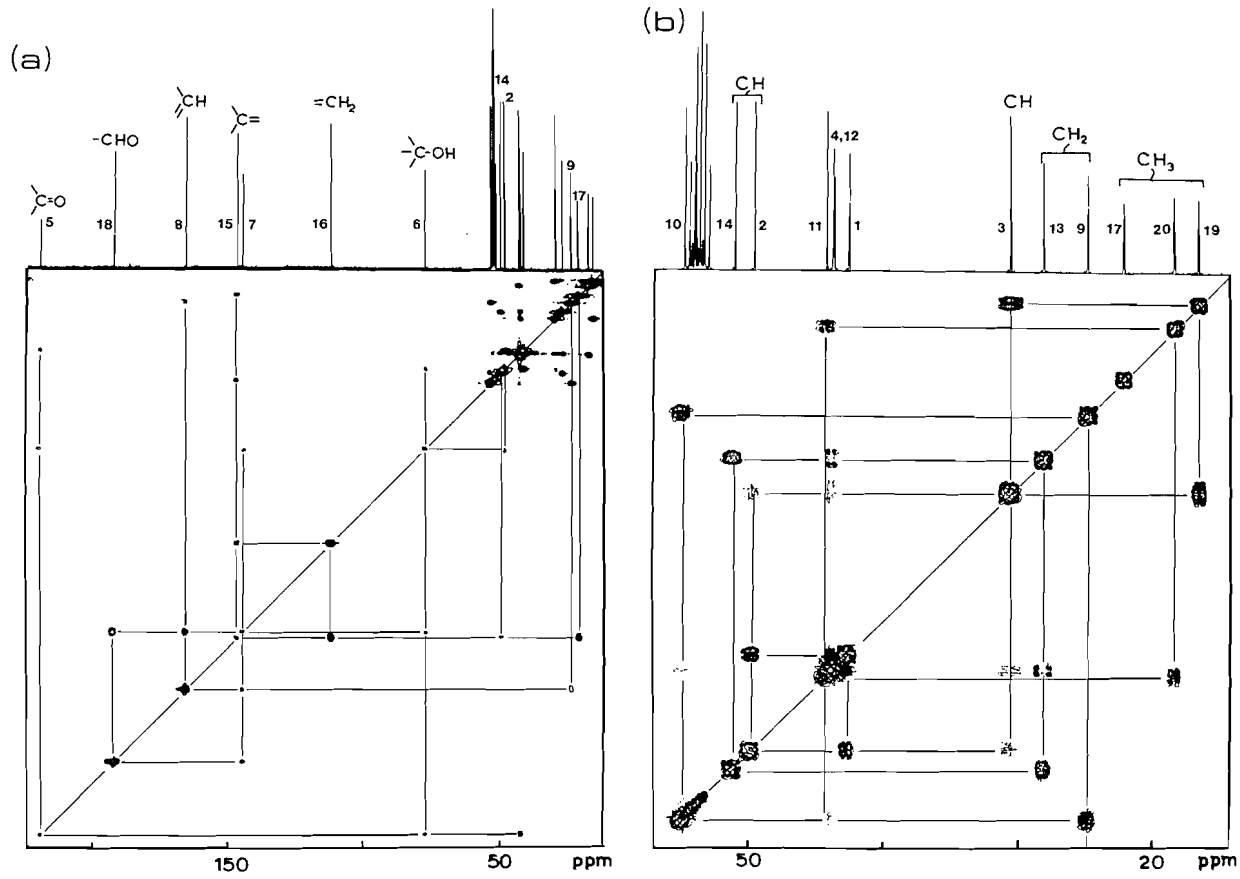

FIG. 1. Contour plots of the ^{13}C COSY spectrum of enriched traversianal: (a) full plot showing connectivities of the carbinyl and sp^2 carbons; (b) an expansion of the sp^3 region of the spectrum. The 1D spectrum of natural **1** is included above each plot for calibration.

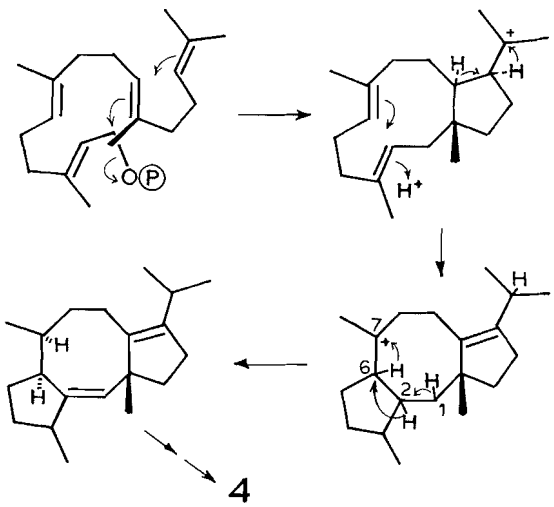

SCHEME 1

this experiment clearly contained isotope-shifted multiplets arising from deuterium directly bonded to labelled carbons at the 2-, 4-, 8-, 12-, 14-, 16-, and 18-positions as well as the three methyl sites, but the situation was not clear for C-10 because of the solvent absorption. Nevertheless, these results are definitely incompatible with a sequence similar to that leading to the fusicoccins for which no directly bonded deuterium would be evident at C-2, -10, and -14 because of hydride shifts. In addition, the absence of any two-bond isotope shifts is consistent with a lack of hydride shifts. It may be noted that two-bond ^2H-induced effects have been employed to identify hydride shifts in other biosynthetic studies (19). In any event, the labelling pattern observed corresponded with that expected for a sequence resembling that found for the ophiobolins. To clarify the picture regarding C-10 and to obtain confirmatory evidence, a second experiment was carried out in which **1**-^2H_x,$^{13}C_y$ was isolated from a culture medium supplemented with [2,2,2-$^2H_3$, 1-$^{13}C_1$]acetate. Its ^{13}C spectrum contained isotope-shifted components arising from ^2H-induced effects through two bonds, i.e., β shifts, for enriched carbons at the 1-, 3-, 7-, 9-, 11-, 13-, and 15-positions. In effect, this experiment reveals the ^2H_x-C-^{13}C fragments arising from incorporation of intact CD_3–$^{13}CO_2$- units and the results show that deuterium is retained through the sequence at C-2, C-10, C-14, C-18, and the three methyl groups. Thus, hydride shifts do not occur from C-2, -10, or -14; this is exactly analogous to the findings for the ophiobolins but contrary to the results for the fusicoccins. The ^2Hmr spectrum of this sample of **1**-^2H_x,$^{13}C_y$ is shown in Fig. 2 together with the proton spectrum. Integration of the deuterium spectrum revealed the relative ^2H content at the various positions to be three at each of the methyl sites (C-17, -19, -20), two at the three methylene positions (C-4, -12, -16), and one at each of C-2, -8, -10, -14, and -18. The signal for the formyl deuterium appears as a doublet because the geminal J_{D-C-C} coupling is sufficiently large to be readily resolved, $J \sim 23$ Hz. All of these data are, therefore, consistent with a biosynthetic sequence closely similar to that for the ophiobolanes although these cannot reveal whether a C-8 to C-15 hydride shift occurred at an intermediate stage.

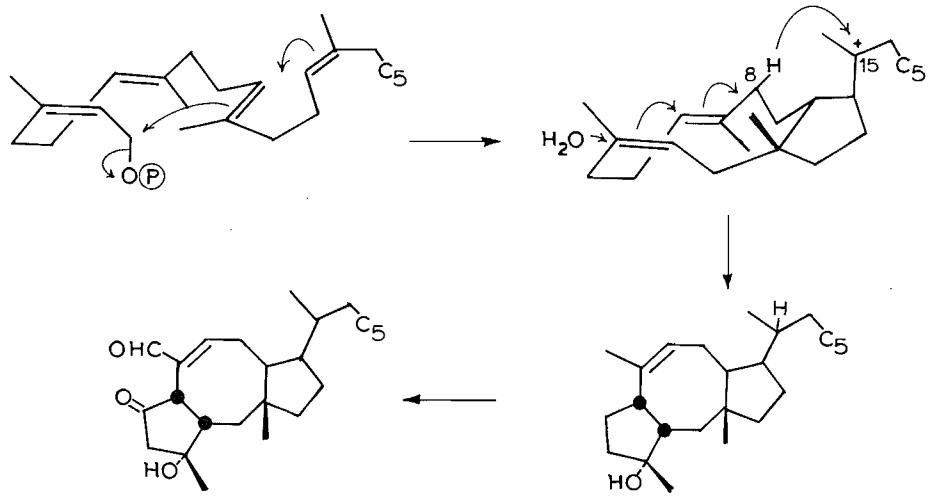

SCHEME 2

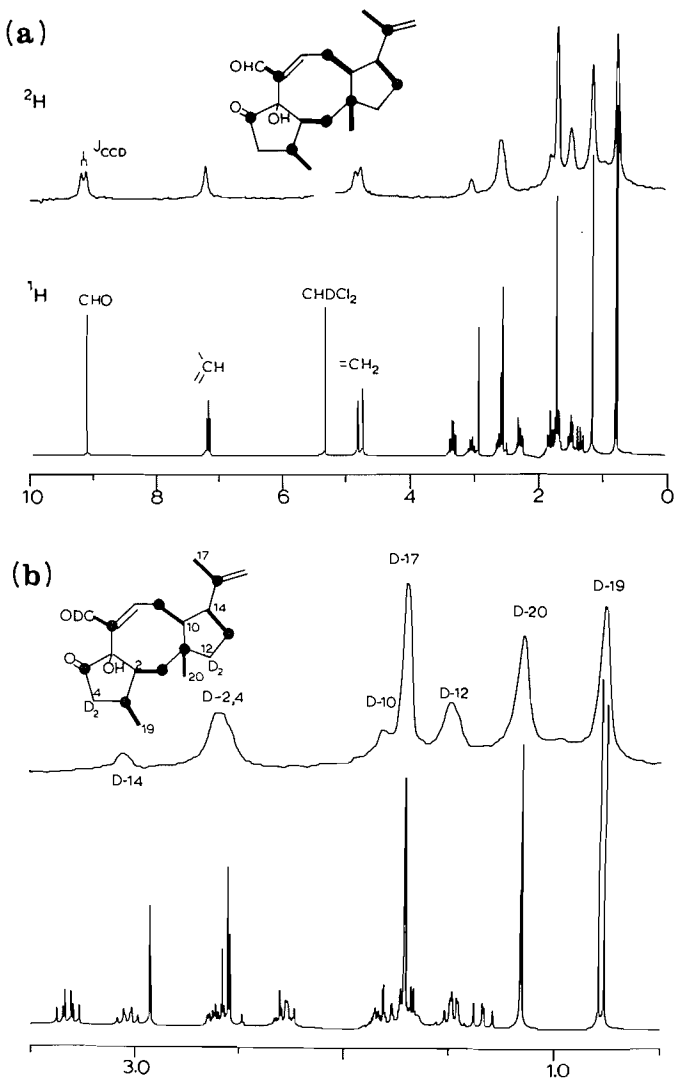

FIG. 2. The ^{2}Hmr spectra of **1**-^2H_x,$^{13}C_y$, arising from [2,2,2-$^2H_3$, 1-$^{13}C_1$]acetate incorporation, shown with the ^{1}H spectra of natural **1**: (a) full spectra, δ 0–10; (b) high field region, δ 0.5–3.5. In the structural formula dark circles indicate enriched carbons while bold bonds denote intact ^2H_x-C-^{13}C units.

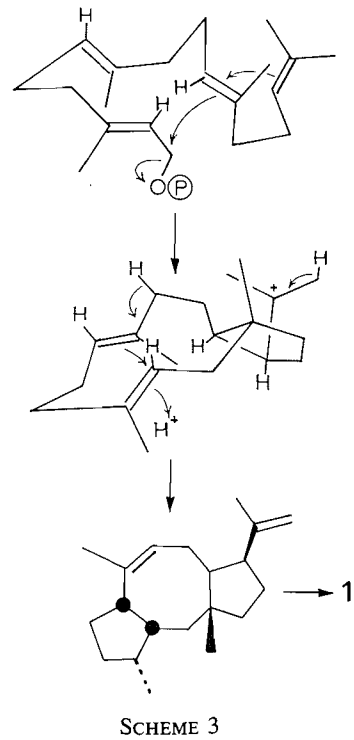

SCHEME 3

While the pathway outlined in Scheme 2 represents the cyclization of *cis*-2-geranylfarnesyl pyrophosphate that is required to generate the observed stereochemistry in ophiobolin A and B, it has been established that the *trans* isomer is efficiently utilized in incorporation experiments. However, the precise stage at which isomerization occurs is not known. It is to be noted that ophiobolins **8**–**10** were isolated from three different organisms and that the stereochemistry of each is different. The stereochemistry of **1** also differs from that of each of these compounds. The α configuration of the 3-methyl group in **1** is opposite to that in the classical ophiobolins A–F and may imply a variation in the biosynthetic pathway. Cyclization of all *trans*-geranylgeranyl pyrophosphate can be envisaged to lead to the observed stereochemistry as shown in Scheme 3. Other variations of this pathway may be involved in the sequences leading to ophiobolins G (**9**) and H, ceroplastol (**10**), and its

Can. J. Chem. Downloaded from www.nrcresearchpress.com by 93.93.197.157 on 09/07/12
For personal use only.

derivatives, since these differ fundamentally in stereochemistry but their biosyntheses have not been investigated.

Although an origin of traversianal from geranylgeranyl pyrophosphate seems most probable, it is not possible to discount at this stage its derivation from a sesterterpene by scission of the extended side chain. The only terpenes previously reported from *Cercospora* spp. appear to be abscisic acid and related compounds from *C. rosicola* (20) and *C. cruenta* (21). The most frequently reported metabolites of *Cercospora* spp. are the polyketide pigments, cercosporin and dothistromin and their derivatives (22, 23), but none of these was detected in our experiments.

Experimental

General purpose solvents were redistilled before use and evaporations were done at the reduced pressure of a water aspirator. Precoated plates of silica gel (Macherey–Nagel Polygram Sil G/UV_{254}, 0.25 mm) were employed for thin-layer chromatography (tlc). Melting points were determined on a Kofler hot stage and are uncorrected. Optical rotations were measured with a Perkin–Elmer 241 photoelectric polarimeter. Shimadzu UV 240 and Pye Unicam PU9516 instruments were used to record uv and ir spectra, respectively. Mass spectra were determined on a Varian MAT 311A system.

The nmr spectra were obtained with a Varian XL-300 system. Although initially some selective decoupling experiments were done to aid analysis, all of the coupling interactions were identified by homonuclear correlation using the HOMCOR pulse sequence of the XL-300 software. The correlated spectrum was obtained using a 1024 × 512 data point matrix transforming 1024 points in both domains with a spectral width of 2068 Hz in both domains. A series of nOe difference spectra were recorded with a spectral width of 2200 Hz, 90° pulses, acquisition time of 2.2 s, and a 20% duty cycle. A total of 24 16-transient blocks, each with four steady-state pulse cycles, was collected at 10 irradiation frequencies, one of which was 5000 Hz off-resonance. Subtraction of the latter free-induction decay (fid) from each of the nine fids containing a saturated absorption before 16K transformation gave the required difference spectra. The ^2H and ^{13}C spectra were obtained at 46.1 and 75.4 MHz, respectively, and the protonation level for each carbon signal was determined by recording the APT spectrum. Specific assignments of the protonated carbon signals were obtained by heteronuclear correlation with the proton spectrum using the HETCOR sequence of the XL software. The ^{13}C–^1H correlation spectrum utilized a 2048 × 128 data matrix with a 14-kHz spectral width for $^{13}C_x$ and a 2.1-kHz width for ^1H transforming 2048 and 512 points, respectively. Assignments for the fully substituted carbons were confirmed from their ^{13}C satellites in the spectrum of **1**-^{13}C isolated from the incorporation experiment with [1,2-$^{13}C_2$]acetate. Additional information on the carbon–carbon connectivities was obtained from ^{13}C–^{13}C correlation and double quantum coherence spectra of this enriched sample. Two ^{13}C COSY experiments utilized the HOMCOR sequence with a 1024 × 256 data point matrix transforming 1024 points in each frequency domain and spectral widths of 16 and 5 kHz in both domains. The 2D-INADEQUATE spectrum was recorded using the CCC2D sequence of the XL software with a 2048 × 128 data point matrix transforming 2048 and 512 points, respectively, with 16-kHz spectral widths in both domains.

The microanalysis was carried out by Guelph Chemical Laboratories Ltd., Guelph, Ont. Labelled sodium acetate precursors for the incorporation experiments were obtained from MSD Isotopes, a division of Merck Frosst Canada Inc., Montreal, P.Q.

Fungal cultures, isolated in 1985 from naturally infected *Trigonella foenum-graecum* L. as described previously (2), were routinely maintained on potato-dextrose agar (PDA) slants kept at room temperature in the dark. Operations on viable fungal material were conducted in a class II, type A biohazard cabinet, employing appropriate aseptic techniques.

Isolation of natural traversianal from PDA cultures

Fragments of mycelium from PDA slants were used to inoculate liquid potato-dextrose medium (24) (40-mL portions in 250-mL Delong flasks) and a mycelial suspension, prepared by homogenizing the contents of three such flasks after 21 days' growth at room temperature in the dark, was then used to inoculate PDA contained in 300 Petri dishes (disposable type, Canlab D2001 L, 10 cm diam; 20 mL/dish). After 15 days' incubation in the dark at room temperature (ca. 25°C), the contents of the dishes were extracted by steeping in MeOH/EtOAc (1:1, 5 L) for several hours. The extract was decanted and the extraction repeated twice with fresh solvent. The combined extracts were strained through cheesecloth, concentrated until mainly aqueous, and extracted 3 times with equal volumes of EtOAc; each extract was washed with the same small portion of water. The residue (945 mg) obtained on evaporation of the combined extracts crystallized from a small volume of EtOAc to give practically pure traversianal (144 mg, mp 228°C). Chromatography of the mother liquors over SiO_2 (Camag DFO, 750 g) with light petroleum ether/EtOAc (1:1, 25-mL fractions) gave another 69 mg of crystalline traversianal (fractions 47–61). In another run, with a 21-day incubation period, a yield of 303 mg of crude traversianal was obtained by crystallization of the extract from 120 Petri dish cultures, together with another 63 mg by chromatography of the mother liquors. Pure traversianal, mp 236–237°C, was obtained by a single recrystallization of the crude product from hot MeOH, but only in low yield. Because of apparent partial decomposition of the material in the MeOH mother liquors, subsequent specimens of traversianal, mp 234–235°C, were obtained by recrystallization from C_6H_6 or EtOAc/CH_2Cl_2; $[\alpha]_D^{24}$ −248 (*c* 1, CH_2Cl_2);uv (EtOH): 234 nm (ε 13 000); ir ($CHCl_3$): 3530 (br), 3075 (w), 3030 (w), 2950, 2925, 2880–2720 (w), 1740 (s), 1678 (s), 1620, 1046, 1032, 893 cm^{-1}; ^1H and ^{13}Cmr: see Table 1; ms *m/e*: 316 (M^+), 301 (M − CH_3), 298 (M − H_2O), 287, 280, 270, 255, 229, 227, 216, 215, 213, 211, 201, 200, 199, 187, 185, 173, 159, 147, 145 (100%). *Exact Mass* calcd. for $C_{20}H_{28}O_3$:316.2038; found: 316.2032. *Anal.* calcd. for $C_{20}H_{28}O_3$: C 75.90, H 8.92, O 15.18; found: C 76.13, H 9.11, O 15.50.

Isolation of labelled traversianal from liquid cultures amended with precursors

Cultures were grown at room temperature in the dark in 1-L Roux bottles, each containing 100 mL potato-dextrose medium (24), which was inoculated with a mycelial suspension of the fungus as described above. In preliminary experiments, individual bottles from a batch of cultures were harvested by filtration on days 4, 7, 11, 14, 16, and 18. Equal aliquots of EtOAc extracts of the filtrates were compared visually by tlc (MeOH–$CHCl_3$, 2:98). Traversianal (red color to vanillin, 0.5% in 60% aqueous phosphoric acid, *Rf* 0.37) was first detected on day 11 with spots reaching maximum intensity on day 16.

(*a*) Each of 15 Roux bottle cultures was treated with 5.0 mL of sterile 0.0408 M sodium [1,2-$^{13}C_2$]acetate (90 at.% ^{13}C) on day 10 and again on day 13, after inoculation. The cultures were filtered on day 16, yielding 106 mg total product on EtOAc extraction. Repeated recrystallization of the crude product from C_6H_6 gave only 5 mg of traversianal-$^{13}C_x$, mp 226–228°C, but another 23 mg, mp 230–232°C after one recrystallization, was obtained by chromatography of the combined mother liquors over SiO_2 (50 g) with 2% MeOH in $CHCl_3$.

(*b*) In an otherwise entirely analogous experiment, 20 cultures were amended with 0.05 M sodium [2,2,2-$^2H_3$, 2-$^{13}C_1$]acetate (98 at.% ^2H, 90 at.% ^{13}C) on days 11 and 13, then harvested on day 17. Direct crystallization and recrystallization of the crude product (54 mg) provided traversianal-^2H_x, $^{13}C_y$, mp 222–225°C, 7 mg, sufficiently pure for spectroscopic examination.

(*c*) Another batch of 20 cultures, amended with 0.05 M sodium [2,2,2-$^2H_3$, 1-$^{13}C_1$]acetate (98 at.% ^2H, 90 at.% ^{13}C) exactly as in (*b*), furnished 77 mg total extract from which 8 mg of traversianal-^2H_x, $^{13}C_y$, mp 222–225°C, was isolated by crystallization.

Acknowledgements

We wish to acknowledge the financial support of the Natural Sciences and Engineering Research Council of Canada and the

Can. J. Chem. Downloaded from www.nrcresearchpress.com by 93.93.197.157 on 09/07/12
For personal use only.

excellent technical assistance of V. M. Richardson and S. Wilson.

1. A. STOESSL, J. B. STOTHERS, and R. C. ZIMMER. J. Chem. Soc. Chem. Commun. 508 (1987).
2. R. C. ZIMMER. Can. Plant Dis. Surv. **64**, 33 (1984).
3. A. BALLIO. *In* Toxins in plant disease. *Edited by* R. D. Durbin. Academic Press, New York. 1981. pp. 395–441.
4. A. STOESSL. *In* Toxins in plant disease. *Edited by* R. D. Durbin. Academic Press, New York. 1981. pp. 109–217.
5. H. G. CUTLER. *In* Bioregulators for pest control. *Edited by* P. A. Hedin. ACS Symp. Ser. No. 276. American Chemical Society, Washington, D.C. 1985. pp. 455–468.
6. J. M. KIM, S. B. HYEON, A. ISOGAI, and A. SUZUKI. Agric. Biol. Chem. **48**, 803 (1984).
7. H. G. CUTLER, F. G. CRUMLEY, R. H. COX, J. P. SPRINGER, R. F. ARRENDALE, R. J. COLE, and P. D. COLE. J. Agric. Food Chem. **32**, 778 (1984).
8. F. SUGAWARA, G. STROBEL, R. N. STRANGE, J. N. SIEDOW, G. D. VAN DUYNE, and J. CLARDY. Proc. Natl. Acad. Sci. U.S.A. **84**, 3081 (1987).
9. A. BAX, R. FREEMAN, T. A. FRENKIEL, and M. H. LEVITT. J. Magn. Reson. **43**, 478 (1981).
10. A. BALLIO, M. BRUFANI, C. G. CASINOVI, S. CERRINI, W. FEDELI, R. PELLICCIARI, B. SANTURBANO, and A. VACIAGO. Experientia, **24**, 631 (1968).
11. T. SASSA, A. TAKAHAMA, and T. SHINDO. Agric. Biol. Chem. **39**, 1729 (1975).
12. T. HASHIMOTO, M. TORI, Z. TAIRA, and Y. ASAKAWA. Tetrahedron Lett. **26**, 6473 (1985).
13. S. HUNECK, G. BAXTER, A. F. CAMERON, J. D. CONNOLLY, and D. S. RYCROFT. Tetrahedron Lett. **24**, 3787 (1983).
14. J. I. OKOGUN, A. A. ADESOMOJU, G. A. ADESIDA, H. J. LINDNER, and G. HABERMEHL. Z. Naturforsch. C: Biosci. **37C**, 558 (1982); A. A. ADESOMOJU, J. I. OKOGUN, M. P. CAVA, and P. J. CARROLL. Phytochemistry, **22**, 2535 (1983).
15. S. NOZOE, M. MORISAKI, K. TSUDA, Y. IITAKA, N. TAKAHASHI, S. TAMURA, K. ISHIBASHI, and M. SHIRASAKA. J. Am. Chem. Soc. **87**, 4968 (1965); L. CANONICA, A. FIECCHI, M. GALLI KIENLE, and A. SCALA. Tetrahedron Lett. 1329 (1966).
16. Y. IITAKA, I. WATANABE, I. T. HARRISON, and S. HARRISON. J. Am. Chem. Soc. **90**, 1092 (1968); T. RIOS and F. G. GOMEZ. Tetrahedron Lett. 2929 (1969).
17. K. D. BARROW, R. B. JONES, P. W. PEMBERTON, and L. PHILLIPS. J. Chem. Soc. Perkin Trans. 1, 1405 (1975); A. BANERJI, R. HUNTER, G. MELLOWS, K. Y. SIM, and D. H. R. BARTON. J. Chem. Soc. Chem. Commun. 843 (1978); G. RANDAZZO, A. EVIDENTE, R. CAPASSO, F. COLANTUONI, L. TUTTOBELLO, and A. BALLIO. Gazz. Chim. Ital. **109**, 101 (1979).
18. S. NOZOE and M. MORISAKI. J. Chem. Soc. Chem. Commun. 1319 (1969); L. CANONICA. *In* Phytotoxins in plant diseases. *Edited by* R. K. S. Wood, A. Ballio, and A. Graniti. Academic Press, New York. 1972. pp. 157–173.
19. A. STOESSL and J. B. STOTHERS. Can. J. Chem. **61**, 1766 (1983).
20. S. J. NEILL, R. HORGAN, D. C. WALTON, and C. A. M. MERCER. Phytochemistry, **26**, 2515 (1987).
21. T. ORITANI, M. NIITSU, T. KATO, and K. YAMASHITA. Agric. Biol. Chem. **49**, 2819 (1985).
22. G. ASSANTE, R. LOCCI, L. CAMARDA, L. MERLINI, and G. NASINI. Phytochemistry, **16**, 243 (1977).
23. F. J. LYNCH and M. J. GEOGHEGAN. Trans. Br. Mycol. Soc. **69**, 496 (1977).
24. A. STOESSL and J. B. STOTHERS. Z. Naturforsch. C: Biosci. **41C**, 677 (1986).
25. M. T. M. CLEMENTS, R. E. KLINCK, S. PEIRIS, A. J. RAGAUSKAS, and J. B. STOTHERS. Can. J. Chem. **66**, 454 (1988).
26. A. STOESSL and J. B. STOTHERS. Annu. Proc. Phytochem. Soc. Eur. **27**, 1 (1987).

Can. J. Chem. Downloaded from www.nrcresearchpress.com by 93.93.197.157 on 09/07/12
For personal use only.

Structural studies of organoboron compounds. XXIX.[1] 6,6-Diethyl-2,2-diphenyl-1,3-dioxa-6-azonia-2-boratacyclooctane monohydrate

WOLFGANG KLIEGEL

Institut für Pharmazeutische Chemie, der Technischen Universität Braunschweig, 3300 Braunschweig, Beethovenstraße 55, Bundesrepublik Deutschland

AND

STEVEN J. RETTIG AND JAMES TROTTER

Department of Chemistry, University of British Columbia, 2036 Main Mall, Vancouver, B.C., Canada V6T 1Y6

Received June 30, 1987

WOLFGANG KLIEGEL, STEVEN J. RETTIG, and JAMES TROTTER. Can. J. Chem. **66**, 1091 (1988).

Details of the preparation and structure of the title compound are given. Crystals of 6,6-diethyl-2,2-diphenyl-1,3-dioxa-6-azonia-2-boratacyclooctane monohydrate are orthorhombic, $a = 7.0322(2)$, $b = 16.3505(7)$, $c = 16.8164(4)$ Å, $Z = 4$, space group $P2_12_12_1$. The structure was solved by direct methods and was refined by full-matrix least-squares procedures to $R = 0.045$ and $R_w = 0.050$ for 2013 reflections with $I \geq 3\sigma(I)$. The monocyclic eight-membered *B*, *N*-betaine is the first to be structurally characterized. The eight-membered chelate ring has a conformation intermediate between the S_4 and *boat–boat* forms which is probably stabilized by transannular C—H···O interactions. The average libration-corrected O—B and B—C bond lengths of 1.500 and 1.639 Å are, respectively, the shortest and longest yet observed for an *O*,*O*-chelate of diphenylboron.

WOLFGANG KLIEGEL, STEVEN J. RETTIG et JAMES TROTTER. Can. J. Chem. **66**, 1091 (1988).

On rapporte les détails de la préparation et de la détermination de la structure du composé mentionné dans le titre. Les cristaux du monohydrate du diéthyl-6,6 diphényl-2,2 dioxa-1,3 azonia-6 borata-2 cyclooctane sont orthorhombiques avec $a = 7{,}0322(2)$, $b = 16{,}3505(7)$ et $c = 16{,}8164(4)$ Å, $Z = 4$ et groupe d'espace $P2_12_12_1$. On a résolu la structure par des méthodes directes et on l'a affinée par la méthode des moindres carrés (matrice entière) jusqu'à des valeurs de $R = 0{,}045$ et $R_w = 0{,}050$ pour 2013 réflexions avec $I \geq 3\sigma(I)$. La *B*,*N*-bétaïne monocyclique à huit chaînons est la première à avoir été caractérisée du point de vue de sa structure. Le chélate cyclique à huit chaîons possède une conformation qui est intermédiaire entre les formes S_4 et *bateau–bateau* et celle-ci est probablement stabilisé par des interactions transannulaires C—H···O. Les longueurs des liaisons O—B et B—C corrigées pour la libration sont respectivement 1,500 et 1,639 Å et ce sont respectivement les liaisons la plus courte et la plus longue qui aient été observées pour un chélate-*O*,*O* du diphénylbore.

[Traduit par la revue]

Introduction

1,3-Dioxa-6-aza-2-boracyclooctanes **1** are known to undergo intramolecular (transannular) N→B coordination to give very stable bicyclo[3.3.0]octane ring systems **2**, confirmed by chemical and physical investigations (1–6). Generally the extent of the N→B interaction depends on the nitrogen and boron substitution as well as on the conformational conditions. The size and the electronic effects of the substituents markedly influence the magnitude of N—B coordination. In accordance with these findings, replacement of the ring nitrogen atom by oxygen or sulphur led to fairly unstable non-crystalline compounds without any detectable transannular bonding (7).

A cyclooctane system without a transannular N→B interaction should be realized by quaternization of both the tertiary amine and boronate groups of **1**. Direct *N*-alkylation and *B*-arylation of the known (8) compound **1/2** seemed disadvantageous, so the synthesis of **3** was carried out by *N*-alkylation of 2-diethylaminoethanol **6** via the addition of oxirane (ethylene oxide) and subsequent trapping of the zwitterionic intermediate **4** as the diphenylboron chelate **3**. The symmetrical cyclic *B*,*N*-betaine structure **3** has been postulated in a preliminary report (9) on the basis of ^{1}H nmr data which suggest magnetically equivalent ethylene moieties within the ring skeleton, consistent with the formation of **3** by insertion of oxirane into the N—B bond of compound **5** (9).[2] Compound **3** is structurally related to the cyclic six-membered *B*,*N*-betaines **7** (12) and **8** (13). Eight-membered ring systems like **3** were also formulated in patents on polymeric (14) and monomeric (15) boric acid esters of aminoalcohols, but to our knowledge no structural proof has yet been presented.

High quality crystals of **3** can be grown from ethanol but ir and ^{1}H nmr data as well as elemental analyses indicate that this compound exists as a monohydrate. This could result from alternative symmetric structures with hydrogen-bonded (**A**) or covalently bound (**B** and **C**) water. Asymmetric structures such as **D** (from a possible *O*-alkylation of the diethylaminoethanol **1** followed by chelate formation with *N*-(hydroxyethyloxyethyl)diethylamine acting as the ligand), **E** (from hydrolytic ring opening of **3**), or **F** (from chelate formation with ethylene glycol as the ligand) would be unlikely in view of the ^{1}H nmr data. Conductivity measurements and osmometric estimations in DMF solution were unclear. An X-ray crystallographic analysis was undertaken to provide a definitive structural assignment.

Experimental

*6,6-Diethyl-2,2-diphenyl-1,3-dioxa-6-azonia-2-boratacyclooctane monohydrate (**3**·H_2O)*

Methods (a) and (b)

Cooled oxirane (ethylene oxide, 0.5 g, 11 mmol) is added to *N*,*N*-diethylaminoethanol (1.17 g, 10 mmol) in 10 mL ethanol. After dissolving (*a*) oxybisdiphenylborane (1.73 g, 5 mmol) or (*b*) triphenylboron (2.42 g, 10 mmol), the solution is kept at room temperature for 1 h. Crystallization of the product occurs spontaneously at room temperature or upon cooling.

Method (c)

N-(2-diphenylboryloxyethyl)diethylamine dihydrate (**5**·2H_2O, 3.17

[1]Part XXVIII: ref. 12.

[2]Compound **5** has been reported as the diphenylborinic acid ester of diethylaminoethanol (10) and probably contains an intramolecular N—B bond as shown for the *N*-unsubstituted derivative (11). Different samples of **5**, prepared by the methods in ref. 10, contain varying amounts of water.

Can. J. Chem. Downloaded from www.nrcresearchpress.com by 93.93.197.157 on 09/07/12
For personal use only.

Can. J. Chem. Downloaded from www.nrcresearchpress.com by 93.93.197.157 on 09/07/12
For personal use only.

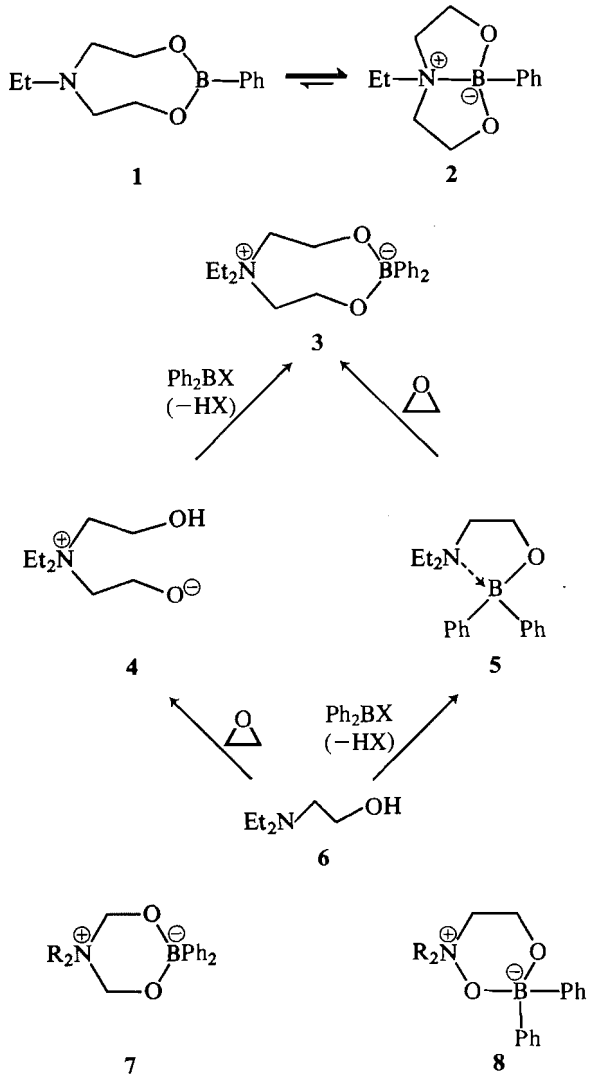

g, 10 mmol) in 15 mL ethanol is mixed with cooled oxirane (0.7 g, 15 mmol) and kept at room temperature for 4 days. Crystallization begins after cooling the reaction mixture.

Yields: (*a*) 41%, (*b*) 40%, (*c*) 60%. Mp (decomp.) 203–205°C (from ethanol). Lit.[3] 203°C. *Anal.* calcd. for **3**·H_2O: C 69.98, H 8.81, B 3.15, N 4.08. Found: C 69.38, H 8.98, B 3.42, N 4.13. The substance gives a blue color reaction with diphenylcarbazone in methanol, indicating the presence of the diphenylboron moiety (16). Ir (KBr): 3360 cm^{-1} (br, associated H_2O). ^1H nmr (90 MHz, d_6-DMSO/TMS): δ(ppm) = 1.12 (t, J = 7 Hz, $2CH_3$) 3.2–3.8 (m, $6CH_2$, H_2O), 6.7–7.4 (m, BPh_2); (60 MHz, $CDCl_3/F_3CCOOH$/TMS): δ(ppm) = 1.33 (t, J = 7 Hz, $2CH_3$), 3.35 (q, J = 7 Hz, $2CH_2$), 3.60 (m, $2CH_2$), 4.65 (m, $2CH_2$), 7.2–7.7 (m, BPh_2), H_2O associated with CF_3COOH; (60 MHz, d_6-acetone/TMS at 70°C): δ(ppm) = 1.29 (t, J = 7 Hz, $2CH_3$), 2.72 (s, $2CH_2$), 3.57 (q, J = 7 Hz, $2CH_2$), 3.76 (s, $2CH_2$), 6.7–7.7 (m, BPh_2), H_2O not detected. ^{11}B nmr (32.1 MHz, DMSO/-Et_2OBF_3): δ = 4.9 ppm. Crystals suitable for X-ray analysis were obtained by recrystallization from ethanol.

X-ray crystallographic analysis

A crystal bounded by the six faces (followed by the distances in mm between parallel faces): ±(0 −1 1), 0.46, ±(1 0 1), 0.40, {0 1 0}, 0.59, was mounted in a general orientation. Unit-cell parameters were refined by least-squares on 2 sin θ/λ values for 25 reflections (2θ = 76–96°) measured on a diffractometer with Cu-$K\alpha$ radiation ($\lambda(K\alpha_1)$ = 1.540562, $\lambda(K\alpha_2)$ = 1.544930 Å). Crystal data at 22°C are as follows:

$C_{20}H_{28}BNO_2 \cdot H_2O$ fw = 343.3

Orthorhombic, a = 7.0322(2), b = 16.3505(7), c = 16.8164(4) Å, V = 1933.5(1) Å^3, Z = 4, ρ_c = 1.179 Mg m^{-3}, F(000) = 744, μ(Cu-$K\alpha$) = 5.76 cm^{-1}. Absent reflections: $h00$, $h \neq 2n$, $0k0$, $k \neq 2n$, and $00l$, $l \neq 2n$, uniquely indicate the space group $P2_12_12_1$ (D_2^4, No. 19).

Intensities were measured with nickel-filtered Cu-$K\alpha$ radiation on an Enraf-Nonius CAD4-F diffractometer. An ω–2θ scan at 1.2–10.0° min^{-1} over a range of (0.90 + 0.14 tan θ) degrees in ω (extended by 25% on both sides for background measurement) was employed. Data were measured to 2θ = 150°. The intensities of three check reflections, measured every 3600 s throughout the data collection, remained constant to within 4%. After data reduction,[4] an absorption correction was applied using the Gaussian integration method (17, 18). Transmission factors ranged from 0.692 to 0.818 for 96 integration points. Of the 2284 independent reflections measured, 2013 (88.1%) had intensities greater than or equal to 3σ(I) above background where $\sigma^2(I) = S +$

TABLE 1. Final positional (fractional × 10^4) and isotropic thermal parameters (U × 10^3 Å^2) with estimated standard deviations in parentheses*

Atom	x	y	z	U_{eq}
O(1)	7416(3)	2175(1)	7154(1)	46
O(2)	4206(2)	2265(1)	6591(1)	41
O(3)	10477(4)	2058(2)	6119(1)	77
N	6218(4)	3810(2)	6285(1)	54
C(1)	4847(5)	2456(2)	5819(2)	48
C(2)	6436(4)	3072(2)	5765(1)	48
C(3)	6219(5)	3610(2)	7170(2)	49
C(4)	7627(4)	2972(2)	7453(2)	51
C(5)[1]	4650(14)	4272(9)	6078(9)	53
C(5′)[2]	3975(17)	4182(11)	6183(10)	55
C(6)[1]	4453(14)	4546(7)	5229(7)	67
C(6′)[2]	3555(17)	4433(8)	5317(8)	65
C(7)[3]	8212(10)	4218(4)	6080(3)	55
C(7′)[4]	7227(13)	4631(5)	6109(5)	54
C(8)[3]	8514(12)	5013(4)	6522(5)	80
C(8′)[4]	9313(16)	4543(8)	6288(8)	83
C(9)	4514(4)	1806(2)	8010(1)	44
C(10)	2633(5)	2019(2)	8151(2)	61
C(11)	1857(6)	2053(3)	8911(2)	73
C(12)	2957(7)	1867(2)	9556(2)	71
C(13)	4832(6)	1651(2)	9447(2)	62
C(14)	5592(5)	1620(2)	8680(2)	53
C(15)	5779(5)	863(2)	6787(2)	48
C(16)	4335(6)	479(2)	6358(2)	59
C(17)	4518(8)	−306(2)	6046(2)	76
C(18)	6181(9)	−736(2)	6166(2)	83
C(19)	7615(8)	−388(2)	6589(3)	82
C(20)	7440(6)	412(2)	6898(2)	64
B	5489(4)	1792(2)	7130(2)	41

*Superscripts refer to site occupancy factors of 0.52, 0.48, 0.59, and 0.41, respectively.

[3]The melting point of this compound had been mistakenly interchanged with that of another compound in a table in ref. 9.

[4]The computer programs used include locally written programs for data processing and locally modified versions of the following: MULTAN 80, multisolution program by P. Main, S. J. Fiske, S. E. Hull, L. Lessinger, G. Germain, J. P. Declercq, and M. M. Woolfson; AGNOST, absorption corrections, by J. A. Ibers; ORFLS, full-matrix least-squares, and ORFFE, function and errors, by W. R. Busing, K. O. Martin, and H. A. Levy; FORDAP, Patterson and Fourier syntheses, by A. Zalkin; ORTEP II, illustrations, by C. K. Johnson.

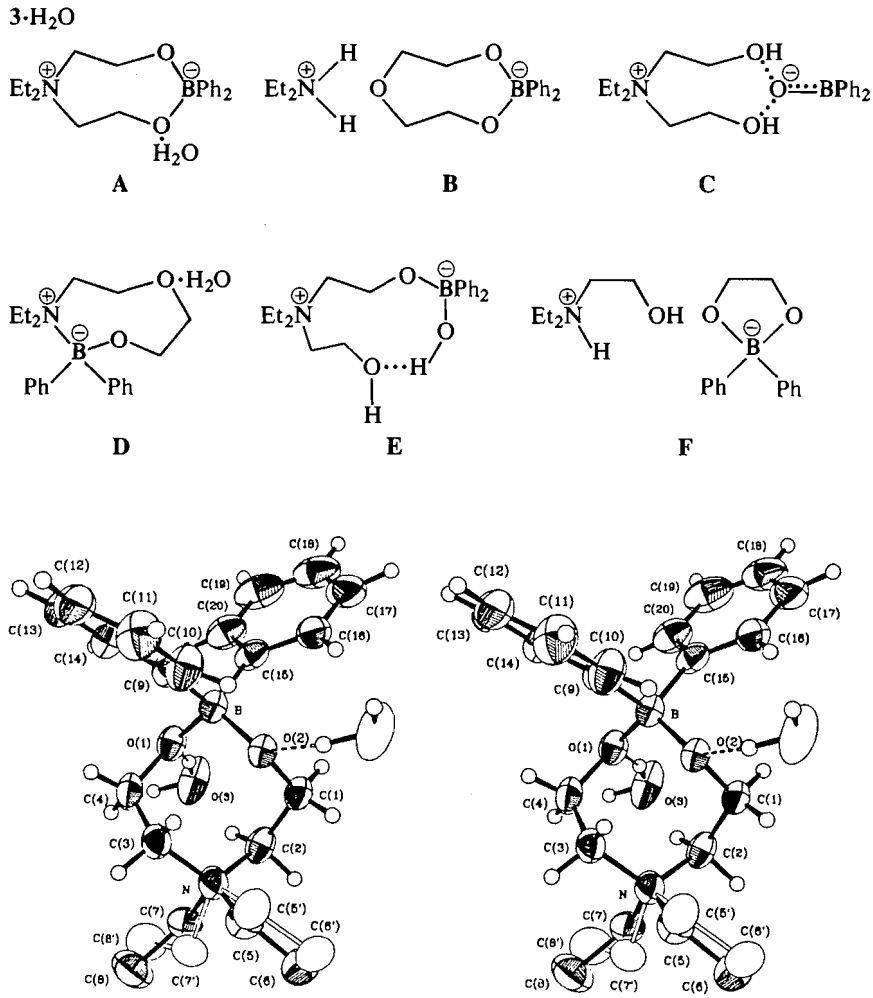

FIG. 1. Stereoscopic view 6,6-diethyl-2,2-diphenyl-1,3-dioxa-6-azonia-2-boratacyclooctane monohydrate; 50% probability thermal ellipsoids are shown for the non-hydrogen atoms. Hydrogen atoms have been assigned arbitrary thermal parameters for the sake of clarity. Broken lines indicate hydrogen bonds.

$2B + (0.04(S - B))^2$ with S = scan count and B = normalized background count.

The structure was solved by direct methods, the coordinates of the non-hydrogen atoms being determined from an E-map. After refinement of the non-hydrogen atoms with anisotropic thermal parameters, anomalous thermal parameters indicated disordering of the N-ethyl groups. A split-atom model was subsequently refined. The site occupancy factors were initially fixed at 0.5 and were subsequently adjusted to give nearly equal average thermal parameters for each group of atoms. In the final stages of refinement the occupancy factors were kept fixed. The ethyl hydrogen atoms were included as fixed atoms (staggered geometry, C—H = 0.98 Å, $U_H \propto U_{\text{bonded atom}}$) and all other hydrogen atoms were refined with isotropic thermal parameters. Scattering factors for all atoms and anomalous scattering factors for O, N, and C were taken from ref. 19. The weighting scheme $w = 1/\sigma^2(F)$, where $\sigma^2(F)$ is derived from the previously defined $\sigma^2(I)$, gave uniform average values of $w(|F_o| - |F_c|)^2$ over ranges of both $|F_o|$ and sin θ/λ and was employed in the final stages of full-matrix refinement of 343 variables. Reflections with $I < 3\sigma(I)$ were not included in the refinement. An isotropic Type I extinction correction (Thornley–Nelmes definition of mosaic anisotropy with a Lorentzian distribution) was applied (20–22). The final value of g was $6.5(2) \times 10^4$. Convergence was reached at $R = 0.045$ and $R_w = 0.050$ for 2013 reflections with $I \geq 3\sigma(I)$. The mirror-image structure was refined in parallel and rejected at the 99.5% significance level (the R and R_w ratios both = 1.006). The function minimized was $\Sigma w(|F_o| - |F_c|)^2$, $R = \Sigma||F_o| - |F_c||/\Sigma|F_o|$ and $R_w = (\Sigma w(|F_o| - |F_c|)^2/\Sigma w|F_o|^2)^{1/2}$.

On the final cycle of refinement the mean and maximum parameter shifts corresponded to 0.02 and 0.31σ, respectively. The mean error in an observation of unit weight was 1.158. The largest peak on the final difference map was 0.18 e Å^{-3}. The final positional and thermal parameters appear in Tables 1 and 5,[5] respectively. Measured and calculated structure factors have been placed in the Depository of Unpublished Data.[5]

The ellipsoids of thermal motion for the non-hydrogen atoms are shown in Fig. 1. The thermal motion has been analysed in terms of the rigid-body modes of translation, libration, and screw motion (23). The rms standard error in the temperature factors σU_{ij} (derived from the least-squares analysis) is 0.0030 Å^2. The structural subunits PhB, the eight-membered ring, and $(—CH_2CH_2)_2N(CH_2CH_3)_2$ were separately analysed (rms ΔU_{ij} = 0.0018–0.0059 Å^2). The appropriate bond distances have been corrected for libration (23, 24), using shape parameters q^2 of 0.08 for all atoms involved. Corrected bond lengths appear in Table 2 along with the uncorrected values; corrected bond angles do not differ by more than 1σ from the uncorrected values given

[5]The structure factor table, Table 5 (anisotropic thermal parameters) and other material mentioned in the text may be purchased from the Depository of Unpublished Data, CISTI, National Research Council of Canada, Ottawa, Ont., Canada K1A 0S2.

Can. J. Chem. Downloaded from www.nrcresearchpress.com by 93.93.197.157 on 09/07/12
For personal use only.

TABLE 2. Bond lengths (Å) with estimated standard deviations in parentheses

Bond	Length Uncorr.	Corr.	Bond	Length Uncorr.	Corr.
O(1)—C(4)	1.403(4)	1.410	C(7′)—C(8′)	1.504(14)	1.509
O(1)—B	1.494(3)	1.501	C(9)—C(10)	1.389(5)	1.398
O(2)—C(1)	1.409(3)	1.414	C(9)—C(14)	1.391(4)	1.399
O(2)—B	1.495(3)	1.499	C(9)—B	1.632(4)	1.635
N —C(2)	1.498(4)	1.505	C(10)—C(11)	1.390(4)	1.394
N —C(3)	1.523(3)	1.528	C(11)—C(12)	1.366(6)	1.373
N —C(5)	1.381(14)	1.385	C(12)—C(13)	1.377(6)	1.386
N —C(5′)	1.699(14)	1.706	C(13)—C(14)	1.396(4)	1.400
N —C(7)	1.591(7)	1.596	C(15)—C(16)	1.394(5)	1.403
N —C(7′)	1.546(8)	1.551	C(15)—C(20)	1.393(5)	1.402
C(1)—C(2)	1.507(4)	1.514	C(15)—B	1.638(4)	1.643
C(3)—C(4)	1.516(4)	1.521	C(16)—C(17)	1.392(4)	1.397
C(5)—C(6)	1.50(2)	1.506	C(17)—C(18)	1.380(7)	1.389
C(5′)—C(6′)	1.54(2)	1.547	C(18)—C(19)	1.359(7)	1.368
C(7)—C(8)	1.512(9)	1.517	C(19)—C(20)	1.413(5)	1.417

TABLE 3. Bond angles (deg) with estimated standard deviations in parentheses

Bond	Angle (deg)	Bonds	Angle (deg)
C(4)—O(1)—B	119.7(2)	N —C(7′)—C(8′)	109.0(8)
C(1)—O(2)—B	118.7(2)	C(10)—C(9)—C(14)	115.8(3)
C(2)—N —C(3)	113.4(2)	C(10)—C(9)—B	124.0(3)
C(2)—N —C(5)	112.0(6)	C(14)—C(9)—B	120.2(3)
C(2)—N —C(5′)	108.9(6)	C(9)—C(10)—C(11)	122.7(3)
C(2)—N —C(7)	97.0(3)	C(10)—C(11)—C(12)	119.9(4)
C(2)—N —C(7′)	122.7(4)	C(11)—C(12)—C(13)	119.5(3)
C(3)—N —C(5)	111.4(6)	C(12)—C(13)—C(14)	120.0(3)
C(3)—N —C(5′)	100.1(6)	C(9)—C(14)—C(13)	122.1(3)
C(3)—N —C(7)	107.6(3)	C(16)—C(15)—C(20)	116.2(3)
C(3)—N —C(7′)	111.9(4)	C(16)—C(15)—B	120.6(3)
C(5)—N —C(5′)	15.8(9)	C(20)—C(15)—B	123.2(3)
C(5)—N —C(7)	114.8(6)	C(15)—C(16)—C(17)	122.8(4)
C(5)—N —C(7′)	81.0(6)	C(16)—C(17)—C(18)	119.6(5)
C(5′)—N —C(7)	130.3(6)	C(17)—C(18)—C(19)	119.4(4)
C(5′)—N —C(7′)	95.5(7)	C(18)—C(19)—C(20)	121.0(4)
C(7)—N —C(7′)	35.9(3)	C(15)—C(20)—C(19)	120.9(4)
O(2)—C(1)—C(2)	116.2(2)	O(1)—B —O(2)	110.3(2)
N —C(2)—C(1)	115.3(2)	O(1)—B —C(9)	110.5(2)
N —C(3)—C(4)	117.1(3)	O(1)—B —C(15)	106.6(2)
O(1)—C(4)—C(3)	117.2(2)	O(2)—B —C(9)	106.9(2)
N —C(5)—C(6)	118.5(9)	O(2)—B —C(15)	109.9(2)
N —C(5′)—C(6′)	111.6(8)	C(9)—B —C(15)	112.6(2)
N —C(7)—C(8)	112.2(5)		

in Table 3. Intra-annular torsion angles defining the conformation of eight-membered ring are listed in Table 4. Bond lengths and angles involving hydrogen and a complete listing of torsion angles (Tables 6–8) are included as supplementary material.[5]

TABLE 4. Intra-annular torsion angles (deg) standard deviations in parentheses

Atoms	Torsion angle (deg)
C(4)—O(1)—B —O(2)	62.9(3)
C(1)—O(2)—B —O(1)	50.3(3)
B —O(2)—C(1)—C(2)	−69.4(3)
O(2)—C(1)—C(2)—N	−44.4(4)
C(3)—N —C(2)—C(1)	63.4(3)
C(2)—N —C(3)—C(4)	40.8(4)
N —C(3)—C(4)—O(1)	−63.1(4)
B —O(1)—C(4)—C(3)	−45.8(3)

Results and discussion

The crystal structure consists of molecules having the originally suggested structure **3A** (9), bridged by hydrogen-bonded water molecules (Fig. 1) to form ribbons extending along the *a*-axis [O(3)—H(O3a)···O(1) and O(3)—H(O3b)···O(2) ($1 + x$, y, z), H···O = 2.06(6) and 1.77(8) Å, O···O = 2.775(3) and 2.761(3) Å, O—H···O = 158(5) and 153(6)°, respectively). These ribbons are reinforced (C(2)—H(2a)···O(3),

Can. J. Chem. Downloaded from www.nrcresearchpress.com by 93.93.197.157 on 09/07/12
For personal use only.

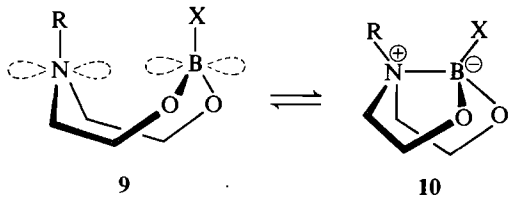

9 10

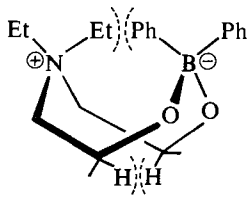

3 boat–boat (bow-stern substitution)

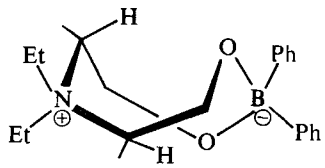

3 boat–boat (flank substitution)

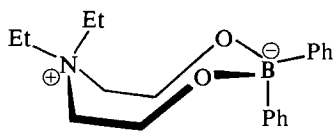

3 boat–chair

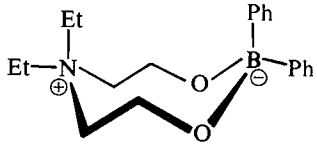

3 crown

H···O = 2.41(3) Å, C···O = 3.344(4) Å, C—H···O = 161(3)°) and cross-linked (C(2)—H(2b)···O(3) ($x - 1/2$, $1/2 - y$, $1 - z$), H···O = 2.34(3) Å, C···O = 3.247(4) Å, C—H···O = 141(2)°) by probable C—H···O hydrogen bonds. The water molecule is thus fully utilized as both a donor and an acceptor of hydrogen bonds.

Compound **3** is the first monocyclic eight-membered *B,N*-betaine to be structurally characterized. Other boracyclooctanes having trivalent boron and nitrogen atoms in the 1- and 5-positions are prone to transannular N→B coordination, forming bicyclo[3.3.0]octanes as shown for several different types of boron heterocycles (3, 25, 26). Structural stabilization, weak in eight-membered cyclic boronates with little or no transannular coordination (5, 7), is achieved in **3** by quaternization of both boron and nitrogen resulting in a zwitterionic salt structure. Dissociative and reassociative processes in solutions of cyclic boronates of bis(2-hydroxyethyl)amines (**9** ↔ **10**) have been monitored by dynamic nmr spectroscopy (5). Opening of the bicyclic structure **10** proceeds via an intermediate cyclooctane system **9** having a *boat–boat* (saddle) conformation. The *boat–boat* conformation of cyclooctane itself is one of five conformations within 2 kcal/mol of the minimum energy *boat–chair* conformation, the former being destabilized with respect to the latter primarily by short transannular contacts between inward-pointing hydrogen atoms (27, 28). In the case of **3** these inward-pointing hydrogen atoms are opposite the ring oxygen atoms and cannot cause an energetically unfavorable interaction. Weak attractive transannular C—H···O interactions (C(2)—H(2a)···O(1) and C(3)—H(3b)···O(2), H···O = 2.41(3) and 2.31(3) Å, C···O = 2.843(3) and 2.791(4) Å, C—H···O = 106(2) and 115(2)°) probably contribute to conformational stability. Both the *boat–boat* and the closely related but less symmetrical S_4 conformations have two types of ring positions: "bow/stern" (inner) and "flank" (outer). Disubstitution of a pair of opposite "bow/stern" positions is sterically unfavorable, thus the substituted N and B atoms of **3** occupy "flank" positions. The conformation actually observed for **3** is intermediate between the *boat–boat* (torsion angles of ±52.5°, bond angles of 118 and 119°) and S_4 (torsion angles alternately ±64.9° and ±37.6°, bond angles of 117 and 118°) conformations (28), but nearer to the latter (mean $\Delta\omega$ and $\Delta\theta$ = 5.1 and 2.2° relative to S_4, 9.7 and 2.7° relative to *boat–boat*). Calculations for cyclooctane show that the S_4 conformation is slightly less strained than the *boat–boat* (28). The structure of **3** provides an example of the S_4 conformation for an eight-membered ring, stabilized by the special arrangement of ring heteroatoms and substitutents. Similar situations have been reported for $[NPR_2]_4$, R = Me (29) and NMe_2 (30), and $[OSeO_2]_4$ (31) which also have S_4 conformations with the substituted atoms occupying "flank" positions.

As observed earlier for compounds of the type **7** (12), the largest deviations from "ideal" intracyclic bond angles occur at the boron and nitrogen atoms. If the eight-membered ring in **3** had an undistorted *boat–boat* conformation the molecule would possess a C_2 axis passing through the N and B atoms. For the S_4 conformation, deviation from C_2 symmetry causes a small energy difference between the "flank" position substituent sites. Although the difference is not statistically significant, the pseudo-axial B—C bond is 0.008(6) Å longer than its pseudo-equatorial counterpart. Significant differences between axial and equatorial B—C bonds have been noted for **7** (12), **8** (13), and a phosphorus analog of **7** (32). The average O—B and B—C distances[6] of 1.500 and 1.639 Å are, respectively, the shortest and longest yet observed for an *O,O*-chelate of "Ph_2B^+" (12, 33–35), indicating that the monoanion derived from **4** is among the strongest known donors for the "Ph_2B^+" cation. Relatively strong O—B binding was also observed for **7** (R = (1/2)($(CH_2)_3$) and Me) (12) where average O—B = 1.510 and 1.518 Å and average B—C = 1.625 and 1.623 Å. The sum of bond lengths involving the boron atoms in *O,O*-chelates of diphenylboron has been found to be 6.331(9) Å for compounds containing five-membered chelate rings (33, 34) and is essentially constant for larger rings; 6.277(9) Å (12, 33), 6.276 Å (35), and 6.278 Å for six-, seven-, and eight-membered rings, respectively.

Unlike the short intraannular C—O distances (average 1.376 Å) observed in compounds **7** (12), the values in **3** (1.410(3) and 1.414(3) Å) are close to the normal C—O single bond distance of 1.43 Å and are in good agreement with those observed in other boron chelates with hydroxyalkyl ligands (3, 11, 13, 25, 36). Some bond lengths and angles involving the disordered *N*-ethyl groups deviate significantly from the expected values. This is probably a result of imperfect modelling of the disorder and is commonly observed in such situations. Both phenyl rings are planar within experimental error and show normal substituent-induced geometric distortions (37).

Acknowledgments

We thank the Natural Sciences and Engineering Research Council of Canada and the Fonds der Chemischen Industrie, Frankfurt am Main, for financial support, and the University of British Columbia Computing Centre for assistance. We are also grateful to Prof. H. Nöth, University of Munich, for running the ^{11}B nmr spectra.

1. H. K. ZIMMERMAN. Adv. Chem. Ser. **42**, 23 (1964).
2. G. B. BUTLER and G. L. STATTON. J. Am. Chem. Soc. **86**, 518 (1964).

[6]Libration corrected bond lengths (esd's assumed equal to those of the uncorrected values) are employed in the discussion and are compared with similarly treated (23) distances unless otherwise stated.

Can. J. Chem. Downloaded from www.nrcresearchpress.com by 93.93.197.157 on 09/07/12
For personal use only.

3. S. J. RETTIG and J. TROTTER. Can. J. Chem. **53**, 1393 (1975).
4. R. CSUK, H. HÖNIG, and C. ROMANIN. Monatsh. Chem. **113**, 1025 (1982).
5. R. CONTRERAS, C. GARCIA, T. MANCILLA, and B. WRACKMEYER. J. Organomet. Chem. **246**, 213 (1983).
6. R. CSUK, N. MÜLLER, and H. STERK. Z. Naturforsch. **40**b, 987 (1985).
7. U. W. GERWARTH and W. WEBER. Syn. React. Inorg. Metal-Org. Chem. **5**, 175 (1975).
8. H. WEIDMANN and H. K. ZIMMERMAN. Liebigs Ann. Chem. **619**, 28 (1958).
9. W. KLIEGEL. Angew. Chem. **80**, 614 (1968).
10. B. SERAFINOWA, B. USTUPSKA-STEFANIAK, and M. MAKOSZA. Roczn. Chem. **35**, 723 (1961).
11. S. J. RETTIG and J. TROTTER. Can. J. Chem. **51**, 1288 (1973).
12. W. KLIEGEL, S. J. RETTIG, and J. TROTTER. Can. J. Chem. **66**, 377 (1988).
13. W. KLIEGEL, S. SARGE, H. K. CAMMANGA, S. J. RETTIG, and J. TROTTER. *In* Reactivity of solids. *Edited by* P. Barret and L. C. Dufor. Mater. Sci. Monogr. **28**, 725 (1985). Full paper in preparation.
14. B. RUDNER and M. S. MOORES. USA Pat. 2976307 (1961); Chem. Abstr. **56**, 321 (1962).
15. T. WEIL. USA Pat. 3256310 (1966); Chem. Zentralbl. **10**, 2106 (1969).
16. R. NEU. Z. Anal. Chem. **176**, 334 (1960).
17. P. COPPENS, L. LEISEROWITZ, and D. RABINOVICH. Acta Crystallogr. **18**, 1035 (1965).
18. W. R. BUSING and H. A. LEVY. Acta Crystallogr. **22**, 457 (1967).
19. International tables for X-ray crystallography. Vol. IV. Kynoch press, Birmingham. 1974. pp. 99–102, 149.
20. P. J. BECKER and P. COPPENS. Acta Crystallogr. Sect. A, **30**, 129 (1974); **30**, 148 (1974); **31**, 417 (1975).
21. P. COPPENS and W. C. HAMILTON. Acta Crystallogr. Sect. A, **26**, 71 (1970).
22. F. R. THORNLEY and R. J. NELMES. Acta Crystallogr. Sect. A, **30**, 748 (1974).
23. V. SCHOMAKER and K. N. TRUEBLOOD. Acta Crystallogr. Sect. B, **24**, 63 (1968).
24. D. W. J. CRUICKSHANK. Acta Crystallogr. **9**, 747 (1956); **9**, 754 (1956); **14**, 896 (1961).
25. S. J. RETTIG, J. TROTTER, W. KLIEGEL, and H. BECKER. Can. J. Chem. **54**, 3142 (1976).
26. W. KLIEGEL, S. J. RETTIG, and J. TROTTER. Can. J. Chem. **62**, 515 (1984).
27. (*a*) J. DALE. Stereochemie and Konformationsanalyse. Verlag Chemie. Weinheim. 1978; (*b*) W. DÖPKE. Dynamische Aspekte der Stereochemie organischer Verbindungen. Akademie-Verlag. Berlin. 1979; (*c*) F. G. RIDDELL. Heterocyclen. Thieme Verlag. Stuttgart. 1982.
28. J. B. HENDRICKSON. J. Am. Chem. Soc. **89**, 7036 (1967); **89**, 7043 (1967); **89**, 7047 (1967).
29. M. W. DOUGILL. J. Chem. Soc. 5471 (1961).
30. G. J. BULLEN. J. Chem. Soc. 3193 (1962).
31. F. C. MIJLHOFF. Acta Crystallogr. **18**, 795 (1965).
32. B. A. ARBUZOV, O. A. ERASTOV, G. N. NIKONOV, A. A. ESPENBETOV, A. I. YANOVSKII, and YU. T. STRUCHKOV. Izv. Akad. Nauk SSSR, Ser. Khim. 1545 (1981); Bull. Acad. Sci. USSR, Div. Chem. Sci. 1243 (1981).
33. C. ORVIG, S. J. RETTIG, and J. TROTTER. Can. J. Chem. **65**, 590 (1987) and references therein.
34. W. O. NELSON, C. ORVIG, S. J. RETTIG, and J. TROTTER. Can. J. Chem. **66**, 132 (1988).
35. W. KLIEGEL, U. LAUTERBACH, S. J. RETTIG, and J. TROTTER. Can. J. Chem. **65**, 1457 (1987).
36. W. KLIEGEL, L. PREU, S. J. RETTIG, and J. TROTTER. Can. J. Chem. **63**, 509 (1985).
37. A. DOMENICANO, P. MURRAY-RUST, and A. VACIAGO. Acta Crystallogr. Sect. B. **39**, 457 (1983) and references therein.

Can. J. Chem. Downloaded from www.nrcresearchpress.com by 93.93.197.157 on 09/07/12
For personal use only.

Synthesis and metal ion complexation behavior of polycarboxylate 18-crown-6 ethers derived from tartaric acid

PHILIP J. DUTTON, THOMAS M. FYLES, AND SUSAN J. MCDERMID
Department of Chemistry, University of Victoria, Victoria, B.C., Canada V8W 2Y2

Received September 17, 1987

PHILIP J. DUTTON, THOMAS M. FYLES, and SUSAN J. MCDERMID. Can. J. Chem. **66**, 1097 (1988).

The metal ion complexation behavior of four 18-crown-6 ethers derived from (+)- and *meso*-tartaric acid is examined. Preparations of a *meso*-crown ether diacid and of a crown ether hexacid from three units of (+)-tartaric acid are described. Acidity constants and stability constants for complexation of metal cations in aqueous solution were determined by potentiometric titration. The complexes are substantially stabilized by favourable electrostatic interactions and are of similar stability to complexes of cryptands and EDTA. The complexation behavior of the series can be rationalized in terms of electrostatic interactions, direct coordination of the cations by at least one carboxylate from the crown ether periphery, and rigidification of the ligands as the anionic charge increases. Distributions of charge influence the relative stability of isomeric complexes. Highly charged polycarboxylate crown ethers are effective, but relatively unselective, cation complexing agents for a range of cations. The complexes are stable to pH 3 and the ligands can be used as simultaneous pH and metal ion buffers.

PHILIP J. DUTTON, THOMAS M. FYLES et SUSAN J. MCDERMID. Can. J. Chem. **66**, 1097 (1988).

On a étudié la complexation d'ions métalliques par quatre éthers 18-couronnes-6 dérivés des acides (+)- et *méso*-tartriques. On décrit les préparations, réalisées à partir trois unités d'acide (+)-tartrique, d'un diacide d'éther couronne *méso* et d'un hexacide d'éther couronne. Utilisant des titrages potentiométriques, on a déterminé les constantes d'acidité et les constantes de stabilité pour la complexation de cations métalliques, dans des solutions aqueuses. Les complexes sont très stabilisés par des interactions électrostatiques favorables et leurs stabilités ressemblent à celles des cryptands et de l'EDTA. Pour rationaliser le comportement des membres de la série vis-à-vis de la complexation, on doit faire appel à des interactions électrostatiques, à la coordination directe des cations par au moins un groupement carboxylate de l'éther couronne de la périphérie et à une rigidification des ligands au fur et à mesure que la charge anionique augmente. Les distributions de charge influencent la stabilité relative des complexes isomères. Pour beaucoup de cations, les éthers couronnes portant plusieurs groupement carboxylates hautement chargés sont des agents de complexation efficaces, mais relativement peu sélectifs. À un pH de 3, les complexes sont stables et on peut utiliser les ligands simultanément comme tampons du pH et des ions métalliques.

[Traduit par la revue]

Can. J. Chem. Downloaded from www.nrcresearchpress.com by 93.93.197.157 on 09/07/12
For personal use only.

The underlying theme in the complexation chemistry of macrocycles, is the control of complex formation by control of ligand structure through synthesis (1, 2). From this perspective, crown ethers derived from (+)-tartaric acid possess a number of appealing features as frameworks for the construction of specific complexing agents. Firstly, the carboxyl groups provide an easy synthetic entry to a wide range of derivatives (3–7). Secondly, the tartaric acid units show a strong conformational preference for an *anti* disposition of the carboxylates and other carboxylate derived groups (8–12). This limits overall conformational flexibility (8, 11, 12) and leads to well-defined conformations in which the carboxylate derived groups lie axial to the plane of the macrocycle (8–12). Lateral interactions between substituent groups and bound substrates are thus favored (3, 4, 13, 14). Finally, the presence of charged groups on the macrocyclic periphery leads to markedly enhanced cation complexation relative to uncharged ligands of similar structure (3, 8, 12). This is primarily a result of a favorable electrostatic interaction between the anionic ligand and the complexed cation (5, 8).

Additional effects may be important. The carboxylates could act as additional ligating sites in a fashion similar to the neutral donor arms of lariat ethers (15, 16). Evidence from infrared and nuclear magnetic resonance spectroscopy (12), from electron spin resonance spectroscopy (11), and from analysis of stability constant data (12, 17) suggests that direct and cooperative carboxylate–cation interactions occur, especially with small cations in solvents of moderate polarity. Such contacts probably distort the crown ether such as seen in the crystal structures of the *syn* and *anti* diacid diamide 18-crown-6 derivatives (9). The di- and tetra-acids (Fig. 1) and their derivatives have overall twofold symmetry. In contrast, the complexes of the parent 18C6 prefer an ideal D_{3d} symmetry (18). Thus, both *RR*18C6A$_2$ and 18C6A$_4$ are incapable of symmetrically interacting with a bound cation, either by direct contact or by indirect coulombic attraction without some distortions of the macrocycle from threefold symmetry. At the same time as complex stability is enhanced by increasing charge on the ligand, the complexation selectivity may be lowered (12) or reversed (19).

Nonetheless, the tetraacid 18C6A$_4$ is capable of binding potassium ion in aqueous solution as effectively as the cryptands (5). The general strategy of electrostatic enhancement of cation binding therefore warrants a detailed examination. To this end, we have examined the crown ethers shown in Fig. 1. The diacid *RR*18C6A$_2$ and tetraacid 18C6A$_4$ have been previously reported (8, 21). For comparison purposes the diacid derived from *meso*-tartaric acid, *RS*18C6A$_2$, was prepared. The series also was extended to the hexaacid 18C6A$_6$, derived from three units of (+)-tartaric acid. This material can bear up to six anionic charges and, in principle, could preserve threefold symmetry in its complexes. This report examines the syntheses of *RS*18C6A$_2$, 18C6A$_6$, and the metal cation complexation behavior of the series in aqueous solutions.

Results and discussion

Synthesis of ligands

The syntheses of *RR*18C6A$_2$ and 18C6A$_4$ have been reported (8, 21, 22); the syntheses of *RS*18C6A$_2$ and 18C6A$_6$ follow directly from previous methods (Fig. 2). In particular, the synthesis of the *meso* crown ether **3** is a simple extension (21) starting from the bis-dimethylamide of *meso*-tartaric acid **1**. The dithallium salt of **1** reacted with pentaethylene glycol dibromide to afford the diamide crown ether **2** in 24% recrystallized yield. Acid hydrolysis gave *RS*18C6A$_2$ (**3**) in nearly quantitative

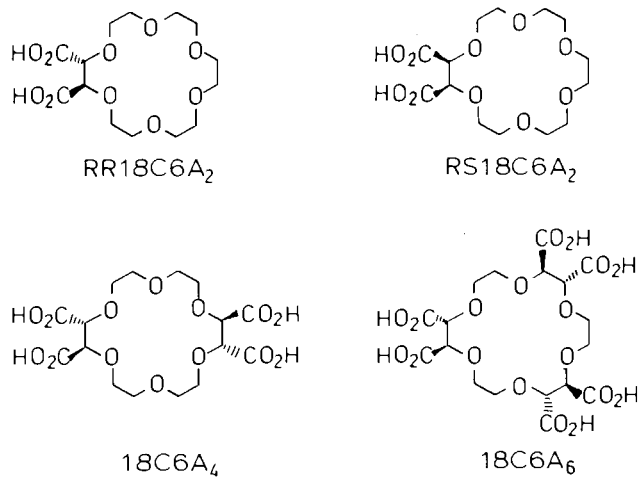

FIG. 1. Structures of the ligands considered with abbreviated names.

yield. Compounds in the *meso* series are significantly easier to crystallize but are otherwise closely similar to previously examined materials from (+)-tartaric acid.

The synthetic plan for $18C6A_6$ (**13**) follows trivially from the structure. Two "half crown" triethylene glycol derivatives, **10** and **11**, are required in the macrocyclization. The derivative **11** has been previously reported (23) and application of similar chemistry was expected to give **10** from a monoprotected tartaramide **5**.

The monoprotection of the tartaramide **4** using one equivalent of thallous ethoxide in DMF followed by treatment with excess benzyl bromide invariably gave close to the theoretical yield of the dibenzyl ether of **4** with only minor amounts of **5**. Partial hydrogenolysis of the dibenzyl ether gave a mixture from which the desired **5** could be isolated by a solvent extraction sequence. A survey of other bases and reaction conditions eventually revealed that the use of one equivalent of sodium hydride with **4**, followed by excess benzyl bromide, produced **5** cleanly without loss of chiral integrity (22, 24). The subsequent coupling of **5** with the tetrahydropyranyl ether of 2-bromoethanol, followed by hydrolysis of the Thp ether **6** gave the alcohol **7** as anticipated (23). Provided that **6** is purified by column chromatography, the alcohol **7** and the tosylate **8** can be adequately purified by a sequence of liquid–liquid extractions (25). Coupling of **8** with a second mole of the sodium salt of **5** gives the "half crown" dibenzyl ether **9**. After column chromatography, **9** is obtained as a crystalline solid. Hydrogenolysis of **9** gives the diol **10**, which can again be purified by a sequence of liquid–liquid extractions.

The final macrocyclization uses sodium hydride as the base to couple **10** and **11** (23) to yield the hexaamide **12** in modest but reliable yields of 20–30%. The product is characterized by the expected simple ^1H and ^{13}C nmr spectra and a strong molecular ion and expected fragmentations in the mass spectrum. Acidic hydrolysis of the amides gives the hexaacid **13** ($18C6A_6$), which was purified by ion exchange and crystallization from water. The hexaacid **13** can be converted to ester and amide derivatives for use in membrane transport experiments; their synthesis will be reported separately.

Determination of complexation constants

Stability constants for metal ion complexation by the polycarboxylate crown ethers were determined by potentiometric titration. The principles have been discussed previously (12, 21); the primary constants determined are cumulative association constants, β_{lmh}, defined by eq. [1] (charges omitted for clarity).

$$[1]\quad lL + mM + hH \rightleftharpoons L_lM_mH_h \qquad \beta_{lmh} = \frac{[L_lM_mH_h]}{[L]^l[M]^m[H]^h}$$

where L = ligand, M = metal ion, H = proton, and l, m, and h are the respective stoichiometric coefficients. Since the ligand and complex activity coefficients are unknown, the β_{lmh} are defined in terms of concentrations. The errors introduced are minimized by use of a high constant ionic strength and low ligand concentration. Of greater chemical utility than the cumulative constants are stepwise formation constants such as apply to the association of a partly protonated ligand with a metal ion. These values can be derived from the β_{lmh} for the system. As an example consider a diprotic ligand H_2L forming two complexes with a metal ion M^+ (i.e., ML^- and HML). The stepwise equilibria of interest are given as eqs. [2]–[5]. The stepwise formation constants K_{a_1}, K_{a_2}, K_{ML}, and K_{HML} are defined in terms of species concentrations and cumulative association constants as indicated. Note as well that the acidity constants follow the convention of *dissociation* while the β_{lmh} values are in term of *association*.

$$[2]\quad H_2L \rightleftharpoons HL^- + H^+ \qquad K_{a_1} = \frac{[HL^-][H^+]}{[H_2L]} = \frac{\beta_{101}}{\beta_{102}}$$

$$[3]\quad HL^- \rightleftharpoons L^{2-} + H^+ \qquad K_{a_2} = \frac{[L^{2-}][H^+]}{[HL^-]} = \frac{1}{\beta_{101}}$$

$$[4]\quad L^{2-} + M^+ \rightleftharpoons ML^- \qquad K_1 = \frac{[ML^-]}{[L^{2-}][M^+]} = \beta_{110}$$

$$[5]\quad HL^- + M^+ \rightleftharpoons HML \qquad K_2 = \frac{[HML]}{[HL^-][M^+]} = \frac{\beta_{111}}{\beta_{101}}$$

The experimental procedure involves the pH-metric titration of the ligand as the free acid with base (Me_4NOH). The resulting titration curve is analysed by a modified version of the program SCOGS (26) to yield β_{10h} and thus the pK_a's for the ligand. Metal ion is then added to the system and the mixture is again titrated. The resulting titration curve, together with the previously determined values of β_{10h}, is again analysed by SCOGS to yield β_{lmh} for the cation. Various checks and controls are outlined in the experimental section and in previous work (12, 21).

The results for the four carboxylate crown ethers are presented in Table 1. The set of β_{lmh} values for each ligand/cation pair permits a calculation of species concentrations as a function of pH. Examples of these curves are given in Fig. 3; Fig. 3*a* shows the protonated forms of $18C6A_6$ in the absence of metal ions while Fig. 3*b* shows the metal containing species present in a potassium ion/$18C6A_6$ mixture. The chief value of such curves is to provide a rapid, visual summary of the species present and their relative importance in describing the solution equilibria. At the concentrations used ($\sim(3–4) \times 10^{-4}$ M in L), any system with log $K > 4.0$ is dominated by the metal complexes of the ligands above pH 3.0. Below pH 3.0 the protonated forms of the free ligands dominate.

The value of log β_{110} for $K^+/18C6A_4$ has been reported previously to be 5.48 (5, 8); our value of 4.5 ± 0.2 is in rather poor agreement with this value. The techniques used differ appreciably; in particular we assess the protonated complexes that were ignored in the previous work. Over the past few years

Can. J. Chem. Downloaded from www.nrcresearchpress.com by 93.93.197.157 on 09/07/12
For personal use only.

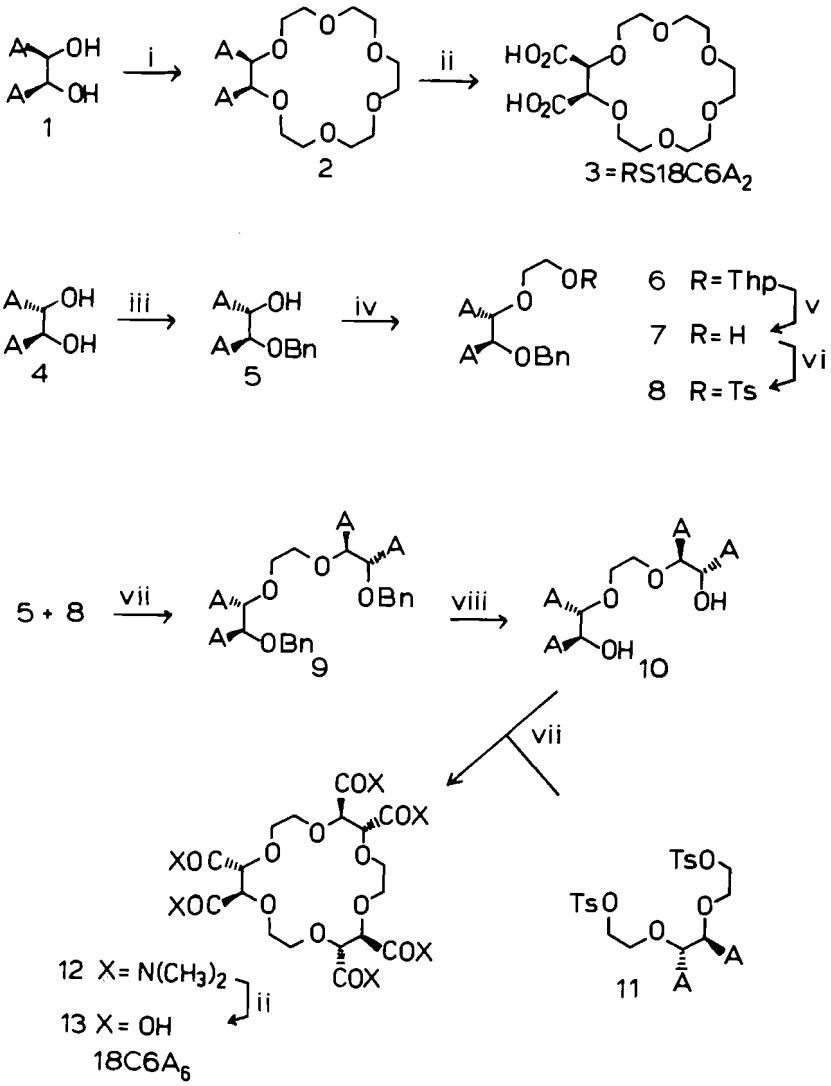

Abbreviations: Bn = benzyl; A = $C—N(CH_3)_2$, Ts = *p*-toluenesul fonyl, Thp = tetrahydropyranyl, DMF = dimethyl formamide

(i) 1. $TlOC_2H_5$/DMF; 2. $BrCH_2(CH_2OCH_2)_4CH_2Br$/DMF/80°C/6 h; (ii) H_3O^+/reflux; (iii) 1. NaH/DMF, 2. BnBr (excess)/80°C/7 h; (iv) 1. $TlOC_2H_5$/DMF, 2. $BrCH_2CH_2OThp$/60°C/15 h; (v) H_3O^+/CH_3OH/reflux; (vi)$TsCl/(C_2H_5)_3N/CH_2Cl_2$; (vii) NaH/DMF/65°C/ 12 h; (viii) H_2/Pd–C

FIG. 2. Synthetic schemes.

we have determined the $K^+/18C6A_4$ and $K^+/RR18C6A_2$ systems several times at different concentrations of ligand. In general, as the ligand concentration increases, so also do the log β_{lmh} values (log β_{110} ($K^+/18C6A_4$) = 4.9 at 1.15×10^{-3} M; = 5.3 at 2.61×10^{-3} M; = 5.4 at 5.0×10^{-3} M). This is undoubtedly a result of the variation in activity coefficients, which we ignore in our analysis. The set of data in Table 1 is designed to minimize this effect and to permit internal comparisons; slightly different values would be obtained at other ligand concentrations.

Factors governing metal ion binding

Table 1 provides insights into the behavior of the polycarboxylate crown ethers both as ligands and as polycarboxylic acids. The acidity constants follow expected trends: the monoprotonated ligands are increasingly weaker acids as the total charge increases. The effect is modest, however, and the fully deprotonated ligands are accessible at pH 5 and greater. Furthermore the half-protonated forms ($H18C6A_2^-$, $H_218C6A_4^{2-}$, $H_318C6A_6^{3-}$) occur as the predominant protonated species over a range of pH centered near 3.5 (see Fig. 3*a*). This is due to monoprotonation of each tartaric acid residue; the second protonation requires more acidic conditions.

The stepwise formation constants clearly exhibit the expected electrostatic enhancement of cation binding. An increase in anionic charge clearly increases the magnitude of the formation constants. There is ample evidence to show this is generally the case: (*i*) divalent ions are bound more strongly than monovalent ions, (*ii*) the complexes of the fully deprotonated ligands with divalent ions show a regular increase in stability with increasing charge, (*iii*) many ligand/cation combinations exhibit a regular decrease in stability constant with ligand protonation. Despite these regularities, however, there are some important exceptions that indicate that other structural effects are important in cation binding.

Firstly, there is a clear indication that the donor set of the ligands is inappropriate for complexation of "softer" cations such as Cd^{2+}, Cu^{2+}, and Zn^{2+} compared to the harder alkali

Can. J. Chem. Downloaded from www.nrcresearchpress.com by 93.93.197.157 on 09/07/12
For personal use only.

Can. J. Chem. Downloaded from www.nrcresearchpress.com by 93.93.197.157 on 09/07/12
For personal use only.

TABLE 1. Logarithm of cumulative stability constants and derived stepwise formation constants[a]

Metal	Stoichiometry			Ligand			
	l	*m*	*h*	*RR*18C6A$_2$	*RS*18C6A$_2$	18C6A$_4$	18C6A$_6$
H^{+b}	1	0	1	4.37	4.75	4.88	5.07
	1	0	2	7.09 (2.72)	7.09 (2.34)	9.17 (4.29)	9.80 (4.73)
	1	0	3	‡	‡	12.01 (2.84)	14.23 (4.43)
	1	0	4	‡	‡	14.14 (2.13)	17.52 (3.29)
	1	0	5	‡	‡	‡	20.19 (2.67)
	1	0	6	‡	‡	‡	21.19 (1.0)[e]
Na^+	1	1	0	3.3	2.5	4.5	5.4
	1	1	1	6.7 (2.4)	*	9.0 (4.1)	10.2 (5.1)
	1	1	2	*	*	11.1 (1.9)	13.8 (4.0)
	1	1	3	‡	‡	*	17.4 (3.2)
K^+	1	1	0	4.2	3.1	4.8	4.1
	1	1	1	7.6 (3.2)	*	9.6 (4.7)	10.4 (5.3)
	1	1	2	*	*	12.6 (3.4)	14.7 (4.0)
	1	1	3	‡	‡	*	17.8 (3.2)
Tl^+	1	1	0	5.7	3.3	3.6	4.4
	1	1	1	9.3 (4.6)	*	9.7 (4.8)	10.9 (5.8)
	1	1	2	*	*	*	14.9 (5.1)
	1	1	3	‡	‡	*	17.8 (3.5)
Ca^{2+}	1	1	0	5.6	4.3	8.6	9.8
	1	1	1	*	*	11.9 (7.0)	13.6 (8.6)
	1	1	2	*	*	*	16.5 (6.7)[f]
Sr^{2+}	1	1	0	5.9	5.8	8.0	10.4
	1	1	1	8.9 (4.2)	8.9 (4.2)	10.9 (6.1)	13.8 (8.8)
	1	1	2	*	*	*	16.6 (6.8)
Ba^{2+}	1	1	0	6.5	5.6	7.2	9.5
	1	1	1	*	*	11.0 (6.2)	13.8 (8.8)
	1	1	2	*	*	*	16.3 (6.5)
Cu^{2+}	1	1	0	[c]	—	5.3	7.1
	1	1	1	*	—	*	11.1 (6.0)
Zn^{2+}	1	1	0	[d]	—	4.0	6.3
	1	1	1	*	—	*	10.2 (5.2)
Cd^{2+}	1	1	0	3.0	—	7.9	9.3
	1	1	1	*	—	10.9 (6.0)	13.6 (8.5)
	1	1	2	*	—	*	16.4 (6.6)

[a]Determined at 25°C, I = 0.05 M with Me_4NCl. Values in parentheses are calculated for the 1:1 association of metal with protonated ligand. The symbol * indicates that the complex of the given stoichiometry was not required to achieve a fit of the experimental data. The symbol ‡ indicates the stoichiometry is inappropriate for the ligand. The dash — indicates the system was not examined. Uncertainty in acidity constants is log $\beta_{10h} \pm 0.1$; in association constants is log $\beta_{lmh} \pm 0.2$.

[b]Logarithm of dissociation constants; follows the convention of pK_a.

[c]log $\beta_{110} \cong 3.9 \pm 0.7$; competition with hydroxo complexes increases uncertainty.

[d]log $\beta_{110} \cong 3.7 \pm 0.7$; competition with hydroxo complexes increases uncertainty.

[e]log $\beta_{106} \pm 0.5$.

[f]log $\beta_{113} = 18.4 \pm 0.5$ (4.1).

metal and alkaline cations. The Ca^{2+}/Cd^{2+} comparison is particularly appropriate since the effective ionic radii of these two ions are closely similar (27) (six coordination: Ca^{2+}, 1.00 Å; Cd^{2+} 0.95 Å; seven coordination: Ca^{2+}, 1.06 Å; Cd^{2+}, 1.03 Å). The surface charge density of the two ions must therefore be closely similar, with a tendency to favor Cd^{2+} in any coulombic interaction. Despite this electrostatic advantage, the Cd^{2+} complexes are all weaker than related Ca^{2+} complexes. In fact the Cd^{2+} complex of *RR*18C6A$_2^{2-}$ is weaker than the complexes of monovalent ions. The Cu^{2+} and Zn^{2+} ionic radii are substantially smaller but the complexes of these ions are also weaker than related Ca^{2+} complexes. Clearly a high anionic charge alone is insufficient to achieve stable complexes.

The second important "irregularity" in the data concerns the Tl^+ complexes of 18C6A$_4^{4-}$ and 18C6A$_6^{6-}$ and the K^+ complex of 18C6A$_6^{6-}$. In each of these cases the monoprotonated complexes are markedly more stable than the complexes of the fully deprotonated ligand. The consequences are readily apparent in Fig. 3*b*; free K^+ passes through a minimum when the monoprotonated complex achieves its maximum concentration. These cases are the interactions of the most highly charged ligands with the cations of lowest surface charge density. On a

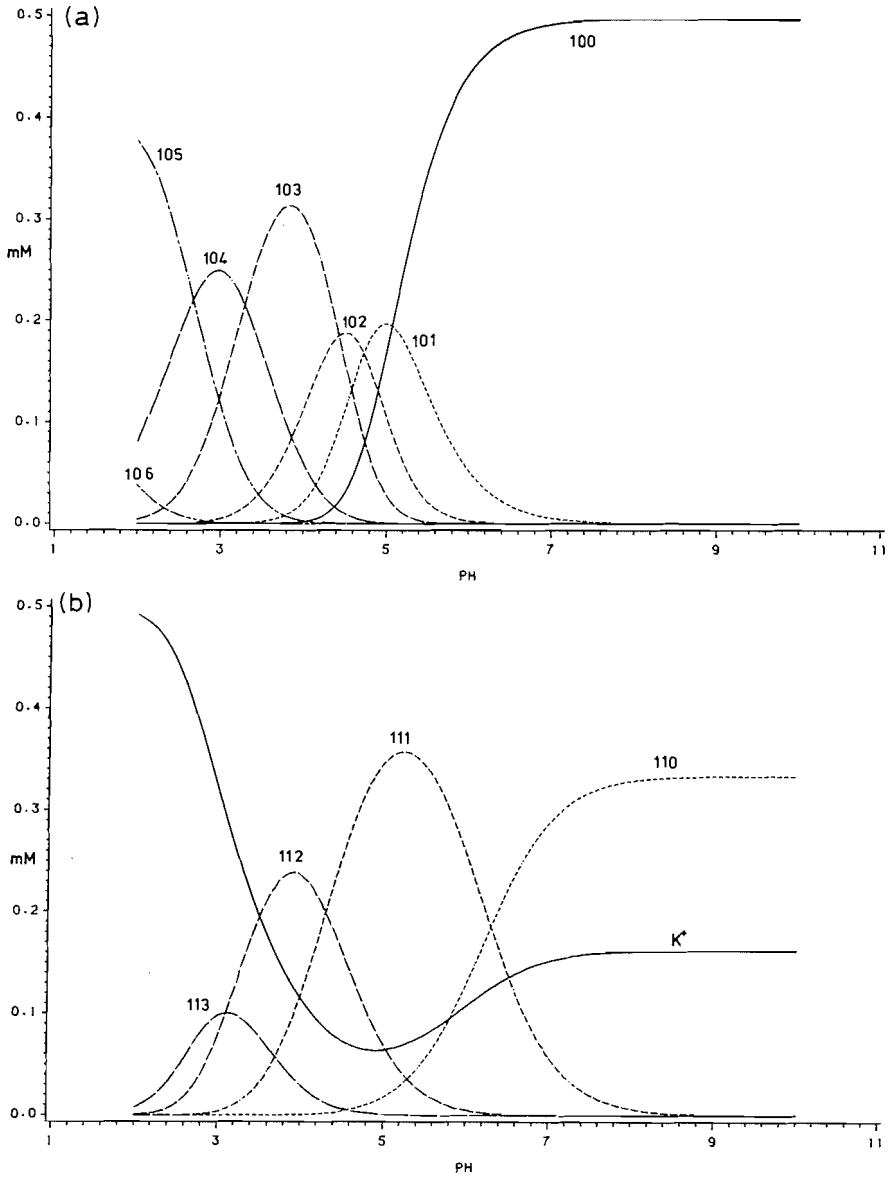

FIG. 3. (a) Protonated forms of $18C6A_6$ as a function of pH; (b) potassium complexes of $18C6A_6$ and free K^+ concentration as a function of pH. $[18C6A_6] = 5 \times 10^{-4}$ *M*, $[K^+] = 5 \times 10^{-4}$ *M*.

purely electrostatic basis Tl^+ and K^+ are least able to organize the donors of the ligand in the face of the strong internal repulsions between the charged carboxylates. The fully deprotonated ligands are thus apparently more rigid than more protonated forms, which can distort to accommodate a range of cations. This is a further example of the principle that "the guest organizes the host" (15, 28).

Since a single deprotonation provokes the effect, it is tempting to argue that one additional donor site is required and that the normal interaction involves seven donor atoms from the ligand. Complexes of moderately charged ligands, or of cations with sufficiently high charge density, easily achieve a seven-coordinate geometry despite the repulsions that occur as the carboxylate moves towards the cation in the macrocycle. For the "irregular" complexes, the energetic cost of this distortion is incompletely compensated by the carboxylate–cation interaction energy. Protonation lowers the total charge, hence reduces the repulsive interactions. Alternatively, the irregular complexes might be simple six-coordinate crown ether complexes.

The issue of carboxylate participation in complexes of charged crown ethers can be examined using the approach described by Eyring and co-workers (17). They divide the total free energy of complexation (ΔG_{tot}) into two components: (*i*) a polyether cavity factor (ΔG_{cav}) due to interaction of the cation only with the crown ether oxygens and (*ii*) an electrostatic interaction (ΔG_{el}) between the cation and the anionic ligand without crown ether participation. The two effects are related to the total free energy change by eq. [6] (17).

$$[6] \quad \Delta G_{tot} = \Delta G_{cav} + \lambda \Delta G_{el}$$

where $\lambda = 0$ for no cation–carboxylate interaction such as occurs with neutral crown ethers, and $\lambda = 1$ for the maximum electrostatic interaction with a fully deprotonated ligand. Intermediate values of λ indicate intermediate degrees of protonation. Squaring eq. [6] yields the relation [7].

$$[7] \quad (\Delta G_{tot})^2 = (\Delta G_{cav})^2 + 2\lambda \Delta G_{cav} \Delta G_{el} + (\lambda \Delta G_{el})^2$$

$(\Delta G_{cav})^2$ is the contribution to metal ion complexation due to the crown ether acting alone, $(\lambda \Delta G_{el})^2$ is the strictly

Can. J. Chem. Downloaded from www.nrcresearchpress.com by 93.93.197.157 on 09/07/12
For personal use only.

TABLE 2. Contributions to ion binding calculated by eq. [7][a]

				Ligand											
	Complex			*RR*18C6A$_2$			*RS*18C6A$_2$			18C6A$_4$			18C6A$_6$		
Metal	*l*	*m*	*h*	%CE	%CO	%EL	%CE	%CO	%EL	%CE	%CO	%EL	%CE	%CO	%EL
Na^+	1	1	0	6	37	57	10	44	46	3	29	68	2	25	73
	1	1	1	44	44	11				9	42	49	4	33	62
	1	1	2							55	38	7	13	46	41
	1	1	3										33	49	18
K^+	1	1	0	23	50	27	43	45	12	18	49	33	25	50	25
	1	1	1	76	22	2				33	49	18	22	50	28
	1	1	2							73	25	2	49	42	9
	1	1	3										76	22	2
Tl^+	1	1	0	16	48	36	47	43	10	40	47	14	27	50	23
	1	1	1	63	33	4				38	47	15	23	50	27
	1	1	2										41	46	13
	1	1	3										78	21	1
Ca^{2+}	1	1	0	1	16	84	1	20	79	0	11	89	1	9	90
	1	1	1							1	20	78	1	15	85
	1	1	2										2	25	73
Sr^{2+}	1	1	0	21	50	29	22	50	28	12	45	43	7	39	54
	1	1	1	78	21	1	78	21	1	35	48	17	16	48	37
	1	1	2										36	48	16
Ba^{2+}	1	1	0	35	48	16	48	43	10	29	50	21	17	48	35
	1	1	1							56	38	6	28	50	22
	1	1	2										59	36	5

[a]%CE, interaction with the crown ether alone; %EL, coulombic metal–ligand interaction; %CO, cooperative interaction of crown ether bound cation with carboxylate.

Can. J. Chem. Downloaded from www.nrcresearchpress.com by 93.93.197.157 on 09/07/12
For personal use only.

coulombic contribution, and $2\lambda\Delta G_{cav}\Delta G_{el}$ is the contribution due to a cooperative interaction of the crown ether and the carboxylates with the cation. This first-order analysis deals only with ion–ligand contributions to ΔG_{tot} and ignores differential solvation effects. Nonetheless eq. [7] provides a convenient means to assess the relative importance of the three contributions to the cation–ligand interaction.

Table 2 provides such an analysis for the alkali metal and alkaline earth complexes of the polycarboxylate crown ethers of Fig. 1. The values of ΔG_{cav} were derived from the literature values for 18-crown-6 complexes of the cations in water (log β_{110}: Na^+, 0.8 (20); K^+, 2.03 (29); Tl^+, 2.27 (29); Ca^{2+}, 0.48 (30); Sr^{2+}, 2.72 (29); Ba^{2+}, 3.87 (29)). The λ values scale to the fraction of protonation, thus half-protonated $H_218C6A_4^{2-}$ has $\lambda = 1/2$ and monoprotonated $H18C6A_6^{5-}$ has $\lambda = 5/6$, etc. The percentage contributions of $(\Delta G_{cav})^2$ (%CE),$(\lambda\Delta G_{el})^2$ (%EL), and $2\lambda\Delta G_{cav}\Delta G_{el}$ (%CO) provide a simple picture of the relative contributions in the ligand–cation interaction.

Since the approach is clearly a first-order approximation and our values of ΔG_{cav} and λ are chosen somewhat arbitrarily, we proceed to examine Table 2 with some caution. A few general conclusions can be readily drawn. Firstly the complexation of Ca^{2+}, and to a lesser extent Na^+, is apparently dominated by the strictly Coulombic component (%EL). This is in accord with both the small size (hence poor "fit") and high surface charge density of these ions. Secondly, the complexes of large cations (K^+, Tl^+, Ba^{2+}) with a modest charge ($\lambda = 0.5$) are dominated by the strictly crown ether contribution (%CE). The electrostatic component in these cases is usually small. Thirdly, in the majority of cases, the cross term for cooperative crown ether and carboxylate interaction (%CO) is quite constant (40–50%) and an important contributor to the cation-ligand interaction. This result is consistent with the view that the normal complexation mode for this series involves a coordinating carboxylate acting in concert with the crown ether oxygens. Finally, the irregular K^+ and Tl^+ complexes noted above are not irregular on Table 2; carboxylate coordination apparently occurs but at the expense of poorly compensated electrostatic repulsions with other non-coordinated carboxylates.

A related consequence of the view that these ligands provide cooperative carboxylate and crown ether binding interactions is the attendant increase in "effective cavity size" compared with a simple six donor atom 18-crown-6. The interrelationship of the number of donors (with their topology) and the effective ionic radius of the bound cation governs binding in flexible neutral ligands (15). The same applies to flexible charged ligands, with the additional complexity that ligand flexibility decreases as charge increases.

To summarize the picture: the ligands normally bind cations with cooperative crown ether and carboxylate donor interactions. Thus a trend favouring larger cations is expected, and found, in the complexes of the diacids *RR*18C6A$_2$ and *RS*-18C6A$_2$. In all cases, the electrostatic interactions favour small, high surface charge cations. Thus as ligand charge increases the trend favoring large cations should reverse (compare Ca^{2+}, Sr^{2+}, Ba^{2+} with *RR*18C6A$_2^{2-}$ and 18C6A$_4^{4-}$). As well as bearing an increased charge, the highly charged forms are enlarged and rigidified by repulsive electrostatic interactions between carboxylates. One consequence is that the complexes of low surface charge cations with highly charged ligands are

destabilized relative to less charged ligands by the energetic demands of moving the carboxylate to the metal ion. Another consequence is to destabilize the complexes of small ions despite their high surface charge. The composite result is a degradation of the selectivity of highly charged ligands such as $18C6A_6^{6-}$.

Comparison of isomeric charged ligands

Tables 1 and 2 also provide a comparison between isomeric ligands, both the configurational isomers, *RR* and *RS*18C6A$_2$, and isomeric distributions of charge, $18C6A_4^{4-}$ vs. $H_2 18C6A_6^{4-}$ for example. The trends generally support the analysis above but provide additional structural insights as well.

Crown ethers derived from *R,R*-(+)-tartaric acid show a marked preference for a diaxial disposition of carboxylates (8–12): the conformational preference of the parent (+)-tartaric acid (31) is carried directly into the crown ethers. We assume the conformations of the parent *meso*-tartaric acid are carried into *RS*18C6A$_2$. This produces one axial and one equatorial carboxylate with a normal *gauche* OCCO dihedral angle (31). Equilibration with an identical form is possible by *gauche*$^+$ to *gauche*$^-$ inversions around the macrocycle. The diaxial conformation of two carboxylates, and two ether oxygens, can be made with CPK molecular models; this is a minor conformer in the parent (31) and involves an unfavourable anti OCCO dihedral angle. Thus it is likely that *RS*18C6A$_2$ bears one axial carboxylate available as a ligating site, and one equatorial carboxylate directed away from the macrocycle. Interconversion of the two is presumably possible in the free ligand, and possibly in the complexes as well.

The complexes of the *meso*-crown ether are generally less stable than those of *RR*18C6A$_2$ by about a factor of 10 on average. Electrostatic stabilization falls off with distance (5) and the equatorial carboxylate is indeed further from the center of the macrocycle than the axial carboxylate, but the pure electrostatic argument fails to account for the data. Certainly the complexes of the dianions should differ, but the complexes of the monoanions, involving one coordinated axial carboxylate, should be closely similar. The *meso*-crown ether forms few detectable protonated complexes and the Tl^+ complex of *RS*18C6A$_2^{2-}$ is in fact weaker than the protonated complex of *RR*H18C6A$_2^-$. If the *meso*-crown ether is in fact equilibrating between a pair of isomers and the complexes have a relatively fixed seven-coordination structure, there will be an unfavourable entropy contribution on complex formation of any type. Since the *RR*-crown ethers have predominantly one conformation, they do not suffer the same unfavourable loss of entropy. This issue would be clarified by a more complete thermodynamic study. Thus in general, the *RS* complexes should be less stable than the *RR* complexes in accord with observation.

Comparisons between other pairs of ligands of like charge reveal that the complexes of the more protonated ligand are less stable by about a factor of 10 despite bearing the same charge and formally bearing the same potential binding sites. Of the dozen cases from Table 1, only the Tl^+ complexes of $18C6A_4^{4-}$ and $H_2 18C6A_6^{4-}$ show the opposite behavior. The more protonated ligands have fewer localized dianionic sites, hence a general electrostatic stabilization effect would be less pronounced. The differences are more marked with divalent cations, in line with an electrostatic component. In addition there must be differences in solvation, especially for comparisons involving fully deprotonated ligands. Intramolecular hydrogen bonding is available to partly protonated ligands but is not possible in fully deprotonated forms. Increased solvation of the free ligand or disruption of hydrogen bonded structures of the free ligand on complexation would act to diminish the formation constant of the complex.

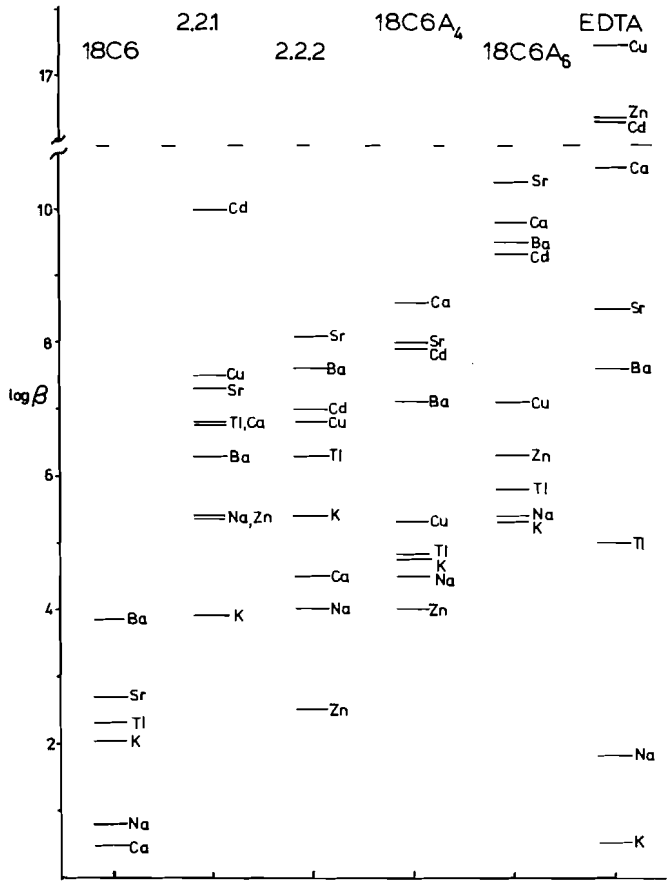

FIG. 4. Comparison of stability constants of crown ethers, cryptands, and EDTA. Literature values (20, 29, 30, 32–34) shown are averaged or "best values" (32). The 18C6A$_4$ and 18C6A$_6$ complexes are the 110 complexes except for Tl^+ and K^+ (18C6A$_6$) where the 111 complexes are more stable.

Comparisons with other metal ion binding ligands

The stepwise formation constants determined are compared with other ligands in Fig. 4. It is clear that the complexes of the charged crown ethers are substantially more stable than those of the parent 18C6 (29, 30) and fall within the range usually associated with the cryptands 2.2.1 and 2.2.2 (33) and the complexone EDTA (32, 34). Direct comparisons of this type must, however, take account of the different set of donors provided by each ligand. Both EDTA and the cryptands provide two nitrogen donors, hence the Cu^{2+}, Cd^{2+}, and Zn^{2+} complexes are particularly stabilized relative to $18C6A_4^{4-}$ and $18C6A_6^{6-}$. Conversely the alkali metal and alkaline earth cation complexes are somewhat disfavoured relative to the same ligands.

With respect to the selectivity of complexation, it is clear that 18C6A$_4$ and 18C6A$_6$ recognize cation charge with relatively little discrimination of cation size. As a result the triad "selectivities" among Ca^{2+}, Sr^{2+}, and Ba^{2+} are poor, especially in comparison to EDTA. Similarly the triad selectivity among Na^+, K^+, and Tl^+ is virtually absent in 18C6A$_4$ and 18C6A$_6$,in poor comparison to the cryptands. It is apparent that 18C6A$_4$

Can. J. Chem. Downloaded from www.nrcresearchpress.com by 93.93.197.157 on 09/07/12
For personal use only.

Can. J. Chem. Downloaded from www.nrcresearchpress.com by 93.93.197.157 on 09/07/12
For personal use only.

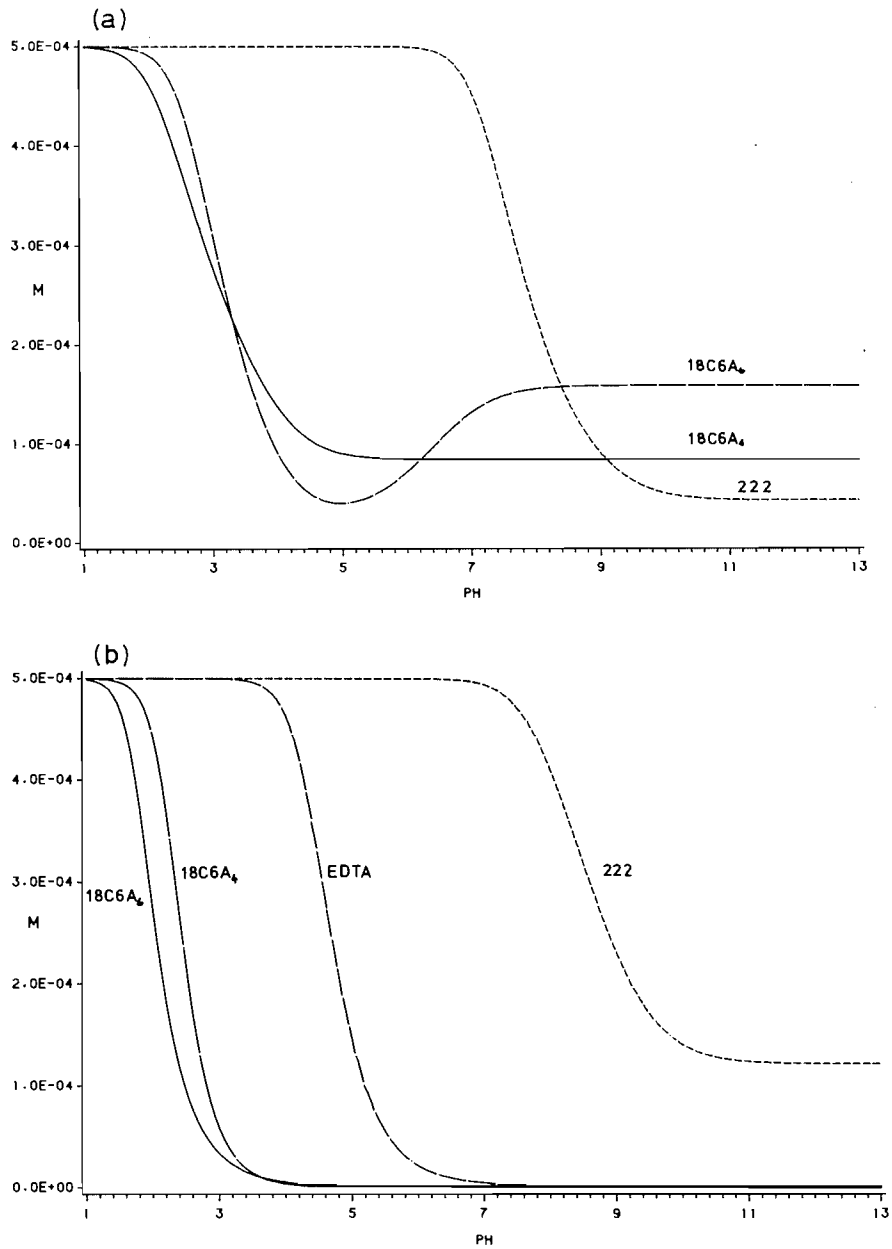

FIG. 5. (a) Calculated free K^+ concentration as a function of pH for 2.2.2 cryptand, $18C6A_4$, and $18C6A_6$ at $[L] = [K^+] = 5 \times 10^{-4}$ M. (b) Calculated free Ca^{2+} concentration as a function of pH for EDTA, 2.2.2 cryptand, $18C6A_4$, and $18C6A_6$ at $[L] = [Ca^{2+}] = 5 \times 10^{-4}$ M.

and $18C6A_6$ are somewhat indiscriminant cation binding agents.

A more unique feature of metal ion complexes of $18C6A_4$ and $18C6A_6$ is their ability to bind cations over a wide pH range. As noted above, the protonated complexes are less stable, but nonetheless do have appreciable stability. In contrast, protonation on nitrogen of the cryptates results in drastic destabilization and decomplexation. The same is true of EDTA. The comparison is readily made in Fig. 5, where free K^+ (Fig. 5*a*) and free Ca^{2+} (Fig. 5*b*) concentrations have been calculated for an equimolar mixture of metal ion and ligand at 5×10^{-4} M as a function of pH. In the K^+ case the concentrations at high pH reflect the order of the stability of the complexes ($2.2.2 > 18C6A_4^{4+} > 18C6A6_6^{6-}$). The minimum in the $18C6A_6$ curve is the result of the greater stability of the monoprotonated complex as discussed above. In any event, it is clear that both polycarboxylate crown ethers can bind K^+ well into acidic solution while 2.2.2 requires strongly basic conditions to achieve a similar result. Similarly the Ca^{2+} results show that pH > 9.5 is required for 2.2.2, pH > 6 for EDTA, while the polycarboxylate crown ethers bind Ca^{2+} to a significant extent even at pH 3.

In addition the polycarboxylate crown ethers have a series of protonation equilibria of the free ligand from pH 5 to 2. One can therefore envisage a simultaneous buffering of protons and metal ions in the pH range of 3–5. As an example consider 1×10^{-3} M $18C6A_6$ at pH 4.5 containing half an equivalent of K^+. Addition of a further one quarter of an equivalent of KOH (to 7.5×10^{-4} M $[K^+]$) provokes a pH change of 0.18 and a pK ($-\log[K^+]$) change of 0.36 (from 1.2 to 2.7×10^{-5} M free K^+). This type of behavior is rare, although some pH buffer systems will bind transition metal ions to produce a similar effect (32).

Can. J. Chem. Downloaded from www.nrcresearchpress.com by 93.93.197.157 on 09/07/12
For personal use only.

Conclusions

In summary, the polycarboxylate crown ethers examined show a range of behaviors with respect to the complexation of metal cations. At the two extremes, small, high charge density cations are bound predominantly by coulombic interaction while larger cations are bound by mono- and dianionic ligands predominantly as normal crown ether complexes. For a large number of cases the two effects act cooperatively to produce stabilized complexes involving direct coordination of the bound cation by at least one carboxylate from the ligand. Comparisons between *RR* and *RS*18C6A$_2$, and between ligands with isomeric charge distributions indicate that the final behaviors observed include entropic and solvation effects as well. Nevertheless, polycarboxylate crown ethers act as effective, if somewhat unselective, ligands for alkali metal and alkaline earth cations. They are as effective at ion binding as the cryptands and EDTA but offer an expanded pH range for complexation.

Experimental

General details

Melting points were taken on a Koefler hot stage microscope (uncorrected). Proton nmr spectra were recorded with a Perkin Elmer R32 (90 MHz, CW) or Bruker WM250 (250 MHz, FT) spectrometer in $CDCl_3$ solvent with Me_4Si as internal standard unless otherwise noted. Carbon spectra were recorded at 93.8 MHz (WM250) in $CDCl_3$ with the central solvent line as standard (77.0 ppm relative to Me_4Si) or in D_2O with CH_3OH as internal standard (49.0 ppm relative to Me_4Si). The mass spectra were recorded with a Finnegan 330 gs–ms instrument with methane chemical ionization. Optical rotations were recorded using a Perkin Elmer polarimeter in 95% ethanol as solvent (concentration in g/100 mL). Elemental analyses were performed by Canadian Microanalytical Services, Vancouver, B.C.

In general, products obtained as oils gave poor microanalyses due to entrapped chlorinated solvent. Solid derivatives and the final compounds, however, gave satisfactory microanalyses.

Materials

(*a*) *meso-N,N,N′,N′*-Tetramethyltartaramide (**1**) was prepared from *meso*-tartaric acid by dimethylammonolysis of the diester; mp 156–160°C; ir (cm^{-1}): 3400 (OH), 1630 (amide I); ^{1}H nmr δ: 5.22 (brs, OH), 4.45 (AA′, CH), 3.03 and 2.85 (2s, NCH_3); ^{13}C nmr δ: 172.4 (C═O), 68.7 (CH), 37.4 and 36.0 (NCH_3); ms (*m/e*); 205 (*M* + 1).

(*b*) 1,14-Dibromo-3,6,9,12-tetraoxatetradecane was prepared from the dichloride (35) by the method of Babler and Spina (36) using H_2CBr_2 and NaBr in DMF; ^{1}H nmr δ: 3.70 and 3.51 (A_2B_2, J_{AB} = 7 Hz, OCH_2CH_2Br), 3.60 (brs, all other protons); ms (*m/e*): 363, 365, 367 ($^{79}Br_2$ *M* + 1, $^{79}Br^{81}Br$ *M* + 1, $^{81}Br_2$ *M* + 1), peaks for the dichloride and chlorobromide absent.

(*c*) 2-(2-Bromoethoxy)tetrahydropyran (23), thallous ethoxide (21), and (2*R*,3*R*)-*N,N,N′,N′*-tetramethyl-2,3-bis(2-(tosyloxy)ethoxy)succinamide (**11**) (23) were prepared as previously. All other materials were commercially available. DMF was dried over activated 4 Å molecular sieves added directly to commercially available solvent.

meso-N,N,N′,N′-Tetramethyl-2,3-carboxamido-1,4,7,10,13,16-hexaoxacyclooctadecane (2)

To a solution of **1** (15.0 g, 0.0734 mol) in dry DMF (600 mL) was added thallous ethoxide (10.8 mL, 0.15 mol) with vigorous stirring at room temperature. After 15 min 1,14-dibromo-3,6,9,12-tetraoxatetradecane (22.2 g, 0.0619 mol) was added. The mixture was stirred at 85°C for 6 h, cooled, and purified using the procedure described previously (21) to yield 9.9 g of crystalline **2**; mp 130°C; ir (cm^{-1}): 1660 (amide), 1110 (C–O); ^{1}H nmr δ: 5.02 (2H, s, CH), 3.74 (20H, br, CH_2O); 3.26 and 3.06 (12H, 2s, NCH_3); ^{13}C nmr δ: 170.0 (C═O), 78.0 (CH), 70.2, 69.8 and 69.7 (CH_2O), 37.3 and 36.3 (NCH_3); ms (*m/e*): 407 (*M* + 1). *Anal.* calcd. for $C_{18}H_{34}N_2O_8$: C 53.19, H 8.43, N 6.89; found: C 53.15, H 8.23, N 6.68.

meso-4,7,10,13,16-Hexaoxacyclooctadecane-2,3-dicarboxylic acid (3)

Compound **3** was prepared from **2** by acidic hydrolysis as described previously (21) in 94% recrystallized yield as the monohydrate; mp 70–73°C (loss of H_2O evident); ir (cm^{-1}): 3700–3000 (OH), 1740 (CO); ^{1}H nmr δ: 4.60 (2H, s, CH), 3.69 (20H, brs, CH_2O); ^{13}C nmr δ: 172.8 (C═O), 79.9 CH, 70.6, 69.8 and 69.6 (CH_2O); ms (*m/e*): 353 (M + 1). *Anal.* calcd. for $C_{14}H_{26}O_{11}$ (**3**·H_2O): C 45.40, H 7.07; found: C 44.96, H 7.00.

(2R,3R)-N,N,N′N′-Tetramethyl-2-benzyloxy-3-hydroxysuccinamide (5)

Sodium hydride (5.2 g, 60% in oil, 130 mmol) was washed with pentane (3×) under an Ar atmosphere. Dry dimethylformamide (DMF, 500 mL) was added and the suspension stirred while tartaramide (**4**) (25 g, 122 mmol) was added as a solid. The suspension was stirred until clear (ca. 1 h) and benzyl bromide (25 g, 150 mmol) was added rapidly. The temperature was raised to 80°C for 7 h. The solvent was removed by evaporation under reduced pressure and the product dissolved in 500 mL of water. The aqueous solution was extracted with 250-mL portions of pentane (2×), Et_2O (2×) (disubstituted side product; ^{1}H nmr δ (2s, 12H, 4 × NCH_3), (brs, 4H, 2 × OCH_2), (s, 2H, 2 × $CHOCH_2$), (s, 10H, 2 × C_6H_5)), and CH_2Cl_2 (3×). The combined CH_2Cl_2 extracts were dried over $MgSO_4$, evaporated, and evacuated overnight at 34–40°C to give the monobenzyl ether (**6**) as a viscous oil (23 g, 78 mmol, 64%): $[\alpha]_D^{22}$ +53.2° (*c* 0.87); ^{1}H nmr and ^{13}C nmr; Table 3; ms (*m/e*): 295 (*M* + 1).

(2R,3R)-N,N,N′,N′-Tetramethyl-2-benzyloxy-3-(2-tetrahydropyranyloxy)ethoxysuccinamide (6)

Thallous ethoxide (5.4 mL, 77 mmol) was added by syringe to a solution of **5** (21 g, 71 mmol) in dry DMF (300 mL). The solution was warmed to 60°C over 1 h and 2-(2-bromoethoxy)tetrahydropyran was added. The reaction proceeded at 60°C for 15 h, was cooled, and the thallous bromide removed by filtration (Celite). The DMF was evaporated, the product evacuated overnight, taken up in CH_2Cl_2, and filtered again. The product after evaporation was preadsorbed on neutral Al_2O_3 (100 g) and loaded on a short (16–20 cm) column of neutral Al_2O_3 (1000 g) packed with CH_2Cl_2. The product was eluted rapidly with 0.5% MeOH/CH_2Cl_2; appropriate fractions were identified by thin-layer chromatography (tlc) (R_f 0.79, 5% MeOH/CH_2Cl_2, Merck silica gel 60 silanized) and combined to give the product as an oil after evaporation and evacuation (22.6 g, 54 mmol, 75%); ^{1}H nmr and ^{13}C nmr: Table 3.

(2R,3R)-N,N,N′,N′-Tetramethyl-2-benzyloxy-3-(2-hydroxy)ethoxysuccinamide (7)

The Thp ether **6** (22 g, 53 mmol) was dissolved in MeOH (200 mL) and concentrated HCl (3 drops) was added. The solution was heated at reflux for 1.5 h. The solvent was evaporated and the product evacuated to give **7** as an oil (18.8 g, 55 mmol, 100%), which was used without further purification; $[\alpha]_D^{22}$ +43.9 (*c* 1.56); ^{1}H nmr and ^{13}C nmr: Table 3.

(2R,3R)-N,N,N′,N′-Tetramethyl-2-benzyloxy-3-(2-tosyloxy)ethoxysuccinamide (8)

The alcohol **7** (8.9 g, 26 mmol) was stirred in CH_2Cl_2/Et_3N (100 mL/6 mL) at 0°C and *p*-toluenesulfonyl chloride (TsCl) (6 g, 31 mmol) was added. The flask was fitted with a drying tube and allowed to warm slowly to room temperature. The reaction was stirred overnight, water was added, and the product extracted into CH_2Cl_2 (3×), washed with cold 10% HCl (2×) and cold saturated sodium bicarbonate, dried over $MgSO_4$, filtered, evaporated, and evacuated. The product was triturated with boiling pentane (12 × 100 mL). The oil obtained (10 g, 20 mmol, 78%) was used without further purification; $[\alpha]_D^{22}$ +23.7 (*c* 2.23); ^{1}H nmr and ^{13}C nmr: Table 3.

(3R,4R,9R,10R)-N,N,N′,N′,N″,N″,N‴,N‴-Octamethyl-3,4,-9,10-tetracarboxamido-2,5,8,11-tetraoxa-1,12-diphenyldodecane (9)

Sodium hydride (3.82 g, 60% NaH in oil, 95.5 mmol) was washed with pentane (3×) under inert atmosphere. Dry DMF (400 mL) was

TABLE 3. ^1H and ^{13}C nuclear magnetic resonance data (δ, (multiplicity, J (Hz)) for compounds **5**–**13**[a]

Compound	Bn ——	OCH ——	CHO —	CH_2 —	CH_2	O ‖ C —	$N(CH_3)_2$	R	
5 ^1H	4.37 and 4.73 (AB, 7.7), 7.3(s)	4.43 (d,3)	4.75 (dd,3,4.8)	—	—	—	2.80,2,82 2.90,3.12	OH 4.0(d,4.8)	
^{13}C	72.4,128.8 128.9,136.7	76.3	69.2	—	—	170.5 171.0	35.9,36.1 37.1,37.2	— —	
6 ^1H	4.7(m) 7.3(s)	4.7(m)		3.4–3.7(m)		—	2.9,3.0 3.1	CH 4.7(m)	$CH_2CH_2CH_2CHO$ 1.6(m), 3.4– 3.7(m)
^{13}C	71.2,127.4 127.5,128.0 137.6	76.2 76.3	77.3 77.6	66.3 68.7	66.5 69.0	169.1	35.4,36.8 36.9	98.4 98.5	19.1,25.1,30.2, 61.7
7 ^1H	4.46 and 4.60 (AB,12) 7.3(s)	4.8(brs)		3.7(s)		—	2.9,3.0 3,1	OH 3.6(s)	
^{13}C	71.4,127.8 128.2,137.2	76.3	77.2	71.4	61.5	169.0 169.3	35.7 36.9	—	
8 ^1H	4.51 and 4.63 (AB,12) 7.3(s)	4.7(s)		3.8–4.1(m)		—	2.8,2.9 3.0	OTS 7.3 and 7.7 (AB,8)	CH_3 2.4
^{13}C	71.3,127.8 128.3,137.5	76.1	77.3	69.0	67.2	168.5 169.1	35.6,37.0 37.1	127.8,129.7 133.0,144.7	21.4
9 ^1H	4.1(brs) 7.3(s)	4.8(s)		3.8(brs)		—	2.8,3.0 3.1	—	
^{13}C	71.5,127.8 128.4,137.9	76.4	77.6	69.5		169.2 169.4	35.6,37.1 37.2	—	
10 ^1H	—	4.8 (dd,5.7,6.2)	4.5 (d,5.7)	3.7(m)		—	2.91,2.92 3.11,3.17	OH 4.3(d,6.2)	
^{13}C	—	69.0	78.4	68.7		170.2 169.3	35.2,35.5 36.6	—	
12 ^1H	—	4.8(s)		3.8(brs)			2.9,3.1		
^{13}C		77.3		69.6		169.4	35.6,37.5	—	
13 $^1H^b$	—	4.3(s)		3.6(m)		—	—	—	
$^{13}C^b$	—	79.8		80.0		173.5	—	—	

[a]$CDCl_3$ relative to TMS unless otherwise indicated. [b]D_2O.

added and the suspension was mechanically stirred while the monobenzyl ether **5** (28.1 g, 95.5 mmol) was added slowly as a solution in dry DMF (500 mL). The mixture was stirred at room temperature until clear, and the tosylate **8** (47 g, 95.5 mmol) in dry DMF (250 mL) was added rapidly. The temperature was raised to 65°C for 12 h, the solvent was evaporated under reduced pressure, and the product evacuated. The product was dissolved in water and extracted with CH_2Cl_2 (3×). The combined CH_2Cl_2 extracts were dried, evaporated, and evacuated to give the product as an oil (50 g, 91 mmol, 95%). Attempts to use the product in unpurified form were unsuccessful. A portion of the original product (20 g, 32.6 mmol) was preadsorbed on deactivated Al_2O_3 (100 g, Brockman III), loaded onto a deactivated Al_2O_3 (1000 g, Brockman III) column packed with CH_2Cl_2, and eluted with a methanol gradient. Product containing fractions (0.25–0.5% MeOH) were identified by tlc (R_f 0.53, 5% MeOH/CH_2Cl_2, Merck silica gel 60 silanized), combined, dried, evaporated, and evacuated to give the solid product (8.5 g, 13.8 mmol, 43%); mp 92–94°C; $[\alpha]_D^{22}$ +57.6 (*c* 1.05); ^1H nmr and ^{13}C nmr: Table 3. *Anal.* calcd. for $C_{32}H_{46}N_4O_8$: C 62.5, H 7.5, N 9.1; found: C 60.2, H 7.4, N 8.8.

*(1R,2R,7R,8R)-N,N,N′,N′,N″,N″,N‴,N‴-Octamethyl-1,2,-7,8-tetracarboxamido-3,6-dioxaoctane-1,8-diol (**10**)*

The dibenzyl ether **9** (6.83 g, 11.1 mmol) was dissolved in 95% EtOH (20 mL) and poured over 10% Pd/C (250 mg, 2 mol% Pd). Two drops HCl were added. The suspension was hydrogenated at 50 psi (1 psi = 6.9 kPa) (Parr apparatus) for 36 h. The catalyst was filtered from the solution and evaporation and evacuation gave a solid. The product was dissolved in H_2O, neutralized with $NaHCO_3$, and continuously extracted with CH_2Cl_2 for 20 h. The organic layer was dried, evaporated, and evacuated to give the product as a gum (4.8 g, 11.1 mmol, 100%); $[\alpha]_D^{22}$ +47.9 (*c* 1.83); ^1H nmr and ^{13}C nmr: Table 3. *Anal.* calcd. for $C_{18}H_{34}N_4O_8$: C 49.8, H 7.8, N 12.9; found: C 48.2, H 7.8, N 12.3.

*(2R,3R,8R,9R,14R,15R)-N,N,N′,N′,N″,N″,N‴,N‴,N^{iv},N^{iv},-N^{v},N^{v}-Dodecamethyl-1,4,7,10,13,16-hexaoxacyclooctadecane-2,3,8,9,14,15-hexacarboxamide (**12**)*

Sodium hydride (0.12 g, 97% as a powder, 4.6 mmol) was handled in a glove bag and charged into a 3-neck 500-mL round-bottomed flask. While under inert atmosphere, dry DMF (20 mL) was added and the suspension was stirred at 0°C. The diol **10** (1 g, 2.3 mmol) was dissolved in dry DMF (30 mL) and added rapidly to the NaH suspension, and the resulting solution was stirred 1 h. The ditosylate **11** (1.38 g, 2.3 mmol) in dry DMF (30 mL) was added rapidly and the reaction allowed to proceed for 9 h at 70°C. The solvent was evaporated and the product evacuated overnight. The product was dissolved in H_2O (100 mL) and extracted with a series of solvents (Et_2O 3 × 100 mL, CH_2Cl_2 3 × 100 mL, continuous CH_2Cl_2). The crude product was

Can. J. Chem. Downloaded from www.nrcresearchpress.com by 93.93.197.157 on 09/07/12
For personal use only.

obtained upon drying, evaporating, and evacuating the continuous extract (0.85 g, 1.2 mmol, 53%).

Products from a variety of cyclizations were combined for chromatography. The combined crude product (3.5 g, 5 mmol) was dissolved in CH_2Cl_2 and loaded onto a neutral Al_2O_3 (200 g) column packed with CH_2Cl_2. The column was eluted with a methanol gradient (0–0.5%, flush with 2.5%). Product was obtained in seven fractions at 0.25% $MeOH/CH_2Cl_2$. The combined fractions were dried, evaporated, and evacuated to give a white powder (2.1 g, 3 mmol, 60%) (cyclization yield 32%); $[\alpha]_D^{22}$ +87.6 (*c* 1.92); ^1H nmr and ^{13}C nmr: Table 3; ms (*m/e*) 691 (*M* + 1). *Anal.* calcd. for $C_{30}H_{54}N_6O_{12}$: C 52.2, H 7.8, N 12.2; found: C 51.5, H 7.7, N 11.9.

*(2R,3R,8R,9R,14R,15R)-1,4,7,10,13,16-Hexaoxacyclooctadecane-2,3,8,9,14,15-hexacarboxylic acid (**13**, 18C6A$_6$)*

The hexaamide **12** (1.9 g, 2.7 mmol) was dissolved in 2.5 M HCl (100 mL) and heated at 80°C for 24 h. The solvent was evaporated and the product evacuated to give a solid that was redissolved in deionized water and passed through a strong acid ion exchange resin (30 g, Dowex 50 × 8–100). Product was obtained by evaporation of the first four fractions as a white solid (1.5 g, 2.8 mmol, 100%). The product was recrystallized from hot deionized H_2O (1.0 g, 1.9 mmol, 70%).

The level of trace contamination by sodium and potassium (by Atomic Absorption Spectroscopy) was not acceptable for the sample used for the potentiometric titration. The hexaacid **14** (0.50 g) was dissolved in doubly distilled deionized H_2O (8 mL) and loaded onto a strong acid ion exchange column (15 g, Dowex 50W × 2 pa, washed with 500 mL of 1 M Fluka Puriss, p.a., H_2SO_4 followed by 2× distilled deionized water until neutral) and eluted with doubly distilled deionized H_2O. Fractions (1 mL) with pH <3 were combined, evaporated, and evacuated to give the product as a white powder (0.464 g, 94%). A sample was recrystallized from 2× distilled deionized water by slow evaporation. The large crystals obtained from water are hydrates; evacuation produces powdery, anhydrous materials used for potentiometric titration and elemental analysis; mp 113–116°C; $[\alpha]_D^{22}$ +122.1 (*c* 1.74); ^1H nmr and ^{13}C nmr: Table 3. *Anal.* calcd. for $C_{18}H_{24}O_{18}$: C 40.9, H 4.6; found: C 40.4, H 3.8.

Stability constant determinations

The general procedures and apparatus have been described previously (12, 21). The pH electrode (Fisher glass electrode) was soaked in tetramethylammonium chloride (TMACl)/HCl solutions for several weeks before initial use and stored in distilled deionized water between uses. The reference electrode (Fisher calomel) was linked to the cell via a porous plug bridge containing 0.05 M TMACl. The electrodes were calibrated with commercially available buffers at pH 2.00 and 6.86 and linearity was checked at pH 4.01. All titrations were performed in a sealed cell under a slight positive pressure of argon. For pK_a determinations, a 5.0-mL solution of ligand free acid ($(3–4) \times 10^{-4}$ M) in 0.05 M TMACl was titrated with standardized TMAOH containing 0.05 M TMACl to beyond the strong acid/strong base end point (~80 μL per ligand equivalent using 2.5×10^{-2} M TMAOH) in 2–4 μL aliquots (20 points per ligand equivalent). The data file was stored and processed as previously (21) to yield β_{10h} for the ligand. For stability constant determinations two procedures were used. One followed the procedure for pK_a determination directly, with the addition of an equivalent of metal chloride solution to the free acid before titration with base. The other used the solution resulting from the pK_a titration by addition of an equivalent of metal chloride to the basic solution. This mixture was titrated with 2.5×10^{-2} M HCl (containing 0.05 M TMACl) back to the starting acidic pH (~20 aliquots per ligand equivalent). The second method is inappropriate for metals that form insoluble hydroxo complexes. The β_{lmh} values determined by the two methods were the same within the experimental uncertainty of log β ± 0.2. Computations of the Cd^{2+}, Zn^{2+}, and Cu^{2+} systems included literature values for chloro and hydroxo complex formation (34): log β (species): 1.90 ($CdCl^+$), 2.44 ($CdCl_2$), 3.15 ($CdCl_3^-$), 3.8 ($CdOH^+$), 4.71 ($ZnOH^+$), 9.86 ($Zn(OH)_2$), 15.5 ($Zn(OH)_3^-$), 5.70 ($CuOH^+$), 13.10 ($Cu(OH)_2$), 16.9 ($Cu_2(OH)_2^{2+}$), 33.7 ($Cu_3(OH)_4^{2+}$). The calculated values for 18C6A$_4$ and 18C6A$_6$ with Zn^{2+}, Cu^{2+}, or Cd^{2+} were relatively insensitive to the literature values chosen. The values calculated for *RR*18C6A$_2$ with the same ions are much more dependent upon the values chosen. Consequently the uncertainties are greater in these cases. Ternary complex species such as 18C6A$_6^{4-}$/$CuOH^+$ (CuLOH) were tolerated by SCOGS and in some cases improved the fit considerably but this may be an artifact of the β values chosen for the hydroxo complexes. Computations of buffer capacity and species distribution as a function of pH used the algorithm COMPLEX (37) adapted for use on an HP85 microcomputer.

Acknowledgements

It is a pleasure to acknowledge the support of the Natural Sciences and Engineering Research Council of Canada through operating grants and a postgraduate scholarship (P.J.D.).

1. J. M. LEHN. Struct. Bonding, **16**, 1 (1973).
2. J. M. LEHN. Science, **227**, 849 (1985); I. O. SUTHERLAND. Chem. Soc. Rev. **15**, 63 (1986); D. J. CRAM. Angew Chem. Int. Ed. Engl. **25**, 1039 (1986).
3. J. M. LEHN. Pure Appl. Chem. **51**, 979 (1979).
4. J. P. BEHR and J. M. LEHN. Helv. Chim. Acta, **63**, 2112 (1980).
5. J. P. BEHR, J. M. LEHN, and P. VIERLING. Helv. Chim. Acta, **65**, 1853 (1982).
6. J. P. BEHR, C. J. BURROWS, R. HENG, and J. M. LEHN. Tetrahedron Lett. **26**, 215 (1985).
7. A. BASAK and H. DUGAS. Tetrahedron Lett. 273 (1986).
8. J. P. BEHR, J. M. GIRODEAU, R. C. HAYWARD, J. M. LEHN, and J. P. SAUVAGE. Helv. Chim. Acta, **63**, 2096 (1980).
9. J. P. BEHR, J. M. LEHN, D. MORAS, and J. C. THEIRRY. J. Am. Chem. Soc. **103**, 701 (1981).
10. J. J. DALY, P. SCHONHOLZER, J. P. BEHR, and J. M. LEHN. Helv. Chim. Acta, **64**, 1444 (1981).
11. H. DUGAS, P. VEROACK, and M. PTAK. Can. J. Chem. **62**, 489 (1984).
12. T. M. FYLES and D. M. WHITFIELD. Can. J. Chem. **62**, 507 (1984).
13. C. SIRLIN. Thèse de Doctorat es Sciences, Unversité Louis Pasteur, Strasbourg, France. 1982.
14. C. SIRLIN. Bull. Soc. Chim. Fr. II, 5 (1984).
15. R. D. GANDOUR, F. R. FRANCZECK, V. J. GATTO, C. MINGANTI, R. A. SCHULTZ, B. D. WHITE, K. A. ARNOLD, D. MAZZOCCHI, S. R. MILLER, and G. W. GOKEL. J. Am. Chem. Soc. **108**, 4078 (1986).
16. G. W. GOKEL, L. ESCHEGOYEN, K. A. ARNOLD, T. P. CLEARY, V. J. GATTO, D. A. GUSTOWSKI, C. HANLON, A. KAIFER, and M. KIM. Adv. Chem. Ser. **215**, 443 (1987).
17. R. J. ADAMIC, E. M. EYRING, S. PETRUCCI, and R. A. BARTSCH. J. Phys. Chem. **89**, 3752 (1985).
18. R. HILGENFELD and W. SAENGER. Top. Curr. Chem. **101**, 1 (1982).
19. C. A. CHANG, J. TWU, and R. A. BARTSCH. Inorg. Chem. **25**, 396 (1986).
20. R. M. IZATT, J. S. BRADSHAW, S. A. NIELSEN, J. D. LAMB, and J. J. CHRISTENSEN. Chem. Rev. **85**, 271 (1985).
21. L. A. FREDERICK, T. M. FYLES, N. P. GURPRASAD, and D. M. WHITFIELD. Can. J. Chem. **59**, 1721 (1981).
22. A. ANANTANARAYAN, V. A. CARMICHAEL, P. J. DUTTON, T. M. FYLES, and M. J. PITRE. Synth. Commun. **16**, 1771 (1986).
23. A. ANANTANARAYAN, P. J. DUTTON, T. M. FYLES, and M. J. PITRE. J. Org. Chem. **51**, 752 (1986).
24. H. O. KALINOWSKI, D. SEEBACH, and G. CRASS. Angew. Chem. Int. Ed. Engl. **14**, 762 (1975).
25. T. M. FYLES, C. A. MCGAVIN, and D. M. WHITFIELD. J. Org. Chem. **49**, 753 (1984).
26. I. G. SAYCE. Talanta, **15**, 1397 (1968); **18**, 653 (1971).
27. R. D. SHANNON. Acta Crystallogr. Sect. A: Cryst. Phys. Diffr. Theor. Gen. Crystallogr. **A32**, 751 (1976).

Can. J. Chem. Downloaded from www.nrcresearchpress.com by 93.93.197.157 on 09/07/12
For personal use only.

28. D. J. CRAM and V. N. TRUEBLOOD. Top. Curr. Chem. **98**, 43 (1981).
29. R. M. IZATT, R. E. TERRY, B. L. HAYMORE, L. D. HANSEN, N. K. DALLEY, A. G. AVONDET, and J. J. CHRISTENSEN. J. Am. Chem. Soc. **98**, 7620 (1976).
30. H. HOILAND, J. A. RINGSETH, and T. S. BRUN. J. Solution Chem. **8**, 779 (1979).
31. J. ASCENSO and V. M. S. GIL. Can. J. Chem. **58**, 1376 (1980).
32. D. D. PERRIN and B. DEMPSEY. Buffers for pH and metal ion control. Chapman and Hall Ltd., London. 1974. Chap. 7.
33. J. M. LEHN and J. P. SAUVAGE. J. Am. Chem. Soc. **97**, 6700 (1975).
34. L. G. SILLEN and A. E. MARTELL. Stability constants of metal-ion complexes. Chem. Soc. Special Publication No. 17 (1964); No. 24 (1971).
35. C. J. PETERSEN. J. Am. Chem. Soc. **89**, 7017 (1967).
36. J. H. BABLER and K. P. SPINA. Synth. Commun. **14**, 1313 (1984).
37. G. GINZBURG. Talanta, **23**, 149 (1976).

Can. J. Chem. Downloaded from www.nrcresearchpress.com by 93.93.197.157 on 09/07/12
For personal use only.

Nucleofugality effects in the pyridine promoted formation of esters from 2-substituted ethanesulfonyl chlorides[1]

JAMES FREDERICK KING, JOHN HENRY HILLHOUSE, TOYANNE MARIE LAURISTON, AND KISHAN CHAND KHEMANI

Department of Chemistry, University of Western Ontario, London, Ont., Canada N6A 5B7

Received October 6, 1987

JAMES FREDERICK KING, JOHN HENRY HILLHOUSE, TOYANNE MARIE LAURISTON, and KISHAN CHAND KHEMANI. Can. J. Chem. **66**, 1109 (1988).

The products of reaction of a series of 10 2-substituted ethanesulfonyl chlorides, X—$CH_2CH_2SO_2Cl$ (1), with neopentyl alcohol and pyridine-d_5 in nitromethane-d_3 showed three reaction pathways depending on the nucleofugality of the substituent, X. These routes lead, respectively, to (*i*) the corresponding neopentyl ester (**4**), via the sulfene (**3**) (low substituent nucleofugality); (*ii*) a mixture of ester **4** and neopentyl ethenesulfonate (**5**), by the same route except for a partial loss of the 2-substituent during trapping of the sulfene (**3**) (intermediate nucleofugality); and (*iii*) a mixture of the ethenesulfonate (**5**) and the pyridino-betylate (**4***g*) esters, arising from initial elimination of HX to form ethenesulfonyl chloride (**2**) followed by its further reaction (high substituent nucleofugality). A set of nucleofugality values closely related to, and partly complementing, those derived by Stirling and co-workers can be estimated from the product ratios in those reactions proceeding (at least in part) by route (*ii*) above. Old reports of anomalous products from 1,2-ethanedisulfonyl chloride (**1***i*) and 2-chloroethanesulfonyl chloride (**1***j*) are simply accounted for on the basis of the initial conversion to ethenesulfonyl chloride (**2**).

JAMES FREDERICK KING, JOHN HENRY HILLHOUSE, TOYANNE MARIE LAURISTON et KISHAN CHAND KHEMANI. Can. J. Chem. **66**, 1109 (1988).

Les produits provenant des réactions d'une série de 10 chlorures d'éthanesulfonyle substitués en position 2, X—$CH_2CH_2SO_2Cl$ (**1**), avec l'alcool néopentylique et la pyridine-d_5, dans le nitrométhane-d_3 proviennent de trois voies différentes qui dépendent de la nucléofugacité du substituant X. Ces voies conduisent respectivement à (*i*) ester néopentylique correspondant (**4**), par la biais du sulfène **3** (lorsque la nucléofugacité du substituant est faible); (*ii*) un mélange de l'ester **4** et l'éthènesulfonate de néopentyle (**5**) qui proviennent de la même voie, excepté pour la perte partielle du substituant en position 2 qui se produit lors du piégeage du sulfène **3** (lorsque la nucléofugacité du substituant est intermédiaire); et (*iii*) un mélange des esters éthènesulfonate (**5**) et pyridinio-bétylate (**4***g*) qui proviennent d'une élimination initiale de HX, conduisant au chlorure d'éthènesulfonyle (**2**), qui est suivie de sa réaction (lorsque la nucléofugacité du substituant est élevée). En se basant sur les rapports des produits qui se forment au cours des réactions (au moins en partie) qui suivent la voie (*ii*) mentionnée plus haut, on peut évaluer un ensemble de valeurs de nucléofugacité qui ressemble et qui complète celui de Stirling et ses collaborateurs. Des rapports antérieurs concernant la formation de produits anormaux à partir des chlorures d'éthanedisulfonyle-1,2 (**1***i*) et de chloro-2 éthanesulfonyle (**1***j*) peuvent facilement être expliqués en se basant sur une conversion initiale en chlorure d'éthènesulfonyle (**2**).

[Traduit par la revue]

Can. J. Chem. Downloaded from www.nrcresearchpress.com by 93.93.197.157 on 09/07/12
For personal use only.

In the course of an extended investigation of the mechanism of sulfonyl transfer (1–4), we have looked at the reactions of a number of 2-substituted ethanesulfonyl chlorides (**1**) with water or alcohols in the presence of tertiary amines, and have been struck by the variation in the nature of the reaction products. We now report a more systematic examination of this reaction with substrates bearing substituents having a sizeable range in nucleofugality (or "leaving group ability"). Our results enable us to (*a*) assign the mechanistic pathways leading to the various observed products, (*b*) estimate nucleofugality values as defined by Stirling and co-workers (5, 6) for some of these leaving groups, and also (*c*) to provide insight into some inadequately explained observations with 1,2-ethanedisulfonyl and 2-chloroethanesulfonyl chlorides (**1***i* and **1***j*) dating back over many years.

Results and discussion

Reaction conditions and products

Compounds **1***a* – **1***j* were treated with pyridine-d_5 and neopentyl alcohol in nitromethane-d_3 at room temperature; the ^{1}Hmr spectrum was run within 20 min and the product composition so determined summarized in Table 1. Neopentyl alcohol was chosen because (*a*) its sulfonic esters are comparatively unreactive and hence less subject to subsequent transformation than those of other alcohols, and (*b*) the neopentyl grouping gives characteristic, uncluttered ^{1}Hmr spectra with both starting materials and products; nitromethane was found to be a suitable solvent capable of keeping both covalent and ionic products in solution. In all cases the products were found to be stable to the conditions of the reaction, i.e., the product composition given in Table 1 is that of the primary, kinetically controlled reaction products.

Reaction pathways to products

Inspection of the results in Table 1 reveals three patterns of reactivity: (*i*) ordinary formation of the corresponding ester (**4**), illustrated by the reactions of **1***a–c*; (*ii*) production of a mixture of the corresponding ester (**4**) and the ethenesulfonate ester (**5**), exemplified by the reactions of the 2-phenylthio- and 2-acetoxyethanesulfonyl chlorides (**1***e* and **1***f*); and (*iii*) generation of a mixture of the ethenesulfonate (**5**) and betylate (**4***g*) esters displayed by the disulfonyl chloride (**1***i*) and 2-chloroethanesulfonyl chloride (**1***j*). Two of these patterns have been observed previously. The first of these is, of course, just the normal formation of alkanesulfonic esters via the sulfene (**3**), i.e., the regular "sulfene route". The third set of products, i.e., the ~2:1 mixture of **5** and **4***g*, has also been obtained from the reaction of ethenesulfonyl chloride under the same conditions (1). The simplest explanation of this result is that these products arise by initial conversion of the starting sulfonyl

[1]Part 31 in the series Organic Sulfur Mechanisms. Part 30: J. F. King, S. M. Loosmore, and J. H. Hillhouse. In preparation.

TABLE 1. Relative proportions of esters (**4**, **4***g*, and **5**) in the reaction of 2-substituted ethanesulfonyl chlorides (**1**) and related compounds[a]

Substrate	Relative proportions 4	4*g*	5	Mechanistic pathway
1*a* (X = H)	100	—	—	Sulfene route (**1** → **3** → **4**)
1*b* (X = HO)	100[b]	—	—	
1*c* (X = $NpOSO_2$)	>95[c]	—	—	
1*d* (X = $PhSO_2$)	97	—	3	Sulfene + elimination route (**1** → **3** → **4** + **5**)
1*e* (X = PhS)	85	—	15	
1*f* (X = MeCOO)	40	—	60	
1*g* (X = pyridinio)	33	(33)	67	Sulfene + elimination and alkene routes[d]
1*h* (X = 3,5-$(NO_2)_2C_6H_3COO$)	9	10	81[e]	
1*i* (X = $ClSO_2$)	—	33	67[f]	Alkene route (**1** → **2** → **3***g* → **4***g* + **5**)
1*j* (X = Cl)	—	32	68	
CH_2=$CHSO_2Cl$ (**2**)	—	33	67	(**2** → **3***g* → **4***g* → **5**)[g]
$ClCH_2CH_2SO_2Br$ (**6**)	—	33	67	Alkene route (like **1***i*)

[a]Conditions: sulfonyl halide (~0.3 M), pyridine-d_5 (1.5–2.0 M), and neopentyl alcohol (~0.6 M) in nitromethane-d_3 at room temperature. Ester ratios were determined from ^{1}Hmr spectra (T-60 or XL-200), which also showed the esters (**4**, **4***g*, and **5**) to be the principal products (usually >90%), often along with small amounts of hydrolysis products.

[b]Actual product composition: **4***b*, 16%, $C_5H_5N^+CH_2CH_2SO_3^-$, 84% (see also ref. 4).

[c]No sign of **4***g* or **5** in the T-60 ^{1}Hmr spectrum.

[d]Incursion of about 20% of the alkene route in the reaction of **1***g* is deduced from labelling experiments described elsewhere (1). In the reaction of **1***h* the ratio of sulfene to alkene routes is ~70:30 with most (87%) of the sulfene (**3***h*) undergoing elimination to give **5** and a small amount (13%) going to **4***h* (see text).

[e]Actual product composition: **5**, 50%; **4***g*, 7%; **4***h*, 7%; neopentyl 3,5-dinitrobenzoate, 13%; pyridinium 2-(3,5-dinitrobenzoyloxy)ethanesulfonate, 7%; pyridinium ethenesulfonate, 16%. The last three probably arise largely by trapping of the sulfene (**3***h*) by the liberated 3,5-dinitrobenzoate anion (cf. ref. 2), followed by further reaction of the resultant mixed anhydrides.

[f]The product showed no sign of any **4***c*, which would have been formed if any **4***i* (=**1***c*) had been produced.

[g]The assignment of this mechanism is discussed elsewhere (1).

chloride into ethenesulfonyl chloride (**2**) (the "alkene route"), followed by vinylogous attack of pyridine on **2** to give the cationic sulfene (**3***g*), which in turn forms the characteristic mixture of ethenesulfonate (**5**) and betylate (**4***g*) (ref. 1, cf. also ref. 3). Reaction of **1***j* with a tertiary amine such as 2,6-lutidine or triethylamine is, in fact, the usual preparative route to **2**, and the transitory presence of **2** in the reaction of **1***j* with pyridine is to be expected. In accord with this we found that **1***i* with 2,6-lutidine gave a product with the characteristic ^{1}Hmr spectrum of **2**.

Except for the special case of **1***g*, the other product composition pattern, namely the mixture of the ethenesulfonate (**5**) and 2-substituted ethanesulfonate (**4**), has evidently not been noted before. The normal esters (**4**) presumably arise from the sulfene (**3**), since the deuterated alcohol yields α-deuterated esters. The ethenesulfonate esters **4***e–f* and **4***h* cannot arise from ethenesulfonyl chloride (**2**) because under these conditions **2** always gives a roughly 2:1 mixture of **5** and **4***g* (1), and the latter is not present in any detectable amount in the reaction products from **1***e*, **1***f*, and **1***h*. Accordingly, we propose that **4***e–f* and **4***h* are formed from the sulfenes (**3***e–f* and **3***h*) by elimination of X^- in the course of the trappng reaction.

Such a proposal requires a mechanistic picture in which it is possible to account for the conversion of 2-acetoxyethanesulfonyl chloride (**1***f*), for example, into the sulfene (**3***f*) without any loss of acetate anion to form **2**, and, at the same time, in the sulfene trapping step to lose acetate anion more quickly than protonation to form the acetoxy-ester (**4***f*). This requirement is nicely consistent with the variable transition state mechanism for elimination reactions, with the conversion of **1***f* into **3***f* proceeding by an E1cB-like E2 reaction, and the trapping of the sulfene (**3***f*) with the alcohol a stepwise process going via a discrete carbanion (**7**, X = AcO), which

$$XCH_2CH_2SO_2OR \leftarrow \underset{\mathbf{4}}{} XCH_2\bar{C}H—SO_2OR \rightarrow \underset{\mathbf{7}}{}$$

$$CH_2{=}CHSO_2OR + X^- \quad (\mathbf{5})$$

either eliminates X^- (AcO^- in this case) to give **5** or is protonated by the (unspecified) proton source to give **4**; this mechanism has already been discussed in connection with the trapping of **3***g* in aqueous media (3). With such a picture only a *partial* negative charge is enough to extrude the comparatively nucleofugal chloride anion from **1***f* to give **3***f* (without any loss of acetate anion to form **2**), but, with the formation of the full negative charge on the carbon in **7** in the sulfene trapping step, loss even of the less nucleofugal acetate anion competes successfully with the alternative reaction, the rapid protonation of the α-sulfonyl carbanion.

The reaction of the 3,5-dinitrobenzoyloxy compound (**1***h*) illustrates the particularly delicate balance between the possible pathways in each of the two stages of the reaction. Since formation of the betylate (**4***g*) from the pyridinio-sulfene (**3***g*) is accompanied by roughly twice the quantity of ethenesulfonate ester (**5**), the 10% yield of **4***g* indicates that about 30% of the total product is formed via **2**, while the remaining 70% arises by direct conversion to the sulfene (**3***h*); the reaction pathways may be summarized as follows: **1** → **3** → **4***h*, 9%; **1** → **3** → **5**, 61%; **1** → **2** → **5**, 20% (total yield of **5**, 81%); **1** → **2** → **4***g*, 10%. Reaction of **1***h* obviously gives the highest yield of **5** of any of the substrates used in this study, but it would appear unlikely

Can. J. Chem. Downloaded from www.nrcresearchpress.com by 93.93.197.157 on 09/07/12
For personal use only.

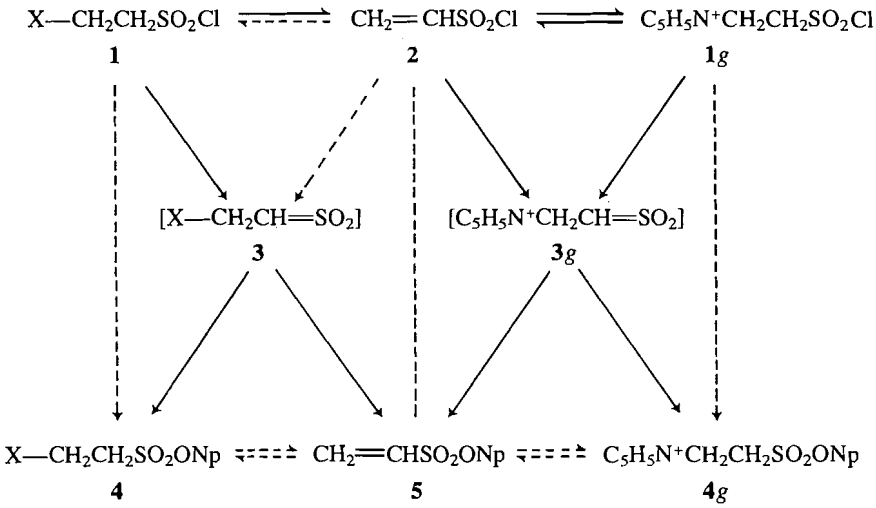

Np = $CH_2C(CH_3)_3$

	X		X
a	H	*f*	$CH_3CO—O$
b	HO	*g*	$C_5H_5N^+$
c	$NpOSO_2$	*h*	$3,5—(NO_2)_2C_6H_3CO—O$
d	$PhSO_2$	*i*	$ClSO_2$
e	PhS	*j*	Cl

SCHEME 1

that direct quantitative formation of **5** can be obtained (with the present conditions, at least) merely be altering the leaving group (X), since increased reactivity in the leaving group would probably lead to more **2** and so to more betylate (**4***g*), whereas diminished reactivity would likely result in more **4** relative to **5**.

In principle, the balance among the different reaction pathways should be alterable by changing the leaving group on the sulfur atom. The reaction of 2-chloroethanesulfonyl bromide (**6**) was looked at with an eye to seeing if the more reactive bromide would lead to preferential formation of the sulfene (**3**, X = Cl) rather than the ethenesulfonyl halide, but the product was the same as that from **2** (see Table 1) and therefore presumably arose by way of ethenesulfonyl bromide and the pyridinio-sulfene (**3***g*).

Other possible pathways

Scheme 1 includes a number of dashed arrows representing reactions which, though a priori reasonable, may be shown to participate, at most, only to a very limited extent under the conditions of this study. As has already been noted above, interconversion of products under the specified conditions is excluded by control experiments. Much longer intervals than those used in the experiments summarized in Table 1, however, may lead to change; the composition of the mixture of **4***g* and **5**, for example, alters from 33:67 to 88:12 on long standing, thereby providing a convenient route to **4***g* (1). Also, the required authentic specimen of **4***j* was obtained by allowing **1***j* to react for 10 days with neopentyl alcohol in CH_2Cl_2 (without added base), i.e., by the direct conversion **1***j* to **4***j*. That such a direct reaction is not important in the presence of pyridine, however, is shown by the deuteration products observed with neopentyl alcohol-*d*. With a 10-fold excess of neopentyl alcohol-*d* (93% NpOD, 7% NpOH), 2-phenylthioethanesulfonyl chloride (**1***e*) gave (in addition to 14% of **5**) a mixture of $PhSCH_2CHDSO_2ONp$ and $PhSCH_2CH_2SO_2ONp$ (**4***e*) in the ratio of 87:13; when one recalls that protons are introduced into the reaction mixture by the formation of the sulfene (**1** → **3**), it is clear that the reaction products are readily accounted for by the sulfene mechanism (**1** → **3** → **4**) without any detectable incursion of the direct displacement reaction. Similar results were encountered in deuteration experiments with **1***g* and **1***h*. Ethanesulfonyl chloride (**1***a*) is the only substrate that shows any sign of the direct displacement process. With a 10-fold excess of NpOD (containing 12% of NpOH) **1***a* gave a 56:44 mixture of the mono- and undeuterated esters, CH_3CHDSO_2ONp and $CH_3CH_2SO_2ONp$ (**4***a*). It seems likely that a portion of this reaction product arises via the direct reaction (**1** → **4**). It should be noted that **1***a* is much the least reactive of the substrates used in this study, with reaction completion requiring more than 22 h as compared with 5 min for the other substrates (**1***b*–*j* and **2**); with such slow sulfene formation it is perhaps not surprising that another process, such as a general base or possibly a nucleophilic catalyzed direct displacement, may enter the picture. The much greater ease of sulfene formation from substrates **1***b*–**1***g* is consistent with the above-mentioned E1cB-like E2 picture, since the substituents *b*–*g* are all distinctly electron withdrawing relative to hydrogen and would be expected to facilitate development of the partial negative charge at C-1. This expectation is in accord with Thomas and Stirling's observation (7) that the rate of the closely related detritiation of $PhSO_2CHTCH_2Z$ with ethoxide in ethanol correlated with the σ^* values of the CH_2Z grouping ($\rho^* = 4.89$).

As has been mentioned elsewhere (1) the interconversion **1***g* ⇌ **2** occurs to a minor extent, leading to some $CH_2=CDSO_2ONp$ in the product. This is not seen in the material from **1***e* or **1***h*, nor do any of the reactions with NpOD show any sign of the dideuterated product, $XCH_2CD_2SO_2ONp$ (which would be expected if any XCH_2CHDSO_2Cl had been formed, cf. refs. 3 and 8); hence other **1** ⇌ **2** interconversions are evidently precluded.

Can. J. Chem. Downloaded from www.nrcresearchpress.com by 93.93.197.157 on 09/07/12
For personal use only.

Can. J. Chem. Downloaded from www.nrcresearchpress.com by 93.93.197.157 on 09/07/12
For personal use only.

The insensitivity of product ratios to changes in concentrations of reagents and the mechanism of trapping of the sulfene (3)

In the hope of gaining insight into the challenging problem of how sulfenes are converted into the final products, we carried out a series of experiments with 2-phenylthioethanesulfonyl chloride (**1***d*) in which the various ingredients of the reaction mixture were systematically altered. The remarkable result was that the product composition changed very little. The ratio of ethenesulfonate to 2-phenylthioethanesulfonate esters (**5**:**4***e*) was not altered (from 16:84) by increasing the concentration of NpOH from 0.66 to 1.53 to 2.70 M; changing the pyridine-d_5 concentration from ~1.5 to 4.2 M lowered the percentage of **4***e* slightly (to 76%), but addition to pyridinium chloride (2.0 M, [pyridine] 3.95 M) made no discernible further change (78% **4***e*). In the presence of NpOD the change in product ratios was less than experimental uncertainty: e.g., with a 51:49 mixture of NpOD:NpOH (in 10-fold excess) the products were **5** (13%), $PhSCH_2CHDSO_2ONp$ (41%), and $PhSCH_2CH_2SO_2ONp$ (46%), and with 93:7 NpOD:NpOH the ratio of the same products as 14:75:11; any isotope effect on either the ratio of **5** to **4***e* or on the isotopic composition of the phenylthio ester would appear to be minimal (i.e., <1.2).

The results would appear to rule out protonation of **7** by NpOH or pyridinium ion from the general body of the solution; uptake of hydrogen ion from the solvent is already excluded by the absence of deuterium in the product from the reaction with NpOH in CD_3NO_3. Recalling our earlier experiments showing that the reaction of phenylsulfene, $PHCH{=}SO_2$, with alcohols is base catalyzed (9), we suggest the following sequence:

$$\underset{\mathbf{3}}{XCH_2CH{=}SO_2} + ROH + B \longrightarrow \underset{\mathbf{7}}{XCH_2\bar{C}HSO_2OR\ \overset{+}{B}H}$$

$$\underset{\mathbf{7}}{XCH_2\bar{C}HSO_2OR\ \overset{+}{B}H} \xrightarrow{k_H} \underset{\mathbf{4}}{XCH_2CH_2SO_2OR} + B$$

$$\underset{\mathbf{7}}{XCH_2\bar{C}HSO_2OR\ \overset{+}{B}H} \xrightarrow{k_E} \underset{\mathbf{5}}{CH_2{=}CHSO_2OR} + B + HX$$

By this scheme the actual hydrogen ion transfer step is a unimolecular ion-pair process. One should note that the ion pair (**7**) as initially formed may be presumed to have the BH^+ ion in the vincinity of the RO group, i.e., well away from the other two sulfonyl oxygens and hence not, in the first instance, in the arrangement preferred for protonation of the α-sulfonyl carbanion (near the C^- in the internal bisector of the O—S—O angle) (cf. ref. 10). Once this latter "preferred" setup is arrived at, it is likely that the hydrogen ion transfer will be extremely fast; we expect on this basis that k_H will not be much influenced by either the particular isotope or the nature of X. It follows that the variation in product ratios from these reactions must be assigned to the intrinsic differences in k_E, the rate constant for the elimination from **7**, and hence that these product ratios may be used to estimate nucleofugalities of the X groups, as discussed in the next section.

Nucleofugalities from product ratios

Stirling and co-workers (5, 6) have placed the "leaving group ability" of nucleofugal groups in alkene-forming reactions on a quantitative basis by examining a series of olefin-forming eliminations of the following general type in which G is a carbanion-stabilizing function like $PhSO_2$, CN, or PhCO, and Z is the "leaving group" or nucleofuge:

$$G{-}CH_2CH_2Z + B^- \underset{k_{-1}[BH]}{\overset{k_1[B^-]}{\rightleftharpoons}} G{-}\bar{C}HCH_2{-}Z \xrightarrow{k_2} G{-}CH{=}CH_2 + Z^-$$

For an $(E1cB)_R$ process (i.e., one in which $k_{-1}[BH] > k_2$) the observed rate constant for the overall conversion of G—CH_2CH_2Z to G—$CH{=}CH_2$ is given by $k_{obs} = k_1k_2/k_{-1}[BH]$, and hence

$$[1] \quad \log k_2 = \log (k_{obs}/k_1) + \log (k_{-1}[BH])$$

Stirling and co-workers define the "leaving group rank" or "nucleofugality" of Z by the function $\log (k_{obs}/k_1) + 11$, i.e., by using the value of $\log k_2$ obtained by assigning $k_{-1}[BH]$ equal to 10^{11}; k_{obs} is obtained by measuring the rate of the overall elimination, and k_1 from the rate of exchange of hydrogens α to G.

In our system it is evident that, if the mechanism in the previous section holds, the product ratio [**5**]/[**4**] is simply equal to k_E/k_H, and hence

$$[2] \quad \log k_E = \log ([\mathbf{5}]/[\mathbf{4}]) + \log k_H$$

If, as we argue above, k_H is insensitive to X, then the function $\log ([\mathbf{5}]/[\mathbf{4}])$ gives a scale of nucleofugalities analogous to Stirling's. The similarities of structure are so great that it is tempting to place our relative results on the same absolute basis by adding the same scaling term, i.e., +11.

The nucleofugalities thus obtained are listed in Table 2. Comparison with Stirling's results, though limited, suggests a measure of correspondence, and at the same time points up some of the difficulties associated with these procedures. The value 9.5 for the phenylsulfonyl group is between those (8.7 and 9.6) derived by Stirling (from reactions in which G = $PhSO_2$ and CN, respectively). That for the acetoxy function (11.2) suggests roughly comparable magnitudes for $k_{-1}[BH]$ and k_2 in the reaction of $AcOCH_2CH_2SO_2Ph$, i.e., a mechanism on the $(E1cB)_I$–$(E1cB)_R$ borderline, in rough accord with the conclusion (which, though reasonable, was not rigorously proved) that this is an $(E1cB)_I$ process (11). It may be noted that the present experiments make it possible to obtain a relative nucleofugality for the acetoxy group, a function for which this is not possible by the Stirling procedure because the appropriate substrates do not react by the requisite $(E1cB)_R$ mechanism.

The nucleofugality of the phenylthio function, relative to that of the phenylsulfonyl group, continues to be puzzling. Stirling (6) reported that PhS was less nucleofugal than $PhSO_2$ in the reactions of Z—CH_2CH_2—CN and about the same in those of Z—$CH_2CH_2SO_2Ph$; we find that PhS is rather *more* nucleofugal than $PhSO_2$ in our system. This anomaly, though by no means fully understood, may well be at least partly steric in origin.

In addition to the above, admittedly approximate, quantitative assignments of nucleofugality, we note that the failure of **1***b* to yield any neopentyl ethenesulfonate (**5**) shows hydroxide to be a weaker nucleofuge than $PhSO_2$. We also saw no sign of **5** from the neopentyloxysulfonyl substrate (**1***c*), but the nmr instrument was less sensitive than that used with the phenylsulfonyl-sulfonyl chloride (**1***d*) and our results do not prove any real difference in nucleofugality between $PhSO_2$ and $NpOSO_2$.

It is also of interest to look at the other end of the reactivity scale represented in this study. In a competition experiment between the disulfonyl chloride (**1***i*) and the chlorosulfonyl chloride (**1***j*) we found that **1***i* reacted almost six times faster than **1***j* (after inclusion of the statistical factor). The chlorosulfonyl

TABLE 2. Nucleofugalities of some of the 2-substituents

Group	log [5]/[4][a]	Nucleofugality[b]
Phenylsulfonyl	−1.5	9.5
Phenylthio	−0.8	10.2
Acetoxy	0.2	11.2
Pyridinio[c]	0.3	11.3
3,5-Dinitrobenzoyloxy[d]	0.8	11.8

[a]Obtained from the yields of **5** and **4** given in Table 1, except as otherwise noted.

[b]Nucleofugality = log ([**5**]/[**4**]) + 11 (see text).

[c]Calculated from the average of the proportions of **4***g* and **5** for the five reactions in Table 1 giving these products (only).

[d]From the ratio [**5**]/[**4***g*] = 61/9 (the respective percentages from **3***g* only), see text.

group, though not commonly regarded as a nucleofuge, has been observed to behave as such in a number of nucleophilic displacements (ref. 12 and refs. cited); the comparative unfamiliarity of reactions involving the loss of the $ClSO_2$ function is due, however, not to low nucleofugality itself but to the ease of other reactions of sulfonyl chlorides such as nucleophilic displacement at sulfur, elimination to form the sulfene, or reduction by nueclophilic attack at the chlorine atom. We must note explicitly that our observations do not permit a numerical assignment of the nucleofugalities of the Cl and $ClSO_2$ groups as defined by Stirling and co-workers. The lack of deuterium in the neopentyl ethenesulfonate formed from **1***j*, NpOD, and pyridine shows that the conversion of **1***j* to **2** is not an $(E1cB)_R$ process, but rather either an E2 or $(E1cB)_I$ reaction, and hence, as Stirling has emphasized (6), not capable of providing a nucleofugality value as defined.

Our results do, as the following argument shows, lead to the conclusion that both the chloro and chlorosulfonyl functions are the most nucleofugal of the 10 groups examined in this study. If we make the reasonable assumption that the sulfonyl chlorides all have the same possible reaction pathways, the finding that **1***h* and **1***j* reacted only by way of **2** can have only two possible causes: (*i*) the sulfene formation (**1** → **3**) is slow for **1***i* and **1***j*, or (*ii*) the C=C bond formation (**1** → **2**) is fast for **1***i* and **1***j*. It is very difficult to imagine, however, how the formation of $ClCH_2CH{=}SO_2$ or $ClSO_2CH_2CH{=}SO_2$ could be so much slower than the analogous reaction yielding $RCOOCH_2CH{=}SO_2$ or, especially, $NpOSO_2CH_2CH{=}SO_2$; this would require a substituent effect leading to quite remarkable differences among similar substituents;[2] it is much simpler to conclude that **1** → **2** is fast with **1***i* and **1***j*, i.e., the chloro and chlorosulfonyl groups are more nucleofugal than 3,5-dinitrobenzoyloxy and the others. The high reactivity of chlorosulfonyl and bromosulfonyl leaving groups relative to other sulfonyl-containing functions has been noted before and ascribed to a fragmentation process in which the SO_2—Hal bond is partly broken in the transition state (14).

Earlier reports of the anomalous reactions of **1**i *and* **1**j

As noted in the introduction there are a number of reports, some dating back to the previous century, describing unexpected reactions of 1,2-ethanedisulfonyl and 2-chloroethanesulfonyl chlorides (**1***i* and **1***j*) (15–22). With nucleophiles of the general formula ZH, such as water, alcohols, or amines, the major products of these reactions were never the orthodox derivatives, $ZSO_2CH_2CH_2SO_2Z$ or $ClCH_2CH_2SO_2Z$, but rather the ethenesulfonate, $CH_2{=}CHSO_2Z$, or the formal product of further addition of ZH, i.e., $ZCH_2CH_2SO_2Z$; thus (*a*) **1***i* with hot water gives mainly SO_2, HCl, and $CH_2{=}CHSO_3H$ (15, 17, 22), and (*b*) **1***j* with aniline yields $CH_2{=}CHSO_2NHPh$ (**8**) and (or) $PhNH_2{}^+CH_2CH_2SO_2NHPh\ Cl^-$ (**9**) (16–21). In the light of the present work it is highly likely that these products arise by initial formation of ethenesulfonyl chloride (**2**) followed by vinylogous reaction to form the sulfene **3** (X = Z^+). If Clutterbuck and Cohen (20) are correct in their assertion that **8** and **9** are both stable to the reaction conditions, then the different ratios of **8** and **9** found under the various reported conditions arise from different ratios of elimination to protonation in the trapping of **3** (X = Z^+). Further work is in order to check aspects of the earlier reports and to sort out the factors that control the variations in product ratios.

Experimental

Instrumentation and methods

Where not otherwise indicated, reagent grade chemicals and solvents were used as received. Melting points were determined on a Reichert Hot Stage and are uncorrected. Infrared spectra were obtained using Beckman 4250 and Bruker IFS 32 FTIR spectrometers and refer to chloroform solutions except as otherwise noted. The ^{1}Hmr spectra were obtained with Varian T60, XL100, XL200, and XL300 spectrometers, with all reported chemical shifts from the latter three instruments. The ^{13}Cmr spectra were run on Varian XL200 and XL300 spectrometers. Spectra recorded in $CDCl_3$ and CD_3NO_2 were calibrated with Me_4Si (TMS) and those recorded in D_2O either with sodium trimethylsilylpropionate (TSP) or sodium trimethylsilylpropanesulfonate (DSS). Mass spectra were run on a Varian MAT-311A spectrometer. The cold finger distillation apparatus used in microdistillation has been described elsewhere (23). Solvent evaporation on work-up was carried out using a Büchi rotary evaporator connected to a water aspirator.

Reactants

(*a*) Ethanesulfonyl chloride (**1***a*), commercial sample distilled, bp 54°C (4 Torr; 1 Torr = 133.3 Pa); ^{1}Hmr δ: 1.57 (t, 3H), 3.82 (q, 2H); neopentyl 2-(chlorosulfonyl)ethanesulfonate (**1***c* = **4***i*) (10), mp 108°C; ^{1}Hmr (CD_3NO_2) δ: 1.12 (s, 9H), 3.89 (t, 2H), 4.06 (s, 2H), 4.35 (t, 2H); 2-(phenylsulfonyl)ethanesulfonyl chloride (**1***d*) (24), mp 172–174°C (lit. (24) mp 173°C); ^{1}Hmr (CD_3NO_2) δ: 3.75–3.95 and 4.1–4.3 (sym A_2B_2 m, 4H), 7.6–8.05 (m, 5H); 2-(phenylthio)ethanesulfonyl chloride (**1***e*) (12); ^{1}Hmr (CD_3NO_2) δ: 3.45–3.62 and 4.15–3.98 (sym m(A_2B_2), 4H), and 7.3–7.57 (m, 5H); 2-acetoxyethanesulfonyl chloride (**1***f*) (25), bp 72–73°C (0.1 Torr); n_D^{25} 1.4639 (lit. (25) n_D 1.4633); ^{1}Hmr ($CDCl_3$) δ: 2.13 (s, 3H), 4.07 (t, 2H), 4.65 (t, 2H); *N*-(2-chlorosulfonylethyl)pyridinium chloride (**1***g*, Cl^-) (3); 2-(3,5-dinitrobenzoyloxy)ethanesulfonyl chloride (**1***h*), see below; 1,2-ethanedisulfonyl chloride (**1***i*) (26), mp 91°C (lit. (26) mp 91°C); ^{1}Hmr (CD_3NO_2) δ: 4.52 (s); 2-chloroethanesulfonyl chloride (**1***j*) (27), bp 58°C (3 Torr); ^{1}Hmr (CD_3NO_2) δ: 4.07–4.14 (app t, 2H) and 4.26–4.33 (app t, 2H). Neopentyl alcohol-*d* was prepared by multiple exchange of a solution of commercial NpOH in organic solution with D_2O; specifically, NpOH (4 g) in D_2O (10 mL) and ether (100 mL), followed by further shaking of the ether layer with three 15-ml D_2O portions, then evaporation of the ether, dissolution in CH_2Cl_2 followed by another D_2O wash (15 mL), followed by separation and evaporation of the CH_2Cl_2 layer, gave 3.1 g of product; deuterium content was estimated at 93% by comparison of the integral of the OH ^{1}Hmr peak (δ 1.72) with the ^{13}C satellite of the CH_2 signal (δ 2.95).

*(b) 2-(3,5-Dinitrobenzoyloxy)ethanesulfonyl chloride (***1**h*)*

3,5-Dinitrobenzoyl chloride (freshly prepared from the acid plus $SOCl_2$ and recrystallized from benzene, mp 73°C; 4.4 g, 19.1 mmol) was fused with sodium 2-hydroxyethanesulfonate (2.5 g, 16.9 mmol)

[2]Orthodox substituent effects have been observed in at least one sulfene-generating reaction: the rates of formation of $ArCH{=}SO_2$ from $ArCH_2SO_2O—C_6H_3—2,4(NO_2)_2$ in an $(E1cB)_I$ reaction process showed an excellent correlation with σ^- (with ρ^- 2.38, r = 0.996) (13).

Can. J. Chem. Downloaded from www.nrcresearchpress.com by 93.93.197.157 on 09/07/12
For personal use only.

Can. J. Chem. Downloaded from www.nrcresearchpress.com by 93.93.197.157 on 09/07/12
For personal use only.

in a Pyrex test tube (25 mL) over a microburner for 5 min. The almost clear hot liquid so obtained was cooled to room temperature and quenched with water (250 mL) by grinding the test tube in a mortar and pestle. The aqueous solution was filtered and washed several times with CH_2Cl_2 (5 × 100 mL) to remove any dinitrobenzoic acid. The aqueous layer was then concentrated to 50 mL on a rotary evaporator. The white crystals of sodium 2-(3,5-dinitrobenzoyloxy)ethanesulfonate that formed within a few hours were removed by filtration and air-dried, mp 307–310°C (5.6 g, 97%); ir (KBr) ν_{max}: 3100 (m), 2960, 2900 (w), 1740 (s) 1635 (m), 1540 (s), 1460 (m), 1350 (s), 1280 (s), 1200 (vs), 1050 (m), 1000 (m), 925 (m), 800 (m), 770 (m), 750 (m), 700 (s) cm^{-1}; ^{1}Hmr (D_2O) δ: 3.47 (t, 2H), 4.81 (t, 2H), 9.18–9.3 (m, 3H); ^{13}Cmr (D_2O) δ: 52.3, 64.6, 126.1, 135.8, 151.4, and 166.9. The salt (1.22 g, 3.57 mmol) was ground with excess PCl_5 (12 g) in a mortar, which was then covered loosely with a watch glass and put in a preheated oven at 210°C for 10 min. The contents of the mortar were then ground again while still hot, whereupon reaction occurred immediately to yield a pasty mass. Water (30 mL) was then added and the aqueous suspension extracted with CH_2Cl_2 (5 × 100 mL). The organic extracts were combined, dried with anhydrous $MgSO_4$, and evaporated to yield a colorless oil that solidified upon cooling (1.133 g, 94%). Recrystallization from chloroform afforded 2-(3,5-dinitrobenzoyloxy)ethanesulfonyl chloride (**1***h*) as white needles (0.909 g, 75%); mp 115–116°C; ir ($CHCl_3$) ν_{max}: 3110 (m), 2980 (w), 1750 (s), 1630 (m), 1550 (vs), 1380 (s), 1345 (vs), 1275 (vs), 1170 (s), 1155 (s), 1070 (m) cm^{-1}; ^{1}Hmr ($CDCl_3$) δ: 4.19–4.25 and 5.01–5.06 (symmetrical multiplet, 4H) and 9.19–9.3 (m, 3H); ^{13}Cmr ($CDCl_3$) δ: 59.4, 63.1, 122.9, 129.5, 132.2, 148.6, and 161.7. *Exact Mass* calcd. for $C_9H_7N_2O_8SCl$: 337.9611; found: 337.9613.

*(c) 2-Chloroethanesulfonyl bromide (**6**)*

2-Chloroethanesulfonyl chloride (**1***j*) (719 mg, 4.41 mmol) was stirred with four equivalents of aqueous (8 mL) sodium sulfite (2.22 g, 17.64 mmol) at 0°C for 18 h. Bromine was then added dropwise until the brownish color of bromine persisted. The reaction mixture was quickly transferred to a separatory funnel and extracted with methylene chloride (5 × 50 mL). The extracts were washed with 5% sodium bisulfite solution until the bromine color had disappeared. The CH_2Cl_2 layer was dried with $MgSO_4$ and the solvent evaporated to yield crude **6** (624 mg, 68%); cold finger vacuum distillation (bath temperature 110°C, 1.4 Torr) gave **6** as a pale yellow liquid (574 mg, 63% yield); ir (film) ν_{max}: 2992 (w), 2930 (w), 1364 (vs) 1310 (m), 1157 (vs), 660 (m) cm^{-1}; ^{1}Hmr (CD_3NO_2) δ: 4.40–4.33 and 4.11–4.04 (m, 4H, A_2B_2) ppm; ^{13}Cmr (CD_3NO_2) δ: 70.7 and 37.6 ppm; *Anal.* calcd. for $C_2H_4O_2BrCl$: C 11.58, H 1.94, S 15.45, Br 38.51, Cl 17.09; found: C11.49, H 1.89, S 15.35, Br 38.70, Cl 17.21.

Neopentyl esters

(a) Previously reported esters

Neopentyl 2-hydroxyethanesulfonate (**4***b*) (4), also, see preparation of **4***h*. *N*-[2-(Neopentyloxysulfonyl)ethyl]pyridinium chloride (**4***g*) 1, 23).

*(b) Neopentyl ethanesulfonate (**4**a)*

Pyridine-d_5 (0.713 mL, 8.32 mmol) was added to a solution of ethanesulfonyl chloride (**1***a*) (214 mg, 1.66 mmol) in nitromethane-d_3 and the reaction mixture allowed to stand for 22 h; work-up followed by careful removal of the last traces of CH_2Cl_2 under reduced presure gave **4***a* as a pale yellow liquid (280 mg, 93%); ir ($CHCl_3$) ν_{max}: 2970 (s), 1550 (m), 1465 (m), 1350 (vs), 1165 (s), 960 (vs), 840 (vs) cm^{-1}; ^{1}Hmr (CD_3NO_2) δ: 1.00 (s, 9H), 1.37 (t, 3H), 3.19 (q, 2H), 3.87 (s, 2H); ^{13}Cmr (CD_3NO_2) δ: 8.7, 26.5, 32.7, 45.1, 80.4. *Anal.* calcd. for $C_7H_{16}O_3S$: C 46.64, H 8.95, S 17.79; found: C 46.84, H 9.31, S 17.65.

*(c) Dineopentyl 1,2-ethanedisulfonate (**4**c)*

Pyridine (0.75 mL, 9.3 mmol) was added to a solution of neopentyl 2-(chlorosulfonyl)ethanesulfonate (**1***c* = **4***i*) (10) (0.60 g, 2.15 mmol) and neopentyl alcohol (0.50 g, 5.5 mmol) in methylene chloride (25 mL) and the mixture allowed to stand for 18 h. The diester (**4***c*) was obtained on work-up as a yellowish solid (0.35 g, 50%), which after recrystallization from ethyl acetate – petroleum ether (bp 60–80°C) melted at 150–152°C; ir (CH_2Cl_2) ν_{max}: 3055 (w), 2955 (m), 2860 (w), 1465 (w), 1349 (s), 1215 (w), 1165 (s), 1149 (s), 938 (vs), 915 (s) cm^{-1}; ^{1}Hmr (CD_3NO_2) δ: 1.01 (s, 9H), 3.57 (s, 2H), 3.94 (s, 2H). *Anal.* calcd. for $C_{12}H_{26}O_6S_2$: C43.62, H 7.93, S 19.41; found: C 43.73, H 8.10, S 19.62.

*(d) Neopentyl 2-(phenylsulfonyl)ethanesulfonate (**4**d)*

A mixture of 2-(phenylsulfonyl)ethanesulfonyl chloride (**1***d*) (202 mg, 0.75 mmol), neopentyl alcohol (132 mg, 1.50 mmol), and pyridine (300 mg, 3.79 mmol) in nitromethane (20 mL) was allowed to stand at room temperature for 19 h. Recrystallization from hexanes of the crude product (158 mg, 65%) obtained after work-up gave **4***d* as white needles, mp 110.5–111°C; ir ($CHCl_3$) ν_{max}: 2960 (m), 1360 (s), 1323 (s), 1164 (s), 1145 (s), 950 (s) cm^{-1}; ^{1}Hmr ($CDCl_3$) δ: 0.98 (s, 9H), 3.63–3.44 (sym m, 4H), 3.95 (s, 2H), 7.61–8.07 (m, 5H); ^{13}Cmr ($CDCl_3$) δ: 25.9, 31.8, 43.2, 50.2, 80.0, 127.9, 130.0, 134.5, 137.6. *Exact Mass* calcd. for $C_{13}H_{20}O_5S_2$: 320.0752; found: 320.0758.

*(e) Neopentyl 2-(phenylthio)ethanesulfonate (**4**e)*

Recrystallization (hexanes) of the crude product (69% yield) obtained from **1***e* exactly as **4***d* was prepared from **1***d* gave needles, mp 71.5–72.5°C; ir ($CHCl_3$) ν_{max}: 2960 (m), 1480 (m), 1440 (w), 1350 (s), 1160 (s), 960 (s), 840 (m) cm^{-1}; ^{1}Hmr ($CDCl_3$) δ: 1.30 (s, 9H), 3.07 (s, 4H), 3.59 (s, 2H), 7.1–7.6 (m, 5H); ^{13}Cmr ($CDCl_3$) δ: 26.0, 27.5, 31.7, 49.7, 78.8, 127.3, 129.2, 130.5, 133.1. *Exact Mass* calcd. for $C_{13}H_{20}O_3S_2$: 288.0854; found: 288.0853.

*(f) Neopentyl 2-acetoxyethanesulfonate (**4**f)*

The mixture of neopentyl ethenesulfonate (**5**) and neopentyl 2-acetoxyethanesulfonate (**4***f*) (obtained from reaction of 2-acetoxyethanesulfonyl chloride (**1***f*) with neopentyl alcohol and triethylamine) was placed under reduced pressure (0.2 Torr, oil bath temperature 90°C) to evaporate the **5** (bp 62°C, 0.02 Torr). The colorless oily residue gave the following data: ir (neat) ν_{max}: 2970 (m), 1750 (s), 1350 (s), 1240 (s), 1160 (s), 1030 (m), 955 (s), 840 (m) cm^{-1}; ^{1}Hmr ($CDCl_3$) δ: 1.00 (s, 9H), 2.09 (s, 3H), 3.46 (t, 2H), 3.91 (s, 2H), 4.49 (t, 2H); (CD_3NO_2) δ: 1.01 (s, 9H), 2.08 (s, 3H), 3.63 (t, 2H), 3.95 (s, 2H), 4.57 (t, 2H). *Anal.* calcd. for $C_9H_{18}O_5S$: C 45.36, H 7.61, S 13.46; found: C 45.41, H 7.52, S 13.31.

*(g) Neopentyl 2-(3,5-dinitrobenzoyloxy)ethanesulfonate (**4**h)*

A mixture of 2-hydroxyethanesulfonyl chloride (**4**) (1.99 g, 13.8 mmol), neopentyl alcohol (12.15 g, 137.8 mmol), and trimethylamine (3.25 g, 55.1 mmol) was allowed to stand at room temperature for 2 h. Conventional work-up followed by removal of the excess alcohol over an extended period on the rotary evaporator gave a crude product (2.5 g, 93%) with spectra appropriate to neopentyl 2-hydroxyethanesulfonate, as follows: ir ($CHCl_3$) ν_{max}: 1352 (vs), 1171 (vs), 967 (vs) cm^{-1}; ^{1}Hmr ($CDCl_3$) δ: 1.00 (s, 9H), 3.38 (t, 2H), 3.91 (s, 2H), 4.06 (t, 2H); ^{13}Cmr ($CDCl_3$) δ: 26.0, 52.3, 56.5, 73.2, 79.1. Reaction of 1 g (5.1 mmol) of this material with 3,5-dinitrobenzoyl chloride, as described above for the preparation of **1***h* followed by work-up gave crude **4***h* (1.7 g, 85%), which after recrystallization from benzene–pentane gave **4***h* as white crystals melting at 90–92°C; ir ($CHCl_3$) ν_{max}: 3095 (m), 1735 (vs), 1625 (m), 1540 (s), 1455 (m), 1350 (vs), 1268 (vs), 1150 (vs), 1067 (m), 950 (vs), 840 (m) cm^{-1}; ^{1}Hmr (CD_3NO_2) δ: 0.99, (s, 9H), 3.77 (s, 2H), 3.99 (s, 2H), 4.87 (t, 2H), 9.09–9.19 (m, 3H); ^{13}Cmr (CD_3NO_2) δ: 2.64, 32.7, 49.6, 61.1, 81.1, 124.0, 130.6, 134.4, 150.0, 163.8. *Exact Mass* calcd. for $C_{14}H_{18}O_9N_2S$: 390.0733; found: 390.0734.

*(h) Neopentyl 2-chloroethanesulfonate (**4**j)*

A solution of 2-chloroethanesulfonyl chloride (**1***j*) (3.5 g, 21.6 mmol) and neopentyl alcohol (1.9 g, 21.6 mmol) in methylene chloride (5 mL) was allowed to stand at 50°C for 10 days. The solvent was evaporated and the oily brown residue distilled under reduced pressure in a short-path cold-finger distillation apparatus (bath temperature 120°C, 0.5 Torr) giving a colorless oil (0.6 g, 15%); ir (neat) ν: 2960 (m), 1355 (s), 1205 (s), 1170 (vs), 995 (s), 935 (s), 845 (m) cm^{-1}; ^{1}Hmr ($CDCl_3$) δ: 1.00 (s, 9H), 3.70 (m, 4H), 3.93 (s, 2H); (CD_3NO_2) δ: 1.02 (s, 9H), 3.62 (m, 2H), 3.92 (m, 2H), 3.96 (s, 2H). *Anal.* calcd. for $C_7H_{15}ClO_3S$: C 39.16, H 7.04, Cl 16.51, S 14.93; found: C 39.31, H 7.09, Cl 16.42, S 15.03.

Can. J. Chem. Downloaded from www.nrcresearchpress.com by 93.93.197.157 on 09/07/12
For personal use only.

Reaction of the 2-substituted ethanesulfonyl chlorides with neopentyl alcohol and pyridine-d_5

Pyridine-d_5 (50–70 μL, 0.6–0.8 mmol) was injected into a solution of the sulfonyl chloride (**1**) (0.10–0.16 mmol) and neopentyl alcohol (0.20–0.26 mmol) in CD_3NO_2 (0.25–0.40 mL) at 37°C and contained in an nmr tube. The ^{1}Hmr spectrum was run (within 5 min), after thorough mixing of the contents of the tube. With **1***c*–**1***j* the reaction was then complete, but with **1***a* and **1***b* the product composition given in Table 1 (determined from integration of Me_3CCH_2O— singlets) was obtained after 18 and 8 h, respectively. The spectra were in all cases found consistent (by comparison with authentic spectra) with the mixture of esters described in Table 1. With **1***e* (which is presumably slightly wet and not readily purified), the spectrum showed peaks corresponding to 18% of the hydrolysis product pyridinium 2-(phenylthio)ethanesulfonate (as shown by comparison with the spectrum of an authentic specimen); with the other reactions small amounts (<5%) of the corresponding hydrolysis products were sometimes in evidence.

The following series of experiments with 2-phenylthioethanesulfonyl chloride (**1***e*) was carried out as above (in CD_3NO_2) using the following quantities given in the order **1***e*, NpOH, pyridine-d_5, total volume, and forming the relative yields of products **4***e*:**5**: (*a*) 72.5 mg (0.307 mmol, 0.033 M), 54 mg (0.613 mmol, 0.66 M), 131 μL (1.53 mmol, 1.65 M), 0.93 mL, gave 84:16; (*b*) 74.7 mg (0.316 mmol, 0.35 M), 55.7 mg (0.632 mmol, 0.70 M), 135 μL (1.59 mmol, 1.77 M), 0.90 mL, gave 82.5:17.5; (*c*) 75.8 mg (0.321 mmol, 0.305 M), 141 mg (1.60 mmol, 1.53 M), 137.5 μL (1.60 mmol, 1.53 M), 1.05 mL, gave 84.6:15.4; (*d*) 68.8 mg (0.29 mmol, 0.27 M), 256 mg (2.80 (mmol, 2.70 M), 124 μL (0.145 mmol, 1.35 M), 1.08 mL, gave 82:18; (*e*) 64.4 mg (0.270 mmol, 0.262 M), 120 mg (1.36 mmol, 1.31 M), 374 μL (4.36 mmol, 4.20 M), 1.04 mL, gave 76:24; (*f*) 58.0 mg (0.245 mmol, 0.245 M), 108 mg (1.23 mmol, 1.23 M), plus a stock solution of pyridinium-d_5 chloride and pyridine-d_5 in CD_3NO_2 to yield a reaction mixture initially 2.05 M and 3.95 M, respectively, total volume 1.0 mL, gave 78:22.

Deuterium labelling experiments

2-Phenylthioethanesulfonyl chloride (**1***e*) (62.3 mg, 0.26 mmol) was mixed with NpOH and NpOD in CD_3NO_2; ^{1}Hmr integration showed a 49:51 ratio of NpOH:NpOD. Pyridine-d_5 was added quickly; initial concentrations of **1***e*, NpOH–NpOD mixture, pyridine-d_5: 0.173, 1.76, 0.88 M; total volume 1.50 mL. The ^{1}Hmr spectrum after 5 min showed (*a*) no sign of unreacted **1***e*, (*b*) ratio of **5** to total (deuterated and undeuterated) neopentyl 2-phenylthioethanesulfonate, 13:86, (*c*) no sign of deuteration on the neopentyl ethenesulfonate; the spectrum after a further 15 min was unchanged. The reaction mixture was worked up by pouring into water and extracting with CH_2Cl_2, followed by drying and evaporation of the solvent. Integration of the two halves of the A_2B_2 pattern in the ^{1}Hmr spectrum of the product ($CDCl_3$, with Eu(fod)$_3$, 41 mg, 0.092 mmol) gave the ratio of $PhSCH_2CH_2SO_2ONp$ to $PhSCH_2CHDSO_2ONp$ as 53:47. A similar experiment with NpOD:NpOH 93:7, the following initial concentrations of the above reagents (same sequence) 0.142, 1.42, 0.707 M, and total volume 1.50 mL, gave a 14:86 ratio of **5** to the phenylthio-ester, with the latter 88% $PhSCH_2CHDSO_2ONp$.

Pyridine-d_5 (47 μL, 0.55 mmol) was added to a solution of **1***h* (37 mg, 0.11 mmol) and NpOD (92% OD, 7% OH) (97.5 mg, 1.09 mmol) in CD_3NO_2 (total volume of solution, 0.86 mL); the C-2 protons of **4***g* and **4***h* appeared as doublets at δ 5.31 and 4.89 in the ^{1}Hmr spectrum, showing them to be largely monodeuterated at C-1, but quantitative estimation of deuteration was not feasible.

The ^{1}Hmr spectra of the following reaction mixtures showed signals appropriate to the indicated product composition: (*a*) from **1***d* (80.4 mg, 0.42 mmol), NpOD (95% OD) (374 mg, 4.20 mmol), pyridine-d_5 (180 μL, 2.10 mmol) in CD_3NO_2 (total volume 1.45 mL), $PhSO_2CH_2CHDSO_2ONp$ 90%, $PhSO_2CH_2CH_2SO_2ONp$ 8%, **5** ~2%; (*b*) the product (total volume 1.11 mL) from **1***j* (36.7 mg, 0.225 mmol), NpOD (95% OD) (201 mg, 2.25 mmol), pyridine-d_5 (97 μL, 1.13 mmol), a roughly 2:1 mixture of **5** (with no sign, i.e. estimated <2%, of $CH_2{=}CDSO_2ONp$) and the betylate, with the C-2 proton signal appearing as a doublet, indicating it to be mostly monodeuterated ($C_5H_5N^+CH_2CHDSO_2ONp$); (*c*) pyridine-d_5 (108 μL, 1.26 mmol) with **1***a* (32.3 mg, 0.25 mmol), NpOD (88% OD) (224 mg, 2.5 mmol) in CD_3NO_2 (total volume 0.69 mL), after 22 h at room temperature, CH_3CHDSO_2ONp 56% and $CH_3CH_2SO_2ONp$ 44%.

Reaction of ethane-1,2-disulfonyl chloride (1i) with 2,6-lutidine

2,6-Lutidine (25 μL, 0.21 mmol) was injected into a solution of the disulfonyl chloride (**1***i*) (36 mg, 0.16 mmol) in $CDCl_3$ (~0.5 mL) in an nmr tube at 37°C. The ^{1}Hmr spectrum was run immediately after thorough mixing and showed the characteristic signals of ethenesulfonyl chloride (**2**) (and the lutidine – lutidinium ion mixture) with no sign of unreacted **1***i*; addition of authentic **2** enhanced the peaks assigned to **2**.

Relative reactivities of 1,2-ethanedisulfonyl and 2-chlorosulfonyl chlorides (1i and 1j)

Pyridine-d_5 (44 μL, 0.52 mmol) was added by microsyringe to a mixture of equivalent amounts (0.52 mmol) of **1***i* (117 mg) and **1***j* (84 mg) with neopentyl alcohol (91 mg, 1.03 mmol) in CD_3NO_2 (0.5 mL) in an nmr tube. The mixture was shaken vigorously and the ^{1}Hmr spectrum run immediately. Integration of the singlet at δ 4.65 due to **1***i* and the pair of triplets at 4.40 and 4.13 due to **1***j*, relative to the sum of the neopentyl methylene singlets at 3.98, 3.80, 3.23 arising from **4***g*, **5**, and unreacted neopentyl alcohol, gave the proportions of unreacted **1***i* and **1***j* as 55 and 95%, respectively. Addition of another 44-μL portion of pyridine led to 8 and 80% of unreacted **1***i* and **1***j*. Values for the rate constant ratio were obtained from the expression

$$k_{1i}/k_{1j} = (\log [1i]/[1i]_0)/(\log [1j]/[1j]_0)$$

and found to be respectively 11.6 and 11.2, from the two sets of results, average, 11.4; the statistically corrected ratio for the rates of elimination to form **2** on a per hydrogen basis from **1***i* vs. **1***j*, 5.7.

Control experiments

(*a*) A solution of **4***f* (30 mg, 0.13 mmol), neopentyl alcohol (18 mg, 0.2 mmol), and pyridine-d_5 (50 μL, 0.6 mmol) in CD_3NO_2 (0.4 mL) showed no observable change in ^{1}Hmr spectrum over a 14-h interval. Pyridinium-d_5 chloride (20 mg, 0.17 mmol) was added; no change in the spectrum was found after a further 4 h. Similar solutions of **4***d*, **4***e*, **4***h*, and **4***j* with pyridine-d_5 and neopentyl alcohol showed unchanged ^{1}Hmr spectra after, respectively, 10, 10, 10, and 90 min at room temperature; after 5 days the solution of **4***j* showed a trace (<5%) of **5** but no sign of **4***g*. (*b*) Pyridine-d_5 (0.1 mL, 0.12 mmol) was added to a solution of **2** (38 mg, 0.3 mmol), neopentyl alcohol (50 mg, 0.57 mmol), and dry acetic acid (6 μL, 0.1 mmol) at 37°C. The ^{1}Hmr spectrum showed **5** (72%) and **4***g* (28%), with no sign of any **4***f*. (*c*) A solution of **1***h* (0.14 mmol) and NpOH (0.14 mmol) in CD_3NO_2 showed no change in ^{1}Hmr spectrum on standing at 50°C for 6 days.

Acknowledgement

We thank the Natural Sciences and Engineering Research Council of Canada for financial support of this work.

1. J. H. HILLHOUSE. Ph.D. thesis, University of Western Ontario, 1982. Chap. 2.
2. J. F. KING. Acc. Chem. Res. **8**, 10 (1975).
3. J. F. KING, J. H. HILLHOUSE, and S. SKONIECZNY. Can. J. Chem. **62**, 1977 (1984).
4. J. F. KING and J. H. HILLHOUSE. Can. J. Chem. **61**, 1583 (1983).
5. D. J. MARSHALL, P. J. THOMAS, and C. J. M. STIRLING. J. Chem. Soc. Perkin Trans. 2, 1898 (1977).
6. C. J. M. STIRLING. Acc. Chem. Res. **12**, 198 (1979).
7. P. J. THOMAS and C. J. M. STIRLING. J. Chem. Soc. Perkin Trans. 2, 1909 (1977).
8. J. F. KING, R. P. BEATSON, and J. M. BUCHSHRIBER. Can. J. Chem. **55**, 2323 (1977)
9. J. F. KING and Y. I. KANG. J. Chem. Soc. Chem. Commun. 52 (1975).

10. E. BLOCK. Reactions of organosulfur compounds. Academic Press, New York. 1978. pp. 50–53.
11. D. R. MARSHALL, P. J. THOMAS, and C. J. M. STIRLING. J. Chem. Soc. Perkin Trans. 2, 1914 (1977).
12. J. F. KING and K. C. KHEMANI. Can. J. Chem. **63**, 619 (1985).
13. J. F. KING and R. P. BEATSON. Tetrahedron Lett. 973 (1975).
14. J. F. KING and D. J. H. SMITH. J. Am. Chem. Soc. **89**, 4803 (1967).
15. W. KÖNIGS. Ber. **7**, 1163 (1874).
16. H. LEYMANN. Ber. **18**, 870 (1885).
17. E. P. KOHLER. Am. Chem. J. **19**, 728 (1897), **20**, 680 (1898).
18. W. AUTENRIETH and P. RUDOLPH. Ber. **34**, 3470 (1901).
19. W. AUTENRIETH and J. KOBURGER. Ber. **36**, 3626 (1903).
20. P. W. CLUTTERBUCK and J. B. COHEN. J. Chem. Soc. **121**, 120 (1922).
21. A. A. GOLDBERG. J. Chem. Soc. 464 (1945).
22. S. M. MCELVAIN, A. JELINEK, and K. RORIG. J. Am. Chem. Soc. **67**, 1578 (1945).
23. J. F. KING, S. M. LOOSMORE, M. ASLAM, J. D. LOCK, and M. J. MCGARRITY. J. Am. Chem. Soc. **104**, 7108 (1982).
24. S. P. MCMANUS, M. R. SMITH, F. T. HERRMANN, and R. A. ABRAMOVITCH. J. Org. Chem. **43**, 647 (1978).
25. R. ANSCHÜTZ. Justus Liebigs Ann. Chem. **415**, 64 (1918).
26. B. C. SAUNDERS. J. Chem. Soc. 684 (1950).
27. A. LE BERRE, A. ETIENNE, and B. DUMAITRE. Bull. Soc. Chim. Fr. 954 (1973).

Can. J. Chem. Downloaded from www.nrcresearchpress.com by 93.93.197.157 on 09/07/12
For personal use only.

Structural studies of organoboron compounds. XXX.[1] 1,9-Dimethyl-3,5,7-triphenyl-2,4,6,8-tetraoxa-1,9-diazonia-5-bora-3,7-diboratatricyclo[5.4.0.0^{3,9}]undecane

HENNING AMT AND WOLFGANG KLIEGEL

Institut für Pharmazeutische Chemie, der Technischen Universität Braunschweig, Beethovenstraße 55, 3300 Braunschweig, Bundesrepublik Deutschland

AND

STEVEN J. RETTIG AND JAMES TROTTER

Department of Chemistry, University of British Columbia, 2036 Main Mall, Vancouver, B.C., Canada V6T 1Y6

Received September 17, 1987

HENNING AMT, WOLFGANG KLIEGEL, STEVEN J. RETTIG, and JAMES TROTTER. Can. J. Chem. **66**, 1117 (1988).

Details of the preparation and physical properties of the title compound are given. Crystals of 1,9-dimethyl-3,5,7- triphenyl-2,4,6,8-tetraoxa-1,9-diazonia-5-bora-3,7-diboratatricyclo[5.4.0.0^{3,9}]undecane are orthorhombic, a = 9.4026(3), b = 9.4663(2), c = 24.7462(9) Å, Z = 4, space group $P2_12_12_1$. The structure was solved by direct methods and was refined by full-matrix least-squares procedures to R = 0.036 and R_w = 0.038 for 1536 reflections with $I \geq 3\sigma(I)$. The three six-membered and two seven-membered rings comprising the tricyclo[5.4.0.0^{5,9}]undecane ring system all have boat or boat-like conformations. Important bond lengths (corrected for libration) are: B(sp^3)—N = 1.649(6) and 1.668(6), B(sp^3)—O(N) = 1.492(5) and 1.497(6), B(sp^3)—O[B(sp^2)] = 1.444(6) and 1.438(5), B(sp^3)—C = 1.600(6) and 1.594(7), B(sp^2)—O = 1.357(6) and 1.370(6), B(sp^2)—C = 1.574(6) Å.

HENNING AMT, WOLFGANG KLIEGEL, STEVEN J. RETTIG et JAMES TROTTER. Can. J. Chem. **66**, 1117 (1988).

On rapporte les détails de la préparation et de la détermination de la structure du composé mentionnné dans le titre. Les cristaux du diméthyl-1,9 triphényl-3,5,7 tétraoxa-2,4,6,8 diazonia-1,9 bora-5 diborata-3,7 tricyclo[5,4,0,0^{3,9}]undécane sont orthorhombiques avec a = 9,4026(3), b = 9,4663(2) et c = 24,7462(9) Å, Z = 4 et groupe d'espace $P2_12_12_1$. On a résolu la structure par des méthodes directes et on l'a affinée par la méthode des moindres carrés (matrice entière) jusqu'à des valeurs de R = 0,036 et R_w = 0,038 pour 1536 réflexions avec $I \geq 3\sigma(I)$. Les trois cycles à six chaînons et les deux cycles à sept chaînons formant le système tricyclo[5.4.0.0^{3,9}]undécane sont tous dans des conformations bateaux ou qui ressemblent à des bateaux. Les longueurs de liaison importantes (corrigées pour la libration) sont: B(sp^3)—N = 1,649(6) et 1,668(6), B(sp^3)—O(N) = 1,492(5) et 1,497(6), B(sp^3)—O[B(sp^2)] = 1,444(6) et 1,438(5), B(sp^3)—C = 1,600(6) et 1,594(7), B(sp^2)—O = 1,357(6) et 1,370(6) et B(sp^2)—C = 1,574(6) Å.

[Traduit par la revue]

Introduction

The condensation of *N,N'*-methylenebis(*N*-methylhydroxylamine) and phenylboronic acid does not lead to the strained tricyclooctane ring system **1** ("dinoradamantane" skeleton) but gives the bicyclooctane **2** (1) as was confirmed by X-ray crystal structure analysis (2). We have now attempted to synthesize a less strained ring-enlarged homolog of **1** with the tricyclononane structure **4** ("nortwistane" skeleton) by reaction of *N,N'*-dihydroxy-*N,N'*-dimethyl-1,2-ethanediamine **3** with phenylboronic acid. The crystalline reaction product turned out to be neither a tricyclic (**4**) nor a bicyclic (**5**) 1:2-condensate of **3** and phenylboronic acid. Quantitative elemental analyses and nmr spectra revealed instead a 1:3-condensation product **6**. Reaction of **3**[2] and phenylboronic acid in a molar ratio of 1:3 gave **6**, expectedly, in better yield. Unfortunately the chemical and spectroscopic data of **6** were not sufficient to decide between possible alternative structures which include the tricycloundecane ring system A (known as the "4-homotwistane" skeleton (4)) and the bicycloundecane B which both incorporate a seven-membered ring. The tricycloundecane C and the bicycloundecane D, containing eight-membered rings, and the monocyclic undecane ring system E having fluxional N—B coordination are also among the possible structures. An X-ray crystallographic analysis has been carried out in order to provide a definitive structural assignment.

Experimental

N,N'-dihydroxy-N,N'-dimethyl-1,2-ethanediamine, 3

A solution of KBH_4 (3.2 g, 60 mmol) in 50 mL of water is added dropwise to a solution of *N,N'*-1,2-ethanediylidenebis(methanamine)-*N,N'*-dioxide (2.3 g, 20 mmol) (3) in 100 mL of water, warmed to 40°C. The reaction mixture is stirred 24 h at room temperature. Tartaric acid (5 g, 25 mL 20% aqueous solution) is added to the reaction mixture until it is weakly acidic. The reaction mixture is then neutralized (pH 7–8) with $NaHCO_3$. The solution is evaporated to dryness and the remaining solid extracted with 4 × 30 mL hot absolute ethanol. Cooling down of the collected ethanolic solutions yields 1.3 g (55%) of colorless crystals. Melting point 157°C (from ethanol). Infrared (KBr): 3190 cm^{-1} (O—H). ^{1}H nmr (d_6-DMSO/TMS) δ(ppm) = 2.51 (s, 2 CH_3), 2.70 (s, CH_2CH_2), 7.76 (s, br, 2 OH). *Anal.* calcd. for $C_4H_{12}N_2O_2$: C 39.99, H 10.07, N 23.31; found: C 39.83, H 10.04, N 22.99.

1,9-Dimethyl-3,5,7-triphenyl-2,4,6,8-tetraoxa-1,9-diazonia-5-bora-3,7-diboratatricyclo[5.4.0.0^{3,9}]undecane, 6A

3 (0.24 g, 2 mmol) and phenylboronic acid ((*a*) 0.48 g, 4 mmol, or (*b*) 0.72 g, 6 mmol) are heated in 50 mL benzene under reflux conditions for 1 h using a Dean–Stark trap for continuous water removal. The solution is then evaporated, and the dry residue dissolved in benzene. After addition of petroleum ether and cooling a colorless substance crystallizes. Yields: (*a*) 0.27 g (42%), (*b*) 0.65 g (76%). Melting point (decomp.) 201–203°C (from acetone/ether/petroleum ether). ^{1}H nmr (d_6-DMSO/TMS): δ(ppm) = 2.71 (s, 2 CH_3), 3.58 and

[1]Part XXIX: ref. 47.

[2]Compound **3** has been synthesized by reduction of the bis(*N*-methyl)nitrone of glyoxal (3) with potassium tetrahydroborate.

Can. J. Chem. Downloaded from www.nrcresearchpress.com by 93.93.197.157 on 09/07/12
For personal use only.

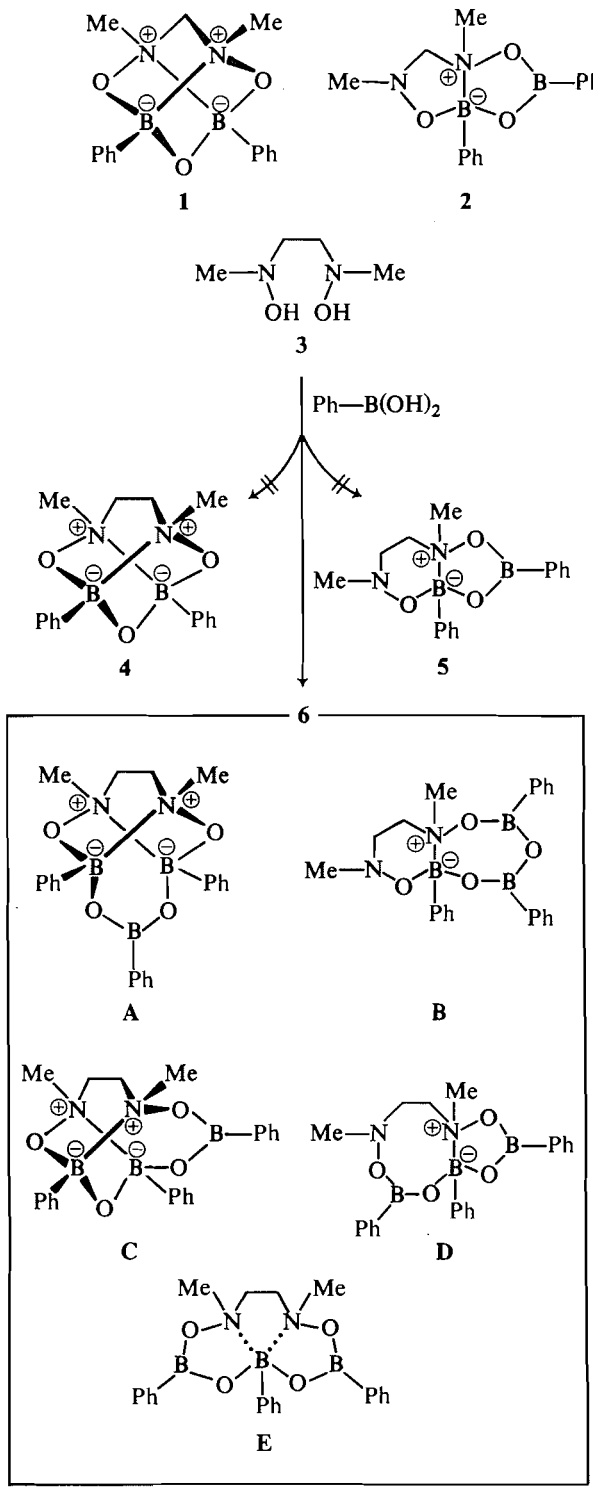

3.78 (m, m, N—CH_2CH_2—N), 7.3–7.4 (m, 9 phenyl-H), 7.8–8.0 (m, 6 phenyl-H). *Anal.* calcd. for $C_{22}H_{25}B_3N_2O_4$: C 63.84, H 6.09, B 7.84, N 6.77; found: C 63.35, H 6.09, B 7.92, N 6.81. Crystals suitable for X-ray analysis were obtained by recrystallization from acetone/ether/petroleum ether (2:1:drops).

X-ray crystallographic analysis

A crystal bounded by the six faces (followed by the distances in mm between parallel faces): {0 0 1}, 0.22, {0 1 0}, 0.32, ±(2 0 1), 0.40, was mounted in a general orientation. Unit-cell parameters were refined by least-squares on 2 sin θ/λ values for 25 reflections (2θ = 50–83°) measured on a diffractometer with Cu-$K\alpha$ radiation ($\lambda(K\alpha_1)$ = 1.540562, $\lambda(K\alpha_2)$ = 1.544390 Å). Crystal data at 22°C are:

$C_{22}H_{25}B_3N_2O_4$ f.w. = 413.9

Orthorhombic, a = 9.4026(3), b = 9.4663(2), c = 24.7462(9) Å, V = 2202.6(1) Å^3, Z = 4, ρ_c = 1.248 Mg m^{-3}, $F(000)$ = 872, μ(Cu-$K\alpha$) = 6.33 cm^{-1}. Absent reflections: $h00$, h odd, $0k0$, k odd, and $00l$, l odd, uniquely indicate the space group $P2_12_12_1$ (D_2^4, No. 19).

Intensities were measured with nickel-filtered Cu-$K\alpha$ radiation on an Enraf-Nonius CAD4-F diffractometer. An ω–2θ scan at 1.7–10.0° min^{-1} over a range of (1.10 + 0.14 tan θ) degrees in ω (extended by 25% on both sides for background measurement) was employed. Data were measured to 2θ = 150°. The intensities of three check reflections, measured every 3600 s throughout the data collection, remained constant to within 4%. After data reduction,[3] an absorption correction was applied using the Gaussian integration method (5, 6). Transmission factors ranged from 0.809 to 0.878 for 120 integration points. Of the 2588 independent reflections measured, 1536 (59.4%) had intensities

TABLE 1. Final positional (fractional × 10^4) and isotropic thermal parameters (U × 10^3 Å^2)* with estimated standard deviations in parentheses

Atom	x	y	z	U_{eq}
O(1)	4223(3)	2327(3)	9705(1)	48
O(2)	2943(3)	3949(3)	9102(1)	50
O(3)	3003(3)	1655(3)	8700(1)	53
O(4)	5309(3)	2810(3)	8582(1)	52
N(1)	4966(4)	1305(4)	9373(1)	50
N(2)	5551(4)	3720(4)	9039(1)	51
C(1)	6821(5)	3116(6)	9310(2)	62
C(2)	6496(5)	1590(5)	9465(2)	59
C(3)	4559(5)	−84(5)	9605(2)	65
C(4)	5840(6)	5128(5)	8803(2)	69
C(5)	4258(5)	4909(5)	9905(2)	52
C(6)	5044(6)	4713(6)	10374(2)	71
C(7)	5004(8)	5695(8)	10791(2)	100
C(8)	4185(9)	6869(8)	10751(3)	112
C(9)	3375(7)	7106(5)	10283(3)	91
C(10)	3459(6)	6128(5)	9872(2)	66
C(11)	1017(4)	3336(5)	8443(2)	48
C(12)	492(5)	4714(5)	8459(2)	60
C(13)	−651(5)	5123(6)	8131(2)	69
C(14)	−1282(5)	4158(6)	7793(2)	69
C(15)	−782(5)	2793(6)	7778(2)	66
C(16)	353(5)	2387(5)	8096(2)	57
C(17)	5102(5)	207(5)	8381(2)	52
C(18)	4236(5)	−925(5)	8241(2)	64
C(19)	4721(7)	−2043(6)	7925(2)	77
C(20)	6080(8)	−2029(6)	7729(2)	82
C(21)	6975(6)	−937(6)	7859(2)	81
C(22)	6483(6)	157(5)	8174(2)	68
B(1)	4164(6)	3739(5)	9443(2)	46
B(2)	2386(6)	2946(6)	8775(2)	49
B(3)	4519(5)	1498(6)	8727(2)	50

*U_{eq} = (1/3) (trace of diagonalized U).

[3]The computer programs used include locally written programs for data processing and locally modified versions of the following: MULTAN 80, multisolution program by P. Main, S. J. Fiske, S. E. Hull, L. Lessinger, G. Germain, J. P. Declercq, and M. M. Woolfson; TLS, thermal motion analysis by V. Schomaker and K. N. Trueblood; AGNOST, absorption corrections, by J. A. Ibers; ORFLS, full-matrix least-squares, and ORFFE, function and errors, by W. R. Busing, K. O. Martin and H. A. Levy; FORDAP, Patterson and Fourier syntheses, by A. Zalkin; ORTEP II, illustrations, by C. K. Johnson.

Can. J. Chem. Downloaded from www.nrcresearchpress.com by 93.93.197.157 on 09/07/12
For personal use only.

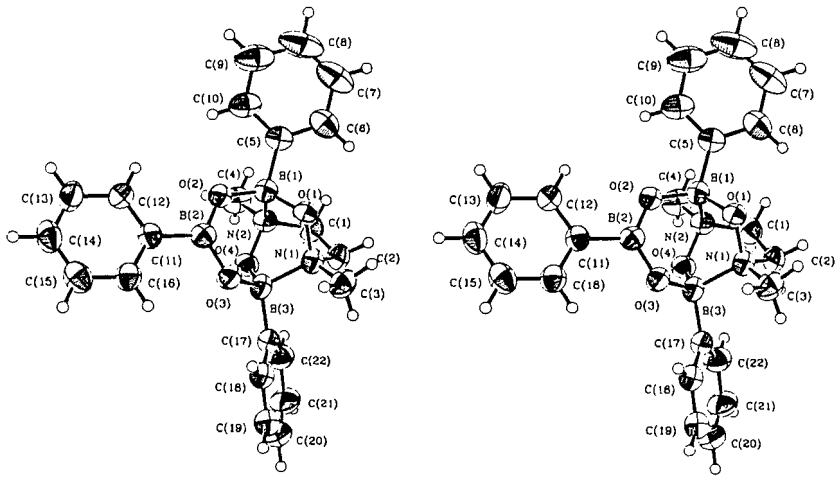

FIG. 1. Stereoscopic view 1,9-dimethyl-3,5,7-triphenyl-2,4,6,8-tetraoxa-1,9-diazonia-5-bora-3,7-diboratatricyclo[5.4.0.0^{3,9}]undecane; 50% probability thermal ellipsoids are shown for the non-hydrogen atoms. Hydrogen atoms have been assigned arbitrary thermal parameters for the sake of clarity.

greater than or equal to $3\sigma(I)$ above background where $\sigma^2(I) = S + 2B + (0.04(S - B))^2$ with S = scan count and B = normalized background count.

The structure was solved by direct methods, the coordinates of all non-hydrogen atoms being determined from an E-map. The non-hydrogen atoms were refined with anisotropic thermal parameters and the hydrogen atoms were fixed in idealized positions (staggered methyls, C(sp^2)—H = 0.97, C(sp^3)—H = 0.98 Å, $U_H \propto U_{\text{bonded atom}}$). Scattering factors for all atoms and anomalous scattering corrections for O, N, and C were taken from ref. 7. The weighting scheme $w = 1/\sigma^2(F)$, where $\sigma^2(F)$ is derived from the previously defined $\sigma^2(I)$, gave uniform average values of $w(|F_o| - |F_c|)^2$ over ranges of both $|F_o|$ and sin θ/λ and was employed in the final stages of full-matrix refinement of 281 variables. Reflections with $I < 3\sigma(I)$ were not included in the refinement. An isotropic Type I extinction correction (Thornley–Nelmes definition of mosaic anisotropy with a Lorentzian distribution) was applied (8–10). The final value of g was $0.80(9) \times 10^4$. Convergence was reached at $R = 0.036$ and $R_w = 0.038$ for 1536 reflections with $I \geq 3\sigma(I)$. For all 2588 reflections $R = 0.077$. A parallel refinement of the mirror-image structure resulted in R factor ratios of 1.009 on both R and R_w. The function minimized was $\Sigma w(|F_o| - |F_c|)^2$, $R = \Sigma||F_o| - |F_c||/\Sigma|F_o|$ and $R_w = (\Sigma w(|F_o| - |F_c|)^2/\Sigma w|F_o|^2)^{1/2}$.

On the final cycle of refinement the mean and maximum parameter shifts corresponded to 0.01 and 0.08σ, respectively. The mean error in an observation of unit weight was 0.691. The largest peak on the final difference map was 0.16 e Å^{-3}. The final positional and thermal parameters appear in Tables 1 and 6,[4] respectively. Measured and calculated structure factors have been placed in the Depository of Unpublished Data.[4] The final F_o and F_c values for the intense reflections indicate the possibility of anisotropic extinction. The application of an anisotropic extinction correction in this case, however, was judged inappropriate since only a small number of reflections was involved, and in only one instance was $||F_o| - |F_c||$ greater than $3\sigma(F)$ (3.7σ for 0 0 2).

The ellipsoids of thermal motion for the non-hydrogen atoms are shown in Fig. 1. The thermal motion has been analysed in terms of the rigid-body modes of translation, libration, and screw motion (11). The rms standard error in the temperature factors σU_{ij} (derived from the least-squares analysis) is 0.0031 Å^2. The structural subunits PhB and the tricycloundecane ring system plus the N-methyl carbon atoms were analysed separately (rms ΔU_{ij} = 0.0024–0.0035 Å^2). The appropriate bond distances have been corrected for libration (11, 12). Corrected bond lengths appear in Table 2 along with the uncorrected values. Corrected values for the bond angles and torsion angles for the tricyclo[5.4.0.0^{3,9}]undecane system are within one standard deviation of the uncorrected values given in Tables 3 and 4. Calculated hydrogen coordinates and thermal parameters (Table 5) and a complete listing of torsion angles (Table 7) are included as supplementary material.

Results and discussion

The crystal structure of **6** consists of discrete molecules separated by normal van der Waals distances. The shortest intermolecular contacts between non-hydrogen atoms are C(2)···C(5)($1/2 + x$, $1/2 - y$, $2 - z$) = 3.346(6), C(3)···C(9)(x, $y - 1$, z) = 3,337(7), and O(1)···C(1)($x - 1/2$, $1/2 - y$, $2 - z$) = 3.348(5) Å. The structure analysis confirms the existence of the tricyclo[5.4.0.0^{3,9}]undecane ring system **6A**, a heteroanalog of the "4-homotwistane" system (4). The tricycloundecane system contains three six-membered rings and two seven-membered rings which all have boat or boat-like conformations (see Table 4). The conformational flexibility of the eleven-membered ring allows the formation of two transannular N→B coordinative bonds, resulting in formation of the symmetric homotwistane analog. In the related cyclooctane system only one transannular N→B bond is formed to give the fused-ring compound **2** (1, 2), the strained tricyclo[3.3.0.0^{3,7}]octane system **1** (D_{2d}-dinoradamantane (13)) not existing under normal conditions in the solid state (2). The tricyclic ring system in **6A** contains two sp^3-hybridized boron atoms with a tetrahedral arrangement of ligands and one sp^2-hybridized boron atom. Incorporation of the latter into the ring system is responsible for distortions from an "ideal" homotwistane skeleton, carbocyclic derivatives of which have been synthesized (14).

Bond lengths[5] involving the tetrahedrally coordinated boron atoms in **6A** may be compared with those observed for six other compounds having a PhBN(sp^3)O$_2$ ligand set (2, 15–18). While the individual bond lengths involving the boron atoms vary considerably in these "PhBN(sp^3)O$_2$" compounds (B—C = 1.582–1.641, O—B = 1.438–1.497, and N—B = 1.649–

[4]The structure factor table, Table 6 (anisotropic thermal parameters) and other material mentioned in the text may be purchased from the Depository of Unpublished Data, CISTI, National Research Council of Canada, Ottawa, Ont., Canada K1A 0S2.

[5]Libration corrected bond lengths (esd's assumed equal to those of the uncorrected values) are employed in the discussion and are compared with similarly treated (11) distances unless otherwise stated.

Can. J. Chem. Downloaded from www.nrcresearchpress.com by 93.93.197.157 on 09/07/12
For personal use only.

Can. J. Chem. Downloaded from www.nrcresearchpress.com by 93.93.197.157 on 09/07/12
For personal use only.

TABLE 2. Bond lengths (Å) with estimated standard deviations in parentheses

Bond	Length		Bond	Length	
	Uncorr.	Corr.		Uncorr.	Corr.
O(1)—N(1)	1.449(4)	1.452	C(6)—C(7)	1.389(7)	1.396
O(1)—B(1)	1.486(5)	1.492	C(7)—C(8)	1.355(9)	1.363
O(2)—B(1)	1.439(6)	1.444	C(8)—C(9)	1.403(9)	1.413
O(2)—B(2)	1.354(6)	1.357	C(9)—C(10)	1.377(7)	1.385
O(3)—B(2)	1.366(6)	1.370	C(11)—C(12)	1.395(6)	1.403
O(3)—B(3)	1.434(5)	1.438	C(11)—C(16)	1.391(6)	1.398
O(4)—N(2)	1.440(4)	1.443	C(11)—B(2)	1.571(6)	1.574
O(4)—B(3)	1.491(6)	1.497	C(12)—C(13)	1.402(6)	1.405
N(1)—C(2)	1.481(6)	1.486	C(13)—C(14)	1.373(6)	1.379
N(1)—C(3)	1.484(6)	1.489	C(14)—C(15)	1.376(7)	1.384
N(1)—B(3)	1.663(6)	1.668	C(15)—C(16)	1.381(6)	1.384
N(2)—C(1)	1.484(5)	1.488	C(17)—C(18)	1.389(6)	1.396
N(2)—C(4)	1.480(5)	1.484	C(17)—C(22)	1.396(7)	1.405
N(2)—B(1)	1.644(6)	1.649	C(17)—B(3)	1.590(7)	1.594
C(1)—C(2)	1.526(7)	1.531	C(18)—C(19)	1.392(7)	1.396
C(5)—C(6)	1.389(6)	1.399	C(19)—C(20)	1.367(8)	1.376
C(5)—C(10)	1.380(6)	1.388	C(20)—C(21)	1.371(7)	1.378
C(5)—B(1)	1.593(6)	1.600	C(21)—C(22)	1.375(6)	1.379

TABLE 3. Bond angles (deg) with estimated standard deviations in parentheses

Bonds	Angle (deg)	Bonds	Angle (deg)
N(1)—O(1)—B(1)	111.8(3)	C(11)—C(12)—C(13)	120.9(5)
B(1)—O(2)—B(2)	124.3(4)	C(12)—C(13)—C(14)	120.0(5)
B(2)—O(3)—B(3)	120.6(4)	C(13)—C(14)—C(15)	119.6(5)
N(2)—O(4)—B(3)	112.9(3)	C(14)—C(15)—C(16)	120.6(5)
O(1)—N(1)—C(2)	105.1(3)	C(11)—C(16)—C(15)	121.3(4)
O(1)—N(1)—C(3)	104.3(3)	C(18)—C(17)—C(22)	115.3(5)
O(1)—N(1)—B(3)	110.5(3)	C(18)—C(17)—B(3)	121.7(4)
C(2)—N(1)—C(3)	110.6(4)	C(22)—C(17)—B(3)	123.0(5)
C(2)—N(1)—B(3)	111.9(4)	C(17)—C(18)—C(19)	122.3(5)
C(3)—N(1)—B(3)	113.8(4)	C(18)—C(19)—C(20)	119.8(5)
O(4)—N(2)—C(1)	104.6(3)	C(19)—C(20)—C(21)	119.9(5)
O(4)—N(2)—C(4)	105.0(3)	C(20)—C(21)—C(22)	119.6(5)
O(4)—N(2)—B(1)	111.0(3)	C(17)—C(22)—C(21)	123.1(5)
C(1)—N(2)—C(4)	112.2(4)	O(1)—B(1)—O(2)	114.2(4)
C(1)—N(2)—B(1)	111.5(3)	O(1)—B(1)—N(2)	103.1(3)
C(4)—N(2)—B(1)	112.1(3)	O(1)—B(1)—C(5)	108.1(4)
N(2)—C(1)—C(2)	108.5(4)	O(2)—B(1)—N(2)	106.1(3)
N(1)—C(2)—C(1)	109.2(4)	O(2)—B(1)—C(5)	111.6(4)
C(6)—C(5)—C(10)	116.8(5)	N(2)—B(1)—C(5)	113.6(4)
C(6)—C(5)—B(1)	122.4(5)	O(2)—B(2)—O(3)	123.0(4)
C(10)—C(5)—B(1)	120.6(4)	O(2)—B(2)—C(11)	117.7(4)
C(5)—C(6)—C(7)	121.1(6)	O(3)—B(2)—C(11)	119.2(4)
C(6)—C(7)—C(8)	120.6(6)	O(3)—B(3)—O(4)	113.4(4)
C(7)—C(8)—C(9)	120.0(6)	O(3)—B(3)—N(1)	107.9(4)
C(8)—C(9)—C(10)	118.1(6)	O(3)—B(3)—C(17)	113.3(4)
C(5)—C(10)—C(9)	123.3(5)	O(4)—B(3)—N(1)	101.4(4)
C(12)—C(11)—C(16)	117.6(4)	O(4)—B(3)—C(17)	109.8(4)
C(12)—C(11)—B(2)	119.6(4)	N(1)—B(3)—C(17)	110.3(4)
C(16)—C(11)—B(2)	122.6(4)		

1.759 Å), the sums of the bond lengths at boron lie within the relatively small range of 6.191–6.297 Å with an average value of 6.228 Å. These bond length sums are sensitive to ring-size and other steric effects and are a good indicator of the overall strain at the boron atom and its substituents. These compounds include monocyclic six-membered boron-containing ring systems (15), fused-ring systems with the N—B bond at the ring junction (2, 16–18), and in the present case a bridged-ring system in which both the B and N atoms occupy bridgehead positions. The average bond length sum in **6A**, 6.191 Å, is the smallest yet observed for a "PhBN(sp^3)O_2" compound and is indicative of a relatively low-strain system. The staggered con-

TABLE 4. Torsion angles (deg) for the tricycloundecane system with estimated standard deviations in parentheses

Atoms	Value (deg)
B(1)—O(1)—N(1)—C(2)	79.9(4)
B(1)—O(1)—N(1)—B(3)	−40.9(4)
N(1)—O(1)—B(1)—O(2)	89.5(4)
N(1)—O(1)—B(1)—N(2)	−25.1(4)
B(2)—O(2)—B(1)—O(1)	−39.0(6)
B(2)—O(2)—B(1)—N(2)	73.8(5)
B(1)—O(2)—B(2)—O(3)	−5.7(7)
B(3)—O(3)—B(2)—O(2)	−31.3(7)
B(2)—O(3)—B(3)—O(4)	−27.2(6)
B(2)—O(3)—B(3)—N(1)	84.3(5)
B(3)—O(4)—N(2)—C(1)	81.8(4)
B(3)—O(4)—N(2)—B(1)	−38.6(4)
N(2)—O(4)—B(3)—O(3)	88.5(5)
N(2)—O(4)—B(3)—N(1)	−26.9(4)
O(1)—N(1)—C(2)—C(1)	−58.3(4)
B(3)—N(1)—C(2)—C(1)	61.7(5)
O(1)—N(1)—B(3)—O(3)	−45.1(5)
O(1)—N(1)—B(3)—O(4)	74.3(4)
C(2)—N(1)—B(3)—O(3)	−161.8(4)
C(2)—N(1)—B(3)—O(4)	−42.4(4)
O(4)—N(2)—C(1)—C(2)	−58.3(4)
B(1)—N(2)—C(1)—C(2)	61.8(5)
O(4)—N(2)—B(1)—O(1)	72.7(4)
O(4)—N(2)—B(1)—O(2)	−47.7(4)
C(1)—N(2)—B(1)—O(1)	−43.6(5)
C(1)—N(2)—B(1)—O(2)	−163.9(4)
N(2)—C(1)—C(2)—N(1)	−9.1(5)

formations about the N—B bonds in **6A** are partially responsible for this. In related systems with fully substituted B and N atoms, steric factors result in less favorable conformations about rather long N—B bonds (2, 15, 16).

The average N—B distance of 1.659 Å in **6A** is the shortest observed for a "PhBN(sp^3)O_2" compound; similar to the values of 1.634 (uncorr.)–1.657 Å observed for relatively strain-free *N,O*-chelates of the type C(sp^2)$_2$BN(sp^3)O (19–24). The bond distances between the tetrahedral boron atoms and the nitrogen-bound oxygen atoms (mean B—O(N) = 1.495(4) Å) are the longest O—B distances yet observed for a "PhBN(sp^3)O_2" compound but are strikingly short compared with corresponding distances of 1.517 (uncorr.)–1.604 Å reported for other boron chelates with *N*-oxide ligands (25–31). The mean B(sp^3)—C distance of 1.597(4) Å in **6A** is close to the uncorrected mean value of 1.602 Å observed for the other "PhBN(sp^3)O_2" compounds (2, 15–18).

The two B(sp^2)—O bonds (1.357(6) and 1.370(6) Å) are relatively short, demonstrating the partial π-bond character resulting from $pp(\pi)$ back-donation from the two oxygen atoms to boron within the trigonal planar phenylboronate system. Similar B(sp^2)—O distances have been reported for the free arylboronic acids $PhB(OH)_2$ (32), mean 1.371(6) Å, and 4-$BrC_6H_4B(OH)_2$ (33), uncorrected mean 1.36 Å. The uncorrected B(sp^2)—O distances in various phenylboronate derivatives range 1.311–1.421 Å with an average value of 1.370 Å (2, 15, 16, 18, 28, 30, 32–42). The B(sp^2)—O—B(sp^3) linkages in **6A** are unique among organoboron compounds in that the B(sp^2)—O distances are normal. This may be ascribed to the fact that both oxygen atoms of the phenylboronate moiety are bonded to B(sp^3) atoms. In all other structurally characterized organoboron compounds containing B(sp^2)—O—B(sp^3) units only one such unit is present, displaying very short B(sp^2)—O bonds (1.311–1.367, uncorrected mean 1.338 Å) and normal B(sp^3)—O distances (1.444–1.495, uncorrected mean 1.471 Å) (2, 15, 16, 18, 28, 40, 42). In the present case it is the B(sp^3)—O[B(sp^2)] bonds which are short at 1.438(5) and 1.444(6) Å.

The B(sp^2)—C distance of 1.574(6) Å is slightly longer than the average uncorrected value of 1.552 Å, but in the range 1.506–1.582 Å observed for other phenylboronate derivatives (2, 15, 16, 18, 28, 30, 32–42). As expected, the B(sp^2)—C bond is shorter than the B(sp^3)—C bonds, indicating a π-interaction between the phenyl ring and the trigonal planar boron atom. The sp^2-hybridized boron atom is displaced 0.026(5) Å from the plane of its substituents and the angle between the normals to the B(2) coordination plane and the associated phenyl mean plane is 7.3°, a typical value for such systems.

It can be concluded that in the case of *N*-methyl and *B*-phenyl substitution the formation of **6A** is favored in the condensation reaction of **3** with phenylboronic acid, even at an adduct ratio of 1:2. **6A** appears to be the thermodynamically most stable structure in this complex-building system. The structure of **6A** can also be interpreted in terms of the boat form of the well-known (43–46) BONBON ring, conformationally locked by the ethylene bridge between the nitrogen atoms, and containing an additional boronate bridge linking the ring boron atoms (see formula **7**).

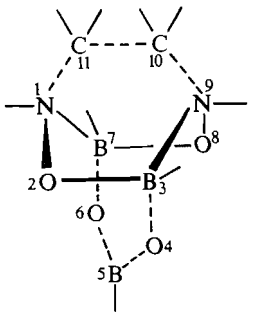

7

tricyclo[5.4.0.0^{3,9}]undecane system containing the BONBON boat partial structure

Acknowledgments

We thank the Natural Sciences and Engineering Research Council of Canada and the Fonds der Chemischen Industrie, Frankfurt am Main, for financial support, and the University of British Columbia Computing Centre for assistance.

1. W. KLIEGEL. J. Organomet. Chem. **253**, 9 (1983).
2. W. KLIEGEL, S. J. RETTIG, and J. TROTTER. Can. J. Chem. **62**, 515 (1984).
3. G. ZINNER, O. HANTELMANN, and U. DYBOWSKI. Chemiker-Zeitg. **97**, 205 (1973).
4. E. OSAWA, K. AIGAMI, N. TAKAISHI, Y. INAMOTO, Y. FUJIKURA, Z. MAJERSKI, P. VON R. SCHLEYER, E. M. ENGLER, and M. FARCASIU. J. Am. Chem. Soc. **99**, 5361 (1977).
5. P. COPPENS, L. LEISEROWITZ, and D. RABINOVICH. Acta Crystallogr. **18**, 1035 (1965).
6. W. R. BUSING and H. A. LEVY. Acta Crystallogr. **22**, 457 (1967).
7. International tables for X-ray crystallography. Vol. IV. Kynoch Press, Birmingham. 1974. pp. 99–102 and 149.
8. P. J. BECKER and P. COPPENS. Acta Crystallogr. Sect. A, **30**, 129 (1974); **30**, 148 (1974); **31**, 417 (1975).

Can. J. Chem. Downloaded from www.nrcresearchpress.com by 93.93.197.157 on 09/07/12
For personal use only.

9. P. COPPENS and W. C. HAMILTON. Acta Crystallogr. Sect. A, **26**, 71 (1970).
10. F. R. THORNLEY and R. J. NELMES. Acta Crystallogr. Sect. A, **30**, 748 (1974).
11. V. SCHOMAKER and K. N. TRUEBLOOD. Acta Crystallogr. Sect. B, **24**, 63 (1968).
12. D. W. J. CRUICKSHANK. Acta Crystallogr. **9**, 747 (1956); **9**, 754 (1956); **14**, 896 (1961).
13. M. NAKAZAI, K. NAEMURA, H. HARADA, and H. NARUTAKI. J. Org. Chem. **47**, 3470 (1982).
14. G. FRATER. Helv. Chim. Acta, **62**, 1893 (1979).
15. M. YALPANI and R. BOESE. Chem. Ber. **116**, 3347 (1983).
16. W. KLIEGEL, D. NANNINGA, S. J. RETTIG, and J. TROTTER. Can. J. Chem. **62**, 845 (1984).
17. S. J. RETTIG and J. TROTTER. Can. J. Chem. **53**, 1393 (1975).
18. S. J. RETTIG, J. TROTTER, W. KLIEGEL, and H. BECKER. Can. J. Chem. **54**, 3142 (1976).
19. S. J. RETTIG and J. TROTTER. Can. J. Chem. **51**, 1288 (1973).
20. S. J. RETTIG and J. TROTTER. Acta Crystallogr. Sect. B. **30**, 2139 (1974).
21. S. J. RETTIG and J. TROTTER. Can. J. Chem. **54**, 3130 (1976).
22. I. CYNKIER and H. HOPE. Acta Crystallogr. Sect. B, **34**, 2990 (1978).
23. I. CYNKIER. Cryst. Struct. Commun. **10**, 797 (1981).
24. R. ALLMANN, E. HOHAUS, and S. OLEJNIK. Z. Naturforsch. Teil B, **37**, 1450 (1982).
25. S. J. RETTIG, J. TROTTER, and W. KLIEGEL. Can. J. Chem. **52**, 2531 (1974).
26. J. C. JANSEN, M. VERHAGE, and H. VAN KONINGSVELD. Cryst. Struct. Commun. **11**, 305 (1982).
27. W. KLIEGEL, D. NANNINGA, S. J. RETTIG, and J. TROTTER. Can. J. Chem. **61**, 2493 (1983).
28. W. KLIEGEL, H.-W. MOTZKUS, S. J. RETTIG, and J. TROTTER. Can. J. Chem. **62**, 838 (1984).
29. W. MARINGGELE, G. M. SHELDRICK, A. MELLER, and M. NOLTMEYER. Chem. Ber. **117**, 2112 (1984).
30. W. KLIEGEL, L. PREU, S. J. RETTIG, and J. TROTTER. Can. J. Chem. **63**, 509 (1985).
31. W. KLIEGEL, S. J. RETTIG, and J. TROTTER. Unpublished results.
32. S. J. RETTIG and J. TROTTER. Can. J. Chem. **55**, 3071 (1977).
33. Z. V. ZVONKOVA and V. P. GLUSKOVA. Kristallografiya, **3**, 559 (1958).
34. H. SHIMANOUCHI, N. SAITO, and Y. SASADA. Bull. Chem. Soc. Jpn. **42**, 1239 (1969).
35. A. H.-J. WANG, I. C. PAUL, K. L. RINEHART, JR., and F. J. ANTOSZ. J. Am. Chem. Soc. **93**, 6275 (1971).
36. F. ZETTLER, H. D. HAUSEN, and H. HESS. Acta Crystallogr. Sect. B, **30**, 1876 (1974).
37. P. J. COX, P. D. CRADWICK, and G. A. SIM. J. Chem. Soc. Perkin Trans. II, 110 (1976).
38. A. GUPTA, A. KIRFEL, G. WILL, and G. WULFF. Acta Crystallogr. Sect. B, **33**, 637 (1977).
39. M. YALPANI, R. BOESE, and D. BLASER. Chem. Ber. **116**, 3338 (1983).
40. W. KLIEGEL, D. NANNINGA, S. J. RETTIG, and J. TROTTER. Can. J. Chem. **61**, 2329 (1983).
41. M. J. BROADHURST, C. H. HASSALL, and G. J. THOMAS. Tetrahedron, **40**, 4649 (1984).
42. W. KLIEGEL, H.-W. MOTZKUS, S. J. RETTIG, and J. TROTTER. Can. J. Chem. **64**, 507 (1986).
43. L. P. KUHN and M. INATOME. J. Am. Chem. Soc. **85**, 1206 (1963).
44. H. J. ROTH and B. MILLAR. Arch. Pharm. Ber. Dt. Pharm. Ges. **297**, 744 (1964).
45. A. SINGH, V. D. GUPTA, G. SRIVASTAVA, and R. C. MEHROTRA. J. Organomet. Chem. **64**, 145 (1974).
46. S. J. RETTIG and J. TROTTER. Can. J. Chem. **61**, 206 (1983).
47. W. KLIEGEL, S. J. RETTIG, and J. TROTTER. Can. J. Chem. **66**, 1091 (1988).

Can. J. Chem. Downloaded from www.nrcresearchpress.com by 93.93.197.157 on 09/07/12
For personal use only.

Synthesis and structural characterization of two triclinic modifications of diethylammonium *trans*-tetrachlorobis(dimethylsulfoxide-*S*)rhodate(III): an example of hydrogen-bond acceptor structural isomerism

SUJATHA N. GAMAGE, BRIAN R. JAMES, STEVEN J. RETTIG, AND JAMES TROTTER
Department of Chemistry, University of British Columbia, 2036 Main Mall, Vancouver, B.C., Canada V6T 1Y6

Received October 1, 1987

SUJATHA N. GAMAGE, BRIAN R. JAMES, STEVEN J. RETTIG, and JAMES TROTTER. Can. J. Chem. **66**, 1123 (1988).

Two crystalline modifications (I and II) of diethylammonium *trans*-tetrachlorobis(dimethylsulfoxide-*S*)rhodate(III) have been isolated from the same reaction mixture. The compound is formed by hydrolysis, in the presence of hydrochloric acid, of an η^1-ylidic enamine complex of rhodium(III), which is made via dehydrogenation of triethylamine in the presence of *mer*-trichlorotris(dimethylsulfoxide)rhodium(III). Crystals of form I are triclinic, $a = 8.1787(7)$, $b = 10.761(1)$, $c = 10.927(1)$ Å, $\alpha = 86.681(6)$, $\beta = 84.879(7)$, $\gamma = 71.814(8)°$, $Z = 2$, space group $P\bar{1}$, and those of form II are triclinic, $a = 7.931(2)$, $b = 9.489(2)$, $c = 13.302(2)$ Å, $\alpha = 102.03(1)$, $\beta = 97.40(1)$, $\gamma = 107.49(1)°$, $Z = 2$, space group $P\bar{1}$. Both structures were solved by Patterson and Fourier methods and were refined by full-matrix least-squares procedures to $R = 0.024$ and 0.060 for 4959 and 4320 reflections with $I \geq 3\sigma(I)$, respectively. Both crystal structures consist of centrosymmetric $[RhCl_4(Me_2SO)_2]^-$ anions and $(NEt_2H_2)^+$ cations, linked by hydrogen bonds to form infinite chains. In form I the hydrogen bonds are all of the type N—H···Cl (H···Cl = 2.50(4) and 2.49(3) Å), while in form II they are all of the type N—H···O (H···O = 2.25(7) and 2.04(6) Å).

SUJATHA N. GAMAGE, BRIAN R. JAMES, STEVEN J. RETTIG et JAMES TROTTER. Can. J. Chem. **66**, 1123 (1988).

A partir d'un seul mélange réactionnel, on a pu isoler deux modifications cristallines (I et II) du diéthylammonium *trans*-tétrachloro bis(diméthylsulfoxyde-*S*) rhodium(III). Le composé se forme par hydrolyse, en présence d'acide chlorhydrique, d'un complexe η^1-ylidique enamine du rhodium(III) qui est préparé via une déshydrogénation de la triéthylamine en présence du *mer*-trichloro tris(diméthylsulfoxyde) rhodium(III). Les cristaux de la forme I sont tricliniques avec $a = 8,1787(7)$, $b = 10,761(1)$ et $c = 10,927(1)$ Å, $\alpha = 86,681(6)$, $\beta = 84,879(7)$ et $\gamma = 71,814(8)°$, $Z = 2$ et groupe d'espace $P\bar{1}$ alors que ceux de la forme II sont tricliniques avec $a = 7,931(2)$, $b = 9,489(2)$ et $c = 13,302(2)$ Å, $\alpha = 102,03(6)$, $\beta = 97,40(1)$ et $\gamma = 107,49(1)°$, $Z = 2$ et groupe d'espace $P\bar{1}$. On a résolu les deux structures à l'aide des méthodes de Patterson et Fourier et on les a affinées par la méthode des moindres carrés (matrice entière) jusqu'à des valeurs de $R = 0,024$ et 0,060 respectivement pour 4959 et 4320 réflexions avec $I \geq 3\sigma(I)$. Les deux structures moléculaires comportent des anions $[RhCl_4(Me_2SO)_2]^-$ centrosymétriques et des cations $(NEt_2H_2)^+$ qui sont réunis par des liaisons hydrogènes formant des chaînes infinies. Dans la forme I, les liaisons hydrogènes sont toutes du type N—H···Cl (H···Cl = 2,50(4) et 2,49(3) Å); par ailleurs, dans la forme II, elles sont toutes du type N—H···O (H···O = 2,25(7) et 2,04(6) Å).

[Traduit par la revue]

Introduction

We have reported recently on reactions in which tertiary amines are dehydrogenated in the presence of *mer*-$RhCl_3(Me_2SO)_3$, in which one of the dimethylsulfoxide ligands is *O*-bonded (Me_2SO) and two are *S*-bonded (Me_2SO) (1, 2). In the case of triethylamine, the dehydrogenation yields an enamine fragment that is stabilized within an η^1-ylidic enamine complex of rhodium(III), **1**, while the "hydrogen" reduces half of the initially present Rh(III) to Rh(I) (1). The reaction stoichiometry is summarized in equation [1], where the Rh(I) product is probably 4-coordinate containing Cl^- and Me_2SO ligands.

[1] $2RhCl_3(Me_2SO)_3 + NEt_3 \rightarrow$

$Rh(I) + 3Cl^- + 2H^+ + 4Me_2SO +$

$RhCl_3(Me_2SO)_2(CH_2CH{=}NEt_2)$ (**1**)

Complex **1** exists in two forms, the *mer-trans* (**1***a*) and the *mer-cis* (**1***b*); both were isolated and the latter was characterized by X-ray analysis (1). On studying the solution chemistry of these complexes, we discovered an acidification/hydrolysis reaction, [2]; subsequent characterization of product **2** by X-ray analysis showed it to exist in two distinct forms which differ in H-bonding interactions between the diethylammonium cation and the anion, which has *trans* geometry.

[2] $1 + H_2O + HCl \rightarrow (NEt_2H_2)[RhCl_4(Me_2SO)_2]$ (**2**) $+ CH_3CHO$

This paper reports on the preparation of **2**, and particularly on the existence of the unusual solid-state isomers. The *trans*-tetrachlorobis(dimethylsulfoxide-*S*)rhodate(III) anion within **2** has been characterized by X-ray analysis previously, but in association with a sodium cation (3) and the hydrogen-bridged cation $[Me_2SO{\cdots}H{\cdots}OSMe_2]^+$ (4).

Experimental

Spectral or reagent grade solvents and chemicals were used throughout. $RhCl_3{\cdot}3H_2O$ was obtained on loan from Johnson, Matthey Ltd. ^1H nmr spectra were recorded on Bruker WP80 or Varian XL100 instruments operating in the FT mode with TMS as internal standard. Infrared spectra were recorded on a Perkin-Elmer 598 or on a Nicolet 5DX FT spectrometer. Elemental analyses were performed by Mr. P. Borda of this department.

Syntheses of *mer*-$RhCl_3(Me_2SO)_3$ and $RhCl_3(Me_2SO)_2(CH_2CH{=}NEt_2)$, **1**, followed literature procedures (1). Dimethylacetamide hydrochloride (DMA·HCl) was prepared by passing gaseous HCl through neat DMA, and recrystallizing the white adduct formed from ethanol (5).

[Cation] trans-*[$RhCl_4(Me_2SO)_2$], cation = NEt_3H^+, $NEt_2H_2^+$ (2)*

(*a*) $RhCl_3(Me_2SO)_3$ (200 mg, 0.45 mmol) and NEt_3 (0.2 mL, 1.4 mmol) were stirred in acetone (25 mL) under Ar overnight, and the solution concentrated to give an off-white precipitate (NEt_3·HCl) and a red–brown solution — which at this stage contains **1** (1). Addition of DMA·HCl (180 mg, 1.5 mmol) and stirring overnight under Ar yielded

Can. J. Chem. Downloaded from www.nrcresearchpress.com by 93.93.197.157 on 09/07/12
For personal use only.

TABLE 1. Crystallographic data[a]

Compound	$(Et_2NH_2)[RhCl_4(Me_2SO)_2]$	$(Et_2NH_2)[RhCl_4(Me_2SO)_2]$
Formula	$C_8H_{24}Cl_4NO_2RhS_2$	$C_8H_{24}Cl_4NO_2RhS_2$
fw	475.12	475.12
Form	I	II
Crystal system	Triclinic	Triclinic
Space group	$P\bar{1}$	$P\bar{1}$
a (Å)	8.1787(7)	7.931(2)
b (Å)	10.761(1)	9.489(2)
c (Å)	10.927(1)	13.302(2)
α (deg)	86.681(6)	102.03(1)
β (deg)	84.879(7)	97.40(1)
γ (deg)	71.814(8)	107.49(1)
V (Å^3)	909.6(2)	913.9(3)
Z	2	2
ρ_c (g/cm^3)	1.735	1.727
F(000)	480	480
μ(Mo-K_α)(cm^{-1})	17.34	17.25
Crystal dimensions (mm)	0.20 × 0.25 × 0.31	0.14 × 0.48 × 0.50
Transmission factors	0.613–0.708	0.494–0.795
Scan type	ω–2θ	ω–2θ
Scan range (deg in ω)	0.70 + 0.35 tan θ	0.90 + 0.35 tan θ
Scan speed (deg/min)	1.1–10.0	2.0–10.0
Data collected	$\pm h, +k, \pm l$	$+h, \pm k, \pm l$
$2\theta_{max}$ (deg)	65	60
Crystal decay	Negligible	Negligible
Unique reflections	6563	5297
Reflections with $I \geq 3\sigma(I)$	4959	4320
Number of variables	250	262
R	0.024	0.060
R_w	0.035	0.077
S	1.71	3.28
Mean Δ/σ (final cycle)	0.02	0.06
Max Δ/σ (final cycle)	0.39	0.58
Residual density (e/Å^3)	0.71	2.71

[a]Temperature 295 K, Enraf-Nonius CAD4-F diffractometer, Mo-K_α radiation (λK_{α_1} = 0.70930, λK_{α_2} = 0.71359 Å), graphite monochromator, takeoff angle 2.7°, aperture (2.0 + tan θ) × 4.0 mm at a distance of 173 mm from the crystal, scan range extended by 25% on both sides for background measurement, $\sigma^2(I) = C + 2B + [0.04(C - B)]^2$ (C = scan count, B = normalized background count), function minimized: $\Sigma w(|F_o| - |F_c|)^2$ where $w = 1/\sigma^2(F)$, $R = \Sigma||F_o| - |F_c||/\Sigma|F_o|$, $R_w = (\Sigma w(|F_o| - |F_c|)^2/\Sigma w|F_o|^2)^{1/2}$, $S = (\Sigma w(|F_o| - |F_c|)^2/(m - n))^{1/2}$. Values given for R, R_w, and S are based on those reflections with $I \geq 3\sigma(I)$.

an orange solution and yellow precipitate. An ir (Nujol) of the crude yellow product showed the presence of $NEt_2H_2^+$ (ν_{N-H} = 3140 cm^{-1}, s), NEt_3H^+ (ν_{N-H} = 2400–2600 cm^{-1}, s) and only a weak peak due to —CH_2—CH=NEt_2 ($\nu_{C=N}$ = 1640 cm^{-1}). Recrystallization from CH_2Cl_2/ether in air yielded $(NEt_3H)[RhCl_4(Me_2SO)_2]$ (40 mg, 20% yield). *Anal.* calcd. for $C_{10}H_{28}Cl_4NO_2RhS_2$: C 23.86, H 5.61, N 2.78; found: C 23.35, H 5.29, N 2.71. ^{1}H nmr (δ, $CDCl_3$, 100 MHz): 1.38 t (9H, CH_3CH_2), 3.13 q (6H, CH_3CH_2), 3.48 s (~11H, *trans*-Me_2SO), 3.53 s (~1H, *cis*-Me_2SO) (6).

The mother liquor from the recrystallization was concentrated to ~1 mL and left in a closed Schlenk tube; after a few days several red crystals appeared (~20 mg). Infrared (KBr): 3140 cm^{-1}, s (ν_{N-H} of $NEt_2H_2^+$), 1128 and 1140 cm^{-1}, s, (ν_{SO} of Me_2SO). X-ray analysis of the crystals (see below) showed them to be two distinct forms with molecular formula $(NEt_2H_2)[trans\text{-}RhCl_4(Me_2SO)_2]$, **2**.

(*b*) The decomposition of **1** (**1***a* or **1***b*) to **2** (see reaction [2]) was monitored by ^{1}H nmr (80 MHz) by dissolving **1** (6 mg, ~0.015 mmol) and DMA·HCl (4 mg, 0.03 mmol) in acetone-d_6 (0.6 mL) which contained ~0.04 mmol H_2O as impurity (δ 2.93 ppm). The resonances of **1** (see ref. 1) and DMA·HCl (δ 2.32, 3H, CH_3CO; 3.10, 6H, $(CH_3)_2N$) were replaced over 2 days by peaks assignable to $NEt_2H_2^+$ (δ 1.4 t, 6H, CH_3CH_2; 3.2 m, 4H, CH_3CH_2), DMA (δ 2.1, CH_3CO; 3.0, 6H, $(CH_3)_2N$) and CH_3CHO (δ 9.8, 1H, CHO, D_2O stable; the CH_3 resonance, expected at δ 2.2, was obscured by resonances of DMA and acetone-d_5). The peak position of Me_2SO remained essentially unchanged (δ 3.5), while the impurity water peak disappeared, presumably as a result of both consumption of the water (reaction [2]) and its proton exchange with those of $NEt_2H_2^+$. A drying of a drop of the nmr solution sample on a NaCl window revealed in the ir the 3140 cm^{-1} peak of $NEt_2H_2^+$ and the absence of $\nu_{C=N}$ of **1** (see above).

X-ray crystallographic analyses

Crystallographic data for the two crystal forms of **2** appear in Table 1. The crystals are red–orange in color, those of form I growing as blocks with faces {1 0 −1}, {0 −1 1}, {1 1 0}, (0 1 −2), and (0 0 1) developed, and those of form II as plates with faces {1 −1 0}, {0 0 1}, and {0 −1 1} developed. Unit-cell parameters were refined by least squares on 2 sin θ/λ values for 25 reflections with 2θ = 45–53° and 45–56° for forms I and II, respectively. The intensities of three standard reflections, measured each hour of X-ray exposure time during the data collections, showed only small random variations for both samples. The data were reduced,[1] and corrected for absorption (numerical integration). Both structures were solved by Patterson and Fourier methods. The non-hydrogen atoms were refined with anisotropic thermal parameters and the hydrogen atoms with isotropic thermal param-

[1]The computer programs used include locally written programs for data processing and locally modified versions of the following: AGNOST, absorption corrections, by J. A. Ibers; ORFLS, full-matrix least-squares, and ORFFE, function and errors, by W. R. Busing, K. O. Martin and H. A. Levy; FORDAP, Patterson and Fourier syntheses, by A. Zalkin; ORTEP II, illustrations, by C. K. Johnson.

Can. J. Chem. Downloaded from www.nrcresearchpress.com by 93.93.197.157 on 09/07/12
For personal use only.

Can. J. Chem. Downloaded from www.nrcresearchpress.com by 93.93.197.157 on 09/07/12
For personal use only.

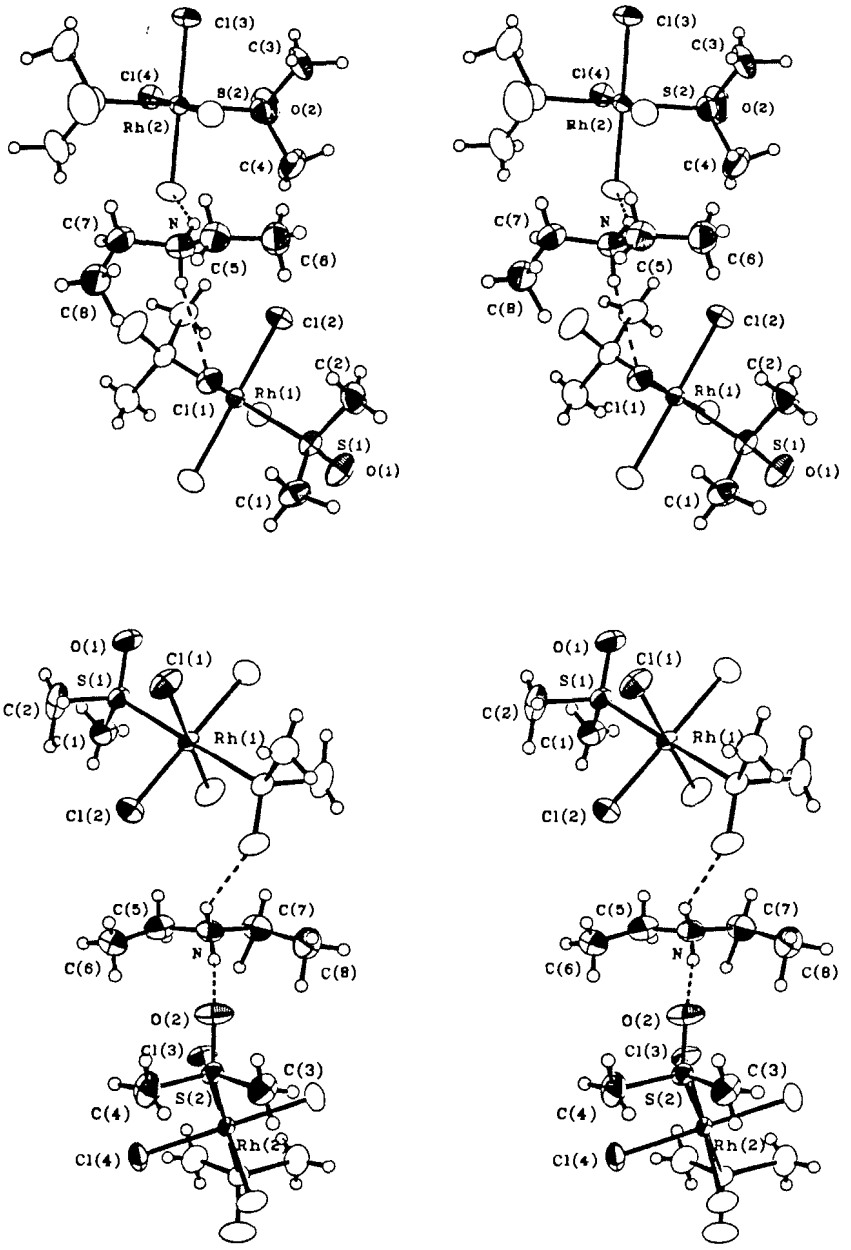

FIG. 1. Stereoscopic views of the structures of **2**, form I (top) and form II (bottom); 50% probability thermal ellipsoids are shown for the non-hydrogen atoms. Hydrogen atoms have been assigned arbitrary thermal parameters for the sake of clarity. Broken lines indicate hydrogen bonds. Shaded non-hydrogen atoms comprise the asymmetric units.

eters, except for those associated with the C(6) methyl group in form I which were fixed in calculated positions (staggered, C—H = 0.98 Å, $U_H \propto U_{\text{bonded atom}}$). Neutral atom scattering factors for all atoms and anomalous scattering corrections for Rh, Cl, and S were taken from ref. 7. The maximum parameter shifts on the final cycles of full-matrix least-squares refinement were associated with hydrogen atoms. The largest peaks on the final difference maps were within 1 Å of the metal atoms. Final positional and isotropic (or equivalent isotropic) thermal parameters are given in Table 2. Bond lengths and angles appear in Table 3. Anisotropic thermal parameters, bond lengths and angles involving hydrogen, torsion angles (Tables 4–7), and measured and calculated structure factors have been placed in the Depository of Unpublished Data.[2]

[2]The structure factor tables and Tables 4–7 may be purchased from the Depository of Unpublished Data, CISTI, National Research Council of Canada, Ottawa, Ont., Canada K1A 0S2.

Results and discussion

The synthetic procedure for isolation of **2** from $RhCl_3(Me_2SO)_3$, coupled with its *in situ* formation from $RhCl_3(Me_2SO)_2(CH_2CH{=}NEt_2)$, **1**, with concomitant generation of CH_3CHO, are most readily rationalized chemically in terms of reactions [1] and [2]. A corresponding slow decomposition of chloro(enamine)palladium(II) complexes in CH_2Cl_2 containing traces of H_2O to give CH_3CHO (or the expected ketone for a coordinated $—CH_2C(Me){=}NEt(^iPr)$ fragment) has been reported (8); these workers suggested a mechanism incorporating initial hydrolysis to a β-oxoalkylpalladium species which then underwent Pd—C bond cleavage by HCl formed in the hydrolysis; details have not appeared, and the nature of the Pd product(s) was not discussed. Added HCl is required for the decomposition of our Rh(III)–enamine complex, reaction [2],

TABLE 2. Final positional (fractional × 10^4, Rh, Cl, and S × 10^5, H × 10^3) and isotropic thermal parameters ($U \times 10^3$ Å^2) with estimated standard deviations in parentheses

Atom	x	y	z	U_{eq}/U_{iso}[a]
		Form I		
Rh(1)	0	0	0	26
Rh(2)	50000	50000	50000	28
Cl(1)	27159(6)	4947(5)	9462(4)	38
Cl(2)	−17240(7)	21902(5)	1541(5)	44
Cl(3)	39824(7)	69691(5)	60372(6)	46
Cl(4)	25013(7)	44848(5)	57336(5)	43
S(1)	13300(6)	4081(5)	−18750(4)	35
S(2)	37161(7)	60351(5)	32396(5)	42
O(1)	625(3)	86(2)	−2956(2)	58
O(2)	1977(3)	6076(3)	3149(3)	83
N	212(3)	2598(2)	3163(2)	46
C(1)	3595(3)	−416(3)	−1964(2)	51
C(2)	1348(4)	2054(3)	−2009(3)	54
C(3)	3718(5)	7684(3)	3096(4)	65
C(4)	5014(6)	5415(5)	1874(3)	80
C(5)	1259(4)	3449(3)	2688(3)	52
C(6)	609(4)	4187(3)	1537(3)	64
C(7)	654(3)	1941(3)	4390(2)	49
C(8)	2470(4)	1074(3)	4362(3)	57
H(N)	−105(5)	309(4)	315(3)	75(11)
H(N′)	52(4)	187(3)	268(3)	78(10)
H(1a)	424(5)	−1(4)	−272(3)	96(11)
H(1b)	392(4)	−23(3)	−122(3)	53(8)
H(1c)	382(5)	−141(4)	−195(3)	76(10)
H(2a)	31(5)	254(4)	−191(4)	72(11)
H(2b)	193(3)	226(3)	−126(3)	47(7)
H(2c)	196(4)	213(3)	−265(3)	63(9)
H(3a)	463(7)	766(5)	335(5)	120(18)
H(3b)	331(5)	830(4)	225(4)	89(12)
H(3c)	286(6)	818(4)	359(4)	89(13)
H(4a)	422(5)	622(4)	130(4)	87(12)
H(4b)	601(5)	567(4)	202(4)	89(13)
H(4c)	488(9)	483(6)	172(6)	127(32)
H(5a)	227(6)	289(5)	279(4)	130(17)
H(5b)	87(6)	403(4)	333(4)	131(15)
H(6a)	132	474	126	78
H(6b)	66	356	90	78
H(6c)	−59	473	171	78
H(7a)	38(4)	248(3)	498(3)	51(8)
H(7b)	−14(4)	149(3)	474(3)	64(9)
H(8a)	319(5)	168(4)	416(3)	77(10)
H(8b)	266(4)	57(3)	347(3)	63(8)
H(8c)	280(7)	56(6)	492(5)	151(19)
		Form II		
Rh(1)	0	0	0	26
Rh(2)	50000	0	50000	25
Cl(1)	9012(22)	−20168(16)	3176(11)	50
Cl(2)	29417(18)	17012(17)	6938(12)	55
Cl(3)	38166(18)	−9826(14)	32008(8)	43
Cl(4)	78713(16)	10202(15)	46614(11)	47
S(1)	−7531(16)	5940(12)	16203(8)	33
S(2)	46432(15)	23250(13)	49111(8)	31
O(1)	469(6)	2040(4)	2368(3)	47
O(2)	5742(6)	3682(4)	5764(3)	52
N	2052(6)	5145(5)	2172(4)	40
C(1)	−873(12)	−880(7)	2261(5)	49
C(2)	−2986(10)	657(10)	1516(6)	61
C(3)	5033(11)	2777(8)	3710(5)	51
C(4)	2352(8)	2222(9)	4819(6)	55
C(5)	3018(10)	5537(7)	1322(5)	51

Can. J. Chem. Downloaded from www.nrcresearchpress.com by 93.93.197.157 on 09/07/12
For personal use only.

TABLE 2 (*concluded*)

Atom	*x*	*y*	*z*	U_{eq}/U_{iso}[a]
C(6)	4949(10)	5651(9)	1581(7)	67
C(7)	244(8)	5334(7)	2071(5)	52
C(8)	−446(12)	5255(10)	3051(7)	65
H(N)	206(9)	431(8)	213(5)	41(16)
H(N′)	263(8)	569(7)	278(5)	36(15)
H(1a)	−6(11)	−92(10)	235(6)	68(28)
H(1b)	−170(9)	−173(8)	193(5)	53(18)
H(1c)	−95(9)	−39(8)	293(6)	55(18)
H(2a)	−394(13)	−42(11)	90(8)	96(28)
H(2b)	−261(14)	112(13)	228(9)	139(42)
H(2c)	−338(14)	101(13)	80(9)	122(36)
H(3a)	508(10)	375(9)	385(5)	62(20)
H(3b)	468(12)	211(11)	315(7)	87(28)
H(3c)	592(11)	263(9)	360(6)	62(22)
H(4a)	190(8)	189(7)	548(5)	45(15)
H(4b)	239(6)	336(6)	478(4)	29(12)
H(4c)	226(13)	185(12)	426(8)	103(36)
H(5a)	233(9)	486(8)	68(5)	47(16)
H(5b)	269(14)	608(11)	115(8)	78(34)
H(6a)	563(12)	630(10)	225(7)	85(25)
H(6b)	551(10)	604(9)	102(6)	76(23)
H(6c)	507(8)	479(7)	170(4)	31(14)
H(7a)	103(12)	677(11)	208(7)	102(29)
H(7b)	−71(8)	457(7)	154(5)	46(15)
H(8a)	60(10)	620(8)	373(6)	65(20)
H(8b)	−28(9)	481(7)	336(5)	30(18)
H(8c)	−153(16)	549(13)	328(9)	148(43)

[a] U_{eq} = (1/3) trace of diagonalized U.

Can. J. Chem. Downloaded from www.nrcresearchpress.com by 93.93.197.157 on 09/07/12
For personal use only.

TABLE 3. Bond lengths (Å) and angles (deg) with estimated standard deviations in parentheses

	Length			Length	
Bond	I	II	Bond	I	II
Rh(1)—Cl(1)	2.3459(4)	2.3309(12)	S(1)—C(2)	1.774(3)	1.778(6)
Rh(1)—Cl(2)	2.3452(5)	2.3371(13)	S(2)—O(2)	1.422(2)	1.472(4)
Rh(1)—S(1)	2.3173(5)	2.3124(10)	S(2)—C(3)	1.773(3)	1.779(6)
Rh(2)—Cl(3)	2.3400(5)	2.3330(11)	S(2)—C(4)	1.786(4)	1.777(6)
Rh(2)—Cl(4)	2.3429(5)	2.3339(11)	N —C(5)	1.482(3)	1.493(8)
Rh(2)—S(2)	2.3294(5)	2.3318(11)	N —C(7)	1.499(3)	1.491(7)
S(1)—O(1)	1.463(2)	1.481(4)	C(5)—C(6)	1.495(4)	1.492(11)
S(1)—C(1)	1.783(2)	1.769(6)	C(7)—C(8)	1.486(4)	1.485(11)

	Angle			Angle	
Bonds	I	II	Bonds	I	I
Cl(1)—Rh(1)—Cl(2)	89.61(2)	90.24(6)	C(1)—S(1)—C(2)	99.74(14)	101.6(4)
Cl(1)—Rh(1)—S(1)	87.75(2)	94.42(4)	Rh(2)—S(2)—O(2)	116.27(11)	117.0(2)
Cl(2)—Rh(1)—S(1)	92.51(2)	90.11(5)	Rh(2)—S(2)—C(3)	111.31(12)	112.3(2)
Cl(3)—Rh(2)—Cl(4)	89.76(2)	90.09(5)	Rh(2)—S(2)—C(4)	111.67(13)	111.7(2)
Cl(3)—Rh(2)—S(2)	90.59(2)	89.89(4)	O(2)—S(2)—C(3)	105.9(2)	106.9(3)
Cl(4)—Rh(2)—S(2)	91.61(2)	86.14(4)	O(2)—S(2)—C(4)	110.8(2)	107.5(3)
Rh(1)—S(1)—O(1)	115.23(8)	115.85(15)	C(3)—S(2)—C(4)	99.5(2)	100.1(4)
Rh(1)—S(1)—C(1)	111.78(9)	111.3(2)	C(5)—N—C(7)	115.0(2)	113.9(5)
Rh(1)—S(1)—C(2)	110.92(10)	112.5(2)	N—C(5)—C(6)	111.8(2)	111.5(6)
O(1)—S(1)—C(1)	108.16(12)	107.0(3)	N—C(7)—C(8)	111.8(2)	110.5(6)
O(1)—S(1)—C(2)	109.88(14)	107.4(3)			

and an alternative mechanism could involve initial protonolysis of the metal–carbon bond, followed by hydrolysis of the incipient unsaturated enamine-derived cation:

$$\mathbf{1} + HCl \rightarrow (CH_3CH{=}NEt_2)[RhCl_4(Me_2SO)_2]$$

[3] $$\downarrow$$

$$CH_3CHO + (NEt_2H_2)[RhCl_4(Me_2SO)_2] \quad (\mathbf{2})$$

Of note is the fact that **2** (with *trans* sulfoxides) is obtained using either **1***a* or **1***b* which have, respectively, *trans*- and *cis*-disposed sulfoxides. The required isomerization in the **1***b* → **2** transformation could be accommodated within the HCl step, if protonation yielded a 5-coordinate $RhCl_3(Me_2SO)_2$ intermediate (square pyramid ⇌ trigonal bipyramid) that subsequently added chloride.

The isolation of $(NEt_3H)[RhCl_4(Me_2SO)_2]$ during procedure (*a*) of the experimental section presumably arises because the excess NEt_3 used makes NEt_3H^+ available as a possible counter-ion when the DMA·HCl is added. Higher yields of **2** could certainly be attained via a synthetic procedure based on reaction [2].

The most unusual finding in this enamine hydrolysis work, however, is the discovery of two distinct crystal forms of complex **2**. Stereoviews of the two structures are shown in Fig. 1. Both structures possess an asymmetric unit consisting of an $(NEt_2H_2)^+$ cation and two crystallographically independent half-anions, the Rh atoms being located at centres of symmetry. Hydrogen-bonded chains of alternating cations and anions are observed in both crystal structures. In form I the ionic species are linked by N—H···Cl hydrogen bonds (N—H(N)···Cl(3)($-x$, $1-y$, $1-z$) and N—H(N′)···Cl(1), H···Cl = 2.50(4) and 2.49(3), N···Cl = 3.356(2) and 3.353(2) Å, N—H···Cl = 143(3) and 154(3)°, respectively) and in form II by N—H···O hydrogen bonds (N—H(N)···O(1) and N—H(N′)···O(2)($1-x$, $1-y$, $1-z$), H···O = 2.25(7) and 2.04(6), N···O = 2.917(6) and 2.856(6) Å, N—H···O = 143(6) and 160(6)°, respectively). The fact that both forms of **2** can be isolated from the same reaction mixture indicates that the strengths of the N—H···Cl and N—H···O hydrogen-bonding networks in the two polymorphs of **2** must be nearly equal. Crystal polymorphism is a common phenomenon and usually results from differing conditions for crystal growth (9). The isolation of more than one crystal form from the same reaction mixture is not without precedent (e.g. ref. 10). In most cases of crystal polymorphism involving hydrogen-bonded systems, the donor–acceptor pairings remain the same while the hydrogen-bonding motifs may (e.g. ref. 11) or may not (e.g. refs. 10, 12) be different in different crystal forms of the same material. In the present example we have the same motif involving different hydrogen-bond acceptors.

Bond distances and angles observed for the *trans*-$[RhCl_4(Me_2SO)_2]^-$ anions in both crystal forms of **2** are in good agreement with those reported for the Na^+ (3) and $[H(Me_2SO)_2]^+$ (4) salts of the same anion. The effects of the different hydrogen-bonding modes in the two crystal forms of **2** are reflected in the Rh—Cl and S=O bond lengths. The mean Rh—Cl distances are longer in the N—H···Cl hydrogen-bonded form I (2.344(3) vs. 2.334(3) Å), while the mean S=O distances are longer in the N—H···O hydrogen-bonded form II (1.477(6) vs. 1.44(3) Å). The $(NEt_2H_2)^+$ cations are also different in the two forms, that in form I having a *GT* local conformation at nitrogen (C—N—C—C torsion angles of −60.6(3) and −173.3(2)°) while in form II the local conformation is *TT* (torsion angles of 167.9(5) and −167.6(6)°).[3]

Acknowledgments

We thank the Natural Sciences and Engineering Research Council of Canada for financial support (operating grants to B.R.J. and J.T.), the University of British Columbia Computing Centre for assistance, and Johnson, Matthey Ltd. for a loan of rhodium.

1. S. N. Gamage, R. H. Morris, S. J. Rettig, and B. R. James. J. Organomet. Chem. **309**, C59 (1986).
2. S. N. Gamage, I. S. Thorburn, R. H. Morris, S. J. Rettig, and B. R. James. J. Chem. Soc. Chem. Commun. 894 (1987).
3. V. I. Sokol, N. D. Rubstova, and A. Y. Gribenyuk. Zhur. Strukt. Khim. **15**, 318 (1974).
4. B. R. James, R. H. Morris, F. W. B. Einstein, and A. Willis. J. Chem. Soc. Chem. Commun. 31 (1980).
5. W. D. Kumler. J. Org. Chem. **83**, 4983 (1961).
6. J. R. Barnes, P. L. Goggin, and R. J. Goodfellow. J. Chem. Res. (M). 1610 (1979).
7. International tables for X-ray crystallography. Vol. IV. Kynoch Press, Birmingham. 1974. pp. 99–102 and 149.
8. R. McCrindle, G. Ferguson, G. J. Arsenault, and A. J. McAlees. J. Chem. Soc. Chem. Commun. 571 (1983); R. McCrindle, G. Ferguson, G. J. Arsenault, A. J. McAlees, and D. K. Stephenson. J. Chem. Res. (S) 360 (1984), and J. Chem. Res. (M) 3301 (1984).
9. J. D. Dunitz. X-ray analysis and the structure of organic compounds. Cornell University Press, Ithaca, N.Y. 1979. p. 321.
10. A. Kapor, B. Ribar, V. Divjakovic, G. Stajer, G. Bernath, and G. Argay. Acta Crystallogr. Sect. C, **43**, 1347 (1987).
11. (*a*) J. A. Kanter and G. Roelofsen. Acta Crystallogr. Sect. B, **32**, 3328 (1976); (*b*) J. A. Kanter, G. Roelofsen, and T. Feenstra. Acta Crystallogr. Sect. B, **32**, 3331 (1976).
12. (*a*) S. J. Rettig and J. Trotter. Can. J. Chem. **51**, 1288 (1973); (*b*) S. J. Rettig and J. Trotter. Can. J. Chem. **54**, 3130 (1976).
13. S. Mizushima. Structure of molecules and internal rotation. Academic Press, New York. 1954.
14. M. W. Dougall and N. L. Paddock. J. Chem. Soc. Dalton Trans. 1022 (1974).

[3]The *GT* (*gauche–trans*) and *TT* (*trans–trans*) terminology for conformations is taken from ref. 13; illustrations can be found also in, for example, ref. 14.

Can. J. Chem. Downloaded from www.nrcresearchpress.com by 93.93.197.157 on 09/07/12
For personal use only.

Diffusion in associating nonelectrolyte mixtures: stepwise aggregation and micelle formation

DEREK G. LEAIST
Department of Chemistry, University of Western Ontario, London, Ont., N6A 5B7 Canada

Received September 28, 1987

DEREK G. LEAIST. Can. J. Chem. **66**, 1129 (1988).

Equations have been developed to predict diffusion coefficients and Onsager coefficients for associating nonelectrolyte solutes in binary or multicomponent solutions with any number of association equilibria. The equations are used to interpret previously reported data for binary diffusion with stepwise association of ethanol and *N*-methylacetamide in carbon tetrachloride solutions. Diffusion of Triton X-100, a non-ionic micelle-forming surfactant, is also analyzed. In contrast to the gradual decrease in the diffusivity caused by stepwise association, formation of micellar aggregates produces a sharp drop in the diffusivity at the critical micelle concentration. The relation between interdiffusion coefficients and intradiffusion coefficients for associating nonelectrolyte solutes is discussed.

DEREK G. LEAIST. Can. J. Chem. **66**, 1129 (1988).

On a développé des équations qui permettent de prédire les coefficients de diffusion et les coefficients d'Onsager de solutés non-électrolytes qui s'associent dans des solutions binaires ou à plusieurs composants et qui comportent n'importe quel nombre d'équilibres d'association. On a utilisé les équations pour interpréter des données rapportées antérieurement pour de la diffusion binaire impliquant une association par étapes de l'éthanol et du *N*-méthylacétamide dans des solutions de tétrachlorure de carbone. On a aussi analysé la diffusion du Triton X-100, un agent de surface non-ionique qui forme des micelles. Par opposition avec la diminution graduelle de la possibilité de diffusion provoquée par cette association par étapes, la formation d'aggrégats micellaires provoque une diminution importante de la possibilité de diffusion à la concentration micellaire critique. On discute de la relation entre les coefficients d'interdiffusion et les coefficients d'intradiffusion pour les solutés non-électrolytes qui s'associent.

[Traduit par la revue]

Can. J. Chem. Downloaded from www.nrcresearchpress.com by 93.93.197.157 on 09/07/12
For personal use only.

Introduction

Many nonelectrolyte solutes associate (1). Aqueous urea, for example, is extensively dimerized (2, 3). In nonpolar solvents, carboxylic acids and phenols form dimers (4–7). Other solutes, such as nucleic acids (8), amides (9–11), and certain dyes (12), associate in a stepwise manner to form chain-like aggregates. Non-ionic surfactants illustrate an extreme case of association in which micellar clusters containing several hundred molecules can form (13–16).

The work reported here was undertaken to study the diffusion behavior of associating nonelectrolytes. The effects of association on diffusion are interpreted by determining changes in the solute mobility and the free energy gradient, the driving force for diffusion.

Binary diffusion of dimerizing solutes (2, 17–20) and ternary diffusion of solutes A and B that form complex AB (21) have already been studied. The equations developed in the present paper extend the earlier treatments to nonelectrolyte mixtures that contain arbitrary numbers of components and association equilibria.

Weinheimer *et al.* (15) have reported an approximate expression for estimating the diffusion coefficient of micelle-forming nonelectrolytes above the critical micelle concentration. The more general expression developed here allows changes in the rate of diffusion to be followed as the concentration is raised or lowered through the critical micelle concentration.

Theory

Consider isothermal diffusion in a nonelectrolyte solution composed of solvent and n different solute species with n_r independent association reactions. The reaction rates are assumed to be rapid compared to diffusion so that chemical equilibrium exists locally. This is a valid assumption provided the chemical relaxation times are small compared to $\epsilon^2/\Delta D$, where ϵ is a characteristic linear dimension of the system and ΔD is the difference between the diffusivities of the reactants and products (22).

Local chemical equilibrium places n_r restrictions on transport of the n solute species. Therefore, only $n - n_r$ solute flows are independent. Interdiffusion in the solution under consideration can be described by using generalized Fick equations for $N = n - n_r$ constituent solute components (23).

$$[1] \quad J_i = -\sum_{k=1}^{N} D_{ik}\nabla C_k$$

J_i and ∇C_k denote the molar flux densities and the gradients in the concentrations of the solute components. Diffusion coefficient D_{ik} measures the flux of component i produced by the gradient in component k.

Onsager's equations (23)

$$[2] \quad J_i = -\sum_{k=1}^{N} L_{ik}\nabla\mu_k$$

relate the fluxes of the solute components to the gradients in the components' chemical potentials. The two sets of transport coefficients are related by the identity

$$[3] \quad D_{ik} = \sum_{q=1}^{N} L_{iq}\partial\mu_q/\partial C_k$$

In general, the N solute components may be transported as monomers, dimers, trimers, etc. (A_1, A_2, A_3, ...), or, in multicomponent mixtures, as complexes formed with other components (A_1B_1, A_2B_1, A_1B_2, ...). In order to estimate the transport coefficients of associating components, it proves convenient to have transport equations

$$[4] \quad j_p = -\sum_{q=1}^{n} l_{pq}\nabla\hat{\mu}_q$$

for each of the n solute species. j_p and $\nabla\hat{\mu}_q$ stand for the molar flux densities and the gradients in the chemical potentials of the various solute species.

If stoichiometric coefficient ν_{ip} denotes the number of moles of constituent component i contained in one mole of species p, then

$$[5] \quad J_i = \sum_{p=1}^{n} \nu_{ip} j_p$$

$$[6] \quad \nabla\hat{\mu}_q = \sum_{k=1}^{N} \nu_{kq} \nabla\mu_k$$

Substitution of eqs. [4] and [6] into eqs. [5] provides the following general relation between the transport coefficients of the components and the species

$$[7] \quad L_{ik} = \sum_{p=1}^{n} \sum_{q=1}^{n} \nu_{ip} l_{pq} \nu_{kq}$$

Equation [7] can be rerewritten as

$$[8] \quad \mathbf{L} = \boldsymbol{\nu} \mathbf{l} \boldsymbol{\nu}^{\mathrm{T}}$$

where $\boldsymbol{\nu}^{\mathrm{T}}$ denotes the transpose of $\boldsymbol{\nu}$, the $N \times n$ matrix of stoichiometric coefficients.

L_{ik} coefficients

It is a valid approximation, especially for dilute solutions, to express the diffusion velocity of each species (v_i) as the product of the mobility of the species (u_i) and the driving force ($-\nabla\hat{\mu}_i$) acting on the species (22).

$$[9] \quad v_i = -u_i \nabla\hat{\mu}_i$$

Since $j_i = c_i v_i$, where c_i denotes the concentration of species i, we have

$$[10] \quad j_i = -c_i u_i \nabla\hat{\mu}_i$$

Comparisons of eqs. [4] and [10] shows that the off-diagonal l_{ik} coefficients ($i \neq k$) may be neglected (24) and that the diagonal elements are given by $l_{ii} = c_i u_i$. Equation [7] then provides the following approximate relation between the Onsager coefficients of the solute components and the mobilities of the diffusing species.

$$[11] \quad L_{ik} = \sum_{q=1}^{n} \nu_{iq} c_q u_q \nu_{kq}$$

Interchanging i and k in eqs. [11] shows that the reciprocal relations $L_{ik} = L_{ki}$ ($i \neq k$) are satisfied.

Cross-coefficient L_{ik} ($i \neq k$) measures the interaction between flows of components i and k. If components i and k take part in a chemical reaction with species q, then the product $\nu_{iq}\nu_{kq}$ is non-zero, and hence the flows of the two components will interact. Conversely, if components i and k do not react with a common species, then rows i and k of $\boldsymbol{\nu}$ are orthogonal and the two components are predicted to diffuse independently.

D_{ik} coefficients

Einstein's equation (23),

$$[12] \quad D_i = RTu_i$$

which relates the diffusion coefficient and the molar mobility of each species, and eqs. [3] and [11] provide the following approximate expressions

$$[13] \quad D_{ik} = (RT)^{-1} \sum_{p=1}^{n} \sum_{q=1}^{n} \nu_{iq} c_i D_q \nu_{pq} \partial\mu_p / \partial C_k$$

for the diffusion coefficients of the solute components (D_{ik}) in terms of the concentrations and diffusion coefficients (D_i) of the species.

In favorable cases, accurate values of D_i can be obtained from analysis of binary or tracer diffusion data (15, 17–19). If this information is unavailable, values of D_i can be estimated from diffusivities for species with similar molecular structures (25). For solute molecules that are large compared to the solvent molecules, diffusivities can be estimated by using Stokes Law (23), $D_i = kT/6\pi\eta a$, where k, T, η, and a denote Boltzmann's constant, temperature, solvent viscosity, and the effective molecular radius.

Results

The equations that have been developed will now be used to interpret binary diffusion of nonelectrolytes that associate in a step-wise manner or form micelles. One example of ternary diffusion with complex-formation will also be treated.

Binary mixtures

Transport in solutions that contain a single solute component will be considered first. In general, the solute molecules can exist as monomers (designated by A_1), dimers (A_2), trimers (A_3), etc. Aggregation of the solute can be represented by the series of association reactions

$$iA_1 = A_i \qquad K_i$$

in which aggregates of i monomers are formed from i free monomers. Choosing total A the constituent solute component and numbering the solute species $1 = A_1$, $2 = A_2$, $3 = A_3$, ..., defines the following stoichiometric coefficients

$$[14] \quad \boldsymbol{\nu} = (1 \quad 2 \quad 3 \quad 4 \ldots)$$

Equation [11] shows that U, the overall molar mobility of the solute, is weighted in favor of the mobilities of the diffusing species as follows

$$[15] \quad U = \sum_{i=1} i^2 c_i u_i / C = L/C$$

The concentrations of the species can be evaluated by using the conditions of chemical equilibrium

$$[16] \quad K_i = c_i / c_i^i$$

and from the total content of solute A

$$[17] \quad C = \sum_{i=1} i c_i$$

Given values of L from eq. [15], the binary diffusion coefficient of the solute can be evaluated from

$$[18] \quad D = L \mathrm{d}\mu / \mathrm{d}C$$

Differentiation of eqs. [16] and [17] and the expression for the solute's chemical potential

$$[19] \quad \mu_1 = \mu_1^0 + RT \ln C_1$$

gives

$$[20] \quad \mathrm{d}\mu/\mathrm{d}C = RT / \sum_{i=1} i^2 c_i$$

Can. J. Chem. Downloaded from www.nrcresearchpress.com by 93.93.197.157 on 09/07/12
For personal use only.

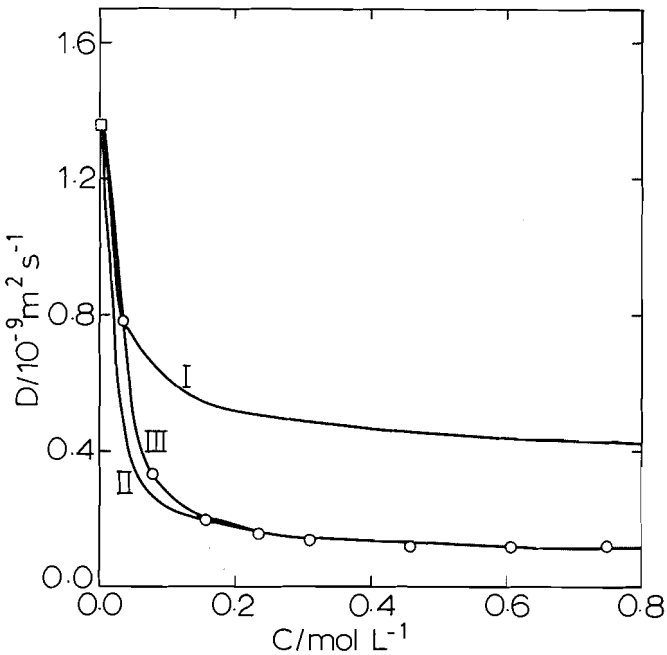

FIG. 1. Diffusion coefficients for *N*-methylacetamide in carbon tetrachloride solutions at 25°C: ○, interdiffusion coefficients measured by Longsworth (25); curve I, predicted values of D, $D_i = D_1 i^{-1/3}$, $K_{12} = 5$ L mol^{-1}, $\bar{K} = 40$ L mol^{-1}; curve II, $D_i = D_1 i^{-0.68}$, $K_{12} = 5$ L mol^{-1}, $\bar{K} = 40$ L mol^{-1}; curve III, $D_i = D_1 i^{-0.68}$, $K_{12} = 1$ L mol^{-1}, $\bar{K} = 25$ L mol^{-1}.

and hence

$$[21] \quad D = \sum_{i=1} i^2 c_i D_i / \sum i^2 c_i$$

Thus D is an $i^2 c_i$-weighted average of the diffusion coefficients of the species.

Equations [15], [17], [18], [20], and [21] have been simplified by dropping subscripts "11" from L and D and subscript "1" from C, U, and μ. In addition, the solute has been assumed to be ideal in the thermodynamic sense.

N-Methylacetamide (NMA) in carbon tetrachloride

Longsworth (25) has used Rayleigh interferometry to measure precise diffusion coefficients for NMA + carbon tetrachloride solutions. Continuous stepwise self-association of NMA in these solutions produces dimers, trimers and larger hydrogen-bonded aggregates. Association of the solute causes D to drop from 1.36×10^{-9} m^2 s^{-1} at infinite dilution to 0.12×10^{-9} m^2 s^{-1} at 0.4 mol L^{-1} and 25°C.

The thermodynamic parameters for self-association of NMA are not known reliably. However, evidence from several independent sources suggests it is a reasonable approximation to use K_2 for the monomer–dimer equilibrium and a second constant, $\bar{K}$, for the subsequent association steps ($i > 2$)

$$A_1 + A_{i-1} = A_i \qquad \bar{K}$$

in which aggregates of i monomers are formed from aggregates of $i - 1$ monomers (9, 10). Since $\bar{K} = K_i/K_{i-1}$, we have $K_i = K_2 \bar{K}^{i-2}$ for $i > 2$. The reported values of K_2 and $\bar{K}$, as inferred from infrared (7, 26, 27) or nmr (10) spectra and from vapor pressure data (28), vary considerably, from about 0.9 to 8 for K_2 and from about 20 to 50 L mol^{-1} for $\bar{K}$, at 25°C.

The value of D_1, the diffusivity of the NMA monomer, was set equal to 1.36×10^{-9} m^2 s^{-1}, the limiting diffusion coefficient of fully-dissociated NMA obtained by Longsworth (25) by extrapolation of D to zero concentration of solute. Values for the diffusivities of the associated NMA species are not available. However, the volume of an aggregate of i monomers is approximately i times larger than the volume of a single monomer. Therefore, values of D_i ($i \geq 2$) can be estimated by using the Stokes law ratios $D_i/D_1 = i^{-1/3}$.

In Fig. 1 the predicted values of D for NMA in carbon tetrachloride (curve I) are compared with the measured D values reported by Longsworth (25). The values of the association constants that were used in the calculations were taken from the middle of the ranges of the reported values: $K_{12} = 5$ L mol^{-1} and $\bar{K} = 40$ L mol^{-1}. Above 0.1 mol L^{-1} NMA, the predicted values of D are significantly too large. This discrepancy might be caused by the higher NMA polymers being more stable than the value adopted for $\bar{K}$ would suggest. In view of the uncertainty in the estimates of the diffusion coefficients of the NMA polymers, this explanation is speculative. For example, the diffusion coefficients of the longer threads of associated NMA molecules will be smaller than the values suggested by Stokes law, which is valid only for spherical particles. To obtain better estimates for the diffusion coefficients of polymeric chains in carbon tetrachloride, Longsworth's (25) limiting diffusivities for the C_7, C_{12}, C_{16}, C_{20}, C_{22}, C_{28}, and C_{32} normal alkanes were used. The plot of ln D_i versus ln i, where i is the number of carbon atoms in the alkane, gave the slope $-0.68(\pm 0.02)$, which suggests $D_i = D_1 i^{-0.68}$. The values of D_2, D_3, ... obtained from this equation together with $K_{12} = 5$ L mol^{-1} and $\bar{K} = 40$ L mol^{-1} were used to calculate the values of D for NMA shown by curve II in Fig. 1. Agreement with the measured values of D is improved remarkably. Below 0.1 mol L^{-1} NMA, however, the calculated D values are too low. This remaining discrepancy can be removed by adjusting the values of the association constants to $K_{12} = 1$ L mol^{-1} and $\bar{K} = 25$ L mol^{-1} (curve III).

Orange II in water

The stepwise association of certain dyes, such as Orange II (29), is described by the isodesmic model in which the stepwise association constant is independent of the size of the aggregate: $\bar{K} = K_i/K_{i-1}$ for $i \geq 2$. In this case the concentrations of the total dye and the dye monomer are related by (29)

$$[22] \quad C = c_1(1 - \bar{K}c_1)^{-2}$$

and D is given by

$$[23] \quad D = \sum_i i^2 \bar{K}^{i-1} c_i^i D_i \Big/ \Big(\sum_i i^2 \bar{K}^{i-1} c_i^i \Big)$$

No experimental binary diffusion coefficients appear to have been reported for isodesmically associating nonelectrolytes.

Ethanol in carbon tetrachloride

Diffusion of ethanol in carbon tetrachloride has also been studied (25, 30, 31). In contrast to the continuous association of NMA or Orange II, association of ethanol molecules proceeds only to the hexamer stage ($K_n(n \geq 7) = 0$). From infrared measurements at 25°C, Coburn and Grunwald (6) obtained the values 0.64, 0.61, 14.3, 27.8, and 54.1 for K_2 through K_6. By extrapolation of diffusion coefficient versus molar volume data for molecules with similar structures, Longsworth (25) assigned the values 1.274×10^{-9}, 0.907×10^{-9}, 0.621×10^{-9}, 0.492×10^{-9}, and 0.464×10^{-9} m^2 s^{-1} to D_2 through D_6. By extrapolation of measured values of D to zero concentration, he also

Can. J. Chem. Downloaded from www.nrcresearchpress.com by 93.93.197.157 on 09/07/12
For personal use only.

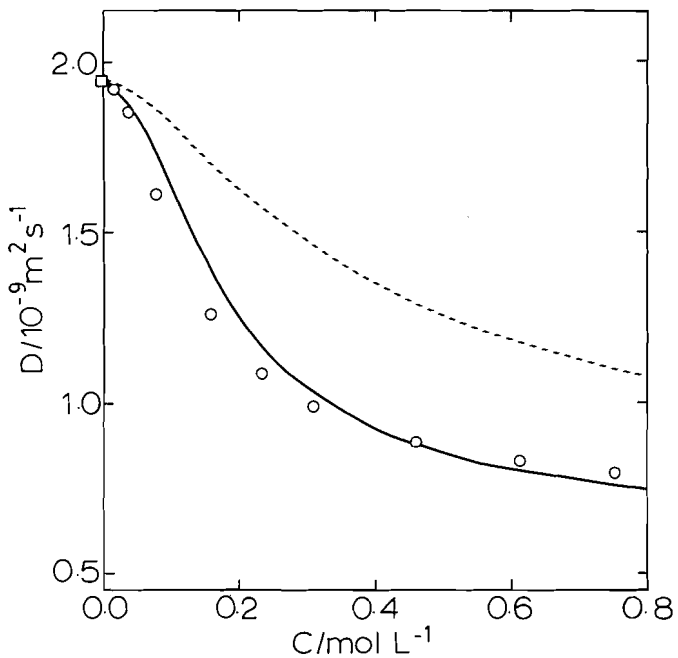

FIG. 2. Diffusion coefficients for ethanol in carbon tetrachloride solutions at 25°C: ○, interdiffusion coefficients measured by Longsworth (25); solid curve, predicted interdiffusion coefficients (eq. [21]); dashed curve, predicted intradiffusion coefficient (eq. [39]).

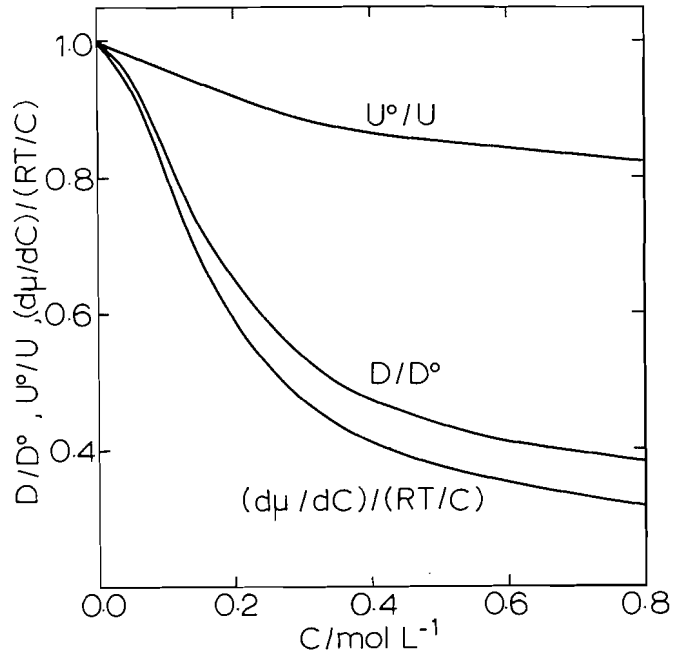

FIG. 3. Comparison of the mobility, diffusion coefficient and thermodynamic factor for ethanol in carbon tetrachloride at 25°C. In the limit $C \rightarrow 0$: $U \rightarrow U^\circ = u_1$; $D \rightarrow D^\circ = D_1$; $C\mathrm{d}\mu/\mathrm{d}C \rightarrow RT/C$.

determined the value 1.95×10^{-9} m^2 s^{-1} for D_1, the diffusion coefficient of the ethanol monomer.

Figure 2 gives a comparison of the predicted values of D which were generated by eq. [21] and the precise optical values measured by Longsworth for ethanol in carbon tetrachloride (25). Agreement is considerably better than that for NMA in carbon tetrachloride, probably because the values of K_i and D_i for the ethanol solutions are known more precisely.

As mentioned earlier, D can be expressed as a product of the mobility and a thermodynamic factor.

$$[24] \quad D = U(C\mathrm{d}\mu/\mathrm{d}C)$$

Figure 3 shows calculated values of the mobility and the thermodynamic factor for diffusion of ethanol in carbon tetrachloride at 25°C. The concentration-dependence of D is seen to be dominated by the thermodynamic factor, which drops as the concentration is raised. By reducing the number of free particles per mole of solute, association leads to lower free energy gradient, the "driving force" for diffusion. At the same time, however, there is less friction per mole of solute if some of the separate solute particles combine into aggregate diffusing particles. This increases the solute's molar mobility. In concentrated solutions, most of the ethanol is transported as hexamers. In this limit, values of D and $C\mathrm{d}\mu/\mathrm{d}C$ approach D_6 and $RT/6$, respectively.

Triton X-100 in water

As a final example of binary diffusion with self-association, transport of a nonionic micelle-forming detergent will be explored. The analysis will be simplified by assuming that the micelles are monodisperse.

Let m stand for the number of monomers held in each micelle. An expression for the diffusion coefficient of the surfactant can be obtained from eq. [21] by saving only those terms containing c_1 or c_m.

Among non-ionic surfactants, diffusion of aqueous Triton X-100 ($(CH_3)_3CCH_2C(CH_3)_2C_6H_4O(CH_2CH_2O)_{10}H$, molecular weight 646 g mol^{-1}) has been most thoroughly studied (15, 16). As the concentration of the surfactant is raised through the critical micelle concentration (cmc) of about 0.25 mmol L^{-1} (14), spherical aggregates containing approximately 140 monomers are formed (13). The diffusion coefficient of the Triton X-100 micelles, D_m is about 0.067×10^{-9} m^2 s^{-1}, the value determined by Weinheimer *et al.* (15) by extrapolation to high concentrations where most of the solute is transported as micelles. The diffusion coefficient of the Triton X-100 monomers, D_1, is difficult to measure because extremely dilute solutions are required to ensure that monomer diffusion is the dominant transport mechanism. At high dilutions, adsorption of solute onto the surfaces of diffusion cells can produce large errors in the measured values of D (15). In the calculations reported here, the value 0.35×10^{-9} m^2 s^{-1} was used for D_1. This estimate was obtained from Stokes law as follows: $D_1 = (140)^{1/3} D_m$. (It is close to the value reported for the diffusion coefficient of polyethylene glycol with molecular weight 600 g mol^{-1} (32).)

Figure 4 gives values of D calculated for aqueous Triton X-100 at 25°C. In this case association, through the thermodynamic factor, produces a sharp drop in D as the concentration is raised through the cmc. Above the cmc, D drops slowly with C and approaches D_m. Formation of submicellar aggregates, which is neglected in the present treatment, would produce a more gradual drop in D at the cmc.

Multicomponent mixtures

The equations developed in this paper can also be used to interpret the transport properties of mixtures containing two or more associating solute components. However, no multicomponent diffusion measurements appear to have been made on such mixtures. The following example merely serves as a brief illustration of how the equations can be applied to the particular case

Can. J. Chem. Downloaded from www.nrcresearchpress.com by 93.93.197.157 on 09/07/12
For personal use only.

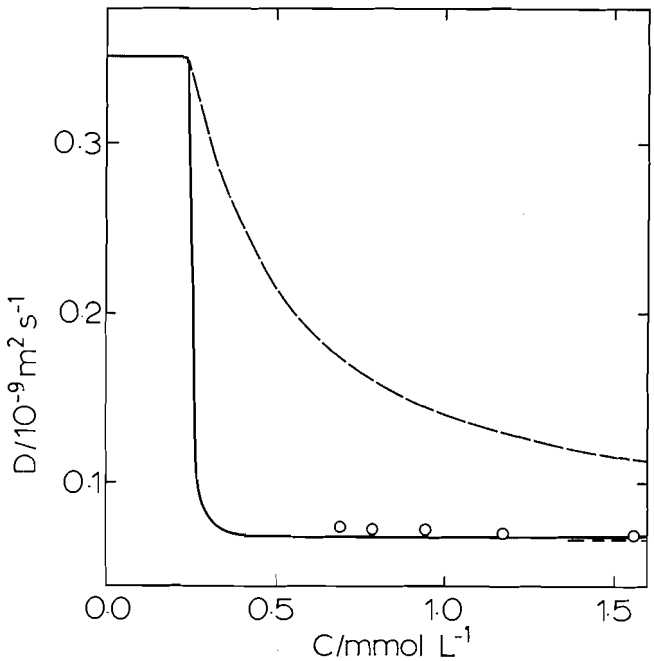

FIG. 4. Diffusion coefficients for aqueous Triton X-100 at 25°C: ○, interdiffusion coefficients measured by Weinheimer *et al.* (15); solid curve, predicted interdiffusion coefficients (eg. [21]); dashed curve, predicted intradiffusion coefficients (eq. [39]). At high concentrations, D approaches D_m, the diffusion coefficient of the micelles (horizontal dashed line).

of mixtures containing two solutes that form a 1:1 complex (21).

$A + B = AB$

If solute monomers A_1 and B_1 associate by forming complex A_1B_1, there are three different solute species and one reaction equilibrium. Only two flows of solute are independent. Diffusion of the solutes is described by ternary flow equations (eqs [1] and [2] with $N = 2$).

If total A and total B are chosen as the constituent solute components and if the solute species are numbered as follows: 1 = A_1, 2 = B_1, and 3 = A_1B_1, then the stoichiometric coefficients are given by

$$[25] \quad \nu = \begin{pmatrix} 1 & 0 & 1 \\ 0 & 1 & 1 \end{pmatrix}$$

Equations [11] and [25] furnish the following expressions for the Onsager coefficients of the solute components

$$[26] \quad L_{11} = (c_1D_1 + c_3D_3)/RT$$

$$[27] \quad L_{12} = L_{21} = c_3D_3/RT$$

$$[28] \quad L_{22} = (c_2D_2 + c_3D_3)/RT$$

Given the concentrations of total A and total B components, c_1 and c_2, respectively, the concentrations of the species can be evaluated by solving the conditions of mass balance and reaction equilibrium: $C_1 = c_1 + c_2$, $C_2 = c_2 + c_3$, $K = c_3/c_1c_2$. Differentiation of the expressions for the chemical potentials of the solute components

$$[29] \quad \mu_i = \mu_i^0 + RT \ln c_i$$

provides

$$[30] \quad \partial\mu_1/\partial C_1 = RT(1 - f_2)/c_1$$

$$[31] \quad \partial\mu_1/\partial C_2 = \partial\mu_2/\partial C_1 = -RTf_2/c_2$$

$$[32] \quad \partial\mu_2/\partial C_2 = RT(1 - f_1)/c_2$$

and hence

$$[33] \quad D_{11} = D_1 + f_2(D_3 - D_1)$$

$$[34] \quad D_{12} = f_1(D_3 - D_1)$$

$$[35] \quad D_{21} = f_1(D_3 - D_2)$$

$$[36] \quad D_{22} = D_2 + f_2(D_3 - D_2)$$

where f_1 and f_2 stand for

$$[37] \quad f_1 = c_2^{-1}/(c_1^{-1} + c_2^{-1} + c_3^{-1})$$

$$[38] \quad f_2 = c_1^{-1}/(c_1^{-1} + c_2^{-1} + c_3^{-1})$$

Equations [33]–[38] can be used to show that the multicomponent diffusivity of each component is not a simple concentration-weighted average of the diffusivities of the species containing that component, i.e. $D_{11} \neq (c_1D_1 + c_3D_3)/(c_1 + c_3)$. f_1 and f_2 can take the values $0 \leq f_i \leq 1$. Consequently, D_{11} and D_{22}, the diffusivities of the components, can take the values $D_3(A_1B_1) \leq D_{11} \leq D_1(A_1)$ and $D_3(A_1B_1) \leq D_{22} \leq D_2(B_1)$.

The expressions for D_{12} and D_{21} suggest that coupled diffusion will be important if the diffusivity of the complex A_1B_1 differs significantly from the diffusivity of species A_1 or B_1. Cross-coefficient D_{12}, for example, gives the flow of component A produced by the gradient in the concentration of component B. Due to the association reaction, an increase in the concentration of component B leads to an increase in the concentration of the complex A_1B_1 and to a corresponding decrease in the concentration of the species A_1. As a result, the gradient in component B (∇C_2) produces a gradient with the same sign in the concentration of the complex A_1B_1 (∇c_3), and an equal but opposite gradient in the concentration of the uncomplexed A_1 species ($\nabla c_1 = -\nabla c_3$). The net coupled flow of component A, which comprises the flow $-D_3(A_1B_1)\nabla c_3$ of complexed A plus the countercurrent flow $D_1(A_1)\nabla c_3$, is therefore proportional to $D_3 - D_1$. As $C_1/C_2 \rightarrow 0$, D_{12} vanishes because the gradient in component B and produce a coupled flow of component A in a solution that does not contain component A. Similarly, D_{21} is proportional to $D_3 - D_2$ and $D_{21} \rightarrow 0$ as $C_2/C_1 \rightarrow 0$.

Discussion

It is tempting to regard the binary diffusion coefficient of a self-associating solute as simply the average of the diffusion coefficients of the various solute species weighted according to the fraction of the total solute carried by each species, i.e.

$$[39] \quad D^* = \sum_i ic_iD_i/\sum_i ic_i = \sum_i ic_iD_i/C$$

In fact, the diffusion coefficient D^* defined in this manner corresponds to the intradiffusion coefficient of the solute (2, 19, 20, 33, 34). Intradiffusion coefficients can be measured by tagging some of the solute molecules with radioactive atoms, then following their motion through an otherwise homogenous solution in which the total concentration of labelled and unlabelled solute is uniform. Intradiffusion can also be measured by using nmr methods (35).

The interdiffusion coefficient (also known as the mutual

Can. J. Chem. Downloaded from www.nrcresearchpress.com by 93.93.197.157 on 09/07/12
For personal use only.

diffusion coefficient), D, studied in this paper, in contrast, describe transport of solute from regions of high concentration to low concentration in non-uniform solutions. Equations [21] and [39] emphasize that D and D^* differ markedly; whereas D is obtained by giving the weight i^2c_i to the diffusion coefficient of an aggregate of i monomers, the weights ic_i give D^*.

The dashed curves in Figs. 2 and 4 give calculated intradiffusion coefficients for ethanol in carbon tetrachloride and for Triton X-100 in water. For a given solution, the interdiffusion coefficient D is smaller than the intradiffusion coefficient D^* because the former is more heavily weighted in favor of the larger aggregates which diffuse relatively slower. If eq. [39] is used to estimate interdiffusion coefficients, the predicted values will be too high. Indeed, this led Longsworth (25) to suspect that association of ethanol is stronger than suggested by infrared measurements. When the diffusivities of the ethanol polymers are weighted according to eq. [21], good agreement with experiment is obtained.

In this paper association constants have been used to predict binary diffusion coefficients. The results for ethanol in carbon tetrachloride suggest that reliable predictions can be made provided reliable estimates of the association constants and the mobilities of the various solute species are available. If reliable mobility estimates are available, as in the case of NMA in carbon tetrachloride, it will be feasible to invert this procedure, namely to use diffusion measurements to determine association constants.

Acknowledgement

This work was supported by the National Sciences and Engineering Research Council of Canada.

1. O. Redlich and A. T. Kister. J. Chem. Phys. **15**, 849 (1947).
2. R. H. Stokes. J. Phys. Chem. **69**, 4012 (1965).
3. J. G. Albright and R. Mills. J. Phys. Chem. **69**, 3120 (1965).
4. N. D. Coggeshall and E. L. Saier. J. Am. Chem. Soc. **73**, 5414 (1951).
5. J. Wenograd and R. A. Spurr. J. Am. Chem. Soc. **79**, 5844 (1957).
6. W. C. Coburn and E. Grunwald. J. Am. Chem. Soc. **80**, 1318 (1958).
7. I. M. Klotz and J. S. Franzen. J. Am. Chem. Soc. **84**, 3461 (1962).
8. H. Høiland, A. Skauge, and I. Stokkeland. J. Phys. Chem. **88**, 6350 (1984).
9. L. A. Laplanche, H. B. Thompson, and M. T. Rogers. J. Phys. Chem. **69**, 1482 (1965).
10. L. L. Graham and C. Y. Chang. J. Phys. Chem. **75**, 776 (1971).
11. L. L. Graham and C. Y. Chang. J. Phys. Chem. **75**, 784 (1971).
12. R. Reeves and S. A. Harkaway. J. Colloid Interface Sci. **64**, 342 (1978).
13. L. M. Kushner and W. D. Hubbard. J. Phys. Chem. **58**, 1163 (1954).
14. A. Ray and G. Nemethy. J. Phys. Chem. **75**, 804 (1971).
15. R. M. Weinheimer, D. F. Evans, and E. L. Cussler. J. Colloid Interface Sci. **80**, 357 (1981).
16. M. Corti and V. Degiorgio. Optics Commun. **14**, 358 (1975).
17. G. T. A. Muller and R. H. Stokes. Trans. Faraday Soc. **53**, 642 (1957).
18. L. A. Dunn and R. H. Stokes. Aust. J. Chem. **18**, 285 (1965).
19. H. Schönert. Z. Phys. Chem. N.F. **119**, 53 (1980).
20. P. C. Carman. J. Phys. Chem. **71**, 2565 (1967).
21. V. Vitagliano and R. Sartorio. J. Phys. Chem. **74**, 2949 (1970).
22. W. H. Stockmayer. J. Chem. Phys. **33**, 1291 (1960).
23. H. J. V. Tyrrell and K. R. Harris. Diffusion in liquids. Butterworths, London. 1984.
24. D. G. Leaist. J. Chem. Soc. Faraday Soc. 1, **78**, 3069 (1982).
25. L. G. Longsworth. J. Colloid Interface Sci. **22**, 3 (1966).
26. K. R. Bhaskar and C. N. R. Rao. Biochim. Biophys. Acta, **136**, 561 (1967).
27. H. Lowenstein, H. Lassen, and A. Hvidt. Acta Chem. Scand. **24**, 1687 (1970).
28. R. D. Grigsby, S. D. Christian, and H. E. Affsprung. J. Phys. Chem. **70**, 1203 (1966).
29. E. L. Cussler. Diffusion. Cambridge University Press, Cambridge. 1984. p. 167.
30. B. R. Hammond and R. H. Stokes. Trans. Faraday Soc. **52**, 781 (1956).
31. D. K. Anderson and A. L. Babb. J. Phys. Chem. **67**, 1362 (1963).
32. L. G. Longsworth. J. Phys. Chem. **67**, 689 (1963).
33. P. J. Dunlop. J. Phys. Chem. **69**, 1693 (1965).
34. R. Mills. Rev. Pure. Appl. Chem. Aust. **11**, 78 (1961).
35. K. R. Harris, R. Mills, P. J. Back, and D. S. Webster. J. Mag. Res. **29**, 473 (1978).

Can. J. Chem. Downloaded from www.nrcresearchpress.com by 93.93.197.157 on 09/07/12
For personal use only.

Étude de la metallation des carbamates d'hydroxy-2,3,4 quinoléines

J. M. JACQUELIN, Y. ROBIN, A. GODARD ET G. QUEGUINER

Institut national supérieur de chimie industrielle de Rouen, Institut national des sciences appliquées, B.P. 8, 76130 Mont-Saint-Aignan, France

Reçu le 16 juin 1987

J. M. JACQUELIN, Y. ROBIN, A. GODARD et G. QUEGUINER. Can. J. Chem. **66**, 1135 (1988).

Les *N,N*-dialkyl *O*-quinolyl-3 ou 4) carbamates sont lithiés régiosélectivement en 4 (respectivement en 3) par le DIPAL dans le THF à −78°C. La métallation de l'isomère substitué en position 2 s'éffectue en *ortho* en utilisant le chélate *S*-BuLi/TMEDA dans le THF à −105°C. L'utilisation d'aldéhydes comme électrophiles a permis de mettre en évidence l'importance de l'encombrement stérique autour de l'atome d'azote de la fonction carbamate. De nombreux dérivés disubstitués ont été préparés.

J. M. JACQUELIN, Y. ROBIN, A. GODARD, and G. QUEGUINER. Can. J. Chem. **66**, 1135 (1988).

When *N,N*-dialkyl *O*-(quinolyl-3 or 4) carbamates are reacted with LDA in THF at −78°C lithiation occurs regioselectively at the *ortho* positions (respectively at C4 and C3). With the 2-substituted isomer better results can be obtained by using *sec*-butyllithium/TMEDA chelate instead of LDA in THF at −105°C. Each of the lithiated intermediates is treated with various electrophiles. The results of experiments with aldehydes afford convincing evidence of the influence of steric hindrance around the nitrogen of the carbamate functional group. Various disubstituted hydroxyquinolines have been prepared.

Can. J. Chem. Downloaded from www.nrcresearchpress.com by 93.93.197.157 on 09/07/12
For personal use only.

Si les réactions d'additions nucléophiles de réactifs organométalliques sur la quinoléine et ses dérivés sont connues depuis longtemps, la métallation directe par ces mêmes composés n'a été que peu étudiée. La réaction d'addition nucléophile concurrente a longtemps masqué la réaction de métallation. Cependant Bouley, Marsais et coll., dans notre laboratoire, sont parvenus à lithier puis à fonctionnaliser des halogéno-quinoléines avec des bons rendements par réaction avec le DIPAL (diisopropylamidure de lithium) (1, 2). Les premières métallations d'hydroxy-quinoléines masquées ont été réalisées par Gilman et Beel en 1951 (3). Cette réaction a notamment permis à Narasinham *et al.* de préparer des alcaloïdes dans la série des furoquinoléines par métallation des méthoxy-2 et diméthoxy-2,4 quinoléines substituées (4). Le groupement orthodirecteur alkoxy n'a cependant permis que l'obtention de faibles rendements en produits lithiés. Récemment, un nouveau groupement orthodirecteur a été utilisé pour la métallation de phénols et de pyridinols par Snieckus et coll. Ils décrivent la métallation de *N,N*-dialkyl *O*-arylcarbamates (5, 6). Pour ces auteurs, le groupement carbamate est plus puissant que les groupes éther et présente une meilleure régiosélectivité lors de la métallation de sites *ortho* non équivalents.[1]

Le groupe *N,N*-dialkylcarbamate, utilisé pour la première fois par Snieckus (7) en série π déficitaire, en tant que groupement orthoorienteur de la métallation des hydroxypyridines, nous a permis de metaller les hydroxyquinoléines substituées sur le noyau benzènique en utilisant la méthode de déplacement (9). Nous décrivons dans cette publication la métallation des hydroxyquinoléines substituées sur le noyau pyridinique.

Résultats et discussion

N,N-*Dialkyl* O-*(quinolyl-2) carbamates* 1

Les *N,N*-dialkyl *O*-(quinolyl-2) carbamates **1** (R = Me; R = Et) sont métallés par action du DIPAL à −78°C. Cependant les lithio-3 quinoléines formées ne réagissent pas avec des électrophiles car elles subissent *in situ* à −78°C un réarrangement anionique conduisant aux hydroxy amides correspondants **2** (R = Me; R = Et). Cette réaction notée, réarrangement anionique de Fries, a été précédemment constatée par Snieckus lors de l'action d'organométalliques sur les *O*-pyridyl carbamates à température ambiante (fig. 1).

Cependant par action du DIPAL sur le carbamate *N,N*-diethylé **1** (R = Et) à une température plus basse (−105°C) et avec l'utilisation du méthanol deutérié comme électrophile, on prépare le *N,N*-diéthyl *O*-((deutério-3) quinolyl-2) carbamate **4** avec un rendement de 40%. La formation du produit **2** (R = Et) n'est pas évitée. L'utilisation du chélate *sec*-butyllithium/-TMEDA (tetramethyl ethylène diamine) comme agent métallant, dans les mêmes conditions de température et de solvant, permet de porter le taux de conversion en composé **4** à 80% (fig. 2). Ayant mis en évidence la formation du dérivé lithié **3** dans les conditions citées plus haut nous avons testé sa réactivité vis à vis d'aldéhydes. Dans tous les cas la substitution a lieu de façon régiosélective sur le carbone 3 (fig. 3). Nous avons isolé les alcools secondaires attendus **5** (R^1 = Et 30%; R^1 = Ph 28%), ainsi qu'un isomère **6** (R^1 = Et 19% ; R^1 = Ph 24%) auquel nous avons attribué une structure de type quinolinone caractérisée par la présence en infrarouge de deux groupes carbonyle à 1700 cm^{-1} et 1660 cm^{-1}. La transformation **5** → **6** peut s'expliquer par l'attaque nucléophile de l'alcoolate intermédiaire sur la fonction carbonyle du composé **5** (fig. 3).

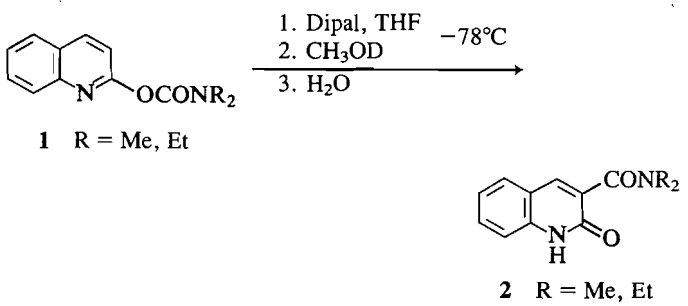

1 R = Me, Et

2 R = Me, Et

FIG. 1

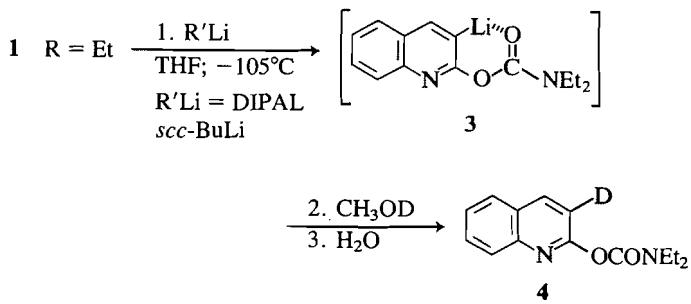

3

4

FIG. 2

1. M. A. J. Miah et V. Snieckus, résultats non publiés.

Printed in Canada / Imprimé au Canada

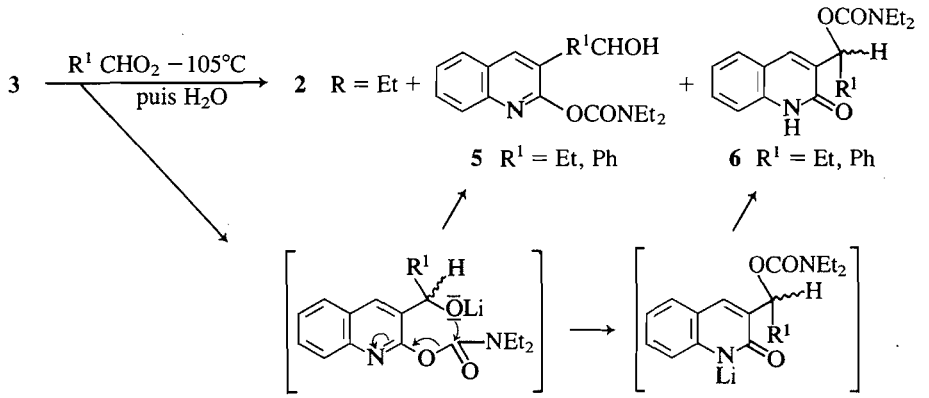

FIG. 3

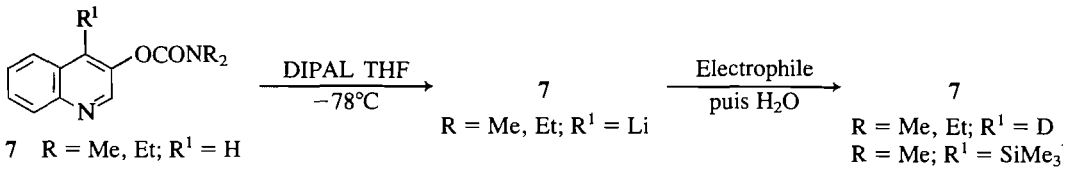

FIG. 4

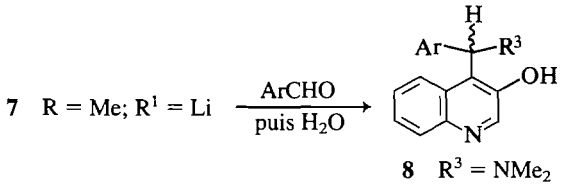

FIG. 5

N,N-*Dialkyl* O-*(quinolyl-3) carbamates* **7**

Les *N,N*-dialkyl *O*-(quinolyl-3) carbamates sont métallés régiosélectivement sur C4 par le DIPAL à −78°C. Les intermédiaires lithiés sont caractérisés sous forme de dérivés deutériés ou silylés obtenus respectivement par action du méthanol deutérié ou du chlorotriméthylsilane à −78°C (fig. 4). La position de métallation est établie en comparant les spectres de rmn ^1H des composés **7**, $R^1 = H$ et $R^1 = D$.

L'absence de tout produit issu d'un réarrangement anionique de Fries montre la bonne stabilité des dérivés lithiés **7** ($R^1 = Li$). De plus les rendements élevés rendent ces réactions très intéressantes en synthèse. Nous avons donc testé la réactivité des quinolyl-lithiums intermédiaires avec plusieurs aldéhydes. Nous avons précédemment montré que la réaction d'aldéhydes aromatiques sur le dérivé lithié du carbamate *N,N*-diméthylé **7** ($R = Me$; $R^1 = Li$) conduisait de façon inattendue aux *N,N*-dimethyl (hydroxy-3 quinolyl)-4 aryl méthane **8** ($R^3 = NMe_2$) avec de bons rendements (Ar = phényl, *para*-méthoxyphényl, *ortho*-méthoxyphényl, diméthoxy-2,4 phényl, chloro-2 phényl, *O*-thiényl, pyridyl-2) (8) (fig. 5).

Rappelons qu'un carbamate **8** ($Ar = C_6H_5$; $R^3 = OCONMe_2$) a pu être isolé lorsque le benzaldéhyde a été utilisé comme électrophile. Cependant ce composé est peu stable et perd facilement une molécule de CO_2 pour donner l'amine **8** ($Ar = C_6H_5$; $R^3 = NMe_2$). L'utilisation des autres aldéhydes donne directement l'amine dans les conditions de la réaction, la même réaction conduite avec le dérive *N,N*-diéthylé **7** ($R = Et$; $R^1 = Li$) et le benzaldéhyde comme électrophile fournit un mélange de carbamate **8** ($Ar = C_6H_5$; $R^3 = OCONEt_2$) et d'amine **8** ($Ar = C_6H_5$; $R^3 = NEt_2$) (fig. 6). Le taux de conversion du réactif est constant (75–80%) mais les proportions amine/carbamate sont variables et dépendent des conditions de traitement du mélange brut réactionnel. Contrairement au dérivé *N,N*-diméthylé la transformation du carbamate *N,N*-diéthylé en amine demande un chauffage prolongé.

Lorsque le *para*-méthoxybenzaldéhyde est utilisé comme électrophile on isole exclusivement le carbamate **8** (Ar = *p*-$MeOC_6H_4$; $R^3 = OCONEt_2$) (fig. 7). Ce composé s'avère stable puisque chauffé dans le xylène pendant 24 h il ne se décarboxyle pas.

L'isolement de carbamates de type **8** ($R^3 = OCONR_2$) permet de proposer un mécanisme en deux étapes :

(*i*) L'obtention du carbamate s'explique par un intermédiaire cyclique obtenu par action de l'alcoolate sur le carbonyle du carbamate initial (fig. 8).

(*ii*) Nous avons envisagé deux mécanismes pour expliquer la décarboxylation, soit une réaction intramoléculaire comprenant l'attaque de l'amine sur le carbone extracyclique dans un intermédiaire cyclique **A**, soit une réaction intermoléculaire avec formation d'une paire d'ions **B** et attaque de l'amine libérée (fig. 9).[2]

Afin de mettre en évidence le mécanisme mis en jeu dans cette derniére étape nous avons effectué la réaction de métallation avec le carbamate *N,N*-diméthylé **7** ($R = Me$; $R^1 = H$) et utilisé le benzaldéhyde comme électrophile. Aprés hydrolyse nous avons, à toutes les étapes du traitement, ajouté de la diéthylamine. Nous avons ainsi obtenu un mélange des deux amines **8** ($Ar = C_6H_5$; $R = NMe_2$, NEt_2). Ce résultat indique qu'un mécanisme intermoléculaire *B* peut être envisagé. Avec l'espèce lithiée issue du carbamate *N,N*-diméthylé **7** ($R = Me$; $R^1 = Li$) les aldéhydes aliphatiques réagissent de façon indentique à celle des aldéhydes aromatiques. Les amines **9** analogues des amines **8** ($R^3 = NMe_2$) sont obtenues avec des rendements de

2. Nous remercions sincèrement Monsieur le professeur V. Snieckus de nous avoir suggéré lors d'une discussion de prendre en considération ce deuxième mécanisme.

Can. J. Chem. Downloaded from www.nrcresearchpress.com by 93.93.197.157 on 09/07/12
For personal use only.

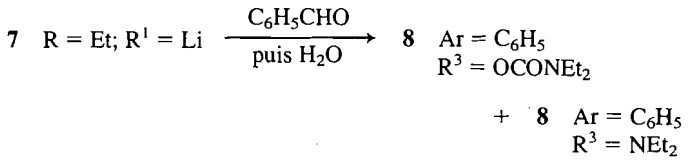

FIG. 6

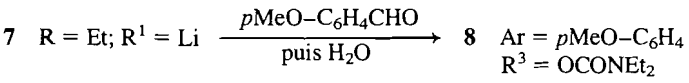

FIG. 7

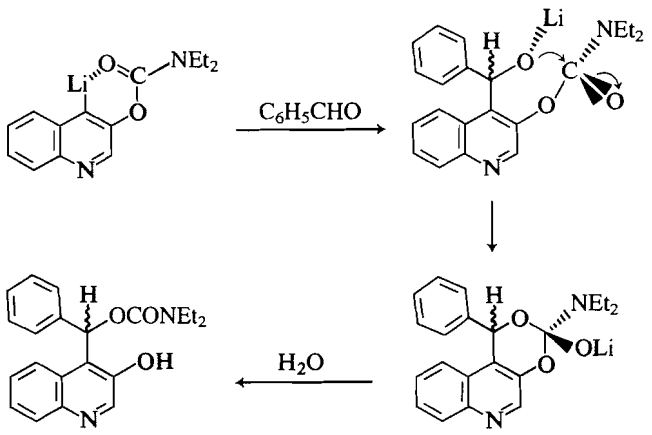

FIG. 8

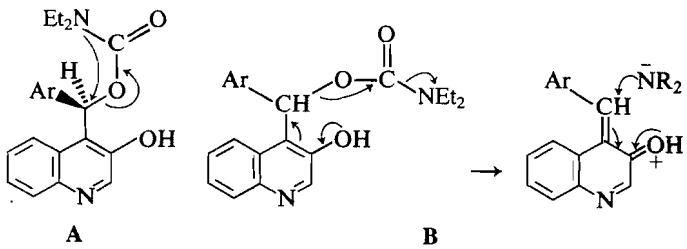

FIG. 9

60%. Ces amines **9** peuvent en outre être transformées en dérivés vinyliques **10** par simple chauffage (fig. 10). Par contre, avec l'espèce lithiée issue du carbamate *N,N*-diéthylé **7** (R = Et; R^1 = Li) l'action des aldéhydes aliphatiques conduit aux alcools secondaires **11** avec des rendements assez faibles (25 et 30%) (fig. 11).

N,N-*Dialkyl* O-*(quinolyl-4) carbamates* **12**

Les *N,N*-dialkyl (*O*-quinolyl-4) carbamates **12** sont métallés par action du DIPAL à −78°C dans le THF. La forme lithiée **12** (R = Me; R^1 = Li) issue du carbamate *N,N*-diméthylé **12** (R = Me; R^1 = H) subit le réarrangement anionique de Fries et conduit à la *N,N*-diméthyl carbamoyl-3 1*H*-quinolone-4 **13** (80%) (fig. 12). L'intermédiaire lithié **12** (R = Et; R^1 = Li) provenant du carbamate diéthylé **12** (R = Et; R^1 = H) ne subit pas ce réarrangement et peut être caractérisé par réaction avec divers électrophiles. Les dérivés substitués en position 3 **12** (R = Et; R^1 = D, Me, $SiMe_3$) sont alors obtenus. Les bons rendements (75–95%) et la parfaite régiosélectivité nous ont amené à faire réagir l'intermédiaire **12** (R = Et; R^1 = Li) avec des réactifs carbonylés : des aldéhydes. Ainsi, après action du propanal, l'alcool secondaire **12** (R = Et; R^1 = CHOH—Et) est

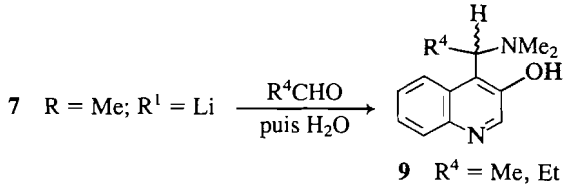

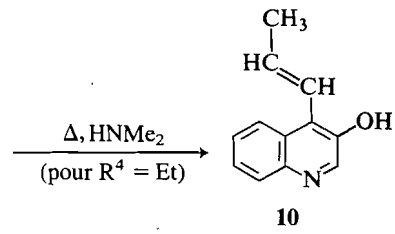

FIG. 10

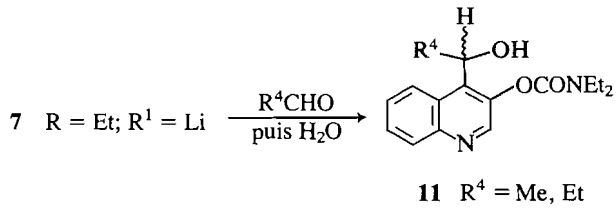

FIG. 11

isolé avec un rendement de 43%. Dans les mêmes conditions, l'action du benzaldéhyde conduit à un mélange de produits que nous n'avons pu séparer et qui, après reflux dans la soude, sont intégralement convertis en un seul dérivé **14**. L'analyse du spectre de rmn ^1H ne permet pas son identification. L'analyse du spectre infrarouge présente une seule vibration attribuée à un groupe carbonyl à 1660 cm^{-1}, caractéristique d'une forme quinolone. L'analyse élémentaire nous permet alors de proposer pour **14** la structure phényl-hydroxyméthyl-3 dihydro-1,4 oxo-4 quinoléine (fig. 12).

Conclusion

Nous avons étendu la méthode de fonctionnalisation proposée par Snieckus dans les séries du benzène et de la pyridine aux carbamates d'hydroxy-2, -3 et -4 quinoléines. L'utilisation d'un groupe orthodirecteur puissant permet dans notre cas l'utilisation du DIPAL moins nucléophile défavorisant les réactions d'addition nucléophile sur le cycle de la quinoléine qui y est très sensible. L'utilisation d'aldéhydes en tant qu'agents électrophiles a montré l'importance de la substitution de l'azote de la fonction carbamate. La mise en oeuvre de cette réaction très régiosélective a permis l'obtention de nombreux dérivés disubstitués. Nous étudions actuellement la possibilité d'utilisation de ces synthons pour la préparation d'alcaloïdes dans la série des furoquinoléines.

Partie expérimentale

Les points de fusion sont déterminés au banc de Kofler. Les spectres infrarouges sont enregistrés sur un spectrophotomètre Beckman Accu-lab TM2. Les microanalyses sont effectuées avec un appareil Carlo Erba CHNOS 1106. Les spectres de rmn ^1H sont enregistrés dans le chloroforme deutérié sauf précision contraire (référence TMS) à 60 MHz sur un appareil Varian EM-360L. **Note** : Dans les conditions d'enregistrement utilisées les sigaux de certains protons mobiles ne peuvent être attribués car ils sont trop étalés. Nous avons noté E pour électrophile.

Can. J. Chem. Downloaded from www.nrcresearchpress.com by 93.93.197.157 on 09/07/12
For personal use only.

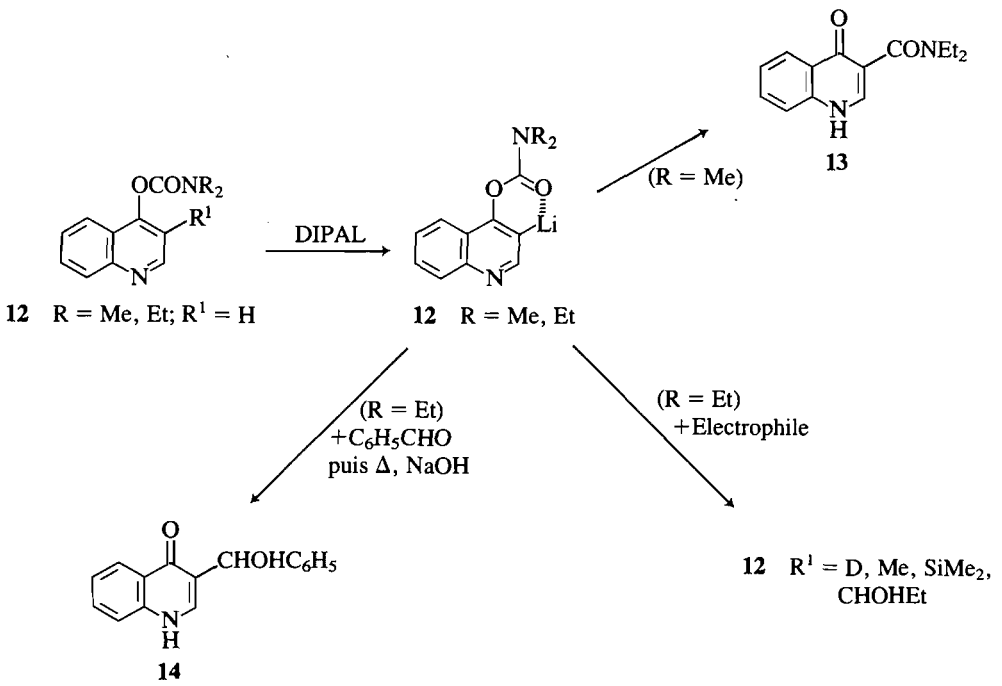

FIG. 12

N,N-*Dialkyl O-(quinolyl-X) carbamates*

Voie A

Dans 30 mL de pyridine, on chauffe durant 12 h 0,05 mol de quinolinol et 0,06 mol de chlorure de *N,N*-dialkylcarbamoyle. Après hydrolyse par 30 mL d'eau, décantation, la phase aqueuse est extraite par 2 × 50 mL de dichlorométhane. Le pyridine résiduelle est éliminée par entraînement azéotropique au toluène et le produit brut et purifié par filtration sur colonne d'alumine neutre (éluant CH_2Cl_2) et recristallisé dans l'hexane.

Voie B

Dans 100 mL de THF anhydre 0,05 mol de quinolinol et 0,06 mol de NaH sont agités 30 min à température ambiante. On introduit alors 0,06 mol de chlorure de *N,N*-dialkyl carbamoyle et le mélange réactionnel est porté à reflux 2 h. Le produit brut est récupéré et purifié de façon indentiques à la voie A.

Voie C

Identique à la voie B en utilisant 3 équivalents d'hydrure de sodium et 3 équivalents de chlorure de *N,N*-dialkyle carbamoyle.

1 (R = Me) : F = 76°C; rendement : 65% (voie B); ir (KBr; cm^{-1}) : 3060, 2920, 1720; rmn ^1H : 2,9(s, 3H, CH_3), 3,05(s, 3H, CH_3), 7,2(d, 1H, H3), 7,6(m, 3H, H5, H6, H7), 8,0 (dd, 1H, H8), 8,15(d, 1H, H4); J_{3-4} = 9 Hz. *Anal.* calc. pour $C_{12}H_{12}N_2O_2$: C 66,65, N 12,95, H 5,59; trouvée : C 66,35, N 12,88, H 5,52.

1 (R = Et) : Huile; rendement : 75% (voie B); ir (KBr; cm^{-1}) : 3050, 2970, 1720; rmn ^1H : 1,2(t, 6H, $2CH_3$), 3,4(q, 2H, CH_2), 3,45(q, 2H, CH_2), 7,2(d, 1H, H3), 7,6(m, 3H, H5, H6, H7), 8,0(dd, 1H, H8), 8,15(d, 1H, H4); $J_{CH_2CH_3}$ = 8 Hz; J_{3-4} ≈ 9 Hz. *Anal.* calc. pour $C_{14}H_{16}N_2O_2$: C 68,83, N 11,47, H 6,60; trouvée : C 69,11, N 11,55, H 6,72.

7 (R = Me; R^1 = H) : F = 76°C; rendement : 72% (voie A); ir (KBr; cm^{-1}) : 3050, 2930, 1725; rmn ^1H : 2,95(s, 3H, CH_3), 3,05(s, 3H, CH_3), 7,5(m, 3H, H5, H6, H7), 7,85(d, 1H, H4), 8,1(dd, 1H, H8), 8,75(d, 1H, H2); J_{2-4} = 2,5 Hz; J_{7-8} = 7,5 Hz; J_{6-8} = 2 Hz. *Anal.* calc. pour $C_{12}H_{12}N_2O_2$: C 66,65, N 12,95, H 5,59; trouvée : C 66,69, N 12,95, H 5,61.

7 (R = Et; R^1 = H) : F = 60°C; rendement : 63% (voie A); ir (KBr; cm^{-1}) : 3070, 2980, 1720; rmn ^1H : 1,33(m, 6H, $2CH_3$), 3,5(m, 4H, $2CH_2$), 7,6(m, 3H, H5, H6, H7), 8,0(d, 1H, H4), 8,15(dd, 1H, H8), 8,8(d, 1H, H2); J_{2-4} = 2,5 Hz. *Anal.* calc. pour $C_{14}H_{16}N_2O_2$: C 68.83, N 11,47, H 6,60; trouvée : C 68,85, N 11,47, H 6,56.

12 (R = Me; R^1 = H) : F < 50°C; rendement : 45% (voie C); ir (KBr; cm^{-1}) : 3060, 2940, 1730; rmn ^1H : 3,05(s, 3H, CH_3), 3,23(s, 3H, CH_3), 7,37(d, 1H, H3), 7,4–7,85(m, 2H, H6, H7), 8,0(dd, 1H, H5), 8,1(dd, 1H, H8), 8,9(d, 1H, H2); J_{2-3} = 5 Hz, J_{5-6} = J_{7-8} = 7,5 Hz; J_{5-7} = J_{6-8} = 2 Hz. *Anal.* calc. pour $C_{12}H_{12}N_2O_2$: C 66,65, N 12,95, H 5,59; trouvée : C 66,90, N 12,85, H 5,38.

12 (R = Et; R^1 = H) : F = 54°C; rendement : 60% (voie C); ir (KBr; cm^{-1}) : 3050, 2960, 1730; rmn ^1H : 1,23(m, 6H, $2CH_3$), 3,4(m, 4H, $2CH_2$), 7,38(d, 1H, H3), 7,4–7,8(m, 2H, H6, H7), 8,0(dd, 1H, H5), 8,1(dd, 1H, H8), 8,86(d, 1H, H2); J_{2-3} = 4,5 Hz; J_{7-8} = J_{5-6} = 8 Hz; J_{5-7} = J_{6-8} = 2 Hz. *Anal.* calc. pour $C_{14}H_{16}N_2O_2$: C 68,83, N 11,47, H 6,60; trouvée : C 68,80, N 11,49, H 6,66.

Techniques générales de métallation

Voie A

À une solution de 0,0050 mol de DIPAL dans 30 mL de THF anhydre, on ajoute à −78°C 0,0045 mol de carbamate dans 8 mL de THF. Après 1 h d'agitation l'électrophile est introduit à cette température et laissé réagir 1 h. Après hydrolyse et extraction au chloroforme à pH neutre le produit brut est purifié par chromatographie liquide sur silice.

Voie B

Une solution de 0,005 mol de chélate *S*-BuLi/TMEDA (préparée à 78°C en coulant la TMEDA dans l'alkyllithium) dans 30 mL de THF est refroidie à −105°C. Le carbamate (0,0045 mol dans 8 mL de THF) est introduit, laissé réagir 1 h, puis l'électrophile est coulé à −105°C. La récupération et la purification du produit brut sont identiques à celles utilisées dans la voie A.

2 (R = Me) (E = MeOD) : F = 220°C; rendement : 90% (voie A); ir (KBr; cm^{-1}) : 3050, 2980, 2930, 1665, 1635; rmn ^1H (DMSO δ ppm/HMDS) : 2,83(s, 3H, CH_3), 2,95(s, 3H, CH_3), 7,2–7,7(m, 4H, H5, H6, H7, H8), 7,95(s, 1H, H4). *Anal.* calc. pour $C_{12}H_{12}N_2O_2$: C 66,65, N 12,95, H 5,59; trouvée : C 66,72, N 13,18, H 5,44.

2 (R = Et) (E = MeOD) : F = 167°C; rendement : 90% (voie A); ir (KBr; cm^{-1}) : 3060, 2980, 2940, 1665, 1630; rmn ^1H : 1,16(t, 3H, CH_3), 1,33(t, 3H, CH_3), 3,36(q, 2H, CH_2), 3,68(q, 2H, CH_2), 7,2–7,7(m, 4H, H5, H6, H7, H8), 7,9(s, 1H, H4). *Anal.* calc. pour $C_{14}H_{16}N_2O_2$: C 68,83, N 11,47, H 6,60; trouvée : C 68,55, N 11,20, H 6,51.

4 (E = MeOD; 5 equiv.) : analyse du produit brut après extraction (bilan massique : 100%) indique la présence du produit **4**. L'intégration

Can. J. Chem. Downloaded from www.nrcresearchpress.com by 93.93.197.157 on 09/07/12
For personal use only.

Can. J. Chem. Downloaded from www.nrcresearchpress.com by 93.93.197.157 on 09/07/12
For personal use only.

du proton H4 sur le spectre de rmn ^1H montre une incorporation du deutérium de 40% par la voie A et de 80% par la voie B; rmn ^1H : 1,2(t, 6H, $2CH_3$), 3,40(q, 2H, CH_2), 3,45(q, 2H, CH_2), 7,5 (m, 3H, H5, H6, H7), 8,0(dd, 1H, H8), 8,15(s, 1H, H4).

5 (R^1 = Et) (E = EtCHO; 5 équiv.) : Huile incolore: rendement : 30% (voie B); ir (film; cm^{-1}) : 3420, 2980, 2940, 1730; rmn ^1H : 1,0(t, 3H, CH_3), 1,35(2t, 6H, CH_3-CH_2—N), 1,85(m, 2H, CHOHCH_2), 3,5(m, 5H, CH_2—N et OH), 4,85(t, 1H, *CH*—OH), 7,4–8,0(m, 4H, H5, H6, H7, H8), 8,33(s, 1H, H4); $J_{CH2-CH3}$ = 7,5 Hz; J_{CH-CH2} = 5 Hz. *Anal.* calc. pour $C_{17}H_{22}N_2O_3$: C 67,55, N 9,27, H 7,28; trouvée : C 67,35, N 8,98, H 6,89.

5 (R^1 = Ph) (E = PhCHO; 1,2 équiv.) : Huile incolore; rendement : 24% (voie B); ir (film; cm^{-1}) : 3400, 2980, 1720; rmn ^1H : 1,2(m, 6H, $2CH_3$), 3,4(m, 4H, $2CH_2$), 4,05(m, 1H, OH), 6,1(s, 1H, *CH*OH), 7,33(s, 5H, phényl), 7,3–8,25(m, 4H, H5, H6, H7, H8), 8,3(s, 1H, H4). *Anal.* calc. pour $C_{21}H_{22}N_2O_3$: C 69,47, N 7,37, H 6,31; trouvée : C 69,45, N 7,59, H 6,19.

6 (R^1 = Et) (E = EtCHO ; 5 equiv.) : F = 141°C; rendement : 19% (voie B); ir (KBr; cm^{-1}) : 2980, 2940, 1700, 1660; rmn ^1H : 0,95–1,5(m, 6H, $3CH_3$), 2,05(m, 2H, CH_2—COH), 3,45(q, 4H, $2CH_2$), 6,10(t, *CH*OH), 7,0–7,7(m, 4H, H5, H6, H7, H8), 7,8(s, 1H, H4); J_{CH-CH2} = 6 Hz; $J_{CH_2-CH_3}$ = 8 Hz. *Anal.* calc. pour $C_{17}H_{22}N_2O_3$: C 67,55, N 9,27, H 7,28; touvée : C 67,33, N 8,95, H 6,91.

6 (R^1 = Ph) (E = PhCHO; 1,2 équiv.) : F = 250°C; rendement : 24% (voie B); ir (KBr; cm^{-1}) : 3400, 2980, 1700, 1660; rmn ^1H : 1,3(m, 6H, $2CH_3$), 3,45(m, 4H, $2CH_2$), 7,2–7,85(m, 9H, H5, H6, H7, H8, phényl), 7,9(s, 1H, H4), 6,06(s, 1H, CH—O). *Anal.* calc. pour $C_{21}H_{22}N_2O_3$: C 69,47, N 7,37, H 6,31; trouvée : C 69,11, N 7,63, H 6,01.

7 (R^1 = D) (E = MeOD ; 5 équiv.) : (Voie A) L'analyse des spectres de rmn ^1H indique la présence des produits deutériés dans tous les cas (R = Me, Et). Le taux d'incorporation du deutérium, déterminé par intégration des signaux des protons H4 est de 80%.

7 (R = Me ; R^1 = D) : rmn ^1H : 2,95(s, 3H, CH_3), 3,05(s, 3H, CH_3), 7,2–7,8(m, 3H, H5, H6, H7), 8,1 (dd, 1H, H8), 8,8(s, 1H, H2).

7 (R = Et; R^1 = D) : rmn ^1H : 1,4(m, 6H, $2CH_3$), 3,4(m, 4H, $2CH_2$), 7,25–8,0(m, 3H, H5, H6, H7), 8,5(s, H2), 8,2(m, 1H, H8).

7 (R = Me; R^1 = $SiMe_3$) (E = $ClSiMe_3$; 1,2 équiv.) : F = 58°C; rendement : 90% (voie A); ir (film; cm^{-1}) : 3060, 2950, 1725, 1260; rmn ^1H : 0,35(s, 9H, $SiMe_3$), 2,85(s, 3H, CH_3), 2,95(s, 3H, CH_3), 7,4(m, 2H, H6, H7), 8,0(m, 2H, H5, H8), 8,55(s, 1H, H2). *Anal.* calc. pour $C_{15}H_{21}N_2O_2Si$: C 62,46, N 9,71, H 6,98; trouvée : C 61,95, N 9,53, H 6,75.

8 (Ar = C_6H_5; R^3 = NEt_2) (E = PhCHO; 1,2 équiv.) : Huile incolore; rendement variable (env. 40%) (voie A); ir (film; cm^{-1}) : 3400, 2970, 1595; rmn ^1H : 1,1(t, 6H, $2CH_3$), 2,85(q, 4H, $2CH_2$), 5,5(s, 1H, CH), 7,05–7,75(m, 7H, phényl, H6, H7), 7,75–8,25(m, 2H, H5, H8), 8,7(s, 1H, H2); $J_{CH_2-CH_3-CH_3}$ = 7 Hz. *Anal.* calc. pour $C_{20}H_{18}N_2O$: C 78,43, N 9,15, H 7,19; trouvée: C 78,39, N 8,94, H 7,13.

8 (Ar = *p*$MeOC_6H_4$; R^3 = $OCONEt_2$) (E = *p*MeOPhCHO; 1,2 équiv.) : F = 133°C; rendement = 53% (taux de conversion 80%) (voie A); ir (KBr; cm^{-1}) : 3400, 2970, 1720; rmn ^1H : 1,15(t, 6H, $2CH_3$), 3,3(q, 4H, $2CH_2$), 3,7(s, 3H, MeO), 4,4(m, 1H, OH), 6,45(s, 1H, CHO), 6,85(d, 2H, H'3, H'5), 7,15–7,85(m, 4H, H'2, H'6, H6, H7), 8,0–8,33(m, 2H, H5, H8), 8,4(s, 1H, H2); $J_{H'2-H'3}$ = 9 Hz; $J_{CH_2-CH_3}$ = 7 Hz. *Anal.* calc. pour $C_{22}H_{24}N_2O_4$: C 69,47, N 7,37, H 6,31; trouvée : C 69,37, N 7,31, H 6,26.

8 (Ar = C_6H_5; R^3 = $OCONEt_2$) (E = PhCHO; 1,2 équiv.) : Huile incolore; rendement variable (voie A); ir (film; cm^{-1}) : 1730, 1715; rmn ^1H : 1,2(t, 6H, $2CH_3$), 3,35(m, 4H, $2CH_2$), 6,65(s, 1H, CH), 7,25–7,9(m, 7H, phényl, H6, H7), 8,05–8,45(m, 2H, H5, H8), 8,7(s, 1H, H2). *Anal.* calc. pour $C_{21}H_{22}N_2O_3$: C 72,0, N 8,0, H 6,28; trouvée : C71,89, N 7,99, H 6,30.

9 (R^4 = CH_3) (E = CH_3CHO; 5 équiv.) : rendement : 60% (voie A); Huile incolore: ir (film; cm^{-1}) : 3050, 2970, 2800, 1595; rmn ^1H : 1,4(d, 3H, CH_3), 2,32(s, 6H, $N(CH_3)_2$), 4,08(q, 1H, CH_3—*CH*), 7,5(m, 2H, H6, H7), 8,0(m, 2H, H5, H8), 8,65(s, 1H, H2); J_{CH_3-CH} = 7,5 Hz. *Anal.* calc. pour $C_{13}H_{16}N_2O$: C72,19, N 12,95, H 7,46; trouvée : C 72,28, N 13,12, H 7,35.

9 (R^4 = Et) (E = CH_3CH_2CHO; 5 équiv.) : Huile incolore; rendement : 58% (voie A); ir (film; cm^{-1}) : 3055, 2970, 2800, 1595; rmn ^1H : 0,75(t, 3H, CH_3), 2,00(dt, 2H, CH_2), 2,40(s, 6H, $N(CH9_3)_2$), 4,10(t, 1H, CH), 7,50(m, 2H, H6, H7), 8,00(m, 2H, H5, H8), 8,65(s, 1H, H2); $J_{CH_3-CH_2}$ = 7,5 Hz; J_{CH_2-CH} = 6 Hz. *Anal.* calc. pour $C_{14}H_{18}N_2O$: C 73,01, N 12,16, H 7,88; trouvée : C 72,56; N 11,64, H 7,84.

11 (R^4 = Me) (E = CH_3—CHO; 3 équiv.) : Huile incolore; rendement : 25% (voie A); ir (film; cm^{-1}) : 3400, 2980, 2965, 1720; rmn ^1H : 1,2(m, 6H, CH_3—CH_2—N), 1,65(d, 3H, CH_3), 3,45(m, 4H, CH_2—N), 3,5–4,0(m, 1H, OH), 5,6(q, 1H, *CH*OH), 7,3–7,8(m, 2H, H6, H7), 8,05(m, 1H, H8), 8,5(s, 1H, H2), 8,65(m, 1H, H5); J_{CH-CH_3} = 7 Hz. *Anal.* calc. pour $C_{16}H_{20}N_2O_3$: C 66,67, N 9,72, H 6,94; trouvée : C 66,67, N 9,51, H 7,05.

11 (R^4 = Et) (E = CH_3—CH_2—CHO; 3 équiv.) : Huile; rendement : 35% (voie A); ir (film, cm^{-1}) : 3400, 2970, 1720; rmn ^1H : 1,0(t, 3H, CH_3), 1,2(t, 6H, CH_3—CH_2—N, 2,0(m, 2H, CH_2-CHO), 3,4(q, 4H, CH_2—N), 4,6(s, 1H, OH); 5,3(t, 1H, *CH*OH), 7,55(m, 2H, H6, H7), 8,0(m, 1H, H8), 8,5(s, 1H, H2), 8,5(m, 1H, H5); $J_{CH_3-CH_2}$ = 7 Hz; J_{CH_2-CH} = 7 Hz. *Anal.* calc. pour $C_{17}H_{22}N_2O_3$: C 67,55, N 9,27, H 7,28; trouvée : C 67,34, N 9,30, H 7,03.

13 Obtenu à partir de **12** (R = Me; R^1 = H) lors de l'utilisation de la méthode de métallation notée voie A; F = 236–237°C; rendement : 80%; ir (KBr; cm^{-1}) : 3440, 2940, 1720, 1660, 1630; rmn ^1H : 3,05(s, 6H, $N(CH_3)_2$), 7,2–7,9(m, 3H, H6, H7, H8), 8,1(s, 1H, H2), 8,4(m, 1H, H5). *Anal.* calc. pour $C_{12}H_{12}N_2O_2$: C 66,65 N 12,95, H 5,59; trouvée : C 66,18, N 12,58, H 5,37.

12 (R = Et; R^1 = D) (E = MeOD) : rendement : 85% (voie A); ir (KBr; cm^{-1}) : 2980, 1725; rmn ^1H : 1,3(m, 6H, CH_3), 3,5(m, 4H, CH_2), 7,4—7,8(m, 2H, H6, H7), 8,0(dd, 1H, H5), 8,12(dd, 1H, H8), 8,86(s, 1H, H2); J_{5-6} = J_{7-8} = 8 Hz; J_{5-7} = J_{6-8} = 2 Hz. *Anal.* calc. pour $C_{14}H_{15}DN_2O_2$: C 68,57, N 11,52, H 6,12; trouvée : C 68,79, N 11,54, H 6,33.

12 (R = Et; R^1 = Me) (E = CH_3I; 10 équiv.) : rendement : 75% (voie A); ir (KBr; cm^{-1}) ; 3050, 2960, 1730; rmn ^1H : 1,33(m, 6H, CH_3), 2,3(s, 3H, CH_3), 3,53(m, 4H, CH_2), 7,55–8,0(m, 3H, H5, H6, H7); 8,15(dd, 1H, H8), 8,85(s, 1H, H2); J_{7-8} = 8 Hz; J_{8-6} = 2 Hz. *Anal.* calc. pour $C_{15}H_{18}N_2O_2$: C 69,76, N 10,85, H 6,97; trouvée : C 69,45, N 10,74, H 6,95.

12 (R = Et; R^1 = $SiMe_3$) (E = $ClSiMe_3$) : Huile incolore; rendement : 95% (voie A); ir (film; cm^{-1}) : 3060, 2975, 1725; rmn ^1H : 0,4(s, 9H, $SiMe_3$), 1,36(t, 6H, CH_3), 3,5(q, 4H, CH_2), 7,3–7,95(m, 3H, H5, H6, H7), 8,15(dd, 1H, H8), 8,95(s, 1H, H2); $J_{CH_2-CH_3}$ = 13 Hz; J_{8-7} = 8 Hz; J_{8-6} = 2 Hz. *Anal.* calc. pour $C_{17}H_{24}N_2O_2Si$: C 64,51, N 8,85, H 7,64; trouvée : C 64,65, N 8,91, H 7,90.

12 (R = Et; R^1 = EtCHOH) (E = EtCHO; 3 équiv.) : rendement : 43% (voie A); ir (film; cm^{-1}) : 3400, 2970, 2940, 1730; rmn ^1H : 1,0(t, 3H, CH_3—CH_2—CH), 1,6(m, 6H, CH_3), 1,6–2,1(m, 2H, CH_2—CH), 3,5(m, 4H, CH_2—N), 4,9(t, 1H, CHOH), 7,3–8,0(m, 3H, H5, H6, H7), 8,15(m, 1H, H8), 9,0(s, 1H, H2); J_{CH-CH_2} = 6 Hz. *Anal.* calc. pour $C_{17}H_{22}N_2O_3$: C 67,55, N 9,27, H 7,28; trouvée : C 67,32, N 8,99, H 7,48.

N,N-*Diméthylcarbamoyl-3 dihydro-1,4 quinolinone-4* ***14***

Le mélange brut issu de la réaction de métallation de **12** (R = Et; R^1 = H) par la voie A et utilisant le benzaldéhyde comme électrophile (1 équivalent) est chauffé à ébullition dans la soude (20%) pendant 2 h. Le composé obtenu a les caractéristiques suivantes : ir (film; cm^{-1}) : 3400, 3300–2600, 1660, 1620; masse molaire déterminée par spectrométrie de masse = 251 g (masse calculée pour **13** : 251,287 g). *Anal.* calc. pour $C_{16}H_{13}NO_2$: C 76,49, N 5,57, H 5,18; trouvée : C 76,27, N 5,71, H 5,08.

Hydroxy-3 (propènyl-1)-4 quinoléine ***10***

Une quantité (100 mg) de l'amine **9** (R^4 = Et) est chauffée à une température supérieure à 150°C. La réaction est suivie grâce au dégagement de diméthylamine. Le rendement est pratiquement quantitatif; F = 189°C; ir (KBr; cm^{-1}); 3060, 2960, 2640, 1575; rmn ^1H : 2,05(dd, 3H, CH_3), 6,7(dm, 2H, CH=CH), 7,45(m, 2H, H6, H7), 7,95(m, 2H, H5, H8), 8,7(s, 1H, H2), 9,7(m, 1H, OH), J_{CH_3-CH} = 3 Hz; $J_{CH=CH}$ = 1 Hz; J_{6-7} = 3 Hz. *Anal.* calc. pour $C_{12}H_{11}NO$: C 77,80, N 7,56, H 5,94, trouvée : C 77,92, N 7,56, H 6,02.

Remerciements

Nous remercions M. le Professeur V. Snieckus pour les discussions fructueuses à propos de ce travail. Ces discussions ont été rendues possibles grâce à un contrat OTAN.

1. F. MARSAIS et G. QUEGUINER. Tétrahédron, **39**, 2009 (1983).
2. F. MARSAIS, E. BOULEY et G. QUEGUINER. J. Organométal. Chem. **171**, 273 (1979).
3. H. GILMAN et J. A. BEEL. J. Am. Chem. Soc. **73**, 32 (1951).
4. (*a*) N. S. NARASIMHAN et M. V. PARADKAR. Chem. Ind. 831 (1967); (*b*) N. S. NARASIMHAN et R. H. ALURKAR. Chem. Ind. 515 (1968); (*c*) N. S. NARASIMHAN, M. V. PARADKAR et R. H. ALURKAR. Tetrahedron, **27**, 1351 (1971); (*d*) N. S. NARASIMHAN et R. S. MALI. Tetrahedron, **30**, 4153 (1974); (*e*) A. C. RANADE, R. S. MALI, R. M. GIDWANI et H. R. DESHPANDE. Chem. Ind. 310 (1977); (*f*) N. S. NARASIMHAN et S. P. BHAGWAT. Synthesis, 903 (1979).
5. M. P. SIBI et V. SNIECKUS. J. Org. Chem. **48**, 1937 (1982).
6. M. A. J. MIAH et V. SNIECKUS. J. Org. Chem. **50**, 5438 (1985).
7. V. SNIECKUS. Lectures in heterocyclic chemistry. *Edited by* R. N. Castle. Heterocorp, Tampa, FL. 1984. p. 95.
8. Y. ROBIN, A. GODARD, et G. QUEGUINER. J. Heterocycl. Chem. Sous presse.
9. Y. ROBIN, A. GODARD, et G. QUEGUINER. J. Organomet. Chem. Sous presse.

Can. J. Chem. Downloaded from www.nrcresearchpress.com by 93.93.197.157 on 09/07/12
For personal use only.

High resolution ^{13}C nuclear magnetic resonance spectra of solid pyrazoles. Application to annular tautomerism

ROBERT FAURE[1] AND ÉMILE-JEAN VINCENT

Laboratoire de chimie organique physique, Université d'Aix-Marseille III, Rue Henri Poincaré, 13397 Marseille CEDEX 13, France

ANDRÉ ROUSSEAU

Centre d'études nucléaires de Grenoble, Centre d'études atomiques, Avenue des martyrs, 85X, 38041 Grenoble CEDEX, France

AND

ROSE MARIA CLARAMUNT AND JOSÉ ELGUERO[1]

Quimica Organica, UNED, and Instituto de Quimica Médica, Juan de la Cierva, 3. 28006 Madrid, Spain

Received April 23, 1987[2]

ROBERT FAURE, ÉMILE-JEAN VINCENT, ANDRÉ ROUSSEAU, ROSA MARIA CLARAMUNT, and JOSÉ ELGUERO. Can. J. Chem. **66**, 1141 (1988).

Carbon-13 nuclear magnetic resonance spectroscopy in the solid state (cross polarization/magic angle spinning technique) is a very suitable method for studying the annular tautomerism of pyrazoles. In all the compounds studied, the tautomerism is frozen and the signals are well resolved except for 3,5-dimethyl-4-nitro pyrazole, which shows broad signals. In the case of 4-substituted derivatives of 3(5)-methylpyrazoles, the tautomer present in the solid state is a 4-X-5 methylpyrazole. 3-Phenyl-5-methylpyrazole (4*H* or 4-methyl) is favoured over the 3-methyl-5-phenyl tautomer.

ROBERT FAURE, ÉMILE-JEAN VINCENT, ANDRÉ ROUSSEAU, ROSA MARIA CLARAMUNT et JOSÉ ELGUERO. Can. J. Chem. **66**, 1141 (1988).

La résonance magnétique nucléaire à haute résolution du carbone-13 à l'état solide (technique polarisation croisée/rotation à l'angle magique) est une méthode parfaitement adaptée à l'étude de la tautomérie annulaire des pyrazoles. Pour tous les composés étudiés, l'échange prototropique est bloqué et les signaux sont fins et bien résolus, à l'exception de ceux du diméthyl-3,5 nitro-4 pyrazole qui sont très élargis. Dans le cas des dérivés du méthyl-3(5) pyrazole substitués en position 4, la structure du tautomère présent en phase cristalline est de la forme X-4 méthyl-5. En ce qui concerne les dérivés du phényl-3(5) méthyl-5(3) pyrazole, l'équilibre tautomère est totalement déplacé vers la forme dans laquelle le méthyle est en position 5.

Can. J. Chem. Downloaded from www.nrcresearchpress.com by 93.93.197.157 on 09/07/12
For personal use only.

Introduction

In a series of papers (1–5), we have shown that high resolution ^{13}C nmr is a valuable tool for the study of tautomerism of azoles in the solid state, and, particularly, of annular tautomerism, i.e., prototropic tautomerism between nitrogen atoms (6*a*). In crystals, generally only one tautomer is present and, very seldom, two functional tautomers linked by hydrogen bonds have been observed by diffraction methods (6*b*). However, no clear example of the existence of two tautomers in a single crystal has been reported for annular tautomerism. In contrast to other types of tautomerism, annular tautomerism often involves two identical entities as in pyrazole **1***a* ⇌ **1***b* and in 3,5-dimethylpyrazole **2***a* ⇌ **2***b* (this is called autotropic rearrangement or degenerate tautomerism (6*c*)).

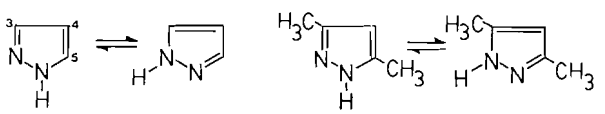

1a **1b** **2a** **2b**

In the case of pyrazole **1** (1) (and of all other "parent" azoles (2)) the equilibrium **1***a* ⇌ **1***b* is frozen at room temperature in the solid state. Only in the case of 3,5-dimethylpyrazole have we observed a dynamic behaviour in the crystal at room temperature (3) by ^{13}C CP/MAS spectroscopy. At low temperature (T = 233 K) the **2***a* ⇌ **2***b* interconversion is frozen (3).

To generalize these observations to other pyrazoles substituted at positions 3 and 5 with identical substituents ("symmetrical" pyrazoles) or different substituents ("asymmetrical" pyrazoles) we have studied 14 *N*-unsubstituted pyrazoles. For comparative purposes, we have also studied an *N*-substituted derivative: 1,5-dimethyl-4-bromopyrazole, **14**CH_3. We must stress that all these pyrazoles are microcrystalline compounds and this, in the case of asymmetric pyrazoles, implies that most probably, only one tautomer will be observed (K_T = 0), although the possibility of a hydrogen bonded dimer (K_T = 1) of the two different tautomers cannot be ruled out.

Results and discussion

In Table 1 we have collected the ^{13}C chemical shifts of NH pyrazoles in the solid state (this work, except **1** (1) and **2** (3)) and in DMSO-d_6 solution (7). The ^{13}C chemical shifts of the corresponding *N*-methyl derivatives are necessary to discuss the annular tautomerism of asymmetric pyrazoles. Three kinds of data concerning these last compounds are given in Table 1: (*i*) literature data (7); (*ii*) some new data of pyrazoles synthesized especially for this work (1,3,5-trimethyl-4-nitropyrazole, **4**CH_3, 1,3-dimethyl-5-bromopyrazole, **17**CH_3, and 1,4,5-trimethyl-3-phenylpyrazole, **23**CH_3); (*iii*) several chemical shifts (in italics in Table 1), which have been estimated from the results of ref. 7.

Symmetrical pyrazoles

In solution, the rapid exchange of the tautomeric proton between both nitrogens (6*d*) leads, in compounds **1–8**, to an isochrony of the signals corresponding to the C-3 and C-5 carbon atoms. For these compounds in the solid state at room temperature we observe well-resolved signals and a clear difference between the chemical shifts of C-3 and C-5, the only exceptions being the 3,5-dimethylpyrazole **2** (3) and 3,5-

[1]Authors to whom correspondence may be addressed.

[2]Revision received November 9, 1987.

Can. J. Chem. Downloaded from www.nrcresearchpress.com by 93.93.197.157 on 09/07/12
For personal use only.

TABLE 1. ^{13}C chemical shifts of NH pyrazoles (solid state and solution) and N—CH_3 pyrazoles (solution)

Compound no.	R^3	R^4	R^5	Solid state, R = H			Solution,[a] R = H			Solution,[a] R = CH_3		
				3	4	5	3	4	5	3	4	5
1	H	H	H	138.7	107.0	128.0	133.7	104.8	133.7	138.5	105.2	130.4
2	CH_3	H	CH_3	12.8(Me)[b]	104.8[b]	10.5 (Me)[b]	11.9 (Me)	103.3	11.9 (Me)	13.1 (Me)	104.2	10.6 (Me)
				147.5[b]		139.3[b]	143.0		143.0	145.0		138.3
3	CH_3	CH_3	CH_3	11.4 (Me)	6.8 (Me)	8.9 (Me)	10.4 (Me)	7.3 (Me)	10.4 (Me)	11.5 (Me)	7.9 (Me)	9.2 (Me)
				147.4	110.7	137.3	140.7	109.2	140.7	144.1	110.3	135.6
4	CH_3	NO_2	CH_3	13.9 (Me)	131.9	12.4 (Me)	12.7 (Me)	130.1	12.7 (Me)	13.4 (Me)	130.1	11.0 (Me)
				147.0[c]		142.0[c]	143.4		144.3			140.5
5	CH_3	Br	CH_3	12.5 (Me)	[d]	10.6 (Me)	10.9 (Me)	92.5	10.9 (Me)	11.8 (Me)	92.4	9.8 (Me)
				145.7		138.1	141.3		141.3	143.9		137.0
6	CH_3	I	CH_3	12.1 (Me)	[d]	10.5 (Me)	12.4 (Me)	61.7	12.4 (Me)	13.6 (Me)	62.0	11.4 (Me)
				149.2		142.5	144.7		144.7	147.2		140.2
7	C_2H_5	CH_3	C_2H_5	13.6 (Me)	7.5 (Me)	13.6 (Me)	13.6 (Me)	7.3 (Me)	13.6 (Me)			
				18.8 (CH_2)	107.1	16.8 (CH_2)	18.6 (CH_2)	107.6	18.6 (CH_2)	—	—	—
				151.6		142.2	146.3		146.3			
8	*t*-C_4H_9	H	*t*-C_4H_9	31.3 (Me)	98.4	31.3 (Me)	30.5 (Me)	96.2	30.5 (Me)			
				32.7 (C)		32.7 (C)	31.0 (C)		31.0 (C)			
				158.6		155.0	156.0		156.0	—	—	—
9	CH_3	NO_2	H							12.9 (Me)	[d]	132.1
				11.2 (Me)	132.4	137.2	11.6 (Me)	132.7	134.7	144.9		
				142.6			141.7					
10	H	NO_2	CH_3							135.4	132.4	11.2 (Me)
												139.9
11	CH_3	Cl	H							*10.8* (Me)	*107.0*	*128.8*
				9.2(Me)	[d]	135.5[c]	9.4 (Me)	107.1	132.4	*143.5*		
				135.5			138.8			*135.0*	*107.4*	*8.7* (Me)
12	H	Cl	CH_3									*134.3*
										11.4 (Me)	91.8	131.0
							10.3 (Me)	92.2	134.7	145.5		
13	CH_3	Br	H	10.4 (Me)	[d]	139.0	140.8					
				139.0						137.3[e]	91.8	9.3 (Me)[f]
14	H	Br	CH_3									136.8[e]
										13.2 (Me)	—	*135.2*
							11.6 (Me)	59.1	139.1	*149.0*		
15	CH_3	I	H	12.6 (Me)	[d]	142.9[c]	144.0					
				142.9[c]						*141.8*	—	*10.8* (Me)
16	H	I	CH_3									*139.8*
										13.2 (Me)	107.2	112.2
17	CH_3	H	Br				10.6 (Me)	106.1	125.1	147.8		
				12.2 (Me)	106.6	[d]	141.3					
				142.9						*122.4*	*106.9*	*10.9* (Me)
18	Br	H	CH_3									*139.1*

Can. J. Chem. Downloaded from www.nrcresearchpress.com by 93.93.197.157 on 09/07/12
For personal use only.

TABLE 1 (*concluded*)

Compound no.	R^3	R^4	R^5	Solid state, R = H			Solution,[a] R = H			Solution,[a] $R = CH_3$		
				3	4	5	3	4	5	3	4	5
19	CH_3	C_6H_5	H	9.9 (Me) 139.4	d (C1′) 127.4 (C2′) 131.8 (C3′) 127.4 (4′) 120.4 (Ph)	133.6	11.5 (Me) 138.3	d (C1′) 126.7 (C2′) 128.6 (C3′) 125.5 (C4′) 118.6 (Ph)	134.0	*12.9* (Me) *145.0*	*118.3*	*128.2*
20	H	C_6H_5	CH_3							*134.6*	*118.7*	*10.2* (Me) *136.1*
21	C_6H_5	H	CH_3	131.7	134.0 132.8 130.0 128.7 127.8 127.4 (Ph)	102.4 102.1	9.90 (Me) 141.9 140.8	133.0 (C1′) 125.4 (C2′) 128.8 (C3′) 127.1 (C4′) 148.5 (Ph)	101.2	11.3 (Me) 142.0	133.8 (C1′) 124.8 (C2′) 128.4 (C3′) 126.9 (C4′) 148.4	102.0	10.7 (Me) 139.6
22	CH_3	H	C_6H_5		127.0 126.4 124.7 124.1 123.2 150.4						13.2 (Me) 146.1	105.1	130.5 (C1′) 128.2 (C2′) 128.6 (C′) 128.1 (C4′) 143.4 (Ph)
23	C_6H_5	CH_3	CH_3								130.9 (C1′) 129.4 (C2′) 128.4 (C3′) 127.9 (C4′) 146.1 (Ph)	8.2 (Me) 112.2	11.5 (Me) 141.1
24	CH_3	CH_3	C_6H_5	(Ph) 136.7 (C1′) 129.4 (C2′) 129.4 (C3′) 129.4 (C4′) 148.5	7.5 (Me) 111.6	8.5 (Me) 138.5	133.6 (C1′) 127.0 (C2′) 128.5 (C3′) 127.0 (C4′) 145.0 (Ph)	8.9 (Me) 109.4	10.2 (Me) 140.9	—	—	—

[a]Solvent: DMSO-d_6.
[b]$T = 233$ K.
[c]Broad signal.
[d]Not observed.
[e]In the solid state, $\delta = 136.7$ ppm.
[f]In the solid state, $\delta = 8.3$ ppm ($\delta N—CH_3 = 28.1$ ppm).

Can. J. Chem. Downloaded from www.nrcresearchpress.com by 93.93.197.157 on 09/07/12
For personal use only.

dimethyl-4-nitropyrazole **4** already described. For the last compound the signals corresponding to C-3 and C-5 are large but still clearly different.

The singular behaviour of compound **4** has two possible explanations: (*i*) a prototropy with a relatively fast exchange rate as in 3,5-dimethylpyrazole **2** (3); (*ii*) an incomplete suppression of the dipolar coupling between ^{14}N and ^{13}C (8). Experiments are on the way (variable temperature studies, nqr, ^{15}N isotopic labelling) to solve this problem[3] but we call attention to the fact that the other 4-nitro derivative **9/10** (see later) shows narrow signals.

The mean value of the C-3 and C-5 carbon chemical shifts measured in the solid state is close to the value observed in solution. The differences ($\delta_{solid} - \delta_{solution}$:**1**, C: −0.3; **2**, CH: −0.3, C: 0.4; **3**, CH: −0.3, C: 1.7; **4**, CH: 0.5, C: 1.1; **5**, CH: 0.7, C: 0.6; **6**, CH: −1.1, C: 1.2; **7**, CH: 0.0, CH: −0.8, C: 0.6; **8**, CH: 0.8; C: 1.7, C: 0.8) are small enough to assume that pyrazoles in the solid state are good models of fixed tautomers.

Thus in the following discussion we shall consider the chemical shifts measured in the solid state identical to those the pyrazole would present in solution if there were no tautomerism.

Taking into account the preceding comment, the *N*-methylation effects will be defined as $\Delta\delta = \delta_{N—CH_3\ (solution)} - \delta_{N—H\ (solid)}$. For symmetric pyrazoles, we have calculated the following $\Delta\delta$ values:

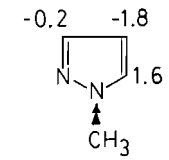

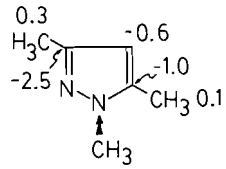

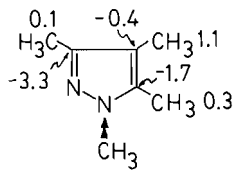

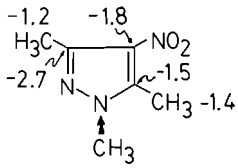

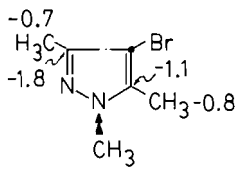

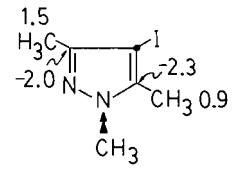

In the case of 3,5-dimethylpyrazoles the effects are quite constant. The averaged values for compounds **2, 3, 4, 5,** and **6** are

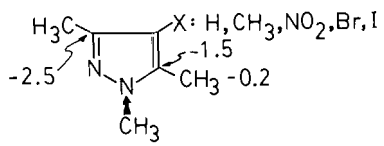

Asymmetrical pyrazoles

For these pyrazoles, both annular tautomers are of different energy and hence the following equilibria must be considered: **9** ⇌ **10, 11** ⇌ **12, 13** ⇌ **14, 15** ⇌ **16, 17** ⇌ **18, 19** ⇌ **20, 21** ⇌ **22**, and **23** ⇌ **24**. In solution, both tautomers are present in relative amounts that depend on the nature of the substituents, the solvent, the temperature, and the concentration (6*e*). During the crystallization process the equilibrium shifts towards the more stable or the less soluble tautomer, and so only one tautomer is expected in the crystal. A remote possibility exists that both tautomers could crystallize together to form a 1:1 mixed crystal.

With the exception of 3(5)-phenyl-5(3)-methylpyrazole **21/22**, the remaining pyrazoles show a unique set of signals, thus confirming the existence of a unique tautomer in the solid state. For some compounds, **13/14, 15/16**, and 1,5-dimethyl-4-bromopyrazole, **14**CH_3, a splitting of the methyl signal is observed. We have not considered these supplementary signals for the determination of the tautomeric structure since (*i*) the last compound, unable to show tautomerism, shows this behaviour also; (*ii*) the splitting is not observed for the other signals; (*iii*) some supplementary carbon resonances in the CP/MAS ^{13}C nmr spectra are not of molecular origin (8, 10).

For asymmetric pyrazoles, the effects (defined previously) due to *N*-methylation are

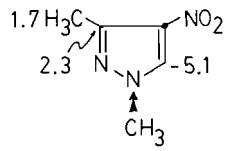

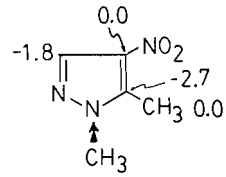

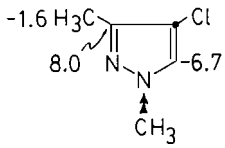

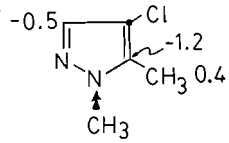

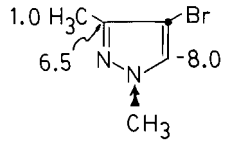

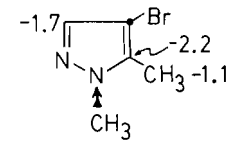

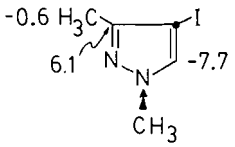

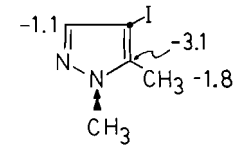

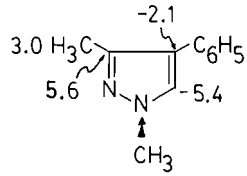

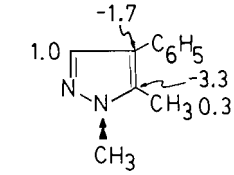

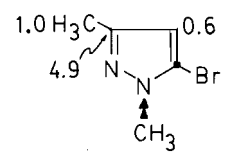

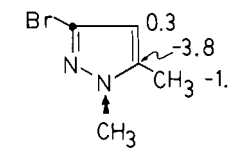

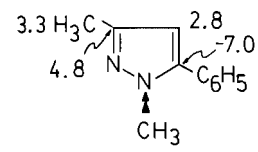

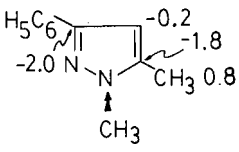

[3] J. Elguero and J. A. S. Smith. Work in progress.

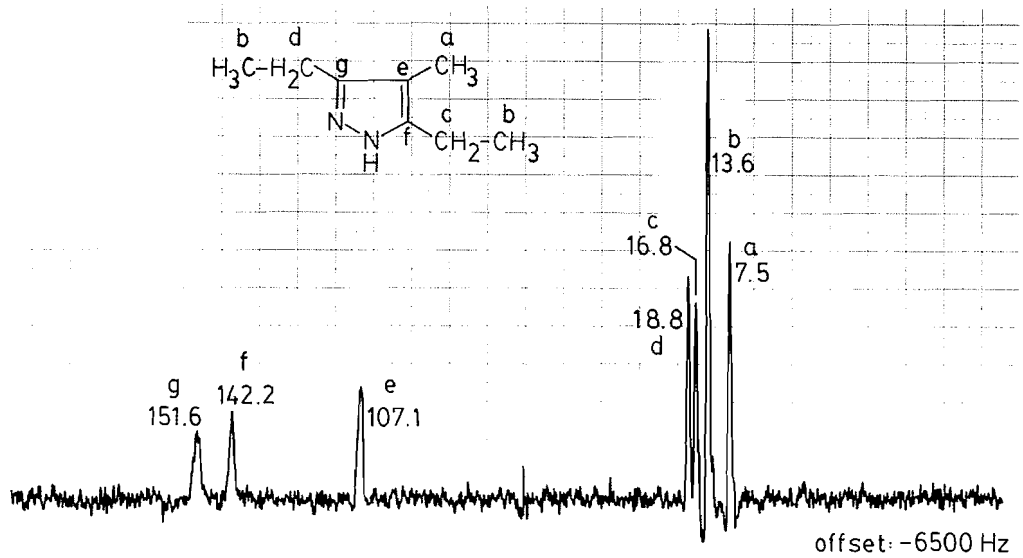

FIG. 1. The ^{13}C nmr spectrum of 3,5-diethyl-4-methylpyrazole **7**.

Comparing these values with those obtained for symmetrical pyrazoles, it can be concluded that:

(*i*) 3(5)-Methylpyrazoles substituted at position 4 by an X group (NO_2, Cl, Br, I, C_6H_5) exist in the solid state as 4-X-5-methylpyrazoles **10, 12, 14, 16,** and **20**. As a matter of fact the averaged Δδ values are, as a whole, comparable to those previously reported for symmetrically substituted pyrazoles.

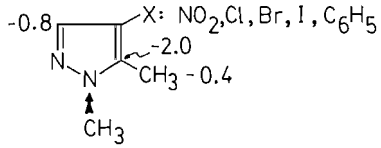

(*ii*) 3(5)-Methyl-5(3)-X-pyrazoles exist in the solid state as 3-X-5-methylpyrazoles **18, 21**, and **23**; the corresponding averaged Δδ values are

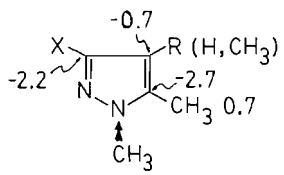

The structure of 3(5)-phenyl-5(3)-methylpyrazole **21/22** was determined by neutron diffraction (11). In the solid state, this compound exists as a cyclic tetramer with the tautomeric proton equidistant from both nitrogen atoms.

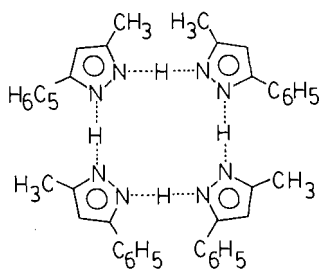

In this case with the neutron diffraction results it is not possible to determine the tautomer present in the solid state. However, the splitting of some carbon resonances observed in the ^{13}C nmr spectrum recorded at 75 MHz is not attributable to a mixture of tautomers **21** and **22**, since it affects essentially the carbon resonances of the phenyl ring. The 12 lines observed for this substituent could correspond to two different conformations of the phenyl in the crystal. In any case, this compound deserves further study.[3]

Conclusion

This study has corroborated the earlier observation (1, 2) that in the solid state "rapid"[4] annular tautomerism is seldom observed. The reasons why a given tautomer is preferred in the solid state are not clearly understood at the present moment. For 3(5)-methylpyrazole (liquid at room temperature), a solution study (12) shows that the 5-methyl tautomer is slightly more stable (54% in hexamethylphosphoramide at −17°C) than the 3-methyl tautomer. The difference in energy is very small, but this preference of the methyl group for position 5, together with the preferences of the bromo and phenyl substituents for position 3 (6*f*), will favour tautomers **18, 21**, and **23**.

Experimental

Spectra were obtained with a Bruker CXP-200 FT nmr spectrometer (Centre d'études nucléaires de Grenoble), operating at an applied field strength of 4.7 T or a ^{13}C resonance frequency of 50.31 MHz. A typical cross-polarization time was 5 ms with a recycle time of 10–15 s. Spectral width, 20.0 kHz. Spinning rate (estimated from the location of spinning sidebands), 3.2–3.5 kHz. Proton decoupling field, ≥ 1.2 mT. The ^{13}C nmr signal of linear poly(ethylene) pellets was used as internal reference (the poly(ethylene) signal was taken as 33.63 ppm downfield from tetramethylsilane (9)). A typical spectrum (3,5-diethyl-4-methylpyrazole **7**) is given in Fig. 1.

Acknowledgements

We wish to thank Drs. G. Hermann and M. Ziliox (Bruker Spectrospin, Wissembourg, France) for recording the spectrum of 3(5)-phenyl-5(3)-methylpyrazole **21/22** on a Bruker MSL-300 spectrometer (Bruker Analytische Messtechnik GmbH, Karlsruhe, Germany).

[4]Rapid in the sense that it produces broad signals at room temperature with 50- to 75-MHz instruments.

Can. J. Chem. Downloaded from www.nrcresearchpress.com by 93.93.197.157 on 09/07/12
For personal use only.

1. J. ELGUERO, A. FRUCHIER, and V. PELLEGRIN. J. Chem. Soc. Chem. Commun. 1207 (1981).
2. R. FAURE, E. J. VINCENT, and J. ELGUERO. Heterocycles, **20**, 1713 (1983).
3. A. BALDY, J. ELGUERO, R. FAURÉ, M. PIERROT, and E. J. VINCENT. J. Am. Chem. Soc. **107**, 5290 (1985).
4. P. BALLESTEROS, J. ELGUERO, R. M. CLARAMUNT, R. FAURE, M. C. FOCES-FOCES, F. H. CANO, and A. ROUSSEAU. J. Chem. Soc. Perkin Trans. 2, 1677 (1986).
5. R. FAURE, E. J. VINCENT, A. ROUSSEAU, and J. ELGUERO. Heterocycles, **26**, 333 (1987).
6. J. ELGUERO, C. MARZIN, A. R. KATRITZKY, and P. LINDA. the tautomerism of heterocycles. Academic Press, New York. 1976; (*a*) pp. 3 and 266; (*b*) pp. 37 and 325; (*c*) p. 268; (*d*) pp. 39 and 247; (*e*) pp. 8 and 272; (*f*) p. 273.
7. P. CABILDO, R. M. CLARAMUNT, and J. ELGUERO. Org. Magn. Reson. **22**, 603 (1984).
8. N. ZUMBULYADIS, P. M. HENRICHS, and R. H. YOUNG. J. Chem. Phys. **75**, 1603 (1981); A. NAITO, S. GANAPATHY, and C. A. MCDOWELL. J. Chem. Phys. **74**, 5393 (1981); J. G. HEXEM, M. H. FREY, and S. J. OPELLA. J. Am. Chem. Soc. **103**, 224 (1981); A. NAITO, S. GANAPATHY, and C. A. MCDOWELL. J. Magn. Reson. **48**, 367 (1982); J. G. HEXEM, M. H. FREY, and S. J. OPELLA. J. Chem. Phys. **77**, 3847 (1982); J. G. HEXEM, M. H. FREY, and S. J. OPELLA. J. Am. Chem. Soc. **105**, 5717 (1983); R. K. HARRIS, P. JONSEN, and K. J. PACKER. Magn. Reson. Chem. **23**, 565 (1985); R. K. HARRIS, P. JONSEN, K. J. PACKER, and C. D. CAMPBELL. Magn. Reson. Chem. **24**, 977 (1986).
9. W. L. EARL and D. L. VANDERHART. J. Magn. Reson. **48**, 35 (1982).
10. C. S. YANNONI. Acc. Chem. Res. **15**, 201 (1982); A. M. CHIPPENDALE, A. MATHIAS, R. S. AUJLA, R. K. HARRIS, K. J. PACKER, and B. J. SAY. J. Chem. Soc. Perkin Trans. 2, 1357 (1983), and references therein.
11. F. H. MOORE, A. H. WHITE, and A. C. WILLIS. J. Chem. Soc. Perkin Trans. 2, 1068 (1975).
12. M. T. CHENON, C. COUPRY, D. M. GRANT, and R. J. PUGMIRE. J. Org. Chem. **42**, 659 (1977).

Can. J. Chem. Downloaded from www.nrcresearchpress.com by 93.93.197.157 on 09/07/12
For personal use only.

Cationic complexes of titanium(III); phosphine substitution reactions

PATRICIA A. SEEWALD, GRAHAM S. WHITE, AND DOUGLAS W. STEPHAN[1]

Department of Chemistry and Biochemistry, University of Windsor, Windsor, Ont., Canada N9B 3P4

Received October 19, 1987

PATRICIA A. SEEWALD, GRAHAM S. WHITE, and DOUGLAS W. STEPHAN. Can. J. Chem. **66**, 1147 (1988).

The Ti(III) compound $[Cp_2Ti(CH_3CN)_2]_2[ZnCl_4]$, **1**, has been prepared and crystallizes in the space group *Pbca* with a = 28.444(11) Å, b = 15.370(4) Å, c = 15.206(5) Å, and Z = 8. The BPh_4 salt (i.e., $[Cp_2Ti(CH_3CN)_2][BPh_4]$, **2**) is a convenient precursor for Ti(III) cationic phosphine complexes. Reaction of **2** with several monodentate phosphines has been monitored by epr spectroscopy. Compound **2** reacts with PMe_3 in a stepwise fashion, to replace the coordinated CH_3CN molecules, yielding $[Cp_2Ti(CH_3CN)(PMe_3)][BPh_4]$, **3**, and $[Cp_2Ti(PMe_3)_2][BPh_4]$, **4**. Complex **4** exhibits a quasi-reversible cyclic voltammogram at −0.40 V vs. SCE, in the presence of excess PMe_3. This is indicative of a Ti(III)/Ti(II) redox couple thus generating the known Ti(II) species $Cp_2Ti(PMe_3)_2$. Similar reactions of **2** with PEt_3 show that only the monosubstitution product $[Cp_2Ti(CH_3CN)(PEt_3)]^+$, is formed even in the presence of excess phosphine. No substitution was seen with either PCy_3 or PPh_3. The steric and electronic factors affecting substitution are briefly considered.

PATRICIA A. SEEWALD, GRAHAM S. WHITE et DOUGLAS W. STEPHAN. Can. J. Chem. **66**, 1147 (1988).

On a préparé le composé du Ti(III) $[Cp_2Ti(CH_3CN)_2]_2[ZnCl_4]$, **1**, et il cristallise dans le groupe d'espace *Pbca*, avec a = 28,444(11), b = 15,370(4) et c = 15,206(5) Å et Z = 8. Le sel de BPh_4 (soit le $[Cp_2Ti(CH_3CN)_2][BPh_4]$, **2**, est un précurseur approprié pour les complexes cationiques phosphious du Ti(III). Faisant appel à la rpe, on a examiné la réaction du compose **2** avec plusieurs phosphines monodentates. La réaction du composé **2** avec la PMe_3 conduit à un remplacement par étapes des molécules de CH_3CN coordonnées et à la formation des composés $[Cp_2Ti(CH_3CN)(PMe_3)]_2[BPh_4]$, **3**, et $[Cp_2Ti(PMe_3)_2]_2[BPh_4]$, **4**. A −0,40 V vs, SCE, en présence d'un excès de PMe_3, le complexe **4** présente un voltampérogramme cyclique pratiquement réversible. Ce resultat suggère l'existence d'un couple redox Ti(III)/Ti(II) qui génère le composé du Ti(II) $Cp_2Ti(PMe_3)_2$. Des réactions similairés du composé avec le PEt_3 indiquent qu'il se forme un seul produit de monosubstitution, le $[Cp_2Ti(CH_3CN)(PEt_3)]^+$, même en présence d'un excès de phosphine. On n'a observé aucune substitution soit avec le PCy_3 soit avec la PPh_3. On discute brièvement de la nature des facteurs stériques et electroniques qui affectent la substitution.

[Traduit par la revue]

Can. J. Chem. Downloaded from www.nrcresearchpress.com by 93.93.197.157 on 09/07/12
For personal use only.

Introduction

Our interest in early transition metal complexes stems from their utility as synthetic precursors to heterobimetallic species (1–11). Such bimetallic complexes are of interest because of their potential applications in catalysis. Recently, in an effort to expand the arsenal of metalloligands available, we described the synthesis and chemistry of some Ti(IV), Zr(IV), and Ti(III) phosphine chalcogenide complexes (12). It is of interest to further develop the monometallic chemistry of Ti(III) with a view to examining chemistry which may subsequently provide synthetic routes to new heterobimetallic complexes. In this vein, we have examined some simple phosphine substitution chemistry of Ti(III) cations. Such cationic Ti(III) complexes are of interest in their own right. Whereas cationic Ti(IV) and Zr(IV) complexes have found numerous applications in the activation of organic substrates (13–16), little of the chemistry of analogous Ti(III) species has been investigated (17).

Experimental section

All preparations were done under an atmosphere of dry, O_2-free N_2. Solvents were reagent grade, distilled from the appropriate drying agents under N_2, and degassed by the freeze–thaw method at least three times prior to use. Electron paramagnetic resonance spectra were recorded on a Varian E-12 spectrometer, using DPPH as the reference. Ultraviolet–visible data were recorded on a Hewlett Packard 8451A diode array spectrophotometer. Cyclic voltammetry experiments were performed using a BAS CV-27 potentiostat. A platinum disk electrode was used and the potentials reported are relative to SCE. $Na[BPh_4]$ was used as the supporting electrolyte. Combustion analyses were performed by Galbraith Laboratories Inc., Knoxville, TN. $[Cp_2Ti(CH_3CN)_2][BPh_4]$, **2**, was prepared by the literature method (17). Cp_2TiCl_2 was purchased from the Aldrich Chemical Co.

Preparation of $[Cp_2Ti(CH_3CN)_2]_2[ZnCl_4]$, 1

Following the procedure of Green and Lucas (18) for the preparation of $Cp_2TiCl_2ZnCl_2TiCp_2$, 8.3 g (33.3 mmol) of Cp_2TiCl_2 was suspended in 200 mL of THF. Zn dust (2.3 g, 35.2 mmol) was added and the mixture was stirred for 4 h. During this time the solution went from its initial red–orange colour to dark green. The solution was filtered and concentrated to 75 mL. Addition of 25 mL of CH_3CN resulted in a colour change to dark blue. Addition of 100 mL of diethyl ether, and allowing the mixture to stand overnight, led to the precipitation of dark blue crystals. The crystals were isolated by filtration. Yield 5.0 g (6.87 mmol, 41%). *Anal.* calcd for $C_{28}H_{32}Cl_4N_4Ti_2Zn$: C 46.22, H 4.43, N 7.70; found: C 45.83, H 4.49, N 7.66. Electron paramagnetic resonance (CH_3CN): g = 1.983; $a\langle^{47}Ti/^{49}Ti\rangle$ = 12.0 G. Visible (CH_3CN; λ, nm (ε, M^{-1} cm^{-1})): 578 (80).

Reaction of 2 with PR_3 (R = Me, Et, Cy, Ph), formation of $[Cp_2Ti(CH_3CN)(PR_3)][BPh_4]$ (R = Me, 3, R = Et, 5)

2 (20 mg, 0.063 mmol) were combined with 1, 2 or excess equivalents of the phosphines. The solutions were stirred overnight and the epr of the reaction mixtures were recorded. Approximate integrations of the epr spectra were obtained from simulations and were used to determine the equilibrium constants. **3**: epr (THF): g = 1.986; $a\langle^{31}P\rangle$ = 20.3 G, $a\langle^{47}Ti/^{49}Ti\rangle$ = 9 G. **5**: epr (THF): g = 1.985; $a\langle^{31}P\rangle$ = 19.3 G, $a\langle^{47}Ti/^{49}Ti\rangle$ = 9 G.

Preparation of $[Cp_2Ti(PMe_3)_2][BPh_4]$, 4

To a solution of 300 mg (0.52 mmol) of **2** in 40 mL of THF was added 220 mg (2.89 mmol) of PMe_3. The mixture was stirred for 48 h. During this time the solution became pale blue in colour. The solution was filtered and pentane was added slowly. On standing, a light blue solid precipitated from solution which was isolated by filtration. Yield 200 mg (59%); mp 255–260°C(dec). *Anal.* calcd for $C_{40}H_{48}BP_2Ti$: C 73.97, H 7.44; found: C 69.54, H 7.17.[2] Electron paramagnetic resonance (THF): g = 1.989; $a\langle^{31}P\rangle$ = 30.0 G, $a\langle^{47}Ti/^{49}Ti\rangle$ = 9.6 G.

[1]Author to whom all correspondence should be addressed.

[2]In this instance poor analytical results were obtained despite recrystallizations and repeated analyses. Such discrepancies have been seen with other Cp_2Ti compounds (6, 7) also see ref. 40.

Can. J. Chem. Downloaded from www.nrcresearchpress.com by 93.93.197.157 on 09/07/12
For personal use only.

TABLE 1. Crystallographic parameters

Formula	$C_{20}H_{32}Cl_4N_4Ti_2Zn$
Crystal colour, form	Dark blue prisms
Crystal system	Orthorhombic
Space group	*Pbca*
a (Å)	28.444(11)
b (Å)	15.206(5)
c (Å)	15.370(4)
Volume (Å^3)	6648(4)
Density (g cm^{-3})	1.45
Z	8
Crystal dimension (mm)	0.44 × 0.44 × 0.46
Absorption coefficient, μ (cm^{-1})	14.50
Radiation λ, Å	Mo Kα (0.71069)
Temperature (°C)	24
Scan speed (deg/min)	2.0–5.0
Scan range (deg)	1.0 below $K\alpha_1$, 1.0 above $K\alpha_2$
Background/scan time ratio	0.5
Unique data	3577
Data $F_o^2 > 3\sigma(F_o^2)$	1596
Number of variables	252
R (%)	6.00
R_w (%)	6.42
Max Δ/σ in final cycle	0.001
Maximum residual electron density (e/Å^3), atom associated	0.74, C25, C29

Cyclic voltammogram (THF with excess PMe_3 added): −0.40 V vs. SCE. Ultraviolet–visible (THF, λ, nm (ε, M^{-1} cm^{-1})): 368 (330).

X-ray data collection and reduction

Dark blue crystals of **1** were obtained by crystallization from CH_3CN/diethyl ether. Diffraction experiments were performed on a four-circle Syntex $P2_1$ diffractometer with graphite-monochromatized Mo Kα radiation. The initial orientation matrix was obtained from 15 machine-centred reflections selected from a rotation photograph. These data were used to determine the crystal system. Partial rotation photographs around each axis were consistent with an orthorhombic crystal system. Ultimately, 30 high-angle reflections ($15° < 2\theta < 25°$) were used to obtain the final lattice parameters and the orientation matrix. Machine parameters, crystal data, and data collection parameters are summarized in Table 1. The observed extinctions were consistent with the space group *Pbca*. $+h$, $+k$, $+l$ data were collected in one shell ($4.5° < 2\theta < 40.0°$). During the data collection three standard reflections were recorded every 197 reflections. The intensities of the standards showed no statistically significant change over the duration of the data collection. The data were processed using the SHELX-76 program package on the computing facilities at the University of Windsor. A total of 1596 reflections with $F_o^2 > 3\sigma F_o^2$ were used in the refinements. No absorption correction was applied to the data.

Structure solution and refinement

Non-hydrogen atomic scattering factors were taken from the literature tabulations (19, 20). The Ti and Zn atom positions were determined using direct methods. The remaining non-hydrogen atoms were located from successive difference Fourier map calculations. The refinement was carried out by using full-matrix least-squares techniques on *F*, minimizing the function $\Sigma w(|F_o| - |F_c|)^2$ where the weight, *w*, is defined as $4F_o^2/\sigma^2(F_o^2)$ and $|F_o|$ and $|F_c|$ are the observed and calculated structure factor amplitudes. In the final cycles of the refinements the metal atoms, Cl, N, and C atoms of the acetonitrile moieties were assigned anisotropic temperature factors. The carbon atoms of the cyclopentadienyl rings were described by isotropic thermal parameters. Hydrogen atom positions were allowed to ride on the carbon to which they are bonded assuming a C—H bond length of 0.95 Å. Hydrogen atom temperature factors were fixed at 1.10 times the isotropic temperature factor of the carbon atom to which they are bonded. In all cases the hydrogen atom contributions were calculated, but not refined. The final values of $R = \Sigma||F_o| - |F_c||/\Sigma|F_o|$ and $R_w = (\Sigma w(|F_o| - |F_c|)^2/\Sigma wF_o^2)^{1/2}$ are given in Table 1. The maximum Δ/σ on any of the parameters in the final cycles of the refinement and the location of the largest peak in the final difference Fourier map calculations are also given in Table 1. The residual electron density was of no chemical significance. The following data are tabulated: positional parameters (Table 2); selected bond distances and angles (Table 3). Thermal parameters (Table S1), hydrogen atom parameters (Table S2) bond distances and angles associated with the cyclopentadienyl rings and $ZnCl_4$ dianion (Table S3) and values of $10|F_o|$ and $10|F_c|$ (Table S4) have been deposited as supplementary material.[3]

Results and discussion

The reduction of Cp_2TiCl_2 by Zn dust is a well known route to the Ti(III) chloro-bridged dimer (18). The intermediate, i.e., $Cp_2TiCl_2ZnCl_2TiCp_2$, in this reaction has been previously described (18). Cleavage of the Zn bridged species by a donor ligand results in the formation of the Ti(III) cations and $[ZnCl_4]^{2-}$. Use of acetonitrile to effect this cleavage results in the formation a dark blue crystalline product, **1**. The epr spectrum of **1** shows a central resonance with a *g* value of 1.983. Hyperfine couplines to ^{49}Ti and ^{47}Ti of 12.0 G are also observed. Based on the spectroscopic data and elemental analyses, **1** is formulated as $[Cp_2Ti(CH_3CN)_2]_2[ZnCl_4]$. This formulation was confirmed by X-ray crystallography (*vide infra*).

An X-ray crystallographic study of **1** revealed that the crystals were made up of orthorhombic unit cells each containing eight formula units. The closest nonbonded distance between the cations and the anion is 2.572 Å (Cl2—H2B). The closest nonbonded distance between cations is 2.523 Å (H2A—H8A). Selected interatomic dimensions are given in Table 3. An ORTEP drawing of the cations is given in Fig. 1. The geometry of the dianion is tetrahedral with Zn—Cl distances averaging 2.268(5) Å. The geometries of the Ti atoms are pseudotetrahedral. Two π-bonded cyclopentadienyl rings and two nitrogen atoms of the acetonitrile moieties comprise the Ti coordination sphere. The Ti—C distances in the two crystallographically distinct cations are not statistically different. The average Ti—C distance is 2.36(2) Å. Ti—N bond distances average 2.16(2) Å. The Cp—Ti—Cp angles are 134.8(5) and 135.1(5)° in the two cations in the asymmetric unit. This is in the range seen in a wide variety of Cp_2MX_2 type complexes (21–36). The N—Ti—N angles in the two independent cations are 80.6(5) and 80.8(5)°, respectively. This angle is similar to that seen in the Ti(III) species $Cp_2Ti(PMe_3)Cl$ (Cl—Ti—P angle 80.4(1)°) (32). It is larger than the O—Ti—O, angles of 78.6 and 76.9° found in the two crystallographically independent cations of $[Cp_2Ti(THF)(acetone)]^+$ (23) yet considerably smaller than the X—M—X angles seen in the other d^1 complexes $[Cp_2MoCl_2]BF_4$ (87.9°) (21) and Cp_2NbCl_2 (85.6°) (21). It is noteworthy that the N—Ti—N angle is also lower than that predicted from the EHMO calculations of Lauher and Hoffman for the X—M—X angles of d^1 Cp_2MX_2 complexes (approximately 85°) (36).

Preliminary attempts to effect phosphine substitution on the cation of **1** showed that the anion was a source of interfering side reactions. Thus, to examine such reactions, it was necessary to employ $[Cp_2Ti(CH_3CN)_2][BPh_4]$. This salt, **2** was prepared by known methods from $[Cp_2TiCl]_2$ (17).

The reaction of **2** with PMe_3 was performed and monitored by

[3]A complete set of data may be purchased from the Depository of Unpublished Data, CISTI, National Research Council of Canada, Ottawa, Ont., Canada K1A 0S2.

TABLE 2. Positional parameters[a]

Atom	x	y	z	Atom	x	y	z
Zn	4113(1)	6104(1)	2818(1)	Til	4238(1)	1931(2)	4233(2)
Ti2	2313(1)	4665(2)	1462(2)	Cl1	4808(1)	6111(4)	3542(3)
Cl2	4118(2)	5168(3)	1670(3)	Cl3	3951(2)	7483(3)	2330(4)
Cl4	3563(2)	5965(3)	3802(3)	N1	4535(2)	2717(8)	3207(9)
N2	4960(5)	1993(10)	4681(10)	N3	2297(5)	3714(9)	431(9)
N4	1559(5)	4593(8)	1263(8)	CO1	4142(7)	967(12)	3047(14)
C1	4735(6)	3105(10)	2728(12)	CO2	4531(6)	711(11)	3476(11)
C2	4994(6)	3598(12)	2044(13)	CO3	4395(7)	403(11)	4292(12)
C3	5349(7)	2005(12)	4836(11)	CO4	3921(6)	520(11)	4353(12)
C4	5850(6)	2071(12)	5078(11)	CO5	3754(7)	857(12)	3559(13)
C5	2243(6)	3219(12)	−101(11)	CO6	3637(7)	2979(13)	4368(14)
C6	2165(7)	2520(11)	780(13)	CO7	3530(6)	2274(12)	4937(12)
C7	1179(7)	4514(11)	1097(11)	CO8	3875(6)	2264(12)	5578(13)
C8	687(6)	4392(11)	849(11)	CO9	4174(7)	2940(12)	5432(13)
C10	4037(7)	3378(14)	4693(14)	C11	2086(6)	4103(10)	2803(10)
C12	2228(5)	3395(10)	2290(9)	C13	2702(5)	3492(10)	2141(10)
C14	2856(6)	4231(10)	2547(10)	C15	2485(6)	4606(12)	2985(11)
C16	2564(7)	6133(12)	1617(12)	C17	2146(6)	6145(11)	1120(11)
C18	2256(6)	5717(11)	359(11)	C19	2718(7)	5450(13)	359(13)
C20	2902(7)	5713(12)	1123(12)				

TABLE 3. Selected bond distances and angles

Bond	Distance (Å)	Bond	Distance (Å)
Til—C01	2.35(2)	Til—C02	2.34(2)
Til—C03	2.37(2)	Til—C04	2.34(2)
Til—C05	2.37(2)	Til—C06	2.35(2)
Til—C07	2.34(2)	Til—C08	2.37(2)
Til—C09	2.41(2)	Til—C10	2.38(2)
Til—N1	2.15(1)	Til—N2	2.17(2)
N1—C1	1.10(2)	N2—C3	1.13(2)
C1—C2	1.49(2)	C3—C4	1.48(2)
Ti2—C11	2.32(2)	Ti2—C12	2.33(1)
Ti2—C13	2.34(2)	Ti2—C14	2.37(2)
Ti2—C15	2.35(2)	Ti2—C16	2.36(2)
Ti2—C17	2.36(2)	Ti2—C18	2.34(2)
Ti2—C19	2.37(2)	Ti2—C20	2.37(2)
Ti2—N3	2.15(1)	Ti2—N4	2.17(2)
N3—C5	1.12(2)	N4—C7	1.12(2)
C5—C6	1.51(2)	C7—C8	1.46(2)

Bonds	Angle (deg)	Bonds	Angle (deg)
Cp1—Til—Cp2	134.8(5)	N1—Til—N2	80.6(5)
Til—N1—C1	172(2)	Til—N2—C3	173(2)
N1—C1—C2	177(2)	N2—C3—C4	176(2)
Cp3—Ti2—Cp4	135.1(5)	N3—Ti2—N4	80.8(5)
Ti2—N3—C5	173(2)	Ti2—N4—C7	174(1)
N3—C5—C6	177(2)	N4—C7—C8	178(2)

[a]The notation Cp1, Cp2, Cp3, and Cp4 refers to the centroid of the respective cyclopentadienyl rings.

epr spectroscopy. Addition of one equivalent of PMe_3 gave rise to a complex epr spectrum (Fig. 2*b*), in which signals arising from three species in equilibria are present. The equilibria involved are given in reactions [1] and [2]. The equilibrium constants for these reactions simplify to $K_{eq_1} = [\mathbf{3}]^2/[\mathbf{2}][PMe_3]$ and $K_{eq_2} = [\mathbf{4}]^2/[\mathbf{3}][PMe_3]$. Estimations of these equilibrium constants were obtained by simulation of the spectrum where 1 equiv. of PMe_3 was added; $K_{eq_1} \simeq 50$, $K_{eq_2} \simeq 10$.

[1] $[Cp_2Ti(CH_3CN)_2]^+ + PMe_3 \rightleftharpoons$

2

$[Cp_2Ti(CH_3CN)(PMe_3)]^+ + CH_3CN$

3

[2] $[Cp_2Ti(CH_3CN)(PMe_3)]^+ + PMe_3 \rightleftharpoons$

3

$[Cp_2Ti(PMe_3)_2]^+ + CH_3CN$

4

In the presence of excess PMe_3, the equilibria shift such that they are dominated by species **3** and **4**. The epr spectrum (Fig. 2*c*) shows resonances arising from only two species. Overlapping doublet and triplet signals are observed. These signals arise from the coupling of the unpaired electron to one or two phosphorus nuclei in **3** and **4**, respectively. The *g* value for **3** is 1.986, while for **4** it is 1.989. The *A* values are 20.3 and 30.0 G for **3** and **4**, respectively. Molecular orbital calculations (36), as well as single crystal epr studies (37) of d^1 complexes of the form Cp_2ML_2 show that the unpaired electron resides in an orbital that is in the TiL_2 plane. The greater *A* value for **4** implies a better overlap of this a_1 Ti orbital (i.e., the singly occupied orbital) with the orbitals on phosphorus. Such an increase in overlap would result from an increase in the L—Ti—L angle. In the case of **4**, steric interactions between the phosphine substituents may account for such an increase. The suggestion of steric effects affecting the L—Ti—L angle is consistent with the geometry changes observed in the structurally related Ti(II) complexes $Cp_2Ti(CO)_2$, $Cp_2Ti(CO)(PMe_3)$, and $Cp_2Ti(PMe_3)_2$ (32, 33, 35).

Compound **4** can be isolated from the equilibrium mixture, where excess PMe_3 is present, by precipitation with hexane. The epr spectrum of **4** in THF shows the expected triplet (Fig. 2*d*). The absence of other signals indicates that, at least in THF, phosphine dissociation does not ocur.

Compounds **2** and **4** were studied by cyclic voltammetry in THF or CH_3CN using a Pt electrode and $Na[BPh_4]$ as the supporting electrolyte. Under these conditions, no reversible

Can. J. Chem. Downloaded from www.nrcresearchpress.com by 93.93.197.157 on 09/07/12
For personal use only.

Can. J. Chem. Downloaded from www.nrcresearchpress.com by 93.93.197.157 on 09/07/12
For personal use only.

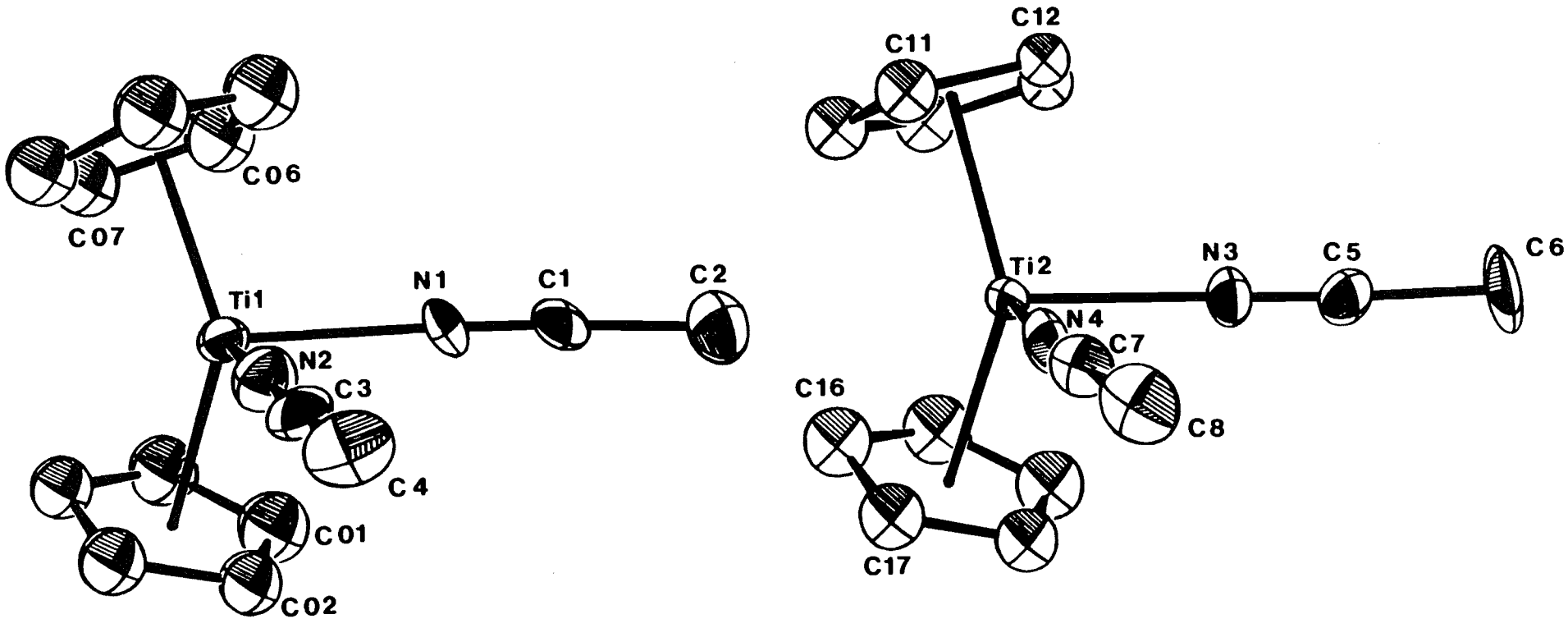

FIG. 1. ORTEP drawing of the cations of **1**, 30% thermal ellipsoids are shown, hydrogen atoms are omitted for clarity.

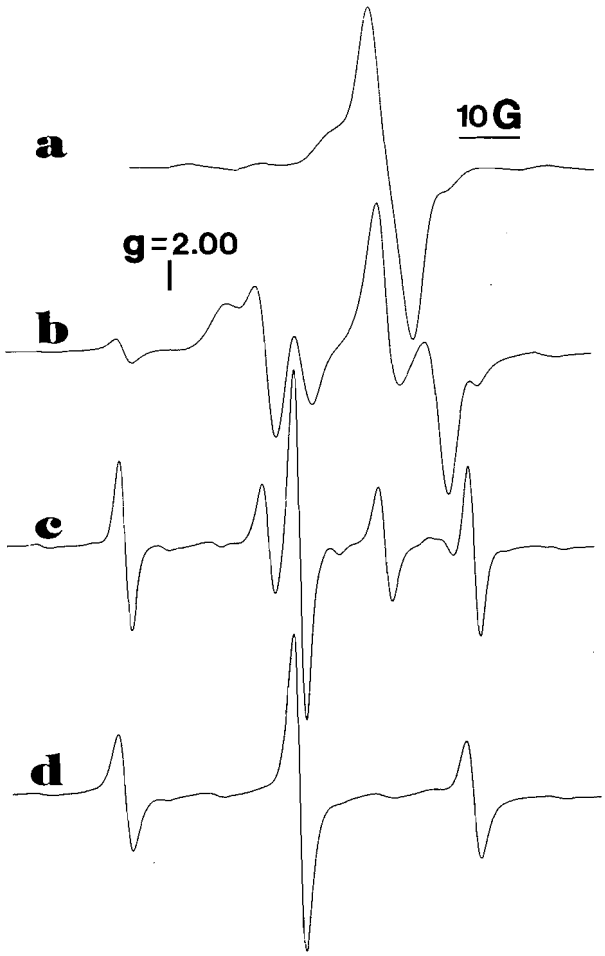

FIG. 2. EPR spectra recorded in THF at 25°C of (*a*) **2** (*b*) the reaction of **2** with 1 equivalent of PMe_3, (*c*) the reaction of **2** with a large excess of PMe_3, (*d*) isolated **4**.

electrochemical features were observed between 0.5 and −1.5 V vs. SCE, despite variations in the scan rate between 50 and 500 mV/s. In the case of **4**, following addition of excess PMe_3, a quasi-reversible redox wave centred at −0.40 V vs. SCE was observed (Fig. 3). The peak separation suggests a one electron process and the potential is consistent with a Ti(III)/Ti(II) redox couple (reaction [3]). Reduction of **4** yields the known compound $Cp_2Ti(PMe_3)_2$, **6**, (33). Rausch *et al.* have described the equilibrium in which dissociation of PMe_3 from **6** occurs (reaction [4]) (34). Presumably the addition of excess PMe_3 inhibits the

[3] $[Cp_2Ti(PMe_3)_2]^+ + e \rightleftharpoons Cp_2Ti(PMe_3)_2$

4 **6**

[4] $Cp_2Ti(PMe_3)_2 \rightleftharpoons Cp_2Ti(PMe_3) + PMe_3$

6 **7**

dissociation of phosphine from the electrochemically generated **6**. In the absence of excess phosphine, **6** is in equilibrium with $Cp_2Ti(PMe_3)$, **7**, and thus the reversible Ti(III)/Ti(II) redox couple is only observed in the presence of excess PMe_3.

Similar substitution reactions of **2** with PEt_3 were performed. The extent of reaction was much less than in the case of the reactions with PMe_3. The epr spectrum of the reaction mixture of **2**, in the presence of excess PEt_3, shows resonances attributable to only two species, the starting compound **2** and $[Cp_2Ti(CH_3CN)(PEt_3)][BPh_4]$, **5**. No evidence of disubstitution was observed.

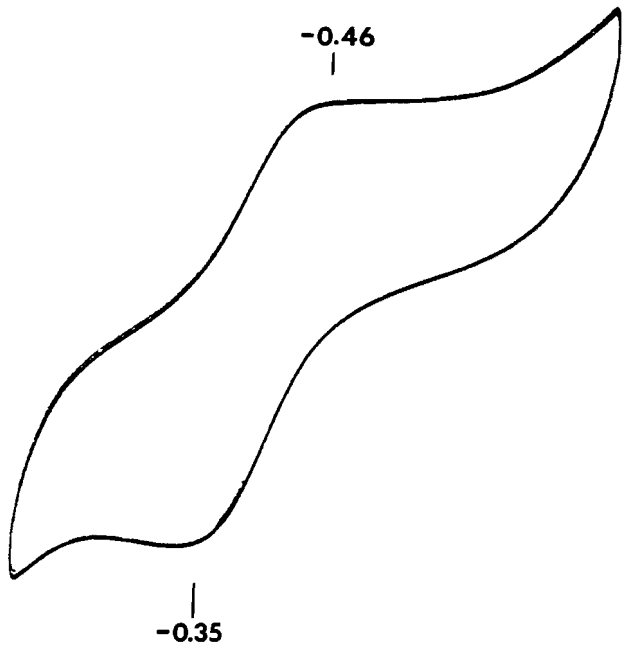

FIG. 3. Cyclic voltammogram of **4** in the presence of excess PMe_3 in THF using $Na[BPh_4]$ as the supporting electrolyte.

Reactions of **2** with PCy_3 or PPh_3 were also examined. Even in the presence of excesses of these phosphines, the epr spectral data were consistent with very limited degrees of reaction. No spectral features attributable to the PCy_3 or PPh_3 analogs of **3** and **4** were discernable, although some broadening of the central resonance arising from **2** was observed.

The greater degree of substitution seen with PMe_3 clearly reflects the favourable basicity and steric properties of this ligand. Since the basicities of PMe_3, PEt_3, and PCy_3 are similar, the degree of substitution in these cases seems to be sterically controlled. Tolman's calculation of the cone angles for these ligand are 118, 132, and 170°, respectively (38). It seems that even small differences in the steric bulk of these ligands inhibits substitution. This presumably arises from the interaction of β hydrogen atoms with the cyclopentadienyl protons. It is noteworthy that similar steric inhibition of substitution reactions has been observed for the reactions of phosphines with $Cp_2Ti(CO)_2$ where only PF_3 gave a disubstitution Ti(II) product (39). With other phosphines (PEt_3, PPh_3) only Ti(II) monosubstitution products could be prepared (i.e., $Cp_2Ti(CO)(PR_3)$ (39).

In the case of attempts to react **2** with PPh_3, both steric (Tolman cone angle 145°) (38) and basicity factors are unfavourable for substitution. It is interesting to note that while no reaction is observed with **2**, substitution to give the related monophosphine Ti(II) complex $Cp_2Ti(CO)(PPh_3)$ does proceeed (39). The instability of the Ti(III) substitution product $[Cp_2Ti(CH_3CN)(PPh_3)]^+$ may reflect the poorer ability of Ti(III) to secure the bonding of PPh_3 via π back donation.

Summary

The crystal and molecular structure of $[Cp_2Ti(CH_3CN)_2]_2[ZnCl_4]$ has been established. Substitution reactions in which phosphines replace the coordinated acetonitrile of this Ti(III) cation are very sensitive to both the steric and electronic nature

Can. J. Chem. Downloaded from www.nrcresearchpress.com by 93.93.197.157 on 09/07/12
For personal use only.

of the phosphine. Of the phosphines employed, only PMe_3 is both basic enough and small enough to afford disubstitution.

Acknowledgements

NSERC of Canada is thanked for financial support of this work. P.A.S. is grateful for the award of a NSERC undergraduate summer research assistantship and G.S.W. is grateful for the award of a NSERC Canada Postgraduate Scholarship.

1. G. S. WHITE and D. W. STEPHAN. Inorg. Chem. **24**, 1499 (1985).
2. L. GELMINI, L. C. MATASSA, and D. W. STEPHAN. Inorg. Chem. **24**, 2585 (1985).
3. L. GELMINI and D. W. STEPHAN. Inorg. Chem. **25**, 1222 (1986).
4. S. J. LOEB, H. A. TAYLOR, L. GELMINI, and D. W. STEPHAN. Inorg. Chem. **25**, 1977 (1986).
5. L. GELMINI and D. W. STEPHAN. Inorg. Chim. Acta, **111**, L17 (1986).
6. T. A. WARK and D. W. STEPHAN. Inorg. Chem. **26**, 363 (1987).
7. G. S. WHITE and D. W. STEPHAN. Organometallics, **6**, 2169 (1987).
8. G. S. WHITE and D. W. STEPHAN. Organometallics. In press.
9. L. GELMINI and D. W. STEPHAN. Organometallics. In press.
10. T. A. WARK, G. S. WHITE, J. S. TSE, and D. W. STEPHAN. Unpublished results.
11. W. L. ZHENG and D. W. STEPHAN. Inorg. Chem. In press.
12. L. GELMINI and D. W. STEPHAN. Organometallics, **6**, 1515 (1987).
13. R. F. JORDAN, W. E. DASHER, and S. F. ECHOLS. J. Am. Chem. Soc. **108**, 1718 (1986).
14. R. F. JORDAN, R. E. LAPOINTE, C. S. BAJGUR, S. F. ECHOLS, and R. WILLETT. J. Am. Chem. Soc. **109**, 4111 (1987).
15. R. F. JORDAN, C. S. BAJGUR, R. WILLETT, and B. SCOTT. J. Am. Chem. Soc. **108**, 7410 (1986).
16. R. F. JORDAN, C. S. BAJGUR, W. E. DASHER, and A. L. RHEINGOLD. Organometallics, **6**, 1041 (1987).
17. R. S. P. COUTTS, B. KAUTZNER, and P. C. WAILES. Aust. J. Chem. **22**, 1137 (1969).
18. M. L. GREEN and C. R. LUCAS. J. Chem. Soc. (D) 1000 (1972).
19. (*a*) D. T. CROMER and J. B. MANN. Acta Crystallogr. Sect. A. Cryst. Phys. Diffr. Theoret. Gen. Crystallogr A**24**, 324 (1968); (*b*) D. T. CROMER and J. B. MANN. Acta Crystallogr. Sect. A.: Cryst. Phys., Diffr., Theor. Gen. Crystallogr. A**24**, 390 (1968).
20. D. T. CROMER and J. T. WABER. International tables for X-ray crystallography. Kynoch Press, Birmingham, England. 1974.
21. K. PROUT, T. S. CAMERON, R. A. FORDER, S. R. CRITCHLEY, B. DENTON, and G. V. REES. Acta Crystallogr. B**30**, 2290 (1974).
22. A. CLEARFIELD, D. K. WARNER, C. H. S. MOLINA, R. ROPAL, and I. BERNAL. Can. J. Chem. **53**, 1622 (1975).
23. R. ALLMAN, V. BATZEL, R. PFEIL, and G. SCHMID. Z. Naturforsch. **31**b, 1329 (1976).
24. C. H. S. MOLINA, A. CLEARFIELD, and I. BERNAL. Inorg. Chem. **13**, 2880 (1974).
25. U. THEWALT and W. LASSER. J. Organomet. Chem. **276**, 341 (1984).
26. R. D. ROGERS, M. M. BENNING, L. K. KURIHARA, K. J. MORIARTY, and M. D. RAUSCH. J. Organomet. Chem. **293**, 51 (1985).
27. R. JUNGST, D. SEKUTOWSKI, J. DAVIES, M. LULY, and G. STUCKY. Inorg. Chem. **16**, 1645 (1977).
28. C. H. S. MOLINA, A. CLEARFIELD, and I. BERNAL. J. Organomet. Chem. **80**, 79 (1974).
29. E. F. EPSTEIN and I. BERNAL. Inorg. Chim. Acta, **7**, 211 (1973).
30. B. R. DAVIES and I. BERNAL. J. Organomet. Chem. **30**, 75 (1971).
31. B. R. DAVIES and I. BERNAL. J. Organomet. Chem. **26**, 229 (1971).
32. L. B. KOOL, D. M. RAUSCH, H. G. ALT, M. HERBERHOLD, U. THEWALT, and B. WOLF. J. Organomet. Chem. **297**, 159 (1985).
33. L. B. KOOL, M. D. RAUSCH, H. G. ALT, M. HERBERHOLD, U. THEWALT, and B. WOLF. Angew. Chem. Int. Ed. Engl. **24**, 394 (1985).
34. L. B. KOOL, M. D. RAUSCH, H. G. ALT, M. HERBERHOLD, U. THEWALT, and B. HONOLD. J. Organomet. Chem. **320**, 37 (1987).
35. J. L. ATWOOD, K. E. STONE, H. G. ALT, D. C. HRNCIR, and M. D. RAUSCH. J. Organomet. Chem. **132**, 367 (1977).
36. J. W. LAUHER and R. HOFFMAN. J. Am. Chem. Soc. **98**, 1729 (1976).
37. J. L. PETERSEN and L. F. DAHL. J. Am. Chem. Soc. **96**, 2248 (1974).
38. C. A. TOLMAN. J. Am. Chem. Soc. **92**, 2953 (1970).
39. B. H. EDWARDS, R. D. ROGERS, D. J. SIKORA, J. L. ATWOOD, and M. D. RAUSCH. J. Am. Chem. Soc. **105**, 416 (1983).
40. A. SHAVER and J. M. MCCALL. Organometallics, **3**, 1823 (1984). R. S. P. COUTTS, J. R. SURTEES, J. R. SWAN, and P. C. WAILES. Aust. J. Chem. **19**, 1377 (1966).

Can. J. Chem. Downloaded from www.nrcresearchpress.com by 93.93.197.157 on 09/07/12
For personal use only.

Electron paramagnetic resonance study of the reactions of the spin trap 3,5-dibromo-4-nitrosobenzenesulfonate[1]

FOR ERRATA SI
V.66 1988 P.3190

PETER SMITH[2] AND JILL SUZANNE ROBERTSON

Paul M. Gross Chemical Laboratory, Department of Chemistry, Duke University, Durham, NC 27706, U.S.A.

Received September 30, 1987

PETER SMITH and JILL SUZANNE ROBERTSON. Can. J. Chem. **66**, 1153 (1988).

Using rapid-mixing, continuous-flow $TiCl_3$-based techniques and also by means of static-sample studies involving the thermal decomposition of symmetric aliphatic azo compounds, we have characterized by electron paramagnetic resonance 22 spin adducts of 3,5-dibromo-4-nitrosobenzenesulphonate, **1**, in aqueous solution at 25°C. These spin adducts, all nitroxides, exhibit a moderately wide range of α-nitrogen and β-CH proton splitting constants, which we discuss in terms of steric and electronic effects. In connection with these studies, blank experiments showed that aqueous solutions of **1** gave no radicals when exposed to light and heat. In addition, we have studied by electron paramagnetic resonance at 25°C static samples of aqueous solutions of **1** both by itself and in the presence of each of several acrylic and methacrylic monomers and in both the presence and absence of light. These solutions yielded radicals, namely, nitroxides, only when containing methacrylic monomers, the presence of light having no effect. These observations support the "ene" addition/oxidation mechanism of nitroxide formation.

PETER SMITH et JILL SUZANNE ROBERTSON. Can. J. Chem. **66**, 1153 (1988).

Opérant en solutions aqueuses, à 25°C, faisant appel à la résonance paramagnétique électronique et utilisant des techniques de mélange rapide, à flux continu et basées sur le $TiCl_3$ ainsi que des études à l'aide d'échantillons statiques impliquant la décomposition thermique de composés azo aliphatiques symétriques, on a caracterisé 22 adduits de spin du dibromo-3,5 nitroso-4 sulfonate, **1**. Ces adduits de spin, tous des nitroxydes, présentent tous un éventail assez large de constantes de couplages avec l'azote en α et le proton CH en β. Pour fins de comparaison, on a démontré que des solutions aqueuses ne contenant que du composé **1** ne donnent pas de radicaux lorsqu'on les expose à la lumière ou à la chaleur. De plus, opérant à 25°C et faisant appel à la résonance paramagnetique electronique, on a étudié dans échantillons statiques du composé **1**, en solutions aqueuses, soit seul ou en présence de plusieurs monomères acryliques et méthacryliques différents, tant en présence qu'en absence de lumières. Ces solutions ne fournissent des radicaux, soit des nitroxydes, que lorsqu'elles contiennent des monomères méthacryliques; la présence de lumière est sans effet. Ces résultats suggèrent que la formation du nitroxyde implique un mécanisme d'addition/oxydation de nature «ene».

[Traduit par la revue]

Introduction

One way of studying a highly reactive radical, R·, in solution in systems where the steady-state concentration is below the usual epr detection limit is the so-called spin trap method (1). This method depends upon the addition to the reaction system of a low concentration of a diamagnetic substance (the spin trap, ST) with high affinity for R·. The product of this trapping reaction, R(ST)·, the spin adduct, must be a particularly persistent (2) radical whose concentration builds to a readily detectable level,

[1] $R\cdot + ST \rightarrow R(ST)\cdot$

The most commonly employed spin traps have been either nitrones or nitroso compounds, yet, although the latter generally yield more informative spin-adduct epr spectra than the former (3–9), few nitroso compounds have seen use in aqueous solution studies. One recently discovered water-soluble nitroso compound is 3,5-dibromo-4-nitrosobenzenesulphonate, Z—N=O, or **1** (10). Although there have been few reports of its use (11–14), the synthesis of **1** is inexpensive and easy and, unlike other nitroso compounds frequently employed (3–5) as spin traps, **1** is insensitive to laboratory light.

Because of the minimal variation of epr splitting constants for adducts of any one spin trap, contrasted with the greater variation of such constants for adducts of a particular radical with different spin traps (3–9), it is advantageous to employ more than one spin trap to attempt to trap a radical of interest. Thus, because a major problem with spin trapping is the unambiguous determination of spin-adduct structures, the introduction of new spin traps whose characteristics will aid in identifying which radical was indeed trapped provides a broader foundation for this technique. In particular, there is a pressing need to obtain and characterize new water-soluble nitroso spin traps to further the study of reactions in aqueous media, for example, biological systems. To that end, we have generated and characterized several spin adducts of **1**. To assist in unambiguous assignment of spin-adduct spectra, we employed rapid-mixing, continuous-flow techniques, first generating and characterizing the radical of interest, R· and then, by allowing an aqueous solution of **1** to enter the flowing stream, trapping and characterizing the spin adduct. Also, as a further unambiguous, static-sample, radical generating method, we used the thermal decomposition of symmetric aliphatic azo compounds. In addition, we investigated the stability of **1** to light, heat, and several olefins. Our results show that **1** traps a wide variety of carbon-centered radicals, is stable to light and heat, and exhibits enophilicity (15, 16) toward certain olefins. Because the spin adducts of **1** display a moderately wide range of values for the splitting constants $a_{\beta\text{-H}}$(CH) and $a_{\alpha\text{-N}}$, which vary with the nature of the radical trapped, it can be a useful and diagnostic spin trap, one that complements spin traps currently in use.

Experimental

The epr spectrometer, its accessories, and the general experimental arrangements and procedures were as before (17), unless otherwise specified. The continuous-flow studies employed a Borg mix-and-flow cell (18) in conjunction with a three-stream continuous-flow system as in earlier work in this laboratory (19). The static-sample investigations employed a Varian V-4548 aqueous-solution sample cell. All samples were at 25.0 ± 1.0°C and all spectra recorded were as the first derivative with a field-modulation amplitude of 2.0×10^{-1} G.

[1]Supported by the National Science Foundation and the North Carolina Board of Science and Technology.

[2]Author to whom correspondence may be addressed.

Printed in Canada / Imprimé au Canada

Can. J. Chem. Downloaded from www.nrcresearchpress.com by 93.93.197.157 on 09/07/12
For personal use only.

We synthesized **1** from 3,5-dibromosulphanilic acid (Aldrich) via the method of Kaur *et al.* (10), recrystallized the crystals so obtained twice from 95% ethanol (Apper Alcohol), and stored the final product (yield, 71%) in the dark at −10°C until used. The substrates examined were methanol (**2**), ethanol (95%) (**3**), isopropanol (**4**), acetone (**5**), trioxane (**6**), acrylic acid (**7**), methyl acrylate (**8**), ethyl acrylate (**9**), butyl acrylate (**10**), methacrylic acid (**11**) methyl methacrylate (**12**), isobutyl methacrylate (**13**), acrylonitrile (**14**), methacrylonitrile (**15**), 2,2′-azobis-(2-methylpropanonitrile) (**16**), 2,2′-azobis-(2-methylbutanonitrile) (**17**), 4,4′-azobis-(4-cyanopentanoic acid) (**18**), 2,2′-azobis-(2,4-dimethylpentanonitrile) (**19**), 2,2′-azobis-(2-ethylbutanonitrile) (**20**), dimethyl-2,2′-azobis-(2-methylpropanoate) (**21**), and 2,2′-azobis-(2-methylpropane) (**22**).

All substrates were either synthesized and purified (20) samples available in our laboratory (**17, 19–21**) or were as received from Apper Alcohol (**3**), Aldrich (**18**), Alfa (**22**), Kodak (**14** and **16**), Mallinckrodt (**2, 4–6**), or Rohm and Haas (**7–13**).

$TiCl_3$–H_2O_2 radical generating system studies

The three-stream, continuous-flow system was as follows: a reducing stream 0.004 M in $TiCl_3$ and an oxidizing stream, 0.1 M in H_2O_2, with both streams 0.02 M in substrate and 0.1 M in H_2SO_4; and a third stream, 0.003 M in **1**, which joined the oxidizing stream via a T-piece and stopcock, S, which allowed these two solutions to mix just prior to entering the cell. With S closed, thus using only the oxidizing and reducing streams, we first optimized the signal from the radical to be trapped, following which, with S open, this signal disappeared and in its place that from the spin-adduct nitroxide appeared. Total flow rates for both processes were 6–7 mL s^{-1}, with those of the oxidizing, reducing, and **1** streams, respectively, in the approximate ratios first 3:1:0, and then 3:1:3. The substrates so studied were **2–15**.

$TiCl_3$–$(CH_3)_3COOH$ radical generating system studies

The procedures and conditions were as for the $TiCl_3$-H_2O_2 work except for the replacement of the H_2O_2 in the oxidizing stream by *tert*-butylhydroperoxide, $(CH_3)_3COOH$ (Aldrich, 70%) (21), in the same concentration, and the omission of substrate from the oxidizing and reducing streams; the total flow rate was 2–3 mL s^{-1}, with the rates of the reducing, oxidizing, and **1** streams, respectively, in the approximate ratios first 1:1:0, and then 1:1:3.

$FeSO_4$–H_2O_2 radical generating system studies

All procedures and conditions were as for the $TiCl_3$–H_2O_2 work except for the replacement of the $TiCl_3$ in the reducing stream by 0.0025 M $FeSO_4 \cdot 7H_2O$ and ethylenediaminetetraacetic acid (1:1) (22–24). The only substrates so examined were **3** and **4**.

Azo-compound thermal decomposition studies

We heated at 100°C for 3 min with stirring a mixture of 25 mL of deionized water containing 2.0×10^{-4} moles of dissolved **1** with the same number of moles of the solid azo compound, then cooled this slurry in a constant temperature bath for 15 min to 25.0 ± 1.0°C, and next removed an aliquot of aqueous layer for epr examination as a static sample. All azo compounds, **16–22**, received this treatment.

In addition, we prepared at 25°C slurries of the type described above and, while keeping the temperature at 25.0 ± 1.0°C, exposed them to radiation from a sunlamp (Kenmore, 275 W, 110–125 V) for periods of 1–3 h. The spectra obtained were identical to those obtained by the thermal decomposition method, but less intense. All spectroscopic data reported refer to thermal decomposition studies. In addition we ran blank experiments for both the thermal and photochemical decomposition studies where the procedures followed were as described, except for the omission of the azo compounds, these giving no signals.

As a further examinination of the stability of **1** to light, we exposed aqueous solutions of **1** to normal laboratory light at room temperature for days and examined them by epr. No detectable signals were present.

*Demonstration of the enophilicity of **1***

We stirred aqueous solutions ca. 5.45 mM in both **1** and olefin at 25.0 ± 1.0°C for a minute and then removed static samples at 30-min intervals over a 3-h period for epr examination. We carried out all the procedures both in the presence of normal laboratory light and under photographic darkroom conditions, there being no observable difference, for example, in intensity or splitting-constant values, between the spectra obtained. The olefins so studied were **7–15** but, as expected, the only ones found to undergo reaction were **11–13** and **15** (15, 16).

Results and discussion

Table 1 presents the numbering scheme for all substrates employed and spin adducts observed. Tables 2–6 summarize the epr spectroscopic data obtained.

Tables 2–4 give the results of all studies involving the use of rapid-mixing, continuous-flow radical generating systems. Of the three such systems employed, only that producing the methyl radical (21) gave a spin-adduct spectrum in the absence of any substrate, namely, that of **23**. The other two systems, which generate ·OH radicals, gave no spin adduct, as expected (3, 10, 13, 14). In the absence of **1**, each substrate treated with an ·OH radical generating system yielded an optimized spectrum consistent with the presence of only one radical, namely, a substrate-derived species. For substrates **2–9**, **11**, **12**, **14**, and **15**, these spectra were in agreement with the literature (27–32); for the rest, **10** and **13**, which do not appear to have received previous epr investigations under conditions comparable to those of our work, the spectra were fully characterizable in terms of the expected (33) single ·OH-addition radicals, **39** and **40**. The epr data for **39** and **40** are in reasonable agreement with those for analogous species taken under comparable conditions, see Table 4 (27, 31, 32). Upon including **1** in the mixing streams, the signal from the substrate-derived radical disappeared and, with one exception, in its place appeared one fully consistent with that of its expected spin adduct, which was thus unambiguously assignable.

This exception was for the $FeSO_4$–H_2O_2/CH_3CH_2OH reaction system:

[2] $Fe(II) + H_2O_2 \rightarrow Fe(III) + \cdot OH + {}^-OH$

[3] $\cdot OH + CH_3CH_2OH \rightarrow \cdot CH(CH_3)OH + H_2O$

[4] $\cdot OH + CH_3CH_2OH \rightarrow \cdot CH_2CH_2OH + H_2O$

Here, although because of the electrophilic character of the hydroxyl radical (24) we would expect the rate constant for [3], k_3, to be greater than k_4, the optimized spectrum was from $\cdot CH_2CH_2OH$, because the reactivity of Fe(III) towards radicals is selective, paralleling stabilities of corresponding carbonium ions (24)

[5] $\cdot CH(CH_3)OH + Fe(III) \rightarrow {}^+CHCH_3OH + Fe(II)$

[6] $\cdot CH_2CH_2OH + Fe(III) \rightarrow {}^+CH_2CH_2OH + Fe(II)$

i.e., $k_5 \gg k_6$. However, on allowing **1** to enter the flowing stream, as the spectrum from $\cdot CH_2CH_2OH$ disappeared, that which took its place was almost entirely from **25**, the spin adduct of $\cdot CH(CH_3)OH$. The kinetic complexity (22–24) of the $FeSO_4$–H_2O_2 radical generating system restricts a detailed analysis of this topic here. However, it is reasonable to expect that $\cdot CH(CH_3)OH$ would be more susceptible to trapping than $\cdot CH_2CH_2OH$ because the α-OH group renders the α-carbon more nucleophilic (34), while steric differences between these two radicals would appear unimportant, and our observations fit this simple expectation. As well as the spectrum from **25**, there was one other present, a low-intensity absorption (5% of the whole) probably corresponding to trapped $\cdot CH_2CH_2OH$, as expected; i.e., $\cdot CH_2CH_2OH$ is the minor product of ·OH attack on CH_3CH_2OH in the absence of any effect from the presence of Fe(III) (24). These results contrast with a recent report (13*b*)

Can. J. Chem. Downloaded from www.nrcresearchpress.com by 93.93.197.157 on 09/07/12
For personal use only.

TABLE 1. Numbering scheme for all substrates and spin adducts

Substrate	Radical trapped, R·	Spin adduct observed, Z—N(O·)—R
—	·CH_3	**23**
2 CH_3OH	·CH_2OH	**24**
3 $CH_2(CH_3)OH$	·$CH(CH_3)OH$	**25**
4 $CH(CH_3)_2OH$	·$C(CH_3)_2OH$	**26**
4 $CH(CH_3)_2OH$	·$CH_2CH(CH_3)OH$	**27**
5 $CH_3C(O)CH_3$	·$CH_2C(O)CH_3$	**28**
6 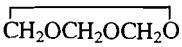	·	**29**
7 $CH_2{=}CH(CO_2H)$	·$CH(CO_2H)CH_2OH$	**30**
8 $CH_2{=}CH(CO_2CH_3)$	·$CH(CO_2CH_3)CH_2OH$	**31**
9 $CH_2{=}CH(CO_2CH_2CH_3)$	·$CH(CO_2CH_2CH_3)CH_2OH$	**32**
10 $CH_2{=}CH[CO_2(CH_2)_3CH_3]$	·$CH[CO_2(CH_2)_3CH_3]CH_2OH$	**33**
11 $CH_2{=}C(CH_3)(CO_2H)$	·$C(CH_3)(CO_2H)CH_2OH$	**34**
12 $CH_2{=}C(CH_3)(CO_2CH_3)$	·$C(CH_3)(CO_2CH_3)CH_2OH$	**35**
13 $CH_2{=}C(CH_3)[CO_2CH_2CH(CH_3)_2]$	·$C(CH_3)[CO_2CH_2CH(CH_3)_2]CH_2OH$	**36**
14 $CH_2{=}CH(CN)$	·$CH(CN)CH_2OH$	**37**
15 $CH_2{=}C(CH_3)(CN)$	·$C(CH_3)(CN)CH_2OH$	**38**
16 $(CH_3)_2(CN)C{-}N{=}N{-}C(CN)(CH_3)_2$	·$C(CN)(CH_3)_2$	**41**
17 $(CH_3CH_2)(CH_3)(CN)C{-}N{=}N{-}C(CN)(CH_3)(CH_2CH_3)$	·$C(CN)(CH_3)(CH_2CH_3)$	**42**
18 $[HO_2C(CH_2)_2](CH_3)(CN)C{-}N{=}N{-}C(CN)(CH_3)[(CH_2)_2CO_2H]$	·$C(CN)(CH_3[(CH_2)_2CO_2H]$	**43**
19 $[(CH_3)_2CHCH_2](CH_3)(CN)C{-}N{=}N{-}C(CN)(CH_3)[CH_2CH(CH_3)_2]$	·$C(CN)(CH_3)[CH_2CH(CH_3)_2]$	**44**
20 $(CH_3CH_2)_2(CN)C{-}N{=}N{-}C(CN)(CH_2CH_3)_2$	·$C(CN)(CH_2CH_3)_2$	**45**
21 $(CH_3O_2C)(CH_3)_2C{-}N{=}N{-}C(CH_3)_2(CO_2CH_3)$	·$(CH_3)_2(CO_2CH_3)$	**46**
22 $(CH_3)_3C{-}N{=}N{-}C(CH_3)_3$	·$C(CH_3)_3$	**47**

TABLE 2. Electron paramagnetic resonance spectroscopic data[a] for Z—N(O·)—R radicals resulting from addition of hydrogen-atom abstraction radicals[b] to **1**

Substrate	Spin adduct	-R	Splitting constants[c, d] (G) α-N	β-H(CH)	*meta*[e]	Δg[f]	ΔH_{pp} (G)
—	**23**	—CH_3[g]	14.32(2)	13.35(2)	0.70(2)	29	0.2
2	**24**	—CH_2OH	13.47(2)	8.94(2)	0.61(2)	28	0.4
3	**25**	—$CH(CH_3)OH$	13.75(2)	9.06(1)	0.58(2)	32	0.4
4	**26**	—$C(CH_3)_2OH$	14.04(2)	—	0.70(2)	31	0.3
4	**27**	—$CH_2CH(CH_3)OH$[h]	14.01(1)	10.60(2)[i]	0.55(2)	24	0.4
5	**28**	—$CH_2C(O)CH_3$	13.07(2)	9.50(2)	0.62(2)	32	0.4
6	**29**	— 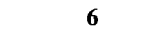	11.96(3)	5.34(2)	—	32	0.8[j]

[a]At 25.0 ± 1.0°C and pH ca. 2.

[b]Except for **23** and **27**, all trapped radicals were hydrogen-atom abstraction species generated by the $TiCl_3$–H_2O_2 radical generating system.

[c]Unless otherwise stated, all protons at a given site are magnetically equivalent.

[d]Each number in parentheses is the standard deviation of the mean, σ_{n-1}, times 10^2 and the maximum error limits are approximately $\pm 2\sigma_{n-1}$ based on the reported error limits for the standard (25).

[e]The two CH phenyl-ring protons.

[f]Δg value = $(g - 2.00600)$ and σ_{n-1} times 10^5 for all radicals is 1. The maximum error limits of the g values are ±0.00006 based on the reported error limits for the standard (25, 26).

[g]$TiCl_3$–$(CH_3)_3COOH$ radical generating system.

[h]$FeSO_4$–H_2O_2 radical generating system. The only comparable study in the literature (10) (for the corresponding spin adducts generated from the deuteriated analogue of **1**, 2,6-dideuterio-3,5-dibromonitrosobenzenesulphonate, **1′**, by photolysis of H_2O_2–$(CH_3)_2CHOH$–**1′**–H_2O mixtures at 20°C) reports that the α-N splitting is 14.0 G and the two β-H(CH) protons are nonequivalent, with a values 9.8 and 11.25 G.

[i]The chiral γ carbon renders these two β-H(CH) protons nonequivalent but, based on the observed ΔH_{pp}, this nonequivalence must be <0.2 G.

[j]This large value is attributable to unresolved splittings, e.g., from *meta*- and δ-CH protons.

published since the completion of our work that the $TiCl_3$– and $FeCl_2$–H_2O_2/CH_3CH_2OH/**1** reaction systems at room temperature both yielded only the spin-adduct spectrum of the ·CH_2CH_2OH radical. The difference between our results and these other findings presumably arises from the use by the other workers (13*b*) of reaction conditions very different from those we followed, namely, static samples and reactant concentrations in general considerably higher than those of our work.

In contrast, using the $FeSO_4$–H_2O_2/$(CH_3)_2CHOH$ reaction system, the optimized radical spectrum was from ·$CH_2CH(CH_3)OH$ and the spectrum in the presence of **1** was fully interpretable as arising from **27**, the spin adduct of this

Can. J. Chem. Downloaded from www.nrcresearchpress.com by 93.93.197.157 on 09/07/12
For personal use only.

TABLE 3. Electron paramagnetic resonance spectroscopic data[a] for Z—N(O·)—R radicals resulting from addition of ·OH-addition radicals[b] to **1**

Substrate	Spin adduct	-R	Splitting constants[c] (G) α-N	β-H(CH)	Δg^d	ΔH_{pp} (G)[e]
7	**30**	—$CH(CO_2H)CH_2OH$	12.99(3)	5.00(2)	37	1.6
8	**31**	—$CH(CO_2CH_3)CH_2OH$	13.07(1)	4.86(1)	37	1.8
9	**32**	—$CH(CO_2CH_2CH_3)CH_2OH$	13.04(2)	5.30(2)	37	1.4
10	**33**	—$CH[CO_2(CH_2)_3CH_3]CH_2OH$	13.25(2)	5.92(2)	35	1.8
11	**34**	—$C(CH_3)(CO_2H)CH_2OH$	12.93(2)	—	45	1.4
12	**35**	—$C(CH_3)(CO_2CH_3)CH_2OH$	12.91(2)	—	39	1.7
13	**36**	—$C(CH_3)[CO_2CH_2CH(CH_3)_2]CH_2OH$	12.92(2)	—	53	1.8
14	**37**	—$CH(CN)CH_2OH$	12.92(3)	5.44(2)	48	1.2
15	**38**	—$C(CH_3)(CN)(CH_2OH$	13.00(2)	—	53	1.8

[a]See Table 2, footnote *a*.
[b]Generated by the $TiCl_3$–H_2O_2 radical generating system.
[c]See Table 2, footnote *d*.
[d]See Table 2, footnote *f*.
[e]The large values of ΔH_{pp} are attributable to unresolved splittings, e.g., from *meta*- and γ-CH protons as well as the γ-CN nitrogen (**37**, **38**) and γ-CH_3 protons (**34–36**, **38**).

TABLE 4. Electron paramagnetic resonance spectroscopic data[a] for radicals resulting from ·OH radical addition to **10** and **13**

Substrate	Radical	Splitting constants[b](G) α-H(CH)	β-H(CH)	γ-H(CH)	g^c
10	**39** ·$CH[CO_2(CH_2)_3CH_3]CH_2OH$	20.22(2)	21.55(2)	1.58(3)	2.00341(2)
13	**40** ·$C(CH_3)[CO_2CH_2CH(CH_3)_2]CH_2OH$	—	20.07(3)[d]	1.66(2)	2.00342(2)

[a]See Table 2, footnote *a*.
[b]See Table 2, footnotes *c* and *d*, and Table 3, footnote *b*.
[c]Each number in parentheses is σ_{n-1} times 10^5; for the maximum error limits of the *g* values see Table 2, footnote *f*.
[d]Five equivalent β-protons.

TABLE 5. Electron paramagnetic resonance spectroscopic data[a] for Z—N(O·)—R radicals resulting from addition of symmetric azo-compound derived radicals to **1**

Substrate	Spin adduct	—R	Splitting constant[b](G) α-N	Δg^c	ΔH_{pp} (G)[d]
16	**41**	—$C(CN)(CH_3)_2$	13.28(3)	35	1.8
17	**42**	—$C(CN)(CH_3)(CH_2CH_3)$	13.32(2)	41	1.7
18	**43**	—$C(CN)(CH_3)[(CH_2)_2CO_2H]$	13.21(4)	52	1.4
19	**44**	—$C(CN)(CH_3)[CH_2CH(CH_3)_2]$	13.59(3)	32	1.4
20	**45**	—$C(CN)(CH_2CH_3)_2$	13.92(3)	20	1.5
21	**46**	—$C(CH_3)_2(CO_2CH_3)$	13.33(4)	33	1.6
22	**47**	—$C(CH_3)_3$	14.24(2)	24	1.5

[a]At 25.0 ± 1.0°C and pH ca. 6.
[b]See Table 2, footnote *d*.
[c]See Table 2, footnote *f*.
[d]The large values of ΔH_{pp} are attributable to unresolved splittings, e.g., from *meta*-CH protons, γ-CN nitrogens (**41–45**), and γ-CH_3 protons (**46**, **47**).

same species. Acknowledging, once more, the kinetic complexity of the $FeSO_4$–H_2O_2 radical generating system, this observation agrees with simple expectation, i.e., the expected greater stability of $^+C(CH_3)_2OH$ over $^+CH_2CH(CH_3)OH$ and the greater steric hindrance to the trapping of $\cdot C(CH_3)_2OH$ over $\cdot CH_2CH(CH_3)OH$.

Table 5 summarizes the results of all static-sample, R—N=N—R thermal decomposition studies. Thermal decomposition of each R—N=N—R compound in the presence of **1** yielded a spin-adduct spectrum fully consistent with trapping the expected single radical (35), R·. There was no evidence for the trapping of >Ċ—C≡N radicals in the >C=C=N· form (36–38), a result in accord with the general finding that nitroso compounds do not readily trap N-centered radicals (3–9, 39) and the relative strengths of C—N and N—N bonds (40).

Two of the spin adducts characterized in this study, **23** and **24**, have been the subject of the already mentioned epr investigation (13*b*) using static samples and the $TiCl_3$– and $FeCl_2$–

Can. J. Chem. Downloaded from www.nrcresearchpress.com by 93.93.197.157 on 09/07/12
For personal use only.

TABLE 6. Electron paramagnetic resonance spectroscopic data[a] for Z—N(O·)—CH_2—C(X)=CH_2 radicals resulting from the enophilic reaction of **1** with methacrylic monomers

Substrate	Radical	—X	Splitting constants[b](G) α-N	β-H(CH)	δ-H(CH)	*meta*[c]	Δg^d	ΔH_{pp} (G)[e]
11	**48**	—CO_2H	13.83(3)	9.97(2),10.35(2)	0.50(2)[e]	0.70(2)	27	0.40
12	**49**	—CO_2CH_3	13.45(2)	8.41(3). 8.93(3)	—	—	37	1.6[f]
13	**50**	—$CO_2CH_2CH(CH_3)_2$	13.58(3)	8.54(2), 8.81(3)	—	—	38	1.6[f]
15	**51**	—CN	13.79(2)	10.97(2),11.17(2)	0.40(2)[e]	0.60(3)	38	0.40

[a]See Table 5, footnote *a*.
[b]See Table 2, footnote *d*. The β-CH protons are magnetically inequivalent.
[c]See Table 2, footnote *e*.
[d]See Table 2, footnote *f*.
[e]Only one δ-CH proton splitting detected.
[f]The large value of ΔH_{pp} is attributable to unresolved splittings, e.g., from *meta*- and δ-CH protons.

H_2O_2 radical generating systems, and there is reasonable agreement between our epr data for these radicals and those of the other work (13*b*). Also, there has been a report of the splitting constants for spin adducts similar to **23**, **24**, **25**, **27**, and **45** where the spin trap used was 2,6-dideuterio-3,5-dibromonitrosobenzenesulfonate, **1′** (10). These trapped radicals were formed (10) from photolysis of H_2O_2–substrate–H_2O mixtures at 20°C and, except in the case of **27**, there is reasonable agreement between these literature values and our data, bearing in mind the difference in solvent conditions. However, for **27**, there is an appreciable difference between our results and the literature with respect to the size of the β-CH_2 proton splittings, see Table 2, a difference for which we are unable to account.

The spectra for **29–38** and **41–47** showed no *meta*-CH proton splittings, consistent with the large ΔH_{pp} values, 0.8–1.8 G, in comparison with those of the spectra from **23–28**, 0.2–0.4 G, for which *meta*-CH proton splittings were clearly resolvable, see Tables 2, 3, and 5.

We would expect the nitroxide function to be sensitive to substituents on the nitrogen (41), as demonstrated by resonance structures,

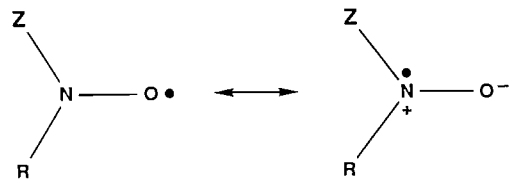

52 53

where structure **52** is favored when the R group is electron withdrawing, either −M or −I (ref. 34, Chaps. 1, 9), and will have lower α-N splittings than structure **53**, which is favored by the presence of an electron-donating, +M or +I, R group. In agreement with this, adducts **24, 25**, and **26** show that as the number of methyl groups is increased, the α-N splitting constant increases, because the methyl group is +M. For groups **28–38** and **41–46** and groups **23–27** and **47**, respectively, the R moieties are of −M and +M character, respectively. Thus, as expected, the average α-N splitting constant for the former, 13.1 G, is lower than that for the latter, 14.0 G. We need to view individual cases in terms of all β substituents and their ability to donate or withdraw electrons. For example, in the case of **29**, for the two ethereal oxygens the electron withdrawal by induction (−I effect) appears to be greater than electron donation by resonance (+M effect) (ref. 34, Chaps. 1, 9), as the α-N splitting constant is very low. While adduct **45** has a strong −M group, it also contains two +M groups, both $-CH_2CH_3$, and these groups account for its seemingly high α-N splitting constant, 13.9 G. As expected on the basis of their −R groups being +M, **23** and **47** have the largest α-N splitting constants.

Ideally, the $a_{\beta\text{-H}}$(CH) values should decrease as the bulk of the trapped group increases (42). This trend holds in general for our data as $a_{\beta\text{-H}}$(CH) values for **29–33** and **37** are considerably smaller than those for **23–25**, **27**, and **28**, which contain much less bulky groups. On these grounds, **23**, as expected, has the highest $a_{\beta\text{-H}}$(CH) value. For **27** and, as previously noted, for spin adducts of 5,5-dimethyl-l-pyrroline-l-oxide (43), the larger $a_{\alpha\text{-N}}$ and $a_{\beta\text{-H}}$(CH) values are probably due to increased spin density on the nitrogen and a decrease in the β-CH dihedral angle caused by intramolecular hydrogen bonding from the hydroxy hydrogen to the nitroxide oxygen (43). A scatter plot (43) of $a_{\alpha\text{-N}}$ versus $a_{\beta\text{-H}}$(CH) values for spin adducts **23–25**, **27–33**, and **37** clearly shows that **1** adequately differentiates between all spin-trap adducts except **30** and **31** and also **32** and **37**.

All the spin-adduct spectra generated in the continuous-flow studies disappeared when the flow was stopped, while the spectra of the azo-compound derived adducts were much more stable, their spectral intensity changing less than 10% over a 3-h period. Check experiments on a solution of **41** prepared in the usual manner, to which a freshly prepared solution of $TiCl_3$, H_2SO_4, and H_2O_2 was quickly added to approximate conditions in the flow studies, showed that the signal from **41** disappeared immediately, suggesting that the source of signal disappearance in the flow studies was from destruction of the spin adducts by components of the $TiCl_3$–H_2O_2 radical generating system, as expected (23, 44). It is interesting to note, however, that the static-sample $TiCl_3$– and $FeCl_2$–H_2O_2/substrate/**1** reaction-system studies previously cited (13*b*) did yield spin adducts sufficiently persistent for epr observation.

Table 6 summarizes the epr results obtained for all substrates susceptible to the enophilicity of **1**, i.e., each methacrylic monomer, CH_2=$C(CH_3)X$, yielded a spectrum fully interpretable in terms of one radical, and this radical, a nitroxide, was that expected to form via the nonphotolytic "ene" addition/oxidation mechanism (15).

The small single proton coupling in **48–51** is attributable to the δ-CH proton oriented toward the oxygen of the nitroxide function. Others have proposed a similar type of 1,6 interaction

Can. J. Chem. Downloaded from www.nrcresearchpress.com by 93.93.197.157 on 09/07/12
For personal use only.

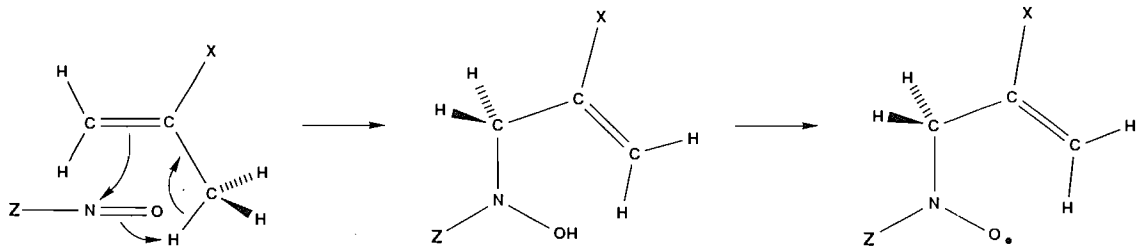

54

in a quasi-six-membered cyclic system to explain hyperfine splitting in certain iminoxyl radicals (45). Although the representation of **54** shown here has the quasi-six-membered ring containing the NO· group, the β-, γ-, and δ-carbons, and one δ-CH hydrogen atom planar, the ring probably is twisted about the β-C/γ-C bond because the β-CH hydrogens are magnetically inequivalent. This is not unreasonable, as construction of models supports the presence of ring strain in a planar configuration.

The spectral intensity of the radicals **48–51** changed less than 10% over the 3-h period of the experiment. Though not formed by a spin-trapping reaction, **48–51** are of the Z—N(O·)—R type and exhibit splittings characteristic of that structure (see Tables 2, 3, and 5); therefore their presence could easily interfere with the detection and characterization of concurrently generated spin adducts, pointing to an important potential limitation in the use of **1**. Chatgilialoglu and Ingold (15) have stressed the caution necessary when observing "spontaneous" reactions between nitroso compounds and olefins, for, in many but not all cases studied, they found that such reactions occurred only in the presence of light. We observed radical formation between **1** and all methacrylic monomers studied both in the presence and the absence of light, indicating that **1** can yield nitroxides by nonphotolytic processes, supporting the "ene" addition/oxidation mechanism (15, 16, 46) of nitroxide formation.

Can. J. Chem. Downloaded from www.nrcresearchpress.com by 93.93.197.157 on 09/07/12
For personal use only.

Acknowledgements

We thank Dr. Kirk R. Maples, now of the National Institute of Environment Health Sciences, for useful discussions. We acknowledge with thanks gift samples of **7–13** from Rohm and Haas Company.

1. E. G. Janzen and B. J. Blackburn. J. Am. Chem. Soc. **90**, 5909 (1968); G. R. Chalfont, M. J. Perkins, and A. Horsfield. J. Am. Chem. Soc. **90**, 7141 (1968); C. Lagercrantz and S. Forschult. Nature, **218**, 1247 (1968).
2. D. Griller and K. U. Ingold. Acc. Chem. Res. **9**, 13 (1976).
3. C. A. Evans. Aldrichimica Acta, **12**, 23 (1979).
4. M. J. Perkins. Adv. Phys. Org. Chem. **17**, 1 (1980).
5. E. G. Janzen. Acc. Chem. Res. **4**, 31 (1971).
6. E. G. Janzen. Free Radicals Biol. **4**, 115 (1980).
7. R. P. Mason. *In* Spin labeling in pharmacology. *Edited by* J. L. Holtzman. Academic Press, New York. 1984. Chap. 2; R. P. Mason and C. Mottley. Electron Spin Reson. (Specialist Periodical Reports), **10B**, 185 (1987).
8. G. R. Buettner. *In* Superoxide dismutase. Vol. 2. *Edited by* L. W. Oberly, CRC Press, Inc., Boca Raton, FL. 1982. p. 63.
9. C. Lagercrantz. J. Phys. Chem. **75**, 3466 (1971).
10. H. Kaur, K. H. W. Leung, and M. J. Perkins. J. Chem. Soc. Chem. Commun. 142 (1981).
11. K. V. Ettinger, A. R. Forrester, and C. H. Hunter. Can. J. Chem. **60**, 1549 (1982).
12. R. A. Floyd and I. Zs-Nagy. Biochim. Biophys. Acta, **709**, 94 (1984).
13. (*a*) T. Ozawa and A. Hanaki. Biochem. Biophys. Res. Commun. **136**, 657 (1986); (*b*) Bull. Chem. Soc. Jpn. **60**, 2304 (1987).
14. K. Stolze and R. P. Mason. Biochem. Biophys. Res. Commun. **143**, 941 (1987).
15. C. Chatgilialoglu and K. U. Ingold. J. Am. Chem. Soc. **103**, 4833 (1981).
16. A. B. Sullivan. J. Org. Chem. **31**, 2811 (1966).
17. P. Smith, K. R. Maples, C. C. Devlin, and G. McCrohan. J. Magn. Reson. **67**, 539 (1986).
18. D. C. Borg. Nature, **201**, 1087 (1964).
19. P. Smith and K. R. Maples. J. Magn. Reson. **65**, 491 (1985).
20. L. B. Gilman. Ph.D. dissertation, Duke University, Durham, NC. 1975.
21. M. F. R. Mulcahy, J. R. Steven, and J. C. Ward. Aust. J. Chem. **18**, 1177 (1965).
22. T. Shiga. J. Phys. Chem. **69**, 3805 (1965).
23. G. Czapski, A. Samuni, and D. Meisel. J. Phys. Chem. **75**, 3271 (1971).
24. C. Walling. Acc. Chem. Res. **8**, 125 (1975).
25. R. J. Faber and G. K. Fraenkel. J. Chem. Phys. **47**, 2462 (1967).
26. J. Q. Adams, S. W. Nicksic, and J. R. Thomas. J. Chem. Phys. **45**, 654 (1966).
27. P. Smith, J. T. Pearson, P. B. Wood, and T. C. Smith. J. Chem. Phys. **43**, 1535 (1965).
28. P. Smith, J. T. Pearson, and R. V. Tsina. Can. J. Chem. **44**, 753 (1966); P. Smith and P. B. Wood. Can. J. Chem. **45**, 649 (1967).
29. R. O. C. Norman and P. R. West. Chem. Soc. B, **389** (1969).
30. A. J. Dobbs, B. C. Gilbert, and R. O. C. Norman. J. Chem. Soc. A, **124** (1971).
31. K. Takakura and B. Rånby. J. Polymer Sci. C, **22**, 939 (1969).
32. H. Fischer. Z. Naturforsch. A: Astrophys. Phys. Phys. Chem. **19A**, 866 (1964).
33. B. Rånby and J. F. Rabek. *In* ESR spectroscopy in polymer research. Springer Verlag, New York. 1977.
34. J. March. *In* Advanced organic chemistry. 3rd ed., John Wiley, New York. 1985. Chap. 5.
35. P. S. Engel. Chem. Rev. **80**, 99 (1980).
36. P. B. Ayscough, B. R. Brooks, and H. E. Evans. J. Phys. Chem. **68**, 3889 (1964).
37. P. Smith and S. Carbone. J. Am. Chem. Soc. **81**, 6174 (1959).
38. M. Talât-Erben and S. Bywater. J. Am. Chem. Soc. **77**, 3710 (1955); **77**, 3712 (1955).
39. J. C. Bevington, P. F. Fridd, and B. J. Tabner. J. Chem. Soc. Perkin Trans. 2, 1389 (1982).
40. J. A. Kerr. Chem. Rev. **66**, 465 (1966).
41. E. G. Janzen. Acc. Chem. Res. **2**, 279 (1969).
42. E. G. Janzen. Top. Stereochem. **6**, 177 (1971).
43. E. G. Janzen and J.I-P. Liu. J. Magn. Reson. **9**, 510 (1973).
44. B. C. Gilbert, R. O. C. Norman, and R. C. Sealy. J. Chem. Soc. Perkin Trans. 2, 824 (1974).
45. B. C. Gilbert, R. O. C. Norman, and D. C. Price. Proc. Chem. Soc. 234 (1964).
46. H. M. R. Hoffman. Agnew. Chem. Int. Ed. Engl. **8**, 556 (1969).

2,6-Di-*tert*-butylpyridine: an unusually weak base in dimethylsulfoxide

ROBERT L. BENOIT, MONIQUE FRÉCHETTE, AND DIANE LEFEBVRE

Département de chimie, Université de Montréal, C.P. 6128, Succursale A, Montréal (Québec), Canada H3C 3J7

Received September 30, 1987

ROBERT L. BENOIT, MONIQUE FRÉCHETTE, and DIANE LEFEBVRE. Can. J. Chem. **66**, 1159 (1988).

The ionization constants of the conjugate acids BH^+ of pyridine, 2-picoline, 2,6-lutidine, and 2,6-di-*tert*-butylpyridine (DTBP) have been determined in Me_2SO. The partition coefficients of the bases B between Me_2SO and water, and the enthalpies of solution and protonation of B in Me_2SO have also been obtained. In contrast to its high basicity in the gas phase, DTBP is an abnormally weak base in Me_2SO ($pK = 0.81$). The factors responsible for this very low basicity are analyzed by considering correlations between the gas-phase, Me_2SO, and aqueous basicities of B and by comparing the transfer parameters for B and BH^+. The solvation of DTBP and $DTBPH^+$ in Me_2SO and in water differs. While the solvation of DTBP in Me_2SO is normal, the enthalpy of solution of $DTBPH^+$ in Me_2SO is abnormally low and close to that of a cation whose solvation is nonspecific. This suggests a much reduced H-bonding between sterically hindered $DTBPH^+$ and the large Me_2SO solvent molecule.

ROBERT L. BENOIT, MONIQUE FRÉCHETTE et DIANE LEFEBVRE. Can. J. Chem. **66**, 1159 (1988).

On a déterminé les constantes d'ionisation dans le Me_2SO des acides conjugués BH^+ de la pyridine, de la picoline-2, de la lutidine-2,6 et de la di-*tertio*-butyl-2,6 pyridine (DTBP). On a aussi obtenu les coefficients de partage des bases B entre le Me_2SO et l'eau, et les chaleurs de solution et de protonation de B dans le Me_2SO. En opposition à sa basicité élevée en phase gazeuse, la DTBP est une base anormalement faible dans le Me_2SO ($pK = 0.81$). On analyse les facteurs responsables de cette très faible basicité en considérant des corrélations entre les basicités de B en phase gazeuse, dans le Me_2SO et dans l'eau, et en comparant les paramètres de transfert de B et BH^+. La solvatation de DTBP et $DTBPH^+$ dans le Me_2SO et l'eau diffère. Alors que la solvatation de DTBP dans le Me_2SO est normale, l'enthalpie de solution de $DTBPH^+$ dans le Me_2SO est anormalement basse et proche de celle d'un cation dont la solvatation est non-spécifique. Ceci suggère une liaison-H très affaiblie entre $DTBPH^+$, empêchée stériquement, et la grosse molécule du solvant Me_2SO.

Can. J. Chem. Downloaded from www.nrcresearchpress.com by 93.93.197.157 on 09/07/12
For personal use only.

Since it was first synthesized by Brown and Kanner (1), 2,6-di-*tert*-butylpyridine (DTBP) has attracted the interest of many researchers because of its unusually low basicity: with its two alkyl substituents, DTBP is nevertheless a weaker base than unsubstituted pyridine in aqueous solution. Brown and Kanner (1) and others (2) proposed that the abnormally low basicity of DTBP was caused by steric hindrance to hydration of $DTBPH^+$. Recent determinations of gas-phase proton affinities of DTBP and other alkyl-substituted pyridines showed that the basicity of DTBP in the gas phase was normal (2, 3), which confirmed that its weak basicity in water was due to solvent effects on DTBP and (or) $DTBPH^+$. A complete analysis of the thermodynamic cycles linking the protonation processes of DTBP and other pyridines in the gas phase and in aqueous solution led Arnett and Chawla (2) to conclude that there was indeed some hindrance to the hydration of $DTBPH^+$ as reflected in its abnormally low enthalpy of hydration. However, more recently Hopkins *et al.* (3), after investigating the protonation of additional *tert*-butylpyridines and repeating the thermodynamic determinations of Arnett and Chawla (2) of DTBP, concluded from their new data that the hydration enthalpy of $DTBPH^+$ was normal but that the corresponding entropy was abnormal; they suggested that the rotation of the water molecule attached to $DTBPH^+$ and of $-CMe_3$ was restricted. These results and conclusions were in agreement with the gas phase studies of Moet-Ner and Sieck (4) on the attachment of one water molecule to a series of pyridinium cations including $DTBPH^+$.

Since, as we have recently shown (5), contrasting solution and protonation thermodynamic data for bases in water and in a nonaqueous solvent such as dimethylsulfoxide (Me_2SO) can lead to new insights into solute–solvent H-bonding interactions, we have now determined the data needed to compare the behaviour of DTBP in both water and Me_2SO. We have also included pyridine (Py), 2-picoline (MePy), and 2,6-lutidine (Me_2Py) in our investigation to broaden the basis of our comparisons, and we are presenting here the results of our potentiometric, spectroscopic (uv and nmr), and calorimetric study.

Experimental

Materials

Pyridine (Anachemia) was used as received. DTBP (Aldrich), MePy (Aldrich), and Me_2Py (Eastman Kodak) were distilled once or twice; Me_2Py was kept under vacuum in a desiccator over P_4O_{10}. The purity of the bases was checked by titration with standardized $HClO_4$ 0.1 M in HCH_3COO and found to be 100.0 ± 0.4% (Py), 98 ± 1% (DTBP), 99.2 ± 0.1% (MePy), and 98 ± 1% (Me_2Py) respectively. Me_2SO (BDH, analytical reagent (0.20% water) and Anachemia, A.C.S. reagent (0.14% water)), *n*-heptane (American Chemicals "all glass redistilled"), and trifluromethanesulfonic acid (HCF_3SO_3) (Aldrich) were used without further purification. Tetraethylammonium perchlorate (Eastman Kodak) was recrystallized in a 4:1 water–ethanol mixture and dried under vacuum at room temperature.

pK_a determinations

Potentiometric titrations of Me_2SO solutions of the pyridines ((1×10^{-2})–0.4 M) with a standardized solution of HCF_3SO_3 in Me_2SO were carried out at 25.0°C. A constant ionic strength was maintained by making the pyridine solutions initially 0.100 M in Et_4NClO_4. The potentiometric apparatus used as well as the calibration of the glass electrode with standardized HCF_3SO_3 have been previously described (6).

A spectrophotometric procedure was also used to determine the pK_{as} of $DTBPH^+$ in Me_2SO. The absorbances of $(0.7–3.0) \times 10^{-4}$ M solutions of DTBP in 0–1 M HCF_3SO in Me_2SO were measured with a PMQ II Zeiss spectrophotometer using 1-cm thermostated cells at 25.0°C. The ionic strength was maintained at 0.1 M by adding Et_4NClO_4 to solutions with acid concentrations lower than 0.1 M. The values of K and the molar absorptivities "ε" of DTBP were obtained from the absorbances measured at 8 wavelengths between 265 and 285 nm using the graphical method of Rossotti and Rossotti (7).

The protonation of DTBP was also studied by ^{13}C nmr using a Bruker WP-80 spectrometer operating at 20.2 MHz (5). ^{13}C spectra in Me_2SO were taken on 0.14–0.29 M solutions of DTBP to which HCF_3SO_3 was added to give acid to base molar ratios from 0 to 30.5 and thus protonate up to 70% of DTBP. The value of K_{as} was calculated from the chemical shift data by the graphical procedure of Rossotti and Rosssotti (7).

Solubility and partition coefficient determinations

The solubility of DTBP in Me_2SO was determined potentiometrical-

Can. J. Chem. Downloaded from www.nrcresearchpress.com by 93.93.197.157 on 09/07/12
For personal use only.

ly. Three separate determinations were made by titrating the saturated solutions with standardized $HClO_4$ 0.1 M in HCH_3COO.

We determined the partition coefficients of Py, MePy, and Me_2Py between water and Me_2SO using *n*-heptane as the common immiscible reference solvent. The partition coefficients of the bases between *n*-heptane and Me_2SO, $P_{h/s}$, and *n*-heptane and water, $P_{h/w}$, were obtained by determining potentiometrically the concentration of each base in Me_2SO and water after equilibration of 5–17 separate 20-mL samples of 0.1–0.95 M solutions in Me_2SO or water with 2, 5, 10, or 20 mL of *n*-heptane. The equilibrium concentration of the bases in *n*-heptane was obtained by difference. The potentiometric titrations of the base solutions were made with $HClO_4$ in HCH_3COO for aqueous Py and MePy and the Me_2SO solution of Me_2Py. The aqueous solution of Me_2Py was titrated with 0.1 or 0.05 M HCl. The base concentrations in *n*-heptane were plotted against the base concentrations in the Me_2SO or aqueous phases to give, by a least-squares procedure, $P_{h/s}$ and $P_{h/w}$ respectively for Py, MePy, and Me_2Py.

Calorimetric measurements

The heats of solution of the liquid pyridines in Me_2SO were measured at 25.00°C with a LKB model 8725-2 isoperibol calorimeter as previously described (6), the amount of the bases dissolved being known from the weight of the glass ampoules. For each base, three to eight separate determinations were made at different concentrations by dissolving (0.2–7.8) $\times 10^{-3}$ mol of base in 100 mL of solvent. The total heats of neutralization were obtained similarly by dissolving (0.25–1.1) $\times 10^{-3}$ mol MePy, Me_2Py, and DTBP in 100 mL of 0.1 M HCF_3SO_3 in Me_2SO.

Results

Ionization constants

The ionization constants K_{as} of the conjugate acids BH^+ in Me_2SO were calculated from the potentiometric neutralization and calibration data by using the program previously described (6). The values of pK_{as} are given in Table 1 together with the corresponding aqueous values pK_{aw} of Hopkins and co-workers (3, 6, 12, 13). No corrections were made for the effect of ionic strength, which would be small for such protonation reactions. For DTBP, pK_{as} was also obtained from the uv absorbance data. Plots of $(\varepsilon - \varepsilon_B)/[H^+]$ were linear, the slopes gave $1/K_{as}$ and the intercept $\varepsilon_{BH^+}/K_{as}$. The pK_{as} value, 0.81 ± 0.07, is in good agreement with the potentiometric value, even though the ionic strength varied from 0.1 to 1.00. The ^{13}C nmr data were treated in a similar manner. However, because of the high DTBP concentration used, corrections had to be made to obtain $[H^+]$ so that the nmr pK_{as} value is less precise but still in fair agreement with the other values. Interestingly, the ^{13}C signals, particularly the C-4 one, were broader when the solutions contained both DTBP and $DTBPH^+$. The slower exchange might indicate some unusual solvent effects on DTBP and $DTBPH^+$, though likely not as marked as for 1,8-bis(dimethylamino)naphthalene and its conjugate acid where separate signals were obtained (5).

Free energies of transfer from water to Me_2SO

The free energies of transfer, $\Delta G^0_{ws}(B)$ (hypothetical 1 M solution as standard state) were obtained for DTBP from its solubility in water as determined by Hopkins *et al.* (3) and our experimental solubility in Me_2SO, 0.29 ± 0.01 M, assuming ideal behaviour. For the more soluble bases Py, MePy, and Me_2Py, ΔG^0_{ws} was calculated from the partition coefficient $P_{s/w}$ obtained by combining the partition coefficients $P_{h/s}$ between Me_2SO and *n*-heptane, which were respectively 0.165 ± 0.007 (Py), 0.368 ± 0.006 (MePy), 0.75 ± 0.06 (Me_2Py), and the partition coefficients $P_{h/w}$ between water and *n*-heptane, 0.36 ± 0.01 (Py,), 1.05 ± 0.03 (MePy), 4.7 ± 0.3 (Me_2Py).

The free energies of transfer of BH^+, $\Delta G^0_{ws}(BH^+)$ were calculated in turn by means of eq. [1] derived from the thermodynamic cycle relating the protonation reaction in water and Me_2SO:

[1] $\Delta G^0_{ws}(BH^+) = \Delta G^0_{ws}(B) + \Delta G^0_{ws}(H^+) + \Delta G^0_{ps} - \Delta G^0_{pw}$

ΔG^0_{ps} and ΔG^0_{pw} are the protonation energies in Me_2SO and water calculated from pK_{2s} and pK_{2w}. The value of $\Delta G^0_{ws}(H^+)$, −19 kJ mol^{-1}, is based on the tetraphenylarsonium-tetraphenylborate (tatb) assumption (8). Our free energies of transfer are given in Table 2.

TABLE 1. Ionization constants K_{2s} and K_{2w} of BH^+ ions at 25°C

BH^+	pK_{as} Me_2SO	pK_{aw} H_2O	$\Delta = pK_{as} - pK_{aw}$	$\Delta G_{pg}(B)$[e] (kJ mol^{-1})
PyH^+[a]	3.45	5.17	−1.72	−889.5
$MePyH^+$	4.01 ± 0.01	5.97[b]	−1.95	−903.3
Me_2PyH^+	4.46 ± 0.03	6.75[b]	−2.29	−917.2
$DTBPH^+$	0.81 ± 0.07[d]	4.95[c]	−4.14	−933.9
	1.0 ± 0.2[d]			
	0.97 ± 0.08[d]			

[a]Reference 6.
[b]References 12, 13.
[c]Reference 3.
[d]Obtained from the uv, potentiometric, and ^{13}C nmr data, respectively.
[e]Reference 4.

TABLE 2. Free energies of transfer[a] (kJ mol^{-1}) of B and BH^+ from water to Me_2SO at 25°C

B	ΔG^0_{ws} (B)	ΔG^0_{ws} (BH^+)
Py	−1.9 ± 0.2	−10.9
MePy	−2.6 ± 0.1	−10.5
Me_2Py	−4.6 ± 0.4	−10.6
DTBP	−22.0	−17.8

[a]Standard state as hypothetical 1 M solution.

Enthalpies of solution and protonation

The values of the bases' enthalpy of solution in water, ΔH^0_w, and of protonation in water, ΔH^0_{pw}, were taken from the literature (3, 9). The plots of the heats of solution of DTBP, MePy, and Me_2Py in Me_2SO and Me_2SO solutions of 0.1 M HCF_3SO_3 against the number of moles dissolved were linear, and the least-squares slopes gave $\Delta H^0_s(B)$ and $\Delta H^0_{ns}(B)$ according to

[2] B(c or l) = B(s)

[3] B(c or l) + H^+(s) = BH^+(s)

A correction was applied for the incomplete protonation of DTBP. The heat of protonation ΔH^0_{ps} corresponding to

[4] B(s) + H^+(s) = BH^+(s)

was obtained by subtracting $\Delta H^0_s(B)$ from $\Delta H^0_{ns}(B)$. The enthalpies of solution and protonation in water and Me_2SO are listed in table 3 together with protonation gas-phase values, ΔH^0_{pg}, taken from a published account (4).

Enthalpies of transfer from water to Me_2SO

The enthalpies of transfer of the bases from water to Me_2SO, $\Delta H^0_{ws}(B)$, were calculated from their enthalpies of solution in both solvents. $\Delta H^0_{ws}(BH^+)$ was obtained from an equation similar to [1] relating the protonation process in both solvents. The value of $\Delta H^0_{ws}(H^+)$, −25.5 kJ mol^{-1}, is based on the tatb

TABLE 3. Enthalpies of solution and enthalpies of protonation (kJ mol^{-1}) of B at 25°C

B	ΔH^0_s(B) Me_2SO	ΔH^0_w(B) H_2O	ΔH^0_{ps} Me_2SO	ΔH^0_{pw} H_2O	$\Delta H^{0\,d}_{pg}$ gas phase
Py	1.17[a]	−9.7[b]	−27.7[a]	−20.1[b]	−922.2
MePy	1.796 ± 0.0009	−12.6[b]	−29.2 ± 0.3	−26.0[b]	−936.0
Me_2Py	2.530 ± 0.007	−15.9[b]	−32.9 ± 0.3	−30.3[b]	−950.2
DTBP	10.7 ± 0.6	4.2[c]	−11 ± 2	−35.6[c]	−966.5

[a]Reference 14.
[b]Reference 9.
[c]Reference 3.
[d]Calculated from the values taken from ref. 4 and with ΔH^0_{pg} for pyridine from ref. 3.

TABLE 4. Free energies and enthalpies of transfer (kJ mol^{-1}) of B from the gas phase to Me_2SO and water, and from water to Me_2SO at 25°C

B	ΔG^0_{gs} (B)	ΔG^0_{gw} (B)	ΔH^0_{gs} (B)	ΔH^0_{gw} (B)	ΔH^0_{ws} (B)
Py	−13.6	−11.7[a]	−38.1	−49.0[a]	10.9
MePy	−14.0	−11.4[b]	−39.7	−54.1[c]	14.4
Me_2Py	−15.9	−11.3[b]	−42.6	−61.0[c]	18.4
DTBP	−16.6	5.4[a]	−45.8	−52.3[a]	6.5

[a]Reference 3.
[b]Calculated from the combined values taken from refs. 2 and 3.
[c]Calculated from the combined values taken from refs. 3 and 9.

TABLE 5. Free energies and enthalpies of transfer (kJ mol^{-1}) of BH^+ from the gas phase to Me_2SO and water, and from water to Me_2SO at 25°C

BH^+	ΔG^0_{gs} (BH^+)	ΔG^0_{gw} (BH^+)	ΔH^0_{gs} (BH^+)	ΔH^0_{gw} (BH^+)	ΔH^0_{ws} (BH^+)
PyH^+	−254.7	−243.7	−298.8	−276.6	−22.2
$MePyH^+$	−244.5	−234.2	−288.1	−273.8	−14.3
Me_2PyH^+	−235.1	−224.6	−280.5	−270.8	−9.7
$DTBPH^+$	−198.9	−181.0	−245.5	−251.1	+5.6

extrathermodynamic assumption (8). The values of ΔH^0_{ws} are given in Tables 4 and 5.

Transfers from the gas phase

The thermodynamic functions ΔP^0_{gw}(B) for the transfer of B from the gas phase to water (Table 4) are from Hopkins *et al.* (3) (Py and DTBP) and Arnett *et al.* (9) (MePy and Me_2Py). The values of $\Delta P^0_{gw}(BH^+)$ given in Table 5 are calculated by means of eq. [5] derived from the thermodynamic cycle relating the protonation in the gas phase and water:

$$[5]\quad \Delta P^0_{gw}(BH^+) = \Delta P^0_{gw}(B) + \Delta P^0_{gw}(H^+) + \Delta P^0_{pw} - \Delta P^0_{pg}$$

ΔP^0_{pw} and ΔP^0_{pg} are the protonation functions in water and in the gas phase respectively (Tables 1 and 3). The values of $\Delta G^0_{gw}(H^+) = -1092.0$ kJ mol^{-1} and that of $\Delta H^0_{gw}(H^+) = -1129.7$ kJ mol^{-1} are taken from ref. 8. The functions for the gas phase – Me_2SO transfers, ΔP^0_{gs}, given in Tables 4 and 5, are obtained from the corresponding ΔP^0_{gw} values and the water – Me_2SO transfer functions ΔP^0_{ws} listed in Tables 2, 4, and 5.

Discussion

It is clear from Table 1 that the upward pK_s trend that is observed when passing from Py to the alkylpyridines, MePy and Me_2Py, is not followed by DTBP; even more than in water, DTBP is an unusually weak base in Me_2SO, since its pK_{as} is some 2.5 units lower than the pK_{as} of Py while the corresponding pK_{aw} difference is only 0.2. The factors responsible for the very weak basicity of DTBP in Me_2SO can best be analyzed, first, by considering different types of correlation between the aqueous, Me_2SO, and gas phase basicities of Py, MePy, Me_2Py, and DTBP and then by comparing the transfer parameters for the bases B and their conjugate acids BH^+.

Correlation of solution and gas phase basicities

Looking at the correlations between Me_2SO and the aqueous basicities, we first note that for Py, MePy, and Me_2Py the pK_{as} are linearly related to pK_{aw} with $pK_{as} = 0.65\ pK_{aw}$ but that the point for DTBP deviates from the line by nearly 2.3 pK units. Then, in the plot[1] of ΔH^0_{ps} against ΔH^0_{pw}, the DTBP point is also off the line by some 25 kJ mol^{-1}. However, given that the basicity of DTBP is abnormal in water, these results do not necessarily indicate that DTBP behaves abnormally in Me_2SO. More definite conclusions can be drawn by comparing gas phase and Me_2SO basicities, since DTBP basicity is normal in the gas phase. In the plot[1] of the gas phase protonation enthalpy ΔH^0_{pg} vs. the Me_2SO protonation free energy ΔG^0_{ps}, the point for DTBP deviates from the line by some 22 kJ mol^{-1} while in the plot of ΔH^0_{pg} vs. ΔH^0_{ps}, the DTBP point is also some 24 kJ mol^{-1} off the line. We conclude from both results that the abnormally low basicity of DTBP in Me_2SO is primarily due to an enthalpy

[1]Not shown here.

Can. J. Chem. Downloaded from www.nrcresearchpress.com by 93.93.197.157 on 09/07/12
For personal use only.

effect with possibly an additional entropy effect. An enthalpy effect was also found to be responsible for the unusual basicity of DTBP in alcohol–water mixtures (10), but in water there was only an entropy effect (3).

We will now compare and contrast the thermodynamic parameters for the transfer of the pyridines B and their conjugate acids BH^+ from the gas phase to Me_2SO and water to analyze further the enthalpy effect.

Transfer of pyridines

First, the ΔG^0_{gs} and ΔH^0_{gs} parameters for the transfer of the pyridines to Me_2SO in Table 4 show a smooth trend towards higher exothermicity when passing from Py to MePy, Me_2Py, *and* DTBP so that there is at least no large abnormality in the solution of DTBP. This is in opposition to its solution behaviour in water where both the corresponding ΔG^0_{gw} and ΔH^0_{gw} exhibit a discontinuity in the trend observed for the other pyridines, the exothermicity being lower than predicted.

These different patterns of solvation for DTBP in Me_2SO and water are of course reflected in the broken trends of the water – Me_2SO transfer parameters ΔG^0_{ws} and ΔH^0_{ws} for the pyridines (Tables 2, 4). The indicated unusual destabilization of DTBP in water may result from weaker H-bonding interactions with the pyridine N because of steric hindrance of the *tert*-butyl groups or because of hydrophobic interactions of the same groups (3). It is worth noting that in the aliphatic series the water – Me_2SO transfer enthalpy of $-CH_3$ groups corresponds to an "extra stabilization" in water (11), as is observed here when passing from Py to MePy and Me_2Py, but not for DTBP, suggesting that poor H-bonding may be the dominant factor in the weaker than expected solvation of DTBP in water.

Transfer of pyridinium cations

The free energy and enthalpy of transfer of BH^+ from the gas phase to Me_2SO in Table 5 show some decrease in exothermicity from PyH^+ to $MePyH^+$ and Me_2PyH^+, and then a much larger decrease for $DTBPH^+$. For the gas phase – water transfers, the picture is different. There is a smooth decrease in exothermicity of ΔH^0_{gw} from PyH^+ to $DTBPH^+$, but a sharp decrease of ΔH^0_{gw} for $DTBPH^+$ and a corresponding large change of ΔS^0_{gw}. Thus while in water it is the entropy of solution of $DTBPH^+$ which is abnormal, as already concluded by Hopkins *et al.* (3) from their analysis of the parameters for a series of *tert*-butyl pyridines, in Me_2SO it is the enthalpy of solution of $DTBPH^+$ which appears to be abnormally low. We therefore suggest that there is a much reduced H-bonding between the large Me_2SO molecule and the sterically hindered $DTBPH^+$ cation. Actually, the solvation enthalpy of $DTBPH^+$ in Me_2SO, -245 kJ mol^{-1}, is close to that of PSH^+ (PS standing for 1,8-bis(dimethylamino)naphthalene), -254 kJ mol^{-1}, whose solvation in Me_2SO appears to be nonspecific (5).

The variations in the pyridine series of the water–Me_2SO transfer parameters $\Delta G^0_{ws} - \Delta H^0_{ws}$ (Tables 2, 4, 5) reflect, of course, the combined changes of $\Delta G^0_{gw} - \Delta H^0_{gw}$ and $\Delta G^0_{gs} - \Delta H^0_{gs}$ so that a direct interpretation would be difficult. Nevertheless, it is interesting to note that the ΔG^0_{ws} values for B and BH^+ (Table 2) show that the larger $pK_{as} - pK_{aw}$ difference observed with DTBP is largely due to a much stronger stabilization in Me_2SO of DTBP than of the other bases B.

To conclude, we can say that the unusually low basicity of DTBP in Me_2SO as evidenced by the sharp pK_{as} decrease to 0.81 (when passing from Py, MePy, and Me_2Py to DTBP) is mainly due to an abrupt decrease in the free energy and enthalpy of solvation of $DTBPH^+$ because of poor H-bonding to solvent molecules. In water, the more moderate pK_{aw} decrease observed for DTBP is caused by a low free energy of solvation of $DTBPH^+$, in turn linked to an abnormal solvation entropy as discussed by Hopkins *et al.* (3) but opposed, in part, by a less negative free energy of solvation of DTBP. As for the lower basicity of Py, MePy, and Me_2Py in Me_2SO than in water, the water–Me_2SO transfer functions show that this is mainly due to the superior basicity of Me_2SO ($\Delta G_{ws}(H^+) = -25$ kJ mol^{-1}) opposed by a lesser stabilization of BH^+ in Me_2SO ($\Delta G^0_{ws} \sim -10$ kJ mol^{-1}). Further work is being carried out on other substituted pyridines to extend the linear relationship found between pK_{2s} and pK_{2w} and to ascertain to what extent the representative points off the correlation line correspond to pyridines with unusual interactions of B and (or) BH^+ with the solvents, as we have found for DTBP.

Acknowledgements

We wish to acknowledge a grant and a scholarship (D.L.) from the Natural Sciences and Engineering Research Council of Canada and financial assistance from the Ministère de l'Éducation. We also thank Professor E. Buncel for his interest in this research and for the gift of MePy and Me_2Py.

1. H. C. Brown and B. Kanner. J. Am. Chem. Soc. **75**, 3865 (1953).
2. E. M. Arnett and B. Chawla. J. Am. Chem. Soc. **101**, 7141 (1979).
3. H. P. Hopkins, D. V. Jahagirdar, P. S. Moulik, D. H. Aue, H. M. Webb, W. R. Davidson, and M. D. Pedley. J. Am. Chem. soc. **106**, 4341 (1984).
4. M. Meot-Ner and L. W. Sieck. J. Am. Chem. Soc. **105**, 2956 (1983).
5. R. L. Benoit, D. Lefebvre, and M. Fréchette. Can. J. Chem. **65**, 996 (1987); R. L. Benoit and M. Fréchette. Thermochim. Acta. In press.
6. R. L. Benoit, D. Boulet, L. Seguin, and M. Fréchette. Can. J. Chem. **63**, 1228 (1985).
7. F. J. C. Rossotti and H. Rossotti. The determination of stability constants. Advanced Chemistry Series. McGraw–Hill, New York. 1961. p. 275.
8. R. L. Benoit and C. Louis. The chemistry of non-aqueous solvents. Vol. V. *Edited by* J. J. Lagowski. Academic Press, New York. 1978, and references therein.
9. E. M. Arnett, B. Chawla, L. Bell, M. Taagepera, W. J. Hehre, and R. W. Taft. J. Am. Chem. Soc. **99**, 5729 (1977).
10. H. P. Hopkins and S. Z. Ali. J. Am. Chem. Soc. **99**, 2069 (1977).
11. M. H. Abraham. J. Am. Chem. Soc. **104**, 2085 (1982), and references therein.
12. H. C. Brown and B. Kanner. J. Am. Chem. Soc. **88**, 986 (1966).
13. H. C. Brown and X. R. Mihm. J. Am. Chem. Soc. **77**, 1723 (1955).
14. R. L. Benoit, M. J. Mackinnon, and L. Bergeron. Can. J. Chem. **59**, 1501 (1981).

Can. J. Chem. Downloaded from www.nrcresearchpress.com by 93.93.197.157 on 09/07/12
For personal use only.

Reactions of 1,2-dehydropyrrolidin-5-one with 1,3-dienes. Synthesis of *dl*-gephyrotoxin 223AB[1]

OLIVER E. EDWARDS,[2] AUSTIN M. GREAVES,[3] AND WING-WAH SY[3]

Chemistry Division, National Research Council of Canada, 100 Sussex Drive, Ottawa, Ont., Canada K1A 0R6

Received August 6, 1987

OLIVER E. EDWARDS, AUSTIN M. GREAVES, and WING-WAH SY. Can. J. Chem. **66**, 1163 (1988).

Evidence is presented that the regiospecific and often stereospecific pseudo-Diels–Alder reactions of 1,3-dienes with *N*-acyl immonium salts, derived from 5-ethoxy-2-pyrrolidinone, are stepwise reactions. 6,7-Dehydroindolizidinones, unsaturated lactam esters, and new indene and furan derivatives are described. A synthesis of *dl*-gephyrotoxin 223AB (indolizidine 223AB) from *trans*-1,3-heptadiene was achieved.

OLIVER E. EDWARDS, AUSTIN M. GREAVES et WING-WAH SY. Can. J. Chem. **66**, 1163 (1988).

On présente des données qui suggèrent que les réactions de pseudo-Diels–Alder régiospécifiques et souvent stéréospécifiques dans dienes-1,3- avec les sels de *N*-acyl-immonium dérivés de l'éthoxy-5 pyrrolidinone-2 sont des réactions par étapes. On décrit des déhydro-6,7 indolizidinones, des esters lactames non-saturés ainsi que de nouveaux dérivés de l'indène et du furanne. On a réalisé une synthèse de la (*dl*)-géophyrotoxine 223AB (indolizidine 223AB) à partir de l'heptadiène-1,3-*trans*.

[Traduit par la revue]

Can. J. Chem. Downloaded from www.nrcresearchpress.com by 93.93.197.157 on 09/07/12
For personal use only.

The apparent Diels–Alder reactions of *N*-acylimines or their salts have been the subject of much study (*la–f* and references therein). The initial objective of the present research was to define the mildest conditions under which intermolecular cycloaddition of simple *N*-acylimines to 1,3-dienes would take place, to obtain products from sensitive dienes. However, despite our success in isolating a steroidal *N*-acylimine with hydrogen on the imine carbon (aldimine) (2) it appeared that simpler *N*-acylaldimines such as **1** are too reactive to be readily isolated (see, however, ref. 3 for more stable electronegatively substituted examples).

We hence attempted to isolate crystalline salts of 1,2-dehydropyrrolidin-2-one **1** using the action of acetyl chloride or acetyl perchlorate on the readily available 5-ethoxy-2-pyrrolidinone **2** (4). Again this failed, although reactions showed that these salts were undoubtedly formed (see method D below).

As a consequence we changed our objective to reaction of salts of **1**, generated *in situ*, with simple 1,3-dienes, with the hope of stereo-controlled natural product synthesis. Preliminary studies using **3** (R = OCHO) or **3** (R = $OCOCH_3$), derived from **2**, as sources of the corresponding salts of **1**, using heat or triethylamine failed to give Diels–Alder adducts with 2,3-dimethylbutadiene. Success was achieved using **2** or **3** with a variety of Brönsted or Lewis acids. Low to good yields of 6,7-dehydroindolizidin-3-ones were obtained from a variety of 1,3-dienes, in addition to monocyclic addition products. In this way a precurser to *dl*-gephyrotoxin 223AB (**4**) (5) and possible precursers for monomorine (**5**) (6) and dendroprimine (**6**) (7) were generated.

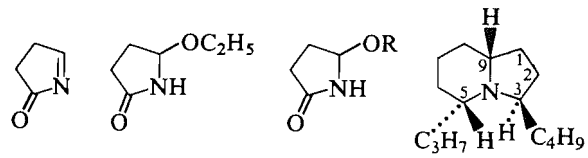

1 **2** **3** **4**

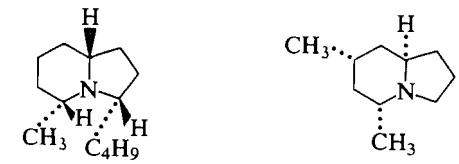

5 **6**

Results

The reaction of **2** with 1,3-dienes using methods A–E, but with some variation in relative concentrations (detailed in the Experimental), will be described under individual dienes. Method A used formic acid as solvent and catalyst; method B used methanesulfonic acid in dichloromethane; method C involved a stirred two-phase system of chloroform and 36% perchloric acid; method D used preformed salts of **1** in acetonitrile; method E was designed for use with acetoxydienes, using boron trifluoride etherate in acetic acid – acetic anhydride mixtures.

Three methods were used for reaction of **2** with isoprene. From reaction in formic acid (method A) an 80% yield of a mixture of two monocyclic formates was isolated. A negligible amount of the 6,7-dehydroindolizidinone **8** was produced. The ratio of the formates was roughly 2:1. That these had structures **7***a* and **7***b* followed from analysis, ^{1}H nmr spectra, and their nearly identical ^{13}C nmr spectra. Proton decoupling experiments showed that the vinyl hydrogen was coupled (J = 7 Hz) with the methylene carrying the formate group and that the 4′-methylene was only significantly coupled to H-5. Use of method C gave a 10% yield of 6,7-dehydro-6-methylindolizidin-3-one **8**. The complex mixture of monocyclic products was not separated. Using method D a 9% yield of **8** was isolated. The main products were monocyclic lactam dienes, which were not characterized.

The structure of **8** followed from its analysis, mass spectrum, and nmr spectra. The fact that the vinyl hydrogen and the 5-methylene of **8** were not coupled located the methyl group on C-6.

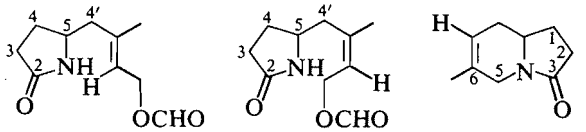

7*a* **7***b* **8**

[1]Issued as NRCC No. 28653.

[2]Present address: Department of Chemistry, Carleton University, Ottawa, Ont., Canada K1S 5B6.

[3]NRCC Research Associates, 1982–1983 (A.M.G.) and 1980–1982 (W.-W. S.).

Can. J. Chem. Downloaded from www.nrcresearchpress.com by 93.93.197.157 on 09/07/12
For personal use only.

The action of formic acid on *trans*-piperylene (method A) gave a 57% yield of monocyclic formates and an 11% yield of a dehydroindolizidinone. The formate mixture was partially separated on silica, giving a 1.5% yield of a crystalline isomer, mp 102°C. This was assigned structure **9** on the basis of analysis and spectra. Its ^{13}C nmr spectrum showed the presence of a secondary formate (doublet at 72.3 ppm) and its ^{1}H nmr spectrum had signals for a vinyl methyl group (doublet at δ 1.7). The other formates were oils, but after hydrolysis and separation on silica gel these gave two crystalline lactam alcohols. One with mp 117°C (35% yield) had a three-hydrogen doublet at δ 1.22, while the other with mp 72°C (23% yield) had a comparable doublet at δ 1.24, clearly indicating with the other spectral evidence that they were stereoisomers with gross structure **10** (R = H). Oxidation of both gave the same conjugated ketone **11**

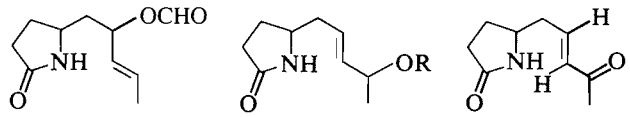

9 **10** **11**

showing that the isomerism was at the secondary alcohol center. The *J* value of 16 Hz for the vinyl hydrogen signal at δ 6.17 showed that the double bond had the *E* configuration. Thus the major formates had structure **10** (R = CHO).

The dehydroindolizidinone was one isomer that from its ^{1}H and ^{13}C nmr spectra clearly had gross structure **12**. By analogy to the chemical shift of the 5-methyl group near the plane of the carbonyl in one of the isomers from 3-methyl-1,3-pentadiene (see below) we conclude that this had an equatorial methyl *anti* to the 9-hydrogen as shown in **12**. It is thus a promising precurser for the synthesis of the trail pheromone of the Pharoah ant, monomorine **5** (6), and its C-3 epimer.

Reaction of **3** with *E*-1,3-heptadiene in formic acid (Method A) gave a 15–20% yield of the desired dehydroindolizidinone **13**, and a mixture of formates that were not separated. The use of method B resulted in a 25% yield of **13**, the remainder being a mixture of lactam dienes that was not further characterized.

The dehydroindolizidinone was one isomer. By analogy to the product from piperylene we assumed that the configuration was that shown in **13** (plus its mirror image) with the 5 and 9 hydrogens *syn* to each other. This was precisely what was needed as a precurser of the proposed structure for gephyrotoxin 223AB (5*a*). As outlined below, the synthesis succeeded (see 5*b* for a preliminary account) and the stereochemistry was confirmed by X-ray analysis (8).

Modest yields of an indolizidinone were obtained from 2,3-dimethylbutadiene. Method A gave a 16% yield of the bicyclic lactam **14** and a 43% yield of a mixture of formates **15***a* and **15***b*

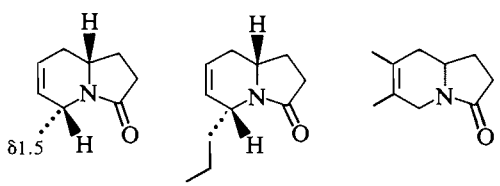

12 **13** **14**

(R = CHO). The ^{1}H nmr spectrum of the formates appeared to be that of one compound, but the ^{13}C nmr spectrum had 24 signals, showing the presence of two isomers. To our surprise, hydrolysis of the formates gave a sharp-melting lactam alcohol, mp 94–95°C. Again its ^{13}C nmr spectrum showed this to be a equimolar mixture of two very similar isomers. The ^{1}H nmr spectrum now showed the presence of two NH groups. We conclude that the isomeric alcohols were **15***a* and **15***b* (R = H) with NH signals at δ 7.7 and δ 8.5 respectively. A comparable yield of **14** (19%) was obtained using method B in benzene with *p*-toluenesulfonic acid.

trans-2-Methyl-1,3-pentadiene gave the highest yield (over 70%) of dehydroindolizidinone of any of the dienes studied, using method A. Although many other products were detected by tlc, only a small amount of formate ester was formed. The bicyclic product was a 1:1 mixture of isomers, separable on silica gel using a 1:1 acetone–hexane mixture. Their very similar ^{1}H and ^{13}C nmr spectra showed them to be stereoisomers with structures **16** and **17**. The assignment of configuration to

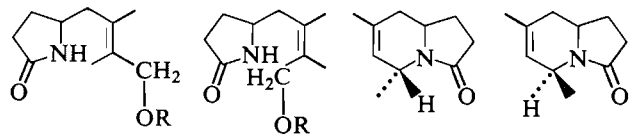

15*a* **15***b* **16** **17**

each was possible because the methyl group in the plane of the carbonyl was deshielded relative to that of it epimer (see **18** and **19**). The structure and stereochemistry of **19** make it a potentially valuable precurser of the orchid alkaloid dendroprimine **6** and its 7-epimer (7).

Reaction of *trans*-3-methyl-1,3-pentadiene with **2** following method A gave little, if any, bicyclic product. Monocyclic formates were produced in 75% yield. The ^{13}C nmr spectrum showed this to be a mixture consisting mainly of two closely related isomers. This and the ^{1}H nmr spectrum (see **20**) are consistent with this structure, with the isomers probably being the epimeric formates (see the piperylene case). Demonstrated couplings are indicated by double-headed arrows.

In reaction of *trans,trans*-2,4-hexadiene using method A, only minor amounts of bicyclic product and a 70% yield of monocyclic lactam formates were produced. The ^{13}C nmr spectrum of the formates showed this to contain two nearly identical stereoisomers. This and the ^{1}H nmr spectrum were consistent with structure **21**, with the isomers likely to be the epimeric formates. In contrast, the use of method C gave 20% of bicyclic product. Only one isomer was formed (^{13}C nmr). The chemical shift of the 5-methyl group and 5-hydrogen are close to those for

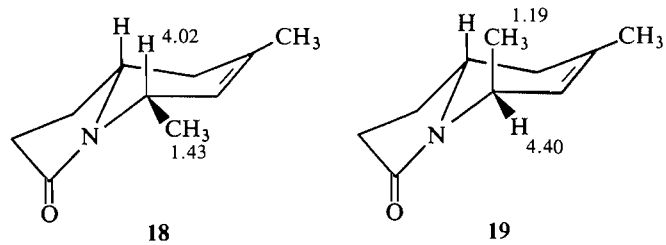

18 **19**

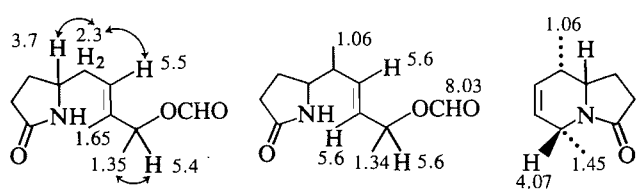

20 **21** **22**

18, hence we assign the stereochemistry shown in **22**, assuming retention of the original diene geometry.

When 1,3-cyclohexadiene reacted with **2** in formic acid following method A, both products of one-bond and of two-bond formation were observed. The one-bond products (42%) were a

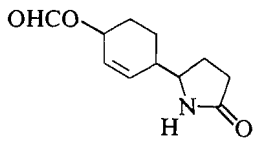

23

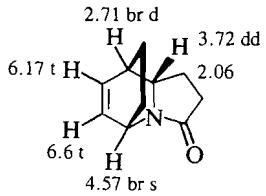

24

mixture of four isomeric formates. The spectra of the mixture were consistent with stereoisomers of structure **23**. In contrast, the two-bond product (40%) gave a single set of ^{13}C nmr signals, hence it was most probably one isomer. We assign structure and stereochemistry shown in **24** to it on the basis of analysis, spectra, and arguments based on maximum orbital overlap in the transition state for cyclization (see Discussion).

No dehydroindolizidinone was detected when 2,3-diphenyl-1,3-butadiene was treated with **2** in formic acid when method A was used. Instead the major products were a mixture of lactam formates and an indene derivative. The formates were hydrolysed, then the mixture separated in silica gel, giving a hydroxy lactam, mp 177°C (24%), and a second, mp 196°C (4%). The former had an uv spectrum (λ_{max} 234 nm, ε 11 800), analysis, and ^1H and ^{13}C nmr spectra consistent with structure **25**. Although the minor alcohol analysed for an isomer of **25**, its uv spectrum (λ_{max} 252 nm, ε 8440) and ^1H nmr signals were unusual. No ^{13}C nmr spectrum was obtained. Structure **26** seems a reasonable possibility, with the two vinyl hydrogens resonating at δ 4.59.

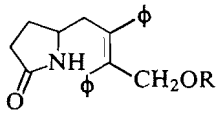

25

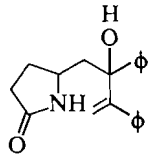

26

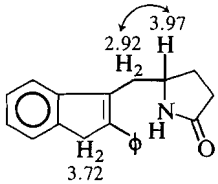

27

The most interesting product (14%) was assigned the substituted indene structure **27** on the basis of analysis, its uv spectrum (λ_{max} 289 nm, ε 14 800), and its ^1H nmr spectra and the coupling indicated by the double-headed arrow. The presence of five singlets between 134 and 145.8 ppm and eight doublets between 119.4 and 128.6 ppm in its ^{13}C nmr spectrum confirmed this structure.

The use of method C converted 2,3-diphenylbutadiene into a mixture of coupling products, which seemed to be dienes corresponding to proton elimination from original allylic cations.

As would be expected if the reaction were electrophilic attack by the *N*-acyl immonium ion from **1**, methods C and D on furan gave the 2-substituted derivative **28**, mp 82–83°C. The use of $Cu(BF_4)_2$ as catalyst in chloroform and **2** as reagent gave **28** and the product **29** of substitution on the two α positions. The simplicity of its ^1H nmr spectrum is suggestive of a *syn* relationship of the pyrrolidinone rings.

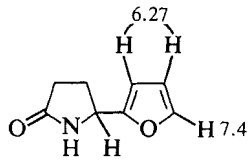

28

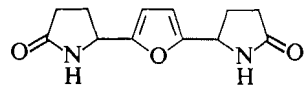

29

Using method E, 1-acetoxy-1,3-butadiene gave predominantly monocyclic coupling products. The major one (33%) was crystalline, mp 111–112°C. Its analysis and spectra were only consistent with structure **30** (see figure). Hydrogenation of **30** over Pd(C) gave mainly simple reduction of the double bond. The acylal hydrogen signal became a triplet (J = 5 Hz) at δ 6.8.

Reaction of the sensitive dienes 2-acetoxy- and 2-trimethylsilyloxy-1,3-butadiene with **2** and **3** (R = OAc) under a variety of conditions gave bad mixtures and no products were characterized.

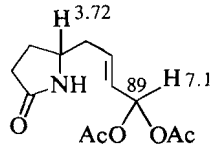

30

Synthesis of *dl*-gephyrotoxin 223AB (**4**) from the dehydroindolizidinone **13** was accomplished in 15% overall yield. The 6,7-dehydro-5-propylindolizidin-2-one **13** was reduced catalytically to **31**. This was transformed using small modifications of a sequence used by Hart and Tsai (8) into **4** (see Flowsheet). The major differences from their procedure was the use of Lawes-

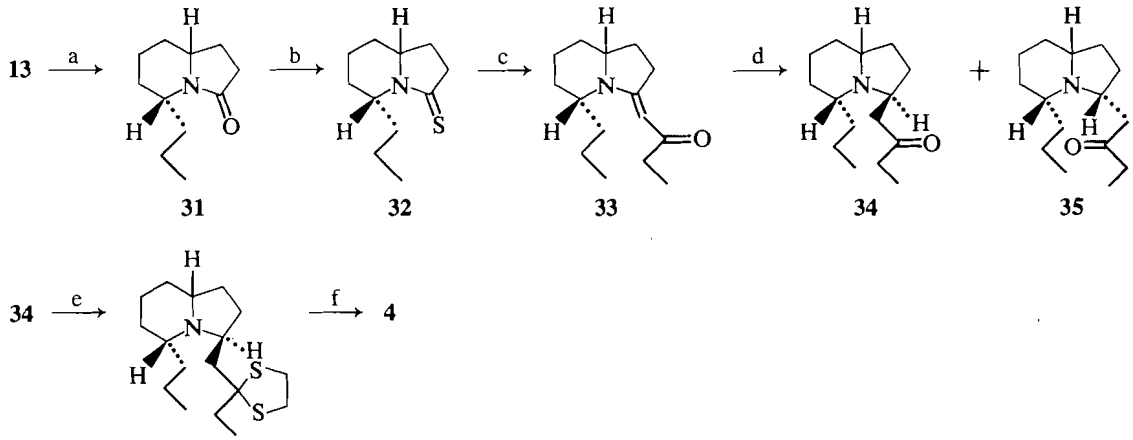

31 32 33 34 35

36

(a) H_2, Pd/C (b) Lawesson's reagent (c) 1-bromo-2-butanone, Et_3N
(d) $NaCNBH_3$,H^+ (e) $HSCH_2CH_2SH$ (f) Ni(R)

FLOWSHEET

Can. J. Chem. Downloaded from www.nrcresearchpress.com by 93.93.197.157 on 09/07/12
For personal use only.

son's reagent (9) to make the thiolactam **32** and of Raney nickel to desulfurize the dithioketal **36**. Both steps were efficient.

Two epimers at C-3 of the saturated keto lactams (**34** and **35**) were produced, distinguished by the fact that one gave a readily crystalline hydrochloride, while the salt of the other remained amorphous. However, it appeared that the amorphous salt was slowly converted into the crystalline one on standing. A mechanism exists for such an interconversion (eq. [1]), but the

[1] 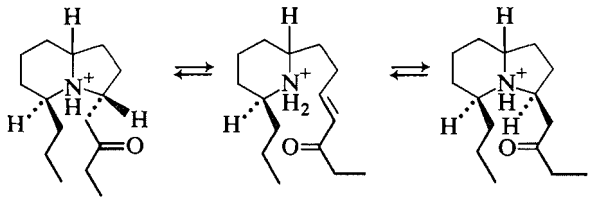

phenomenon has not been rigorously examined. The crystalline salt was used for subsequent reactions, and fortunately proved to have the desired stereochemistry shown in **34**.

The final product had the same gc retention time as authentic gephyrotoxin-223AB[4] and gave a ^{13}C nmr spectrum identical to that found by Professor Tokuyama and co-workers for natural toxin (10). The ^{13}C nmr spectrum differed significantly from that reported by Macdonald for his synthetic isomer (11) but agreed well with that reported by Royer and Husson (12) for their synthetic optically active toxin. The structure and relative stereochemistry of the hydrobromide of our synthetic base **4** was determined by Pryzbylska and Ahmed (13) using X-ray crystallography.

A parallel series of transformations has been used to convert **12** into analogues of **32** and **33**, thus paving the way to a synthesis of *dl*-monomorine (unpublished work in these laboratories).

Discussion

The apparent Diels–Alder reactions of *N*-acyl imines or their salts have been the subject of much study. Both intermolecular and intramolecular examples have been provided (1*a–f*, and references therein). In the cases where Brönsted or Lewis acids catalysed the reactions, highly polarized acyl immonium salts[5] were present, and the possibility exists that the reactions were stepwise cationic additions. Indeed, in our own cases, the production of varying amounts of products in which only one carbon–carbon bond had been formed, the internal attack on an aromatic ring (for 2,3-diphenyl-1,3-butadiene) (see also ref. 15), and the substitution of furan all argue for a stepwise process. The regiochemistry and stereochemistry of the Diels–Alder-type products can equally well be accounted for with this mechanism (see below). The high temperature intramolecular reactions of Weinreb and Levin (1e) (in the presence of the weak acetic acid) stand a better chance of being true Diels–Alder reactions of the transient *N*-acyl imines.

The regiochemistry of the formate ester production is consistent with attack of the *N*-acyl immonium ion on an unsubstituted end of the 1,3-diene, if available. In all unsymmetrical cases except that of isoprene, this appeared to give the thermodynamically more stable cation. However, calculation of the relative energy of the cations **A** and **B** from isoprene favored **B** by 6 kcal/mol.[6] But the formate arose from **A**, hence kinetic factors determined the site of attack.

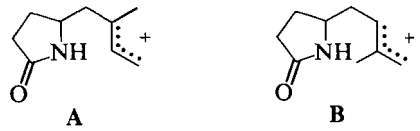

A **B**

The regiochemistry of dehydroindolizidinone formation, however, was consistent in all cases with attack on the least substituted end of the diene, leading to formation of the most substituted (lowest energy) delocalized allylic cation.

The yield of dehydroindolizidinones, using method A (formic acid), from the various dienes studied, varied from traces (isoprene) to over 70% (2-methyl-1,3-pentadiene). This is not simply a consequence of the rotamer populations in the diene. Herman[6] has calculated that only 2,3-dimethyl-1,3-butadiene has more *s-cis* than *s-trans* rotamer present at room temperature. It is also not related to the barrier to rotation or relative stability of the two delocalized allylic cations (see discussion below). Thus the origin of the difference is subtle, and may reflect nonbonded interactions in a reaction complex or transition state.

The factors involved in determining the relative stereochemistry of the bicyclic products can be illustrated with the cases of *trans*-piperylene, *trans*-1,3-heptadiene, and *trans*-2-methyl-1,3-pentadiene. The dehydroindolizidinones from the first two were essentially pure **37** (R = CH_3 and C_3H_7 respectively). These are the thermodynamically more stable isomers, but also those expected from maximum secondary orbital overlap corresponding to the Diels–Alder *endo* rule (see **38**).

That the orbital overlap is a dominant factor is supported by the case of 2-methyl-1,3-pentadiene. We suggest that in this case the steric repulsion between the 2-methyl group and a methylene group of the immonium ion as in **38** partially overrides the electronic effect, resulting in an equal contribution to the transition state of an orientation depicted in **39**. This

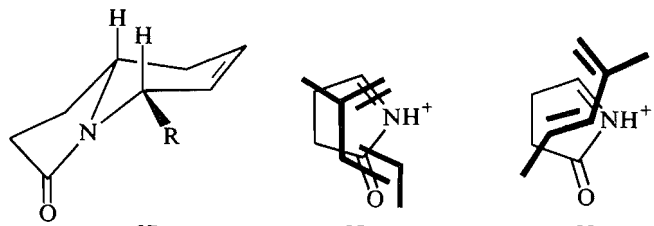

37 **38** **39**

rationalizes the fact that nearly equal amounts of stereoisomers **16** and **17** were formed.

Both Krow *et al.* (1*f*) and Weinreb and Levin (1*e*) have invoked similar secondary orbital interactions to account for the stereochemistry they encountered in their apparent Diels–Alder reactions.

If the reactions are stepwise and the above arguments are correct, our steric results demand a good retention of stereochemistry in the initially formed allylic cations. Thus little or no rotation about the 2,3 bond takes place in the cations derived from **38** and its analogues from *trans*-piperylene and *trans*-2-methyl-1,3-heptadiene (see **40**). Herman[6] has estimated a barrier of around 15 kcal/mol (average of the two barrier heights) to rotation in the case where $R^2 = R^3 = CH_3$ (from 2-methyl-1,3-pentadiene) and R^2 = H, $R^3 = CH_3$ (from isoprene), but somewhat higher (17–21 kcal/mol) for the other dienes studied. This is adequate to provide retention of configuration in a stepwise process.

A further test of this steric control would be the geometry of

[4]We cordially thank Dr. T. F. Spande for making this observation and for other exchanges of information.

[5]In accord with traditional usage for amines, an imine should give rise to an immonium salt, not an imminium salt as has often been used.

[6]We warmly thank L. Herman for these calculations, to be reported in a thesis submitted as partial requirement for the Ph.D. degree, Department of Chemistry, Carleton University.

Can. J. Chem. Downloaded from www.nrcresearchpress.com by 93.93.197.157 on 09/07/12
For personal use only.

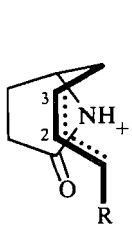

40*a*

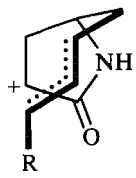

40*b*

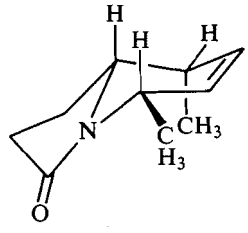

41

the product from *E,E*-2,4-hexadiene. The dehydroindolizidinone from this had the 5- and 9-hydrogens *syn* (see **41**), as expected for a reaction orientation related to **38**. Thus we predict that the 8-methyl group would be *anti* to the 9-hydrogen as in **41**. Unfortunately we have no evidence defining its configuration.

Our synthesis of (±) gephyrotoxin 223AB (now called indolizidine 223AB) compares favorably in yield and the use of readily available starting materials with the ingenious approaches devised by others (11, 12). The requirement of final resolution to obtain optically active material may make it inferior in practice to the synthesis of Royer and Husson (12). Synthesis of other stereoisomers of gephyrotoxin 223AB have been reported by Hart and Tsai (8), and by Stevens and Lee (16).

The above reactions should be capable of extension to other bicyclic systems fused through nitrogen, using such readily available *N*-acyl imine precursers as **42** (17) and **43** (4).

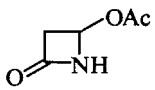

42

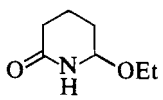

43

Experimental

Separations were done on tlc silica gel with 13% $CaSO_4$ binder and fluorescent indicator, either in a column or 1000-μm plates, or on "flash" silica gel (50–63 μm). Infrared spectra were determined on a Perkin–Elmer model 257 grating spectrometer using dichloromethane solutions. The ^1H and ^{13}C nmr spectra were recorded using a Bruker WP-80 FT spectrometer with deuterochloroform as solvent and TMS as reference. Mass spectra were obtained using electron impact (EI), courtesy of the Ottawa–Carleton mass spectrometry center. Yields were calculated on the basis of the 5-ethoxy-2-pyrrolidinone or 5-acetoxy-2-pyrrolidinone used.

Reagents

5-Ethoxy-2-pyrrolidine 2

This was prepared from succinimide in a manner similar to that of Speckamp and co-workers (4). Simultaneous slow addition of hydrogen chloride in absolute ethanol and solid sodium borohydride, keeping the pH between 4 and 8 and cooling (0–5°C), was necessary to produce moderate yields (ca. 50%).[7] Purification of the ether-soluble product was achieved by passage in ether through a short bed (10-fold weight ratio) of activity II alumina, followed by concentration to small volume and addition of hexane. It formed large prisms, mp 56–58°C, and gave ^1H nmr signals at δ 8.1 (br, NH), 4.97 (br m, 1H), 3.5 (br m, 2H), 2.3 (m, 4H), and 1.20 (t, 3H, J = 7 Hz). More polar fractions yielded needles, mp 63–65°C, which from their ^1H nmr spectra were a 1:1 eutectic of succinimide and **2**.

5-Acetoxy-2-pyrrolidinone 3 (R = Ac)

A solution of 127 mg of 5-ethoxy-2-pyrrolidinone (**2**) in 1 mL of acetic acid and 0.75 mL of acetic anhydride was held at 70°C for 4 h. The reagents were removed under reduced pressure of 0.1 Torr (1 Torr = 133.3 Pa). The oily product (126 mg) gave ^1H nmr signals at δ 7.98 (br, NH), 6.05 (1H, m), 2.8–2.1 (4H, m), and 2.18 (3H, s). It was never obtained completely pure.

E-*1,3-Heptadiene*

A commercial sample (Wiley Organics) gave ^{13}C nmr signals at 137.5, 135.3, 131.2, 114.6, 34.7, 22.5, and 13.7 ppm. It thus appeared to be one isomer, which on the basis of the geometry of derived products (see gephyrotoxin-223AB) had the *E* configuration of the internal double bond.

E-*2-Methyl-1,3-pentadiene*

The commercial sample used (Aldrich) gave ^{13}C nmr signals at 142.2, 134.3, 125.4, 113.8, 18.7, and 18.1 ppm.

1-Acetoxy-1,3-butadiene

A commerical sample (Aldrich) was freshly distilled under reduced pressure. It was an approximately 60:40 mixture of two isomers according to its ^1H nmr spectrum. The main isomer give signals at δ 7.5 (1 H, d, J = 12 Hz), a complex set of signals between 6.5 and 4.6 (4H) and 2.2 (3H, s).

General conditions for 1,3-diene reactions[8]

Method A

A mixture of 301 mg of 5-ethoxy-2-pyrrolidinone **2**, 805 mg of freshly distilled 2,3-dimethyl-1,3-butadiene, 4 mL of 98% formic acid, and 0.6 mL of dichloromethane gave two phases. This was stirred under argon for 3 h. A trace of upper phase persisted. The solvents and the bulk of the formic acid were removed *in vacuo* in 35°C. The residue was dissolved in 15 mL of dichloromethane. The solution was washed with 3 mL of water, then 3 mL of saturated sodium bicarbonate solution. The aqueous layers were washed twice with 15-mL portions of dichloromethane. The organic layers yielded 710 mg of pleasant-smelling oil. This was hydrolysed for 1 h using 326 mg of potassium carbonate in 2 mL of water and 1 mL of methanol (stirring, room temperature). The bulk of the methanol was removed under reduced pressure, then the products were extracted into dichloromethane (3 × 7 mL). The 660 mg of oil recovered from the CH_2Cl_2 was absorbed from this solvent onto 40 g of silica gel. Elution with CH_2Cl and 0.75% methanol in chloroform gave products derived from the diene alone. A 5% methanol in chloroform mixture eluted products less polar than the desired bicyclic product **14**, followed by fractions rich in this compound (447 mg). This was followed by 64 mg of crystalline hydroxy lactam **15** (R = H). The fractions rich in **14** were separated on five silica gel plates using 5% methanol in chloroform into (*a*) 175 mg of a mixture of **14** with a monocyclic product with ν_{max} 3420 and 1696 cm^{-1} (not identified), and (*b*) 102 mg, rich in hydroxy lactam **15** (R = H). The mixture (*a*) was separated on 1000-m alumina plates using 4% ethanol in chloroform. The yield of bicyclic lactam **14** was 45 mg (12%) and of the crystalline lactam **15** (R = H) was 166 mg (39%).

If the crude reaction product was not hydrolysed the product could be separated on silica gel to give **14** (16%) and the formate **15** (R = OCHO) (43%). See also the detail for 2,3-diphenyl-1,3-butadiene.

Method B

Separate solutions of 5.6 g of *trans*-piperylene, 3.27 g of 5-ethoxy-2-pyrrolidinone in 9 mL of dry methylene chloride, and 3.13 g of methanesulfonic acid in 3 mL of methylene chloride were cooled to 0°C, then mixed. The resulting solution was left at 0°C for 64 h, then added to a stirred mixture of 10 mL of chloroform and 20 mL of water. The mixture was carefully neutralized using solid sodium bicarbonate. The layers were separated, and the aqueous layer extracted with three 30-mL volumes of chloroform. The chloroform extracts were washed with 10 mL of saturated brine, dried, and distilled. The residue was adsorbed from methylene chloride onto 200 g of silica gel and the products eluted with 25% ethyl acetate in methylene chloride. Three hundred millilitres of solvent eluted 787 mg of products derived from piperylene alone. Five percent ethanol in methylene chloride (600 mL) eluted 226 mg of unidentified products. The next 300 mL eluted 2.2 g rich in the desired bicyclic adduct but containing more polar and less polar compounds. These were removed on 1000-μm silica gel plates

[7]We thank Paul Desilets for experiments on these conditions. We were unable to obtain the high yields reported in ref. 4.

[8]These are illustrated using specific dienes.

Can. J. Chem. Downloaded from www.nrcresearchpress.com by 93.93.197.157 on 09/07/12
For personal use only.

Can. J. Chem. Downloaded from www.nrcresearchpress.com by 93.93.197.157 on 09/07/12
For personal use only.

using 5% ethanol in chloroform. The desired dehydroindolizidinone **12** weighed 530 mg (14%). See also the detail for 1,3-heptadiene.

Method C

A solution of 65 mg of 5-ethoxy-2-pyrrolidinone **2** and 200 mg of *E,E*-2,4-hexadiene in 1 mL of chloroform was cooled to −10°C. To this was added 0.5 mL of 36% perchloric acid. The mixture was stirred at −10°C for 1 week. Chloroform was added, followed by saturated sodium bicarbonate solution to neutralize the acid. The solution was dried using anhydrous sodium sulfate. The products were separated on a silica gel plate using 5% ethanol in chloroform, giving 17 mg (20%) of the dehydroindolizidinone **22**. The other major products derived from **2** appeared to be monocyclic dienes, but were not further characterized.

Method D

A solution of 123 mg of acetyl chloride in 1 mL of dry benzene was added to a solution of 300 mg of silver perchlorate in 2 mL of dry benzene. Silver chloride separated. The mixture was filtered through sintered glass under dry argon into a solution of 190 mg of ethoxy lactam **1** in 1 mL of benzene. A precipitate formed. The bulk of the benzene was removed under reduced pressure, then a solution of 217 mg of isoprene in 3 mL of dry acetonitrile was added. The mixture was left under argon for 4 days at room temperature. The solvent was evaporated, the products extracted into dichloromethane (filtered), then the solution and washings stirred with 1 mL of saturated sodium bicarbonate solution. The water was absorbed using anhydrous sodium sulfate, then the dichloromethane removed. The 263 mg of residue was adsorbed from dichloromethane onto 7 g of silica gel. The products were eluted successfully with dichloromethane, 0.5% methanol in chloroform, then 5% methanol in chloroform. The 70 mg rich in bicyclic lactam (tlc) was further separated on a 100-μm silica gel plate using 7% methanol in chloroform. The desired bicyclic product **8** (ca. 20 mg, 9%) was still contaminated with a slightly more polar product (ν_{max} 3430 and 1687 cm^{-1}), which was probably a monocyclic diene.

In other experiments using the same ratio of silver perchlorate but only half the molar equivalent of acetyl chloride, the yield of bicyclic lactam **8** remained at 9%, but a new product with slightly lower R_f in silica gel was isolated and characterized as a trimer of the *N*-acyl imine **1** with mp 205°C.

Method E

5-Acetoxy-2-pyrrolidinone **3** (R = Ac) was prepared from 127 mg of **2** as described above. This was combined with 300 mg of freshly distilled 1-acetoxy-1,3-butadiene in 0.75 mL of acetic acid and 0.4 mL of acetic anhydride. To this was added 60 mg of boron trifluoride etherate. The clear solution was left for 5 h at room temperature under argon, then the solvents removed under 0.1 Torr at 40°C. Water and dichloromethane were added, followed by enough sodium bicarbonate to bring the pH to 7 (stirring). The dichloromethane layer was separated, then the aqueous layer extracted twice with the same solvent. The organic extracts yielded 131 mg of an oil that crystallized on standing. The crystals were collected using an acetone–hexane mixture. The mother liquors were separated on a silica gel plate giving more of the crystals. The isolated yield of crude lactam acylal **30** was 70 mg (28%), mp 108–110°C.

Reactions of specific dienes

Isoprene

Using method A (516 mg of **2**, 25 mL of 98% formic acid, and 1.5 mL of isoprene for 2 h at room temperature), an 83% yield of the monocyclic formate **7** was obtained, and only a trace of indolizidinone was detected.

Using method C (65 mg of **2**, 200 mg of isoprene, 0.5 mL of 36% perchloric acid, and 0.5 mL of chloroform stirred 7 days at −10°C), a 10% yield of the indolizidinone **8** was obtained.

See also method D, above.

5,9-syn-6,7-Dehydro-6-methylindolizin-2-one 8

This was an oil with ν_{max} 1668 cm^{-1} and ^1H nmr signals at δ 5.40 (1H, br s), 4.24 (1 H, d, J = 5 Hz), 3.56 (1H, br s), 3.49 (1H, d, J = 5 Hz), 2.40 (ca. H, m), 2.12 (ca. H, br s), and 1.71 (3H, s). The vinyl hydrogen was not coupled to any of the other three low-field hydrogens.

Its ^{13}C nmr spectrum had signals at δ 173(s), 131(s), 117(d), 53(d), 40(t), 37(t), 30.5(t), 22.5(t), and 23(q). It gave m/z 152 (9), 151 (75) (M^+), 150 (15), 136 (51), 108 (24), 96 (17), 94 (23), 84 (37), 68 (100). *Anal.* calcd. for $C_9H_{13}NO$: C 71.49, H 8.67, N 9.26; found: C 71.66, H 8.84, N 9.16.

1-Hydroxy-3-methyl-4-(5'-oxo-2'-pyrrolidinyl)-but-2-en-1-ol formate 7

This was a viscous oil with ν_{max} 3430, 1723, and 1700 cm^{-1}. It gave ^1H nmr signals at δ 8.06 (1H, s), 7.1 (br s, NH), 5.43 (1H, t, J = 7 Hz), 4.69 (2H, d, J = 8 Hz), 3.82 (1H, m), and 1.75 (3H, s). Irradiation at δ 2.27 reduced the multiplet at 3.8 to a broad singlet; the doublet at 4.69 collapsed to a singlet when δ 5.4 was irradiated, and irradiation at 4.7 collapsed the triplet at 5.4 to a singlet. Its ^{13}C nmr spectrum had signals at δ 178.0(s), 160.7(d), 138.3(s), 121.0(d), 60.1(t), 52.2(d), 46.5(t), 30.1(t), 26.7(t), and 16.5(q) ppm. Extra signals for a minor isomer were present at 138.8, 121.6, 59.9, 52.5, 26.9, and 23.5 ppm with the same multiplicities as the major peaks. *Anal.* calcd. for $C_{10}H_{15}NO_3$: C 60.89, H 7.67, N 7.10; found: C 61.07, H 7.83. N 7.24.

trans-*Piperylene*

See also method B above.

Following method A(3 g of **2**, 8 mL of *trans*-piperylene in 35 mL of 98% formic acid, 2 h at room temperature), 4 g of less volatile products were obtained. Separation on 160 g of silica gel gave 2.6 g (57%) of monocyclic formates and 600 mg rich in indolizidinone. Further separation of the latter fraction using tlc plates and 5% ethanol in chloroform as solvent gave 369 mg (11%) of bicyclic lactam **12**.

The monocyclic formate was a mixture of at least four isomers. Separation on a 50-fold ratio of silica gel using 5% ethanol in chloroform gave 67 mg (1.5%) of crystalline lactam formate **9**, mp 103°C, as an early eluate. The other isomers were not cleanly separated. Comparison of their ^{13}C nmr spectra showed such close similarity that they were most likely stereoisomers. The mixture was hydrolysed using potassium carbonate in aqueous methanol and the lactam alcohols separated on silica gel, giving 1.4 g (35%) of **10***a* (R = H), mp 117°C, and 0.9 g (23%) of its isomer **10***b* (R = H), mp 72°C.

2-Hydroxy-1-(5'-oxo-2'-pyrrolidinyl)-3-pentene formate 9

This had mp 102–103°C and ν_{max} 3420, 3210, 172) (sh), and 1692 cm^{-1}. Its ^1H nmr spectrum had signals at δ 8.08 (1H, s), 6.71 (br s, NH), 5.2–6.0 (3H, m), 3.69 (1H, m), and 1.72 (3H, d, J = 4 Hz). Its ^{13}C nmr spectrum had signals at δ 178.0(s), 160.5(d), 130.7(d), 128.2(d), 72.3(d), 50.75(d), 41.6(t), 27.5(t), and 17.6(q). *Anal.* calcd. for $C_{10}H_{15}NO_3$: C 60.89, H 7.67, N 7.10; found: C 61.02, H 7.74, N 6.97.

This gave an amorphous lactam alcohol with a ^1H nmr spectrum different from either isomer described below.

Major formates 10 (R = CHO)

This mixture gave ^1H nmr signals at δ 8.08 (1H, s), 7.02 (1H, br s), 5.1–5.8 (3H, m), 3.5–3.9 (1H, m), 1.35 (3H, d, J = 6 Hz). The methyl group was coupled to a proton resonating at δ 5.5. Its ^{13}C nmr spectrum had signals at δ 178.3(s), 160.2(d), 132.6(d), 128.1(d), 70.53(d), 70.46(d), 53.7(d), 39.0(t), 30.0(t), 26.2(t), and 20.0(q) ppm. The signals at 70.53 and 70.46 correspond to epimers at the carbon carrying the formate ester.

*4-Hydroxy-1-(5'-oxo-2'pyrrolidinyl)-2-pentene 10*a (*R = H*)

This had mp 116–117°C and gave ^1H nmr signals at δ 8.57 (NH), 5.6 (2H, br m), 4.53 (1H, OH), 4.24 (1H, m), 3.7 (1H, br m), and 1.22 (3H, d, J = 6 Hz). Its ^{13}C nmr spectrum had signals at δ 179.6(s), 138.9(s), 126.4(s), 68.9(s), 55.2(s), 40.0(t), 31.0(t), 27.15(t), and 22.9(q) ppm. *Anal.* calcd. for $C_9H_{15}NO_2$: C 63.88, H 8.94, N 8.28; found C 63.72, H 9.01, N 8.18.

*4-Hydroxy-1-(5'-oxo-2'-pyrrolidinyl)-2-pentene 10*b (*R = H*)

This crystallized from concentrated ethyl acetate solution, and had mp 70–72°C. It had ν_{max} 3600, 3380, 3220, and 1685 cm^{-1} and gave ^1H nmr signals at δ 7.59 (NH), 5.68 (2H, m), 4.27 (1H, m), 3.79 (1H, t), 3.33 (1H, br s), 1.68 (1H, br s), and 1.24 (3H, d, J = 6 Hz). The

hydrogen resonating at 4.27 was coupled to the methyl group (δ 1.24). Its ^{13}C nmr spectrum had signals at δ 179.2(s), 138.0(d), 125.0(d), 67.6(d), 54.6(d), 39.0(t), 30.7(t), 26.9(t), and 22.8(q) ppm. Its EI mass spectrum gave no parent ion. The base peak was at *m/z* 84. Its CI mass spectrum gave peaks at *m/z* 170 (*M* + 1) and 152 (*M* − 18).

*Oxidation of **10**a and **10**b*

To a solution of 31 mg of **10***b* in 2 mL of dichloromethane was added 855 mg of active manganese dioxide (18) (dried at 45°C *in vacuo*). After the mixture had been stirred 1.25 h, 5 mL of 10% methanol in chloroform was added, then the solid removed by filtration. The filtrate and washings were evaporated, giving 30 mg of residue. This was purified on a 500-μm silica gel plate using 10% methanol in chloroform, giving 20 mg in a main zone. This crystallized from ethyl acetate – ether mixtures, mp 65–68°C. Jones oxidation of **10***b* in acetone gave a 30% yield of the same product.

Manganese dioxide oxidation of ***10a*** as above gave a product with mp 64–67°C. The products from both isomers proved identical (mixture mp and comparison of ir and ^1H nmr spectra).

*Keto-lactam **11***

This had mp 65–68°C and ν_{max} 3420, 3200, 1699, 1675, and 1631 cm^{-1}. Its EI mass spectrum gave no parent ion. The base peak was at *m/z* 84 ($C_4H_6NO^+$). Its CI mass spectrum (ether) gave *M* + 1 at *m/z* 168 and *M* −18 at *m/z* 149. Its ^1H nmr spectrum gave signals at δ 6.88–6.57 (1H, m), 6.55 (br m, NH), 6.17 (1H, d, *J* = 16 Hz), 3.81 (1H, m), and 2.26 (3H, s) superimposed on a 6H multiplet.

E-*1,3-Heptadiene*

The use of method A gave a mixture of formate esters with ^1H nmr signals at δ 8.0 (1H, s), 7.0 (1H, NH), 5.9–5.1 (3H, m), 3.7 (1H, m), and 0.9 (3H, t) typical of the monocyclic lactam formates described from other dienes. The yield of dehydroindolizidinone **13** (ca. 15%) was lower than that using method B, hence the latter method was used in preparative work.

In a minor modification of method B, 5.8 g (45 mmol) of **2** and 17 g (180 mmol) of *E*-1,3-heptadiene in 40 mL of dry dichloromethane was cooled to −5°C. A solution of 4.7 g (49 mmol) of methanesulfonic acid in 15 mL of dichloromethane was added to this with stirring during 15 min. The mixture was stirred at 0°C for 120 h. Separation of the products on silica gel gave two pairs of ethoxy lactams, corresponding to the formate esters from method A, and 1.3 g of pure **13** followed by 0.76 g of **13** contaminated with monocyclic adducts. The latter was purified using silica gel plates, giving a total yield of 1.7 g (21%) of **13**.

*5,9-*syn*-6,7-Dehydro-5-(1'-propyl)indolizidine-3-one (**13**)*

This distilled over a short path of 95°C under 0.05 Torr as a colorless oil. It had ν_{max} 1677 cm^{-1} and ^1H nmr signals at δ 5.75 (2H, m), 4.1 (1H, br), and 3.47 (1H, m), with peaks at 2.29, 1.00, and 0.90. Its ^{13}C nmr spectrum had signals at δ 175.4(s), 129.0(d), 123.9(d), 55.6(d), 52.5(d), 34.5(t), 31.8(t), 31.1(t), 26.6(t), 16.7(t), and 13.9(q). Its mass spectrum gave peaks at *m/z* 179 (5.3), 164 (2.9), 150 (12), 137 (39), 136 (99), and 108 (100). *Anal*, calcd. for $C_{11}H_{17}NO$: 73.70, H 9.56, N 7.81; found: C 73.52, H 9.43, N 7.69.

2,3-Dimethyl-1,3-butadiene

See method A above. The yield of the dehydroindolizidine **14** was around 16%.

*7,8-Dehydro-7,8-dimethylindolizidin-2-one **14***

This was an oil with ν_{max} 1670 cm^{-1}. It gave ^1H nmr signals at δ 4.3, 4.0, 3.56 and 3.2 (br, 3H total), and 1.68 (6H, s). Its ^{13}C nmr spectrum had signals at δ 173.4(s), 123.5(s), 121.7(s), 53.0(d), 44.0(t), 38.1(t), 29.7(t), 24.8(t), 18.7(q), and 15.7(q) ppm. It gave *m/z* 165 (100), 150 (100), 122 (34), 108 (29), 94 (23), 84 (51), 82 (100), and 67 (100). *Anal.* calcd. for $C_{10}H_{15}NO$: C 72.69, H 9.15, N 8.48; found: C 72.47, H 9.01, N 8.29.

*2,3-Dimethyl-4(2'-oxopyrrolidin-5'-yl)-but-2-en-1-ol formate **15** (R = CHO)*

This was an oil distilling over a short path at 150°C, 0.25 Torr. It had ν_{max} 3420, 1718, and 1698 cm^{-1} and gave ^1H nmr signals at δ 8.20 (1H, s) 7.8 (1H, br s), 4.70 (2H, s), 3.85 (1H, br m), and 1.80 (6H, s). Its ^{13}C nmr spectrum had signals at δ 178.2, 161.1, 132.3, 131.8, 126.3, 126.2, 64.9, 64.4, 53.2, 53.0, 52.9, 41.4, 41.1, 30.9, 30.6, 30.5, 30.3, 27.3, 27.1, 27.0, 19.1, 18.5, 17.0, and 16.9 (24 signals, i.e., two isomers). Hydrolysis of this formate in methanol containing potassium carbonate gave the crystalline alcohol **15** (R = H), mp 93°C.

*2,3-Dimethyl-4-(2'-oxopyrrolidin-5'-yl)-but-2-en-1-ol (**15** R = H)*

After recrystallization from acetone–hexane, **15** had mp 94–95°C. It had ν_{max} 3600, 3380, 3220, 3050, and 1680 cm^{-1} and gave ^1H nmr signals at δ 8.45 (0.5H, m), 7.7 (0.5H, m), 3.4–4.6 (4H), 1.9–2.2 (6H), and 1.80 (6H, s) and ^{13}C nmr signals at δ 179.7, 179.0, 131.9, 131.8, 128.3, 127.9, 63.9, 62.6, 53.5, 41.65, 41.1, 30.9, 27.9, 27.4, 19.1, 17.8, 17.4, and 17.0 (18 signals). It was thus a 1:1 mixture of two isomers. *Anal.* calcd. for $C_{10}H_{12}NO_2$: C 65.54, H 9.35, N 7.64; found: C 65.40, H 9.28, N 7.51.

trans-*2-Methyl-1,3-pentadiene*

Method A was followed. A mixture of 2.5 g of ethoxylactam **2**, 4.68 g of freshly distilled *trans*-2-methyl-1,3-pentadiene, and 20 mL of 98% formic acid was stirred under argon for 5 h. Initial cooling was needed to maintain the temperature near 20°C. The reaction mixture was still in two phases. The lower phase was separated, the upper phase washed with 5 mL of formic acid, and the layers again separated. The bulk of the formic acid was removed *in vacuo* and the work-up done as in method A. The 2.25 g (70% calcd. as **16**) of product recovered was predominantly a mixture of the two lactams **16** and **17** in a 1:1 ratio (^1H nmr). These were separated on 100 g of tlc silica gel using a 1:1 mixture of acetone in hexane for elution. Overlapping fractions were separated on 1000-μm tlc plates.

*5,9-*syn*-6-7-Dehydro-5,7-dimethylindolizidin-3-one **16***

The isomer with higher R_f on silica gel (30% acetone in hexane) was an oil, which was distilled over a short path at ca. 90°C, 0.03 Torr. It had ν_{max} 1668 cm^{-1} and gave ^1H nmr signals at δ 5.34 (1H, s), 4.0 (1H, br s), 3.5 (1H, br m), 1.8 (3H, s), and 1.43 (3H, d, *J* = 4 Hz); ^{13}C nmr spectrum, δ: 175.4(s), 130.7(s), 124.7(d), 55.9(d), 48.3(d), 36.9(t), 31.3(t), 26.5(t), 23.0(q), 20.5(q). Its mass spectrum had *m/z* 165 (25) (M^+), 150 (100), and 122 (24). *Anal.* calcd. for $C_{10}H_{15}NO$: C 72.69, H 9.15, N 8.48; found: C 72.44, H 9.03, N 8.33.

*5,9-*anti*-6,7-Dehydro-5,7-dimethylindolizidin-3-one **17***

The isomer with the lower R_f on silica gel (30% acetone–hexane) was distilled over a short path at ca. 90°C, 0.03 Torr. It had ν_{max} 1662 cm^{-1} and gave ^1H nmr signals at δ 5.35 (1H, s), 4.4 (1H, br s), 3.7 (1H, br m), 1.7 (3H, s), 1.15 (3H, d, *J* = 6.6 Hz); ^{13}C nmr spectrum, δ: 173(s), 130.7(s), 123.5(d), 50.0(d), 45.5(d), 37.2(t), 30.0(t), 25.0(t), 23.0(q), and 19.0(q). Its mass spectrum had *m/z* 165(33) (M^+), 150 (100), and 122 (26). *Anal.* calcd. for $C_{10}H_{15}NO$: C 72.69, H 9.15, N 8.48; found: C 72.42, H 9.36, N 8.20.

3-Methyl-1,3-pentadiene

Using method A (65 mg of **2**, 210 mg of 3-methyl-1,3-pentadiene in 3 mL of 98% formic acid for 2 h at room temperature), 80 mg (75%) of monocyclic formate **20** was obtained as an oil.

*5-(5'-Oxo-2'pyrrolidinyl)-3-methylpent-3-en-2-ol formate **20***

This gave ν_{max} 3440, 3220, 1720, and 1695 cm^{-1} and ^1H nmr signals at δ 8.08 (1H, s), 7.13 (1H, br s), 5.4 (2H, m), 3.70 (1H, m), 1.65 (3H, s), and 1.35 (3H, d, *J* = 6.6 Hz). The methyl doublet at δ 1.35 was coupled with a proton resonating near 5.4 (*CH*OCHO) and the singlet at 3.7 and the vinyl hydrogen near 5.5 were coupled to a methylene group resonating near 3.3. Its ^{13}C nmr spectrum showed it to be a mixture of two stereoisomers in nearly equal amounts. The major isomer gave signals at δ 178.4(s), 160.4(d), 137.2(s), 122.5(d), 75.3(d), 54.1(d), 34.5(t), 30.2(t), 26.5(t), 19.0(q), and 12.1(q). *Anal.* calcd. for $C_{11}H_{17}NO_3$: C 62.54, H 8.11, N 6.63; found: C 62.34, H 8.02, N 6.47.

E,E-*2,4-Hexadiene*

Use of method A (61 mg of ethoxy lactam **2**, 190 mg of 2,4-hexadiene in 3 mL of 98% formic acid for 2 h at room temperature) resulted in formation of 71 mg (70%) of monocyclic formate **21**. Little if any dehydroindolizinone was formed.

Can. J. Chem. Downloaded from www.nrcresearchpress.com by 93.93.197.157 on 09/07/12
For personal use only.

Can. J. Chem. Downloaded from www.nrcresearchpress.com by 93.93.197.157 on 09/07/12
For personal use only.

As described above, a 20% yield of the dehydroindolizidinone **22** was formed using method C.

*5-(5'-Oxo-2'-pyrrolidinyl)-hex-3-en-2-ol formate **21***

This was an oil with ν_{max} 3440, 3220, 1720, and 1691 cm^{-1} and ^1H nmr signals at δ 8.03 (1H, s), 7.65 (br s, NH), 5.56 (main peak of a 3H, mult.), 3.51 (1H, m), 1.34 (3H, d, J = 6 Hz), and 1.06 (3H, d, J = 6.6 Hz). Its ^{13}C nmr spectrum showed it to be a mixture of two very similar isomers. The main one gave signals at δ 178.9(s), 160.3(d), 134.1(d), 130.6(d), 70.7(d), 59.0(d), 41.9(d), 30.3(t), 24.2(t), 20.4(q), and 16.3(q). *Anal.* calcd. for $C_{11}H_{17}NO_3$: C 62.54, H 8.11, N 6.63; found: C 62.23, H 7.94, N 6.72.

*5,8,9-*syn*-6,7-Dehydro-5,8-dimethylindolizidin-3-one (**22**)*

This was an oil with ν_{max} 1675 (s) and 1650 (w) cm^{-1} and ^1H nmr signals at δ 6.1–5.4 (2H, m), 4.07 (1H, br), 3.69 (1H, br), 1.45 (3H, d, J = 6 Hz), and 1.0 (3H, d, J = 7 Hz). The methyl group resonating at 1.45 was coupled with the proton at 4.07, but the methyl at 1.0 was not strongly coupled with any low-field proton. It gave ^{13}C nmr signals at δ 176.8(s), 130.1(d), 129.5(d), 58.7(d), 48.9(d), 32.5(d), 31.2(t), 21.8(t), 21.0(q), and 14.3(q). Its mass spectrum had peaks at m/z 165 (M^+) (36), 150 (77), 122 (14), 108 (8), 94 (11), 84 (58), and 82 (100). The compound was distilled over a short path *in vacuo* for analysis. *Anal.* calcd. for $C_{10}H_{15}NO$: C 72.69, H 9.15, N 8.48; found: C 72.45, H 8.98, N 8.30.

1,3-Cyclohexadiene

Method A was used (65 mg of **2**, 190 mg of cyclohexadiene, and 0.5 mL of 98% formic acid stirred for 4 h at room temperature). After separation on silica gel, using 5% methanol in chloroform, 33 mg (40%) of tricyclic product and 44 mg (42%) of the bicyclic formate were obtained.

*8,9-*syn*-6,7-Dehydro-5,8-ethanoindolizidin-3-one (**24**)*

This distilled over a short path at 50–60°C under 0.1 Torr. It had ν_{max} 1675 cm^{-1} and gave ^1H nmr signals at δ 6.6 and 6.17 (1H each, pseudo triplets, J_1 = 8 Hz and J_2 = 5 Hz from decoupling experiments), 4.57 (1H, br s), 3.72 (1H, dd, J_1 = 9 Hz, J_2 = 5 Hz), and 2.71 (1H, br d, J = 6 Hz). The following couplings were demonstrated: 6.6–6.17; 6.6–4.57; 6.17–2.71; 3.72–2.1. It gave ^{13}C nmr signals at δ 178.1(s), 136.8(d), 130.7(d), 60.1(d), 44.8(d), 35.0(d), 31.8(t), 28.5(t), 24.5(t), and 22.9(t). Its mass spectrum had peaks at m/z 163 (5), 134 (9), 106 (5), 84 (100), 80 (88), and 79 (57). *Anal.* calcd. for $C_{10}H_{13}NO$: C 73.59, H 8.03, N 8.58; found: C 73.41, H 7.95, N 8.73.

*4-(5'-Oxo-2'-pyrrolidinyl)-cyclohex-2-en-1-ol formate (**23**)*

The ^{13}C nmr spectrum of this product showed it to be a mixture of four stereoisomers with correct chemical shifts and multiplicities for **23**. Its ^1H nmr spectrum had signals near δ 8.1 (CHO), 7.4–8.1 (NH), 5.95, 5.82 (vinyl hydrogens), 5.33 (CHN), and 3.6 (CHO-). It was not further characterized.

2,3-Diphenylbuta-1,3-diene

The diene (897 mg, mp 47°C) (19) and 563 mg of ethoxy lactam **2** in 3 mL of dichloromethane and 4 mL of formic acid formed two oil layers. This mixture was stirred under argon for 29 h. An extra 201 mg of ethoxy lactam **2** was added, then stirring continued (total time 71 h). The bulk of the solvent and formic acid were removed on a rotating evaporator at 50°C. The residue was dissolved in dichloromethane, then washed free of acid using aqueous sodium carbonate. The 1.12 g of oil recovered from the dichloromethane was adsorbed on a column of 15 g of tlc silica gel. Dichloromethane eluted 451 mg of diphenylbutadiene, followed by 136 mg of nitrogen-free products (formate esters). Chloroform containing 5% (v/v) of methanol eluted 505 mg of condensation products. This solvent and 10% methanol in chloroform eluted 71 mg of a mixture of more polar products, which was not further investigated.

The 505 mg contained the indene derivative **27** and two formoxy amides. This was partially separated on four 1000-μm silica gel plates using 5% methanol in chloroform. A small zone (R_f 0.7, 51 mg) contained a lactam (1682 cm^{-1}) and gave a weak NH band. It was not identified. Bands rich in indene (R_f 0.6, 218 mg) and formate ester (R_f 0.5, 80 mg) were still mixtures. They were combined and hydrolysed by refluxing for 1 h in aqueous methanol containing potassium carbonate. The product was again separated on three 1000-μm silica gel plates using 7% methanol in chloroform, giving 90 mg of indene **27** (R_f 0.65), 167 mg of hydroxy lactam **25** (R_f 0.5), and 30 mg of hydroxy lactam **26** (R_f 0.3).

In a parallel run, the indene **27** and formate mixture was carefully separated on a 50-fold ratio of flash silica gel using 5% methanol in chloroform, giving quite pure indene **27** in the early eluates and formoxy lactam **25** (R = H) as a more strongly adsorbed fraction.

*2,3-Diphenyl-4-(5'-oxo-2'pyrrolidinyl)but-2-en-1-ol formate (**25**, R = OCHO)*

This was an oil with ν_{max} 3420, 1721, and 1692 cm^{-1} and λ_{max} 233 nm, ε 11 000, Its ^1H nmr spectrum had signals at δ 7.84 (1H, s), 5.85 (br, s, NH), 4.72 (2H, s), and 3.4 (1H, t, J = 5 Hz). Its ^{13}C nmr spectrum had signals at δ 177.8(s), 160.6(d), a cluster of doublets at 127.7–129.0, 141.3, 139.5, and 135.4 (singlets), 65.6(t), 52.7(d), 42.0(t), 29.9(t), and 27.0(t). This was hydrolysed by potassium carbonate in aqueous methanol to the hydroxy lactam **25** (R = H).

*2,3-Diphenyl-4-(5'-oxo-2'-pyrrolidinyl)but-2-en-1-ol (**25**, R = H)*

Yield 24%. This crystallized from acetone as buttons, mp 176–177°C. It had ν_{max} 3380, 3220, and 1675 cm^{-1} and λ_{max} 234 nm, ε 11 800. It gave ^1H nmr signals at δ 87 (1H, br s), 7.1–7.7 (10H, m), 3.8–4.4 (3H, m, includes the OH signal) reduced to a pair of doublets at 3.90 and 4.34 (J = 11 Hz) when exchanged with D_2O, 3.4 (1H, t, J = Hz), and 1.3–2.7 (6H, m), and ^{13}C nmr signals at δ 180.0(s), 141.0(s), 140.3(s), 140.2(s), 137.5(s), 129.0, 128.6, 127.3, 126.9 (aryl doublets), 65.1(t), 53.3(d), 42.0(t), 31.0(t), and 27.1(t). *Anal.* calcd. for $C_{20}H_{21}NO_2$: C 78.14, H 6.89, N 4.56; found: C 77.96, H 6.91, N 4.17.

When warmed with a formic acid – acetic anhydride mixture this gave the formate ester (**25**, R = CHO) described above.

*2,3-Diphenyl-4-(5'-oxo-2-pyrrolidinyl)but-1-en-3-ol (**26**)*

Yield 4%. It crystallized from methanol–acetone mixtures as short needles, mp 195–196°C. It had ν_{max} 3430, 3300, and 1684 cm^{-1} and λ_{max} 252 nm, ε 8440. Its ^1H nmr spectrum had signals at δ 7.07 (10H), 6.55 (br s, NH), 4.59 (2H, m), 3.59 (1H, br m), 2.6–3.2 (2H, m,), 2.4 (OH), 2.0–2.6 (4H, m). *Anal.* calcd. for $C_{20}H_{21}NO_2$: C 78.14, H 6.89, N 4.56; found: C 78.02, H 7.02, N 4.38.

*2-Phenyl-3-(5'-oxo-2'-pyrrolidinylmethyl)indene (**27**)*

Yield 14%. This remained as a thick oil with λ_{max} 289 nm, ε 14 800, λ_{min} 248 nm and λ_{max} 227 nm. It had ν_{max} 3424 and 1694 cm^{-1} and ^1H nmr signals at δ 7.37 (10H), 6.41 (br s, NH), 3.97 (1H, m), 3.72 (2H, s), 2.92 (2H, d, J = 6.7 Hz), and 2.12 (4H, br s). The signals at δ 3.97 and 2.9 were coupled. It gave ^{13}C nmr signals at δ 177.8(s), 145.8(s), 143.9(s), 142.6(s), 137.2(s), 134.8(s), 128.6, 128.4, 128.2, 127.3, 126.5, 125.0, 123.7, 119.4 (doublets), 53.6(d), 42.3(t), 32.8(t), 30.0(t), and 27.2(t). *Anal.* calcd. for $C_{20}H_{19}NO$: C 83.01, H 6.62, N 4.84; found: C 82.88, H 6.70, N 4.72.

Furan

Method C (259 mg of **2**, 425 mg of furan, 1 mL of 30% perchloric acid, 1.5 mL of chloroform for 2 h) gave 251 mg (83%) of crude 5-(2'-furyl)-2-pyrrolidinone **28**, mp 75°C.

Method D (304 mg of **2**, 242 mg of silver perchlorate, 1.5 mL of benzene, and 117 mg of acetyl chloride, then 325 mg of furan in 1 mL of dry acetonitrile, left 4 h at room temperature. After addition of 197 mg of furan the mixture was left for 0.5 h) gave 153 mg of products. After separation on 6 g of silica gel the only compound identified was 70 mg (39%) of **28**.

Copper fluoroborate catalysis

A mixture of 202 mg of **2**, 345 mg of $Cu(BF_4)_2$, and 210 mg of dry furan in 1 mL of dry ethanol-free chloroform gave a green gum and colorless solution. This was stirred for 3 h at room temperature. The solution was diluted with dichloromethane, then washed successively with water (3 mL) and saturated sodium bicarbonate solution (3 mL). Repeated extraction (3×) of the aqueous layers gave 167 mg of oil. This was separated on two 1000-μm silica gel plates using 8% methanol in chloroform giving 40 mg of **28** (17%) and 39 mg of 2,5-bis-(5'-oxo-2'-pyrrolidinyl)furan **29**. The combined aqueous layers were evaporated to near dryness. Dichloromethane was added, then the

Can. J. Chem. Downloaded from www.nrcresearchpress.com by 93.93.197.157 on 09/07/12
For personal use only.

remaining water removed using sodium sulfate. A further 41 mg, rich in **29**, was obtained. The total yield of **29** was 70 mg (19%).

*2-(5'-Oxo-2'-pyrrolidinyl)furan (**28**)*

This crystallized as rectangular prisms from acetone–hexane, mp 82–83°C. It gave ^{1}H nmr signals at δ 7.4 (1H, M), 6.78 (1H, br s, NH), 6.27 (2H, m), 4.80 (1H, poorly resolved triplet), and 2.33 (4H, m). *Anal.* calcd. for $C_8H_9NO_2$: C 63.56, H 6.00, N 9.27; found: C 63.66, H 5.93, N 9.12.

*2,5-Bis(5'-oxo-2'-pyrrolidinyl)furan (**29**)*

This was an oil with ν_{max} 3430, 3210, and 1700 cm^{-1}. It gave ^{1}H nmr signals at δ 6.8 (2H, NH), 6.1 (2H, s), 4.8 (2H, m), and 2.0–2.7 (8H).

1-Acetoxy-1,3-butadiene

Method E (see above) gave no significant amount of bicyclic product, and the only compound characterized was the acylal **30** (28%). A comparable yield of **30** was obtained when **2** was used as the reagent. In a large run the only other product obtained reasonably pure (7% yield) was also a lactam acylal with higher R_f than **30**. Only two acetoxy groups were present (^{1}H nmr and probably 12 other carbons), hence it appeared to arise from two diene molecules and one molecule of **2**. No structure was deduced.

*1,1-Diacetoxy-4-(5'-oxy-2'-pyrrolidinyl)but-2-ene (**30**)*

After recrystallization from ethyl acetate this had mp 111–112°C and ν_{max} 3420, 3200, 1760, and 1699 cm^{-1}. It gave ^{1}H nmr signals at δ 7.0 (1H, d, J = 5 Hz), 6.8 (1H, br s, NH), 6.15–5.3 (2H, m), 3.72 (1H, m), and 2.1 (6H, s). Its ^{13}C nmr spectrum had signals at δ 178.3(s), 168.7(s), 132.5(d), 127.0(d), 89.2(d), 53.5(d), 39.1(t), 30.1(t), 26.5(t), and 20.8(q). *Anal.* calcd. for $C_{12}H_{17}NO_5$: C 56.46, H 6.71, N 5.49; found: C 56.29, H 6.66, N 5.39.

Hydrolysis of **30** using a saturated solution of sodium bicarbonate in 1:1 methanol–water gave a mixture containing an unsaturated aldehyde with ν_{max} 3420, 3330, and 1690 cm^{-1} and a ^{1}H nmr doublet at δ 9.65 (J = 7 Hz). It was not further characterized.

Lactam acylal of unknown structure

This amorphous product had ν_{max} 1760, 1680, and 1650 cm^{-1} and ^{1}H nmr signals at δ 7.1 (1H, d, J = 5 Hz), 6.3–5.3 (4H, m), 4.5 (1H, br), 3.65 (1H, br), 2.1 (6H, s). Its ^{13}C nmr spectrum had signals at δ 173.8(s), 168.6(s), 133.2(d), 127.0(d), 126.5(d), 125.0(d), 89.3(d), 51.0(d), 49.1(d), 36.3(t), 32.1(t), 30.0(t), 25.1(t) and 20.9(1) (14 signals).

Synthesis of gephyrotoxin 223AB

*5,9-syn-5(1'-Propyl)indolizidin-3-one (**31**)*

Unsaturated lactam **13** (679 mg) in 5 mL of ethanol was added to a suspension of 136 mg of 30% palladium on charcoal in 15 mL of ethanol, which had been previously saturated with hydrogen. The mixture was shaken under hydrogen. An initial rapid uptake of 30 mL of hydrogen was followed by slower reaction. After 2 h, 81 mL of hydrogen had been absorbed. The solution was filtered through a bed of Celite, and the filtrate and washings evaporated, leaving 620 mg of colorless oil. This was further purified by adsorption from dichloromethane onto a column of 50 g of silica gel (flash). Elution with 10% ethyl acetate and 2% ethanol in dichloromethane gave 24 mg of impurities, then 554 mg of quite pure (tlc on silica, 5% ethanol in chloroform) saturated lactam. An analytical sample was prepared by purification on 1000-μm silica gel plates (5% ethanol in chloroform) followed by distillation at 95°C, 0.05 Torr. It gave ^{1}H nmr signals at δ 3.2 (2H br), 2.2, 1.0, and 0.98. Its ^{13}C nmr spectrum had signals at δ 174.0(s), 59.5(d), 57.2(d), 34.4, 31.8, 31.6, 29.5, 24.9, 22.6, 19.8 (triplets), and 13.9(q). *Anal.* calcd. for $C_{11}H_{19}NO$: C 72.88, H 10.57, N 7.73; found: C 73.06, H 10.55; N 7.90.

Thiolactam 32

A mixture of 377 mg of dihydrolactam **31** and 512 mg of Lawesson's reagent (10) in 8 mL of pure dry dimethoxyethane was stirred under argon for 2 h. A further 88 mg of Lawesson's reagent was then added, and the solution left overnight at 5°C. Thin-layer chromatography still showed the presence of some starting material, so the mixture was heated to 50°C for 15 min. The bulk of the dimethoxyethane was removed under reduced pressure, then the thick oil adsorbed from dichloromethane onto 50 g of silica gel (flash). Sulphurous impurities (30 mg) were followed by 406 mg of crystalline solid. This was distilled over a short path at 135°C, 0.02 Torr, giving 390 mg (95%) of crystalline thiolactam. This had mp 52°C and ν_{max} (film) 1675 cm^{-1}. Its ^{1}H nmr spectrum had signals at δ 0.8–2.5 (ca. 14H), 2.75–3.05 (2H, m), 3.65–4.0 (1H, m), and 4.15–4.45 (1H, m). Its ^{13}C nmr spectrum had signals at δ 13.9(q), 14.7, 19.9, 21.6, 27.7, 29.4, 32.7, 44.2 (triplets), 46.2(d), 54.8(d), and 198.5(s). Its mass spectrum had m/z 197 (90), 196 (25), 168 (26), 164 (27), 155 (100), and 122 (74). *Anal.* calcd. for $C_{11}H_{19}NS$: C 66.97, H 9.71, N 7.10, S 16.22; found: C 67.08, H 9.81, N 7.20, S 16.25.

α,β-Unsaturated ketone 33

A solution of 437 mg of crystalline thiolactam **32** and 495 mg of 1-bromo-2-butanone in 5 mL of dry ether was prepared. The solution became milky and in 2.5 h an oil had separated. The ether layer was separated and evaporated. An ether extraction of the residue left more insoluble gum. The combined ether-insoluble product was dissolved in 5 mL of dry dichloromethane. Triphenylphosphine (597 mg) was added, followed by a solution of 451 mg of dry triethylamine in 2 mL of dry dichloromethane. The mixture became warm and a yellow color developed. This was left overnight at room temperature (now burgundy color). The solvent was removed *in vacuo* leaving a mush of crystals and oil. This was suspended in 10 mL of 10% ethyl acetate in hexane. The crystals were removed by filtration, then washed with 5 mL of the same solvent. The filtrate was evaporated, then extracted with more 10% ethyl acetate in hexane. This left a small amount of dark tar. The solution gave 685 mg of reddish brown oil. This was adsorbed from CH_2Cl_2 on 30 g of tlc silica gel and eluted with 20% ethyl acetate in dichloromethane. Early eluates gave 121 mg of orange crystals, followed by the desired product (567 mg). This was distilled over a short path at 150°C, 0.2 Torr, giving 434 mg (83%) of thick yellow oil. This had λ_{max} 308 nm, ε 31 000, and ν_{max} (film) 1652 and 1550 cm^{-1}. Its ^{1}H nmr spectrum had signals at δ 1.05 (3H, t, J = 7 Hz), 1.3–3.1 (15H), 3.3–3.85 (3H), and 4.85–5.15 (1H, m). Its ^{13}C nmr had signals at δ 88(d), 163.5(s), and 197.2(s). Its mass spectrum had m/z 235 (21), 206 (73), 192 (26), 164 (30), 138 (21), and 136 (100). *Anal.* calcd for $C_{15}H_{25}NO$: C 76.54, H 10.7, N 5.95; found: C 76.32, H 10.82, N 5.88.

Keto bases 34 and 35

The α,β-unsaturated keto base **33** (433 mg) was dissolved in 3 mL of methanol containing 141 mg of sodium cyanoborohydride. Bromocresol green indicator was added. A 2 N solution of hydrogen chloride in methanol was added dropwise with stirring until the solution remained yellow. After a total of 1 h the solution was evaporated, sodium carbonate solution added, and the product extracted into dichloromethane. The 456 mg of product was converted to its sulfate in methanol, then the solvent removed *in vacuo*. A cold solution of the salt in 4 mL of acetone was oxidized with a small excess of Jones' reagent (20); the excess after 10 min was destroyed with 2-propanol. The acetone solution and chromium salts yielded 379 mg of dichloromethane-soluble light brown oil. This was converted to its hydrochloride in methanol, the solvent removed, then acetone added. Addition of ether gave some crystalline hydrochloride. The remainder was separated on three 1000-μm silica gel plates using 15% ethanol in chloroform. A narrow blue band was followed by a zone rich in the crystalline hydrochloride, then one rich in amorphous hydrochloride. The crystalline hydrochloride from both zones (acetone–ether or ethyl acetate) was combined with the first crop of crystals, giving 200 mg (40%) of the hydrochloride of **34**. The amorphous hydrochloride (mainly that of **35**) weighed 198 mg (39%).

Keto base 34

The base liberated from the pure crystalline hydrochloride was an oil with ν_{max} 1712 cm^{-1} (film) and ^{1}H nmr signals at δ 2.8–3.3 (1H, m), 2.2–2.7 (4H, m), 1.13, 1.08, and 0.98. Its ^{13}C nmr spectrum had signals at δ 210.1(s), 55.8, 54.3, 52.9, 46.7, 37.0, 32.5, 29.8, 27.9, 23.4, 20.8, 19.2, 14.4, and 7.7. *Anal.* calcd. for $C_{15}H_{27}NO$: C 75.89, H 11.46, N 5.90; found: C 75.91, H 11.47, N 6.03.

Its hydrochloride crystallized from acetone–ether as needles or tiny prisms with mp 154°C, ν_{max} ($CHCl_3$) 1715 cm^{-1}, and ^{1}H nmr signals at δ 4.45 (1H br) and 3.85 (1H br). It gave ^{13}C nmr signals at δ 206, 63.3,

59.7, 56.0, 39.8, 36.8, 32.5, 27.8, 27.3, 27.1, 26.6, 22.5, 18.5, 13.5, and 7.2.

Keto base 35

The base liberated from the amorphous hydrochloride was an oil with ν_{max} 1712 cm^{-1} (film) and ^1H nmr signals at δ 3.7–4.0 (1H, br), 2.0–2.7 (7H, m), 1.16, 1.07, and 0.96. Its ^{13}C nmr spectrum had signals at δ 211.5(s), 59.4(d), 56.9(d), 55.0(d), 39.1, 37.0, 36.1, 32.3, 30.8, 29.7, 27.5, 24.7, 18.9, 14.6, and 7.9. It gave *m/z* 237 (3.2), 194 (100), 166 (90), and 122 (46). *Anal.* calcd. for $C_{15}H_{27}NO$: C 75.89, H 11.46, N 5.90; found: C 75.92, H 11.27, N 5.98.

Ethylene thioketal hydrochloride 36

Crystalline keto base **34** hydrochloride (mp 153°C, 78 mg) was dissolved in 1 mL of dry ethanol-free chloroform, then 0.3 mL of 1,2-ethanedithiol and 0.4 mL of freshly distilled $BF_3 \cdot Et_2O$ added. The mixture was left at room temperature for 4 h, then evaporated *in vacuo*. The semisolid residue was dissolved in dichloromethane, then the solution washed with dilute aqueous sodium hydroxide. The base recovered from the dichloromethane extracts was converted to its hydrochloride using HCl in methanol. The methanol was evaporated and the product crystallized from ethyl acetate, giving 93 mg, mp 173°C (90%). This was recrystallized for analysis from dichloromethane – ethyl acetate, giving tiny rosettes, mp 172–174°C. It gave ^1H nmr signals at δ 4.25 (1H, br m) and 3.32 (4H, s). *Anal.* calcd. for $C_{17}H_{32}ClNS_2$: C 58.35, H 9.22, N 4.00; found: C 60.37, H 9.62, N 4.10.

dl-*Gephyrotoxin 223AB* (*4*)

To a solution of 105 mg of ethylenethioketal **36** in 4.5 mL of absolute ethanol was added 430 mg of freshly prepared W2 Raney nickel (14). The suspension was refluxed under argon for 3.5 h, cooled, then filtered through a bed of Celite. The filtrate and ethanol washings were acidified using hydrogen chloride in ethanol, then evaporated under reduced pressure. The residue (66 mg, 87%) crystallized. This was purified on a 1000-μm silica gel plate using 15% ethanol in chloroform for development. A faint mauve band (R_f 0.6) was followed by the toxin hydrochloride. The 49 mg (63%) of salt crystallized from ethyl acetate – ether as flat needles, mp 129–131°C. The base liberated from the hydrochloride distilled over a short path at 95°C under 0.4 Torr. It gave ^{13}C nmr signals in $CDCl_3$ at δ 59.1, 58.6, 56.7, 36.0, 32.5, 31.1, 30.2, 29.3, 26.5, 25.1, 24.8, 23.0, 19.0, 14.6, and 14.2. In C_6D_6 the signals were at δ 59.0, 58.7, 56.4, 36.6, 33.1, 31.5, 30.8, 29.6, 27.1, 25.3, 23.4, 18.7, 14.9, and 14.4 (apparently two signals near 25 ppm were coincident).

The spectrum in deuteriochloroform was nearly identical to that reported by Royer and Husson (12) for their synthetic isomer, and to that recorded for natural gephyrotoxin 223AB by Professor T. Tokuyama and co-workers (10) (see glc comparison for the salt).

dl-*Gephyrotoxin 223AB hydrochloride* (*4 hydrochloride*)

The analytic specimen, mp 131°C, gave ^1H nmr signals at δ 3.85 (1H, br), 2.95 (2H, b), 2.08, 2.0, and 0.94 (center of a poorly resolved triplet) and ^{13}C nmr signals at δ 62.9(d), 59.95(d), 59.6(d), 32.6(t), 27.9(t), 27.54(t), 27.46(t), 27.36(t), 26.4(t), 24.9(t), 22.9(t), 22.4(t), 18.7(t), 13.7(q), and 13.6(q).

Comparison with various stereoisomers (glc) was kindly made by T. F. Spande[4] using a 30.5-m glass capillary column with SP-1000 stationary phase at 140°C, helium carrier gas, and flame ionization detector. The hydrochloride was shown to contain 98.6% of gephyrotoxin 223AB (**4**) (5*E*,9*E* isomer) and 1.4% of the 5*E*,9*Z* diastereoisomer.[9]

dl-*Gephyrotoxin 223AB hydrobromide*: A solution of the free base in methanol was acidified with hydrogen bromide in methanol, the solvent removed *in vacuo*, and the salt recrystallized from acetone. It formed flat needles with mp 147–150°C. Good-sized crystals grown slowly from acetone were used for X-ray crystallography (13). Its mass spectrum gave peaks at *m/z* 223 (2.8) (M^+), 222 (2.7), 180 (93), and 166 (100).

[9]This stereochemical designation gives the relation (*Z* = *syn*, *E* = *anti*) of the 5- and 9-hydrogens to the 3-hydrogen.

Acknowledgements

We thank Professor J. W. ApSimon for his hospitality, enabling completion of this work, R. J. Kolt and K. Bourque for ^{13}C nmr spectra, H. Seguin for the microanalyses, and Paul Desilets for exploratory experiments.

1. (*a*) R. Merten and G. Müller. Chem. Ber. **97**, 682 (1964); (*b*) M. P. Cava, C. K. Wilkins, D. R. Dalton, and K. Bessho. J. Org. Chem. **30**, 3772 (1965); (*c*) P. M. Quan, T. K. B. Karns, and L. D. Quin. J. Org. Chem. **30**, 2769 (1965); (*d*) S. M. Weinreb and R. R. Staib. Tetrahedron, **38**, 3087 (1982); (*e*) S. M. Weinreb and J. I. Levin. Acc. Chem. Res. **18**, 16 (1985); (*f*) G. R. Krow, K. J. Henz, and S. W. Szczepanski. J. Org. Chem. **50**, 1888 (1985).
2. W. A. Court, O. E. Edwards, C. Grieco, W. Rank, and T. Sano. Can. J. Chem. **53**, 463 (1975).
3. R. Albrecht, G. Kresze, and B. Mlakar. Chem. Ber. **97**, 483 (1964); S. Breuer, T. Bernath, and D. Ben-Ishai. Tetrahedron Lett. 4569 (1966); M. E. Jung, K. Shishido, L. Light, and L. Davis. Tetrahedron Lett. **22**, 4607 (1981); J. S. Millership and H. Suschitzky. Chem. Commun. 1496 (1971); D. S. Pearce, M. J. Lock, and H. W. Moore. J. Am. Chem. Soc. **97**, 6181 (1975); D. Vor Der Brück, R. Bühler, and H. Plieninger. Tetrahedron, **28**, 791 (1972); H. Poisel. Chem. Ber. **110**, 948 (1977); C. Shin. Y. Sato, H. Ohmatsu, and J. Yoshimura. Bull. Chem. Soc. Jpn. **54**, 1137 (1981); W. Steglich, K. Burger, M. Dürr, and E. Burgis. Chem. Ber. **107**, 1488 (1974).
4. J. C. Hubert, J. B. P. A. Wijnberg, and W. A. Speckamp. Tetrahedron, **31**, 1437 (1975).
5. (*a*) T. F. Spande, D. J. Hart, J. W. Daly, Y.-M. Tsai, and T. L. Macdonald. Experientia, **37**, 1242 (1981); (*b*) J. W. Daly and T. F. Spande. *In* Alkaloids: chemical and biological perspectives. Vol. 4. *Edited by* S. W. Pelletier. John Wiley and Sons Inc., New York. 1986. pp. 118–123.
6. J. E. Oliver and P. E. Sonnett. J. Org. Chem. **39**, 2662 (1974); J. H. Jones, M. S. Blum, and H. M. Fales. Tetrahedron, **38**, 1949 (1982).
7. L. Blomquist, K. Leander, B. Lüning, and J. Rosenblum. Acta. Chem. Scand. **26**, 3203 (1972).
8. D. J. Hart and Y.-M. Tsai. J. Org. Chem. **47**, 4403 (1982).
9. K. Clausen, M. Thorsen, and S.-O. Lawesson. Tetrahedron, **37**, 3635 (1981).
10. J. W. Daly, T. F. Spande, N. Whittaker, R. J. Highet, D. Feigl, N. Nishimori, T. Tokuyama, and C. W. Myers. J. Nat. Prod. (Lloydia), **49**, 265 (1986).
11. T. L. Macdonald. J. Org. Chem. **45**, 193 (1980).
12. J. Royer and H.-P. Husson. Tetrahedron Lett. **26**, 1515 (1985).
13. M. Pryzbylska and F. R. Ahmed. Crystallogr. Sect. C: Cript. Struct. Commun. **C42**, 832 (1986).
14. R. Mozingo. Org. Synth. Coll. Vol. **3**, 181 (1955).
15. D. Ben-Ishai and E. Goldstein. Tetrahedron, **27**, 3119 (1971).
16. R. V. Stevens and A. W. M. Lee. J. Chem. Soc. Chem. Commun. 103 (1982).
17. K. Clausz, D. Grimm, and G. Prossel. Justus Liebigs Ann. Chem. 539 (1974).
18. J. Attenburrow, A. F. B. Cameron, J. H. Chapman, R. M. Evans, B. A. Hems, A. B. A. Jansen, and T. Walker. J. Chem. Soc. 1094 (1952).
19. K. Alder and J. Haydn. Justus Liebigs Ann. Chem. **570**, 201 (1950; **570**, 212 (1950).
20. K. Bowden, I. M. Heilbron, E. R. H. Jones, and B. C. L. Weedon. J. Chem. Soc. 39 (1946).

Can. J. Chem. Downloaded from www.nrcresearchpress.com by 93.93.197.157 on 09/07/12
For personal use only.

Anthosterones A and B, ring A contracted steroids from the sponge *Anthoracuata graceae*

MARK TISCHLER, STEPHEN W. AYER, AND RAYMOND J. ANDERSEN[1]
Departments of Chemistry and Oceanography, University of British Columbia, Vancouver, B.C., Canada V6T 1W5

AND

JOHN F. MITCHELL AND JON CLARDY[1]
Department of Chemistry – Baker Laboratory, Cornell University, Ithaca, NY 14853-1301, U.S.A.

Received September 3, 1987

MARK TISCHLER, STEPHEN W. AYER, RAYMOND J. ANDERSEN, JOHN F. MITCHELL, and JON CLARDY. Can. J. Chem. **66**, 1173 (1988).

Four new steroids, anthosterone A (**5**), anthosterone B (**6**), and the Δ^4-3,6-diketo steroids **7** and **8**, have been isolated from the sponge *Anthoarcuata graceae*. The structures of anthosterones A (**5**) and B (**6**) were deduced from their spectral data and verified via single crystal X-ray diffraction analysis on **5**. The proposed structures for steroids **7** and **8** were based on spectral analysis and confirmed by synthesis of a model compound **12**. Anthosterones A and B represent the first examples of a new type of ring A contraction in a steroid nucleus.

MARK TISCHLER, STEPHEN W. AYER, RAYMOND J. ANDERSEN, JOHN F. MITCHELL et JON CLARDY. Can. J. Chem. **66**, 1173 (1988).

À partir de l'éponge *Anthoarcuata graceae*, on a isolé quatre nouveaux stéroïdes, l'anthostérone A (**5**), l'anthostérone B (**6**) et les Δ^4 dicéto-3,6 stéroïdes **7** and **8**. On a déterminé les structures des anthostérones A (**5**) et B (**6**) en se basant sur leurs données spectrales et on les a vérifiées à l'aide d'une analyse par diffraction de rayons-X sur un cristal unique du composé **5**. On a proposé les structures des stéroïdes **7** et **8** en se basant sur des analyses spectrales et on les a confirmées en procédant à la synthèse du composé modèle **12**. Les anthostérones A et B sont les premiers exemples de stéroïdes comportant un nouveau type de contraction du cycle A.

[Traduit par la revue]

Can. J. Chem. Downloaded from www.nrcresearchpress.com by 93.93.197.157 on 09/07/12
For personal use only.

Marine sponges continue to be a prolific source of interesting new steroids (1). Commonly encountered features in these compounds include: (*i*) A-nor skeletons of general structures **1** (2) and **2** (3), (*ii*) additional oxygenation of both the nucleus and the side chain (4), and (*iii*) side chains that have been extensively modified by alkylation and (or) degradation (5).

Several years ago we reported the isolation of the two cholestenone derivatives **3** and **4** from skin extracts of the dorid nudibranch *Aldisa sanguinea cooperi* (6). Specimens of *A. cooperi* are normally found deeply embedded in the sponge *Anthoarcuata graceae* from which they obtain nutrition and cryptic pigmentation. As part of an ongoing investigation of the origins of nudibranch skin chemistry (7), we undertook a careful examination of the steroids present in extracts of *A. graceae* to determine if compounds **3** and **4** were being sequestered by the nudibranchs directly from their sponge diet. As previously reported (6), we failed to find any evidence for the presence of either **3** or **4** in *A. graceae* extracts; however, we have found four new steroids, compounds **5–8**, whose structures are presented in this manuscript.

Anthoarcuata graceae was collected by hand using SCUBA on shallow rocky reefs (−2 to −15 m) along the shoreline of the Deer Group of Islands in Barkley Sound, British Columbia. Freshly collected sponge was homogenized in a Waring blender with methanol and extracted at room temperature for periods of up to a week. The methanol was removed via vacuum filtration, concentrated *in vacuo* to an aqueous suspension, and the suspension was partitioned between water and dichloromethane. The resulting sponge solids were extracted three additional times with dichloromethane at 1-day intervals. Combination and reduction of all the dichloromethane solutions gave a dark red oil. Fractionation of the red oil by sequential application of silica-gel flash, Sephadex LH-20, reverse phase hplc, and preparative thin-layer silica-gel chromatographies gave pure samples of anthosterones A (**5**) and B (**6**) and the Δ^4-3,6-diketosteroids **7** and **8**.

Anthosterone A (**5**), obtained as white needles (mp 142–143°C) from acetonitrile, gave a parent ion in the EI hrms at m/z 442.3083 daltons that was consistent with a molecular formula of $C_{28}H_{42}O_4$ (ΔM + 0.4 mmu). The ultraviolet spectrum of **5** showed a single absorption with λ_{max} 250 nm (ε 12 500), and its infrared spectrum had absorption bands at 3532, 1744, and 1717 cm^{-1} that were assigned to alcohol, ester carbonyl, and α,β-unsaturated cyclopentenone carbonyl functionalities respectively. A methyl resonance at δ 3.79 (s) ppm in the ^1H nmr spectrum of **5**, in conjunction with a mass spectral fragment at m/z 383 daltons ($M^+ - 59$; CO_2CH_3) and the ester carbonyl stretch in the infrared spectrum, indicated that anthosterone A was a methyl ester. The remainder of the ^1H nmr spectrum of **5** was typical of a steroid. Resonances at δ 0.73 (s), 0.96 (d, J = 6.7 Hz), and 1.21 (s) ppm were assigned to the C18, C21, and C19 methyl protons respectively. A pair of resonances at δ 1.69 (s) and 1.62 (s) ppm assigned to the protons on olefinic methyl groups at C26 and C27, and an olefinic resonance at δ 5.10 (t, J = 8 Hz) ppm assigned to H24, revealed that anthosterone A had a standard Δ^{24} steroid side chain. An intense fragment ion at m/z 329 daltons (rel. int. 41%, $M^+ - (C_8H_{15} + H_2)$) in the mass spectrum of **5** (8), and a close agreement between the chemical shifts of ^{13}C nmr resonances assigned to the side-chain carbons of **5** (Table 2) and values for model compounds (9) confirmed the nature of the side chain.

Subtracting the methoxy carbon of the ester functionality from the 28 carbons in the molecular formula of anthosterone A (**5**) left the 27 carbons of a standard steroid skeleton. All of the

[1]Authors to whom correspondence may be addressed.

Can. J. Chem. Downloaded from www.nrcresearchpress.com by 93.93.197.157 on 09/07/12
For personal use only.

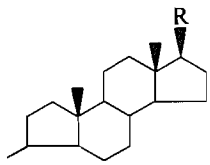

1

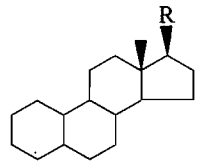

2

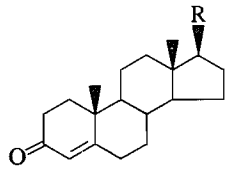

3 R = 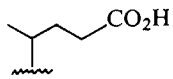

4 R = 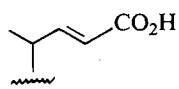

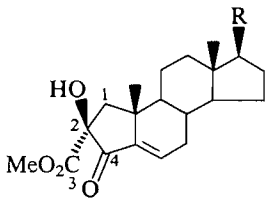

5 R = 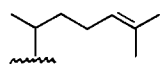

6 R = 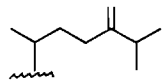

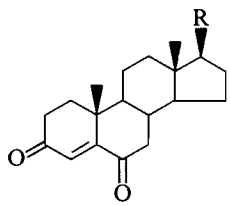

7 R = 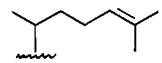

8 R = 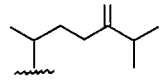

12 R = 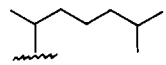

one-carbon appendages of the standard skeleton (carbons 18, 19, 21, 26, and 27) could be accounted for in the ^{1}H nmr spectrum of **5** as indicated above, and it was apparent that there were no additional alkyl substituents in the side chain. We concluded, therefore, that the primary carbon represented by the methyl ester carbonyl had been exposed by a contraction of one of the rings of the nucleus.

A number of additional fragments of **5** could be identified from spectral data. The ^{1}H nmr resonances at δ 2.10 (d, J = 13.3 Hz) and 2.19 (d, J = 13.3 Hz) ppm were assigned to a pair of spin-isolated geminal protons. The ^{13}C nmr resonances at δ 200.9 (s), 145.1 (s), and 136.3 (d) ppm, an ^{1}H nmr resonance at δ 6.73 (t, J = 3.3 Hz) ppm, the ir band at 1717 cm^{-1}, and the uv chromophore were assigned to an α,β-disubstituted-α,β-unsaturated ketone. Finally, a ^{13}C nmr resonance at δ 79.9 (s) ppm and the OH stretching band in the ir spectrum were assigned to a tertiary alcohol.

We were able to construct only the three candidate structures **5, 9**, and **10** that could accommodate all the identified fragments of anthosterone A. Nuclear magnetic resonance experiments allowed us to eliminate two of the possible structures. Application of a soft pulse to the geminal proton at δ 2.19 ppm in a SINEPT experiment, optimized for polarization transfer through 2- and 3-bond ^{1}H,^{13}C couplings (J = 7 Hz), showed transfer to the ester carbonyl (δ 173.4), the ketone carbonyl (δ 200.9), the tertiary carbinol (δ 79.9), and the fully substituted olefinic (δ 145.1) carbon resonances. The observed polarization transfer to the ester carbonyl carbon would require a highly improbable six-bond ^{1}H,^{13}C coupling in structure **10**. An ^{1}H COSY spectrum of anthosterone A showed a correlation between the downfield doublet of the isolated geminal spin system at δ 2.19 ppm and the methyl resonance at δ 1.21 ppm assigned to the protons on the C19 methyl group. The observed correlation could only be attributed to a W coupling between the C19 methyl protons and an α proton on Cl of structure **5**. With the constitution of anthosterone A (**5**) in hand, all that remained was to determine the relative stereochemistry at C2. This was accomplished by carrying out an acetylation reaction on anthosterone B (**6**).

Anthosterone B (**6**), obtained as white needles (mp 155–157°C, acetonitrile), gave a parent ion at m/z 456.3236 daltons in the EI ms appropriate for a molecular formula of $C_{29}H_{44}O_4$ (ΔM + 0.5 mmu). It was apparent from the ^{1}H (Table 1) and ^{13}C nmr (Table 2) spectra of **6** that it contained the same ring A contracted nucleus as anthosterone A (**5**). The ^{1}H nmr resonances at δ 1.04 (d, J = 6.5 Hz, 6H), 4.67 (s), and 4.73 (s) ppm could be assigned to isopropyl and olefinic methylene fragments in the side chain of anthosterone B (**6**). Mass spectral fragments at m/z 382 ($M^+ - (CO_2CH_3 + CH_3)$) and 298 (382 − C_6H_{12} via a McLafferty rearrangement) daltons indicated that the olefinic methylene was at C24 of the side chain. Comparison of the chemical shifts of the ^{13}C nmr resonances assigned to the side chain carbons of **6** (Table 2) with the chemical shifts of the corresponding carbons in model compounds confirmed this assignment (10). Acetylation of anthosterone B (**6**) with acetic

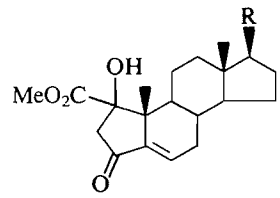

9

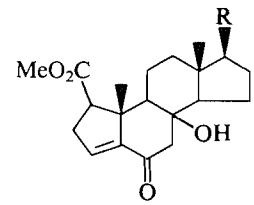

10

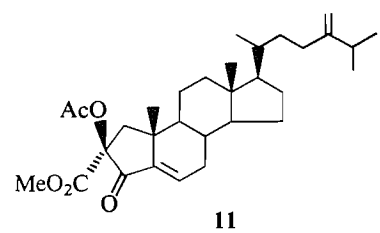

11

anhydride and pyridine gave the mono acetate **11**. The ^{1}H nmr resonance assigned to the C19 methyl protons showed an upfield shift (δ 1.20 in **6**; δ 1.10 in **11**) and the resonances assigned to the Cl methylene protons showed a downfield shift (δ 2.10 and 2.18 in **6**; δ 2.47 and 2.65 in **11**) in the spectrum of acetate **11**. These acetylation shifts confirmed the spatial proximity of the tertiary alcohol, isolated methylene, and C19 methyl groups in **6**, and they required that the tertiary alcohol and the C19 methyl group be *cis* to each other. The complete structures of anthosterones A and B could therefore be represented as **5** and **6**.

To verify that our structural assignments for **5** and **6** were correct, we subjected anthosterone A (**5**) to single crystal X-ray diffraction analysis.

Crystal data:

$C_{28}H_{42}O_4$ fw = 442.64

Orthorhombic, $P2_12_12_1$, a = 8.576(1), b = 8.378(1), c = 36.312(4) Å, V = 2609.0 Å^3, ρ_c = 1.127 g cm^{-3}, μ = 5.45 cm^{-1}, (20°C; CuKα; λ = 1.5418 Å).

All unique diffraction maxima in one octant of the limiting sphere with 0° < 2θ <114° were collected from a crystal of approximate size 0.15 × 0.20 × 0.40 mm using CuKα radiation and 1.5° ω-scans. Variable scan speeds (based on pre-scans) were applied (1.5–28.0°/min). The intensities of three check

TABLE 1. ^{1}H nuclear magnetic resonance assignments, recorded at 400 MHz in $CDCl_3$. Chemical shifts are in ppm from internal TMS

Proton on carbon no.	5	6	7	8	12
1	2.10, d, J = 13.3 Hz	2.10, d, J = 13.5 Hz	—	—	—
	2.19, d, J = 13.3 Hz	2.18, d, J = 13.5 Hz	—	—	—
4	—	—	6.19, s	6.17, s	6.19, s
5	6.73, t, J = 3.3 Hz	6.73, t, J = 3.3 Hz	—	—	—
18	0.73, s	0.73, s	0.73, s	0.73, s	0.74, s
19	1.21, s	1.20, s	1.17, s	1.17, s	1.19, s
21	0.96, d, J = 6.7 Hz	0.97, d, J = 6.5 Hz	0.95, d, J = 6 Hz	0.96, d, J = 7 Hz	0.94, d, J = 6 Hz
24	5.10, t, J = 8 Hz	—	5.09, t, J = 6 Hz	—	—
26	1.69, s	1.04, d, J = 6.5 Hz	1.69, s	1.02, d, J = 8 Hz	0.87, d, J = 6 Hz
27	1.62, s	1.04, d, J = 6.5 Hz	1.61, s	1.02, d, J = 8 Hz	—
28	3.79, s	4.67, bs	—	4.68, bs	—
		4.73, bs	—	4.76, bs	—
29	—	3.77, s	—	—	—

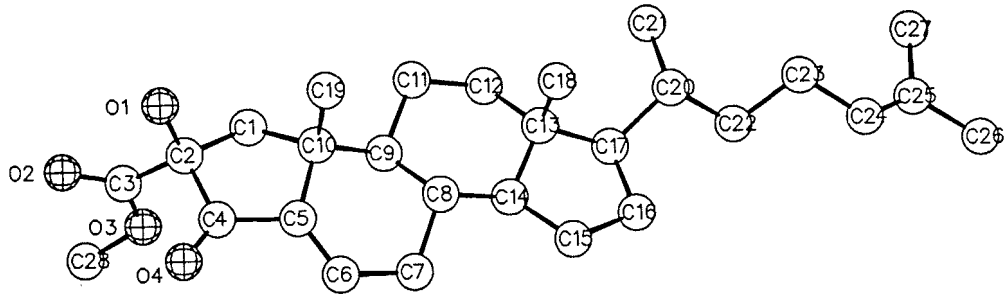

FIG. 1. A computer generated perspective drawing of Anthosterone A (**5**).

TABLE 2. Partial ^{13}C nmr assignments, recorded in $CDCl_3$ at 75 MHz. Chemical shifts are in ppm from internal TMS

Carbon no.	5	6	7	8	12
2	79.9	79.9	—	—	—
3	173.4	173.4	199.6	199.6	199.4
4	200.9	200.9	125.5	125.4	125.3
5	145.1	145.1	161.1	161.0	161.0
6	136.3	136.3	202.4	202.3	202.3
24	125.1	156.8	124.9	156.7	—
25	131.1	33.8	127.1	—	—
26	17.7	21.9	—	—	—
27	25.8	21.8	—	—	—
28	53.4	106.0	—	106.1	—
29	—	53.4	—	—	—

reflections (0,0,10; 4,0,0; 0,0,2) were monitored at every 100 reflections during the data collection. No decrease of the intensities of the check reflections was observed and their variation was less than 10%. Of the 2061 reflections measured, only 929 (45%) were judged observed ($|F_o| > 3\sigma(F_o)$) due to the poor quality of the crystal.[2]

A phasing model was found using direct methods, and recycling of a plausible molecular fragment revealed the entire heavy atom structure. Isotropic block diagonal least squares for the non-hydrogen atoms were terminated at R = 0.105. Block diagonal least-squares refinements with anisotropic non-hydrogen atoms and isotropic hydrogens have converged to a conventional crystallographic residual of 0.075, R_w = 0.098, S = 1.151. The function minimized was $\Phi = \Sigma\, w\Delta F^2$, where $w = 1/\sigma(F)^2$. The hydroxyl hydrogen atom was located in a difference map, all other hydrogen atomic positions were generated from assumed geometries, and the isotropic temperature factors for the hydrogen atoms were calculated from the B(eq) value of the atom to which they were bonded (B(H) = 1.1B(eq), Å^2). The highest peak in the final difference electron density map was 0.48 e Å^{-3}. No hydrogen atomic parameters were refined and no absorption correction was applied. The X-ray experiment did not define the absolute configuration. A computer generated perspective drawing of the final X-ray model is given in Fig. 1, the positional parameters and B(eq) values for the non-hydrogen atoms are given in Table 3, bond distances and angles are shown in Table 4. Additional crystallographic information is available.[3]

Two additional steroids, **7** and **8**, which had Δ^4-3,6-diketo nuclei and side chains identical to those found in anthosterones A (**5**) and B (**6**) respectively, were also isolated from *A. graceae* extracts. Steroid **7**, obtained as needles from acetonitrile (mp 92–93°C), gave a parent ion in the EI ms at m/z 396.3034 daltons that was consistent with a molecular formula of $C_{27}H_{40}O_2$ (ΔM − 0.4 mmu). An olefinic proton resonance at δ 6.19 (s) ppm in the ^{1}H nmr, carbonyl and olefinic carbon resonances at δ 202.4 (s), 199.6 (s), 161.1 (s), and 125.5 (d)

[2]All crystallographic calculations were done on a PRIME 9950 computer operated by the Cornell Chemistry Computing Facility. Principal programs employed are given in ref. 11.

[3]Atomic coordinates for this structure have been deposited and may be purchased from the Depository of Unpublished Data, CISTI, National Research Council of Canada, Ottawa, Ont., Canada K1A 0S2.

Can. J. Chem. Downloaded from www.nrcresearchpress.com by 93.93.197.157 on 09/07/12
For personal use only.

TABLE 3. Final positional parameters ($\times 10^4$) and B(eq) values for the non-hydrogen atoms for compound **5** with their e.s.d's

Atom	*x/a*	*y/b*	*z/c*	*B*(eq)	Atom	*x/a*	*y/b*	*z/c*	*B*(eq)
O1	5253(12)	11144(10)	3000(2)	10.0(3)	C13	5008(14)	5455(13)	4576(3)	7.3(4)
O2	7944(13)	11458(12)	2633(3)	11.6(4)	C14	5338(15)	4633(14)	4211(3)	7.5(4)
O3	9046(11)	9407(10)	2913(2)	9.8(3)	C15	4595(15)	2970(16)	4248(3)	7.9(4)
O4	5714(13)	8095(11)	2572(2)	11.1(4)	C16	4835(17)	2560(14)	4657(3)	8.1(4)
C1	6613(17)	9583(15)	3468(3)	8.6(4)	C17	5394(14)	4116(12)	4853(3)	6.8(3)
C2	6402(17)	9970(15)	3055(3)	8.7(4)	C18	3190(14)	5926(15)	4606(3)	7.6(4)
C3	7876(17)	10400(16)	2852(3)	9.3(5)	C19	3679(17)	9025(15)	3607(4)	10.3(5)
C4	5784(17)	8364(18)	2887(3)	9.4(5)	C20	4665(15)	4261(14)	5259(3)	7.5(3)
C5	5432(17)	7230(15)	3204(3)	8.7(5)	C21	5325(19)	5741(17)	5474(3)	10.2(5)
C6	5436(18)	5646(16)	3185(3)	9.7(5)	C22	5203(16)	2773(15)	5464(3)	8.2(4)
C7	5396(16)	4659(13)	3518(3)	7.7(4)	C23	4461(18)	2659(15)	5854(3)	9.4(5)
C8	4991(14)	5641(14)	3876(3)	7.5(4)	C24	4760(18)	1036(16)	6018(3)	9.4(5)
C9	5858(16)	7191(16)	3882(3)	8.0(4)	C25	5096(17)	728(17)	6346(3)	10.1(5)
C10	5352(18)	8263(14)	3554(3)	8.5(4)	C26	5374(20)	−921(19)	6525(4)	11.4(6)
C11	5723(17)	8075(14)	4265(3)	8.6(5)	C27	5530(27)	1964(22)	6632(4)	14.8(8)
C12	5992(15)	6972(15)	4592(3)	8.0(4)	C28	10429(25)	9960(21)	2694(4)	13.3(7)

TABLE 4. Bond lengths (Å) and angles (°) for compund **5**

Bond	Length	Bond	Length	Bond	Length
O1—C2	1.41(2)	O2—C3	1.19(2)	O3—C3	1.32(2)
O3—C28	1.44(2)	O4—C4	1.17(1)	C1—C2	1.54(2)
C1—C10	1.58(2)	C2—C3	1.51(2)	C2—C4	1.57(2)
C4—C5	1.52(2)	C5—C6	1.33(2)	C5—C10	1.54(2)
C6—C7	1.47(2)	C7—C8	1.58(2)	C8—C9	1.50(2)
C8—C14	1.51(2)	C9—C10	1.55(2)	C9—C1	1.58(2)
C10—C19	1.58(2)	C11—C12	1.52(2)	C12—C13	1.53(2)
C13—C14	1.52(2)	C13—C17	1.54(2)	C13—C18	1.61(2)
C14—C15	1.54(2)	C15—C16	1.54(2)	C16—C17	1.56(2)
C17—C20	1.61(2)	C20—C21	1.57(2)	C20—C22	1.52(2)
C22—C23	1.56(2)	C23—C24	1.51(2)	C24—C25	1.25(2)
C25—C26	1.55(2)	C25—C27	1.51(2)		

Bond	Angle	Bond	Angle	Bond	Angle
C3—O3—C28	116.0(7)	C2—C1—C10	105.0(7)	O1—C2—C1	111.6(6)
O1—C2—C3	110.4(7)	O1—C2—C4	107.9(7)	C1—C2—C3	115.4(7)
C1—C2—C4	103.7(7)	C3—C2—C4	107.3(7)	O2—C3—O3	122.9(8)
O2—C3—C2	123.1(8)	O3—C3—C2	113.7(7)	O4—C4—C2	124.4(8)
O4—C4—C5	127.5(8)	C2—C4—C5	107.9(6)	C4—C5—C6	125.8(6)
C4—C5—C10	106.4(6)	C6—C5—C10	127.0(6)	C5—C6—C7	121.5(7)
C6—C7—C8	112.9(6)	C7—C8—C9	110.8(6)	C7—C8—C14	109.2(5)
C9—C8—C14	112.1(6)	C8—C9—C10	110.6(6)	C8—C9—C11	112.5(6)
C10—C9—C11	112.5(6)	C1—C10—C5	101.5(6)	C1—C10—C9	111.5(6)
C1—C10—C19	111.3(6)	C5—C10—C9	107.2(6)	C5—C10—C19	111.6(7)
C9—C10—C19	113.2(7)	C9—C11—C12	113.1(6)	C11—C12—C13	113.0(6)
C12—C13—C14	108.0(5)	C12—C13—C17	117.5(5)	C12—C13—C18	109.1(6)
C14—C13—C17	101.5(6)	C14—C13—C18	110.5(6)	C17—C13—C18	110.0(6)
C8—C14—C13	114.4(6)	C8—C14—C15	119.7(6)	C13—C14—C15	104.8(6)
C14—C15—C16	103.4(6)	C15—C16—C17	107.1(6)	C13—C17—C16	104.1(5)
C13—C17—C20	117.4(5)	C16—C17—C20	111.2(5)	C17—C20—C21	112.0(6)
C17—C20—C22	105.5(6)	C21—C20—C22	107.2(6)	C20—C22—C23	111.7(6)
C22—C23—C24	110.2(6)	C23—C24—C25	126.9(6)	C24—C25—C26	128.3(8)
C24—C25—C27	124.6(8)	C26—C25—C27	106.6(7)		

ppm in the ^{13}C nmr, carbonyl and olefinic double bond stretching bands at 1686 and 1643 cm^{-1} in the ir, and a uv chromophore with a λ_{max} at 249 nm were assigned to the Δ^4-3,6-diketo functionality in **7**. Compound **12**, prepared by Jones oxidation of cholesterol (12), served as a model for the Δ^4-3,6-diketo nucleus of **7**. The nmr, ir, and uv data collected on **12** were in excellent agreement with those assigned to the ene dione functionality of **7**. The ^1H nmr resonances at δ 1.61 (s, 3H), 1.69 (s, 3H), and 5.09 (t, J = 6 Hz, 1H) in the spectrum of **7** were assigned to the protons on C26, C27, and C24 of a Δ^{24} steroid

Can. J. Chem. Downloaded from www.nrcresearchpress.com by 93.93.197.157 on 09/07/12
For personal use only.

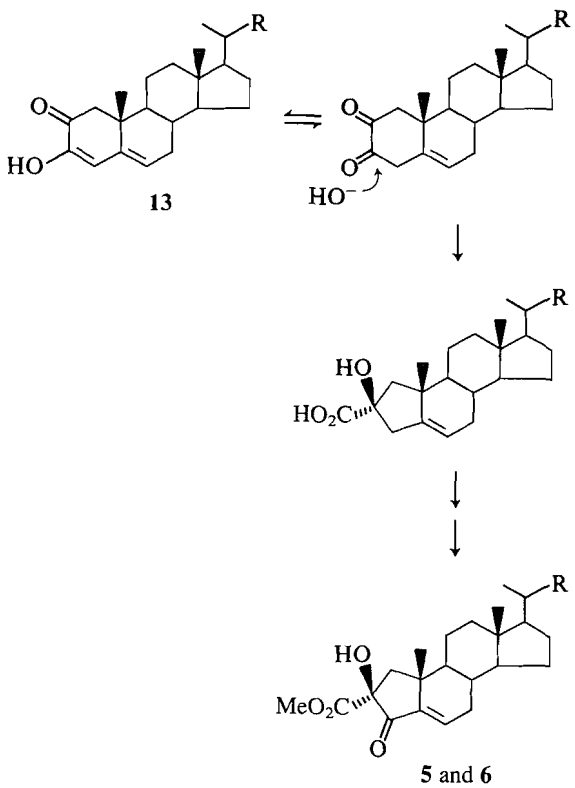

SCHEME 1

side chain. An intense mass spectral fragment at m/z 283 daltons ($M^+ - C_8H_{17}$ (side chain)) confirmed the nature of the side chain in **7** (8).

Steroid **8**, also obtained as needles from acetonitrile (mp 111–112°C), gave a parent ion in the EI ms at m/z 410.3182 daltons consistent with a molecular formula of $C_{28}H_{42}O_2$(ΔM − 0.5 mmu). It was immediately apparent from the ^1H and ^{13}C nmr spectra of **8** that it shared the Δ^4-3,6-diketo steroid nucleus with **7** and the $\Delta^{24,28}$ olefinic methylene side-chain functionality with **6** (Tables 1 and 2). The ms and uv data for this steroid were also consistent with structure **8**.

Anthosterones A (**5**) and B (**6**) apparently represent the first examples of ring A contracted steroids in which there is a one-carbon appendage at C2 of the cyclopentane ring. All previously reported examples have a one-carbon appendage at C3 (i.e., general structure **1**). A benzilic acid rearrangement on an α diketone such as **13** represents a possible ring contraction step in the biosynthesis of the anthosterone nucleus (Scheme 1). The Δ^4-3,6-diketone nucleus in steroids **7** and **8** has not been previously reported from a natural source.

Experimental

The nmr spectra were recorded on Varian XL 300 and Bruker WH-400 spectrometers. Me_4Si was used as an internal standard. Low resolution mass spectra were recorded on an AEI MS902 spectrometer and high resolution mass spectra on an AEI MS50 spectrometer. The ir spectra were recorded on a Perkin Elmer 1710 Fourier transform spectrometer. The uv spectra were recorded on a Bausch and Lomb Spectronic 2000 instrument. Optical rotation measurements were recorded on a Perkin Elmer 141 polarimeter.

Merck silica gel (230–400 mesh) was used for flash chromatography and a Whatman Magnum 9 Partisil 10 ODS-3 column was used for preparative hplc. Sephadex LH 20 was used for molecular exclusion chromatography.

Anthoarcuata graceae (1.2 kg dry wt.) was collected with the aid of SCUBA on shallow rocky reefs (−2 to −15 m) in the Deer Group of Islands in Barkley Sound, British Columbia. Freshly collected sponge was immediately immersed in methanol (8L) and homogenized in a Waring blender. After extraction at room temperature for 1 week, the methanol was removed via vacuum filtration, concentrated *in vacuo* to an aqueous suspension (250 mL), and the suspension was partitioned between brine (750 mL) and dichloromethane (4 × 300 mL). The resulting sponge solids were extracted three additional times with dichloromethane (1.5 L) at 1-day intervals. The combined dichloromethane solutions were dried over Na_2SO_4, filtered, and concentrated *in vacuo* to give a dark red oil (46.9 g, 3.9% dry wt.).

Flash chromatography (step gradient from 100% hexane to 30% ethyl acetate/ 70% hexane) on the red oil gave a fraction containing a mixture of steroids, fats, and pigments. Sephadex LH20 chromatography (eluent 55% methanol/ 45% chloroform) largely removed the fats and pigments from the steroid mixture. Reverse phase hplc (eluent 10% water/90% aectonitrile) separated the steroid fraction, obtained from LH20, into two major fractions that each contained a mixture of two steroids. The fast running hplc fraction contained steroids **6** and **8**, while the slow running hplc fraction contained steroids **5** and **7**. Preparative tlc (silica gel, eluent: 5% methanol/95% dichloromethane) separated anthosterone B (**6**) from steroid **8**, and anthosterone A (**5**) from steroid **7**.

Anthosterone A (**5**): 7 mg, 6 × 10^{-4}% dry wt; mp 142–143°C (CH_3CN); uv (CH_3CN) λ_{max}: 250 nm (ε 12 500); ir ($CHCl_3$, cast): 3532, 3021, 2951, 2869, 1744, 1717, 1648 cm^{-1}; ^1H nmr (Table 1); ^{13}C nmr (Table 2) δ: 200.9, 173.4, 145.1, 136.3, 131.1, 125.1, 79.9, 56.3, 56.0, 55.9, 53.4, 49.7, 46.7, 42.9, 39.9, 36.1, 35.6, 32.3, 32.2, 28.1, 25.8, 24.7, 24.4, 22.1, 21.8, 18.7, 17.7, 12.0 ppm; EI hrms M^+: 442.3083 ($C_{28}H_{42}O_4$, ΔM + 0.4 mmu); EI lrms m/z: 442, 427, 383, 358, 329, 298, 283, 95, 81, 69(100%), 55.

Anthosterone B (**6**): 5 × 10^{-4}% dry wt; mp 155–157°C (CH_3CN); uv (CH_3CN) λ_{max}: 249 nm (ε 12 030); ir ($CHCl_3$, cast): 3022, 2929, 2856, 1744, 1717, 1643, cm^{-1}; ^1H nmr (Table 1); ^{13}C nmr (Table 2) δ: 200.9, 173.4, 156.8, 145.1, 136.3, 106.0, 79.9, 56.3, 55.9, 53.4, 49.6, 46.7, 42.9, 39.9, 39.3, 35.7, 34.6, 33.8, 32.3, 32.2, 31.0, 28.1, 24.3, 22.1, 22.0, 21.9, 21.8, 18.7, 12.0 ppm; EI hrms M^+: 456.3236 ($C_{29}H_{44}O_4$, ΔM + 0.5 mmu); EI lrms m/z: 456, 382, 367, 298, 269.

Acetylation of anthosterone B

Anthosterone B (**6**) (2.8 mg) was stirred overnight at room temperature in a mixture of pyridine (0.4 mL) and acetic anhydride (0.2 mL). The pyridine/acetic anhydride mixture was removed *in vacuo* to give anthosterone B acetate (**11**) in quantitative yield as a white solid. *Acetate* (**11**): ^1H nmr ($CDCl_3$) δ: 0.72(s, 3H), 0.97(d, J = 8 Hz, 3H), 1.03(d, J = 8 Hz, 6H), 1.10(s, 3H), 2.16(s, 3H), 2.47(d, J = 14 Hz, 1H), 2.65(d, J = 14 Hz, 1H), 3.76 (s, 3H), 4.67(bs, 1H), 4.73(s, 1H), 6.81(t, J = 4 Hz, 1H); EI hrms M^+: 498.3347 ($C_{31}H_{46}O_5$, ΔM 0.0 mmu).

Ene dione **7**: 3 × 10^{-4}% dry wt; mp 92–93°C; uv (CH_3CN) λ_{max}: 249 nm (ε 11 600); ir ($CHCl_3$, cast): 3031, 2956, 1686, 1643, 1606 cm^{-1}; ^1H nmr (Table 1); ^{13}C nmr (Table 2); EI hrms M^+: 396.3034 ($C_{27}H_{40}O_2$, ΔM + 0.4 mmu); EI lrms m/z 396, 326, 283, 243.

Ene dione **8**: 3 × 10^{-4}% dry wt; mp 111–112°C (CH_3CN); uv (CH_3CN) λ_{max}: 249 nm (ε 12 500); ^1H nmr (Table 1); ^{13}C nmr (Table 2); EI hrms M^+: 410.3182 ($C_{28}H_{42}O_2$, ΔM − 0.5 mmu); EI lrms m/z 410,327, 326, 312, 311, 283, 257.

Ene dione **12**: Prepared according to the literature (12); mp 132–134°C (CH_3CN); ir ($CHCl_3$, cast): 2953, 2871, 1685, 1606 cm^{-1}; ^1H nmr (Table 1); ^{13}C nmr (Table 2); EI hrms M^+: 398.3186 ($C_{27}H_{42}O_2$, ΔM − 0.1 mmu).

Acknowledgements

The authors wish to thank Mike LeBlanc and the staff of the Bamfield Marine Station for assistance in the collection of *A. graceae*. Financial support at UBC was provided by a grant from the Natural Sciences and Engineering Research Council of Canada to R.J.A. The Cornell authors thank the New York State Sea Grant and NIH CA24487 for financial support.

Can. J. Chem. Downloaded from www.nrcresearchpress.com by 93.93.197.157 on 09/07/12
For personal use only.

1. (*a*) J. R. PROUDFOOT, X. LI, and C. DJERASSI. J. Org. Chem. **50**, 2026 (1985); (*b*) S. B. SEIDEL, J. R. PROUDFOOT, C. DJERASSI, D. SICA, and G. SODANO. Steroids, **47**, 49 (1986).
2. (*a*) L. MINALE and G. SODANO. J. Chem. Soc. Perkin Trans. 1, 2308 (1974); (*b*) M. L. EGGERSDORF, W. C. M. C. KOKKE, C. W. CRANDELL, J. E. HOCHLOWSKI, and C. DJERASSI. J. Org. Chem. **47**, 5304 (1982).
3. (*a*) L. MINALE and G. SODANO. J. Chem. Soc. Perkin Trans. 1, 1888 (1974); (*b*) S. POPOV, R. M. K. CARLSON, A. WEGMAN, and C. DJERASSI. Tetrahedron Lett. 3491 (1976).
4. (*a*) A. MALORNI, L. MINALE, and R. RICCIO. Nouv. J. Chim. **2**, 351 (1975); (*b*) P. KOCH, C. DJERASSI, V. LAKSHMI, and F. J. SCHMITZ. Helv. Chim. Acta, **66**, 2431 (1983).
5. (*a*) W. C. M. C. KOKKE, C. TARCHINI, D. B. STIERLE, and C. DJERASSI. J. Org. Chem. **44**, 3385 (1979); (*b*) I. L. STOILOV, J. THOMPSON, and C. DJERASSI. Tetrahedron Lett. **27**, 4821 (1986).
6. S. W. AYER and R. J. ANDERSEN. Tetrahedron Lett. **23**, 1039 (1982).
7. D. E. WILLIAMS, S. W. AYER, and R. J. ANDERSEN. Can. J. Chem. **64**, 1527 (1986), and references therein.
8. S. WYLLIE and C. DJERRASI. J. Org. Chem. **33**, 305 (1968).
9. (*a*) O. TANAKA and R. KASAI. Prog. Chem. Org. Nat. Prod. **46**, 1 (1984); (*b*) L. MINALE and R. RICCIO. Tetrahedron Lett. 2711 (7976).
10. J. A. FINDLAY and A. D. PATIL. Can. J. Chem. **63**, 2406 (1985).
11. G. VAN DUYNE. FOBS86. Cornell University, Ithaca, NY 1986; P. MAIN, S. E. HULL, L. LESSINGER, G. GERMAIN, J. P. DECLERCQ, and M. M. WOOLFSON. Multan 80. University of York, England; K. HIROTSU and E. ARNOLD. BLS78A. Cornell University, Ithaca, NY. 1981; G. VAN DUYNE. PL1PLOT. Cornell University, Ithaca, NY. 1984; TABLES. Cornell University, Ithaca, NY. 1986.
12. (*a*) B. ACHARI, E. ALI, P. P. GHOSH DASTIDAR, and S. C. PAKRASHI. J. Indian Chem. Soc. **51**, 419 (1974); (*b*) D. J. ABERHART and E. CASPI. J. Biol. Chem. **246**, 1387 (1971).

Can. J. Chem. Downloaded from www.nrcresearchpress.com by 93.93.197.157 on 09/07/12
For personal use only.

Thermodynamics of alkanoate + alkane binary mixtures. Concentration dependence of excess heat capacities and volumes[1]

MERCEDES PINTOS, RAMON BRAVO, MARIA CARMEN BALUJA, AND MARIA INMACULADA PAZ ANDRADE
Departamento de Fisica Fundamental, Facultad de Ciencias, Universidad de Santiago de Compostela, Santiago de Compostela, Spain

AND

GENEVIÈVE ROUX-DESGRANGES AND JEAN-PIERRE E. GROLIER
Laboratoire de Thermodynamique et Cinétique Chimique (UA CNRS 434), Université Blaise Pascal Clermont-Ferrand, F - 63170 Aubière, France

Received October 23, 1987

This paper is dedicated to Professor J. A. Morrison

MERCEDES PINTOS, RAMON BRAVO, MARIA CARMEN BALUJA, MARIA INMACULADA PAZ ANDRADE, GENEVIÈVE ROUX-DESGRANGES and JEAN-PIERRE E. GROLIER. Can. J. Chem. **66**, 1179 (1988).

Excess molar volumes, V^E, and excess molar heat capacities at constant pressure, C_p^E, have been obtained for some *n*-alkanoate + *n*-alkane mixtures at 298.15 K from density and volumetric heat capacity measurements using liquid-flow techniques. The alkanoates selected were *n*-propyl methanoate, methyl ethanoate, ethyl ethanoate, methyl propanoate, methyl butanoate, methyl pentanoate, and methyl octanoate. V^E are positive for all systems and rather symmetric. The composition dependence of C_p^E is typically of the ω-shaped type with two minima, more or less pronounced, which are separated by a positive part in the case of the more polar esters, i.e. *n*-propyl methanoate and methyl ethanoate. These results are discussed in terms of possible changes in conformation of both the ester and the *n*-alkane.

MERCEDES PINTOS, RAMON BRAVO, MARIA CARMEN BALUJA, MARIA INMACULADA PAZ ANDRADE, GENEVIÈVE ROUX-DESGRANGES et JEAN-PIERRE E. GROLIER. Can. J. Chem. **66**, 1179 (1988).

Les volumes d'excès, V^E, et les capacités calorifiques d'excès, C_p^E, ont été obtenus pour quelques mélanges *n*-alcanoate + *n*-alcane à 298.15 K à partir de mesures des densités et des capacités calorifiques volumiques, à l'aide de techniques à écoulement de liquide. Les alcanoates choisis ont été le méthanoate de *n*-propyle, l'éthanoate de méthyle, l'éthanoate d'éthyle, le propanoate de méthyle, le butanoate de méthyle, le pentanoate de méthyle et l'octanoate de méthyle. Les volumes d'excès sont positifs et plutôt symétriques pour tous les systèmes. La variation avec la concentration des capacités calorifiques d'excès est représentée par des courbes avec deux minima plus ou moins marqués qui sont séparés par une partie positive dans le cas des esters les plus polaires tels que le méthanoate de propyle et l'éthanoate de méthyle. Ces résultats sont interprétés en terme de changements de conformations possibles, à la fois dans l'ester et l'alcane.

Can. J. Chem. Downloaded from www.nrcresearchpress.com by 93.93.197.157 on 09/07/12
For personal use only.

Binary mixtures of the type (an alkanoate + an *n*-alkane) have been investigated fairly extensively from a thermodynamic point of view. For our part, we have measured a number of heats of mixing and excess volumes (1), and recently we published a review paper (2) analysing the information available in the literature about the thermodynamic properties of this class of mixtures in terms of a quasi-chemical group contribution model. Ten years ago Dusart *et al.* (3) measured the excess volumes of binary mixtures with *n*-heptane of a series of methylalkanoates to investigate a possible cyclization of alkanoates in an aliphatic medium. With the availability of calorimetric techniques for precise measurements of heat capacities such mixtures are good candidates for a systematic study of these properties which are rather sensitive to molecular motions and interactions. Surprisingly, no data could be found for the heat capacities of such mixtures and this lack of information prevented us to extend the correlation of thermodynamic properties in a range of temperatures (2).

However, the main reason for the present investigation has to be found in our interest in binary liquid mixtures having an alkane as one component and a simple organic compound, Y, as the other. Indeed quite interesting mixing behavior has been observed with mixtures of the type (Y + an alkane) depending on the nature of second component Y. We have experimentally established that mixtures of this type usually exhibit a strong concentration dependence of excess heat capacities, C_p^E, (i.e. with mole fraction x of component Y). For example, if Y is a α,ω-dichloroalkane (4–6), a cyclic ether (7), or an alkanone (8) the $C_p^E(x)$ curves in the case of an *n*-alkane as second component are more or less ω-shaped (curves with two minima). Such behavior was also found by Benson and co-workers (9, 10) for Y being an aliphatic ether. Patterson and Saint-Victor (11) confirmed these results in the case of an alkanone. A similar concentration dependence has been observed in case of the more polar nitrobenzene and benzonitrile by Lainez *et al.* (12). Interestingly enough Patterson and co-workers (11) have shown that this type of concentration dependence also exists when the alkane is a branched alkane, what we indeed confirm with the binary mixtures (an alkanoate + a branched alkane) (13).

We have discussed this general behavior of thermodynamic properties in terms of destruction or creation of "order" and/or whenever possible, induced conformational changes in liquid *n*-alkanes, with respect to the situation existing in the pure liquid, and in terms of the change in the population of *gauche/trans* conformations (14). When Y is a "flexible" molecule which itself exhibits conformational equilibria, we suggested that cooperative induced conformational molecular "arrangements" may take place between Y and the aliphatic chains of the *n*-alkane (8). Therefore of particular interest were the studies of binary mixtures of a flexible molecule Y with a flexible cycloalkane such as cyclohexane. Indeed similar behavior (ω-shaped $C_p^E(x)$ curves) was also observed for 1,2-dichloroethane + cyclohexane and + methylcyclohexane (15),

[1]Communicated in part at the 42nd Annual Calorimetry Conference, Boulder, CO, U.S.A., July 26–31, 1987.

Printed in Canada / Imprimé au Canada

TABLE 1. Densities ρ and molar isobaric heat capacities C_p of component liquids at 298.15 K

Liquid	ρ (kg m^{-3}) Experimental	ρ (kg m^{-3}) Literature	C_p (J K^{-1} mol^{-1}) Experimental	C_p (J K^{-1} mol^{-1}) Literature
n-Heptane	679.51[o]		224.781[o]	
n-Decane	726.15	726.30,[a] 726.25,[b] 726.11[e]	313.13	314.54,[c] 313.56,[d] 314.56[b]
n-Tetradecane	759.31	759.12,[f] 759.28[a]	433.53	434.20,[g] 436.91[f]
Propyl methanoate	895.17	899.60,[h] 895.25[i]	172.10	171.42[i]
Methyl ethanoate	926.79	927.90,[b] 927.30[j]	141.34	143.90,[k] 138.50,[l] 140.56[m]
Ethyl ethanoate	894.37	894.00,[h] 894.55,[b] 894.45[j] 894.28[i]	168.94	169.30,[i] 167.70[k] 169.60[n]
Methyl propanoate	909.01	909.00,[h] 907.69[i] 909.32[j]	171.21	172.7,[i] 174.50[k] 173.60[b] 169.00[l]
Methyl butanoate	892.17	892.60[j]	198.16	200.80,[k] 199.20[l]
Methyl pentanoate	884.66	885.22[j]	226.11	229.30[k]
Methyl octanoate	872.30		314.23	

[a]Reference 23. [b]Reference 24. [c]Reference 25. [d]Reference 26.
[e]Reference 27. [f]Reference 21. [g]Reference 4. [h]Reference 28.
[i]Reference 17. [j]Reference 3. [k]Reference 29. [l]Reference 30.
[m]Reference 31. [n]Reference 32.
[o]Values from Fortier *et al.* (22) adopted for the *n*-heptane used as the ultimate reference liquid in all our density and heat capacity measurements.

even more pronounced for 1,4-dioxane + cyclohexane (16) and, just recently, for a series of alkanoates with cyclohexane (17). On the ground of the results observed with branched alkanes Patterson and co-workers (11) have been advocating a more general explanation in terms of non-randomness which in our view most likely involves the conformational changes. Furthermore we agree with these authors that the closeness of the upper critical solution temperature (UCST) is an extreme case of non-randomness which would explain the marked concentration dependence observed when component Y is strongly polar (11–13).

Against this background of experimental studies and possible explanations we have determined the excess volumes, V^E, and the C_p^E of binary mixtures of some alkanoates with an *n*-alkane. As previously (17) the aliphatic esters were selected in order to make a comparative study between different isomers, namely in the $C_4H_8O_2$ series, *n*-propyl methanoate, ethyl ethanoate, and methyl propanoate. We also selected a polar 3-carbon alkanoate, methyl ethanoate, to compare with the more polar *n*-propyl methanoate. In addition, three methyl alkanoates of increasing chain length, methyl butanoate, methyl pentanoate, and methyl octanoate were chosen to investigate the influence of chain length on the concentration dependence of V^E and C_p^E.

The present paper reports C_p^E at 298.15 K for eleven binary mixtures: *n*-propyl methanoate ($HCOOC_3H_7$) with *n*-heptane and *n*-decane, ethyl ethanoate ($CH_3COOC_2H_5$) with *n*-heptane, *n*-decane, and *n*-tetradecane, methyl propanoate ($C_2H_5COOCH_3$) with *n*-heptane and *n*-decane, and with *n*-heptane only, methyl ethanoate (CH_3COOCH_3), methyl butanoate ($C_3H_7COOCH_3$), methyl pentanoate ($C_4H_9COOCH_3$), and methyl octanoate ($C_7H_{15}COOCH_3$). In addition, V^E are reported at the same temperature for the same systems but *n*-propyl methonate with *n*-decane which has been published elsewhere (18).

Experimental

Component liquids

Sources of the primary materials were as follows: ethyl ethanoate (puriss. p.a., with purity > 99.5 mol%), methyl propanoate (purum, with purity > 99 mol%), *n*-heptane (puriss. p.a. with purity > 99.5 mol%), *n*-decane (purum, with purity > 99 mol%), and *n*-tetradecane (puriss p.a., with purity > 99 mol%) from Fluka, propyl methanoate (synth., with purity > 98 mol%) and methyl ethanoate (synth., with purity > 99 mol%) from Merck. All these component liquids were used without further purification. The three methyl alkanoates, (butanoate, pentanoate, and octanoate) were prepared by direct esterification of the corresponding carboxylic acids, double distilled and purified chromatographically. Prior to the experimental measurements, the component liquids were carefully dried with molecular sieve beads (Union Carbide Type 4 A) from Fluka.

Density and heat capacity measurements

Mixtures were prepared by mass. The possible error in the mole fractions is estimated to be less than 10^{-4}. Densities, ρ, of the pure liquids and their mixtures were determined with a vibrating-tube densimeter (Sodev, model 02 D) operated in the flow mode. Before each series of measurements, the instrument was calibrated using a vacuum and doubly distilled and degassed water for which we used the density ρ(298.15 K) = 997.047 kg m^{-3} (19).

Excess molar volumes of a mixture with mole fraction x of the alkanoate

$$[1] \quad V^E = V - xV_1 - (1 - x)V_2$$

were obtained from the density ρ of the mixture according to the relation

$$[2] \quad V^E = xM_1(\rho^{-1} - \rho_1^{-1}) + (1 - x)M_2(\rho^{-1} - \rho_2^{-1})$$

where V_i, M_i, and ρ_i denote respectively the molar volume, molar mass, and density of pure component i (1 for alkanoate, 2 for *n*-alkane). Isobaric heat capacities per unit volume C_p/V were measured with a Picker flow calorimeter (from Setaram) equipped with gold cells, using the stepwise procedure. They were converted to isobaric molar heat capacities C_p using our densities. Isobaric excess molar heat capacities were then calculated from

$$[3] \quad C_p^E = C_p - xC_{p1} - (1 - x)C_{p2}$$

where C_{pi} is the molar heat capacity of pure component i.

For the vibrating-tube densimeter and the flow calorimeter, temperature control was better than ±0.003 K. Details of the experimental techniques and of the accuracy attainable for non-electrolyte mixtures may be found in previous publications; see, for example, refs. 20 and 21.

Can. J. Chem. Downloaded from www.nrcresearchpress.com by 93.93.197.157 on 09/07/12
For personal use only.

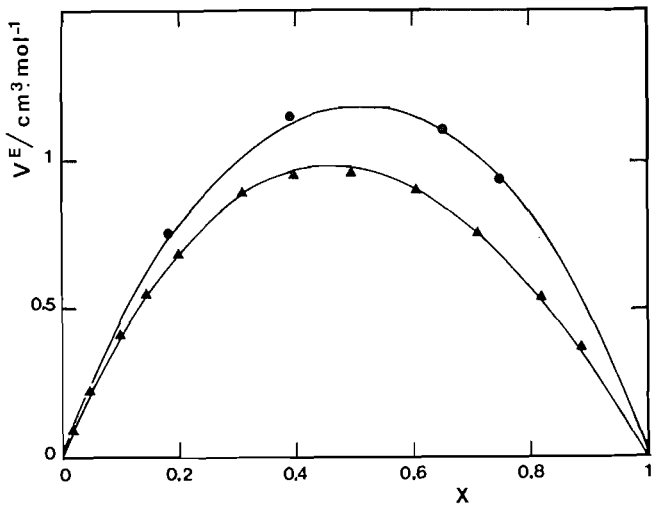

FIG. 1. Experimental excess molar volumes, V^E, at 298.15 K for xHCOOC$_3$H$_7$ + $(1-x)$C$_n$H$_{2n+2}$; ▲, n = 7; the curve was calculated from eq. [4] with coefficients from Table 3. ●, n = 10; the curve represents the smoothing function given by Sarmiento *et al.* (18).

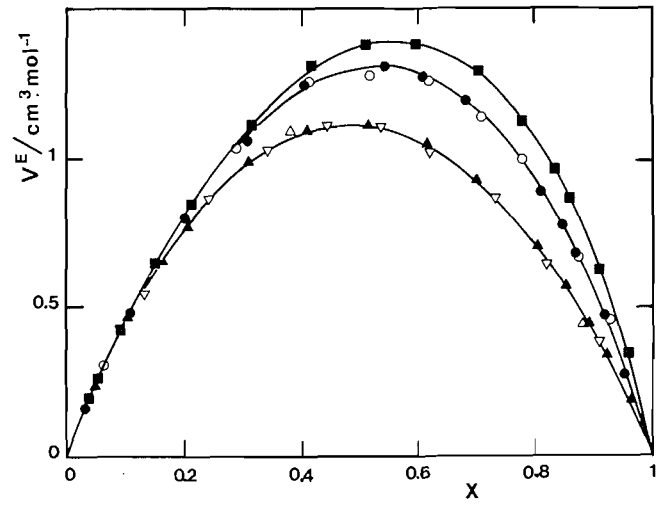

FIG. 2. Experimental excess molar volumes, V^E, at 298.15 K for xCH$_3$COOC$_2$H$_5$ + $(1-x)$C$_n$H$_{2n+2}$. With n = 7: ▲, present results; ▽, Grolier *et al.* (1); △, Dusart *et al.* (3). With n = 10: ●, present results; ○, Grolier *et al.* (1). With n = 14: ■, present results. The curves were calculated from eq. [4] with coefficients from Table 3.

Results and discussion

Experimental densities and heat capacities of the pure liquids are given in Table 1, where some literature values are given for comparison. Small discrepancies can be observed between the results from different sources but the overall agreement is satisfactory and we believe that our present results, particularly for the heat capacities of pure alkanoates, constitute reliable new data for these class of component liquids.

Experimental results for the excess molar volumes and the excess molar heat capacities at constant pressure are given in Table 2, while graphical representations are provided by Figs. 1–9. For each mixture, the excess quantities are fitted with a smoothing function of the form

$$[4]\quad Q^E = x(1-x)\sum_{i=0}^{n-1} A_i(2x-i)^i$$

where either $Q^E = V^E/(\text{cm}^3\ \text{mol}^{-1})$, or $Q^E = C_p^E/(\text{J K}^{-1}\ \text{mol}^{-1})$

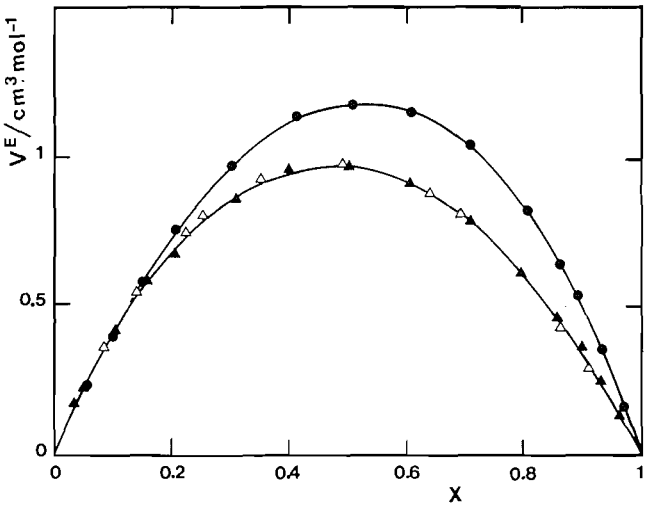

FIG. 3. Experimental excess molar volumes, V^E, at 298.15 K for xC$_2$H$_5$COOCH$_3$ + $(1-x)$C$_n$H$_{2n+2}$. With n = 7: ▲, present results; △, Dusart *et al.* (8). With n = 10: ●, present results. The curves were calculated from eq. [4] with coefficients from Table 3.

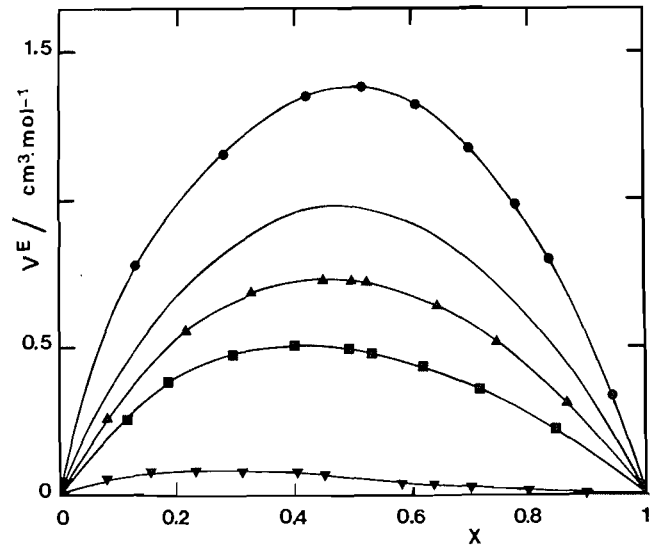

FIG. 4. Experimental excess molar volumes, V^E, at 298.15 K for methyl alkanoates with n-heptane: xC$_m$H$_{2m+1}$COOCH$_3$ + $(1-x)$-C$_7$H$_{16}$: ●, m = 1; ▲, m = 3; ■, m = 4; ▼, m = 7. Full curve without experimental points is for m = 2 (see Fig. 3). All the curves were calculated from eq. [4] with coefficients from Table 3.

The coefficients A_i, and the corresponding standard deviations $s(Q^E)$ are given in Table 3. These coefficients were used to obtain the calculated curves in the figures.

The excess molar volumes are positive for all the systems and show the usual concentration dependence of mixtures of alkanoates with n-alkanes (1, 3), as well as the familiar decrease of V^E when the alkylated part of the alkanoate increases (see Figs. 1 to 4). This decrease, in a given series of alkanoates, corresponds to a dilution of the ester group. Of particular interest is the different behavior of C$_4$H$_8$O$_2$ alkanoates with the same n-alkane. For example, propyl methanoate and methyl propanoate exhibit practically identical V^E with n-haptane (Figs. 1 and 3) in contrast ethyl ethanoate leads to more positive V^E. This is an indication that V^E results from the competition of different effects, e.g., size, polarity, chemical structure, which cancel out in the same way in the case of the propyl methanoate and methyl propano-

Can. J. Chem. Downloaded from www.nrcresearchpress.com by 93.93.197.157 on 09/07/12
For personal use only.

TABLE 2. Excess molar volumes, V^E, and excess molar isobaric heat capacities, C_p^E, for some alkanoate + *n*-alkane mixtures at 298.15 K

xHCOOC$_3$H$_7$ + (1 − x)C$_7$H$_{16}$			xHCOOC$_3$H$_7$ + (1 − x)C$_{10}$H$_{22}$			xCH$_3$COOCH$_3$ + (1 − x)C$_7$H$_{16}$		
x	V^E (cm^3 mol^{-1})	C_p^E (J K^{-1} mol^{-1})	x	V^E (cm^3 mol^{-1})	C_p^E (J K^{-1} mol^{-1})	x	V^E (cm^3 mol^{-1})	C_p^E (J K^{-1} mol^{-1})
0.0170	0.0877	—	0.0438	—	−0.503	0.1251	0.7827	−0.387
0.0481	0.2261	−0.249	0.0794	—	−0.564	0.2794	1.1580	−0.018
0.0964	0.4133	−0.142	0.1082	—	−0.561	0.4173	1.3523	0.618
0.1444	0.5474	0.036	0.1558	—	−0.365	0.5172	1.3824	0.947
0.1995	0.6777	0.325	0.1815	0.7400	−0.311	0.6084	1.3225	1.023
0.3077	0.8842	0.787	0.2844	—	0.134	0.6994	1.1728	0.831
0.3966	0.9488	1.051	0.3892	1.1491	0.511	0.7739	0.9862	0.530
0.4962	0.9514	1.132	0.5066	—	0.845	0.8305	0.8008	0.224
0.6049	0.8954	1.132	0.6538	1.0951	0.815	0.9434	0.3250	−0.092
0.7106	0.7524	0.897	0.7470	0.9376	0.669			
0.8208	0.5338	0.536	0.8033	—	0.441			
0.8835	0.3728	0.300	0.8622	—	0.201			
			0.8995	—	0.084			
			0.9513	—	−0.098			

xCH$_3$COOC$_2$H$_5$ + (1 − x)C$_7$H$_{16}$			xCH$_3$COOC$_2$H$_5$ + (1 − x)C$_{10}$H$_{22}$			xCH$_3$COOC$_2$H$_5$ + (1 − x)C$_{14}$H$_{30}$		
x	V^E (cm^3 mol^{-1})	C_p^E (J K^{-1} mol^{-1})	x	V^E (cm^3 mol^{-1})	C_p^E (J K^{-1} mol^{-1})	x	V^E (cm^3 mol^{-1})	C_p^E (J K^{-1} mol^{-1})
0.0332	0.1672	−0.046	0.0310	0.165	−0.200	0.0366	0.187	−0.55
0.0535	0.2586	−0.094	0.0557	0.271	−0.431	0.0548	0.258	−0.85
0.1044	0.4667	—	0.1092	0.487	−0.796	0.0918	0.417	−1.80
0.1581	0.6480	−0.313	0.1531	0.649	−0.985	0.1477	0.654	−2.74
0.2048	0.7754	−0.320	0.2022	0.807	−1.078	0.2118	0.842	−3.23
0.3082	0.9817	−0.187	0.3099	1.064	−1.163	0.3152	1.112	—
0.4080	1.0928	0.006	0.4030	1.256	−0.919	0.4139	1.306	−3.60
0.5120	1.1042	0.105	0.5407	1.314	−0.642	0.5106	1.381	−3.20
0.6149	1.0403	—	0.6096	1.272	−0.555	0.5973	1.380	−2.70
0.7005	0.9227	−0.085	0.6837	1.195	−0.496	0.7030	1.304	−2.15
0.8022	0.6992	−0.217	0.8120	0.897	−0.521	0.7803	1.123	−1.94
0.8513	0.5592	−0.198	0.8460	0.778	−0.527	0.8326	0.971	−1.78
0.8910	0.4338	−0.175	0.8738	0.689	−0.491	0.8617	0.867	—
0.9194	0.3281	−0.161	0.9201	0.472	−0.449	0.9129	0.618	−0.98
0.9579	0.1779	−0.092	0.9536	0.287	−0.345	0.9573	0.343	−0.66

xC$_2$H$_5$COOCH$_3$ + (1 − x)C$_7$H$_{16}$			xC$_2$H$_5$COOCH$_3$ + (1 − x)C$_{10}$H$_{22}$			xC$_3$H$_7$COOCH$_3$ + (1 − x)C$_7$H$_{16}$		
x	V^E (cm^3 mol^{-1})	C_p^E (J K^{-1} mol^{-1})	x	V^E (cm^3 mol^{-1})	C_p^E (J K^{-1} mol^{-1})	x	V^E (cm^3 mol^{-1})	C_p^E (J K^{-1} mol^{-1})
0.0356	0.1703	−0.233	0.0483	0.2116	−0.488	0.0811	0.2656	−0.477
0.0496	0.2296	−0.330	0.0553	0.2348	−0.539	0.2124	0.5509	−0.723
0.1039	0.4237	−0.574	0.0984	0.4033	−0.853	0.3292	0.6821	−0.678
0.1591	0.5903	−0.673	0.1514	0.5910	−1.104	0.4440	0.7288	−0.563
0.2058	0.6781	—	0.2048	0.7629	−1.244	0.4952	0.7247	−0.543
0.3102	0.8636	−0.562	0.3103	0.9781	−1.310	0.5246	0.7173	−0.517
0.3979	0.9622	−0.334	0.4093	1.1373	−1.155	0.6457	0.6350	−0.444
0.5056	0.9749	−0.308	0.5059	1.1771	−1.013	0.7465	0.5171	−0.379
0.6047	0.9140	−0.285	0.6044	1.1590	−0.817	0.8665	0.3097	−0.281
0.7138	0.7815	−0.239	0.7087	1.0544	−0.655			
0.7973	0.6098	−0.308	0.8061	0.8262	−0.612			
0.8552	0.4686	−0.281	0.8620	0.6470	−0.577			
0.8924	0.3679	−0.217	0.8922	0.5436	−0.516			
0.9273	0.2483	−0.216	0.9329	0.3591	−0.419			
0.9601	0.1358	−0.155	0.9699	0.1726	−0.233			

Can. J. Chem. Downloaded from www.nrcresearchpress.com by 93.93.197.157 on 09/07/12
For personal use only.

TABLE 2 (*concluded*)

xC$_4$H$_9$COOCH$_3$ + (1 − x)C$_7$H$_{16}$			xC$_7$H$_{15}$COOCH$_3$ + (1 − x)C$_7$H$_{16}$		
x	V^E (cm^3 mol^{-1})	C_p^E (J K^{-1} mol^{-1})	x	V^E (cm^3 mol^{-1})	C_p^E (J K^{-1} mol^{-1})
0.1129	0.2607	−0.567	0.0749	0.0472	−0.476
0.1829	0.3803	−0.665	0.1522	0.0691	−0.722
0.2914	0.4678	−0.688	0.2279	0.0754	−0.839
0.4023	0.5023	−0.600	0.3100	0.0708	−0.868
0.4919	0.4894	−0.547	0.4017	0.0712	−0.822
0.5357	0.4771	−0.538	0.4451	0.0669	−0.763
0.6173	0.4338	−0.505	0.5870	0.0294	−0.674
0.7161	0.3560	−0.464	0.6367	0.0245	−0.600
0.8449	0.2214	−0.336	0.6960	0.0186	−0.559
			0.7962	0.0142	−0.325
			0.9012	0.0028	−0.191

TABLE 3. Coefficients, A_i, and standard deviations, s, for least-squares representations of V^E and C_p^E by eq. [4]*

Composition	Q^E	A_0	A_1	A_2	A_3	A_4	$s(Q^E)$
x HCOOC$_3$H$_7$							
+ (1 − x)C$_7$H$_{16}$	V^E	3.8243	−0.5116	0.4476	−0.2006		0.0090
	C_p^E	4.586	0.442	−1.955	3.308	−7.189	0.025
+ (1 − x)C$_{10}$H$_{22}$	C_p^E	3.126	2.881	−2.969	2.185	−10.022	0.040
x CH$_3$COOCH$_3$							
+ (1 − x)C$_7$H$_{16}$	V^E	5.5364	0.1347	0.2518	−1.8105	2.4950	0.0054
	C_p^E	3.629	5.181	−9.203	−4.423		0.015
x CH$_3$COOC$_2$H$_5$							
+ (1 − x)C$_7$H$_{16}$	V^E	4.4379	−0.2688	0.4355	−0.1225		0.0024
	C_p^E	0.430	0.967	−8.008	−1.142	6.243	0.014
+ (1 − x)C$_{10}$H$_{22}$	V^E	5.2163	0.5948	0.6463	0.2837		0.012
	C_p^E	−2.924	4.644	−5.907	−4.679		0.031
+ (1 − x)C$_{14}$H$_{30}$	V^E	5.5136	1.1251	0.8155	0.7321	0.7794	0.010
	C_p^E	−12.777	11.034	−11.882	−10.552	8.761	0.12
x C$_2$H$_5$COOCH$_3$							
+ (1 − x)C$_7$H$_{16}$	V^E	3.8905	0.2352	0.3905	−0.4276		0.0086
	C_p^E	−1.144	1.531	−5.096	0.991		0.036
+ (1 − x)C$_{10}$H$_{22}$	V^E	4.7334	0.4774	0.5933	0.2612		0.0080
	C_p^E	−4.032	4.184	−3.891	−2.731	−2.623	0.014
xC$_3$H$_7$COOCH$_3$							
+ (1 − x)C$_7$H$_{16}$	V^E	2.8943	−0.4668	0.3150	−0.1067		0.0012
	C_p^E	−2.118	1.523	−3.361	1.090		0.009
x C$_4$H$_9$COOCH$_3$							
+ (1 − x)C$_7$H$_{16}$	V^E	1.9556	−0.6247	0.3580			0.0040
	C_p^E	−2.197	0.938	−3.264	1.607		0.008
x C$_7$H$_{15}$COOCH$_3$							
+ (1 − x)C$_7$H$_{16}$	V^E	0.1994	−0.3487	0.1896			0.0050
	C_p^E	−2.984	1.710	−1.853	1.745		0.025

*Units for V^E, cm^3 mol^{-1}; C_p^E, J K^{-1} mol^{-1}.

ate. Also as expected, for a given alkanoate, the excess molar volumes become more positive as the length of the *n*-alkane increases (Figs. 1–3).

The present V^E data at 298.15 K agree well with our previous results (1) in the case of ethyl ethanoate and methyl propanoate, as well as with the results of Dusart *et al.* (3) (see Figs. 2 and 3). These latter authors have also measured V^E for the two systems methyl butanoate and methyl pentanoate with *n*-heptane (3). Their results (not shown in Fig. 4) agree also well with ours. These three sets of data have been obtained with similar vibrating-tube densimeters and the overall agreement between these results is normal.

No direct measurements of excess molar heat capacities could be found for any of the systems investigated here and the most remarkable aspect of this work relates to the composition dependence of these properties. For all esters the $C_p^E(x)$ curves show the now well-known ω-shaped concentration dependence with a more or less marked double minimum (Figs. 5 to 9).

Can. J. Chem. Downloaded from www.nrcresearchpress.com by 93.93.197.157 on 09/07/12
For personal use only.

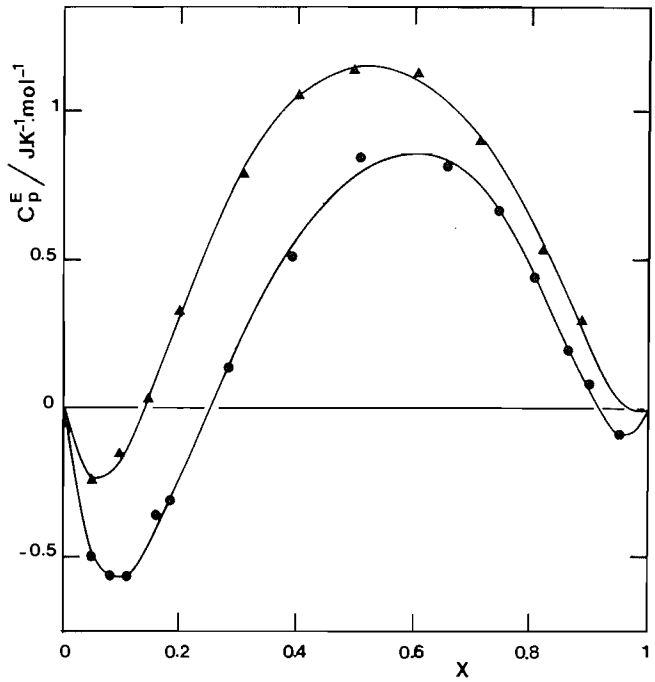

FIG. 5. Experimental excess molar isobaric heat capacities, C_p^E, at 298.15 K for $x\text{HCOOC}_3\text{H}_7 + (1 - x)\,\text{C}_n\text{H}_{2n+2}$; ▲, $n = 7$; ●, $n = 10$. The curves were calculated from eq. [4] with coefficients from Table 3.

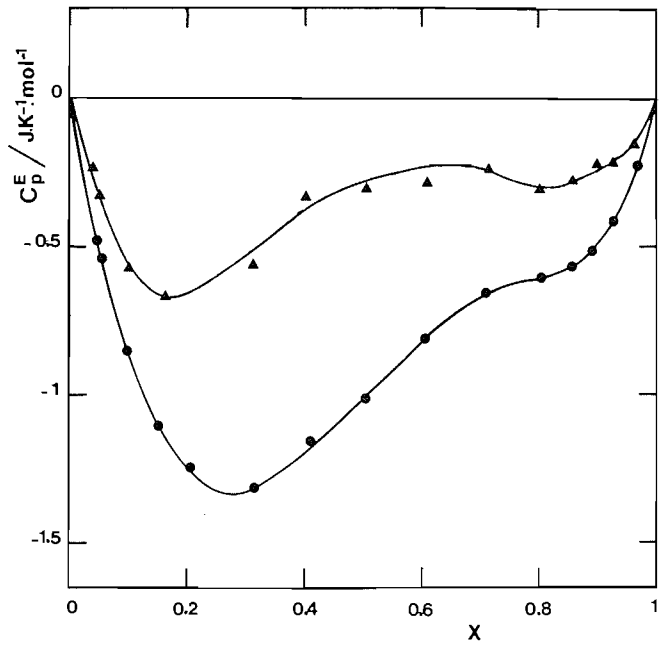

FIG. 7. Experimental excess molar isobaric heat capacities, C_p^E, at 298.15 K for $x\text{C}_2\text{H}_5\text{COOCH}_3 + (1 - x)\text{C}_n\text{H}_{2n+2}$; ▲, $n = 7$; ●, $n = 10$. The curves were calculated from eq. [4] with coefficients from Table 3.

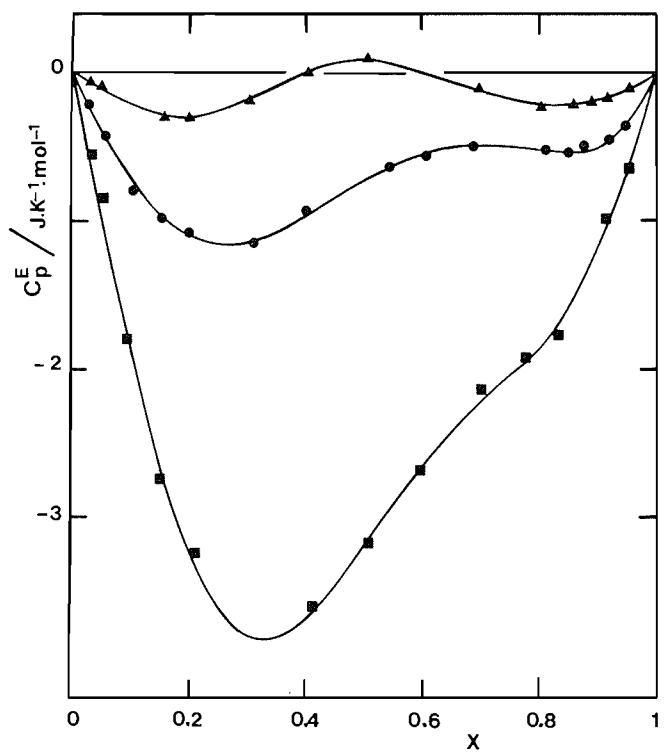

FIG. 6. Experimental excess molar isobaric heat capacities, C_p^E, at 298.15 K for $x\text{CH}_3\text{COOC}_2\text{H}_5 + (1 - x)\text{C}_n\text{H}_{2n+2}$; ▲, $n = 7$; ●, $n = 10$; ■, $n = 14$. The curves were calculated from eq. [4] with coefficients from Table 3.

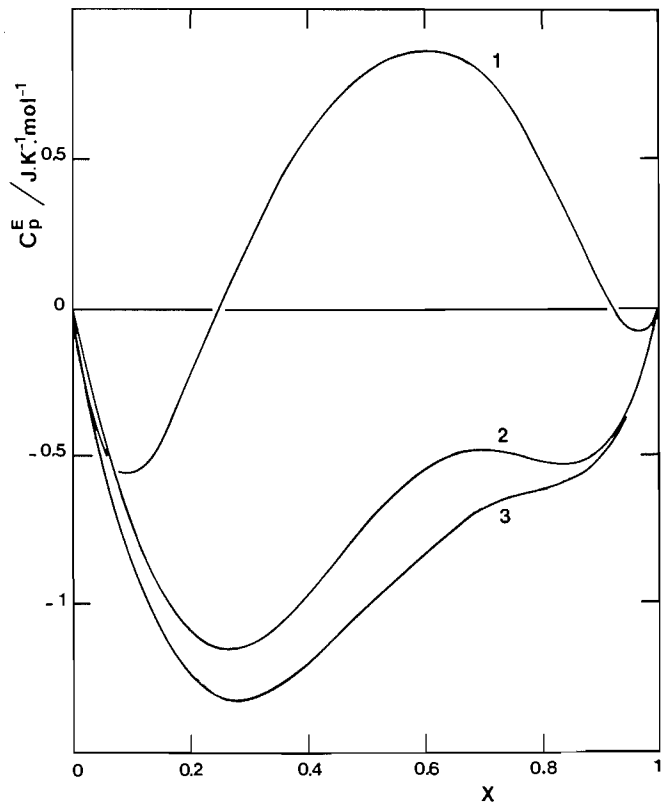

FIG. 8. Excess molar isobaric heat capacities, C_p^E, at 298.15 K for isomeric alkanoates with *n*-decane: $x\text{RCOOR}' + (1 - x)\text{C}_{10}\text{H}_{22}$: *1*, HCOOC_3H_7; *2*, $\text{CH}_3\text{COOC}_2\text{H}_5$; *3*, $\text{C}_2\text{H}_5\text{COOCH}_3$. All the curves were calculated from eq. [4] with coefficients from Table 3. The actual experimental points are given in Figs. 5–7.

Can. J. Chem. Downloaded from www.nrcresearchpress.com by 93.93.197.157 on 09/07/12
For personal use only.

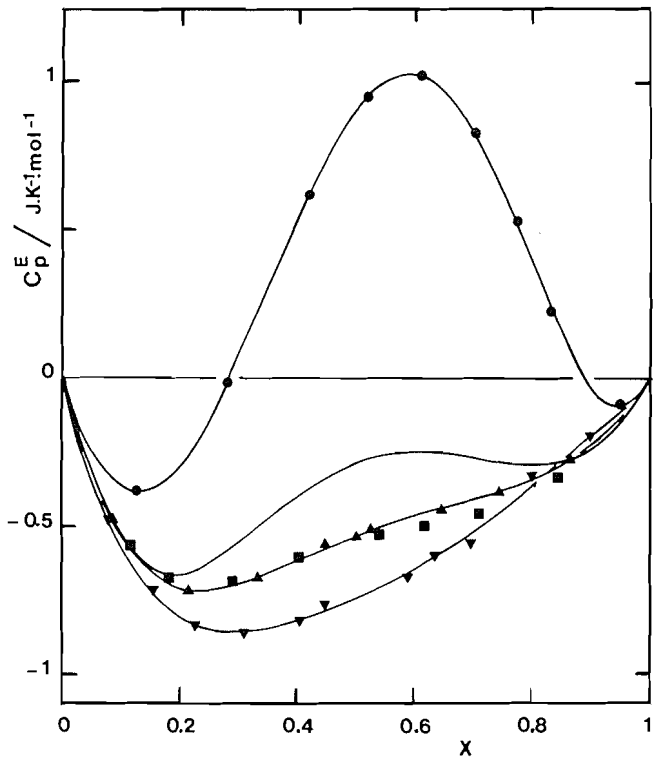

FIG. 9. Experimental excess molar isobaric heat capacities, C_p^E, at 298.15 K for methyl alkanoates with *n*-heptane: $xC_mH_{2m} + {}_1COOCH_3 + (1-x)C_7H_{16}$: ●, $m = 1$; ▲, $m = 3$; ■, $m = 4$; ▼, $m = 7$. Full curve without experimental points is for $m = 2$ (see Fig. 6). All the curves were calculated from eq. [4] with coefficients from Table 3.

The present behavior, even more pronounced, is similar to the observation made for mixtures of alkanoates with cyclohexane (17). In particular, a positive part in the $C_p^E(x)$ curves appears in the central range of concentration in the case of the smaller, more polar, esters: namely, propyl methanoate, methyl ethanoate and, to a less extent, ethyl ethanoate. This would be typical of the non-randomness advocated by Patterson and co-workers (11) to explain the large positive C_p^E values observed for mixtures containing a polar alkanone, like acetone. This positive part can be a pronounced sharp maximum, almost a peak, as observed with very polar substances like benzonitrile or nitrobenzene (12) in *n*-alkanes near the UCST. This strong concentration dependence almost vanishes when the anisotropy of the polar group (here the ester group) is "diluted" and thus becomes less effective on the aliphatic environment. This is indeed observed with either a given alkanoate in alkanes of increasing chain length, see Figs. 5, 6, and 7, or with alkanoates of increasing alkyl chain length in a given *n*-alkane (Fig. 9). Typically the ω-shape is no more present in the case of methyl octanoate in *n*-heptane (Fig. 9).

As indicated in the Introduction we tentatively interpret the present results as a possible consequence of the modification of the percentage of the *gauche/trans* conformations in *n*-alkanes upon addition of a solute which itself can exhibit conformers of different polarity, depending on its concentration in the mixture. For alkanoates, these possible conformers (or rotamers) correspond to molecular internal rotation around the C—O bond. A large body of studies supports this contention (33–36) and, as expected, propyl methanoate which has the highest dipole moment ($\mu = 1.91$ D) leads to the strongest concentration dependence. This is clearly shown in Fig. 8 where the three $C_4H_8O_2$ isomers are compared in admixture to *n*-decane: the C_p^E curve becomes more negative, and therefore less ω-shpaed, the smaller the dipole moment.

In conclusion our present results seem to confirm the effect on C_p^E of cooperative induced conformational arrangements already observed with mixtures containing alkanones (in alkanes) (8) or alkanoates (in cyclohexane (17).

Acknowledgments

This work was performed within the frame of the Spanish–French treaty on scientific and technical cooperation. Three of us (M.P., R.B., and M.C.B.) gratefully acknowledge the financial support by the French Embassy in Madrid and the University of Santiago de Compostela. We also are indebted to Mrs. Piekarski (University of Limoges) for carrying out some density measurements.

1. J.-P. E. GROLIER, D. BALLET, and A. VIALLARD. J. Chem. Thermodyn. **6**, 895 (1974).
2. H. V. KEHIAIAN, R. BRAVO, M. PINTOS BARRAL, M. I. PAZ ANDRADE, R. GUIEU, and J.-P. E. GROLIER. Fluid Phase Equilib. **17**, 187 (1984).
3. O. DUSART, C. PIEKARSKI, S. PIEKARSKI, and A. VIALLARD. J. Chim. Phys. **73**, 837 (1976).
4. A. LAINEZ, G. ROUX-DESGRANGES, J.-P. E. GROLIER, and E. WILHELM. Fluid Phase Equilib. **20**, 47 (1985).
5. A. LAINEZ, E. WILHELM, G. ROUX-DESGRANGES, and J.-P. E. GROLIER. J. Chem. Thermodyn. **17**, 1153 (1985).
6. A. LAINEZ, J.-P. E. GROLIER, and E. WILHELM. Thermochim. Acta, **91**, 243 (1985).
7. J.-P. E. GROLIER, A. INGLESE, and E. WILHELM. J. Chem. Thermodyn. **16**, 67 (1984).
8. J.-P. E. GROLIER and G. C. BENSON. Can. J. Chem. **62**, 949 (1984).
9. K. KIMURA, P. D'ARCY, M. E. SUGAMORI, and G. C. BENSON. Thermochim. Acta, **64**, 149 (1983).
10. G. C. BENSON, M. K. KUMARAN, T. TRESZCZANOWICZ, P. J. D'ARCY, and C. J. HALPIN. Thermochim. Acta, **95**, 59 (1985).
11. M. E. SAINT-VICTOR and D. PATTERSON. Fluid Phase Equilib. **35**, 237 (1987).
12. A. LAINEZ, M. RODRIGO, A. H. ROUX, J.-P. E. GROLIER, and E. WILHELM. Calorim. Anal. Therm. **16**, 153 (1985).
13. R. BRAVO, M. PINTOS, M. I. PAZ ANDRADE, G. ROUX-DESGRANGES, and J.-P. E. GROLIER. 42nd Annual Calorimetry Conference, Boulder, CO, U.S.A., July 26–31, 1987. Paper N° 30.
14. E. WILHELM. Thermochim. Acta, **94**, 47 (1985).
15. E. WILHELM, J.-P. E. GROLIER, and M. H. KARBALAI GHASSEMI. Thermochim. Acta. **28**, 59 (1979).
16. A. INGLESE, J.-P. E. GROLIER, and E. WILHELM. Fluid Phase Equilib. **15**, 287 (1984).
17. E. JIMENEZ, L. ROMANI, M. I. PAZ ANDRADE, G. ROUX-DESGRANGES, AND J.-P. E. GROLIER. J. Solution Chem. **15**, 879 (1986).
18. F. SARMIENTO, M. I. PAZ ANDRADE, G. ROUX-DESGRANGES, and J.-P. E. GROLIER. Int. Data Ser. Selec. Data Mixts. Ser. A, **1**, 66 (1985).
19. G. S. KELL. J. Chem. Eng. Data, **20**, 97 (1975).
20. J.-P. E. GROLIER, E. WILHELM, and M. H. HAMEDI. Ber. Bunsenges. Phys. Chem. **82**, 1282 (1978).
21. A. H. ROUX, J.-P. E. GROLIER, A. INGLESE, and E. WILHELM. Ber. Bunsenges. Phys. Chem. **88**, 986 (1984).
22. J.-L. FORTIER, G. C. BENSON, and P. PICKER. J. Chem. Thermodyn. **8**, 289 (1976).
23. Selected values of Physical and Thermodynamic properties of

Can. J. Chem. Downloaded from www.nrcresearchpress.com by 93.93.197.157 on 09/07/12
For personal use only.

hydrocarbons and related compounds. American Petroleum Institute Research Project 44. Carnegie Press, Pittsburg. 1953. Table 20 *d*. (Part 1). p. 288.
24. J. A. RIDDICK and W. B. BUNGER. Organic solvents: Tech. Chem. Ser., 3rd ed. Vol 2. Wiley-Interscience, New York 1970.
25. Selected values of properties of hydrocarbons and related compounds. American Institute Research Project 44. Thermodynamics Research Center, Texas A & M University, College Station, Texas. October 31, 1979. Table 23-2 (1-205). p. 1.
26. J. A. GATES, R. H. WOOD, J. C. COBOS, C. CASANOVA, A. H. ROUX, G. ROUX-DESRANGES, and J.-P. E. GROLIER. Fluid Phase Equilib. **27**, 137 (1986).
27. J. R. GOATES, J. B. OTT, and R. B. GRIGG. J. Chem. Thermodyn. **13**, 907 (1979).
28. Selected values of properties of hydrocarbons and related compounds. Thermodynamics Research Center Data Project, Texas A & M University College Station, Texas. December 31, 1969. Table 23-2-1.
29. R. FUCHS. J. Chem. Thermodyn. **11**, 959 (1979).
30. R. SHAW. J. Chem. Eng. Data, **14**, 461 (1969).
31. M. COSTAS and D. PATTERSON. J. Chem. Soc. Faradey Trans. I, **81**, 635 (1985).
32. M. COSTAS and D. PATTERSON. J. Chem. Soc. Faraday Trans. I, **81**, 2381 (1985).
33. R. J. B. MARSDEN and L. E. SUTTON. J. CHEM. SOC. 1383 (1936).
34. J. M. O'GORMAN, W. SHAND, JR., and V. SCHOMAKER. J. Am. Chem. Soc. **72**, 4222 (1950).
35. M. OKI and H. NAKANISHI. Bull. Chem. Soc. Jpn. **44**, 3144 (1971).
36. A. G. PINKOS and A. Y. LIN. J. Molecular Struct. **24**, 9 (1975).

Can. J. Chem. Downloaded from www.nrcresearchpress.com by 93.93.197.157 on 09/07/12
For personal use only.

Excess partial molar enthalpies of *tert*-butanol in water–*tert*-butanol mixtures

YOSHIKATA KOGA

Department of Chemistry, University of British Columbia, Vancouver, B.C., Canada V6T 1Y6

Received September 9, 1987

This paper is dedicated to the late Professor J. A. Morrison

YOSHIKATA KOGA. Can. J. Chem. **66**, 1187 (1988).

Excess partial molar enthalpies of *tert*-butanol (TBA) in water–*tert*-butanol mixtures were measured at 20.00, 26.90, 45.17, and 59.49°C in the water-rich region, and at 30.00°C for the entire range. The results together with those of the previous work, (Y. Koga. Can. J. Chem. **64**, 206 (1986)), appear to support the following views: At $X_{TBA} \approx 0$, TBA molecules form hydrogen bonds with H_2O molecules, and they enhance the structure of the hydrogen bond network of H_2O. The latter effect is of very long range; the enthalpic repulsion between solutes is already operative via enhancement of hydrogen bond network when two TBA molecules are separated by 12 H_2O molecules. This enthalpic repulsion becomes stronger as the concentration of TBA increases. At a certain threshold, $X_{TBA} \approx 0.03$ at 30.00°C for example, the new scheme in which solutes tend to associate sets in, and for $X_{TBA} > 0.06$ this scheme becomes predominant. The effect of higher temperature is to shift this threshold to the lower values of X_{TBA}. Therefore, it is probable that a lower critical solution temperature may exist at a temperature higher than the boiling points of the solution. It was also shown that if species of $TBA(H_2O)_k$ type persist, they exhibit a hard-sphere nature in terms of enthalpic interaction among themselves.

YOSHIKATA KOGA. Can. J. Chem. **66**, 1187 (1988).

Opérant à 20,00, 26,90, 45,17 et 59,49°C et à des concentrations riches en eau ainsi qu'à 30,00°C à toutes les concentrations, on a mesuré les enthalpies molaires partielles en excès du *tert*-butanol (ATB) dans des mélanges eau/*tert*-butanol. Il semble que les résultats obtenus, pris de concert avec ceux de notre travail antérieur (Y. Koga, Can. J. Chem. **64**, 206 (1986)), sont en accord avec les conclusions suivantes: à une $X_{ATB} \approx 0$, les molécules d'ATB forment des liaisons hydrogènes avec les molécules de H_2O et elles augmentent ainsi la structure du réseau de liaisons hydrogènes de H_2O. Ce dernier effet agit à une très grande distance; la répulsion entre les solutés qui dûe à l'entropie se fait déjà sentir, par le biais d'une augmentation du réseau de liaisons hydrogènes, lorsque deux molécules d'ATB sont séparées par 12 molécules de H_2O. Lorsque la concentration en ATB augmente, cette répulsion dûe à l'enthalpie augmente aussi. A un nouveau seuil, par exemple, à une $X_{ATB} \approx 0.03$ et à 30,00°C, il s'établit un nouveau schéma d'association entre les solutés et à une $X_{ATB} > 0{,}06$, ce schéma devient prédominant. Lorsqu'on augmente la température, ce seuil se déplace vers des valeurs plus faibles de X_{ATB}. Il est donc probable qu'une température de solution critique plus faible puisse exister lorsque les températures d'ébullition de la solution sont plus élevées. On a aussi démontré que, si les espèces du type $ATB(H_2O)_k$ persistent, elles présentent une nature de sphère dure en termes d'interaction enthalpiques entre elles.

[Traduit par la revue]

Introduction

In a previous article in this journal (1) (called paper I hereinafter) excess partial molar enthalpies[1] of *tert*-butanol (TBA) in water–*tert*-butanol mixtures, H_m^E(TBA), at 26.90°C were reported. It was shown that in terms of excess partial molar enthalpies and their temperature dependence there were two regions bound at about $X_{TBA} = 0.06$, X_{TBA} being the mole fraction of *tert*-butanol. In the water-rich region, $X_{TBA} < 0.06$, H_m^E(TBA) depends sharply on X_{TBA} and C_p^E(TBA) ($= \partial H_m^E(TBA)/\partial T$) is large and positive ($\sim$250 J K^{-1} mol^{-1}). In the region, $X_{TBA} > 0.06$, H_m^E(TBA) is small and nearly constant ($\pm$1 kJ mol^{-1}) and C_p^E(TBA) is also nearly constant at ~ -30 J K^{-1} mol^{-1}. The peculiarity of TBA–H_2O mixtures is thus promient in the water-rich region, while in the rest of the X_{TBA} regions the TBA molecules in the mixture find themselves in the situation not very different from that in pure TBA.

In the present work are reported the additional results of H_m^E(TBA) at 30.00°C and also at 20.00, 26.90, 45.17, and 59.49°C in the water-rich region. While the system of TBA–H_2O has been subjected to numerous investigations for a long time, recent measurements (2, 3) on thermodynamic quantities that are proportional to a second derivative of the free energy with respect to appropriate variables, appear to add some new insights. Indeed, Sakurai has presented an alternative explanation to the classical "iceberg" formation using accurate values of partial molar volumes of TBA and H_2O in the entire range of mole fraction (3). The excess partial molar enthalpy, H_m^E(TBA), is one of such quantities and provides direct information on the solute–solvent and the solute–solute interaction potentials, which no doubt is important in gaining an additional insight.

In theory, the excess partial molar enthalpy can be obtained graphically by the Bakhuis–Rooseboom (21) method from the data of excess (integral) molar enthalpies of the mixture. However, existing data for the TBA–H_2O mixtures (4) are not so closely netted in terms of the mole fraction that an accurate graphical differentiation is not possible, particularly in the water-rich region. For the very close proximity to $X_{TBA} = 0$, the apparent molar enthalpies were fitted to a virial expansion (5, 6) from which excess partial molar enthalpies can be calculated. However, the applicability of such expression is limited to the very water-rich region only. Thus, it was elected to measure the excess partial molar enthalpies directly for the entire range of mole fraction in paper I (1). The present paper is an extention thereof. In the event that excess partial molar enthalpies of H_2O in the mixtures become available, the excess (integral) molar enthalpies and the apparent molar enthalpies are calculated from the measured excess partial molar enthalpies of H_2O and those

[1]In paper I, a conventional term, the differential heat of dilution, and a notation, Δh, were used. In this paper, however, in accordance with the recommendations by the IUPAC Commissions on Thermodynamics, use will be made of the term, the excess partial molar enthalpy with the notation, H_m^E(TBA) instead. Thus H_m^E(TBA) in this paper is the same as Δh in paper I. By the same token, ΔC_p ($= \partial \Delta h/\partial T$) in paper I is the same as $C_P^E(TBA)$ ($= \partial H_m^{EE}(TBA)/\partial T$) in this paper.

Can. J. Chem. Downloaded from www.nrcresearchpress.com by 93.93.197.157 on 09/07/12
For personal use only.

of TBA, and can then be compared directly with the existing data (4–6).

Experimental

The excess partial molar enthalpies were measured by means of an LKB Bromma 8700 precision calorimetry system. Two separate sets of measurements were made. For the runs at 20.00, 26.90, and 30.00°C, the same procedure as described elsewhere was employed (1, 18). Briefly, a glass ampoule containing about 1 mL of purified TBA was broken in about 90 g of the mixture. For the runs at 45.17 and 59.49°C about 1 mL of TBA (BDH assured, analytical reagent) was introduced from a 5 mL buret, through a heat exchanger immersed in the bath and into the so-called titration cell (~100 mL) provided with the apparatus. In the series of addition of TBA from the buret, the accurate amount of TBA for the first one is always uncertain, although correction was made to account for a small amount of additional TBA introduced due to the thermal expansion of TBA in the heat exchanger. The data of the first run in each series was therefore discarded. This uncertainty about the amount of the first dose of TBA causes uncertainties in the values of X_{TBA} in the subsequenty runs. However, it was estimated to be at most 0.5% at the lowest mole fraction studied.

The excess partial molar enthalpies were calculated as $H_m^E(TBA) = \Delta H/\Delta n_{TBA}$, where ΔH is the enthalpy change of the mixture due to the addition of a small amount Δn_{TBA} (~0.01 mol) of TBA. Since the increment, Δn_{TBA} is very small in comparison with the total amount of the mixture, typically about 4 mol, the above relation, $H_m^E(TBA) = \Delta H/\Delta n_{TBA}$, should hold. This was checked by reducing Δn_{TBA} to 0.007 mol for the two runs at 26.90°C of this work. As shown later, the data points with the two different sets of increments appear to lie on the smooth curve within the experimental error. The error limit in H_m^E(TBA) obtained by the ampoule method was estimated to be 0.5% of the resulting value with the upper bound ±0.05 kJ mol^{-1} for the results, the absolute value of which are larger than 10 kJ mol^{-1} and with the lower bound ±0.015 kJ mol^{-1} for those smaller than 3 kJ mol^{-1}. The buret method was found to be not as accurate, with an estimate of error ±0.2 kJ mol^{-1}. To test the consistency between the two methods, three runs by the buret method were conducted at 30.00°C. As shown below, the results appeared consistent within the stated error limits.

Results and discussion

The excess partial molar enthalpies of TBA in TBA–H_2O mixtures are tabulated in Table 1, together with the data of paper I (1) in which only graphical presentation was made. The values of H_m^E(TBA) were plotted against X_{TBA} in the water-rich region in Fig. 1. Figure 2 is an enlarged view at close proximity of the origin for the ampoule runs at 26.90 and 30.00°C. In the figure the two data points at 26.90°C of this work in which Δn_{TBA} was reduced to 0.007 mol seem to lie on the smooth curve drawn through the data points of paper I (1) within experimental error. In paper I (1), Δn_{TBA} was 0.01 mol. Hence it was concluded that the relation $H_m^E(TBA) = \Delta H/\Delta n_{TBA}$ holds with $\Delta n_{TBA} = 0.01$ mol. Scatter of the data for 20.00°C is due to the fact that TBA solidifies in ampoules and there appears to be an additional work done on solid TBA when the ampoule is broken by the saphire needle. Such effect depends on the way the solid is formed and it is not controllable. Other than the data at 20.00°C, all the points appeared to be on smoothly drawn curves within the respective error limits. In Fig. 3 are shown the values of H_m^E(TBA) read off the smooth curves at various values of X_{TBA}, including those extrapolated to $X_{TBA} = 0$, against temperature.

As mentioned above, there are no data for the excess partial molar enthalpies for this mixture available in literature to compare directly with the present results. For $X_{TBA} < 0.05$ at 25°C, however, the apparent relative molar enthalpies, ϕ_L, are fitted to a virial expansion with respect to molality, m (6). Since

[1] $$H_m^E(TBA) - H_m^E(TBA, X_{TBA} = 0) = \partial(m\phi_L)/\partial m$$

an indirect comparison is possible. For $X_{TBA} > 0.05$, on the other hand, the excess molar (integral) enthalpies, H_m^E are compiled at various temperatures (4), but the data are not netted closely enough for an accurate graphical differentiation. When the excess partial molar enthalpies of H_2O in the mixture, $H_m^E(H_2O)$, become available, the values of H_m^E are calculated and a direct comparison will be possible. At present, however, the present data at 30.00°C were compared in an approximate manner with those obtained from the excess molar enthalpies compiled by Westmeier (4). Namely, the data of the excess molar enthalpies at 30°C (4) were plotted, through which a smooth curve was drawn using a flexible ruler, and H_m^E were estimated by the Bakhuis–Rooseboom method (21).

Such comparisons are summarized in Table 2. In column 2 are listed the values of H_m^E(TBA) of this work at 25°C, which were read off from Fig. 3. Column 3 contains the values of H_m^E(TBA) calculated as, by virtue of eq. [1],

[2] $$H_m^E(TBA) - H_m^E(TBA, X_{TBA} = 0) = 2mh_{xx} + 3m^2h_{xxx} + 4m^3h_{xxxx}$$

for $m < 3$ mol kg^{-1}, or $X_{TBA} < 0.05$, with the virial coefficients determined by Desnoyers *et al.* (6). For the value of H_m^E(TBA, $X_{TBA} = 0$) at 25°C, that by Desnoyers *et al.* at 26.0°C (6) was corrected by the value of C_p^E(TBA) at 25°C calculated using the apparent molar heat capacity of deVisser *et al.* (22). See Table 3, below. In column 4 are given the values of H_m^E(TBA) read off the smooth curve drawn through the present data points at 30.00°C, Fig. 1 showing a portion $X_{TBA} < 0.06$. In column 5 are listed the values of H_m^E(TBA) calculated from Westmeier's excess molar enthalpies (4) as mentioned above. In spite of the crudeness, the comparison between columns 2 and 3 and that between columns 4 and 5 are reasonable. While the virial expansion obtained by Desnoyers *et al.* (6), i.e. eq. [2], is applicable only in the range $X_{TBA} < 0.05$, the value calculated at $X_{TBA} = 0.06$ in column 2, 0.43 kJ mol^{-1}, and its difference from the observed value in column 1, −2.0 kJ mol^{-1}, serve to suggest the limitation of the virial expansion in understanding the nature of the mixture in the entire concentration range.

The value of the excess partial molar enthalpy at the infinite dilution, $H_m^E(TBA, X_{TBA} = 0)$, −17.4 kJ mol^{-1} at 25°C, should include the energetic gain for a TBA molecule to break hydrogen bondings to TBA molecules in the pure TBA liquid and to form hydrogen bondings to surrounding H_2O molecules in the mixture. There should also be an additional effect that a solute TBA makes on the solvent H_2O. Theoretical estimates (8, 9) indicate that the TBA–H_2O potential is −25.6 kJ mol^{-1} when TBA acts as the proton donor and H_2O the acceptor and is −21.7 kJ mol^{-1} in the opposite case, while the TBA–TBA potentials are −20 kJ mol^{-1} in both cases regardless of which acts as the proton donor or the acceptor. Thus, the energetic gain in exchange of hydrogen bondings amounts to −7.3 kJ mol^{-1}. The remaining −10.1 kJ mol^{-1} in H_m^E(TBA, $X_{TBA} = 0$) should therefore be attributed to some structural enhancement, i.e. formation of extra hydrogen bonds, in the solvent H_2O caused by a TBA molecule (2, 20). The temperature dependence of the energies of hydrogen bonds is small. Therefore, the values of $C_p^E(TBA) (= \partial H_m^E(TBA)/\partial T)$ in the water-rich region should be due mainly to the temperature dependence of the latter effect, which is likely to be high.

In passing, the heat of fusion of TBA at 20.0°C is estimated as

Can. J. Chem. Downloaded from www.nrcresearchpress.com by 93.93.197.157 on 09/07/12
For personal use only.

TABLE 1. Excess partial molar enthalpies of *tert*-Butanol

X_{TBA}	H_m^E(TBA)/kJ mol^{-1}
T = 20.00°C, ampoule method	
0.00039	−13.97
0.00133	−13.92
0.00422	−13.54
0.00562	−13.38
0.00727	−13.29
0.00839	−13.57
0.00913	−13.20
0.01638	−11.94
0.01714	−11.84
T = 26.90°C, ampoule method	
0.001854	−16.88
0.003064	−16.63
T = 26.90°C, ampoule method/ previous work (1)	
0.00105	−16.88
0.00316	−16.62
0.00523	−16.53
0.00730	−16.08
0.01629	−14.63
0.01846	−14.17
0.02067	−13.68
0.02989	−11.25
0.03206	−10.55
0.04026	−7.64
0.04207	−6.96
0.04218	−6.96
0.04416	−6.40
0.04412	−6.22
0.04609	−5.70
0.04809	−5.01
0.05151	−4.00
0.05167	−4.02
0.05385	−3.33
0.06575	−1.37
0.06802	−1.15
0.07991	−0.41
0.09246	0.02
0.1119	0.29
0.1394	0.57
0.1718	0.70
0.2059	0.83
0.2417	0.90
0.2788	0.97
0.3225	1.01
0.3636	1.03
0.4077	1.03
0.5605	0.80
0.7304	0.43
0.8817	0.12
T = 30.00°C, ampoule method	
0.000852	−16.09
0.00264	−15.86
0.00447	−15.62
0.00625	−15.39
0.00811	−15.19
0.01059	−14.83
0.01261	−14.47

TABLE 1 (*concluded*)

X_{TBA}	H_m^E(TBA)/kJ mol^{-1}
0.01860	−13.46
0.02062	−12.94
0.02262	−12.54
0.03383	−9.30
0.03602	−8.57
0.04530	−5.28
0.04725	−4.66
0.06293	−1.43
0.1010	0.14
0.1975	0.80
0.3044	0.90
0.4148	0.93
0.4177	0.91
0.5572	0.75
0.6246	0.61
0.7386	0.41
0.8142	0.26
T = 30.00°C, buret method	
0.00213	−15.84
0.00283	−16.12
0.00746	−15.20
T = 45.17°C, buret method	
0.00176	−12.71
0.00355	−12.51
0.00381	−12.60
0.00577	−12.42
0.00770	−12.03
0.01804	−9.95
0.02011	−9.65
0.02212	−9.19
0.02186	−9.02
0.02463	−8.54
0.02616	−7.63
0.02854	−7.44
0.03697	−4.82
0.03930	−4.23
0.04149	−3.64
0.05855	−1.34
0.06123	−1.11
0.06398	−0.91
0.06644	−0.78
T = 59.49°C, buret method	
0.00237	−9.87
0.00249	−9.54
0.00429	−9.62
0.00453	−9.49
0.00646	−9.26
0.00838	−9.00
0.01280	−7.98
0.01519	−7.77
0.01732	−7.25
0.01968	−6.85
0.03264	−4.06
0.03532	−3.38
0.04495	−2.09
0.04724	−1.77
0.05498	−1.26
0.05745	−1.05

Can. J. Chem. Downloaded from www.nrcresearchpress.com by 93.93.197.157 on 09/07/12
For personal use only.

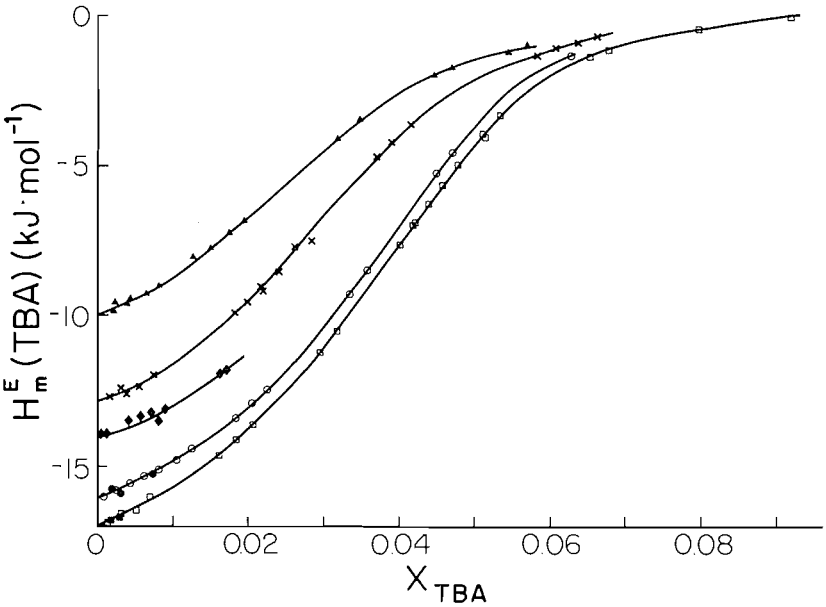

FIG. 1. The excess partial molar enthalpies of *tert*-butanol (TBA) in H_2O–TBA mixtures, H_m^E(TBA), against the mole fraction X_{TBA}. ▲, 59.49°C (buret); ×, 45.17°C (buret); ○, 30.00° (ampoule); ●, 30.00°C (buret); □, 26.90°C (ampoule/previous work (1)); ■, 26.90°C (ampoule); ◆, 20.00°C (ampoule).

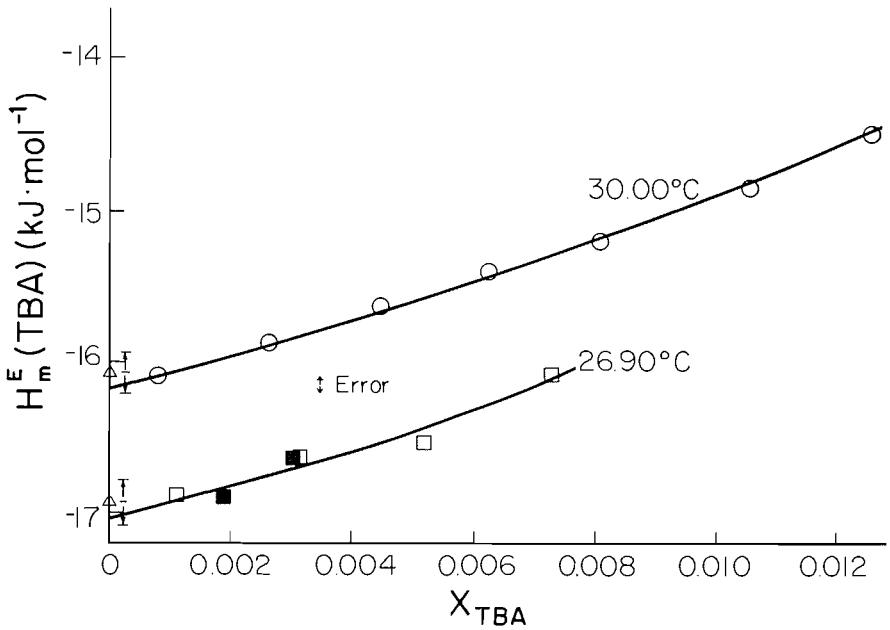

FIG. 2. The excess partial molar enthalpies of *tert*-butanol (TBA) in H_2O–TBA mixtures, H_m^E(TBA), against the mole fraction, X_{TBA}. The enlarged view of ampoule runs at 26.90 and 30.00°C. ○, ■, this work; □, previous work (1); △, ref. 7.

3.8 kJ mol^{-1} from the difference between the actual value and the extrapolated value of H_m^E(TBA, X_{TBA} = 0) to 20.0°C, as shown in Fig. 3.

As pointed out above, X_{TBA} = 0.06 is the boundary at 26.90°C which separates the two regions (1); for $X_{TBA} < 0.06$, H_m^E(TBA) depends sharply on X_{TBA} and C_p^E(TBA) (= $\partial H_m^E(\text{TBA})/\partial T$) is large, while for $X_{TBA} > 0.06$ they both become small and nearly constant. Figure 1 shows that such a boundary shifts towards a smaller value in X_{TBA} as the temperature is raised. Indeed, Fig. 3 suggests at about 100°C the boundary becomes very close to X_{TBA} = 0. Namely, the second scheme, in which TBA molecules in the mixture find themselves in a not very different environment than that in the pure TBA, dominates in almost the entire range of X_{TBA}. This suggests association of TBA molecules and hence the possible existence of a lower critical solution temperature above the boiling point (10). This is a very probable explanation on the abnormal enhancement in the concentration fluctuations (11–14) and the maxima in the correlation lengths (2, 10, 14) in the middle range of X_{TBA}.

Estimates of C_p^E(TBA) as $\Delta H_m^E(\text{TBA})/\Delta T$ were made from the two smooth curves of H_m^E(TBA) drawn through the points measured at 26.90°C (1) and 30.00°C. They are listed in column 4 of Table 3, which complements the data in paper I (1). The

Can. J. Chem. Downloaded from www.nrcresearchpress.com by 93.93.197.157 on 09/07/12
For personal use only.

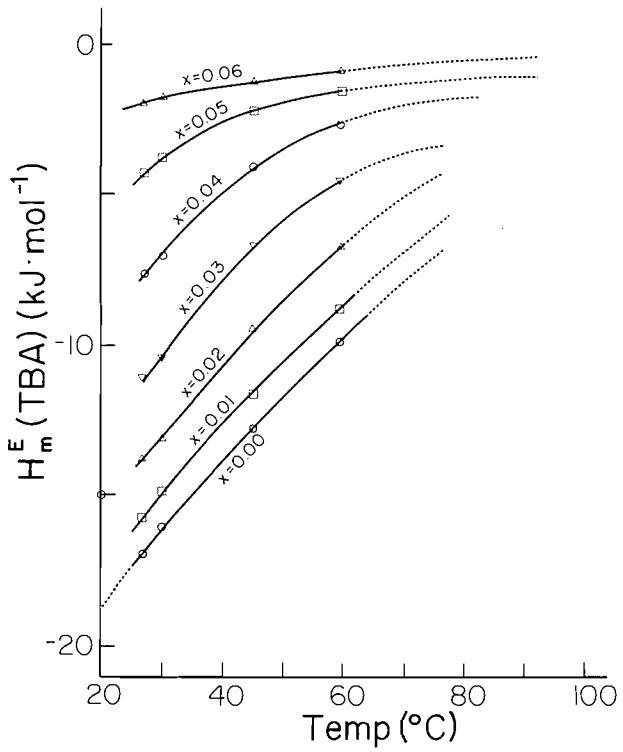

FIG. 3. The excess partial molar enthalpies of *tert*-butanol (TBA) in H_2O–TBA mixtures, H_m^E(TBA), against temperature at various values of X_{TBA}.

values of X_{TBA} in the table were so chosen that at a close proximity of X_{TBA} the actually measured values of H_m^E(TBA) for both temperatures are available. This is to minimize errors introduced in drawing a smooth curve. This method of obtaining C_p^E(TBA) inevitably causes a large error, an estimate of which is also given in column 4 of Table 3. While the data for the apparent molar heat capacities of the mixture, ϕ_c, are available in literature (22), there are no data for the partial molar heat capacities to compare directly with the present results. Thus an attempt was made to make an approximate comparison as follows: The data of ϕ_c at 25°C and 40°C (22) obtained from the Depository of Unpublished Data, CISTI, NRC, were plotted against X_{TBA}, and slopes at appropriate values of X_{TBA} were obtained graphically. C_p^E(TBA) was then calculated as,

$$[3]\quad C_p^E(\text{TBA}) = \phi_c + X_{TBA}(1 - X_{TBA})(\partial\phi_c/\partial X_{TBA}) - \phi_c(X_{TBA} = 1)$$

The resulting values are listed in columns 5 and 6 for 25°C and 40°C, respectively. The latter method of obtaining C_p^E(TBA) is superior if the data points for ϕ_c are closely netted, which is the case for $X_{TBA} < 0.04$ at 25°C and for $X_{TBA} < 0.055$ at 40°C (22). Thus, the fact that the present data do not show a maximum in the range $X_{TBA} < 0.05$ may be attributed to the large error involved in the method. However, the data in columns 4, 5, and 6 agree in the general trend of C_p^E(TBA) that $X_{TBA} \approx 0.06$ marks a sharp boundary above which C_p^E(TBA) is small, negative, and virtually constant.

The solute–solute interaction in the mixture in comparison with that in pure TBA is expressed as $(\delta H_m^E(\text{TBA})/\delta n_{TBA})$, which in the water-rich region is approximately equal to $(\delta H_m^E(\text{TBA})/\partial X_{TBA})$. Thus, the slopes of the smooth curves in Fig. 1 were obtained graphically as $(\partial H_m^E(\text{TBA})/\partial X_{TBA})$ with $\partial X_{TBA} = 0.002$ and shown in Fig. 4. The slopes do not appear to approach zero smoothly towards $X_{TBA} = 0$ though they may do so at much smaller value of X_{TBA} than the range covered in the present work. Arnett, Kover, and Carter (7) claimed that at 25°C the values of H_m^E(TBA) were constant within the error limit ±0.06 kJ mol^{-1} for $X_{TBA} < 2 \times 10^{-4}$. The present data clearly

TABLE 2. Comparison of H_m^E(TBA)

	H_m^E(TBA)/kJ mol^{-1}					
(1)	(2) This work	(3)	(4) This work	(5)	(6)	(7)
X_{TBA}	25°C	(*a*) 25°C	30°C	(*b*) 30°C	(*c*) 26°C	(*d*) 25°C
0.0	−17.4	−17.30			−17.050	−17.46
0.01	−16.2	−16.20				
0.02	−14.3	−14.40				
0.03	−11.6	−11.87				
0.04	−8.1	−8.58				
0.05	−4.7	−4.48				
0.06	−2.0	(0.43)	−1.75	−1.5		
0.075			−0.55	−0.55		
0.1			0.13	0.16		
0.2			0.80	0.80		
0.3			0.91	0.90		
0.4			0.92	0.90		
0.5			0.84	0.88		
0.6			0.66	0.75		
0.7			0.50	0.51		
0.8			0.27	0.23		
0.9			0.06	0.05		

[a]Calculated using the data in ref. 6. See text.
[b]Calculated using the data in ref. 4. See text.
[c]Reference 6.
[d]Reference 7.

TABLE 3. Comparison of C_p^E(TBA)

	H_m^E(TBA)/kJ mol^{-1}		C_p^E(TBA)/J K^{-1} mol^{-1}			
(1)	(2)	(3)	(4)	(5)	(6)	(7)
X_{TBA}	This work 30.0°C	This work 26.9°C	This work 28.45°C	(*a*) 25°C	(*a*) 40°C	(*b*) 25°C
0.0	−16.03	−16.90	281±35	252	219	275
0.002	−15.83	−16.76	300±35	254	222	
0.004	−15.60	−16.46	277±35	256	225	
0.006	−15.37	−16.24	281±35	259	228	
0.018	−13.48	−14.24	245±35	274	240	
0.02	−13.05	−13.80	242±35	276	241	
0.0328	−9.54	−10.14	194±30	301	238	
0.044	−5.72	−6.36	206±25	298	173	
0.048	−4.42	−5.03	197±25	263	146	
0.063	−1.45	−1.70	81±20	58	43	
0.1	0.10	0.14	−10±15	3	6	
0.2	0.80	0.83	−10±15	−15	−6	
0.3	0.91	1.00	−30±15	−13	−7	
0.41	0.92	1.01	−30±15	−11	−8	
0.56	0.74	0.81	−20±15	−5	−2	
0.735	0.42	0.43	−3±15	1	0	

[a]Calculated from the data of ref. 22. See text.
[b]Reference 7.

Can. J. Chem. Downloaded from www.nrcresearchpress.com by 93.93.197.157 on 09/07/12
For personal use only.

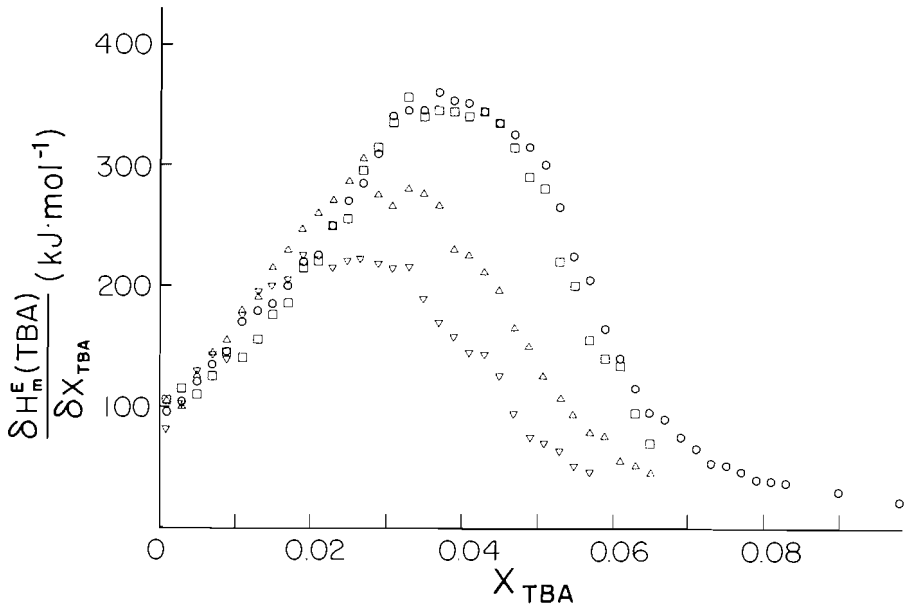

FIG. 4. The slopes of the curves of H_m^E(TBA) vs. X_{TBA}, i.e. $\delta H_m^E(TBA)/\delta X_{TBA}$, against the mole fraction, X_{TBA}. ○, 26.90°C; □, 30.00°C; △, 45.17°C; ▽, 59.49°C.

show as in Figs. 2 and 4, that at least at about $X_{TBA} = 0.001$ the slopes are non-zero and positive. This implies that the solute–solute interaction is repulsive in terms of enthalpy and is operating already at $X_{TBA} = 0.001$, i.e. the solute–solute interaction is effectively of very long range.

If TBA molecules are randomly distributed among H_2O molecules without any preferential association, a given TBA molecule is surrounded by $(1 - X_{TBA})/X_{TBA}$ H_2O molecules on average. Assuming that such H_2O molecules surround a TBA molecule in a spherical fashion, the radius, n_r, in terms of number of H_2O molecules may then be defined as

$$[4] \quad (4/3)\pi n_r^3 = (1 - X_{TBA})/X_{TBA}$$

In Fig. 5 are plotted the values of $\delta H_m^E(TBA)/\delta X_{TBA}$ against n_r. $n_r \approx 1.6$ marks a strikingly sharp rise in the solute–solute interaction, indicating a hard-sphere behaviour of the species of a TBA molecule surrounded by H_2O molecules with $n_r \approx 1.6$. Such hard-sphere radii, n_r*, were estimated from Fig. 5 to be 1.55, 1.68, and 1.77 at 26.90, 45.17, and 59.49°C, respectively. In terms of the number, k, in the species of TBA$(H_2)_k$ type, these values of n_r* correspond to 16, 20, and 23 at the respective temperatures. These values compare favourably with those obtained by Iwasaki *et al.* (13) by light scattering technique, i.e. $k = 15 \sim 19$ at 17.5°C and $k = 21 \sim 25$ at 63°C (13). Note, however, that this alone does not support the persistence of such species in the entire concentration range.

As can also be seen in Fig. 5, the value of $\delta H_m^E(TBA)/\delta X_{TBA}$ is ~100 kJ mol^{-1} at $n_r = 6$. Namely, the solute–solute repulsive interaction is already operative when two solutes are separated by about 12 H_2O molecules on average. Such a long range interaction is only possible via the hydrogen bond network of water (15–17). That the hydrogen bond network in pure H_2O extents to the entire bulk is well documented (15–17). Additional evidence has been given recently in the excess partial molar enthalpies of H_2O and D_2O in H_2O–D_2O mixtures (18). In spite of the fact that the strength of the hydrogen bonds and the probability of those intact are higher in D_2O, the measured excess partial molar enthalpies of H_2O and those of D_2O are

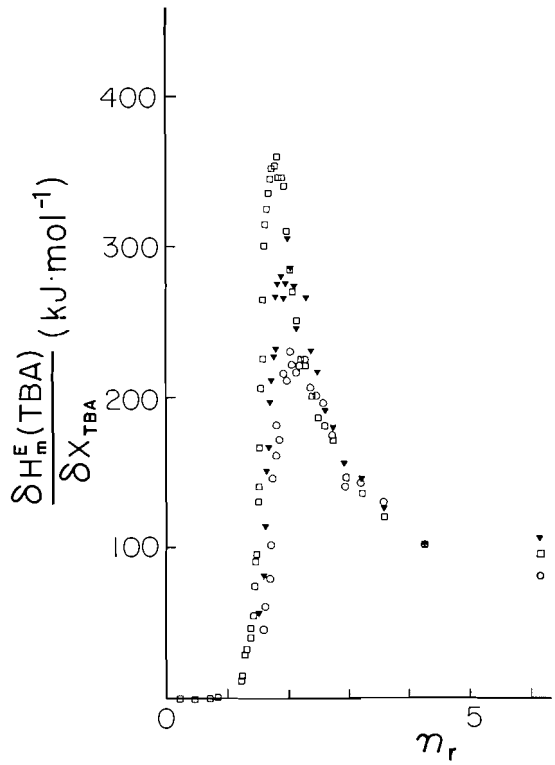

FIG. 5. The slopes of the curves of H_m^E(TBA) vs, X_{TBA}, i.e., δH_m^E(TBA/δX_{TBA}, against n_r defined by eq. [4]. □, 26.90°C; ▼, 45.17°C; ○, 59.49°C.

perfectly symmetric with respect to interchange of H_2O and D_2O. The resulting excess molar enthalpies of H_2O–D_2O, $H_m^E\{xH_2O + (1 - x)D_2O\}$, were expressed as,

$$[5] \quad H_m^E = A_1 x(1 - x)$$

with $A_1 = 132.3$ J mol^{-1} at 25.00°C (18). Namely, the intermolecular interactions in H_2O–D_2O mixture can be described by the mean-field type expression, which is rigorously correct

Can. J. Chem. Downloaded from www.nrcresearchpress.com by 93.93.197.157 on 09/07/12
For personal use only.

when the interaction is weak and infinite in range (19). Thus a TBA molecule causes structure enhancement (2, 8, 9, 20) in the surrounding H_2O molecules and this effect entails at least six H_2O molecules away via the hydrogen bond network.

Both Figs. 4 and 5 show the effect of temperature on the solute–solute interaction energy. Namely, at the low end of X_{TBA} or at large values of n_r, the effect of temperature is not apparent. However, the increase of the solute–solute interaction as X_{TBA} increases is cut short at higher temperatures and it appears that the second scheme in which H_m^E(TBA) as well as $\delta H_m^E(TBA)/\delta X_{TBA}$ becomes small sets in, i.e. TBA molecules tend to associate. From Fig. 5, these thresholds appear to be 0.02 at 59.49, 0.025 at 45.17, and 0.03 at 30.00°C. Indeed, a recent molecular dynamics calculation (9) showed a tendency that TBA molecules associate already at $X_{TBA} = 0.03$.

Thus a probable scenario for mixing TBA into H_2O may be as follows: AT $X_{TBA} \approx 0$, a TBA molecule forms hydrogen bonds with H_2O molecules and rearranges the surrounding H_2O molecules to enhance the network structure of H_2O. The latter exothermic effect is as significant as the hydrogen bond formation. At least at $X_{TBA} = 0.001$, the structure enhancement extend the entire bulk of the solution and an additional TBA molecule has an enthalpic difficulty to settle into an already somewhat enhanced structure of the solution. Thus H_m^E(TBA) increases and $\delta H_m^E(TBA)/\delta X_{TBA}$ also increases. Then at a certain threshold, $X_{TBA} = 0.02$ at 59.49, 0.025 at 45.17, and 0.03 at 30.00°C, this first scheme becomes unfavourable as compared to the second scheme whereby TBA molecule tend to associate. Beyond the threshold the second scheme starts to set in. Above a boundary somewhat higher than the threshold, 0.06 at 30.00°C, the second scheme dominates and the solution consists of clustered TBA molecules.

While the scenario presented here is not entirely new (23), the partial molar enthalpies and their derivatives with respect to X_{TBA}, Figs. 4 and 5, provide for the first time the threshold of X_{TBA} above which the solute–solute enthalpic repulsion start to die down, and the temperature dependence of such threshold value. Figure 5 also shows clearly a hard-sphere nature of the species of $TBA(H_2O)_k$ type, if such species persist. Thus, although much has been known about this mixture, it is still worthwhile to measure accurately the quantities that are proportional to the higher order derivatives of the free energy in the entire concentration range.

Acknowledgement

I wish to thank Professors D. H. Dolphin and L. G. Harrison for allowing me to use their facilities and many colleagues in Department of Chemistry, U.B.C., for kindly lending chemicals and incidentals. However, it is Professor James A. Morrison that has provided me with constant support and encouragement that have kept my research program somehow going since my lucky encounter with him 15 years ago. I do not have enough vocabulary to express my gratitude to him propertly. So, in the simplest possible way:

Thank you for everything, Jim!

1. Y. Koga. Can. J. Chem. **64**, 206 (1986).
2. T. M. Bender and R. Pecora. J. Phys. Chem. **90**, 1700 (1986).
3. M. Sakurai. Bull. Chem. Soc. Jpn. **60**, 1 (1987).
4. S. Westmeier. Chem. Techn. **29**, 218 (1977).
5. F. Franks, M. Pedley, and D. S. Reid. J. Chem. Soc. Faraday 1, **72**, 359 (1977).
6. J. E. Desnoyers, G. Perron, L. Avedikian, and J.-P. Morel. J. Sol. Chem. **5**, 631 (1976).
7. E. M. Arnett, W. B. Kover, and J. V. Carter. J. Am. Chem. Soc. **91**, 4028 (1969).
8. K. Nakanishi, K. Ikari, S. Okazaki, and H. Touhara. J. Chem. Phys. **80**, 1656 (1984).
9. H. Tanaka, K. Nakanishi, and H. Touhara. J. Chem. Phys. **81**, 4065 (1984).
10. G. W. Euliss and C. M. Sorensen. J. Chem. Phys. **80**, 4767 (1984).
11. H. D. Bale, R. E. Shepler, and D. K. Sorgen. Phys. Chem. Liquids, **1**, 181 (1968).
12. K. Iwasaki and T. Fujiyama. J. Phys. Chem. **81**, 1908 (1977).
13. K. Iwasaki and T. Fujiyama. J. Phys. Chem. **83**, 463 (1979).
14. Y. Koga. Chem. Phys. Lett. **111**, 176 (1984).
15. G. Nemethy and H. A. Scheraga. J. Chem. Phys. **41**, 680 (1964).
16. H. E. Stanley and J. Texeira. J. Chem. Phys. **73**, 3404 (1980).
17. Y. Marcus and A. Ben-Naim. J. Chem. Phys. **83**, 4744 (1985).
18. Y. Koga. J. Chem. Thermodyn. **19**, 571 (1987).
19. H. E. Stanley. *In* Introduction to phase transitions and critical phenomena. Oxford Press, Oxford. 1971. Sec. 5.6.
20. H. Uedaira and J. Kida. Nippon Kagaku Kaishi, **1982**, 539 (1982).
21. I. Prigogine and R. Defay. *In* Chemical thermodynamics. *Translated by* D. H. Everett. Longmans, London. 1965. p. 7.
22. C. Devisser, C. Perron, and J. E. Desnoyers. Can. J. Chem. **55**, 856 (1977).
23. F. Franks and J. E. Desnoyers. *In* Water science reviews. 1. *Edited by* F. Franks. Cambridge University Press, Cambridge. 1985. p. 171.

Can. J. Chem. Downloaded from www.nrcresearchpress.com by 93.93.197.157 on 09/07/12
For personal use only.

Metal ion catalysis of the decomposition of transient 2-carboxy-2,5-cyclohexadienones in aqueous solution

OSWALD S. TEE[1] AND N. RANI IYENGAR

Department of Chemistry, Sir George Williams Campus, Concordia University, Montréal, P.Q., Canada H3G 1M8

Received September 10, 1987

OSWALD S. TEE and N. RANI IYENGAR. Can. J. Chem. **66**, 1194 (1988).

Bromide ion induced debromination of the anion of 4-bromo-4-methyl-2,5-cyclohexadienone-2-carboxylic acid (**1**) is catalyzed by cupric ions and ferric ions. Similarly, the enolization of the anion of the benzocyclohexadienone **3**, which is formed during the bromination of 1-naphthol-2-carboxylic acid, is catalyzed by some metal ions. The origin of the catalysis in these reactions is strong metal ion binding to the incipient dianion products that are of the salicylate type. Evidence for this is that the efficiency of the metal (and hydrogen) ion catalysis parallels the stability of the analogous complexes with the salicylate dianion.

OSWALD S. TEE et N. RANI IYENGAR. Can. J. Chem. **66**, 1194 (1988).

La débromation, induite par l'ion bromure, de l'anion de l'acide bromo-4 méthyl-4 cyclohexadiène-2,5 one-2 carboxylique (**1**) est catalysée par les ions cuivrique et ferrique. De la même manière, l'énolisation de l'anion de la benzacyclohexadiènone **3**, qui se forme lors de la bromation de l'acide naphtol-1 carboxylique-2, est catalysée par quelques ions métalliques. La catalyse dans ces réactions est due à la forte liaison des ions métalliques avec les produits dianioniques qui se forment et qui sont du type salicylate. Le fait que l'efficacité de la catalyse par les ions métalliques (ou l'hydrogène) soit parallèle à la stabilité des complexes analogues avec le dianion salicylate est en accord avec la conclusion précédente.

[Traduit par la revue]

Can. J. Chem. Downloaded from www.nrcresearchpress.com by 93.93.197.157 on 09/07/12
For personal use only.

Labile cyclohexadienones can be observed during the aqueous bromination of phenols lacking electron-withdrawing groups (1–4). Two types of dienone are formed and they decompose by different reactions, depending on the phenol. Where the starting phenol has no *para* substituent a transient 4-bromo-2,5-cyclo-hexadienone is formed, which enolizes to the 4-bromo product (1–3). On the other hand, with *p*-alkylphenols, part of the initial fast bromine attack occurs *ipso* to the alkyl group, leading to a 4-alkyl-4-bromo-2,5-cyclohexadienone, an "ipso-dienone" (4, 5), which cannot enolize and which decomposes by debromination (1, 4).

Two particularly interesting examples of the above types of intermediates that we have found are the cyclohexadienones **1** and **3**, derived from bromine attack on certain salicylic acids. The bromide ion induced debromination of the ipso-dienone **1** (→ $\mathbf{2}^-$, eq. [1]) is greatly facilitated by the 2-carboxyl group (4, 6). Similarly, the enolization of the benzocyclohexadienone **3** (→ $\mathbf{4}^-$, eq. [2]) is catalyzed by its internal carboxyl group and by

[1] 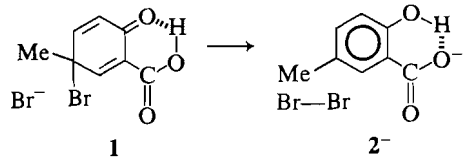

1 **2⁻**

[2] 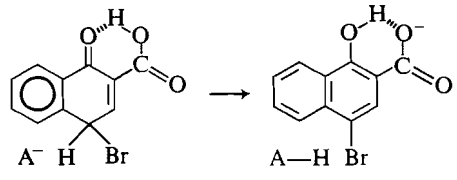

3 **4⁻**

external bases (3). We hereby report that the debromination of **1** and the enolization of **3** are also catalyzed by some metal ions.

We were prompted to look for such behaviour by the ongoing interest in enzymic and non-enzymic metal ion catalyzed reactions (7, 8) and by the knowledge that salicylate dianions form weak to strong complexes with various metal ions (9). It was anticipated that the binding of metal ions to the anions of **1** and **3** ($\mathbf{1}^-$ and $\mathbf{3}^-$) would be relatively weak whereas binding to the dianions of the products ($\mathbf{2}^{2-}$ and $\mathbf{4}^{2-}$) should be considerably stronger (9). Therefore, assuming that metal ion binding to the transition states of the reactions $\mathbf{1}^- \rightarrow \mathbf{2}^{2-}$ and $\mathbf{3}^- \rightarrow \mathbf{4}^{2-}$ is intermediate in strength, catalysis of these reactions by metal ions should occur, in favourable cases.

Since the early work of Pedersen (10) on the enolization of β-keto esters, various workers have shown that enolization (and closely related reactions such as the decarboxylation of β-keto acids) can be catalyzed by metal ions (11–14). The early studies tended to emphasize the binding abilities of the substrates but it is now clear that metal ion binding to the incipient products is of more importance (11–14). The present work provides further evidence that this is the case but the novel aspect of the work arises because the reactants **1** and **3** are labile intermediates.

The decomposition reactions [1] and [2] are energetically favourable and inherently fast (1–4, 6). Therefore, reactant-like transition states are to be expected and it is by no means clear that they will have sufficient product character that an increase in metal ion binding will lower their energies significantly.

Results

Our results for the effect of metal ions on the rate of debromination of the ipso-dienone **1** are summarized in Table 1. For ease of comparison, the observed first-order rate constants (k^{obs}) are presented together with the values (k^{calc}) expected in the absence of metal ions, calculated from the kinetic parameters obtained in our earlier study of **1** (6). Significant enhancements of rate were found with cupric ions and ferric ions but little or no effect[2] was observed with Zn^{2+}, Ni^{2+}, Mg^{2+}, and Co^{2+} ions.[3]

[1]Author to whom correspondence may be addressed.

[2]With nickel and zinc ions the rates are somewhat lower than expected. This may be due to a small effect on the partitioning of bromine attack (see later).

[3]With added Al^{3+} ions complex behaviour was observed, which was not pursued.

TABLE 1. The effect of metal ions on the rate of decomposition of 4-bromo-4-methyl-2,5-cyclohexadienone-2-carboxylic acid (**1**)[a]

Ion	[ion] (mM)	pH	k^{obs} (s^{-1})	k^{calc} (s^{-1})
Cu^{2+}	0.5	2.78	1.59	1.70
		3.79	0.470	0.407
		4.23	0.279	0.164
		4.67	0.285	0.0621
		4.91	0.278	0.0361
		5.09	0.262	0.0239
		5.20[b]	0.189	0.0186
	0.2	4.69	0.129[c]	0.0593
	0.4		0.271	
	0.6		0.299	
	0.8		0.468	
	1.0[b]		0.559	
Fe^{3+}	0.1	3.01	1.38	1.37
		3.75	0.728	0.439
		4.18	0.538	0.183
		4.64	0.354	0.0664
		4.98[b]	0.163	0.0308
	0.03	4.67	0.175[c]	0.0621
	0.05		0.201	
	0.07		0.262	
	0.10[b]		0.383	
Zn^{2+}	0.5	2.78	1.45	1.70
		3.79	0.269	0.407
		4.67	0.0454	0.0621
Ni^{2+}	0.5	4.23	0.117	0.164
		4.69	0.0403	0.0593
Mg^{2+}	0.5	4.91	0.0448	0.0361
Co^{2+}	0.5	4.91	0.0474	0.0361

[a]At 25°C, I = 0.11 M, in aqueous solution containing 0.1 M KBr.[2,3] The values of k^{calc} (for reaction in the absence of metal ions) are calculated from constants obtained earlier (6).

[b]Experiments at higher pH or [metal ion] were precluded by the unfavorable optical properties of the solutions.

[c]The dependence of k^{obs} on [ion] is linear.[4,5]

For both Cu^{2+} and Fe^{3+} the dependence of k^{obs} on the metal ion concentration at fixed pH is reasonably linear.[4, 5]

The extent of catalysis by metal ions varies with pH, as shown in Fig. 1. Presented there are appropriate rate data from Table 1, superimposed on the rate profile for the decomposition of the ipso-dienone **1** in the absence of metal ions. This profile (curve a, Fig. 1) corresponds to reaction of the undissociated form of **1** (pK_a = 3.06); reaction of the anion $\mathbf{1}^-$ is not important at the acidities studied (6). However, as seen in Fig. 1, this is no longer the case when the reaction medium contains either cupric ions (0.5 mM) or ferric ions (0.1 mM). For these ions there is a significant amount of catalysis only at acidities where the ipso-dienone **1** largely exists as its anion, $\mathbf{1}^-$. Thus, the rate data are consistent with the simple reaction of the metal ion with the anion of the substrate.

The catalysis by ferric ions decreases above pH 4.5. This is probably due to the presence of an equilibrium of the hydrated

[4]For cupric ions at pH 4.69 (Table 1): intercept = 0.0121 (sd = 0.0396); slope = 568 (sd = 6); r = 0.984.

[5]For ferric ions at pH 4.67 (Table 1): intercept = 0.0654 (sd = 0.0300); slope = 3040 (sd = 440); r = 0.979.

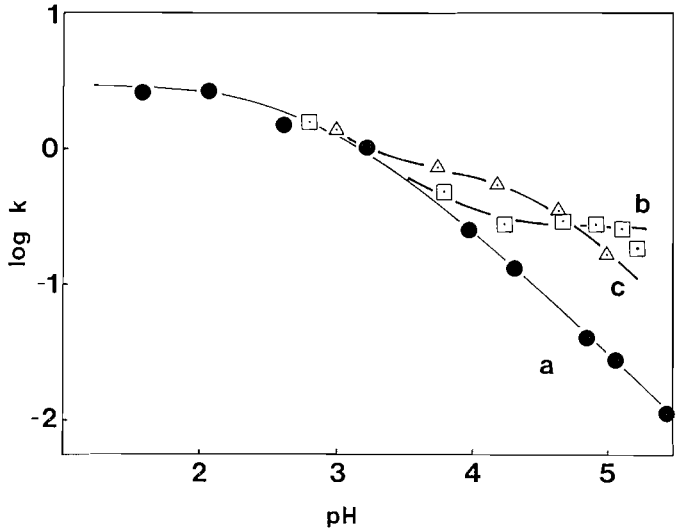

FIG. 1. pH dependence of the debromination of the dienone **1**: (a) in the absence of added metal ions (data from ref. 6); (b) in the presence of 0.5 mM cupric ions; (c) in the presence of 0.1 mM ferric ions.

ferric ion, which undergoes deprotonation in the pH range studied:

[3] $Fe(H_2O)_6^{3+} \rightleftharpoons Fe(H_2O)_5(OH)^{2+} + H^+$; pK_1 = 2.46 (9)

[4] $Fe(H_2O)_5(OH)^{2+} \rightleftharpoons Fe(H_2O)_4(OH)_2^{+} + H^+$; pK_2 = 4.70 (9)

At the acidities where the catalysis is most evident the dominant form of the ferric ion is $Fe(H_2O)_5(OH)^{2+}$ and this appears to be the form involved in the catalysis since the rate drops off with pH above pK_2, as discussed below.

In the absence of added metal ions and at fixed [Br^-] the pH dependence of the rate constant for the decomposition of **1** may be described by eq. [5], where k_1 is the rate constant for reaction of undissociated **1** and K_a is its acid dissociation constant.

$$[5] \quad (k^{obs})_0 = k_1[H^+]/(K_a + [H^+])$$

When ferric ions are present an additional term must be added to take account of the metal ion catalysis and the equilibria in eqs. [3] and [4] so that:

$$[6] \quad k^{obs} = (k^{obs})_0 + \frac{k_{cat}[Fe^{3+}]_t f_A K_1[H^+]}{([H^+]^2 + K_1[H^+] + K_1K_2)}$$

where $f_A = K_a/(K_a + [H^+])$ is the fraction of **1** existing at its anion. The derivation of eq. [6][6] assumes that the reactive form of the iron is $Fe(H_2O)_5(OH)^{2+}$. This assumption is necessary to reproduce the decrease in ferric ion catalysis that occurs when pH > pK_2. No catalysis by $Fe(H_2O)_6^{3+}$ is evident, presumably because of an unfavourable combination of the equilibria [3], [4], and the dissociation of **1**. The data in Fig. 1 correspond to a value of $k_{cat} \sim 5000\ M^{-1}\ s^{-1}$ for catalysis by $Fe(H_2O)_5(OH)^{2+}$.

The catalysis of the decomposition of **1** by cupric ions shows a plateau (k_{cat} = 570 $M^{-1}\ s^{-1}$) between pH 4 and 5 but the rate decreases slightly at higher pH. This decrease may be due to the

[6]In eq. [6] the quantity $[Fe^{3+}]_t$ is the total concentration of added iron (which is in large excess over [**1**]). For convenience we ignore the presence of the excess of 5-methylsalicylic acid (see Experimental). Any complexation involving this species will reduce the effective value of $[Fe^{3+}]_t$ but since the effect should be constant it should not affect our interpretation.

Can. J. Chem. Downloaded from www.nrcresearchpress.com by 93.93.197.157 on 09/07/12
For personal use only.

Can. J. Chem. Downloaded from www.nrcresearchpress.com by 93.93.197.157 on 09/07/12
For personal use only.

TABLE 2. The effect of cupric ions on the rate of bromination of 5-methylsalicylic acid (**2**)[a]

pH	k_2^{obs} (M^{-1} s^{-1})	k_2^{calc} (M^{-1} s^{-1})
0.13	3310	2350
1.09	2.53×10^4	2.13×10^4
2.09	1.74×10^5	1.95×10^5
2.76	1.25×10^6	6.80×10^5
3.85	2.21×10^6	1.80×10^6

[a]At 25°C, I = 0.11 M (KBr). Values of k_2^{obs} were determined in the presence of 0.1 mM cupric ions. The values of k_2^{calc} were calculated from the parameters of the rate profile for **2** in the absence of added metal ions, given earlier (6).

onset of the first ionization of the hydrated cupric ion:

[7] $Cu(H_2O)_6^{2+} \rightleftharpoons Cu(H_2O)_5(OH)^+ + H^+$; $pK_1 = 7.34$ (9)

In contrast to the behaviour of **1**, no catalysis by cupric ions (0.5 mM) was found for the decay of the analogous ipso-dienone lacking the 2-carboxyl group, formed during the reaction of *p*-methylphenol with bromine (1, 4). Thus, the 2-carboxyl group seems to be necessary for the occurrence of metal ion catalysis of the debromination of **1**.

The decomposition of **1** is a more complex reaction than is implied by eq. [1]. This arises because the debromination step produces 5-methylsalicylic acid (**2**) and bromine, which then react again, and the bromine attack is partitioned between *ortho* attack (~90%) and *para* (*ipso*) attack (~10%). Ultimately, all of the bromine is converted to the *o*-substituted product, 3-bromo-5-methylsalicylic acid (eq. [8]).

[8] $\mathbf{1} + Br^- \underset{k_p}{\overset{k_d}{\rightleftarrows}} \mathbf{2}^- + Br_2 \xrightarrow{k_0}$ product

This mechanism, which is amply supported by a variety of evidence (1, 4, 6), means that the rate constant for the decomposition of **1** (eq. [9]) contains the term: $k_o/(k_o + k_p)$, which represents the

[9] $k^{obs} = k_d k_o[Br^-]/(k_o + k_p)$

fraction of *ortho* bromine attack. This fraction, which is about 0.9 (4, 6), will be insensitive to the presence of metal ions as long as k_o and k_p do not vary markedly. As far as we can tell, this is the case.

Experiments carried out over a range of acidities (Table 2) showed that the second-order rate constants for the attack of bromine on 5-methylsalicylic acid **2** in the presence of 0.1 mM cupric ions are very close to those observed in their absence. Fitting to the data gives $k_2 = 2.9 \times 10^6$ M^{-1} s^{-1} for reaction of the anion $\mathbf{2}^-$ and $pK_a = 3.12$, compared to the values of $k_2 = 2.1 \times 10^6$ M^{-1} s^{-1} and $pK_a = 3.08$ that were found previously (6); this means that $k_2 = (k_o + k_p)$ is little changed by the cupric ions. Therefore, assuming that k_o and k_p are affected to a similar extent, the effect of the metal ions on k^{obs} for the decay of **1** (eq. [9]) is almost solely due to their effect on the rate constant of the debromination step, k_d.

The effects of added metal ions on the rate of enolization of the benzocyclohexadienone **3** were also studied and the results are presented in Table 3. Only in the pH region 4–6 were modest amounts of catalysis observed for Cu^{2+}, Fe^{3+}, and possibly Al^{3+}; outside this region the normal reaction (3) is dominant.

TABLE 3. The effect of metal ions on the rate of enolization of the benzocyclohexadienone **3**[a]

Ion	[ion] (mM)	pH	k^{obs} (s^{-1})	k^{calc} (s^{-1})
Cu^{2+}	0.1[b]	3.83	12.4	14.3
		4.21	7.40	6.52
		5.08	2.39	1.05
		5.68	1.25	0.369
		6.17	0.342	0.214
		6.72	0.218	0.161
		7.17	0.182	0.147
		7.30	0.177	0.146
	0.1[b]	56.2	1.33[c]	0.403
	0.2		2.58	
	0.3		3.48	
	0.5		6.32	
Fe^{3+}	0.1	3.76	16.8	16.4
		4.13	10.6	7.72
		4.63	3.81	2.66
		5.05	1.16	1.11
		5.67	0.409	0.374
		6.11	0.182	0.225
		6.70	0.149	0.162
		7.08	0.130	0.149
Al^{3+}	0.1[d]	4.80	1.52	1.85
		5.15	1.01	0.912
		5.62	0.701	0.403
		6.16	0.171	0.216
		6.71	0.134	0.161
		7.09	0.125	0.149
Zn^{2+}	0.1	5.68	0.276	0.369
Ni^{2+}			0.326	
Mg^{2+}			0.285	
Co^{2+}			0.284	

[a]At 25°C, I = 0.11 M, in 0.1 M aqueous KBr. The values of k^{calc} (for reaction in the absence of metal ions) are calculated from constants presented earlier (3).
[b]For $[Cu^{2+}] > 0.1$ mm the absorbance traces became increasingly noisy due to the large background absorbance.
[c]The dependence of k^{obs} on [ion] is linear.[7]
[d]At higher $[Al^{3+}]$ complex behaviour was observed.

For cupric ions the catalysis is maximal around pH 5.5 and the dependence of the rate on the [ion] is linear.[7] Above pH 6 this catalysis diminishes, probably due to the approach to the equilibrium [7], and the rate constants approach those observed in the absence of added metal ions (3). Likewise, the catalysis by Fe^{3+} and Al^{3+} ions, which is only apparent in a limited range of pH, is probably attenuated by the equilibria [3] and [4], and their analogues for Al^{3+} (9).

The enolizations of **3** and of its anion $\mathbf{3}^-$ are catalyzed by general bases (3). As seen by the results of experiments carried out in acetate buffers (Table 4) this also *seems* to be the case when cupric ions are present. However, the slopes of the buffer plots and the variation of these slopes with pH are virtually the same as those observed previously for reaction in the absence of added cupric ions (3).[8] Therefore, we conclude that increasing the buffer concentration simply increased the rate of the normal

[7]For cupric ions at pH 5.62 (Table 2): intercept = 0.0246 (sd = 0.2225); slope = 12400 (sd = 700); r = 0.9967.

[8]As previously, the data obtained in buffers are consistent with reaction of either acetate ion on the undissociated form of **3** or acetic acid on the anion of **3**. Of these two interpretations, the former is preferred, for reasons given previously (3).

TABLE 4. Dependence of the rate of the enolization of **3** on the acetate buffer concentration in the presence of cupric ions[a]

		k^{obs} (s^{-1})		
[buffer] (M)	pH =	4.32	4.85	5.30
0.01		2.83	1.86	1.26
0.05		4.75	2.67	1.66
0.10		6.86	3.32	2.31
0.15		9.04	4.39	2.92
	Intercept =	2.45	1.70	1.11
	Slope =	44.1	17.5	12.0
	r =	0.9997	0.9956	0.9989

[a]At 25°C, I = 1.0 M (NaCl), $[Cu^{2+}]$ = 0.1 mM. The intercepts, slopes, and correlation coefficients are from the least-squares analysis of k^{obs} vs. [buffer].

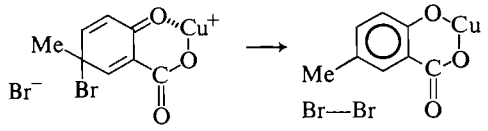

SCHEME 1

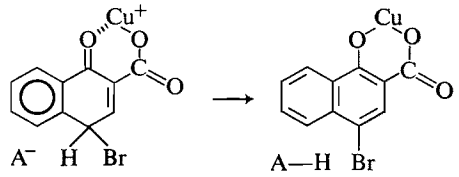

SCHEME 2

TABLE 5. Constants for metal ion complexation and for the catalysis of the debromination of the anion of the dienone **1**[a]

Ion	pK_M	k_{cat} (M^{-1} s^{-1})
Fe^{3+}	16.35	~5000
Al^{3+}	14.11	—[b]
H^+	13.61	3010
Cu^{2+}	10.60	570
Ni^{2+}	6.95	—[c]
Zn^{2+}	6.85	—[c]
Co^{2+}	6.72	—[d]
Mg^{2+}	Small	—[d]

[a]Values of pK_M (20°C) for the complexation of ions with the dianion of salicylic acid[10] in aqueous solution are taken from the literature (9). The catalytic constants (k_{cat}) are for reaction in 0.1 M aqueous KBr at 25°C.
[b]Complex behaviour observed.
[c]No catalysis observed.
[d]There may be weak catalysis (see Table 1).

reaction relative to that of the metal ion catalyzed reaction. This should be the case if the third-order rate constant for catalysis by acetate ions and protons is greater than the analogous rate constant for acetate and cupric ions. Such is almost certainly the case since the catalytic constant for the proton (k_{cat} = 1.1 × 10^5 M^{-1} s^{-1} (3)) at low buffer concentration is almost 10 times that for Cu^{2+} (k_{cat} = 1.2 × 10^4 M^{-1} s^{-1}).[7] Therefore, even though the cupric ion catalyzed enolization of the anion $\mathbf{3}^-$ is probably susceptible to catalysis by buffer bases, it is difficult to observe such with only 0.1 mM of cupric ions at pH 4–5 because of the competition from proton catalysis.

Discussion

The results presented above indicate that the debromination of $\mathbf{1}^-$ and the enolization of $\mathbf{3}^-$ are catalyzed by some metal ions. However, the effects are relatively modest as the metal ions can barely compete with catalysis by protons under the conditions used.[9] The rate data are consistent with electrophilic catalysis (7) occurring through mechanisms analogous to those shown in eqs. [1] and [2] but in which the place of the carboxyl proton is taken by a metal ion. These mechanisms are shown in Schemes 1 and 2, using the cupric ion for illustrative purposes.

The dependences of the catalyzed rates on [metal ion] are linear over the concentration ranges studied and they show no downward curvature, which would be indicative of the onset of saturation.[4,5,7] Thus, the binding of the substrate anions ($\mathbf{1}^-$ and $\mathbf{3}^-$) to both Cu^{2+} and Fe^{3+} must be relatively weak with dissociation constants ≫1 mM. In contrast, the binding of these cations to the product dianions ($\mathbf{2}^{2-}$ and $\mathbf{4}^{2-}$) must be very much stronger, judging by stability constants in the literature (9). As shown by the constants[10] in Table 5, the binding of Fe^{3+}, Al^{3+}, and Cu^{2+} to the salicylate dianion ($\mathbf{S}^{2-}$) is very strong and comparable in strength to the binding of the proton. In contrast, the binding of the other metal ions, which do not show catalysis, is several orders of magnitude weaker.

Table 5 also lists the catalytic constants for Fe^{3+}, Cu^{2+}, and the proton in the debromination of $\mathbf{1}^-$. These values increase in a regular manner with the ability of the ion to form complexes with $\mathbf{S}^{2-}$ and so they provide good evidence that binding of the cation to the incipient product dianion $\mathbf{2}^{2-}$ is the primary factor that determines catalytic ability. The slope of log k_{cat} versus pK_M is about 0.2,[11] which implies that only a small part of the potential binding energy to $\mathbf{2}^{2-}$ is available at the transition state of the reaction. Nevertheless, this can be a significant amount of energy, as shown below.

The proton catalyzed debromination of the anion $\mathbf{1}^-$ actually involves the conversion of **1** into $\mathbf{2}^-$ (eq. [1]) (6). This reaction is accompanied by a *large* change in pK_a of about 13.61 − 3.06 = 10.55,[12] which is equivalent to an increase in the binding energy of the proton of 14.4 kcal/mol at 25°C. Even if only 20% of this energy is available for stabilization of the transition state of the debromination, a rate increase of 130 may accrue. In fact, the actual rate increase is 2300 times, relative to the proton catalyzed debromination of 4-bromo-4-methyl-2,5-cyclohexadienone (6). The difference between these two factors is probably due to an additional effect of the carboxyl group of **1**, since electron withdrawal by this group should facilitate the abstraction of Br^+ from **1** by bromide ion (eq. [1]).

Enolization of the anion $\mathbf{3}^-$ is catalyzed by Cu^{2+} ions and probably be Fe^{3+} and Al^{3+} ions, also. However, at acidities

[9]Higher concentrations of cupric or ferric ions gave solutions with unfavorable optical properties (due to turbidity or high background absorbance), which precluded the measurements of rates.

[10]The stability constants in Table 5 are $pK_M = -\log(K_M)$, where $K_M = [M^{n+}][S^{2-}]/[MS^{(n-2)+}]$ is the dissociation constant of the metal ion – salicylate dianion complex (9).

[11]We note that this slope is quite close to the Brønsted α of 0.27 for the general acid catalyzed debromination of 4-bromo-4-methyl-2,5-cyclohexadienone (4).

Can. J. Chem. Downloaded from www.nrcresearchpress.com by 93.93.197.157 on 09/07/12
For personal use only.

Can. J. Chem. Downloaded from www.nrcresearchpress.com by 93.93.197.157 on 09/07/12
For personal use only.

where such catalysis might compete with proton catalysis, the amounts of these ions are limited by unfavourable equilibria (eg., eqs. [3], [4], and [7]). Only in the case of Cu^{2+} was a reasonable amount of catalysis detected and its k_{cat} is about 10 times smaller than that for the proton (see Results). Thus, as found for the debromination of the dienone anion $\mathbf{1}^-$, the catalytic efficiency of an ion parallels its ability to bind salicylate dianions.

The energy considerations that apply to the ion catalyzed enolization of the anion $\mathbf{3}^-$ are similar to those discussed above for the debromination of $\mathbf{1}^-$. From the k_{cat} values for the proton and Cu^{2+} catalyzed enolization of $\mathbf{3}^-$, the slope of log k_{cat} vs. pK_M is 0.32. Assuming the same pK_a change of 10.55,[12] in going from **3** to $\mathbf{4}^-$, 32% of the increase in the binding energy of the proton corresponds to a rate increase of 2400 times. The actual increase for the proton catalyzed reaction of $\mathbf{3}^-$ is much larger, being 2×10^5 (3). Again, the difference betwen these two values may arise because of electron withdrawal by the 2-carboxyl group of **3**.

Our results have broad similarities to various earlier studies of electrophilic catalysis by metal ions. For example, the enolizations of β-keto esters (10), 2-acetylpyridine (11), and of acetonyl phosphonates (12) can be catalyzed by metal ions. Similarly, the decarboxylation of β-keto carboxylate anions can be promoted with metal ions (7*c*, 13, 14) and we note that the catalytic constants show a reasonable correlation with the stability constants for the metal ion complexes of the incipient product anions (7*c*). In suitable cases, divalent metal ions may also afford *electrophilic* catalysis of ester hydrolysis (15), as distinct from cases where the catalysts function by delivering a metal-bound OH^- to the ester (or amide) carbonyl (7*c*, 16) or in some other way (17).[13]

The present results emphasize that any reaction that produces a salicylate-type dianion in its rate-limiting step has the potentiality for electrophilic catalysis by metal ions, as well as by the proton. However, the extent to which a significant amount of metal ion catalysis actually occurs depends primarily on whether it can compete with proton catalysis. This, in turn, depends on various binding constants, the substrate pK_a, and the pHs at which the reaction can be studied. Only under favourable circumstances can ions such as Cu^{2+} or Fe^{3+}, which strongly bind to the product dianion, compete with the proton as the electrophilic catalyst.

It is also noteworthy that for the ions H^+, Cu^{2+}, and Fe^{3+} the strength of binding to the product dianions is so great that its partial expression in the transition states is significant, even though the transition states in question are "early" and reactant-like.

Experimental

The basic approach used was as in our previous studies of the dienones **1** and **3** (3, 6). Rate measurements were made at 25°C, using the same stopped-flow apparatus and data acquisition system as in other recent work (1–4, 6). One of the drive syringes of the stopped-flow apparatus contained a solution of bromine in the desired aqueous medium while the other contained the substrate necessary to generate the dienone (see below) in the same medium, containing the metal ion. The metal ions were introduced into solution as their chloride salts except for the use of ferric nitrate and aluminium sulphate.

The ipso-dienone was generated *in situ* in the stopped-flow apparatus from bromine (0.1 mM) and 5-methylsalicylic acid (**2**) (0.5 mM) in aqueous buffer containing 0.1 M KBr (total $I = 0.11$ M). Since only about 10% of the attack of bromine on **2** is *ipso*, the initial concentration of **1** was about 0.01 mM, much less than the concentration of the added metal ions. The disappearance of **1** was monitored at 250 nm (6)

Similarly, the benzocyclohexadienone **3** was generated *in situ* from 1-naphthol-2-carboxylic acid (0.1 mM) and bromine (0.05 mM) in the desired medium and its enolization was monitored as a decay at 270 nm (3). For the pH and metal ion dependence studies the total ionic strength $I = 0.11$ M (0.01 M buffer salt + 0.1 M KBr), whereas for the buffer catalysis studies $I = 1.0$ M ([buffer salt] + [NaCl]). Because of the very low solubility of 1-naphthol-2-carboxylic acid in water, experiments could not be carried out at pHs below 3.5, where it is not appreciably ionized (3).

Acknowledgements

The authors thank the Natural Sciences and Engineering Research Council of Canada for an operating grant to O.S.T. and Mr. Bryan Takasaki for carrying out exploratory work.

1. O. S. Tee, N. R. Iyengar, and M. Paventi. J. Org. Chem. **48**, 759 (1983).
2. O. S. Tee and N. R. Iyengar. J. Am. Chem. Soc. **107**, 455 (1985).
3. O. S. Tee and N. R. Iyengar. Can. J. Chem. **65**, 1714 (1987).
4. O. S. Tee, N. R. Iyengar, and J. M. Bennett. J. Org. Chem. **51**, 2585 (1986).
5. A. Fischer and G. N. Henderson. Can. J. Chem. **57**, 552 (1979); Can. J. Chem. **61**, 1045 (1983).
6. O. S. Tee and N. R. Iyengar. J. Org. Chem. **50**, 4468 (1985).
7. (*a*) T. C. Bruice and S. Benkovic. Bioorganic mechanisms. Vol. 1 and 2. W. A. Benjamin, New York. 1966; (*b*) W. P. Jencks. Catalysis in chemistry and enzymology. McGraw–Hill, New York. 1969; (*c*) M. L. Bender. Mechanisms of homogeneous catalysis from protons to proteins. Wiley, New York. 1971. Chap 8.
8. C. Walsh. Enzymatic reaction mechanisms. W. H. Freeman, San Francisco. 1979; M. N. Hughes. The inorganic chemistry of biological processes. 2nd ed. Wiley, Chichester, U.K. 1981; A. Fersht. Enzyme structure and mechanism. 2nd ed. W. H. Freeman, New York. 1985.
9. (*a*) L. G. Sillen and A. E. Martell (*Editors*). Stability constants of metal ion complexes. Chemical Society, London. 1964 and 1971. (Chem. Soc. Special Publication, Nos. 17 and 25); (*b*) D. D. Perrin. Nature **182**, 741 (1958).
10. K. J. Pedersen. Acta Chem. Scand. **2**, 252, 385 (1948).
11. B. G. Cox. J. Am. Chem. Soc. **96**, 6823 (1974).
12. R. Kluger, M. K. Wong, and A. K. Dodds. J. Am. Chem. Soc. **106**, 1113 (1984), and references therein.
13. S.-J. Tsai and D. L. Leussing. Inorg. Chem. **26**, 2620 (1987), and references therein.
14. C. R. Grissom and W. W. Cleland. J. Am. Chem. Soc. **108**, 5582 (1986), and references therein.
15. T. H. Fife and T. J. Przystas. J. Am. Chem. Soc. **107**, 1041 (1985), and references therein.
16. T. H. Fife and T. J. Przystas. J. Am. Chem. Soc. **108**, 4631 (1986), and references therein.
17. J. Suh and K. H. Chun. J. Am. Chem. Soc. **108**, 3057 (1986).

[12]Based on the second pK_a of salicylic acid (= 13.61)(9*b*) and the pK_a of **1** (= 3.06) (6). The pK_a of **3** must be close to 3.0, also (3).

[13]Recently, another type of catalysis was found for the hydrolysis of 3-carboxyaspirin (17). There, metal ions promote the overall reaction by inhibiting reverse intramolecular acyl transfer; they do so by forming a strong metal ion – salicylate dianion complex with the anhydride intermediate (17).

Chemical electrochemical mechanism. Electrochemical reduction of some pyrazolidine-3,5-diones in DMSO. Relation between voltammetric behavior and ^{1}H nuclear magnetic resonance spectra

CHRISTINE HERRENKNECHT AND ELISABETH GUERNET-NIVAUD
Laboratoire de Chimie Analytique et d'Electrochimie Organiques Centre d'Etudes Pharmaceutiques, rue Jean-Baptiste Clement, F-92296 Chatenay-Malabry Cedex, France

OLIVIER LAFONT
Laboratoire de Chimie Organique, Centre de Pharmacochimie du Madrillet, Faculté de Médecine et de Pharmacie de Rouen, F-76800 Saint-Etienne du Rouvray, France

AND

MICHEL GUERNET AND CLAIRE GUEUTIN
Laboratoire de Chimie Analytique et d'Electrochimie Organiques Centre d'Etudes Pharmaceutiques, rue Jean-Baptiste Clement, F-92296 Chatenay-Malabry Cedex, France

Received June 4, 1987[1]

CHRISTINE HERRENKNECHT, ELISABETH GUERNET-NIVAUD, OLIVIER LAFONT, MICHEL GUERNET, and CLAIRE GUEUTIN. Can. J. Chem. **66**, 1199 (1988).

In DMSO (TEAP), phenylbutazone, oxyphenbutazone, and kebuzone, pyrazolidine-3,5-dione species are irreversibly reduced in two steps at the mercury electrode. The total reduction process is monoelectronic with production of the enolate carbanion. A chemical–electrochemical mechanism is proposed, each step is attributed to one of the tautomeric forms, ketoenol (E) and diketone (D). The tautomeric equilibrium constants (K = [E]/[D]) are reached both by linear sweep voltammetry at 30 V s^{-1} and by FT ^{1}H NMR and the global apparent acidity constants are determined by potentiometry.

CHRISTINE HERRENKNECHT, ELISABETH GUERNET-NIVAUD, OLIVIER LAFONT, MICHEL GUERNET et CLAIRE GUEUTIN. Can. J. Chem. **66**, 1199 (1988).

Phénylbutazone, oxyphenbutazone et kébuzone, dérivés de la pyrazolidinedione-3,5 se réduisent à une électrode de mercure en deux étapes dans le DMSO (TEAP). Le transfert irréversible, globalement monoélectronique conduit à la forme carbanion énolate. Un mécanisme c.e. est proposé, chaque étape correspond à une des formes tautomères, cétoénol (E) ou dicétone (D). Les constantes de l'équilibre cétoénolique (K = [E]/[D]) sont atteintes aussi bien par voltamétrie linéaire à 30 V s^{-1} que par FT ^{1}H RMN, les constantes d'acidité globales apparentes sont déterminées par potentiométrie.

Introduction

Continuing our study on pyrazolidine-3,5-diones of pharmaceutical interest, we report some new results of electroreduction at the mercury electrode and ^{1}H NMR spectroscopy of phenylbutazone **1**, oxyphenbutazone **2**, and kebuzone **3**, in a dipolar aprotic medium such as dimethylsulfoxide (DMSO). These compounds present a hydrogen atom in α-position of two carbonyl groups. The lability of this hydrogen induces weak acidity and prototropic tautomerism of keto–enol type (see Scheme A).

Electrochemical behaviors of β-diketones are largely described in protic media, but the authors were mainly interested by protonation or hydration reaction of tautomeric forms (1, 2). In DMSO, in the case of diphenylpropanediones, a 0.5 electron process yielding the conjugated base and pinacol was reported (3).

In a previous investigation of title compounds in ethanol ($LiClO_4$), we noted the influence of tautomerism on electron transfer (4). The difference occurring in the limiting currents was related to the apparent pK_a values and suggested the attribution of the single cathodic wave to the keto–enol form; the diketone form was masked by the background discharge.

In the present article, linear voltammetry at the hanging drop mercury electrode in DMSO was used in order to elucidate the redox mechanism and reach the tautomeric equilibrium constants (Scheme A), FT ^{1}H NMR confirmed voltammetric values.

Results and discussion

The reduction of **1**, **2**, and **3** at the dropping mercury electrode in DMSO exhibited two well-defined waves (Fig. 1). The half-wave potentials ($E_{1/2}$) of the former (ca. −1.4 V) and the latter (ca. −1.9 V) were very similar for these three compounds, but a big discrepancy was observed in the intensities of the limiting currents (i_l) for equimolecular concentrations, although it was assumed that all the species had identical diffusion coefficients; i_{l1} assignable to the first step increased from oxyphenbutazone to phenylbutazone and kebuzone while the second step i_{l2} decreased. The total intensity ($i_{l1} + i_{l2}$) remained constant. The slopes of the linear plot of log $(i_l - i)/i$ versus E for these monoelectronic waves varied from 116 to 140 mv per unit of logarithm, thus proving a non nernstian transfer.

Exhaustive coulometry needed one Faraday per mole, the potential being applied upon the first (−1.5 V) or the second step (−2.2 V): the decrease of the more easily reducible form brought about the disappearance of the less reducible one.

These data could be interpreted as a chemical–electrochemical reduction process, each step being attributed to one of the tautomeric forms. In such mechanisms different variations of i_l with mercury column height (H) were expected according to the possible participation of the thermodynamic (K) and/or kinetic (k_f and k_b) constants in the overall values of current intensities (5). Two characteristic types of behavior are described; if K is the only constant involved, the plot of i_l versus $H^{1/2}$ is linear, whereas i_l is independent of H when only k_f and k_b are involved.

Pyrazolidine-3,5-diones showed an intermediate dependency of i_{l1} on H: a linear function with $H^{1/3}$ indicated a non diffusion-

[1]Revision received December 11, 1987.

Can. J. Chem. Downloaded from www.nrcresearchpress.com by 93.93.197.157 on 09/07/12
For personal use only.

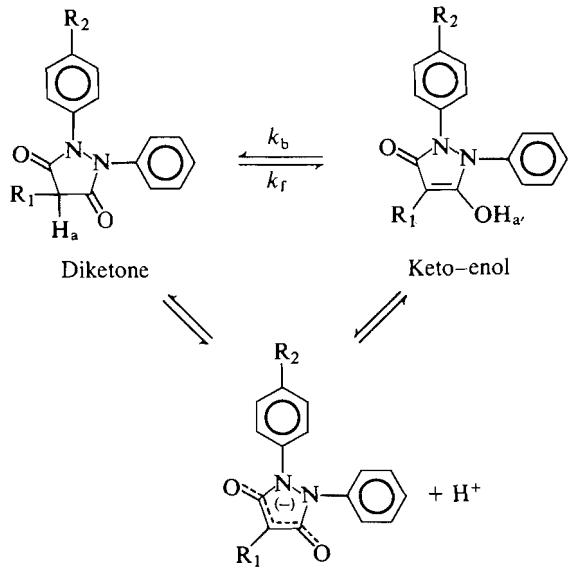

$$K_a = \frac{[H^+]\,[\text{anion}]}{[\text{Keto–enol}] + [\text{Diketone}]}$$

$$K = \frac{[\text{Keto–enol}]}{[\text{Diketone}]} = \frac{K_f}{K_b}$$

1 : $R_1 = -\underset{b}{CH_2}-\underset{c}{CH_2}-\underset{d}{CH_2}-\underset{e}{CH_3}$, $R_2 = H$

2 : $R_1 = -\underset{b}{CH_2}-\underset{c}{CH_2}-\underset{d}{CH_2}-\underset{e}{CH_3}$, $R_2 = OH$

3 : $R_1 = -\underset{b}{CH_2}-\underset{c}{CH_2}-CO-\underset{e}{CH_3}$, $R_2 = H$

SCHEME A

controlled first step and supported the notion that the initial transfer is governed by the tautomeric equilibrium K as well as by kinetic constants k_f and k_b.

These results were compared with those provided by linear sweep voltammetry. Current–potential curves were recorded over a range of scan rates (v) from 0.1 to 30 V s^{-1}: current intensities were rather scan-rate independent when v is lower than 10 V s^{-1}, indicating a kinetic behavior; when increasing v (>10 V s^{-1}), they became a linear function of $v^{1/2}$, a pure diffusion-controlled process was then obtained and peak currents (i_{p1} and i_{p2}) were directly related to the concentration of each tautomeric form in solution (6).

In order to attribute each reduction step to the convenient tautomeric form we undertook a spectroscopic study. When the usual concentrations were used for ^1H NMR study (i.e. 3×10^{-1} mol L^{-1}), ketoenolic forms of these derivatives could not be observed (7). FT ^1H NMR spectroscopy performed in the same concentration range as voltammetry (i.e. 2×10^{-3} mol L^{-1}, in DMSO-d_6) allowed us to identify the two tautomeric forms in solution. Chemical shifts, spin–spin couplings, relative integration intensities, and assignments of the side chains protons are listed in Table 2. For kebuzone homonuclear double irradiation unambiguously permitted the attribution of H_b and H_c signals (Table 3). The populations of the keto and enol tautomers were determined from the intensity of the H_b signals in both forms,

TABLE 1. Limiting currents (i_l) and half-wave potentials ($E_{1/2}$) of the first and the second cathodic steps (vs. Ag/AgCl)

	1st step		2nd step	
Compounds	i_l (μA)	$E_{1/2}$ (V)	i_l (μA)	$E_{1/2}$ (V)
Oxyphenbutazone	0.100	−1.38	0.645	−2.00
Phenylbutazone	0.285	−1.37	0.460	−1.94
Kebuzone	0.465	−1.36	0.280	−1.91

except for kebuzone where the H_c resonance was used (Table 3). The shielding effect of 0.1 ppm observed on the H_c, signal of ketoenol **3** was consistent with the formation of hydrogen bonding involving the C=O group of the side chain. Taking into account the accuracy of the measurements, a satisfactory correlation appeared between the ^1H NMR estimations of the relative ratios of ketoenol and diketo forms for the three compounds and the linear voltammetry ratios i_{p1}/i_{p2} measured at a sweep rate of 30 V s^{-1} (Table 4). It follows that this ratio intensity represents a good estimate of ketoenol and diketone relative concentrations.

Consequently, one may assume that the two polarographic waves correspond respectively to the ketoenol (−1.4 V) and diketone reduction (−1.9 V). The following chemical–electrochemical mechanism is proposed:

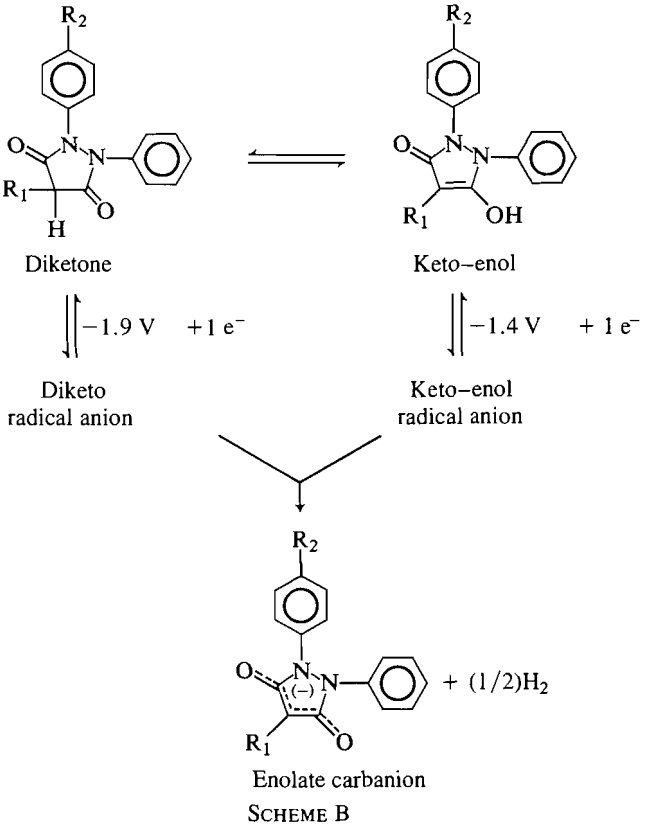

SCHEME B

The quantitative generation of the enolate carbanion by rapid elimination of half a molecule of hydrogen per mole of radical anion was proved by ultraviolet experiments. The same evolution of uv spectra appeared either during exhaustive coulometry or by adding an alkaline agent. Before electrolysis or in neutral solution the wavelength of the maximum of absorption of pyrazolidine-3,5-dione derivatives was less than 250 nm and therefore their absorption was masked by the solvent cut-off. Either

Can. J. Chem. Downloaded from www.nrcresearchpress.com by 93.93.197.157 on 09/07/12
For personal use only.

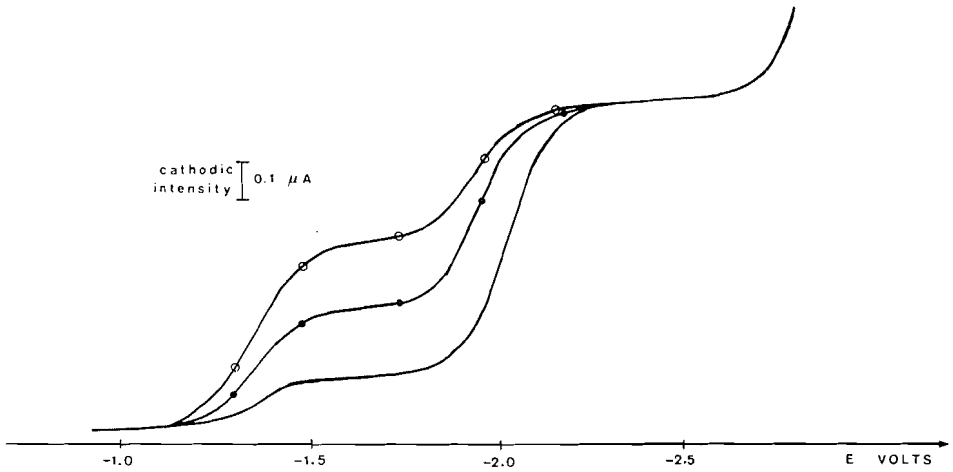

FIG. 1. Direct current polarographic curves i (μA) = $f(E)$(V vs. Ag/Ag^+) of 2×10^{-3} mol L^{-1} oxyphenbutazone (—), phenylbutazone (—●—), and kebuzone (—⊖—) in DMSO TEAP (drop time 1 s, mercury column height 55 cm).

TABLE 2. Chemical shifts (δ),* multiplicities (M),† relative integration intensities (RI), and assignments‡ of ^1H NMR spectra aliphatic signals

Phenylbutazone, **1**			Oxyphenbutazone, **2**			Kebuzone, **3**			
δ	M	RI	δ	M	RI	δ	M	RI	Assignments
3.867	t	0.70	3.786	t	0.76	3.858	t	0.55	a
1.902	dt	1.63	1.886	dt	1.75	2.068	dt	1.30	b
2.152	t	0.41	2.147	t	0.30	2.356	t	0.65	b′
1.380	m	2.00	1.387	m	2.00	2.708	t	1.35	c
						2.604	t	0.70	c′
1.306	tq	2.00	1.312	tq	2.00	—			d,d′
0.859	t	3.00	0.868	t	3.00	2.102	s	3.00	e
						2.086	s		e′

*ppm relative to TMS.
†d = doublet; t = triplet; s = singlet; q = quadruplet; m = multiplet; dt = doublet of triplet; tq = triplet of quadruplet.
‡b′, c′, d′, e′ are the protons of ketoenol form corresponding to b, c, d, and e for the diketo form (Scheme A).

TABLE 3. Assignments of side chain proton signals of kebuzone by homonuclear double irradiation

	Multiplicity of signal*						
Proton irradiated	a	b	b′	c	c′	e	e′
None	t	dt	t	t	t	s	s
a	—	t	t	t	t	s	s
c′	t	dt	s	t	—	s	s
c	t	d	t	—	t	s	s

*t = triplet; d = doublet; s = singlet; dt = doublet of triplet.

after electrolysis or in an alkaline medium, a bathochromic shift appeared, consistent with the enolate carbanion formation (λ_m = 270 nm, $\epsilon_M = 2.1 \times 10^5$ for phenylbutazone). The irreversibility of the cathodic process was proved because no complementary anodic peak was observed even at potential scan rate as high as 30 V s^{-1}. This observation confirmed the high-rate irreversible evolution of the radical anion to the enolate carbanion which is not oxidizable in the solvent limits.

On the other hand, in a previous report (4), we assumed that in an ethanolic medium an increase of K was related to a decrease of pK_a' (Scheme A). In order to strengthen this assumption, we evaluated in DMSO the apparent pK_a' values for the three

TABLE 4. i_{p1}/i_{p2} ratios (linear sweep voltammetry at 30 V s^{-1}). K values (^1H FT NMR) and pK_a' (potentiometry)

Compounds	i_{p1}/i_{p2}	K	pKa′
Phenylbutazone	0.30	0.25	6.9
Oxyphenbutazone	0.15	0.15	7.6
Kebuzone	0.59	0.52	6.3

compounds by potentiometry. If one considers the results listed in Table 4, pK_a' values decrease from oxyphenbutazone to phenylbutazone and kebuzone while corresponding K values increase. In this series, as it was expected, the acidic dissociation of —O—H enol bond is easier than that of the corresponding —C—H bond. The relative increase of K in kebuzone may be attributed to hydrogen bondings which would stabilize the ketoenol form.

Experimental

Solvents, electrolytes, and reagents

Phenylbutazone, oxyphenbutazone (Ciba-Geigy), and kebuzone (Beytout) were employed without further purification. Their identities were checked by IR and NMR spectra and their purity by TLC on glass plates coated with fluorescent silicagel (Merck) (solvent of migration: cyclohexane/methylisobutylketone/anhydrous acetic acid 80/35/5 — Rf:phenylbutazone 0.77, oxyphenbutazone 0.40, kebuzone 0.25).

Can. J. Chem. Downloaded from www.nrcresearchpress.com by 93.93.197.157 on 09/07/12
For personal use only.

Salicylic acid (Fluka), sodium salicylate (Merck), benzoic acid (Prolabo), sodium benzoate (Merck) were employed without further purification.

Dimethylsulfoxide (DMSO): (*i*) spectroscopic grade (Merck) for voltammetric determinations; (*ii*) DMSO-d_6 (CEA, 99.99% purity) for NMR.

Tetraethylammonium perchlorate (TEAP) (Fluka) was purified according to the method described by Kolthoff and Coetzee (8). Tetrabutylammonium hydroxide (TBAH) (Merck) was used without further purification.

Apparatus

Polarographic measurements were made on a PRG5 Tacussel potentiostat coupled with an EPL1 Tacussel recorder. The three-electrode jacketed cell used was of conventional design and was thermostated at 25 ± 0.1°C. For polarography, the working electrode consisted of an MPO Tacussel dropping mercury electrode with an adjustable drop time. A platinum wire served as auxilliary electrode. An Ag/AgCl reference electrode and sample compartment were separated by a TEAP/solvent bridge.

Cyclic voltammetric triangular wave forms were obtained from a GSTP3 Tacussel function generator. A hanging drop mercury electrode (Kemula type) was used as the working electrode while reference and counter electrodes were identical to those described above. Data were recorded on an R 5103M Tektronik oscilloscope.

For controlled potential electrolysis, a mercury pool ca. 1 cm deep and 12 cm^2 in area was placed in the cell, a large surface platinum auxilliary electrode was used in the anodic compartment separated by a solvent bridge containing the background electrolyte. The reference electrode was the same as that described above. Potentials were imposed by a PRT 202X Tacussel potentiostat. The quantity of electricity used was measured using an IG5 Tacussel integrator.

Potentiometric pK_a' measurements were carried out at a hydrogen platinum electrode Pt151 Tacussel, using an Ag/AgCl reference electrode. The potentials were measured at 25 ± 0.1°C using a Tacussel S70 As/N millivoltmeter.

The ultraviolet technique was carried out with a Pye-Unicam SP 800 spectrometer.

The ^1H NMR technique was carried out with a BRUCKER FT 500 MHz spectrometer.

Procedures

For all the electrochemical experiments, the pyrazolidine-3,5-diones solutions, in which the background electrolyte was 2×10^{-1} mol L^{-1} TEAP, were about 2×10^{-3} mol L^{-1}. The solutions were purged with nitrogen and kept under a blanket of nitrogen during the recording. Cyclic voltammograms were recorded at different potential scan rates (0.1 to 30 V s^{-1}). For controlled potential electrolysis, nitrogen was continuously bubbled through the solution during electrolysis and a magnetic stirrer was used.

The potentiometric pK_a' determinations were carried out in DMSO 10^{-2} mol L^{-1} solutions after addition of half an equivalent of TBAH. The electrode was calibrated with DMSO solutions of salicylate and benzoate buffers (9).

The ultraviolet measurements were carried out on electrochemical solutions with 0.1 mm optical path cells.

The NMR spectra were recorded at 30°C using DMSO-d_6 2×10^{-3} mol L^{-1} solutions.

Acknowledgments

The authors are grateful to the CIBA-GEIGY and BEYTOUT companies for generously providing samples. Thanks are also expressed to Pr. D. Davoust (University of Paris VI) for NMR spectra.

1. M. B. Fleury, J. Tohier, and P. Zuman. J. Electroanal. Chem. **143**, 253 (1983).
2. J. P. Segretario, N. Sleszynski, and P. Zuman. J. Electroanal. Chem. **214**, 259 (1986).
3. R. C. Buchta and D. H. Evans. J. Electrochem. Soc. **117**, 1494 (1970).
4. C. Gueutin, E. Nivaud, P. Boucly, and M. Guernet. Can. J. Chem. **59**, 759 (1981).
5. J. M. Saveant. Bull. Soc. Chim. Fr. **2**, 471 (1967).
6. J. M. Saveant. Rev. Chim. Miner. **5**, 477, (1968).
7. M. Woodruff and J. B. Polya. Austral. J. Chem. **31**, 1855 (1978).
8. I. M. Kolthoff and J. F. Coetzee. J. Am. Chem. Soc. **79**, 870 (1957).
9. J. Courtot-Coupez and M. Le Demezet. Bull. Soc. Chim. Fr. **3**, 1033 (1969).

Can. J. Chem. Downloaded from www.nrcresearchpress.com by 93.93.197.157 on 09/07/12
For personal use only.

Structure and conformation of 5′-chloro-5′-deoxyarabinosylcytosine: X-ray, ^{1}H and ^{13}C nmr analyses[1]

GEORGE I. BIRNBAUM

Division of Biological Sciences, National Research Council of Canada, Ottawa, Ont., Canada K1A 0R6

AND

MILOŠ BUDĚŠÍNSKÝ AND JIŘÍ BERÁNEK

Institute of Organic Chemistry and Biochemistry, Czechoslovak Academy of Sciences, Flemingovo 2, 166 10 Prague 6, Czechoslovakia

Received October 7, 1987

GEORGE I. BIRNBAUM, MILOŠ BUDĚŠÍNSKÝ, and JIŘÍ BERÁNEK. Can. J. Chem. **66**, 1203 (1988).

Crystals of 5′-chloroarabinosylcytosine, an inhibitor of nucleic acid synthesis, belong to the orthorhombic space group $P2_12_12_1$, and the cell dimensions are $a = 6.801(1)$, $b = 9.698(2)$ and $c = 16.497(3)$ Å. X-ray intensity data were measured on a diffractometer and the structure was determined by direct methods. Least-squares refinement, which included all hydrogen atoms, converged at $R = 0.032$ for 1251 observed reflections. The conformation about the glycosyl bond is *anti*, the furanose ring adopts a C3′ *endo*/C4′ *exo* pucker and the conformation of the side chain is *gauche*$^+$, stabilized by an intramolecular C6—H···Cl5′ hydrogen bond. ^{1}H and ^{13}C nmr spectra confirm the *anti* conformation about the glycosyl bond. In D_2O solution there is an approximately equal population of *N*- and *S*-type conformers of the furanose ring and a *trans* > *gauche*$^+$ > *gauche*$^-$ distribution of the 5′-CH_2Cl side chain rotamers.

GEORGE I. BIRNBAUM, MILOŠ BUDĚŠÍNSKÝ et JIŘÍ BERÁNEK. Can. J. Chem. **66**, 1203 (1988).

Les cristaux de la chloro-5′ arabinosylcytosine, un inhibiteur de la synthèse de l'acide nucléique, appartiennent au groupe d'espace orthorhombique $P2_12_12_1$, avec $a = 6{,}801(1)$, $b = 9{,}698(2)$ et $c = 16{,}497(3)$ Å. On a mesuré les intensités de diffraction par les rayons-X et on a déterminé la structure par des méthodes directes. L'affinement par le méthode des moindres carrés, incluant tous les atomes d'hydrogène, converge vers $R = 0{,}032$ pour 1251 réflexions observées. La conformation autour de la liaison glycosyle est *anti*, le cycle furannose adopte une conformation C3′ *endo*/C4′ *exo* et la chaîne latérale, qui est stabilisée par une liaison hydrogène intramoléculaire C6—H···C15′, est *gauche*$^+$. Les spectres rmn du ^{1}H et du ^{13}C confirment la présence d'une conformation *anti* autour de la liaison glycosyle. En solution dans le D_2O, les proportions des conformères des types N et S du cycle furannose sont approximativement égales alors que la distribution des rotamères de la chaîne latérale 5′-CH_2Cl est la suivante: *trans* > *gauche*$^+$ > *gauche*$^-$.

[Traduit par la revue]

Introduction

Having recently carried out X-ray and nmr analyses of 2′,5′-anhydroarabinosylcytosine (1), we turned our attention to 5′-chloroarabinosylcytosine (2), another analog of the antileukemic agent arabinosylcytosine (ara-C). Of all biologically active nucleoside analogs we studied (3), this compound is the most potent and specific inhibitor of DNA synthesis in L1210 cells. Also, its penetration through the intestinal wall is faster and it is metabolically more stable (4, 5) than the parent ara-C. This could be its fundamental advantage, particularly for oral applications. It was recently found that 5′-chloroarabinosylcytosine (5′-Cl-ara-C) could be directly phosphorylated to ara-C-5′-trihosphate (6), the biologically active form of ara-C (7, 8). Unusual properties, both chemical and/or biological, were also observed in some other 5′-chloro derivatives of nucleoside analogs, eg. 5′-chloro-5-fluorouridine (9) and 5′-chloro-6-azauridine (10). It appeared of interest, therefore, to carry out a detailed physico-chemical study of 5′-Cl-ara-C, a representative member of such a group of nucleoside analogs. In contrast to the rigid molecule of 2′,5′-anhydroarabinosylcytosine (1), one would not expect a large measure of agreement between the solid-state and solution conformations of the flexible 5′-Cl-ara-C molecule.

Experimental

5′-Chloroarabinosylcytosine was prepared as previously described (2) and crystallized from water to give colorless prisms. Precession photographs indicated the orthorhombic space group $P2_12_12_1$. A crystal measuring 0.3 × 0.5 × 0.6 mm was mounted on an Enraf-Nonius CAD-4 diffractometer; the crystal data are as follows:

$C_9H_{12}N_3O_4Cl$ mw = 261.67

Orthorhombic, $a = 6.801(1)$, $b = 9.698(2)$, $c = 16.497(3)$ Å, $V = 1088.0(4)$ Å^3, $\rho_c = 1.60$ g cm^{-1}, $Z = 4$ (20°C, MoKα_1, $\lambda = 0.70930$ Å), $F(000) = 544$, μ(MoKα) = 3.56 cm^{-1}.

Unit cell dimensions were determined from a least-squares refinement of the angular settings of 25 reflections with $20 < \theta < 26°$. Intensities were measured at room temperature (20°C) with Nb-filtered MoKα radiation, using $\omega/2\theta$ scans with variable scan ranges and speeds. Two standard reflections were measured at regular intervals; their intensities fluctuated by ±1%. Both *hkl* and *hkl̄* reflections with $\theta \leq 27.5°$ were measured and averaged. Of the 1464 unique reflections in the dataset there were 1252 (85.5%) with $I \geq 3\sigma(I)$ which were considered observed. The intensities were corrected for Lorentz and polarization factors; absorption corrections were unnecessary.

The structure was determined by direct methods with the aid of the computer program MULTAN78 (11). Atomic parameters of non-hydrogen atoms were refined by block-diagonal least squares with anisotropic temperature parameters. All hydrogen atoms were located on difference Fourier maps and their parameters refined with isotropic temperature factors. The scattering factors were taken from the International tables for X-ray crystallography (12) and the chlorine and oxygen curves were corrected for anomalous dispersion. Throughout the refinement the function $\Sigma w(|F_o| - |F_c|)^2$ was minimized and a factor of 0.8 applied to all shifts. The following weighting scheme was used during the final stages: $w = w_1 \cdot w_2$, where $w_1 = 1$ for $|F_o| \leq 15$, $w_1 = 15/|F_o|$ for $|F_o| > 15$; and $w_2 = \sin^2\theta/0.14$ for $\sin^2\theta < 0.14$, w_2, = 1 for $\sin^2\theta \geq 0.14$. This scheme made the average values of $w(\Delta F^2)$ independent of $|F_o|$ and $\sin^2\theta$. The strongest reflection (004) suffered from secondary extinction effects and was given zero weight. After the

[1]NRC No. 28916.

Can. J. Chem. Downloaded from www.nrcresearchpress.com by 93.93.197.157 on 09/07/12
For personal use only.

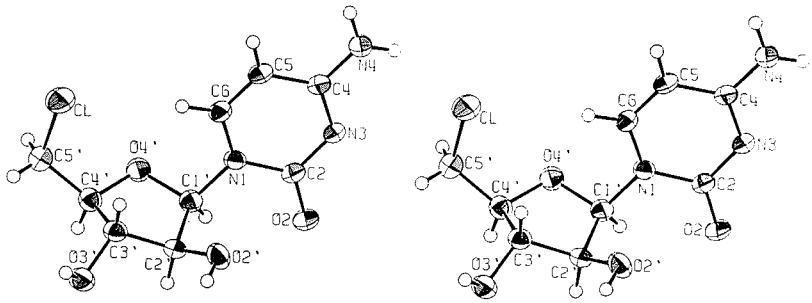

FIG. 1. Stereoscopic view of 5′-chloroarabinsylcytosine; the ellipsoids correspond to 50% probability.

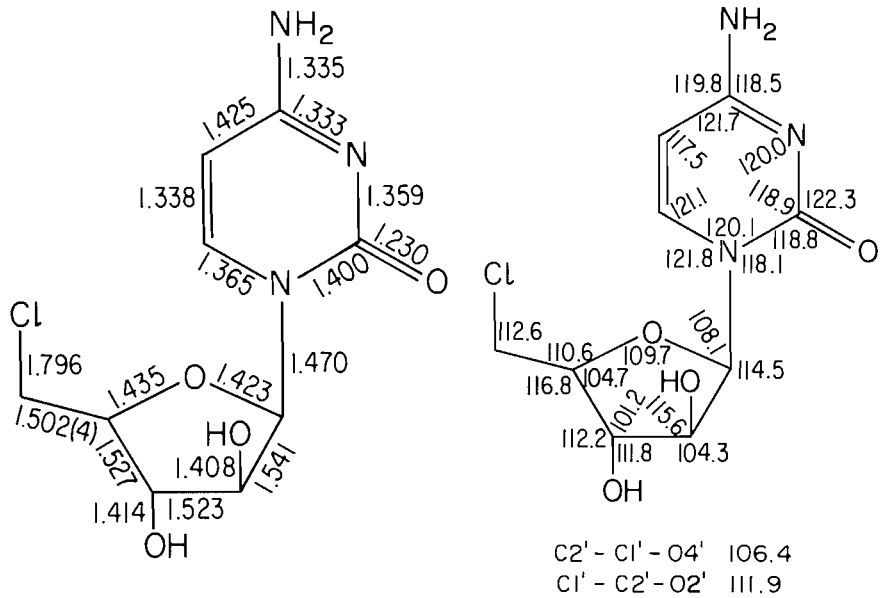

FIG. 2. (Left) Bond distances (in Å); unless otherwise indicated, their estimated standard deviations (esd's) are 0.003 Å. (Right) Bond angles (in deg); their esd's are 0.2°.

final cycle the average parameter shift equalled 0.15σ and the largest 0.45σ. The final conventional residual index R is 0.032 and the weighted index R_w is 0.036 for 1251 observed reflections. A final difference Fourier map showed no significant features. Atomic coordinates are listed in Table 1. Anisotropic temperature parameters and a list of observed and calculated structure factors are available from the Depository of Unpublished Data.[2]

^{1}H and ^{13}C nmr spectra were measured on a Varian XL-200 FT-NMR spectrometer at frequencies of 200 and 50.3 MHz, respectively. Solutions of ~ 5 mg (for ^{1}H nmr) and 50 mg (for ^{13}C nmr) of 5′-Cl-ara-C in 0.4 mL of DMSO-d_6 were used. DMSO was used as an internal reference and the signals were recalculated to a δ-scale, using δ_H(DMSO) = 2.50 and δ_C(DMSO) = 39.7 ppm. In addition, the 400-MHz ^{1}H nmr spectrum of a saturated solution of 5′-Cl-ara-C (≤2 mg) in D_2O (0.4 mL) was measured on a Bruker AM 400 FT-NMR instrument, using HDO as internal reference (δ_H = 4.80 ppm). Selective decoupling on proton H1′ was used for the determination of its coupling constants in both ^{1}H and ^{13}C nmr spectra. The proton chemical shifts and coupling constants were checked using a spectrum-simulation procedure (standard program SPIN on Varian XL-200 instrument). Carbon-13 chemical shifts and the number of directly bonded protons were determined from the "attached proton test" ^{13}C nmr spectrum (13). The coupling constants J(C,H) were extracted from the proton-coupled ^{13}C nmr spectrum with nOe enhancement

[2]These tables may be purchased from the Depository of Unpublished Data, CISTI, National Research Council, Ottawa, Ont., Canada K1S 0S2.

Results and discussion

Solid-state structure

A stereoscopic view of the molecule is shown in Fig. 1. Figure 2 shows the bond lengths and bond angles while the Newman projections (Fig. 3) display the torsion angles. The pyrimidine ring is not exactly planar; the largest deviations from the mean plane (χ^2 = 1110.8) are 0.040(2) and −0.041(2) Å for N1 and C2, respectively. The bond lengths and bond angles of the cytosine base are in excellent agreement with previously found values (14). The conformation about the glycosyl bond is, as usual, *anti* with χ_{CN} [C6—N1—C1′—O4′] = 30.7(3)°. This is in good agreement with the average value of χ_{CN} in arabinonucleosides (15). The furanose ring adopts the C3′ *endo*/C4′ *exo* ($^3T_4$) pucker with a phase angle of pseudorotation (P) of 33.5° and a maximum amplitude of puckering (τ_m) of 36.8°. Again we note that, in contrast to ribonucleosides, there is no correlation betwen the ring pucker and χ_{CN} (15). The conformation about C4′—C5′ is *gauche*$^+$, possibly stabilized by an intramolecular hydrogen bond (15). Bond lengths and bond angles in the arabinose moiety have commonly observed values and require no comments.

As mentioned above, there is an intramolecular hydrogen bond in which H6 is donated to C15′. While C6—H···O5′ hydrogen bonds have been found in many crystal structures (16), the observation of an C6—H···C15′ bond apears to be

Can. J. Chem. Downloaded from www.nrcresearchpress.com by 93.93.197.157 on 09/07/12
For personal use only.

TABLE 1. Final atomic parameters[a]

Atom	x	y	z	U_{eq}/U^b
N1	3259(3)	36891(20)	61857(12)	260
C2	3843(3)	50466(23)	63447(13)	277
O2	5597(2)	53423(19)	62951(12)	371
N3	2452(3)	59935(20)	65435(12)	283
C4	589(3)	56039(23)	66431(13)	282
N4	−746(3)	65638(22)	68256(16)	385
C5	4(3)	41989(26)	65680(17)	339
C6	1366(3)	32899(24)	63294(15)	309
C1′	4752(3)	27138(23)	58918(14)	287
C2′	5846)3)	19228(23)	65645(14)	292
O2′	5713(3)	26001(19)	73173(11)	399
C3′	4970(3)	4784(26)	65349(14)	291
O3′	6338(3)	−5336(19)	67843(12)	375
C4′	4456(4)	3533(24)	56367(14)	310
O4′	3790(3)	17030(18)	54085(10)	330
C5′	2959(4)	−7182(27)	54108(17)	387
C15′	616(1)	−4269(8)	58827(5)	488
HN41	−41(6)	742(4)	680(2)	23(9)
HN42	−198(5)	633(4)	685(2)	18(8)
H5	−121(7)	399(4)	666(3)	30(10)
H6	109(5)	239(3)	624(2)	5(7)
H1′	560(5)	322(3)	559(2)	5(6)
H2′	717(5)	182(4)	636(2)	16(8)
HO2′	628(6)	212(4)	765(2)	23(9)
H3′	380(5)	43(4)	686(2)	12(7)
HO3′	577(7)	−110(4)	711(2)	24(10)
H4′	557(5)	14(3)	541(2)	9(7)
H5′	269(7)	−71(4)	483(3)	30(10)
H5″	330(6)	−152(4)	563(2)	17(8)

[a]The x and U_{eq} parameters of the non-hydrogen atoms were multiplied by 10^4, the y and z coordinates by 10^5; all hydrogen atom parameters were multiplied by 10^3.

[b]In Å^2; U_{eq} is $(1/3)(U_{11} + U_{22} + U_{33})$.

novel. In their review of C—H···X bonds in crystal structures determined by neutron diffraction Taylor and Kennard (16*a*) listed 13 C—H···Cl bonds with H···Cl distances in the range 2.569–2.944 Å. The corrected H···*A* distances listed in Table 2 were calculated following the normalization of C—H, N—H, and O—H bonds to their nominal values of 1.09, 1.04, and 0.97 Å, respectively (17). It can be seen that the H6···C15′ distance is well within this range. The C6—H6···C15′ angle (174°) lends futher support to the existence of this hydrogen bond. C15′ is also involved in a fairly strong intermolecular hydrogen bond, accepting a proton from N4. This hydrogen bond could stabilize the C4-amino group and thus slow down the deamination, and the resulting deactivation, of 5′-Cl-ara-C. We can now explain our earlier observation (4–6) that 5′-Cl-ara-C is more stable than ara-C.

The hydrogen bonding network can be represented schematically as follows:

C—H···Cl5′···H41—N4 O3′—H···O2′—H···N3

O2···H42

The molecular packing in the crystal is shown in Fig. 4. Apart from hydrogen bonds, there are no abnormally short intermolecular distances and there is no base stacking.

Solution conformation

^{1}H and ^{13}C nmr spectra were studied to determine the solution conformation of 5′-Cl-ara-C. The proton spectrum in DMSO-

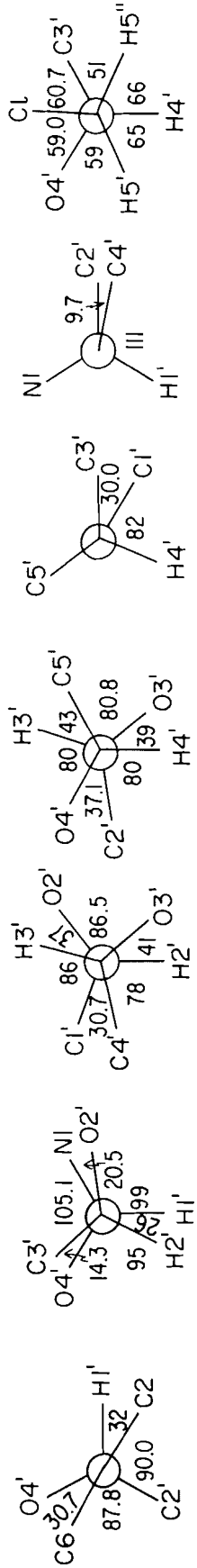

FIG. 3. Newman projections along N1—C1′, C1′—C2′, C2′—C3′, C3′—C4′, C4′—O4′, O4′—C1′, and C4′—C5′; the esd's are 0.2–0.3° for torsion angles which do not involve hydrogen atoms and 2–3° for those which do.

Can. J. Chem. Downloaded from www.nrcresearchpress.com by 93.93.197.157 on 09/07/12
For personal use only.

TABLE 2. Distances and angles for hydrogen bonds[a]

			Distances, Å			Angles, deg
D	*A*	*A at*	*D*···*A*	H···*A*	H···A_{corr}	*D*—H···*A*
C6—H6···Cl5′		*x*, *y*, *z*	1.714	2.82	2.63	174
N4—HN41···Cl5′		*x*, 1 + *y*, *z*	3.434	2.67	2.52	146
N4—HN42···O2		−1 + *x*, *y*, *z*	2.890	2.11	1.97	146
O3′—HO3′···O2′		1 − *x*, −1/2 + *y*, 3/2 − *z*	2.724	1.87	1.76	170
O2′—HO2′···N3		1 − *x*, 1/2 + *y*, 3/2 − *z*	2.742	1.92	1.77	179

[a]The esd's are 0.003 Å, 0.04 Å, and 2–4° for *D*···*A*, H···*A*, and *D*—H···*A*, respectively.

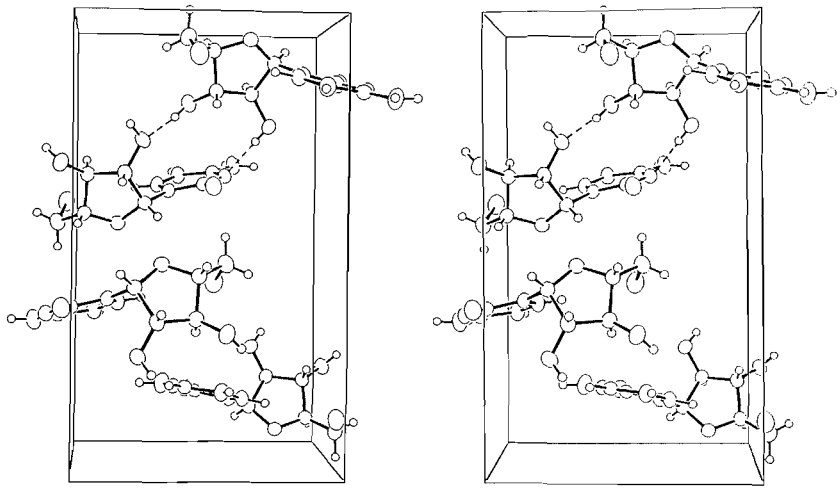

FIG. 4. Stereoscopic view of the molecular packing in the crystal; the directions of the axes are *x* ⊙, *y* →, *z* ↑. Dashed lines are intermolecular hydrogen bonds.

d_6 showed a strongly coupled spin system of H3′, H4′, H5′, and H5″ protons at δ 3.72–3.96 which made the analysis of related parameters very difficult. Much better resolution of signals was achieved in D_2O solution. Proton chemical shifts and coupling constants used for a conformational analysis (see Table 3) were therefore obtained from a 400 MHz spectrum in D_2O. Carbon-13 nmr spectra were mesured only in DMSO-d_6 because of the very low solubility of 5′-Cl-ara-C in D_2O.

Pentose ring

We followed the method of de Leeuw and Altona (18) for determining the relative population of *N*- and *S*-type puckers in th conformational equilibrium. Using $P_N = 16.6°$, $P_S = 159.6°$, $\tau_N = \tau_S = 36°$ (recommended for arabinosides (18)), we estimated an *N*/*S* conformer ratio of 0.45/0.55. The r.m.s. deviation between calculated (18) and observed *J*(1′2′), *J*(2′3′) and *J*(3′4′) values (Table 3) amounts to 0.21 Hz. Subsequently, we repeated the calculation with the parameters for the *N*-conformer corresponding to those found in the crystal structure ($P_N = 33.5°$, $\tau_N = 36.8°$). Assuming $\tau_S = \tau_N$, we optimized P_S and the *N*/*S* ratio for the best fit with the experimental *J* values. The results thus obtained ($P_S = 159°$, *N*/*S* ratio 0.46/0.54) are not much different from the original ones, but the r.m.s. deviation between observed and calculated coupling constants decreased to 0.07 Hz, a value which is comparable to the experimental error of *J*'s. This means that in D_2O solution 5′-Cl-ara-C exists as a nearly equally populated mixture of *N* (C3′ *endo*, ^3E) and *S* (C2′ *endo*, ^2E) conformers. This result agrees with the general conformational behaviour of arabinosides in which no distinct preference for either conformer has been found in solution (18) or in the solid state (15). Our *J* values and *N*/*S* ratio are very similar to those reported for 3′-Me-ara-A and 3′,5′-diMe-ara-A (18, 19).

Exocyclic 5′-CH_2Cl

The conformation about the C4′—C5′ bond in nucleosides can be interpreted in terms of rapid rotational averaging among three staggered rotamers, viz. *gauche*$^+$ (g^+), *trans* (*t*) and *gauche*$^-$ (g^-) (20). The rotamer populations can be calculated (21) from the observed couplings *J*(4′5′) and *J*(4′5″), and values of 11.5 and 1.5 Hz (for J_t and J_g, respectively) are generally used for 5′-OH nucleosides (21). In our case of a 5′-Cl derivative, we have to correct the *J* values for the effect of different substituent electronegativity. Using Bystrov's (22) equation $J_{corr} = J(1 - 0.1\Delta E)$ with $\Delta E = E_{Cl} - E_O = -0.35$, we obtained corrected values $J_t = 11.9$ and $J_g = 1.55$ Hz. From these values and the experimental values *J*(4′5′) = 4.35 and *J*(4′5″) = 5.9 Hz, we calculated the approximate rotamer populations given in Table 4. The values for the *gauche*$^-$ and *trans* rotamers were obtained by assigning the H5′ and H5″ protons according to the published convention (23). The population of the *gauche*$^+$ rotamer is slightly lower than in ara-C, presumably because the relatively weak C—H···Cl hydrogen bond would not play a significant role in D_2O solution. On the other hand, the population of the *gauche*$^-$ rotamer, energetically unfavourable in normal nucleosides (15), is somewhat higher owing to the decreased electronegativity of the substituent at C5′.

Orientation about the glycosyl bond

The proton decoupled "attached proton test" ^{13}C nmr spec-

Can. J. Chem. Downloaded from www.nrcresearchpress.com by 93.93.197.157 on 09/07/12
For personal use only.

TABLE 3. Proton and carbon-13 nmr data

Proton	Chemical shifts (ppm) DMSO-d_6	Chemical shifts (ppm) D_2O	Coupling constants (Hz) in D_2O[a] H,H	J(H,H)
H5	5.71	6.14	5,6	7.65
H6	7.48	7.87	5,1′	0.4
HN4	7.12		6,1′	0.2
H1′	6.12	6.34	1′,2′	4.75
H2′	4.02	4.52	2′,3′	3.55
H3′		4.31	3′,4′	4.85
H4′	3.72–3.96[b]	4.28	4′,5′	4.35
H5′		4.05	4′,5″	5.9
H5″		3.98	5′,5″	12.1
HO2′	5.62[c]			
HO3′	5.64[c]			

Carbon	Chemical shifts (ppm)	Coupling constants (Hz) C,H	^1J(C,H)	C,H	J(C,H)[d]	C,H	J(C,H)[d]
C2	155.40			C2,H6	5.8	C2,H1′	1.3
C4	165.86			C4,H5	1.6	C4,H6	9.2
C5	93.16	C5,H5	173.0	C5,H6	2.5		
C6	143.15	C6,H6	182.7	C6,H5	3.0	C6,H1′	5.5
C1′	86.92	C1′,H1′	167				
C2′	77.66	C2′,H2′	151				
C3′	74.66	C3′,H3′	152				
C4′	84.16	C4′,H4′	154				
C5′	44.68	C5′,H5′	152.5				
		C5′,H5″	152.5				

[a]The absolute values of J are given.
[b]Strongly coupled four-spin system.
[c]These values may be interchanged.
[d]Long-range J(C,H) were determined only for cytosine carbons.

TABLE 4. Conformational properties of 5′-Cl-ara-C and ara-C in D_2O solution

Compound	Pentose ring population N	Pentose ring population S	Exocyclic 5′-CH_2X population g^+	Exocyclic 5′-CH_2X population g^-	Exocyclic 5′-CH_2X population t	Glycosyl bond orientation τ(C6—N1—C1—H1′)
5′-Cl-ara-C	0.45	0.55	0.31	0.27	0.42	140°
ara-C[a]	0.50	0.50	0.37	0.19	0.44	[b]

[a]Data taken from refs. 19 and 20.
[b]The value is not given.

trum in DMSO-d_6 afforded nine signals. Their structural assignment (Table 3) was done on the basis of numbers of directly bonded protons, chemical shift arguments, and a comparison with ^{13}C nmr data of cytosine nucleosides and arabinofuranose derivatives. All one-bond couplings J(C,H) were determined from the proton-coupled ^{13}C nmr spectrum. Long-range couplings J(C,H) were established only for cytosine carbons because sugar carbons gave poorly resolved multiplets. The orientation about the glycosyl bond can be estimated from ^3J(C6, H1′) and ^3J(C2, H1′) couplings. As in our preceding work on 2′5′-anhydro-ara-C (1), we found a significantly higher value of the former (5.5 vs. 1.3 Hz). This indicates a preference for the *trans* orientation of the fragment C6—N1—C1′—H1′. The approximate values calculated (24) for the torsion angles C6—N1—C1′—H1′ and C2—N1—C1′—H1′ (140 and 40°, respectively) are in good agreement with the values 150(2) and 32(2)° obtained from the X-ray analysis (Table 4).

Acknowledgements

Apart from MULTAN78 (11), all crystallographic computations were carried out with programs written by Ahmed *et al.* (25). Figures 1 and 4 were drawn with the ORTEP program of Johnson (26).

1. G. I. BIRNBAUM, M. BUDĚŠÍNSKÝ, and J. BERÁNEK. Can. J. Chem. **65**, 271 (1987).
2. H. HŘEBABECKÝ, J. BROKEŠ, and J. BERÁNEK. Collect. Czech. Chem. Commun. **45**, 599 (1980).
3. J. BERÁNEK and E. M. ACTON. Collect. Czech. Chem. Commun. **49**, 2551 (1984).
4. J. BERÁNEK. Drugs Exptl. Clin. Res. **12**, 355 (1986).
5. L. NOVOTNÝ, H. FARGHALI, M. RYBA, I. JANKŮ, and J. BERÁNEK. Cancer Chemother. Pharmacol. **13**, 195 (1984).
6. K. FANG, D. H. W. HO, N. BROWN, R. A. NEWMAN, and J. BERÁNEK. Abst. No. 1301, 78th Annual Meeting of the Amer-

Can. J. Chem. Downloaded from www.nrcresearchpress.com by 93.93.197.157 on 09/07/12
For personal use only.

ican Association for Cancer Research (AACR), Atlanta, GA, March 1987.
7. M. Y. Chu and G. A. Fischer. Biochem. Pharmacol. **11**, 423 (1962).
8. J. J. Furth and S. S. Cohen. Cancer Res. **28**, 2061 (1968).
9. (*a*) H. Hřebabecký and J. Beránek. Nucleic Acids Res. **5**, 1029 (1978); (*b*) L. Novotný, H. Farghali, I. Janků, and J. Beránek. Cancer Chemother. Pharmacol. In press.
10. P. Drašar and J. Beránek. Nucleic Acids Res. Spec. Publ. **4**, 179 (1978).
11. P. Main, S. E. Hull, L. Lessinger, G. Germain, J.-P. Declercq, and M. M. Woolfson. MULTAN78, University of York, England, and University of Louvain, Belgium. 1978.
12. International tables for X-ray crystallography. Vol. IV. Kynoch Press, Birmingham. 1974.
13. C. Le Cocq and J.-Y. Lallemand. J. Chem. Soc. Chem. Commun. 150 (1981).
14. R. Taylor and O. Kennard. J. Am. Chem. Soc. **104**, 3209 (1982).
15. G. I. Birnbaum and D. Shugar. *In* Topics in nucleic acid structure. Part 3. *Edited by* S. Neidle. Macmillan, London. 1987. p. 1.
16. (*a*) R. Taylor and O. Kennard. J. Am. Chem. Soc. **104**, 5063 (1982). (*b*) G. I. Birnbaum, K. L. Sadana, W. J. P. Blonski, and F. E. Hruska. J. Am. Chem. Soc. **108**, 1671 (1986). (*c*) G. I. Birnbaum, J. Giziewicz, E. J. Gabe, T.-S. Lin, and W. H. Prusoff. Can. J. Chem. **65**, 2135 (1987).
17. R. Taylor and O. Kennard. Acc. Chem. Res. **17**, 320 (1984).
18. F. A. A. M. De Leeuw and C. Altona. J. Chem. Soc. Perkin II 375 (1982).
19. I. Ekiel, M. Remin, E. Darzynkiewicz, and D. Shugar. Biochim. Biophys. Acta, **562**, 177 (1979).
20. H. M. Berman. *In* Topics in nucleic acid structure. *Edited by* S. Neidle. Macmillan, London. 1981. p. 1.
21. D. B. Davies. Prog. NMR Spectr. **12**, 135 (1978).
22. V. F. Bystrov. Usp. Khim. **41**, 512 (1972).
23. M. Remin and D. Shugar. Biochem. Biophys. Res. Commun. **48**, 636 (1972).
24. V. F. Bystrov, Yu. D. Gavrilov, and V. N. Solkan. J. Magn. Reson. **19**, 123 (1975).
25. F. R. Ahmed, S. R. Hall, M. E. Pippy, and C. P. Huber. J. Appl. Crystallogr. **6**, 309 (1973).
26. C. K. Johnson. ORTEP-II. Report ORNL-5138, Oak Ridge National Laboratory, Oak Ridge, TN. 1976.

Can. J. Chem. Downloaded from www.nrcresearchpress.com by 93.93.197.157 on 09/07/12
For personal use only.

Photochemistry of cyclic α-hydroxy ketones. III. The nature of the photoproducts from 5-hydroxy-5β-cholest-3-en-6-one and the relationship of these to the photoproducts from analogous saturated 5-hydroxycholestan-6-ones[1]

PETER YATES AND SHIRLEY STIVER
Lash Miller Chemical Laboratories, University of Toronto, Toronto, Ont., Canada M5S 1A1

Received October 29, 1987

PETER YATES and SHIRLEY STIVER. Can. J. Chem. **66**, 1209 (1988).

Photolysis of 5-hydroxy-5β-cholest-3-en-6-one (**2**) in hexanes gave 5-oxo-5,6-seco-cholest-3-en-6-al (**13**) and [(1*R*, 4*R*, 7a*R*)-1-(1*S*,5-dimethylhexyl)-7a-methyl-2,3,3a,4,7,7a-hexahydro-1*H*-inden-4-yllacetaldehyde (**14**). Similar irradiation of **13** gave **14** and a small amount of 5-hydroxy-*B*-nor-5β-cholest-3-ene-6α-carbaldehyde (**15**). The structures of **13** and **15** were confirmed by independent synthesis: the former from cholesteryl acetate via 3β-acetoxy-6,6-dimethoxy-5,6-seco-cholestan-5-one and the latter from **13** by treatment with methanolic sodium methoxide. Photolysis of 5-deuteroxy-5β-cholest-3-en-6-one (**26**) in hexanes gave the -CDO analogues of the aldehydes **13**, **14**, and **15**. These observations are interpreted in terms of α-cleavage of the C-5 — C-6 bond of **2** to give an acyl allyl diradical, which undergoes O—H hydrogen abstraction to give **13**. The occurrence of α-cleavage as the major reaction pathway is attributed to the increased stabilization of the alkyl radical center by the hydroxyl substituent. The preference for O—H rather than C—H abstraction in the diradical is attributed to the planar nature of the allyl radical center. The indenylacetaldehyde **14** is considered to arise via a Norrish type II reaction of **13**, while the formation of *B*-nor aldehyde **15** is ascribed to a "dark" aldol reaction of **13**.

PETER YATES et SHIRLEY STIVER. Can. J. Chem. **66**, 1209 (1988).

La photolyse de l'hydroxy-5 5β-cholestène-3 one-6 (**2**) dans des hexanes conduit à l'oxo-5 séco-5,6 cholestène-3 al-6 (**13**) et au [(1*R*, 4*R*, 7a*R*) (diméthyl-1*S*,5 hexyl)-1 méthyl-7a hexahydro-2,3,3a,4,7,7a 1*H*-indènyl-4] acétaldéhyde (**14**). En procédant à une irradiation semblable du composé **13**, on obtient le produit **14** ainsi qu'une faible quantité d'hydroxy-5 *B*-nor 5β-cholestène-3 carbaldéhyde-6α (**15**). On a confirmé les structures des composés **13** et **15** en procédant à leurs synthèses; le premier a été préparé à partir de l'acétate de cholestéryle, via l'acétoxy-3β diméthoxy-6,6 séco-5,6 cholestanone-5, alors que pour le deuxième on a soumis le composé **13** à un traitement par du méthanolate de potasssium en milieu méthanolique. La photolyse de la deutéroxy-5 5β-cholestène-3 one-6 (**26**) dans des hexanes conduit aux analogues -CDO des aldéhydes **13**, **14** et **15**. On interprète ces observations en fonction d'un clivage-α, de la liaison C-5/C-6 du composé **2**, qui conduirait à un diradical acyle allyle qui subirait un enlèvement d'hydrogène du O—H pour donner le composé **13**. Pour expliquer le fait que la voie principale de la réaction implique un clivage-α, on suggère qu'elle est due à une augmentation de la stabilisation du centre radicalaire alkyle par le substituant hydroxyle. Le fait que, dans le diradical, l'hydrogène du O—H est enlevé plutôt que celui du C—H est attribué à la nature planaire du centre radicalaire allylique. On considère que l'indènylacétaldéhyde **14** provient d'une réaction Norrish type II du composé **13** alors que la formation du *B*-nor aldéhyde **15** serait le résultat d'une réaction aldolique "à la noirceur" du composé **13**.

[Traduit par la revue]

Can. J. Chem. Downloaded from www.nrcresearchpress.com by 93.93.197.157 on 09/07/12
For personal use only.

Introduction

As an extension of our studies of the photochemistry of α-hydroxy ketones of type **1** (1, 3) we have investigated the photochemistry of the β,γ-unsaturated α-hydroxy ketone, 5-hydroxy-5β-cholest-3-en-6-one (**2**), whose synthesis we have

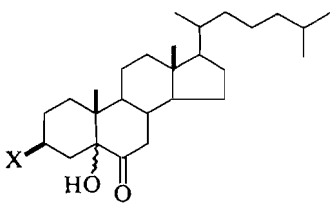

1

X = OAc, H, or OBn

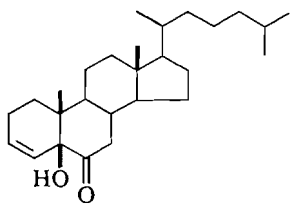

2

recently reported (4). There have been few previous reports on the photochemistry of such ketones. Sasaki *et al.* (5) observed that direct irradiation of 1-hydroxy-bicyclo[3.2.2]nona-3,5-dien-2-ones of type **3** gave products of type **5** that were considered to be formed via intermediates of type **4**, themselves formed from **1** by 1,3-acyl shifts (Scheme 1). Carlson and

[1]For paper II, see ref. 1; for a preliminary communication concerning part of this work, see ref. 2.

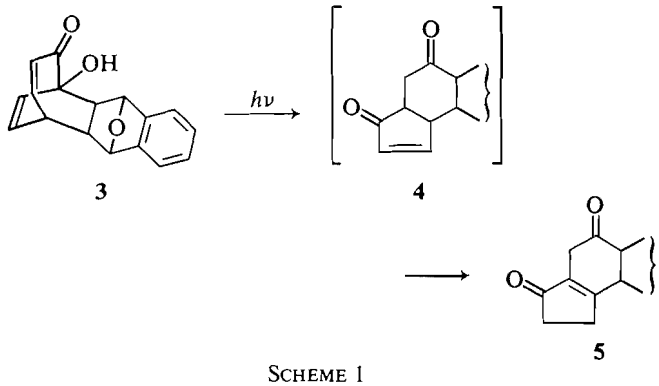

3 **4** **5**

SCHEME 1

Prabhu (6) found that direct irradiation of 2-hydroxy-2-(2-methyl-1-propenyl)cyclohexanone (**6**) gave the aldehyde **8** as the major product and the cyclo-octane-1,4-dione **9** as a minor product. The latter was again considered to be formed via a 1,3 acyl shift, while the major product was thought to arise via α-cleavage of **6** to give the diradical **7**, followed by a 1,5 hydrogen shift (Scheme 2).

Hancock *et al.* (7) have carried out the most detailed mechanistic investigation of the photochemistry of β-γ-unsaturated α-hydroxy ketones. They observed that direct irradiation of 1-acetyl-2-cyclohexen-1-ol (**10**) gave 3-acetylcyclohexanone

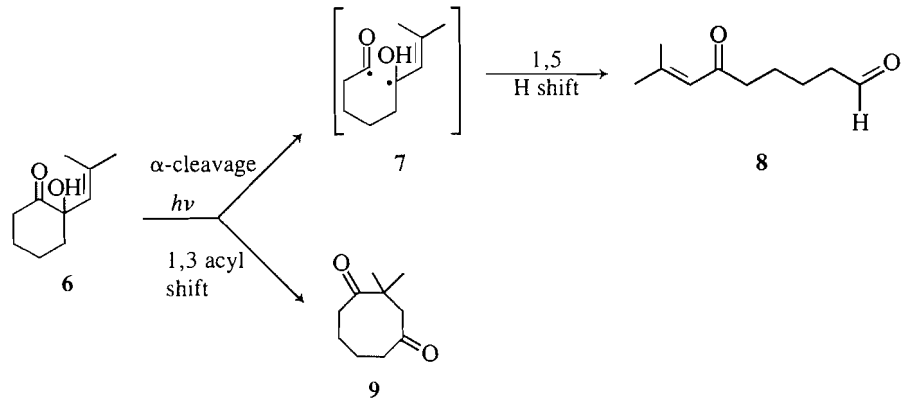

SCHEME 2

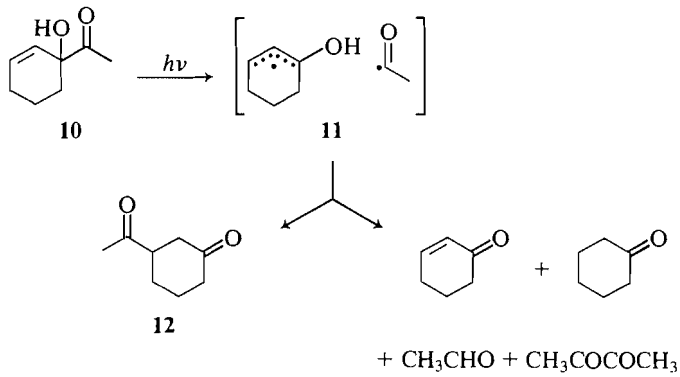

SCHEME 3

(**12**) as the major product. The presence of cyclohexanone, 2-cyclohexen-1-one, acetaldehyde, and biacetyl among the minor products led them to propose that the 1,3 acyl shift involved in the conversion of **10** to **12** proceeded stepwise via α-cleavage to the acyl allyl radical pair **11**, followed by recombination to give **12** (Scheme 3).

Results

Photolysis of 5-hydroxy-5β-cholest-3-en-6-one (2)

Photolysis of **2** in alcoholic solvents led to intractable product mixtures. However, when the irradiation was carried out in hexanes two photoproducts could be isolated, the 5,6-seco-aldehyde **13** and the indenylacetaldehyde **14**, in 40 and 10% yield, respectively. The indenylacetaldehyde **14** was a secondary product, since it was formed from photolysis of the seco-aldehyde **13** in hexanes, which also gave a small amount of the β-nor aldehyde **15** (Scheme 4). In both irradiations the mass balance of isolated products was poor.

The structural assignment for the indenylacetaldehyde **14** was based on its ir and ^{1}H nmr spectra, in conjunction with its molecular composition, $C_{20}H_{34}O$. At 200 MHz, the signals of the two vinyl protons in the ^{1}H nmr spectrum of **14** were resolved into two multiplets at δ 5.45–5.52 (width = 16 Hz) and 5.58–5.68 (width = 19 Hz). In its mass spectrum the base peak with *m/z* 133 is attributed to the ion **17**, derived from McLafferty rearrangement of the molecular ion and further cleavage of the resultant ion **16** as depicted in Scheme 5.

The structural assignment for the seco-aldehyde **13** is based on its spectra and is confirmed by an independent synthesis. In its ir spectrum carbonyl-stretching bands at 5.80 and 5.97 μm witness the presence of both aldehyde and α,β-unsaturated ketone functions. Vinyl proton signals at δ 5.83 (br d, J = 10 Hz) and 6.80 (br m, width = 22 Hz) in its ^{1}H nmr spectrum are characteristic of the α,β-unsaturated ketone system. Two conformations, **13***A* and **13***B*, are available to the cyclohexenone ring of **13**. Models show that in conformer **13***A*, the C-19 methyl group resides in the deshielding region of the C-5 carbonyl group and the relatively low-field chemical shift observed for the C-19 methyl resonance of **13** (δ 1.10) suggests that **13** prefers to exist as conformer **13***A*. This places the more bulky substituent at C-10 in an axial orientation, as observed to result from the "2-alkyl ketone effect" in cyclohexanones (8). Compound **13** exhibits a base peak at *m/z* 110 in its mass spectrum; this peak is attributed to the very stable ion **18** derived from a McLafferty rearrangement of the molecular ion.

A monosemicarbazone **19** of **13** was prepared and its mixture melting point with an authentic sample (*vide infra*) was undepressed. The molecular composition of **19**, $C_{28}H_{47}O_2N_3$, verifies the presence of a single semicarbazone group. Although the enone and semicarbazone carbonyl-stretching bands in the ir spectrum of **19** are not resolved, the absence of an aldehydic carbonyl-stretching band at ~5.80 μm and the presence of an *H*—C=N signal at δ 6.90 (t, J = 6Hz) in its ^{1}H nmr spectrum establishes that it is the aldehydic carbonyl group of **13** that has been derivatized.

The structural assignment for the *B*-nor aldehyde **15** is based on its spectra and confirmed by independent synthesis (*vide infra*). In its ^{1}H nmr spectrum, the appearance of an aldehydic proton signal at δ 9.70 as a doublet (J = 3.5 Hz) suggested the ring-contracted *B*-nor structure. Assignment of the stereochemistry at C-5 and C-6 in **15** proved a difficult task. Irradiation at δ 9.70 collapsed a doublet of doublets at δ 2.41 (J = 9.5, 3.5 Hz), ascribed to the C-6 methine proton, to a doublet (J = 9.5 Hz); however, the 9.5-Hz coupling constant between the C-6 and C-8 methine protons is compatible with the dihedral angles measured from Dreiding models of all four diastereomers of **15**, and thus does not provide a basis for stereochemical assignment at either C-5 or C-6.

Assignment of the stereochemistry at C-5 in **15** was arrived at as follows. Hydrogenation over Adams catalyst in ethyl acetate gave the saturated *B*-nor aldehyde **20**, whose spectra are in accord with expectation. Examination of the chemical shifts of the C-19 methyl protons in the ^{1}H nmr spectra of a variety of Δ^3-unsaturated and analogous saturated steroids indicates that in 5α-steroids, hydrogenation of a Δ^3 double bond leads to a downfield shift of the C-19 methyl signal (9) whereas an upfield shift of this signal accompanies similar hydrogenation in the 5β series (9, 10). On this basis the C-19 methyl signals at δ 0.96 and 0.87 in the ^{1}H nmr spectra of the unsaturated and saturated

Can. J. Chem. Downloaded from www.nrcresearchpress.com by 93.93.197.157 on 09/07/12
For personal use only.

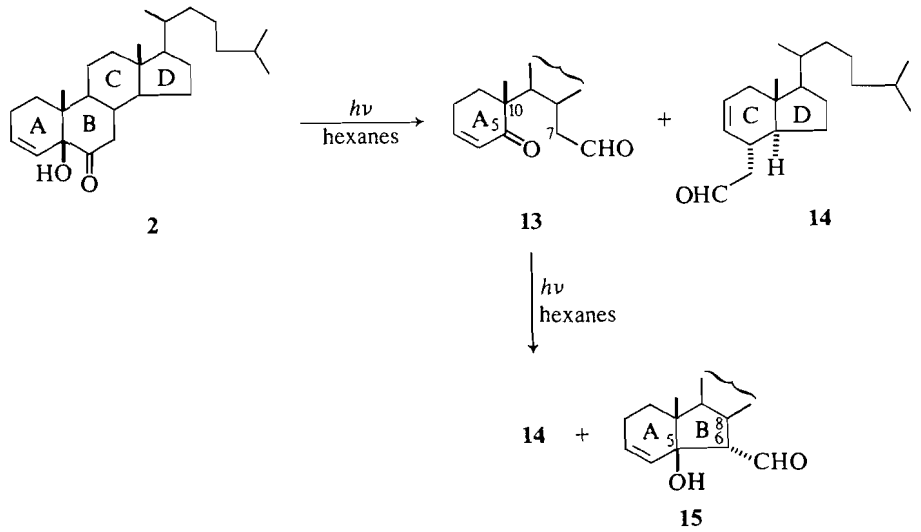

2 13 14 14 + 15

SCHEME 4

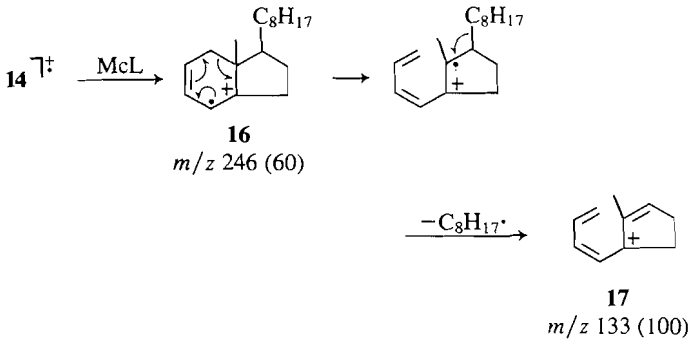

16
m/z 246 (60)

17
m/z 133 (100)

SCHEME 5

aldehydes **15** and **20**, respectively, signify the β stereochemistry of the hydroxyl groups at C-5 in these compounds.

With the 5β configuration for the C-5 hydroxyl group assigned, the α and β configurations of the C-6 formyl group can be distinguished, for in the β configuration, but not the α, the aldehyde would be expected to be strongly hydrogen bonded. The presence of both sharp and broad hydroxyl-stretching bands in the ir spectra and the appearance of the hydroxyl signals as broad multiplets in the ^{1}H nmr spectra suggest that the hydroxyl groups in **15** and **20** are not strongly hydrogen bonded; thus the C-6 formyl group in each is tentatively assigned the α configuration.

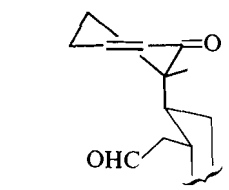

13*A*

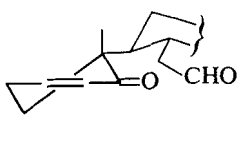

13*B*

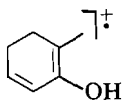

18
m/z 110 (100)

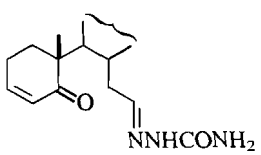

19

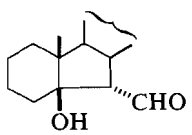

20

This assignment is supported by the lanthanide-induced shifts (LIS) in the ^{1}H nmr spectrum of **20**. Upon addition of a small amount of Sievers' reagent ($Eu(fod)_3$) the C-6 methine proton signal underwent a large downfield shift (Δδ 0.6) while only a negligible downfield shift (Δδ 0.03) was observed for the aldehydic proton signal. These differential shifts indicate that the europium complex is coordinated to the hydroxyl group at C-5 and not to the carbonyl group of the aldehyde (11, 12), since a substantial deshielding of the aldehydic proton via a contact shift would have been expected from coordination of the shift reagent to the latter (12, 13). Bidentate coordination of the shift reagent to both the 5β-hydroxyl and 6-formyl groups is expected for the β, but not the α, stereochemistry of the formyl group. Thus, the negligible LIS shift observed for the aldehydic proton further suggests the α configuration for the 6-formyl group.

The structural assignment for the seco-aldehyde **13** was confirmed by an independent synthesis as outlined in Scheme 6. Ozonolysis of cholesteryl acetate (**21**) with reductive work-up with dimethyl sulfide gave the acetoxy keto aldehyde **22**, which was converted to its dimethyl acetal **23** with triethyl orthoformate and a catalytic quantity of *p*-toluenesulfonic acid (14). Alternatively, addition of these reagents in the reductive work-up of the ozonolysis product gave the dimethyl acetal **23** directly in quantitative yield. In the ^{1}H nmr spectra of both **22** and **23** the appearance of the C-3 methine proton signals as narrow multiplets ($W_{1/2}$ = 8 Hz) evidenced the preference of these 5,6-seco-cholestan-5-ones for the conformations **22***A* and **23***A*, respectively. In this conformation the bulkier substituent at C-10 adopts the axial orientation in accord with the 2-alkyl ketone effect (*vide supra*).

β-Elimination of the acetoxyl group from **23** to give the acetal enone **24** was effected with 1,8-diazabicyclo[5.4.0]undec-7-ene (DBU), and the aldehyde functionality was regenerated by the procedure of Conia and co-workers (15), using aqueous oxalic acid in a slurry of silica gel in dichloromethane. The aldehyde **13** thus obtained was identical with the major photoproduct isolated from irradiation of **2**.

An attempt to prepare the Δ^3-unsaturated *B*-nor aldehyde **15** by an alumina-induced aldol condensation (16) of **13** yielded instead the diene-6-carboxaldehyde **25** (Scheme 7). This was identified by the presence of well-separated vinyl proton signals at δ 6.18 and 6.93 and an aldehydic proton signal as a singlet at δ 10.03 in its ^{1}H nmr spectrum.

Can. J. Chem. Downloaded from www.nrcresearchpress.com by 93.93.197.157 on 09/07/12
For personal use only.

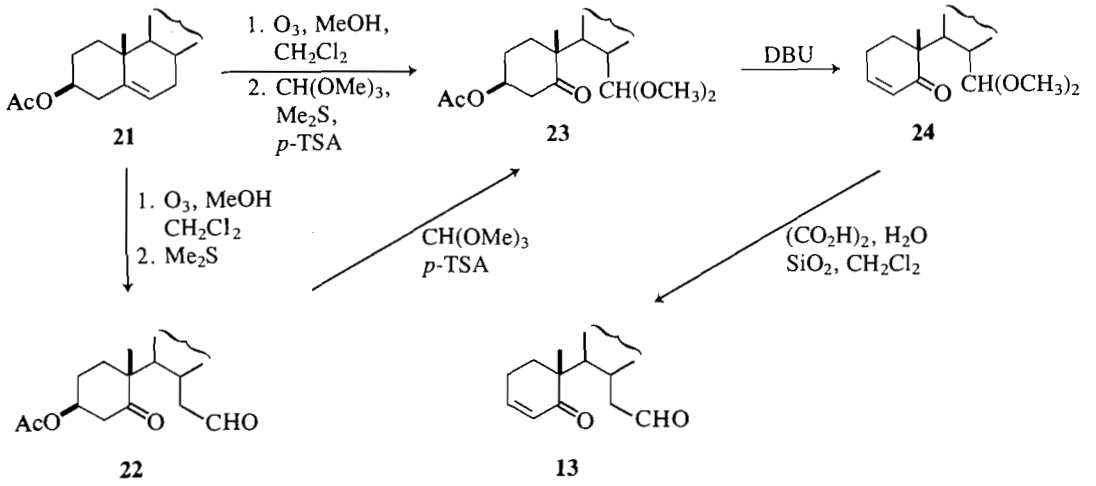

SCHEME 6

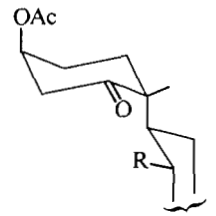

22A R = CHO
23A R = $CH(OCH_3)_2$

Aldol condensation of **13** without concomitant dehydration was achieved by brief treatment with methanolic sodium methoxide (Scheme 7). The *B*-nor aldehyde **15** thus obtained was identical with that isolated as a minor product from the irradiation of **13**.

Photolysis of 5-deuteroxy-5β-cholest-3-en-6-one (26)

To explore further the photoconversion of 5-hydroxy-5β-cholest-3-en-6-one (**2**) to the seco-aldehyde **13** and the indenylacetaldehyde **14**, the photolysis of **26**, the *O*-deuterated derivative of **2**, was investigated. Irradiation of an anhydrous solution of **26** in hexanes was found to give the deuterated seco-aldehyde **27** together with the deuterated indenylacetaldehyde **28** and the deuterated *B*-nor aldehyde **29** (Scheme 8). Weak aldehydic C–D stretching bands at 4.82 μm in the ir spectrum of each evidenced the presence of deuterium at the aldehydic site. The ^1H nmr spectra of **27**, **28**, and **29** were identical to the spectra of their undeuterated analogues **13**, **14**, and **15**, respectively, with the exception that the aldehydic proton signal in each was substantially diminished. Comparison

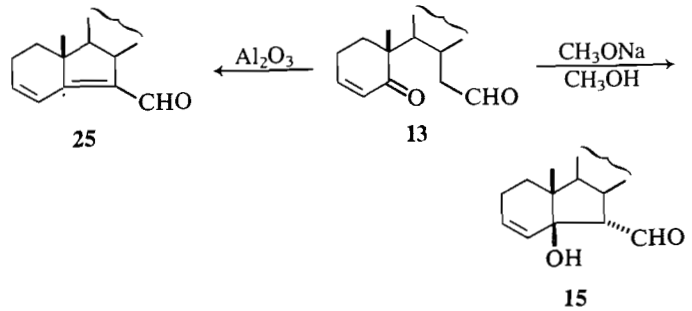

SCHEME 7

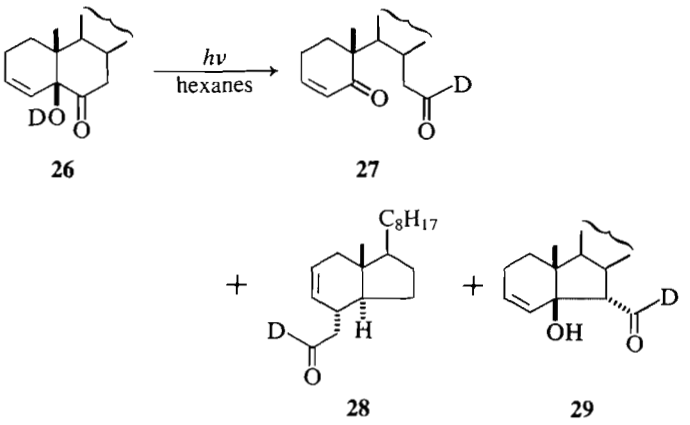

SCHEME 8

of the extent of deuterium incorporation into the aldehydic sites in **27** and **28**, as determined from their ^1H nmr spectra, with the total deuterium content calculated from their mass spectra established that the deuterium label in these aldehydes resided completely in the aldehydic site and indicated that the starting **26** was deuterated to the extent of 75–80%. There was no evidence for the formation of any of the ring A deuterated aldehydes **30** and **31**, whose formation could be envisaged to occur by other pathways.

However, since the deuterated aldehydes were isolated by silica gel column chromatography, we could not exclude the possibility that if deuterium label had been introduced into ring A, yielding aldehyde **30** or **31**, it might have been lost via

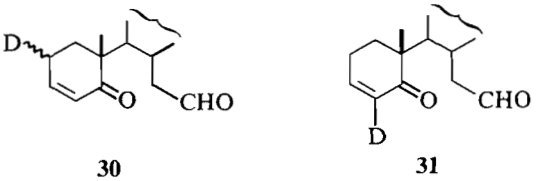

enolization and exchange during chromatography. We therefore sought to obtain higher deuterium incorporation by the addition of a small amount of deuterium oxide to the solvent hexanes used in the irradiation of **26**. These conditions could have led to additional deuterium incorporation at C-2, C-4, and C-7 in **27**,

Can. J. Chem. Downloaded from www.nrcresearchpress.com by 93.93.197.157 on 09/07/12
For personal use only.

but, in the event, no such further deuteration was observed and **27** and **28** were obtained with 89% and 96% d_1 incorporation, as evidenced by their mass spectra. Their ^{1}H nmr spectra showed no trace of aldehydic proton signals. Thus it can be concluded that the deuterium label in **27** and **28** resides only in the aldehydic sites, and that the former is formed to the exclusion of the ring A deuterated analogues **30** and **31**.

Discussion

As noted in the Introduction, direct irradiation of certain β,γ-unsaturated α-ketols has been observed to lead to reactions that proceed via [1,3] acyl migration, a process typical of the singlet excited states of β,γ-unsaturated ketones (17). Debate regarding the role of discrete diradicals arising from α-cleavage in these [1,3] acyl migrations has not yet been resolved (17), although many features of the photochemical behavior of β,γ-unsaturated ketones can be most simply explained by this model.

The propensity of excited β,γ-unsaturated carbonyl chromophores to react via the [1,3] acyl shift mode has been correlated with the relative rate constants for α-cleavage and intersystem crossing from the singlet $n\pi^*$ state (18). α-Cleavage is in turn assisted when the angle between the two planes formed by the carbonyl and olefinic groups is decreased from 180°C, since the incipient unfilled orbital formed in the transition state for α-cleavage can overlap better with the ethylenic π system (18). This arrangement of the π systems is manifested by a hyperchromic effect of the $n\pi^*$ band in the ultraviolet spectrum. From a quantitative perspective, Beugelmans and co-workers (19) have noted that β,γ-unsaturated ketones with $n\pi^*$ molecular extinction coefficients greater than 100 react via [1,3] acyl migration, whereas those with coefficients less than 50 undergo photoreaction by alternative pathways.

We have shown that irradiation of the Δ^3-unsaturated ketol **2** affords, as the major product, the seco-aldehyde **13** (Scheme 9). Deuterium labelling studies (*vide infra*) are in accord with the formation of **13** via an α-cleavage mechanism giving the diradical **32**. The $n\pi^*$ ultraviolet maximum of ketol **2** (λ_{max} 283 (ε = 83)) has an extinction coefficient slightly smaller than that suggested by Beugelmans and co-workers as indicative of α-cleavage. However, in the Δ^3-unsaturated ketol **2**, α-cleavage is considered to be further favored by the radical-stabilizing effect of the α-hydroxyl group. This suggestion is not without precedent for, although the effects of α-substitution in β,γ-unsaturated ketone photolyses are relatively unexplored, Engel *et al.* (20) have noted that increasing α-substitution in β,γ-unsaturated ketones promotes a [1,3] acyl migration at the expense of a [1,2] acyl shift, an observation that they attributed to an increase in the rate of α-cleavage with α-methyl substitution.

In the case of the photolysis of 1-acetylcyclohex-2-en-1-ol (**10**) (Scheme 3), Hancock *et al.* (7) concluded that the predominant photoreaction involves α-cleavage followed by 1,3-recombination of the radical pair thus formed, while O—H abstraction by the acyl radical represents a minor pathway.

In contrast, abstraction of the O—H hydrogen to give aldehyde **13** represents the major disproportionation reaction of diradical **32** formed in the irradiation of **2**. The formation of diketone **33**, the expected product of 1,3-diradical recombination (Scheme 9), was not observed in the photolysis of **2**, although it cannot be excluded that some **33** was formed and underwent further photolysis to unisolated products.

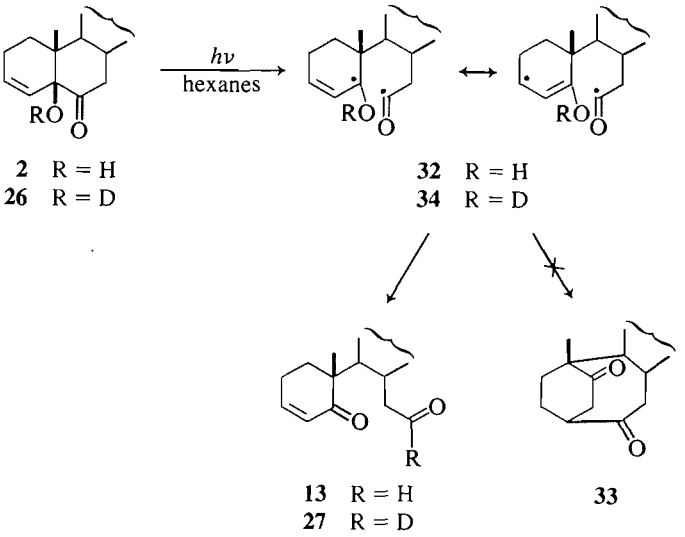

SCHEME 9

Our deuterium labelling studies showed that irradiation of **26**, the *O*-deuteroxy analogue of **2**, gives the α-deutero aldehyde **27**. This establishes that the aldehyde **13** is formed from **2** via α-cleavage to the diradical **32** (Scheme 9). Three pathways can be envisaged for the conversion of **32** to **13**: (*i*) hydroxyl hydrogen abstraction by the acyl radical, (*ii*) C-2 hydrogen abstraction by this radical, and (*iii*) tautomerization of the enol function to the corresponding ketonic function, followed by C-4 hydrogen abstraction by the acyl radical. For the *O*-deutero ketol **26** these imply the product labeling patterns shown in Scheme 10. The fact that the deutero aldehyde **27** was the only product observed and that the deuterated ring A products **35** and **36** could not be detected provides strong evidence that pathway *i* is predominant by far.[2] Several factors are considered to contribute to the selective abstraction of the hydroxyl hydrogen. While each abstraction involves an eight-membered ring transition state, the close proximity of the hydroxyl hydrogen to the acyl radical immediately following α-cleavage is considered to favor this abstraction. Abstraction of the hydroxyl hydrogen, unlike the alternative C—H abstractions, leads directly to the formation of a thermodynamically favored carbonyl bond. It may be noted that an analogous pathway may be involved in the conversion of **7** and **8**, rather than that earlier proposed (Scheme 2) (6).

Interestingly, the disproportionation reactions of the diradicals formed from α-cleavage of the Δ^3-unsaturated 5β-steroidal ketol **2** and of the saturated 5α and 5β steroidal ketols **1** are different, the former involving O—H abstraction leading to the keto aldehyde **13** and the latter C—H abstraction to give a ketene **38** (Scheme 11) (3). This difference in behavior is attributed to the planar geometry, imposed by delocalization, of the allylic radical moeity of **32**. This projects the O—H group towards the acyl radical favoring abstraction of this hydrogen. In contrast, the nonplanar geometry of the hydroxyl substituted alkyl radical

[2]The ratio of **27** to **36** that would result from pathway *iii* would depend on the stereoselectivity associated with the ketonization and abstraction steps. Each step would have to be completely stereospecific for only **27** or **36** to be formed. Although we cannot exclude absolutely the formation of solely product **27** by this route, such complete stereoselectivity seems exceedingly unlikely.

Can. J. Chem. Downloaded from www.nrcresearchpress.com by 93.93.197.157 on 09/07/12
For personal use only.

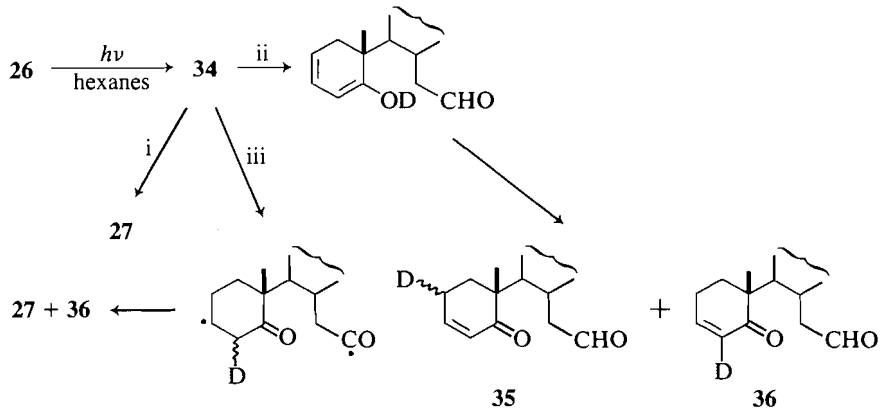

SCHEME 10

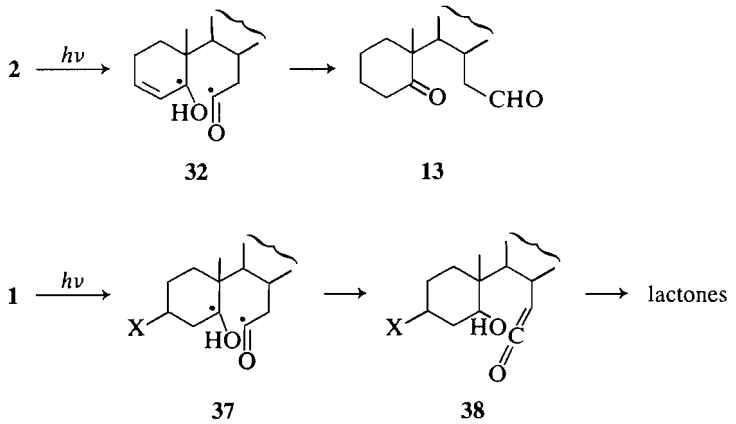

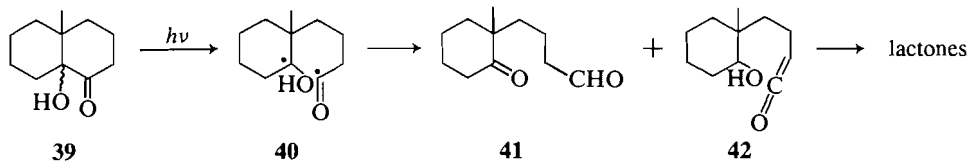

SCHEME 11

center in the saturated steroidal ketol diradicals **37** holds the O—H bond away from the acyl radical (3), inhibiting this mode of disproportionation,[3, 4]

The indenylacetaldehyde **14**, a secondary photoproduct from the irradiation of **2**, is considered to arise from a Norrish II reaction of **13** (Scheme 12). Models indicate that there are three γ-hydrogens that satisfy the geometric requirements for abstraction by the excited α,β-unsaturated enone carbonyl group: the C-11α, and C-11β hydrogens and the hydrogen at C-8 (23). Formation of **14**, resulting from abstraction of a secondary,

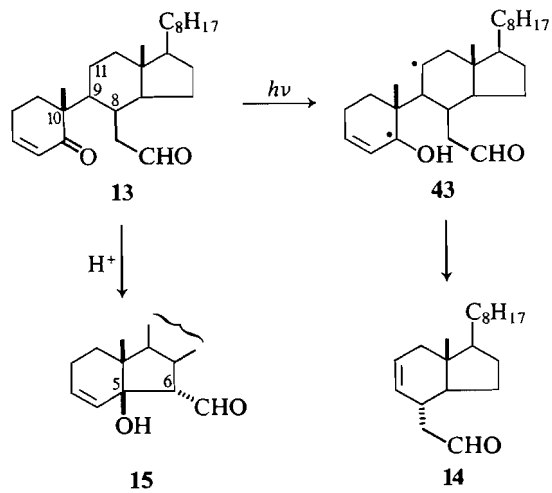

SCHEME 12

[3]In our examination of molecular models, a bent rather than a linear acyl radical was used, for this has been calculated and experimentally shown to be the preferred geometry of the acyl radical (21, 22).

[4]Other possible factors are contraindicated by the observation that the diradicals **40** produced from α-cleavage during irradiation of the bicyclic α-ketols **39** reacted partially by O—H abstraction giving the keto aldehyde **41** as well as by C—H abstraction giving the ketene **42** (Scheme 11).

Can. J. Chem. Downloaded from www.nrcresearchpress.com by 93.93.197.157 on 09/07/12
For personal use only.

C-11, hydrogen atom rather than the tertiary, C-8, hydrogen atom, is attributed to the ability of the resulting diradical **43** to assume a favorable conformation for cleavage of the C-9—C-10 bond, which is not attainable by the corresponding diradical formed by C-8 hydrogen abstraction. The photoconversion of **13** and **14** is of considerable intrinsic interest since it involves a Norrish Type II reaction of a 6-substituted 2-cyclohexenone, a reaction without precedent insofar as we are aware.

The *B*-nor aldehyde **15** is considered to arise from a "dark" aldol reaction of the primary photoproduct **13** (Scheme 12). The pH of the photolysate following irradiation of **2** was found to be acidic, and the aldol condensation is considered to proceed by addition of the protonated enone carbonyl group of **13** to the enol of the aldehyde moiety. Such a route accounts for the observed stereochemistry of **15** at C-5 and C-6.

Conclusions

We have shown that the photolysis of the β,γ-unsaturated α-hydroxy ketone **2** proceeds via α-cleavage to an acyl allyl diradical, which undergoes hydrogen transfer from the hydroxyl group to the acyl radical center to give the keto aldehyde **13**. Two features of this reaction pathway are noteworthy: (*i*) the occurrence of α-cleavage as the major reaction pathway rather than a 1,3 acyl shift, the most frequently observed photochemical reaction pathway for β,γ-unsaturated ketones, and (*ii*) the occurrence of OH hydrogen abstraction in the diradical intermediate to the exclusion of CH hydrogen abstraction. The first feature is attributable to the additional stabilization of the allyl radical center by interaction with the oxygen atom of the hydroxyl group, thus favoring α-cleavage. The second feature is attributed to the planarity of the allyl radical center, which favors transfer of the hydroxyl hydrogen atom to the nearby acyl radical center, rather than transfer of hydrogen from the more distant C-2, C-4, or C-7 sites. The maintenance of the propinquity of the hydroxyl hydrogen and the acyl radical center is ascribable to restriction of rotation about the C-9—C-10 bond in the diradical intermediate as postulated in the cases of the saturated steroidal analogues of **2** (3). The formation of hydroxy ketenes rather than keto aldehydes in the saturated cases is attributable to the nonplanar nature of the alkyl radical center in the alkyl acyl diradicals formed as intermediates.

The secondary photochemical reaction of **13** to give **14** is considered to be a Norrish type II reaction. Formation of **14** results from abstraction of a secondary C-11 hydrogen atom; tertiary C-8 hydrogen abstraction, which would lead to an olefinic isomer of **14**, was not observed. Preferential abstraction from C-11 is attributed to the ability of the diradical intermediate thus formed to adopt a conformation that is favorable for cleavage of the C-9—C-10 bond.

The formation of the *B*-nor aldehyde **15** from **13** is attributable to a dark aldol reaction, catalyzed by an acidic species formed during the photolysis. Its formation could presumably be supressed by carrying out the photolysis in the presence of sodium bicarbonate (24).

Returning to the primary photochemical reaction of **2**, the formation of **13**, we conclude that in general α-cleavage will be favored over the 1,3-diacyl shift reaction in related cyclic β,γ-unsaturated α-hydroxy ketone systems, but that the exclusive formation of a keto aldehyde rather than a ketene-derived product may depend on the specific nature of the ring system into which the three functionalities are incorporated.

Experimental[5]

Irradiation of 5-hydroxy-5β-cholest-3-en-6-one (2) in hexanes. Formation of 5-oxo-5,6-seco-cholest-3-en-6-al (13) and [1R, 4R, 7aR)-1-(1S,5-dimethylhexyl)-7a-methyl-2,3,3a,4,7,7a-hexahydro-1H-inden-4-yl]acetaldehyde (14)

A solution (3 × 14 cm) of **2** (189 mg, 0.47 mmol) in hexanes (65 mL) was irradiated in a Pyrex tube under argon at 300 nm for 4 h. The colorless photolysate was washed with saturated aqueous sodium bicarbonate (10 mL) and saturated aqueous sodium chloride (3 × 5 mL), dried over anhydrous magnesium sulfate, and concentrated to give a colorless oil (175 mg). The oil was flash chromatographed on silica gel (2 × 16 cm) with hexanes – ethyl acetate (9:1 v/v) as eluent. Compound **14** (13.5 mg, 10%) was eluted first, as a colorless oil that resisted crystallization; ir λ_{max}: 3.70 (w), 5.81 μm; ^{1}H nmr δ: 0.70 (s, 3H, C-7a Me), 0.88 (d, J = 6 Hz), 2.40 (m), 5.20–5.83 (m, width = 40 Hz, 2H), 9.80 (nar m, $W_{1/2}$ = 4 Hz, 1H); ^{1}H nmr (200 MHz) δ: 0.71 (s, 3H, C-7a Me), 0.87 (d, J = 6 Hz, 6H), 0.92 (d, J = 6 Hz, 3H), 1.00–2.58 (m, 19H), 5.45–5.52 (m, width = 16 Hz, 1H), 5.58–5.68 (m, width = 19 Hz, 1H), 9.80 (nar m, $W_{1/2}$ = 5 Hz, 1H), ms m/z: 290 (42), 133 (100). *Exact Mass* calcd. for $C_{20}H_{34}O$: 290.2610; found: 290.2613.

A small amount of unconsumed starting ketol **2** (15 mg, 8%) was eluted next. This was followed by **13** (75 mg, 40%), obtained as a colorless oil that resisted crystallization; ir λ_{max}: 3.69 (w), 5.80, 5.97 μm; ^{1}H nmr δ: 0.70 (s, C-18 Me), 1.10 (s, C-19 Me), 5.83 (br d, J = 10 Hz, 1H), 6.80 (br m, width = 22 Hz, 1H), 9.60 (m, $W_{1/2}$ = 3 Hz, 1H); ms m/z: 400 (4), 110 (100). *Exact Mass* calcd. for $C_{27}H_{44}O_2$: 400.3341; found: 400.3343. The ir, ^{1}H nmr, ^{13}C nmr, and mass spectra of the seco-aldehyde **13** isolated from photolysis of the ketol **2** were identical to those of **13** prepared by an independent route (*vide infra*).

*Irradiation of 13. Formation of 14 and 5-hydroxy-*B*-nor-5β-cholest-3-ene-6α-carbaldehyde (15)*

A solution (4 × 19 cm) of **13** (547 mg, 1.37 mmol) in hexanes (180 mL) was degassed with argon for 1.5 h, and the solution was irradiated in Pyrex at 300 nm for 22 h. The colorless photolysate was washed with saturated aqueous sodium bicarbonate (1 × 15 mL) and saturated aqueous sodium chloride (4 × 20 mL), dried over anhydrous sodium sulfate, and concentrated to give a yellow oil (460 mg). Thin-layer chromatography of the oil with hexanes – ethyl acetate (4:1 v/v) evidenced two predominant spots and a host of smaller spots. The oil was flash chromatographed under nitrogen pressure on a silica gel column (2 × 12 cm) with hexanes – ethyl acetate (95:5 v/v) as eluent. Compound **14** (71 mg, 18%) was eluted first as a colorless oil. Further elution gave an impure 1:1 mixture of unconsumed seco-aldehyde **13** and *B*-nor aldehyde **15** (153 mg). The mixture of **13** and **15** was purified by flash chromatography under nitrogen pressure on silica gel (1.5 × 16 cm) with chloroform–methanol (99.5:0.5 v/v) as eluent. The oil obtained (70 mg) was flash chromatographed again under nitrogen pressure on a silica gel column (1.5 × 18 cm) with chloroform – diethyl ether (97:3 v/v) as eluent to give **15** (38 mg, 7%) as a colorless oil that resisted crystallization; ir λ_{max}: 2.78 (sh, w), 2.88 (br, w), 5.82 μm; ^{1}H nmr δ: 0.70 (s, C-18 Me), 0.97 (s, C-19 Me), 1.90 (m, OH), 2.42 (dd, J = 10, 4 Hz), 5.70 (nar m, $W_{1/2}$ = 2 Hz, 2H), 9.72 (d, J = 3 Hz, 1H); ^{1}H nmr (200 MHz) δ: 0.71 (s, C-18 Me), 0.86 (d, J = 7 Hz, C-26,27 Me), 0.91 (d, J = 6 Hz, C-21 Me), 0.96 (s, C-19 Me), 2.41 (dd, J = 9.5, 3.5 Hz, 1H), 5.64–5.79 (m, width = 31 Hz, 2H), 9.70 (d, J = 3.5 Hz, 1H); ms m/z: 400 (6), 110 (100). *Exact Mass* calcd. for $C_{27}H_{44}O_2$: 400.3341; found: 400.3340.

The indenylacetaldehyde **14** (49 mg, 0.17 mmol) was treated with a solution of semicarbazide hydrochloride (100 mg, 0.90 mmol) and sodium acetate trihydrate (150 mg, 1.10 mmol) in water (1 mL). Diethyl ether (1 mL) and 95% ethanol (1 mL) were added, and the solution was allowed to stand at room temperature for 24 h. Diethyl ether (20 mL) and saturated aqueous sodium bicarbonate (5 mL) were added to the resulting white suspension. The aqueous phase was ex-

[5]For a general description of the experimental procedures used, see ref. 3.

Can. J. Chem. Downloaded from www.nrcresearchpress.com by 93.93.197.157 on 09/07/12
For personal use only.

Can. J. Chem. Downloaded from www.nrcresearchpress.com by 93.93.197.157 on 09/07/12
For personal use only.

tracted with diethyl ether (2 × 10 mL, 1 × 5 mL), and the combined ethereal solutions were washed with water (3 × 5 mL), dried over anhydrous sodium sulfate, and concentrated to give a white solid (58 mg). Crystallization from hexanes–ethanol gave the *semicarbazone of* ***14*** as white crystals, mp 167–170°C; ir λ_{max}: 2.96 (sh, w), 3.07 (br, w), 5.92, 6.40 μm; ^{1}H nmr δ: 0.67 (s, C-7a Me), 0.87 (d, J = 6 Hz, 6H), 5.52 (m, 4H, H—C=C—H and $CONH_2$, signal corresponding to 2H moves upfield on dilution), 7.05 (t, J = 6 Hz, 1H, H—C=N), 9.33 (nar m, $W_{1/2}$ = 4 Hz, 1H, C=N—NH, moves upfield on dilution); ms *m/z*: 347 (17), 101 (100). *Exact Mass* calcd. for $C_{21}H_{37}ON_3$: 347.2936; found: 347.2920.

*Ozonolysis of cholesteryl acetate (**21**). Formation of 3β-acetoxy-5-oxo-5,6-seco-cholestan-6-al (**22**)*

A stirred solution of **21** (500 mg, 1.17 mmol) in dichloromethane–methanol (95:5 v/v; 150 mL) cooled in an absolute ethanol – Dry Ice bath to −35 to −40°C was treated with an unstandardized stream of ozone for 1.5 h, at which point a starch – potassium iodide test of the effluent from the reaction flask became positive. The flask was flushed with argon, and the reaction mixture was treated with dimethyl sulfide (2.0 mL, 27 mmol). The solution was allowed to warm gradually to room temperature overnight under a slow stream of argon. The reaction mixture was washed with saturated aqueous sodium chloride (1 × 50 mL) and water (4 × 25 mL), dried over anhydrous sodium sulfate, and concentrated to give **22** (546 mg) as a pale yellow oil in quantitative yield; ir λ_{max}: 3.67 (w), 5.78, 5.85 μm; ^{1}H nmr δ: 0.70 (s, C-18 Me), 1.03 (s, C-19 Me), 2.02 (s), 5.33 (nar m, $W_{1/2}$ = 8 Hz, 1H), 9.62 (br s, 1H); ms *m/z*: 460 (3), 110 (100).

*3β-Acetoxy-6,6-dimethoxy-5,6-seco-cholestan-5-one (**23**)*

*(i) Ozonolysis of **21** with a dimethyl sulfide/p-toluenesulfonic acid/trimethyl orthoformate work-up*

A stirred solution of **21** (3.00 g, 7.00 mmol) in dichloromethane–methanol (95:5 v/v; 200 mL) cooled in an absolute ethanol – Dry Ice bath to −40°C was treated with an unstandardized stream of ozone. After 6 h, a starch – potassium iodide test of the effluent gas from the reaction mixture became positive. The flask was flushed with argon, and dimethyl sulfide (6.0 mL, 82 mmol), trimethyl orthoformate (3.6 mL, 33 mmol), and *p*-toluenesulfonic acid monohydrate (58 mg, 0.31 mmol) were added. The reaction mixture was allowed to warm gradually to room temperature overnight under a flow of argon and poured into saturated aqueous sodium bicarbonate (25 mL). The organic phase was washed with water (7 × 50 mL), dried over anhydrous sodium sulfate, and concentrated to give **23** (3.66 g) as a yellow oil in quantitative yield; ir λ_{max}: 5.77, 5.86, 7.29 (m) μm; ^{1}H nmr δ: 0.67 (s, C-18 Me), 1.05 (s, C-19 Me), 2.00 (s), 3.20 (s, 6H), 4.43 (t, J = 6 Hz, 1H), 5.37 (nar m, $W_{1/2}$ = 8 Hz, 1H); ms *m/z*: 506 (1), 75 (100). *Exact Mass* calcd. for $C_{31}H_{54}O_5$: 506.3971; found: 506.3947.

*(ii) From the seco-aldehyde **22***

A stirred solution of **22** (3.29 g, 7.15 mmol) and *p*-toluenesulfonic acid monohydrate (44 mg, 0.23 mmol) in anhydrous methanol (30 mL) under an argon atmosphere and cooled to −23°C in a carbon tetrachloride – Dry Ice bath was treated with trimethyl orthoformate (3.5 mL, 32 mmol). The reaction mixture was stirred in the cold bath for 4 h and poured into saturated aqueous sodium bicarbonate (10 mL). The methanol was removed on a rotary evaporator under water aspirator pressure. Water (50 mL) was added to the residue, and the mixture was extracted with diethyl ether (1 × 50 mL, 3 × 25 mL). The combined ethereal extracts were washed with water, dried over anhydrous sodium sulfate, and concentrated to give a colorless oil (3.35 g) comprising **23** contaminated with approximately 15% of **22**. This material gave satisfactory results in its reaction with 1,8-diazabicyclo[5.4.0]undec-7-ene (DBU) (*vide infra*).

*6,6-Dimethoxy-5,6-seco-cholest-3-en-5-one (**24**)*

A solution of **23** (3.66 g, 7.23 mmol) and 1,8-diazabicyclo-[5.4.0]undec-7-ene (DBU) (4.5 mL, 30 mmol) in heanes (100 mL) was stirred at room temperature under an argon atmosphere for 19 h. The reaction mixture was poured into 2 *N* hydrochloric acid (25 mL), and the aqueous phase was extracted with hexanes (2 × 25 mL). The combined organic phases were washed with 2 *N* hydrochloric acid (5 mL), saturated aqueous sodium bicarbonate (25 mL), and water (4 × 15 mL), dried over anhydrous sodium sulfate, and concentrated to give a yellow oil (3.30 g). High performance liquid chromatography of the oil on a PrepPak-500 silica gel column (Waters Scientific; 5.7 × 30 cm) with dichloromethane – ethyl acetate (98:2 v/v) as eluent gave **24** (2.39 g, 74%) as a colorless oil that resisted crystallization; ir λ_{max}: 5.97, 7.28 (m), 8.99 (br) μm; ^{1}H nmr δ: 0.67 (s, C-18 Me), 1.15 (s, C-19 Me), 3.28 (s) and 3.32 (s) (6H), 4.40 (t, J = 5 Hz, 1H), 5.90 (br d, J = 10 Hz, 1H), 6.73 (br m, width = 20 Hz, 1H); ms *m/z*: 446 (1), 75 (100). *Exact Mass* calcd. for $C_{29}H_{50}O_3$: 446.3760; found: 446.3789.

*5-Oxo-5,6-seco-cholest-3-en-6-al (**13**)*

A slurry of 70–230 mesh silica gel (Brinkmann; 9.0 g) in dichloromethane (15 mL) was treated dropwise with aqueous 7% oxalic acid (890 μL). The acid-treated silica gel was stirred for 15 min, and a solution of **24** (734 mg, 1.65 mmol) in dichloromethane (15 mL) was added. The reaction mixture was stirred at room temperature under an argon atmosphere for 2 h and neutralized by the addition of solid sodium bicarbonate (2.5 g). The mixture was filtered, and the collected solids were washed with dichloromethane (4 × 15 mL). The combined filtrate and washings were washed with water (10 mL), dried over anhydrous sodium sulfate, and concentrated to give **13** (547 mg, 83%) as a colorless oil that resisted crystallization. The ir, ^{1}H nmr, ^{13}C nmr, and mass spectra were identical to those of **13** isolated from photolysis of 5-hydroxy-5β-cholest-3-en-6-one (**2**) (*vide supra*).

*5-Oxo-5,6-seco-cholest-3-en-6-al 6-semicarbazone (**19**)*

Compound **13** (200 mg, 0.05 mmol) was treated with a solution of semicarbazide hydrochloride (400 mg, 3.59 mmol) and sodium acetate trihydrate (600 mg, 4.41 mmol) in water (4 mL). Diethyl ether (5 mL) and 95% ethanol (5 mL) were added, and the resulting solution was stirred at room temperature for 2.5 h. The diethyl ether was removed on the rotary evaporator under reduced pressure, and the resulting white suspension was allowed to stand at 0°C overnight. The precipitate was filtered and washed with methanol–water (1:1 v/v; 40 mL) to give **19** as a white solid. Crystallization from 95% ethanol gave **19** (47 mg, 21%) as white needles, mp 189–194°C (dec. slowly); ir λ_{max}: 2.87 (sh, w), 3.01 (sh, w), 5.92, 6.39 (m) μm; ^{1}H nmr δ: 0.68 (s, C-18 Me), 1.12 (s, C-19 Me), 5.50 (m, 2H, $CONH_2$, moves upfield on dilution), 5.85 (br d, J = 10 Hz, 1H), 6.77 (m) and 6.90 (t, J = 6 Hz, H—C=N) (2H), 8.70 (m, 1H, C=N—NH, moves upfield on dilution); ms *m/z*: 457 (4), 81 (100). *Exact Mass* calcd. for $C_{28}H_{47}O_2N_3$: 457.3668; found: 457.3680. *Anal.* calcd for $C_{28}H_{47}O_2N_3$: C 73.47, H 10.35, N 9.18; found: C 73.43, H 10.40, N 9.18.

*Treatment of 5-oxo-5,6-seco-cholest-3-en-6-al (**13**) with alumina. Formation of B-nor-cholesta-3,5-diene-6-carbaldehyde (**25**)*

A mixture of **13** (340 mg, 0.85 mmol) and neutral, activity I, 70–230 mesh alumina (Merck; 3.4 g) in benzene (10 mL) was stirred at room temperature under an argon atmosphere for 7 h. The resulting yellow suspension was filtered, and the alumina was washed with chloroform. The filtrate and washings were concentrated to give **25** (251 mg, 77%) as a yellow solid; ir λ_{max}: 6.03, 6.23 (m) μm; ^{1}H nmr δ: 0.77 (s, C-18 Me), 0.93 (s, C-19 Me), 6.18 (dt, J = 10, 4 Hz, 1H), 6.93 (br d, J = 10 Hz, 1H), 10.03 (s, 1H).

A solution of **25** (29 mg, 0.08 mmol) in diethyl ether (2 mL) was added to a filtered solution of 2,4-dinitrophenylhydrazine (250 mg, 1.26 mmol) in methanol (5 mL) and concentrated sulfuric acid (0.4 mL). After 45 min the orange-red crystals that had formed were filtered and washed with aqueous methanol and water (30 mL) until the washings were no longer acidic to pH paper. Flash chromatography of the solid (41 mg) on silica gel with chloroform as eluent gave the *(2,4-dintrophenyl)hydrazone of **25*** (19 mg, 44%). Crystallization from hexanes – ethyl acetate gave orange crystals, mp 273–275°C (dec.; the crystals became red at 265–271°C and melted to give a dark red liquid) (lit. (25) mp 262–264°C (dec.) (benzene)).

Can. J. Chem. Downloaded from www.nrcresearchpress.com by 93.93.197.157 on 09/07/12
For personal use only.

*Reaction of 5-oxo-5,6-seco-cholest-3-en-6-al (**13**) with sodium methoxide. Formation of 5-hydroxy-*B*-nor-5β-cholest-3-ene-6α-carbaldehyde (**15**)*

Under an argon atmosphere, a solution of sodium methoxide in methanol, prepared by the addition of sodium (28 mg, 1.2 mmol) to anhydrous methanol (15 mL), was treated dropwise with a solution of **13** (373 mg, 0.93 mmol) in anhydrous methanol (10 mL). The solution was allowed to stand at room temperature for 35 min and poured into water (10 mL). The methanol was removed on a rotary evaporator under water aspirator pressure, and saturated aqueous sodium chloride (10 mL) was added to the residue. The mixture was extracted with diethyl ether (1 × 50 mL, 3 × 15 mL), and the combined ethereal extracts were washed with saturated aqueous sodium chloride (10 × 5 mL) and water (2 × 10 mL), dried over anhydrous sodium sulfate, and concentrated to give **15** (347 mg, 94%) as a yellow-orange oil. The ir, ^{1}H nmr, and ^{13}C nmr spectra were identical to those of **15** isolated from photolysis of **13** (*vide supra*).

Compound **15** (43 mg, 0.11 mmol) was treated with a solution of semicarbazide hydrochloride (100 mg, 0.90 mmol) and sodium acetate trihydrate (150 mg, 1.10 mmol) in water (1 mL). Diethyl ether (1 mL) and 95% ethanol (1 mL) were added to give a homogeneous solution, which was allowed to stand, unstoppered, at room temperature for 30 min. A white precipitate formed, and the reaction mixture was stoppered and allowed to stand at room temperature overnight. Saturated aqueous sodium bicarbonate (5 mL) was added to the white suspension, and the mixture was extracted with diethyl ether (4 × 15 mL). The combined ethereal phases were washed with water (3 × 5 mL), dried over anhydrous sodium sulfate, and concentrated to give the *semicarbazone of **15*** (41 mg, 87%) as a white solid. Crystallization from methanol–water gave white crystals, mp 208–210°C (dec.); ir λ_{max}: 3.05 (br, w), 5.90, 6.38 (m) μm; ms *m/z*: 457 (1), 55 (100). *Exact Mass* calcd. for $C_{28}H_{47}O_2N_3$: 457.3668; found: 457.3662. *Anal.* calcd. for $C_{28}H_{47}O_2N_3 \cdot 0.5$ MeOH: C 72.25, H 10.43, N 8.87; found: C 72.32, H 10.34, N 8.73.

*Hydrogenation of **15**. Formation of 5-hydroxy-*B*-nor-5β-cholestane-6α-carbaldehyde (**20**)*

A solution of **15** (249 mg, 0.62 mmol) in ethyl acetate (30 mL) was stirred with platinum oxide monohydrate (Alfa; 34 mg) at room temperature under 1 atmosphere (101.3 kPa) of hydrogen for 7 h. The reaction mixture was filtered through anhydrous magnesium sulfate, and the magnesium sulfate was washed with ethyl acetate (8 × 10 mL). The combined filtrate and washings were concentrated to give **20** (234 mg, 94%) as a colorless oil. The oil was flash chromatographed under nitrogen pressure on a silica gel column (2 × 16 cm) with hexanes – ethyl acetate (9:1 v/v) as eluent to give **20** (137 mg, 55%) as a colorless oil that resisted crystallization; ir λ_{max}: 2.76 (sh, w), 2.85 (br, w), 3.64 (w), 5.84 μm; ^{1}H nmr δ: 0.70 (s, C-18 Me), 0.87 (s, C-19 Me), 2.10 (m, OH), 9.80 (nar m, $W_{1/2}$ = 4 Hz, 1H); ^{1}H nmr (benzene-d_6, 200 MHz) δ: 0.62 (s, C-18 Me), 0.86 (s, C-19 Me), 0.94 (d, *J* = 7 Hz, C-26,27 Me), 0.98 (d, *J* = 7 Hz, C-21 Me), 1.95 (br d, *J* = 12 Hz), 2.04 (dd, *J* = 9, 3 Hz superimposed on a br s), 2.10 (dd, *J* = 9, 9Hz), 9.68 (d, *J* = 3 Hz); ^{1}H nmr (benzene-d_6 with added Eu(fod)$_3$, 200 MHz) δ: 0.69 (s, C-18 Me), 0.95 (d, *J* = 7 Hz, C-26,27 Me), 1.01 (d, *J* = 6 Hz, C-21 Me), 1.18 (s, C-19 Me), 2.02 (br d, *J* = 13 Hz), 2.46 (dd, *J* = 9.5, 10 Hz), 2.63 (dd, *J* = 8.5, 3 Hz), 9.70 (d, *J* = 3 Hz); ms *m/z*: 402 (9), 112 (100). *Exact Mass* calcd. for $C_{27}H_{46}O_2$: 402.3498; found: 402.3468.

A solution of semicarbazide hydrochloride (300 mg, 2.69 mmol) and sodium acetate trihydrate (450 mg, 3.31 mmol) in water (3 mL) was added to **20** (120 mg, 0.30 mmol). The homogeneous solution, obtained by the addition of diethyl ether (2 mL) and 95% ethanol (2 mL), was allowed to stand at room temperature overnight. The reaction mixture was poured into saturated aqueous sodium bicarbonate (10 mL) and extracted with chloroform (1 × 50 ml, 4 × 15 mL) and diethyl ether (1 × 100 mL). The combined organic phases were washed with saturated aqueous sodium chloride, dried over anhydrous sodium sulfate, and concentrated to give the *semicarbazone of **20*** (124 mg, 91%) as a white solid. Crystallization from methanol gave the semicarbazone as white needles, mp 213–215°C (dec.); ms *m/z*: 459 (41), 263 (100). *Exact Mass* calcd. for $C_{28}H_{49}O_2N_3$: 459.3825; found: 459.3832. *Anal.* calcd. for $C_{28}H_{49}O_2N_3$: C 73.15, H 10.74, N 9.14; found: C 72.91, H 10.85, N 9.09.

*Irradiation of 5-deuteroxy-5β-cholest-3-en-6-one (**26**) in anhydrous hexanes. Formation of [(1R,4R,7aR)-1-(1S,5-dimethylhexyl)-7a-methyl-2,3,3a,4,7,7a-hexahydro-1H-inden-4-yl]-(1-deutero)-acetaldehyde (**28**), 5-oxo-5,6-seco-cholest-3-en-(6-deutero)-6-al (**27**), and 5-hydroxy-B-nor-5β-cholest-3-ene-6α-(deutero)carbaldehyde (**29**)*

In a separatory funnel, a solution of **2** (189 mg, 0.47 mmol) in hexanes (200 mL) was treated successively with a solution of anhydrous potassium carbonate in deuterium oxide (99.8%, Aldrich; 1 × 100 mg K_2CO_3 in 1.5 mL D_2O, 1 × 100 mg K_2CO_3 in 3 mL D_2O, 1 × 100 mg K_2CO_3 in 5 mL D_2O) and deuterium oxide (2 × 5 mL). The organic phase was added to a flask pretreated with deuterium oxide, a short path distillation apparatus was fitted, and the hexanes – deuterium oxide azeotrope (bp ~ 64°C; ~1 mL) and hexanes (125 mL) were distilled at atmospheric pressure under an argon atmosphere. The residue (75 mL) was added via cannula under argon to a Pyrex photolysis tube pretreated with deuterium oxide. The solution (3 × 14 cm) was degassed with argon for 30 min and irradiated at 300 nm for 5.5 h. The colorless photolysate was washed with water (10 mL), saturated aqueous sodium bicarbonate (5 mL), and saturated aqueous sodium chloride (3 × 10 mL), dried over anhydrous sodium sulfate, and concentrated to give a colorless oil (203 mg). The oil was flash chromatographed on a silica gel column (2 × 16 cm) under argon pressure. Elution with chloroform – diethyl ether (99.5: 0.5 v/v) gave **28** (19 mg, 14%) as a colorless oil; ir λ_{max}: 4.82 (w), 5.84 μm; ^{1}H nmr δ: 0.72 (s, 3H, C-7a Me), 0.87 (d, *J* = 6 Hz), 2.42 (m), 5.53 (m, 2H), 9.88 (m, 0.19H); ms *m/z*: 291 (31), 133 (100); d_0 17%, d_1 81%, d_2 1%. *Exact Mass* calcd. for $C_{20}H_{33}DO$: 291.2672; found: 291.2657.

Further elution gave unconsumed **2** (65 mg, 34%) as a white solid followed by a mixture of **2** and the deuterated seco-aldehyde **27** (90 mg). Still further elution gave a mixture of the deuterated seco-aldehyde **27** and the deuterated *B*-nor aldehyde **29** (32 mg). The mixture of **2** and **27** was flash chromatographed again under argon pressure with chloroform – diethyl ether (99.5:0.5 v/v) as eluent to give another 4 mg of **2** (2%; total 36%) and **27** (46 mg, 24%) as a colorless oil; ir λ_{max}: 4.83 (w), 5.84, 5.97 μm; ^{1}H nmr (200 MHz) δ: 0.69 (s, C-18 Me), 0.85 (d, *J* = 6 Hz, C-26,27 Me), 0.89 (d, *J* = 7 Hz, C-21 Me), 1.08 (s, C-19 Me), 2.25 (dd, *J* = 18, 3.5 Hz), 2.53 (dd, *J* = 18, 5 Hz, 1H), 5.83 (ddd, *J* = 10, 3, 1 Hz, 1H), 6.78 (br d, *J* = 10 Hz, 1H), 9.58 (m, 0.17H); ms *m/z*: 401 (4), 110 (100); d_0 25%, d_1 72%, d_2 3%. *Exact Mass* calcd. for $C_{27}H_{43}DO_2$: 401.3404; found: 401.3422.

The mixture of **27** and **29** was flash chromatographed under argon pressure on a silica gel column (2 × 16 cm) with chloroform – diethyl ether (99:1 v/v) to give a further 9 mg of **27** (5%; total 29%) and **29** (10 mg, 5%); ir λ_{max}: 2.79 (sh, w), 2.91 (br, w), 4.82 (w), 5.89 μm; ^{1}H nmr δ: 0.72 (s, C-18 Me), 0.97 (s, C-19 Me), 5.73 (nar m, $W_{1/2}$ = 2 Hz, 2H), no aldehyde signal detected at δ 9.72; ms *m/z*: 401 (4), 110 (100); d_0 20%, d_1 77%, d_2 3%. *Exact Mass* calcd. for $C_{27}H_{43}DO_2$: 401.3404; found: 401.3408.

*Irradiation of 5-deuteroxy-5β-cholest-3-en-6-one (**26**) in hexanes in the presence of deuterium oxide. Formation of **27**, **28**, and **29***

In a separatory funnel, a solution of **2** (47 mg, 0.12 mmol) in hexanes (20 mL) was treated with a solution of anhydrous potassium carbonate in deuterium oxide (99.8%, Aldrich; 3 × 35 mg K_2CO_3 in 5 mL D_2O, 1 × 50 mg K_2CO_3 in 3 mL D_2O) and deuterium oxide (2 × 1 mL). Deuterium oxide (2 mL) was added, and the two-phase mixture was added via cannula under argon to a Pyrex photolysis tube pretreated with deuterium oxide. The solution (3 × 6 cm) was degassed with argon for 30 min and irradiated with stirring at 300 nm for 6 h. The photolysate was diluted with hexanes (25 mL), and the solution was washed with water (10 mL), saturated aqueous sodium bicarbonate (1 × 5 mL), and saturated aqueous sodium chloride (5 × 5 mL), dried

over anhydrous sodium sulfate, and concentrated to give a colorless oil (47 mg) that partially solidified. Flash chromatography under argon pressure on a silica gel column (1.5 × 15 cm) with chloroform – diethyl ether (99.5:0.5 v/v) as eluent gave **28** (11 mg, 32%) as a colorless oil; ^{1}H nmr δ: 0.72 (s, 3H, C-7a Me), 0.87 (d, J = 6 Hz), 2.42 (m), 5.53 (m, 2H), no aldehyde signal observed at δ 9.88; ms: d_0 2%, d_1 96%, d_2 2%. Further elution gave **27** (7 mg, 15%); ^{1}H nmr (200 MHz) δ: 0.69 (s, C-18 Me), 0.86 (d, J = 7 Hz, C-26,27 Me), 0.89 (d, J = 7 Hz, C-21 Me), 1.08 (s, C-19 Me), 2.25 (dd, J = 18, 3.5 Hz), 2.53 (dd, J = 18, 5 Hz, 1H), 5.83 (ddd, J = 10, 3, 1 Hz, 1H), 6.78 (br d, J = 10 Hz, 1H), no aldehyde signal observed at δ 9.58 even when the spectrum was amplified by a factor of 15; ms: d_0 5%, d_1 89%, d_2 4%. Still further elution gave a mixture of **27** and **29**, which was rechromatographed under the same conditions to give **29** (11 mg, 24%) as a colorless oil.

Acknowledgments

We thank the Natural Sciences and Engineering Research Council of Canada for financial support of this work and for the award of a postgraduate fellowship to S.S., and Imperial Oil Limited for the award of a Graduate Research Fellowship to S.S.

1. P. Yates and S. Stiver. Can. J. Chem. **66**, 476 (1988).
2. S. Stiver and P. Yates. Tetrahedron Lett. **27**, 2215 (1986).
3. S. Stiver and P. Yates. Can. J. Chem. **66**, 214 (1988).
4. P. Yates and S. Stiver. Can. J. Chem. **65**, 2203 (1987).
5. T. Sasaki, K. Kanematsu, and K. Hayakawa. J. Chem. Soc. Perkin Trans. 1, 1951 (1972); T. Sasaki, K. Kanematsu, K. Hayakawa, and A. Kondo. J. Org. Chem. **38**, 4100 (1973).
6. R. G. Carlson and A V. Prabhu. J. Org. Chem. **39**, 1753 (1974).
7. K. G. Hancock, J. T. Lau, and P. L. Wylie. Tetrahedron Lett. 4149 (1974); K. G. Hancock, P. L. Wylie, and J. T. Lau. J. Am. Chem. Soc. **99**, 1149 (1977).
8. E. L. Eliel. Stereochemistry of carbon compounds. McGraw–Hill, New York. 1962. p. 240; E. L. Eliel, N. L. Allinger, S. J. Angyal, and G. A. Morrison. Conformational analysis. John Wiley, New York. 1965. pp. 112–113.
9. D. Lavie, S. Greenfield, Y. Kashman, and E. Glotter. Isr. J. Chem. **5**, 151 (1967); G. M. L. Cragg, C. W. Davey, D. N. Hall, G. D. Meakins, E. E. Richards, and T. L. Whateley. J. Chem. Soc. (C), 1266 (1966).
10. J. E. Bridgeman, P. C. Cherry, A. S. Clegg, J. M. Evans, E. R. H. Jones, A. Kasal, V. Kumar, G. D. Meakins, Y. Morisawa, E. E. Richards, and P. D. Woodgate. J. Chem. Soc. (C), 250 (1970); G. W. Kabalka, R. Hutchins, N. R. Natale, D. T. C. Yang, and V. Broach. Org. Synth. **59**, 42 (1980).
11. O. Hofer. *In* Topics in stereochemistry. Vol. 9. *Edited by* N. L. Allinger and E. L. Eliel. John Wiley, New York. p. 140.
12. A. F. Cockerill, G. L. O. Davies, R. C. Harden, and D. M. Rackham. Chem. Rev. **73**, 553 (1973).
13. L. M. Jackman and S. Sternhell. Applications of nuclear magnetic resonance spectroscopy in organic chemistry. 2nd ed. Pergamon, New York. 1969. pp. 102–103.
14. J. Gauthier and P. Deslongchamps. Can. J. Chem. **45**, 297 (1967).
15. F. Huet, A. Lechevallier, M. Pellet, and J. M. Conia. Synthesis, 63 (1978).
16. K. Tanabe and Y. Morisawa. Chem. Pharm. Bull. **11**, 536 (1963).
17. S. S. Hixson, P. S. Mariano, and H. E. Zimmerman. Chem. Rev. **73**, 531 (1973); W. G. Dauben, G. Lodder, and J. Ipaktschi. Top. Curr. Chem. **54**, 73 (1975); K. N. Houk. Chem. Rev. **76**, 1 (1976).
18. J. R. Williams and G. M. Sarkisian. J. Chem. Soc. Chem. Commun. 1564 (1971).
19. J. Pusset, M. T. Le Goff, and R. Beugelmans. Tetrahedron, **31**, 643 (1975).
20. P. S. Engel, M. A. Schexnayder, H. Ziffer, and J. I. Seeman. J. Am. Chem. Soc. **96**, 924 (1974).
21. A. G. Davies and R. Sutcliffe. J. Chem. Soc. Perkin Trans. 2, 819 (1980).
22. N. J. Turro. Modern molecular photochemistry. Benjamin/Cummings, Menlo Park, CA. 1978. pp. 224–228, 537; N. J. Turro, W. E. Farneth, and A Devaquet. J. Am. Chem. Soc. **98**, 7425 (1976).
23. N. J. Turro and D. S. Weiss. J. Am. Chem. Soc. **90**, 2185 (1968); J. C. Dalton, K. Davies, N. J. Turro, D. S. Weiss, J. A. Barltrop, and J. D. Coyle. J. Am. Chem. Soc. **93**, 7213 (1971).
24. G. Roussi and R. Beugelmans. Tetrahedron Lett. 1333 (1972); P. Yates. J. Photochem. **5**, 91 (1976).
25. K. Tanabe, R. Hayashi, and R. Takasaki. Chem. Pharm. Bull. **9**, 1 (1961).

Can. J. Chem. Downloaded from www.nrcresearchpress.com by 93.93.197.157 on 09/07/12
For personal use only.

Enzyme catalysed hydrolysis of chlorophenoxypropionates

ROBERT CHÊNEVERT[1] AND LINDA D'ASTOUS

Département de chimie, Faculté des sciences et de génie, Université Laval, Québec (Québec), Canada G1K 7P4

Received September 16, 1987

ROBERT CHÊNEVERT and LINDA D'ASTOUS. Can. J. Chem. **66**, 1219 (1988).

We report on the enzymatic hydrolysis of methyl 2-phenoxypropionate and of the following chlorinated derivatives: methyl *o*-chloro-, *m*-chloro-, *p*-chloro-, and *o,p*-dichloro-2-phenoxypropionates. α-Chymotrypsin, lipase, and pig liver esterase have an *R* enantioselectivity whereas subtilisin has an *S* enantioselectivity. Enantiomeric excesses (e.e.) cover a wide range (from 5 to 100%).

ROBERT CHÊNEVERT et LINDA D'ASTOUS. Can. J. Chem. **66**, 1219 (1988).

Nous décrivons l'hydrolyse enzymatique du phénoxy-2 propionate de méthyle et de ses dérivés chlorés suivants : *o*-chloro, *m*-chloro, *p*-chloro et *o,p*-dichloro phénoxy-2 propionates de méthyle. La lipase, l'estérase et la α-chymotrypsine hydrolysent sélectivement l'isomère *R* alors que la subtilisine montre une sélectivité inverse. Les excès énantiomériques (e.e.) sont très variables (de 5 à 100%).

Can. J. Chem. Downloaded from www.nrcresearchpress.com by 93.93.197.157 on 09/07/12
For personal use only.

Introduction

The use of enzymes as catalysts in synthetic organic chemistry is being increasingly exploited by chemists (1). Hydrolases that are readily available and do not require cofactor regeneration are particularly valuable in asymmetric synthesis. In recent years, several hydrolytic enzymes have been used for the resolution of racemates (2) or the enantiotopic group differentiation in meso compounds (3). We report here a study on the resolution of chlorophenoxypropionates by hydrolases. Chlorophenoxyalkanoic acids and derivatives are plant growth regulators (herbicides) (4). They have an influence on lipid metabolism and are hypolipidemic and hypocholesterolemic agents (5). They also have a morphogenic activity on insects (6). Their structure has been incorporated in synthetic or semisynthetic penicillins (7). There is always a more or less pronounced difference in biological activity between the D and L forms. For instance, the D-(+)-4-chlorophenoxypropionic acid is an auxin 100 times more active than the L-(−) isomer (8).

Results and discussion

The racemic ester substrates (+)-(**1**–**5**) were prepared by esterification of the commercially available corresponding acids with methanol in the presence of 2,2-dimethoxy propane and *p*-toluenesulfonic acid. Preparative-scale (5–6 mmol) enzyme catalysed hydrolyses were performed in buffered aqueous solutions at pH 7–8. The enzymatic saponification was indicated by the decrease of pH, which was maintained at its initial value by the addition of a dilute sodium hydroxide solution. The reactions were monitored from the consumption of the base and terminated at the 50%-of-hydrolysis point. The unreacted esters were recovered from the reaction mixtures by extraction with ether at pH 7–8. The product acids that are present in the aqueous phase as sodium salts were isolated after acidification to pH 2 and extraction with ether. Acids were converted to their methyl esters before the determination of their optical purity. Enantiomeric excess (e.e.) values were determined by ^{1}H nmr analysis using tris[3-(heptafluoropropylhydroxymethylene)-*d*-camphorato]europium(III) as a chiral shift reagent. In every case, well-resolved signals were obtained for the ester methyl protons. Absolute configurations were assigned by comparison with the optical rotation signs reported in the literature (8*b*, 9). The results are summarized in Tables 1 and 3 (experimental part). Recovery yields ranged from 70 to 99% of the amount estimated to be present based on acid released. α-Chymotrypsin, subtilisin, lipase, and esterase are enantioselective, and enantiomeric excesses cover a wide range from 5 to 100%. Esterase is the most active enzyme but its enantioselectivity is much lower than other enzymes. The dichlorophenoxyester **5** is more resistant to hydrolysis and poor enantioselectivities were found with all enzymes. Klibanov and co-workers (2*b*, 10) reported the resolution of 2-(*p*-chlorophenoxy)propionic acid by asymmetric hydrolysis and by esterification or transesterification with immobilized lipase or free lipase in dry organic media. Table 1 reports the e.e.'s that are consistently achievable under the usual reaction conditions. These reactions have not been optimized and Table 2 shows how manipulation of reaction conditions can sometimes be used to improve enantiomeric purities if the enantioselectivity of the enzyme under the usual conditions is inadequate. To avoid non-enzymatic hydrolysis, we kept the pH constant (pH 7–8) and changed the ionic strength and the nature of the electrolytes. Both sodium and calcium ions are activators of lipases (11). Sodium ions suppress enzyme inhibition by interfacial charge effects. The role of calcium ions is more complex. Calcium ions bind to the enzyme and affect the enzyme–substrate association. Calcium ions can also remove the unionized fatty acids from the interface where the reaction occurs, through the formation of insoluble calcium carboxylates. Since the values of enantiomeric excess increase with the extent of conversion (12), it is possible to improve the optical purity of the unreacted ester by extending reaction times, but at the expense of decreased yield. For example, α-chymotrypsin catalysed hydrolysis of methyl 2-phenoxypropionate gave a 66% e.e. at 50% conversion and a >90% e.e. at 70% conversion. Acids can be prepared with higher values of e.e. by carrying hydrolyses to low conversions. Whichever the desirable isomer, the other one can be readily racemized and recycled. Methyl esters were racemized by a

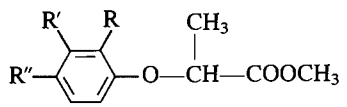

	R=H	R′=H	R″=H
1			
2	Cl	H	H
3	H	Cl	H
4	H	H	Cl
5	Cl	H	Cl

[1]Author to whom correspondence may be addressed.

TABLE 1. Enzyme catalysed hydrolyses of phenoxypropionates

	% ee (abs. conf.)[a]							
	α-Chymotrypsin		Subtilisin		Lipase		Esterase	
Substrate	Recovered ester	Acid product	Recovered ester	Acid product	Recovered ester	Acid product	Recovered ester	Acid product
1	66 (*S*)	70 (*R*)	56 (*R*)	46 (*S*)	61 (*S*)	48 (*R*)	10 (*S*)	7 (*R*)
2	80 (*S*)	75 (*R*)	24 (*R*)	35 (*S*)	36 (*S*)	39 (*R*)	5 (*S*)	4 (*R*)
3	100 (*S*)	87 (*R*)	50 (*R*)	40 (*S*)	24 (*S*)	27 (*R*)	5 (*S*)	6 (*R*)
4	48 (*S*)	59 (*R*)	37 (*R*)	30 (*S*)	100 (*S*)	89 (*R*)	26 (*S*)	22 (*R*)
5	30 (*S*)	17 (*R*)	13 (*R*)	19 (*S*)	27 (*S*)	20 (*R*)	11 (*S*)	10 (*R*)

[a]Average values of three runs.

TABLE 2. Lipase catalyzed hydrolyses of methyl 2-(4-chlorophenoxy)propionate. Optimization of enantiomeric excess via condition control

Conditions (for a 50-mL solution)	Recovered ester (% ee)[a]
Phosphate buffer pH 7.00	44
Phosphate buffer pH 8.00	64
Borate buffer pH 8.00	69
Borate buffer pH 8.00	
NaCl (4 mmol)	59
$CaCl_2$ (0.06 mmol)	55
NaCl (4 mmol), $CaCl_2$ (0.03 mmol)	59
NaCl (4 mmol), $CaCl_2$ (0.06 mmol)	70
NaCl (4 mmol), $CaCl_2$ (0.09 mmol)	100
NaCl (4 mmol), $CaCl_2$ (0.12 mmol)	64
NaCl (4 mmol), $CaCl_2$ (0.15 mmol)	59

[a]Average values of three runs.

brief treatment with sodium methoxide in methanol. The corresponding acids can be recycled by esterification prior to racemization by using the same procedure.

The *R* enantiomers are better substrates for α-chymotrypsin and this stereoselectivity can be rationalized in terms of Cohen's active site model (13) as shown in Fig. 1. When the α-NHR group of an amino acid ester substrate is replaced by a new group like a methyl group, the L-enantiomers (*R*) bind as shown with the usual ar-aryl group and n-ester interactions unchanged. The methyl group is too large to fit the restricted h-site and only the L-isomer (*R*) is readily hydrolyzed. Although the methyl group can be accommodated at the am-site, it does not bind there because there is no formation of hydrogen bond, as occurs when the substituent is an amino group. It is noteworthy that the selectivity of subtilisin is different from that of chymotrypsin. Both serine proteases have a similar active center and often have the same stereoselectivity, the substrate specificity of subtilisin being broader than that of chymotrypsin. Lipase and esterase have an *R* stereoselectivity like chymotrypsin. No well-defined active site models are available for these enzymes. However, several studies have shown that a better enantioselectivity is obtained when the acid component of the ester is larger than an *n*-propyl group or when the alcohol component of the ester is a methyl or a small group (2*d*, 14). We found that the enantioselectivity decreases when the methyl group in chlorophenoxypropionates is replaced by an ethyl or an *n*-propyl group.

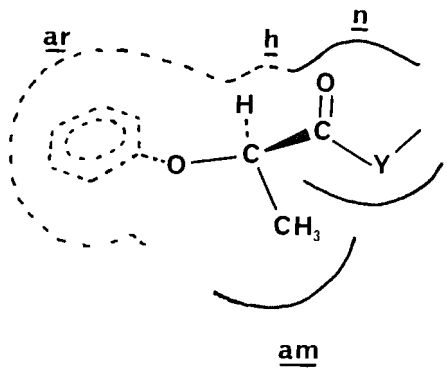

FIG. 1. Schematic representation of the binding of an L-phenoxypropionate in the active site of α-chymotrypsin.

Experimental

α-Chymotrypsin (E.C. 3.4.21.1, type II), subtilisin (E.C. 3.4.21.14, Carlsberg, protease type VIII), lipase (E.C. 3.1.1.13, type VII), and esterase (E.C. 3.1.1.1, porcine liver) were purchased from Sigma. Phenoxypropionic acids and $Eu(hfc)_3$ were purchased from Aldrich. The nmr studies were performed on a Varian XL-200 spectrometer. Optical rotations were measured with a Jasco DIP-360 digital polarimeter. Elemental analyses were carried out in a Carlo Erba Strumentazione-1106 apparatus.

Esterification of phenoxypropionic acids, general procedure

The acid (0.125 mol), 2,2-dimethoxypropane (0.185 mol), and a catalytic amount of *p*-toluenesulfonic acid (15 mg) were dissolved in dry methanol (0.185 mol). The solution was stirred magnetically for 4 h at 55°C under a dry atmosphere. Acetone and methanol were evaporated and the crude ester was distilled under reduced pressure (~1 Torr; 1 Torr = 133.3 Pa). The yields were in the range 70–100%. *Methyl 2-phenoxypropionate* (**1**): bp 75–76°C (0.65 Torr); ir (neat) ν_{max}: 3100–3000, 2960, 1765, 1740, 1300–1055 cm^{-1}; ^1H nmr δ: 1.62 (3H, d, J = 7 Hz), 3.74 (3H, s), 4.77 (1H, q, J = 7 Hz), 6.84–6.91 (2H, m), 6.93–7.01 (1H, m), 7.22–7.32 (2H, m); ^{13}C nmr δ: 18.54, 52.19, 72.36, 114.85, 121.40, 129.35, 157.27, 172.44; ms *m/e* (rel. intensity): 180 (39, M^+), 121 (100), 77(39). *Anal.* calcd. for $C_{10}H_{12}O_3$: C 66.65, H 6.71; found: C 66.37, H 6.62%. *Methyl 2-(2-chlorophenoxy)propionate* (**2**): bp 97–98°C (0.70 Torr); ir (neat) ν_{max}: 3070, 3000, 2960, 1760, 1295–1045, 750 cm^{-1}; ^1H nmr δ: 1.67 (3H, d, J = 7 Hz), 3.74 (3H, s), 4.77 (1H, q, J = 7 Hz), 6.84 (1H, dd, J_o = 8 Hz, J_m = 2 Hz), 6.92 (1H, td, J_o = 8 Hz, J_m = 2 Hz), 7.16 (1H, td, J_o = 8 Hz, J_m = 2 Hz), 7.36 (1H, dd, J_o = 8 Hz, J_m = 2 Hz); ^{13}C nmr δ: 19.08, 52.90, 74.56, 115.71, 123.08, 124.26, 128.08, 131.01, 153.76, 172.44; ms *m/e* (rel. intensity): 214 (60, M^+), 155 (100), 128 (72). *Anal.* calcd. for $C_{10}H_{11}O_3Cl$: C 55.96, H 5.17; found: C 55.72, H 5.01%. *Methyl 2-(3-chlorophenoxy)propionate* (**3**): bp 89–90°C (0.65 Torr); ir (neat) ν_{max}: 3080, 3000, 2960, 1760, 1740, 1280–1050 cm^{-1}; ^1H nmr δ: 1.61 (3H, d, J = 7 Hz), 3.75 (3H, s), 4.74 (1H, q, J = 7 Hz),

Can. J. Chem. Downloaded from www.nrcresearchpress.com by 93.93.197.157 on 09/07/12
For personal use only.

TABLE 3. Enzymatic hydrolyses of phenoxyesters: reaction times and yields[a]

Substrate	Enzyme	Reaction time (h)	Recovered ester, % yield	Acid product, % yield
1	α-Chymotrypsin	22	94	81
	Subtilisin	23	76	99
	Lipase	10	79	96
	Esterase	5	82	96
2	α-Chymotrypsin	42	93	77
	Subtilisin	94	90	99
	Lipase	36	77	95
	Esterase	10	90	95
3	α-Chymotrypsin	29	75	78
	Subtilisin	70	78	93
	Lipase	10	82	95
	Esterase	6	76	98
4	α-Chymotrypsin	36	85	71
	Subtilisin	25	77	72
	Lipase	12	99	98
	Esterase	5	78	96
5	α-Chymotrypsin	50	92	94
	Subtilisin	160	94	93
	Lipase	160	83	92
	Esterase	13	74	95

[a]Average values of three runs.

6.74 (1H, ddd, J_o = 8 Hz, J_m = 2 Hz, 1 Hz), 6.87 (1H, t, J_m = 2 Hz), 6.96 (1H, ddd, J_o = 8 Hz, J_m = 1 Hz), 7.18 (1H, t, J_o = 8 Hz); ^{13}C nmr δ: 18.45, 52.33, 72.54, 113.07, 115.56, 121.64, 130.17, 134.74, 158.00, 171.90; ms *m/e* (rel. intensity): 214 (43, M^+), 157 (31), 155 (100). *Anal.* found. for $C_{10}H_{11}O_3Cl$: C 55.75, H 5.06%. *Methyl 2-(4-chlorophenoxy)propionate* (**4**): bp 100–101°C (1.50 Torr); ir (neat) ν_{max}: 3100–3000, 2960, 1760, 1745, 1285–1050, 825, 665 cm^{-1}; ^{1}H nmr δ: 1.58 (3H, d, J = 7 Hz), 3.72 (3H, s), 4.70 (1H, q, J = 7 Hz), 6.77 (2H, AA'XX', J_A = 3 Hz, J_X = 3 Hz, J_o = 9 Hz), 7.19 (2H, AA'XX', J_A = 3 Hz, J_X = 3 Hz, J_o = 9 Hz); ^{13}C nmr δ: 18.46, 52.30, 72.71, 116.24, 126.31, 129.26, 155.93, 172.04; ms *m/e* (rel. intensity): 214 (58, M^+), 155 (100), 128 (66). *Anal.* found. for $C_{10}H_{11}O_3Cl$: 55.69, H 4.98%. *Methyl 2-(2,4-dichlorophenoxy)propionate* (**5**): bp 110–111°C (1.10 Torr); ir (neat) ν_{max}: 3100–3000, 2955, 1760, 1285–1045, 865, 800 cm^{-1}; ^{1}H nmr δ: 1.64 (3H, d, J = 7 Hz), 3.73 (3H, s), 4.71 (1H, q, J = 7 Hz), 6.75 (1H, d, J_o = 9 Hz), 7.10 (1H, dd, J_o = 9 Hz, J_m = 3 Hz), 7.34 (1H, d, J_m = 3 Hz); ^{13}C nmr δ: 18.41, 52.41, 74.25, 115.95, 124.59, 126.90, 127.37, 130.10, 152.02, 171.50; ms *m/e* (rel. intensity): 248 (25, M^+), 162 (100), 135 (36). The physical properties and spectroscopic data of compound **5** were compared to those in the literature (15).

This esterification procedure has been used for the preparation of the substrates and esterification of product acids prior to the determination of their optical purities by nmr spectroscopy.

Enzyme-catalysed hydrolyses of phenoxyesters, general procedure

The ester (5 or 6 mmol) was suspended in a buffered aqueous solution (50 mL) at room temperature (20°C). The enzyme was added and the pH was maintained at its initial value by addition of 0.1 M aqueous NaOH from a burette. The reaction was stopped at the 50%-of-hydrolysis point. The mixture was first extracted at initial pH with ether (3 × 50 mL) to remove the unchanged ester. The aqueous mixture was then acidified to pH 2.0 with 2 M hydrochloric acid and was again extracted with ether (3 × 50 mL) to remove the product acid. The ether extracts were dried on magnesium sulfate and evaporated. Details pertaining to each enzyme are the following: α-chymotrypsin: substrate (5 mmol), enzyme (200 mg), solvent (phosphate buffer, pH 7.00); subtilisin: substrate (6 mmol), enzyme (15 mg), solvent (phosphate buffer, pH 7.70); lipase: substrate (5 mmol), enzyme (70 mg), solvent (phosphate buffer, pH 8.00, 10 mmol NaCl, 0.15 mmol $CaCl_2$); esterase: substrate (5 mmol), enzyme (200 units), solvent (borate buffer, pH 8.00, 10 mmol NaCl, 0.15 mmol $CaCl_2$). Reaction times and yields are reported in Table 3.

Racemization of methyl esters

A small amount of sodium (23 mg, 1 mmol) was added to 25 mL of dry methanol. When all the sodium had reacted, the optically active ester (5 mmol) was added and the solution was stirred under reflux for 30 min. After cooling to room temperature, most of the methanol was evaporated and water was added. The aqueous phase was extracted with ether and the ethereal solution was dried over magnesium sulfate and evaporated. The remainder was optically inactive (checked by nmr analysis in the presence of Eu(hfc)$_3$) and the yields were higher than 90%.

Acknowledgements

We acknowledge the financial support of this work by the Natural Sciences and Engineering Research Council of Canada and the Ministère de l'éducation du Québec.

1. (*a*) J. B. JONES. Tetrahedron, **42**, 3351 (1986); (*b*) G. M. WHITESIDES and C. H. WONG. Angew. Chem. Int. Ed. Engl. **24**, 617 (1985); (*c*) A. R. BATTERSBY. Chem. Br. **20**, 611 (1984); (*d*) A. M. KLIBANOV. Science, **219** 722 (1983); (*e*) G. M. WHITESIDES and C. H. WONG. Aldrichimica Acta, **16**, 27 (1983).
2. (*a*) S. RAMASWAMY, R. A. H. F. HUI, and J. B. JONES. J. Chem. Soc. Chem. Commun. 1545 (1986); (*b*) G. KIRCHNER, M. P. SCOLLAR, and A. M. KLIBANOV. J. Am. Chem. Soc. **107**, 7072 (1985); (*c*) M. SCHNEIDER, N. ENGEL, and H. BOENSMANN. Angew. Chem. Int. Ed. Engl. **23**, 64 (1984); (*d*) W. E. LADNER and G. M. WHITESIDES. J. Am. Chem. Soc. **106**, 7250 (1984).
3. (*a*) D. BREIGOFF, K. LAUMEN, and M. P. SCHNEIDER. J. Chem. Soc. Chem. Commun. 1523 (1986); (*b*) J. B. JONES, R. S. HINKS, and P. G. HULTIN. Can. J. Chem. **63**, 452 (1985); (*c*) F. BJORKLING, J. BOUTELJE, S. GATENBECK, K. HULT, T. NORIN, and P. SZMULIK. Tetrahedron, **41**, 1347 (1985); (*d*) Y. F. WANG,

Can. J. Chem. Downloaded from www.nrcresearchpress.com by 93.93.197.157 on 09/07/12
For personal use only.

C. S. CHEN, G. GIRDAUKAS, and C. J. SIH. J. Am. Chem. Soc. **106**, 3695 (1984).
4. R. CREMLYN. Pesticides. Preparation and mode of action. Wiley, Chichester. 1978. p. 143.
5. (*a*) H. KATOH, S. NAKAJIMA, Y. KAWASHIMA, H. KOZUKA, and M. UCHIYAMA. Biochem. Pharmacol. **33**, 1081 (1984); (*b*) T. F. WHAYNE and D. T. WITIAK. J. Med. Chem. **16**, 228 (1973).
6. B. D. HAMMOCK, E. KURVANO, A. KETTERMAN, R. H. SCHEFFRAHN, S. N. THOMPSON, and D. SALLUME. J. Agric. Food Chem. **26**, 166 (1978).
7. Y. G. PERRON, W. F. MINOR, C. T. HOLDREGE, W. J. GOTTSTEIN, J. C. GODFREY, L. B. CRAST, R. B. BABEL, and L. C. CHENEY. J. Am. Chem. Soc. **82**, 3934 (1960).
8. (*a*) C. R. WORTHING. The pesticide manual. 6th ed. BCPC Publication, London. 1979. p. 329; (*b*) A. FREDGA, A. M. WEIDLER, and C. GRÖNWALL. Ark. Kemi, **17**, 265 (1960).
9. (*a*) M. MATELL. Ark. Kemi, **4**, 473 (1952); (*b*) D. T. WITIAK, T. C. L. HO, R. E. HACKNEY, and W. E. CONNOR. J. Med. Chem. **11**, 1086 (1968); (*c*) W. J. GOTTSTEIN and L. C. CHENEY. J. Org. Chem. **30**, 2072 (1965).
10. B. CAMBOU and A. M. KLIBANOV. Biotechnol. Bioeng. **26**, 1449 (1984).
11. (*a*) P. DESNUELLE. *In* The enzymes. Vol. VII. *Edited by* P. O. Boyer. Academic Press, New York. 1972. Chap. 19; (*b*) H. BROCKERHOFF. Lipolytic enzymes. Academic Press, New York. 1974. Chap. 4.
12. C. S. CHEN, Y. FUJIMOTO, G. GIRDAUKAS, and C. J. SIH. J. Am. Chem. Soc. **104**, 7294 (1982).
13. (*a*) S. G. COHEN. Trans. N.Y. Acad. Sci. **31**, 705 (1969); (*b*) A. R. FERSHT, D. M. BLOW, and J. FASTREZ. Biochemistry, **12**, 2035 (1973); (*c*) J. B. JONES and J. F. BECK. Applications of biochemical systems in organic chemistry. *Edited by* J. B. Jones, C. J. Sih, and D. Perlman. Wiley, New York. 1976. p. 107.
14. (*a*) E. GUIBÉ-JAMPEL, G. ROUSSEAU, and J. SALAÜN. J. Chem. Soc. Chem. Commun. 1080 (1987); (*b*) Q. M. GU, C. S. CHEN, and C. J. SIH. Tetrahedron Lett. **27**, 1763 (1986).
15. C. H. VAN PETEGHEM and A. M. HEYNDRICKX. J. Assoc. Off. Anal. Chem. **58**, 1001 (1975).

Can. J. Chem. Downloaded from www.nrcresearchpress.com by 93.93.197.157 on 09/07/12
For personal use only.

Conductivity and ionic association of tetraalkylammonium halides in *tert*-butanol–water mixture at 25°C

AIJAZ AHMAD ANSARI[1] AND M. R. ISLAM[2]
Department of Chemistry, Aligarh Muslim University, Aligarh-202001, India

Received July 23, 1987[3]

AIJAZ AHMAD ANSARI and M. R. ISLAM. Can. J. Chem. **66**, 1223 (1988).

The molar conductivities of Pr_4NBr, Bu_4NBr, Pr_4NI, and Bu_4NI have been measured in *tert*-butanol–water (*t*-BuOH–H_2O) mixtures ($61.30 \geq D \geq 16.50$) over the maximum concentration range ($2 \times D^3 \times 10^{-7}$ mol dm^{-3}) along with the densities and viscosities of the solvent mixtures at 25°C. The conductance data have been analysed by using the Fuoss-1978 (F78) conductance equation and the results compared with the values obtained from the Justice (J), Pitt's (P), and Fuoss–Onsager–Skinner (FOS) equations. Molar conductivities at infinite dilution (Λ_0), the thermodynamic ion association constants (K_A) and the distance or ion-size parameters (R^0 or a^0) are evaluated from these data. The F78 equation fitted the data better and yielded K_A and R values which are in accord with the ion-association theories. The interpretation of these parameters is discussed to provide some insight on the magnitude of the ionic association and the ion–solvent interaction.

AIJAZ AHMAD ANSARI et M. R. ISLAM. Can. J. Chem. **66**, 1223 (1988).

Opérant à 25°C et dans des mélanges de *tert*-butanol/eau (*tert*-BuOH/H_2O), ($61.30 \geq D \geq 16.50$), on a mesuré les conductivités molaires du Pr_4NBr, du Bu_4NBr, du Pr_4NI et du Bu_4NI sur un éventail maximal de concentrations ($2 \times D^3 \times 10^{-7}$ mol dm^{-3}); on a aussi déterminé les densités et les viscosités des mélanges de solvant. On a analysé les données de conductance à l'aide de l'équation de conductance de Fuoss-1978 (F78) et on a comparé les résultats aux valeurs obtenues à l'aide des équations de Justice (J), de Pitt (P) et de Fuoss–Onsager–Skinner (FOS). Utilisant ces données, on a évalué les conductivités molaires à dilution infinie (Λ_0), les constantes thermodynamiques d'association ionique (K_A) ainsi que les paramètres de distance ou de grosseur ionique (R^0 ou a^0). La meilleure corrélation est obtenue à l'aide de l'équation F78 et elle fournit des valeurs de K_A et de R qui sont en accord avec les théories d'association ionique. Dans le but de comprendre l'amplitude de l'association ionique et de l'interaction ion–solvant, on discute de l'interprétation de ces paramètres.

[Traduit par la revue]

Introduction

In investigating the electrical conductances of dilute electrolytic solutions in various pure and mixed solvents (1–3) the concentration–conductance data have been adequately explained by the Fuoss–Onsager equation (4) using ion–ion and ion–solvent interactions. The magnitude and nature of such interactions have been interpreted in terms of the limiting molar conductance, the ion-size parameter, and the ionic-association constant. The solvent properties like viscosity and dielectric constant have also been taken into account in determining the extent of such interactions. However, the implication of precise conductance data to the above has revealed the discrepancy between the parameters calculated using experimental data and those derived theoretically. Consequently, the Fuoss–Hsia equation (5) emerged as one of the equations which succeeded in explaining the conductance behaviour. Although Justice (6) extended this equation for long-range interactions by including the higher order concentration terms, its unique solution does not give reasonable values for the ion-size parameter in higher dielectric constant medium. While Fuoss primitive model (7) based on the formation of contact-ion-pair has been applied to 1:1 electrolytes, which are either unassociated or associated in dilute solutions, but discarded later on as the short-range interactions were counted twice. Finally, Fuoss (8, 9) proposed the theory of diffusion-controlled steady state which has two main features: (*a*) the unpaired ions surrounded by only solvent molecules within their Gurney cosphere diameter and (*b*) the paired ions within their cosphere, which are of two catagories, viz., those whose next neighbours are solvent molecules behave as a dipole while those whose next neighbours are ions of opposite charge give rise to the formation of contact ion-pairs contributing only to charging current.

The anomalous physical properties of *t*-BuOH–H_2O mixtures have attracted much attention, and there are numerous thermodynamic data available in the literature (10–13) in comparison with other alcohol–water mixtures. Of these, the differential heats of dilution could provide direct information about the energetics of the solute–solute interaction, or the hydrophobic interaction. It would, therefore, be worthwhile to undertake the measurement of electrical conductance of tetraalkylammonium halides in *t*-BuOH–H_2O mixtures in order to examine the suitability of F78 conductance equation over those of the Justice (14), Pitt's (15, 16), and FOS (17) conductance equations to provide a better understanding of the mechanism of the observed conductivity behaviour of associated and unassociated electrolytes.

Experimental

Reagent grade *t*-BuOH (E. Merck) was purified (18) until the measured density, 0.7808 g cm^{-3} viscosity, 4.462 cP, and specific conductance ($0.5–2 \times 10^{-8}$ ohm^{-1} cm^{-1} at 25°C were found to be comparable with those of the corresponding literature values (19). This freshly purified solvent was used for the preparation of the solvent mixtures with triply distilled water (sp. conductance, 2.3×10^{-6} ohm^{-1} cm^{-1}). The density and viscosity measurements of solvent mixtures were made with an accuracy of ±0.002% and ±0.13%, respectively, as reported earlier (20). Pr_4NBr (Fluka, AG), Pr_4NI, Bu_4NBr, and Bu_4NI (Estman, AG) were used as solute.

Conductance measurements were carried out by Impedence Bridge, 1608-A (General Radio & Co., U.S.A.) at a constant frequency of 1 kHz with a stated accuracy of ±0.05–0.005%. Other apparatus and procedure used for conductance measurements have been described elsewhere (21, 22). The overall reproducibility of the conductance measurement was found to be ±0.025%.

The solvent mixtures and solutions were prepared under pure and dry

[1]Author to whom correspondence should be addressed.

[2]Present address: Department of Chemistry, University of Kashmir, Srinagar (J. & K.), India.

[3]Revision received December 15, 1987.

Can. J. Chem. Downloaded from www.nrcresearchpress.com by 93.93.197.157 on 09/07/12
For personal use only.

TABLE 1. Physical properties of t-BuOH–H_2O mixtures at 25°C

Wt% of t-BuOH	ρ (g cm^{-3})	η (cP)	D	q^* (A°)
10	0.9818	1.5056	70.0	3.82
20	0.9672	2.3089	61.30	4.57
30	0.9447	3.1234	52.50	5.25
40	0.9223	3.7967	43.90	6.38
50	0.9003	4.3113	35.40	7.94
60	0.8764	4.7147	27.50	10.18
70	0.8528	4.8353	21.40	13.09
80	0.8288	4.7302	16.50	16.98
90	0.8045	4.3552	12.40	—
100	0.7808	4.4618	9.90	—
	(0.78053)†	(4.5200)†		

*Bjerrum distance.
†Reference 19.

nitrogen atmosphere in a dry box. The dielectric constants of the solvent mixtures used for analysis were taken from the literature (23).

Results and discussion

The physical properties of the solvents used are listed in Table 1. The molar conductivities, Λ (Ω^{-1} cm^2 mol^{-1}) of Pr_4NBr, Bu_4NBr, Pr_4NI, and Bu_4NI in t-BuOH–H_2O mixtures of different compositions are given in Table 2 as a function of concentration, C (mol dm^{-3}) at 25°C.

The concentration dependence of conductance data for all salts have been first analysed in terms of F78 conductance equation (8, 9) which gives three adjustable parameters Λ_0, K_A, and R by the following set of equations:

$$[1] \quad \Lambda = [1 - \alpha(1 - \gamma)][\Lambda_0(1 + RX) + EL]$$

$$[2] \quad K_R = (1 - \alpha)(1 - \gamma)/C\gamma^2 f^2 = (4\pi NR^3/3000)\exp(\beta/R)$$

$$[3] \quad K_S = \alpha/(1 - \alpha)$$

$$[4] \quad K_A = 1 - \gamma/C\gamma^2 f^2 = K_R/(1 - \alpha)$$

and the activity coefficient, f, is given by

$$[5] \quad -\ln f = \beta\kappa/2(1 + \kappa R)$$

Here R is the Gurney cosphere diameter (24) and RX and EL are the relaxation and hydrodynamic terms, respectively. Other terms have their usual significance. Details of computational methods are given elsewhere (21, 22).

Similarly, each set of conductance data has been analysed using Justice's modification (14) of the Fuoss–Hsia equation (5), and constants derived by Fernandez–Prini (25). The Fuoss–Hsia equation is given by

$$[6] \quad \Lambda = \Lambda_0 - S(\alpha C)^{1/2} + E\alpha C \ln(\alpha C) + J_1\alpha C - J_2(\alpha C)^{3/2} - \Lambda\alpha C f_\pm^2 K_A$$

where α is the degree of dissociation, $f_\pm$ is the mean molar activity coefficient, and all other terms have their usual significance. The thermodynamic association constant is defined by

$$[7] \quad K_A = (1 - \alpha)/\alpha^2 C f_\pm^2$$

where the activity coefficient for the neutral ion pair is taken as unity. Activity coefficients were calculated from the Debye–Hückel equation

$$[8] \quad \ln f_\pm^2 = -A(\alpha C)^{1/2}/\{1 + BR_j(\alpha C)^{1/2}\}$$

As proposed by Justice (14), the distance parameter, R_j in eq. [8] has been taken as the Bjerrum distance, q. The calculation of eq. [6] has been carried out by a pit-mapping method (26) in which Λ_0, R_j, and K_A are varied until a minimum is located for the standard error of estimate. This latter quantity, σ_Λ is defined by

$$[9] \quad \sigma_\Lambda = \{\Sigma(\Lambda_{obs} - \Lambda_{calc})^2/(N - 3)\}^{1/2}$$

The set of conductance data analysed using F78 and J equations has also been analysed using Pitt's (P) equation (15, 16),

$$[10] \quad \Lambda = \left[\Lambda_0 - \frac{Z^2e^2\kappa}{(1 + \kappa a)}\left(\frac{N\,10^9}{3\pi\eta_0 C^2}\right)\right] \times \left[1 - \frac{Z^2e^2\kappa}{3DkT(1 + \sqrt{2})(1 + \kappa a)(\sqrt{2} + \kappa a)}\right] - \frac{Z^4e^4\kappa^2}{3D^2k^2T^2}\left[\Lambda_0 S_1 - \frac{T_i}{(1 + \kappa a)}\left(\frac{NDkT\,10^9}{3\pi\eta_0 C^2}\right)\right]$$

where $q = Z^2e^2\kappa/DkT$, $\kappa^2 = 8\pi nZ^2e^2/DkT$, and n = number of positive and negative charges, N is Avogadro's Number, η_0 is the solvent viscosity, C is the velocity of light, a is the ion-size parameter, and other symbols have their usual meaning.

In the same way, each set of conductance data was then analysed by using FOS equation (17).

$$[11] \quad \Lambda = \Lambda_0 - S(C\gamma)^{1/2} + EC\gamma\log(6E'_1C\gamma) + LC\gamma - K_AC\gamma f_\pm^2\Lambda$$

for associated electrolytes. The symbols used have their usual meaning. The least-squares method have been used for calculation as proposed by Kay (27, 28).

The values of the best-fit parameters of the limiting molar conductance, Λ_0, association constant, K_A, and the distance parameter, R, or ion-size parameter, a^0, along with σ_Λ% thus computed which correspond to minimum standard deviation from F78, J, P and FOS conductance equations are recorded in Table 3(*a*) to (*d*) respectively. All calculations have been carried out on a VAX-11/780 computer.

A comparison of different available conductance equations has been made here with respect to their applicability to the measured conductances. The values of Λ_0 obtained for all the salts through the F78 and J methods of treatment of conductance data are found to be almost close to each other with an average deviation of $\sim\pm0.02$% while those obtained by using the P and the FOS conductance equations have an average deviation of $\sim\pm0.06$% and $\sim\pm0.11$%, respectively. An inspection of Table 3 reveals an apparently normal behaviour of tetraalkylammonium salts in the various solvent mixtures, i.e., Λ_0 decreases with increasing size of the tetraalkylammonium ions in the order $Pr_4\overset{+}{N} > Bu_4\overset{+}{N}$ and with decreasing dielectric constant of the solvent mixtures. This is in agreement with the earlier findings (1, 2, 21, 22, 26–30) in several pure and mixed solvents and can be attributed to the size and hydrophobic solvation of cations which increase in the order $Me_4\overset{+}{N} < Et_4\overset{+}{N} < Pr_4\overset{+}{N} < Bu_4\overset{+}{N}$, so that the mobility should be in the reverse order.

The computed values of association constant, K_A, obtained for all the salts under study through F78 equation (Table 3*a*) are 30%, 43.2%, and 48.8% higher than those obtained from J (Table 3*b*), P (Table 3*c*), and FOS (Table 3*d*) equations, respec-

Can. J. Chem. Downloaded from www.nrcresearchpress.com by 93.93.197.157 on 09/07/12
For personal use only.

TABLE 2. Molar conductivities, Λ (Ω^{-1} cm^2 mol^{-1}) and molar concentrations, C (mol dm^{-3}) of Pr_4NBr, Bu_4NBr, Pr_4NI, and Bu_4NI in t-BuOH–H_2O mixtures at 25°C

Pr_4NBr		Bu_4NBr		Pr_4NI		Bu_4NI	
$C/10^{-4}$	Λ	$C/10^{-4}$	Λ	$C/10^{-4}$	Λ	$C/10^{-4}$	Λ
			20 Wt% t-BuOH+H_2O				
437.500	38.674	292.573	37.567	471.503	34.800	409.008	32.390
349.960	39.960	248.680	38.454	377.503	36.062	327.207	33.780
291.633	40.980	198.949	39.618	269.430	37.895	233.719	35.780
218.724	42.490	142.106	41.242	209.556	39.178	181.781	37.194
174.979	43.685	110.526	42.344	188.600	39.692	148.729	38.272
145.815	44.426	90.430	43.156	157.166	40.550	111.546	39.610
109.361	45.650	77.511	43.730	117.873	41.802	89.236	40.730
87.488	46.506	67.822	44.210	99.261	42.490	74.363	41.500
72.906	47.150	54.257	44.930	85.725	43.040	63.739	42.110
62.490	47.652			78.581	43.352		
			40 Wt% t-BuOH + H_2O				
156.231	25.993	127.790	27.260	155.520	25.780	151.923	23.365
112.485	27.114	108.629	27.872	124.416	26.400	129.134	23.890
93.737	27.686	86.903	28.670	105.753	26.815	103.307	24.596
70.302	28.528	72.419	29.230	88.127	27.265	86.089	25.140
56.241	29.140	54.314	30.190	66.095	27.920	64.566	25.945
46.867	29.600	43.451	30.820	49.571	28.520	48.424	26.676
35.150	30.250	36.209	31.304	39.656	28.930	38.739	27.189
28.120	30.690	27.156	31.980	28.375	29.485	27.670	27.865
			60 Wt% t-BuOH + H_2O				
37.555	17.432	41.496	16.102	41.213	16.650	41.691	16.986
27.039	17.930	29.877	16.636	29.672	17.205	30.017	17.684
19.313	18.402	24.897	16.915	21.193	17.713	21.440	18.336
15.021	18.712	18.672	17.314	16.483	18.060	16.675	18.778
11.265	19.030	14.004	17.676	13.186	18.335	13.340	19.140
9.012	19.250	11.203	17.930	9.418	18.712	9.528	19.624
6.437	19.548	8.002	18.270	7.325	18.945	7.410	19.940
5.006	19.733	6.223	18.485	5.860	19.142	5.928	20.190
4.095	19.870	5.091	18.624	4.185	19.397	4.234	20.510
		4.307	18.765				
			70 Wt% t-BuOH + H_2O				
17.181	14.485	17.790	12.900	17.629	14.180	16.530	13.330
14.603	14.752	15.121	13.170	14.984	14.472	14.050	13.606
11.682	15.090	12.096	13.522	11.987	14.860	11.240	13.977
9.735	15.350	10.080	13.795	9.989	15.150	9.366	14.270
7.301	15.730	8.640	14.015	7.491	15.582	7.024	14.696
5.840	15.986	6.720	14.346	5.992	15.890	5.619	15.003
4.866	16.200	5.498	14.588	5.243	16.060	4.682	15.230
3.649	16.470	4.651	14.776	4.194	16.324	3.511	15.541
			80 Wt% t-BuOH + H_2O				
8.678	9.975	8.825	9.485	8.844	11.385	8.717	10.775
7.818	10.160	7.501	9.765	7.517	11.710	7.845	10.980
6.254	10.530	6.000	10.120	6.013	12.140	6.276	11.390
5.211	10.833	5.000	10.410	5.010	12.475	5.230	11.720
4.466	11.070	4.285	10.640	4.294	12.750	4.482	11.980
3.907	11.272	3.749	10.835	3.757	12.975	3.486	12.390
3.125	11.590	2.999	11.144	3.005	13.336	3.137	12.555
2.604	11.830	2.499	11.380	2.504	13.610	2.614	12.824

Can. J. Chem. Downloaded from www.nrcresearchpress.com by 93.93.197.157 on 09/07/12
For personal use only.

tively. This uncertainty stems purely from the ambiguities in the theories and at present it is not possible to suggest the superiority of one equation over that of the other. An inspection of Table 3 shows that the K_A values for Pr_4NBr, Bu_4NBr, Pr_4NI, and Bu_4NI are found to increase with decrease in the dielectric constant of the medium (21, 22). However, the association constants obtained for Pr_4NBr and Bu_4NBr from F78 and J equations and to those of Pr_4NI and Bu_4NI from F78, J, P, and FOS conductance equations in t-BuOH–H_2O mixtures are an exponential function of the dielectric constant of the medium as is evident from the linear plots of log K_A vs. $1/D$ (Fig. 1). But, on the other hand, we get a concave curve for Pr_4NBr and Bu_4NBr when K_A obtained from P and FOS equations which is beyond explanation and also is contrary to the Justice–Bjerrum theory.

Furthermore, a perusal of Table 3 reveals that the K_A values

Can. J. Chem. Downloaded from www.nrcresearchpress.com by 93.93.197.157 on 09/07/12
For personal use only.

TABLE 3. (*a*) Best-fit parameters for Pr_4NBr, Bu_4NBr, Pr_4NI, and Bu_4NI in *t*-BuOH–H_2O mixtures at 25°C using the F78 conductance equation

Salt	Λ_0 (Ω^{-1} cm^2 mol^{-1})	K_A (dm^3 mol^{-1})	R (A°)	σ_Λ%
		20 Wt% *t*-BuOH		
Pr_4NBr	53.10±0.030	15.78	6.84	0.05
Bu_4NBr	50.17±0.006	19.18	7.45	0.01
Pr_4NI	49.61±0.005	18.90	7.85	0.008
Bu_4NI	48.74±0.040	26.70	8.44	0.06
		40 Wt% *t*-BuOH		
Pr_4NBr	34.01±0.007	35.28	8.46	0.01
Bu_4NBr	35.71±0.030	43.40	9.24	0.06
Pr_4NI	32.21±0.007	27.07	8.56	0.01
Bu_4NI	31.10±0.005	40.85	9.38	0.01
		60 Wt% *t*-BuOH		
Pr_4NBr	21.01±0.002	193.88	13.78	0.01
Bu_4NBr	19.94±0.005	113.38	15.52	0.03
Pr_4NI	20.59±0.003	115.07	15.80	0.01
Bu_4NI	21.98±0.002	149.22	16.25	0.01
		70 Wt% *t*-BuOH		
Pr_4NBr	18.06±0.006	247.36	16.44	0.02
Bu_4NBr	16.67±0.001	313.03	18.60	0.004
Pr_4NI	18.25±0.004	296.42	16.84	0.01
Bu_4NI	17.29±0.009	326.73	17.25	0.03
		80 Wt% *t*-BuOH		
Pr_4NBr	14.15±0.007	948.16	19.78	0.02
Bu_4NBr	13.61±0.006	997.12	20.98	0.02
Pr_4NI	16.19±0.005	955.73	19.48	0.01
Bu_4NI	15.38±0.005	981.51	19.85	0.01

(*b*) Best-fit parameters for Pr_4NBr, Bu_4NBr, Pr_4NI, and Bu_4NI in *t*-BuOH–H_2O mixtures at 25°C using the J conductance equation

Salt	Λ_0 (Ω^{-1} cm^2 mol^{-1})	K_A (dm^3 mol^{-1})	R_j (A°)	σ_Λ%
		20 Wt% *t*-BuOH		
Pr_4NBr	53.04±0.036	10.59	3.99	0.05
Bu_4NBr	50.21±0.006	13.73	2.60	0.03
Pr_4NI	49.58±0.003	12.43	3.50	0.006
Bu_4NI	48.59±0.045	18.64	2.96	0.08
		40 Wt% *t*-BuOH		
Pr_4NBr	33.99±0.006	24.62	5.88	0.01
Bu_4NBr	35.78±0.024	32.69	5.40	0.05
Pr_4NI	32.24±0.005	17.09	5.83	0.01
Bu_4NI	31.10±0.003	28.43	5.41	0.009
		60 Wt% *t*-BuOH		
Pr_4NBr	21.01±0.002	52.58	10.06	0.009
Bu_4NBr	19.95±0.003	62.43	9.85	0.01
Pr_4NI	20.59±0.003	61.76	10.02	0.01
Bu_4NI	21.97±0.003	92.03	9.54	0.01
		70 Wt% *t*-BuOH		
Pr_4NBr	18.05±0.005	167.42	12.68	0.02
Bu_4NBr	16.67±0.001	214.95	11.87	0.005
Pr_4NI	18.25±0.002	217.19	11.60	0.01
Bu_4NI	17.32±0.006	250.70	10.09	0.03
		80 Wt% *t*-BuOH		
Pr_4NBr	14.10±0.003	763.88	15.52	0.02
Bu_4NBr	13.58±0.004	808.57	14.43	0.02
Pr_4NI	16.14±0.001	776.02	15.64	0.006
Bu_4NI	15.35±0.003	803.14	15.06	0.01

(*c*) Best-fit parameters for Pr_4NBr, Bu_4NBr, Pr_4NI, and Bu_4NI in *t*-BuOH–H_2O mixtures at 25°C using the P conductance equation

Salt	Λ_0 (Ω^{-1} cm^2 mol^{-1})	K_A (dm^3 mol^{-1})	a (A°)	σ_Λ%
		20 Wt% *t*-BuOH		
Pr_4NBr	52.82±0.043	8.71	2.51	0.09
Bu_4NBr	49.92±0.034	11.18	2.65	0.07
Pr_4NI	49.20±0.053	9.80	2.50	0.11
Bu_4NI	48.20±0.076	15.60	2.54	0.15
		40 Wt% *t*-BuOH		
Pr_4NBr	33.88±0.016	20.19	3.28	0.04
Bu_4NBr	35.56±0.042	26.16	3.24	0.10
Pr_4NI	32.13±0.016	12.65	3.42	0.05
Bu_4NI	30.96±0.022	22.99	3.28	0.06
		60 Wt% *t*-BuOH		
Pr_4NBr	20.98±0.004	39.16	5.50	0.03
Bu_4NBr	19.91±0.006	47.43	5.39	0.05
Pr_4NI	20.56±0.005	47.95	5.45	0.03
Bu_4NI	21.92±0.008	75.44	5.16	0.05
		70 Wt% *t*-BuOH		
Pr_4NBr	18.01±0.007	135.26	6.65	0.03
Bu_4NBr	16.60±0.007	173.99	6.43	0.03
Pr_4NI	18.18±0.009	174.99	6.39	0.04
Bu_4NI	17.23±0.015	199.42	6.42	0.07
		80 Wt% *t*-BuOH		
Pr_4NBr	14.05±0.008	670.54	7.76	0.03
Bu_4NBr	13.52±0.011	698.39	7.79	0.05
Pr_4NI	16.09±0.006	688.15	7.70	0.02
Bu_4NI	15.28±0.008	703.92	7.70	0.03

(*d*) Best-fit parameters for Pr_4NBr, Bu_4NBr, Pr_4NI, and Bu_4NI in *t*-BuOH–H_2O mixtures at 25°C using the FOS conductance equation

Salt	Λ_O (Ω^{-1} cm^2 mol^{-1})	K_A (dm^3 mol^{-1})	α (A°)	σ_Λ%
		20 Wt% *t*-BuOH		
Pr_4NBr	52.96±0.080	8.81	2.95	0.15
Bu_4NBr	50.15±0.040	12.92	4.14	0.07
Pr_4NI	49.50±0.040	10.99	3.40	0.08
Bu_4NI	48.54±0.166	17.92	4.20	0.32
		40 Wt% *t*-BuOH		
Pr_4NBr	33.94±0.020	18.74	3.36	0.05
Bu_4NBr	35.75±0.090	29.82	4.90	0.25
Pr_4NI	32.19±0.020	10.88	3.20	0.06
Bu_4NI	31.06±0.020	23.78	4.06	0.06

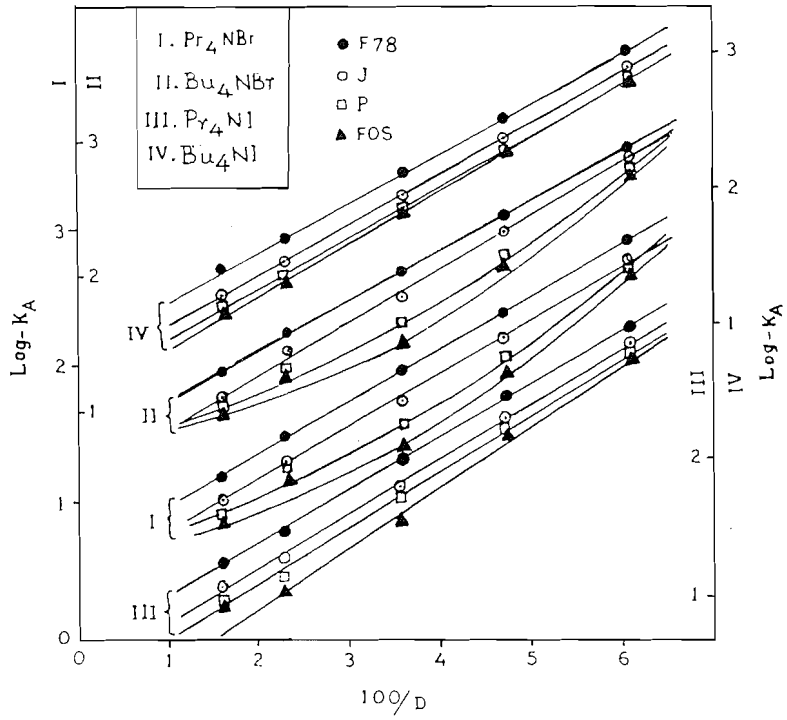

FIG. 1. Dependence of K_A on dielectric constant, D, in t-BuOH–H_2O mixtures at 25°C.

TABLE 3 (*concluded*)

Salt	Λ_O (Ω^{-1} cm^2 mol^{-1})	K_A (dm^3 mol^{-1})	a (A°)	σ_Λ%
		60 Wt% t-BuOH		
Pr_4NBr	20.99±0.004	25.07	4.22	0.02
Bu_4NBr	19.93±0.007	35.24	4.43	0.03
Pr_4NI	20.56±0.008	33.48	4.20	0.04
Bu_4NI	21.94±0.005	67.33	4.86	0.02
		70 Wt% t-BuOH		
Pr_4NBr	18.02±0.020	105.65	5.28	0.11
Bu_4NBr	16.64±0.005	156.70	5.96	0.03
Pr_4NI	18.22±0.015	159.35	5.90	0.08
Bu_4NI	17.31±0.020	205.62	7.26	0.11
		80 Wt% t-BuOH		
Pr_4NBr	14.08±0.022	624.70	6.98	0.15
Bu_4NBr	13.56±0.030	681.46	7.83	0.22
Pr_4NI	16.10±0.014	630.78	6.72	0.08
Bu_4NI	15.31±0.026	666.13	7.35	0.16

for all the salts in a given dielectric constant increase with increasing size of the ions and follow the order $Pr_4\overset{+}{N} < Bu_4\overset{+}{N}$ as expected (19, 31–34). Moreover, an increase in ionic-association with increasing the proportion of t-BuOH may be ascribed to the predominant solvation of cations with one of the solvent molecules which control the extent of ion-pairing in t-BuOH–H_2O mixtures.

The distance parameter or Gurney cosphere diameter, R (Table 3*a*) obtained from the F78 equation for Pr_4NBr, Bu_4NBr, Pr_4NI, and Bu_4NI are found to be larger compared to those of the distance of closest approach, R_j (Table 3*b*) and the ion-size parameter, α^0 (Table 3*c* and *d*) calculated from J, P, and FOS conductance equations, respectively. The values of distance or ion-size parameters obtained in the case of 20 wt% t-BuOH from J, 20 and 40 wt% t-BuOH from P, and 20, 40, and 60 wt% t-BuOH from FOS equations are smaller than the crystallographic radius of the ion pair which explain the inadequacy of the theories. However, the R values computed through the F78 equation are reasonable and higher than the Bjerrum distance, q, whereas $R_j \leq q$ and a^0 are less than q. Consequently, it is evident from Table 3 that the values of R or a^0 do not show any significant variation with the size of the cations or the anions but are found to increase with decrease in the dielectric constant of the medium which, in turn, indicates that the increase in ionic association (35, 36).

Thus, in the light of the above discussion it can be concluded that the F78 conductance equation seems to be better suited in explaining the behaviour of electrolytic solutions in all respects because it includes the solvated radii of ions present in the solution in diffuse steady state and gives significantly better fit parameters as compared to the other conductance equations.

Acknowledgements

The authors are indebted to Professors R. M. Fuoss, R. L. Kay, and J. C. Justice for sending the details of their equations and computer programs. I thank Professor A. D. Pethybridge, University of Reading (U.K.), for the personal communication and his invaluable suggestions on the distance parameters. We would also like to thank Professor N. Islam for his helpful discussion, Professor M. T. Ahmad, Z. H. Engg. College, AMU Aligarh, for the use of an impedence bridge and C.S.I.R., Government of India, for granting a Senior Research Fellowship.

1. R. L. KAY and D. F. EVANS. J. Phys. Chem. **76**, 366 (1966); **76**, 2325 (1966).
2. D. F. EVANS and P. GARDAM. J. Phys. Chem. **72**, 3281 (1968); **73**, 158 (1969).

Can. J. Chem. Downloaded from www.nrcresearchpress.com by 93.93.197.157 on 09/07/12
For personal use only.

3. K. MIYOSHI and T. TOMINAGA. J. Phys. Chem. **77**, 519 (1973).
4. R. M. FUOSS and L. ONSAGER. J. Phys. Chem. **61**, 668 (1957).
5. R. M. FUOSS and K. L. HSIA. Proc. Natl. Acad. Sci. USA, **57**, 1550 (1967).
6. J. C. JUSTICE and R. M. FUOSS. J. Phys. Chem. **67**, 1707 (1963).
7. R. M. FUOSS. J. Am. Chem. Soc. **80**, 3163 (1958); **81**, 2659 (1959).
8. R. M. FUOSS. J. Phys. Chem. **82**, 2427 (1978).
9. R. M. FUOSS. Proc. Natl. Acad. Sci. USA, **75**, 16 (1978).
10. E. M. ARNETT. Physico-chemical process in mixed aqueous solvents. *Edited by* F. Frank. Heinemann, London 1967. p. 105.
11. F. FRANKS. *In* Water, a comprehensive treatise. Vol. 4. *Edited by* F. Frank. Plenum Press, New York. 1975. Chapt. 1.
12. J. JUILLARD. J. Chem. Soc. Faraday Trans. 1, **78**. 37 (1982).
13. Y. KOGA. Can. J. Chem. **64**, 206 (1986).
14. J. C. JUSTICE. J. Chim. Phys. **65**, 353 (1968).
15. E. PITTS. Proc. R. Soc. A. **217**, 43 (1953).
16. E. PITTS, B. E. TABOR, and J. DALY. Trans. Faraday Soc. **65**, 849 (1969).
17. R. M. FUOSS, L. ONSAGER, and J. F. SKINNER. J. Phys. Chem. **69**, 2581 (1965).
18. M. K. CHANTOONI, JR. and I. M. KOLTHOFF. J. Phys. Chem. **82**, 994 (1978).
19. T. L. BROADWATER and R. L. KAY. J. Phys. Chem. **74**, 3802 (1970).
20. M. R. ISLAM and A. A. ANSARI. Ind. J. Chem. **21A**, 1057 (1982).
21. M. R. ISLAM and A. A. ANSARI. J. Electrochem. Soc. To be published.
22. A. A. ANSARI and M. R. ISLAM. Can. J. Chem. In press.
23. H. S. HARNED and B. B. OWEN. The physical chemistry of electrolytic solution. Reinhold Publishing Corporation, New York. 1958.
24. R. M. FUOSS. J. Phys. Chem. **81**, 1829 (1977).
25. R. M. FUOSS and F. ACCASCINA. Electrolytic conductance, Interscience, New York. 1959.
26. M. SALOMON and E. PLICHTA. Electrochim. Acta, **28**, 1681 (1983).
27. R. L. KAY. J. Am. Chem. Soc. **82**, 2099 (1960).
28. R. L. KAY, C. S. ZAWOSKI, and D. F. EVANS. J. Phys. Chem. **69**, 4208 (1965).
29. S. M. A. MATESICH, J. A. NADAS, and D. F. EVANS. J. Phys. Chem. **74**, 4568 (1970).
30. T. L. BROADWATER and D. F. EVANS. J. Phys. Chem. **73**, 3985 (1969).
31. W. H. LEE and R. J. WHEATON. J. Chem. Soc. Faraday Trans. II, **75**, 1128 (1979).
32. P. BERONIUS. Acta Chem. Scand. A, **34**, 309 (1980).
33. R. L. KAY and T. L. BROADWATER. J. Solution Chem. **5**, 57 (1976).
34. R. L. KAY, T. VITUCCIO, C. ZAWOYSKY, and D. F. EVANS. J. Phys. Chem. **70**, 2336 (1966).
35. J. C. JUSTICE. J. Phys. Chem. **79**, 454 (1975).
36. A. D. PETHYBRIDGE and S. S. TABA. J. Chem. Soc. Faraday Trans. 1, **76**, 368 (1980).

Can. J. Chem. Downloaded from www.nrcresearchpress.com by 93.93.197.157 on 09/07/12
For personal use only.

Mechanisms of long-range $^{13}C,^{13}C$ spin–spin coupling in thioanisole and its derivatives. Conformational applications

TED SCHAEFER AND GLENN H. PENNER
Department of Chemistry, University of Manitoba, Winnipeg, Man., Canada R3T 2N2

Received September 8, 1987

TED SCHAEFER and GLENN H. PENNER. Can. J. Chem. **66**, 1229 (1988).

The ^{13}C nuclear magnetic resonance chemical shifts and the long-range $^{13}C,^{13}C$ spin–spin coupling constants are reported for 23 thioanisole derivatives enriched in ^{13}C at the methyl position. For *para* and *meta* substituted thioanisole derivatives, $^nJ(C,C)$ (n being the formal number of bonds intervening between the coupled nuclei) can be related to functions of the angle by which the thiomethyl group twists out of the aromatic plane. For $n = 3, 4, 5$, the ensuing relationships yield estimates of the twofold barriers to rotation about the C(1)—S bond. The barrier is lower in ethyl phenyl sulfide than in thioanisole derivatives. Complications arise for *ortho* substituted thioanisole derivatives but estimates of the torsional motion about the C(1)—S bond can be obtained from the observed $^nJ(C,C)$. Among the complications is the expected fact that $^3J(C,C)$, which is shown to be larger in the *cis* than the *trans* orientation of the intervening bonds ("anti-Karplus" behaviour), is perturbed by the substituent attached to the coupled nucleus. It is confirmed that in 2-hydroxythioanisole the thiomethyl group is oriented effectively perpendicular to the benzene plane, attributable to a stereospecific hydrogen bond between the hydroxyl group and the 3*p* lone-pair on the sulfur atom. In acetone-d_6 solution, an equilibrium exists between this conformation and one in which an intermolecular hydrogen bond exists with solvent molecules. In the latter, the thiomethyl group prefers a coplanar orientation. In 2-aminothioanisole, the thiomethyl group twists out of the plane by about 60° so as to optimize the N—H. . .3*p* interaction. This twist angle is changed very little in acetone-d_6 solution because the second N—H bond can hydrogen bond to the solvent molecules without disrupting the intramolecular N—H. . .3*p* interaction. It is also shown that the chemical shift of the ^{13}C nucleus in the methyl group is a good conformational indicator in *meta* and *para* substituted thioanisoles. Therefore it can be used as such for molecules in which $^nJ(C,C)$ is difficult to find, in 1,4-dithiomethylbenzene, for example.

TED SCHAEFER et GLENN H. PENNER. Can. J. Chem. **66**, 1229 (1988).

On a mesuré les déplacements chimiques en résonance magnétique nucléaire du ^{13}C ainsi que les constantes de couplage spin–spin à longue distance $^{13}C,^{13}C$ pour 23 dérivés du thioanisole enrichis en ^{13}C dans la position du méthyle. Pour les dérivés du thioanisole substitués en positions *para* ainsi que *méta*, les constantes $^nJ(C,C)$, pour lesquelles n correspond au nombre de liaisons formelles intervenant entre les noyaux qui sont couplés, peuvent être reliées aux fonctions de l'angle de torsion du groupement thiométhyle par rapport au plan aromatique. Pour $n = 3, 4$ ou 5, les relations qui en dérivent permettent d'évaluer les barrières binaires à la rotation autour de la liaison C(1)—S. La barrière est plus faible dans le cas du sulfure d'éthyle et de phényle que dans les cas des dérivés du thioanisole. On fait face à des complications avec les dérivés du thioanisole substitués en *ortho*; toutefois, les évaluations du mouvement de torsion autour de la liaison C(1)—S peuvent être obtenues à partir des constantes $^nJ(C,C)$ observées. Parmi les complications rencontrées, mentionnons le fait attendu que la constante $^3J(C,C)$, qui est plus grande dans l'orientation *cis* des liaisons intermédiaires que dans l'orientation *trans* (comportement anti-Karplus), est perturbée par la présence du substituant attaché au noyau couplé. Il est confirmé que, dans l'hydroxy-2 thioanisole, le groupement thiométhyle est effectivement orienté d'une façon perpendiculaire au plan du benzène et que ce fait est attribuable à une liaison hydrogène stéréospécifique entre le groupement hydroxyle et la paire d'électrons 3*p* libre de l'atome de soufre. En solution dans l'acétone-d_6, il existe un équilibre entre cette conformation et celle dans laquelle il existe une liaison hydrogène intermoléculaire avec les molécules du solvant. Dans cette dernière, le groupement thiométhyle existe d'une façon préférentielle dans l'orientation coplanaire. Dans l'amino-2 thioanisole, l'angle de torsion du groupement thiométhyle par rapport au plan du benzène est de 60° et, dans cette conformation, l'interaction N—H. . .3*p* est optimale. En solution dans l'acétone-d_6, cet angle de torsion ne subit pas beaucoup de changement; ce résultat est dû au fait que la deuxième liaison N—H peut former une liaison hydrogène avec les molécules de solvant sans déranger l'interaction N—H. . .3*p* intramoléculaire. On a aussi démontré que le déplacement chimique du noyau ^{13}C du groupement méthyle est un bon indicateur conformationnel pour les dérivés du thioanisole substitués en positions *méta* ainsi que *para*. On peut donc en conclure qu'il peut être utilisé tel quel pour des molécules dans lesquelles la constante $^nJ(C,C)$ est difficile à déterminer comme, par exemple, dans le cas du dithiométhyl-1,4-benzène.

[Traduit par la revue]

Introduction

Long-range spin–spin coupling constants between ^1H and ^{13}C nuclei in the side chain and ^1H and ^{13}C nuclei in the ring provide conformational information about thiophenol and thioanisole derivatives (1–3). For example, in derivatives of **1** (R = H) the predominantly twofold barrier to rotation about the C(1)—S bond is sensitive to the nature of the *para* substituent. Thus, in thiophenol V_2 is 3.4 kJ mol^{-1} (4) with a planar, $\theta = 0°$, conformation as the most stable, while in *p*-nitrothiophenol V_2 increases to 9 kJ mol^{-1}. This increase in V_2 may be attributed to a larger mobile bond order of the C(1)—S bond in the nitro derivative. In *p*-aminothiophenol this mobile bond order decreases so much that the most stable conformer has θ as 90° (3).

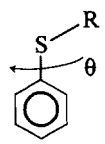

$\theta = 0°$

1

These conclusions are based on $^4J(H,H)$, the coupling constant over four formal bonds between the *ortho* and sulfhydryl protons. It is assumed (1, 3) that $^4J(H,H)$ is proportional to $\sin^2\theta$ and a hindered rotor model is used to relate the expectation value of $\sin^2\theta$ to V_2. The value of $^4J(H,H)$ at $\theta = 90°$ is obtained from 2-hydroxythiophenol, **2** (R = H), in which a stereospecific intra-

Can. J. Chem. Downloaded from www.nrcresearchpress.com by 93.93.197.157 on 09/07/12
For personal use only.

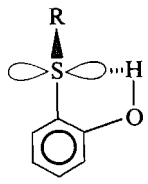

2

molecular hydrogen bond between the hydroxyl group and the 3*p* orbital on the sulfur atom forces the S—H bond into a plane perpendicular to the molecular plane (5).

V_2 in thiophenol derivatives is also sensitive to *meta* substituents and the observed changes are qualitatively understandable (1) in terms of perturbation molecular orbital theory (6). For these molecules both ^4J(H,H) and ^6J(H,H) are employed as indicators of V_2.

In thioanisole and its derivatives, the indicator in the side chain is the ^{13}C nucleus in the methyl group. The value of $^6J_{90}$ in the equation, $^6J(H,C) = {}^6J_{90} \sin^2 \theta$, is estimated from the observed coupling constants between the ^{13}C nucleus of the methyl group and the *para* proton in molecules like 2,6-dichloro- or 2,6-dibromothioanisole (2). In derivatives of 4-fluorothioanisole, the *para* proton is replaced by the ^{19}F nucleus in the coupling scheme (2). ^6J(H,C) or ^6J(C,F) are measurable with the INEPT pulse sequence (7) or in the presence of ^{1}H broadband decoupling.

In the presence of *para* substituents other than hydrogen or fluorine, other indicator nuclei are required. These might be the remaining ring protons or ^{13}C nuclei in the benzene ring. Enrichment with ^{13}C in the methyl group allows a relatively facile measurement of ^nJ(C,C) if the ring protons are decoupled during the measurement. The use of model compounds may establish the θ dependence of ^nJ(C,C), and expectation values of the appropriate functions of θ may then give information about the internal rotational potential in the thioanisole derivatives of interest.

In this paper, such measurements are reported for 15 symmetrically substituted thioanisole derivatives, and for some 2-substituted thioanisole derivates. It turns out that ^5J(C,C) is a good conformational indicator. When the resonance peaks of the 4-^{13}C nucleus is broad (nitro or amino groups), other ^nJ(C,C) values provide conformational conclusions. It is also shown that the *ortho* hydroxyl and amino substituents differ significantly in the changes they cause in θ of the thiomethyl group on formation of O—H. . .S and N—H. . .S intramolecular hydrogen bonds.

Experimental

All ^{13}C enriched precursors came from MSD Isotopes and had a minimum isotopic purity of 95 at.%. The ^{13}C enriched thioanisoles were easily prepared as follows. About 0.1 g of sodium metal was added to 10 mL of absolute methanol, followed by addition of 2 mmol of the thiophenol derivative. Then 2.3 mmol (0.33 g) of $^{13}CH_3I$ was added while stirring the solution and the latter was continued for 15 min. Addition of water gave a cloudy suspension. Extraction with ether, drying over anhydrous $MgSO_4$, and filtration was followed by rotary evaporation. Ethylation of thiophenols used 2.3 mmol (0.36 g) of $CH_3{}^{13}CH_2I$.

Samples for nmr analysis, at concentrations in the solvents as given in the tables, were transferred to 10 mm od nmr tubes for ^{13}C nmr and to 5 mm od tubes for ^{1}H nmr. All solutions contained small amounts of tetramethylsilane as a reference. The sample tubes were degassed by the freeze–pump–thaw procedure and were then flame-sealed.

All nmr spectra were accumulated on an AM300 Bruker spectrometer at a probe temperature of 300 K. In proton-decoupled ^{13}C nmr, 128–256 free induction decays were additively stored, while 400–2800 decays were needed for proton-coupled ^{13}C nmr experiments. The actual number of added decays depended on the concentration of the ^{13}C enriched material. For reasons of cost, the concentration was sometimes too low to accumulate acceptable spectra of ^{13}C nuclei not bonded to hydrogen atoms in a reasonable time span. Acquisition times varied between 20 and 30 s; for example, a spectral width of 100 Hz was assigned to a 4K data region to give an acquisition time of 20.5 s. Some free induction decays were zero-filled to twice the original data region before Fourier transformation, using a small amount of Gaussian multiplication. The ^{1}H nmr spectra were the result of 8–32 accumulated decays with acquisition times as long as 40 s. The linewidths at half height of the ^{1}H and ^{13}C nmr spectra typically fell between 0.05 and 0.25 Hz. Relative signs of some coupling constants were determined by partial decoupling (8) experiments. The ^{13}C and ^{1}H excitation frequencies were 75.486 and 300.135 MHz, respectively.

Spectral analyses were performed with a locally modified version of the computer program NUMARIT (9). INDO MO FPT computations (10, 11) of coupling constants employed Amdahl 470/V8, 580/5850, or 5870 systems, as did the spectral analytical procedures.

Results and discussion

Tables 1–5 present chemical shift and coupling constant data relevant to the discussion below. In these tables, signs in parentheses are assumed while those not in parentheses are obtained from double resonance experiments. Figure 1 demonstrates the sign determination for $^3J(^{13}CH_3, {}^{13}C\text{-}2) \equiv {}^3J$(C,C) in 3,5-dichlorothioanisole-α-^{13}C.

$^nJ(C,C)$ *as a function of* θ

INDO MO FPT computations of long-range coupling constants in benzene derivatives are very useful as semiquantitative indicators of their θ dependence (2, 12–14). Quantitative agreement with experiment is relatively rare because of the parameterization of this semiempirical method and because the geometry assumed in the computations may well be different from the true geometry.

The computations for thioanisole, at 15° intervals of θ, yield numbers that can be fit by the expressions, $^5J(C,C)/Hz = 0.05(2) + 1.67(4) \sin^2 \theta$, $^4J(C,C)/Hz = -0.32(2) - 1.46(2) \sin^2 \theta + 0.17(2) \sin^2 (\theta/2)$, and $^3J(C,C)/Hz = 2.25(4) - 0.63(5) \sin^2 \theta + 0.50(5) \sin^2 (\theta/2)$. The equation for ^5J(C,C) indicates a σ–π mechanism for this coupling constant, just as for ^6J(H,C) to the *para* proton (2). The coefficient of $\sin^2 \theta$ is much too large, however, and, as argued previously for other coupling constants (12, 14, 15), the term independent of θ may well be an artifact of the calculation. The equation for ^4J(C,C) implies a large and negative σ–π component and a small σ electron component (16, 17), proportional to $\sin^2 (\theta/2)$. For an evenfold barrier, the expectation value of $\sin^2 (\theta/2)$ is 0.5, so that a distinction between a term in $\sin^2 (\theta/2)$ and a term independent of θ is impossible to establish for the compounds in Table 1. The equation ^3J(C,C) is an alternative representation of the Karplus equation (18), usually written in terms of cos θ, cos 2θ, and a constant term (trigonometric identities). With these hints about the conformational behaviour of ^nJ(C,C), the experimental values in Tables 1–3 can be discussed as follows.

Consider ^5J(C,C). The largest number in Table 1, 0.91 Hz, is that for 2,6-dimethylthioanisole. In the 2,6-dichloro derivative ^5J(C,C) drops to 0.77 Hz. The chloro and methyl substituents are often (19) taken to have very similar steric requirements. The two ^5J(C,C) values here indicate, on the face of it, that the

Can. J. Chem. Downloaded from www.nrcresearchpress.com by 93.93.197.157 on 09/07/12
For personal use only.

TABLE 1. ^{13}C nuclear magnetic resonance chemical shifts and $^nJ(^{13}C,^{13}C)$ in some symmetrical thioanisole derivatives at 300 K

Parameter	H[a]	H[b]	2,6-diF[c]	2,6-diCl[d]	3,5-diCl[e]	4-F[f]	4-Cl[g]	4-Br[h]
($S^{13}CH_3$)	15.45	15.88	17.78	18.32	14.80	16.56	15.58	15.43
(C_1)	139.57	139.04	113.59	135.16	114.14	134.83	138.59	138.24
(C_2)	127.13	126.75	163.68	141.42	124.55	129.74	128.52	138.77
(C_3)	129.68	128.72	112.59	129.71	135.59	116.58	129.57	132.50
(C_4)	125.66	124.87	130.79	131.32	125.09	161.01	130.92	118.62
$^2J(^{13}C,C_1)$	(−)1.38	(−)1.42	(−)1.76	(−)2.11	−1.39[o]	(−)1.42	(−)1.38	(−)1.40
$^3J(^{13}C,C_2)$	(+)2.95	(+)2.93	(+)1.29	(+)1.33	+3.25	(+)2.70	(+)2.95	(+)2.97
$^4J(^{13}C,C_3)$	(+)0.28	(+)0.24	(−)0.55	−0.69	(+)0.42	0.10	(+)0.25	(+)0.27
$^5J(^{13}C,C_4)$	(+)0.20	(+)0.22	(+)0.63	+0.77	+0.11	(+)0.33	(+)0.26	(+)0.21

	4-CH_3[i]	4-*t*-Bu[j]	4-OCH_3[k]	4-NH_2[l]	4-NO_2[l]	3,5-diCl–4-OCH_3[m]	3,5-diCl–4-OH[n]	2,6-diMe[p]
($S^{13}CH_3$)	16.06	15.83	17.65	19.18	—	15.78	—	18.16
(C_1)	135.90	135.88	130.11	—	—	—	—	135.69
(C_2)	127.73	127.29	130.64	132.24	126.04	127.13	128.29	143.03
(C_3)	130.38	126.53	115.46	115.80	124.54	130.22	—	128.70
(C_4)	135.51	148.66	159.20	—	—	150.38	—	128.77
$^2J(^{13}C,C_1)$	(−)1.40	(−)1.40	(−)1.46	—	—	—	—	(−)1.99
$^3J(^{13}C,C_2)$	(+)2.74	(+)2.78	(+)2.34	(+)1.94	(+)3.35	(+)3.01	(+)2.67	(+)1.15
$^4J(^{13}C,C_3)$	(+)0.14	(+)0.18	0.10	0.10	(+)0.47	(+)0.23	—	(−)0.82
$^5J(^{13}C,C_4)$	(+)0.31	(+)0.28	(+)0.41	—	—	(+)0.18	—	(+)0.91

[a] 2.7 mol% in acetone-d_6.
[b] 7.0 mol% in CS_2/10 mol% C_6D_{12}/0.5 mol% TMS.
[c] 2.8 mol% in acetone-d_6. The $^{13}C,^{19}F$ coupling constants are $^1J = -246.10$, $^2J_{1F} = 21.98$, $^2J_{3F} + {}^4J_{3F} = 22.70$, $^3J_{2F} = 5.26$, $^3J_{4F} = 10.36$, and $^4J(CH_3,F) = \pm 3.57$ Hz. The signs are based on data in refs. 51 and 52. $^5J(^{13}CH_3,H\text{-}3)$ and $^6J(^{13}CH_3,H\text{-}4)$ are (+)0.212(3) and (−)0.412(2) Hz, respectively.
[d] 2.6 mol% in acetone-d_6.
[e] 3.4 mol% in acetone-d_6.
[f] 4.0 mol% in acetone-d_6. The $^{13}C,^{19}F$ coupling constants are $^1J = -242.71$, $^2J = 22.11$, $^3J = 7.88$, $^4J = 3.17$, and $^6J = 0.47$ Hz.
[g] 5.1 mol% in acetone-d_6.
[h] 4.5 mol% in acetone-d_6.
[i] 3.0 mol% in acetone-d_6; $^6J(SCH_3,CH_3)$ is ± 0.07 Hz.
[j] 5.3 mol% in acetone-d_6.
[k] 3.5 mol% in acetone-d_6. $^7J(SCH_3,OCH_3)$ is less than 0.05 Hz in magnitude.
[l] About 2 mol% in acetone-d_6.
[m] 3.5 mol% in acetone-d_6. $^7J(SCH_3,OCH_3)$ is $\pm 0.09_3$ Hz.
[n] 2.0 mol% in acetone-d_6.
[o] Signs in parentheses are assumed, those not in parentheses are determined by double resonance experiments.
[p] 17 mol% in acetone-d_6; δ(2-CH_3) is 21.75, $^4J(CH_3,CH_3)$ is less than 0.1 Hz.

methyl groups cause $\langle\theta\rangle$ to be nearer 90° than do the two *ortho* chlorine atoms. There are some experiments, for example, on *ortho* disubstituted isopropyl benzene derivatives (19, 20), that agree that a methyl has larger steric requirements than a chlorine substituent. Yet, a methyl group is a better π electron donor than a chlorine substituent, therefore possibly causing a larger θ for the SCH_3 group (compare ^5J(C,C) for 4-methyl and 4-chlorothioanisole in Table 1). Hence the larger apparent $\langle\theta\rangle$ value in the 2,6-dimethyl derivative might arise for electronic instead of steric reasons. Furthermore, it is possible that the relatively electronegative chlorine substituents have an intrinsic effect on ^5J(C,C), as distinct from a conformational one (see below).

In 2-hydroxythioanisole ^5J(C,C) is also 0.91 Hz for a CCl_4 solution (Table 3). For reasons given in the introduction, this molecule is expected to have the perpendicular ($\theta \sim 90°$) conformation (see **2**). Note that ^4J(C,C) in **2** (R = CH_3) is the same for C-3 and C-5 (Table 3), as expected for such a conformation, as is $^5J(H,^{13}CH_3)$ for H-3 and H-5 (Table 4). Also $^6J(H\text{-}4,^{13}CH_3)$, a coupling proportional to $\sin^2\theta$, is −0.56 Hz in **2** (R = CH_3), to be compared with −0.54 Hz in 2,6-dibromothioanisole (2).

None of these molecules is rigid, of course, that is with $\langle\theta\rangle$ as 90°. Geometry-optimized STO-3G MO computations for 2,6-dichlorothioanisole give an energy difference of 31.3 kJ mol^{-1} between the planar and perpendicular forms, corresponding to a $\langle\sin^2\theta\rangle$ of 0.957. This number implies a $^5J_{90}$(C,C) of 0.80 Hz, much smaller than the observed ^5J(C,C) in 2-hydroxythioanisole or 2,6-dimethylanisole. If a substantial fourfold component of the barrier exists in the 2,6-dichloro derivative, with a sign opposite to the twofold component, as computed for 2,6-difluorothioanisole (2), then $\langle\sin^2\theta\rangle$ will be larger for a given V_2 than if V_4 is zero (this is easily seen pictorially by adding curves for V_2 and V_4 to yield a potential curve that clearly drives $\langle\theta\rangle$ towards 90°). If such a situation also exists in the 2,6-dimethyl derivative, any barrier derived from $\langle\sin^2\theta\rangle$, as indicated by ^5J(C,C), will be quite uncertain. Because of these ambiguities concerning the form of the internal rotational potential in the diortho-substituted molecules, and because of the further ambiguity connected with intrinsic substituent perturbations of ^5J(C,C), it is most likely best to write eq. [1] in which $^5J_{90}$(C,C) is taken as the maximum observed value of ^5J(C,C). The use of eq. [1] to obtain V_2 values in *meta* or *para* substituted derivatives of the thioanisole will therefore yield lower limits to

Can. J. Chem. Downloaded from www.nrcresearchpress.com by 93.93.197.157 on 09/07/12
For personal use only.

TABLE 2. ^{13}C nuclear magnetic resonance chemical shifts and $^{n}J(^{13}C,^{13}C)$ for some ethyl phenyl sulfides at 300 K

Parameter	H[a]	4-CH_3[b]	4-OCH_3[c]
$\delta(^{13}CH_2)$	27.61	28.34	29.85
$\delta(CH_3)$	14.63	14.76	14.91
$\delta(C_1)$	137.71	133.84	127.32
$\delta(C_2)$	129.43	130.37	133.64
$\delta(C_3)$	129.72	130.39	115.36
$\delta(C_4)$	126.41	136.46	159.87
$^1J(^{13}C,CH_3)$	35.05	35.40	35.46
$^2J(^{13}C,C_1)$	(−)1.40	(−)1.41	(−)1.46
$^3J(^{13}C,C_2)$	(+)2.20	(+)2.05	(+)1.68
$^4J(^{13}C,C_3)$	<0.05	(−)0.09	(−)0.23
$^5J(^{13}C,C_4)$	(+)0.34	(+)0.43	(+)0.54

[a]2.4 mol% in acetone-d_6.
[b]2.5 mol% in acetone-d_6, $\delta(4\text{-}CH_3) = 20.91$, $^6J(CH_2,CH_3) = \pm 0.15$ Hz.
[c]3.1 mol% in acetone-d_6, $\delta(OCH_3) = 55.51$, $^7J(CH_2,OCH_3) < 0.05$ Hz.

V_2 (see below).

[1] $$^5J(C,C)/Hz = 0.91 \langle \sin^2 \theta \rangle$$

Both $^5J(C,C)$ and $^6J(H,^{13}CH_3)$ are assumed to be pure $\sigma-\pi$ coupling constants (dependent only on $\sin^2 \theta$). In Table 5 numbers for these coupling constants are given for a variety of compounds. A linear relationship, with a correlation coefficient of 0.9995, exists between these coupling constants and is given by eq. [2]. This proportionality implies that, for neutral molecules, the hyperfine coupling parameters, Q^C_{CH} and Q^H_{CH}, which represent transmission of unpaired spin density from the aromatic π orbitals to the sites of the ring ^{13}C or ^1H nuclei, respectively, are of opposite sign. In aromatic free radicals Q^C_{CH} and Q^H_{CH} are positive and negative, respectively (23, 24).

[2] $$^5J(C,C) = -1.50\, ^6J(H,^{13}CH_3) + 0.02$$

Equation [2] implies that $^5J(C,C)$ and $^6J(H,^{13}CH_3)$ undergo proportional intrinsic substituent perturbations but, of course, cannot yield a value of $^5J(C,C)$ at a θ of 90° in thioanisole. Nor does eq. [2] prove that the form of eq. [1] is correct. The undetectable $^5J(C,C)$ and $^6J(H,^{13}CH_3)$ in anisole (Table 5) are consistent with a very small, if any, angle-independent term in eq. [1]).

Turning to $^4J(C,C)$ and reiterating that $\langle \sin^2 (\theta/2) \rangle$ is 0.5 for an evenfold barrier (symmetrically substituted molecules), the theoretical calculations above imply a proportionality between $^4J(C,C)$ and $\sin^2 \theta$ for the molecules in Table 1. Consequently, a linear regression between $^4J(C,C)$ and $^5J(C,C)$ is in order, yielding eq. [3] for 13 points ($r = 0.992$). It should be noted that $^4J(C,C)$ is measured as negative in 2,6-dichlorothioanisole and that the other signs of $^4J(C,C)$ in Table 1 are assumed; the INDO MO FPT computations agree that the $\sigma-\pi$ component of $^4J(C,C)$, proportional to $\sin^2 \theta$, is negative. In view of eq. [1], it follows that $^4J(C,C)$ is given by eq. [4]. The way in which the constant term in eq. [3] breaks into a term in $\sin^2 (\theta/2)$ and, possibly, an angle-independent term, cannot be determined from this approach.

[3] $$^4J(C,C)/Hz = -1.66\, ^5J(C,C) + 0.62$$

[4] $$^4J(C,C)/Hz = 1.51 \langle \sin^2 \theta \rangle + 0.62$$

Again, from the theoretical numbers for ^3J, a linear relationship between it and ^5J is expected and found, as in eq. [5].

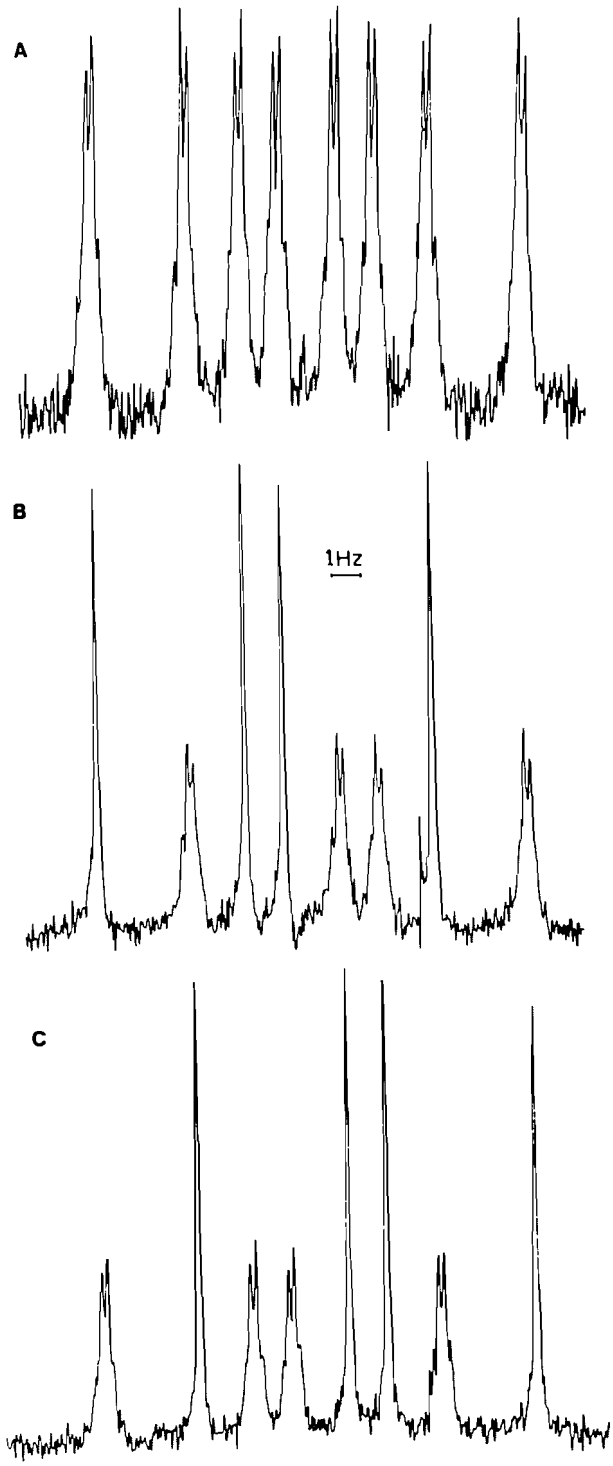

FIG. 1. Part A displays half of the ^{13}C nmr spectrum of C-2 in 3,5-dichlorothioanisole-α-^{13}C as a 3.4 mol% solution in acetone-d_6 at 300 K and 75.486 MHz. No attempt at peak width optimization is present here. The eight quartets arise from large, ca. 8 Hz, couplings to H-4 and H-6 and a 3-Hz coupling to the α ^{13}C nucleus. The quartet structure is caused by a coupling interaction with the methyl protons. In B the methyl proton peaks at high frequency are being irradiated (partial decoupling). The collapse of quartets of C-2 occurs in the high-frequency band of the doublets arising from coupling to the α ^{13}C nucleus. In C the methyl proton peaks at low frequency, corresponding to a spin state of the α ^{13}C nucleus opposite to that in B, are being irradiated. These experiments demonstrate that $^1J(^1H,\alpha\text{-}^{13}C)/^3J(^{13}CH_3,^{13}C\text{-}2)$ is positive, which yields the absolute value of ^3J given that ^1J is positive.

Can. J. Chem. Downloaded from www.nrcresearchpress.com by 93.93.197.157 on 09/07/12
For personal use only.

TABLE 3. ^{13}C nuclear magnetic resonance chemical shifts and $^nJ(^{13}C,^{13}C)$ in Hz for some 2-X-thioanisoles at 300 K

Parameter	2-OH[a]	2-OH[b]	2-OCH_3[c]	2-NH_2[d]	2-F[e]	2-Br[f]	2-OH-α-CH_3[g]
$\delta(S^{13}CH_3)$	19.70	16.11	14.23	17.56	14.85	15.38	14.90
$\delta(C_1)$	120.72	124.60	128.17	119.63	126.64	140.82	118.72
$\delta(C_2)$	156.93	155.92	157.10	147.30	160.71	121.68	157.73
$\delta(C_3)$	115.04	115.44	109.66	114.38	115.76	133.30	115.00
$\delta(C_4)$	130.76	128.00	126.36	128.96	127.53	126.46	131.05
$\delta(C_5)$	120.54	121.07	121.90	118.33	125.69	128.91	120.39
$\delta(C_6)$	134.94	129.99	126.34	136.16	128.77	126.27	136.16
$^2J(^{13}C,C_1)$	(−)1.75	(−)1.42	(−)1.25	(−)1.72	(−)1.35	(−)1.11	(−)1.64
$^3J(^{13}C,C_2)$	(+)1.13	—	(+)1.38	(+)1.10	(+)1.63	(+)2.21	(+)1.01
$^4J(^{13}C,C_3)$	(−)0.77	<0.5	<0.05	(−)0.65	±0.09	<0.1	(−)0.72
$^5J(^{13}C,C_4)$	(+)0.91	(+)0.46	(+)0.25	(+)0.76	(+)0.29	<0.05	(+)0.86
$^4J(^{13}C,C_5)$	(−)0.76	<0.1	±0.36	(−)0.59	±0.23	±0.60	(−)0.74
$^3J(^{13}C,C_6)$	(+)1.26	(+)2.99	(+)4.01	(+)1.68	(+)3.52	+4.19	(+)1.05

[a]4.0 mol% in CCl_4/C_6D_{12}.
[b]5.2 mol% in acetone-d_6; peaks are relatively broad.
[c]4.2 mol% in acetone-d_6; $^5J(CH_3,CH_3)$ is less than 0.05 Hz.
[d]3.6 mol% in CCl_4/C_6D_{12}.
[e]5.0 mol% in acetone-d_6. The $^{13}C,^{19}F$ coupling constants are $^1J = -242.25$, $^2J_{1F} = 17.08$, $^2J_{3F} = 21.59$, $^3J_{4F} = 7.73$, $^4J_{5F} = 3.53$, $^3J_{6F} = 2.63$, and $^4J(CH_3,F) = \pm 2.33$ Hz.
[f]3.8 mol% in acetone-d_6.
[g]5.0 mol% in CCl_4/C_6D_{12}. $^1J(CH_2,CH_3)$ is 34.9 Hz.

TABLE 4. ^1H nuclear magnetic resonance spectral parameters for 2-hydroxythioanisole-α-^{13}C and 2-aminothioanisole-α-^{13}C at 300 K

Parameter	2-OH[a,g]	2-NH_2[b]	Parameter	2-OH	2-NH_2
ν_3[c]	2068.337(1)[d]	2032.252(1)	$^5J_{36}$	0.387(1)	0.380(2)
ν_4	2148.495(1)	2109.156(1)	$^4J_{C6}$	−0.532(2)	−0.371(2)[f]
ν_5	2032.271(1)	1985.451(1)	$^5J_{C5}$	0.186(2)[e]	0.117(2)[f]
ν_6	2218.340(1)	2184.863(1)	$^5J_{C3}$	0.187(2)[e]	0.183(2)[f]
$^3J_{34}$	8.177(1)	8.035(2)	$^6J_{C4}$	−0.563(2)	−0.421(4)[f]
$^3J_{45}$	7.368(1)	7.284(2)	Transitions calcd.	128	160
$^3J_{56}$	7.712(1)	7.710(2)	Transitions assigned	118	159
$^4J_{35}$	1.331(1)	1.348(2)	Largest difference	0.017	0.018
$^4J_{46}$	1.676(1)	1.552(2)	Error (rms)	0.005	0.006

[a]4.5 mol% in CCl_4, containing also 10.0 mol% of C_6D_{12} and 0.5 mol% TMS. δ(OH) is 6.49 ppm.
[b]3.0 mol% in acetone-d_6 containing 0.5 mol% TMS.
[c]In Hz at 300.135_2 Hz to high frequency of TMS.
[d]Numbers in parentheses are standard deviations in the last significant figure.
[e]Signs determined by double resonance procedures.
[f]Signs determined by weak irradiation experiments.
[g]Rapid hydroxyl proton exchange.

[5] $^3J(C,C)/Hz = -2.74\,^5J(C,C) + 3.55$

Here $r = 0.995$, but 2,6-difluorothioanisole is omitted from the analysis because it deviates strongly (0.15 Hz in 1.29 Hz) from the regression line. The probability of an intrinsic substituent perturbation is apparent. It follows that $^3J(C,C)$ is related to $\sin^2\theta$ by eq. [6]. The constant term is a composite of a term in $\sin^2(\theta/2)$ and an *apparent* angle-independent term (for free rotation both $\langle\sin^2\theta\rangle$ and $\langle\sin^2(\theta/2)\rangle$ become 0.5 and $^3J(C,C)$ would be 2.31 Hz).

[6] $^3J(C,C)/Hz = -2.49\langle\sin^2\theta\rangle + 3.55$

Rotational barriers from $^nJ(C,C)$

Equations [1], [4], and [6] yield $\langle\sin^2\theta\rangle$ for the molecules in Table 1. For thioanisole the available evidence suggests an almost purely twofold barrier to rotation about the C(1)—S bond (2). A hindered rotor model (25, 26) relates V_2 to $\langle\sin^2\theta\rangle$. In the present instance 31 free rotor basis functions were employed, the population distributions were computed at 300 K, and tables of $\langle\sin^2\theta\rangle$ and V_2 were constructed at intervals of 0.42 kJ mol^{-1} in V_2 for a range of reduced moments of inertia. For values of the latter appropriate to the compounds in Tables 1 and 2, $\langle\sin^2\theta\rangle$ is insensitive to their precise value relative to other errors involved in the deduction of the barrier heights.

In Table 6 the barriers are presented as deduced from $^nJ(C,C)$. The lower limit of the twofold barrier in thioanisole itself is 6.3 ± 0.2 kJ mol^{-1} if the simple average of the three numbers is taken. The true error in these numbers is difficult to assess reliably. Between a V_2 of 0 and about 12 kJ mol^{-1}, the hindered rotor model has a reasonably steep dependence of V_2 on $\langle\sin^2\theta\rangle$ at 300 K and is in principle quite accurate (±0.1 kJ mol^{-1}). Therefore the uncertainty in $^nJ_{90}(C,C)$ and the experimental

Can. J. Chem. Downloaded from www.nrcresearchpress.com by 93.93.197.157 on 09/07/12
For personal use only.

TABLE 5. Values in Hz of $^5J(^{13}C,C\text{-}4)$ and of $^6J(H\text{-}4,^{13}C)$ for some anisole, thioanisole, and benzyl cyanide derivatives

Substituent	^5J	^6J	Substituent	^5J	^6J
$O^{13}CH_3$	<0.03[a]	<0.03[b]	2,6-diCl-$S^{13}CH_3$	0.77	−0.52[e]
$S^{13}CH_3$	0.20	−0.15[c]	2,6-diBr-$O^{13}CH_3$	0.94[a]	−0.63[f]
$CH_2^{13}CN$[d]	0.51	−0.36	2,6-diF-$CH_2^{13}CN$[d]	0.95	−0.65
2,6-diF-$S^{13}CH_3$	0.62	−0.42[e]	2,6-diCl-$CH_2^{13}CN$[d]	1.08	−0.72

[a]Unpublished results from this laboratory, acetone-d_6 solution.
[b]Reference 21, in both acetone-d_6 and CS_2/C_6D_{12} solutions.
[c]Reference 2, in benzene-d_6 solution.
[d]Reference 22, in benzene-d_6 solution.
[e]Reference 2, in acetone-d_6 solution.
[f]Reference 21, 50 v/v % in benzene-d_6.

TABLE 6. Lower limits to the twofold barriers to rotation about the C(1)—S bond in thioanisole and some of its *meta* and *para* and α-methyl substituted derivatives

	V_2[a, b]				V_2[a, b]		
		via				via	
Substituent	^5J	^4J	^3J	Substituent	^5J	^4J	^3J
H	6.5	6.3	6.1	4-NO_2	—	14.6	17.6
4-Br	6.5	6.5	6.5	3,5-diCl	12.4	11.5	12.4
4-Cl	4.8	6.3	6.2	3,5-diCl-4-OH	—	—	3.1
4-*t*-Bu	4.2	4.7	4.2	3,5-diCl-4-OCH_3	7.8	5.6	7.0
4-CH_3	3.4	4.0	3.8	α-CH_3	2.2	—[c]	1.4
4-F	2.9	—[c]	3.4	4-CH_3-α-CH_3	0.0	—	0.2
4-OCH_3	1.0	—[c]	0.3	4-OCH_3-α-CH_3	−2.7[d]	−2.0[d]	−2.8[d]
4-NH_2	—	—[c]	−3.1[d, e]				

[a]In kJ mol^{-1}.
[b]Based on $\langle \sin^2 \theta \rangle$ derived from $^{3,4,5}J(C,C)$ and eqs. [1], [4], and [6].
[c]Too small a ^4J to observe accurately (Tables 1 and 2).
[d]These are upper limits to the barrier, the stable conformation having θ as 90°.
[e]V_2 values for 1,4-dithiomethyl benzene, 3,5-ditrifluoromethylthioanisole, 4-thiomethylbenzaldehyde, and 4-hydroxymethylthioanisole are derived in the text from the chemical shift of the ^{13}C nucleus of the methyl group. In the order above, they are 4.6, 8.7, 12.6, and 5.6 kJ mol^{-1}.

error in $^nJ(C,C)$ would appear to be a major source of inaccuracy. The $^nJ(C,C)$ were in general reproducible to within 0.01 Hz in repeated measurements. $^5J(C,C)$ in thioanisole is therefore the same in CS_2 and acetone-d_6 solutions to within experimental error. Clearly, the uncertainties in the $^nJ_{90}(C,C)$ numbers will introduce some relatively major errors in V_2. Thus, if $^5J_{90}(C,C)$ is as large as 1.00 Hz, V_2 in thioanisole rises to 7.2 kJ mol^{-1}. Such a value of $^5J_{90}(C,C)$ corresponds to an apparent V_2 of 15.9 kJ mol^{-1} in 2,6-dimethylthioanisole and of only 6.4 kJ mol^{-1} in the 2,6-dichloro derivative. Intuitively, these latter numbers appear as unreasonably small. Perhaps, therefore, the individual V_2 values in Table 6 will be only about 10% too low from this source of error, the error in $^nJ_{90}(C,C)$ introducing an error roughly proportional to V_2 in the range from zero to about 12 kJ mol^{-1}.

Another major source of error in the V_2 numbers in Table 6 may well be the intrinsic substituent perturbations of $^nJ(C,C)$, particularly of those in which the substituent is bonded to the atom containing a coupled nucleus. For example, in 4-chlorothioanisole the value of V_2 based on $^5J(C,C)$ is 1.4 kJ mol^{-1} lower than those based on $^{3,4}J(C,C)$, whereas in 4-*tert*-butylthioanisole the V_2 values from the three coupling constants agree much more closely among themselves. However, the data in Table 6 in general do not support an attribution of intrinsic substituent perturbations of $^nJ(C,C)$ to a unique substituent parameter such as electronegativity, for example. Nevertheless, such perturbations are present; see the V_2 values for the 3,5-dichloro-4-methoxy derivative, for example.

The geometry-optimized STO-3G MO calculations (2) have V_2 as 6.2 kJ mol^{-1} for thioanisole, but their reliability has not been assessed by computations with sufficiently large basis sets. The V_2 based on $^6J(H,^{13}CH_3)$ was given previously as 5.4 ± 0.4 kJ mol^{-1} (2). It must be revised because eq. [2] implies a minimum magnitude for $^6J_{90}(H,^{13}CH_3)$ of 0.59 Hz, instead of the 0.56 Hz assumed before (2). The revised V_2 is then 6.0 kJ mol^{-1}. The present set of numbers for V_2 may be compared with earlier theoretical and experimental approaches to the barrier in thioanisole, yielding values (27, 28) between 1 and 26 kJ mol^{-1} (see also references cited in ref. 2).

The barriers in the *para* substituted derivatives in Table 6 follow the expectations based on the notion that π electron donors decrease the mobile bond order of the C(1)—S bond (the S—CH_3 group is itself a weak π electron donor) and therefore reduce the magnitude of V_2; π electron acceptors therefore increase V_2. According to the data in Table 6, the *tert*-butyl group is a weaker π donor than a methyl group. The nitro

Can. J. Chem. Downloaded from www.nrcresearchpress.com by 93.93.197.157 on 09/07/12
For personal use only.

substituent causes a large increase in V_2, the true value of this increase being somewhat uncertain because V_2 now lies in a range in which $\langle \sin^2 \theta \rangle$ changes less rapidly with V_2 (at a V_2 of 17 kJ mol^{-1}, $\langle \sin^2 \theta \rangle$ decreases by only 0.005 for an increase in V_2 of 0.84 kJ mol^{-1}). It is noteworthy, however, that the V_2 in *p*-nitrothioanisole is derived from ^3J(C,C) and ^4J(C,C) because ^5J(C,C) is obscured by broad C-4 peaks (quadrupolar relaxation of the ^{14}N nucleus causing a decrease in T_2 by scalar relaxation of the second kind). Broad C-4 peaks also occur in *p*-aminothioanisole, in which the strongly π-electron donating amino substituent stabilizes the perpendicular conformation of the thiomethyl moiety ($\theta = 90°$ for the ground state). This result follows from ^3J(C,C), whose value implies a ^4J(C,C) of +0.09 Hz, in agreement with observation. It follows that the planar ground state of thioanisole is a consequence of $3p \ldots \pi$ conjugation, which overcomes repulsion between the methyl group and the *ortho* C—H bonds.

The large V_2 in 3,5-dichlorothioanisole (2) found from $^6J(H,^{13}CH_3)$ is confirmed by the numbers in Table 6, although the error is relatively large. This result has been discussed (2) in terms of perturbation molecular orbital theory. If a 4-hydroxy substituent is added to this compound, then it is this substituent which dominates V_2. The same conclusion was reached for the thiophenol derivative (1). Phenomenologically, the *para* substituent is a first-order perturber and dominates the *meta* substituent, a second-order perturber. It would be useful to have an independent confirmation of this conclusion.

A hydroxy group flanked by two chlorine substituents remains in the aromatic plane, allowing full conjugation. A methoxy group in the same position lies predominantly perpendicular to that plane (21) and hence will not conjugate as strongly with the aromatic π system. Consequently, V_2 in 3,5-dichloro-4-methoxythioanisole rises to about 7 kJ mol^{-1} from the 3 kJ mol^{-1} in 3,5-dichloro-4-hydroxythioanisole.

Because of the probable presence of significant fourfold components of the internal barriers in the 2,6-di-X derivatives, various ratios of V_2 to V_4 being compatible with a given $\langle \sin^2 \theta \rangle$, it is best to conclude only that the perpendicular conformation of the thiomethyl group is most stable for X = F, Cl, CH_3; the ^nJ(C,C) imply that this stability increases in the indicated order. The ^3J(C,C) values are apparently decreased by electronegative substituents at the *ortho* positions, just as expected from the behaviour of other vicinal coupling constants, those between ^{13}C and ^{1}H nuclei, for instance (29). Such a decrease is also noticeable in 2-hydroxythioanisole in which ^3J(C,C-3) is 0.1 Hz smaller than ^3J(C,C-6) in Table 3. A decrease in ^3J(C,C) is therefore also expected on substitution of a methyl group for hydrogen on the side chain, as in 2-hydroxy-α-methylthioanisole; this decrease does occur (Table 3).

In this compound, ^5J(C,C) is 0.86 Hz. Then, if this number is taken as an approximation to $^5J_{90}$(C,C), lower limits to V_2 for the compounds in Table 2 are obtainable: 2.2, 0.0, and −2.7 kJ mol^{-1}, respectively, for ethyl phenyl sulfide and its 4-methyl and 4-methoxy derivatives. The conclusion seems inescapable that the barriers to rotation about the C(1)—S bonds in these compounds are about 3 kJ mol^{-1} lower than in the corresponding thioanisoles (Table 6). Furthermore, the stable conformer in 4-methoxyphenyl ethyl sulfide is almost certainly the one in which the *S*-ethyl group lies in a plane perpendicular to that of benzene ($^5J_{90}$(C,C) would have to be greater than 1.08 Hz for a coplanar stable form).

^4J(C,C) is calculated as 0.05, −0.09, and −0.28 Hz for the three compounds in the order given above, in rough agreement with the values in Table 2. To calculate ^4J(C,C) the coefficient of $\langle \sin^2 \theta \rangle$ in eq. [4] must be reduced by a factor of 0.86/0.91. The observed ^4J(C,C) of 0.23 Hz in the 4-methoxy derivative suggests a barrier of −2.0 kJ mol^{-1}, that is, in agreement with a perpendicular conformer indicated by ^5J(C,C).

A plot of ^3J(C,C) versus ^5J(C,C) for these ethyl phenyl sulfides fits ^3J/Hz = −3.01 ^5J(C,C) + 3.32 with a correlation coefficient of 0.997, significant at the 95% confidence level. Conversion to an equation in $\langle \sin^2 \theta \rangle$ has it that ^3J(C,C)/Hz = −2.59 $\langle \sin^2 \theta \rangle$ + 3.32. V_2 values follow as 1.4, 0.2, and −2.8 kJ mol^{-1} in the order 4-H, 4-CH_3, and 4-OCH_3. Note that these are lower limits for 4-H and 4-CH_3; for 4-OCH_3 the number implies an upper limit to the extent of stabilization of the perpendicular conformer.

2-X-Thioanisole derivatives

The internal rotational potentials about the C(1)—S bond in 2-X-thioanisole derivatives have onefold as well as twofold components; there may also be higher odd and evenfold harmonics. Equations [4] and [6] for ^4J and ^3J are then no longer valid. For ^3J(C,C) the constant term of 3.55 Hz in eq. [6] also contains the term $0.5J_{180}$. A crude approach to the problem assumes that 2-bromothioanisole takes on the planar conformation **3**, in which θ is zero from the aspect of C-4, C-5, and C-6 and is 180° for C-2 and C-3. A further approximation assumes that 2-hydroxythioanisole (CCl_4 solution) has conformation **2** with θ as 90°. ^5J(C,C) in the bromine compound is less than 0.05 Hz, implying a $\langle \sin^2 \theta \rangle$ probably less than 0.05, so that only small amplitude oscillations occur about the C(1)—S bond (the dipole moment of **3** has been interpreted in terms of θ being 45° (*29a*)).

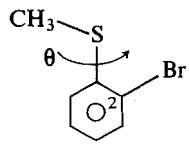

3

From ^3J(C,C) in these two compounds, but ignoring that for C-2 in 2-bromothioanisole, one may write

$$^3J(C,C)/\text{Hz} = 4.3 - 2.4 \langle \sin^2 \theta \rangle - 1.4 \langle \sin^2 (\theta/2) \rangle$$

in reasonable agreement with eq. [6] for which $\langle \sin^2 (\theta/2) \rangle$ is 0.5. The new relationship has ^3J(C,C) for C-2 in 2-bromothioanisole as 2.9 Hz, compared to the measured value of 2.2 Hz. The reason for the discrepancy lies in the following facts. Computations of ^3J(H,C) for the methyl protons in 2-fluorotoluene, for example (29), yield smaller couplings to C-2 than for C-6 and may be attributed to the presence of the directly bonded fluorine substituent; compared to similar computations on toluene, the substituent perturbations at C-6 are much smaller than at C-2. Furthermore, the substituent effect on ^3J(H,C) is dependent on θ, being a minimum near 90°. Presumably a similar situation holds for the thioanisole derivatives.

An INDO MO FPT computation on 2-fluorothioanisole, for a geometry very similar to that given by STO-3G MO optimized calculations (2), gives a reduction of over 0.4 Hz at C-2 for θ = 180° relative to thioanisole, whereas at θ = 90° the two ^3J(C,C) values differ by 0.1 Hz at most (see below for further complications). Thus, the very similar values of ^3J(C,C) in 2-hydroxythioanisole, that for C-2 being about 0.1 Hz smaller than that for C-6, are a consequence of a θ very near 90°. In the 2-bromo derivative, the large discrepancy of 0.7 Hz in ^3J(C,C) for C-2 is connected with the nearly planar conformation.

Can. J. Chem. Downloaded from www.nrcresearchpress.com by 93.93.197.157 on 09/07/12
For personal use only.

Can. J. Chem. Downloaded from www.nrcresearchpress.com by 93.93.197.157 on 09/07/12
For personal use only.

In 2-fluorothioanisole, ^5J(C,C) suggests relatively large librations about the C(1)—S bond, $\langle \sin^2 \theta \rangle$ being 0.32 and arcsin $\langle \sin^2 \theta \rangle^{1/2}$ is 34°. A true $\langle \sin^2 \theta/2 \rangle$ is not available; yet, if the obvious approximation is made, then ^3J(C,C) is calculated as 3.4 Hz for C-6. The observed value is 3.5 Hz. For C-2, ^3J becomes 2.3 Hz and the observed 1.6 Hz yields a discrepancy of 0.7 Hz. That this difference is the same as that for the less electronegative bromine substituent may well have to do with the larger average θ in the fluorine compound. Similar remarks apply to the 2-methoxy derivative, although the calculated ^3J(C,C) values are in much poorer agreement with experiment.

The experimental relationship above has ^3J(C,C) as smaller at θ = 180° than at θ = 0°, the opposite behaviour from the usual Karplus equation. Indeed, the INDO MO FPT calculations agree with the normal form, the coefficient of the term in $\sin^2(\theta/2)$ being positive. It may be noted that these computations were performed on the STO-3G geometries (2) and that a standard geometry (30) gave ^3J(C,C) larger at θ = 0° than at θ = 180°C. Because the true geometry is not known and because the computed ^3J(C,C) are really quite sensitive to the C(1)—S bond length and the C(2)—C(1)—S angle, it is best to rely on the unequivocal experimental indications of the "anti-Karplus" behaviour of ^3J(C,C) in thioanisole. A recent discussion (31) of the coupling mechanisms of ^3J(C,C) should be consulted for the intricacies that are involved.

Again, ^4J(C,C) displays a larger magnitude at θ = 0° than at θ = 180° (see 2-bromothioanisole in Table 3). Further, ^4J(C,C) is very nearly zero at θ = 180°, possibly just the opposite of expectations based on intuition (see the 2-methoxy and 2-bromo derivatives in Table 3). It does appear, however, that the substituent at C-2 has a large influence on this result. Note that ^4J(C,C) for 2-hydroxythioanisole in CCl_4 solution, where θ ~ 90° and a substituent effect is expected to be minimal (see ^3J(C,C) above), is the same for C-3 and C-5. The INDO MO FPT calculations do imply a very small, negative ^4J(C,C) at θ = 180°, −0.15 Hz, and −0.32 Hz at θ = 0°. Equation [4], based on the symmetrically substituted molecules, could be written as

$$^4J(\mathrm{C,C})/\mathrm{Hz} = 1.51 \langle \sin^2 \theta \rangle + a + b \langle \sin^2 (\theta/2) \quad [4]$$

where $a + b \langle \sin^2 (\theta/2) \rangle = a + 0.5b = 0.6$ Hz. In 2-bromothioanisole, of course, $\langle \sin^2 (\theta/2) \rangle$ and $\langle \sin^2 \theta \rangle$ are near zero for C-5 and ^4J(C,C) is ±0.6 Hz. The positive sign is consistent with the treatment of ^4J(C,C) in the previous section. In that event, the coefficient of $\langle \sin^2 (\theta/2) \rangle$ must be very near zero, yielding eq. [4] as an approximation for C-5 in the *ortho* substituted thioanisoles. However, the very small or vanishing ^4J(C,C) for C-3 is not reproduced by this relationship. It is therefore best to conclude that, for near-planar conformations at least, an electronegative substituent at C-2 reduces ^4J(C,C) drastically, that is, for θ ~ 180°.

2-Hydroxythioanisole

In CCl_4 solution, the ^nJ(H,C) and ^nJ(C,C) numbers for the 2-hydroxy derivative (Tables 3 and 4) are consistent with a perpendicular conformation of the thiomethyl group, that is, with θ very near 90°. In acetone-d_6 solution, the solvent molecules compete with the 3*p* lone-pair on sulfur for hydrogen bonding to the hydroxyl group. If an equilibrium exists between **4***a* and **4***b*, then ^nJ(C,C) should lie between the values observed for 2-methoxythioanisole, in which the SCH_3 group is favored to lie in the aromatic plane, and those for 2-hydroxythioanisole in CCl_4 solution. This is confirmed by the data in Table 3. The lifetime of an intermolecular hydrogen bond in solution at

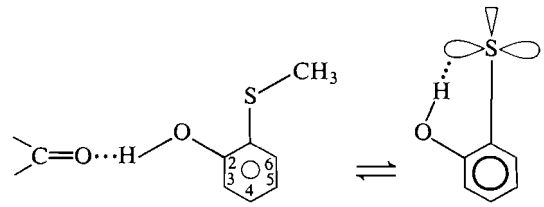

4*a* **4***b*

ambient temperatures is apparently less than 10^{-7} s (32, 33). δ(C-6) is 130.0, while (Table 3) it is 134.9 in CCl_4 solution and is 126.3 for 2-methoxythioanisole, which will roughly mimic the chemical shift of C-6 in **4***a* (C-6 is *meta* to the hydroxyl group and will be least influenced by the orientational behaviour of the latter). In other words, the rate process involved in the **4***a* ⇌ **4***b* equilibrium must be characterized by a rate constant of at least 2500 s^{-1} at 300 K (34). The barrier to internal rotation about the C—O bond in phenol is about 14.5 kJ mol^{-1} (4). The intermolecular hydrogen bond between phenol and cyclohexanone or acetone in CCl_4 solution has a free energy of formation of about −6.5 kJ mol^{-1} (35, 36). In the present situation the medium is acetone-d_6, however, and the two forms, **4***a* and **4***b*, may be stabilized by different amounts than in CCl_4 solution. An empirical relationship (37) has been used previously (38–40) to estimate the energy of hydrogen bond formation for hydroxyl groups in phenol derivatives: $\Delta\delta(\mathrm{OH}) = (-0.4 \pm 0.2) + E/\mathrm{kcal\ mol^{-1}}$, where Δδ(OH) is the chemical shift relative to the δ(OH) of 4.3 in phenol at infinite dilution in CCl_4 near 300 K (41). δ(OH) for 2-hydroxythioanisole in acetone-d_6 solution is 8.35 at 300 K; in CCl_4 solution it is 6.49. The population of **4***a* is assessed below at 0.64 ± 0.04. Hence δ(OH) of **4***a* is implied as 9.4 ± 0.2, ignoring any solvent effect on the shift of the proton in the hydrogen bond. Consequently, a *very rough* estimate of the enthalpy of formation of **4***a* is −23 ± 2 kJ mol^{-1}, to be compared with −20 ± 1 kJ mol^{-1} derived from calorimetric and vibrational information (35, 36). The entropy of formation of the intermolecular hydrogen bond in **4***a* is roughly −45 J mol^{-1} K^{-1} (35, 36). A free energy of activation of (6.5 + 14.5) kJ/mol for the interconversion of **4***a* and **4***b* is therefore taken as reasonable. At 300 K, the rate constant is then enormous (34) relative to any chemical shift difference between corresponding ^{13}C nuclei at 75 MHz in **4***a* and **4***b*.

The equilibrium populations of **4***a* and **4***b* can be estimated from some of the ^{13}C nmr chemical shifts, as well as from some of the ^nJ(C,C) in Tables 1 and 3. Assume that the nmr parameters for 2-methoxythioanisole are a measure of those in **4***a* and that those for the CCl_4 solution of 2-hydroxythioanisole characterize **4***b*. Then ^5J(C,C) and ^3J(C,C) yield the fractional population of **4***b* as 0.32 and 0.37, respectively. δ(C-4) and δ(C-6), least affected by the hydroxyl group, gave 0.37 and 0.42, respectively. $\delta(CH_3)$ yields 0.34. The ^{13}C chemical shifts that are subject to larger substituent effects from the hydroxyl group, namely, those of C-1, C-2, C-3, and C-5, are contraindicated as a measure of the populations of **4***a* and **4***b*. Of course, the thiomethyl group is changing its orientation drastically between **4***a* and **4***b* and that is what predominantly causes the alterations in the selected nmr indicators above. The average of the five estimates is 0.36 ± 0.04 (standard deviation) for the fractional population of **4***b*. The free energy difference at 300 K is therefore 1.4^{-3}_{+5} kJ mol^{-1}, **4***a* more stable. The free energy of interconversion estimated above would necessitate extremely low temperatures, about 100 K, to characterize **4***a* and **4***b* by their individual nmr spectra.

Can. J. Chem. Downloaded from www.nrcresearchpress.com by 93.93.197.157 on 09/07/12
For personal use only.

On the questionable assumption that δ(OH) of **4***b* in CCl_4 solution is a measure of the enthalpy of the O—H. . . .S intramolecular hydrogen bond, one has -10.9 kJ mol^{-1}. However, this estimate should presumably be corrected for the energy necessary to twist the thiomethyl group out of the molecular plane by roughly 90°, δ(OH) itself not being a measure of this energy. In thioanisole, V_2 is at least 6.1 kJ mol^{-1} (Table 6) but, of course, the hydroxy group will lower the $3p\ldots\pi$ conjugation in 2-hydroxythioanisole. The energy of twist is difficult to estimate, so that the O—H. . .3*p* bond may have an energy of at least 11 kJ mol^{-1}. This is higher than the energy of the O—H. . .O bond in 2-hydroxyanisole (42), in agreement with Schroeder–Lippencott potential functions (43) and with δ(OH) in the anisole derivative (44).

If the chemical shift difference between the hydroxyl protons in **4***a* and **4***b* is taken as a measure of their enthalpy difference, then the latter follows from the empirical relationship as 12.1 ± 0.8 kJ mol^{-1}. The free energy difference of **4***a* and **4***b*, being 1.4 ± 0.5 kJ mol^{-1}, implies an entropy difference at 300 K of 35.7 ± 4.5 J mol^{-1} K^{-1}. This estimate is somewhat lower in magnitude than the 45.2 ± 4.2 J mol^{-1} K^{-1} for free phenol and its complex with acetone in CCl_4 solution (36). As pointed out by Jaffé (45), the entropy change on formation of the intramolecular hydrogen bond in 2-halophenols is very small. Actually, **4***b* is favored by an entropy term of R ln 2 relative to a conformer with a coplanar thiomethyl group, so that firmer conclusions must be left in abeyance.

Finally, if there were no change in entropy on formation of **4***b*, then the present considerations would suggest a free energy barrier to conversion of **4***b* to a free, coplanar form (in which the hydroxyl group points away from the thiomethyl group) of 14.5 + 11 or about 25 kJ mol^{-1}. This is compatible with the discussion above concerning the rate processes leading to broadening of the ^{13}C nmr peaks.

2-Aminothioanisole

In 2-aminothioanisole in CCl_4 solution (Table 3) a stereospecific intramolecular hydrogen bond to the 3*p* lone-pair need not twist the thiomethyl group into a perpendicular conformation because the amino group has a pyramidal geometry. From the most recent structural data on aniline and derivatives (46, 47), the angle φ in **5** can be calculated (48) as 25°. The barrier to rotation about the C—N bond in aniline is near 21 kJ mol^{-1} (49). The thiomethyl group is not a strong electron donor; donation of π electron density would lower the C—N rotational barrier.

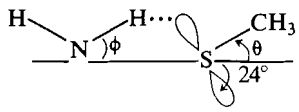

5

The barrier about the C(1)—S bond will be lowered by the amino group, however (see Table 6), so that the thiomethyl group can easily twist out of the benzene plane to optimize the intramolecular hydrogen bond indicated in **5**. The twist angle, θ, can be approximated from ^5J(C,C), being 0.76 Hz. Then arc sin $\langle\sin^2\theta\rangle^{1/2}$ is 66°, so that the 3*p* lone-pair would twist out of plane by about 24°, that is by about 66° away from its perpendicular orientation in a planar thioanisole molecule. In aniline, the barrier to inversion is only about 6 kJ mol^{-1} (50). Therefore an inversion at nitrogen is no doubt also occurring in **5**, which would entail oscillatory motion about the C(1)—S bond.

The estimate of 66° for θ based on ^5J(C,C) can be checked with, for example, ^3J(C,C) for C-6. The two relationships used in this paper yield an average of 1.67 ± 0.20 Hz for an angle of 66°, to be compared with the value in Table 3 of 1.68 Hz. ^4J(C,C) for C-5 yields an arc sin $\langle\sin^2\theta\rangle^{1/2}$ of 64°.

When dissolved in acetone-d_6, the second N—H bond, not involved in the intramolecular hydrogen bond in 2-aminothioanisole, can bond to solvent molecules. Therefore, unlike 2-hydroxythioanisole, the intramolecular hydrogen bond in the amino derivative need not be broken. Indeed, $^6J(H,CH_3)$ in such a situation is -0.42 Hz (Table 4) and arc sin $\langle\sin^2\theta\rangle^{1/2}$ is 60°. Further, assume that $^5J(H,CH_3)$ behaves like $^5J(H,CH_3)$ in toluene (16,17) and can be written as $^5J(H,CH_3) = A\langle\sin^2\theta\rangle + B\langle\sin^2(\theta/2)\rangle$. The data in Table 4 yield A as 0.116(4) and B as 0.136(4) Hz if $\langle\sin^2(\theta/2)\rangle$ is estimated on the assumption of two rigid molecules in Table 4, 90° and 60° for θ. Finally, on the assumption that $\delta(CH_3)$ is proportional to $\langle\sin^2\theta\rangle$, that its values in 2-methoxythioanisole, 14.23, and in 2-hydroxythioanisole, 19.70, correspond to $\langle\sin^2\theta\rangle$ values of 0.275 and unity, respectively (obtained from ^5J(C,C)), the equation in $\delta(CH_3)$ becomes $\delta = 12.2 + 7.54\langle\sin^2\theta\rangle$. The δ of 17.56 for 2-aminothioanisole then has arc sin $\langle\sin^2\theta\rangle^{1/2}$ as 58°. This result encourages the following approach to conformational deductions about thioanisole derivatives for which only $\delta(CH_3)$ is conveniently measurable.

δ(CH$_3$) as a conformational indicator

$\delta(CH_3)$ for the *para* substituted thioanisoles in Table 1, and including also the 3,5-dichloro derivative, is related to ^3J(C,C) by δ/ppm = $-3.46\ ^3J$(C,C)/Hz + 25.75 (nine points with a correlation coefficient of 0.991). Combined with eq. [6], this relationship should yield $\langle\sin^2\theta\rangle$ for the 4-thiomethyl, 3,5-ditrifluoromethyl, 4-carboxaldehyde, and 4-hydroxymethyl thioanisole derivatives; $\delta(CH_3)$ is 15.99, 14.99, 14.49, and 15.81, respectively, for dilute acetone-d_6 solutions. Consequently, $\langle\sin^2\theta\rangle$ is 0.293, 0.177, 0.119, and 0.272 for these compounds, corresponding to twofold barriers of 4.6, 8.7, 12.6, and 5.6 kJ mol^{-1}, respectively, for 4-SCH_3, 3,5-diCF_3, 4-CHO, and 4-CH_2OH derivatives of thioanisole. Comparison with the V_2 estimates in Table 6 suggests that the thiomethyl group is a weak π electron donor, as expected, that the CHO group is a somewhat weaker π electron acceptor than is the nitro group, and that the hydroxymethyl group is a weaker electron donor than is the methyl group; this is also reasonable. The CF_3 groups are not as effective as chlorine substituents at the *meta* position in raising the barrier to internal rotation about the C(1)—S bond. The present relationship between $\delta(CH_3)$ and ^3J(C,C) cannot be applied to most *ortho* substituted derivatives in Tables 1 and 3 because of proximity and other substituent perturbations of both parameters.

^{2}J(C,C) values

This coupling constant is not very sensitive to the average angle θ, as demonstrated by its near constancy in the *para* and *meta* substituted derivatives of thioanisole in Table 1. It increases in magnitude by 0.5 Hz in 2,6-dimethylthioanisole, but is also sensitive to proximate substituent perturbations, as can be seen by its magnitude in the 2-hydroxy derivative. ^2J(C,C) is negative in 3,5-dichlorothioanisole and most likely also negative for all the other molecules in Tables 1–3.

Acknowledgement

We are grateful to the Natural Sciences and Engineering Research Council of Canada for financial assistance.

1. T. SCHAEFER, J. D. BALEJA, and G. H. PENNER. Can. J. Chem. **63**, 2471 (1985).
2. T. SCHAEFER and J. D. BALEJA. Can. J. Chem. **64**, 1376 (1986).
3. T. SCHAEFER and T. A. WILDMAN. Chem. Phys. Lett. **80**, 280 (1981).
4. N. W. LARSEN and F. M. NICOLAISEN. J. Mol. Struct. **22**, 29 (1974).
5. T. SCHAEFER, T. A. WILDMAN, and S. R. SALMAN. J. Am. Chem. Soc. **102**, 107 (1980).
6. A. PROSS and L. RADOM. Prog. Phys. Org. Chem. **13**, 1 (1981).
7. G. A. MORRIS and R. FREEMAN. J. Am. Chem. Soc. **101**, 760 (1979).
8. J. P. MAHER and D. F. EVANS. Proc. Chem. Soc. London, 208 (1961).
9. J. S. MARTIN, A. R. QUIRT, and K. E. WORVILL. The nmr program library. Daresbury Laboratory, Daresbury, U.K.
10. J. A. POPLE, J. W. MCIVER, JR., and N. S. OSTLUND. J. Chem. Phys. **49**, 2960 (1968); **49**, 2965 (1968).
11. P. DOBOSH and N. S. OSTLUND. QCPE, **11**, 281 (1975).
12. R. WASYLISHEN and T. SCHAEFER. Can. J. Chem. **50**, 1852 (1972).
13. M. BARFIELD, C. J. HALLICK, K. HATA, S. STERNHELL, and P. W. WESTERMAN. J. Am. Chem. Soc. **105**, 2178 (1983).
14. T. SCHAEFER, J. PEELING, and G. H. PENNER. Can. J. Chem. **61**, 2773 (1983).
15. T. SCHAEFER, J. PEELING, G. H. PENNER, A. LEMIRE, and R. SEBASTIAN. Can. J. Chem. **63**, 24 (1985).
16. T. SCHAEFER and R. LAATIKAINEN. Can. J. Chem. **61**, 2785 (1983).
17. T. SCHAEFER, R. SEBASTIAN, and G. H. PENNER. Can. J. Chem. **63**, 2597 (1985).
18. M. KARPLUS. J. Am. Chem. Soc. **85**, 2870 (1963).
19. H. FÖRSTER and F. VÖGTLE. Angew. Chem. Int. Ed. Engl. **16**, 429 (1977).
20. A. MANNSCHRECK and L. ERNST. Chem. Ber. **104**, 228 (1971).
21. T. SCHAEFER, R. LAATIKAINEN, T. A. WILDMAN, J. PEELING, G. H. PENNER, J. BALEJA, and K. MARAT. Can. J. Chem. **62**, 1592 (1984).
22. T. SCHAEFER and G. H. PENNER. Can. J. Chem. **64**, 2013 (1986).
23. H. M. MCCONNELL and D. B. CHESNUT. J. Chem. Phys. **28**, 107 (1958).
24. M. KARPLUS and G. K FRAENKEL. J. Chem. Phys. **35**, 1312 (1961).
25. W. J. E. PARR and T. SCHAEFER. Acc. Chem. Res. **13**, 400 (1980).
26. P. B. AYSCOUGH, M. S. BRICE, and R. E. D. MCCLUNG. Mol. Phys. **20**, 41 (1971).
27. T. MATSUSHITA, Y. OSAMURA, N. MISAWA, K. NISHIMOTO, and Y. ISUNO. Bull. Chem. Soc. Jpn. **52**, 2521 (1979).
28. P. PALMIERI, F. FULLINI, B. VELINO, and C. ZAULI. Gazz. Chim. Ital. **105**, 919 (1975).
29. R. WASYLISHEN and T. SCHAEFER. Can. J. Chem. **51**, 961 (1973); (*a*) H. LUMBROSO, CH. LIEGEOIS, L. TESTAFERRI, and M. TIECCO. J. Mol. Struct. **144**, 121 (1986).
30. J. A. POPLE and M. S. GORDON. J. Am. Chem. Soc. **89**, 4253 (1967).
31. M. L. SEVERSON and G. E. MACIEL. J. Magn. Reson. **57**, 248 (1984).
32. K. ENDO, B. KNUETTEL, I. MORISHIMA, T. INUBUSHI, and T. YONEZAWA. Chem. Phys. Lett. **31**, 387 (1975).
33. K. ENDO, I. MORISHIMA, and T. YONEZAWA. J. Chem. Phys. **67**, 4760 (1977).
34. J. SANDSTRÖM. Dynamic nmr spectroscopy. Academic Press, New York. 1982. Chaps. 6 and 7.
35. J. N. SPENCER, J. A. ADREFSKY, J. NAGHDI, L. PATTI, and J. F. TRADER. J. Phys. Chem. **91**, 2959 (1987).
36. F. FRITSCHE. Ber. Bunsen-ges. Phys. Chem. **68**, 459 (1964).
37. T. SCHAEFER. J. Phys. Chem. **79**, 1888 (1975).
38. T. TAKASUKA and Y. MATSUI. J. Chem. Soc. Perkin Trans. 2, 1743 (1979).
39. J. REUBEN. J. Am. Chem. Soc. **108**, 1735 (1986).
40. T. SCHAEFER, D. M. MCKINNON, R. SEBASTIAN, J. PEELING, G. H. PENNER, and R. P. VEREGIN. Can. J. Chem. **65**, 908 (1987).
41. V. S. GRIFFITHS and G. SOCRATES. J. Mol. Spectrosc. **21**, 302 (1966).
42. G. L. CARLSON and W. G. FATELEY. J. Phys. Chem. **77**, 1157 (1973).
43. W. R. SNYDER, H. D. SCHREIBER, and J. N. SPENCER. Spectrochim. Acta, Part A, **29**, 1225 (1973).
44. T. SCHAEFER and T. A. WILDMAN. Can. J. Chem. **57**, 450 (1979).
45. H. H. JAFFÉ. J. Am. Chem. Soc. **79**, 2373 (1957).
46. G. ROUSSY and A. NONAT. J. Mol. Spectrosc. **118**, 180 (1986).
47. M. COLAPIETRO, A. DOMENICANO, G. PORTALONE, G. SCHULTZ, and I. HARGITTAI. J. Phys. Chem. **91**, 1728 (1987).
48. A. WOLF, U. VOETS, and H.-H. SCHMIDKE. Theor. Chim. Acta (Berlin), **54**, 229 (1980).
49. N. W. LARSEN, E. L. HANSEN, and F. M. NICOLAISEN. Chem. Phys. Lett. **43**, 584 (1976).
50. J. M. HOLLAS, M. R. HOWSON, T. RIDLEY, and L. HALONEN. Chem. Phys. Lett. **98**, 611 (1983).
51. V. WRAY, L. ERNST, and E. LUSTIG. J. Magn. Reson. **27**, 1 (1977).
52. W. S. BREY, L. W. JAQUES, and H. J. JAKOBSEN. Org. Magn. Reson. **12**, 243 (1979).

Can. J. Chem. Downloaded from www.nrcresearchpress.com by 93.93.197.157 on 09/07/12
For personal use only.

Ethyl cation transfer from diethylchloronium to alkyl aromatics studied by high pressure mass spectrometry

PEGGY JANE MATHEWS AND JOHN A. STONE
Chemistry Department, Queen's University, Kingston, Ont., Canada K7L 3N6

Received September 22, 1987

PEGGY JANE MATHEWS and JOHN A. STONE. Can. J. Chem. **66**, 1239 (1988).

Diethylchloronium ($(C_2H_5)_2Cl^+$) has been formed in a high pressure (2–4 Torr) ion source using a C_2H_5Cl/CH_4 mixture. $(C_2H_5)_2Cl^+$ reacts with C_2H_5Cl (E_a = 22 ± 2 kcal mol^{-1}) at temperatures above 500 K to give *t*-$C_4H_9^+$. The reaction of $(C_2H_5)_2Cl^+$ with B (B = benzene, toluene, isopropylbenzene, mesitylene) yields mainly $C_2H_5B^+$ at temperatures below 500 K but BH^+ is also formed at higher temperatures. The further reactions of $C_2H_5B^+$ include proton transfer to B yielding BH^+ (mesitylene), hydride transfer from B (isopropylbenzene), and reaction with C_2H_5Cl yielding $(C_2H_5)_2B^+$ (toluene and benzene) and $(C_2H_5)_3B^+$ (benzene). The rate constants for the reaction $(C_2H_5)_2Cl^+ + B \rightarrow C_2H_5B^+ + C_2H_5Cl$ increase in the order of increasing reaction exothermicity (mesitylene > isopropylbenzene > toluene > benzene). Mesitylene has a negative temperature coefficient, isopropylbenzene has no temperature coefficient, and toluene and benzene show positive temperature coefficients of reaction rate constants consistent with the double well potential theory for gas phase S_N2 reactions.

PEGGY JANE MATHEWS et JOHN A. STONE. Can. J. Chem. **66**, 1239 (1988).

Utilisant un mélange de C_2H_5Cl/CH_4 dans une source ionique à haute pression (2 à 4 Torr), on a formé l'ion diéthylchloronium ($(C_2H_5)_2Cl^+$). L'ion $(C_2H_5)_2Cl^+$ réagit avec le C_2H_5Cl (E_a = 22 ± 2 kcal mol^{-1}) à des températures supérieures à 500 K et il y a formation de *tert*-$C_4H_9^+$. A des températures allant jusqu'à 500 K, la réaction du $(C_2H_5)_2Cl^+$ avec les molécules B (B = benzène, toluène, isopropylbenzène et mésitylène) fournit principalement les ions $C_2H_5B^+$; toutefois, à des températures plus élevées, il y a formation des ions BH^+. Parmi les réactions subséquentes des ions $C_2H_5B^+$, on observe un transfert de protons à B conduisant à l'ion BH^+ (mésitylène), un transfert d'hydrure provenant de B (isopropylbenzène) et une réaction avec le C_2H_5Cl conduisant aux ions $(C_2H_5)_2B^+$ (toluène et benzène) et $(C_2H_5)_3B^+$ (benzène). Les constantes de vitesse pour la réaction $(C_2H_5)_2Cl^+ + B \rightarrow C_2H_5B^+ + C_2H_5Cl$ augmentent avec le rendement thermique positif de la réaction (mésityléne > isopropylbenzène > toluène > benzène). Pour ce qui est des coefficients de température des constantes des vitesses de réaction, celui du mésitylène est négatif alors que l'isopropylbenzène n'en a pas et que ceux du toluène et du benzène sont positifs; ces résultats sont en accord avec la théorie du potentiel à double puits pour les réactions S_N2 en phase gazeuse.

[Traduit par la revue]

Introduction

Dialkylhalonium ions have been shown to be excellent alkylating agent for aromatic hydrocarbons in both gas and liquid phases (1–4). Dimethylchloronium ($CH_3ClCH_3^+$) has been extensively studied in the gas phase because it is very readily prepared from methane/methyl chloride mixtures in a chemical ionization (CI) source (3, 4). It reacts with bases in the gas phase by methyl cation transfer.

[1] $CH_3ClCH_3^+ + B \rightarrow CH_3Cl + BCH_3^+$

Such reactions are bimolecular nucleophilic displacement (S_N2) reactions, the base B displacing methyl chloride from the chloronium ion. For example, reaction [1] is highly exothermic (>30 kcal mol^{-1}) for bases such as dimethyl ether and ammonia and reaction occurs at almost every collision (4). However, with the aromatic bases benzene, toluene, and isopropyl benzene, although the exothermicities of the reactions are still of the same magnitude the reaction efficiencies (the measured rate constant k divided by the collision rate constant k_c as calculated by the average dipole orientation (ADO) theory (5)) are far less than unity (4). For B = benzene the reaction efficiency increases with increasing temperature (positive temperature coefficient) while for B = toluene or isopropylbenzene the reaction efficiency decreases with increasing temperature (negative temperature coefficient). A series of relative rate determinations for B = benzene, toluene, and mesitylene for which reaction exothermicity increases in the order given suggested that the magnitude of the negative temperature dependence increases with increasing exothermicity (6).

The above observations are strong supporting evidence for the double well potential model first set out in some detail by Brauman and co-workers (7, 8) and well summarized by Magnera and Kerbale (9). In this model, reaction [1] is considered to occur in several steps as in reaction [2] and Fig. 1. There is initial formation of an ion–molecule complex $CH_3ClCH_3^+ \cdots B$ (rate constant k_c) which can either return to products (rate constant k_b) or pass over the central chemical barrier (rate constant k_p) to give the complex $CH_3Cl \cdots CH_3B^+$ which subsequently decomposes to products. In these highly exothermic reactions k_{-p} is considered to be negligibly small ($k_{-p} \ll k_p$) so that once the system passes over the barrier methyl cation transfer occurs irreversibly.

[2] $$CH_3ClCH_3^+ + B \underset{k_b}{\overset{k_c}{\rightleftharpoons}} CH_3ClCH_3^+ \cdots B \underset{k_{-p}}{\overset{k_p}{\rightleftharpoons}} CH_3Cl \cdots CH_3B^+ \overset{k_d}{\rightarrow} CH_3Cl + CH_3B^+$$

The steady-state assumption $d[CH_3^+ClCH_3 \cdots B]/dt = 0$ yields the overall rate constant k where $k = (k_c k_p)/(k_b + k_p)$ and reaction efficiency $k/k_c = k_p/(k_b + k_p)$. When the reaction exothermicity is sufficiently large the level of the top of the central barrier relative to the reactants energy level, ΔE^0, is large and negative, facilitating passage over the chemical barrier. When ΔE^0 is positive, return to reactants over the centrifugal barrier is favoured and the reaction has an activation energy $\approx \Delta E^0$. When ΔE^0 is small and negative the central barrier may still be rate controlling since entropic considerations favour return to reactants rather than formation of a constrained transition state at the top of the barrier in which the carbon being transferred to B is in a pentacoordinated state.

Can. J. Chem. Downloaded from www.nrcresearchpress.com by 93.93.197.157 on 09/07/12
For personal use only.

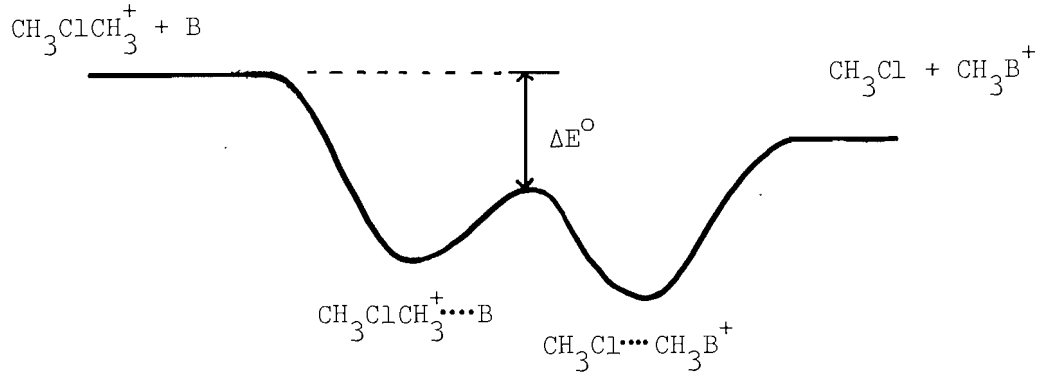

FIG. 1. The reaction coordinate for an ionic gas phase nucleophilic displacement reaction.

The use of different aromatic bases with a common chloronium ion enables the reaction exothermicity and hence ΔE^0 to be varied in a regular manner (3, 4). In this paper we seek additional evidence for the model by using the same series of bases but a different chloronium ion, namely diethylchloronium. S_N2 reactions with aromatic base B lead to the formation of $BC_2H_5^+$ in a reaction whose exothermicity will be different to that of the analogous reaction [1].

[3] $C_2H_5ClC_2H_5^+ + B \rightarrow C_2H_5Cl + C_2H_5B^+$

The order of reactivity of the different bases should be, according to the model, the same for $(C_2H_5)_2Cl^+$ and $(CH_3)_2Cl^+$ but the temperature coefficients should change with change of ΔE^0.

$(C_2H_5)_2Cl^+$ is the exclusive long-lived ion in C_2H_5Cl/CH_4 mixtures under most ion source conditions whereas CH_3Cl/CH_4 mixtures lead to both $(CH_3)_2Cl^+$ and $C_2H_5ClCH_3^+$, each of which reacts with aromatics, the latter ion forming $BC_2H_5^+$ (4, 6). The ion chemistry resulting from $C_2H_5^+$ addition may be followed using C_2H_5Cl/CH_4 mixtures without the complications resulting from a concurrent reaction.

Experimental

The mass spectrometer with pulsed electron beam and high pressure ion source (1–5 Torr, 300–600 K) has been described previously (10). Samples are prepared in a heated 5 L flask at a total pressure of ~700 Torr (1 Torr = 133 Pa) and are bled into the ion source via a heated leak valve and a heated glass line. A typical sample contained 6.6 mol% ethyl chloride, 1.4 mol% sulfurhexafluoride to capture thermalized electrons and hence increase ion residence time in the ion source, and 92 mol% methane. A small amount of an aromatic base was also added when required, ranging from 0.001–0.005 mol% in typical cases but for the very unreactive base, benzene, as much as 0.39% was used.

The aromatic bases were reagent grade and were used as received. Methane (99.99% pure) and ethyl chloride (99.7%) were from Matheson, Canada while the sulfur hexafluoride (Instrument Grade) was from Liquid Carbonic, Canada.

Results and discussion

The ion chemistry in methane/ethyl chloride mixtures

In mixtures containing only methane, ethyl chloride, and sulfur hexafluoride it is assumed that the major product, the diethylchloronium ion, is formed from the two methane reagent ions, CH_5^+ and $C_2H_5^+$, in a manner analogous to that for dimethylchloronium in a CH_4/CH_3Cl mixture (4).

[4] $CH_5^+ + C_2H_5Cl \rightarrow CH_4 + C_2H_5ClH^+$
$\Delta H^0 = -40$ kcal mol^{-1}

[5] $C_2H_5^+ + C_2H_5Cl \rightarrow C_2H_5ClH^+ + C_2H_4$
$\Delta H^0 = -9$ kcal mol^{-1}

[6] $C_2H_5ClH^+ + C_2H_5Cl \rightarrow C_2H_5ClC_2H_5^+ + HCl$

[7] $C_2H_5^+ + C_2H_5Cl \xrightarrow{M} C_2H_5ClC_2H_5^+$

In calculating the enthalpy changes for reactions [4] and [5] the proton affinity (PA) of C_2H_5Cl is taken as 172 kcal mol^{-1} (11) and other PA values are from ref. 12. Reactions [4] and [5] being typical, high exothermic proton transfer reactions involving ions with localized charges proceed at or near collision rates (13). The rate constant for reaction [6] has been reported as 5.5×10^{-10} cm^3 molecule^{-1} s^{-1} (14) which gives a half life for $C_2H_5ClH^+$ of $\sim 2 \times 10^{-7}$ s in a typical sample at 4 Torr and 300 K. This ion was not observed since $C_2H_5ClC_2H_5^+$ is generated well within 50 μs, the earliest observation time after the ionizing electron pulse. At low pressure under ion cyclotron resonance (ICR) conditions (< 10^{-4} Torr) $C_2H_5^+$ reacts with ethyl chloride mainly by proton transfer but isotopic experiments demonstrate the participation of an intermediate but unobserved complex in which hydrogen migration occurs (14). The stabilized complex was not observed under ICR conditions but the formation of the diethylchloronium ion by reaction [7] is probable at 1–4 Torr. The similar direct addition of $C_2H_5^+$ to methyl chloride has been suggested (4).

At 300 K $(C_2H_5)_2Cl^+$ is the only abundant ion in the mass spectrum of methane/ethyl chloride mixtures. A non-chlorine-containing ion of m/z 57 is also present but is of very low intensity (<1%). $(C_2H_5)_2Cl^+$ is the major ion present at all temperatures below 580 K. The relative intensity of m/z 57 shows little change with temperature up to 500 K but above this temperature its yield increases very rapidly and it becomes the major ion above 580 K. Luczynski and Wincel (15) reported the presence of m/z 57, which they identified as $C_4H_9^+$ but assigned no structure, in ethyl chloride at 403 K and 0.01–0.10 Torr. They proposed that it was formed by the unimolecular decomposition of excited $(C_2H_5)_2Cl^+$. No mode of excitation was suggested.

[8] $C_2H_5ClC_2H_5^+* \rightarrow C_4H_9^+ + HCl.$

If this were a thermal decomposition then the normalized intensity of m/z 57 might be expected to decrease as the total pressure is decreased which is contrary to what is observed. Figure 2 shows the normalized yields of ions at high temperature in a typical methane/ethyl chloride mixture. $(C_2H_5)_2Cl^+$ decays linearly with time to yield mainly m/z 57 and smaller amounts of m/z 55 and 69, none of which contains chlorine. The slope of

Can. J. Chem. Downloaded from www.nrcresearchpress.com by 93.93.197.157 on 09/07/12
For personal use only.

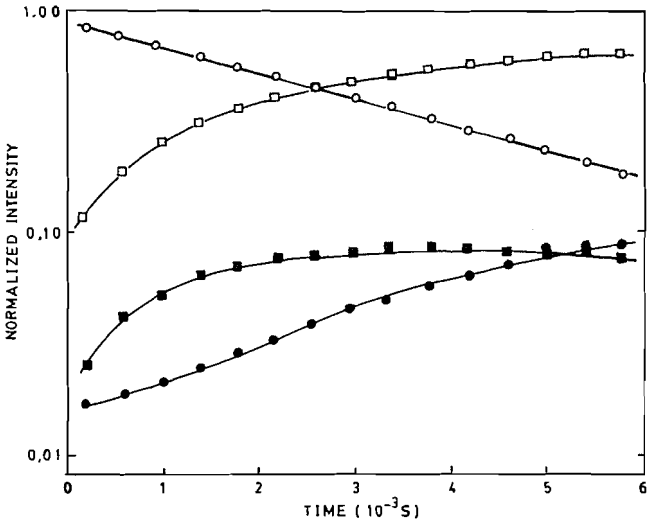

FIG. 2. The normalized ion intensities after a 50 μs pulse of ionizing electrons in a $C_2H_5Cl/SF_6/CH_4$ (0.065/0.017/0.928) mixture at 4.6 Torr and 571 K. ○, $(C_2H_5)_2Cl^+$; □, $C_4H_9^+$ (*m/z* 57); ■, $C_4H_7^+$ (*m/z* 55); ●, $C_5H_9^+$ (*m/z* 69).

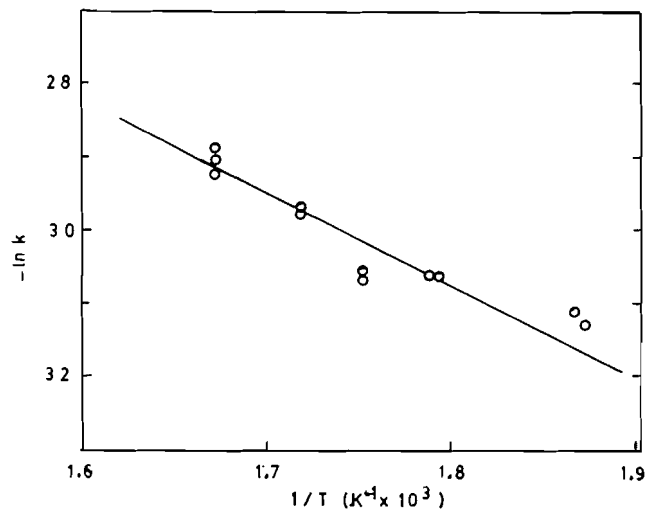

FIG. 3. Arrhenius plot for the reaction $(C_2H_5)_2Cl^+ + C_2H_5Cl \rightarrow C_4H_9^+ + C_2H_5Cl + HCl$.

the decay curve increases with increasing ethyl chloride concentration. The data fit a second order rate expression of the form

$$[9] \quad \frac{-d[(C_2H_5)_2Cl^+]}{dt} = k_{10}[(C_2H_5)_2Cl^+][C_2H_5Cl]$$

k_{10} is very small ($<10^{-13}$ cm^3 molecule^{-1} s^{-1}) and is independent of total pressure in the range 2.5 to 4.7 Torr but is strongly dependent on temperature. The Arrhenius plot of Fig. 3 yields an activation energy of 22 ± 2 kcal mol^{-1}. The overall reaction should therefore be written as [10] rather than [8].

[10] $(C_2H_5)_2Cl^+ + C_2H_5Cl \rightarrow C_2H_5Cl + C_4H_9^+ + HCl$

The standard enthalpy change for this reaction is of course the same as that for reaction [8]. This enthalpy change may be calculated provided that a value for $\Delta H_f^0((C_2H_5)_2Cl^+)$ is known. Reaction [7] was never observed as an equilibrium reaction so that a measurement of the binding energy of $C_2H_5^+$ to C_2H_5Cl which would lead to $\Delta H_f^0((C_2H_5)_2Cl^+)$ could not be made. An estimate of this enthalpy of formation may however be obtained. The standard enthalpy changes for reactions [11] and [12] are, respectively, −68 (16) and −30.7 kcal mol^{-1} (17)

[11] $CH_3^+ + CH_3Cl \rightleftharpoons (CH_3)_2Cl^+$

[12] $C_2H_5^+ + CH_3Cl \rightleftharpoons C_2H_5ClCH_3^+$

This leads to $\Delta H_f^0((CH_3)_2Cl^+) = 172$ kcal mol^{-1} and $\Delta H_f^0(C_2H_5ClCH_3^+) = 164$ kcal mol^{-1}. ΔH^0 for reaction [13] is then −71 kcal mol^{-1}.

[13] $CH_3^+ + C_2H_5Cl \rightleftharpoons C_2H_5ClCH_3^+$

This enthalpy of binding of CH_3^+ to C_2H_5Cl is 3 kcal mol^{-1} greater than that to CH_3Cl, which may be attributed to the slightly greater polarizability of the larger C_2H_5Cl. The difference in binding energies of $C_2H_5^+$ to CH_3Cl and C_2H_5Cl should be much the same as that for CH_3^+ so that a value of $\Delta H^0 = -34$ kcal mol^{-1} for reaction [7] is reasonable. This leads to $\Delta H_f^0((C_2H_5)_2Cl^+) = 155$ kcal mol^{-1}. The measured activation energy for reaction [10] of 22 kcal mol^{-1} is considerably less than $D(C_2H_5^+—ClC_2H_5)$ so that there are no conditions under which reaction [7] can be observed as an equilbrium and therefore $D(C_2H_5^+—ClC_2H_5)$ cannot be directly determined.

If $C_4H_9^+$ is the *t*-butyl cation then $\Delta H_{10}^0 = -11$ kcal mol^{-1} while if it is the *sec*-butyl cation then $\Delta H_{10}^0 = +6$ kcal mol^{-1}. The structure of $C_4H_9^+$ will be discussed later.

The ion chemistry in methane/ethyl chloride/aromatic mixtures

The primary reaction between aromatic B and $(C_2H_5)_2Cl^+$ is $C_2H_5^+$ transfer (reaction [3]). A typical mass spectrum is shown in Fig. 4*a* while Figs. 4*b* to 8 show time-resolved data. No adducts of formula $B\cdot(C_2H_5)_2Cl^+$ were observed under any conditions. Toluene$\cdot(CH_3)_2Cl^+$ has been observed in methane/methyl chloride/toluene mixtures at temperatures below 240 K (4), and equilibrium measurements yielded $D((CH_3)_2Cl^+—C_7H_8) = 12.3$ kcal mol^{-1}. There is no reason why the binding energies for the analogous $B\cdot(C_2H_5)_2Cl^+$ ion–neutral complexes would be significantly greater than this value and hence such complexes would not be observable in our available temperature range of 300–600 K.

The initial $B\cdot C_2H_5^+$ adduct is an *ipso*-protonated arenium ion. All the available evidence suggests that hydrogen migration occurs very rapidly to yield an ion with a tetrahedral or close to tetrahedral CH_2 group (2, 9).

[14] $(C_2H_5)_2Cl^+ +$ 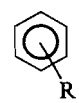 $\longrightarrow C_2H_5Cl +$ 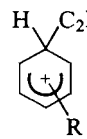

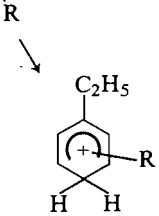

The structure of the final product may be described by the positions of the CH_2 and C_2H_5 groups relative to the site(s) of R. The preferred position of ethylation will be *para* to R in toluene and isopropylbenzene by analogy with other gas phase systems

Can. J. Chem. Downloaded from www.nrcresearchpress.com by 93.93.197.157 on 09/07/12
For personal use only.

Can. J. Chem. Downloaded from www.nrcresearchpress.com by 93.93.197.157 on 09/07/12
For personal use only.

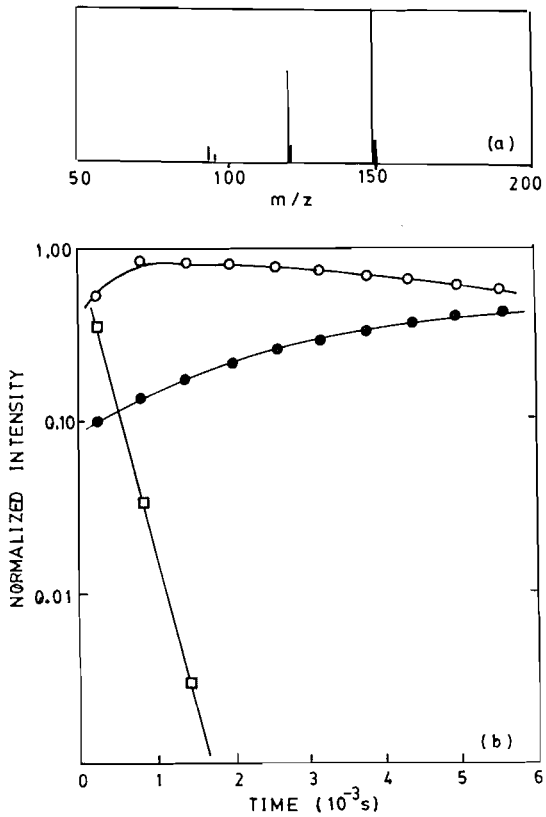

FIG. 4. (*a*) Mass spectrum of a mesitylene/$C_2H_5Cl/SF_6/CH_4$ (4×10^{-5}/0.072/0.014/0.914) mixture at 4.86 Torr and 306 K. (*b*) The normalized ion intensities after a 50 μs pulse of ionizing electrons for the same system. □, $(C_2H_5)_2Cl^+$; ○, $C_2H_5C_6H_3(CH_3)_3^+$ (*m/z* 149); ●, $C_6H_4(CH_3)_3^+$ (*m/z* 121).

(18–20). The site of CH_2 giving the most stable structure is then determined by the positions of C_2H_5 and R and the nature of R. The final stable $B \cdot C_2H_5^+$ structures which are assumed to be formed and for which reaction enthalpies can be calculated are:

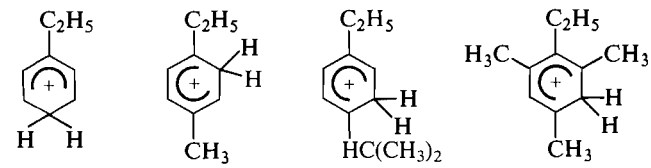

benzene toluene isopropylbenzene mesitylene

$C_2H_5^+$ transfer to initially yield the *ipso*-protonated species will be up to 7 kcal mol^{-1} less exothermic (18). The ion chemistries of the systems containing the individual aromatics are sufficiently different to warrant separate descriptions.

Mesitylene

This compound gives the simplest mass spectrum at any temperature (Fig. 4*a*). There are only two major product ions, $B \cdot C_2H_5^+$ (*m/z* 149) and BH^+ (*m/z* 121). The time-resolved, normalized ion yields in Fig. 4*b* show that $(C_2H_5)_2Cl^+$ disappears in a pseudo first order reaction giving *m/z* 149 which in turn disappears in a much slower pseudo first order proton transfer reaction to give *m/z* 121.

[15] $(C_2H_5)_2Cl^+ + (CH_3)_3C_6H_3 \rightarrow C_2H_5Cl + (CH_3)_3C_6H_3C_2H_5^+$ (*m/z* 149)
$\Delta H^0 = -33$ kcal mol^{-1}

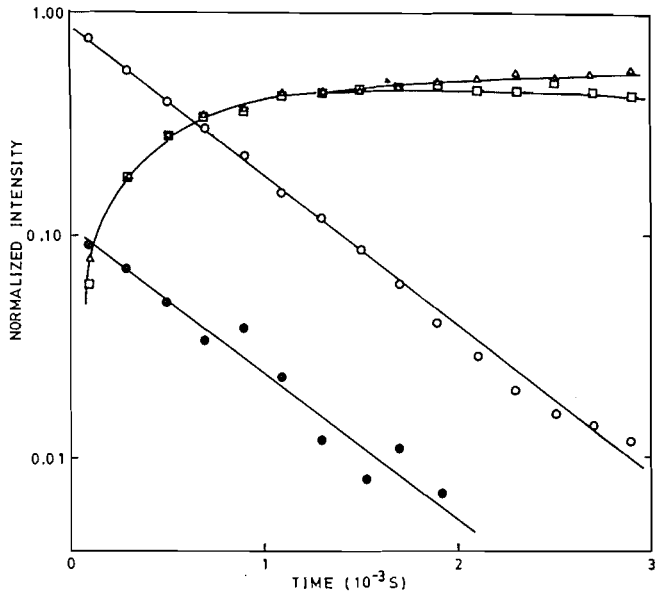

FIG. 5. The normalized ion intensities after a 50 μs pulse of ionizing electrons in a mesitylene/$C_2H_5Cl/SF_6/CH_4$ (9.9×10^{-5}/ 0.066/ 0.014/0.920) mixture at 4.39 Torr and 572 K. ○, $(C_2H_5)_2Cl^+$; ●, $C_4H_9^+$ (*m/z* 57); □, $C_2H_5C_6H_3(CH_3)_3^+$ (*m/z* 149); △, $C_6H_4(CH_3)_3^+$ (*m/z* 121).

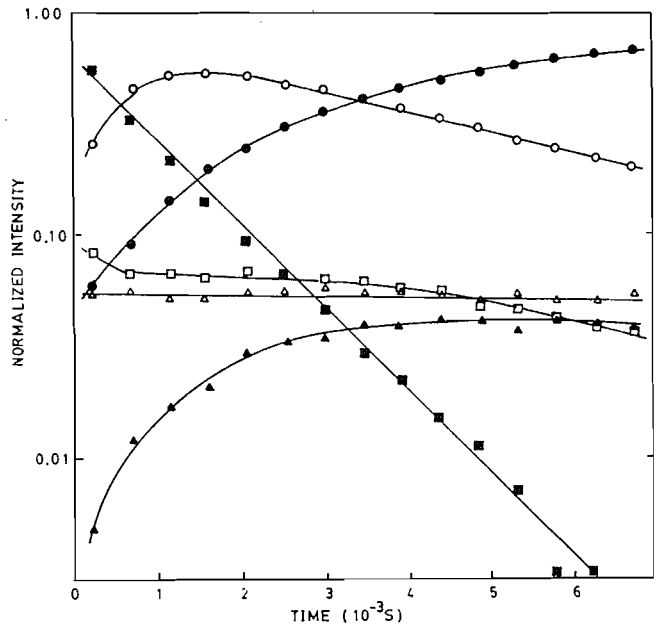

FIG. 6. The normalized ion intensities as functions of time after a 50 μs ionizing pulse of electrons in an isopropylbenzene/C_2H_5Cl/SF_6/-CH_4 (2.3×10^{-4}/0.007/0.007/0.986) mixture at 4.40 Torr and 296 K. ■, $(C_2H_5)_2Cl^+$; ○, $C_2H_5C_6H_5C_3H_7^+$ (*m/z* 149); ●, $C_9H_{11}^+$ (*m/z* 119); □, $C_9H_{13}^+$ (*m/z* 121); △, $C_{12}H_{19}^+$ (*m/z* 163); ▲, $C_{10}H_{15}^+$ (*m/z* 135).

[16] $(CH_3)_3C_6H_3C_2H_5^+ + (CH_3)_3C_6H_3 \rightarrow (CH_3)_3C_6H_2C_2H_5 + (CH_3)_3C_6H_4^+$ (*m/z* 121)
$\Delta H^0 = +4$ kcal mol^{-1}

The enthalpy changes for these and subsequent reactions have been obtained using tabulated standard enthalpies of formation of neutrals from ref. 21 and of ions from ref. 12. For species with no tabulated data, standard enthalpies were calculated as described in Appendix 1.

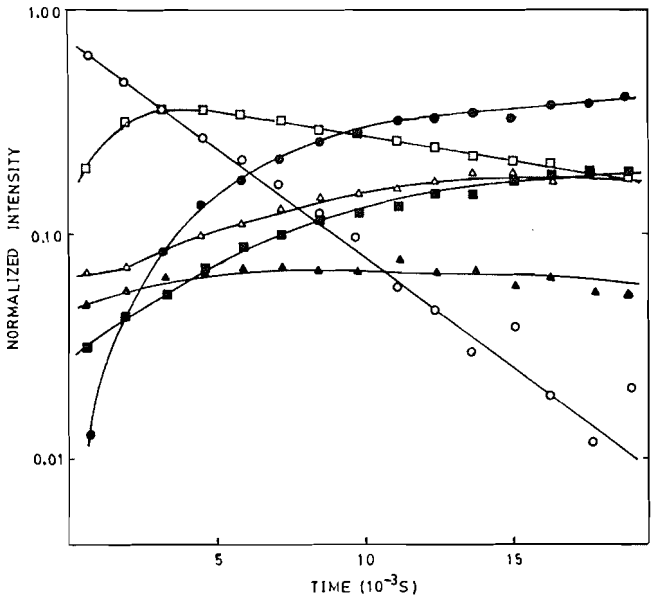

FIG. 7. The normalized ion intensities after a 50 μs pulse of ionizing electrons in a toluene/C_2H_5Cl/SF_6/CH_4 (3.6×10^{-4}/0.068/0.015/0.918) at 4.46 Torr and 303 K. ○, $(C_2H_5)_2Cl^+$; □, $C_2H_5C_6H_5CH_3^+$ (m/z 121); ●, $C_{12}H_{21}$ (m/z 177); △, m/z 184; ■, $C_{11}H_{17}^+$ (m/z 149); ▲, $C_6H_6CH_3^+$ (m/z 93).

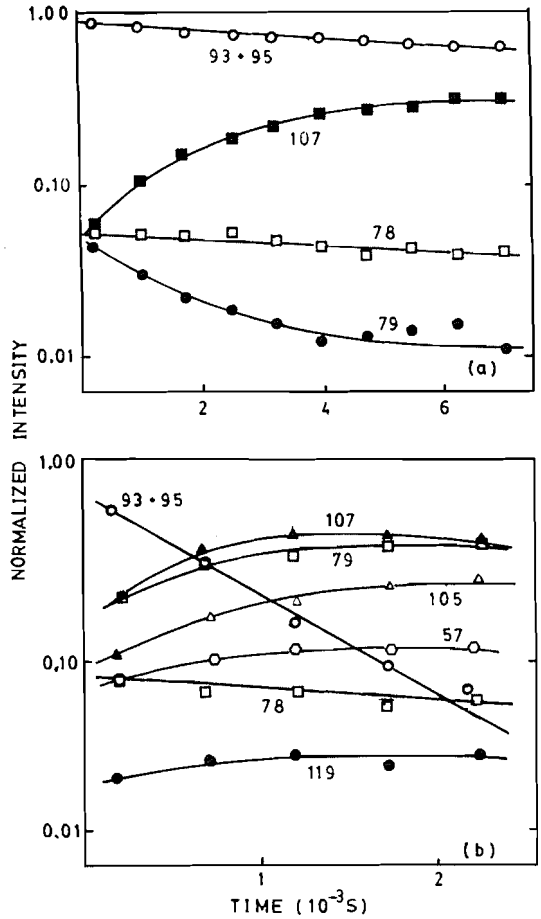

FIG. 8. The normalized ion intensities after a 50 μs ionizing pulse of electrons in a benzene/C_2H_5Cl/SF_6/CH_4 mixture: (*a*) (0.002/0.066/0.021/0.913) 4.70 Torr, 378 K; (*b*) (0.002/0.070/0.013/0.917) 4.60 Torr, 574 K. $(C_2H_5)_2Cl^+$ (m/z 93 + 95); $C_6H_6C_2H_5^+$ (m/z 107); $C_6H_6^+$ (m/z 78); $C_6H_7^+$ (m/z 79); $C_8H_9^+$ (m/z 105); $C_4H_9^+$ (m/z 57); $C_9H_{11}^+$ (m/z 119).

Reaction [16] is slightly endothermic and is consequently quite slow but the reverse reaction does not occur since there is essentially no $(CH_3)_3C_6H_3C_2H_5$ present in the system. The rate constant for this reaction was not measured but it was observed to proceed more slowly at high than at low temperature. Negative temperature coefficients for rate constants of slightly endothermic proton transfer reactions involving aromatic hydrocarbons have been previously observed (20). Such behaviour is a consequence of charge delocalization in the reactant ion.

At high temperature when $C_4H_9^+$ is also present proton transfer, reaction [17], also occurs and the yield of m/z 121 increases (Fig. 5).

[17] $C_4H_9^+ + (CH_3)_3C_6H_3 \rightarrow C_4H_8 + (CH_3)_3C_6H_4^+$

This reaction is exothermic by 5 kcal mol^{-1} if $C_4H_9^+$ is the *t*-butyl cation and by 21 kcal mol^{-1} if it is the *s*-butyl cation. In either case the reaction will occur at or near to the collision rate. The parallel decays of m/z 57 and 93 shows their interdependence via reaction [10]. At considerably lower mesitylene concentrations than that of Fig. 5 the build-up of the $C_4H_9^+$ fractional yield (via reaction [10]) is observed at short reaction times before its decay parallel with that of $(C_2H_5)_2Cl^+$

Isopropylbenzene

$B \cdot C_2H_5^+$ (m/z 149) is the major initial ion at low temperatures but at long reaction times it is replaced by m/z 119 (Fig. 6) which is the major ion at long reaction times at all temperatures. Since the yield of BH^+ (m/z 121), ring protonated *i*-propylbenzene, changes little with time at low temperature, the thermal decomposition of this ion can be ruled out as a source of m/z 119. This latter ion is formed either by the pyrolysis of m/z 149 or by the reaction of m/z 149 with isopropylbenzene. The latter is the case since the rate of decay of m/z 149 increases with increasing isopropylbenzene concentration, the reaction being pseudo first order with rate constant 6×10^{-12} cm^3 $molecule^{-1}$ s^{-1} at 300 K. The structure of m/z 119 is of course not directly determined in an experiment such as this; the ion was found not to react further. Two possibilities are ethyltropylium and the α,α-dimethylbenzyl cation. We favour the latter, formed by dissociative proton transfer.

[18] 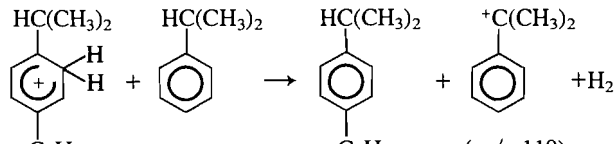

(m/z 149) (m/z 119)

$\Delta H° = 12$ kcal mol^{-1}

The reaction is significantly endothermic but is favoured by a large increase in entropy ($\Delta n = +1$). The possibility of the occurrence of such a process was tested using isopropylbenzene alone. Methane chemical ionization of this molecule forms mainly the ring protonated ion (m/z 121). This in turn slowly reacts with the neutral molecule to give m/z 119 ($k \sim 10^{-12}$ cm^3 $molecule^{-1}$ s^{-1} at 300 K) in a reaction which may be formulated.

[19] 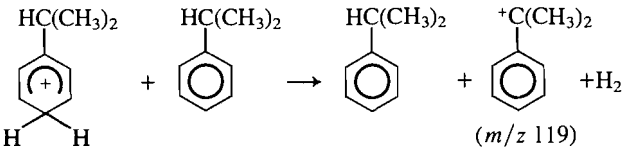

(m/z 121) (m/z 119)

$\Delta H° = 12$ kcal mol^{-1}

Can. J. Chem. Downloaded from www.nrcresearchpress.com by 93.93.197.157 on 09/07/12
For personal use only.

m/z 119 again showed no further reaction. For comparison purposes m/z 119 was also formed by the protonation of α-methylstyrene using methane chemical ionization. This ion will have the same structure as that shown in reaction [18] since protonation of styrene is exclusively on the olefinic side chain (22). Once again m/z 119 did not react further but did react very slowly ($k < 10^{-12}$ cm^3 molecule^{-1} s^{-1} at 400 K) with cyclohexene. Ausloos and co-workers (23) found that the benzyl cation ($C_6H_5CH_2^+$) reacts very efficiently with cyclohexene ($k/k_c = 0.5$ at 320 K) and with about the same efficiency with alkyl benzenes. The two extra methyl groups in m/z 119 obviously confer considerably stability on the benzyl cation just as methyl substituents do on the methyl cation.

The occurrence of significantly endothermic entropy driven ionic reactions such as [18] and [19] has been debated (24). A likely explanation is that a proton is transferred in the initially formed ion–molecule complex yielding H_2 and m/z 119 which is solvated by the neutral product molecule. As long as this solvation energy is greater than the endothermicity, reaction with loss of H_2 can readily occur. Equilibration with the bath gas molecules leads to the break-up of the solvation complex. Under our ion source conditions we do not expect to observe such weakly bound (~12 kcal mol^{-1}) complexes.

m/z 135 which can be formulated $C_2H_5C_6H_5C_2H_5^+$ is formed at low temperature only. It could be the $C_2H_5^+$ adduct of a C_8H_{10} impurity or more probably the product of a displacement reaction involving m/z 149 and ethyl chloride.

[20] 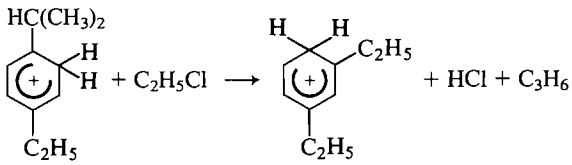

m/z 163 may be formulated as $C_6H_5(C_3H_7)_2^+$. The mechanism of its formation and that of m/z 135 ($C_{10}H_{15}$) are unknown.

At high temperature the system becomes very complex, major reaction channels involve the addition of $C_2H_5^+$ followed by the loss of either propylene yielding m/z 107 or propane yielding m/z 105. Such displacement reactions have been observed following protonation (13). The major ion at short reaction times is ring protonated isopropylbenzene which once again slowly reacts to give m/z 119.

Toluene

Protonated toluene ($C_7H_9^+$, m/z 93) is isobaric with $(C_2H_5)_2^{35}Cl$ and it was therefore necessary to obtain time-resolved information on the diethylchloronium ion by monitoring the smaller isotopic peak $(C_2H_5)_2^{37}Cl^+$ at m/z 95. The information from this ion was then also used to deconvolute m/z 93 and obtain the time-resolved contribution of $C_8H_9^+$. At low temperature $B \cdot C_2H_5^+$ (m/z 121) ultimately yields m/z 177 at long reaction time (Fig. 7). This latter ion could be formed in reactions similar to reaction [20] but since displacement of an olefin is not possible, only loss of HCl occurs.

[21] 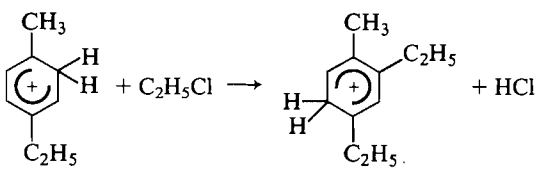

(m/z 121) (m/z 149)

[22] m/z 149 + C_2H_5Cl → 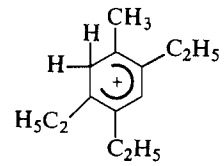 + HCl

(m/z 177)

Neither m/z 149 nor m/z 177 is observed at high temperature, presumably because the required collision complexes do not have a long enough lifetime for the elimination reactions to occur. As with isopropylbenzene a loss of alkane, in this case methane, leads at high temperature to the formation of a small amount of m/z 105 but BH^+ and $BC_2H_5^+$ are the major products.

Benzene

The reaction between benzene and $(C_2H_5)_2Cl^+$ is so slow that up to 0.39 mol% benzene was required in some of the experiments. This was considerably more than was required for the study of the other aromatics. At low temperature, Fig. 8*a*, $BC_2H_5^+$ (m/z 107) is the major product and there is a small yield of m/z 135 corresponding to $(C_2H_5)_2C_6H_5^+$ which could be formed by the reaction of the adduct with ethyl chloride.

[23] $C_2H_5C_6H_6^+ + C_2H_5Cl \rightarrow (C_2H_5)_2C_6H_5^+ + HCl$
$\Delta H^0 = -8$ kcal mol^{-1}

Some BH^+ (~ 4% total ionization) is formed presumably by reaction with precursors of $(C_2H_5)_2Cl^+$. At the highest temperatures the ion chemistry becomes more complex (Fig. 8*b*). As with the other alkylaromatics, the protonated molecule is a major product and indeed at very low benzene concentrations it is the major product.

The two stable forms of $C_4H_9^+$ are the *t*-butyl and *sec*-butyl cations (25). Proton transfer from *t*-$C_4H_9^+$ (PA(*i*-C_4H_8) = 196 kcal mol^{-1}) is endothermic with benzene (PA 181 kcal mol^{-1}), toluene (PA 190 kcal mol^{-1}), and isopropylbenzene (PA 192 kcal mol^{-1}) but is exothermic with mesitylene (PA 201 kcal mol^{-1}). Proton transfer from *sec*-$C_4H_9^+$ (PA(2-C_4H_8) = 179 kcal mol^{-1}) is exothermic to all of the aromatic hydrocarbons under study. We find that proton transfer from *t*-$C_4H_9^+$ to mesitylene occurs with high efficiency at a rate about one half the collision rate at 581 K, with toluene the reaction efficiency is about 1% while no proton transfer occurs with benzene. At high temperatures when $C_4H_9^+$ is formed by reaction [10], BH^+ is one of the two major products for all the aromatics. This ion is not formed by proton transfer from $C_4H_9^+$ in the case of benzene since the observed yields of $C_4H_9^+$ are those expected from reaction [10] alone. Toluene shows a very slow reaction with $C_4H_9^+$, isopropylbenzene reacts a little faster while mesitylene reacts fastest of all. This behaviour indentifies $C_4H_9^+$ as *t*-$C_4H_9^+$. This is consistent with extensive studies on the isomerization of *sec*-$C_4H_9^+$ to *t*-$C_4H_9^+$ (25). Even if the former ion were the immediate product of reaction [10], the high temperature and the presence of the dipolar ethyl chloride ($\mu_D = 2.1$ D) would cause very rapid isomerization (26).

The protonating agent at high temperatures must be the diethylchloronium ion itself. The rate constants for disappearance of $(C_2H_5)_2Cl^+$ by reaction with aromatic at high temperature are in the order benzene < toluene ≈ isopropyl benzene < mesitylene (*vide infra*) which will also be the order of rate constants for reaction to yield BH^+. The reaction mechanism is not known, a possible one being

Can. J. Chem. Downloaded from www.nrcresearchpress.com by 93.93.197.157 on 09/07/12
For personal use only.

Can. J. Chem. Downloaded from www.nrcresearchpress.com by 93.93.197.157 on 09/07/12
For personal use only.

[24] $(C_2H_5)_2Cl^+ + M \rightarrow C_2H_5Cl + C_2H_4 + MH^+$

The exothermicities for different B are (kcal mol^{-1}) benzene +15, toluene +7, isopropylbenzene +5, and mesitylene −4 which are consistent with the order of reaction rate constants. The use of these values in an expression for the rate constant of the form $k \approx k_c$ [exp $(-\Delta H^0/RT)$] gives rate constants of approximately the correct order of magnitude for toluene and isopropylbenzene but a value for benzene which is too small by several orders of magnitude. There is a large entropy change for this reaction which may, as discussed earlier, be described as an entropy driven reaction. The participation of product ion solvation may again be the explanation for the measurable, but low rate of reaction.

The kinetics of $C_2H_5^+$ transfer

The rate constants for the decay of $(C_2H_5)_2Cl^+$ in these systems was measured by two different methods. The most common method employed in high pressure mass spectrometry, which we call the normalization method, uses the slopes of the pseudo first order decays of $(C_2H_5)_2Cl^+$ from plots such as those in Figs. 4–8. The actual value of the slope for a given system depends on the precision with which all the different ions in the system are monitored. When there are many ions to monitor in a complex spectrum over an extended period of time there is the possibility of error which arises from a variation in ion source conditions. In addition, the rate constants obtained are for the overall disappearance of $(C_2H_5)_2Cl^+$ and not solely for the reaction of interest, namely, reaction with aromatic.

The second method, which we call the standard addition method and which has been described in detail (4), provides the rate constant for reaction with aromatic only. $(C_2H_5)_2Cl^+$ disappears by reactions [10] and [14] and also by diffusion to the walls with rate constant k_d

$$[25] \quad \frac{-d[(C_2H_5)_2Cl^+]}{dt} = (k_{10}[C_2H_5Cl] + k_{14}[B] + k_d)[(C_2H_5)_2Cl^+]$$

Under fixed ion source conditions $[C_2H_5Cl]$ and [B] are constant and taking the $(C_2H_5)_2Cl^+$ ion current i to be proportional to ion concentration, eq. [25] becomes pseudo first order.

$$[26] \quad -\frac{di}{dt} = k'i \text{ where } k' = k_{10}[C_2H_5Cl] + k_{14}[B] + k_d$$

Such behaviour is shown in Fig. 9 for a fixed C_2H_5Cl concentration and increasing concentration of aromatic. The experiment is performed by making up a $C_2H_5Cl/SF_6/CH_4$ mixture in the reservoir and monitoring the ion current due to $(C_2H_5)_2Cl^+$ as a function of time after the ionizing electron pulse. A known amount of aromatic is added and the current is monitored again. With increasing aromatic concentration the slope of the decay curve increases as described by eq. [25]. Under these conditions $k' = k'' + k_{14}[B]$ where $k'' = k_{10}[C_2H_5Cl] + k_d$. A plot of k' vs. [B] then yields a straight line with slope k_{14}. Plots for benzene at different temperatures are shown in Fig. 10. It is to be noted that both slope and intercept increase with increasing temperature. The increase in the size of the intercept is mainly due to an increase in k_d since the term $k_{10}[C_2H_5Cl]$ is of importance only at the highest temperatures.

The Arrhenius type plots shown in Fig. 11 for mesitylene, toluene, and benzene were obtained by the standard additions method while the plot for *i*-propylbenzene was obtained by the normalization method. Figure 12 compares the two methods of

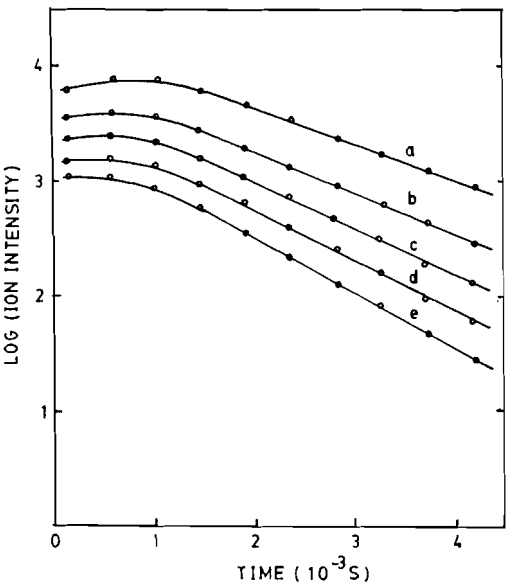

FIG. 9. The intensities of the $C_2H_5^+$ adduct of benzene ($C_6H_6C_2H_5^+$, m/z 107) after 60 μs ionizing pulses of electrons for $C_2H_5Cl/SF_6/CH_4$ (0.035/0.007/0.958) mixtures at 4.58 Torr and 512 K. The mole fractions of benzene are (*a*) 0, (*b*) 0.0005, (*c*) 0.0009, (*d*) 0.0014, and (*e*) 0.0019. The slope of the linear portion of each decay curve is equal to k', the pseudo first order rate constant for the disappearance of $(C_2H_5)_2Cl^+$.

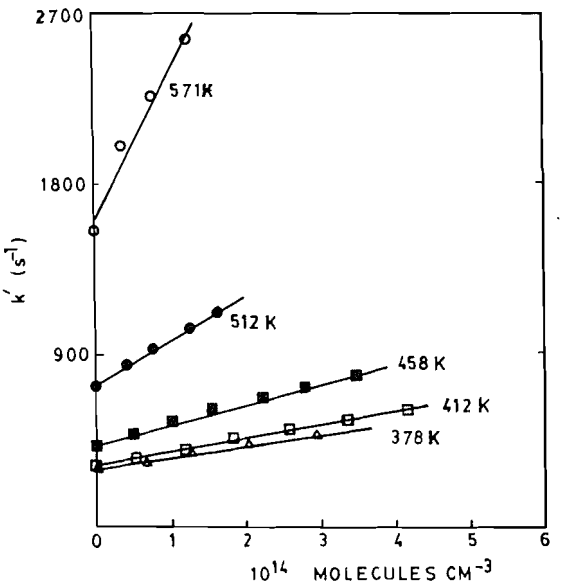

FIG. 10. Plots of $k' = k_{10}[C_2H_5Cl] + k_{14}[C_6H_6] + d_d$ versus benzene concentration at 4.58 Torr.

determining rate constants for mesitylene and benzene. It is evident that, except at the highest temperatures, there is good agreement between the two methods. There is a noticeable concentration dependence in the results obtained for benzene using the normalization method and a very slight dependence for mesitylene. The dependence for benzene increases with increasing temperature. Benzene has a much smaller rate constant for reaction with $(C_2H_5)_2Cl^+$ than does mesitylene and greater concentrations of benzene were therefore required for the same extent of reaction. In the standard addition method there is a noticeable non-linearity in the plot of k' versus ben-

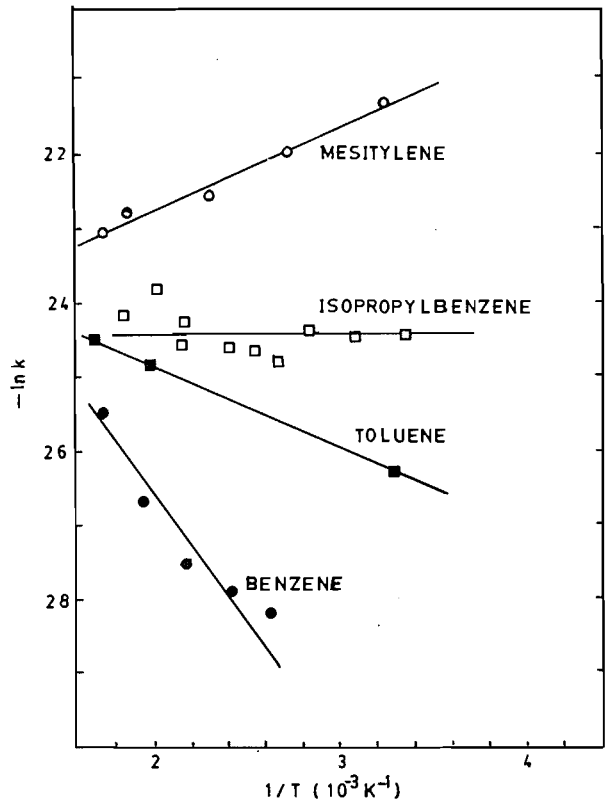

FIG. 11. Arrhenius plots for the reaction $(C_2H_5)_2Cl^+ + B \rightarrow BC_2H_5^+ + C_2H_5Cl$. Data for isopropylbenzene were obtained using the normalization method, the remainder were obtained using the standard addition method.

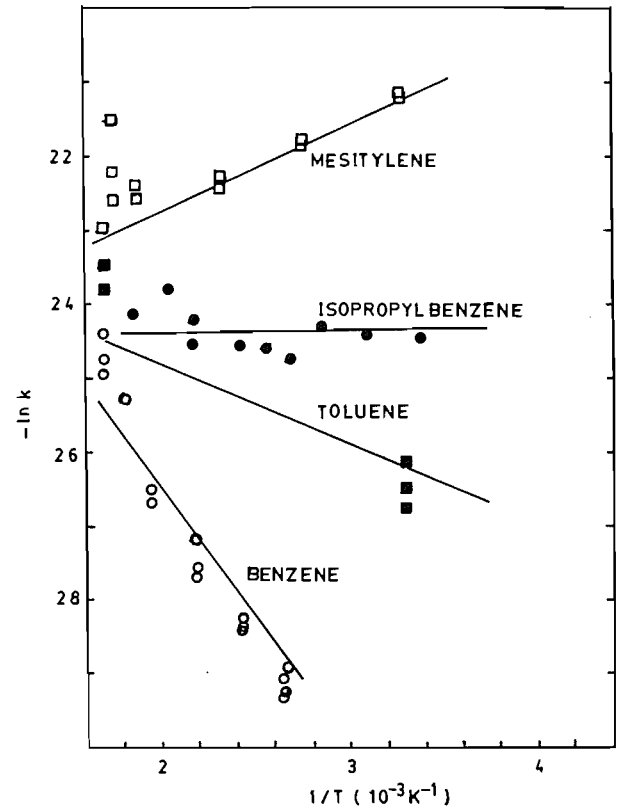

FIG. 12. Arrhenius plots for the reaction $(C_2H_5)_2Cl^+ + B \rightarrow BC_2H_5^+ + C_2H_5Cl$. Data for all aromatics were obtained by the normalization method (see text); the lines are those from Fig. 11. Comparison of the two sets of data illustrates the deviation of the normalized data at high temperatures due to the increased rate of disappearance of $(C_2H_5)_2Cl^+$ via reaction [10]. For benzene the value of k at a given temperature increases with increasing benzene concentration as shown, the lowest point at a given temperature is for the lowest benzene concentration.

zene concentration at the high concentration end which may be attributed to an increase in k_d since the diffusion coefficient of $(C_2H_5)_2Cl^+$ is reduced as the concentration of polarizable benzene molecules becomes significant. The error caused by this effect was minimized by limiting the benzene concentration range, especially at the high temperatures where k_d is large. The error due to this effect was, under these circumstances, less than the experimental errors inherent in measuring rate constants of value less than 10^{-12} cm^3 molecule^{-1} s^{-1}. The very marked deviation between the results for the two methods for all aromatics at the highest temperatures is because the normalization method measures the rate of disappearance of $(C_2H_5)_2Cl^+$ by both reactions [10] and [14]. For systems such as this involving competitive reactions the standard addition method of obtaining reaction rate constants is preferred. It does not, as does the normalization method, give information on product type and relative yields of products; the two methods are complementary when the full kinetic picture is required.

The rate of $C_2H_5^+$ addition at any temperature in the experimental range increases in the order benzene < toluene < isopropylbenzene < mesitylene. This is the order of increasing gas phase basicity of the aromatic substrate as measured by proton affinity. The same order was observed for the relative rates of CH_3^+ transfer from $(CH_3)_2Cl^+$ to aromatic hydrocarbons (6). Alkylation of toluene by $(C_2H_5)_2Cl^+$ in SO_2ClF solution at 195 K was found to be five times faster than alkylation of benzene (1) suggesting that there is a similar mechanism for alkylation in both gas and liquid phases.

The slowness of ethyl cation transfer from $(C_2H_5)_2Cl^+$ to an aromatic molecule is consistent with the mechanism discussed in the introduction for CH_3^+ transfer from $(CH_3)_2Cl^+$, i.e., the double well potential curve is appropriate as a description of the reaction path. The rate constants for transfer to benzene and toluene increase with increasing temperature while that for mesitylene decreases and the rate constant for transfer to isopropylbenzene is independent of temperature. All reactions are very exothermic (Table 1) and the analysis proposed by Sen Sharma and Kebarle (4) would have the energy level of the central maximum (chemical transition state) below the level of the reactants only for mesitylene. The positive activation energies for benzene and toluene show that the central maximum is above the reactant energy level; that for isopropylbenzene is at or close to the same level as the reactants.

It is at first somewhat surprising that the rate constants at 305 K for $C_2H_5^+$ transfer from $(C_2H_5)_2Cl^+$ to benzene, toluene, and isopropylbenzene are smaller than those for CH_3^+ transfer from $(CH_3)_2Cl^+$. This is in contrast to the observation of Sen Sharma and Kebarle (4) that $C_2H_5^+$ transfer from $CH_3ClC_2H_5^+$ to benzene, toluene, and isopropylbenzene is faster at 305 K than is CH_3^+ transfer from $(CH_3)_2Cl^+$. They suggested that the internal barrier will be smaller for transfer of the more weakly bound $C_2H_5^+$ ($D(C_2H_5^+—ClCH_3) = 30.7$ kcal mol^{-1} (27)) to a given aromatic. Sen Sharma and Kebarle could not measure the dependence of the rate constant for $C_2H_5^+$ transfer from $C_2H_5ClCH_3^+$ to aromatic molecules at higher temperatures because of problems engendered by its dissociation. Although

Can. J. Chem. Downloaded from www.nrcresearchpress.com by 93.93.197.157 on 09/07/12
For personal use only.

TABLE 1. Thermodynamic data for the reaction $(C_2H_5)_2Cl^+ + B \rightarrow C_2H_5B^+ + C_2H_5Cl$

B	$\Delta H_f^0(B)^a$	$\Delta H_f^0(C_2H_5B^+)^a$	ΔH^{0a}
Benzene	20	181	−20.1
Toluene	12	173	−21.1
Isopropylbenzene	7	161	−27.1
Mesitylene	−4	145	−32.1

[a]Units, kcal mol^{-1}.

$(CH_3)_2Cl^+$ reacts more rapidly with a given aromatic at 305 K than does $(C_2H_5)_2Cl^+$, it does not necessarily do so at a higher temperature because of the different temperature dependences of the rate constants. Thus at 450 K transfer of $C_2H_5^+$ from $(C_2H_5)_2Cl^+$ to toluene and isopropylbenzene is faster than CH_3^+ transfer from $(CH_3)_2Cl^+$. CH_3^+ transfer to benzene still has the higher rate constant. All these CH_3^+ and $C_2H_5^+$ transfers are highly exothermic and the absolute value of the exothermicity is obviously not the sole criterion determining the relative rates with which they react with a given aromatic. In solution it is found that S_N2 displacements are more facile at a methyl than at a methylene group (28). This has been ascribed to a steric interaction (29), the chemical transition state for CH_3^+ transfer is less crowded than that for $C_2H_5^+$ transfer. Such a steric interaction in the gas phase would lead to a lower density of states at the central barrier for $C_2H_5^+$ transfer compared with CH_3^+ transfer for a given ΔE^0, ensuring a lower rate of ethylation. However, as argued earlier, the value of ΔE^0 is also different for $(CH_3)_2Cl^+$ and $(C_2H_5)_2Cl^+$ (and also presumably for $C_2H_5ClCH_3^+$) with the same aromatic; the change of electrophile therefore affects both the entropy and the energy of the transition state.

The trend of increasing rate constant with increasing exothermicity of reaction does, however, hold for each alkylating agent with the same series of aromatic bases over the temperature range 300–600 K.

Can. J. Chem. Downloaded from www.nrcresearchpress.com by 93.93.197.157 on 09/07/12
For personal use only.

1. G. A. OLAH. Halonium ions. Wiley Interscience, New York. 1975.
2. M. SPERANZA and N. PEPE. J. Chem. Soc. Perkin Trans. **2**, 1179 (1979).
3. J. A. STONE, M. S. LIN, and J. VARAH. Can. J. Chem. **59**, 2412 (1982).
4. D. K. SEN SHARMA and P. KEBARLE. J. Am. Chem. Soc. **104**, 19 (1982).
5. T. SU and M. T. BOWERS. Int. J. Mass Spectrom. Ion Phys. **12**, 347 (1973).
6. J. A. STONE, W. M. SPLINTER, and D. E. SPLINTER. Can. J. Chem. **100**, 5826 (1984).
7. W. N. OLMSTEAD and J. I. BRAUMAN. J. Am. Chem. Soc. **101**, 3715 (1979).
8. J. M. JASINSKI and J. I. BRAUMAN. J. Am. Chem. Soc. **102**, 2906 (1980).
9. T. F. MAGNERA and P. KEBARLE. *In* Ionic processes in the gas phase. *Edited by* M. A. Almoster Ferreira. D. Reidel Publishing Co. 1982. p. 135.
10. J. A. STONE and D. E. SPLINTER. Can. J. Chem. **59**, 1779 (1981).
11. W. L. JORGENSEN. J. Am. Chem. Soc. **99**, 280 (1977).
12. S. G. LIAS, J. F. LIEBMAN, and R. D. LEVIN. J. Phys. Chem. Ref. Data, **13**, 695 (1984).
13. A. G. HARRISON. Chemical ionization mass spectrometry. CRC Press Inc. Boca Raton, FA. U.S.A. (1983).
14. J.L. BEAUCHAMP, D. HOLTZ, S. D. WOODGATE, and S. L. PATT. J. Am. Chem. Soc. **94**, 2798 (1972).
15. Z. LUCZYNSKI and H. WINCEL. Int. J. Mass Spectrom. Ion Phys. **14**, 29 (1974).
16. T. B. MCMAHON. Private communication.
17. D. K. SEN SHARMA and P. KEBARLE. J. Am. Chem. Soc. **100**, 5826 (1978).
18. J. L. DEVLIN, J. F. WOLF, R. W. TAFT, and W. J. HEHRE. J. Am. Chem. Soc. **98**, 1990 (1976).
19. F. CACACE, G. DE PETRIS, S. FORNARINI, and P. GIACOMELLO. J. Am. Chem. Soc. **108**, 7495 (1986).
20. J. A. STONE, X. LI, and P. A. TURNER. Can. J. Chem. **64**, 2021 (1986).
21. J. B. PEDLEY and J. RYLANCE. Sussex-N.P.L. Computer analysed thermochemical data: organic and organometallic compounds. Univ. of Sussex. 1977.
22. A. G. HARRISON, R. HOURIET, and T. T. TIDWELL. J. Org. Chem. **49**, 1302 (1984).
23. P. AUSLOOS, J.-A. A. JACKSON, and S. G. LIAS. Int. J. Mass Spectrom. Ion Phys. **33**, 269 (1980).
24. M. HENCHMAN. *In* Structure reactivity and thermochemistry of ions. *Edited by* P. Ausloos and S. G. Lias. D. Reidel, Dordrecht. 1986. p. 381.
25. P. AUSLOOS and S. G. LIAS. Int. J. Mass Spectrom. Ion. Proc. **58**, 165 (1984).
26. S. G. LIAS, D. M. SHOLD, and P. AUSLOOS. J. Am. Chem. Soc. **102**, 2540 (1980).
27. D. K. SEN SHARMA, S. M. DE HOJER, and P. KEBARLE. J. Am. Chem. Soc. **107**, 3757 (1985).
28. A. STREITWEISER. Chem. Rev. **56**, 571 (1956).
29. C. K. INGOLD. Q. Rev. Chem. Soc. **11**, 1 (1957).

Appendix I

Standard enthalpies of formation were not available for several of the neutral molecules and ions discussed in this paper. Estimates of such enthalpies were made as follows.

The following standard enthalpies of formation of alkyl aromatics are from ref. 21 (units kcal mol^{-1}): benzene 20, toluene 12, ethylbenzene 7, isopropylbenzene 1, and mesitylene −4. Single substituents decrease the enthalpy for formation of benzene by the following amounts: methyl 8, ethyl 13, *i*-propyl 19 kcal mol^{-1}. If substituent contributions are strictly additive then mesitylene (1,3,5-trimethylbenzene) with three methyl groups is calculated to have a standard enthalpy of formation of $20 - 3 \times 8 = -4$ cal mol^{-1}, which is identical with the experimental value. The other two trimethylbenzene isomers have only slightly different values viz. 1,2,3-trimethylbenzene −2 kcal mol^{-1} and 1,2,4-trimethylbenzene −3.3 kcal mol^{-1} i.e. geometrical isomerism has little effect on the standard enthalpy of formation. With the above values for the substituents, calculated standard enthalpies are usually within ±2 kcal mol^{-1} of known experimental values. For example the value calculated for ethyltoluene is −1 kcal mol^{-1} and the experimental values for *o*-, *m*-, and *p*-ethyltoluene are respectively, 0, 0, and −1 kcal mol^{-1}.

The standard enthalpies of formation of ions were obtained, where possible, from the literature (mainly ref. 12) and if not available they were estimated using estimated proton affinities as follows. An alkyl substituent increases the proton affinity of benzene, in general the larger the alkyl group the higher the proton affinity. Thus PA(benzene) = 181.3, PA(toluene) = 189.8, PA(ethylbenzene) = 191.6, and PA(isopropylbenzene) = 192.1 kcal mol^{-1}. Protonation is assumed to occur *para* to the alkyl group leading to the following stabilization energies for a *para* substituent: methyl 8.5, ethyl 10.3, and *i*-propyl 10.8 kcal mol^{-1}. Relative to stabilization by methyl (= 1.00) the stabilization efficiencies increase for ethyl by a factor of 1.21

and for *i*-propyl by 1.27. When more than one methyl substituent is present both their number and sites relative to the site of protonation determine the proton affinity (18, 20). The following stabilization enthalpies have been assigned for a methyl substituent: *ortho* 6.4, *meta* 2.6, and *para* 7.6 kcal mol^{-1} (20). This value for *p*-methyl is slightly lower than the value given above but the difference is within the spread of values of experimental proton affinities used in obtaining the evaluated proton affinity. For ethyl and isopropyl substituents, the stabilization enthalpy is assumed to be that for methyl multiplied by the stabilization efficiency eg for a *meta*-ethyl substituent it is $2.6 \times 1.21 = 3.1$ kcal mol^{-1}. The $C_2H_5^+$ is presumed to add *para* to the alkyl group on toluene and isopropylbenzene and at an unsubstituted site on mesitylene. The *ipso*-hydrogen then transfers to the nonsubstituted site on the aromatic ring that leads to the maximum stabilization enthalpy. For example, the addition of ethyl cation to isopropylbenzene is assumed to lead to protonated 1-ethyl-4-isopropylbenzene. The proton affinity of this molecule is calculated using the following stabilization enthalpies: *ortho*-propyl $6.4 \times 1.27 = 8.1$ kcal mol^{-1}, *meta*-ethyl $2.6 \times 1.21 = 3.1$ kcal mol^{-1}, i.e. PA(1-ethyl-4-isopropylbenzene) = 181.3 + 8.1 + 3.1 = 192.5 kcal mol^{-1}. For polymethylbenzenes such calculations agree with experimental values to better than ±2 kcal mol^{-1} (20). Similar error limits should hold for the ethyl and isopropylbenzenes but there is no experimental data to check this assumption. For aromatic B the following data have been estimated (kcal mol^{-1}).

B	PA(B)[a]	$\Delta H_f^0(B)$[a]	$\Delta H_f^0(BH^+)$[a]
4-Ethyltoluene	192	−1	173
1-Ethyl-4-isopropyl benzene	193	−12	161
1,3,5-Methyl-2-ethyl benzene	204	−17	145

[a]Units, kcal mol^{-1}.

Can. J. Chem. Downloaded from www.nrcresearchpress.com by 93.93.197.157 on 09/07/12
For personal use only.

A Raman and infrared spectroscopic study of triethylenediamine (DABCO) and its protonated forms

DAVID A. GUZONAS AND DONALD E. IRISH

Guelph–Waterloo Center for Graduate Work in Chemistry, Waterloo Campus, University of Waterloo, Department of Chemistry, Waterloo, Ont., Canada N2L 3G1

Received August 6, 1987

DAVID A. GUZONAS and DONALD E. IRISH. Can. J. Chem. **66**, 1249 (1988).

The Raman and infrared spectra of DABCO have been measured as a function of the pH, and the vibrational bands of the two protonated forms of DABCO have been tabulated and assigned. The frequencies of several of the Raman bands were found to exhibit substantial shifts upon protonation, and the appearance of the Raman spectrum in the region between 900 and 1100 cm^{-1} in particular shows differences which can be used to differentiate between the three forms of DABCO. The values of the two pK_a's were determined from the intensity versus pH plots for the three species.

DAVID A. GUZONAS et DONALD E. IRISH. Can. J. Chem. **66**, 1249 (1988).

On a mesuré les spectres Raman et infrarouges du DABCO en fonction du pH; on présente sous forme de tableaux les positions des bandes de vibration des deux formes protonées du DABCO et on en fait l'attribution. On a trouvé que, par protonation, les fréquences de plusieurs bandes observées dans le Raman subissent des déplacements importants; en particulier, les bandes qui apparaissent entre 900 et 1100 cm^{-1} du spectre Raman permettent de différencier les trois formes du DABCO. On a déterminé les deux pK_a à partir des courbes des intensités en fonction du pH des trois espèces.

[Traduit par la revue]

Can. J. Chem. Downloaded from www.nrcresearchpress.com by 93.93.197.157 on 09/07/12
For personal use only.

Introduction

As part of a detailed study of the surface enhanced Raman scattering (SERS) of the diamine, 1,4-diazabicyclo[2.2.2]-octane, abbreviated DABCO, at a silver electrode (1) the effect of the bulk solution pH on the SER spectrum has been investigated (2). This necessitated knowledge of the vibrational spectra of the protonated forms of DABCO, which is not available in the literature, and prompted this study of the infrared and unenhanced Raman spectra of this molecule as a function of pH.

DABCO can exist in three forms in aqueous solution, depending upon the pH, viz.:

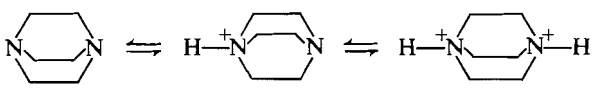

Although the effect of protonation on the ^{13}C and ^{15}N nmr spectra of DABCO (3) and the effect of pH on the molecular motion of DABCO (4) have been studied, the Raman spectra of the two protonated forms have not been discussed in the literature. A very brief discussion of the infrared spectra of the salts of the diprotonated forms can be found in studies of the ligand properties of DABCO and $DABCOH_2^{2+}$ by Quagliano *et al.* (5) and Yokobayashi *et al.* (6).

The DABCO molecule has 54 ($3 \times 20 - 6$) vibrational degrees of freedom; the molecule is believed to be of D_{3h} symmetry (7, 8), and thus the irreducible representation is (activities given in parentheses, ia for inactive)

$$\Gamma_{vib} = 6a_1'(R) + 3a_2'(ia) + 4a_1''(ia) + 5a_2''(IR) + 9e'(R,IR) + 9e''(R)$$

There are therefore a total of 24 Raman-allowed modes and 14 infrared-allowed modes, including 9 coincidences, as well as seven modes inactive in both spectroscopies. Six of the Raman bands should be polarized. The Raman and/or infrared spectra of DABCO have been reported by a number of authors, the earliest study being of the infrared spectrum by Farkas *et al.* (9). The Raman spectra of DABCO in benzene and water, and the infrared spectrum of the solid were reported by Weiss *et al.* (7); at about the same time the infrared spectra of the gas phase, solution and solid state and Raman spectra of saturated solutions in chloroform and benzene were reported by Marzocchi *et al.* (10). A normal co-ordinate analysis of DABCO, azabicyclo[2.2.2]octane (ABCO), and bicyclo[2.2.2]octane (BCO) was performed by Bruesch (11), and an accompanying infrared and Raman study was reported by Bruesch and Gunthard (12). However, a substantial number of the expected Raman bands were not found by any of the above researchers. McDivett and Humphrey (13) also reported the infrared and Raman spectra of DABCO and some DABCO complexes; again, a large number of Raman bands were not observed, including most of the nine expected e'' modes. A more complete Raman study was reported by Ernstbrunner *et al.* (14), who also performed a new normal co-ordinate calculation in which the force constants were refined until the observed and calculated band frequencies were in good agreement. The normal coordinate analysis and band assignments for Ernstbrunner *et al.* were therefore used in this paper as a starting point for the assignments of the protonated DABCO species. Unfortunately, these authors do not report the calculated frequencies of the inactive modes or of the modes which were not observed, and do not report the observed Raman frequencies in the C—H stretching region. There are therefore a few unanswered questions concerning the band assignments of DABCO; as well, the infrared and Raman spectra of the two protonated forms need to be characterized.

The distribution diagram for a 1.0 *M* DABCO aqueous solution is shown in Fig. 1, calculated using the literature values of the pK_a's, $pK_{a_1} = 8.82$ and $pK_{a_2} = 2.97$ (15); see also Larson *et al.* (16). It can be seen that there exist pH values at which only one of the three species is present in the solution at concentrations greater than about 1%, which facilitates the analysis of the infrared and Raman spectra.

Experimental

Raman spectra were obtained using a digital drive, Jarrell-Ash, 25-100 spectrometer (1 meter double Czerny-Turner monochromator),

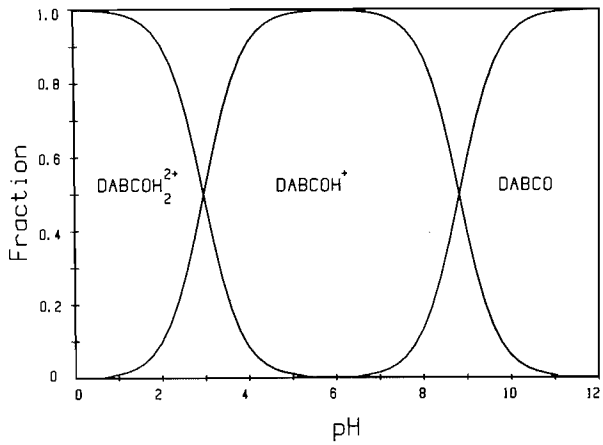

FIG. 1. Fractional composition of aqueous 1.0 *M* DABCO as a function of pH.

TABLE 1. Raman band positions in several solvents (solvent acceptor number given in parentheses)*

Mode	Benzene (8.2)	Acetonitrile (19.3)	Chloroform (23.1)	Methanol (41.3)	Water (54.8)
ν_{36}	332	332	—	329	332
ν_{27}	424	422	422	421	424
ν_{35}	577	577	576	575	577
ν_6	—	598	603	626	630
ν_5	805	804	802	803	806
ν_4	962	964	967	981	983
ν_{24}	1062	1062	1060	—	1062
ν_{23}	1296	—	1296	—	1301
ν_{22}	1321	1320	—	—	1328
ν_3	1332	—	1337	—	1352
ν_2	1453	—	1453	—	1458

*—, obscured by solvent bands.

with an RCA 31034 photomultiplier tube and an SSR model 1105/1120 photon counting system. The 514.5 nm line of a Spectra Physics model 165-03 argon ion laser was used for excitation. The spectrometer was controlled by, and data collected on, a Commodore PET model 2001 computer. A DEC Pro 380 computer interfaced to a VAX 11/785 via ETHERNET was used to perform curve resolution and factor analysis, the latter being done using the TARGET™ factor analysis package obtained from Malinowski (17, 18).

Infrared spectra were obtained using a BOMEM DA 3.02 FTIR spectrometer, using a globar source, KCl beamsplitter, and a liquid nitrogen cooled Hg–Cd–Te detector.

Solutions were prepared from distilled water. DABCO was obtained from Aldrich and purified by recrystallization from low boiling petroleum ether before use. The solution pH was adjusted using 12 *M* HCl and 50% w/v NaOH, the pH being measured with a Fisher Accumet model 800 pH meter. The Raman samples were contained in 0.05 mm o.d. melting point tubes; the solutions were filtered using Millipore BD 0.06 μm polyvic filters before injection into the tubes. The infrared spectra were measured using a liquid cell with AgCl windows.

Results and discussion

Solvent shifts in the Raman spectrum of DABCO

In order to obtain information on the solute–solvent interactions of DABCO Raman spectra of DABCO dissolved in a number of solvents were obtained. Table 1 lists the positions of the strongest Raman bands in these solvents, arranged in order of solvent acceptor number (19). While most of the bands show only random one or two wavenumber shifts with changes in solvent, several bands, viz., ν_6, ν_4, and ν_3, show substantial shifts to higher wavenumber upon going from benzene (non-polar, non-hydrogen bonding, low acceptor number) to water (polar, hydrogen bonding, high acceptor number). As seen in Table 1, there is a clear relationship between the acceptor number and the band position of these three bands. Since DABCO is known to strongly hydrogen-bond, the observed shifts are undoubtedly caused in large part by the hydrogen-bonding of DABCO to the solvent. These bands have been previously assigned to the totally symmetric skeletal deformation (ν_6), the νCC/ωCH$_2$ (ν_4), and the ωCH$_2$/νCC (ν_3) (14). That the solvent–DABCO interaction is reflected most strongly in the frequency of ν_3, ν_4, and ν_6 can be understood in terms of the through-bond interactions of the lone-pair orbitals (20). Because of the favourable position of the two nitrogen atoms of DABCO, the lone pair orbitals interact via the carbon–carbon framework; molecular orbital calculations show that the lone pair electrons are 42% on the carbon–carbon framework (21). Any changes in the interactions of the lone pairs with the solvent will clearly alter the degree of mixing of the lone pair MO's with the C—C σ MO, and therefore alter the electron density on the C—C bonds as well as the N—C bonds. Since ν_3 and ν_4 both contain substantial amounts of the C—C stretching co-ordinate, these two bands will be particularly sensitive to changes in the environment of the lone-pairs. Similarly, since the anti-symmetric combination of the lone pair orbitals was shown (20) to be coupled to the NCC bond angle, and thus to ν_6, the sensitivity of ν_6 to solvent effects is also understandable. These observations suggest that the frequencies of these bands are good indicators of the extent of the interaction of the lone pairs, an upward shift in the frequency correlating with an increase in the strength of the interaction.

Infrared and Raman spectra of the protonated forms of DABCO

Raman spectra were obtained of solutions whose pH values differed by about 0.5 pH units, while infrared spectra were obtained only at pH values where each of the three forms could be studied in isolation. In both studies three distinct spectra were found, as seen in Figs. 2 and 3; the Raman spectra smoothly change from the DABCO spectra at high pH through the monoprotonated and then the diprotonated forms as the pH is lowered. The spectra of the three species are, not surprisingly, fairly similar in overall appearance, but do exhibit small band shifts, intensity changes, and some substantial changes in the spectral region from 900 to 1400 cm^{-1}, as indicated in Table 2. Because of the presence of a large number of bands in the C—H stretching region, some of which are overtones of the C—H wagging modes, no definitive assignment of a number of the Raman and infrared bands appearing in this region was possible.

Before turning to a discussion of the spectra, it is necessary to consider the effect of changes in the symmetry of DABCO upon protonation. The species DABCOH$^+$ is probably of C_{3v} symmetry while the diprotonated form is assumed to be of D_{3h} symmetry like the neutral DABCO. A correlation diagram summarizing the changes in activity to be expected based on these symmetries is presented in Fig. 4, and one can make some simple predictions from this figure concerning changes to be anticipated in the infrared and Raman spectra upon protonation.

Upon monoprotonation, the five a_2'', infrared-allowed, Raman-forbidden modes of DABCO become both infrared- and Raman-allowed; thus the Raman spectrum of the monoprotonated form could contain five new *polarized* bands, assuming

Can. J. Chem. Downloaded from www.nrcresearchpress.com by 93.93.197.157 on 09/07/12
For personal use only.

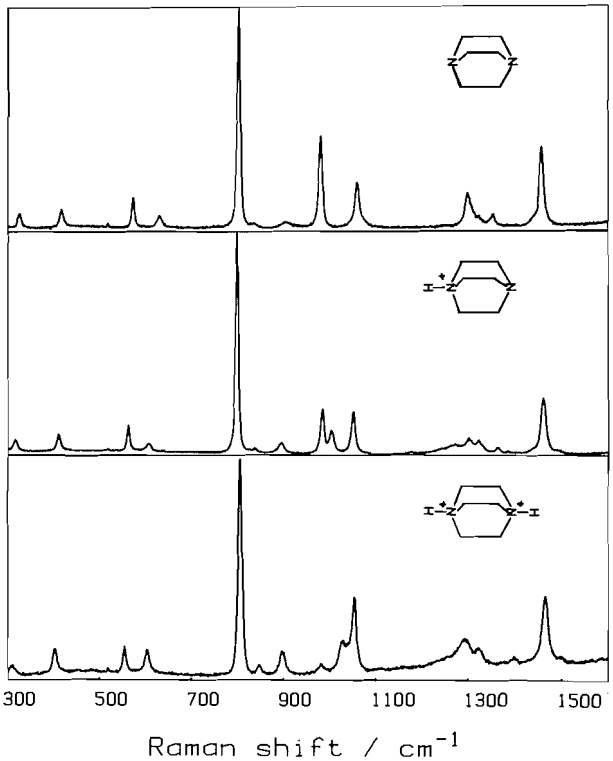

FIG. 2. Raman spectra from 300 to 1600 cm^{-1} of DABCO and its two protonated forms.

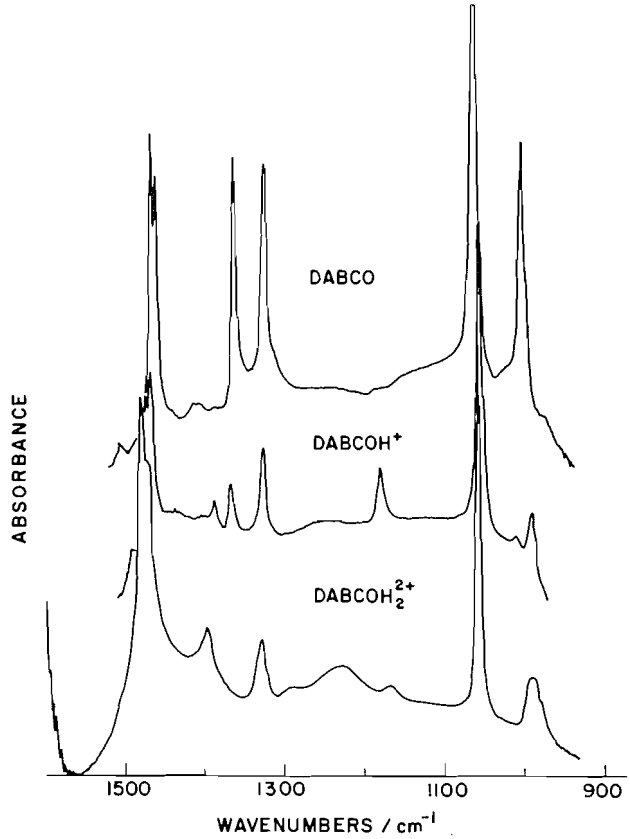

FIG. 3. Infrared spectra from 900 to 1600 cm^{-1} of DABCO and its two protonated forms.

observable intensity, as well as two new bands due to the N^+H group. The infrared spectrum is expected to become much more complex because the a_1' and e' modes (15 in total) become allowed in the monoprotonated species. Upon diprotonation, the infrared and Raman spectra are expected to resemble the spectra of the unprotonated DABCO species except for the addition of bands due to the N^+H groups, three bands being Raman active and two being infrared active.

There is a close structural similarity between the monoprotonated DABCO species and the monoamine azabicyclo-[2.2.2]octane (ABCO) that can be utilized to aid in the assignment of the former. As well, the similarity between the molecules bicyclo[2.2.2]octane (BCO), $ABCOH^+$, and the diprotonated DABCO has been exploited. The band assignments of Bruesch and Gunthard (12) for ABCO and BCO were thus useful in assigning the bands of the protonated DABCO species.

The 300 to 850 cm^{-1} region

The Raman bands ν_{36}, ν_{27}, ν_{35}, and ν_6 at 332, 424, 577, and 630 cm^{-1}, respectively, in the unprotonated DABCO spectrum shift to lower wavenumber in the sequence DABCO > $DABCOH^+$ > $DABCOH_2^{2+}$. These vibrations are associated with changes in the NC_3 bond angles; the addition of first one and then two protons affects both the mass at the nitrogen atoms and the bonding electron distribution. Note, however, ν_6, at 630 cm^{-1} in DABCO, which shows a shift to *higher* wavenumber when the strength of the solvent–DABCO interaction increases, shows the same downward shift in frequency as the other cage deformation (NCC bending) modes; the conversion of lone pair electron density to localized σ bond density must cause this change in force constant. The cage-breathing mode at 806 cm^{-1} in the unprotonated form undergoes a small shift to lower frequency (801 cm^{-1}) upon monoprotonation, due most likely to the increase of the mass at the nitrogen atom. On diprotonation, this band is observed to increase in frequency to 809 cm^{-1}, this shift possibly arising from a redistribution of electron density in the diprotonated species, not unexpected since there are now no lone-pair orbitals left for through-bond interaction. In the same spectral region, a new band is seen in the Raman spectrum as a weak shoulder at ≈760 cm^{-1}; this band is polarized and corresponds to $\nu_{18}(a_2'')$ of the unprotonated DABCO, now Raman-allowed and totally symmetric, as expected from the correlation diagram. Two weak bands, at 831 and 911 cm^{-1} in the unprotonated DABCO, are also seen in the Raman spectra of the monoprotonated form, at 841 and 896 cm^{-1}, and at 852 and 903 cm^{-1} in the diprotonated DABCO.

The 850 to 1200 cm^{-1} region

The spectral region from 950 to 1100 cm^{-1} exhibits perhaps the most distinctive and, as far as identification is concerned, useful changes upon protonation, as can be seen in Fig. 5. For the monoprotonated species, a new Raman band at 1005 cm^{-1} is seen, in addition to bands at 987 and 1053 cm^{-1} which occur at 1002 (IR), 983, and 1060 cm^{-1} for the unprotonated species. This new Raman band corresponds to $\nu_{10}(a_2'')$ which becomes Raman-allowed in $DABCOH^+$; at the same time ν_4 at 983 cm^{-1} in DABCO becomes allowed in the infrared spectrum of the monoprotonated species (987 (R), 991 (IR)). The Raman bands at 987 and 1005 cm^{-1} are both polarized as expected. These changes can all be understood in terms of a reduction of the symmetry of DABCO from D_{3h} to C_{3h} upon monoprotonation.

More puzzling are the spectral changes observed upon diprotonation. Raman bands are observed at 987, 1033, and

Can. J. Chem. Downloaded from www.nrcresearchpress.com by 93.93.197.157 on 09/07/12
For personal use only.

Can. J. Chem. Downloaded from www.nrcresearchpress.com by 93.93.197.157 on 09/07/12
For personal use only.

TABLE 2. Vibrational band positions and assignments of DABCO and its protonated forms*

		DABCO			$DABCOH^+$		$DABCOH_2^{2+}$	
Symmetry	Mode	Raman	Infrared	Assignment	Raman	Infrared	Raman	Infrared
a_1'								
	ν_1	2889	—	$\nu_s CH_2$	?	?	2880	?
	ν_2	1457	—	δCH_2	1488	1492	1513	—
	ν_3	1352	—	$\nu CH_2/\nu CC$	1364	1365	1407	—
	ν_4	983	—	$\nu CC/\omega CH_2$	987	991	1033	—
	ν_5	806	—	$\nu_s NC_3$	801	+	809	—
	ν_6	630	—	Skel def	608	+	605	—
a_2''								
	ν_{14}	—	2885	$\nu_s CH_2$	?	?	—	?
	ν_{15}	—	1467	δCH_2	?	1475	—	1481
	ν_{16}	—	1364	ωCH_2	1383	1386	—	1397
	ν_{17}	—	1002	Skel def	1005	1007	—	990
	ν_{18}	—	783	$\nu_s NC_3$	760	+	—	786
e'	ν_{19}	?	?	$\nu_{as} CH_2$	?	?	?	?
	ν_{20}	?	?	$\nu_s CH_2$	?	?	?	?
	ν_{21}	1457	1461	δCH_2	1475	1475	1476	1471
	ν_{22}	1321	1324	ωCH_2	1325	1327	1330	1326
	ν_{23}	1299	1301	τCH_2	1301	?	1299	1299
	ν_{24}	1060	1061	$\nu_{as} NC_3$	1053	1056	1061	1058
	ν_{25}	911	910	νCC	896	+	903	+
	ν_{26}	831	834	ρCH_2	841	+	852	+
	ν_{27}	424	+	$\delta_{as} NC_3$	411	+	404	+
e''								
	ν_{28}	?	?	$\nu_{as} CH_2$	?	?	?	?
	ν_{29}	?	?	$\nu_s CH_2$	?	?	?	?
	ν_{30}	1446	—	?	1458	?	1476	—
	ν_{31}	1323	—	ωCH_2	1320	?	1320	—
	ν_{32}	1311	—	?	?	?	?	—
	ν_{33}	1130	—	?	1178	1180	1169	—
	ν_{34}	982	—	?	987	991	987	—
	ν_{35}	577	—	$\delta_{as} NC_3$	563	+	555	—
	ν_{36}	332	—	ρNC_3	318	+	312	—

*N^+H stretches: 2500–2800, broad in ir, weak in R; N^+H bends: 1200–1300, broad in ir and Raman. +: band not observed, below window cutoff; —: band not active. ?: no assignment possible.

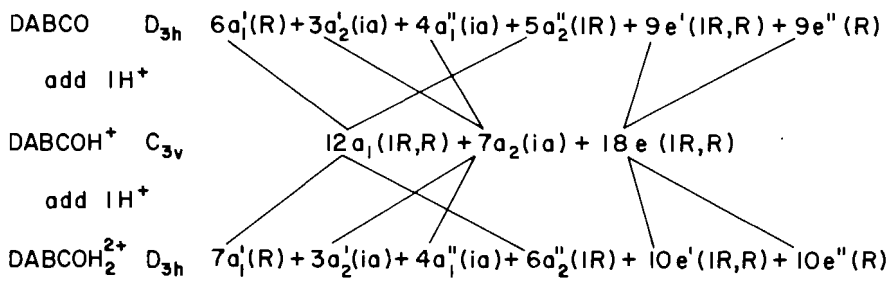

FIG. 4. Correlation diagram for DABCO and its two protonated forms.

1061 cm^{-1} with only the band at 1033 cm^{-1} being polarized. Two bands, one at 1058 cm^{-1} and the other a broad band at 990 cm^{-1}, are observed in the infrared spectrum. If $DABCOH_2^{2+}$ is of D_{3h} symmetry as proposed, then only one polarized Raman band is expected, as observed; this means that the band at 1033 cm^{-1} must be ν_4 *shifted* by 46 cm^{-1} from its position in the unprotonated and monoprotonated species. The same behavior is observed upon protonation of ABCO, which rules out an explanation based on the interaction of two closely-spaced, positively-charged, nitrogen atoms. A plausible hypothesis is that diprotonation in DABCO and monoprotonation in ABCO removes the mixing of the lone-pair orbitals and the σ_{C-C} orbitals, thus radically altering the C—C bond length and/or strength and leading to the observed shift in the frequency of ν_4. Monoprotonation does not produce such an effect since one lone pair (or the equivalent thereof delocalized over the entire framework) is left unchanged; Cralk and George (3) have proposed that a rapid exchange

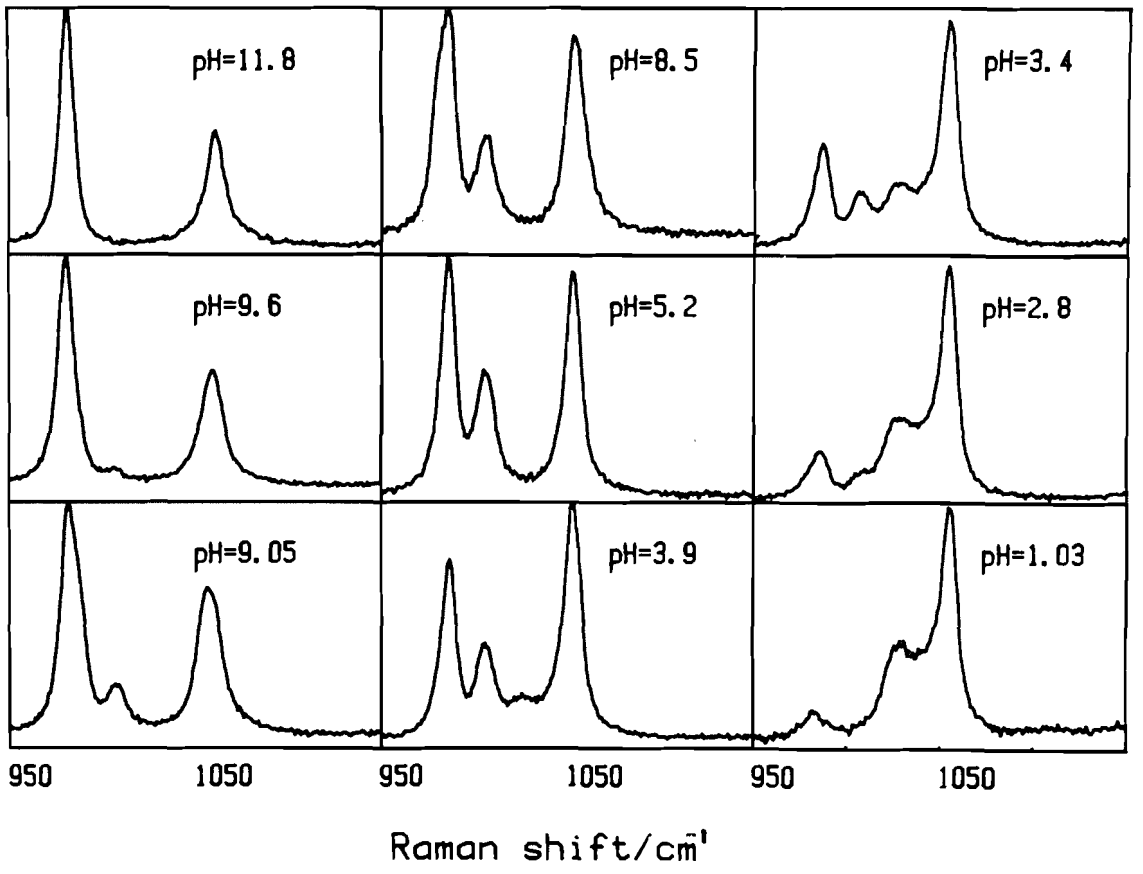

FIG. 5. Raman spectra from 950 to 1100 cm^{-1} of DABCO at the pH values specified.

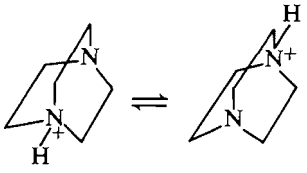

occurs in $DABCOH^+$ since the two nitrogens appear equivalent in NMR. Because the monoprotonated species conforms to the selection rules expected for C_{3v} symmetry in the Raman and infrared spectra, the exchange process above must be slow on a vibrational timescale; however, such an exchange would still leave the equivalent of one lone pair involved in the through-bond interaction, which could account for the unshifted value of ν_4 in the monoprotonated species compared to the unprotonated DABCO.

One anomaly still exists in the Raman spectrum of this region, namely, the appearance of a depolarized band at 987 cm^{-1}; this is the position at which ν_4 is found in the mono- and unprotonated DABCO's, and thus no band should be observed at this position if the band at 1033 cm^{-1} is correctly assigned as ν_4. Since the band observed at 987 cm^{-1} is not polarized, while the band at 1033 cm^{-1} is, the assignment of the latter to ν_4 is undoubtedly correct which leaves the assignment of the band at 987 cm^{-1} still open. The infrared band at this position is not Raman-allowed under D_{3h} symmetry. It is therefore suggested that this band be assigned to one of the missing e'' modes of DABCO; this band would be obscured in the unprotonated species by the much stronger ν_4 band at the same frequency. It is on this basis that the assignment of this band was made. This proposal can be verified by utilizing the sensitivity of ν_4 to solvent changes; the Raman spectrum of DABCO in carbon tetrachloride could not be obtained because of a photochemical process, previously reported by Weiss *et al.* (7); acetonitrile was therefore used as a solvent. In spite of the presence of interfering solvent bands in the 1000 cm^{-1} region, there does appear to be a weak band at about 995 cm^{-1} which could be the missing e'' mode. It is easier to see that this is the case by using ABCO instead of DABCO, as the former exhibits the same changes on monoprotonation as DABCO does on diprotonation, and a band is seen in the spectrum of the protonated ABCO at 987 cm^{-1}, similar to that observed in diprotonated DABCO. The C—C stretch of ABCO occurs at 987 cm^{-1} in water and is lowered to 967 cm^{-1} in carbon tetrachloride; in this solvent a weak band is observed at 991 cm^{-1}, as expected from the preceding argument. Thus the assignment of the band at 987 cm^{-1} to an e'' mode, previously unreported, appears reasonable.

Another unassigned band is found at 1178 cm^{-1} in the Raman spectrum of the monoprotonated DABCO and at 1169 cm^{-1} for the diprotonated form; it also appears with considerable intensity in the infrared spectrum of the monoprotonated species, and is weaker in the infrared spectrum of the diprotonated form. This band is tentatively assigned to another of the missing e'' modes.

N^+H vibrations

The spectral region between 1200 and 1600 cm^{-1} exhibits a number of changes on protonation, the most important of which is the appearance of a broad feature in both the infrared and

Can. J. Chem. Downloaded from www.nrcresearchpress.com by 93.93.197.157 on 09/07/12
For personal use only.

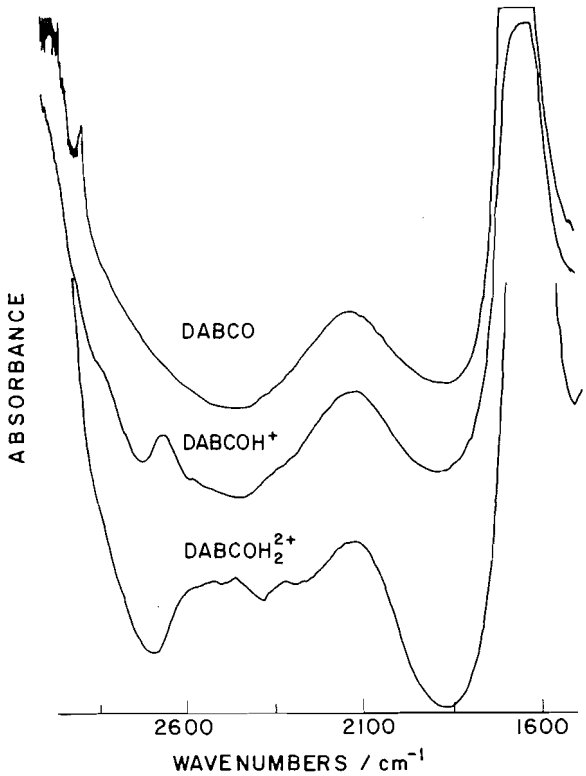

FIG. 6. Infrared spectra of the NH^+ stretching region of DABCO and its two protonated forms.

Raman spectra due to the N^+H group; at this point it is therefore useful to discuss the vibrational bands which arise from this group. The irreducible representations of the protonated species given in the correlation diagram show that upon monoprotonation, two bands due to the N^+H group arise, one of a_1 symmetry and the other of e species, and both should be present in the infrared and Raman spectra. Upon diprotonation, two further bands are expected thus giving rise to a total of four modes attributable to the vibration of the two N—H groups; the irreducible representation for the modes due to this group only is

$$\Gamma_{vib} = 1a_1'(R) + 1a_2''(IR) + 1e'(IR,R) + 1e''(R)$$

Ebsworth and Sheppard (22) discussed the infrared spectra of protonated amine salts, and gave the following frequencies for the stretching and deformation modes of trimethyl ammonium iodide:

$$\nu_s(N^+H) = 2725\ cm^{-1} \qquad \delta(N^+H) = 1418\ cm^{-1}$$

Brissette and Sandorfy (23) discussed the N^+H stretching vibration of several tertiary amines; in the solid state the centre of the broad band assigned to the N^+H stretch is found at about 2600 cm^{-1} for triethylamine and 2450 cm^{-1} for tri-*n*-butylamine hydrochloride, while in aqueous solution the same two bands are found at 2570 and 2640 cm^{-1}, respectively (Chenon and Sandorfy, ref. 24). Quagliano *et al.* (5) discussed the infrared spectrum of the diprotonated dabconium cation and assigned the N^+H stretching mode to a broad, intense infrared absorption between 1800 and 2800 cm^{-1}.

The infrared spectra of the N^+H stretching region of the three forms of DABCO in water are shown in Fig. 6. The analogous Raman spectra are shown in Fig. 7. It is apparent from the infrared spectra that the band at 2666 cm^{-1}, which appears upon monoprotonation, ought to be assigned to the N^+H stretching mode since it falls at about the same frequency as found for other protonated tertiary amines. Upon diprotonation this band becomes a broad, structured feature extending from below 2200 cm^{-1} to above 2700 cm^{-1}, evidence for considerable hydrogen bonding with the solvent water molecules, and it is assigned to the antisymmetric N^+H vibration. The Raman spectrum is less easily interpreted, since even the spectrum of the unprotonated species exhibits bands in this region. Upon monoprotonation several weak bands appear in this region, one at 2656 cm^{-1} which may correspond to the 2666 cm^{-1} band observed in the infrared spectrum. This leaves the identity of the band seen at 2761 cm^{-1} a mystery. Upon diprotonation a pair of Raman bands at 2761 and 2789 are observed and may represent the N^+H symmetric stretch. Because of the low intensity of these bands and the evidence of solvent interactions which causes them to become broad, it is safest to simply assign the N^+H stretch to bands between 2300 and 2800 cm^{-1} and leave the assignment of particular bands to particular modes unstated. To confirm that these bands do correspond to the N^+H stretches, the infrared and Raman spectra of $DABCOD_2^{2+}$ in D_2O

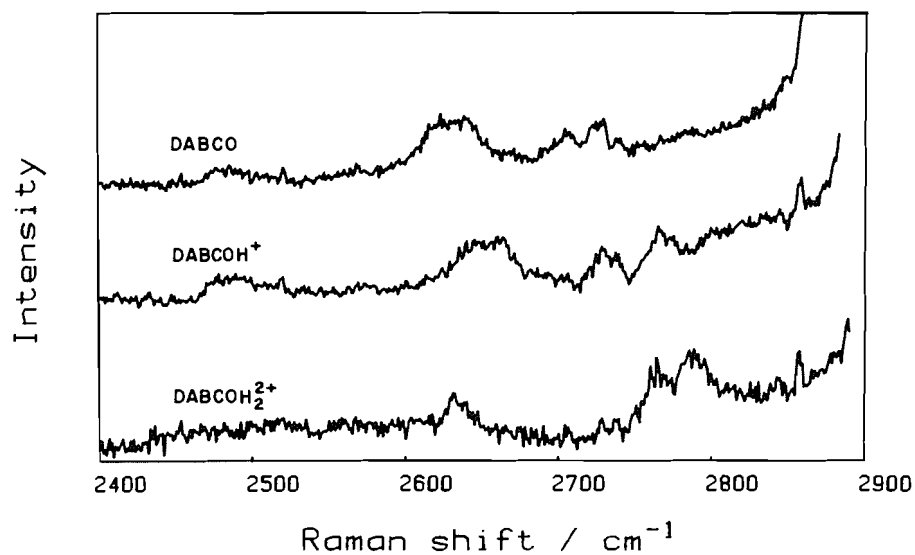

FIG. 7. Raman spectra of the NH^+ stretching region of DABCO and its two protonated forms.

Can. J. Chem. Downloaded from www.nrcresearchpress.com by 93.93.197.157 on 09/07/12
For personal use only.

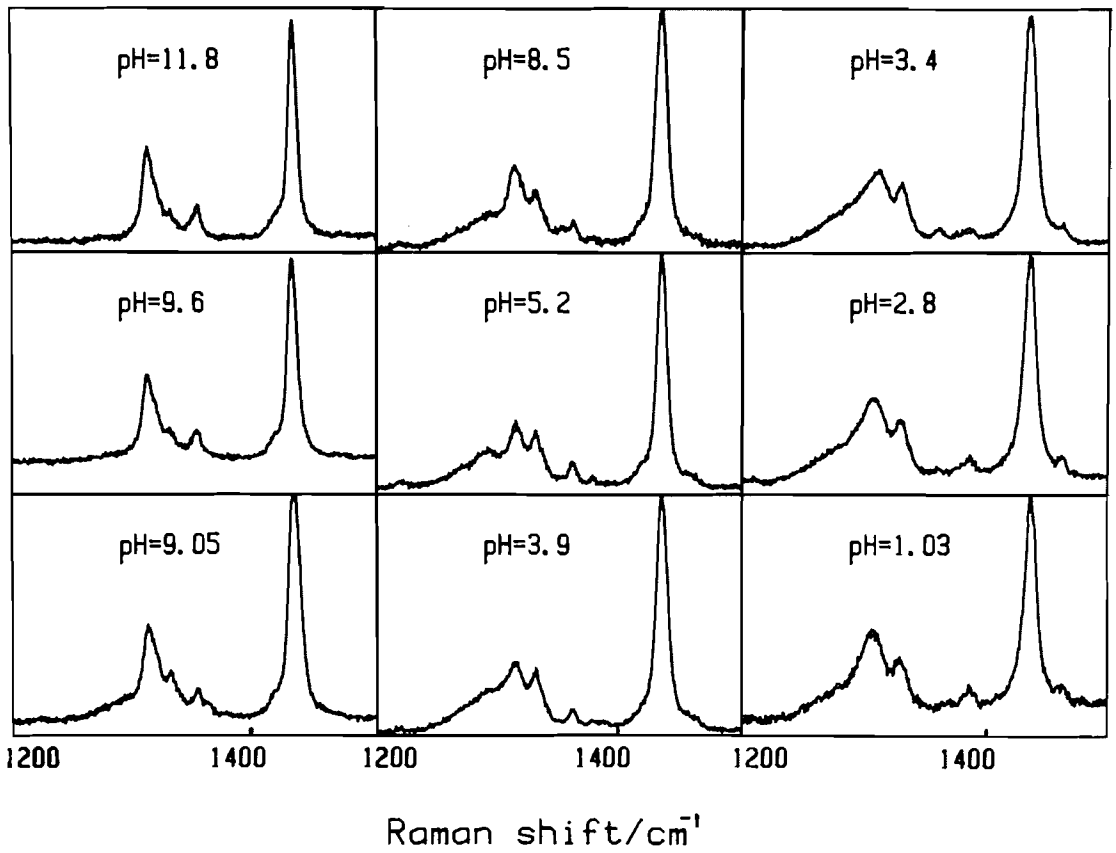

FIG. 8. Raman spectra of the CH scissors and wagging region (1200 to 1500 cm^{-1}) of DABCO at the pH values specified.

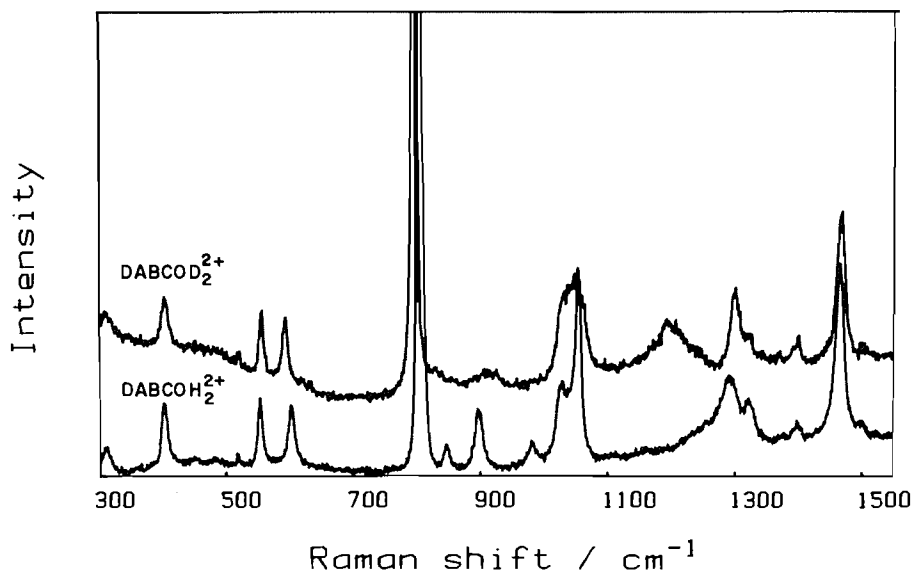

FIG. 9. Raman spectra of DABCO, protonated and deuteriated, at pH $\approx$ 0, in H_2O and D_2O.

were obtained. The N^+D stretches are expected to occur at $\approx 1970\ cm^{-1}$ if the above assignment is correct, and indeed the infrared and Raman spectra of the di-deuterated species show a number of bands between 1700 and 2100 cm^{-1} not seen in the spectrum of DABCO in D_2O. Thus the assignment of the N^+H stretching modes seems correct.

Turning now to the N^+H bending modes, Fig. 8 shows the Raman spectra of the region 1250 to 1450 cm^{-1}. One can see that a broad band appears in the spectra of both protonated species, centered around 1275 cm^{-1}; a similar band (or group of bands) appears in the infrared spectra, as seen in Fig. 3. That these bands are due to the N^+H bending modes can be verified by again turning to the spectra obtained in D_2O. Figure 9 shows the Raman spectra of $DABCOH_2^{2+}$ and $DABCOD_2^{2+}$, and as expected the broad band at $\approx 1275\ cm^{-1}$ is shifted in the deuteriated species, although its new location is not clear (the

Can. J. Chem. Downloaded from www.nrcresearchpress.com by 93.93.197.157 on 09/07/12
For personal use only.

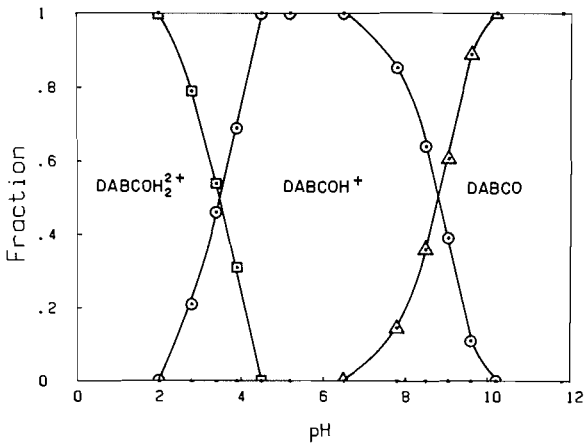

FIG. 10. Fractional composition of aqueous 2.0 *M* DABCO as a function of pH, obtained from Raman band areas.

broad band at about 1200 cm^{-1} arises from the D_2O bending mode). Interestingly, the Raman spectrum of $DABCOD_2^{2+}$ exhibits a number of intensity changes and band shifts compared to the spectrum of $DABCOH_2^{2+}$; their origins are not clear. For example, bands at 852, 903, and 987 cm^{-1} in the spectrum of the latter species become broad and weak in the spectrum of the former. As well, the infrared- and Raman-active band at 1061 cm^{-1} in the $DABCOH_2^{2+}$ spectrum shifts to 1043 cm^{-1} and merges with ν_4 to form a broad, poorly resolved feature in the Raman spectrum. At the same time the band at 852 cm^{-1} which is weak in the Raman is strong in the infrared spectrum, while weak bands appear in the infrared at 911 and 976 cm^{-1}.

No definitive explanation for these changes can be given at this time; it is suggested that coupling of the N^+D bending modes, which are of *e'* and *e''* species and which plausibly could lie between 900 and 1000 cm^{-1}, to modes of *e'* or *e''* species in this region occurs. The four modes which are observed to be affected are of these species. It is clear, however, that in spite of these unresolved changes, the spectra of the $DABCOD_2^{2+}$ confirm the assignment of the broad feature in both the Raman and infrared spectra of $DABCOH_2^{2+}$ at $\approx$1280 cm^{-1} to the N^+H bending modes.

Returning then to Fig. 8, most of the C—H wagging modes, which lie between 1300 and 1360 cm^{-1} and the C—H scissors modes between 1440 and 1470 cm^{-1} in DABCO exhibit shifts to higher wavenumber upon protonation, the shifts being of the order of up to 50 cm^{-1} for some of the bands. For example, ν_3 at 1352 cm^{-1} in DABCO shifts to 1364 cm^{-1} upon monoprotonation and to 1407 cm^{-1} upon diprotonation, while ν_{16} at 1364 cm^{-1} in DABCO shifts to 1383 cm^{-1} in the monoprotonated and 1397 cm^{-1} in the diprotonated form. The other C—H wagging modes do not show such large shifts. The C—H scissors modes all shift to higher wavenumber, the greatest shift being that of a polarized band which appears as a shoulder at 1488 cm^{-1} in the monoprotonated species and as a weak, polarized band at 1513 cm^{-1} in the diprotonated species; it can be assigned to ν_2 on the basis of its polarized Raman spectrum, the total band shift from DABCO to $DABCOH_2^{2+}$ being 56 cm^{-1}. Note that the bands which undergo the greatest shift with protonation appear to be the totally symmetric modes.

The results of the above discussions on the various spectral regions are summarized in Table 2, which lists the best assignments of all of the observed infrared and Raman bands of the three forms of DABCO. The mode numbering used in the

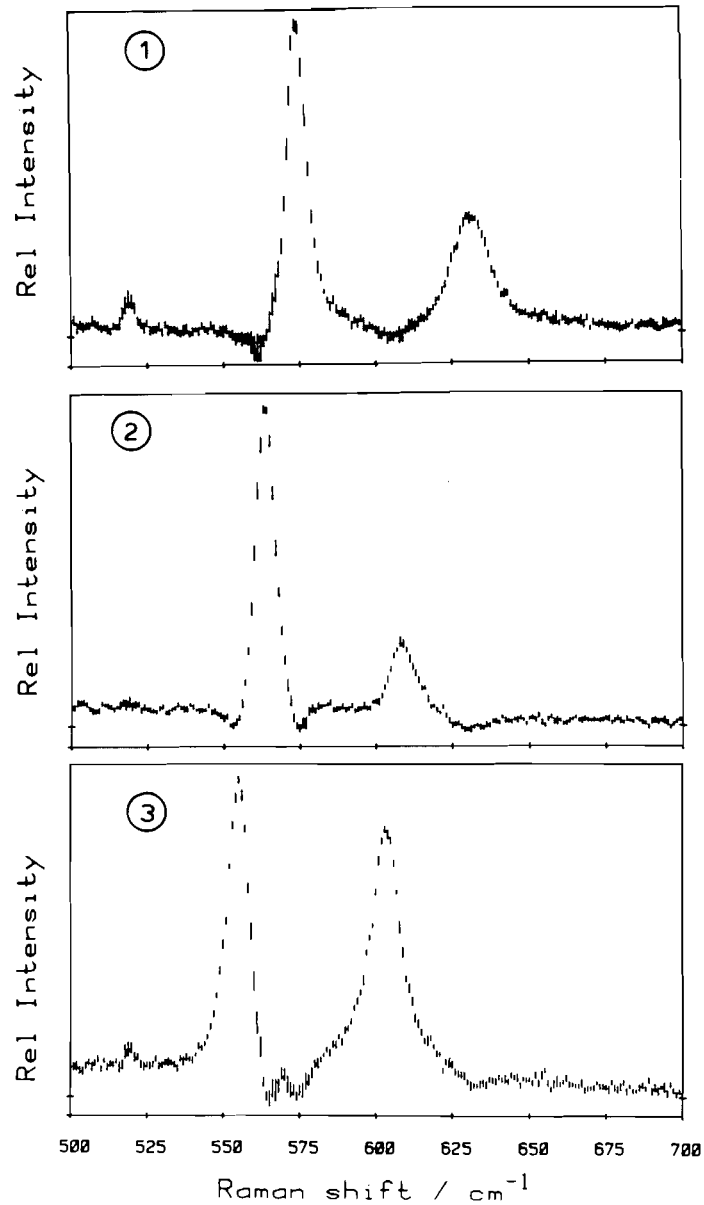

FIG. 11. Spectra of DABCO (*1*), $DABCOH^+$ (*2*), and $DABCOH_2^{2+}$ (*3*) isolated by key factor spectral isolation analysis.

table is that for unprotonated DABCO in order to provide a direct comparison of the band positions of the different species; the modes arising from the N^+H group(s) are listed at the end of the table, without any attempt to identify the species of the mode. Assignments are based on those of Ernstbrunner *et al.*; note, however the difference in the numbering of the modes between Table 2 and ref. 14.

Intensity changes with solution pH

It was interesting to see if it was possible to estimate values for the pK_a's from the Raman spectral data. In order to do this, it was necessary to find a Raman band which could be used as a measure of the concentration of the species of interest; ideally the band chosen should exhibit a reasonably large frequency shift and little change in absolute intensity. The best candidates for this task are any one of the three lowest frequency cage deformation modes ν_{27}, ν_{35}, or ν_{36}; ν_{35} at 577 cm^{-1} was chosen, and the band areas of each of the components repre-

Can. J. Chem. Downloaded from www.nrcresearchpress.com by 93.93.197.157 on 09/07/12
For personal use only.

senting the different DABCO protonated species was obtained. These areas were used to calculate the percentage of each of the three species DABCO, $DABCOH^+$, and $DABCOH_2^{2+}$, the results being plotted in Fig. 10. If one assumes that the molar scattering coefficients of the three species are identical, then the point at which the curves cross, which represents 50% abundance, should occur at the pH value equal to the pK_a for the equilibrium between the two species in question. In this manner, the following values were obtained:

$$pK_{a_1} = 3.2 \quad (2.97)$$

$$pK_{a_2} = 9.0 \quad (8.82)$$

These values are compared to the literature values in parentheses. The most obvious reason for the discrepancy is the change in the molar scattering coefficient upon protonation; there is no reason to expect the values of this factor to remain unchanged when DABCO is protonated. In fact, the data indicate that the molar scattering coefficients of these bands decrease successively on protonation. Also, for the large (2 *M*) concentration used in these experiments the activity coefficients should not be neglected.

An attempt was also made to use factor analysis to obtain the DABCO distribution diagram, using the same spectral region in the input data matrix. The principle component analysis correctly chose three as the number of components present, and the key factor spectral isolation program was able to reproduce the spectra of the three components (Fig. 11); these compare very well with the known spectra of the three protonated species. The relative concentrations obtained, however, did not produce a very sensible distribution curve above pH 6, and it appears that curve resolution was a superior method for obtaining the distribution diagram from the Raman data.

Acknowledgements

This work was supported by grants from the Natural Sciences and Engineering Research Council of Canada. D.A.G. is grateful for the award of an Ontario Graduate Scholarship. Thanks are expressed to Dr. M. Krell for assistance with the factor analysis.

1. D. E. Irish, D. A. Guzonas, and G. F. Atkinson. Surf. Sci. **158**, 314 (1985).
2. D. A. Guzonas. Ph.D. Thesis. University of Waterloo, Waterloo, Ont. 1987.
3. D. J. Cralk and C. L. George. J. Phys. Chem. **86**, 3893 (1982).
4. A. M. Amorim Da Costa. J. Mol. Struct. **141**, 347 (1986).
5. J. V. Quagliano, A. K. Banerjee, V. L. Goedken, and L. M. Vallarino. J. Am. Chem. Soc. **92**, 182 (1969).
6. H. Yokobayashi, K. Nagase, and K. Sone. Bull. Chem. Soc. Jpn. **51**, 2569 (1978).
7. G. S. Weiss, A. S. Parkes, E. R. Nixon, and R. E. Hughes. J. Chem. Phys. **41**, 3759 (1964).
8. N. Gonohe, N. Yatsuda, N. Mikami, and M. Ito. Bull. Chem. Soc. Jpn. **55**, 2796 (1982).
9. A. Farkas, G. A. Mills, W. E. Erner, and H. B. Maerker. J. Chem. Eng. Data, **4**, 334 (1959).
10. M. P. Marzocchi, G. Sbrana, and G. Zerbi. J. Am. Chem. Soc. **87**, 1429 (1965).
11. P. Bruesch. Spectrochim. Acta, **22**, 867 (1966).
12. P. Bruesch and Hs. H. Gunthard. Spectrochim. Acta, **22**, 877 (1966).
13. J. R. McDivett and G. L. Humphrey. Spectrochim. Acta, **30A**, 1021 (1974).
14. E. E. Ernstbrunner, R. B. Girling, W. E. L. Grossman, and R. E. Hester. J. Chem. Soc. Faraday II, **74**, 501 (1978).
15. P. Paoletti, J. H. Stern, and A. Vacca. J. Phys. Chem. **69**, 3759 (1965).
16. J. W. Larson, G. L. Bertrand, and L. G. Hepler. J. Chem. Eng. Data, **11**, 595 (1966).
17. E. R. Malinowski. Target 85 Programs, Lake Hiawatha, N.J. (1985).
18. E. R. Malinowski. Anal. Chim. Acta, **134**, 129 (1982).
19. V. Gutman. The donor–acceptor approach to molecular interactions. Plenum Press, New York. 1978.
20. E. Heilbronner and K. A. Muszkat. J. Am. Chem. Soc. **90**, 3818 (1970).
21. R. Hoffmann, A. Imamura, and J. W. Hehre. J. Am. Chem. Soc. **90**, 1499 (1968).
22. E. A. V. Ebsworth and N. Sheppard. Spectrochim. Acta, **13**, 261 (1959).
23. C. Brissette and C. Sandorfy. Can. J. Chem. **38**, 34 (1960).
24. B. Chenon and C. Sandorfy. Can. J. Chem. **36**, 1181 (1958).

Can. J. Chem. Downloaded from www.nrcresearchpress.com by 93.93.197.157 on 09/07/12
For personal use only.

Nucleic acid related compounds. 53. Synthesis and biological evaluation of 2′-deoxy-β-*threo*-pentofuranosyl nucleosides. "Reversion to starting alcohol" in Barton-type reductions of thionocarbonates[1]

MORRIS J. ROBINS,[2] DANUTA MADEJ, FRITZ HANSSKE, AND JOHN S. WILSON
Department of Chemistry, University of Alberta, Edmonton, Alta., Canada T6G 2G2

GILLES GOSSELIN, MARIE-CHRISTINE BERGOGNE, AND JEAN-LOUIS IMBACH
Laboratoire de chimie bio-organique, Unité associée n° 488 du Centre national de la recherche scientifique, Université des sciences et techniques du Languedoc, Place Eugène-Bataillon, 34060 Montpellier CEDEX, France

AND

JAN BALZARINI AND ERIK DE CLERCQ
Rega Institute for Medical Research, Katholieke Universiteit Leuven, B-3000 Leuven, Belgium

Received August 28, 1987

MORRIS J. ROBINS, DANUTA MADEJ, FRITZ HANSSKE, JOHN S. WILSON, GILLES GOSSELIN, MARIE-CHRISTINE BERGOGNE, JEAN-LOUIS IMBACH, JAN BALZARINI, and ERIK DE CLERCQ. Can. J. Chem. **66**, 1258 (1988).

Treatment of selectively 3′,5′-protected β-D-xylofuranosyl nucleosides (**4**) with phenyl chlorothionocarbonate and DMAP followed by hydrogenolysis of the resulting (2′-*O*-phenoxythiocarbonyl) phenyl thionocarbonate esters (**6**) with tributylstannane/AIBN, and deprotection, gave 2′-deoxy-β-D-*threo*-pentofuranosyl nucleosides (**7**). Formation of a by-product bis(nucleosid-2′-yl)thionocarbonate dimer (**8**) was detected in the uracil nucleoside reaction sequence. Its subsequent reduction provides one explanation for "reversion to starting alcohol" in Barton-type deoxygenation reactions. Only the guanine 2′-deoxynucleoside analogue (**7***b*) had (weak) antiviral activity (against herpes simplex virus type 1).

MORRIS J. ROBINS, DANUTA MADEJ, FRITZ HANSSKE, JOHN S. WILSON, GILLES GOSSELIN, MARIE-CHRISTINE BERGOGNE, JEAN-LOUIS IMBACH, JAN BALZARINI et ERIK DE CLERCQ. Can. J. Chem. **66**, 1258 (1988).

La réaction des nucléosides de β-D-xylofurannosyle protégés sélectivement en 3′,5′ (**4**) avec du chlorothionocarbonate de phényle et du DMAP, suivie d'une hydrogénolyse des esters thionocarbonates de (*O*-phénoxythiocarbonyl-2′) de phényle (**6**) avec le tributylstannane/AIBN et d'une déprotection, conduit aux nucléosides du désoxy-2′ β-D-*thréo*-pentofurannosyle (**7**). Dans la suite de réactions impliquant le nucléoside d'uracile, on a détecté la formation du dimère du thionocarbonate de bis-(nucléosidyl-2′) (**8**) comme sous-produit. Sa réduction subséquente permet d'expliquer la «réversion vers l'alcool de départ» qui est observée dans des réactions de désoxygénation du type de Barton. L'analogue désoxy-2′ nucléoside de la guanine (**7***b*) est le seul à présenter une activité antivirale (faible) (contre le virus herpès simplex de type 1).

[Traduit par la revue]

Methods for the synthesis of β-D-xylofuranosyl nucleosides via base-sugar coupling (ref. 1, and references therein) and for selective 2′-deoxygenation of nucleosides (2) have been developed by us previously. We now report combination of these approaches to give 2′-deoxy-β-D-*threo*-pentofuranosyl nucleosides (**7**) and their evaluation for antiviral activity in several cell systems.

In the pioneering studies of the Cambridge group, Michelson and Todd (3) reported preparation of the O2,C3′-cyclonucleoside of thymidine and its hydrolysis to give 1-(2-deoxy-β-D-*threo*-pentofuranosyl)thymine (**7***e*) in 1955. Fox and Miller (4) and Horwitz *et al.* (5) later described careful characterization of this product. An analogous procedure was employed (6) for the preparation of 1-(2-deoxy-β-D-*threo*-pentofuranosyl)uracil (**7***d*).

Goodman and co-workers (7) first prepared 9-(2-deoxy-β-D-*threo*-pentofuranosyl)adenine (**7***a*) (and its 3′-deoxy isomer) by nucleophilic ring opening (oxirane) of 9-(2,3-anhydro-β-D-lyxofuranosyl)adenine with benzylthiolate followed by desulfurization. Analogous (acid-catalyzed) ring opening with bromide followed by hydrogenolysis with tributylstannane gave alternative access to the isomeric adenine 2′-(**7***a*) and 3′-deoxy-*threo* nucleoside products (8). Ikehara's 8-mercaptoadenine-S8,C2′-cyclonucleoside desulfurization approach (9) has also provided the 2′-deoxy-*threo* compound (**7***a*). We (10) have more recently described a reductive rearrangement route to these analogues.

In the present study, condensation of 1,2-di-*O*-acetyl-3,5-di-*O*-benzoyl-α-D-xylofuranose (**1**) (11)[3] with the five major nucleic acid bases (**2***a–e*) under appropriate conditions (protection, catalyst, solvent, etc.) gave the 2′-*O*-acetyl-3′,5′-di-*O*-benzoyl-β-D-xylofuranosyl nucleoside derivatives (**3**) in moderate to good yields (1).[4]

Selective deacetylation of O2′ was effected by the Ishido procedure with hydrazine hydrate in buffered acetic acid/pyridine (11, 14) to give the 3′,5′-di-*O*-benzoyl derivatives (**4**). Direct treatment of **4***a,d,e* and the N^2-acetyl derivative of **4***b* with phenyl chlorothionocarbonate and 4-(dimethylamino)pyridine (DMAP) in acetonitrile (2) gave the corresponding 2′-*O*-(phenoxythiocarbonyl) derivatives **6***a,d,e* and N^2-acetyl-**6***b*. Barton-type deoxygenative hydrogenolysis of these thiono-

[1]For the previous paper in this series, see ref. 23.

[2]Author to whom inquiries may be addressed at the Department of Chemistry, Brigham Young University, Provo, Utah 84602, U.S.A.

[3]For condensations, alternative use of 1-*O*-acetyl-2,3,5-tri-*O*-benzoyl-α-D-xylofuranose (12) was equally effective. However, the noncrystalline preparation (13) of "tetra-*O*-acetyl-D-xylofuranose" contained significant quantities of pyranose and other contaminants (1*a*) and should be avoided.

[4]See the experimental section for compound **3***e*. Syntheses of **3***a,c,d* and the N^2-acetyl derivative of **3***b* are described in ref. 1.

Can. J. Chem. Downloaded from www.nrcresearchpress.com by 93.93.197.157 on 09/07/12
For personal use only.

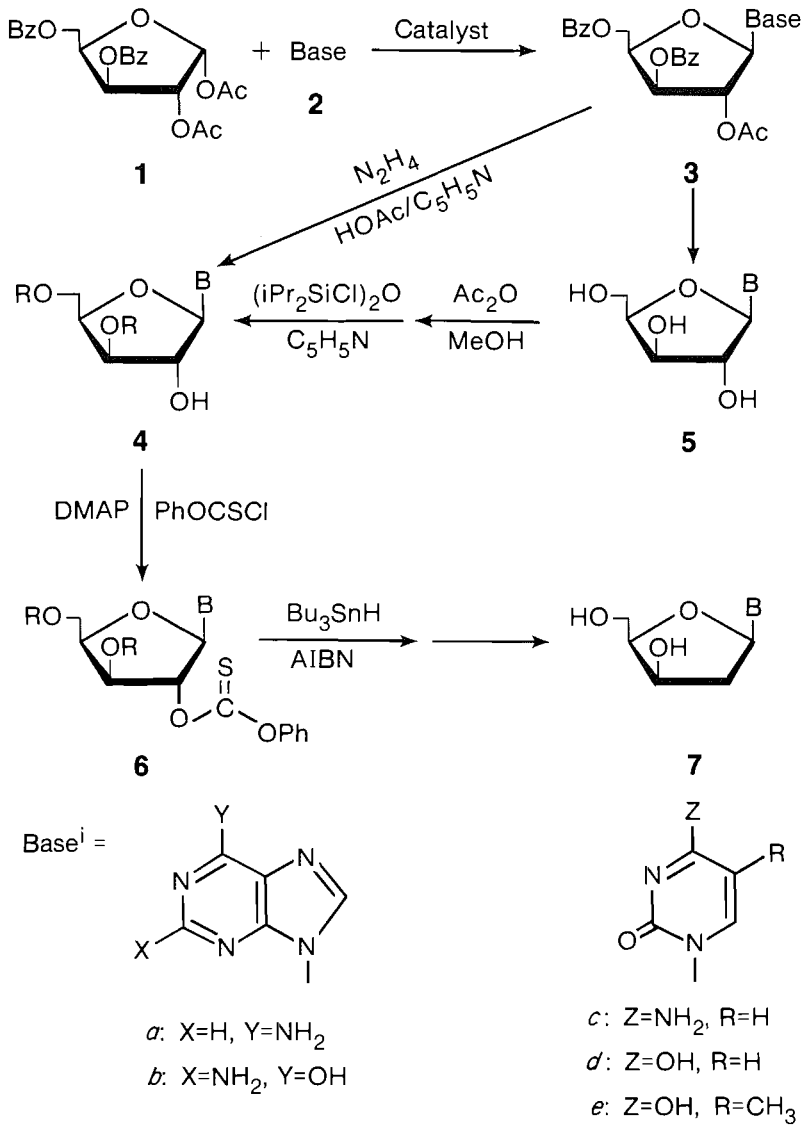

[i]The keto tautomers of the indicated enol bases predominate almost exclusively in aqueous solutions.

SCHEME 1

carbonate esters[5] with tributylstannane (and AIBN, α,α′-azobisisobutyronitrile, initiator) in toluene at 80°C (2) followed by deprotection gave the desired 2′-deoxy-β-D-*threo*-pentofuranosyl products (**7***a*,*b*,*d*,*e*).

The cytosine nucleoside (**4***c*) underwent N^4 thionoacylation and subsequent side reactions as observed previously with cytidine (2*b*). Therefore, **3***c* was fully deprotected (1*a*) and the resulting 1-(β-D-xylofuranosyl)cytosine (**5***c*) was selectively N^4-acetylated with acetic anhydride in methanol at reflux (2*b*, 15) and then converted to its 3′,5′-*O*-(1,1,3,3-tetraisopropyldisiloxan-1,3-diyl) derivative (**4***c*; R = $[Si(iPr)_2]_2O$; B = N^4-acetyl-*c*) (1*b*, 2*b*, 16, 17). Thionoacylation at O2′, hydrogenolysis, and deprotection gave **7***c*.

In the original Barton deoxygenation of alcohols, "reversion" of thiono esters to starting alcohols was observed (18, 19). We did not detect this side reaction in our 2′-deoxygenations of 2′-*O*-(phenoxythiocarbonyl) ribonucleosides with AIBN initiated hydrogenolyses using tributylstannane (2). However, in the present work, formation of parent β-D-xylofuranosyl nucleosides (**5**) was observed after O2′-thionoacylation, hydrogenolysis, and deprotection of **4**.

Isolation of a dimeric nucleosid-2′-yl thionocarbonate ester (**8**) in the uracil series provided an explanation for this result. Apparently, the less hindered O2′ region of the α-face of β-D-xylofuranosyl nucleosides (relative to β-D-ribonucleosides with a bulky *cis*-vicinal O3′ function) allows transesterification of the free 2′-hydroxyl group of one nucleoside with the phenyl thionocarbonate moiety of a second 2′-*O*-(phenoxythiocarbonyl) nucleoside derivative (with expulsion of the less basic phenoxide) to give **8**. The ^{13}C nmr spectrum of this product had peaks corresponding to one thiocarbonyl carbon, two identically shifted pairs of benzoyl carbonyl carbons, and an identically shifted dimeric nucleoside carbon skeleton. This compound (**8**) had tlc migration slightly slower than the

[5]The N^2-acetyl-**6***b* compound was further solubilized by trimethylsilylation with *N*,*O*-bis(trimethylsilyl)trifluoroacetamide before the hydrogenolysis step.

Can. J. Chem. Downloaded from www.nrcresearchpress.com by 93.93.197.157 on 09/07/12
For personal use only.

TABLE 1. Characteristic data for compounds **7***a–e*

Compound	Melting point (°C)	Ultraviolet max[a] (nm) (ε)	^{1}H nmr (δ ppm)[b] H2′	H2″	H3′	H1′	^{13}C nmr (δ ppm)[b] C4′	C1′	C3′	C5′	C2′
7*a*	234–235	260 (15 000)	2.25	2.77	4.33	6.25	85.53	83.29	69.69	60.39	41.11
7*b*	>300	253 (12 300)	2.18	2.71	4.35	6.06	84.96	81.68	68.98	59.78	40.77
7*c*	153–155	272 (8500) 230 (7600)	1.80	2.50	4.20	6.00	84.97	84.97	68.93	59.69	41.37
7*d*	170–171	261 (10 100)	1.87	2.55	4.24	6.05	85.01	83.75	68.46	59.41	40.74
7*e*	174–175	266 (9600) 208 (9500)	1.85	2.60	4.25	6.07	84.95	83.65	68.88	59.79	40.89

[a]MeOH as solvent.
[b]Me_2SO-d_6 as solvent with Me_4Si as internal standard.

Can. J. Chem. Downloaded from www.nrcresearchpress.com by 93.93.197.157 on 09/07/12
For personal use only.

2′-*O*-(phenoxythiocarbonyl) monomer derivative (**6**), and could be separated by preparative tlc. Analytical tlc evidence for the formation of analogous dimeric thionocarbonates was observed in other cases also.

Barton first demonstrated that tributylstannane-mediated hydrogenolysis of a 2′,3′-*O*-thiocarbonyl derivative of adenosine gave a mixture of 2′- (major) and 3′-deoxy products (20). Analogous reduction of dimeric derivatives of **8** followed by

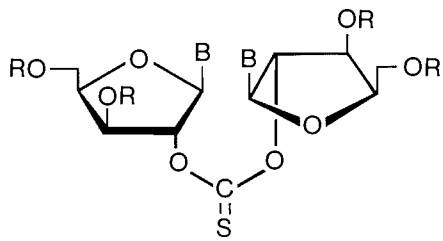

8

deprotection would produce one equivalent of 2′-deoxynucleoside (**7**) and one of the parent β-D-xylofuranosyl starting material (**5**).

Compounds **7***a–e* (Table 1) were evaluated against a variety of viruses: herpes simplex virus types 1 and 2, vaccinia virus, vesicular stomatitis virus, Coxsackie virus type B4, polio virus type 1, parainfluenza virus type 3, reovirus type 1, Sindbis virus, and Semliki forest virus in the appropriate (primary rabbit kidney, HeLa, and (or) Vero) host cell cultures (21*a*). Except for the 3′-epimer (**7***b*) of 2′-deoxyguanosine, which inhibited herpes simplex virus type 1 in primary rabbit kidney cells at a concentration of 70 μg/mL but was not cytotoxic at concentrations up to 400 μg/mL, no antiviral activity was noted with any compound in any system at a concentration lower than 200 μg/mL. Similarly, no significant protective activity was observed with any of the compounds when examined against the cytopathogenicity of human immunodeficiency virus (HIV) in ATH8 cells (21*b*) at a concentration of 100 μ*M* (~25 μg/mL).

Experimental

Biological assays in cell culture

The viruses, cell types, and methods have been described (21).

Chemical synthesis

General procedures and instrumentation used have been described (1*a*, 2*b*). See ref. 1*a* for syntheses of compounds **3***a*,*d* and **5***c*; ref. 1*b* for N^2-acetyl-**3***b* and **4***b* (R = Bz) and **3***c*; and ref. 11 for **4***a* (R = Bz). The nmr spectra were determined in Me_2SO-d_6 solutions with Me_4Si as internal reference unless otherwise noted.

*9-(2-Deoxy-β-D-*threo*-pentofuranosyl)adenine (7*a*)*

A solution of 951 mg (2 mmol) of **4***a* (R = Bz) (11), 400 μL (499 mg, 2.89 mmol) of PhOCSCl, and 500 mg (4.1 mmol) of DMAP in 40 mL of CH_3CN was stirred overnight at ambient temperature. Solvent was evaporated and the residue was partitioned between EtOAc/H_2O. The organic phase was washed with ice-cold 1 *N* HCl/H_2O, H_2O, saturated $NaHCO_3$/H_2O, saturated NaCl/H_2O, dried (Na_2SO_4), filtered, and evaporated to dryness. The resulting solid foam was dissolved in 10 mL of dry $PhCH_3$, evaporated *in vacuo*, and this process was repeated to give 9-(3,5-di-*O*-benzoyl-2-*O*-phenoxythiocarbonyl-β-D-xylofuranosyl)adenine as a crisp colorless tlc homogeneous solid foam.

This **6***a* (R = Bz) was dissolved in 20 mL of dry $PhCH_3$ and heated with 0.8 mL (866 mg, 2.97 mmol) of Bu_3SnH and 60 mg (0.37 mmol) of AIBN for 8 h at 80°C. The solution was evaporated and the tlc homogeneous residue was stirred with 5% NaOMe/MeOH at ambient temperature until deprotection was complete (tlc). The solution was evaporated and the residue was dissolved in a minimum volume of H_2O and applied to a column of Dowex 1X2(OH^-) resin (50 mL). Elution with H_2O and evaporation of appropriately pooled fractions gave 420 mg (84%) of crude **7***a*. Crystallization of this product from MeOH/Et_2O (diffusion) (22) gave 388 mg (77%) of **7***a*: mp 234–235°C (lit. (7) mp 218.9–219.5°C); uv (MeOH) max 260 nm (ε 15 000), min 227 nm (ε 3000); ^{1}H nmr δ: 2.25 (dd, $J_{1'-2'}$ = 2 Hz, $J_{2'-2''}$ = 14.5 Hz, 1, H2′), 2.77 ("sept", $J_{1'-2''}$ = 9.5 Hz, $J_{2''-3'}$ = 5 Hz, 1, H2″), 3.65 (m, 2, H5′, 5″), 3.90 (m, 1, H4′), 4.33 (m, 1, H3′), 4.68 (t, 1, OH5′), 5.97 (d, 1, OH3′), 6.25 (dd, 1, H1′), 7.33 (bs, 2, NH_2), 8.15 (s, 1, H8), 8.35 (s, 1, H2); ^{13}C nmr δ: 156.23 (C6), 152.76 (C2), 148.86 (C4), 140.83 (C8), 118.05 (C5), 85.53 (C4′), 83.29 (C1′), 69.69 (C3′), 60.39 (C5′), 41.11 (C2′); ms *m/z*: 251.1013 (M^+ 251.1018). *Anal.* calcd. for $C_{10}H_{13}N_5O_3$ (251.2): C 47.81, H 5.22, N 27.88; found: C 47.95, H 5.16, N 27.74.

*9-(2-Deoxy-β-D-*threo*-pentofuranosyl)guanine (7*b*)*

A mixture of 533.5 mg (1 mmol) of N^2-acetyl-**4***b* (R = Bz) (1*b*), 200 μL (250 mg, 1.45 mmol) of PhOCSCl, 366 mg (3 mmol) of DMAP, and 100 mL of CH_3CN was stirred for 6 h at ambient temperature. Thin-layer chromatography showed disappearance of starting material with formation of product N^2-acetyl-**6***b* (R = Bz) and ~20% of dimeric thionocarbonate (**8**; R = Bz, B = N^2-acetyl-*b*). This reaction mixture was evaporated and worked up as described above for the conversion **4***a* → **6***a* (R = Bz), except that ice-cold 10% HOAc in saturated NaCl/H_2O was substituted for the 1 *N* HCl/H_2O wash.

The crude N^2-acetyl-9-(3,5-di-*O*-benzoyl-2-*O*-phenoxythiocarbonyl-β-D-xylofuranosyl)guanine (**6***b*; R = Bz, B = N^2-acetyl-*b*) was dissolved in 24 mL of dry dimethylformamide (DMF) and treated with 2.4 mL (2.3 g, 9 mmol) of $CF_3C(=NSiMe_3)(OSiMe_3)$[5] for 30 min at 70°C. The residue obtained after evaporation *in vacuo* was dissolved in 10 mL of dry $PhCH_3$ and treated with 670 μL (725 mg, 2.49 mmol) of Bu_3SnH and 49 mg (0.3 mmol) of AIBN for 36 h at 80°C. The solution was evaporated and the residue was stirred with 20 mL of MeOH for 3 h. The mixture was evaporated and separated by preparative tlc

Can. J. Chem. Downloaded from www.nrcresearchpress.com by 93.93.197.157 on 09/07/12
For personal use only.

(silica, MeOH/$CHCl_3$, 1:9). Elution of the appropriate band and deprotection with NH_3/MeOH gave the title compound, which was crystallized from H_2O to give 85 mg (31%) of **7***b*: mp >300°C; uv (MeOH) max 253 nm (ε 12 300), min 221 nm (ε 2900); ^{1}H nmr δ: 2.18 (dd, $J_{1'-2'}$ = 2 Hz, $J_{2'-2''}$ = 14.5 Hz, 1, H2′), 2.71 ("sept", $J_{1'-2''}$ = 8.5 Hz, $J_{2''-3'}$ = 5.3 Hz, 1, H2″), 3.68 (m, 2, H5′, 5″), 3.90 (m, 1, H4′), 4.35 (bs, 1, H3′), 4.69 (bs, 1, OH5′), 5.45 (bs, 1, OH3′), 6.06 (dd, 1, H1′), 6.50 (bs, 2, NH_2), 7.98 (s, 1, H8), 10.66 (bs, 1, NH); ^{13}C nmr δ: 156.62 (C6), 153.50 (C2), 150.50 (C4), 136.04 (C8), 116.37 (C5), 84.96 (C4′), 81.68 (C1′), 68.98 (C3′), 59.78 (C5′), 40.77 (C2′); ms (FAB) *m/z*: 268 (23%, *M* + 1). *Anal.* calcd. for $C_{10}H_{13}N_5O_4 \cdot 0.25\,H_2O$ (271.7): C 44.20, H 5.01, N 25.77; found: C 44.29, H 4.90, N 25.87.

*1-(2-Deoxy-β-D-*threo*-pentofuranosyl)cytosine (7*c*)*

A mixture of 243 mg (1 mmol) of **5***c* (1*a*), 0.24 mL of Ac_2O, and 25 mL of absolute MeOH was heated at reflux for 5 h (with further hourly additions of 0.24 mL of Ac_2O). The residual powder obtained after evaporation of the solution and drying was dissolved in 5 mL of pyridine and treated with 0.36 mL (360 mg, 1.14 mmol) of $(i\mathrm{Pr_2SiCl})_2O$ for 24 h at ambient temperature. The solution was evaporated and the residue was partitioned between EtOAc and H_2O. The organic phase was washed with saturated $NaHCO_3/H_2O$, saturated NaCl/H_2O, dried (Na_2SO_4), filtered, and evaporated. The vacuum-dried residual N^4-acetyl-1-[3,5-*O*-(1,1,3,3-tetraisopropyldisiloxan-1,3-diyl)-β-D-xylofuranosyl]cytosine (**4***c*; R = $(i\mathrm{Pr_2Si})_2O$, B = N^4-acetyl-*c*) was dissolved in 10 mL of CH_3CN and treated with 250 μL (312 mg, 1.81 mmol) of PhOCSCl and 978 mg (8 mmol) of DMAP for 3 h at ambient temperature. The solution was evaporated and the residue worked up as in the above procedure for conversion of **4***a* to **6***a* (R = Bz), except that ice-cold 1% HOAc in saturated NaCl/H_2O was substituted for the 1 *N* HCl/H_2O wash.

The crude dry foam containing N^4-acetyl-1-[2-*O*-phenoxythiocarbonyl-3,5-*O*-(1,1,3,3-tetraisopropyldisiloxan-1,3-diyl)-β-D-xylofuranosyl]cytosine (**6***c*; R = $(i\mathrm{Pr_2Si})_2O$, B = N^4-acetyl-*c*) was dissolved in 10 mL of dry $PhCH_3$ and heated with 620 μL (671 mg, 2.3 mmol) of Bu_3SnH and 49 mg (0.3 mmol) of AIBN for 24 h at 80°C. Successive deprotection (2*b*) with Bu_4NF/THF and NH_3/MeOH and evaporation gave a residue that was partitioned between Et_2O and H_2O. The aqueous phase was concentrated and applied to a column of Dowex 1X2(OH^-) resin. Elution with H_2O and evaporation of appropriately pooled fractions gave 113 mg (50%) of the title product, which was crystallized from MeOH/Et_2O (diffusion) (22) to give **7***c*: mp 153–155°C; uv (MeOH) max 272, 230 nm (ε 8500; 7600), min 251 nm (ε 6100); ^{1}H nmr δ: 1.80 (dd, $J_{1'-2'}$ = 2 Hz, $J_{2'-2''}$ = 14.5 Hz, 1, H2′), 2.50 ("sept", $J_{1'-2''}$ = 8.5 Hz, $J_{2''-3'}$ = 5.5 Hz, 1, H2″), 3.60–3.85 (m, 3, H4′, 5′, 5″), 4.20 (m, 1, H3′), 4.70 (bs, 1, OH5′), 5.15 (bs, 1, OH3′), 5.70 (d, J_{5-6} = 7.5 Hz, 1, H5), 6.00 (dd, 1, H1′), 7.06 (bs, 2, NH_2), 7.82 (d, 1, H6); ^{13}C nmr δ: 165.73 (C4), 155.49 (C2), 142.03 (C6), 93.48 (C5), 84.97 (C1′, C4′), 68.93 (C3′), 59.69 (C5′), 41.37 (C2′); ms *m/z*: 227.0906 (M^+ 227.0906). *Anal.* calcd. for $C_9H_{13}N_3O_4$ (227.2): C 47.57, H 5.77, N 18.49; found: C 47.27, H 5.54, N 18.72.

Further elution of the Dowex 1X2(OH^-) column with MeOH/H_2O gave 74 mg (30%) of starting **5***c* (presumably arising from hydrogenolysis of a derivative of dimeric **8**).

*1-(3,5-Di-O-benzoyl-β-D-xylofuranosyl)uracil (4*d*; R = Bz)*

To a solution of 6.00 g (12.1 mmol) of **3***d* (1*a*) in 105 mL of HOAc/C_5H_5N (1:4) was added 1.8 mL (1.86 g, 37.1 mmol) of $N_2H_4 \cdot H_2O$. The solution was stirred for 18 h at ambient temperature and 56 mL of Me_2CO was added. Stirring was continued for 2 h, the solution was evaporated, and the residue was partitioned between H_2O (200 mL) and EtOAc (2 × 250 mL). The combined organic phase was washed with saturated $NaHCO_3/H_2O$, H_2O, dried (Na_2SO_4), filtered, and evaporated. The resulting solid foam was chromatographed on a column of silica (EtOAc/CH_2Cl_2, 4:6). Evaporation of appropriate fractions gave 4.5 g (80%) of the title product, which was crystallized from PhH to give **4***d* (R = Bz): mp 94–97°C; uv (95% EtOH/H_2O) max 263, 230 nm (ε 8600, 25 000), min 251 nm (ε 7300); ^{1}H nmr ($CDCl_3$) δ: 4.6, 4.8, 5.0 (m, 4, H3′, 4′, 5′, 5″), 5.4–5.8 (m, 3, OH2′, H2′, H5; J_{5-6} = 8.4 Hz with D_2O exchange), 5.83 (s, 1, H1′), 7.2–8.1 (m, 11, Ph's and H6), 10.5 (bs, 1, H3); ms *m/z*: 452 (M^+). *Anal.* calcd. for $C_{23}H_{20}N_2O_8 \cdot 0.7H_2O$ (465.0): C 59.41, H 4.64, N 6.02; found: C 59.33, H 4.38, N 6.07.

*1-(2-Deoxy-β-D-*threo*-pentofuranosyl)uracil (7*d*)*

A mixture of 452.4 mg (0.97 mmol) of **4***d* (R = Bz) hydrate, 261 μL (326 mg, 1.89 mmol) of PhOCSCl, 427 mg (3.5 mmol) of DMAP, and 10 mL of CH_3CN was stirred for 6 h at ambient temperature. Evaporation was followed by work-up as described above for the conversion **4***a* → **6***a* (R = Bz), except ice-cold 1% HOAc in saturated NaCl/H_2O was substituted for the 1 *N* HCl/H_2O wash.

The resulting light-yellow solid foam containing **6***d* (R = Bz) was dissolved in 20 mL of dry $PhCH_3$ and heated with 620 μL (671 mg, 2.3 mmol) of Bu_3SnH and 49 mg (0.3 mmol) of AIBN for 24 h at 80°C. The solution was evaporated and the residue was deprotected by stirring with 540 mg (10 mmol) of NaOMe in 20 mL of MeOH overnight at ambient temperature. This solution was evaporated and the residue partitioned between Et_2O and H_2O. The aqueous phase was neutralized to pH 6.0 with Amberlite 120(H^+) resin, filtered, and evaporated. The residue was chromatographed on a column of silica (MeOH/$CHCl_3$, 1:1) and the product crystallized from absolute EtOH to give 157 mg (71%) of **7***d*: mp 170–171°C (lit. (6) mp 163–165°C); uv (MeOH) max 261 nm (ε 10 100), min 231 nm (ε 2200); ^{1}H nmr δ: 1.87 (dd, $J_{1'-2'}$ = 2.0 Hz, $J_{2'-2''}$ = 14.5 Hz, 1, H2′), 2.55 ("sept", $J_{1'-2''}$ = 8.5 Hz, $J_{2''-3'}$ = 5.2 Hz, 1, H2″), 3.56–3.87 (m, 3, H4′, 5′, 5″), 4.24 (m, 1, H3′), 4.70 ("t", $J_{OH5'-5',5''}$ = 5.5 Hz, 1, OH5′), 5.27 (d, $J_{OH3'-3'}$ = 3.3 Hz, 1, OH3′), 5.65 (d, J_{5-6} = 8 Hz, 1, H5), 6.05 (dd, 1, H1′), 7.92 (d, 1, H6), 11.26 (bs, 1, H3); ^{13}C nmr δ: 163.13 (C4), 150.46 (C2), 141.30 (C6), 101.06 (C5), 85.01 (C4′), 83.75 (C1′), 68.46 (C3′), 59.41 (C5′), 40.74 (C2′); ms *m/z*: 228.0746 (M^+ 228.0746). *Anal.* calcd. for $C_9H_{12}N_2O_5$ (228.2): C 47.37, H 5.30, N 12.28; found: C 47.27, H 5.34, N 11.90.

In the above thioacylation reaction of **4***d* → **6***d* (R = Bz), a second slightly slower migrating (tlc) product was formed in ≳10% yield. It was isolated in essentially pure form by preparative tlc and its ^{13}C nmr spectrum was taken and compared with that of **6***d* (R = Bz). This provides clear evidence for the formation of a dimeric thionocarbonate (**8***d*; R = Bz): δ: 191.11 (C=S), 165.24, 164.32 (2 × 2 C=O), 162.86 (C4), 150.21 (C2), 140.41 (C6), 133.84, 133.42, 129.48, 129.07, 128.99, 128.69, 128.60 (4 × Ph's), 102.15 (C5), 87.83 (C1′), 86.66 (C4′), 77.81 (C2′), 74.73 (C3′), 61.66 (C5′); ^{13}C nmr (**6***d*; R = Bz) δ: 193.11 (C=S), 165.26, 164.43 (2 × C=O), 162.83 (C4), 153.01 (C2), 140.30 (C6), 133.88, 133.44, 127.78, 129.46, 129.08, 129.01, 128.72, 128.62, 128.37, 126.88, 121.49 (3 × Ph's), 102.29 (C5), 87.39 (C1′), 86.67 (C4′), 77.45 (C2′), 74.77 (C3′), 61.80 (C5′).

*1-(2-O-Acetyl-3,5-di-O-benzoyl-β-D-xylofuranosyl)thymine (3*e*)*

To a mixture of 17.96 g (40.6 mmol) of **1** (11) and 5.12 g (40.6 mmol) of thymine (**2***e*) in 650 mL of dry CH_3CN were added 6.92 mL (5.29 g, 32.8 mmol) of $(Me_3Si)_2NH$ and 4.04 mL (3.46 g, 31.8 mmol) of Me_3SiCl, followed by 5.69 mL (12.7 g, 48.6 mmol) of $SnCl_4$. The resulting clear solution was heated for 45 min at reflux while protected from moisture and then cooled to ambient temperature and filtered. The filtrate was evaporated *in vacuo* and 500 mL of $CHCl_3$ was added. This solution was shaken with 350 mL of saturated $NaHCO_3/H_2O$ and the resulting emulsion was filtered using Celite. The filter aid was washed with hot $CHCl_3$ (2 × 200 mL) and the combined organic phase was washed with H_2O (3 × 200 mL), dried (Na_2SO_4), and evaporated. The resulting solid foam (20.6 g) was chromatographed on a column of silica (EtOAc/CH_2Cl_2, 18:82) and appropriate fractions were pooled and evaporated to give 9.5 g (46%) of the title compound, which crystallized from PhH/$i\mathrm{Pr_2O}$ to give **3***e*: mp 87–88°C; uv (95% EtOH/H_2O) max 266, 230 nm (ε 8400; 21 100), min 252 nm (ε 7100); ^{1}H nmr ($CDCl_3$) δ: 1.77 (s, 3, CH_3), 2.16 (s, 3, Ac), 4.7 (m, 3, H4′, 5′, 5″), 5.4 (m, 1, H3′), 5.7 (m, 1, H2′), 6.15 (d, $J_{1'-2'}$ = 2.9 Hz, 1, H1′), 7.2–7.7 and 7.9–8.1 (m, 11, 2 × Bz and H6), 9.48 (bs, 1, H3); ms *m/z*: 508 (M^+). *Anal.* calcd. for

$C_{26}H_{24}N_2O_9 \cdot C_6H_6$ (586.6): C 65.52, H 5.16, N 4.78; found: C 65.38, H 5.05, N 4.85.

*1-(3,5-Di-O-benzoyl-β-D-xylofuranosyl)thymine (**4**e; R = Bz)*

A solution of 5.6 g (9.5 mmol) of **3***e* solvate in 95 mL of $HOAc/C_5H_5N$ (1:4) was treated with 1.63 mL (1.68 g, 33.6 mmol) of $N_2H_4 \cdot H_2O$ and worked up as described above for the conversion of **3***d* → **4***d* (R = Bz). Addition of $CHCl_3$ to the resulting solid foam resulted in crystallization of 4.1 g of the title product. Column chromatography (silica, $EtOAc/CH_2Cl_2$, 4:6) afforded an additional 0.6 g (total 4.7 g, 84%) of **4***e* (R = Bz): mp 97–99°C; uv (95% $EtOH/H_2O$) max 268, 229 nm (ε 6900; 10 100), min 252 nm (ε 6000); ^1H nmr (Me_2SO-$d_6/CDCl_3$) δ: 1.76 (s, 3, CH_3), 4.4 (m, 1, H4′), 4.8 (m, 3, H2′, 5′, 5″), 5.5 (m, 1, H3′), 5.94 (d, $J_{1'-2'}$ = 1.9 Hz, 1, H1′), 6.3 (bs, 1, OH2′), 7.3–7.7 and 7.8–8.1 (m, 11, 2 × Bz and H6), 11.2 (bs, 1, H3); ms *m/z*: 466 (M^+). *Anal.* calcd. for $C_{24}H_{22}N_2O_8 \cdot CHCl_3$ (585.8): C 51.26, H 3.96, N 4.78; found: C 50.93, H 3.92, N 4.55.

*1-(2-Deoxy-β-D-*threo*-pentofuranosyl)thymine (7*e*)*

A mixture of 466 mg (1 mmol) of **4***e* (R = Bz), 250 μL (312 mg, 1.81 mmol) of PhOCSCl, 488 mg (4 mmol) of DMAP, and 10 mL of CH_3CN was stirred for ~20 min at ambient temperature and then worked up as described above for the conversion **4***d* → **6***d* (R = Bz).

The resulting solid foam was subjected to hydrogenolysis as described above for **6***d* (R = Bz) and the resulting oily residue was deprotected by stirring with 20 mL of NH_3/MeOH overnight at ambient temperature. Evaporation and partitioning of the residue between Et_2O and H_2O was followed by evaporation of the aqueous phase and column chromatography of the residue (silica, $MeOH/CHCl_3$, 2:8). Evaporation of appropriately pooled fractions and crystallization of the residue from $MeOH/Et_2O$ (diffusion) (22) gave 190 mg (78%) of **7***e*: mp 174–175°C (lit. (5) mp 170–171°C); uv (MeOH) max 266, 208 nm (ε 9600; 9500), min 233 nm (ε 2200); ^1H nmr δ: 1.77 (s, 3, CH_3), 1.85 (dd, $J_{1'-2'}$ = 2.2 Hz, $J_{2'-2''}$ = 14.5 Hz, 1, H2′), 2.60 ("sept", $J_{1'-2''}$ = 8.5 Hz, $J_{2''-3'}$ = 5.5 Hz, 1, H2″), 3.60–3.85 (m, 3, H4′, 5′, 5″), 4.25 (m, 1, H3′), 4.70 ("t", $J_{OH5'-5',5''}$ = 5.5 Hz, 1, OH5′), 5.26 (d, $J_{OH3'-3'}$ = 3.5 Hz, 1, OH3′), 6.07 (dd, 1, H1′), 7.82 (d, $J_{allylic}$ = 1.2 Hz, 1, H6), 11.24 (bs, 1, H3); ^{13}C nmr δ: 163.99 (C4), 150.77 (C2), 137.35 (C6), 108.83 (C5), 84.95 (C4′), 83.65 (C1′), 68.88 (C3′), 59.79 (C5′), 40.89 (C2′), 12.63 (CH_3); ms *m/z*: 242.0905 (M^+ 242.0903). *Anal.* calcd. for $C_{10}H_{14}N_2O_5$ (242.2): C 49.58, H 5.83, N 11.56; found: C 49.29, H 5.88, N 11.37.

Acknowledgements

We thank the Natural Sciences and Engineering Research Council of Canada, the National Cancer Institute of Canada, and the University of Alberta for generous support of this work.

1. (*a*) G. Gosselin, M.-C. Bergogne, J. de Rudder, E. De Clercq, and J.-L. Imbach. J. Med. Chem. **29**, 203 (1986); (*b*) G. Gosselin, M.-C. Bergogne, J. de Rudder, E. De Clercq, and J.-L. Imbach. J. Med. Chem. **30**, 982 (1987).
2. (*a*) M. J. Robins and J. S. Wilson. J. Am. Chem. Soc. **103**, 932 (1981); (*b*) M. J. Robins, J. S. Wilson, and F. Hansske. J. Am. Chem. Soc. **105**, 4059 (1983).
3. A. M. Michelson and A. R. Todd. J. Chem. Soc. 816 (1955).
4. J. J. Fox and N. C. Miller. J. Org. Chem. **28**, 936 (1963).
5. J. P. Horwitz, J. Chua, J. A. Urbanski, and M. Noel. J. Org. Chem. **28**, 942 (1963).
6. J. P. Horwitz, J. Chua, M. Noel, and M. A. DaRooge. J. Med. Chem. **7**, 385 (1964).
7. A. P. Martinez, W. W. Lee, and L. Goodman. J. Org. Chem. **31**, 3263 (1966).
8. R. Mengel and H. Wiedner. Chem. Ber. **109**, 1395 (1976).
9. M. Ikehara, Y. Nakahara, and S. Yamada. Chem. Pharm. Bull. **19**, 538 (1971).
10. F. Hansske and M. J. Robins. J. Am. Chem. Soc. **105**, 6736 (1983).
11. G. Gosselin and J.-L. Imbach. J. Heterocycl. Chem. **19**, 597 (1982).
12. (*a*) J. J. Fox, N. Yung, J. Davoll, and G. B. Brown. J. Am. Chem. Soc. **78**, 2117 (1956); (*b*) T. Tkaczynski, J. Smejkal, and F. Sorm. Collect. Czech. Chem. Commun. **29**, 1736 (1964); (*c*) C. Nakayama and M. Saneyoshi. Nucleosides Nucleotides, **1**, 139 (1982).
13. (*a*) P. Chang and B. Lythgoe. J. Chem. Soc. 1992 (1950); (*b*) E. J. Reist and L. Goodman. Biochemistry, **3**, 15 (1964); (*c*) B. L. Kam, J.-L. Barascut, and J.-L. Imbach. Carbohydr. Res. **69**, 135 (1979).
14. Y. Ishido, N. Nakazaki, and N. Sakairi. J. Chem. Soc. Perkin Trans. 1, 2088 (1979).
15. K. A. Watanabe and J. J. Fox. Angew. Chem. Int. Ed. Engl. **5**, 579 (1966).
16. W. T. Markiewicz. J. Chem. Res. Synop. 24 (1979); J. Chem. Res. Miniprint, 181 (1979).
17. M. J. Robins, J. S. Wilson, L. Sawyer, and M. N. G. James. Can. J. Chem. **61**, 1911 (1983).
18. D. H. R. Barton and S. W. McCombie. J. Chem. Soc. Perkin Trans. 1, 1574 (1975).
19. E. M. Acton, R. N. Goerner, H. S. Uh, K. J. Ryan, D. W. Henry, C. E. Cass, and G. A. LePage. J. Med. Chem. **22**, 518 (1979).
20. D. H. R. Barton and R. Subramanian. J. Chem. Soc. Perkin Trans. 1, 1718 (1977).
21. (*a*) E. De Clercq, J. Descamps, G. Verhelst, R. T. Walker, A. S. Jones, P. F. Torrence, and D. Shugar. J. Infect. Dis. **141**, 563 (1980); (*b*) J. Balzarini, H. Mitsuya, E. De Clercq, and S. Broder. Int. J. Cancer, **37**, 451 (1986).
22. M. J. Robins, R. Mengel, R. A. Jones, and Y. Fouron. J. Am. Chem. Soc. **98**, 8204 (1976).
23. R. Zou and M. J. Robins. Can. J. Chem. **65**, 1436 (1987).

Can. J. Chem. Downloaded from www.nrcresearchpress.com by 93.93.197.157 on 09/07/12
For personal use only.

Isotope effects in nucleophilic substitution reactions. VI. The effect of ion pairing on the transition state structure of S_N2 reactions

KENNETH CHARLES WESTAWAY[1] AND ZHU-GEN LAI
Chemistry Department, Laurentian University, Sudbury, Ont., Canada P3E 2C6

Received September 10, 1987

KENNETH CHARLES WESTAWAY and ZHU-GEN LAI. Can. J. Chem. **66**, 1263 (1988).

Spectroscopic and conductivity studies of sodium thiophenoxide solutions in four different solvents and the secondary α-deuterium kinetic isotope effects found in the presence of 15-crown-5 ether demonstrate that the secondary α-deuterium kinetic isotope effect and transition state structure for the S_N2 reaction between sodium thiophenoxide and *n*-butyl chloride are significantly different, depending on whether the ionic reactant is a solvent-separated ion-pair complex or a free ion. In all three solvents in which the form of the ionic reactant changes, a smaller isotope effect and tighter transition state are found for the reaction with the ion-pair complex.

KENNETH CHARLES WESTAWAY et ZHU-GEN LAI. Can. J. Chem. **66**, 1263 (1988).

On a réalisé des études basées sur la spectroscopie ou sur la conductivité de solutions de thiophénolate de sodium dans quatre solvants différents et on a mesuré des effets isotopiques cinétiques secondaires des deutérium en α en présence d'éther 15-couronne-5; l'ensemble de ces résultats démontre que l'effet isotopique cinétique secondaire du deutérium en α ainsi que la structure de l'état de transition de la réaction S_N2 du thiophénolate de sodium avec le chlorure de *n*-butyle sont assez différentes suivant qu'il s'agit d'une paire ionique complexe séparée par un solvant ou d'un ion libre. Dans les trois solvants où il se produit des changements dans la forme des réactifs ioniques, la paire ionique complexe conduit à un plus petit effet isotopique et à un état de transition plus compact.

[Traduit par la revue]

Can. J. Chem. Downloaded from www.nrcresearchpress.com by 93.93.197.157 on 09/07/12
For personal use only.

Introduction

Westaway, Waszczylo, Smith, and Rangappa (1) recently reported that the magnitude of the secondary α-deuterium kinetic isotope effect for an S_N2 or E2 reaction can be concentration dependent, i.e., can change markedly when the concentration of an ionic reactant is altered. For example, the secondary α-deuterium kinetic isotope effect in the S_N2 reaction between *n*-butyl chloride and sodium thiophenoxide in DMF, eq. [1], changes from 1.129 ± 0.010 when the sodium thiophenoxide concentration is 4.0×10^{-3} M to 1.085 ± 0.011 when the sodium thiophenoxide concentration is increased to 8.6×10^{-3} M.

[1] $Na^+ {}^-SC_6H_5 + CH_3CH_2CH_2CL_2Cl \rightarrow CH_3CH_2CH_2CL_2SC_6H_5 + Na^+ {}^-Cl$ (L = H, D)

The authors suggested that the change in the kinetic isotope effect (transition state structure) was the result of a change in the state of the reacting anion from a free thiophenoxide ion to a sodium thiophenoxide ion pair. The work in this paper demonstrates that the change in the magnitude of the secondary α-deuterium kinetic isotope effect for the S_N2 nucleophilic substitution reaction between *n*-butyl chloride and thiophenoxide ion is, indeed, due to a change in the form of the reacting nucleophile from a free thiophenoxide ion to a solvent-separated sodium thiophenoxide ion-pair complex.

Results and discussion

Proof of an ion pair and a free ion reaction

The concentration dependence found for the secondary α-deuterium kinetic isotope effect in the S_N2 (2) reaction between sodium thiophenoxide and *n*-butyl chloride was tentatively attributed to a change in the form of the reacting ion from a sodium thiophenoxide ion pair to a free thiophenoxide ion (1). Conductivity measurements (3), nmr spectroscopy (4, 5), and uv spectroscopy (6, 7) have been used to study the phenomenon of ion pairing. Two of these techniques, uv spectroscopy and conductivity measurements, have been used to determine the concentration ranges where sodium thiophenoxide exists as an ion-pair complex and as a free ion in four different solvents.

Conductivity measurements

The conductance of sodium thiophenoxide solutions of different concentrations was measured in four different solvents, DMSO, DMF, methanol, and diglyme. At low sodium thiophenoxide concentrations, the conductance versus concentration plot was linear. However, at higher concentrations, the plot changed to a concave curve, Fig. 1. The concentration where the slope of the conductance versus concentration plot begins to decrease was taken as the concentration where the form of the sodium thiophenoxide changed from a pair of free ions to an ion-pair complex. The downward curve is found because the conductance resulting from the ion-pair complex is much lower than that caused by the two free ions. The approximate[2] concentrations where the sodium thiophenoxide changes from free ions to an ion-pair complex in each solvent are given in Table 1. The change in the state of the salt occurred at reasonably high concentrations, i.e., at approximately 2.1×10^{-2} M and 6.8×10^{-3} M, in the highly polar aprotic solvents DMSO and DMF, respectively. The change in the form of the salt occurred at significantly lower concentrations, i.e., at approximately 2.3×10^{-4} M, in the less polar methanol. No change in the form of the salt was detected in diglyme and it appears that the sodium thiophenoxide exists as an ion-pair complex in diglyme at all of the concentrations used in this study.

Ultraviolet spectroscopy

The changes that occurred in the uv spectrum when the concentration of the sodium thiophenoxide was varied were also used to determine (confirm) the concentrations where the sodium thiophenoxide changed from a free ion to an ion-pair

[1]Author to whom correspondence may be addressed.

[2]The concentrations are approximate because it is difficult to tell exactly where the curvature begins.

Can. J. Chem. Downloaded from www.nrcresearchpress.com by 93.93.197.157 on 09/07/12
For personal use only.

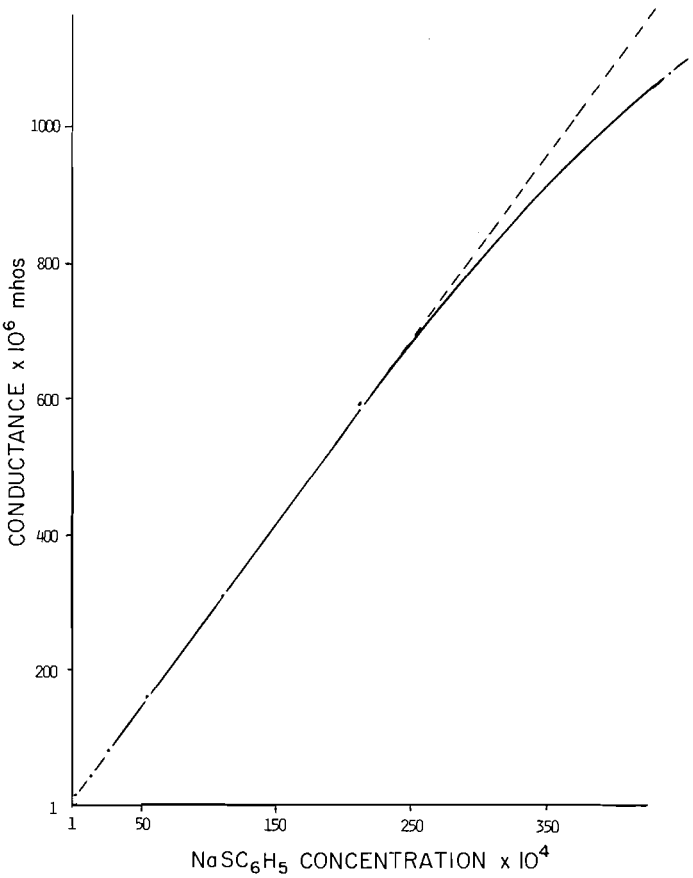

FIG. 1. The conductance versus the sodium thiophenoxide concentration in DMSO at 20°C. Similar curves at different sodium thiophenoxide concentrations were found in methanol and DMF.

TABLE 1. The approximate concentrations where conductivity measurements indicate that sodium thiophenoxide changes from a free ion to an ion-pair complex in DMSO, DMF, methanol, and diglyme at 20°C

Solvent	Concentration where conductivity measurements indicate sodium thiophenoxide changes from free ions to an ion-pair complex (mol/L)
DMSO	2.1×10^{-2}
DMF	6.8×10^{-3}
CH_3OH	2.3×10^{-4}
Diglyme	None

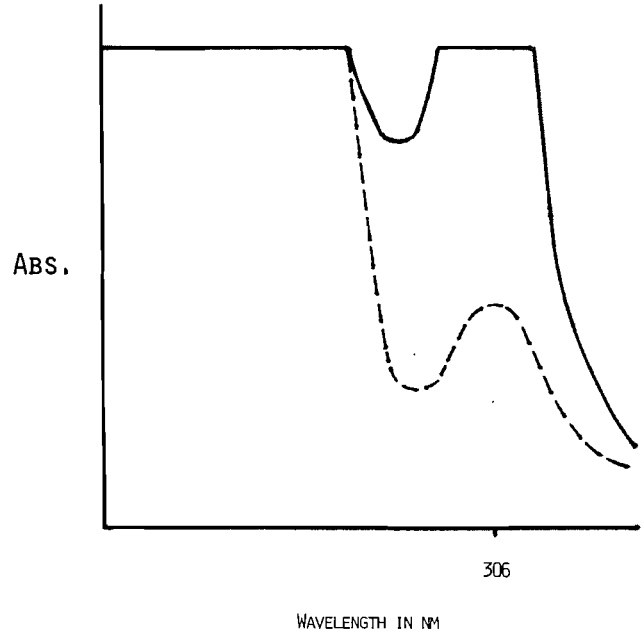

FIG. 2. The ultraviolet spectrum of a 1.2×10^{-2} M solution of the sodium thiophenoxide ion-pair complex on the 0–2 scale (—) and a 6.0×10^{-3} M solution of the free thiophenoxide ion on the 0–1 scale (– – –) in DMF. The same spectral maxima were observed in DMSO at different concentrations.

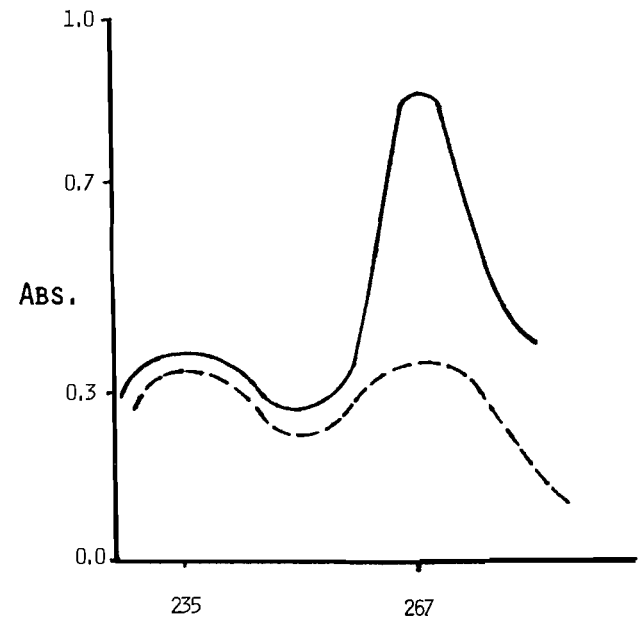

FIG. 3. The ultraviolet spectrum of a 1.2×10^{-4} M solution of the sodium thiophenoxide ion-pair complex (—) and a 6.0×10^{-5} M solution of the free thiophenoxide ion (– – –) in methanol at 20°C.

complex. Two different types of behaviour were observed in these experiments. In DMSO and DMF, the maximum absorbance changed from 306 nm at high concentrations, where the sodium thiophenoxide exists as an ion-pair complex, to a lower wavelength at lower concentrations, where the sodium thiophenoxide exists as free ions, Fig. 2. For example, the change in the form of the ion is demonstrated by the large change in the absorbance (molar extinction coefficient) at 306 nm, i.e., the very large peak found on the 0–2 absorbance scale when the sodium thiophenoxide concentration is 2.5×10^{-2} M is small on the 0–1 scale when the concentration of the sodium thiophenoxide is reduced by a factor of two. Since the molar extinction coefficient is not concentration dependent, the ion-pair complex that causes the absorbance at 306 nm must have been converted to free ions that absorb at a lower wavelength. The maximum absorbance for the free ion, which is hidden by the solvent absorbance, Fig. 2, appears to be near 260 nm. The λ_{max} for the free thiophenoxide ion was found by measuring the ultraviolet spectrum of the salt in 1-mm cells with a DMF–methanol or DMSO–methanol solution in the reference cell. The change in the uv spectrum (the form) of the sodium thiophenoxide occurs between 1.2×10^{-2} M and $6 \times$

TABLE 2. The concentration where the sodium thiophenoxide changes from an ion-pair complex to free ions in DMSO, DMF, methanol, and diglyme at 20°C

Solvent	Concentration where the sodium thiophenoxide changes[a]	
	From an ion-pair complex to free ions using uv spectroscopy	From fee ions to an ion-pair complex using conductivity
DMSO	1.9×10^{-2}	2.1×10^{-2}
DMF	9.0×10^{-3}	6.8×10^{-3}
CH_3OH	9.8×10^{-5}	2.3×10^{-4}
Diglyme	None	None

[a]Since the form of the thiophenoxide ion changes with concentration very rapidly (*vide infra*) these concentrations should be almost identical.

10^{-3} M in DMF and between 2.5×10^{-2} M and 1.2×10^{-2} M in DMSO.

In methanol, the uv spectrum of the sodium thiophenoxide ion-pair complex has a small absorbance at 235 nm and a strong absorbance at 267 nm, Fig. 3. The free ion, on the other hand, has a single absorbance at 235 nm. Thus, the shift from an ion-pair complex to a free ion occurs when the maximum absorbance changes from 267 nm at a sodium thiophenoxide concentration of $>1.3 \times 10^{-4}$ M, where the sodium thiophenoxide is present as an ion-pair complex, to 235 nm, when the sodium thiophenoxide concentration is 6.5×10^{-5} M. The sodium thiophenoxide exists as free ions at concentrations of $<6.5 \times 10^{-5}$ M.

The concentration ranges where uv spectroscopy indicates the sodium thiophenoxide changes from free ions to an ion-pair complex are given in Table 2. Again, the change from an ion-pair complex to free ions occurred at the highest concentrations in DMSO and DMF. The change in the form of the salt occurred at much lower concentrations in methanol and was not observed at any of the concentrations used in diglyme. Finally, a comparison of the concentrations where the conductivity and the uv results indicate sodium thiophenoxide changes from an ion-pair complex to free ions, Table 2, shows that the agreement between the two methods is excellent.

An interesting observation is the higher energy absorbance found in the uv spectra of the free ion. Although this relationship was not expected, CNDO/2 calculations of the energies of the highest occupied and lowest unoccupied π molecular orbitals of the free thiophenoxide ion and the sodium thiophenoxide ion pair in methanol suggest that the observed uv absorbances are correct. In fact, the calculated difference between the excitation wavelengths of the free ion and ion pair are almost equal to the observed differences in the wavelengths. This also supports the assignment of the ion pair and the free ion in the uv spectra.

Ion pairing and the secondary α-deuterium kinetic isotope effect

Once the concentration ranges in which the different forms of the nucleophilic species existed in the different solvents were known, the secondary α-deuterium kinetic isotope effects for the S_N2 reaction between *n*-butyl chloride and sodium thiophenoxide were determined at sodium thiophenoxide concentrations where the uv and conductivity studies indicated that the nucleophile existed as a free ion and as a solvent-separated ion-pair complex. The results in Table 3 indicate that the magnitude of the isotope effect changes in every solvent when the form of the thiophenoxide ion changes. It is important to note that there is no change in the kinetic isotope effect in diglyme even though the changes in concentration of the sodium thiophenoxide were larger than those made in the other solvents. This obviously is because the sodium thiophenoxide reacts as an ion pair at all concentrations in diglyme.

The isotope effects measured in the different solvents are interesting for another reason. A plot of the sodium thiophenoxide concentration where the secondary α-deuterium kinetic isotope effect (the form of the ionic reactant changes from an ion-pair complex to free ions) changes in DMSO, DMF, and methanol versus the dielectric constant of the solvent, Fig. 4, has a correlation coefficient of 0.9986 for the least-squares straight line. Although the data for this plot have only been obtained from three solvents, the very high correlation coefficient suggests that the concentrations where ion pairing becomes important can be estimated for a particular salt from the dielectric constant of the solvent. This relationship is to be expected, because the association constant for a salt in organic solvents is linearly related to the dielectric constant of the solvent (8).

The hypothesis that the magnitude of the secondary α-deuterium kinetic isotope effect is dependent on the form of the reacting anion was further confirmed by measuring the secondary α-deuterium kinetic isotope effects for the S_N2 *n*-butyl chloride – sodium thiophenoxide reaction in the presence of 15-crown-5 ether. The 15-crown-5 ether solvates sodium ions extremely well (9) and ensures that the sodium thiophenoxide exists as free ions even at concentrations where it usually exists as an ion-pair complex. When the 15-crown-5 ether was added to a reaction in which the sodium thiophenoxide was normally present as the ion-pair complex in DMF, Table 4, the secondary α-deuterium kinetic isotope effect changed markedly. In fact, the isotope effect of 1.127 ± 0.016 found in the presence of 15-crown-5 ether at high sodium thiophenoxide concentrations, where the sodium thiophenoxide usually reacts as an ion-pair complex, is identical to the $k_H/k_D = 1.129 \pm 0.010$ found when the thiophenoxide reacts as a free ion. An experiment was also done to ensure that the 15-crown-5 ether does not affect the isotope effect in the free ion reaction, Table 4. The secondary α-deuterium kinetic isotope effect of 1.128 ± 0.013 in the crown ether reaction, at concentrations where the sodium thiophenoxide usually reacts as a free ion, demonstrates that the change in the isotope effect is, indeed, the result of the change in the form of the reacting ion and not due to the 15-crown-5 ether.

Finally, the secondary α-deuterium kinetic isotope effects were measured at several different sodium thiophenoxide concentrations to ensure that the isotope effect only changed when the form of the reacting anion was altered and not when the sodium thiophenoxide concentrations were changed. The α-deuterium kinetic isotope effects found for a wide range of sodium thiophenoxide concentrations in DMF, Table 5, Fig. 5, show that the isotope effect changes very rapidly at a specific concentration (where the conductivity and uv spectroscopy indicate that the form of the reacting anion changes) and then remains constant when the concentration of the salt is either increased or decreased. Thus, the change in the secondary α-deuterium kinetic isotope effect (transition state structure) only occurs over a very narrow range of concentrations when the form of the nucleophile changes. It is important to note that the changes in the secondary α-deuterium kinetic isotope effects occur at the concentrations where the conductivity and

Can. J. Chem. Downloaded from www.nrcresearchpress.com by 93.93.197.157 on 09/07/12
For personal use only.

TABLE 3. The rate constants and secondary α-deuterium kinetic isotope effects[a] measured for the S_N2 reactions between *n*-butyl chloride and sodium thiophenoxide in DMSO, DMF, methanol, and diglyme at 20°C

$[NaSC_6H_5]$ (mol/L)	k_H (L/mol-s)	k_D (L/mol-s)	$(k_H/k_D)_\alpha$
	DMSO free ion		
1.1×10^{-2}	$(2.927 \pm 0.017)^b \times 10^{-2}$	$(2.617 \pm 0.013)^b \times 10^{-2}$	1.118 ± 0.009^c
5.5×10^{-3}	$(3.168 \pm 0.005) \times 10^{-2}$	$(2.844 \pm 0.021) \times 10^{-2}$	1.114 ± 0.007
	DMSO ion pair		
2.5×10^{-2}	$(3.424 \pm 0.004) \times 10^{-2}$	$(3.311 \pm 0.006) \times 10^{-2}$	1.034 ± 0.002
	DMF free ion		
$(4.0\text{–}4.1) \times 10^{-3}$	$(6.131 \pm 0.043) \times 10^{-2}$	$(5.432 \pm 0.033) \times 10^{-2}$	1.129 ± 0.010
3.1×10^{-3}	$(6.136 \pm 0.045) \times 10^{-2}$	$(5.457 \pm 0.006) \times 10^{-2}$	1.124 ± 0.008
	DMF ion pair		
8.6×10^{-3}	$(4.352 \pm 0.022) \times 10^{-2}$	$(4.011 \pm 0.034) \times 10^{-2}$	1.085 ± 0.011
$(0.94\text{–}1.8) \times 10^{-2}$	$(4.503 \pm 0.063) \times 10^{-2}$	$(4.156 \pm 0.068) \times 10^{-2}$	1.083 ± 0.023
	CH_3OH free ion		
$(4.4\text{–}6.7) \times 10^{-5}$	$(3.396 \pm 0.022) \times 10^{-5}$	$(3.001 \pm 0.017) \times 10^{-5}$	1.132 ± 0.010
	CH_3OH ion pair		
$(9.3\text{–}9.9) \times 10^{-3}$	$(2.457 \pm 0.016) \times 10^{-5}$	$(2.233 \pm 0.011) \times 10^{-5}$	1.100 ± 0.009
2.9×10^{-2}	$(2.408 \pm 0.011) \times 10^{-5}$	$(2.190 \pm 0.004) \times 10^{-5}$	1.100 ± 0.005
	Diglyme ion pair		
1.8×10^{-3}	$(3.235 \pm 0.120) \times 10^{-3}$	$(2.839 \pm 0.200) \times 10^{-3}$	1.139 ± 0.091
3.5×10^{-3}	$(4.009 \pm 0.054) \times 10^{-3}$	$(3.501 \pm 0.112) \times 10^{-3}$	1.145 ± 0.039
3.7×10^{-3}	$(4.825 \pm 0.140) \times 10^{-3}$	$(4.238 \pm 0.085) \times 10^{-3}$	1.139 ± 0.040
3.8×10^{-3}	$(5.627 \pm 0.087) \times 10^{-3}$	$(4.927 \pm 0.031) \times 10^{-3}$	1.142 ± 0.019

[a]Each isotope effect was determined with a different batch of solvent and often by a different worker.
[b]The errors are the standard deviation of at least three different kinetic runs.
[c]The error is $1/k_D[(\Delta k_H)^2 + (k_H/k_D)^2 \times (\Delta k_D)^2]^{1/2}$ where Δk_H and Δk_D are the standard deviations for the rate constants for the undeuterated and deuterated substrates, respectively (1).

uv spectroscopy indicate that the form of the reacting sodium thiophenoxide changes, Tables 2 and 4. What is surprising is how sharply the form of the nucleophile changes, i.e., the isotope effects and uv spectra suggest that the reacting nucleophile is completely different when the concentration of the salt changes by a factor of two.

Since the secondary α-deuterium kinetic isotope effect changes when, and only when, the form of the reacting nucleophile changes, the change in the secondary α-deuterium kinetic isotope effect must be due to a change in the form of the reacting ion (nucleophile) from a free ion to a solvent-separated ion-pair complex.

Type of ion pair

If one is to understand the effect of ion pairing on the secondary α-deuterium kinetic isotope effect and transition state structure of an S_N2 reaction, it is important to know the form of the ion pair. One way of determining the type of ion pair is to determine how a change in the cation affects the uv spectrum of the ion pair (6, 7). If a contact ion pair is present, a change in cation, e.g., from lithium to cesium, will cause a large shift in the λ_{max} of the ion pair. With a solvent-separated ion pair, on the other hand, the cation and the chromophore are separated and a change in cation has little or no effect on the λ_{max}. Accordingly, the uv spectra of lithium, sodium, and cesium thiophenoxides were measured in DMSO, DMF, methanol, and diglyme, at concentrations where the salts were known to exist as the ion-pair complex. The λ_{max} for these salts, Table 6, was independent of the cation in DMSO, DMF, and methanol. Thus, the ion-pair reactant in these three solvents is the solvent-separated ion pair.

Although the situation is different in diglyme, it appears that the solvent-separated ion pair is also the reacting species when sodium thiophenoxide is used in this solvent. The uv spectrum of the lithium thiophenoxide ion-pair complex, with a λ_{max} at 325 nm, is significantly different from that for the sodium and cesium thiophenoxide ion-pair complexes, which have a weak λ_{max} at 304 ± 2 nm. This suggests that the lithium salt exists as a contact ion pair in diglyme. However, sodium and cesium thiophenoxide, which have almost identical uv spectra, appear to exist as solvent-separated ion-pair complexes in diglyme. Thus, the sodium thiophenoxide appears to exist as a solvent-separated ion-pair complex in all of the solvents used in this study.

Although the uv spectra of the alkali metal thiophenoxides show that the sulfur end of the ion-pair reactant is a solvent-separated ion pair, the extremely sharp change in the uv spectrum and in the secondary α-deuterium kinetic isotope

Can. J. Chem. Downloaded from www.nrcresearchpress.com by 93.93.197.157 on 09/07/12
For personal use only.

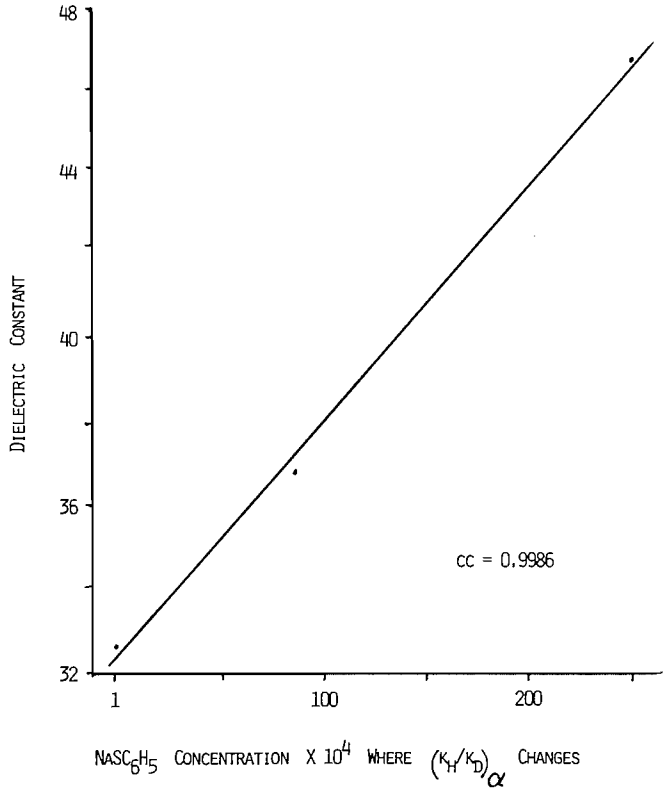

FIG. 4. A plot of the dielectric constant of the solvent versus the sodium thiophenoxide concentration where the secondary α-deuterium kinetic isotope effect changes.

effects with concentration indicates that the solvent-separated ion pair is not simple. In fact, if the ion pair consisted of a pair of ions, one would have to change the concentration of the salt by nearly 1000 times to convert most of the free ion into the ion pair. The extremely rapid change in the form of the reacting anion suggests that the solvent-separated ion pair must exist as a complex consisting of several solvent-separated sodium thiophenoxide ion pairs, eq. [2].

[2] $m\,Na^+ + m\,SC_6H_5^- \rightleftarrows (Na^+(solvent)_n\,(SC_6H_5^-))_m$

All of the experimental findings are consistent with such an equilibrium. First, the form of the reacting anion would change rapidly with concentration if this equilibrium existed. Thus, the rapid change that is observed in the uv spectra and in the secondary α-deuterium kinetic isotope effects, is expected. The conductivity data are also consistent with the formation of the ion-pair complex because the conductance of a complex ion is lower than that of the free ions (10). Finally, the ion-pair complex cannot form in the presence of 15-crown-5 ether because the sodium ions are complexed by the crown ether. Thus, the secondary α-deuterium kinetic isotope effects in the reactions containing 15-crown-5 ether should be identical to those found in the free ion reactions. This is observed.

Effect of a change in the form of the nucleophile on transition state structure

In each solvent where the reacting nucleophile changes, the secondary α-deuterium kinetic isotope effect is smaller in the reaction involving the ion-pair complex, i.e., the isotope effect is reduced from 1.12 for the free ion reaction to 1.03 in the ion-pair complex reaction in DMSO, from 1.13 to 1.08 in DMF,

TABLE 4. The effect of adding 15-crown-5 ether on the secondary α-deuterium kinetic isotope effects[a] in the ion-pair and free ion S_N2 reaction between *n*-butyl chloride and sodium thiophenoxide in DMF at 20°C

$[NaSC_6H_5]$ (mol/L)	k_H (L/mol-s)	k_D (L/mol-s)	$(k_H/k_D)_\alpha$
	DMF free ion, no 15-crown-5 ether		
$(4.0–4.1) \times 10^{-3}$	$(6.131 \pm 0.043)^b \times 10^{-2}$	$(5.432 \pm 0.033)^b \times 10^{-2}$	1.129 ± 0.010^c
3.1×10^{-3}	$(6.136 \pm 0.045) \times 10^{-2}$	$(5.457 \pm 0.006) \times 10^{-2}$	1.124 ± 0.008
	DMF ion pair, no 15-crown-5 ether		
8.6×10^{-3}	$(4.352 \pm 0.022) \times 10^{-2}$	$(4.011 \pm 0.034) \times 10^{-2}$	1.085 ± 0.011
$(0.94–1.8) \times 10^{-2}$	$(4.503 \pm 0.063) \times 10^{-2}$	$(4.156 \pm 0.068) \times 10^{-2}$	1.083 ± 0.023
	DMF with 15-crown-5 ether at concentrations where sodium thiophenoxide usually reacts as a solvent-separated ion pair		
9.3×10^{-3}	5.304×10^{-2}	4.668×10^{-2}	1.136^d
$(0.97–1.1) \times 10^{-2}$	$(4.763 \pm 0.045) \times 10^{-2}$	$(4.225 \pm 0.046) \times 10^{-2}$	1.127 ± 0.016^e
	DMF with 15-crown-5 ether at concentrations where sodium thiophenoxide reacts as a free ion		
$(3.2–4.0) \times 10^{-3}$	$(6.136 \pm 0.056) \times 10^{-2}$	$(5.438 \pm 0.042) \times 10^{-2}$	1.128 ± 0.013^e

[a]Each isotope effect was determined with a different batch of solvent and often by a different worker.
[b]Standard deviation from at least three kinetic runs.
[c]The error is $1/k_D[(\Delta k_H)^2 + (k_H/k_D)^2 \times (\Delta k_D)^2]^{1/2}$ where Δk_H and Δk_D are the standard deviations for the rate constants for the undeuterated and deuterated substrates, respectively (1).
[d]Using 2.2 equivalents of 15-crown-5 ether. The kinetic isotope effect was calculated from only one k_H and one k_D.
[e]Using 1.1 equivalents of 15-crown-5 ether.

Can. J. Chem. Downloaded from www.nrcresearchpress.com by 93.93.197.157 on 09/07/12
For personal use only.

Can. J. Chem. Downloaded from www.nrcresearchpress.com by 93.93.197.157 on 09/07/12
For personal use only.

TABLE 5. The secondary α-deuterium kinetic isotope effects found using several different concentrations of sodium thiophenoxide in the S_N2 reaction between *n*-butyl chloride and sodium thiophenoxide in DMF at 20°C

$[NaSC_6H_5]$ (mol/L)	$(k_H/k_D)_\alpha$
1.8×10^{-2}	1.087[a]
1.2×10^{-2}	1.079[a]
9.4×10^{-3}	1.084[a]
8.6×10^{-3}	1.085±0.011[b]
4.1×10^{-3}	1.129±0.010
3.1×10^{-3}	1.124±0.008

[a]These isotope effects were calculated from single rate constants measured for the deuterated and undeuterated substrates. The average isotope effect over this range of concentrations is 1.084 ± 0.023.

[b]The error is $1/k_D[(\Delta k_H)^2 + (k_H/k_D)^2 \times (\Delta k_D)^2]^{1/2}$ where Δk_H and Δk_D are the standard deviations for the rate constants for the undeuterated and deuterated substrates, respectively (1).

and from 1.13 to 1.10 in methanol. The C_α—H(D) out-of-plane bending vibrations, which are primarily responsible for determining the magnitude of a secondary α-deuterium kinetic isotope effect (11), will be the same in the initial state of every reaction. As a result, the different secondary α-deuterium kinetic isotope effects for the free ion and ion-pair complex reactions reflect differences in the energy of the C_α—H(D) out-of-plane bending vibrations in the S_N2 transition states (transition state structure). Since a smaller secondary α-deuterium kinetic isotope effect is observed when the C_α—H(D) out-of-plane bending vibrations are sterically hindered (higher energy) in the transition state, it appears that the S_N2 transition states for the solvent-separated ion-pair complex reactions are more sterically crowded than those for the free ion reactions. Although the sodium atom of the ion-pair complex could

TABLE 6. The absorption wavelength for the lithium, sodium, and cesium thiophenoxide ion pairs in DMSO, DMF, methanol, and diglyme at 20°C

	λ_{max} (nm)			
Salt	DMSO	DMF	CH_3OH	Diglyme
$C_6H_5S^-\ Li^+$	305	308	266	325
$C_6H_5S^-\ Na^+$	305	308	267	302
$C_6H_5S^-\ Cs^+$	305	307	267	306

increase the steric crowding around the C_α—H(D) bonds (the energy of the out-of-plane bending vibrations) in the S_N2 transition state of the ion-pair reaction, these isotope effects are more likely the result of a tighter transition state with shorter α-carbon–nucleophile and (or) α-carbon – leaving group bonds. This rationale is preferred because the sodium atom of the solvent-separated ion-pair complex is some distance away from the α carbon in the transition state. This separation between the sodium ion of the solvent-separated ion-pair complex and the C_α—H(D) transition state bonds is required because (*i*) the secondary α-deuterium kinetic isotope effects are large and normal, indicating that the transition states are loose with reasonably long α-carbon–nucleophile and α-carbon – leaving group bonds; (*ii*) the sodium atom of the solvent-separated ion pair is separated from the sulfur by at least one solvent molecule, and is far from the large, tetrahedral sulfur atom and, therefore, from the smaller α carbon; and (*iii*) the sodium ion will be associated with a nonreacting lone pair of electrons on the sulfur atom and will not be near the bonding electrons in the transition state. Since the sodium ion will not be near the lone pair of sulfur electrons that are forming the bond or to the very short C_α—H(D) bonds on the S----Cα----Cl axis of the S_N2 transition state, it should not affect the C_α—H(D) out-of-plane bending vibrations in the transition state. As a

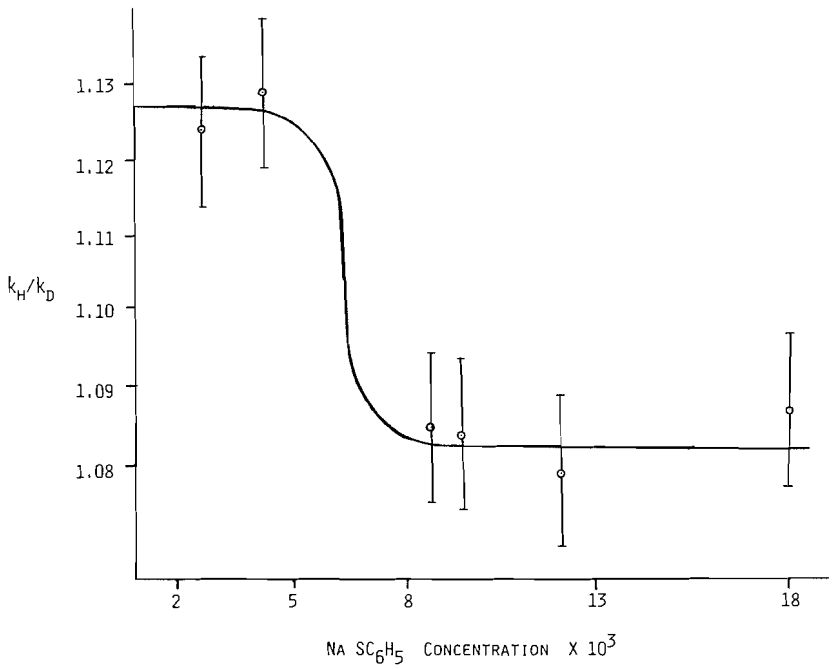

FIG. 5. The secondary α-deuterium kinetic isotope effect for the S_N2 reaction between sodium thiophenoxide and *n*-butyl chloride in DMF at 20°C versus the sodium thiophenoxide concentration.

TABLE 7. The rate constants and Hammett ρ values for the free ion and ion-pair S_N2 reactions between *n*-butyl chloride and a series of *para*-substituted sodium thiophenoxides in DMF at 20°C

para Substituent on the nucleophile	$k_{free\ ion} \times 10^2$ (L/mol-s)	$k_{ion\ pair} \times 10^2$ (L/mol-s)
CH_3O^-	22.75±0.18	16.84±0.42
CH_3^-	12.32±0.19	10.68±0.27
H^-	6.131±0.043	4.503±0.063
Cl^-	2.059±0.056	1.847±0.026
ρ	−2.05±0.08	−1.93±0.09
Correlation coefficient	0.998	0.998

result, the smaller isotope effects in the ion-pair complex reactions must indicate that the transition states for these reactions are tighter than those for the free ion reactions. This is, in fact, expected because the negative charge on the nucleophilic atom of the ion pair is less than that of a free thiophenoxide ion[3] and the sulfur atom should have to be closer to the α carbon before it distorts the α-carbon–chlorine bond and displaces the leaving group. Thus, these results suggest that the S_N2 transition states for the ion-pair complex reactions are tighter, with shorter nucleophile–α-carbon and (or) α-carbon–leaving group bonds, than those in the free ion reactions.

It is important to note, however, that the secondary α-deuterium kinetic isotope effect for the reaction of the ion-pair complex in diglyme appears to be slightly larger (k_H/k_D = 1.14) than that for the free ion reactions (k_H/k_D = 1.126 ± 0.007). Thus, the ion-pair transition state in diglyme appears to be looser than that for the free ion reactions. This may arise because the sodium thiophenoxide ion pair is very weakly solvated in the slightly polar diglyme and the influence of the nucleophilic sulfur is felt at larger distances from the α-carbon.

The Hammett ρ values, obtained by changing the *para* substituent on the nucleophile, were determined for both the ion-pair complex and the free ion reactions, Table 7, in an effort to learn more about the relative lengths of the α-carbon–nucleophile bonds in the S_N2 transition states of these reactions. Although the Hammett ρ value for the free ion reaction is slightly larger, the free ion and ion-pair complex ρ values are statistically the same. Thus, this technique does not appear to be useful in distinguishing between the lengths of the α-carbon–nucleophile bonds in the free ion and ion-pair transition states.

Finally, it is interesting to investigate the magnitude of the change in the isotope effects for the ion-pair complex and the free ion reactions in the different solvents. The change in the secondary α-deuterium kinetic isotope effect when the form of the reacting ion changes is large in the dipolar aprotic solvents, DMSO and DMF, and much smaller in the protic solvent, methanol. The change in the magnitude of the isotope effect might be smaller in methanol because hydrogen bonding to the thiophenoxide ion in methanol lowers the electron density on the sulfur atom of the free ion in the same way the sodium ion does in the ion-pair complex. If this is so, the negative charge on the sulfur of the thiophenoxide ion in the free ion reaction in methanol will be lower than that on the free ions in DMSO and DMF where the anion is only weakly solvated. As a result, one would expect the change in charge on the nucleophilic sulfur atom (the change in the magnitude of the secondary α-deuterium kinetic isotope effect) to be smaller in going from the free "solvated" ion reaction to the ion-pair complex reaction in methanol than in the dipolar aprotic solvents, DMSO and DMF.

[3]Z.-g. Lai and K. C. Westaway. Submitted to Can. J. Chem.

Conclusions

The results obtained from spectroscopic and conductivity measurements of sodium thiophenoxide solutions in four different solvents, as well as the secondary α-deuterium kinetic isotope effects found with 15-crown-5 ether, demonstrate that the secondary α-deuterium kinetic isotope effects in the S_N2 reaction between sodium thiophenoxide and *n*-butyl chloride are significantly different when the ionic reactant is a solvent-separated ion-pair complex than when this reactant is a free ion. In all three solvents in which the form of the ionic reactant changes, a smaller isotope effect and tighter transition state are found for the reaction involving the ion pair complex.

Experimental

Preparation of reagents

Solvents

Oxygen, which reacts with the thiophenoxide ion, was removed from each solvent by bubbling extra-dry nitrogen through the solvent for 1 h. The DMSO and DMF were dried, and distilled in glass grade solvents purchased from Caledon Laboratories. Diglyme was purchased from Eastman. The DMSO was used directly. The diglyme and the DMF were further purified by distillation from sodium thiophenoxide in an extra-dry nitrogen atmosphere. Analar methanol was distilled in an extra-dry nitrogen atmosphere before use. The 15-crown-5 ether purchased from Parrish Chemical Co. was used without further purification.

para-*Substituted sodium thiophenoxides*

The preparation of these salts is described elsewhere (13).

n-*Butyl chloride*

Reagent grade *n*-butyl chloride was distilled and stored under extra-dry nitrogen.

n-*Butyl-1,1*-d_2 *chloride*

Methyl butyrate: 20 g (0.62 mol) of methanol was added dropwise to a cold mixture of 92 g (1.04 mol) of butyric acid and 15 mL of concentrated sulfuric acid. When the addition was complete, the mixture was refluxed overnight and then poured into 150 mL of a 4.0 M solution of sodium hydroxide. The organic layer was separated and washed twice with 100 mL of water, once with 100 mL of a 5% sodium bicarbonate solution, and twice with 100-mL portions of water. After drying over anhydrous magnesium sulfate, the organic layer was distilled to give 26.4 g (41.4%) of methyl butyrate, bp 100–101°C (lit.(14) bp 102.3°C).

n-*Butyl-1-1*d_2 *alcohol*: 1.2 L of dry (freshly distilled from lithium aluminum hydride) ether was placed in a 2-L three-necked flask fitted with a condenser and a dropping funnel, which were both sealed with a drying tube. Lithium aluminum deuteride (Merck) (10 g, 0.238 mol) was added to the dry ether and a solution comprised of 41.4 g (0.402 mol) of methyl butyrate and 200 mL dry ether was added, dropwise, from the dropping funnel. When all of the ester had been added, the mixture was refluxed overnight. Then the mixture was cooled and the excess lithium aluminum deuteride decomposed by adding a 10% solution of sulfuric acid in water, dropwise, until the mixture was homogeneous. The ether layer was separated and the aqueous layer was extracted twice with 200 mL of ether. The ether layers were combined, washed twice with 50 mL of water, once with 50 mL of 5% sodium bicarbonate, and again with 50 mL of water. After most of the ether had been removed on a rotary evaporator, distillation of the alcohol gave two fractions, bp 80–114°C and 114–116°C. The 80–114°C fraction was redistilled and the 114–116°C fraction collected. This gave 19.3 g (53%) of *n*-butyl-1,1-d_2 alcohol, bp 114–116°C (lit.(14) bp 117°C).

Can. J. Chem. Downloaded from www.nrcresearchpress.com by 93.93.197.157 on 09/07/12
For personal use only.

Can. J. Chem. Downloaded from www.nrcresearchpress.com by 93.93.197.157 on 09/07/12
For personal use only.

An nmr analysis indicated that the alcohol was more than 98.5% deuterated at the one position.

n-*Butyl-1,1*-d_2 *chloride*: 30 g (0.25 mol) of thionyl chloride was cooled to 5°C and 18.8 g (0.25 mol) of *n*-butyl-1,1-d_2 alcohol was added dropwise. When the addition was complete, 15 drops of pyridine were added and the mixture was heated at 70°C for 5 h. Three condensers were used to keep losses to a minimum. The reaction mixture was poured into 40 mL of water and the organic layer was separated, washed twice with 50 mL of water, twice with 50 mL of 10% sodium hydroxide, and twice with 50 mL of water. After the product had been dried over anhydrous magnesium sulfate, a distillation gave 18.7 g (79%) of *n*-butyl-1,1-d_2 chloride, bp 76–77°C (lit. (14) bp 78.4°C). An nmr analysis indicated that the sample was at least 99% deuterated at the α-carbon.

Conductivity and ultraviolet measurements

The solutions used for the conductivity and uv spectroscopy studies were prepared in a nitrogen atmosphere to prevent oxidation of the thiophenoxide ion. A 50-mL volumetric flask was filled with extra-dry nitrogen and weighed accurately. Then the sodium thiophenoxide and the 50 mL volumetric flask were placed in a IR^2 glove bag, which was filled, evacuated, and refilled with extra-dry nitrogen. Between 10 and 170 mg (7.6×10^{-5} and 1.3×10^{-3} mol depending on the solvent) of sodium thiophenoxide was placed in the volumetric flask. The flask was resealed, removed from the glove bag, and reweighed accurately.

The flask containing the sodium thiophenoxide, 10 50-mL volumetric flasks, three 50-mL glass-stoppered Erlenmeyer flasks, 10 25-mL pipettes, a 1-mL pipette, and the appropriate oxygen-free solvent were placed in the glove bag under a nitrogen atmosphere (*vide supra*). The solvent was added to the volumetric flask containing the sodium thiophenoxide and 1-mL samples of this solution were pipetted into the three 50-mL Erlenmeyer flasks. Then, 25 mL of this solution was pipetted into a new volumetric flask and diluted to 50 mL. This procedure was repeated until 11 solutions of varying concentration had been made. When all 10 dilutions were made, the glove bag was opened, the concentration of the thiophenoxide ion in the original solution was determined by titrating with standard mercury II nitrate (15), and the uv spectrum and the conductance of each solution were determined.

The uv spectra were recorded on Hitachi Perkin–Elmer 124 double beam and Beckman DU-65 spectrophotometers. The uv spectra in DMSO and DMF were recorded in 1-mm quartz cells to reduce the absorbance from the solvent. The spectra in methanol were recorded in 10-mm quartz cells. Methanol was used in the reference cell throughout the study.

The conductance of the sodium thiophenoxide solutions was determined by two methods. One method involved using a conductivity bridge that was capable of measuring resistances between 0.1 and 110 000 ohms to within 0.1% (16). The second method was used to measure very high resistances, i.e., up to several million ohms. This was done by measuring the current, I, in microamps, which passed through a conductivity cell when a known voltage, V, was placed across the cell. The conductance of the solution (1/R) is equal to I/V. The conductivity bridge method was used for the solutions in DMSO and DMF. The second method was used for the methanol solutions.

Kinetic measurements

All of the apparatus was cleaned with cleaning solution and distilled water and then dried at 140°C. To ensure a water-free environment, the apparatus was either sealed while hot or was cooled in a desiccator.

A stoppered 250-mL Erlenmeyer was filled with extra-dry nitrogen and weighed accurately. This flask, a bottle of sodium thiophenoxide, a spatula, a crude balance, and some Kimwipes were placed in an IR^2 glove bag. The bag was sealed and the tops removed from the Erlenmeyer and the sodium thiophenoxide. Then the bag was filled with extra-dry nitrogen, evacuated, and refilled. The appropriate amount (between 2 and 730 mg, depending on the solvent) of sodium thiophenoxide was placed in the Erlenmeyer flask, which was sealed, removed from the glove bag, and weighed accurately.

The Erlenmeyer containing the sodium thiophenoxide, an adapter fitted with a serum cap, a bottle of purified (*vide supra*) solvent, and a 250-mL graduated cylinder were placed in a glove bag, which was filled, evacuated, and refilled with extra-dry nitrogen. Approximately 220 mL of solvent was added to the Erlenmeyer and the flask was stoppered with the adapter and the serum cap. This solution was stored in a nitrogen atmosphere overnight.

The sodium thiophenoxide solution, two 125-mL Erlenmeyer flasks fitted with adapters and serum caps, three stoppered, 50-mL Erlenmeyer flasks, a 75-mL and a 5-mL pipette, and a rubber bulb were placed in the glove bag under a nitrogen atmosphere (*vide supra*). Then 75 mL of the sodium thiophenoxide solution was pipetted into each 125-mL Erlenmeyer flask and 5 mL of the sodium thiophenoxide solution was placed in each 50-mL Erlenmeyer flask.

The reaction vessels were temperature equilibrated for at least 0.75 h at 20.00 ± 0.02°C. The purity of the sodium thiophenoxide solution was determined by titrating the 5-mL samples with standard mercury II nitrate (15). Finally, the kinetic run was begun by injecting the appropriate amount of *n*-butyl chloride through the serum cap with an airtight syringe. The end of the syringe containing the *n*-butyl chloride was sealed with a rubber serum cap and weighed accurately before and after the addition of the *n*-butyl chloride.

The same general procedure was used in the kinetic runs with 15-crown-5 ether. The only difference was that approximately 1.1 equivalents (relative to the sodium thiophenoxide) of the 15-crown-5 ether was added to the reaction flask with a gastight syringe a few minutes before the *n*-butyl chloride was added.

The kinetic data were obtained by withdrawing aliquots of the reaction mixture at various times throughout the run. These samples were analyzed in two different ways. Ultraviolet spectroscopy was used for the fast reactions in DMSO, DMF, and diglyme. An electrochemical titration (17) was used for the extremely slow reactions with relatively high concentrations of sodium thiophenoxide in methanol.

In the uv method, 1-mL aliquots of the reaction mixture were withdrawn with a 1-mL gastight syringe fitted with a 6-in. needle. Each sample was quenched by diluting it to 50 mL with a 0.13% mixture (v/v) of sulfuric acid in methanol. The absorbance was followed at 262 nm using the 0.13% solution of sulfuric acid in methanol in the reference cell. The procedure used for determining the rate constants has been described previously (11).

In the electrochemical method, 5-mL aliquots were withdrawn with a 5-mL gastight syringe fitted with a 6-in. needle and quenched by diluting them to 25 mL with methanol. Both the chloride ion and the thiophenoxide ion were titrated with standard 0.1 M silver nitrate. The endpoint for the chloride titration was at 250 mV, whereas the endpoint for the thiophenoxide ion was at −100 mV. The rate constant was calculated using the chloride ion concentrations and the normal equation for a second-order reaction that is first order in each reactant (12).

Acknowledgements

The authors gratefully acknowledge the financial support provided by the Natural Sciences and Engineering Research Council of Canada. The authors also wish to thank Mr. Wade Elford and Ms. Bonnie Gleason who measured the conductivity and uv spectra of the thiophenoxide salts.

1. K. C. Westaway, Z. Waszczylo, P. J. Smith, and K. S. Rangappa. Tetrahedron Lett. **26**, 25 (1985).
2. D. G. Graczyk, J. W. Taylor, and C. R. Turnquist. J. Am. Chem. Soc. **100**, 7333 (1978).
3. M. N. Islam and K. T. Leffek. J. Chem. Soc. Perkin Trans. 2, 952 (1977).
4. D. H. O'Brien, C. R. Russell, and A. J. Hart. J. Am. Chem. Soc. **98**, 7427 (1976).
5. J. W. Burley and R. N. Young. J. Chem. Soc. Perkin Trans. 2, 1006 (1972).

6. E. BUNCEL, B. C. MENON, and J. P. COLPA. Can. J. Chem. **57**, 999 (1979).
7. E. BUNCEL and B. MENON. J. Org. Chem. **44**, 317 (1979).
8. J. E. GORDON. The organic chemistry of electrolyte solutions. J. Wiley and Sons, New York. 1975. p. 386.
9. J. J. CHRISTENSEN, D. J. EATOUGH, and R. M. IZATT. Chem. Rev. **74**, 351 (1974).
10. R. J. WILLIAMS, J. N. PHILLIPS, and K. J. MYSELS. Trans. Faraday Soc. **51**, 728 (1955).
11. K. C. WESTAWAY and Z. WASZCZYLO. Can. J. Chem. **60**, 2500 (1982).
12. K. J. LAIDLER. Chemical kinetics. 2nd ed. McGraw-Hill Book Company, New York, NY. 1965. p. 9.
13. K. C. WESTAWAY and S. F. ALI. Can. J. Chem. **57**, 1089 (1979).
14. R. C. WEAST and M. J. ASTLE (*Editors*). CRC Handbook of Chemistry and Physics. 61st ed. CRC Press, Boca Raton, FL. 1980–1981.
15. K. C. WESTAWAY and R. A. POIRIER. Can. J. Chem. **53**, 3216 (1975).
16. H. A. JOLY and K. C. WESTAWAY. Can. J. Chem. **64**, 1206 (1986).
17. D. G. GRACZYK and J. W. TAYLOR. J. Am. Chem. Soc. **96**, 3255 (1974).

Can. J. Chem. Downloaded from www.nrcresearchpress.com by 93.93.197.157 on 09/07/12
For personal use only.

Platinum and palladium complexes of $[R_2PCH_2P(Y)R'_2]$ and $[R_2PCHP(Y)R'_2]^-$ ligands, Y = O, S, or Se: ^{13}C, ^{31}P, ^{77}Se, and ^{195}Pt nuclear magnetic resonance studies and the crystal and molecular structures of *trans*-$[PtCl(PEt_3)\{Bu^t_2PCH_2P(O)Me_2\}][ClO_4]$ and *trans*-$PtCl(PEt_3)\{Ph_2PCH_2P(S)Bu^t_2\}][ClO_4]$

DAVID ERIC BERRY, JANE BROWNING, KEITH ROGER DIXON,[1] AND ROBERT WAYNE HILTS
Department of Chemistry, University of Victoria, Victoria, B.C., Canada V8W 2Y2

Received October 20, 1987

DAVID ERIC BERRY, JANE BROWNING, KEITH ROGER DIXON, and ROBERT WAYNE HILTS. Can. J. Chem. **66**, 1272 (1988).

Reactions of the bisphosphine monochalcogenides, $[Ph_2PCH_2P(Y)R_2]$, Y = O, S, or Se, R = Ph, Pr^i, or Bu^t, with the chloro-bridged dimers $[M_2Cl_4(PR'_3)_2]$, M = Pd or Pt, R′ = Et or Bu^n, in the presence of either $NaClO_4$ or $NaBF_4$ yield perchlorate and fluoroborate salts of the complex cations *cis*- and *trans*-$[PtCl(PR'_3)\{Ph_2PCH_2P(Y)R_2\}]^+$. In many cases both *cis* and *trans* isomers (defined by the relative orientation of the two M—P bonds) are obtained and the precise isomer distribution is a sensitive function of the substituents. Corresponding neutral complexes, *cis*- and *trans*-$[PtCl(PR'_3)\{Ph_2PCHP(Y)R_2\}]$, can be synthesized either by deprotonation of the cations using NaH or by use of the salts $Li[Ph_2PCHP(Y)R_2]$ in the initial bridge cleavage reactions. These and related complexes are characterized by complete ^{13}C, ^{31}P, ^{77}Se, and ^{195}Pt NMR studies and by two crystal structure determinations. The complexes **I**, *trans*-$[PtCl(PEt_3)\{Bu'_2PCH_2P(O)Me_2\}][ClO_4]$, and **II**, *trans*-$[PtCl(PEt_3)\{Ph_2PCH_2P(S)Bu'_2\}][ClO_4]$, crystallize in the monoclinic space group $P2_1/c$, respective cell dimensions: a = 15.579(2), b = 13.590(3), c = 13.578(1) Å; β = 105.96(1)°; and a = 14.002(4), b = 16.366(5), c = 15.524(5) Å; β = 106.01(3)°. Complete X-ray diffraction studies show that both complexes contain closely square planar platinum centres with the $R_2PCH_2P(Y)R'_2$ ligands coordinated via phosphorus and the Y atom so as to form five-membered chelate rings. The molecular dimensions suggest that the bond to sulphur is stronger than that to oxygen and exerts a larger *trans* influence.

DAVID ERIC BERRY, JANE BROWNING, KEITH ROGER DIXON, et ROBERT WAYNE HILTS. Can. J. Chem. **66**, 1272 (1988).

En présence soit de $NaClO_4$ ou de $NaBF_4$, les chalcogénures de bisphosphines, $[Ph_2PCH_2P(Y)R_2]$ dans lesquels Y = O, S ou Se et R = Ph, *i*-Pr ou *tert*-Bu, réagissent avec les dimères pontés par le chlore, $[M_2Cl_4(PR'_3)_2]$ dans lesquels M = Pd ou Pt et R′ = Et ou *n*-Bu, pour donner les perchlorates et les fluoroborates des cations complexes *cis*- et *trans*-$[PtCl(PR'_3)\{Ph_2PCH_2P(Y)R_2\}]^+$. Dans plusieurs cas, on obtient les deux isomères *cis* et *trans* (définis par rapport à l'orientation des deux liaisons M—P) et la distribution précise des isomères est très sensible à la nature des substitutants. On peut synthétiser les complexes neutres correspondants, *cis*- et *trans*-$[PtCl(PR'_3)\{Ph_2PCHP(Y)R_2\}]$, soit par une déprotonation des cations à l'aide de NaH soit en utilisant les sels de $Li[Ph_2PCHP(Y)R_2]$ lors des réactions initiales de clivage des ponts. On a caractérisé ces complexes ainsi que d'autres à l'aide d'études rmn complètes du ^{13}C, du ^{31}P, du ^{77}Se et du ^{195}Pt ainsi que par deux déterminations de structures cristallines. Les complexes **I**, *trans*-$[PtCl(PEt_3)\{tert\text{-}Bu_2PCH_2P(O)Me_2\}][ClO_4]$, et **II**, *trans*-$[PtCl(PEt_3)\{Ph_2PCH_2P(S)tert\text{-}Bu_2\}][ClO_4]$,cristallisent dans le groupe d'espace monoclinique $P2_1/c$ avec les dimensions respectives suivantes: a = 15,579(2), b = 13,590(3) et c = 13,578(1) Å et β = 105,96(1)° et a = 14,002(4), b = 16,366(5) et c = 15,524(5) Å et β = 106,01°. Les études complètes de diffraction des rayons-X démontrent que les deux complexes contiennent des centres de platine qui sont assez près du plan carré et que les ligands $R_2PCH_2P(Y)R'_2$ sont coordonnés au phosphore et à l'atome Y pour former des cycles de chélates à cinq chaînons. Les dimensions des molécules suggèrent que le liaison avec le soufre est beaucoup plus forte que celle avec l'oxygène et qu'elle exerce une influence trans beaucoup plus forte.

[Traduit par la revue]

Introduction

The potentially bidentate ligands, $[R_2PCH_2P(Y)R'_2]$, Y = O, S, or Se, were first synthesised and studied by Grim and co-workers approximately ten years ago (1–5). These authors reported extensive ^{31}P nuclear magnetic resonance (NMR) data including coordination complexes of the ligands with chromium, molybdenum and tungsten carbonyls. Subsequent to these studies very few coordination complexes of these ligands have been described in the literature, except for very recent reports of the reaction of $[Ph_2PCH_2P(O)Ph_2]$ with $[PtCl_2(COD)]$ (6), and of formation of $[Ph_2PCH_2P(Se)Ph_2]$ platinum complexes by selenium extrusion from complexes of the diselenide (7). Moreover, no X-ray structural studies of $[R_2PCH_2P(Y)R'_2]$ complexes have been reported.

We became interested in these ligands as part of a wide-ranging study of platinum group metal complexes involving ligands such as **1**, **2**, or **3**, which are loosely analogous to acetylacetone or acetylacetonate (8, 9). Some of this work had shown particularly interesting dynamic stereochemistry in cases

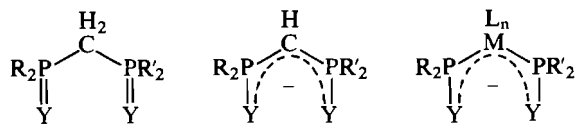

1 **2** **3**

where the ligands were bound by one strong, relatively inert, bond and one weaker, relatively labile, bond (9, 10). For example, **2** can be bound to a metal via a strong bond to carbon and a relatively weak bond to a Y atom. The $[R_2PCH_2P(Y)R'_2]$ ligands are further examples of this possibility since the most likely mode of coordination is a five-membered chelate ring with a strong bond to the PR_2 group and a weaker bond to the Y atom.

The present paper describes studies of a wide range of platinum and palladium complexes of $[R_2PCH_2P(Y)R'_2]$ and $[R_2PCHP(Y)R'_2]^-$ ligands. These appear to be the first examples of platinum group complexes of the anionic ligands, although mercury complexes of $[Ph_2PCHP(Y)Ph_2]^-$, Y = S or Se, have been described recently (11, 12). Characterization is primarily by detailed NMR studies but we also report the crystal and molecular structures of two of the complexes, **I**, *trans*-

[1]Author to whom correspondence should be addressed.

Can. J. Chem. Downloaded from www.nrcresearchpress.com by 93.93.197.157 on 09/07/12
For personal use only.

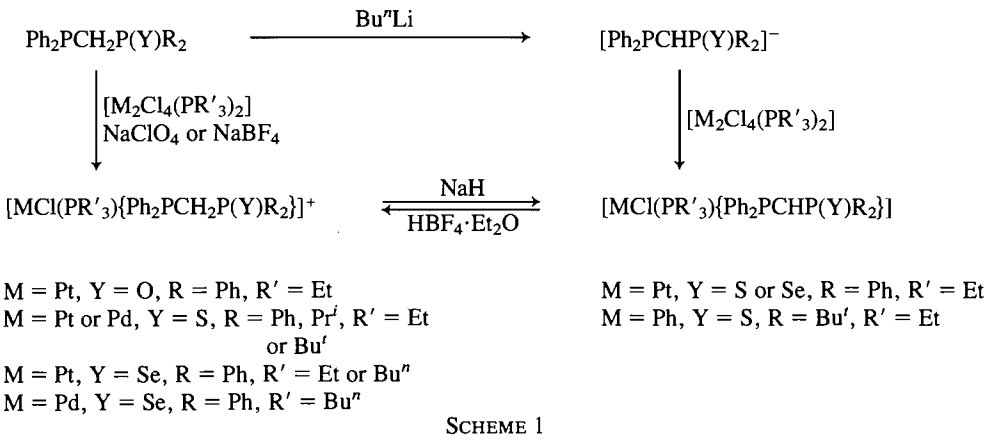

SCHEME 1

$[PtCl(PEt_3)\{Bu^t_2PCH_2P(O)Me_2\}][ClO_4]$ and, **II**, *trans*-$[PtCl(PEt_3)\{Ph_2PCH_2P(S)Bu^t_2\}][ClO_4]$. Future publications will deal with complexes of the same ligands with other platinum group metals and with the platinum group coordination chemistry of the related $[R_2P(Y)CH_2P(Y)R'_2]$ and $[R_2P(Y)CHP(Y)R'_2]^-$ ligands.

Results and discussion

(A) Synthesis

The ligands, $[Ph_2PCH_2P(Y)Ph_2]$ were prepared as previously described (1–3). For Y = O or S, $P(Y)Ph_3$ was reacted with methyl lithium to yield $[Ph_2P(Y)CH_2]Li$, followed by combination of the lithium salt with Ph_2PCl, and for Y = Se, $[Ph_2PCH_2PPH_2]$ was oxidized by elemental selenium (3). Previous preparations of the alkyl derivatives, $[Ph_2PCH_2P(S)R_2]$, R = Pr^i or Bu^t, have utilised similar procedures with $[Ph_2P(S)CH_2]Li$ and R_2PCl followed by sulphur transfer reactions (4). However, we have found it more satisfactory to obtain these ligands by reaction of $[Ph_2PCH_2]Li$ with R_2PCl followed by oxidation of the resulting $[Ph_2PCH_2PR_2]$ under reflux in benzene with one mole of elemental sulphur. The much higher reactivity of the dialkylphosphino group relative to the diphenylphosphino group ensures exclusive formation of the desired product.

Cleavage reactions of the chloro-bridged dimers, $[M_2Cl_4(PR'_3)_2]$, proceed in high yield under mild conditions with the above ligands or the derived anions, $[Ph_2PCHP(Y)R_2]^-$, to yield the extensive series of platinum and palladium complexes detailed in Scheme 1. The resulting square planar complexes have been fully characterized, primarily by the ^{31}P NMR data and the two crystal structure determinations discussed below. Comments on ^{13}C, ^{77}Se, and ^{195}Pt data are also given below. All of the complexes contain five-membered chelate rings in which the ligand is bound via one phosphorus atom and the chalcogen, but the distribution of isomers varies widely with the substituents. We have chosen to designate structures such as **5** and **6** as *cis* or *trans* respectively, depending on the relative orientation of the two M—P bonds.

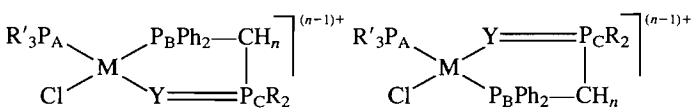

5 (*cis*)

6 (*trans*)

In our work, the actual distribution of *cis* and *trans* isomers was a very sensitive function of the metal and of the substituents. For example, $[PtCl(PEt_3)\{Ph_2PCH_2P(S)Bu^t_2\}]^+$ was obtained exclusively as the *trans* isomer whereas the analogous Pr^i and palladium complexes were exclusively *cis*. In many other cases isomer mixtures were obtained and we were not able to discern any general patterns. Details of the isomers obtained are presented in the ^{31}P NMR and experimental sections.

As outlined in Scheme 1, the synthesis of complexes containing $[Ph_2PCH_2P(S)R_2]^-$ ligands was accomplished either by cleavage of a metal dimer by the lithium salt of the ligand, or by sodium hydride deprotonation of the corresponding $Ph_2PCH_2P(S)R_2$ complex. The latter route demonstrates the enhanced acidity of the coordinated ligand since sodium hydride does not deprotonate the free ligands. Moreover, the reversal of these deprotonations by $HBF_4.Et_2O$ provides an important confirmation of the assigned structures. Our previous studies using $Ph_2P(S)CH_2P(S)Ph_2$ and related ligands showed that deprotonation of the ligand sometimes led to a change from S,S to S,C coordination (9). Thus, it is also important, and somewhat disappointing, to note that none of the present complexes showed any evidence of this effect.

Successful synthesis of complexes of the anionic ligands was limited to platinum, since the greater lability of palladium gave complex mixtures of products under similar conditions. Selenium analogs of the sulphur complexes were accessible only by the sodium hydride route because the salt, $Li[Ph_2PCHP(Se)Ph_2]$, proved highly unstable.

During the course of the work, we obtained several other complexes which, while not strictly within the format of Scheme 1, are closely related. Thus, *trans*-$[PtCl(PEt_3)\{Ph_2P(S)CH_2PPr^i_2\}]^+$ resulted from cleavage of $[Pt_2Cl_4(PEt_3)_2]$ by the appropriate ligand, and *trans*-$[PtCl(PEt_3)\{Bu^t_2PCH_2P(O)Me_2\}]^+$ was obtained by inadvertent oxidation during an attempted preparation of $[PtCl(PEt_3)\{Bu^t_2PCH_2PMe_2\}]^+$. More interesting were a series of reactions using $[Ph_2PCH_2P(O)Ph_2]$, since the weaker coordinating ability of oxygen for platinum gave a more complex reaction pattern than that observed for the sulphur analogs. The initial product of reaction of $[Ph_2PCH_2P(O)Ph_2]$ with $[Pt_2Cl_4(PEt_3)_2]$, either alone or in the presence of $NaClO_4$, was *trans*-$[PtCl_2(PEt_3)\{Ph_2PCH_2P(O)Ph_2\}]$ in which the ligand is coordinated only via phosphorus and has a "dangling" P(O) group. ^{31}P NMR studies showed that during purification procedures this complex tends to convert to the corresponding *cis* isomer. The ^{31}P NMR spectrum of this *cis* isomer is broad at ambient temperature but sharp at −35°C. This suggests that a chloride ligand is labilized by the *trans* effect of phosphorus and exchanges rapidly with the dangling P(O) group, leading to broadening of the phosphorus resonances. Further, in the presence of $NaClO_4$, the chloride is completely displaced by

Can. J. Chem. Downloaded from www.nrcresearchpress.com by 93.93.197.157 on 09/07/12
For personal use only.

TABLE 1. Phosphorus-31 nuclear magnetic resonance parameters for the complexes, $[MCl(P_AR'_3)\{Ph_2P_BCH_nP_C(Y)PR_2\}]^{(n-1)+}$*

M	Y	R	R′	*n*	StereoChem	Notes	δ(P_A)	δ(P_B)	δ(P_C)	*J*(P_A—P_B)	*J*(P_A—P_C)	*J*(P_B—P_C)	*J*(Pt—P_A)	*J*(Pt—P_B)	*J*(Pt—P_C)
Pt	O	Ph	Et	2	*cis*	a,c	4.80	14.08	65.40	18.3	h	12.2	3595	3575	h
Pt	S	Ph	Et	2	*cis*	a,c	12.67	17.30	49.86	15.8	6.0	25.4	3061	3637	h
Pt	S	Ph	Et	1	*cis*	d	7.64	20.44	45.48	14.3	6.3	80.5	3206	3508	41.9
Pt	S	Pr^i	Et	2	*cis*	a,c	13.03	21.45	81.19	14.4	6.4	12.0	3049	3652	27.3
Pd	S	Ph	Et	2	*cis*	b,c	32.18	37.73	48.52	2.9	7.2	31.6			
Pd	S	Pr^i	Et	2	*cis*	a,c	31.68	39.94	80.07	0	7.6	16.1			
Pd	S	Bu^t	Et	2	*cis*	a,c	31.04	42.77	90.95	0	7.4	10.0			
Pt	Se	Ph	Et	2	*cis*	b,c	13.07	18.06	32.07	14.6	5.8	29.8	3035	3695	h
Pt	Se	Ph	Et	1	*cis*	d	7.46	20.31	22.28	13.1	7.3	87.4	3189	3546	28.9
Pt	Se	Ph	Bu^n	2	*cis*	b,c	5.25	18.14	32.20	14.5	6.9	29.6	3009	3714	h
Pd	Se	Ph	Et	2	*cis*	b,c	28.51	31.55	37.81	7.9	3.3	37.3			
Pt	S	Ph	Et	2	*trans*	b,c	16.69	20.75	63.60	421.0	36.5	54.6	2395	2302	103.5
Pt	S	Ph	Et	1	*trans*	e	13.66	32.59	58.67	430.5	44.4	117.0	2331	2326	49.5
Pt	S	Pr^i	Et	2	*trans*	a,c	16.42	30.51	98.19	431.1	34.7	37.2	2408	2332	112.3
Pt	S	Bu^t	Et	2	*trans*	a,c	16.66	40.62	110.25	436.5	34.9	30.4	2402	2361	129.6
Pt	S	Bu^t	Et	1	*trans*	e	13.40	38.86	99.82	434.5	39.3	84.6	2315	2412	77.3
Pd	S	Ph	Et	2	*trans*	b,c	26.18	12.97	63.42	480.8	65.4	37.7			
Pd	S	Pr^i	Et	2	*trans*	a,c	25.95	31.44	99.23	491.6	36.2	45.0			
Pd	S	Bu^t	Et	2	*trans*	a,f	26.53	39.63	112.55	496.7	36.2	38.7			
Pt	Se	Ph	Bu^n	2	*trans*	b,c	7.15	23.94	44.08	419	37.7	60.3	2365	2313	111.9
Pd	Se	Ph	Et	2	*trans*	b,c	24.63	26.16	45.93	406	42.3	71.2			
trans-[PtCl(PEt$_3$)-{$Bu^t_2PCH_2P(O)Me_2$}]$^+$						a,c	17.12	51.03	103.91	411.0	21.1	19.4	2543	2246	h
trans-[PtCl(PEt$_3$)-{$Ph_2P(S)CH_2PPr^i_2$}]$^+$						b,c	16.19	51.05	68.16	401.2	41.7	42.3	2326	2202	88.3
trans-[PtCl$_2$(PEt$_3$)-{$Ph_2PCH_2P(O)Ph_2$}]						g	18.86	12.62	29.81	485.2	h	13.8	2577	2434	42
cis-[PtCl$_2$(PEt$_3$)-{$Ph_2PCH_2P(O)Ph_2$}]						c	5.63	1.44	24.95	17.1	h	22.7	3386	3845	116.2

*The labelling scheme is shown in structures **5** and **6**. Chemical shifts (δ) are quoted in ppm relative to 85% H_3PO_4. All shifts were positive. Coupling constants (*J*) are in Hz.

†*a*, ClO_4^- salt; *b*, BF_4^- salt; *c*, $CDCl_3$ solution; *d*, C_6D_6 solution; *e*, tetrahydrofuran solution with external C_6D_6 lock; *f*, CH_2Cl_2 solution with external C_6D_6 lock; *g*, acetone solution with external C_6D_6 lock; *h*, not resolved.

Can. J. Chem. Downloaded from www.nrcresearchpress.com by 93.93.197.157 on 09/07/12
For personal use only.

the P(O) group and the ultimate product is *cis*-[PtCl(PEt$_3$){$Ph_2PCH_2P(O)Ph_2$}][ClO_4] as indicated in Scheme 1. Chloride displacement by the P(O) group of the [Ph_2PCH_2-$P(O)Ph_2$] ligand also occurs in its reaction with the chloro-bridged complex, [$Pt_2Cl_2(PEt_3)_4$][ClO_4]$_2$, which yields the chelate complex, [$Pt(PEt_3)_2$\{$Ph_2PCH_2P(O)Ph_2$\}][ClO_4]$_2$, under ambient conditions. Comparable behaviour has been reported recently in reactions of [$Ph_2PCH_2P(O)Ph_2$] with [$PtCl_2$(COD)] where the initial product *cis*-[$PtCl_2$\{$Ph_2PCH_2P(O)Ph_2$\}] can be converted to [Pt\{$Ph_2PCH_2P(O)Ph_2$\}$_2$] by chloride abstraction using silver nitrate (6).

(B) Nuclear Magnetic Resonance

1. General

Data derived from ^{31}P, ^{13}C, ^{77}Se, and ^{195}Pt NMR spectra are collected in Tables 1–3. The most extensive set is for ^{31}P since the high sensitivity of this nucleus enabled us to obtain spectra even for isomers available only as small percentage of reaction mixtures. For ^{13}C the only significant data are for the carbon of the P—CH_n—P groups and only these parameters have been included in the tables. The following discussion deals first with some general trends and then with the detail of individual assignments. The labelling scheme used is shown in structures **5** and **6**. Those assignments which are not specifically discussed rest upon similar arguments and upon the internal consistency of the various series of complexes shown in Table 1.

The assignments shown in Tables 1–3 lead to several useful generalisations: (*i*) Coordination of the [$Ph_2PCH_2P(Y)R_2$] ligands results, as expected (13), in extensive deshielding of the directly coordinated phosphorus with coordination shifts ranging from 42–50 ppm in *cis* platinum complexes and 58–68 ppm in *cis* palladium complexes. The *trans* complexes of the two metals experience a common range of coordination shifts from 58–68 ppm. The indirectly coordinated phosphorus of the $P_C(Y)$ group is less strongly affected, with coordination shifts ranging from 1–16 ppm in *cis* complexes of both metals and 16–37 ppm in *trans* complexes. The phosphine oxide complex, *cis*-[PtCl(PEt$_3$){$Ph_2PCH_2P(O)Ph_2$}]$^+$, is an exception here with a coordination shift for the P(O) phosphorus of +36.4 ppm. Coordination also causes deshielding of the carbon of the P_B—C—P_C group, especially in *cis* complexes where the range is 10–13 ppm compared with only 2–3 ppm in *trans* complexes. When the Y atom is selenium (Table 3), it also is deshielded by coordination. The last major effect of coordination is a sharp decrease in the magnitude of the two bond P_B—C—P_C coupling, for example changing from 76.2 Hz in [Ph_2PCH_2-$P(S)Ph_2$] to 25.2 Hz in *cis*-[PtCl(PEt$_3$){$Ph_2PCH_2P(S)Ph_2$}]$^+$. This change could be a normal result of the change in coordination number at phosphorus, since we note that in [$Ph_2P(O)CH_2$-$P(S)Ph_2$] the coupling is only 15.6 Hz (3) and it is also generally known that P^V—C—P^V couplings are smaller than P^{III}—C—P^{III} (14*a*). However, in the case of the metal complex there is also the possibility of a contribution of opposite sign from the P—Y—M—P pathway.

TABLE 2. Carbon-13 and platinum-195 nuclear magnetic resonance parameters for ligands, $[Ph_2CH_nP(Y)R_2]^{(2-n)-}$ and complexes, $[MCl(P_AR'_3)\{Ph_2P_BCH_nP_C(Y)PR_2\}]^{(n-1)+}$*

M	Y	R	R′	*n*	StereoChem	Notes	δ(PCP) (ppm)	^1J(C—P(Y)) (Hz)	^1J(C—PPh$_2$) (Hz)	δ(^{195}Pt) (ppm)	Ξ(^{195}Pt) (MHz)
	O	Ph		2		a	31.25	68.0	33.3		
	S	Ph		2		a	34.94	54.6	31.8		
	S	Ph		1		b	19.65	115.6	18.0		
	S	Pr^i		2		a	27.67	53	35		
	S	Bu^t		2		a	24.63	39.2	30.6		
	Se	Ph		2		a	35.18	47.2	32.4		
Pt	S	Ph	Et	2	*cis*	a,d	45.03	49.8	34.8	−78.10	21.398329
Pt	S	Ph	Et	1	*cis*	c	31.75	114.5	48.8	−50.93	21.398910
Pt	S	Pr^i	Et	2	*cis*	a,d	38.41	~39	~39	−53.16	21.398862
Pd	S	Ph	Et	2	*cis*	a,e	47.04	50.1	26.5		
Pd	S	Pr^i	Et	2	*cis*	a,d	39.38	39.2	29.8		
Pt	Se	Ph	Et	2	*cis*	a,e,f	46.53	44.7	34.7	−131.22	21.397192
Pt	Se	Ph	Et	1	*cis*	c	34.19	103.8	84.9	−100.86	21.397842
Pt	Se	Ph	Bu^n	2	*cis*	a,e,f	~47			−108.58	21.397676
Pd	Se	Ph	Et	2	*cis*	a,e,g	48.36	44.6	27.6		
Pt	S	Ph	Et	1	*trans*	c,h				108.05	21.402312
Pt	S	Bu^t	Et	2	*trans*	a,d	27.23	37.0	26.4	119.40	21.402555
Pd	S	Pr^i	Et	2	*trans*	a,d	29.08	40.9	18.3		
Pt	Se	Ph	Et	2	*trans*	a,e,f	~34			−48.62	21.398960
Pt	Se	Ph	Bu^n	2	*trans*	a,e,f	34.23	47.4	25.8	−29.10	21.399377
$[Ph_2P(S)CH_2PPr^i_2]$						a	26.73	56.4	37.8		
trans-$[PtCl(PEt_3)\{Ph_2P(S)CH_2PPr^i_2\}]^+$						a,e	21.58	57.1	18.4	−154.99	21.403317
trans-$[PtCl(PEt_3)\{Bu^t_2PCH_2P(O)Me_2\}]^+$						a,d,i				1080.29	21.423118

*The labelling scheme is shown in structures **5** and **6**. Chemical shifts (δ) are quoted in ppm relative to tetramethylsilane for ^{13}C or to 21.4 MHz for ^{195}Pt. Coupling constants (*J*) are in Hz.

†*a*, $CDCl_3$ solution; *b*, lithium salt, d_8-tetrahydrofuran solution; *c*, C_6D_6 solution; *d*, ClO_4^- salt; *e*, BF_4^- salt; *f*, in ^{13}C spectra of the *cis*/*trans* mixtures, $[PtCl(PEt_3)\{Ph_2PCH_2P(Se)Ph_2\}]^+$ and $[PtCl(PBu^n_3)\{Ph_2PCH_2P(Se)Ph_2\}]^+$, the principal peaks were due to the *cis*-Et and *trans*-Bu^n compounds but very weak peaks at ~34 and ~47 ppm, respectively, were probably due to the other isomers; *g*, a very weak ^{13}C resonance at ~36 ppm was probably due to the *trans* isomer; *h*, ^{13}C spectrum was too weak to observe; *i*, ^{13}C spectrum was not recorded.

TABLE 3. Selenium-77 nuclear magnetic resonance parameters for $[Ph_2PCH_2P(Se)Ph_2]$ and the complexes, $[MCl(P_AR'_3)\{Ph_2P_BCH_nP_C(Se)PPh_2\}]^{(n-1)+}$*

M	R′	*n*	StereoChem	Notes	δ(^{77}Se) (ppm)	Ξ(^{77}Se) (MHz)	^1J(Se—Pt) (Hz)	^1J(Se—P$_C$) (Hz)	^2J(Se—P$_A$) (Hz
Pt	Et	2	*cis*	a,c	+36.17	19.072213	249	510	104
Pt	Et	1	*cis*	b	+166.62	19.074701	127	421.2	102.9
Pd	Et	2	*cis*	a,c	+72.61	19.072908		524	125
Pt	Bu^n	2	*trans*	a,c	−6.81	19.071393	190	501	22
Pd	Et	2	*trans*	a,c	+21.87	19.071940		514	d
$Ph_2PCH_2P(Se)Ph_2$				b	−283.35	19.066119		730	

*The labelling scheme is shown in structures **5** and **6**. Chemical shifts (δ) are quoted in ppm relative to $Se(CH_3)_2$ at 19.071523 MHz. Coupling constants (*J*) are in Hz.

†*a*, $CDCl_3$ solution; *b*, C_6D_6 solution; *c*, BF_4^- salt; *d*, not resolved.

The data also enable us to establish a *trans* influence order for the P(Y) groups. Thus in *cis*-$[PtCl(PEt_3)\{Ph_2PCH_2P(Y)Ph_2\}]^+$ complexes, the ^1J(Pt—P$_A$) couplings *trans* to the coordinated Y atom are Y = O, 3959; Y = S, 3061; Y = Se, 3035 Hz; indicating that the *trans* influence order is Se > S ≫ O.

(*ii*) Deprotonation of the initial complexes results in several effects. The couplings, ^2J(P$_B$—C—P$_C$), ^1J(P$_C$(Y)—C), and ^2J(Pt—Y—P$_C$) all increase and the carbon of the P$_B$—C—P$_C$ group becomes more shielded. For example these parameters change from 25.4, 49.8, <10 Hz, and 45.03 ppm, respectively, in *cis*-$[PtCl(PEt_3)\{Ph_2PCH_2P(S)Ph_2\}]^+$ to 80.5, 114.5, 41.9 Hz, and 31.75 ppm, in the corresponding neutral complex, *cis*-$[PtCl(PEt_3)\{Ph_2PCHP(S)Ph_2\}]$. These changes are consistent with the increased electron density being located primarily in the C—P$_C$—Y region of the molecule and indicate contributions from both resonance forms of the ligand: Ph_2P—C$^-$(H)—P(=S)R$_2$ and Ph_2P—C(H)=P(—S$^-$)R$_2$.

(*iii*) Variation of the substitution pattern of the $[Ph_2PCH_2P(Y)R_2]$ ligand affects mainly δ(P$_C$) and ^2J(P$_B$—C—P$_C$) with other parameters being little changed. Increased shielding of P$_C$(Y) is accompanied by increased coupling in the sequences O ≪ S < Se and Bu^t < Pr^i ≪ Ph.

2. Phosphorus-31 NMR spectra

(i) cis *complexes*

These spectra basically consist of three doublets of doublets,

Can. J. Chem. Downloaded from www.nrcresearchpress.com by 93.93.197.157 on 09/07/12
For personal use only.

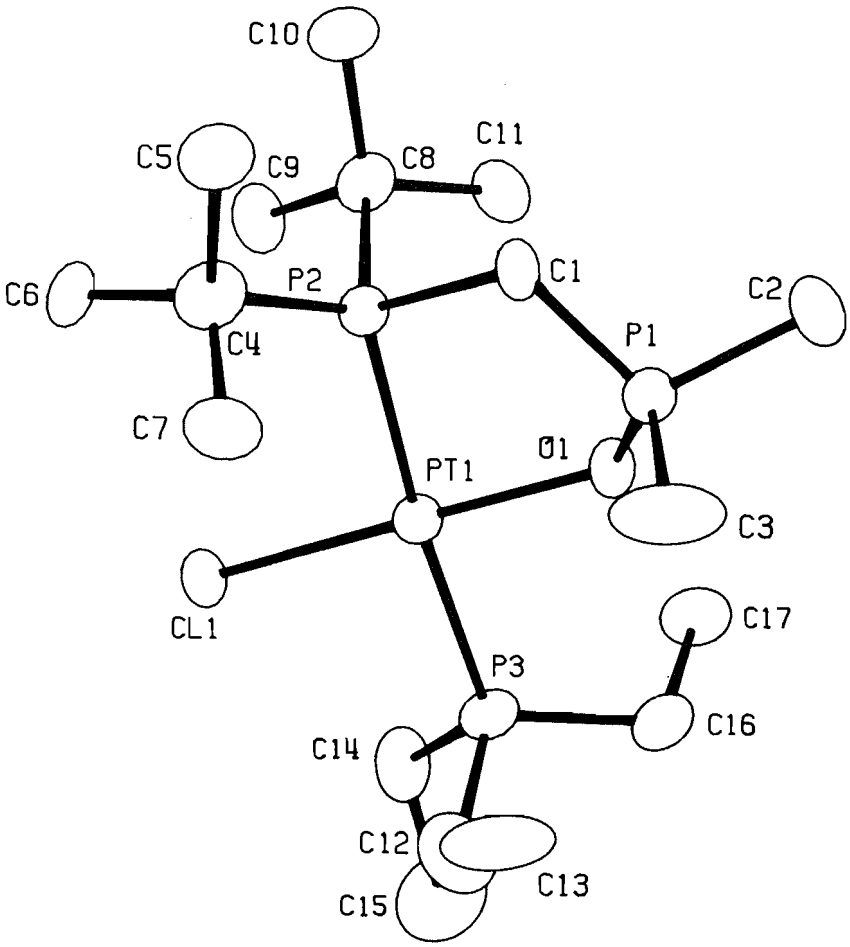

FIG. 1. ORTEP plot of compound **I**, *trans*-[PtCl(PEt$_3$){Bu$^t_2$PCH$_2$P(O)Me$_2$}][ClO$_4$].

easily analyzed as first order AMX spin systems but somewhat more difficult to assign to the appropriate phosphorus atoms in the molecules. For example, in *cis*-[PtCl(PEt$_3$){Ph$_2$PCH$_2$P(S)Ph$_2$}]$^+$ the three doublets of doublets occur at 12.67, 17.30, and 49.86 ppm relative to H_3PO_4. Using the labelling shown in structure **5** the resonance at 49.86 ppm is unambiguously assigned to P_C by the absence of any large (one-bond) coupling to ^{195}Pt, but the problem is to distinguish P_A and P_B. A PPh$_2$ group coordinated in a five-membered ring is expected to undergo a large deshielding coordination shift (up to 60 ppm) (13). Since the PPh$_2$ group in the uncoordinated ligand occurs at −27.87 ppm, this suggests that the more deshielded resonance (17.30 ppm) is the PPh$_2$ group (P_B). This assignment then gives 12.67 ppm for the PEt$_3$ ligand (P_A), consistent with values in similar complexes (e.g. [Pt$_2$Cl$_4$(PEt$_3$)$_2$] at 11.85 ppm). We also obtain $^2J(P_B—P_C) > {}^3J(P_A—P_C)$, as expected for a two bond relative to a three bond coupling and consistent with the large value (76.2 Hz) of $^2J(P_B—P_C)$ in the uncoordinated ligand. Finally, when the complex is deprotonated to form *cis*-[PtCl(PEt$_3$){Ph$_2$PCHP(S)Ph$_2$}] the only really significant change in NMR parameters is an increase in the value of $^2J(P_B—P_C)$ from 25.4 to 80.5 Hz, thus confirming the complete assignment.

For the *cis* palladium complexes the assignments are made slightly more difficult by the absence of a suitable magnetically active metal isotope, but the normal expectation (14*b*) is that palladium phosphorus complexes are deshielded relative to their platinum analogs (e.g. in our work [Pd$_2$Cl$_4$(PEt$_3$)$_2$] is at 48.42 ppm relative to its Pt analog at 11.85 ppm). Thus for *cis*-[PdCl(PEt$_3$){Ph$_2$PCH$_2$P(S)Ph$_2$}]$^+$, assignment of P_A and P_B at 32.18 and 37.73 ppm, respectively, is consistent with deshielding from the above platinum analog. Moreover, when the substituent at the P(S) group is changed from Ph to Pr^i to Bu^t the most significant NMR changes are in $\delta(P_C)$, 48.52 to 80.07 to 90.95 ppm, and $^2J(P_B—P_C)$, 31.6 to 16.1 to 10.0 Hz, thus confirming the assignments of P_B and P_C.

(ii) trans *complexes*

These spectra are basically similar to those of the *cis* complexes except that, using the labelling of structure **6**, P_A and P_B are now closely coupled because of the large two-bond *trans* coupling, and the spectra appear as ABX spin systems. These were fully analyzed by computer simulation in all cases and the large $^2J(P_A—P_B)$ values in these *trans* complexes form the major basis of our stereochemical assignments. The problem of distinguishing between P_A and P_B is similar to that in the *cis* complexes and the arguments are similar to those above. Most importantly in, for example *trans*-[PtCl(PEt$_3$){Ph$_2$PCH$_2$P(S)Ph$_2$}]$^+$, it is the resonance at 20.75 ppm whose coupling to P_C changes dramatically (from 54.6 to 117.0 Hz) on deprotonation, thus establishing this coupling as $^2J(P_B—P_C)$ and $\delta(P_B)$ as 20.75 ppm.

(iii) [Pt(PEt$_3$)$_2${*Ph$_2$CH$_2$P(O)Ph$_2$*}*]*

Relatively little information can be obtained from the ^{31}P NMR spectrum of this complex because the large *trans* ^2J(P—Pt—P) coupling produces a deceptively simple pattern even at 101.3 MHz. The phosphorus of the PEt$_3$ group *trans* to

Can. J. Chem. Downloaded from www.nrcresearchpress.com by 93.93.197.157 on 09/07/12
For personal use only.

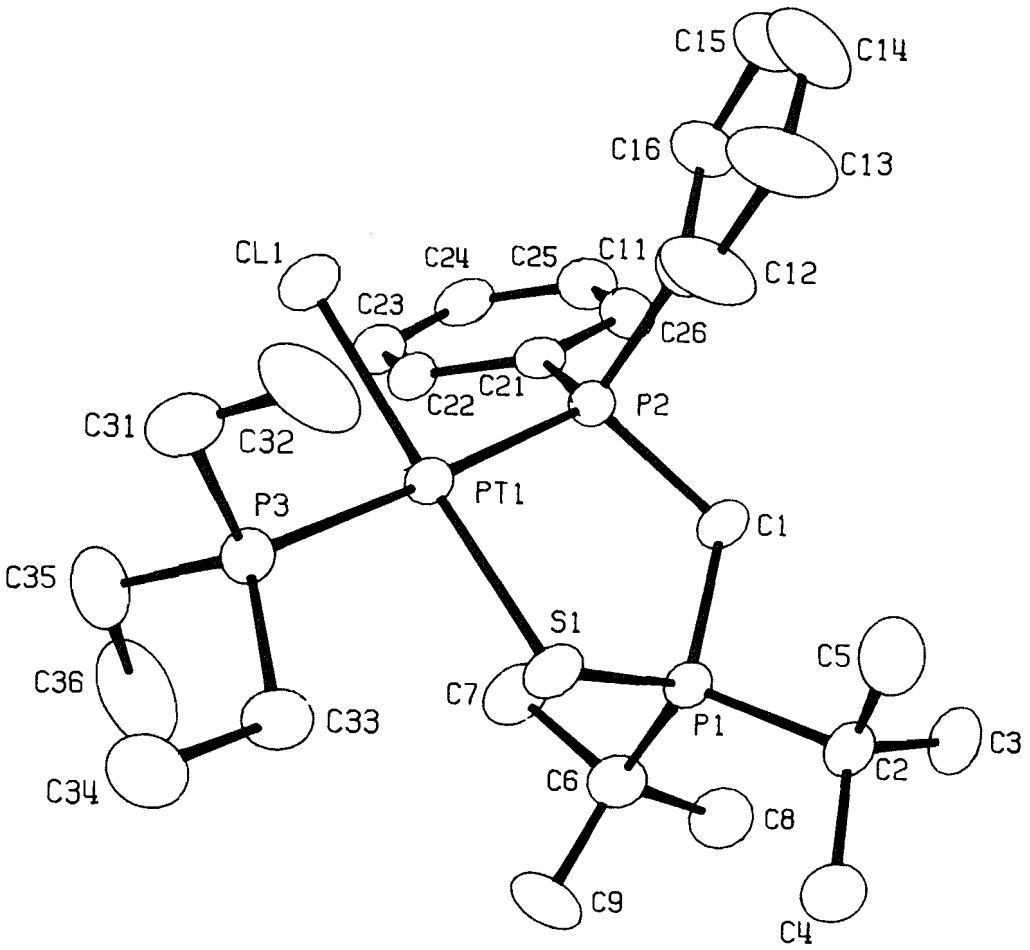

FIG. 2. ORTEP plot of compound **II**, *trans*-[PtCl(PEt$_3$){Ph$_2$PCH$_2$P(S)Bu$^t_2$}][ClO$_4$].

oxygen appears at 0.88 ppm as a triplet (19.8 Hz) due to two averaged couplings, ^2J(P—M—P)$_{cis}$. The phosphorus of the P(O) group is a similarly averaged triplet (16.8 Hz) at 71.58 ppm, and the mutually *trans* phosphorus atoms of the PPh$_2$ group and the remaining PEt$_3$ appear centred at 25.55 ppm as two closely spaced triplets (18.3 Hz). These are probably the centre lines of a closely coupled AB spin system, with the triplet structure arising from averaged couplings to the other two phosphorus atoms. The weak outer lines of the AB system are not observed and hence the individual chemical shifts and the ^2J(P—M—P)$_{trans}$ coupling cannot be obtained. The spectrum also shows ^{195}Pt sidebands which yield ^1J(Pt—PEt$_3$)$_{trans\ to\ O}$, 3561 Hz; ^1J(Pt—PEt$_3$)$_{trans\ to\ P}$ and ^1J(Pt—PPh$_2$), 2350 and 2460 Hz. For the latter pair it is not possible to say which is which, and finally ^2J(Pt—P(O)) is not resolved.

3. ^{13}C, ^{77}Se, and ^{195}Pt NMR spectra

In general these were simple first order spectra and assignments presented no particular problems. In the ^{13}C spectra the larger of the two couplings to the P—CH$_n$—P(Y) carbon was assigned to the coupling to the P(Y) phosphorus on the basis of previous results (3). The electronegative chalcogenide substituent is expected to raise the effective nuclear charge at phosphorus and also to modify the phosphorus hybridization so as to raise *s* orbital participation in the C—P bond. The ^{195}Pt spectra showed the expected first order patterns from coupling to phosphorus and served mainly to confirm the ^{31}P assignments.

The ^{77}Se spectra (Table 3) were mostly simple patterns with doublet coupling due to ^1J(Se—P$_C$), doubled again by ^2J(Se—M—P$_A$) and with first order ^{195}Pt sidebands. The $^{2/3}J$(Se—P$_B$) couplings were not resolved. As expected ^2J(Se—M—P$_A$) is much larger when the two atoms are mutually *trans*. The only complication is in the spectrum of *cis*-[PtCl(PEt$_3$){Ph$_2$PCHP(Se)Ph$_2$}], where increased ^2J(P$_B$—C—P$_C$) coupling combined with a reduced value for ^1J(Pt—Se) results in a complex non-first order multiplet. Computer simulation of the spectrum was successful using the parameters given in Tables 1 and 3, with the addition of $^{2/3}J$(Se—P$_B$) = −4 Hz and with the use of negative signs for ^2J(P$_A$—P$_B$) and ^3J(P$_A$—P$_C$). However, considerable caution is necessary since this may not be a unique solution.

(C) X-Ray crystal structures

The atom labelling schemes and structures of single cations of compounds **I**, *trans*-[PtCl(PEt$_3$){Bu^{t}PCH$_2$P(O)Me$_2$}][ClO$_4$], and **II**, *trans*-[PtCl(PEt$_3$){Ph$_2$PCH$_2$P(S)Ph$_2$}][ClO$_4$], are shown in Figs. 1 and 2, respectively. Fractional atomic coordinates and isotropic temperature parameters, bond lengths and bond angles are collected in Tables 4–7, and further Tables have been deposited, including: structure factors, anisotropic temperature parameters, complete bond lengths and angles, and selected intermolecular distances.[2]

[2]Copies of these tables may be purchased from the Depository of Unpublished Data, CISTI, National Research Council of Canada, Ottawa, Ont., Canada K1A 0S2.

Can. J. Chem. Downloaded from www.nrcresearchpress.com by 93.93.197.157 on 09/07/12
For personal use only.

Can. J. Chem. Downloaded from www.nrcresearchpress.com by 93.93.197.157 on 09/07/12
For personal use only.

TABLE 4. Fractional atomic coordinates and temperature parameters for compound **I**, *trans*-[PtCl(PEt$_3$){Bu$^t_2$PCH$_2$P(O)Me$_2$}][ClO$_4$]*

Atom	x/a	y/b	z/c	U_{eq}†
Pt (1)	30167 (4)	457 (6)	−22617 (5)	508 (3)
Cl (1)	3854 (4)	1310 (4)	−2650 (4)	68 (2)
P (1)	1433 (4)	−932 (4)	−1712 (4)	61 (2)
P (2)	2513 (3)	880 (4)	−1026 (4)	49 (2)
P (3)	3395 (4)	−899 (4)	−3482 (4)	65 (2)
O (1)	2342 (9)	−1133 (9)	−1911 (11)	67 (6)
C (1)	1499 (11)	175 (14)	−965 (14)	59 (7)
C (2)	1155 (18)	−1957 (17)	−1004 (20)	103 (14)
C (3)	542 (16)	−763 (23)	−2888 (18)	117 (13)
C (4)	2071 (14)	2179 (16)	−1335 (18)	79 (10)
C (5)	1449 (15)	2510 (16)	−626 (19)	88 (11)
C (6)	2887 (15)	2917 (14)	−1176 (18)	84 (11)
C (7)	1526 (15)	2148 (17)	−2455 (15)	77 (9)
C (8)	3315 (13)	737 (15)	245 (16)	63 (8)
C (9)	4242 (13)	1187 (15)	241 (17)	76 (9)
C (10)	2979 (15)	1201 (17)	1126 (16)	84 (10)
C (11)	3469 (15)	−401 (15)	449 (17)	65 (9)
C (12)	2751 (21)	−549 (20)	−4757 (20)	108 (14)
C (13)	1759 (19)	−455 (25)	−4880 (20)	121 (14)
C (14)	4566 (18)	−748 (19)	−3576 (22)	106 (14)
C (15)	4726 (20)	−1292 (26)	−4493 (28)	166 (21)
C (16)	3258 (16)	−2205 (17)	−3367 (20)	93 (12)
C (17)	3830 (16)	−2651 (17)	−2328 (20)	93 (12)
Cl (2)	−1188 (4)	763 (6)	−1899 (5)	87 (3)
O (2)	−605 (13)	1125 (16)	−2375 (19)	168 (14)
O (3)	−836 (18)	−76 (18)	−1354 (22)	206 (18)
O (4)	−1378 (27)	1324 (26)	−1275 (21)	322 (27)
O (5)	−1908 (20)	503 (34)	−2648 (23)	301 (24)

*Estimated standard deviations are given in parentheses. Coordinates $\times 10^n$ where $n = 5$ for Pt and 4 otherwise; temperature parameters $\times 10^n$ where $n = 4$ for Pt and 3 otherwise.

†U_{eq} = the equivalent isotropic temperature parameter = $(1/3)\ \Sigma_i\Sigma_j U_{ij} a_i^* a_j^* (\boldsymbol{a}_i \cdot \boldsymbol{a}_j)$.

In both structures the $R_2PCH_2P(Y)R'_2$ ligand coordinates via phosphorus and the Y atom so as to form a five-membered chelate ring. The platinum coordination is closely square-planar with all five atoms of the coordination plane within −0.036 to +0.038 Å of the least squares plane for **I**, and within −0.10 to +0.02 Å for **II**. The chelate ligands lie in twisted conformations so that P(1) is above the coordination plane, 0.763 Å for **I** and 0.524 Å for **II**. The associated Pt(1)—Y—P(1) angles are 117.3(7) and 107.2(1)°, respectively, and the twist also raises C(1) above the coordination plane by 0.677 Å for **I** and by 0.174 Å for **II**. The chelate ligand geometries are closely similar with respective values of P(1)—C(1), 1.80(2) and 1.824(7) Å, P(2)–C(1), 1.87(2) and 1.860(7) Å, and P(1)—C(1)—P(2), 108.7(9) and 112.8(4)°. The bond lengths are within the normal ranges for P—C single bonds (ref. 15, p. 7). The precise character of the P—Y bonds is more problematical. Some lengthening of these bonds on coordination is expected (16) and previous authors have suggested that a P—S bond of 2.013(2) Å in a palladium complex of P(S)Et$_2$Ph is long enough to suggest extensive participation of the R_3P^+—S^- resonance form rather than $R_3P{=}S$ (17). Among simple phosphorus compounds, the lengths for P—O bonds in P_4O_{10}, 1.604 (single) and 1.439 (double), and for P—S bonds in P_4S_{10}, 2.097 (single) and 1.908 (double), appear to be fairly typical (ref. 15, pp. 7, 65, 74). Thus, the distances observed in the present complexes, P—O 1.536(13), and P—S 2.045(2) Å, are rather closer to single bond rather than double bond lengths. The most closely comparable complex in the literature is probably, [CuCl{Ph$_2$P(S)CH$_2$P(S)Ph$_2$}], in which the P—S lengths are 1.970(2) and 1.974(3) Å (18).

Within the coordination sphere, the relative strengths of the Pt—S and Pt—O bonds are of interest in that platinum is expected to be more strongly bound by the soft sulphur base than by the harder oxygen base. Comparison of the P—O and P—S lengths (1.536(13) and 2.045(2) Å, respectively) suggests that the covalent radius of S is greater than that of O by about 0.5Å. However, the Pt—S bond (2.282(2) Å) is only 0.24 Å longer than the Pt—O bond (2.044(11) Å), consistent with a relatively greater strength for the Pt—S bond. This greater strength for the Pt—S bond is also reflected in the trans influence sequence S ≫ O, which has been demonstrated above by the ^{31}P coupling constants. In the structural data the trans influence is shown by the Pt—Cl lengths 2.304(2) Å (*trans* to O) and 2.326(2) Å (*trans* to S).

Experimental section

(A) Synthetic and spectroscopic studies

Data relating to the characterization of the complexes are given in the Tables, the Results section and in the preparative descriptions below. Microanalysis was by the Canadian Microanalytical Service, Vancouver, B.C., Canada. ^{31}P nuclear magnetic resonance spectra were recorded in appropriate solvents (Table 1) at either 24.3 MHz using a Nicolet TT14 Fourier transform spectrometer with a Varian HA60 magnet and an external C_6D_6 lock signal or at 101.3 MHz using a Bruker WM250 Fourier transform spectrometer locked to the solvent deuterium resonance. ^{13}C, ^{77}Se, and ^{195}Pt spectra were recorded at 62.9, 47.7, and 53.5 MHz, respectively, in $CDCl_3$ solution using the Bruker instrument. For all nuclei protons were decoupled by broad band ("noise") irradiation at appropriate frequencies. ^{31}P chemical shifts were measured relative to external P(OMe)$_3$ and are reported in parts per million relative to 85% H_3PO_4 using a conversion factor of +141 ppm. ^{13}C, ^{77}Se, and ^{195}Pt chemical shifts are reported in ppm relative to Si(CH$_3$)$_4$, Se(CH$_3$)$_2$ (19.071523 MHz (19),[3] and $\Xi(^{195}Pt)$ = 21.4 MHz (20), respectively. Positive values are deshielded relative to the references. Simulated NMR spectra were calculated on an IBM 3031 computer and plotted on a Calcomp 1039 plotter. The programs used were a locally constructed package based on the UEAITR and NMRPLOT programs from the literature (21, 22).

All operations were carried out at ambient temperature (ca. 25°C) under an atmosphere of dry nitrogen using standard Schlenk tube techniques. Solvents were dried by reflux over appropriate reagents (calcium hydride for dichloromethane, molecular sieves or K_2CO_3 for acetone, and potassium/benzophenone for diethyl ether, tetrahydrofuran, toluene, benzene, and hexane) and were distilled under nitrogen prior to use. Recrystallizations from solvent pairs were by dissolution of the complex in the first solvent (using about double the volume required for complete solution) followed by dropwise addition of sufficient second solvent to cause turbidity at ambient temperature. Crystallization was then completed either by continued very slow dropwise addition of the second solvent or, in those cases where a temperature is indicated in the detailed descriptions below, by setting the mixture aside at a reduced temperature.

The complexes, [M$_2$Cl$_4$(PR$_3$)$_2$], M = Pt, R = Et or Bu^n, or M = Pd, R = Et (23) and the ligands [Ph$_2$PCH$_2$P(Y)Ph$_2$], Y = O, S, or Se, and [Ph$_2$P(S)CH$_2$PPr$^i_2$] were prepared as previously described (1–3). The ligands [Ph$_2$PCH$_2$P(S)R$_2$], R = Pr^i or Bu^t, were obtained by reaction of the known diphosphines, [Ph$_2$PCH$_2$PR$_2$] (24), with one mole equivalent of elemental sulphur under reflux in benzene for 2 h.

[3]This value is misquoted as 19.091523 MHz in the widely used secondary reference, C. Mcfarlane and W. McFarlane. *In* NMR and the Periodic Table. *Edited by* R. K. Harris and B. E. Mann. Academic Press, London. 1978. p. 402.

TABLE 5. Selected interatomic distances (Å) and bond angles (deg) for compound **I**, *trans*-[PtCl(PEt$_3$){Bu$^t_2$PCH$_2$P(O)Me$_2$}][ClO$_4$]*

Atoms		Distance	Atoms			Angle
Cl (1)	—Pt (1)	2.304 (4)	P (2)	—Pt (1)	—Cl (1)	97.2 (2)
P (2)	—Pt (1)	2.332 (5)	P (3)	—Pt (1)	—Cl (1)	88.7 (2)
P (3)	—Pt (1)	2.297 (5)	P (3)	—Pt (1)	—P (2)	173.8 (2)
O (1)	—Pt (1)	2.044 (11)	O (1)	—Pt (1)	—Cl (1)	176.4 (4)
O (1)	—P (1)	1.536 (13)	O (1)	—Pt (1)	—P (2)	85.3 (4)
C (1)	—P (1)	1.80 (2)	O (1)	—Pt (1)	—P (3)	88.9 (4)
C (2)	—P (1)	1.81 (2)	C (1)	—P (1)	—O (1)	109.6 (7)
C (3)	—P (1)	1.82 (2)	C (1)	—P (1)	—C (3)	107.5 (11)
C (1)	—P (2)	1.87 (2)	C (1)	—P (1)	—C (2)	109.2 (10)
C (4)	—P (2)	1.90 (2)	C (2)	—P (1)	—O (1)	108.8 (10)
C (8)	—P (2)	1.84 (2)	C (2)	—P (1)	—C (3)	109.1 (13)
C (12)	—P (3)	1.81 (3)	C (3)	—P (1)	—O (1)	112.7 (10)
C (14)	—P (3)	1.88 (2)	C (1)	—P (2)	—Pt (1)	103.8 (6)
C (16)	—P (3)	1.80 (2)	C (4)	—P (2)	—Pt (1)	117.8 (7)
			C (4)	—P (2)	—C (1)	103.1 (9)
			C (8)	—P (2)	—Pt (1)	110.3 (7)
			C (8)	—P (2)	—C (1)	105.5 (9)
			C (8)	—P (2)	—C (4)	114.6 (10)
			C (12)	—P (3)	—Pt (1)	111.0 (9)
			C (14)	—P (3)	—Pt (1)	115.8 (8)
			C (14)	—P (3)	—C (12)	101.5 (14)
			C (16)	—P (3)	—Pt (1)	115.4 (8)
			C (16)	—P (3)	—C (12)	107.1 (13)
			C (16)	—P (3)	—C (14)	104.8 (11)
			P (1)	—O (1)	—Pt (1)	117.3 (7)
			P (2)	—C (1)	—P (1)	108.7 (9)

*Estimated standard deviations are given in parentheses.

Can. J. Chem. Downloaded from www.nrcresearchpress.com by 93.93.197.157 on 09/07/12
For personal use only.

Colourless crystals of the monosulphide ligands were obtained in yields ranging from 60–80% by recrystallization from ethanol.

The lithium salts Li[Ph$_2$PCHP(Y)R$_2$], Y = S, R = Ph, Pr^i, Bu^t, Y = O, R = Ph, were prepared by dropwise addition of a slight excess (ca. 1.1–1.2 molar equivalents) of *n*-butyl lithium (1.5 *M* in hexane) to stirred solutions of [Ph$_2$PCH$_2$P(Y)R$_2$] in tetrahydrofuran. ^{31}P and ^{13}C NMR spectra confirmed that the required anions were the sole phosphorus containing products.

^{31}P NMR data for the metal complexes used as starting materials were recorded in CH_2Cl_2 solution: [Pd$_2$Cl$_4$(PEt$_3$)$_2$], δ(P) +49.52 ppm, [Pt$_2$Cl$_4$(PEt$_3$)$_2$], δ(P) +11.85 ppm, *J*(Pt—P) 3832 Hz, [Pt$_2$Cl$_2$(PEt$_3$)$_4$][BF$_4$]$_2$, δ(P) +19.62 ppm, *J*(Pt—P) 3585 Hz. For the neutral ligands ^{31}P data were recorded in chloroform and for the anionic ligands in tetrahydrofuran. The following data are given in the order, δ(P)R$_2$ (ppm), δ(P(Y))R$_2$ (ppm), ^{2}*J*(PP) (Hz): [Ph$_2$PCH$_2$P(O)Ph$_2$], −28.12, +29.00, 51.3; [Ph$_2$PCHP(O)Ph$_2$]$^-$, −18.77, +38.99, 148.8; [Ph$_2$PCH$_2$P(S)Ph$_2$], −27.87, +40.38, 76.2; [Ph$_2$PCHP(S)Ph$_2$]$^-$, −10.22, +51.04, 162.7; [Ph$_2$PCH$_2$P(Se)Ph$_2$], −27.04, +30.76, 83.2; [Ph$_2$PCH$_2$P(S)Pr$^i_2$], −27.63, +66.20, 52.9; [Ph$_2$PCHP(S)Pr$^i_2$]$^-$, −13.04, +73.25, 139.7; [Ph$_2$PCH$_2$P(S)Bu$^t_2$], −24.64, +75.89, 52.8; [Ph$_2$PCHP(S)Bu$^t_2$]$^-$, −5.74, +89.37, 132.3. Many of these species have been reported previously and where ^{31}P data are available (1–3, 25), or data are in good agreement.

(1) [MCl(PR$_3$){R$'_2$PCH$_2$P(Y)PR$''_2$}][Z], M = Pt or Pd, R = Et or Bu^n, R$'$, R$''$ = Ph, Pr^i, or Bu^t, Y = S or Se, Z = BF$_4^-$ or ClO$_4^-$

These complexes were obtained by reaction of the appropriate ligand with a dinuclear metal complex, [M$_2$Cl$_4$(PR$_3$)$_2$], in the presence of NaClO$_4$.H$_2$O or NaBF$_4$. The procedures were all similar to the following representative example and yields were in the range 70–90% based on conversion of the metal dimers.

A solution of [Ph$_2$PCH$_2$P(S)Bu$'_2$] (0.171 g, 0.454 mmol) in acetone (10 mL) was added dropwise to a stirred solution of [Pt$_2$Cl$_4$(PEt$_3$)$_2$] (0.175 g, 0.227 mmol) and NaClO$_4$.H$_2$O (0.064 g, 0.457 mmol) in acetone (25 mL). After 2 h the mixture was filtered to remove precipitated NaCl and the solvent removed *in vacuo*. The residue was washed with diethyl ether and recrystallized from dichloromethane/diethyl ether to give *trans*-[PtCl(PEt$_3$){Ph$_2$PCH$_2$P(S)Bu$'_2$}][ClO$_4$] as pale yellow crystals (0.279 g, 0.338 mmol). *Anal.* calcd. for C$_{27}$H$_{45}$Cl$_2$O$_4$P$_3$PtS: C 39.3, H 5.50; found: C 39.2, H 5.45.

The representative example described above was obtained exclusively as the *trans* isomer, which we have designated as the isomer in which the two metal–phosphorus bonds are mutually *trans*. The other related complexes showed considerable variation in the isomer mixture obtained. Usually ^{31}P NMR spectra of the initial reaction products showed the presence of both possible isomers whereas the final crystals were often single isomers. In the characterization details given below the isomers are indicated as in the following example, Isomers: reaction mixture, *c*20/*t*80; crystals, *c*0/*t*100, where the numbers indicate percentages of *cis* and *trans* isomers.

[PtCl(PEt$_3$){Ph$_2$PCH$_2$P(S)Ph$_2$}][ClO$_4$]

Recrystallization: tetrahydrofuran/diethyl ether/−18°C. Isomers: reaction mixture, *c*100/*t*0; crystals, *c*100/*t*0 *Anal.* calcd. for C$_{31}$H$_{37}$Cl$_2$O$_4$P$_3$PtS: C 43.1, H 4.31; found: C 43.3, H 4.79.

[PtCl(PEt$_3$){Ph$_2$PCH$_2$P(S)Pr$^i_2$}][ClO$_4$]

Recrystallization: dichloromethane/diethyl ether/−18°C. Isomers: reaction mixture, *c*50/*t*50; crystals, *c*100/*t*0 *Anal.* calcd. for C$_{25}$H$_{41}$Cl$_2$O$_4$P$_3$PtS: C 37.7, H 5.19; found: C 37.9, H 5.12.

[PdCl(PEt$_3$){Ph$_2$PCH$_2$P(S)Ph$_2$}][BF$_4$]

Recrystallization: tetrahydrofuran/diethyl ether/−18°C. Isomers: reaction mixture, *c*60/*t*40; crystals, *c*60/*t*40 *Anal.* calcd. for C$_{31}$H$_{37}$BClF$_4$P$_3$PdS: C 48.8, H 4.89; found: C 49.0, H 4.75.

[PdCl(PEt$_3$){Ph$_2$PCH$_2$P(S)Pr$^i_2$}][ClO$_4$]

Recrystallization: dichloromethane/diethyl ether/−18°C. Isomers: reaction mixture, *c*50/*t*50; crystals, *c*50/*t*50 *Anal.* calcd. for C$_{25}$H$_{41}$Cl$_2$O$_4$P$_3$PdS: C 42.4, H 5.84; found: C 42.6, H 5.76.

[PdCl(PEt$_3$){Ph$_2$PCH$_2$P(S)Bu$^t_2$}][ClO$_4$]

Recrystallization: acetone/diethyl ether/−18°C. Isomers: reaction

Can. J. Chem. Downloaded from www.nrcresearchpress.com by 93.93.197.157 on 09/07/12
For personal use only.

TABLE 6. Fractional atomic coordinates and temperature parameters for compound **II**, *trans*-[PtCl(PEt$_3$){Ph$_2$CH$_2$P(S)Bu$^t_2$}][ClO$_4$]

Atom	x/a	y/b	z/c	U_{eq}
Pt (1)	60353 (2)	35780 (1)	28641 (2)	497 (1)
Cl (1)	5190 (1)	4801 (1)	2440 (2)	77 (1)
Cl (2)	971 (2)	3830 (1)	2139 (2)	76 (1)
S (1)	6873 (1)	2409 (1)	3413 (2)	71 (1)
P (1)	8106 (1)	2364 (1)	2951 (1)	53 (1)
P (2)	7419 (1)	4142 (1)	2581 (1)	49 (1)
P (3)	4589 (1)	3063 (1)	3107 (1)	60 (1)
O (1)	1564 (7)	4112 (7)	1626 (8)	198 (7)
O (2)	556 (10)	4427 (7)	2543 (9)	204 (7)
O (3)	152 (8)	3432 (7)	1708 (8)	198 (7)
O (4)	1462 (9)	3260 (10)	2756 (12)	273 (11)
C (1)	8465 (5)	3403 (4)	2753 (6)	63 (3)
C (2)	9157 (5)	1948 (5)	3868 (5)	68 (3)
C (3)	10151 (6)	2015 (6)	3639 (7)	89 (4)
C (4)	8951 (7)	1054 (6)	4062 (8)	112 (5)
C (5)	9219 (8)	2488 (7)	4715 (6)	103 (5)
C (6)	7808 (7)	1778 (5)	1885 (5)	77 (3)
C (7)	7150 (8)	2358 (6)	1145 (6)	94 (4)
C (8)	8793 (8)	1546 (6)	1619 (7)	89 (4)
C (9)	7192 (8)	1008 (6)	1945 (7)	106 (5)
C (11)	7936 (5)	4931 (4)	3398 (5)	63 (3)
C (12)	7889 (11)	4811 (7)	4254 (7)	123 (6)
C (13)	8271 (12)	5402 (7)	4928 (7)	144 (7)
C (14)	8558 (10)	6138 (8)	4738 (8)	123 (6)
C (15)	8522 (9)	6316 (6)	3863 (9)	107 (5)
C (16)	8195 (7)	5728 (5)	3152 (7)	87 (4)
C (21)	7283 (5)	4541 (4)	1463 (4)	53 (2)
C (22)	6363 (5)	4441 (4)	804 (4)	57 (2)
C (23)	6266 (6)	4707 (5)	−59 (5)	67 (3)
C (24)	7060 (6)	5094 (4)	−276 (5)	71 (3)
C (25)	7988 (6)	5195 (5)	378 (6)	74 (3)
C (26)	8095 (5)	4903 (4)	1245 (5)	65 (3)
C (31)	4018 (7)	3758 (5)	3753 (8)	98 (5)
C (32)	4752 (11)	3913 (9)	4694 (9)	146 (7)
C (33)	4699 (7)	2081 (5)	3687 (7)	89 (4)
C (34)	3729 (8)	1776 (7)	3843 (8)	110 (5)
C (35)	3650 (7)	2916 (7)	2046 (7)	100 (4)
C (36)	4012 (10)	2314 (10)	1451 (8)	155 (7)

*Estimated standard deviations are given in parentheses; coordinates $\times 10^n$ where $n = 5$ for Pt and 4 otherwise; temperature parameters $\times 10^n$ where $n = 4$ for Pt and 3 otherwise.

†U_{eq} = the equivalent isotropic temperature parameter = $(1/3)\,\Sigma_i\Sigma_j U_{ij} a^* a_j^* (\boldsymbol{a}_i \cdot \boldsymbol{a}_j)$.

mixture, *c*60/*t*40; crystals, *c*100/*t*0 *Anal.* calcd. for $C_{27}H_{45}Cl_2O_4P_3PdS$: C 44.1, H 6.16; found: C 43.4, H 5.97.

[PtCl(PEt$_3$){Ph$_2$PCH$_2$P(Se)Ph$_2$}][BF$_4$]

Recrystallization: tetrahydrofuran/diethyl ether/25°C. Isomers: reaction mixture, *c*80/*t*20; crystals, *c*80/*t*20 *Anal.* calcd. for $C_{31}H_{37}BClF_4P_3PtSe$: C 41.4, H 4.15; found: C 42.1, H 4.10.

[PtCl(PBu$^n_3$){Ph$_2$PCH$_2$P(Se)Ph$_2$}][BF$_4$]

Recrystallization: tetrahydrofuran/diethyl ether/25°C. Isomers: reaction mixture, *c*20/*t*80; crystals, *c*20/*t*80 *Anal.* calcd. for $C_{37}H_{49}BClF_4P_3PtSe$: C 45.2, H 5.02; found: C 45.2, H 4.92.

[PdCl(PEt$_3$){Ph$_2$PCH$_2$P(Se)Ph$_2$}][BF$_4$]

Recrystallization: tetrahydrofuran/diethyl ether/25°C. Isomers: reaction mixture, *c*70/*t*30; crystals, *c*70/*t*30 *Anal.* calcd. for $C_{31}H_{37}BClF_4P_3PdSe$: C 46.0, H 4.60; found: C 46.4, H 4.77.

[PtCl(PEt$_3$){Ph$_2$P(S)CH$_2$PPr$^i_2$}][BF$_4$]

Recrystallization: tetrahydrofuran/diethyl ether/25°C. Isomers: reaction mixture, *c*0/*t*100; crystals, *c*0/*t*100 *Anal.* calcd. for $C_{25}H_{41}BClF_4P_3PtS$: C 38.3, H 5.27; found: C 38.3, H 5.07.

(2) [Ph$_2$PCH$_2$P(O)Ph$_2$] complexes

(*i*) A preparation of [PtCl(PEt$_3$){Ph$_2$PCH$_2$P(O)Ph$_2$}][ClO$_4$] was attempted by reacting the ligand with [Pt$_2$Cl$_4$(PEt$_3$)$_2$] in a procedure similar to (*1*) above for the sulphur analog. In this case, however, the products were more complex. The initial product in all reactions, both in the presence of NaClO$_4$ and with no added salts, was shown by ^{31}P NMR to be *trans*-[PtCl$_2$(PEt$_3$){Ph$_2$PCH$_2$P(O)Ph$_2$}]. A crystalline sample of this yellow product was obtained as the first precipitate in a fractional crystallization from acetone/pentane in the presence of NaClO$_4$. The second (colourless) precipitate in this procedure was *cis*-[PtCl(PEt$_3$){Ph$_2$PCH$_2$P(O)Ph$_2$}][ClO$_4$].

During work-up procedures, but before the fractional crystallization, the solutions also showed ^{31}P NMR evidence for a third product, *cis*-[PtCl$_2$(PEt$_3$){Ph$_2$PCH$_2$P(O)Ph$_2$}], which could not be isolated in crystalline form.

trans-*[PtCl$_2$(PEt$_3$){Ph$_2$PCH$_2$P(O)Ph$_2$}]*

Anal. cald. for $C_{31}H_{37}Cl_2OP_3Pt$: C 47.5, H 4.75; found: C 47.8, H 4.84%. Melting point 146–148°C.

cis-*[PtCl(PEt$_3$){Ph$_2$PCH$_2$P(O)Ph$_2$}][ClO$_4$]*

Anal. calcd. for $C_{31}H_{37}Cl_2O_5P_3Pt$: C 43.9, H 4.40, Cl 8.4; found: C 44.3, H 4.50, Cl 8.8. Melting point 250–252°C.

(ii) [Pt(PEt$_3$)$_2${Ph$_2$PCH$_2$P(O)Ph$_2$}][ClO$_4$]$_2$

A solution of [Ph$_2$PCH$_2$P(O)Ph$_2$] (0.25 g, 0.62 mmol) in CH$_2$Cl$_2$/acetone (10 mL) was added dropwise to a stirred solution of [Pt$_2$Cl$_2$(PEt$_3$)$_4$][ClO$_4$]$_2$ (0.35 g, 0.31 mmol) and NaClO$_4$.H$_2$O (0.20 g, 1.4 mmol) in CH$_2$Cl$_2$/acetone (25 mL). After 15 h the mixture was filtered to remove precipitated NaCl and the solvent removed *in vacuo*. The residue was extracted into dichloromethane and crystallized by addition of diethyl ether to give [Pt(PEt$_3$)$_2${Ph$_2$PCH$_2$P(O)Ph$_2$}]-[ClO$_4$]$_2$.CH$_2$Cl$_2$. Recrystallization: dichloromethane/diethyl ether. *Anal.* calcd. for $C_{38}H_{54}Cl_4O_9P_4Pt$: C 40.9, H 4.88; found: C 40.8, H 5.00. Melting point 252–253°C.

(3) trans-*[PtCl(PEt$_3$){Bu$^t_2$PCH$_2$P(O)Me$_2$}][ClO$_4$]*

This complex was prepared by inadvertent oxidation of the ligand during some related work with [Bu$^t_2$PCH$_2$PMe$_2$] complexes.

A solution of [Bu$^t_2$PCH$_2$PMe$_2$] (0.33 g, 1.5 mmol) in acetone (15 mL) with NaClO$_4$.H$_2$O (0.18 g, 1.3 mmol) was added dropwise to a stirred solution of [Pt$_2$Cl$_4$(PEt$_3$)$_2$] (0.28 g, 0.36 mmol) in acetone (25 mL). After 6 h the solvent was removed *in vacuo* and the residue extracted with dichloromethane. Dropwise addition of hexane to the extract yielded an oily first precipitate which was discarded and a crystalline second precipitate. The second precipitate was extracted into benzene, the solvent removed *in vacuo* and the resulting residue recrystallized from dichloromethane/hexane to give *trans*-[PtCl(PEt$_3$){Bu$^t_2$PCH$_2$P(O)Me$_2$}][ClO$_4$] as pale yellow crystals. *Anal.* calcd. for $C_{17}H_{41}Cl_2O_5P_3Pt$: C 29.8, H 6.04; found: C 29.1, H 5.86.

(4) [Ph$_2$PCHP(Y)R$_2$]$^-$ complexes

(i) [PtCl(PEt$_3$){Ph$_2$PCHP(S)Ph$_2$}]

This complex was prepared by two different routes:

(*a*) Sodium hydride (0.100 g, 3.33 mmol, 80% in oil) and *cis*-[PtCl(PEt$_3$){Ph$_2$PCH$_2$P(S)Ph$_2$}][BF$_4$] (0.180 g, 0.211 mmol) were stirred in tetrahydrofuran for 3 h. After filtration to remove unreacted sodium hydride, the solvent was removed *in vacuo* and the resulting yellow residue extracted with benzene (20 mL). Evaporation of the extract under reduced pressure gave a yellow oil which was converted to a free flowing yellow solid, [PtCl(PEt$_3$){Ph$_2$PCHP(S)Ph$_2$}] (0.113 g, 0.148 mmol), by washing with hexane (3 × 10 mL). Recrystallization: tetrahydrofuran/diethyl ether. Isomers: reaction mixture, *c*80/*t*20; crystals, *c*80/*t*20 *Anal.* calcd. for $C_{31}H_{36}ClP_3PtS$: C 48.7, H 4.75; found: C 49.4, H 4.80.

(*b*) *n*-Butyl lithium (1.5 *M* in hexane, 0.87 mL, 1.30 mmol) was added dropwise to a stirred solution of [Ph$_2$PCH$_2$P(S)Ph$_2$] (0.541 g, 1.30 mmol) in tetrahydrofuran (5 mL) and the resulting yellow solution was added to a solution of [Pt$_2$Cl$_4$(PEt$_3$)$_2$] (0.500 g, 0.648 mmol) in tetrahydrofuran (10 mL). After 2 h, the solvent was removed *in vacuo* and the residue washed with hexane (3 × 10 mL) to leave [PtCl(PEt$_3$){Ph$_2$PCHP(S)Ph$_2$}] (0.874 g, 1.144 mmol).

TABLE 7. Selected interatomic distances (Å) and bond angles (deg) for compound **II**, *trans*-[PtCl(PEt$_3$){Ph$_2$CH$_2$P(S)Bu$^t_2$}][ClO$_4$]*

Atoms		Distance	Atoms			Angle
Cl (1)	—Pt (1)	2.326 (2)	S (1)	—Pt (1)	—Cl (1)	174.8 (1)
S (1)	—Pt (1)	2.282 (2)	P (2)	—Pt (1)	—Cl (1)	89.4 (1)
P (2)	—Pt (1)	2.296 (2)	P (2)	—Pt (1)	—S (1)	92.0 (1)
P (3)	—Pt (1)	2.319 (2)	P (3)	—Pt (1)	—Cl (1)	87.7 (1)
P (1)	—S (1)	2.045 (2)	P (3)	—Pt (1)	—S (1)	91.0 (1)
C (1)	—P (1)	1.824 (7)	P (3)	—Pt (1)	—P (2)	177.0 (1)
C (2)	—P (1)	1.871 (7)	P (1)	—S (1)	—Pt (1)	107.2 (1)
C (6)	—P (1)	1.857 (9)	C (1)	—P (1)	—S (1)	108.9 (2)
C (1)	—P (2)	1.860 (7)	C (2)	—P (1)	—S (1)	108.0 (3)
C (11)	—P (2)	1.816 (7)	C (2)	—P (1)	—C (1)	105.8 (3)
C (21)	—P (2)	1.814 (7)	C (6)	—P (1)	—S (1)	109.1 (3)
C (31)	—P (3)	1.838 (9)	C (6)	—P (1)	—C (1)	109.6 (4)
C (33)	—P (3)	1.829 (8)	C (6)	—P (1)	—C (2)	115.2 (4)
C (35)	—P (3)	1.817 (9)	C (1)	—P (2)	—Pt (1)	112.6 (2)
			C (11)	—P (2)	—Pt (1)	110.3 (2)
			C (11)	—P (2)	—C (1)	102.5 (3)
			C (21)	—P (2)	—Pt (1)	117.1 (2)
			C (21)	—P (2)	—C (1)	104.0 (3)
			C (21)	—P (2)	—C (11)	109.2 (3)
			C (31)	—P (3)	—Pt (1)	113.2 (3)
			C (33)	—P (3)	—Pt (1)	116.2 (3)
			C (33)	—P (3)	—C (31)	105.4 (4)
			C (35)	—P (3)	—Pt (1)	110.3 (3)
			C (35)	—P (3)	—C (31)	105.2 (5)
			P (35)	—P (3)	—C (33)	105.7 (5)
			P (2)	—C (1)	—P (1)	112.8 (4)

*Estimated standard deviations are given in parentheses.

(ii) [PtCl(PEt$_3$){Ph$_2$PCHP(Se)Ph$_2$}]

This complex was prepared in 85% yield by reaction of sodium hydride with [PtCl(PEt$_3$){Ph$_2$PCH$_2$P(Se)Ph$_2$}][BF$_4$] in a procedure identical with method *i(a)* above for the sulphur analogue. Recrystallization: tetrahydrofuran/diethyl ether. Isomers: reaction mixture, *c*100/*t*0; crystals, *c*100/*t*0 *Anal.* calcd. for C$_{31}$H$_{36}$ClP$_3$PtSe: C 45.9, H 4.47; found: C 46.2, H 4.74.

(iii) trans-*[PtCl(PEt$_3$){Ph$_2$PCHP(S)Bu$^t_2$}]*

This complex was prepared by reaction of sodium hydride with *trans*-[PtCl(PEt$_3$){Ph$_2$PCH$_2$P(S)Bu$^t_2$}][ClO$_4$] in a procedure identical with method *i(a)* above for the phenyl analogue. The product was identified by ^{31}P NMR.

(iv) Reactions with fluoroboric acid

Approximately two-fold molar excesses of HBF$_4$.Et$_2$O were added dropwise to stirred solutions of *cis*(85%)/*trans*(15%)-[PtCl(PEt$_3$){Ph$_2$PCHP(S)Ph$_2$}] and *cis*-[PtCl(PEt$_3$){Ph$_2$PCHP(Se)Ph$_2$}], respectively, in diethyl ether (5 mL). The resulting immediate yellow precipitates were identified by ^{31}P NMR as essentially quantitative yields of the corresponding *cis*-[PtCl(PEt$_3$){Ph$_2$PCH$_2$P(Y)Ph$_2$}][BF$_4$] complexes.

(B) X-ray data collection

Compounds **I**, *trans*-[PtCl(PEt$_3$){Bu$^t_2$PCH$_2$P(O)Me$_2$}][ClO$_4$], and **II**, *trans*-[PtCl(PEt$_3$){Ph$_2$PCH$_2$P(S)Bu$^t_2$}][ClO$_4$], were prepared as described above and crystals suitable for study by X-ray diffraction were grown for **I** by recrystallization from dichloromethane/hexane, and for **II** by vapour diffusion of diethyl ether into a solution of the complex in dichoromethane. Preliminary photographic work was carried out with Weissenberg and precession cameras using Cu K$_\alpha$ radiation. After establishment of symmetry and approximate unit cells the crystals were transferred to diffractometers (see below). The unit cells were refined by least-squares methods employing respectively 25 and 23 pairs of centering measurements at $\pm 2\theta$ in the ranges $|2\theta|$ = 35–40° and $|2\theta|$ = 18–47°. The crystals were mounted approximately along the *a* and *c* axes respectively. The crystal data at approximately 24°C were as follows:

Compound **I**

Monoclinic, space group $P2_1/c$; a = 15.579(2), b = 13.590(3), c = 13.578(1) Å; β = 105.96(1)°; V(cell) = 2764(2) Å^3; D_m = 1.644 g cm^{-3} (flotation in CCl$_4$/CHBr$_3$), D_c = 1.647 g cm^{-3}; formula C$_{17}$H$_{41}$Cl$_2$O$_5$P$_3$Pt; M_r = 684.43; Z = 4; asymmetric unit = one molecule.

Compound **II**

Monoclinic, space group $P2_1/c$; a = 14..002(4), b = 16.366(5), c = 15.524(5) Å; β = 106.01(3)°; V(cell) = 3419(2) Å^3; D_m = 1.58 g cm^{-3} (flotation in CCl$_4$/CHBr$_3$), D_c = 1.60 g cm^{-3}; formula C$_{27}$H$_{45}$Cl$_2$O$_4$P$_3$PtS; M_r = 824.63; Z = 4; asymmetric unit = one molecule. For both crystals intensity measurements were collected for two reciprocal space octants (h unrestricted, $k \geq 0$, $l \geq 0$) up to 2θ = 50°.

For compound **I** the diffractometer was an Enraf-Nonius CAD4 instrument using graphite monochromated Mo K$_\alpha$ radiation and the NRCCAD modification of the ENRAF-NONIUS program (26). Measurements used the "Profile" $\omega/2\theta$ scan developed by Grant and Gabe (27), with scan rate 2.06° min^{-1} over a range of (0.80 + 0.34 tan θ) degrees in ω. Three standard reflections (−2, 3, 4; −2, −4, 0; and −6, −3, 1) were measured every hour to check crystal stability and three others (−8, 0, 4; 0, −10, 0; and −2, 6, 2) were measured every 500 reflections to check crystal orientation. There was no evidence of deterioration in either set of measurements. Approximate dimensions of the crystal were 0.83 × 0.12 × 0.09 mm. Lorentz and polarization factors were applied and the data were corrected for absorption using an empirical method based on a scan of ϕ Eulerian. Reflections with intensity less than 4.0$\sigma(I)$ were removed from the data set to give a final file containing 2523 reflections.

For compound **II** the diffractometer was a Picker 4-circle instrument automated with a PDP11/10 computer and using Zr filtered Mo K$_\alpha$

Can. J. Chem. Downloaded from www.nrcresearchpress.com by 93.93.197.157 on 09/07/12
For personal use only.

radiation ($\lambda = 0.71069$ Å). A $\theta/2\theta$ step scan was used with 160 steps of 0.01° in 2θ, counting for 0.25 s per step. Background measurements were for 20 s at each end of the scan. Each batch of 50 reflections was preceded by the measurement of three standard reflections (0, 0, 4; 5, 0, 0; and 0, −8, 0;). The Lorentz and polarization factors were applied and each batch was scaled to maintain the sum of the standards constant. There was no evidence of sample decomposition during the data collection. Absorption corrections were applied with a numerical integration procedure utilizing an 8 × 8 × 16 Gaussian grid. The crystal shape was defined by perpendicular distances to crystal faces from a central origin as follows: ±{1$\bar{1}$0}, 0.1144 mm; ±{110}, 0.1144 mm; ±{001}, 0.5013 mm. The absorption coefficient was 43.36 cm^{-1} and the range of transmission factors 0.33–0.43. Reflections with intensity less than $2.0\sigma(I)$ were removed from the data set to give a final file containing 5279 reflections.

(C) Structure solution and refinement

The structures were found and refined using the SHELX-76 program package (28), and illustrations were drawn using ORTEP (29). The atomic scattering factors used were for neutral atoms, with corrections for anomalous dispersion (30). The structures were solved by direct methods, developed by standard Fourier synthesis procedures using difference maps, and refined by the method of least squares minimising $\Sigma w\Delta^2$ where $\Delta = ||F_o| - |F_c||$. The weights were obtained from counting statistics using $w = 1/(\sigma^2(F) + 0.001F^2)$. For compound **I** there were 253 parameters to be determined from 2523 independent observations, and for compound **II**, 343 parameters from 5279 independent observations. Hydrogen atoms were not located. All non-hydrogen atoms were treated anisotropically and convergence was obtained with maximum shift/esd ratios of 0.060 and 0.249 for **I** and **II**, respectively. The respective residuals were $R = 0.0650$ and 0.0444, and $R_w = (\Sigma w\Delta^2/\Sigma wF_o^2)^{1/2} = 0.0632$ and 0.0463. The final difference maps had maxima of +1.4 and +0.79 e $Å^{-3}$ and minima of −1.2 and −0.32 e $Å^{-3}$ and gave no indication that any material had been overlooked.

Acknowledgements

We thank the Natural Sciences and Engineering Research Council of Canada and the University of Victoria for research grants, Mrs. C. Greenwood for recording NMR spectra, and Dr. G. W. Bushnell and Mrs. K. A. Beveridge for invaluable assistance with the X-ray crystallography.

1. S. O. Grim, L. C. Satek, C. A. Tolman, and J. P. Jesson. Inorg. Chem. **14**, 656 (1975).
2. S. O. Grim and J. D. Mitchell. Inorg. Chem. **16**, 1762 (1977).
3. S. O. Grim and E. D. Walton. Inorg. Chem. **19**, 1982 (1980).
4. S. O. Grim, P. H. Smith, I. J. Colquhoun, and W. McFarlane. Inorg. Chem. **19**, 3195 (1980).
5. I. J. Colquhoun, S. O. Grim, W. McFarlane, J. D. Mitchell, and P. H. Smith. Inorg. Chem. **20**, 2516 (1981).
6. S. J. Higgins, R. Taylor, and B. L. Shaw. J. Organomet. Chem. **325**, 285 (1987).
7. P. Peringer and J. Schwald. J. Chem. Soc. Chem. Commun. 1625 (1986).
8. D. E. Berry, K. A. Beveridge, J. Browning, G. W. Bushnell, and K. R. Dixon. Can. J. Chem. **64**, 1903 (1986).
9. J. Browning, G. W. Bushnell, K. R. Dixon, and A. Pidcock. Inorg. Chem. **22**, 2226 (1983).
10. J. Browning, K. A. Beveridge, G. W. Bushnell, and K. R. Dixon. Inorg. Chem. **25**, 1987 (1986).
11. P. Peringer and M. Lusser. J. Organomet. Chem. **312**, C61 (1986).
12. M. Lusser and P. Peringer. Inorg. Chim. Acta, **127**, 151 (1987).
13. P. E. Garrou. Chem. Rev. **81**, 229 (1981).
14. K. R. Dixon. *In* Multinuclear NMR. *Edited by* Joan Mason. Plenum Press, New York. 1987. (*a*) p. 395. (*b*) p. 388.
15. D. E. C. Corbridge. The structural chemistry of phosphorus. Elsevier, Amsterdam. 1974.
16. P. B. Hitchcock, J. F. Nixon, I. Silaghi-Dumitrescu, and I. Haiduc. Inorg. Chim. Acta, **96**, 77 (1985).
17. L. C. Satek, H. L. Ammon, and J. M. Stewart. Acta Crystallogr. B, **31**, 2691 (1975).
18. E. W. Ainscough, H. A. Bergen, A. M. Brodie, and K. A. Brown. J. Chem. Soc. Dalton Trans. 1649 (1976).
19. W. McFarlane and R. J. Wood. J. Chem. Soc. Dalton Trans. 1397 (1972).
20. R. G. Kidd and R. J. Goodfellow. *In* NMR and the Periodic Table. *Edited by* R. K. Harris and B. E. Mann. Academic Press, London. 1978. p. 249.
21. R. B. Johannsen, J. A. Ferreti, and R. K. Harris. J. Magn, Reson. **3**, 84 (1970).
22. J. D. Swalen. *In* Computer programmes for chemistry. Vol. I. *Edited by* D. F. Detar. W. A. Benjamin, New York. 1968.
23. R. J. Goodfellow and L. M. Venanzi. J. Chem. Soc. 7533 (1965).
24. S. O. Grim and J. D. Mitchell. Inorg. Chem. **16**, 1770 (1977).
25. S. W. Carr and R. Colton. Aust. J. Chem. **34**, 35 (1981).
26. Y. Le Page, E. J. Gabe, and P. S. White. NRCCAD modification of the ENRAF-NONIUS program, Chemistry Division, National Research Council of Canada, Ottawa, Canada.
27. D. F. Grant and E. J. Gabe. J. Appl. Crystallogr. **11**, 114 (1978).
28. G. M. Sheldrick. SHELX-76. A computer program for crystal structure determination. University of Cambridge, Cambridge, England. 1976.
29. C. K. Johnson. ORTEP: A Fortran thermal ellipsoid plot program for crystal structure illustrations. ORNL-3794, Oak Ridge National Laboratory, Oak Ridge, U.S.A. 1965.
30. D. T. Cromer and J. T. Waber. *In* International tables for X-ray crystallography. Vol. IV. *Edited by* A. Ibers and W. C. Hamilton. Kynoch Press, Birmingham, England. 1974. pp. 99, 148.

Can. J. Chem. Downloaded from www.nrcresearchpress.com by 93.93.197.157 on 09/07/12
For personal use only.

Excess molar enthalpies of binary mixtures containing esters of fatty acids

SANTOS OTIN, IGNACIO SENAR, MA JOSÉ SORIANO, AND CELSO GUTIERREZ LOSA
Departamento de Química Física, Facultad de Ciencias, Universidad de Zaragoza, 50009 Zaragoza, Spain

Received September 15, 1987

SANTOS OTIN, IGNACIO SENAR, MA JOSÉ SORIANO, and CELSO GUTIERREZ LOSA. Can. J. Chem. **66**, 1283 (1988).

Excess molar enthalpies H_m^E, at 310.15 K and 101.32 kPa, have been determined for the binary mixtures: lauric acid ethyl ester +, stearic acid ethyl ester +, oleic acid ethyl ester +, linoleic acid ethyl ester + *n*-hexadecane, + toluene, or + ethyl alcohol, and elaidic acid ethyl ester + *n*-hexadecane or + toluene.

The results show that H^E of ester + *n*-hexadecane mixtures increases with decreasing chain length and with increasing unsaturation of the ester molecule. Ester + toluene mixtures are slightly exothermic and ester + alcohol are strongly endothermic, with H_m^E values ranging from 1535 to 1740 J mol^{-1} at the maximum.

SANTOS OTIN, IGNACIO SENAR, MA JOSÉ SORIANO et CELSO GUTIERREZ LOSA. Can. J. Chem. **66**, 1283 (1988).

Opérant à 310,15 K et 101,32 kPa, on a déterminé les enthalpies molaires en excès, H_m^E, des mélanges binaires : ester éthylique de l'acide laurique +, ester éthylique de l'acide stéarique +, ester éthylique de l'acide oléique + et ester éthylique de l'acide linoléique + *n*-hexadécane, + toluène ou + alcool éthylique ainsi que de l'ester éthylique de l'acide élaidique + *n*-hexadécane ou + toluène.

Les résultats indiquent que le H^E des mélanges d'esters + *n*-hexadécane augmentent avec une diminution de la longueur de la chaîne et avec l'augmentation du degré d'insaturation de la molécule d'ester. Les mélanges d'esters + toluène sont légèrement exothermiques alors que les mélanges d'esters + alcool sont fortement endothermiques; les valeurs de H_m^E varient de 1535 à un maximum de 1740 J mol^{-1}.

[Traduit par la revue]

Can. J. Chem. Downloaded from www.nrcresearchpress.com by 93.93.197.157 on 09/07/12
For personal use only.

Introduction

In recent years, the application of thermodynamics of liquid mixtures has been often extended to systems of biological interest. These "biothermodynamic" studies refer specially to the behaviour of aminoacids and peptides, and their terminal derivatives, but, in general, include biological macromolecules and the components of cellular membranes, too.

The present paper is a contribution to the study of some interactions in the apolar zone of the membranes, which basically are those existing between the side chains of aminoacids and the hydrocarbon chain of lipids in the double layer. In such interactions, hydrophobicity of the aminoacid will play a fundamental role, but other factors, such as chain length in lipids, the number and location of unsaturations (if they exist) and their geometric isomerism, are also important.

We report here on the calorimetric behaviour of mixtures containing ethyl ester derivatives of some aliphatic acids which differ either in their chain length (lauric and stearic acids), or in the number of unsaturations (oleic and linoleic acids), or in their geometric isomerism (oleic and elaidic acids). The apolar zone in the esters lies in the hydrocarbon chain, and the carboxylate group can be located between both the polar and the apolar zones. As second component of the mixtures we have first used *n*-hexadecane and then, toluene and ethyl alcohol, as they represent, respectively, the side chain (RH) of the aminoacids $H_2N(R)CHCOOH$ phenylalanine (strongly hydrophobic) and treonine (moderately hydrophobic).

We measured the excess molar enthalpy H^E of the mixtures at 310.15 K and 101.32 kPa.

As far as we know, there exist no previous measurements on these mixtures.

Experimental

The esters used were Sigma products (better than 99 mol% purity). *n*-Hexadecane, toluene, and ethyl alcohol were Merck-Schuchardt (better than 99.5% purity). No purification was attempted, because of the difficulty of handling the esters.

Refractive index measurements for the sodium D-line were carried out to ±0.00002 with an Abbe refractometer, and the experimental values of static dielectric constants at 2 MHz, were obtained using a DM01 Dipolometer (Kahl Scientific Inst. Corp.) using the heterodyne beat method (accuracy of ±1%). Refractive indices and static dielectric constants of the pure liquids are given in Table 1.

Excess molar enthalpies were obtained using an isobaric and quasi-isothermic calorimeter (1). Electric energy was measured to better than 0.5%, and the temperature of the water thermostat was controlled to within ±0.002 K. The calorimeter was checked with *n*-hexane + cyclohexane, the agreement with the reported data (2) being better than 0.5% over the central range of concentration.

Results

Table 2 contains the experimental values of H^E for each mixture at 310.15 K. The results for ester + *n*-hexadecane, or + toluene were fitted by least squares to a Redlich–Kister type polynomial

$$[1] \quad H^E = x(1-x)\sum_{i=0}^{i} A_i(1-2x)^i$$

and, in the case of ester + ethyl alcohol mixtures, H^E values were fitted to a Mrazek and van Ness (4) type polynomial

$$[2] \quad H^E = x(1-x)\sum_{i=0}^{i} A_i(1-x)^{i/2}$$

where x is, in both cases, the mole fraction of ester. The values of the coefficients A_i and the standard deviations $\sigma(H^E)$ given by

$$[3] \quad \sigma(H^E) = [\Sigma(H^E - H^E_{exp})^2/(N-n)]^{1/2}$$

where N is the number of experimental points and n the number of coefficients A_i, are reported in Table 3.

Printed in Canada / Imprimé au Canada

Can. J. Chem. Downloaded from www.nrcresearchpress.com by 93.93.197.157 on 09/07/12
For personal use only.

TABLE 1. Static dielectric constants ε_s and refractive indices n^D of pure esters

Compound	T/K	ε_s	T/K	n^D This work	n^D Lit. (3)
Lauric acid ethyl ester	303.15	3.4371	293.15	1.43098	1.4311
	308.15	3.4012			
	313.15	3.3709			
Stearic acid ethyl ester	308.15	3.0667	313.15	1.43537	1.4292
	313.15	3.0454			
Oleic acid ethyl ester	303.15	3.2030	298.15	1.44861	1.4449
	308.15	3.1774			
	313.15	3.1526			
Elaidic acid ethyl ester	303.15	3.2255	298.15	1.44872	1.445
	308.15	3.2034			
	313.15	3.1829			
Linoleic acid ethyl ester	303.15	3.2929	298.15	1.45742	
	308.15	3.2716			
	313.15	3.2531			

TABLE 2. Experimental values of H^E for the studied mixtures at 310.15 K

x	H^E/J mol^{-1}	x	H^E/J mol^{-1}	x	H^E/J mol^{-1}	x	H^E/J mol^{-1}
x lauric acid ethyl ester + $(1-x)$ n-hexadecane							
0.0909	151	0.3917	495	0.5100	503	0.7023	373
0.1331	235	0.4294	511	0.5585	483	0.7237	365
0.2044	333	0.4691	509	0.5875	461	0.8146	259
0.2590	402	0.4860	504	0.6204	444	0.8916	154
0.3044	448						
x stearic acid ethyl ester + $(1-x)$ n-hexadecane							
0.0474	54	0.4209	310	0.5396	318	0.7354	204
0.1395	157	0.4482	320	0.6053	292	0.8064	155
0.2419	236	0.4876	321	0.6826	241	0.9155	64
0.3279	284						
x oleic acid ethyl ester + $(1-x)$ n-hexadecane							
0.0923	200	0.3005	425	0.5923	459	0.7022	389
0.1856	332	0.4081	467	0.6222	453	0.7985	274
0.2436	386	0.4562	480	0.6840	418	0.9544	56
x elaidic acid ethyl ester + $(1-x)$ n-hexadecane							
0.0988	203	0.4091	394	0.6000	392	0.7354	276
0.2100	315	0.4340	406	0.6693	337	0.8481	159
0.2906	357	0.5041	411				
x linoleic acid ethyl ester + $(1-x)$ n-hexadecane							
0.0506	171	0.2296	575	0.4749	692	0.8111	357
0.1160	384	0.3067	650	0.6012	618	0.9054	171
0.1874	537	0.3939	686	0.7011	530		
x lauric acid ethyl ester + $(1-x)$ toluene							
0.0800	−16	0.3669	−49	0.5842	−52	0.7631	−41
0.1411	−31	0.4400	−57	0.6262	−50	0.8486	−30
0.2558	−41	0.5255	−56	0.6735	−50	0.9527	−12
x stearic acid ethyl ester + $(1-x)$ toluene							
0.0769	12	0.3130	16	0.5422	−6	0.7400	−21
0.2051	18	0.4503	3	0.6227	−13	0.8479	−21
x oleic acid ethyl ester + $(1-x)$ toluene							
0.0980	−22	0.4106	−56	0.5228	−58	0.8463	−29
0.1825	−35	0.4938	−59	0.6709	−48	0.9647	−11
0.2883	−43						

TABLE 2 (*concluded*)

x	H^E / J mol^{-1}	x	H^E / J mol^{-1}	x	H^E / J mol^{-1}	x	H^E / J mol^{-1}
			x elaidic acid ethyl ester + $(1 - x)$ toluene				
0.0963	−35	0.4182	−98	0.6000	−97	0.8530	−65
0.2000	−72	0.4903	−95	0.7239	−89	0.9338	−33
0.2893	−86						
			x linoleic acid ethyl ester + $(1 - x)$ toluene				
0.0960	−36	0.3113	−71	0.5535	−78	0.7654	−55
0.1886	−52	0.4125	−77	0.6322	−68	0.9012	−35
0.2442	−67	0.5038	−78				
			x lauric acid ethyl ester + $(1 - x)$ ethyl alcohol				
0.0585	364	0.4138	1462	0.6539	1490	0.8181	1151
0.1424	741	0.4942	1546	0.7029	1401	0.8655	966
0.2005	972	0.5531	1529	0.7636	1275	0.9160	710
0.2710	1197	0.5849	1535	0.7817	1250	0.9432	502
0.3371	1339	0.6248	1494				
			x stearic acid ethyl ester + $(1 - x)$ ethyl alcohol				
0.0490	384	0.3188	1505	0.5414	1722	0.7640	1517
0.1022	688	0.3733	1562	0.5669	1724	0.7936	1413
0.1451	903	0.3981	1611	0.6116	1725	0.8519	1138
0.2012	1137	0.4402	1655	0.6649	1697	0.8939	831
0.2529	1325	0.5144	1711	0.7115	1605		
			x oleic acid ethyl ester + $(1 - x)$ ethyl alcohol				
0.0912	588	0.3021	1435	0.5427	1677	0.7817	1406
0.1430	896	0.4194	1618	0.6335	1659	0.8828	995
0.2011	1139	0.5094	1680	0.7343	1524		
			x linoleic acid ethyl ester + $(1 - x)$ ethyl alcohol				
0.0633	429	0.3598	1585	0.5100	1741	0.8080	1319
0.1231	765	0.3985	1640	0.6002	1702	0.8813	954
0.1938	1126	0.4837	1734	0.7012	1615	0.9259	622
0.2928	1445						

TABLE 3. Values of the A_i parameters of eq. [1] or [2] and standard deviations $\sigma(H^E)$/J mol^{-1} at 310.15 K

Mixture	A_0	A_1	A_2	A_3	A_4	$\sigma(H^E)$
$(1 - x)$ *n*-hexadecane +						
x lauric acid ethyl ester	2006	−437	−164	392	−400	4.5
x stearic acid ethyl ester	1269	−248	−359	1	8	4.5
x oleic acid ethyl ester	1928	−75	131	−744	−192	5.3
x elaidic acid ethyl ester	1638	−142	−253	−929	527	5.4
x linoleic acid ethyl ester	2707	−629	1144	−605	−1527	13.2
$(1 - x)$ toluene +						
x lauric acid ethyl ester	−218	8.4	−35.4	−30.0	2.7	1.9
x stearic acid ethyl ester	−6.9	−203	10.0	−21.9	−43.8	0.4
x oleic acid ethyl ester	−219	40.9	−53.8	−107		3.4
x elaidic acid ethyl ester	−405	−4.1	−105	−106		3.2
x linoleic acid ethyl ester	−308	50.4	−124	−69.4		3.4
$(1 - x)$ ethyl alcohol +						
x lauric acid ethyl ester	11212	−3010	−25032	35165	−11731	19
x stearic acid ethyl ester	−4589	95332	−226547	205183	−61131	16
x oleic acid ethyl ester	4310	58148	−194051	223453	−85629	12
x linoleic acid ethyl ester	−620	81552	−229216	247279	−91840	10

Can. J. Chem. Downloaded from www.nrcresearchpress.com by 93.93.197.157 on 09/07/12
For personal use only.

Can. J. Chem. Downloaded from www.nrcresearchpress.com by 93.93.197.157 on 09/07/12
For personal use only.

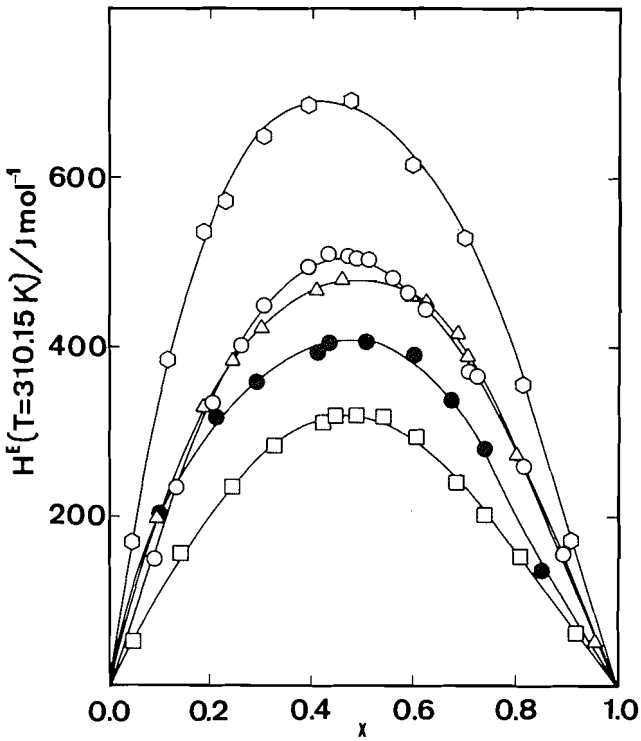

FIG. 1. Excess molar enthalpies H^E(310.15 K) of *n*-hexadecane + (○) lauric acid ethyl ester; + (□) stearic acid ethyl ester; + (△) oleic acid ethyl ester; + (●) elaidic acid ethyl ester; + (⬡) linoleic acid ethyl ester.

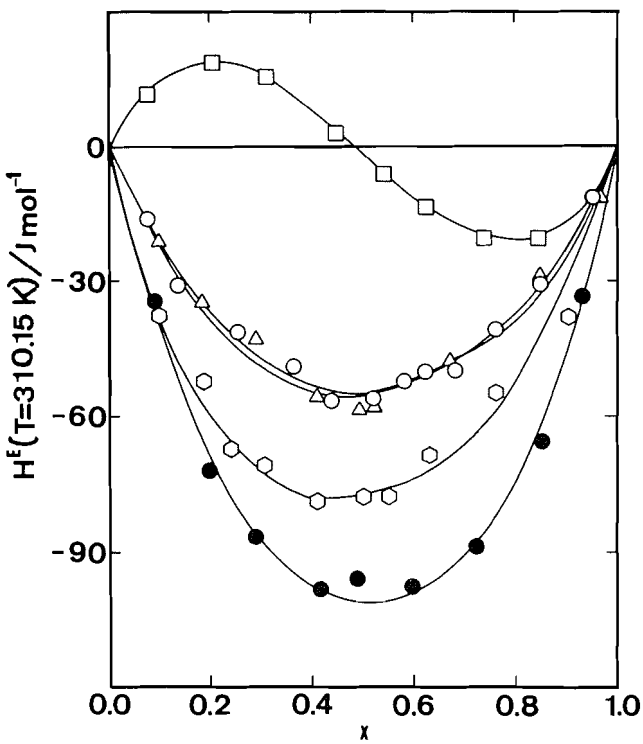

FIG. 2. Excess molar enthalpies H^E(310.15 K) of toluene + (○) lauric acid ethyl ester; + (□) stearic acid ethyl ester; + (△) oleic acid ethyl ester; + (●) elaidic acid ethyl ester; + (⬡) linoleic acid ethyl ester.

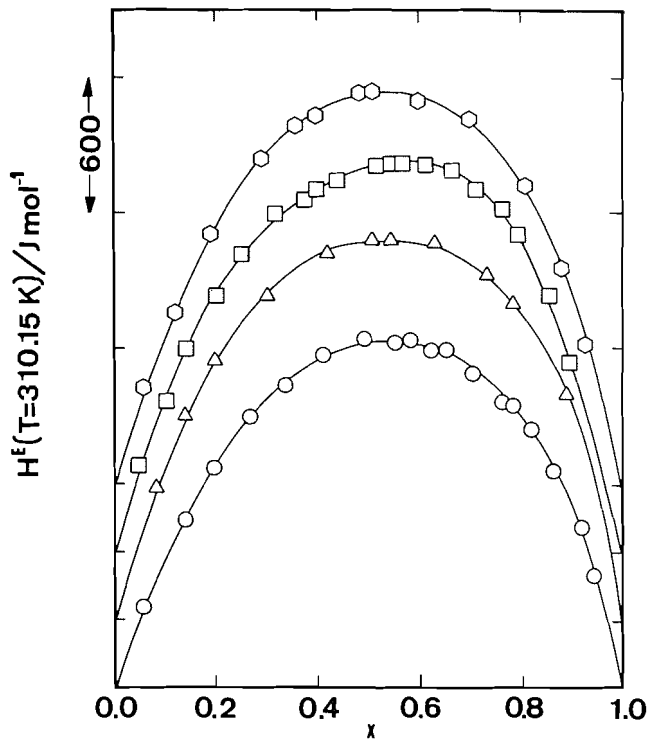

FIG. 3. Excess molar enthalpies H^E(310.15 K) of ethyl alcohol + (○) lauric acid ethyl ester; + (□) stearic acid ethyl ester; + (△) oleic acid ethyl ester; + (⬡) linoleic acid ethyl ester.

All the results are plotted in Figs. 1–3 where the solid lines are those calculated from smoothing equations.

Discussion

As Fig. 1 shows, H^E of a saturated ester + *n*-hexadecane increases when the chain length of the ester decreases, in accord with a "dilution" effect of the carboxylate group ("size effect").

When a double bond is introduced into an ethyl stearate molecule, a new positive contribution to H^E of the corresponding mixtures (ethyl *cis*- or *trans*-oleate + *n*-hexadecane) appears. Since comparison of the H^E values of (*n*-alkane + *n*-alkane) and (*n*-alkane + *n*-alkene) reveals an increase in H^E_{max} ranging from 10 to 100 J mol^{-1} (by short chains) (5), it is explainable that *cis*- or *trans*-oleate + *n*-hexadecane to be more entothermic than ethyl stearate + *n*-hexadecane (about 150 and 90 J mol^{-1} at the maximum, respectively). With the present data it is, however, not so easy to explain why ethyl *cis*-oleate + *n*-hexadecane is a little more endothermic than ethyl *trans*-oleate + *n*-hexadecane. The greater electrical asymmetry of the *cis* isomer might probably play a role as the other component of the mixture is a non polar one. It is to be expected that the aliphatic – double bond interaction in ethyl *cis*-oleate + *n*-hexadecane will be stronger than that in ethyl elaidate + *n*-hexadecane as the elaidate molecules will show a more compact packing.

Ester + toluene mixtures show a remarkable exothermic effect relative to *n*-hexadecane (ranging from 350 to 780 J mol^{-1}, at $x = 0.5$), which can be put down to the possibility of formation of n–π complexes between free electrons of carboxylate group and the aromatic π system; with unsaturated esters, an additional effect exists coming from the π(double bond)–π′(aromatic) interaction.

The behaviour of ethyl alcohol + ester mixtures is clearly the most difficult to explain (Fig. 3). In the mixing process two opposite effects take place: (*i*) an endothermic effect owing to the disappearance of both hydrogen bonds in the alcohol and dipole–dipole interactions in the ester, and (*ii*) an exothermic effect mainly coming from the formation of new hydrogen bonds between the carboxylate group and alcohol molecules. Molar enthalpy of formation of hydrogen bonds in normal alcohols is estimated to be $-23.5\ \text{kJ mol}^{-1}$ (6) and Nagata *et al.* (7) give the value of $-18.4\ \text{kJ mol}^{-1}$ for the molar energy of the ester–alcohol hydrogen bonds. Besides, it was shown (8) that in the absence of any other effects (as "orientational order" effect), the energy of alcohol–alcohol and ester–alcohol hydrogen bonds is almost independent of the aliphatic chain length. We do not know any reference about the calorimetric value for ethyl alcohol + *n*-hexadecane; however, it is known that ethyl alcohol + *n*-nonane is strongly endothermic ($H^{E}_{x=0.5} = 1000\ \text{J mol}^{-1}$) (9) and that the value of H^{E} increases with increasing length of the hydrocarbon chain. This information together with our results on the *n*-hexadecane + ester mixtures, points to a weak exothermic effect of the OH(alcohol)–COOR(ester) interaction and also to a rather small influence of a double bond in the ester (OH–π interaction). In fact, ethyl alcohol + ethyl stearate, + ethyl oleate, or + ethyl linoleate show quite similar values of H^{E}_{max}, ranging from 1680 to $1750\ \text{J mol}^{-1}$.

1. C. Gutiérez Losa and M. Gracia. Rev. Acad. Cienc. Fís.-Quím. Natur. Zaragoza, **26**, 101 (1971).
2. M. B. Ewing, K. N. Marsh, R. H. Stokes, and C. W. Tuxford. J. Chem. Thermodyn. **2**, 751 (1970).
3. Handbook of chemistry and physics. 64th ed. CRC Press, FL 33431 USA.
4. R. V. Mrazek and H. C. van Ness. Am. Inst. Chem. Eng. J. **7**, 190 (1961).
5. J. P. E. Grolier. Int. DATA Ser. Sel. DATA Mixtures. Sér. A, 43 (1975); 221 (1974); 66 (1976); L. Kudryavseva, M. Kuus, H. Vlit, and O. Eisen. Int. DATA Ser. Sel. DATA Mixtures, Sér. A, 13 (1981).
6. I. Brown, W. Fock, and F. Smith. Aus. J. Chem. **17**, 1106 (1964); P. Pérez, F. Royo, M. Gracia, and C. Gutiérrez Losa. J. Chem. Thermodyn. **17**, 711 (1985).
7. I. Nagata, M. Nagashima, K. Kazuma, and M. J. Nakagawa. J. Chem. Eng. Jpn. **8**, 261 (1975).
8. J. P. E. Grolier and A. Viallard. J. Chim. Phys. **68**, 1442 (1971).
9. H. C. Van Ness and M. M. Abbott. Int. DATA Ser. Sel. DATA Mixtures. Sér. A, 14 (1976).

Can. J. Chem. Downloaded from www.nrcresearchpress.com by 93.93.197.157 on 09/07/12
For personal use only.

The proton affinity of triethylsilanol obtained by proton transfer equilibrium measurements using a high pressure mass spectrometer

XIAOPING LI AND JOHN A. STONE
Chemistry Department, Queen's University, Kingston, Ont., Canada K7L 3N6

Received July 8, 1987

XIAOPING LI and JOHN A. STONE. Can. J. Chem. **66**, 1288 (1988).

The proton affinity (PA) of triethylsilanol has been determined by equilibrium proton transfer measurements using a high pressure mass spectrometer. The reference bases were naphthalene and *m*-xylene which have the required low affinities for trialkylsilylium. van't Hoff plots were used to obtain PA($(C_2H_5)_3SiOH$) = 197.9 ± 0.4 kcal mol^{-1}. This value is used to recommend that PA($(CH_3)_3SiOH$) ≈ 192 kcal mol^{-1}. $(C_2H_5)_3Si^+$ has been produced by the protonation of $(C_2H_5)_4Si$ and the enthalpy change for the reaction $(C_2H_5)_3SiOH_2^+ \rightleftharpoons (C_2H_5)_3Si^+ + H_2O$ has been determined to be 32 ± 1 kcal mol^{-1} which gives $\Delta H_f^0((C_2H_5)_3Si^+)$ = 135 kcal mol^{-1}. A value of ~141 kcal mol^{-1} is recommended for $\Delta H_f^0((CH_3)_3Si^+)$.

XIAOPING LI et JOHN A. STONE. Can. J. Chem. **66**, 1288 (1988).

Utilisant un spectromètre de masse à haute pression et des mesures d'équilibre de transfert protonique, on a déterminé l'affinité protonique (AP) du triéthylsilanol. Comme bases de référence, on a utilisé le naphtalène et le *m*-xylène dont les affinités pour l'ion trialkylsilylium sont suffisamment basses. On a utilisé des courbes de van't Hoff pour déterminer l'AP($(C_2H_5)_3SiOH$) = 197,9 ± 0,4 kcal mol^{-1}. On utilise cette valeur pour recommander que l'AP($(CH_3)_3SiOH$) ≈ 192 kcal mol^{-1}. On a produit l'ion $(C_2H_5)_3Si^+$ par protonation du $(C_2H_5)_4Si$ et on a déterminé que le changement d'enthalpie pour la réaction $(C_2H_5)_3SiOH_2^+ \rightleftharpoons (C_2H_5)_3Si^+ + H_2O$ est égal à 32 ± 1 kcal mol^{-1}; on peut en déduire que le $\Delta H_f^0((C_2H_5)_3Si^+)$ = 135 kcal mol^{-1}. On recommande une valeur de ~141 kcal mol^{-1} pour le $\Delta H_f^0((CH_3)_3Si^+)$.

[Traduit par la revue]

Introduction

The gas phase proton affinity of a molecule is determined with best accuracy by measuring the equilibrium constant for proton transfer to a reference base of similar proton affinity. In this manner the proton affinities of a large number of organic molecules have been determined and these data are compiled in several publications (1–3). A few proton affinity values for organosilicon compounds are present in the most comprehensive and consistent compilation (3) but all the data were obtained by other than the equilibrium method and the values listed are approximate ones. A major problem in using the equilibrium method is that due to the electropositive nature of silicon, protonated organosilicon compounds tend to transfer a silicon-containing cation rather than the proton, thus preventing the setting up of proton transfer equilibria. In order for the equilibrium method to be feasible the reference base must have a proton affinity in the correct range and also have a relatively low affinity for the silicon-containing cation. We have previously shown that alkyl aromatics, with proton affinities in the range 183–205 kcal mol^{-1}, have relatively low affinities for $(CH_3)_3Si^+$ (4) and have used them to determine the proton affinity of hexamethyldisiloxane by the equilibrium method (5). In this paper we report the first determination of the proton affinity of a silanol, triethylsilanol, by the same method.

Theoretical calculations suggest that an α-silyl group, except at oxygen, is a destabilizing species which lowers the proton affinity of a molecule (6). There was no difference between the calculated proton affinities of methanol and silanol but significant differences for nitrogen- and phosphorus-containing molecules. There is no reported experimental proton affinity measurement for silanol but there are two quite different values for the proton affinity of trimethylsilanol. Clemens and Munson (7) estimated the value as 197 ± 2 kcal mol^{-1}. They used methane/tetramethylsilane/water mixtures in a chemical ionization (CI) source. Protonated trimethylsilanol is formed by the following reactions:

[1] $CH_5^+ + (CH_3)_4Si \dashrightarrow 2CH_4 + (CH_3)_3Si^+$

[2] $(CH_3)_3Si^+ + H_2O \rightleftharpoons (CH_3)_3SiOH_2^+$

With excess water, equilibrium [2] is far to the right. Bases (B) of increasing proton affinity were introduced into the ion source via a gas chromatograph and significant amounts of BH^+ were observed for bases with proton affinities greater than 199 kcal mol^{-1}. This value was taken to be the upper limit of PA($(CH_3)_3SiOH$). The authors point out that their results could be ambiguous since competing reactions might have obscured proton transfer to bases of lower proton affinity.

We obtained ΔH_2^0 = −30.1 kcal mol^{-1} by direct measurement (8) and used $\Delta H_f^0((CH_3)_3Si^+)$ = 150.5 kcal mol (9) and $\Delta H_f^0((CH_3)_3SiOH)$ = −119.4 kcal mol^{-1} (10) to obtain PA($(CH_3)_3SiOH$) = 183.7 kcal mol^{-1}. This value is substantially lower than the upper limit suggested by Clemens and Munson but depends not only on the accuracy of the experimental value of ΔH_2^0 but also on the accuracy of the standard enthalpies of formation of $(CH_3)_3Si^+$ and $(CH_3)_3SiOH$. The former has been discussed by Walsh (11) who suggests a value of 145 ± 6 kcal mol^{-1}, the lower bound of which would raise PA($(CH_3)_3SiOH$) to 195 kcal mol^{-1}.

A direct determination of the proton affinity of trimethylsilanol would be appropriate to settle both the above experimental discrepancy and to check the validity of the theoretical calculation. Unfortunately, trimethylsilanol is not commercially available and is also relatively unstable with respect to our experimental conditions but triethylsilanol is more stable, is commercially available, and was, therefore, used in this study. In addition tetraethylsilane is also commercially available, allowing the determination of the binding energy of $(C_2H_5)_3Si^+$ to water and hence providing a check on the value we previously obtained for $(CH_3)_3Si^+$.

Experimental

The high pressure mass spectrometer equipped with pulsed electron beam has been described previously as has the method of sample

Can. J. Chem. Downloaded from www.nrcresearchpress.com by 93.93.197.157 on 09/07/12
For personal use only.

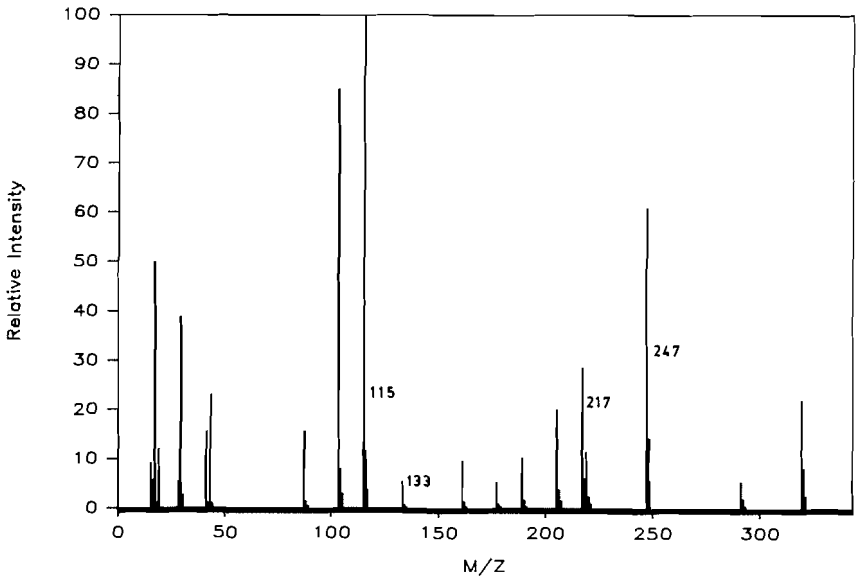

FIG. 1. Mass spectrum of $(C_2H_5)_3SiOH$ (6×10^{-3} mol%) in CH_4 at 4.1 Torr and 585 K.

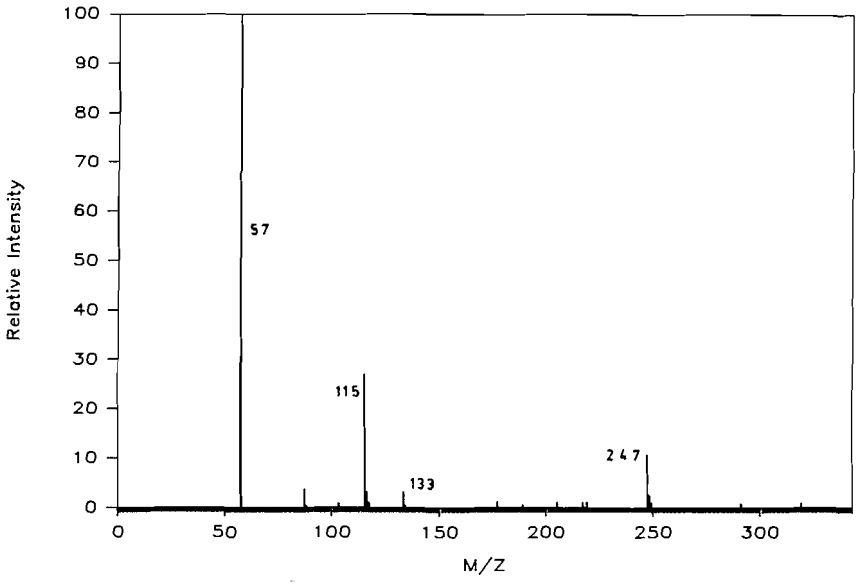

FIG. 2. Mass spectrum of $CH_4/i\text{-}C_4H_{10}/(C_2H_5)_3SiOH$ (92:8:1.5 $\times$ 10^{-3}) at 4.0 Torr and 585 K.

preparation and data collection (12). The pumping of the ion source housing has been improved by the addition of a second 4 in. diffusion pump.

Pre-mixed samples are flowed from a heated reservoir via a heated metering valve into the ion source. Time-resolved spectra are obtained by pulsing the electron beam on for ~50 μs and off for ~10 ms. The ions of each m/z value leaving the ion exit slit are collected as functions of time after the electron pulse using ion counting equipment and a multi-channel analyzer. Data are processed using a personal computer.

Triethylsilanol and tetraethylsilane from Petrarch Systems, Inc., were used without further purification. The *m*-xylene and naphthalene were from the Aldrich Chemical Company, Inc. No ions attributable to impurities in these chemicals were observed in this work. The methane (99.99%) and isobutane (99.5%) which were used as buffer gases were from Matheson Gas Products Canada.

Results and discussion

The CI spectrum of triethylsilanol is dependent on both the type and pressure of the protonating reagent gas and the ion source temperature. Figures 1, 2, and 3 show the effects of reagent gas at a temperature near the experimental maximum of 600 K. In methane as buffer gas the major ions from triethylsilanol result from protonation by the reagent ions CH_5^+ and $C_2H_5^+$ at either ethyl or oxygen, while in methane/isobutane protonation by $t\text{-}C_4H_9^+$ is predominantly at oxygen. Time-resolved spectra show the following reactions leading to the major ions seen in the spectrum (BH^+ is a reagent ion)

[3a] $(C_2H_5)_3SiOH + BH^+ \dashrightarrow (C_2H_5)_3SiOH_2^+ * + B$

[3b] $\dashrightarrow (C_2H_5)_2SiOH^+ + C_2H_6 + B$ (m/z 103)

[4a] $(C_2H_5)_3SiOH_2^+ * \dashrightarrow (C_2H_5)_3Si^+ + H_2O$ (m/z 115)

[4b] $\overset{M}{\dashrightarrow} (C_2H_5)_3SiOH_2^+$ (m/z 133)

Can. J. Chem. Downloaded from www.nrcresearchpress.com by 93.93.197.157 on 09/07/12
For personal use only.

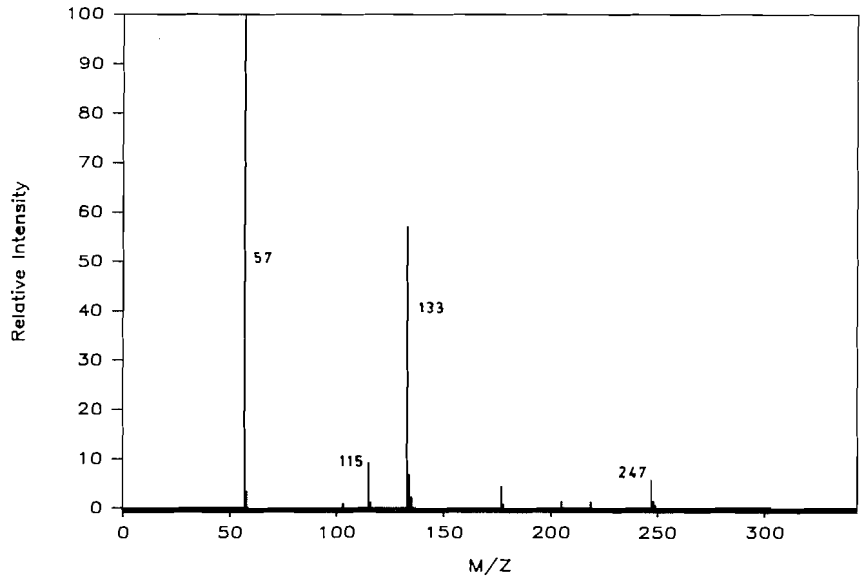

FIG. 3. Mass spectrum of $CH_4/i\text{-}C_4H_{10}/(C_2H_5)_3SiOH/H_2O$ (87:8:1.5 × 10^{-3}:5) at 4.1 Torr and 586 K.

[5] $(C_2H_5)_2SiOH^+ + (C_2H_5)_3SiOH \rightarrow (C_2H_5)_2SiOSi(C_2H_5)_3^+ + H_2O$ (m/z 217)

[6] $(C_2H_5)_3Si^+ + (C_2H_5)_3SiOH \xrightarrow{M} (C_2H_5)_3SiO(H)Si(C_2H_5)_3^+$ (m/z 247)

Using PA($(C_2H_5)_3SiOH$) = −197.9 kcal mol^{-1} (*vide infra*) the enthalpies of proton transfer from the reagent ions B to $(C_2H_5)_3SiOH$ (reaction [3a]) are: CH_5^+ −66 kcal mol^{-1}, $C_2H_5^+$ −35 kcal mol^{-1}, and $t\text{-}C_4H_9^+$ −2 kcal mol^{-1}. The increasing site selectivity for protonation noted above is, as expected, correlated with the exothermicity of the reactions, the more basic site, oxygen being preferred when $t\text{-}C_4H_9^+$ is the protonating agent. A similar behaviour was observed with hexamethyldisiloxane, protonation on both methyl and oxygen occurring in methane but only oxygen protonation in methane/isobutane mixtures (5).

There is only a small yield of m/z 133 ($(C_2H_5)_3SiOH_2^+$) in methane when highly exothermic proton transfer to oxygen leads to m/z 115 and 247 via reactions [4a] and [6] (Fig. 1). In methane/isobutane the relative yield of m/z 133 increases but at 585 K (Fig. 2) m/z 115 and 247 still predominate. This is due to the thermal dehydration of $(C_2H_5)_3SiOH_2^+$ as discussed later. At temperatures lower than 500 K, this dissociation is negligible and proton transfer from $t\text{-}C_4H_9^+$ to triethylsilanol leads to m/z 133 alone. The presence of water in the reagent gas reduces the intensity of m/z 115 and therefore of m/z 247 by reversing the thermal dehydration. Figure 3 shows that a methane/isobutane/water mixture gives the high fractional yield of protonated triethylsilanol which is necessary for proton transfer equilibrium studies.

At low temperatures in a methane/isobutane buffer gas, triethylsilanol (M) yields mainly MH^+ which is further solvated to M_2H^+ and M_3H^+. As with the analogous alcohols this behaviour places a lower limit on the temperature range over which proton transfer equilibria may be studied. Since the yields of M_2H^+ and M_3H^+ increase with increasing concentration of M the equilibrium measurements were made with the minimum amount of M present. This was assured by having reference bases of lower proton affinity then triethylsilanol. The chosen bases, which must be aromatic, were *m*-xylene and naphthalene. Equilibria were studied over the temperature range 360–560 K for triethylsilanol/*m*-xylene and 440–580 K for triethylsilanol/naphthalene. The proton transfer equilibrium between *m*-xylene and naphthalene could be studied over the full range of temperature accessible to the instrument, i.e. 300–600 K.

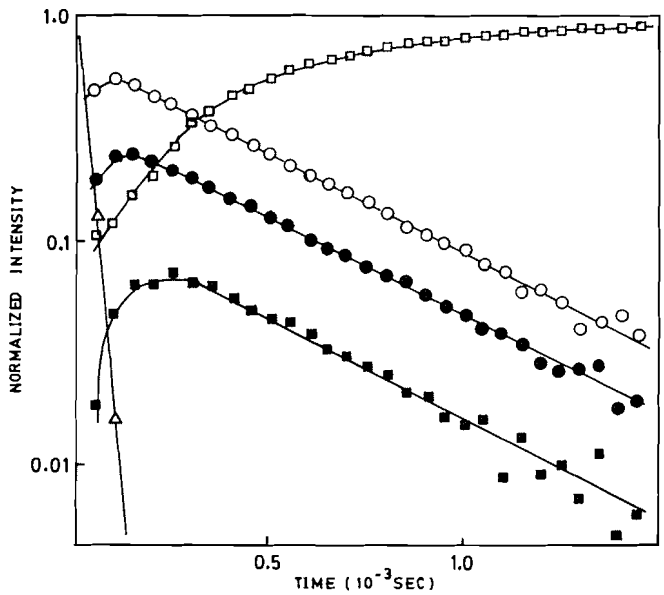

FIG. 4. Normalized ion intensities as functions of time after a 50 μs pulse of ionizing electrons in $CH_4/i\text{-}C_4H_{10}/m\text{-xylene}/(C_2H_5)_3SiOH$ (92:8:1.3 × 10^{-1}:5.8 × 10^{-3}), 3.5 Torr, 453 K. △ $t\text{-}C_4H_9^+$ (m/z 57), ○ $C_8H_{11}^+$ (m/z 107), ● $(C_2H_5)_3SiOH_2^+$ (m/z 133), ■ $((C_2H_5)_3SiOH)_2H^+$ (m/z 265), □ $(C_2H_5)_3SiO(H)Si(C_2H_5)_3^+$ (m/z 247).

A typical temporal profile of normalized ion intensities after a short ionizing electron pulse is shown in Fig. 4. Although m/z 247 is the dominant ion at long reaction time, the rate of its

Can. J. Chem. Downloaded from www.nrcresearchpress.com by 93.93.197.157 on 09/07/12
For personal use only.

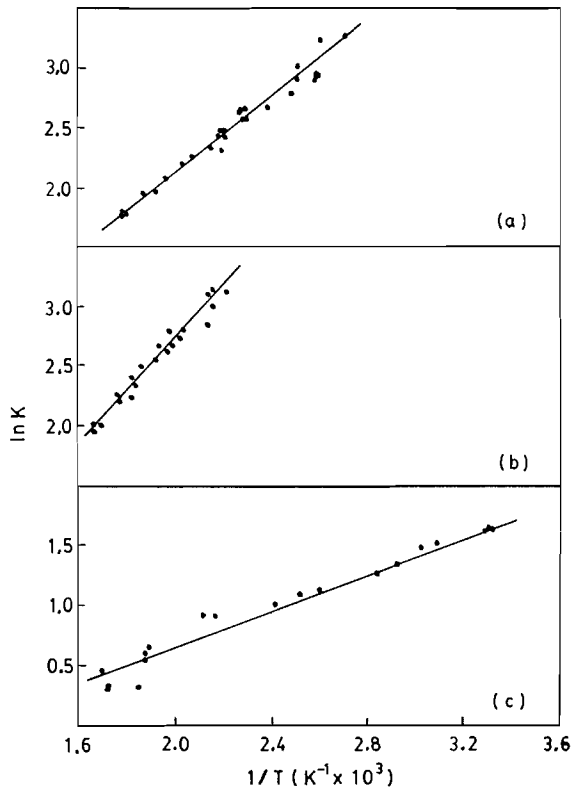

FIG. 5. van't Hoff plots for proton transfer equilibria of the form $B_1H^+ + B_2 \rightleftharpoons B_1 + B_2H^+$). (*a*) B_1 = *m*-xylene, B_2 = triethylsilanol; (*b*) B_1 = naphthalene, B_2 = triethylsilanol; (*c*) B_1 = naphthalene, B_2 = *m*-xylene. Each line is a least-squares fit to the data points which were obtained from results obtained using several different sample compositions over an extended period of time. The number of different samples were (*a*) 8, (*b*) 7, and (*c*) 4.

TABLE 1. Standard enthalpy and entropy changes for proton transfer

	$-\Delta H^0$ kcal mol^{-1}		$-\Delta S^0$ cal K^{-1} mol^{-1}	
Triethylsilanol				
	3.0±0.1		1.7±0.3	
m-Xylene		4.0±0.2		2.6±0.4
	1.5±0.1		1.9±0.1	
Naphthalene				

production is sufficiently small compared with the rate of proton exchange (reaction [7]) that the equilibrium is not disturbed.

[7] $(C_2H_5)_3SiOH_2^+ + C_8H_{10} \rightleftharpoons (C_2H_5)_3SiOH + C_8H_{11}^+$

The calculated equilibrium constant at a given temperature is independent of both ion source pressure (2–4 Torr) and ratio of neutral molecules (varied by a factor of five). The standard enthalpy and standard entropy changes for the three equilibria are obtained from the van't Hoff plots of Fig. 5. The results, which are presented in Table 1, show acceptable internal consistency although not as good as is usually obtained with organic compounds. We attribute this to the smaller than usual temperature range that was used for the two equilibria involving triethylsilanol.

The slow formation of m/z 247 at 453 K, the temperature at which the data in Fig. 4 were taken, could be by reaction [6]. However, $(C_2H_5)_3Si^+$ was not observed in the mass spectrum and its steady state concentration must therefore have been extremely low and would be even lower at lower temperatures when m/z 247 is still present. The probable mechanism of formation of m/z 247 in this mixed system is the dehydration of the nascent proton bound dimer.

[8] $(C_2H_5)_3SiOH_2^+ + (C_2H_5)_3SiOH \dashrightarrow ((C_2H_5)_3SiOH)_2H^+ *$

[9a] $((C_2H_5)_3SiOH)_2H^+ * \dashrightarrow (C_2H_5)_3SiO(H)Si(C_2H_5)_3^+ + H_2O$ (m/z 247)

[9b] $\xrightarrow{M} ((C_2H_5)_3SiOH)_2H^+$ (m/z 265)

The analogous reaction is well known in alcohols (13). Figure 4 shows that the proton bound dimer (m/z 265) decays in parallel with protonated triethylsilanol (m/z 133) and therefore these two ions are in equilibrium with each other; the formation of m/z 247 is so slow as not to disturb this equilibrium.

To fix the proton affinity of triethylsilanol, an acceptable value for the proton affinity of either *m*-xylene or naphthalene is required. The gas phase basicity of *m*-xylene has been measured by the equilibrium method using ion cyclotron resonance but only the value is quoted, no details of the reference bases etc. are given (14). The evaluated proton affinity is 195.9 kcal mol^{-1} which is 1.2 kcal mol^{-1} greater than the evaluated proton affinity of naphthalene (3), a difference which is in fair agreement with the 1.55 kcal mol^{-1} of Table 1. There are problems, however, in accepting the absolute values quoted for *m*-xylene and naphthalene since, for example, a value from each of two different laboratories is used in obtaining the evaluated proton affinity of naphthalene, and one of these finds a difference between the proton affinities of naphthalene and toluene of only 1.7 kcal mol^{-1} (15). The evaluated difference is 4.9 kcal mol^{-1} (3). We recently measured the proton affinity of *m*-xylene as 194.9 kcal mol^{-1} relative to PA(mesitylene) = 201 kcal mol^{-1} (5). We have reconfirmed this value which is 1.0 kcal mol^{-1} below that quoted above. Using our value, the proton affinity of triethylsilanol is 197.9 ± 0.4 kcal mol^{-1} and that of naphthalene is 193.3 ± 0.6 kcal mol^{-1}.

The proton affinity of trimethylsilanol may be estimated from that of triethylsilanol. An ethyl group is more polarizable than a methyl group and is therefore better able to stabilize a positive charge on an adjacent site as shown by the following pairs of proton affinities (units kcal mol^{-1}) $(CH_3)_3N$ (225.1), $(C_2H_5)_3N$ (232.2); $(CH_3)_3P$ (227.1), $(C_2H_5)_3P$ (231.7); C_2H_5OH (188.3), n-C_3H_7OH (191.2) (3). Replacing one methyl by one ethyl increases the proton affinity by roughly 2 kcal mol^{-1}. With PA($(C_2H_5)_3SiOH$) = 198 kcal mol^{-1}, an estimated value of PA($(CH_3)_3SiOH$) is 192 kcal mol^{-1} leading to $\Delta H_f^0((CH_3)_3Si^+)$ = 142 kcal mol^{-1}, which is in the range of values, 146 ± 5 kcal mol^{-1}, suggested by Walsh (11). This estimated value for PA($(CH_3)_3SiOH$) is preferable to our earlier value of 183.7 kcal mol^{-1} which was based on the enthalpy change for reaction [2] and Szepes and Baer's indirect measurement of $\Delta H_f^0((CH_3)_3Si^+)$ = 150.5 kcal mol (9). Walsh (11) has discussed the uncertainties involved in the interpretation of the latter data and notes that slightly different values are obtained for $\Delta H_f^0((CH_3)_3Si^+)$ when data for its production from different compounds are used. It is readily apparent that many more direct determinations of the thermochemical properties of

Can. J. Chem. Downloaded from www.nrcresearchpress.com by 93.93.197.157 on 09/07/12
For personal use only.

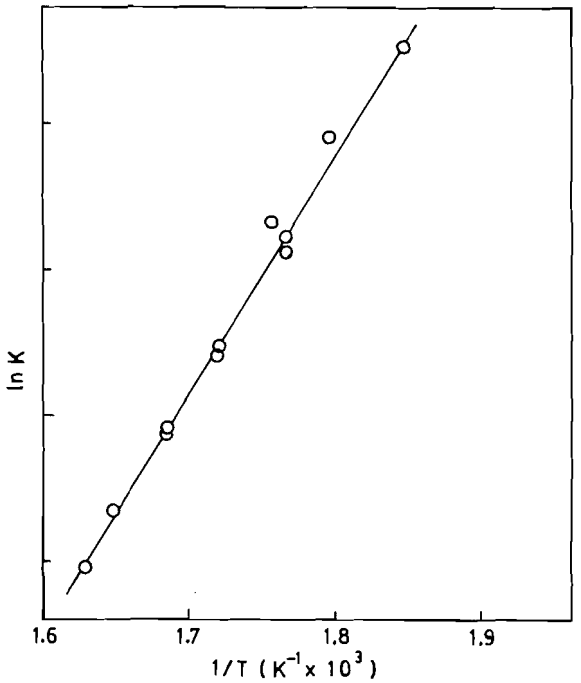

FIG. 6. van't Hoff plot for the equilibrium $(C_2H_5)_3Si^+ + H_2O \rightleftharpoons (C_2H_5)_3SiOH_2^+$.

silicon compounds, both ionic and neutral, are required in order to provide a firm base for organosilicon chemistry.

The condensation of triethylsilylium with water

Upon methane chemical ionization, tetraethylsilane, like tetramethylsilane, loses an alkyl group to yield the trialkylsilylium cation.

[10] $(C_2H_5)_4Si + CH_5^+ \dashrightarrow (C_2H_5)_3Si^+ + C_2H_6 + CH_4$

In the presence of water triethylsilylium is in equilibrium with protonated triethylsilanol

[11] $(C_2H_5)_3Si^+ + H_2O \rightleftharpoons (C_2H_5)_3SiOH_2^+$

The equilibrium constant, K, was measured over a range of temperatures to yield the van't Hoff plot in Fig. 6. K is defined in terms of the ratio of ion currents at long reaction time when equilibrium has been attained, and the pressure P_{H_2O} of water vapour in the ion source. The standard pressure P^0 is one atmosphere.

$$[12] \quad k = \frac{i_{(C_2H_5)_3SiOH_2^+}}{i_{(C_2H_5)_3Si^+}(P_{H_2O}/P^0)}$$

From the plot the standard enthalpy of binding of water to triethylsilylium is -32 ± 1 kcal mol^{-1} and the standard entropy change is -35 ± 3 cal K^{-1} mol^{-1}. These values are consistent with the designation of the adduct as protonated triethylsilanol. In particular, the large entropy change shows the formation of a "tight" structure with Si—O bonding rather than a "looser" structure which would be associated with a water/triethylsilylium complex (16). The numbers are very close to the 31 ± 2 kcal mol^{-1} and 27 ± 3 cal K^{-1} mol^{-1} observed for the association of water with trimethylsilylium. A slightly lower binding energy was expected for triethylsilylium compared with trimethylsilylium because of the greater stabilizing effect on a charge centre of an ethyl compared with a methyl. For example, we found that the binding energies of water to $(CH_3)_3Ge^+$ and $(C_2H_5)_3Ge^+$ were 28.6 ± 0.5 and 24.9 ± 0.5 kcal mol^{-1}, respectively (17). The wider error limits for $(CH_3)_3Si^+$ (30.1 ± 1.9 kcal mol^{-1}) and $(C_2H_5)_3Si^+$ (32 ± 1 kcal mol^{-1}) are due to the smaller temperature range encompassed by the van't Hoff plot and are such that the true order could be the reverse of the stated one. The difference between the values for the trimethyl- and triethylsilicon-containing ions appears to be considerably less than for the germanium-containing ions.

The above data may be used to estimate the standard enthalpy of formation of the triethylsilylium ion. The standard enthalpy of formation of triethylsilanol is not known but with $\Delta H_f^0((CH_3)_3SiOH) = -119.4$ kcal mol^{-1} and assuming that substitution of an ethyl for a methyl on silicon decreases the enthalpy of formation by 1.2 kcal mol^{-1} ($\Delta H_f^0((CH_3)_4Si = -58.7$ kcal mol^{-1} and $\Delta H_f^0((C_2H_5)_4Si) = -63.5$ kcal mol^{-1} (10)) then $\Delta H_f^0((C_2H_5)_3SiOH) \approx -123$ kcal mol^{-1}. This value, combined with $PA((C_2H_5)_3SiOH) = 198$ kcal mol^{-1}, gives $\Delta H_f^0((C_2H_5)_3Si^+) = 135$ kcal mol^{-1}. The error limits in this calculation are difficult to assess, but the value is probably good to better than ± 5 kcal mol^{-1}. This value of 135 kcal mol^{-1} supports a value of 140–145 kcal mol^{-1} for $\Delta H_f^0((CH_3)_3Si^+)$ if, as discussed earlier, 2 kcal mol^{-1} is assigned as the stabilization energy of an ethyl compared with a methyl substituent on a siliconium centre.

Acknowledgement

The authors thank the Natural Sciences and Engineering Research Council of Canada for financial assistance.

1. D. H. AUE and M. T. BOWERS. *In* Gas phase ion chemistry. Vol. 2. *Edited by* M. T. Bowers. Academic Press, New York. 1979. pp. 1–51.
2. R. WALDER and J. L. FRANKLIN. Int. J. Mass Spectrom. Ion Phys. **36**, 85 (1980).
3. S. G. LIAS, J. F. LIEBMAN, and R. D. LEVIN. J. Phys. Chem. Ref. Data, **13**, 695 (1984).
4. A. C. WOJTYNIAK and J. A. STONE. Int. J. Mass Spectrom. Ion Proc. **74**, 59 (1986).
5. X. LI and J. A. STONE. Can. J. Chem. **65**, 2454 (1987).
6. M. L. HENDEWERK, R. FREY, and D. A. DIXON. J. Phys. Chem. **87**, 2026 (1983).
7. D. CLEMENS and B. MUNSON. Anal. Chem. **57**, 2022 (1985).
8. J. A. STONE, A. C. M. WOJTYNIAK, and W. WYTENBURG. Can. J. Chem. **64**, 575 (1986).
9. L. SZEPES and T. BAER. J. Am. Chem. Soc. **106**, 273 (1984).
10. J. B. PEDLEY and J. RYLANCE. Sussex – N.P.L. Computer analysed thermochemical data: organic and organometallic compounds. University of Sussex. 1977.
11. R. WALSH. J. Phys. Chem. **90**, 389 (1986).
12. J. A. STONE and D. E. SPLINTER. Can. J. Chem. **59**, 1779 (1981).
13. L. M. BASS, R. D. CATES, M. F. JARROLD, N. J. KIRCHNER, and M. T. BOWERS. J. Am. Chem. Soc. **105**, 7024 (1983).
14. J. L. DEVLIN, J. F. WOLF, R. W. TAFT, and W. J. HEHRE. J. Am. Chem. Soc. **98**, 1990 (1976).
15. M. MEOT-NER. J. Phys. Chem. **84**, 2716 (1980).
16. M. MEOT-NER, M. M. ROSS, and J. E. CAMPANA. J. Am. Chem. Soc. **107**, 4839 (1985).
17. J. A. STONE and W. J. WYTENBURG. Can. J. Chem. **65**, 2146 (1987).

Can. J. Chem. Downloaded from www.nrcresearchpress.com by 93.93.197.157 on 09/07/12
For personal use only.

The photochemistry of the rhodizonate dianion in aqueous solution

G. IRACI AND M. H. BACK

Ottawa–Carleton Chemistry Institute, University of Ottawa Campus, Ottawa, Ont., Canada K1N 6N5

Received August 12, 1987

G. IRACI and M. H. BACK. Can. J. Chem. **66**, 1293 (1988).

The photochemistry of the rhodizonate dianion at 483 nm has been studied in aqueous solution at pH 8.3. In the absence of oxygen no reaction was observed. In the presence of oxygen, 6.2×10^{-5} *M*, the dianion was consumed with a quantum yield of 0.044. The oxidation apparently did not involve the formation of $O_2(^1\Delta_g)$. Electron transfer from the excited dianion was observed with methyl viologen.

G. IRACI et M. H. BACK. Can. J. Chem. **66**, 1293 (1988).

Opérant en solution aqueuse, à un pH de 8,3 et à une longueur d'onde de 482 nm, on a étudié la photochimie du dianion rhodizonate. En l'absence d'oxygène, on n'a pas observé de réaction. En présence d'oxygène, $6{,}2 \times 10^{-5}$ *M*, le dianion est consommé avec un rendement quantique de 0,044. Il ne semble pas que l'oxydation implique la formation d'$O_2(^1\Delta_g)$. Avec le viologène de méthyle, on a observé un transfert d'électrons.

[Traduit par la revue]

Can. J. Chem. Downloaded from www.nrcresearchpress.com by 93.93.197.157 on 09/07/12
For personal use only.

Introduction

Rhodizonic acid, $H_2C_6O_6$, is one of the series of cyclic oxocarbons whose dianions are stabilized by electron delocalization to the extent of possessing aromatic properties (1, 2). The dianions all show strong π–π^* absorption giving an absorption band with a characteristic double maximum. In rhodizonic dianion the strongest absorption is at 483 nm ($\epsilon = 3.3 \times 10^4$ L mol^{-1} cm^{-1}) (3) which makes it of interest for solar energy conversion. It is known that aerated aqueous solutions of rhodizonic acid are unstable and in basic solution conversion to croconic acid takes place (1). The disappearance of rhodizonic dianion is accelerated by exposure to visible light (4, 5) but it appears that no systematic study of the photolysis of rhodizonic, or of any of the oxocarbons, has been reported. The present paper describes a brief investigation of the behaviour of the rhodizonic dianion in aqueous solution following absorption of light at 483 nm.

Experimental

Solutions of sodium rhodizonate (Aldrich Chemical Co.) were degassed and photolyzed in a 1-cm quartz spectrophotometer cell, using a tungsten lamp and monochromator. Dissolved oxygen was analyzed by the Winkler method (6). Fluorescence was measured using a SLM 8000 Fluorescence Spectrophotometer.

Flash photolysis experiments were performed with a model 858 Flash Kinetic Spectrometer from Applied Photophysics Ltd., supplied by Photochemical Research Associates. London, Ont. The transient absorption was measured with a Tektronix 2235 100 MHz oscilloscope and photographed with Polaroid Type 667 film. The flash duration to half maximum was 150 μs.

Results

Both acidic and basic solutions of rhodizonic acid were unstable. In basic solution, pH > 10, croconic acid was formed in the presence of oxygen, while in the absence of oxygen the tetrahydroxyquinone tetra-anion, identified by its maxima at 380 and 270 nm, was formed (Fig. 1). This product had previously been observed only in an electrochemical reduction reaction (7).

De-oxygenated solutions (5×10^{-5} *M*, pH 8.3) were stable for several days and irradiation at 483 nm caused no measurable disappearance of the dianion. In the presence of oxygen, however, the rhodizonic dianion disappeared upon irradiation but the only product identified was croconic acid, which accounted for < 10% of the decomposition. An unstable product was tentatively identified from its absorption maximum (280 nm) (4) as cyclohexanehexone.

The light intensity at 483 incident on the reaction cell was measured using the potassium ferrioxalate actinometer (8) and the average value, from five experiments, was $6.2 \pm 0.3 \times 10^{14}$ quanta s^{-1}. Quantum yields for the disappearance of rhodizonate dianion were measured at two concentrations of oxygen and are shown in Table 1.

Photolyses were also performed in partially de-oxygenated solutions in the presence of two compounds, maleic acid and 3-methyl-1,3-pentadiene, which are expected to react efficiently with any $O_2(^1\Delta_g)$ generated in the system (9, 10). The rate of reaction of rhodizonate was unaffected by the presence of either compound. Unless the rate of reaction of $O_2(^1\Delta_g)$ with rhodizonic dianion is much faster than with either of these reactants, it appears that the photooxidation of the rhodizonic dianion occurs by a direct reaction rather than through the intermediate formation of $O_2(^1\Delta_g)$.

De-oxygenated solutions of rhodizonate excited at 483 nm showed only a very weak fluorescence with a maximum intensity at 584 nm. As a rough estimate, less than 1% of the excited ions formed by absorption at 483 nm decayed by emission of fluorescence.

De-oxygenated solutions of rhodizonate in a Pyrex cell at concentrations in the range 5×10^{-4} to 15×10^{-4} *M* were subjected to flash photolysis using a broad spectrum of visible light, and a broad transient absorption band was observed with a maximum at 640 nm. The lifetime of the transient was, however, scarcely longer than the duration of the flash (~150 μs) and further investigation was not practical with this apparatus.

Solutions of rhodizonate ($1.5 - 3.0 \times 10^{-4}$ *M*) and methyl viologen ($1.3 \times 10^{-3} - 1.3 \times 10^{-2}$ *M*) were flash-photolyzed in the Pyrex cell and a transient absorption was observed in the region of 610 nm. This absorption was not present after flash photolysis of the rhodizonate alone at these concentrations and suggests that the methyl viologen monocation was formed following flash photolysis by electron transfer from an excited $C_6O_6^{2-}$ species.

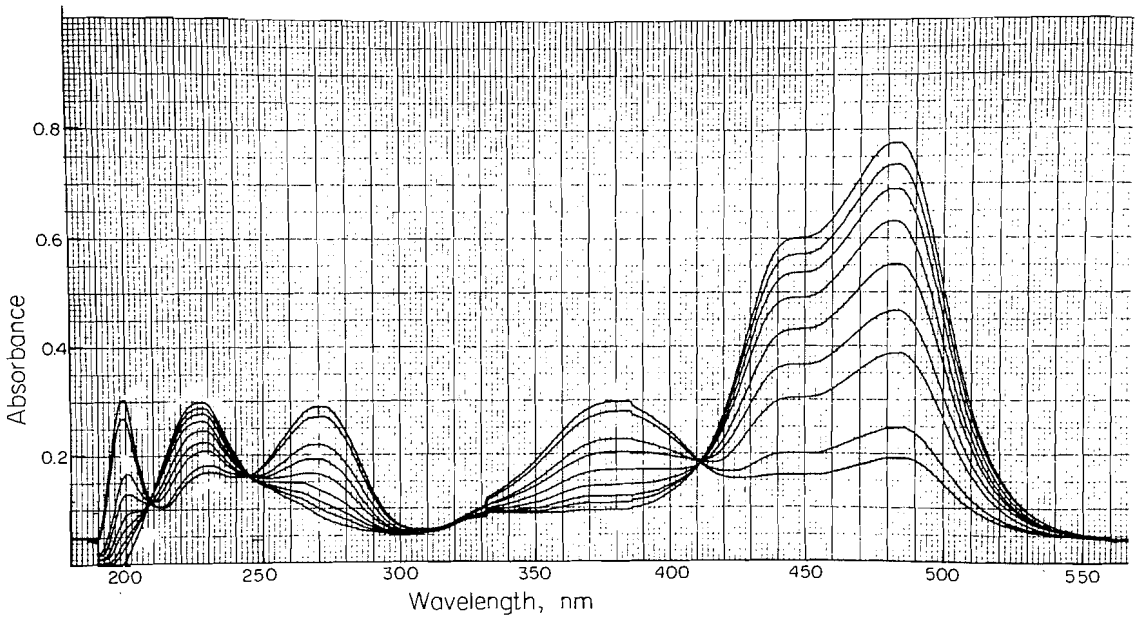

FIG. 1. Absorption spectra of a de-aerated solution of sodium rhodizonate (2.3×10^{-5} *M*) at pH 10.9. Decreasing absorptions at 483 and 227 nm are due to rhodizonate dianion while increasing absorptions at 380 and 270 nm are due to tetrahydroxy quinone. The spectra record reaction times of 0, 5, 10, 20, 35, 55, 75, 150, and 180 min.

TABLE 1. Quantum yields for the disappearance of rhodizonate dianion

$[Rh^{2-}]$ (*M*)	$[0_2]$ (*M*)	$-d[Rh^{2-}]/dt$ ($M\ s^{-1}$)	ϕ
2.5×10^{-5}	6.2×10^{-5}	1.2×10^{-8}	0.044 ± 0.005
2.5×10^{-5}	9.5×10^{-6}	9.0×10^{-9}	0.031 ± 0.006

Conclusions

No photodecomposition of rhodizonic dianion at 483 nm and at pH 8.3 occurs in the absence of oxygen and the quantum yield of fluorescence is less than 1%. Irradiation of the dianion in the presence of oxygen leads to its disappearance, and the croconate ion is a minor product. The photooxidation probably does not proceed through formation of $O_2(^1\Delta_g)$. If the excited rhodizonate reacts with oxygen at a diffusion-controlled rate, ($\sim 10^9\ M^{-1}\ s^{-1}$) the quantum yield for its disappearance indicates a lifetime of the order of 10^{-6} s, which, together with the lack of fluorescence, suggests involvement of the triplet state.

Acknowledgments

The authors acknowledge financial support from the Natural Sciences and Engineering Research Council of Canada. They thank Dr. R. A. Back for helpful discussions, Dr. A. G. Szabo for the use of his fluorescence spectrophotometer, both at the National Research Council, Canada, and Dr. A. D. Westland for suggesting the analytical method for oxygen.

1. R. WEST (*Editor*). Oxocarbons. Academic Press, New York. 1980.
2. R. WEST and J. NIU. Non-benzenoid aromatics. Vol. 1. *Edited by* J. Snyder. Academic Press, New York. 1969. p. 311; R. West. Isr. J. Chem. **20**, 300 (1980).
3. E. PATTON and R. WEST. J. Phys. Chem. **74**, 2512 (1970).
4. R. A. CHALMERS and G. M. TELLING. Microchim. Acta, **6**, 1126 (1967).
5. L. J. SILVESTRI, R. E. HURST, L. SIMPSON, and J. M. SETTINE. Anal. Biochem. **123**, 303 (1982).
6. D. A. SKOOG and D. M. WEST. Fundamentals of analytical chemistry. Saunders College Publishing, Philadelphia. 1982. p. 772.
7. J. MOIROUX, D. ESCOURROU, and M. B. FLEURY. J. Electroanal. Chem. **116**, 333 (1980).
8. J. G. CALVERT and J. N. PITTS. Photochemistry. John Wiley and Sons, New York. 1966.
9. R. HIGGINS, C. S. FOOTE, and H. CHENG. Oxidation of organic compounds. Adv. Chem. Ser. **77**, 102 (1968).
10. B. R. MONROE. J. Am. Chem. Soc. **103**, 7253 (1981).

Can. J. Chem. Downloaded from www.nrcresearchpress.com by 93.93.197.157 on 09/07/12
For personal use only.

Excess molar volumes, speeds of sound, and isentropic compressibilities of binary mixtures of furfural with some aromatic hydrocarbons

HOMENDRA NAOREM AND S. K. SURI[1]

Department of Chemistry, Indian Institute of Technology, Hauz Khas, New Delhi – 110 016, India

Received September 16, 1987

HOMENDRA NAOREM and S. K. SURI. Can. J. Chem. **66**, 1295 (1988).

Molar excess volumes of mixing and isentropic compressibilities for the binary mixtures of furfural with benzene, toluene, ethylbenzene, and *o*-, *m*-, and *p*-xylenes at 308.15 K have been measured. The results reveal that geometric factors are predominant in determining the solution behaviour of the binary mixtures under investigation.

HOMENDRA NAOREM et S. K. SURI. Can. J. Chem. **66**, 1295 (1988).

Opérant à 308,15 K, on a mesuré les volumes molaires en excès de mélange et les compressibilités isentropiques des mélanges binaires du furfural avec le benzène, le toluène, l'éthylbenzène et les *o*-, *m*- et *p*-xylènes. Les résultats révèlent que les facteurs géométriques prédominent dans la détermination du comportement en solution des mélanges binaires étudiés.

[Traduit par la revue]

Can. J. Chem. Downloaded from www.nrcresearchpress.com by 93.93.197.157 on 09/07/12
For personal use only.

Introduction

In earlier communications from this laboratory (1–3) we reported the excess molar volumes of binary mixtures of different hydrocarbons with tetrahydrofuran, cyclohexanone, dioxane, etc. A perusal of literature reveals that studies on hydrocarbon–furfural mixtures are scanty. As a part of our investigation, it was, therefore, considered worthwhile to study the mixture behaviour of furfural with some hydrocarbons. In this manuscript, we report the results of our studies on the excess molar volumes and isentropic compressibilities of binary mixtures of furfural with benzene, toluene, ethylbenzene, *o*-xylene, *m*-xylene, and *p*-xylene at 308.15 K over the entire composition range. The present study aims to provide some information on binary mixtures containing furfural with a view to understanding the nature of interaction present in these mixtures.

Experimental

The aromatic hydrocarbons (Fluka, AG Grade) were purified by established procedures (4). Commercial grade furfural was distilled under vacuum and the middle fraction boiling at constant temperature was collected. The solvents were stored in brown glass bottles and fractionally distilled using a column of 15 theoretical plates immediately before use. The purities of the liquids were checked by comparing the measured densities and refractive indexes with those reported in the literature (4, 5); agreement was within 5×10^{-5} g cm^{-3} and 4×10^{-4} respectively.

The excess molar volumes, V^E, were computed from the experimental density data. The densities of liquids and liquid mixtures were measured using a vibrating tube digital densimeter model DMA 60/602 (Anton Paar, Austria). The temperature of the liquid under investigation was maintained at 308.15 ± 0.01 K with the help of a closed-loop circulating ultra-thermostat. Duplicate densities were reproducible to within 5×10^{-5} g cm^{-3}, which propagates an uncertainty of ±0.005 cm^3 mol^{-1} in the V^E values.

The isentropic compressibility, k_s, was computed from the ultrasonic speed of sound, u, of the solution, which in turn was measured with a single crystal interferometer (model F-81, Mittal Enterprise, India) operating at a frequency of 2 MHz. The error in the measurement of u was estimated to be around 0.15%. This generates an uncertainty of ±2 TPa^{-1} in the k_s values reported in this paper.

Results and discussion

The excess molar volumes of the aforesaid systems are recorded in Table 1 and graphically represented in Fig. 1. The

[1]Author to whom correspondence may be addressed.

TABLE 1. Molar excess volumes, V^E (cm^3 mol^{-1}), for binary mixtures of furfural with some aromatic hydrocarbons at 308.15 K

x	V^E (cm^3 mol^{-1})	x	V^E (cm^3 mol^{-1})
x Furfural + $(1-x)$ benzene			
0.0672	−0.023	0.5620	−0.108
0.2082	−0.066	0.6652	−0.103
0.2751	−0.088	0.8072	−0.062
0.3528	−0.101	0.9284	−0.024
0.4552	−0.113		
x Furfural + $(1-x)$ toluene			
0.0857	−0.036	0.6802	−0.144
0.2344	−0.098	0.7596	−0.118
0.3053	−0.126	0.8593	−0.082
0.3720	−0.147	0.9164	−0.055
0.5304	−0.162		
x Furfural + $(1-x)$ ethylbenzene			
0.0916	−0.016	0.5716	−0.052
0.1733	−0.028	0.6448	−0.051
0.2378	−0.036	0.7479	−0.038
0.3957	−0.049	0.8948	−0.018
0.4752	−0.058		
x Furfural + $(1-x)$ *o*-xylene			
0.0853	0.019	0.5976	0.024
0.1887	0.039	0.7308	0.001
0.2941	0.052	0.8544	−0.013
0.4381	0.040	0.9530	−0.008
0.5498	0.035		
x Furfural + $(1-x)$ *m*-xylene			
0.0888	−0.004	0.6550	−0.040
0.2724	−0.026	0.7319	−0.034
0.3749	−0.038	0.8487	−0.018
0.4821	−0.042	0.8945	−0.016
0.5578	−0.044		
x Furfural + $(1-x)$ *p*-xylene			
0.1862	−0.056	0.6551	−0.088
0.2889	−0.080	0.7328	−0.075
0.3716	−0.094	0.8687	−0.041
0.5058	−0.099	0.9631	−0.012
0.5939	−0.095		

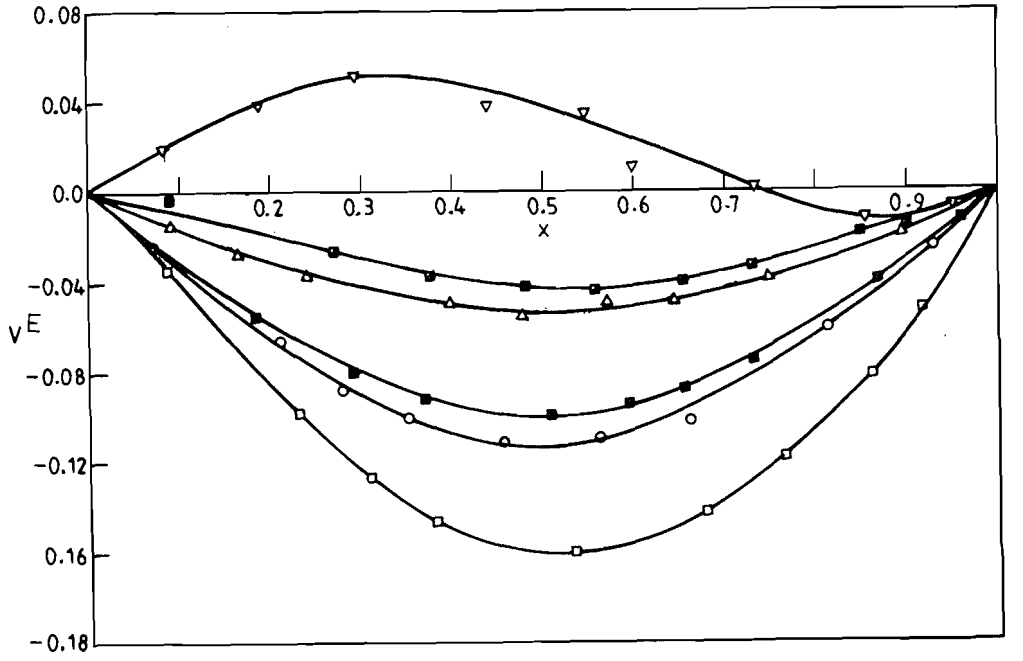

FIG. 1. Molar excess volumes, V^E, as a function of composition at 308.15 K for the binary mixtures of furfural with various aromatic hydrocarbons: ○, benzene; □, toluene; △, ethylbenzene; ◪, *m*-xylene; ▽, *o*-xylene; ■, *p*-xylene.

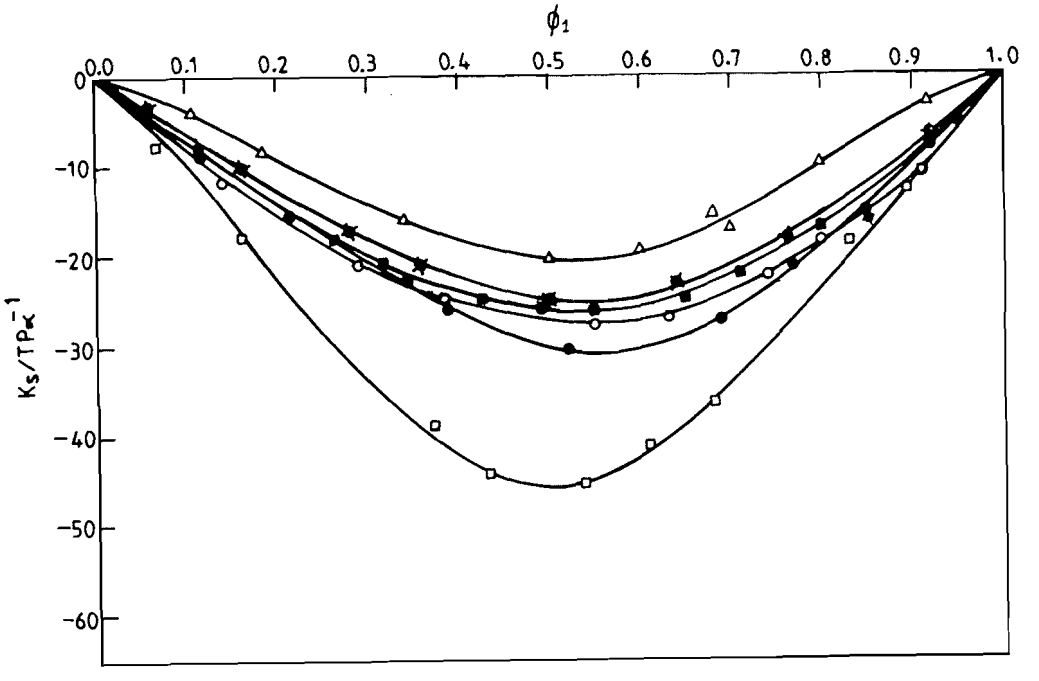

FIG. 2. Values of K_s against volume fraction of furfural for the binary mixtures of furfural with aromatic hydrocarbons at 308.15 K. ●, benzene; □, toluene; ■, ethylbenzene; △, *o*-xylene; ○, *m*-xylene; ⊗, *p*-xylene.

TABLE 2. Values of the parameters in eq. [1] and the standard deviation $\sigma(V^E)$

x Furfural +	A_0	A_1	A_2	A_3	$\sigma(V^E)$ (cm^3 mol^{-1})
$(1-x)$ Benzene	−0.4546	−0.0059	0.1280	0.0151	0.002
$(1-x)$ Toluene	−0.6425	−0.0740	0.1161	−0.0801	0.004
$(1-x)$ Ethylbenzene	−0.2136	−0.0121	0.0368	0.0216	0.002
$(1-x)$ *o*-Xylene	0.1487	−0.2674	−0.1437	0.0420	0.004
$(1-x)$ *m*-Xylene	−0.1691	−0.0167	0.0599	−0.0796	0.003
$(1-x)$ *p*-Xylene	−0.3961	−0.0008	0.0675	0.0009	0.002

Can. J. Chem. Downloaded from www.nrcresearchpress.com by 93.93.197.157 on 09/07/12
For personal use only.

TABLE 3. Volume fraction ϕ, density ρ, sound velocity u, isentropic compressibility k_s, and its deviation K_s as calculated from eq. [3] for furfural + an aromatic hydrocarbon at 308.15 K

ϕ	ρ (g cm^3)	u (m s^{-1})	k_s (TPa^{-1})	K_s (TPa^{-1})
ϕ Furfural + (1 − ϕ) benzene				
0.0	0.86257	1255	735	—
0.1217	0.89760	1270	691	−9
0.2153	0.92508	1284	656	−16
0.3457	0.96270	1304	611	−23
0.3905	0.97548	1312	595	−26
0.5173	1.01114	1335	555	−30
0.6932	1.05949	1366	506	−27
0.7684	1.07979	1375	490	−21
0.8525	1.10222	1386	472	−15
0.9217	1.12048	1395	458	−8
1.00	1.14372	1404	444	—
ϕ Furfural + (1 − ϕ) toluene				
0.0	0.85281	1257	742	—
0.0647	0.87283	1266	715	−8
0.1598	0.90186	1281	676	−18
0.3704	0.96040	1324	593	−39
0.4271	0.98708	1332	571	−44
0.5425	1.01387	1359	534	−46
0.6102	1.03802	1362	519	−41
0.6813	1.05326	1374	503	−36
0.8342	1.09647	1386	475	−18
0.8965	1.11793	1391	462	−13
1.00	1.14372	1404	444	—
ϕ Furfural + (1 − ϕ) ethylbenzene				
0.0	0.85360	1280	715	—
0.1142	0.88676	1291	676	−8
0.2662	0.93099	1311	625	−18
0.3161	0.94558	1319	608	−21
0.4251	0.97715	1333	576	−24
0.5481	1.01306	1351	541	−26
0.6497	1.04266	1366	514	−25
0.7098	1.06002	1372	501	−22
0.8024	1.08670	1385	480	−17
0.9512	1.12989	1399	452	−5
1.00	1.14372	1404	444	—
ϕ Furfural + (1 − ϕ) *o*-xylene				
0.00	0.86676	1309	673	—
0.1052	0.89581	1316	645	−4
0.1834	0.91728	1323	623	−8
0.3480	0.96272	1342	577	−16
0.5024	1.00558	1361	537	−21
0.5997	1.03263	1369	517	−19
0.6811	1.05546	1375	501	−17
0.7038	1.06165	1377	497	−15
0.8060	1.09016	1385	478	−10
0.9152	1.11094	1400	459	−4
1.00	1.14372	1404	444	—
ϕ Furfural + (1 − ϕ) *m*-xylene				
0.00	0.85117	1283	714	—
0.1417	0.89954	1294	664	−12
0.2887	0.93596	1318	615	−21
0.3841	0.96393	1332	585	−25
0.4898	0.99488	1345	556	−26
0.5503	1.01258	1356	537	−28
0.6324	1.03654	1367	516	−27
0.7406	1.06810	1380	492	−22
0.8000	1.08542	1387	479	−19
0.9086	1.11706	1398	458	−11
1.00	1.14372	1404	444	—
ϕ Furfural + (1 − ϕ) *p*-xylene				
0.00	0.84783	1272	729	—
0.0588	0.86527	1277	709	−3
0.1669	0.89727	1289	671	−10
0.2838	0.93214	1305	630	−18
0.3564	0.95383	1315	606	−21
0.4992	0.99653	1336	562	−25
0.6424	1.03894	1357	523	−23
0.7668	1.07505	1375	492	−18
0.8502	1.09959	1389	471	−16
0.9205	1.12049	1393	460	−7
1.00	1.14372	1404	444	—

experimental V^E values were fitted into the smoothing equation:

$$[1]\quad V^E/x(1-x) = A_0 + A_1(2x-1) + A_2(2x-1)^2 + A_3(2x-1)^3$$

where x is the mole fraction of furfural in the mixture. The values of the parameters A_0, A_1, A_2, and A_3 were evaluated by the method of least squares and are given in Table 2, along with the standard deviation $\sigma(V^E)$. Since the $\sigma(V^E)$ values for all the mixtures studied are less than the experimental uncertainty involved, eq. [1] may be taken to represent the experimental results.

The k_s values reported in Table 3 were computed using the relation

$$[2]\quad k_s = (u^2 \cdot \rho)^{-1}$$

where u is the speed of sound and ρ is the density of the solution. In the last column of Table 3 are recorded the values of K_s, the deviation in isentropic compressibility, given by the expression

$$[3]\quad K_s = k_s - \phi_1 k_{s,1} - \phi_2 k_{s,2}$$

where the subscripts 1 and 2 represent the component molecules of the binary mixtures and ϕ_i is the volume fraction of the component i in the mixture. The K_s values were fitted into the polynomial:

$$[4]\quad K_s/\phi_1 \cdot \phi_2 = B_0 + B_1(\phi_1 - \phi_2) + B_2(\phi_1 - \phi_2)^2 + B_3(\phi_1 - \phi_2)^3$$

The values of the adjustable parameters B_0, B_1, B_2, and B_3 obtained by the method of least squares are included in Table 4 along with the standard deviation $\sigma(K_s)$. Figure 2 shows the graphical representation of the variation of K_s with the volume fraction of furfural, ϕ_1.

It is observed from Table 1 that the V^E values for all the mixtures studied (except those containing *o*-xylene) are negative over the entire composition range. For mixtures containing *o*-xylene, a plot of V^E vs. x yields an S-shaped curve and V^E becomes negative only at the furfural end. Further, the substitution of an alkyl group in the benzene ring influences $V^E_{0.5}$, the excess molar volume at equimolar concentration, in

Can. J. Chem. Downloaded from www.nrcresearchpress.com by 93.93.197.157 on 09/07/12
For personal use only.

TABLE 4. Values of the parameters in eq. [4] and standard deviation $\sigma(K_s)$

ϕ Furfural +	B_0	B_1	B_2	B_3	$\sigma(K_s)$/TPa^{-1}
$(1-\phi)$ Benzene	−117	−32	30	21	1
$(1-\phi)$ Toluene	−176	−4	71	11	2
$(1-\phi)$ Ethylbenzene	−104	−16	17	−4	1
$(1-\phi)$ *o*-Xylene	−80	−8	52	1	2
$(1-\phi)$ *m*-Xylene	−108	−12	−8	−14	1
$(1-\phi)$ *p*-Xylene	−101	−23	26	−8	1

the following order: toluene < benzene < ethylbenzene. The methyl substitution in toluene influences $V^E_{0.5}$ in the order toluene < *p*-xylene < *m*-xylene < *o*-xylene. To the best of our knowledge, no data have been reported in the literature for the excess volumes and isentropic compressibilities of any of the binary mixtures under investigation, to compare with our results.

The overall volumetric effects in a binary mixture may be attributed to geometric and interaction factors. These arise from the differences in size and shape and cohesive energy of the component molecules (6, 7). The excess volumes, unlike the excess enthalpies, H^E, are more sensitive to geometrical effects (8), and a significant contribution of these geometric factors to the volumetric behaviour of these mixtures is also reflected in the V^E values of xylene solutions. The results of H^E studies on these systems will be published elsewhere.

Isentropic copressibilities presented in Table 3 show that K_s values for all the mixtures studied are negative over the entire composition range. The values suggest that "intermolecular spaces" in the mixtures, as defined by Jacobson (9), might decrease from benzene to a xylene.

1. S. K. SURI. Can. J. Chem. **59**, 2839 (1981).
2. B. CHAWLA, R. PRAKASH, and S. K. SURI. Can. J. Chem. **61**, 1647 (1983).
3. S. K. SURI and V. RAMAKRISHNA. Indian J. Chem. **7**, 490 (1969).
4. J. A. RIDDICK and W. B. BUNGER. Techniques of organic chemistry. Vol. II. Organic solvents. Wiley–Interscience, New York. 1970.
5. J. TIMMERMANS. Physico-chemical constants. Vol. II. Elsevier, Amsterdam. 1965.
6. R. P. RASTOGI, I. NATH, and I. MISHRA. J. Phys. Chem. **71**, 1277 (1967).
7. R. K. NIGAM and P. P. SINGH. Trans. Faraday Soc. **65**, 950 (1969).
8. L. PIKKARAINEN. J. Chem. Eng. Data, **32**, 429 (1987).
9. B. JACOBSON. Ark. Kemi, **2**, 177 (1953).

Can. J. Chem. Downloaded from www.nrcresearchpress.com by 93.93.197.157 on 09/07/12
For personal use only.

A single-crystal electron spin resonance study of the cyclic 1,2,4,3,5-trithiadiazolyl radical, $S_3N_2^{+\bullet}$

K. F. PRESTON AND J.-P. CHARLAND
Division of Chemistry, National Research Council of Canada, Ottawa, Ont., Canada K1A 0R9

AND

L. H. SUTCLIFFE
Chemistry Department, Royal Holloway and Bedford New College, Egham, Surrey, UK TW20 OEX

Received December 2, 1987

K. F. PRESTON, J.-P. CHARLAND, and L. H. SUTCLIFFE. Can. J. Chem. **66**, 1299 (1988).

An anisotropic ESR signal detected in single crystals of 5-methyl-1,3,2,4-dithiazolylium hexafluoroarsenate ($CH_3\overline{CNSNS}^+AsF_6^-$) is shown to be that of 1,2,4,3,5-trithiadiazolyl, $S_3N_2^{+\bullet}$. The **g**- and ^{14}**N**-hyperfine tensors for this radical were established in the monoclinic *abc** crystal-axis system from spectral measurements at room temperature on aligned single crystals. Agreement of the principal values of the tensors with those obtained in our earlier studies by simulation of powder spectra is excellent. The **g**-tensor (2.0021, 2.0072, 2.0248) and the two ^{14}**N**-tensors (25.4, 0.8, 0.8 MHz) are collinear within experimental error and lie with minimum *g* and maximum hyperfine perpendicular to the plane of the host cation. The electronic structure of the radical deduced from our earlier studies ($^2A_2$ in C_{2v}) is confirmed, and the impurity is shown to substitute for the host cation in the anticipated manner.

K. F. PRESTON, J.-P. CHARLAND et L. H. SUTCLIFFE. Can. J. Chem. **66**, 1299 (1988).

On démontre que le signal rpe anisotrope qui est détecté dans les cristaux uniques de l'hexafluoroarsenate de méthyl-5 dithiazolylium-1,3,2,4 ($CH_3\overline{CNSNS}^+AsF_6^-$) est dû au trithiadiazolyl-1,2,4,3,5, $S_3N_2^{+\bullet}$. Utilisant des mesures spectrales effectuées à la température ambiante, sur des monocristaux alignés, on a déterminé les tenseurs **g** et hyperfins du ^{14}**N** de ce radical dans l'axe cristallin du système monoclinique *abc**. Il existe un accord excellent entre les valeurs principales des tenseurs et celles qui ont été obtenues au cours de nos études antérieures effectuées par simulation des spectres de poudre. A l'intérieur des erreurs expérimentales, le tenseur **g** (2,0021, 2,0072 et 2,0248) et les deux tenseurs du ^{14}**N** (25,4, 0,8 et 0,8 MHz) sont colinéaires et se trouvent à la valeur minimale de g et à la valeur maximale du tenseur hyperfin perpendiculaire au plan du cation hôte. On a confirmé la structure électronique du radical qui avait été déduite à partir de nos études antérieures ($^2A_2$ dans C_{2v}) et on démontre que l'impureté se substitue au cation hôte de la manière anticipée.

[Traduit par la revue]

Introduction

The vast majority of free-radical structures have been determined from spectroscopic measurements made on samples of liquid or solid solutions, or of both types of sample. Rarely is it possible to carry out the ultimate spectroscopic measurement on an aligned single crystal containing the free radical as an impurity. Such single-crystal determinations by ESR spectroscopy provide additional and invaluable information in the principal directions of tensors, which cannot be extracted from powder data (1*a*, 2, 3). Structural similarities between the free radical and the host often predetermine the location of the radical within the crystal structure, so that the experimental principal directions in the crystal axis system may be transformed into an axis system of the free radical itself (1*a*, 2–4). Armed with both principal values and directions of the **g**- and hyperfine tensors in a molecular axis system, the spectroscopist can usually unequivocally establish the ground-state geometry and electronic wavefunction of the free radical. An added advantage of measurements on a single crystal, of course, is the lack of ambiguity associated with the spectral analysis of powder samples.

Much of the early literature on the chemical applications of ESR spectroscopy was concerned with the class of radicals commonly referred to as cyclic π radicals (1*b*). Although almost exclusively populated by carbocyclics, one of the simplest members of this class of free radicals is, in fact, inorganic, viz. the cyclic sulphur nitride $S_3N_2^{+\bullet}$ (5–10). This free radical is remarkably persistent and is a common by-product of the reactions of sulphur–nitrogen compounds in polar solvents (9). Liquid-phase and powder spectra of this species suitably enriched in ^{33}S and ^{15}N have been interpreted (8–11) in terms of a planar π radical (Fig. 1) in which the unpaired electron occupies an orbital of the A_2 representation in C_{2v} symmetry.

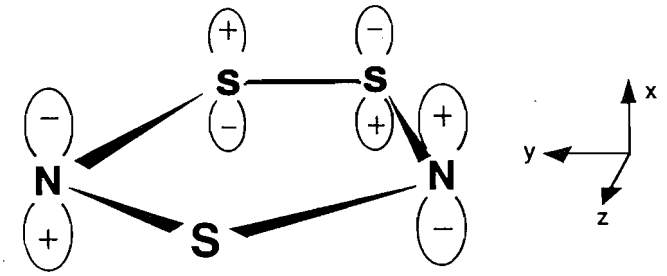

FIG. 1. The $^2A_2$ SOMO of $S_3N_2^+$.

Experimental

5-Methyl-1,3,2,4-dithiadiazolylium hexafluoroarsenate (V) was prepared according to a literature method (12) from acetonitrile (May and Baker, HPLC grade) and S_2N^+ AsF_6^-, kindly provided by Dr. A. G. Kendrick of Durham University. The dithionitronium salt is very reactive and can produce the $S_3N_2^{+\bullet}$ radical in high concentrations with, for example, tetrahydrofuran (11). Hence by using a slight excess of this salt in the preparation of $CH_3\overline{CNSNS}^+AsF_6^-$ some $S_3N_2^+$ radical (its identity being proved by ESR — see below) was introduced

[1]NRCC No. 28712.

Can. J. Chem. Downloaded from www.nrcresearchpress.com by 93.93.197.157 on 09/07/12
For personal use only.

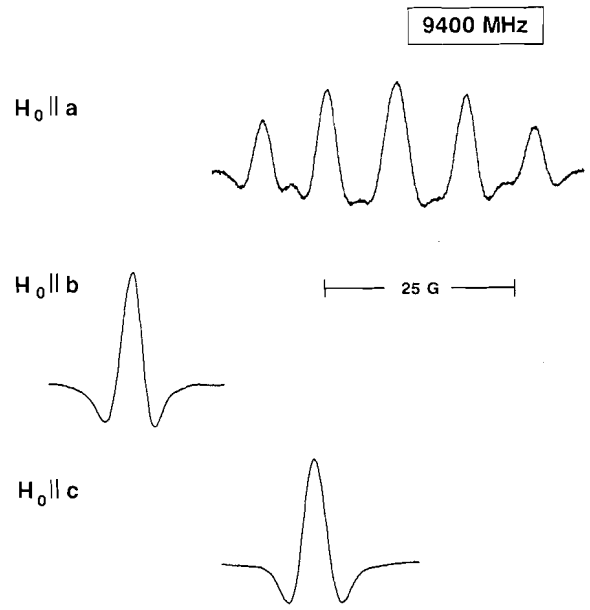

FIG. 2. Second-derivative ESR spectra at 25°C for H_0 parallel to the crystal axes a,b,c^* of 5-Me-1,3,2,4-dithiadiazolylium hexafluoroarsenate.

into the crystal: crystals were obtained by recrystallisation from liquid sulphur dioxide (BDH).

Good single crystals (needle axis ≈2–3 mm) were selected with the aid of a polarizing microscope. One of these was attached with epoxy resin to the gear wheel of a two-circle goniometer (4, 13). Other crystals were aligned on a Nonius diffractometer according to the established crystal structure (12). Such crystals were sealed in the ends of 4 mm quartz tubes so that the tube axis was one of the orthogonal axes abc^* of the monoclinic ($P2_1/c$) crystal (12), and a second crystal axis lay in a known direction in the plane perpendicular to the tube. Contact of the crystals with air was minimized by carrying out most of the manipulations under an atmosphere of very dry nitrogen in a dry box.

The single crystal, either mounted on the two-circle goniometer or sealed into the end of a quartz tube, was placed at the centre of the rectangular resonant cavity of a Varian E-12 spectrometer. Dry nitrogen was passed through the cavity during the course of the measurements to limit deterioration of the crystal. Magnetic field intensity was determined with a Cyclotron Corporation gaussmeter and microwave frequency with a Systron–Donner digital counter. Since the linewidth of the signal increased at sub-ambient temperatures, measurements were confined to room temperature.

Results

Examination of single crystals of 5-methyl-1,3,2,4-dithiadiazolylium hexafluoroarsenate prepared as described above revealed the presence of an intense ESR spectrum. For an arbitrary orientation of the d.c. magnetic field, the spectrum consisted of two sets of quintets each having the 1:2:3:2:1 intensity ratio characteristic of interaction of a single unpaired electron with two equivalent ^{14}N ($I = 1$) nuclei. Certain orientations (Fig. 2) of the crystal resulted in a coalescence of the spectrum to that of a single quintet, and others in the collapse of the nuclear hyperfine in one or both of the quintets to a single broad resonance. No orientation could be found for which the ESR spectrum either consisted of more than two sets or indicated inequivalence of the two ^{14}N nuclei. This behaviour conformed with that anticipated for the two magnetically inequivalent sites of a monoclinic crystal, and showed furthermore that the two ^{14}N hyperfine tensors of the radical are parallel (4).

The method of spectral coalescences (4) was used successfully to locate the b axis of the monoclinic ($P2_1/c$) crystal: a particularly narrow coalescence showing no resolved hyperfine structure was chosen as a tentative y axis (4), and it was found that the spectrum remained coalesced (i.e. only one site observed) throughout the plane (xz) perpendicular to that axis. Axes x and z were chosen corresponding to the minimum and maximum in the least-squares best fit (3, 4) to the g^2 data (Fig. 3) for the xz plane. The ESR spectra from crystallographically-aligned samples were then examined and it was found that to within the experimental error in measured g (one standard deviation ±0.0002), the initially chosen axes x,y,z corresponded to the orthogonal crystal axes a,b,c^*. Subsequent measurements made with the two-circle goniometer were then referred to the crystal axis system. Spectra were recorded as a function of angular departure from a crystal axis in each of the three crystal planes, and were analyzed to yield values of g^2 and g^2a^2 for each site. Exact analysis for the ^{14}N hyperfine coupling was not possible for the bc^* plane since the hyperfine was not resolved for any direction in that plane. Crude estimates of the ^{14}N coupling constants for that plane were obtained by spectral simulation using the linewidth (3.0 G) determined for the spectrum of a single site showing a well-resolved hyperfine manifold. The values of g^2 and g^2a^2 exhibited the usual sinusoidal behaviour (Fig. 3) within a plane; least-squares fitting procedures were used (3, 4) to determine the best-fit diagonal and off-diagonal tensor components in the abc^* basis (Table 1). Relative signs of the off-diagonal elements of the two matrices were established in the approved manner by the comparison of measured and predicted values of g^2 and g^2a^2 for the skew direction (1,1,1) in the abc^* basis (4).

Following diagonalization of the $\mathbf{g}^2$ matrix, which yielded the principal values and directions of $\mathbf{g}$ (Table 1), the $\mathbf{g}$-matrix was assembled in the crystal axis system. The $\mathbf{a}^2$ matrix was generated by pre- and post-multiplication of $\mathbf{g}^2\mathbf{a}^2$ by $\mathbf{g}^{-1}$ (4), and was diagonalized to give principal values and directions of the ^{14}N tensor (Table 1).

In order to ascertain the origin of the paramagnetic "impurity", the reagents used in the preparation of the host material were examined by ESR spectroscopy. It was quickly established that the reagent $NS_2^+AsF_6^-$, as expected, contained a free-radical impurity. When dissolved in liquid SO_2, it exhibited an isotropic spectrum of two equivalent ^{14}N nuclei with (at 0°C) $g = 2.0115$, $a_{14}(2) = 8.98$ MHz. An identical spectrum was obtained from a solution of a host crystal in SO_2. Evidently the radical can easily be incorporated into the host during the crystallization process.

Discussion

A comparison of the principal values and of the isotropic values of $\mathbf{g}$ and $\mathbf{a}_{14}$ with those reported (8–10) for the cyclic inorganic radical $S_3N_2^{+\bullet}$ (Table 2) leaves no doubt whatsoever as to the identity of the radical detected in this single-crystal study. The added directional information obtained from the single crystal substantiates the structural and electronic symmetry assignments made for trithiadiazolylium on the basis of powder and solution spectra alone.

Dealing firstly with the principal values, we note the excellent agreement between the three components of the $\mathbf{g}$-tensor determined here and the values deduced from powder spectra of $S_3N_2^{+\bullet}$ (9, 10). The maximum principal value of the ^{14}N

Can. J. Chem. Downloaded from www.nrcresearchpress.com by 93.93.197.157 on 09/07/12
For personal use only.

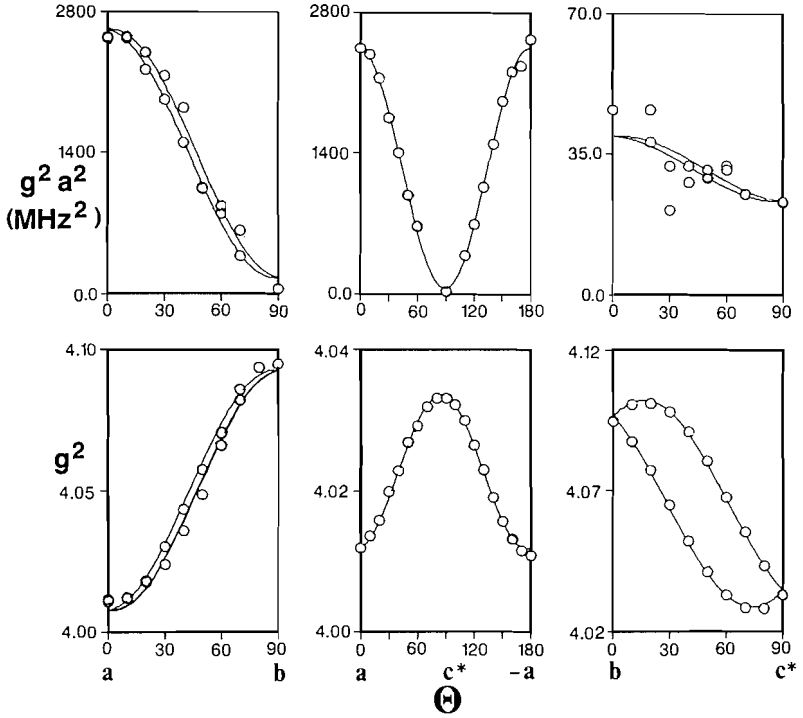

FIG. 3. Plots of g^2 and g^2a^2 (MHz^2) against angle for the three orthogonal planes of the crystal. Least-squares best-fit sine curves have been drawn through the experimental points (circles).

TABLE 1. The $\mathbf{g}^2$ and hyperfine tensors $\mathbf{ga}^2\mathbf{g}/MHz^2$ for the radical $S_3N_2^+$ in a crystal of 5-Me-1,3,2,4-dithiadiazolylium hexafluoroarsenate; principal values of $\mathbf{g}$ and hyperfine interactions in MHz and their direction cosines in the abc^* axis system

	Tensor			Principal values and direction cosines of $\mathbf{g}$, $\mathbf{a}_{14}(2)$		
	a	*b*	*c**	*x*	*y*	*z*
				2.0021	2.0072	2.0248
$\mathbf{g}^2$	4.0086	±0.0033	0.0000	0.9983	−0.0469	−0.0347
	±0.0033	4.0939	±0.0197	∓0.0468	∓0.2879	∓0.9565
	0.0000	±0.0197	4.0349	0.0349	0.9565	−0.2896
				25.4	2.3	2.9 MHz
$\mathbf{ga}_{14}^2\mathbf{g}$	2585	∓118	45	0.9988	0.0212	0.0446
$2^{14}\mathbf{N}$	∓118	39	∓1	∓0.0462	±0.0835	±0.9954
	45	∓1	23	0.0174	−0.9963	0.0844

TABLE 2. Comparison of spectral parameters for $S_3N_2^+$

Matrix	*T*/K	g_{xx} a_{xx}[a]	g_{yy} a_{yy}	g_{zz} a_{zz}	g_{iso} a_{iso}	Reference
$CH_3\overline{CNSNS}^+$	298	2.0021	2.0072	2.0248		This work
AsF_6^-		25.4	<2.3	<2.9		
D_2SO_4	110	2.0013	2.0062	2.0250		10
		25.7	<1.5	<1.5		
SO_2	273				2.0115	This work
					8.98	
CH_2Cl_2	300?				2.01	8
					8.86	
D_2SO_4	295				2.0111	10
					8.98	

[a]Hyperfine interaction in MHz of two equivalent ^{14}N nuclei.

Can. J. Chem. Downloaded from www.nrcresearchpress.com by 93.93.197.157 on 09/07/12
For personal use only.

TABLE 3. Certain bond lengths and direction cosines in the *abc** axis system of the 5-Me-1,3,2,4-dithiadiazolylium hexafluoroarsenate crystal

Bond	Length (nm)	Direction cosines		
		a	*b*	*c**
S_1—N_2	0.1634	−0.1092	−0.9934	0.0342
S_1—C_1	0.1773	0.1226	0.0980	−0.9876
S_2—N_2	0.1581	−0.0663	0.3901	0.9184
S_2—N_1	0.1571	0.1911	0.7802	−0.5956
N_1—C_1	0.1323	−0.0069	0.8984	0.4391
Perpendicular to cation plane		0.9860	−0.0979	0.1349
Bisector $N_1S_2N_2$		0.1016	0.9579	0.2684

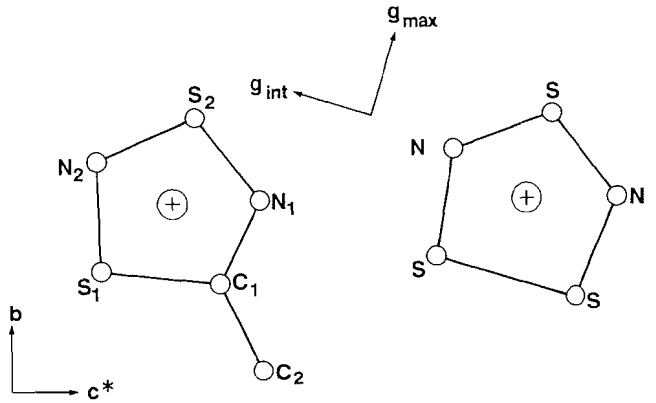

FIG. 4. Projection along *a* of the host cation structure, and the presumed orientation of the impurity cation radical $S_3N_2^{+\bullet}$.

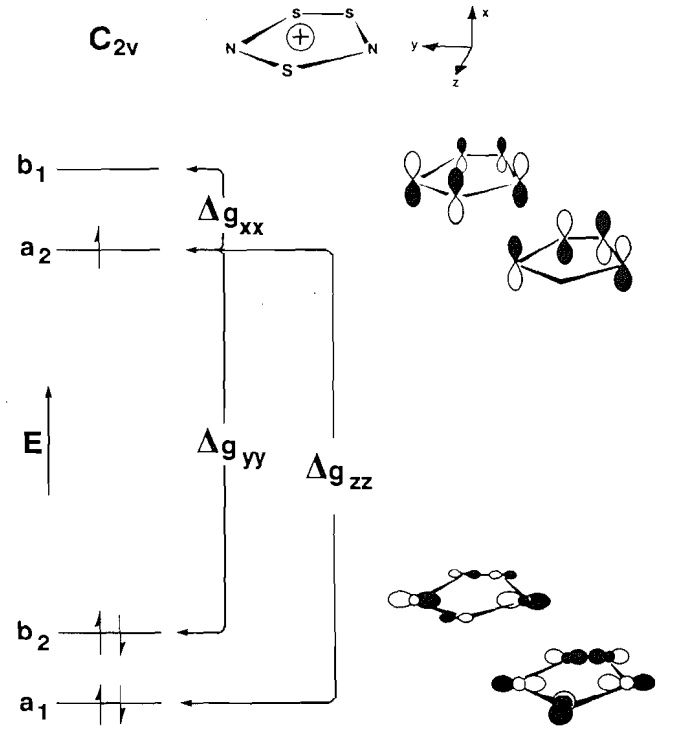

FIG. 5. Hückel molecular orbitals and symmetry-allowed *g* shifts for $S_3N_2^{+\bullet}$.

hyperfine interaction, a_{xx}, is also in good accord with the powder value, but the remaining two values seem to be larger than the limits imposed by the line-widths of the powder spectrum (Table 2). Hyperfine coupling to the ^{14}N nuclei was not resolved in the *yz* (*bc**) plane (Figs. 2, 3), and only crude estimates of its value were made (Fig. 3) from line-width measurements and simulations. Furthermore, with such small couplings the contribution from the ^{14}N nuclear Zeeman interaction (≈1 MHz) to the "observed" splittings cannot be ignored (3). A better estimate of the very small hyperfine interactions, a_{yy} and a_{zz}, can be obtained from a comparison of the isotropic value, measured in SO_2 or D_2SO_4 near room temperature (Table 2), and the value of a_{xx}. In this manner we obtain a $^{14}\mathbf{N}$ tensor of (25.4, 0.8, 0.8) MHz with standard errors of 0.1 MHz in each component, providing the tensor is perfectly axial.

Considering next the principal directions of the **g**- and $^{14}\mathbf{N}$ hyperfine tensors, we note that since **g** is distinctly rhombic, all three principal directions are well defined. In the case of the $^{14}\mathbf{N}$ tensors, the proximity, the uncertainty and the small magnitudes of a_{yy} and a_{zz} result in ill-defined directions for those two components. Nevertheless, they are found to lie 12° from g_{yy} and g_{zz}, respectively. The direction of unique and maximum hyperfine is, of course, very well defined; it lies only 1° from g_{xx}. We conclude, therefore, that to within the experimental error (±2°) all three tensors are collinear.

In Table 3 we have assembled some directions in the *abc** basis of the host crystal (12) which are germane to the present discussion. The perpendicular to the host cation plane lies 6.5° from g_{xx} and 7.4° from a_{xx}. g_{xx} (maximum *g*) lies 4.0° from the bisector of $N_1S_2N_2$, and g_{yy} lies 11.9° from C_1S_1. If we accept the π-radical description (Fig. 1) of $S_3N_2^+$ in which g_{min} and a_{max} lie perpendicular to the radical plane and g_{max} lies along the (*z*) two-fold axis (9, 10) we see (Fig. 4) that the impurity radical cation has substituted for the host cation in the manner most expected. Since this particular orientation accounts for both powder and single-crystal data and corresponds to the predictions (see below) of simple molecular orbital calculations, we feel that the assignment of $^2A_2$ in C_{2v} for the electronic ground-state wavefunction of $S_3N_2^{+\bullet}$ can be accepted with a high degree of confidence.

The assignment of the in-plane *g* values, given without justification in our earlier work (9, 10), is corroborated by the present data if the orientation of Fig. 4 is in fact correct. Molecular orbital calculations at the Hückel and INDO levels give some support for the assignment of g_{max} to the two-fold axis. Figure 5 shows the upper filled and the lowest unoccupied molecular orbitals predicted by an energy optimized Hückel calculation, and indicates the symmetry-allowed *g* shifts which may arise through spin–orbit interactions of the half-filled a_2 level with neighbouring levels. (INDO predictions are similar and do not alter the conclusions reached here regarding *g* shifts.) The Stone formula (14) tells us that the *g* shift is proportional to the spin–orbit interaction and inversely proportional to the difference in energy between ground and excited states. Since the spin–orbit coupling constant for sulphur is roughly 5 times that for nitrogen (15), the *g* shifts in $S_3N_2^{+\bullet}$ are essentially determined by sulphur orbital components in the ground and excited states. At first glance, the proximity of the b_1 level suggests a significant *negative* shift for $H_0//x$, but the orbital compositions of a_2 and b_1 are inappropriate: *both* are made up

Can. J. Chem. Downloaded from www.nrcresearchpress.com by 93.93.197.157 on 09/07/12
For personal use only.

of p_x atomic orbitals, so that spin–orbit interaction is zero to first approximation. Similarly, energy considerations alone (Fig. 5) would suggest that the (positive) g shift along y should exceed that along z. However, the b_2 orbital has very little contribution from p_z atomic orbitals which generate the spin–orbit interaction about y. In contrast, the a_1 orbital has important S $3p_y$ components which are responsible for the considerable positive g shift when $H_0 // z$. Qualitatively, therefore, the molecular orbital predictions match the experimental **g** tensor extremely well: maximum g is predicted to lie along the two-fold axis (z); g_{xx} and g_{yy} are predicted to lie very near to the free-spin value with small negative and positive departures therefrom, respectively.

Ideally, it would be desirable to study the ESR spectrum of $S_3N_2^{+\bullet}$ in a single crystal of its dimer $S_6N_4^{2+}$, whose crystal structure is well-established (16). The dimer is known to contain small amounts of the radical (16) but unfortunately, it has not proven possible to grow a crystal of sufficient size for our purposes. However, it may be feasible to use a host more symmetrical than $CH_3\overline{CNSNS}^+$ such as the salts of $R\overline{CSNSC}R^+$, where R = H, CH_3 etc. Unfortunately, in spite of our successes (10) in labelling $S_3N_2^+$ with sulphur-33 and nitrogen-15, there does not appear to be a practicable way of introducing the labelled radical into a single crystal.

Acknowledgements

We would like to express our gratitude to Dr. A. G. Kendrick of Durham University for the gift of a sample $S_2N^+AsF_6^-$: K.F.P. and L.H.S. are also indebted to NATO for a travel award.

1. J. E. WERTZ and J. R. BOLTON. Electron spin resonance: elementary theory and applications. McGraw-Hill, New York. 1972. (*a*) Chap. 7; (*b*) Chaps. 5, 6.
2. J. R. MORTON. Chem. Rev. **64**, 453 (1964).
3. H. A. FARACH and C. P. POOLE. Adv. Magn. Reson. **5**, 229 (1971).
4. J. R. MORTON and K. F. PRESTON. J. Magn. Reson. **52**, 457 (1983).
5. D. CHAPMAN and A. G. MASSEY. Faraday Soc. **58**, 1291 (1962).
6. D. A. C. MCNEIL, M. MURRAY, and M. C. R. SYMONS. J. Chem. Soc. A, 1019 (1967).
7. S. A. LIPP, J. J. CHANG, and W. L. JOLLY. Inorg. Chem. **9**, 1970 (1970).
8. R. J. GILLSEPIE, P. R. IRELAND, and J. E. VEKRIS. Can. J. Chem. **53**, 3147 (1975).
9. S. A. FAIRHURST, K. F. PRESTON, and L. H. SUTCLIFFE. Can. J. Chem. **62**, 1124 (1984).
10. (*a*) S. A. FAIRHURST, K. M. JOHNSON, L. H. SUTCLIFFE, K. F. PRESTON, A. J. BANISTER, Z. V. HAUPTMAN, and J. PASSMORE. J. Chem. Soc. Dalton Trans. 1465 (1986); (*b*) K. M. JOHNSON, K. F. PRESTON, and L. H. SUTCLIFFE. In preparation.
11. S. A. FAIRHURST, A. HULME-LOWE, K. M. JOHNSON, L. H. SUTCLIFFE, J. PASSMORE, and M. J. SCHRIVER. Magn. Reson. Chem. **23**, 828 (1985).
12. G. K. MACLEAN, J. PASSMORE, M. N. S. RAO, M. J. SCHRIVER, P. S. WHITE, D. BETHELL, R. S. PILKINGTON, and L. H. SUTCLIFFE. J. Chem. Soc. Dalton Trans. 1405 (1985).
13. J. R. MORTON, K. F. PRESTON, and S. J. STRACH. Rev. Sci. Instrum. **52**, 1358 (1981).
14. A. J. STONE. Proc. R. Soc. A**271**, 424 (1963).
15. J. R. MORTON, J. R. ROWLANDS, and D. H. WHIFFEN. National Physical Laboratory Report BPR13. 1962.
16. R. W. H. SMALL, A. J. BANISTER, and Z. V. HAUPTMAN. J. Chem. Soc. Dalton Trans. 1379 (1984).

Can. J. Chem. Downloaded from www.nrcresearchpress.com by 93.93.197.157 on 09/07/12
For personal use only.

Electron thermalization distance distribution in liquid carbon monoxide: electron capture

G. RAMANAN AND GORDON R. FREEMAN
Chemistry Department, University of Alberta, Edmonton, Alta., Canada T6G 2G2

Received November 13, 1987

G. RAMANAN and GORDON R. FREEMAN. Can. J. Chem. **66**, 1304 (1988).

Electron thermalization in X irradiated liquid CO is truncated by electron capture to form an anion, as it is in liquid N_2. The thermalization distance distribution in these two liquids is a modified exponential, rather than the modified Gaussian obtained in liquid hydrocarbons where electron capture does not occur. The density normalized distance parameter $b_{EP}d$ in CO was constant, 2.8×10^{-6} kg/m^2, at densities $2.7 \gtrsim d/d_c > 2.0$, but increased somewhat at lower densities, reaching 3.3×10^{-6} kg/m^2 at $d/d_c = 1.4$. The thermalization distances in CO are about two thirds those in N_2 at the same density. Electrons are captured more readily by CO than by N_2.

G. RAMANAN et GORDON R. FREEMAN. Can. J. Chem. **66**, 1304 (1988).

Comme il a été observé antérieurement dans le N_2 liquide, la thermalisation des électrons dans le CO liquide irradié par des rayons-X est tronquée par une capture d'électron qui forme un anion. Dans ces deux liquides, la distribution de la distance de thermalisation est une exponentielle modifiée plutôt que la distribution de Gauss modifiée observée dans les hydrocarbures liquides dans lesquels la capture d'électron ne se produit pas. Dans le CO, à des densités $2{,}7 \gtrsim d/d_c > 2{,}0$, le paramètre de distance normalisé pour la densité, $b_{EP}d$, est constant à $2{,}8 \times 10^{-6}$ kg/m^2; toutefois, à des densités plus faibles, cette valeur augmente pour atteindre $3{,}3 \times 10^{-6}$ kg/m^2 à $d/d_c = 1{,}4$. A la même densité, la distance de thermalisation dans le CO est environ les deux tiers de celle dans le N_2. Il se produit une capture plus rapide des électrons dans le CO que dans le N_2.
[Traduit par la revue]

Introduction

The distribution of electron thermalization distances in X irradiated liquid nitrogen has been found to be non Gaussian (1), which is different from those in hydrocarbons (2). The distribution is mainly a one-dimensional exponential, attributed to truncation of the electron thermalization process by electron capture (3). Carbon monoxide is isoelectronic with nitrogen, and both form transient anions with low energy electrons, carbon monoxide at 0.27 aJ (1.7 eV) and nitrogen at 0.37 aJ (2.3 eV) (4). We therefore chose carbon monoxide for a comparative study.

The rotational constants for CO and N_2 are $B = 3.9 \times 10^{-23}$ J and 3.6×10^{-23} J, respectively, and the vibrational quanta are also similar, respectively 4.4×10^{-20} and 4.3×10^{-20} J (5). The electric moments are more different: dipole 3.7×10^{-31} C m (6) and zero; quadrupole 6.0×10^{-40} C m^2 (7) and 5.1×10^{-40} C m^2 (8) for CO and N_2, respectively. Thus rotational and vibrational excitation by low energy electrons are more efficient for CO (4*b*, 9) than for N_2 (10) in the gas phase, and presumably also in the liquid phase. One might therefore expect shorter thermalization distances in liquid carbon monoxide than in liquid nitrogen at the same density.

Experimental

Materials

Matheson Research Grade CO (99.99%) with sub ppm levels of oxygen, methane, ethane, and hydrogen, and other impurities like carbon dioxide (<5 ppm), nitrogen (~35 ppm), propane (~35 ppm), and dimethyl ether (~15 ppm), was used after purification. The CO from the cylinder was passed through a column of KOH pellets previously degassed in the high vacuum line at an elevated temperature (heated with a brush flame while watching the pressure gauge). This CO was then passed through cold traps kept in liquid oxygen (~90 K), to reduce the condensable impurities. The standard technique of reducing sub ppm levels of oxygen by keeping over a potassium mirror was not possible due to the rapid reaction of this metal with CO (11–13) to give a sequence of colored substances ending in a black solid. The indication that our method of purification reduced the impurity to acceptable levels was indicated by the linear electron current transient (ECT) signal obtained in a low pressure sample.

Sample preparation, irradiation, and dosimetry

The CO was transferred in the vacuum line by distillation with liquid nitrogen as coolant.

The amount of material transferred into the cell was measured in a calibrated burette at a known temperature (77.3 K). From the volume and density, the mass of the material put into the cell was known (6.08 ± 0.04 g).

The conductance cell was of the high pressure type (14). Its internal volume including the tip of the capillary that had been sealed after filling was 21.6 ± 0.1 cm^3. The volume was measured by filling with distilled water using calibrated syringes. The distance between the electrodes was 3.3×10^{-3} m and the cell constant was 12.9 m^{-1} (measured by a four wire capacitance bridge, Electro Scientific Industries model 273, calibrated by a General Radio precision capacitance model 1422-CD).

The cell was accurately positioned in a cylindrical Dewar covered with a styrofoam top, all in a Faraday cage. The method of temperature control was described earlier (15) with one essential difference. The electrical connection through the 1 cm thick glass cell wall to the collector electrode was a 2 mm OD Kovar tube, sealed at the electrode end, which took a 30 gauge copper–constantan thermocouple (calibrated) inside the cell to within ~2 mm of the electrode surface. The recorded temperatures are those at the electrode. The temperature differences between different places on the outside surface of the cell were up to ±0.4 K due to inhomogeneities in the flow of thermostating gas. The temperature registered inside the Kovar tube was usually 0.1 K higher than the average of the three temperatures measured at the top, middle and bottom of the outside surface of the cell.

The irradiations were with 300 ns pulses of 1.7 MeV (270 fJ) X rays which delivered 1.0×10^{11} eV/g (1.6×10^{-5} J/kg) to the sample. Dosimetry was done with lithium fluoride thermoluminescent crystals between the electrodes of a dummy cell that had the same geometry as the conductance cell. The crystals were calibrated against the Fricke dosimeter (16). Energy absorption in liquid CO was calculated from that in the Fricke solution by multiplying by the ratio of the electron densities. The numbers of moles of electrons per gram are CO, 0.500; Fricke solution, 0.554.

Can. J. Chem. Downloaded from www.nrcresearchpress.com by 93.93.197.157 on 09/07/12
For personal use only.

TABLE 1. Electron thermalization distances b_{EP} and mobilities μ_- in liquid CO

T (K)	d (kg/m^3)	d/d_c	ϵ	b_{EP} (nm)	$10^3 G_{fi}^{0a}$	μ_- (10^{-7} m^2/V s)	η (μPa.s)
77.3	805	2.69	1.572	3.5	1.8	0.91	173
83.5	781	2.60	1.552	3.6	2.2	1.17	145
84.7	775	2.58	1.547	3.7	2.4	1.2	140
89.9	752	2.51	1.528	3.8	2.8	1.5	120
93.2	737	2.46	1.515	3.8	3.0	1.7	111
94.7	730	2.43	1.510	3.9	3.2	1.8	106
100.2	701	2.34	1.486	4.1	4.0	2.1	92
103.7	685	2.28	1.472	4.2	4.4	2.3	84
106.7	668	2.23	1.460	4.3	4.9	2.5	78.5
111.7	638	2.13	1.436	4.6	6.1	2.8	67.7
113.1	628	2.09	1.428	4.6	6.3	2.9	65.0
118.1	593	1.98	1.401	4.8	7.5	3.4	56.2
119.0	587	1.96	1.397	4.9	7.8	3.5	55.3
122.1	561	1.86	1.375	5.3	9.5	3.7	50.0
124.7	532	1.77	1.355	5.7	11.5	4.0	45.9
125.8	520	1.73	1.346	5.8	11.9	4.1	44.5
128.3	487	1.62	1.322	6.3	15	4.4	39.6
130.5	450	1.50	1.295	7.0	18	4.7	33.3
131.2	433	1.44	1.283	7.5	22	4.9	30.8
132.9[b]	300[b]	1.00	—	—	—	—	18.0[b]

[a]Assuming $G_{tot} = 3.1$ and $y_0 = 1$ nm.
[b]Critical fluid: T_c, d_c, and assume η_c equals that of nitrogen.

Free ion yields and ion mobilities

The free ions produced in the liquid by each pulse of radiation were measured by sweeping them from the sensitive volume by an electric field and integrating the charges. A low drift integrator (17) and a Nicolet 1170 waveform digitizer were used. Separate measurements were made with positive and negative applied voltages. For a given magnitude of voltage, the amount of charge collected was the same for the positive and negative applied voltages within 5%; the average was used at each voltage to calculate the yield.

The ion mobilities were measured by a time of flight method (18, 19).

Physical properties

Values of the density, d, of liquid CO under its vapor pressure at various temperatures were obtained from ref. 20.

Values of the dielectric constant, ϵ, were calculated from the Mosotti–Clausius relation and the densities using $\epsilon = 1.572$ and $d = 805$ kg/m^3 at 77.3 K as the basis. This value of the ϵ was obtained by measuring the capacitance of the cell filled with liquid N_2 and then with liquid CO at 77.3 K; $\epsilon(N_2) = 1.431$ (1). Our value of $\epsilon = 1.539$ for liquid CO at 84.9 K compares with 1.55 reported earlier (21).

Values of the viscosity of liquid CO are not available in the literature. We have approximated them by using values for N_2 at the same T/T_c (Table 1).

Results

Free ion yields

Yields were measured in the liquid under its vapor pressure at temperatures from 77.3 to 131.2 K (Figs. 1 and 2). The data at 77.3 K were taken with the cell immersed in liquid nitrogen, whereas the rest were taken with the thermoregulated nitrogen gas flowing through the Dewar vessel. The attenuation of the X ray beam by the liquid nitrogen bath was estimated by putting methanol in the Dewar during dosimetry (density 790 kg/m^3 at 295 K), because the LiF crystals had to be irradiated at room temperature. The attenuation factor was 1.15, after adjusting for the different electron densities of nitrogen (0.500 mol/g) and methanol (0.562 mol/g).

Measurements in the liquid nitrogen bath were used as a monitor from day to day. The four sets of free ion yield values agreed within 2%.

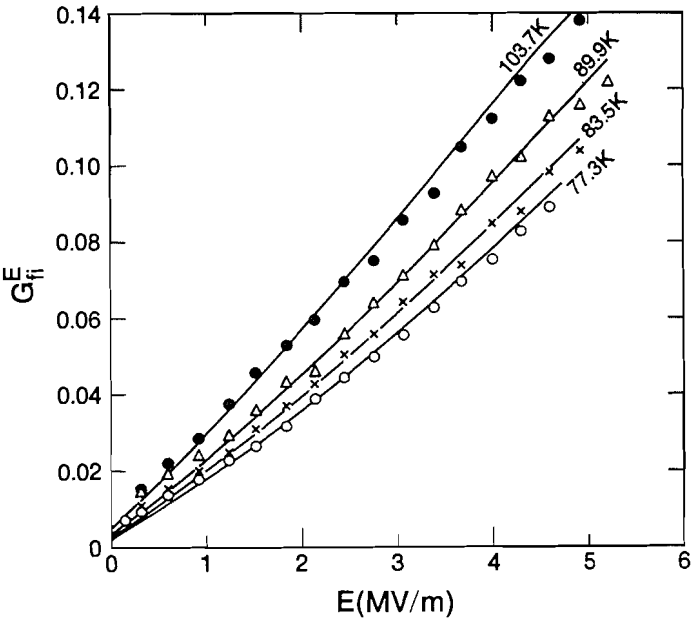

FIG. 1. Free ion yields in liquid CO at the temperatures indicated. The lines were calculated from eqs. [1]–[5], using parameter values from Table 1.

Ion mobilities

The ion mobilities in liquid carbon monoxide were measured at temperatures ranging from 77.3 to 131.2 K. The variation of ion current with time showed a single slope even at high fields, indicating little difference between anion and cation mobilities. The mobilities are independent of applied field strength over the range 0.3–5.2 MV/m, and are listed in Table 1.

Can. J. Chem. Downloaded from www.nrcresearchpress.com by 93.93.197.157 on 09/07/12
For personal use only.

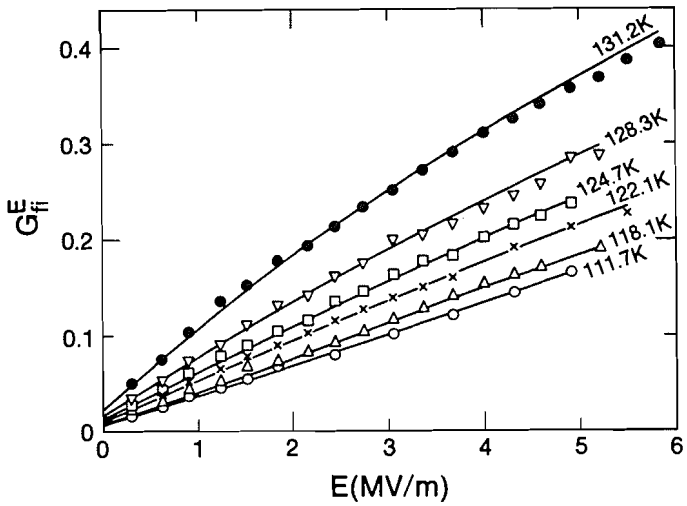

FIG. 2. Free ion yields in liquid CO at the temperatures indicated. Lines calculated as in Fig. 1.

Discussion

Free ion yields and electron thermalization distances

Information about the distribution function $F(y)$ of electron thermalization distances y in irradiated liquids can be obtained from the field and temperature dependences of the free ion yields (1, 22–24). The relevant equations relate the measured yield G^E_{fi} at applied field strength E to the total ionization yield G_{tot} and the probability $\phi^E_{fi}(y)$ that an electron with thermalization distance y escapes geminate neutralization and becomes a free ion.

$$[1] \quad G^E_{fi} = G_{tot} \int_0^\infty F(y)\phi^E_{fi}(y)dy$$

where

$$[2] \quad \phi^E_{fi}(y) = \phi^0_{fi}(y)[1 + f(E,y,T)]$$

where $\phi^0_{fi}(y)$ is the escape probability at zero applied field,

$$[3] \quad \phi^0_{fi}(y) = \exp(-r_c/y)$$

where $r_c = \xi^2/4\pi\epsilon_0\epsilon k_B T$ is the distance (value of y) at which the coulombic attraction between the ion and electron in a pair equals the average thermal energy $k_B T(J)$, ξ is the protonic charge (C), ϵ_0 is the permittivity of vacuum, and ϵ is the relative permittivity of the medium between the two charges. The function $f(E,y,T)$ describes the fractional increase of G^E_{fi} with increasing E,

$$[4] \quad f(E,y,T) = e^{-\beta y} \sum_{n=1}^{\infty} \frac{(\beta y)^n}{(n+1)!} \sum_{j=0}^{n-1} (n-j) \frac{(r_c/y)^{j+1}}{(j+1)!}$$

where $\beta = \xi E/k_B T$.

Equation [4] is based on an assumption that each ion–electron pair is sufficiently far from other pairs that each electron is coulombically influenced only by its sibling ion, although for a fraction of the electrons this is not true. Furthermore, the value of G_{tot} in eq. [1] is taken equal to that in the gas phase, although the value in the liquid phase is probably a fraction larger. The errors caused by these two assumptions tend to cancel each other (25).

The distribution function $F(y)$ is chosen by fitting eqs. [1] to [4] to measured ion yields. Our recent paper on liquid N_2 (1) describes several Gaussian and exponential forms of $F(y)$, designated YG, YGP, YEC, YE, and YEP. The free ion yields

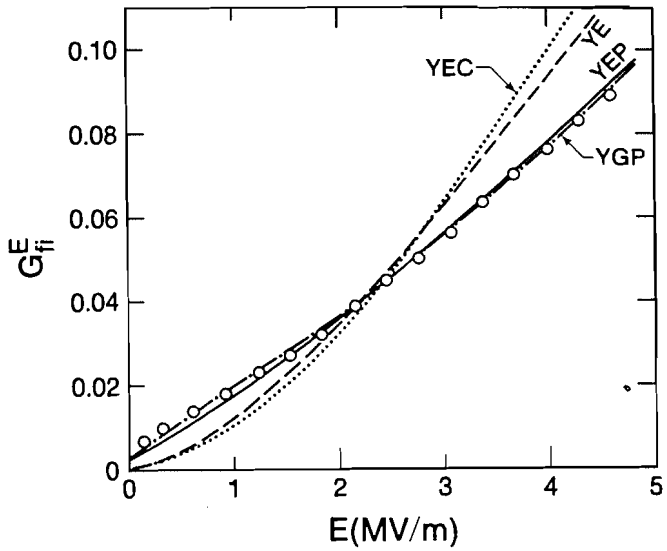

FIG. 3. Effect of distribution of electron thermalization distances on field dependence of calculated free ion yields in liquid CO at 77.3 K. ○, experimental. Lines calculated from eqs. [1]–[4] and the $F(y)$ distributions indicated (1): —, YEP; ----, YE; ...., YEC: -·-·, YGP. Parameter values are in Table 2.

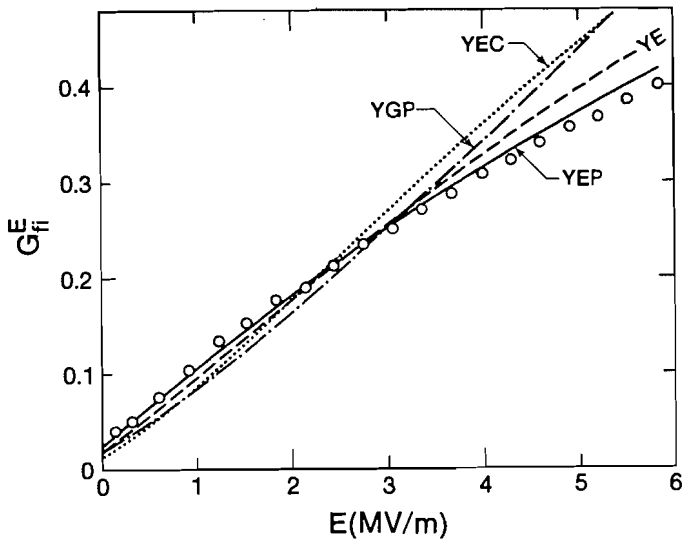

FIG. 4. Experimental (○) and calculated free ion yields in liquid CO at 131.2 K. Symbols as in Fig. 3.

in liquid nitrogen could not be fitted with Gaussian or simple exponential distributions. A similar disagreement occurs for liquid CO (Figs. 3 and 4).

The function YEP that fits the N_2 data (1) also provides the best fit to the CO data over the range of temperatures (Figs. 3 and 4). The distribution YEP is

$$[5] \quad F(y) = \begin{cases} \text{YE} & , 0 < (y - y_0) < 3.5b_{EP} \\ \text{YE} + 0.74\, b^2_{EP}/(y - y_0)^3, & (y - y_0) > 3.5b_{EP} \end{cases}$$

where YE is

$$[6] \quad F(y) = \begin{cases} 0 & , y < y_0 \\ b^{-1}_{EP} \exp[(y_0 - y)/b_{EP}], & y > y_0 \end{cases}$$

where y_0 is taken as 1 nm.

Values of the dispersion parameters of the four functions used

Can. J. Chem. Downloaded from www.nrcresearchpress.com by 93.93.197.157 on 09/07/12
For personal use only.

TABLE 2. Parameter values for curves in Figs. 3 and 4

T (K)	Distribution[a]	$10^3 G_{fi}^{0b}$	b (nm)	bd (10^{-6} kg/m^2)
77.3	YEP[c]	1.8	3.5	2.8
	YE[c]	0.4	4.9	4.0
	YEC	0.3	3.3	2.7
	YGP	2.3	5.7	4.6
131.2	YEP[c]	21	7.5	3.3
	YE[c]	15	8.9	3.9
	YEC	12	5.5	2.4
	YGP	17	9.9	4.3

[a]Reference 1.
[b]Assume $G_{tot} = 3.1$.
[c]Assume $y_0 = 1$ nm.

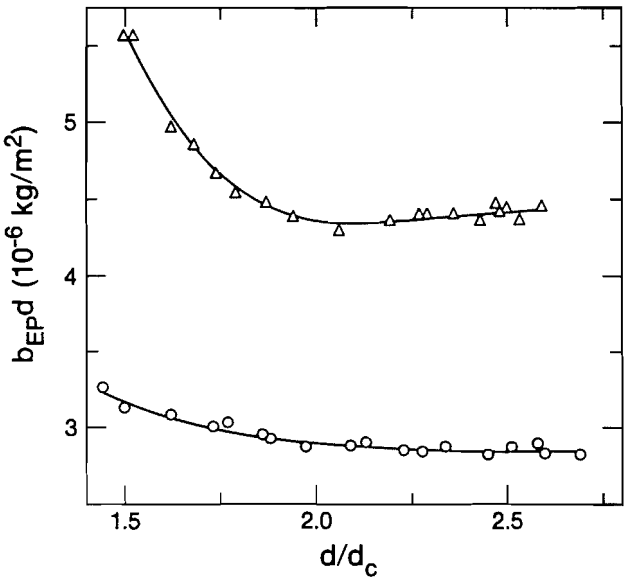

FIG. 5. Electron thermalization distances normalized for liquid density, $b_{EP}d$, as functions of d/d_c, where d_c refers to the critical fluid. △, N_2, d_c = 312 kg/m^3 (1); ○, CO, d_c = 300 kg/m^3.

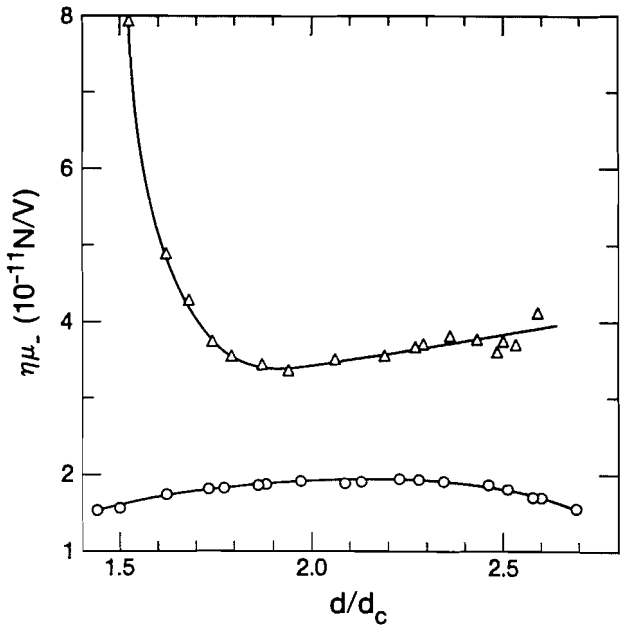

FIG. 6. Anion mobility normalized for liquid viscosity, $\eta\mu_-$, as a function of d/d_c. Symbols as in Fig. 5.

to calculate the curves in Figs. 3 and 4 are listed in Table 2. The values of b_{EP} are also listed in Table 1.

Density dependence of electron thermalization distances

The liquid was under its vapor pressure, so as the temperature was increased from 77.3 to 131.2 K the density decreased from 805 to 433 kg/m^3 (d/d_c from 2.69 to 1.44). The density normalized thermalization distance $b_{EP}d$ decreases with increasing density in the low density liquid, but is constant at $d/d_c > 2.0$ (Fig. 5). The values of $b_{EP}d$ in dense CO are about 1.5 times smaller than those in N_2, and the variation at $d/d_c < 2.0$ is less (Fig. 5). Thus electron thermalization occurs more rapidly in liquid CO than in liquid N_2, as expected.

We conclude that the electron thermalization process in liquid CO is truncated by electron capture to form an anion, as it is in liquid N_2.

The viscosity normalized mobility of the anions in liquid N_2 increased rapidly at $d/d_c < 1.7$, whereas it remained low in that density region of liquid CO (Fig. 6). This confirms that electron capture occurs more readily in liquid CO than in N_2.

Acknowledgement

We thank the staff of the Radiation Research Centre for their excellent technical assistance.

1. G. RAMANAN and G. R. FREEMAN. J. Chem. Phys. **87**, 319 (1987).
2. J.-P. DODELET, K. SHINSAKA, U. KORTSCH, and G. R. FREEMAN. J. Chem. Phys. **59**, 2376 (1973).
3. A. MOZUMDER and M. TACHIYA. J. Chem. Phys. **62**, 979 (1975).
4. (*a*) G. J. SCHULZ. Phys. Rev. **116**, 1141 (1959); (*b*) J. E. LAND. J. Appl. Phys. **49**, 5716 (1978).
5. G. HERZBERG. Spectra of diatomic molecules. Van Nostrand, London. 1950. p. 520.
6. C. A. BURRUS. J. Chem. Phys. **28**, 427 (1958).
7. L. JANSEN, A. MICHELS, and J. M. LUPTON. Physica, **24**, 347 (1954).
8. D. E. STOGRYN and A. P. STOGRYN. Mol. Phys. **11**, 371 (1966).
9. R. D. HAKE and A. V. PHELPS. Phys. Rev. **158**, A70 (1967).
10. A. G. ENGELHARDT, A. V. PHELPS, and C. G. RISK. Phys. Rev. **135**, A1566 (1964).
11. H. N. GILBERT. Chem. Eng. News, **26**, 2660 (1948).
12. M. B. NEIMAN and V. A. SHUSHUNOV. Dokl. Akad. Nauk. SSSR, **60**, 1347 (1950).
13. W. F. SAGER, A. FATIADI, P. C. PARKS, D. G. WHITE, and T. P. PERROS. J. Inorg. Nucl. Chem. **25**, 187 (1963).
14. J.-P. DODELET and G. R. FREEMAN. Can. J. Chem. **55**, 2264 (1977).
15. M. A. FLORIANO and G. R. FREEMAN. J. Chem. Phys. **85**, 1603 (1986).
16. N. GEE and G. R. FREEMAN. Phys. Rev. A, **28**, 3568 (1983).
17. R. J. GARDNER. Rev. Sci. Instrum. **58**, 1540 (1987).
18. T. WADA and G. R. FREEMAN. Conference on Electrical Insulation and Dielectric Phenomena. Ann. Rep. 1980. National Academy Press, Washington, DC. p. 386.
19. N. GEE, M. A. FLORIANO, T. WADA, S. S.-S. HUANG, and G. R. FREEMAN. J. Appl. Phys. **57**, 1097 (1985).
20. J. G. HUST and R. B. STEWART. Natl. Bur. Stand. Techn. Note, 202, U.S. GPO, Washington, DC, 1963.
21. W. L. WILLIS. Cryogenics, **6**, 279 (1966).
22. J.-P. DODELET, P. G. FUOCHI, and G. R. FREEMAN. Can. J. Chem. **50**, 1617 (1972).
23. J.-P. DODELET and G. R. FREEMAN. J. Chem. Phys. **60**, 4657 (1974).
24. J. CASANOVAS, R. GROB, J. ORETET, and A. SHAMSALDIN. J. Chim. Phys. **80**, 325 (1983).
25. G. R. FREEMAN. *In* Kinetics of nonhomogeneous processes. *Edited by* G. R. Freeman. Wiley-Interscience, New York. 1987. Chap. 2.

Can. J. Chem. Downloaded from www.nrcresearchpress.com by 93.93.197.157 on 09/07/12
For personal use only.

Hydrolysis of phenyltellurium(VI) fluorides and X-ray crystal and molecular structures of Ph_3TeF_2OH

ALEXANDER F. JANZEN, KOHRSHED ALAM, AND MEEHAE JANG
Department of Chemistry, University of Manitoba, Winnipeg, Man., Canada R3T 2N2

BARRY J. BLACKBURN
Department of Chemistry, University of Winnipeg, Winnipeg, Man., Canada R3B 2E9

AND

ANTHONY S. SECCO
Department of Chemistry, University of Manitoba, Winnipeg, Man., Canada R3T 2N2

Received November 17, 1987

ALEXANDER F. JANZEN, KOHRSHED ALAM, MEEHAE JANG, BARRY J. BLACKBURN, and ANTHONY S. SECCO. Can. J. Chem. **66**, 1308 (1988).

The hydrolysis of $PhTeF_5$, *trans*-Ph_2TeF_4, and *mer*-Ph_3TeF_3 is described. The hydrolysis products $PhTeF_4OH$, Ph_2TeF_3OH, and Ph_3TeF_2OH were identified by ^{19}F nmr and mass spectrometry and, in the case of Ph_3TeF_2OH, by X-ray crystallographic analysis. Ph_3TeF_2OH has non-equivalent fluorines and the conditions under which stereoselective fluorine exchange occurs are described.

Crystals of Ph_3TeF_2OH are triclinic, $P\bar{1}$, $a = 8.791(2)$, $b = 9.832(2)$, $c = 11.147(2)$ Å, $\alpha = 95.51(2)$, $\beta = 102.01(2)$, $\gamma = 112.56(2)°$, and $Z = 2$. The structure was determined from a Patterson map and refined to an R value of 0.026 for 2562 observed data. The coordination about Te is described as octahedral with two phenyl groups *trans* to each other and the third phenyl *trans* to a fluorine. The molecule exhibits the longest Te(VI)—F bond known, 2.011(2) Å. This same F which undergoes the more rapid exchange in solution is involved in H-bonding in the crystal, linking centrosymmetrically related molecules into dimers where OH...F is 1.90(3) Å and O—H...F is 177(4)°. However, H-bonding is not responsible for the stereoselective fluorine exchange in solution.

ALEXANDER F. JANZEN, KOHRSHED ALAM, MEEHAE JANG, BARRY J. BLACKBURN et ANTHONY S. SECCO. Can. J. Chem. **66**, 1308 (1988).

On décrit l'hydrolyse du $PhTeF_5$, du *trans*-Ph_2TeF_4 et du *mer*-Ph_3TeF_3. Pour identifier les produits d'hydrolyse, le $PhTeF_4OH$, le Ph_2TeF_3OH et le Ph_3TeF_2OH, on a fait appel à la rmn du ^{19}F et à la spectrométrie de masse et, dans le cas du Ph_3TeF_2OH, à la diffraction des rayons-X. Le Ph_3TeF_2OH comporte des fluors qui ne sont pas équivalents et on décrit les conditions dans lesquelles il se produit un échange stéréosélectif du fluor.

Les cristaux du Ph_3TeF_2OH sont tricliniques, groupe d'espace $P\bar{1}$ avec $a = 8{,}791(2)$, $b = 9{,}832(2)$ et $c = 11{,}147(2)$ Å, $\alpha = 95{,}51(2)$, $\beta = 102{,}01(2)$, $\gamma = 112{,}56(2)°$ et $Z = 2$. On a déterminé la structure à partir d'une carte de Paterson et on l'a affinée jusqu'à une valeur de R de 0,026 pour 2562 réflexions observées. On décrit la coordination autour du Te comme octaédrique avec deux groupements phényles *trans* l'un par rapport à l'autre et le troisième phényle *trans* par rapport à un fluor. Dans cette molécule, on a observé la plus longue liaison Te(VI)—F connue, 2,011(2) Å. Dans le cristal, l'atome de fluor qui subit un échange rapide en solution est impliqué dans une liaison hydrogène; cette liaison associe des molécules liées d'une façon centrosymétrique et conduit à des dimères dans lesquels la liaison OH...F est égale à 1,90(3) Å et l'angle O—H...F est de 177(4)°. Toutefois, la liaison hydrogène n'est pas responsable de l'échange stéréosélectif de fluor qui se produit en solution.

[Traduit par la revue]

Introduction

The synthesis of organotellurium(VI) compounds (1–3), including a series of phenyltellurium(VI) fluorides prepared in our laboratory (4), has made these compounds available for chemical and structural study. We have carried out an investigation of the hydrolysis of $PhTeF_5$, *trans*-Ph_2TeF_4, and *mer*-Ph_3TeF_3 and determined the X-ray structure of one of the hydrolysis products, Ph_3TeF_2OH. The fluorine ligands in Ph_3TeF_2OH are non-equivalent and stereoselective Te—F bond cleavage may be studied by ^{19}F nmr and compared with the nmr and structural studies reported for the *mer*-Ph_3TeF_3–$Ph_3TeF_2^+$ system (5).

Experimental

Synthesis

^{19}F nmr spectra were recorded on a Bruker WH90 spectrometer at 84.66 MHz with C_6F_6 (−162.9 ppm) as an internal reference. ^{125}Te nmr spectra were recorded on a Bruker AM300 spectrometer at 94.76 MHz using Ph_2Te (692 ppm with respect to Me_2Te) as an external reference. Mass spectra were obtained on a Finnegan 1015 quadrupole instrument. XeF_2 was obtained from PCR Research Chemicals Inc. $PhTeF_5$, Ph_2TeF_4, and Ph_3TeF_3 were prepared from XeF_2 and PhTeTePh, Ph_2TeF_2, and Ph_3TeF, respectively, as described previously (4, 5).

cis- *and* trans-*$PhTeF_4OH$*

H_2O (0.20 mmol) was added to a solution of $PhTeF_5$ (0.19 mmol) in acetonitrile (0.3 mL) in an nmr tube fitted with a Teflon insert and closed with a plastic cap. The mixture was kept at room temperature for 1 h with occasional gentle shaking. ^{19}F nmr examination of the reaction mixture shows the formation of *cis*- and *trans*-$PhTeF_4OH$. The *cis*-to-*trans* ratio was approximately 1:3 and the combined yield was about 70%, as determined by nmr peak integration.

Nuclear magnetic resonance data are shown in Table 1. Mass spectrum of 1:3 mixture of *cis*- and *trans*-$PhTeF_4OH$, m/z: 300 (M^+), 281 ($M^+ - F$), 223 ($M^+ - Ph$).

Ph_2TeF_3OH

H_2O (0.10 mmol) was added to *trans*-Ph_2TeF_4 (0.08 mmol) in CD_3CN (2 mL) in a Teflon-lined nmr tube. After 5 days at 25°C, Ph_2TeF_3OH (20%) and unreacted Ph_2TeF_4 (80%) were present. Nuclear magnetic resonance data in Table 1; ms m/z: 358 (M^+).

Can. J. Chem. Downloaded from www.nrcresearchpress.com by 93.93.197.157 on 09/07/12
For personal use only.

TABLE 1. ^{19}F nmr data of some phenyltellurium(VI) compounds*

Compound	Spin system	Chemical shift F^a	F^b	F^c	$J(F^aF^b)$	$J(F^aF^c)$	$J(F^bF^c)$	$J(TeF^a)$	$J(TeF^b)$	Solvent
cis-$PhTeF_4OH$, **1***a*	ABC_2	−28	−44	−52	147	116	105			CD_3CN
trans-$PhTeF_4OH$, **1***b*	A_4	−47						3445		CD_3CN
Ph_2TeF_3OH, **2**	AB_2	−32	−63		33			2960	2726	CD_2Cl_2
Ph_3TeF_2OH, **3**	AB	−3	−76		55			2500	2100	CD_2Cl_2

*Chemical shifts in ppm from $CFCl_3$ and coupling constants in Hz.

Ph_3TeF_2OH

Ph_3TeF_2OH was often observed as a minor component in samples of Ph_3TeF_3, Ph_3TeF_2Cl, $Ph_3TeF_2{}^+PF_6{}^-$, and Ph_4TeF_2. It was crystallized from dichloromethane solution and identified by X-ray crystallography, ^{19}F nmr (Table 1) and ms, m/z: 416 (M^+), 399 ($M^+ - OH$), 339 ($M^+ - Ph$).

X-ray crystallographic analysis of Ph_3TeF_2OH

$C_{18}H_{16}OF_2Te$ fw = 413.92

Triclinic, $P\bar{1}$, a = 8.791(2), b = 9.382(2), c = 11.147(2) Å, α = 95.51(2), β = 102.01(2), γ = 112.56(2), V = 814.6(4) Å^3, Z = 2, ρ_c = 1.687 g cm^{-3}, ρ_0 not measured, μ = 18.5 cm^{-1}, (21°C; MoKα, λ = 0.71073 Å).

Reflection data from a single crystal of Ph_3TeF_2OH grown from dichloromethane were collected on a Nicolet $R3m$ automated diffractometer. Data were collected with the ω–2θ mode in the range $3° \leq 2 \leq 50°$, exploring the $\pm h$, $\pm k$, $\pm l$ region of reciprocal space. Of the 3042 reflections measured 2879 were considered unique after symmetry equivalents were averaged, R_{sym} = 0.013. The 2564 observed reflections had $I \geq 1.5\sigma(I)$, where $\sigma(I) = R[S + B_L + B_R]$, R = scan rate, S = total scan count, and B_L, B_R = left and right background counts. Data were corrected for Lorentz and polarization effects. An empirical absorption correction based on the reflection intensity measurements at 36 different azimuthal angles for 10 reflections was also applied. Other aspects of data collection were as reported in an earlier publication (5).

A Patterson map revealed the positions of the Te and both F atoms. Refinement of these atoms, followed by difference Fourier syntheses yielded the remaining atoms. The complete list of atoms was refined by full-matrix least-squares procedures[1] with the Te corrected for anomalous dispersion (6). Non-hydrogens were refined with anisotropic temperature parameters, whereas, hydrogens were assumed to undergo isotropic thermal motion. Convergence was reached at R = 0.027 and R_w = 0.020 where $R = \Sigma||F_o| - k|F_c||/\Sigma|F_o|$ and $R_w = [\Sigma w(|F_o| - k|F_c|)^2/\Sigma w|F_o|^2]^{1/2}$. A weighting analysis confirmed the use of the weights $w = 1/\sigma^2(F_o)$ in the function $\Sigma w(|F_o| - k|F_c|)^2$ which was minimized throughout the refinement. It was apparent at this stage that the two reflections for which the attenuator was required during data collection were in poor agreement with their calculated, F_c, values. Because of uncertainty in the operation of the attenuator it was decided that the two low angle reflections $\bar{2}01$ and $\bar{1}21$ should be eliminated from the data set. The final cycle of refinement yielded values of R = 0.026 and R_w = 0.020 for 2562 observed data and R = 0.032 and R_w = 0.020 when the 2877 observed and unobserved data were included. Mean and maximum shifts were 0.072 and 0.492σ, respectively, and the goodness of fit, S = 1.570. A final difference map showed a maximum peak of 0.484 e$^-$/Å^3 located between Te and C(13), and three troughs −1.06 e$^-$/Å^3 (0.239, 0.276, 0.209), −1.02 e$^-$/Å^3 (0.110, 0.222, 0.247), and −0.645 e$^-$/Å^3 (0.102, 0.199, 0.166) symmetrically positioned and forming a triangle about, and in a plane with the Te atom. The mean plane through the three troughs and the Te atom lies approximately 34° away from the mean plane through Te, F(1), O, C(1), and C(13) with the $\bar{T}e$...trough(3) vector pointing towards H(O). These troughs may be due to the inadequacy of ellipsoids in describing the anisotropic thermal motion of the Te atom and that higher order functions may be required for a more detailed description of the motion. Scattering factors for Te, C, and O were from ref. 7 while those for hydrogen were from ref. 8. Final atomic positional parameters are given in Table 2.[2] Thermal

TABLE 2. Final positional parameters (fractional × 10^5, O and C × 10^4) and isotropic thermal parameters (Å^2 × 10^3) with estimated standard deviations in parentheses

Atom	x	y	z	U_{eq}*
Te	14185(3)	23173(3)	20400(2)	48
F(1)	26789(25)	21162(22)	36281(17)	63
F(2)	12498(26)	1993(21)	13113(17)	66
O	185(3)	2454(3)	439(2)	62
C(1)	3783(5)	3164(4)	1571(3)	53
C(2)	3903(6)	2631(5)	417(4)	68
C(3)	5436(6)	3271(6)	123(4)	76
C(4)	6831(6)	4426(6)	969(4)	74
C(5)	6721(6)	4939(6)	2118(4)	75
C(6)	5190(5)	4319(5)	2425(4)	65
C(7)	1612(4)	4542(4)	2853(3)	48
C(8)	1457(4)	5600(4)	2124(3)	53
C(9)	1580(5)	7037(4)	2673(4)	68
C(10)	1877(6)	7416(5)	3926(4)	78
C(11)	2051(8)	6383(7)	4648(5)	102
C(12)	1900(7)	4924(5)	4118(4)	87
C(13)	−819(5)	954(4)	2530(3)	56
C(14)	−854(6)	−142(5)	3269(4)	68
C(15)	−2325(7)	−951(5)	3607(4)	84
C(16)	−3731(7)	−693(6)	3211(5)	93
C(17)	−3734(7)	385(6)	2454(5)	92
C(18)	−2265(6)	1216(5)	2124(5)	78

*U_{eq} is equal to one third the trace of the diagonalized anisotropic temperature factor matrix.

[1]Computation was carried out on the University of Manitoba Computer Services Department's Amdahl 580/5850 mainframe computer using locally written programs and SHELXTL (version 4) for processing, and modified versions of the following programs for structure refinement and calculations. ORFLS: W. R. Busing; K. O. Martin; H. A. Levy. Report ORNL-TM-305, 1962; Oak Ridge National Laboratory, Oak Ridge, TN. FORDAP: A. Zalkin. ORFFE: W. R. Busing; K. O. Martin; H. A. Levy. Report ORNL-TM-306, 1964; Oak Ridge, National Laboratory, Oak Ridge, TN. ORTEP II: C. K. Johnson. Report ORNL-TM-306-5138, 1976; Oak Ridge National Laboratory, Oak Ridge, TN.

[2]Tables of hydrogen positional and thermal parameters, anisotropic thermal parameters, bond lengths, and angles involving phenyl carbons and involving hydrogens, torsion angles, and observed and calculated structure factor amplitudes may be purchased from the Depository of Unpublished Data, CISTI, National Research Council of Canada, Ottawa, Ont., Canada K1A 0S2.

Can. J. Chem. Downloaded from www.nrcresearchpress.com by 93.93.197.157 on 09/07/12
For personal use only.

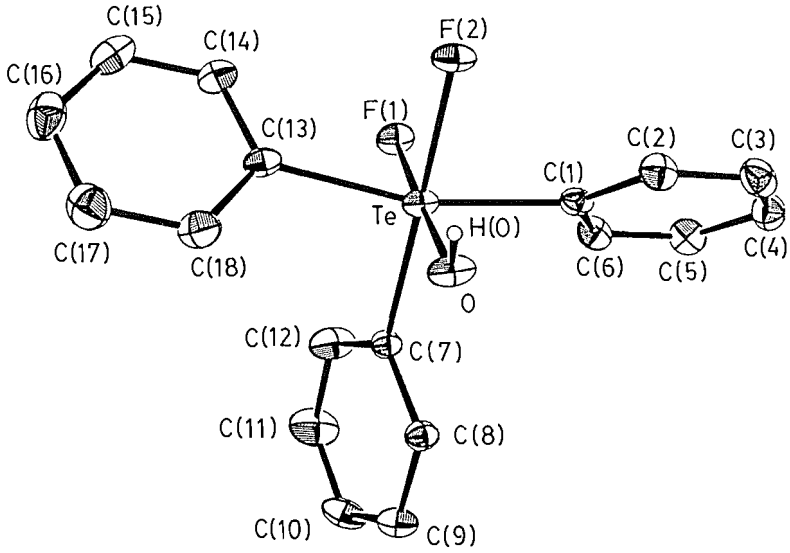

FIG. 1. ORTEP drawing of the Ph_3TeF_2OH molecule. Atoms are represented by thermal ellipsoids at the 50% probability level.

motion analysis (9) in terms of rigid-body modes of translation, libration, and screw motion indicated some independent motion of the PhTe groups and the C_3TeF_2O moiety.

Discussion

The hydrolysis of $PhTeF_5$ was carried out in acetonitrile solution at 25°C in the presence of 1 equiv. of H_2O,

[1] $$PhTeF_5 + H_2O \xrightarrow[CH_3CN]{} PhTeF_4OH + HF$$

and the product $PhTeF_4OH$ consisted of a 1:3 mixture of *cis* **1***a* and *trans* **1***b* isomers in a combined yield of 70%. The ABC_2 and A_4 ^{19}F nmr spectra (Table 1) establish the geometry of *cis* **1***a* and *trans* **1***b* isomers.

trans-Ph_2TeF_4 hydrolysed more slowly than $PhTeF_5$ and the

[2] $$trans\text{-}Ph_2TeF_4 + H_2O \xrightarrow[CH_3CN]{} Ph_2TeF_3OH + HF$$

product Ph_2TeF_3OH, **2**, was formed in 20% yield after 5 days at 25°C. Only one AB_2 ^{19}F nmr spectrum (Table 1) was observed but three isomeric structures are possible for Ph_2TeF_3OH. Since each of the three isomers is expected to have an AB_2 spin system, therefore, we cannot establish which isomer is the hydrolysis product.

The hydrolysis product Ph_3TeF_2OH, **3**, was present as a minor contaminant in samples of *mer*-Ph_3TeF_3, Ph_3TeF_2Cl, $Ph_3TeF_2^+PF_6^-$, and Ph_4TeF_2 and its AB ^{19}F nmr spectrum is consistent with structure **3**.

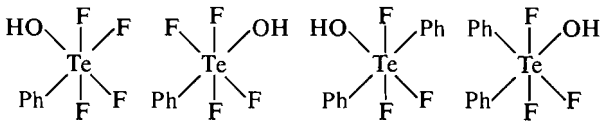

1*a* **1***b* **2***a* **2***b*

2*c* **3**

TABLE 3. Selected bond angles (deg) with estimated standard deviations in parentheses

Bonds	Angle (deg)	Bonds	Angle (deg)
F(1)—Te—F(2)	87.50(8)	F(2)—Te—C(13)	83.17(11)
F(1)—Te—O	177.92(10)	O—Te—C(1)	92.68(12)
F(1)—Te—C(1)	86.52(11)	O—Te—C(7)	90.86(11)
F(1)—Te—C(7)	91.19(10)	O—Te—C(13)	93.91(13)
F(1)—Te—C(13)	86.44(11)	C(1)—Te—C(7)	96.60(13)
F(2)—Te—O	90.49(9)	C(1)—Te—C(13)	165.37(12)
F(2)—Te—C(1)	83.74(11)	C(7)—Te—C(13)	96.35(13)

TABLE 4. Selected bond lengths (Å) with estimated standard deviations in parentheses

	Length			Length	
Bond	Uncorr.	Corr.	Bond	Uncorr.	Corr.
Te—F(1)	1.951(2)	1.958	Te—C(1)	2.119(4)	2.124
Te—F(2)	2.011(2)	2.016	Te—C(7)	2.123(3)	2.129
Te—O	1.929(2)	1.937	Te—C(13)	2.110(4)	2.115

Ph_3TeF_2OH molecules (Fig. 1) exist in a conformation similar to molecules of *mer*-Ph_3TeF_3 (5) which is best described by the distorted octahedral bonding about the central Te atom with the phenyls oriented so as to minimize the intramolecular steric strain. The *trans* phenyl groups adopt a bent propeller arrangement. They form a dihedral angle of 92° between the mean planes of the rings and form a C—Te—C angle of 165.37(12)° (Table 3) compared to the corresponding angles of 109° and 167.98(11)° in Ph_3TeF_3. Despite the increased twist of the phenyls and the closing of the C—Te—C angle, intramolecular contacts between these phenyls and the equatorial F are very similar to those in the trifluoride structure. The contacts are able to be maintained as a result of the long Te—F(2) bond of 2.011(2) Å (Table 4).

Can. J. Chem. Downloaded from www.nrcresearchpress.com by 93.93.197.157 on 09/07/12
For personal use only.

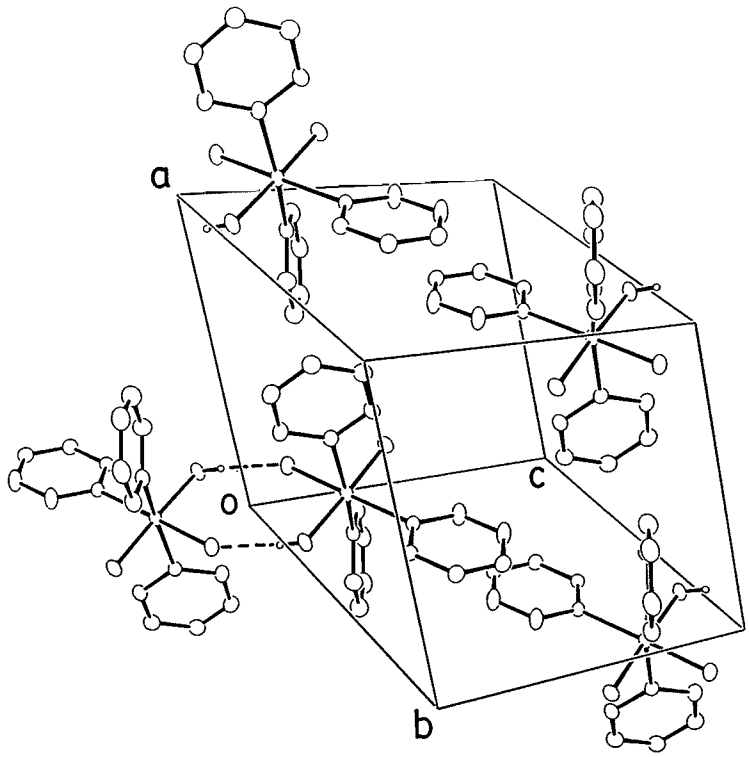

FIG. 2. ORTEP packing diagram of Ph_3TeF_2OH molecules with dashed lines indicating H bonding.

Both Te—F bond lengths (2.011(2) Å, 1.951(2) Å) are significantly longer than their counterparts (1.954(2) Å, 1.915(2) Å), respectively) in Ph_3TeF_3 (5) but there is no accompanying increase in Te—C bond lengths. Since it is unlikely that packing forces would affect bond lengths to this extent, it is reasonable to suggest that the 2–3% difference in Te—F bond lengths is due to the replacement of F by OH but how the OH decreases the electron density in the Te—F bonds is unclear. One explanation may be a $(d–p)\pi$ interaction between the Te and O as suggested for $Te(OTeF_5)_4$ (10). It is of interest to note that the Te(VI)—F bond length of 1.954 Å in Ph_3TeF_3 was the longest known and is now superseded by the 2.011 Å Te(VI)—F bond in the present compound.

An additional minor difference between the conformations of Ph_3TeF_2OH and Ph_3TeF_3 is manifested in the amount of twist of the C(7)—phenyl ring about the Te—C(7) bond. The twist is defined by the torsion angles O—Te—C(7)—C(8) (−21.6°) and F(1)—Te—C(13)—C(18) (−10.5°) in the respective compounds. The extra 11° twist in the hydroxide molecule is required to reduce the steric interaction between H(C8) and the OH group which is bulkier, and protrudes further over the phenyl than the corresponding fluoride ligand in Ph_3TeF_3.

The Te(VI)—O(H) bond length of 1.929(3) Å can be compared to the only other known Te(VI)—O(H) distances of 1.904(5) Å and 1.937(5) Å found in $H_2Te_2O_6$ (11). While the former is considerably shorter, the latter is not significantly different from that in the present structure. Lindqvist *et al.* (11) have suggested that the variation in Te(VI)—O(H) bond lengths in $H_2Te_2O_6$ results from a difference in π bonding between Te and each of the hydroxy groups. If the bond length can be used as an indicator for π bonding, it appears that such bonding does not occur to a large extent in Ph_3TeF_2OH.

Crystal packing (Fig. 2) is dictated by hydrogen bonding linking centrosymmetrically related molecules into dimers via O—$H(x,y,z)\ldots F(2)(\bar{x},\bar{y},\bar{z})$ (and by symmetry $F(2)(x,y,z)\ldots H$—$O(\bar{x},\bar{y},\bar{z})$) and by π–π interactions resulting from [C(1)]-phenyl$(x,y,z)\ldots$[C(1)]phenyl$(1-x, 1-y, \bar{z})$ overlap. The hydrogen bonded dimers have H...F distances of 1.90(3) Å and O—H...F angles of 177(4)° compared with tetravalent $H_2Te_2O_3F_4$ where H bonds link the molecules in a diamond network and the respective values are 1.6 Å and 164° (12).

The phenyl...phenyl stacking, where the interplanar spacing is 3.46 Å, links H-bonded dimers into a chain along the [110] direction. Similar stacking is observed in Ph_3TeF_3 (5) and Ph_2TeCl_2 (13).

The AB ^{19}F nmr spectrum of **3** is consistent with the solid state structure as determined by X-ray crystallography. Since the fluorines are non-equivalent, the relative rate of Te—F^a versus Te—F^b bond cleavage may be studied by ^{19}F nmr and the results compared with the stereoselective exchange observed in the *mer*-Ph_3TeF_3–$Ph_3TeF_2^+$ system (5).

Under certain conditions, no intra- or intermolecular fluorine exchange can be observed by ^{19}F nmr and **3** is thus a "rigid" molecule in solution. For example, re-crystallizing **3** from CH_2Cl_2 or treating solutions of **3** with NaF stops all fluorine exchange. As found previously, treatment with NaF or R_4NCl also stopped fluorine exchange in the *mer*-Ph_3TeF_3–$Ph_3TeF_2^+$ system (5) because any five-coordinate Te(VI) cation was converted to a six-coordinate Te(VI) compound.

On standing for several days in glass nmr tubes, intermolecular fluorine exchange in **3** was observed by ^{19}F nmr. This exchange leads to loss of F^a—F^b and Te—F^a coupling but retention of Te—F^b coupling, as shown in Fig. 3, and these results demonstrate that Te—F^a bonds are cleaved more rapidly than Te—F^b bonds in the exchange process. This behaviour resembles that observed in the *mer*-Ph_3TeF_3–$Ph_3TeF_2^+$ system

Can. J. Chem. Downloaded from www.nrcresearchpress.com by 93.93.197.157 on 09/07/12
For personal use only.

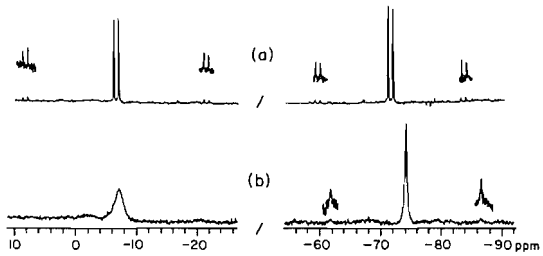

FIG. 3. ^{19}F nmr spectrum of Ph_3TeF_2OH, **3**: (*a*) in the absence of fluorine exchange. Fluorine–tellurium couplings given in Table 1. (*b*) with exchange, showing loss of F^a—F^b and Te—F^a coupling but retention of Te—F^b coupling.

and we propose a similar mechanism, namely, initial formation of cation **4**, followed by a rapid equilibrium involving a fluorine-bridged intermediate **5** in which F^a occupies the bridging position.

[3] $$Ph_3TeF_2OH \xrightarrow[\text{e.g. HF}]{\text{Lewis acid}} Ph_3TeFOH^+AF^-$$

[4] 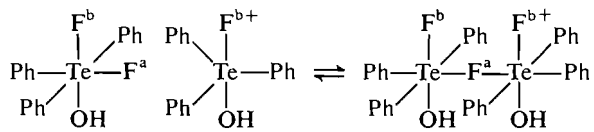

3 **4** **5**

We assume that a Lewis acid such as HF, or Si or B fluorides which are produced by the reaction of HF with glass, reacts with **3** to give cation **4**; although **4** could not be observed directly, it was found that treatment of an exchanging sample of **3** with NaF stopped exchange and regenerated "rigid" **3**, presumably because any cation **4** was converted to **3**. Reactions of phenyltellurium(VI) fluorides with PF_5 can generate cations such as $Ph_3TeF_2^+$ (5) or Ph_3TeFCl^+,[3] but the use of PF_5 would be inappropriate for the synthesis of Ph_3TeFOH^+ because of the presence of the hydroxy group.

Those features in the Ph_3TeF_3–$Ph_3TeF_2^+$ system (5) which were assumed to be important for the observation of stereoselective fluorine exchange are also present in the Ph_3TeF_2OH–Ph_3TeFOH^+ system, namely, the presence of three phenyl substituents which prevents the scrambling of F^a and F^b ligands, significantly longer Te—F^a bonds (2.011 Å in **3**) than Te—F^b bonds (1.951 Å in **3**), and a F^a-bridged intermediate **3** which minimizes the steric interactions among six phenyl substituents.

Although hydrogen-bonding leads to dimerized Ph_3TeF_2OH molecules in the solid state, such hydrogen-bonding cannot be responsible for stereoselective fluorine exchange because re-crystallized samples of **3** show no fluorine exchange in solution.

[3]M. Jang and A. F. Janzen. Unpublished results.

Acknowledgments

The financial assistance of the Natural Sciences and Engineering Research Council of Canada (NSERC) and the Petroleum Research Fund, administered by the American Chemical Society, is gratefully acknowledged. The purchase of an AM300 NMR spectrometer was made possible by grants from NSERC and the Manitoba Health Research Council. We also thank the University of Manitoba Geological Sciences Department for use of X-ray diffraction facilities and the Computer Services Department for assistance.

1. (*a*) C. D. DESJARDINS, C. LAU, and J. PASSMORE. J. Inorg. Nucl. Chem. Lett. **10**, 151 (1974); (*b*) C. LAU, J. PASSMORE, E. K. RICHARDSON, T. K. WHIDDEN, and P. S. WHITE. Can. J. Chem. **63**, 2273 (1985).
2. R. S. MICHALAK, S. R. WILSON, and J. C. MARTIN. J. Am. Chem. Soc. **106**, 7529 (1984).
3. G. KLEIN and D. NAUMANN. J. Fluor. Chem. **30**, 259 (1985).
4. K. ALAM and A. F. JANZEN. J. Fluor. Chem. **27**, 467 (1985).
5. A. S. SECCO, K. ALAM, B. J. BLACKBURN, and A. F. JANZEN. Inorg. Chem. **25**, 2125 (1986).
6. D. T. CROMER and D. LIBERMAN. J. Chem. Phys. **53**, 1891 (1970).
7. D. T. CROMER and J. B. MANN. Acta Crystallogr., Sect. A: Cryst. Phys., Diffr. Theor., Gen. Crystallogr. A**24**, 321 (1968).
8. R. F. STEWART, E. R. DAVIDSON, and W. T. SIMPSON. J. Chem. Phys. **42**, 3175 (1965).
9. V. SCHOMAKER and K. N. TRUEBLOOD. Acta Crystallogr., Sect. B: Struct. Crystallogr. Cryst. Chem. B**24**, 63 (1969).
10. H. PRITZKOW and K. SEPPELT. Inorg. Chem. **16**, 2685 (1977).
11. O. LINDQVIST and J. MORET. Acta Crystallogr., Sect. B: Struct. Crystallogr. Cryst. Chem. B**29**, 956 (1973).
12. J. C. JUMAS, M. MAURIN, and E. PHILIPPOT. J. Fluor. Chem. **8**, 329 (1976).
13. N. W. ALCOCK and W. D. HARRISON. J. Chem. Soc. Dalton Trans. 215 (1982).

Can. J. Chem. Downloaded from www.nrcresearchpress.com by 93.93.197.157 on 09/07/12
For personal use only.

Structural and electronic origin of the conformational behavior of biphenyl-like α-diimine ligands. A theoretical study

VINCENZO BARONE AND CAMILLA MINICHINO
Dipartimento di Chimica, Università di Napoli, via Mezzocannone 4, I-80134 Napoli, Italy
SÁNDOR FLISZÁR
Département de Chimie, Université de Montréal, C.P. 6210, Succ. A, Montréal (Qué), Canada H3C 3V1
AND
NINO RUSSO
Dipartimento di Chimica, Università della Calabria, I-87030 Arcavacata di Rende (Cosenza), Italy

Received July 14, 1987[1]

VINCENZO BARONE, CAMILLA MINICHINO, SÁNDOR FLISZÁR, and NINO RUSSO. Can. J. Chem. **66**, 1313 (1988).

The conformational behavior of aromatic α-diimines has been analyzed by means of *ab initio* computations making use of the standard STO-3G minimal basis set. The absolute minimum of the potential energy curve always corresponds to the planar *trans* conformation and a secondary minimum is also found for a non planar cisoid conformation. An alternate analysis, rooted in bond energy calculations explicitly involving the charges of the bond-forming atoms, indicates that bonded rather than nonbonded interactions are responsible for the observed conformational preferences.

VINCENZO BARONE, CAMILLA MINICHINO, SÁNDOR FLISZÁR, et NINO RUSSO. Can. J. Chem. **66**, 1313 (1988).

Une étude conformationelle *ab initio*, conduite en base minimale STO-3G, est présentée pour une série d' α-diimines aromatiques. La conformation planaire trans correspond dans tous les cas au minimum absolu de la courbe de potentiel, un minimum secondaire étant observé pour la forme cisoïde non planaire. Une analyse complémentaire, basée sur des calculs d'énergies de liens en termes de charges électroniques, montre que ce sont les interactions liées (par opposition a celles entre atomes non liés) qui sont responsables pour les préférences conformationelles observées.

Can. J. Chem. Downloaded from www.nrcresearchpress.com by 93.93.197.157 on 09/07/12
For personal use only.

Introduction

Transition metal complexes of aromatic α-diimine ligands such as 2,2′-bipyridine (bpy) have found extensive applications in preparative and analytical chemistry for almost a century (1–3) and are currently receiving further attention in view of solar energy conversion and storage (4, 5) and of modelling intermediates in transition metal catalyzed reactions (6, 7). In this connection, since the replacement of CH groups by N atoms leads to more electron-deficient compounds, attention has turned to coupled diazines, such as 4,4′-bipyrimidine (bpm), 2,2′-bipyrazine (bpz), or 3,3′–bipyridazine (bpd). Although the complexing ability of these ligands is essentially related to their ionization potentials and electron affinities (8, 9), for such flexible molecules the conformation assumed upon complexation often does not correspond to the equilibrium conformation of the free ligand. This consideration stimulated several experimental investigations about the conformational behavior of heteroaromatic systems consisting of two rings linked together by essentially single bonds (10–13). Only the neighborhood of potential energy minima can be well characterized by these techniques, the rest of the potential energy curve remaining ill defined. Theoretical computations do not suffer from this problem and the only limitation to their systematic use is the definition of the best compromise between reliability of the results and computational costs. There is now a general consensus on the use of non empirical computations employing minimal or split valence basis sets (13–18) in the rigid rotor approximation (14–16).

Ab initio studies at these levels have been recently performed in a systematic and comprehensive way for biphenyl (14, 17, 18), bipyridines (13, 19, 20), bipyrimidines (21, 22), phenylpyridines (19), phenylpyrimidines (23), bipyrroles (24, 25), bifurans (15, 26), furylpyrroles (26), phenylpyrroles (27), and bithienyls (28). These studies have shown that the complete torsional potential of nonfused biheterocycles is transferable with a high degree of accuracy among molecules with the same *ortho* substituents, irrespective of the nature of *meta* and *para* groups. On these grounds all the bihexaheterocyclic systems have been grouped into five classes (14), whose serial number corresponds to the number (0 to 4) of *ortho* nitrogen atoms. Two situations are actually possible when there are two nitrogen atoms in *ortho* positions, and the corresponding classes are labelled 2 (when the two nitrogen atoms are on the same ring) or 2′ (when the two nitrogen atoms belong to different rings). Only molecules belonging to class 2′ (i.e. α-diimines) are characterized by a torsional potential which is intrinsically not symmetric around $\theta = 90°$, irrespective of possible asymmetries at *meta* positions. This characteristic implies a doubling of the number of points to be computed for a comparable fitting of the potential and has prevented till now a systematic study of this class. The main object of the present paper is to present a systematic study of this kind and to analyze the results in terms of simple interpretative models. As we shall see, the significant electron redistribution, which accompanies conformational changes, requires the use of a refined model explicitly accounting for the variations of bond energies.

Computational procedure

The torsional potentials of the title molecules were computed by the internal STO-3G basis set (29) of the GAUSSIAN/82 package (30) using structures of the different rings optimized at the STO-3G level (9) and a CC inter-ring distance of 1.50 Å.

The torsional angle θ between the planes of the two rings was spanned in steps of 30°. The different sets of conformational

[1]Revision received December 16, 1987.

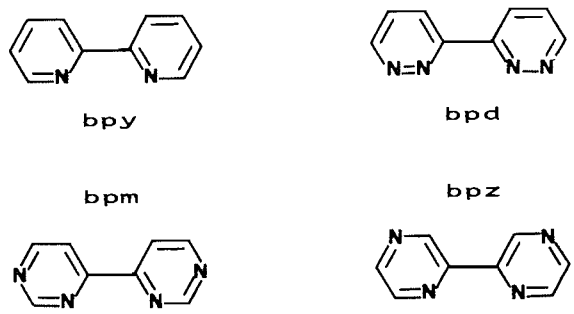

FIG. 1. Aromatic α-diimines investigated.

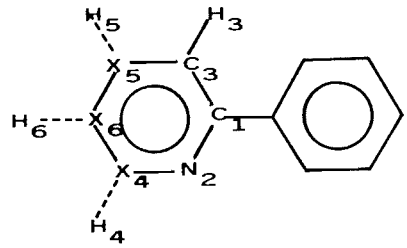

FIG. 2. Atom numbering of aromatic α-diimines. X4, X5, and X6 are either C or N atoms.

energies $V(\theta)$ (expressed as the total energies $E(\theta)$ minus the energy $E(0°)$ of the planar *cis* conformation) have been fitted by a truncated Fourier expansion

$$V(\theta) = \Sigma \tfrac{1}{2}V_j[1 - \cos(j\theta)]$$

This fitting allows a quantitative comparison of different molecules and the analytical location of the extreme points on the potential energy curve (10, 14, 25, 26). Furthermore, the physical origin of the low-order potential constants is well recognized (14).

Results

The structures, labelling, and atom numbering of the ligands studied in this work are shown in Figs. 1 and 2. The conformational energies and their six-term Fourier expansions are collected in Table 1 together with the location and relative energies of the critical points of the torsional curves obtained from these expansions. From these data it is apparent that the V_5 and V_6 potential constants play only a negligible role, so that four potential constants are sufficient for an accurate description of the conformational behavior of the title molecules. As a matter of fact, the relative weights of the odd and even potential constants are very similar in these molecules.

From a general point of view, the most striking feature of the results of Table 2 is the very similar torsional potential computed for all the title molecules. Closer inspection of the results, however, reveals a decrease of the *cis–trans* energy difference in going from bpy to the various diazines. Furthermore the value of this barrier is particularly low for bpz.

In agreement with the experimental data for 2,2′-bipyridine (14,31–36) the planar *trans* arrangement always corresponds to the absolute energy minimum. With respect to biphenyl, the loss of steric interactions between the *ortho* hydrogens (at $\theta = 180°$) now favors the planar structure. A second minimum at $\theta = 43 \pm 2°$ is revealed by STO-3G computations. The energy difference and the barrier between the two minima amount to 6 ± 1 and 1.5 ± 0.5 kcal mol^{-1}, respectively, and the position of the second minimum is similar to the minimum conformation of

TABLE 1. Conformational characteristics of molecules of class 2′*

Parameter	Value			
	bpy	bpd	bpm	bpz
$E(0°)$	−486.13399	−517.57330	−517.62894	−517.62512
$V(30°)$	−3.1	−1.7	−2.1	−2.1
$V(60°)$	−3.3	−1.5	−1.8	−1.7
$V(90°)$	−2.6	−1.0	−1.1	−0.8
$V(120°)$	−4.9	−3.4	−3.3	−2.9
$V(150°)$	−8.3	−6.9	−6.7	−6.1
$V(180°)$	−9.5	−8.2	−8.0	−7.3
V_1	−6.7	−6.3	−5.9	−5.1
V_2	2.5	3.2	3.1	3.1
V_3	−2.1	−1.5	−1.6	−1.6
V_4	−1.7	−1.0	−1.2	−1.3
V_5	−0.7	−0.4	−0.5	−0.5
V_6	−0.4	−0.2	−0.2	−0.2
θ_{min}	45°	42°	42°	41°
V_{min}	−3.9	−2.1	−2.5	−2.5

*The molecules are labelled as in Fig. 1. Energy differences with respect to planar *cis* conformations ($V(\theta)$) and potential terms (V_i) are in kcal mol^{-1} and angles in degrees. For all the molecules the absolute energy minimum corresponds to the planar *trans* conformation ($\theta = 180°$), so that only values for the secondary minimum are reported.

biphenyl. Visibly, the nitrogen lone pair interaction in the planar *cis* conformation of these molecules causes a destabilization similar in nature to that occurring between the *ortho* hydrogens in the planar form of the molecules belonging to class 0. In fact, the energy differences between the second minimum at $\theta \approx 43°$ and the *cis* conformation from one side ($E_1 = 3 \pm 1$ kcal mol^{-1}), or the maximum conformation at $\theta = 90°$ from the other side ($E_2 = 1.5 \pm 0.5$ kcal mol^{-1}), are similar to those found for molecules of class 0 ($E_1 = 3.5$, $E_2 = 2.3$ kcal mol^{-1} for eight molecules (14)).

In agreement with electron diffraction data for 2,2′-bipyridine (36), the planar *cis* form represents the absolute maximum of the potential energy curve. The energy difference between the two planar forms is particularly significant (9 ± 1 kcal mol^{-1}) and can be expressed in terms of variations of (*i*) bond energies and (*ii*) nonbonded interactions between atoms belonging to different rings.

The data of Table 2 show a significant electron redistribution between *cis* and *trans* conformations, which, however, essentially involves the N and H *ortho* atoms. In particular there is a net N → H charge transfer in each *cis* conformation, while the contrary occurs in the corresponding *trans* form. This transfer reduces N ... N and H ... H repulsions in the *cis* conformation, and increases N ... N attractions in the *trans* form. Although the involvement of the sole *ortho* groups explains the similarity of conformational behavior for the molecules belonging to the same class (i.e., with the same *ortho* substituents) the differences in electrostatic interactions between the *cis* and *trans* conformations are reasonably expected to be of minor import (37–39).

Let us now examine how the relative energies of *cis* and *trans* conformations can be affected by electron redistributions. Several studies (37, 40) indicate that the individual bond energies of ground-state molecules are (to a good approximation) linearly dependent on the charges of the bond-forming atoms, i.e.,

$$\epsilon_{ij} = \epsilon_{ij}^0 + a_{ij}\Delta q_i + a_{ji}\Delta q_j$$

Can. J. Chem. Downloaded from www.nrcresearchpress.com by 93.93.197.157 on 09/07/12
For personal use only.

TABLE 2. STO-3G Mulliken populations (q_i in me) and energy difference, $V(180°)$, between *cis* and *trans* conformations (in kcal mol^{-1}) obtained from complete computations or from eq. [1]*

	Value							
	bpy		bpd		bpm		bpz	
Parameter	*cis*	*trans*	*cis*	*trans*	*cis*	*trans*	*cis*	*trans*
q_{C1}	97	98	92	90	109	108	90	88
q_{N2}	−226	−251	−121	−148	−223	−248	−209	−231
q_{C3}	−75	−66	−63	−56	−83	−76	25	32
q_{H3}	72	95	80	106	79	102	85	105
q_{X4}	34	32	−132	−137	131	130	28	27
q_{H4}	76	73			87	84	88	86
q_{X5}	−51	−51	−61	−62	48	47	−221	−222
q_{H5}	73	74	84	85	87	88		
q_{X6}	−72	−73	26	26	−234	−235	28	28
q_{H6}	73	72	96	95			87	86
$V(180°)$, STO-3G	9.5		8.2		8.0		7.3	
$V(180°)$, eq. [1]	10.6		12.0		9.6		7.4	

*The labelling of the molecules and the numbering of the atoms are defined in Figs. 1 and 2. The values of the a_{ij}'s in kcal mol^{-1} me^{-1} are −0.083 (C—H), −0.358 (C—C), −0.480 (C—N), −0.587 (N—N), −0.632 (H—C), and −0.497 (N—C).

where ϵ_{ij}^0 is for a reference bond with net charges q_i^0 and q_j^0 at atoms i and j, respectively, whereas ϵ_{ij} corresponds to modified charges, $q_i = q_i^0 + \Delta q_i$ and $q_j = q_j^0 + \Delta q_j$. The a_{ij} and a_{ji} parameters (Table 2, Appendix 1) measure the effect of unit charge variations at atom i (bonded to j) and j (bonded to i), respectively.

The derivation of the ϵ_{ij}^0's can be avoided in the present context. Indeed, if only bonded terms are important, the energy difference $V(180)$ between the *cis* and *trans* conformations of the same molecule is

$$V(180) = \left(\sum_{i<j} \epsilon_{ij}\right)^{cis} - \left(\sum_{i<j} \epsilon_{ij}\right)^{trans}$$

$$= \sum_i \sum_j a_{ij} (\Delta q_i^{cis} - \Delta q_i^{trans})$$

$$= \sum_i \sum_j a_{ij} (q_i^{cis} - q_i^{trans})$$

i.e.,

$$[1] \quad V(180) = \sum_i (\Delta' q_i \sum_j a_{ij})$$

where $\Delta' q_i = q_i^{cis} - q_i^{trans}$. The use of eq. [1] involves the computation of reliable net charges. Mulliken's approximation is appropriate because[2] $\Delta' q_i = \Delta' q_i^{\text{Mulliken}}$. The required level of sophistication, using correlated wave functions constructed from extended and carefully optimized basis sets (41, 42), is out of computational reach for the molecules at hand for which we only know Mulliken populations obtained from the STO-3G basis set with standard orbital exponents. On the other hand, past experience (37, 40–42) indicates that the Δq_i's obtained in this manner correlate with their corrected counterparts satisfying charge–energy relationships with great accuracy. On these grounds, we tentatively scale our STO-3G results as follows

$$\Delta' q_i \simeq \frac{1}{2} \Delta' q_i^{\text{STO-3G}}$$

and subsequently show that this approximation suffices to bring the present results in line with the vast body of evidence gathered so far concerning the role of electronic charges in determining molecular energies (37, 40–42).

[2]In a Mulliken-type charge analysis not involving the classical equipartitioning of overlap populations between dissimilar atoms, the net charge of each individual atom must be corrected depending on what is bonded to it (37). These corrections cancel in the differences between net charges of homologous atoms in *cis* and *trans* conformers.

TABLE 3. The calculation of the *cis–trans* energy difference of bipyridazine (bpd)*

Atom	$\Delta' q_i$, me	$\Sigma_j a_{ij}$	$\Sigma_j a_{ij} \Delta' q_i$
C1	0		0
N2	−13.4	−1.08	14.5
C3	3.5	−0.80	−2.8
H3	12.7	−0.63	−8.0
N4	−2.4	−1.08	2.6
C5	−0.2	−0.80	0.2
H5	0.7	−0.63	−0.4
C6	0.3	−0.92	−0.3
H6	−0.4	−0.63	0.2

*The sum of the $\Sigma_j a_{ij} \Delta' q_i$ terms, 6.0 kcal/mol, is taken twice in order to account for the changes occurring in both cycles. The atom numbering is that of Fig. 2.

The energy differences between the *cis* and *trans* forms of the title molecules were now computed from eq. [1], using the appropriate a_{ij} and $\Delta' q_i$ results. An example is given in Table 3. The final energy calculations indicated in Table 2 are, indeed, similar to those derived from straightforward conventional STO-3G computations. The general trends are satisfactorily reproduced with the exception of bpd. This can be possibly traced back to the notorious weakness of STO-3G calculations using standard orbital exponents in situations dealing with adjacent atoms carrying lone pairs (43).

This result offers new insight into the origin of the energy differences between the conformers considered in our study.

Can. J. Chem. Downloaded from www.nrcresearchpress.com by 93.93.197.157 on 09/07/12
For personal use only.

Can. J. Chem. Downloaded from www.nrcresearchpress.com by 93.93.197.157 on 09/07/12
For personal use only.

Discussion

Ab initio computations have led to a comprehensive picture describing the conformational behavior of aromatic α-diimines. The *trans* forms are significantly favored over their *cis* counterparts, with a relatively shallow local minimum for a torsional angle of $\theta \approx 43°$. The conformational behavior of nonfused heterocycles appears to be adequately represented by three or four term Fourier expansions. Similar two-term expansions which are often used in experimental studies provide much poorer (and sometimes incorrect) results.

In an assessment of the reason why the *trans* form should be preferred over the *cis* conformer in the molecules considered here, one can easily be drawn to interpretations invoking steric repulsions, namely those involving the nitrogen lone pairs. As a corollary, this type of argument contracts to a consideration of nonbonded interactions between the atoms of one cycle with those of the other cycle. Our results are not there to dispute the involvement of "nonbonded interactions," but rather to examine their physical nature and the energetic effect accompanying them.

In the first place, it is clear that the molecular wave function differs depending upon what conformer is considered and, hence, also its square, and, therefore, the distribution of electronic charge. This is, indeeed, what is observed in our SCF charge analyses.

A school of thought could now suggest to interpret the conformational behavior in terms of electrostatic interactions between nonbonded atoms. The general failure of this type of approach, and its reasons, are well known from numerical analyses: with the use of realistic atomic charges, it simply turns out that electrostatic effects would usually be far too small to provide satisfactory explanations and, occasionally, even lead to wrong predictions (39). On the other hand, it also seems to reflect a lack of logics to consider variations of electronic charges at the individual atoms and their rôle in conformational effects solely in terms of nonbonded interactions and, at the same time, treat the problem as if any interaction between bonded atom pairs was to remain unaffected by the charges carried by these atoms.

This is precisely where our alternate energy analysis steps in. The effects on the bonded terms resulting from changes of electron populations were explicitly taken into account. It now appears, though our rough charge analyses cannot provide great precision, that the differences in bond energies do, indeed, discriminate between the *cis* and *trans* conformers. They do account for at least the major part of the energy differences revealed by conventional SCF calculations. Briefly, the *trans* forms are more stable than their *cis* counterparts primarily because the bond energies of the former are larger than those of the latter.

The direct comparison between planar forms offers no difficulty because the conjugation between the two rings should remain essentially the same in each planar form. This would no longer hold true for nonplanar forms, largely because the link between the two cycles would suffer from a partial suppression of conjugative stabilization, as in biphenyl (44). Thus restricting our considerations to the planar forms, it suffices, for an off-hand rough diagnosis, to observe the directions of the partial charge transfers. When the atom whose Σa_{ij} value is most negative gains electronic charge at the expense of atoms with less negative Σa_{ij} sums, the final result is one of a thermochemical stabilization. Accordingly the most stable *trans* conformer has more negative nitrogen atoms than its *cis* counterpart, a result satisfying common chemical intuition. The prime sources from which nitrogen gains electronic charge are the hydrogen atoms.

Our account of the electronic origin of energy changes associated with conformational preferences illustrates the prevailing weight of bonded over nonbonded energy contributions. This insight complements the information which can be derived from conventional SCF energy analyses.

Acknowledgments

S. F. thanks the Authorities of the Università di Napoli for their hospitality and the Natural Sciences and Engineering Research Council of Canada for financial support.

1. A. A. SCHILT. Applications of 1,10-phenanthrolyne and related compounds. Pergamon, London. 1969.
2. W. R. MCWHINNIE and J. D. MILLER. Adv. Inorg. Radiochem. **12**, 135 (1969).
3. F. BLAU. Ber. Dtsch. Chem. Ges. **21**, 1077 (1888); Monatsch. Chem. **10**, 375 (1889).
4. K. KALYAMASUNDARAN. Coord. Chem. Rev. **46**, 159 (1982).
5. M. SERPONE, G. PONTARINI, M. A. JAMIESON, F. BOLLETTA, and M. MAESTRI. Coord. Chem. Rev. **50**, 209 (1983).
6. J. T. BURTON, R. J. PUDDEPHAT, M. L. JONES, and J. A. IBERS. Organometallics, **2**, 1487 (1983).
7. J. A. SCOTT and R. J. PUDDEPHAT. Inorg. Chim. Acta, **89**, L27 (1984).
8. M. J. S. DEWAR. The molecular orbital theory of organic chemistry. McGraw-Hill, New York. 1969.
9. V. BARONE, C. CAULETTI, M. GHEDINI, F. LELJ, and M. N. PIANCASTELLI. In press.
10. A. ALMENNINGEN, O. BASTIANSEN, L. FERNHOLT, B. N. CYVIN, S. J. CYVIN, and S. SAMDAL. J. Mol. Struct. **128**, 59 (1985).
11. K. VINODGOPAL and W. R. LEENSTRA. J. Phys. Chem. **89**, 3824 (1985).
12. G. BREWER and E. SUIN. Inorg. Chem. **24**, 4580 (1985).
13. V. BARONE, F. LELJ, C. CAULETTI, M. N. PIANCASTELLI, and N. RUSSO. Mol. Phys. **49**, 599 (1983).
14. V. BARONE, F. LELJ, and N. RUSSO. Int. J. Quantum Chem. **29**, 541 (1986).
15. E. ORTÍ, J. SÁNCHEZ-MARÍN, and F. TOMÁS. Theochem, **108**, 199 (1984).
16. E. VON NAGY-FELSOBUKI. Chem. Phys. Lett. **127**, 245 (1986).
17. J. ALMLÖF. Chem. Phys. **6**, 135 (1974).
18. G. H. PENNER. THEOCHEM, **137**, 191 (1986).
19. V. BARONE, F. LELJ, L. COMMISSO, N. RUSSO, C. CAULETTI, and M. N. PIANCASTELLI. Chem. Phys. **96**, 435 (1985).
20. M. YAGI, K. MAKIGUCHI, A. OHNUKI, K. SUZUKI, J. HIGUCHI, and S. NAGASE. Bull. Chem. Soc. Jpn. **58**, 252 (1985).
21. V. BARONE, C. CAULETTI, F. LELJ, M. N. PIANCASTELLI, and N. RUSSO. J. Am. Chem. Soc. **104**, 4571 (1982).
22. V. BARONE, F. LELJ, N. RUSSO, and P. L. CRISTINZIANO. Unpublished results.
23. V. BARONE, L. COMMISSO, F. LELJ, and N. RUSSO. Tetrahedron, **41**, 1915 (1985).
24. E. ORTÍ, J. SÁNCHEZ-MARÍN, and F. TOMÁS. Theochem, **124**, 307 (1985).
25. E. ORTÍ, J. SÁNCHEZ-MARÍN, and F. TOMÁS. Theoret. Chim. Acta, **69**, 41 (1986).
26. E. ORTÍ, J. SÁNCHEZ-MARÍN, M. MERCHAN, and F. TOMÁS. J. Phys. Chem. **91**, 545 (1987).
27. N. RUSSO, M. TOSCANO, V. BARONE, and C. MINICHINO. J. Chim. Phys. **84**, 735 (1987).
28. V. BARONE, F. LELJ, N. RUSSO, and M. TOSCANO. J. Chem. Soc. Perkin Trans. II, 907 (1986).
29. W. J. HEHRE, R. F. STEWARD, and J. A. POPLE. J. Chem. Phys. **51**, 2657 (1969).
30. J. S. BINKLEY, M. J. FRISCH, D. J. DEFREES, K. RAGHAVACHARI, R. A. WHITESIDE, H. B. SCHLEGEL, E. M. FLUDER, and J. A. POPLE. GAUSSIAN 82. Carnegie-Mellon University. 1982.

31. L. L. MERRITT, JR., and E. D. SCHROEDER. Acta Crystallogr. **9**, 801 (1956).
32. C. W. N. CUMPER, R. F. A. GINNAN, and A. I. VOGEL. J. Chem. Soc. 1188 (1962).
33. K. NAKAMOTO. J. Phys. Chem. **64**, 1420 (1960).
34. S. CASTELLANO, H. GÜNTHER, and S. EBERSOLE. J. Phys. Chem. **69**, 4166 (1965).
35. T. M. SPOTSWOOD and C. I. TANZER. Aust. J. Chem. **20**, 1227 (1967).
36. O. BASTIANSEN and M. TRAETTEBERG. Tetrahedron, **17**, 147 (1962).
37. S. FLISZÁR. Charge distributions and chemical effects. Springer Verlag, New York. 1983.
38. B. M. PETTITT and M. KARPLUS. J. Am. Chem. Soc. **107**, 1166 (1985).
39. A. VEDANI and J. D. DUNITZ. J. Am. Chem. Soc. **107**, 7653 (1985).
40. S. FLISZÁR. J. Am. Chem. Soc. **102**, 6946 (1980).
41. S. FLISZÁR. Int. J. Quantum Chem. **29**, 305 (1986).
42. C. MIJOULE, J. M. LECLERCQ, S. ODIOT, and S. FLISZÁR. Can. J. Chem. **63**, 1741 (1985).
43. A. VEILLARD. Theoret. Chim. Acta, **18**, 21 (1970).
44. S. FLISZÁR, G. CARDINAL, and N. A. BAYKARA. Can. J. Chem. **64**, 1074 (1986).
45. S. FLISZÁR, M. FOUCRAULT, M. T. BÉRALDIN, and J. BRIDET. Can. J. Chem. **59**, 1074 (1981).
46. D. A. CASE, M. COOK, and M. KARPLUS. J. Chem. Phys. **73**, 3294 (1980).
47. S. FLISZÁR, G. CARDINAL, and M. T. BÉRALDIN. J. Am. Chem. Soc. **104**, 5287 (1982).
48. M. COMEAU, M. T. BÉRALDIN, E. C. VAUTHIER, and S. FLISZÁR. Can. J. Chem. **63**, 3226 (1985).

Appendix

The a_{ij} parameter is deduced from the formula (37, 40)

$$a_{ij} = \frac{3}{7}\left[\frac{(\partial E_i^{vs}/\partial N_i)^0 - (1/2)(\partial^2 E_i^{vs}/\partial N_i^2)^0 \Delta q_i}{v_i K_i^{mol}} - Z_j^{eff} < r_{ij}^{-1} >^0\right]$$

where Z^{eff} are effective nuclear charges ($Z^{eff} = 1, 4, 5$ for H, C, and N, respectively), v_i is the number of atoms attached to i, and $<r_{ij}^{-1>0}$ is the average inverse distance between the N_i electrons of atom i and the nucleus of atom j. K_i^{mol} is 1/2 for H, 0.4287 for C, and 0.4260 for N (37, 40, 45). The factor 3/7 translates nuclear–electronic into total (potential + kinetic) energy changes. Since the second-order term is negligible for H, C, and N, all the a_{ij}'s used in this work can be treated as constants.

The derivatives of the valence state energies for hydrogen and carbon are taken from ref. 44, whereas those of nitrogen are taken from ref. 46, namely, $\partial E^{\sigma}{}_N/\partial N_N = -0.29$ and $\partial E^{\pi}{}_N/\partial N_N = -0.26$ a.u. When the charges vary at both the σ and π levels, we have (37)

$$a_{ij}\,\Delta q_i = a^{\sigma}{}_{ij}\,\Delta q^{\sigma}{}_i + a^{\pi}{}_{ij}\,\Delta q^{\pi}{}_i$$

Taking advantage of the relationship (47)

$$\Delta q^{\sigma}{}_i = m_i \Delta q^{\pi}{}_i$$

it follows that

$$a_{ij} = (m_i a^{\sigma}{}_{ij} + a^{\pi}{}_{ij})/(1 + m_i)$$

The value of m_C was taken from ref. 44 and the value for nitrogen was computed from the STO-3G charges of pyridine derivatives given in ref. 48. Although the m_N values obtained using standard or optimized orbital exponents differ significantly from one another (−0.418 vs. −0.234) it is noteworthy that the values computed for a_{NC} and a_{NN} are virtually unaffected by the value selected for m. Similarly, any uncertainty concerning our selection of the $(\partial E/\partial N)$ derivatives for nitrogen has only a marginal effect on the final a_{NC} and a_{NN} values, not exceeding ~0.05 kcal mol^{-1} me^{-1}. This comes from the fact that the leading term in the expression of a_{ij} is represented by $(3/7)\,Z_j^{eff} < r_{ij}^{-1} >^0$. The set of a_{ij} values used in the present study is indicated in Table 2.

Can. J. Chem. Downloaded from www.nrcresearchpress.com by 93.93.197.157 on 09/07/12
For personal use only.

Comparison of STO-3G and 3-21G *ab initio* harmonic force fields for ethane, propane, dimethyl ether, and cyclobutane: effects of geometry and scaling on calculated frequencies, eigenvectors, and infrared absorption intensities

R. ANTHONY SHAW, CHARLES URSENBACH, ARVI RAUK, AND HAL WIESER[1]

Department of Chemistry, University of Calgary, Calgary, Alta., Canada T2N 1N4

Received August 13, 1987

R. ANTHONY SHAW, CHARLES URSENBACH, ARVI RAUK, and HAL WIESER. Can. J. Chem. **66**, 1318 (1988).

Ab initio harmonic force fields were calculated for ethane, propane, dimethyl ether, and cyclobutane at the STO-3G and 3-21G levels. The calculated frequencies, displacement eigenvectors, and calculated infrared absorption intensities were compared as they derive from force constants that were (*i*) unscaled; (*ii*) scaled to fit observed vibrational frequencies reported in the literature; (*iii*) evaluated at the optimized geometries; and (*iv*) evaluated at structures for which the bond lengths were corrected from the optimized geometries according to published procedures. A total of nine combinations of *ab initio* force field/reference geometry/**G**-matrix geometry were investigated for each of the four molecules. The ability of scaling factors as the only variables to predict vibrational parameters from STO-3G and 3-21G force fields was explored. Conditions were examined for which the scaling factors are satisfactorily transferable among different molecules.

R. ANTHONY SHAW, CHARLES URSENBACH, ARVI RAUK et HAL WIESER. Can. J. Chem. **66**, 1318 (1988).

On a calculé les champs de force harmonique *ab initio* de l'éthane, du propane, de l'éther diméthylique et du cyclobutane à des niveaux STO-3G et 3-21G. Les fréquences calculées, les déplacements des vecteurs fondamentaux ainsi que les intensités calculées des absorptions infrarouges sont comparées à celles obtenues à l'aide de constantes de forces : (*i*) qui ne sont pas graduées; (*ii*) qui sont graduées de façon à s'ajuster aux fréquences de vibration rapportées dans la littérature; (*iii*) qui ont été évaluées à l'aide de géométries optimisées et (*iv*) qui ont été évaluées à l'aide de structures pour lesquelles les longueurs des liaisons avaient été corrigées à partir de géométries optimisées en fonction de procédures publiées. Pour chacune des molécules, on a examiné un total de neuf combinaisons de champs de force *ab initio*/géométrie de référence/géométrie de matrice **G**. On a exploré la possibilité d'utiliser uniquement les facteurs scalaires pour prédire les paramètres vibrationnels à partir des champs de force de niveaux STO-3G et 3-21G. On a examiné les conditions pour lesquelles les facteurs scalaires sont transférés d'une façon satisfaisante entre les différentes molécules.

[Traduit par la revue]

Introduction

Over the past 15 years a number of *ab initio* harmonic vibrational force fields have been published (for reviews, see ref. 1). A general procedure for their evaluation has evolved, which involves the following steps: (*i*) selection of a basis set for the force constant evaluation; (*ii*) specification of a reference geometry about which the force constants are to be calculated; (*iii*) evaluation of the force constants via a second differentiation of the energy with respect to either Cartesian or suitable internal (local symmetry) coordinates, and subsequent calculation of vibrational frequencies. Frequently, it is necessary to proceed further by (*iv*) scaling of the *ab initio* force constants in local symmetry coordinates; and (*v*) optimizing the scaling factors to provide agreement between observed and calculated vibrational frequencies. For the purpose of scaling, the force constants are grouped according to type (e.g., CC stretch, CH stretch, CH_2 deformation, etc.) and are then scaled within each group following previous experience with similar types of coordinates.

The most difficult aspect of developing empirical force fields is the assignment of interaction constants (i.e., off-diagonal elements of the force constant matrix). From early theoretical work, it is evident that even basis sets of moderate size are sufficient to calculate the interaction constants with high accuracy (2–4). However, the diagonal force constants are overestimated even near the Hartree–Fock limit (5, 6) and as a consequence the *ab initio* force field must be scaled to reproduce experimentally observed frequencies. The final scaled force field is generally insensitive to improvements in the basis set beyond the simplest "split valence" (3-21G or 4-21G) level (7). Results obtained with the minimal STO-3G basis set have been criticized on the grounds that the diagonal force constants, and hence the vibrational frequencies, are overestimated to a significantly greater extent than for split valence basis sets, and its use in this regard has been limited (3, 4, 8–16). The majority of these reports present only unscaled STO-3G frequencies, with just three attempting to scale the STO-3G force field (10, 14, 16).

With respect to the choice of reference geometry, it has been argued on theoretical grounds that the experimental r_e structure is the most appropriate (17). In practice, such experimental data are rarely available. An alternative and more straightforward choice is the optimized structure for the chosen basis set. Extensive comparisons between optimized 4-21G and experimental geometries show that the *ab initio* bond lengths generally differ systematically from the experimental ones (4, 8, 19). It has become common practice to apply systematic "corrections" to the bond lengths, as first suggested by Blom and Altona (4). However, the actual benefits of such corrections for the purpose of vibrational analysis are not obvious in view of other approximations involved. These include the use of limited basis sets, invocation of the harmonic approximation, and the necessity of scaling the force field in any case to match observed frequencies.

Scaling of the calculated force field is intended to compensate for systematic errors that ensue from the practical necessity to use approximate uncorrelated wavefunctions (Hartree–Fock with limited basis set), and must be accomplished in such a manner as to retain the physical information available from the theory. For example, one procedure uniformly scales the entire force constant matrix by a constant, bringing the calculated frequencies in closer agreement with those observed while leaving unchanged the descriptions of the nuclear vibrational

[1]Author to whom correspondence may be addressed.

Can. J. Chem. Downloaded from www.nrcresearchpress.com by 93.93.197.157 on 09/07/12
For personal use only.

TABLE 1. Summary of force field/geometry combinations

Set no.	Basis set used in *ab initio* force constant calculation	Reference geometry about which *ab initio* force constants are calculated	Geometry used in calculation of **G** matrix	Abbreviation used in text
1	STO-3G	STO-3G	STO-3G	STO/STO/STO
2	STO-3Gcorr[a]	STO-3G	STO-3G	STOcorr/STO/STO
3	STO-3G	STO-3G	3-21corr[b]	STO/STO/321c
4	STO-3Gcorr[a]	STO-3G	3-21corr[b]	STOcorr/STO/321c
5	STO-3G	3-21corr[b]	3-21corr[b]	STO/321c/321c
6	STO-3Gcorr[a]	3-21corr[b]	3-21corr[b]	STOcorr/321c/321c
7	3-21G	3-21G	3-21G	321/321/321
8	3-21G	3-21G	3-21corr[b]	321/321/321c
9	3-21G	3-21corr[b]	3-21corr[b]	321/321c/321c

[a] "Corr" used in connection with STO-3G implies a correction of certain elements of the STO-3G force field to achieve closer agreement between scaled STO-3G and 3-21G force constants (see text).

[b] "Corr" used in connection with 3-21G implies corrections of optimized 3-21G bond lengths using procedures documented in the literature (18, 19).

Can. J. Chem. Downloaded from www.nrcresearchpress.com by 93.93.197.157 on 09/07/12
For personal use only.

displacements. Calculated intensities in this case are not affected. If the force fields are expressed in internal coordinates, the scale factors are generally different for bond stretching, angle bending, and torsional deformations. A body of experience based on combined theoretical and experimental investigations on small molecules already exists from which initial scaling factors may be chosen and transferred to new molecules of interest. To interpret congested spectra for which the majority of assignments are impossible to determine with any confidence from experimental data alone, it is desirable that the initial set of scale factors be sufficiently accurate to calculate most frequencies to within $10\,cm^{-1}$.

In the following we describe extensive comparisons of *ab initio* harmonic force fields calculated at the STO-3G and 3-21G levels for ethane, propane, dimethyl ether, and cyclobutane, for all of which the vibrational spectra are well documented in the literature. Our objective was to examine systematically the effects on the calculated frequencies, displacement eigenvectors, and absorption intensities, of scaling the force constants to reproduce the observed vibrational data, and of varying the reference geometry at which the **F** and **G** matrices are evaluated. For practical applications the results indicate: (*i*) for what purposes scaling is advisable and (or) necessary; (*ii*) whether optimized or corrected geometries are to be preferred; (*iii*) to what extent scaling factors optimized for one molecule are transferable to structurally similar or different molecules; and (*iv*) whether and with what compromise STO-3G force fields could be substituted when necessary for practical considerations.

Calculations

Force constants and geometry optimizations

The procedures adopted here for evaluating the various force fields were guided by our aim to quantify the influence of various choices for determining the force constants. Accordingly, for each molecule the force fields differ in terms of: (*i*) the basis set used to calculate the force constants; (*ii*) the reference geometry adopted for calculating the force constants, optimized for the basis set used or employing the "corrected" 3-21G structures; and (*iii*) the reference geometry adopted for calculating the **G** matrix. The "corrected" 3-21G structures were derived by adjusting the optimized bond lengths, a procedure intended to compensate for systematic deviations between optimized and experimental structures (4, 8, 19). The C—H and C—O bond lengths were adjusted by +0.005 and −0.023 Å, respectively. For the C—C bond length we used the procedure recommended by Pulay *et al.* for the 4-21G basis (19), according to which $\Delta R_{C-C} = 0.16(R^{calc}_{C-C} - 1.45\,Å)$.

The structures used for steps (*ii*) and (*iii*) need not be identical. We have examined two alternatives for each of the 3-21G and STO-3G basis sets. With one, both the **F** matrix (i.e., the force constants) and the **G** matrix are evaluated at the same (optimized) structure, while with the second the **F** matrix, evaluated at the optimized geometry, is used with **G** calculated with the "corrected" geometry. Our aim for this comparison was to assess the effect of changing the reference geometry for either the **F** or the **G** matrix separately.

In this manner we examined three alternative procedures for each basis set (Table 1). Systematic comparisons of individual elements of STO-3G force fields with corresponding 3-21G values further suggested that a uniform correction, as described in a following section, should be applied to certain of the STO-3G force constants. We designated this kind of a force field as STOcorr in Table 1.

All *ab initio* Cartesian force constants and optimized geometries were evaluated using the Gaussian 82 program (20). The force constants were transformed to a non-redundant set of local symmetry coordinates via the method prescribed by Fogarasi and Pulay (1*a*). The optimized geometries are summarized in Tables 2–4, and the local symmetry coordinate definitions in Tables 5–8. The vibrational secular equation was then solved using the standard Wilson **GF** formalism, and finally the local symmetry force constants were adjusted via least-squares refinement of a number of scaling factors to fit the observed frequencies. The scaling procedure adopted is that of Pulay *et al.* (19) according to which

$$[1] \quad F_{ij} = (C_i C_j)^{1/2} K_{ij}$$

where K_{ij} and F_{ij} denote the unscaled and scaled *ab initio* force constants, respectively, and C_i is the scaling factor for the local symmetry coordinate i. Least-squares optimization of the scaling factors was accomplished using a program that minimizes the rms deviation between observed and calculated frequency parameters, $\lambda_i = 4\pi^2 c^2 \nu_i^2$, with the observed parameters weighted by $1/(\lambda_i^{obs})^2$. Molecules included in the

TABLE 2. Optimized *ab initio* and experimental bond lengths (Å) and angles (degrees)

Parameter	STO-3G	3-21G	321c	4-21G[a,b]	4-31G[c]	r_z[d,e]	r_s[f,g]
Ethane							
CH	1.086	1.084	1.089	1.083	1.083	1.095	
CC	1.538	1.542	1.528	1.541	1.529	1.531	1.526
HCH	108.2	108.1	108.1	108.0	107.7	107.4	
Propane							
CH of CH_3 (ip)[h]	1.086	1.084	1.089	1.083	1.083	1.098	1.089
(op)[h]	1.086	1.085	1.089	1.084	1.084	1.098	1.094
CH of CH_2	1.089	1.085	1.090	1.083	1.085	1.097	1.096
CC	1.541	1.541	1.526	1.541	1.530	1.534	1.526
CCH (ip)[h]	110.6	111.2	111.2	111.2	111.4	111.0	111.8
(op)[h]	110.7	110.5	110.5	110.6	110.8	111.0	110.6
HCH of CH_2	107.1	107.2	107.2	107.0	106.4	107.8	106.1
CCC	112.5	111.6	111.6	112.3	112.6	112.0	112.4

[a]Reference 19.
[b]Reference 30.
[c]Reference 4*a*.
[d]Reference 31.
[e]Reference 32.
[f]Reference 33.
[g]Reference 34.
[h]In-plane (ip) and out-of-plane (op) with respect to the CCC plane.

TABLE 3. Optimized *ab initio* and experimental bond lengths (Å) and angles (degrees) of dimethyl ether

Parameter	STO-3G	3-21G	321c	4-21-0*[a]	4-21G[b]	4-31G[c]	r_s[d]
CH (ip)[e]	1.092	1.079	1.084	1.081	1.079	1.077	1.091
(op)[e]	1.095	1.086	1.091	1.087	1.085	1.085	1.100
CO	1.434	1.433	1.410	1.415	1.440	1.421	1.410
OCH (ip)[e]	107.4	106.9	106.9	107.2	106.6	107.0	107.2
(op)[e]	112.1	111.5	111.5	111.6	111.2	111.3	110.8
COC	119.5	113.9	113.9	111.2	113.8	115.9	111.7
H(ip)CH(op)						109.2	109.5
COCH(op)	60.9	60.7	60.7	60.8	60.7		

[a]Reference 35.
[b]Reference 36.
[c]Reference 37.
[d]Reference 38.
[e]In-plane (ip) and out-of-plane (op) with respect to the COC plane.

refinements were propane-h_8, -d_2, and -d_6, ethane-h_6 and -d_6, dimethyl ether-h_6 and -d_6, and cyclobutane-h_8 and -d_8. The vibrational frequencies and assignments were taken from the literature (4, 21, 22). The optimized scaling factors are summarized in Table 9.

Absorption intensities

The charge flow model, as formulated by Abbate *et al.* for calculating dipole and vibrational rotatory strengths (23), was used for evaluating the theoretical infrared absorption intensities. This theory is formally equivalent to the electro-optical parameter (EOP) method (see, for example, ref. 24) employed by Gussoni *et al.* (25) for interpreting and reproducing the experimental intensities of both ethane and propane. The EOPs of ref. 25 were converted to the charge flow formalism,[2] and were then used to calculate the dipole strengths, D_j, and integrated infrared absorption intensities, A_j, for propane and ethane via:

$$[2]\quad D_j = \frac{e^2 h}{4\pi c \nu_j}\left[\sum_A Z_A^0 \boldsymbol{t}_{A,j} + \sum_{\alpha,k} \boldsymbol{r}_{AB}\frac{\partial \xi_\alpha}{\partial R_k} L_{kj}\right]^2$$

$$[3]\quad A_j = 8\pi^3 N D_j \nu_j / 3hc$$

where Z_A^0 = equilibrium net charge of atom A; $\boldsymbol{t}_{A,j} = \partial \boldsymbol{r}_A / \partial Q_j$ is the Cartesian displacement vector of atom A accompanying unit displacement in normal coordinate Q_j, i.e., the appropriate element of the Cartesian eigenvector matrix; $\boldsymbol{r}_{AB}$ = a vector joining atoms A and B in the direction BA, defining bond α; $\partial \xi_\alpha / \partial R_k$ = the flow of positive charge from atom B to atom A in response to unit increase in coordinate R_k; L_{kj} = the appropriate element in the conventional **L** matrix ($= \partial R_k / \partial Q_j$). The expression for D_j is equivalent to that given by Abbate *et al.* (23).

Analogous charge flow parameters have not been derived for either dimethyl ether or cyclobutane, so that the intensities in

[2]The parameters so derived have been deposited as supplementary material, and may be purchased from the Depository of Unpublished Data, CISTI, National Research Council of Canada, Ottawa, Ont., Canada K1A 0S2.

Can. J. Chem. Downloaded from www.nrcresearchpress.com by 93.93.197.157 on 09/07/12
For personal use only.

TABLE 4. Optimized *ab initio* and experimental bond lengths (Å) and angles (degrees) of cyclobutane

Parameter	STO-3G	3-21G	321c	4-21G[a]	421c[a]	4-31G[b]	6-31G*[b]
CH (axial)	1.0865	1.0817	1.0867	1.081	1.086	1.082	1.085
CH (equatorial)	1.0867	1.0800	1.0850	1.080	1.085	1.080	1.084
CC	1.5532	1.5690	1.5500	1.567	1.548	1.554	1.557
HCH	108.72	109.90	109.90	109.4	109.4	108.5	108.3
CH_2 rocking angle	1.36	4.40	4.40			3.8	4.4
q[c]	0.0771	0.232	0.229	(24.1)	(24.1)	0.205	0.234
	El. Diff.[d]	r_z[e]	r_g[e]	nmr[f]			
CH	1.092	1.093	1.109	1.133			
CC	1.548	1.552	1.554	1.548			
HCH	110	106.4	106.4	108.1			
CH_2 rocking angle	0.34	6.2	6.2	4			
q[c]	(35)	(27.9)	(27.9)	(27.0)			

[a]Reference 39.
[b]Reference 40.
[c]Denotes either perpendicular distance between ring diagonals (in Å), or puckering dihedral angle (degrees) when given in brackets.
[d]Electron diffraction structure (41).
[e]Reference 42.
[f]Reference 43.

TABLE 5. Definitions of local symmetry coordinates of ethane

No.	Definitions[a,b]
1	CC stretch
2	C1–H3 stretch
3	C2–H4 stretch
4	C1–H5 stretch
5	C1–H6 stretch
6	C2–H7 stretch
7	C2–H8 stretch
8	CH_3 sym. def. (1), α(3-1-5) + α(3-1-6) + α(5-1-6) − β(3-1-2) − β(5-1-2) − β(6-1-2)
9	CH_3 sym. def. (2) α(7-2-8) + α(4-2-7) + α(4-2-8) − β(4-2-1) − β(7-2-1) − β(8-2-1)
10	CH_3 asym. def. (1) 2α(5-1-6) − α(3-1-6) − α(3-1-5)
11	CH_3 asym. def. (2) 2α(7-2-8) − α(4-2-7) − α(4-2-8)
12	CH_3 asym. def. (1) α(3-1-5) − α(3-1-6)
13	CH_3 asym. def. (2) α(4-2-8) − α(4-2-7)
14	CH_3 rock (1) 2β(3-1-2) − β(5-1-2) − β(6-1-2)
15	CH_3 rock (2) 2β(4-2-1) − β(7-2-1) − β(8-2-1)
16	CH_3 rock (1) β(5-1-2) − β(6-1-2)
17	CH_3 rock (2) β(7-2-1) − β(8-2-1)
18	C1–C2 torsion τ(3-1-2-8) + τ(5-1-2-7) + τ(6-1-2-4)

[a]See Fig. 1 for atom numbering.
[b]All coordinates were normalized. Normalization constants are not shown.

these cases were evaluated assuming fixed partial charges Z^0 (STO-3G Mulliken population analysis) on each atom, i.e., no terms of the type $\partial\xi_\alpha/\partial R_k$ were included. While the intensities calculated in this fashion generally do not agree well with the experimental values, they are considered adequate for the present purpose.

Comparison of calculated quantities

It is impossible to list all the relevant calculated eigenvectors, intensities, etc. for all force fields. Their accuracy was therefore assessed by comparing with the same quantities obtained with the scaled 321/321c/321c force field (see Table 1 for definitions used to designate the various force fields). While this choice may appear to be arbitrary, we concur with the opinion expressed by Pulay *et al.* (26) that properly scaled quantum mechanical force fields derived using medium sized split-valence basis sets "probably represent the limiting accuracy that can be achieved within the harmonic approximation". Their chosen method, which in our notation would be designated 421/421c/421c, is virtually equivalent to our 321/321c/321c combination. Accordingly the eigenvectors, calculated intensities, and force constants for a given force field n are assessed in terms of their average percent deviations from the scaled 321/321c/321c parameters (i.e., the reference set) as follows:

intensities:

$$[4]\quad \Delta A_n/\% = \frac{\sum_i |A_{i,n} - A_{i,\mathrm{ref}}|}{\sum_i A_{i,\mathrm{ref}}} \times 100$$

including only infrared active transitions;

eigenvectors:

$$[5]\quad \Delta L_n/\% = \frac{\sum_{i,j} |L_{i,j,n} - L_{i,j,\mathrm{ref}}|}{\sum_{i,j} |L_{i,j,\mathrm{ref}}|} \times 100$$

excluding all $L_{i,j} = 0$;

force constants:

$$[6]\quad \Delta F_n/\% = \frac{\sum_{i,j} |F_{i,j,n} - F_{i,j,\mathrm{ref}}|}{\sum_{i,j} |F_{i,j,\mathrm{ref}}|} \times 100$$

including only unique symmetry allowed force constants. The frequencies calculated with each combination were compared with experimental numbers, and the accuracy assessed in a similar fashion:

$$[7]\quad \Delta \nu_n/\% = \frac{\sum_i |\nu_{i,\mathrm{obs}} - \nu_{i,n}|}{\sum_i \nu_{i,\mathrm{obs}}} \times 100$$

Can. J. Chem. Downloaded from www.nrcresearchpress.com by 93.93.197.157 on 09/07/12
For personal use only.

TABLE 6. Definitions of local symmetry coordinates of propane

No.	Definitions[a,b]
1	C1–C2 stretch
2	C1–C3 stretch
3	C2–H4 stretch
4	C2–H5 stretch
5	C2–H6 stretch
6	C1–H7 stretch
7	C1–H8 stretch
8	C3–H9 stretch
9	C3–H10 stretch
10	C3–H11 stretch
11	CCC bend $5\theta(2\text{-}1\text{-}3) - \beta(7\text{-}1\text{-}2) - \beta(8\text{-}1\text{-}2) - \beta(7\text{-}1\text{-}3) - \beta(8\text{-}1\text{-}3) - \alpha(7\text{-}1\text{-}8)$
12	CH_2 scissor $4\alpha(7\text{-}1\text{-}8) - \beta(7\text{-}1\text{-}2) - \beta(8\text{-}1\text{-}2) - \beta(7\text{-}1\text{-}3) - \beta(8\text{-}1\text{-}3)$
13	CH_2 wag $\beta(7\text{-}1\text{-}2) + \beta(8\text{-}1\text{-}2) - \beta(7\text{-}1\text{-}3) - \beta(8\text{-}1\text{-}3)$
14	CH_2 rock $\beta(7\text{-}1\text{-}2) - \beta(8\text{-}1\text{-}2) + \beta(7\text{-}1\text{-}3) - \beta(8\text{-}1\text{-}3)$
15	CH_2 twist $\beta(7\text{-}1\text{-}2) - \beta(8\text{-}1\text{-}2) - \beta(7\text{-}1\text{-}3) + \beta(8\text{-}1\text{-}3)$
16	CH_3 sym. def. (2) $\alpha(5\text{-}2\text{-}4) + \alpha(5\text{-}2\text{-}6) + \alpha(4\text{-}2\text{-}6) - \beta(4\text{-}2\text{-}1) - \beta(5\text{-}2\text{-}1) - \beta(6\text{-}2\text{-}1)$
17	CH_3 sym. def. (3) $\alpha(9\text{-}3\text{-}10) + \alpha(9\text{-}3\text{-}11) + \alpha(10\text{-}3\text{-}11) - \beta(9\text{-}3\text{-}1) - \beta(10\text{-}3\text{-}1) - \beta(11\text{-}3\text{-}1)$
18	CH_3 asym. def. (op) (2) $2\alpha(6\text{-}2\text{-}5) - \alpha(4\text{-}2\text{-}5) - \alpha(4\text{-}2\text{-}6)$
19	CH_3 asym. def. (op (3) $2\alpha(10\text{-}3\text{-}11) - \alpha(9\text{-}3\text{-}10) - \alpha(9\text{-}3\text{-}11)$
20	CH_3 asym. def. (ip) (2) $\alpha(4\text{-}2\text{-}5) - \alpha(4\text{-}2\text{-}6)$
21	CH_3 asym. def. (ip) (3) $\alpha(9\text{-}3\text{-}10) - \alpha(9\text{-}3\text{-}11)$
22	CH_3 rock (op) (2) $2\beta(1\text{-}2\text{-}4) - \beta(1\text{-}2\text{-}5) - \beta(1\text{-}2\text{-}6)$
23	CH_3 rock (op) (3) $2\beta(1\text{-}3\text{-}9) - \beta(1\text{-}3\text{-}10) - \beta(1\text{-}3\text{-}11)$
24	CH_3 rock (ip) (2) $\beta(1\text{-}2\text{-}5) - \beta(1\text{-}2\text{-}6)$
25	CH_3 rock (ip) (3) $\beta(1\text{-}3\text{-}10) - \beta(1\text{-}3\text{-}11)$
26	C1–C2 torsion $\tau(4\text{-}2\text{-}1\text{-}8) + \tau(5\text{-}2\text{-}1\text{-}7) + \tau(6\text{-}2\text{-}1\text{-}3)$
27	C1–C3 torsion $\tau(9\text{-}3\text{-}1\text{-}7) + \tau(10\text{-}3\text{-}1\text{-}2) + \tau(11\text{-}3\text{-}1\text{-}8)$

[a]See Fig. 1 for atom numbering.
[b]All coordinates were normalized. Normalization constants are not shown.

and

$$[8] \quad \Delta\nu_n/\mathrm{cm}^{-1} = \frac{\sum_i |\nu_{i,\mathrm{obs}} - \nu_{i,n}|}{k_\nu}$$

including only the k_ν observed frequencies.

Tables 10–13 summarize the results for both the scaled and unscaled force fields listed in Table 1, while Table 14 summarizes separately an analogous comparison for the four symmetry blocks of propane.

Scaled STO-3G and 3-21G force constants

Since in all scaled force fields corresponding diagonal force constants are generally within 2% or better (see ΔF_n (diag.) of Tables 10–13), the interaction constants may be compared directly. Such a comparison is provided in Table 15. The interaction constants listed in the first two columns were obtained by scaling (eq. [1]) to fit the frequencies separately for the four molecules using either the 3-21G or STO-3G basis sets evaluated at the same corrected 3-21G reference geometry. It is seen that while the STO-3G stretch/stretch interactions are unreliable, often differing in sign as well as magnitude, the bend/bend constants adopt comparable values. The stretch/bend interactions, which are of significant magnitude (i.e., greater than 0.05 mdyn/Å), are underestimated by a nearly constant factor. This last observation suggests the possibility of first correcting the STO-3G constants as they are obtained from the *ab initio* calculations, and then optimizing the force field by scaling using eq. [1]. A multiplicative correction factor of 1.48 was derived on the basis of the comparisons presented here as well as with the appropriate force constants for oxetan.[3] The "corrected" force constants derived in this fashion are listed under STOcorr in Table 15, and are identified as such throughout this report.

TABLE 7. Definitions of local symmetry coordinates of dimethyl ether

No.	Definitions[a,b]
1	C3–O stretch
2	C2–O stretch
3	C2–H4 stretch
4	C2–H5 stretch
5	C2–H6 stretch
6	C3–H7 stretch
7	C3–H8 stretch
8	C3–H9 stretch
9	COC bend
10	CH_3 sym. def. (2) $\alpha(4\text{-}2\text{-}5) + \alpha(4\text{-}2\text{-}6) + \alpha(5\text{-}2\text{-}6) - \beta(1\text{-}2\text{-}4) - \beta(1\text{-}2\text{-}5) - \beta(1\text{-}2\text{-}6)$
11	CH_3 sym. def. (3) $\alpha(7\text{-}3\text{-}8) + \alpha(7\text{-}3\text{-}9) + \alpha(8\text{-}3\text{-}9) - \beta(1\text{-}3\text{-}7) - \beta(1\text{-}3\text{-}8) - \beta(1\text{-}3\text{-}9)$
12	CH_3 asym. def. (ip) (2) $2\alpha(5\text{-}2\text{-}6) - \alpha(4\text{-}2\text{-}5) - \alpha(4\text{-}2\text{-}6)$
13	CH_3 asym. def. (ip) (3) $2\alpha(8\text{-}3\text{-}9) - \alpha(7\text{-}3\text{-}8) - \alpha(7\text{-}3\text{-}9)$
14	CH_3 asym. def. (op) (2) $\alpha(4\text{-}2\text{-}5) - \alpha(4\text{-}2\text{-}6)$
15	CH_3 asym. def. (op) (3) $\alpha(7\text{-}3\text{-}8) - \alpha(7\text{-}3\text{-}9)$
16	CH_3 rock (ip) (2) $2\beta(1\text{-}2\text{-}4) - \beta(1\text{-}2\text{-}5) - \beta(1\text{-}2\text{-}6)$
17	CH_3 rock (ip) (3) $2\beta(1\text{-}3\text{-}7) - \beta(1\text{-}3\text{-}8) - \beta(1\text{-}3\text{-}9)$
18	CH_3 rock (op) (2) $\beta(1\text{-}2\text{-}5) - \beta(1\text{-}2\text{-}6)$
19	CH_3 rock (op) (3) $\beta(1\text{-}3\text{-}8) - \beta(1\text{-}3\text{-}9)$
20	O–C2 torsion $\tau(4\text{-}2\text{-}1\text{-}3) + \tau(5\text{-}2\text{-}1\text{-}3) + \tau(6\text{-}2\text{-}1\text{-}3)$
21	O–C3 torsion $\tau(7\text{-}3\text{-}1\text{-}2) + \tau(8\text{-}3\text{-}1\text{-}2) + \tau(9\text{-}3\text{-}1\text{-}2)$

[a]See Fig. 1 for atom numbering.
[b]All coordinates were normalized. Normalization constants are not shown.

For propane, the calculation of infrared absorption intensities first required transformation of the force constants, reported by Snyder (27) and adopted by Gussoni *et al.* (25) for the evaluation of the electro-optical parameters, from internal valence coordinates to the local symmetry coordinates used in the *ab initio* force field. The symmetrized empirical force constants are listed in Table 16, together with the corresponding optimized scaled 3-21G and STOcorr values. The agreement between the diagonal force constants is evident and with certain minor discrepancies, particularly for the CH_2 rock, the corresponding empirical values are in good accord with the *ab initio* results. Among the interaction force constants, with the exception of the STOcorr stretch/stretch interactions, the general agreement between the *ab initio* results is excellent. There are a number of empirical interaction constants, most notably the C–C stretch/CH_2 scissor, C–C stretch/CH_3 symmetric deformation, and CH_2 scissor/CH_3 symmetric deformation, that are in poor accord with the *ab initio* results. It seems unlikely that the scaled *ab initio* force fields should be in error for these particular cases, especially in view of the otherwise good agreement between empirical and *ab initio* results, and so it is likely that in these instances the empirically derived force constants are in error.

[3]R. A. Shaw, N. Ibrahim, and H. Wieser, unpublished results.

Can. J. Chem. Downloaded from www.nrcresearchpress.com by 93.93.197.157 on 09/07/12
For personal use only.

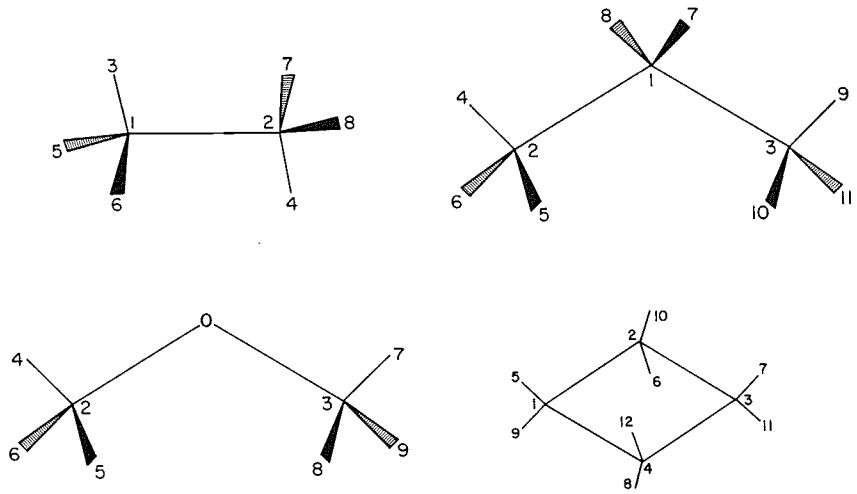

FIG. 1. Atom numbering used in the coordinate definitions given in Tables 5–8.

TABLE 8. Definitions of local symmetry coordinates of cyclobutane

No.	Definitions[a,b]
1	C1–C2 stretch
2	C2–C3 stretch
3	C3–C4 stretch
4	C4–C1 stretch
5	C1–H5 stretch
6	C2–H6 stretch
7	C3–H7 stretch
8	C4–H8 stretch
9	C1–H9 stretch
10	C2–H10 stretch
11	C3–H11 stretch
12	C4–H12 stretch
13	CH_2 scissor (1) $5\alpha(5\text{-}1\text{-}9) - \theta(4\text{-}1\text{-}2)$
14	CH_2 scissor (2) $5\alpha(6\text{-}2\text{-}10) - \theta(3\text{-}2\text{-}1)$
15	CH_2 scissor (3) $5\alpha(7\text{-}3\text{-}11) - \theta(4\text{-}3\text{-}2)$
16	CH_2 scissor (4) $5\alpha(8\text{-}4\text{-}12) - \theta(1\text{-}4\text{-}3)$
17	CH_2 wag (1) $\beta(5\text{-}1\text{-}4) + \beta(9\text{-}1\text{-}4) - \beta(5\text{-}1\text{-}2) - \beta(9\text{-}1\text{-}2)$
18	CH_2 wag (2) $\beta(6\text{-}2\text{-}3) + \beta(10\text{-}2\text{-}3) - \beta(6\text{-}2\text{-}1) - \beta(10\text{-}2\text{-}1)$
19	CH_2 wag (3) $\beta(7\text{-}3\text{-}2) + \beta(11\text{-}3\text{-}2) - \beta(7\text{-}3\text{-}4) - \beta(11\text{-}3\text{-}4)$
20	CH_2 wag (4) $\beta(8\text{-}4\text{-}1) + \beta(12\text{-}4\text{-}1) - \beta(8\text{-}4\text{-}3) - \beta(12\text{-}4\text{-}3)$
21	CH_2 rock (1) $\beta(5\text{-}1\text{-}4) - \beta(9\text{-}1\text{-}4) + \beta(5\text{-}1\text{-}2) - \beta(9\text{-}1\text{-}2)$
22	CH_2 rock (2) $\beta(6\text{-}2\text{-}3) - \beta(10\text{-}2\text{-}3) + \beta(6\text{-}2\text{-}1) - \beta(10\text{-}2\text{-}1)$
23	CH_2 rock (3) $\beta(7\text{-}3\text{-}2) - \beta(11\text{-}3\text{-}2) + \beta(7\text{-}3\text{-}4) - \beta(11\text{-}3\text{-}4)$
24	CH_2 rock (4) $\beta(8\text{-}4\text{-}1) - \beta(12\text{-}4\text{-}1) + \beta(8\text{-}4\text{-}3) - \beta(12\text{-}4\text{-}3)$
25	CH_2 twist (1) $\beta(5\text{-}1\text{-}4) - \beta(9\text{-}1\text{-}4) - \beta(5\text{-}1\text{-}2) + \beta(9\text{-}1\text{-}2)$
26	CH_2 twist (2) $\beta(6\text{-}2\text{-}3) - \beta(10\text{-}2\text{-}3) - \beta(6\text{-}2\text{-}1) + \beta(10\text{-}2\text{-}1)$
27	CH_2 twist (3) $\beta(7\text{-}3\text{-}2) - \beta(11\text{-}3\text{-}2) - \beta(7\text{-}3\text{-}4) + \beta(11\text{-}3\text{-}4)$
28	CH_2 twist (4) $\beta(8\text{-}4\text{-}1) - \beta(12\text{-}4\text{-}1) - \beta(8\text{-}4\text{-}3) + \beta(12\text{-}4\text{-}3)$
29	Ring def. $\theta(4\text{-}1\text{-}2) - \theta(1\text{-}2\text{-}3) + \theta(2\text{-}3\text{-}4) - \theta(3\text{-}4\text{-}1)$
30	Pucker $\tau(1\text{-}2\text{-}3\text{-}4) - \tau(2\text{-}3\text{-}4\text{-}1) + \tau(3\text{-}4\text{-}1\text{-}2) - \tau(4\text{-}1\text{-}2\text{-}3)$

[a]See Fig. 1 for atom numbering.
[b]All coordinates were normalized. Normalization constants are not shown.

Such discrepancies are reflected in the calculated absorption intensities (Table 17) for the A_1 scissor (ν_4), CH_3 symmetric deformation (ν_6), and C–C stretching (ν_8) modes, which are increased by 70%, 20%, and 140%, respectively, when the scaled 3-21G force field is substituted for the empirical one. The B_2 CH_3 symmetric deformation mode, ν_{24}, is similarly affected. These observations suggest that even the most carefully derived empirical force fields, although satisfactory in reproducing observed vibrational frequencies, are considerably less reliable than scaled *ab initio* force fields for the purpose of calculating infrared absorption intensities.

Reference geometry effects

The most objective measure of the accuracy of a force field is the fit of observed to calculated frequencies. Only minor variations occur among the three scaled 3-21G force fields, amounting to 0.5 ± 0.1% (Tables 10–13). Most importantly, the eigenvectors and calculated intensities are reproducible with an average percent deviation of 4.3% at worst. Since this is well below the usual uncertainty inherent in infrared intensity calculations, we conclude that for practical purposes when a force field is scaled to fit observed spectra it is not necessary to adjust the optimized 3-21G structure prior to evaluating the force constants except as noted below. The compromise approach, namely evaluating the force constants about the optimized geometry and then using the corrected structure for calculating the **G** matrix (321/321/321c), generally yields results comparable to the 321/321/321 combination.

Exceptions to this generalization are molecules for which the chosen basis set yields an optimized structure that is different from the r_e geometry in some significant aspect. For example, this is the case for cyclobutane for which STO-3G appreciably underestimates the ring dihedral angle compared to 3-21G (see Table 4). As demonstrated in Table 15 the scaled STO-3G force constants are decidedly more accurate when calculated at the corrected 3-21G reference geometry (STOcorr/321c/321c) than when evaluated at the optimized STO-3G structure (STOcorr/STO/STO). The most convincing evidence favoring the use of the more reliable reference geometry of the two is the resulting improvement in the fit of observed to calculated frequencies. The eigenvectors and calculated intensities are similarly brought into better agreement with the reference values (i.e., 321/321c/321c), with their average deviations being reduced by factors of about 2.5 and 4, respectively (24.4 to 10.7%, and 23.0 to 5.6%, respectively; see Table 13).

3-21G scaling factors

The scaling process serves to correct for the overestimation of the *ab initio* diagonal force constants. A simpler alternative is to scale the *ab initio* frequencies. It is well documented, however, that some types of force constants are systematically overestimated to a greater extent than others. The scaling of the force constants using different factors for different types of

Can. J. Chem. Downloaded from www.nrcresearchpress.com by 93.93.197.157 on 09/07/12
For personal use only.

Can. J. Chem. Downloaded from www.nrcresearchpress.com by 93.93.197.157 on 09/07/12
For personal use only.

TABLE 9. Optimized scaling factors for ethane (ET), propane (PR), dimethyl ether (DM), and cyclobutane (CB)

(*a*) Methylene modes

Force Field	Scissor		Rock		Wag		Twist	
	PR	CB	PR	CB	PR	CB	PR	CB
STOcorr/STO/STO	0.65	0.66	0.73	0.62	0.70	0.64	0.69	0.70
STOcorr/STO/321c	0.66	0.66	0.72	0.64	0.70	0.64	0.70	0.71
STOcorr/321c/321c	0.65	0.66	0.70	0.69	0.68	0.66	0.68	0.68
321/321/321	0.78	0.79	0.83	0.85	0.79	0.79	0.78	0.78
321/321/321c	0.79	0.79	0.84	0.86	0.80	0.79	0.78	0.78
321/321c/321c	0.78	0.78	0.79	0.77	0.76	0.76	0.76	0.75

(*b*) Methyl modes

Force Field	Sym. Def.			Asym. Def.			Rock			Torsion		
	PR	ET	DM	PR	ET	DM	PR	ET	DM	PR	ET	DM
STOcorr/STO/STO	0.66	0.67	0.70	0.63	0.63	0.65	0.69	0.70	0.78	0.93	0.85	0.78
STOcorr/STO/321c	0.66	0.67	0.71	0.64	0.64	0.64	0.69	0.70	0.77	0.94	0.86	0.72
STOcorr/321c/321c	0.65	0.66	0.71	0.63	0.63	0.66	0.66	0.68	0.77	0.53	0.60	3.66
321/321/321	0.78	0.78	0.78	0.77	0.77	0.76	0.79	0.80	0.85	0.86	0.87	0.94
321/321/321c	0.78	0.79	0.79	0.78	0.77	0.76	0.79	0.80	0.85	0.86	0.88	0.93
321/321c/321c	0.76	0.77	0.77	0.77	0.76	0.76	0.76	0.76	0.81	0.50	0.56	0.63

(*c*) Other modes

Force Field	C–C stretch			CCC (COC) bend			C–O stretch	C–H stretch			
	PR	ET	CB	PR	CB	DM	DM	PR	ET	DM	CB
STOcorr/STO/STO	0.68	0.69	0.61	0.81	0.88	(0.73)	0.69	0.64	0.65	0.66	0.64
STOcorr/STO/321c	0.68	0.69	0.61	0.80	0.81	(0.68)	0.69	0.64	0.65	0.66	0.64
STOcorr/321c/321c	0.64	0.66	0.61	0.76	0.73	(0.95)	0.63	0.65	0.66	0.64	0.64
321/321/321	0.96	0.99	0.95	0.85	0.84	(1.04)	0.90	0.83	0.84	0.83	0.81
321/321/321c	0.96	0.99	0.95	0.84	0.81	(1.01)	0.90	0.83	0.84	0.83	0.81
321/321c/321c	0.89	0.92	0.87	0.80	0.82	(0.99)	0.80	0.86	0.86	0.86	0.84

TABLE 10. Summary of force fields for ethane[a]

	Force field	ΔL_n/% (eq. [5])	ΔA_n/% (eq. [4])	$\Delta\nu_n$ (eqs. [7], [8])		ΔF_n (eq. [6])/%		
				cm^{-1}	%	Diag.	Interact.	Overall
Unscaled:	STO/STO/STO	5.5	3.5	412.5	23.8	50.5	35.7	48.8
	STOcorr/STO/STO	2.9	1.9	406.1	23.4	50.5	53.6	50.9
	STO/STO/321c	5.4	3.0	410.5	23.7	50.5	35.7	48.8
	STOcorr/STO/321c	2.6	1.4	404.1	23.3	50.5	53.6	50.9
	STO/321c/321c	5.7	3.0	415.4	24.0	52.5	35.5	50.6
	STOcorr/321c/321c	2.7	1.4	409.1	23.6	52.5	55.3	52.8
Scaled:	STO/STO/STO	4.6	3.5	22.3	1.3	1.0	48.6	6.3
	STOcorr/STO/STO	1.3	1.9	21.3	1.2	0.7	29.6	3.9
	STO/STO/321c	4.6	2.9	22.5	1.3	0.9	48.6	6.3
	STOcorr/STO/321c	1.2	1.4	21.5	1.2	0.6	29.6	3.9
	STO/321c/321c	5.0	3.0	21.7	1.2	0.9	47.6	6.1
	STOcorr/321c/321c	1.6	1.5	20.3	1.2	0.6	28.3	3.7
Unscaled:	321/321/321	1.3	1.0	183.3	10.6	13.4	19.5	14.1
	321/321/321c	1.1	0.2	180.1	10.4	13.4	19.5	14.1
	321/321c/321c	0.6	0.2	183.4	10.6	15.6	22.1	16.3
Scaled:	321/321/321	1.1	1.1	8.7	0.5	0.1	4.1	0.6
	321/321/321c	0.8	0.2	8.9	0.5	0.1	4.4	0.6
	321/321c/321c	0.0	0.0	8.4	0.5	0.0	0.0	0.0

[a]See eqs. [4]–[8] for definitions of ΔL_n, ΔA_n, $\Delta\nu_n$, and ΔF_n.

TABLE 11. Summary of force fields for propane[a]

	Force field	ΔL_n/% (eq. [5])	ΔA_n/% (eq. [4])	$\Delta\nu_n$ (eqs. [7], [8]) cm^{-1}	$\Delta\nu_n$ (eqs. [7], [8]) %	ΔF_n (eq. [6])/% Diag.	ΔF_n (eq. [6])/% Interact.	ΔF_n (eq. [6])/% Overall
Unscaled:	STO/STO/STO	16.9	20.3	387.7	24.1	51.4	43.1	50.4
	STOcorr/STO/STO	11.5	17.5	381.5	23.8	51.4	60.6	52.4
	STO/STO/321c	15.7	19.2	385.6	24.0	51.4	43.1	50.4
	STOcorr/STO/321c	10.8	16.1	379.4	23.6	51.4	60.6	52.4
	STO/321c/321c	17.7	18.6	394.6	24.6	52.5	41.6	51.2
	STOcorr/321c/321c	11.0	15.6	388.3	24.2	52.5	63.1	53.7
Scaled:	STO/STO/STO	19.3	20.3	12.7	0.8	2.0	50.9	7.8
	STOcorr/STO/STO	8.8	17.4	11.1	0.7	0.8	35.5	4.9
	STO/STO/321c	19.5	19.3	13.0	0.8	1.8	50.9	7.6
	STOcorr/STO/321c	9.4	16.1	11.0	0.7	0.6	35.5	4.8
	STO/321c/321c	19.1	18.7	13.1	0.8	1.7	47.7	7.1
	STOcorr/321c/321c	8.3	15.5	11.3	0.7	0.5	33.3	4.4
Unscaled:	321/321/321	9.3	3.6	173.8	10.8	18.7	19.7	18.8
	321/321/321c	8.9	3.0	171.0	10.6	18.7	19.7	18.8
	321/321c/321c	6.8	1.0	176.5	11.0	19.1	22.1	19.5
Scaled:	321/321/321	3.3	2.9	5.9	0.4	0.5	5.5	1.0
	321/321/321c	3.1	2.2	6.1	0.4	0.3	5.6	0.9
	321/321c/321c	0.0	0.0	7.1	0.4	0.0	0.0	0.0

[a]See Table 10.

TABLE 12. Summary of force fields for dimethyl ether[a]

	Force field	ΔL_n/% (eq. [5])	ΔA_n/% (eq. [4])	$\Delta\nu_n$ (eqs. [7], [8]) cm^{-1}	$\Delta\nu_n$ (eqs. [7], [8]) %	ΔF_n (eq. [6])/% Diag.	ΔF_n (eq. [6])/% Interact.	ΔF_n (eq. [6])/% Overall
Unscaled:	STO/STO/STO	21.1	33.4	321.2	21.7	48.8	40.8	47.7
	STOcorr/STO/STO	20.5	23.2	311.9	21.1	48.8	68.2	51.3
	STO/STO/321c	23.9	37.2	328.0	22.2	48.8	40.8	47.7
	STOcorr/STO/321c	22.5	25.6	318.6	21.5	48.8	68.2	51.3
	STO/321c/321c	18.9	32.4	336.0	22.7	52.3	46.2	51.5
	STOcorr/321c/321c	19.1	19.0	326.4	22.1	52.3	75.3	55.3
Scaled:	STO/STO/STO	15.5	28.2	8.5	0.6	2.2	44.2	7.6
	STOcorr/STO/STO	13.4	14.6	8.2	0.6	2.6	39.3	7.3
	STO/STO/321c	16.1	28.5	10.9	0.7	1.6	44.4	7.1
	STOcorr/STO/321c	15.3	16.5	10.6	0.7	2.1	38.3	6.7
	STO/321c/321c	13.8	22.8	11.9	0.8	2.1	46.8	7.9
	STOcorr/321c/321c	12.0	11.7	11.0	0.7	2.5	45.0	8.0
Unscaled:	321/321/321	8.3	6.8	156.0	10.5	16.8	17.1	16.9
	312/321/321c	8.2	6.8	152.7	10.3	16.8	17.1	16.9
	321/321c/321c	3.5	2.7	167.8	11.3	19.6	21.3	19.9
Scaled:	321/321/321	1.8	1.8	6.9	0.5	0.5	7.7	1.5
	321/321/321c	1.9	2.2	7.0	0.5	0.4	7.9	1.3
	321/321c/321c	0.0	0.0	6.8	0.5	0.0	0.0	0.0

[a]See Table 10.

local symmetry coordinates can therefore change not only the absolute magnitudes of the frequencies but also their relative positions.

Scaling also has the effect of altering the eigenvectors relative to those derived with unscaled constants, as is illustrated by comparing the scaled vs. unscaled 321/321c/321c force fields of Tables 10–13. The difference in the average deviation (ΔL_n) between the two varies from less than 1% in ethane, for which the high symmetry is the dominant factor determining the nature of the normal modes, to 7% in propane, for which the largest discrepancies arise in the A_1 and B_2 symmetry species with average deviations of 11 and 9.5% respectively (see Table 14). Calculated absorption intensities for A_1 and B_2 modes are therefore influenced to a greater extent by scaling than the B_1 modes. As illustrated in Table 17, the calculated intensities for ν_8 (symmetric C–C stretch), ν_{26} (asymmetric C–C stretch), and ν_{27} (CH_3 rock) are doubled, halved, and tripled, respectively, upon scaling. The reason that these modes are particularly affected can be attributed to the need for scaling the C–C stretching force constants by a relatively larger factor (i.e., less

Can. J. Chem. Downloaded from www.nrcresearchpress.com by 93.93.197.157 on 09/07/12
For personal use only.

TABLE 13. Summary of force fields for cyclobutane[a]

	Force field	ΔL_n/% (eq. [5])	ΔA_n/% (eq. [4])	$\Delta\nu_n$ (eqs. [7], [8]) cm^{-1}	$\Delta\nu_n$ (eqs. [7], [8]) %	ΔF_n (eq. [6])/% Diag.	Interact.	Overall
Unscaled:	STO/STO/STO	24.1	22.9	392.0	24.4	55.9	61.4	56.5
	STOcorr/STO/STO	17.7	16.0	386.4	24.1	55.9	79.6	58.4
	STO/STO/321c	23.2	12.5	389.7	24.3	55.9	61.4	56.5
	STOcorr/STO/321c	18.0	6.5	384.1	23.9	55.9	79.6	58.4
	STO/321c/321c	16.0	13.3	393.2	24.5	56.0	52.6	55.7
	STOcorr/321c/321c	11.7	6.4	387.6	24.2	56.0	75.3	58.1
Scaled:	STO/STO/STO	22.5	27.3	20.8	1.3	3.8	59.8	9.7
	STOcorr/STO/STO	24.4	23.0	20.9	1.3	3.5	55.4	9.0
	STO/STO/321c	20.8	15.5	19.2	1.2	2.8	59.9	8.8
	STOcorr/STO/321c	27.0	13.3	19.6	1.2	2.6	54.9	8.2
	STO/321c/321c	12.7	11.2	15.3	1.0	1.7	49.3	6.8
	STOcorr/321c/321c	10.7	5.6	13.6	0.8	1.3	41.0	5.5
Unscaled:	321/321/321	7.4	6.7	175.0	10.9	19.5	19.9	19.6
	321/321/321c	7.8	7.8	173.0	10.8	19.5	19.9	19.6
	321/321c/321c	4.8	5.0	179.3	11.2	20.3	22.2	20.5
Scaled:	321/321/321	3.6	3.5	8.9	0.6	0.7	5.5	1.2
	321/321/321c	3.8	4.3	8.7	0.5	0.6	5.7	1.1
	321/321c/321c	0.0	0.0	10.3	0.6	0.0	0.0	0.0

[a]See Table 10.

scaling) than the bending vibrations (~0.96 vs. 0.8, respectively). In general, the extent to which the calculated intensity of a particular vibration will be changed by scaling will depend on the relative magnitudes of the scaling factors for the coordinates that are involved in that vibration.

It is desirable that the scaling factors employed in the initial prediction be sufficiently reliable to enable one to assign the observed absorptions at the outset with confidence. That required level of accuracy is attainable only when the factors are optimized for specific coordinates, implying that they should be refined independently for all coordinates that are not symmetry equivalent. For example, although the scissoring, rocking, wagging, and twisting modes of a methylene group all consist of angle bending motions, four separate scaling factors should be refined independently. Indeed, as the calculations reveal, the refined 321/321/321 factors for three of these (i.e., scissor, wag, and twist in Table 9) are similar in magnitude (0.78–0.79), independent of the mode and compound, while the rocking factor is larger for both propane and cyclobutane. The significance of such differences may be demonstrated by observing that if 0.79 were used instead of 0.84 for a hypothetical "pure" rocking mode, the latter's position would be predicted to occur at 970 rather than 1000 cm^{-1}. If this region of the spectrum were congested, the result would likely be a misassignment of the relevant mode to an observed band at lower frequency.

In addition, it is reasonable to expect that the scaling factors may be sensitive to the chemical environment of a particular moiety. For the molecules investigated here, the methyl groups in propane and dimethyl ether provide the opportunity for such a comparison. As seen in Table 9, of the three methyl deformations, the rocking mode requires a larger scaling factor for the ether, indicating that the adjacent oxygen atom does have an effect.

One particularly desirable feature of scaling factors would be their transferability. This is perhaps the most important aspect to consider in deciding among the various options. If scaling factors refine to virtually identical values when fit individually and independently to the observed frequencies of a set of molecules, it may be safely assumed that the vibrational spectra of other species encompassing the same coordinates may be predicted with the same level of accuracy.

The optimized scaling factors of Table 9 indicate that from the point of view of their transferability, there is little to choose among the three alternative procedures. For each of the four CH_2 deformation modes, the analogous refined scaling factors are within 0.02 of one another at worst. The same applies to the CH_3 deformations of ethane and propane. A wider range is evident among the C–C stretch scaling factors optimized for ethane, propane, and cyclobutane; however, the range of values is the same in all three cases and hence from the point of view of transferability none of the three procedures emerges as being preferable to the other two.

STO-3G force fields

As anticipated, the unscaled STO-3G frequencies are markedly higher, and the eigenvectors and calculated infrared absorption intensities uniformly less accurate than the corresponding unscaled 3-21G values. While scaling of the force constants in the same manner as for 3-21G improves the calculated frequencies, the eigenvectors and intensities remain unacceptable (Tables 12–15). Inclusion of the stretch/bend correction factor (STOcorr) serves to bring the scaled STO-3G eigenvectors and intensities into much better accord with the 3-21G results. For each molecule, excepting only cyclobutane for the reasons given earlier, ΔA_n and (or) ΔL_n (eqs. [3] and [4]) are reduced by a factor of two or better for the STOcorr/STO/STO force field as compared to the uncorrected STO/STO/STO. The apparently marginal improvement in ΔA_n of propane is due to the damping effect of the large C–H stretching intensities, which are poorly reproduced by the uncorrected force field and are virtually unaffected by the adjusted stretch/bend interaction constants that distinguish the STOcorr from the STO force field.

Can. J. Chem. Downloaded from www.nrcresearchpress.com by 93.93.197.157 on 09/07/12
For personal use only.

TABLE 14. Average deviations in eigenvectors, intensities, and frequencies by symmetry block for propane[a]

	Force field	A_1 Symmetry species			A_2 Symmetry species		
		ΔL_n/% (eq. [5])	ΔA_n/% (eq. [4])	$\Delta \nu_n$/% (eq. [7])	ΔL_n/% (eq. [5])	ΔA_n/% (eq. [4])	$\Delta \nu_n$/% (eq. [7])
Unscaled:	STO/STO/STO	22.0	40.8	23.8	5.7		24.4
	STOcorr/STO/STO	20.8	37.7	23.3	5.0		24.3
	STO/STO/321c	18.9	40.8	23.7	5.5		24.2
	STOcorr/STO/321c	18.3	36.8	23.3	5.0		24.1
	STO/321c/321c	21.8	40.6	24.0	5.4		25.6
	STOcorr/321c/321c	20.3	37.1	23.6	5.1		25.5
Scaled:	STO/STO/STO	21.2	41.2	0.7	3.8		0.8
	STOcorr/STO/STO	14.7	37.0	0.6	3.2		0.8
	STO/STO/321c	21.9	41.5	0.7	3.7		0.8
	STOcorr/STO/321c	15.6	36.2	0.6	2.8		0.8
	STO/321c/321c	21.4	41.3	0.7	3.8		0.8
	STOcorr/321c/321c	15.3	36.9	0.6	3.1		0.9
Unscaled:	321/321/321	17.1	6.5	10.9	0.6		11.5
	321/321/321c	16.6	5.6	10.7	0.5		11.3
	321/321c/321c	13.0	1.1	10.8	0.1		12.5
Scaled:	321/321/321	4.9	5.6	0.4	1.1		0.4
	321/321/321c	4.7	4.6	0.4	0.6		0.4
	321/321c/321c	0.0	0.0	0.4	0.0		0.5

	Force field	B_1 Symmetry species			B_2 Symmetry species		
		ΔL_n/% (eq. [5])	ΔA_n/% (eq. [4])	$\Delta \nu_n$/% (eq. [7])	ΔL_n/% (eq. [5])	ΔA_n/% (eq. [4])	$\Delta \nu_n$/% (eq. [7])
Unscaled:	STO/STO/STO	4.8	3.4	24.1	29.1	22.7	24.3
	STOcorr/STO/STO	6.0	2.0	24.0	8.9	17.4	23.7
	STO/STO/321c	4.6	2.5	24.1	28.9	19.8	24.1
	STOcorr/STO/321c	5.8	1.1	24.0	9.5	14.5	23.4
	STO/321c/321c	5.1	2.5	24.7	32.8	17.0	24.5
	STOcorr/321c/321c	5.8	1.2	24.5	7.8	11.3	23.9
Scaled:	STO/STO/STO	4.1	3.2	0.7	42.1	22.4	0.9
	STOcorr/STO/STO	4.8	1.9	0.8	8.7	18.5	0.7
	STO/STO/321c	4.4	2.3	0.7	41.8	19.3	1.0
	STOcorr/STO/321c	5.4	1.0	0.8	9.4	15.7	0.6
	STO/321c/321c	3.3	2.4	0.7	41.7	16.4	1.0
	STOcorr/321c/321c	4.0	1.1	0.7	6.7	11.8	0.7
Unscaled:	321/321/321	2.3	1.1	10.4	11.6	4.3	10.7
	321/321/321c	2.1	0.4	10.3	11.0	4.0	10.5
	321/321c/321c	2.6	0.3	10.6	7.0	2.2	10.7
Scaled:	321/321/321	2.6	1.2	0.5	3.3	2.4	0.3
	321/321/321c	2.5	0.4	0.5	3.2	2.2	0.3
	321/321c/321c	0.0	0.0	0.7	0.0	0.0	0.3

[a]See Table 10.

The marked improvement in ΔL_n thus reflects, not only for propane but for all four molecules, alterations in the nature of lower frequency mid-infrared modes.

The modes most affected by the stretch/bend correction should be those involving simultaneous displacement of both bending and skeletal stretching coordinates. For propane, the in-phase and out-of-phase C–C stretching coordinates transform as A_1 and B_2 respectively, and so it is within these symmetry species that the STOcorr force fields should be more accurate than the uncorrected STO-3G. Table 14 confirms this to be the case. Modes comprising the A_2 and B_1 symmetry species, i.e., virtually pure bending modes, are adequately described by the uncorrected STO-3G force field and a affected little by the stretch/bend correction. Although not presented explicitly here, analogous behaviour is found for each of the other three molecules. For ethane the species A_{1g} (C–C stretch), for dimethyl ether A_1 and B_2 (C–O in-phase and out-of-phase stretch), and for cyclobutane A_1, B_1, and E (ring C–C stretching) are all substantially better described by the STOcorr than the uncorrected STO-3G force field.

As for the 3-21G case, the frequencies, eigenvectors, and intensities for the scaled STOcorr force fields are little affected by changing the reference geometry from the optimized (STO-3G) to corrected 3-21G structure for ethane, propane, and

Can. J. Chem. Downloaded from www.nrcresearchpress.com by 93.93.197.157 on 09/07/12
For personal use only.

TABLE 15. Selected scaled *ab initio* interaction force constants[a]

Molecule	Force constant	321/321c/321c	STO/321c/321c	STOcorr/321c/321c
	Stretch/stretch			
Ethane:	CC/CH	0.0809	−0.0031	−0.0031
	CH/CH	0.0572	−0.0105	−0.0106
Propane:	CC/CC	0.1180	0.0732	0.0708
	CH/CH (ip/op)	0.0551	−0.0478	−0.0481
	CH/CH (CH_2)	0.0650	−0.0443	−0.0445
Dimethyl ether:	CO/CO	−0.0347	−0.1521	−0.1599
	CO/CH (ip)	0.1238	0.0960	0.0988
	CO/CH (op)	0.2186	0.1568	0.1613
	CH/CH (ip/op)	0.0604	−0.0443	−0.0446
	CH/CH (op/op)	0.0771	−0.0374	−0.0376
Cyclobutane:	CC/CC (adj.)	0.0411	−0.0467	−0.0468
	CC/CC (opp.)	0.1550	0.0104	0.0104
	CH/CH	0.0536	−0.0531	−0.0534
	CC/CH (eq)	0.0705	−0.0101	−0.0101
	CC/CH (ax)	0.0757	−0.0057	−0.0057
	Bend/bend			
Ethane:	CH_3 rock/CH_3 rock	0.1230	0.1336	0.1335
	CH_3 sym. def./CH_3 sym. def.	0.0243	0.0212	0.0211
Propane:	CCC/CH_3 rock	0.1106	0.1156	0.1153
	CH_2 wag/CH_3 rock	−0.0475	−0.0525	−0.0543
	CH_2 rock/CH_3 rock	−0.0809	−0.0904	−0.0903
	CH_2 twist/CH_3 rock	−0.0923	−0.0971	−0.0970
	CH_3 rock/CH_3 rock	0.0303	0.0257	0.0257
Dimethyl ether:	CH_3 asym. def./CH_3 rock	−0.0636	−0.0503	−0.0502
	CH_3 asym. def./CH_3 rock	0.0333	0.0276	0.0276
Cyclobutane:	CH_2 wag/CH_2 twist	−0.0574	−0.0562	−0.0572
	CH_2 rock/CH_2 twist	−0.0493	−0.0548	−0.0551
	CH_2 rock/ring def.	−0.0540	−0.0532	−0.0531
	CH_2 twist/CH_2 twist (adj.)	0.0694	0.0748	0.0753
	Stretch/bend			
Ethane:	CC/CH_3 sym. def.	−0.3437	−0.2303	−0.3448
	CH/CH_3 sym. def.	0.0708	0.0418	0.0629
	CH/CH_3 asym. def.	−0.1273	−0.0738	−0.1092
	CH/CH_3 rock	0.1041	0.0519	0.0768
Propane:	CC/CCC	0.1931	0.1507	0.2184
	CC/CH_2 scissor	−0.1195	−0.0873	−0.1276
	CC/CH_2 wag	0.2943	0.2044	0.3072
	CC/CH_3 sym. def.	−0.3276	−0.2225	−0.3318
	CH/CH_3 asym. def.	−0.1261	−0.0720	−0.1066
	CH/CH_3 rock	0.0898	0.0448	0.0663
Dimethyl ether:	CO/COC	0.4667	0.3789	0.5803
	CO/CH_3 sym. def.	−0.5094	−0.3801	−0.5871
	CO/CH_3 rock	0.1251	0.1213	0.1836
	CH/CH_3 asym. def.	−0.1284	−0.0723	−0.1072
	CH/CH_3 rock	0.0862	0.0725	0.1074
Cyclobutane:	CC/CH_2 scissor	−0.1279	−0.0933	−0.1391
	CC/CH_2 wag	−0.2237	−0.1437	−0.2155
	CC/CH_2 twist	0.0923	0.0724	0.1075
	CH (eq)/CH_2 scissor	0.0936	0.0643	0.0960
	CH (ax)/CH_2 scissor	0.0837	0.0585	0.0873
	CH (eq)/CH_2 rock	0.0744	0.0347	0.0514
	CH (ax)/CH_2 rock	−0.1008	−0.0525	−0.0779

[a]In units of mdyn/Å (stretch), mdyn Å/rad^2 (bend), mdyn/rad (stretch–bend).

Can. J. Chem. Downloaded from www.nrcresearchpress.com by 93.93.197.157 on 09/07/12
For personal use only.

TABLE 16. Comparison of *ab initio* and empirical force constants for propane[a]

Force constant	321/321c/321c[b]	STOcorr/321c/321c[b]	Snyder[c]
CC stretch	4.309	4.333	4.532
CH stretch (CH_3)	4.813/4.795	4.786/4.769	4.699
CH stretch (CH_2)	4.768	4.755	4.538
CCC bend	0.894	0.905	0.996
CH_2 scissor	0.585	0.586	0.559
CH_2 wag	0.642	0.643	0.623
CH_2 rock	0.786	0.789	0.703
CH_2 twist	0.647	0.639	0.661
CH_3 sym. def.	0.560	0.560	0.548
CH_3 asym. def.	0.561/0.559	0.563/0.561	0.539
CH_3 rock	0.649/0.659	0.644/0.658	0.649
CH_3 torsion	0.030	0.030	0.024
CC/CC	0.118	0.071	0.083
CC/CCC bend	0.193	0.218	0.248
CC/CH_2 scissor	−0.120	−0.128	−0.034
CC/CH_2 wag	0.294	0.307	0.271
CC/CH_3 sym. def.	−0.328	−0.331	−0.213
CH/CH (CH_3 ip/op)	0.055	−0.048	0.032
CH/CH (CH_2)	0.065	−0.044	0.019
CCC bend/CH_2 scissor	0.005	−0.010	0.040
CCC bend/CH_3 sym. def.	−0.016	−0.015	0.012
CCC bend/CH_3 rock	0.111	0.115	0.121
CH_2 scissor/CH_3 sym. def.	0.008	0.006	−0.111
CH_2 scissor/CH_3 rock	0.026	0.023	0.023
CH_2 wag/CH_3 sym. def.	−0.020	−0.019	0.011
CH_2 wag/CH_3 rock	−0.047	−0.054	−0.056
CH_2 rock/CH_3 rock	−0.078	−0.089	−0.089
CH_2 twist/CH_3 rock	−0.092	−0.097	−0.096

[a]In units of mdyn/Å (stretch), mdyn Å/rad^2 (bend), mdyn/rad (stretch–bend).
[b]Scaled using optimized scaling factors of Table 9.
[c]Reference 27. All non-zero force constants obtained by symmetrizing the reported internal valence force constants are included.

dimethyl ether. In each of these cases the ΔL_n and ΔA_n for the scaled STOcorr/321c/321c combination are only marginally better than the corresponding STOcorr/STO/STO parameters (see Tables 10–12). In general, the refined STOcorr scaling factors (Table 9) exhibit a reasonably good degree of reproducibility, with similar trends as previously noted in the context of 3-21G. Among the methyl deformation modes, the three scaling factors refine to similar values for both propane and ethane, with the magnitudes of the scaling factors increasing reproducibly in the order asymmetric deformation < symmetric deformation < rocking. As for 3-21G, the last mentioned is higher for dimethyl ether, reflecting the presence of the neighboring oxygen atom.

Some major discrepancies occur for the refined STOcorr/STO/STO scaling factors of cyclobutane as compared to those of ethane and propane, particularly for the C–C stretching, CCC bending, and CH_2 rocking and wagging vibrations. As noted earlier in the context of reference geometry effects, the STO-3G ring dihedral angle in cyclobutane is significantly in error (Table 4), and the scaled STOcorr/STO/STO force constants and derived quantities do not compare well with the corresponding 3-21G results. It is of interest to note in this connection, the CH_2 rocking, CH_2 wagging, and CCC bending scaling factors refine to very similar values for both cyclobutane and propane when the force constants are reevaluated at the more accurate, corrected 3-21G structure (STOcorr/321c/321c). The C–C stretching factor remains appreciably lower for cyclobutane than for ethane and propane, probably reflecting the inaccuracy of the C–C/C–C interaction force constants. These observations indicate that while relatively small corrections of bond lengths are generally not necessary, large errors in molecular angles should be corrected empirically prior to evaluating the force constants. Analogous behaviour has been noted by Schlegel *et al.* (3) when they calculated the force field of ammonia using the 4-31G basis set. In that case the calculated H—N—H angle is much larger than the experimental value (113.7 vs. 107.3°). The corresponding diagonal bending force constant, which is appreciably lower when evaluated at the theoretical structure, reproduces the "experimental" constant with the level of accuracy expected for the 4-31G basis (i.e., marginally overestimated) when calculated at the experimental geometry.

Conclusions

While it is well known that *ab initio* force constants calculated at the 3-21G level can be scaled to reproduce observed vibrational frequencies, the results presented here indicate that a reasonably flexible scaling procedure is required. Such a properly devised procedure then provides a level of accuracy for the vibrational eigenvectors sufficient for calculating infrared absorption intensities. The choice of reference geometry at which the force constants are evaluated is less critical in this regard. Small corrections to the optimized bond lengths lead to negligible changes in the scaled force constants, and in other vibrational parameters derived from them. However, if the optimized structure is known to be in significant

Can. J. Chem. Downloaded from www.nrcresearchpress.com by 93.93.197.157 on 09/07/12
For personal use only.

TABLE 17. Propane intensities calculated using different force fields[a]

		Intensity/cm mol^{-1} × 10^3				
		STO/321c/321c		321/321c/321c		
ν	ν_{obs}/cm^{-1}	Unscaled	Scaled[c]	Unscaled	Scaled	Snyder[b]
	A_1					
1	2977	4351	4528	5362	5352	3908
2	(2923)	1906	1820	273	269	822
3	2887	1587	1567	2353	2361	2767
4	1476	278	284	264	247	425
5	1462	33	37	1	18	28
6	1392	468	372	369	381	438
7	1158	133	165	167	151	157
8	869	49	29	17	27	60
9	369	22	24	21	22	21
	B_1					
15	2973	10157	10272	10303	10292	4871
16	2968	35	0	30	37	5467
17	1472	1083	1001	953	958	1241
18	1192	22	26	34	31	37
19	748	212	210	189	192	225
20	268	1	0	1	0	1
	B_2					
21	2968	2003	2018	2335	2331	1981
22	2887	3168	3157	2842	2849	2891
23	1464	7	3	1	1	4
24	1378	1	153	156	140	119
25	1338	401	234	241	258	258
26	1054	20	46	82	38	37
27	922	103	90	46	85	82

[a]Using charge flow formalism; see eqs. [2] and [3].
[b]Empirical force field of ref. 27, using their assumed structure. This essentially reproduces the calculated propane intensities of ref. 25.
[c]STOcorr/321c/321c, i.e., the stretch/bend interaction force constants corrected by the factor of 1.48 prior to scaling. See text.

error in some aspect, such as dihedral angles of cyclic molecules for example, force constants are better evaluated at a more accurate reference structure.

Another criterion that might be anticipated to favor one choice of reference geometry over the other is the transferability of scaling factors. We note that the C–C stretching force constants are calculated less accurately at the corrected structure than at the optimized one, as reflected by the optimized scaling factors averaging 0.90 (0.89, 0.92, 0.87 for PR, ET, and CB, respectively, in Table 9) and 0.97 (0.96, 0.99, 0.95), respectively, for the two alternatives. For the three relevant molecules these scaling factors are lowered by the same amount, their relative magnitudes remaining the same, when the geometry is adjusted. The uncertainty in vibrational frequencies calculated by transferring the average of the optimized factors hence appears to be the same for both instances. However, the values chosen empirically for adjusting the bond lengths in many cases may be subject to appreciable uncertainties, particularly for unusual structures (18, 28). Such uncertainties would then be reflected as noticeable variations in the refined scaling factors. For this reason, we prefer to use consistently optimized structures. The scaling factors derived in this manner should then reflect mainly the systematic deficiencies of the basis set (and Hartree–Fock wavefunctions in general).

It has become clear that the scaling factor for any particular type of coordinate is not a universally transferable parameter, but may be influenced by the chemical and (or) geometrical environment surrounding a particular moiety. This has been demonstrated in the present work by the discrepancy between the refined CH_3 rocking factors for propane and dimethyl ether, as well as in our previous determination of a scaled 3-21G force field for oxetan.[4] In the latter case, for example, scaling factors refined for analogous CH_2 bending modes in the α and β positions assume significantly different values. These examples illustrate that assuming a single factor to be appropriate for all CH_2 or CH_3 bending modes may lead to significant differences in certain scaled force constants and hence to appreciable errors in calculated frequencies. Retrospectively, useful relationships among individually refined scaling factors may emerge. One persistent observation that we have made in this and other studies using the 3-21G basis, is that the refined CH_2 twisting and wagging factors are generally within 0.01 of one another for

[4]R. A. Shaw, N. Ibrahim, and H. Wieser, unpublished results.

Can. J. Chem. Downloaded from www.nrcresearchpress.com by 93.93.197.157 on 09/07/12
For personal use only.

any individual methylene group. This suggests that these two modes could be scaled with a common factor. Although for the molecules discussed here this factor is equivalent to that for CH_2 scissoring, we have encountered instances where they differ. The CH_2 rocking vibration generally needs a factor higher than the other methylene deformations.

The STO-3G basis set is deficient in that the stretch/stretch interaction force constants are inaccurate, often differing in sign from 3-21G, and the stretch/bend interaction force constants are significantly underestimated. We suggest that the scaling of the STO-3G force constants, using the same procedure as for 3-21G, should be preceded by multiplying all stretch/bend constants by a factor of about 1.48. The calculated frequencies, eigenvectors, and absorption intensities obtained in this manner approach the accuracy of scaled 3-21G force fields throughout the mid- and far-infrared regions. The inaccuracy of the stretch/stretch interactions is noticeable primarily in the C–H stretching region, where the STO-3G frequencies and particularly the vibrational eigenvectors are completely unreliable.

We conclude by suggesting that the potential accuracy of scaled *ab initio* force fields for predicting vibrational frequencies may be fully realized by defining and optimizing scaling factors individually for each type of vibrational coordinate, for a number of small molecules containing diverse structural and chemical features. Significant differences among the optimized factors should be recognized and correlated with structural and (or) chemical influences. For the reasons outlined above, the consistent use of the optimized geometry for force field calculations should facilitate such correlations, and hence emerge as the preferred procedure. An alternative presented by Pulay *et al.* (28), namely to use high quality calculations for determining the equilibrium geometry and then a basis set of more moderate size for evaluating the force constants, is equally consistent but is impractical at this time for any but the smallest molecules.

Finally, it should be stressed that we have concerned ourselves primarily with ascertaining the role of force field uncertainties when evaluating vibrational frequencies and intensities. We have not addressed the separate problem of using *ab initio* methods for calculating molecular dipole moment derivatives, i.e., terms of the type $\partial\mu/\partial X$ or $\partial\mu/\partial R$. It is well known that split valence basis sets of medium size can be expected to provide order of magnitude estimates for these quantities (19, 26), while the STO-3G basis appears to be much less accurate (29).

Can. J. Chem. Downloaded from www.nrcresearchpress.com by 93.93.197.157 on 09/07/12
For personal use only.

Acknowledgements

R.A.S. wishes to acknowledge the award of postgraduate scholarships from the City of Calgary/McMahon Stadium Society and the Natural Sciences and Engineering Research Council of Canada (NSERCC) during the tenure of which most of this work was carried out. We are further indebted to the Academic Computing Services of the University for access to the Honeywell/Multics and CDC Cyber 205 computing systems. This research is supported by NSERCC operating grants to A.R. and H.W., both of which are hereby gratefully acknowledged.

1. (*a*) G. Fogarasi and P. Pulay. *In* Vibrational spectra and structure. Vol. 14. *Edited by* J. R. Durig. Elsevier Publishing, Amsterdam. 1985. pp. 125–219; (*b*) G. Fogarasi and P. Pulay. Annu. Rev. Phys. Chem. **35**, 191 (1984); (*c*) P. Pulay. *In* The force concept in chemistry. *Edited by* B. M. Deb. Van Nostrand Reinhold, New York. 1981. pp. 449–480; (*d*) P. Pulay. *In* Applications of electronic structure theory. *Edited by* H. F. Schaefer III. Plenum, New York. 1977. pp. 153–185.
2. P. Pulay and W. Meyer. J. Mol. Spectrosc. **40**, 59 (1971).
3. H. B. Schlegel, S. Wolfe, and F. Bernardi. J. Chem. Phys. **63**, 3632 (1975).
4. C. E. Blom and C. Altona. Mol. Phys. (*a*) **31**, 1359 (1976); (*b*) **31**, 1377 (1976).
5. W. Meyer and P. Pulay. J. Chem. Phys. **56**, 2109 (1972).
6. P. Pulay and W. Meyer. J. Chem. Phys. **57**, 3337 (1972).
7. G. Fogarasi and P. Pulay. Acta Chim. Acad. Sci. Hung. **108**, 55 (1981).
8. M. D. Newton, W. A. Lathan, W. J. Hehre, and J. A. Pople. J. Chem. Phys. **52**, 4064 (1970).
9. D. Steele. Mol. Phys. **38**, 145 (1979).
10. T. C. Jao, I. Scott, and D. Steele. J. Mol. Spectrosc. **92**, 1 (1982).
11. C. Pouchan, D. Liotard, A. Dargelos, and M. Chaillet. J. Chim. Phys. **73**, 1046 (1976).
12. C. Pouchan, A. Dargelos, and M. Chaillet. J. Chim. Phys. **75**, 595 (1978).
13. P. Pulay, G. Fogarasi, and J. E. Boggs. J. Chem. Phys. **74**, 3999 (1981).
14. K. W. Hipps and R. D. Poshusta. J. Phys. Chem. **86**, 4112 (1982).
15. A. Korminicki, F. Pauzat, and Y. Ellinger. J. Phys. Chem. **87**, 3847 (1983).
16. Y. Nishimura, M. Tsuboi, S. Kato, and K. Morokuma. J. Am. Chem. Soc. **103**, 1354 (1981).
17. R. H. Schwendeman. J. Chem. Phys. **44**, 2115 (1966).
18. L. Schafer, C. Van Alsenoy, and J. N. Scarsdale. J. Mol. Struct. **86**, 349 (1982).
19. P. Pulay, G. Fogarasi, F. Pang, and J. E. Boggs. J. Am. Chem. Soc. **101**, 2550 (1979).
20. J. S. Binkley, M. J. Frisch, D. J. Defrees, K. Raghavachari, R. A. Whiteside, H. B. Schlegel, L. M. Fluder, and J. A. Pople. Department of Chemistry, Carnegie–Mellon University, Pittsburgh, PA. 1983.
21. C. E. Blom, C. Altona, and A. Oskam. Mol. Phys. **34**, 557 (1977).
22. A. Annamalai and T. A. Keiderling. J. Mol. Spectrosc. **109**, 46 (1985).
23. S. Abbate, L. Laux, J. Overend, and A. Moscowitz. J. Chem. Phys. **75**, 3161 (1981).
24. G. Zerbi, M. Gussoni, S. Abbate, and P. Jona. Vibrational intensities in infrared and Raman spectroscopy. *Edited by* W. B. Person and G. Zerbi. Elsevier, Amsterdam. 1982.
25. M. Gussoni, S. Abbate, R. Sanvito, and G. Zerbi. J. Mol. Struct. **75**, 177 (1981).
26. P. Pulay, G. Fogarasi, G. Pongor, J. E. Boggs, and A. Vargha. J. Am. Chem. Soc. **105**, 7037 (1983).
27. R. G. Snyder. J. Chem. Phys. **47**, 1316 (1967).
28. P. Pulay, J. Lee, and J. E. Boggs. J. Chem. Phys. **79**, 3382 (1983).
29. B. A. Hess, Jr., L. J. Schaad, and P. L. Polavarapu. J. Am. Chem. Soc. **106**, 4348 (1984).
30. J. N. Scarsdale, C. Van Alsenoy, and L. Schafer. J. Mol. Struct. **86**, 277 (1982).
31. K. Kuchitsu. J. Chem. Phys. **49**, 4456 (1968).
32. T. Iijima. Bull. Chem. Soc. Jpn. **45**, 1291 (1972).
33. E. Hirota, K. Matsamura, M. Imachi, M. Fujio, Y. Tsuno, and C. Matsamura. J. Chem. Phys. **66**, 2660 (1977).
34. D. R. Lide, Jr. J. Chem. Phys. **33**, 1514 (1960).
35. J. E. Boggs, M. Altman, F. R. Cordell, and Y. Dai. J. Mol. Struct. **94**, 373 (1983).
36. J. O. Williams, J. N. Scarsdale, L. Schafer, and H. J. Geise. J. Mol. Struct. Theochem. **76**, 11 (1981).

37. C. E. BLOM, L. P. OTTO, and C. ALTONA. Mol. Phys. **32**, 1137 (1976).
38. U. BLUKIS, P. H. KASAI, and R. MYERS. J. Chem. Phys. **38**, 2753 (1963).
39. G. BANHEGYI, G. FOGARASI, and P. PULAY. J. Mol. Struct. **89**, 1 (1982).
40. D. CREMER. J. Am. Chem. Soc. **99**, 1307 (1977).
41. A. ALMENNINGEN, O. BASTIANSEN, and P. N. SKANCKE. Acta Chem. Scand. **15**, 711 (1961); P. N. SKANCKE. Ph.D. thesis, University of Oslo, 1960.
42. T. EGAWA, S. YAMAMOTO, T. FUKUYAMA, and K. KUCHITSU. 11th Austin Symposium on Molecular Structure. Austin, TX. March 1986. Paper S10.
43. S. MEIBOOM and L. C. SNYDER. J. Am. Chem. Soc. **89**, 1038 (1967); J. Chem. Phys. **52**, 3857 (1970).

Can. J. Chem. Downloaded from www.nrcresearchpress.com by 93.93.197.157 on 09/07/12
For personal use only.

Thin-layer steady-state voltammetry under control by diffusion and migration

CHRISTA L. COLYER, PAUL J. J. CONNELLY, HEATHER L. GORDON, AND KEITH B. OLDHAM
Department of Chemistry, Trent University, Peterborough, Ont., Canada K9J 7B8

Received December 15, 1987

CHRISTA L. COLYER, PAUL J. J. CONNELLY, HEATHER L. GORDON, and KEITH B. OLDHAM. Can. J. Chem. **66**, 1333 (1988).

Measurements of steady-state currents in thin-layer cells provide an opportunity to apply a stringent test of theories of electrochemical transport by simultaneous diffusion and migration. We have applied such a test and find the theory to be vindicated.

CHRISTA L. COLYER, PAUL J. J. CONNELLY, HEATHER L. GORDON et KEITH B. OLDHAM. Can. J. Chem. **66**, 1333 (1988).

Les mesures de courants à l'état stationnaire effectuées sur des cellules en couche mince fournissent une occasion d'appliquer un test rigoureux aux théories du transport électrochimique par diffusion et migration simultanées. On a appliqué un tel test et on a trouvé que la théorie est justifiée.

[Traduit par la revue]

Can. J. Chem. Downloaded from www.nrcresearchpress.com by 93.93.197.157 on 09/07/12
For personal use only.

Introduction

Apart from studies employing rotating disc electrodes, voltammetry is generally carried out under transient conditions with diffusion being the sole transport mode. There are good reasons for these choices. Transient, rather than steady-state, conditions are selected because the latter are not usually attained experimentally without the participation of (deliberate or natural) convective transport. Two considerations persuade electrochemists to use excess supporting electrolyte and thereby inhibit migratory transport: first, the mathematical problem of predicting the voltammetric current is lessened when diffusion is the only transport mode; second, unwelcome ohmic polarization is alleviated when migration is minimized.

The present interest in microelectrodes has changed the picture somewhat. Small electrodes permit a steady state to be reached in times small enough that natural convection is not a problem (1). Moreover, ohmic polarization is held not to be as serious at microelectrodes and therefore studies with such electrodes have sometimes been carried out in the presence of little or no supporting electrolyte (2, 3). Thus the time seems opportune for an examination of voltammetry under steady-state conditions with both diffusion and migration contributing to the transport process. For experimental convenience, however, we do not use microelectrodes in the present study. Instead, the early attainment of a steady state is ensured by a small interelectrode separation.

The laws of transport by combined diffusion–migration have been tested under voltammetric conditions only rarely (4–6). Such a test is the object of the present study. The charge numbers of the participating ions, both electroactive and electroinactive, are important parameters in studies involving migration, but here we shall treat theoretically only the case that is employed experimentally: a dipositive electroactive cation and univalent supporting ions. To achieve a steady state in a thin-layer cell requires that the anode and cathode reactions be mutual converses, and we have chosen the reactions

[1] $\mathrm{M} \rightarrow \mathrm{M}^{2+}(\mathrm{aq}) + 2e$

and

[2] $\mathrm{M}^{2+}(\mathrm{aq}) + 2e \rightarrow \mathrm{M}$

to ensure this, with both electrodes being of metal M. To prevent electrolysis altering the surface geometry of the electrodes it is desirable that the electrode metal be a liquid and for this reason we have selected mercury as the electrode metal. Liquid electrodes cause difficulty with the gravitational stability of the thin-layer cell but this has been overcome by the tactic described in the experimental section of the article.

Theory

Our object here is to derive the steady-state voltammetric relationship, i.e., the equation that interrelates the potential ΔE of the two-electrode thin-layer cell to the steady-state current i that flows through it. This equation will contain the initial concentrations of the electroactive and supporting cations as parameters. The same steady state is achieved by applying a known ΔE and observing the resultant current i as by applying a known i and observing the resultant ΔE. The former is the more appropriate description of our experimental procedure but the appreciation of this theoretical section is aided by regarding the current as being imposed on the cell and treating potential as the dependent variable.

Of course, in practice, the steady state is preceded by a transient phase in which local concentrations, fluxes, and potentials are functions of time. The present treatment will ignore this transient phase entirely, because our interest is confined to the time-independent final state.

Cell geometry

Figure 1 diagrams the cell, which consists of two electrodes of metal M, each of area A and separated by a uniform distance L, the intervening space being filled by electrolyte solution. Meters monitor the cell current i and the interelectrode potential ΔE. A distance coordinate x is erected normal to the electrode surfaces, with its origin at the cell centre such that $x = -L/2$ corresponds to the anode and $x = L/2$ to the cathode.

Solution composition

The electrolyes MA_2 and BA are strong and therefore the solution contains the ions B^+, M^{2+}, and A^- as the only solutes; we shall use the subscripts 1, 2, and 3 to denote these three ions. The superscript "b" will denote conditions before electrolysis, while "a" and "c" will refer to conditions at the anode and cathode respectively once the steady state is attained. Because of the electroneutrality requirement, initial ion concentrations are interrelated by

[3] $$0 = \sum_j z_j c_j^{\mathrm{b}} = c_1^{\mathrm{b}} + 2c_2^{\mathrm{b}} - c_3^{\mathrm{b}}$$

where z_j denotes the charge number of ion j. The absence of a subscript will refer to the total ion content, thus:

[4] $$c^{\mathrm{b}} = \sum_j c_j^{\mathrm{b}} = c_1^{\mathrm{b}} + c_2^{\mathrm{b}} + c_3^{\mathrm{b}} = 2c_1^{\mathrm{b}} + 3c_2^{\mathrm{b}}$$

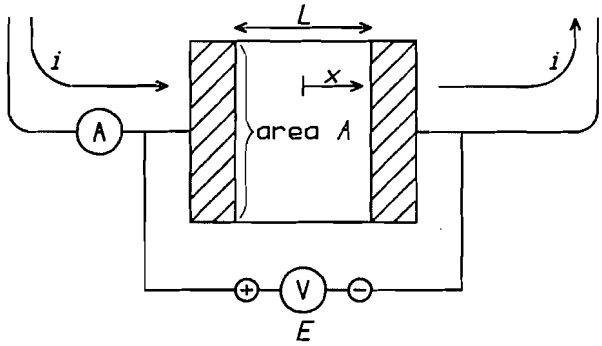

FIG. 1. Geometry of the steady-state cell.

In the steady state, the concentrations of B^+, M^{2+}, and A^-, as well as the total ion concentration, vary with distance and we shall emphasize this functional dependence by writing $c_1(x)$, $c_2(x)$, and $c_3(x)$, as well as $c(x)$. Since the total amount of each ion is conserved during electrolysis, the relationship

$$[5] \quad \int_{-\frac{1}{2}L}^{\frac{1}{2}L} c_j(x)\,dx = Lc_j^b \qquad j = 1,2,3$$

must be obeyed. Moreover, electroneutrality will hold locally, as well as globally, so that

$$[6] \quad 0 = \sum_j z_j c_j(x) = c_1(x) + 2c_2(x) - c_3(x)$$

We shall have occasion to refer to the local total ion concentration and the local ionic strength. These are

$$[7] \quad c(x) = \sum_j c_j(x) = c_1(x) + c_2(x) + c_3(x)$$

and

$$[8] \quad \mu(x) = \tfrac{1}{2}\sum_j z_j^2 c_j(x) = \tfrac{1}{2}c_1(x) + 2c_2(x) + \tfrac{1}{2}c_3(x)$$

respectively.

Ion fluxes

Each ion is subjected to a diffusive flux and a migratory flux. The diffusive flux is given by Fick's first law and equals $-D_j dc_j(x)/dx$ where D_j is the diffusion coefficient of ion j and the negative sign indicates that diffusion occurs down the concentration gradient $dc_j(x)/dx$. The migratory flux is proportional to the local concentration $c_j(x)$ of the ion, to its mobility u_j, and to the local electric field $-d\phi(x)/dx$ where $\phi(x)$ is the electric potential in the solution at distance x from the cell's midplane. The direction of the electrostatic force acting on each ion depends on the sign of its charge and this is taken into account by including the factor $|z_j|/z_j$ in the expression for the migratory flux. Hence the total flux experienced by each ion is

$$[9] \quad J_j = -D_j \frac{d}{dx}c_j(x) - \frac{|z_j|}{z_j}u_j c_j(x)\frac{d}{dx}\phi(x)$$

Recognize that, in the steady state, each ion flux is independent not only of time but also of position in the cell, so that we have written J_j rather than $J_j(x)$.

The Nernst–Einstein relationship (7) links the diffusion coefficient of an ion to its mobility by the identity $RTu_j = F|z_j|D_j$. When this is used to eliminate u_j from eq. [9], one arrives at

$$[10] \quad \frac{J_j}{D_j} = -\frac{d}{dx}c_j(x) - z_j c_j(x)\frac{F}{RT}\frac{d}{dx}\phi(x)$$

after division by D_j.

Because the ions B^+ and A^- are not involved in electrode reactions, their steady-state fluxes J_1 and J_3 must be zero. The flux of M^{2+}, however, is proportional to the current density i/A and is given by application of Faraday's law to reaction [1] or [2] as $J_2 = i/(2AF)$. Hence, the forms adopted by eq. [10] on application to each of the three ions are

$$[11] \quad 0 = -\frac{d}{dx}c_1(x) - c_1(x)\frac{F}{RT}\frac{d}{dx}\phi(x)$$

$$[12] \quad \frac{i}{2AFD_2} = -\frac{d}{dx}c_2(x) - 2c_2(x)\frac{F}{RT}\frac{d}{dx}\phi(x)$$

and

$$[13] \quad 0 = -\frac{d}{dx}c_3(x) + c_3(x)\frac{F}{RT}\frac{d}{dx}\phi(x)$$

respectively. These equations will later enable us to determine the ways in which $\phi(x)$ and each $c_j(x)$ depend on distance and will ultimately lead to an expression for the interelectrode potential difference ΔE.

Concentration interrelationships

Elimination of the field-dependent term between eqs. [11] and [13] leads to

$$[14] \quad \frac{dc_1(x)}{c_1(x)} + \frac{dc_3(x)}{c_3(x)} = 0$$

which implies that $\ln\{c_1(x)\} + \ln\{c_3(x)\}$ is invariant, so that

$$[15] \quad c_1(x)c_3(x) = \text{constant}$$

The constant in this last result is independent not only of x but also of the current i. It must, therefore, equal the product $c_1^b c_3^b$ of the concentrations of B^+ and A^- prior to electrolysis. Hence

$$[16] \quad c_1(x)c_3(x) = c_1^b c_3^b$$

This latest equation interrelates two of the three local ion concentrations. Equation [7] provides another relationship linking the $c_j(x)$ values to the total concentration $c(x)$. A third interrelationship is provided by the electroneutrality condition, eq. [6]. Using these three interrelationships one can, for example, eliminate $c_2(x)$ and $c_3(x)$, and generate the quadratic equation $c_1^2(x) - 2c(x)c_1(x) + 3c_1^b c_3^b = 0$, which solves to give the local concentration of B^+ to be

$$[17] \quad c_1(x) = c(x) - [c^2(x) - 3c_1^b c_3^b]^{1/2}$$

Similarly one may derive expressions for the local concentrations of M^{2+}

$$[18] \quad c_2(x) = \tfrac{2}{3}[c^2(x) - 3c_1^b c_3^b]^{1/2} - \tfrac{1}{3}c(x)$$

or of A^-

$$[19] \quad c_3(x) = \tfrac{1}{3}[c^2(x) - 3c_1^b c_3^b]^{1/2} + \tfrac{1}{3}c(x)$$

in terms of the local total concentration $c(x)$.

The surd that occurs in eqs. [17]–[19] has a simple interpretation: it equals the local ionic strength. That this is so follows by making the weighted sum of the three equations, with weights as specified by eq. [8]:

$$[20] \quad \mu(x) = \tfrac{1}{2}c_1(x) + 2c_2(x) + \tfrac{1}{2}c(x) = [c^2(x) - 3c_1^b c_3^b]^{1/2}$$

Total concentration

The condition of local electroneutrality, eq. [6], leads to the cancellation of all terms that involve the field when eqs. [11],

Can. J. Chem. Downloaded from www.nrcresearchpress.com by 93.93.197.157 on 09/07/12
For personal use only.

[12], and [13] are straightforwardly summed. The simple result

$$[21] \quad \frac{i}{2AFD_2} = -\frac{d}{dx}[c_1(x) + c_2(x) + c_3(x)] = -\frac{d}{dx}c(x)$$

shows that the gradient of the local total concentration is a constant. One integration leads to

$$[22] \quad c(x) = \sum_j c_j(x) = \text{constant} - \frac{ix}{2AFD_2}$$

and a second, between $x = -L/2$ and $x = L/2$, produces

$$[23] \quad \sum_j \int_{-\frac{1}{2}L}^{\frac{1}{2}L} c_j(x)\, dx = L(\text{constant})$$

Each of the integrals in eq. [23] may be evaluated as Lc_j^b by recourse to eq. [5], so that the constant term turns out to be simply c^b. The profile of the total concentration thus emerges from eq. [22] as

$$[24] \quad c(x) = c^b - \frac{ix}{2AFD_2}$$

Ion concentration profiles

The profiles of individual ion concentrations follow by substitution of expression [24] into each of eqs. [17]–[19]. For example

$$[25] \quad c_2(x) = \frac{2}{3}\left[\left(c^b - \frac{ix}{2AFD_2}\right)^2 - 3c_1^b c_3^b\right]^{1/2} - \frac{c^b}{3} + \frac{ix}{6AFD_2}$$

Unlike the profile of the total ion concentration, none of the profiles of individual ion concentrations is linear. An example of the shapes encountered is found in Figure 2.

A surprising result is discovered when $x = 0$ is substituted into eq. [25] and its $c_1(x)$ and $c_3(x)$ cohorts. In each case one finds, after considerable algebra, that $c_j(0) = c_j^b$. In other words, this means that the ion concentrations at the cell midplane in the steady state are unchanged from their values prior to electrolysis.

Limiting current

As i is increased, concentration polarization of M^{2+} at the cathode increases; that is, $c_2(L/2)$ diminishes. At some critical value of i, the limiting current i_l, $c_2(L/2)$ or c_2^c becomes zero. The cell cannot sustain a steady-state current exceeding this critical value.

To determine i_l, we set $c_2(L/2)$ equal to zero in eq. [25]. This leads to the expression

$$[26] \quad i_l = \frac{4AFD_2}{L}[c^b - 2(c_1^b c_3^b)^{1/2}]$$

If we regard the solution as composed of a concentration c_1^b of the electrolyte BA and a concentration c_2^b of the salt MA_2, then the limiting current is more usefully written as

$$[27] \quad i_l = \frac{4AFD_2}{L}(2c_1^b + 3c_2^b - 2[c_1^b(c_1^b + 2c_2^b)]^{1/2})$$

Two limiting cases of eq. [27] are of interest. The "unsupported" case corresponds to the virtual absence of supporting electrolyte so that c_1^b is negligible; eq. [27] reduces to

$$[28] \quad i_l \simeq \frac{12AFD_2c_2^b}{L} \qquad c_2^b \gg c_1^b$$

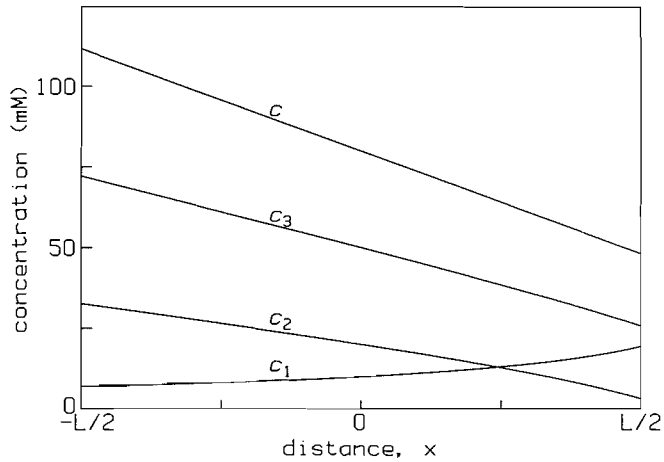

FIG. 2. The total concentration profile and the individual concentration profiles of the NO_3^-, Hg_2^{2+}, and H^+ ions for initial concentrations $c_3^b = 50$ mM, $c_2^b = 20$ mM, and $c_1^b = 10$ mM. The current is 90% of the limiting current.

in this case. The other limit, corresponding to the "fully supported" case when supporting electrolyte is in excess, may be deduced from eq. [27] by binomially expanding $[c_1^b(c_1^b + 2c_2^b)]^{1/2} = c_1^b[1 + (2c_2^b/c_1^b)]^{1/2}$ as $c_1^b[1 + (c_2^b/c_1^b) - (c_2^b/c_1^b)^2/8 + \ldots]$. Thence

$$[29] \quad i_l \simeq \frac{4AFD_2c_2^b}{L} = i_d \qquad c_2^b \ll c_1^b$$

Here we use the i_d symbol to denote the diffusion-limited current, because only diffusion is important in transporting M^{2+} when the concentration of supporting electrolyte massively exceeds that of the electroactive ion.

Comparison of eqs. [28] and [29] shows that, in the totally unsupported case, the limiting current is three times as large as the diffusion current. To discuss intermediate cases, it is useful to define the "support ratio" (8)

$$[30] \quad \text{support ratio} = \rho = \frac{\text{concentration of electroinactive ions excluding counter ions}}{\text{concentration of electroactive ions plus counter ions}} = \frac{c_1^b + (c_3^b - 2c_2^b)}{c_2^b + 2c_2^b} = \frac{2c_1^b}{3c_2^b}$$

As the support ratio increases from zero to infinity, the i_l/i_d ratio ranges from 3 down to 1. Table 1 shows some intermediate values calculated from the relationship

$$[31] \quad i_l = 3\{1 + \rho - [\rho(\rho + 4/3)]^{1/2}\}i_d$$

Notice that i_l is exactly twice i_d for a support ratio of one sixth.

Concentration polarization

The concentration of M^{2+} at the anode exceeds that at the cathode when the cell is undergoing steady-state electrolysis. Nernst's law reveals that this gives rise to a potential difference

$$[32] \quad \Delta E_{conc} = \frac{RT}{2F} \ln \{c_2^a/c_2^c\}$$

between the electrodes, the anode being positive. In writing this result we ignore any discrepancy between activity coefficients at the two electrodes. Steady-state values of the concentrations c_2^a and c_2^c can be found by substituting $x = -L/2$ and $x = L/2$, respectively, into eq. [25]. This gives

Can. J. Chem. Downloaded from www.nrcresearchpress.com by 93.93.197.157 on 09/07/12
For personal use only.

Can. J. Chem. Downloaded from www.nrcresearchpress.com by 93.93.197.157 on 09/07/12
For personal use only.

TABLE 1. The (limiting current)/(diffusion current) ratio as a function of the support ratio $\rho = 2c_1^b/3c_2^b$

ρ	i_l/i_d
0	3
Small	$3 - (12\rho)^{1/2}$
0.001	2.893
0.002	2.851
0.005	2.770
0.010	2.682
0.020	2.566
0.050	2.361
0.100	2.164
0.200	1.939
0.500	1.628
1.000	1.417
2.000	1.254
5.000	1.118
10.00	1.063
Large	$1 + (2/3\rho)$
∞	1

$$[33]\quad \frac{2}{3}\left[\left(c^b \pm \frac{iL}{4AFD_2}\right)^2 - 3c_1^b c_3^b\right]^{1/2} - \frac{c^b}{3} \mp \frac{iL}{12AFD_2}$$

where upper signs refer to c_2^a, lower signs to c_2^c. Notational economies result from using the expression $i_d = 4AFD_2c_2^b$ for the diffusion current to replace the denominators of the terms that involve the current. After factoring $c_2^b/3$, expressions [33] then become

$$[34]\quad c_2^a \text{ or } c_2^c = \frac{c_2^b}{3}\left(2\left[\left(\frac{c^b}{c_2^b} \pm \frac{i}{i_d}\right)^2 - \frac{3c_1^b c_3^b}{(c_2^b)^2}\right]^{1/2} - \frac{c^b}{c_2^b} \mp \frac{i}{i_d}\right)$$

The c^b/c_2^b terms may be replaced by $3(1 + \rho)$, where ρ is the support ratio $2c_1^b/3c_2^b$, and similarly $3c_1^b c_3^b/(c_2^b)^2$ may be replaced by $9\rho(4 + 3\rho)/4$. After making these replacements, substitution into eq. [32] of the expressions for c_2^a and c_2^c leads to

$$[35]\quad \Delta E_{conc} = \frac{RT}{2F}(\ln[\{4(1 + \rho + i/3i_d)^2 - 4\rho - 3\rho^2\}^{1/2} - 1 - \rho - i/3i_d] - \ln[\{4(1 + \rho - i/3i_d)^2 - 4\rho - 3\rho^2\}^{1/2} - 1 - \rho + i/3i_d])$$

This complicated expression cannot be further simplified. Moreover, attempts to invert eq. [35] to give an explicit formula for i/i_d lead only to a quartic equation $(i/i_d)^4 + \alpha_3(i/i_d)^3 + \alpha_2(i/i_d)^2 + \alpha_1(i/i_d) + \alpha_0 = 0$ in which the α coefficients are elaborate functions of ρ and $\exp(2F\Delta E_{conc}/RT)$. The solution of this equation to give an explicit expression for i/i_d would be extremely complicated and was not pursued.

Potential profile

We have yet to address the question of how the local potential $\phi(x)$ varies across the cell. Because only differences in ϕ are significant, we are free to choose any particular plane as the location of zero potential; we select the midplane, so that $\phi(0) = 0$.

Equation [13] may be rewritten

$$[36]\quad \frac{F}{RT}d\phi(x) = d\ln\{c_3(x)\}$$

and integrated to

$$[37]\quad \frac{F\phi(x)}{RT} = \frac{F}{RT}[\phi(x) - \phi(0)] = \ln\{c_3(x)\} - \ln\{c_3(0)\} = \ln\{c_3(x)/c_3^b\}$$

Analogous to eq. [25], the concentration profile of A^- is

$$[38]\quad c_3(x) = \frac{1}{3}\left[\left(c^b - \frac{ix}{2AFD_2}\right)^2 - 3c_1^b c_3^b\right]^{1/2} + \frac{c^b}{3} - \frac{ix}{6AFD_2}$$

which may be combined with eq. [37] to give

$$[39]\quad \phi(x) = \frac{RT}{F}\left(\ln\left\{\left[\left(c^b - \frac{ix}{2AFD_2}\right)^2 - 3c_1^b c_3^b\right]^{1/2} + c^b - \frac{ix}{2AFD_2}\right\} - \ln[3c_3^b]\right)$$

for the potential profile. This may be expressed somewhat more concisely in terms of an inverse hyperbolic cosine (9)

$$[40]\quad \phi(x) = \frac{RT}{F}\left(\text{arcosh}\left[\left(c^b - \frac{ix}{2AFD_2}\right)\Big/(3c_1^b c_3^b)^{1/2}\right] - \frac{1}{2}\ln(3c_3^b/c_1^b)\right)$$

Figure 3 provides an example of the potential profile.

Ohmic polarization

The difference $\phi^a - \phi^c$ represents the potential between the solution layers immediately adjacent to the anode and the cathode. This is the ohmic polarization or "iR drop" experienced by the cell. To determine the magnitude of ϕ^a or ϕ^c, one need only substitute $x = -L/2$ or $x = L/2$ into eq. [40]. Thereby one finds

$$[41]\quad \Delta E_{ohm} = \phi^a - \phi^c = \frac{RT}{F}\left(\text{arcosh}\left[\left(c^b + \frac{iL}{4AFD_2}\right)\Big/(3c_1^b c_3^b)^{1/2}\right] - \text{arcosh}\left[\left(c^b - \frac{iL}{4AFD_2}\right)\Big/(3c_1^b c_3^b)^{1/2}\right]\right)$$

Some simplification results from introducing the expression for the diffusion current $i_d = 4AFD_2c_2^b/L$, namely

$$[42]\quad \Delta E_{ohm} = \frac{RT}{F}\left(\text{arcosh}\left[\left(\frac{c^b}{c_2^b} + \frac{i}{i_d}\right)\Big/\frac{(3c_1^b c_3^b)^{1/2}}{c_2^b}\right] - \text{arcosh}\left[\left(\frac{c^b}{c_2^b} - \frac{i}{i_d}\right)\Big/\frac{(3c_1^b c_3^b)^{1/2}}{c_2^b}\right]\right)$$

There are terms in this equation similar to those found in eq. [34] and once more we may replace c^b/c_2^b by $3(1 + \rho)$ and $(3c_1^b c_3^b)^{1/2}/c_2^b$ by $3[\rho(1 + 3\rho/4)]^{1/2}$. Using the formula (9) for the difference of two inverse hyperbolic cosines, one may then invert eq. [42] to yield

$$[43]\quad \frac{i}{3i_d} = \left[(1 + \rho)^2 \tanh^2\left(\frac{F}{2RT}\Delta E_{ohm}\right) - \rho\left(1 + \frac{3\rho}{4}\right)\sinh^2\left(\frac{F}{2RT}\Delta E_{ohm}\right)\right]^{1/2}$$

The relationship between the potential difference ΔE_{ohm} and the current i is distinctly nonlinear, as illustrated in Fig. 4.

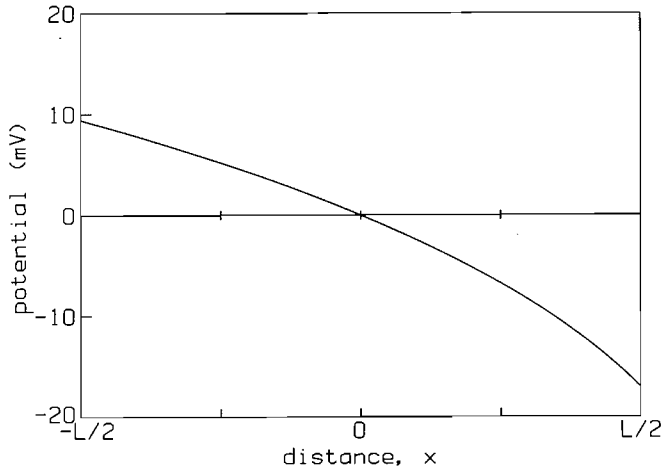

FIG. 3. The potential profile under the conditions of Fig. 2.

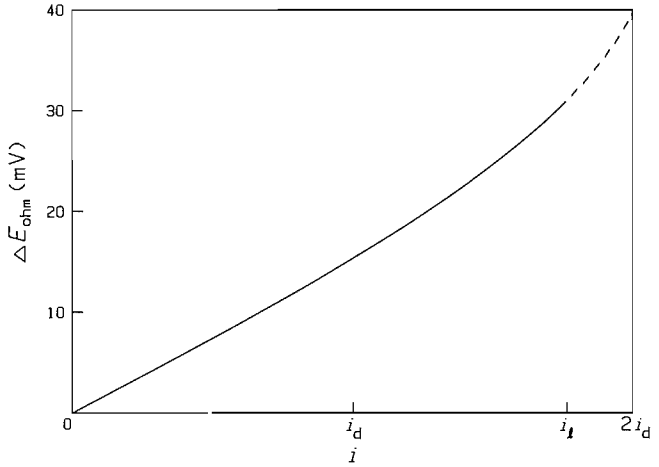

FIG. 4. The ohmic overpotential as a function of current for the solution composition described under Fig. 2. The dashed portion is inaccessible because the current cannot exceed i_l.

Thus the phrase "ohmic polarization" must not be interpreted as implying that Ohm's Law is obeyed.

Cell potential

Because the equilibrium interelectrode potential difference of the cell is zero, any potential difference existing in the steady state may be ascribed to polarizations. Of the three polarizations, ohmic, concentration, and activation, that afflict electrochemical cells, the choice of the Hg_2^{2+}/Hg electrode, for which reactions [1] and [2] are known to be very fast (10), permits us to ignore activation polarization. Thus the total cell potential ΔE contains only two terms, ΔE_{conc} and ΔE_{ohm}, due to concentration and ohmic polarizations, respectively.

After replacement of the terms c^b/c_2^b and $3c_1^bc_3^b/(c_2^b)^2$ by their $3(1 + \rho)$ and $9\rho[1 + (3\rho/4)]$ equivalents, addition of eqs. [35] and [42] produces, after some rearrangements

$$[44]\quad \Delta E = \frac{RT}{F}\left(\ln\left[\frac{[4(1+\rho+i/3i_d)^2 - \rho(4+3\rho)]^{1/2} - 1 - \rho - i/3i_d}{[4(1+\rho-i/3i_d)^2 - \rho(4+3\rho)]^{1/2} - 1 - \rho + i/3i_d}\right]^{1/2} + \operatorname{arcosh}\left[\frac{1+\rho+i/3i_d}{[\rho+(3\rho^2/4)]^{1/2}}\right] - \operatorname{arcosh}\left[\frac{1+\rho-i/3i_d}{[\rho+(3\rho^2/4)]^{1/2}}\right]\right)$$

as the final expression for the cell potential. Recall that we use the abbreviations $i_d = 4AFD_2c_2^b/L$ for the diffusion current and $\rho = 2c_1^b/3c_2^b$ for the support ratio, c_1^b and c_2^b being the initial concentrations of the supporting cation B^+ and the electroactive cation M^{2+}, respectively.

Though it is complicated, eq. [44] does provide an analytical solution to the problem that we posed. It permits us to calculate the cell potential for any applied current i and for any chosen values of the concentration parameters c_1^b and c_2^b. An example is shown as Fig. 5.

Unsupported limit

It is of interest to determine the forms acquired by eqs. [35] and [42], and thence by [44], as the support ratio $2c_1^b/3c_2^b$ approaches zero. One finds

$$[45]\quad \Delta E_{conc} \rightarrow \frac{RT}{2F}\ln\left[\frac{3i_d + i}{3i_d - i}\right] = \frac{RT}{F}\operatorname{artanh}\left[\frac{i}{3i_d}\right]$$

and (unless i approaches $3i_d$)

$$[46]\quad \Delta E_{ohm} \rightarrow \frac{RT}{F}\ln\left[\frac{3i_d + i}{3i_d - i}\right] = \frac{2RT}{F}\operatorname{artanh}\left[\frac{i}{3i_d}\right]$$

so that, in this limit, the ohmic polarization is exactly twice the concentration polarization.

Hence the equation of the totally unsupported steady-state voltammogram is

$$[47]\quad \Delta E = \Delta E_{conc} + \Delta E_{ohm} = \frac{3RT}{F}\operatorname{artanh}\left[\frac{i}{3i_d}\right] = \frac{3RT}{F}\operatorname{artanh}\left[\frac{iL}{12AFD_2c_2^b}\right]$$

or equivalently

$$[48]\quad \frac{iL}{12AFD_2c_2^b} = \frac{i}{3i_d} = \tanh\left[\frac{F\Delta E}{3RT}\right] = 1 - \frac{2}{1+\exp(2F\Delta E/3RT)}$$

Fully supported limit

Here we seek the limiting form of eq. [44] as $\rho \rightarrow \infty$, that is, as the concentration of electroinactive ions overwhelms the M^{2+} concentration. One finds that, in this limit

$$[49]\quad \Delta E_{conc} \rightarrow \frac{RT}{2F}\ln\left[\frac{i_d + i}{i_d - i}\right] = \frac{RT}{F}\operatorname{artanh}\left[\frac{i}{i_d}\right]$$

whereas

$$[50]\quad \Delta E_{ohm} \rightarrow \frac{4RTi}{3F\rho i_d} \rightarrow 0$$

Hence the equation of the fully supported voltammogram is

Can. J. Chem. Downloaded from www.nrcresearchpress.com by 93.93.197.157 on 09/07/12
For personal use only.

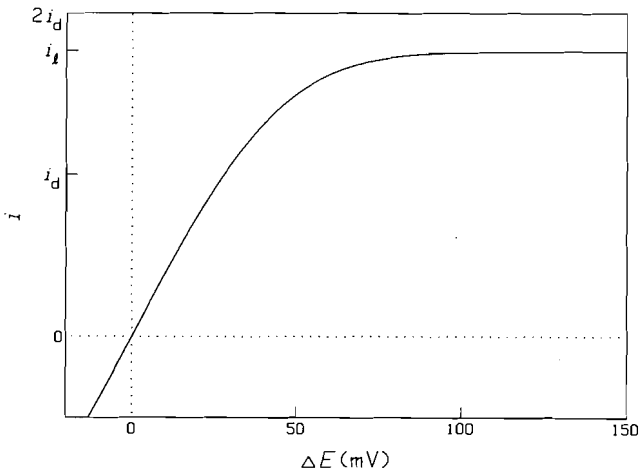

FIG. 5. Current as a function of the cell potential for the solution composition described under Fig. 2.

$$[51]\quad \Delta E = \Delta E_{conc} + \Delta E_{ohm} = \frac{RT}{F}\,\text{artanh}\left[\frac{i}{i_d}\right] = \frac{RT}{F}\,\text{artanh}\left[\frac{iL}{4AFD_2c_2^b}\right]$$

or equivalently

$$[52]\quad \frac{iL}{4AFD_2c_2^b} = \frac{i}{i_d} = \tanh\left[\frac{F\Delta E}{RT}\right] = 1 - \frac{2}{1 + \exp(2F\Delta E/RT)}$$

which agrees with established theory (11, 12).

Experimental

The theory we have just presented presupposes parallel pools of the liquid metal mercury separated by a thin layer of electrolyte solution. Of course, three liquid phases cannot be maintained in this configuration. To overcome this difficulty we absorbed the electrolyte in an inert porous disc, which was then sandwiched between the mercury pools. The effect of the porous medium on the steady-state theory can be interpreted in terms of a "uniform tortuosity" model (11). This simple, but surprisingly successful, model envisages the pore structure as a bundle of non-intersecting tubules, all of length λL, which penetrate the porous matrix from one surface to the other. Thus each L in our theory is to be replaced by λL, where λ is the "tortuosity factor" of the medium, a number somewhat larger than unity. A second effect arises from the space-filling aspect of the porous matrix: the effective area for interelectrode transport is diminished from A to $A\theta/\lambda$, where θ is the porosity of the medium, equal to the fraction of the total volume that is void. Hence, according to the uniform tortuosity model, eq. [43] remains valid provided that the definition of the diffusion current is modified to

$$[53]\quad i_d = 4AFD_2c_2^b\theta/\lambda^2 L$$

Cell

Details of the thin-layer cell have been described previously (12). The soaked porous disc was clamped between two abutting plastic annuli, so as to create three chambers, as illustrated in Fig. 6. The anode and cathode chambers contain mercury pools that serve as opposing electrodes, each with an area of 1134 mm^2. The peripheral chamber encloses the protruding edge of the porous disc. Careful measurements (12) gave 272 ± 14 μm as the thickness L of the porous matrix under the conditions of the experiments.

Solutions

Stock solutions of $Hg_2(NO_3)_2/HNO_3$ and HNO_3 were prepared

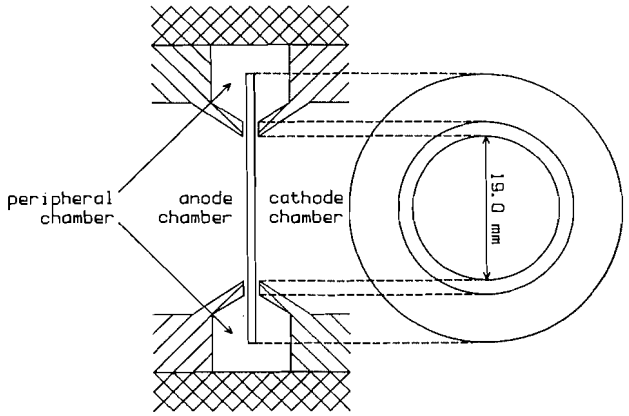

FIG. 6. Diagram illustrating the construction of the cell.

volumetrically from concentrated HNO_3 and gravimetrically from $Hg_2(NO_3)_2 \cdot 2H_2O$: they were deaerated by the passage of argon and stored under argon and over mercury. Soaking solutions were prepared by appropriate dilution of mixed stock solutions. Generally Hg_2^{2+} concentrations ranged between 10 and 30 mM; supporting electrolyte concentrations ranged from 112 mM down to a lower limit dictated by the hydrolysis of Hg(II) as discussed below.

In a few experiments NO_3^- was replaced by ClO_4^-: no discernable difference resulted.

To avoid high acidity, some diffusion current measurements were made in solutions containing excess KNO_3, in addition to $Hg_2(NO_3)_2$ and HNO_3. The theory suggests that the identity of the supporting monovalent cation is unimportant, so that substitution of some H^+ by K^+ should be without effect. Experiments confirmed this prediction.

Procedure

Whatman No. 5 filter paper circles were used as the porous discs. To remove soluble impurities, the papers were soaked in repeatedly renewed deionized water and then air dried. As described in ref. 12, the papers were soaked in electrolyte solution using a technique that avoided air pockets being trapped within the pores.

The soaked disc was mounted in the cell prior to assembly. After cell assembly, all three chambers were flushed with argon and the two electrode chambers were then filled with mercury using the careful technique described elsewhere (12).

In some preliminary experiments, erratic currents were obtained that we believe have an origin in common with polarographic maxima (13). Large electroosmotic forces must operate in our cell, and it appears that their sign is such as to push the solution towards the cathode. Normally these forces do not result in any movement of the electrolyte solution because mercury from the anode cannot enter the pores to replace the migrating solution. However, it appears that the standard soaking and wiping procedure leaves sufficient solution adhering to the surface of the matrix that small pockets, sustained by electroosmosis, can develop between the mercury cathode and the matrix itself. Motion within these pockets is, we believe, responsible for the anomalous currents. To obviate this effect, dry argon was circulated through the peripheral chamber for a sufficient time: water evaporated into the argon and the excess solution was thereby wicked away from the electrode interface. If the drying was continued for too long, a precipitous fall in current ensued; a "sufficient" length of time was one that just failed to cause this condition.

In principle it makes no difference to the steady state how one proceeds from the initial unpolarized cell to the final condition of a constant interelectrode potential ΔE. The simplest route—a single potential step—was, however, considered unsuitable because the large initial currents that flow with this technique might "stress" the system. Accordingly, we imposed a "capped ramp" signal in which the potential rose from an initial zero value to the final ΔE value at a rate of 2.0 mV s^{-1}, and was thereafter held constant. The eventual steady-state current, i, was read from a chart recording of the chronoamperogram. A PARC model 170 electrochemistry system was employed

Can. J. Chem. Downloaded from www.nrcresearchpress.com by 93.93.197.157 on 09/07/12
For personal use only.

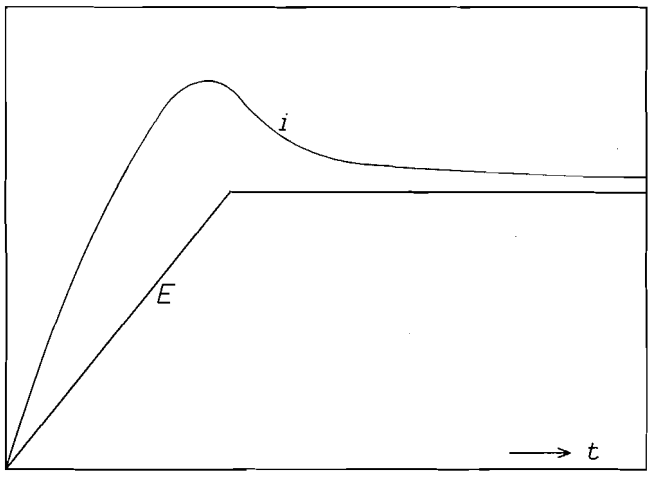

FIG. 7. Illustrating the capped ramp signal and the current response. The pertinent potential and current are the constant values at long times.

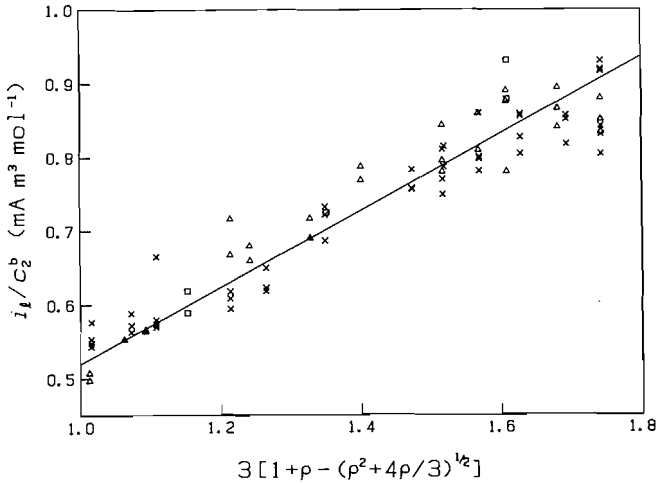

FIG. 8. Results of experiments in Classes III and IV. Mercurous ion concentrations are as follows: □, c_2^b = 10 mM; ×, c_2^b = 18 mM; △, c_2^b = 30 mM. The straight line is the linear regression through the origin.

both to apply the capped ramp signal and to monitor the cell response, as exemplified in Fig. 7.

The cell was not thermostated. Experiments were conducted at an ambient temperature close to 294 K.

Hydrolysis

From literature values (14) of the equilibrium constant for the $Hg_2^{2+}(aq) \rightleftarrows Hg^{2+}(aq) + Hg(l)$ disproportionation, the solubility product of the $HgO(s) + H_2O(l) \rightleftarrows Hg^{2+}(aq) + 2OH^-(aq)$ dissolution, and the ionic product of the $H_2O(l) \rightleftarrows H^+(aq) + OH^-(aq)$ dissociation, one calculates an equilibrium constant

$$[54] \quad K = \frac{[H^+]^2}{[Hg_2^{2+}]} = 3.1 \times 10^{-5} \text{ mol L}^{-1}$$

for the hydrolysis reaction

$$[55] \quad Hg_2^{2+}(aq) + H_2O(l) \rightleftarrows HgO(s) + Hg(l) + 2H^+(aq)$$

This implies that hydrolysis will occur at small support ratios. Quantitatively, eq. [54] predicts that one needs

$$[56] \quad \rho > \frac{3.7 \times 10^{-3} \text{ mol}^{1/2} \text{ L}^{-1/2}}{(c_2^b)^{1/2}}$$

to ensure that hydrolysis does not occur in the bulk solution.

However, the situation is worse than eq. [56] suggests because, as Fig. 2 demonstrates, the Hg_2^{2+} concentration at the anode is greater than its bulk value, while the H^+ concentration there is less than c_1^b. Both these factors encourage hydrolysis and, in fact, we observed a yellow precipitate at the anode for solutions of borderline composition. Of course, results are invalid when hydrolysis occurs.

This unfortunate circumstance places a lower limit on the support ratios that can be studied. The smallest value of ρ that we employed successfully was 0.355.

Results

Our experiments have three independent variables: the imposed interelectrode potential ΔE, the support ratio ρ, and the concentration c_2^b of the electroactive Hg_2^{2+} species. There is one dependent variable, the steady-state current i. Because there is no reason to believe that i will not be proportional to c_2^b, at constant values of ΔE and ρ, we will express our results in terms of the ratio i/c_2^b as a function of the two independent variables ΔE and ρ. In fact, the experimental i/c_2^b ratios were independent of c_2^b.

Limiting cases are approached at high values of ΔE and at both high and low values of ρ. Thus, one can delineate six possible classes of experiment, as shown in Table 2, of which two are inaccessible. The nomenclature of the remaining four classes is established in the table. Of the 143 experiments conducted in this study, 49 were in Class I, 14 in Class II, 74 in Class III and 6 in Class IV.

Analysis of experiments in Classes III and IV

In these classes we have total concentration polarization and therefore the measured steady-state currents are limiting currents. Accordingly, eq. [31] should apply, so that we expect

$$[57] \quad \frac{i_l}{c_2^b} = 3[1 + \rho - (\rho^2 + 4\rho/3)^{1/2}]\frac{i_d}{c_2^b}$$

A plot of i_l/c_2^b versus $3[1 + \rho - (\rho^2 + 4\rho/3)^{1/2}]$ is shown as Fig. 8. There is considerable scatter but a clear linear relationship emerges. A regression through the origin yields a correlation coefficient of 0.9988 and a gradient of

$$[58] \quad \frac{i_d}{c_2^b} = (5.20 \pm 0.26) \times 10^{-4} \text{ A m}^3 \text{ mol}^{-1}$$

Analysis of experiments in Classes II and IV

In these classes supporting electrolyte is in large excess and therefore eq. [51] should hold. This may be rewritten as

$$[59] \quad \frac{i}{c_2^b} = \frac{i_d}{c_2^b} \tanh \frac{F\Delta E}{RT}$$

Figure 9 is a plot of i/c_2^b versus $\tanh(F\Delta E/RT)$ for the 20 data from Classes II and IV. The regression line has a slope (with standard error) of

$$[60] \quad \frac{i_d}{c_2^b} = (5.44 \pm 0.20) \times 10^{-4} \text{ A m}^3 \text{ mol}^{-1}$$

the correlation coefficient being 0.9993.

Analysis of experiments in Class I

In this class we have neither excess supporting electrolyte nor concentration polarization, so that the full equation [44] applies without simplification. Thus it is this class that affords the most stringent test of the theory.

Because it is impossible to invert eq. [44] to obtain an explicit formula for i_d, a more circuitous analysis was adopted. Starting from a guessed value of $i/3i_d$, an estimate of ΔE_{conc} was

Can. J. Chem. Downloaded from www.nrcresearchpress.com by 93.93.197.157 on 09/07/12
For personal use only.

TABLE 2. Classification of experiments

	Unsupported (small ρ)	Modest support (intermediate ρ)	Fully supported (ρ ≥ 41)
Not concentration polarized (modest ΔE)	Inaccessible because of hydrolysis	Class I $i/c_2^b = f(\rho,\Delta E)$	Class II $i/c_2^b = f(\Delta E)$
Concentration polarized ($\Delta E \geq 500$ mV)	Inaccessible because of hydrolysis	Class III $i/c_2^b = i_l/c_2^b = f(\rho)$	Class IV $i/c_2^b = i_l/c_2^b = i_d/c_2^b =$ constant

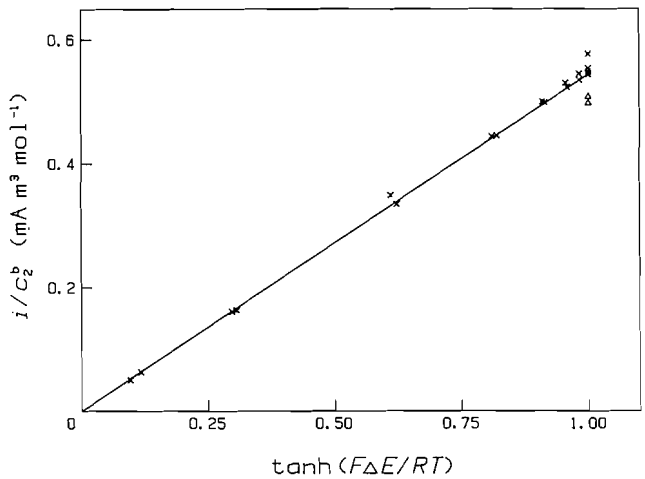

FIG. 9. Results of experiments in Classes II and IV. Symbols and line have the same significance as in Fig. 8.

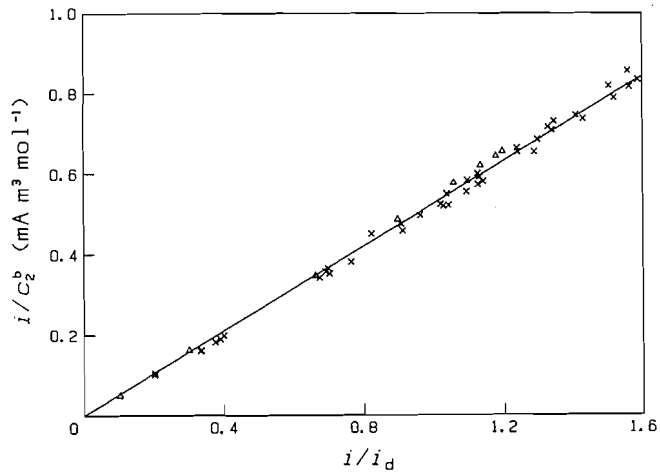

FIG. 10. Results of experiments in Class I. Symbols and line have the same significance as in Fig. 8.

calculated via eq. [35]. This was then subtracted from the measured ΔE to obtain an estimate of ΔE_{ohm}. This, in turn, was substituted into eq. [43] to yield a second value of $i/3i_d$, as illustrated in scheme [61]

$$[61]\quad \frac{i}{3i_d} \xrightarrow{\text{eq. [35]}} \Delta E_{conc} \xrightarrow[\text{from } \Delta E]{\text{subtract}} \Delta E_{ohm} \xrightarrow{\text{eq. [43]}} \frac{i}{3i_d}$$

On this basis a revised estimate of $i/3i_d$ was arrived at and the procedure was iterated until the input and output of scheme [61] were identical. Values of i/c_2^b were then plotted versus i/i_d, producing the graph shown as Fig. 10. A linear regression through the origin leads to the slope

$$[62]\quad \frac{i_d}{c_2^b} = (5.28 \pm 0.15) \times 10^{-4}\ \text{A m}^3\ \text{mol}^{-1}$$

with a correlation coefficient of 0.9996.

Comparison of values

The values of i_d/c_2^b summarized in eqs. [58], [60], and [62] are in total agreement with each other, the compromise value

$$[63]\quad \frac{i_d}{c_2^b} = (5.3 \pm 0.1) \times 10^{-4}\ \text{A m}^3\ \text{mol}^{-1}$$

applying to all. The agreement between the three values represents a successful outcome of this study.

According to eq. [53], the experimental value of $(5.3 \pm 0.1) \times 10^{-4}$ A m^3 mol^{-1} is to be associated with the constant $4AFD_2\theta/(\lambda^2 L)$. Using measured values of A and L, as reported in the experimental section, and a literature value (12, 15) of $(9.5 \pm 0.1) \times 10^{-10}$ m^2 s^{-1} for D_2, we calculate $\theta/\lambda^2 = 0.35 \pm 0.03$, which agrees perfectly with the porosity value $\theta = 0.748 \pm 0.008$ and a tortuosity factor of about 1.45, as determined previously (12) for similar porous media.

Discussion

Experiments performed with porous media do not have a high degree of reproducibility, as the scatter in Figs. 8, 9, and 10 will attest. Nevertheless, it is evident that the linear relationships that are predicted for these three diagrams are obeyed. Moreover, it is clear from the lack of any dependance in the figures on the concentration symbols that the same linear relationship holds irrespective of the mercurous ion concentration.

We believe that the fact that, to within experimental error, all three graphs have an identical slope and that this slope is precisely what theory would predict is a convincing proof that the theory is correct. Recall the steady-state data were collected over wide ranges of mercurous ion concentration, hydrogen ion concentrations, and applied potential, so that we have exercised the theory as strenuously as possible.

Conclusion

We conclude that existing electrochemical theory is capable of predicting the results of steady-state voltammetry, whether or not supporting electrolyte is in excess. The theory must take into account concentration and ohmic polarizations, as well as activation polarization where this is encountered.

Acknowledgements

This research was generously funded by an Operating Grant from the Natural Sciences and Engineering Research Council

Can. J. Chem. Downloaded from www.nrcresearchpress.com by 93.93.197.157 on 09/07/12
For personal use only.

of Canada (NSERC) and early phases were also supported by the Defence Research Board of the Canadian Department of National Defence. The summertime participation in this research by undergraduate students was made possible by grants from NSERC and Canadian Industries Limited. Invaluable technical assistance was provided by Jan Myland.

1. A. M. BOND, K. B. OLDHAM, and C. G. ZOSKI. J. Electroanal. Chem. In press.
2. A. M. BOND, M. FLEISCHMANN, and J. ROBINSON. J. Electroanal. Chem. **168**, 299 (1984).
3. M. CISZKOWSKA and Z. STOJEK. J. Electroanal. Chem. **213**, 189 (1986).
4. M. GOTO, M. GRENNESS, and K. B. OLDHAM. Bull. Chem. Soc. Jpn. **50**, 1950 (1977), and references cited therein.
5. C. E. VALLET and J. BRAUNSTEIN. J. Phys. Chem. **81**, 2438 (1977).
6. M. GOTO, M. GRENNESS, and K. B. OLDHAM. J. Electrochem. Soc. **126**, 50 (1979).
7. A. J. BARD and L. R. FAULKNER. Electrochemical methods: fundamentals and applications. John Wiley, New York. 1980. p. 121.
8. K. B. OLDHAM and C. G. ZOSKI. *In* Comprehensive chemical kinetics. Vol. 26. *Edited by* C. H. Bamford and R. G. Compton. Elsevier, Amsterdam. 1986. p. 118.
9. J. SPANIER and K. B. OLDHAM. An atlas of functions. Hemisphere, Washington, DC. and Springer Verlag, Berlin. 1987. Chap. 31.
10. N. TANAKA and R. TAMAMUSHI. Electrochim. Acta, **9**, 963 (1964).
11. K. B. OLDHAM and L. E. TOPOL. J. Phys. Chem. **71**, 3007 (1967).
12. M. A. ARMITAGE, G. A. BRYDON, P. J. J. CONNELLY, C. J. E. FARINA, H. L. GORDON, K. B. OLDHAM, and T. YANAGI. Can. J. Chem. **58**, 1966 (1980).
13. H. H. BAUER. *In* Electroanalytical chemistry. Vol. 8. *Edited by* A. J. Bard. Marcel Dekker Inc., New York, NY. 1975. p. 170.
14. D. C. HARRIS. Quantitative chemical analysis. W. H. Freeman and Co., San Francisco, CA. 1982. pp. 68, 661.
15. B. SHARIFKER and G. HILLS. J. Electroanal. Chem. **130**, 81 (1981).

Can. J. Chem. Downloaded from www.nrcresearchpress.com by 93.93.197.157 on 09/07/12
For personal use only.

Adrian L. Schwan and John Warkentin. Reactions of 4-*tert*-butyl-5-methylene-3,3-dimethyl-Δ^1-1,2,4-triazoline with dimethyl acetylenedicarboxylate. Can. J. Chem. **65**, 1200 (1987).

Corrections in Table 1, under spectral data for **3**:

For 2.55 (2, 9H), read 1.55 (2, 9H). For 2.66 (s, 3H), read 1.66 (s, 6H). For 234, in the right-hand column, read 224.

Can. J. Chem. Downloaded from www.nrcresearchpress.com by 93.93.197.157 on 09/07/12
For personal use only.

A quantitative examination of the photoisomerization of some protonated phenols

RONALD F. CHILDS[1] AND BAHA E. GEORGE
Department of Chemistry, McMaster University, Hamilton, Ont., Canada L8S 4M1
Received August 5, 1987

RONALD F. CHILDS and BAHA E. GEORGE. Can. J. Chem. **66**, 1343 (1988).

The photoisomerization of a series of protonated, methyl substituted phenols to protonated bicyclo[3.1.0]hexenones has been examined. These reactions, which were carried out in CF_3SO_3H as a strong acid solvent at ambient temperatures, provide a convenient route to a variety of bicyclo[3.1.0]hexenones. The quantum yields for these photoisomerizations vary from 0.018 for protonated 3,5-dimethylphenol to 0.65 for protonated 2,6-dimethylphenol. This variation in efficiency can be understood in terms of a competition between ring opening, to regenerate the starting phenol, or cyclopropyl migration, to give product, of an initially formed intermediate.

RONALD F. CHILDS et BAHA E. GEORGE. Can. J. Chem. **66**, 1343 (1988).

On a étudié les photo-isomérisations d'une série de méthyl-phénols protonés qui conduisent aux formes protonées de bicyclo[3.1.0]hexènones. Ces réactions qu'on a effectuées à la température ambiante, dans le CF_3SO_3H qui agit comme solvant acide fort, offrent une voie d'accès intéressante à une variété de bicyclo[3.1.0]hexènones. Les rendements quantiques de ces photo-isomérisations varient de 0,018, dans le cas du diméthyl-3,5 phénol, à 0.65, dans le cas du diméthyl-2,6 phénol. On peut interpréter cette variation en fonction d'une compétition entre une ouverture de cycle qui regénère le phénol de départ et une réaction qui conduit au produit et qui implique la migration du cyclopropyle d'un intermédiaire qui se formerait initialement.

[Traduit par la revue]

Can. J. Chem. Downloaded from www.nrcresearchpress.com by 93.93.197.157 on 09/07/12
For personal use only.

Most often on dissolution of a phenol in a strong acid medium, proton attachment occurs on the carbon *para* to the oxygen atom of the phenol to give what can be considered to be an *O*-protonated cyclohexa-2,5-dienone, eq. [1] (1). These

[1] 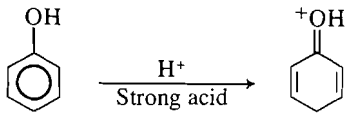

protonated phenols are stable in solution provided the strong acid solvent is a non-oxidizing and non-sulphonating medium. Triflic acid, CF_3SO_3H, meets these criteria and is an excellent medium for these cations, with solutions being stable for long periods even at elevated temperatures (2). The only limitation on the use of triflic acid would seem to be its lower acidity compared to the other commonly used super-acid solvents (3) and the requirement for a more acidic medium to ensure ring protonation of some of the least basic phenols.

Ring protonated phenols have been shown to photoisomerize to give protonated bicyclo[3.1.0]hexenones on irradiation, eq. [2] (4, 5). This transformation parallels the analogous photo-

[2] 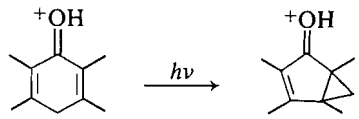

rearrangements of neutral (6) and protonated cyclohexa-2,5-dienones (7) and provides a convenient preparative route to a wide variety of bicyclohexenones that have one or no substituents at C6.

An important feature of these photoisomerizations of protonated phenols is that the products of the reactions are also photochemically active and are converted back to a protonated phenol on irradiation. This overall process can lead to the production of an isomer of the original starting protonated phenol.

Protonated bicyclohexenones, the initial photoproducts of the isomerization of these protonated phenols, can also be converted back to a protonated phenol thermally. In many instances the activation energies for these isomerizations are large and the acid solutions have to be heated to relatively high temperatures for the thermal isomerizations to proceed. Indeed, the thermal stability and highly exothermic nature of these rearrangements (8) have led us to suggest that the photochemical and reverse thermal isomerizations of protonated phenols are potential candidates for a solar energy, photochemical/latent heat storage system (9). To evaluate the potential use of protonated phenols for solar energy storage it is important to know considerably more about the photoreactions themselves. For this purpose we have undertaken a quantitative examination of the photoisomerization of a series of methyl substituted protonated phenols. The results of this study are reported here.

Results and discussion

Characterization of the protonated phenols

The methyl substituted phenols **1–10** were protonated by dissolving them in CF_3SO_3H at 25°C. The resulting cations, **1*H*–10*H***, were characterized by comparison of their ^1H nmr spectra with those reported previously for the same cations in

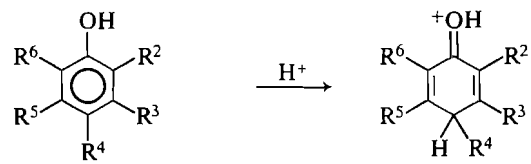

	R^2	R^3	R^4	R^5	R^6	
1	Me	H	H	H	Me	**1*H***
2	Me	H	H	Me	H	**2*H***
3	Me	Me	H	H	H	**3*H***
4	H	Me	H	Me	H	**4*H***
5	Me	Me	H	Me	H	**5*H***
6	Me	Me	H	H	Me	**6*H***
7	Me	Me	Me	Me	H	**7*H***
8	Me	Me	Me	H	Me	**8*H***
9	Me	Me	H	Me	Me	**9*H***
10	Me	Me	Me	Me	Me	**10*H***

[1]Author to whom correspondence may be addressed.

FSO_3H at low temperature (1). Apart from **7**, in every case the spectra were entirely consistent with the formation of the C4 protonated cations **1***H*–**6***H*, and **8***H*–**10***H*. With **7**, in addition to **7***H*, the C6 protonated material **7***H′* was shown to be present in small amounts (5%).

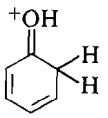

7*H′*

One difference that was observed between the room temperature ^1H nmr spectra of these cations in CF_3SO_3H at room temperature, as compared to those obtained in FSO_3H at low temperatures, was the line shapes of some of the resonances associated with ring protons. In most cases no coupling was detected between the H4 protons and adjacent protons on the C3, C5, or C4 methyl groups in these cations in CF_3SO_3H, in contrast to that found when FSO_3H was used as the solvent. The absence of this coupling suggests that relatively rapid exchange of the H4 proton with solvent is occurring in triflic acid (10). This exchange can be sufficiently rapid on the nmr time scale to lead in certain cases to a very significant degree of line broadening of the H4 resonances. As the temperature of the samples is lowered there is a reduction in the half-width of the resonances associated with H4. These effects are most pronounced in the ^1H nmr spectra of **1***H* and **8***H*. For example, the nmr spectrum of **8***H* at room temperature shows the resonances of both H4 and H5 to be very broad and the C4 methyl resonance to be a singlet, Fig. 1, suggesting at this temperature the occurrence of an intermolecular exchange of H4 with the acid medium and either an intramolecular exchange of H4 with H5 or direct exchange of H5 with the solvent. It is not known whether the difference in behaviour between the rates of exchange of H4 in the two acid media results from the difference in their acidities (3) or is associated with the difference in temperature under which the spectra were obtained. The freezing point of CF_3SO_3H and the reactivity of FSO_3H towards these cations at temperatures above −20°C make a direct experimental test of these factors difficult.

A further point to note with respect to the ^1H nmr spectra of these protonated phenols is the position of the resonances associated with the H4 protons. In those cases where there is a methylene group at C4 resonance is typically found at ca. 4.0 ppm. In the three cases where there is a methyl group at C4, the methine proton is found upfield of this position at ca. 3.6 ppm. Normally it is expected that a methine proton would be found at lower chemical shift than a comparably situated methylene proton. A likely reason for this unusual reversal is that the cations with a methyl group at C4 (**7***H*, **8***H*, and **10***H*) are not planar but rather adopt a conformation to which the C4 carbon is tilted out of the plane of the ring carbons so as to minimize interaction of the C4 methyl with the groups at C3 and C5. This twisting effect would move the C4 methine proton into the plane of the other ring carbons, Fig. 2, and as such it would be in a different magnetic environment relative to the methylene protons of the other cations. A comparable twisting of the six-membered ring has been suggested to take place with protonated hexamethylbenzenium cation (11). It is interesting to note that the chemical shift discrepancy noted above is also found in the parent benzenium ions, which have a single methyl substituent at the saturated ring carbon (10).

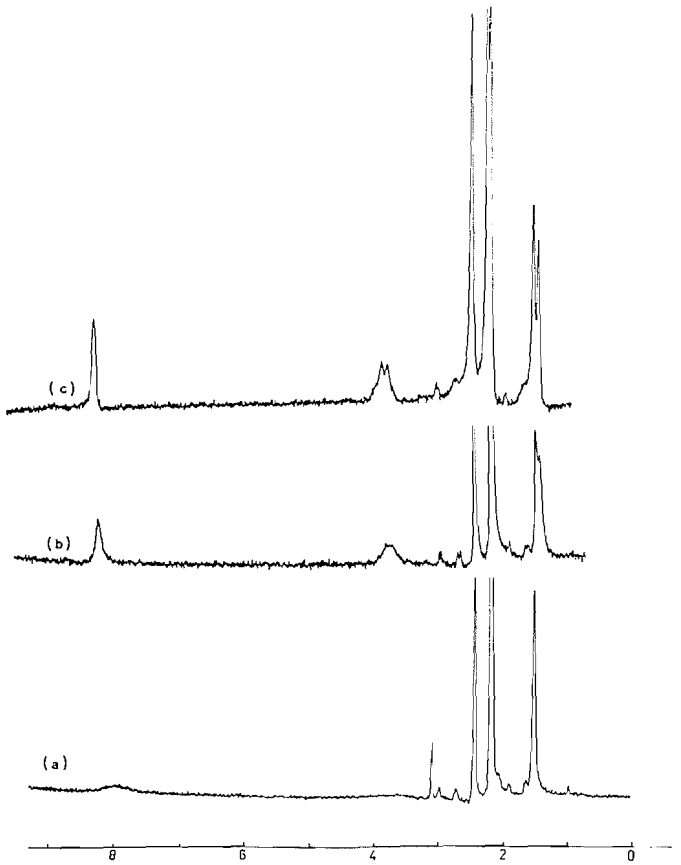

FIG. 1. The ^1H nmr spectra of **8***H*. (a) Room temperature: (b) 0°C; (c) −20°C.

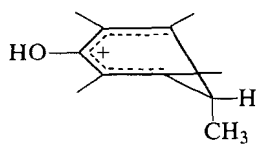

FIG. 2. Conformation of a protonated phenol with a methyl group at C4.

The uv spectra of the acid solutions of the protonated phenols are summarized in Table 1. In all cases a strong absorption band was observed between 300 and 330 nm. The position of this band is characteristic of oxygen protonated cyclohexa-2,5-dienones (11). In the case of solutions of **7**, a further weak absorption band was observed at 385 nm (log ε 2.63). Protonated cyclohexa-2,4-dienones exhibit absorption spectra in this region and the presence of this second band in the spectrum of **7** in CF_3SO_3H is consistent with the presence of **7***H′* in addition to **7***H*.

Photoisomerization of protonated phenols. Qualitative aspects

Irradiation of solutions of the protonated methyl substituted phenols at room temperature in triflic acid led to the formation of isomeric protonated bicyclo[3.1.0]hexenones and, in certain instances, isomeric phenols, Table 2. The products were identified on the basis of the ^1H nmr spectra of the protonated species and the subsequent isolation and characterization of the bicyclic ketones, see Tables 3, 4, and 6 and the experimental section. Some of these bicyclic ketones have been previously characterized and where this is the case it is noted in the tables.

Can. J. Chem. Downloaded from www.nrcresearchpress.com by 93.93.197.157 on 09/07/12
For personal use only.

TABLE 1. Ultraviolet spectra of protonated phenols and bicyclo[3.1.0]hexenones

Compound	λ^{max} (nm)	Log ϵ^{max}
1*H*	304	3.72
2*H*	300	3.78
3*H*	305	3.75
4*H*	306	3.87
5*H*	328	3.61
6*H*	326	3.43
7*H*	385,310	2.63,4.06
8*H*	324	3.79
9*H*	328	3.99
10*H*	329	3.72
13*H*	330	3.50
17*H*[a]	336	3.50
18*H*[a]	332	3.40
20*H*[a]	332	3.65

[a]In H_2SO_4.

TABLE 2. Summary for photoisomerizerations of protonated phenols

Protonated phenol	Time of irradiation (h)	Total isomerization (%)	Products[a,b] (%)
1*H*[c]	48	70	**11**(100)
2*H*[c]	216	60	**12**(35), others(65)
3*H*[d]	48	60	**13**(95), **23**(5)
4*H*[c]	288	<5	Unidentified products
5*H*[c]	253	<20	Unidentified products
6*H*[c]	40	60	**16**(82), **22**(16), others(2)
6*H*[d]	72	90	**16**(83), **24**(17)
8*H*[c]	40	85	**19**(53), **17**(18), **18**(9), **9**(20)
8*H*[d]	32	85	**19**(28), **17**(29), **18**(19), **25**(7), **8** and **9**(19)
9*H*[c]	40	85	**19**(53), **17**(18), **18**(9), **9**(20)
10*H*[c]	8	66	**20**(100)

[a]Expressed as a percentage of total products.
[b]After neutralization of the irradiated solution with base.
[c]In CF_3SO_3H (room temperature).
[d]In FSO_3H at −78°C.

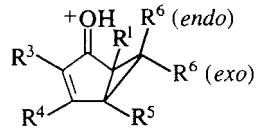

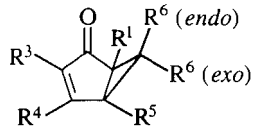

	R^1	R^3	R^4	R^5	R^6 *exo*	R^6 *endo*	
11*H*	Me	Me	H	H	H	H	**11**
12*H*	Me	H	Me	H	H	H	**12**
13*H*	H	Me	Me	H	H	H	**13**
14*H*	H	H	Me	Me	H	H	**14**
15*H*	H	Me	Me	Me	H	H	**15**
16*H*	Me	Me	Me	H	H	H	**16**
17*H*	Me	Me	Me	H	H	Me	**17**
18*H*	Me	Me	Me	H	Me	H	**18**
19*H*	Me	Me	Me	Me	H	H	**19**
20*H*	Me	Me	Me	Me	H	Me	**20**
23*H*	Me	H	H	Me	H	H	**23**
24*H*	Me	Me	H	Me	H	H	**24**
25*H*	Me	Me	H	Me	H	Me	**25**

In the case of the photoisomerization of **8***H*, two primary products, **17***H* and **18***H*, were obtained in which the stereochemistry of the C6 methyl group was the only difference. These two cations were distinguished by the positions of the resonances of these methyl substituents on C6 in comparison with other protonated and neutral bicyclohexenones (12). As has been noted before, with this type of photoisomerization of protonated phenols or benzenium ions themselves, the major isomer formed has the methyl group in the C6 *endo* position (13). Such a preference is consistent with the nonplanar conformation of the starting cations as was discussed above.

The reversible nature of these reactions is well exemplified in the photoisomerizations of the tetramethyl phenols **8***H* and **9***H*. The change in composition versus length of irradiation of **9***H* is shown in Fig. 3. Initially, the decrease of **9***H* is matched by the formation of **19***H*. The proportion of this bicyclic product rises to little over 50% and then drops to what appears to be a limiting value of 46%. As the reaction proceeds, protonated bicyclic ketones, **17***H* and **18***H*, are produced as well as **8***H*.

At longer irradiation times it would appear that a photostationary state involving all five cations is being reached. This can be seen from the data presented in Fig. 4. Ultimately a solution with the same composition was reached, upon irradiation of **8***H*, as was obtained starting with **9***H*. These interconversions of the tetramethyl substituted cations can be understood in terms of the processes depicted in Scheme 1. That the protonated bicyclic ketones will absorb light under the conditions used is seen on examination of their uv spectra given in Table 1.

The photoisomerization of protonated durenol, **9***H*, has also been investigated by Baeckstrom *et al.* (5). In addition to the formation, after quenching, of **19** and two unidentified ketones, presumably **17** and **18**, they also reported the formation of a trimethylphenol (2%) and 2,3,4,5-tetramethylphenol (7%). Under the conditions used in this work, neither of these latter two products was present in the reaction mixture. It should be noted that in our earlier work on the irradiation of **9***H*, using a super-pressure mercury lamp and a longer wavelength cut-off filter, only **8***H* was detected as a product (3). These photoisomerizations with a variety of absorbing and potentially photoreactive species present can be particularly sensitive to the wavelength of the light used for the isomerizations.

In the case of protonated 3,5-dimethylphenol, **4***H*, no characterizable photoproducts could be detected even after prolonged irradiations of the acid solutions. The photoisomerization of **5***H* yielded several minor products and these were not characterized.

In addition to the stereoselectivity exhibited at C6 of the product cations, the unsymmetrical arrangement of methyl groups at carbons 2, 3, 5, and 6 of **2***H*, **3***H*, **6***H*, and **8***H* means that products may result from the formation of the cyclopropyl ring between either C2,3 or C5,6. With triflic acid as a solvent, the product detected at room temperature was in each case that in which the number of methyl groups on the double bond of the bicyclic ketone product was maximized. However, with **3***H* and **6***H*, the protonated phenols **21***H* and **22***H*, respectively, were also formed in low amounts during the photoisomerizations. These two protonated phenols cannot arise from a further photoisomerization of **13***H* or **16***H* and suggest that **23***H* and

Can. J. Chem. Downloaded from www.nrcresearchpress.com by 93.93.197.157 on 09/07/12
For personal use only.

TABLE 3. ^{1}H nuclear magnetic resonance shifts of bicyclo[3.1.0]hexenones[a]

Compound	H1	H3	H4	H5	H6 *endo*	H6 *exo*	Coupling constants (Hz)
11	(1.40)	(1.65)	7.26d	2.16m	1.22m	1.30m	$J_{4,5} = 2.0$
11*H*	(1.70)	(1.85)	8.45d	3.55m	2.35m	2.95m	$J_{4,5} = 2.1$
12	(1.40)	5.35bs	(2.13)	[c]	1.25m	1.34m	$J_{CH_2} = 3.2$; $J_{5,CH_2} =$ 3.3 and 6.7
13	2.23m	(1.55)	(2.05)	2.11m	1.17m	1.43m	
13*H*	3.27m	(1.77)	(2.45)	3.55m	2.35m	2.60m	
16	(1.33)	(1.51)	(1.95)	1.88m	1.11m	1.20m	$J_{CH_2} = 3.20$, $J_{5,CH_2} = 3.1$ and 6.3
16*H*	(1.67)	(1.77)	(2.42)	3.35m	2.25m	2.75m	$J_{CH_2} = 3.0$, $J_{5,CH_2} = 3.0$ and 6.2
17	(1.35)	(1.63)	(1.98)	(2.13)d	(0.97)d	1.75m	$J_{5,6} = 7.3$; $J_{CH_3,H6} = 6.2$
17*H*	(1.68)	(1.90)	(2.40)	3.50d	(1.25)d	3.35m	$J_{5,6} = 7.0$; $J_{CH_3,H6} = 6.2$
18	(1.39)	(1.58)	(2.08)	1.64d	1.32m	(1.1)d	$J_{5,6} = 2.3$; $J_{CH_3,H6} = 5.8$
18*H*	(1.68)	(1.81)	(2.43)	3.23d	2.83m	(1.35)d	$J_{5,6} = 2.5$; $J_{CH_3,H6} = 6.0$
19	(1.33)	(1.47)	(1.96)	(1.20)	0.83d	1.17d	$J_{CH_2} = 3.0$
19*H*	(1.65)	(1.80)	(2.40)	(1.60)	1.92d	2.85d	$J_{CH_2} = 3.2$
20	(1.34)	(1.63)	(1.92)	(1.25)	(0.94)d	1.41q	$J_{CH_3H6} = 6.4$
20*H*	(1.65)	(1.90)	(2.35)	(1.62)	(1.20)d	2.90q	$J_{CH_3,H6} = 6.4$
23	(1.25)	5.38d	7.23d	(1.14)	0.75d	[c]	$J_{CH_2} = 3.1$; $J_{3,4} = 6.0$
24	(1.35)	(1.56)d	6.95q	(1.24)	0.85d	1.31d	$J_{CH_3,H4} = 1.3$; $J_{CH_2} = 3.0$
24*H*[b]	(1.71)	(1.81)d	8.23q	(1.67)	2.18d	3.26d	$J_{CH_3,H4} = 1.4$; $J_{CH_2} = 3.5$
25	(1.35)	(1.65)d	6.9d	(1.20)	(0.97)d	1.43q	$J_{CH_3,H6} = 6.4$; $J_{CH_3,H4} = 1.4$
25*H*[b]	(1.70)	(2.03)	8.0	(1.65)	(1.36)d	2.20	$J_{CH_3,H6} = 6.4$

[a]Ketones in $CDCl_3$; protonated ketones in CF_3SO_3H; bs = broad singlet, d = doublet, q = quartet, m = multiplet. All the nmr spectra were recorded at room temperature unless otherwise specified. Values in brackets refer to CH_3 group.
[b]At −10°C.
[c]Position uncertain.

TABLE 4. ^{13}C nuclear magnetic resonance data for bicyclo[3.1.0]hexenones[a]

Compound	Chemical shift (ppm) C1	C2	C3	C4	C5	C6	Methyl carbons				
11	29.4	208.0	135.8	155.7	27.3	42.8	13.1	10.1			
11*H*	40.2	226.0	131.0	186.4	40.8	76.2	10.7	8.7			
12	28.3	[b]	123.8	168.8	33.8	41.7	19.2	13.8			
13	24.4	206.6	129.5	168.2	30.8	34.0	16.3	7.6			
16*H*	29.0	205.3	129.5	166.1	31.2	40.2	16.4	14.0	8.3		
16*H*	37.4	219.6	131.1	209.6	41.9	70.8	19.4	10.4	6.6		
17	34.3	207.0	133.2	163.5	36.9	46.2	17.1	14.7	7.6	7.2	
18	34.4	208.4	129.3	168.2	38.2	48.0	16.3	14.5	8.7	7.9	
19	32.5	208.0	128.4	169.4	33.6	46.8	13.5	11.5	10.3	7.6	
19*H*	40.9	219.5	129.8	209.2	47.0	76.8	17.6	9.5	7.2	5.7	
20	37.1	207.7	132.6	165.3	38.7	54.4	14.6	13.1	11.6	8.4	7.3
24	31.9	208.6	134.7	159.2	33.6	48.8	13.3	10.5	10.0		

[a]Ketones in $CDCl_3$ or CD_2Cl_2; protonated ketones in CF_3SO_3H.
[b]Position uncertain.

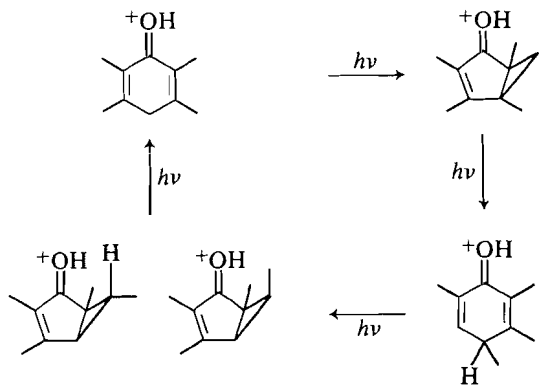

SCHEME 1

24*H* could be formed during the photoreactions but not survive the reaction conditions. Indeed, previous work on the photoisomerization of **6***H* at low temperature using FSO_3H as a solvent has shown that **24***H* is formed as a minor product of the reaction. In this work it was shown that triflic acid solutions of **24***H* were stable up to −10°C but at higher temperatures it rearranged thermally to form **22***H* (3). Irradiations of **3***H* and **8***H* in FSO_3H at low temperature also led to the formation of minor amounts of the less stable isomers **23***H* and **25***H* respectively.

Photoisomerization of protonated phenols. Quantitative aspects

The quantum efficiencies for the photoisomerizations of a number of protonated phenols and the reverse ring opening of

Can. J. Chem. Downloaded from www.nrcresearchpress.com by 93.93.197.157 on 09/07/12
For personal use only.

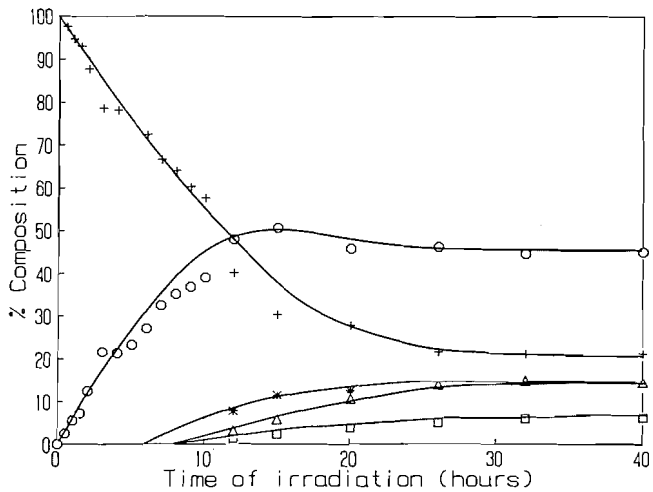

FIG. 3. Photoisomerization of **9***H* as a function of irradiation time. +, **9***H*; ○, **19***H*; *, **8***H*; △, **17***H*; □, **18***H*.

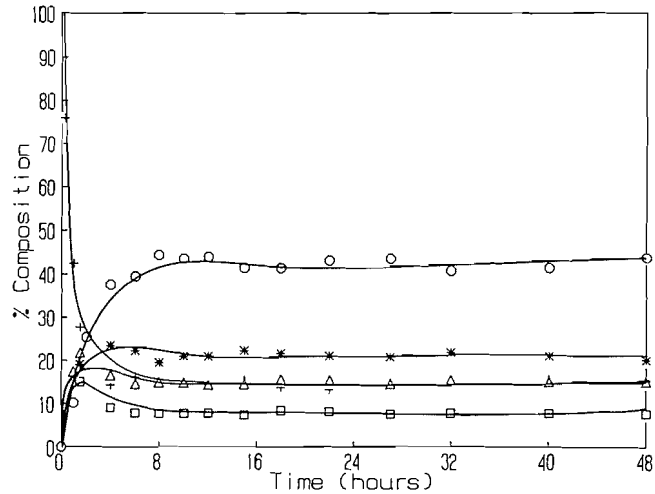

FIG. 4. Photoisomerization of **8***H* as a function of irradiation time. +, **8***H*; ○, **19***H*, *, **9***H*; △, **17***H*; □, **18***H*.

protonated bicyclic ketones were measured, Table 5. In each case the composition of the solutions was determined by quenching the acid solutions and carrying out quantitative analyses by glpc. In all cases the degree of conversion was kept below 10% and no correction was made for any back reaction.

The effect of dissolved oxygen on the reactions was determined by comparing reactions in which the oxygen had been removed by purging with argon with those using aerated samples. As can be seen from the results in Table 5, oxygen has no detectable effect on these reactions, consistent with the earlier suggestions that these reactions involve singlet or short-lived triplet excited states.

As can be seen on examination of the data in Table 5, at least over the range of systems studied here the quantum efficiency of the ring opening of the protonated bicyclic ketones is insensitive to the positions and number of methyl substituents. In each case

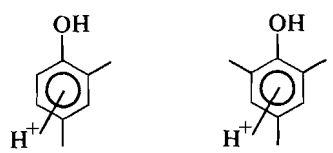

21*H* **22***H*

TABLE 5. Quantum yields[a]

Reaction	Quantum yield	
	Aerated	Degassed
1*H* → **11***H*	0.65 ± 0.02	
3*H* → **13***H*	0.38 ± 0.02	0.38 ± 0.03
4*H* → product	0.018 ± 0.001	
6*H* → **16***H*	0.50 ± 0.01	
8*H* → **17***H* + **18***H* 2 : 1	0.49 ± 0.01	
9*H* → **19***H*	0.24 ± 0.01	0.24 ± 0.01
10*H* → **20***H*	0.20 ± 0.03	0.19 ± 0.02
13*H* → **3***H*	0.16 ± 0.01	
16*H* → **6***H*	0.24 ± 0.02	
19*H* → **8***H*	0.20 ± 0.01	0.19 ± 0.01
20*H* → **10***H*	0.21 ± 0.01	0.21 ± 0.01

[a]Measured relative to the photodecomposition of potassium ferrioxalate at 313 nm.

the measured quantum efficiency is close to 0.2. The seeming insensitivity of the efficiency of this ring-opening reaction stands in marked contrast to the relatively large changes that are observed with the photoisomerizations of the protonated phenols, which in the systems studied here range from a low of 0.018 to a high of 0.65, a factor over nearly 40.

In examining the changes of the efficiencies of the photoisomerizations of the protonated phenols it is clear that there are some definite trends present. It is clear that the isomerization reaction is favoured by the presence of methyl groups at carbons 2 and 6 and hindered by methyls at carbons 3 and 5. Thus, comparing the series **1***H* (0.65), **6***H* (0.50), and **9***H* (0.24), there is a consistent drop in the efficiency of conversion to the corresponding protonated bicyclic ketone as methyl groups are successively added to the *meta* positions. The reverse effect is seen in comparing the effect of the addition of a methyl group to the *ortho* position(s), for example comparing **3***H* (0.38) with **1***H* (0.65) or **4***H* (0.018) with **9***H* (0.24). These effects are large and well beyond the experimental uncertainty of the measurements. In contrast, the quantum efficiencies for the isomerizations of **9***H* and **10***H* or **6***H* and **8***H* are essentially the same, indicating that groups at C4 are relatively unimportant.

Why are such large effects observed? In seeking to answer such a question it is necessary to know the mechanism of the reaction. In the case of the directly comparable photoisomerizations of cross-conjugated cyclohexadienones there is very strong evidence to indicate that the reactions proceed via an initial bonding between C3 and C5 followed by a ground state cyclopropyl migration to give the bicyclohexenone (6). It is particularly interesting that the effect of methyl substituents on the efficiencies of the photoisomerization of cross-conjugated cyclohexadienones is exactly the same as found here with the protonated systems and it would seem most likely that a similar two-step isomerization pathway holds in these latter systems (14).

If it is assumed that the photoisomerization of the protonated phenols discussed here proceeds as shown in Scheme 2, then it is possible to account for the observed variations in quantum efficiency on the basis of a competition between ring opening of the ground state intermediate formed in the reaction and cyclopropyl migration to give the protonated bicyclic product.

From the work described in the accompanying paper on the thermal isomerization of deuterated **19***H* it is clear that the

Can. J. Chem. Downloaded from www.nrcresearchpress.com by 93.93.197.157 on 09/07/12
For personal use only.

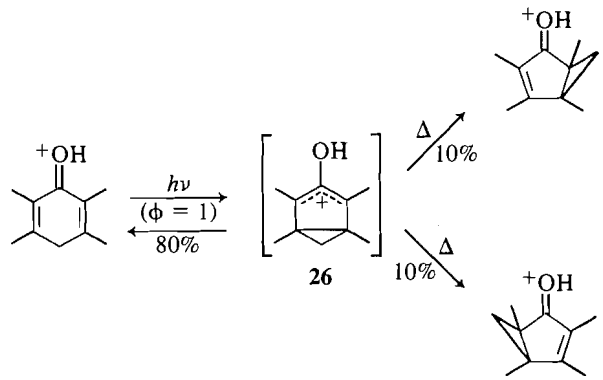

SCHEME 2

relative rates of ring opening and cyclopropyl migration in the intermediate **26** are very closely matched, with ring opening being favoured by a factor of 4 as compared to migration. Such a ratio between these rate constants should also hold in the photochemical reaction if **26** is formed as a ground state intermediate. This means that if the first photochemical step of the reaction is assumed to have an efficiency of 1.00, then the maximum efficiency observed for the formation of **19***H* should be 0.2 with the remainder of **26** reverting to starting material. The observed quantum efficiency for the conversion of **9***H* to **19***H* is 0.24 + 0.02. The agreement between these two numbers suggests that this analysis is correct.

On the basis of this result with **9***H*, if we further assume that the efficiencies of the first photochemical step in these isomerizations of protonated phenols are high and approach 1 in each case, then the effect of the placement of methyl substituents can be understood. The work described in the accompanying paper suggested that when an intermediate such as **26** has methyl substituents at C3 and C5, the bridgehead positions, then ring opening will be facile. Conversely, the presence of methyls at the vinylic positions C2 and C6 will retard ring opening. If the barriers to ring opening and cyclopropyl migration in these photochemically generated intermediates are close, then the effect of *ortho* and *meta* substituents on the overall quantum efficiencies can be accounted for. It is interesting that Schuster and Liu (14) have provided evidence for a similar competition between ring opening and cyclopropyl migration of the corresponding zwitterion involved in the photoisomerization of neutral 2,5-cyclohexadienones.

Conclusion

In conclusion, it should be noted that the combination of relatively high quantum efficiencies and overall freedom of these photoisomerizations from side reactions make these photoisomerizations attractive from a synthetic perspective. In general, bicyclo[3.1.0]hexenones are not easy materials to prepare and this room temperature photoisomerization provides convenient access to a variety of methyl substituted derivatives of these bicyclic ketones. In using these reactions for synthetic purposes it is important to stress that the bicyclo[3.1.0]hexenones are very volatile materials and that great care should be taken not to lose material during the evaporation of solvent during work-up manipulations. It is also advisable, for maximum yields of the bicyclic materials, that the reactions be monitored and stopped at the appropriate point, to minimize subsequent photoreactions that can complicate the purification steps.

TABLE 6. Infrared and mass spectral data of the bicyclic ketones

Compound	Infrared (cm^{-1})	Mass spectrum (m/e) obs.	calcd.
12	1701	122.0699	122.0732
16	1694	136.0867	136.0888
17	1641	150.1030	150.1045
18	1703	150.1047	150.1045
20	1695	164.1210	164.1201
25	1701	150.1070	150.1045

Experimental

General

The ^1H nmr spectra were recorded in Varian EM 390 and Bruker WM-250 spectrometers. The absorption spectra were obtained on Tracor Northern DA RSS system or Hewlett Packard 8451A spectrometers. The gc analyses were carried out on Varian 3700 and Hewlett Packard 5790A gas chromatographs. A 1/8 in. × 8 ft copper column packed with 2% OV17 on Chromosorb W (Column A) and a 1/8 in. × 10 ft stainless steel column packed with 10% Flourad FC 431 on Chromosorb W (Column B) were used in the gc analyses. An Aerograph model A-90-P3 gas chromatograph with a 1/4 in. × 5 ft copper column packed with 10% OV17 on Chromosorb W (Column C) column was used for preparative separation.

FSO_3H and CF_3SO_3H were obtained commercially and the former acid distilled prior to use. Cyclohexane was distilled over $LiAlH_4$ and pyridine was refluxed over solid KOH and distilled. Phenols **1**–**6** and **9** were obtained commercially and purified by sublimation before use. 2,3,4,6-Tetramethylphenol (15), 2,3,4,5-tetramethylphenol (16), and pentamethylphenol (15) were prepared by published procedures.

Protonation

Samples were protonated by the addition of cooled FSO_3H (−78°C) or CF_3SO_3H (0°C) to weighed amounts of phenols in nmr tubes cooled in a Dry Ice – acetone bath (FSO_3H) or an ice bath (CF_3SO_3H). Solution was achieved by mixing the contents of the tubes with a thin glass rod.

Photoisomerizations

These were carried out using a Rayonet photoreactor (Southern New England Ultraviolet Co.) equipped with 253.7-nm or 300-nm lamps. For low temperature irradiations the samples contained in 5-mm quartz nmr tubes were cooled in a partially silvered quartz Dewar held at −70°C with a FTS Flexicool FC2084P1 refrigeration unit.

Preparative scale irradiations were carried out using the appropriate phenol (2 g) dissolved in CF_3SO_3H (10 mL). The reaction mixtures were stirred during irradiation. Aliquots were withdrawn periodically to check the progress of the reaction using ^1H nmr spectroscopy. The reaction mixtures were quenched by pouring into $NaHCO_3$/ether at −78°C (FSO_3H) or at 0°C (CF_3SO_3H). Organic products were extracted into ether and careful removal of ether gave the products. Care should be taken during ether removal to prevent loss of volatile products.

The products were analysed (quantitative) by analytical gc and the components of the mixtures were separated by preparative gc. The ir and mass spectral data for the bicyclic ketones are given in Table 6.

Analysis of tetramethyl phenols

Acid solutions resulting from irradiations of **8***H* and **9***H* were quenched and the products isolated as outlined above. Following the removal of volatile ketones, the residue (10 mg) was dissolved in dry pyridine (1 mL). To 10 μL of this solution in a screw cap septum reacti-vial 100 μL of bis(trimethylsilyl)trifluoroacetamide was added, and the mixture was allowed to stand at room temperature for 1/2 h. Gas chromatographic analysis of the products (Column B) showed the presence of two components. These were identified as silyl derivatives

Can. J. Chem. Downloaded from www.nrcresearchpress.com by 93.93.197.157 on 09/07/12
For personal use only.

of durenol and isodurenol by comparison with authentic samples. Detector response was checked using mixtures of known composition.

Quantum yield measurements

The light source used in this work was an Osram HBO 200-W super-pressure mercury lamp with a Kratos LPS 25T power supply. Wavelength selection (313 nm) was achieved using a Kratos GM100 grating monochromator with entrance and exit slits set for a 24-nm bandwidth. The filter used was an Optikon filter no. 313FS10-25 with a high wavelength cutoff at 325-nm. The parallel beam from the monochromator was split by a quartz plate (7.5 cm square, 1.5 mm thick) fixed at 45° to the beam inside a light-tight box. Samples were contained in quartz "Lollipop cells". The samples were prepared by weighing the phenol or ketone (5–10 mg) into the sample container and dissolving in CF_3SO_3H (0.5 mL).

The quantum yields were measured at 313 nm with potassium ferrioxalate actinometry. The percent conversion, in all cases, was less than 10% and the quantum yields were not corrected for back reaction. After irradiation the neutral photoproducts were recovered by the procedure described above. The degree of conversion of the starting material was determined by analytical gc using Column B.

The quantum yield for the conversion of each protonated phenol to the corresponding protonated bicyclo[3.1.0]hexenones was measured at least three times and the mean values and the errors (standard deviation from the mean) are given in Table 5. The quantum yields for the conversion of protonated bicyclo[3.1.0]hexenones to protonated phenols were measured twice and the two values averaged to give the quantity given in Table 5. The error was estimated at 10%.

Acknowledgement

This work was supported by grants from the Natural Sciences and Engineering Research Council of Canada.

1. G. A. Olah and Y. K. Mo. J. Org Chem, **38**, 353 (1973); R. F. Childs and B. D. Parrington. Can. J. Chem. **52**, 3303 (1974); S. M. Blackstock, K. E. Richards, and G. J. Wright. Can. J. Chem. **52**, 3313 (1974).
2. R. F. Childs and B. E. George. Can. J. Chem. **66**, 1350 (1988).
3. G. Grondin, R. Sagnes, and A. Commeyras. Bull. Soc. Chim. Fr. 1779 (1976); R. D. Howells and J. D. McCown. Chem. Rev. **77**, 67 (1977); H. Bakoss, R. Ranson, R. Roberts, and A. Sadri. Tetrahedron, **38**, 623 (1982).
4. R. F. Childs and B. D. Parrington. Chem Commun. 1581 (1970); R. F. Childs, B. D. Parrington, and M. Zeya. J. Org. Chem. **44**, 4912 (1979); R. F. Childs, G. Shaw, and A. Varadarajan. Synthesis, 198 (1982).
5. P. Baekstrom, U. Jacobson, B. Koutek, and T. Norin. J. Org. Chem. **50**, 3728 (1985).
6. H. E. Zimmerman. Adv. Photochem. **1**, 183 (1963); K. Schaffner. Adv. Photochem. **4**, 81 (1966); D. I. Schuster. Acc. Chem. Res. **11**, 65 (1978).
7. J. W. Pavlik and R. J. Pasteris. J. Am. Chem. Soc. **96**, 6107 (1974); N. Filipescu and J. W. Pavlik. J. Am. Chem. Soc. **92**, 6062 (1970).
8. R. F. Childs, M. Mahendran, S. D. Zweep, G. S. Shaw, S. K. Chadda, N. A. D. Burke, B. E. George, R. Faggiani, and C. J. L. Lock. Pure Appl. Chem. **58**, 111 (1986).
9. R. F. Childs, D. L. Mulholland, M. Zeya, and A. Goyal. Sol. Energy, **30**, 155 (1983).
10. (*a*) D. M. Brouwer, E. L. Mackor, and C. MacLean. Carbonium Ions, **1**, 837 (1970); (*b*) V. A. Koptyug. Top. Current Chem. 122 (1984).
11. D. M. Brouwer, C. MacLean, and E. L. Mackor. Disc. Faraday Soc. **39**, 121 (1965).
12. E. C. Friedrich. J. Org. Chem. **33**, 413 (1968); V. P. Vitullo. J. Org. Chem. **34**, 224 (1969).
13. R. F. Childs, M. Sakai, B. Parrington, and S. Winstein. J. Am. Chem. Soc. **96**, 6403 (1974); R. F. Childs and S. Winstein. J. Am. Chem. Soc. **96**, 6409 (1974).
14. D. I. Schuster and K.-C. Liu. Tetrahedron, **37**, 3329 (1981); D. I. Schuster and K. U. Prahbu. J. Am. Chem. Soc. **96**, 3511 (1974); D. I. Schuster and D. J. Patel. J. Am. Chem. Soc. **90**, 5145 (1968).
15. S. R. Finn and J. W. G. Musty. J. Soc. Chem. Ind. London, Suppl. Issue No. 1, S_3 (1950).
16. H. Kakshinumunty and M. Santappa. J. Org. Chem. **27**, 1839 (1962).

Can. J. Chem. Downloaded from www.nrcresearchpress.com by 93.93.197.157 on 09/07/12
For personal use only.

Thermal isomerizations of protonated bicyclo[3.1.0]hexenones

RONALD F. CHILDS[1] AND BAHA E. GEORGE
Department of Chemistry, McMaster University, Hamilton, Ont., Canada L8S 4M1

Received August 5, 1987

RONALD F. CHILDS and BAHA E. GEORGE. Can. J. Chem. **66**, 1350 (1988).

The thermal isomerization of a wide range of protonated methyl substituted bicyclo[3.1.0]hex-3-en-2-ones to protonated phenols has been examined using triflic acid as a strong acid solvent. The rate constants and activation energies of these isomerizations have been determined. The barriers to the isomerizations were shown to be dependent on the number and position of the methyl substituents. The results show that three different mechanisms are needed to account for these isomerizations, two of which involve a preliminary circumambulatory rearrangement prior to ring opening and the other process involving a direct ring opening of the initial protonated bicyclohexenone to give an intermediate *meta*-protonated phenol.

RONALD F. CHILDS et BAHA E. GEORGE. Can. J. Chem. **66**, 1350 (1988).

Opérant dans l'acide triflique qui agit comme solvant fortement acide, on a étudié l'isomérisation thermique d'un grand nombre de bicyclo[3.1.0]hexène-3 ones-2 substituées par des groupements méthyles en phénols protonés. On a déterminé les constantes de vitesse ainsi que les énergies d'activation de ces isomérisations. On a démontré que les barrières à ces isomérisations dépendent du nombre et de la position des substituants méthyles. Les résultats démontrent que trois mécanismes différents sont nécessaires pour expliquer ces isomérisations : deux impliquent une transposition circumambulatoire préliminaire précédant l'ouverture du cycle alors que l'autre processus implique une ouverture directe du cycle de la bicyclohexènone protonée initiale conduisant à un phénol intermédiaire protoné en *méta*.

[Traduit par la revue]

Can. J. Chem. Downloaded from www.nrcresearchpress.com by 93.93.197.157 on 09/07/12
For personal use only.

The thermal isomerization of bicyclo[3.1.0]hexenyl cations to the isomeric benzenium ions is a well-known reaction (1–4). This $4e^-$ disrotatory electrocyclic reaction is formally forbidden in the ground state and as a consequence these reactions, despite their strongly exothermic nature, involve relatively high activation energies (5).

When these bicyclic cations bear a hydroxy substituent, the corresponding thermal isomerization to hydroxybenzenium cations appears to be more complicated than that of the parent benzenium ions. The isomerization of the hexamethyl substituted cation, **1**, has been studied in detail (1, 6). Careful studies with deuterium labeled derivatives showed that this reaction proceeds by a circumambulation of the cyclopropyl ring around the five-membered ring followed by a higher energy ring-opening reaction of the unobserved intermediate **3**. There have been no further reports of studies of the ring-opening reactions of other protonated bicyclo[3.1.0]hexenones and it is not clear whether the isomerization pathway observed with **1** is a general feature of these systems.

In the isomerization of **1** the direct ring-opening reaction to give **4** and thence **5** is of higher energy than the observed pathway involving **3**. The indirect route involving the intermediacy of **3** does not eliminate the need for the disrotatory electrocyclic ring opening and questions arise as to why this is the preferred isomerization pathway and how much higher in energy is the direct pathway involving **4**. As the barriers to circumambulation in these types of cation are dependent on the substituents at C6 (1, 7), it seems likely that the pathway for this type of isomerization could be altered by changes in the substitution pattern of the protonated bicyclic ketones.

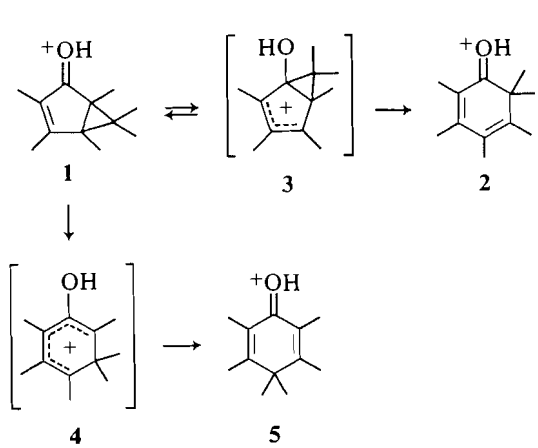

SCHEME 1

In this present work we report the results of an examination of the isomerization of a wide range of different methyl substituted protonated bicyclo[3.1.0]hexenones and show that ring opening to yield a protonated phenol is a common reaction. However, it is also clear that there are a range of mechanisms at play and that subtle changes in the substitution pattern of the starting bicyclic ketone can dramatically alter the direction of the ring-opening reaction.

Results

The bicyclic ketones **6–14** were prepared by irradiation of the corresponding protonated phenols in triflic acid as previously described (8). Dissolution of the ketones in triflic acid yielded solutions of the corresponding protonated materials **6*H*–14*H***. Except in the cases of **10*H*** and **12*H***, the acid solutions of these protonated ketones were stable at room temperature.

The thermal isomerizations of these protonated ketones in triflic acid were examined by nmr spectroscopy. The products of isomerization were identified by comparison of the nmr spectra of the products with those of authentic protonated phenols, and in several cases these assignments were confirmed by isolation of the phenol following neutralization of the acid solution. The rate of isomerization was measured by heating the samples in a constant temperature bath and monitoring the changes in the ^1H nmr spectra as a function of time. No side products were detected during the course of these isomerizations and in each case good first-order kinetics were observed. The results of these studies are summarized in Table 1.

[1]Author to whom correspondence may be addressed.

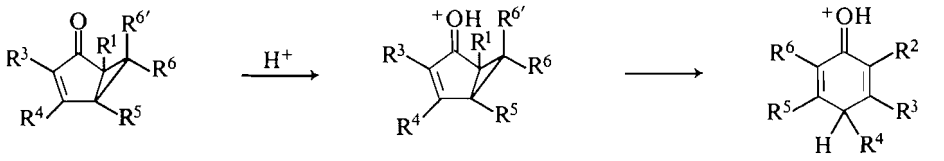

6–14 **6*H*–14*H*** **15*H*–21*H***

	R^1	R^3	R^4	R^5	R^6	$R^{6'}$		R^2	R^3	R^4	R^5	R^6
6	Me	Me	Me	Me	H	Me	**6*H***					
7	Me	Me	Me	Me	H	H	**7*H***					
8	Me	Me	Me	H	H	Me	**8*H***					
9	Me	Me	Me	H	Me	H	**9*H***					
10	Me	Me	H	Me	H	Me	**10*H***					
11	Me	Me	Me	H	H	H	**11*H***					
12	Me	Me	H	Me	H	H	**12*H***					
13	H	Me	Me	H	H	H	**13*H***					
14	Me	Me	H	H	H	H	**14*H***					
							15*H*	Me	Me	Me	Me	Me
							16*H*	Me	Me	H	Me	Me
							17*H*	Me	Me	Me	H	Me
							18*H*	Me	Me	H	H	Me
							19*H*	Me	H	Me	H	Me
							20*H*	Me	Me	H	H	H
							21*H*	Me	H	H	Me	H

TABLE 1. Isomerizations of protonated bicyclohexenones

Starting ion	Product	Rate constant × 10^5 (s^{-1}) 60°C ∓0.5	100°C ∓0.5	Other	(°C)	$G^{\neq}$ kcal/mol
1	**2**	—	—	91	(10)	20.5[a]
6*H*	**15*H***	7.3∓0.3	530∓50	—		25.8∓0.8
7*H*	**16*H***	6.0∓0.4	290∓20	—		26.2∓0.8
8*H*	**16*H***	1.7∓0.1	—	—		26.7∓0.8
9*H*	**17*H***	31∓0.2	—	—		24.9∓0.7
10*H*	**17*H***	—	—	52∓3	(20)	21.5∓0.5
11*H*	**18*H***	0.33∓0.06	28∓2	—		27.9∓0.9
12*H*	**19*H***	—	—	52∓6	(30)	22.4∓0.6
13*H*	**20*H***	—	0.87∓0.2	—		30.7∓1
14*H*	**21*H***	—	54∓4	—		27.2∓0.8

[a]Reference 1.

To check for the occurrence of circumambulation in **7*H***, the deuterated cation **22*H*** was prepared. Treatment of **7** with CD_3O^-/CD_3OD led to the formation of **22**, which on protonation in triflic acid gave **22*H***. This solution was heated at 60°C until some 40% of **22*H*** had isomerized to **23*H***. Careful analysis of the ^1H nmr spectra of the resulting solution showed that there was a small increase in the relative intensity of the resonance due to the residual undeuterated C4 methyl group of **22*H*** at δ 1.40, which could be attributed to the formation of **22*H'***. As it is possible that some of the growth of this signal results from a slow exchange of deuterium in **22*H*** with solvent, it can only be stated with certainty that the rate of circumambulation of **22*H*** to give **22*H'*** cannot be faster than the growth in this resonance. Thus the maximum rate constant for this scrambling process is $7.8 \pm 0.8 \times 10^{-6}\ s^{-1}$ at 60°C.

The stability of the various protonated phenols in CF_3SO_3H was determined by heating the acid solutions to the temperatures used to study the isomerizations of the protonated bicyclic ketones. Only one phenol, **17*H***, was observed to rearrange under these conditions. In the case of **17*H*** it isomerized to **16*H*** at 60°C with a first-order rate constant of $3.2 \times 10^{-6}\ s^{-1}$. This isomerization is slower than that of the conversion of **8*H*** to **16*H*** ($k = 1.7 \times 10^{-5}\ s^{-1}$ at 60°C) meaning that **17*H*** could have

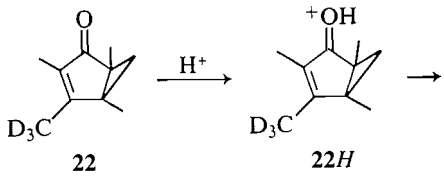

22 **22*H***

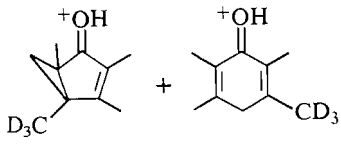

22*H'* **23*H***

been detected if it had been produced as an initial product of the rearrangement of the protonated bicyclic ketone.

Discussion

It is clear from the results presented above that all of the protonated bicyclohexenones studied isomerize on heating to give protonated phenols. The barriers to these isomerizations are relatively high and elevated temperatures are required for most of the reactions. From the data given in Table 1 it can be seen that there is a wide spread of free energies of activation

Can. J. Chem. Downloaded from www.nrcresearchpress.com by 93.93.197.157 on 09/07/12
For personal use only.

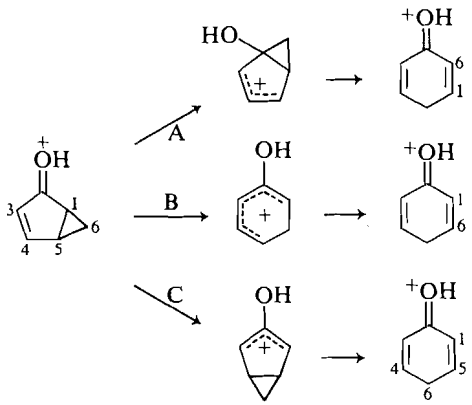

SCHEME 2

associated with these reactions. Only one product is observed in each case and the reactions occur with no detectable loss of material. This is remarkable in terms of the rather extreme conditions of acid and temperature that were employed and the results point to the usefulness of triflic acid as a non-oxidizing strong acid medium for high temperature carbocation rearrangements.

In principle there are three ways in which the ring opening of a protonated bicyclo[3.1.0]hexenone can take place. As is shown in Scheme 2, the cyclopropyl carbon C6 can potentially end up in the *ortho*, *meta*, or *para* positions of the protonated phenol. The first of these reactions, path A, involves insertion of C6 into the *ortho* position. This corresponds to the reaction seen by Hart and co-workers with **1** (6). Path B involves an initial ring opening of the bicyclohexenone followed by a subsequent rearrangement of the initially formed *meta*-protonated phenol to give the more stable isomer. The last example, path C, is a reaction comparable to that described by Hart; however, in this instance, the cyclopropane carbon has migrated to the ring position opposite to the hydroxy function.

The control experiments show that solutions of the protonated phenols in triflic acid are stable when heated to the same temperatures under which the thermal isomerizations of the bicyclic cations were conducted. This means that while there can be proton reorganization on the phenolic rings, the positions of the methyl groups remain unchanged once the ring opening of the bicyclic ketones has occurred. Thus the positions of the methyl groups in the products as compared to the starting bicyclic ketones indicate the location of C6, the cyclopropane carbon.

The methyl substitution pattern present in some systems does not enable a clear differentiation between the three isomerization pathways to be made. However, in the reactions of **7***H*, **9***H*, **12***H*, and **14***H* the results are unambiguous. The isomerization of **14***H* to **21***H* corresponds to the involvement of path A. The conversion of **12***H* to **19***H* is a direct ring-opening process, path B, while the formation of **16***H* and **17***H* from **7***H* and **9***H*, respectively, provides clear-cut examples of the intervention of path C.

While the overall course of these ring-opening reactions would seem clear, questions arise as to how these reactions take place and what factors determine the relative activation energies of each pathway in a particular case. The occurrence of cyclopropyl circumambulations in bicyclo[3.1.0]hexenyl cations and protonated bicyclo[3.1.0]hexenones is a well-established isomerization process. Furthermore, while the intermediate **3** has not been directly observed in the isomerization of **1**, there is excellent evidence for its existence in the very careful work of Hart and colleagues. Similarly, in this work the detection of scrambling of deuterium in the isomerization of **22***H* would again indicate the presence of a circumambulatory rearrangement and it is highly suggestive that the intermediate **24** is involved in this ring-opening process. It would thus seem likely that the ring openings by paths A and C, as shown in Scheme 2, take place by an initial circumambulatory step followed by an electrocyclic ring opening.

It is possible to account for the products obtained in pathways A and C on the basis of single-step mechanisms. While such mechanisms cannot be ruled out on the basis of the existing results, it would seem very unlikely that they are involved in these rearrangements, particularly as it has been shown that they do not occur in the isomerization of alkyl substituted bicyclo[3.1.0]hexenyl cations nor indeed with the analogous isomerizations of the isoelectronic bicyclo[2.1.0]pentenes to cyclopentadienes (9).

In examining the factors determining the preference for isomerization by the various pathways shown in Scheme 2, it is useful to consider first the direct ring-opening reaction, path B. The one clear-cut example of the operation of this pathway is the conversion of **12***H* to **19***H*. The rate-determining step in this isomerization will be the initial electrocyclic ring opening to yield **25**. The subsequent hydride shift, whether it be an inter- or intramolecular process, will be fast.

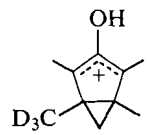

24

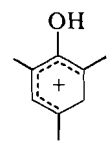

25

Previous work on the isomerization of bicyclo[3.1.0]hexenyl cations has shown that the addition of an *endo* methyl group to C6 has a small rate-accelerating effect on the ring-opening reaction (1). In this present work, the addition of an *endo* methyl group to C6 of **12***H* gives **10***H*. The positions of the methyl groups in **10***H* do not permit an unequivocal identification of which isomerization path is followed. However, as the isomerization of **10***H* proceeds with the same rate constant as that of **12***H* but at a temperature 10° lower than the latter system, it would seem likely that **10***H* also isomerizes by path B.

In contrast to the straightforward reaction path for the isomerization of **12***H*, both **7***H* and **14***H* undergo a different type of ring opening. Protonated ketone **7***H* only differs from **12***H* by the presence of a methyl group at C4 of the latter cation. The effect of this methyl group is to cause **7***H* to isomerize by path C. On the other hand, the formal removal of the the C5 methyl group from **12***H* gives **14***H*, and this cation isomerizes by path A. The addition of a methyl group to C4 or removal from C5 of **12***H* must raise the barrier of the direct ring-opening reaction by at least 3.8 or 4.8 kcal/mol, respectively. These are very large effects for the introduction or removal of a methyl group on the barrier in an electrocyclic reaction.

The effect of a methyl group at C4 would seem to result from changes in the relative stabilities of the starting bicyclic cations. A C4 methyl group in **7***H* would stabilize this cation and presumably raise the barrier to isomerization with respect to **12***H*. A comparable effect of a methyl group on the barriers to the electrocyclic ring opening with the penta- and 1,2,3,5-tetramethyl-bicyclo[3.1.0]hexenyl cations has been reported (2). It is interesting that similar but smaller effects have been

Can. J. Chem. Downloaded from www.nrcresearchpress.com by 93.93.197.157 on 09/07/12
For personal use only.

Can. J. Chem. Downloaded from www.nrcresearchpress.com by 93.93.197.157 on 09/07/12
For personal use only.

noted by Klärner and Adamsky on the barrier to the ring opening of substituted bicyclo[2.1.0]pentenes by the introduction of a methyl group at the 2 position (10, 11).

Related studies on the ring openings of bicyclo[2.1.0]pentenes and cyclobutenes show that methyl substituents at the bridgehead positions lower the barrier to the ring-opening reactions (12–15). In the present case, methyl groups at C1 or C5 of the bicyclic cations will have relatively little effect on the stability of the starting cations. However, they are ideally placed to stabilize the initially formed intermediate in Path B of these reactions and so lower the barrier to isomerization by this route. The absence of a C5 methyl group in the case of **14***H* causes the energy barrier for the direct electrocyclic ring opening to be greater than 27.2 kcal/mol, as compared to 22.4 kcal/mol for **12***H*.

The importance of the two methyl groups on the bridgehead carbons for the direct ring-opening reaction can also be seen in the photoisomerization of **20***H*. Irradiation of a solution of **20***H* in FSO_3H at −70°C leads to the formation of a mixture of **13***H* (95%) and **26** (5%). When this same photoisomerization is carried out in triflic acid at room temperature, **13***H* and **27** are formed in the same ratio. As there was no change in the light source or in any other conditions in the irradiation other than temperature, it is clear that **26** is thermally unstable at room temperature and isomerizes to **27** via path B.

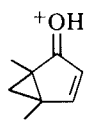

26

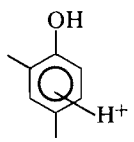

27

In examining the effect of substituents on the barriers to isomerization by paths A and C, it is important to know which is the rate-determining step in the two reactions. In the case of **1** the work of Hart (8) clearly establishes that the circumambulatory step is a relatively low energy process and that the ring opening of the intermediate is the rate-determining step. The effect of C6 methyl substituents on the circumambulatory reactions of bicyclo[3.1.0]hexenyl cations is well established (1). In general, an *exo* methyl substituent at C6 greatly accelerates the circumabulatory process in a bicyclo[3.1.0]hexenyl cation while an *endo* methyl group has a much smaller effect. These effects have been previously discussed in terms of both the steric requirements for these concerted reactions and the need for charge-stabilizing substituents at C6.

The effect of substituents at C6 in the ions studied here is clearly seen in the various isomerizations summarized in Table 1. In the case of the isomerization of **7***H*, it is clear that the barriers for circumambulation and ring opening via path C are now very comparable. The increase in the barrier to circumambulation of **7***H* (26.2 kcal/mol) as compared to that of **1** (17.4 kcal/mol) is not unexpected in view of the difference in substitution at C6 in the two cations.

While the substituent patterns in **8***H* and **11***H* do not allow an unambiguous definition of the isomerization pathways, comparison of the effect of the C6 substituents on the rate of isomerization of these ions as compared to **9***H* supports the suggestion that they isomerize via a two-step process in which the barrier to circumambulation determines the overall rate of the reaction. In particular, it should be noted that **9***H*, which isomerizes by path C, has the lowest isomerization barrier. This is consistent with the presence of an C6 *exo* methyl substituent in this ion. It is also interesting that the barrier to isomerization of **6***H* is the same as that of **7***H*. In the former case the pathway by which isomerization occurs is not known; however, in view of the behavior of both **1** and **7***H* it would seem likely that **6***H* also isomerizes by either pathway A or C. If this is the case then the *endo* C6 substituent on **6***H* is not having much effect on the barrier to circumambulation, as would be expected from the previous results.

Previous work has shown that **28** rearranges to **29** at 10°C,

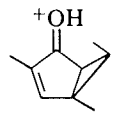

28

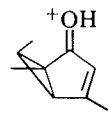

29

indicating that in this case circumambulation is a lower energy process than any of the ring-opening pathways (8). However, in this present work neither **10***H* nor **12***H* undergoes circumambulatory rearrangements in preference to direct ring opening. It is interesting that **28** lacks the second methyl substituent at the bridgehead positions that would seem to be a requirement for the operation of path B.

One further feature of these ring openings that deserves mention is the choice of ring opening between paths A and C. Once the barrier to ring opening by a direct reaction, path B, becomes of higher energy than the circumambulatory routes, then there formally is a choice between two related paths, A and C. One thing that is clear from the results presented above is that the stability of the intermediates involved in paths A and C is not of major importance in determining the course of the reactions. This is clearly shown in comparing the isomerization of **1**, **14***H*, and **7***H*. Indeed the contrasting behavior of **1** and **7***H* is difficult to understand from a single perspective and points to the subtle blend of factors that are at play in these ions in determining the course of the ring-opening reactions.

Experimental

The nmr spectra were obtained using Varian EM390 and Bruker WM-250 instruments. The bicyclic ketones were prepared as described in the accompanying paper (16). Product identification was made by comparison with authentic samples of the various phenols.

Preparation of carbocations

The cation precursor, ca. 10 mg, in an nmr tube was cooled in an ice bath (0°C). CF_3SO_3H (0.5 mL), cooled previously to 0°C, was added dropwise. Dissolution of the base was achieved as the solution was slowly brought to ambient temperature.

Quenching acid solutions

The CF_3SO_3H solution containing the cation was added to a rapidly stirred aqueous solution of $NaHCO_3$. The organic material was extracted into ether (3 × 5 mL) and the combined extracts washed with water (2 × 5 mL) and dried over $MgSO_4$. The solvent was removed carefully by evaporation through a 7-cm Vigreux column using a steam bath. The products were analysed by gc using a 10% Flourad FC 431 on a Chromosorb W column as described in the accompanying paper (16).

Synthesis of 1,3,5-trimethyl-4-methyl-d_3-bicyclo[3.1.0]hexenone, 22

This compound was prepared from **7** using a procedure similar to that outlined by Hart *et al.* (17). The bicyclic ketone **7** (50 mg) was dissolved in $NaOCD_3$ (0.5 mL CD_3OD/50 mg Na). The solution was left at 25°C and its ^1H nmr spectrum examined periodically. After 1 h the methyl signal at δ 1.96 had disappeared and no further change in the nmr spectrum was observed after several hours. The trideuterio ketone was isolated by pouring the solution into 5 mL of CH_2Cl_2 and washing with ice water (3 × 5 mL). After drying ($MgSO_4$) the solvent was

evaporated slowly through a 7-cm Vigreux column to give **22** as an oil; ^{1}H nmr ($CDCl_3$) δ: 1.47 (s, 3H, CH_3), 1.33 (s, 3H, CH_3), 1.20 (s, 3H, CH_3), 1.16 (d, 1H, J = 3 Hz), 0.83 (d, 1H, J = 3 Hz).

Thermal stability of bicyclo[3.1.0]hexenones in CF_3SO_3H

Each ketone (ca. 10 mg) was dissolved in CF_3SO_3H according to the above method. The resultant solutions were examined by ^{1}H nmr at various temperatures between 34 (probe temperature) and 100°C for cations **6***H*, **7***H*/**8***H*, **9***H*, **11***H*, **13***H*, and **14***H* and between 0 and 30°C for cations **10***H* and **12***H*. Normally, the bath or probe temperature was increased from the lowest value by increments of 10°C until an isomerization was observed. The isomerization was followed by ^{1}H nmr spectroscopy. Products were identified by ^{1}H nmr and by gc after quenching the acid solution.

Isomerization rate constants

The rate constants for the conversion of the protonated bicyclic ketones **6***H*, **7***H*, **8***H*, **9***H*, **11***H*, and **14***H* to their isomeric phenols at 60°C were determined by dissolving the ketone (ca. 10 mg) in CF_3SO_3H (0.40 mL) and adding a small amount of $(CH_3)_4N^+BF_4^-$ as an internal standard. This mixture was placed into a medium-walled nmr tube. The sample was heated in a Haake A81 constant temperature bath and at various time intervals the sample was cooled quickly to 25°C and its ^{1}H nmr spectrum obtained. The relative concentration of the starting material was determined by comparison with the signal due to the internal standard and the first-order rate constant calculated. Each determination was repeated at least in duplicate.

Acknowledgement

This work was supported by grants from the Natural Sciences and Engineering Research Council of Canada.

1. R. F. Childs and S. Winstein. J. Am. Chem. Soc. **96**, 6409 (1974); **90**, 3146 (1968).
2. R. F. Childs, M. Sakai, B. D. Parrington, and S. Winstein. J. Am. Chem. Soc. **96**, 6403 (1974).
3. I. S. Isaev, V. I. Mamatyuk, L. I. Kuzubova, T. A. Gordymova, and V. A. Koptyug. Zh. Org. Khim. **6**, 2482 (1970); V. A. Koptyug, L. I. Kuzubova, I. S. Isaev, and V. I. Mamtyuk. Zh. Org. Khim. **6**, 2258 (1970); V. A. Koptyug, L. I. Kuzubova, I. S. Isaev, and V. I. Mamatyuk. J. Chem. Soc. D: 389 (1969); Zh. Org. Khim. **6**, 1843 (1970); V. A. Koptyug. Top. Curr. Chem. **122**, 211 (1984).
4. P. Vogel, M. Saunders, N. M. Hasty, Jr., and J. A. Berson. J. Am. Chem. Soc. **93**, 1551 (1971).
5. R. F. Childs and D. L. Mulholland. J. Am. Chem. Soc. **105**, 96 (1983).
6. D. W. Swatton and H. Hart. J. Am. Chem. Soc. **89**, 5075 (1967); H. Hart, T. R. Rogers, and J. Griffiths. J. Am. Chem. Soc. **91**, 754 (1969).
7. R. F. Childs. Tetrahedron, **38**, 567 (1982).
8. R. F. Childs, B. D. Parrington, and M. Zeya. J. Org. Chem. **52**, 3303 (1974); R. F. Childs, G. S. Shaw, and A. Varadarajan. Synthesis, **3**, 198 (1982).
9. G. D. Andrews and J. Baldwin. J. Am. Chem. Soc. **99**, 4853 (1977); W. E. Farneth, M. B. D'Amore, and J. I. Brauman. J. Am. Chem. Soc. **98**, 5546 (1976).
10. F. Klärner and F. Adamsky. Chem. Rev. **116**, 299 (1983).
11. F. Klärner and F. Adamsky. Angew. Chem. Int. Ed. Engl. **18**, 674 (1979).
12. H. M. Frey, B. M. Pope, and R. F. Skinner. Trans. Faraday Soc. **63**, 1166 (1967); H. M. Frey. Trans. Faraday Soc. **60**, 83 (1964).
13. M. J. S. Dewar and S. Kirschwer. J. Chem. Soc. Chem. Commun. 461 (1975).
14. R. Breslow, J. Napierski, and A. H. Schmidt. J. Am. Chem. Soc. **94**, 5906 (1972).
15. R. Criegee and H. Gruner. Angew. Chem. Int. Ed. Engl. **7**, 467 (1969).
16. R. F. Childs and B. E. George. Can. J. Chem. **66**, 1343 (1988).
17. H. Hart, P. M. Collins, and A. J. Waring. J. Am. Chem. Soc. **88**, 1005 (1966).

Can. J. Chem. Downloaded from www.nrcresearchpress.com by 93.93.197.157 on 09/07/12
For personal use only.

The importance of ground state conformation in the photoisomerizations of protonated enones

RONALD F. CHILDS,[1] MAILVAGANAM MAHENDRAN, CHRISTOPHER BLACKBURN, AND GREGORY ANTONIADIS
Department of Chemistry, McMaster University, Hamilton, Ont., Canada L8S 4M1
Received October 21, 1987

RONALD F. CHILDS, MAILVAGANAM MAHENDRAN, CHRISTOPHER BLACKBURN, and GREGORY ANTONIADIS. Can. J. Chem. **66**, 1355 (1988).

The conformations of several protonated enones have been determined by low temperature ^{13}C nuclear magnetic resonance spectroscopy. Information on the ground state conformation has been used to understand the differences in the photochemistry of these systems. Photoisomerizations of **4** and **5** have been examined. In the case of **4**, irradiation leads only to the formation of the *Z* isomer **16**; protonated dihydrofuran **13** was not observed. In the case of **5**, both the *Z* isomer **17** and protonated dihydrofuran **14** were observed. The protonated dihydrofuran **14** was produced from the start of the reaction. It is concluded from these and previous results that for the photocyclization to occur the starting cation must exist in an *s-cis* conformation in the ground state.

RONALD F. CHILDS, MAILVAGANAM MAHENDRAN, CHRISTOPHER BLACKBURN et GREGORY ANTONIADIS. Can. J. Chem. **66**, 1355 (1988).

Faisant appel à la résonance magnétique nucléaire du ^{13}C, à basse température, on a déterminé les conformations de plusieurs ènones protonées. On a utilisé les informations relatives aux conformations dans l'état fondamental pour comprendre les différences observées lors de la photochimie de ces systèmes. On a étudié les photo-isomérisations des composés **4** et **5**. Dans le cas du composé **4**, l'irradiation ne conduit qu'à la formation de l'isomère-*Z* (**16**); on n'observe pas de formation du dihydrofuranne protoné **13**. Dans le cas du composé **5**, on observe la formation de l'isomère-*Z* **17** ainsi que celle du dihydrofuranne protoné **14**. La formation du dihydrofuranne **14** commence dès le début de la réaction. Sur la base de ces résultats et d'autres obtenus antérieurement, on en conclut que la photo-isomérisation ne peut se produire que si le cation de départ existe dans la conformation *s-cis*, à l'état fondamental.

[Traduit par la revue]

Protonated enones and their oxygen alkylated analogues undergo a variety of photoisomerizations upon irradiation (1). The primary photoreactions of the acyclic cations are *E*/*Z* isomerizations about their C=C and C=O partial double bonds (2). A second type of reaction, occurring with systems containing an isopropyl group at the β-position, is cyclization to form a protonated dihydrofuran (3). These reactions are illustrated in Scheme 1. All of these photoisomerizations of protonated enones involve π,π* excited states.

One feature of the cyclization reaction of **1** is that ring closure has been shown to take place only from the 2-*Z* isomer,[2] **2**. A mechanism that could account for this observation would involve hydrogen abstraction by oxygen from the γ position. Such a 1,5-hydrogen abstraction reaction would parallel that commonly found in the photoreactions of unprotonated enones (4). However, deuterium labelling experiments showed that such a process did not occur with these protonated systems but instead that the C4 isopropyl hydrogen migrates exclusively to C3 of the starting enone (5). This hydrogen migration can be considered to involve a photochemically initiated 1,2 hydride shift from C4 to C3.

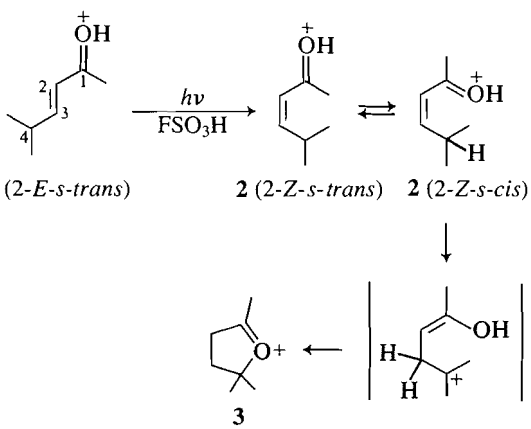

1 (2-*E*-*s*-*trans*) **2** (2-*Z*-*s*-*trans*) **2** (2-*Z*-*s*-*cis*)

3

SCHEME 1

The photochemical interconversion of **1** and **2** will involve a common, twisted excited state. It is likely that the hydride shift from C4 to C3 also occurs from this twisted excited state or a closely related ground state species. As such it is difficult to see why the ground state conformation about the 2–3 bonds of these cations can determine that **2** but not **1** undergoes photochemically induced ring closure to give **3**. Rather it would seem most likely that the critical feature is the ground state conformation about the C1—C2 bonds of these protonated ketones.

Calculations on acrolein indicate that the barriers to rotation about the C2—C3 bond are increased in the π,π* excited states as compared to the ground state (6). This means that in the case of the cyclization reaction shown in Scheme 1, which involves π,π* excited states, ring closure can only occur upon excitation of cations that have an *s-cis* conformation in the ground state. As a result, one possible reason for the photochemical cyclization of **2** as compared to **1** is that the relative proportions of the *s-cis* and *s-trans* conformations of these protonated enones might depend on the configuration of the C2—C3 bond.

In this paper we describe a series of experiments that, in the first place, determine the conformation about the C1—C2 bonds of several of these cations using low temperature nmr methods. Second, the photochemistry of these cations has been shown to correlate with the known conformational preferences.

[1]Author to whom correspondence may be addressed.

[2]To facilitate comparison a common, nonsystematic numbering system for enones has been used, with the carbonyl carbon always being C1, and α and β carbons, C2 and C3, respectively (see figures).

Can. J. Chem. Downloaded from www.nrcresearchpress.com by 93.93.197.157 on 09/07/12
For personal use only.

TABLE 1. Proton chemical shifts of enones[a]

Compounds	Temperature (°C)	Solvent	Chemical shifts, ppm H1	H2	H3	H4	H5	R[b]	Coupling constants, Hz $J_{1,2}$	$J_{2,3}$	$J_{3,4}$	$J_{4,5}$
4	−68	FSO_3H	9.18d	7.08dd	8.76dd	3.10m	(1.30)d	—	9.9	15.3	6.0	6.9
5	−68	FSO_3H	—	7.15d	8.61dd	2.94m	(1.28)d	(1.52)s	—	14.5	6.3	6.5
7	−68	FSO_3H	—	7.15d	8.60m	(2.40)d	—	(1.45)s	—	15.5	6.0	—
9	34	$CDCl_3$	—	5.70–6.20m		3.60m	(1.10)d	(2.20)s	—	11.9	—	6.5
10	34	$CDCl_3$	9.50d	6.10dd	6.85dd	2.60m	(1.20)d	—	9.5	15.0	6.0	6.9
11	34	$CDCl_3$	—	6.50d	7.00dd	2.50m	(1.15)d	(1.20)s	—	15.0	6.0	7.0
12	34	$CDCl_3$	—	6.45d	6.90m	(1.85)d	—	(1.15)s	—	15.0	6.0	—
13	−20	FSO_3H	—	3.99t	2.35t	—	(1.89)s	—	—	7.5	—	—
14	34	FSO_3H	—	3.90t	2.45t	—	(1.80)s	(1.48)s	—	7.5	—	—
16	−68	FSO_3H	9.64d	6.90dd	8.35dd	3.49m	(1.32)d	—	10.8	11.7	9.2	6.6
17	−68	FSO_3H	—	7.00d	7.66dd	3.58m	(1.22)d	(1.40)s	—	10.5	6.5	6.5

[a]When solvent is FSO_3H, $(CH_3)_4N^+BF_4^-$, used as internal standard, is taken as δ3.10; chemical shifts in brackets refer to methyl group resonances; s, singlet; d, doublet; dd, doublet of doublets; t, triplet, m, multiplet.
[b]Substituent on Cl.

Results and discussion

Preparation of protonated enones

The protonated enones studied were **1**, **2** and **4**–**7**. These cations were chosen because the groups attached to the carbonyl group, hydrogen, methyl, and *tert*-butyl, provide a wide range of steric requirements (7). Of these, cations **1** and **6** have been reported previously and **2** generated as a mixture with **1** and **3**.

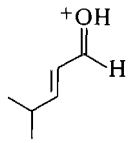
4

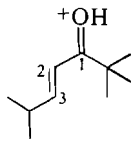
5

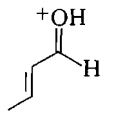
6

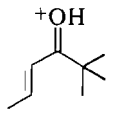
7

Dissolution of the enones **8**–**12** in FSO_3H at low temperature led to the formation of cations **1**, **2**, **4**, **5**, and **7**. The low temperature ^1H nmr spectra of these cations were consistent with the indicated structures, Table 1 (8). In the case of **1**, **2**, and **6** the spectra obtained were identical to those previously reported (3, 14).

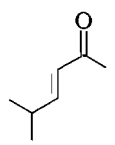
8

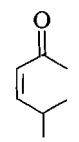
9

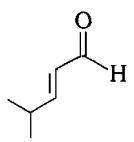
10

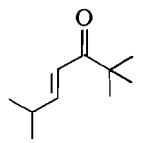
11

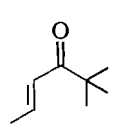
12

As was expected from the behaviour of **1**, cations **4** and **5** rearrange on heating the acid solutions to yield the corresponding protonated dihydrofurans **13** and **14**, respectively. The identity of the products was established by comparison of their ^1H nmr spectra with those of other protonated dihydrofurans (3, 9). These isomerizations proceeded in high yield with no other products being detected. The first-order rate constants for these isomerizations were determined by monitoring changes in the nmr spectra as a function of time.

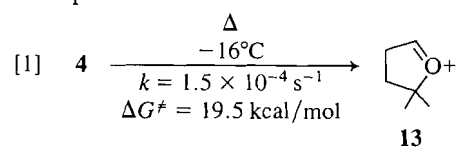
[1] **4** $\xrightarrow[k = 1.5 \times 10^{-4}\ s^{-1}]{\Delta \quad -16°C}$ **13**
$\Delta G^{\neq} = 19.5$ kcal/mol

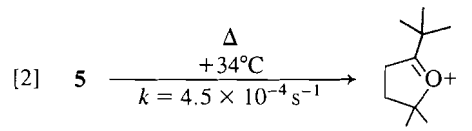
[2] **5** $\xrightarrow[k = 4.5 \times 10^{-4}\ s^{-1}]{\Delta \quad +34°C}$ **14**

Heating solutions of **6** and **7** to 25°C did not lead to the formation of any rearranged products. A darkening of solutions of **6** was noted under these conditions.

Conformational studies

It has been shown by Mullen *et al.* that rotation about the C1—C2 bond of protonated enones is slowed sufficiently at −80°C that it is possible to observe non-averaged ^{13}C nmr spectra of both conformations (10). At even lower temperatures interconversion of the two conformers about the C=O partial double bond is almost stopped on the nmr time scale (10, 12). Thus these workers showed that protonated enone, **15**, which

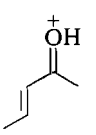
15

serves as a good model for **1**, exists predominantly in the *s-trans* conformation (75%) in equilibrium with the *s-cis* conformer (25%) (11).

The critical features determining the conformational preferences of protonated enones are the groups attached to the carbonyl carbon and the *Z* substituent in the β-carbon. The *E* substituent on the β-carbon is unimportant (11) and, rather than **4** and **5**, for the purposes of these conformational studies cations

Can. J. Chem. Downloaded from www.nrcresearchpress.com by 93.93.197.157 on 09/07/12
For personal use only.

TABLE 2. ^{13}C nuclear magnetic resonance of enones[a]

Compound	Solvent	Temperature (°C)	Chemical shifts in ppm C1	C2	C3	C4	C5	C1a	C1a'
6	FSO_3H/SO_2ClF	0– −105	206.1	130.4	193.2	23.6	—	—	—
7	FSO_3H/SO_2ClF	0	224.3	123.9	176.8	20.6	—	43.0	24.4
		−85	222.8	121.8	177.3	24.4	—	42.9	21.0
			225.2*	124.2*	172.3*				
		−105	224.5	123.6	177.3	26.9	—	42.9	21.0
			221.7*	121.8*[b]	172.3*				
9	FSO_3H/SO_2ClF	−85	218.4	120.9	190.0	28.9	19.8	33.2	—
				124.0*	191.24*[b]		18.6*	35.2*	—
		−105	218.4	120.9	188.32	28.9	19.8	33.1	—
				124.0*	190.7*		18.6*	35.4*	—
12	$CDCl_3$	25	197.6	121.7	153.9	21.7	—	31.4	26.3

[a]External standard C_6D_6/dioxane at room temperature taken as 128.0.
[b]Broad * minor component.

2, **6**, and **7** were used, as their thermal stability permitted studies to be made over a wide range of temperatures.

The low temperature ^{13}C nmr spectra of FSO_3H/SO_2ClF solutions of **2**, **6**, and **7**, are given in Table 2. Cooling solutions of **7** led to changes in its ^{13}C nmr spectra that were qualitatively similar to those observed for **15**. However, they differed in the proportion of the C1—C2 conformations present. Analysis of the changes observed showed that at −85°C, **7** exists as a mixture containing 80% of the *s-cis* and 20% *s-trans* conformers. As was found by Mullen *et al.*, further broadening and splitting of the resonances associated with the *s-trans* conformer occurred as the temperature of the sample was lowered to −105°C.

Similar changes were observed in the low temperature nmr spectra of **2**. This cation was shown to consist of 88% of the *s-cis* and 12% of the *s-trans* conformers.

No change was observed in the nmr spectra of **6** on cooling to −105°C, indicating that this cation exists predominantly in one conformation. In the absence of two signals for the different conformations it is difficult to make an absolute identification. However, it would be expected that the *s-trans* conformation would be the most stable. In the case of a protonated aldehyde an *E* conformation about the C=O bond would be greatly preferred, and no broadening or splitting of any of the carbon resonances would be expected as the temperature is lowered (13).

It is clear from these observations that a substantial difference in the ground state conformations of cations **1** and **2** would be expected. The *s-trans* conformation will be preferred with **1** whereas the *s-cis* conformation will dominate for **2**.

Underlying this conclusion, however, is the question of what is the determining factor lying behind these changes in conformation of the C1—C2 bond of these cations. The steric requirement of the substituents is clearly important. This is shown by comparison of the series of cations **6**, **15**, and **7** in which, as the substituent attached to the carbonyl carbon is varied from H to methyl to *tert*-butyl, the proportion of the *s-cis* conformer is increased relative to the *s-trans*. This pattern follows the results found for the related allyl cations in which the key determinant in deciding the conformational preference of these systems is the 1,3 interaction of the *Z* groups on the terminal carbons (14).

In the case of **7**, where the carbonyl substituent is a *tert*-butyl group, it is interesting to note that while the *s-cis* conformer predominates there is still some 20% of the *s-trans* form present. This contrasts with the situation found with the corresponding neutral ketone **12**. Examination of the ir spectrum of **12** shows that it exhibits only a single carbonyl absorption at 1695 cm^{-1}, indicating that the molecule exists essentially completely in the *s-cis* conformation (11). It would seem that an "OH" group in a protonated carbonyl compound has an effective steric requirement that is somewhat comparable to a *tert*-butyl group. Examination of the crystal structures that have been reported for protonated carbonyl compounds shows that in each case an exceptionally strong hydrogen bond is formed between the OH proton and an electronegative atom in the counterion (15). In general, there is little difference in the ^{13}C nmr spectra of protonated carbonyl compounds in the solid state and highly polar solvents such as FSO_3H, and it would seem that this specific hydrogen bonding situation is maintained in solution. In other words, in terms of its three-dimensional shape, a more appropriate model for the OH group of a protonated carbonyl compound would be $-OHOSO_2F$.

A group such as $-OHOSO_2F$ would have a rather unusual steric requirement in that it would be large at a relatively long distance from the carbon to which it is attached. As such it would have quite different properties than a group such as methyl, and this could account for the switch in the preferred conformation of **1** as compared to **2**.

Photoisomerizations

The photoisomerizations of **4** and **5** were examined at low temperatures in FSO_3H. In the case of **4**, λ_{max} 260 nm, irradiation at 254 nm led to the formation of a new cation, which was identified by its low temperature ^1H nmr spectrum as **16**, Table 1. The proton/proton coupling constant between H(2) and H(3) was 11.7 Hz, a value typical of a *Z* configuration about the C2—C3 bond of a protonated enone. A photostationary state was set up between **4** and **16**, consisting of 35% of the former and 65% of the latter ion. No evidence could be found for the formation of **13** as a product of these photoisomerizations, even on prolonged irradiations.

Irradiation of **5**, λ_{max} 279 nm, gave two additional cations. One of these was identified as **14** by comparison of the ^1H nmr spectra of the mixture with those obtained from the thermal rearrangement of **5**. The second product was shown to be the

Can. J. Chem. Downloaded from www.nrcresearchpress.com by 93.93.197.157 on 09/07/12
For personal use only.

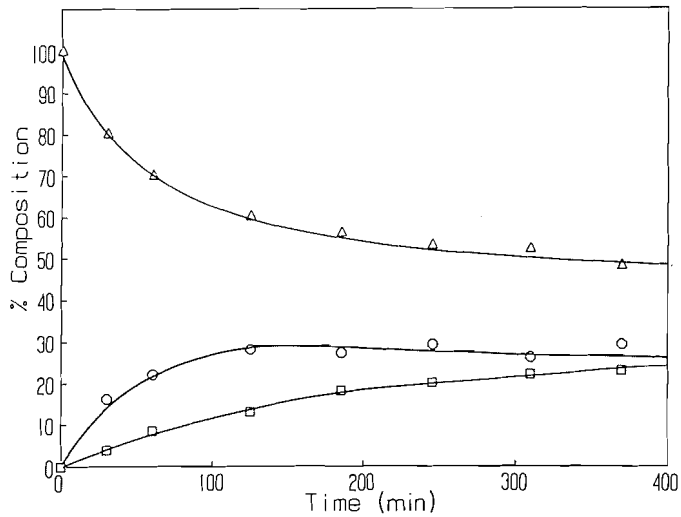

FIG. 1. Photoisomerization of **5** as a function of irradiation time (**5**, △; **17**, ○; **14**, □.)

2-*Z* isomer **17** by its characteristic nmr spectrum, Table 1. As can be seen from the data given in Fig. 1, **14** is produced from the start of the irradiation. This indicates that **14** is produced from both **5** and **17**.

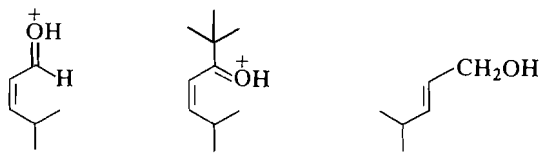

16 **17** **18**

The formation of the cyclic product from both **5** and **17**, but not from **4** or **16**, is entirely consistent with ground state conformational control of these photoreactions and the results fully substantiate the suggestion made earlier to account for the photo-induced cyclization of **2**, but not **1**, to **3** (2). It is quite clear with these protonated enones that photochemically induced ring closure by the bonding of the oxygen atom to the cation center at C4 requires an *s-cis* conformation in the ground state.

Experimental

General

The ^1H nmr spectra were obtained on Varian EM390 and Bruker WM-250 spectrometers. The ^{13}C nmr spectra were recorded on a Bruker WM-250 spectrometer. Samples were protonated by adding cooled FSO_3H to weighed amounts of compounds in nmr tubes cooled in a Dry Ice – acetone bath.

Syntheses

Aldehyde **10** (16), the precursor to **4**, was obtained by oxidation of 4-methyl-pent-2-en-1-ol **18** with pyridinium dichromate.

Condensation of 1-bromopinacolone with isobutryaldehyde in the presence of zinc, followed by dehydration of the initially formed alcohol with iodine, led to the formation of **11** (17).

A similar series of reactions using the bromoketone and acetaldehyde yielded **12** (17). The crude product was purified by distillation; ir(neat): 1695 and 1630 cm^{-1}.

3-Z-5-Methyl-hex-3-en-2-one

A pentane solution (50 mL) of **8** (500 mg) was irradiated (254 nm) for 12 h at −60°C. The solvent was removed under reduced pressure to yield a mixture of *Z* and *E* isomers. The *Z* compound was separated by preparative layer chromatography (silica; 20% ether/petroleum ether). The *Z* isomer obtained was further purified by distillation to yield pure *Z*-enone **9** (150 mg); ir(liquid film); 1700, 1625 cm^{-1}; M^+ calcd. for $C_7H_{12}O$: 112.0888; found: 112.0879.

Photoisomerizations were carried out using a Rayonet photoreactor and 253.7-nm lamps. The samples, contained in 5-mm quartz nmr tubes, were cooled in a partially silvered quartz Dewar held at −70°C. The reaction was followed by low temperature ^1H nmr spectroscopy.

1. R. F. CHILDS. Rev. Chem. Intermed. **3**, 285 (1980).
2. R. F. CHILDS and M. E. HAGAR. Can. J. Chem. **58**, 1788 (1980); R. F. CHILDS and A. W. COCHRANE. J. Org. Chem. **46**, 1086 (1981).
3. R. F. CHILDS, T. DICLEMENTE, E. F. LUND-LUCAS, T. J. RICHARDSON, and C. V. ROGERSON. Can. J. Chem. **61**, 856 (1983).
4. C. S. K. WAN and A. C. WEEDON. J. Chem. Soc. Chem. Commun. 1235 (1981); S. L. ENG, R. RICHARD, C. S. K. WAN, and A. C. WEEDON. J. Chem. Soc. Chem. Commun. 236 (1983); N. C. YANG and M. J. JORGENSEN. Tetrahedron Lett. 1203 (1964).
5. R. F. CHILDS and G. S. SHAW. J. Chem. Soc. Chem. Commun. 261 (1983).
6. A. DEVAQUET. J. Am. Chem. Soc. **94**, 5160 (1972); R. R. BIRGE and P. A. LEERMAKERS. J. Am. Chem. Soc. **94**, 8105 (1972); J. F. GIRAF and C. P. LILLYA. Mol. Photochem. **9**, 227 (1979); R. J. LONCHARICH, T. R. SCHWARTZ, and K. N. ITOUK. J. Am. Chem. Soc. **109**, 14 (1987).
7. R. F. W. BADER, M. T. CARROL, J. R. CHEESEMAN, and C. CHANG. J. Am. Chem. Soc. In press; E. L. ELIEL. *In* Stereochemistry of carbon compounds. McGraw–Hill, New York, NY. 1962. p. 236.
8. R. F. CHILDS, E. F. LUND, G. MARSHALL, W. MORRISEY, and C. V. ROGERSON. J. Am. Chem. Soc. **98**, 5924 (1976); R. F. CHILDS, D. L. MULHOLLAND, and A. NIXON. Can. J. Chem. **60**, 801 (1982).
9. D. M. BROUWER, J. A. VAN DOON, and A. A. KIFFEN. Recl. Trav. Chem. Pays-Bas, **94**, 198 (1975); C. U. PITTMAN, JR. and S. P. MCMANUS. J. Am. Chem. Soc. **91**, 5915 (1969).
10. K. MULLEN, E. KOTZAMZANI, H. SCHMICKLER, and B. FREI. Tetrahedron Lett. **25**, 5623 (1984).
11. A. F. KLUGE and P. LILLYA. J. Org. Chem. **36**, 1977 (1971); K. NOACK and R. N. JONES. Can. J. Chem. **39**, 2225 (1961); M. E. KRONENBERG and HAVINGA. Recl. Trav. Chim. Pays-Bas, **84**, 17 (1965).
12. D. CREMER, J. GAUSS, R. F. CHILDS, and C. BLACKBURN. J. Am. Chem. Soc. **107**, 2435 (1985); C. BLACKBURN, R. F. CHILDS, D. CREMER, and J. GAUSS. J. Am. Chem. Soc. **107**, 2442 (1985).
13. G. A. OLAH, Y. HALPERN, Y. K. MO, and G. LIANG. J. Am. Chem. Soc. **94**, 3554 (1972).
14. N. L. ALLINGER and J. H. SIEFEST. J. Am. Chem. Soc. **97**, 752 (1975).
15. M. SUNDARALINGAM and A. K. CHWANG. Carbonium Ions. Vol. 5, Wiley–Interscience, New York. 1976. p. 2428; R. F. CHILDS, M. MAHENDRAN, S. D. ZWEEP, G. S. SHAW, S. K. CHADDA, N. A. D. BURKE, B. E. GEORGE, R. FAGGIANI, and C. J. L. LOCK. Pure Appl. Chem. **58**, 111 (1986).
16. Y. CHRETIE-BESSIEVE and H. LEOLTE. C. R. Hebd. Seances Acad Sci. **255**, 723 (1962).
17. C. H. HEATHCOCK, M. A. HENDERSON, D. A. OARE, and M. A. SANNER. J. Org. Chem. **50**, 3019 (1985).

Can. J. Chem. Downloaded from www.nrcresearchpress.com by 93.93.197.157 on 09/07/12
For personal use only.

Synthesis of a β-diketone from a dithioacetal. A model study for the synthesis of an ionomycin fragment

KEVIN P. SHELLY AND LARRY WEILER[1]

Department of Chemistry, University of British Columbia, Vancouver, B.C., Canada V6T 1Y6

Received December 2, 1987

KEVIN P. SHELLY and LARRY WEILER. Can. J. Chem. **66**, 1359 (1988).

The anions of dithioacetals react with epoxides to give β-hydroxydithioketals, which can be oxidized and hydrolyzed to β-diketones. This sequence is applied to a model study of the synthesis of the C-5 to C-15 fragment of the antibiotic ionomycin.

KEVIN P. SHELLY et LARRY WEILER. Can. J. Chem. **66**, 1359 (1988).

Les anions des dithioacétals réagissent avec les époxydes; cette réaction fournit des β-hydroxydithiocétals qui peuvent être oxydés et finalement hydrolysées en β-dicétones. Cette série de réactions a été appliquée à une étude modèle de la synthèse du fragment C-5 à C-15 de l'antibiotique ionomycine.

[Traduit par la revue]

Introduction

In 1978, Liu *et al.* reported the production and isolation of the antibiotic ionomycin from *Streptomyces conglobatus* (1*a*; see also 1*b*). The antibiotic was isolated as its calcium salt from a broth concentrate that had been adjusted to pH 12 with sodium hydroxide. This illustrated the high affinity of ionomycin for calcium ions, which was verified by subsequent studies (2). Ionomycin chelates dipositive ions as a dibasic acid, whereas the few other known ionophores that chelate divalent cations do so as monobasic acids. The structure of ionomycin (**1**) was determined from spectroscopic data and an X-ray structure analysis of the calcium salt (3). Ionomycin (**1**) was found to be a polyether compound with a β-diketone and a carboxyl group. These latter two functional groups are ionized in the calcium salt and together with three other oxygen atoms encapsulate the calcium cation in an octahedral coordination site.

Several reports of the synthesis of ionomycin fragments have already occurred (4–8). None of these reports deals with the generation of the β-diketone moiety. At this time we would like to report our model studies on the preparation of two fragments corresponding to carbons 5–9 and 10–15 of ionomycin (**1**), the fusion of these two fragments, and the generation of the requisite β-diketone unit.[2]

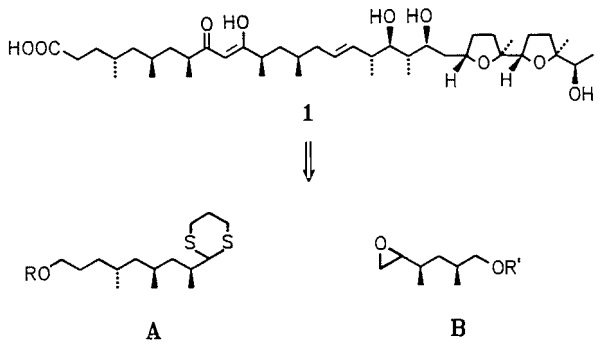

Our retrosynthetic analysis of the left-hand side of ionomycin (**1**) led us to consider the use of a dithiane to link subunits A and B together with the expectation that subsequent transformations would yield the desired β-diketone. Dithianes have been used extensively in organic synthesis (10) following the discovery of their metallation and subsequent reaction with electrophiles by Seebach and Corey (11). These authors noted that epoxides "are opened very slowly" by dithiane anions and they suggested storage of the reaction mixture at low temperature for up to 1 week. In spite of that warning of their sluggish reactivity, the opening of epoxides by dithiane anions has been used in the synthesis of natural products (12). These two examples involved either a simple epoxide or a simple dithiane moiety. We planned to employ both a complex dithiane and complex epoxide in the key alkylation.

Results and discussion

The dithiane **2** was prepared from isobutyraldehyde following the procedure of Seebach and Corey (11). By careful control of the concentration and time for the metallation reaction, we were able to obtain high isolated yields of product **3** from the reaction with 1,2-epoxybutane after a few hours. The ease of this reaction was encouraging, although it was achieved employing both a very simple dithiane and epoxide as models.

Initially we studied the oxidation of **3** with pyridinium chlorochromate. However, the isolated yields of keto dithiane **4** were disappointing (ca. 40%). We then turned our attention to pyridinium dichromate, which previously had been used to oxidize a hydroxy dithiane (13). Using similar conditions to Corey and Schmidt we could obtain yields of **4** in the 80% range. The β-keto dithiane **4** was hydrolyzed using mercury(II) (14) to give the β-diketone **5** in about 50% yield. Since there are

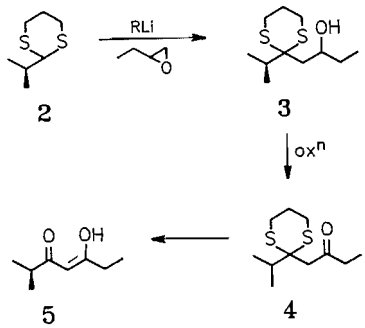

numerous techniques available to hydrolyse dithianes, we did not invest any time in trying to improve the yield in this simple model.

meso-2,4-Dimethylglutaric anhydride (**6**) was prepared according to the method of Allinger (15). Methanolysis (16) of **6** gave poor yields of the monomethyl ester **7**. Elemental analysis

[1]Author to whom correspondence may be addressed.

[2]These results have been reported in ref. 9.

Can. J. Chem. Downloaded from www.nrcresearchpress.com by 93.93.197.157 on 09/07/12
For personal use only.

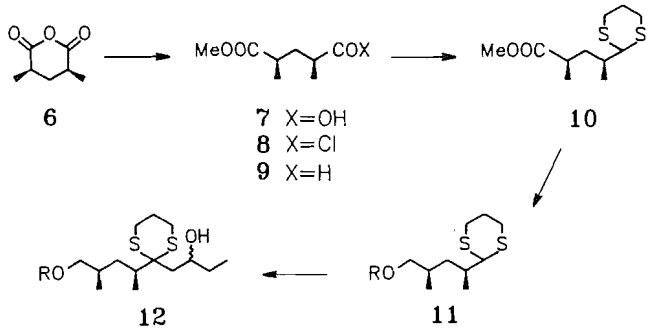

of **6** showed that under our experimental conditions one mole of water had crystallized with the anhydride. This problem was overcome by Kugelrohr distillation of the hydrated anhydride. Subsequent methanolysis of the distilled anhydride afforded the desired monoester **7** in over 90% yield. The acid chloride **8** was readily prepared and was stable and easy to handle. Rosenmund reduction of **8** to **9** had to be carried out under controlled conditions (17). Because of the instability of the aldehyde **9**, it was not isolated but was used immediately after preparation. Treatment of **9** with 1,3-dithiolpropane gave the dithiane **10** in over 60% yield from **8**. Reduction of the ester in **10** and protection gave the silyl ether **11**.

The dithiane **11** was metallated and reacted with 1,2-epoxybutane as above in the preparation of **3**. We were unable to isolate any product under these conditions, but we did recover **11** in high yield. A deuterium oxide quench of the attempted metallation of **11** showed that the carbanion formation using *n*-butyllithium as base was unsuccessful. At this stage we embarked on an extensive study of the effect of base, solvent, time, ligand addition, and temperature on the metallation of **11**. Using *tert*-butyllithium in *n*-heptane with the addition of at least one equivalent of tetramethylethylenediamine resulted in about 50% incorporation of deuterium in **11** on quenching. We were unable to increase the amount of deuterium incorporation by further refining the experimental conditions. This could be due to complete formation of the lithiated dithiane, which then forms an aggregate that on protonation gives a very stable 1:1 complex of the lithio dithiane anion and the neutral dithiane.

The incomplete incorporation of deuterium on quenching a carbanion has been known for several years (18) and is not good evidence for the lack of formation of such anions. Enolate carbanions are frequently only partially quenched by D^+ sources. It has been suggested that this is due to the formation of enolate amine complexes, which result in reprotonation of the carbanion rather than deuteration (19). These complexes are stable and crystalline, and X-ray studies have been carried out on a number of these compounds. The X-ray structure of the TMEDA complex of the lithium anion of the benzaldehyde dithiane shows that this carbanion forms similar complexes to the above enolates (20). We suggest a similar mechanism for the incomplete incorporation of deuterium into the dithane carbanions as for the enolate carbanions.

We returned to the use of *n*-butyllithium as base and found that addition of TMEDA in THF resulted in levels of deuterium incorporation approaching 75% when the metallated reaction mixture was quenched with deuterium oxide. Generation of the anion from **11** under these conditions and alkylation with 1,2-epoxybutane gave the product **12** in up to 75% yield by gc.

Methylenation of the aldehyde **9** with a Wittig reagent did not proceed efficiently. This problem was solved by carrying out the methylenation using the Lombardo modification (21) of the Nozaki reagent (22). In this way we were able to obtain the olefin **13** in about 40% yield from **8**. Epoxidation of **13** gave a diastereomeric mixture of epoxides **14**, which were not separated. Reaction of the epoxides **14** with the metallated dithiane **11** under the above conditions gave about 10% yield of the products **15** and **16**. Deuteration studies showed that generation of the dithiane carbanion was not the problem and we speculated that deprotonation of the ester in **14** might be competing with alkylation of the epoxide moiety. As a result, the epoxides **17** were prepared from **13** by reduction of the ester,

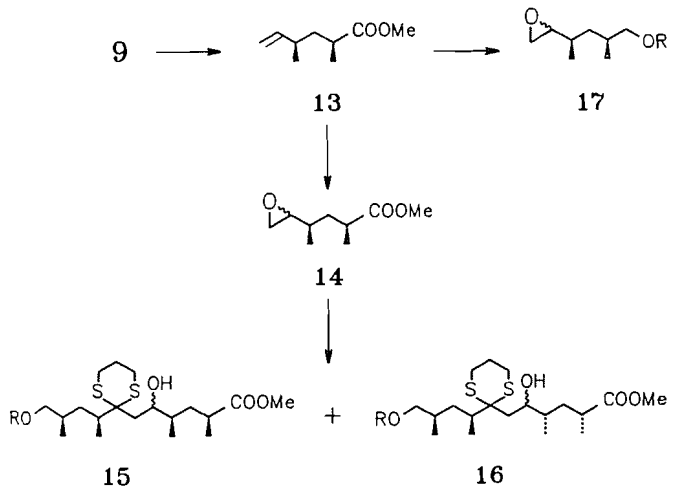

protection, and epoxidation. A gc analysis of **17** showed that the diastereomeric epoxides were formed in a ratio 65:35. Since the asymmetric centre at C-5 in **17** is destined to become an sp^2 carbon, the epimeric mixture was carried forward.

Generation of the anion from **11**, followed by reaction with **17**, gave the β-hydroxy dithianes **18** and **19** in 40% yield along with about 40% recovered dithiane **11**. We then experienced some difficulty in the oxidation of **18** and **19**. As a result we investigated the hydrolysis and subsequent oxidation to generate the β-diketone functionality. Hydrolysis of **18** and **19** with methyl iodide (23) followed by a Moffat oxidation gave the β-diketones **20** and **21** in 25% isolated yield, along with about 50% unreacted β-hydroxy ketones from the Moffat oxidation. The structure proof of **20** and **21** came from an analysis of their spectroscopic data. We were able to separate the diastereomers of the *tert*-butyldimethylsilyl enol ethers of **20** and **21** by capillary column gc. The ratio of the two diastereomers was 55:45. We have not been able to determine which diastereomer predominates. Nor could we detect any spectral differences between **20** and **21** even on a 400-MHz ^{1}H nmr spectrum.

Thus these model studies indicate that the coupling of a dithiane and an epoxide, followed by hydrolysis of the dithiane and oxidation, would appear to be a viable route to the β-diketone of ionomycin. The use of optically pure starting materials would avoid the formation of diastereomers such as **20** and **21**. The synthesis and coupling of such units is under active investigation. The two protecting groups in **20** and **21** are identical, to simplify the product identification. However, they would be different in the actual subunits corresponding to A and B.

Can. J. Chem. Downloaded from www.nrcresearchpress.com by 93.93.197.157 on 09/07/12
For personal use only.

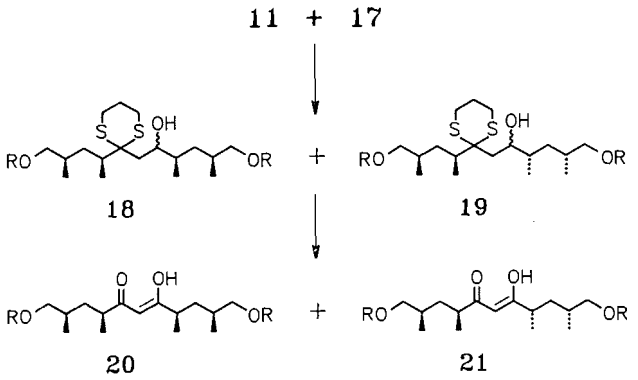

Experimental

General

Melting points were determined on a Kofler micro heating stage and are uncorrected. Kugelrohr distillations were performed by means of a Büchi Kugelrohr thermostat. Infrared spectra were recorded on a Perkin–Elmer model 710B spectrophotometer. Solution spectra were performed using a sodium chloride solution cell of 0.2 mm thickness. Absorption positions are given in cm^{-1} and are calibrated by means of the 1601 cm^{-1} band of polystyrene. The proton nuclear magnetic resonance spectra were taken in deuterochloroform solution and recorded on a Bruker WP-80 (80 MHz) instrument unless otherwise specified. The 400-MHz spectra were recorded on a Bruker WH-400 instrument, the 270-MHz spectra were recorded on a home-built unit consisting of an Oxford instrument 63.4 KG superconducting magnet and a Nicolet 32K computer, and the 60-MHz spectra on an EM-360 instrument. Signal positions are given in parts per million downfield from tetramethylsilane using the δ scale. Signal multiplicity, coupling constants, and intgrated areas are indicated in parentheses. Low resolution mass spectra were determined on either a Varian MAT CH4B or Kratos MS50 mass spectrometer. Spectra are quoted as *m/z* values. The major ion fragmentations are reported as percentages of the base peak. High resolution mass measurements were determined using a Kratos MS50 mass spectrometer. Gas–liquid chromatography was performed on a Hewlett Packard model 5880A gas chromatograph using a 12 m × 0.2 mm column of OV-101 or Carbowax 20M. The flow rate was 1.0 mL/min or 2.4 mL/min and helium was used as the carrier gas. In all cases a flame ionization detector was used. Microanalyses were performed by Mr. P. Borda, Microanalytical Laboratory, University of British Columbia, Vancouver.

Silica gel $PF_{254+366}$ supplied by E. Merck Co. was used for preparative tlc. The plates were ca. 1 mm in thickness. Analytical tlc was performed on commercial, precoated silica gel plates (silica gel 60 F_{254}) supplied by E. Merck Co. Visualization was effected by a combination of uv fluorescence, iodine vapour, or a 2 M sulfuric acid spray. Flash chromatography (24) was performed using silica gel 60, 230–400 mesh ASTM, supplied by E. Merck Co.

All reactions involving air or moisture sensitive reagents were performed under an atmosphere of dry nitrogen using either oven or flame-dried glassware. All reaction products were dried by allowing the solutions to stand over anhydrous magnesium sulfate. The petroleum ether used was of boiling range ca. 30–60°C. Dry solvents and reagents were prepared as follows: acetonitrile and methylene chloride by distillation from phosphorus pentoxide; benzene, boron trifluoride etherate, dimethylsulfoxide, 2,6-dimethylpyridine, diethyl methylmalonate, 1,2-epoxybutane, ethyl 2-bromoisobutyrate, *n*-heptane, and hexamethylphosphoramide by distillation from calcium hydride; dichloroacetic acid by storage over anhydrous magnesium sulfate followed by filtration and distillation; dimethylformamide by distillation from barium oxide followed by storage over 4A molecular sieves; dicyclohexylcarbodiimide and oxalyl chloride were distilled before use; ethanol by refluxing over magnesium ethoxide followed by distillation; ethyl ether and tetrahydrofuran by refluxing over lithium aluminum hydride followed by distillation; methanol by refluxing over magnesium methoxide followed by distillation; tetramethylethylenediamine by distillation from potassium hydroxide.

n-Butyllithium and *tert*-butyllithium were obtained from Aldrich Chemical Company, Inc. The alkyllithium solutions were standardized by titration against 1,3-dipheny1-2-propanone tosylhydrazone in THF (25).

1,1-(Propane-1',3'-dithio)-2-methyl propane (2)

A 1-L flask was charged with 36 mL isobutyraldehyde (0.4 mol), 800 mL chloroform, and 40 mL 1,3-dithiolpropane (0.4 mol). The solution was stirred for 1 h under an atmosphere of nitrogen, then cooled to −20°C. Boron trifluoride etherate (24.6 mL, 0.2 mol) was added, and the reaction was allowed to warm to room temperature overnight. The organic layer was washed three times each with water, potassium hydroxide solution, and water and was dried over anhydrous magnesium sulfate. Removal of the solvent under reduced pressure yielded a yellow oil. Distillation at reduced pressure (90°C/3 Torr; 1 Torr = 133.3 Pa) gave 51 g of compound **2** (71% yield) as a pale yellow oil; ir ($CHCl_3$): 1460, 1415, 1280, 1190, and 910 cm^{-1}; ^1H nmr ($CDCl_3$) δ: 1.03 (d, *J* = Hz, 6H), 1.67–2.23 (m, 3H), 2.70–2.93 (m, 4H), 3.98 (d, *J* = 6 Hz, 1H); mass spectrum: (*a*) high resolution calcd. for $C_7H_{14}S_2$: 162.0537 amu; found: 162.0535; (*b*) low resolution *m/z* (rel. intensity): 162 (M^+, 41), 121 (12), 119 (100), 55 (14), 45 (18), and 41 (22).

5,5-(Propane-1',3'-dithio)-6-methyl heptan-3-ol (3)

A 50-mL flask was charged with 0.81 g of the dithiane (5.0 mmol) and 25 mL THF. The stirred solution was cooled to −20°C under a nitrogen atmosphere and 4.0 mL *n*-butyllithium (1.4 M in hexane, 5.6 mmol) was added dropwise. After stirring for 2.5 h at −20°C, the reaction flask was stored at −10°C for 16 h. The solution was then warmed to 0°C, and 0.43 mL of 1,2-epoxybutane (5.0 mmol) was added. After 5 h, the mixture was concentrated under reduced pressure. Water was added and the aqueous phase was extracted three times with ethyl ether. The combined organic extracts were washed with water, brine solution, and water, dried over anhydrous magnesium sulfate, and filtered. Removal of the solvent under reduced pressure afforded 1.06 g of the alcohol **3** (90% yield) as a white crystalline solid. Preparative tlc of a small amount of this material using petroleum ether:ethyl acetate (6:1) gave **3** as white powdery crystals, mp 65–66°C; ir ($CHCl_3$): 3425, 1460, 1420, 1385, 1130, 1060,and 990 cm^{-1}; ^1H nmr ($CDCl_3$) δ: 1.03 (t, *J* = 7 Hz, 3H), 1.06 (d, *J* = 7 Hz, 3H), 1.24 (d, *J* = 7 Hz, 3H), 1.35–2.55 (m, 7H), 2.75–3.00 (m, 4H), 3.75 (bs, 1H, exchangeable with D_2O), 3.75–4.10 (m, 1H); mass spectrum: (*a*) high resolution calcd. for $C_{11}H_{22}OS_2$: 234.1112 amu; found: 234.1108; (*b*) low resolution *m/z* (rel. intensity): 234 (M^+, 24), 191 (79), 161 (18), 135 (12), 133 (100), 107 (13), 73 (13), 69 (20), 59 (25), 57 (29), and 41 (40).

5,5-(Propane-1',3'-dithio)-6-methylheptan-3-one (4)

A 100-mL flask was charged with 11.32 g pyridinium dichromate (30.0 mmol) and 25 mL DMF. The resulting solution was cooled to 0°C and the alcohol **20** (1.0 g, 4.3 mmol) was added to this solution. After 11 h at 0°C, the reaction mixture was poured into 150 mL water. The aqueous phase was extracted several times with ethyl ether. The combined organic phases were washed four times with water, dried over anhydrous magnesium sulfate, and the solvent was removed under reduced pressure giving 0.84 g of the crude ketone (85% yield). Preparative tlc of a small amount of this material using petroleum ether:ethyl acetate (8:1) gave **4** as a colourless oil; ir ($CHCl_3$): 1710, 1460, 1355, 1230, 1140, and 1110 cm^{-1}; ^1H nmr ($CDCl_3$) 270 MHz, δ: 1.04 (t, *J* = 7 Hz, 3H), 1.22 (d, *J* = 6.5 Hz, 6H), 1.79–2.12 (m, 2H), 2.41–2.56 (m, 1H), 2.59 (q, 2H), 2.73–3.01 (m, 4H), 3.16 (s, 2H); mass spectrum: (*a*) high resolution calcd. for $C_{11}H_{20}OS_2$: 232.0955 amu; found: 232.0942; (*b*) low resolution *m/z* (rel. intensity: 232 (M^+, 22), 189 (72), 175 (13), 133 (29), 107 (18), 69 (16), 57 (100), 41 (37), and 29 (66).

Can. J. Chem. Downloaded from www.nrcresearchpress.com by 93.93.197.157 on 09/07/12
For personal use only.

Can. J. Chem. Downloaded from www.nrcresearchpress.com by 93.93.197.157 on 09/07/12
For personal use only.

2-Methyl-3,5-heptanedione (5)

A 100-mL flask was charged with 2.61 g mercuric chloride (9.6 mmol), 1.05 g mercuric oxide (4.8 mmol), and 10 mL acetonitrile. To this suspension was added the dithiane **4** (1.0 g, 4.3 mmol) in 30 mL acetonitrile and 3 mL water. After heating to reflux for 2 h, ethyl ether was added and the mixture was filtered. The solvent was removed under reduced pressure until 50 mL remained. After cooling this solution in an ice bath, it was added to a mixture of 20 g ice and 6 mL concentrated hydrochloric acid. The organic layer was separated and the aqueous phase was washed three times with ethyl ether. The combined organic extracts were dried over anhydrous magnesium sulfate, filtered,and solvent was removed under reduced pressure to yield a brown oil. Kugelrohr distillation (80°C/20 Torr) yielded 0.32 g of the β-diketone **5** (52% yield) as a colourless oil; ir ($CHCl_3$): 1730, 1680, 1560, 1465, and 1155 cm^{-1}; ^1H nmr ($CDCl_3$) 60 MHz, δ: 0.90–1.33 (m, 9H), 2.07–2.70 (m, 3H), 3.50 (s, 0.26H), 5.40 (s, 0.74H).

meso-*2,4-Dimethylglutaric anhydride (6)*

2,4-Dimethylglutaric acid (26) (8.14 g, 0.05 mmol) was heated to 100°C with 10.8 mL acetic anhydride for 2 h. Removal of the volatile materials under reduced pressure, followed by Kugelrohr distillation of the resulting oil (80–140°C/0.1 Torr) afforded 7 g (97% yield) of a mixture of *meso-* and *dl*-anhydrides. This material was dissolved in 10 mL warm ethyl acetate and filtered. The filtrate was washed six times with 10-mL portions of ethyl acetate. The combined ethyl acetate washings were reduced to a volume of 50 mL. Crystallization by allowing the solution to stand afforded 2.76 g *meso*-anhydride **6** as a white crystalline solid, mp 93.5–94°C (lit. (26) mp 94–95°C); ir ($CHCl_3$): 1818, 1770, 1080, and 1020 cm^{-1}.

Methyl (2S,4R*)-2,4-dimethylglutarate (7)*

A 50-mL flask, fitted with a reflux condenser, was charged with 3.07 g (21.6 mmol) **6** and 15 mL dry methanol. The resulting solution was heated to reflux and stirred overnight, after which the methanol was removed under reduced pressure. Vacuum distillation (102°C/0.2 Torr) yielded 3.41 g of the monoacid **7** (91% yield), as a colourless oil; ir ($CHCl_3$): 2990, 1735, 1715, 1460, 1280, and 1175 cm^{-1}; ^1H nmr ($CDCl_3$) δ: 1.18 (d, J = 6 Hz, 3H), 1.20 (d, J = 6 Hz, 3H), 1.53 (q, 1H), 2.10 (q, 1H), 2.38–2.78 (m, 2H), 3.67 (s, 3H), 11.33 (bs, 1H); mass spectrum: (*a*) high resolution calcd. for $C_8H_{12}O_3$ ($M^+ - H_2O$): 156.0787 amu; found: 156.0784; (*b*) low resolution m/z (rel. intensity): 156 ($M^+ - H_2O$, 7), 143 (32), 142 (21), 128 (47), 115 (33), 114 (45), 101 (39), 88 (49), 69 (100), 59 (50), 57 (36), 56 (71), 45 (62), and 41 (67).

Methyl (2R,4S*)-4-chloromethanoyl-2-methylpentanoate (8)*

The monoacid **7** (3.21 g, 18.5 mmol) was stirred in 15 mL of dry benzene in a 3-necked 100-mL flask fitted with an equal pressure addition funnel and a nitrogen inlet. A catalytic amount of DMF was added (15 μL), followed by 2.42 mL oxalyl chloride (27.7 mmol) in 5 mL benzene over 30 min. After 3 h, the benzene was removed by distillation. Vacuum distillation (52°C/0.2 Torr) afforded 3.26 g of the acid chloride (92% yield) as a colourless oil; ir (CCl_4): 1800, 1745, 1460, 1200, and 1180 cm^{-1}; ^1H nmr ($CDCl_3$) δ: 1.21 (d, J = 6 Hz, 3H), 1.32 (d, J = 6 Hz, 3H), 1.58 (q, 1H), 2.21 (q, 1H), 2.94 (q, 1H), 3.70 (s, 3H); mass spectrum: (*a*) high resolution calcd. for $CH_{10}O_2Cl$ ($M^+ - OCH_3$): 161.0370 amu; found: 161.0361; (*b*) low resolution m/z (rel. intensity): 161 ($M^+ - OCH_3$, 10), 157 (35), 129 (31), 128 (32), 73 (25), 69 (100), 59 (41), 56 (48), and 41 (56).

Methyl (2S,4R*)-2,4-dimethyl-5,5-(propane-1',3'-dithio)-pentanoate (10)*

A 50-mL flask was charged with 80 mg 9% Pd/C catalyst (15 mg per mmol acid chloride), 18 mL THF, and 0.6 mL 2,6-dimethylpyridine (5 mmol). The acid chloride **8**, 0.985 g (5.1 mmol), in 7 mL THF was added and the system was hydrogenated for 8 h at atmospheric pressure. The reaction was filtered through Celite, and the solid was washed with ethyl ether. The filtrate was reduced to a volume of 10–15 mL. Then 50 mL ethyl ether was added and the organic layer was washed three times with cold 0.2 N hydrochloric acid, three times with sodium bicarbonate solution, ammonium chloride solution twice, brine, and water. The organic phase was dried over anhydrous magnesium sulfate, filtered, and the solvent removed under reduced pressure to a volume of 5–10 mL. This solution was transferred to a 50-mL flask fitted with a nitrogen inlet. Chloroform (15 mL) was added, followed by 0.51 mL 1,3-dithiolpropane (5.1 mmol). After 1 h stirring at room temperature the solution was cooled to −20°C. Boron trifluoride etherate (0.315 mL, 2.56 mmol) was added and the reaction was allowed to warm to room temperature overnight, after which chloroform was added. The organic layer was washed with water, then three times each with potassium hydroxide solution and water. The organic layer was dried over anhydrous magnesium sulfate, filtered, and the solvent was removed under reduced pressure to give a yellow oil. Flash chromatography (3:1, petroleum ether:ethyl acetate) provided 787 mg of the dithiane **10** (62% yield) as a pale yellow oil; ir ($CHCl_3$): 1735, 1460, 1390, 1280, 1180, and 1150 cm^{-1}; ^1H nmr ($CDCl_3$) δ: 1.15 (t, 6H), 1.33–1.60 (m, 1H), 1.68–2.23 (m, 4H), 2.34–2.70 (m, 1H), 2.78–3.03 (m, 4H), 3.68 (s, 3H), 4.13 (d, J = 3 Hz, 1H); mass spectrum: (*a*) high resolution calcd. for $C_{11}H_{20}O_2S_2$: 248.0905 amu; found: 248.0905; (*b*) low resolution m/z (rel. intensity): 248 (M^+, 26), 121 (17), 119 (100), 106 (10), 73 (15), 59 (15), 45 (21), and 41 (32).

(2S,4R*)-2,4-Dimethyl-5,5-(propane-1',3'-dithio)-pentan-1-ol*

A 50-mL 2-necked flask was charged with 191 mg lithium aluminum hydride (5 mmol) and 8 mL ethyl ether, under a nitrogen atmosphere. The suspension was cooled to 0°C, and then 635 mg of the ester **10** (2.56 mmol) in 7 mL ethyl ether was added. After 30 min at 0°C and 90 min at room temperature, the reaction was carefully quenched with dilute hydrochloric acid. Ethyl ether was added and the organic layer was separated. The aqueous phase was washed three times with ethyl ether. The combined ether extracts were dried over anhydrous magnesium sulfate, filtered, and the solvent was removed under reduced pressure to give a yellow oil. Flash chromatography (1:1, petroleum ether:ethyl acetate) provided 492 mg of the alcohol (87% yield) as a pale yellow oil; ir ($CHCl_3$): 3475, 1460, 1420, 1380, 1275,and 1015 cm^{-1}; ^1H nmr ($CDCl_3$) δ: 1.00 (d, J = 9 Hz, 3H), 1.05 (d, J = 9 Hz, 3H), 1.58–2.33 (m, 6H), 2.15 (bs, 1H, exchangeable with D_2O), 2.73–3.05 (m, 4H), 3.28–3.68 (m, 2H), 4.15 (d, J = 3 Hz, 1H); mass spectrum: (*a*) high resolution calcd. for $C_{11}H_{20}OS_2$: 220.0956 amu; found: 220.0957; (*b*) low resolution m/z (rel. intensity): 220 (M^+, 23), 121 (15), 120 (10), 119 (100), 73 (14), 55 (13), 45 (22),and 41 (35).

(2S,4R*)-2,4-Dimethyl-5,5-(propane-1',3'-dithio)-1-[(*tert*-butyldimethylsilyl)oxy]-pentane (11)*

To a solution of the above alcohol (0.48 g, 2.2 mmol) in 3 mL methylene chloride was added 2,6-dimethylpyridine (0.51 mL, 4.4 mmol) at 0°C under nitrogen. After 5 min, *tert*-butyldimethylsilyl trifluoromethane sulfonate (0.75 mL, 3.3 mmol) was added and the reaction was stirred for 30 min at 0°C and 2.5 h at room temperature. The reaction was diluted with ethyl ether, washed with 0.2 N hydrochloric acid twice, sodium bicarbonate solution twice, ammonium chloride solution, and water. The organic layer was dried over anhydrous magnesium sulfate, filtered, and the solvent was removed under reduced pressure giving a yellow oil. Kugelrohr distillation (140°C/0.2 Torr) afforded 0.708 g **11** as a colourless oil (97% yield); ir ($CHCl_3$): 1465, 1455, 1240, 920, and 825 cm^{-1}; ^1H nmr ($CDCl_3$) 270 MHz, δ: 0.07 (s, 6H), 0.95 (s, d, 12H), 1.13 (d, J = 6 Hz, 3H), 1.63–2.22 (m, 6H), 2.84–3.05 (m, 4H), 3.35–3.59 (ddd, 2H), 4.20 (d, J = 4 Hz, 1H); mass spectrum: (*a*) high resolution calcd. for $C_{16}H_{34}OS_2Si$: 334.1820 amu; found: 334.1825; (*b*) low resolution m/z (rel. intensity): 334 (M^+, 2), 319 (2), 279 (12), 278 (19), 277 (91), 171 (22), 165 (25), 149 (11), 129 (10), 119 (77), 113 (37), 95 (23), 91 (11), 75 (100), 73 (46), and 41 (20).

Can. J. Chem. Downloaded from www.nrcresearchpress.com by 93.93.197.157 on 09/07/12
For personal use only.

(6S,8R*)-6,8-Dimethyl-9-[(*tert*-butyldimethylsilyl)oxy]-5,5-(propane-1',3'-dithio)-nonan-3-ol (**12**)*

The dithiane **11** (137 mg, 0.41 mmol) was stirred in 1 mL THF at −35°C. *n*-Butyllithium (0.34 mL, 1.45 M in hexane, 0.49 mmol) was added, followed by tetramethylethylenediamine (0.074 mL, 0.49 mmol). After 1 h, hexamethylphosphoramide (0.107 mL, 0.62 mmol) was added and a deep yellow coloured solution was observed. This colour faded upon addition of 1,2-epoxybutane (0.106 mL, 1.23 mmol). The solution was stirred at −35°C for 1 h, then stored at −20°C for 48 h. The reaction was diluted with water and ethyl ether. The organic layer was washed with copper sulfate solution, sodium chloride solution, and ammonium chloride solution, dried over anhydrous magnesium sulfate, and filtered. Removal of the solvent under reduced pressure afforded 93 mg of an oil, which by gc analysis was 75% product **12** and 20% starting dithane **11**. Flash chromatography using methylene chloride gave a pure sample of **12**; ir ($CHCl_3$): 3400, 1465, 1260, 1090, and 840 cm^{-1}; ^1H nmr ($CDCl_3$) δ: 0.04 (s, 6H), 0.77–2.24 (m, 19H), 0.87 (s, 9H), 2.72–3.04 (m, 4H), 3.32–4.19 (m, 4H); mass spectrum: (*a*) high resolution calcd. for $C_{20}H_{42}O_2S_2S_1$: 406.2398 amu; found: 406.2391 amu; (*b*) low resolution *m/z* (rel. intensity): 406 (M^+, 32), 349 (19), 291 (21), 193 (60), 192 (68), 191 (100), 165 (41), 133 (81), 109 (65), 75 (79), 73 (88), 59 (82), and 55(60).

Methylenation reagent

The active methylene complex was prepared by a slight modification of Lombardo's method (21). A 500-mL 2-necked flask, fitted with an equal pressure addition funnel, was charged with 11.5 g zinc dust, 100 mL THF, and 4.04 mL methylene bromide under nitrogen. The slurry was cooled to −40°C. Titanium tetrachloride (4.6 mL) was poured into the addition funnel and, over 30 min, was added dropwise to the slurry. As the addition of the titanium tetrachloride is very vigorous, it is recommended to leave the addition funnel stopperless. After 2 h stirring at −40°C, the grey slurry was warmed to 0°C, and stirred for 24 h. The active methylene complex can be stored between 0 and 5°C for up to 2 weeks.

Methyl (2R,4S*)-2,4-dimethyl-5-hexenoate (**13**)*

A 100-mL 3-necked flask was charged with 0.18 g 9% Pd/C catalyst (15 mg per mmol acid chloride), 40 mL THF, and 1.35 mL 2,6-dimethylpyridine (11.6 mmol). The acid chloride **8**, 2.25 g (11.7 mmol), in 15 mL THF was added and the system was hydrogenated for 8 h at atmospheric pressure. The reaction was filtered through Celite and the solid was washed with methylene chloride. The filtrate was reduced to a volume of 10–15 mL. Then 50 mL methylene chloride was added and the organic layer was washed three times with cold 0.2 N hydrochloric acid, three times with sodium bicarbonate solution, ammonium chloride solution twice, brine, and water. The organic phase was dried over anhydrous magnesium sulfate, filtered, and the solvent removed under reduced pressure to a volume of 50 mL. The methylene complex stirred at 0°C was added portionwise, using a pipette, to this methylene chloride solution of the aldehyde **9**. Conversion to the alkene **13** is instantaneous and can be monitored by gc or tlc analysis. After complete conversion, the black solution was poured into 150 mL saturated solution of sodium bicarbonate and 300 mL ethyl ether. The mixture was stirred for 2 h until the solution was white with a black solid evident. The organic layer was separated and the aqueous layer was washed a few times with ethyl ether. The combined organic extracts were dried over anhydrous magnesium sulfate, filtered, and the solvent was removed under reduced pressure to give a yellow oil. Flash chromatography using methylene chloride provided 729 mg of the alkene **13** as a pale yellow oil (40% yield); ir ($CHCl_3$): 135, 1650, 1460, 110, and 920 cm^{-1}; ^1H nmr ($CDCl_3$) δ: 1.03 (d, J = 7 Hz, 3H), 1.11 (d, J = 7 Hz, 3H), 1.28–2.65 (m, 4H), 3.65 (s, 3H), 4.83–5.13 (m, 2H), 5.38–5.88 (m, 1H); mass spectrum: (*a*) high resolution calcd. for $C_8H_{13}O$ ($M^+ - OCH_3$): 125.0966 amu; found: 125.0974; (*b*) low resolution *m/z* (rel. intensity): 156 (M^+, 5), 125 (10), 124 (8), 101 (12), 97 (20), 96 (13), 88 (100), 81 (12), 69 (26), 57 (27), 55 (63), 41 (36), and 29 (24).

Methyl (2S,4R*)-2,4-dimethyl-5,6-epoxyhexanoate (**14**)*

To a stirred solution of the alkene **13** (593 mg, 3.80 mmol) in 20 mL methylene chloride at 0°C, was added 1.18 g (6.84 mmol) metachloroperoxybenzoic acid. The reaction was allowed to warm to room temperature slowly and was left stirring overnight. The reaction was diluted with methylene chloride and washed once with sodium bicarbonate solution, sodium thiosulfate solution, three times with sodium bicarbonate solution, and finally water. The organic layer was dried over anhydrous magnesium sulfate, filtered, and the solvent removed under reduced pressure giving an oil. Flash chromatrography using methylene chloride provided 492 mg of the epoxide **14** (75% yield) as a pale yellow oil; ir ($CHCl_3$): 1735, 1460, and 1170 cm^{-1}; ^1H nmr ($CDCl_3$) 60 MHz, δ: 0.86–1.79 (m, 9H), 2.39–2.86 (m, 4H), 3.66 (s, 3H).

Methyl (2S,4R*,8S*,10R*)-2,4,8,10-tetramethyl-5-hydroxy-7,7-(propane-1',3'-dithio)-11-[(*tert*-butyldimethylsilyl)oxy]-undecanoate (**15**) and its diastereomer **16***

The dithiane **11** (160 mg, 0.48 mmol) was stirred in 2 mL THF at −35°C. *n*-Butyllithium was added (0.41 mL, 1.45 M in hexane, 0.60 mmol), followed by tetramethylethylenediamine (0.09 mL, 0.60 mmol). After 1 h, hexamethylphosphoramide (0.125 mL, 0.72 mmol) was added and a deep yellow colour was observed. After 1 h, the epoxide **14** (93 mg, 0.54 mmol) in 0.125 mL hexamethylphosphoramide and 1 mL THF were added to the reaction. After 4 h, the reaction was worked up as for **12** to give 164 mg of an oil, which by tlc analysis was predominantly the starting dithiane **11**. Preparative tlc using petroleum ether:ethyl acetate (3:1) gave 30 mg of products **15** and **16** (12% yield); ^1H nmr δ: 0.04 (s, 6H), 0.69–2.94 (m, 28H), 0.87 (s, 9H), 3.29–4.09 (m, 4H), 3.64 (s, 3H); mass spectrum: low resolution *m/z* (rel. intensity): 506 (M^+, 6), 417 (20), 291 (49), 259 (45), 185 (14), 159 (100), 133 (34), 127 (63), 75 (59), 74 (48), 73 (50), and 55 (46).

(2R,4S*)-2,4-Dimethyl-5-hexen-1-ol*

Lithium aluminum hydride (0.185 g, 4.9 mmol) was stirred in 8 mL ethyl ether at 0°C. The alkene **13** (0.38 g, 2.4 mmol) in 7 mL ethyl ether was added. After 30 min at 0°C and 90 min at room temperature, the reaction was carefully quenched with dilute hydrochloric acid. Ethyl ether was added and the organic layer was separated. The aqueous phase was washed three times with ethyl ether. The combined ether extracts were dried over anhydrous magnesium sulfate, filtered, and the solvent was removed under reduced pressure to give a yellow oil. Flash chromatography using methylene chloride afforded 0.174 g of the desired alcohol (56% yield) as a yellow oil; ir ($CHCl_3$): 3480, 1650, 1460, 1380, 1020, and 920 cm^{-1}; ^1H nmr ($CDCl_3$) δ: 0.90 (d, J = 6 Hz, 3H), 0.98 (d, J = 6 Hz, 3H), 1.13–1.88 (m, 2H), 2.03–2.49 (m, 2H), 2.45 (bs, 1H, exchangeable with D_2O), 3.30–3.63 (m, 2H), 4.80–5.15 (m, 2H), 5.40–5.90 (m, 1H); mass spectrum: (*a*) high resolution calcd. for C_7H_{13} ($M^+ - CH_2OH$): 97.1017 amu; found: 97.1021; (*b*) low resolution *m/z* (rel. intensity): 128 (M^+, 1), 97 (18), 95 (41), 71 (47), 70 (29), 69 (22), 68 (42), 58 (43), 57 (21), 56 (35), 55 (100), 43 (33), 41 (54), 39 (22), 31 (30), and 29 (36).

(2R,4S*)-2,4-Dimethyl-1-[(*tert*-butyldimethylsilyl)oxy]-hex-5-ene*

To a solution of the above alcohol (159 mg, 1.24 mmol) in 1.5 mL methylene chloride was added 2,6-dimethylpyridine (0.29 mL, 2.55 mmol) at 0°C under nitrogen. After 5 min *tert*-butyldimethylsilyl trifluoromethane sulfonate (0.43 mL, 1.9 mmol) was added, and the reaction was stirred for 30 min at 0°C and 2.5 h at room temperature. The reaction was diluted with ethyl ether, washed with 0.2 N hydrochloric acid twice, sodium bicarbonate solution twice, ammonium chloride solution, and water. The organic layer was dried over anhydrous magnesium sulfate, filtered, and the solvent was removed under reduced pressure giving a yellow oil. Flash chromatography (10:1, petroleum ether:ethyl acetate) afforded 270 mg of the silyl ether (90% yield) as a colourless oil; ir ($CHCl_3$): 1650, 1480, 1260, 950, and 840 cm^{-1}; ^1H nmr ($CDCl_3$) 400 MHz, δ: 0.09 (s, 6H), 0.92 (d, J = 6 Hz, 3H), 0.95 (s, 9H), 1.02–1.11 (m, 1H), 1.05 (d, J = 6 Hz, 3H),

Can. J. Chem. Downloaded from www.nrcresearchpress.com by 93.93.197.157 on 09/07/12
For personal use only.

1.39–1.48 (m, 1H), 1.63–1.75 (m, 1H), 2.23–2.34 (m, 1H), 3.37–3.51 (ddd, 2H), 4.92–5.05 (m, 2H), 5.61–5.72 (m, 1H); mass spectrum: (*a*) high resolution calcd. for $C_{10}H_{21}OSi$ ($M^+ - t$Bu): 185.1376 amu; found: 185.1369; (*b*) low resolution *m/z* (rel. intensity): 185 ($M^+ - t$Bu, 57), 115 (14), 76 (12), 75 (100), 73 (27), 55 (11), and 41 (11).

(2R,4S*)-2,4-Dimethyl-1-[(*tert*-butyldimethylsilyl)oxy]-5,6-epoxy hexane (**17**)*

To a stirred solution of the above alkene (253 mg, 1.04 mmol) in 6 mL methylene chloride at O°C, was added 543 mg (3.14 mmol) metachloroperoxybenzoic acid. The reaction was allowed to warm to room temperature slowly and was left stirring overnight. The reaction was diluted with methylene chloride and washed once with sodium bicarbonate solution, sodium thiosulfate solution, three times with sodium bicarbonate solution, and finally, with water. The organic layer was dried over anhydrous magnesium sulfate, filtered, and the solvent was removed under reduced pressure, giving a yellow oil. Flash chromatography (3:1, petroleum ether:ethyl ether) provided 231 mg of the epoxide **17** (86% yield) as a pale yellow oil; ir ($CHCl_3$): 1460, 1255, 1090, 830, and 770 cm^{-1}; ^1H nmr ($CDCl_3$) δ: 0.05 (s, 6H), 0.83–1.13 (m, 8H), 0.93 (s, 9H), 1.38–1.93 (m, 2H), 2.40–2.85 (m, 3H), 3.33–3.48 (m, 2H); mass spectrum: (*a*) high resolution calcd. for $C_{10}H_{21}O_2Si$ ($M^+ - t$Bu): 201.1335 amu; found: 201.1323; (*b*) low resolution *m/z* (rel. intensity): 201 ($M^+ - t$Bu, 16), 171 (30), 145 (22), 129 (13), 115 (28), 109 (22), 105 (12), 89 (20), 75 (100), and 73 (26).

(2S,4R*,8S*,10R*)-2,4,8,10-Tetramethyl-1,11-[di(*tert*-butyldimethylsilyl)oxy]-7,7-(propane-1′,3′-dithio)-undec-5-ol (**18**) and its diastereomer **19***

The dithiane **11** (114 mg, 0.34 mmol) was stirred in 1 mL THF at −40°C. *n*-Butyllithium (0.17 mL, 2.2 M in hexane, 0.37 mmol) was added, followed by tetramethylethylenediamine (TMEDA, 0.06 mL, 0.41 mmol), producing a faint yellow coloured solution. After 1 h, hexamethylphosphoramide (HMPA, 0.09 mL, 0.51 mmol) was added and a deep yellow coloured solution was observed. After 15 min, the reaction was cooled to −78°C. The epoxide **17** (96 mg, 0.37 mmol) in 1 mL THF was added dropwise. The reaction was stirred for 30 min at −78°C, 30 min at −40°C, 2 h at −10°C, and was stored at −2°C for 40 h. The reaction was diluted with water and ethyl ether. The organic layer was washed with sodium chloride solution, ammonium chloride solution, dried over anhydrous magnesium sulfate, and filtered. Removal of the solvent under reduced pressure afforded an orange oil. Flash chromatography (methylene chloride) gave the following compounds, in order of elution: (*a*) dithiane **11** (49 mg, 43%); (*b*) β-hydroxy dithianes **18** and **19** as a pale yellow oil (79 mg, 39% yield, 69% based on recovered starting dithiane); ir ($CHCl_3$): 3450, 1470, 1260, 1050, 910, and 820 cm^{-1}; ^1H nmr ($CDCl_3$) δ: 0.05 (s, 12H), 0.80–1.27 (m, 16H), 0.93 (s, 18H), 1.30–2.33 (m, 8H), 2.60–2.95 (m, 4H), 3.20–3.65 (m, 5H), 3.73–4.05 (m, 1H); mass spectrum: (*a*) high resolution calcd. for $C_{30}H_{64}O_3S_2Si_2$: 592.3834 amu; found: 592.3834; (*b*) low resolution *m/z* (rel. intensity): 592 (M^+, 3), 535 (10), 377 (20), 359 (15), 246 (19), 245 (100), 187 (29), 185 (26), 165 (16), 145 (11), 133 (19), 115 (15), 113 (99), 109 (22), 107 (13), 95 (27), 75 (58), 73 (41), and 55 (15).

(2R,4S*,8R*,10S*)-2,4,8,10-Tetramethyl-1,11-[di(*tert*-butyldimethylsilyl)oxy]-7-hydroxy-undec-5-one and its diastereomer*

The β-hydroxy dithianes **18** and **19** (39 mg, 0.07 mmol) and 18 mg calcium carbonate (0.4 mmol) were stirred in 5 mL acetonitrile and 2 mL water. Methyl iodide (1 mL) was added and the reaction was heated to reflux for 17 h. The solvents were removed under reduced pressure and water was added to the residual material. The aqueous phase was washed three times with ethyl ether. The combined organic extracts were dried over anhydrous magnesium sulfate, filtered, and the solvent was removed under reduced pressure to give a yellow oil. Flash chromatography (4:1, petroleum ether:ethyl ether) provided 18 mg of the β-hydroxy ketones (54% yield); ir ($CHCl_3$): 1710, 1460, 1390, 1260, 1110, and 840 cm^{-1}; ^1H nmr ($CDCl_3$) δ: 0.05 (s, 12H), 0.80–2.15 (m, 20H), 0.93 (s, 18H), 2.48–2.70 (m, 2H), 3.33–3.53 (m, 5H), 3.80–4.05 (m, 1H); mass spectrum: (*a*) high resolution calcd. for $C_{23}H_{49}O_4Si_2$ ($M^+ - t$Bu); 445.3170 amu; found: 445.3170; (*b*) low resolution *m/z* (rel. intensity): 445 ($M^+ - t$Bu, 11), 427 (9), 313 (5), 295 (6), 287 (7), 246 (10), 245 (57), 243 (12), 221 (15), 203 (17), 201 (24), 188 (12), 187 (94), 185 (30), 113 (100), 109 (37), 95 (49), 85 (43), 83 (31), 75 (86), 73 (59), and 57 (47).

(2R,4S*,8R*,10S*)-2,4,8,10-Tetramethyl-1,11-[di(*tert*-butyldimethylsilyl)oxy]-undec-5,7-dione (**20**) and its diastereomer **21***

The above β-hydroxy ketones (10 mg, 0.02 mmol) were stirred in 0.2 mL dimethylsulfoxide and 0.2 mL methylene chloride. Dicyclohexylcarbodiimide (DCC, 25 mg, 0.12 mmol) was added and after it dissolved, 0.8 μL (0.01 mmol) dichloroacetic acid was added. Petroleum ether was added, and the organic layer was washed with water and aqueous oxalic acid. The combined aqueous layers were washed once with petroleum ether. All the organic extracts were dried over anhydrous magnesium sulfate, filtered, and concentrated affording a pasty solid. Flash chromatography (40:1, petroleum ether:ethyl ether) provided, in order of elution: (*a*) product β-diketones **20** and **21** (2.5 mg, 25% yield, 75% based on recovered starting material); (*b*) starting β-hydroxy ketone (5 mg, 50%). The β-diketones **20** and **21** were characterized by the following spectral data: ir ($CHCl_3$): 1600, 1460, 1260, 1060, and 1020 cm^{-1}; ^1H nmr ($CDCl_3$) 400 MHz, δ: 0.03 (s, 12H), 0.90 (d, s, 24H), 1.08–1.18 (m, 2H), 1.14 (d, J = 8 Hz, 6H), 1.56–1.66 (m, 2H), 1.72–1.81 (m, 2H), 2.40–2.50 (m, 2H), 3.34–3.46 (m, 4H), 5.47 (s, 1H); mass spectrum: (*a*) high resolution calcd. for $C_2H_{56}O_4Si_2$: 500.3719 amu; found: 500.3718; (*b*) low resolution *m/z* (rel. intensity): 500 (M^+, 2), 485 (4), 445 (12), 444 (33), 443 (100), 311 (40), 244 (14), 243 (71), 185 (49), 115 (11), 109 (11), 95 (11), 85 (30), 75 (74), 73 (57), 69 (21), and 55 (16).

Acknowledgements

We are grateful to the Natural Sciences and Engineering Research Council of Canada for financial support of this work.

1. (*a*) W. C. Liu, D. S. Slusarchyk, G. Astle, W. H. Trejo, W. E. Brown, and E. Meyers. J. Antibiot. **31**, 815 (1978); (*b*) E. Meyers, D. S. Slusarchyk, and W. C. Liu. U.S. Patent 38733693 (1975); Chem. Abstr. **83**, 41512a (1975).
2. C. Liu and T. E. Hermann. J. Biol. Chem. **253**, 5892 (1978).
3. B. K. Toeplitz, A. I. Cohen, P. T. Funke, W. L. Parker, and J. Z. Gougoutas. J. Am. Chem. Soc. **101**, 3344 (1979).
4. (*a*) D. Nicoll-Griffith and L. Weiler. J. Chem. Soc. Chem. Commun. 659 (1984); (*b*) C. Spino and L. Weiler. Tetrahedron Lett. **28**, 731 (1987).
5. P. G. M. Wuts, R. D'Costa, and W. Butler. J. Org. Chem. **49**, 2582 (1984).
6. (*a*) D. A. Evans, M. M. Morrissey, and R. L. Dow. Tetrahedron Lett. **26**, 6005 (1985); (*b*) D. A. Evans and R. L. Dow. Tetrahedron Lett. **27**, 1007 (1986); (*c*) D. A. Evans, E. B. Sjogren, J. Batroli, and B. L. Dow. Tetrahedron Lett. **27**, 4957 (1986).
7. S. L. Schreiber and Z. Wang. J. Am. Chem. Soc. **107**, 5303 (1985).
8. S. Hanessian and P. J. Murray. Can. J. Chem. **64**, 2231 (1986).
9. K. P. Shelly. M.Sc. thesis, University of British Columbia, Vancouver, B.C. 1984.
10. B. Grobel and D. Seebach. Synthesis, 357 (1977).
11. D. Seebach and E. J. Corey. J. Org. Chem. **40**, 231 (1975), and references therein.
12. (*a*) H. Redlich, B. Schneider, and W. Francke. Tetrahedron Lett. **21**, 3009 (1980); (*b*) M. Hirayama, K. Gamoh, and N. Ikekawa. J. Am. Chem. Soc. **104**, 3735 (1982).
13. E. J. Corey and G. Schmidt. Tetrahedron Lett. 399 (1979).
14. E. J. Corey and D. Crouse. J. Org. Chem. **33**, 298 (1968).

15. N. L. ALLINGER. J. Am. Chem. Soc. **81**, 232 (1959).
16. A. ZAMOJSKI. Rocz. Chem. **40**, 451 (1966).
17. P. A. BARTLETT and J. L. ADAMS. J. Am. Chem. Soc. **102**, 337 (1980).
18. P. L. CREGER. J. Am. Chem. Soc. **92**, 1396 (1970).
19. T. LAUBE, J. D. DUNITZ, and D. SEEBACH. Helv. Chim. Acta, **68**, 1373 (1985).
20. R. AMSTUTZ, J. D. DUNITZ, and D. SEEBACH. Angew. Chem. Int. Ed. Engl. **20**, 465 (1981).
21. L. LOMBARDO. Tetrahedron Lett. **23**, 4293 (1982).
22. K. TAKAI, Y. HOTTA, K. OSHIMA, and H. NOZAKI. Tetrahedron Lett. 2417 (1978).
23. M. FETIZON and M. JURION. J. Chem. Soc. Chem. Commun. 382 (1972).
24. W. C. STILL, M. KAHN, and A. MITRA. J. Org. Chem. **43**, 2923 (1978).
25. M. F. LIPTON, C. M. SORENSEN, A. C. SADLER, and R. H. SHAPIRO. J. Organomet. Chem. **186**, 155 (1980).
26. K. VON AUWERS and J. F. THORPE. Ann. **285**, 310 (1895).

Can. J. Chem. Downloaded from www.nrcresearchpress.com by 93.93.197.157 on 09/07/12
For personal use only.

Products and reaction paths in the liquid phase oxidation of trans-1,2-dichloroethene with oxygen

KARL GRIESBAUM,[1] MICHAEL P. HAYES, AND VERA WERLI

Engler-Bunte-Institut, Bereich Petrochemie, Universität Karlsruhe (TH), D-7500 Karlsruhe, Germany

Received September 21, 1987

KARL GRIESBAUM, MICHAEL P. HAYES, and VERA WERLI. Can. J. Chem. **66**, 1366 (1988).

Ultraviolet initiated liquid phase oxidation of neat *trans*-1,2-dichloroethene (**1***a*) with oxygen at 30°C afforded ca. 45% of the combined C1-products CO, CO_2, and phosgene as well as nine oxygenated and nine non-oxygenated chlorinated organic products. Major oxygenated products were *cis*- and *trans*-2,3-dichlorooxirane (**6***a*, *b*) and 1,2,2-trichloroethyl formate (**13**); minor products were e.g., *meso* and *rac* bis(1,2,2-trichloroethyl) ether (**11***c*, *d*) and dichloromethyl 1,2,2-trichloroethyl ether (**12**). The mode of formation of all products is rationalized by a unified reaction scheme.

KARL GRIESBAUM, MICHAEL P. HAYES et VERA WERLI. Can. J. Chem. **66**, 1366 (1988).

Le dichloro-1,2 éthène *trans* (**1***a*) à l'état pur, à 30°C, soumis à une oxydation par l'oxygène, catalysée par la lumière ultraviolette, fournit des produits en C1 (comme le CO, le CO_2 et le phosgène) avec un rendement global d'environ 45% ainsi que neuf produits organiques chlorés qui sont oxygénés et neuf qui ne sont pas oxygénés. Les produits oxygénés principaux sont les dichloro-2,3 oxiranes *cis* et *trans* (**6***a* et **6***b*) et le formiate de trichloro-1,2,2 éthyle (**13**); parmi les produits mineurs, on note les isomères *méso* et *rac* de l'éther bis(trichloro-1,2,2 ethylique) (**11***c* et **11***d*) et l'éther dichlorométhoxy-1 trichloro-1,2,2 éthane (**12**). On rationalise le mode de formation de tous les produits à l'aide d'un schéma réactionnel unifié.

[Traduit par la revue]

Can. J. Chem. Downloaded from www.nrcresearchpress.com by 93.93.197.157 on 09/07/12
For personal use only.

Introduction

Oxidation reactions of the chloriated ethenes vinyl chloride (1–4), 1,1-dichloroethene (5–7), 1,2-dichloroethene (8–11), trichloroethene (12–15), and tetrachloroethene (16, 17) with oxygen have been examined under a variety of conditions and aspects. While earlier studies were concerned with industrial aspects such as the production of chlorinated acetaldehydes (1, 6) or chlorinated acetyl chlorides (14), recent work has been focused on health (15) and environmental (4, 10, 18) aspects. Thus, it has been claimed that chloroethenes may be metabolized via potentially carcinogenic chlorinated epoxides (15) on the one hand, and that they may be a significant cause for the phenomenon called forest decline (18).

From the information that is currently available, it appears that photosensitized oxidations of chloroethenes with oxygen in the gas phase result predominantly in the cleavage of the carbon skeleton to give C1-products such as carbon monoxide and phosgene, whereas bulk phase liquid oxidations give the corresponding chlorooxiranes and (or) chlorinated oxo compounds by ring-opening isomerizations of the former.

In connection with a program concerned with the chemistry of halogenated epoxides (19), we tried to make use of the liquid phase oxidation of *trans*-1,2-dichloroethene (**1***a*) to prepare larger amounts of the stereoisomeric 2,3-dichlorooxiranes (**6***a*, *b*) that had been reported (8, 9) as products of this reaction. This led us to the observations reported below.

Results and discussion

trans-1,2,-Dichloroethene (**1***a*) was treated with oxygen at pressures of 1.4 bar (1 bar = 100 kPa) at 30°C. In the dark, no reaction products could be detected after 46 h of exposure, whereas under uv irradiation **1***a* was gradually consumed (Fig. 1, curve 1), in line with previous experience (8, 9). The reaction could be accelerated by the admixture of chlorine to the oxygen feed (Fig. 1, curves 2 and 3).

Oxidation of **1***a* with oxygen in the absence of added chlorine afforded the volatile inorganic products HCl, CO, CO_2, and phosgene, along with a liquid that contained the organic products **2** – **13** in the proportions shown in Table 1. Furthermore, small amounts of formic acid, mono- and dichloroacetic acid, and, in cases of incomplete conversions of **1***a*, variable amounts of **1***b* were formed. Oxidation of **1***a* with oxygen in the presence of equimolar amounts of chlorine afforded the same products, albeit in considerably different proportions, along with compounds **14** – **17** (Table 1). In addition to the above mentioned products, small amounts of a solid precipitated during the oxidation reaction and ca. 25 – 30% of a viscous residue remained after distillation of the liquid reaction products, neither of which have been characterized.

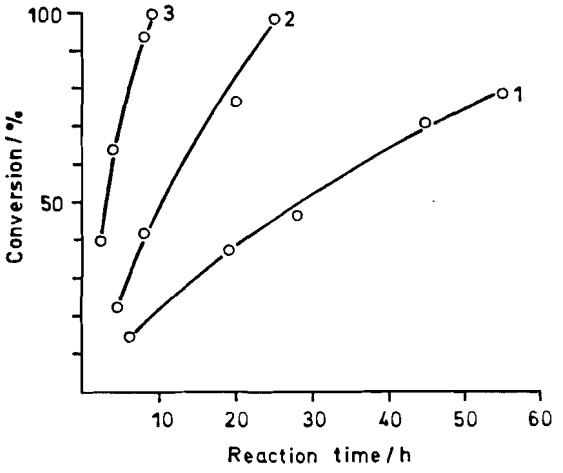

FIG. 1. Conversion vs. reaction conditions in the uv initiated liquid phase oxidation of *trans*-1,2-dichloroethene with oxygen at 30°C. O_2 flow rate, 6 mL/min. (1) O_2; (2) $O_2/Cl_2 = 6$; (3) $O_2/Cl_2 = 1$.

The organic products **1***b* and **2** – **17** were identified by glc and gc/ms analyses of the liquid product mixtures. In addition, compounds **1***b*, **2**, **4** – **7**, **10** – **13**, **16**, and **17** were isolated and characterized by their ^1H nmr and ir spectra. Formic acid as well as mono- and dichloroacetic acid were identified as the corresponding methyl esters after treatment of the product mixtures with diazomethane and subsequent glc and gc/ms

[1]Author to whom correspondence may be addressed.

Printed in Canada / Imprimé au Canada

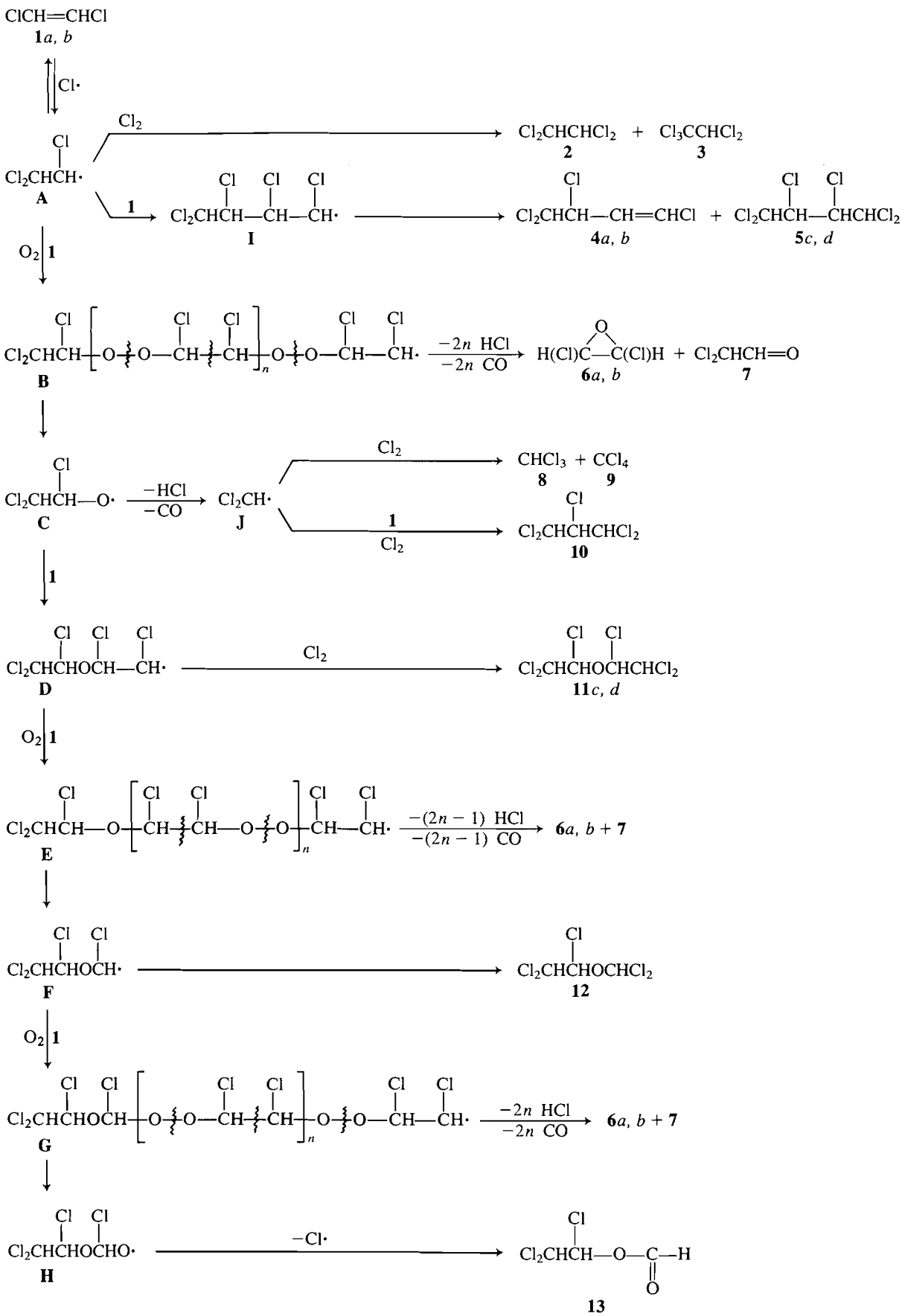

a: *trans*; *b*: *cis*; *c*: *meso*; *d*: *rac*

SCHEME 1

Can. J. Chem. Downloaded from www.nrcresearchpress.com by 93.93.197.157 on 09/07/12
For personal use only.

TABLE 1. Relative proportions and analytical data of organic products from the liquid phase oxidation of TRANS-1,2-idchloroethane (**1***a*)

Products	Reagent O_2 (68)[a]	Reagent O_2/Cl_2 (99)[a]	gc-t_R min	Mass spectral data (m/e)
2	6.9	49.3	13.8	172, 170, 168, 166 $(M)^+$; 87, 85, 83 $(M/2)^+$
3	0.6	4.7	12.6	210, 208, 206, 204, 202, 200 $(M)^+$; 123, 121, 119, 117 $(CCl_3)^+$
4*a*	0.6	Trace	23.5	200, 198, 196, 194, 192, $(M)^+$; 113, 111, 109 $(M - CHCl_2)^+$
4*b*	0.2	Trace	20.8	
5*c*	1.5	2.0	30.3	197, 195, 193, 191 $(M - HCl_2)^+$; 149, 147, 145, 143 $(M - CHCl_2 - HCl)^+$
5*d*	4.3	2.1	28.4	
6*a*	42.4	8.0	3.9	116, 114, 112 $(M)^+$; 50, 48 $(CHCl)^+$
6*b*	9.0	1.5	8.6	
7	0.3	1.6	4.9	116, 114, 112, $(M)^+$; 87, 85, 83 $(M - CHO)^+$
8	0.1	Trace	3.3	
9	0.2	Trace	2.4	
10	0.8	Trace	21.8	149, 147, 145, 143 $(M - HCl_2)^+$; 100, 98, 96 $(M - CHCl_2 - Cl)^+$; 87, 85 83 $(CHCl_2)^+$
11*c*	0.3	2.8	34.5	252, 250, 248, 246, 244, 242 $(M - HCl)^+$; 137, 135, 133, 131 $(C_2H_2Cl_3)^+$
11*d*	0.7	3.4	42.3	
12	3.1	4.9	25.9	137, 135, 133, 131 $(M - OCHCl_2)$; 87, 85, 83 $(CHCl_2)^+$
13	29.2	1.3	18.3	117, 115, 113 $(M - CO - Cl)^+$; 67, 65 $(CHO + HCl)^+$; 29 $(CHO)^+$
14	—	0.5	5.3	115, 113, 111 $(M - Cl)^+$; 86, 84, 82 $(M - HCOCl)^+$
15	—	14.6	7.6	115, 113, 111 $(M - Cl)^+$; 87, 85, 83 $(M - COCl)^+$
16	—	2.7	37.4	171, 169, 167, 165 $(Cl_3CCHCl)^+$; 135, 133, 131 $(Cl_2CHCHCl)^+$
17	—	0.5	31.2	151, 149, 147 $(M - CHCl_2CO)^+$; 137, 135, 133, 131 $(M - Cl_2CHCOO)^+$ 115, 113, 111 $(Cl_2CHCO)^+$; 87, 85, 83 $(CHCl_2)$

[a]Percent conversion.

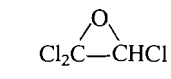

14

15

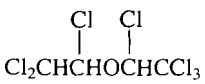

16

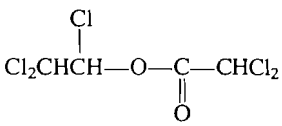

17

analyses; in addition, mono- and dichloromethyl acetate were isolated from such mixtures.

The structure assignment of the hitherto unknown trichloroethyl formate (**13**) was supported by its facile solvolysis with ethanol to give ethyl formate, as well as the hemiketal (**18***a*) and the ketal (**18***b*) of dichloroacetaldehyde. The structures of **4***a* and **4***b* were substantiated by ozonolysis in methanol, which—in line with the results of the ozonolysis of other substrates containing chloro-substituted double bonds (20)—yielded **20**, probably by HCl-catalyzed dehydration of **19** (21).

It is evident from the foregoing results that the liquid phase oxidation of **1***a* provides a considerably larger variety of products than had been recognized in previous investigations concerned with the oxidation of this or other chloroethenes. In particular, the oxygenated products **11** – **13**, but also the non-oxygenated product **10**, had not been reported before in the oxidation of **1***a*. All of the products obtained in this investigation can be logically explained by applying and extending a reaction scheme that had been proposed by Mayo for liquid phase oxidations of both chlorinated (13) and non-chlorinated (22) olefins. According to this proposal (Scheme 1) the reaction starts with the addition of chlorine atoms to substrate **1***a* to give radical **A** as the first and key intermediate for all products.

18

a: R = H; *b*: R = C_2H_5

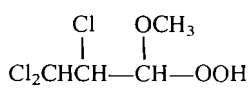

19

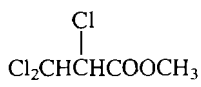

20

The oxygenated products are explained by the following reaction steps: Alternating reactions of **A** with oxygen and **1** afford radicals of type **B**, which in turn are cleaved to give **6***a*, **6***b*, **7** (by isomerization of **6**), and radical **C** for $n=0$, and **6***a*, **6***b*, **7**, **C**, CO, and HCl for $n \geq 1$. Radical **C** could provide additional **7** by loss of chlorine. On the basis of the low proportion of **7** in the reaction mixture (Table 1) we assume, however, that the major reaction path of **C** in the bulk phase proceeds via **D** to give radicals of type **E**, which in turn are cleaved to give additional CO, HCl, **6***a*, **6***b*, and **7**, as well as radical **F**. Finally, alternating reactions of **F** with oxygen and **1** give radicals of type **G**. Cleavage of the latter provides still more CO, HCl, **6***a*, **6***b*, and **7**, along with radical **H**, which by loss of chlorine affords **13**. Radicals **D** and **F** can also be intercepted by chlorine to give products **11** and **12**, respectively.

The non-oxygenated products are explained by the following reactions: Radical **A** can react by loss of chlorine to give **1***b* in addition to the starting material **1***a*. Furthermore, **A** can react with chlorine to give **2** and **3**, or with **1** via radical **I** to give structures **4** and **5**. Radical **C** can undergo cleavage to give CO, HCl, and radical **J** (10), which in turn leads to **8** + **9** by reaction with chlorine and to **10** by addition to **1**, followed by reaction of the ensuing radical with chlorine.

Of the additional products that were obtained when **1***a* was oxidized in the presence of added chlorine, **14** is formed by chlorination of **6**, as we have shown independently, and **16** is

Can. J. Chem. Downloaded from www.nrcresearchpress.com by 93.93.197.157 on 09/07/12
For personal use only.

Can. J. Chem. Downloaded from www.nrcresearchpress.com by 93.93.197.157 on 09/07/12
For personal use only.

assumed to be formed by chlorination of **11**. Compound **15** can arise both from the isomerization of **14** (15) and from oxidation of **2**, which was the single major product from the reaction of **1***a* with oxygen and chlorine (Table 1). We have shown that the conversion of **2** into **15** occurs not only in the gas phase (23), but also in the liquid phase oxidation under the conditions that were applied for the oxidation of **1***a*. Finally, compound **17** could possibly be formed by reaction of **6** with **15**.

The reaction sequence proposed in Scheme 1 draws support from the fact that the proportion of **11** + **12** + **16** in relation to that of the combined other oxidation products **6** + **7** + **13** + **14** + **15** is increased from ca. 1:20 in the oxidation of **1***a* with oxygen alone to ca. 1:2 in the joint reaction of **1***a* with oxygen and chlorine. This result is indicative of a competition between chlorine and oxygen for the intermediate radicals **D** and **F**.

A material balance of the products obtained from the oxidation with oxygen alone showed that the carbon contained in **1***a* was converted into CO with 37.8% and into CO_2 with 5.1% selectivity. This means that ca. 43% of **1***a* has suffered cleavage of the double bond. Furthermore, the relative amounts of CO + CO_2 on the one hand, and of **6** + **7** + **13** + **15** on the other hand, indicate that in radicals **B** and **E** the number *n* of the respective repeating units is, on the average, between one and two. This means that the incipient peroxy radical **21**, which is

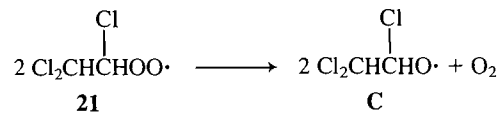

derived from the reaction of **A** with oxygen, is effectively trapped by the excess substrate **1***a*. By contrast, in the gas phase oxidation of **1** (10), radicals of type **21** have been reported to react with themselves by loss of oxygen to give, among other products, radical **C**, which in turn is cleaved to give CO, HCl, and radical **J**.

The assumed initiation of the oxidation of **1***a* by chlorine atoms (Scheme 1) has been well documented in the literature. These chlorine atoms probably arise from light-induced decomposition of **1***a* by direct C—Cl cleavage and (or) via the intermediate formation of HCl. In line with this assumption is the fact that the oxidation of **1***a* is inhibited in the absence of light (see above) and also in the presence of an added base. Thus, treatment of **1***a* with oxygen at 30°C under uv irradiation gave no detectable amounts of products in the presence of ca. 2 molar equivalents of 1,4-diazabicyclo[2.2.2]octane (DABCO).

Experimental

General methods

The ^{1}H nmr spectra were recorded on a Bruker WP 60, ir spectra on a Beckman Acculab 1, and gc/ms spectra on a Varian MAT 111 instrument. The glc analyses were carried out on a Varian model 1400 instrument (column 0.35 × 300 cm; 2.5% Nitrilesiliconoil XE on Chromosorb G; 60–160°C at 4°C/min). The pgc separations were performed on a Perkin Elmer F 21 instrument. Conditions: (*a*) column 0.8 × 500 cm; 5% Nitrilesiliconoil XE on Chromosorb G; 90–180°C at 3°C/min; (*b*) column 0.8 × 350 cm; 2.5% Nitrilesiliconoil XE 60 on Chromosorb G; 140–180°C at 1.5°C/min; (*c*) column 0.8 × 500 cm; 2.5% Nitrilesiliconoil XE 60 on Chromosorb G; 100°C; (*d*) column 0.8 × 500 cm; 2.5% Nitrilesiliconoil XE 60 on Chromosorb G; 90–180°C at 3°C/min.

Oxidation procedure

The oxidations were carried out in cylindrical glass reactors of appropriate (20, 55, 110, 300 mL) capacity. Each reactor was equipped with a surrounding cooling mantle, a coaxially arranged water-cooled 125-W medium pressure uv immersion lamp (Philips HPK 125) having a quartz mantle, a frit for the dispersion of oxygen, and a sampling device. The oxygen was dried over silica gel and molecular sieve and then passed through the reactor at a pressure of ca. 1.4 atmospheres (1 atm = 101.3 kPa) and at a flow rate of 6 mL/min, in one case also at 18 mL/min (Fig. 1). The exit gases from the reactor were sequentially passed through a condenser kept at −50°C, two cold traps, each kept at −78°C, for the condensation of remaining organic material, a solution of 1 N aqueous potassium hydroxide for the removal of HCl, CO_2, and phosgene, a fixed bed reactor of copper oxide kept at 600°C for the conversion of CO into CO_2, and, finally, a solution of 1 N aqueous potassium hydroxide for the absorption of CO_2. The proportions of HCl and CO_2 in the exit gases were determined by titration of the first KOH solution by an established procedure (24); the proportion of CO resulted from titration of the second KOH solution.

Commercial **1***a* (Fluka) was, for each experiment, washed 3 times with water to remove added stabilizer, sequentially dried over sodium sulfate and phosphorus pentoxide, and distilled through a 100-cm packed column; the fraction boiling at 47.5°C was collected.

Oxidation of **1**a *with oxygen*

(*a*) *Identification of products*

In a 55-mL reactor, 70.0 g of **1***a* was treated with oxygen at 30°C for 56 h, while the progress of the reaction was monitored by glc analysis at regular intervals (Fig. 1). The reaction reached a conversion of 79% and produced 17.8 g (42.9% based on the amount of **1***a* converted) of HCl, 12.2 g (37.8%) of CO, 3.1 g (5.1%) of CO_2, 10.8 g of a liquid condensate in the traps kept at −78°C, and 34.5 g of a liquid material in the reactor. The glc and gc/ms analyses of the latter product showed the presence of **1***a* and **1***b* as well as **2** – **13** in the proportions reported in Table 1. A sample of the liquid condensate reacted spontaneously with methanol. The glc and gc/ms analyses of the product after the reaction had ceased showed the presence of **1***a* and of **1***b* as major, and of methyl formate (*m*/*e* = 60; 32; 31; 29), chloromethyl carbonate (*m*/*e* = 96, 94; 65, 63; 59), and dimethyl carbonate (*m*/*e* = 90; 59; 45) as minor components. The latter two components are derived from phosgene.

(*b*) *Isolation of* **1**b, **2**, **6**a, **6**b, **7**, *and* **13** *and identification of chloro-, dichloroacetic, and formic acid*

A sample of 29.5 g of the liquid material in the reactor was distilled through a 10-cm Vigreux column by gradually lowering the pressure and increasing the bath temperature. By pgc (condition *a*), **1***b*, **2**, **6***a*, **6***b*, and **7** were isolated from a fraction of 8.6 g boiling at 24°C/33 Torr (1 Torr = 133.3 Pa), and **13** was isolated from a fraction of 2.0 g boiling at 30–31°C/4 Torr. A fraction of 1.7 g boiling at 31–39°C/0.25 Torr was treated with a solution of diazomethane in ether. When gas evolution had ceased, the ether was removed in a rotary evaporator. The glc and gc/ms analyses of the residue showed the presence of methyl formate, and methylchloro and methyldichloro acetate. From this residue methylchloro and methyldichloro acetate were isolated by pgc (conditions *a*).

The isolated products **1***a*, **2**, **6***a* (25), **6***b* (25), **7**, and methylchloro and methyldichloro acetate have been identified based on the identity of their ^{1}H nmr spectra with those of authentic samples.

1,2,2-Trichloroethyl formate (**13**): Colorless liquid; ir (film): 1755 (C=O) cm^{-1}; ^{1}H nmr ($CDCl_3$, Me_4Si) δ: 5.92 (dd, *J* = 3.9 and 0.4 Hz, 1H), 6.76 (dd, *J* = 3.9 and 0.9 Hz, 1H), 8.20 (dd, *J* = 0.9 and 0.4 Hz 1H); ms, see Table 1. *Anal.* calcd. for $C_3H_3OCl_3$: C 20.31, H 1.70, O 18.04, Cl 59.95; found: C 20.44, H 1.72, O 17.98, Cl 59.85.

(*c*) *Isolation of* **4**a, **4**b, **5**c, **5**d, ***10***, *and* **12**

In a 300-mL reactor 300 g of **1***a* was oxidized for 60 h under the conditions reported above to give 165 g of liquid product, which was submitted to a vacuum distillation. From a fraction of 3.7 g boiling at 42–45°C/4–5 Torr compounds **4***a*, **4***b*, **10**, and **12** were isolated by pgc (condition *a*). From a fraction of 3.2 g boiling at 82°C/5 Torr, compound **5***c* was isolated by crystallization at room temperature, and **5***d* by pgc separation (condition *a*) of the mother liquor.

The isolated products **4***a* (26), **4***b* (26), **5***c* (27), and **10** (28) were

identified by comparison of their ^{1}H nmr spectra with those of published data.

Dichloromethyl 1,2,2-trichloroethyl ether (**12**): Colorless liquid; ir (CCl_4): 1375, 1305, 1290, 1215, 1095, 1060, 985, 835, 705 cm^{-1}; ^{1}H nmr ($CDCl_3$, Me_4Si) AB system with δ_A 5.85, δ_B 6.04, J_{AB} = 3.29 Hz (2H), 7.22 (s, 1H); ms data, see Table 1. *Anal.* calcd. for $C_3H_3OCl_5$: C 15.51, H 1.30, O 6.89, Cl 76.30; found: C 15.64, H 1.25, O 6.66, Cl 76.45.

Oxidation of **1**a *with oxygen in the presence of chlorine*

(*a*) *Identification of products*

In a 110-mL reactor, 122 g of **1***a* was treated with an equimolar mixture of oxygen and chlorine at 30°C for 10 h; glc and gc/ms analyses showed the presence of compounds **2**–**17** in the proportions reported in Table 1.

(*b*) *Isolation of* **11**c, **11**d, **16**, *and* **17**

From the combined liquid material of two reactions, 117 g was submitted to a vacuum distillation. From a fraction of 5.9 g, gained at 3 Torr and bath temperatures of 80–160°C and which was collected at −5°C, compounds **11***c*, **11***d*, **16**, and **17** were isolated by pgc (condition *b*).

meso-*Bis(1,2,2-trichloroethyl) ether* (**11**c): ^{1}H nmr ($CDCl_3$, Me_4Si) AB system with δ_A 5.88, δ_B 5.99, J_{AB} = 3.5 Hz; (C_6D_6, Me_4Si) δ_A 4.99, δ_B 5.39, J_{AB} = 3.2 Hz). *Anal.* calcd. for $C_4H_4OCl_6$: C 17.11, H 1.44, O 5.70, Cl 75.75; found: C 17.46, H 1.40, O 6.69, Cl 74.32.

rac-*Bis(1,2,2-trichloroethyl) ether* (**11**d): ^{1}H nmr ($CDCl_3$, Me_4Si) δ: 5.85 (s); (C_6D_6, Me_4Si) AB system with δ_A 4.87, δ_B 5.01, J_{AB} = 4.0 Hz. *Anal.* calcd. for $C_4H_4OCl_6$: C 17.11, H 1.44, Cl 75.75; found: C 17.56, H 1.38, Cl 74.12.

The stereochemical assignments of **11***c* and **11***d* are only made by analogy with **5***c* and **5***d*, in which the isomer with the larger coupling constant was assigned the racemic structure.

1,2,2,2-Tetrachloroethyl 1,2,2-trichloroethyl ether (**16**): ^{1}H nmr ($CDCl_3$, Me_4Si) AB system with δ_A 5.88, δ_B 6.33, J_{AB} = 3.4 Hz (2H), 6.01 (s, 1H).

1,2,2-Trichloroethyl dichloroacetate (**17**): AB system with δ_A 5.91, δ_B 6.64, J_{AB} = 4.2 Hz (2H), 6.06 (s, 1H).

Solvolysis of **13** *with ethanol*

A solution of 0.88 g (5 mmol) of **13** in 0.92 g (20 mmol) of ethanol was kept stirring in a closed vessel for 6 h. Preparative gc separation (condition *c*) provided ethyl formate, **18***a* and **18***b*. These were identified by comparison of their ^{1}H nmr spectra with known data in the case of ethyl formate (29*a*) and **18***b* (29*b*), and with that of authentic **18***a* (δ 1.26, t; 3.74, q; 4.81, d; 5.66, d).

Ozonolysis of **4**a *and* **4**b *in methanol*

A mixture of 0.91 g (5 mmol) of **4***a* and **4***b* (1:2) and 5.5 mL of a 1 N solution of anhydrous hydrogen chloride in methanol was ozonized at −78°C until the solution turned blue, and then warmed up to room temperature. Methanol was largely removed by distillation at normal pressure to give a residue consisting of two phases. From the lower phase, 0.4 g (42%) of **20** was isolated by pgc (condition *d*).

Methyl 2,3,3-trichloropropionate (**20**): ir (film): 1760 (C=O) cm^{-1}; ^{1}H nmr ($CDCl_3$, Me_4Si) δ: 3.86 (s, 3H), 4.61 (d, J = 7.5 Hz, 1H), 6.02 (d, 1H).

Chlorination of **6**

In a 20-mL reactor, 5.6 g of a mixture of **6***a* and **6***b* was treated with a stream of chlorine in nitrogen under uv irradiation at 30°C. After 23 h glc analysis showed the presence of **14** and of tetrachlorooxirane, as shown by coinjection with authentic samples.

Oxidation of **2**

In a 20-mL reactor, 18.2 g of **2** was treated with oxygen under the conditions that were applied for the oxidation of **1***a*. After 6 h, glc and ^{1}H nmr analyses of the product mixture (15.9 g) showed the presence of unreacted **2** (81%) and of the products **3** (6%), **8** (1%), and **15** (12%). The assignment of **15** was confirmed by the formation of methyl dichloroacetate upon addition of methanol to the mixture.

Inhibition of the oxidation of **1**a *by base*

A solution of 1.4 g (12.5 mmol) of 1,4-diazabicyclo[2.2.2]octane (DABCO) in 60 g (625 mmol) of **1***a* was treated with oxygen under the usual oxidation conditions. The solution turned yellow and small amounts of solid material precipitated on the reactor walls. After 84 h of continuous oxygenation, glc analysis showed only the peak of **1***a* to the exclusion of any oxidation products.

Acknowledgment

Support of this work by the Sonderforschungsbereich 62 is gratefully acknowledged.

1. Austrian Patent No. 164028 (1948).
2. G. A. Razuvaev and K. S. Minsker. J. Gen. Chem. USSR, **28** 957 (1958).
3. M. Lederer. Agnew. Chem. **71**, 162 (1959).
4. J. P. H. Müller and F. Korte. Chemosphere, **6**, 341 (1977).
5. R. C. Reinhardt. Chem. Eng. News, **28**, 1236 (1947).
6. German Patent No. 746451 (1944).
7. E. Sanhueza and J. Heicklen. J. Photochem. **4**, 17 (1975).
8. J. H. Futrell and A. S. Newton. J. Am. Chem. Soc. **80**, 4424 (1958).
9. F. Österreicher. Doctoral dissertation, University of Vienna (1967).
10. E. Sanhueza and J. Heicklen. Int. J. Chem. Kinet. **7**, 589 (1975).
11. K. L. Müller and H. J. Schumacher. Z. Phys. Chem. Abt. B, **37**, 365 (1937).
12. G. Huybrechts and L. Meyers. Trans. Faraday Soc. **62**, 2191 (1966).
13. F. R. Mayo and M. Honda. Prep. Gen. Pap.—Am. Chem. Soc. Div. Petrol. Chem. **13** (2), C-5 (1968).
14. German Patent No. 2533181 (1975).
15. S. A. Kline and B. L. Van Duuren. J. Heterocycl. Chem. **14**, 455 (1977).
16. G. Huybrechts, J. Olbrechts, and K. Thomas. Trans. Faraday Soc. **63**, 1647 (1967).
17. D. M. Frankel, C. E. Johnson, and H. M. Pit. J. Org. Chem. **22**, 1119 (1957).
18. H. Frank and W. Frank. Experientia, **42**, 1267 (1986).
19. K. Griesbaum, P. M. Scaria, and T. Döhling. J. Org. Chem. **51**, 1302 (1986), and references cited therein.
20. H. Keul and K. Griesbaum. Can. J. Chem. **58**, 2049 (1980).
21. K. Griesbaum and H. Keul. Angew. Chem. **87**, 748 (1975).
22. F. R. Mayo. J. Am. Chem. Soc. **80**, 2645 (1958).
23. J. W. Spence and P. L. Hanst. J. Air Pollut. Control Assoc. **28**, 250 (1978).
24. C. A. Rojahn. Quantitative Analyse. Steinkopff-Verlag, Darmstadt, FRG. 1939. p. 137.
25. K. Griesbaum, R. Kibar, and B. Pfeffer. Liebigs Ann. Chem. 214 (1975).
26. L. O. Moore. J. Phys. Chem. **74**, 3603 (1970).
27. R. J. Abraham and J. R. Monasterios. J. Chem. Soc. Perkin Trans 2, 699 (1975).
28. N. S. Bhacca, D. P. Hollis, L. F. Johnson, E. A. Pier, and J. N. Shovlery. High resolution nmr spectra catalog, Varian Associates. 1962. Compound No. 241.
29. C. J. Pouchert and J. R. Campbell. The Aldrich library of spectra. Aldrich Chemical Co, Milwaukee, WI. (*a*) Vol. 3. 1974. p. 19; (*b*) Vol. 1. 1974. p. 141.

Can. J. Chem. Downloaded from www.nrcresearchpress.com by 93.93.197.157 on 09/07/12
For personal use only.

On the role of partition and surface reactions in the adsorption of binary liquid mixtures on silica gel

PREM P. SINGH[1] AND KRISHAN K. SHARMA
Department of Chemistry, Maharshi Dayanand University, Rohtak – 124001, India

Received June 4, 1987[2]

PREM P. SINGH and KRISHAN K. SHARMA. Can. J. Chem. **66**, 1371 (1988).

The adsorption behaviour of benzene (A), toluene (A), *p*-xylene (A), and *o*-xylene (A) in their binary mixtures with *o*-chlorotoluene (B) on silica gel has been studied at 308.15 K. The data have been analysed in terms of a model that assumes that partition and surface reactions play an important role in the adsorption process, and have revealed that while both partition and surface reactions dictate the adsorption (U-shaped isotherms) of *o*-chlorotoluene (OCTE) (B) from benzene (A) or toluene (A) + OCTE (B) mixtures, the adsorption of A and B entities of *p*-xylene (A) or *o*-xylene (A) + OCTE (B) mixtures (S-shaped isotherms) onto the silica gel surface is governed primarily by the distribution process and secondarily by the surface reaction.

PREM P. SINGH et KRISHAN K. SHARMA. Can. J. Chem. **66**, 1371 (1988).

Opérant à 308,15 K, on a étudié le comportement du benzène (A), du toluène (A), du *p*-xylène (A) et de l'*o*-xylène (A) dans leurs mélanges binaires avec l'*o*-chlorotoluène (B) lors de leur adsorption sur le gel de silice. On a analysé les données en fonction d'un modèle qui fait l'hypothèse que la partition ainsi que les réactions de surface jouent un rôle important dans le processus d'adsorption. Les données démontrent que la partition ainsi que les réactions de surface déterminent l'adsorption (isothermes en U) de l'*o*-chlorotoluène (OCTE) (B) à partir de mélanges de benzène (A) ou toluène (A) + OCTE (B); toutefois, l'adsorption des entités A et B à partir de mélanges de *p*-xylène (A) ou d'*o*-xylène (A) + OCTE (B) (isothermes en S) sur la surface de gel de silice est principalement déterminée par un processus de distribution et d'une façon secondaire par la réaction de surface.
[Traduit par la revue]

Introduction

The analysis of the adsorbed phase when binary liquid mixtures are equilibrated with inert solids has invoked considerable theoretical interest (1–6). While some (1, 2) of these approaches assume that the non-ideality of the bulk liquid phase is responsible for the imperfection of the surface phase, others (3–6) maintain that the heterogeneity of the solid phase also plays an important role in solution adsorption. None of these approaches (1–6), however, take into consideration the role of partition (7) and surface reactions (7) in the adsorption process, and the failure of the present approaches (1–6) to explain the S-shaped adsorption isotherms may be traced to the neglect of these important factors. The present work was undertaken to highlight the role of (*i*) partition and (*ii*) surface reactions in the solution adsorption process.

Experimental

Analytical grade benzene (E. Merck), toluene (E. Merck), *o*-xylene (E. Merck), *p*-xylene (E. Merck), and *o*-chlorotoluene (J. T. Baker Chemicals Co., U.S.A.) were purified as suggested elsewhere (8). The purity of the final samples was checked by measuring their densities at 298.15 ± 0.01 K, which agreed to within ±0.00005 g cm^{-3} with the literature values (9–12). Since the surface properties of these reagents were involved in the present work, we also determined their surface tension at 293.15 ± 0.01 K before and after adsorption (for 72 h at 308.15 ± 0.2 K) on silica gel (0.3 g in 10 mL of the pure liquid) by a modified double capillary rise method (13). The radii of the two capillaries (r_1 = 0.0151 cm and r_2 = 0.0801 cm) were determined from the lengths and weights of mercury threads. The lengths of the mercury threads were read by a cathetometer (M/s OSAW, India) that could read to ±0.001 cm. The uncertainty in the measured surface tension values is about 0.27% at the worst. The surface tension values of benzene, toluene, *p*-xylene, and OCTE before and after adsorption, along with the corresponding literature values (12, 14, 15), are recorded in Table 1.

The adsorbent used was silica gel (without binder) (100–120 mesh) supplied by M/s Glaxo Laboratories, India. It was dried at 393.15 K for 72 h. Portions of known weight (0.15–0.3 g) of silica gel were placed in glass ampoules and degassed for 24 h under 10^{-5} Torr pressure (1 Torr = 133.3 Pa). These ampoules were then filled with 5.0 mL of binary solutions of known composition (by weight), sealed, and then placed (for 72 h) in an air thermostat maintained at 308.15 ± 0.2 K. The liquid phase was subsequently separated from the solid and the change in composition of the solution due to adsorption was determined by a Carl Zeiss interferometer maintained at 308.15 K. For this purpose preliminary composition of the solution, after adsorption, was first determined from plots of composition vs. refractive indices (determined by an Abbé refractometer maintained at 308.15 ± 0.01 K). (The refractometer readings were reproducible to better than ±0.0002 and the compositions were accurate to ±0.1 mol% at the worst.) The final composition of this solution was determined by comparing it with a solution of known composition (by weight) using the Carl Zeiss interferometer and the calibration curves that were first drawn (using this interferometer). The interferometer readings were reproducible to ±1 unit and the changes in composition (on the mole fraction scale) are believed to be accurate to better than 3 × 10^{-4}.

TABLE 1. Comparison of the measured surface tension of the reagents before and after adsorption on silica gel at 293.15 ± 0.01 K, with their corresponding literature values

	Surface tension (dynes cm^{-1})			
Reagent	Before adsorption	After adsorption	Lit. value	Ref.
Benzene	28.86	28.85	28.88	14
Toluene	28.53	28.54	28.52	14
p-Xylene	28.48	28.48	28.50	15
OCTE	33.42	33.42	33.44	12

Results and discussion

The experimental results are recorded in Table 2. It is apparent from Table 1 that while *o*-chlorotoluene (OCTE) is adsorbed preferentially from benzene (A) or toluene (A) +

[1]Author to whom correspondence may be addressed.
[2]Revision received January 15, 1988.

Can. J. Chem. Downloaded from www.nrcresearchpress.com by 93.93.197.157 on 09/07/12
For personal use only.

Can. J. Chem. Downloaded from www.nrcresearchpress.com by 93.93.197.157 on 09/07/12
For personal use only.

TABLE 2. Measured adsorption data of the various (A + B) liquid mixtures on silica gel at 308.15 K

$x_{A(l)}$	n_A[a]	n_B[a]	m (g)	$\Delta x_{A(l)}$[b]
		Benzene (A) + OCTE (B)		
0.1286	0.0057	0.0387	0.2070	−0.0365
0.2428	0.0110	0.0343	0.2862	−0.0772
0.3576	0.0167	0.0300	0.2170	−0.0924
0.4680	0.0227	0.0258	0.2665	−0.0920
0.5677	0.0281	0.0214	0.2235	−0.0753
0.6621	0.0339	0.0173	0.2950	−0.0729
0.8395	0.0455	0.0087	0.2150	−0.0335
		Toluene (A) + OCTE (B)		
0.1111	0.0048	0.0384	0.2731	−0.0169
0.2156	0.0094	0.0342	0.2812	−0.0544
0.3205	0.0141	0.0299	0.2014	−0.0516
0.4263	0.0191	0.0257	0.3290	−0.0867
0.5234	0.0235	0.0214	0.2380	−0.0616
0.7221	0.0330	0.0127	0.2210	−0.0359
0.8137	0.0380	0.0087	0.2807	−0.0404
		o-Xylene (A) + OCTE (B)		
0.1003	0.0043	0.0386	0.1938	0.0147
0.1935	0.0082	0.0342	0.1791	0.0295
0.2933	0.0124	0.0299	0.1518	0.0217
0.3885	0.0164	0.0258	0.2140	0.0223
0.4941	0.0208	0.0213	0.1976	−0.0141
0.5947	0.0252	0.0172	0.2100	−0.0217
0.6883	0.0290	0.0131	0.2202	−0.0333
0.7956	0.0334	0.0086	0.2495	−0.0344
0.8313	0.0401	0.0081	0.2144	−0.0287
		p-Xylene (A) + OCTE (B)		
0.0956	0.0041	0.0388	0.2620	0.0056
0.1939	0.0082	0.0341	0.3470	0.0239
0.2898	0.0122	0.0299	0.2840	0.0248
0.3895	0.0164	0.0257	0.3059	0.0245
0.4904	0.0204	0.0212	0.2736	0.0204
0.6916	0.0287	0.0128	0.3189	−0.0450
0.7248	0.0295	0.0112	0.2600	−0.0350
0.8395	0.0330	0.0063	0.2800	−0.0349
0.8935	0.0369	0.0044	0.3019	−0.0250

[a] In mol for 5 mL of solution.
[b] $\Delta x_{A(l)} = x_{A(l)initial} - x_{A(l)final}$.

OCTE (B) mixtures, *o*-xylene (A) or *p*-xylene (A) is adsorbed preferentially in the range $x_A^l \leq 0.5$ and OCTE is adsorbed preferentially in the rest of the composition range from *o*-xylene (A) or *p*-xylene (A) + OCTE (B) mixtures. Again, while the extent of OCTE (B) adsorption is greater from toluene (A) + OCTE (B) mixtures than that from benzene (A) + OCTE (B) mixtures, OCTE (B) is adsorbed (in the range $x_A^l > 0.5$) to a greater extent from its binary mixtures with *p*-xylene (A) than from those with *o*-xylene (A). The transition from the U-shaped isotherms in benzene (A) or toluene (A) + OCTE (B) mixtures to S-shaped isotherms for *o*-xylene (A) or *p*-xylene (A) + OCTE (B) mixtures when these mixtures are equilibrated with silica gel highlights the influence of $-CH_3$ substituents in the benzene ring on their adsorption on silica gel in the presence of OCTE (B).

Since specific molecular adsorption and chemical reactions with the surface of silica gel are determined (16) by surface hydroxyl groups and as these groups are the most accessible (ref. 16, p. 131) for interaction, we first recorded the infrared spectrum (in KBr pellets) of the present silica gel (Fig. 1) to understand the state of the surface -OH groups. The infrared spectrum of the present silica gel (Fig. 1) showed four characteristic absorption bands at 3420, 1625, 1100, and 800 cm^{-1}. While the very strong absorption band at 1100 cm^{-1} is due (17) to the asymmetric stretching vibrations of the Si—O—Si moiety, the weak absorption band at 800 cm^{-1} is due (18) to the Si—O—Si bending mode and the weak absorption at 1625 cm^{-1} is due (19) to the in-plane deformation of the -OH group. The band at 3420 cm^{-1} has been attributed (20) to -OH stretching vibration of molecular water. The position of the band at 1625 cm^{-1} also compares (20) favourably (at 1627 cm^{-1}) with the H—O—H bending vibrations in liquid water. Further, since the band at 3500 cm^{-1} observed in the spectra of some silica surfaces has been assigned (21) to the H—O—Si(^)—O—H moiety, we assume that the band at 3420 cm^{-1} in the infrared spectrum of the present silica gel is also due to this entity.

Further, aromatic hydrocarbons with their π-electron clouds have weak hydrogen-bond base characteristics (22). If specific interactions can occur (23–27) between the surface -OH groups and the π-electron clouds of the constituents of the present (A + B) mixtures, it is apparent that the adsorption of A and (or) B on the surface of silica gel must involve (ref. 20, p. 132) an acid–base type of interaction between the surface $-\bar{O}—H^+$ groups of the H—O—Si(^)—O—H moiety and the π-electron clouds of the basic adsorbate(s).

The presence of a $-CH_3$ substituent in *o*-chlorotoluene (OCTE) (B) would then require (28) (due to hyperconjugation) that there be an excess of charge at its *o* and *p* positions. Evidently the extent to which this happens in an (A + B) mixture would be dictated by the molecular entity A. Since the accumulation of charge at the *o* and *p* positions of OCTE (B) would be greater in the presence of toluene (A) than in the presence of benzene (A), and as B would now be more basic than the normal forms of benzene or toluene (A), it follows that compared to benzene (A) or toluene (A), OCTE (B) should be adsorbed preferentially on the silica gel surface and that the extent to which this happens should be greater in the presence of toluene (A) than in the presence of benzene (A). The experimental excess adsorption data of benzene (A) or toluene (A) + OCTE (B) mixtures lends credence to this conjecture. Again, as OCTE in the present situation would be expected to have only one electron-rich center

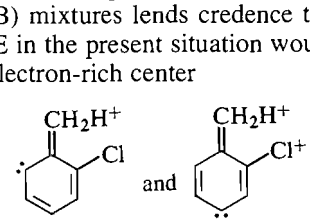

I

it follows that in the adsorption of OCTE (B) from benzene (A) or toluene (A) + OCTE (B) mixtures on silica gel only one -O—H of the H—O—Si(^)—O—H moiety is involved.

On the other hand, the presence of two $-CH_3$ substituents *para* to each other, as in *p*-xylene, would cause the creation of two electron-rich centres,

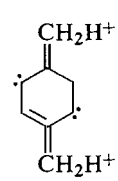

II

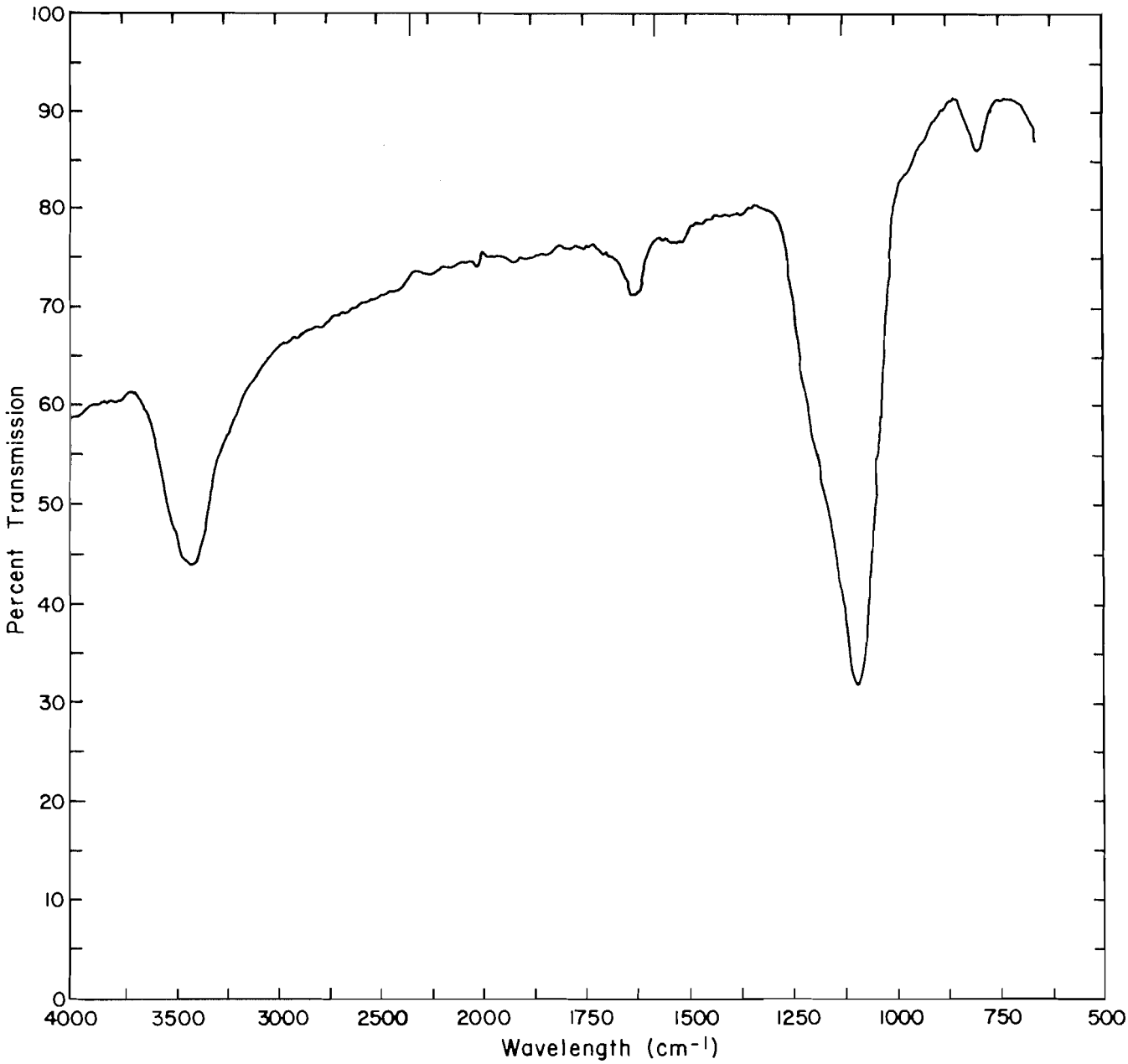

FIG. 1. Infrared spectrum (in KBr pellets) of silica gel.

The weak absorption band at 1700 cm^{-1} observed in the infrared spectrum (in KBr pellets) of pure *p*-xylene or *o*-xylene adsorbed on silica gel (Fig. 2) may be due to species like

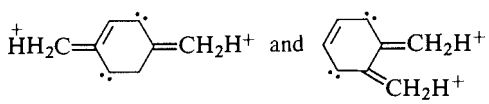

III

The extent to which this happens should evidently be greater in *p*-xylene than in *o*-xylene and should be dictated by the concentration of OCTE (B). Thus while the large excess of OCTE would cause *p*-xylene in the *p*-xylene (A) + OCTE (B) mixture to exist, in increasing proportion, in the **II** form, the increasing proportion of *p*-xylene would also cause OCTE to exist in increasing proportions, in the forms:

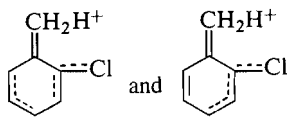

IV

Since the **II** form of *p*-xylene would be expected to be a stronger base than the

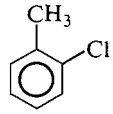

V

form of OCTE, it follows that at low mole fractions of *p*-xylene, *p*-xylene should be adsorbed preferentially and that this should decrease as the mole fraction of x_A in the *p*-xylene (A) + OCTE

Can. J. Chem. Downloaded from www.nrcresearchpress.com by 93.93.197.157 on 09/07/12
For personal use only.

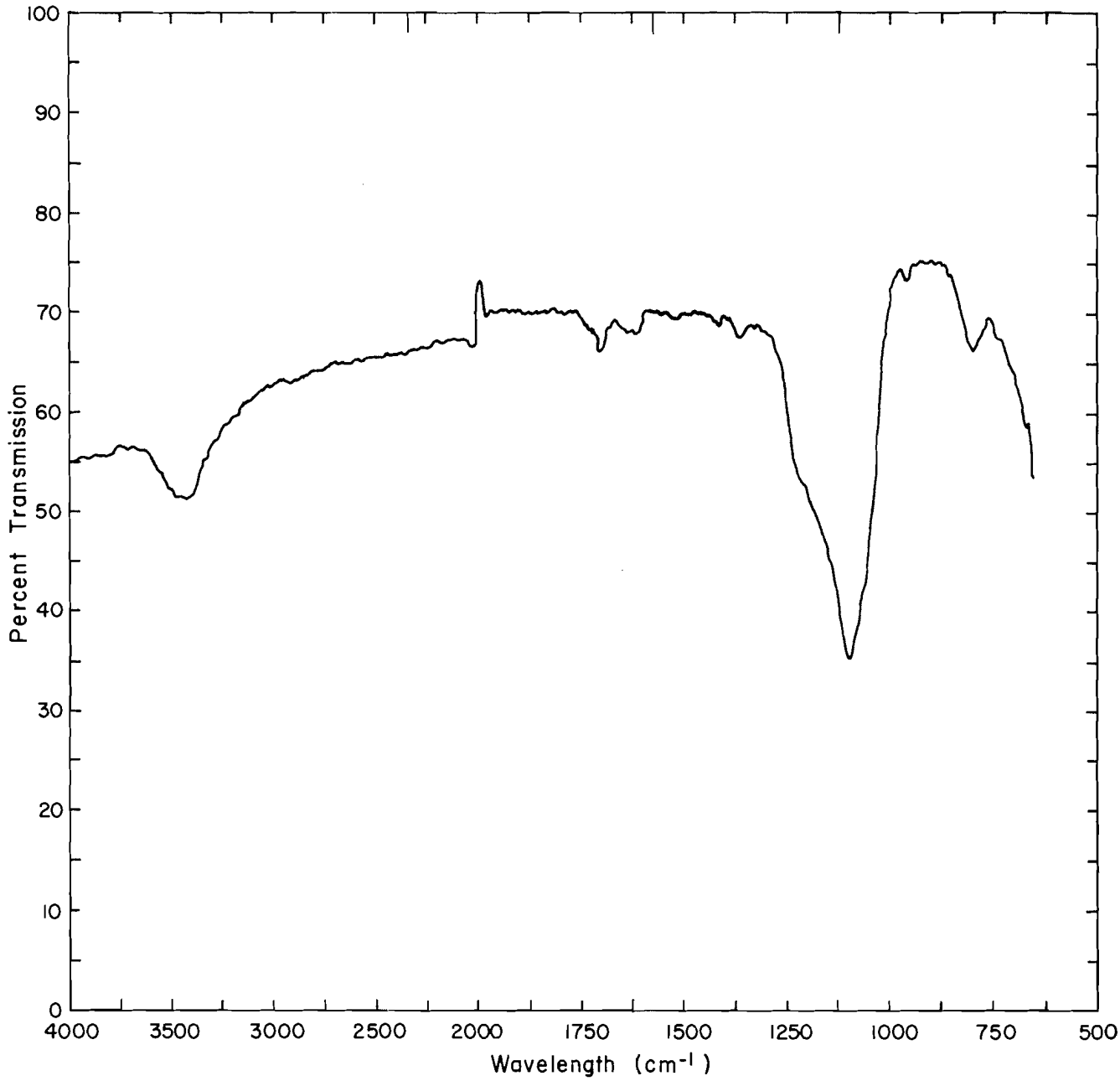

FIG. 2. Infrared spectrum (in KBr pellets) of *p*-xylene (after adsorption on silica gel).

(B) mixture increases. Again as the **IV** forms of OCTE, in the presence of large x_A, would be more basic than the

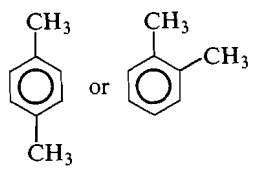

VI

forms of *p*-xylene or *o*-xylene, it follows that at high x_A, OCTE should be adsorbed preferentially and that this effect should be greater in the *p*-xylene (A) + OCTE (B) mixture than in the *o*-xylene (A) + OCTE (B) mixture, as has indeed been observed. If the postulated formation of increased proportions of the **IV** forms of OCTE as the concentration of *p*-xylene is increased is valid, then one would envisage that the Cl center of these species should also interact with the O-H entity (or entities) of the H—O—Si—OH moiety. The fact that a new weak band has been observed at 2300 cm^{-1} in the infrared spectrum (in KBr pellets) of the *p*-xylene (A) + OCTE (B) mixture adsorbed on silica gel (Fig. 3) at $x_A = 0.8935$, and a band at 2300 cm^{-1} can be assigned (29) to hydrogen-bonded hydrogen chloride molecules, lends credence to such a type of interaction. Again, because the infrared spectrum of the *p*-xylene (A) + OCTE (B) mixture adsorbed on silica gel exhibits a reasonably intense band at 1700 cm^{-1} (with no new band at 2300 cm^{-1}) corresponding to $x_A = 0.1939$ (Fig. 4), and because the intensity of the band at 1700 cm^{-1} decreases while a new weak band appears at 2300 cm^{-1} corresponding to $x_A = 0.8935$, it appears that while at low x_A *p*-xylene is adsorbed

Can. J. Chem. Downloaded from www.nrcresearchpress.com by 93.93.197.157 on 09/07/12
For personal use only.

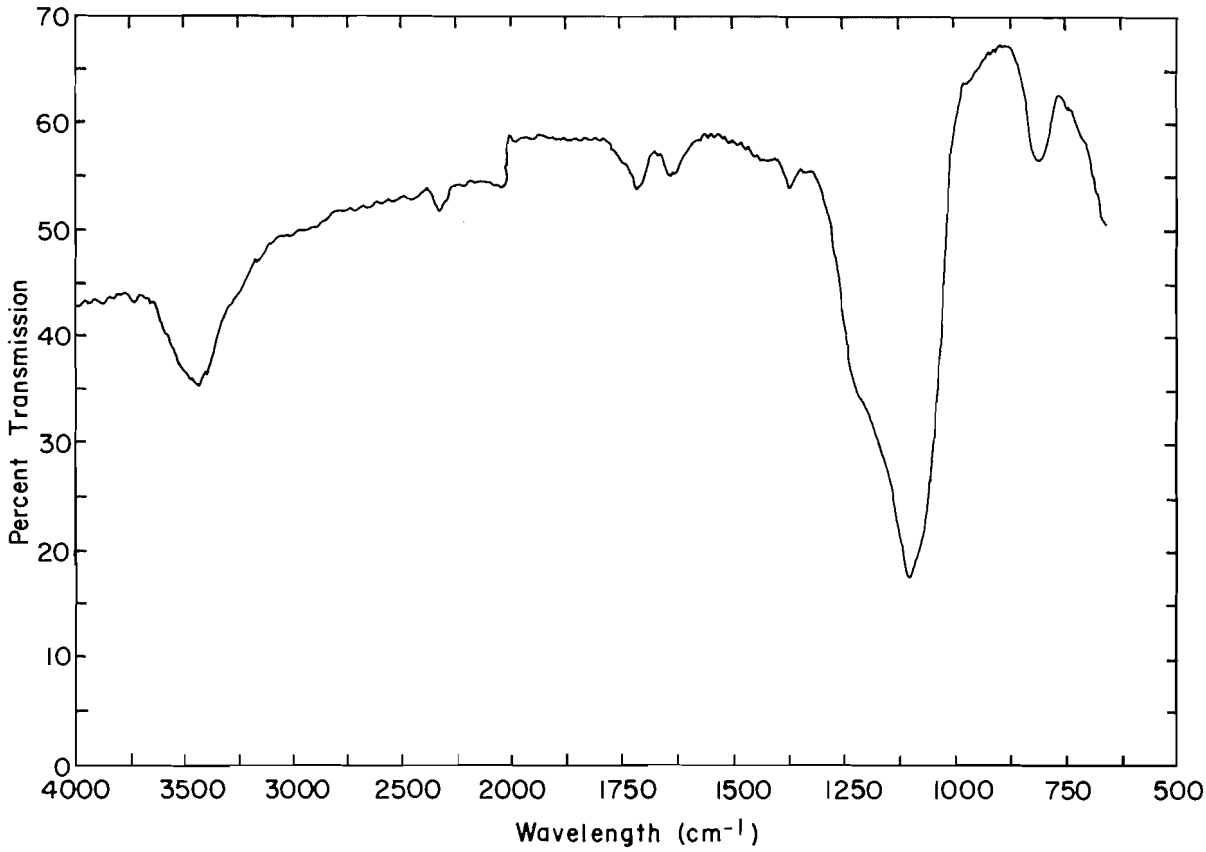

FIG. 3. Infrared spectrum (in KBr) pellets) of *p*-xylene + OCTE ($x_{p\text{-xylene}} = 0.8935$) mixture adsorbed on silica gel).

preferentially, at high x_A it is the OCTE that is preferentially adsorbed. Further, as *p*-xylene (A) or *o*-xylene (A) and OCTE (B) in *p*-xylene (A) or *o*-xylene (A) + OCTE (B) mixtures has been postulated to have two electron-rich centers, it follows that both -OH groups of the O—H—Si—O—H moiety should be involved in the adsorption process characterizing the *p*-xylene (A) + OCTE (B) mixtures.

If the preferential adsorption of B from an (A + B) mixture on a solid (S) surface causes no appreciable changes in the composition of A, and if the addition of a degassed solid S to an (A + B) liquid mixture causes absorption of B, which subsequently undergoes surface reaction on S, then the preferential adsorption of B on the silica gel (S) may involve (*i*) the distribution of B(l) between two immiscible phases, A(l) and S, and (*ii*) the interaction of a part of the absorbed B(l) molecules with the surface -OH groups. Consequently if $(N_{B(l)})_S$ represents the total number of moles of B(l) per gram of the S phase, then

$$[1] \quad (N_{B(l)})_S = \begin{array}{l}\text{number of moles of B(l) per gram of S that are}\\ \text{free in the body of S + number of moles of B(l)}\\ \text{per gram of S due to the surface reaction}\end{array}$$

The "equilibrium constant", K, of the surface reaction

$$[2] \quad x(B(l))_S \rightleftharpoons y(B^\sigma)_S$$

would then be given by

$$[3] \quad K = (n_B^g)_S^y (\gamma^\sigma{}_{B(l)})_S^y / (n_{B(l)})_S^x (\gamma_{B(l)})_S^x$$

where $(\gamma^\sigma{}_{B(l)})_S$ and $(n_B^g)_S$ represent, respectively, the activity coefficient and the number of moles of B(l) per gram of S that are adsorbed on the surface of S; $(\gamma_{B(l)})_S$ and $(n_{B(l)})_S$ are the corresponding quantities of B(l) entity that exist free in the body of S. Since no method is available to evaluate $(\nu^\sigma{}_{B(l)})_S$ and $(\gamma_{B(l)})_S$ we assume that $(\gamma_B^g)_S/(\gamma_{B(l)})_S \approx 1$, so that eq. [3] reduces to

$$[4] \quad K = (n_B^g)_S^y / (n_{B(l)})_S^x$$

If ξ is the extent of the surface reaction, then the number of moles of B(l) per gram of S due to the surface reaction would be $x\xi$, so that eq. [1] yields

$$[5] \quad (N_{B(l)})_S = (n_{B(l)})_S + x\xi$$

But as $(n_B^g)_S = y\xi$, eq. [4] yields

$$[6] \quad K = (y\xi)^y / (n_{B(l)})_S^x$$

so that

$$[7] \quad \xi = K^{1/y} (n_{B(l)})_S^{x/y} / y$$

Equation [5] then yields

$$[8] \quad (N_{B(l)})_S = (n_{B(l)})_S + \frac{x}{y} \cdot K^{1/y} (n_{B(l)})_S^{x/y}$$

Again, as no reaction is assumed to occur between A and B in the liquid phase, and as B(l) distributes itself between the A(l) and S phases, we define a "distribution coefficient", K_d, as

$$[9] \quad K_d = \frac{(n_{B(l)})_S}{(n_{B(l)})_{\equiv \text{m in A(l)}}}$$

where $(n_{B(l)})_{\equiv \text{m in A(l)}}$ refers to the number of moles of B(l) per mL of the total liquid phase in the equilibrium state. Consequently

Can. J. Chem. Downloaded from www.nrcresearchpress.com by 93.93.197.157 on 09/07/12
For personal use only.

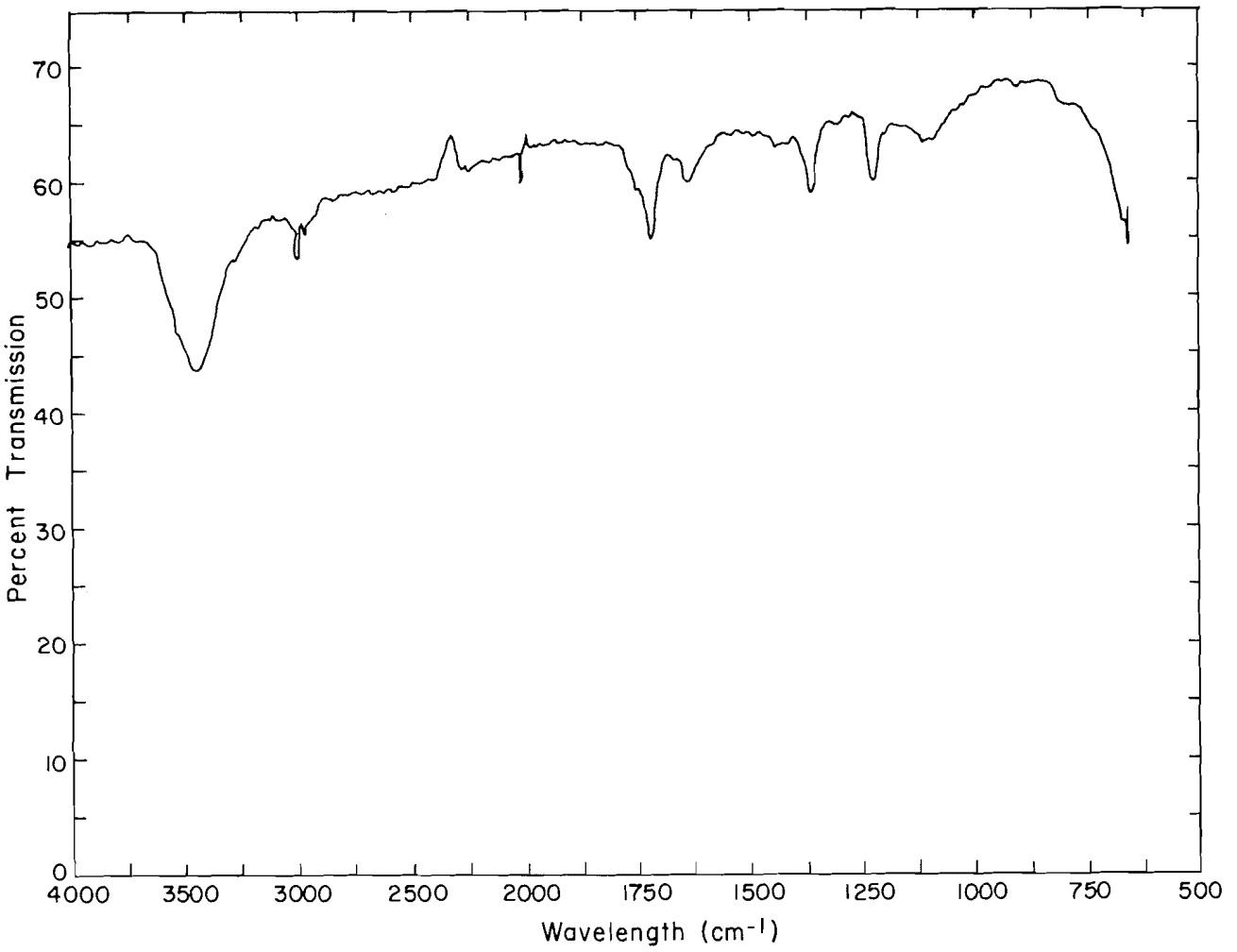

FIG. 4. Infrared spectrum (in KBr pellets) of *p*-xylene + OCTE ($x_{p\text{-xylene}} = 0.1939$) mixture adsorbed on silica gel.

[10] $(n_{B(l)})_S = K_d \cdot (n_{B(l)})_{\equiv \text{m in A(l)}}$

Hence expression [8] yields

[11] $$(N_{B(l)})_S = [K_d(n_{B(l)})_{\equiv \text{m in A(l)}})] + \frac{x}{y} \cdot K^{1/y}(K_d)^{x/y}(n_{B(l)})^{x/y}_{\equiv \text{m in A(l)}}$$

or

[12] $$\frac{(N_{B(l)})_S}{(n_{B(l)})_{\equiv \text{m in A(l)}}} = K_d + \frac{x}{y} \cdot K^{1/y}(K_d)^{x/y}(n_{B(l)})^{(x/y)-1}_{\equiv \text{m in A(l)}}$$

Evaluation of K_d and K from eq. [12] thus requires a knowledge of $(N_{B(l)})_S$ and $(n_{B(l)})_{\equiv \text{m in A(l)}}$. Since the equilibrium mole fraction $x_{B(l)_m}$ in the A(l) is known and if $n_{A(l)}$ is the number of moles of A(l) per mL of the liquid phase, then

[13] $$x_{B(l)_m} = \frac{(n_{B(l)})_{\equiv \text{m in A(l)}}}{(n_{A(l)} + (n_{B(l)})_{\equiv \text{m in A(l)}}}$$

or

[14] $$(n_{B(l)})_{\equiv \text{m in A(l)}} = \frac{x_{B(l)_m} \cdot n_{A(l)}}{1 - x_{B(l)_m}}$$

Hence

[15] $(N_{B(l)})_S = (n_{B(l)})_{\text{initial in A(l)}} - (n_{B(l)})_{\equiv \text{m in A(l)}}$

Since all the relevant quantities in eq. [12] can be deduced from the experimental adsorption data, it should be possible to evaluate the K_d and K parameters of the adsorption process.

We now consider two cases:

Case (*i*): $x = 1$, $y = \frac{1}{2}$ so that eq. [12] reduces to

[16] $$\frac{(N_{B(l)})_S}{(n_{B(l)})_{\equiv \text{m in A(l)}}} = K_d + 2K^2K_d^2(n_{B(l)})_{\equiv \text{m in A(l)}}$$

Case (*ii*): $x = 1$, $y = 2$, so that eq. [12] yields

[17] $$\frac{(N_{B(l)})_S}{(n_{B(l)})_{\equiv \text{m in A(l)}}} = K_d + 0.5K^{0.5}(K_d)^{0.5}(n_{B(l)})^{-0.5}_{\equiv \text{m in A(l)}}$$

Since, in the adsorption of OCTE (B) from benzene (A) or toluene (A) + OCTE (B) mixtures onto the silica surface, one -OH group of the H—O—Si—O—H moiety of the silica gel is assumed to be involved per molecule of OCTE, and if the basic arguments in deriving eq. [12] are valid, then according to eq. [16] a plot of Q $(=(N_{B(l)})_S/(n_{B(l)})_{\equiv \text{m in A(l)}}$ vs. Z $(=(n_{B(l)})_{\equiv \text{m in A(l)}})$ should be a straight line of slope $2K^2K_d^2$ and intercept K_d. This was indeed found to be true of the adsorption of OCTE (B) on silica gel from its binary mixtures with benzene (A) or toluene (A) (Fig. 5); the relevant K_d and K values are recorded in Table 3.

On the other hand, as the adsorption of OCTE (B) or *p*-xylene (A) or *o*-xylene (A) into the silica gel surface from the *p*-xylene (A) or *o*-xylene (A) + OCTE (B) mixtures is assumed to involve the interaction of both -OH groups of the

Can. J. Chem. Downloaded from www.nrcresearchpress.com by 93.93.197.157 on 09/07/12
For personal use only.

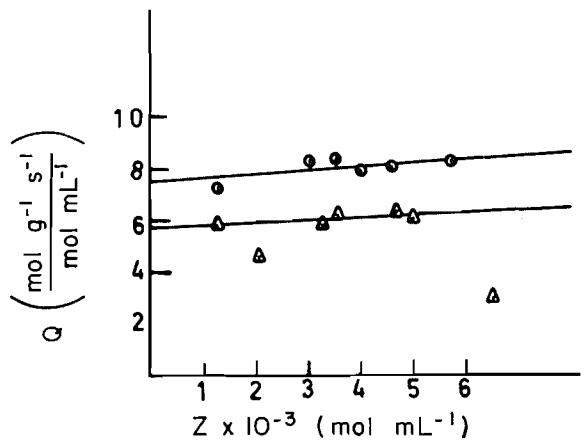

FIG. 5. Plot of Q vs. Z for benzene + OCTE (⊙) and toluene + OCTE (△) adsorbed on silica gel at 308.15 K.

TABLE 3. The distribution coefficient, K_d, and the equilibrium constant, K, of the surface reaction, for the B and (or) A entity of the various (A + B) mixtures adsorbed on silica gel at 308.15 K

System	K_d (mL g^{-1})	K
Benzene (A) + OCTE (B)	7.54	1.075
Toluene (A) + OCTE (B)	5.70	1.24
o-Xylene (A) + OCTE (B)	0.7 (for B) 1.8 (for A)	0.132 (for B) 0.01655 (for A)
p-Xylene (A) + OCTE (B)	0.4 (for B) 1.0 (for A)	0.2152 (for B) 0.01145 (for A)

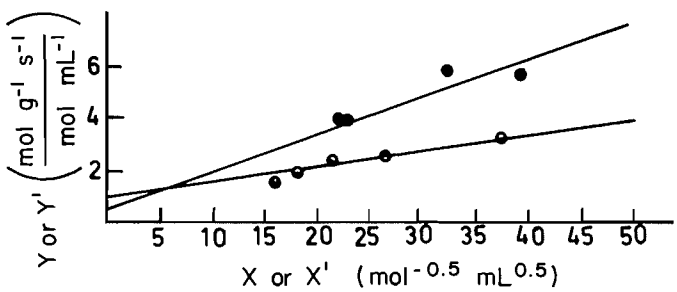

FIG. 6. Plot of Y or Y' vs. X or X' for *p*-xylene + OCTE mixture adsorbed on silica gel at 308.15 K.

H—O—Si—O—H moiety, then according to eq. [17], a plot of $Y\,(=(N_{B(l)})_S/(n_{B(l)})_{\equiv m \text{ in } A(l)})$ vs. $X\,(=(n_{B(l)})^{-0.5}_{\equiv m \text{ in } A(l)})$ and a plot of $Y^1\,(=(N_{A(l)})_S/n_{A(l)})_{\equiv m \text{ in } B(l)})$ vs. $X^1\,(=(n_{A(l)})^{-0.5}_{\equiv m \text{ in } B(l)})$ (utilizing the necessary relevant data) should be straight lines. This was found to indeed be true of the adsorption of A and B entities of the *p*-xylene (A) or *o*-xylene(A) + OCTE (B) mixtures on the silica gel surface (Figs. 6, 7); the relevant K_d and K values are recorded in Table 3.

Examination of Table 3 thus clearly reveals that while the adsorption of OCTE on the silica gel surface from benzene (A) or toluene (A) + OCTE (B) mixtures is dictated by both the distribution and the surface complexation reaction processes, the adsorption of A and B entities of the *p*-xylene (A) or

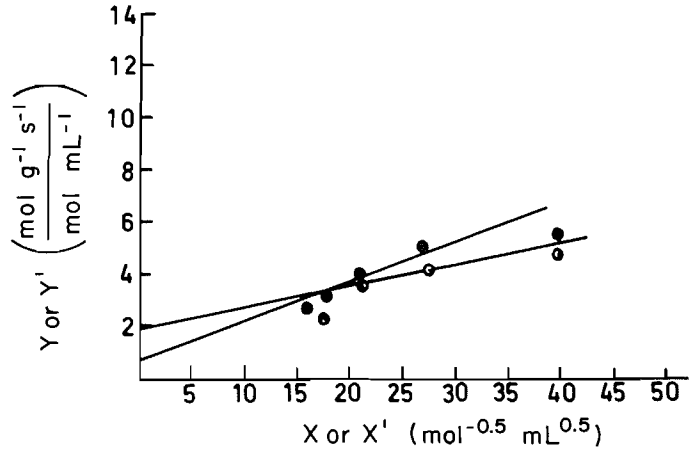

FIG. 7. Plot of Y or Y' vs. X or X' for *o*-xylene + OCTE mixture adsorbed on silica gel at 308.15 K.

o-xylene (A) + OCTE (B) mixtures onto the silica gel surface is governed primarily by the distribution process and secondarily by surface reaction processes. Further, the variation of the distribution coefficient K_d of OCTE (B) between A(l) and the solid phase (S) for benzene (A) or toluene (A) or the *o*-xylene (A) or *p*-xylene (A) + OCTE (B) mixtures in the order benzene > toluene > *o*-xylene > *p*-xylene suggests that the partitioning of OCTE (B) between the A(l) and S phases is dictated by $-CH_3$ substituents in the benzene ring. This is understandable. The adsorption of OCTE (B) from benzene (A) or toluene (A) or *o*-xylene (A) or *p*-xylene (A) + OCTE (B) mixtures onto the silica gel has been postulated to involve the **IV** species of OCTE, and because toluene (A), *p*-xylene (A), and *o*-xylene (A) can exist (due to hyperconjugation) in the

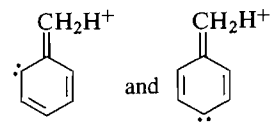

VII

and **III** forms respectively and these species also have electron-deficient centers, the relative strengths of which vary in the order *p*-xylene > *o*-xylene > toluene, it is apparent that the partitioning of OCTE (B) between the A(l) and S phases in the present study should vary in the order benzene > toluene > *o*-xylene > *p*-xylene. This would of necessity require that A(l) and B(l) be characterized by some sort of mutual interaction. A recent study (30) on the molar excess volumes and excess enthalpies of benzene (A) or toluene (A) or *p*-xylene (A) or *o*-xylene (A) + OCTE (B) liquid mixtures indeed has suggested that weak specific interactions (probably contact charge-transfer type) do take place between the components of these mixtures. Since the interactions between the A and B components of the present (A + B) mixtures in the liquid phase are very weak (activity coefficients of A and B in the bulk phase of the (A + B) mixtures are all close to unity (30)), it is reasonable to assume that their presence does not seriously jeopardize the mathematical arguments of the present analysis. The K_d and K values for the adsorption of A and B entities of the *p*-xylene or *o*-xylene (A) + OCTE (B) mixtures on the silica gel surface further suggest that the S-shaped adsorption isotherms characterizing these mixtures are dependent on the relative partitioning abilities of the A and B entities and that the surface reaction plays a relatively minor part.

Can. J. Chem. Downloaded from www.nrcresearchpress.com by 93.93.197.157 on 09/07/12
For personal use only.

The present study has thus revealed that any comprehensive theory of adsorption must take into consideration not only the partitioning abilities of the A and or B components of the (A + B) mixtures but also their ability to undergo surface reactions on the solid surface. Perhaps the non-ideality of the bulk liquid phase may also be an important factor.

Acknowledgements

The authors express their thanks to the Head of the Chemistry Department and the Authorities of Maharshi Dayanand University, Rohtak, for providing the necessary research facilities. The authors also express their gratitude to Professor D. H. Everett, F.R.S., and Dr. J. M. Haynes of the University of Bristol, U.K., for determining the surface area of the silica gel. Thanks are also due to Dr. J. K. Makrandi for helpful discussions.

1. G. SCHAY and L. G. NAGY. Acta Chim. Acad. Sci. Hung. **50**, 207 (1966).
2. D. H. EVERETT. Trans. Faraday Soc. **61**, 2478 (1965).
3. A. ZCHUCHOWITZKY. Acta Physicochim. URSS. **8**, 531 (1938).
4. W. RUDZINSKI and S. PARTYKA. J. Chem. Soc. Faraday Trans. 1, **77**, 2577 (1981).
5. W. RUDZINSKI, L. ZALTAR, J. ZAJAC, E. WOLFRAM, and PASZLI. J. Colloid Interface Sci. **96**, 339 (1983).
6. R. SIPS. J. Chem. Phys. **16**, 490 (1948).
7. H. G. CASSIDY. *In* Techniques of organic chemistry. Vol. V. Adsorption and chromatography. *Edited by* A. Weissberger. Interscience, New York. 1950. p. 34.
8. A. I. VOGEL. *In* A textbook of practical organic chemistry. English Book Soc., Longmans, London. 1983. p. 172.
9. J. SINGH, H. C. PFLUG, and G. C. BENSON. J. Phys. Chem. **72**, 1939 (1968).
10. B. G. KYLE and T. M. REED. J. Am. Chem. Soc. **30**, 6170 (1958).
11. A. F. FORZIATI and F. D. ROSSINI. J. Res. Natl. Bur. Stand. U.S. **43**, 473 (1949).
12. J. TIMMERMANS. *In* Physico-chemical constants of pure organic compounds. Elsevier, Amsterdam. 1950. p. 297.
13. A. M. JAMES and F. E. PRICHARD. *In* Practical physical chemistry. Longman Group Ltd., Harlow, Essex. 1974. p. 29.
14. M. HENNAULT-ROLAND and L. LEK. Bull. Soc. Chem. Belg. **40**, 177 (1931).
15. G. W. SMITH. J. Phys. Chem. **48**, 168 (1944).
16. A. V. KISELEV and V. I. LYGIN. *In* Infrared spectra of surface compounds. *Translated from Russian by* N. Kaner. John Wiley and Sons, New York. 1975. p. 79.
17. N. WRIGHT and M. J. HUNTER. J. Am. Chem. Soc. **69**, 803 (1947).
18. A. L. SMITH. Spectrochim. Acta, **16**, 87 (1960).
19. H. W. KOHLSCHUTTER and K. UNGER. *In* Thin layer chromatography. 2nd ed. *Edited by* E. Stahl. Springer Verlag, Berlin. 1969. p. 12.
20. M. L. HAIR. *In* Infrared spectroscopy in surface chemistry. Marcel Dekker, New York. 1967. p. 83.
21. J. A. HOCKEY and B. A. PETHICA. Trans. Faraday Soc. **57**, 2247 (1961).
22. N. B. CULTHUP, S. E. WIBERLEY, and L. H. DALY. *In* Introduction to infrared and Raman spectroscopy. Academic Press, New York. 1975. p. 217.
23. M. FOLMAN and D. J. C. YATES. Proc. R. Soc. London, A: **246**, 32 (1958).
24. V. I. LYGIN and A. V. KISELEV. Colloid. J. **23**, 250 (1961).
25. N. N. AVGUL and A. V. KISELEV. *In* Chemistry and physics of carbon. Vol. 6. Dekker, New York. 1970. p. 1.
26. L. B. PERI. J. Phys. Chem. **70**, 2937 (1966).
27. J. A. HOCKEY. Chem. Ind. (London), 57 (1965).
28. R. L. MORRISON and R. N. BOYD. *In* Organic chemistry. Prentice–Hall of India, New Delhi. 1969. p. 393.
29. D. COOK. J. Am. Chem. Soc. **80**, 49 (1958).
30. H. P. DAHIYA, P. P. SINGH, and S. DAGAR. Fluid Phase Equilibr. **33**, 191 (1987).

Can. J. Chem. Downloaded from www.nrcresearchpress.com by 93.93.197.157 on 09/07/12
For personal use only.

Conformational changes in serine on methylmercury complexation

MARIE-CLAUDE CORBEIL AND ANDRÉ L. BEAUCHAMP

Département de Chimie, Université de Montréal, C.P. 6128, Succ. A, Montréal (Qué.) Canada H3C 3J7

Received October 19, 1987

MARIE-CLAUDE CORBEIL and ANDRÉ L. BEAUCHAMP. Can. J. Chem. **66**, 1379 (1988).

The CH_3Hg^+ cation forms a zwitterionic complex $CH_3Hg[HOCH_2CH(NH_2)CO_2$—N,O,O] with serine in aqueous solution. X-ray diffraction ($P2_12_12_1$, $a = 5.821$, $b = 8.052$, $c = 14.307$ Å, $R = 0.021$) shows that mercury is linearly bonded to the NH_2 end of the amino acid, whereas one carboxylate oxygen and the side-chain hydroxyl group establish secondary Hg—O bonds. Coordination leads to characteristic changes in the infrared and Raman spectra of serine. From the ^1H and ^{13}C nmr spectra, N-coordination is found to be retained in aqueous solution, whereas the ligand conformation observed in the solid accounts for 76% of the conformer distribution.

MARIE-CLAUDE CORBEIL and ANDRÉ L. BEAUCHAMP. Can. J. Chem. **66**, 1379 (1988).

Le cation CH_3Hg^+ forme un complexe zwiterionique $CH_3Hg[HOCH_2CH(NH_2)CO_2$—N,O,O] avec la sérine en solution aqueuse. La diffraction des rayons X ($P2_12_12_1$, $a = 5{,}821$, $b = 8{,}052$, $c = 14{,}307$ Å, $R = 0{,}021$) montre que le mercure est lié de façon linéaire à l'extrémité NH_2 de l'acide aminé, alors que l'un des oxygènes carboxylates et la fonction hydroxyle de la chaîne latérale établissent des liaisons secondaires Hg—O. La coordination introduit des changements caractéristiques dans les spectres infrarouge et Raman de la sérine. Les spectres rmn ^1H et ^{13}C indiquent que la coordination du métal à l'azote persiste en solution aqueuse et que le complexe adopte à 76% la conformation observée à l'état solide.

Can. J. Chem. Downloaded from www.nrcresearchpress.com by 93.93.197.157 on 09/07/12
For personal use only.

Introduction

When bonded to flexible ligands containing extra free donor groups, the methylmercury(II) cation is expected to have an influence on the ligand conformation, since the linearly-coordinated Hg atom tends to satisfy its residual Lewis acidity by forming secondary bonds near the equatorial plane perpendicular to the CH_3—Hg—L direction. We are currently examining the effect of CH_3Hg^+ coordination on the conformation of protein components. Conditions and sites for primary coordination have been studied by using ligands like glycine, alanine (1), and glycylglycine (2), which are devoid of functionalized side chains. In the present paper, complexation with serine, which contains a —CH_2OH side chain, is being examined.

Experimental section

Reagents

L-Serine (from Nutritional Biochemicals Corporation) was used without further purification. The source of CH_3Hg^+ ions was the hydroxide CH_3HgOH (1 *M* aqueous solution from Alfa Inorganics).

Vibrational spectroscopy

The Raman spectra, excited by the 514.5 nm line from a Spectra Physics Model 165 argon ion laser, were recorded at Université Laval on a Spex Model 1400 microcomputer-controlled spectrometer. The samples were contained in capillary tubes which were mounted on a motor shaft and rotated at high speed in the laser beam. The laser power at the sample was 200 mW for free serine and 25 mW for the complex to prevent decomposition. The spectra were recorded at 5 cm^{-1} spectral slit width, with a 2 s integration time at each 2 cm^{-1} frequency increment.

The infrared spectra were recorded as KBr pellets on a FTIR Nicolet 7199 instrument equipped with a HeNe class II laser with a resolution of 1 cm^{-1} and 200 scans per spectra.

Nuclear magnetic resonance spectroscopy

The ^1H and ^{13}C nmr spectra were obtained with the Bruker WH-400 spectrometer of the Centre Régional de RMN à Haut Champ located at the Université de Montréal. The samples were dissolved in D_2O (Cambridge Isotope Lab., 99.83% isotopic purity). DSS and 1,4-dioxane were used as external references for the ^1H and ^{13}C spectra, respectively. The concentration of the solutions was ~0.15 *M*.

Preparations

CH_3Hg(L-ser): 1 mmol (105 mg) of L-serine was dissolved in 1.0 mL of 1 *M* aqueous CH_3HgOH. Absolute ethanol (10 mL) was added. After a few hours at room temperature and in open air (hood), colorless needles precipitated. Yield: 150 mg (48%). *Anal.* calcd. for $C_4H_9HgNO_3$: C 15.03, H 2.84, Hg 62.74; N, 4.38; found (Schwarzkopf Lab.): C 15.28, H 2.89, Hg 62.33, N 4.20.

O,N-Deuterated L-serine-d_4 and CH_3Hg(L-ser-d_3) were obtained by exchange with heavy water.

Crystal data

$C_4H_9HgNO_3$ fw = 319.71

Orthorhombic, $P2_12_12_1$, $a = 5.821(2)$, $b = 8.052(1)$, $c = 14.307(3)$ Å, $V = 670.6$ Å^3, $Z = 4$, $D_c = 3.166$ g cm^{-3}, λ(MoK$\bar{\alpha}$) = 0.71069 Å, μ(MoKα) = 228.8 cm^{-1}, $T = 293$ K.

Crystallographic measurements and structure determination

A crystal of dimensions (mm) 0.05 (between 011 and 011) × 0.05 (011–011) × 0.11 (100–100) was used for X-ray work. The space group and cell parameters were initially determined from precession and cone-axis photographs. Accurate cell parameters and intensity data were obtained with an Enraf-Nonius CAD4 diffractometer, as described elsewhere (3). The six standard reflections monitored during the experiment showed random fluctuations within ±1.7%. A total of 713 *hkl* reflections was measured ($2\theta \leq 50°$). Inspection of the full data set confirmed the systematic absences noted on the films ($h00$, $h \neq 2n$; $0k0$, $k \neq 2n$; $00l$; $l \neq 2n$), unambiguously identifying $P2_12_12_1$ as the space group. After removal of the 16 systematic absences, the data set consisted of 697 independent reflections, of which 675 were used to solve the structure ($I \geq 3\,(\sigma(I))$. The data were corrected for the Lorentz effect, polarization, and absorption (Gaussian integration, grid 8×8×8, transmission range: 0.24–0.44).

The structure was solved by the heavy-atom method and refined on $|F_o|$. The mercury atom was located from a Patterson map and the non-hydrogen atoms were found on the difference Fourier (ΔF) map phased on Hg. Isotropic refinement by full-matrix least squares converged to $R = \Sigma\|F_o| - |F_c\|/\Sigma|F_o| = 0.052$ and $R_w = [\Sigma w(|F_o| - |F_c|)^2/\Sigma w|F_o|^2]^{1/2} = 0.069$. At this stage, it was checked that the absolute configuration was that of the L enantiomer of serine. Refinement was completed by block-diagonal least squares. The hydrogen atoms on the amino, methine, and methylene groups were fixed at idealized positions (C—H = 0.95 Å, N—H = 0.87 Å, $B_{iso} = 4.0$ Å^2). The methyl and hydroxyl hydrogens were not visible in the ΔF map. The hydrogen parameters were not refined, but their

TABLE 1. Refined coordinates ($\times 10^3$, Hg$\times 10^5$) and equivalent isotropic temperature factors ($\times 10^3$)

Atom	X	Y	Z	U_{eq}
Hg(1)	22757(6)	2570(5)	−4885(3)	34
O(6)	−164(1)	−74(1)	−137	34
O(7)	−251(1)	−304(1)	−216(1)	47
O(8)	119(1)	−322(1)	−25	38
N(2)	289(1)	−104(1)	−176	30
C(1)	190(2)	172(1)	70(1)	45
C(3)	143(2)	−252(1)	−190(1)	27
C(4)	200(2)	−381(1)	−114(1)	32
C(5)	−112(2)	−205(1)	−181(1)	30

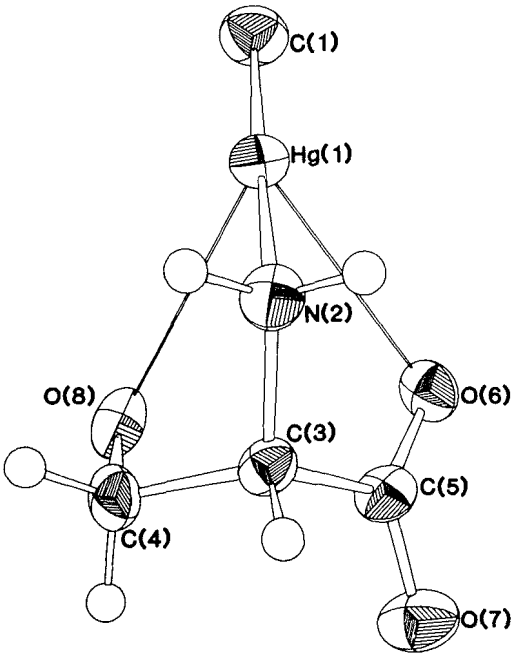

FIG. 1. Numbering scheme and structure of $CH_3Hg[HOCH_2CH(NH_2)(CO_2—N,O,O]$ complex with L-serine. The thin bonds correspond to Hg...O contacts. The thermal ellipsoids for the non-hydrogen atoms correspond to 50% probability. The methylene and methine hydrogens are represented by open spheres of arbitrary size. The methyl and hydroxyl hydrogens were not located.

coordinates were recalculated after each least-square cycle. Anisotropic refinement of all non-hydrogen atoms converged to $R = 0.021$, $R_w = 0.026$, and a goodness-of-fit ratio of 1.15. The final ΔF map was featureless, and the general background was below ± 0.55 e/Å^3.

The scattering curves were from standard sources. The f' and f'' contributions of Hg to anomalous dispersion were included in structure-factor calculation (4). The refined coordinates and equivalent isotropic temperature factors are listed in Table 1.

Results and discussion

Description of the structure

The CH_3Hg(L-ser) complex is represented in Fig. 1, with the numbering scheme used. Interatomic distances and bond angles are listed in Table 2.

The CH_3Hg^+ ion has replaced an ammonium proton of serine. The metal shows a linear coordination (C(1)—Hg—N(2) = 174.0(4)°), with a Hg—N(2) distance (2.128)(7) Å) similar to those reported for this type of complexes (1, 2). Mercury also makes two intramolecular contacts with oxygen

TABLE 2. Interatomic distances and bond angles

Atoms	Distance (Å)
C(1)—Hg(1)	2.08(1)
Hg(1)—N(2)	2.128(7)
N(2)—C(3)	1.48(1)
C(3)—C(4)	1.54(1)
C(3)—C(5)	1.54(1)
C(4)—O(8)	1.44(1)
C(5)—O(6)	1.26(1)
C(5)—O(7)	1.24(1)

Bonds	Angle (deg)
C(1)—Hg(1)—N(2)	174.0(4)
Hg(1)—N(2)—C(3)	114.5(6)
N(2)—C(3)—C(4)	108.9(7)
N(2)—C(3)—C(5)	110.2(7)
C(3)—C(4)—O(8)	109.4(7)
C(4)—C(3)—C(5)	108.4(7)
C(3)—C(5)—O(6)	118.6(8)
C(3)—C(5)—O(7)	116.0(8)
O(6)—C(5)—O(7)	125.5(9)

atoms. The first one with the O(6) carboxylate oxygen at 2.726(6) Å (Table 3) is common for methylmercury — amino acid complexes, since it has been observed in complexes with alanine (1), methionine (5), and tyrosine (6). A second contact involves the hydroxylic oxygen O(8) at 2.890(8) Å. This appears to be the first example of intramolecular tridentate coordination for serine. Some very weak Zn...OH interaction may be present for one of the ligands in the Zn(L-ser)$_2$ chelate (7), but with an adjacent molecule in the polymeric structure. The present complex also appears to be only the second example of a CH_3Hg^+ hydroxylic oxygen interaction, the previous example being a Hg...OH contact of 2.680(6) Å $[CH_3Hg(L—N, 0)]NO_3$, where L is tris(*N*-methylimidazol-2-yl)methanol (8).

In presence of mercury, light-atom positions cannot be determined with high accuracy. Considering the esd's, the bond lengths and angles of L-serine (9–11) are not significantly affected by complexation.

A stereo view of the unit cell is given in Fig. 2. Two molecules related by a 2_1 axis parallel to *a* are connected via hydroxyl groups forming moderately strong O(8)—H...O(6) hydrogen bonds (O...O = 2.769(9) Å) and a normal Hg—O(8) contact of 3.000(7) Å (Table 3). This pair is anchored to four similar pairs in the unit cell by symmetry equivalent N(2)—H(21)...O(7) hydrogen bonds (N...O = 2.88(1) Å). The pairs of molecules are repeated by the *a* translation, generating an infinite chain in which propagation is mainly achieved by weak N(2)—H(22)...O(7) interactions (N...O = 3.18(1) Å).

In the crystal structures of serine (9–11) and most of its complexes (7, 12–17), the role of the —OH group is restricted to intermolecular hydrogen bonding. Hence, the orientation of the CH_2—OH bond is not controlled by coordinative interactions, but by hydrogen bonding. The three low-energy conformations of serine are shown in structures **I**–**III**. Conformation **III** is found in the crystals of L-serine (9, 10), DL-serine (9, 11, and L-serine monohydrate (11), and for chelate rings in various metal complexes (7, 14, 16). In this conformation, the —OH group is *gauche* to the $—CO_2^-$ and NH_2 groups. The other common conformation **I** (OH *anti* to CO_2^-) has been observed

Can. J. Chem. Downloaded from www.nrcresearchpress.com by 93.93.197.157 on 09/07/12
For personal use only.

TABLE 3. Distances and angles in the hydrogen bonds and Hg...O contacts

Atoms	Distance (Å)	Bonds	Angle (deg)
		Hydrogen bonds	
N(2)—H(21)...O(7)[a]	2.88(1)	C(3)—N(2)—O(7)[a]	124.1(6)
N(2)—H(22)...O(7)[b]	3.18(1)	C(5)[a]—O(7)[a]—N(2)	108.0(4)
O(8).....O(6)[c]	2.769(9)	C(3)—N(2)—O(7)[b]	93.0(5)
		C(5)[b]—O(7)[b]—N(2)	134.5(4)
		C(4)—O(8)—O(6)[c]	119.4(5)
		C(5)[c]—O(6)[c]—O(8)	105.9(6)
		Hg...O contacts	
Hg(1)...O(6)	2.726(6)	Hg(1)—O(6)—C(5)	106.0(6)
Hg(1)...O(8)	2.890(8)	N(2)—Hg(1)—O(6)	66.5(3)
Hg(1)...O(8)[c]	3.000(7)	C(1)—Hg(1)—O(6)	117.2(3)
		Hg(1)—O(8)—C(4)	98.3(5)
		N(2)—Hg(1)—O(8)	70.3(2)
		C(1)—Hg(1)—O(8)	115.4(3)
		Hg(1)—O(8)[c]—C(4)[c]	112.3(5)
		N(2)—Hg(1)—O(8)[c]	84.6(3)
		C(1)—Hg(1)—O(8)[c]	95.8(4)

[a] $-x,\frac{1}{2}+y,-\frac{1}{2}-z$.
[b] $1+x,y,z$.
[c] $\frac{1}{2}+x,-\frac{1}{2}-y,-z$.

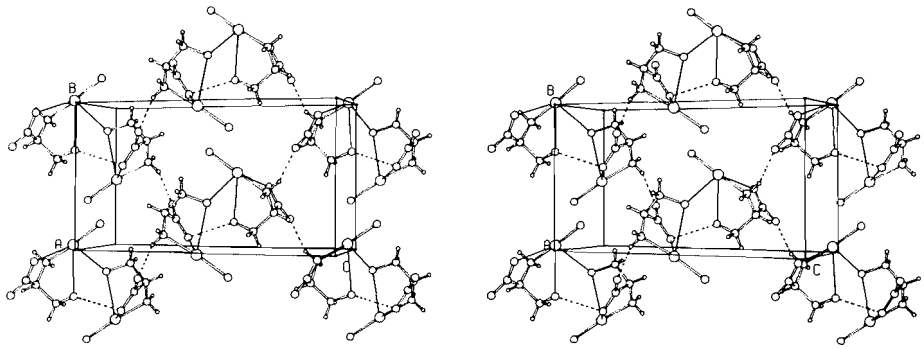

FIG. 2. Stereo view of the unit cell of CH_3Hg(L-serine) down the *a* axis. Atoms can be identified from Fig. 1. Full lines correspond to Hg...O contacts and dottted lines to hydrogen bonds.

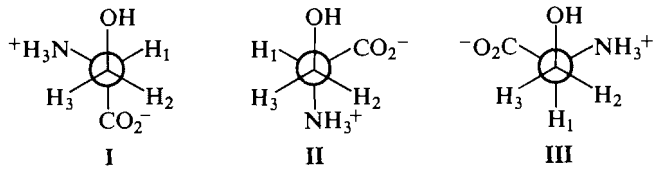

in several chelates (12, 13, 15–17), sometimes in the presence of a second chelate ring with conformation **III**. The only example of conformation **II** is found in Zn(L-ser)$_2$ (7) for the ligand providing chain propagation in the polymeric structure: this serine forms an O/N chelate with one Zn atom and uses the other carboxylate oxygen to strongly coordinate to a nearby Zn atom, whereas the —OH group is weakly interacting with the latter Zn atom, as mentioned above. These constraints probably force an atypical conformation in the amino acid.

The present CH_3Hg(L-ser) complex adopts conformation **III**, with N(2)—C(3)—C(4)—O(8) and C(5)—C(3)—C(4)—O(8) angles of 70.0(9)° and −49.9(9)°, respectively. However, this time, the preference for conformation **III** probably originates mainly from intramolecular Hg...O interactions.

Deviation from planarity in the N—C—CO_2 backbone remains within 2° in uncoordinated serine (9–11). In chelates, coordination introduces a twist about the C—C bond, generally increasing the N—C—C=O torsion angle to the 19–24° range (7, 14–17), although extreme values of 7° (12) and 42° (13) have been noted. The CH_3Hg(L-ser) complex lies in the normal region, with a N(2)—C(3)—C(5)—O(6) angle of −21(1)°.

Vibrational spectroscopy

The spectra of DL-serine and five deuterated derivatives have been empirically assigned by Madec, Lauransan, and Garrigou-Lagrange (18). Those of L-serine and its ND_3/OD derivative have also been reported by the same group, who briefly commented on the differences compared to the racemic material (19). Our results for L-serine and L-serine-d_4 are in good agreement with those reported by these authors.[1] On the basis of a normal coordinate analysis, Machida, Izumi, and Kagayama (20) have proposed for DL-serine assignments which have been recently reexamined and generally confirmed by Susi and co-workers (21). The approximate assignments used for the L-isomer have been directly transferred from the interpretation of Machida *et al.* for the DL-isomer (20), with only a few changes. These authors assigned a band at 1249 cm^{-1} to the δ(OH) mode for DL-serine. However, since this band for

Can. J. Chem. Downloaded from www.nrcresearchpress.com by 93.93.197.157 on 09/07/12
For personal use only.

TABLE 4. Infrared and Raman wavenumbers (cm^{-1}) for CH_3Hg(L-ser) and CH_3Hg(L-ser-d_3)[a]

Ch_3HgSer		$CH_3HgSer\text{-}ND_2,OD$		
Infrared	Raman	Infrared	Raman	Assignment
~3400 sh		—	—	ν(OH)
3173 s,b	3166 w,b	—	—	$\nu_a(NH_2)$
3065 s,b	3078 w,b	—	—	$\nu_s(NH_2)$
	3006 m	3005 m	3010 m	
2962 w	2948 s	2958 m	2962 s	ν(CH), $\nu(CH_2)$
2936 w			2946 vs	
2928 m	2928 vs	2928 m	2927 vs	$\nu(CH_3(Hg))$
2893 w	2892 m	2885 m	2886 m	$\nu_s(CH_2)$
		~2550 sh,b	—	ν(OD)
—	—	2372 m	2380 w,sh	$\nu_a(ND_2)$
—	—	2273 m	2280 w,b	$\nu_s(ND_2)$
1594 vs	1602 w	1591 vs		$\nu_a(CO_2^-)$
1594 vs	1602 w	—	—	$\partial(NH_2)$
1466 m	1466 m	1466 m	1466 w	$\partial(CH_2)$
1416 m	1416 m	1406 s	1405 w	$\nu_s(CO_2^-)$
1380 s	1388 w	—	—	
1349 w	1346 s	1358 s	1356 m	∂(CH), $\tau(NH_2)$
1326 s	1316 s	1323 s	1320 m	and $\tau(CH_2)$
1303 m		1292 m	1296 w	
1223 w	1224 w,sh	1243 m	1244 w	$\omega(CH_2)$
~1190 w		—	—	∂(OH)
1212 m	1204 vs	1207 vw	1208 vs	$\partial(CH_3(Hg))$
—	—	1193 m		$\partial(ND_2)$
1164 s	1164 m	—	—	$\omega(NH_2)$
1097 m	1096 m	1092 s	1104 w	
1048 s	1046 w	1038 m	1030 w	
985 w	982 m	958 w		ν skeletal
918 w	916 m	934 m	930 w	
—	—	~930 sh		$\tau(ND_2)$
—	—	847 w		∂(OD)
874 w	878 s			$\rho(CH_2)$
—	—	829 w		$\omega(ND_2)$
819 s	824 m	806 m	820 w	$\omega(CO_2^-)$
792 m		788 m		$\rho(CH_3(Hg))$
701 m	704 w	690 m		$\partial(CO_2^-)$
		635 w		
647 w,b		—	—	$\rho(NH_2)$ + t(OH)
580 w				∂ skeletal
562 m	560 vs	~560 sh	565 vs	ν(Hg−C)
	553 m,sh		554 vs	$\rho(CO_2^-)$
469 m	476 vs	447 m	453 vs	ν(Hg−N)
	374 w		350 w	
	292 m		290 m	∂ skeletal

[a]Abbreviations: v,very; s, strong; m, medium; w, weak; b, broad; sh, shoulder. Vibration types: ν, stretching; ∂, bending; ρ, rocking; ω, wagging; τ, twisting, t, torsion; s, symmetric; a, antisymmetric.

L-serine is not removed, but simply shifted from 1246 to 1265 cm^{-1} on deuteration, we assigned it to the $\omega(CH_2)$ vibration, which was assumed to coincide with the a $\rho(NH_3^+)$ vibration at 1176 cm^{-1} for DL-serine. The broad feature at 1216 cm^{-1} for L-serine , removed by deuteration, would then correspond to the δ(OH) mode, as proposed by Madec *et al.* (19). The δ(OD) vibration could correspond to one of the components, probably the first, of the pair of weak infrared bands at 875 and 838 cm^{-1}, the other component being due to a $\rho(ND_3^+)$ motion.

The wavenumbers for the (CH_3Hg)(L-ser) complex are listed in Table 4. Figures of the spectra are part of the supplementary material.[1] The assignments are largely based on the normal coordinate analysis carried out on the Cu(II) and Zn(II) complexes of DL-serine by Machida *et al.* (22).

The presence of the CH_3Hg^+ group in the compound is evidenced from the characteristic bands at 2928 (ir,R,υ), 1210 (ir,R,δ), and 790 cm^{-1} (ir,ρ) of the Hg-bonded methyl group (1, 2). The υ(Hg—CH_3) and υ(Hg—N) modes produce very strong Raman bands at 560 and 476 cm^{-1}, respectively, that is the

[1]A complete set of data may be purchased from the Depository of Unpublished Data, CISTI, National Research Council of Canada, Ottawa, Ont., Canada K1A 0S2.

Can. J. Chem. Downloaded from www.nrcresearchpress.com by 93.93.197.157 on 09/07/12
For personal use only.

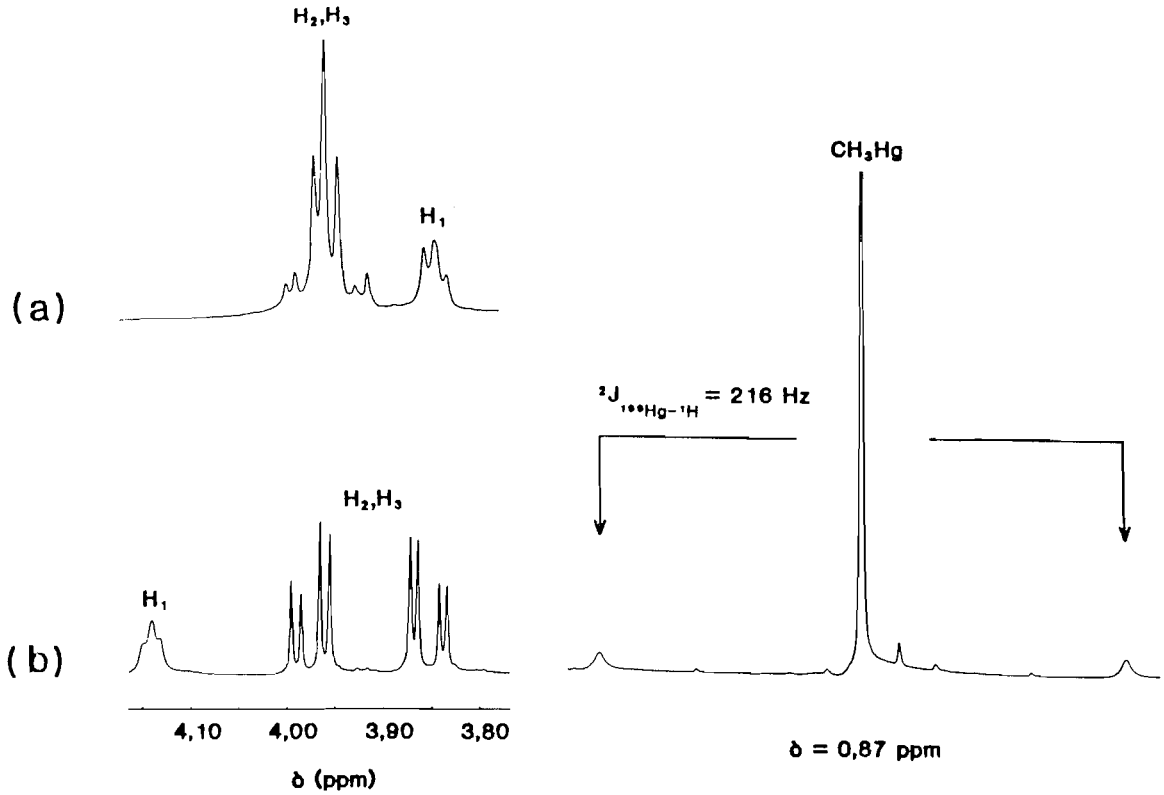

FIG. 3. 400-MHz ^{1}H nmr spectra of water solutions of (*a*) L-serine (pH 7.4) and (*b*) CH_3Hg(L-serine) (pH 8.0).

same positions as for CH_3Hg(gly) and CH_3Hg(L-ala) in solution (1). It is noteworthy that the υ(Hg—N) mode undergoes a $-20\,cm^{-1}$ shift upon deuteration. A similar effect has been noted for the CH_3Hg^+ complexes with methionine (5).

In the CH_3Hg(L-ser) complex, one of the NH_3^+ protons is replaced by a CH_3Hg^+ group. Accordingly, the high frequency υ(N—H) massif of L-serine is shifted upward by complexation as usual (22, 23). The NH_3^+ deformation modes at 1639, 1620, 1500 (δ), 1181, and 1130 (ρ) cm^{-1} are replaced by vibrations of the coordinated NH_2 group. The $\delta(NH_2)$ and $\upsilon_a(CO_2^-)$ modes both contribute to the strong infrared peak at $1600\,cm^{-1}$. The $\delta(ND_2)$ counterpart probably gives rise to the weaker infrared feature at $1193\,cm^{-1}$ in the spectrum of the N,O–d_3 derivative. The $\omega(NH_2)$ band is observed at $1164\,cm^{-1}$ and shifted to $829\,cm^{-1}$ by deuteration. This mode occurs at the same position for various serine chelates (22, 23).

No individual band can be assigned to the $\tau(NH_2)$ mode, but it likely contributes to the strong bands in the $1250–1390\,cm^{-1}$ region by coupling with the $\delta(CH_2)$ and δ(CH) motions, as indicated by Machida *et al.* (22). Evidence for this comes from the disappearance of one of the strong bands in this region upon deuteration, and from the presence of a broad low-wavenumber shoulder at ca. $930\,cm^{-1}$, assigned to $\tau(ND_2)$ mode, which would correspond to an ideally uncoupled $\tau(NH_2)$ mode at $1300\,cm^{-1}$. The $\rho(NH_2)$ band could not be identified with certainty, but it could contribute to the very broad infrared absorption between 600 and $700\,cm^{-1}$, which is removed by deuteration.

The crystal structure shows that the coordinated ligand adopts a conformation favoring the formation of a moderately strong secondary Hg—O bond with the hydroxylic oxygen. This does not appreciably affect the δ(OH) vibration, but the low-frequency torsion mode of the free ligand has become a genuine γ(OH) deformation mode, which should now occur at a much higher wavenumber. For instance, in solid ethanol, it is observed at $\sim 660\,cm^{-1}$ (24). It is likely that the γ(OH) mode of the complex contributes to the broad infrared absorption at $600–700\,cm^{-1}$ mentioned above.

The υ_a and υ_s carboxylate vibrations are not appreciably shifted from their positions in the free ligand, which was anticipated since this group is not involved in the primary coordination of mercury. The ρ, ω, and δ modes, which are usually more sensitive to hydrogen bonding and Hg...carboxyl contacts, are affected to a greater extent.

Nuclear magnetic resonance spectroscopy

Figure 3*a* shows the ^{1}H nmr spectrum of L-serine. Inequivalence of the methylene protons (H_2 and H_3) produces an ABX multiplet for the CH_2—CH fragment. The coupling constants and chemical shifts were refined by spectral simulation using the spectrum analysis program PANIC (25). The refined data given in Table 5 are similar to those reported earlier (26).

The ^{1}H nmr spectrum of the methylmercury complex (Fig. 3*b*) shows a CH_3Hg^+ signals at 0.87 ppm, accompanied by a pair of satellites resulting from coupling with ^{199}Hg (17% natural abundance). the $^2J(^{199}Hg—^1H)$ coupling constant of 216 Hz is common for complexation to nitrogen in amino acids (27). Displacement of an amino hydrogen by the less electron-attracting mercury produces a downfield shift of 0.31 ppm for the methine (H_1) signal, while protons H_2 and H_3 are not greatly affected. However, the slight upfield shift (−0.09 ppm) of one of these two protons increases the signal separation which turns the L-serine ABX spectrum into an AMX pattern. With glycine and alanine, methylmercury complexation gave similar shifts:

Can. J. Chem. Downloaded from www.nrcresearchpress.com by 93.93.197.157 on 09/07/12
For personal use only.

TABLE 5. ^{1}H nmr parameters of the CH_2—CH fragment of serine and its methylmercury complex

Parameter	Fragment	Value	
		L-ser	CH_3Hg(L-ser)
^{1}H δ(ppm)	H_1	3.83	4.13
	H_2	3.96	3.96
	H_3	3.93	3.84
	CH_3Hg	—	0.87
^{13}C δ(ppm)	CH	57.2	58.6
	CH_2	61.0	62.6
	CO_2^-	173.3	176.9
	CH_3Hg	—	−1.9
J(Hz)	$J(H_1—H_2)$	4.1(3)	4.2(2)
	$J(H_1—H_3)$	5.5(3)	3.2(2)
	$J(H_2—H_3)$	−12.4(3)	−12.1(2)
	$J(C—H_2)$	—	7.3(4)
	$J(C—H_3)$	—	2.9(4)

TABLE 6. Populations of the rotational isomers for serine and its methylmercury complex

Compound	P_I	P_{II}	P_{III}
L-ser	0.28	0.16	0.56
CH_3Hg(L-ser)	0.07	0.17	0.76

the methylene protons of glycine were downfield shifted by 0.14 ppm, the methine proton of alanine by 0.41 ppm, while its methyl protons were not affected (1).

The vicinal coupling constants $^3J(H_1—H_2)$ and $^3J(H_1—H_3)$ provide information on the conformation of the molecule (28, 29). Serine has three possible rotational isomers whose Newman projection down the CH—CH_2 bond are shown in structures **I** to **III**.

To each rotamer corresponds a set of $^3J(H_1—H_2)$ and $^3J(H_1—H_3)$ coupling constants reflecting its conformation. However, rotation about the CH—CH_2OH bond is fast on the nmr time scale, so that the observed coupling constants are averaged over the three rotamers. The weighted average values are given by eq. [1] and [2],

$$[1] \quad {}^3J(H_1—H_2) = P_I J_g + P_{II} J_t + P_{III} J_g$$

$$[2] \quad {}^3J(H_1—H_3) = P_I J_t + P_{II} J_g + P_{III} J_g$$

where $^3J(H_1—H_2)$ and $^3J(H_1—H_3)$ are the observed coupling constants, J_g and J_t are the coupling constants corresponding to *gauche* and *trans* interactions, respectively, and P_i is the fractional population of rotamer i.

With $(P_I + P_{II} + P_{III})$ normalized to unity, eq. [1] and [2] become:

$$[3] \quad P_I = [{}^3J(H_1—H_3) - J_g] \,/\, (J_t - J_g)$$

$$[4] \quad P_{II} = [{}^3J(H_1—H_2) - J_g] \,/\, (J_t - J_g)$$

$$[5] \quad P_{III} = 1 - P_I - P_{II}$$

However, to use these equations, unambiguous assignment of the H_2 and H_3 signals is a prerequisite. This can be achieved by using the ^3J(C—H) vicinal coupling constants between the carboxylate carbon and the CH_2 protons. These coupling constants are also weighted averages over the three conformations:

$$[6] \quad {}^3J(C—H_2) = P_I J_g + P_{II} J_g + P_{III} J_t$$

$$[7] \quad {}^3J(C—H_3) = P_I J_g + P_{II} J_t + P_{III} J_g$$

The following set of equations, where J_g and J_t now represent ^3J(C—H) constants, can be deduced as above:

$$[8] \quad P_{II} = [{}^3J(C—H_3) - J_g]/(J_t - J_g)$$

$$[9] \quad P_{III} = [{}^3J(C—H_2) - J_g]/(J_t - J_g)$$

$$[10] \quad P_I = 1 - P_{II} - P_{III}$$

From the experimental ^3J(H—H) coupling constants and eqs [3] and [4], two sets of P_I, P_{II}, and P_{III} values can be calculated, depending on the assignments for H_2 and H_3. In a same way, the ^3J(C—H) coupling constants and eqs [8] and [9] give two sets of populations, one of which must coincide with one of those obtained from ^{1}H spectrum. From this common set, ambiguity is removed. This method has been applied to several amino acids, including serine (30).

From the observed values of $^3J(H_1—H_2)$ and $^3J(H_1—H_3)$ of Table 5, the populations of Table 6 were calculated, assuming the J_t and J_g values (13.3 and 2.4 Hz for H—H, 10.0 and 1.2 Hz for C—H) proposed by Martin (11).

According to Ogura *et al.* (32), **III** is the major conformation of serine over the whole pH range. Interestingly, this is also the conformation observed in the solid state by X-ray diffraction (9–11). From our results (Table 5), we calculate that **III** accounts for 56% of free serine in solution. For CH_3Hg(L-ser), the population of **III** raises to 76% at the expense of rotamer **I**, whose population decreases from 28% to 7%. Therefore, the conformer observed in the crystal structure described above remains by far the most important contributor in solution.

Concluding remarks

The CH_3Hg^+ cation binds to the NH_2 group of serine as it generally does with amino acids. The Hg...O secondary bond with a carboxylate oxygen observed in the crystal structure also occurs commonly. In this serine complex, the —OH group is suitably oriented to form an extra intramolecular Hg...O secondary bond, thereby leading to tridentate binding. In order for the three coordinating interactions to take place simultaneously, serine must adopt conformation **III**, in which the three donor atoms occupy the same region of space and can cluster around Hg.

Conformation **III** is already the most populated (56%) in aqueous solutions of free serine. Its contribution is raised to 76% for the CH_3Hg(L-ser) complex. Stabilization of this conformer probably originates mainly in the Hg...O contacts. Besides the contribution to cohesion due to the contacts themselves, the chelate effect provides a favorable contribution to the tridentate coordination. However, the Hg...O contacts are not strong to the point that the molecule is frozen in conformation **III** exclusively. Disruption of the Hg...O contacts can probably be balanced to some extent by hydration: Hg...OH_2 contacts could be acceptable alternatives to those formed with serine, whereas hydrogen bonding with water could satisfy the residual basicity of the —OH and —CO_2^- groups. Nevertheless, the overall effect observed in this work is a definite enrichment in the conformer **III** observed in the crystal, and it is clear that the orientation of the —CH_2OH side chain is affected by the presence of coordinated mercury.

Can. J. Chem. Downloaded from www.nrcresearchpress.com by 93.93.197.157 on 09/07/12
For personal use only.

Acknowledgments

We wish to thank M. J. Olivier and M. Simard who collected the X-ray data, and R. Savoie, M. Pigeon, and S. Alex (Université Laval) who kindly provided the Raman spectra. We are also grateful to M. T. Phan Viet for valuable suggestions concerning the nmr study. This work was made possible by grants from NSERC and FCAR.

1. M. C. Corbeil, A. L. Beauchamp, S. Alex, and R. Savoie. Can. J. Chem. **64**, 1876 (1986).
2. S. Alex, R. Savoie, M. C. Corbeil, and A.L. Beauchamp. Can. J. Chem. **64**, 148 (1986).
3. F. Bélanger-Gariépy and A. L. Beauchamp. J. Am. Chem. Soc. **102**, 3461 (1980).
4. D. T. Cromer and J. B. Mann. Acta Crystallogr. A**24**, 321 (1968); R. F. Stewart, E. R. Davidson, and W. T. Simpson. J. Chem. Phys. **42**, 3175 (1965); D. T. Cromer. Acta Crystallogr. **18**, 17 (1965).
5. Y. S. Wong, A. J. Carty, and P. C. Chieh. J. Chem. Soc. Dalton Trans. 1157 (1977).
6. N. W. Alcock, P. A. Lampe, and P. Moore. J. Chem. Soc. Dalton Trans. 1324 (1978).
7. D. Van der Helm, A. F. Nicholas, and C. G. Fisher. Acta Crystallogr. B**26**, 1172 (1970).
8. A. J. Canty, J. M. Patrick, and A. H. White. J. Chem. Soc. Dalton Trans. 1873 (1983).
9. T. J. Kistenmacher, G. A. Rand, and R. E. Marsh. Acta Crystallogr. B**30**, 2573 (1974).
10. E. Benedetti, C. Pedone, and A. Sirigu. Cryst. Struct. Commun. **1**, 35 (1972).
11. M. N. Frey, M. S. Lehmann, T. F. Koetzle, and W. C. Hamilton. Acta Crystallogr. B**29**, 876 (1973).
12. Y. Sasada, A. Takenaka, and T. Furuya. Bull. Chem. Soc. Jpn. **56**, 1745 (1983).
13. W. Petri, J. Meder, M. Girnth-Weller, K. Bartel, V. Bejenke, G. Huttner, and W.Beck. Chem. Ber. **115**, 846 (1982).
14. D. van der Helm and W. A. Franks. Acta Crystallogr. B**25**, 451 (1969).
15. I. A. Dyakon, S. V. Donu, L. F. Chapurina, and A. S. Avilov. Kristallografiya, **29**, 384 (1984).
16. R. S. Vagg. Acta Crystallogr. B**35**, 341 (1979).
17. D. van der Helm and M. B. Hossain. Acta Crystallogr. B**25**, 457 (1969).
18. C. Madec, J. Lauransan, and C. Garrigou-Lagrange. Can. J. Spectrosc. **23**, 166 (1978).
19. C. Madec, J.Lauransan, and C. Garrigou-Lagrande. C.R. Acad. Sci. Ser B, **288**, 69 (1979).
20. K. Machida, M. Izumi, and A.Kagayama. Spectrochim. Acta, **35**A, 1333 (1979).
21. H. Susi, D. M. Byler, and W. V. Gerasimowicz. J. Mol. Struct. **102**, 63 (1983).
22. J. Odo, M. Nishio, Y. Saito, Y. Tanaka, and K. Machida. Chem. Pharm. Bull. **31**, 3802 (1983).
23. Y. Inomata, T. Inomata, and T. Moriwaki. Bull. Chem. Soc. Jpn. **44**, 365 (1971).
24. Y. Mikawa, J. W. Brasch, and R. J. Jakobsen. Spectrochim. Acta, **27**A, 529 (1971).
25. PANIC. Standard Bruker program.
26. G. Wider, R. Baumann, K. Nagayama, R. R. Ernst, and K. Wuthrich. J. Mag. Reson. **42**, 73 (1981); M. Kainosho and K. Ajisaka. J. Am. Chem. Soc. **97**, 5630 (1975).
27. D. L. Rabenstein, R.Ozubko, S. Libich, C. A. Evans, M. T. Fairhurst, and C. Suvanrakorn, J. Coord. Chem. **3**, 263 (1974).
28. W. A. Thomas. Ann. Rep. NMR Spectrosc. **6**B, 1, 233 (1976).
29. V. F. Bystrov. Prog. NMR Spectroscopy, **10**, 41 (1976).
30. W. G. Espersen and R. B. Martin. J. Phys. Chem. **80**, 741 (1976); P. E. Hansen, J. Feeney, and G. C. K. Roberts. J. Mag. Reson. **17**, 249 (1975); M. C. Reddy, B. P. Nagi Reddy, K. R. Sridharan, and J. Ramakrishna. Org. Mag. Reson. **22**, 464 (1984); B. P. Mikhova, M. F. Simeonov, and S. L. Spassov. Mag. Reson. Chem. **23**, 474 (1985).
31. R. B. Martin. J. Phys. Chem. **83**, 2404 (1979).
32. H. Ogura, Y. Arata, and J. Fujiwara. J. Mol. Spectrosc. **23**, 76 (1967).

Can. J. Chem. Downloaded from www.nrcresearchpress.com by 93.93.197.157 on 09/07/12
For personal use only.

Regioselective synthesis of 2-pyrazolines and pyrazoles from ethyl α-cyanocinnamates

HAMDI M. HASSANEEN AND HIYAM A. H. MOUSA

Girls College, Science Department, General Presidency for Girls Education, Riyadh, Saudi Arabia

AND

SALEH T. EZMIRLY AND AHMAD S. SHAWALI[1]

Department of Chemistry, Faculty of Science, King Abdulaziz University, P.O. Box 9028, Jeddah 21413, Saudi Arabia

Received September 24, 1987

HAMDI M. HASSANEEN, HIYAM A. H. MOUSA, SALEH T. EZMIRLY, and AHMAD S. SHAWALI. Can. J. Chem. **66**, 1386 (1988).

The cycloaddition of nitrilimines **1***a–e* to ethyl α-cyanocinnamate **6***a* furnished the 2-pyrazoline derivatives **11***a–e* respectively. Similar reactions of **1***a–e* with ethyl α-cyano-*p*-nitrocinnamate **6***b* yielded 1,3-disubstituted 4-(*p*-nitrophenyl)-5-ethoxycarbonylpyrazoles **14***a–e*, via elimination of hydrogen cyanide from their precursors, the 2-pyrazoline derivatives **13***a–e*, respectively. The structures of the cycloadducts **11** and **14** were supported by spectral (^{13}C and ^{1}H nuclear magnetic resonance and infrared) and analytical data.

HAMDI M. HASSANEEN, HIYAM A. H. MOUSA, SALEH T. EZMIRLY et AHMAD S. SHAWALI. Can. J. Chem. **66**, 1386 (1988).

Le cycloaddition des nitrilimines **1***a–e* sur l'α-cyanocinnamate d'éthyle (**6***a*) conduit aux divers dérivés **11***a–e* de la pyrazoline-2. Des réactions semblables entre les composés **1***a–e* et l'α-cyano *p*-nitrocinnamate d'éthyle (**6***b*) conduisent aux (*p*-nitrophényl)-4 éthoxycarbonyl-5 pyrazoles disubstitués **14***a–e*, par le biais de l'élimination de cyanure d'hydrogène à partir des dérivés pyrazolines-2 (**13***a–e*) qui sont leurs précurseurs. On a déduit les structures des cycloadduits **11** et **14** en se basant sur leurs spectres (résonance magnétique nucléaire du ^{13}C et du ^{1}H ainsi que infrarouge) et sur des données analytiques.

[Traduit par la revue]

Introduction

Nitrilimines **1***a–f* are well-known 1,3-dipoles and their reactions with a variety of mono- and di-substituted ethylenes **2–4** have been extensively investigated (1). However, reactions of **1** with trisubstituted ethylenes **5** have received little if any attention (2, 3). Here we wish to report the results of the study of the cycloadditions of ethyl α-cyanocinnamate **6***a* and its *p*-nitro derivative **6***b* with nitrilimines **1***a–e* (Scheme 1). Our aim in studying the dipolarophilicity of **6** was to explore the effect of the α-cyano group on the regiochemistry of the cycloaddition of ethyl cinnamate **7**. The reactions of the latter ester with diphenylnitrilimine **1***a* (3) and with *N*-phenyltrifluoroacetonitrilimine **1***f* (4) yielded, in each case, a mixture of the two possible isomers **9** and **10** (Scheme 2).

Results and discussion

The reactions of nitrilimines **1***a–e*, generated *in situ* by treatment of the corresponding hydrazidoyl halides **8***a–e* with triethylamine, with **6***a* were carried out in refluxing chloroform. Thin-layer chromatographic analysis of the reaction mixture on silica gel with a mixture of carbon tetrachloride and chloroform (5:1.5 v/v) as eluent showed the formation of only one product. This was confirmed by ^{1}H nmr analysis of the crude reaction product, in which only one methine singlet signal was observed. These findings indicate that the reactions studied are regiospecific, yielding one of the two possible regioisomers **11** or **12** (Scheme 3). The structures of the cycloadducts were assigned on the basis of their spectral (ir, ^{13}C nmr, and ^{1}H nmr) and elemental analyses (Tables 1–3). The distinction between the two structures **11** and **12** was made on the basis of the nitrile absorption in the infrared spectra. Aliphatic nitriles activated by a nitrogen or an oxygen atom in the α-position (4, 10), such as the 5-cyano-2-pyrazoline derivatives, exhibit no nitrile absorption in their infrared spectra (11). On the other hand, the nitrile group in the 4-cyano-substituted 2-pyrazoline and pyrazole derivatives is ir active, showing a strong band in the 2100–2400 cm^{-1} region (12). In the infrared spectra of the products isolated from the reaction of **1***a–e* with **6***a* the nitrile absorption was absent. Therefore they were assigned the 5-cyano-5-ethoxycarbonyl-substituted 2-pyrazoline structure **11**. This assignment is supported by ^{13}C nmr spectra (5). For example, compounds **11***a–e* showed four characteristic lines assignable to C-3(s, δ141.1–142.6), C-4 (d, δ62.1–64.5), C-5 (s, δ71.1–74.0), and CN (s, δ211.6) ppm (Table 2). The ^{1}H nmr spectra of the cycloadducts showed, in each case, one characteristic singlet near δ5.0 ppm assignable to the methine proton at the 4-position in **11**. The methine chemical shift at the 5-position in **12** is expected to appear at lower field (13). Attempts to prepare an authentic sample of **12** for comparison purposes failed, however.

The reaction of ethyl α-cyano-*p*-nitrocinnamate **6***b* with **1***a–e* under the same conditions proceeded to give 4-(*p*-nitrophenyl)-5-ethoxycarbonyl-1,3-disubstituted pyrazoles **14***a–e* respectively (Table 3). The latter products undoubtedly resulted via thermal elimination of hydrogen cyanide from the corresponding cycloadducts **13***a–e* (Scheme 4). The assigned structures **14***a–e* were supported by analytical and spectral data (Tables 1–3). In the ^{1}H nmr spectra, the products **14***a–e* showed no signals due to 4-H or 5-H characteristic of 2-pyrazoline derivatives (6). In the ir spectra, the products **14***a–e* revealed in each case a strong absorption band near 1720 cm^{-1} due to an α,β-unsaturated ester carbonyl group (Table 1). The ^{13}C nmr spectra of **14***a–e*, while revealing the absence of nitrile carbon, had three characteristic lines near δ 140.2–147.0 (s), 131.3–131.7 (s), 138.7–140.0 (s) ppm assignable to C-3, C-4, and C-5 atoms of the pyrazole ring, respectively (Table 2) (5).

These results indicate that ethyl α-cyanocinnamates **6***a–b*, unlike ethyl cinnamate **12**, react with nitrilimines **1***a–e* regiospecifically in each case. These results may be interpreted by HOMO–LUMO interaction of **1** and dipolarophile **6** (7). The α-cyano group, being electron withdrawing, tends to lower the HOMO and LUMO energies, particularly the LUMO energy in this case, thus causing greater dipole (HOMO) – dipolarophile

[1]Author to whom correspondence may be addressed.

Printed in Canada / Imprimé au Canada

Can. J. Chem. Downloaded from www.nrcresearchpress.com by 93.93.197.157 on 09/07/12
For personal use only.

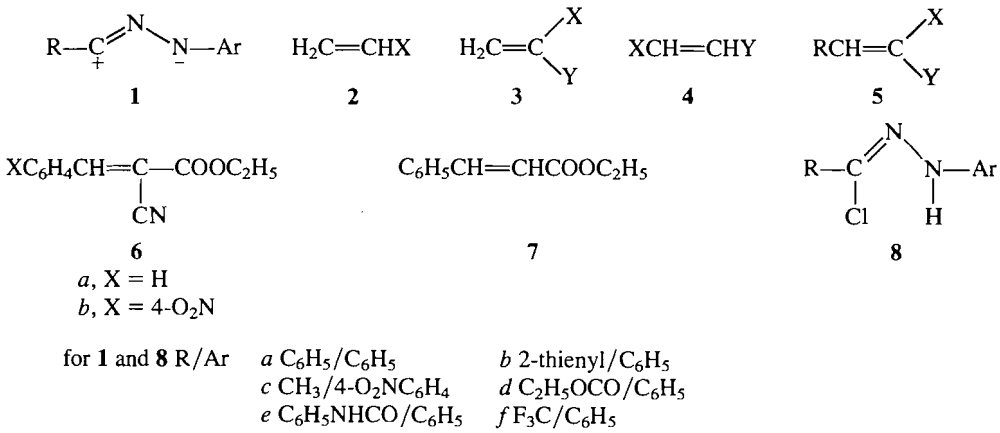

for **1** and **8** R/Ar *a* C_6H_5/C_6H_5 *b* 2-thienyl/C_6H_5
c $CH_3/4\text{-}O_2NC_6H_4$ *d* C_2H_5OCO/C_6H_5
e C_6H_5NHCO/C_6H_5 *f* F_3C/C_6H_5

SCHEME 1

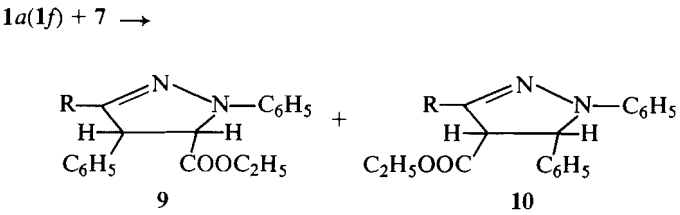

SCHEME 2

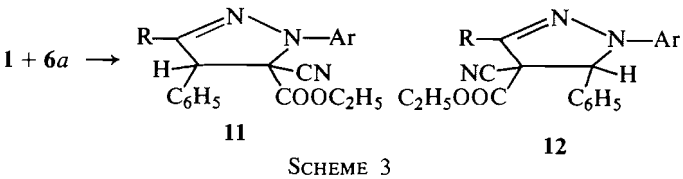

SCHEME 3

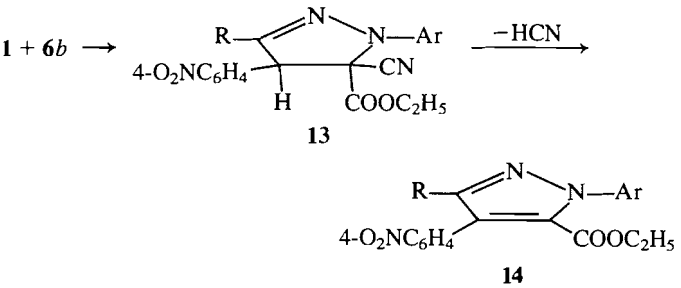

SCHEME 4

(LUMO) control of orientation (8). Furthermore, the α-cyano group decreases the LUMO coefficient at the site of attachment (8) so that the difference between the LUMO coefficients of the α- and β-carbon atoms becomes larger in **6** than in **7**. Consequently, the largest bonding interaction in the transition state arises between the carbon atom of the nitrilimine **1** and the β-carbon atom of **6**, thereby leading exclusively to the formation of the cycloadducts **11** and **13**.

Regarding the mechanism of elimination of hydrogen cyanide from **13** to give **14**, it is difficult to say anything conclusively except that it is similar to thermal elimination of hydrazoic acid from 1,3,4-triphenyl-5-benzoyl-5-azido-2-pyrazoline (2). The observation that such elimination occurs easily from **13** and not from **11** seems to be due to the higher acidity of the 4-H in **13**.

TABLE 1. The ^{1}H nmr and ir spectral data of the 2-pyrazolines **11***a–e* and pyrazole derivatives **14***a–e*

Compound No.	^{1}H nmr ($CDCl_3$)[a,b] δ, ppm	Infrared (KBr) ν,cm^{-1}
11*a*	1.2 (t,3H), 4.20(q,2H), 5.2 (s,1H)	1740
11*b*	1.2 (t,3H), 4.25(q,2H), 5.6 (s,1H)	1740
11*c*	1.15(t,3H), 2.0(s,3H), 4.2 (q,2H) 5.70(s,1H)	1760
11*d*	1.15(t,3H), 1.30(t,3H), 4.20(q,2H), 4.36(q,2H), 5.03(s,1H)	1760, 1700
11*e*	1.30(t,3H), 4.15(q,2H), 5.2 (s,1H)	1750, 1650, 3340
14*a*	0.95(t,3H), 4.00(q,2H)	1715
14*b*	1.00(t,3H), 4.15(q,2H)	1720
14*c*	1.00(t,3H), 2.30(s,3H), 4.20(q,2H)	1720
14*d*	0.90(t,3H), 1.20(t,3H), 4.00(q,2H) 4.30(q,2H)	1720, 1700
14*e*	1.00(t,3H), 4.10(q,2H)	1720, 1675, 3330

[a]All compounds exhibited aromatic proton multiplet signals in the region 7.0 – 8.4 ppm.
[b]The value of coupling constant *J* for the triplet (t) and the quartet (q) signals is 7 Hz.

Experimental

All melting points were measured on a Bockmonoscop hot-stage type melting point apparatus and are uncorrected. The infrared spectra were recorded in potassium bromide on a Zeiss infrared spectrophotometer model IMT16. The ^{1}H nmr spectra were obtained in deuterated chloroform with a Varian EM-390 90-MHz spectrometer. The ^{13}C nmr spectra were obtained from 1 M deuterated chloroform solutions on a JEOL JNM FX 100 spectrometer using tetramethylsilane as internal reference. Microanalyses were performed on a Perkin Elmer elemental analyzer model 240-B at the microanalytical laboratory of King Abdulaziz University. The hydrazidoyl halides **1***a–e* (1) and the dipolarophiles **6***a–b* (9) were prepared as described in the literature.

*1-Aryl-3-*R*-4-phenyl-5-cyano-5-ethoxycarbonyl-2-pyrazolines***11***a–e. General method*

To a stirred solution of the appropriate hydrazidoyl halide **1** (5 mmol) and ethyl α-cyanocinnamate **6***a* (5 mmol) in chloroform (40 mL) was added triethylamine (0.7 mL, 5 mmol) at room temperature. The mixture was then refluxed for 10–12 h and cooled. The reaction mixture was washed three times with water, and the organic layer was collected, dried over anhydrous sodium sulfate, and then filtered. The solvent was evaporated under reduced pressure and the residue was triturated with a little methanol, whereupon it solidified. The crude

Can. J. Chem. Downloaded from www.nrcresearchpress.com by 93.93.197.157 on 09/07/12
For personal use only.

TABLE 2. ^{13}C nuclear magnetic resonance data of the 2-pyrazolines **11***a–e* and pyrazole derivatives **14***a–e*

Compound No.	δ, ppm[a]						
	CN	CO	C-3	C-4	C-5	OCH_2R	CH_3R
11*a*	211.6(s)	165.6(s)	142.3(s)	63.9(d)	73.3(s)	63.2(t)	13.8(q)
11*b*	211.5(s)	165.4(s)	142.6(s)	64.5(d)	73.5(s)	64.0(t)	13.8(q)
11*c*	211.6(s)	165.0(s)	141.1(s)	67.5(d)	71.1(s)	64.7(t)	13.9(q) 14.1(q)
11*d*	211.5(s)	165.2(s)	141.8(s)	62.1(d)	74.0(s)	63.3(t)	14.2(q)
11*e*	211.5(s)	164.5(s) 157.3(s)	141.1(s)	62.3(d)	73.5(s)	64.5(t)	13.9(q)
14*a*		159.4(s)	140.2(s)	131.5(s)	139.7(s)	61.6(t)	13.5(q)
14*b*		158.7(s)	147.0(s)	131.7(s)	140.0(s)	61.5(t)	13.4(q)
14*c*		159.0(s)	144.2(s)	131.4(s)	138.7(s)	61.9(t)	13.6(q) 12.3(q)
14*d*		161.1(s) 158.5(s)	141.3(s)	131.3(s)	139.7(s)	61.4(t) 61.8(t)	13.4(q) 14.1(q)
14*e*		158.7(s) 158.4(s)	143.1(s)	131.3(s)	139.6(s)	61.9(t)	13.4(q)

[a]All compounds exhibit lines assignable to the phenyl ring carbons.

TABLE 3. Physical constants of 2-pyrazolines **11***a–e* and pyrazoles **14***a–e*

Compound No.	Melting point,°C	Yield, %	Molecular formula	Anal. calcd. (found), %		
				C	H	N
11*a*	107	80	$C_{25}H_{21}N_3O_2$	75.92 (75.75)	5.35 (5.19)	10.62 (10.70)
11*b*	156	70	$C_{23}H_{19}N_3O_2S$	68.81 (69.00)	4.69 (4.69)	10.47 (10.50)
11*c*	148	83	$C_{20}H_{18}N_4O_4$	63.48 (63.22)	4.79 (4.80)	14.81 (14.67)
11*d*	96	72	$C_{22}H_{21}N_3O_4$	67.50 (67.33)	5.41 (5.28)	10.73 (10.51)
11*e*	200	75	$C_{26}H_{22}N_4O_3$	71.22 (71.14)	5.06 (5.00)	12.78 (12.81)
14*a*	197	80	$C_{24}H_{19}N_3O_4$	69.72 (69.67)	4.14 (4.00)	10.16 (10.10)
14*b*	187	85	$C_{22}H_{17}N_3O_4S$	62.99 (63.05)	4.09 (4.10)	10.02 (10.10)
14*c*	150	70	$C_{19}H_{16}N_4O_6$	57.57 (57.75)	4.07 (4.12)	14.13 (13.91)
14*d*	125	75	$C_{21}H_{19}N_3O_6$	61.61 (61.72)	4.68 (4.55)	10.26 (10.32)
14*e*	170	80	$C_{25}H_{20}N_4O_5$	65.78 (65.53)	4.42 (4.24)	12.27 (12.11)

product was collected and subjected to tlc and ^1H nmr analyses, indicating the presence of only one regioisomeric product (see Discussion). Crystallization of the crude product from ethanol yielded the corresponding 2-pyrazoline derivatives **11** in 75–85% yield. The compounds prepared, **11***a–e*, together with their physical constants are listed in Table 3.

*1-Aryl-3-*R*-4-(*p*-nitrophenyl)-5-ethoxycarbonylpyrazoles,* ***14***a–e

These were prepared by the same general procedure described above for the preparation of **11***a–e*, using ethyl α-cyano-*p*-nitrocinnamate **6***b* (5 mmol) in place of ethyl α-cyanocinnamate **6***a*. Work-up of the reaction mixture afforded the pyrazoles **14***a–e* in 70–80% yield (Table 3).

1. (*a*) A. S. SHAWALI. Heterocycles, **20**, 2239 (1983); (*b*) A. S. SHAWALI and C. PARKANYI. J. Heterocycl. Chem. **17**, 833 (1980); (*c*) P. CARAMELLA and P. GRUNANGER. 1,3-Dipolar cycloaddition chemistry. Vol. 1. *Edited by* A. Padwa. Wiley–Interscience, New York. 1984. Chap. 3.
2. G. L'ABBE and G. MATHYS. J. Heterocycl. Chem. **11**, 613 (1974).
3. W. FLIEGE, R. GRASHEY, and R. HUISGEN. Chem. Ber. **117**, 1194 (1984).
4. K. TANAKA, S. MAENO, and K. MITSUHASHI. Chem. Lett. 543 (1982).
5. G. C. LEVY and G. L. NELSON. Carbon-13 nuclear magnetic resonance for organic chemists. Wiley–Interscience, New York. 1972; L. F. JOHNSON and W. C. JANKOWSKY. Carbon-13 nuclear magnetic resonance spectra. Wiley, New York. 1972.
6. R. SUSTMANN, R. HUISGEN, and H. HUBER. Chem. Ber. **100**, 1802 (1967).
7. K. N. HOUK, J. SIMS, C. R. WATTS, and L. J. LUSKUS. J. Am. Chem. Soc. **95**, 7301 (1973).

Can. J. Chem. Downloaded from www.nrcresearchpress.com by 93.93.197.157 on 09/07/12
For personal use only.

8. K. N. HOUK, J. SIMS, R. E. DUKE, JR., R. W. STROZIER, and J. K. GEORGE. J. Am. Chem. Soc. **95**, 7287 (1973).
9. G. JONES. Organic reactions. Vol. 15. *Edited by* R. Adams. Wiley, New York. 1967. pp. 204–599, and references cited therein.
10. G. BUTT, J. CILMI, P. M. HOOBIN, and R. D. TOPSON. Spectrochim. Acta, Part A: **36**A, 521 (1980); B. H. THOMAS and W. J. ORVILLE. *J. Mol. Struct.* **7**, 123 (1971).
11. A. S. SHAWALI and A. O. ABDELHAMID. Bull. Chem. Soc. Jpn. **49**, 321 (1976); S. T. EZMIRLY and A. S. SHAWALI. J. Heterocycl. Chem. **25**, 257 (1988).
12. A. S. SHAWALI. J. Heterocycl. Chem. **14**, 375 (1977); A. S. SHAWALI, H. M. HASSANEEN, M. SAMI, and H. M. FAHHAM. J. Heterocycl. Chem. **13**, 1137 (1976).
13. R. SUSTMAN, R. HUISGEN, and H. HUBER. Chem. Ber. **100**, 1802 (1967); T. SHIMIZU, Y. HAYASHI, T. NISHIO, and K. TERAMURA. Bull. Chem. Soc. Jpn. **57**, 787 (1984).

Can. J. Chem. Downloaded from www.nrcresearchpress.com by 93.93.197.157 on 09/07/12
For personal use only.

Nuclear analogs of β-lactam antibiotics. Synthesis of 6,6-disubstituted acylaminopenems[1]

JACQUES BANVILLE,[2] PHILIPPE LAPOINTE, BERNARD BELLEAU,[3] AND MARCEL MENARD

Antiinfective Chemistry Department, Pharmaceutical Research and Development Division, Bristol–Myers Co., 100 Industrial Blvd., Candiac, P.Q., Canada J5R 1J1

Received October 2, 1987

JACQUES BANVILLE, PHILIPPE LAPOINTE, BERNARD BELLEAU, and MARCEL MENARD. Can. J. Chem. **66**, 1390 (1988).

The preparation of 6α-methyl-2-methyl-6β-phenoxyacetamidopenem-3-carboxylate, 6α-methoxy-2-methyl-6β-phenoxyacetamidopenem-3-carboxylate, and 6α-methoxy-2-methyl-6β-phenylmalonylamidopenem-3-carboxylate from penicillin V and 6-aminopenicillanic acid is described. These penems have been isolated and characterized as their sodium or potassium salt. The chemical stability of the above compounds was determined as their half-life in aqueous buffer. In this way, it was found that the 6α-methyl analog was more stable than the parent 6-monosubstituted acylaminopenem while the remaining analogs were of comparable stability.

JACQUES BANVILLE, PHILIPPE LAPOINTE, BERNARD BELLEAU et MARCEL MENARD. Can. J. Chem. **66**, 1390 (1988).

On décrit la préparation du méthyl-6α méthyl-2 phénoxyacétamido-6β pénemcarboxylate-3, du méthoxy-6α méthyl-2 phénoxyacétamido-6β pénemcarboxylate-3 et du méthoxy-6α méthyl-2 phénylmalonylamido-6β carboxylate-3 à partir de la pénicilline V et de l'acide amino-6 pénicillanique. Ces pénems ont été isolés et caractérisés sous forme de sels de sodium ou de potassium. La demi-vie de ces produits dans un tampon aqueux indique leur stabilité chimique. On a trouvé, de cette façon, que l'analogue méthyl-6α est plus stable que l'acylaminopénem monosubstitué en position 6 tandis que les deux autres analogues ont une stabilité comparable.

Can. J. Chem. Downloaded from www.nrcresearchpress.com by 93.93.197.157 on 09/07/12
For personal use only.

The first penems to be synthesized by Woodward and co-workers (1) were acylaminopenem-3-carboxylic acids of the type **1** (R = H, Me, Ph). These compounds were found to be quite unstable and had little antibacterial activity. Since the 6-unsubstituted penems **2***a* (2) and especially the penems **2***b* (3) having the 6-hydroxyethyl substitution of thienamicin (4) were chemically more stable and had a more interesting spectrum of biological activity, little attention has been given to the preparation of 6-acylamino penems. It has been shown that the introduction of a substituent, especially a methoxyl group, at the 6 or 7 position of, respectively, a penicillin or a cephalosporin results in an improvement in the chemical and enzymatic stability (3*b*). To see what effect a 6-substituent would have on the stability and activity of a 6-acylamino penem, we undertook the synthesis of penems **3***a* and **3***b*. As well, the effects of different acyl groups in the 6-acylamino side chain (**3***c*) were examined. When we initiated this study, none of these products had been reported in the literature. Recently, though, the preparation of the protected 6α-methoxy-2-methyl-6β-phenoxyacetamido penem-3-carboxylate **16** has been described (5). However, in this case, the corresponding deprotected penem could not be obtained. We were able to prepare and characterize the deprotected 6,6-disubstituted penems **3***a*, **3***b*, and **3***c*, using Woodward's approach (1) for the preparation of 6-acylamino penems from penicillin V.

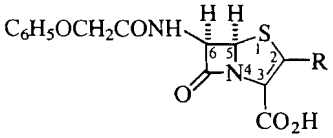

1

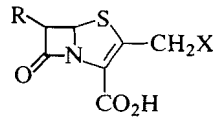

2 *a*, R = H
b, R = CH_3CHOH (*trans R*)

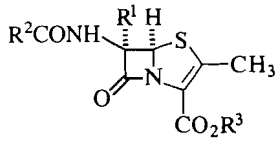

3 *a*, $R^1 = CH_3$, $R^2 = C_6H_5OCH_2$, R^3 = Na or K
b, $R^1 = OCH_3$, $R^2 = C_6H_5OCH_2$, R^3 = Na
c, $R^1 = OCH_3$, $R^2 = C_6H_5CHCO_2Na$, R^3 = Na

The first compound to be prepared by the above mentioned approach was the 6α-methyl-2-methyl-6β-phenoxyacetamido-penem-3-carboxylate **3***a*. In the case of penicillin, the introduction of an α-methyl group had a marked effect on the chemical stability of the β-lactam ring (6). The rate of the basic hydrolysis of 6-methyl-penicillin V methyl ester is four times slower than the unsubstituted compound.

The presence of the α-methyl group did not introduce a major problem, since the configuration at positions 5 and 6 of the penicillin nucleus is the same in the penem. The introduction of a 6α-alkyl substituent via a Schiff base is a well-documented process in penicillin chemistry (6, 7) and we used this approach. First, *N*-benzylidene-6-aminopenicillanic acid **4***a* (7*a*) was protected as its methyl ester **4***b* by treatment with diazomethane. Then, to introduce the 6-methyl group, we found Bohme's procedure (6) (potassium *tert*-butoxide, methyl iodide) to be the most satisfactory. Removal of the benzylidene group from **4***c* by exchange with 2,4-DNPH·TSOH in ethanol (7*c*) followed by acylation with phenoxyacetyl chloride gave the acylated compound **5***a* in a 59% yield from **5***c*. This compares favorably with the results of Dolfini and co-workers (6) who reported a 23% yield of acylated material by direct acylation of the Schiff base. The next step required oxidation of the sulfur of the thiazolidine ring and subsequent opening of this ring. Oxidation of **5***a* with *m*-chloroperbenzoic acid gave in high yield (90%) the two isomeric sulfoxides **5***b* and **5***c* (ratio 76:24 respectively) and these were separated by chromatography. Based on previous proton nmr studies (8) of penicillin "*R*" and "*S*" sulfoxides, the major isomer **5***b* was assigned the *S* stereochemistry and

[1]Work presented at the 67th Annual CIC Conference held in Montreal, June 3–6, 1984.

[2]Author to whom correspondence may be addressed.

[3]Present address: McGill University, Montreal.

TABLE 1. ^{1}H magnetic resonance of the sulfoxides **5***b* and **5***c* (60 MHz, $CDCl_3$, chemical shift values in ppm)

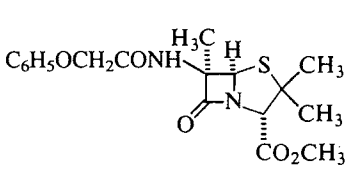

5*a*

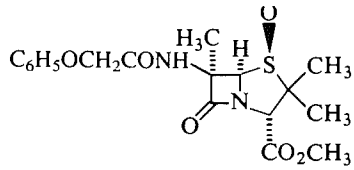

5*b* *S*

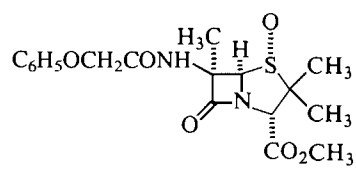

5*c* *R*

	5*a*	**5***b* *S*	**5***c* *R*
CH_3-2	1.45 and 1.48	1.25 and 1.70	1.30 and 1.66
H-3	4.41	4.63	4.53
H-5	5.43	4.83	4.56
CH_3-6	1.85	1.91	1.80
CH_2	4.5	4.51	4.53
C_6H_5	6.7–7.4	6.8–7.5	6.8–7.5
CO_2CH_3	3.78	3.85	3.83

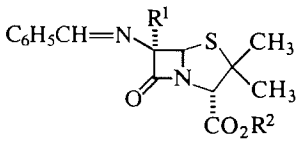

4 *a*, $R^1 = R^2 = H$
b, $R^1 = H$, $R^2 = CH_3$
c, $R^1 = R^2 = CH_3$

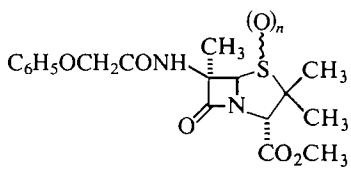

5 *a*, $n = 0$
b, $n = 1$ β-sulfoxide *S*
c, $n = 1$ α-sulfoxide *R*

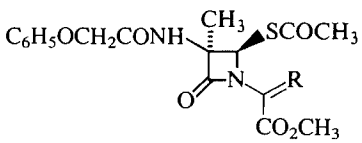

6 *a*, R = =C(CH3)2
b, R = O
c, R = $P(C_6H_5)_3$

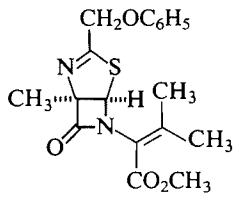

7

the minor, more polar, isomer **5***c* the *R* stereochemistry. Specifically, a downfield shift for the proton at position 3 due to a "*syn*-axial" effect (8*c*) is observed in the case of *S* isomer **5***b* (Table 1). Also, as has been noted by Barton for the 6-monosubstituted sulfoxides, the H-5 proton in both 6-disubstituted sulfoxides shows an upfield shift that is greater in the case of the *R* isomer. The latter upfield shift was attributed to shielding brought about by a *trans* orientation of the H-5 proton with respect to the lone pair of the sulfur atom.

We found that the two isomeric sulfoxides, **5***b* and **5***c*, behaved differently when subjected to ring-opening conditions (acetic anhydride, trimethylphosphite (9)). The major *S* isomer **5***b* reacted more slowly (105°C, 10 h) than the *R* isomer **5***c* and gave, after isomerization of the butenoate double bond with triethylamine, the thioester **6***a* in less than 30% yield. The main product isolated from this reaction was the thiazoline **7**. However, when the *R* sulfoxide **5***c* was subjected to the same conditions, the rearrangement was complete in 2 h and **6***a* was obtained in a 45% yield after isomerization. In this case, the thiazoline **7** was formed in trace amounts only.

To increase the proportion of the *R* sulfoxide **5***c* in the oxidation of **5***a*, different oxidizing agents were examined (Table 2). When sodium periodate was used, the ratio of *R* to *S* was lowered to 17:83. However, when the oxidation was conducted with ozone in a mixture of acetone and water (10), the *R* sulfoxide **5***c* predominated (ratio *R*:*S* > 95:5 by ^{1}Hmr). Steric effects direct the approach of the ozone molecule, and the α-methyl group seems to enhance this effect.

The butenoate **6***a* was then cleaved with ozone and the resulting alkoxalyl derivative **6***b* treated with methanol to give the azetidinone **8** in a 50% yield from **6***a*. The phosphorane **6***c* was obtained using Woodward's original procedure. Reaction of **8** with *p*-nitrobenzyl glyoxylate afforded a diastereomeric mixture of hemiaminals **9***a*, which, upon successive treatment with thionyl chloride and triphenyl phosphine, gave the phosphorane **6***c* in a 45% overall yield from **8**. Upon being heated in toluene at 100°C for 48 h, the phosphorane **6***c* was smoothly converted to the penem **10** in a 72% yield after chromatography.

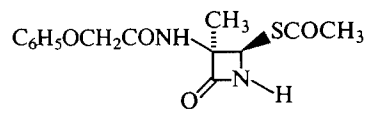

8

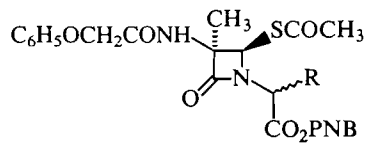

9 *a*, R = OH
b, R = Cl

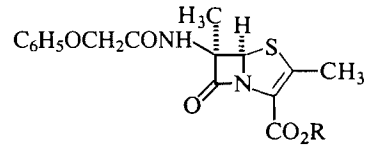

10 R = PNB
3*a* R = Na, K

Hydrogenolysis of the *p*-nitrobenzyl ester in a two-phase system consisting of ether, tetrahydrofuran, and an aqueous phosphate buffer gave the penem as the salt **3***a* (40% yield after purification by reversed phase column chromatography). No attempt has been made to prepare the carboxylic acid. The ultraviolet spectrum of **3***a* possesses the characteristic absorption of

Can. J. Chem. Downloaded from www.nrcresearchpress.com by 93.93.197.157 on 09/07/12
For personal use only.

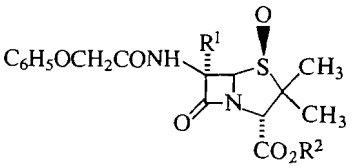

11 *a*, $R^1 = H$, $R^2 = CH_3$
b, $R^1 = OCH_3$, $R^2 = CH_3$
c, $R^1 = H$, $R^2 = PNB$
d, $R^1 = OCH_3$, $R^2 = PNB$

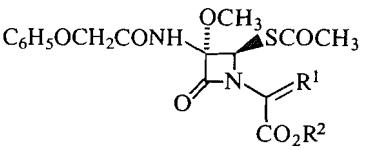

12 *a*, $R^1 = =C(CH_3)_2$, $R^2 = CH_3$
b, $R^1 = =C(CH_3)_2$, $R^2 = PNB$
c, $R^1 = O$, $R^2 = CH_3$
d, $R^1 = O$, $R^2 = PNB$
e, $R^1 = P(C_6H_5)_3$, $R^2 = PNB$

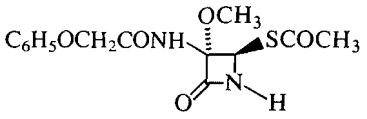

13

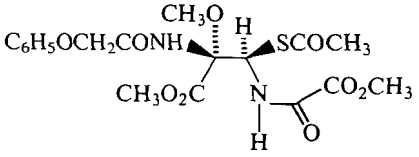

14

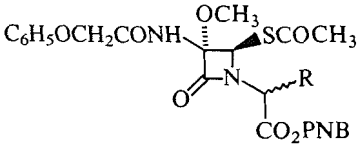

15 *a*, R = OH
b, R = Cl

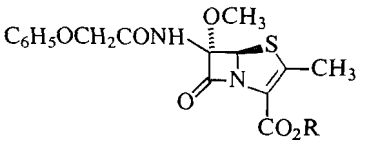

16 R = PNB
3*b* R = Na

PNB = *p*-nitrobenzyl

TABLE 2. Stereochemistry of the oxidation of **5***a* in **5***b* and **5***c*

Oxidizing agent	Ratio **5***b* (*S*):**5***c* (*R*)
m-Chloroperbenzoic acid	76:24
$NaIO_4$	83:17
O_3	<5 : >95

penems at 297 nm, and the absorption of 1770 cm^{-1} in the infrared spectrum is characteristic of a strained β-lactam.

The 6-methoxy penem **3***b* was obtained by a route similar to that described for the 6-methyl penem. Numerous methods for the introduction of a 6β or a 7β methoxy substituent into, respectively, a penicillin or a cephalosporin have been described (11). In this case, the 6-methoxy penicillins **11***a* and **11***c* were chosen as starting materials. The two 6β-methoxy sulfoxides **11***b* (42%) and **11***d* (12) (71%), were readily obtained via the procedure of Koppel and Koehler (13). Opening of the thiazoline ring of **11***b* and **11***d* followed by isomerization under basic conditions gave the two azetidinones **12***a* (60%) and **12***b* (55%). These were then treated with ozone to give the respective alkoxalyl derivatives, **12***c*, (97%) and **12***d* (85%). Methanolysis of the alkoxalyl derivative **12***c* under neutral conditions gave only traces of the desired azetidinone **13**. The major product that was obtained was the ring-opened product **14**. Even methanolysis at −20°C in the presence of a catalytic amount of triethylamine resulted in opening of the β-lactam ring. However, in the presence of aqueous acid (THF, 1 N HCl), **12***c* was slowly converted to the azetidinone **13** (40% completion after 8 h; evaluated by ^{1}Hmr) and the latter could be isolated in a 36% yield.

A more convenient route to the hemiaminal **15***a* was by the direct reduction of the alkoxalyl **12***c* with diborane (1). Treatment of **15***a* with thionyl chloride and pyridine followed by triphenylphosphine and 2,6-lutidine gave the phosphorane **12***e* in 12% overall yield from **12***b*. Cyclization of **12***e* was effected by heating in toluene to give the crystalline penem **16** in a 55% yield. Hydrogenolysis of the *p*-nitrobenzyl ester **16** was conducted as before to give the deprotected penem **3***b* (61%). This material was purified by chromatography on reversed phase silica gel and the lyophilized, amorphous product showed reasonable stability at room temperature. Its ultraviolet (297 nm) and infrared (1759 cm^{-1}) spectra are consistent with the proposed structure.

We were also interested in the effect produced by varying the acylamino substituents of those penems. The combination of a methoxyl group with an α-carboxythienyl-acetamido group (as in temocillin) or various arylmalonylamino groups at position 6 of penicillins results in compounds that have very interesting antibacterial activity (11*a*, pp. 326–364; 14). However, because the thienyl moiety was not compatible with the ozonolysis step in our synthetic scheme, we undertook the preparation of the 6α-methoxy-6-phenylmalonylamidopenem **3***c*.

Our first approach to the preparation of **3***c* was to take advantage of the various intermediates that had been generated in the synthesis of the phenoxyacetamido penem **3***b*. Direct cleavage of the acylamino side chain followed by introduction of the desired acyl group was not examined because racemization problems at position 7 were encountered when this was attempted in the case of the cephamycins (15). The possibility of trans-acylation was examined. However, attempts to convert **12***b* into its diacylated derivative by treatment of this material with an acid chloride in presence of an acid scavenger (16) were not successful. Accordingly, introduction of the phenylmalonyl group at an earlier stage of the synthesis was examined.

The possible introduction of the desired acyl side chain via a sulfenimine intermediate as described by Gordon *et al.* (17) was then examined. Indeed, reaction of the sulfenimine **17** with triphenylphosphine and mercuric acetate in methanol followed by acylation with phenylmalonyl chloride mono-*p*-nitrobenzyl ester gave **18** (63%). Oxidation of **18** with *m*-chloroperbenzoic acid gave the two isomeric sulfoxides **19***a* and **19***b* in a 19:9 ratio (93%). The two sulfoxides were also a mixture of epimers at the malonyl center.

Can. J. Chem. Downloaded from www.nrcresearchpress.com by 93.93.197.157 on 09/07/12
For personal use only.

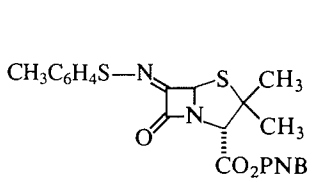

17

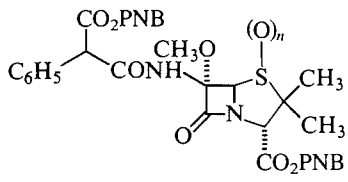

18 $n = 0$
19 *a*, $n = 1$, α-sulfoxide
b, $n = 1$, β-sulfoxide

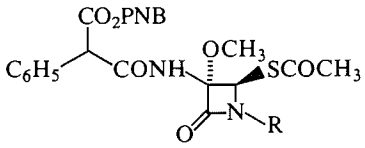

20 *a*, R = $COCO_2PNB$
b, R = H
c, R = $CHOHCO_2PNB$

The oxalimide **20***a* and the azetidinone **20***b* could be obtained in a similar manner to that described for the preparation of the phenoxyacetamido derivative **13**. However, all subsequent attempts to obtain the phosphorane analog of **12***e* were unsuccessful. That is, reduction of the oxalimide **20***a* to **20***c* ($NaBH_4$–AcOH (18), since diborane reduction did not work in this case), followed by reaction with thionyl chloride and triphenylphosphine, only resulted in the formation of decomposition products no longer containing a β-lactam ring. Furthermore, the hemiaminal **20***c* could not be obtained by reaction of **20***b* with *p*-nitrobenzyl glyoxylate due to the instability of the β-lactam ring under the reaction conditions.

We then turned to examining alternative methods for the preparation of the penem nucleus. After considering the available methods (19), Betty's procedure involving 1,5 ring closure (20) of the penem by nucleophilic attack of sulfur at C-4 of an azetidinone was considered most promising. This method required the specific formation of the 4α-chloroazetidinone **24**, which should then be closed to the penem having the correct stereochemistry at position 5.

Heating the mixture of sulfoxides **19***a* and **19***b* with 2-mercaptobenzothiazole gave the disulfide **21** (Scheme 1). Ozonolysis of the terminal olefin gave the enol **22**, which was then treated with triphenylphosphine to form the oxazoline **23***a*. This product was more easily purified as the mesylate **23***b*, which was obtained in a 39% overall yield from **19**. Ring opening of the oxazoline with hydrochloric acid gave only one product, the α-chloroazetidinone **24** in 48% yield. Attack by the chloride ion on the less encumbered α face of the oxazoline results in the formation of the α-chloro isomer.

Reaction of this chloroazetidinone **24** with hydrogen sulfide and triethylamine gave the penem **25** in a low yield (25%). This penem, like most of the intermediates in this sequence, was relatively unstable on silica gel and was obtained contaminated with the degradation product, the thiazole **26***a*. Simultaneous deprotection of both ester groups by hydrogenolysis gave the penem **3***c* as its sodium salt (30% yield after chromatography on reversed phase silica gel). This product was also contaminated by the thiazole **26***b* (ratio of penem to thiazole, 75:25 by ^{1}Hmr). The malonyl penem was more unstable than the two that had been previously prepared and, even as a dry powder, underwent decomposition over the period of a few days. The carbonyl frequency of the β-lactam is at 1765 cm^{-1} and the proton nmr indicated a 1:1 mixture of epimers at the malonyl side chain.

The half-life in a pH 7.4 buffer solution at 37°C of the penems prepared above is a good indication of their chemical stability (3*a*). The parent 6-monosubstituted acylaminopenem **1** (R = CH_3) prepared by Woodward has a half-life of 1.5 h under these conditions. The 6α-methoxypenems **3***b* and **3***c* were comparable, having half-lives of 1.2 and 1.6 h respectively. Introduction of a 6α-methoxy group did not seem to have much of an effect on the stability of the penem. However, the 6α-methyl group did, since the 6α-methylpenem **3***a* had a half-life of 12 h under these conditions. This greater stability is also reflected in the ease with which this compound could be synthesized relative to the α-methoxy analogs. In vivo, all three penems **3***a*, **3***b*, and **3***c* showed only weak activity against Gram-positive and Gram-negative strains of bacteria.

Experimental

Melting points were determined on a Gallenkamp melting point apparatus and are not corrected. The ultraviolet spectra were recorded

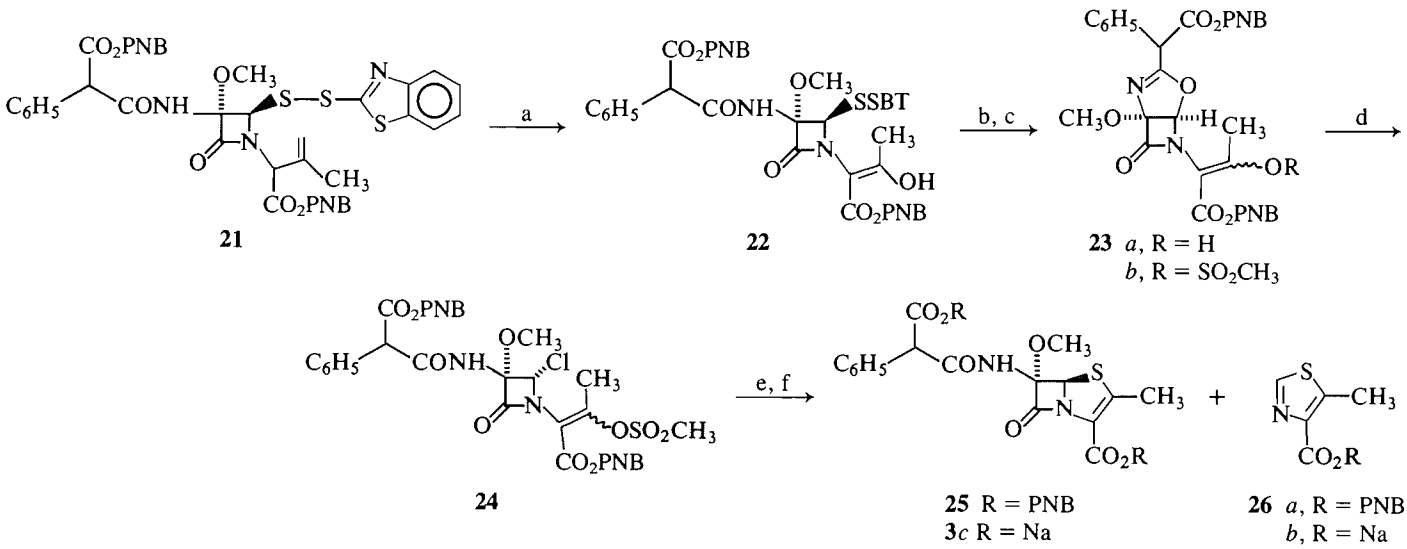

21 22 23 *a*, R = H; *b*, R = SO_2CH_3 24 25 R = PNB; 3*c* R = Na 26 *a*, R = PNB; *b*, R = Na

(a) O_3; Me_2S; (b) $P(Ph)_3$; (c) CH_3SO_2Cl; (d) HCl; (e) H_2S, Et_3N; (f) H_2, Pd/C

SCHEME 1

Can. J. Chem. Downloaded from www.nrcresearchpress.com by 93.93.197.157 on 09/07/12
For personal use only.

Can. J. Chem. Downloaded from www.nrcresearchpress.com by 93.93.197.157 on 09/07/12
For personal use only.

on a Pye Unicam SP8-100 uv/vis spectrophotometer. The infrared spectra were recorded on a Perkin–Elmer 267 grating infrared spectrophotometer. Optical rotations were measured with a Perkin–Elmer model 141 polarimeter. The ^{1}H nuclear magnetic resonance spectra were taken with either a Varian EM-360 (60 MHz) or a Varian CFT-20 (80 MHz) nmr spectrometer. Tetramethylsilane was employed as the internal standard and chemical shifts were reported in parts per million (δ) relative to the internal standard. Tetrahydrofuran was freshly distilled from lithium aluminum hydride. Solvents were reagent grade and had been stored over molecular sieves (4Å) before use. *p*-Nitrobenzyl glyoxylate (21) was prepared from di-*p*-nitrobenzyl fumarate by ozonolysis (CH_2Cl_2, −78°C) followed by reduction with dimethyl sulfide (22). *p*-Nitrobenzyl 6-phenoxyacetamidopenicillanate-1-β-oxide **11***c* was obtained by esterification of the potassium salt of penicillin V with *p*-nitrobenzyl bromide followed by oxidation with *m*-chloroperbenzoic acid by a method similar to the one described by Baldwin and Abraham and co-workers (27). Column chromatography was carried out on silica gel (230–400 mesh, Merck) or on reversed phase silica gel (μ-Bondapak C_{18}, 55–105 μm, Waters) for the penem salts **3***a*, **3***b*, and **3***c*. Microanalyses were performed by Micro-Tech Laboratories, Skokie, Illinois, U.S.A. The half-lives of the penems **3***a*, **3***b*, and **3***c* were determined by uv at 37°C for 10^{-4} M solutions using the method of Woodward (3*a*).

Methyl N-*benzylidene-6-aminopenicillanate* (**4**b) (7*b*)

A suspension of *N*-benzylidene-6-aminopenicillanic acid (**4***a*) (7*a*) (108.0 g, 0.375 mol) in ether (2.1 L) was cooled to 5°C and treated dropwise with a cold solution of diazomethane (18 g, 0.43 mol, prepared from Diazald, Aldrich Chemical Co.) in ether (1.5 L). The solution obtained was then concentrated under vacuum and the residual solid was triturated with cold hexanes to give 102.7 g (86%) of the title material **4***b* as a white solid; ir (Nujol) ν_{max}: 1760 (C=O β-lactam), 1740 (CO ester), and 1635 (C=N) cm^{-1}; ^{1}Hmr ($CDCl_3$, 60 MHz) δ: 1.51 and 1.68 (2s, 2 × 3H, CH_3-2), 3.85 (s, 2H, CO_2CH_3-3), 4.43 (s, 1H, H-3), 5.37 (dd, J = 2 Hz, J = 4 Hz, 1H, H-6), 5.63 (d, J = 4 Hz, H-5), 7.3–7.9 (m, 5H, aromatic), and 8.65 (d, J = 2 Hz, 1H, CH=N) ppm.

Methyl N-*benzylidene-6-amino-6α-methylpenicillanate* (**4**c) (6)

A solution of methyl *N*-benzylidene-6-aminopenicillanate (**4***b*) (102.5 g, 0.32 mol) in dry 1,2-dimethoxyethane (1.4 L) was cooled to −40°C and treated with iodomethane (320 mL). Potassium *tert*-butoxide (36.3 g, 0.32 mol) was then added in portions over 5 min and the mixture was stirred at −40°C for 2 h. The red solution was then diluted with CH_2Cl_2 (2 L) and washed several times with water and brine. The organic phase was dried ($MgSO_4$) and evaporated to give 106 g (100%) of an oil, which solidified upon standing. This material was used as such for the next step: ir (Nujol) ν_{max}: 1765 (C=O β-lactam), 1750 (C=O ester), and 1635 (C=N) cm^{-1}; ^{1}Hmr ($CDCl_3$, 60 MHz) δ: 1.43 and 1.52 (2s, 2 × 3H, CH_3-2), 1.78 (s, 3H, CH_3-6), 3.77 (s, 3H, CO_2CH_3-3), 4.30 (s, 1H, H-3), 5.3 (s, 1H, H-5), 7.2–7.8 (m, 5H, aromatic), and 8.63 (s, 1H, CH=N) ppm.

Methyl 6α-methyl-6-phenoxyacetamidopenicillanate (**5**a)

A mixture of *p*-toluenesulfonic acid monohydrate (61.4 g, 0.32 mol) and finely ground 2,4-dinitrophenylhydrazine (75.8 g, containing 20% water) in anhydrous EtOH (1.4 L) was stirred at 22°C for 30 min. Then a solution of **4***c* (106.0 g, 0.32 mol) in EtOH (1 L) was added and the heterogenous mixture was stirred for 50 min. The solid formed was filtered and washed with EtOH. The filtrate and the washings were concentrated under vacuum to give a solid. Trituration with ether and filtration gave 127.7 g of the intermediate methyl 6α-methyl-6β-aminopenicillanate *p*-toluenesulfonate salt. The salt was dissolved in CH_2Cl_2 (1.4 L), cooled to 0°C, and treated successively with a solution of phenoxyacetyl chloride (60.5 g, 0.355 mol) in CH_2Cl_2 (0.5 L) and a solution of KH_2PO_4 (155 g) in cold water (1.4 L). The mixture was stirred vigorously for 30 min at 5°C, treated with pyridine (29 mL), and stirred for another 15 min. The organic phase was separated and the aqueous phase was extracted with CH_2Cl_2. The combined organic phases were washed with cold HCl (0.1 N), saturated $NaHCO_3$, and then brine. After drying (Na_2SO_4), evaporation of the solvent gave an oil, which was purified by filtration through a short pad of silica gel (500 g) followed by high-pressure liquid chromatography (hplc, Waters Associates Prep LC/system 500 using PrepPak-500/silica cartridges, elution CH_2Cl_2:EtOAc, 9:1). The title compound **5***a* was obtained as a pale yellow foam: 71.6 g (59%) (lit. (6) 23% by direct acylation of the Schiff base). The spectral data were in accordance with those already described.

Methyl 6α-methyl-6-phenoxyacetamidopenicillanate-1β- and -1α-oxide (**5**b *and* **5**c)

Method A: Oxidation with m-*chloroperbenzoic acid*

A solution of methyl 6α-methyl-6-phenoxyacetamidopenicillanate **5***a* (2.30 g, 6.1 mmol) in CH_2Cl_2 (30 mL) was cooled in an ice–water bath and treated dropwise with a solution of *m*-chloroperbenzoic acid (1.23 g of 85%, 6.1 mmol) in CH_2Cl_2 (15 mL). After 30 min at 5°C, the mixture was washed successively with cold 5% $NaHCO_3$, brine, and then dried ($MgSO_4$). The oil obtained after evaporation of the solvent was chromatographed on silica gel (100 g) using a mixture of toluene and ethyl acetate (gradient 8:2 to ethyl acetate). The β-sulfoxide **5***b* eluted first and was obtained as a white foam: 1.60 g (68%); $[\alpha]_D^{25}$ +284° (*c* 1.0, $CHCl_3$); ir (film) ν_{max}: 3300 (NH), 1780 (C=O β-lactam), 1750 (C=O ester), 1665 and 1520 (amide), and 1050 (S—O) cm^{-1}.

The more polar α-sulfoxide **5***c* was obtained as a solid, which was recrystallized from a mixture of ethyl acetate and hexanes to give 0.50 g (21%) of a white solid: mp 109–110°C; $[\alpha]_D^{25}$ +155° (*c* 1.0, $CHCl_3$); ir (KBr) ν_{max}: 3400 (NH), 1790 (C=O β-lactam), 1750 (C=O ester), 1670 and 1520 (amide), and 1050 (S—O) cm^{-1}. *Anal.* calcd. for $C_{18}H_{22}N_2O_6S$: C 54.81, H 5.62, N 7.10, S 8.13; found: C 54.63, H 5.57, N 7.55, S 8.10.

Method B: Oxidation with sodium metaperiodate

A solution of **5***a* (0.115 g, 0.3 mmol) in MeOH (1 mL) was cooled in an ice–water bath and treated with a solution of $NaIO_4$ (0.064 g, 0.30 mmol) in water (0.2 mL). The resulting mixture was slowly warmed up to 22°C and stirred for 18 h. The precipitate that formed was filtered and washed with MeOH. Evaporation of the filtrate gave the sulfoxide as a foam. The ^{1}Hmr of the crude product indicated that an 83:17 mixture of β- and α-sulfoxides had been obtained.

Method C: Oxidation with ozone

A solution of **5***a* (71.6 g, 0.189 mol) in a mixture of acetone–water (1:1, 1 L) was cooled to 0–5°C and treated with a stream of ozone until the starting material disappeared (tlc). The solution was then flushed with N_2 and extracted with CH_2Cl_2 (1 L). The aqueous phase was extracted twice with CH_2Cl_2 (100 mL) and then the combined organic phases washed successively with 3% aqueous sodium thiosulfate and brine. After drying (Na_2SO_4), evaporation of the solvent gave a solid that was triturated with hexanes to give 61.0 g (82%) of the α-sulfoxide **5***c*. The β-sulfoxide was not detected by ^{1}Hmr (60 MHz).

*Methyl α-(4*R*-acetylthio-3*R*-methyl-3-phenoxyacetamido-2-azetidinon-1-yl)-β-methylcrotonate* **6**a)

A. By rearrangement of the α-sulfoxide **5**c

A solution of methyl 6α-methyl-6-phenoxyacetamidopenicillanate 1α-oxide **5***c* (10.0 g, 25.4 mmol) in toluene (250 mL) was treated with acetic anhydride (20 mL, 0.21 mol) and trimethyl phosphite (9.25 g, 74.5 mmol) and then heated at 85°C for 3 h. The solvent and excess reagents were evaporated *in vacuo* and the last traces of reagents removed by coevaporation with toluene. The residual oil was diluted with ethyl acetate (100 mL), washed with water, cold 5% $NaHCO_3$, and brine, and dried ($MgSO_4$). The solution was concentrated to approximately 20 mL, cooled in an ice–water bath, and then treated with triethylamine (0.8 mL, 5.7 mmol). After 4 h at 0–5°C, the reaction mixture was diluted with ethyl acetate (100 mL), washed with cold 5% aqueous AcOH, 5% $NaHCO_3$, and brine, and dried ($MgSO_4$). The solvent was evaporated and the residue chromatographed on silica gel (400 g) using a mixture of CH_2Cl_2 and ethyl acetate (4:1) as eluent. The title material **6***a* was obtained as a clear oil: 4.80 g (45%); ir (film) ν_{max}: 1775 (C=O β-lactam), 1720 (sh C=O ester), 1690 (C=O amide and thioester), and 1520 (amide) cm^{-1}; ^{1}Hmr ($CDCl_3$, 60 MHz) δ: 1.76 (s, 3H, CH_3-3 of azetidinone), 2.16, 2.23, and 2.26

Can. J. Chem. Downloaded from www.nrcresearchpress.com by 93.93.197.157 on 09/07/12
For personal use only.

(3s, 3 × 3H, CH_3 of crotonate and $SCOCH_3$-4 of azetidinone), 3.81 (s, 3H, CO_2CH_3), 4.5 (s, 2H, CH_2 of phenoxyacetyl), 5.66 (s, 1H, H-4 of azetidinone), and 6.7–7.5 (m, 6H, aromatic and NH) ppm.

B. By rearrangement of the β-sulfoxide **5**b

A solution of the β-sulfoxide **5***b* (0.175 g, 0.44 mmol) in toluene (1.5 mL) was treated with trimethyl phosphite (0.15 mL) and acetic anhydride (0.27 mL) and heated at 105°C for 10 h. After work-up and isomerization as above, chromatography on silica gel gave 0.080 g (43%) of thiazoline **7** as an oil and 0.055 g (30%) of the thioester **6***a*. Thiazoline **7**: ir (film) ν_{max}: 1700 (C=O β-lactam), 1715 (C=O ester), 1650 and 1595 cm^{-1}; ^{1}Hmr ($CDCl_3$, 60 MHz) δ: 1.56, 1.73, and 2.16 (3s, 3 × 3H, CH_3 of crotonate and CH_3-3 of azetidinone), 3.70 (s, 3H, CO_2CH_3), 4.7 (s, 2H, CH_2 of phenoxyacetyl), 5.70 (s, 1H, H-4 of azetidinone), and 6.8–7.3 (m, 5H, aromatic) ppm.

N-*Methoxalyl-4*R-*acetylthio-3*R-*methyl-3-phenoxyacetamido-2-azetidinone* **6**b

A solution of methyl α-(4*R*-acetylthio-3*R*-methyl-3-phenoxyacetamido-2-azetidinon-1-yl)-β-methylcrotonate **6***a* (4.20 g, 10.0 mmol) in a mixture of CH_2Cl_2 (100 mL) and MeOH (25 mL) was cooled to −25°C and treated with ozone until a light blue color persisted. The reaction mixture was then flushed with N_2, treated with methyl sulfide (2.5 mL), and allowed to warm up to 22°C. The mixture was diluted with CH_2Cl_2 (100 mL), washed successively with 3% aqueous sodium bisulfite and brine, and dried ($MgSO_4$). Evaporation of the solvent gave 4.0 g of the crude *N*-methoxalylazetidinone **6***b* as white foam. This product was used as such for the next step: ir (film) ν_{max}: 1815 and 1750 (C=O), 1700 (br, C=O ester, amide and thioester), and 1520 (C=O amide) cm^{-1}; ^{1}Hmr ($CDCl_3$, 60 MHz) δ: 1.80 (s, 3H, CH_3-3), 2.33 (s, 3H, $SCOCH_3$-4), 3.93 (s, 3H, CO_2CH_3), 4.56 (s, 2H, CH_2 of phenoxyacetyl), 5.80 (s, 1H, H-4), and 6.8–7.4 (m, 6H, NH and aromatic) ppm.

*4*R-*Acetylthio-3*R-*methyl-3-phenoxyacetamido-2-azetidinone* **8**

A solution of the crude *N*-methoxalyl azetidinone **6***b* (4.0 g) in a mixture of MeOH (300 mL), EtOAc (30 mL), and water (6 mL) was stirred at 22°C for 18 h. The solvent was then concentrated *in vacuo* and the residue was partitioned between EtOAc (150 mL) and water. The organic phase was dried ($MgSO_4$) and concentrated *in vacuo* to give a crude product that was chromatographed on silica gel (75 g). Elution with toluene–EtOAc (1:2) gave 1.53 g (50%) of the azetidinone **8** as a white solid. Recrystallization from EtOAc gave white needles: mp 118–119°C; $[\alpha]_D^{22}$ −20° (*c* 1.0, $CHCl_3$); ir (KBr) ν_{max}: 3320 (NH), 1780 (C=O β-lactam), 1680 and 1660 (C=O amide and thioester), and 1520 (C=O amide) cm^{-1}; ^{1}Hmr ($CDCl_3$, 80 MHz) δ: 1.77 (s, 3H, CH_3-3), 2.32 (s, 3H, $SCOCH_3$-4), 4.54 (s, 2H, CH_2 of phenoxyacetyl), 5.41 (s, 1H, H-4), 6.1 and 6.7 (bs, 2 × 1H, NH), and 6.8–7.5 (m, 5H, aromatic) ppm. *Anal.* calcd. for $C_{14}H_{16}N_2O_4S$: C 54.53, H 5.23, N 9.08, S 10.40; found: C 54.64, H 5.21, N 9.04, S 10.11.

p-*Nitrobenzyl (4*R-*acetylthio-3*R-*methyl-3-phenoxyacetamido-2-azetidinon-1-yl)triphenylphosphoranylidene acetate* **6**c

A suspension of azetidinone **8** (1.53 g, 4.96 mmol) and *p*-nitrobenzyl glyoxylate monohydrate (1.25 g, 5.46 mmol) in CH_2Cl_2 (30 mL) was cooled to 0–5°C and treated with triethylamine (35 μL, 0.25 mmol). After 1 h, the resulting solution was diluted with CH_2Cl_2, and washed with cold 0.1 N HCl and brine. After drying ($MgSO_4$), evaporation gave 2.7 g of the crude hemiaminal **9***a* as an oil; ir (film) ν_{max}: 3300 (br), 1770 (C=O β-lactam), 1690 (C=O), and 1520 (C=O amide) cm^{-1}; ^{1}Hmr ($CDCl_3$, 80 MHz) (mixture of two diastereoisomers in a 1:1 ratio) δ: 1.69 and 1.73 (2s, 3H, CH_3-3 of azetidinone), 2.22 and 2.32 (2s, 3H, $SCOCH_3$), 4.54 (s, 2H, CH_2 of phenoxyacetyl), 5.35 (m, 2H, CH_2 of *p*-nitrobenzyl), 5.52 and 5.55 (2s, 1H, H-4 of azetidinone), 6.7 (br s, 1H, NH), and 6.9–8.3 (m, 9H, aromatic) ppm.

Thionyl chloride (0.38 mL, 5.26 mmol) was added dropwise over 5 min to a cooled (−20°C) solution of the crude hemiaminal **9***a* (2.7 g) and pyridine (0.45 mL, 5.56 mmol) in dry tetrahydrofuran (60 mL). After 15 min, the white precipitate that formed was filtered on a Celite pad and washed with benzene. The filtrate and washings were combined and concentrated *in vacuo*. The residue was rapidly purified on a silica gel pad (40 g) using a mixture of CH_2Cl_2:EtOAc, 3:1, as eluent. Evaporation gave 2.39 g (85% from **8**) of *p*-nitrobenzyl (4*R*-acetylthio-3*R*-methyl-3-phenoxyacetamido-2-azetidinon-1-yl) chloro acetate **9***b* (4:3 mixture of diastereoisomers by ^{1}Hmr) as a clear oil: ir (film) ν_{max}: 1790, 1770 (C=O), 1690 (C=O amide and thioester), and 1520 (amide) cm^{-1}; ^{1}Hmr ($CDCl_3$, 80 MHz) δ: 1.72 (s, 3H, CH_3-3 of azetidinone), 2.21 and 2.31 (2s, 3H, $SCOCH_3$), 4.55 (s, 2H, CH_2 of phenoxyacetyl), 5.32 and 5.38 (2s, 2H, CH_2 of *p*-nitrobenzyl), 5.66 and 5.77 (2s, 1H, H-4 of azetidinone), 6.16 and 6.26 (2s, 1H, H-2 of acetate), 6.6 (br s, 1H, NH), and 6.8–8.2 (br s, 1H, NH) ppm.

A solution of the epimeric chloro compounds **9***b* (0.95 g, 1.77 mmol) in dry tetrahydrofuran (50 mL) was treated with triphenylphosphine (1.0 g, 3.81 mmol) and 2,6-lutidine (0.25 mL, 2.14 mmol) and the resulting mixture was heated at 50°C under N_2 for 66 h. The solvent was then evaporated and the residue dissolved in EtOAc (200 mL). The solution was washed successively with cold 0.1 N HCl, cold 1% $NaHCO_3$, and brine, and dried ($MgSO_4$). Evaporation and chromatography of the residue on silica gel (40 g, elution with toluene:EtOAc 1:1–1:3) gave 1.20 g (88%) of the title phosphorane **6***c* as an oil: ir (film) ν_{max}: 1770 (C=O β-lactam), 1690 (br), 1620 (br), and 1520 (amide) cm^{-1}.

p-*Nitrobenzyl (5*R*) 6*R-*methyl-2-methyl-6-phenoxyacetamidopenem-3-carboxylate* ***10***

A solution of the phosphorane **6***c* (1.20 g, 1.57 mmol) in toluene (800 mL) was heated under N_2 and in the presence of a small crystal of hydroquinone, at 100°C for 48 h. The solvent was then concentrated *in vacuo* and the residue was chromatographed on silica gel (60 g). Elution with a mixture of toluene and EtOAc (85:15) gave 0.550 g (72%) of the penem **10** as a white foam: $[\alpha]_D^{25}$ +302° (*c* 1.06, $CHCl_3$); uv (EtOH) λ_{max} (ε): 307 (10 700), 274 (sh), 268 (15 000), and 262 (15 000) nm; ir (film) ν_{max}: 1787 (C=O β-lactam), 1707 (C=O ester), 1668 and 1517 (amide), and 1325 (NO_2) cm^{-1}; ^{1}Hmr ($CDCl_3$, 80 MHz) δ: 1.83 (s, 3H, CH_3-6), 2.35 (s, 3H, CH_3-2), 4.51 (s, 2H, CH_2 of phenoxyacetyl), 5.33 (ABq, J_{AB} = 13.6, $\Delta\nu$ = 17.8, CH_2 of *p*-nitrobenzyl), 5.74 (s, 1H, H-5), 6.8–7.4 (m, 5H, aromatic), 7.59 (d, *J* = 8.8 Hz, 2H, H-2 of *p*-nitrobenzyl), and 8.23 ppm (d, *J* = 8.8 Hz, 2H, H-3 of *p*-nitrobenzyl). *Anal.* calcd. for $C_{23}H_{21}N_3O_7S$: C 57.14, H 4.38, N 8.69, S 6.63; found: C 56.94, H 4.60, N 8.69, S 6.50.

*(5*R*) 6*R-*Methyl-2-methyl-6-phenoxyacetamidopenem-3-carboxylic acid, sodium–potassium salt* **3**a

A solution of *p*-nitrobenzyl (5*R*) 6*R*-methyl-2-methyl-6-phenoxyacetamidopenem-3-carboxylate **10** (0.150 g, 0.31 mmol) in a mixture of tetrahydrofuran (15 mL), ether (30 mL), water (15 mL), and pH 7 phosphate buffer (20 mL of a 0.05 M solution, KH_2PO_4–NaOH) was hydrogenated over 0.3 g of 10% Pd on activated carbon in a Parr apparatus under a pressure of 45 psi (1 psi = 6.9 kPa) at room temperature for 1.5 h. The mixture was then filtered through a Celite pad, and the aqueous phase, after evaporation of traces of organic solvent *in vacuo*, was chromatographed at 0–5°C on reversed phase silica gel (2 × 18 cm). Elution with water and then a mixture of water–CH_3CN, 9:1, gave 0.053 g (48%) of the penem **3***a* as a white powder after lyophilization: $[\alpha]_D^{22}$ +321° (*c* 0.88, H_2O); uv (H_2O, pH 7.4 phosphate buffer) λ_{max} (ε based on K salt): 297 (7850), 274 (7200), 267 (7700), and 260 (7500) nm; ir (KBr) ν_{max}: 1770 (C=O β-lactam), 1675 and 1520 (amide), and 1600 (br, carboxylate) cm^{-1}; ^{1}Hmr (D_2O, 80 MHz) δ: 1.69 (s, 3H, CH_3-6), 2.19 (s, 3H, CH_3-2), 4.69 (CH_2 of phenoxyacetyl overlapping with HDO), 5.67 (s, 1H, H-5), and 6.9–7.4 ppm (m, 5H, aromatic). By uv, at 37°C, the half-life of this penem was determined to be 12 h at pH 7.4.

p-*Nitrobenzyl 6α-methoxy-6β-phenoxyacetamidopenicillanate-1-β-oxide* ***11*** d (12)

This product was obtained via a slight modification (23) of the Koppel and Koehler's method (13).

A solution of *p*-nitrobenzyl 6-phenoxyacetamidopenicillanate-1-β-oxide (**11***c*) (20.0 g, 39.8 mmol) in dry CH_2Cl_2 (300 mL) was cooled to −30°C and treated with freshly prepared *tert*-butyl hypochlorite (24).

Can. J. Chem. Downloaded from www.nrcresearchpress.com by 93.93.197.157 on 09/07/12
For personal use only.

Then lithium methoxide (43.8 mmol, prepared by dissolving lithium, 0.30 g, in MeOH, 35 mL) was added dropwise over 1 h. After another hour at −30°C, acetic acid (2.5 mL) was added and the solution was washed with 5% cold aqueous $NaHCO_3$, 5% $Na_2S_2O_3$, and brine, and dried (Na_2SO_4). Evaporation left an oil, which was chromatographed on silica gel (200 g). Elution with a mixture of toluene and EtOAc (7:3) gave 15.1 g (71%) of **11***d* as an oil: ir (film) ν_{max}: 1788 (C=O β-lactam), 1753 (C=O ester), 1688 and 1521 (amide), and 1350 (NO_2) cm^{-1}; ^{1}Hmr ($CDCl_3$, 60 MHz) δ: 1.13 and 1.6 (2s, 2 × 3H, CH_3-2), 3.46 (s, 3H, OCH_3-6), 4.53 (s, 2H, CH_2 of phenoxyacetyl), 4.63 (s, 1H, H-3), 5.0 (s, 1H, H-5), 5.3 (s, 2H, CH_2 of *p*-nitrobenzyl), 6.8–7.4 (m, 6H, NH and aromatic), 7.53 (d, J = 9.0 Hz, 2H, H-2 of *p*-nitrobenzyl), and 8.23 (d, J = 9.0 Hz, 2H, H-3 of *p*-nitrobenzyl) ppm.

Methyl 6α-methoxy-6β-phenoxyacetamidopenicillanate-1β-oxide ***11***b (12)

Starting with methyl 6-phenoxyacetamidopenicillanate **11***a* (25) (3.80 g, 10.0 mmol) and using the same procedure as was used to prepare **11***d*, we obtained 1.73 g (42%) of **11***b* as an oil: ir (film) ν_{max}: 1788 (C=O β-lactam), 1755 (C=O ester), 1690 and 1510 (amide) cm^{-1}; ^{1}Hmr ($CDCl_3$, 60 MHz) δ: 1.23 and 1.66 (2s, 2 × 3H, CH_3-2), 3.5 (s, 3H, OCH_3-6), 3.83 (s, 3H, CO_2CH_3-3), 4.58 (s, 2H, CH_2 of phenoxyacetyl), 4.60 (s, 1H, H-3), 5.0 (s, 1H, H-5), and 6.7–7.6 (m, 6H, NH and aromatic) ppm.

p-*Nitrobenzyl α-(4*R*-acetylthio-3*S*-methoxy-3-phenoxyacetamido-2-azetidinon-1-yl)-β-methylcrotonate* ***12***b

A solution of sulfoxide **11***d* (15.0 g, 28.0 mmol) in toluene (250 mL) was treated with trimethyl phosphite (12.4 g, 0.1 mol) and acetic anhydride (26.7 mL, 0.28 mol) at 96°C for 24 h. Work-up as for **6***a* followed by isomerization (EtOAc 50 mL, Et_3N 0.8 mL, 3 h) and chromatography gave 8.69 g (55%) of **12***b* as a syrup: $[\alpha]_D^{22}$ +20° (*c* 1.14, $CHCl_3$); ir (film) ν_{max}: 1780 (C=O β-lactam), 1715 (sh, C=O ester), 1695 and 1520 (amide), and 1345 (NO_2) cm^{-1}; ^{1}Hmr ($CDCl_3$, 60 MHz) δ: 2.16 and 2.3 (2s, 3H and 6H, CH_3 of crotonate and $SCOCH_3$), 3.5 (s, 3H, OCH_3-3), 4.53 (s, 2H, CH_2 of phenoxyacetyl), 5.30 (s, 2H, CH_2 of *p*-nitrobenzyl), 5.93 (s, 1H, H-4), 6.8–7.4 (m, 6H, NH and aromatic), 7.56 (d, J = 9.0 Hz, 2H, H-2 and *p*-nitrobenzyl), and 8.20 (d, J = 9.0 Hz, 2H, H-3 of *p*-nitrobenzyl) ppm.

*Methyl α-(4*R*-acetylthio-3*S*-methoxy-3-phenoxyacetamido-2-azetidinon-1-yl)-β-methylcrotonate* ***12***a

Using the same procedure described above for **12***b*, 10.3 g (72.1 mmol) of **11***b* gave 6.59 g (60%) of **12***a* as an oil: $[\alpha]_D^{20}$ +55° (*c* 1.08, $CHCl_3$); ir (film) ν_{max}: 1772 (C=O β-lactam), 1715 (sh C=O ester), 1700 and 1520 (amide) cm^{-1}; ^{1}Hmr ($CDCl_3$, 60 MHz) δ: 2.15, 2.26 and 2.3 (3s, 3 × 3H, CH_3 of crotonate and $SCOCH_3$), 3.6 and 3.76 (2s, 2 × 3H, OCH_3-3 and CO_2CH_3), 4.53 (s, 2H, CH_2 of *p*-nitrobenzyl), 6.0 (s, 1H, H-4), and 6.8–7.5 (6H, NH and aromatic) ppm. *Anal.* calcd. for $C_{20}H_{24}N_2O_7S$: C 55.03, H 5.54, N 6.42, S 7.34; found: C 54.85, H 5.47, N 6.25, S 6.86.

N-p-*Nitrobenzoxalyl 4*R*-acetylthio-3*S*-methoxy-3-phenoxyacetamido-2-azetidinone* ***12***d

Ozonolysis of 2.60 g (4.66 mmol) of **12***h* in a mixture of CH_2Cl_2 (80 mL) and MeOH (10 mL) at −20°C and work-up as described above for **6***b* gave 2.40 g (97%) of **12***d* as a clear oil; $[\alpha]_D^{23}$ +17° (*c* 0.98, $CHCl_3$); ir (film) ν_{max}: 1822 and 1760 (C=O β-lactam, oxalyl), 1710 (br, C=O ester, amide), 1525 (amide), and 1350 (NO_2) cm^{-1}; ^{1}Hmr ($CDCl_3$, 60 MHz) δ: 2.36 (s, 3H, $SCOCH_3$), 3.6 (s, 3H, OCH_3-3), 4.60 (s, 2H, CH_2 of phenoxyacetyl), 5.40 (s, 2H, CH_2 of *p*-nitrobenzyl), 6.0 (1H, s, H-4), 7.0–7.6 (m, 6H, NH and aromatic), 7.56 (d, J = 8.8 Hz, 2H, H-2 of *p*-nitrobenzyl), and 8.4 (d, J = 8.8 Hz, H-3 of *p*-nitrobenzyl) ppm.

N-*Methoxalyl 4*R*-acetylthio-3*S*-methoxy-3-phenoxyacetamido-2-azetidinone* ***12***c

Ozonolysis of 0.736 g (1.68 mmol) of the crotonate **12***a* at −20°C in methanol (25 mL) and work-up as described above for **6***b* gave 0.602 g (85%) of **12***c as a clear oil: ir (film)* ν_{max}: 1820 and 1755 (C=O β-lactam and oxalyl), 1710 (br, C=O ester, amide, and thioester), and 1510 (sh, amide) cm^{-1}; ^{1}Hmr ($CDCl_3$, 60 MHz) δ: 2.37 (s, 3H, $SCOCH_3$), 3.63 (s, 3H, OCH_3-3), 3.96 (s, 3H, CO_2CH_3), 4.63 (s, 2H, CH_2 of phenoxyacetyl), 6.03 (s, 1H, H-4), and 6.8–7.6 (m, 6H, NH and aromatic) ppm.

*4*R*-Acetylthio-3*S*-methoxy-3-phenoxyacetamido-2-azetidinone* ***13***

A solution of *N*-methoxalyl 4*R*-acetylthio-3*S*-methoxy-3-phenoxyacetamido-2-azetidinone **12***c* (0.677 g, 1.85 mmol) in tetrahydrofuran (10 mL) was treated with 1 M aqueous HCl (2 mL) and stirred at 22°C for 8 h. The reaction mixture was diluted with EtOAc, washed with brine, and dried (Na_2SO_4). Evaporation of the solvent and chromatography of the residue on silica gel (20 g, elution toluene–EtOAc 1:1) gave 0.180 g (36%) of the title azetidinone **13** as a solid. Recrystallization from a mixture of ether and hexanes gave white needles: mp 123–124°C (lit. (*5a*) mp 136–139°C); ir (KBr) ν_{max}: 3260 (NH), 1778 (C=O β-lactam), and 1681 (amide) cm^{-1}; ^{1}Hmr ($CDCl_3$, 80 MHz) δ: 2.34 (s, 3H, $SCOCH_3$), 3.58 (s, 3H, OCH_3-3), 4.58 (s, 2H, CH_2 of phenoxyacetyl), 5.58 (s, 1H, H-4), 6.3 (br, 1H, NH), and 6.8–7.4 (m, 5H, aromatic) ppm. *Anal.* calcd. for $C_{14}H_{16}N_2O_5S$: C 51.84, H 4.97, N 8.63, S 9.88; found: C 51.44, H 4.96, N 8.39, S 9.58.

p-*Nitrobenzyl (4*R*-acetylthio-3*S*-methoxy-3-phenoxyacetamido-2-azetidinon-1-yl)triphenylphosphoranylidene acetate* ***12***e

A solution of *N*-*p*-nitrobenzoxalyl 4*R*-acetylthio-3*S*-methoxy-3-phenoxyacetamido-2-azetidinone **12***d* (2.40 g, 4.52 mmol) in tetrahydrofuran (40 mL) was cooled to 0–5°C and treated with 6.8 mL (6.8 mmol) of a 1 M solution of B_2H_6 in tetrahydrofuran (Aldrich Chemical Co.). After 1 h, the reaction mixture was quenched by addition of aqueous NH_4Cl solution (20 mL) and extracted with CH_2Cl_2. After drying (Na_2SO_4), evaporation gave 2.09 g of crude hemiaminal **15***a* as an oil. This product was unstable on silica gel and was used as is for the next step: ir (film) ν_{max}: 1760 (C=O β-lactam), 1700 (C=O) and 1520 (amide) cm^{-1}.

Thionyl chloride (0.27 mL, 3.74 mmol) was added dropwise over 5 min to a cooled (−27°C) solution of the crude hemiaminal **15***a* and pyridine (0.30 mL, 3.74 mL) in dry tetrahydrofuran (40 mL). After 15 min, the solid that formed was filtered through a Celite pad and washed with tetrahydrofuran (20 mL). The combined filtrates were concentrated *in vacuo* and chromatographed on silica gel (30 g). Elution with a mixture of CH_2Cl_2 and ethyl acetate (8:2) gave 0.71 g (34% from **12***d*) of *p*-nitrobenzyl (*4R*-acetylthio-3*S*-methoxy-3-phenoxyacetamido-2-azetidinon-1-yl) chloro acetate **15***b* as a clear oil. The ^{1}Hmr indicated a 2:1 mixture of diastereoisomers: ir (film) ν_{max}: 1794 (C=O β-lactam), 1766 (C=O ester), 1700 (C=O thioester and amide), and 1526 (amide) cm^{-1}; ^{1}Hmr ($CDCl_3$, 60 MHz) δ: 2.23 and 2.3 (2s, 3H, $SCOCH_3$), 3.56 (s, 3H, OCH_3-3), 4.56 (s, 2H, CH_2 of phenoxyacetyl), 5.33 and 5.36 (2s, 2H, CH_2 of *p*-nitrobenzyl), 5.86 and 5.93 (2s, 1H, H-4 of azetidinone), 6.13 and 6.16 (2s, 1H, H-2 of acetate), 6.7–7.3 (m, 6H, aromatic and NH), 7.52 (d, J = 8.5 Hz, 2H, H-2 of *p*-nitrobenzyl), and 8.20 (d, J = 8.5 Hz, 2H, H-3 of *p*-nitrobenzyl) ppm.

A solution of the chloro acetate **15***b* (0.70 g, 1.27 mmol) in tetrahydrofuran (45 mL) was treated with triphenylphosphine (1.04 g, 3.96 mmol) and 2,6-lutidine (0.112 g, 1.04 mmol) and heated under N_2 at 53°C for 48 h. The solvent was evaporated *in vacuo*, the residue dissolved in CH_2Cl_2, washed with cold 0.1 N aqueous HCl, cold 1% aqueous $NaHCO_3$, and brine. After drying (Na_2SO_4), evaporation of the solvent gave a residue that was chromatographed on silica gel (2 × 14 cm). Elution with a mixture of CH_2Cl_2 and EtOAc (7:3) gave 0.361 g (36% from **15***b*) of the title phosphorane **12***e* as a gum: ir (film) ν_{max}: 1770 (C=O β-lactam), 1700 (C=O), 1625 and 1600, 1520 (amide), and 1350 (NO_2) cm^{-1}.

p-*Nitrobenzyl (5*R*) 6*S*-methoxy-2-methyl-6-phenoxyacetamidopenem-3-carboxylate* ***16***

A solution of the phosphorane **12***e* (0.360 g, 0.46 mmol) in dry toluene (200 mL) was maintained at 98°C under N_2 for 24 h. The solvent was then concentrated to ~10 mL and this was chromato-

Can. J. Chem. Downloaded from www.nrcresearchpress.com by 93.93.197.157 on 09/07/12
For personal use only.

graphed on silica gel (20 g). Elution with a mixture of toluene and EtOAc (8:23) gave 0.129 g (55%) of the title penem **16** as a white solid. Recrystallization from a mixture of CH_2Cl_2 and ether gave white cubes: mp 152–153°C (lit. (5*a*) mp 152–153°C); $[\alpha]_D^{22}$ +235° (*c* 0.44, $CHCl_3$); uv (EtOH) λ_{max} (ε): 308 (8300), 274 (sh), 268 (12 200), and 262 (sh) nm; ir (KBr) ν_{max}: 1785 (C=O β-lactam), 1704 (C=O ester), 1670 and 1513 (C=O amide), 1585, 1493, and 1323 (NO_2) cm^{-1}; ^{1}Hmr ($CDCl_3$, 80 MHz) δ: 2.33 (s, 3H, CH_3-2), 3.51 (s, 3H, OCH_3-6), 4.56 (s, 2H, CH_2 of phenoxyacetyl), 5.34 (ABq, J_{AB} = 13.6 Hz, $\Delta\nu$ = 17 Hz, CH_2 of *p*-nitrobenzyl), 5.92 (s, 1H, H-5), 6.7–7.4 (m, 5H, aromatic), 7.60 (d, *J* = 8.8 Hz, 2H, H-2 of *p*-nitrobenzyl), 7.78 (br s, 1H, NH), and 8.20 (d, *J* = 8.8 Hz, 2H, H-3 of *p*-nitrobenzyl) ppm. *Anal.* calcd. for $C_{23}H_{21}N_3O_8S$: C 55.30, H 4.24, N 8.41, S 6.42; found: C 55.36, H 4.28, N 8.36, S 6.49.

Sodium (5R) 6S-methoxy-2-methyl-6-phenoxyacetamidopenem-3-carboxylate ***3b***

A solution of *p*-nitrobenzyl (5*R*) 6*S*-methoxy-2-methyl-6-phenoxyacetamidopenem-3-carboxylate **16** (0.095 g, 0.19 mmol) in a mixture of tetrahydrofuran (5 mL), ether (15 mL), water (15 mL), pH 7.0 phosphate buffer (4 mL of a 0.5 M solution), and sodium bicarbonate (0.015 g, 0.19 mmol) was hydrogenated over 0.15 g of 10% Pd on activated carbon under 45 psi of H_2 at ~15°C for 3 h. The catalyst was removed by filtration through a Celite pad and the aqueous phase was chromatographed at 0–5°C on reversed phase silica gel (2 × 8 cm). Elution with a mixture of H_2O and CH_3CN (9:1) gave 0.045 g (61%) of the penem **3***b* as a white amorphous powder after lyophilization: $[\alpha]_D^{22}$ +150° (*c* 0.44, H_2O); uv (H_2O, pH 7.4 phosphate buffer) λ_{max} (ε): 297 (4900), 272 (5200), 265 (5700), and 259 (5700) nm; ir (KBr) ν_{max}: 1759 (C=O β-lactam), 1688 (C=O of amide), and 1620 (br, carboxylate) cm^{-1}; ^{1}Hmr (D_2O, 80 MHz) δ: 2.16 (s, 3H, CH_3-2), 3.44 (s, 3H, OCH_3-6), 4.67 (s, 2H, CH_2 of phenoxyacetyl), 5.86 (s, 1H, H-5), and 6.8–7.4 (m, 5H, aromatic) ppm. By uv, at 37°C the half-life of this penem was determined to be 1.2 h in a pH 7.4 phosphate buffer.

p-*Nitrobenzyl 6α-methoxy-6β-[α-(*p*-nitrobenzyloxycarbonyl)phenylacetamido]penicillanate* ***18***

A solution of *p*-nitrobenzyl 6-*p*-toluenesulfenimidopenicillanate (**17**) (13.7 g, 29.1 mmol) (17) in dry CH_2Cl_2 (500 mL) was treated at 24°C with triphenylphosphine (22.8 g, 87.0 mmol) and a solution of mercuric acetate (9.23 g, 29.0 mmol) in methanol (100 mL). After 3.5 h, the solvent was evaporaed and the residue dissolved in CH_2Cl_2 (300 mL). Propylene oxide (180 mL) and pyridine (9 mL) were added and the mixture cooled to −10°C. Then a solution of phenylmalonyl chloride mono-*p*-nitrobenzyl ester (87.6 mmol) in CH_2Cl_2 (70 mL) (prepared by mono-esterification of the commercial phenylmalonic acid with *p*-nitrobenzyl alcohol (26) to give the phenylmalonic acid mono-*p*-nitrobenzyl ester (mp 128–129°C), followed by reaction of the mono-ester (27.6 g, 87.6 mmol) in CH_2Cl_2 (70 mL) with oxalyl chloride (7.7 mL) and a drop of *N*,*N*-dimethylformamide at 22°C for 2 h and evaporation) was added dropwise over 10 min and the resulting mixture was stirred for 3 h at −10°C. The reaction mixture was filtered through a Celite pad, which was then washed with CH_2Cl_2. The filtrate and the washings were washed with cold saturated aqueous $NaHCO_3$, brine, and dried (Na_2SO_4). Evaporation of the solvent gave an oil, which was chromatographed on silica gel (200 g). Elution with a mixture of toluene and EtOAc (9:1–7:3) gave 12.6 g (63%) of the title material **18** as a clear oil. The ^{1}Hmr indicated a 1:1 mixture of diastereoisomers: ir (film) ν_{max}: 1778 (C=O β-lactam), 1750 (C=O ester), 1695 and 1520 (amide), and 1350 (NO_2) cm^{-1}; ^{1}Hmr ($CDCl_3$, 80 MHz) δ: 1.24, 1.28, and 1.23 (3s, 2 × 3H and 6H, CH_3-2), 3.36 and 3.38 (2s, 2 × 3H, OCH_3-6), 4.41 and 4.46 (2s, 1H, CH of malonyl), 4.67 and 4.69 (2s, 1H, H-3), 5.28 (s, 4H, CH_2 of *p*-nitrobenzyl), 5.52 and 5.54 (s, 1H, H-5), and 7.2–8.3 (m, 14H, NH and aromatic) ppm. *Anal.* calcd. for $C_{32}H_{30}N_4O_{11}S$: C 56.63, H 4.46, N 8.26, S 4.72; found: C 56.63, H 4.48, N 8.05, S 4.73.

p-*Nitrobenzyl 6α-methoxy-6β-[α-(*p*-nitrobenzyloxycarbonyl)phenylacetamido]penicillanate-1β- and -1α-oxide (****19****b and* ***19****a)*

m-Chloroperbenzoic acid (3.09 g, 17.9 mmol) was added in small portions over 30 min to a solution of 6α-methoxy penicillanate **18** (12.2 g, 17.9 mmol) in CH_2Cl_2 (250 mL) at −20°C. After 1 h at −20°C, the mixture was washed with cold aqueous saturated $NaHCO_3$, brine, and dried (Na_2SO_4). Evaporation of the solvent gave an oil, which was chromatographed on silica gel (300 g). Elution with a mixture of toluene and EtOAc (7:3) gave 10.65 g (85%) of the major β-oxide **19***b* as an oil: ir (film) ν_{max}: 1785 (C=O β-lactam), 1750 (C=O ester), 1680 and 1515 (amide), and 1345 (NO_2) cm^{-1}; ^{1}Hmr ($CDCl_3$, 80 MHz) (mixture of epimers at the malonyl side chain in 1:1 ratio) δ: 1.12 and 1.59 (2s, 2 × 3H, CH_3-2), 3.38 (s, 3H, OCH_3-6), 4.6, 4.62, 4.65, 4.75, 4.90, and 4.93 (6s, total 3H, H-3, H-5 and CH of malonyl), 5.27 and 5.32 (br s, 4H, CH_2 of *p*-nitrobenzyl), and 7.1–8.3 (m, 13H, aromatic) ppm. *Anal.* calcd. for $C_{32}H_{30}N_4O_{12}S$: C 55.33, H 4.35, N 8.05, S 4.61; found: C 55.0, H 4.24, N 7.97, S 4.61. Further elution with the same solvent system gave 1.01 g (8%) of the minor α-sulfoxide **19***a* as a solid, which was crystallized from a mixture of toluene and CH_2Cl_2: mp 160–165°C (dec); ir (KBr) ν_{max}: 1788 (C=O β-lactam), 1750 and 1740 (sh) (C=O ester), 1690 and 1520 (amide), and 1350 (NO_2) cm^{-1}; ^{1}Hmr ($CDCl_3$, 80 MHz) (mixture of epimers at the malonyl side chain in 1:1 ratio) δ: 1.12, 1.17, 1.20, and 1.22 (4s, 6H, CH_3-2), 3.45 and 3.50 (2s, 3H, OCH_3-6), 4.50, 4.53, 4.66, 4.71, 4.84, and 4.92 (6s, 3H, H-3, H-5 and CH of malonyl), 5.29 (br s, 4H, CH_2 of *p*-nitrobenzyl), and 7.2–8.3 (m, 13H, aromatic) ppm. *Anal.* calcd. for $C_{32}H_{30}N_4O_{12}S$: C 55.33, H 4.35, N 8.05, S 4.61; found: C 55.39, H 4.39, N 8.03, S 4.63.

Disulfide ***21***

A mixture of *p*-nitrobenzyl 6α-methoxy-6β-[α-(*p*-nitrobenzyloxycarbonyl)phenylacetamido]penicillanate-1β-oxide (**19***b*) (5.50 g, 7.99 mmol) and 2-mercaptobenzothiazole (1.34 g, 8.0 mmol) in toluene (160 mL) was heated under reflux for 5 h. The solvent was evaporated and the residual oil (6.60 g) was used as such for the next step. Attempted purification on silica gel led to isomerization of the β double bond; ir (film) ν_{max}: 1775 (C=O β-lactam), 1740 (C=O ester), 1680 and 1520 (amide), and 1345 (NO_2) cm^{-1}; ^{1}Hmr ($CDCl_3$, 60 MHz) δ: 1.90 (br s, 3H, CH_3 of 3-butenoate), 3.50 (br s, 3H, OCH_3), and 7.1–8.3 (m, aromatic) ppm.

Enol ***22***

A solution of the disulfide **21** (6.60 g, 7.83 mmol) in CH_2Cl_2 (120 mL) was cooled to −78°C and treated with a stream of ozone until a yellow-green solution was obtained. The mixture was then stirred at −78°C for 15 min, flushed with N_2, and treated with methyl sulfide (2 mL). The solution was allowed to warm up to 22°C and washed successively with 10% aqueous solution bisulfite (100 mL) and brine. After drying (Na_2SO_4), evaporation gave 6.0 g of the title material **22** as an oil. Since the product was strongly absorbed on silica gel, the crude material was used as such for the next step. Chromatography of a sample on silica gel (elution toluene:EtOAc 6:4) gave the title enol **22** as an oil; ir (film) ν_{max}: 3300 (OH), 1780 (C=O β-lactam), 1755 (C=O ester), 1675 and 1520 (amide), and 1345 (NO_2) cm^{-1}; ^{1}Hmr ($CDCl_3$, 80 MHz) (mixture of epimers ratio 1:1 at the malonyl side chain) δ: 2.32 (br s, 3H, CH_3 acetoacetate), 3.45 and 3.50 (2s, 3H, OCH_3), 4.7 and 4.75 (2s, 1H, H of malonyl), 5.1 and 5.3 (br s, CH_2 of *p*-nitrobenzyl and H-4), and 7.2–8.3 (m, aromatic) ppm.

Oxazoline ***23***b

Triphenylphosphine (1.02 g, 3.90 mmol) was added over 15 min to a solution of the crude enol **22** (3.30 g, 3.90 mmol) in ethyl acetate (30 mL) that had been cooled to 0°C. The resulting mixture was stirred at 0°C for 30 min. Mesyl chloride (0.60 mL, 7.8 mmol) and triethylamine (1.08 mL, 7.8 mmol) were then added over 5 min. After 1.5 h at 0°C, the reaction mixture was diluted with EtOAc (300 mL), washed with brine, and dried (Na_2SO_4). Evaporation of the solvent gave a dark violet gum, which was rapidly chromatographed on silica gel (2.5 × 20 cm; this product was relatively unstable on silica gel). Elution with a mixture of CH_2Cl_2 and EtOAc 9:1 gave 1.10 g (39% from the enol **22**) of the oxazoline **23***b* as a light yellow oil: ir (film) ν_{max}: 1790 (C=O β-lactam), 1730 (C=O ester), 1675, 1605, 1520, and 1345 cm^{-1}; ^{1}Hmr ($CDCl_3$, 80 MHz) δ: 2.63 (s, 3H, CH_3 of

crotonate), 3.1 and 3.16 (2s, 3H, CH_3 of mesylate), 3.58 (s, 3H, OCH_3), 5.3 (br, CH_2 of *p*-nitrobenzyl), 6.06 and 6.1 (2s, 1H, H-4), and 7.2–8.4 (m, aromatic) ppm.

Chloro azetidinone 24

A solution of the oxazoline **23***b* (1.10 g, 1.52 mmol) in dry CH_2Cl_2 (40 mL) was treated with a stream of dry HCl for 2.5 h. The reaction mixture was then concentrated *in vacuo* and chromatographed on silica gel (2 × 18 cm). Elution with a mixture of CH_2Cl_2 and EtOAc (9:1) gave 0.55 g (48%) of the chloro azetidinone **24** as a clear oil; $[\alpha]_D^{22}$ +30° (*c* 2.5, $CHCl_3$); ir (film) ν_{max}: 1788 (C=O β-lactam), 1730 (C=O ester), 1690 and 1520 (amide), and 1350 (NO_2) cm^{-1}; ^{1}Hmr ($CDCl_3$, 80 MHz) (mixture of epimers at the malonyl side chain, ratio 1:1) δ: 2.68 (s, 3H, CH_3 of crotonate), 3.15 and 3.17 (2s, 3H, CH_3 of mesylate), 3.48 and 3.51 (2s, 3H, OCH_3), 4.61 and 4.63 (2s, 1H, H of malonate), 5.27 (s, 4H, CH_2 of *p*-nitrobenzyl), 6.11 and 6.15 (2s, 1H, H-4 of azetidinone), and 7.1–8.2 (m, 14H, aromatic) ppm.

p-*Nitrobenzyl (5*R*) 6*S*-methoxy-2-methyl-6-[α-(*p*-nitrobenzyloxycarbonyl)phenylacetamido]penem-3-carboxylate 25*

A solution of triethylamine (0.106 mL, 0.76 mmol) in dry THF (5 mL) was cooled to −20°C and hydrogen sulfide was bubbled through the solution for 5 min. Then *N*,*N*-dimethylformamide (1 mL) and the chloroazetidinone **24** (0.290 g, 0.38 mmol) in THF (2 mL) were added and the mixture was stirred at −20°C for 30 min. The reaction mixture was then diluted with EtOAc (25 mL), washed with cold brine, and dried (Na_2SO_4). Evaporation of the solvent gave an oil, which was rapidly chromatographed on silica gel (2 × 10 cm, elution with toluene–EtOAc 85:15) to give 0.070 g (~25%) of the title penem **25** as an oil. This product was relatively unstable on silica gel and was contaminated by the thiazole **26***a* (ratio penem:thiazole = 7:3 by ^{1}Hmr); ir (film) ν_{max}: 1785 (C=O β-lactam), 1740 (C=O ester), 1700 (broad), 1520 and 1445 (NO_2) cm^{-1}; ^{1}Hmr ($CDCl_3$, 80 MHz) penem **25** (mixture of epimers ratio 1:1 at the malonyl side chain) δ: 2.22 and 2.29 (2s, 3H, CH_3-2), 3.39 and 3.43 (2s, 3H, OCH_3-6), 4.68 (s, 1H, H of malonyl), 5.29 (br s, CH_2 of *p*-nitrobenzyl), 5.81 and 5.83 (2s, 1H, H-5), and 7.2–8.2 (m, aromatic) ppm; thiazole **26***a* δ: 2.8 (s, CH_3), 5.47 (s, CH_2 of *p*-nitrobenzyl), and 8.8 (br s, H-2) ppm.

*Disodium (5*R*) 6*S*-2-methyl-6-(α-carboxyphenylacetamido)penem-3-carboxylate 3*c

A solution of the crude penem ester **25** (0.070 g, mixture of penem **25** and thiazole **26***a* in a 7:3 ratio) in a mixture of tetrahydrofuran (8 mL), ether (15 mL), pH 7.0 phosphate buffer (5 mL of a 0.05 M solution), ice (15 g), and 0.017 g (0.2 mmol) of $NaHCO_3$ was hydrogenated over 0.2 g of 10% Pd on activated carbon under 45 psi of H_2 at 15°C for 1.5 h. The reaction mixture was then filtered through a Celite pad and the aqueous phase was chromatographed on reversed phase silica gel (1.5 × 11 cm) using cold water (0–5°C) as eluent. Freeze-drying of the uv active fractions gave 0.015 g (~30%) of the title material as a white amorphous powder. By ^{1}Hmr this product contained 25% (mole ratio) of the thiazole **26***b*; uv (H_2O pH 7.4 phosphate buffer) λ_{max}: 299 (4100) and 250 (4700) nm; ir (KBr) ν_{max}: 1765 (C=O β-lactam), 1670 (amide), and 1600 (br, carboxylate) cm^{-1}; ^{1}Hmr (D_2O, 80 MHz) penem **3***c* (mixture of epimers at the malonyl side chain in a 1:1 ratio) δ: 2.13 and 2.17 (2s, 3H, CH_3-2), 3.40 and 3.54 (2s, 3H, OCH_3-6), 4.51 and 4.61 (2s, 1H, H of malonyl), 5.80 and 5.82 (2s, 1H, H-5) ppm; thiazole **26***b* δ: 2.60 (s, CH_3) and 8.61 (s, H-2) ppm.

By uv at 37°C, the half-life of this penem was determined to be 1.6 h in a pH 7.4 phosphate buffer. At 22°C the half-life increased to 6.6 h. This penem was unstable even in the dry form and decomposed at 0°C after a few days.

Acknowledgements

We would like to thank Drs. H. Mastalerz and A. Martel for helpful discussions in the course of this work and also during the preparation of this manuscript. We also thank Mr. G. Lacasse for running the 80-MHz ^{1}Hmr spectra.

1. I. Ernest, J. Gosteli, C. W. Greengrass, W. Holick, D. E. Jackman, H. R. Pfaendler, and R. B. Woodward. J. Am. Chem. Soc. **100**, 8214 (1978).
2. (*a*) M. Lang, K. Prasad, W. Holik, J. Gosteli, I. Ernest, and R. B. Woodward. J. Am. Chem. Soc. **101**, 6296 (1979); (*b*) I. Ernest, J. Gosteli, and R. B. Woodward. J. Am. Chem. Soc. **101**, 6301 (1979); (*c*) H. R. Pfaendler, J. Gosteli, and R. B. Woodward. J. Am. Chem. Soc. **101**, 6303 (1979).
3. (*a*) H. R. Pfaendler, J. Gosteli, and R. B. Woodward. J. Am. Soc. **102**, 2039 (1979); (*b*) W. Durckheimer, J. Blumbach, R. Lattrell, and K. H. Scheunemann. Angew. Chem. Int. Ed. Engl. **24**, 180 (1985).
4. G. Albers-Schonberg, B. H. Arison, O. D. Hensens, J. Hirshfield, K. Hoogsteen, E. A. Kaczka, R. E. Rhodes, J. S. Kahan, F. M. Kahan, R. W. Ratcliffe, E. Walton, L. J. Ruswinkle, R. B. Morin, and B. G. Christensen. J. Am. Chem. Soc. **100**, 6491 (1978).
5. (*a*) E. Perrone and R. Stoodley. J. Chem. Soc. Commun. 933 (1982); (*b*) J. R. Irving, E. Perrone, and R. J. Stoodley. Tetrahedron Lett. **24**, 2501 (1983); (*c*) B. G. Christensen and F. P. DiNinno. U.S. Patent No. 4,215,124 (1980).
6. E. H. W. Bohme, H. E. Applegate, J. B. Ewing, P. T. Funke, M. S. Puar, and J. E. Dolfini. J. Org. Chem. **38**, 230 (1973).
7. (*a*) R. Reiner and P. Zeller. Helv. Chim. Acta, **51**, 1905 (1968); (*b*) E. H. W. Bohme, H. E. Applegate, B. Toeplitz, J. E. Dolfini, and J. Z. Gougoutas. J. Am. Chem. Soc. **93**, 4324 (1971); (*c*) R. A. Firestone, N. Schelechow, D. B. R. Johnston, and B. G. Christensen. Tetrahedron Lett. 375 (1972).
8. (*a*) R. D. G. Cooper, P. V. DeMarco, J. C. Cheng, and N. D. Jones. J. Am. Chem. Soc. **91**, 1408 (1969); (*b*) R. D. G. Cooper, P. V. DeMarco, and D. O. Spry. J. Am. Chem. Soc. **91**, 1528 (1969); (*c*) D. H. R. Barton, F. Comer, and P. G. Sammes. J. Am. Chem. Soc. **91**, 1529 (1969); (*d*) R. A. Archer and P. V. DeMarco. J. Am. Chem. Soc. **91**, 1530 (1969).
9. L. D. Hatfield, J. Fisher, F. L. Jose, and R. D. G. Cooper. Tetrahedron Lett. 4897 (1970).
10. D. O. Spry. J. Org. Chem. **37**, 793 (1972).
11. (*a*) E. M. Gordon and R. B. Sykes. *In* Chemistry and biology of β-lactam antibiotics. Vol. 1. *Edited by* R. B. Morin and M. Gorman. Academic Press, New York. 1982. pp. 218–364; (*b*) F. A. Jung, W. R. Pilgrim, J. P. Poyser, and P. J. Siret. *In* Topics in antibiotic chemistry. Vol. 4. *Edited by* P. G. Sammes. John Wiley and Sons, New York. 1980. pp. 196–211.
12. J. E. Baldwin, F. J. Urban, R. D. G. Cooper, and F. L. Jose. J. Am. Chem. Soc. **95**, 2401 (1973).
13. G. A. Koppel and R. E. Koehler. J. Am. Chem. Soc. **95**, 2403 (1973).
14. R. J. Ponsford, M. J. Basker, G. Burton, A. W. Guest, F. P. Harrington, P. H. Milner, M. J. Pearson, T. C. Smale, and A. U. Stachulski. *In* Recent advances of the chemistry of β-lactam antibiotics. *Edited by* A. G. Brown and S. M. Roberts. The Royal Society of Chemistry, London. 1985. pp. 32–51.
15. W. H. W. Lunn, R. W. Burchfield, T. K. Elzey, and E. V. Mason. Tetrahedron Lett. 1307 (1974).
16. L. M. Weinstock, S. Karady, F. E. Roberts, A. M. Hoinowski, G. S. Brenner, T. B. K. Lee, W. C. Lumma, and M. Sletzinger. Tetrahedron Lett. 3979 (1975).
17. E. M. Gordon, H. W. Chang, C. M. Cimarusty, B. Toeplitz, and J. Z. Gougoutas. J. Am. Chem. Soc. **102**, 1690 (1980).
18. M. Aratani and M. Hashimoto. J. Am. Chem. Soc. **102**, 6171 (1980).
19. I. Ernest. *In* Chemistry and biology of β-lactam antibiotics. Vol. 2. *Edited by* R. B. Morin and M. Gorman. Academic Press, New York. 1982. pp. 315–360.
20. S. Betty, H. G. Davies, and J. Kitchin. *In* Recent advances of the chemistry of β-lactam antibiotics. *Edited by* G. I. Gregory. The Royal Society of Chemistry, London. 1981. pp. 349–358.

Can. J. Chem. Downloaded from www.nrcresearchpress.com by 93.93.197.157 on 09/07/12
For personal use only.

21. E. G. BRAIN, A. J. EGLINGTON, J. H. C. NAYLER, N. F. OSBORNE, R. SOUTHGAVE, and P. TOLLIDAY. J. Chem. Soc. Perkin Trans. 1, 2479 (1977).
22. M. MENARD and A. MARTEL. U.S. Patent No. 4,282,150 (1981).
23. M. MURAKAMI, I. ISAKA, and T. KASHIWAGI. U.S. Patent No. 4,051,126 (1977).
24. M. J. MINTZ and C. WALLING. Org. Synth. Collect. Vol. **5**, 184 (1973).
25. R. B. MORIN, B. G. JACKSON, R. A. MUELLER, E. R. LAVAGNINO, W. B. SCANLON, and S. L. ANDREWS. J. Am. Chem. Soc. **91**, 1401 (1969).
26. K. D. HARDY. Ger. Offen. 1,901,918 (1969); Chem. Abstr. **71**, 124426d (1969).
27. J. E. BALDWIN, B. CHAKRAVARTI, L. D. FIELD, J. A. MURPHY, K. R. WHITTEN, E. P. ABRAHAM, and G. JAYATILAKE. Tetrahedron, **38**, 2773 (1982).

Can. J. Chem. Downloaded from www.nrcresearchpress.com by 93.93.197.157 on 09/07/12
For personal use only.

1-β-Methylcarbapenem intermediates.[1] Stereoselective synthesis of (3*S*,4*R*)-3-[(1*R*)-1-*tert*-butyldimethylsilyloxyethyl]-4-[(1*R*)-3-methoxycarbonyl-1-methyl-2-oxopropyl]azetidin-2-one and its related chemistry

MASAKI ENDO[2] AND ROBERT DROGHINI

Chemical Process Development, Bristol–Myers Pharmaceutical Research and Development Division, 100 Industrial Blvd., Candiac, P.Q., Canada J5R 1J1

Received October 13, 1987

MASAKI ENDO and ROBERT DROGHINI. Can. J. Chem. **66**, 1400 (1988).

A chiral intermediate bearing the 1-β-methyl moiety (**14***a*) for 1-β-methylcarbapenem antibiotics (**1**) was prepared by stereoselective aldol-type reaction between 4-acetoxyazetidinone **3***a* and the dianion (or corresponding bissilyl enol ether) of a 3-oxopentanoate **12** or **13** in the presence of a metal salt. A major side reaction has also been elucidated.

MASAKI ENDO et ROBERT DROGHINI. Can. J. Chem. **66**, 1400 (1988).

On a préparé un intermédiaire chiral portant la portion méthyl-1β (**14***a*) des antibiotiques méthyl-1β carbapénème (**1**) en faisant appel à une réaction stéréosélective de type aldol entre l'acétoxy-4 azétidinone (**3***a*) et le dianion (ou l'éther énolique bissylilé correspondant) d'un oxo-3 pentanoate (**12** ou **13**), en présence d'un sel métallique. On a aussi expliqué une réaction secondaire importante.

[Traduit par la revue]

Introduction

The 1-β-methylcarbapenems (**1**) are chemically and metabolically more stable than their carbapenem progenitors (**2**)

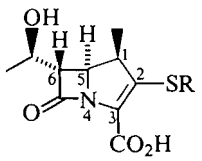

1

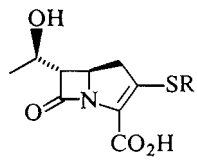

2

while still retaining high antimicrobial activity (1). This discovery has led to intense efforts to stereoselectively introduce the β-methyl function onto carbapenem precursors (1–8, 10).

Two general approaches to this problem account for most of successful syntheses to date (Scheme 1). The more popular is the aldol-type reaction between the chiral 4-acetoxyazetidinone **3***a* (9) or the 4-chloroazetidinone **3***b* (6) and metal enolates or silyl enol ethers **4** (R = auxiliary group) affording compound **5** (2–6). The other is stereoselective reduction of olefinic esters **6** and propargyl alcohols **8** to give **7** (7, 8) and **9** (10) respectively. These approaches then require several transformations of the 4-substituent of the azetidinone to produce the key intermediate **10***a* (1*a*), which, after diazo-transfer and intramolecular cyclization, yields the important carbapenem precursor **11** (1*a*).

It appeared to us that an aldol-type reaction between **3***a* and the dianion (or corresponding bissilyl enol ether) of a 3-oxopentanoate **12** or **13** would afford **10***a* directly. Therefore, we investigated the stereochemical outcome of these reactions (Scheme 2).

Results and discussion

Huckin and Weiler (11) demonstrated that the dianions of β-ketoesters generated by using one equivalent of sodium

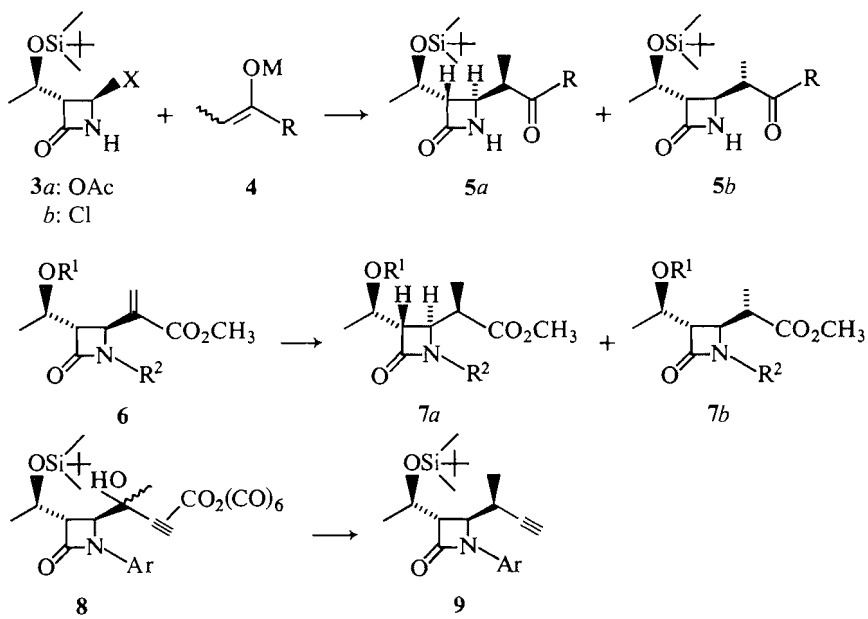

SCHEME 1

[1]Part I, see ref. 6.

[2]Author to whom correspondence may be addressed.

Can. J. Chem. Downloaded from www.nrcresearchpress.com by 93.93.197.157 on 09/07/12
For personal use only.

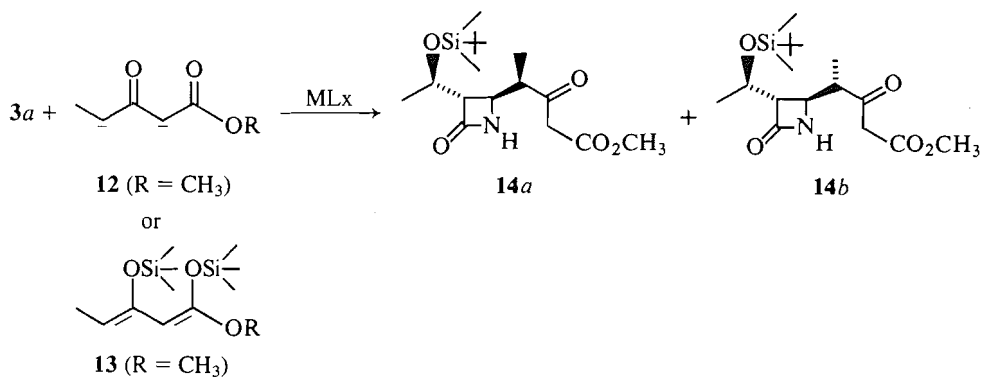

SCHEME 2

hydride and one equivalent of *n*-butyllithium react with alkylating agents to produce only γ-alkylated products in good yields. Based on the above report, we carried out a series of coupling reactions of 4-acetoxyazetidinone **3***a* with the dianion

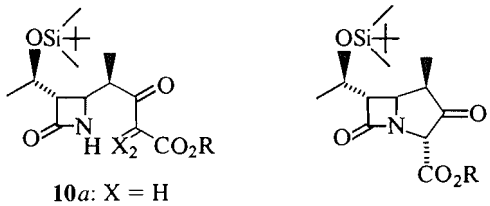

12 of methyl 3-oxopentanoate in the presence of Lewis acid (Scheme 2).

The dianion **12** generated by following Weiler's procedure (11) was cooled to −30 to −40°C and was quenched with Lewis acid, presumably to form the metal enolate **12***a* (eq. [1]).

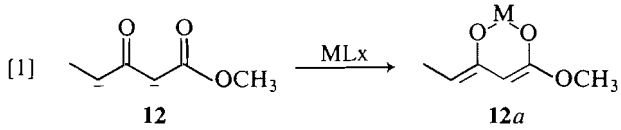

The enolate **12***a* formed at −30 to −40°C reacted with 4-acetoxyazetidinone **3***a* to give a mixture of **14***a* and **14***b*.

According to the results shown in Table 1, all reactions went in favor of the β-isomer **14***a*. In particular, zinc chloride, tri-*n*-butylborane, and tin(II) chloride were found to be good reagents.

It should be noted that exclusion of Lewis acid gave only decomposition products at the usual reaction temperatures, but at −70°C, β-rich product was nevertheless obtained.

The generally low yields could largely be explained by the formation of a stable, crystalline by-product identified as the 2-pyridone **15**. Also observed in these reactions was a compound that converted to **15** on attempts to isolate it in pure form. This precursor was tentatively identified as the amide **16** by ^{1}H nmr.[3] It seemed likely that **16** derived from the 2-azetidinone **17**, product of alkylation at the α-site of dianion **12**.

To confirm this sequence, an independent synthesis of **17** was attempted. Lewis acid-mediated coupling of **3***a* with silyl enol

[3]Data for ^{1}H nmr (200 MHz, $CDCl_3$), δ: 0.83, 0.90 (2s, 6H, CH_3Si), 0.86 (s, 9H, CH_3CSi), 1.10 (t, J = 7.2 Hz, 3H, CH_2CH_3), 1.18 (d, J = 6.2 Hz, 3H, CH_3CHOSi), 2.68 (m, 2H, CH_2CH_3), 3.47 (dd, J = 5.6 and 10.4 Hz, 1H, CHC=), 3.83 (s, 3H, CO_2CH_3), 4.26 (m, 1H, CH_3CHOSi), 5.38, 6.50 (2s, 1H, NH_2), 6.94 (d, J = 10.4 Hz, 1H, CH=).

TABLE 1. Results of coupling reaction with **12**

Entry	MLx	**14***a*/**14***b*[a]	Yield (%)[b]
1	$ZnCl_2$	78:22	75
2	$B(n\text{-}Bu)_3$	93:7	28
3	$SnCl_2$	88:12	30
4	$Ti(i\text{-}PrO)_4$	60:40	66
5	$ZrCp_2Cl_2$	74:26	10
6	$MgCl_2$	60:40	26 (100)[c]
7	—	73:23	38

[a]The ratio was determined by hplc (column: Hypersil; column length: 100 mm; solvent: 25% EtOAc/hexane; detection: uv 260 nm).
[b]Isolated yield by chromatography.
[c]Adjusted for unreacted starting material.

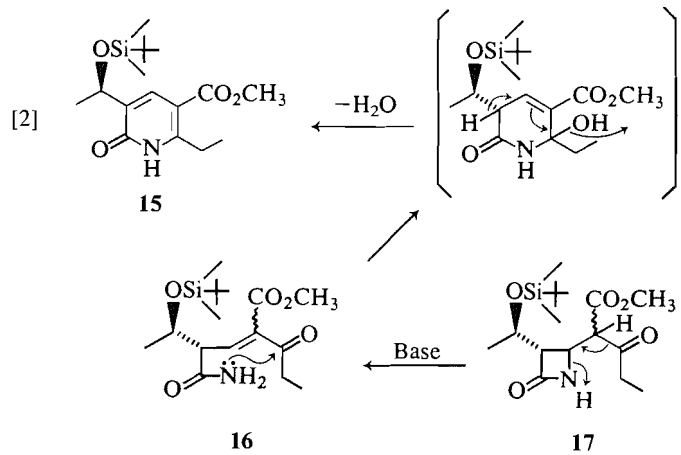

ether **18** (12) gave only traces of desired product. However, **17** was obtained in good yield under the essentially neutral conditions of the Reformatsky-type reaction shown in Scheme 3. Thus the enol ether **18** (12), prepared *in situ* at 0°C from the reaction of methyl 3-oxopentanoate with trimethylsilyl triflate, was reacted with one equivalent of bromine to yield α-bromopentanoate **19** in quantitative yield. Compound **19** was then treated with activated zinc dust at −15°C to form the zinc enolate **20** (13), which immediately reacted with 4-acetoxyazetidinone **3***a* to produce the α-alkylated product **17** (*R*/*S*) in 83% yield (after recrystallization).

It was then possible to show that base treatment of **17** (TEA, 23°C, 24 h) gave 94% of a crystalline compound identical to the major by-product identified as **15**. Furthermore, nmr analysis of the reaction after 30 min clearly showed the presence of compound **16**.

Can. J. Chem. Downloaded from www.nrcresearchpress.com by 93.93.197.157 on 09/07/12
For personal use only.

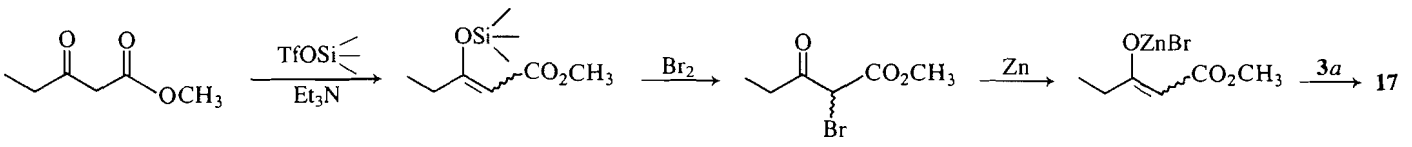

18 19 20

SCHEME 3

The dianion **12** is a very strong base and is considered a hard nucleophile, while the bissilyl enol ether **13** is a soft nucleophile (12). The silyl enol ether **13** would therefore be expected to give a better controlled reaction. Indeed, the reaction of 4-acetoxyazetidinone **3***a* with **13** in the presence of metal salt was much cleaner compared to that of the dianion **12**, and good β-selectivity was also obtained. Furthermore, no α-alkylation was observed.

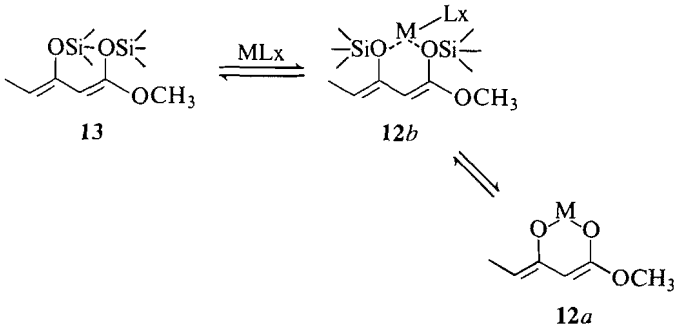

13 **12***b* **12***a*

The reaction probably first involves metal exchange and (or) interaction between **13** and a metal salt MLx. The mixture of **13** and **12***a*,*b* then reacts with 4-acetoxyazetidinone **3***a* to give the coupled products **14***a* and **14***b* (Scheme 2). The results are shown in Table 2.

There was a clear difference in the stereoselectivity when tin(II) and tin(IV) salts were employed (entries 1–4). Tin(II) chloride and triflate favored the β isomer, particularly with THF as solvent, while tin(IV) chloride (a stronger Lewis acid) completely reversed the β/α ratio. Similar results were obtained using zinc compounds (entries 5, 6). Diethyl zinc gave good β-selectivity, while zinc chloride, a Lewis acid, favored the α isomer. Thus far, Lewis acids would seem to disfavor β-selectivity. However, boron trichloride, a Lewis acid, showed β-selectivity, as did boron trifluoride (entries 8, 9). On the other hand trialkylboranes such as tri-*n*-butylborane were α-selective (entry 7). Titanium(IV) and silicon compounds were also found to favor slightly the β isomer.

The β-ketoester diastereomers **14***a* and **14***b*, separated by chromatography, were shown to exist as keto/enol tautomers in solution (Scheme 4). The ^{1}H nmr spectra indicated 17% of the enol form for the 1-β-methyl isomer **14***a* and 52% enol for the α-methyl isomer. The ir spectrum in $CHCl_3$ clearly showed the enol form (ν_{OH} = 3410 cm^{-1}).

In carbapenem or penem syntheses it is desirable to protect the carboxylic acid with groups such as allyl or *p*-nitrobenzyl, which may be removed under mild conditions at or near the end of the reaction sequence (1*a*, 14). Therefore the methyl ester of the 1-β-methylcarbapenem intermediate **14***a* was transformed into its allyl ester **23** by simple ester exchange in 50% yield. The allyl ester **23** was then diazotized to give the key 1-β-methylcarbapenem intermediate **24** in 97% yield (1*a*) (Scheme 5). When the diazotization of **14***a* was carried out first, it proceeded well. However, the following transesterification did not work at all.

TABLE 2. Results of coupling reaction with **13**

Entry	MLx	**14***a*/**14***b*[a]	Yield (%)[b]	Solvent
1	$SnCl_2$	69:31	70	THF
2	$SnCl_2$	58:42	70	CH_2Cl_2
3	$Sn(TfO)_2$	73:27	41	THF
4	$SnCl_4$	27:73	15.1[c]	THF
5	$ZnCl_2$	33:67	75	CH_2Cl_2
6	$ZnEt_2$	73:27	33[c]	THF
7	$B(n\text{-}Bu)_3$	20:80	100	THF
8	$BF_3 \cdot Et_2O$	60:40	54 (80)[d]	THF
9	BCl_3 (cat.)	76:24	28 (100)[d]	THF
10	$MgBr_2 \cdot Et_2O$	83:17	8[c]	THF
11	$TiCl_2(TfO)_2$	64:36	23	THF
12	$TfOSiMe_3$ (cat.)	57:43	75	CH_2Cl_2

[a]The ratio was determined by hplc (conditions: see Table 1).
[b]Isolated yield by chromatography.
[c]Estimated yield by hplc.
[d]Adjusted for unreacted starting material.

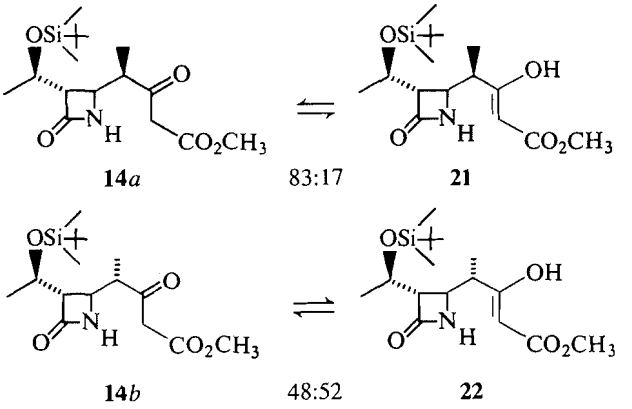

14*a* 83:17 **21**

14*b* 48:52 **22**

SCHEME 4. Tautomerism of the α-ketoesters **14***a* and **14***b*.

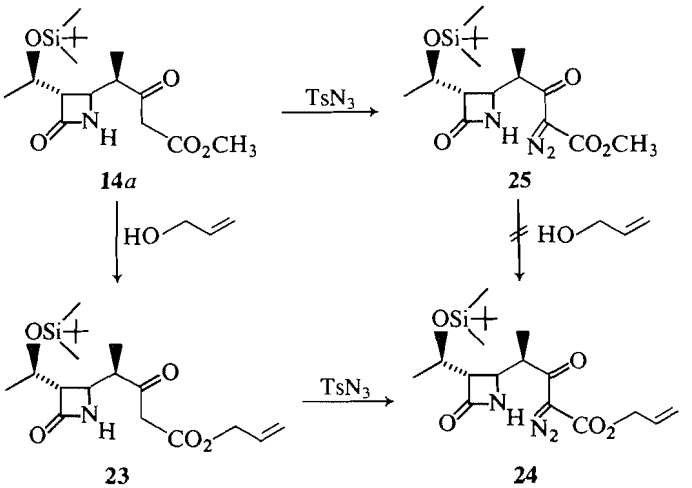

14*a* **25** **23** **24**

SCHEME 5

Can. J. Chem. Downloaded from www.nrcresearchpress.com by 93.93.197.157 on 09/07/12
For personal use only.

In summary, a useful chiral intermediate **14***a* for 1-β-methylcarbapenem antibiotics **1** has been prepared directly and stereoselectively by coupling 4-acetoxyazetidinone with the dianion or a bissilyl enol ether of methyl 3-oxopentanoate.

Experimental

*(3S,4R)-3-[(1R)-1-*tert*-Butyldimethylsilyloxyethyl]-4-[(1R)-3-methoxycarbonyl-1-methyl-2-oxopropyl]azetidin-2-one (**14**a + **14**b)*

Some typical procedures for both the dianion and the bissilyl enolate processes are described.

Via the dianion process

Example 1, using tin(II) chloride

To a suspension of sodium hydride (0.192 g, 4 mmol, 50% in mineral oil) in dry THF (10 mL) at −10 to −5°C under nitrogen atmosphere was added dropwise a solution of methyl 3-oxopentanoate (0.52 g, 4 mmol) in dry THF (1 mL), maintaining the temperature at −5 to 0°C. The resulting slurry was stirred at −5 to 0°C for 15 min, giving a colorless solution in 5–10 min. Then *n*-butyllithium (2.58 mL, 4 mmol, 1.55 M solution in hexane) was added dropwise, maintaining the temperature at −5 to 0°C. It was stirred for 15 min. The yellow dianion solution (**12**) was then cooled to −45°C and anhydrous tin(II) chloride (0.76 g, 4 mmol) was added all at once. As soon as the tin(II) chloride was added, a precipitation took place as the temperature started rising to −35°C, and it gradually dissolved back into the solution. The cloudy solution was stirred at −45 to −35°C for 0.5 h and a solution of 4-acetoxyazetidinone **3***a* (9) (0.574 g, 2 mmol) in dry THF (1 mL) was added. The resulting solution was allowed to warm up to room temperature and stirred for 1.5 h. Thin-layer chromatography (tlc) (silica gel, petroleum ether – ether 3:2 as solvent, uv and molybdate solution for visualization) showed completion of reaction. The reaction mixture was diluted with ether (70 mL), washed successively with 1 N hydrochloric acid (30 mL), saturated sodium bicarbonate (30 mL), and brine (30 mL), dried over anhydrous magnesium sulfate, and concentrated to give an oil (0.87 g), which was chromatographed on silica gel (ether – petroleum ether 1:1), yielding 0.22 g (30%) of the title compound with a β/α ratio of 88:12 and the pyridone **15** (0.19 g, 28%).

Both pure isomers **14***a* and **14***b* were isolated by further chromatography for characterization.

*β-Isomer **14**a*: mp 67–68°C (recrystallized from hexane); $[\alpha]_D^{23}$ −2.4° (*c* 0.46, $CHCl_3$); ir ($CHCl_3$): 3415 (OH, enol), 1755 (β-lactam), 1735 (CO_2CH_3, keto), 1712 (CO, keto), 1655 (CO_2CH_3, enol), and 1625 (C=C, enol) cm^{-1}; ^1H nmr (200 MHz, $CDCl_3$) δ: 0.04, 0.05 (2s, 6H, CH_3Si keto + enol), 0.85 (s, 9H, CH_3CSi keto + enol), 1.11–1.21 (4 overlapping d, *J* = 6.3 and 7.1 Hz for keto form, 6H, CH_3CHOSi keto + enol and $CH_3CH{=}O$, $CH_3CHC(OH){=}$), 2.40 (m, 0.17H, $CH_3CHC(OH){=}$), 2.89, 2.95 (overlapping dd and m, *J* = 2.3 and 4.7 Hz, 1.83H, H-3 keto + enol and $CH_3CHC{=}O$), 3.52 (q, *J* = 15.8 Hz, 1.66 Hz, $COCH_2CO_2$), 3.72 (overlapping s and m, 3.17H, CO_2CH_3 keto + enol and H-4 enol), 3.92 (dd, *J* = 2.3 and 4.5 Hz, 0.83H, H-4 keto), 4.16 (m, 1H, CH_3CHOSi keto + enol), 5.02 (s, 0.17H, =CH), 5.80 (br s, 0.83H, NH keto), 5.93 (br s, 0.17H, NH enol); mass spectrum (C.I.) *m/e*: 358 $(M + H)^+$. *Anal.* calcd. for $C_{17}H_{31}NO_5Si$ (357.492): C 57.12, H 8.74, N 3.92; found: C 57.10, H 8.86, N 3.86.

*α-Isomer **14**b*: mp 82–83°C (recrystallized from hexane); $[\alpha]_D^{23}$ +6.1° (*c* 0.49, $CHCl_3$); ir ($CHCl_3$): 3415 (OH, enol), 1755 (β-lactam), 1735 (CO_2CH_3, keto), 1712 (CO, keto), 1650 (CO_2CH_3, enol), and 1625 (C=C, enol) cm^{-1}; ^1H nmr (200 MHz, $CDCl_3$) δ: 0.05, 0.06 (2s, 6H, CH_3Si keto + enol), 0.85, 0.86 (2s, 9H, CH_3CSi keto + enol), 1.20 (m, 6H, CH_3CHOSi keto + enol and $CH_3CHC{=}O$, $CH_3CHC(OH){=}$), 2.31 (m, 0.52H, $CH_3CHC(OH){=}$), 2.65–2.80 (overlapping m and dd, 1.42H, $CH_3CHC{=}O$ and H-3 keto + enol), 3.52 (s, 0.84H, $COCH_2CO_2$), 3.68 (2 overlapping dd, 1H, H-4 keto + enol), 3.73 (s, 3H, CO_2CH_3 keto + enol), 4.15 (m, 1H, CH_3CHOSi keto + enol), 5.40 (s, 0.52H, =CH), 5.84 (br s, 0.52H, NH enol), 5.92 (br s, 0.48H, NH keto); mass spectrum (C.I.) *m/e*: 358 $(M + H)^+$. *Anal.* calcd. for $C_{17}H_{31}NO_5Si$ (357.492): C 57.12, H 8.74, N 3.92; found: C 56.66, H 8.95, N 3.99.

*Pyridone **15***: mp 104–105°C (recrystallized from *i*-PrOH–H_2O 2:3); ir ($CHCl_3$): 1712, 1645 cm^{-1}; ^1H nmr (200 MHz, $CDCl_3$) δ: 0.03, 0.08 (2s, 6H, CH_3Si), 0.92 (s, 9H, CH_3CSi), 1.30 (t, *J* = 7.5 Hz, 3H, CH_2CH_3), 1.37 (d, *J* = 6.2 Hz, 3H, CH_3CHO), 3.07 (m, 2H, CH_2CH_3), 3.83 (s, 3H, CO_2CH_3), 4.94 (d of q, *J* = 1.0 and 6.2 Hz, 1H, CH_3CHO), 8.18 (d, *J* = 1 Hz, =CH), 11.18 (br s, 1H, NH); mass spectrum (C.I.) *m/e*: 340 $(M + H)^+$. *Anal.* calcd. for $C_{17}H_{29}NO_4Si$ (339.484): C 60.14, H 8.69, N 4.12; found: C 59.73, H 8.58, N 3.95.

Example 2, using zinc chloride

The dianion solution of **12** (4 mmol, produced as described in Example 1) was cooled to −40°C, to which was added zinc chloride (0.68 g, 5 mmol, fused-dry). The mixture was stirred at −40 to −10°C for 15 min to give a cloudy solution. Then, a solution of 4-acetoxyazetidinone **3***a* (0.574 g, 2 mmol) in dry THF (1 mL) was added. The resulting solution was stirred at room temperature for 1 h. Disappearance of the starting 4-acetoxyazetidinone was shown by tlc. The reaction mixture was worked up as described in Example 1, yielding 0.54 g (75%) of the title compound with a β/α ratio of 78:22.

*Example 3, using tri-*n*-butylborane*

The dianion solution of **12** (4 mmol, produced as described in Example 1) was cooled to −70°C. To this was added dropwise a solution of 4-acetoxyazetidinone **3***a* (0.574 g, 2 mmol) and $(n\text{-Bu})_3B$ (1 mL, 1 M solution in THF) in dry THF (5 mL) over 10 min, and the resulting yellow solution was stirred at −70 to −65°C for 2 h. The reaction mixture was treated with a mixture of pH 7 buffer (4 mL), methanol (5 mL), and 30% H_2O_2 (1 mL) at room temperature for 1 h, then extracted with ether. The ether extract was washed with brine, 10% $NaHSO_3$, and brine, respectively, dried over anhydrous magnesium sulfate, and concentrated *in vacuo* to give an oil (0.58 g), which was chromatographed on silica gel (ether – petroleum ether 1:1), yielding the title compound (0.21 g, 28%); hplc showed β:α = 93:7.

Example 4, without Lewis acid

The dianion solution of **12** (4 mmol, produced as described in Example 1) was cooled to −70°C. To this was added a solution of 4-acetoxyazetidinone **3***a* (0.574 g, 2 mmol) in dry THF (2 mL). The resulting solution was stirred at −70°C for 1 h. Thin-layer chromatography (silica gel, ether – petroleum ether 3:2, uv and a molybdate solution for visualization) showed no starting 4-acetoxyazetidinone **3***a*. The reaction was then quenched with 6 N hydrochloric acid (10 mL) and the reaction mixture was worked up in the same manner as described in Example 1, yielding the title compound (0.27 g, 38%, β:α 77:23).

Via the bissilyl enolate process

Example 5, using tin(II) chloride

To a solution of 1,3-bis(trimethylsilyloxy)-1-methoxypenta-1,3-diene (**13**) (12) (0.466 g, 1.7 mmol) in dry THF (10 mL) at −40°C under N_2 was added anhydrous tin(II) chloride (0.323 g, 1.7 mmol). The slurry was stirred at −40 to −10°C for 25 min, and then a solution of 4-acetoxyazetidinone **3***a* (0.287 g, 1 mmol) in dry THF (1 mL) was added. The resulting solution was stirred at room temperature for 3 h. The reaction mixture was diluted with ether (70 mL), washed with brine (5×), dried over anhydrous magnesium sulfate, and concentrated to give a colorless oil (0.57 g), which was chromatographed on silica gel eluting with ether – petroleum ether 1:1, then ether alone, giving the title compound (0.25 g, 70%, β:α 69:31).

*Example 6, using tri-*n*-butylborane*

To a solution of 1,3-bis(trimethylsilyloxy)-1-methoxypenta-1,3-diene (**13**) (12) (0.274 g, 1 mmol) in dry THF (5 mL) at −70°C under N_2 was added $(n\text{-Bu})_3B$ (1 mL, 1 M solution in THF) and it was stirred at −70°C for 0.5 h. 4-Acetoxyazetidinone **3***a* (0.17 g, 0.59 mmol) was then added. The resulting solution was allowed to warm up and stirred at room temperature for 18 h. The reaction mixture was worked up as described in Example 3, affording the title compound (0.22 g, 100%, β:α 20:80).

Can. J. Chem. Downloaded from www.nrcresearchpress.com by 93.93.197.157 on 09/07/12
For personal use only.

*(3S,4R)-3-[(1R)-1-*tert*-Butyldimethylsilyloxyethyl]-4-(1-methoxycarbonyl-2-oxo-butan-1-yl]azetidin-2-one (**17**)*

Zinc dust (0.65 g, 10 mmol) was activated by washing with 1 N hydrochloric acid and dry THF (5×). The activated zinc dust was stirred in dry THF (10 mL) at −20°C under N_2 atmosphere. To this was added dropwise a solution of 4-acetoxyazetidinone **3***a* (0.574 g, 2 mmol) and methyl 2-bromo-3-oxopentanoate (**19**) (1.254 g, 6 mmol) in dry THF (5 mL) over 10 min. The slurry was stirred at −15 to 0°C for 3 h. The reaction mixture was filtered on Celite. The filtrate was diluted with ether (70 mL), washed successively with 1 N hydrochloric acid and brine (4×), dried over anhydrous magnesium sulfate, and concentrated to give an oil, which was chromatographed on silica gel eluting with ether–petroleum ether 1:1, then ether alone, affording the title compound as a diastereomeric mixture (55:44, 0.46 g, 83%); mp 81–83°C (recrystallized from hexane); ^{1}H nmr (200 MHz, $CDCl_3$) δ: 0.05 (s, 6H, CH_3Si), 0.85, 0.86 (2s, 9H, CH_3CSi), 1.03–1.11 (overlapping 2d and 2t, 6H, CH_3CHOSi and CH_3CH_2), 2.49, 2.55 (2q, J = 7.2 Hz, 2H, CH_2CH_3), 2.88, 2.92 (2dd, J = 2.7, 3.3 and 2.5, 5.0 Hz, 1H, H-3), 3.56, 3.74 (2d, J = 9.6 and 8.2 Hz, 1H, $CHCO_2CH_3$), 3.74, 3.75 (2s, 3H, CO_2CH_3), 4.12–4.24 (overlapping m and 2dd, 2H, CH_3CHOSi and H-4), 5.91, 5.96 (br s, 1H, NH); mass spectrum (C.I.) m/e: 358 $(M + H)^+$. *Anal.* calcd. for $C_{17}H_{31}NO_5Si$ (357.198): C 57.12, H 8.74, N 3.92; found: C 57.52, H 8.88, N 4.02.

*Methyl 2-bromo-oxopentanoate (**19**)*

To a solution of methyl 3-oxopentanoate (13.0 g, 0.1 mol) and triethylamine (12.12 g, 0.12 mol) in dry dichloromethane (150 mL) at −5°C under nitrogen atmosphere was added dropwise trimethylsilyltriflate (26.66 g, 0.12 mol). The resulting yellow solution was stirred at 0–5°C for 1.5 h. To this solution (containing enol ether **18** (12)) was added dropwise a solution of bromine (16.0 g, 0.1 mol) in dichloromethane (60 mL). The resulting solution was stirred at 0°C for 1 h. The reaction mixture was washed with water (4×), dried over anhydrous magnesium sulfate, and concentrated to give an oil (21.0 g). The crude oil was distilled under reduced pressure, yielding **19** (14.32 g, 68%); bp 51–54°C/0.5 Torr (1 Torr = 133.3 Pa); ^{1}H nmr (200 MHz, $CDCl_3$) δ: 1.12 (t, J = 7.2 Hz, 3H, CH_3CH_2), 2.79 (q, J = 7.2 Hz, 2H, CH_3CH_2), 3.82 (s, 3H, CO_2CH_3), 4.81 (s, 1H, CHBr).

*(3S,4R)-3-[(1R)-1-*tert*-Butyldimethylsilyloxyethyl]-4-[(1R)-3-allyloxycarbonyl-1-methyl-2-oxopropyl]azetidin-2-one (**23**)*

A solution of methyl ketoester **14***a* (223 mg, 0.625 mmol) in allyl alcohol (25 mL) was heated in oil bath at 100–110°C for 17 h with removal of methanol/allyl alcohol. The remaining solution was concentrated under reduced pressure to give an oil (260 mg), which was chromatographed on silica gel (30% ethyl acetate in heptane), giving the title compound (120 mg, 50%); mp 75–76°C (recrystallized from hexane); $[\alpha]_D^{23}$ −21.9° (*c* 0.63, $CHCl_3$); ^{1}H nmr (200 MHz, $CDCl_3$) δ: 0.05, 0.06 (2s, 6H, CH_3Si keto + enol), 0.86 (s, 9H, CH_3CSi keto + enol), 1.11–1.22 (4 overlapping d, 6H, CH_3CHOSi keto + enol and $CH_3CHC{=}O$, $CH_3CHC(OH){=}$), 2.41 (m, 0.24H, $CH_3CHC(OH){=}$), 2.90, 2.96 (overlapping dd and m, J = 2.6 and 4.5 Hz, 1.76H, H-3 keto + enol and $CH_3CHC{=}O$), 3.55 (q, J = 15.8 Hz, 1.52H, $COCH_2CO_2$), 3.81 (dd, J = 2.2 and 6.4 Hz, 0.24H, H-4 enol), 3.94 (dd, J = 2.3 and 4.5 Hz, 0.76H, H-4 keto), 4.17 (m, 1H, CH_3CHOSi keto + enol), 4.63 (m, 2H, $CO_2CH_2CH{=}$), 5.06 (s, 0.24H, $C(OH){=}CHCO_2$), 5.23–5.38 (m, 2H, $CH{=}CH_2$), 5.80–6.00 (m, 2H, $CH{=}CH_2$ and NH); mass spectrum (C.I.) m/e: 384 $(M + H)^+$. *Anal.* calcd. for $C_{19}H_{33}NO_5Si$ (383.565): C 59.50, H 8.67, N 3.65; found: C 59.51, H 8.94, N 3.70.

*(3S,4R)-3-[(1R)-1-*tert*-Butyldimethylsilyloxyethyl]-4-[(1R)-3-allyloxycarbonyl-3-diazo-1-methyl-2-oxopropyl]azetidin-2-one (**24**)*

To a solution of β-ketoester **23** (0.19 g, 0.5 mmol) in dry acetonitrile (3 mL) at room temperature were added *p*-toluenesulfonyl azide (0.127 g, 0.65 mmol) and triethylamine (0.051 g, 0.5 mmol). The resulting solution was stirred for 18 h. The reaction mixture was diluted with ether (50 mL), then washed successively with 1 N hydrochloric acid, and brine (2×), dried over anhydrous magnesium sulfate, and concentrated to give the white crystalline title compound (0.20 g, 97%); mp 102–104°C (recrystallized from hexane); $[\alpha]_D^{23}$ −19.3° (*c* 0.62, $CHCl_3$); ^{1}H nmr (200 MHz, $CDCl_3$) δ: 0.04, 0.05 (2s, 6H, CH_3Si), 0.85 (s, 9H, CH_3CSi), 1.16, 1.18 (2 overlapping d, J = 6.3 and 6.7 Hz, 6H, CH_3CHOSi and $CH_3CHC{=}O$), 2.96 (dd, J = 1.3 and 4.1 Hz, 1H, H-3), 3.84–3.96 (overlapping m and dd, 2H, $CH_3CHC{=}O$ and H-4), 4.17 (m, 1H, CH_3CHOSi), 4.71 (m, 2H, $CO_2CH_2CH{=}$), 5.27–5.39 (m, 2H, $CH{=}CH_2$), 5.86–5.95 (m, 2H, $CH{=}CH_2$ and NH); mass spectrum (C.I.) m/e: 410 $(M + H)^+$. *Anal.* calcd. for $C_{19}H_{31}N_3O_5Si$ (409.562): C 55.72, H 7.63, N 10.25; found: C 55.67, H 7.77, N 10.13.

*(3S,4R)-3-[(1R)-1-*tert*-Butyldimethylsilyloxyethyl]-4-[(1R)-3-methoxycarbonyl-3-diazo-1-methyl-2-oxopropyl]azetidin-2-one (**25**)*

The title compound was prepared in the same manner as described in the preparation of compound **24** in quantitative yield; mp 105–106°C (recrystallized from hexane); ^{1}H nmr (200 MHz, $CDCl_3$) δ: 0.04, 0.05 (2s, 6H, CH_3Si), 0.84 (s, 9H, CH_3CSi), 1.15 (d, J = 4.5 Hz, 3H, $CH_3CHC{=}O$), 1.17 (d, J = 4.1 Hz, 3H, CH_3CHOSi), 2.95 (dd, J = 1.3 and 4.1 Hz, 1H, H-3), 3.82 (s, 3H, CO_2CH_3), 3.89 (overlapping m and dd, 2H, $CH_3CHC{=}O$ and H-4), 4.17 (m, 1H, CH_3CHOSi), 5.86 (br s, 1H, NH); mass spectrum (C.I.) m/e: 384 $(M + H)^+$. *Anal.* calcd. for $C_{17}H_{29}N_3O_5Si$ (383.316): C 53.27, H 7.57, N 10.96; found: C 53.24, H 7.74, N 10.95.

*Base-catalyzed rearrangement of **17** to pyridone **15***

A solution of compound **17** (50 mg, 0.14 mmol) and triethylamine (0.02 mL, 0.14 mmol) in dichloromethane (2 mL) was stirred at room temperature for 24 h. The reaction mixture was diluted with dichloromethane (20 mL), washed successively with 1 N hydrochloric acid (10 mL), saturated sodium bicarbonate (10 mL), and water (2 × 10 mL), dried over anhydrous magnesium sulfate, and concentrated to give a white crystalline solid whose ^{1}H nmr spectrum and physical properties were identical to that of pyridone **15**. Yield 43 mg (94%).

Acknowledgements

The authors would like to thank Dr. J. L. Douglas for advice during the course of this work, and D. Dodsworth for the mass spectral analyses.

1. (*a*) D. H. Shih, L. Baker, L. Cama, and B. G. Christensen. Heterocycles, **21**, 29 (1984); (*b*) D. H. Shih, J. A. Fayter, L. D. Cama, B. G. Christensen, and J. Hirshfield. Tetrahedron Lett. **26**, 583 (1985).
2. K. Fujimoto, Y. Iwano, and K. Hirai. Tetrahedron Lett. **26**, 89 (1985).
3. L. M. Fuentes, I. Shinkai, and T. N. Salzmann. J. Am. Chem. Soc. **108**, 4675 (1986).
4. Y. Nagao, T. Kumagai, S. Tamai, T. Abe, Y. Kuramoto, T. Taga, S. Aoyagi, Y. Nagase, M. Ochiai, Y. Inoue, and E. Fujita. J. Am. Chem. Soc. **108**, 4673 (1986).
5. R. Deziel and D. Favreau. Tetrahedron Lett. **27**, 5687 (1986).
6. M. Endo. Can. J. Chem. **65**, 2140 (1987).
7. T. Iimori and M. Shibasaki. Tetrahedron Lett. **27**, 2149 (1986).
8. C. U. Kim, B. Luh, and R. A. Partyka. Tetrahedron Lett. **28**, 507 (1987).
9. (*a*) A. Yoshida, T. Hayashi, N. Takeda, S. Oida, and E. Ohki. Chem. Pharm. Bull. **29**, 2899 (1981); (*b*) A. Martel and J. P. Daris. U.S. Patent No. 4,596,677 (1986); (*c*) M. Endo. Synth. Commun. **17**, 1029 (1987).
10. J. S. Prasad and L. S. Liebeskind. Tetrahedron Lett. **28**, 1857 (1987).
11. S. N. Huckin and L. Weiler. J. Am. Chem. Soc. **96**, 1082 (1974).
12. T. H. Chan and P. Brownbridge. Tetrahedron, **37**, 387 (1981).
13. K. Maruoka, S. Hashimoto, Y. Kitagawa, H. Yamamoto, and H. Nozaki. J. Am. Chem. Soc. **99**, 7705 (1977).
14. R. Deziel. Tetrahedron Lett. **28**, 4371 (1987).

Can. J. Chem. Downloaded from www.nrcresearchpress.com by 93.93.197.157 on 09/07/12
For personal use only.

Fused heterocycles from *o*-acylbenzenethiol derivatives

DAVID M. MCKINNON AND KINGSLEY R. LEE
Chemistry Department, University of Manitoba, Winnipeg, Man., Canada R3T 2N2

Received November 18, 1987

DAVID M. MCKINNON and KINGSLEY R. LEE. Can. J. Chem. **66**, 1405 (1988).

The oximes of 2-acylthioanisole derivatives may be conveniently converted into 1,2-benzisothiazoles by acetic anhydride in pyridine. 3-(2-Methylthiophenyl)-1,2-benzisothiazole, prepared by this method, has been further converted into the 1,2-benzisothiazolo[2,3-*b*]-1,2-benzisothiazolium system. The phenylhydrazones of certain 2-acylthioanisoles are also cyclized by polyphosphoric acid to 2-(2-methylthio)phenylindoles, which are further converted into benzo[*b*]thieno[3,2-*b*]indoles by demethylation and oxidation.

DAVID M. MCKINNON et KINGSLEY R. LEE. Can. J. Chem. **66**, 1405 (1988).

Sous l'influence de l'anhydride acétique dans la pyridine, on peut facilement transformer les oximes de dérivés de l'acyl-2 thioanisole en benzisothiazoles-1,2. Utilisant cette méthode, on a préparé le (méthyl-2 thiophényl)-3 benzisothiazole-1,2 qu'on a utilisé pour préparer le système benzisothiazolo-1,2 [2,3-*b*]benzisothiazole-1,2 ium. Sous l'influence de l'acide polyphosphorique, on peut cycliser un certain nombre de phénylhydrazones d'acyl-2 thioanisoles en (méthyl-2 thio)-2 phénylindoles qui, par déméthylation et oxydation, peuvent être transformés en benzo[*b*] thiéno[3,2-*b*] indoles.

[Traduit par la revue]

Can. J. Chem. Downloaded from www.nrcresearchpress.com by 93.93.197.157 on 09/07/12
For personal use only.

Introduction

In connection with our interest in isothiazoles, we wished to examine certain fused systems where the nitrogen atom forms a bridgehead to another heterocyclic ring. One of the most synthetically appealing methods to certain 1,2-benzisothiazole precursors **1** appeared to be from the readily accessible oximes of 2-(methylthiophenyl) ketones **2**.

Results and discussion

A number of variations of this method have been reported, involving heating the aromatic esters (1, 2), *p*-toluenesulfonate esters (1), or thionocarbamate esters (2) of the oximes. The conversions may also be effected in polyphosphoric acid (3). However, these methods suffer some disadvantages in that either products may be inconvenient to separate, there could be realkylation on nitrogen, or conditions are too drastic for certain compounds. What is required is that the hydroxy group of the oxime be converted into a suitable leaving group by esterification, and that the eliminated ester be volatile and nonreactive.

These conditions are supplied by the use of the acetate ester of the oxime, and we have found that heating the oximes **3***a–f* of the ketones **2***a–f* in an acetic anhydride/pyridine mixture converts them into 1,2-benzisothiazoles **1***a–f* in good to excellent yields. The intermediate oxime acetates may be isolated, but on longer heating the elimination is completed. Reaction mixtures become dark, but yields of 1,2-benzisothiazoles are not seriously compromised.

The method appears to be of fairly wide scope, allowing the synthesis of a number of aryl- and alkyl-1,2-benzisothiazoles, but failed for the oxime **3***g* of methyl 2-(2-methylthiophenyl)-2-oxoacetate **2***g*. Instead, 2-methylthiobenzonitrile was formed by elimination.

Starting ketones were available by Friedel–Crafts acylation of aryl methyl sulfides, or from 2-methylthiobenzoyl chloride. For the oxime **3***g*, benzo[*b*]thiophene-2,3-dione was converted by treatment with dimethyl sulfate in base to 2-(2-methylthiophenyl)-2-oxoacetic acid. This esterified in methanol with sulfuric acid to the ketoester **2***g*, which was converted to **3***g* by treatment with hydroxylamine. While the use of *tert*-butyl sulfides might give even better yields of 1,2-benzisothiazoles (2), many suitable methyl sulfides are available or more readily prepared.

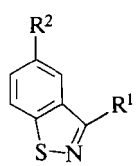

1

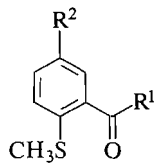

2

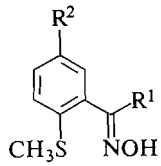

3

a $R^1 = CH_3$, $R^2 = H$
b $R^1 = R^2 = CH_3$
c $R^1 = CH_2CH_3$, $R^2 = CH_3$
d $R^1 = C_6H_5$, $R^2 = H$
e $R^1 = C_6H_5$, $R^2 = CH_3$
f $R^1 = CH_2CH_2CO_2CH_3$, $R^2 = CH_3$
g $R^1 = CO_2CH_3$, $R^2 = H$
h $R^1 = CH_2CH_2CO_2H$, $R^2 = CH_3$
i $R^1 = C_6H_4OSCH_3$, $R^2 = H$

It was also of interest, since the related system **4** may be made (4) by oxidation of 2-(2-mercaptophenyl)pyridine (5), to use this method to prepare the novel 1,2-benzisothiazolo[2,3-*b*]-1,2-benzisothiazolium system **6**, via the 1,2-benzisothiazole **7***a*. A suitable starting ketone was not available by Friedel–Crafts procedures, but 2,2′-dichlorobenzophenone reacted with sodium methanethiolate to form 2,2′-bis(methylthio)benzophenone **8***a*. Under more severe conditions only thioxanthenone was obtained. The ketone reacted slowly with hydroxylamine to give the oxime **3***i*, which was also contaminated with the isothiazole **7***b*. However, the latter was more efficiently made by the acetic anhydride/pyridine procedure on the oxime **3***i*. Attempted direct demethylation and oxidation of the 1,2-benzisothiazole **7***b* to the system **5** did not succeed. It was recovered from perchloric acid. Accordingly demethylation was achieved via a Pummerer rearrangement of the sulfoxide **7***c* to the acetoxy sulfide **7***d*. This hydrolysed in acid to the mercaptan **7***a*. Probably dealkylation of a *tert*-butylthio sulfide **7***e* might have been easier (3) but 2,2′-bis(*tert*-butylthio)benzophenone (**3***b*), prepared from 2,2′-dichlorobenzophenone and 1,1-dimethylethanethiolate, could not be converted to an oxime. Reaction of 2,2′-dichlorobenzophenone with less *tert*-butylmercaptan gave the chloro *tert*-butylthioketone **8***c*.

When the mercaptan **7***a* was treated with iodine, a dark red solid was obtained, which crystallized from nitromethane

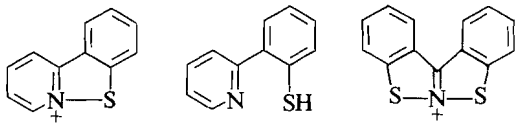

4 5 6

as fine red prisms. While the analysis of this material was consistent with the triiodide **6**, X = I_3, and the mass spectrum showed an intense ion at $M^+ = 242$, the ^{1}H nmr spectrum in acetone was not consistent with a symmetrical structure, i.e., eight different protons were evident. In view of its solubility properties, this material does appear to be a salt, although it could not be converted to a perchlorate. The methylthio precursor **7***b* also demonstrated a large ion at $M^+ = 242$, by demethylation.

These ketones **2***a,b,c* also permitted the synthesis of three 2-(2-methylthiophenyl)indoles **9***a,b,c*, via their phenylhydrazones **10***a,b,c* respectively. Previous attempts to synthesize these types by Fischer indolization procedures failed (5), but we found that cyclization to the indoles was readily effected in polyphosphoric acid, as suggested in ref. 6. These dealkylated by treatment with sodium in liquid ammonia to the mercaptans **9***d,e,f* respectively. While oxidation of suitable mercapto- or thio-amines to isothiazoles is a versatile method of synthesis (7), treatment of **9***d,e* with iodine gave, not the indolo[1,2-*b*]-

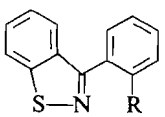

7

a R = SH
b R = SCH_3
c R = $SOCH_3$
d R = SCH_2OCOCH_3

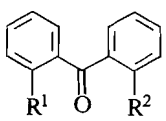

8

a $R^1 = R^2 = SCH_3$
b $R^1 = R^2 = SC(CH_3)_3$
c $R^1 = SC(CH_3)_3$, R^2 = Cl

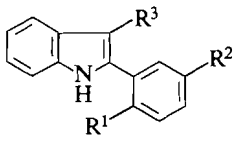

9

a $R^1 = SCH_3$, $R^2 = R^3 = H$
b $R^1 = SCH_3$, $R^2 = CH_3$, $R^3 = H$
c $R^1 = SCH_3$, $R^2 = R^3 = CH_3$
d $R^1 = SH$, $R^2 = R^3 = H$
e $R^1 = SH$, $R^2 = CH_3$, $R^3 = H$
f $R^1 = SH$, $R^2 = R^3 = CH_3$
g $R^1 = SOCH_3$, $R^2 = CH_3$, $R^3 = H$

1,2-benzisothiazoles **11***a,b*, but the benzo[*b*]thieno[3,2-*b*]indoles **12***a,b* respectively. These cyclizations therefore correspond to various sulfenylation reactions of indoles (8). Even the sterically hindered mercaptan **9***f* failed to produce an isothiazole, and what appear to be decomposition products were obtained. If electrophilic attack of a sulfur cation at carbon-3 had occurred, then reaction intermediates could not aromatize and decomposition would be expected. This method represents a new approach to the system **12**. A previous method (9) involved indole formation as a last stage in the reaction sequence.

The benzothienoindole **12***b* was also made by acid treatment of the sulfoxide **9***g*. We saw no evidence of the formation of a

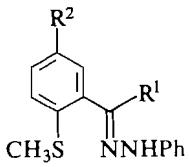

10

a R^1 = H, $R^2 = CH_3$
b $R^1 = R^2 = CH_3$
c $R^1 = CH_3$, $R^2 = CH_2CH_3$

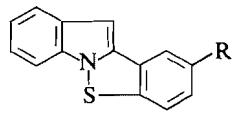

11

a R = H
a R = CH_3

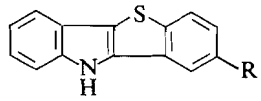

12

a R = H
b R = CH_3

benzothiopyranoindole, which might have been produced by cyclization of an intermediate in a Pummerer rearrangement of **9***g*. These results are similar to some observed for 1-(2-alkylsulfinylaryl)pyrroles (10).

Experimental

Unless otherwise stated, ^{1}H nmr spectra were obtained in deuteriochloroform solution using tetramethylsilane as an internal standard, on Varian model EM360 or AM 300 spectrometers. Mass spectra were obtained on a V.G. 707E spectrometer. Infrared spectra were recorded on a Perkin Elmer model 881 spectrophotometer. Thick layer chromatography was performed on Merck type 60 PF 254 silica gel. Where necessary, solutions were dried over anhydrous magnesium sulfate.

Preparation of ketones **2**a–f

The ketones **2***a,b,c* were prepared by reported methods (1, 11, 12) respectively. Others were prepared by the methods described herein.

*Preparation of 1-(5-methyl-2-methylthiophenyl)propanone (***2**c*)*

To methyl 4-methylphenyl sulfide (27.6 g, 0.2 mol) in dichloromethane (100 mL), at −20°C, was added propanoyl chloride (18.5 g, 0.2 mol), followed by portionwise addition of anhydrous aluminum chloride (26.8 g, 0.2 mol) over 5 min. The mixture was allowed to attain room temperature and left for 48 h. The dark red mixture was poured over dilute hydrochloric acid in ice, and extracted with methylene chloride. The evaporated dried extract gave a yellow oil, which was distilled at 0.5 Torr (1 Torr = 133.3 Pa). The fraction of boiling range 115–120°C was collected. It crystallized on cooling and was recrystallized from cyclohexane as colorless prisms, mp 40–41°C (58%). The ir spectrum of **2***c*: 1666 (C=O str) cm^{-1}; ^{1}H nmr, δ: 1.25, 2.92 (3H, t, 2H, q, resp. the ethyl group), 2.39, 2.42 (two 3H, s, the S- and C-methyls), 7.20–7.62 (3H, bands, the aromatic protons) ppm; mass spectrum, *M* calcd.: 194; found, M^+: 194. *Anal.* calcd. for $C_{11}H_{14}SO$: C 68.06, H 7.22, S 16.49; found: C 68.12, H 7.25, S 16.29.

*Preparation of 2-methylthiobenzophenone (***2** d*)*

To 2-methylthiobenzoyl chloride (18.6 g, 0.1 mol) in dry benzene (200 mL) was added anhydrous aluminum chloride (13.4 g, 0.1 mol), and the mixture allowed to stand 16 h. The mixture was poured over dilute hydrochloric acid in ice, and the organic layer separated, dried, and evaporated to a yellow oil that was distilled at 0.35 Torr. The fraction of boiling range 162–167°C was collected. On cooling, this deposited a small amount (50 mg) of thioxanthenone, which was removed by filtration. Otherwise the ketone was fairly pure (81%).

The ir spectrum: 1667 (C=O) cm^{-1}; ^{1}H nmr, δ: 2.38 (3H, s, the S-methyl), 7.20–7.95 (9H, bands, the aromatic protons) ppm; mass spectrum, *M* calcd.: 228; found, M^+: 228.

This compound was identical (R_f, spectroscopic properties) with a sample prepared from 2-mercaptobenzophenone (13) for which different nmr spectral data have been reported.

Can. J. Chem. Downloaded from www.nrcresearchpress.com by 93.93.197.157 on 09/07/12
For personal use only.

Can. J. Chem. Downloaded from www.nrcresearchpress.com by 93.93.197.157 on 09/07/12
For personal use only.

Preparation of 4-(5-methyl-2-methylthiophenyl)-4-oxobutanoic acid (2b)

To a solution of methyl 4-methylphenyl sulfide (27.4 g, 0.2 mol) and succinic anhydride (20.04 g, 0.2 mol) in methylene chloride (150 mL) was added anhydrous aluminum chloride (29.3 g, 0.22 mol). The mixture was let stand 48 h, then poured over dilute hydrochloric acid in ice. The organic layer was separated and extracted with 20% sodium hydroxide solution. On acidification this gave the desired acid, which crystallized from benzene as colorless prisms, mp 132°C (48%); ^{1}H nmr, δ: 2.41 (two 3H, s, the S- and C-methyls), 2.78, 3.33 (two 2H, t, the methylene protons), 7.33–7.80 (3H, bonds, the aromatic protons) ppm; mass spectrum, *M* calcd.: 238; found, M^+: 238. *Anal.* calcd. for $C_{12}H_{14}SO_3$: C 60.50, H 5.88, S 13.45; found: C 60.53, H 6.02, S 13.33.

Preparation of methyl 4-(5-methyl-2-methylthiophenyl)-4-oxobutanoate (2f)

The acid **2***h* (9.52 g, 0.04 mol) prepared above, in methanol (60 mL) and concentrated sulfuric acid (1 drop), was heated under reflux 4 h. The solution was evaporated to 20 mL volume, and allowed to stand. The desired ester crystallized as pale yellow prisms. These were collected and recrystallized from cyclohexane as pale yellow prisms, mp 73–74°C (80%); ^{1}H nmr of **2***f*, δ: 2.41, 2.42 (two 3H, s, the S- and C-methyl protons), 3.73 (3H, s, the O-methyl protons), 2.78, 3.33 (two 2H, t, the methylene protons), 7.32–7.80 (3H, bands, the aromatic protons) ppm; mass spectrum, *M* calcd.: 252; found, M^+: 252. *Anal.* calcd. for $C_{13}H_{16}SO_3$: C 61.90, H 5.56, S 12.70; found: C 61.81, H 5.38, S 12.71.

Preparation of methyl 2-(2-methylthiophenyl)-2-oxoethanoate (2g)

Benzo[*b*]thiophene-2,3-dione (16.4 g, 0.1 mol) (14) was dissolved with stirring in 20% aqueous sodium hydroxide solution (100 mL) and treated with dimethyl sulfate (19.2 g, 0.15 mol). After 30 min the solution was acidified with concentrated hydrochloric acid. The crude acid precipitated as a viscous, dark yellow oil. It was dissolved in methanol (100 mL), concentrated sulfuric acid (2 drops) was added, and it was allowed to stand for 4 weeks. The mixture was poured into water and extracted with chloroform. This was washed with base and water, and dried. Evaporation gave a yellow-brown oil, which was purified by chromatography in benzene giving **2***g* as a dark yellow oil (89%); ^{1}H nmr of **2***g*, δ: 2.57 (3H, s, the S-methyl group), 3.97 (3H, s, the O-methyl group), 7.10–7.91 (4H, bands, the aromatic protons) ppm; mass spectrum, *M* calcd.: 210; found, M^+: 210. *Anal.* calcd. for $C_{10}H_{10}SO_3$: C 57.14, H 4.76, S 15.24; found: C 57.08, H 4.83, S 15.50.

Preparation of 2,2′-bis(methylthio)benzophenone (8a)

To a solution of sodium methoxide in methanol (from sodium (1 g) in methanol (20 mL)) was added excess methanethiol, and the mixture evaporated to dryness. The solid was dissolved in bis(2-methoxyethyl) ether (25 mL) in a pressure bottle, and to it added liquid methanethiol (10 mL) and 2,2′-dichlorobenzophenone (5.02 g, 0.02 mol). The mixture was heated at 100°C for 24 h, then poured into water. A yellow oil precipitated and crystallized on standing. It was collected and recrystallized from a toluene:cyclohexane 1:1 mixture as yellow prisms, mp 100–101°C (86%); ^{1}H nmr of **8***a*, δ: 2.47 (6H, s, the S-methyl protons), 7.05–7.60 (8H, bands, the aromatic protons) ppm; mass spectrum, *M* calcd.: 274; found, M^+: 274. *Anal.* calcd. for $C_{15}H_{14}S_2O$: C 65.69, H 5.11, S 23.36; found: C 65.65, H 5.02, S 23.51.

At 150°C, without excess methanethiol, only thioxanthenone was isolated.

*Preparation of 2,2′-bis(*tert*-Butylthio)benzophenone (8b)*

This was performed as for **8***a*. The product was recrystallized from cyclohexane as yellow prisms, mp 110°C (96%); ^{1}H nmr of **8***b*, δ: 1.30 (18H, s, the *tert*-butyl protons), 7.18–7.58 (8H, bands, the aromatic protons) ppm; mass spectrum, *M* calcd.: 358; found, M^+: 358. *Anal.* calcd. for $C_{21}H_{26}S_2O$: C 70.39, H 7.26, S 17.88; found: C 70.22, H 7.13, S 18.05.

When equivalent quantities of 2,2′-dichlorobenzophenone and sodium 1,1-dimethylethanethiolate were used in the above procedure, work-up gave **8***c* as a yellow oil. This was purified by chromatography using benzene as an eluent (81%). The ^{1}H nmr spectrum of **8***c*, δ: 1.21 (9H, s, the *tert*-butyl protons), 7.17–7.59 (8H, bands, the aromatic protons) ppm; mass spectrum, calcd. for two isotopes, *M*: 306, 304; found, M^+: 306, 304. *Anal.* calcd. for $C_{17}H_{17}ClSO$: C 66.78, H 5.58, Cl 11.16, S 10.51; found: C 66.83, H 5.49, Cl 11.32, S 10.29.

Preparation of ketoximes 3a–g

The ketones prepared above, dissolved in an approximately 20-fold weight of a pyridine:ethanol 1:1 mixture, with an equal weight of hydroxylamine hydrochloride, were heated under reflux for 24 h for benzophenones, and 4 h for the other compounds. Mixtures were worked up by addition to ice-cold 20% hydrochloric acid. Solids were collected and liquids isolated by chloroform extraction. No analyses were taken but in all cases mass spectral and nmr data were consistent with pure oximes or mixtures of their geometrical isomers. Yields were usually high (90–95%).

Melting points (oximes) are as follows: **3***a* (106–108°C); **3***b* (103°C); **3***d* (130°C); **3***e* (133–136°C); **3***g* (102–104°C). Other oximes were either oils or melting ranges were too broad to be diagnostic.

Preparation of 2,2′-bis-methylthiobenzophenone oxime (3i)

The ketone **2***h* (5.48 g, 0.02 mol) in pyridine (20 mL) and hydroxylamine hydrochloride (6 g) was heated under gentle reflux for 1 week. The mixture was added to concentrated hydrochloric acid (20 mL) in ice (100 g), and a sticky solid precipitated. This was collected and crystallized from methanol giving **3***i* as pale yellow prisms, mp 136–137°C (56%). Chromatography of the mother liquor using a benzene:chloroform 10:1 mixture as an eluent gave, in reverse order of elution, more oxime (20%), starting ketone (8%), and a fast running material that crystallized on standing. It was recrystallized from cyclohexane, giving **7***b* as pale yellow prisms, mp 80°C (15%).

The ^{1}H nmr spectrum of **3***i*, δ: 2.43, 2.48 (two 3H, s, the S-methyl protons), 3.70 (1H, br, the oxime proton), 7.05–7.50 (8H, bands, the aromatic protons) ppm; mass spectrum, *M* calcd.: 289; found, M^+: 289. *Anal.* calcd. for $C_{15}H_{15}NS_2O$: C 62.28, H 5.19, N 4.84, S 22.15; found: C 62.21, H 5.30, N 4.62, S 22.04.

The ^{1}H nmr spectrum of **7***b*, δ: 2.35 (3H, s, the S-methyl protons), 7.20–8.04 (8H, bands, the aromatic protons) ppm; mass spectrum, *M* calcd.: 257; found, M^+: 257. In addition, a large ion at M^+ 242 (M^+ − 15) was evident. *Anal.* calcd. for $C_{14}H_{11}NS_2$: C 65.37, H 4.28, N 5.45, S 24.90; found: C 65.42, H 4.31, N 5.28, S 24.79.

Preparation of 1,2-benzisothiazoles 1a–f, 7b

The ketoximes **3** (1 g) in pyridine (20 mL) and acetic anhydride (2 g) were heated under reflux 24 h. Mixtures were diluted with 50% concentrated hydrochloric acid in water and extracted with chloroform. Where necessary this was treated with charcoal. Drying and evaporation gave the desired 1,2-benzisothiazoles. 3-Aryl-1,2-benzisothiazoles crystallized on standing and were recrystallized from methanol. Others were purified by chromatography or distillation. The results are summarized in Table 1. All compounds gave mass spectra consistent with their formulae.

If mixtures are heated for 1 h, the oxime acetates may be isolated.

Reaction of methyl 2-(2-methylthiophenyl)-2-oxoacetate oxime (3g) with acetic anhydride to form 2-methylthiobenzonitrile

The ketoester oxime (4.46 g, 0.02 mol) was heated with pyridine and acetic anhydride by the general procedure above. Work-up gave a colorless oil that crystallized on standing. It was recrystallized from cyclohexane as colorless needles, mp 36°C (83%). The compound was identical (mixture mp, spectroscopic properties) with an authentic specimen (16).

Preparation of 3-(2-methylsulfinylphenyl)-1,2-benzisothiazole (7c)

3-(2-Methylthiophenyl)-1,2-benzisothiazole (1.028 g, 4.0 mmol) in acetone (20 mL) was treated with the equivalent quantity of *m*-chloroperoxybenzoic acid in acetone (20 mL) and warmed 5 min. The solution was evaporated to dryness and partitioned between chloroform and saturated sodium carbonate solution. The former was

Can. J. Chem. Downloaded from www.nrcresearchpress.com by 93.93.197.157 on 09/07/12
For personal use only.

TABLE 1. Preparation of 1,2-benzoisothiazoles **1***a–f*, **7***b* from oximes **3**

Product	Starting oxime	Yield (%)	Melting point (bp) (°C)	Formula	*Anal.* calcd. (found)				^{1}H nmr (in ppm)
					C	H	N	S	
1*a*	**3***a*	95	(243)*	C_8H_7NS	—	—	—	—	2.72 (3H, s), 7.27–8.10 (8H, bands)
1*b*	**3***b*	90	(262)	C_9H_9NS	66.26 (66.18)	5.52 (5.61)	8.59 (8.63)	19.60 (19.49)	2.38 (3H, s), 2.59 (3H, s), 7.10–7.85 (3H, bands)
1*c*	**3***c*	76	(62, 0.2mm)	$C_{10}H_{11}NS$	67.80 (67.91)	6.21 (6.36)	7.91 (8.07)	18.08 (18.13)	1.45 (3H, t), 3.11 (2H, q), 2.52 (3H, s), 7.25, 8.01 (3H, bands)
1*f*	**3***f*	83	§	$C_{12}H_{13}NSO_2$	61.28 (61.35)	5.53 (5.46)	5.96 (6.09)	13.62 (13.32)	2.36 (3H, s), 2.85, 3.13 (two 2H, t), 3.65 (3H, s), 7.05–7.80 (3H, bands)
1*d*	**3***d*	93	71†	$C_{13}H_9NS$	—	—	—	—	7.40–8.35 (9H bands)
1*e*	**3***e*	94	70	$C_{14}H_{11}NS$	74.67 (74.53)	4.89 (5.01)	6.22 (6.03)	14.22 (14.27)	2.81 (3H, s), 7.16–7.99 (8H, bands)
7*b*	**3***i*	92‡							

*Also converted to hydrochloride, mp 116°C (lit. (15) mp 116°C).
†Literature (15) mp 71°C.
‡For further data see this work (above).
§This was purified by chromatography and isolated as an oil.

dried and evaporated to an oil, which was purified by chromatography in methylene chloride, giving **7***c* as a colorless oil (83%); ^{1}H nmr of **7***c*, δ: 3.01 (3H, s, the S-methyl protons), 7.30–8.53 (8H, bands, the aromatic protons) ppm; mass spectrum, *M* calcd. 273; found, M^+: 273. *Anal.* calcd. for $C_{14}H_{11}NS_2O$: C 61.54, H 4.03, N 5.13, S 23.44; found: C 61.66, H 4.07, N 5.01, S 23.29.

*Preparation of 3-(2-acetoxymethylthiophenyl)-1,2-benzisothiazole (**7**d)*

A solution of the sulfoxide **7***c* (1.09 g, 4.0 mmol) in acetic anhydride (10 mL) and *p*-toluenesulfonic acid (50 mg) was heated under reflux 1 h, then added to a stirred solution of sodium bicarbonate and left for 1 h. The dried chloroform extract of this mixture was evaporated, giving **7***d* as a pink oil, further purified by chromatography in a benzene:chloroform 1:1 mixture (93%). The ^{1}H nmr spectrum of **7***d*, δ: 2.07 (3H, s, the acetoxy protons), 5.37 (2H, s, the methylene protons), 7.13–8.16 (8H, bands, the aromatic protons) ppm; mass spectrum, *M* calcd.: 315; found, M^+: 315. In addition, a large ion at M^+ 242 was evident. *Anal.* calcd. for $C_{16}H_{13}NS_2O_2$: C 60.95, H 4.13, N 4.44, S 20.32; found: C 61.08, H 4.40, N 4.41, S 20.18.

*Preparation of 3-(2-mercaptophenyl)-1,2-benzisothiazole (**7**a)*

The acetate **7***d* (0.63 g, 2.0 mmol) in methanol (10 mL) and concentrated hydrochloric acid (1 mL) was heated under reflux in a nitrogen atmosphere for 3 h. The solution was decanted from a tarry precipitate and evaporated *in vacuo*. The product was then dissolved in chloroform, washed with aqueous sodium bicarbonate solution, and dried. Evaporation gave a smelly reddish oil. No further purification of this was attempted, but the nmr spectrum indicated only peaks in the mercaptan and aromatic ranges (73%).

Iodine oxidation of 3-(2-mercaptophenyl)-1,2-benzisothiazole

The crude product from above (0.283 g, 1 mmol) in ethanol (5 mL) was treated dropwise with a saturated solution of iodine in ethanol until precipitation was complete. The dark red precipitate was collected and recrystallized from nitromethane as fine, dark red prisms, mp 162°C (61%). This material, tentatively **6**, X = I_3, was insoluble in ether, benzene, and chloroform. It was slightly soluble in acetone.

The nmr spectrum of **6** (X = I_3) in acetone indicated a series of bands, δ 7.43–8.46 ppm, consistent with eight different aromatic protons. The mass spectrum, M^+ calcd.: 242; found, M^+: 242. *Anal.* calcd. for $C_{13}H_8NS_2I_3$: C 25.04, H 1.28, N 2.25, S 10.27, I 61.16; found: C 24.98, H 1.30, N 2.20, S 10.32, I 60.98. An attempt to convert this material to a perchlorate in acetic acid failed.

*Preparation of phenylhydrazones of ketones **2**a–c*

Equivalent quantities of ketones, phenylhydrazine hydrochloride, and sodium acetate in ethanol were heated under reflux for 1 h. Mixtures were poured over ice and products collected or extracted with chloroform. Solid products were recrystallized from ethanol. They were not analysed.

Compounds (mp), yields are as follows: **10***a* (118°C; lit. (5) mp 86°C) 86%; **10***b* (115°C) 80%; **10***c* (oil) 70%.

*Cyclization of phenylhydrazones **10**a–c to indoles **9**a–c*

General procedure

The phenylhydrazones (2 g) in polyphosphoric acid (40 mL) were heated at 100°C for 2 h, with occasional stirring. Mixtures were diluted with water and products extracted with ethyl acetate. These extracts were washed with sodium bicarbonate solution, dried, and evaporated to give crude indoles, which were recrystallized from ethanol. Data are summarized below.

*2-(2-Methylthiophenyl)indole (**9**a)*

This was obtained as colorless prisms, mp 124–125°C (65%); ^{1}H nmr, δ: 2.40 (3H, s, the S-methyl protons), 6.89 (1H, s, the indole proton), 7.14–7.90 (8H, bands, the aromatic protons), 9.15 (1H, br s, the N-H proton) ppm; mass spectrum, *M* calcd.: 239; found, M^+: 239. *Anal.* calcd. for $C_{15}H_{13}NS$: C 75.31, H 5.44, N 5.86, S 13.39; found: C 75.36, H 5.40, N 5.99, S 13.42.

*2-(5-Methyl-2-methylthiophenyl)indole (**9**b)*

This was obtained as colorless prisms, mp 107–108°C (71%); ^{1}H nmr, δ: 2.33 (3H, s, the C-methyl protons), 2.38 (3H, s, the

S-methyl protons), 6.85 (1H, s, the indole proton), 7.01–7.78 (7H, bands, the aromatic protons), 9.15 (1H, br s, the N-H proton) ppm; mass spectrum, *M* calcd.: 253; found, M^+: 253. *Anal.* calcd. for $C_{16}H_{15}NS$: C 75.89, H 5.93, N 5.53, S 12.65; found: C 75.83, H 6.09, N 5.46, S 12.62.

*3-Methyl-2-(2-methylthio-5-methylphenyl)indole (**9**c)*

This was obtained as colorless prisms, mp 96–98°C (78%); ^{1}H nmr, δ: 2.25, 2.28, 2.34 (three 3H, s, the C and S methyl groups), 7.05–7.70 (7H bands, the aromatic protons), 8.17 (1H, br s, the N-H proton) ppm; mass spectrum, *M* calcd.: 267; found, M^+: 267. *Anal.* calcd. for $C_{17}H_{17}NS$: C 76.40, H 6.37, N 5.24, S 11.99; found: C 76.41, H 6.29, N 5.18, S 11.82.

*Preparation of benzo[b]thieno[3,2-b]indole (**12**a)*

The indole **9***a* (0.478 g, 2.0 mmol) in ether (10 mL) was added to liquid ammonia (50 mL), and sodium (60 mg) was added in small pieces until a permanent blue color appeared. After 1 h ethanol (5 mL) was added, and the ammonia allowed to evaporate. The mixture was acidified with dilute hydrochloric acid and extracted with ether. The dried solvent gave, on evaporation, 2-(2-mercaptophenylindole) (**10***d*) as an oil. This was not further characterized. It was dissolved in acetic acid (2 mL), treated with a saturated solution of iodine in ethanol (2 mL), and let stand 16 h. The mixture was added to a solution of sodium bisulfite and sodium bicarbonate in water and extracted with ether. The dried extract gave the crude indole **12***a* on evaporation. It was recrystallized from cyclohexane as small colorless prisms, mp 250–252°C (lit. (9) mp 250–252°C) (46%).

*Preparation of 8-methylbenzo[b]thieno[3,2-b]indole (**12**b)*

This was prepared as above, using the indole **9***b*. The product **12***b* was obtained as colorless prisms, mp 220–222°C (lit. (9) mp 222–224°C (62%).

*Cleavage and oxidation of 3-methyl-2-(2-methylthio-5-methylphenyl)-indole (**9**c)*

Performed as above, the iodine oxidation gave only a complex mixture, which was not further examined.

*2-(2-Methylsulfinyl-5-methylphenyl)indole (**9**g)*

To the indole **9***b* (5.06 g, 2.0 mmol) in acetone (10 mL) was added a solution of the equivalent quantity of *m*-chloroperbenzoic acid in acetone (10 mL), and the solution refluxed gently 30 min. The mixture was poured into saturated sodium bicarbonate solution and extracted with chloroform. The dried extract gave **9***g* on evaporation, which was recrystallized from ethanol as colorless prisms, mp 184–185°C (55%); ^{1}H nmr, δ: 2.45 (6H, two superimposed singlets, the S- and C-methyl protons), 6.75–7.95 (8H, bands, the indole and aromatic protons), 10.67 (1H, br s, the N-H proton) ppm; mass spectrum, *M* calcd.: 269; found, M^+: 269. *Anal.* calcd. for $C_{16}H_{15}NSO$: C 71.38, H 5.58, N 5.20, S 11.90; found: C 71.22, H 5.46, N 5.31, S 12.08.

*Conversion of 2-(2-methylsulfinyl-5-methylphenyl)indole into 8-methylbenzo[b]thieno[3,2-b]indole (**12**b)*

The sulfoxide **9***g*, (100 mg, 0.37 mmol) in acetic acid (10 mL), saturated with hydrogen chloride, was heated under reflux 1 h, neutralized with aqueous sodium bicarbonate solution, and extracted with chloroform. The dried extract gave the benzothienoindole **12***b* on evaporation, identical (mixture mp, mass spectrum, nmr) to a sample prepared above (56%).

Acknowledgements

We wish to thank Mr. K. Marat and Mr. T. Wolowiec for the preparation of nmr spectra, Mr. W. Buchannon for mass spectra, and the Natural Sciences and Engineering Research Council of Canada for financial support.

1. R. J. CRAWFORD and C. WOO. J. Org. Chem. **31**, 1655 (1966).
2. A. J. LAWSON. Phosphorus Sulfur, **12**, 357 (1982).
3. K. CLARKE, C. G. HUGHES, and R. M. SCROWSTON. J. Chem. Soc. Perkin Trans. 1, 356 (1973).
4. D. M. McKINNON, K. A. DUNCAN, A. M. McKINNON, and P. A. SPEVACK. Can. J. Chem. **63**, 882 (1985).
5. E. W. McCLELLAND and J. L. D'SILVA. J. Chem. Soc. 227 (1932).
6. B. ROBINSON. *In* The Fischer indole synthesis. John Wiley and Sons, New York. 1982.
7. D. L. PAIN, B. J. PEART, and K. R. H. WOOLDRIDGE. *In* Isothiazoles and their benzo-derivatives. *In* Comprehensive heterocyclic chemistry. Vol. 6. part 17. *Edited by* K. Potts. Pergamon Press, Oxford. 1984.
8. R. A. JONES. *In* Pyrroles and their benzo-derivatives. ii. Reactivity. *In* Comprehensive heterocyclic chemistry. Vol. 4. part 3. *Edited by* C. W. Bird and G. W. H. Cheeseman. Pergamon Press, Oxford. 1984.
9. K. E. CHIPPENDALE, B. IDDON, and H. SUSCHITZKY. J. Chem. Soc. Perkin Trans. 1, 2023 (1972).
10. D. K. BATES and R. T. WINTERS. The synthesis of pyrrolo[2,1-*c*]benzothiazoles and pyrrolo[2,1-*c*]benzothiazines from a common precursor. Presented to 10th International Congress of Heterocyclic Chemistry, Waterloo, Canada. 1985.
11. K. AUWERS and F. ARNDT. Chem. Ber. **42**, 537 (1909).
12. F. KROLLPFEIFFER, H. HARTMANN, and F. SCHMIDT. Annalen, **563**, 15 (1949).
13. K. A. SCHELLENBERG and F. H. WESTHEIMER. J. Org. Chem. **30**, 1859 (1965).
14. D. PAPA, E. SCHWENK, and H. F. GINSBERG. J. Org. Chem. **14**, 723 (1949).
15. A. RICCI and A. MARTANI. Ann. Chim. (Rome), **53**, 577 (1963).
16. E. W. McCLELLAND and L. A. WARREN. J. Chem. Soc. 2621 (1929).

Can. J. Chem. Downloaded from www.nrcresearchpress.com by 93.93.197.157 on 09/07/12
For personal use only.

Variational transition state calculation: collision energy dependence of the M + RX → MX + R (M = alkali, X = halogen, R = radical) reaction family[1]

J. ALONSO, L. BAÑARES, M. MENÉNDEZ, AND A. GONZÁLEZ UREÑA

Departamento de Química Física, Facultad de Química, Universidad Complutense de Madrid, 28040 Madrid, Spain

Received May 27, 1987

J. ALONSO, L. BAÑARES, M. MENÉNDEZ, and A. GONZÁLEZ UREÑA. Can. J. Chem. **66**, 1410 (1988).

A variational transition state theory has been developed to account for the kinetic energy dependence of the reaction cross-section which is valid for the case where experiments are carried out at different, but fixed, collision energies. One of the main aspects of the present work is the inclusion of non-collinear configurations for the transition state.

Analytical expressions for $\sigma_R(E_T)$ averaged over the angle of attack are presented and several model calculations where carried out for the M + RX → MX + R reaction family with an orientational dependence of the energy barrier. The relative success of the present model calculations has been rationalized considering the possibility that long range interactions, via alignment forces, would favour the collinear approach regardless of the initial angle of attack.

J. ALONSO, L. BAÑARES, M. MENÉNDEZ et A. GONZÁLEZ UREÑA. Can. J. Chem. **66**, 1410 (1988).

On a mis au point une théorie variationnelle de l'état de transition pour expliquer le fait que la réaction de section droite dépend de l'énergie cinétique; cette théorie est valide dans les cas où les expériences sont faites à des énergies de collision différentes, mais fixes. Un des principaux aspects de ce travail est l'inclusion de configurations qui ne sont pas colinéaires pour l'état de transition.

On présente des expressions analytiques pour les valeurs de $\sigma_R(E_T)$ moyennes suivant l'angle d'attaque et on a effectué plusieurs calculs modèles pour la famille de réactions M + RX → MX + R, suivant l'orientation de la barrière d'énergie. On rationalise le succès relatif de nos calculs modèles en suggérant que des interactions à longue distance, par le biais d'alignement de forces, favorisent l'approche colinéaire quel que soit l'angle initial d'attaque.

[Traduit par la revue]

Can. J. Chem. Downloaded from www.nrcresearchpress.com by 93.93.197.157 on 09/07/12
For personal use only.

I. Introduction

In a previous study (1) a microcanonical transition state theory was developed to account for the kinetic energy dependence of the reaction cross-section, that is the excitation function, $\sigma_R(E_T)$, of atom–diatom exchange reactions. Essentially a variational transition state theory model was considered valid for quasi-collinear configurations on LEPS energy surfaces. A test was performed to the excitation function for Cl + CH_3I → ClI + CH_3 (2), which yields satisfactory results in the interpretation of its collision energy dependence.

The present paper is an extension of that treatment for non-collinear configurations of the transition state. Analytical expressions for the excitation function averaged over the angle of attack are presented and several model calculations were carried out with an orientational dependence of the reaction barrier of the linear form $E = E_0 + E_0'(1 - \cos\gamma)$. Applications were made to the M + RX → MX + R family of reactions for which an extensive body of data is available from molecular beam experiments (3–10). Therefore we have an excellent opportunity to test the present treatment.

We anticipate that the present theory is useful to predict the collision energy dependence of the reaction cross-section with no or small negative energy dependence, i.e. those systems without sharp maximum in their excitation functions. In these latter cases the theory is not good enough to predict such post-maximum decline in $\sigma_R(E_T)$ as a result, perhaps, of some dynamic effect absent in our statistical treatment even though the location of the transition state varied (see, for example, ref. 11) on the reaction coordinate.

One interesting result is that the quasi-collinear configuration seems to be more capable of reproducing the observed behaviour of $\sigma_R(E_T)$ in the near post-threshold range. This has been rationalized by the possibility that, over this low energy range, long range interaction via alignment forces, it would favour the collinear approach regardless of the initial angle of attack.

[1]This work was performed with support of the Comisión Interministerial de Ciencia y Tecnología of Spain (Project PB85/0007).

Printed in Canada / Imprimé au Canada

II. Theory

Microcanonical variational transition state theory (μVTST)

Our starting point is the variational TST rate constant $k(E)$ for the microcanonical ensemble of A, BC pairs at total energy E, given by (11)

$$[1] \qquad k_{\mu VTST}(E) = \kappa(E)\frac{N^+(E - V^+(s^*))}{h\rho(E)}$$

where h is Planck's constant, $\rho(E)$ is the density of states of reactants per unit energy and volume, $N^+(E - V^+(s^*))$ is the minimum in the total number of internal states of the transition state, within the active modes, excluding the reaction coordinate, and energy less than or equal to $E - V^+$, where V^+ is the potential energy of transition state, along the reaction coordinate s and s^* is the location of this minimum in the energy path. $\kappa(E)$ is the transmission coefficient, which is traditionally assumed to be independent of energy and equal to unity.

To obtain analytical expressions for $N^+(E - V^+(s^*))$ and $k_{\mu VTST}(E,s^*)$ two cases were considered: the quasi-collinear model (1), where only collinear configurations of the ABC system were included and the bent, non-collinear model, where allowance was made for bent transition states, including an orientational dependence of the reaction barrier as a result of the bending potential for the A..B..C triatomic system.

A. Quasi-collinear model (1)

This model considers a configuration on the triatomic ABC system whose minimum energy (or reaction path) is the collinear one at transition state configuration. For a strictly collinear configuration only symmetric and asymmetric stretching modes ν_S and ν_A are relevant, but in the realistic three-dimensional situation, when slight deviations from collinearity contribute, the doubly degenerate bending mode ν_B is also active.

TABLE 1. Microcanonical reaction cross-section expressions for triatomic quasi-collinear configurations (see text for details)

Case	Stretch: Harmonic	Stretch: Morse	Bending	β	$F(z)$
A0		0	0	$\pi I^{\ddagger} D_e$	z
A1		0	1	$\frac{\pi I^{\ddagger} D_e^2}{2(h\nu_B)}$	z^2
A2		0	2	$\frac{\pi I^{\ddagger} D_e^3}{6(h\nu_B)^2}$	z^3
A3	1		0	$\frac{\pi I^{\ddagger} D_e^2}{2(h\nu_S)}$	z^2
A4	1		1	$\frac{\pi I^{\ddagger} D_e^3}{6(h\nu_S)(h\nu_B)}$	z^3
A5	1		2	$\frac{\pi I^{\ddagger} D_e^4}{24(h\nu_S)(h\nu_B)^2}$	z^4
B1		1	0	$\frac{\pi I^{\ddagger} D_e}{2x_e}$	$z - \frac{2}{3}(1 - (1 - z)^{3/2})$
B2		1	1	$\frac{\pi I^{\ddagger} D_e^2}{2x_e(h\nu_B)}$	$\frac{z^2}{2} - \frac{2}{3}z + \frac{4}{15}(1 - (1 - z)^{5/2})$
B3		1	2	$\frac{\pi I^{\ddagger} D_e^3}{12x_e(h\nu_B)^2}$	$\frac{z^3}{2} - \frac{4}{5}z(1 + (1 - z)^{5/2}) + \frac{16}{35}(1 - (1 - z)^{7/2})$

At the internal energy $E_{int}^{\ddagger}$ the density of internal states of the activated complex is (12, 13)

$$[2] \qquad \rho(E_{int}^{\ddagger}) = \frac{2I^{\ddagger}}{\hbar^2} N_{vib}(E_{int}^{\ddagger})$$

where $N_{vib}(E_{int}^{\ddagger})$ is the total number of vibrational states of the activated complex with energy $E_{int}^{\ddagger}$ and $I^{\ddagger}$ is the moment of inertia.

This density was obtained by compounding the number of vibrational states $N_{vib}(E_{int}^{\ddagger})$ with the density of rotational states $\rho_{rot} = 2I^{\ddagger}/\hbar^2$ for the transition state.

For the present case in which all vibrational modes (i.e. $(\nu_S + 2\nu_B)$) are considered active (13)

$$[3] \qquad \rho(E_{int}^{\ddagger}) = \frac{I^{\ddagger}}{3\hbar^2}\left(\frac{1}{h\nu_B}\right)^2 \frac{1}{h\nu_S} E_{int}^{\ddagger 3}$$

where the asymmetric stretch is taken as the reaction coordinate and the harmonic approximation is used for the symmetric stretch and bending modes.

If the more realistic Morse-oscillator approximation (1) is used for the symmetric stretch motion, the above density becomes (1, 13)

$$[4] \qquad \rho(E_{int}^{\ddagger}) = \frac{I^{\ddagger} D_e^2}{\hbar^2 (h\nu_B)^2 2x_e}\left\{\frac{1}{2}\left(\frac{E_{int}^{\ddagger}}{D_e}\right)^2 + \frac{2}{3}\frac{E_{int}^{\ddagger}}{D_e}\left(1 - \frac{E_{int}^{\ddagger}}{D_e}\right)^{3/2} - \frac{4}{15}\left(1 - \left(1 - \frac{E_{int}^{\ddagger}}{D_e}\right)^{5/2}\right)\right\}$$

where x_e is the anharmonicity constant (12), $x_e = h\nu_S/4D_e$ and ν_S, D_e are the vibrational frequency and dissociation energy of the oscillator, respectively.

The sum of states $N(E - V(s))$ is obtained by integrating [4] up to the total available energy, $E - V(s)$,

$$[5] \qquad N(E - V(s)) = \int_0^{E - V(s)} \rho(E_{int}^{\ddagger}) dE_{int}^{\ddagger} = \frac{I^{\ddagger} D_e^3}{6x_e \hbar^2 (h\nu_B)^2} F(z)$$

where

$$[6] \qquad F(z) = \frac{z^3}{2} - \frac{4}{5}z(1 + (1 - z)^{5/2}) + \frac{16}{35}(1 - (1 - z)^{7/2})$$

and

$$[7] \qquad z(s) = \frac{E - V(s)}{D_e}$$

is the reduced available energy.

The $F(z)$ functions for the cases where different subsets of the total number of modes are active are summarized in Table 1. In this table two cases are considered: case A where all the internal degrees of freedom of ABC complex are treated as harmonic oscillators; case B is the same but the stretching motion is described by the Morse-oscillator model.

Excitation function expressions

Since we are primarily interested in the collision energy dependence of the cross section, we restrict ourselves here to the case of a low and constant reactant internal energy E_{int} (e.g. as controlled by the nozzle conditions for a supersonic beam). In this case one can split $\rho(E)$ as follows:

$$[8a] \qquad \rho(E) = \rho_T(E_T) N_{int}(E_{int})$$

where

$$[8b] \qquad E = E_T + E_{int}$$

Can. J. Chem. Downloaded from www.nrcresearchpress.com by 93.93.197.157 on 09/07/12
For personal use only.

Can. J. Chem. Downloaded from www.nrcresearchpress.com by 93.93.197.157 on 09/07/12
For personal use only.

where $\rho_T(E_T)$ is the reactant translational density of states and $N_{int}(E_{int})$ the sum of states of the target molecules BC. They are given by (1)

$$[9] \quad \rho_T(E_T) = A_T E_T^{1/2} = (\mu^{3/2}/2^{1/2}\pi^2\hbar^3)E_T^{1/2}$$

and, within the rigid-rotor Morse-oscillator approximation for BC, by

$$[10] \quad N_{int}(E_{int}) = \left(\frac{1}{2x_e^R}\right)\left(1 - \left(\frac{D_e^R - E_V}{D_e^R}\right)^{1/2}\right)\left(\frac{E_R}{hcB_e}\right)$$

where the vibrational and rotational energies of BC, E_V and E_R, are taken fixed and x_e^R, D_e^R stand for the anharmonicity constant and dissociation energy of the (diatom) reactant, respectively.

In these cases where the reactants have different, but fixed collision energies, a corresponding cross-section $\sigma_R(E)$ can be defined given the μVTST rate (eqs. [1] and [5]) as follows

$$[11] \quad \sigma_R(E) = \frac{k^{\ddagger}(E,s^*)}{v} = \left(\frac{\mu}{2E_T}\right)^{1/2}\frac{N^{\ddagger}(E,s^*)}{h\rho(E)}$$

where μ is the reduced mass of the reactant.

Substituting eqs. [9] and [10] into eq. [11] yields a cross-section expression as a function of E_T, E_V, and E_R. In the idealized situation, which is approximated by many experiments, the target molecule is in the vibrational and rotational ground state (i.e. cold), in which case $N_{int}(E_{int}) \rightarrow 1$. In this case the excitation function reduces to

$$[12] \quad \sigma_R(E) = \sigma_R(E_T) = \beta F(z)/\mu E_T$$

where the expressions for β and $F(z)$ are given in Table 1 for the cases of fully and partially active internal modes. We are concerned with translational effects and so we employ the simplified version of eq. [12].

(B) Bending potential effect: dependence of reaction barrier on orientation angle

In the previous treatment no allowance was made for any orientation angle dependence of the reaction barrier. To include it let us consider a configuration of the triatomic ABC system specified by the angle γ as shown in Fig. 1. The total reaction cross-section can be obtained by

$$[13] \quad \sigma_R(E) = \frac{\int_{-1}^{+1}\sigma_R(E,\gamma)\,d(\cos\gamma)}{\int_{-1}^{+1}d(\cos\gamma)}$$

where

$$[14] \quad \sigma_R(E,\gamma) = \left(\frac{\mu}{2E_T}\right)^{1/2}\frac{N^{\ddagger}(E - V^{\ddagger}(s^*,\gamma))}{h\rho(E)}$$

Note that $N^{\ddagger}(E - V^{\ddagger}(s^*,\gamma))$ now measures the minimum number of energetically available internal states of the transition state at the molecular configuration specified by γ.

In the present work we have considered as valid the quasi-collinear approximation described above. Essentially it is equivalent to assume that the maximum angle of approach, γ_{max}, leading to reaction always occurs at molecular configurations where the normal vibrational modes of the triatomic molecule can be described by those of the linear triatomic molecule. So, the same cases as in the quasi-collinear model can be described here.

With respect to $V^{\ddagger}(s,\gamma)$, it can be approximated by a linear function of cosine (14), i.e.,

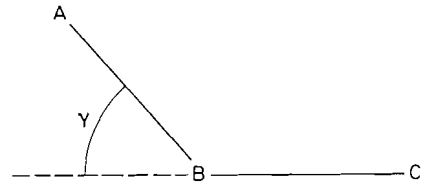

FIG. 1. Bent configuration for the ABC triatomic at the specified γ angle.

$$[15] \quad V(s,\gamma) = V(s) + V'(s)(1 - \cos\gamma)$$

This function has been used (14–16) successfully to fit experimental and calculated data on the orientation dependence of the reaction threshold.

With this assumption and using the harmonic approximation, with all modes considered active, one gets

$$[16a] \quad N(E - V(s,\gamma_{max})) = \int_{\cos\gamma_{max}}^{+1} C\cdot(E - V(s) - V'(s)(1 - \cos\gamma))^4 d(\cos\gamma)$$

where

$$[16b] \quad C = \frac{I^{\ddagger}}{12(h\nu_B)^2(h\nu_S)\hbar^2}$$

and so

$$[17] \quad N(E - V(s,\gamma_{max})) = \frac{I^{\ddagger}D_e^5}{240\,V'(s)(h\nu_B)^2(h\nu_S)}F(z,x)$$

where $z(s)$ is defined by eq. [7] and

$$[18] \quad x(s) = \frac{V'(s)(1 - \cos\gamma_{max})}{D_e}$$

being $z(s) - x(s)$ the reduced available energy at γ_{max}.

The functions $F(z,x)$ for the cases where different subsets of the total number of modes are active are summarized in Table 2. As in Table 1 two cases are considered: internal modes as harmonic oscillators (case A) and stretching motion described by the Morse-oscillator model (case B).

As in the quasi-collinear model, the corresponding cross-section $\sigma_R(E)$ results

$$[19] \quad \sigma_R(E) = \sigma_R(E_T) = \beta F(z,x)/\mu E_T$$

where the expressions for β and $F(z,x)$ are given in Table 2 for the cases of fully and partially active internal modes.

We should point out that section II.B does not include the angular terms of the transition state configurations again. Essentially what it does is to modify the potential energy barrier as a function of the bending angle, i.e. it takes into consideration an orientational dependence of the reaction barrier or, equivalently, the potential energy value as a function of the bending angle. If we use the harmonic approximation, the number of internal states is given by

$$N_{int} = \left(\frac{E - V^{\ddagger}(s)}{h\nu_B}\right)$$

where $E - V^{\ddagger}(s)$ is the total energy available for the transition state. For the results described in section I and Table 2, $V(s)$ has been taken as the collinear $V^{\ddagger}(s)$ value. In section II.B what we have done is to account for an orientational dependence of $V(s)$, i.e. $V(s,\gamma) = V(s) + V(s)'(1 - \cos\gamma)$. We have used

TABLE 2. Microcanonical reaction cross-section expressions for triatomic non-collinear configurations (see text for details)

Case	Stretch: Harmonic	Stretch: Morse	Bending	β	$F(z,x)$
A0	0		0	$\frac{\pi I^{\ddagger} D_e^2}{4V'}$	$z^2 - (z-x)^2$
A1	0		1	$\frac{\pi I^{\ddagger} D_e^3}{12V'(h\nu_B)}$	$z^3 - (z-x)^3$
A2	0		2	$\frac{\pi I^{\ddagger} D_e^4}{48V'(h\nu_B)^2}$	$z^4 - (z-x)^4$
A3	1		0	$\frac{\pi I^{\ddagger} D_e^3}{12V'(h\nu_S)}$	$z^3 - (z-x)^3$
A4	1		1	$\frac{\pi I^{\ddagger} D_e^4}{48V'(h\nu_S)(h\nu_B)^2}$	$z^4 - (z-x)^4$
A5	1		2	$\frac{\pi I^{\ddagger} D_e^5}{240V'(h\nu_S)(h\nu_B)^2}$	$z^5 - (z-x)^5$
B1		1	0	$\frac{\pi I^{\ddagger} D_e^2}{4x_e V'}$	$\frac{1}{2}(z^2 - (z-x)^2 - \frac{2}{3}x + \frac{4}{15}((1-z-x)^{5/2} - (1-z)^{5/2})$
B2		1	1	$\frac{\pi I^{\ddagger} D_e^3}{12x_e V'(h\nu_B)}$	$\frac{z^3-(z-x)^3}{2} - (z^2-(z-x)^2) + \frac{4}{5}x + \frac{8}{35}((1-z)^{7/2} - (1-z-x)^{7/2})$
B3		1	2	$\frac{\pi I^{\ddagger} D_e^4}{24x_e V'(h\nu_B)^2}$	$\frac{z^4-(z-x)^4}{8} - \frac{z^2-(z-x)^2}{10} + \frac{16}{35}x + \frac{8}{35}(z(1-z)^{7/2} - (z-x)(1-z-x)^{7/2}) + \frac{48}{315}((1-z)^{9/2} - (1-z-x)^{9/2})$

this procedure because the bending potential for these systems are not known.

In ordinary treatments, perhaps more rigorous than the present one, the orientational dependence of the potential energy is intrinsically considered by the calculation of $E - V^{\ddagger}(s)$ at different bending angles. On the other hand, potentials of the linear form in $\cos\gamma$ described above, are currently used in the literature. We realize that this procedure may be a grossly classical approximation, but it does imply repetition in counting the angular terms. It only introduces an orientational angle dependence of the reaction barrier rather than use the same collinear value for all the bent configurations of the activated complex. This can be proven as follows. Let us take, for example, the A0 case in both approximations, as described in Tables 1 and 2. The former considers the same collinear E_0 for all the bent configurations. The latter uses the angle dependence described by the linear terms in cosine of γ. If we adopt the limit $V' \to 0$, which physically means taking the same E_0 value for all the non-collinear configurations, Table 2 results reduce to those in Table 1. For example, in the case A0 one gets

$$\frac{\pi I^{\ddagger} D_e^2}{4V'(s)}(z^2 - (z-x)^2) \xrightarrow[(V'(s)\to 0)]{} \pi I^{\ddagger} D_e z$$

(Table 2 result) ⟶ (Table 1 result)

It is obvious that the same result could not be achieved if we would have incorporated twice the angular terms.

Potential energy surface (PES)

The potential energy surface (PES) was taken to be of the extended LEPS form

$$[20] \quad E = Q_1 + Q_2 + Q_3 - 2^{-1/2}|(J_1 - J_2)^2 + (J_2 - J_3)^2 + (J_3 - J_1)^2|^{1/2}$$

where

$$[21] \quad Q_i = \frac{1}{2}\left({}^1\Sigma_i + \frac{1 - S_i}{1 + S_i}{}^3\Sigma_i\right)$$

$$[22] \quad J_i = \frac{1}{2}\left({}^1\Sigma_i - \frac{1 - S_i}{1 + S_i}{}^3\Sigma_i\right)$$

and where diatomic singlet and triplet potential-energy curves are given by Morse and anti-Morse functions

$$[23] \quad {}^1\Sigma = D_e|\exp(-2\beta(R - R_e)) - 2\exp(-\beta(R - R_e))|$$

$$[24] \quad {}^3\Sigma = \tfrac{1}{2}D_e|\exp(-2\beta(R - R_e)) + 2\exp(-\beta(R - R_e))|$$

The diatomic parameters D_e, β, R_e were taken from the literature, and the Sato parameters S_i were adjusted to give a

Can. J. Chem. Downloaded from www.nrcresearchpress.com by 93.93.197.157 on 09/07/12
For personal use only.

TABLE 3. Potential parameters for the different LEPS surfaces used and some properties of collinear A:B:C at the saddle point

Compound	D_e/kcal mol^{-1}	R_e/Å	β/Å^{-1}
CH_3I	54.00	2.14	1.704
CH_3Br	67.80	1.94	1.731
C_2H_5Br	65.49	1.94	2.087
CH_3K†(Na)	20.00	2.40	1.620
C_2H_5K*	30.00	3.00	0.700
KI	76.60	3.05	0.760
NaI	69.55	2.71	0.892
KBr	90.47	2.80	0.747

System	Sato parameters			Saddle point configuration		Threshold energy
	S_{AB}	S_{BC}	S_{AC}	R_{AB}/bohr	R_{BC}/bohr	E_0/eV
K + CH_3Br	−0.015	−0.090	0.000	7.88	3.79	0.23
K + C_2H_5Br	0.200	−0.280	0.370	6.40	3.98	0.10
K + CH_3I	0.176	−0.300	0.000	7.24	4.27	0.04
Na + CH_3I	0.150	−0.190	0.000	6.65	4.19	0.04

*Estimated values.
†From ref. 17.

classical barrier height V_0 equal to the measured threshold energies. The LEPS parameters are listed in Table 3.

The minimum energy or reaction path was then found (1, 11) by using the gradient of the potential to calculate the paths of steepest descent from the saddle point to reactants ($s < 0$), and products ($s > 0$), where the distance from the saddle point along this path is s. Two new coordinates were defined at each s:x^s is the tangent to the reaction path at s, and u^s is perpendicular to x^s. Then a Morse potential $V(u^s)$ was fitted to the local vibrational potential $V(u^s; x^s = 0)$:

$$V(u^s) = D(s)|1 - \exp(-\beta(s)u^s)|^2$$

in terms of the Morse parameters $D(s) = V(A + B + C) - V^{\ddagger}(s)$ and $\beta(s)$. For a given action Ah, the local vibrational energy is

$$\epsilon(A,s) = h\nu_s(s)A(1 - A/\beta(s))$$

Further, the frequency of the bending motion was determined at each s as described elsewhere (1, 11).

We thus calculated $\nu_s(s)$, $\nu_B(s)$ and hence $N(E,s)$ for each value of E in intervals of s and found its minimum $N^{\ddagger}(E - V(s^*))$. The same search procedure was repeated at different E.

To account for the non-collinear configurations we have used the angle-averaged expressions of section II.B and particularly eq. [19] with the corresponding $F(z,x)$ from Table 2. To carry out such calculation an orientational angle dependence of the reaction barrier of the linear form described by eq. [15] was used.

III. Results and discussion

The present theoretical approach was applied to the collision energy dependence of the M + RX → MX + R family of reactions where M = alkali, R = radical, and X = halogen. A significant body of data is now available for this family from molecular beams experiments (10). The results are presented for each system separately.

(A) K + CH_3Br → KBr + CH_3 (6)

This reaction has been studied by Bernstein and co-workers (6) and its excitation function shows an Arrhenius behaviour with an energy threshold value of 0.24 eV.

Figure 2 shows the contour map of the collinear LEPS PES obtained by fitting the Sato parameters to obtain the experimental threshold. The minimum energy path is indicated by the dashed curve. Figure 3 shows the experimental versus theoretical excitation functions. The best fit was obtained with no vibrational degrees of freedom as active mode (hereafter the vibrationally adiabatic case), i.e. case A0 of Table 2. This is shown by the solid line. The dashed line represents the model calculation using the stretching degree of freedom as active, i.e. assuming energy transfer between the motion along the reaction coordinate and the stretching motion. It seems clear that this choice gives poorer results than in the previous case.

Figure 4 displays the same excitation function comparison but now the calculation have been carried out including non-collinear configurations. These were performed by using the angle-average cross-section described in section II.B with an orientational dependence of the reaction barrier. To carry out these calculations some value of the E_0' was required. Unfortunately no reliable threshold parameter has been reported so far. In the present work we have used $E_0' = 0.07$ eV which is close to the one reported for analogous systems, as for example, the Rb + CH_3I reaction (4, 15).

As can be seen in Fig. 4, once again the vibrationally adiabatic case describes much better the experimental behaviour than does the non-adiabatic one. Nevertheless a cross comparison of Figs. 3 and 4 indicates that the calculations using the collinear approach give a better representation of the experimental results than those obtained with non-collinear configurations.

(B) K + C_2H_5Br → KBr + C_2H_5 (7, 8)

This excitation function was measured in our laboratory (9)

Can. J. Chem. Downloaded from www.nrcresearchpress.com by 93.93.197.157 on 09/07/12
For personal use only.

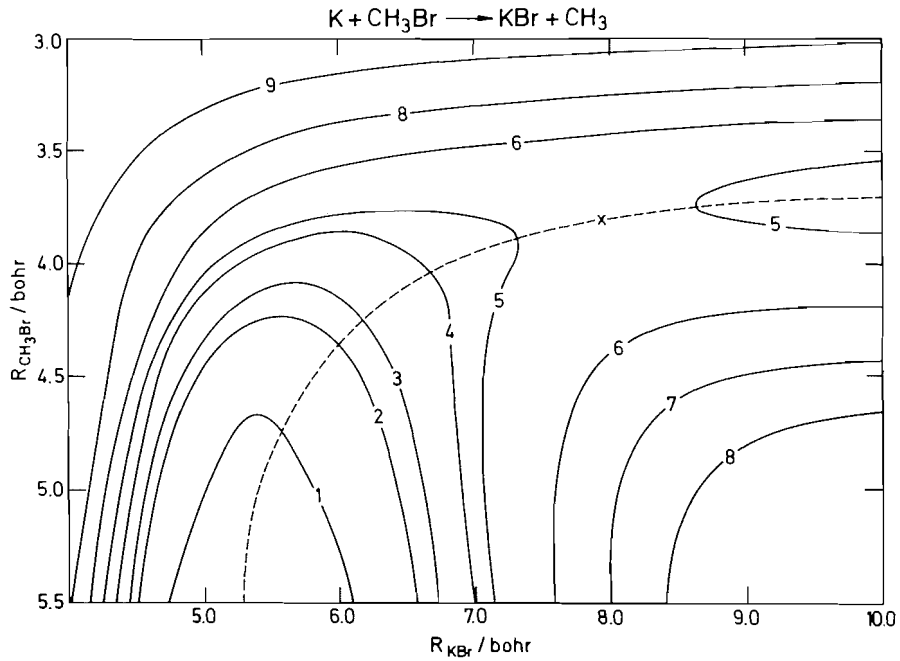

FIG. 2. Potential energy surface for the collinear reaction K + $CH_3Br \rightarrow KBr + CH_3$. The energy contours are as follows (in kJ mol^{-1}): (*1*) −50, (*2*) −20, (*3*) −10, (*4*) 10, (*5*) 20, (*6*) 50, (*7*) 75, (*8*) 100, (*9*) 200. The LEPS parameters used in the present calculation are described in Table 3. Dashed line corresponds to the reaction path.

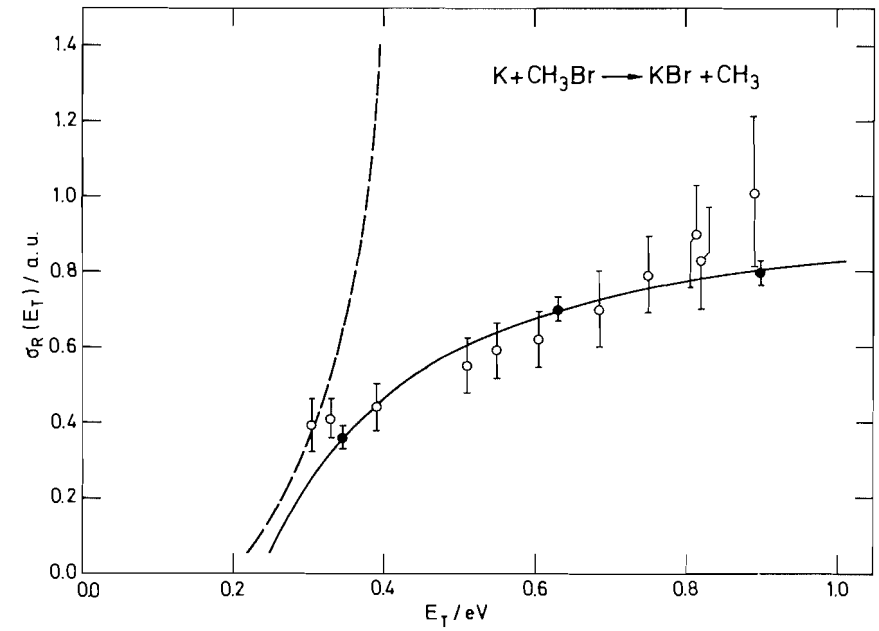

FIG. 3. Excitation function for the K + $CH_3Br \rightarrow KBr + CH_3$ reaction. Open circles: experimental points from ref. 6. Solid line: present model calculation, using the quasi-collinear model without vibrational excitation (case A0, Table 1). Dashed line: result of considering the stretching mode active (case A3, Table 1). Solid circles: present trajectory results scaled at E_T = 61 kJ mol^{-1}. The actual trajectory calculation value at this energy is σ_R = 26.4 $Å^2$. The μTST value is σ_R = 40.7 $Å^2$.

and it is displayed in Fig. 5 together with the same type of calculation described in Fig. 3, but now using the LEPS potential built with the same procedure as before and with the parameters listed in Table 3. Note how a better overall representation of the experimental excitation function is achieved in the vibrationally adiabatic case with the quasi-collinear model. Figure 6 shows the same comparison as Fig. 4, but now for the present system. An E_0' value of 0.07 eV was also used. A comparison between Figs. 5 and 6 furnishes analogous conclusions to the previous case with respect to the validity of the collinear approach in the present model calculation.

(C) Na(K) + $CH_3I \rightarrow$ Na(K)I + CH_3 (3, 9)

These two excitation functions have been measured by the

Can. J. Chem. Downloaded from www.nrcresearchpress.com by 93.93.197.157 on 09/07/12
For personal use only.

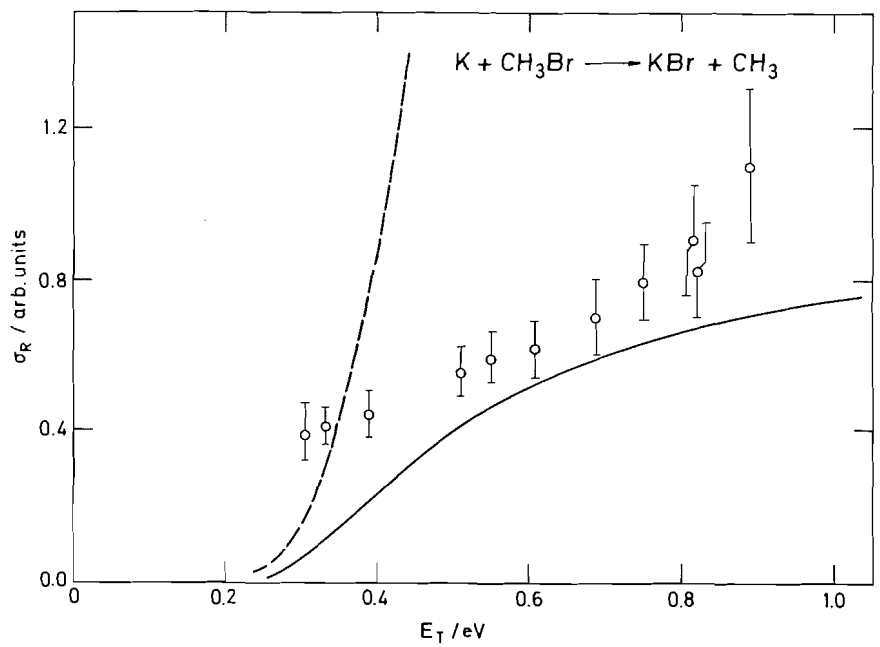

FIG. 4. Same presentation as in Fig. 3 but now using the angle average cross-section, with an orientational dependence of the reaction barrier. Solid line is the model prediction using case A0 of Table 2, i.e. no vibrational activation; dashed line is the result of using case A3 of Table 2.

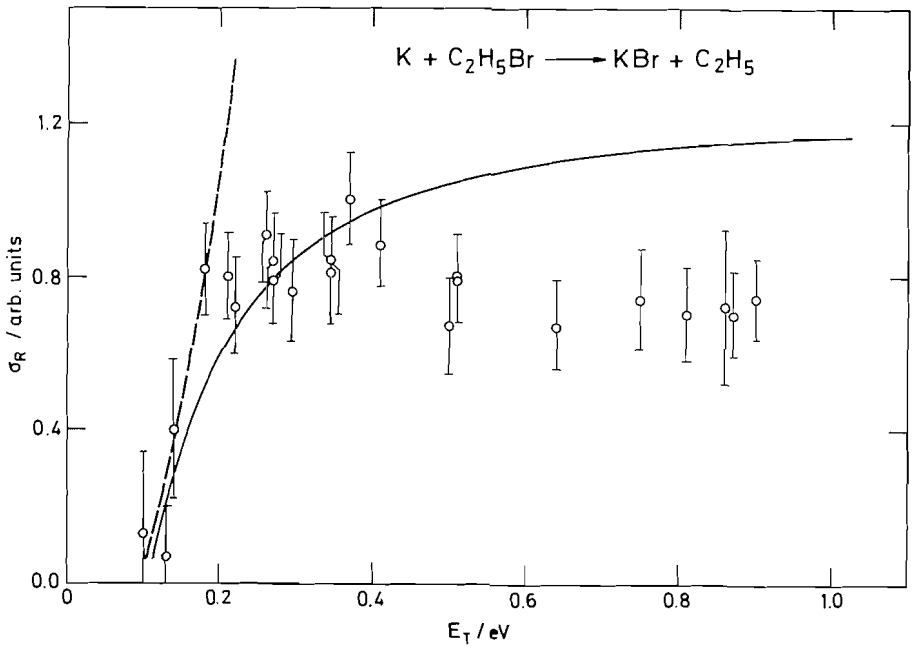

FIG. 5. Same presentation as in Fig. 3 but now for the $K + C_2H_5Br \rightarrow KBr + C_2H_5$ reaction. Open circles are experimental points from ref. 8. Solid line is the vibrationally adiabatic case (quasi-collinear configuration). Dashed line represents the result of the case A3 in Table 1, i.e. the model prediction when one considers the stretching mode as active one.

molecular beam method (3, 9). We have grouped them because they represent clear examples where a maximum in the collision energy dependence of the reaction cross-section was found. In fact the post-maximum decline in the excitation function has drawn considerable theoretical attention. Several mechanisms have been reported to account for this translational feature being the recrossing mechanism one of the most widely proposed (10, 17).

Figures 7 and 8 show the LEPS potential for these systems built using the parameters of Table 3. Theoretical and experimental data of these excitation functions are displayed in Figs. 9 and 10 for the Na and K reactions, respectively. From inspection of these two figures the following comments can be made:

(*a*) None of the cases used in the present model calculation are able to predict the maximum and post-maximum decline in the reaction cross-section. It seems clear that variational

Can. J. Chem. Downloaded from www.nrcresearchpress.com by 93.93.197.157 on 09/07/12
For personal use only.

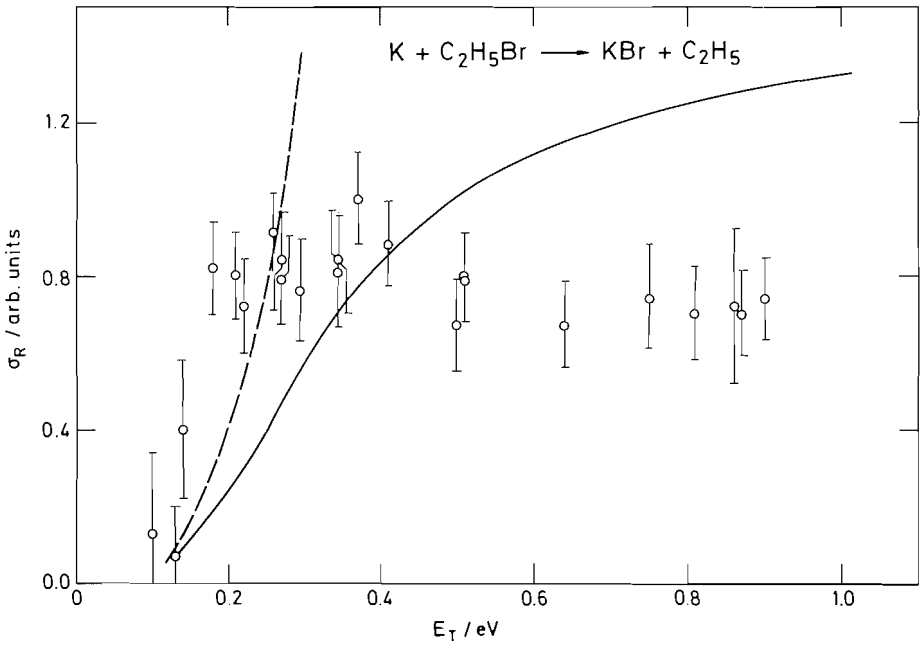

FIG. 6. Same presentation as in Fig. 4 but for the $K + C_2H_5Br \rightarrow KBr + C_2H_5$ reaction.

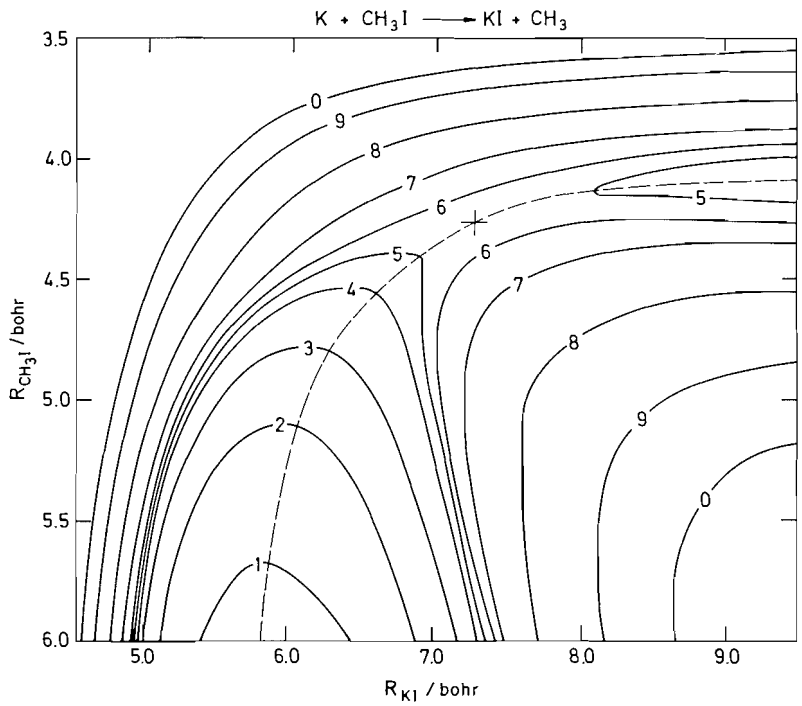

FIG. 7. Potential Energy Surface for the collinear reaction $K + CH_3I \rightarrow KI + CH_3$. The energy contours are as follows (in kJ mol^{-1}): (*1*) −50, (*2*) −25, (*3*) −10, (*4*) 0, (*5*) 3, (*6*) 5, (*7*) 10, (*8*) 25, (*9*) 50, (*0*) 75. The LEPS parameters used in the present calculation are described in Table 3. The dashed line corresponds to the reaction path.

transition state calculation at least within the approximation presently used is unable to account for this negative collision energy dependence. Even though one takes advantage of the variational location of the transition state, as in the present work, some dynamic effects seem to be still absent in our treatment to reproduce the observed behaviour of the excitation function.

(*b*) Once again the vibrationally adiabatic case seems to offer the better prediction of the experimental collision energy dependence of the reaction cross-section, at least before a maximum in $\sigma_R(E_T)$.

(*c*) Since for the K reaction absolute data on the reaction cross-section are available, a comparison of these absolute

Can. J. Chem. Downloaded from www.nrcresearchpress.com by 93.93.197.157 on 09/07/12
For personal use only.

Can. J. Chem. Downloaded from www.nrcresearchpress.com by 93.93.197.157 on 09/07/12
For personal use only.

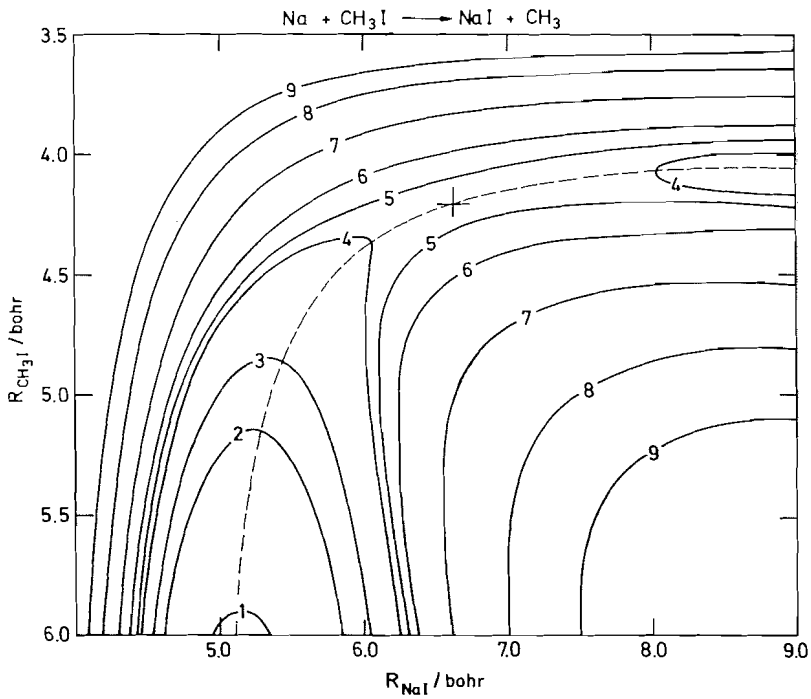

FIG. 8. Same presentation as in Fig. 7 but for the N + $CH_3I \rightarrow$ NaI + CH_3. The energy contours are as follows (in kJ mol^{-1}): (*1*) −40, (*2*) −20, (*3*) −10, (*4*) 3, (*5*) 5, (*6*) 10, (*7*) 25, (*8*) 50, (*9*) 75. The LEPS parameters used are described in Table 3. The dashed line corresponds to the reaction path.

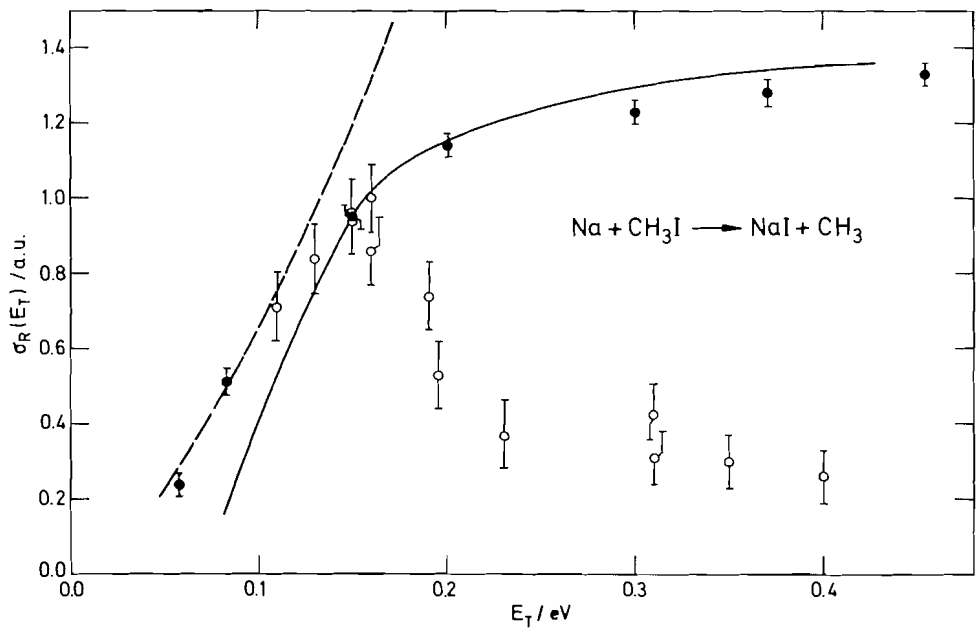

FIG. 9. Excitation Function for the Na + $CH_3I \rightarrow$ NaI + CH_3 reaction. Open symbols: experimental points from ref. 9. Solid and dashed line as in Fig. 3. Closed symbols: quasiclassical trajectory simulation scaled at E_T = 14.6 kJ mol^{-1}, being the calculated value σ_R (E_T = 14.6 kJ mol^{-1}) = 16.1 $Å^2$.

values is also possible. The best quantitative results are obtained for the quasi-collinear vibrationally adiabatic model, as long as one uses the two degrees of freedom associated with the linear transition state configuration as described by cases A3 or B1 of Table 2.

(D) Near threshold behaviour

Figures 11 and 12 show an interesting comparison of the four excitation functions already mentioned in the near threshold range. The representation is the quantity $\sigma_R(E_T).E_T$ versus E_T. Theoretical calculations include: (*a*) solid line: quasi-collinear model, where only the collinear reaction barrier was used. (*b*) Dashed line represents the same calculation but using the angle average cross-section with an orientation dependence for the reaction barrier of the type $E_{th} = E_0 + E_0'(1 - \cos \gamma)$. (*c*) Closed circles represent trajectory calculation results (see

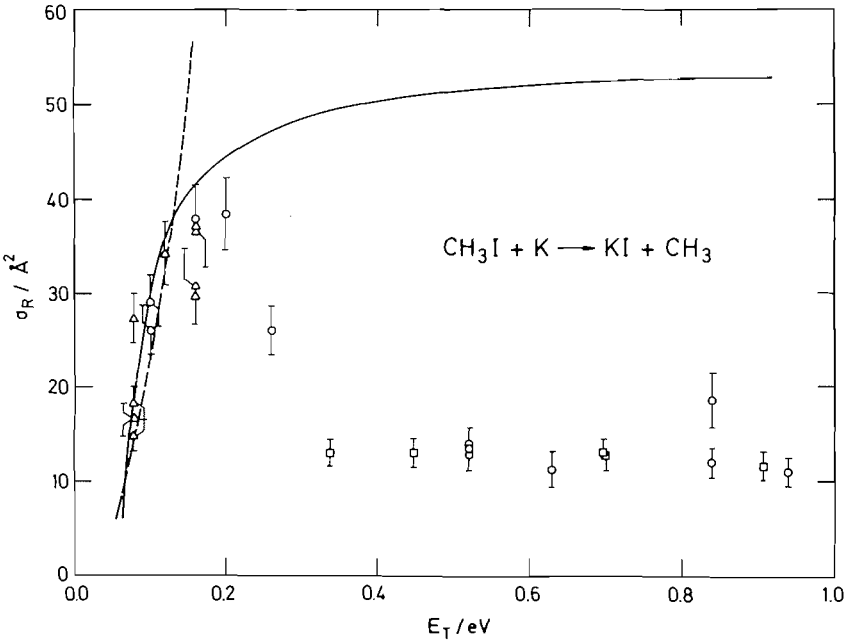

FIG. 10. Same presentation as in Fig. 9 but for the $K + CH_3I \rightarrow KI + CH_3$ reaction. Symbols: experimental data from ref. 3.

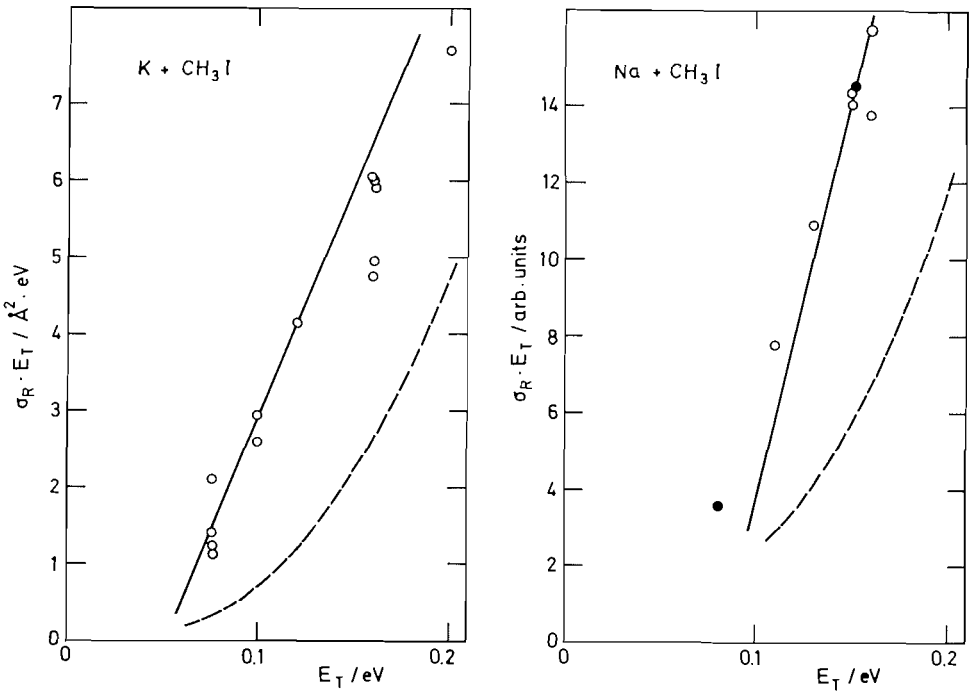

FIG. 11. Theoretical and experimental data on $\sigma(E_T)^* E_T$ versus E_T for the indicated reaction over the near threshold range. All the calculations have been carried out considering the spread of the collision energy reported in the experiments. Symbols are experimental data from the same references as in previous figures. Solid line is quasi-collinear calculation. Dashed line is the angle average cross-section with the orientational dependence of the reaction barrier. See text for comments. Solid circles are present trajectory calculation results, i.e. low energy results from Fig. 9.

below) that seem to be in good agreement with experimental data.

For a better illustration these functionalities are shown in Fig. 13. All the calculations were convoluted considering the spread of the collision energy as reported in the respective molecular beam experiment from where data were taken. It is known that (14) the post-threshold law should show a quadratic dependence on the energy excess $(E_T - E_0)$ if one uses a linear functionality with respect to $\cos\gamma$, as described earlier, as well as in the rotating rod model (18). From inspection of Figs. 11 and 12 one may conclude that the best fit of the data is always obtained by the calculation carried out with the collinear configuration (i.e. E_0 instead of $E_0 + E_0'(1 - \cos\gamma)$).

It seems as if over this post-threshold range where the

Can. J. Chem. Downloaded from www.nrcresearchpress.com by 93.93.197.157 on 09/07/12
For personal use only.

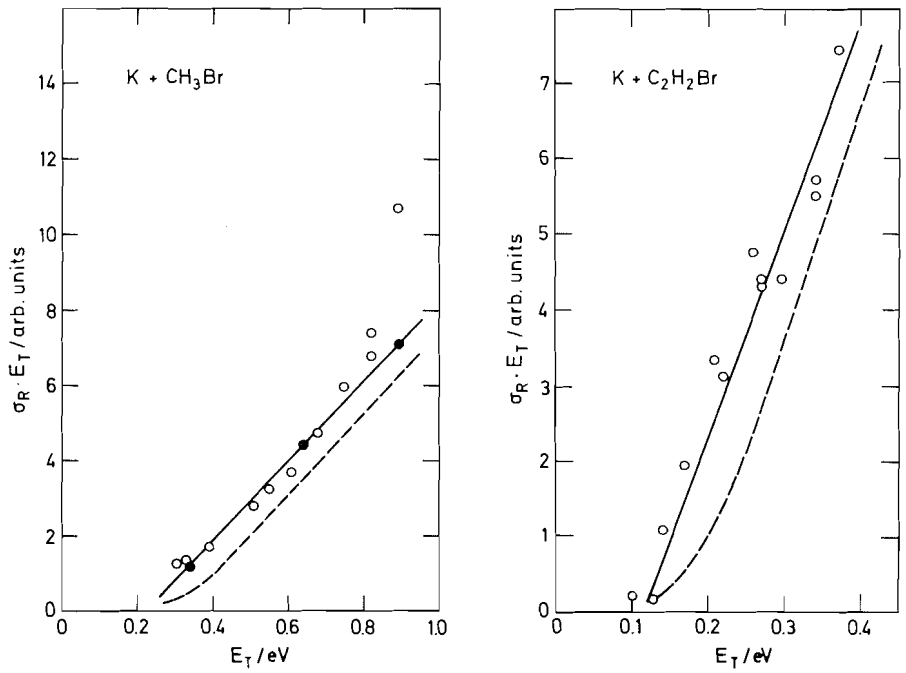

FIG. 12. Same presentation as in Fig. 11 for the indicated reactions. Solid circles are present trajectory calculation results.

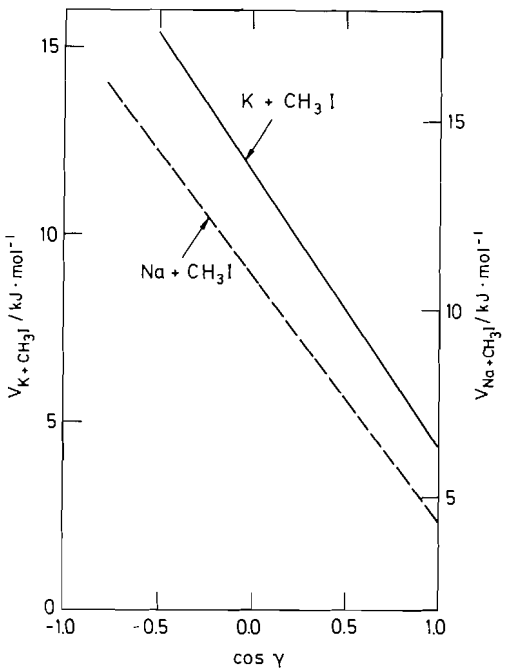

FIG. 13. Orientational dependence of the reaction barrier for the indicated reactions. Solid line: K reaction with $E_0' = 0.07$ eV. Dashed line: Na reaction with $E_0' = 0.067$ eV.

collision energy is low, and the reaction time correspondingly large, long range orientational interactions (via bending interactions, i.e. alignment forces) would select the collinear configuration for the transition state regardless of the initial angle of approach. Of course, excitation function with fixed reactants geometry as it is currently studied (19) will clarify this point, so care should be taken with this interpretation and the satisfactory fit of the excitation functions should not be over-interpreted. In fact trajectory calculations (20) have shown that only right above the threshold can one see the quadratic energy dependence of $\sigma_R(E_T)$.

(E) Comparison with quasi-classical trajectory calculations

Since, except for the CH_3Br case, the calculations using the variational transition state theory fail to reproduce the observed maxima in the cross-section, we think it is worthwhile to compare the present theoretical calculations with quasi-classical trajectory simulations on the same (assumed physical) potential energy surface. This comparison would provide a clear way to distinguish between the goodness of the μTST and that of the primitive LEPS surface used.

Two set of calculations using the quasi-classical trajectory method have been carried out for the K and Na plus CH_3I reactions. The potential energy surface used were of the LEPS extended form and their parameters are listed, as it was already mentioned, in Table 3. The program and method of calculation was the same as the one used in ref. 21, therefore we omit details for brevity.

Figure 3 shows trajectory calculation result for the reaction cross-section and three different collision energies (solid circles are used for a better display) for the $K + CH_3Br \rightarrow KBr + CH_3$ reaction. The theoretical values were reduced by a factor of 1.5 in order to normalize the quasi-classical trajectory results to those μTST. Except for this factor one can see the excellent agreement between both theories and the experimental results as far as the collision energy dependence of the reaction cross-section is concerned.

On the other hand, the fact that in the $Na + CH_3I$ case both calculations, as shown in Fig. 9, fail to reproduce the experimental excitation function values, is a clear indication that the disagreement is mainly due to the wrong (assumed) PES rather than to a failure of the μTST treatment here adopted. Work is in progress to build a more suitable potential energy surface from which one could reproduce the experimental cross sections by using both theoretical treatments.

Can. J. Chem. Downloaded from www.nrcresearchpress.com by 93.93.197.157 on 09/07/12
For personal use only.

Acknowledgment

A.G.U. thanks J. C. Whitehead for providing the quasi-classical trajectory program used in the present work.

1. L. BAÑARES, J. ALONSO, M. MENZINGER, and A. GONZÁLEZ UREÑA. J. Chem. Soc. Faraday Trans. 2, **82**, 1033 (1986).
2. S. M. A. HOFFMAN, D. J. SMITH, A. GONZÁLEZ UREÑA, T. A. STEELE, and R. GRICE. Mol. Phys. **53**, 1067 (1984).
3. M. E. GERSH and R. B. BERNSTEIN. J. Chem. Phys. **55**, 4461 (1971); **56**, 6131 (1972).
4. H. E. LITVAK, A. GONZÁLEZ UREÑA, and R. B. BERNSTEIN. J. Chem. Phys. **61**, 738 (1974); **61**, 4091 (1974).
5. F. J. AOIZ, V. J. HERRERO, and A. GONZÁLEZ UREÑA. Chem. Phys. **59**, 61 (1981).
6. H. F. PANG, K. T. WU, and R. B. BERNSTEIN. J. Chem. Phys. **54**, 2088 (1977); K. T. WU, H. F. PANG, and R. B. BERNSTEIN. J. Chem. Phys. **61**, 1064 (1978).
7. V. J. HERRERO, V. SAEZ RÁBANOS, and A. GONZÁLEZ UREÑA. Mol. Phys. **47**, 725 (1982).
8. V. J. HERRERO, V. SAEZ RÁBANOS, and A. GONZÁLEZ UREÑA. J. Phys. Chem. **88**, 2399 (1984).
9. V. SAEZ RÁBANOS, E. VERDASCO, V. J. HERRERO, and A. GONZÁLEZ UREÑA. J. Chem. Phys. **81**, 5725 (1984).
10. A. GONZÁLEZ UREÑA. Adv. Chem. Phys. **66**, 213 (1987).
11. (*a*) B. C. GARRETT and D. G. TRUHLAR. J. Chem. Phys. **83**, 1052 (1979); (*b*) D. G. TRUHLAR and B. C. GARRETT. Ann. Rev. Phys. Chem. **35**, 159 (1984).
12. G. HERZBERG. Molecular spectra and molecular structure. Vol. I. Spectra of diatomic molecules. (Van Nostrand Reinhold, New York. 1950).
13. P. J. ROBINSON and K. A. HOLBROOK. Unimolecular reactions. Wiley, London. 1972.
14. R. D. LEVINE and R. B. BERNSTEIN. Chem. Phys. Lett. **105**, 467 (1984).
15. R. B. BERNSTEIN. J. Chem. Phys. **82**, 3656 (1985).
16. N. C. BLAIS, R. B. BERNSTEIN, and R. D. LEVINE. J. Phys. Chem. **89**, 10 (1985).
17. R. A. LABUDDE, P. J. KUNTZ, R. B. BERNSTEIN, and R. D. LEVINE. J. Chem. Phys. **59**, 6286 (1973).
18. N. AGMON. Chem. Phys. **45**, 249 (1980); **61**, 189 (1981).
19. H. JALINK, D. H. PARKER, K. H. MEIWES-BROER, and S. STOLTE. J. Phys. Chem. **90**, 552 (1986).
20. R. GOTTING, H. R. MAYNE, and J. P. TOENNIES. J. Chem. Phys. **80**, 2230 (1984).
21. I. W. FLETCHER and J. C. WHITEHEAD. J. Chem. Soc. Faraday Trans. 2, **77**, 2329 (1981).

Can. J. Chem. Downloaded from www.nrcresearchpress.com by 93.93.197.157 on 09/07/12
For personal use only.

Enzymes in organic synthesis. 44.[1] Stereoselective pig liver esterase-catalyzed hydrolyses of 3-substituted glutarate diesters of compactin-synthon interest[2]

LISTER K.-P. LAM AND J. BRYAN JONES
Department of Chemistry, University of Toronto, Toronto, Ont., Canada M5S 1A1

Received December 7, 1987

LISTER K.-P. LAM and J. BRYAN JONES. Can. J. Chem. **66**, 1422 (1988).

Pig liver esterase-catalyzed hydrolyses of dimethyl 3-hydroxy-, 3-methoxyethoxymethoxy-, and 3-benzyloxyglutarates occur with enantiotopic stereoselectivity to give the corresponding acid-ester products of 16–40% enantiomeric excess (ee). The results also provide another example of reversal of PLE-stereoselectivity.

LISTER K.-P. LAM et J. BRYAN JONES. Can. J. Chem. **66**, 1422 (1988).

Les hydrolyses, catalysées par l'estérase du foie de porc, des hydroxy-3, méthoxyéthoxyméthoxy-3 et benzyloxy-3 glutarates de diméthyle se produisent avec une stéréosélectivité énantiotopique et elles fournissent les produits acide-esters correspondants avec un excès énantiomérique (eé) de 16–40%. Les résultats fournissent aussi un autre exemple de renversement de la stéréosélectivité de l'EFP.

[Traduit par la revue]

Compactin (**1**) and related compounds are potent inhibitors of HMG-CoA reductase, the rate-limiting enzyme in cholesterol biosyntheses (2*a*), and are consequently able to reduce plasma cholesterol levels in animals, including humans (2*b*). This property, combined with the very low toxicity (2), has elicited great interest in compactin and its analogues as hypocholesteremic drugs. As a result, the synthesis of compactins remains a very active field (3).

Chiral acid-esters such as **3***a* are potentially useful synthons for the therapeutically vital (4) lactone moiety of compactin. Our previous work on pig liver esterase (PLE)-catalyzed hydrolyses of 3-substituted glutarate diesters **2** had shown that enantiotopically selective hydrolyses could be effected to give acid-esters **3** of up to 97% enantiomeric excess (ee) (5). This encouraged us to evaluate the potential of PLE-catalyzed hydrolyses of the 3-oxygenated glutarate diesters **2***b–d* for the production of the potential compactin-lactone synthons **3***b–d*.

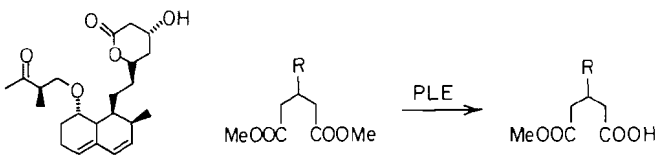

1 **2** **3**

a, R = Me
b, R = OH
c, R = OMEM
d, R = $OCH_2C_6H_5$

Results

Diesters **2***b–d* were prepared in good yields by unexceptional methods. Each proved to be a reasonable substrate for PLE, having rates of hydrolyses (relative to that of the reference standard ethyl butyrate = 100) of 17 for **2***b*, 2 for **2***c*, and 4 for **2***d*. The preparative-scale hydrolyses of **2***b–d* proceeded smoothly to give high yields of the corresponding acid-esters **3***b–d*. The results are summarized in Table 1.

The absolute configurations of **3***b–d* were established by their correlations with (−)-(*R*)- and (+)-(*S*)-**3***b* of known (6) stereochemistry. The ee's of Table 1 were determined on the acid-esters **3***b* derived from **3***b–d* during the absolute configuration assignments, via their conversions to their (*S*)-1-phenethanamide derivatives **4** by the method of Heathcock and co-workers (7), followed by ^1H nmr examinations of the *tert*-butyl and methoxyl resonances.

TABLE 1. PLE-catalyzed hydrolyses of **2***b–d*[a]

Substrate	Product (% yield, % ee)
2*b*	(+)-(3*S*)-**3***b* (87, 16)
2*c*	(+)-(3*R*)-**3***c* (92, 39)
2*d*	(−)-(3*S*)-**3***d* (87, 40)

[a]At pH 7, 20°C.

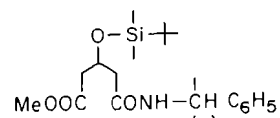

4

Discussion

The easily removable methoxyethoxymethyl (MEM) and benzyl functions were chosen as the hydroxyl-protecting groups for substrates **2***c,d* because of their stability during the acidic work-up involved in the enzyme-catalyzed reactions, and to avoid stereochemical complications introduced by the use of other common, but chiral, protecting groups. Substrates **2***b,c* were readily prepared by standard methods. However, due to the sensitivity of dimethyl 3-hydroxyglutarate (**2***b*) to base, benzylation attempts using sodium hydride – benzyl bromide conditions were unsuccessful in the preparation of **2***d*, and the acid-catalyzed procedure of Iversen and Bundle (8) was used instead. It was found that $BF_3 \cdot Et_2O$ was a more effective benzylation catalyst than the triflic acid used originally (8).

Although the relative rates of PLE-catalyzed hydrolyses of **2***b–d* were significantly slower than that of the ethyl butyrate

[1]For Part 43, see ref. 1.

[2]Abstracted from the Ph.D. thesis of L.K.-P.L., University of Toronto, Toronto, Ont. 1986.

Can. J. Chem. Downloaded from www.nrcresearchpress.com by 93.93.197.157 on 09/07/12
For personal use only.

Can. J. Chem. Downloaded from www.nrcresearchpress.com by 93.93.197.157 on 09/07/12
For personal use only.

standard, each still remained a good candidate for preparative-scale reactions.[3]

The results of the preparative-scale experiments (Table 1) show that the ee levels are significantly increased by the conversion of the C3-OH group of **2***b* to the more bulky O-MEM and O-benzyl functions of **2***c* and **2***d* respectively. This ee increase on functionalization, and the reversal of stereoselectivity observed, parallel the observations recorded in the 3-amino- and 3-alkylglutarate series (5, 9). Rationalizing the many stereospecificity reversals within different series of substrates documented (5, 9, 10) for PLE now represents a formidable interpretative challenge.

There is interest (11, 12) in **3***b* as a chiral precursor of important target molecules other than compactin, with esterase-based methods complementing those involving reductions of β-ketoesters (13, 14).

While the current PLE-catalysis approach has not yet reached its goal of producing enantiomerically pure **3***b*,[4] further increases in ee levels should be attainable by control of reaction conditions (5, 15) and, by analogy with the 3-amino series (9), by different O-functionalization of **2***b*. Interestingly, when 3-methyl (16*a*) or 2,4-dimethyl (16*b*) substituents are present in **2***b* of 2,4-dimethyl (16*b*) substituents are present in **2***b*, PLE-catalyzed hydrolyses yield acid-esters of high ee's (16).

Experimental

The instrumentation and general purification and analytical methods used were as described previously (5). PLE (EC 3.1.1.1) was Sigma Chemical Company Type II (Lot 123F-0240). Unless noted otherwise, ir spectra were for films, and ^{1}H nmr and $[\alpha]_D^{25}$ measurements were taken on $CDCl_3$ and $CHCl_3$ solutions respectively.

Preparation of substrates

Dimethyl 3-hydroxyglutarate (**2***b*) was obtained in 80% yield by reduction (6) with $NaBH_4$ of dimethyl 3-ketoglutarate (Aldrich); **2***b* had bp 138–140°C (8 Torr; 1 Torr = 133.3 Pa); ir: 3430, 1740 cm^{-1}; ^{1}H nmr δ: 2.58 (4H, d, J = 6 Hz), 3.63 (1H, br s, OH), 3.75 (6H, s), and 4.48 (1H, quintet, J = 6.2 Hz) ppm.

*Dimethyl 3-methoxyethoxymethoxyglutarate (2*c*)*

Triethylamine (100 mL, 0.72 mol) was added dropwise with stirring at 20°C to a mixture of dimethyl 3-hydroxyglutarate (**2***b*, 5 g, 28.4 mmol) and methoxyethoxymethyl chloride (13.3 g, 107 mmol) at 25°C. The mixture was then refluxed for 1.5 days, filtered, and the solvent removed by rotoevaporation. The residual oil was taken up in diethyl ether (30 mL), and washed with saturated aqueous $NaHCO_3$ (10 mL) and then with brine (10 mL). The ether layer was dried ($MgSO_4$), filtered, and the solvent was removed by rotoevaporation. The crude oil was purified by flash chromatography (ether:hexanes (1:1) elution), followed by Kugelrohr distillation to afford dimethyl 3-methoxyethoxymethoxyglutarate (**2***c*, 6.9 g, 92% yield), bp 89–91°C (0.15 Torr); ir: 1736 cm^{-1}; ^{1}H nmr δ: 2.63 (4H, d, J = 6 Hz), 3.33 (3H, s), 3.37–3.77 (4H, m), 3.65 (6H, s), 4.38 (1H, quintet, J = 6 Hz), and 4.72 (2H, s) ppm. *Anal.* calcd. for $C_{11}H_{20}O_7$: C 49.99, H 7.63; found: C 49.97, H 7.61%.

*Dimethyl 3-benzyloxyglutarate (2*d*)*

Boron trifluoride – diethyl ether (catalytic amount, 0.05 mL) was added with stirring to a solution of dimethyl 3-hydroxyglutarate (**2***b*, 1.76 g, 10 mmol) and benzyl trichloroacetimidate (5.05 g, 20 mmol) in cyclohexane–CH_2Cl_2 (2:1; 100 mL). The reaction was kept for 3 h at 23°C prior to addition of more cyclohexane (100 mL). The organic layer was then filtered and washed with saturated aqueous $NaHCO_3$ (2 × 50 mL) and then with brine (50 mL). The dried ($MgSO_4$) solution was filtered, and the solvent was removed by rotoevaporation. The crude oil obtained was purified by flash chromatography (ethyl acetate:hexanes (1:10) elution) and then Kugelrohr-distilled to give dimethyl 3-benzyloxyglutarate (**2***d*, 1.87 g, 70% yield), bp 126–130°C (0.2 Torr); ir: 1739 cm^{-1}; ^{1}H nmr δ: 2.63 (4H, d, J = 6 Hz), 3.68 (6H, s), 4.32 (1H, quintet, J = 6 Hz), 4.58 (2H, s), and 7.32 (5H, s) ppm. *Anal.* calcd. for $C_{14}H_{18}O_5$: C 63.13, H 6.81; found: C 62.80, H 6.94%.

*PLE-catalyzed hydrolyses of 2*b–d

The relative rates of hydrolyses of **2***b–d* were determined as described previously (17).

The preparative-scale reactions were performed according to the standard procedure for symmetrical diester substrates (5). The results obtained (summarized in Table 1) were as follows:

Dimethyl 3-hydroxyglutarate (**2***b*, 1.0 g, 5.68 mmol) with PLE (400 units) for 80 min gave methyl hydrogen (3*S*)-3-hydroxyglutarate (**3***b*, 800 mg, 87% yield, 16% ee), bp 124–126°C (0.2 Torr); $[\alpha]_D^{25}$ +0.13° (*c* 15) (lit. (6) $[\alpha]_D^{22}$ −1.7° (*c* 12.5) for (3*R*)-**3***b*); ir: 3450–2610, 1734, 1715 cm^{-1}; ^{1}H nmr δ: 2.60 (4H, d, J = 6 Hz), 3.73 (3H, s), 4.45 (1H, quintet, J = 6 Hz), and 7.17 (2H, br s) ppm. *Anal.* calcd. for $C_6H_{10}O_5$: C 44.45, H 6.22; found: C 44.33, H 6.07%.

Dimethyl 3-methoxyethoxymethoxyglutarate (**2***c*, 750 mg, 2.84 mmol) with PLE (200 units) for 11 h yielded methyl hydrogen (3*R*)-3-methoxyethoxymethoxyglutarate (**3***c*, 655 mg, 92% yield, 39% ee), bp 140–145°C (0.25 Torr); $[\alpha]_D^{25}$ +1.0° (*c* 25); ir: 3430–2610, 1736, 1714 cm^{-1}; ^{1}H nmr δ: 2.68 (4H, d, J = 6 Hz), 3.37 (3H, s), 3.40–3.80 (4H, m), 3.68 (3H, s), 4.37 (1H, quintet, J = 6 Hz), 4.77 (2H, s), and 8.99 (1H, br s) ppm. *Anal.* calcd. for $C_{10}H_{18}O_7$: C 48.00, H 7.25; found: C 47.39, H 7.16%.

Dimethyl 3-benzyloxyglutarate (**2***d*, 500 mg, 1.88 mmol) with PLE (132 units) for 12 h afforded methyl hydrogen (3*S*)-3-benzyloxyglutarate (**3***d*, 410 mg, 87% yield, 40% ee), bp 145–147°C (0.2 Torr); $[\alpha]_D^{25}$ −0.3° (*c* 10); ir: 3440–2680, 1736, and 1714 cm^{-1}; ^{1}H nmr δ: 2.68 (2H, d, J = 6 Hz), 2.69 (2H, d, J = 6 Hz), 3.70 (3H, s), 4.32 (1H, quintet, J = 6 Hz), 4.60 (2H, s), 7.33 (5H, s), and 10.38 (1H, br s) ppm. *Anal.* calcd. for $C_{13}H_{16}O_5$: C 61.90, H 6.39; found: C 61.03, H 6.52%.

Absolute configuration determinations

Correlations were to the known (6) (−)-(3*R*)-**3***b*.

*Of (+)-3*c

The cleavage method of Boeckman and Potenza (18) was used. (+)-Methyl hydrogen methoxyethoxymethoxyglutarate (**3***c*, 635 mg, 2.54 mmol) in dry CH_2Cl_2 (10 mL) was treated dropwise with *o*-phenylene bromoboronate (19) in CH_2Cl_2 (0.2 M, 12.7 mL, 2.54 mmol) at 20°C. After stirring at 20°C for 30 min the mixture was treated with water (10 mL) and stirred for another 20 min. The reaction mixture was then extracted with ethyl acetate (4 × 50 mL), and the organic phase dried ($MgSO_4$), filtered, and rotoevaporated. The Kugelrohr distillation gave (−)-(3*R*)-**3***b* (339 mg, 82% yield), bp 123–128°C/0.2 Torr; $[\alpha]_D^{25}$ −0.43° (*c* 7.5, $CHCl_3$) (lit. (6) $[\alpha]_D^{22}$ −1.7° (*c* 12.5) for (3*R*)-**3***b*); ir and ^{1}H nmr identical to spectra obtained for (+)-(3*S*)-**3***b* above.

*Of (−)-3*d

A mixture of (−)-(3*S*)-monomethyl 3-benzyloxyglutarate ((−)-(3*S*)-**3***d*, 252 mg, 1.0 mmol) and pre-equilibrated 10% Pd/C (75 mg) in 95% ethanol (12 mL) was hydrogenated at 23°C and atmospheric pressure (20). Hydrogen uptake (1 equiv.) ceased after 12 h. The mixture was then filtered and rotoevaporated to give (+)-(3*S*)-**3***b* (146 mg, 90% yield), bp 122–125°C (0.2 Torr); $[\alpha]_D^{25}$ +0.78° (*c* 5.0); ir and ^{1}H nmr identical with those of (+)-(3*S*)-**3***b* above.

Enantiomeric excess determinations

The method of Rosen *et al.* (7) was used, using ^{1}H nmr measurements on the amides **4** obtained from (+)-(3*S*)- or (−)-(3*R*)-**3***c* above and (*S*)-1-phenylethanamine. The ee values obtained (accuracy: ±1%) are recorded in Table 1.

[3]Any ester with a rate of hydrolysis ≥ 0.02% of that of ethyl butyrate will work satisfactorily in synthetic-scale conversions.

[4]The 16% ee level of **2***b* attained in this study matches that reported by Tamm and co-workers (11). Under normal conditions, we do not observe higher ee levels (12) with any of our current PLE batches.

The properties of the reference amide diastereomers, separated by flash chromatography, are as follows:

(3*S*,1′*S*)-**4**: ^{1}H nmr (200 MHz) δ: 0.03 (3H, s), 0.07 (3H, s), 0.86[5] (9H, s, *t*-Bu), 1.47 (3H, d, J = 7.0 Hz), 2.39 (1H, d of d, J = 5.1, 14.8 Hz), 2.45 (1H, d, J = 1.6 Hz), 2.48 (1H, d, J = 0.8 Hz), 2.55 (1H, d of d, J = 5.1, 14.8 Hz), 3.65[5] (3H, s, -OMe), 4.50 (1H, m), 5.13 (1H, m), 6.60 (1H, br d, J = 7.6 Hz), and 7.32 (5H, m) ppm.

(3*R*,1′*S*)-**4**: ^{1}H nmr (200 MHz) δ: 0.03 (3H, s), 0.07 (3H, s), 0.80[5] (9H, s, *t*-Bu), 1.50 (3H, d, J = 7.0 Hz), 2.39 (1H, d of d, J = 5.3, 14.9 Hz), 2.59 (2H, d, J = 5.9 Hz), 3.68[5] (3H, s, -OMe), 4.52 (1H, m), 5.12 (1H, m), 6.60 (1H, br d, J = 7.6 Hz), and 7.31 (5H, m) ppm.

Acknowledgements

The generous support of the Natural Sciences and Engineering Research Council of Canada and the Bickell Foundation, and the awards of a Gollop Memorial and University of Toronto Open Fellowships (to L.K.-P.L.) are gratefully acknowledged.

1. L. K.-P. LAM and J. B. JONES. J. Org. Chem. In press.
2. (*a*) A. ENDO. Pharmacol. Ther. **31**, 257 (1987); J. Med. Chem. **28**, 401 (1985); (*b*) A. YAMAMOTO, H. SUDO, and A. ENDO. Atherosclerosis, **35**, 259 (1980).
3. (*a*) A. P. KOZIKOWSKI and C.-S. LI. J. Org. Chem. **52**, 3541 (1987); (*b*) P. A. GRIECO, R. LIS, R. E. ZELLE, and J. FINN. J. Am. Chem. Soc. **108**, 5908 (1986); (*c*) G. E. KECK and D. F. KACHENSKY. J. Org. Chem. **51**, 2487 (1986); (*d*) J. S. PRASAD, D. L. J. CLIVE, and G. V. J. DA SILVA. J. Org. Chem. **51**, 2717 (1986); (*e*) G. E. STOCKER, A. W. ALBERTS, P. S. ANDERSON, E. J. CRAGOE, A. A. DEAN, J. L. GILFILLAN, J. HIRSHFIELD, W. J. HOLTZ, W. F. HOFFMAN, J. W. HUFF, T. J. LEE, F. C. NOVELLO, J. D. PRUGH, C. S. ROONEY, R. C. SMITH, and A. K. WILLARD. J. Med. Chem. **29**, 170 (1986); (*f*) J. D. PRUGH, S. C. ROONEY, A. A. DEANA, and H. G. RAMJIT. J. Org. Chem. **51**, 648 (1986); (*g*) T. ROSEN and C. H. HEATHCOCK. J. Am. Chem. Soc. **107**, 3731 (1985); (*h*) S. D. BURKE, J. O. SAUNDERS, J. A. OPLINGER, and C. W. MURTIASHAW. Tetrahedron Lett. **26**, 1131 (1985).
4. A. SATO, A. OGISO, H. NOGUCHI, S. MITSUI, I. KANEKO, and Y. SHIMADA. Chem. Pharm. Bull. **28**, 1509 (1980).
5. L. K. P. LAM, R. A. H. F. HUI, and J. B. JONES. J. Org. Chem. **51**, 2047 (1986).
6. S. G. COHEN and E. KHEDOURI. J. Am. Chem. Soc. **83**, 4228 (1961).
7. T. ROSEN, M. WATANABE, and C. H. HEATHCOCK. J. Org. Chem. **49**, 3657 (1984).
8. T. IVERSEN and D. R. BUNDLE. J. Chem. Soc. Chem. Commun. 1240 (1981).
9. K. ADACHI, S. KOBAYASHI, and M. OHNO. Chimia, **40**, 311 (1986).
10. (*a*) G. SABBIONI and J. B. JONES. J. Org. Chem. **52**, 4565 (1987); (*b*) F. BJORKLING, J. BOUTELJE, F. GATENBECK, K. HULT, T. NORIN, and P. SZMULIK. Tetrahedron, **41**, 1347 (1986).
11. P. MOHR, N. WAESPE-SARCEVIC, and C. TAMM. Helv. Chim. Acta, **66**, 2501 (1983); P. MOHR, L. ROESSLEIN, and C. TAMM. Helv. Chim. Acta, **70**, 142 (1987).
12. D. W. BROOKS and J. T. PALMER. Tetrahedron Lett. **24**, 3059 (1983).
13. C. J. SIH and C. S. CHEN. Angew. Chem. Int. Ed. Engl. **23**, 570 (1984); W. R. SHIEH, A. S. GOPALAN, and C. J. SIH. J. Am. Chem. Soc. **107**, 2993 (1985).
14. D. W. BROOKS, N. C. DE LEE, and R. PEEVEY. Tetrahedron Lett. **41**, 2623 (1984).
15. Y. F. WANG, C. S. CHEN, G. GIRDAUKAS, and C. J. SIH. J. Am. Chem. Soc. **106**, 3695 (1984).
16. (*a*) F.-C. HUANG, L. F. H. LEE, R. S. D. METTAL, P. R. RAVIKUMAR, J. A. CHANG, C. J. SIH, E. CASOU, and C. R. ECK. J. Am. Chem. Soc. **97**, 4144 (1975); (*b*) C.-S. CHEN, Y. FUJIMOTO, and C. J. SIH. J. Am. Chem. Soc. **103**, 3580 (1981); C.-S. CHEN, Y. FUJIMOTO, G. GIRDAUKAS, and C. J. SIH. J. Am. Chem. Soc. **104**, 7294 (1982).
17. J. B. JONES, R. S. HINKS, and P. G. HULTIN. Can. J. Chem. **63**, 452 (1985).
18. R. K. BOECKMAN, JR. and J. C. POTENZA. Tetrahedron Lett. **26**, 1411 (1985).
19. W. GERRARD, M. F. LAPPERT, and B. A. MOUNTFIELD. J. Chem. Soc. 1529 (1959).
20. C. H. HEATHCOCK and R. RATCLIFFE. J. Am. Chem. Soc. **93**, 1746 (1971).

[5]Used in ee determination.

Can. J. Chem. Downloaded from www.nrcresearchpress.com by 93.93.197.157 on 09/07/12
For personal use only.

Reaction of $Me_3SnCu \cdot Me_2S$ with terminal alkynes. Preparation of 2-trimethylstannyl-1-alkenes

EDWARD PIERS AND J. MICHAEL CHONG

Department of Chemistry, University of British Columbia, 2036 Main Mall, University Campus, Vancouver, B.C., Canada V6T 1Y6

Received December 7, 1987

EDWARD PIERS and J. MICHAEL CHONG. Can. J. Chem. **66**, 1425 (1988).

Reaction of ω-substituted terminal alkynes **5** with (trimethylstannyl)copper(I)·dimethyl sulfide (**1**) under suitable reaction conditions provides good to excellent yields of the corresponding 2-trimethylstannyl-1-alkenes **6**.

EDWARD PIERS et J. MICHAEL CHONG. Can. J. Chem. **66**, 1425 (1988).

La réaction, dans des conditions appropriées, d'alcynes terminaux substitués en ω (**5**) avec du diméthylsulfure de (triméthylstannyl)cuivre (I) (**1**) fournit les triméthylstannyl-2 alcènes-1 correspondants (**6**) avec des rendements qui vont de bons à excellents.

[Traduit par la revue]

Can. J. Chem. Downloaded from www.nrcresearchpress.com by 93.93.197.157 on 09/07/12
For personal use only.

Introduction

The reactions of various alkylcopper(I) reagents with terminal alkynes have been investigated in detail and have been applied to the synthesis of structurally diverse alkenes, dienes, and related substances (1, 2). In general, the alkylcopper(I) species add to the triple bond in a regioselective, *cis* fashion, with the alkyl group and the copper moiety being transferred to C-2 and C-1, respectively, of the 1-alkyne substrate.

Fleming *et al.* (3) have reported that lower order silylcuprates such as $(Me_2PhSi)_2CuLi$ or $(Me_2PhSiCuCN)Li$ add to terminal alkynes with *cis* stereochemistry but with low regioselectivity. In contrast, the higher order cuprate $[(Me_2PhSi)_2CuCN]Li_2$ adds to 1-alkynes stereo- (*cis*) and regioselectively to produce intermediates in which the dimethyl(phenyl)silyl group is attached exclusively to C-1 (3). Thus, interestingly, the regioselectivity of silylcupration of terminal alkynes with the higher order silylcuprate is opposite to that of carbocupration with a variety of alkylcopper(I) reagents (1, 2).

Recently we described the preparation of a number of (trimethylstannyl)copper(I) reagents (e.g., **1**–**4**) and reported

$Me_3SnCu \cdot Me_2S$	$[Me_3SnCuY]Li$
1	**2** Y = SPh
	3 Y = C≡CC(OMe)Me_2
	4 Y = CN

that these species transfer efficiently the trimethylstannyl group to the β carbon of a variety of α,β-unsaturated carbonyl compounds (4). Ongoing investigations into the chemical reactivity of **1**–**4**, along with our desire to prepare ω-substituted 2-trimethylstannyl-1-alkenes, led to a study of the reaction of (trimethylstannyl)copper(I)·dimethyl sulfide (**1**) with 1-alkynes. We report herein the results of this study.[1]

Results and discussion

For our initial experiments, we chose the substrate 8-tetrahydropyranyloxy-1-octyne (**5***a*)[2] (see Chart 1). This compound is a relatively high-boiling, nonvolatile substance and, therefore, any starting material remaining in a crude product mixture would be detected very readily.

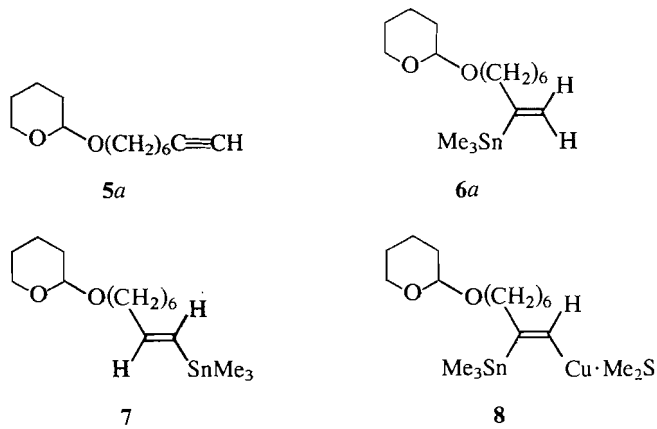

5*a* **6***a* **7** **8**

CHART 1

Reaction of the 1-alkyne **5***a* with 1.5 equivalents of $Me_3SnCu \cdot Me_2S$ (**1**) in tetrahydrofuran (THF) at −78°C for 6 h, followed by suitable work-up, afforded an oil that contained (gas–liquid chromatographic analysis), in addition to hexamethylditin, a 31:65:4 mixture of the starting material **5***a* and two products, respectively. The major product, obtained by flash chromatography (7) of the mixture on silica gel, was shown to be the 2-trimethylstannyl-1-alkene **6***a*. On the basis of subsequent work (*vide infra*), the minor product was, presumably, the (*E*)-1-trimethylstannyl-1-alkene **7**, although this substance was not isolated.

When the reaction of **5***a* with reagent **1** was allowed to proceed for 17 h (−78°C), the composition of the crude product mixture was very similar to that given above. On the other hand, much more starting material (crude product composition 74(**5***a*):25(**6***a*):1(**7**)) was recovered when the reaction mixture was quenched (NH_4Cl, H_2O) after only 2 h. When the reaction was carried out at a higher temperature (−63°C) for 6 h, the isolated material consisted of a 29:67:4 mixture of **5***a*, **6***a*, and **7**, respectively.

The fact that the reaction of reagent **1** with the terminal alkyne **5***a* did not go to completion even after extended reaction times seemed to indicate that the reaction is reversible and that the equilibrium favors only marginally the vinylcopper(I) intermediate **8**. Some evidence for a reversible process was obtained by treating the reaction mixture (after a reaction time of 6 h at −78°C) with iodine instead of a proton source. In this experiment, the starting material **5***a* was recovered in 94%

[1]For a preliminary account of this work, see ref. 5.

[2]This material is readily prepared by reaction of lithium acetylide – ethylenediamine complex with 1-bromo-6-tetrahydropyranyloxyhexane. We are very grateful to Professor L. Weiler and Ms. M. E. Alderdice for a generous gift of the latter compound (see also ref. 6).

TABLE 1. Conversion of 1-alkynes **5** into 2-trimethylstannyl-1-alkenes **6**

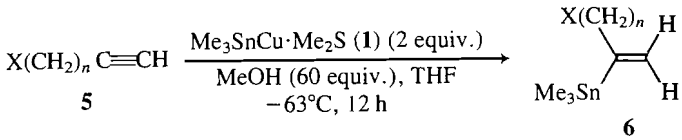

5 6

Entry	Substrate 5			Product 6 (yield, %)[a]	
		n	X		
1	*a*	6	OTHP[b]	*a*	(84)
2	*b*	4	OH	*b*	(85)
3	*c*	4	Cl	*c*	(80)
4	*d*	3	OSiBu^{t}Me$_2$	*d*	(82)
5	*e*	3	OH	*e*	(88)
6	*f*	3	Cl	*f*	(79)
7	*g*	2	OSiBu^{t}Me$_2$	*g*	(81)
8	*h*	2	OH	*h*	(82)[c]
9	*i*	2	Cl	*i*	(59)[d]
10[e]	*j*	1	OTHP[b]	*j*	(58)[f]
11[e]	*k*	1	OSiBu^{t}Me$_2$	*k*	(51)[g]

[a]Yields refer to isolated, purified product. The reactions were performed on a 0.2-mmol scale.

[b]THP = 2-tetrahydropyranyl.

[c]When the reaction was performed on a 1-mmol scale, **6***h* was obtained in 81% yield and (*E*)-4-trimethylstannyl-3-buten-1-ol (**9**) was isolated in 8% yield.

[d]Also isolated (preparative gas–liquid chromatography) was a small sample of (*E*)-4-chloro-1-trimethylstannyl-1-butene (**10**).

[e]This reaction was carried out at −78°C in the absence of methanol (see text).

[f]Also isolated (22%) was (*E*)-3-tetrahydropyranyloxy-1-trimethylstannylpropene (**11**).

[g]Also isolated (20%) was (*E*)-3-*tert*-butyldimethylsiloxy-1-trimethylstannylpropene (**12**).

yield. This result may be rationalized by postulating that the strong electrophile iodine pulls the equilibrium towards the starting material by destroying the (trimethylstannyl)copper(I) reagent **1** faster than it reacts with the intermediate vinylcopper(I) species **8**. We[3] and others (9) have made similar observations with the reactions of (trimethylstannyl)copper(I) reagents with α,β-acetylenic esters. The latter processes appear to be reversible since, although the initial equilibria probably lie far "to the right," treatment of the reaction mixtures with electrophiles such as bromine or iodine provides high yields of the starting materials (α,β-acetylenic esters). On the other hand, high yields of β-trimethylstannyl α,β-unsaturated esters are obtained if the reaction mixtures are treated with a proton source such as methanol (9–11).

It is known (4, 9–11) that (trimethylstannyl)copper(I) reagents are very weak bases in THF and react very slowly, if at all, with weak proton donors such as methanol. On the other hand, as noted above, vinylcopper(I) species formed by addition of (trimethylstannyl)copper(I) to α,β-acetylenic esters are readily protonated by methanol (9–11). Therefore, in the hope of "driving" the reaction of the 1-alkyne **5***a* with reagent **1** to completion, varying amounts of methanol were added to the reaction mixture. After some experimentation, it was found that **5***a* could be converted efficiently (84% yield) into the 2-trimethylstannyl-1-alkene **6***a* by reaction with 2 equivalents of reagent **1** (THF, −63°C, 12 h) in the presence of 60 equivalents of methanol. Subjection of other 1-alkynes **5** to the same reaction conditions gave good to excellent yields of the corresponding 2-trimethylstannyl-1-alkenes **6**. The appropriate data are summarized in Table 1.

A number of comments should be made regarding the chemical reactions summarized in Table 1. Some of the starting materials (**5***b*,*e*,*f*,*h*) are commercially available, while others were either known substances (**5***c*,*d*,*i*,*k*; references 12–15, respectively) or were prepared readily (**5***a*, see footnote 2; **5***g*, reaction of *tert*-butyldimethylsilyl chloride with **5***h* in the presence of imidazole in *N*,*N*-dimethylformamide; **5***j*, reaction of 2-propyn-1-ol with dihydropyran in the presence of *p*-toluenesulfonic acid in benzene) from known materials.

In the conversions involving substrates **5***a–h* (Entries 1–8), gas–liquid chromatographic analyses of the crude products showed that, in each case, a small amount (~2–10%) of a second product was present. However, when the product mixtures were subjected to (slow) column chromatography on silica gel, only the major products **6** were isolated. Apparently the minor products were rather unstable to chromatography and were destroyed on the column. Nevertheless, when the reaction summarized in Entry 8 was repeated on a larger scale (see footnote *c*, Table 1) and flash chromatography (7) was carried out on the resultant 9:1 mixture of products, the minor product was obtained in 8% yield. On the basis of its spectra, this material was identified as (*E*)-4-trimethylstannyl-3-buten-1-ol (**9**). Of particular note was the proton nuclear magnetic resonance (^{1}H nmr) spectrum of **9**, which exhibited signals due to two vicinal olefinic protons (H_A and H_B in **9**) with a mutual coupling constant of 18.5 Hz. Other excellent evidence for the constitution and stereochemistry of **9** was provided by the magnitude of the coupling constant ($^3J_{Sn-H} \sim 72$ Hz) between the ^{117}Sn and ^{119}Sn isotopes and H_B. This value is typical of alkenes having a trimethylstannyl group and a proton in a *cis* relationship (16).

On the basis of the isolation and characterization of the product **9** and analogous substances from reactions summarized in Entries 9–11 (*vide infra*), it is highly likely that the minor products formed from the reactions of **5***a–g* with $Me_3SnCu\cdot Me_2S$ (**1**) (Entries 1–7) are the corresponding (*E*)-1-trimethylstannyl-1-alkenes. Thus, in each case, there is a small amount of $Me_3SnCu\cdot Me_2S$ addition of the acetylenic linkage regioisomeric with that leading to the major product **6**. This addition evidently takes place with the expected (1–3) *cis* stereochemistry to give, after protonation of the vinylcopper(I) species, the corresponding (*E*)-1-alkene.

The additions of $Me_3SnCu\cdot Me_2S$ (**1**) to the 1-alkynes **5***i–k* (Entries 9–11) are significantly less regioselective than those involving substrates **5***a–h*. Reaction of **5***i* with **1** provides the 2-trimethylstannyl-1-alkene **6***i* and the (*E*)-1-trimethylstannyl-1-alkene **10** in a ratio of 4:1. A small sample of the latter substance, isolated by preparative gas–liquid chromatography, exhibited the expected spectral properties. In similar fashion, the reactions of $Me_3SnCu\cdot Me_2S$ (**1**) with the 2-propyn-1-ol derivatives **5***j* and **5***k* gave, in each case, a mixture of regioisomeric products (**6***j* and **11** (7:3) and **6***k* and **12** (72:28), respectively). The (*E*)-1-trimethylstannyl-1-alkenes **11** and **12** were obtained in yields of 22 and 20%, respectively, and were spectrally characterized. Thus, it is evident that placement of an electron-withdrawing group close to the triple bond reduces the regioselectivity of the addition of $Me_3SnCu\cdot Me_2S$ (**1**) to the alkyne function.

It should also be noted that the reactions of **1** with the substrates **5***j* and **5***k* proceed to completion at −78°C (6 h) in the *absence* of a proton source (methanol) (see footnote *e*, Table 1).

[3]Unpublished work carried out by J. M. Chong. See also ref. 8.

Can. J. Chem. Downloaded from www.nrcresearchpress.com by 93.93.197.157 on 09/07/12
For personal use only.

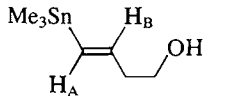

9

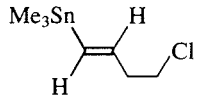

10

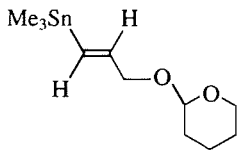

11

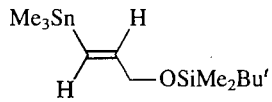

12

Thus, not only are these processes relatively nonregioselective, but they do not require the presence of a proton source for the efficient conversion of starting material to products.

The reaction characteristics summarized above may be rationalized qualitatively as follows. The addition of **1** to **5** is expected (1–3) to occur in a *cis* fashion and, if the reaction is reversible, the two possible regioisomeric intermediates **13** and **14** would be in equilibrium with one another. When the electronegative group X is separated from the triple bond by a number of carbon atoms, the intermediate **13** is appreciably more stable than **14**. Thus, not unexpectedly, it appears that the polar carbon–copper(I) bond prefers to be associated with the terminal carbon atom (C-1) rather than with C-2. However, when electronegative groups are placed near to the alkyne function (e.g., Cl in **5***i*, OR in **5***j* and **5***k*), the intermediate **14** is inductively stabilized to a greater extent than **13**.[4] Therefore, the energy difference between the two intermediates is reduced and the proportion of the (*E*)-1-trimethylstannyl-1-alkenes (**10**–**12**) in the product mixtures increases.

Finally, it may be noted that the electron-withdrawing effect of a propargylic OR group can also be invoked to rationalize the fact that the reactions of **1** with **5***j* and **5***k* (Table 1, Entries 10 and 11) proceed to completion even in the absence of a proton source. Thus, in these cases, the intermediates **13** and **14** (n = 1, X = OR) are, apparently, stabilized sufficiently to allow the (potentially) reversible reactions to lie very largely (or completely) to the right.

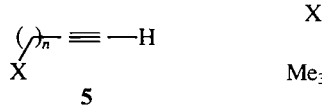

5

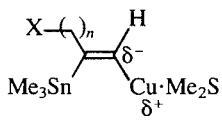

13

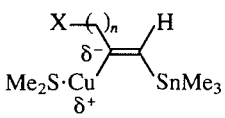

14

Conclusion

Reaction of (trimethylstannyl)copper(I)·dimethyl sulfide (**1**) with ω-substituted 1-alkynes **5** under suitable conditions provides good to excellent yields of the corresponding 2-trimethylstannyl-1-alkenes **6**. We have shown and reported in preliminary form (17) that some of the latter substances serve as excellent precursors of novel, synthetically useful bifunctional reagents. The details of these and other related studies will be reported in the near future.

[4]A referee suggested that coordination between the X and Cu atoms in **14** might assist in stabilizing the intermediate. This suggestion is entirely reasonable.

Experimental

General information

Distillation temperatures, which refer to short path (Kugelrohr) distillations, are uncorrected. Infrared (ir) spectra were recorded on Perkin Elmer models 710 or 710B spectrophotometers and were calibrated using the 1601 cm^{-1} band of a polystyrene film. Proton nuclear magnetic resonance (^1H nmr) spectra were taken on $CDCl_3$ solutions and were recorded at 80 MHz (Bruker WP-80 spectrometer) or at 400 MHz (Bruker WH-400 spectrometer). Signal positions are given in δ units and, for compounds containing Me_3Sn or *t*-$BuMe_2Si$ groups, were measured relative to the chloroform signal (δ 7.25). The tin–proton coupling constants (J_{Sn-H}) are given as an average of the ^{117}Sn and ^{119}Sn values. High resolution mass spectra were recorded with Kratos/AEI MS 50 or MS 902 spectrometers. For compounds containing the Me_3Sn group, molecular mass measurements are based on ^{120}Sn and were made on the (M^+ − Me) peak.

8-Tetrahydropyranyloxy-1-octyne (5a)

To a cool (10°C), stirred suspension of lithium acetylide – ethylenediamine complex (5.81 g, 60 mmol) in 40 mL of dry dimethyl sulfoxide (argon atmosphere) was added, dropwise, 13.25 g (50 mmol) of 1-bromo-6-tetrahydropyranyloxyhexane (see footnote 2). After the addition was complete, the dark brown slurry was warmed to room temperature and stirred for 2 h. Water (25 mL) was added dropwise. The mixture was diluted with water (100 mL) and then was extracted with ether (3 × 100 mL). The combined extracts were washed with water (3 × 50 mL), dried ($MgSO_4$), and concentrated. Distillation (air-bath temperature 105–110°C/0.9 Torr (1 Torr = 133.3 Pa)) of the residual yellow oil afforded 8.12 g (77%) of the 1-alkyne **5***a* as a colorless oil that exhibited ir (neat): 3290, 2100, 1140, 1120, 1080, 1035 cm^{-1}; ^1H nmr (80 MHz) δ: 1.2–1.9 (m, 14H), 1.93 (t, 1H, J = 2.5 Hz), 2.0–2.4 (m, 2H), 3.2–4.1 (m, 4H), 4.55 (br s, 1H). *Exact Mass* calcd. for $C_{13}H_{22}O_2$: 210.1620; found: 210.1607.

General procedure for the addition of $Me_3SnCu\cdot Me_2S$ (1) to 1-alkynes (5). Preparation of 2-trimethylstannyl-1-alkenes (6)

To a cold (−78°C), stirred solution of $Me_3SnCu\cdot Me_2S$ (**1**) (0.4 mmol) in 3 mL of dry THF (argon atmosphere) was added sequentially a dry THF solution (0.5 mL) of the 1-alkyne **5** (0.2 mmol) and dry methanol (0.5 mL, 12 mmol). The dark red reaction mixture was stirred at −78°C for 10 min and at −63°C for 12 h. Saturated aqueous ammonium chloride (pH 8) (5 mL) and ether (20 mL) were added and the mixture was allowed to warm to room temperature with vigorous stirring. Stirring was continued until the aqueous phase became deep blue. The layers were separated and the aqueous phase was extracted with ether (2 × 5 mL). The combined organic extracts were washed with saturated aqueous ammonium chloride (pH 8) (2 × 5 mL) and dried ($MgSO_4$). Removal of the solvent afforded a crude oil that, on the basis of gas–liquid chromatographic analysis, consisted of a mixture of hexamethylditin, a major product, and a minor (1–20%) product. Subjection of this oil to conventional or flash (7) column chromatography on silica gel, followed by concentration of the appropriate fractions and bulb-to-bulb distillation of the residual material, furnished the 2-trimethylstannyl-1-alkene **6**. In most cases, the minor product (the corresponding (*E*)-1-trimethylstannyl-1-alkene) was not isolated.

8-Tetrahydropyranyloxy-2-trimethylstannyl-1-octene (6a)

Following the general procedure, 8-tetrahydropyranyloxy-1-octyne (**5***a*) (39 mg, 0.2 mmol) was converted into a 95:5 mixture of two products. Subjection of the crude oil to flash chromatography on silica gel (2 × 15 cm column, elution with 1:20 ether – petroleum ether), followed by distillation (air-bath temperature 115–120°C/0.7 Torr) of the oil thus obtained gave 59 mg (84%) of the vinylstannane **6***a* as a colorless oil. This material exhibited ir (neat): 1140, 1120, 1080, 1040, 915, 770 cm^{-1}; ^1H nmr (80 MHz) δ: 0.13 (s, 9H, $^2J_{Sn-H}$ = 53 Hz), 1.1–1.9 (m, 14H), 2.1–2.4 (m, 2H), 3.2–4.0 (m, 4H), 4.5–4.7 (m, 1H), 5.12 (br d, 1H, J = 3 Hz, $^3J_{Sn-H}$ = 70 Hz), 5.63 (dt, 1H, J = 3, 1.5 Hz, $^3J_{Sn-H}$ = 156 Hz). *Exact Mass* calcd. for $C_{15}H_{29}O_2Sn$ (M^+ − Me): 361.1190; found: 361.1203.

Can. J. Chem. Downloaded from www.nrcresearchpress.com by 93.93.197.157 on 09/07/12
For personal use only.

Can. J. Chem. Downloaded from www.nrcresearchpress.com by 93.93.197.157 on 09/07/12
For personal use only.

*5-Trimethylstannyl-5-hexen-1-ol (**6**b)*

Conversion of 5-hexyn-1-ol (**5***b*) (24 mg, 0.2 mmol) into a 97:3 mixture of two products was accomplished via the general procedure. Column chromatography of the crude mixture on silica gel (7 g, elution with 1:3 ether – petroleum ether) and distillation (air-bath temperature 80–83°C/12 Torr) of the oil obtained afforded 54 mg (85%) of the alcohol **6***b* as a colorless oil that exhibited ir (neat): 3300 (br), 1060, 920, 770 cm^{-1}; ^1H nmr (80 MHz) δ: 0.17 (s, 9H, $^2J_{Sn-H}$ = 53 Hz), 1.25 (t, 1H, *J* = 5 Hz), 1.4–1.7 (m, 4H), 2.32 (br t, 2H, *J* = 7 Hz), 3.65 (dt, 2H, *J* = 5, 6 Hz), 5.14 (dt, 1H, *J* = 3, 1 Hz; $^3J_{Sn-H}$ = 70 Hz), 5.65 (dt, 1H, *J* = 3, 1.5 Hz; $^3J_{Sn-H}$ = 152 Hz). *Exact Mass* calcd. for $C_8H_{17}OSn$ (M^+ − Me): 249.0302; found: 249.0302.

*6-Chloro-2-trimethylstannyl-1-hexene (**6**c)*

By means of the general procedure, 6-chloro-1-hexyne (**5***c*) (12) (22.5 mg, 0.2 mmol) was converted into a 92:8 mixture of two products. Subjection of this material to column chromatography (4 g of silica gel, elution with petroleum ether) gave a colorless liquid that, upon distillation (air-bath temperature 55–58°C/12 Torr) afforded 44 mg (80%) of the chloro alkene **6***c*. This liquid exhibited ir (neat): 1440, 920, 775 cm^{-1}; ^1H nmr (80 MHz) δ: 0.17 (s, 9H, $^2J_{Sn-H}$ = 53 Hz), 1.4–2.0 (m, 4H), 2.32 (br t, 2H, *J* = 7 Hz, $^3J_{Sn-H}$ = 50 Hz), 3.55 (t, 2H, *J* = 6 Hz), 5.17 (dt, 1H, *J* = 2.5, 1 Hz; $^3J_{Sn-H}$ = 70 Hz), 5.67 (dt, 1H, *J* = 2.5, 1.2 Hz; $^3J_{Sn-H}$ = 150 Hz). *Exact Mass* calcd. for $C_8H_{16}{}^{35}ClSn$ (M^+ − Me): 264.9957; found: 264.9952.

*5-tert-Butyldimethylsiloxy-2-trimethylstannyl-1-pentene (**6**d)*

Following the general procedure, 5-*tert*-butyldimethylsiloxy-1-pentyne (**5***d*) (13) (45 mg, 0.2 mmol) was transformed into a 95:5 mixture of two products. Column chromatography (7 g silica gel, elution with petroleum ether) of this material provided a colorless oil that, upon distillation (air-bath temperature 98–103°C/12 Torr), yielded 68 mg (82%) of the ether alkene **6***d*; ir (neat): 1260, 1105, 840, 780 cm^{-1}; ^1H nmr (80 MHz) δ: 0.07 (s, 6H), 0.17 (s, 9H, $^2J_{Sn-H}$ = 53 Hz), 0.92 (s, 9H), 1.5–1.7 (m, 2H), 2.35 (br t, 2H, *J* = 7.5 Hz), 3.62 (t, 2H, *J* = 6 Hz), 5.16 (br d, 1H, *J* = 2.5 Hz, $^3J_{Sn-H}$ = 72 Hz), 5.68 (dt, 1H, *J* = 2.5, 1 Hz; $^3J_{Sn-H}$ = 152 Hz). *Exact Mass* calcd. for $C_{13}H_{29}OSiSn$ (M^+ − Me): 349.1010; found: 249.1011.

*4-Trimethylstannyl-4-penten-1-ol (**6**e)*

4-Pentyn-1-ol (**5***e*) (16 mg, 0.2 mmol) was converted, via the general procedure, into a 98:2 mixture of two products. The crude product was chromatographed on silica gel (7 g, elution with 1:3 ether–petroleum ether). Distillation (air-bath temperature 72–76°C/12 Torr) of the oil thus obtained produced 43 mg (88%) of the alcohol **6***e*, which exhibited ir (neat): 3300 (br), 1060, 920, 775 cm^{-1}; ^1H nmr (80 MHz) δ: 0.20 (s, 9H, $^2J_{Sn-H}$ = 53 Hz), 1.42 (t, 1H, *J* = 5.5 Hz), 1.5–1.9 (m, 2H), 2.40 (br t, 2H, *J* = 7 Hz), 3.68 (dt, 2H, *J* = 5.5, 6 Hz), 5.20 (dt, 1H, *J* = 2.5, 1 Hz; $^3J_{Sn-H}$ = 70 Hz), 5.72 (dt, 1H, *J* = 2.5, 1 Hz; $^3J_{Sn-H}$ = 150 Hz). *Exact Mass* calcd. for $C_7H_{15}OSn$ (M^+ − Me): 235.0145; found: 235.0134.

*5-Chloro-2-trimethylstannyl-1-pentene (**6**f)*

By means of the general procedure, 5-chloro-1-pentyne (**5***f*) (20 mg, 0.2 mmol) was converted into a 9:1 mixture of two products. Column chromatography (4 g of silica gel, elution with petroleum ether) of this material, followed by distillation (air-bath temperature 55–60°C/12 Torr) of the oil thus obtained, afforded 42 mg (79%) of the chloro alkene **6***f*; ir (neat): 1440, 920, 770 cm^{-1}; ^1H nmr (80 MHz) δ: 0.16 (s, 9H, $^2J_{Sn-H}$ = 53 Hz), 1.7–2.1 (m, 2H), 2.19 (br t, 2H, *J* = 7 Hz), 3.52 (t, 2H, *J* = 6.5 Hz), 5.22 (dt, 1H, *J* = 2.5, 1 Hz; $^3J_{Sn-H}$ = 70 Hz), 5.72 (dt, 1H, *J* = 2.5, 1 Hz; $^3J_{Sn-H}$ = 148 Hz). *Exact Mass* calcd. for $C_7H_{14}{}^{35}ClSn$ (M^+ − Me): 252.9840; found: 252.9823.

*4-tert-Butyldimethylsiloxy-2-trimethylstannyl-1-butene (**6**g)*

Following the general procedure, 4-*tert*-butyldimethylsiloxy-1-butyne (**5***g*) (35 mg, 0.2 mmol) was converted into a 92:8 mixture of two products. Column chromatography (8 g of silica gel, elution with petroleum ether) of the crude product and distillation (air-bath temperature 97–105°C/12 Torr) of the oil thus obtained furnished 54 mg (81%) of the alkene ether **6***g*; ir (neat): 1250, 1100, 920, 840, 775 cm^{-1}; ^1H nmr (80 MHz) δ: 0.08 (s, 6H), 0.16 (s, 9H, $^2J_{Sn-H}$ = 53 Hz), 0.92 (s, 9H), 2.50 (br t, 2H, *J* = 7 Hz), 3.65 (t, 2H, *J* = 7 Hz), 5.22 (br d, 1H, *J* = 2.5 Hz, $^3J_{SnH}$ = 71 Hz), 5.70 (dt, 1H, *J* = 2.5, 1 Hz; $^3J_{Sn-H}$ = 150 Hz. *Exact Mass* calcd. for $C_{12}H_{27}OSiSn$ (M^+ − Me): 335.0854; found: 335.0856.

*3-Trimethylstannyl-3-buten-1-ol (**6**h)*

(a) "Small" scale

Following the general procedure, 3-butyn-1-ol (**5***h*) (15 mg, 0.2 mmol) was converted into a 92:8 mixture of two products. Subjection of the crude product mixture to flash chromatography (6 g of silica gel, elution with 1:3 ether – petroleum ether), followed by distillation (air-bath temperature 65–70°C/12 Torr) of the oil thus obtained, produced 42 mg (82%) of the alcohol **6***h*; ir (neat): 3300 (br), 920, 770 cm^{-1}; ^1H nmr (80 MHz) δ: 0.18 (s, 9H, $^2J_{Sn-H}$ = 53 Hz), 1.46 (t, 1H, *J* = 6 Hz), 2.55 (br t, 2H, *J* = 6 Hz, $^3J_{Sn-H}$ = 51 Hz), 3.66 (dt, 2H, *J* = 6, 6 Hz), 5.32 (dt, 1H, *J* = 1.2, 1 Hz; $^3J_{Sn-H}$ = 70 Hz), 5.77 (dt, 1H, *J* = 1.2, 1 Hz; $^3J_{Sn-H}$ = 148 Hz). *Exact Mass* calcd. for $C_6H_{13}OSn$ (M^+ − Me): 220.9989; found: 220.9986.

(b) "Large" scale

To a cold (−78°C), stirred solution of $Me_3SnCu\cdot Me_2S$ (**1**) (2.0 mmol) in 15 mL of dry THF (argon atmosphere) was added sequentially a dry THF solution (1 mL) of 3-butyn-1-ol (**5***h*) (70 mg, 1.0 mmol) and methanol (2.5 mL, 62 mmol). The dark red reaction mixture was stirred at −78°C for 10 min and at −63°C for 12 h. Work-up as described in the general procedure produced a colorless oil that consisted of hexamethylditin and a 9:1 mixture of two products (gas–liquid chromatographic analysis). Flash chromatography (17 g of silica gel, elution with 1:3 ether – petroleum ether) gave 191 mg (81%) of the less polar, major product **6***h* (spectra identical with those summarized above) and 19 mg (8%) of the more polar, minor product **9** (distillation temperature 65–70°C/12 Torr). The latter oil exhibited ir (neat): 3350 (br), 1600, 1050, 990, 775 cm^{-1}; ^1H nmr (400 MHz) δ: 0.13 (s, 9H, $^2J_{Sn-H}$ = 54 Hz), 1.45 (t, 1H, *J* = 6 Hz), 2.42 (ddt, 2H, *J* = 6.2, 1.2, 6 Hz), 3.69 (dt, 2H, *J* = 6, 6 Hz), 5.96 (dt, 1H, *J* = 18.5, 6.2 Hz; $^3J_{Sn-H}$ = 72 Hz), 6.11 (dt, 1H, *J* = 18.5, 1.2 Hz; $^2J_{Sn-H}$ = 84 Hz). *Exact Mass* calcd. for $C_6H_{13}OSn$ (M^+ − Me): 220.9989; found: 220.9994.

*4-Chloro-2-trimethylstannyl-1-butene (**6**i) and (E)-4-chloro-1-trimethylstannyl-1-butene (**10**)*

Following the general procedure, 4-chloro-1-butyne (**5***i*) (14) (17 mg, 0.2 mmol) was transformed into a mixture of two products in a ratio of 4:1. Chromatography of the crude mixture on silica gel (8 g, elution with petroleum ether), followed by distillation (air-bath temperature 55–60°C/12 Torr) of the less polar oil gave 28 mg (59%) of the major product **6***i* as a colorless oil; ir (neat): 1615, 925, 775 cm^{-1}; ^1H nmr (80 MHz) δ: 0.24 (s, 9H, $^2J_{Sn-H}$ = 53 Hz), 2.50 (br t, 2H, *J* = 7 Hz, $^3J_{Sn-H}$ = 47 Hz), 3.58 (t, 2H, *J* = 7 Hz), 5.32 (dt, 1H, *J* = 2.2, 1 Hz; $^3J_{Sn-H}$ = 68 Hz), 5.78 (dt, 1H, *J* = 2.2, 1 Hz; $^3J_{Sn-H}$ = 144 Hz). *Exact Mass* calcd. for $C_6H_{12}{}^{35}ClSn$ (M^+ − Me): 238.9650; found: 238.9651.

A small sample of the minor, more polar product **10** was obtained from the appropriate chromatography fractions by preparative gas–liquid chromatography. This material exhibited ir ($CHCl_3$): 1600, 780 cm^{-1}; ^1H nmr (400 MHz) δ: 0.13 (s, 9H, $^2J_{Sn-H}$ = 54 Hz), 2.60 (ddt, 2H, *J* = 1.2, 6, 7 Hz), 3.57 (t, 2H, *J* = 7 Hz), 5.96 (dt, 1H, *J* = 18.5, 6 Hz; $^3J_{Sn-H}$ = 71 Hz), 6.11 (dt, 1H, *J* = 18.5, 1.2 Hz; $^2J_{Sn-H}$ = 82 Hz). *Exact Mass* calcd. for $C_6H_{12}{}^{35}ClSn$ (M^+ − Me): 238.9650; found: 238.9657.

*3-Tetrahydropyranyloxy-2-trimethylstannylpropene (**6**j) and (E)-3-tetrahydropyranyloxy-1-trimethylstannylpropene (**11**)*

To a cold (−78°C), stirred solution of $Me_3SnCu\cdot Me_2S$ (**1**) (1.5 mmol) in 12 mL of dry THF (argon atmosphere) was added a solution of 3-tetrahydropyranyloxypropyne (**5***j*) (140 mg, 1 mmol) in dry THF (1 mL) and the dark red mixture was stirred at −78°C for 6 h. Methanol

(0.5 mL), saturated aqueous ammonium chloride (pH 8) (5 mL), and ether (40 mL) were added and the vigorously stirred mixture was allowed to warm to room temperature. Stirring was continued until the aqueous phase became deep blue. The phases were separated and the organic phase was washed with saturated aqueous ammonium chloride (pH 8) (2 × 10 mL) and then was dried ($MgSO_4$). Removal of the solvent gave an oil that contained hexamethylditin and two products in a ratio of 7:3 (gas–liquid chromatographic analysis). Flash chromatography of this material on silica gel (2 × 15 cm column, elution with 1:15 ether – petroleum ether) provided 177 mg (58%) of the major, less polar product **6***j* (distillation temperature 103–110°C/12 Torr) and 67 mg (22%) of the minor, more polar product **11** (distillation temperature 105–115°C/12 Torr).

Compound **6***j* exhibited ir (neat): 1140, 1120, 1030, 775 cm^{-1}; ^1H nmr (80 MHz) δ: 0.20 (s, 9H, $^2J_{Sn-H}$ = 54 Hz), 1.4–2.0 (m, 6H), 3.70 (m, 2H), 4.28 (m, 2H), 4.67 (m, 1H), 5.30 (dt, 1H, J = 2.5, 1.5 Hz; $^3J_{Sn-H}$ = 71 Hz), 5.86 (dt, 1H, J = 2.5, 1 Hz; $^3J_{Sn-H}$ = 146 Hz). *Exact Mass* calcd. for $C_{10}H_{19}O_2Sn$ (M^+ − Me): 291.0407; found: 291.0408.

Compound **11** exhibited ir (neat): 1600, 1030, 910, 875, 775 cm^{-1}; ^1H nmr (400 MHz) δ: 0.14 (s, 9H, $^2J_{Sn-H}$ = 54 Hz), 1.50–1.68 (m, 4H), 1.70–1.79 (m, 1H), 1.82–1.93 (m, 1H), 3.48–3.54, 3.86–3.92 (m, m, 1H each), 4.01 (ddd, 1H, J = 13, 5.2, 1.2 Hz; $^4J_{Sn-H}$ = 11 Hz), 4.27 (ddd, 1H, J = 13, 4.8, 1.5 Hz; $^4J_{Sn-H}$ = 11 Hz), 4.65 (t, 1H, J = 7 Hz), 6.11 (ddd, 1H, J = 19, 5.2, 4.8 Hz; $^3J_{Sn-H}$ = 71 Hz), 6.29 (ddd, 1H, J = 19, 1.2, 1.5 Hz; $^2J_{Sn-H}$ = 82 Hz). *Exact Mass* calcd. for $C_{10}H_{19}O_2Sn$ (M^+ − Me): 291.0407; found: 291.0406.

*3-*tert*-Butyldimethylsiloxy-2-trimethylstannylpropene (**6**k) and (*E*)-3-*tert*-butyldimethylsiloxy-1-trimethylstannylpropene (**12**)*

To a cold (−78°C), stirred solution of $Me_3SnCu \cdot Me_2S$ (**1**) (1.3 mmol) in 10 mL of dry THF (argon atmosphere) was added a solution of 3-*tert*-butyldimethylsiloxypropyne (**5***k*) (15) (147 mg, 0.86 mmol) in 1 mL of dry THF and the dark red mixture was stirred at −78°C for 6 h. Saturated aqueous ammonium chloride (pH 8) (5 mL) and ether (40 mL) were added and further work-up proceeded as described above. Gas–liquid chromatographic analysis of the crude product showed that it consisted of a mixture of hexamethylditin and two products in a ratio of 72:28. Flash chromatography of this material on silica gel (2 × 15 cm column, elution with petroleum ether) provided 161 mg (51%) of the less polar major product (**6***k*) (distillation temperature 90–95°C/12 Torr) and 59 mg (20%) of the more polar minor product **12** (distillation temperature 93–98°C/12 Torr).

Compound **6***k* exhibited ir (neat): 1460, 1260, 1080, 860, 840, 780 cm^{-1}; ^1H nmr (80 MHz) δ: 0.07 (s, 6H), 0.15 (s, 9H, $^2J_{Sn-H}$ = 54 Hz), 0.92 (s, 9H), 4.32 (dd, 2H, J = 2, 1 Hz; $^3J_{Sn-H}$ = 33 Hz), 5.21 (dt, 1H, J = 2.5, 2 Hz; $^3J_{Sn-H}$ = 71 Hz), 5.81 (dt, 1H, J = 2.5, 1 Hz; $^3J_{Sn-H}$ = 148 Hz). *Exact Mass* calcd. for $C_{11}H_{25}OSiSn$ (M^+ − Me): 321.0697; found: 321.0686.

Compound **12** exhibited ir (neat): 1600, 1260, 1130, 1100, 850, 780 cm^{-1}; ^1H nmr (400 MHz) δ: 0.09 (s, 6H), 0.14 (s, 9H, $^2J_{Sn-H}$ = 54 Hz), 0.94 (s, 9H), 4.20 (dd, 2H, J = 4.1, 1.6 Hz; $^4J_{Sn-H}$ = 14 Hz), 6.08 (dt, 1H, J = 19, 4.1 Hz; $^3J_{Sn-H}$ = 73 Hz), 6.24 (dt, 1H, J = 19, 1.6 Hz, $^2J_{Sn-H}$ = 84 Hz). *Exact Mass* calcd. for $C_{11}H_{25}OSiSn$ (M^+ − Me): 321.0697; found: 321.0698.

Acknowledgements

Financial support and a postgraduate scholarship (to J.M.C.) from the Natural Sciences and Engineering Research Council of Canada are gratefully acknowledged.

1. J. F. Normant and A. Alexakis. Synthesis, 841 (1981).
2. E. Erdik. Tetrahedron, **40**, 641 (1984).
3. I. Fleming, T. W. Newton, and T. Roessler. J. Chem. Soc. Perkin Trans. 1, 2527 (1981).
4. E. Piers, H. E. Morton, and J. M. Chong. Can. J. Chem. **65**, 78 (1987).
5. E. Piers and J. M. Chong. J. Chem. Soc. Chem. Commun. 934 (1983).
6. D. Savoia, E. Tagliavini, C. Trombini, and A. Umani-Ronchi. J. Org. Chem. **45**, 3227 (1980).
7. W. C. Still, M. Kahn, and A. Mitra. J. Org. Chem. **43**, 2923 (1978).
8. E. Piers and J. M. Chong. J. Org. Chem. **47**, 1602 (1982).
9. S. D. Cox and F. Wudl. Organometallics, **2**, 184 (1983).
10. E. Piers and H. E. Morton. J. Org. Chem. **45**, 4263 (1980).
11. E. Piers, J. M. Chong, and H. E. Morton. Tetrahedron Lett. **22**, 4905 (1981).
12. C. Dupuy and J.-M. Surzur. Bull. Soc. Chim. Fr. II-353 (1980).
13. C. H. Lin and S. J. Stein. Synth. Commun. **6**, 503 (1976).
14. J. D. Roberts and R. H. Mazur. J. Am. Chem. Soc. **73**, 2509 (1976).
15. M. W. Logue and K. Teng. J. Org. Chem. **47**, 2549 (1982).
16. A. J. Leusink, H. A. Budding, and J. W. Marsman. J. Organomet. Chem. **9**, 285 (1967).
17. E. Piers and V. Karunaratne. J. Org. Chem. **48**, 1774 (1983); J. Chem. Soc. Chem. Commun. 935 (1983); Can. J. Chem. **62**, 629 (1984); J. Chem. Soc. Chem. Commun. 959 (1984); E. Piers and B. W. A. Yeung. J. Org. Chem. **49**, 4567 (1984); Can. J. Chem. **64**, 2475 (1986).

Can. J. Chem. Downloaded from www.nrcresearchpress.com by 93.93.197.157 on 09/07/12
For personal use only.

Thermolysis of trimethylsilyl esters: an ultraviolet photoelectron spectroscopy study

NICK HENRY WERSTIUK, MICHAEL A. BROOK, AND PETER HÜLSER
Department of Chemistry, McMaster University, Hamilton, Ont., Canada L8S 4M1

Received August 19, 1987

NICK HENRY WERSTIUK, MICHAEL A. BROOK, and PETER HÜLSER. Can. J. Chem. **66**, 1430 (1988).

The thermolytic behaviour of trimethylsilyl trifluoromethanesulfonate, **1**, trimethylsilyl trifluoroacetate, **2**, and trimethylsilyl acetate, **3**, has been investigated by ultraviolet photoelectron spectroscopy. Acetate **3** undergoes decomposition only to a small extent at 800°C via the mechanism shown in Scheme 1 (X = Si); only acetic acid and starting material are detected. In contrast

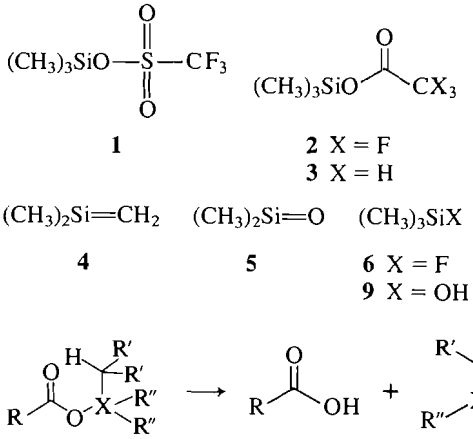

SCHEME 1

with this result, **1** and **2** decompose completely at 725–800°C and yield products which cannot be derived via the mechanism shown in Scheme 1. Evidence is presented to support our proposal that the thermolysis of **1** yields trimethylsilyl fluoride, **6**, and difluorooxathirane dioxide, **7**, as primary products. The photoelectron spectra of **1, 2, 3, 6** and trimethylsilanol, **9**, are presented. Molecular orbital eigenvalues of dimethylsilene, **4**, dimethylsilanone, **5** (calculated using AMPAC and Gaussian 82), **6** and **9** (AMPAC) are reported. Molecular orbital contour diagrams are given for selected MOs of **6** and **9**.

NICK HENRY WERSTIUK, MICHAEL A. BROOK et PETER HÜLSER. Can. J. Chem. **66**, 1430 (1988).

Faisant appel à la spectroscopie ultraviolette photoélectronique, on a étudié le comportement thermolytique des trifluorométhanesulfonate (**1**), trifluoroacétate (**2**) et acétate (**3**) de triméthylsilyle. A 800°C, l'acétate **3** ne subit qu'une faible décomposition qui se produit par le biais de départ. Par opposition à ce résultat, les composés **1** et **2** se décomposent complètement, à des températures allant de 725 à 800°C, et ils fournissent des produits dont on ne peut pas expliquer la formation en se basant sur le schéma 1. On présente des données qui supportent notre hypothèse selon laquelle la thermolyse du composé **1**

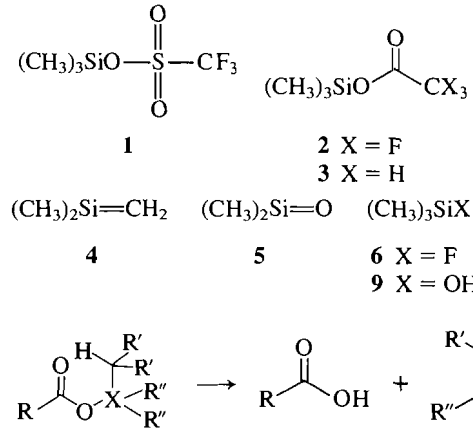

SCHÉMA 1

fournirit du fluorure de triméthylsilyle (**6**) ainsi que le dioxyde du difluorooxathirane (**7**) comme produits primaires. On rapporte les spectres photoélectroniques des composés **1, 2, 3, 6** ainsi qui du triméthylsilanol (**9**). On rapporte aussi les valeurs fondamentales des orbitales moléculaires du diméthylsilène (**4**), de la diméthylsilanone (**5**) (calculées à l'aide de l'AMPAC et de la Gaussienne 82), ainsi que des composés **6** et **9** (AMPAC). On rapporte enfin des diagrammes de contour d'orbitales moléculaires choisies des composés **6** et **9**.

[Traduit par la revue]

Can. J. Chem. Downloaded from www.nrcresearchpress.com by 93.93.197.157 on 09/07/12
For personal use only.

Can. J. Chem. Downloaded from www.nrcresearchpress.com by 93.93.197.157 on 09/07/12
For personal use only.

Introduction

The thermolysis of carboxylic acid esters has been the subject of extensive mechanistic studies (1, 2). In general, the reaction occurs via a six-membered ring transition state and yields an alkene and a carboxylic acid (Scheme 1, X = C). Although tetrakis (trifluoroacetates) of silicon, germanium, tin, lead, and titanium have been shown to decompose thermally via a different mechanism (3), there have been no reported studies of silyl esters such as trimethylsilyl trifluoromethanesulfonate **1** (TMSOTf), trimethylsilyl trifluoroacetate, **2** (TMSTFA), and trimethylsilyl acetate, **3** (TMSOAc).

In our continuing studies on transients (4) in the gas phase, the thermolyses of **1**, **2**, and **3** were investigated by ultraviolet photoelectron spectroscopy (UPS) to establish whether or not dimethylsilene, **4**, and/or dimethylsilanone, **5**, both highly reactive, elusive molecules, are formed by thermolysis of the esters. The former — only its lowest IE (7.98 eV) has been obtained experimentally (5) — would be expected to arise via a typical ester decomposition of **2** or **3** (Scheme 1, X = Si). The latter, not yet detected in the gas phase by UPS, could be formed via the mechanism shown in Scheme 2: cleavage of the relatively weak SiC bond (~318 kJ/mol) (6) of **2** or **3** would yield an oxygen stabilized silyl radical which by β-scission would give **5** and the acyl radical. If the same mechanism were to apply to the thermal decomposition of **1**, the corresponding sulfonyl radical and **5** would be formed.

In this paper we show that while acetate **3** decomposes thermally via the classical route, the thermolyses of **1** and **2**, driven by silicon–fluorine bond formation, proceed via a different mechanism.

Experimental

Preparation of silyl compounds

TMSOTf, **1**, obtained from Aldrich Chem. Co. was used without further purification upon freshly opening a vial.

TMSTFA, **2**, was prepared using a modified procedure of Sartori (3). Trimethylsilyl chloride (3.42 g, 32 mmol) and trifluoroacetic acid (3.22 g, 28 mmol) were heated at reflux for 2 h during which time the temperature of the vapor phase increased from 57 to 90°C. TMSTFA (4.28 g, 79.9%) was distilled from the reaction mixture. ^{1}H nmr ($CDCl_3$): δ 0.35 (s, 9H). **1** and **2** displayed a single peak in the ^{1}H nmr and on this basis were assumed to be >95% pure.

TMSOAc **3** was prepared as described by Schuyten *et al.* (7) and purified by preparative gas chromatography (GC).

TMSF, **6**, and TMSOH, **9**, were prepared according to the procedure of Sommer *et al.* (8); TMSOH was purified by preparative gas chromatography.

Thermolysis studies

The thermolysis apparatus and the photoelectron (p.e.) spectrometer used in this study are described in a previous publication (4). Thermolyses were carried out at a pressure of approximately 1×10^{-3} Torr. In each case, a p.e. spectrum of the total thermolysate was obtained initially. Subsequently, the thermolysate was condensed in a U-trap cooled with liquid nitrogen and the components separated by a low-temperature distillation (4) which was monitored by recording p.e. spectra.

Theoretical calculations

Calculations of the molecular orbital eigenvalues (MOEs) and molecular orbital contour plots (MOCs) were carried out on VAX 8600 and 11/780 computers. The initial geometries of TMSOH and dimethylsilanone were obtained using the molecular modelling packages CHEMGRAF (9) or MODEL (10). These provide an interactive graphics environment for performing molecular mechanics structural energy minimizations using MODEL generalized force constants or MM2/MMP2 force constants (11). This procedure greatly facilitated construction of input files for the AMPAC calculations (12). For TMSF the experimental geometry was used (13), and for dimethylsilene the DZ + d SCF structure (14) was used. The final geometries and MOEs of **1–9** were calculated using the MNDO hamiltonian of AMPAC. MOCs of TMSF and TMSOH were obtained using the programs DENSITY (density plots from MOPAC (QCPE 455) calculations, ref. 15) which uses an output file from AMPAC, and DRAW (molecular drawing program (QCPE 456), ref. 16) which generates a plot of the contours. The *ab initio* calculations on **4** and **5** were carried out using GAUSSIAN 82 (17) with a 6-31G* basis set. MOCs were displayed on an IBM XT compatible microcomputer, equipped with a Princeton HX-12E color monitor and a Genoa Spectra enhanced graphics card, running Grafpoint TGRAF-05 software (18). This system emulates a Tektronix 4105 color terminal. Plots of the MOCs were obtained by a screen dump to a dot-matrix printer.

Results

Thermolysis of TMSOTf, 1

The p.e. spectra of **1** and its thermolysate obtained at 725°C are given in Fig. 1 as 1(*A*) and 1(*B*), respectively. It is evident that conversion to products is essentially complete under these conditions. When the thermolysate was trapped by liquid nitrogen as 300 scans were accumulated over several hours, no discernible spectrum over background was obtained. When a low-temperature distilation was carried out, spectra 1(Cl) and 1(D) were obtained after only a slight warming of the trap. Subtraction of spectrum 1(D) from 1(Cl) yielded 1(C2) which corresponds closely to the spectrum of $CH_2{=}CF_2$ (19). Based on the number of scans accumulated during the distillation of the product giving rise to spectrum 1(Cl), however, it is a minor component. 1(D) is the spectrum of COF_2 (20). Further warming yielded spectrum 1(E1), then 1(F). Subtraction of spectrum 1(F) from 1(E1) yielded 1(E2), which is the spectrum of SO_2 (21). The identity of the component giving rise to spectrum 1(F), a major product of thermolysis, was initially unknown. Since the p.e. spectra of TMSF and TMSOH were also unknown prior to this study, the compounds were prepared from $(CH_3)_3SiCl$ and the molecular orbital eigenvalues (MOEs) calculated using AMPAC and are given in Tables 1 and 2, respectively. While the eigenvalues of these compounds correlated reasonably well with the experimentally determined IEs, the p.e. spectrum of TMSF, **6** was identical to spectrum 1(F) thereby identifying the fluoride as a major product of thermolysis. The p.e. spectrum of TMSOH is shown in Fig. 2.

Thermolysis of TMSTFA, 2

The p.e. spectra of **2** and its thermolysate, produced at 790°C, are shown in Fig. 3 as 3(A) and 3(B), respectively. As was the case in the thermolysis of **1**, TMSF, identified by the broad band at 11 eV and the general features of spectrum 3(B), is a major product; CO_2 (IEs 13.8, 17.5–18.0, 18.1), and what appears to be CO (IEs 14.0, 16.5–17.5) (21) are the other directly identifiable products. To obtain a more accurate analysis of the products, the thermolysate was trapped by liquid nitrogen as 200 scans were accumulated. Although a spectrum with a good signal-to-noise ratio was obtained, it did not correspond to CO, CHF_3, CF_4, $CH_3{-}CF_3$, or $CF_3{-}CF_3$, all possible products of thermolysis. As the trap was warmed slowly, spectrum 3(C) was obtained, followed by spectrum 3(D), 3(E1), 3(F), and 3(G). Spectra 3(C) and 3(D) are composed of CO_2, COF_2 (see 1(D)), and $CF_2{=}CF_2$, the latter identified by the broad peak with fine structure centered at approximately 10.5 eV and differentiated

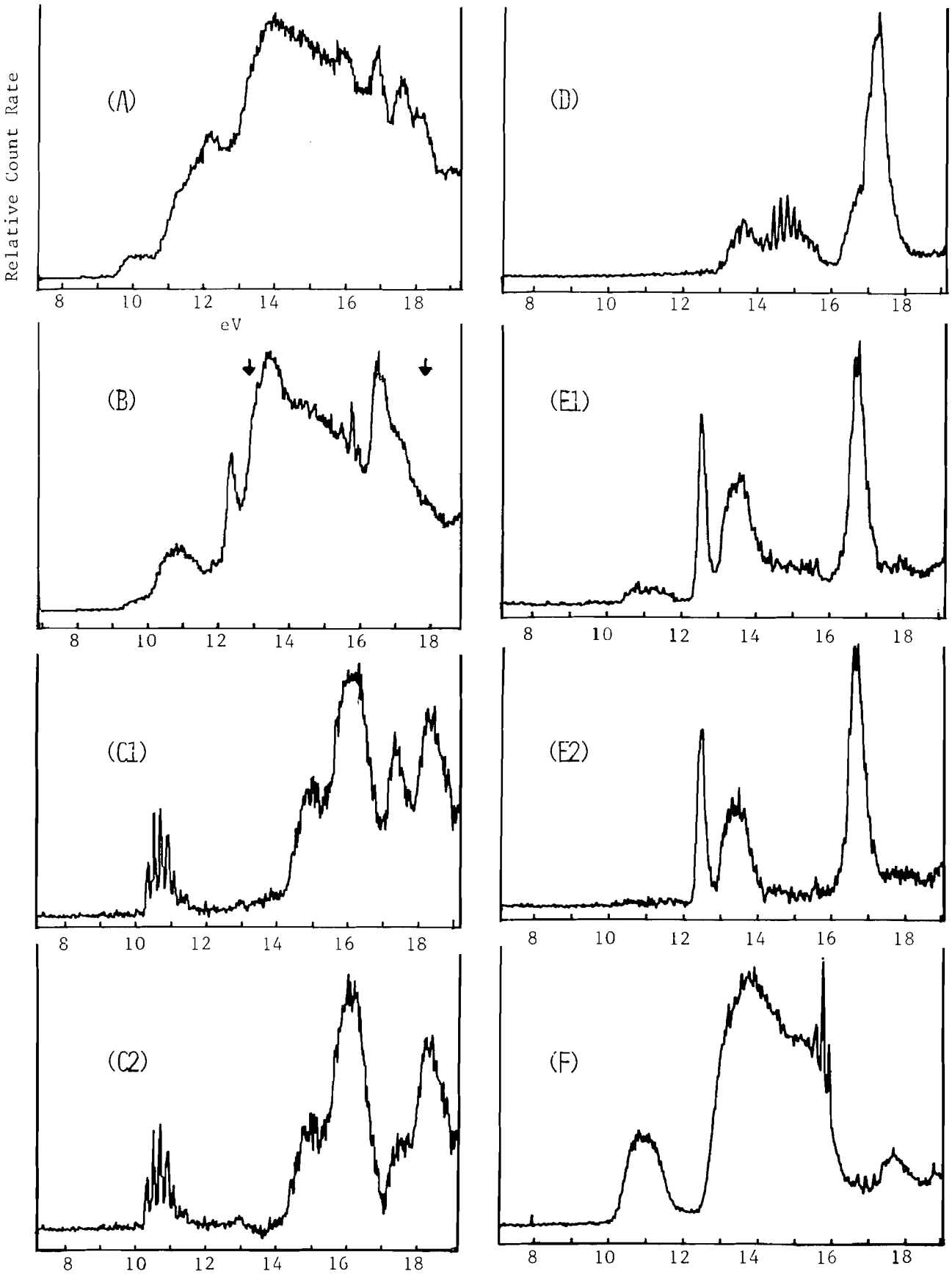

FIG. 1. 1(A), p.e. spectrum of **1**; 1(B), p.e. spectrum of the thermolysate of **1**; spectra of the components of the thermolysate: 1(C1); 1(C2), CH_2F_2; 1(D), COF_2; 1E(I); 1E(2), SO_2; 1(F), TMSF.

Can. J. Chem. Downloaded from www.nrcresearchpress.com by 93.93.197.157 on 09/07/12
For personal use only.

Can. J. Chem. Downloaded from www.nrcresearchpress.com by 93.93.197.157 on 09/07/12
For personal use only.

TABLE 1. Molecular orbital eigenvalues and ionization energies of trimethylsilyl flouride, **6**

Eigenvalue		
MNDO[a,b]	6-31G*[a,b]	IE (eV)
11.31	11.86 (10.91)[c]	11.0
11.31	11.86 (10.91)	
13.72	14.46 (13.30)	
13.89	14.68 (13.51)	
14.00	14.68 (13.51)	
14.00	14.89 (13.70)	
14.21	15.30 (14.07)	12.8–16.3
14.21	15.30 (19.07)	
14.59	16.01 (14.73)	
15.26	17.47 (16.07)	
15.26	17.47 (16.07)	
16.26	14.59 (18.02)	

[a]The experimental geometry was used.
[b]Only MOEs less than 21 eV are reported.
[c]92% of Koopman's theorem.

TABLE 2. Molecular orbital eigenvalues and ionization energies of trimethylsilanol, **9**

MNDO[a,b]	IE (eV)
10.92	~10.0
11.22	~10.5
12.67	12.2
12.68	
13.66	
13.76	
13.91	12.5–16.0
14.03	
14.19	
14.37	
14.54	
18.28	17.8

[a]Only MOEs less than 21 eV are reported.
[b]The MNDO optimized geometry was used in the calculation.

from $CF_2{=}CH_2$ (see Fig. 1 (C2)) by the fact that the σ and fluorine lone pair bands appear at higher energies than the corresponding bands for $CF_2{=}CH_2$ (19). Spectra 3(E1) and 3(F) correspond to CO_2 (21) and 3(G) is the spectrum of TMSF. Subtraction of 3(F) from 3(E1) gave 3(E2) which is the spectrum of COF_2 (20). Although it appears that CO is one of the products (*vide supra*), it was not detected during the trapping or during the low-temperature distillation. The reason for this is not obvious. To establish whether or not the α-lactone, **8** (Scheme 4) — a potential intermediate — could be detected, TMSTFA was thermolyzed at 720°C and the products were trapped over a period of 3 h. Figure 4 is the spectrum of the thermolysate before the products were trapped. The small peak at 18.1 eV establishes that only a small amount of CO_2 is produced at this temperature. Low-temperature distillation of the thermolysate yielded no additional components other than those observed at 790°C.

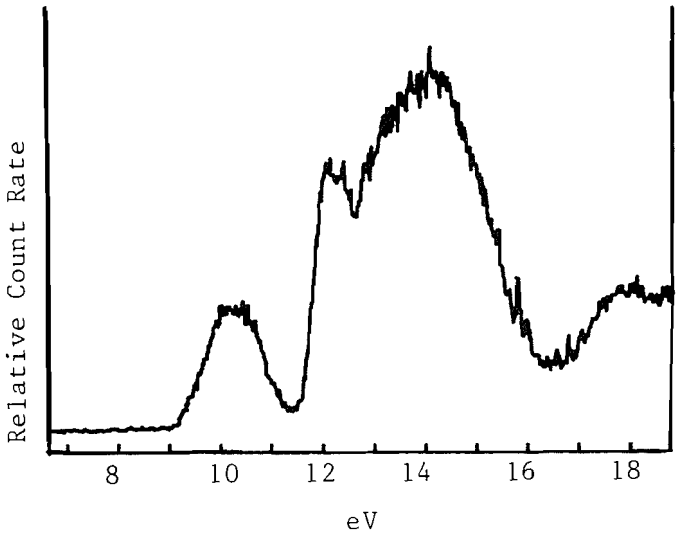

FIG. 2. Photoelection spectrum of TMSOH.

Thermolysis of TMSOAc, 3

Spectra 5(A) and 5(B) of Fig. 5 correspond to **3** and its thermolysate obtained at 800°C. It is evident from these spectra that TMSOAc decomposes only to a minor extent under the conditions employed in this study. Subtraction of 5(A) from 5(B) yielded a spectrum with a low signal-to-noise ratio (IEs 10.9, 12.1, 15.0, and 17.1) which identified acetic acid as a product (21).

Theoretical calculations

The MOEs calculated for TMSF, TMSOH, dimethylsilene **4**, and dimethylsilanone **5**, along with the experimentally obtained IEs for TMSF and TMSOH, are given in Tables 1–4. Figures 6 and 7 show selected MOCs for TMSF and TMSOH obtained using AMPAC, DENSITY and DRAW.

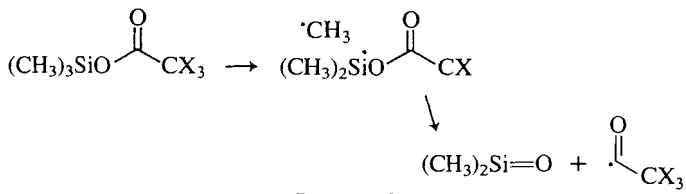

SCHEME 2

Discussion and conclusions

Thermolysis of TMSOTf

This study establishes clearly that the strong SiF bond (~807 kJ mol^{-1}) (6) determines the course of the thermolyses of TMSOTf and TMSTFA. Possible mechanisms for thermolysis of TMSOTf and TMSTFA are shown in Scheme 3 (pathways *a* and *b*) and Scheme 4 (pathways *a* and *b*), respectively. In the case of TMSOTf, it is significant that no SO_3 is observed in the spectrum of the thermolysate or during the low temperature distillation; SO_3 exhibits sharp bands at 12.8 and 17.9 eV indicated by the arrows in spectrum 1(B) as well as broad bands at 13.8 and 14.9 (22, 23). If TMSOTf decomposes via pathway *a* (Scheme 3), then COF_2 could be formed by singlet $:CF_2$ stripping oxygen from SO_3. The absence of SO_3 in the thermolysis mixture requires that the reaction be nearly quantitative, an unreasonable expectation based on the high reactivity and instability of $:CF_2$. That is, $:CF_2$ would also be expected to react via other channels such as dimerization, polymerization, and inser-

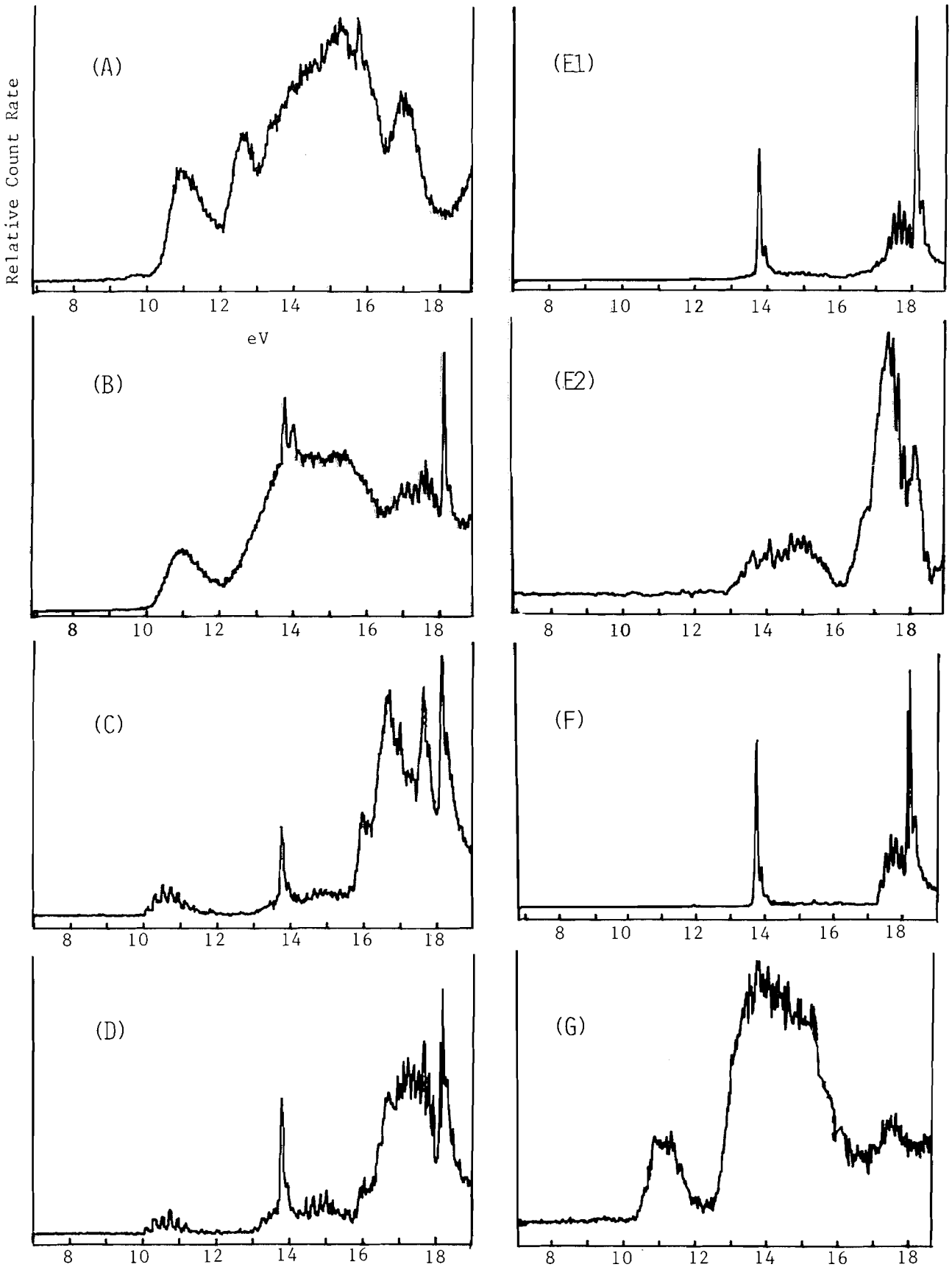

FIG. 3. 3(A), p.e. spectrum of **2**. 3(B), p.e. spectrum of the thermolysate of **2**; spectra of the components of the thermolysate; 3(C) and 3(D) composed of C_2F_4, COF_2, and CO_2; 3(E1); 3(E2), COF_2; 3(F), CO_2; 3(G), TMSF.

Can. J. Chem. Downloaded from www.nrcresearchpress.com by 93.93.197.157 on 09/07/12
For personal use only.

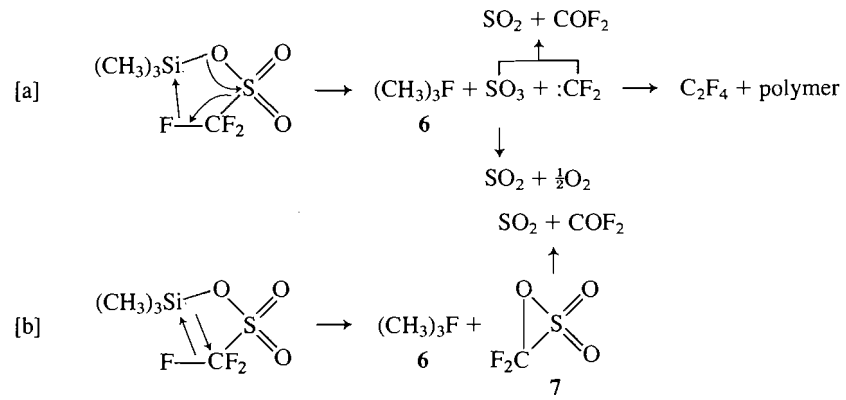

SCHEME 3

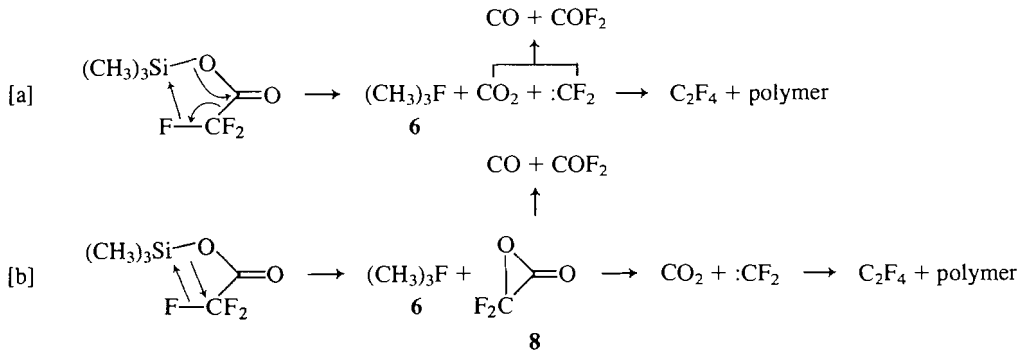

SCHEME 4

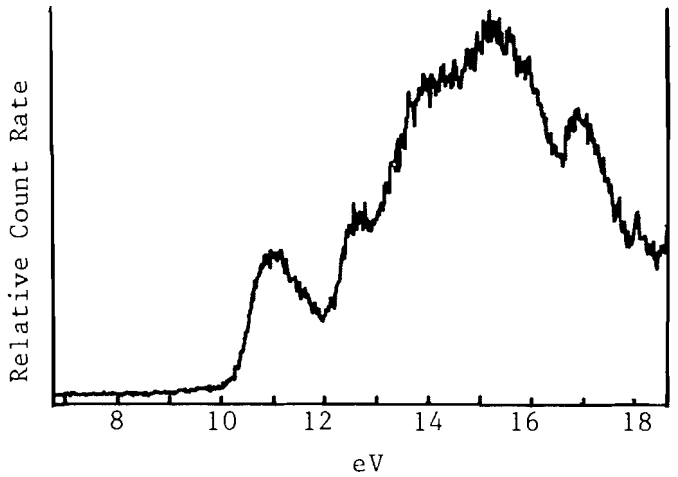

FIG. 4. Photoelectron spectrum of the thermolysate of **2** at low conversion.

tion into SiC bonds of the starting ester. The only other route to SO_2 involves thermal extrusion of an oxygen atom from SO_3. This is possible, as indicated by studies of the high-temperature thermolyses of metal sulfates: SO_3 given off as a primary product along with the metal oxide and at 700°C, is almost completely converted to SO_2 and O_2 (24–28). However, O_2 was not detected either in the spectrum of the total thermolysate (spectrum (1B)) or during the trapping with liquid nitrogen; the lowest IE band of O_2 is a series of well-resolved vibrational components beginning at 12 eV. Furthermore, neither O_2 or SO_3 was detected even at 630°C when the thermolysate was passed through a dry-ice/acetone trap. Under these conditions, as was the case at 720°C, TMSF and SO_2 were clearly identified as the major products.

We take these observations as support for our view that TMSOTf decomposes predominantly via pathway *b* to form 3,3-difluoro-oxathiirane dioxide **7** which extrudes SO_2 to give COF_2 (Scheme 3). This is also supported by the fact that attempts to prepare oxathiirane dioxide have been unfruitful (29). Although the yield of COF_2 is substantially less than the yields of SO_2 and TMSF based on the number of scans collected for each substrate, this must be due to the instability of COF_2 at 720°C. That pathway *b* is the mechanism of decomposition of TMSOTf is further supported by the work of Ainsworth *et al.* (30). They showed by ^{18}O labelling that ketene alkyl trialkylsilyl acetals decompose thermally via a four-membered ring transition state (Scheme 5).

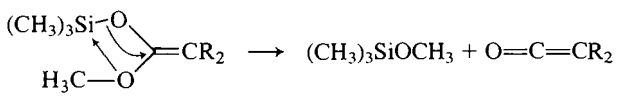

SCHEME 5

The formation of $CH_2{=}CF_2$ as a minor product rather than $CF_2{=}CF_2$ is unexpected; the compounds are easily distinguished by UPS. Since Bell and co-workers (31) have shown that β-trifluoroethylsilanes decompose thermally to yield $CH_2{=}CF_2$ and fluorosilane, it is conceivable that this product arises from a silane such as $R_2XSiCH_2CF_3$. While the exact

Can. J. Chem. Downloaded from www.nrcresearchpress.com by 93.93.197.157 on 09/07/12
For personal use only.

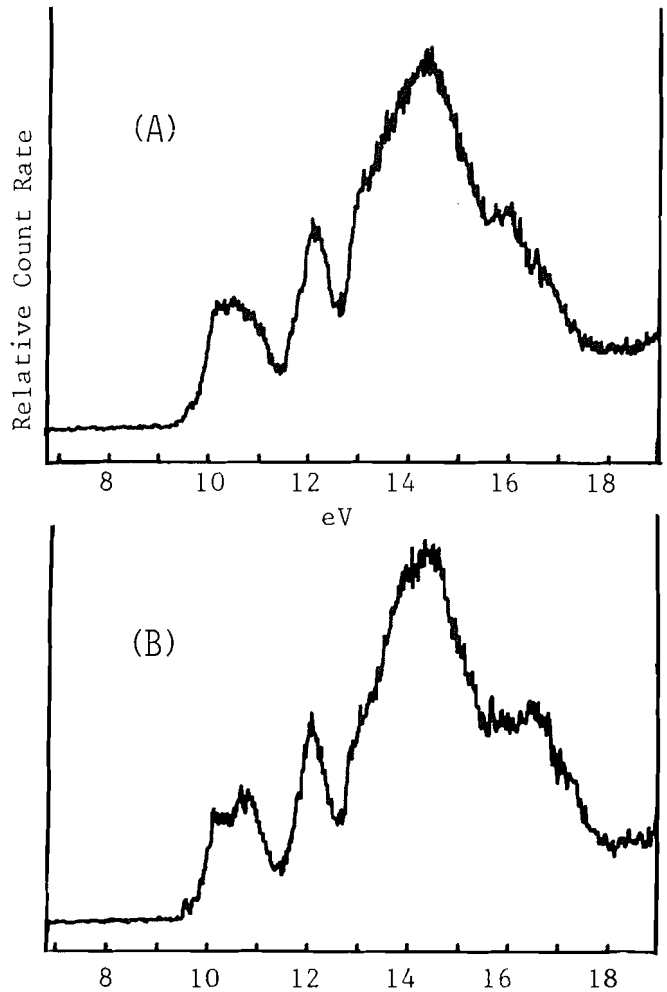

FIG. 5. 5(A), p.e. spectrum of **3**; 5(B) p.e. spectrum of the thermolysate of **3** at low conversion.

source of such a silane is unknown, the starting material is a potential source of $\cdot CF_3$ and dimethylsilene.

Our results contrast with the observations of Voronkov *et al.* on the thermolysis of bis(trimethylsilyl)sulfate ($(CH_3)_3SiO)_2SO_2$) at 200°C at room pressure (32). In that case, the major products were hexamethyldisiloxane, trimethylsilyl methanesulfonate ($(CH_3)_3SiOSO_2CH_3$), and tetramethyl-1,2-bis(mesyloxy)disiloxane ($(CH_3SO_2OSi(CH_3)_2)O$). It is clear that the absence of the driving force provided by the formation of the SiF bond results in a changeover in the mechanism of thermal decomposition of trimethylsilyl esters.

Thermolysis of TMSTFA

In keeping with the mechanism proposed for the thermolysis of TMSOTf, we propose that TMSTFA decomposes predominantly via pathway *b* (Scheme 4). The small amount of COF_2 that is observed could be formed via the reaction of $:CF_2$ with CO_2 or by extrusion of CO from α-lactone, **8**. However, unlike TMSOTf (*vide supra*), the decomposition of TMSTFA yields $CF_2{=}CF_2$, presumably by the dimerization of $:CF_2$. To determine whether or not TMSTFA decomposes via pathway *b*, an attempt was made to detect α-lactone, **8**, by thermolyzing TMSTFA at 720°C, a temperature at which only a small amount of CO_2 is formed (Fig. 4). However, no products other than those observed at 790°C were detected upon low temperature distillation of the thermolysate. If the lactone is a primary product of thermolysis, it decomposes at 720°C — not an unreasonable expectation considering that α-lactones are highly strained.

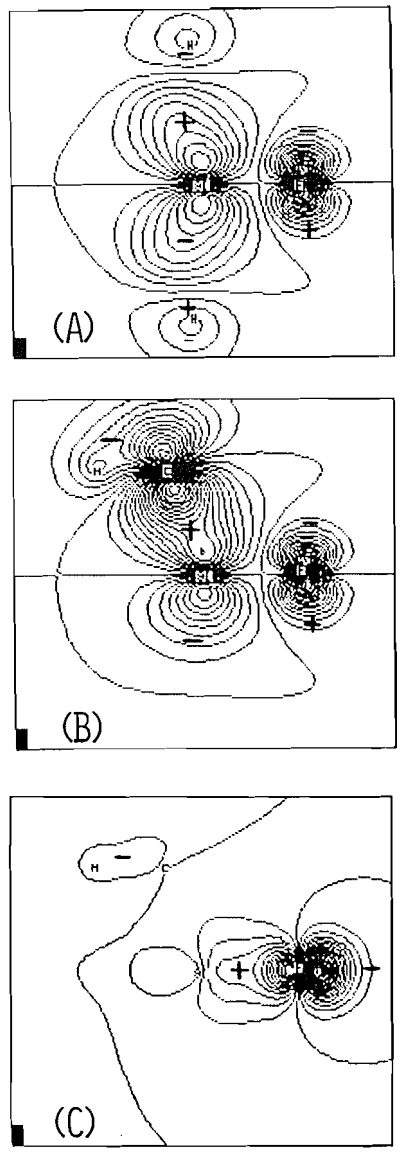

FIG. 6. Molecular orbital contours (MOCs); 6(A), MO 16 of TMSF in the *xz* plane, contour interval 0.05; 6(B), MO 15 of TMSF in the *xy* plane, contour interval 0.05; 6(C), MO 5 of TMSF in the *xy* plane, contour interval 0.125.

Thermolysis of TMSOAc

While TMSOTf and TMSTFA decompose completely at temperatures below at 790°C, TMSOAc undergoes only partial decomposition at 800°C yielding acetic acid as the only detectable product. Although the formation of acetic acid requires dimethylsilene, **4**, as a coproduct, no peak was observed at 7.9 eV where the lowest ionization energy of dimethylsilene is expected (5). That **4** is not detected is presumably due to the low conversion and its reactivity (5). The inertness of TMSOAc, probably a consequence of the high SiO bond energy, contrasts with the reactivity of *tert*-butyl acetate that decomposes readily to 2-methylpropene and acetic acid at 300°C at higher pressures (2).

Molecular orbital eigenvalues and molecular orbital contours TMSF and TMSOH

For AMPAC and GAUSSIAN 82 (6-31G*) calculations on

Can. J. Chem. Downloaded from www.nrcresearchpress.com by 93.93.197.157 on 09/07/12
For personal use only.

Can. J. Chem. Downloaded from www.nrcresearchpress.com by 93.93.197.157 on 09/07/12
For personal use only.

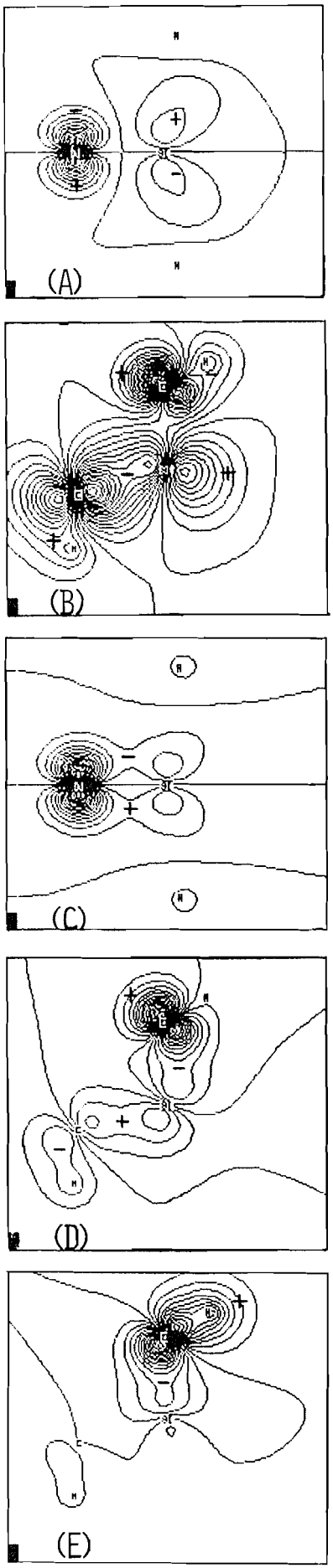

FIG. 7. MOCs; 7(A), MO 16 of TMSOH in the *xz* plane, contour interval 0.125; 7(B), MO 15 of TMSOH in the *xy* plane, contour interval 0.05; 7(C), MO 14 of TMSOH in the *xz* plane, contour interval 0.125; 7(D), MO 13 TMSOH in the *xy* plane, contour interval 0.125; 7(E), MO 5 of TMSOH in the *xy* plane, contour interval 0.125.

TMSF, the experimentally obtained geometry (13) was used. In the case of TMSOH, the MNDO optimized geometry given in Fig. 8 was used because an experimentally determined geometry was not available. As shown in Table 1, the correlation between the experimentally obtained IEs of TMSF and MOEs obtained by AMPAC and GAUSSIAN 82 is good, and, in fact, the MOEs were used to identify TMSF (*vide supra*) as a major product of thermolysis. The molecular orbital contours (MOCs) of MO 16 (HOMO) and MO 15 of TMSF which are degenerate and which are characterized by the broad peak at 11 eV of spectrum 1(F), are shown in Fig. 6 and 6(A) and 6(B), respectively. Both MOs have $\sigma_{SiC}n_F$ character. As shown by the MOC plot in Fig. 6(C), MO 5, characterized by the peak at 17.8 eV, has n_F character.

The MOEs of TMSOH, **9** obtained by AMPAC are given in Table 2. Again, as in the case of TMSF, the correlation between the MOEs and the IEs is good. The MOCs of MO 16 (HOMO) and MO 15 of TMSOH, characterized by the unsymmetrical broad band centered at 10.5 eV of spectrum 2, are shown in Fig. 7 as 7(A) and 7(B), respectively. The HOMO has n_O character while MO 15 is predominately σ_{SiC} in character. MOs 14 and 13, which are degenerate according to AMPAC (Table 2) and which are characterized by the peak at 12.2 eV in spectrum 2, are shown as in 7(C) and 7(D), respectively. MO 5 characterized by the peak at 17.7 eV has σ_{OH} character as shown by the MOC plot given in 7(E).

*Dimethylsilene, **4***

The MOEs of dimethylsilene calculated using AMPAC and GAUSSIAN 82 (6-31G*) from the geometry calculated at the DZ + d SCF level (14) are given in Table 3. Only the lowest IE (7.9 eV) of dimethylsilene has been observed because the photoelectron spectrum was recorded for a mixture obtained by thermolysis (5). At first glance, the MOE of the HOMO of **4** obtained at the 6-31G* level appears to correlate reasonably well with the experimental value (7.98 eV) of the lowest IE (5). However, when 92% of Koopman's theorem is taken, which usually yields better correlations (33), the MOE (7.26 eV) is considerably lower than the experimental value. Furthermore, the MOEs calculated by AMPAC are usually high by approximately 0.5 eV at low IEs, thereby placing the lowest MOE at approximately 7.5 eV, again considerably lower than the experimental value. The reason for the difference between the experimental and calculated values is not evident. The AMPAC calculation also provided support for the view of Schaefer and co-workers (14) that the geometry of dimethylsilene obtained by electron diffraction (34) is in error. The MOE of the HOMO obtained using this geometry is 7.58 eV, substantially lower than the experimental value. Taking into account the overestimation by AMPAC of MOEs at low binding energies (0.5 eV), the predicted value should be at approximately 7.1 eV, thereby establishing that the geometry obtained by electron diffraction, at least as far as the length of the SiC double bond is concerned, is in error.

Dimethylsilanone

The MOEs of dimethylsilanone calculated using AMPAC and GAUSSIAN 82 (6-31G*) are given in Table 4. For the

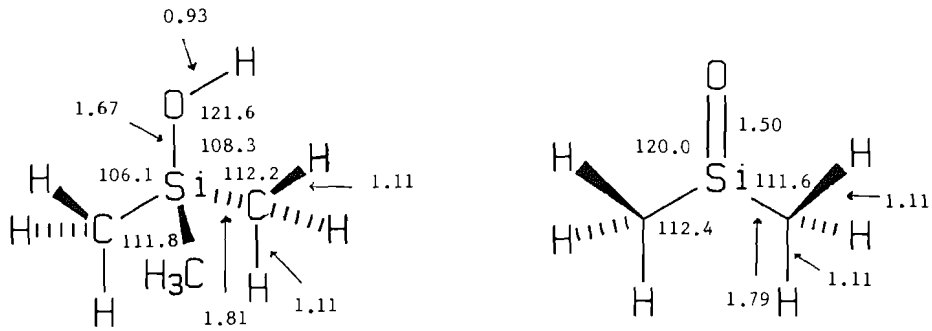

FIG. 8. Bond angles and bond lengths of TMSOH and dimethylsilanone.

TABLE 3. Molecular orbital eigenvalues of dimethylsilene, **4**

MNDO[a] (DZ + d)[b]	6-31G*[a] (DZ + d)[b]	MNDO[a] (Electron diffraction)[c]
7.97	7.89 (7.26)[d]	7.58
11.30	12.11 (11.14)	11.26
11.98	12.62 (11.61)	11.40
13.66	14.58 (13.41)	13.76
14.02	15.14 (13.93)	13.92
14.18	15.43 (14.19)	14.10
14.26	15.57 (14.32)	14.12
14.28	15.62 (14.33)	14.12
14.51	16.90 (15.55)	14.30

[a]Only the MOEs les than 22 eV are reported.
[b]The geometry obtained at the DZ + d level (14) was used in this calculation.
[c]The geometry obtained by electron diffraction (34) was used in this calculation.
[d]92% of Koopman's theorem.

TABLE 4. Molecular orbital eigenvalues of dimethylsilanone, **5**

MNDO[a,b]	6-31G*[a,c]
10.15	11.11 (10.22)[d]
11.05	11.56 (10.63)
12.57	13.20 (12.14)
12.96	13.41 (12.34)
14.28	15.65 (14.90)
14.31	15.67 (14.42)
14.50	16.10 (14.81)
14.55	16.14 (14.85)
14.67	17.10 (15.73)

[a]Only the MOEs below 22 eV are reported.
[b]The MNDO optimized geometry was used in the calculation.
[c]The STO-3G optimized geometry was used in the calculation.
[d]92% of Koopman's theorem.

semi-empirical calculations, the geometry generated by CHEMGRAF was optimized using MNDO (AMPAC) and is given in Fig. 8. For the *ab initio* calculations the STO-3G optimized geometry was used. As in the case of acetone, MO 12 (HOMO) has n_O character and MO 11 is π_{SiO}. However, the separation is considerably less (0.9 eV, AMPAC; 0.4 eV, 6-31G*) than the separation in acetone. This is largely due to a shift of the π_{SiO} MO to higher energy.

Conclusions

Thermolysis studies show that, where possible, formation of a strong SiF bond provides a driving force for thermal decomposition of trimethylsilyl esters. We plan to exploit this to synthesize highly reactive silicon containing species in the gas phase and in solution.

Acknowledgements

Financial support by the Natural Sciences and Engineering Council of Canada and the awarding of a scholarship to P.H. by the Deutscher Akademischer Austauche Dienst (DAAD) is gratefully acknowledged. We wish to thank the McMaster Institute for Materials Research for the use of CHEMGRAF.

1. C. H. DEPUY and R. W. KING. Chem. Rev. 431 (1960).
2. R. TAYLOR. J. Chem. Soc. Perkin II, 1025 (1975) and references cited therein.
3. P. SARTORI and M. WEIDENBRUCH. Chem. Ber. **100**, 2049 (1967).
4. N. H. WERSTIUK. Can. J. Chem. **64**, 2175 (1986).
5. J. M. DYKE, G. D. JOSLAND, R. A. LEWIS, and A. MORRIS. J. Phys. Chem. **86**, 2913 (1982).
6. E. COLVIN. Silicon in organic synthesis. Butterworths, London. 1981. Chapt. 2, p. 4.
7. H. A. SCHUYTEN, J. W. WEAVER, and J. D. REID. J. Am. Chem. Soc. **69**, 2110 (1947).
8. L. H. SOMMER, E. W. PIETRUSZA, and F. C. WHITMORE. J. Am. Chem. Soc. **68**, 2282 (1946).
9. K. DAVIES. CHEMGRAF. Chemical Crystallography Laboratory, Oxford University. *Developed by* Chemical Design Ltd., 200 Route 17 S Suite 120, Mahwah, N.J. 07430, U.S.A.
10. W. C. STILL. MODEL. Columbia University. *Modified by* K. Steliou (Version 2.7), Département de Chimie, Université de Montréal, C.P. 6128 succursale A, Montréal, Canada H3C 3J7.
11. MM2/MMP2 QCPE 395. QCPE packages are available from QCPE, Chemistry Department, Indiana University, Bloomington, IN 47401, U.S.A.
12. AMPAC: Austin Method 1 Package (QCPE 506). Dewar Research Group and J. P. Stewart. QCPE Bull. **6**, 24 (1986).
13. B. REMPFER, H. OBERHAMMER, and N. AUNER. J. Am. Chem. Soc. **108**, 3893 (1986).
14. Y. YOSHIOKA, J. D. GODDARD, and H. F. SCHAEFER, III. J. Am. Chem. Soc. **103**, 2452 (1981).
15. J. J. P. STEWART. QCPE Bull. **5**, 59 (1985).
16. D. M. STORCH. QCPE Bull. **5**, 61 (1985).
17. J. S. BINKLEY, M. FRISCH, K. RAGHAVACHIRI, D. DEFREES, R. WHITESIDE, E. FLUDER, R. SEEGER, and J. A. POPLE. GAUSSIAN 82. Release H, Department of Chemistry, Carnegie-Mellon University, Pittsburgh, 1982.
18. TGRAF-05: Available from Grafpoint, 4340 Stevens Creek Boulevard, San Jose, CA 95129, U.S.A.
19. R. F. LAKE and H. THOMPSON. Proc. R. Soc. London A, **315**, 323 (1970).

Can. J. Chem. Downloaded from www.nrcresearchpress.com by 93.93.197.157 on 09/07/12
For personal use only.

20. J. W. RABALAIS. *In* Principles of ultraviolet photoelectron spectroscopy. J. Wiley and Sons, New York. 1977. p. 323.
21. K. KIMURA, S. KATSUMATA, Y. ACHIBA, T. YAMAZAKI, and S. IWATA. Handbook of HeI photoelectron spectra of fundamental organic molecules. Japan Scientific Societies Press, Tokyo. 1981.
22. R. L. DEKOCK and D. R. LLOYD. J. Chem. Soc. D, 526 (1973).
23. G. W. MINES and R. K. THOMAS. Proc. R. Soc. Lond. A **336**, 355 (1972).
24. D. W. JOHNSON, JR. and P. K. GALLAGHER. J. Am. Ceram. Soc. **54**, 461 (1971).
25. D. W. JOHNSON, JR. and P. K. GALLAGHER. Thermochim. Acta, **6**, 333 (1973).
26. H. A. PAPAZIAN, P. J. PIZZOLATO, and R. R. ORRELL. Thermochim. Acta, **4**, 97 (1972).
27. H. A. PAPAZIAN, P. J. PIZZOLATO, and R. R. ORRELL. Thermochim. Acta, **6**, 337 (1973).
28. L. W. COLLINS, E. K. GIBSON, and W. W. WENDLANDT. Thermochim. Acta, **11**, 177 (1975).
29. U. ZOLLER. Chemistry of heterocyclic compounds. Vol. 42. Part 1, Small ring heterocycles. *Edited by* A. Hassner. J. Wiley and Sons, New York. 1983. Chapt. III.
30. C. AINSWORTH, F. CHEN, and Y.-N. KUO. J. Organomet. Chem. **46**, 75 (1972).
31. T. N. BELL, R. BERKLEY, A. E. PLATT, and A. G. SHERWOOD. CAN. J. CHEM. **52**, 3158 (1974).
32. M. G. VORONKOV, E. A. MALETINA, V. K. ROMAN, and A. I. ALBANOV. Izv. Akad. Nauk SSSR, Ser. Khim. 935 (1982).
33. C. R. BRUNDLE, M. B. ROBIN, N. A. KUEBLER, and H. BASCH. J. Am. Chem. Soc. **94**, 1451 (1972).
34. P. G. MAHAFFY, R. GUTOWSKY, and L. K. MONTGOMERY. J. Am. Chem. Soc. **102**, 2854 (1980).

Can. J. Chem. Downloaded from www.nrcresearchpress.com by 93.93.197.157 on 09/07/12
For personal use only.

The effect of the water–cation interaction on the polarisability and second hyperpolarisability of hydrated Li^+. A comparative study

J. WAITE AND M. G. PAPADOPOULOS

National Hellenic Research Foundation, 48, Vas. Constantinou Avenue, GR-116 35 Athens, Greece

Received September 18, 1987

J. WAITE and M. G. PAPADOPOULOS. Can. J. Chem. **66**, 1440 (1988).

The CHF-PT-EB-CNDO method has been used to compute the polarisability and second hyperpolarisability of the hydrated lithium cation with one and two hydration shells. The effect of the $Li^+ \ldots (H_2O)_n$ interaction on these properties is discussed and the main findings are confirmed in hydrated Na^+, Be^{2+}, and Al^{3+}.

J. WAITE et M. G. PAPADOPOULOS. Can. J. Chem. **66**, 1440 (1988).

On a utilisé la méthode CHF-PT-EB-CNDO pour calculer la polarisabilité et la seconde hyperpolarisabilité du cation du lithium hydraté avec une ainsi qu'avec deux couches d'hydratation. On discute de l'effet de l'interaction $Li^+ \ldots (H_2O)_n$ sur ces propriétés et on confirme les principales conclusions avec les ions Na^+, Be^{2+} et Al^{3+} hydratés.

[Traduit par la revue]

I. Introduction

The nature of short-range (5 Å or less) interactions between water and ions has been a matter of long-standing chemical interest (1, 2). One important problem which has attracted the attention of theorists is the change induced in the structure and properties of water and ion due to their interaction (3–5). The objective of this article is to report and analyse the effect of the water–cation interaction on the static electric polarisability (6), α, and hyperpolarisability (6), γ, of some hydrated cations.[1] These properties have been chosen because, first, they depend to a great extent on the outer regions of the charge cloud (e.g. the valence electrons generally account for at least 90% of the polarisability of an atom or molecule (7)), which are mainly affected by the intermolecular interaction and second, the change in the hyperpolarisability resulting from the above interaction has not been reported before.

This study has been performed by employing hydrated Li^+ with one and two hydration shells as a test model. Calculations of the properties (α and γ) of other hydrated cations (Na^+, Be^{2+}, Al^{3+}) have also been performed in order to check the validity of the findings in $Li^+(H_2O)_4$. The first hydration shell is formed from four water molecules tetrahedrally placed (8–10). The properties of this and $Li^+(H_2O)_{12}$, which contains the second hydration shell (11), have been calculated and the effect of the outer water sheath on the interaction hyperpolarisability has been demonstrated. In addition the interaction property values for various configurations of $Li^+(H_2O)_n$, where $n = 2$ and 4 are compared.

There have been several studies analysing other interesting aspects of the water–cation interactions (3, 4, 12, 13). For example, the charge transfer from the water cluster to the cation and the polarization of the electronic charge distribution of $(H_2O)_n$ by the positively charged atom (4). The present findings contribute to the formation of a more comprehensive view concerning the water–cation interaction.

[1]The average polarisability α and second hyperpolarisability γ are given by (6*a*):

$$\alpha = \tfrac{1}{3}(\alpha_{xx} + \alpha_{yy} + \alpha_{zz})$$

$$\gamma = \tfrac{1}{5}(\gamma_{xxxx} + \gamma_{yyyy} + \gamma_{zzzz} + 2\gamma_{xxyy} + 2\gamma_{xxzz} + 2\gamma_{yyzz})$$

where x, y, and z define Cartesian components. Expressions for the relevant tensor components, in terms of which α and γ are defined are given in ref. 6*b* and *c*.

The computations have been performed using the CHF-PT-EB-CNDO method (14–18). The basis set was optimized to the experimental α and γ values of H_2O (19) in order to reasonably reproduce the charge distribution of water and in particular its outer regions which are of importance for the proposed study.

II. Computational method

The computations have been performed using the CHF-PT-EB-CNDO method, which has been shown to give polarisability and hyperpolarisability results in satisfactory agreement with experimental values (14–16, 18a, 20).

The CHF-PT-EB-CNDO method relies on: (*a*) An extended basis CNDO/2 wave function (EB-CNDO) (21); (*b*) The coupled Hartree–Fock perturbation theory (CHF-PT) of McWeeny and co-workers (6*b*, *c*); (*c*) The optimisation of the basis set with respect to the hyperolarisability (and/or polarisability) of some judiciously chosen model compound(s). This basis set is subsequently used for the computation of the polarisability and the hyperpolarisability of compounds with similar structure.

The CHF-PT-EB-CNDO method, through the optimisation of the basis set, with respect to some experimental values, allows (at least to some extent) for the effect of electron correlation.

It is considered that CHF-PT-EB-CNDO provides the proper apparatus for the first approach to the considered problem since: (*a*) It is known that an accurate description of intermolecular interactions depends mainly on the outer regions of the molecules. However, ample evidence has been provided, for a wide variety of compounds, that these parts are satisfactorily described by CHF-PT-EB-CNDO (14–16, 18*a*, 20). (*b*) An essential part of our method is the optimisation of the basis set, in some model compound(s), so that the computed properties (α and γ) approach as closely as possible the experimental values. This optimisation procedure helps to ensure the physically correct description of the polarised charge cloud, at least of the isolated molecule (14–16, 18*a*, 20); (*c*) The analysis of the results utilises ratios and differences of property values and thus the effect of any systematic errors in their absolute values is reduced.

It is noted that the deficiency of standard CNDO/2 (21) to give accurate absolute values for properties like equilibrium geometries (22, 23) is not relevant to our objective as we are interested in differences in property (α, γ) values and ratios. Furthermore, while our method uses the CNDO (21) approx-

Printed in Canada / Imprimé au Canada

Can. J. Chem. Downloaded from www.nrcresearchpress.com by 93.93.197.157 on 09/07/12
For personal use only.

TABLE 1. Polarisabilities and hyperpolarisabilities of H_2O[a] (in a.u.[b])

H				O							
1s	2s	2p	3d	2s	2p	3s	3p	3d	4f	α	γ
0.8	0.38	0.475		1.975	1.975					9.82	2310
1.3	0.08	0.285		1.35	1.35	0.48	0.612			9.81	2300
0.81	0.08	0.287		1.57	1.57	0.5	0.6			9.89	2330
1.0	0.5	0.5		2.275	2.275			1.517		9.54	
1.0	0.5	0.5		1.975	1.975			1.317		10.8	
1.0	0.5	0.5	0.333	2.275	2.275			1.517	1.317		1960
1.0	0.5	0.5	0.333	1.975	1.975			1.317	0.988		1970
Experimental values										9.82 (19a)	2310±119 (19b)

[a]For computation the following geometry has been used: R_{OH} = 1.8142 a.u. and ∠HOH = 104.45°.
[b]1. a.u. of polarisability ≃ 0.148176 × 10^{-24} esu ≃ 0.164867 × 10^{-40} C^2 m^2 J^{-1}; 1 a.u. of second hyperpolarisability ≃ 0.503717 × 10^{-39} esu ≃ 0.623597 × 10^{-64} C^4 m^4 J^{-3}.

Can. J. Chem. Downloaded from www.nrcresearchpress.com by 93.93.197.157 on 09/07/12
For personal use only.

imations it also employs the above stated optimisation principle, making a reasonably accurate determination of non-linearities possible.

Within the set of options and approximations which define the CHF-PT-EB-CNDO method, we have performed a considerable amount of computational experimentation employing the water molecule as a test model. Basis sets involving up to *d* orbitals for H and up to *f* for O have been used, a small but representative set of which is given in Table 1.

Detailed analysis on an extensive set of data, referring to several molecules, has shown that high l AOs like *d* and *f* orbitals are sufficient (they can lead to reasonable results) but not necessary within a semiempirical framework, in particular if one takes advantage of the flexibility and freedom allowed within such schemes (14–16, 18*a*, 20*b*). Analysis of the computations on H_2O has led to the following, optimised basis:

H: 1*s*(0.8), 2*s*(0.38), 2*p*(0.475)

O: 2*s*(1.975), 2*p*(1.975)

For the considered cations (Li^+, Na^+, Be^{2+}, and Al^{3+}) we have used Burns' exponents (24), which have been shown to give, in general, reasonable results for α and γ (16, 18*a*, 20*a*).

The geometric models (coordinates) were built by employing data from the literature (mainly from refs. 1 and 11). Detailed information is given in the footnotes of Table 2 and Figs. 1–4. The coordinates of all the studied hydrated ions are available on request.

The same geometric elements (bond lengths and angles) have been used for all the hydrated cations. This choice facilitates the comparison of trends found in hydrated Li^+ with those determined using the other hydrated cations (Na^+, Be^{2+}, and Al^{3+}).

The convergence criteria for the iterative computation of $R^{(0)}$, $R^{(1)}$, and $R^{(2)}$ (where these are the zeroth order density matrix and its first and second order corrections respectively) are given in refs. 17 and 18*a*.

III. Results and discussion

We have defined the index:

$$[1] \quad p'_{int} = \frac{p[M^{v+}(H_2O)_n] - p[(H_2O)_n]}{p[M^{v+}(H_2O)_n]} \times 100$$

where p'_{int} is either α'_{int} or γ'_{int} and *v* is 1, 2, or 3. This index gives the property arising from the interaction of the cation, M^{v+}, with the water cluster, $(H_2O)_n$, as percent of the property of $M^{v+}[(H_2O)_n]$. The above index helps to systematically analyse the interaction properties of the considered hydrated cations.

TABLE 2. The interaction polarisability, α'_{int}, and hyperpolarisability, γ'_{int}, of hydrated Li^+, Na^+, Be^{2+}, and Al^{3+}

Hydrated cation	Configuration			
	Linear		Tetrahedral or cluster	
	α'_{int}	γ'_{int}	α'_{int}	γ'_{int}
$Li^+(H_2O)_4$[a,c]	−1.72	7.42	−8.13	−11.0
$Na^+(H_2O)_4$[c]	−1.14	9.01	−5.33	−5.52
$Be^{2+}(H_2O)_4$[c]	−1.96	80.7	−19.2	−43.3
$Al^{3+}(H_2O)_4$[c]	—	—	−18.8	−52.2
$Li^+(H_2O)_{12}$[d]	—	—	−4.0	−5.64

[a]Tetrahedral configuration of $Li^+(H_2O)_4$ (Fig. 3) (8–10). The Li^+ is placed at the center of the tetrahedron. The Li^+ ... O line bisects the ∠HOH, with the hydrogens away from the Li^+. The planes of the water molecules are such that the hydrogen atoms are maximally separated. The O...O distance is 5. a.u. (1) and Li^+ ... O distance is 4 a.u.
[b]Linear configuration of $Li^+(H_2O)_4$ (**6** in Fig. 2). The Li^+, the first H_2O (that is the water which is nearest to the Li^+), and the third H_2O lie on the same plane. The second and the last H_2O (the one furthest from Li^+) lie on the plane which is perpendicular to the previous plane.
[c]The geometries of the hydrated Na^+, Be^{2+}, and Al^{3+} are the same as that used for $Li^+(H_2O)_4$, Fig. 3.
[d]The $Li^+(H_2O)_{12}$ cluster (Fig. 4) is built from the tetrahedral $Li^+(H_2O)_4$ by associating one water molecule with each hydrogen. The added water is in a plane perpendicular to that of the water to which it is bonded and the peripheral water's ∠HOH is bisected by the extension of H—O bond of the inner water.

The results of Table 2 show that the contribution of the property (polarisability or hyperpolarisability) which is due to the interaction between Li^+ or Na^+ and $(H_2O)_n$ to the property of $M^+(H_2O)_n$ is small.

Practically it seems that the properties of the hydrated monovalent cations Li^+ or Na^+ can be approximated by the properties of the hydration shell itself. It is also observed (Table 2) that the interaction properties which are due to interaction of Be^{2+} or Al^{3+} with $(H_2O)_4$, contribute to the property (α, γ) of $M^{v+}(H_2O)_4$, considerably more than the interaction properties associated with Li^+ or Na^+.

It is emphasized that the interaction hyperpolarisabilities are much greater than the property of the cation itself. For example, it has been found that:

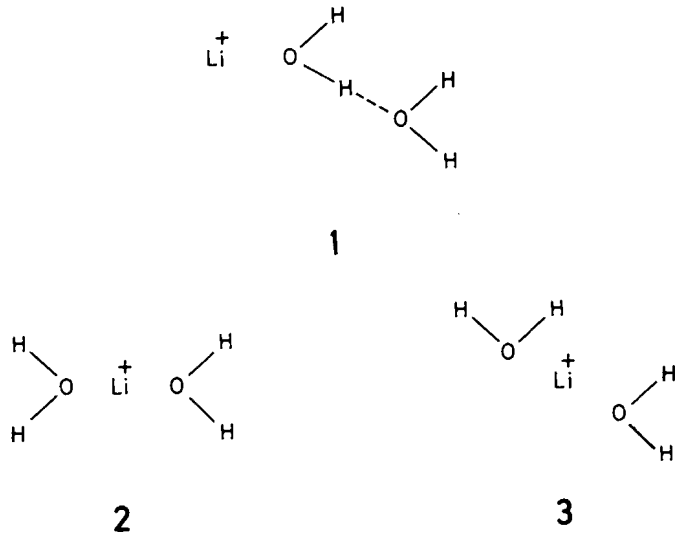

FIG. 1. Structure of three different configurations of $Li^+(H_2O)_2$. In **1** the outer water is perpendicular to the plane of Li^+ and the inner water molecule. The configuration **2** is planar. In **3** the two water molecules have the arrangement defined in the tetrahedral cluster (Table 2, footnote *a* and Fig. 3).

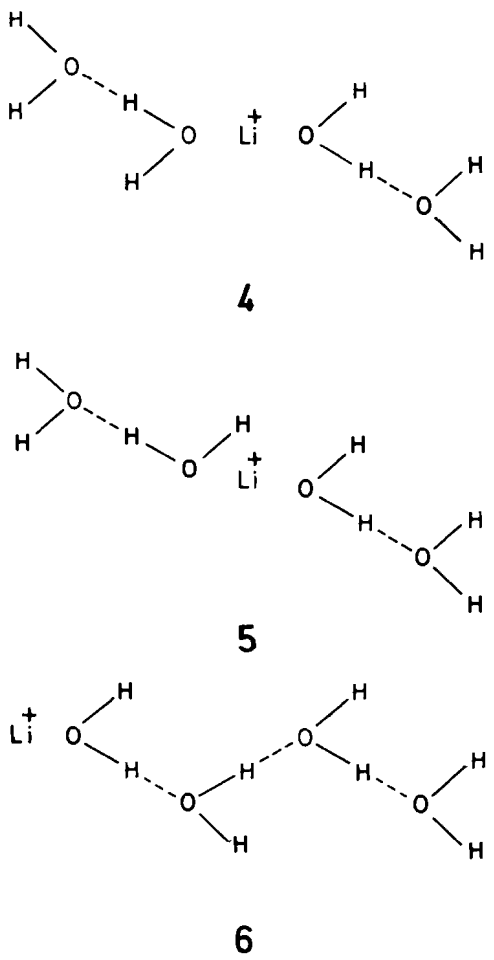

FIG. 2. Three configurations of $Li^+(H_2O)_4$. In **4**, Li^+ and the two adjacent water molecules are planar (as in **3** of Fig. 1). The planes of the two outer water molecules are perpendicular to this plane. In **5** the four water molecules and Li^+ have the geometry which corresponds to a segment of $Li^+(H_2O)_{12}$. In **6** the linear configuration of $Li^+(H_2O)_4$ is presented (geometric details are given in Table 2, footnote *b*).

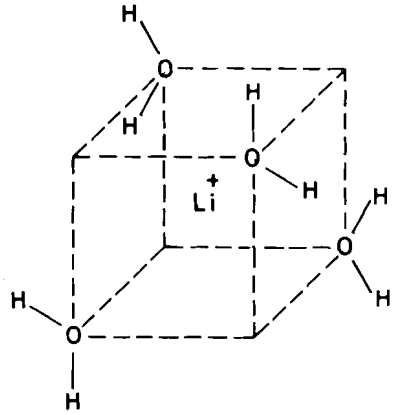

FIG. 3. Tetrahedral configuration of $Li^+(H_2O)_4$. Geometric details are given in Table 2, footnote *a*.

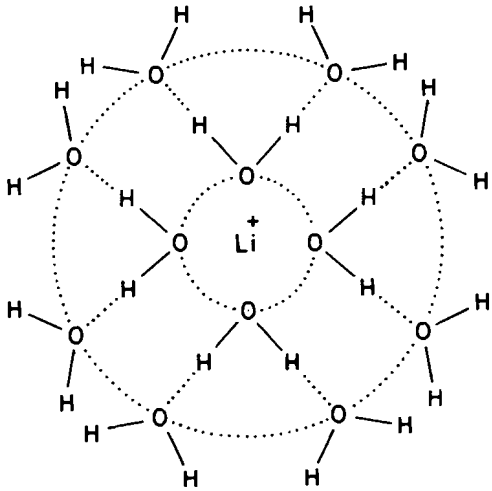

FIG. 4. Structure of $Li^+(H_2O)_{12}$ (11).

[2] $\gamma[Li^+(H_2O)_4]_{tet} - \gamma[(H_2O)_4]_{tet} = -1800$ a.u.

[3] $\gamma[Li^+(H_2O)_4]_{lin} - \gamma[(H_2O)_4]_{lin} = 1700$ a.u.

[4] $\gamma[Li^+(H_2O)_{12}] - \gamma[(H_2O)_{12}] = -5500$ a.u.

while γ of Li^+ is 0.24 a.u. (25*a*).

Thus the effect of environmental interactions on the nonlinear electric properties of hydrated cations is expected to be of fundamental importance for their understanding. The magnitude of the interaction polarisability is also large in comparison to that of the isolated cation. For example we have:

[5] $\alpha[Li^+(H_2O)_{12}] - \alpha[(H_2O)_{12}] = -11$ a.u.

while the polarisability of Li^+ is approximately 0.19 a.u. (25).

The results of Tables 2 and 3 show:

[6] $\alpha[M^{\nu}(H_2O)_4]_{lin} > \alpha[M^{\nu+}(H_2O)_4]_{tet}$

[7] $\alpha[(H_2O)_4] > \alpha[M^{\nu+}(H_2O)_4]$

[8] $\gamma[M^{\nu+}(H_2O)_4]_{lin} > \gamma[M^{\nu+}(H_2O)_4]_{tet}$

[9] $\gamma[M^{\nu+}(H_2O)_4]_{lin} > \gamma[(H_2O)_4]_{lin}$

[10] $\gamma[(H_2O)_4]_{tet} > \gamma[M^{\nu+}(H_2O)_4]_{tet}$

The results of Table 3 show the remarkable variation of α and γ of $M^{\nu+}(H_2O)_4$, where $M^{\nu+} = Li^+$, Na^+, or Be^{2+}, is depen-

Can. J. Chem. Downloaded from www.nrcresearchpress.com by 93.93.197.157 on 09/07/12
For personal use only.

TABLE 3. Ratios of the polarisability and the hyperpolarisability in linear and tetrahedral configurations

Hydrated cation	$\alpha_{linear}/\alpha_{tetrahedral}$	$\gamma_{linear}/\gamma_{tetrahedral}$
$Li^+(H_2O)_4$	1.44	1.48
$Na^+(H_2O)_4$	1.42	1.43
$Be^{2+}(H_2O)_4$	1.59	(9.17)[a]

[a]This ratio is currently under investigation.

TABLE 4. The effect of changes in configuration on α'_{int} and γ'_{int} of $Li^+(H_2O)_n$

Lithium–water cluster	Identification	α'_{int}	α'_{int}
$Li^+(H_2O)_2$	Fig. 1, **1**	−4.66	4.60
	Fig. 1, **2**	−5.14	−3.75
	Fig. 1, **3**	−6.46	−9.35
$Li^+(H_2O)_4$	Fig. 2, **4**	−1.85	15.6
	Fig. 2, **5**	−2.35	6.30
	Fig. 2, **6**	−1.72	7.42
	Fig. 3	−8.13	−11.0

dent on the shape of the configuration. Furthermore, the results of Table 4 show that changes in the configuration of the hydrated cation may induce a considerable change in the contribution of the interaction properties to α or γ of the hydrated species.

It has been found that for the linear configuration the polarisability of $Li^+(H_2O)_4$ is less than that of $(H_2O)_4$ while the reverse is true for the hyperpolarisability (Table 2). The above trends are also shown in the results of the hydrated Na^+ and Be^{2+} (Table 2, linear configuration). The hyperpolarisability results are remarkable, since the formal addition of positive charge usually decreases the property values due to the contraction of the charge cloud (26). Presumably the polarisation of the waters' valence electrons overrides this effect for the hyperpolarisability.

It has been found that:

$$[11] \quad \frac{\gamma[(H_2O)_{12}]}{3 \times \gamma[(H_2O)_4]_{tet}} \simeq 2$$

This result demonstrates the important effect of the water–water interaction on the hyperpolarisability of the H-bonded cluster. It is added that the considerable effect of the environmental interactions, in strongly associating liquids, on the electric non-linearities has been experimentally demonstrated (27).

The intermolecular interactions in water clusters constitute a cooperative process (that is each interaction enhances the next one) (28). Apparently the addition of each water molecule acts to further polarise the electron distribution within the cluster (29). This cooperative effect has also been observed for hydrogen bond energies, dipole moments (29), and polarisabilities (28).

Clementi *et al.* found that for $Li^+(H_2O)_2$ the non-additivity correction to the total interaction energy is satisfactorily approximated by the induction energy (30). This approximation is completed by a short-range exponential repulsive term. The above model has also been successfully applied to larger hydration numbers (30). The long-range induction energy has been used to explain the main contribution to the non-additive part of the interaction energy in $(H_2O)_3$ (31).

IV. Conclusions

The effect of the water–Li^+ interaction on the polarisability and hyperpolarisability of the hydrated ion has been studied by employing various clusters, simulating the first and second hydration shells. For the computation of the properties (α and γ) the CHF-PT-EB-CNDO method has been used, which has been shown to give satisfactory results for the polarisability and hyperpolarisability of a large number of molecules belonging to several families (alkanes (14), polyenes (15), amides (28) etc.). Considering that the computation of accurate molecular hyperpolarisabilities is a very difficult task (elaborate *ab initio* treatments have only been used for atoms, diatomics, and triatomics), we have taken many precautions to safeguard the validity of the findings which are mainly trends and phenomena.

The computational work has been performed mainly on hydrated Li^+, but for confirmation (within the employed methodology) and generalisation of the observations, the properties of hydrated Na^+, Be^{2+}, and Al^{3+} have also been calculated.

In summary it is noted: (*a*) The first direct computational evidence has been presented for the magnitude of the effect which is due to the interaction $M^{v+} \ldots (H_2O)_n$, on the polarisability and hyperpolarisability of hydrated M^{v+}. It has been demonstrated in the case of $Li^+(H_2O)_n$ that the interaction property (α, γ) is much greater than the property of the cation itself in isolation. (*b*) Changes in the configuration of the hydrated cation may induce a remarkable variation in the interaction hyperpolarisability. We found that for the linear configuration the unexpected trend: $\gamma[M^{v+}(H_2O)_4] > \gamma[(H_2O)_4]$. (*c*) Comparing the changes induced in the electric properties due to the water–cation interaction, the greater sensitivity of the hyperpolarisability becomes clear. Thus one may define indices in terms of the hyperpolarisabilities (like γ'_{int} that has been employed in the present work) which may serve as powerful probes of solute-solvent interactions. (*d*) The cooperative character of the water–water interactions on the hyperpolarisability has been demonstrated.

The present results illustrate the importance of the solute–solvent interaction in the study of hyperpolarisabilities of positively charged species in solution and complement previous studies where the interacting systems were neutral (18*c*, 23). The reported findings are expected to be of importance in the rationalization of trends and phenomena in terms of polarisation theory.

1. M. D. NEWTON and S. EHRENSON. J. Am. Chem. Soc. **93**, 4971 (1971).
2. A. K. SOPER, G. W. NEILSON, J. E. ENDERBY, and R. A. HOWE. J. Phys. C, **10**, 1793 (1977).
3. D. G. BOUNDS. Mol. Phys. **54**, 1335 (1985).
4. A. PULLMAN, B. PULLMAN, and H. BERTHOD. Theor. Chim. Acta, **47**, 175 (1978).
5. P. KOLLMAN. J. Am. Chem. Soc. **99**, 4876 (1977).
6. (*a*) A. D. BUCKINGHAM and B. J. ORR. Q. Rev. Chem. Soc. **21**, 195, (1967); (*b*) R. MCWEENY. Phys. Rev. **126**, 1028 (1962); (*c*) G. DIERCKSEN and R. MCWEENY. J. Chem. Phys. **44**, 3554 (1966); J. L. DODDS, R. MCWEENY, W. T. RAYNES, and J. P. RILEY. Mol. Phys. **33**, 611 (1977).
7. T. M. MILLER and B. BEDERSON. Adv. Atom. Mol. Phys. **13**, 1 (1977).
8. K. H. MICHAELIAN and M. MOSKOVITS. Nature, **273**, 135 (1978).
9. P. A. KOLLMAN and I. D. KUNTZ. J. Am. Chem. Soc. **96**, 4766 (1974).

Can. J. Chem. Downloaded from www.nrcresearchpress.com by 93.93.197.157 on 09/07/12
For personal use only.

10. GY. I. SZÁSZ, K. HEINZINGER, and G. PÁLINKÁS. Chem. Phys. Lett. **78**, 194 (1981).
11. B. M. RODE, G. J. REIBNEGGER, and S. FUJIWARA. J. Chem. Soc. Faraday II, **76**, 1268 (1980).
12. G. H. F. DIERCKSEN and W. P. KRAEMER. Theor. Chim. Acta, **23**, 387 (1972).
13. (*a*) H. KISTENMACHER, H. POPKIE, and E. CLEMENTI. J. Chem. Phys. **61**, 799 (1974); (*b*) G. H. F. DIERCKSEN, W. P. KRAEMER, and B. O. ROOS. Theor. Chim. Acta, **36**, 249 (1975); (*c*) G. PÁLINKÁS and K. HEINZINGER. Chem. Phys. Lett. **126**, 251 (1986); (*d*) T. L. MATHERS and N. R. KESTNER. Int. J. Quant. Chem. Quant. Chem. Symp. **9**, 297 (1986); (*e*) M. ARBMAN, H. SIEGBAHN, L. PETTERSSON, and P. SIEGBAHN. Mol. Phys. **54**, 1149 (1985).
14. C. A. NICOLAIDES, M. PAPADOPOULOS, and J. WAITE. Theor. Chim. Acta, **61**, 427 (1982).
15. M. G. PAPADOPOULOS, J. WAITE, and C. A. NICOLAIDES. J. Chem. Phys. **77**, 2527 (1982).
16. J. WAITE, M. G. PAPADOPOULOS, and C. A. NICOLAIDES. J. Chem. Phys. **77**, 2536 (1982).
17. J. WAITE and M. G. PAPADOPOULOS. J. Mol. Struct. **108**, 247 (1984).
18. (*a*) J. WAITE and M. G. PAPADOPOULOS. J. Chem. Phys. **82**, 1427 (1985); (*b*) J. WAITE and M. G. PAPADOPOULOS. J. Chem. Soc. Faraday Trans. II, **81**, 433 (1985); (*c*) J. WAITE and M. G. PAPADOUPOULOS. Chem. Phys. Lett. **114**, 539 (1985).
19. (*a*) A. J. SADLEJ. Mol. Phys. **34**, 731 (1977); (*b*) J. F. WARD and C. K. MILLER. Phys. Rev. A, **19**, 826 (1979).
20. (*a*) J. WAITE and M. G. PAPADOPOULOS. J. Chem. Phys. **80**, 3503 (1984); (*b*) M. G. PAPADOPOULOS and J. WAITE. J. Chem. Phys. **82**, 1435 (1985).
21. J. A. POPLE and D. L. BEVERIDGE. Approximate molecular orbital theory. McGraw Hill, New York. 1970.
22. S. N. MOHAMMAD and A. J. HOPFINGER. Int. J. Quant. Chem. **22**, 1189 (1982).
23. V. A. ZUBKOV, B. I. KOLEGOV, and T. M. BIRSHTEIN. Russ. Chem. Rev. **52**, 1057 (1983).
24. G. BURNS. J. Chem. Phys. **41**, 1521 (1964).
25. (*a*) M. N. GRASSO, K. T. CHUNG, and R. P. HURST. Phys. Rev. **167**, 1 (1968); (*b*) C. POUCHAN and D. M. BISHOP. Phys. Rev. A, **29**, 1 (1984).
26. J. WAITE and M. G. PAPADOPOULOS. J. Phys. Chem. **89**, 2292 (1985).
27. (*a*) I. LEDOUX and J. ZYSS. Chem. Phys. **73**, 203 (1982); (*b*) B. F. LEVINE and C. G. BETHEA. J. Chem. Phys. **65**, 2429 (1976).
28. J. WAITE and M. G. PAPADOPOULOS. J. Chem. Phys. **83**, 4047 (1985).
29. S. SCHEINER and J. F. NAGLE. J. Phys. Chem. **87**, 4267 (1983).
30. E. CLEMENTI, H. KISTENMACHER, W. KOLOS, and S. ROMANO. Theor. Chim. Acta, **55**, 257 (1980).
31. E. CLEMENTI, W. KOLOS, G. C. LIE, and G. RANGHINO. Int. J. Quant. Chem. **17**, 377 (1980).

Can. J. Chem. Downloaded from www.nrcresearchpress.com by 93.93.197.157 on 09/07/12
For personal use only.

Equilibrium and kinetic studies of a chemical model of active transport: Membrane transport of potassium salts by cryptand carriers driven by potassium ion complexation

THOMAS M. FYLES AND STEVEN P. HANSEN
Department of Chemistry, University of Victoria, Victoria, B.C., Canada V8W 2Y2

Received October 6, 1987

THOMAS M. FYLES and STEVEN P. HANSEN. Can. J. Chem. **66**, 1445 (1988).

A theoretical framework of energy transduction in membranes was used as a point of departure for the design of a simple chemical model of primary active transport (reaction pumping). In the model, cryptand carriers transport potassium salts across a bulk liquid membrane, driven by the complexation of potassium by a dicarboxylate crown ether in one aqueous phase. Both the equilibrium position and kinetic behavior of the model system could be predicted from the theoretical framework. Experimental verification of the predictions confirms the fitness of the theoretical framework and provides a design tool for the formulation of new membrane transport systems.

THOMAS M. FYLES et STEVEN P. HANSEN. Can. J. Chem. **66**, 1445 (1988).

On a utilisé un cadre de référence théorique de l'énergie de transduction dans les membranes comme point de départ pour élaborer un modèle chimique simple du transport actif primaire (réaction de pompage). Dans ce modèle, le transport des sels de potassium à travers une membrane liquide globale est effectué par un cryptand qui y est entraîné par la complexation du potassium, à partir d'une phase aqueuse, par un éther couronne portant deux groupements carboxylates. On peut prédire la position de l'équilibre ainsi que le comportement cinétique du système modèle à partir du cadre de référence théorique. Une vérification expérimentale des prédictions permet de confirmer l'utilité du cadre théorique et fournit un outil pour élaborer la formulation de nouveaux systèmes de transport membranaire.

[Traduit par la revue]

Can. J. Chem. Downloaded from www.nrcresearchpress.com by 93.93.197.157 on 09/07/12
For personal use only.

1. Introduction

Energy transduction achieved by the coupling of chemical reactions to membrane transport processes is a central concept in membrane bioenergetics (1, 2). The most prominent example is the "chemiosmotic" hypothesis of Mitchell (3), first applied to oxidative phosphorylation. The concept now includes all aspects of (primary) active transport, group translocation, and light driven processes (4, 5). Although the concept is simple, the molecular details of natural active transport systems are exquisitely complex (4, 5).[1] Molecular and mechanistic complexity, joined with the formidable mathematics of some theoretical treatments (4), provide little guidance for the elaboration of abiotic applications or, indeed, for biomimetic model studies.

In contrast, Goddard (7) has recently proposed a unified model that describes both the equilibrium and the kinetic behavior of transporter mediated energy transduction systems. The model is conceptually simple and provides the general case, applicable in specific cases to both natural (6) and abiotic (8) membrane transport systems. More importantly, the conceptual framework and derived kinetic and thermodynamic relationships can be used predictively in the design or evaluation of new membrane transport systems. The general case can be succinctly stated in a form that reveals the requirements for each chemical entity in the system, readily leading to the assignment of explicit chemical identities for each component of the new transport system. Our first venture in using this framework as a design tool for the elaboration of new transport systems is centered on a system exhibiting primary active transport. Our goals are to illustrate how the approach can work in a simple case and to examine the interplay between theory and experiment. It is important neither to be seduced by the simplicity of the theory, nor repelled by the complexities of the flux equations. A reasoned examination of simple predictions of the theory will serve to balance the two tendencies and will serve to buttress future development of more complex systems.

1.1 Conceptual model

The basic schematic mechanisms for secondary active transport (gradient pumping), for primary active transport (reaction pumping), and for reaction coupling are given in Fig. 1. These follow directly from Goddard (7). The carrier (or in general, the transporter) is confined to the membrane and serves as the sole means of transport of the species A and B either together (symport) or in opposite directions (antiport). Numerous examples of abiotic secondary active transport (gradient pumping) are known, especially those involving crown ether and cryptand carriers (8–10). The most common examples involve cation–anion symport mediated by lipophilic cation complexing agents (10) and cation–proton antiport mediated by ionizable cation complexing agents (9). Examination of Fig. 1 reveals the strong similarities between the three cases. Indeed the sole difference between gradient pumping and reaction pumping is that the species A is intercepted by some C in the right aqueous phase. For any A and C, a formal equilibrium with AC can be written, which embodies the free energy of the AC "bond". It is this reaction free energy that energizes the active transport. At the same time, however, the formation of AC is seen to be a device for controlling the free A concentation at some (low) level in the right aqueous phase. From the equilibrium viewpoint, reaction pumping is thus just a special case of gradient pumping (or vice versa) and the two systems can in principle be interconverted by addition, or deletion, of a suitable reactant C.

All three systems of Fig. 1 can be represented by a single generalized cycle involving composite solution species S and P on the left, S′ and P′ on the right, and the transporter Q(Q′) in the membrane. The flux across the membrane (J) is related to the solution concentrations, interfacial reaction rates, and transporter translocation rates by eq. [1] (7):[2]

$$[1] \quad \hat{C}(K - K') = \{2\hat{R} + (1/k + \hat{R})(K + K') + 2KK'/k + (R - R')(K - K')\}J$$

[1]The entire volume (ref. 6) is devoted to the sodium–potassium pump.

[2]Equation [1] is somewhat different from equation 3.17 of ref. 7; this version is correct (J. D. Goddard, personal communication).

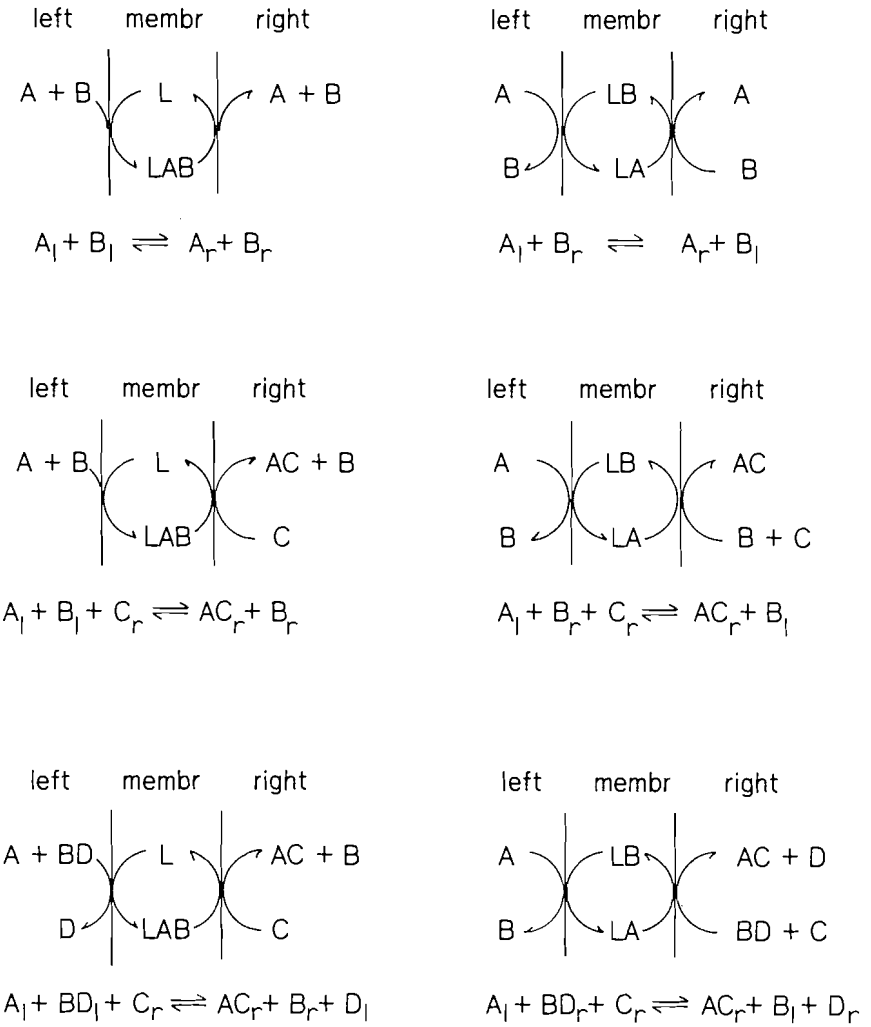

FIG. 1. Schematic mechanisms of gradient pumping (top), reaction pumping (middle), and reaction coupling (bottom). L is a membrane bound carrier that facilitates the transport of solutes A and B through the membrane. The symport case is on the left, the antiport is on the right. The equilibria denote the overall equilibrium condition of the transport.

where $\hat{C}$ is the total transporter concentration at any point in the membrane, $1/k$ (and $1/k'$) are the transport resistances for transporter translocation, R and R' are the equivalent resistances of the interfacial reactions away from equilibrium (thus $\hat{R} = R + R' + 1/k'$), and K and K' describe the equilibria at the left and right interfaces in terms of extraction constants and the solution concentrations (7).

Equation [1] is a completely general form, which should apply to the full range of natural and abiotic transport systems. It allows for, but does not compel, membrane asymmetry (1, 2) ($K \neq K'$, $R \neq R'$, $k \neq k'$). It allows for transport limited by reaction rate (R, R'), by diffusion or translocation (k, k'), or by a combination of the two rate limiting processes. It does not, however, allow for "leaky" transport. The membrane is impermeable to the species S, P in the absence of transporter, hence the coupling is predicted to be perfectly efficient with strict reversibility preserved. For the development of new abiotic transport systems, it serves as a fundamental point of departure.

2. Chemical model of active transport

We wish to examine a simple, reversible reaction pumping case at and near equilibrium. This will permit an assessment of both the overall equilibrium position as well as the kinetic predictions of eq. [1]. For experimental convenience, concentrations near 10^{-3} M are required for all species. This implies that the association constant of AC should be $\log K = 4$–6. If a weaker association were chosen then the unbound A would be significant. A stronger association drives the transport cycle strongly in one sense, requiring large opposing gradients to achieve equilibrium. In this context we note that the free energy of hydrolysis of ATP (AC) to ADP and inorganic phosphate (A + C) provides approximately 30 kJ of energy as the driving force for transport under physiological conditions (11). This corresponds to an association constant of $\log K = 5.3$. In general, a tenfold concentration gradient of an ionic solute correponds to a membrane potential of 59.2 mV (at 298 K) or to a free energy requirement of 5.7 kJ to create the gradient. The energy demands of active transport are modest, and easily accessible with common reagents.

Drawing on the close analogy between the sections of Fig. 1 and the large body of available work on artificial symport and antiport gradient pumping (9, 10), we chose to examine the symport transport system sketched in Fig. 2. Initially crown ether carriers were envisaged. However, the kinetic analysis (below) suggested that the values of the extraction constants

Can. J. Chem. Downloaded from www.nrcresearchpress.com by 93.93.197.157 on 09/07/12
For personal use only.

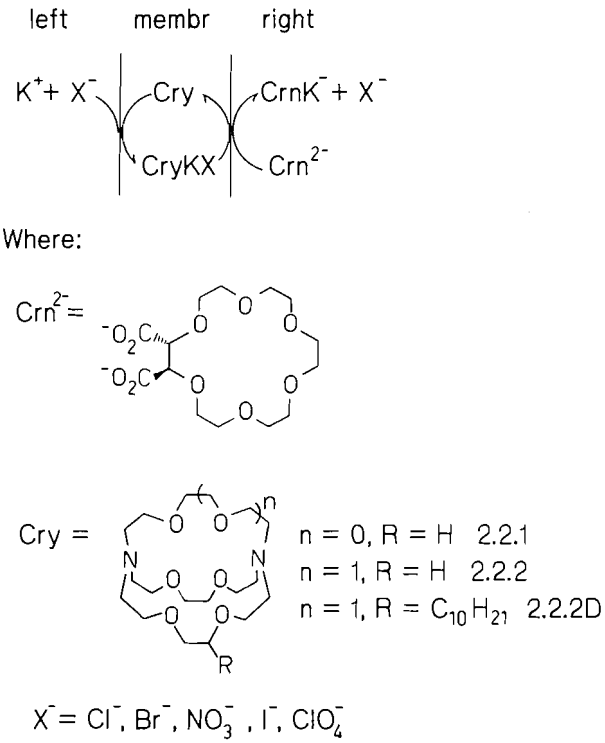

FIG. 2. Schematic mechanism of the chemical model of reaction pumping.

required would be higher than normally accessible with crown ethers and simple potassium salts (12). Consequently, cryptand carriers, with their greater extraction constants, were utilized. Commercially available carriers and a range of common potassium salts provide a distribution of values of extraction constant, controlled by the nature of the anion (12). The dicarboxylate crown ether (13) (Crn) shown in Fig. 2 was chosen as the species C; thus AC represents the potassium complex of this crown ether. The formation constant of the 1:1 complex is $\log K_{110} = 4.6$ in water at 5×10^{-3} M (14). Both aqueous phases must be buffered at a basic pH to prevent protonation of the cryptand carrier (Cry) (pK_a (2.2.2) = 9.6) (15). In such basic solutions, the complexation equilibria of Crn can be simply represented as the formation of the 1:1 complex without need to consider the ligand pK_a or the protonated complexes of the ligand (14).

The use of a polycarboxylate crown ether to control the internal potassium and sodium ion concentrations in an emulsion membrane experiment has been previously reported (40); this case and related cases will be discussed in the Conclusions.

2.1 Equilibrium position

The overall equilibrium state of the system of Fig. 2 can be represented by eq. [2],

[2] $K_l^+ + X_l^- + Crn_r^{2-} \rightleftharpoons CrnK_r^- + X_r^-$

which defines an equilibrium constant K_{eq} (eq. [3]) in terms of concentrations (strictly activities of the various species).

$$[3] \quad K_{eq} = \frac{[CrnK^-]_r[X^-]_r}{[K^+]_l[X^-]_l[Crn^{-2}]_r}$$

The complex $CrnK^-_r$ is in equilibrium with K_r^+ and Crn_r^{2-} (eq. [4]) with defined equilibrium constant K_{110}.

$$[4] \quad Crn_r^{2-} + K_r^+ \rightleftharpoons CrnK_r^- \quad K_{110} = \frac{[CrnK^-]_r}{[Crn^{2-}]_r[K^+]_r}$$

Substitution of $[CrnK^-]_r$ from eq. [4] into eq. [3] gives eq. [5].

$$[5] \quad K_{eq} = K_{110}\,\frac{[K^+]_r[X^-]_r}{[K^+]_l[X^-]_l}$$

The ratio of concentrations (activities) that appears in eq. [5] is the same as the "overall equilibrium constant" defined for the gradient pumping symport case of Fig. 1. In a simple gradient pumping system, the overall equilibrium constant is unity, by definition (7). Thus the value of K_{eq} (eq. [3]) is numerically equal to K_{110} (eq. [4]). At total concentrations of $[K^+]_{tot} = 2 \times 10^{-3}$ M and $[Crn^{2-}]_{tot} = 5 \times 10^{-3}$ M, the potassium is 99.2% complexed. Thus, to a good approximation, $[CrnK^-]_r \simeq [K^+]_{tot,r}$ and $[Crn^{2-}]_r = [Crn^{2-}]_{tot,r} - [K^+]_{tot,r}$. This provides a means to determine K_{eq} experimentally from the total measured concentrations of K^+ and X^- in each phase, according to eq. [6].

$$[6] \quad K_{eq} = \frac{[K^+]_{tot,r}[X^-]_r}{[K^+]_l[X^-]_l([Crn^{2-}]_{tot,r} - [K^-]_{tot,r})}$$

The experimental value of K_{eq} can then be compared to an independently measured value of K_{110}.

2.2 Flux behavior

For experimental simplicity we chose a U-tube bulk liquid membrane. We follow the analysis of Behr, Kirch, and Lehn (8) in defining the characteristics of the liquid membrane. We assume here, and demonstrate experimentally (see Experimental), that the transport is limited by diffusion. This means that the interfacial reactions are fast and $R = R' = 0$. For a simple diffusional process, k and k' are defined by Fick's law. We assume the membrane is symmetric, thus $k = k' = D/l$ where D is a general diffusion coefficient, equal for all species in the membrane, and l is the diffusion thickness of the unstirred boundary layers adjacent to the interfaces (8). Substitution of these constraints into eq. [1] yields eq. [7].

$$[7] \quad J\left(\frac{2l}{\hat{C}D}\right) = \frac{(K - K')}{(1 + K)(1 + K')}$$

We note that $\hat{C}$ is the total carrier concentration at every point (L_0 in ref. 8), hence the bracketed term on the left of eq. [7] is simply $1/J_{max}$, the reciprocal of the maximal flux the system can exhibit under the imposed experimental conditions (8). Equation [7] thus defines the term J/J_{max} in parallel with the analysis of Behr, Kirch, and Lehn (8).

Finally, chemical identities can be assigned to generate explicit forms for K and K'. Since membrane symmetry is assumed (8), K_{ex}, defined by eq. [8], applies at both interfaces:

[8] $K^+(aq) + X^-(aq) + Cry(org) \rightleftharpoons CryKX(org)$

$$K_{ex} = \frac{[CryKX(org)]}{[K^+(aq)][X^-(aq)][Cry(org)]}$$

and eq. [7] becomes eq. [9].

$$[9] \quad \frac{J}{J_{max}} = \frac{K_{ex}(F - G)}{(1 + K_{ex}F)(1 + K_{ex}G)}$$

where

$$[10] \quad F = [K^+]_l[X^-]_l$$

$$[11] \quad G = \frac{[CrnK^-]_r[X^-]_r}{K_{110}[Crn^{2-}]_r}$$

Equation [9] is a close relative of the equations independently

Can. J. Chem. Downloaded from www.nrcresearchpress.com by 93.93.197.157 on 09/07/12
For personal use only.

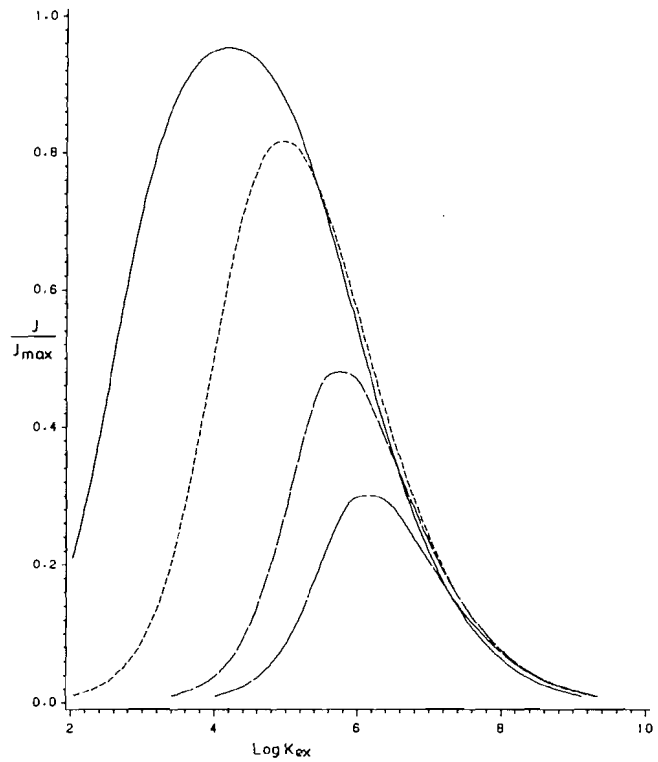

FIG. 3. J/J_{max} as a function of log K_{ex} showing the effect of the left-hand aqueous phase composition of the transport behavior for the cell: variable [KX], pH 9.6 $\|$ 1×10^{-3} M Cry $\|$ 2×10^{-3} M KX, 5×10^{-3} M Crn, pH 9.6, for 1% total transport. ———, [KX] = 5×10^{-2} M; -----, [KX] = 1×10^{-2} M; – – –, [KX] = 2.0×10^{-3} M; – – [KX] = 1×10^{-3} M.

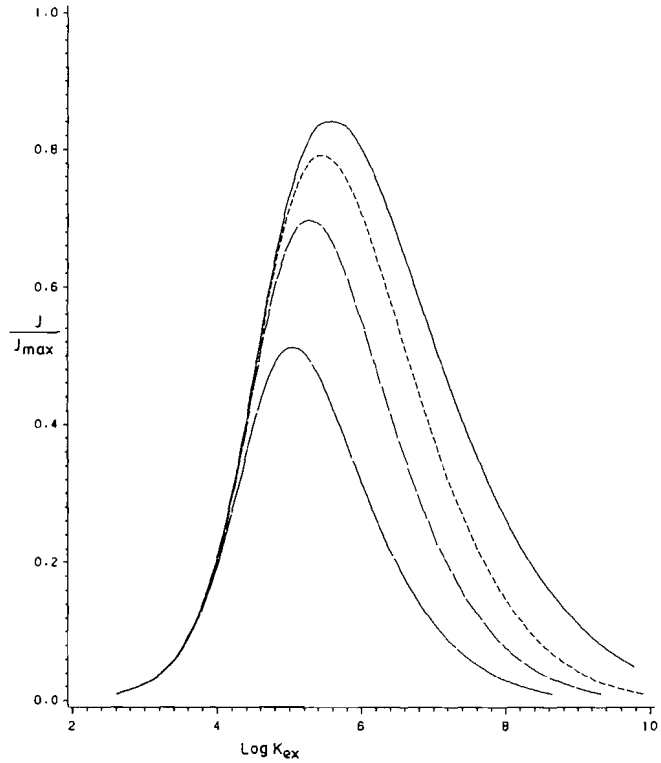

FIG. 4. J/J_{max} as a function of log K_{ex} showing the effect of $[X^-]_r$ on the transport behavior of the cell: 5×10^{-3} M KX, pH 9.6 $\|$ 1×10^{-3} M Cry $\|$ 2×10^{-3} MK^+, 5×10^{-3} M Crn, variable $[X^-]$, pH 9.6, for 1% total transport. ———, $[X^-] = 0$; ------ $[X^-] = 5 \times 10^{-4}$ M; – – – $[X^-] = 2 \times 10^{-3}$ M; – –, $[X^-] = 5 \times 10^{-3}$ M.

developed (8) for the symport and antiport cases of gradient pumping. Using K and K' as defined for gradient pumping, eq. [7] also yields eqs. (8) and (9) of ref. 8 for the symport and antiport respectively.

As previously derived (8, 12), eq. [9] is a quadratic in K_{ex} and may be solved as follows: 1. For a given fraction of transport (f), the total concentrations in both aqueous phases may be derived from the initial concentrations. Using these concentrations in the right compartment, the values for stability and acidity constants of Crn, the pH, and the mass balance equations, the equilibrium concentrations $[Crn^{2-}]_r$ and $[CrnK^-]_r$ can be calculated (16). 2. The terms F and G (eqs. [10] and [11]) are thus defined and the two roots (K_{ex}) of eq. [9] can be solved for a cycle of values of J/J_{max} (8, 12). 3. Finally, the results are plotted as a bell-shaped curve of J/J_{max} as a function of log K_{ex}. This procedure permits a computational survey of the flux behavior of the system expected for various initial conditions, values of K_{110}, or extents of transport.

The normalized flux, J/J_{max}, is a bell-shaped function of log K_{ex}. At low values of the extraction constant, the extraction of KX into the organic phase is poor and the flux is low. As K_{ex} increases, the flux increases up to a maximum at an optimal value of K_{ex} (K_{ex}(opt)). At this point the concentration gradients in the unstirred boundary layers are symmetric and equal, and the carrier is half saturated (8). A further increase in K_{ex} results in a decrease in flux as the carrier holds KX in the organic phase.

Figure 3 illustrates the influence of the concentrations in the left aqueous phase. Below K_{ex}(opt), the flux varies with the product $[K^+]_l[X^-]_l$ and a Michealis–Menton analysis will apply. (8). At values of K_{ex} greater than K_{ex}(opt) the flux is independent of the left aqueous phase composition, hence saturation kinetics do not apply. Similarly, the flux is a function of the concentration of the anion in the right aqueous phase as shown in Fig. 4. As $[X^-]_r$ increases there is a marked decrease in the flux for systems with log K_{ex} > log K_{ex}(opt). Behavior such as this is not found in gradient pumping cases and provides an additional experimental test. Figure 5 illustrates that the flux depends on the extent of transport, falling ultimately to zero in the equilibrium limit. The curves are symmetrical about K_{ex}(opt), in contrast to symport gradient pumping but similar to antiport gradient pumping (8). This suggests that initial rate methods should be used with some caution since the concentrations are nowhere strictly linear functions of time. Figure 6 shows the variation expected for a variation of carrier concentration. This set is similar to related gradient pumping cases. Note that J_{max} is a linear function of carrier concentration, hence the absolute transport rate is slower at the lower concentrations but the rate relative to a given amount of carrier is greater at lower concentration for systems above log K_{ex}(opt).

3. Experimental tests of the model

The equilibrium state of the experimental system is in principle easy to assess. In practice, however, these experiments were complicated by the very low rates of transport for near equilibrium conditions; the flux depends upon the concentration gradients, which are shallow near equilibrium. As a consequence, experiments take several weeks to reach equilibrium. Small amounts of evaporation or acidification by atmospheric CO_2 strongly perturb the calculation of K_{eq} by eq. [6]. In addition, although the Br^- and ClO^-_4 cases initially proceed more rapidly

Can. J. Chem. Downloaded from www.nrcresearchpress.com by 93.93.197.157 on 09/07/12
For personal use only.

Can. J. Chem. Downloaded from www.nrcresearchpress.com by 93.93.197.157 on 09/07/12
For personal use only.

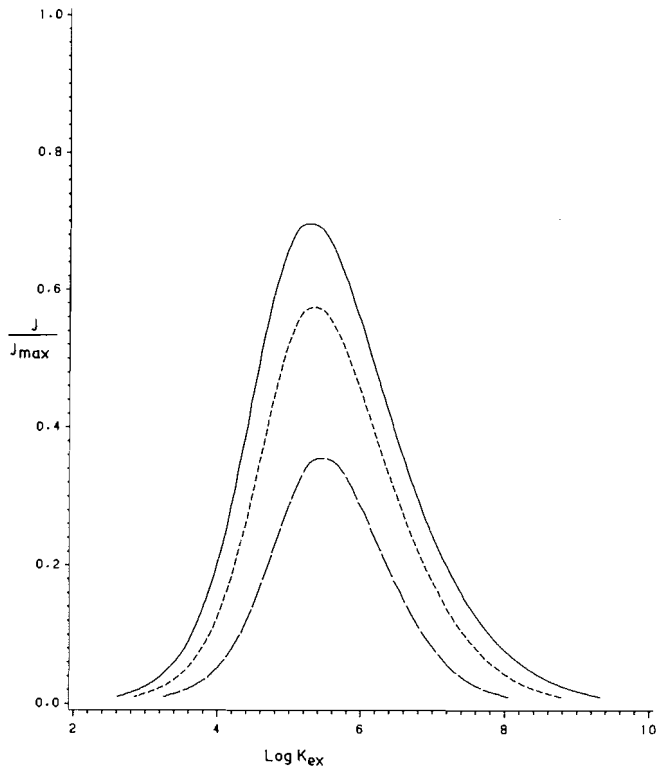

FIG. 5. J/J_{max} as a function of log K_{ex} showing the effect of the fraction of transport on the behavior of the system for the cell 5×10^{-3} M KX $\|$ 1×10^{-3} M Cry $\|$ 2×10^{-3} M KX, 5×10^{-3} Crn, pH 9.6. ——— $f = 1\%$; ----- $f = 25\%$; – – – $f = 50\%$.

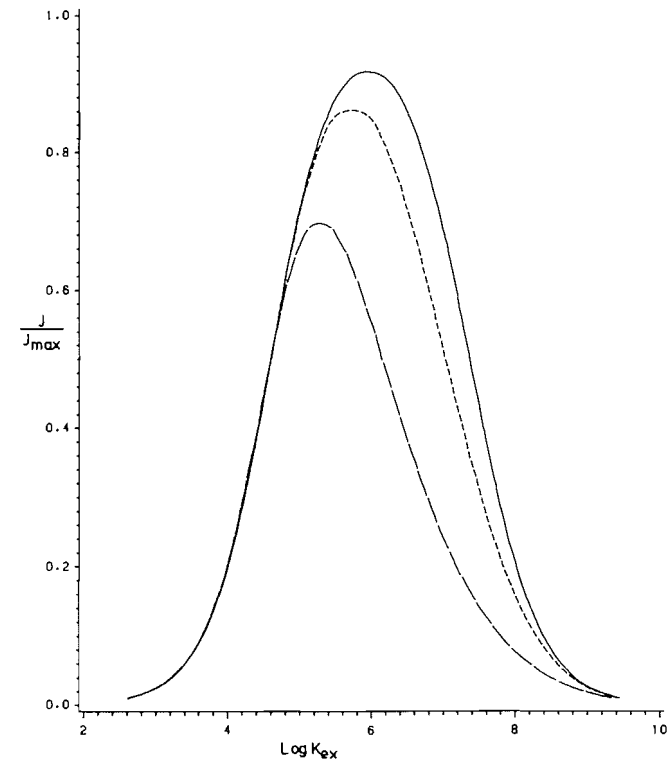

FIG. 6. J/J_{max} as a function of log K_{ex} showing the effect of variable carrier concentration on the cell: 5×10^{-3} M KX, pH 9.6 $\|$ vary [Cry] $\|$ 2×10^{-3} M KX, 5×10^{-3} Crn, pH 9.6. ———, [Cry] = 1×10^{-5} M; ---- [Cry] = 10^{-4} M; – – – [Cry] = 10^{-3} M.

than the Cl^- system (due to favorable log K_{ex}), an appreciable amount of potassium is held in the organic phase. This eventuality is ignored in the derivation of eq. [6]. The effect is minimized by use of Cl^- as anion, engendering even longer experimental times.

Nevertheless, the equilibrium of a KCl system was reached in 5–7 weeks using a sealed cell. The initial conditions were 2.0×10^{-3} M KCl, pH 9.60 $\|$ 1.0×10^{-3} M 2.2.2D in $CHCl_3$ $\|$ 2.0×10^{-3} M KCl, 5.0×10^{-3} M Crn, pH 9.6. The equilibrium state for these conditions is calculated to be $[KCl]_{l,eq} = 4.5 \times 10^{-4}$ M, $[KCl]_{r,eq} = 3.55 \times 10^{-3}$ M. The experimental values are: $[K^+]_l = (4.31 \pm 0.05) \times 10^{-4}$ M, $[Cl^-]_l = (4.5 \pm 0.1) \times 10^{-4}$ M, $[K^+]_{r,tot} = (3.51 \pm 0.05) \times 10^{-3}$ M, and $[Cl^-]_r = (3.57 \pm 0.1) \times 10^{-3}$ M. Substitution of these values into eq. [6] yields an experimental value of log $K_{eq} = 4.64 \pm 0.05$, in comparison to log $K_{110} = 4.6 \pm 0.2$ (14). Similar experiments using KBr or $KClO_4$ yield somewhat higher values of log K_{eq} (4.79, 4.84), complicated by potassium extraction as noted above. Nevertheless, the agreement of theory with experiment lies within or near the limit of the experimental uncertainties.

3.1 Determination of J_{max}

The term J_{max} contains the parameters D and l, neither of which is readily accessible. The value of J_{max} may be determined in the same way as in an enzyme kinetics experiment, from the variation in flux as a function of substrate concentration. In the present case the substrate is the left aqueous phase concentration $[K^+]_l[X^-]_l$ (12). The procedure is only valid if $K_{ex} < K_{ex}(opt)$ (8), but J_{max} should be a constant for all systems at equal carrier concentration and equal stirring behavior (18). The Eadie–Hofstee form of the Michealis–Menton equation was used (17) (eq. [12])

$$[12] \quad J = \frac{-1}{K_{ex}} \left(\frac{J}{[K^+]_l[X^-]_l} \right) + J_{max}$$

and J_{max} was determined as the intercept of a plot of J as a function of $J/([K^+]_l[X^-]_l)$. The systems examined are given in Table 1; six of the seven cases cluster around 3.4×10^{-6} mol m^{-2} s^{-1} but the seventh (2.2.2/KCl) is much lower. In this case, much higher salt concentrations were required to achieve useful rate variation. Further, the carrier 2.2.2 is water soluble and may be salted out into the aqueous solution. This would lower [Cry(org)] and thus lower J_{max}. Ignoring this one case, the average of the other six is $(3.40 \pm 0.17) \times 10^{-6}$ mol m^{-2} s^{-1}, taken to apply to all 12 systems examined.

3.2 Determination of K_{ex}

For systems where saturation kinetics apply, K_{ex}, defined by eq. [2], can be evaluated from the slope of the plot of eq. [12]. This method is inappropriate for systems with $K_{ex} > K_{ex}(opt)$ and extraction constants were determined directly. Two types of experiments were done for each carrier/salt pair. In one set a strongly basic (pH 11.7) aqueous phase was used. Under these conditions, protonation of the cryptand can be ignored and eq. [13] applies for equal phase volumes of organic and aqueous phases.

$$[13] \quad K_{ex} = \frac{(M - M_{eq})}{(L - M + M_{eq})(M_{eq})(M_{eq})}$$

where L is the total initial carrier concentration, M is the total initial potassium concentration, and M_{eq} is the equilibrium aqueous phase potassium ion concentration. In a second set of two-phase extraction experiments, the solution pH and carrier

TABLE 1. Transport flux and extraction constants determined[a]

Entry	Cry	X	Conditions[b]	J	J_{max}	log K_{ex}	J/J_{max}
1	2.2.2D	Cl	A	3.30			
2	2.2.2D	Cl	B	1.65			
3	2.2.2D	Cl	C	0.63	3.45	3.95[c]	0.18
4	2.2.2D	Br	A	3.28			
5	2.2.2D	Br	B	2.81			
6	2.2.2D	Br	C	2.09	3.30	4.84[c]	0.61
7	2.2.2D	Br	E	0.21			
8	2.2.2D	Br	F	2.06			
9	2.2.2D	Br	G	1.04			
10	2.2.2D	NO_3	B	2.92			
11	2.2.2D	NO_3	C	2.20	3.12	4.89[c]	0.65
12	2.2.2D	NO_3	D	0.73			
13	2.2.2D	I	C	0.64		7.4[d]	0.19
14	2.2.2D	I	B	0.61			
15	2.2.2D	I	F	0.23			
16	2.2.2D	ClO_4	C	0.58		7.4[d]	0.17
17	2.2.2	ClO_4	F	0.33			
18	2.2.2	Cl	A	1.12			
19	2.2.2	Cl	H	1.56	1.73[e]	2.90[c]	
20	2.2.2	Cl	I	0.58			
21	2.2.2	Cl	C	<0.10			<0.03
22	2.2.2	Br	A	3.35			
23	2.2.2	Br	B	2.64			
24	2.2.2	Br	C	1.47	3.44	4.48[c]	0.43
25	2.2.2	NO_3	A	3.42			
26	2.2.2	NO_3	B	2.99			
27	2.2.2	NO_3	C	2.08	3.62	4.9[f]	0.61
28	2.2.2	ClO_4	C	0.49		7.5[d]	0.14
29	2.2.2	I	C	0.59		7.2[d]	0.17
30	2.2.1	I	A	3.11			
31	2.2.1	I	B	2.64			
32	2.2.1	I	C	1.54	3.50	4.50[c]	0.45
33	2.2.1	ClO_4	C	2.16		5.7[d]	0.64

[a]For the cell: variable $[KX]_l$, pH 9.6, glycine/MTEAOH ‖ 1.0×10^{-3} M Cry ‖ 5.0×10^{-3} M Crn, variable $[KX]_r$, pH 9.6, glycine/MTEAOH at 25 ± 0.5°C stirring at 400 rpm. Units of J: 10^{-6} mol m^{-2} s^{-1}; uncertainties: J ± 10%, log K_{ex} ± 0.5.

[b]Condition: $[KX]_l$, $[KX]_r$; A: 5.0×10^{-2}, 2.0×10^{-3}; B: 1.0×10^{-2}, 2.0×10^{-3}; C; 5.0×10^{-3}, 2.0×10^{-3}; D: 2.0×10^{-3}, 2.0×10^{-3}; E: 1.0×10^{-3}, 2.0×10^{-3}; H: 1.0×10^{-1}, 2.0×10^{-3}; I: 2.5×10^{-2}, 2.0×10^{-3}; F: 5.0×10^{-3}, 4.0×10^{-3}; G: 5.0×10^{-3} M KBr, 4.0×10^{-3} M $KClO_4$.

[c]Determined by eq. [20].

[d]Direct determination by eqs. [21] and [22]. Results from two methods at each of two concentrations averaged.

[e]See text; salting out of Cry probable.

[f]Averaged value: 4.72[c] and 5.1[b].

concentration were identical to the transport experiment. Since the pH is close to the carrier pK_a, these values were corrected to account for partial protonation according to eq. [14],

$$[14] \quad K_{ex} = \frac{(M - M_{eq})}{(L - M + M_{eq})(M_{eq})^2}\left(1 + \frac{pH}{pK_a}\right)$$

where the pK_a is for the first protonation of the carrier. Further protonation and partitioning of partly protonated species were ignored. The values of log K_{ex} derived from the two sets of experiments agreed to ±0.1 in all cases. Values averaged between two initial potassium concentrations are given in Table 1.

3.3 Flux behavior of the model

The initial concentrations in the standard experiment were $[KX]_l = 5 \times 10^{-3}$ M, pH 9.6 ‖ 1.0×10^{-3} M Cry in $CHCl_3$ ‖ $[KX]_r = 2.0 \times 10^{-3}$ M, [Crn] = 5.0×10^{-3} M, pH 9.6. As noted above, the potassium on the right is 99.2% complexed; at 20% transport this only drops to 98.8%. The potassium on the right is virtually entirely complexed throughout the experiment. The observed fluxes for 12 directly comparable cases at 5% total transport are given in Table 1. Experimental pairs of J/J_{max} and log K_{ex} are compared with the theoretical curve in Fig. 7. The agreement is quite good, especially on the saturation kinetics side. The lack of suitable systems with log K_{ex} > log K_{ex}(opt) limits the number of independent points on the other side of the bell curve.

The anion dependence of flux predicted in Fig. 4 can be observed experimentally. However, as the transport proceeds, $[X^-]_r$ increases quite rapidly. Thus the flux decreases after a brief induction period. The net result is a sigmoidal curve of $[K^+]_r$ vs. time, which is difficult to reliably quantify. Attempts to buffer $[X^-]_l$ at some low value were messy and unreliable, but in qualitative agreement with Fig. 4. Alternatively, the flux can be markedly suppressed by addition of ClO_4^- or I^- to the right-hand aqueous phase, not only of systems containing these same counterions (entries 13, 15; 16, 17) but also in a Br^- system (entries 8, 9). In the latter case, ClO_4^- on the right inhibits Br^- transport from left to right even though no ClO_4^- can be detected

Can. J. Chem. Downloaded from www.nrcresearchpress.com by 93.93.197.157 on 09/07/12
For personal use only.

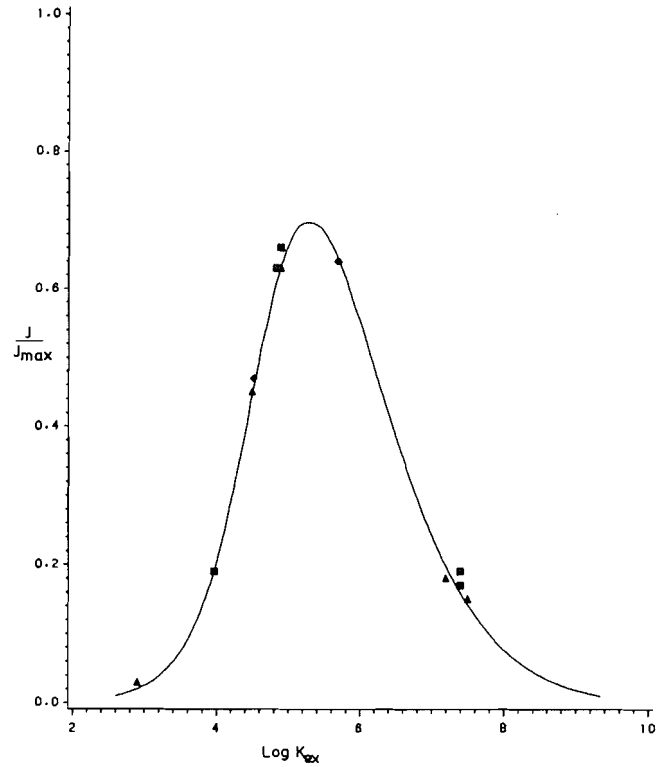

FIG. 7. J/J_{max} as a function of log K_{ex}. Experimental points from Table 1, condition C. Theoretical curve calculated for condition C at 5% total transport. ■ 2.2.2D as carrier; ▲ 2.2.2 as carrier; ◆ 2.2.1 as carrier.

in the left aqueous phase. This is entirely consistent with the model. That a saturable process occurs for $K_{ex} < K_{ex}(opt)$ is implicitly demonstrated by the determination of J_{max} and K_{ex} by eq. [12]. The converse case is demonstrated by the KI/2.2.2D system (entries 13, 14), consistent with the calculation presented in Fig. 3.

4. Conclusions

Taken together, the experimental results provide strong confirmation that the development from eq. [1] as outlined above is a reliable predictor of the kinetic and equilibrium behavior to be expected of systems derived from Fig 1. It is perhaps less clear that the experimental system examined is in fact an "active" transport system within the sense of a biochemical definition. Certainly no covalent bond lysis occurs, as the paradigm of ATP hydrolysis would require. Nonetheless, transport is clearly coupled to a reaction free energy change, that of the complexation of K^+ by Crn^{2-}, and the transport ceases when the equilibrium condition of eq. [3] is satisfied. The gradients present at equilibrium are balanced by the reaction free energy change as would occur in an isolated Na^+/K^+ pump energized by ATP hydrolysis. The distinction is to focus attention upon what the ΔG achieves rather than upon where it came from.

Within this context it is of interest to examine previous reports of active transport as well as other reports in which the question of active transport was not addressed. The most obvious of the latter are the reports of Izatt and co-workers on the transport of cations across emulsion membranes driven by suitable complexing anions in the internal phase (19–21). The system is formally identical to the one presented here; the authors discuss the role of the complexing anion and stability of the metal ion complexes formed in determining the extent of transport. From the viewpoint of active transport this is equivalent to varying the available reaction free energy, which controls varying the magnitude of the concentration gradient that can be achieved at equilibrium. The brief report involving polycarboxylate crown ethers as complexing agents (40) must also fall in this class. However, the pH of the internal phase of the system is not reported and it is unclear what the full driving force might be. Cation complexation in an unbuffered system would result in deprotonation (14) and acidification of the internal phase. The net result would be to diminish the ability of the crown ether to bind further potassium or sodium internally.

When one of the transported species is a proton, in cation–proton antiport systems for example, use of buffer solutions to maintain a target pH gradient results in formal similarities to primary active transport. In these cases AC is some acid in equilibrium with its conjugate base C. Extent of transport should then be determined by the pK_a of the acid. This has not been explicitly demonstrated, as the buffer components are usually regarded as uninteresting and are commonly used in excess with respect to the transported ions (17). An antiport reaction pumping scheme for ammonia, exploiting acid/base behavior, has been described by Selegny and Langevin (22). These authors focus on membrane asymmetry as the essential principle, but the system can equally well be represented according to Fig. 1 and eq. [1]. An earlier glucose transport system, also asymmetric, can similarly be cast in the form of Fig. 1 and eq. [1] (23).

Of the systems claiming to involve active transport, the majority of cases are examples of gradient pumping (9). Systems that are unambiguous examples of reaction pumping all involve electron transport coupled to cation symport (24) or anion antiport (25–27). One of the latter has been examined near equilibrium, where an anion gradient has been shown to drive a redox process (25), as anticipated by Fig. 1. This is akin to reaction coupling, as are other reports of electron transport (28, 29). The equilibrium and kinetic behavior of these systems probably also follows the predictions from eq. [1]; curves such as Figs. 3–6 would thus involve a composite electron transfer/extraction equilibrium constant. These electrochemically driven processes are in contrast to numerous electrochemically (30–33) or photochemically (34–37) switched transport processes. The distinction between redox or light *driven* transport and redox or light *switched* transport turns on the utilization of the input energy. In a driven transport process the energy is used for gradient creation. In switching, the carrier or substrate is prepared for efficient extraction or release; any "uphill" transport that occurs is a result of gradient pumping.

It is clear that some good examples of reaction pumping and reaction coupling have been demonstrated. However, examples involving transport of substrates other than electrons or protons, such as the model outlined in this report, have not been widely investigated. At the same time these are the cases that will yield useful separation and reaction coupling applications. The carriers required for numerous types of substrates are known (9). The procedure outlined in this report will assist in the design of systems incorporating these known carriers for new transport systems.

Experimental

The carriers utilized were commercially available (Merck) and were used as received. Potassium salts and other buffer components were of analytical grade. The crown ether, *R,R*-(+)-1,4,7,10,13,16-hexaoxacyclooctadecane-2,3-dicarboxylic acid (Crn) was prepared and purified as previously described (13, 14). The buffers utilized

Can. J. Chem. Downloaded from www.nrcresearchpress.com by 93.93.197.157 on 09/07/12
For personal use only.

Can. J. Chem. Downloaded from www.nrcresearchpress.com by 93.93.197.157 on 09/07/12
For personal use only.

methyl tris(hydroxyethyl)ammonium ($MTEA^+$) as a non-extractable cation and were prepared from $MTEA^+OH^-$, which was prepared as previously described (38). A stock buffer solution was prepared from glycine by addition of MTEAOH to reach a final pH of 9.6 and then made to volume to contain 2×10^{-2} M glycine. The stock solution was diluted by 1:2 for the solutions used for transport and extractions, which therefore contained 1×10^{-2} M glycine/$\sim 5 \times 10^{-3}$ M $MTEA^+$. Potassium analyses were done using atomic emission as previously described (17). Anion analyses were done by anion chromatography using the system previously described (39).

Equilibrium position of transport

These experiments used the U-tube cell described previously (17) sealed with serum caps on either arm. Only the organic phase in the base of the cell was stirred (magnetic stirrer); the aqueous solutions were slowly mixed by convection and viscous drag at the interfaces. The initial conditions were as follows: left aqueous phase, 8.0 mL, 2.0 $\times 10^{-3}$ M KX, glycine/MTEAOH (10^{-2} M gly), pH 9.6 ‖ 12.0 mL membrane phase ($CHCl_3$) containing 1.0×10^{-3} M carrier ‖ right aqueous phase, 8.0 mL, 2.0×10^{-3} M KX, 5.0×10^{-3} M Crn, glycine/MTEAOH (10^{-2} M gly), pH 9.6. The initial solutions were analysed for potassium and anion concentrations. The cell was sealed, and the pressure in both arms was equalized with needles through the serum caps, which were then withdrawn. The cell was thermostatted at 25.0 ± 0.5°C, and the organic phase was stirred at 400 ± 1 rpm for periods ranging up to 8 weeks. Samples (25 μL) were withdrawn periodically and checked for change in potassium ion concentration. When no further change was noted over a period of 7–10 days, the cell was opened, the pH was checked, and multiple samples were withdrawn for potassium and anion concentration determination. A sample of the organic phase was evaporated and analysed for potassium. The systems examined were (salt, carrier, length of experiment, log K_{eq} calculated by eq. [6], residual potassium in the membrane expressed as % carrier saturation): $KClO_4$, 2.2.2D, 3 weeks, 4.84, 65%; KBr, 2.2.2D, 3 weeks, 4.79, 35%; KCl, 2.2.2D, 7 weeks, 4.64, 7%.

Kinetic behavior

The transport experiments, analytical procedures and transport rate determinations followed procedures previously described (17). The initial conditions are given in the footnotes to Table 1; all solutions contained glycine/MTEAOH pH 9.6 (10^{-2} M glycine). Additional experimental tests included the following: 1. A repeat of entry 6 with no cryptand carrier, which gave no detectable transport. Thus the dicarboxylate crown cannot act as a carrier. 2. Multiple repeats of entry 6 at stirring rates of 100, 200, and 600 rpm; fluxes of 1.41, 1.81, and 2.43 $\times 10^{-6}$ mol m^{-2} s^{-1} show that the rate is a function of stirring, hence is controlled by diffusion (18) as assumed. 3. A repeat of entry 6 with carrier concentrations of 5×10^{-4} M and 2×10^{-3} M; fluxes of 1.21 and 3.87 $\times 10^{-6}$ mol m^{-2} s^{-1} indicate that the rate is a function of carrier concentration (approximately first order in carrier (17)) as required by the mechanism assumed. 4. Several repeats of entries 22–24 at different buffer concentrations; no detectable change in flux from the values reported.

Determination of log K_{ex}

In a small stoppered test tube, immersed in a constant temperature bath, was placed 0.500 mL of the carrier solution in $CHCl_3$ (5×10^{-4} M or 1×10^{-3} M) followed by 0.500 mL of an aqueous solution of potassium salt (5×10^{-4} M, 1×10^{-3} M, or 2×10^{-3} M KX in glycine/MTEAOH pH 9.6 (10^{-2} M gly) or 10^2 M MTEAOH pH 11.7). The mixture was stirred on a vortex mixer for 60 s, equilibrated in the constant temperature bath for 5 min, and the aqueous phase was sampled in triplicate (50–100 μL). The mixing/equilibration/sampling procedure was repeated. The six samples were diluted and analysed for potassium by atomic emission. Initial concentrations of potassium were determined by atomic emission from the stock solutions used. Values of K_{ex} were calculated for each sample using eq. [13] or [14] and averaged within each set of triplicates. In general the two sets agreed within log K_{ex} ± 0.05 and were averaged. This result suggests that 60 s of mixing is sufficient to reach equilibrium. The concentration range is best suited for log K_{ex} 5.5–7.5 and the calculations are most reliable for approximately 50% extraction; for lower values of log K_{ex} the pair of experimental values from 1×10^{-3} M and 2×10^{-3} M KX solutions were averaged and reported in Table 1; for higher values of log K_{ex} the results from 5.0×10^{-4} M and 1.0×10^{-3} M KX solutions were averaged. Agreement between eqs. [13] and [14] at a given concentration was good (log K_{ex} ± 0.1) but agreement between pairs of concentrations was less satisfactory (log K_{ex} ± 0.3). The values reported in Table 1 are reliable to log K_{ex} ± 0.5, as assessed from replicate experiments from separate solution preparations. The extraction stoichiometry was assumed to be 1:1 in all cases. This was confirmed by an nmr extraction experiment utilizing 2.2.2D in $CDCl_3$ and $KClO_4$ in D_2O. The ^1H nmr spectrum changed with added $KClO_4$ up to one equivalent but was constant thereafter, consistent with the formation of a 1:1 complex.

Calculations of theoretical curves

The general procedure follows those reported previously (8, 12) and the methods outlined in the text. The equilibrium concentrations for the right aqueous phase were calculated using the algorithm of COMPLEX (16), the total concentrations and the pH, and the values of cumulative association constants for Crn: log $\beta_{101} = 4.48$, log $\beta_{102} = 7.42$, log $\beta_{110} = 4.60$ (= log K_{110}), log $\beta_{111} = 8.07$. For a given fraction of transport f, the total concentrations can be calculated, followed by the equilibrium concentrations as required for eqs. [10] and [11]. A further correction for diffusion resistance in the aqueous unstirred layers must also be applied as in eq. [15] (8, 12).

$$[15] \quad G = \frac{[CrnK^-][X^-]_r}{K_{110}[Crn^{2-}]_r} + \frac{C}{2}\left(\frac{J}{J_{max}}\right)$$

With the terms defined, and $y = J/J_{max}$, eq. [9] can be cast as a quadratic in K_{ex} ($AK_{ex}^2 + BK_{ex} + C = 0$) where $A = yFG$, $B = ((F + G)y + G - F)$, and $C = y$. Repeated solutions for K_{ex} with an increment of 0.01 y yields points for the curves of Fig. 3–7. Interpolation used a cubic spline procedure.[3]

Acknowledgements

The ongoing support of the Natural Sciences and Engineering Research Council of Canada, and of the University of Victoria, is gratefully acknowledged.

1. M. Hofer. Transport across biological membranes. Pitman. London. 1981.
2. M. D. Houslay and K. K. Stanley. Dynamics of biological membranes. J. Wiley and Sons, New York. 1982.
3. P. Mitchell. Biochem. Soc. Trans. **4**, 399 (1974), and references therein.
4. H. V. Westerhof and K. VanDam. Curr. Top. Bioenerg. **9**, 2 (1979).
5. E. Heinz. Curr. Top. Membr. Transp. **16**, 249 (1982).
6. W. P. Jencks. Curr. Top. Membr. Transp. **19**, 1 (1983).
7. J. D. Goddard. J. Phys. Chem. **89**, 1825 (1985).
8. J. P. Behr, M. Kirch, and J. M. Lehn. J. Am. Chem. Soc. **107**, 241 (1985).
9. M. Okahara and Y. Nakatsuji. Top. Curr. Chem. **128**, 37 (1985).
10. R. M. Izatt, G. A. Clark, J. S. Bradshaw, J. D. Lamb, and J. J. Christensen. Sep. Purif. Methods, **15**, 21 (1986).
11. H. R. Mahler and E. H. Cordes. Biological chemistry. 2nd ed. Harper and Row, New York. 1971. pp. 23–25.
12. T. M. Fyles. Can. J. Chem. **65**, 884 (1987).
13. L. A. Frederick, T. M. Fyles, N. P. Gurprasad, and D. M. Whitfield. Can. J. Chem. **59**, 1724 (1981).
14. P. J. Dutton, T. M. Fyles and S. J. McDermid. Can. J. Chem. **66**, 1097 (1988).

[3]The curves were plotted using the GPLOT procedure of SAS/GRAPH; SAS/GRAPH Users Guide, SAS Institute, Cary, North Carolina, 1981.

15. J. M. LEHN and J. P. SAUVAGE. J. Am. Chem. Soc. **97**, 6700 (1975).
16. G. GINZBURG. Talanta, **23**, 149 (1976).
17. T. M. FYLES, V. A. MALIK-DIMER, C. A. MCGAVIN, and D. M. WHITFIELD. Can. J. Chem. **60**, 2259 (1982).
18. T. M. FYLES. J. Membr. Sci. **24**, 229 (1985).
19. J. J. CHRISTENSEN, S. P. CHRISTENSEN, M. P. BIEHL, S. A. LOWE, J. D. LAMB, and R. M. IZATT. Sep. Sci. Technol. **18**, 363 (1983).
20. R. M. IZATT, D. V. DEARDON, D. W. MCBRIDE, JR., J. L. OSCARSON, J. D. LAMB, and J. J. CHRISTENSEN. Sep. Sci. Technol. **18**, 1113 (1983).
21. R. M. IZATT, R. L. BRUENING, G. A. CLARK, J. D. LAMB, and J. J. CHRISTENSEN. J. Membr. Sci. **28**, 77 (1986).
22. E. SELEGNY and D. LANGEVIN. J. Chem. Res. (S), 278 (1978); (M), 3466 (1978).
23. G. BROUN, D. THOMAS, and E. SELEGNY. J. Membr. Biol. **8**, 313 (1972).
24. J. J. GRIMALDI and J. M. LEHN. J. Am. Chem. Soc. **101**, 1333 (1979).
25. T. SHINBO, M. SUGIURA, N. KANO, and Y. KOBATAKE. J. Membr. Sci. **9**, (1981).
26. A. OHKI, M. TAKAGI, and K. UENO. Chem. Lett. 1591 (1980).
27. A. L. ATHAYDE and C. F. IVORY. J. Membr. Sci. **24**, 309 (1985).
28. S. S. ANDERSON, I. G. LYLE, and R. PATERSON. Nature, **259**, 147 (1976).
29. J. J. GRIMALDI, S. BOILEAU, and J. M. LEHN. Nature, **265**, 229 (1977).
30. A. OHKI, T. TAKEDA, M. TAKAGI, and K. UENO. Chem. Lett. 1529 (1982).
31. A. OHKI, T. TAKEDA, M. TAKAGI, and K. UENO. J. Membr. Sci. **15**, 231 (1983).
32. T. SAJI and I. KINOSHITA. J. Chem. Soc. Chem. Commun. 716 (1986).
33. L. ECHEVERRIA, M. DELGADO, V. J. GATTO, G. W. GOKEL, and L. ECHEGOYEN. J. Am. Chem. Soc. **108**, 6825 (1986).
34. S. SHINKAI, T. MINAMI, Y. KUSANO, and O. MANABE. J. Am. Chem. Soc. **104**, 1967 (1982).
35. S. SHINKAI and O. MANABE. Top. Curr. Chem. **121**, 67 (1984).
36. S. SHINKAI, K. MIYAZAKI, and O. MANABE. J. Chem. Soc. Perkin Trans. 1, 449 (1987).
37. T. SHIMIDZU and M. YOSHIKAWA. J. Membr. Sci. **13**, 1 (1983).
38. T. M. FYLES and C. A. MCGAVIN. Anal. Chem. **54**, 2103 (1982).
39. L. M. DULYEA, T. M. FYLES, and G. D. ROBERTSON. J. Membr. Sci. **34**, 87 (1987).
40. R. M. IZATT, G. C. LINDH, R. L. BRUENING, J. S. BRADSHAW, J. D. LAMB, and J. J. CHRISTENSEN. Pure. Appl. Chem. **58**, 1453 (1986).

Can. J. Chem. Downloaded from www.nrcresearchpress.com by 93.93.197.157 on 09/07/12
For personal use only.

Proton transfer reactions between *ortho*-methyl substituted derivatives of 4-nitrophenylphenylcyanomethane and nitrogen bases in acetonitrile solvent

KENNETH T. LEFFEK AND PRZEMYSLAW PRUSZYNSKI[1]

Department of Chemistry, Dalhousie University, Halifax, N.S., Canada B3H 4H6

Received January 4, 1988

KENNETH T. LEFFEK and PRZEMYSLAW PRUSZYNSKI. Can. J. Chem. **66**, 1454 (1988).

Equilibrium constants, rate constants, primary deuterium isotope effects, and activation parameters have been measured for the proton transfer reactions in acetonitrile solvent of 4-nitrophenylphenylcyanomethane and 2-methyl-4-nitrophenylphenylcyanomethane with tetramethylguanidine base and for the reactions of 2-methyl-4-nitrophenylphenylcyanomethane and 2,6-dimethyl-4-nitrophenylphenylcyanomethane with 1,5-diazabicyclo[5.4.0]undec-7-ene base. Introduction of the *ortho*-methyl groups in the substrate molecule caused significant reductions in the equilibrium and rate constants. The expected rise in the kinetic primary deuterium isotope effect was not observed when the first *ortho*-methyl group was introduced, but a 20% increase did accompany the introduction of the second *ortho*-methyl group. Enthalpy of activation measurements indicated that there was no increase in the proton tunnelling contribution to the isotope effect when the amount of steric hindrance is increased with *ortho*-methyl groups.

KENNETH T. LEFFEK et PRZEMYSLAW PRUSZYNSKI. Can. J. Chem. **66**, 1454 (1988).

Opérant dans l'acétonitrile comme solvant, on a mesuré les constantes d'équilibre, les constantes de vitesse, les effets isotopiques primaires du deutérium ainsi que les paramètres d'activation pour les réactions de transfert de proton des nitro-4 et méthyl-2 nitro-4 phénylphénylcyanométhanes avec la base tétraméthylguanidine ainsi que pour les réactions des méthyl-2 nitro-4 et diméthyl-2,6 nitro-4 phénylphénylcyanométhanes avec la base diaza-1,5 bicyclo[5.4.0]undécène-7. L'introduction des groupements méthyles en *ortho* des molécules de substrat provoque des diminutions importantes des constantes d'équilibre ainsi que de vitesse. Lorsqu'on a ajouté le premier groupement méthyle en *ortho*, on n'a pas observé l'augmentation prévue de l'effet isotopique cinétique primaire du deutérium; toutefois, l'introduction du second groupement méthyle en *ortho* provoque une augmentation de 20%. Des mesures d'enthalpie d'activation permettent de déduire qu'une augmentation de l'encombrement stérique, provoquée par la présence de groupements méthyles en *ortho*, ne conduit pas à une augmentation de la contribution de l'effet tunnel du proton.

[Traduit par la revue]

Introduction

Recent kinetic studies of proton transfer reactions from 4-nitrophenylphenylcyanomethane and its ring substituted derivatives in aprotic solvents have shown substantial primary deuterium isotope effects ($k_H/k_D > 10$ at 25°C) indicating a possible significant contribution to the rate constants from proton tunnelling (1). Changes in the rate constant for proton transfer accompanying *para* substitution of the second phenyl ring (2) and variation of the solvent (3) led to the conclusion that the transition state for the reaction came early on the reaction pathway and that the developing negative charge was localized on the central carbon atom. Thus, the carbanionic transition state retains most of the tetrahedral structure of the substrate molecule.

This work is now extended to a study of the steric effects of *ortho*-substituted methyl groups on the phenyl ring carrying the *para* nitro group. Consideration of enhanced primary deuterium isotope effects as a manifestation of steric effects was proposed by Lewis and Funderburk in 1967 (4), but no clear relationship has become apparent. Work done on secondary kinetic deuterium isotope effects in the 1960s and early 1970s, particularly on the configurational inversion of biphenyls, showed that effects arising from steric hindrance (5, 6) did not necessarily increase when very large amounts of steric hindrance were involved (7, 8).

Steric effects on proton transfer reactions from carbon acids have been observed (9, 10), particularly with the highly hindered base 2,7-dimethoxy-1,8-bis(dimethylamino)naphthalene, but no specific study of steric effects in these reactions has been carried out.

[1]Visiting Scientist 1986–1987.

Results and discussion

Three substrate molecules were used, 4-nitrophenylphenylcyanomethane (**1**), 2-methyl-4-nitrophenylphenylcyanomethane (**2**), and 2,6-dimethyl-4-nitrophenylphenylcyanomethane (**3**). The proton transfer reaction rate constants for **1** and **2** were measured with tetramethylguanidine base (TMG) but the reaction of **3** was too slow to be measured. Substrates **2** and **3** reacted at convenient rates with 1,5-diazabicyclo[5.4.0]undec-7-ene (DBU) but substrate **1** was too fast to be measured with this base. The three substrates can be compared using both of these nitrogen bases overlapping the series with substrate **2**.

The reactions were carried out in acetonitrile solvent and the substrates gave a product with a single broad strong absorption peak at 590 nm for **1**, 597 nm for **2**, and 671 nm for **3** characteristic of the carbanions of the acid substrates. The large absorption peak shift for the 2,6-dimethyl substituted product is probably due to steric inhibition of the tendency of the carbanion to assume a nearly planar structure. The absorbance measurements of the equilibrium mixtures were fitted to the Hildebrand–Benesi equation [1] for an ion-pair product, where a and b are the initial concentrations of the acid and base repectively and A is the equilibrium absorbance.

$$[1] \quad a/A = \frac{1}{Kb\epsilon} + \frac{1}{\epsilon}$$

The equilibrium constant K and the molar absorptivity ϵ were derived from a plot of a/A vs. $1/b$. The 2-methyl substrate **2** with TMG gave $K = 300 \pm 60$ dm^3 mol^{-1} at 25°C (ϵ 24 000), a considerably lower value than that previously reported (1) for the unsubstituted substrate **1** of 6000 dm^3 mol^{-1} (ϵ 40 000). This

Can. J. Chem. Downloaded from www.nrcresearchpress.com by 93.93.197.157 on 09/07/12
For personal use only.

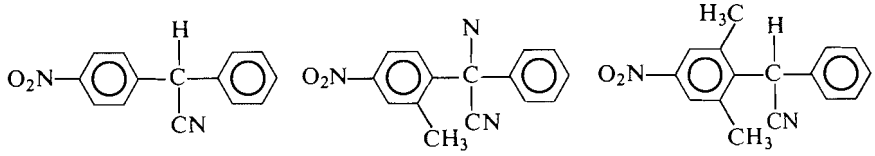

1 2 3

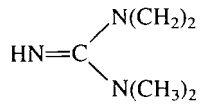

(TMG)

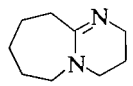

(DBU)

would be expected as a result of the steric inhibition to planarity in the carbanion by the 2-methyl group and also, as a minor contribution, the electron releasing character of that group.

The reaction of DBU with the 2-methyl substrate **2** gave $K = 3500 \pm 700$ dm^3 mol^{-1} at 25°C (ε 37 000) and the addition of the second *ortho*-methyl group in substrate **3** decreased the equilibrium constant to 100 ± 20 dm^3 mol^{-1} (ε 15 000). This change is again consistent with increased steric inhibition to planarity in the carbanion.

The pseudo-first-order rate constants were measured under conditions of a large excess of base using a stopped-flow spectrophotometer, by monitoring the increase of the product concentration at the wavelength corresponding to the product peak. The carbanion formed from the 2-methyl substrate **2** decompsed slowly but no decomposition was detectable at times less than 2 min, whereas the kinetic measurements (10 half-lives) were always complete in less than 2 s.

The pseudo-first-order rate constants, k_{obs}, were fitted to eq. [2] for an equilibrium of the type shown in eq. [3], by a least-squares calculation to yield k_2 and k_b, the rate constants for the forward and backward reactions.

$$[2] \quad k_{obs} = k_2[\text{Base}] + k_b$$

$$[3] \quad \geq C{-}H + N\!\!\leq \underset{k_b}{\overset{k_2}{\rightleftharpoons}} \geq C^- HN^+\!\!\leq$$

These results are shown in Table 1 for five different temperatures for the normal and deuterated analogues of substrates **2** and **3**. The results (1) for substrate **1** at 25°C are included for comparison. The ratio k_2/k_b gives the equilibrium constant K. For the 2-methyl substrate **2** with TMG, $k_2/k_b = 220 \pm 30$ dm^3 mol^{-1} at 25°C for the proton transfer reaction, in satisfactory agreement with the value of 300 ± 60 obtained from the equilibrium measurements. The slow decomposition of the carbanion from this substrate may introduce a slight error in the 300 value, but such an error would be in the direction to increase the value of K.

For the reactions with DBU base, the dimethyl substrate **3** gave $k_2/k_b = 86 \pm 6$ dm^2 mol^{-1} at 25°C, in good agreement with the value of 100 ± 20 from the equilibrium measurements. The methyl substrate **2** gave $k_2/k_b = 2000 \pm 200$ dm^3 mol^{-1} at 25°C, whereas the equilibrium measurements gave 3500 ± 700. However, the experimental error of the Hildebrand–Benesi method may be significantly larger than the statistical value quoted, since K is determined from the slope of the graph $(1/K\varepsilon)$. When $K = 3500$ dm^3 mol^{-1} and $\varepsilon = 37\,000$ the slope is 7.7×10^{-9}. In these circumstances the difference between k_2/k_b of 2000 and 3500 determined for K from the equilibrium measurements may not be significant.

Comparison of the second-order rate constants for the reaction with TMG base shows that the introduction of one *ortho*-methyl group reduces the rate, relative to the unsubstituted substrate, by a factor of 18 at 25°C. However, the primary deuterium isotope effect is essentially unchanged. The second *ortho*-methyl group causes another rate constant reduction in the reaction with DBU base of a factor of 18 at 25°C but in this case the primary deuterium isotope effect is increased by about 20%. The second *ortho*-methyl group decreases the acid strength of the carbon acid and therefore shifts the transition state so that it comes later along the reaction path. This transition state is more planar and more symmetrical, corresponding to greater loss of zero-point energy and larger primary isotope effect. This is not expected to be a large effect (11) and would be offset by some steric inhibition of C—H and C—D vibrational frequencies in the intial state, which would result in smaller isotopic rate ratio. The increased isotope effect is also qualitatively in agreement with an enhanced contribution from proton tunnelling to the rate of the reaction as a consequence of a narrower energy barrier to reaction in the presence of considerable steric hindrance. It is plausible that such an effect would have a threshold and not appear until the steric hindrance reached a particular level with the introduction of the second *ortho*-methyl group.

The activation parameters and the effect of deuterium substitution on them are shown in Table 2. These results show that the major part of the rate constant change for proton transfer when *ortho*-methyl groups are introduced into the substrate molecule is due to increases in the enthalpy of activation, confirming that the effect is predominantly steric in origin. The deuterium isotope effect on the enthalpy of activation is generally greater than the 1.1 kcal mol^{-1} that is expected from the complete loss of the C—H (C—D) stretching vibration in the transition state. However, the three measurements carried out on the methyl substituted substrates all show a slightly smaller enthalpy isotope effect than that obtained for the unsubstituted molecule (1). This demonstrates that there is no evidence for increased tunnelling in this system when the amount of steric hindrance is increased with *ortho*-methyl groups. Thus, although the rates of the reactions are changed by the increased steric hindrance and also the isotope effects to some extent, the width of the barrier to reaction, which controls the amount of proton tunnelling, does not seem to be altered.

Experimental

Materials

p-Nitrophenylphenylcyanomethane and its deuterated analogue were prepared as described previously (1).

Can. J. Chem. Downloaded from www.nrcresearchpress.com by 93.93.197.157 on 09/07/12
For personal use only.

Can. J. Chem. Downloaded from www.nrcresearchpress.com by 93.93.197.157 on 09/07/12
For personal use only.

TABLE 1. Rate constants for the proton transfer reaction from methyl substituted 4-nitrophenylphenylcyanomethanes to nitrogen bases in acetonitrile solvent

(*a*) 4-Nitrophenylphenylcyanomethane and tetramethylguanidine

Temperature (°C)	10^3[Base] (M)	$k_{obs}(s^{-1})$	$10^{-3}k_2(dm^3\ mol^{-1}\ s^{-1})$	$k_b(s^{-1})$	k_H/k_D
Proton transfer					
25.0	0.49–1.97	5.4–16.9	7.86±0.2	1.5±0.2	
Deuteron transfer					
25.0	0.11–0.44	1.3–3.7	0.73±0.03	0.44±0.08	10.7

(*b*) 2-Methyl-4-nitrophenylphenylcyanomethane and tetramethylguanidine

Temperature (°C)	10^3[Base] (M)	$k_{obs}(s^{-1})$	$k_2(dm^3\ mol^{-1}\ s^{-1})$	$k_b(s^{-1})$	k_H/k_D
Proton transfer					
15.0	6.5–32.35	4.0–12.2	315±12	2.1	
20.0	6.5–32.35	4.3–13.8	366±5	2.0	
25.0	6.5–32.35	4.7–16.1	440±7	2.0	
30.0	6.5–32.35	5.6–18.2	509±37	2.4	
35.0	6.5–32.35	6.5–21.8	590±9	2.7	
Deuteron transfer					
10.0	5.0–25.0	0.16–0.61	22.8±1.6	0.064	
15.0	5.0–40.0	0.17–1.15	27.2±0.6	0.058	11.6±0.5
20.0	5.0–50.0	0.23–1.76	34.4±0.3	0.043	10.6±0.2
25.0	5.0–50.0	0.28–2.15	43.8±1.9	0.004	10.0±0.5
30.0	10.0–40.0	0.62–2.18	51.6±1.2	0.12	9.9±0.7

(*c*) 2-Methyl-4-nitrophenylphenylcyanomethane and 1,5-diazabicyclo[5.4.0]undec-7-ene

Temperature (°C)	10^4[Base] (M)	$k_{obs}(s^{-1})$	$10^{-3}k_2(dm^3\ mol^{-1}\ s^{-1})$	$k_b(s^{-1})$	k_H/k_D
Proton transfer					
10.0	5.0–30.0	18.0–74.2	21.8±0.1	5.6	
15.0	5.0–30.0	20.4–80.4	23.6±0.5	8.2	
20.0	5.0–30.0	23.2–92.5	27.1±0.8	10.4	
25.0	5.0–30.0	27.7–103.5	29.3±0.9	14.6	
30.0	5.0–30.0	32.2–120	33.7±0.2	17.2	
Deuteron transfer					
10.0	10.4–52.0	2.0–10.1	1.91±0.05	0.04	11.4±0.3
15.0	10.4–52.0	2.1–11.9	2.27±0.09	0.13	10.4±0.5
20.0	10.4–52.2	2.6–13.4	2.61±0.03	0.20	10.4±0.3
25.0	10.4–52.0	2.8–15.5	3.05±0.03	0.30	9.6±0.3
30.0	10.4–52.0	3.3–17.2	3.57±0.08	0.41	10.0±0.2

(*d*) 2,6-Dimethyl-4-nitrophenylphenylcyanamethane and 1,5-diazabicyclo[5.4.0]undec-7-ene

Temperature (°C)	10^3[Base] (M)	$k_{obs}(s^{-1})$	$10^{-2}k_2(dm^3\ mol^{-1}\ s^{-1})$	$k_b(s^{-1})$	k_H/k_D
Proton transfer					
10.0	4.0–21.0	10–29	10.4±0.4	7.3	
15.0	4.0–21.0	15–36	11.9±0.6	11.4	
20.0	4.0–21.0	19–43	13.9±0.4	14.0	
25.0	4.0–21.0	22–52	16.0±0.7	18.5	
30.0	4.0–21.0	27–55	18.3±0.7	22.8	
Deuteron transfer					
10.0	10.0–50.0	0.76–3.92	0.77±0.01		13.5±0.6
15.0	10.0–50.0	0.94–4.91	0.96±0.04		12.4±0.8
20.0	10.0–48.0	1.15–5.61	1.14±0.05		12.2±0.6
25.0	10.0–48.0	1.30–6.46	1.35±0.02		11.8±0.6
30.0	10.0–48.0	1.57–8.33	1.75±0.06		10.5±0.6

Can. J. Chem. Downloaded from www.nrcresearchpress.com by 93.93.197.157 on 09/07/12
For personal use only.

TABLE 2. Activation parameters for the proton and deuteron transfer reaction from methyl substituted 4-nitrophenylphenylcyanomethanes to nitrogen bases in acetonitrile solvent

(*a*) 4-Nitrophenylphenylcyanomethane and tetramethylguanidine

Parameter	H-transfer		D-transfer
$\Delta H\ddagger$(kcal mol^{-1})	3.7±0.2		5.9±0.2
$\Delta S\ddagger$(cal mol^{-1} deg^{-1})	−28.3±0.7		−25.6±0.8
$(\Delta H\ddagger_D - \Delta H\ddagger_H)$		2.2±0.3	
$(\Delta S\ddagger_D - \Delta S\ddagger_H)$		+2.7±1.1	

(*b*) 2-Methyl-4-nitrophenylphenylcyanomethane and tetramethylguanidine

Parameter	H-transfer		D-transfer
$\Delta H\ddagger$(kcal mol^{-1})	5.0±0.1		6.6±0.3
$\Delta S\ddagger$(cal mol^{-1} deg^{-1})	−29.7±0.4		−28.9±1.0
$(\Delta H\ddagger_D - \Delta H\ddagger_H)$		1.6±0.3	
$(\Delta S\ddagger_D - \Delta S\ddagger_H)$		+0.8±1.0	

(*c*) 2-Methyl-4-nitrophenylphenylcyanomethane and 1,5-diazabicyclo[5.4.0]undec-7-ene

Parameter	H-transfer		D-transfer
$\Delta H\ddagger$(kcal mol^{-1})	3.1±0.2		4.3±0.2
$\Delta S\ddagger$(cal mol^{-1} deg^{-1})	−27.6±0.8		−28.2±0.6
$(\Delta H\ddagger_D - \Delta H\ddagger_H)$		1.2±0.3	
$(\Delta S\ddagger_D - \Delta S\ddagger_H)$		−0.6±1.0	

(*d*) 2,6-Dimethyl-4-nitrophenylphenylcyanomethane and 1,5-diazabicyclo[5.4.0]undec-7-ene

Parameters D-transfer	H-transfer		
$\Delta H\ddagger$(kcal mol^{-1})	4.3±0.1		6.1±0.3
$\Delta S\ddagger$(cal mol^{-1} deg^{-1})	−29.4±0.2		−28.1±1.2
$(\Delta H\ddagger_D - \Delta H\ddagger_H)$		1.8±0.3	
$(\Delta S\ddagger_D - \Delta S\ddagger_H)$		1.3±1.2	

(2-Methyl-4-nitrophenyl)phenylcyanomethane was prepared by the following synthetic route: 2-methyl-4-nitroaniline (0.1 mol) was treated with a solution of 20 g of concentrated H_2SO_4 in 80 mL of water and cooled to 0–5°C. Then 7 g of $NaNO_2$ in 12–15 mL of water was added dropwise and the resulting diazonium salt kept in ice. Cuprous bromide solution was prepared by dissolving 6.3 g of $CuSO_4$, 2 g of clean copper turnings, 15.2 g of NaBr, and 3–4 g of concentrated H_2SO_4 in 100 mL of water. This mixture was heated for 3–4 h until the solution acquired a yellowish colour. The solution was placed in a flask fitted with a steam distillation head, and steam was passed. The cold solution of diazonium salt was then added dropwise. The crude product of 2-bromo-5-nitrotoluene obtained in the steam distillate was purified by washing its ether solution with NaOH solution (to remove phenol) and then by column chromatography on silica gel. Finally it was recrystallized from methanol; mp 78°C; ^{1}H nmr δ(ppm): 2.46 (s, 3H), 7.66–8.14 (m, 3H).

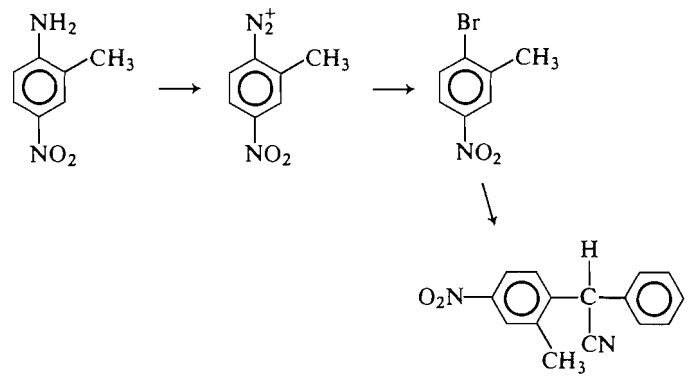

This material was reacted with phenylcyanomethane using the procedure of Davis and Pizzini (12). 2-Bromo-5-nitrotoluene (7.7 g) was dissolved in 56 g of pyridine and 24 g of a paste, obtained by grinding 12 g KOH with 12 g of pyridine, was added. This mixture was kept at 5°C and 4.6 g of phenylcyanomethane was added. The reaction mixture was stirred overnight and the temperature maintained below 0°C. Then 30 mL of benzene was added and the resulting precipitate was filtered, washed with ether, dissolved in water, and finally acidified by acetic acid. The dark colour disappeared and an oily product was formed. This product, after purification by column chromatography, was dissolved in a small amount of chloroform and poured slowly into excess pentane. Yellow crystals were formed, which were then recrystallized from methanol; mp 73–74.5°C; ^{1}H nmr δ(ppm): 2.38 (s, 3H), 5.40 (s, 1H), 7.33–8.17 (m, 8H).

The deuterated analogue was obtained by exchanging 200 mg of the carbon acid with a solution of NaOD in a solution of 25% D_2O in dioxan. After about 2–3 min the reaction mixture was neutralized by several drops of DCl in D_2O. The solvents were then evaporated and the organic part was separated from the NaCl by washing with dry chloroform. The chloroform was then evaporated and the residue dissolved in dioxan. This procedure was repeated four times. A high degree of deuteration was indicated by the disappearance of the proton nmr signal at 5.40 ppm. The mass spectrum indicated 96% deuteration.

(2,6-Dimethyl-4-nitrophenyl)phenylcyanomethane was prepared by the following synthetic route: pure 2,6-dimethylaniline (17.4 g) was dissolved in 112 mL of pyridine (dried over NaOH and distilled) and 31 g of *p*-toluenesulfonylchloride was added. The reaction mixture was refluxed for 2 h and then poured into 700 mL of 2 N HCl; the precipitate was filtered and recrystallized twice from ethanol. Yield 82%, mp 137°C; ^{1}H nmr δ(ppm): 2.03 (s, 6H), 2.4 (s, 3H), 6.2 (s, 1H), 7.03–7.7 (m, 7H).

The nitration step was carried out using a modification of the method of Bambenek (13). A mixture of the sulfonamide (15.3 g), nitric acid, and glacial acetic acid was refluxed for 10 min, after which 5–7 mL of fuming nitric acid was added to initiate the nitration. After heating for a further 6 to 7 min the reaction mixture was cooled and diluted with water. The solid material was filtered and washed with cold water. The crude product was recrystallized from ethanol; yield 66.4%, mp 162–164°C (lit. (14) mp 167°C); ^{1}H nmr δ(ppm): 2.17 (s, 6H), 2.47 (s, 3H), 6.43 (s, 1H), 7.23–7.93 (m, 6H).

The nitrated sulfonamide (19.2 g) was dissolved in concentrated H_2SO_4 (190 mL) and heated at 50°C for 1 h, then cooled and poured into 500 g of ice. The precipitate was decolourized with charcoal in ethanol and recrystallized as yellow needles; yield 50%, mp 165.2°C; ^{1}H nmr δ(ppm): 2.17 (s, 6H), 4.03 (br s, 2H), 7.8 (s, 2H). This 2,6-dimethyl-4-nitroaniline (5 g) was dissolved in a solution of concentrated H_2SO_4 (4.1 mL) in water (30 mL). This solution was cooled to 0–5°C and $NaNO_2$ solution (2.7 g in 4.7 mL H_2O) was added slowly. The diazonium salt thus formed was then added to a CuBr solution, prepared as described above, and the mixture was steam distilled. The distillate was washed with NaOH and the residue filtered to yield about 3 g of crude 2,6-dimethyl-4-nitrobromobenzene; ^{1}H nmr δ(ppm): 2.53 (s, 6H), 7.97 (s, 2H).

This product (2.5 g) was dissolved in pyridine (20 mL) and a paste, obtained by grinding 4.2 g of KOH in 4.2 g pyridine, was added. The mixture was cooled to −5°C and 1.5 g of phenylcyanomethane was added with stirring. The stirring was continued for 10 h with the reaction flask cooled in ice, then 20 mL benzene was added. The resulting precipitate was filtered and the crude product washed with benzene and ether. This product was dissolved in about 100 mL water

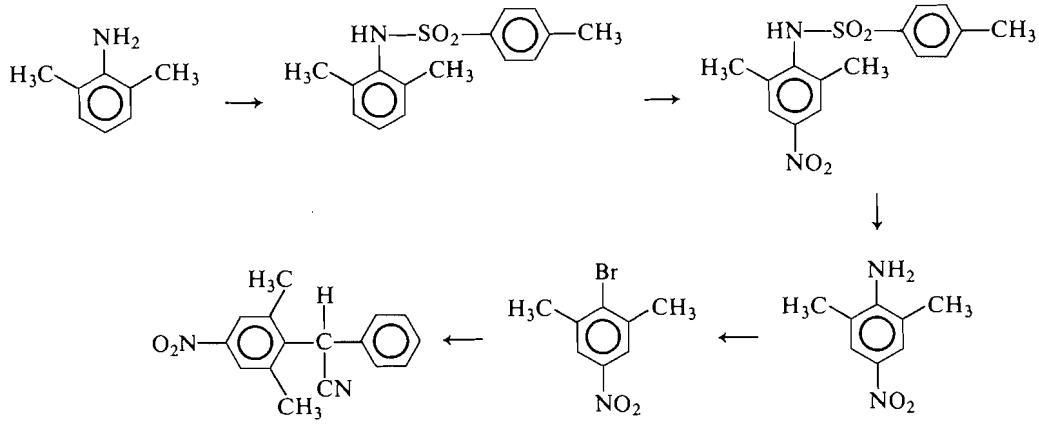

and then precipitated by the addition of acetic acid. The yellow solid was washed with water and dried. Yield 1 g (35%), mp 116–117°C; ^{1}H nmr δ(ppm); 2.36 (s, 6H), 5.67 (s, 1H), 6.90–7.37 (m, 5H), 7.83 (s, 2H).

Deuteration of the 2,6-dimethyl-4-nitrophenylphenylcyanomethane was accomplished using a solution of 5 mg of metallic sodium in a mixture of 10 mL D_2O and 10 mL dioxane. About 200 mg of the carbon acid was dissolved in 2 mL of dioxane and 2 mL of the above solution. After 1 min the coloured solution was neutralized with several drops of DCl in D_2O. The solvents were evaporated and the carbon acid was separated from NaCl by extraction with chloroform. After evaporation of the chloroform, the procedure was repeated four times. The nmr signal at 5.67 ppm disappeared, and the mass spectrum indicated 98% deuteration.

Reagent grade acetonitrile was purified by the method of O'Donnell *et al.* (15) with a final fractional distillation from P_2O_5.

Tetramethylguanidine was dried with KOH and then fractionally distilled under reduced pressure. The middle fraction, about 25% of the total, was used.

1,8-Diazabicyclo[5.4.0]undec-7-ene was dried with KOH and fractionally distilled under reduced pressure.

Equilibrium measurements

The absorbance at equilibrium was measured for a series of reactions with a constant acid concentration of either 1×10^{-5} M or 4.7×10^{-5} M, and different base concentrations in excess of the acid concentration by factors ranging from 23 to 1000, using a Cary 219 spectrophotometer.

Kinetic measurements

The reaction rate constants were measured with a Durrum–Gibson stopped-flow spectrophotometer using acid concentrations of 1×10^{-5} or 2×10^{-5} M with base concentrations shown in Table 1. The pseudo-first-order rate constants were obtained as described previously (2).

Acknowledgement

The authors are grateful to Mr. R. Vaidya for technical assitance.

1. A. Jarczewski, P. Pruszynski, and K. T. Leffek. Can. J. Chem. **61**, 2029 (1983).
2. M. Hojatti and K. T. Leffek. Can. J. Chem. **62**, 2653 (1984).
3. M. Hojatti and K. T. Leffek. Can. J. Chem. **64**, 2365 (1986).
4. E. S. Lewis and L. H. Funderburk. J. Am. Chem. Soc. **89**, 2322 (1967).
5. L. Melander and R. E. Carter. J. Am. Chem. Soc. **86**, 295 (1964).
6. L. Melander and R. E. Carter. Acta Chem. Scand. **18**, 1138 (1964).
7. C. Heitner and K. T. Leffek. Can. J. Chem. **44**, 2567 (1966).
8. K. T. Leffek. Can. J. Chem. **45**, 2115 (1967).
9. K. T. Leffek and P. Pruszynski. Can. J. Chem. **59**, 3034 (1981).
10. A. Jarczewski, P. Pruszynski, M. Kazi, and K. T. Leffek. Can. J. Chem. **62**, 954 (1984).
11. L. Melander and W. H. Saunders, Jr. Reaction rates of isotopic molecules. John Wiley & Sons, New York. 1980. p. 131.
12. R. B. Davis and L. C. Pizzini. J. Org. Chem. **85**, 1884 (1960).
13. M. A. Bambenek. Recl. Trav. Chim. Pays-Bas, **82**, 97 (1963).
14. B. M. Wepster. Recl. Trav. Chim. Pays-Bas, **28**, 92 (1909).
15. J. F. O'Donnell, J. T. Ayers, and C. K. Mann. Anal. Chem. **37**, 1161 (1965).

Can. J. Chem. Downloaded from www.nrcresearchpress.com by 93.93.197.157 on 09/07/12
For personal use only.

Absorption and photoacoustic spectroscopies of lutein and zeaxanthin Langmuir–Blodgett films in connection with the Haidinger's brushes

C. N. N'SOUKPOÉ-KOSSI AND R. M. LEBLANC

Centre de recherche en photobiophysique, Université du Québec à Trois-Rivières, Case postale 500, Trois-Rivières (Qué.), Canada G9A 5H7

Received November 12, 1987

C. N. N'SOUKPOÉ-KOSSI and R. M. LEBLANC. Can. J. Chem. **66**, 1459 (1988).

The molecular state of a single monolayer of lutein, zeaxanthin, and of a mixture of lutein and L-α-phosphatidylcholine-β-oleoyl-γ-stearoyl has been investigated using absorption and photoacoustic spectroscopies. Both methods, confirmatively, reveal that the two carotenoids are mostly in a monomer state coexisting with carotenoid crystals. We observe that the absorption as well as the photoacoustic bands are red-shifted relative to the bands in solution. The absorption bands are found to peak at mean values of 440.0, 464.8, and 503.8 ± 0.5 nm for lutein, and at 452.7, 475.9, and 513.7 ± 0.5 nm for zeaxanthin. The photoacoustic peaks are situated at 444.0, 467.2, and 502.4 ± 0.5 nm for lutein, and 455.4, 473.8, and 509.0 ± 0.5 nm for zeaxanthin. Diluting lutein monolayer with the phospholipid results into a blue-shift of the absorption bands compared with those of the pure carotenoid monolayer and the macular pigment spectra. The results are discussed in connection with the Haidinger's brushes. It is concluded that lutein molecules might not be mixed with membrane lipids in the macular tissue, but form a monolayer protruding from the Henle fiber membranes to form the Haidinger's brushes in the macula.

C. N. N'SOUKPOÉ-KOSSI et R. M. LEBLANC. Can. J. Chem. **66**, 1459 (1988).

Faisant appel à des méthodes spectroscopique d'absorption et photoacoustique, on a étudié l'état moléculaire d'une monocouche simple de lutéine, de zéaxanthine ainsi que d'un mélange de lutéine et de la L-α-phosphatidyl β-oléoyl γ-stéaroyl choline. Les deux méthodes confirment que les deux caroténoïdes existent principalement dans un état monomère qui coexiste avec des cristaux de caroténoïde. On a observé que, par rapport aux bandes en solution, l'absorption ainsi que les bandes photoacoustiques sont déplacées vers le rouge. On a trouvé que les bandes d'absorption ont une intensité maximale à des valeurs moyennes de 440,0, 464,8 et 503,8 ± 0,5 nm pour la lutéine et à 452,7, 475,9 et 513,7 ± 0,5 nm pour la zéaxanthine. Les pics photoacoustiques sont situés à 444,0, 467,2 et 502,4 ± 0,5 nm pour la lutéine et à 455,4, 473,8 et 509,0 ± 0,5 nm pour la zéaxanthine. Lors de la dilution de la monocouche de lutéine avec le phospholipide, les bandes observées sont déplacées vers le bleu par rapport à celles obtenues dans le spectre de la monocouche de caroténoïde pur ainsi dans celui du pigment maculeux. On discute des résultats en fonction des brosses de Haidinger. On en conclut que les molécules de lutéine ne sont peut être pas mélangées avec les lipides membranaires dans le tissu maculeux; toutefois, elles forment une monocouche faisant saillie par rapport aux fibres membranaires de Henle et elles conduisent à la formation des brosses de Haidinger dans la macule.

[Traduit par la revue]

Introduction

The presence of carotenoids has often been observed in biological membranes (1–4). They belong to the most widely distributed pigments in the animal kingdom (1, 5, 6). Particularly seen in photosynthetic units (1, 2), in vertebrate retina macula (3, 4, 7–9) and in cone oil droplets of some animals (10–14), they are linked with photoprotection of photosensitive pigments (15–20). Among them, lutein and zeaxanthin are the most widespread carotenoid alcohols in nature which are responsible for the yellow colour of human retina macula (9), the site of localization of the structures responsible for Haidinger's brushes (21). The brushes are attributed to the directional organization of the carotenoid molecules in the membranes of Henle's fibers (i.e. the inner segments of cone receptor cells (21)). Because of their great ability to absorb light quanta due to their polyenic chain, carotenoids can easily be studied by photometric methods. Yet, their spectroscopic properties are far from clear. It has been observed that carotenoids undergo changes in their molecular state which are associated with changes in their spectroscopic properties (21–27). Most of these studies have been performed in solution and liposomes, and it has been reported that carotenoids could be in some aggregate state (23, 25–27, 28–30) or crystalline state (21, 31) depending on the experimental conditions. The monolayer model has also been employed to study properties of carotenoid molecules (29, 31–38).

One important question to be answered would certainly be: what is the aggregation state of the carotenoids in the macular tissue? The monolayer model (Langmuir–Blodgett films) is known to match the packing pattern of molecules in biological membranes or similar structures. The comparison of the spectroscopic properties of the carotenoids in Langmuir–Blodgett films with those of the macular pigments can answer the above question and help us better understand the structural organization underlying the important role of protection against photooxidation ascribed to the macular pigments. To do this, two independent spectroscopic methods, i.e., absorption and photoacoustic spectroscopies have been used in conjunction with the monolayer methodology.

Materials

All the solvents used were distilled as follows: benzene (BDH Chemicals, Montréal, Québec, Canada) at 80°C in a glass bead column, and ethanol (Les Alcools de Commerce Ltée, Ville St-Laurent, Québec, Canada) at 78.5°C in a Vigreux column; the first 200 mL served to rinse the column. Water used for the monolayer work has been first filtered and deionized in a nanopure Barnstead column (Fisher Chem. Co., Montréal, Québec, Canada) to obtain specific resistivity of 16–18 MΩ cm and then bidistilled in a quartz distillation system (Heraeus Quarzschmelze BmbH Produktbereich Infrarot, Hanau 1, W. Germany): the surface tension was equal to or higher than 71 mN m^{-1}. Zeaxanthin was obtained from Hoffmann-La Roche Co. (Basle, Switzerland). Highly purified all-*trans*-lutein was supplied by Drs. Bone and Landrum of the International University of Florida (Miami, U.S.A.). The spectrophotometric measurements were per-

Can. J. Chem. Downloaded from www.nrcresearchpress.com by 93.93.197.157 on 09/07/12
For personal use only.

Can. J. Chem. Downloaded from www.nrcresearchpress.com by 93.93.197.157 on 09/07/12
For personal use only.

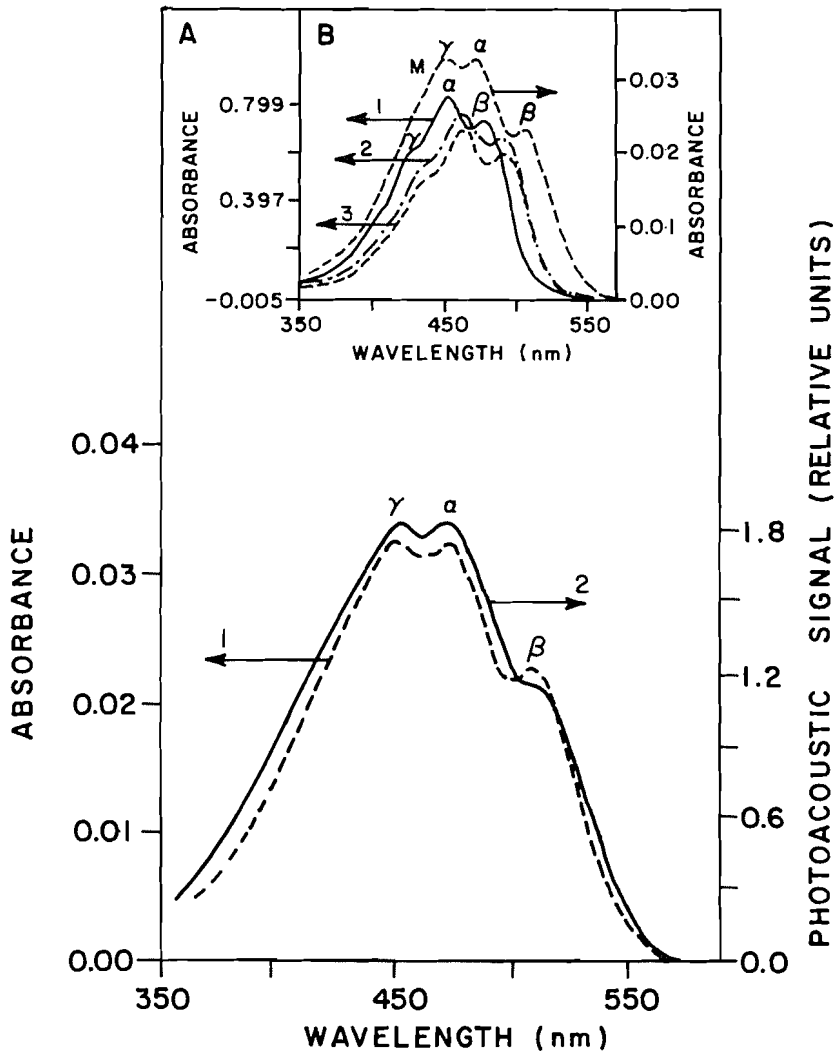

FIG. 1. (*A*) Absorption (curve 1) and photoacoustic (curve 2) spectra of a zeaxanthin single monolayer. (*B*) Absorption spectra of zeaxanthin solution in ethanol (curve 1), benzene (curve 2) and in benzene–ethanol (9:1, v:v) mixture (curve 3). Concentration: 6.40×10^{-5} mol dm^{-3}; pathlength: 1 mm. Curve M is the absorption spectrum for a single monolayer.

formed with a Perkin-Elmer 553 spectrophotometer. For the photoacoustic determinations, a home-made photoacoustic spectrometer (39–43) provided with Challenger II or Apple II computer was utilized. The power of the incident beam given by a xenon lamp (Conrad-Anovia, West Germany) was about 5 to 15 W m^{-2} in the spectral range used, i.e., from 350 to 600 nm.

Methods

Monolayer preparation

The carotenoid (lutein or zeaxanthin) were dissolved in a mixture of benzene: ethanol (9:1, v:v) which has been at first bubbled with argon. The solutions were stored in small vials (~3 mL) filled with argon and closed with mininert valves (Chromatographic Specialties Ltd., Brockville, Ont., Canada). The concentrations of the solutions were adjusted to $(2–4) \times 10^{-4}$ mol dm^{-3}. The fresh solution, protected against light by wrapping the vial with aluminium foil was used within 3 days under argon or nitrogen atmosphere to avoid oxidative damage. A Langmuir-type film balance provided with a vibration-free hydraulic deposition system (44) was used. As solid support for the monolayers, we used two quartz disks, 2.54 cm in diameter (Esco Product Inc., Oak Ridge, New Jersey, U.S.A.) joined face-to-face along their rims by paraffin wax. This arrangement allows for adsorption of a single monolayer on only one face of each slide when lifted from the subphase. The support was immersed into the aqueous subphase, the carotenoid solution (~150 μL) spread at the interface and after having waited for about 10 min, the molecules were compressed at a speed of $\sim 10^{17}$ Å^2 min^{-1} to the desired pressure (i.e., 5 and 25 mN m^{-1}). The support was then lifted without vibration with the hydraulic deposition device at a speed of 0.61 cm min^{-1} and constant surface pressure (5 or 25 mN m^{-1}). The reason for depositing the monolayer at these surface pressures comes from the interest to know about the state of the monolayers below and above a *plateau* observed at about 5 mN m^{-1} in the π–*A* isotherm (N'soukpoé-Kossi *et al.*, submitted for publication). After the deposition, the slides were separated carefully and mounted in a special holder which was placed in an aluminium foil-wrapped beaker in the presence of argon. The monolayers were immediately analyzed by two independent methods (absorption and photoacoustic spectroscopies) to avoid introduction of spurious instrumental signals in the results.

Spectroscopic measurements

All of the absorption measurements were performed under nitrogen atmosphere, at normal incidence, and at temperature between 23 and 25°C. The absorption spectra were recorded from 350 to 600 nm at a speed of 60 nm min^{-1}, bandwidth: 1 nm. The wavelength of peaks and subpeaks, and their intensity ratios (spectral ratios) were compared with those of spectra in solutions, in PVA, in liposomes and *in vivo* tissue. The absorption coefficients (α') and the optical absorption length ($\mu_{\alpha'}$) of the monolayers were also calculated.

The photoacoustic (PA) measurements were carried out at normal incidence and room temperature. The PA spectra were recorded from

TABLE 1. Spectral ratios

Sample	State	Measurement	⟨α (nm)⟩	⟨β (nm)⟩	⟨γ (nm)⟩	$\left\langle \frac{\alpha}{\beta} \right\rangle$	$\left\langle \frac{\alpha}{\gamma} \right\rangle$
Zeaxanthin	Ethanol solution*	Absorption	451.0	478.0	426.0	1.2	1.4
	Benzene solution*	Absorption	463.0	492.0	435.0	1.1	1.4
	Benzene–ethanol (9:1, v:v) solution*	Absorption	462.7	492.0	435.0	1.2	1.4
	Monolayer	Absorption	475.9	513.7	452.7	1.5	1.0
		PAS	473.8	509.0	455.4	1.5	1.0
	Monolayer solubilized in benzene–ethanol (9:1, v:v)	Absorption	461.5	492.0	436.0	1.2	1.4
Lutein	Ethanol solution*	Absorption	445.0	472.3	424.0	1.1	1.4
	Benzene solution*	Absorption	455.7	484.2	433.7	1.1	1.4
	Benzene–ethanol (9:1, v:v) solution*	Absorption	456.1	486.2	434.0	1.1	1.5
	Monolayer	Absorption	464.8	503.8	440.0	1.7	0.9
		PAS	467.2	502.4	444.0	1.6	1.0
	Monolayer solubilized in benzene–ethanol (9:1, v:v)	Absorption	454.6	482.8	430.0	1.2	1.5
Lutein–PC(1:1)	Benzene–ethanol (9:1, v:v) solution	Absorption	456.0	485.0	432.0	1.2	1.5
	Monolayer dep. π: 5 mN m^{-1}	Absorption	450.0	479.2	425.3	1.3	1.1
	25 mN m^{-1}	Absorption	450.0	484.0	418.0	1.3	1.0
	Monolayer solubilized in benzene–ethanol (9:1, v:v)	Absorption	452.0	482.5	429.0	1.2	1.5
Lutein (results from other laboratories)							
	In PVA†	Absorption	464.0	491.0	440.0	1.1	1.2
	In liposomes†	Absorption	451.0	482.0	427.0	1.4	1.1
	In vivo‡	Absorption	460.0	485.0	433.0	1.2	1.1

*Concentrations of the carotenoids range from 4.8×10^{-6} to 6.5×10^{-5} mol dm^{-3}.
†Calculated from data in ref. 21.
‡Calculated from data in ref. 3.

350 to 600 nm at a speed of 50 nm min^{-1} at a modulation frequency of 100 Hz; the bandwidth was 10 nm and time constant of the lock-in amplifier was 1.25 s. Usually, the PA spectra were measured on the same monolayers as the ones used for absorption. However, sometimes one of the pair of slides bearing the monolayer was used for absorption and the other one for photoacoustic spectroscopy. The PA spectra for the carotenoids were normalized against that of carbon black under the same experimental conditions. Details of the theory and methods of photoacoustic spectroscopy are reviewed elsewhere (45, 46).

Results

The carotenoid monolayers were observed to be very unstable: when the compression was stopped, a drop in the surface pressure occurred. To prevent this drop in pressure we deposited the monolayer onto the support immediately after the desired pressure was reached and maintained the surface pressure constant by keeping the compression on. The deposition ratio was found to be usually greater than 1.2 indicating that some unidentified process responsible for reduction of surface pressure was in course. This instability was observed for pure monolayers of lutein and zeaxanthin. The addition of a phospholipid stabilized the films: this stabilizing effect was true for lutein mixed with L-α-phosphatidylcholine-β-oleoyl-γ-stearoyl for carotenoid molar ratio of 0.10 to 0.50. Zeaxanthin has not been tested for this stabilizing effect.

The absorption and photoacoustic spectra of a pure zeaxanthin monolayer are shown in Fig. 1*A* and the absorption spectra in solution in Fig. 1*B*. We notice that all spectra display three peaks and subpeaks in the visible that we name α, β, and γ in the decreasing order of their intensities in solution. The peaks are bathoshifted in the monolayer (Fig. 1*B*, curve M) compared with solution (Fig. 1*B*, curves 1, 2, 3), and excellent accordance is observed between absorption and PA spectra of the monolayer (Fig. 1*A*, curve 1 vs. curve 2). The absorption and PA bands have been characterized not only by their positions, but also by their respective spectral ratios (i.e., α/β and α/γ). The mean values were found to be 452.7, 475.9, and 513.7 ± 0.5 nm for the absorption bands, and 455.4, 473.8, and 509.0 ± 0.5 nm for PA bands. The spectral ratios are shown in Table 1.

The results obtained for a lutein monolayer are shown in Fig. 2. Figure 2*A* represents the absorption (curve 1) and PA (curve 2) spectra of a pure lutein monolayer with average values of 440.0, 464.8, and 503.8 ± 0.5 nm for the absorption bands, and 444.0, 467.2, and 502.4 ± 0.5 nm for the PA bands. Similar to zeaxanthin, we observed a bathoshift for the spectra of the

Can. J. Chem. Downloaded from www.nrcresearchpress.com by 93.93.197.157 on 09/07/12
For personal use only.

Can. J. Chem. Downloaded from www.nrcresearchpress.com by 93.93.197.157 on 09/07/12
For personal use only.

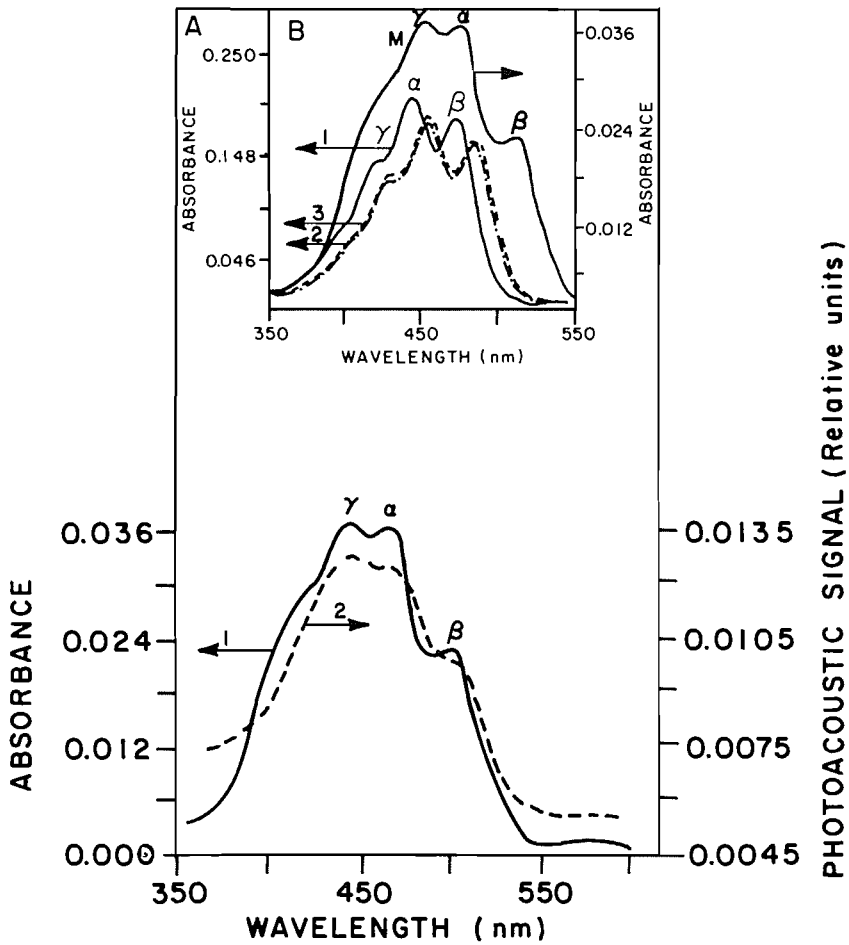

FIG. 2. (*A*) Absorption (curve 1) and photoacoustic (curve 2) spectra of a lutein single monolayer. (*B*) Absorption spectra of lutein solution in ethanol (curve 1), benzene (curve 2) and in benzene–ethanol (9:1, v:v) mixture (curve 3). Concentration: 1.85×10^{-5} mol dm^{-3}; pathlength: 1 mm. Curve M is the absorption spectrum of a single monolayer.

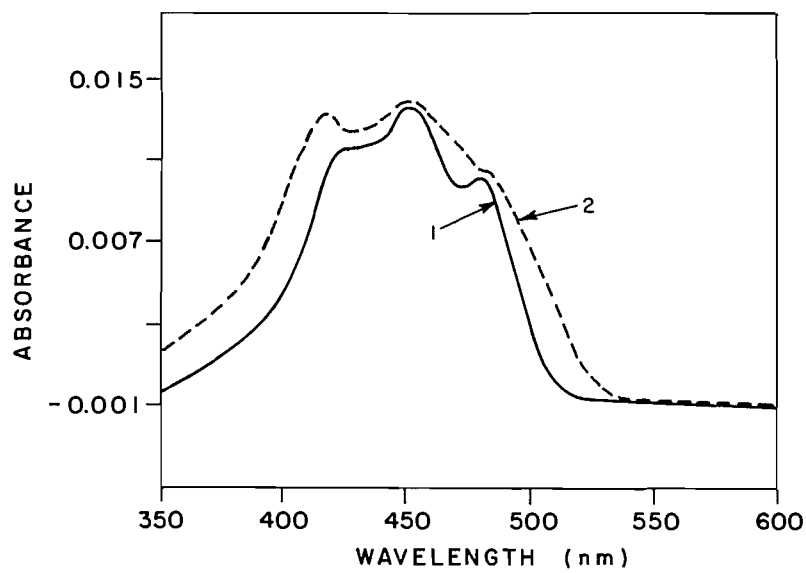

FIG. 3. Absorption spectra of two monolayers of lutein mixed with L-α-phosphatidylcholine-β-oleoyl-γ-stearoyl (1:1, mol:mol) deposited at a surface pressure of 5 mN m^{-1} (curve 1) and at 25 mN m^{-1} (curve 2).

monolayer in comparison with solution (Fig. 2*B*) resembling the absorption spectrum *in vivo* shown in Fig. 4, curve 4. Here also, a good agreement is observed between absorption and PA spectra of the monolayer (see positions of peaks and their relative intensities in Table 1).

Now, it appears interesting to investigate the packing pattern of carotenoid molecules in monolayer. To do this, we have measured the absorption spectra of mixtures of lutein and phosphatidylcholine. The molar ratios of lutein were 0.50, 0.40, 0.30, 0.25, 0.16, and 0.10. The deposition surface pressures

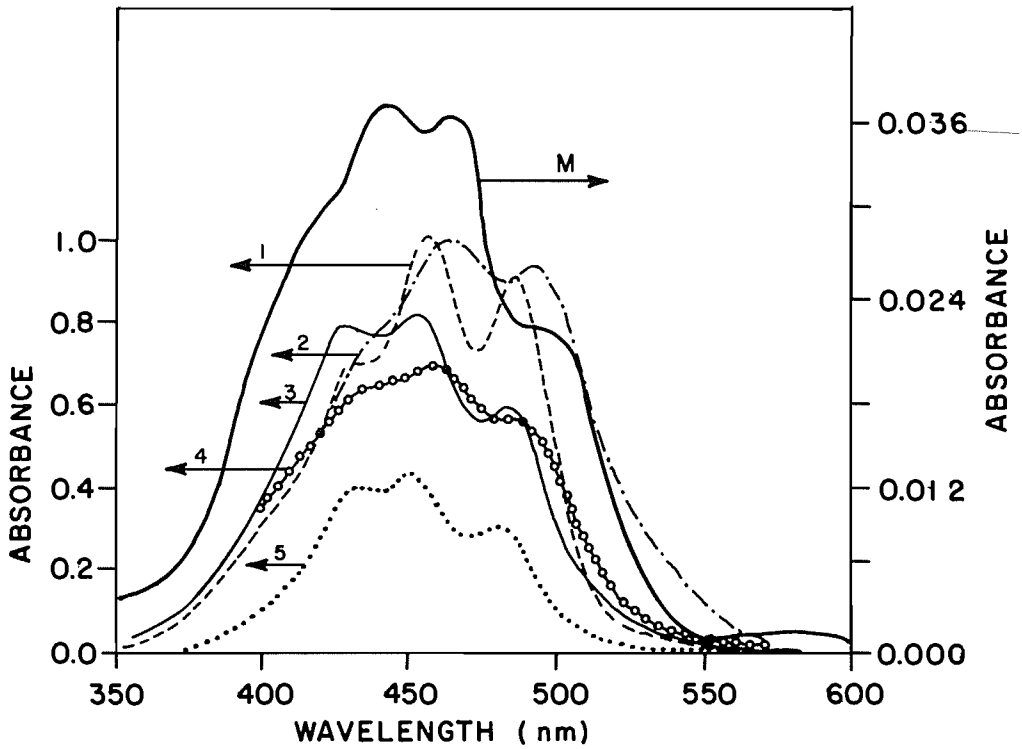

FIG. 4. Absorption spectra of lutein in different media: in benzene-ethanol (9:1, v:v) solution (curve 1), in polyvinyl alcohol (curve 2, taken from ref. 21), in mixed monolayer (lutein–PC, 1 mol:1 mol) at 5 mN m^{-1} (curve 3), *in vivo* (curve 4, taken from ref. 3), in phospholipid liposomes (curve 5, taken from ref. 21), and in a single monolayer (curve M).

were 5 and 25 mN m^{-1}. Among all the molar ratios tried, only two (0.50, 0.40) gave a measurable signal in absorption. The absorption spectra of monolayers deposited at 5 and 25 mN m^{-1} for lutein–PC (molar ratio of 0.50) mixture are shown in Fig. 3. There is no significant difference between the two curves (λ of peaks are 425.3, 450.0, and 479.2 ± 0.5 nm for 5 mN m^{-1}, and 418.0, 450.0, and 484.0 ± 0.5 nm for 25 mN m^{-1}). The absorption spectra have shifted to blue relative to pure lutein monolayer and fairly well reproduce the absorption bands in liposomes (Fig. 4; curve 3 vs. curve 5: curve 3 is the absorption spectrum of the mixed monolayers deposited at a surface pressure of 5 mN m^{-1} and curve 5 is that for lutein-containing liposomes (21)). The blue-shift amounts to 14.6 to 24.5 nm depending on the band, the largest shift occurring for β-bands. The spectral ratios are indicated in Table 1. Attempts to record the photoacoustic spectra of mixed lutein–phospholipid monolayer were unsuccessful, the signal being too weak and too noisy.

In some of our experiments we oberved deformation of the absorption spectra with a concomitant deformation of PA signals compared with what we usually obtained. Examples of this are given in Fig. 5. In Fig. 5*A*, we can see the appearance of a shoulder at about 425.0 nm for zeaxanthin (curve 1) and at about 410 nm for lutein monolayers (curve 2), or in a more pronounced form with a well-defined peak at 380.0 nm (Fig. 5*A*, curve 3). Curve 4 in Fig. 5*A* is another case of deformation of the absorption band (of lutein monolayer). In all these cases, when the monolayer is dissolved into benzene–ethanol (9:1, v:v) mixture, the absorption spectrum of fresh solution is restored as indicated in Fig. 5*C* where curve 1 is the spectrum of fresh lutein solution and curve 2 is that of the solubilized lutein monolayer. This clearly indicates that there was no chemical change in the molecules, but only a change in the state. In Fig. 5*B* we see the absorption and photoacoustic spectra of a typical monolayer displaying this peculiar blue-shift. As discussed later, the growth of these shorter-wavelength peaks is caused by the crystallization of the carotenoids.

To set a basis of comparison for further work, some photometric parameters have been derived. For instance, the extinction coefficient[1] of the carotenoid monolayer has been found to be 9.43×10^7 cm^2 mol^{-1} (or 1.57 $Å^2$ $molecule^{-1}$) for pure zeaxanthin and 8.27×10^7 cm^2 mol^{-1} (or 1.37 $Å^2$ $molecule^{-1}$) for pure lutein, using a molecular area at 25 mN m^{-1} of 37 $Å^2$/molecule for zeaxanthin and 41.5 $Å^2$/molecule for lutein. The mean absorbance (A) was 0.042 and 0.031 for zeaxanthin and lutein monolayers, respectively. The unexpectedly lower absorbance value obtained for lutein monolayer compared with that of zeaxanthin probably reveals the presence of much more pinholes in lutein than in zeaxanthin monolayers.

If we know the thickness of the monolayer, the coefficient of optical absorption ($\alpha' = 2.3A/l$), a useful photoacoustic parameter, can be easily calculated. According to Zsako *et al.* (37), the length of carotenoid molecule is 32.0 Å and the molecular diameter, D, is 7.82 Å. Considering that in the monolayer, zeaxanthin and lutein molecules form an angle, θ, of 47.1° and 48.6°, respectively, with the plane of the support (N'soukpoé-Kossi *et al.*, submitted for publication), the thickness of their monolayers comes to be 32 Å $\sin\theta + D\cos\theta$; that gives 28.7 Å for zeaxanthin monolayer and 29.2 Å for lutein monolayer. Therefore, $\alpha'_{Zea} = 3.3 \times 10^5$ cm^{-1} and $\alpha'_{Lut} = 2.4 \times 10^5$ cm^{-1}.

[1]The extinction coefficients in ethanol solution as deducted from the results of Strain (47) are 1.442×10^8 cm^2 mol^{-1} and 1.448×10^8 cm^2 mol^{-1} for zeaxanthin and lutein, respectively. The fact that the absorption coefficients we have found for the monolayers are lower than those in solution may be an indication of inhomogeneity, e.g. presence of empty spaces in the monolayer film, or/and the consequence of different interaction media.

Can. J. Chem. Downloaded from www.nrcresearchpress.com by 93.93.197.157 on 09/07/12
For personal use only.

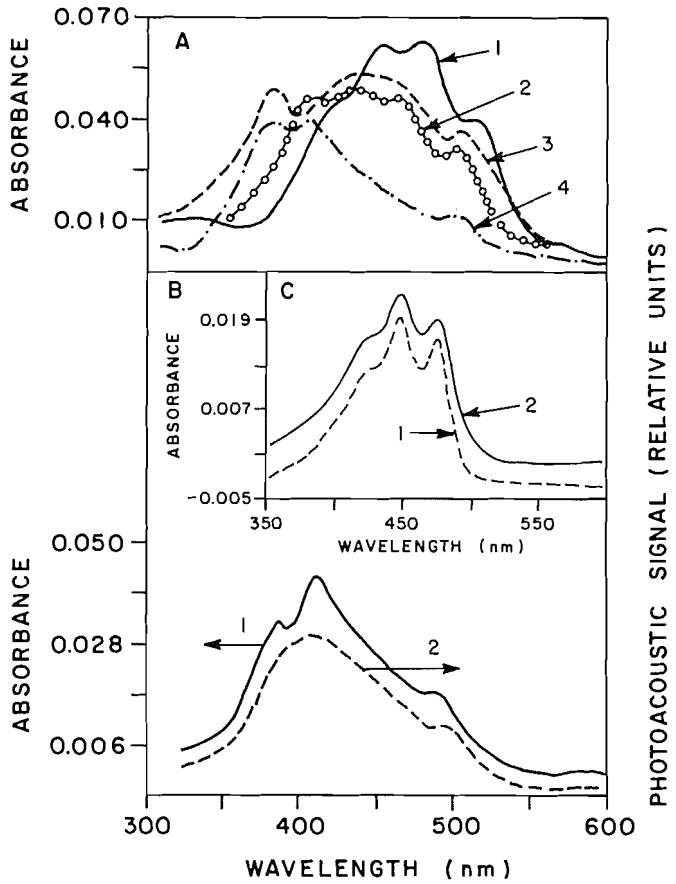

FIG. 5. (*A*) Absorption spectra showing different degrees of crystallization of a single zeaxanthin monolayer (curve 1) and of single lutein monolayers (curves 2 through 4). (*B*) Absorption (curve 1) and photoacoustic (curve 2) spectra of a typical crystallized lutein monolayer. (*C*) Absorption spectra of fresh lutein solution (curve 1) and of crystallized lutein monolayer dissolved in benzene–ethanol (9:1, v:v) mixture (curve 2).

The optical absorption length, $\mu_{\alpha'} = \alpha'^{-1}$ (45) is found to be 30.3 nm for zeaxanthin and 41.2 nm for lutein. The optical absorption length is much larger than the thickness. Under these circumstances, it is quite normal that electronic and PA spectra coincide as we observed, since the carotenoid monolayers are transparent from photoacoustic point of view. The small discrepancy observed between the absorption band maxima and the corresponding photoacoustic ones could simply be accounted for by the lesser resolution power for the PA spectrometer and bandwidth of which was set at 10 nm in order to obtain greater and noise-free signal while the bandwidth of the spectrophotometer was 1 nm.

Discussion

Stability of the carotenoid Langmuir–Blodgett films

One of the more striking features of carotene and carotenoid-monolayers is probably their instability reflected by rapid drop in the surface pressure as soon as the compression is stopped (32). But mixed with phospholipid, lutein forms stable monolayers as we point out in this paper in contrary to the observation reported by Lejeune and Tric (31) on β-carotene mixed with some fatty acid. The failure of the preparation of mixed monolayer of β-carotene and fatty acid has been explained by the absence of polar group in β-carotene that could interact with fatty acid polar groups (31). Two years later, Pincus *et al.* (33) succeeded in preparing stable monolayers of β-carotene mixed with arachidic acid which were easily transferred onto glass slides. In 1978, Ohnishi *et al.* (48) reported the work on monolayers of β-carotene mixed with barium stearate. In the case of lutein which possesses a polar group at each end, strong interactions with the polar head group of the lecithin are possible thereby favouring formation of stable monolayers.

Spectroscopic properties of the carotenoid Langmuir–Blodgett films

Of great importance are the spectroscopic properties of carotenoid monolayers in order to know their state and organization in the films. We begin by discussing about the shift of the absorption spectrum of the carotenoid monolayer relative to solution. As indicated in Figs. 1 and 2, the absorption and photoacoustic spectra of zeaxanthin (Fig. 1*A* vs. Fig. 1*B*) and of lutein (Fig. 2*A* vs. Fig. 2*B*) monolayers are shifted toward red relative to the spectra of solutions. Compared with ethanolic-solution spectra, the mean shift was 29.0 nm for zeaxanthin and 22.7 nm for lutein. The shift was smaller compared with benzene or benzene:ethanol (9:1, v:v) solutions, i.e., 17.3 nm for zeaxanthin and 11.4 nm for lutein monolayers. The largest shift was observed for β-band in all cases (Table 1). This bathochromicity of the monolayers can be explained by π–π electron interactions along the polyenic chains due to close packing of the molecules in a "head-to-tail" manner (49). If this is so, we should expect a decrease of the magnitude of the red-shift when the monolayer is diluted, with a concomitant change in the spectral ratios. In order to investigate the packing model of the carotenoid molecules in the monolayer, the absorption spectra of lutein when mixed with L-α-phosphatidylcholine-β-oleoyl-γ-stearoyl were measured. The results presented in Fig. 3 clearly support the "head-to-tail" model according to which reduction of the magnitude of the red-shift would be observed (49). Indeed, the absorption spectra of mixed monolayers of lutein and L-α-phosphatidylcholine-β-oleoyl-γ-stearoyl are blue-shifted relative to pure lutein monolayer and the macular tissue. The intermolecular interactions involved here resulted in changes in the spectral ratios of the absorption spectra compared with solutions (see Table 1). In the diluted monolayers (especially at 5 mN m^{-1}), the spectral ratios match fairly well those calculated for liposomes (Table 1) according to the results of Bone and Landrum (21). Since the fine structure of the absorption spectra is due to vibrational modes, it is worth noting how much the intermolecular interactions in monolayers affect the relative intensities of these vibrational peaks.

Similar results concerning the bathochromicity have been reported for PVA films incorporated with lutein (21) as depicted in Fig. 4, curve 2 and on mixed monolayers of β-carotene and barium stearate (48). Our results, which are in accordance with these two papers, do not support entirely those of Lejeune and Tric (31). Rather, they observed a blue-shift in the absorption spectra of carotenoid aldehydes (β-apo 2′ carotenal and apo 4′ carotenal) monolayers deposited on glass slides at surface pressure 6, 8, 11, and 14 mN m^{-1}. A gradual blue-shift was observed for the unique peak from 430 nm to 417 nm. We occasionally have observed this kind of blue-shift for zeaxanthin and lutein monolayers (Fig. 5) which we consider to be due to crystallization of the monolayer. As we have recently observed, some crystallization may occur in the carotenoid film (Fig. 5) and was most visible in the π–*A* isotherm. This phenomenon was also observed by many authors in solution especially in presence of water (22, 24–27, 30) and by Lejeune and Tric (31) in air–water

Can. J. Chem. Downloaded from www.nrcresearchpress.com by 93.93.197.157 on 09/07/12
For personal use only.

Can. J. Chem. Downloaded from www.nrcresearchpress.com by 93.93.197.157 on 09/07/12
For personal use only.

interfacial β-carotene. Such hypsochromicity assigned to crystalline state of the carotenoid (21) can be explained by the excitonic coupling theory of McRae and Kasha (49). We believe that this crystallization process is responsible for the instability of the monolayer that was reflected by the drop in surface pressure.

The spectral similarity is intriguing between the crystallized lutein that we observed and the P410 pigment reported by Snodderly *et al.* (3) from microspectrophotometric recordings in the retinal macula of macaque monkeys. Both have absorbance maximum at 410 nm. At this time we do not see any objection against the P410 pigment being lutein crystals in the macular tissue.

From these observations some general conclusions can be drawn: (*1*) pure carotenoid monolayers present absorption and photoacoustic spectra red-shifted compared with solution and resemble the *in vivo* situation; (*2*) the spectrum in liposome can be reproduced by diluting the carotenoid monolayers; (*3*) the lutein molecules are arranged in a "head-to-tail" manner in the monolayer; (*4*) the spectral ratios which are reversed in monolayer relative to solution are reversible upon dilution; (*5*) in presence of water, a number of carotenoids and particularly lutein crystallize.

Molecular organization of lutein in the macula

The results presented here raise a number of questions: how are the carotenoid molecules organized in the macular tissue? In what state are they present? Do they exist as pure compounds or mixed with other pigments or lipids? Based solely on its spectral characteristics, human macula pigment has been identified as lutein (7, 8). But, quite recently, it has been found that human macula is most probably composed of lutein and zeaxanthin in almost equal quantities (9). Surprisingly, the absorption spectrum that we recorded for pure lutein monolayer matches fairly well that of the macula of macaque monkeys (3). Could this imply that lutein is the only carotenoid of macaque macula or probably the predominant one? This hypothesis could be tenable considering that the absorption spectrum of macaque macula presents only three peaks like lutein. This point remains to be clarified by other independent methods.

Now, the similarity between the macular spectrum and that of the lutein monolayer strongly suggests that the macular carotenoids, whatever they be, are highly organized, and most probably, in a monomolecular layer, in a "head-to-tail" manner. This assertion is in accordance with the finding that the macular tissue is dichroic (4). It may reasonably be assumed that the carotenoid layer is embedded in a lipid bilayer (21, 24). But, the blue-shift that we observed in the absorption spectra of mixed lutein and phosphatidylcholine monolayers compared with that of the macular pigment seems inconsistent with this hypothesis. Besides, it is hard to figure out a lipid bilayer structure in which carotenoid molecules would be incorporated when they have to lie at an angle of about 48° (N'soukpoé-Kossi *et al.*, submitted for publication) relative to the plane of the bilayer.

One further point to be made with respect to the molecular arrangement of carotenoid in the native tissue is the relationship between the carotenoid molecules and the Henle fiber membranes. As already reported (50, 51) the carotenoid molecules should be aligned at an acute angle to the membrane plane. In the dichroic macula (4), the greatest absorption was observed when the plane of polarization of the incident light was perpendicular to the axes of the Henle fibers, thereby accounting for the formation of the Haidinger's brushes. It has been proposed (21) that a fraction of the carotenoid molecules are aligned perpendicular to the cylindrically shaped fiber membranes. The remainder was assumed to have random orientations. We have calculated that, for a fiber as a whole to absorb light more strongly which is polarized perpendicular to its axis, rather than parallel, this angle would have to exceed approximately 35°. Our measured angles (N'soukpoé-Kossi *et al.*, submitted for publication) are equal to or greater than 45°, in accordance with these calculations and macula dichroism measurements (4). Since the macular pigment appears to be highly organized and does not seem to be really mixed with lipids as reflected by our results, it can consequently be suggested that the pigment is arranged in a monolayer protruding from the Henle fiber membrane at a mean angle of 48° forming the Haidinger's brushes. This seems to be a reasonable conclusion based on the similarities between the spectroscopic properties of the Langmuir–Blodgett carotenoid films, on those of the macular pigments and on dichroic properties of the macula.

Conclusion

We have given a reasonable concept of the macular structure. While a definite characterization of this system should wait for additional work, we expect this hypothesis to stimulate further investigations. It is very interesting that carotenoid monolayers exhibit spectroscopic properties similar to those of the macular pigment. As characterized, carotenoid monolayers represent a useful tool for the study of macular carotenoids. The use of photoacoustic spectroscopy, apart from supporting the absorption data, adds an especially interesting advantage. Being a non-destructive probe, it can be conveniently applied to *in vivo* samples and any material for which conventional spectroscopic methods are not suitable.

Acknowledgments

The authors would like to thank Drs. R. A. Bone and J. T. Landrum of the International University of Florida for having supplied lutein samples for this study. We are also grateful to Miss Louise Leblanc for her help in the course of this research and to Drs. S. Hotchandani and J.-J. Max for commenting on this paper. This work was supported by the Natural Sciences and Engineering Research Council of Canada and the Fonds pour la Formation de Chercheurs et l'Aide à la Recherche.

1. T. W. Goodwin. The comparative biochemistry of the carotenoids. Chapman and Hall, London. 1952.
2. M. Nishimura and K. Takamatsu. Nature, **180**, 699 (1957).
3. D. M. Snodderly, P. K. Brown, F. C. Delori, and J. D. Auran. Invest. Ophthalmol. Vis. Sci. **25**, 660 (1984).
4. D. M. Snodderly, J. D. Auran, and F. C. Delori. Invest. Ophthalmol. Vis. Sci. **25**, 674 (1984).
5. P. Karrer and E. Jucker. Carotenoids. Elsevier, New York. 1950.
6. T. W. Goodwin. *In* Chemical zoology 6 (pt. B). *Edited by* M. Florkin. Academic Press, New York. 1976. pp. 279–306.
7. G. Wald. Science, **101**, 653 (1945).
8. G. Wald. Documenta Ophthalmol. **3**, 94 (1949).
9. R. A. Bone, J. T. Landrum, and S. L. Tarsis. Vision Res. **25**, 1531 (1985).
10. P. A. Liebman and A. M. Granda. Vision Res. **11**, 105 (1971).
11. P. A. Liebman. *In* Handbook of sensory physiology. Vol. VII. Part I. Photochemistry of vision. *Edited by* H. J. A. Dartnall. Springer-Verlag, Berlin. 1972. pp. 481–528.
12. P. A. Liebman. Nature (London), **253**, 370 (1975).
13. T. Ohtsuka. Science, **229**, 874 (1985).

14. D. JOHNSTON and R. A. HUDSON. Biochim. Biophys. Acta, **424**, 235 (1976).
15. E. FUJIMORI and R. LIVINGSTON. Nature, **180**, 1036 (1957).
16. H. CLAES and T. O. M. NAKAYAMA. Z. Naturforsch. **14**b, 746 (1959).
17. C. S. FOOTE, Y. C. CHANG, and R. W. DENNY. J. Am. Chem. Soc. **92**, 5216 (1970).
18. N. I. KINSKY. Photophysiology, **3**, 123 (1968).
19. N. I. KINSKY. Pure Appl. Chem. **51**, 649 (1979).
20. K. KIRSCHFELD. Proc. R. Soc. Lond. B**216**, 71 (1982).
21. R. A. BONE and T. J. LANDRUM. Vision Res. **24**, 103 (1984).
22. A. HAGER. Planta, **91**, 38 (1970).
23. V. R. SALARES, N. M. YOUNG, P. R. CAREY, and H. J. BERNSTEIN. J. Raman Spectrosc. **6**, 282 (1977).
24. H. T. YAMAMOTO and A. D. BANGHAM. Biochim. Biophys. Acta, **507**, 119 (1978).
25. R. MENDELSOHN and R. W. VAN HOLTEN. Biophys. J. **27**, 221 (1979).
26. S. TAKAGI, K. TAKEDA, and M. SHIROISHI. Agric. Biol. Chem. **46**, 2217 (1982).
27. S. TAKAGI and K. TAKEDA. Agric. Biol. Chem. **47**, 1435 (1983).
28. M. BUCHWALD and W. P. JENCKS. Biochemistry, **7**, 834 (1968).
29. V. A. SINESHCHEHOV, F. F. LITVIN, and M. DAS. Photochem. Photobiol. **15**, 187 (1972).
30. M. CHÉRON and J. BOLARD. C.R. Acad. Sci. Paris, t. **292** (série III, No 211), 1125 (1981).
31. V. LEJEUNE and C. TRIC. J. Chim. Phys. Physicochim. Biol. **68**, 105 (1971).
32. R. M. LEBLANC and B. H. ORGER. Biochim. Biophys. Acta, **275**, 102 (1972).
33. M. PINCUS, S. WINDREICH, and I. R. MILLER. Biochim. Biophys. Acta, **311**, 317 (1973).
34. R. REICH, R. SCHEERER, K.-U. SEWE, and H. T. WITT. Biochim. Biophys. Acta, **449**, 285 (1976).
35. K.-U. SEWE and R. REICH. Z. Naturforsch. **32**c, 161 (1977).
36. E. CHIFU and M. TOMOAIA-COTISEL. Rev. Roum. Chim. **24**, 979 (1979).
37. J. ZSAKO, E. CHIFU, and M. TOMOAIA-COTISEL. Gazz. Chim. Ital. **109**, 663 (1979).
38. M. TOMOAIA-COTISEL, E. CHIFU, V. TAMA, and V. MARCULETIU. Rev. Roum. Chim. **25**, 175 (1980).
39. D. DUCHARME, A. TESSIER, and R. M. LEBLANC. Rev. Sci. Instrum. **50**, 42 (1979).
40. R. CARPENTIER, B. LARUE, and R. M. LEBLANC. Arch. Biochem. Biophys. **222**, 403 (1983).
41. D. FRACKOWIAK, S. HOTCHANDANI, and R. M. LEBLANC. Photochem. Photobiol. **42**, 559 (1985).
42. F. BOUCHER and R. M. LEBLANC. Photochem. Photobiol. **41**, 459 (1985).
43. F. BOUCHER, R. M. LEBLANC, S. SAVAGE, and B. BEAULIEU. Appl. Opt. **25**, 515 (1986).
44. G. MUNGER, L. LORRAIN, G. GAGNÉ, and R. M. LEBLANC. Rev. Sci. Instrum. **58**, 285 (1987).
45. A. ROSENCWAIG. *In* Advances in electronics and electron physics. Vol. 46. *Edited by* L. Marton. Academic, New York. 1978, pp 207–311.
46. D. CAHEN, G. BULTS, H. GARTY, and S. MALKIN. J. Biochem. Biophys. Methods, **3**, 293 (1980).
47. H. H. STRAIN. Leaf xanthophylls. Carnegie Institution, Washington, D.C. 1938.
48. T. OHNISHI, M. HATAKEYAMA, N. YAMAMOTO, and H. TSUBOMURA. Bull. Chem. Soc. Jpn. **51**, 1714 (1978).
49. E. G. MCRAE and M. KASHA. *In* Physical processes in radiation biology. *Edited by* L. Augenstein and R. Rosenberg. Academic Press, New York. 1964. pp. 22–42.
50. J. BRETON and E. ROUX. Biochem. Biophys. Res. Commun. **45**, 557 (1971).
51. J. BRETON, M. MICHEL-VILLAZ, and G. PAILLOTIN. Biochim. Biophys. Acta, **314**, 42 (1973).

Can. J. Chem. Downloaded from www.nrcresearchpress.com by 93.93.197.157 on 09/07/12
For personal use only.

Tautomerism of bis(2-benzothiazolyl)methanes

CARMEN AVENDAÑO[1] AND MARÍA TERESA RAMOS
Departamento de Química Orgánica y Farmacéutica, Facultad de Farmacia, Universidad Complutense, 28040-Madrid, Spain

JOSÉ ELGUERO AND MARÍA LUISA JIMENO
Instituto de Química Médica, Consejo Superior de Investigaciones Científicas, Juan de la Cierva 3, 28006-Madrid, Spain

JUANA BELLANATO
Instituto de Optica, Consejo Superior de Investigaciones Científicas, Serrano 121, 28006-Madrid, Spain

AND

FELICIANA FLORENCIO
Departamento de Rayos X, Instituto de Química Física, Serrano 119, 28006-Madrid, Spain

Received July 28, 1987[3]

This paper is dedicated to Dr. John T. Edward

CARMEN AVENDAÑO, MARÍA TERESA RAMOS, JOSÉ ELGUERO, MARÍA LUISA JIMENO, JUANA BELLANATO, and FELICIANA FLORENCIO. Can. J. Chem. **66**, 1467 (1988).

Tautomerism of dibenzothiazolylmethane (**1**) and its *C*-methyl derivative (**2**) has been studied by ^{1}H nuclear magnetic resonance, ultraviolet, and infrared spectroscopy using *C*,*C*-dimethyl (**3**) and *N*-methyl (**4**) derivatives as model compounds of the "CH" and "NH" forms, respectively. X-ray diffraction analysis of the "fixed" *N*-methyl derivative **4** shows that it corresponds to the *Z-sE* isomer **4***b*$_2$. The CH tautomers are unstable in solution and they slowly isomerize into a mixture of NH tautomers that depends on the solvent and on the *C*-substituent (H or CH_3).

CARMEN AVENDAÑO, MARÍA TERESA RAMOS, JOSÉ ELGUERO, MARÍA LUISA JIMENO, JUANA BELLANATO et FELICIANA FLORENCIO. Can. J. Chem. **66**, 1467 (1988).

Faisant appel à la résonance magnétique nucléaire du ^{1}H ainsi qu'à la spectroscopie ultaviolette et infrarouge et utilisant les dérivés *C*,*C*-diméthylé (**3**) et *N*-méthylé (**4**) comme modèles, on a étudié la tautomérie du dibenzothiazolylméthane (**1**) et de son dérivé *C*-méthylé (**2**). Une étude par diffraction des rayons-X effectuée sur le dérivé *N*-méthyle «figé» (**4**) démontre qu'il correspond à l'isomère *Z-sE* (**4***b*$_2$). En solution, les tautomères CH sont instables et ils s'isomérisent lentement en un mélange des tautomères NH dont la composition dépend du solvant et du substituant porté par le carbone (H ou CH_3).

[Traduit par la revue]

Introduction

In a previous work on the synthesis of aryl(heteroaryl)dibenzothiazolylmethanes (**2**, R = aryl or heteroaryl, R′ = H) (1), we reported that their ^{1}H nmr spectra, even at 300 MHz, were extremely complex and time dependent. This is due to the superimposition of two phenomena: CH/NH tautomerism and air oxidation to carbinols or even to ketones (R = H). In this paper only the first problem will be examined. We report here a careful study of the tautomerism of dibenzothiazolylmethane **1** and its *C*-methyl derivative **2** as a preliminary and necessary step in understanding the more complex case of the aryl(heteroaryl) substituted compounds.

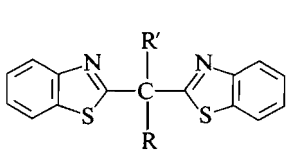

a

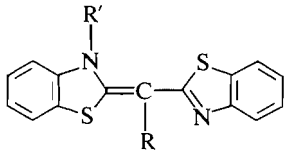

b

1 R = R′ = H
2 R′ = H; R = CH_3
3 R = R′ = CH_3 **4** R′ = CH_3; R = H

Although the tautomerism of diquinolylmethanes has been studied in detail (2), the question of whether unsubstituted dibenzothiazolylmethane (DBM, **1**) and its derivatives with one substituent attached to the methane carbon atom only exist in the CH form (*a*, R′ = H), or whether they are capable of tautomerizing to the enamine NH form (*b*, R′ = H), has given rise to some speculations, often based on insufficient experimental evidence (3–5). Because of conjugation, the *b* forms, which are heterocyclic analogues of enaminoketones, have barriers to rotation of comparable energy about both C—C bonds (6), justifying the possible existence of four isomers (b_1–b_4) when R′ ≠ H.

If R′ = H, prototropy must also be considered. In this case, tautomerism of b_1 and b_3 isomers yields the same compounds, b_1 and b_3, respectively (autotropic prototropy). The only difference is that in the *E-sE* structure, the activation energy of

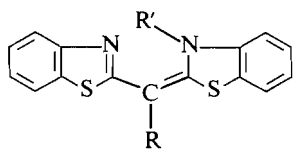

b_1
E-sE

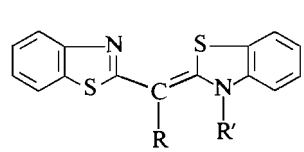

b_2
Z-sE

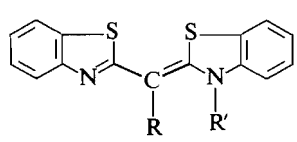

b_3
Z-sZ

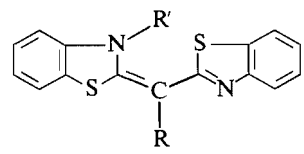

b_4
E-sZ

[1]Author to whom correspondence may be addressed.
[2]Revision received February 8, 1988.

Printed in Canada / Imprimé au Canada

Can. J. Chem. Downloaded from www.nrcresearchpress.com by 93.93.197.157 on 09/07/12
For personal use only.

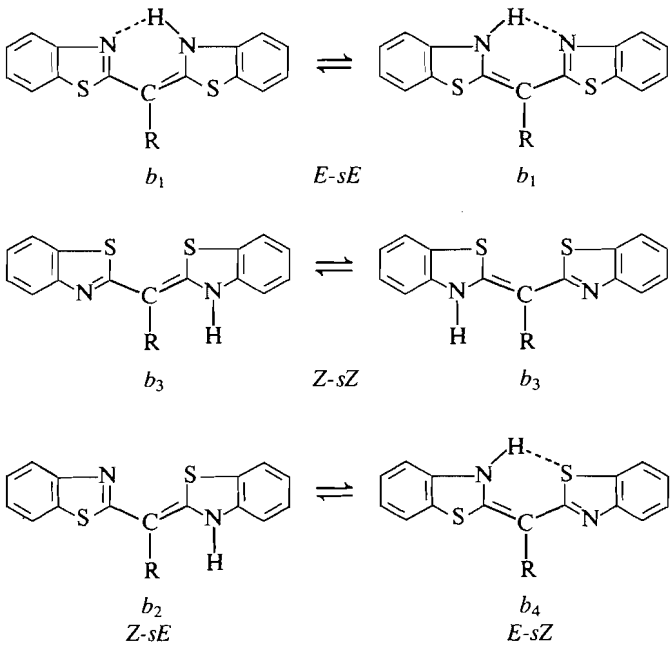

SCHEME 1

the intramolecular $b_1 \rightleftarrows b_1$ process should be very low (as in the enol form of β-diketones) and only averaged signals should be expected in nmr, whereas in the case of *Z-sZ* isomer the $b_3 \rightleftarrows b_3$ intermolecular interconversion would be relatively slow (Scheme 1). Finally, tautomerism interconverts b_2 and b_4 structures. In conclusion, when R′ = H, at most three different structures can be observed in ^{1}H nmr: *E-sE*, *Z-sZ*, and *Z-sE* (or *E-sZ*).

Compounds **3** and **4** have been chosen as fixed *a* and *b* tautomers respectively, **1** and **2** being representatives of compounds capable of tautomerism. Finally, compound **5** (R = CH_3), the cyanine dye obtained by methylation of **4**, is also included in this study.

The structural analysis was undertaken by ^{1}H nmr, uv, and ir spectroscopy in all cases and by X-ray diffraction analysis for compound **4**.

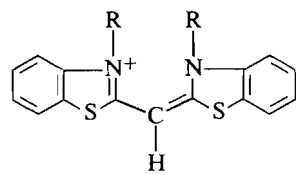

5*a*, *E-sE*

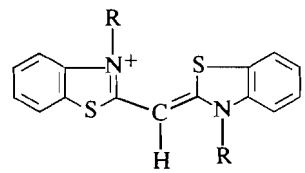

5*b*, *Z-sE*(*E-sZ*)

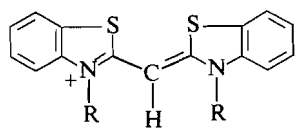

5*c*, *Z-sZ*

Experimental

Synthesis

Compounds **1**, **4**, and **5** were obtained following literature references (7, 8). Compound **2** was prepared by two different methods: by using *o*-aminothiophenol and diethyl methylmalonate in polyphosphoric acid (according to experimental conditions described for analogous compounds in ref. 1) and by the cross-coupling reaction of 2-chlorobenzothiazole with 2-ethylbenzothiazole in the presence of *n*-butyllithium.[3] Both methods afforded a syrup, identified as **2***a*, which solidified on standing. From this solid, chromatography over aluminium oxide (eluent: hexane/ethyl acetate, 9:1) yielded a compound, mp 165°C, identified as **2***b*.

Compound **3** was obtained as a minor product in the reaction of diethyl dimethylmalonate with *o*-aminothiophenol following the experimental conditions described in ref. 1 (the main product was 2-isopropylbenzothiazole as the result of a monocondensation–decarboxylation reaction). Its melting point was identical to that given for this compound in ref. 3 (132°C), in contrast to ref. 4, which gives 157°C.

X-ray crystallographic analysis of compound 4

A crystal of about 0.1 × 0.2 × 0.3 mm was mounted along the long axis. The cell dimensions were refined from 47 general reflections with the Bragg angle $\theta_{max} = 48°$ on an Enraf–Nonius CAD4 diffractometer. Crystal data are

$C_{16}H_{12}N_2S_2$ fw = 296.40

Monoclinic, $P2_1/a$, $a = 14.868(1)$, $b = 10.850(1)$, $c = 8.653(1)$ Å, $\beta = 104.65(1)°$, $V = 1350.5(3)$ Å^3, $Z = 4$, $\rho_c = 1.458$ g cm^{-3}, CuK_α, $\lambda = 1.5418$ Å (graphite monochromator), $\mu = 34.180$ cm^{-1}, $F(000) = 616$.

A total of 2371 independent reflections were measured in the range $2 < \theta < 65°$ (above this value, the reflections were very weak), of which 1973 were considered as observed with the criterion $I > 2\sigma(I)$. Two standard reflections were measured every 90 min. No decomposition was detected during processing; corrections were made for Lorentz and polarization effects, but not for extinction.

Structure was solved by direct and Fourier methods and refined by full-matrix, least-squares procedures, minimizing $\Sigma w(\Delta F)^2$ with isotropic temperature factors on all the atoms. An absorption correction following the DIFABS procedure (10) was applied to isotropically refined data, maximum and minimum absorption factors being 0.973 and 0.782 respectively. Refinement was continued by full-matrix least-squares with anisotropic temperature factors on all atoms including the hydrogen atoms (from difference synthesis) with isotropic temperature factors, and it converged with $R = 0.055$ and $R_w = 0.053$. The function minimized was $\Sigma w(|F_o| - |F_c|)^2$ with $w = k/\sigma_1^2\sigma_2^2$, $\sigma_1 = a_1 + b_1(F_o)$, $\sigma_2 = a_2 + b_2(\sin\theta/\lambda)$, and $k = 0.569$ (11); $(\Delta/\sigma)_{max} = 0.05$, residual electron density in final difference map 0.20 e Å^{-3}, $s = 1.48$.

The atomic scattering factors are taken from the literature (12). The computations were performed on a VAX 11/750 using MULTAN 80 (13) and XRAY 76 (14) programs.

^{1}H nuclear magnetic resonance study

The ^{1}H nmr spectra were obtained on a Varian XL-300 spectrometer operating at 300 MHz and on a Bruker AM-200 spectrometer operating at 200 MHz, using $CDCl_3$ and DMSO-d_6 as solvents and TMS as internal standard.

The typical instrumental parameters were as follows: sweep width, 3000 Hz; flip angle, 52°; acquisition time, 5 s; and data size, 32 K.

To assign and determine chemical shifts and coupling constants, computer assisted analyses of the four-, five-, and eight-spin systems were performed with the iterative program PANIC 81 on a Bruker Aspect 2000 computer. The eight-spin systems were treated like two subsystems of four spins, using an additional routine for obtaining the experimental envelope. The errors in the chemical shifts and coupling constants were estimated to be ±0.04 Hz and ±0.06 Hz respectively and the standard deviation between the observed and calculated line frequencies was 0.07 Hz.

Infrared spectra

Infrared spectra were recorded on a Perkin–Elmer 599B spectrophotometer. Indene and polystyrene were used for instrument calibration. All compounds were compressed into KBr pellets. Spectra in deuterated dimethylsulfoxide, deuterated chloroform, and carbon tetrachloride solutions at different dilutions were also recorded.

[3]A similar reaction using *n*-butylmagnesium bromide instead of butyllithium has been reported (3).

Can. J. Chem. Downloaded from www.nrcresearchpress.com by 93.93.197.157 on 09/07/12
For personal use only.

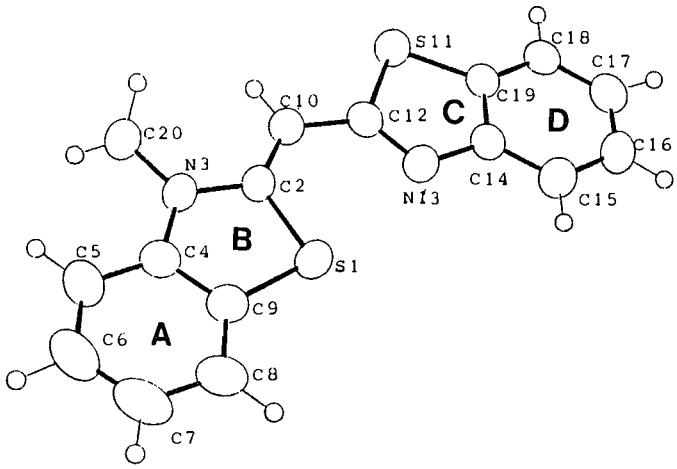

FIG. 1. A view of a molecule of compound $4b_2$ with atom numbering.

Raman spectra were measured for some samples on a Jobin Yvon U 1000 (5145 Å) spectrometer in the solid state and in $CDCl_3$ solutions.

Ultraviolet spectra

Ultraviolet spectra were recorded in ethanol (10^{-5}–10^{-6} M solutions) between 500 and 200 nm on a Bausch and Lomb Spectronic 2000 spectrophotometer.

Results and discussion

X-ray study

Crystallographic numbering (Fig. 1) has been used in this section and in Tables 1 and 2. Figure 1 shows a projection of compound **4** that corresponds to the *Z-sE* isomer b_2. Table 1 gives the final atomic coordinates while interatomic distances and interbond and torsion angles are given in Table 2.[4] The molecular rings are planar (mean torsion angles 0.7(7), 0.7(4), 1.3(5), and 1.2(7)° for A, B, C, and D rings respectively). The two fused rings that form each benzothiazolyl group are situated approximately in a plane (the dihedral angles between the two six- and five-membered rings are 0.8(1) and 1.6(1)° respectively). The two benzothiazolyl groups form a dihedral angle of 3.95(6)° and the C_2—C_{10}—C_{12}—S_{11} and N_3—C_2—C_{10}—C_{12} torsion angles are 177.1(4) and 179.2(4)° respectively, corresponding to a *Z-sE* structure. Stereogeometry of this molecule is consistent with that found in other benzothiazole rings (15, 16).

There is no intra- or intermolecular interaction between the molecular atoms, therefore the molecular packing is only realized by van der Waals forces.

^1H nuclear magnetic resonance study

One of the main problems of this study was to assign the H4 and H7 benzothiazole protons. This assignment has been tentatively reported for benzothiazole itself by comparison with its 4-nitro derivative as δ H4 (8.23 ppm) > δ H7 (8.12 ppm) in CCl_4 (17). Solvent effects for 2-methylbenzothiazole have shown that the polarity of the solvent has a greater influence on the H7 proton than on the H4 (18, 19). Our data support these results and also show a new criterion for assigning protons H4 and H7 in benzothiazoles: $J_{45} > J_{67}$. This question will be discussed at the end of this section. Tables 3 and 4 contain the

[4]Lists of structure factors, hydrogen coordinates, and other material may be purchased from the Depository of Unpublished Data, CISTI, National Research Council of Canada, Ottawa, Ont., Canada K1A 0S2.

TABLE 1. Coordinates and thermal parameters

Atom	x	y	z	U_{eq}*
S1	0.5734(1)	0.3599(1)	0.3429(1)	446(4)
S11	0.6254(1)	0.7155(1)	0.0357(1)	472(4)
N3	0.4137(2)	0.4673(3)	0.3042(4)	406(12)
N13	0.6787(2)	0.5163(3)	0.1971(4)	412(12)
C2	0.4984(3)	0.4823(4)	0.2677(5)	373(13)
C4	0.4071(3)	0.3611(4)	0.3878(4)	421(14)
C5	0.3306(3)	0.3240(5)	0.4387(6)	537(18)
C6	0.3389(4)	0.2165(6)	0.5253(6)	650(21)
C7	0.4200(5)	0.1485(6)	0.5606(6)	694(23)
C8	0.4967(4)	0.1848(4)	0.5082(6)	560(18)
C9	0.4881(3)	0.2920(4)	0.4208(5)	446(15)
C10	0.5192(3)	0.5780(4)	0.1853(5)	437(15)
C12	0.6073(3)	0.5911(4)	0.1518(5)	400(14)
C14	0.7523(3)	0.5541(4)	0.1397(5)	407(14)
C15	0.8374(3)	0.4938(5)	0.1652(5)	490(16)
C16	0.9031(3)	0.5381(5)	0.0930(6)	547(18)
C17	0.8855(3)	0.6412(5)	−0.0032(6)	532(18)
C18	0.8024(3)	0.7035(4)	−0.0266(6)	475(16)
C19	0.7365(3)	0.6601(4)	0.0456(5)	395(14)
C20	0.3387(3)	0.5546(5)	0.2517(6)	495(18)

*$U_{eq} = (1/3)\Sigma(U_{ij}.a_i^*.a_j^*.a_i.a_j.\cos(a_i,a_j)) \times 10^4$.

TABLE 2. Bond lengths (Å) and bond angles (deg)

Bond	Length (Å)	Bond	Length (Å)
S1—C2	1.750(4)	S1—C9	1.743(5)
S11—C12	1.744(4)	S11—C19	1.738(4)
N3—C2	1.383(6)	N3—C4	1.377(6)
N3—C20	1.447(6)	N13—C12	1.314(5)
N13—C14	1.374(6)	C2—C10	1.339(6)
C4—C5	1.379(7)	C4—C9	1.386(6)
C5—C6	1.375(8)	C6—C7	1.380(9)
C7—C8	1.387(9)	C8—C9	1.376(6)
C10—C12	1.419(6)	C14—C15	1.391(6)
C14—C19	1.395(6)	C15—C16	1.374(8)
C16—C17	1.380(7)	C17—C18	1.378(7)
C18—C19	1.372(7)		

Bond	Angle (deg)	Bond	Angle (deg)
C2—S1—C9	90.4(2)	C12—S11—C19	89.3(2)
C4—N3—C20	124.1(4)	C2—N3—C20	121.7(4)
C2—N3—C4	114.1(4)	C12—N13—C14	111.4(4)
S1—C2—N3	110.9(3)	N3—C2—C10	124.0(4)
S1—C2—C10	125.1(3)	N3—C4—C9	112.8(4)
N3—C4—C5	125.9(4)	C5—C4—C9	121.3(4)
C4—C5—C6	117.1(5)	C5—C6—C7	121.8(5)
C6—C7—C8	121.4(5)	C7—C8—C9	116.7(5)
C4—C9—C8	121.8(5)	S1—C9—C8	126.4(4)
S1—C9—C4	111.8(3)	C2—C10—C12	122.4(4)
N13—C12—C10	126.5(4)	S11—C12—C10	118.7(3)
S11—C12—N13	114.8(3)	N13—C14—C19	115.1(4)
N13—C14—C15	125.3(4)	C15—C14—C19	119.6(4)
C14—C15—C16	119.1(4)	C15—C16—C17	120.6(5)
C16—C17—C18	120.9(5)	C17—C18—C19	118.8(4)
C14—C19—C18	120.9(4)	S11—C19—C18	129.7(3)
S11—C19—C14	109.4(3)		

Can. J. Chem. Downloaded from www.nrcresearchpress.com by 93.93.197.157 on 09/07/12
For personal use only.

TABLE 3. ^{1}H nuclear magnetic resonance data in $CDCl_3$ and DMSO-d_6 of compounds **1***a*, **2***a* (200 MHz), and **3***a* (300 MHz)

			δ (ppm)											
			$CDCl_3$						DMSO-d_6					
Compound	R	R′	H4	H5	H6	H7	R	R′	H4	H5	H6	H7	R	R′
1*a*	H	H	8.052	7.492	7.393	7.855	4.96		8.002	7.452	7.525	8.098	5.10	
2*a*	CH_3	H	8.050	7.473	7.368	7.838	2.081	5.134	8.020	7.446	7.525	8.084	1.969	5.335
3	CH_3	CH_3	8.054	7.472	7.365	7.834	2.152		8.028	7.527	7.448	8.076	2.079	

	J (Hz)											
	$CDCl_3$						DMSO-d_6					
Compound	J_{45}	J_{46}	J_{47}	J_{56}	J_{57}	J_{67}	J_{45}	J_{46}	J_{47}	J_{56}	J_{57}	J_{67}
1*a*	8.17	1.15	0.61	7.27	1.26	8.02	8.15	1.25	0.73	7.26	1.19	8.07
2*a**	8.14	1.30	0.72	7.27	1.24	8.03	8.15	1.18	0.66	7.15	1.20	8.02
3	8.25	1.12	0.61	7.26	1.19	8.05	8.26	1.20	0.67	7.24	1.24	8.09

*J_{CHCH_3}(Hz): 7.12 ($CDCl_3$), 7.20 (DMSO-d_6).

TABLE 4. ^{1}H nuclear magnetic resonance data of compound **4** in $CDCl_3$ (200 MHz) and in DMSO-d_6 (300 MHz)

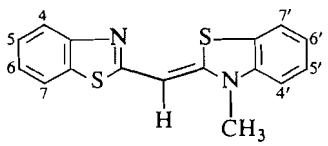

	δ (ppm)		*J* (Hz)		
Proton	$CDCl_3$	DMSO-d_6		$CDCl_3$	DMSO-d_6
H4	7.889	7.893	J_{45}	8.16	8.03
H5	7.370	7.387	J_{46}	1.11	1.31
H6	7.172	7.204	J_{47}	0.55	0.67
H7	7.715	7.747	J_{56}	7.26	7.28
H4′	6.896	7.350	J_{57}	1.24	1.29
H5′	7.236	7.365	J_{67}	7.90	7.99
H6′	7.030	7.121	$J_{4'5'}$	8.16	8.40
H7′	7.474	7.756	$J_{4'6'}$	0.95	0.83
CH	5.905	6.326	$J_{4'7'}$	0.40	0.43
CH_3	3.380	3.584	$J_{5'6'}$	7.51	7.62
			$J_{5'7'}$	1.21	1.30
			$J_{6'7'}$	7.66	7.76
			$J_{4'CH_3}$	0.30	Not visible

TABLE 5. ^{1}H nuclear magnetic resonance data of compound **2***b* (mp 165°C) in $CDCl_3$ (300 MHz) and in DMSO-d_6 (200 MHz)

	δ (ppm)		*J* (Hz)		
Proton	$CDCl_3$	DMSO-d_6		$CDCl_3$	DMSO-d_6
H4	7.911	7.875	J_{45}	8.31	8.27
H5	7.437	7.492	J_{46}	1.20	1.16
H6	7.354	7.434	J_{47}	0.63	0.61
H7	7.787	8.036	J_{56}	7.17	7.12
CH_3	2.63	2.57	J_{57}	1.26	1.20
NH	Not visible		J_{67}	8.02	8.09
			J_{5NH}		0.8
			J_{7NH}		0.3

TABLE 6. ^{1}H nuclear magnetic resonance data of compound **5** in DMSO-d_6 (200 MHz)

Proton	δ (ppm)		*J* (Hz)
H4	7.890	J_{45}	8.47
H5	7.693	J_{46}	0.54
H6	7.509	J_{47}	0.35
H7	8.222	J_{56}	7.33
CH_3	4.03	J_{57}	1.07
CH	6.715	J_{67}	7.99

chemical shifts and coupling constants of model compounds **3** (as a CH fixed form *a*) and **4** (as an NH fixed form *b*) respectively.

Protons H4 and H7 of **3** were assigned according to the downfield shift of H7 in DMSO-d_6 (Table 3). In ref. 3 only the value for the methyl group was reported.

In compound **4**, the chemical shifts of protons H4′ and H7′ are very different in the $CDCl_3$ and DMSO-d_6 spectra (Table 4). The H4′ proton has a rather low chemical shift in $CDCl_3$ and appears as a broad singlet because of a long-distance coupling constant with the *N*-methyl protons. This coupling has been checked by double irradiation.

The spectra of **1** in DMSO-d_6 and in $CDCl_3$ are given in Table 3. In both solvents, only the CH tautomer (**1***a*) was observed for this compound. The methylene protons appeared at δ 4.96 and 5.10 ppm in $CDCl_3$ and DMSO-d_6 respectively. A δ value of 4.92 ppm has been reported for the $CDCl_3$ solution of compound **1** (20). The spectrum in $CDCl_3$, obtained after several days, is characterized by a singlet at 7.14 ppm, besides the methylene signal at 4.96 ppm. The 7.14-ppm signal was attributed to the vinyl hydrogen of a *b* form. A broad signal at 8.45 ppm could be assigned to the NH proton of this tautomer. Leaving aside oxidation products, it is easy to calculate the following populations by measuring the integrals at 4.96 and 7.14 ppm: 78% of NH and 22% of CH tautomers. However, the CH/NH tautomerization is so slow that the aforementioned proportions may not correspond to the equilibrium mixture.

The two forms isolated for compound **2** gave different ^{1}H nmr

Can. J. Chem. Downloaded from www.nrcresearchpress.com by 93.93.197.157 on 09/07/12
For personal use only.

TABLE 7. Infrared and Raman characteristic frequencies (cm^{-1}) for compounds **1–5**

Compound	Medium	ν(N—H) Free	ν(N—H) Bonded	Benzothiazole bands I	II	III		Other ring bands	
1*a*	KBr			1592 w[a]	1553 w		1502 s	1453 m	1432 s
	$CDCl_3$			1599 vw	1561 vw		1508 m	1457 w	1435 m
1*b*$_1$	KBr		~3200 br[b]	1592 w	1560 sh	1550 vs		1450 s	1433 s
	$CDCl_3$		[c]	1599 w	1560 sh	1553 s-vs		1453 m	1438 s
	CCl_4		~3270 br[b]	[d]	[d]	[d]		[d]	[d]
1*b*$_4$	KBr		3200–2400 br[b]	[d]	[d]		1497 s	[d]	[d]
	$CDCl_3$		3100–2400 br[b]	[d]	[d]		1488	[d]	[d]
	CCl_4		3100–2400 br[b]	[d]	[d]		1490 m	[d]	[d]
2*a*	(Film)			1595 w	1558 w		1504 s	1455 s	1435 s
	KBr			[d]	1558 w		1505 s	1455 s	1435 vs
	$CDCl_3$			1595 w	1558 w		1504 m	1455 m	1435 s
2*b*$_1$	KBr		[c]	1587 vw	1554 vw		1492 m 1480 m	1453 m	1432 s
	$CDCl_3$		[c]	[d]	1555 vw		~1495 w	1453 w	1433 m
3*a*	KBr			1585 vw	1554 w		1491 vs	1452 m	1435 s
	Solid (Raman)			1595 vw	1558 w		1503 vs	1458 w	1440 w
	$CDCl_3$			1594 vw	1560 vw		1500 m	1454 w	1435 m
	$CHCl_3$ (Raman)			1595 vw	1560 w		1510 vs	1458 w	1440 w
4*b*$_2$	KBr			1592 m 1585 m	[e]	1555 vs	1491 vs 1473 vs	1450 s	1437 s
	Solid (Raman)			1590 sh 1587 w	1556 sh	1550 w	1490 vs 1475 sh	1452 m	1438 m
	$CDCl_3$			1593 w	1562 sh	1553 vs	1491 s 1474 vs	1454 s	1438 s
	$CHCl_3$ (Raman)			1590 w,pp	1559 w,pp	1550 sh,pp	1490 vs,pp 1475 w,pp	1453 w,pp	1438 m,pp
5	KBr			1590 w	[e]	1528 vs		1465 m	1432 w
	$(CD_3)_2SO$			1590 w	1542 w	1520 vs		1465 m	[c]

[a]Abbreviations: s, strong; m, medium; w, weak; v, very; sh, shoulder; br, broad; pp, partially polarized.
[b]Assigned to the intramolecularly bonded NH group. See text.
[c]Not detected.
[d]Not measured.
[e]Overlapped by the strong "benzothiazole III band".

spectra. The solid one gave the parameters shown in Table 5. This form was characterized as the NH or *b* tautomer, mainly because the methyl protons appeared as a singlet. The NH proton was not clearly visible since it is included in the aromatic region of the spectrum.

The spectrum of the syrup **2** is characteristic of the CH tautomer **2***a* with its methyl signals at 2.08 and 1.97 ppm (doublet) and its CH proton at 5.13 and 5.34 ppm (quartet) in $CDCl_3$ and DMSO-d_6, respectively (Table 3). The values in $CDCl_3$ solution were in agreement with ref. 3. On standing, the spectrum of the chloroform solution changes: the doublet (CH_3) and the quartet (CH) decrease until they disappear, while two methyl singlets of progressively increasing intensities (δ 2.63 and 2.82 ppm) appear. At the end of the process, these two singlets correspond to populations of 44 and 56%, respectively. The 2.63-ppm signal is due to the isolated NH tautomer (Table 5), the other one (2.82 ppm) must correspond to another NH tautomer. In DMSO-d_6 solution, tautomer **2***a* was indefinitely stable (2 weeks).

A comparison of the above results with literature reports on benzothiazole and 2-methylbenzothiazole (18) concerning the assignment criteria (see above) shows: (*i*) the chemical shifts criterion, δ H4 > δ H7 in chloroform and δ H7 > δ H4 in DMSO-d_6 is fulfilled by all compounds save the *N*-methyl derivative **4**; (*ii*) the coupling constants criterion, $J_{45} > J_{67}$, is always valid.

For the monomethinecyanine **5** (R = CH_3), three different isomers can be proposed. G. Scheibe *et al.* (21) have described the analogous compound **5** (R = C_2H_5) as the *Z-sZ* isomer on the basis of the calculated oscillator strength value *f*. Since only one signal corresponding to the methyl protons was observed in the ^1H nmr spectrum of **5** (Table 6), a symmetrical (which excludes **5***b*) and planar structure must be present in solution. Since **5***a* is sterically crowded, we agree with Scheibe's conclusion about the *Z-sZ* structure, **5***c*, of the cyanine here studied.

Infrared study

Table 7 shows the characteristic ir bands of compounds **1–5**, including some Raman data.

According to the literature, the benzothiazole ring in 2-methylbenzothiazole was characterized (22) by three absorption

Can. J. Chem. Downloaded from www.nrcresearchpress.com by 93.93.197.157 on 09/07/12
For personal use only.

Can. J. Chem. Downloaded from www.nrcresearchpress.com by 93.93.197.157 on 09/07/12
For personal use only.

bands in the 1600–1500 cm^{-1} infrared region at 1592 (w), 1560 (m), and 1534 (s) cm^{-1}, which were respectively attributed to "thiazole I", aromatic $\nu C{=}C$, and "thiazole II". However, coupling between $\nu C{=}N$ and $\nu C{=}C$ makes it difficult to distinguish individual vibrations. Several other ir spectroscopic studies on benzothiazoles have been published and the fundamental vibrations assigned (23).

The three "benzothiazole bands" for compound **3** appeared at 1585 (vw), 1554 (w), and 1491 (vs) cm^{-1} in the solid state and were slightly shifted to higher frequencies in chloroform solution (1594 (vw), 1560 (vw), and 1500 (m) cm^{-1}). The Raman pattern in this region was similar.

The ir spectrum of compound **4** in the solid state was characterized by a very strong broad band at 1555 cm^{-1} (weak in Raman), a weak double band with maxima at 1592 and 1585 cm^{-1}, and two strong bands at 1491 and 1473 cm^{-1}. The results in chloroform and carbon tetrachloride were similar. According to literature data for compound **5** (24), the strong ir band at 1555 cm^{-1} of **4** can be assigned to coupled vibrations in the planar N=C—C=C system while the strong band at 1491 cm^{-1}, which is the predominant band in Raman, may also be related with this vibrational mode.

Infrared data for compound **1** in the solid state and in chloroform solution pointed to the same *a* structure as compound **3** discussed above, this assignment being in accordance with the ^1H nmr study. However, important changes took place in the spectrum of the chloroform solution (0.05 M) after several days. The intensity of the band at ca. 1505 cm^{-1} decreased and a strong new band appeared at ca. 1555 cm^{-1}. Results suggest a tautomeric transformation $\mathbf{1}a \rightarrow \mathbf{1}b_1$ in chloroform solution, although it must be remarked that the νN—H absorption could not be unequivocally assigned here. (A weak broad absorption band at ca. 3270 cm^{-1} was observed in some experiments.) When compound **1** was studied as a very dilute CCl_4 solution (0.002 M) and also at a greater concentration (0.025 M), a new broad complex absorption between 3100 and 2400 cm^{-1} was observed after several hours. These results pointed to the formation of the b_4 form (Scheme 1) with an intramolecular N—H···S hydrogen bond. This type of hydrogen bonding has been described in the literature (25, 26). It must be remarked that this b_4 structure is not very stable in the solid state. In fact, on recovering the substance from solution to make a KBr pellet, a large proportion of the b_1 form was obtained.

The ir spectrum of compound **2** obtained as a syrup (see Experimental) was similar to that of compound **3**. In accord with this fact and with ^1H nmr data, this form was characterized as **2***a*.

Surprisingly enough, the NH form **2***b* gave an ir spectrum that, in the 1600–1400 cm^{-1} region, was similar to that of the CH form as a solid and in chloroform solutions, and no NH absorption could be clearly detected. However, according to ^1H nmr data, it must be a *b* form, probably a b_1 structure.

Ultraviolet study

The uv absorption data of compounds **1–5** in ethanolic solution are summarized in Table 8. Two different absorption patterns were observed for model compounds **3** and **4**. Compound **3**, a fixed *a* form, showed four bands with maxima at 292, 282, 258, and 219 nm, similar to those described for benzothiazole itself and other 2-substituted benzothiazoles in 95% ethanol (27). On the other hand, compound **4**, a fixed *b* form, exhibited, in addition to the absorptions in the above-mentioned region (slightly shifted), two new strong bands at the edge of the visible region of the spectrum, corresponding to a more conjugated structure.

TABLE 8. Ultraviolet data of compounds **1–5** in ethanolic solution

Compound	λ	ε	Compound	λ	ε
1	428	2574	**3**	292	3894
	404	2133		282	6018
	346	6670*		258	18307
	295	4953		219	46374
	283	5591	**4**	397	52807
	257	12923		380	51332
	217	41098		273	11407
2*a*	293	4778		265	12981
	283	6371		236	19766
	258	13804		222	33140
	218	34908	**5**	422	71036
				216	89089

*Not observable in fresh solutions.

The CH tautomer **2***a* (syrup) gave, as expected, the same absorption pattern as compound **3**. Due to the low solubility of compound **2***b* in ethanol, a saturated solution was recorded. The absorption bands found at 294, 282, 262, and 217 nm can be explained if the registered spectrum corresponds exclusively to the solubilized CH tautomer.

The data for compound **1** showed the presence of both isomers, the CH form being predominant. Finally, compound **5** (R = Me) showed two maxima, one of them in the visible region (24), in agreement with the greater conjugation of this cyanine dye.

Conclusions

The conclusive and circumstantial evidence concerning the tautomeric equilibrium data on compounds **1** and **2** is summarized below:

	Solvent		
Compound	$CDCl_3$	DMSO	Ethanol
1	22% **1***a* – 78% $\mathbf{1}b_1$	**1***a*	**1***a*
2	44% $\mathbf{2}b_1$ – 56% $\mathbf{2}b_4$	**2***a*	**2***a*

The stabilization of the CH tautomer *a* in polar solvents is similar to that observed for β-diketones (28). The effect of the *C*-methyl group, lowering the stability of the CH tautomer, is opposite to that reported for β-diketones (*C*-methylacetylacetone is less enolized than acetylacetone (9)). Since compound **2***a* tautomerized more quickly than compound **1***a* it is possible that the 22% of **1***a* that remains after several days could disappear after a longer period. However, oxidation problems in chloroform preclude carrying out the experiment under normal conditions.

The equilibrium between the conjugated tautomers *b* shows that intramolecularly hydrogen-bonded forms b_1 and b_4 are the most stable. The effect of the *C*-methyl group (stabilization of b_4) is difficult to rationalize. It may result from a steric effect between R and the sulfur atoms in b_1, but experiments with more bulky R groups would be necessary to assess this hypothesis.

Acknowledgements

One of the authors (M.T.R.) gratefully acknowledges a

research grant from the Spanish "Plan de Formación de Personal Investigador".

1. M. T. RAMOS, C. AVENDAÑO, and J. ELGUERO. J. Heterocycl. Chem. **24**, 247 (1987).
2. G. SCHEIBE and E. DALTROZZO. Diquinolylmethane and its analogs. *In* Adv. Heterocycl. Chem. Vol. 7. Academic Press, New York. 1966.
3. F. BABUDRI, S. FLORIO, G. INGROSSO, and A. M. TURCO. Heterocycles, **24**, 2215 (1986).
4. A. I. KIPRIANOV, L. P. YAKOLEVA, and YU S. ROZUM. Zh. Obshch. Khim. (J. Gen. Chem.), **22**, 302 (1952).
5. D. E. RYAN and B. K. AFGHAN. Anal. Chim. Acta, **44**, 115 (1969).
6. M. OKI. Applications of dynamic NMR spectroscopy to organic chemistry. VCH Publishers, Inc., Weinheim, West Germany. 1985. pp. 111 and 120.
7. CH. RAI and J. B. BRAUNWARTH. J. Org. Chem. **26**, 3434 (1961).
8. W. H. MILLS. J. Chem. Soc. **121**, 455 (1922).
9. G. ALLEN and R. A. DWEK. J. Chem. Soc. B, 161 (1966).
10. N. WALKER and D. STUART. Acta Crystallogr. Sect. A: Found. Crystallogr. **A39**, 158 (1983).
11. M. MARTÍNEZ-RIPOLL and F. H. CANO. (1975) PESOS. A computer program. Instituto Rocasolano, C.S.I.C., Serrano 119, Madrid, Spain.
12. International tables for X-ray crystallography. Vol. IV. Kynoch Press, Birmingham. 1974. pp. 99 and 149.
13. P. MAIN, S. J. FISKE, S. E. HULL, L. LESSINGER, G. GERMAIN, J. P. DECLERQ, and M. M. WOLFSON. MULTAN program, Universities or York, England, and Louvain, Belgium. 1976.
14. J. M. STEWART, F. A. KUNDELL, and J. C. BALDWIN. The X RAY SYSTEM Computer Program, University of Maryland, College Park, MD. 1976.
15. R. A. ZINGARO and E. A. MEYERS. Cryst. Struct. Commun. **9**, 1167 (1980).
16. J. Z. GOUGOUTAS. Cryst. Struct. Commun. **9**, 529 (1980).
17. L. LUNAZZI, F. TADDEI, and P. E. TODESCO. Boll. Sci. Fac. Chim. Ind. Bologna, **23**, 99 (1965).
18. F. L. TOBIASON and J. H. GOLDSTEIN. Spectrochim. Acta, Part A: **23A**, 1385 (1967).
19. A. R. KATRITZKY and Y. TAKEUCHI. Org. Magn. Reson. **2**, 569 (1970).
20. R. GUGLIELMETTI, E. J. VINCENT, and J. METZGER. Bull. Soc. Chim. Fr. 4195 (1967).
21. G. SCHEIBE, H. J. FRIEDRICH, and G. HOHLNEICHER. Angew Chem. **73**, 383 (1961).
22. P. BASSIGNANA, C. COGROSSI, and M. GANDINO. Spectrochim. Acta, **19**, 1885 (1963).
23. J. C. PANIZZI, G. DAVIDOVICS, R. GUGLIELMETTI, G. MILLE, J. METZGER, and J. CHOUTEAU. Can. J. Chem. **49**, 956 (1971).
24. A. LEIFER, D. BONIS, M. BOEDNER, P. DOUGHERTY, M. KORAL, and J. E. LUVALLE. Appl. Spectrosc. **20**, 289 (1966), and references therein.
25. U. DABROWSKA and J. DABROWSKI. Adv. Mol. Relax. Processes, **5**, 81 (1973), and references therein.
26. K. SZULZEWSKY, B. SCHULZ, S. KULPE, and J. KREUTZMANN. Acta Crystallogr. Sect. C: Cryst. Struct. Commun. **C40**, 280 (1984), and references therein.
27. A. CERNIANI and R. PASSERINI. J. Chem. Soc. 2261 (1954).
28. M. Y. ROGERS and J. L. BURDETT. Can. J. Chem. **43**, 1516 (1965).

Can. J. Chem. Downloaded from www.nrcresearchpress.com by 93.93.197.157 on 09/07/12
For personal use only.

Photochemistry of α-chloro- and α-bromoacetophenone. Determination of extinction coefficients for halogen–benzene complexes[1]

W. G. McGimpsey and J. C. Scaiano

Division of Chemistry, National Research Council of Canada, Ottawa, Ont., Canada K1A 0R6

Received November 26, 1987

W. G. McGimpsey and J. C. Scaiano. Can. J. Chem. **66**, 1474 (1988).

The photochemical dehalogenation of α-haloacetophenones (Cl, Br) in benzene solution has been examined under conditions of continuous and pulsed laser irradiation. Product and quantum yield studies indicate that carbon-halogen bond cleavage occurs with quantum yields of 0.88 and 0.41 for α-chloro- and α-bromoacetophenone, respectively. These values are based on trapping studies in which the $PhC(O)\dot{C}H_2$ radicals produced photochemically are scavenged by hydrogen donors such as benzenethiol. Laser flash photolysis studies lead to intense transient signals due to benzene–halogen complexes. Combination of transient data and quantum yields lead to extinction coefficients of 1 800 and 23 700 M^{-1} cm^{-1} for the chlorine (490 nm) and bromine (550 nm) complexes, respectively.

W. G. McGimpsey et J. C. Scaiano. Can. J. Chem. **66**, 1474 (1988).

Opérant dans des conditions continues ainsi que pulsées par irradiation au laser, on a étudié la déshalogénation photochimique des α-haloacétophénones (Cl et Br) en solution dans le benzène. Les résultats relatifs tant à la nature des produits qu'aux rendements quantiques indiquent que les clivages des liaisons carbone-halogène des α-chloro et α-bromoacétophénones se produisent avec des rendements quantiques respectifs de 0,88 et de 0,41. Ces valeurs sont basées sur des études de piégeage dans lesquelles les radicaux $PhC(O)CH_2\cdot$, qui sont produits d'une façon photochimique, sont piégés par des donneurs d'hydrogène comme le benzènethiol. Les études de photolyse éclair au laser conduisent à la production de signaux transitoires intenses qui sont dûs aux complexes benzène–halogène. Les données relatives à la combinaison des espèces transitoires ainsi qu'aux rendements quantiques permettent de déterminer que les coefficients d'extinction sont respectivement de 1 800 et 23 700 M^{-1} cm^{-1} pour les complexes du chlore (490 nm) et du brome (550 nm).

[Traduit par la revue]

Introduction

Aryl alkyl ketones are known to undergo efficient homolytic β-cleavage when substituted at the α-position with a suitable leaving group. A number of published studies have shown that α-phenoxy and α-thiophenoxyacetophenones as well as related systems undergo this process (1–3). It has also been established that excited carbonyl compounds can sensitize homolytic C—X cleavage in intermolecular as well as intramolecular systems. An example of the former is provided by the decomposition of carbon tetrachloride sensitized by aliphatic ketones (4). Intramolecular sensitization leading to C—Cl bond cleavage occurs in a variety of alkyl ketones (5) as well α-chloroacetophenone which is used as a photochemical source of chlorine atoms (6). However, in spite of this application, the photochemistry of α-haloacetophenones has not been examined in detail before.

The initial motivation for this work resulted from the need to establish reliable extinction coefficients for halogen–benzene complexes, as well as to identify reactions involving C—Cl and C—Br cleavage that could be used as reference processes in laser flash photolysis studies. In particular, our interests center on the cleavage of C—X bonds from upper triplet states.[2] While the details of these studies are beyond the scope of this paper, suffice to say that the results reported herein provide adequate quantitative data to allow the use of α-haloacetophenones as reference compounds or actinometers in the study of other transient processes leading to the generation of halogen atoms in solution.

The formation of complexes between halogen atoms (Cl, Br, and I) and aromatics in solution and in matrices has been well established in the literature (8). For benzene, the visible absorption maxima of these complexes are ~490 (Cl·) (8, 9), 540–550 (Br·) (8, 10), and 500 nm (I·) (8, 11). Also, it has recently been shown that at least the $[Cl\cdot,C_6H_6]$ complex has a strong absorption band in the uv region ($\lambda_{max} < 360$ nm) (6).

In this paper we report the results of a study of the photochemistry of α-chloroacetophenone and α-bromoacetophenone in benzene solution in which we combine laser flash photolysis data with product and quantum yield studies.

Experimental

Materials

Benzene (Aldrich Gold Label), cyclohexane (BDH Omnisolv), benzenethiol (Aldrich Gold Label), valerophenone (Aldrich), benzyl bromide (Aldrich), and dodecane (Aldrich) were used as received. α-Bromoacetophenone (BrACP) and α-chloroacetophenone (ClACP) (Aldrich) were recrystallized twice from hexane.

CW irradiations: product studies, quantum yield determinations

(i) Product studies

Typical samples contained either 1 *M* cyclohexane or 0.05 *M* benzenethiol as hydrogen donors. Samples were deaerated by passing a stream of dry nitrogen through the solution for several minutes. Irradiations were carried out using a photochemical reactor with Rayonet lamps supplying light in the 300 or 350 nm wavelength regions. Irradiations at 350 nm were performed with samples contained in quartz cells. Typical irradiation times were 5–10 min corresponding to ~10–20% conversion of starting material. Irradiations carried out at 300 nm were performed with samples contained in quartz cells which were in turn placed in Pyrex test tubes. This modification was necessary because the lamp profile indicated the presence of a considerable intensity in the 254 nm region; Pyrex effectively filters these wavelengths. Typical irradiation times at 300 nm were shorter than for the 350 nm lamps (2–3 min) reflecting the greater lamp intensity and the larger ground state extinction coefficient at 300 nm.

Gas chromatographic analysis was performed using a Perkin Elmer

[1]NRCC No. 28378.

[2]We have measured quantum yields for dehalogenation of naphthalenes following excitation of the triplet state in two-laser experiments (7).

Can. J. Chem. Downloaded from www.nrcresearchpress.com by 93.93.197.157 on 09/07/12
For personal use only.

Can. J. Chem. Downloaded from www.nrcresearchpress.com by 93.93.197.157 on 09/07/12
For personal use only.

8320 capillary instrument equipped with a 12 meter BP10 on vitreous silica column. Retention times for the product mixtures were compared with those of authentic samples. Further corroboration for the identity of products was given by GC–MS analysis.

(ii) Quantum yield determinations

Quantum yield determinations were carried out using valerophenone as a chemical actinometer: irradiation results in production of acetophenone by the Norrish Type II mechanism ($\Phi = 0.30$ in benzene (12)). Samples of BrACP, ClACP, and valerophenone were prepared and their absorption spectra were obtained in the range 280–400 nm. Attempts were made to match the optical density for all three samples at 350 or 300 nm. Corrections were made for band intensity and for band shape relative to the lamp profile, i.e., absorption bands were integrated and multiplied by the integral of the lamp profile. The resulting product was used as a correction factor.

The GC peak areas for acetophenone were quantified by use of an internal standard (dodecane) and the area ratios obtained for the BrACP and ClACP were compared with that of valerophenone in order to obtain $\Phi_{PhC(O)\dot{C}H_2}$, the quantum yield of carbon–halogen bond cleavage. For irradiations carried out in benzene containing 1 *M* cyclohexane the areas of the acetophenone and benzyl halide peaks were included in the calculation of $\Phi_{PhC(O)\dot{C}H_2}$ because both products are derived from the $PhC(O)\dot{C}H_2$ radical (*vide infra*). For irradiations carried out in the presence of benzenethiol, only the acetophenone peaks were used in the calculation of $\Phi_{PhC(O)\dot{C}H_2}$.

Laser flash photolysis studies

A full description of the experimental set up used is given elsewhere (13). Samples of ClACP and BrACP (7×10^{-3} *M*) in benzene were irradiated with the pulses from an excimer laser (308 nm, ~4 ns, <40 mJ/pulse). Solutions were flowed through a specially constructed 7×7 mm^2 quartz cell. The flow system was required to ensure that a fresh volume of solution was irradiated by each laser pulse. Transient absorption spectra were obtained point-by-point with conventional monochromator-photomultiplier detection as well as by using an EG & G optical multichannel analyzer (OMA) equipped with a gated image intensifier (20 ns gate) and controlled by an EG & G 1461 interface.

Extinction coefficient information for the π-complexes was obtained by comparing the optical density of the π-complex with that of the coloured form of Aberchrome-540 produced by 308 nm excitation (14) (monitored at 494 nm). Both the haloacetophenone and Aberchrome-540 measurements were carried out using the same flow cell in order to minimize the effect of changing the experimental geometry.

Phosphorescence

Phosphorescence spectra were obtained at 77 K in degassed glasses using a Perkin Elmer LS-5 spectrofluorimeter. Excitation wavelengths were 300 nm for both ClACP and BrACP. Samples were contained in 0.5 mm i.d. cylindrical quartz cells which were placed in a rectangular quartz Dewar containing liquid nitrogen.

Results and discussion

All studies reported in the various subsections have been carried out under oxygen-free conditions. Unless otherwise indicated the temperatures are 20–22°C for time-resolved studies and ~30°C for product and quantum yield determinations.

Phosphorescence

The phosphorescence spectra of ClACP and BrACP were examined in a methylcyclohexane glass at 77 K. The spectra are relatively well resolved (see Fig. 1) and lead to triplet energies of 69.8 ($\lambda_{0,0}$ = 409 nm) and 68 kcal/mol ($\lambda_{0,0}$ = 421 nm) for ClACP and BrACP, respectively. These triplet energies are somewhat lower than that of acetophenone (73.7 kcal/mol) (15). Well-resolved ketone phosphorescence is typically associated with nπ* character and on this basis we assign ClACP and BrACP triplets as nπ*. The spectrum obtained for BrACP is substantially weaker than that of ClACP. This observation is indicative of a reduced triplet population and may be the result of efficient singlet state dehalogenation. This observation is corroborated by the laser flash photolysis results (*vide infra*).

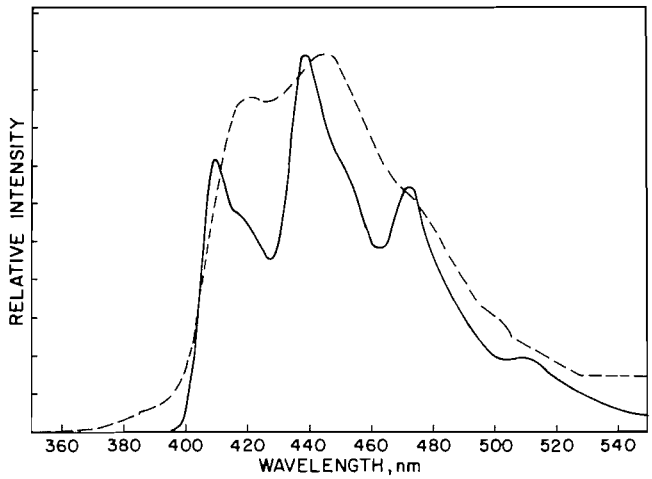

FIG. 1. Phosphorescence spectra from α-chloroacetophenone (—) and α-bromoacetophenone (- - -) in a methylcyclohexane glass at 77 K.

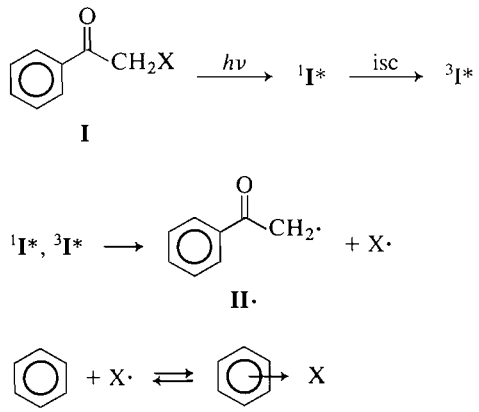

SCHEME 1

Product studies

These studies were carried out in benzene containing ~10^{-2} *M* α-haloacetophenone and either 0.05 *M* benzenethiol or 1 *M* cyclohexane which were used as hydrogen donors. Recent work by Wagner *et al.* (2) has shown that 0.05 *M* benzenethiol is sufficient to quantitatively trap all of the $PhC(O)\dot{C}H_2$ radicals produced during the β-cleavage of α-substituted acetophenones. The reactions which are expected to take place following initial excitation of α-haloacetophenone in the presence of these quenchers are given in Schemes 1 and 2. The initially produced excited singlet state may undergo intersystem crossing to the triplet manifold or β cleavage, yielding radical **II** ($PhC(O)\dot{C}H_2$) and the halogen atom $\dot{X}$. The triplet state may also undergo β cleavage to give **II** and thus, $\Phi_{PhC(O)\dot{C}H_2}$ represents the sum of all products resulting from reaction of **II**. The fate of **II** is given in Scheme 2 and involves hydrogen abstraction in the presence of hydrogen donors as well as a "neophyl-like" rearrangement suggested by the detection of other products (16, 17) (*vide infra*). It should be noted that the neophyl-like product was observed only in the benzene–cyclohexane experiments.

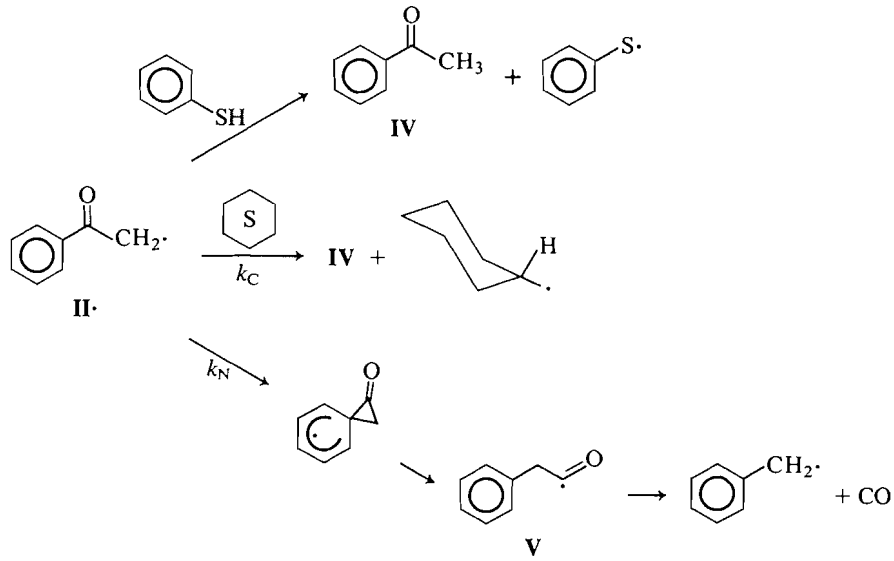

SCHEME 2

Hydrogen abstraction should be slower from cyclohexane than from benzenethiol, thus allowing the rearrangement reactions to compete more efficiently.

The major product of the photolysis using benzenethiol or cyclohexane as radical scavengers was found to be acetophenone (**IV**). When cyclohexane was used as the hydrogen donor the yield of benzyl halide (**VI**), the neophyl-derived product, was 25–30% relative to acetophenone. Thus, under our experimental conditions abstraction from cyclohexane is ca. twice as fast as the rearrangement of $PhC(O)\dot{C}H_2$. For the latter the rate constant k_N (see Scheme 2) been estimated as $10\ M^{-1}\ s^{-1}$ (16, 17). Since the cyclohexane concentration is $1\ M$, we obtain $k_c \sim 20\ M^{-1}\ s^{-1}$ for the abstraction by **II** from cyclohexane at room temperature. Toluene, the other major product of neophyl-like rearrangement is not detectable under our GC conditions.

On the other hand, reaction with benzenethiol is much cleaner with the only major product being acetophenone. It should be noted that another species observed by GC in the benzenethiol experiments initially believed to be a photochemical radical coupling product was shown to be produced thermally, possibly by a non-radical mechanism:

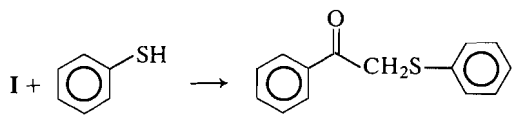

Following carbon–halogen bond cleavage, a certain percentage of $\dot{X}$ undergoes in cage recombination to regenerate the starting material. This process is not detectable by our time resolved methods and does not contribute to the quantum yield, $\Phi_{PhC(O)\dot{C}H_2}$. Following cage escape, $\dot{X}$ is scavenged by benzene resulting in the formation of the π-complex. Decay of this species may take place by reaction with the hydrogen donors present. Alternatively, the π-complex may dissociate yielding $\dot{X}$ which can also undergo hydrogen abstraction from hydrogen donors (chlorine atoms are much more reactive towards hydrogen donors than bromine atoms).[3] Free Cl· atoms abstract from 2,3-dimethylbutane at a nearly diffusion-controlled rate (6).

[3]The activation energy for hydrogen abstraction by Cl· is ~1 kcal/mol while for Br· it is $E_a \sim 14$ kcal/mol (5*c*).

TABLE 1. Quantum yield studies in benzene at 30°C

Substrate	Scavenger	Excitation (nm)	Φ_{ACP}	Φ_{PhCOCH_2}[a]
ClACP	PhSH (0.05 *M*)	350	0.88	0.88
ClACP	PhSH (0.05 *M*)	300	0.64	0.64
ClACP	C_6H_{12} (1 *M*)	350	0.50	0.65
BrACP	PhSH (0.05 *M*)	350	0.41	0.41
BrACP	PhSH (0.05 *M*)	300	0.38	0.38
BrACP	C_6H_{12} (1 *M*)	350	0.27	0.36

[a]This value is identical to Φ_{ACP} for experiments using benzenethiol as a hydrogen donor. For experiments with cyclohexane this value incorporates production of benzyl halide.

Quantum yield studies

Quantum yield determinations were carried out using the formation of acetophenone (ACP) from valerophenone as an actinometer and taking $\Phi_{ACP} = 0.30$ in benzene at room temperature (12). This particular actinometer has two advantages: first, the system of interest and the actinometer yield the same main product (i.e., acetophenone); and second, the absorption spectrum of valerophenone, although not identical to the spectra of ClACP or BrACP is in fact very similar to these spectra and hence, matching of absorbances at 350 nm was not difficult. Our quantum yields are summarized in Table 1, where Φ_{ACP} refers to the quantum yield for acetophenone production. The quantum yields for initial, out-of-cage production of $PhC(O)\dot{C}H_2$, $\Phi_{PhC(O)\dot{C}H_2}$ are also included. For the experiments using benzenethiol as hydrogen donor, this quantity is identical to Φ_{ACP} since acetophenone is the only detectable photochemical product. For experiments using cyclohexane, $\Phi_{PhC(O)\dot{C}H_2}$ includes contributions due to acetophenone production as well as benzyl halide production (neophyl). There is a larger error associated with this value since one cannot assume that all neophyl-derived benzyl radicals led to the formation of benzyl halide. Presumably these radicals may also react with hydrogen donors to yield toluene, which was not distinguishable under our GC conditions. We find the quantum yields at 300 and 350 nm for BrACP to be the same within experimental error. However, the yield at 300 nm for ClACP is lower (0.64 compared with 0.88). There may be more error associated with

Can. J. Chem. Downloaded from www.nrcresearchpress.com by 93.93.197.157 on 09/07/12
For personal use only.

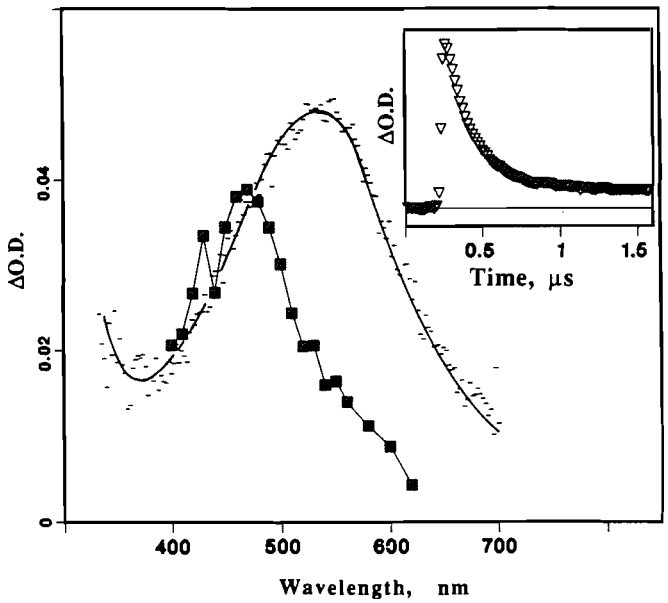

FIG. 2. Transient spectrum of the halogen–benzene complex monitored 1 μs after laser excitation of ClACP (λ_{max} 490 nm) and BrACP (λ_{max} 550 nm) in benzene. Insert: Decay of triplet ClACP monitored at 360 nm.

the 300 nm measurements, since matching of ClACP, BrACP, and valerophenone absorbances is more difficult at this wavelength. Furthermore, irradiations at 300 nm were carried out in Pyrex cells, which adds to the difficulty of compensating for the lamp profile. For these reasons we feel that the 350 nm results are more reliable.

In addition, the values of $\Phi_{PhC(O)\dot{C}H_2}$ obtained in the benzenethiol experiments are believed to be more reliable than those obtained in the cyclohexane experiments because in the latter our analysis does not measure the extent of neophyl-derived toluene under our experimental conditions.

Laser flash photolysis

Laser excitation of ClACP (typically 7×10^{-3} *M*) at 308 nm in benzene leads to its readily detectable triplet state which can be conveniently monitored at 360 nm (not λ_{max}). The triplet lifetime was 155 ± 15 ns and was concentration independent in the range examined (0.0028 to 0.014 *M*), indicating that self-quenching is unimportant in this concentration range. Figure 2 (see insert) illustrates a typical time profile for triplet decay. The formation of a new band centered at 490 nm accompanies triplet decay. This band can be readily characterized as that due to the benzene–chlorine complex on the basis of assignments made in the literature (6, 8). The transient spectrum obtained 1.0 μs after laser excitation is illustrated in Fig. 2.

When the same type of experiments are repeated with BrACP we also observe the formation of the corresponding halogen atom–benzene complex, now centered at 550 nm (see Fig. 2). However, in this case the formation of the complex is "instantaneous" within our time resolution and no signals that we could attribute to triplet BrACP were detected.

In an attempt to determine the triplet lifetimes using indirect techniques, we used 337 nm excitation and carried out quenching experiments using 1-methylnaphthalene (MeN) as a quencher. Under these conditions only the ketone is excited directly by the laser, provided that only moderate concentrations of MeN are used, and the formation of triplet MeN occurs as a result of triplet energy transfer, i.e.

$$[1] \quad XACP^* + MeN \xrightarrow{k_q} XACP + MeN^*$$

The formation of MeN* can be conveniently monitored at 420 nm. The absorbance due to MeN* (A_{420}) before significant triplet decay takes place is related to the rate constant for quenching, k_q, and the lifetime of the ketone triplet, τ_T, according to:

$$[2] \quad \frac{1}{A_{420}} = \alpha + \frac{\alpha}{k_q \tau_T [MeN]}$$

where α is a constant which includes experimental parameters and the quantum yield of intersystem crossing for XACP. This analysis led to $k_q\tau_T = 2090 \pm 430\, M^{-1}$ for ClACP, corresponding to $k_q = (1.34 \pm 0.36)\, 10^{10}\, M^{-1}\, s^{-1}$.

When the same type of experiments were repeated with BrACP we did not find any evidence for sensitized formation of MeN* at quencher concentrations of up to 0.3 *M*. Higher concentrations of MeN cannot be used because direct excitation of the quencher becomes a problem even at 337 nm. It is clear that either the triplet yield is extremely low (suggesting singlet state cleavage), or its lifetime is so short (i.e., $\tau_T \leq 0.1$ ns) that it cannot sensitize MeN before it decays. This observation is consistent with the phosphorescence results which also suggest a low triplet yield.

Another set of experiments was performed in order to verify the monophotonic nature of the $PhCOCH_2$—Cl cleavage under conditions of laser excitation. It is clear that a monophotonic process does take place, since lamp irradiation (*vide supra*) readily leads to photocleavage. The question addressed here is whether lamp and laser photocleavage involve the same process; this is a precondition if quantum yields derived from lamp experiments are to be combined with laser-derived data. In order to achieve this we measured the transient absorption due to the coloured form of Aberchrome-540 (at 494 nm) and the π-complex (at 490 nm after complete formation), as a function of the laser dose, which was adjusted with a calibrated set of neutral density filters. The laser dose was changed by a factor of 9. Plots of the Aberchrome-540 and π-complex absorbances versus the laser dose are shown in Fig. 3. The linearity of these plots indicates that Aberchrome-540 and the π-complex formation have the same dependence on excitation dose. Since Aberchrome-540 formation is known to be monophotonic (14) it can be safely assumed that the same applies to the chlorine–benzene complex.

Similar experiments have been performed in the BrACP system and the results are also shown in Fig. 3.

Determination of transient extinction coefficients

Aberchrome-540 has been developed for use as an actinometer by Heller and Langan (18). We have recently tested and extended this technique for laser applications (14). Aberchrome-540 involves the phototransformation shown in reaction [3] which occurs with $\Phi = 0.20$ in toluene at room temperature.

[3] 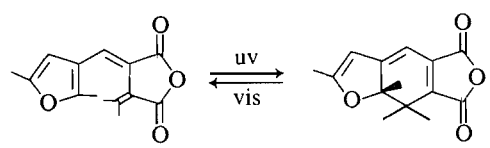

This actinometer is ideally suited for these experiments, since the wavelength maximum for the coloured form (494 nm) is very close to the wavelength maxima for the halogen-benzene

Can. J. Chem. Downloaded from www.nrcresearchpress.com by 93.93.197.157 on 09/07/12
For personal use only.

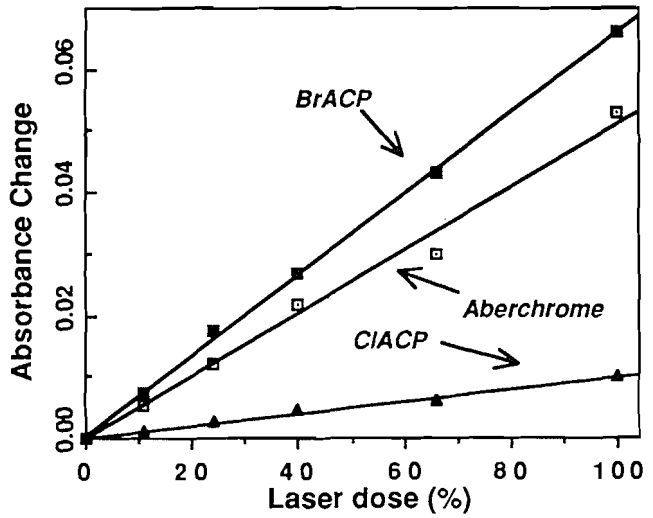

FIG. 3. Transient change in absorbance induced by 308 nm excitation of matched samples of ClACP (in benzene, monitored at 490 nm), BrACP (in benzene, monitored at 550 nm), and Aberchrome-540 (in toluene, monitored at 494 nm). The laser dose was adjusted with a calibrated set of neutral density filters.

complexes. This technique yields the product $\Phi_{complex}\epsilon_{complex}$; the values obtained were 9700 M^{-1} cm^{-1} (550 nm) and 1600 M^{-1} cm^{-1} (490 nm) for the bromine and chlorine complexes, respectively. We now assume that the quantum yield for complex formation, $\Phi_{complex}$, has the same value as $\Phi_{PhC(O)\dot{C}H_2}$, since in pure benzene all the halogen atoms that escape the geminate cage are expected to form a complex with the solvent. For example in the case of Cl· the rate of association with benzene has been measured as 6.0×10^9 M^{-1} s^{-1} (6). Thus, combining the values given above with the 350 nm data from Table 1 we obtain ϵ values of 23 700 and 1 800 M^{-1} cm^{-1} for bromine and chlorine complexes, respectively. All data in this section have been obtained by extrapolation to zero laser dose following the procedures described elsewhere (14). Errors are estimated as ±15%.

Conclusions

Our results indicate that C—X cleavage in α-haloacetophenones is a fast and efficient process which, in the case of ClACP occurs predominantly or exclusively from the triplet state, while for BrACP it may take place from an extremely short lived triplet and/or from the singlet state. The carbon centered radical, $PhC(O)\dot{C}H_2$ can be readily trapped by benzenethiol or by cyclohexane; in the latter case, trapping is competitive with a neophyl-like rearrangement leading to $PhCH_2\dot{C}O$ radicals which subsequently decarbonylate. The cleavage of the C—X bond has been shown to be a monophotonic process under both lamp and laser irradiation. The benzene–halogen complexes have extinction coefficients of 23 700 and 1 800 M^{-1} cm^{-1} for bromine and chlorine, respectively. These extinction coefficients provide needed data to allow the study of other dehalogenation processes using laser techniques.

Acknowledgement

Thanks are due to Mr. S. E. Sugamori for technical assistance.

1. Y. SABORI, T. YOSHIMOTO, and K. MINAMI. Nippon Kagaku Zasshi, **89**, 1248 (1968).
2. P. J. WAGNER and M. J. LINDSTROM. J. Am. Chem. Soc. **109**, 3062 (1987).
3. J. C. SCAIANO and J. C. NETTO-FERREIRA. J. Photochem. **32**, 253 (1986).
4. J. O. PAVLIK, P. I. PLOOARD, A. C. SOMERSALL, and J. E. GUILLET. Can. J. Chem. **51**, 1435 (1973).
5. (*a*) H. MORRISON and L. DE CARDENAS. J. Org. Chem. **52**, 2590 (1987); (*b*) W. R. BERGMARK, C. BARNES, J. CLARK, S. PAPARIAN, and S. MARYNOWSKI. J. Org. Chem. **50**, 5612 (1985); (*c*) P. C. PUROHIT and H. R. SONAWANE. Tetrahedron, **37**, 873 (1981).
6. N. J. BUNCE, K. U. INGOLD, J. P. LANDERS, J. LUSZTYK, and J. C. SCAIANO. J. Am. Chem. Soc. **107**, 5464 (1985).
7. W. G. MCGIMPSEY and J. C. SCAIANO. To be published.
8. R. E. BÜHLER. Rad. Res. Rev. **4**, 233 (1972).
9. R. E. BÜHLER and M. EBERT. Nature (London), **214**, 1220 (1967).
10. J. M. BOSSY, R. E. BÜHLER, and M. EBERT. J. Am. Chem. Soc. **92**, 1099 (1970).
11. T. A. GOVER and G. PORTER. Proc. R. Soc. (London), Ser. A. **262**, 476 (1961).
12. P. J. WAGNER, P. A. KELSO, A. E. KEMPPAINEN, J. M. MCGRATH, H. N. SCHOTT, and R. G. ZEPP. J. Am. Chem. Soc. **94**, 7500 (1972).
13. J. C. SCAIANO. J. Am. Chem. Soc. **102**, 7747 (1980).
14. For a full description of the use Aberchrome-540 as an actinometer in laser flash photolysis studies, see: V. WINTGENS, L. J. JOHNSTON, and J. C. SCAIANO. J. Am. Chem. Soc. **110**, 511 (1988).
15. S. L. MUROV. Handbook of photochemistry. Marcel Dekker, New York. 1973.
16. G. BRUNTON, H. C. MCBAY, and K. U. INGOLD. J. Am. Chem. Soc. **99**, 4447 (1977).
17. D. GRILLER and K. U. INGOLD. Acc. Chem. Res. **13**, 317 (1980).
18. H. G. HELLER and J. R. LANGAN. J. Chem. Soc. 341 (1981).

Can. J. Chem. Downloaded from www.nrcresearchpress.com by 93.93.197.157 on 09/07/12
For personal use only.

Facile preparations of 4-fluororesorcinol

PATRICE C. BÉLANGER,[1] C. K. LAU, HAYDN W. R. WILLIAMS, C. DUFRESNE, AND JOHN SCHEIGETZ
Medicinal Chemistry Department, Merck Frosst Canada Inc., P.O. Box 1005, Pointe-Claire/Dorval (Qué.), Canada H9R 4P8

Received September 9, 1987

PATRICE C. BÉLANGER, C. K. LAU, HAYDN W. R. WILLIAMS, C. DUFRESNE, and JOHN SCHEIGETZ. Can. J. Chem. **66**, 1479 (1988).

Two facile methods for preparing 4-fluororesorcinol have been developed. In the first method, the direct fluorination of 1,3-dimethoxybenzene with trifluoromethyl hypofluorite carried out in Freon 11 at −78°C afforded 2,4-dimethoxyfluorobenzene. Demethylation by heating under reflux in 48% HBr in acetic acid gave 4-fluororesorcinol in an overall yield of 60%. The second method involved the fluorination of 2,6-dimethoxyacetophenone by trifluoromethyl hypofluorite in Freon 11 at −78°C, leading to 2,6-dimethoxy-3-fluoroacetophenone. On heating under reflux in 48% HBr in acetic acid, 4-fluororesorcinol was obtained in an overall yield of 74%. The latter is the method of choice for preparing 4-fluororesorcinol.

PATRICE C. BÉLANGER, C. K. LAU, HAYDN W. R. WILLIAMS, C. DUFRESNE et JOHN SCHEIGETZ. Can. J. Chem. **66**, 1479 (1988).

On a mis au point deux méthodes faciles de préparer le fluoro-4 résorcinol. Dans la première méthode, on a procédé à une fluoration directe du diméthoxy-1,3 benzène par l'hypofluorite de trifluorométhyle dans le Freon-11, à −78°C, et on a ainsi obtenu le diméthoxy-2,4 fluorobenzène. La déméthylation, par chauffage au reflux avec du HBr à 48% dans l'acide acétique, conduit au fluoro-4 résorcinol avec un rendement global de 60%. La deuxième méthode implique une fluoration de la diméthoxy-2,6 acétophénone par l'hypofluorite de trifluorométhyle dans le Freon-11, à −78°C, qui fournit la diméthoxy-2,6 fluoro-3 acétophénone. Par chauffage au reflux avec du HBr à 48% dans l'acide acétique, on obtient le fluoro-4 résorcinol avec un rendement global de 74%. Cette dernière méthode est la méthode de choix pour préparer le fluoro-4 résorcinol.
[Traduit par la revue]

Introduction

Fluorination of aromatic compounds is of great interest chemically and biochemically. Replacing hydrogen by the isosteric fluorine is commonly utilized in the design of new drugs (1, 2) to elevate hydrophilicity and to modify metabolism and bioavailability. In one of our projects, a method of preparing 4-fluororesorcinol was needed and it had to be rapid, efficient, and potentially applicable to large-scale preparation.

Aromatic fluorination by electrophilic sources of fluorine has been the subject of several recent reviews (3). It is normally achieved by performing the Balz–Schiemann reaction (4, 5) or via electrophilic fluorination with reagents such as trifluoromethyl hypofluorite (6), acetyl hypofluorite (7), or xenon difluoride (8).

A survey of literature revealed that there are only a few reported syntheses (8) of 4-fluororesorcinol **4** or of its corresponding dimethyl ether **2** (9) and that the use of the Balz–Schiemann reaction (4, 5), if attempted, has not been reported. Direct fluorination of resorcinol with xenon difluoride (8) gave a monofluoro product whose structure has yet to be confirmed. Fluorination of 1,3-dimethoxybenzene **5** with acetyl hypofluorite (7) gave a 40% yield of 2,4-dimethoxyfluorobenzene **2**, and also 1,5-difluoro-2,4-dimethoxybenzene **6**.

We wish to present two facile and different approaches to the preparation of 4-fluororesorcinol **4**, which have been successful in our hands and are amenable to large-scale preparations.

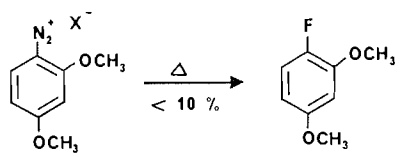

1 **2**

a $X^- = BF_4^-$

b $X^- = PF_6^-$

[1]Author to whom correspondence may be addressed.

Discussion

The Balz–Shiemann reaction (4, 5) involves a controlled thermal decomposition of a diazonium fluoroborate and is the most commonly used method of preparing fluoroaromatic compounds.

The advantage of this reaction resides in the fact that the product is a monofluorinated species, unlike those electrophilic fluorination methods that usually give a mixture of mono and polyfluorinated products. With readily available 2,4-dimethoxyaniline, the Balz–Schiemann reaction (4, 5) was considered the logical route to prepare the desired 2,4-dimethoxyfluorobenzene **2**, and consequently 4-fluororesorcinol **4**. The diazonium fluoroborate **1***a* was prepared accordingly (4*a*), and its pyrolysis investigated under a wide variety of conditions.

On heating the fluoroborate **1***a* slowly from 150 to 200°C, less than a 10% yield of 2,4-dimethoxyfluorobenzene **2** was isolated, the residue being intractable tarry materials. In an attempt to control the heating evenly, **1***a* was mixed well with fine washed sand and the mixture was heated at 165°C, but, again, only tarry materials resulted. Pyrolysis of **1***a* under vacuum (20 Torr; 1 Torr = 133.3 Pa) at 200°C also failed to give any desired product. Interestingly, the pyrolysis of **1***a* in refluxing *N*,*N*-dimethylformamide or xylene gave 1,3-dimethoxybenzene **5**. Substitution of hydrogen for the diazonium group during pyrolysis occurred as reported in other cases by Niemann *et al.* (9). Pyrolysis in Dowtherm (10) at 150–200°C gave only tarry materials. Reaction of **1***a* with cuprous chloride as a catalyst in aqueous acetone at room temperature (11) gave instead small amounts of 2,4-dimethoxychlorobenzene. Pyrolysis of aryl diazonium hexafluorophosphate salts **1***b* has been reported (12) to give better yields of aryl fluorides, but in our hands only a small amount of 1,3-dimethoxybenzene **5** was

Can. J. Chem. Downloaded from www.nrcresearchpress.com by 93.93.197.157 on 09/07/12
For personal use only.

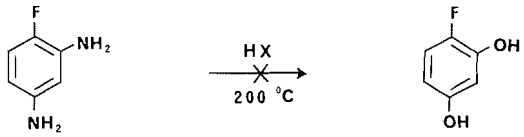

X = Cl, HSO_4, H_2PO_4

isolated when **1***b* was pyrolyzed at 140°C. The reaction of aryltriazenes with 70% hydrogen fluoride in pyridine (13) is another modification of the Balz–Schiemann reaction that was attempted, but again without success. Photolytic decomposition of aryl diazonium fluoroborates in fluoroboric acid at 0°C, although reported to be a more reliable process (14), gave also tarry materials.

Since the decomposition of diazonium salts **1***a* and **1***b* did not give the desired 2,4-dimethoxyfluorobenzene **2**, other approaches were investigated. One such alternative would utilize an aryl compound already substituted with a fluorine at the appropriate position. Thus, the Bucherer reaction (15) was tried on 2,4-diaminofluorobenzene **3**. Heating a solution of the latter in either hydrochloric, sulfuric, or phosphoric acid in a sealed tube at 200°C for 6 h resulted only in polymeric materials.

Direct fluorination of 1,3-dimethoxybenzene **5** with electrophilic fluorinating agents was then considered. Treatment of resorcinol with trifluoromethyl hypofluorite at −78°C did not afford any of the desired 4-fluororesorcinol **4** but reaction of 1,3-dimethoxybenzene **5** with this fluorinating reagent in Freon 11 at −78°C gave a 5:1 mixture of 2,4-dimethoxyfluorobenzene **2** and of 1,5-difluoro-2,4-dimethoxybenzene **6**, together with 15% of the starting material **5**. The two products were found to be easily separable by silica gel chromatography, making the reaction applicable to large-scale preparation.

After demethylating **2** by heating under reflux with 48% hydrobromic acid in acetic acid (16), 4-fluororesorcinol **4** was obtained in 87% yield.

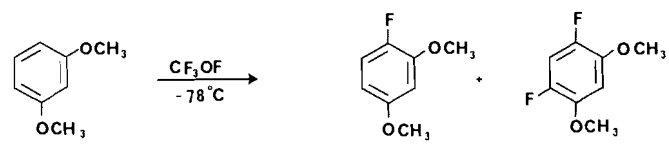

5 **2** **6**

This approach is therefore an interesting alternative, as the overall yield is of the order of 60%. Although 1,3-dimethoxybenzene **5** appears to be somewhat too reactive towards an electrophilic reagent such as trifluoromethyl hypofluorite, careful monitoring of the reaction and careful addition of the reagent will ensure a good product ratio.

Deactivation of 1,3-dimethoxybenzene **5** would permit a better control of this electrophilic substitution reaction and minimize polyfluorination. The deactivation can be achieved by the use of the electron-withdrawing acetyl substituent, reported to be labile under acidic or basic conditions in dihydroxybenzene derivatives (17). Thus, 2,6-dimethoxyacetophenone **8**, readily prepared by methylation of 2,6-dihydroxyacetophenone **7**, reacted readily with trifluoromethyl hypofluorite in Freon 11 at −78°C to give 90% yield of 2,6-dimethoxy-3-fluoroacetophenone **9**.

It was also interesting to observe that in this case, contrary to 2,4-dimethoxyfluorobenzene **2**, the two methoxy groups are readily assignable since the 6-methoxy is a singlet at 3.80 ppm

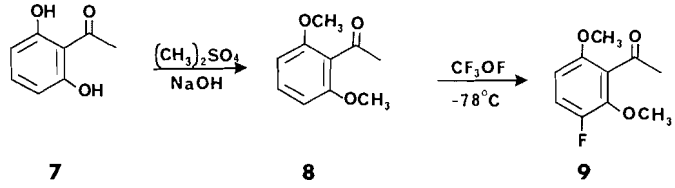

7 **8** **9**

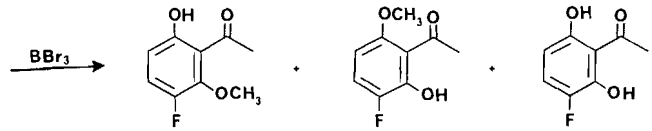

10 **11** **12**

whereas the 2-methoxy is a doublet with a coupling constant of 2 Hz. Such coupling constants have been reported (18) in similar cases.

Removal of the methoxy and of the acetyl groups can be achieved readily by refluxing a solution of 2,6-dimethoxy-3-fluoroacetophenone **9** in a mixture of 48% hydrobromic acid and acetic acid for a period of 2–3 h.

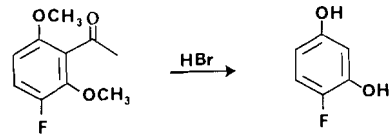

9 **4**

Under these conditions, the methyl groups are assumed to be removed to yield the corresponding 2,6-dihydroxy-3-fluoroacetophenone **12** and, in a subsequent step, a deacylation via a mechanism involving the keto–enol equilibrium of the 1,3-dihydroxy system takes place, leading to **4**.

It is of interest to note that treatment of 2,6-dimethoxy-3-fluoroacetophenone **9** with boron tribromide (19) in dichloromethane at 0°C for 2 h led to a mixture of 3 products readily separable by silica gel chromatography. The two isomeric monomethoxy derivatives **10** (minor) and **11** (major) were readily distinguished by the fluorine methyl coupling constant of 2 Hz when the methoxy is *ortho* to the fluoro group. The third product isolated was found to be 2,6-dihydroxy-3-fluoroacetophenone **12**.

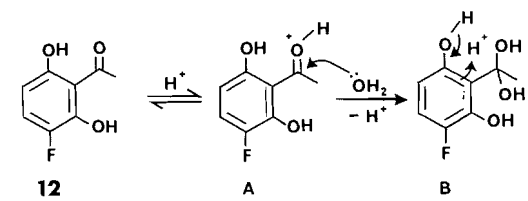

12 **A** **B**

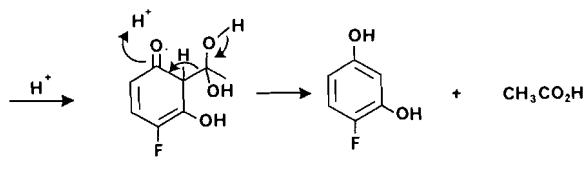

C **4**

Similar results were obtained when 2,4-dimethoxyfluorobenzene **2** was treated with boron tribromide, thus providing a method of preparing monomethoxy derivatives **13** and **14**.

Thus, by carrying out the fluorination on the 2,6-dimethoxyacetophenone **8**, aromatic fluorination with trifluoromethyl hypofluorite was easily controlled and, when combined with

Can. J. Chem. Downloaded from www.nrcresearchpress.com by 93.93.197.157 on 09/07/12
For personal use only.

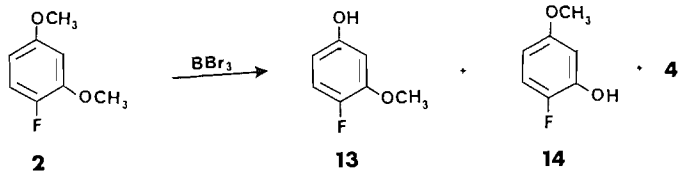

2 13 14

the hydrolysis of the resulting 2,6-dimethoxy-3-fluoroacetophenone **9** by 48% hydrobromic acid in acetic acid, it gave a rapid, efficient preparation of 4-fluororesorcinol **4** that can easily be scaled up. This approach is the preferred route to 4-fluororesorcinol **4**.

Experimental

Melting points were taken on a Thomas Hoover apparatus in open capillary tubes and are uncorrected. A Varian EM-390 spectrometer was used to record nmr spectra in deuterochloroform, unless indicated otherwise. Proton chemical shifts are relative to tetramethylsilane (TMS) as internal standard. Elemental analyses were performed by Guelph Chemical Laboratories Ltd., Guelph, Ontario. Silica gel chromatographic separations were carried out in the flash chromatography mode following the indications of Clark Still (20) using British Drug House silica gel of 200 mesh size. All reactions as well as column chromatography were monitored routinely with the aid of thin-layer chromatography (tlc) using precoated 0.25-mm silica gel GF plates (Analtech), visualizing them by uv, and then charring with sulfuric acid.

Preparation of 2,4-dimethoxyfluorobenzene 2

In a Teflon reaction vessel, a solution of 1,3-dimethoxybenzene **5** (1.5 g; 10.9 mmol) in Freon 11 (50 mL) was cooled to −78°C and trifluoromethyl hypofluorite was bubbled through the solution slowly, monitoring the reaction by tlc. The mixture was poured onto a silica gel column and elution with 7% ethyl acetate in hexane gave 1.0 g (68%) of 2,4-dimethoxyfluorobenzene **2** as an oil and 0.2 g of unreacted 1,3-dimethoxybenzene **5**. For compound **2**, ^{1}H nmr: 3.77 (s, 3H, CH_3), 3.87 (s, 3H, CH_3), 6.37 (pair of triplets, $J_{H5,F}$ = 5 Hz, $J_{H3,H5}$ = 3 Hz, and $J_{H5,H6}$ = 9 Hz, 1H, H5), 6.57 (d of d, $J_{H3,F}$ = 7.2 Hz, $J_{H3,H5}$ = 3 Hz, H3), 7.00 (d of d, $J_{H6,F}$ = 11.2 Hz, $J_{H5,H6}$ = 9 Hz, 1H, H6). *Anal.* calcd. for $C_8H_9FO_2$: C 61.53, H 5.81, F 12.17; found: C 61.51, H 5.95, F 12.40.

1,5-Difluoro-2,4-dimethoxybenzene **6** (0.2 g) was also isolated, mp 98–99°C (lit. (7*d*) mp 99°C); ^{1}H nmr: 3.87 (s, 6H, $2CH_3$), 6.63 (t, $J_{H3,F}$ = 8 Hz, H3), 6.90 (t, $J_{H6,F}$ = 12 Hz, 1H, H6). *Anal.* calcd. for $C_8H_8F_2O_2$: C 55.17, H 4.63, F 21.82; found: C 55.24, H 4.86, F 21.97.

Preparation of 4-fluororesorcinol 4

To a solution of 2,4-dimethoxyfluorobenzene **2** (0.4 g, 2.6 mmol) in glacial acetic acid (2 mL) was added 48% hydrobromic acid (2 mL) and the mixture was refluxed for a period of 4 h. The resulting mixture was concentrated *in vacuo* and the residue was dissolved in a small volume of methylene chloride and chromatographed on silica gel. Elution with 15% ethyl acetate in hexane afforded 0.29 g (87%) of 4-fluororesorcinol **4**, mp 97–98°C; ^{1}H nmr: 6.32 (pair of triplets, $J_{H5,F}$ = 5 Hz, $J_{H3,H5}$ = 3 Hz, and $J_{H5,H6}$ = 9 Hz, 1H, H5), 6.55 (d of d, $J_{H3,F}$ = 7.2 Hz, $J_{H3,H5}$ = 3 Hz, 1H, H3), 7.00 (d of d, $J_{H6,F}$ = 11.2 Hz, $J_{H5,H6}$ = 9 Hz, 1H, H6). *Anal.* calcd. for $C_6H_5FO_2$: C 56.25, H 3.93, F 14.83; found: C 56.73, H 4.28, F 14.75.

Preparation of 2,6-dimethoxyacetophenone 8

To a solution of 2,6-dihydroxyacetophenone **7** (3.0 g, 20 mmol) in aqueous sodium hydroxide (7.5 N, 100 mL) maintained at 60°C was added dropwise over a period of 30 min dimethylsulfate (20 mL). The mixture was then cooled to room temperature; the solid was filtered, washed well with water, and air-dried to yield 2,6-dimethoxyacetophenone **8** (3 g, 82%), mp 58–59°C; ^{1}H nmr: 2.50 (s, 3H, CH_3), 3.83 (s, 6H, $2CH_3$), 6.60 (d, $J_{H3,H4}$ = 9 Hz, 2H, H3 and H5), 7.33 (t, $J_{H3,H4}$ = $J_{H4,F}$ = 9 Hz, 1H, H4). *Anal.* calcd. for $C_{10}H_{12}O_3$: C 66.65, H 6.71; found: C 66.31, H 6.99.

Preparation of 2,6-dimethoxy-3-fluoroacetophenone 9

In a Teflon reaction vessel, a solution of 2,6-dimethoxyacetophenone **8** (1.40 g, 7.7 mmol) in Freon 11 (50 mL) was cooled to −78°C and trifluoromethyl hypofluorite was bubbled through the solution slowly, while monitoring the reaction by tlc. The cold reaction mixture was poured onto a silica gel column and elution with 7% ethyl acetate in hexane gave 1.2 g (91%) of 2,6-dimethoxy-3-fluoroacetophenone **9** and 0.2 g of unreacted 2,6-dimethoxyacetophenone **8**. For compound **9**, ^{1}H nmr: 2.47 (s, 3H, CH_3), 3.80 (s, 3H, CH_3), 3.97 (d, J = 2 Hz, 3H, CH_3), 6.57 (d of d, $J_{H4,H5}$ = 9 Hz, $J_{H5,F}$ = 3 Hz, 1H, H5), 7.07 (d of d, $J_{H4,H5}$ = 9 Hz, $J_{H4,F}$ = 11 Hz, 1H, H4). *Anal.* calcd. for $C_{10}H_{11}FO_3$: C 60.60, H 5.59, F 9.59; found: C 60.40, H 5.70, F 9.20.

Demethylation of 9 with boron tribromide

To a solution of 2,6-dimethoxy-3-fluoroacetophenone **9** (0.5 g; 2.5 mmol) in methylene chloride (3 mL) cooled to −78°C, a 1 M solution of boron tribromide in methylene chloride (3 mL) was added. The mixture was allowed to warm to room temperature and was stirred at that temperature for 30 min. It was then cooled to −78°C and methanol (3 mL) was added. The resulting mixture was chromatographed on silica gel, and eluted with 15% ethyl acetate in hexane. It gave successively 3-fluoro-2-methoxy-6-hydroxyacetophenone **10** (28 mg) as an oil, 3-fluoro-2-hydroxy-6-methoxyacetophenone **11** (287 mg), mp 87–88°C, and 2,6-dihydroxy-3-fluoroacetophenone **12** (61 mg), mp 134–135°C.

3-Fluoro-6-hydroxy-2-methoxycetophenone 10: ^{1}H nmr: 2.70 (s, 3H, CH_3), 4.03 (d, J = 2 Hz, 3H, CH_3), 6.60 (d of d, $J_{H4,H5}$ = 9 Hz, $J_{H5,F}$ = 5 Hz, 1H, H5), 7.20 (d of d, $J_{H4,H5}$ = 9 Hz, $J_{H4,F}$ = 11 Hz, 1H, H4). *Anal.* calcd. for $C_9H_9FO_3$: C 58.69, H 4.92, F 10.32; found: C 58.84, H 4.92, F 10.12.

3-Fluoro-2-hydroxy-6-methoxyacetophenone 11: ^{1}H nmr: 2.70 (s, 3H, CH_3), 3.90 (d, J = 2 Hz, 3H, CH_3), 6.30 (d of d, $J_{H4,H5}$ = 9 Hz, $J_{H5,F}$ = 5 Hz, 1H, H5), 7.25 (d of d, $J_{H4,H5}$ = 9 Hz, $J_{H4,F}$ = 11 Hz, 1H, H4). *Anal.* calcd. for $C_9H_9FO_3$: C 58.69, H 4.92, F 10.32; found: C 58.83, H 4.98, F 10.20.

2,6-Dihydroxy-3-fluoroacetophenone 12: ^{1}H nmr: 2.77 (s, 3H, CH_3), 6.37 (d of d, $J_{H4,H5}$ = 9 Hz, $J_{H5,F}$ = 5 Hz, 1H, H5), 7.17 (d of d, $J_{H4,H5}$ = 9 Hz, $J_{H4,F}$ = 11 Hz, 1H, H4). *Anal.* calcd. for $C_8H_7FO_3$: C 56.42, H 4.14, F 11.16; found: C 56.31, H 4.22, F 11.40.

Preparation of 4-fluororesorcinol 4

To a solution of 2,6-dimethoxy-3-fluoroacetophenone **9** (0.4 g; 2.0 mmol) in glacial acetic acid (2 mL) was added 48% hydrobromic acid (2 mL) and the mixture was refluxed for a period of 4 h. The resulting mixture was concentrated *in vacuo* and the residue was dissolved in a small volume of methylene chloride and chromatographed on silica gel. Elution with 15% ethyl acetate in hexane afforded 0.21 g (81%) of 4-fluororesorcinol **4**, mp 97–98°C, found to be identical to that prepared above.

Demethylation of 2 with boron tribromide

To a solution of 2,4-dimethoxy-3-fluorobenzene **2** (0.5 g, 2.5 mmol) in methylene chloride (3 mL) cooled to −78°C, a 1 M solution of boron tribromide in methylene chloride (3 mL) was added. The mixture was allowed to warm to room temperature and was stirred at that temperature for 30 min. It was then cooled to −78°C and methanol (3 mL) was added. The resulting mixture was chromatographed on silica gel and eluted with 15% ethyl acetate in hexane. It gave successively **2** (19 mg), 4-hydroxy-2-methoxy-fluorobenzene **13** (31 mg) as an oil, 2-hydroxy-4-methoxy-fluorobenzene **14** (314 mg) as an oil, and 4-fluororesorcinol **4** (53 mg), mp 97–98°C.

4-Hydroxy-2-methoxy-fluorobenzene 13: ^{1}H nmr: 3.77 (s, 3H, CH_3), 6.32 (pair of triplets, $J_{H5,F}$ = 5 Hz, $J_{H3,H5}$ = 3 Hz, and $J_{H5,H6}$ = 9 Hz, 1H, H5), 6.60 (d of d, $J_{H3,F}$ = 7.2 Hz, $J_{H3,H5}$ = 3 Hz, 1H, H3), 7.00 (t, $J_{H6,F}$ = $J_{H5,H6}$ = 9 Hz, 1H, H6). *Anal.* calcd. for $C_7H_7FO_2$: C 59.15, H 4.96, F 13.37; found: C 59.46, H 5.59, F 13.00.

2-Hydroxy-4-methoxyfluorobenzene 14: ^{1}H nmr: 3.63 (s, 3H, CH_3), 6.30 (pair of triplets, $J_{H5,F}$ = 5 Hz, $J_{H3,H5}$ = 3 Hz, and $J_{H5,H6}$ = 9 Hz, 1H, H5), 6.63 (d of d, $J_{H3,F}$ = 7.2 Hz, $J_{H3,H5}$ = 3 Hz, 1H, H3),

Can. J. Chem. Downloaded from www.nrcresearchpress.com by 93.93.197.157 on 09/07/12
For personal use only.

7.00 (t, $J_{H6,F} = J_{H5,H6} = 9$ Hz, 1H, H6). *Anal.* calcd. for $C_7H_7FO_2$: C 59.15, H 4.96, F 13.37; found: C 59.22, H 5.30, F 13.63.

Acknowledgements

The authors wish to express their thanks to Dr. Yvan Guindon, formerly with Merck Frosst Canada Inc., now with Bio-Mega, Canada, for his support throughout this work and to Mr. L. R. Perkins and J. Kollonitsch, Merck Sharp and Dohme Research Laboratories, Rahway, NJ, for their helpful advice and suggestions.

1. Carbon–fluorine compounds: chemistry, biochemistry and biological activities. Ciba-Foundation Symposium, Associated Scientific Publisher, Amsterdam. 1972.
2. (*a*) R. FILLER. Chem.-Tech. (Heidelberg) **4**, 752 (1974); (*b*) T. B. PATRICK. J. Chem. Educ. **56**, 228 (1979); (*c*) R. FILLER and Y. KOBAYASHI (*Editors*). Biomedicinal aspects of fluorine chemistry. Elsevier, Amsterdam. 1982.
3. (*a*) H. VYPEL. Chimia, **39**, 305 (1985); (*b*) A. HAAS and M. LIEB. Chimia, **39**, 134 (1985); (*c*) S. PURRINGTON, B. S. KAGAN, and T. B. PATRICK. Chem. Rev. **86**, 997 (1986).
4. (*a*) G. BALZ and G. SCHIEMANN. Ber. Dtsch. Chem. Ges. B: **60**, 1186 (1927); (*b*) A. ROE. Org. React. **5**, 193 (1949).
5. R. L. FERN and C. A. VANDERWERF. J. Am. Chem. Soc. **72**, 4809 (1950).
6. M. HUDLICKY. Chemistry of organic fluorine compounds. 2nd ed. Ellis Horwood, Chichester, England. 1976.
7. (*a*) C. M. SHARTS and W. A. SHEPPARD. Org. React. **21**, 243 (1974); (*b*) T. B. PATRICK, G. L. CANTRELL, and C. CHANG. J. Am. Chem. Soc. **101**, 7434 (1979); (*c*) R. H. HESSE. Isr. J. Chem. **17**, 60 (1978); (*d*) O. LERMAN, Y. TOR, D. HEBEL, and S. ROZEN. J. Org. Chem. **49**, 806 (1984).
8. S. P. ANAND, L. A. QUARTERMAN, H. H. HYMAN, K. G. MIGLIORESE, and R. FILLER. J. Org. Chem. **40**, 807 (1975).
9. C. NIEMANN, A. A. BENSON, and J. F. MEAD. J. Am. Chem. Soc. **63**, 2204 (1941).
10. S. M. SPATZ. J. Org. Chem. **26**, 4158 (1961).
11. E. D. BERGMAN, S. BERKOVIC, and R. IKAN. J. Am. Chem. Soc. **78**, 6037 (1956).
12. K. G. RUTHERFORD, W. REDMOND, and J. R. RIGAMONTI. J. Org. Chem. **26**, 5149 (1961).
13. M. N. ROSENFELD and D. A. WIDDOWSON. Chem. Commun. 914 (1979).
14. K. L. KIRK. J. Org. Chem. **41**, 2373 (1976), and references cited therein.
15. (*a*) N. L. DRAKE. Org. React. **1**, 105 (1947); (*b*) S. PATAI (*Editor*). Chemistry of the amino group. Interscience, London. 1968. p. 37.
16. L. LONG, JR. and A. BURGER. J. Org. Chem. **6**, 852 (1941).
17. P. R. SARAIYA and R. C. SHAH. Proc. Indian Acad. Sci. **31**, 213 (1950).
18. J. BURDON. Tetrahedron, **21**, 1101 (1965).
19. J. F. W. MCOMIE and M. L. WATTS. Chem. Ind. 1658 (1963).
20. W. CLARK STILL, M. KAHN, and A. MITRA. J. Org. Chem. **43**, 2923 (1978).

Can. J. Chem. Downloaded from www.nrcresearchpress.com by 93.93.197.157 on 09/07/12
For personal use only.

Interaction of diiodine with some tetra-substituted dithiooxamides. Crystal and molecular structure of bis(morpholinothiocarbonyl)bis(diiodine)

DAVIDE ATZEI, PAOLA DEPLANO,[1] AND EMANUELE F. TROGU
Istituto di Chimica Generale, Inorganica ed Analitica dell'Università di Cagliari, Via Ospedale 72, 09124 Cagliari, Italy

FRANCESCO BIGOLI AND MARIA ANGELA PELLINGHELLI
Istituto di Chimica Generale dell'Università di Parma, Centro Studio per la Strutturistica Diffrattometrica del C.N.R., Via delle Scienze, 43100 Parma, Italy

AND

ALBERTO VACCA
I.S.S.E.C.C., Consiglio Nazionale delle Ricerche, Via J. Nardi 39, 50132 Firenze, Italy

Received September 1, 1987

DAVIDE ATZEI, PAOLA DEPLANO, EMANUELE F. TROGU, FRANCESCO BIGOLI, MARIA ANGELA PELLINGHELLI, and ALBERTO VACCA. Can. J. Chem. **66**, 1483 (1988).

The reaction of some tetra-substituted dithiooxamides $R_2NC(S)C(S)NR_2$ (R = CH_3:Me_4dto; R = C_2H_5:Et_4dto; R_2N = OC_4H_8N:Mo_2dto) with diiodine has been investigated by spectrophotometric methods in $CHCl_3$. The formation in solution of 1:1 and 1:2 charge-transfer (c.t.) complexes between the reagents has been observed. A new computer program, derived from "SUPERQUAD" (P. Gans, A. Sabatini, and A. Vacca. J. Chem. Soc. Dalton Trans. 1195 (1985)), has been applied to evaluate the formation constants. The 1:2 c.t. complexes have been isolated in the solid state, and an X-ray structure analysis of the $[OC_4H_8NC(S)C(S)NC_4H_8O]\cdot 2I_2$ compound indicated that the crystals are triclinic, space groups $P\bar{1}$, with a = 14.659(6), b = 15.111(6), c = 9.317(5) Å, α = 92.29(2), β = 99.71(2), γ = 99.48(2)° and Z = 4. In particular the torsion angle S—C—C—S (≈90°) shows that the conformation of the dithiooxamide is *not trans*.

DAVIDE ATZEI, PAOLA DEPLANO, EMANUELE F. TROGU, FRANCESCO BIGOLI, MARIA ANGELA PELLINGHELLI et ALBERTO VACCA. Can. J. Chem. **66**, 1483 (1988).

Opérant en solution chloroformique et utilisant des méthodes spectrophotométriques, on a étudié la réaction de quelques dithiooxamides tétrasubstituées ($R_2NC(S)C(S)NR_2$ (R = CH_3:Me_4dto; R = C_2H_5:Et_4dto; R_2N = OC_4H_8:Mo_2dto) avec l'iode. En solution, on a observé que les réactifs forment des complexes de transfert de charge (t.c.) 1:1 et 1:2. Dans le but d'évaluer les constantes de formation, on a appliqué un nouveau programme d'ordinateur dérivé du «SUPERQUAD» (P. Gans, A. Sabatini et A. Vacca. J. Chem. Soc. Dalton Trans. 1195 (1985)). On a isolé le complexe de t.c. 1:2 à l'état solide; une analyse par diffraction des rayons-X du composé $[OC_4H_8NC(S)C(S)NC_4H_8O].2I_2$ indique que les cristaux sont tricliniques, groupe d'espace $P\bar{1}$ avec a = 14,659(6), b = 15,111(6) et c = 9,317(5) Å, α = 92,29(2), β = 99,71(2) et γ = 99,48(2)° et Z = 4. On note, en particulier, que l'angle de torsion S—C—C—S (≈90°) démontre que la conformation du dithiooxamide n'est *pas* trans.

[Traduit par la revue]

Introduction

Diiodine (I_2) forms molecular compounds of the charge-transfer (c.t.) type, with a variety of molecules containing nitrogen, sulphur or selenium heteroatoms. Moreover, these c.t. complexes may be key intermediates in the oxidative mechanism of these molecules by means of I_2.

In recent studies about these reactions, in particular we have used molecules containing one or more thioamide groups: i.e. both the non-coordinated $[R_2NC(S)SSC(S)NR_2]$ = tetraalkyl-thiuram disulphide (1), and $[R_2NC(S)S^-]$ = dialkyl dithio-carbamato anion, which is coordinated to the transition metals Cr(III) (2), Co(III) (3), Fe(III) (4), Mn(III) (5).

The obtained results showed that (*i*) despite the several electron donor sites available in the molecule, the carbonyl sulphur is the site of interaction with I_2, and in solution no stoichiometries higher than 1:1 have been observed (in the explored concentration range); (*ii*) the carbonyl sulphur retains basic properties even though coordinated to transition metals; (*iii*) the c.t. complexes may evolve to give oxidation products, and it was possible to isolate them and determine their structures as cations having poly-iodides as counter ions.

As a progression, we are investigating the behaviour of dithiooxamides, and we here report on the results obtained with tetraalkyl dithiooxamides.

Experimental

Materials

Twice sublimed diiodine was purchased from Carlo Erba. $CHCl_3$ was Merck Reagent Grade and dried over 4 Å molecular sieves before use. Tetra-substituted dithiooxamides were prepared according to literature (6). The compound $[OC_4H_8NC(S)C(S)NC_4H_8O]\cdot 2I_2$ was obtained as red–brown lustrous crystals on slow evaporation of a $CHCl_3$ solution of $[OC_4H_8NC(S)C(S)NC_4H_8O]$ and I_2 in a 1:2.5 ratio. *Anal.* calcd. for $C_{10}H_{16}I_4N_2O_2S_2$: C 15.64, H 2.10, N 3.65; found: C 15.60, H 2.19, N 3.69.

The elemental analyses were performed by Istituto di Chimica Farmaceutica, Università di Cagliari.

The other adducts have been obtained analogously. Infrared data (KBr pellets) are as follows. $[Mo_2dto]\cdot 2I_2$: 2965m, 2920w, 2900w, 2855m, 1510s, 1500s, 1490s, 1457w, 1433vs, 1385m, 1357m, 1330vw, 1300m, 1285s, 1270vs, 1260vs, 1240vs, 1225s, 1200s, 1175m, 1125s, 1110vs, 1060s, 1025vs, 980s, 915w, 908w, 890w, 860s, 840m, 765s, 660w, 640s, 610m, 540s, 500m, 475w, 395wbr, 310w, 290w,br.

$[Et_4dto]\cdot 2I_2$: 2997w, 2975m, 2935m, 2875w, 1528 ÷ 1500vs broad, 1450sh, 1435vs, 1380s, 1355m, 1287s, 1273vs, 1227vs, 1198vs, 1163w, 1142m, 1113s, 1098sh, 1073m, 1060sh, 1010w, 968vs, 928vs, 905vs, 858s, 805w, 780m, 750vs, 640m, 623m, 545sh, 483sh, 405m, 340vw, 305vw.

$[Me_4dto]\cdot 2I_2$: 2963w, 2925mw, 2859w, 1561vs, 1553vs, 1526vs, 1443w, 1432w, 1397vs, 1273s, 1255sh, 1242s, 1184m, 1152s,

Printed in Canada / Imprimé au Canada

Can. J. Chem. Downloaded from www.nrcresearchpress.com by 93.93.197.157 on 09/07/12
For personal use only.

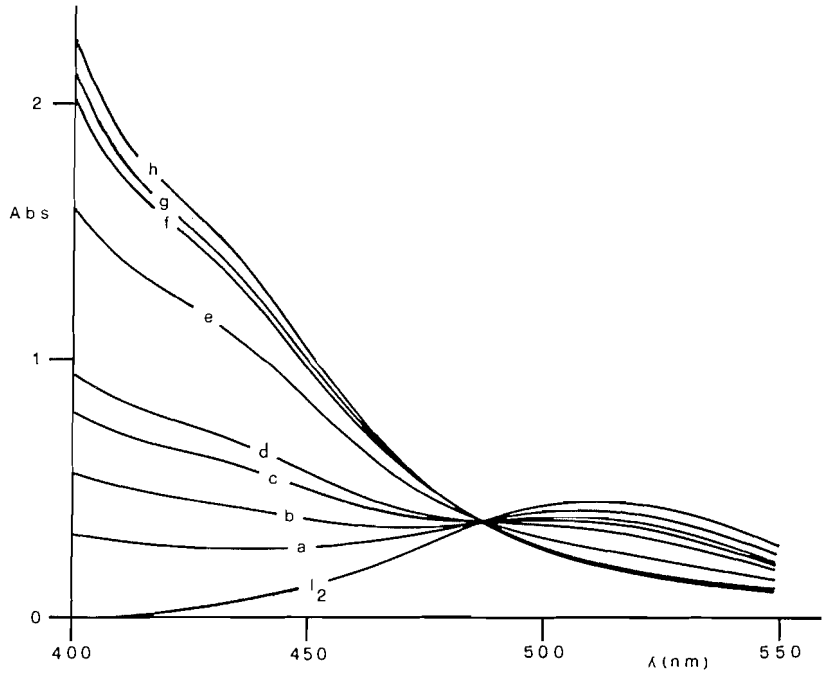

FIG. 1. Visible spectra at 283 K in 1 cm cell of $CHCl_3$ solutions containing constant amounts of I_2 (5×10^{-4} mol dm^{-3}) and variable Me_4dto concentrations in the ratios: *a* = 1:0.5; *b* = 1:1; *c* = 1:1.5; *d* = 1:2; *e* = 1:5; *f* = 1:10; *g* = 1:12; *h* = 1:15.

1112vs, 1046w, 972vs, 899w, 818vs, 621m, 568m, 514w, 437m, 375w, 313m.

Infrared spectra were recorded using a Perkin-Elmer model 983 spectrophotometer.

Spectrophotometric measurements

The electronic spectra were measured on $CHCl_3$ solutions with a Varian model Cary 2300 spectrophotometer equipped with an automatic system of data acquisition at different temperatures in the range 10 to 35°C.

A set of eight $CHCl_3$ solutions containing a constant diiodine concentration ($\approx 5 \times 10^{-4}$ mol dm^{-3}) and variable dithiooxamide concentrations (ranging from 2.5×10^{-4} to 1×10^{-2} mol dm^{-3}) (see Fig. 1) was prepared and the spectra recorded between 400 and 550 nm using 1 cm silica cells. Another set of twelve solutions was prepared with a constant concentration of dithiooxamide ($\approx 5 \times 10^{-4}$ mol dm^{-3}) and diiodine concentrations in the range $2.5 \times 10^{-4} - 2.5 \times 10^{-2}$ mol dm^{-3}; the relevant spectra were measured in the range 240–400 nm with 1 mm silica cells (see Fig. 2).

Calculations

The experimental points used in calculations have been taken from the recorded spectra at 10 nm intervals, the total number of the data being always greater than 95 for each system at each temperature.

A new computer program written in FORTRAN has been used to refine simultaneously equilibrium constants and molar extinction coefficients from the spectrophotometric measurements. The sum of the squared residuals of the optical densities is minimized by the Gauss–Newton least-squares method using unit weights, all the derivatives being obtained analytically. The program is designed to be as general and flexible as possible: the stoichiometry of the species formed can be varied by simple input information; the observed quantities may refer either to individual spectra (batch experiments) or points of spectrophotometric titrations; each spectrum may contain absorption data read at different wavelengths. The number of wavelengths per spectrum is not rigid and may change from one spectrum to another. A detailed description of the program will be the subject of a future publication (7). Calculations were carried out using a GOULD 32/27 computer at I.S.S.E.C.C., Firenze.

X-ray crystallography

Crystal data are as follows:

$C_{10}H_{16}I_4N_2O_2S_2$ mw = 767.987

Triclinic, a = 14.659(6), b = 15.111(6), c = 9.317(5) Å, α = 92.29(2); β = 99.71(2), γ = 99.48(2)° (by least-squares refinement from the θ values of 28 reflections accurately measured) U = 2002(2) Å^3, Z = 4, D_c = 2.549 g cm^{-3}, $F(000)$ = 1400, Mo-K_α radiation (λ = 0.71073 Å), μ(Mo-K_α) = 63.66 cm^{-1}, space group $P\bar{1}$. Crystal dimensions: 0.09 × 0.20 × 0.28 mm^3.

Data collection and processing

Siemens AED diffractometer, niobium-filtered Mo-K_α radiation, θ–2θ scan mode, 4829 unique reflections measured ($+h$, $\pm k$, $\pm l$), ($2.5 \leq \theta \leq 22°$), 2626 observed ($I \geq 2\sigma(I)$), data corrected for absorption (8) (maximum and minimum values 1.049664, 0.993898) and extinction (maximum and minimum values 1.005226, 0.977286).

Structure analysis and refinement

Patterson and heavy-atom methods were used, blocked full-matrix least-squares refinement was carried out with anisotropic thermal parameters for all the non hydrogen atoms excluding those of the morpholinic rings. Hydrogen atoms were placed in their geometrically calculated positions and their coordinates were introduced in the last cycle as fixed contributors. The weighting scheme used in the final cycles was $w = 0.6438/(\sigma^2(F_o) + 0.002250F_o^2)$. The final R and R' values were 0.0455 and 0.0545, respectively. The final electron-density difference synthesis showed no peaks >0.93 and <−0.90 e Å^{-3}. Scattering factors and corrections for anoma-

Can. J. Chem. Downloaded from www.nrcresearchpress.com by 93.93.197.157 on 09/07/12
For personal use only.

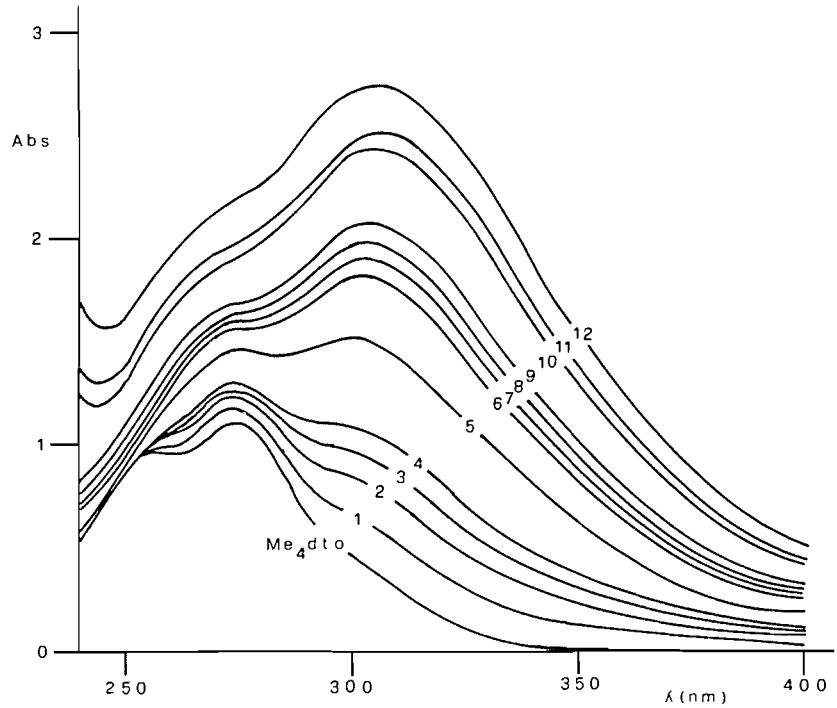

FIG. 2. Ultraviolet spectra at 283 K in 0.1 cm cell of $CHCl_3$ solutions containing constant amounts of Me_4dto (5.08×10^{-4} mol dm^{-3}) and variable diiodine concentrations in the ratios: *1* = 1:0.5; *2* = 1:1; *3* = 1:1.5; *4* = 1:2; *5* = 1:5; *6* = 1:10; *7* = 1:12; *8* = 1:15; *9* = 1:19; *10* = 1:38; *11* = 1:46; *12* = 1:62.

TABLE 1. Fractional atomic co-ordinates ($\times 10^4$) with estimated standard deviations in parentheses for the non-hydrogen atoms

Atom	*X/a*	*Y/b*	*Z/c*	Atom	*X/a*	*Y/b*	*Z/c*
I11	−1565(1)	740(1)	5934(1)	I12	4082(1)	4085(1)	1132(2)
I21	−3278(1)	249(1)	6776(2)	I22	2224(1)	4247(1)	709(2)
I31	27(1)	3707(1)	4477(2)	I32	4575(1)	1374(1)	−9(2)
I41	−60(1)	4462(1)	1766(2)	I42	4196(1)	706(1)	−2919(2)
S11	193(4)	1175(3)	4829(6)	S12	6042(4)	3964(4)	1261(6)
S21	77(4)	3104(3)	7275(6)	S22	4872(4)	1960(4)	2950(6)
O11	3336(11)	3401(10)	5346(17)	O12	8091(10)	1504(9)	725(16)
O21	1003(10)	890(9)	1.1138(15)	O22	6939(13)	3582(11)	7446(19)
N11	1824(11)	2207(9)	6050(16)	N12	6981(10)	2635(9)	1835(16)
N21	585(10)	1677(9)	8460(15)	N22	6080(12)	3261(11)	4585(20)
C11	942(13)	1891(11)	6066(19)	C12	6337(13)	3083(13)	2131(20)
C21	550(12)	2191(11)	7354(19)	C22	5792(12)	2764(12)	3323(21)
C31	2490(13)	2786(12)	7184(21)	C32	7301(15)	1937(14)	2716(22)
C41	2872(16)	3604(15)	6530(25)	C42	7453(15)	1200(14)	1705(24)
C51	2684(16)	2879(15)	4253(25)	C52	7671(16)	2131(15)	−147(25)
C61	2274(15)	1991(14)	4736(24)	C62	7550(14)	2913(13)	703(22)
C71	104(13)	1808(12)	9667(21)	C72	5528(19)	3132(17)	5801(30)
C81	695(15)	1751(14)	1.1110(23)	C82	6106(21)	2886(19)	6946(33)
C91	1574(16)	856(14)	1.0059(25)	C92	7518(19)	3661(17)	6263(30)
C101	957(13)	816(12)	8567(20)	C102	6956(16)	3923(15)	4964(25)

lous dispersion were taken from ref. 9. Calculations were performed on the CYBER 76 computer of CINECA (Casalecchio, Bologna) with financial support from the University of Parma, and on the GOULD-SEL 32/77 computer of the "Centro di Studio per la Strutturistica Diffrattometrica del C.N.R. (Parma)" using the SHELX-76 systems of computer programs (10) and the programs ABSORB (11), PARST (12), PLUTO (13), and ORTEP (14).

The final atomic fractional co-ordinates are given in Table 1; selected bond distances and angles are in Table 2.[1]

[1]The measured and calculated structure factors, fractional atomic co-ordinates for the H atoms, anisotropic thermal parameters, and other material mentioned in the text, may be purchased from the Depository of Unpublished Data, CISTI, National Research Council of Canada, Ottawa, Ont., Canada K1A 0S2.

Can. J. Chem. Downloaded from www.nrcresearchpress.com by 93.93.197.157 on 09/07/12
For personal use only.

TABLE 2. Selected bond distances (Å) and angles (deg) with e.s.d.'s in parentheses

Molecule 1		Molecule 2	
Bond	Distance	Bond	Distance
I11—I21	2.751(2)	I12—I22	2.738(2)
I31—I41	2.805(3)	I32—I42	2.787(3)
I11—S11	2.920(6)	I12—S12	2.892(6)
I31—S21	2.789(6)	I32—S22	2.801(6)
S11—C11	1.67(2)	S12—C12	1.67(2)
S21—C21	1.64(2)	S22—C22	1.64(2)
C11—C21	1.50(3)	C12—C22	1.52(3)
C11—N11	1.31(2)	C12—N12	1.31(3)
C21—N21	1.31(2)	C22—N22	1.34(2)
N11—C31	1.46(2)	N12—C32	1.45(3)
N11—C61	1.53(3)	N12—C62	1.48(3)
N21—C71	1.45(3)	N22—C72	1.50(4)
N21—C101	1.49(2)	N22—C102	1.47(3)

Molecule 1		Molecule 2	
Bonds	Angle	Bonds	Angle
I21—I11—S11	175.5(1)	I22—I12—S12	173.9(2)
I41—I31—S21	174.7(1)	I42—I32—S22	176.5(2)
I11—S11—C11	107.7(7)	I12—S12—C12	112.4(7)
I31—S21—C21	108.6(7)	I32—S22—C22	109.6(7)
S11—C11—C21	115.5(1.3)	S12—C12—C22	117.2(1.4)
S11—C11—N11	127.7(1.4)	S12—C12—N12	124.7(1.5)
S21—C21—C11	118.8(1.3)	S22—C22—C12	120.4(1.4)
S21—C21—N21	124.5(1.4)	S22—C22—N22	125.8(1.5)
C11—C21—N21	116.7(1.5)	C12—C22—N22	113.4(1.6)
C21—C11—N11	116.8(1.6)	C22—C12—N12	118.1(1.7)
C11—N11—C31	127.3(1.6)	C12—N12—C32	123.5(1.6)
C11—N11—C61	120.8(1.6)	C12—N12—C62	121.2(1.5)
C31—N11—C61	112.0(1.5)	C32—N12—C62	114.6(1.5)
C21—N21—C71	122.3(1.5)	C22—N22—C72	120.4(1.8)
C21—N21—C101	127.1(1.5)	C22—N22—C102	125.5(1.8)
C71—N21—C101	109.8(1.4)	C72—N22—C102	114.0(1.8)

Results and discussion

The addition of diiodine to R_4dto is accompanied by a drastic change in the uv–visible spectrum of the solution, and a new c.t. maximum appears near 300 nm, while the characteristic band of the free diiodine is "blue shifted" (see Fig. 1, 2) and an isosbestic point is observed.

The spectrophotometric data obtained between 400 and 550 nm for the solutions with constant diiodine concentration and variable dithiooxamide concentration could be interpreted quite satisfactorily by assuming that the 1:1 species is the only adduct present. This was verified for all the dithiooxamides investigated at all the temperatures. The values of log K_1 are listed in Table 3. The interpolations of the plots of these quantities against $1/T$ (linear correlation coefficients greater than 0.99) allowed a sufficiently precise determination of the enthalpy of formation of the 1:1 adducts and consequently of the calculation of the entropy changes. The values of the thermodynamic functions shown in Table 3 are very close in the three examined dithiooxamides.

The spectral data measured in the range 240–400 nm on the solutions containing constant dithiooxamide concentrations and variable diiodine concentrations are clearly consistent with the stepwise addition of diiodine to the ligand. They have been used

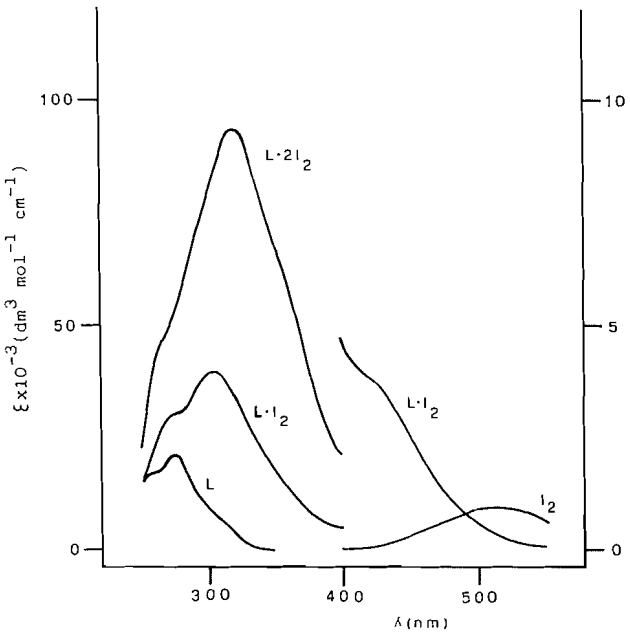

FIG. 3. Calculated uv–vis spectra of 1:1 and 1:2 adducts between Me_4dto and diiodine at 283 K in $CHCl_3$ solutions.

to calculate the formation constant of both of the 1:1 and 1:2 adducts together with the corresponding molar absorption coefficients of the adducts (see Fig. 3). Unfortunately the experimental errors in the observed data did not allow a precise determination of these quantities. However, the following overall values of log K_1 and log $K_1 \cdot K_2$ were obtained at 10°C: 2.87 ± 0.01 and 4.05 ± 0.06 for Me_4dto, 3.00 ± 0.01 and 4.39 ± 0.05 for Et_4dto, 2.45 ± 0.05 and 3.8 ± 0.2 for Mo_2dto.

The principal ir bands are listed in the Experimental part.

In Table 4 the thioamide (I) band with a major ν(CN) contribution, and (IV) band with a high ν(CS) contribution are assigned according to Desseyn and Herman (15).

Structural evidence shows that S atoms have the donor role in the molecule (see later), and that there is an extensive delocalization within the NCS moieties (but not along the carbon–carbon skeleton between them). Previously reported structural studies on some dithiooxamides have shown similar features (16–18).

The ir results reflect this situation. In fact, a significant positive shift is observed in the thioamide(I) ν(CN) band due to the coordination, while the thioamide(IV) ν(CS) band is less affected. The other bands do not undergo any significant shifts.

Because of the π-electron flow from the N atom to the S, the electronic delocalization through the system

allows to compensate the decrease of the bond order CS as a consequence of the coordination: therefore the ν(CS) is less affected by the coordination than expected.

As a consequence of the electron delocalization, the basicity of the parent amine should affect the association constants of the c.t. complexes. For the limited data so far available, a correlation between log K_1 and the pK_A of the parent amines in the protonated form seems to exist (pK_A = 8.492, 10.774, and 10.993 and 298 K for morpholine, dimethylamine, and

Can. J. Chem. Downloaded from www.nrcresearchpress.com by 93.93.197.157 on 09/07/12
For personal use only.

TABLE 3. Logarithms of the equilibrium constants, enthalpy (kcal mol^{-1}), and entropy changes (cal K^{-1} mol^{-1}) for the formation of 1:1 adducts between dithio-oxamides (L) and diiodine in $CHCl_3$ solution

	log K_1						
L	10°C	15°C	20°C	25°C	35°C	ΔH^0	ΔS^0
Mo_2dto	2.294(6)	2.227(9)	2.095(9)	2.062(8)	1.88(1)	−6.4(5)	−12(2)
Me_4dto	2.928(4)	2.848(5)	2.774(5)	2.700(4)	2.541(5)	−6.1(1)	−8.2(5)
Et_4dto		2.917(7)	2.830(8)	2.748(7)	2.597(7)	−6.5(1)	−9.3(3)

TABLE 4. Principal ir bands (cm^{-1}) for the R_4dto + I_2 system

	R_2N = Mo		R = Me		R = Et	
L	ν(CN)	ν(CS)	ν(CN)	ν(CS)	ν(CN)	ν(CS)
R_4dto[a]	1505sh 1480s	855ms	1525s	823m	1492s	870s
[R_4dto·$2I_2$][a]	(1510–1500–1490)s,br	860s	(1561–1553–1526)vs	818vs	(1528–1500)vs,br	858s
R_4dto[b]	1480		1525		1492	
R_4dto + I_2[b] (1:1)	1510 < 1485		1527		1525 ≈ 1499	
R_4dto + I_2[b] (1:2)	1512 ≈ 1485		1550sh 1530		1525 > 1499	
R_4dto + I_2[b] (1:5)	1512 > 1488		1550 ≈ 1530		1525 1500 sh	

[a]As KBr pellets.
[b]In solution of CH_2Cl_2 (for transparency reasons); [R_4dto] = 1.10^{-2} mol dm^{-3}.

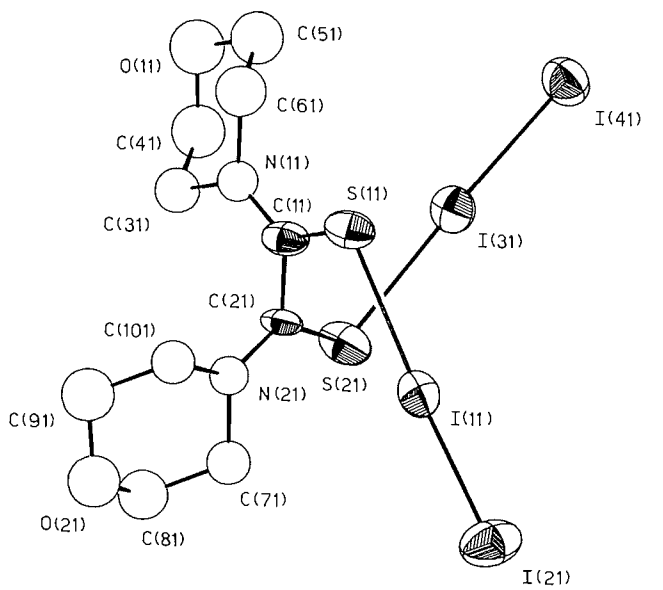

FIG. 4. Perspective view of the molecule **1**. Thermal ellipsoids are drawn at the 50% probability level.

diethylamine, respectively) (19), while the ΔH^0 values are very close in the three dithiooxamides studied.

A more extensive investigation, using parent amines with pK_A varying in more extensive range, and *N,N'*-disubstituted dithiooxamides, to study the effect of the basicity of the parent amine and of hydrogen bonding is in project.

Crystal and molecular structure

The title compound, whose molecular structure is shown in Fig. 4 together with the atomic numbering scheme, is a neutral molecular compound belonging to the series with the two S as heteroatoms in the donor and with the two diiodine molecules as acceptors.

Excluding the S(1i)—I(1i)—I(2i) moieties (where i = 1,2 for molecule **1** and **2**, respectively), the two crystallographically independent molecules of the adduct are related by a pseudo-glide roughly parallel to (0 1 0) at (1/4)*b*. Moreover, they appear similar for several reasons. The bond distances and angles are in good agreement; in the

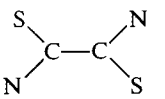

moieties the usual sp^2 hybridization is observed for the C and N atoms and the hybridization at S is essentially sp^3. In each molecule the S(1i)—I(1i) distance is greater than S(2i)—I(3i), and consequently the correlated I(1i)—I(2i) distance is shorter than I(3i)—I(4i). This is the result of the contacts involving the terminal iodine atoms; in fact the longest I—I bond distance is observed when the contacts are approximately in the I—I bond direction. Similar bond distances were observed in [benzyl sulphide]·I_2 (20), in [$Co(C_5H_5N)_4(NCS)_2$]·$2(I_2)$ (21), in [1,4-dithiane]$2(I_2)$ (22), in [2(merocyanine)]·I_2 (23), in dithia[3.3.1]propellane·$2I_2$, and in dithia[3.3.2]propellane·$2I_2$ (24). In addition, despite the large variation in S—I distance, a similar correlation (excluding only one couple of values in dithia[3.3.1]propellane·$2I_2$: S—I 2.852(2) and I—I 2.797(1) Å) and no appreciable change in the C=S distance were observed in the above mentioned and in several other compounds (Herbstein and Schwotzer (25) and references therein).

Besides the intermolecular contacts, the most significant differences between the two independent molecules regard the values of the C(1i)—S(1i)—I(1i) angles (107.7(7)° and 112.4(7)°, respectively) and of the torsion angles around S—C; 148(1)° is observed for I(12)—S(12)—C(12)—N(12) and −30(2)° for I(12)—S(12)—C(12)—C(22), while the values of all the other

Can. J. Chem. Downloaded from www.nrcresearchpress.com by 93.93.197.157 on 09/07/12
For personal use only.

Can. J. Chem. Downloaded from www.nrcresearchpress.com by 93.93.197.157 on 09/07/12
For personal use only.

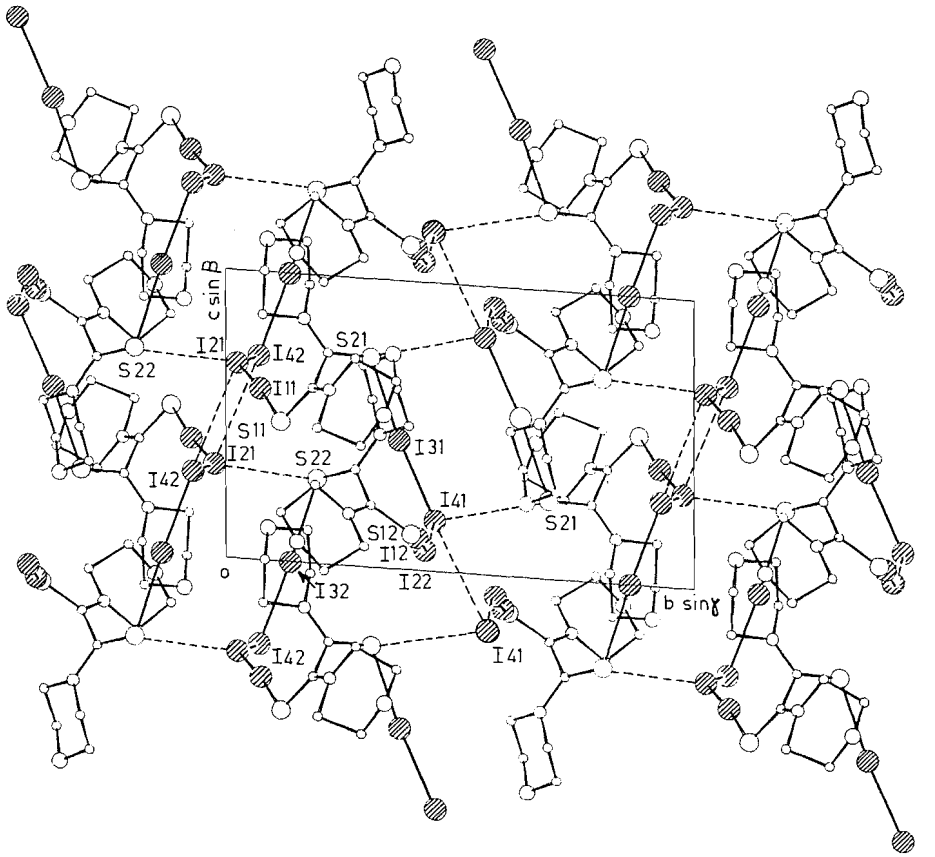

FIG. 5. Projection of the structure along [100].

corresponding angles are about 180° and 0°, respectively. This is determined by the contact I(22)···I(41) 3.705(3) Å.

The pseudo C_2 symmetry observed in molecule **1**, excluding the COC morpholinic moieties, lacks in molecule **2** owing to the above-mentioned I(22)···I(41) interaction. This contact is also responsible of the non-planarity of the C(22)C(12)S(12)I(12) fragment. In the other CCSI planar fragments interactions I(1i)···C(2i) and I(3i)···C(1i) less than the Van der Waals radii sum are observed (I(11)···C(21) 3.51(2), I(31)···C(11) 3.52(2), I(32)···C(12) 3.60(2) Å) while the contact I(12)···C(22) is 3.83(2) Å.

The conformation of these *N,N,N',N'*-tetrasubstituted molecules is the most favourable to yield the minimum hindrance: the values of the S—C—C—S torsion angles are −91(2) and 94(2)°, respectively.

On the contrary, in the uncomplexed molecule and in some metal-complexes of dioxamides, dithiooxamides, and *N,N'*-disubstituted dioxamides and dithiooxamides, the *trans* conformation is determined by contacts which can be considered as intramolecular N—H···S hydrogen bonds.

Contacts of type I···I (as the menthioned I(22)···I(41), I(21)···I(42) $(-x, -y, -z)$ 3.758(3), I(21)···I(42) $(x-1, y, z+1)$ 3.931(3), I(41)···I(41) $(-x, 1-y, -z)$ 3.746(3) Å); I···S (I(21)···S(22) $(-x, -y, 1-z)$ 3.790(6), I(41)···S(21) $(-x, 1-y, 1-z)$ 3.755(5) Å); I···C_{morph} (I(41)···C(62) $(x-1, y, z)$ 3.83(2), I(22)···C(31) $(x, y, z-1)$ 3.99(2) Å); S···S (S(11)···S(11) $(-x, -y, 1-z)$ 3.54(7) Å); O···C_{morph} (O(12)···C(71) $(1+x, y, z-1)$ 3.23(3), O(22)···C(62) $(x, y, 1+z)$ 3.26(3) Å), and C_{morph}···C_{morph} (C(52)···C(82) $(x, y, z-1)$ 3.59(4), C(61)···C(81) $(x, y, z-1)$ 3.73(3) Å) are important in determining the molecular three-dimensional packing.

The first four values show that there are I_2···I_2 secondary interactions which are appreciably shorter than the sum of the Van der Walls radii. Similar unusual interactions were recently observed in dithia[3.3.1]propellane·$2I_2$ (3.720(1) Å) and in our tris(morpholinecarbodithioato-*S,S'*)manganese(IV)pentaiodide dichloromethane (2/1) (26) (3.795(3) and 3.877(3) Å), where however V-shaped I_5^- units of the type I_2···I^-···I_2 are present and where the interactions involve a terminal iodine of a unit and an internal iodine of another unit.

Excluding the I(22) atom, each of the other three terminal iodine interacts with the adjacent iodines in such a way to present a roughly planar T-shaped arrangement; moreover each of them is involved in a contact of type I···S or I···C_{morph} in a direction quite perpendicular to the corresponding T-shaped disposition.

The interactions between the T-shaped arrangements originate others of type

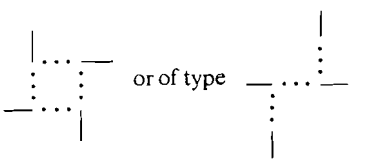

(— indicates the I_2 molecule) as well showed in Fig. 5. The values of the I—I···I angles (I(11)—I(21)···I(42) $(-x, -y, -z)$ 150.8(1)°, I(31)—I(41)···I(41) $(-x, 1-y, -z)$ 174.8(1)°, I(12)—I(22)···I(41) 156.7(1)°, I(32)—I(42)···I(21) $(1+x, y, z-1)$ 170.8(1)°) indicate that the interactions deviate

significantly from linearity and they are in good agreement with those observed in dithia[3.3.1]propellane·$2I_2$ (154.2(1)°) and in tris(morpholinecarbodithioato-*S*,*S*′)manganese(IV)pentaiodide dichloromethane (2/1) (155.9(1) and 176.7(1)°).

Acknowledgment

We thank the Consiglio Nazionale delle Ricerche and the Ministero della Pubblica Istruzione for support in this work.

1. F. Bigoli, M. A. Pellinghelli, G. Crisponi, P. Deplano, and E. F. Trogu. J. Chem. Soc. Dalton Trans. 1349 (1985).
2. G. Crisponi, P. Deplano, V. Nurchi, and E. F. Trogu. Polyhedron, **3**, 1241 (1984).
3. G. Crisponi, P. Deplano, and E. F. Trogu. Inorg. Chim. Acta, **75**, 135 (1984).
4. G. Crisponi, P. Deplano, and E. F. Trogu. J. Chem. Soc. Dalton Trans. 365 (1986).
5. F. Bigoli, P. Deplano, M. A. Pellinghelli, and E. F. Trogu. J. Chem. Soc. Dalton Trans. In press.
6. R. N. Hurd, G. De La Mater, G. C. McElheny, R. J. Turner, and V. H. Wallingford. J. Org. Chem. **26**, 3980 (1961) and references therein.
7. A. Sabatini and A. Vacca. To be published.
8. N. Walker and D. Stuart. Acta Crystallogr. Sect. A, **39**, 158 (1983).
9. International tables for X-ray crystallography. Vol. 4. Kynoch Press, Birmingham. 1974. pp. 99, 149.
10. G. Sheldrick. SHELX 76. A program for crystal structure determination. University of Cambridge. 1976.
11. F. Ugozzoli. ABSORB: Comput. Chem. **11**, 109 (1987).
12. M. Nardelli. Comput. Chem. **7**, 95 (1983).
13. W. D. S. Motherwell. PLUTO. University of Cambridge. 1976.
14. C. K. Johnson. ORTEP Report ORNL-3794, revised. Oak Ridge National Laboratory, TN. 1965.
15. H. O. Desseyn and M. A. Herman. Spectrochim. Acta, **23**A, 2457 (1967).
16. B. Long, P. Markey, and P. J. Wheatley. Acta Crystallogr. **7**, 140 (1954).
17. P. J. Wheatley. J. Chem. Soc. 396 (1956).
18. A. Christensen, H. J. Geise, and B. J. Vandor Veken. Bull. Chem. Soc. Belg. **84**, 1173 (1975).
19. R. M. Smith and A. E. Martell. Critical stability constants. Vols. 2 and 5. Plenum Press, New York. 1975–1982.
20. Chr. Romming. Acta Chem. Scand. **14**, 2145 (1960).
21. H. Hartl and S. Steidl. Z. Naturforsch. **32**B, 6 (1977).
22. G. Y. Chao and J. D. McCullough. Acta Crystallogr. **13**, 727 (1960).
23. M. Bois d'Enghien-Peteau, J. Meunier, and M. Van Meerssche. J. Chim. Phys. Phys. Chim. Biol. **65**, 1221 (1968).
24. F. H. Herbstein, P. Ashkenazi, M. Kaftory, M. Kapon, G. M. Reisner, and D. Ginsburg. Acta Crystallogr. B**42**, 575 (1986).
25. F. H. Herbstein and W. Schwotzer. J. Am. Chem. Soc. **106**, 2367 (1984).
26. P. Deplano, E. F. Trogu, F. Bigoli, and M. A. Pellinghelli. J. Chem. Soc. Dalton Trans. 2407 (1987).

Can. J. Chem. Downloaded from www.nrcresearchpress.com by 93.93.197.157 on 09/07/12
For personal use only.

The conformational behaviour of ^5J_m(F,CH) in 3,5-difluoro derivatives of toluene, ethylbenzene, and cumene. Applications

TED SCHAEFER, CRAIG S. TAKEUCHI, AND STEVEN ERIC SVEINSON[1]
Department of Chemistry, University of Manitoba, Winnipeg, Man., Canada R3T 2N2

Received November 24, 1987

TED SCHAEFER, CRAIG S. TAKEUCHI, and STEVEN ERIC SVEINSON. Can. J. Chem. **66**, 1490 (1988).

The CNDO/2 and INDO MO FPT values for ^5J_m(F,CH$_3$) in 3-fluoro- and 3,5-difluorotoluene are exactly reproduced by $A\cos^2\theta + B\sin^2\theta + C\sin^2(\theta/2)$. Here θ is the angle by which the α C—H bond twists out of the benzene plane. Adjustment of A, B, and C to give an agreement with experiment for 3,5-difluorotoluene yields an equation, best considered empirical, which is tested by ^5J(F,CH) in 3,5-difluoroethylbenzene and 3,5-difluoroisopropylbenzene. The equation reproduces ^5J(F,CH) in these two compounds, the values of $\langle\sin^2\theta\rangle$ being derived from ^6J_p(H,CH), the spin–spin coupling constants over six bonds between the α and *para* ring protons. ^5J(F,CH) is obtained for the asymmetrical compounds, 2,3-difluorobenzylidene diacetate and 2-bromo-5-fluorobenzylidene diacetate. It is shown how ^5J(F,CH) in the latter can discriminate between two conformers, each of which, on the basis of ^6J(H,CH), will be characterized by a large degree of torsion about the C(1)—C_{sp^3} bond.

TED SCHAEFER, CRAIG S. TAKEUCHI et STEVEN ERIC SVEINSON. Can. J. Chem. **66**, 1490 (1988).

On peut reproduire exactement les valeurs calculées par CNDO/2 et INDO MO FPT pour les ^5J_m(F,CH$_3$) des fluoro-3 et difluoro-3,5 toluènes, grâce à l'équation $A\cos^2\theta + B\sin^2\theta + C\sin^2(\theta/2)$ dans laquelle θ correspond à l'angle qui existe entre la liaison C—H en α et le plan du benzène. L'ajustement des paramètres A, B, et C afin d'obtenir une concordance avec l'expérience effectuée sur le difluoro-3,5 toluène fournit une équation que l'on doit considérer comme empirique et que l'on a vérifiée à l'aide des ^5J(F,CH) des difluoro-3,5 éthyl (et isopropyl) benzènes. Pour ces deux composés, l'équation reproduit les valeurs des ^5J(F,CH); les valeurs de $\langle\sin^2\theta\rangle$ ont été obtenues à partir des valeurs de ^6J_p(H,CH), les constantes de couplage spin–spin à travers six liaisons entre les protons α et ceux présents en position *para* sur le cycle. On a déterminé les ^5J(F,CH) des composés asymétriques suivants : le diacétate du difluoro-2,3 benzylidène et le diacétate du bromo-2 fluoro-5 benzylidène. On a démontré que, dans ce dernier cas, les ^5J(F,CH) permettent de choisir entre deux conformères qui, sur la base des ^6J(H,CH), seront caractérisés par une torsion importante autour de la liaison (C1)—C_{sp^3}.

[Traduit par la revue]

Introduction

The mechanisms of the spin–spin coupling constants between the methyl and ring protons in toluene are understood in terms of σ–π and σ electron contributions (1–4). The coupling constants have been written as (in Hz)

$$[1]\quad {}^6J_p(\mathrm{H,CH_3}) = {}^6J^{\pi}_{90}\langle\sin^2\theta\rangle = -1.20\langle\sin^2\theta\rangle$$

$$[2]\quad {}^5J_m(\mathrm{H,CH_3}) = {}^5J^{\pi}_{90}\langle\sin^2\theta\rangle + {}^5J^{\sigma}_{180}\langle\sin^2(\theta/2)\rangle = 0.336\langle\sin^2\theta\rangle + 0.322\langle\sin^2(\theta/2)\rangle$$

$$[3]\quad {}^4J_o(\mathrm{H,CH_3}) = {}^4J^{\pi}_{90}\langle\sin^2\theta\rangle + {}^4J^{\sigma}\langle\cos^2\theta\rangle = -1.08\langle\sin^2\theta\rangle - 0.32\langle\cos^2\theta\rangle$$

In these equations the coefficients of the expectation values of $\sin^2\theta$ represent the σ–π components, while those of $\langle\cos^2\theta\rangle$ and $\langle\sin^2(\theta/2)\rangle$ are the σ components. The angle θ measures the out-of-plane twist of the α C—H bond. Relationships of this kind are useful in the description of the conformational behaviour of a variety of benzyl and benzal compounds (4, 5).

Replacement of hydrogen by a fluorine atom in the phenyl group of toluene leads to ^{1}H,^{19}F coupling constants analogous to the ^{1}H,^{1}H interactions in eqs. [1]–[3]. ^6J_p(F,CH$_3$) is thought to be dominated by a σ–π mechanism, i.e., it has a $\sin^2\theta$ dependence (1, 6). Unlike ^6J_p(H,CH$_3$), it is positive because the hyperfine interaction parameter, $Q^{\mathrm{F}}_{\mathrm{CF}}$, is of opposite sign to $Q^{\mathrm{H}}_{\mathrm{CH}}$. ^4J_o(F,CH$_3$) has a complex dependence on θ, part of the complexity arising from proximate interactions (7, 8) whose conformational dependence is still somewhat uncertain (8).

The substantial magnitudes of ^6J_p(F,CH$_3$) and ^4J_o(F,CH$_3$), being +1.15 Hz in 4-fluorotoluene and +2.0 Hz in 2-fluorotoluene, respectively, stand in sharp contrast to ^5J_m(F,CH$_3$) ≡ ^5J = −0.25 Hz in 3-fluorotoluene (9). It was argued that ^5J arises from a near cancellation of a positive, stereospecific, σ electron component by a negative σ–π contribution. INDO MO FPT computations do imply a large negative ^5J_m near θ = 90° (9) and a larger positive ^5J_m at θ = 180° (zigzag or all-*trans* bond arrangement). For a standard geometry the average ^5J_m is computed as +0.2 Hz (9). In a partially restricted molecular orbital calculation (10), designed to separate σ and σ–π contributions to ^5J_m, support for a negative σ–π component is adduced. Its contribution to ^5J_m is computed as −0.63 Hz, a reasonable magnitude when compared to the σ–π contribution to ^6J_p(F,CH$_3$). However, the net result then is that the σ contribution to ^5J_m has a θ dependence resembling that of a modified Karplus curve, with a slightly negative minimum near θ = 70°, and values near 0.6 and 2.3 Hz at θ = 0° and 180°, respectively. The following discussion takes an essentially empirical approach to ^5J_m, with a view to its use in conformational analysis.

TABLE 1. The CNDO/2 and INDO MO FPT values in Hz for ^5J(F,CH) in 3,5-difluorotoluene for a standard[a] geometry

θ/deg[b]	CNDO/2	INDO	θ/deg[b]	CNDO/2	INDO
0	0.60	0.388	105	0.23	−0.833
15	0.54	0.253	120	0.52	−0.193
30	0.40	−0.109	135	0.87	0.589
45	0.22	−0.580	150	1.21	1.339
60	0.06	−1.010	165	1.45	1.878
75	−0.01	−1.251	180	1.54	2.073
90	0.05	−1.203			

[a]Reference 21.
[b]See **1** for the angle θ.

Explicitly, and with reference to the compounds to be discussed in this work, the INDO MO FPT values for 3,5-difluorotoluene are given in Table 1. The angle θ is defined in **1**.

The INDO values in Table 1 are fit precisely by eq. [4], the

[1]Undergraduate research participant, winter of 1985–1986.

Can. J. Chem. Downloaded from www.nrcresearchpress.com by 93.93.197.157 on 09/07/12
For personal use only.

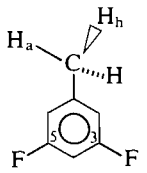

F(3): $\theta = 180°$ for H_a, 60° for H_b
F(5): $\theta = 0°$ for H_a, 120° for H_b

1

maximum deviation being 0.02 Hz with an average deviation of 0.007 Hz. This relationship could be considered as arising from a $\sigma-\pi$ component, proportional to $\sin^2\theta$ and two σ components, one proportional to $\cos^2\theta$ and the other to $\sin^2(\theta/2)$. In other words, one would have eq. [5], in which ${}^5J_0^\sigma$

$$[4]\quad {}^5J_m(\mathrm{F,CH_3})/\mathrm{Hz} = 0.388 - 2.433\sin^2\theta + 1.685\sin^2(\theta/2)$$

$$[5]\quad {}^5J_m(\mathrm{F,CH_3})/\mathrm{Hz} = {}^5J_0^\sigma\cos^2\theta + {}^5J_{90}^\pi\sin^2\theta + {}^5J_{180}^\sigma\sin^2(\theta/2) = {}^5J_0^\sigma + ({}^5J_{90}^\pi - {}^5J_0^\sigma)\sin^2\theta + {}^5J_{180}^\sigma\sin^2(\theta/2)$$

is 0.388 Hz, ${}^5J_{90}^\pi = -2.045$ Hz, and ${}^5J_{180}^\sigma = 1.685$ Hz. The sixfold internal barrier to rotation in **1** is surely less than 200 J/mol (11, 12), so that $\langle\sin^2\theta\rangle$ and $\langle\sin^2(\theta/2)\rangle$ are both[2] 0.5. Equation [4] therefore yields 0.014 Hz for ${}^5J_m$. The observed value is −0.294 Hz (see below). Because there is no obvious reason to single out a given component in eq. [4], the observed number can be reproduced by a decrease of 0.308 Hz in each of the computed values in Table 1. This procedure yields eq. [6].

$$[6]\quad {}^5J_m(\mathrm{F,CH_3})/\mathrm{Hz} = 0.080 - 2.433\langle\sin^2\theta\rangle + 1.685\langle\sin^2(\theta/2)\rangle = A + B\langle\sin^2\theta\rangle + C\langle\sin^2(\theta/2)\rangle$$

This equation implies, but does not establish, a very small value of ${}^5J_m$ at $\theta = 0°$.

The CNDO/2 MO FPT results in Table 1 are accurately reproduced by eq. [7]. The form of eq. [7] is that of eq. [4]. It is

$$[7]\quad {}^5J_m(\mathrm{F,CH_3})/\mathrm{Hz} = 0.597 - 1.021\sin^2\theta + 0.940\sin^2(\theta/2)$$

sometimes assumed that CNDO/2 calculations yield σ electron contributions to coupling constants, whereas INDO includes the π electron contributions. The difference between eqs. [4] and [7] has a coefficient of −1.4 Hz in the $\sin^2\theta$ term. For fast internal rotation, therefore, the $\sigma-\pi$ contribution would be −0.7 Hz, in close agreement with the PRMO approach (10). Certainly, a ${}^5J_{90}^\pi$ of −2.3 Hz (see eqs. [5] and [6]) appears to be much too large in magnitude, so that the coefficients in eq. [6] should be treated as empirical.

Now, for ${}^5J_m(\mathrm{H,CH_3})$ in toluene, all the experimental evidence is consistent with a zero value at $\theta = 0°$ (3, 4). Yet, both INDO and CNDO/2 compute significant values at this angle. Furthermore, the CNDO/2 numbers obey a curve analogous to that of eq. [6]. When it is noted that eq. [6], having a very small value at $\theta = 0°$, reproduces ${}^5J_m(\mathrm{F,CH_3})$ in **1**, the suspicion arises that the substantial computed numbers at this angle are artifacts. Equation [6] will be taken as an operational conformational equation.

One approach to a test of eq. [6] involves **2** and **3**, the 3,5-difluoro derivatives of ethylbenzene and isopropylbenzene.

[2]Because of the threefold symmetry of the methyl group, this statement is true as long as the barrier is small enough to yield an averaged chemical shift of the three protons.

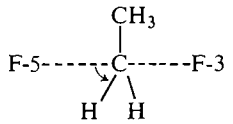

2, $\theta = 30°$

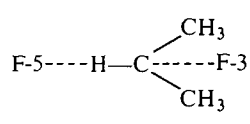

3, $\theta = 0°$

The most stable conformers are indicated in **2** and **3** and $\langle\sin^2\theta\rangle$ values are available from ${}^6J_p(\mathrm{H,CH})$. The internal barriers about the C_{sp^2}—C_{sp^3} bonds are predominantly twofold with some fourfold character. Therefore $\langle\sin^2(\theta/2)\rangle$ is 0.5. As a consequence, the presence of a ${}^5J_0^\sigma$ is not ascertainable from ${}^5J_m$ in **1**, **2**, and **3**. Ideally, a *rigid* molecule like **4** is needed for this purpose.

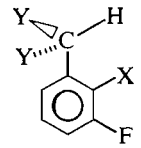

4

This paper gives the analyses of the ^{1}H and ^{19}F nmr spectra of **1**–**3** and of two molecules of type **4**, discusses the ensuing ${}^5J$ values in terms of the preceding equations, and illustrates how ${}^5J$ might be used in conformational analysis.

Experimental

Compounds

The starting materials, 3,5-difluorobenzyl bromide, 3,5-difluoroacetophenone, and 3,5-difluorobenzoic acid were obtained from Fluorochem Ltd. The 3,5-difluorotoluene, **1**, was prepared from the bromide via the Grignard, while 3,5-difluoroethyl benzene, **2**, came from the acetophenone precursor by a modification of the Wolf–Kishner method, exactly as described in ref. 13. The 3,5-difluoroisopropylbenzene, **3**, resulted from the benzoic acid derivative by a procedure described in detail for the corresponding 2,6-difluoro compounds (14, 15). The products gave unmistakable ^{1}H and ^{19}F nmr spectra.

Samples

Compounds **1**, **2**, and **3** were dissolved in CS_2/C_6D_{12}/TMS/C_6F_6 mixtures (see Table 1 for exact compositions) and transferred to 5 mm od nmr sample tubes by filtration through a wad of cotton wool. Degassing of the sample tubes by a number of freeze/thaw/pump cycles was followed by flame-sealing.

Spectral accumulations

The ^{1}H and ^{19}F nmr spectra were acquired on a Bruker AM300 nmr spectrometer at a probe temperature of 300 K. Wide sweepwidth survey spectra were used to reference them with respect to TMS and C_6F_6. Each spectral region was then examined in detail, with sweepwidth and data region adjusted to given acquisition times of approximately 41 s. As many as 32 scans were acquired. Zero filling to twice the original data region was done before transforming the FIDs using small amounts of Gaussian and Lorentzian multiplications. Intrinsic linewidths at half-height were often as small as 0.05 Hz (while decoupling methyl protons for **2** and **3**) after this resolution enhancement, but more typically were 0.07–0.08 Hz. Partial decoupling experiments (16) were used to determine the sign of ${}^5J_m(\mathrm{F,CH})$ in **1**–**3**.

CNDO/2 and INDO MO FPT computations of coupling constants (17, 18) were performed on an Amdahl 470 system.

Results and discussion

Spectral analyses

The ^{1}H and ^{19}F nmr spectra were analyzed with the local version of the computer program NUMARIT (19). The spectral parameters appear in Table 2. Although reasonably high precision was attained, as indicated by the standard deviations of the parameters, the particular AA′XX′B nature of the ring nuclei entailed relatively large correlations between two

Can. J. Chem. Downloaded from www.nrcresearchpress.com by 93.93.197.157 on 09/07/12
For personal use only.

TABLE 2. ^1H and ^{19}F nmr spectral parameters of 3,5-difluoro derivatives of toluene, ethylbenzene, and isopropylbenzene in CS_2 solution at 300 K

Parameter	3,5-di-F-CH_3[a]	3,5-diF-CH_2CH_3[a]	3,5-di-F-isopropyl[b]
$\nu(CH_3)$[c]	698.788(0)[g]	368.801(1)[d]	370.610(3)[e]
$\nu_2 = \nu_6$	1974.780(0)	1982.139(0)	1992.763(1)
ν_F[f]	14675.91(1)	14743.7(1)	14799.67(1)
ν_4	1943.119(0)	1943.709(0)	1943.830(1)
$^3J_{2F}$	9.028(0)	9.162(1)	9.412(1)
$^3J_{4F}$	8.894(0)	8.843(0)	8.763(1)
$^4J_{26}$	1.416(1)	1.433(1)	1.482(2)
$^4J_{24}$	2.335(0)	2.337(1)	2.336(1)
$^4J_{35}$	6.644(1)[h]	6.577(1)[i]	6.523(2)[j]
$^5J_{2F}$	−0.916(0)[h]	−0.905(0)[i]	−0.909(1)[j]
^4J_o(H,CH)	−0.694(0)	−0.651(1)	−0.590(2)
^5J_m(F,CH)	−0.294(0)	−0.067(1)	0.362(2)
^6J_p(H,CH)	−0.588(0)	−0.463(1)[l]	−0.245(2)[m]
Calculated transitions	512	2432	2936
Assigned transitions	472	1438	1008
Peaks observed	213	306	Many[k]
Root-mean-square deviation	0.004	0.008	0.018

[a]2.5 mol% in CS_2, containing also 10.0 mol% C_6D_{12}, 0.25 mol% TMS, and 0.25 mol% C_6F_6.
[b]Approximately 1 mol% in the above mixture.
[c]At 300.135 MHz to high frequency of TMS.
[d]$\nu(CH_2)$ is 784.110(1) Hz.
[e]ν(CH) is 853.592(2) Hz.
[f]At 282.365 MHz, to high frequency of C_6F_6.
[g]Numbers in parentheses are standard deviations in the last significant figure, as given by NUMARIT.
[h]$^4J_{35}$ correlates with $^5J_{2F}$ by 0.511.
[i]$^4J_{35}$ correlates with $^5J_{2F}$ by 0.340.
[j]$^4J_{35}$ correlates with $^5J_{2F}$ by 0.340.
[k]The spectra were examined under conditions where the methyl protons were coupled and uncoupled to other nuclei.
[l]$^6J(F,CH_3)$ is ±0.14 Hz.
[m]$^6J(F,CH_3)$ is ±0.123(1) Hz.

coupling constants within the phenyl moiety (see Table 2). Fortunately, these coupling constants are not of immediate interest in the discussion below.

Figure 1 illustrates the sign determination of ^5J_m(F,CH) in **2** and **3**.

$^5J_m \equiv {}^5J_m$(F,CH) in 1, 2, and 3

In eq. [6] the terms A, B, and C have been adjusted to fit the ^5J of −0.294 Hz in **1**. For **2** and **3**, the expectation values of $\langle\sin^2(\theta/2)\rangle$ are both 0.5, the geometry-optimized STO-3G MO computations[3] yielding evenfold internal rotational barriers (20). The expectation values of $\langle\sin^2\theta\rangle$ are derived from ^6J_p(H,CH) via eq. [1]. In **1**, $^6J_p(H,CH_3)$ is −0.588(0) Hz, implying $^6J^{\pi}_{90}$ as −1.176 Hz. A recent discussion of $^6J^{\pi}_{90}$ in ethylbenzene (20) indicates a small reduction in $^6J^{\pi}_{90}$ in the presence of a methyl substituent on the α carbon atom, implying that $^6J^{\pi}_{90}$ is −1.137 Hz in **2**. Then $\langle\sin^2\theta\rangle$ in **2** follows as 0.463/1.137 or 0.407. If a second methyl substituent causes a further reduction in $^6J^{\pi}_{90}$, then $\langle\sin^2\theta\rangle$ in **3** becomes 0.245/1.098 or 0.223. Substitution of these estimates of $\langle\sin^2\theta\rangle$ into eq. [6] gives −0.068 Hz for ^5J_m in **2** and 0.380 Hz in **3**. The measurements give −0.067(1) and 0.362(2) Hz, respectively (Table 2). In our opinion, the model is therefore satisfactory.

[3]We thank Glenn Penner for the unpublished computations on isopropylbenzene. Because of the symmetry of **1**, **2**, and **3**, no odd components are expected for rotation about their C_{sp^2}—C_{sp^3} bonds; such components would cause $\langle\sin^2(\theta/2)\rangle$ to differ from 0.5.

Of course, if methyl substitution causes a reduction in the magnitude of $^6J^{\pi}_{90}$ in **2** and **3**, then a similar reduction in the $^5J^{\pi}_{90}$ component of ^5J_m is possible. However, the concomitant changes in the other components of ^5J_m are unknown. In ethylbenzene, $^5J_m(H,CH_2)$ is given by eq. [2], implying compensatory effects on $^5J^{\pi}_{90}$ and $^5J^{\sigma}_{180}$ (20) by the methyl group. It appears that eq. [6] is best treated as an empirical equation, with the possibility that the reasonably good agreement with the experimental data for **1**, **2**, and **3** is fortuitous.

Further examination of equation [6]

2,7-Difluorofluorene

An unpublished analysis in this laboratory of the ^1H nmr spectrum of the rigid 2,7-difluorofluorene in CS_2 solution gives $^5J_m(F,CH_2)$ as −1.06(1) Hz. An STO-3G MO structure of fluorene, with full geometry optimization, yields the HCH angle of the methylene group as 107.3° and the relevant angle θ as almost exactly 60°. An INDO MO FPT calculation on 2-fluorofluorene, assuming the STO-3G structure and a C—F bond length of 1.33 Å, gives $^5J_m(F,CH_2)$ as −0.76 Hz. The simplest approach to this number assumes that $^5J_m(F,CH_2)$ is again computed as too large, algebraically, by 0.31 Hz (compare eq. [4] with eq. [6]) and that the adjusted value should therefore be −1.07 Hz, as observed.

However, it is also noted that $^6J_{90}$(H,CH) for 2-fluorofluorene is −0.93 Hz, the measured value of ^6J(H,CH) being −0.72 Hz, whereas it is −1.20 Hz in toluene (4). Therefore it is unlikely that eq. [6] for toluene derivatives will apply quantitatively to $^5J(F,CH_2)$ in 2,7-difluorotoluene. It does not.

Can. J. Chem. Downloaded from www.nrcresearchpress.com by 93.93.197.157 on 09/07/12
For personal use only.

Can. J. Chem. Downloaded from www.nrcresearchpress.com by 93.93.197.157 on 09/07/12
For personal use only.

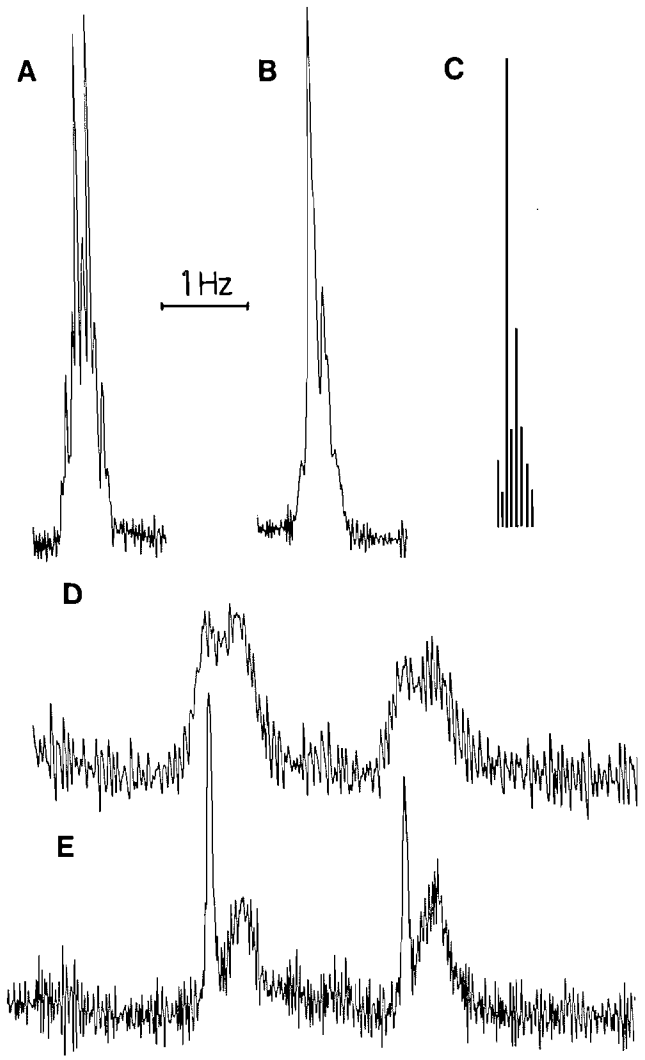

FIG. 1. A multiplet from the ^{19}F nmr spectrum of 3,5-difluoroethylbenzene is displayed in A. In the absence of coupling interactions with the ethyl protons this multipliet would be a single peak. $|^6J(F,CH_3)|$ is ca. 0.14 Hz and $|^5J(F,CH_2)|$ is ca. 0.07 Hz. In B the same multiplet appears under conditions where the high-field peak of the methyl proton resonance is irradiated. In other words, the methyl protons are undergoing classical (16) partial decoupling for a given spin state of the methylene protons, say $|-\frac{1}{2},-\frac{1}{2}|$. In C, a first-order reconstruction of the spectrum in B is presented in which it is assumed that $^5J(F,CH_2)/^3J(CH_2,CH_3) < 0$. The salient point is that the two most prominent peaks, having an intensity ratio of 7:3, appear in the correct sequence. If the coupling ratio above were positive, then the observed spectrum would appear as the mirror image of B. Because ^3J is positive, it follows that $^5J(F,CH_2)$ is negative. In D a pair of doublets is shown from the ^{19}F nmr spectrum of 3,5-difluoroisopropylbenzene. The peaks are broad due to unresolved coupling to six methyl protons. In E the same pair of doublets appears under conditions in which the low-field high-frequency methyl protons are being decoupled for one spin state of the methine proton. The spacing within a doublet, ca. 0.35 Hz, arises from $^5J(F,CH)$. It follows that $^5J(F,CH)/^3J(CH,CH_3) > 0$ and hence that $^5J(F,CH)$ is positive.

Nevertheless, the large negative $^5J(F,CH_2)$ in this molecule is reassuring qualitatively; in **1**, **2**, and **3** this coupling constant ranges from -0.3 to $+0.4$ Hz whereas eq. [6] implies rather large negative values for a large $\sin^2\theta$.

2,3-Difluorobenzylidene diacetate

The existence of a significant ^5J_m at $\theta = 0°$ is now tested as follows. Unfortunately, numerous attempts at the synthesis of **4** (Y = CH_3, X = Cl or F) ended in failure. However, 2,3-difluorobenzylidene diacetate (Y = $OC(O)CH_3$, X = F in **4**) could be prepared from the commercial benzaldehyde derivative in the usual way. The latter was also converted to 2,3-difluorotoluene in the manner described above for the preparation of 3,5-difluoroethylbenzene (13).

The full analysis of the ^1H and ^{19}F nmr spectra of a 3.9 mol% solution of 2,3-difluorotoluene in the CS_2/C_6D_{12} solvent mixture gave $^5J_m(H,CH)$ and $^6J_p(H,CH)$ as 0.328(2) and $-0.575(2)$ Hz, respectively. The threefold symmetry of the methyl group allows the conclusion (eq. [1]) that $^6J^{\pi}_{90}$ is -1.15 Hz in this molecule, whereas it is -1.20 Hz in toluene. Therefore $^5J^{\pi}_{90}$ in eq. [2] becomes 0.322 Hz and hence $^5J^{\sigma}_{180}$ is 0.334 Hz. $^5J_m(F,CH_3)$ is $-0.170(1)$ Hz in 2,3-difluorotoluene, algebraically larger than in 3-fluorotoluene (9). In accordance with the procedure used to arrive at eq. [6], its first term is to be changed to 0.204 Hz to reproduce the coupling in 2,3-difluorotoluene. With these calibration points, it is now possible to consider $^5J_m(F,CH)$ in 2,3-difluorobenzylidine diacetate. Values of $\langle\sin^2\theta\rangle$ and $\langle\sin^2(\theta/2)\rangle$ are found from $^6J(H,CH)$ and $^5J(H,CH)$.

In this molecule, $^6J_p(H,CH)$ is $-0.185(3)$ Hz for a 3.7 mol% solution in the CS_2/C_6D_{12} solvent mixture. The value of $^6J_{90}$ will be smaller in magnitude than for toluene. The electronegativity of the $OC(O)CH_3$ substituent is apparently (22) very near that of the OCH_3 group, the latter causing a reduction of -0.18 Hz in $^6J_{90}$ relative to toluene (see the discussion in a previous section). It appears unlikely that a second $OC(O)CH_3$ will reduce $^6J_{90}$ in an additive fashion. Choosing the reduction of $^6J_{90}$ by the second $OC(O)CH_3$ group to be half that caused by the first $OC(O)CH_3$ group, admittedly somewhat arbitrarily, yields $^6J_{90}$ as -0.930 (1.15/1.20) or -0.891 Hz. Then $\langle\sin^2\theta\rangle$ follows as 0.208. $^5J_m(H,CH)$ is 0.338(3) Hz and the requisite substitutions then imply $\langle\sin^2(\theta/2)\rangle$ as 0.857 and hence that $^5J_m(F,CH)$ is -0.06 Hz (remember that $\sin^2(\theta/2)$ in this connection becomes $1 - 0.857$, the C—H bond of the side chain lying mainly *cis* to the *ortho* C—F bond). In the ^{19}F nmr spectrum of 2,3-difluorobenzylidene diacetate, $^5J(F,CH)$ produces a doublet splitting of rather less than 10% of the peak height. Hence the observed splitting of 0.04(1) Hz is compatible with the existence of a ^5J_o, that is, with a small positive $^5J_m(F,CH)$ at $\theta = 0°$.

In acetone solution, $^5J_m(F,CH)$ is found as $-0.147(2)$ Hz for this compound. The above procedure yields a predicted value of -0.180 Hz, indicating a significant $^5J^{\sigma}_0$. In the acetone solution, $^5J_m(H,CH)$ and $^6J_p(H,CH)$ are 0.357(2) and $-0.202(2)$ Hz, respectively. The intricacies of the above procedure, although logical, may give rise to doubts about its validity. Suppose, therefore, that the spectral data for 2,3-difluorotoluene were unavailable and that eqs. [1] and [2], applicable to toluene, were used to obtain $\langle\sin^2\theta\rangle$ and $\langle\sin^2(\theta/2)\rangle$. Then $\langle\sin^2\theta\rangle$ for 2,3-difluorobenzylidene diacetate in acetone-d_6 solution would follow as $-0.202/-1.20$ or 0.168 and $\langle\sin^2(\theta/2)\rangle$ as 0.067, the latter from eq. [2] and the measured $^5J(H,CH)$ of 0.357 Hz in the diacetate. Hence eq. [6] would yield $^5J(F,CH)$ as -0.216 Hz, again compatible only with a significant positive value of $^5J(F,CH)$ at $\theta = 0°$.

It appears that empirical equations of type [6] are compatible with the conformational properties of **4** (Y = $OC(O)CH_3$, X = F) deduced from the long-range proton–proton coupling constants and that, therefore, they can be used in conformational analysis. However, as remarked in the introduction, the

identification of the coefficient of $\langle \sin^2 \theta \rangle$ as a pure $\sigma-\pi$ term is questionable.

A conformation application of $^5J(F,CH)$

For 2-bromo-5-fluorobenzylidene diacetate, ^5J(H,CH) is small, 0.04 Hz, and badly resolved. Furthermore, its spectral analytical value correlates strongly, by 0.51, with the chemical shift of H-3, 2238.675 Hz, and by 0.29 with ^3J(H-3,H-4). The magnitude of ^5J(H,CH) is therefore uncertain. However, ^5J(F,CH) is 1.037(0) Hz (CS_2 solution), implying as expected that a conformer predominates in which the methine C—H bond is situated near the bromine substituent. Equation [6] indicates 1.76 Hz for a rigid conformer of this kind, **5**, because θ is then

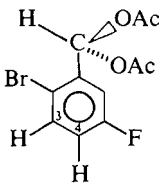

$\theta = 0°$ for H-3
$\theta = 180°$ for F

5

zero. Of course, the conformer is not rigid and the torsion about the C(1)—C_{sp^3} bond is also indicated by ^6J(H,CH), being −0.231(0) Hz.

If no reference molecule except toluene is available and no corrections are made to ^6J(H,CH), then $\langle \sin^2 \theta \rangle$ is 0.192 = −0.231/−1.20. Then arc sin $\langle \sin^2 \theta \rangle^{1/2}$ is 26°, indicating substantial torsion about the exocyclic bond. If $^6J_{90}$ is taken as −0.930(1.252/1.204) or −0.97 Hz (in 2-chloro-5-fluorotoluene, ^6J(H,CH) is −0.626(3) Hz (9) and the factor −0.930 is taken from the previous discussion), then $\langle \sin^2 \theta \rangle$ is 0.238; hence arc sin $\langle \sin^2 \theta \rangle^{1/2}$ is 29°. Further, if this value is taken as indicating θ as 151° for the term in $\sin^2(\theta/2)$ of eq. [6], then ^5J(F,CH) follows as 1.08 Hz, compared to the measured 1.04 Hz. Thus, although ^6J(H,CH) yields an estimate of the torsion it does not discriminate between **5** and a conformer obtained from **5** by rotation of 180° about the C(1)—C_{sp^3} bond. Equation [6] and ^5J(F,CH) do discriminate between these conformers and, apparently, provide a rough measure of the nonplanarity of the correct conformer. In some compounds, of course, ^6J(H,CH) would not be available because of substitution at the site in question.

Acknowledgements

We are grateful to the Natural Sciences and Engineering Research Council of Canada for financial assistance and to the referees for valuable criticism.

1. R. Wasylishen and T. Schaefer. Can. J. Chem. **50**, 1852 (1972).
2. M. Barfield, C. J. Fallick, K. Hata, S. Sternhell, and P. W. Westerman. J. Am. Chem. Soc. **105**, 2178 (1983).
3. T. Schaefer and R. Laatikainen. Can. J. Chem. **61**, 2785 (1983).
4. T. Schaefer, R. Sebastian, and G. H. Penner. Can. J. Chem. **63**, 2597 (1985).
5. W. J. E. Parr and T. Schaefer. Acc. Chem. Res. **13**, 400 (1980).
6. R. Wasylishen and T. Schaefer. Can. J. Chem. **49**, 94 (1971).
7. R. E. Wasylishen and M. Barfield. J. Am. Chem. Soc. **97**, 4545 (1975).
8. T. Schaefer, R. Sebastian, R. P. Veregin, and R. Laatikainen. Can. J. Chem. **61**, 29 (1983).
9. T. Schaefer, W. Danchura, and W. Niemczura. Can. J. Chem. **56**, 2233 (1978).
10. J. C. Facelli, C. G. Giribet, and R. H. Contreras. Org. Magn. Reson. **19**, 138 (1982).
11. H. D. Rudolph, H. Dreizler, A. Jaeschke, and P. Wendling. Z. Naturforsch. A: Astrophys. Phys. Phys. Chem. **22**, 940 (1967).
12. K. Okujama, N. Mikami, and M. Ito. J. Phys. Chem. **89**, 5617 (1985).
13. A. Vogel. Textbook of practical organic chemistry. 4th ed. Longman Group Limited, London. 1978. pp. 600–606.
14. T. Schaefer, R. P. Veregin, R. Laatikainen, R. Sebastian, K. Marat, and J. L. Charlton. Can. J. Chem. **60**, 2611 (1982).
15. R. P. Veregin. M.Sc. thesis. University of Manitoba, 1982.
16. J. P. Maher and D. F. Evans. Proc. Chem. Soc. (London), 208 (1961).
17. J. A. Pople, J. W. McIver, and N. S. Ostlund. J. Chem. Phys. **49**, 2965 (1968).
18. P. Dobosh and N. S. Ostlund. QCPE, **11**, 281 (1975).
19. A. R. Quirt and J. S. Martin. J. Magn. Reson. **5**, 318 (1971); J. S. Martin, A. R. Quirt, and K. E. Worvill. The NMR program library. Daresbury Laboratory, Daresbury, U.K.
20. T. Schaefer, G. H. Penner, and R. Sebastian. Can. J. Chem. **65**, 873 (1987).
21. J. A. Pople and M. S. Gordon. J. Am. Chem. Soc. **89**, 4253 (1971).
22. S. Marriott, W. F. Reynolds, R. W. Taft, and R. D. Topsom. J. Org. Chem. **49**, 959 (1984).

Can. J. Chem. Downloaded from www.nrcresearchpress.com by 93.93.197.157 on 09/07/12
For personal use only.

Theoretical and experimental data on the internal rotational potential in isopropylbenzene

TED SCHAEFER, RUDY SEBASTIAN, AND GLENN H. PENNER
Department of Chemistry, University of Manitoba, Winnipeg, Man., Canada R3T 2N2

Received December 17, 1987

TED SCHAEFER, RUDY SEBASTIAN, and GLENN H. PENNER. Can. J. Chem. **66**, 1495 (1988).

Geometry-optimized STO-3G MO computations of the internal rotational potential about the C_{sp^2}—C_{sp^3} bond in isopropylbenzene yield V (kJ/mol) as $14.1(3)\sin^2\psi - 2.8(3)\sin^2 2\psi + 1.4(3)\sin^2 3\psi$; ψ is the angle by which the α C—H bond deviates from the benzene plane. This result provides no support for the very low internal barrier once hypothesized from microwave data for isopropylbenzene in the vapor phase, nor for the local minimum at $\psi = 90°$ inferred from hyperfine coupling constants in π electron radicals of isopropylbenzene derivatives. An alternative explanation in the literature for such microwave spectra is therefore a more likely one. Similar MO computations with the 6-31G basis at three values of ψ can be fit by $13.40\sin^2\psi - 2.61\sin^2\psi$ for the energies in kJ/mol. In CS_2 and acetone-d_6 solutions, the long-range proton–proton coupling constants imply the independence of the rotational potential of solvent polarity and also that the barrier is rather lower than that computed for the free molecule. An apparent twofold barrier of 6.5 kJ/mol is consistent with the coupling constants but so is a combination of twofold and fourfold barrier components amounting to 9.7, −3.5 and 7.2, −1.5 kJ/mol. The coupling constants do not allow discrimination among these possibilities. The internal rotational potential is not altered significantly in the presence of a 4-hydroxyl substituent in isopropylbenzene.

TED SCHAEFER, RUDY SEBASTIAN et GLENN H. PENNER. Can. J. Chem. **66**, 1495 (1988).

Des calculs d'OM STO-3G optimisés pour la géométrie ont été réalisés pour déterminer le potentiel de la rotation interne autour de la liaison C_{sp^2}—C_{sp^3} de l'isopropylbenzène et ils permettent d'établir que V (kJ/mol) = $14,1(3)\sin^2\psi - 2,8(3)\sin^2 2\psi + 1,4(3)\sin^2 3\psi$; ψ est l'angle par lequel la liaison C—H α dévie du plan du benzène. Ces résultats ne peuvent pas être utilisés pour confirmer la barrière interne très faible qui avait été suggérée sur la base de données de micro-onde obtenues à l'aide d'isopropylbenzène en phase vapeur ni le minimum local à $\psi = 90°$ qui avait été suggéré à partir de constantes de couplages hyperfins dans les radicaux d'électrons π de dérivés de l'isopropylbenzène. L'autre explication qui avait été proposée dans la littérature pour de tels spectres micro-ondes est donc plus probable. Des calculs semblables d'OM effectués au niveau 6-31G, à trois valeurs de ψ, conduisent à des énergies (en kJ/mol) qui peuvent être représentées par l'équation $13,40\sin^2\psi - 2,61\sin^2\psi$. En solutions dans le CS_2 ou dans l'acétone-d_6, les constantes de couplage proton–proton à longue distance impliquent que le potentiel à la rotation ne dépend pas de la polarité du solvant et que la barrière est vraisemblablement plus faible que celle calculée pour la molécule libre. Une barrière apparente binaire de 6,5 kJ/mol est en accord avec les constantes de couplage; toutefois, une combinaison de composantes de barrières binaire et quaternaire qui s'élèvent à 9,7, −3,5 et 7,2 et −1,5 kJ/mol fournit aussi un tel accord. Les constantes de couplage ne permettent pas de départager entre ces deux possibilités. La présence d'un substituant hydroxy-4 sur l'isopropylbenzène ne modifie pas le potentiel à la rotation interne d'une façon importante.

[Traduit par la revue]

Introduction

The recent literature contains some interesting and somewhat contradictory information on the potential function governing the internal rotation of the isopropyl group about the C_{sp^2}—C_{sp^3} bond linking it to the benzene ring. In a number of radicals containing the cumyl moiety (1), the temperature dependence of the hyperfine coupling interaction with the methine proton was interpreted to mean that **2** lies 5–7 kJ/mol above **1** in energy and that **3** lies at a local minimum in the potential energy, being 2.5–3.3 kJ/mol less stable than **1**. It was suggested that the rotational potential arises mainly from steric repulsion between the rotating methyl group and the neighbouring aromatic C—H bonds in the anion, cation, and neutral radicals. Apparently, the electronic structures of the radicals have only a small influence on the potential. A study of the isopropylbenzene anion radical (2) found the energy difference between **1** and **3** to be 1.6 kJ/mol.

The hyperfine coupling parameters for the ^{13}C nuclei in the methyl groups in the nickel acetylacetonate complexes of 4-isopropylaniline (3) yielded an (assumed) twofold potential (**1** → **3**) of 6.3 kJ/mol for the internal barrier to rotation of the isopropyl group. For the uncomplexed aniline derivative, the ^{13}C spin-lattice relaxation times indicated 11.7 ± 0.4 kJ/mol as the magnitude of the internal barrier.

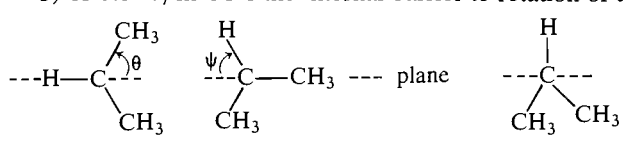

1 **2** **3**

The long-range spin–spin coupling constant over six bonds between the methine and *para* ring protons in 3,5-dibromoisopropylbenzene was consistent with a twofold internal barrier of 8.4 ± 0.8 kJ/mol (4).

All these measurements were made on solutions. Although they differ as to the forms and magnitudes of the internal rotational potentials, the authors all agree that **1** is the most stable conformer. Furthermore, the electron diffraction patterns of isopropylbenzene (5) and of its 4-carboxaldehyde derivative (6) in the vapor phase unambiguously imply **1** as the conformation of the alkyl group.

On the other hand, low-resolution microwave spectra of 4-isopropylbenzaldehyde, also for the vapor, are consistent with a twofold internal barrier of 1.0 ± 0.6 kJ/mol, in strong contrast with the data for solutions and implying (7) a marked phase dependence of the rotational potential; but see below.

Now, *ab initio* molecular orbital computations have had some success in establishing the internal rotational potential in hydrocarbons like styrene (8, 9, 18) and ethylbenzene (10). For the latter, energies for geometry-optimized conformations at the STO-3G and 6-31G levels of theory gave twofold components to the internal barrier about the C_{sp^2}—C_{sp^3} bond as 6.6 and 6.0 kJ/mol, respectively, while the fourfold components were 0.8 and 1.2 kJ/mol, of opposite sign to the twofold magnitudes.

Can. J. Chem. Downloaded from www.nrcresearchpress.com by 93.93.197.157 on 09/07/12
For personal use only.

TABLE 1. ^{1}H nuclear magnetic resonance spectral parameters for 2.5 mol% solutions of isopropylbenzene in CS_2 and acetone-d_6 solutions at 300 MHz and 300 K

Parameter	Value		Parameter	Value	
$\nu(CH_3)^a$	365.941(1)[b]	367.727(1)[c]	^4J(H,CH)	−0.559(1)[b]	−0.569(1)[c]
ν(C—H)	843.640(1)	867.045(1)	^5J(H,CH)	0.298(1)	0.293(1)
ν_2	2123.181(1)	2171.273(1)	^6J(H,CH)	−0.256(1)	−0.252(1)
ν_3	2140.074(1)	2180.856(1)	^5J(H,CH_3)	±0.030(2)	±0.040(2)
ν_4	2105.948(1)	2144.995(1)	^6J(H,CH_3)	±0.005(2)	±0.008(2)
^3J(H,CH_3)	6.910(1)	6.931(1)[d]	^7J(H,CH_3)	±0.000(2)	±0.000(2)
$^3J_{23}$	7.742(1)	7.760(1)	Calculated transitions	2655	2569
$^3J_{34}$	7.402(1)	7.413(1)	Assigned transitions	1401	1124[e]
$^4J_{26}$	1.983(1)	1.995(1)	Observed peaks	140	142[e]
$^4J_{24}$	1.254(1)	1.255(1)	Largest difference	0.037	0.024
$^4J_{35}$	1.464(1)	1.469(1)	Root-mean-square deviation	0.013	0.009
$^5J_{25}$	0.575(1)	0.590(1)			

[a]In Hz at 300.135 MHz to high frequency of internal TMS.
[b]In CS_2, containing also 10 mol% of C_6D_{12} and 0.5 mol% TMS.
[c]In acetone-d_6, containing also 0.5 mol% TMS.
[d]Numbers in parentheses are standard deviations in the last significant figure.
[e]Transitions were assigned to all observed peaks; there are many degeneracies because of the methyl protons.

The long-range spin–spin coupling constants (10) for ethylbenzene indicated a barrier in solution in rough agreement with these computations for the isolated molecules.

Accordingly, it appears that STO-3G MO computations are useful in an attempt to establish the magnitude and shape of the internal rotational potential in isopropylbenzene, that is, whether it is indeed very low and whether **2** represents a local minimum. STO-3G MO computations were performed at 15° intervals of the angle ψ, allowing flexibility of the methyl group rotations about their local C—C bonds, among other geometrically optimizational motions. 6-31G computations were done at only three values of the angle ψ because of constraints on computing time.

In addition, the ^{1}H nmr spectra of isopropylbenzene in CS_2 and acetone solutions were analyzed precisely as 12-spin systems. The long-range proton coupling constants provide some information about the internal motion of the isopropyl group. The ^{1}H nmr spectrum of 4-isopropylphenol is also reported, to ascertain any perturbation of the internal barrier in the presence of a substituent that interacts significantly with the electrons in the benzene ring.

Experimental

A 2.5 mol% solution of isopropylbenzene in CS_2, containing 10 mol% of cyclohexane-d_{12} and 0.5 mol% of tetramethylsilane, was transferred to a 5 mm od nmr tube. The solution was degassed by the freeze–pump–thaw procedure and was then flame-sealed. A 2.5 mol% solution in acetone-d_6 was treated similarly. The ^{1}H nmr spectra were accumulated on an AM 300 spectrometer at a probe temperature of 300 K. The recording technique was identical to that described recently (11) and yielded linewidths at half-height of approximately 0.04 Hz for the *para* ring protons. The *ortho* and *meta* protons were slightly coupled to the methyl protons and the magnitudes of these coupling constants were estimated by spectral simulation (Table 1).

A 2.0 mol% of 4-isopropylphenol in CCl_4, containing ca. 5 mol% of tetramethylsilane, was subjected to ^{1}H nmr on an HA 100 spectrometer at a probe temperature of 305 K. The spectrum was calibrated in a manner described in detail previously (12).

The STO-3G MO computations were done with the program MONSTERGAUSS (13) on an Amdahl 470 system. The carbon atoms of the benzene ring were constrained to a planar hexagon during complete optimization of the side-chain geometries for seven conformations about the C_{sp^2}—C_{sp^3} bond (30 h of cpu time). The imposed constraint is unlikely to perturb significantly the computed internal potential (14). CNDO/2 and INDO MO computations (15*a*) on the STO-3G MO geometries were also performed with the Amdahl 470. Finally, 6-31G MO computations at ψ equal to 0°, 45°, and 90° employed the program GAUSSIAN 82 (15*b*,*c*) on an Amdahl 5870.

Results

Spectral analyses

These were performed with the computer program NUMARIT (16), extensively modified by R.S. Table 1 presents the ^{1}H nmr spectral parameters of isopropylbenzene, as obtained from analyses of the complete spectra arising from the 12-spin system. Figure 1 displays the calculated and observed spectra of most of the transitions arising from the *para* proton. The linewidth at half-height is very near 0.04 Hz.

For the 2.0 mol% solution of 4-isopropylphenol in CCl_4 solution, the germane coupling constants are −0.546(7) and 0.271(7) Hz, respectively, for ^4J(H,CH) and ^5J(H,CH). These long-range coupling constants are sensitive to the conformation of the isopropyl group.

The theoretical barrier

Table 2 presents the computed energies for seven conformations about the C_{sp^2}—C_{sp^3} bond. The STO-3G MO results can be fit by $V(\psi)/\text{kJ mol}^{-1} = (14.10 \pm 0.29)\sin^2\psi - (2.77 \pm 0.29)\sin^2 2\psi + (1.39 \pm 0.28)\sin^3 3\psi$. The quoted errors are given at the 95% confidence interval. There are significant fourfold and sixfold components in the computed internal barrier. Just as for ethylbenzene (10), the fourfold component is of opposite sign to the predominant twofold component. The computed barrier profile does not display a local minimum at $\psi = 60°$ (conformation **2**), suggesting that such a minimum, indicated by the hyperfine coupling constants of the radicals discussed above, either does not occur for the diamagnetic molecules or arises from solvent effects. Furthermore, the STO-3G results do not agree with the very small barrier once deduced from the microwave spectra at low resolution; but see the conclusions.

According to the 6-31G optimizations, the conformations at ψ equal 45° and 90° are 4.09 and 13.40 kJ/mol less stable than that at $\psi = 0°$. These energies are fit by $13.40\sin^2\psi - 2.61\sin^2 2\psi$, again yielding a fourfold component of the barrier

Can. J. Chem. Downloaded from www.nrcresearchpress.com by 93.93.197.157 on 09/07/12
For personal use only.

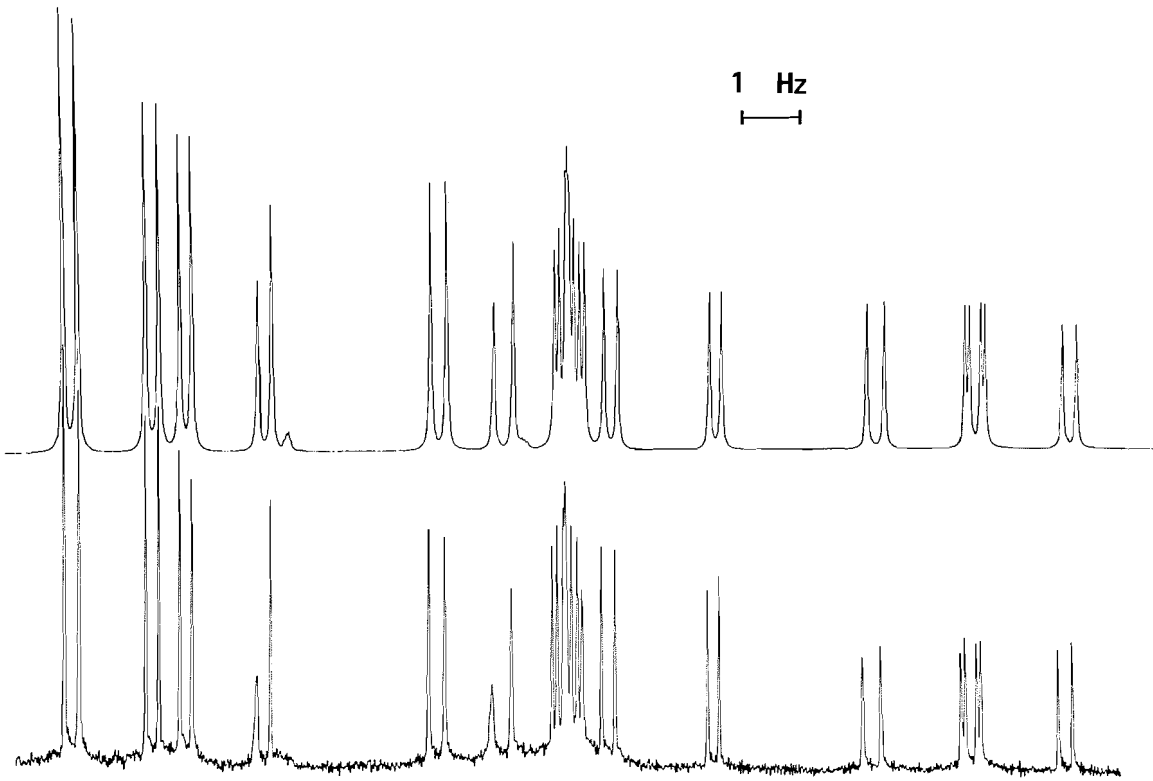

FIG. 1. The observed and computed ^{1}H nmr spectra of the *para* proton are displayed for a 2.5 mol% solution of isopropylbenzene in CS_2 solution (spectral parameters as in Table 1). The linewidths at half-height are near 0.04 Hz in the experimental spectrum.

of opposite sign to that of the twofold component. These components must have the same sign and, of course, different relative magnitudes if a local minimum is to exist at $\psi = 90°$.

The 6-31G structure is shown in Fig. 2 for $\psi = 0°$, the only constraint in the optimization procedure being a planar phenyl moiety; this was also the constraint at 45° and 60°. The computed geometry appears reasonable (see figure caption).

The long-range coupling constant, $^6J(H,CH)$

The coupling constant between the methine proton and the *para* ring proton, ^6J(H,CH), is independent of solvent and is −0.254(2) Hz in isopropylbenzene (Table 1). Such a coupling constant obeys the relationship, $^6J = {}^6J_{90}\langle\sin^2\psi\rangle$, where $^6J_{90}$ is the magnitude of ^6J when the methine C—H bond lies in a plane perpendicular to the aromatic ring (17). The expectation value of $\sin^2\psi$ can be computed as a function of the internal barrier, either quantum mechanically (17) or classically. For toluene, $^6J_{90}$ is −1.20 Hz (11). $^6J_{90}$ is reduced in magnitude by electronegative substituents attached to the α carbon atom. A methyl substituent, as in ethylbenzene (10), reduces the magnitude of $^6J_{90}$ to 1.16 Hz. On the assumption that two methyl substituents yield $^6J_{90}$ as −1.12 Hz (additivity assumption), $\langle\sin^2\psi\rangle$ follows as 0.229. For a hindered rotor model, the apparent twofold barrier is then 6.5 kJ/mol. If $^6J_{90}$ is −1.20 Hz, as in toluene, then the apparent twofold barrier is 7.1 kJ/mol.

Based on a classical averaging procedure, which also yields $\langle\sin^2\psi\rangle$ as 0.229 for a V_2 of 6.5 kJ/mol, the observed ^6J is compatible with twofold and fourfold components of 4.5 kJ/mol and −4.5 kJ/mol, respectively. In view of the MO computations, equal magnitudes of these barrier components seem unlikely. Other possible combinations of V_2 and V_4 are 9.7 and −3.5 kJ/mol, respectively, and 7.2 and −1.0 kJ/mol. These possibilities appear reasonable, although the coupling constant cannot be used to discriminate between them.

TABLE 2. Theoretical energies for various conformations of isopropylbenzene

	Relative energy/kJ mol^{-1}		
ψ/deg[a]	STO-3G MO[b]	STO-3G//CNDO[c]	STO-3G//INDO[c]
0	0.00[d]	0.00[e,g]	0.00[f,h]
15	1.05	0.89	0.92
30	2.98	2.88	2.96
45	4.71	3.29	4.01
60	8.63	8.89	8.68
75	13.29	13.90	13.52
90	15.23	17.14	16.62

[a]The angle by which the α C—H bond of the isopropyl group rotates out of the benzene plane.
[b]Full optimization of the side-chain geometry (see Experimental).
[c]Computed for the STO-3G geometries.
[d]Total energy of −343.634 297 au.
[e]Total energy of −73.155 342 au.
[f]Total energy of −70.875 791 au.
[g]The relative CNDO energies are fit by $V(\psi)$/kJ mol^{-1} = 15.3 $\sin^2\psi$ − 4.0 $\sin^2 2\psi$ + 1.7$_5$ $\sin^2 3\psi$ with errors of 0.5 kJ mol^{-1} at the 95% confidence level. See text for the definition of ψ.
[h]The INDO energies can be fit by $V(\psi)$/kJ mol^{-1} = 14.8 $\sin^2\psi$ − 3.8 $\sin^2 2\psi$ + 1.8 $\sin^2 3\psi$; errors as in footnote *g*.

The 6-31G MO potential above corresponds to a $\langle\sin^2\psi\rangle$ of 0.153, the expectation value of ψ being 20° at 300 K. ^6J very clearly indicates that this value of $\langle\sin^2\psi\rangle$ is too small. If the theory is correct, then the solvents *decrease* the internal barrier, whereas it has been suggested that the solvent would cause a dramatic increase in the barrier (7). It may be noted that the

Can. J. Chem. Downloaded from www.nrcresearchpress.com by 93.93.197.157 on 09/07/12
For personal use only.

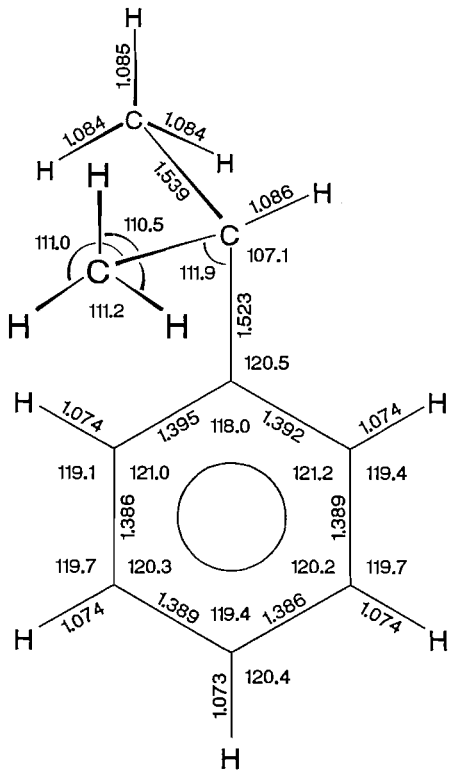

FIG. 2. The computed 6-31G geometry is displayed for the low-energy conformation of isopropylbenzene plane. The total energy is −347.681 397 au, reached during a geometry optimization procedure in which the phenyl nuclei are constrained to a plane. The C—H bonds of the methyl groups, as expected, take on staggered arrangements about neighbouring bonds and there are the usual parallel 1,3 arrangements between two pairs of C—H bonds on different methyl groups. The computed bond angles within the phenyl moiety are close to those (21–23) deduced from the substituent parameter for a methyl group as deduced from X-ray diffraction measurements. The *ortho* C—H bond nearest the methyl groups does not appear to move away significantly from the side chain but, of course, does so as rotation about the C_{sp^2}—C_{sp^3} bond brings the methyl groups nearer.

hyperfine splitting constant for the methine proton in the cation π radical of an isopropylbenzene derivative (1) corresponds to a $\langle\sin^2\psi\rangle$ of 0.222. Perhaps an MO calculation with a much larger basis set is warranted (the 6-31G computations needed 37.3 h of cpu time on the Amdahl 5870).

The other long-range coupling constants

For toluene, ^4J(H,CH) has been written as $-1.08\langle\sin^2\psi\rangle - 0.32\langle\cos^2\psi\rangle$, the first term representing the σ,π contribution and the second a σ component (19). Both expectation values are 0.5, so that ^4J becomes −0.70 Hz, as observed (11). The coefficient of $\langle\sin^2\psi\rangle$ should be multiplied by 1.12/1.20 if it is to apply to isopropylbenzene (see ^6J above). Consequently, ^4J in the latter becomes $-1.01(0.229) - 0.32(0.771)$ or −0.478 Hz, to be compared with the observed value of −0.559(1) Hz (Table 1). To obtain agreement with experiment, the coefficient of $\langle\cos^2\psi\rangle$ must be −0.43 Hz.

A similar discrepancy occurs for ^5J(H,CH). In toluene, ^5J(H,CH) is reproduced by $0.336\langle\sin^2\psi\rangle + 0.322\langle\sin^2(\psi/2)\rangle$, the second term representing the σ electron component (11, 20). This relationship yields 0.233 Hz for ^5J(H,CH) in isopropylbenzene when the coefficient of $\langle\sin^2\psi\rangle$ is reduced by 1.12/1.20 (note that $\langle\sin^2(\psi/2)\rangle$ is 0.5 for any combination of V_2 and V_4). To reproduce the observed value of 0.298(1) Hz in Table 1, the coefficient of $\langle\sin^2(\psi/2)\rangle$ is required to be 0.45 Hz. In other words, the magnitudes of the σ electron components of ^4J and ^5J increase by very nearly the same ratio relative to toluene.

Apparently, ^4J(H,CH) in isopropylbenzene is given by $-1.01\langle\sin^2\psi\rangle - 0.43\langle\cos^2\psi\rangle$ or $-0.43 - 0.58\langle\sin^2\psi\rangle$. In 4-isopropylphenol, ^4J is −0.546(7) Hz, corresponding to a $\langle\sin^2\psi\rangle$ of 0.20(2) if twice the standard deviation of ^4J is taken as a measure of accuracy.[1] It does not appear that the barrier to internal rotation about the C_{sp^2}—C_{sp^3} bond is significantly altered by the hydroxyl substituent. It therefore seems unlikely that the apparently very low barrier reported for 4-isopropylbenzaldehyde in the vapor phase (7) has its origin in a substituent effect.

Conclusion

Ab initio molecular orbital calculations at the STO-3G and 6-31G level do not support the suggestion of a very low internal barrier to rotation about the C_{sp^2}—C_{sp^3} bond in isopropylbenzene. It therefore appears, as pointed out by a referee, that an alternative explanation (24) for the microwave data (7) of isopropylbenzene is more likely. For molecules of this size, the relative intensities of low resolution microwave spectra are not easily related to internal rotational barriers and may well reflect the threshold energy for intramolecular vibrational redistribution. Hence the data (7) are not contradictory to the results of the present work. The long-range proton–proton coupling constants for isopropylbenzene in CS_2 and acetone solutions cannot discriminate between a purely twofold barrier and one containing an additional significant fourfold component. They are consistent with V_2 and V_4 combinations of 9.7 and −3.5 kJ/mol, respectively, as well as with 7.2 and −1.0 kJ/mol; the twofold components are rather smaller than those obtained from the geometry-optimized molecular orbital energies.

Acknowledgments

We are grateful to the Natural Sciences and Engineering Research Council of Canada for financial assistance and to the referees for instructive comments on the microwave spectral interpretations.

1. F. NEMOTO, N. TSUZUKI, K. MUKAI, and K. ISHIZU. J. Phys. Chem. **85**, 2450 (1981).
2. M. T. JONES, S. METZ, and T. C. KUECHLER. Mol. Phys. **33**, 717 (1977).
3. C. CHACHATY, A. FORCHIONI, and J. C. RONFARD-HARET. Mol. Phys. **31**, 325 (1976).
4. T. SCHAEFER, W. J. E. PARR, and W. DANCHURA. J. Magn. Reson. **25**, 167 (1977).
5. L. V. VILKOV, N. I. SADOVA, and S. S. MOCHALOV. Dokl. Akad. Nauk, **179**, 896 (1968).
6. J. BRUNVOLL, M. KOLONITS, R. K. BOHN, and I. HARGITTAI. J. Mol. Struct. **131**, 177 (1985).
7. N. S. TRUE, M. S. FARAG, R. K. BOHN, M. A. MACGREGOR, and J. RADHAKRISHMAN. J. Phys. Chem. **87**, 4622 (1983).
8. T. SCHAEFER and G. H. PENNER. Chem. Phys. Lett. **114**, 526 (1985).
9. C. W. BOCK, M. TRACHTMAN, and P. GEORGE. Chem. Phys. **93**, 431 (1985).
10. T. SCHAEFER, G. H. PENNER, and R. SEBASTIAN. Can. J. Chem. **65**, 873 (1987).
11. T. SCHAEFER, R. SEBASTIAN, and G. H. PENNER. Can. J. Chem. **63**, 2597 (1985).

[1] In 4-methoxytoluene, ^4J(H,CH) is −0.699(1) Hz for a CS_2 solution, as compared to −0.702(1) Hz in toluene (11), implying no marked perturbation of ^4J(H,CH) by a *para* oxygen substituent.

Can. J. Chem. Downloaded from www.nrcresearchpress.com by 93.93.197.157 on 09/07/12
For personal use only.

12. T. SCHAEFER and R. SEBASTIAN. J. Magn. Reson. **41**, 395 (1980).
13. M. R. PETERSEN and R. A. POIRIER. MONSTERGAUSS. Department of Chemistry, University of Toronto, Toronto, Ontario. 1981.
14. T. SCHAEFER and G. H. PENNER. J. Mol. Struct. (Theochem), **138**, 305 (1986).
15. (*a*) P. DOBOSH and N. S. OSTLUND. QCPE, **11**, 281 (1975); (*b*) W. J. HEHRE, L. RADOM, P. V. R. SCHLEYER, and J. A. POPLE. *Ab initio* molecular orbital theory. Wiley, New York. 1986; (*c*) J. S. BINKLEY, M. J. FRISCH, D. J. DEFREES, K. RAHGAVACHARI, R. A. WHITESIDE, H. B. SCHLEGEL, E. M. FLUDER, and J. A. POPLE. Department of Chemistry, Carnegie–Mellon University, Pittsburgh, PA.
16. A. R. QUIRT and J. S. MARTIN. J. Magn. Reson. **5**, 318 (1971); J. S. MARTIN, A. R. QUIRT, and K. E. WORVILL. The nmr program library. Daresbury Laboratory, Daresbury, U.K.
17. W. J. E. PARR and T. SCHAEFER. Acc. Chem. Res. **13**, 400 (1980).
18. J. M. HOLLAS, H. MUSA, T. RIDLEY, P. H. TURNER, K. H. WEISENBERGER, and V. FAWCETT. J. Mol. Spectrosc. **94**, 437 (1982).
19. M. BARFIELD, C. J. FOLLICK, K. HATA, S. STERNHELL, and P. W. WESTERMAN. J. Am. Chem. Soc. **105**, 2178 (1983).
20. T. SCHAEFER and R. LAATIKAINEN. Can. J. Chem. **61**, 2785 (1983).
21. A. DOMENICANO and P. MURRAY-RUST. Tetrahedron Lett. 2283 (1979).
22. R. NORRESTAM and L. SCHEPPER. Acta Chem. Scand. Ser. A: **A35**, 91 (1981).
23. T. M. KRYGOWSKI, G. HÄFELINGER, and J. SCHULE. Z. Naturforsch. B: Anorg. Chem. Org. Chem. **41B**, 895 (1986).
24. N. S. TRUE. Chem. Phys. Lett. **101**, 326 (1983).

Can. J. Chem. Downloaded from www.nrcresearchpress.com by 93.93.197.157 on 09/07/12
For personal use only.

Preparation, chemical and electrochemical reduction of pyrido[2,3-*b*]quinoxalines and pyrido[3,4-*b*]quinoxalines

JOSEPH ARMAND AND LINE BOULARES
Laboratoire de Physicochimie des Solutions, E.N.S.C.P., 11 Rue Pierre et Marie Curie, 75231 Paris CEDEX 05, France

CHRISTIAN BELLEC
Laboratoire de Chimie des Hétérocycles, Université Pierre et Marie Curie, 4 Place Jussieu, 75230 Paris CEDEX 05, France

AND

JEAN PINSON
Laboratoire d'Electrochimie, Université Paris VII, 2 Place Jussieu, 75251 Paris CEDEX 05, France

Received October 22, 1987

JOSEPH ARMAND, LINE BOULARES, CHRISTIAN BELLEC, and JEAN PINSON. Can. J. Chem. **66**, 1500 (1988).

The reaction of 2,3-diaminopyridine with the dimeric 4,5-dimethylcyclohexa-3,5-dien-1,2-dione gives 7,8-dimethylpyrido[2,3-*b*]quinoxaline, **1**, in good yields; in the same way 3,4-diaminopyridine gives the 7,8-dimethylpyrido[3,4-*b*]quinoxaline **2**. The electrochemical reduction of **1** and **2** in hydroorganic medium gives the 5,10-dihydro compounds **6** and **7**; **1** and **2** present a single $2e^-$ polarographic wave, in contrast to phenazine which shows two monoelectronic waves. The catalytic hydrogenation of **1** and **2** gives **6** and **7** and does not involve the pyridinic ring as in the case of pyridopyrazines. $AlLiH_4$ does not react with **2** but **1** is reduced into the 1,2-dihydro derivative **8**. The behavior of **1** and **2** is thus different from that of pyridopyrazines (which give the 1,2,3,4-tetrahydro compounds) and from that of phenazine (which gives the 5,10-dihydro derivative). $NaBH_4$ reacts with pyridopyrazines to give, according to the substituents, 1,2- or 5,6-dihydro or 1,2,3,4-tetrahydro derivatives. Methylmagnesium chloride reacts with **1** to give a mixture of 2-methyl-1,2-dihydro, 2,6,7-trimethyl, and 4,6,7-trimethylpyrido[2,3-*b*]quinoxaline. In the case of **2**, 4,6,7-trimethylpyrido[3,4-*b*]quinoxaline is obtained.

JOSEPH ARMAND, LINE BOULARES, CHRISTIAN BELLEC et JEAN PINSON. Can. J. Chem. **66**, 1500 (1988).

L'action de la diamino-2,3 pyridine sur la diméthyl-4,5 cyclohexadiène-3,5 dione-1,2 sous forme dimère fournit avec un bon rendement la diméthyl-7,8 pyrido[2,3-*b*]quinoxaline **1**. En utilisant la diamino-3,4 pyridine on obtient la diméthyl-7,8 pyrido[3,4-*b*]quinoxaline **2**. En milieu hydroorganique la réduction électrochimique de **1** et **2** fournit les dérivés dihydro-5,10 : **6** et **7**; **1** et **2** présentent une seule vague polarographique de $2e^-$ contrairement à la phénazine qui donne deux vagues monoélectroniques. L'hydrogénation catalytique de **1** et **2** fournit **6** et **7** et ne concerne donc pas le noyau pyridine comme dans le cas des pyridopyrazines. $AlLiH_4$ est sans action sur **2** alors que **1** fournit le dérivé dihydro-1,2 : **8**; le comportement de **1** et **2** diffère de celui des pyridopyrazines (qui donnent des dérivés tétrahydro-1,2,3,4) et de la phénazine (qui fournit le dérivé dihydro-5,10). Avec $NaBH_4$ **1** fournit un mélange de **6** et **8** tandis que **2** donne le dérivé tétrahydro-1,2,3,4. L'action de $NaBH_4$ sur les pyridopyrazines a été également étudiée : selon la nature du substituant des dérivés dihydro-1,2, tétrahydro-1,2,3,4 ou dihydro-5,6 sont obtenus. Le chlorure de méthylmagnésium conduit dans le cas de **1** à un mélange de dérivé dihydro-1,2 méthyl-2, de triméthyl-2,6,7 pyrido [2,3-*b*] quinoxaline et de triméthyl-4,6,7 pyrido [2,3-*b*] quinoxaline et dans le cas de **2** à la triméthyl-4,6,7 pyrido [3,4-*b*] quinoxaline.

N-Heterocyclic compounds present interesting electrochemical behaviour. Their electrochemical reduction allows one to obtain semi reduced compounds and permits the observation of rearrangements between these reduced compounds (1, 2). Combined with other means of reduction, it allows one to prepare selectively reduced compounds. Small structural changes may induce very different chemical behaviours. We now report the reactions of pyrido[2,3-*b*]quinoxalines and pyrido[3,4-*b*]-quinoxalines. The reduction and other chemical properties of these compounds have never been investigated, this may be related to their difficult preparation. We describe easier synthetic routes to these compounds. In the case of the chemical and electrochemical reduction of pyridoquinoxalines different behaviours could be forecasted: (*i*) reduction of the pyrazinic ring as in the case of phenazine, (*ii*) reduction of either the pyridinic or the pyrazinic ring as in the case of pyrido[2,3-*b*]-pyrazines, (*iii*) reduction following a mechanism not yet observed. The three types of reactions can be brought into play depending on which reagent is used. Thus the condensed benzene ring could exert an important influence on the reduction of pyridopyrazines.

Results and discussion

Preparation

Pyrido[2,3-*b*]quinoxalines have been prepared either by cyclization of 2-anilino-3-nitropyridine or of 2-toluidino-3-nitropyridine (3) or by condensation of ketones such as R—CO—CH_3 with 2-formyl-3-aminoquinoxaline (4). The few pyrido[3,4-*b*]quinoxalines which are known have been obtained by cyclization of 3-amino-4-(2-aminoanilino)pyridine (5) or of 3-amino-4-(2-aminotoluidino)pyridine (3). In view of the rather low yields and the complicated experiments, we looked for alternative routes to prepare these compounds. We reacted 2,3- and 3,4-diaminopyridine with a quinone: 4,5-dimethylcyclohexa-3,5-dien-1,2-dione. When the quinone is used as a monomer, only traces of pyridoquinoxalines are obtained, but when the quinone is present in a dimeric form, pyridoquinoxalines **1** and **2** are obtained in good yields.

Electrochemical reduction

We had previously investigated the electrochemical reduction of pyrido[2,3-*b*]pyrazines **3** and of pyrido[3,4-*b*]pyrazines **4** (6) and we were interested to see how the presence of a fused

Printed in Canada / Imprimé au Canada

Can. J. Chem. Downloaded from www.nrcresearchpress.com by 93.93.197.157 on 09/07/12
For personal use only.

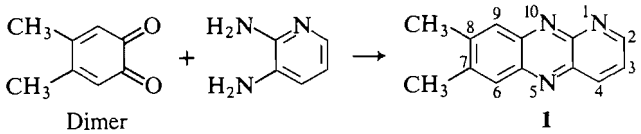

Dimer 1

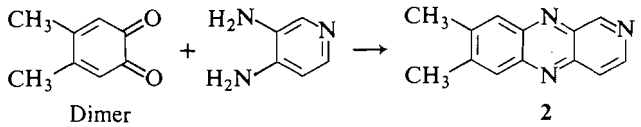

Dimer 2

benzene ring in the 2,3-positions would influence the reduction mechanism of **3** and **4**.

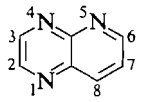

3

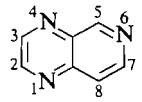

4

The comparison of the electrochemical behaviour of **1** and **2** with that of phenazine **5** is also of interest.

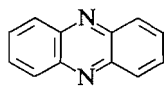

5

*7,8-Dimethylpyrido[2,3-*b*]quinoxaline 1*

In aprotic medium (very dry acetonitrile or DMSO) **1** shows by cyclic voltammetry a first reversible monoelectronic peak: $E_1^0 = -1.10$ V/SCE in acetonitrile, which is followed by a second monoelectronic irreversible peak $E_{Pc_2} = -1.69$ V/SCE. The same voltammetric pattern is observed in the more basic solvent DMSO: $E_1^0 = -1.10$ V/SCE, $E_{Pc_2} = -1.85$ V/SCE. The voltammogram of phenazine in DMSO is similar: $E_1^0 = -1.10$ V/SCE and $E_{Pc_2} = -1.71$ V/SCE. In both cases, the transfer of a second electron leads to a very basic dianion which can abstract a proton from the solvent or from the supporting electrolyte (7) (one can note the small negative shift of the second peak when changing the solvent from acetonitrile to the more basic DMSO). The same potential is observed for both couples $\mathbf{1}/\mathbf{1}^{\cdot-}$ and $\mathbf{5}/\mathbf{5}^{\cdot-}$, the nitrogen atom on the pyridinic ring does not influence the reducibility of the system while pyridopyrazines are more easily reducible than quinoxalines.

In protic medium (H_2O–MeOH 50/50), **1** shows a two-electron wave between pH 1 and 13. Between pH 1 and 6.55, $E_{1/2}$ varies according to $E_{1/2} = 0.20 - 0.087$pH and according to $E_{1/2} = 0.01 - 0.058$pH between pH 6.55 and 13. A controlled potential electrolysis at pH 7.4 allows one to obtain the reduction product: 5,10-dihydropyrido[2,3-*b*]quinoxaline, **6**, which shows a $2e^-$ anodic wave the $E_{1/2}$ of which is near that of **1**. Thus the reduction scheme can be written as:

$$\mathbf{1} + 2e^- + 3H^+ \rightleftharpoons [\mathbf{6}]H^+ \qquad 1 < pH < 6.55$$

$$\mathbf{1} + 2e^- + 2H^+ \rightleftharpoons \mathbf{6} \qquad 6.55 < pH < 13$$

Two comments can be made on the previous results: (*i*) the reduction product **6** is similar to that obtained from phenazine:

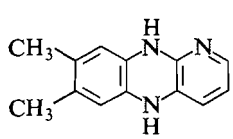

6

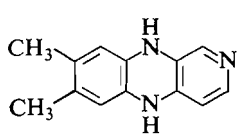

7

5,10-dihydrophenazine. However, there are some differences concerning the polarographic patterns. In the case of **5** (8*a*, 8*b*), two monoelectronic waves are observed in acidic medium up to pH 4 while a single bielectronic wave is observed for **1**.

The two monoelectronic waves observed for phenazine in acidic medium have been assigned to the stepwise reduction of a diprotonated species (8*a*):

$$PH^+ + H^+ \rightleftharpoons PH_2^{2+}$$

$$PH_2^{2+} + e \rightarrow PH_2^{+\cdot} \qquad \text{1st wave}$$

$$PH_2^{+\cdot} + e \rightarrow PH_2 \qquad \text{2nd wave}$$

The pK_a of phenazinium ion is 1.23 (9) and that of the diprotonated species have been estimated to be about −5 (8*a*). In the case of **1**, the first protonation must occur on the pyridinium nitrogen as in the case of pyrido[2,3-*b*]pyrazine (10) for which the pK_a has been measured as $pK_a = 1.2$ (11). In order to observe two one-electron waves for **1**, the two nitrogens of the pyrazine ring should be protonated; the corresponding species should then be triprotonated which is highly unlikely. (*ii*) In aqueous medium at pH > 7 or in an acetonitrile–phenol solvent, we had shown previously (6) that the reduction product of pyrido[2,3-*b*]pyrazines, **3**, undergo a rearrangement leading to a 5,8-dihydro derivative:

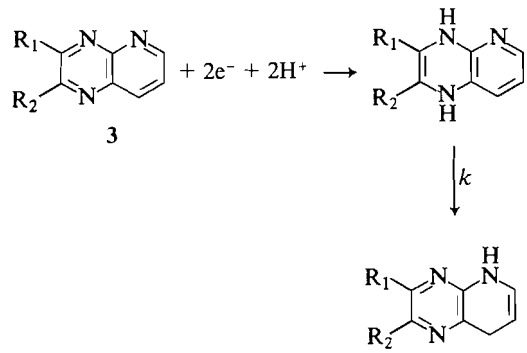

3

In the case of **1**, the electrolysis carried out in a water–methanol or an acetonitrile–phenol medium leads only to compound **6**, the internal rearrangement involving the pyridine ring does not occur. The additional presence of a fused benzene ring in the case of **1** strongly stabilizes the 5,10-dihydro derivative.

*7,8-Dimethylpyrido[3,4-*b*]quinoxaline, 2*

The electrochemistry of **2** is similar to that of **1**. In aprotic medium (very dry acetonitrile), one observes by cyclic voltammetry a first reversible monoelectronic peak ($E_1^0 = -1.05$ V/SCE) followed by a second irreversible cathodic peak ($E_{Pc_2} = -1.88$ V/SCE). In protic medium (water–methanol 50/50), a two-electron polarographic wave is observed which corresponds to the reduction into 5,10-dihydro-7,8-dimethylpyrido[3,4-*b*]-quinoxaline, **7**, obtained through a preparative electrolysis. The half-wave potentials shift with pH as:

$$E_{1/2} = +0.30 - 0.087\text{pH} \qquad 1 < pH < 8.95$$

$$E_{1/2} = +0.04 - 0.058\text{pH} \qquad 8.95 < pH < 13$$

and the reduction schemes are

$$\mathbf{4} + 2e^- + 3H^+ \rightleftharpoons [\mathbf{7}]H^+ \qquad 1 < pH < 8.95$$

$$\mathbf{4} + 2e^- + 2H^+ \rightleftharpoons \mathbf{7} \qquad 8.95 < pH < 13$$

No intramolecular rearrangement involving the pyridine ring is observed for **7**; this could be expected as rearrangements occur

Can. J. Chem. Downloaded from www.nrcresearchpress.com by 93.93.197.157 on 09/07/12
For personal use only.

in the case of 1,4-dihydropyrido[2,3-*b*]pyrazines but not in the case of 1,4-dihydropyrido[3,4-*b*]pyrazines.

Chemical reductions

Catalytic hydrogenation over Pd/C

Both with **1** and **2**, the addition of one mole of hydrogen is observed leading respectively to **6** and **7**:

1 → **6**
2 → **7** (H_2, Pd/C)

In the case of pyrido[2,3-*b*]pyrazines (6, 10) the hydrogenation involves either the pyrazine or the pyridine ring with addition of 2 mol of hydrogen to give a tetrahydrogenated compound. Phenazine yields the 5,10-dihydro derivative (12).

Reduction with $LiAlH_4$

In the case of pyrido[2,3-*b*]pyrazines, **3**, and pyrido[3,4-*b*]-pyrazines, **4** (13, 14), with alkyl or aryl substituents, the reduction with $LiAlH_4$ leads exclusively to 1,2,3,4-tetrahydro derivatives of the pyrazine ring. Reduction of **1** only yields the 1,2-dihydro compound, **8**, where only the pyridine ring is reduced. No reaction is observed in the case of **2**.

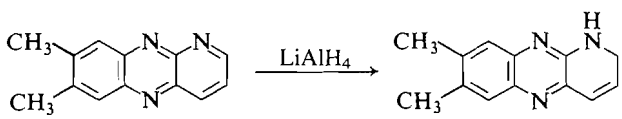

The $LiAlH_4$ reduction of **1** and **2** is different from that of pyridopyrazines as well from that of phenazine which give the 5,10-dihydro compound (15).

Reduction with $NaBH_4$ of pyrido pyrazines and pyrido quinoxalines

The reaction of $NaBH_4$ with pyrido pyrazines has only been described in the case of pyrido[2,3-*b*]pyrazine (which gives the 1,2,3,4-tetrahydro derivative) (16); no results are given concerning substituted pyrido[2,3-*b*] or pyrido[3,4-*b*]-pyrazines.

The reaction of $NaBH_4$ with pyrido[2,3-*b*]pyrazines, **9** and **10**, gives the 1,2-dihydro and 1,2,3,4-tetrahydro derivatives.

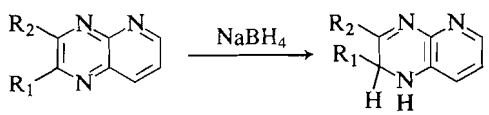

9a: $R_1 = H$; $R_2 = C_6H_5$ → **10***a*
9*b*: $R_1 = R_2 = C_6H_5$ → **10***b*

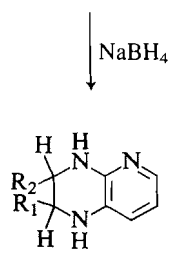

11*a*
11*b*

Compound **10***a* can be easily prepared but **10***b* is obtained only as a mixture with **11***b*. In the case of 2,3-diphenylpyrido-[3,4-*b*]pyrazine, **12**, the 1,2- (or 3,4-) dihydro derivative, **13**, is obtained first and then the 1,2,3,4-tetrahydro derivative, **14**.

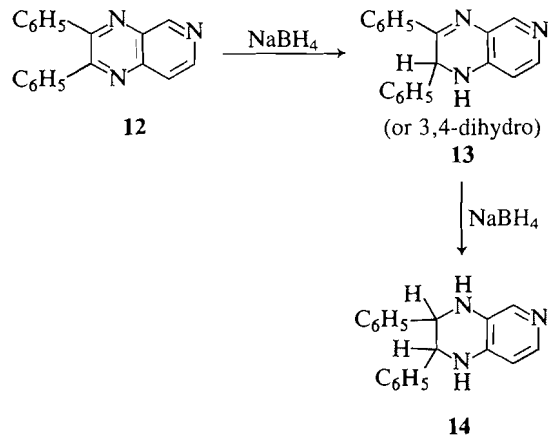

In the case of pyrido[2,3-*b*]pyrazines with a bromine atom in the 7-position, the reduction may involve the pyridine ring. The 2,3-dimethyl-7-bromopyrido[2,3-*b*]pyrazine, **15**, gives the 1,2,3,4-tetrahydro derivative **16** but the 2,3-diphenyl-7-bromopyrido[2,3-*b*]pyrazine, **17**, gives the 5,6-dihydro derivative, **18**, and the 3-phenyl-7-bromopyrido[2,3-*b*]pyrazine, **19**, gives a mixture of the 1,2-dihydro derivative **20** and of the 5,6-dihydro derivative **21**.

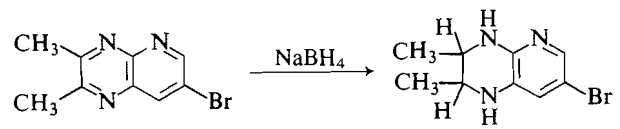

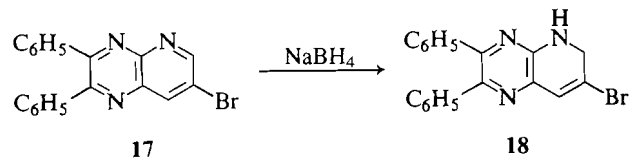

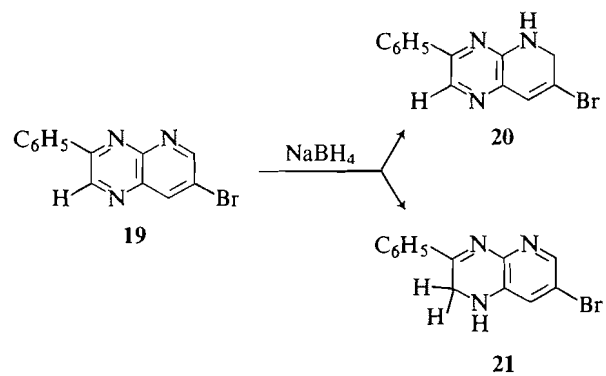

The reaction of $NaBH_4$ with pyridoquinoxalines depends upon the position of nitrogen on the pyridine ring. In the case of **1**, one obtains a mixture of 1,2- and 5,10-dihydro derivatives while **2** leads to a compound tetrahydrogenated on the pyridine ring.

Can. J. Chem. Downloaded from www.nrcresearchpress.com by 93.93.197.157 on 09/07/12
For personal use only.

Can. J. Chem. Downloaded from www.nrcresearchpress.com by 93.93.197.157 on 09/07/12
For personal use only.

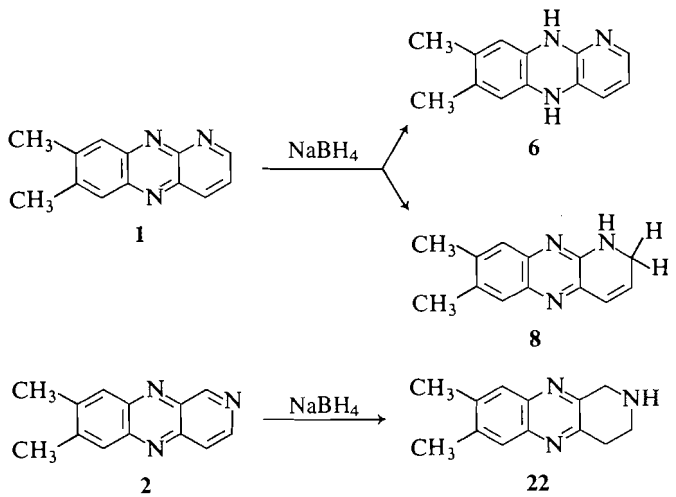

1 6 8 2 22

These results show that in the case of 2,3-alkyl- or aryl-substituted pyridopyrazines the pyrazine ring is more reactive than the pyridine ring towards $NaBH_4$, but the introduction of a bromine atom in position 7 or that of a fused benzene ring in the 2,3 positions levels off the reactivity of both rings.

Reaction of organo magnesium compounds

The reaction of Grignard reagents with pyrido[2,3-*b*]pyrazines has been described (13, 17). The results depend both on the substituents of the heterocyclic compounds and on the Grignard reagent. The reaction can take place either on the pyrazine or on the pyridine ring with addition of one or two moles of the reagent.

Phenylmagnesium bromide does not react with pyridoquinoxalines but methyl magnesium chloride reacts with **1** and **2**. **1** gives a mixture of **23**, **24**, and **26** which can be separated by chromatography. The intermediate compound **25** is too easily oxidized to be isolated.

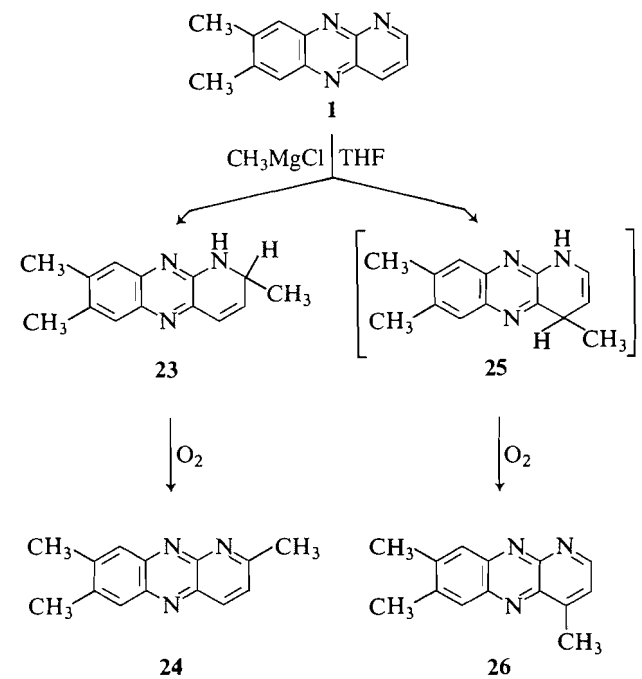

1 23 25 24 26

In the case of **2**, compound **28** is obtained but the intermediate **27** is too oxidizable to be isolated.

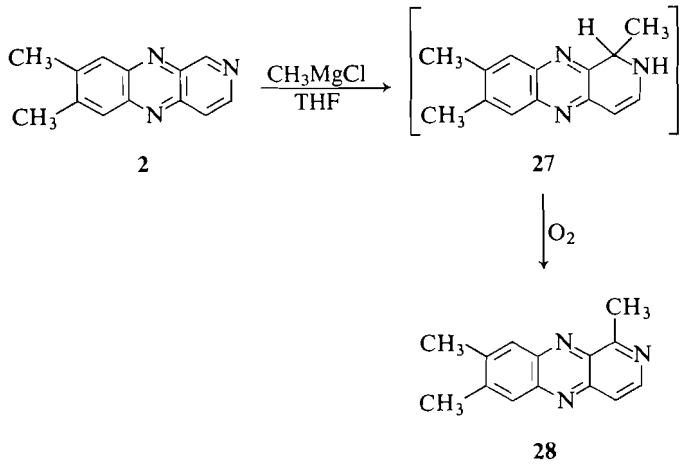

2 27 28

Experimental

Melting points are uncorrected. ^{1}H-nmr spectra were recorded on a Bruker WH80, a Varian A60, and a Bruker 250 MHz spectrometer using tetramethylsilane (TMS) as internal standard. The apparatus and techniques used for the electrochemical studies and pH measurements have been described previously (6). All the potentials are referred to the saturated-calomel electrode (SCE); the temperature of the solutions was 20°C. Acetonitrile used in the cyclic voltammetric experiments was distilled under vacuum and dried over activated alumina. The solutions were desoxygenated with nitrogen dried over phosphorus pentoxide. The microanalyses were performed by the "Service de Microanalyse, Université Pierre et Marie Curie". The following abbreviations are used in reporting nmr results: s = singlet, d = doublet, t = triplet, q = quadruplet, m = multiplet. All the compounds described gave correct elemental analysis.

Preparation of 7,8-dimethylpyrido[2,3-b]quinoxaline, 1

A mixture of 2,3-diaminopyridine (327 mg) and 4,5-dimethyl-3,5-cyclohexadien-1,2-dione dimer (18) (411 mg) in 15 mL of methanol was kept at room temperature for 12 days. The solvent was evaporated and the solid residue was extracted five times with 100 mL of hexane. Hexane was then evaporated to give 527 mg of **1** (84% yield); mp 142–144°C dec. ^{1}H nmr ($CDCl_3$): 7-CH_3 + 8-CH_3, s, 2.55 ppm (6H); 3-H, m, 7.72 ppm (1H); 6-H + 9-H, 2 br s, 7.99 and 8.09 ppm (2H); 4-H, d × d, 8.55 ppm (1H), J_{3-4} = 8 Hz, J_{2-4} = 2 Hz; 2-H, m, 9.29 ppm (1H).

Preparation of 7,8-dimethylpyrido[3,4-b]quinoxaline, 2

A mixture of 3,4-diaminopyridine (327 mg) and 4,5-dimethyl-3,5-cyclohexadien-1,2-dione dimer (18) (411 mg) in 15 mL of methanol was kept at room temperature for 10 days, then at 0°C for 1 day. The solid which precipitated was filtered. The nmr spectrum in $CDCl_3$ shows that it is a mixture of **2** and of one or several intermediate products which give quantitatively **2** after 2 days in solution. Thus a solution of the solid in 10 mL of chloroform was kept at room temperature for 2 days and then evaporated to give 445 mg of **2** (71% yield); mp 178–180°C dec. ^{1}H nmr ($CDCl_3$) 7-CH_3 + 8-CH_3, s, 2.59 ppm (6H); 4-H + 6-H + 9-H, m, 7.95–8.10 ppm (3H); 3-H, d, 8.78 ppm (J = 6 Hz) (1H); 1-H, s, 9.72 ppm (1H).

Electrolysis of 1: preparation of 6

An electrolysis was carried out at pH = 7.4 and E = −0.6 V. The cathodic compartment contained 209 mg of **1** in 100 mL of solution (methanol 50%). At the end of the electrolysis (1.9 F per mol), the precipitate in the cell was filtered under nitrogen, washed with water, and dried to give 150 mg of 5,10-dihydro-7,8-dimethylpyrido[2,3-*b*]-quinoxaline, **6**; mp 175°C dec. ^{1}H nmr (DMSO-d_6): 7-CH_3 + 8-CH_3, s, 1.85 ppm (6H); 6-H + 9-H, 2s, 5.95 and 6.07 ppm (2H); 3-H + 4-H, m, 6.15–6.30 ppm (2H); 2-H, q, 7.05 ppm (1H); 5-H + 10-H, broad s, 7.52 and 8.00 ppm (2H) exchanged with D_2O. The electrolysis of **1** (1.19×10^{-3} M) was also performed on platinum grid in the

compartment of a uv spectrometer. In acetonitrile in the presence of phenol (10^{-2} *M*) at $E = -1.0$ V/SCE the final spectrum is identical to that of **6** (λ_{max} = 369 nm, ε = 12 100, shoulder λ = 352 nm, ε = 10 000). Upon reoxidation of $E = -0.5$ V/SCE **1** is reobtained quantitatively.

Electrolysis of 2, preparation of 7

An electrolysis was carried out at pH = 7.20 and $E = -0.6$ V. The cathodic compartment contained 209 mg of **2** in 100 mL of solution (methanol 50%). At the end of the electrolysis (2.1 F per mol), the cathodic solution which contained a solid in suspension was chilled at 0°C and filtered under nitrogen. The precipitate was washed with water and dried to give 135 mg of 5,10-dihydro-7,8-dimethylpyrido[3,4-*b*]quinoxaline, **7**, mp 185°C dec.; ^{1}H nmr (DMSO-d_6): 7-CH_3 + 8-CH_3, s, 1.85 ppm (6H); 4-H + 6-H + 9-H, m, 5.92–5.95 ppm (3H); 1-H, s, 7.09 ppm (1H); 3-H, d, 7.40 ppm (J = 6 Hz) (1H); 5-H + 10-H, 2 broad s, 7.48 and 7.99 ppm, (2H) exchanged with D_2O.

Catalytic hydrogenation of 1 and 2

Catalytic hydrogenation was carried out at room temperature with 20 mg of **1** in 1 mL of DMSO-d_6 in the presence of 20 mg of 10% Pd/C. After 2 h of stirring and consumption of 1 mol of H_2/mol of **1**, the solution was centrifugated. Its nmr spectrum shows that **1** has given **6** quantitatively. With the same procedure, **2** gives **7** quantitatively.

Reduction of 1 with $LiAlH_4$: preparation of 8

$LiAlH_4$ (250 mg) was added slowly to a solution of **1** (209 mg) in freshly distilled tetrahydrofuran (40 mL). After 24 h of stirring at room temperature, the mixture was quenched with 5 mL of water and filtered. The solution was extracted with 50 mL of chloroform. The organic layer was dried on Na_2SO_4 then evaporated to give 153 mg of **8**; mp 155°C dec. ^{1}H nmr (DMSO-d_6): 7-CH_3 + 8-CH_3, s, 2.28 ppm (3H); 2-CH_2, m, 4.45 ppm (2H); 3-H + 4-H, m, 6.2–6.35 ppm (2H); 6-H + 9-H, 2s, 7.02 and 7.23 ppm (2H); 1-H, br s, 7.11 ppm (1H) exchanged with D_2O.

Reduction of 1 with $NaBH_4$

$NaBH_4$ (130 mg) was added to a solution of **1** (130 mg) in ethanol (15 mL). After 16 h of stirring at room temperature, the mixture was poured under nitrogen into 50 mL of deoxygenated water. Ethanol was evaporated under nitrogen in vacuum, the precipitate was filtered under nitrogen and dried to give 90 mg of a solid which was shown by nmr to be a mixture of **6** (35%) and **8** (65%).

Reduction of 2 with $NaBH_4$

$NaBH_4$ (130 mg) was added to 130 mg of **2** in 15 mL of ethanol. After 4 days of stirring at 40°C, the mixture was poured into 20 mL of water. Ethanol was evaporated under vacuum and the solution was extracted with 100 mL of chloroform. The organic layer was dried then evaporated to give a solid (80 mg) which was shown by nmr to be a mixture of **2** (25%) and of 7,8-dimethyl-1,2,3,4-tetrahydropyrido[3,4-*b*]quinoxaline, **22** (75%) which were separated by chromatography. ^{1}H nmr of **22** ($CDCl_3$): 7-CH_3 + 8-CH_3, s, 2.50 ppm (6H); 1-CH_2 + 3-CH_2 + 4-CH_2, 2m, centered at 3.35 and 4.38 ppm (4H + 2H); 6-H + 9-H, br s, 7.71 ppm (2H); NH, br s at 2.80 ppm exchanged with D_2O.

Reduction of 3-phenylpyrido[2,3-b]pyrazine, 9a, with $NaBH_4$

Preparation of dihydro derivative 10a

$NaBH_4$ (300 mg) was added to a solution of **9***a* (300 mg) in 25 mL of ethanol. After 2 h of stirring at room temperature the mixture was poured into 80 mL of water. The yellow precipitate was filtered, washed with water, and dried to give 246 mg of 1,2-dihydro-3-phenylpyrido[2,3-*b*]pyrazine, **10***a*: mp 190°C. ^{1}H nmr (DMSO-d_6): 2-CH_2, s, 4.52 ppm (2H); 1-H, br s, 6.53 ppm (1H) exchanged with D_2O; 7-H + 8-H, m, centered at 7.03 ppm (2H); 6-H + 3-Ph, m, 7.55–8.35 ppm (6H).

Preparation of tetrahydroderivative 11a

With the same work-up but after stirring for 19 h, 260 mg of 1,2,3,4-tetrahydro-3-phenylpyrido[2,3-*b*]pyrazine, **11***a* (6), was obtained.

Reduction of 2,3-diphenylpyrido[2,3-b]pyrazine, 9b, with $NaBH_4$

Using the same procedure, $NaBH_4$ (200 mg) and **9***b* (200 mg) were stirred at room temperature in 20 mL of ethanol for 5 h. The solid obtained (175 mg) was shown by nmr to be a mixture of **9***b* (15%), 1,2-dihydroderivative, **10***b* (45%) (14), *cis* and *trans* tetrahydro derivatives, **11***b* (40%) (11, 14). With the same work-up but after 72 h, the solid obtained (170 mg) was shown by nmr to be a mixture of *cis* (65%) and *trans* (35%) tetrahydro derivatives **11***b*.

Reduction of 2,3-diphenylpyrido[3,4-b]pyrazine, 12, with $NaBH_4$

$NaBH_4$ (250 mg) was added to a solution of **12** (250 mg) in 20 mL of ethanol. After 4 h of stirring at room temperature, the mixture was poured into 80 mL of water. The precipitate was filtered, washed with water, and dried to give 215 mg of 1,2- or 3,4-dihydro-2,3-diphenylpyrido[2,3-*b*]pyrazine, **13** (6). With the same work-up but after stirring 72 h, 226 mg of *cis*-1,2,3,4-tetrahydro-2,3-diphenylpyrido-[3,4-*b*]pyrazine, **14** (6), was obtained.

Reduction of 7-bromo-2,3-dimethylpyrido[2,3-b]pyrazine, 15, with $NaBH_4$

$NaBH_4$ (200 mg) was added to a solution of **15** (150 mg) in 15 mL of ethanol. After 4 h of stirring at room temperature, the mixture was poured into 100 mL of water, then extracted with 100 mL of chloroform. The organic layer was dried and evaporated to give 70 mg of a solid which was shown by nmr to be a mixture of the *cis*-1,2,3,4-tetrahydro derivative (60%) (14) and the *trans*-1,2,3,4-tetrahydro derivative (40%) (17).

Reduction of 7-bromo-2,3-diphenylpyrido[2,3-b]pyrazine, 17, with $NaBH_4$

With the same procedure as for **15**, 130 mg of 7-bromo-5,6-dihydro-2,3-dimethylpyrido[2,3-*b*]pyrazine, **18** (14), was obtained.

Reduction of 7-bromo-3-phenylpyrido[2,3-b]pyrazine, 19, with $NaBH_4$

Employing the same procedure used with **15**, 115 mg of a solid was obtained. It was shown by nmr to be a mixture of 7-bromo-5,6-dihydro-3-phenylpyrido[2,3-*b*]pyrazine, **20** (65%) (14), and 7-bromo-1,2-dihydro-3-phenylpyrido[2,3-*b*]pyrazine, **21** (35%) (14).

Reaction of 1 with methylmagnesium chloride: preparation of 23, 24, and 26

A mixture of 209 mg of **1** (10^{-3} mol) 1.4 mL of a 3 *M* solution of CH_3MgCl in tetrahydrofuran (Aldrich) in 15 mL of anhydrous THF was stirred at room temperature for 30 min. The solution was quenched with 15 mL of a 5 *M* solution of NH_4Cl. The THF was evaporated and the precipitate was filtered, washed with water, and dried (195 mg). The solid was a complex mixture from which were isolated by column chromatography over silica (eluent: ethyl acetate – methanol 94/6) **23** (45%) mp 138–142°C dec. **24** (10%) and **26** (12%). ^{1}H nmr of **23** ($CDCl_3$): 2-CH_3, d, 1.44 ppm (3H); 7-CH_3 + 8-CH_3, s, 2.34 ppm (6H); 2-H, m, 4.77 ppm (1H); 1-H, br s, 5.55 ppm (1H) exchanged with D_2O; 3-H, d × d, 6.12 ppm (1H) J_{3-4} = 10 Hz, J_{2-3} = 4 Hz; 4-H, d, 6.57 ppm (1H) J_{3-4} = 10 Hz; 6-H + 9-H, 2s, 7.22 and 7.46 ppm (2 × 1H). ^{1}H nmr of **24** ($CDCl_3$): 7-CH_3 + 8-CH_3, s, 2.58 ppm (6H); 2-CH_3, s, 2.95 ppm (3H); 3-H, d, 7.60 ppm (1H) J_{3-4} = 9 Hz; 6-H + 9-H, 2s, 8.05 and 8.07 ppm (2H); 4-H, d, 8.41 ppm (1H) J_{3-4} = 9 Hz. ^{1}H nmr of **26** ($CDCl_3$): 7-CH_3 + 8-CH_3, s, 2.57 ppm (6H); 3-CH_3, s, 2.91 ppm (3H); 3-H, d, 7.54 ppm (1H) J_{2-3} = 4 Hz; 6-H + 9-H, 2s, 7.97 and 8.04 ppm (2 × 1H); 2-H, d, 9.13 ppm (1H) J_{2-3} = 4 Hz.

Reaction of 2 with methylmagnesium chloride: preparation of 28

With the same procedure as for **1** but after stirring for 1.5 h, 158 mg of 1,7,8-trimethylpyrido[3,4-*b*]quinoxaline, **28**, was obtained; mp 180°C dec. ^{1}H nmr ($CDCl_3$): 7-CH_3 + 8-CH_3, s, 2.59 ppm (6H); 1-CH_3, s, 3.21 ppm (3H); 4-H, d, 7.85 ppm (J = 6 Hz) (1H); 6-H + 9-H, 2s, 7.97 and 8.07 ppm (2 × 1H); 3-H, d, 8.61 ppm (J = 6 Hz) (1H).

Can. J. Chem. Downloaded from www.nrcresearchpress.com by 93.93.197.157 on 09/07/12
For personal use only.

1. (*a*) J. ARMAND, L. BOULARES, C. BELLEC, and J. PINSON. Can. J. Chem. **60**, 2797 (1982); **62**, 1028 (1984); (*b*) J. ARMAND and J. PINSON. Physical methods in heterocyclic chemistry. John Wiley, New York. 1984. p. 427.
2. J. ARMAND, K. CHEKIR, N. PLE, G. QUEGUINER, and M. P. SIMONNIN. J. Org. Chem. **46**, 4754 (1981) and references therein.
3. R. G. R. BACON and S. D. HAMILTON. J. Chem. Soc. Perkin I, 1965 (1974).
4. E. LIPPMANN and D. STEINER. Z. Chem. **22**, 256 (1982).
5. V. PETROW, J. SAPER, and B. STURGEON. J. Chem. Soc. 2540 (1949).
6. J. ARMAND, K. CHEKIR, and J. PINSON. Can. J. Chem. **56**, 1804 (1978).
7. D. T. SAWYER and R. Y. KOMAI. Anal. Chem. **44**, 715 (1972).
8. (*a*) D. N. BAILEY, D. M. HERCULES, and D. K. ROE. J. Electrochem. Soc. **116**, 190 (1969); (*b*) R. C. KAYE and H. E. STONEHILL. J. Chem. Soc. 3240 (1952).
9. A. ALBERT, R. GOLDACRE, and J. PHILLIPS. J. Chem. Soc. 2240 (1948).
10. J. M. COSMAO, N. COLLIGNON, and G. QUEGUINER. Can. J. Chem. **60**, 2785 (1982).
11. A. ALBERT and G. B. BARLIN. J. Chem. Soc. C, 5737 (1963).
12. L. BIRKOFER and A. BIRKOFER. Ber. **85**, 286 (1952).
13. D. BOUTTE, G. QUEGUINER, and P. PASTOUR. C.R. Acad. Sci. Ser. C, **273**, 1529 (1971).
14. N. VINOT and P. MAITTE. Bull. Soc. Chim. Fr. 3100 (1973).
15. F. BOHLMANN. Ber. **85**, 390 (1952).
16. R. C. BUGLE and R. A. OSTERYOUNG. J. Org. Chem. **44**, 1719 (1979).
17. N. VINOT and P. MAITTE. Bull. Soc. Chim. Fr. 251 (1976).
18. L. HORNER and K. STURM. Ann. Chem. **597**, 1 (1955).

Can. J. Chem. Downloaded from www.nrcresearchpress.com by 93.93.197.157 on 09/07/12
For personal use only.

Thiophenophane–metal complexes. I. Preparation, X-ray structure, and cyclic voltammetry of 2,5,8-trithia[9](2,5)thiophenophane, L, and of its metal complex cation bis(2,5,8-trithia[9](2,5)thiophenophane-S^2,S^3]copper(I), $[CuL_2]^+$ [1]

C. Robert Lucas,[2] Liu Shuang, and Michael J. Newlands
Department of Chemistry, Memorial University of Newfoundland, St. John's, Nfld., Canada A1B 3X7

and

Jean-Pierre Charland and Eric J. Gabe
Division of Chemistry, National Research Council of Canada, Ottawa, Ont., Canada K1A 0R9

Received October 5, 1987

C. Robert Lucas, Liu Shuang, Michael J. Newlands, Jean-Pierre Charland, and Eric J. Gabe. Can. J. Chem. **66**, 1506 (1988).

Preparation of the thiophenophane $C_{10}H_{14}S_4$, (L), and syntheses of its copper(I) complex $[CuL_2]ClO_4$ or $[CuL_2]BF_4$ are described. The ^{13}C and ^1H nmr spectra of L and the ir spectra (4000–200 cm^{-1}) of $[CuL_2]ClO_4$ and $[CuL_2]BF_4$ are reported. The molecular structures of L and $[CuL_2]ClO_4$ have been determined. For L: space group $P2_1/a$, a = 7.9347(2) Å, b = 18.7479(3) Å, c = 8.8596(2) Å, β = 108.446(2)°, Z = 4, R_f = 0.048, and R_w = 0.034. For $[CuL_2]ClO_4$: space group $P2_1/c$, a = 9.4363(1) Å, b = 18.2768(3) Å, c = 16.2157(3) Å, β = 96.520(2)°, Z = 4, R_f = 0.056, and R_w = 0.037. The Cu(I) complex has distorted tetrahedral coordination geometry; its perchlorate anion is non-coordinating and disordered. The Cu—S bond lengths lie in the range 2.301–2.392 Å and the S—Cu—S angles in the range 92.43–150.26°. Cyclic voltammetry of $[CuL_2]ClO_4$ (10^{-3} mol/L in dimethylsulfoxide, 0.1 mol/L Et_4NClO_4, glassy carbon working electrode, platinum counter electrode, aqueous saturated calomel reference electrode against which the ferrocenium/ferrocene potential under similar conditions was 400 mV) shows a quasi-reversible oxidation ($E_{1/2}$ = 0.150 V, ΔE_p = 170 mV at 50 mV/s). Thiophene's effect as a sub-unit in a small macrocycle upon properties of the latter is discussed.

C. Robert Lucas, Liu Shuang, Michael J. Newlands, Jean-Pierre Charland et Eric J. Gabe. Can. J. Chem. **66**, 1506 (1988).

On décrit la préparation du thiophénophane $C_{10}H_{14}S_4$, (L), ainsi que la synthèse de ses complexes du cuivre(I), $[CuL_2]ClO_4$ ou $[CuL_2]BF_4$. On rapporte les spectres rmn du ^{13}C et du ^1H du ligand L ainsi que les spectres ir (4000–200 cm^{-1}) des complexes $[CuL_2]ClO_4$ et $[CuL_2]BF_4$. On a déterminé les structures moléculaires du ligand L et du complexe $[CuL_2]ClO_4$. Pour le ligand L : groupe d'espace $P2_1/a$, a = 7,9347(2), b = 18,7479(3) et c = 8,8596(2) Å, β = 108,446(2)°, Z = 4, R_f = 0,048 et R_w = 0,034. Pour le complexe $[CuL_2]ClO_4$: groupe d'espace $P2_1/c$, a = 9,4363(1), b = 18,2768(3) et c = 16,2157(3) Å, β = 96,520(2)°, Z = 4, R_f = 0,056 et R_w = 0,037. Le complexe du Cu(I) possède une géométrie de coordination tétraédrique; son anion perchlorate ne donne pas de coordination et il est désordonné. Les longueurs des liaisons Cu—S varient de 2,301 à 2,392 Å et les angles S—Cu—S de 92,43 à 150,26°. La voltammétrie cyclique du complexe $[CuL_2]ClO_4$ (10^{-3} mol/L dans le diméthylsulfoxyde, Et_4NClO_4 à 0,1 mol/L, électrode de carbone vitreux, contre-électrode de platine et électrode de référence de calomel saturé en solution aqueuse contre laquelle le potentiel du couple ferrocénium/ferrocène était de 400 mV dans des conditions semblables) présente une oxydation quasi-réversible ($E_{1/2}$ = 0,150 V, ΔE_p = 170 mV à 50 mV/s). On discute de l'effet du thiophène, agissant comme sous-unité d'un petit macrocycle, sur les propriétés de ce dernier.

[Traduit par la revue]

Introduction

Metal complexes of thioether ligands have been studied for several years (1) but recently there has been quickening interest in them due in part to the recognition of coordinated methionine sulfur in "blue" copper proteins (2) and in part to an enhanced awareness of applications for sulfur compounds in a variety of technologies and medicine (3). Our interest in these molecules is an extension of investigations over several years (4–6) into the organometallic, coordination, and organic chemistry of sulfur compounds.

Evidence concerning the preparation, structure, stability, and redox properties of macrocyclic thioether complexes is accumulating (7–9) and it is of interest to determine the effects of a thiophene sub-unit on these ligands and their complexes. This paper reports the first results of such a study and deals with the preparation, structure and some properties of the macrocycle L (Fig. 1) and its copper(I) complex ion $[CuL_2]^+$ (Fig. 2).

Experimental

Reagents were obtained from the Aldrich Chemical Co. Inc. or from Morton Thiokol, Alfa Products Inc. and were used without further purification. Spectroscopic data were obtained using the following instruments: ir, Perkin Elmer Model 283; nmr, General Electric 300-NB; mass spectra, VG micromass 7070 HS; cyclic voltammetry, BAS CV27 Voltammograph and a Houston 2000 Omnigraph X-Y recorder. Electrochemical measurements were carried out under a nitrogen atmosphere and at room temperature in dimethyl sulfoxide. Solution concentrations were 10^{-3} mol/L in complex and 0.1 mol/L in supporting electrolyte (tetraethylammonium perchlorate). Voltammograms were recorded using a glassy carbon working electrode, a platinum counter electrode and an aqueous saturated calomel reference electrode checked periodically relative to a 1.0×10^{-3} mol/L solution of ferrocene in dimethylsulfoxide containing 0.1 mol/L Et_4NClO_4 for which the ferrocenium/ferrocene reduction potential was 400 mV.

[1] NRCC No. 28785.

[2] To whom all correspondence should be addressed.

Can. J. Chem. Downloaded from www.nrcresearchpress.com by 93.93.197.157 on 09/07/12
For personal use only.

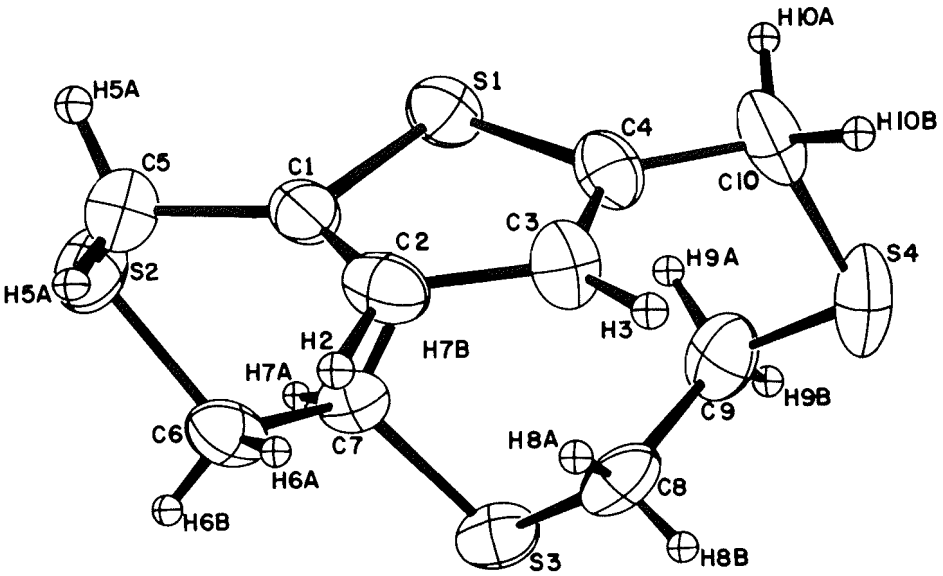

FIG. 1. ORTEP (25) drawing of L ($C_{10}H_{14}S_4$).

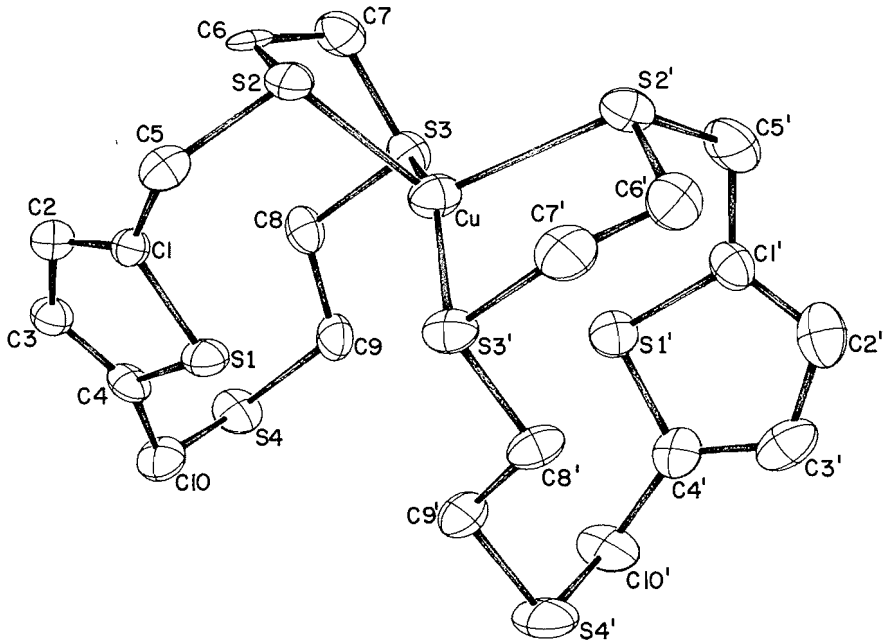

FIG. 2. ORTEP drawing of $[CuL_2]^+$.

The reference electrode was separated from the bulk of the solution by a porous Vycor tube. Junction potential corrections were not used. X-ray diffraction data were collected using an Enraf Nonius CAD-4 diffractometer. Analyses were performed by Canadian Microanalytical Service Ltd.

Preparative

(a) $C_{10}H_{14}S_4$ (ligand L)

Sodium (1.15 g, 50.0 mmol) was dissolved in commercial absolute ethanol (500 mL) under an atmosphere of dry nitrogen and 2-mercaptoethyl sulfide (3.85 g, 24.9 mmol) was added. The mixture was refluxed for 10 min. Over 8 h, a solution of purified 2,5-bis(chloromethyl)thiophene (4.52 g, 25.0 mmol) (10) in commercial absolute ethanol (200 mL) was added dropwise with stirring to the refluxing mixture. (It is important that the reagents for this preparation be pure or the yield will be low. Purification of 2,5-bis(chloromethyl)thiophene can be achieved by washing the crude brown liquid with saturated sodium carbonate solution and then water until the washings are neutral, drying over anhydrous $MgSO_4$ and recrystallizing from petroleum ether.) Refluxing and stirring were continued for a further 4 h. Volatiles were removed on a rotary evaporator and the residue was taken up in CH_2Cl_2, washed with water several times, dried over anhydrous $CaCl_2$ and taken to dryness. The yellow solid was recrystallized twice from benzene to give white needles, mp 151–153°C. Yield 3.6 g (55%). Mass spectrum: major peaks at m/e = 262 and 110 corresponding to $[C_{10}H_{14}S_4]^+$ and $[C_6H_6S]^+$. Nuclear magnetic resonance: ($CDCl_3$, ppm from TMS int. std., assignments based on $^{13}C-^1H$ heteronuclear correlation and attached proton test, position identification from Fig. 1), ^{13}C: 140.2 C1—C4, 128.1 C2—C3, 31.6 C7—C8, 31.4 C5—C10, 30.2 C6—C9; ^1H: 6.92(s) C2—C3 (2H), 3.95(s) C5—C10

Can. J. Chem. Downloaded from www.nrcresearchpress.com by 93.93.197.157 on 09/07/12
For personal use only.

Can. J. Chem. Downloaded from www.nrcresearchpress.com by 93.93.197.157 on 09/07/12
For personal use only.

TABLE 1. Crystal data for $[CuL_2]ClO_4$ and for L

Parameter	Value	
	L	$[CuL_2]ClO_4$
Empirical formula	$C_{10}H_{14}S_8$	$C_{20}H_{28}ClCuO_4S_8$
Formula weight	263.27	687.44
Crystal dimensions, mm	0.30 × 0.30 × 0.50	0.20 × 0.20 × 0.30
Space group	Monoclinic $P2_1/a$	Monoclinic $P2_1/c$
a, Å	7.9347(2)[a]	9.4363(1)
b, Å	18.7479(3)	18.2768(3)
c, Å	8.8596(2)	16.2157(3)
β, deg	108.446(2)	96.520(2)
Z (molecules/cell)	4	4
F(000) electrons	608.28	1059.89
Volume, Å^3	1254.50	2777.95
d_{calc}, g/cm^3	1.394	1.644
Linear absolute coefficient, mm^{-1}	0.70	1.29
Radiation (MoKα), Å	λ = 0.70930	λ = 0.70930
2θ(max), deg	49	44.9
No. reflections measured	2182	4151
No. of unique reflections	2174	3589
No. unique reflections, $I_{net} > n\sigma(I_{net})$	1337 (n = 3.0)	2539 (n = 2.5)
Last least-square cycle calculated with	28 atoms	65 atoms
	184 parameters	411 parameters
	1337 reflections	2539 reflections
R_f (sig. refl.)	0.048[b]	0.056[b]
R_w (sig. refl.)	0.034[c]	0.037[c]
Goodness of fit (last cycle)	2.407[d]	2.997[d]
R_f (all refl.)	0.080[b]	0.081[b]
R_w (all refl.)	0.036[c]	0.039[c]
Maximum shift/σ	0.002	0.394
Last D-map:		
deepest hole, e/Å^3	−0.260	−0.990
highest peak, e/Å^3	0.310	0.970
Secondary extinction coefficient	0.581149	
σ	0.051029	

[a]Throughout this article, esd's are in parentheses and refer to the last digit printed.
[b]$R_f = \Sigma||F_o| - |F_c||/\Sigma|F_o|$.
[c]$R_w = [\Sigma w(|F_o| - |F_c|)^2/\Sigma(w|F_o|)^2]^{1/2}$ where $w = 1/\sigma^2 I$.
[d]Goodness of fit = $[\Sigma w(|F_o| - |F_c|)^2/(\text{number of reflections} - \text{number of parameters.})]^{1/2}$.

(4H), 2.55(t) C9—C6 (4H) J = 8.4 Hz, 2.22(t) C7—C8 (4H) J = 8.4 Hz.

(b) $[CuL_2]ClO_4$

Method A

Solutions of ligand L (300 mg, 1.14 mmol) in CH_2Cl_2 (5 mL) and of $Cu(ClO_4)_2 \cdot 6H_2O$ (185 mg, 0.500 mmol) in acetonitrile/commercial absolute ethanol (1:1) (15 mL) were mixed. The resulting green solution was filtered and left to stand in a 100 mL beaker for one week. The pale yellow crystals were collected by filtration, washed with dichloromethane and diethyl ether, and dried in air. Melting point 170°C (dec). Yield 175 mg (51%). Infrared: (Nujol mull) 1412(s), 1246(m), 1192(m), 1180(w), 1135(w), 1075(vs), 1021(m), 1016(m), 910(vw), 900(vw), 870(w), 824(s), 810(s), 763(w), 691(s), 686(s), 660(m), 617(s), 570(w), 492(w), 446(vw), 410(w), 348(vw), 315(vw), 272(w), 265(w), 250(w) cm^{-1}. *Anal.* calcd. for $C_{20}H_{28}ClCuO_4S_8$: C 34.9, H 4.10, Cu 9.24, S 37.3; found: C 34.9, H 4.10, Cu 9.05, S 35.4.

Method B

Cuprous chloride (25 mg, 0.25 mmol) was dissolved in acetonitrile (10 mL) and a solution of $AgClO_4$ (52 mg, 0.25 mmol) in acetonitrile (5 mL) was added. The mixture was filtered and to the filtrate was added a solution of ligand L (131 mg, 0.500 mmol) in CH_2Cl_2 (5 mL). The resulting suspension was filtered and the filtrate was left to evaporate slowly, giving pale yellow crystals identical to those produced by Method A as shown by ir, mp, and elemental analysis. Yield 125 mg (73%).

(c) $[CuL_2]BF_4$

Preparations of this compound are analogous to those for the perchlorate salt already described, although the yield by Method A is low. By Method B, the yield is 115 mg (68%). Melting point 165°C (dec). Infrared (Nujol mull) similar to perchlorate salt except that bands at 1075 and 617 cm^{-1} have been replaced by bands at 1050(vs) and 521(w) cm^{-1}. *Anal.* calcd. for $C_{20}H_{28}BCuF_4S_8$: C 34.3, H 3.84; found: C 34.0, H 3.81.

X-ray studies

A summary of crystal data for L and for $[CuL_2]ClO_4$ is in Table 1. The diffraction intensities were collected at 295 K with graphite monochromatized MoKα radiation using the θ/2θ scan technique with profile analysis (11) at a scan speed of 4°/min. Three standards were measured after every 100 reflections and no significant crystal decay was detected. Space groups were uniquely determined by systematic absences. Unit cell parameters in Table 1 were obtained by a least-squares refinement of the setting angles for 21 reflections (60° ≤ 2θ ≤ 89°) for $[CuL_2]ClO_4$ and for 46 reflections (50° ≤ 2θ ≤ 79°) for

TABLE 2. Selected distances (Å) and angles (deg) in L

Bond	Distances	Bonds	Angle
S(1)—C(1)	1.737(5)	C(1)—S(1)—C(4)	91.7(3)
S(1)—C(4)	1.721(5)	C(5)—S(2)—C(6)	101.7(3)
S(2)—C(5)	1.805(8)	C(7)—S(3)—C(8)	101.2(3)
S(2)—C(6)	1.816(7)	C(9)—S(4)—C(10)	102.4(3)
S(3)—C(7)	1.814(6)	S(1)—C(1)—C(2)	109.8(4)
S(3)—C(8)	1.800(7)	S(1)—C(1)—C(5)	120.6(5)
S(4)—C(9)	1.800(8)	C(2)—C(1)—C(5)	129.5(5)
S(4)—C(10)	1.840(8)	C(1)—C(2)—C(3)	115.2(5)
C(1)—C(2)	1.344(9)	C(1)—C(2)—H(2)	122(3)
C(1)—C(5)	1.485(8)	C(3)—C(2)—H(2)	120(3)
C(2)—C(3)	1.406(9)	C(2)—C(3)—C(4)	111.6(5)
C(2)—H(2)	0.89(4)	C(2)—C(3)—H(3)	128(3)
C(3)—C(4)	1.363(8)	C(4)—C(3)—H(3)	120(3)
C(3)—H(3)	0.94(5)	S(1)—C(4)—C(3)	111.6(4)
C(4)—C(10)	1.505(8)	S(1)—C(4)—C(10)	119.2(4)
C(5)—H(5A)	0.94(5)	C(3)—C(4)—C(10)	128.8(5)
C(5)—H(5B)	0.88(5)	S(2)—C(5)—C(1)	115.3(5)
C(6)—C(7)	1.529(9)	S(2)—C(5)—H(5A)	96(3)
C(6)—H(6A)	1.04(4)	S(2)—C(5)—H(5B)	104(3)
C(6)—H(6B)	0.89(4)	C(1)—C(5)—H(5A)	112(3)
C(7)—H(7A)	1.19(5)	C(1)—C(5)—H(5B)	104(3)
C(7)—H(7B)	1.10(4)	H(5A)—C(5)—H(5B)	123(5)
C(8)—C(9)	1.53(1)	S(2)—C(6)—C(7)	112.2(4)
C(8)—H(8A)	0.92(5)	S(2)—C(6)—H(6A)	104(2)
C(8)—H(8B)	0.85(5)	S(2)—C(6)—H(6B)	106(3)
C(9)—H(9A)	1.02(5)	C(7)—C(6)—H(6A)	109(2)
C(9)—H(9B)	0.77(4)	C(7)—C(6)—H(6B)	114(3)
C(10)—H(10A)	1.02(5)	H(6A)—C(6)—H(6B)	109(4)
C(10)—H(10B)	1.18(6)	S(3)—C(7)—C(6)	111.8(4)
S(1)—S(3)	4.579(3)	S(3)—C(7)—H(7A)	110(2)
S(2)—S(4)	6.662(3)	S(3)—C(7)—H(7B)	109(2)
		C(6)—C(7)—H(7A)	107(2)
		C(6)—C(7)—H(7B)	114(2)
		H(7A)—C(7)—H(7B)	104(3)
		S(3)—C(8)—C(9)	114.2(5)
		S(3)—C(8)—H(8A)	115(3)
		S(3)—C(8)—H(8B)	110(3)
		C(9)—C(8)—H(8A)	109(3)
		C(9)—C(8)—H(8B)	101(3)
		H(8A)—C(8)—H(8B)	104(4)
		S(4)—C(9)—C(8)	114.7(5)
		S(4)—C(9)—H(9A)	109(3)
		S(4)—C(9)—H(9B)	101(3)
		C(8)—C(9)—H(9A)	114(3)
		C(8)—C(9)—H(9B)	112(4)
		H(9A)—C(9)—H(9B)	103(4)
		S(4)—C(10)—C(4)	112.8(4)
		S(4)—C(10)—H(10A)	121(3)
		S(4)—C(10)—H(10B)	95(3)
		C(4)—C(10)—H(10A)	108(3)
		C(4)—C(10)—H(10B)	104(3)
		H(10A)—C(10)—H(10B)	113(4)

L. Lorentz and polarization factors were applied but no corrections were made for absorption.

The structures were solved with MULTAN (12) plus a difference Fourier map and refined by full-matrix least-squares with counting statistics weights. H-atom positions were calculated but their parameters were not refined. All heavier atoms were refined anisotropically. All calculations were performed with the NRC VAX Crystal Structure programs (13). Scattering factors were taken from the International tables for X-ray crystallography (14). The final atomic positional parameters, the equivalent isotropic temperature factors and important bond lengths are listed in Tables 2–5. Anisotropic thermal parameters, a full listing of bond lengths and bond angles, and final structure factors are available as supplementary data.[3] Figures 1 and 2 show the molecules and the atomic numbering schemes. In $[CuL_2]ClO_4$, three oxygen atoms of each ClO_4^- ion are disordered. Two distinct positions

[3]A complete set of data may be purchased from the Depository of Unpublished Data, CISTI, National Research Council of Canada, Ottawa, Ont., Canada K1A 0S2.

Can. J. Chem. Downloaded from www.nrcresearchpress.com by 93.93.197.157 on 09/07/12
For personal use only.

Can. J. Chem. Downloaded from www.nrcresearchpress.com by 93.93.197.157 on 09/07/12
For personal use only.

TABLE 3. Positional and thermal parameters for $L(C_{10}H_{14}S_4)$

Atom	X	Y	Z	B_{iso}[a]
S1	0.9406(2)	0.22119(8)	0.8252(2)	3.83(7)
S2	1.0287(2)	0.15259(9)	1.2073(2)	5.33(9)
S3	0.6086(2)	0.02644(8)	0.8642(2)	4.92(9)
S4	0.6356(2)	0.1335(1)	0.4234(2)	6.8(1)
C1	1.1173(7)	0.1672(3)	0.9287(6)	3.5(3)
C2	1.1730(8)	0.1286(3)	0.8257(7)	3.9(3)
C3	1.0756(7)	0.1385(3)	0.6643(7)	3.9(3)
C4	0.9430(7)	0.1872(3)	0.6453(6)	3.8(3)
C5	1.1884(9)	0.1701(4)	1.1051(8)	4.9(4)
C6	0.9082(9)	0.0770(3)	1.0962(8)	4.4(3)
C7	0.7143(8)	0.0951(3)	1.0071(7)	4.0(3)
C8	0.6804(9)	0.0510(4)	0.6980(9)	4.7(4)
C9	0.5730(9)	0.1116(4)	0.5961(9)	5.3(4)
C10	0.7952(9)	0.2066(4)	0.4966(7)	5.2(4)
H2	1.246(6)	0.092(2)	0.857(6)	4(1)
H3	1.091(6)	0.116(3)	0.575(5)	5(1)
H5A	1.218(7)	0.217(3)	1.143(6)	6(2)
H5B	1.264(7)	0.134(3)	1.131(6)	5(2)
H6A	0.974(5)	0.066(2)	1.014(5)	3(1)
H6B	0.924(6)	0.041(2)	1.165(5)	4(1)
H7A	0.640(6)	0.101(3)	1.104(5)	6(1)
H7B	0.697(5)	0.147(2)	0.946(5)	4(1)
H8A	0.800(6)	0.061(2)	0.721(5)	4(1)
H8B	0.662(7)	0.017(3)	0.631(6)	5(2)
H9A	0.569(6)	0.157(2)	0.658(5)	5(1)
H9B	0.474(6)	0.102(3)	0.559(5)	3(1)
H10A	0.754(7)	0.257(3)	0.509(6)	6(2)
H10B	0.861(7)	0.201(3)	0.395(6)	9(2)

[a] B_{iso} is the mean of the principal axes of the thermal ellipsoid.

of each of these three oxygen atoms were refined with isotropic thermal parameters and occupancy factors of 0.5.

Results and discussion

Traditional synthetic methods for macrocyclic compounds possessing heterocyclic sub-units have been reviewed (15). Synthesis of ligand L was carried out in 55% yield by a traditional high dilution S_N2 cyclization (reaction [1]). Ring closure

[1] 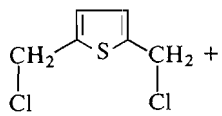

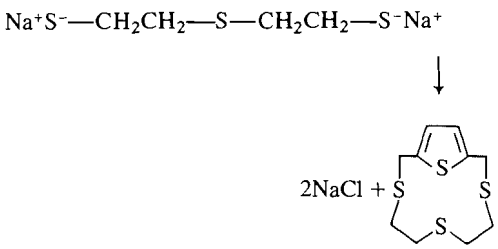

to a 12-membered macrocycle is the preferred process in ethanol for no trace of the 24-membered macrocycle containing two thiophene sub-units was detected. Successful cyclization, however, depends upon the purity of the reagents (see Experimental) and even small amounts of impurities seem to have a significant, adverse effect on the yield. Although the preparation of this compound and a complex of it with copper(II) have been reported (16), there is some discrepancy between the properties of that substance and the material described herein.

TABLE 4. Selected distances (Å) and angles (deg) in $[CuL_2]^+$

Bond	Distances	Bonds	Angle
Cu—S(2)	2.359(3)	S(2)—Cu—S(3)	92.84(9)
Cu—S(3)	2.307(3)	S(2)—Cu—S(2′)	109.49(9)
Cu—S(2′)	2.392(3)	S(2)—Cu—S(3′)	105.22(9)
Cu—S(3′)	2.301(3)	S(3)—Cu—S(2′)	103.76(9)
S(1)—C(1)	1.738(9)	S(3)—Cu—S(3′)	150.3(1)
S(1)—C(4)	1.727(9)	S(2′)—Cu—S(3′)	92.43(9)
S(2)—C(5)	1.83(1)	C(1)—S(1)—C(4)	91.8(5)
S(2)—C(6)	1.80(1)	Cu—S(2)—C(5)	108.7(3)
S(3)—C(7)	1.81(1)	Cu—S(2)—C(6)	98.6(4)
S(3)—C(8)	1.82(1)	C(5)—S(2)—C(6)	101.5(5)
S(4)—C(9)	1.82(1)	Cu—S(3)—C(7)	96.2(4)
S(4)—C(10)	1.83(1)	Cu—S(3)—C(8)	114.0(3)
S(1′)—C(1′)	1.72(1)	C(7)—S(3)—C(8)	100.7(5)
S(1′)—C(4′)	1.71(1)	C(9)—S(4)—C(10)	101.9(5)
S(2′)—C(5′)	1.83(1)	C(1′)—S(1′)—C(4′)	92.8(5)
S(2′)—C(6′)	1.80(1)	Cu—S(2′)—C(5′)	111.7(4)
S(3′)—C(7′)	1.80(1)	Cu—S(2′)—C(6′)	98.2(4)
S(3′)—C(8′)	1.81(1)	C(5′)—S(2′)—C(6′)	101.5(5)
S(4′)—C(9′)	1.814(9)	Cu—S(3′)—C(7′)	95.6(4)
S(4′)—C(10′)	1.83(1)	Cu—S(3′)—C(8′)	113.5(4)
C(1)—C(2)	1.34(1)	C(7′)—S(3′)—C(8′)	100.2(5)
C(1)—C(5)	1.50(1)	C(9′)—S(4′)—C(10′)	103.1(5)
C(2)—C(3)	1.43(1)	S(1)—C(4)—C(3)	111.7(7)
C(3)—C(4)	1.38(1)	S(1)—C(4)—C(10)	119.4(8)
C(4)—C(10)	1.48(1)	C(3)—C(4)—C(10)	128.5(9)
C(6)—C(7)	1.49(2)	S(2)—C(5)—C(1)	114.8(6)
C(8)—C(9)	1.53(2)	S(2)—C(6)—C(7)	114.3(8)
C(1′)—C(2′)	1.36(2)	S(3)—C(7)—C(6)	115.1(7)
C(1′)—C(5′)	1.50(2)	S(3)—C(8)—C(9)	110.4(7)
C(2′)—C(3′)	1.44(2)	S(4)—C(9)—C(8)	112.9(7)
C(3′)—C(4′)	1.34(2)	S(4)—C(10)—C(4)	114.5(7)
C(4′)—C(10′)	1.50(2)	S(1′)—C(1′)—C(2′)	110.4(8)
C(6′)—C(7′)	1.49(2)	C(2′)—C(1′)—C(5′)	127(1)
C(8′)—C(9′)	1.53(2)	S(1′)—C(4′)—C(3′)	111.1(8)
		S(1′)—C(4′)—C(10′)	119.3(8)
		C(3′)—C(4′)—C(10′)	129(1)
		S(2′)—C(5′)—C(1′)	114.9(7)
		S(2′)—C(6′)—C(7′)	113.8(8)
		S(3′)—C(7′)—C(6′)	115.9(8)
		S(1)—C(1)—C(5)	120.8(7)
		C(2)—C(1)—C(5)	128.5(9)
		S(3′)—C(8′)—C(9′)	110.8(7)
		S(4′)—C(9′)—C(8′)	112.2(7)
		S(4′)—C(10′)—C(4′)	113.5(7)

It has been shown (17) that cavity size and orientation of the non-bonding pairs of electrons on the donor atoms of a macrocyclic ligand are factors of major importance to the formation, stability, and properties of its complexes. Conformational changes required in a ligand upon complex formation or upon a change in oxidation state of a coordinated metal atom reveal themselves as kinetic barriers which must be overcome or as thermodynamic penalties which must be paid during these processes. Inclusion of a thiophene sub-unit in a macrocycle should impose limitations on the possible orientations of donor atom electron pairs and on the size and shape of the cavity. The effect of these limitations on the molecular structures of the free ligand (Fig. 1) and a copper(I) complex (Fig. 2) were examined by X-ray methods.

The free ligand consists of a puckered polythioether chain

TABLE 5. Positional and thermal parameters for $[CuL_2]ClO_4$

Atom	X	Y	Z	B_{iso}[a]
Cu	0.7698(1)	0.04730(6)	0.78953(7)	3.54(6)
Cl1	0.0861(4)	0.1785(2)	0.5577(2)	5.6(2)
OClO1	0.087(2)	0.2553(9)	0.554(1)	7.0(4)
OClO2	0.078(1)	0.1626(5)	0.4771(6)	12.8(3)
OClO3	0.064(3)	0.130(1)	0.616(1)	13.2(7)
OClO5	0.182(2)	0.131(1)	0.596(1)	9.4(5)
OClO6	−0.066(3)	0.153(1)	0.554(2)	17.1(9)
OClO7	0.239(3)	0.202(1)	0.581(1)	12.9(7)
OClO8	0.020(2)	0.237(1)	0.591(1)	8.3(5)
S1	0.5015(3)	0.0201(1)	0.6379(1)	3.3(1)
S2	0.8854(2)	−0.0108(1)	0.6857(1)	3.0(1)
S3	0.7134(3)	−0.0624(1)	0.8482(1)	3.3(1)
S4	0.2541(3)	−0.0921(2)	0.7624(2)	4.1(1)
S1′	0.5875(3)	0.0875(1)	0.9513(2)	3.6(1)
S2′	0.9441(3)	0.0998(1)	0.8909(2)	3.6(1)
S3′	0.7021(3)	0.1600(1)	0.7356(1)	3.4(1)
S4′	0.3047(3)	0.2158(2)	0.8417(2)	5.05(2)
C1	0.6238(9)	−0.0289(5)	0.5873(5)	2.9(5)
C2	0.567(1)	−0.0923(6)	0.5582(6)	3.8(6)
C3	0.425(1)	−0.1057(6)	0.5767(6)	3.3(5)
C4	0.3759(9)	−0.0486(5)	0.6212(5)	3.2(5)
C5	0.774(1)	−0.0021(6)	0.5867(6)	3.1(5)
C6	0.853(1)	−0.1045(6)	0.7128(7)	3.4(6)
C7	0.846(1)	−0.1167(6)	0.8029(7)	3.8(6)
C8	0.550(1)	−0.1038(6)	0.7995(6)	3.3(5)
C9	0.421(1)	−0.0572(6)	0.8151(6)	3.6(6)
C10	0.244(1)	−0.466(7)	0.6624(6)	4.1(6)
C1′	0.739(1)	0.1288(5)	0.9999(5)	3.4(5)
C2′	0.705(1)	0.1931(7)	1.0346(7)	4.3(7)
C3′	0.554(1)	0.2087(6)	1.0211(6)	4.2(6)
C4′	0.480(1)	0.1576(5)	0.9758(5)	3.5(5)
C5′	0.885(1)	0.0984(7)	0.9949(6)	4.6(6)
C6′	0.917(1)	0.1945(6)	0.8625(7)	4.4(6)
C7′	0.866(1)	0.2059(6)	0.7731(7)	4.3(6)
C8′	0.578(1)	0.2077(6)	0.7941(7)	3.5(6)
C9′	0.429(1)	0.1749(6)	0.7773(6)	3.9(6)
C10′	0.329(1)	0.1604(7)	0.9363(7)	4.4(6)

[a] B_{iso} is the mean of the principal axes of the thermal ellipsoid.

extending in space at roughly 60° to the plane defined by the thiophene ring. The macrocyclic ring's cavity is roughly triangular with the S2—S4 distance (6.662 Å) representing the base and the S3—S1 distance (4.579 Å) representing the height of the triangle. These dimensions may be compared with those of the cavities in the series of complexes of the type $Cu^{II}([n]aneS_4)^{2+}$ where n = 12 to 16 (18). In that series a ring of at least 14 members was found necessary to achieve a cavity of 4.61 Å which was the minimum that would accommodate Cu(II) co-planar with the four S-donors. In its solid state conformation, ligand L has no capability as a macrocyclic ligand not because of the size of its cavity, however, but because its cavity is shielded on one side by hydrogens on C9 and C7 and on the other by hydrogens on C8 and C6. Furthermore, all lone pairs of electrons on all sulfur atoms are exocyclic and are oriented in such a way that no two sites may bond to the same metal atom simultaneously. As a ligand in solution, the molecule might coordinate in a monodentate manner at several sites and so form a polymer, or a conformational change might occur so that the ligand becomes multidentate.

From models it can be seen that rigidity of the C10—thiophene—C5 portion of the molecule prevents conformations in which more than two thioether sulfurs may be coordinated simultaneously to the same metal atom. Thus, the solid state structure of ligand L suggests that its complexes should be polymeric if the barrier to conformational rearrangement is large. If the barrier is small, complex formation should be accompanied by conformational change to achieve chelate formation and in both cases, the possibility of coordination by thiophene sulfur must at least be considered although such behaviour is not common.

In acetonitrile mixed with either ethanol or dichloromethane, ligand L forms a complex of copper(I), $[CuL_2]ClO_4$ in which conformational change, mainly involving inversion at S3 and C8 of the free ligand has occurred. After the inversions, electron pairs of S3 and S2 are correctly oriented to form a five-membered chelate ring with copper (Fig. 2). The complex can be prepared directly from copper(I) salts or by alcohol reduction of copper(II) salts in presence of the ligand.

The copper atom is coordinated by two pairs of thioether sulfurs, each pair lying in a separate ligand molecule so that the coordination geometry about copper is distorted tetrahedral. When two coordinated sulfurs are in the same ligand molecule, the S—Cu—S angle is compressed to ~92° (Table 3) as is often found in 5-membered chelate rings of copper(I) complexes (19, 20). When the sulfurs are in different ligand molecules, the S—Cu—S angles are close to the tetrahedral value except for one which is opened to ~150° to alleviate crowding of hydrogens on C8, C8′, C9, and C9′, all of which have C—H vectors pointing into the middle of the ion's structure. The Cu—S bond lengths vary between 2.301 and 2.392 Å with an average length of 2.340 Å. These results may be compared to those from the cation $[Cu^{I}([15]aneS_5)]^{+}$ (19) which range from 2.243 to 2.338 Å with an average of 2.286 Å or those from bis(3,6-dithiaoctane)copper(I) tetrafluoroborate (20) which range from 2.280 to 2.318 Å with an average of 2.303 Å. There are no major changes in bond lengths within ligand L as a result of its coordination to copper and the greatest changes in bond angles are those associated with formation of the chelate ring. The failure of ligand L to use all its possible coordination sites is reminiscent of the behaviour of $[14]aneS_4$ with copper(I) (21) or mercury(II) (22). In the case of $[Cu([14]aneS_4)]^{+}$, only three sulfurs are used because of the strain that would be introduced if all four were coordinated to one copper atom while for $(HgCl_2)_2([14]aneS_4)$ only two sulfurs coordinate to each mercury atom due to the presence of chloride which forms stronger bonds than sulfur to mercury(II). In the case of ligand L, the use of all three thioether sulfurs is precluded by the orientation of their non-bonding electron pairs (*vide supra*).

The ir spectrum of the complex as its perchlorate has a very strong band at 1075 cm^{-1} and a strong band at 617 cm^{-1} corresponding to $\nu 3$ and $\nu 4$, respectively, of ionic perchlorate. In the analogous tetrafluoroborate, these bands vanish and are replaced by equivalent ones at 1050 and 521 cm^{-1}. Between 450 and 200 cm^{-1}, only weak bands at 446, 410, 348, 315, 265, and 250 cm^{-1}, also found in the free ligand's spectrum were detected except for a weak band at 272 cm^{-1}. This band, which is not found in the free ligand's spectrum or in the spectra of other complexes of L,[4] is tentatively assigned to a Cu—S stretching vibration.

Cyclic voltammetry for $[CuL_2]ClO_4$ showed a single quasi-reversible redox wave (Fig. 3) ($E_{1/2}$ = 0.150 V vs. aqueous SCE against which the ferrocenium/ferrocene potential under

[4] C. R. Lucas and L. Shuang. Unpublished results.

Can. J. Chem. Downloaded from www.nrcresearchpress.com by 93.93.197.157 on 09/07/12
For personal use only.

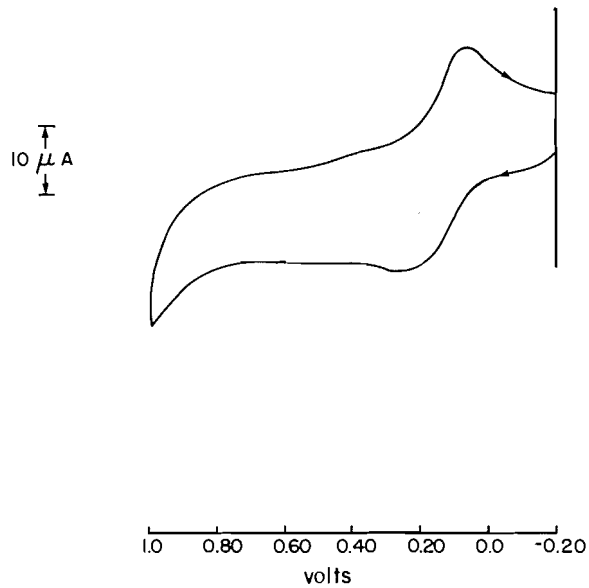

FIG. 3. Cyclic voltammogram of $[CuL_2]ClO_4$.

similar conditions was 400 mV; ΔE_p = 170 mV at 50 mV/s) associated with a Cu^I/Cu^{II} process. Solutions of the free ligand under similar conditions show no redox activity in the voltage range −1.5 to +0.8 V vs. aqueous SCE. Although measured under somewhat different conditions, a series of open chain and macrocyclic tetrathioether complexes of copper have been reported (23) to show $E_{1/2}$ for a Cu^{II}/Cu^I process in the range 0.46 to 0.66 V vs. SCE. Stabilization of copper(I) relative to copper(II) by ligand L would therefore seem to be less effective than that achieved by either open-chain or macrocyclic tetrathioethers in which all four sulfurs bound to the metal are in one ligand molecule.

In conclusion, it has been shown that presence of the rigid thiophene sub-unit as part of a small macrocyclic ring limits the conformations available to that ligand and so prevents "nesting" or "perching" of a metal ion as is often the case in small macrocyclic ring complexes (24). The coordination environment of a complexed Cu(I), although consisting of four coordinated thioether sulfurs, is different from that found in open-chain or macrocyclic tetrathioethers and this difference is reflected in the redox properties of the complex. It seems reasonable to assume that this observation may be exploited to design macrocyclic ligand complexes with enforced stereochemistry or other special characteristics. Details of these and other studies currently in progress will be reported shortly.

Acknowledgements

Financial support for this work was provided by Memorial University as a Hatcher Scholarship (L.S.) and as an operating grant (C.R.L.). Some of the latter was derived from the University President's NSERC fund. The assistance of Dr. Sanat K. Mandal in the cyclic voltammetry is gratefully acknowledged.

1. S. G. MURRAY and F. R. HARTLEY. Chem. Rev. **81**, 365 (1981).
2. P. M. COLMAN, H. C. FREEMAN, J. M. GUSS, M. MURATA, V. S. NORRO, J. A. M. RAMSHAW, and M. P. VENKATAPPA. Nature, **272**, 319 (1978).
3. A. MULLER and B. KREBS (*Editors*). Sulfur, its significance for chemistry, for the geo-, bio- and cosmosphere and technology. Elsevier, Amsterdam. 1984.
4. C. R. LUCAS and M. E. PEACH. Can. J. Chem. **48**, 1869 (1970).
5. C. R. LUCAS. J. Organomet. Chem. **236**, 281 (1982).
6. C. R. LUCAS, M. J. NEWLANDS, E. J. GABE, and F. L. LEE. Can. J. Chem. **65**, 898 (1987).
7. I. R. YOUNG, L. A. OCHRYMOWYCZ, and D. B. RORABACHER. Inorg. Chem. **25**, 2576 (1986).
8. A. J. BLAKE, R. O. GOULD, A. J. HOLDER, T. I. HYDE, A. J. LAVERY, M. O. ODULATE, and M. SCHRODER. Chem. Commun. 118 (1987).
9. S. C. RAWLE and S. R. COOPER. Chem. Commun. 308 (1987).
10. J. M. GRIFFING. J. Am. Chem. Soc. **70**, 3416 (1948).
11. D. F. GRANT and E. J. GABE. J. Appl. Crystallogr. **11**, 114 (1978).
12. G. GERMAIN, P. MAIN, and M. M. WOOLFSON. Acta Crystallogr. A**27**, 368 (1971).
13. E. J. GABE, F. L. LEE, and Y. LEPAGE. *In* Crystallographic computing 3. *Edited by* G. Sheldrick, G. Kruger, and R. Goddard. Clarendon Press, Oxford. 1985. p. 167.
14. International tables for X-ray crystallography. Vol. IV. Kynoch Press, Birmingham, England. 1974. p. 99. Table 2.2B.
15. G. R. NEWKOME, J. D. SAUER, J. M. ROPER, and D. C. HAGER. Chem. Rev. **77**, 513 (1977).
16. E. WEBER and F. VOGTLE. Liebigs Ann. Chem. 891 (1976).
17. R. M. IZATT, J. S. BRADSHAW, S. A. NIELSEN, J. D. LAMB, and J. J. CHRISTENSEN. Chem. Rev. **85**, 271 (1985).
18. V. B. PETT, L. L. DIADDARIO, JR., E. R. DOCKAL, P. W. CORFIELD, C. CECCARELLI, M. D. GLICK, L. A. OCHRYMOWYCZ, and D. B. RORABACHER. Inorg. Chem. **22**, 3661 (1983).
19. P. W. R. CORFIELD, C. CECCARELLI, M. D. GLICK, I. W.-Y. MOY, L. A. OCHRYMOWYCZ, and D. B. RORABACHER. J. Am. Chem. Soc. **107**, 2399 (1985).
20. E. N. BAKER and G. E. NORRIS. J. Chem. Soc. Dalton Trans. 877 (1977).
21. L. L. DIADDARIO, JR., E. R. DOCKAL, M. D. GLICK, L. A. OCHRYMOWYCZ, and D. B. RORABACHER. Inorg. Chem. **24**, 356 (1985).
22. N. W. ALCOCK, N. HERRON, and P. MOORE. J. Chem. Soc. Dalton Trans. 394 (1978).
23. E. R. DOCKAL, T. E. JONES, W. F. SOKOL, R. J. ENGERER, D. B. RORABACHER, and L. A. OCHRYMOWYCZ. J. Am. Chem. Soc. **98**, 4322 (1976).
24. A. D. BEVERIDGE, A. J. LAVERY, M. D. WALKINSHAW, and M. SCHRODER. J. Chem. Soc. Dalton Trans. 373 (1987).
25. C. K. JOHNSON. ORTEP-II: A thermal-ellipsoid plot program for crystal structure illustrations. ORNL-5138. Oak Ridge National Laboratory, Oak Ridge, TN, U.S.A. 1976.

Can. J. Chem. Downloaded from www.nrcresearchpress.com by 93.93.197.157 on 09/07/12
For personal use only.

La photochimie de l'isoprène gazeux dans la région de l'ultraviolet très lointain

HÉLÈNE DESLAURIERS, SYLVAIN DUFOUR ET GUY J. COLLIN[1]

Département des sciences fondamentales, Université du Québec à Chicoutimi, Chicoutimi (Québec), Canada G7H 2B1

Reçu le 5 janvier 1988

HÉLÈNE DESLAURIERS, SYLVAIN DUFOUR et GUY J. COLLIN. Can. J. Chem. **66**, 1513 (1988).

On a mesuré les rendements des produits observés dans la photochimie de l'isoprène éclairé à 184,9, 213,8 et 228,8 nm sous des pressions variant de 1 à 400 Torr. On observe aux trois longueurs d'onde le processus de fragmentation de la liaison C—CH_3 avec formation concomitante des radicaux méthyle et CH_2=CCH=CH_2. Ce dernier radical est en résonance électronique avec le radical allènique CH_2=C=$CHCH_2$. Ce processus a un rendement quantique de 0,83 ± 0,08 à 213,8 nm. L'intermédiaire responsable de cette fragmentation a un temps de vie de l'ordre de 20 ns à 184,9 nm. On observe aussi de petites quantités équivalentes d'une part d'éthylène et de C_3H_4 ($\Phi \cong 0{,}050$) et d'autre part de propène et d'acétylène ($\Phi \cong 0{,}023$). Tous les rendements des produits mesurés décroissent avec l'augmentation de la pression. À ces réactions de fragmentation, il faut ajouter des réactions d'isomérisation particulièrement à 228,8 nm. Les pentadiène-1,4 et -1,3, ainsi que le méthyl-3 butadiène-1,2 sont de ces isomères. Les courbes de type Stern–Volmer sont différentes dans chacun des cas et présentent des courbures importantes, indiquant la complexité des mécanismes réactionnels. Les temps de vie des intermédiaires ont été évalués à 2 ns ou moins.

HÉLÈNE DESLAURIERS, SYLVAIN DUFOUR, and GUY J. COLLIN. Can. J. Chem. **66**, 1513 (1988).

Yields of various products have been measured in the photolysis of isoprene at 184.9, 213.8, and 228.8 nm and at pressures between 1 and 400 Torr. At each wavelength, the major process is the rupture of a C—CH_3 bond, which leads to the formation of methyl and CH_2=C=$CHCH_2$. The quantum yield for this process is 0.83 ± 0.08 at 213.8 nm. The lifetime of the intermediate involved in this process is 20 ns at 184.9 nm. Similar quantities of ethylene and C_3H_4 ($\Phi \cong 0.050$) and propene and acetylene ($\Phi \cong 0.023$) are measured. All the measured yields decrease with an increase in the pressure. In addition to these fragmentation processes, isomerization reactions are also observed, particularly at 228.8 nm. They lead to the formation of 1,3- and 1,4-pentadiene as well as 3-methyl-1,2-butadiene. The Stern–Volmer plot for each isomer is different and each plot shows a strong negative curvature, indicating the complexity of the reaction process. The lifetime of each intermediate is 2 ns or less.

Can. J. Chem. Downloaded from www.nrcresearchpress.com by 93.93.197.157 on 09/07/12
For personal use only.

Introduction

La photochimie des diènes conjugués a été depuis longtemps placée sous la loupe de plusieurs laboratoire. Déjà, en 1933, l'isopropène gazeux a été irradié avec un arc au mercure et un solide blanc avait été observé (1). Plus récemment, ces études ont été reprises et une documentation, assez importante relativement à la photochimie dans le proche uv et à 253,7 nm (photosensibilisation), du butadiène-1,3 et de ses homologues substitués existe (2). Plusieurs réactions de fragmentation ont été considérées dans le cas de la photolyse directe du butadiène-1,3. Dans celui de l'isoprène, des réactions d'isomérisation (3) et de dimérisation (4) ont été observées. Cependant, peu d'attention a, semble-t-il, été apportée à la photochimie directe de l'isoprène dans la région de l'ultraviolet lointain (en deça de son seuil d'absorption) (5). Dans ce dernier travail, nous mentionnions que la réaction principale de fragmentation implique la rupture de la liaison C—CH_3 avec un rendement de 0,70 ± 0,05 dans la région du spectre électromagnétique située entre 174 et 147 nm. Il faut ajouter que la diminution de la longueur d'onde (donc de l'augmentation de l'énergie du photon incident) favorise la fragmentation subséquente du radical C_4H_5 :

[1] iso-C_5H_8 + $h\nu \Rightarrow$ (iso-C_5H_8)**

[2] (iso-C_5H_8)** $\Rightarrow$ CH_3 + C_4H_5*, k_2

[3] C_4H_5* $\Rightarrow$ C_4H_4 + H

[4] C_4H_5* + M $\Rightarrow$ C_4H_5 + M

Le rendement en vinylacétylène, C_4H_4, suit une loi de type Stern–Volmer : $[\Phi(C_4H_4)]^{-1} = a + bP$, où P est la pression dans le réacteur (5, 6). Plus récemment, la photolyse de l'isoprène a été étudiée à 123,6 nm : elle montre une fragmentation primaire et secondaire très importante en plus de la photoionisation (7). Il faut enfin rappeler que nous avions observé la formation d'isomères lorsque l'isoprène est photoéclairé dans la région de son seuil d'absorption, c'est-à-dire entre 220 et 235 nm, bien qu'à ce moment, des doutes subsistaient quant à leur identification.

Après avoir repris l'étude de la photochimie du butadiène-1,3 à 213,8 nm, c'est-à-dire assez proche de son seuil d'absorption,[2] nous reprenons ici celle de l'isoprène entre 185 et 229 nm pour mieux en cerner les mécanismes réactionels et, si possible, les généraliser.

Partie expérimentale

(a) Photoirradiation

Les techniques expérimentales sont bien connues. Les lampes (Philipps) à mercure, à zinc et à cadmium émettent principalement et respectivement à 184,9, 213,8 et 228,8 nm (9), entre le seuil de transmission du quartz (≅180 nm) et celui d'absorption de l'isoprène (≅240 nm) (2). Les photoirradiations durent en général quelques minutes, de telle sorte que le taux de transformation (nombre de photons entrant dans la cellule/nombre de molécules d'isoprène) demeure inférieur à 1%. L'actinométrie a été réalisée à 184,9 et à 213,8 nm par comparaison en photolysant dans les mêmes conditions l'éthylène ou l'éthanethiol respectivement à 184,9 et à 213,8 nm et elle a été décrite (9). Aucune actinométrie n'a été réalisée à 228,8 nm. Toutes les irradiations ont été réalisées à la température de la chambre : T = 20 ± 2°C. Les coefficients d'absorption ont été mesuré à l'aide d'un monochromateur McPherson d'un demi-mètre.

(b) Produits chimiques

L'isoprène est un produit A.P.I. (99,96 ± 0,03%). Plusieurs ampoules ont été utilisées. Les principales impuretés observées dans une ampoule particulièrement sale sont les suivantes : pentadiène-1,4, 0,024%; *trans*- et *cis*-pentadiène-1,3, 0,030% et 0,091%; méthyl-

1. Auteur à qui adresser toute correspondance.

2. S. Dufour, H. Deslauriers, G. J. Collin, G. De Maré et R. Poirier. En préparation.

TABLEAU 1. Photolyse de l'isoprène à 184,9 nm. Rendements quantiques

Isoprène (Torr)[a]	1,7	1,7	1,7	1,7	1,7	6,00
Oxygène (Torr)	—	0,34	0,26	—	—	—
SF_6 (Torr)	—	—	100	100	—	—
DI (Torr)	—	—	—	—	0,17	0,60
Méthane	0,014	0,00	0,002	0,0024	0,30	0,13
Acétylène	0,031	0,023	0,011	0,010	0,02	0,03
Ethylène	0,07	0,052	0,026	0,030	0,065	0,080
Ethane	0,055	0,00	0,00	0,022		
Propène	0,025	0,022	0,010	0,009	0,027	0,025
Allène	0,014	0,014	0,006	0,005	0,010	0,014
Propyne	0,032	0,038	0,017	0,014	0,027	0,040
Butadiène-1,3	0,00	0,00	0,00	0,00	0,078	0,033
Butadiène-1,2	0,00	0,006	0,004	0,00	0,025	0,00
Pentadiène-1,3	n.m.[c]	tr.[b]	≅0,02	≅0,02	n.m.	n.m.
Méthyl-3 butène-1	—	—	—	—	0,26	0,86
Méthyl-2 butène-2	—	—	—	—	1,71	5,67

[a]1 Torr ≡ 133 N m^{-2}.
[b]Traces.
[c]Non mesuré.

TABLEAU 2. Photolyse de l'isoprène à 213,8 nm. Rendements quantiques

Isoprène (Torr)[a]	1,7	1,7	1,7	1,7	5,1	10,2
Oxygène (Torr)	—	0,17	0,20	—	—	—
SF_6 (Torr)	—	—	100	—	—	—
DI (Torr)	—	—	—	0,17	1,0	1,0
Méthane	0,007	0,0025	0,00	0,40	0,22	0,06
Acétylène	0,026	0,024	0,0011	0,028	0,018	0,008
Ethylène	0,058	0,054	0,0043	0,09	0,067	0,015
Ethane	0,059	0,00	0,00	0,00	0,03	0,008
Propène	0,0214	0,022	0,009	0,035	0,014	0,009
Allène	0,010	0,010	0,0007	0,014	0,007	0,005
Propyne	0,029	0,038	0,0022	0,038	0,023	0,015
Butadiène-1,3	<0,001	<0,001	<0,001	0,10	0,066	0,016
Butadiène-1,2	0,00	0,00	0,00	0,048	0,008	0,00
Pentadiène-1,3[b]	0,010	n.m.[c]	0,002	n.m.	0,015	n.m.
Méthyl-3 butadiène-1,2	0,0015	n.m.	0,0009	0,048	0,008	0,00
Méthylvinylacétylène	0,00	0,00	0,00	0,008	0,005	0,006
Méthyl-3 butène-1	0,00	0,00	0,00	0,06	0,19	0,38
Méthyl-2 butène-2	0,00	0,00	0,00	n.m.	2,29	4,5

[a]1 Torr ≡ 133 N m^{-2}.
[b]*trans*.
[c]Non mesuré.

2-butène-2, 0,030% et le méthyl-3-butène-1, 0,0050%. Ces proportions varient d'un échantillon à l'autre. L'oxygène (99,99%), l'hexafluorure de soufre (99,99%) et l'oxyde nitrique (99%) viennent de chez Matheson et l'iodure de deutérium provient de chez Merck Sharp & Dohme du Canada. Ces produits ont été utilisés tels que reçus, après dégasage à la température de l'azote liquide quand leur pression de vapeur saturante le permet.

(c) Analyses

Toutes les analyses ont été réalisées par chromatographie en phase gazeuse (10).

Résultats

Les coefficients d'absorption de l'isoprène ont été mesuré aux trois longueurs d'onde d'intérêt. Ces coefficients sont de 8 170 ± 500 et 7 000 ± 500 $dm^3\,mol^{-1}\,cm^{-1}$, respectivement, à 184,9 et à 228,8 nm. Il y a absorption complète à 213,8 nm avec une pression de 0,4 Torr (1 Torr = 133 N m^{-2}) à travers un chemin optique de 10 cm. Ces coefficients sont en accord avec le spectre d'absorption connu de l'isoprène (11).

(a) Photochimie à 184,9 nm

Les principaux produits formés en présence d'oxygène et de diverses quantités de soufre hexafluoré sont l'éthylène, les C_3H_4 (allène + propyne), l'acétylène et le propène ainsi que des traces de divers isomères (tableau 1). En présence de soufre hexafluoré seulement, aux produits déjà identifiés s'ajoutent l'éthane et le méthyl-2 pentène-2. Lorsque 10% de DI est ajouté à l'isoprène, des quantités importantes de méthane ainsi que de méthyl-3 butène-1 et de méthyl-2 butène-2 apparaissent. Il faut aussi noter une forte dépendance des rendements qui décroissent avec l'augmentation de la pression. Il faut enfin ajouter la ressemblance des rendements en acétylène et en propène d'un part et en éthylène et en C_3H_4 d'autre part.

Can. J. Chem. Downloaded from www.nrcresearchpress.com by 93.93.197.157 on 09/07/12
For personal use only.

TABLEAU 3. Photolyse de l'isoprène à 228,8 nm. Rendements relatifs

Isoprène (Torr)[a]	0,85	10,22[b]	10,22	1,7	1,7	1,7	1,7	0,85	1,7[c]
Oxygène (Torr)	—	—	0,85	0,40	—	—	0,25	—	—
Oxyde nitrique (Torr)	—	—	—	—	0,50	—	—	—	—
Soufre hexafluoré (Torr)	—	—	—	—	—	100	300		
DI (Torr)	—	—	—	—	—	—	—	0,17	0,35
Méthane	0,00	0,00	0,00	0,00	0,00	0,0	0,00	6,00	2,8
Acétylène	1,22	0,16	0,15	0,86	0,71	0,011	0,006	0,80	0,53
Ethylène	2,50	0,55	0,49	2,0	1,6	0,080	0,030	1,97	1,26
Ethane	2,02	0,13	0,00	0,00	0,0	0,022	0,00	0,10	0,03
Propène	1,10	0,16	0,14	0,84	0,68	0,011	0,004	0,85	0,48
Allène	0,45	0,10	0,093	0,37	0,29	0,014	0,004	0,33	0,20
Propyne	1,90	0,40	0,26	1,40	1,15	0,052	0,021	1,15	0,77
Butadiène-1,3	0,17	0,03	0,009	0,01	0,05	0,03	0,00	0,88	0,35
Butadiène-1,2	0,00	0,00	0,00	0,00	0,00	0,00	0,00	0,35	0,08
trans-Pentadiène-1,3	0,88	0,28	0,18	0,92	0,96	0,13	0,10	0,73	0,43
cis-Pentadiène-1,3	2,72	0,45	0,13	0,90	0,96	0,10	0,06	0,63	0,55
Méthyl-3 butadiène-1,2	n.m.[d]	n.m.	0,07	n.m.	n.m.	0,06	0,04	n.m.	n.m.
Méthylvinylacétylène	0,21	0,28	0,35	0,37	0,27	0,19	0,25	0,10	0,13
Inconnu	n.m.	n.m.	0,25	0,27	0,21	n.m.	0,08	n.m.	n.m.
Pentadiène-1,4	0,70	0,36	0,31	0,78	0,68	0,07	0,03	0,30	0,31

[a]1 Torr ≡ 133 N m^{-2}.
[b]Pentyne-2 : 0,34; diméthyl-2,3 butène-1 : 0,31; méthyl-2 pentène-1 : 0,31 et -2 : 0,13.
[c]Méthyl-3 butène-1 : 0,97 et méthyl-2 butène-2 : 3,41.
[d]Non mesuré.

(b) Photochimie à 213,8 et à 228,8 nm

Les résultats rapportés dans les tableaux 2 et 3 sont très similaires à ceux déjà observés et commentés à 184,9 nm. Par exemple : $\Phi(C_3H_4)/\Phi(C_2H_4) = 0,89$ ($\sigma = 0,07$) et $\Phi(C_2H_2)/\Phi(C_3H_6) = 1,10$ ($\sigma = 0,10$) à 213,8 nm. Ces mêmes valeurs sont égales à 0,79 ($\sigma = 0,10$) et 1,08 ($\sigma = 0,08$) à 228,8 nm. Ces résultats seront également rapportés mais de façon plus détaillée dans de prochaines figures. Enfin il faut mentionner l'importance relativement grande des rendements en isomères de l'isoprène à 228,8 nm comparativement à ce qui est observé à plus courtes longueurs d'onde : tableaux 1–3.

Discussion

(a) Fragmentation : produits formés seulement en présence de DI

Que ce soit en présence ou en l'absence d'oxygène, les rendements quantiques des produits sont faibles puisqu'aucun de ceux-ci n'atteint 0,06! Au contraire, en présence d'iodure de deutérium, on observe une formation très importante de méthane, de méthyl-3 butène-1 et surtout de méthyl-2 butène-2 (tableaux 1–3). On peut raisonnablement expliquer la formation de méthane par la réaction de transfert d'un atome d'hydrogène (ici de deutérium) du DI vers le radical méthyle (12) :

[5] $CH_3 + HI \Rightarrow CH_4 + I\cdot$

Ce processus a été amplement observé et utilisé pour identifier la présence de radicaux et en mesurer les rendements (13, 14). Ainsi le rendement quantique $\Phi(CH_3)$ est au moins de 0,3–0,4 (tableaux 1 et 2). Il faut ajouter un effet de pression tout à fait évident : le rendement décroît avec l'augmentation de pression du monomère. Ces résultats peuvent s'expliquer sur la base du mécanisme de type Stern–Volmer (6). Aux réactions [1] et [2] s'ajoutent les réactions suivantes :

[6] $(\text{iso-}C_5H_8)^{**} + M \Rightarrow C_5H_8 + M, \quad k_6$

et

$$[\Phi(CH_3)]^{-1} = [\Phi_0(CH_3)]^{-1}\cdot(1 + k_6/k_2\cdot[M])$$

où k_2 et k_6 sont respectivement les constantes de vitesse des réactions de fragmentation (1er ordre) ou de stabilisation par collision (2ème ordre) de l'espèce excitée $(\text{iso-}C_5H_8)^{**}$ et Φ_0 est le rendement obtenu par extrapolation à pression nulle. La figure 1 résume les observations expérimentales. Il faut tout d'abord remarquer la bonne tenue des droites Stern–Volmer dans chacun des cas. Par extrapolation à pression nulle, on obtient $[\Phi_0(CH_3)]^{-1} \cong [\Phi_0(CH_4)]^{-1} = 2,2 \pm 0,2$ et $1,2 \pm 0,2$, respectivement, à 184,9 et à 213,8 nm. Ainsi une réaction majeure observable à ces deux longueurs d'onde est la réaction [2] tout au moins à basse pression : $\Phi_0(CH_3) = 0,46 \pm 0,05$ et $0,8 \pm 0,2$, respectivement, à 184,9 et à 213,8 nm (tableau 4). En outre, l'interception de ces droites Stern–Volmer avec l'axe des pressions est une mesure (exprimée en unités de pression) du rapport $-k_2/k_6$. En utilisant un rayon moléculaire de 0,583 nm pour l'isoprène (15) (σ(isoprène) ≅ σ(méthyl-3 butène-1) = 0,583 nm), on obtient une vitesse de collision $\omega = 1,58 \times 10^7$ s^{-1}. Les vitesses de fragmentation ainsi calculés de la molécule excitée $(\text{iso-}C_5H_8)^{**}$ sont donc de l'ordre de $(2–3) \times 10^{-8}$ s^{-1} (tableau 4). Les temps de vie sont similaires à celui calculé pour le diméthyl-2 butène-2 photoexcité à 193,2 nm : 70 ns (16), mais beaucoup plus longs que ceux d'autres hexènes ou méthylpentènes excités à 184,9 nm : 0,35–5 ns (17). La présence de deux liaisons conjuguées a très certainement un effet stabilisant sur la molécule photoexcitée.

La formation des butadiène-1,3 et -1,2 en présence de DI constitue une preuve de ce mécanisme. On s'attend en effet à ce qu'une part des radicaux C_4H_5 libérés par les processus [2]–[4] soient interceptés au moins partiellement dans une réaction analogue à la réaction [5], bien qu'il ne soit pas assuré que cette réaction soit quantitative étant donnée la compétition que peut

Can. J. Chem. Downloaded from www.nrcresearchpress.com by 93.93.197.157 on 09/07/12
For personal use only.

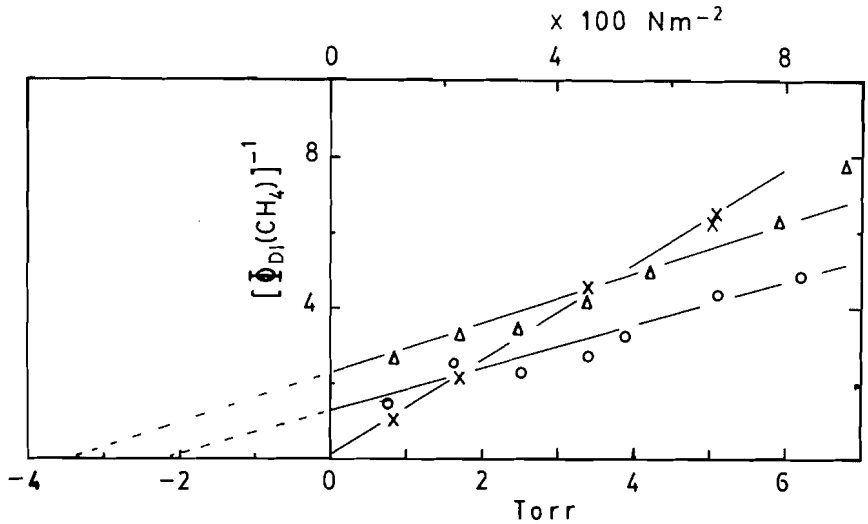

FIG. 1. Inverse du rendement quantique du méthane en fonction de la pression du monomère et en présence de DI (10%) : 184,9 nm, △; 213,8 nm, ○ et 228,8 nm, × (échelle arbitraire). Contrairement à ce que pourrait laisser croire cette dernière droite, son ordonnée à l'origine n'est pas zéro, mais bien positive. L'absence de rendements quantiques ne permet pas d'en préciser davantage cette ordonnée à l'origine.

TABLEAU 4. Photolyse de l'isoprène. Fragmentation d'une liaison C—CH_3

λ (nm)	Équation de Stern–Volmer[a] a	b	r^2	b^{-1}	$-k_2/k_6$ (Torr)	Temps de vie (10^{-8} s)
184,9	0,648	2,18	0,99	0,46	3,4	2
213,8	0,576	1,20	0,95	0,83	2,1	3
228,8	[b]	[b]	0,98	[b]	0,1	80[c]

[a] $f = aP + b$, où [P] ≡ Torr.
[b] Absence de rendements quantiques.
[c] Précision dérisoire.

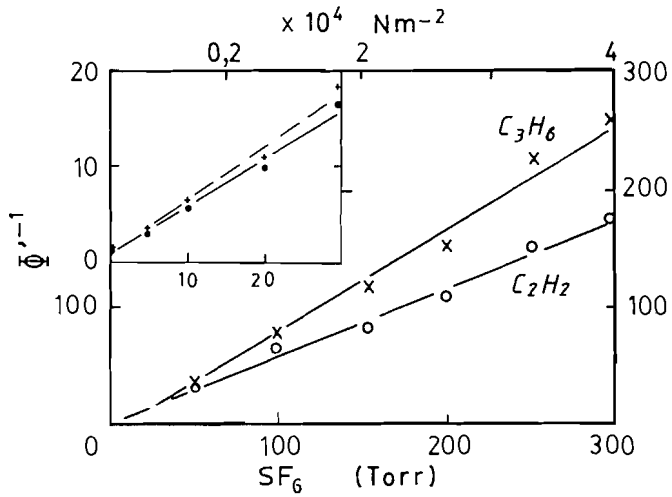

FIG. 2. Inverse des rendements des produits en fonction de la pression du soufre hexafluoré à 228,8 nm : ○, $[\Phi'(C_2H_2)]^{-1} = -0{,}35 + 0{,}58\,P$, $r = 0{,}99$; ●, $[\Phi'(C_2H_2)]^{-1} = +0{,}48 + 0{,}51\,P$, $r = 0{,}99$; ×, $[\Phi'(C_3H_6)]^{-1} = -18{,}0 + 0{,}92\,P$, $r = 0{,}99$; +, $[\Phi'(C_3H_6)]^{-1} = +0{,}32 + 0{,}57\,P$, $r = 0{,}99$.

offrir l'isoprène vis-à-vis certains radicaux (14). La présence des butadiène-1,3 et -1,2 est en accord avec la structure de l'isoprène après perte de son groupe méthyle. Il y a en effet possibilité de résonance électronique entre les structures $CH_2{=}CCH{=}CH_2$ et $CH_2{=}C{=}CHCH_2$ (18), et l'interception par DI conduit aux deux butadiènes mentionnés. Quant aux méthyl-2 butène-2 et méthyl-3 butène-1 dont les rendements quantiques peuvent dépasser l'unité (tableaux 1 et 2), ils sont probablement le résultat d'un mécanisme en chaîne impliquant soit des atomes d'hydrogène, soit d'iode, ou les deux en même temps (19).

(b) Fragmentation : produits formés en présence d'oxygène

Ce sont essentiellement des produits en C_2 et C_3 (tableaux 1–3). Compte tenu des rendements observés, on peut proposer les réactions suivantes où sont exclues les espèces radicalaires thermalisées puisque celles-ci seraient normalement interceptées par l'oxygène moléculaire.

[7] $(\text{iso-}C_5H_8)^{**\text{ ou v}} \Rightarrow C_2H_4 + C_3H_4$

[8] $(\text{iso-}C_5H_8)^{**\text{ ou v}} \Rightarrow C_2H_2 + C_3H_6$

[9] $(\text{iso-}C_5H_8)^{**\text{ ou v}} \Rightarrow C_2H_3^* + C_3H_5^*$

[10] $C_2H_3^* \Rightarrow C_2H_2 + H$

[11] $C_3H_5^* \Rightarrow C_3H_4 + H$

[12] $C_2H_3^*$ ou $C_3H_5^* + M \Rightarrow C_2H_3$ ou $C_3H_5 + M$

Le comportement Stern–Volmer des rendements des produits «moléculaires» s'explique par la stabilisation de l'intermédiaire isoprène excité ou bien par celle du radical chaud (vibrationnellement excité). Si les deux intermédiaires participent à la formation de l'acétylène et de l'éthylène et s'ils sont suceptibles de stabilisation par collision, une courbure positive ou négative à la droite de Stern–Volmer peut éventuellement être observée (20) : figures 2–4. Il faut ajouter que les réactions [9], [10] et [11] ne peuvent se réaliser simultanément car l'énergie initiale des photons est insuffisante pour satisfaire aux exigences thermodynamiques requises par la rupture de trois liaisons. Cela peut expliquer les différences sensibles dans les rendements en acétylène et propène particulièrement à 213,8 et 228,8 nm (voir résultats). Il faut en outre ajouter que les réactions de fragmentation moléculaires demandent une isomérisation préalable de la molécule photoexcitée. Ainsi,

[8a] $(CH_2{=}C(CH_3)CH{=}CH_2)^{**\text{ ou v}}$
$\Rightarrow (CH_3C(CH_3){-}CH{=}CH)^{**\text{ ou v}}$

Can. J. Chem. Downloaded from www.nrcresearchpress.com by 93.93.197.157 on 09/07/12
For personal use only.

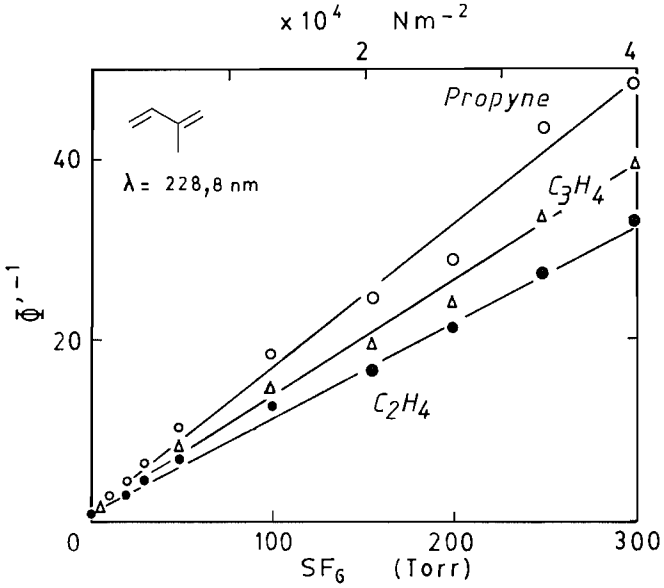

FIG. 3. Inverse des rendements des produits en fonction de la pression du soufre hexafluoré à 228,8 nm : ○, $[\Phi'(CH_3C{\equiv}CH)]^{-1} = 1{,}15 + 0{,}157\,P$, $r = 0{,}99$; △, $[\Phi'(C_3H_4)]^{-1} = 0{,}805 + 0{,}127\,P$, $r = 1{,}00$; ●, $[\Phi'(C_2H_4)]^{-1} = 0{,}809 + 0{,}106\,P$, $r = 1{,}00$.

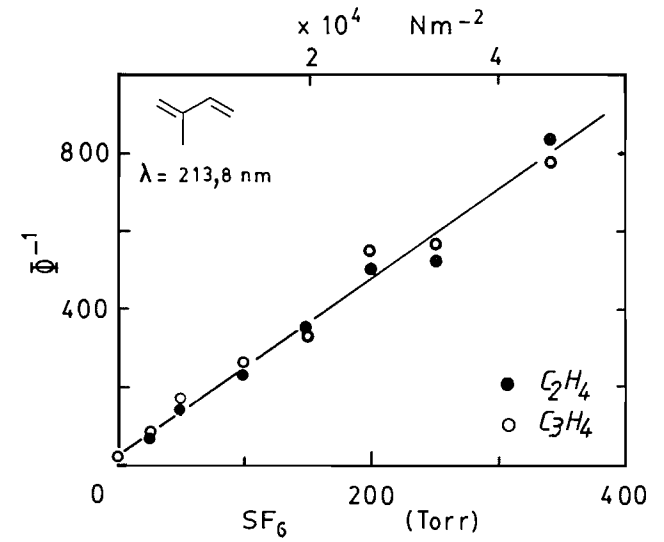

FIG. 4. Inverse des rendements quantiques des produits en fonction de la pression du soufre hexafluoré à 213,8 nm : ●, $[\Phi(C_2H_4)]^{-1} = 18{,}5 + 2{,}30\,P$, $r = 0{,}99$; ○, $[\Phi(C_3H_4)]^{-1} = 48{,}5 + 2{,}25\,P$, $r = 0{,}99$.

[8*b*] $(CH_3C(CH_3)—CH{=}CH)^{**\,ou\,v} \Rightarrow CH_3CCH_3 + CH{\equiv}CH$

[8*c*] $CH_3CCH_3 \Rightarrow CH_3CH{=}CH_2\cdot$

Il en est de même des réactions [7] et [9]. Les résultats sont insuffisants pour apprécier l'importance relative de chacun des processus [7]–[11]. Enfin deux autres produits sont formés avec des rendements qui dépendent fortement de la pression entre 0 et 10 Torr de soufre hexafluoré, puisqu'ils demeurent relativement stables. L'un de ces produits est le méthyl-3 butène-3 yne-1 (méthylvinylacétylène) et l'autre n'a pu être identifié (figure 5).

[13] $(CH_2){=}C(CH_3)CH{=}CH_2)^{**\,ou\,v} \Rightarrow CH_2{=}C(CH_3)C{\equiv}CH + H_2$

Compte tenu de l'énergie disponible à 228,8 nm (523 kJ mol^{-1}),

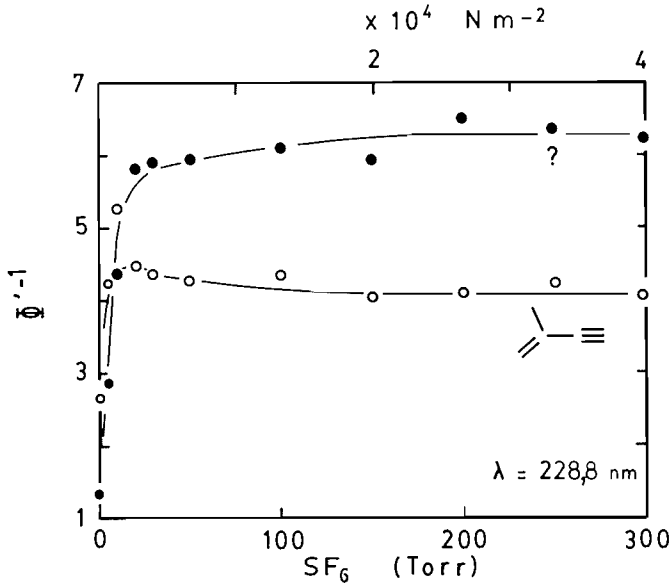

FIG. 5. Inverse des rendements des produits en fonction de la pression du soufre hexafluoré à 228,8 nm : ○, $[\Phi'(\text{Méthylvinylacétylène})]^{-1}$; ●, $[\Phi'(\text{Inconnu})]^{-1}$.

la réaction précédente produit, sinon exclusivement, de l'hydrogène moléculaire plutôt que monoatomique. La fragmentation à partir d'un état électronique excité à courte durée de vie pourrait être responsable de la formation qui apparaît indépendante de la pression, tandis que celle qui est fortement affectée par la pression provient d'un état excité à très long temps de vie.

(c) Fragmentation : produits formés en l'absence d'oxygène ou de DI

La formation d'éthane doit être mise au compte de la recombinaison entre une partie des radicaux méthyles. Une autre partie de ces radicaux réagit avec les autres radicaux présents, comme ceux, par exemple, provenant de l'addition de l'atome d'hydrogène sur le monomère. La présence de ces atomes d'hydrogène est observable à travers la formation de diverses oléfines en C_6. Provenant des réactions [3], [10] et [11], ces atomes s'additionnent sur l'isoprène et forment divers radicaux allylliques C_5H_9. Ceux-ci, à leur tour se recombinent entre eux ou avec les radicaux méthyles. Ces réactions sont responsables de la formation de monooléfines substituées en C_6, et dont certaines ont pu être observées. Ce sont le diméthyl-2,3 butène-1 et les méthyl-2 pentène-1 et -2.

[14] $H + \text{iso-}C_5H_8 \Rightarrow (CH_3)_2CCH{=}CH_2$ ou $(CH_3)_2C{=}CHCH_2$

[15] $H + \text{iso-}C_5H_8 \Rightarrow CH_2{=}C(CH_3)CHCH_3$ ou $CH_2C(CH_3){=}CHCH_3$

[16] $(CH_3)_2CCH{=}CH_2 + CH_3 \Rightarrow (CH_3)_3CCH{=}CH_2$

[17] $CH_2{=}C(CH_3)CHCH_3 + CH_3 \Rightarrow (CH_3)_2CHC(CH_3){=}CH_2$

[18] $(CH_3)_2C{=}CHCH_2 + CH_3 \Rightarrow (CH_3)_2C{=}CHCH_2CH_3$

[19] $CH_2C(CH_3){=}CHCH_3 + CH_3 \Rightarrow CH_3CH_2C(CH_3){=}CHCH_3$

(d) Isomérisation à 228,8 nm

Les représentation Stern–Volmer des rendements en isomères, $[\Phi(x)]^{-1} = f(\text{pression})$, sont loin d'être linéaires : figures 6–8. On observe en général une courbure négative plus ou moins prononcée dans la zone de pression située vers 50 Torr de soufre hexafluoré. Il n'est pas aisé, a priori, d'expliquer ces observations puisque plusieurs raisons peuvent être invoquées

Can. J. Chem. Downloaded from www.nrcresearchpress.com by 93.93.197.157 on 09/07/12
For personal use only.

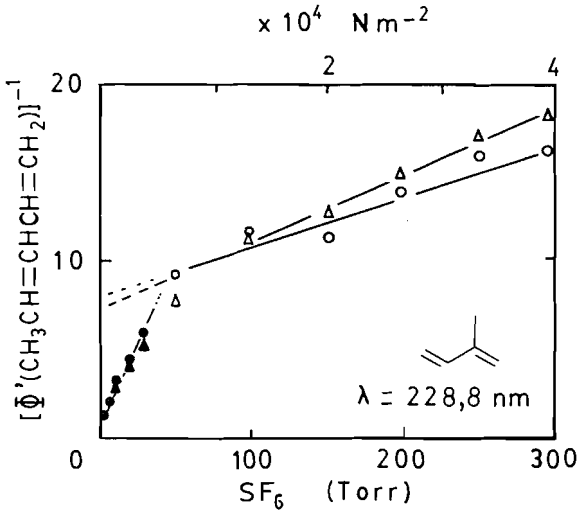

FIG. 6. Inverse des rendements des produits en fonction de la pression du soufre hexafluoré à 228,8 nm : ○, $[\Phi'(\textit{trans}\text{-Pentadiène-1,3})]^{-1} = 7{,}96 + 0{,}028\,P$, $r = 0{,}96$; ●, $[\Phi'(\textit{trans}\text{-Pentadiène-1,3})]^{-1} = 1{,}33 + 0{,}155\,P$, $r = 1{,}00$; △, $[\Phi'(\textit{cis}\text{-Pentadiène-1,3})]^{-1} = 6{,}25 + 0{,}042\,P$, $r = 0{,}99$; ▲, $[\Phi'(\textit{cis}\text{-Pentadiène-1,3})]^{-1} = 1{,}29 + 0{,}14\,P$, $r = 1{,}00$.

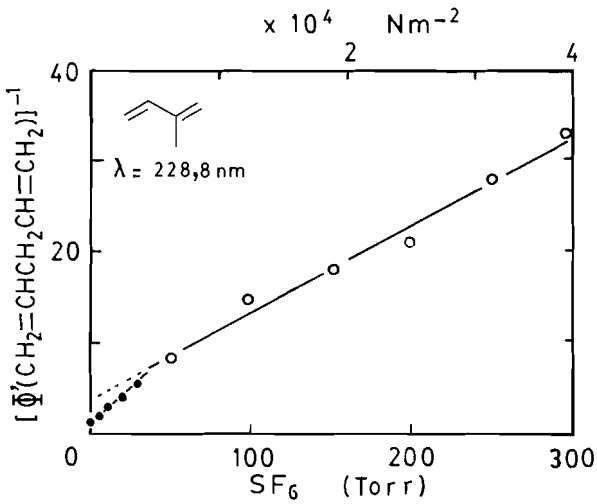

FIG. 7. Inverse des rendements des produits en fonction de la pression du soufre hexafluoré à 228,8 nm : ○, $[\Phi'(C_5H_8\text{-}1,4)]^{-1} = 3{,}43 + 0{,}097\,P$, $r = 0{,}99$; ●, $[\Phi'(C_5H_8\text{-}1,4)]^{-1} = 1{,}25 + 0{,}14\,P$, $r = 1{,}00$.

(6). On ne peut retenir, tout d'abord, une distribution énergétique relativement large des molécules photoexcitées puisque celles-ci contiennent, outre l'énergie thermique initiale (≅20 kJ mol^{-1}), l'énergie du photon incident, soit 523 kJ mol^{-1} (5,44 eV). Une première possibilité peut être retenue : chacun de ces isomères serait le résultat de deux mécanismes réactionnels indépendants et tout à fait différents. La courbe serait alors la «somme» de deux courbes Stern–Volmer indépendantes, comme nous l'avions proposé dans le cas de la photochimie des butènes vers 163–174 nm (21). Dans ce cas, et à haute pression, les courbes Stern–Volmer sont de la forme ($y = a + bP$) : $[\Phi']^{-1} = [\Phi_0']^{-1} + [\Phi_0']^{-1} k_s[P]/k_d$. Du rapport a/b, on obtient la valeur du rapport k_d/k_s pour les différents intermédiaires apparaissant dans les figures 6–8 (tableau 5). Les temps de vie des intermédiaires ainsi calculés sont de l'ordre de, ou inférieur à, la nanoseconde, donc beaucoup plus courts que

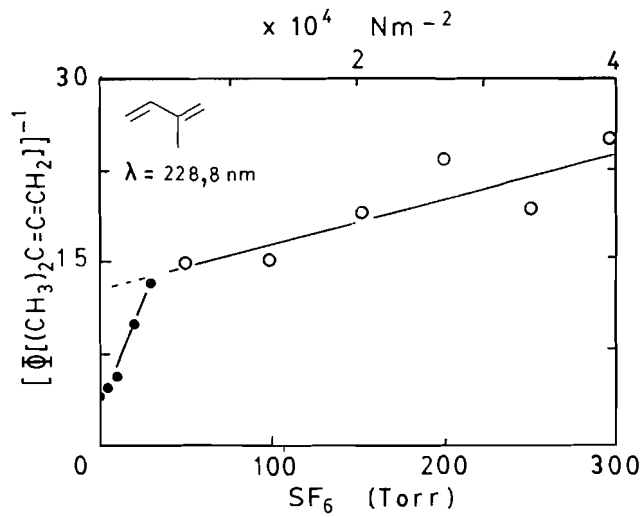

FIG. 8. Inverse du rendement en méthyl-3 butadiène-1,2 en fonction de la pression du soufre hexafluoré à 228,8 nm : ○, $[\Phi']^{-1} = 12{,}7 + 0{,}097\,P$, $r = 0{,}84$; ●, $[\Phi']^{-1} = 3{,}62 + 0{,}32\,P$, $r = 0{,}99$.

TABLEAU 5. Photolyse de l'isoprène. Isomérisation du monomère à 228,8 nm

Isomère	k_s/k_d (Torr)	Temps de vie (10^{-10} s)[a]
trans-Pentadiène-1,3	285	2,3
cis-Pentadiène-1,3	150	4,4
Pentadiène-1,4	35	19
Méthyl-2 butadiène-1,2	130	5,1

[a]Rayon moléculaire de SF_6 : 0,55 nm ($\sigma(SF_6)$ = 0,55 nm. Voir référence 15) et $\omega = 1{,}5 \times 10^7$ s^{-1}.

celui mesuré pour l'intermédiaire responsable de la rupture de la liaison C—CH_3. La même approche pourrait être appliquée à la portion «basse pression» des courbes Stern–Volmer. Cependant, le nombre de données, combiné à la précision expérimentale, enlève une grande part de crédibilité aux résultats obtenus. Une autre explication, tout aussi plausible, réside dans un mécanisme de faisant intervenir successivement deux états excités différents, chacun de ces deux états étant suceptibles d'être stabilisés par collision (20).

[20] $(\text{iso-}C_5H_8)^{**} \Rightarrow \text{iso-}C_5H_8^*$

[21] $\text{iso-}C_5H_8^* \Rightarrow \text{iso-}C_5H_8^v$

[22] $\text{iso-}C_5H_8^* + M \Rightarrow \text{iso-}C_5H_8 + M$

[23] $\text{iso-}C_5H_8^v + M \Rightarrow \text{iso-}C_5H_8 + M$

[24] $\text{iso-}C_5H_8^v \Rightarrow (M_i)^v$

[25] $\text{iso-}C_5H_8^v \Rightarrow (M_i)^v$

[26] $(M_i)^v + M \Rightarrow M_i + M$

Si la molécule $(\text{iso-}C_5H_8)^{**}$ formée dans le processus de photoexcitation, reaction [1], représente un état électronique excité, on n'en connaît pas la nature exacte. Mentionnons qu'à l'énergie incidente utilisée plusieurs états électroniques singulets, et éventuellement triplets (?), sont disponibles (22). On ne peut guère en dire plus de l'état électronique $\text{iso-}C_5H_8^*$. Quant à l'état fondamental vibrationnellement excité, il est identifié par l'exposant v. La molécule M_i est un isomère de l'isoprène,

Can. J. Chem. Downloaded from www.nrcresearchpress.com by 93.93.197.157 on 09/07/12
For personal use only.

isomère qui peut prendre plusieurs configurations différentes. Il en résulte que les mécanismes disponibles sont tout aussi nombreux, sinon plus. Il faut ajouter que si ce dernier mécanisme est convenable, il requiert des paires d'intermédiaires excités différents puisque, hormis pour le couple *cis-* et *trans*-pentadiène-1,3 (figure 6), il ne semble pas y avoir de constance entre les rapports de rendements observés (figures 6–8). Par contre, on peut raisonablement estimer que les premiers états excités stabilisés par collision sont ceux de l'isoprène. En effet, et contrairement à ce qui a été observé, par exemple, dans le cas du tétraméthyléthylène photoexcité dans la région de 185–229 nm où les rendements en isomères croissent avec l'augmentation de la pression (23), dans le cas présent les rendements en isomères décroissent avec l'augmentation de la pression. Une situation également différente a été observée dans le cas du cyclopentène (8).

Remerciements

Nous tenons à exprimer notre reconnaissance au Conseil de recherche en sciences naturelles et en génie du Canada qui a financé cette étude ainsi que Emploi et Immigration Canada qui ont chacun payé une partie des salaires (H.D. et S.D.).

1. S. C. Lind et R. Livingston. J. Am. Chem. Soc. **55**, 1036 (1933).
2. J. G. Calvert et J. N. Pitts, Jr. *Dans* Photochemistry. J. Wiley and Sons, Inc., New York. 1967, et les références qui y sont citées.
3. R. Srinivasan. J. Am. Chem. Soc. **84**, 4141 (1962); R. Srinivasan et S. Boué. Tetrahedron Lett. **3**, 203 (1970); S. Boué et R. Srinivasan. Mol. Photochem. **4**, 93 (1972).
4. G. S. Hammond et R. S. H. Liu. J. Am. Chem. Soc. **85**, 477 (1963).
5. R. Demers, G. J. Collin et H. Gagnon-Deslauriers. Can. J. Chem. **56**, 1864 (1978).
6. W. Forst. *Dans* Theory of unimolecular reactions. *Éditeur* : E. M. Loebl. Academic Press, New York, NY. 1973. pp. 235 et suivantes.
7. V. Lang et R. D. Doepker. Can. J. Chem. **62**, 1731 (1984).
8. W. Makulski et G. J. Collin. J. Phys. Chem. **91**, 708 (1987).
9. G. J. Collin, H. Deslauriers et A. Więckowski. J. Phys. Chem. **85**, 944 (1981).
10. H. Deslauriers et G. J. Collin. Can. J. Chem. **63**, 3168 (1985).
11. W. C. Price et A. D. Walsh. Proc. R. Soc. London. A: **174**, 220 (1940); L. C. Jones, Jr. et L. W. Taylor. Anal. Chem. **27**, 228 (1955).
12. P. Ausloos, R. E. Rebbert et S. G. Lias. J. Photochem. **2**, 267 (1973/74).
13. G. J. Collin et K. Bukka. J. Photochem. **6**, 381 (1976/77).
14. Z. Diaz et R. D. Doepker. J. Phys. Chem. **81**, 1442 (1977).
15. J. O. Hirschefelder, C. F. Curtiss et R. B. Bird. *Dans* Molecular theory of gases and liquids. J. Wiley and Sons, New York, NY. 1964.
16. N. Shimo, N. Nakashima, N. Ikeda et K. Yoshihara. J. Photochem. **32**, 279 (1986).
17. G. J. Collin. Adv. Photochem. **14**, 135 (1988).
18. P. J. Gorton et R. Walsh. J. Chem. Soc. Chem. Commun. 782 (1972).
19. P. Kebarle. J. Chem. Phys. **39**, 2218 (1963).
20. J. A. Barltrop et J. D. Coyle. *Dans* Principles of photochemistry. J. Wiley and Sons, New York, NY. 1978. pp. 152–154.
21. G. J. Collin et A. Wieckowski. J. Photochem. **8**, 103 (1978).
22. M. B. Robin. *Dans* Higher excited states of polyatomic molecules. Vol. II. Academic Press, New York, NY. 1975. pp. 166–180; Vol. III. 1985. pp. 324–328, et les références citées.
23. G. J. Collin et H. Deslauriers. Can. J. Chem. **61**, 1510 (1983).

Can. J. Chem. Downloaded from www.nrcresearchpress.com by 93.93.197.157 on 09/07/12
For personal use only.

Excess molar volumes of methyl alkanoate with *n*-alkanols at 298.15 K

J. ORTEGA AND J. D. GARCIA

Cátedra de Termodinámica y Fisicoquímica, Escuela Superior de Ingenieros Industriales, Polytechnic University of Canarias, Spain

Received October 6, 1987

J. ORTEGA and J. D. GARCIA. Can. J. Chem. **66**, 1520 (1988).

This work reports on the excess molar volumes at 298.15 K of fifteen binary systems formed by $\{xC_mH_{2m+1}CO_2CH_3$ $(m = 1, 2, 3) + (1 - x)C_nH_{2n+1}(OH)$ $(n = 6, 7, 8, 9, 10)\}$. The V_m^E values were calculated using densities obtained in a vibrating-tube densimeter, the excess molar volumes being positive for all these systems. A qualitative interpretation of the results is presented on the basis of the appearance of specific interactions between the —CO—O— groups of the ester and the —OH of the *n*-alkanol.

J. ORTEGA et J. D. GARCIA. Can. J. Chem. **66**, 1520 (1988).

Dans ce travail, on a déterminé les volumes molaires en excès, à 298,15 K, de quinze systèmes binaires formés par $\{xC_mC_{2m+1}CO_2CH_3$ $(m = 1, 2$ ou $3) + (1 - x)C_nH_{2n+1}(OH)$ $(n = 6, 7, 8, 9$ ou $10)\}$. Les valeurs de V_m^E ont été calculées en utilisant les densités qui ont été obtenues à l'aide d'un densimètre à tube vibrant; les volumes molaires en excès sont positifs pour tous les systèmes. On présente une interprétation qualitative des résultats qui est basée sur l'apparition d'interactions spécifiques entre les groupements —CO—O— des esters et —OH des *n*-alcools.

[Traduit par la revue]

Introduction

In previous papers (1–3) data of the V_m^E were presented for several binary systems of aliphatic esters with *n*-alkanols, in which the volumetric behaviour of this type of mixtures was analysed and the results obtained were qualitatively justified. As was stated in the above-mentioned articles, we are particularly interested in confirming the considerations put forward on the behaviour of the —CO—O— ester group. For this purpose it is also necessary to consider the effects of the interactions of compounds having the same functional group with other type of substances, such as *n*-alkanes (4, 5). This interaction is analysed using other excess thermodynamic functions such as H_m^E and G_m^E.

A summary of the studies published to date reveals that there are at least two effects in the interactions of an ester with non-electrolytes. The first and most prominent effect for any ester is that an increase in the V_m^E value is a function of the length of the chain of the binary component in the non-electrolyte. However, the second effect due to the ester is attributed to a specific interaction which causes the decrease of the V_m^E as the number of carbons of the ester increase, for both R_1 and R_2 in R_1—CO—O—R_2.

In this work we studied the changes in volume produced upon mixing methyl alkanoates, starting from acetate to butanoate, with normal alkanols, from hexan-1-ol to decan-1-ol, at a temperature of 298.15 K and at atmospheric pressure. The data presented here will contribute to the study of binary mixtures of ester + *n*-alkanols, providing additional information on the behaviour of the liquid state of these types of compounds.

Experimental

Component liquids

Both the esters and the *n*-alkanols were supplied by Fluka. The characteristics indicated by the manufacturer for the products employed were "purum" > 99 mol% for all the methyl alkanoates, "puriss" > 99.5 mol% for hexan-1-ol, heptan-1-ol, octan-1-ol, and decan-1-ol and "purum" > 98 mol% for nonan-1-ol. All products were dried prior to use with a molecular sieve (Union Carbide, Type A4, by Fluka) and partially degassed with ultrasound. After these operations, the purity of the liquids was tested and the values of density and refractive index determined at 298.15 K. The comparison of these values with those found in the literature is presented in Table 1, a good agreement being obtained for both esters and *n*-alkanols.

Determinations of excess volumes

The binary mixtures over the entire range of concentrations were prepared by weighing, using hermetically sealed vials to avoid evaporation. The molar fractions, x, of the ester were determined with an error of less than 2×10^{-5}. The excess volumes, determined indirectly from the densities, were calculated with

$$[1] \quad V_m^E/(\text{cm}^3\ \text{mol}^{-1}) = (\Sigma x_i M_i)/\rho - \Sigma(x_i M_i/\rho_i)$$

where ρ is the density of the mixture and ρ_i, x_i, and M_i are, respectively, the density, the molar fraction, and the molecular mass of compound i. The molecular masses were determined to within $\pm 10^{-4}$ units and the densities to within ± 0.01 kg m^{-3}. On this basis, the V_m^E values were calculated with an accuracy above ± 0.001 cm^3 mol^{-1}.

For the determination of the densities an Anton Paar digital densimeter, model DMA-55, was used, which was calibrated for each mixture using bidistilled water and *n*-nonane as standard substances, as proposed in an earlier work (9). The densimeter was thermostated by a Heto Birdkerod ultrathermostat which controlled the temperature automatically to within ± 0.01 K.

Results

The V_m^E values of the fifteen systems $\{xC_mH_{2m+1}CO_2CH_3$ $(m = 1, 2, 3) + (1 - x)C_nH_{2n+1}(OH)$ $(n = 6, 7, 8, 9, 10)\}$ are given in Table 2 as a function of the ester concentration, x. These data were correlated by means of the following equation:

$$[2] \quad V_m^E/(\text{cm}^3\ \text{mol}^{-1}) = x(1 - x)\Sigma A_i[x/(x + k(1 - x))]^i \qquad i = 0, 1, 2, \ldots$$

The values of the A_i coefficients were determined, for a constant value of k, by the least-squares method and employing an F-test to evaluate the confidence of each coefficient and optimize the grade of eq. [2]. The equation thus obtained was analysed for the different values of the parameter k in an attempt to minimizing the standard deviation, $s(V_m^E)$, of the experimental data and therefore give the best fit. The parameters of the equation that give the best fit for each system are presented in Table 3, while Fig. 1 shows the distribution of the curves obtained for the fifteen systems studied.

Discussion

No data have been found of V_m^E at 298.15 K for the mixtures studied here. As was expected for this type of systems, all the

Printed in Canada / Imprimé au Canada

Can. J. Chem. Downloaded from www.nrcresearchpress.com by 93.93.197.157 on 09/07/12
For personal use only.

TABLE 1. Densities, ρ, and refractive indices, n_D, of component liquids at 298.15 K

Component	ρ/(kg m^{-3}) This work	ρ/(kg m^{-3}) Literature	n_D This work	n_D Literature
Methyl acetate, $CH_3CO_2CH_3$	927.04	927.3[a] 927.9[b]	1.3588	1.3589[a,b]
Methyl propanoate, $C_2H_5CO_2CH_3$	908.43	909.0[a]	1.3740	1.3742[a]
Methyl butanoate, $C_3H_7CO_2CH_3$	892.37	892.6[a]	1.3851	1.3847[a]
Hexan-1-ol, $C_6H_{13}(OH)$	815.26	816.2[a] 815.34[b]	1.4160	1.4161[a] 1.4157[b]
Heptan-1-ol, $C_7H_{15}(OH)$	818.71	818.6[a] 818.7[c]	1.4223	1.4225[a] 1.4223[b]
Octan-1-ol, $C_8H_{17}(OH)$	821.67	822.3[a] 821.6[c]	1.4270	1.4276[a,b]
Nonan-1-ol, $C_9H_{19}(OH)$	824.78	824.7[a,c]	1.4315	1.4319[a,c]
Decan-1-ol, $C_{10}H_{21}(OH)$	826.42	826.3[a,c]	1.4349	1.4353[a,c]

[a]Reference 6.
[b]Reference 7.
[c]Reference 8.

Can. J. Chem. Downloaded from www.nrcresearchpress.com by 93.93.197.157 on 09/07/12
For personal use only.

excess molar volumes were positive. For any one ester, the V_m^E values increase almost linearly with the number of carbon atoms of the *n*-alkanol; however, the opposite effect takes place when the number of carbon atoms of the ester increases on either side of the —CO—O— group. The first of the effects mentioned, the size effect, takes place also in mixtures of ester + *n*-alkane (4) and is justified by the steric hinderance brought about by the increase of the *n*-alkanol chain. If this fact is considered together with the dissociation of the polymers of the *n*-alkanol, by way of the hydrogen bonds, against the inertia presented by the *n*-alkanes it is found that, with an equal number of carbon atoms, the following is verified for any one ester: V_m^E, *n*-alkane > V_m^E, *n*-alkanol.

It was considered worthwhile to compare the V_m^E values in the interactions of the certain *n*-alkanol with different esters having the same empirical expression. This work shows clearly that the V_m^E values of methyl butanoate are very similar to those of ethyl propanoate (3) and propyl acetate (10) when mixed with the same *n*-alkanols. However, the differences become more significant when the comparison is made of esters with fewer carbon atoms, such as of methyl acetate and ethyl formate (2) upon mixing, as before, with the same *n*-alkanols. These greater differences seem logical since, quantitatively, the V_m^E values are quite high and their absolute error increased considerably. Thus the volumetric effects for R_1—CO—O—R_2 type molecules are the same when substituents R_1 and R_2 are interchanged. Leaving aside esters with a low number of carbon atoms, special considerations would also have to be made when comparing systems containing esters that form pseudocycles, as will be discussed forthwith.

The preceding paragraph bears relation to the second of the aspects pointed out at the beginning of this section, and which proves to be characteristic of those compounds containing a =C=O carbonyl group. We are referring to the decrease in the V_m^E values with the increase in the number of carbon atoms of the ester, for any one *n*-alkanol. This interesting aspect also appears in mixtures of aliphatic ketones with *n*-alkanes (5), and even when one of the radicals of the ketone or of the ester is substituted by phenyl groups (5). The evolution of the results obtained here for the V_m^E is analogous to that of thermodynamic magnitudes of mixtures, such as H_m^E and G_m^E (11). The sequence

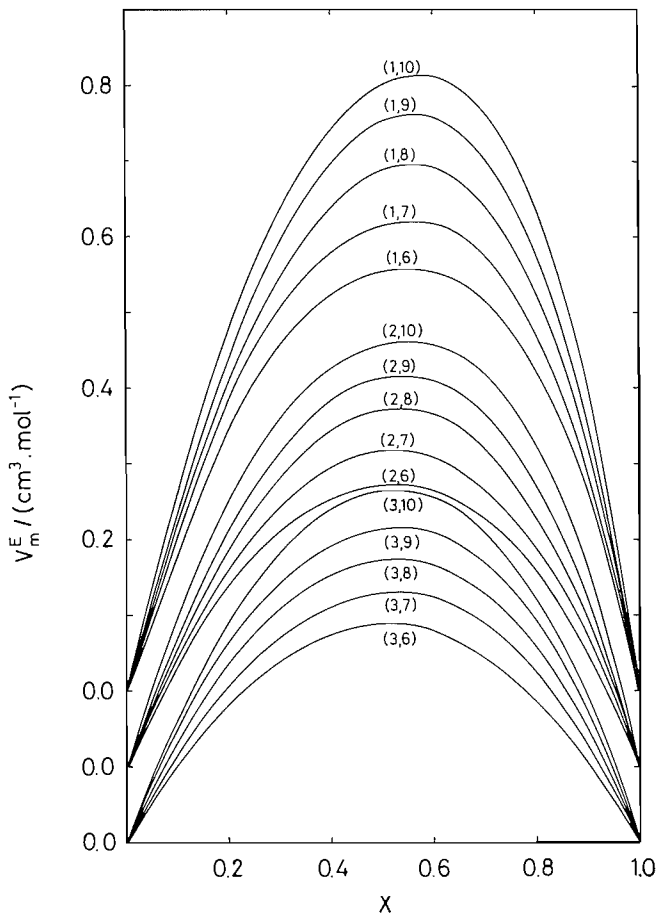

FIG. 1. V_m^E curves at 298.15 K calculated by eq. [2] for the binary systems, (*m*,*n*) {$xC_mH_{2m+1}CO_2CH_3$ (*m* = 1, 2, 3) + (1 − *x*)$C_nH_{2n+1}(OH)$ (*n* = 6, 7, 8, 9, 10)}.

observed in the V_m^E for the mixtures of methyl acetate, methyl propanoate, and methyl butanoate with *n*-alkanols can be explained taking into account that the basic nature of the carbonyl group increases with the length of the chain of the methyl ester, the interactions between the molecules of the ester

TABLE 2. Excess molar volumes, V_m^E, for x (methyl alkanoate) + $(1 - x)$*n*-alkanol at 298.15 K

x	V_m^E / cm^3 mol^{-1}	x	V_m^E / cm^3 mol^{-1}	x	V_m^E / cm^3 mol^{-1}	x	V_m^E / cm^3 mol^{-1}
			$x CH_3CO_2CH_3 + (1 - x)C_6H_{13}(OH)$				
0.05989	0.1046	0.38112	0.5172	0.63782	0.5431	0.84078	0.3653
0.10768	0.1950	0.42925	0.5421	0.67458	0.5259	0.87909	0.3001
0.18823	0.3311	0.47974	0.5520	0.70626	0.5085	0.89682	0.2642
0.23961	0.3974	0.51784	0.5581	0.75105	0.4722	0.97879	0.0662
0.28965	0.4526	0.55541	0.5592	0.76707	0.4569	—	—
0.33586	0.4921	0.60554	0.5529	0.81773	0.3982	—	—
			$x CH_3CO_2CH_3 + (1 - x)C_7H_{15}(OH)$				
0.02486	0.0467	0.40114	0.5825	0.65920	0.5946	0.84211	0.4009
0.12931	0.2667	0.44655	0.6025	0.70030	0.5715	0.87310	0.3401
0.19033	0.3700	0.49450	0.6181	0.72046	0.5567	0.91776	0.2414
0.24347	0.4472	0.54288	0.6239	0.76157	0.5165	0.94393	0.1716
0.28623	0.4943	0.57632	0.6202	0.78842	0.4803	—	—
0.35327	0.5553	0.62983	0.6073	0.81491	0.4442	—	—
			$x CH_3CO_2CH_3 + (1 - x)C_8H_{17}(OH)$				
0.05910	0.1345	0.43034	0.6646	0.67532	0.6541	0.91751	0.2707
0.13348	0.2936	0.49074	0.6874	0.74677	0.5928	0.93137	0.2317
0.20746	0.4210	0.52875	0.6967	0.77347	0.5582	0.94978	0.1758
0.24943	0.4864	0.56241	0.6962	0.81022	0.5012	—	—
0.29672	0.5446	0.60085	0.6887	0.83390	0.4596	—	—
0.37780	0.6262	0.64527	0.6732	0.87541	0.3733		
			$x CH_3CO_2CH_3 + (1 - x)C_9H_{19}(OH)$				
0.06092	0.1473	0.44063	0.7304	0.72364	0.6750	0.92096	0.2845
0.14869	0.3418	0.49772	0.7554	0.77046	0.6189	0.93968	0.2220
0.22316	0.4805	0.54441	0.7611	0.80155	0.5683	0.96040	0.1536
0.30640	0.6028	0.60369	0.7557	0.85765	0.4578	—	—
0.33793	0.6430	0.63423	0.7438	0.87214	0.4192	—	—
0.40928	0.7096	0.67403	0.7202	0.89430	0.3615	—	—
			$x CH_3CO_2CH_3 + (1 - x)C_{10}H_{21}(OH)$				
0.06801	0.1833	0.46602	0.	0.73221	0.7251	0.93075	0.2880
0.12876	0.3309	0.52597	0.8119	0.74920	0.7069	0.94286	0.2456
0.18891	0.4612	0.57080	0.8158	0.77934	0.6629	0.96892	0.1427
0.22535	0.5277	0.62567	0.8021	0.82275	0.5844	0.98496	0.0698
0.30218	0.6389	0.64756	0.7949	0.85868	0.5046	—	—
0.35019	0.6976	0.68229	0.7737	0.91353	0.3475	—	—
			$x C_2H_5CO_2CH_3 + (1 - x)C_6H_{13}(OH)$				
0.05013	0.0669	0.34360	0.3368	0.62406	0.3557	0.86461	0.1914
0.09197	0.1279	0.38758	0.3516	0.66624	0.3402	0.87672	0.1754
0.14477	0.1869	0.43539	0.3669	0.71042	0.3188	0.93608	0.1045
0.19489	0.2401	0.47972	0.3728	0.75105	0.2933	—	—
0.25230	0.2845	0.55455	0.3721	0.78062	0.2702	—	—
0.30696	0.3201	0.59641	0.3641	0.82371	0.2341	—	—
			$x C_2H_5CO_2CH_3 + (1 - x)C_7H_{15}(OH)$				
0.09297	0.1376	0.36592	0.3834	0.60919	0.4048	0.85592	0.2263
0.14970	0.2100	0.45816	0.4155	0.64289	0.3910	0.91417	0.1498
0.16422	0.2243	0.51982	0.4203	0.68067	0.3741	0.96350	0.0708
0.21776	0.2815	0.54390	0.4184	0.73424	0.3418	—	—
0.28258	0.3362	0.58682	0.4104	0.79724	0.2886	—	—
			$x C_2H_5CO_2CH_3 + (1 - x)C_8H_{17}(OH)$				
0.06157	0.1035	0.46662	0.4700	0.67176	0.4364	0.91310	0.1727
0.14626	0.2224	0.49643	0.4737	0.72228	0.4007	0.91836	0.1634
0.21477	0.3059	0.52016	0.4771	0.74344	0.3813	0.93849	0.1269
0.29831	0.3838	0.58105	0.4707	0.80248	0.3252	0.96130	0.0819
0.32696	0.4041	0.58847	0.4695	0.83913	0.2802	—	—
0.36875	0.4325	0.64032	0.4508	0.87185	0.2383	—	—

Can. J. Chem. Downloaded from www.nrcresearchpress.com by 93.93.197.157 on 09/07/12
For personal use only.

TABLE 2 (*concluded*)

x	V_m^E / cm^3 mol^{-1}	x	V_m^E / cm^3 mol^{-1}	x	V_m^E / cm^3 mol^{-1}	x	V_m^E / cm^3 mol^{-1}
			$xC_2H_5CO_2CH_3 + (1 - x)C_9H_{19}(OH)$				
0.04588	0.0834	0.34772	0.4562	0.61667	0.5055	0.89721	0.2222
0.09059	0.1572	0.41324	0.4928	0.67019	0.4827	0.92810	0.1629
0.13270	0.2232	0.44507	0.5037	0.72360	0.4437	0.95270	0.1099
0.17882	0.2882	0.50464	0.5168	0.76617	0.4028	0.97836	0.0498
0.22952	0.3502	0.55466	0.5195	0.80060	0.3672	—	—
0.28973	0.4117	0.57680	0.5163	0.84880	0.3007	—	—
			$xC_2H_5CO_2CH_3 + (1 - x)C_{10}H_{21}(OH)$				
0.06159	0.1271	0.33801	0.4942	0.59867	0.5590	0.84847	0.3534
0.11484	0.2289	0.38476	0.5256	0.65283	0.5408	0.87091	0.3180
0.16981	0.3153	0.42741	0.5421	0.71156	0.5067	0.90757	0.2460
0.22432	0.3821	0.47137	0.5569	0.75250	0.4739	0.94209	0.1596
0.26685	0.4315	0.53541	0.5645	0.81026	0.4103	0.96437	0.1047
			$xC_3H_7CO_2CH_3 + (1 - x)C_6H_{13}(OH)$				
0.08583	0.0900	0.29734	0.2392	0.54791	0.2856	0.83870	0.1562
0.12701	0.1281	0.31171	0.2465	0.60743	0.2758	0.89260	0.1104
0.13491	0.1351	0.37669	0.2706	0.66048	0.2560	0.91016	0.0943
0.16739	0.1606	0.44373	0.2867	0.69940	0.2396	0.94365	0.0605
0.21640	0.1935	0.48151	0.2903	0.73613	0.2222	—	—
0.24462	0.2108	0.50626	0.2881	0.81302	0.1746	—	—
			$xC_3H_7CO_2CH_3 + (1 - x)C_7H_{15}(OH)$				
0.05114	0.0635	0.31802	0.2819	0.61294	0.3191	0.86135	0.1685
0.11733	0.1378	0.34335	0.2928	0.66402	0.3008	0.91216	0.1155
0.15428	0.1722	0.38993	0.3106	0.73098	0.2701	0.92603	0.0968
0.18168	0.1952	0.46550	0.3267	0.75749	0.2505	0.97335	0.0381
0.22291	0.2272	0.50890	0.3305	0.80330	0.2142	—	—
0.28338	0.2644	0.57165	0.3280	0.83847	0.1904	—	—
			$xC_3H_7CO_2CH_3 + (1 - x)C_8H_{17}(OH)$				
0.07662	0.1054	0.34724	0.3350	0.61481	0.3602	0.88937	0.1606
0.08424	0.1178	0.39640	0.3541	0.67487	0.3364	0.93277	0.1057
0.17110	0.2120	0.44836	0.3635	0.70387	0.3236	0.97377	0.0422
0.20948	0.2452	0.50852	0.3737	0.73596	0.3038	—	—
0.24836	0.2758	0.52009	0.3742	0.77618	0.2748	—	—
0.29691	0.3107	0.57343	0.3694	0.85456	0.2034	—	—
			$xC_3H_7CO_2CH_3 + (1 - x)C_9H_{19}(OH)$				
0.06509	0.1056	0.32133	0.3601	0.58465	0.4104	0.85827	0.2249
0.11170	0.1654	0.36873	0.3822	0.65417	0.3901	0.88879	0.1869
0.18973	0.2546	0.41846	0.4012	0.66619	0.3862	0.93148	0.1229
0.20236	0.2683	0.46252	0.4098	0.71985	0.3534	0.94571	0.0973
0.28291	0.3350	0.50013	0.4153	0.80551	0.2851	0.96551	0.0648
			$xC_3H_7CO_2CH_3 + (1 - x)C_{10}H_{21}(OH)$				
0.03400	0.0609	0.39014	0.4383	0.63538	0.4432	0.92034	0.1601
0.08259	0.1384	0.43615	0.4562	0.68045	0.4220	0.95046	0.1093
0.16249	0.2481	0.48533	0.4653	0.72670	0.3874	0.97857	0.0488
0.24093	0.3329	0.53105	0.4679	0.77336	0.3479	—	—
0.28844	0.3760	0.55993	0.4636	0.81709	0.3024	—	—
0.33435	0.4075	0.60240	0.4556	0.86770	0.2371	—	—

weakening, to allow a greater contact between the *n*-alkanol and the ester. This effect causes the positive contribution to the V_m^E values of the mixture to decrease progressively.

Upon plotting the excess molar volumes at infinite dilution of the *n*-alkanols, $V_{m,2}^{E\infty}$, as a function of m in $C_mH_{2m+1}CO_2CH_3$, the distribution of points appears as shown in Fig. 2, where the values of $V_{m,2}^{E\infty}$ are also presented for *n*-heptane with different methyl alkanoates (Dusart *et al.* (5)). No values are available for methyl pentanoate or methyl hexanoate, but it seems that the $V_{m,2}^{E\infty}$ obtained with methyl butanoate are slightly higher than expected, a behaviour analogous to that reported by Dusart *et al.* and which can be readily observed in the graph. This anomaly of methyl butanoate was explained by the formation of an intramolecular cyclization in the molecule of the ester, a

Can. J. Chem. Downloaded from www.nrcresearchpress.com by 93.93.197.157 on 09/07/12
For personal use only.

TABLE 3. Coefficients of eq. [1] and standard deviations, $s(V_m^E)/(cm^3\ mol^{-1})$

System		K	A_0	A_1	A_2	A_3	$s(V_m^E)$
$xCH_3CO_2CH_3$	$+ (1-x)C_6H_{13}(OH)$	0.568	1.5048	4.4289	−9.3945	6.6289	0.0011
	$+ (1-x)C_7H_{15}(OH)$	0.481	1.7701	4.3014	−9.3208	6.6518	0.0014
	$+ (1-x)C_8H_{17}(OH)$	0.876	2.3832	1.1698	−2.1743	2.4662	0.0015
	$+ (1-x)C_9H_{19}(OH)$	0.766	2.4304	1.9885	−3.5541	3.3271	0.0016
	$+ (1-x)C_{10}H_{21}(OH)$	0.832	2.8395	1.1495	−2.8836	3.7286	0.0016
$xC_2H_5CO_2CH_3$	$+ (1-x)C_6H_{13}(OH)$	0.440	1.3453	1.3189	−3.0734	2.1287	0.0018
	$+ (1-x)C_7H_{15}(OH)$	1.061	1.6304	0.1698	−0.2555	0.5427	0.0009
	$+ (1-x)C_8H_{17}(OH)$	2.569	1.7501	0.6580	−0.5651	0.4859	0.0011
	$+ (1-x)C_9H_{19}(OH)$	0.574	1.8153	0.9363	−1.9027	1.6655	0.0012
	$+ (1-x)C_{10}H_{21}(OH)$	0.826	2.2182	0.2774	−1.7411	2.4389	0.0020
$xC_3H_7CO_2CH_3$	$+ (1-x)C_6H_{13}(OH)$	0.251	1.2720	−0.6689	1.1292	−0.5961	0.0012
	$+ (1-x)C_7H_{15}(OH)$	0.241	1.2196	0.8109	−1.8948	1.2934	0.0016
	$+ (1-x)C_8H_{17}(OH)$	0.675	1.5225	−0.1059	−0.2237	0.5223	0.0014
	$+ (1-x)C_9H_{19}(OH)$	0.648	1.7214	−0.1931	−0.2886	0.7384	0.0013
	$+ (1-x)C_{10}H_{21}(OH)$	7.810	1.7983	0.6444	−0.2014	0.3333	0.0013

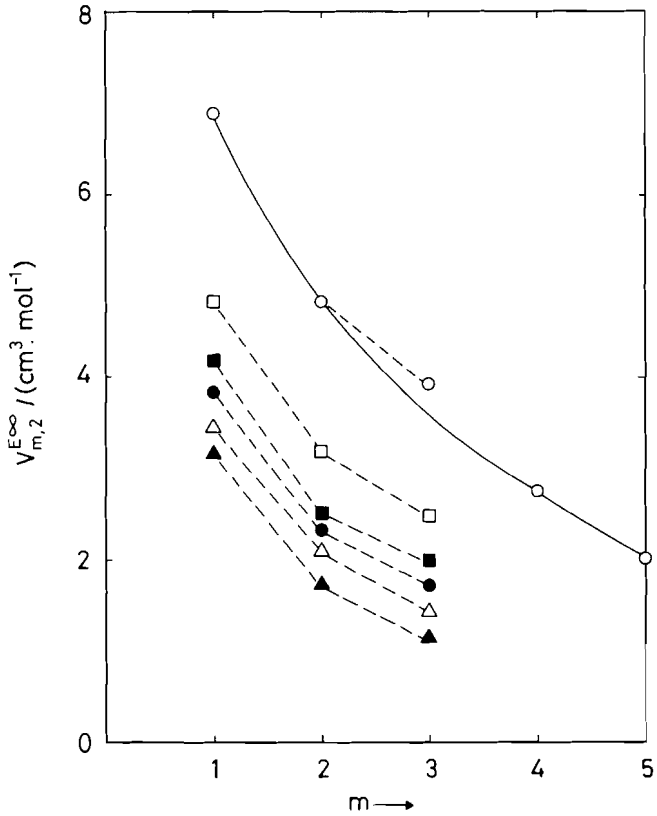

FIG. 2. Plots of $V_{m,2}^E$ for alkan-1-ols $C_nH_{2n+1}(OH)$: (▲), $n = 6$; (△), $n = 7$; (●), $n = 8$; (■), $n = 9$; (□), $n = 10$ in methyl alkanoates, $C_mH_{2m+1}CO_2CH_3$ (m = 1, 2, 3) as a function of m. (○), Values obtained by Dusart *et al.* (5) for mixtures of *n*-heptane with methyl alkanoates.

relatively stable 6-atom cycle being formed. This cyclization causes the solute–solvent interactions to decrease and, moreover, produces a shortening of its apparent volume, originating the increase of the excess volume at infinite dilution. In this case, the formation of the quasi-cycle by a hydrogen bond may be enhanced by the presence of the —OH group in the *n*-alkanol.

1. J. ORTEGA, M. I. PAZ-ANDRADE, E. RODRIGUEZ-NUÑEZ, and L. ROMANI. Aust. J. Chem. **38**, 1435 (1985).
2. J. ORTEGA, R. BRAVO, E. JIMENEZ, and M. I. PAZ-ANDRADE. J. Chem. Thermodyn. **18**, 403 (1986).
3. J. ORTEGA. J. Indian Chem. Soc. **63**, 961 (1986).
4. J.-P. E. GROLIER, O. BALLET, and A. VIALLARD. J. Chem. Thermodyn. **6**, 895 (1974).
5. O. DUSART, C. PIEKARSKI, S. PIEKARSKI, and A. VIALLARD. J. Chim. Phys. **73**, 837 (1976).
6. TRC Tables-Nonhydrocarbons. Thermodynamic Research Center, Texas A&M University, College Station, TX. 1985.
7. J. A. RIDDICK, W. B. BUNGER, and T. K. SAKANO. Organic solvents. Techniques of chemistry. Vol. 11. 4th ed. Wiley-Interscience, New York. 1986.
8. R. C. WILHOIT and B. J. ZWOLINSKI. J. Phys. Chem. Ref. Data, Vol. 11. 1973. Supplement No. 1.
9. J. ORTEGA, J. S. MATOS, M. I. PAZ-ANDRADE, and E. JIMENEZ. J. Chem. Thermodyn. **17**, 1127 (1985).
10. J. ORTEGA, J. A. PEÑA, and M. I. PAZ-ANDRADE. Aust. J. Chem. **39**, 1685 (1986).
11. H. V. KEHIAIAN, R. BRAVO, M. P. BARRAL, M. I. PAZ-ANDRADE, R. GRIEN, and J.-P. E. GROLIER. Fluid Phase Equilibria, **17**, 187 (1984).

Can. J. Chem. Downloaded from www.nrcresearchpress.com by 93.93.197.157 on 09/07/12
For personal use only.

Étude des courants périodiques observés lors de la dissolution électrochimique du nickel en présence d'ions iodure et chlorure en milieu aqueux

LI BEN LE[1] ET OLIVIER VITTORI[2]

Laboratoire d'électrochimie analytique, Unité associée n° 417 du Centre national de la recherche scientifique, Laboratoire des interphases, Université Lyon 1, 43 boulevard du 11 novembre 1918, 69622 Villeurbanne CEDEX, France

Reçu le 24 novembre 1987

LI BEN LE et OLIVIER VITTORI. Can. J. Chem. **66**, 1525 (1988).

Faisant appel à la voltamétrie à faible balayage (<2 mV/s), on a étudié l'électrodissolution du nickel en présence d'ions chlorure et iodure. On a observé que la vitesse de dissolution du nickel est liée à la concentration en chlorure et que l'addition d'iodure modifie la forme des courbes. On a noté que des oscillations du courant se produisent après un délai qui devient plus court au fur et à mesure de l'augmentation de la concentration en iodure. Si la concentration en iodure est maintenue à un niveau faible, ces oscillations se produisent sur un large éventail de potentiels. Une augmentation de cette concentration supprime les oscillations et il apparaît alors deux pics; le plus cathodique devient de plus en plus important. On discute de l'effet produit par l'addition d'agents de surface; le *p*-octylbenzènesulfonate de sodium est le seul à supprimer les oscillations, même à faible concentration alors que l'amidon agit progressivement de 1 à 40 g/L. Les changements de couleur qu'on note à la surface du nickel durant les oscillations suggèrent qu'il se produit une dissolution préférentielle aux jonctions des grains. Ceci explique la couleur noire qu'on peut observer en alternance avec l'aspect métallique; le nickel se couvre alors de particules finement divisées qui se dissolvent rapidement. L'iodure qui apparaît occasionnellement à de tels potentiels anodiques est probablement impliqué dans le processus de dissolution.

LI BEN LE and OLIVIER VITTORI. Can. J. Chem. **66**, 1525 (1988).

Electrodissolution of nickel in the presence of chloride and iodide ions has been investigated using low sweep voltammetry (<2 mV/s). It has been observed that the rate of dissolution of nickel is related to the concentration of chloride, and that addition of iodide modifies the shape of the curves. Oscillations of the current are noticed after a delay shortened by increasing the iodide concentration. These oscillations occur over a wide range of potential provided the iodide concentration is kept low. Increasing this concentration suppresses the oscillations, while two peaks appear, the more cathodic becoming progressively larger. Addition of some surfactants is discussed and progressively larger. Addition of some surfactants is discussed and only SOBS (sodium *p*-octylbenzene sulfonate) suppresses the oscillations even at low concentration, while starch acts progressively from 1 to 40 g/L. Changes of color of the nickel surface during the oscillations suggests a preferential dissolution at the grain boundaries, explaining the black color observed alternatively with a metallic appearance, the nickel being at this time covered with finely divided particles that dissolve quickly. Iodide, appearing only occasionally at such anodic potentials, is probably involved in the dissolution process.

Can. J. Chem. Downloaded from www.nrcresearchpress.com by 93.93.197.157 on 09/07/12
For personal use only.

L'étude du comportement anodique des métaux est un vaste domaine d'un grand intérêt pour les études de corrosion, comme l'a souligné Rangarajan et coll. (1). Cet auteur a rassemblé un grand nombre d'exemples de courants périodiques apparaissant lors d'un balayage anodique des potentiels, en milieu aqueux. Ce phénomène est observé avec différents métaux tels que le zinc (2), l'or (3), le fer (4), et le nickel (5). Sauf pour le zinc qui présente des oscillations en milieu alcalin, tous les autres exemples ont été décrits en milieu acide (1, 3–5). D'autres études dans les acides chlorhydrique et sulfurique ne citent pas de telles oscillations mais soulignent le rôle des ions chlorure dans l'accélération du processus de corrosion (6–9). Un comportement identique a été signalé dans des mélanges méthanol – acide chlorhydrique (10) ou en milieu neutre (11). Dans ce dernier cas un film protecteur d'oxyde peut apparaitre, mais la présence d'ions chlorure, bromure et fluorure a une grande influence sur la vitesse de destruction du film. Plusieurs tentatives pour donner une explication théorique satisfaisante au comportement du nickel ont été proposées récemment par Saraby-Reintjes (11), mais les modèles requièrent la connaissance de plusieurs constantes du système et de ce fait se révèlent difficiles à appliquer. Il apparait aussi que la corrosion par piqûre du nickel est influencée par la taille des grains comme l'ont souligné Cid et Petit (12), qui ont traité thermiquement du nickel polycristallin pour accroitre la taille des grains. Ainsi la corrosion se produit en général d'abord aux joints de grains et se trouve très ralentie après un tel traitement.

Dans le présent article on décrit les oscillations du courant qui peuvent être observées quand un fil de nickel est immergé dans une solution d'ions chlorure dans laquelle la concentration en ion iodure est croissante, et que le potentiel appliqué est rendu progressivement anodique.

Partie expérimentale

Les balayages de potentiel ont été appliqués avec un polarographe Tacussel (France), type PRG5, associé à un enregistreur EPL2 de même marque. Les vitesses usuelles ont été 1 ou 2 mV/s. Une cellule a trois électrodes a été employée, avec une électrode de référence au calomel, saturée. L'électrode auxiliaire était un fil de platine et l'électrode de travail un fil de nickel de 0,5 mm de diamètre de pureté 99,99% Aldrich (U.S.A.). La longueur immergée était de 5 mm dans tous les essais et la surface de l'électrode de 7,85 mm^2.

Les réactifs ont été choisis de qualité analytique. Le pH des solutions a été a vérifié et trouvé situé entre 6 et 7, exception faite pour NH_4Cl 1 M (tableau 2), pour lequel il était de 5. L'eau était déionisée puis distillée. L'oxygène n'était pas chassé par l'azote, et les essais ont été effectués à 20 ± 0,1°C.

Résultats et discussion

Le potentiel de départ a été fixé à −0,1 V/ecs, une valeur à laquelle aucune réaction électrochimique ne se produit. La vitesse maximum de balayage n'a jamais excédé 2 mV/s pour s'approcher des conditions d'un état quasi-stationnaire lors de la dissolution. Les courbes intensité–potentiel tracées dans des solutions de concentration croissante en KCl montrent que le

1. Adresse présente : Université de Hangzhou, section de chimie, Hangzhou, République populaire de Chine.

2. Auteur à qui toute correspondance doit être adressée.

Printed in Canada / Imprimé au Canada

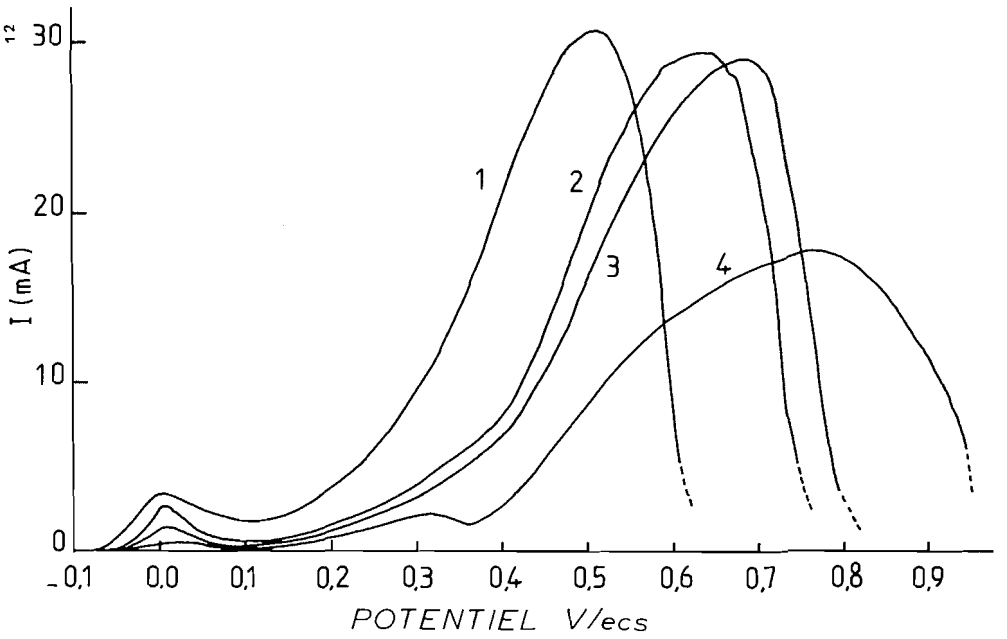

FIG. 1. Courbes de dissolution électrochimique du nickel en fonction de la concentration en ions chlorure. Courbes : 1, 2,68 M; 2, 1,34 M; 3, 1,00 M; 4, 0,67 M.

nickel se dissout progressivement plus rapidement. On observe toujours un premier pic proche de 0,0 V/ecs, dont l'importance est en relation avec la concentration des ions chlorure, et si celle-ci est faible le pic n'est pas observable (figure 1). Il semble que ce pic peu important correspond à la formation d'une couche d'hydroxyde de nickel $Ni(OH)_2$ en surface. Le second pic très intense correspond à la dissolution totale du nickel (figure 1). En solution non agitée on observe sous le fil de nickel la formation d'une colonne liquide verticale de densité supérieure à celle de la solution. Cette observation visuelle est d'autant plus nette que la dissolution est importante. La faible stabilité des ions complexes du nickel en présence d'ions chlorure et iodure incline a penser que le nickel est simplement sous forme d'aquocomplexes.

Les ions Ni^{2+} formés descendent par gravité au fond de la cellule, où ils réagissent avec les ions hydroxyles apparus à l'électrode auxiliaire qui est alors cathodique. L'hydroxyde de nickel apparait progressivement mais le pH au voisinnage du fil de nickel ne varie pas si la cellule est de dimension suffisante (environ 100 mL d'électrolyte support), et si l'électrode auxiliaire n'est pas trop proche. La correction de chute ohmique ne s'impose pas ici compte tenu de la conductivité élévée de l'électrolyte et de la faible vitesse de balayage.

Une concentration de 1 M en KCl a été retenue pour l'étude de l'influence des ions iodure. Un essai préliminaire dans KI 0,024 M, soit 4 g/L, a montré que le nickel ne se dissout que très lentement. L'addition de quantités croissantes de KI dans KCl 1 M révèle une grande différence par rapport aux tracés précédents dans KCl seul (figure 2). En premier on n'observe plus le pic de faible intensité, à 0,0 V/ecs, mais on remarque que la dissolution débute assez brutalement vers +0,15 V/ecs. Puis la courbe intensité–potentiel devient quasi-rectiligne et de pente positive. La figure 3 montre l'évolution progressive des courbes. Il faut noter l'apparition d'oscillations de façon assez brutale au sommet de la partie rectiligne. Le potentiel auquel se produisent ces oscillations est d'autant moins anodique que la concentration en ions iodure s'accroit. Sur la figure 3 les oscillations sont schématisées pour simplifier le dessin. En fait

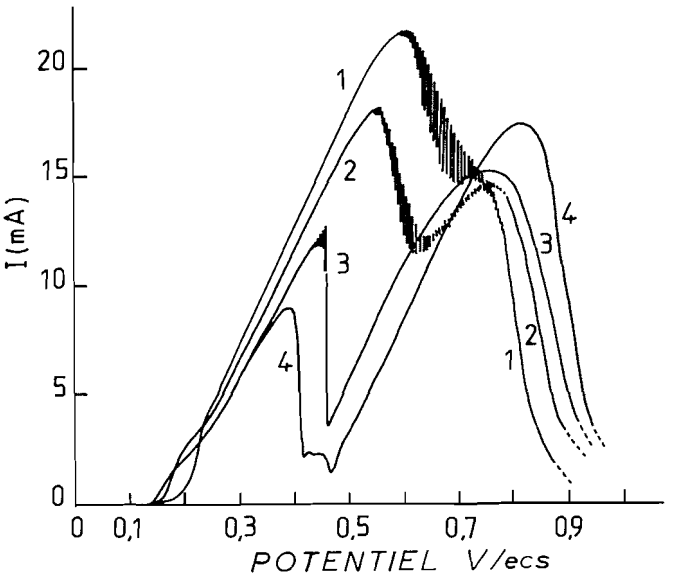

FIG. 2. Courbes de dissolution électrochimique du nickel en fonction de la concentration en ions iodure, pour une concentration constante en ions chlorure ([KCl] = 1 M). Courbes : 1, 0,012 M; 2, 0,024 M; 3, 0,048 M; 4, 0,12 M.

leur fréquence fait que l'enregistrement apparait comme une zone teintée et il faut augmenter nettement la vitesse d'enregistrement pour les discerner. Durant les oscillations le courant moyen décroit et un second pic se forme d'importance croissante avec l'augmentation de la concentration en ion iodure.

Parallèlement on constate que la zone d'oscillations diminue pour pratiquement disparaitre si $[I^-] > 0,12$ M environ. Les deux pics sont alors toujours observables et la dissolution est totale. Durant les oscillations on observe que lorsque le courant décroît le fil est de couleur métallique et lorsqu'il croît la couleur devient noire. Des examens sur plaque de nickel de 0,5 cm^2 de surface ont confirmé cette observation. La dissolution du fil reste progressive et de symétrie radiale.

Can. J. Chem. Downloaded from www.nrcresearchpress.com by 93.93.197.157 on 09/07/12
For personal use only.

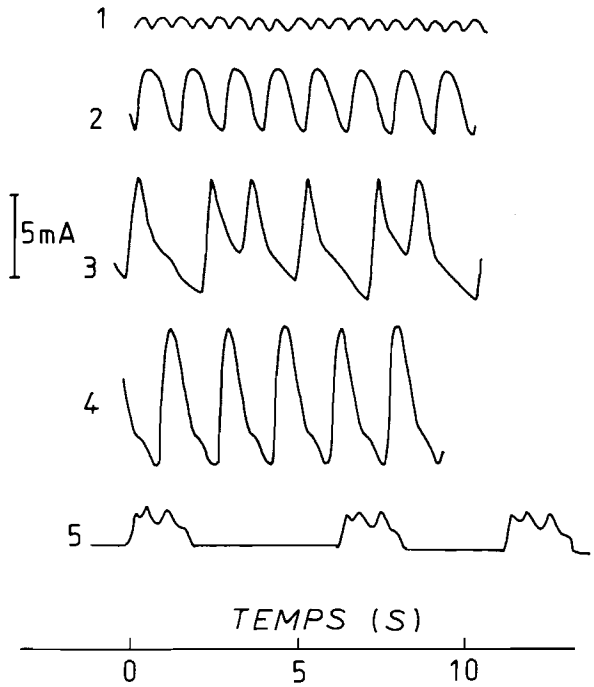

FIG. 3. Observation des oscillations de courant en milieu KCl 1 M pour une concentration en ions iodure de 0,096 M, à différents potentiels. 1, 640 mV; 2, 660 mV; 3, 700 mV; 4, 750 mV; 5, 860 mV.

On note l'apparition d'iode sous la forme I_3^- lors des oscillations et pas avant dans la partie rectiligne croissante du courant. De nouveau la densité plus élevée de la colonne liquide sous le fil de nickel permet l'accumulation d'iode au fond de la cellule. Toutefois les quantités d'iode formé restent très faibles, ce qui indique qu'il ne s'agit ici que d'une réaction secondaire minoritaire. Pour observer plus précisément les oscillations on a balayé en potentiel jusqu'à la zone où elles se produisent, puis enregistré à grande vitesse en maintenant le potentiel fixe. En fait la valeur moyenne du courant reste élevée (figure 3). On constate sur la figure 3 que ces oscillations sont assez régulières à court terme : 10–20 oscillations, mais elles évoluent un peu au cours du temps. Parfois une oscillation irrégulière apparait. La forme du courant dépend du potentiel appliqué et de la concentration en iodure. On a même constaté entre des trains d'oscillations des périodes de quelques secondes durant lesquelles le courant reste constant (exemple à +0,86 V/ecs, figure 3.)

L'étude par fluorescence X d'une plaque de nickel de 5 mm de coté, soumise à des balayages de potentiels arrêtés à +0,45 et +0,55 V/ecs dans KCl 1 M et KI 0,024 M montre que $Ni(OH)_2$ est présent (raie à 0,2340 nm). Le nickel seul donne deux raies à 0,2020 et 0,1750 nm. Si on se réfère à la courbe 2, figure 3, on constate que 0,45 V/ecs est situé avant les oscillations tandis que +0,55 V/ecs est au début de celles-ci. Ceci montre que les ions iodure attaquent essentiellement le nickel métal. Comme l'alternance de couleur, métallique et noire, traduit lors des oscillations le passage d'un état poli à un état granulaire avec de très fines particules (type nickel de Raney), on est conduit à penser que ce sont les joints de grains qui sont préférentiellement attaqués.

Lors de changements alternés de la couleur de la surface il a été observé, par examen à la loupe, que l'iode se forme quand la surface du nickel a l'aspect métallique, ce qui provoque des variations de teinte de la colonne liquide sous l'électrode.

TABLEAU 1. Influence de quelques agents tensioactifs

Composé tensioactif	Concentration (g/L)	Influence
Bromure de *N*-cétyltriméthylammonium	1	Sans
	7	Faible
Chlorure de benzenethonium	1	Sans
	8	Faible
SDS, dodécylsulfate de sodium	1	Faible
Alizarine sulfonate de sodium	1	Sans
SOBS *p*-octylbenzene sulfonate de sodium	1	Oui
Amidon	1–40	Oui

Ces observations suggèrent un double mécanisme pour la dissolution du nickel lorsqu'il est porté à un potentiel suffisamment négatif pour que deux réactions se produisent.

Dans la partie montante de la courbe *i–E* et jusqu'au début des oscillations il se produit la réaction simple :

$$Ni \rightarrow Ni^{2+} + 2e$$

Compte tenu de la valeur du produit de solubilité de $Ni(OH)_2$ qui est de l'ordre de 10^{-14} et du fait que le milieu KCl + KI peut être considéré neutre, la formation de l'hydroxyde en surface s'explique par le fait que c'est en surface que la concentration instantannée de Ni^{2+} est la plus forte. Quand la zone des oscillations débute, une deuxième réaction concurrence la première :

$$3I^- \rightarrow I_3^- + 2e$$

Cependant la faible quantité d'iode observée suggère qu'il y a réaction chimique selon :

$$Ni + I_3^- \rightarrow Ni^{2+} + 3I^-$$

Cette réaction se produit préférentiellement aux joints de grains que l'on peut considérer comme plus fragiles que les microcristaux. Ceci est en accord avec les remarques de Cid et Petit (12) qui indiquaient que le recuit du nickel diminuait la corrosion par piqûre.

Comme il s'agit d'un phénomène qui se produit à l'interface métal–solution, on peut penser que l'addition de composés organiques, tels que les agents tensioactifs, peut modifier ou supprimer les oscillations en limitant l'apparition d'iode, ou en uniformisant l'attaque du nickel. Comme le montre le tableau 1 plusieurs composés à la concentration de 1 g/L ont été essayés. Il s'avère que seuls le SOBS, ou *p*-octylbenzenesulfonate de sodium, et l'amidon provoquaient une disparition des oscillations. Le SOBS est très actif car dés 0,001 M (figure 4) il fait disparaitre les fluctuations de courant tandis que l'amidon a un rôle progressif entre 1 et 40 g/L. Tous les agents tensioactifs n'ont pas été testés sur une large gamme de concentration et on s'est limité à ceux qui donnaient le résultat le plus net à 1 g/L. Les sels d'ammonium quaternaire qui sont chargés positivement ne peuvent s'adsorber à ces potentiels et sont donc sans influence. On peut également signaler que l'addition de faibles quantités de thiourée supprime les oscillations et décale la courbe vers les potentiels cathodiques, c'est à dire rend plus aisée la dissolution du nickel et parait inhiber l'action des ions iodure (figure 4).

Enfin on a recherché d'autres milieux salins dans lesquels les oscillations pouvaient apparaitre (tableau 2). Deux remarques peuvent être faites. La première est que seuls les milieux riches en ions chlorure ou bromure permettent les oscillations à la

Can. J. Chem. Downloaded from www.nrcresearchpress.com by 93.93.197.157 on 09/07/12
For personal use only.

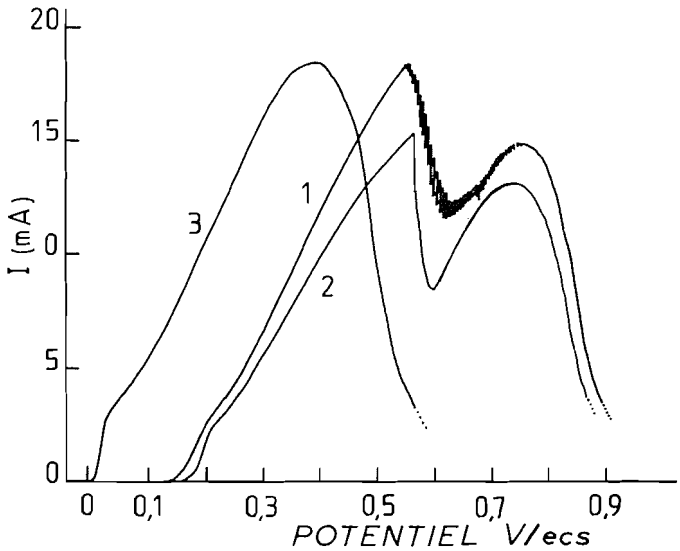

FIG. 4. Courbes de dissolution électrochimique du nickel en milieu KCl 1 M en présence d'ions iodure 0,024 M. Courbe 1 : sans additif; courbe 2 : avec 0,0001 M de SOBS; courbe 3 : avec 0,0026 M de thiourée.

TABLEAU 2. Milieux donnant des oscillations

Système	Concentration (g/L)	Oscillations
KCl 1 M + KI	2	Oui
KBr 1 M + KI	2	Oui
NaCl 1 M + NaI	2	Oui
NH_4Cl 1 M + NH_4I	2	Oui
NH_4Cl 1 M + KI	2	Oui
KCl 1 M + KF	4	Non
KCl 1 M + KBr	2	Non
KF 1 M + KI	2	Non
$(NH_4)_2SO_4$ 1 M + NH_4I	2	Non
$NH_4OOC\text{-}CH_3$ 1 M + KI	2	Non

condition d'être associés aux ions iodure. La seconde est que la présence d'ions iodure n'est pas une condition suffisante puisque les milieux sulfate et acétate n'ont pas permis d'observer la moindre oscillation. L'insolubilité de certains sels ne peut être évoquée puisqu'avec les ions chlorure, iodure, acétate et sulfate, le nickel donne des composés très solubles, et le fluorure moins soluble (4 g/L) ne peut intervenir dans un blocage partiel de la dissolution, qui reste totale dans toutes les expériences.

En conclusion, l'étude de l'oxydation anodique du nickel en présence d'ions chlorure et iodure a révélé un comportement particulier du métal, et les oscillations du courant ont été attribuées à des réactions parallèles avec formation intermédiaire d'iode, dont la réactivité se manifeste par une attaque du métal dans ses zones les moins résistantes.

1. K. S. INDIRA, S. K. RANGARAJAN et K. S. G. DOSS. J. Electroanal. Chem. **21**, 57 (1969).
2. R. C. V. PIATTI, J. J. PODESTA et A. J. ARVIA. Electrochim. Acta, **25**, 827 (1980).
3. J. J. PODESTA, R. C. V. PIATTI et A. J. ARVIA. Electrochim. Acta, **24**, 633 (1979).
4. J. J. PODESTA, R. C. V. PIATTI et A. J. ARVIA. J. Electrochem. Soc. **126**, 1363 (1979).
5. J. OSTERWALD et H. G. FELLER. Electrochim. Acta, **7**, 523 (1962).
6. A. BENGALI et K. NOBE. J. Electrochem. Soc. **126**, 1118 (1979).
7. M. ZAMIN et M. B. IVES. J. Electrochem. Soc. **121**, 1141 (1974).
8. D. D. N. SINGH et M. K. BANERJEE. Corrosion, **42**, 156 (1986).
9. K. CARR, S. BAER et C. A. MELENDRES. Corrosion, **42**, 307 (1986).
10. B. MACDOUGALL et M. J. GRAHAM. J. Electrochem. Soc. **132**, 2553 (1985).
11. A. SARABY-REINTJES. Electrochim. Acta, **30**, 387 (1985); **30**, 403 (1985).
12. M. CID et M. C. PETIT. Proceedings of the 5th Intern. Symposium on Passivity. Elsevier, Bombranes, France. 1983. p. 335.

Can. J. Chem. Downloaded from www.nrcresearchpress.com by 93.93.197.157 on 09/07/12
For personal use only.

Kinetics of crystal growth of calcium sulfate dihydrate. The influence of polymer composition, molecular weight, and solution pH

ZAHID AMJAD
The BFGoodrich Company, Avon Lake, Technical Center, Avon Lake, OH 44012, U.S.A.

Received October 23, 1987

ZAHID AMJAD. Can. J. Chem. **66**, 1529 (1988).

A seeded crystal growth technique has been used to study the influence of solution pH and temperature ranging from 25 to 50°C on the performance of polymers of varying functional groups as calcium sulfate dihydrate ($CaSO_4.2H_2O$, gypsum) crystal growth inhibitors. Results indicate that at constant temperature and at a constant solution pH, crystallization in the presence of polyacrylic acids is preceded by an initial slow growth reaction, hereafter called induction period, following which crystal growth of gypsum proceeds with a rate close to that in pure supersaturated solution. Results suggest that at a constant pH, polyacrylic acid concentration, molecular weight, and temperature greatly affect the duration of induction period. Kinetic data collected as a function of solution pH in the range 2.5 to 9.0 suggest that solution pH has a marked effect on the induction period. The observed dependence of induction period on solution pH may be explained in terms of the degree of ionization of polyacrylic acid. Among the polymers of varying functional groups studied, i.e. carboxyl, sulfonate, acrylamide, dimethyldiallylammonium, etc., only those polymers having carboxyl group showed marked inhibitory activity for the growth of gypsum crystals.

ZAHID AMJAD. Can. J. Chem. **66**, 1529 (1988).

On a fait appel à une technique de croissance de cristaux ensemencés pour étudier l'influence du pH de la solution ainsi que de la température (allant de 25 à 50°C) sur la performance de polymères portant divers groupements fonctionnels comme inhibiteurs de la croissance de cristaux du sulfate de calcium dihydraté ($CaSO_4.2H_2O$, gypse). Les résultats indiquent que, à température constante et à un pH de solution constant, la cristallisation en présence d'acides polyacryliques est précédée par une réaction initiale de croissance qui est lente, appelée par la suite période d'induction, et qui est suivie par une croissance du cristal de gypse se produisant à une vitesse qui est proche de celle qui est observée avec une solution sursaturée pure. Les résultats suggèrent que, à des pH constants, la concentration en acide polyacrylique, le poids moléculaire et la température influencent beaucoup la période d'induction. Les données cinétiques recueillies en fonction du pH allant de 2,5 à 9,0 suggèrent que le pH de la solution a une influence marquée sur la période d'induction. On peut expliquer cette observation en fonction du degré d'ionisation de l'acide polyacrylique. Parmi les polymères portant divers groupements fonctionnels, comme carboxyle, sulfonate, acrylamide, diméthyldiallylammonium, etc, seuls les polymères portant des groupements carbonyles présentent une activité inhibitrice marquée sur la croissance des cristaux de gypse.

[Traduit par la revue]

Can. J. Chem. Downloaded from www.nrcresearchpress.com by 93.93.197.157 on 09/07/12
For personal use only.

Introduction

Considerable attention has been given to the various forms of calcium sulfate crystallizing from aqueous solution as affected by temprature, pH, solution stoichiometric ratio of lattice ions, and impurities level (1–4). These and other important factors involved in the nucleation and growth of calcium sulfate dihydrate ($CaSO_4.2H_2O$, gypsum), hemihydrate ($CaSO_4.\frac{1}{2}H_2O$, plaster of Paris), and anhydrite ($CaSO_4$) should have direct application to the control and inhibition of scale formation in industrial water systems, oil production, geothermal, and desalination systems (5–7). In many cases the deposition of hard crystalline scale on heat transfer surfaces results in decreased thermal efficiency of the system. To preclude an excessive rise of operating costs, scale formation has to be prevented.

The effectiveness of a number of inhibitors in preventing or reducing the crystallization of calcium sulfate has been the subject of numerous investigations. McCartney and Alexander (8) have examined the effect of a number of polyelectrolytes on the growth rate of calcium sulfate dihydrate. It was found that polymers-containing carboxyl groups such as carboxymethyl cellulose, aliginic acid, polymethacrylic acid, and polyacrylic acid were particularly effective as $CaSO_4 \cdot 2H_2O$ crystal growth inhibitors. Kuntz (9) arrived at similar conclusions after studying the effect of various protein hydrolyzates and their synthetic analogues on the crystallization of calcium sulfate.

The influence of molecular weight on the polyelectrolytes on the precipitation of $CaSO_4.2H_2O$ from aqueous solutions have been the subject of numerous investigations. Jones (10) in his study on the effect of molecular weight (50 000 – 400 000) of carboxymethyl cellulose (CMC) reported that high molecular weight CMC polymers were the least effective and the effectiveness increases as the molecular weight of the polymer decreases. Flesher *et al.* (11) in their study on the evaluation of a variety of polyelectrolytes at high temperature, as $CaSO_4.2H_2O$ scale inhibitors showed that the efficiency of the polyelectrolyte decreases with increasing molecular weight in the range 2 000 – 750 000. Amjad (12) in a recent study on the influence of polyacrylates in controlling $CaSO_4.2H_2O$ dihydrate scale formation on heat transfer surfaces reported that the molecular weight of the polyacrylate plays an important role in the inhibition of $CaSO_4.2H_2O$ crystal growth from aqueous solution. The amount of $CaSO_4.2H_2O$ scale deposited on heat exchanger was found to be higher in the case of higher molecular weight polyacrylate (mw = 240 000) than that obtained in the presence of 2 100 molecular weight polyacrylate.

Several studies have been reported on the influence of solution pH on the performance of polymeric and non-polymeric inhibitors on the crystal growth of sparingly soluble salts. Recently Griffiths *et al.* (13) have shown that the performance of phosphonic acids as $CaSO_4.2H_2O$ crystal growth inhibitor improves with increasing pH, and have attributed this improvement to an increase in the degree of deprotonation. Leung and Nancollas (14), using seeded growth technique, arrived at similar conclusions after studying the effect of benzene polycarboxylic acids on the crystal growth of $BaSO_4$. Recently,

TABLE 1. Analytical characteristics of polymers

Polymer	Composition	Acronym	Mol. wt.
Commercial-A	Poly(acrylic acid) (K-XP75)	P-AA	2 600
Commercial-B	Poly(acrylic acid) (K-XP74)	P-AA	6 000
Experimental-C	Poly(acrylic acid)	P-AA	10 000
Experimental-D	Poly(acrylic acid)	P-AA	22 000
Experimental-E	Poly(acrylic acid)	P-AA	50 000
Experimental-F	Poly(acrylic acid)	P-AA	800
Experimental-G	Poly(acrylamide)	P-Am	6 000
Experimental-H	Poly(dimethyldiallylammonium chloride)	P-DMDAAC	6 000
Experimental-I	Poly(isopropylacrylamide)	P-iPrAm	10 000
Experimental-J	Poly(2-acrylamido-2-methyl propane sulfonic acid)	P-SA	10 000

Sheehan and Nancollas (15) have examined the effect of pH in the range 6–9 on the growth rate of $CaC_2O_4.H_2O$ in the presence of polyacrylate. It was found that the rate of growth was independent of solution pH over the pH range studied. Because of the recent interest in the inhibitory effect of polymeric carboxylic acids as crystal growth inhibitors for sparingly soluble salts, in the present work the seeded growth method has been used to investigate the influence of solution pH in the range 2.5–9.0, on the rate of $CaSO_4.2H_2O$ crystal growth in the presence of poly(acrylic acid) (mw 2 600 – 50 000), poly(acrylamide), poly(isopropylacrylamide), poly(2-acrylamido 2-methylpropane sulfonic acid), and poly(dimethyldiallylammonium chloride).

Experimental

Reagent grade chemicals and grade A glassware were used. Stock solutions of calcium chloride and sodium sulfate were prepared using distilled water, filtered through 0.22-μm filter paper (Millipore Corp.) and analyzed as described previously (4). The polymers used in this study were selected from the range of commercial and experimental (BFGoodrich Chemical) materials. Polymer concentrations given in this report are on dry polymer basis. All polymers were tested under equal growth conditions, i.e. at the same supersaturation and pH of the bulk solution. Some of the polymers were also tested at different pH values. Buffers employed for pH control were acetic acid/sodium acetate, trihydroxymethylaminomethane/trishydroxymethylaminomethane hydrochloride, and ammonia/ammonium chloride. pH was measured at 25°C using a Brinkmann pH meter (model 632, Brinkmann Instruments, Westbury, NY) equipped with a pair of glass and calomel electrodes. The system was calibrated before each set of measurements and checked afterwards, against NBS standard buffers. Calcium ion analyses were performed by standard EDTA titration.

Calcium sulfate dihydrate crystals were prepared (4) by the slow dropwise addition of 500 mL of 0.2 *M* calcium chloride solution to 500 mL 0.2 *M* sodium sulfate solution at 70°C. The crystals were washed repeatedly with distilled water until free of chloride ions and were aged at least six months before being filtered to get dry powder for use in the crystal growth experiments. The crystals were characterized by X-ray powder diffraction.

As described elsewhere (1, 4, 16) the seeded crystal growth of a sparingly soluble salt provides a sensitive and reproducible technique for the evaluation of inhibitor effects. The technique involves the addition of a fixed amount of seed crystals to a metastable solution of the inorganic salt followed by periodic analysis for changes in the salt concentration. In the present study, seeded crystal growth experiments were conducted in a stirred double-walled glass cell maintained at 25°C, containing a metastable calcium sulfate solution. The metastable solution (150 mL) was prepared by carefully mixing equimolar volumes of calcium chloride and sodium sulfate such that the final $CaSO_4$ solution concentration would be 3.50×10^{-2} *M*. Solution pH was controlled by the addition of buffers at a total conjugate acid/base concentration of 2.0×10^{-3} *M*, a concentration at which the influence of the buffering components on the rate of crystal growth was proved to be negligible. Polymers were added after the addition of $CaCl_2$, but before the addition of Na_2SO_4, as dilute solutions in water. Crystal growth was initiated in these supersaturated solutions by the addition of a known weight of seed crystals and the reaction monitored by analyzing aliquots of the filtered (0.22 micron filter, Millipore) solution for calcium by EDTA titration.

Results and discussion

The analytical characteristics of the polymers and the experimental conditions used in this study are summarized in Tables 1 and 2, respectively. The typical curves for calcium concentrations against time are shown in Fig. 1. It can be seen that the growth of $CaSO_4.2H_2O$ takes place immediately upon the addition of gypsum seed crystals to the metastable supersaturated solutions. The rate of crystal growth, R, of $CaSO_4.2H_2O$ from supersaturated solutions containing equivalent concentration of ions has been found to follow an equation of the form

$$[1] \quad R = -\mathrm{d}Ca/\mathrm{d}t = ks(T\mathrm{Ca} - T_e\mathrm{Ca})^2$$

in which TCa is total calcium concentration at time t, T_eCa is the equilibrium solubility value, k is a rate constant, s is a function of number of available growth sites present in the seed crystals, and t is the time in minutes. Figure 2 illustrates the linearity of the plots of the integrated form of eq. [1]. Reproducibility is illustrated by the agreement between the results of experiments 2 and 5, respectively. Results of experiments 3 and 5 in Table 2 indicate that the rate of crystallization is directly proportional to the amount of seed crystals added initially. This confirms that crystallization occurred only on the added seed material, without any secondary nucleation or spontaneous precipitation.

Studies were made on the rate of $CaSO_4.2H_2O$ seed crystal growth at 25°C and pH values from 2.5 to 9.0 in buffered calcium sulfate supersaturated solutions. Typical plots of the data plotted according to the integrated form of eq. [1] are shown in Fig. 3. Rate data summarized in Table 2 show that in the pH range 3.5–9.0, second-order rate constant is independent of solution pH, indicating that the bisulfate ion, which was suggested to be rate controlling in the crystallization of the hemihydrate at higher temperatures (7), had a negligible influence on the seeded crystal growth of calcium sulfate dihydrate. Results presented in Table 2 for seeded growth experiments conducted in buffered solution show that rate

Can. J. Chem. Downloaded from www.nrcresearchpress.com by 93.93.197.157 on 09/07/12
For personal use only.

TABLE 2. Kinetic data for calcium sulfate dihydrate crystal growth in the presence of polymers

		$TCaSO_4 = 3.50 \times 10^{-2}\ M$					
Expt.	Polymer	Dosage (ppm)	Seed (mg)	T (°C)	pH	Induction time (min)	10 ks (M^{-1} min^{-1})
2	None	0	200	25	5.5[a]	0	5.65
3	None	0	320	25	5.5[a]	0	9.55
5	None	0	197	25	5.5[a]	0	5.89
8	None	0	200	25	2.5	0	5.55
10	P-AA (comm. B)	0.25	200	25	2.5	0	5.08
4	P-AA (comm. B)	0.50	198	25	2.5	0	5.46
12	P-AA (comm. B)	1.0	202	25	2.5	0	5.26
13	None	0	199	25	3.5	0	5.83
16	P-AA (comm. B)	0.25	198	25	3.5	170	6.10
14	None	0	201	25	4.5	0	5.95
20	P-AA (comm. B)	0.25	199	25	4.5	210	6.26
18	None	0	202	25	5.5	0	5.83
23	P-AA (comm. B)	0.25	203	25	5.5	230	6.02
26	None	0	200	25	6.5	0	6.35
21	P-AA (comm. B)	0.25	202	25	6.5	225	5.96
30	None	0	202	25	7.0	0	5.75
28	P-AA (comm. A)	0.25	200	25	7.0	520	6.04
25	P-AA (comm. B)	0.10	198	25	7.0	42	5.93
32	P-AA (comm. B)	0.25	201	25	7.0	240	5.88
33	P-AA (comm. B)	0.35	197	25	7.0	552	6.01
29	P-AA (comm. B)	1.0	202	25	7.0	>1200	—
31	P-AA (exp. C)	0.25	200	25	7.0	125	6.20
36	P-AA (exp. D)	0.25	201	25	7.0	12	6.30
34	P-AA (exp. D)	0.35	199	25	7.0	48	5.98
37	P-AA (exp. E)	0.25	198	25	7.0	0	5.88
39	P-AA (exp. E)	0.25	200	25	7.0	10	6.15
40	P-AA (exp. F)	0.25	203	25	7.0	140	5.79
38	P-DMDAAC (exp. G)	0.25	200	25	7.0	0	6.22
27	P-Am (exp. H)	0.25	202	25	7.0	0	6.12
35	P-iPrAm (exp. J)	0.25	203	25	7.0	0	5.97
24	P-SA (exp. I)	0.25	201	25	7.0	0	6.05
41	None	0	200	25	8.0	0	6.32
42	P-AA (comm. B)	0.25	199	25	8.0	245	6.25
44	None	0	198	25	9.0	0	5.85
46	P-AA (comm. B)	0.25	197	25	9.0	260	6.19
48	None	0	199	35	7.0	0	12.5
49	P-AA (comm. A)	0.25	200	35	7.0	180	12.8
52	P-AA (comm. B)	0.25	202	35	7.0	86	11.5
51	P-AA (exp. C)	0.25	197	35	7.0	43	11.9
56	P-AA (exp. D)	0.25	198	35	7.0	21	13.1
54	P-AA (exp. E)	0.25	200	35	7.0	5	12.8
57	P-AA (exp. F)	0.25	203	35	7.0	48	11.3
59	None	0	197	50	7.0	0	16.1
62	P-AA (comm. A)	0.25	199	50	7.0	62	15.5
61	P-AA (comm. B)	0.25	201	50	7.0	33	16.7
60	P-AA (exp. C)	0.25	198	50	7.0	10	15.1
64	P-AA (exp. D)	0.25	204	50	7.0	5	15.9
66	P-AA (exp. E)	0.25	196	50	7.0	0	17.1
65	P-AA (exp. F)	0.25	202	50	7.0	26	17.8

[a]Unbuffered solution.

constants are within ±6% of that in the unbuffered solution. This suggests that buffering components at a total conjugate acid/base concentration of $2.0 \times 10^{-3}\ M$ does not have any significant effect on the rate of crystal growth.

Table 2 summarizes the results of crystal growth experiments made in the presence of polymers. Figure 4 illustrates typical growth curves at pH 7.0 in the presence of commercial polymer B (mw 6 000). As shown in Fig. 5, the crystallization reaction in the presence of 0.25 ppm of commercial polymer B is preceded by an induction period of 240 min after which the rate commences with a measurable rate. Figure 4 further indicates that an increase in polymer concentration only results in a prolongation of the induction period and at a 1.0 ppm polymer concentration, the rate of crystallization was completely inhibited for at least 20 h. Table 2 also shows data on induction periods as a function of polymer concentration for commercial polymer B. It can be seen (exps. 25, 32, 33, 39, Table 2) that the duration of the induction period is greatly increased by increasing the polymer concentrations.

Representative plots of the integrated form of eq. [1] in the

Can. J. Chem. Downloaded from www.nrcresearchpress.com by 93.93.197.157 on 09/07/12
For personal use only.

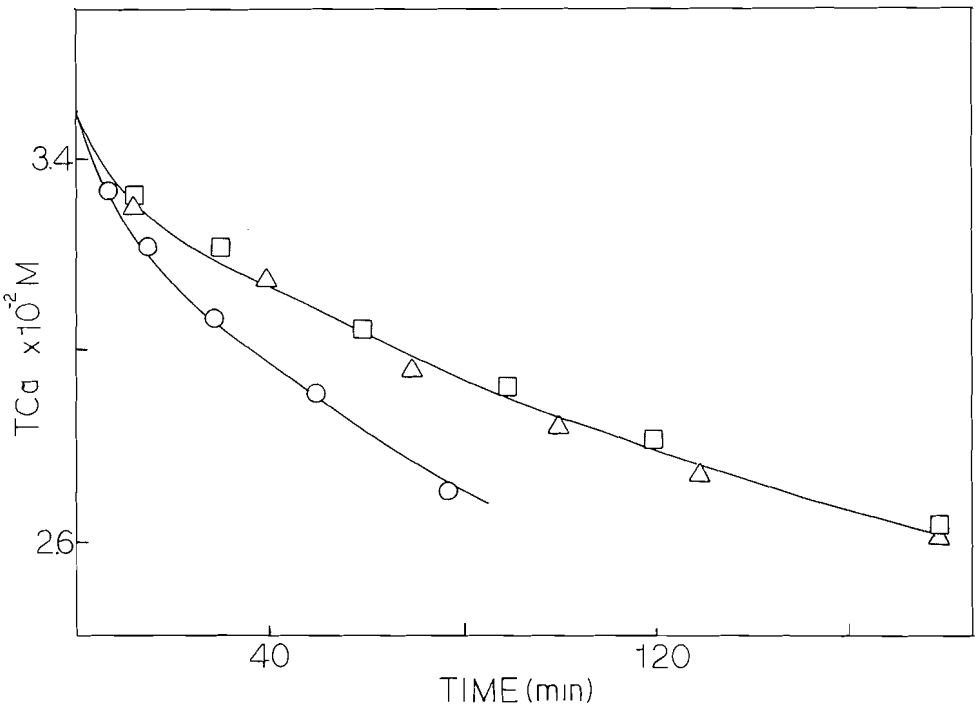

FIG. 1. Plots of total calcium (TCa) against time. The effect of seed concentration: (□) 200 mg, (△) 197 mg, (○) 320 mg, 25°C.

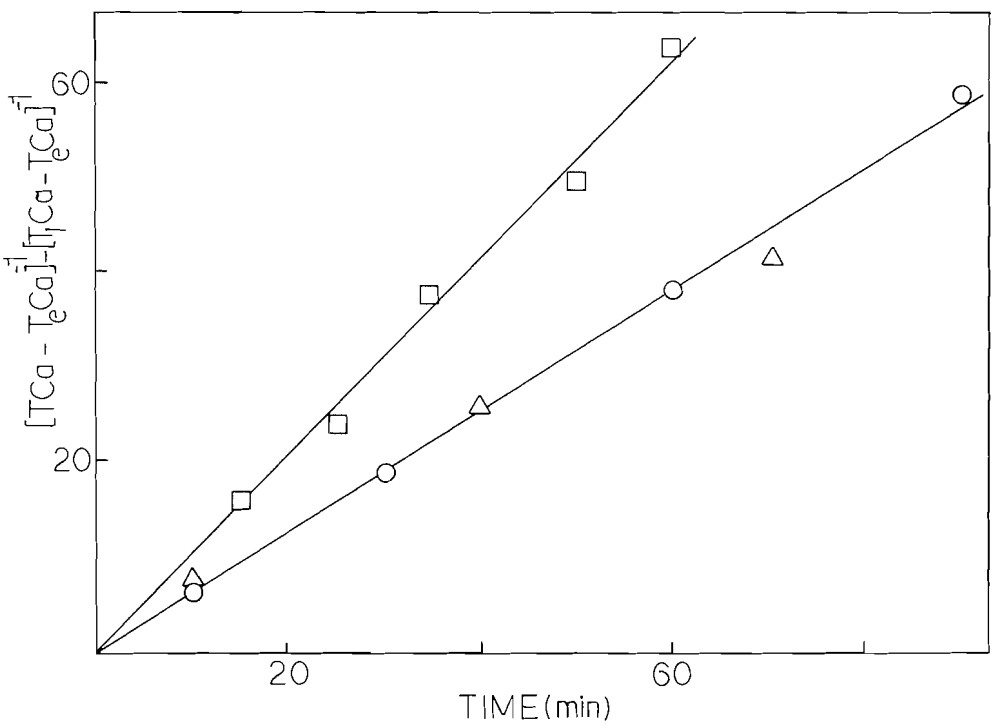

FIG. 2. Kinetic plots of eq. [1] for the $CaSO_4 . 2H_2O$ crystal growth: (○) 200 mg, (△) 197 mg, (□) 320 mg, 25°C.

presence of varying concentration of commercial polymer B shown in Fig. 5 demonstrate the success of this rate equation in interpreting the results in the presence polymer. As shown in Table 2 the rate of crystal growth of $CaSO_4 . 2H_2O$ following the induction period has very little correlation with the concentration of polymer. A similar temporarily growth inhibition was reported in the seeded growth of $CaSO_4 . 2H_2O$ in the presence of phosphonates, polyphosphonates, and other polyelectrolytes (17, 18). It is also interesting to note that seeded growth of $BaSO_4$ in the presence of trace amount of sodium tripolyphosphate, Liu and Nancollas (19) found that crystallization reaction following the initial induction period takes place at a rate comparable to the rate of crystallization from pure solution.

The influence of pH on the performance of several phosphonic acids as $CaSO_4 . 2H_2O$ crystal growth inhibitors has been recently studied by seeded growth technique (13). Results of this study show that an increase in the pH of the crystal growth medium over a pH 4 to 9 range brings about an improvement in

Can. J. Chem. Downloaded from www.nrcresearchpress.com by 93.93.197.157 on 09/07/12
For personal use only.

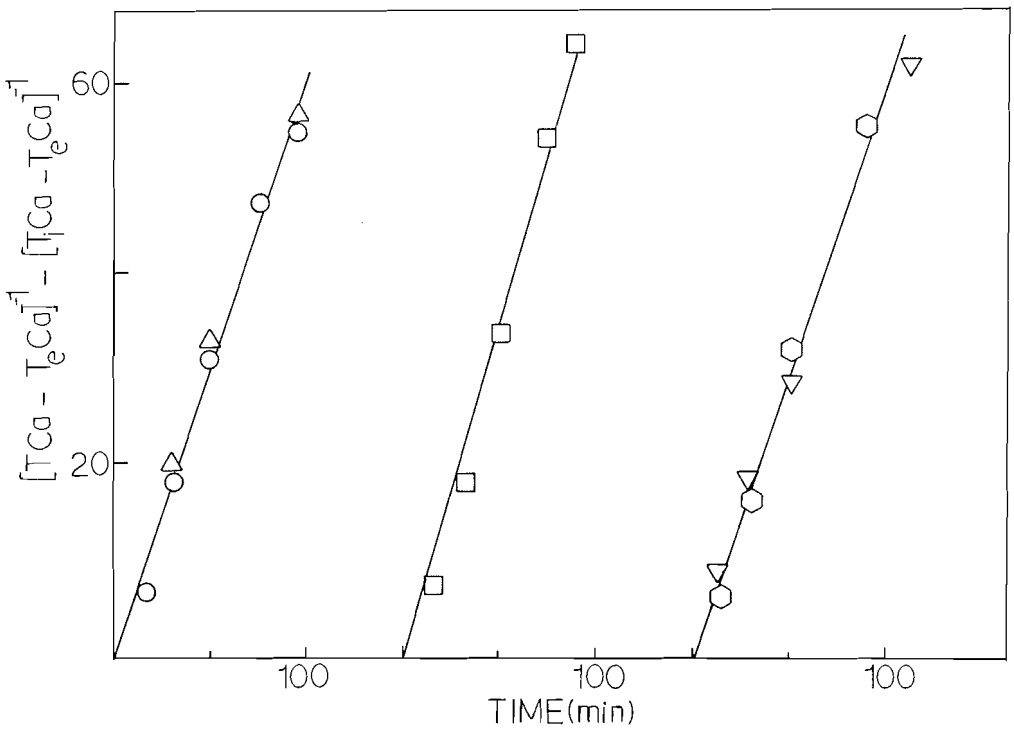

FIG. 3. Kinetic plots of eq. [1] for the $CaSO_4.2H_2O$ crystal growth as a function of solution pH. (○), (△) pH 7.0 (buffered), (□), pH 5.5 (unbuffered), (▽) pH 6.5 (buffered), (⬡) pH 8.5 (unbuffered), 25°C.

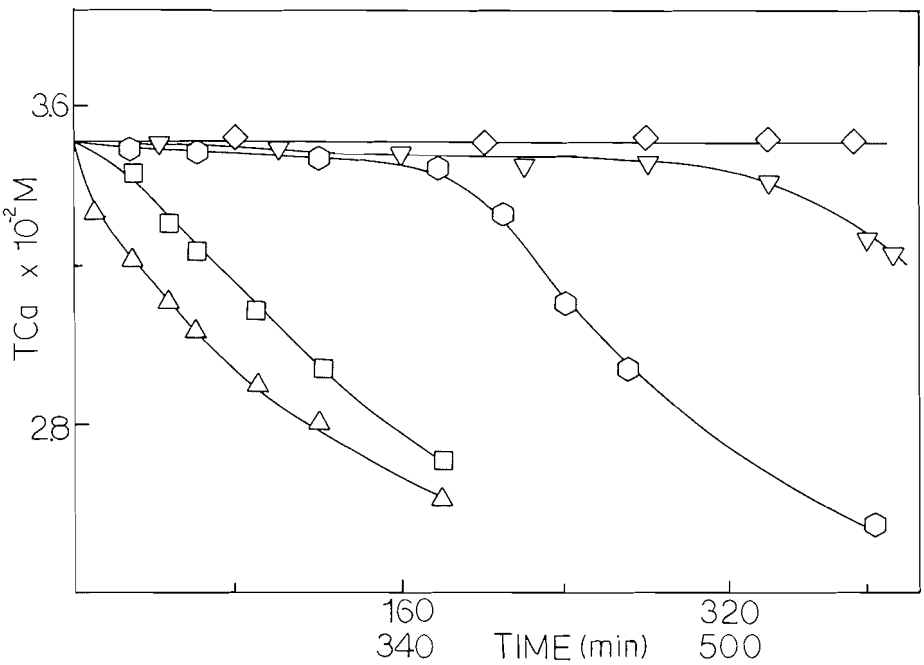

FIG. 4. Plots of *T*Ca as a function of time in the presence of comm-B polyacrylate at pH 7.0, 25°C. The effect of polymer concentration (ppm): (△) 0.0, (□) 0.10, (⬡) 0.25, (▽) 0.35, (◇) 1.0, (0.35 ppm and 1.0 ppm lower time scale).

inhibitor performance that runs parallel to the phosphonic acid titration curve.

For polymeric inhibitors, such as polyacrylic acids, the degree of deprotonation should, just as phosphonate inhibitors, be considered in explaining their action. Unfortunately their acid dissociation constants are not available. It can nevertheless be expected that the affinity of polymeric inhibitor molecules towards the crystal surface should also be influenced by the solution pH due to the dissociation of the carboxylic acid group.

The effect of the solution pH on the crystal growth of $CaSO_4.2H_2O$ in the presence of commercial polymer B was studied using the seeded growth technique. The results presented in Table 2 indicate that at constant temperature and polymer concentration (0.25 ppm), the induction time is strongly dependent upon solution pH. For example, the induction times observed at pH 2.5, 3.5, 5.5, 7.0, and 9.0 are 0, 170, 230, 240, and 260, respectively. Data in Table 2 demonstrates the ineffectiveness (induction time <2 min), of commercial poly-

Can. J. Chem. Downloaded from www.nrcresearchpress.com by 93.93.197.157 on 09/07/12
For personal use only.

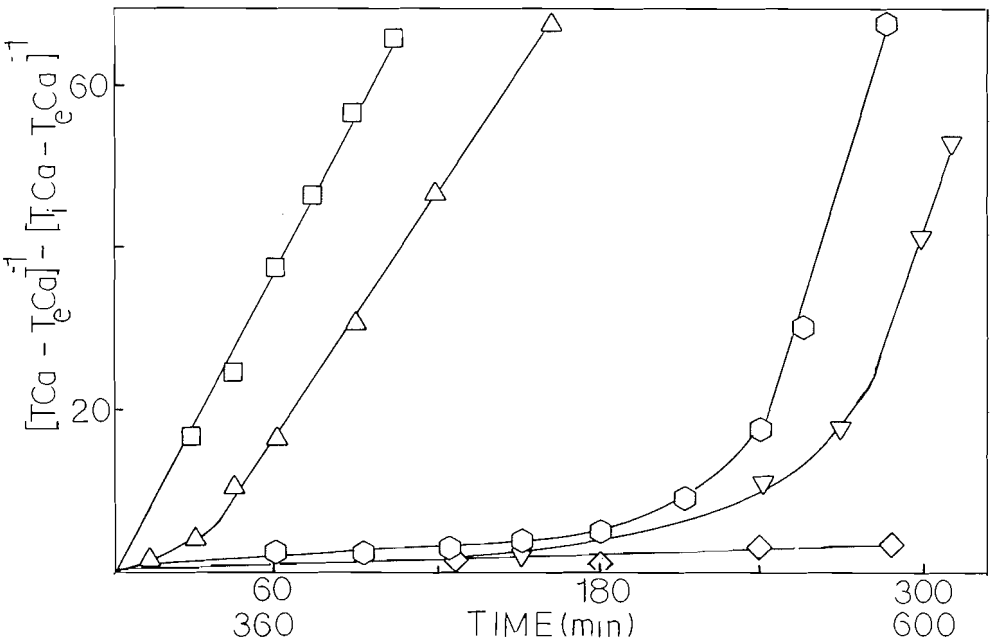

FIG. 5. Kinetic plots of eq. [1] for the growth of $CaSO_4.2H_2O$ in the presence of varying concentration of comm-B polyacrylate at pH 7.0, 25°C. (□) 0.0, (△) 0.10, (◯) 0.25, (▽) 0.35, (◇) 1.0 (0.35 ppm and 1.0 ppm lower time scale).

mer B as an $CaSO_4.2H_2O$ crystal growth inhibitor at pH 2.5 and at 0.25 to 1.0 ppm of polymer concentration. It should be noted that under similar conditions at pH 7.0 induction times observed for commercial polymer B at 0.25 and 1.0 ppm were 240 and >1200 min respectively. The poor inhibitory performance exhibited by commercial polymer B at pH 2.5 may be explained due to insignificant deprotonation of carboxylic acid group at this pH value. Although it has been reported (20) that adsorption capacity of polyelectrolyte increases with decreasing pH values, the absence of induction time or relatively poor performance of commercial polymer B at pH 2.5 may be explained due to insufficient electrostatic interaction of inhibitor molecule at the crystal surface, since at pH 2.5 inhibitor molecule will have very low anionic charge density. Thus at low pH values polymeric inhibitor i.e. commercial polymer B acts like non-ionic polymer and perhaps acquires a loopy configuration at the crystal surface.

As shown in Table 2 the induction times observed for commercial polymer B at 0.25 ppm concentration are 0, 170, and 230, at pH 2.5, 3.5, and 5.5, respectively. However, upon raising the solution pH from 5.5 to 7 to 9, no significant increase in induction times were observed. This suggests that the deprotonation of commercial polymer-B may near complete at pH = 6 or higher.

The influence of polymer structure as $CaSO_4.2H_2O$ crystal growth inhibitor at 0.25 ppm concentration and at pH 7.0 was also studied at the same calcium sulfate supersaturation. Kinetic data for polymers of varying functional group, i.e. acrylamide, isopropylacrylamide, 2-acrylamido-2-methylsulfonic acid, and quarternaryamine, etc., are summarized in Table 2. The results on these polymers (exps. 38, 27, 24, 35) which do not contain carboxyl group show that at 0.25 ppm of polymer concentration these polymers do not show any significant effect on both the induction period and the rate of crystal growth.

The effect of the molecular weight of polyacrylates at a concentration of 0.25 ppm was studied using the seeded growth technique. The results are presented in Table 2. Typical growth curves in the presence of polyacrylates of varying molecular weight are shown in Fig. 6. Data shown in Table 2 indicates that at pH 7.0, 25°C, and constant polymer concentration, the induction time increases with decreasing molecular weight from 20 000 to 2 600 and thereafter decreases with decreasing molecular weight (2 600 – 800). In addition, the rates of crystal growth in the presence of polyacrylates of varying molecular weight (Table 2) are within ±7% of the rate in pure solution. Figure 7 illustrates the effect of molecular weight of polyacrylates on the induction period at various temperatures. It can be seen that an increase in temperature only results in reduction of induction period.

Recently, the influence of a variety of polyelectrolytes in controlling scale formation has attracted the attention of several investigators. It is generally agreed that the polyelectrolytes which have an effect on controlling scale formation are highly substituted with carboxyl groups. In addition, it has also been shown that one of the factors determining the effectiveness of a polyelectrolyte is its molecular weight. Williams and Ruehrwein (21) suggested that molecular weight influences the kinetics of adsorption of the polyelectrolyte onto the growing crystals. It was postulated that there should be an optimum molecular weight for a given polyelectrolyte at which maximum effect would be obtained. In the discussion on the effect of a variety of polyelectrolytes on crystal growth of $CaSO_4.2H_2O$, Smith and Alexander (22) suggested that the adsorbed polymer molecules acted as immobile impurities on the crystal surface and that they inhibited crystal growth by reducing the rate of step movement across the crystal surface. In addition, growth inhibition was found to be strongly dependent on the structure and the molecular weight of the polyelectrolyte. Based upon the results for the similar molecular weight polyelectrolyte, Smith and Alexander (22) reported that polyacrylic acid was more effective than polymethacrylic acid. Furthermore, growth inhibition results for series of experiments with styrene maleic anhydride copolymers suggest an optimum effectiveness with molecular weight of 1600 for this polyelectrolyte. Recently

Can. J. Chem. Downloaded from www.nrcresearchpress.com by 93.93.197.157 on 09/07/12
For personal use only.

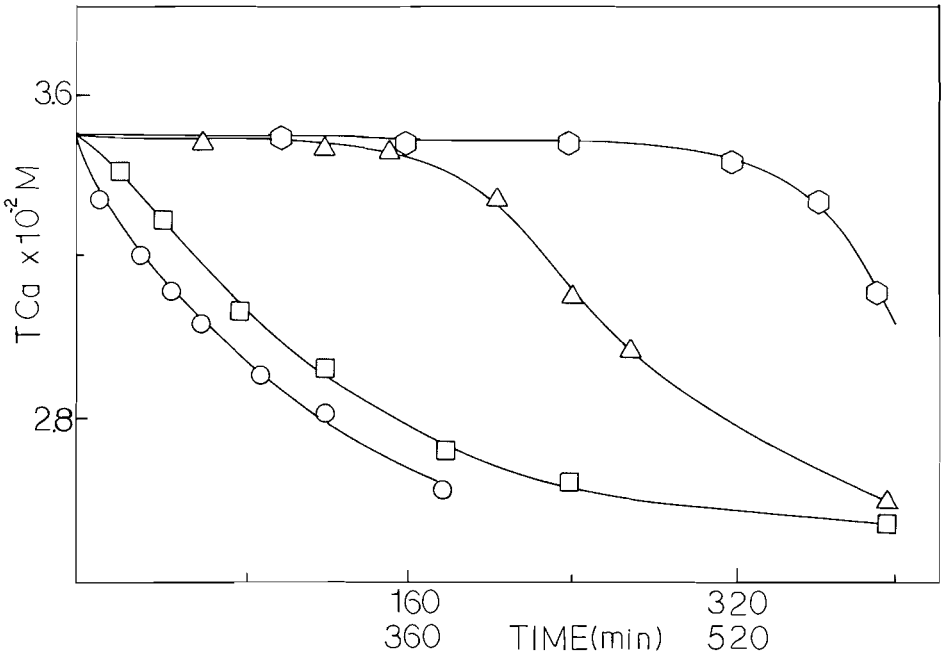

FIG. 6. Plots of TCa against time for $CaSO_4.2H_2O$ crystal growth in the presence of 0.25 ppm polyacrylate at pH 7.0, 25°C. The effect of polymer molecular weight (○) control (no polymer), (□) 22 000, (△) 6 000, (⬡) 2 600, (2 600 mol. wt. — lower time scale).

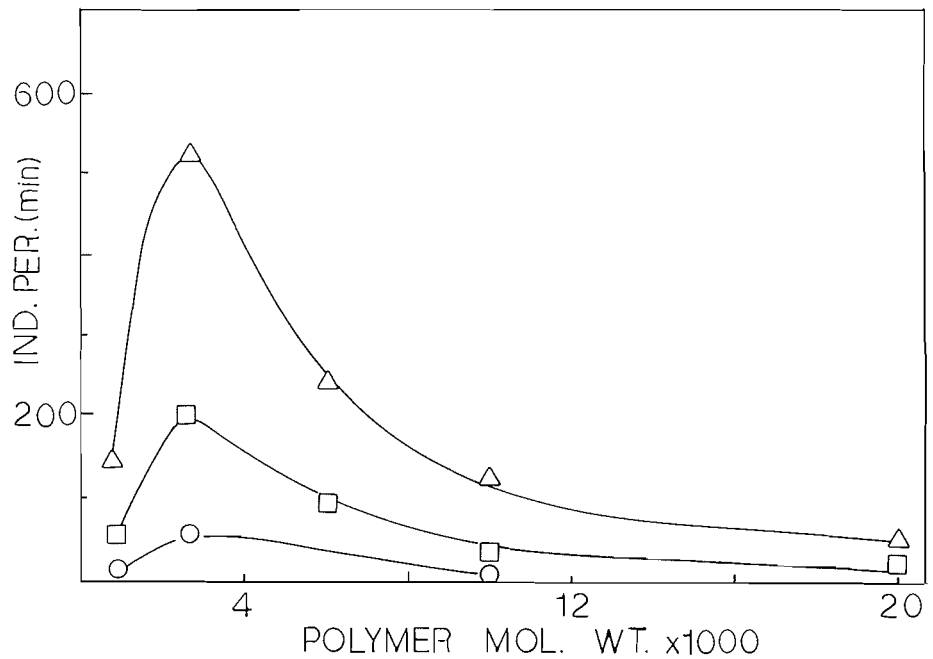

FIG. 7. Relationships of induction periods with polyacrylate molecular weight for the crystal growth of $CaSO_4.2H_2O$ at varying temperature (°C): (△) 25, (□) 35, (○) 50; polymer concentration = 0.25 ppm, pH 7.0.

Libutti *et al.* (23) in their study on the evaluation of polyacrylates as antiscalants for cooling water applications showed that the rate of fouling increases with an increase in molecular weight in the range 2 000 – 100 000.

In summary, the results presented in this paper on the influence of polymers of varying functional groups as $CaSO_4.2H_2O$ crystal growth inhibitors, show that the most effective inhibitors are those which are highly anionic in nature (e.g., carboxyl group in polyacrylic acid) whereas cationic charged polymers do not exhibit any significant inhibitory activity. This observation is consistent with results of earlier investigations on the effect of various anionic charged additives such as polyphosphate, phosphonate, polyaspartic acid, and phosphonocarboxylic acid, as crystal growth inhibitors for barium sulfate, calcium carbonate, and calcium oxalate.

The results presented in this paper on $CaSO_4.2H_2O$ crystal growth inhibition by polyacrylic acid suggest an optimum effectiveness with molecular weight of ~2 000. At values below 2 000 a marked decrease in the polyacrylic acid effectiveness occurs with decreasing molecular weight, which can be due to a decreasing number of bonding possibilities. The same tendency is observed with increasing values of the molecular

Can. J. Chem. Downloaded from www.nrcresearchpress.com by 93.93.197.157 on 09/07/12
For personal use only.

weight above ~2 000. This is rather surprising since the number of bonding possibilities increases with increasing chain lengths. It is not likely that large molecules adopt a "loopier" configuration with less effective bonds than smaller ones, since even very high molecular weight polyelectrolytes appear to be able to adopt a flat configuration upon the crystal surface, in spite of the entropy lost in a flat configuration (20). The phenomenon of a markedly decreasing polyacrylic acid effectiveness with increasing molecular weight above ~2 000 can thus not be explained. Adsorption studies are currently underway in our labs to better understand the role of molecular weight of polyacrylic acid and acrylic acid-based copolymers of varying compositions and functional groups in inhibiting crystal growth of sparingly soluble salts in aqueous solutions. In the industrial application of these polymers as scale inhibitors, the presence of induction period observed for crystal growth in the presence of polyacrylic acids, may be perfectly acceptable provided that the induction period is longer than the period required for scale protection.

Mechanism of $CaSO_4.2H_2O$ crystal growth inhibition

The marked effect of P-AA on the induction period preceding the crystal growth of gypsum from supersaturated solution may be attributed due to one or more of the following factors: (*1*) P-AA may change the ionic strength of the solution and hence the effective solubility of the calcium sulfate; (*2*) P-AA may form stable complexes with calcium ion and reduce supersaturation; (*3*) the inhibitor may be adsorbed on the crystal surface either generally or at the active growth sites.

Under the experimental conditions employed in the present investigation the presence of induction period preceding the crystal growth must be attributed to the surface adsorption factor rather than calcium–P-AA complex formation or the concomitant increase in ionic strength of the supersaturated solution in the presence of poly(acrylic acid).

The results discussed in this paper on $CaSO_4.2H_2O$ crystal growth inhibition by a variety of inhibitors suggest that those inhibitors under this study can be classified into the following two general categories: (*a*) Those such as poly(isopropylacrylamide), poly(acrylamide), and poly(2-acrylamido-2-methyl-2 propane sulfonic acid), and poly(dimethyldiallyl ammonium chloride), which have no pronounced effect on the rate of $CaSO_4.2H_2O$ crystal growth and show induction period of less than 2–5 min. (*b*) Those such as poly(acrylic acid) which also exhibit no significant effect on the rate of $CaSO_4.2H_2O$ crystal growth but show rather well-defined induction periods (few to several hundred minutes). In addition, the duration of the induction periods is greatly influenced by changing the concentration of poly acrylic acid.

The striking effect of the polyacrylic acid on the induction periods with subsequent growth of $CaSO_4.2H_2O$ observed in the present study may be explained by an incorporation of polyacrylic acid into the growing crystals. During the induction period, most of the active growing sites may be poisoned by adsorbed polyacrylic acid molecules. However, some of the growth sites of lower energy may still be free to grow, and the reaction proceeds at a very slow rate. The changes in solution concentration during this stage may be too small to be detected. After these slowly advancing steps cover the poisoned sites, the adsorbed molecules are incorporated into growing crystal and the crystal growth can resume at a rate comparable to that of unpoisoned systems.

Acknowledgement

The author wishes to thank Dr. William F. Masler for polymer synthesis, Glenn Evans for experimental assistance, and The BFGoodrich Company, Specialty Polymers & Chemicals Division for support in publishing this work.

1. G. H. NANCOLLAS, M. M. REDDY, and F. TSAI. J. Crystal Growth, **20**, 125 (1973).
2. D. HASSON and J. ZAHAVI. Ind. Eng. Chem. Fundamentals, **9**, 1 (1970).
3. M. TADROS and I. MAYES. J. Colloid Interface Sci. **72**, 245 (1979).
4. Z. AMJAD. Desalination, **54**, 263 (1985).
5. P. H. RALSTON. J. Pet. Tech. **21**, 1029 (1969).
6. P. F. ROLFE. Desalination, **1**, 539 (1966).
7. A. E. AUSTIN, J. F. MILLER, N. A. RICHARD, and J. F. KIRCHER. Desalination, **16**, 331 (1975).
8. E. R. MCCARTNEY and A. E. ALEXANDER. J. Colloid Sci. **13**, 383 (1958).
9. R. A. KUNTZE. Nature (London), **211**, 406 (1966).
10. L. W. JONES. Corrosion, **17**, 232 (1961).
11. P. FLESHER, E. L. STREATFIELD, A. S. PEARCE, and O. D. HYDES. 3rd Int. Symp. Freshwater Sea, **1**, 493 (1970).
12. Z. AMJAD. 4th Mexican Water Conference, Mexico City, Mexico. 1984. Paper 84-19.
13. D. W. GRIFFITHS, S. D. ROBERTS, and S. T. LIU. Int. Symp. Oilfield Geothermal Chem. Society of Petroleum Engineers, 1979. Paper 7861.
14. W. H. LEUNG and G. H. NANCOLLAS. J. Inorg. Nucl. Chem. **40**, 187 (1978).
15. M. S. SHEEHAN and G. H. NANCOLLAS. Investigative Urology, **17**, 446 (1980).
16. S. T. LIU and G. H. NANCOLLAS. J. Crystal Growth, **6**, 281 (1970).
17. S. T. LIU and G. H. NANCOLLAS. J. Colloid Interface Sci. **52**, 593 (1975).
18. B. R. SMITH and F. SWEET. J. Colloid Interface Sci. **37**, 612 (1971).
19. S. T. LIU and G. H. NANCOLLAS. J. Colloid Interface Sci. **52**, 582 (1975).
20. M. C. CAFE and I. D. ROBB. J. Colloid Interface Sci. **86**, 411 (1982).
21. F. V. WILLIAMS and R. A. RUEHRWEIN. J. Am. Chem. Soc. **79**, 4898 (1957).
22. B. R. SMITH and A. E. ALEXANDER. J. Colloid Interface Sci. **34**, 81 (1970).
23. B. L. LIBUTTI, J. G. KNUDSEN, and R. W. MUELLER. Corrosion/84, National Association of Corrosion Engineers, Houston, Texas. Paper 179.

Can. J. Chem. Downloaded from www.nrcresearchpress.com by 93.93.197.157 on 09/07/12
For personal use only.

COMMUNICATION

2-Picolyl thioesters; a useful synthon for the preparation of 1-β-alkyl carbapenem intermediates[1]

ALAIN MARTEL,[2] JEAN-PAUL DARIS, CAROL BACHAND, JACQUES CORBEIL, AND MARCEL MENARD
Bristol–Myers Pharmaceutical Group, 100 Industrial Boulevard, Candiac (Qué.), Canada J5R 1J1

Received January 19, 1988

ALAIN MARTEL, JEAN-PAUL DARIS, CAROL BACHAND, JACQUES CORBEIL, and MARCEL MENARD. Can. J. Chem. **66**, 1537 (1988).

In this study, a highly stereoselective preparation of (3*S*,4*S*)-3-[(1*R*)-1-*tert*-butyldimethylsilyloxyethyl]-4-[(1*R*)-1-carboxyethyl]-azetidin-2-one (**2**) is reported. It involves a Lewis acid mediated condensation of (3*S*,4*R*)-4-acetoxy-3-[(1*R*)-1-*tert*-butyldimethylsilyloxyethyl]azetidin-2-one (**3**) with simple *O*-silylenol ethers of thiopropionates. From all the examples reported in this paper the 2-picolyl thiopropionate or similar arrangements were found to be essential for this stereoselection. Finally, a mechanism involving chelation control seems to be operative.

ALAIN MARTEL, JEAN-PAUL DARIS, CAROL BACHAND, JACQUES CORBEIL et MARCEL MENARD. Can. J. Chem. **66**, 1537 (1988).

Dans ce travail, on rapporte une préparation hautement stéréosélective de la (3*S*,4*S*)-[(1*R*)-*tert*-butyldiméthylsilyloxy-1 éthyl]-3 [(1*R*)-carboxy-1 éthyl]-4 azétidinone-2 (**2**). Cette synthèse implique une condensation, sous l'influence d'un acide de Lewis, de la (3*S*,4*R*)-acétoxy-4 [(1*R*)-*tert*-butyldiméthylsilyloxy-1 éthyl]-3 azétidinone-2 (**3**) avec des éthers énoliques *O*-silylés simples de l'acide thiopropionique. En se basant sur tous les exemples rapportés dans cette publication, on a trouvé que le thiopropionate de picolyle-2 ou des composés semblables sont essentiels pour obtenir cette stéréosélectivité. Enfin, il semble que le mécanisme implique un contrôle par une chélation.

[Traduit par la revue]

The recent report, by Shih *et al.* (1), that a 1-β-methyl group imparts enzymatic as well as chemical stability to the carbapenem nucleus **1** has stimulated a rapid development of synthetic methods (2) directed towards the preparation of the key intermediate **2**. Although highly diastereoselective preparations of **2** have been recently published (2*i*,*j*,*k*), there remains a need for more efficient methods. Therefore an investigation of the C-4 alkylation of 4-acetoxyazetidinone **3** with simple *O*-enolsilyl ethers of thiopropionates **4** (Scheme 1) was initiated. Even though similar couplings have been reported (2*c*), poor or no β-diastereoselection was achieved. In this paper we would like to report a highly diastereoselective preparation of derivative **2** via a Lewis acid mediated condensation of 4-acetoxyazetidinone with simple *O*-silylenol ethers of thiopropionates.[3]

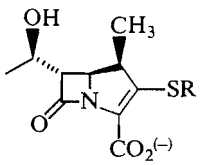

1

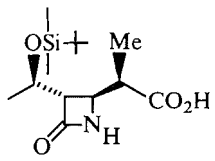

2

Preparation (see Experimental) of enol ethers **4**, generally obtained as mixtures of *E*/*Z* isomers, occurred upon trapping the enolates of thiopropionates **6** with *tert*-butyldimethylsilyl triflate (3). Reaction of these enol ethers **4** with the 4-acetoxyazetidinone **3** in the presence of $ZnCl_2$ afforded derivatives **5** with various α/β ratios, which are listed in Table 1.

In examples 1, 2, 3, 4, 6, 7, and 9 the α-methyl isomer **5** (R^2 = Me) was obtained as the major product. Formation of the α-methyl isomer **5** can be rationalized as occurring (4) via a 6-membered transition state as depicted in **7**. Here the steric interaction between the methyl group of the incoming nucleophile and H-3 of azetidinone **4** is minimized when the methyl group takes the pseudo equatorial position, thus leading to the α-methyl isomer **5**.

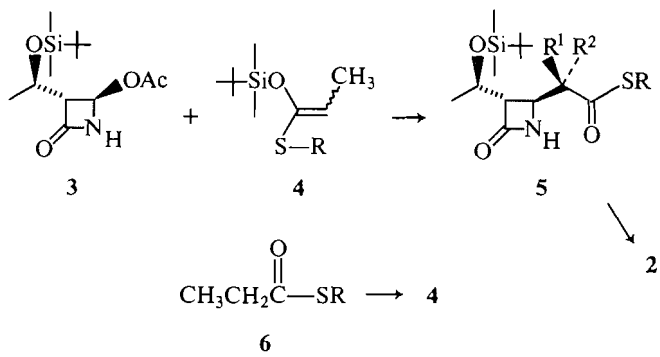

3 **4** **5** **2** **6**

SCHEME 1

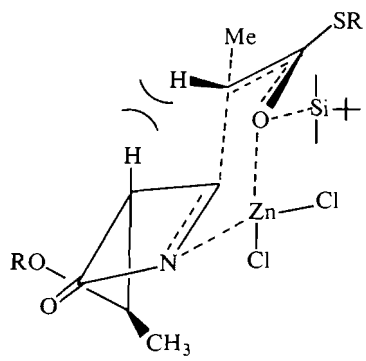

7

In examples 10, 11, 12, and 14 the β-methyl isomer **5** (R^1 =

[1]Work presented at the 70th Annual CIC Conference held in Quebec City, June 7–11, 1987.

[2]Author to whom correspondence may be addressed.

[3]This work is part of a Bristol–Myers U.S. Patent Application submitted on February 1985.

Can. J. Chem. Downloaded from www.nrcresearchpress.com by 93.93.197.157 on 09/07/12
For personal use only.

Can. J. Chem. Downloaded from www.nrcresearchpress.com by 93.93.197.157 on 09/07/12
For personal use only.

TABLE 1.

	R group in **4**, **5**, **6**		α:β in **5**	Yield of **5**
1.	*tert*-Butyl		92:8	74
2.	Phenyl		90:10	91
3.	CH_3SCH_2-		98:—	76
4.	MEM-		86:14	67
5.	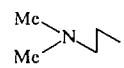		1:1	49
6.	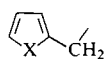	X = O	85:15	100
7.		X = S	81:19	84
8.		4-yl	60:40	58
9.		3-yl	92:8	37
10.		2-yl	13:87	80
11.	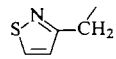		25:75	65
12.	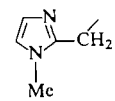		1:9	85
13.	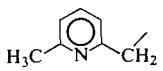		6:4	66
14.	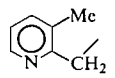		—:>98	85–90

Me) was formed either as the major isomer or almost in a stereospecific manner (example 14). It is suggested that the ability of Zn(II) to form a chelate (see structure **8**) with the sulfur and nitrogen[4] atoms of the thioester is essential for high β-methyl stereoselection. Factors interfering with this chelation bring about a reduction in selectivity. For example, changing the N-heteroatom for O or S resulted in complete loss of β-methyl selectivity (examples 10, 12 vs. examples 6 and 7). Disruption of the chelate (steric factors) was apparent in example 5 and more strikingly in example 13 where the 6′-methyl group could interfere with the ligand around Zn. In this latter case the α/β ratio was 6:4 (see structure **9**). Alternatively, introduction of a 3′-methyl group (see structure 10) appears to favor the formation of the chelate **8** (example 14), and therefore a greater proportion of β-methyl isomer **5** was obtained relative to that for the parent compound (example 10).

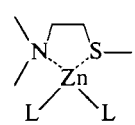

8

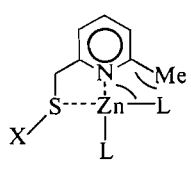

9

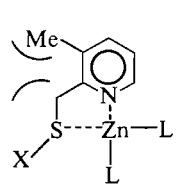

10

[4]There are ample literature precedents for chelates of type **8** (see ref. 5).

The effect of enol geometry on the stereochemical outcome of the reaction was examined in one case (example 14). The two geometric isomers of **4**-14 were separated (column chromatography) and reacted individually with azetidinone **3**. A high β-methyl stereoselectivity (>98%) was observed with the *Z*(O)-enol (isomer B, **4**-14) (assignment tentative) and an 84:16 ratio of β/α isomers was found with the *E*(O)-enol (isomer A, **4**-14) (6). This excellent β-methyl stereoselectivity was tentatively rationalized as resulting from the reaction occurring via a linear transition state such as **11** in which the Lewis acid is not intimately involved with the silyloxy group (2*d*, 7).

In summary, a highly stereoselective preparation of the β-methyl carbapenem precursor **2** has been developed. A mechanism involving chelation control seems to be operative. The 2-picolyl thiopropionates or similar structural arrangements were found to be essential for this stereoselection.

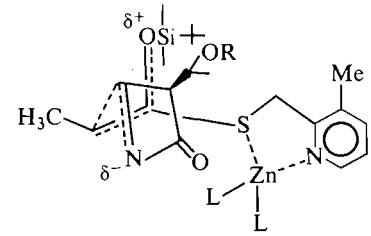

11

Experimental

Base treatment (TEA) of thiopropionates **6** in CH_2Cl_2 and subsequent quenching with TBDMS–OTf gave enol **4** in generally good yields (60–95%). In the case of the 3-methyl-2-picolyl thiopropionate, formation of the enolate required a stronger base (LiHMDS, THF, −78°C). Coupling of **4** (2 equiv.) with the azetidinone **3** was started at 0°C (ice bath) under N_2 using $ZnCl_2$ (2 equiv.) as the Lewis acid. The mixture was allowed to stir at ca. 20°C for 18 h and then worked up (see Table 1). Generation of acid **2** occurred upon treatment of **5** in THF with aqueous NaOH in the presence of H_2O_2.

All new compounds gave ir, ^{1}Hmr, and combustion analyses consistent with their assigned structures.

Physical data of selected derivatives

4-*10*: Mixture of 2 isomers (45:55); ir (CH_2Cl_2) ν_{max}: 1635 (double bond) and 1595 (ar) cm^{-1}; ^{1}Hmr ($CDCl_3$) δ: 8.55–6.95 (4H, m, ar), 4.98 (1H, 5 lines, isomeric H-vinyl), 4.04 and 3.97 (2H, 2s, isomeric -CH_2-), 1.54 and 1.55 (3H, 2d, J = 6.9 Hz, J = 6.7 Hz, isomeric -CH_3), 0.99 and 0.95 (9H, 2s, *tert*-butyl), 0.19 and 0.23 (6H, 2s, dimethyl) ppm.

4-*14*: A 2:8 mixture of 2 isomers; *isomer A* (R_f 0.75, 25% ether – petroleum ether): ir (CH_2Cl_2) ν_{max}: 1635 (olefin) cm^{-1}; ^{1}Hmr ($CDCl_3$, 80 MHz), δ: 8.40–8.34 (1H, m, H-aromatic), 7.37–7.06 (2H, m, H-aromatic), 5.03 (1H, d, J = 6.8 Hz, olefinic-H), 4.10 (2H, s, CH_2), 2.38 (3H, s, CH_3), 1.56 (3H, d, J = 6.8 Hz, CH_3), 0.96 (9H, s, *tert*-butyl-Si), 0.20 (6H, s, $(CH_3)_2$-Si) ppm; *isomer B* (R_f 0.68, 25% ether – petroleum ether): ir (CH_2Cl_2) ν_{max}: 1635 (olefin) cm^{-1}; ^{1}Hmr (80 MHz, $CDCl_3$) δ: 8.39, 8.34 (1H, m, H-aromatic), 7.37–6.95 (2H, m, H-aromatic), 5.00 (1H, q, J = 6.8 Hz, olefinic-H), 4.04 (2H, s, CH_2), 2.35 (3H, s, CH_3), 1.34 (3H, d, J = 6.8 Hz, CH_3), 0.97 (9H, s, *tert*-butyl-Si), 0.21 (6H, s, $(CH_3)_2$-Si) ppm.

5-*10*: (88.7% oil, 80% crystalline, heptane) mp 55–58°C; an 87:13 mixture of β- and α-methyl isomers. *β-methyl*: ir (CH_2Cl_2) ν_{max}: 3410 (N-H), 1765 (β-lactam), 1682 (thioester), and 1594 (ar) cm^{-1}; ^{1}Hmr ($CDCl_3$) δ: 5.82 (1H, s, N-H), 4.30 (2H, s, -CH_2), 4.30–4.00 (1H, m, H-1′), 3.88 (1H, dd, J = 2.2 Hz, J = 6.4 Hz, H-4), 3.15–2.7 (2H, m, H-3, -CH—C—S-), 1.25 (3H, d, 6.9 Hz, CH_3-2′), 1.07 (3H, d, J = 6.3 Hz, -CH_3), 0.86 (9H, s, *tert*-butyl), 0.05 (6H, dimethyl-Si-) ppm. *α-methyl*: ir (CH_2Cl_2) ν_{max}: 3410 (N-H), 1765 (β-lactam C=O) and

1680 (thioester) cm^{-1}; ^{1}Hmr (80 MHz, $CDCl_3$) δ: 8.55, 8.54, 8.50, 8.49 (1H, m, H-arom), 7.75, 7.72, 7.65, 7.62, 7.55, 7.53 (1H, m, H-arom), 7.22–7.00 (2H, m, H-arom), 6.21 (1H, 6s, N-H), 4.42, 4.29, 4.25 (2H, part of ABq, J = 14 Hz, CH_2-S), 4.17, 4.09, 4.08 (1H, m, part of H-1), 3.78, 3.75, 3.66, 3.63 (1H, dd, J = 2.0 Hz, J = 9.6 Hz, H-4), 2.95–2.55 (2H, m, H-3, H-1″), 1.31, 1.22 (3H, d, J = 7.0 Hz, CH_3), 1.26, 1.18 (3H, d, J = 6.2 Hz, CH_3), 0.87 (9H, s, *tert*-butyl-Si), 0.07 (6H, $(CH_3)_2$-Si) ppm.

Acknowledgments

We would like to thank Professor B. Belleau of McGill University, and Drs. H. Mastalerz, R. Vanga, and J. Banville for helpful discussions.

1. D. H. Shih, F. Baker, L. Cama, and B. G. Christensen. Heterocycles, **21**, 29 (1984).
2. (*a*) D. H. Shih, J. A. Fayter, L. D. Cama, B. G. Christensen, and J. Hirshfield. Tetrahedron Lett. **26**, 583 (1985); (*b*) D. H. Shih, L. Cama, and B. G. Christensen. Tetrahedron Lett. **26**, 587 (1985); (*c*) T. Shibata, K. Iino, T. Tanaka, T. Hashimoto, Y. Kameyama, and Y. Sugimura. Tetrahedron Lett. **26**, 4739 (1985); (*d*) H. Fliri and C. P. Mak. J. Org. Chem. **50**, 3438 (1985); (*e*) J. Knight, P. J. Parsons, and R. Southgate. J. Chem. Soc. Chem. Commun. 78 (1986); (*f*) T. Iimori and M. Shibasaki. Tetrahedron Lett. **27**, 2149 (1986); (*g*) Y. Ito, T. Kawabata, and T. Terashima. Tetrahedron Lett. **27**, 5751 (1986); (*h*) T. Kawabata, Y. Kimura, Y. Ito, and S. Terashima. Tetrahedron Lett. **27**, 6241 (1986); (*i*) T. Chiba, M. Nagatsuma, and T. Nakai. Chem. Lett. 1343 (1985); (*j*) Y. Nagao, T. Kumagai, S. Tamai, T. Abe, Y. Kuramoto, T. Taga, S. Aoyagi, Y. Nagase, M. Ochiai, Y. Inoue, and E. Fujita. J. Am. Chem. Soc. **108**, 4673 (1986); (*k*) L. M. Fuentes, I. Shinkai, and T. N. Saltzmann. J. Am. Chem. Soc. **108**, 4675 (1986); (*l*) R. Deziel and D. Favreau. Tetrahedron Lett. **27**, 5687 (1986); (*m*) M. Hatanaka. Tetrahedron Lett. **28**, 83 (1987); (*n*) C. Kim, B. Luh, and R. A. Partyka. Tetrahedron Lett. **28**, 507 (1987); (*o*) Y. Nagao, T. Kumagai, T. Abe, M. Ochiai, T. Taga, K. Machida, and Y. Inoue. J. Chem. Soc. Chem. Commun. 602 (1987); Y. Ito and S. Terashima. Tetrahedron Lett. **28**, 6625 (1987).
3. Y. Ueda, G. Roberge, and V. Vinet. Can. J. Chem. **62**, 2936 (1984).
4. T. H. Chan, T. Aida, P. W. K. Lau, V. Gorys, and D. N. Harpp. Tetrahedron Lett. 4029 (1979), and references cited therein.
5. P. Nanjappan and A. W. Czarnik. J. Am. Chem. Soc. **109**, 1826 (1987), and references cited therein.
6. C. S. Wilcox and R. E. Babslom. J. Org. Chem. **49**, 1451 (1984), and reference cited therein.
7. C. H. Heathcock, K. T. Hug, and L. A. Flippin. Tetrahedron Lett. **25**, 5973 (1984).

Can. J. Chem. Downloaded from www.nrcresearchpress.com by 93.93.197.157 on 09/07/12
For personal use only.

Vol. 65, 1987

Peter Taylor and Vincent Lopata. Some phase relationships between basic bismuth chlorides in aqueous solutions at 25°C. Page 2824. The order of Figs. 1, 2, 4, and 5 has been reversed. The correct arrangement is as follows:

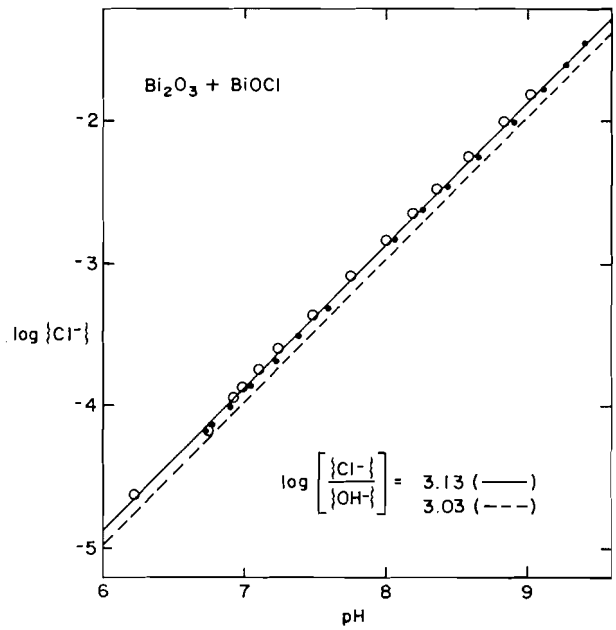

FIG. 1. Measured pH and chloride activity of solutions in contact with α-Bi_2O_3 + BiOCl. First titration, ○; second titration, ●; increasing pH and $\{Cl^-\}$ corresponds to successive additions of NaOH.

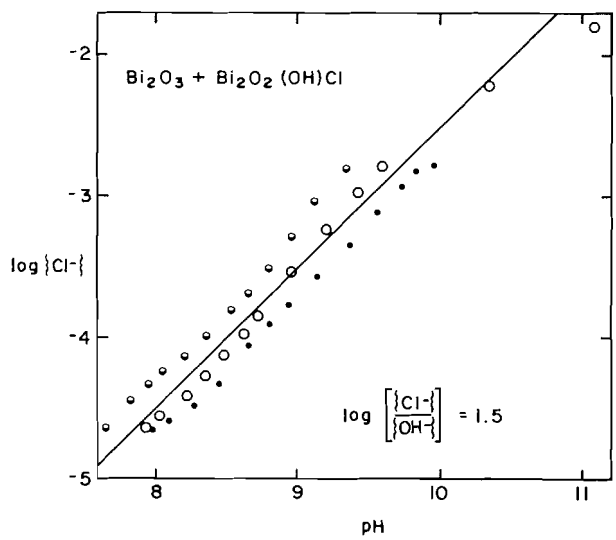

FIG. 2. Measured pH and chloride activity of solutions in contact with α-Bi_2O_3 + "$Bi_2O_2(OH)Cl$". Oxide pretreated with HCl (○) or NaCl (◒, ●).

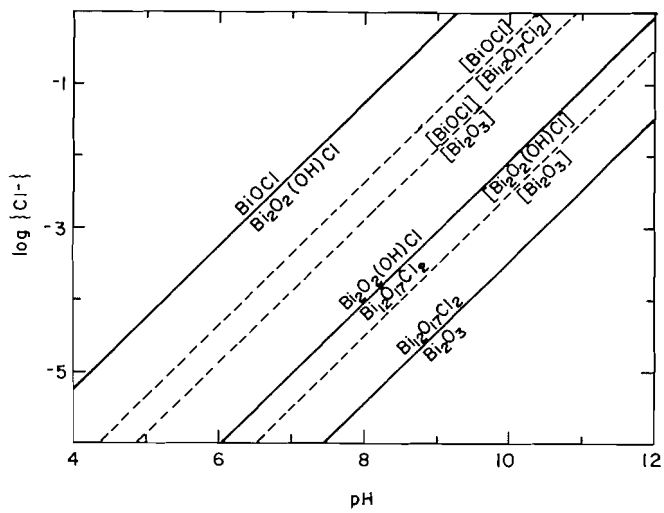

FIG. 4. Phase relationships between α-Bi_2O_3, $Bi_{12}O_{17}Cl_2$, "Bi_2O_2-(OH)Cl", and BiOCl, calculated from equilibrium data in Figs. 1 to 3.

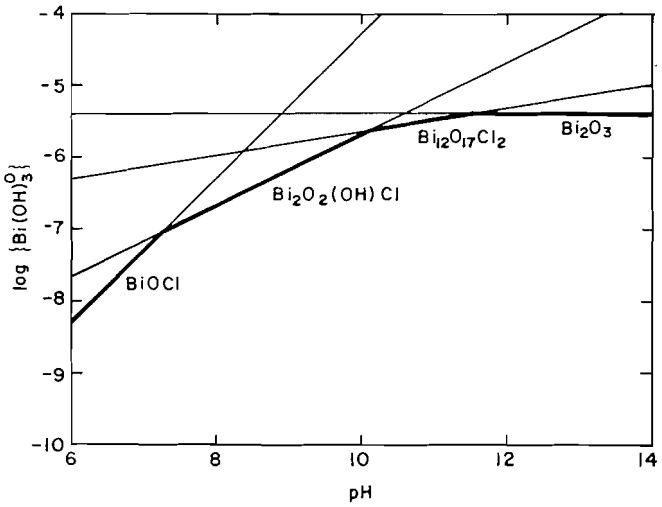

FIG. 5. Calculated $Bi(OH)_3^0$ activities in contact with bismuth oxide and oxychlorides at a Cl^- activity of 10^{-2} mol dm^{-3}, as a function of pH. For any change in log $\{Cl^-\}$, change the pH scale by an equal and opposite quantity. The $Bi(OH)_3^0$ activity approximates total bismuth within the pH limits 7–13. Bold portions of lines represent the range over which each solid is stable.

Can. J. Chem. Downloaded from www.nrcresearchpress.com by 93.93.197.157 on 09/07/12
For personal use only.

The prototropic equilibria in pentenylphosphonic systems

AGNES M. MODRO AND TOMASZ A. MODRO[1]
Department of Chemistry, University of Pretoria, Pretoria 0002, South Africa

Received December 21, 1987

AGNES M. MODRO and TOMASZ A. MODRO. Can. J. Chem. **66**, 1541 (1988).

Dialkyl 2-chloropentylphosphonates, $C_3H_7CHClCH_2P(O)(OR)_2$, and monoalkyl 2-chloropentylphosphonic acids, $C_3H_7CHClCH_2PO_2H(OR)$, have been dehydrohalogenated by strong bases to the corresponding pentenylphosphonic compounds. In all cases the kinetically controlled product was shown to be the *E*-1-pentenylphosphonic derivative. The α,β-unsaturated products underwent base-catalysed isomerization to the thermodynamically controlled *E*-2-pentenylphosphonic systems, thus indicating that the PO_3R_2 and PO_3R^- groups destabilize (relative to hydrogen) the adjacent olefinic bond. The hydrogen–deuterium isotope exchange was studied for the α,β- and β,γ-unsaturated products and the results obtained were in full agreement with the isomerization results.

AGNES M. MODRO et TOMASZ A. MODRO. Can. J. Chem. **66**, 1541 (1988).

Sous l'influence de bases fortes, les chloro-2 pentylphosphonates de dialkyle, $C_3H_7CHClCH_2P(O)(OR)_2$, ainsi que les acides chloro-2 pentylphosphoniques monoalkylés, $C_3H_7CHClCH_2PO_2H(OR)$, subissent une réaction de déshydrohalogénation conduisant aux composés pentènylphosphoniques correspondants. On a démontré que, dans tous les cas, le produit de contrôle cinétique est le dérivé pentène-1(*E*) phosphonique. Sous l'influence du milieu basique, les produits α,β-insaturés subissent une isomérisation conduisant aux systèmes pentène-2(*E*) phosphoniques qui sont thermodynamiquement plus stables; ces résultats indiquent que, par rapport à l'hydrogène, les groupements PO_3R_2 et PO_3R^- déstabilisent la double liaison adjacente. On a étudié l'échange isotopique hydrogène/deutérium sur les produits α,β- et β,γ-insaturés; les résultats obtenus sont en parfait accord avec les résultats des isomérisations.

[Traduit par la revue]

Structural effects on the prototropic equilibria in allylic systems (eq. [1]) have been studied for more than six decades and are discussed in detail in classical monographs on physical organic chemistry (see, for example, ref. 1). Analysis of the free energy change for reaction [1] allowed Hine (2) to determine the "Double-Bond Stabilisation Parameter" for various substituents. According to Hine's and other (3) data, the olefinic bond can be stabilized by resonance donors as well as acceptors, the OR and CO_2R substituents being the respective examples. The only substituent listed as distinctly *destabilizing* (relative to hydrogen) the vinylic system is the methylsulfonyl group; for X = Pr, Y = SO_2Me, the equilibrium constant for reaction [1] was found (4) to be greater than 99.

[1] $\underset{\mathbf{1}a}{X{-}CH_2{-}CH{=}CH{-}Y} \overset{K}{\rightleftharpoons} \underset{\mathbf{1}b}{X{-}CH{=}CH{-}CH_2{-}Y}$

The effect of phosphorus-containing functional groups on the stability of the corresponding propenylic systems is not well established. For the phosphonium group, PR_3^+, the effect on the stability of the propenylphosphonium derivatives depends on substituents at phosphorus (5). While allyltriphenylphosphonium ion (**1***a*, X = PPh_3^+; Y = H) in the presence of a base isomerizes easily and completely to the corresponding vinylic product (**1***b*), the tri-*n*-butylphosphonium analogue (**1***a*, X = PBu_3^+; Y = H) is stable under the same conditions. Reactions of electrophiles with delocalized carbanions obtained by deprotonation of allylphosphonic diamidates (6), diesters (7), or tertiary phosphine oxides (8) show low chemoselectivity and give both α- and γ-substituted products depending on the groups at phosphorus and on the nature of other substituents present in the allylic system.

In this paper we report our studies of the pentenylphosphonic system (**2**) obtained by the dehydrohalogenation of the 2-chloropentylphosphonic derivative **3**. The chemistry of 2-halogenophosphonic acids attracts considerable attention (9) because of the well-known (10) fragmentation of their dianions to alkenes and metaphosphate species, the reaction responsible for the plant-growth regulating properties of 2-chloroethylphosphonic acid (Ethephon) (11). We were, however, interested in base-promoted reactions of **3** proceeding with the retention of the P—C bond, to determine the structure of the elimination products and the possibility of their mutual interconversion.

[2] $\underset{\mathbf{3}}{C_3H_7CHCl{-}CH_2{-}P(O)X_2} \xrightarrow{-HCl} \underset{\mathbf{2}}{C_5H_9P(O)X_2}$

Results and discussion

Dialkyl (**3***b*) and monoalkyl (**3***c*) esters of 2-chloropentylphosphonic acid (**3***a*) were prepared from 1-pentene according to Scheme 1.

Diethyl 2-chloropentylphosphonate (**4**) (**3***b*, R = Et) does not undergo any change when heated as a neat liquid for 12 h at 115°C. It has also been found resistant to base-promoted elimination when heated in pyridine for 90 h at 70°C or in benzene in the presence of the "proton sponge" (14) for 70 h at 50°C. Ester **4** and its dimethyl analogue **5** (**3***b*, R = Me) could,

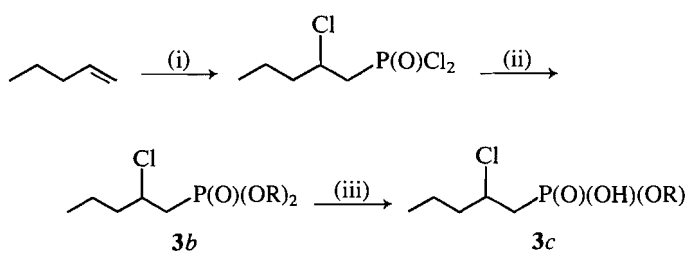

3*b* **3***c*

(i) PCl_5, C_6H_6, followed by P_4O_{10} (9*a*)
(ii) ROH, C_5H_5N, C_6H_6 (12)
(iii) NaI, Me_2CO (13)

SCHEME 1

[1]Author to whom correspondence may be addressed.

Printed in Canada / Imprimé au Canada

Can. J. Chem. Downloaded from www.nrcresearchpress.com by 61.7.252.67 on 09/07/12
For personal use only.

however, be easily converted to the pentenyl derivatives (**2**) by means of stronger bases such as alkoxide ions or butyllithium. When **4** or **5** was treated with strictly 1 mole-equivalent of a base (to ensure the neutrality of the final reaction mixture) at room temperature for 2–3 h, the high-resolution ^{1}H nmr spectra of the products revealed that the *E*-1-pentenylphosphonic esters **2***a* and **2***b* were the exclusive products of the elimination reaction (eq. [3]).

[3] 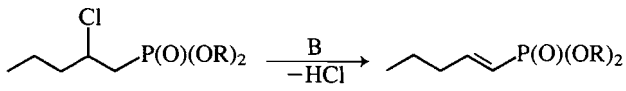

4, R = Et **2***a*, R = Et

B = EtONa/EtOH; EtOK/EtOH; $(EtO)_2Mg$/EtOH; *t*-BuOK/*t*-BuOH; KOH/EtOH; BuLi/C_6H_{14}

5, R = Me **2***b*, R = Me

B = MeONa/MeOH; BuLi/C_6H_{14}

Since the pK_a value for the α-methylene groups in **4** and **5** should be of the order of 20 (15), the regioselectivity of elimination results from the difference in the acidity of the hydrogen atoms at C1 and C3, while the configuration of the products follows the usual (16) stereochemical requirements for the E2 reaction. Esters **2***a* and **2***b* could be easily purified by high-vacuum distillation without any structural changes. However, when incubated at room temperature in an alcohol containing the corresponding sodium alkoxide (1 mole-equivalent) for ca. 60 h, **2***a* and **2***b* isomerized completely to the corresponding *E*-2-pentenyl-1-phosphonic derivatives, **2***c* and **2***d* (eq. [4]).

[4] 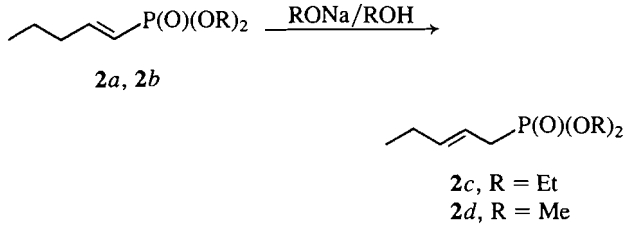

2*a*, **2***b*

2*c*, R = Et
2*d*, R = Me

The same result was obtained when dehydrohalogenation of **4** and **5** was carried out for longer periods in the presence of excess base. In this case, however, if the base used was the RONa/ROH system, up to 20% of the substitution product (**6**) was found in the reaction mixture (eq. [5]). The formation of ethers (**6**) could be eliminated by using *t*-BuOK/*t*-BuOH as a dehydrohalogenating agent; β,γ-unsaturated phosphonates **2***c*, **2***d* were then the exclusive reaction products. It is obvious that the α,β-unsaturated phosphonates (**2***a*, **2***b*) and the β,γ-unsaturated compounds (**2***c*, **2***d*) correspond respectively to the kinetic and thermodynamic products of the dehydrohalogenation of the precursors **4** and **5**. Our results therefore identify the dialkoxyphosphoryl group, $P(O)(OR)_2$, as a substituent strongly destabilizing an olefinic bond and indicate that, similar to the methylsulfonyl,[2] the PO_3R_2 group interacts with adjacent centers mostly via its inductive effect with only a minor resonance component.

[2]For the SO_2Me group the ratio of the resonance to the inductive substituent constants, $\sigma_R^0/\sigma_I = 0.10$, while for the CO_2Et group the corresponding ratio is as high as 0.60 (17).

[5] 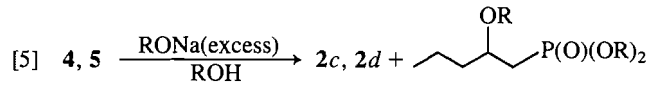

6*a*, R = Et
6*b*, R = Me

Isomerization of α,β- to β,γ-unsaturated phosphonates proceeds via the allylic carbanion intermediate **7** (eq. [6]). According to this scheme, the allylic positions of both substituents, i.e. methylene groups α, γ, and δ, should be susceptible to the hydrogen–deuterium exchange. Ester **2***b* was incubated at room temperature in methanol-d_4 containing an excess of CD_3ONa. After 5 h the ^{1}H nmr spectrum of the solution revealed that the isomerization to **2***d* was complete, and that 100% of the H/D exchange took place at C_α and 23% at C_δ; however, no exchange at C_γ was observed. The absence of the exchange at C_γ shows that in eq. [6] $k_2 \gg k_{-1}$, i.e., the carbanion **7**, once formed, is protonated exclusively at C_α. Additional support for the high rate of isomerization relative to the exchange was provided by the behavior of the β,γ-unsaturated ester **2***d*. When incubated in the CD_3OD/CD_3ONa solution, **2***d* did not, as expected, undergo any isomerization but showed H/D exchange at positions α and δ. The relative rate of the exchange at these two positions was determined as $k(\alpha)/k(\delta) \approx 160$, and can be taken as a measure of the difference in acidities of the two respective methylene groups. After 5 h of incubation the exchange at the δ position in **2***d* was ca. 20%, very close to the conversion observed under the same conditions for C_δ (23%) when **2***b* was used as a precursor for **2***d*. These results indicate that eq. [6] involves fast isomerization, followed by fast exchange at C_α and slow at C_δ of the isomerization product.

The monoanion of the monoester (**3***c*, R = Me) was dehydrohalogenated under the same conditions as neutral esters **2***a* and **2***b* and yielded the *E*-1-pentenylphosphonic derivative **2***e* as the exclusive elimination product (eq. [7]). The regio- and stereoselectivity of the reaction was determined from the high-resolution ^{1}H nmr spectrum of **2***e*. When an excess of the base was used in reaction [7] or when **2***e* was incubated in methanol containing MeONa (3 mole-equivalents) at 40°C for up to 46 h, no isomerization to the β,γ-unsaturated compound was observed. The β,γ-unsaturated isomer **2***f* was then prepared by the demethylation of the stable isomer of the dimethyl ester, **2***d* (eq. [8]). Product **2***f* was also resistant to the isomerization; it remained unchanged after incubation in methanolic MeONa (2 mole-equivalents) at 40°C for 33 h. Stability of both **2***e* and **2***f* toward base-catalysed interconversion implied very slow deprotonation of the corresponding allylic methylene groups to give the necessary allylic carbanion, most likely the result of the insufficiently strong effect of the negatively charged substituent on the acidity of allylic hydrogens. This conclusion was confirmed by exchange experiments; neither **2***e* nor **2***f* showed any evidence of the H/D exchange after incubation in methanol-d_4 containing 6- to 13-fold excess of CD_3ONa at room temperature for 144 h. However, the H/D exchange at the allylic positions in both isomers could be observed under more basic conditions, e.g., in solutions of CD_3ONa (3.6 mole-equivalents) in DMSO-d_6 (18). Allylic phosphonate **2***f* after 20 h at 40°C gave no evidence of isomerization but exchanged completely at the α-CH_2, and to the extent of 30% at the δ-CH_2 group. The most informative results were obtained after incubation of the vinylic derivative **2***e* under the same conditions. In this case the

Can. J. Chem. Downloaded from www.nrcresearchpress.com by 61.7.252.67 on 09/07/12
For personal use only.

Can. J. Chem. Downloaded from www.nrcresearchpress.com by 61.7.252.67 on 09/07/12
For personal use only.

[6] $MeCH_2CH_2CH{=}CHP \underset{+H^+,\ k_{-1}}{\overset{-H^+,\ k_1}{\rightleftharpoons}} MeCH_2\dot{C}HCHCHP \underset{-H^+,\ k_{-2}}{\overset{+H^+,\ k_2}{\rightleftharpoons}} MeCH_2CH{=}CHCH_2P$

7

P = $P(O)(OR)_2$

[7] 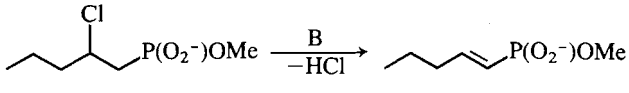

3c **2e**

B = MeONa/MeOH; EtONa/EtOH; *t*-BuOK/*t*-BuOH.

[8] **2d** $\xrightarrow{NaI}$

2f

complete isomerization took place and the isomerized product incorporated 100% of D at C_α, ca. 5% of D at C_δ, and ca. 90% of D at the γ-olefinic carbon (eq. [9]). The high yield (90%) of the H/D exchange at C_γ together with the low (5%) degree of exchange at C_δ indicate that in the case of the ionic substrate **2e**

[9] 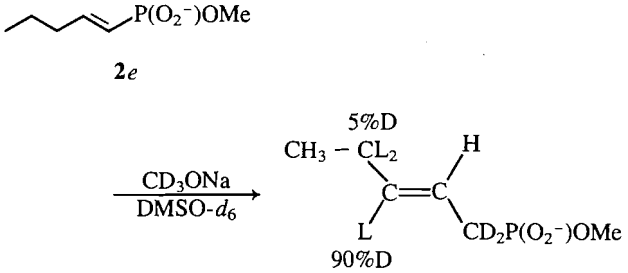

2e

2f, L = H or D

the reaction involves fast exchange at C_γ, accompanied by slow isomerization, i.e., $k_2 < k_{-1}$ (eq. [6]). This result can be easily explained in terms of charge distribution in the allylic carbanion **7**, in which (opposite to the case of the diester **2b**) most of the negative charge is located on C_γ, away from the anionic substituent. Since the isomerized product **2f** is formed slowly, only a low degree of exchange is observed at position δ.[3]

In conclusion, our results enable us to classify both phosphonic substituents, the neutral diester $P(O)(OR)_2$ and the ionic monoester $P(O_2^-)OR$, as *deactivating* (relative to hydrogen) the adjacent olefinic bond. In both cases, under conditions of sufficiently high basicity, both α,β-unsaturated systems, formed in the elimination as products of the kinetic control, rearrange completely to the thermodynamically stable β,γ-unsaturated derivatives.

As expected, the dehydrohalogenation of the free 2-chloropentylphosphonic acid **3a** could not be studied because of its fragmentation (10) according to eq. [10].

[10] 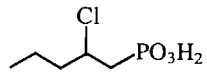

3a

Experimental

All solvents and commercially available reagents were purified by distillation immediately before use. The following media were used for recording ^1H nmr spectra: $CDCl_3$ (Aldrich, Gold Label, 99.8 at.% D); methanol-d_4 (Merck, min. 99%); DMSO-d_6 (Aldrich, Gold Label, 99.9 at.% D); deuterium oxide (Merck, min. 99.75%) containing the required quantity of NaOD (Wilmad Glass, 40% in D_2O, min. 99.0% D). Solutions of sodium alkoxides in alcohols were prepared by dissolving the required quantity of sodium in the corresponding alcohol under nitrogen with exclusion of moisture. Solution of CD_3ONa in DMSO-d_6 was obtained by preparing the solution of sodium methoxide in methanol, evaporation of methanol under reduced pressure, and dissolving the residue in DMSO-d_6 under nitrogen with exclusion of moisture. All reactions were carried out with rigorous exclusion of moisture. Bulb-to-bulb distillations were carried out using a Buchi GKR-50 glass tube oven. Elemental analyses (C, H) were performed at the University of Cape Town using a Heraeus Universal combustion analyser.

The nmr (^1H, ^{13}C, ^{31}P) spectra were recorded on a superconducting FT Bruker AC300 spectrometer with TMS (^1H, ^{13}C) or trimethyl phosphate (^{31}P) as internal standards.

Substrates

2-Chloropentylphosphonic dichloride was obtained by following the procedure given (9*a*) for 2-chloropropylphosphonic dichloride; 67%, bp 86–88°C (1 Torr; 1 Torr = 133.3 Pa); n_D^{20} 1.4906; ^1H nmr ($CDCl_3$) δ: 0.94 (3H, t, J_{HH} 6.5 Hz, CH_3), 1.25–1.72 (2H, m, δ-CH_2), 1.72–2.08 (2H, m, γ-CH_2), 2.51 (2H, d of d, J_{HP} 18.8 Hz, J_{HH} 6.8 Hz, α-CH_2), 4.37 (1H, t of t, J_{HH} 7.3, 6.7 Hz, β-CH); ^{31}P nmr ($CDCl_3$) δ: 40.0 ppm.

Diethyl 2-chloropentylphosphonate (4) was prepared according to the procedure for 2-phenylvinylphosphonates (12); 84%, bp 140°C (0.45 Torr); n_D^{20} 1.4470; ^1H nmr ($CDCl_3$) δ: 0.94 (3H, t, J_{HH} 6.5 Hz, ω-CH_3), 1.34 (6H, t, J_{HH} 7.0 Hz, 2 × CH_3 of Et), 1.30–1.65 (2H, m, δ-CH_2), 1.65–2.00 (2H, m, γ-CH_2), 2.32 (2H, d of d, J_{HP} 19.5 Hz, J_{HH} 6.5 Hz, α-CH_2), 4.13 (4H, quint, $J_{HP} = J_{HH}$ 8.6 Hz, 2 × OCH_2), 4.00–4.40 (1H, m, β-CH). *Anal.* calcd. for $C_9H_{20}O_3PCl$: C 44.5, H 8.3%; found: C 44.4, H 8.1%.

Dimethyl 2-chloropentylphosphonate (5) was prepared as **4**; 71%, bp 84°C (0.85 Torr); n_D^{20} 1.4537; ^1H nmr ($CDCl_3$) δ: 0.94 (3H, t, J_{HH} 6.4 Hz, ω-CH_3), 1.38–1.65 (2H, m, δ-CH_2), 1.65–2.02 (2H, m, γ-CH_2), 2.28 (2H, d of d, J_{HP} 20.5 Hz, J_{HH} 6.5 Hz, α-CH_2), 3.77 (6H, d, J_{HP} 11.0 Hz, 2 × OCH_3), 4.00–4.50 (1H, m, β-CH). *Anal.* calcd. for $C_7H_{16}ClO_3P$: C 39.2, H 7.5%; found: C 40.0, H 7.5%.

Methyl 2-chloropentylphosphonic acid (3c) was prepared by demethylation of **5** with sodium iodide (13) followed by the isolation of the free acid as described in the literature (20); 88%, oil; ^1H nmr ($CDCl_3$) δ: 0.94 (3H, t, J_{HH} 6.7 Hz, ω-CH_3), 1.27–1.82 (2H, m, δ-CH_2), 1.45–2.00 (2H, m, γ-CH_2), 2.31 (2H, d of d, J_{HP} 18.7 Hz,

[3]As one of the referees pointed out, 100% D exchange occurring at C_α in **2f** is interesting in view of the fact that a carbanion α to the PO_3Me^- group is destabilized. For **2f** to exchange it has to become deprotonated either at C_α or C_δ. In the first case most of the negative charge is indeed located at C_γ, but it is only C_α that becomes reprotonated, as it yields the thermodynamically stable (observed) β,γ-unsaturated product. In case of the deprotonation at C_δ, it is this carbon atom which undergoes reprotonation (and exchange); protonation at C_β would yield unobserved γ,δ-unsaturated products. The exchange results indicate that deprotonation of C_α in **2f** is favoured over the deprotonation of C_δ.

Can. J. Chem. Downloaded from www.nrcresearchpress.com by 61.7.252.67 on 09/07/12
For personal use only.

J_{HH} 6.8 Hz, α-CH_2), 3.72 (3H, d, J_{HP} 11.0 Hz, OCH_3), 4.00–4.50 (1H, m, β-CH), 10.34 (1H, bs, OH). *Anal.* calcd. for $C_6H_{14}ClO_3P$: C 35.9, H 7.0%; found: C 36.1, H 7.1%. Na salt of **3***c*: ^{1}H nmr (D_2O) δ: 0.90 (3H, t, J_{HH} 6.7 Hz, ω-CH_3), 1.12–1.82 (2H, m, δ-CH_2), 1.53–1.98 (2H, m, γ-CH_2), 2.19 (2H, d of d, J_{HP} 17.2 Hz, J_{HH} 7.0 Hz, α-CH_2), 3.56 (3H, d, J_{HP} 10.5 Hz, OCH_3), 4.00–4.48 (1H, m, β-CH).

*2-Chloropentylphosphonic acid (**3**a)* was prepared according to the procedure given (9*a*) for 2-chloropropylphosphonic acid; 13%, mp 95.0–95.8°C (from $CHCl_3$/pet. ether); ^{1}H nmr (acetone-d_6) δ: 0.94 (3H, t, J_{HH} 6.7 Hz, ω-CH_3), 1.35–1.73 (2H, m, δ-CH_2), 1.60–1.83 (2H, m, γ-CH_2), 2.35 (2H, d of d, J_{HP} 20.0 Hz, J_{HH} 8.0 Hz, α-CH_2), 4.19–4.39 (1H, m, β-CH), 11.1 (2H, bs, 2 × OH). *Anal.* calcd. for $C_5H_{12}ClO_3P \cdot H_2O$: C 29.4, H 6.9%; found: C 29.1, H 6.1%.

*Preparation of **2**a*

Compound **4** (0.002 mol) was dissolved in 0.9 mL of a 2.2 M solution of sodium ethoxide in ethanol and the solution was incubated at 25°C for 3 h. Water (10 mL) was added (pH of the aqueous solution was 7.0) and the mixture was extracted with chloroform (4 × 3 mL). After drying ($MgSO_4$) and evaporating the solvent under reduced pressure the product was purified by bulb-to-bulb distillation at oven temperature 100–130°C (1 Torr); 62%, n_D^{25} 1.4392; ^{1}H nmr ($CDCl_3$) δ: 0.94 (3H, t, J_{HH} 6.5 Hz, ω-CH_3), 1.33 (6H, t, J_{HH} 7.0 Hz, 2 × CH_3 of EtO), 1.40–1.70 (2H, m, δ-CH_2), 2.08 (2H, d of t, J_{HH} 6.8, 6.7 Hz, γ-CH_2), 4.08 (4H, quint, J_{HP} = J_{HH} 7.8 Hz, 2 × CH_2 of EtO), 5.53 (1H, d of d of t, J_{HP}(*gem*) 21.2 Hz, J_{HH}(*trans*) 17.3 Hz, J_{HH}(1,3) 1.7 Hz, α-CH), 6.67 (1H, d of d of t, J_{HP}(*cis*) 22.1 Hz, J_{HH}(*trans*) 17.3 Hz, J_{HH}(1,2) 6.7 Hz, β-CH) (literature values for CH_2=CH—P(O)$(OEt)_2$: J_{HP}(*gem*): 22.3 Hz (21); 22.0 Hz (22); J_{HH}(*trans*): 18.7 Hz (21, 22); J_{HP}(*cis*): 25.1 Hz (21); 25.0 Hz (22)); ^{13}C nmr ($CDCl_3$) δ: 13.4 (CH_3 of C_5H_9), 16.1 (d, J_{CP} 6.2 Hz, 2 × CH_3 of EtO), 20.8 (C_δ), 36.0 (d, J_{CP} 21.7 Hz, C_γ), 61.3 (d, J_{CP} 5.3 Hz, 2 × CH_2 of EtO), 116.7 (d, J_{CP} 186.2 Hz, C_α), 153.5 (d, J_{CP} 4.1 Hz, C_β) (literature (23) values for CH_2=CH—P(O)$(OEt)_2$: δ 16.7 (d, J_{CP} 7.3 Hz, CH_3 of EtO), 61.7 (d, J_{CP} 5.9 Hz, OCH_2), 127.9 (d, J_{CP} 182.1 Hz, C_α), 134.9 (d, J_{CP} 1.9 Hz, C_β)); ^{31}P nmr ($CDCl_3$) δ: 16.6. *Anal.* calcd. for $C_9H_{19}O_3P$: C 52.4, H 9.3%; found: C 52.3, H 9.1%.

*Preparation of **2**c*

Compound **2***a* (0.002 mol) was dissolved in 0.9 mL of a 2.2 M (1 mole-equivalent) solution of EtONa in EtOH and the solution was incubated at 25°C for 63 h. The product was recovered as for **2***a* and purified by bulb-to-bulb distillation at oven temperature 130°C (0.8 Torr); 69%, n_D^{25} 1.4372; ^{1}H nmr ($CDCl_3$) δ: 0.96 (3H, t, J_{HH} 7.0 Hz, ω-CH_3), 1.29 (6H, t, J_{HH} 7.5 Hz, 2 × CH_3 of EtO), 1.90–2.20 (2H, m, δ-CH_2), 2.53 (2H, d of d, J_{HP} 22.5 Hz, J_{HH} 7.5 Hz, α-CH_2), 4.08 (4H, quint, J_{HP} = J_{HH} 7.8 Hz, 2 × CH_2 of EtO), 5.40 (1H, d of t, J_{HH}(*trans*) 20.0 Hz, J_{HH}(allyl) 7.5 Hz, γ-CH), 5.62 (1H, m, β-CH); ^{13}C nmr ($CDCl_3$) δ: 13.5 (CH_3 of C_5H_9), 16.4 (d, J_{CP} 6.0 Hz, 2 × CH_3 of EtO), 25.6 (d, J_{CP} 2.7 Hz, δ-CH_2), 30.4 (d, J_{CP} 138.9 Hz, α-CH_2), 61.8 (d, J_{CP} 6.4 Hz, 2 × CH_2 of EtO), 117.4 (d, J_{CP} 11.1 Hz, γ-CH), 137.6 (d, J_{CP} 14.2 Hz, β-CH) (literature (19) values for CH_2=CH—CH_2—P(O)$(OEt)_2$: J_{PC} 138.7 Hz, J_{POC} 6.7 Hz, J_{POCC} 5.3 Hz); ^{31}P nmr ($CDCl_3$) δ: 26.1. *Anal.* found: C 52.2, H 9.2%.

When **2***c* was prepared directly from **4** and 2 mole-equivalents of EtONa, and isolated as before, the product contained, besides **2***c*, 17% of diethyl 2-ethoxypentyl-1-phosphonate (**6***a*), as determined by the signal of the ether OCH_2 group (δ 3.53, quart, J_{HH} 7.3 Hz) in the ^{1}H nmr spectrum of the reaction product.

*Preparation of **2**b* was carried out as for **2***a* and the product was distilled at oven temperature 90°C (0.5 Torr); 75%, n_D^{25} 1.4478; ^{1}H nmr ($CDCl_3$) δ: 0.94 (3H, t, J_{HH} 6.5 Hz, ω-CH_3), 1.20–1.80 (2H, m, δ-CH_2), 2.23 (2H, d of t, J_{HH} 7.0, 6.8 Hz, γ-CH_2), 3.72 (6H, d, J_{HP} 11.0 Hz, 2 × OCH_3), 5.60 (1H, d of d of t, J_{HP}(*gem*) 21.2 Hz, J_{HH}(*trans*) 17.2 Hz, J_{HH}(1,3) 1.6 Hz, α-CH), 6.81 (1H, d of d of t, J_{HP}(*cis*) 22.1 Hz, J_{HH}(*trans*) 17.2 Hz, J_{HH}(1,2) 6.4 Hz, β-CH). *Anal.* calcd. for $C_7H_{15}O_3P$: C 47.2, H 8.4%; found: C 47.0, H 8.3%.

*Preparation of **2**d*

Compound **5** (5.0 g, 0.0233 mol) was dissolved in 10 mL of the 2.2 M (1.3 mole-equivalents) solution of *t*-BuOK in *t*-BuOH and incubated at 25°C for 47 h. *tert*-Butanol was removed under reduced pressure, ice water (5 mL) was added, and the mixture was extracted with chloroform (3 × 5 mL). After drying ($MgSO_4$) and evaporation of solvent, **2***d* was purified by bulb-to-bulb distillation at oven temperature 100°C (0.2 Torr); 63%, n_D^{25} 1.4460; ^{1}H nmr ($CDCl_3$) δ: 0.99 (3H, t, J_{HH} 7.3 Hz, ω-CH_3), 1.82–2.30 (2H, m, δ-CH_2), 2.61 (2H, d of d, J_{HP} 21.2 Hz, J_{HH} 6.7 Hz, α-CH_2), 3.75 (6H, d, J_{HP} 10.8 Hz, 2 × OCH_3), 5.42 (1H, d of t, J_{HH}(*trans*) 20.1 Hz, J_{HH}(allyl) 7.5 Hz, γ-CH), 5.65 (1H, m, β-CH). *Anal.* found: C 47.1, H 8.2%.

*Preparation of **2**e*

Compound **3***c* (3.8 g, 0.019 mol) was dissolved in 15 mL of the 2.2 M (2 mole-equivalents) solution of *t*-BuOK in *t*-BuOH and stirred at 25°C for 45 h. *tert*-Butanol was removed under reduced pressure, ice water (10 mL) was added, and the solution was made acidic with trifluoroacetic acid and extracted with chloroform (4 × 5 mL). After drying ($MgSO_4$) and removing the solvent, **2***e* was obtained as free acid; 80%, oil; ^{1}H nmr ($CDCl_3$) δ: 0.93 (3H, t, J_{HH} 6.7 Hz, ω-CH_3), 1.49 (2H, t of quart, J_{HH} 8.1, 7.8 Hz, δ-CH_2), 2.16 (2H, d of t, J_{HH} 7.0, 6.7 Hz, γ-CH_2), 3.69 (6H, d, J_{HP} 11.3 Hz, 2 × OCH_3), 5.68 (1H, d of d of t, J_{HP}(*gem*) 21.5 Hz, J_{HH}(*trans*) 16.9 Hz, J_{HH}(1,3) 1.3 Hz, α-CH), 6.77 (1H, d of d of t, J_{HP}(*cis*) 22.3 Hz, J_{HH}(*trans*) 16.9 Hz, J_{HH}(1,2) 6.7 Hz, β-CH), 9.75 (1H, bs, OH). *Anal.* calcd. for $C_6H_{13}O_3P$: C 43.9, H 7.9%; found: C 44.0, H 7.9%.

*Preparation of **2**f*

Compound **2***f* was prepared from **2***d* (1.85 g, 0.0104 mol) by demethylation with NaI (2 mole-equivalents) in acetone (17 mL). After refluxing the solution for 30 h and cooling, the sodium salt of **2***f* precipitated out. The product was filtered off, washed thoroughly with cold acetone, and dried; 88%; ^{1}H nmr (methanol-d_4) δ: 0.97 (3H, t, J_{HH} 7.5 Hz, ω-CH_3), 1.72–2.36 (2H, m, δ-CH_2), 2.36 (2H, d of d, J_{HP} 20.2 Hz, J_{HH} 7.2 Hz, α-CH_2), 3.54 (3H, d, J_{HP} 10.5 Hz, OCH_3), 5.39–5.62 (2H, overlapping m, β-H, γ-H). *Anal.* calcd. for $C_6H_{12}O_3NaP$: C 38.7, H 6.5%; found: C 39.0, H 6.5%.

Free acid **2***f* was obtained from the sodium salt by acidification (CF_3CO_2H) and extraction with chloroform; 96%, oil, n_D^{25} 1.4528.

*Fragmentation of **3**a*

Compound **3***a* (0.020 g, 0.0001 mol) was dissolved in D_2O (0.6 mL), a 40% solution of NaOD in D_2O (0.02 mL, 2.8 mole-equivalents) was added, and the solution was left at 25°C for 15 min. The mixture was then extracted with chloroform-*d* (0.6 mL), the $CDCl_3$ solution was dried ($MgSO_4$), and ^{1}H nmr of this solution revealed the presence of 1-pentene as the sole reaction product; δ: 0.91 (3H, t, J_{HH} 6.5 Hz, CH_3), 1.41 (2H, t of quart, J_{HH} 6.5, 6.7 Hz, 4-CH_2), 2.05 (2H, d of t, J_{HH} 6.7, 6.5 Hz, 3-CH_2), 4.90–5.15 (2H, m, 1-CH_2), 5.82 (1H, t of quart, J_{HH} 6.5, 7.3 Hz, 2-CH).

H/D exchange experiments were carried out by dissolving substrates in the required medium in an nmr tube, sealing the tube, placing it in a thermostated water bath, and periodically recording the ^{1}H nmr spectrum. The percentage of the exchange was determined from the integral of the remaining signal of the exchanging group relative to the intensities of signals of the non-exchanging groups.

Acknowledgements

Financial assistance of the University of Pretoria and the Council for Scientific and Industrial Research is gratefully acknowledged.

1. C. K. Ingold. Structure and mechanism in organic chemistry. Cornell University Press, Ithaca, NY. 1953. Chap. X; D. J. Cram. Fundamentals of carbanion chemistry. Academic Press, New York. 1965. Chap. V.
2. J. Hine. Structural effects on equilibria in organic chemistry. Wiley–Interscience, New York. 1975. Chap. 8.

3. R. PAUL, M. FLUCHAIRE, and G. COLLARDEAU. Bull. Soc. Chim. Fr. 668 (1950).
4. D. E. O'CONNOR and W. I. LYNESS. J. Am. Chem. Soc. **86**, 3840 (1964).
5. P. T. KEOUGH and M. GRAYSON. J. Org. Chem. **29**, 631 (1964).
6. E. J. COREY and D. E. CANE. J. Org. Chem. **34**, 3053 (1969).
7. H. AHLBRECHT, W. FARNUNG, and M. SIMON. Chem. Ber. **117**, 2622 (1984).
8. M. MALEKI and J. A. MILLER. Tetrahedron Lett. **22**, 3789 (1981).
9. (*a*) M. J. GREGORY and G. M. C. HIGGINS. J. Chem. Soc. Perkin Trans. 2, 711 (1974); (*b*) K. C. CALVO and J. M. BERG. J. Am. Chem. Soc. **106**, 4202 (1984); K. C. CALVO and F. H. WESTHEIMER. J. Am. Chem. Soc. **106**, 4205 (1984).
10. J. A. MAYNARD and J. M. SWAN. Proc. Chem. Soc. London, 1394 (1963); Aust. J. Chem. **16**, 596 (1963).
11. C. A. STUTTE. Plant growth regulators. Am. Chem. Soc., Washington, DC. 1977.
12. K. N. ANISIMOV and A. N. NESMEYANOV. Izv. Akad. Nauk SSSR, Otd. Khim. Nauk, 999 (1955); Chem. Abstr. **50**, 11267 (1956).
13. L. ZERVAS and I. DILARIS. J. Am. Chem. Soc. **77**, 5354 (1955).
14. R. W. ALDER, P. BOWMAN, W. R. S. STEELE, and D. R. WINTERMAN. J. Chem. Soc. Chem. Commun. 723 (1968).
15. L. M. PEVZNER, V. M. IGNAT'EV, and B. I. IONIN. J. Gen. Chem. USSR, **52**, 1703 (1982).
16. J. MARCH. Advanced organic chemistry. 3rd ed. J. Wiley, New York. 1985. Chap. 17.
17. R. A. Y. JONES. Physical and mechanistic organic chemistry. 2nd ed. Cambridge University Press, London. 1984. p. 66.
18. D. J. CRAM, R. RICKBORN, C. A. KINGSBURY, and P. HABERFIELD. J. Am. Chem. Soc. **83**, 3678 (1961).
19. J. R. LLINAN, E. J. VINCENT, and G. PEIFFER. Bull. Soc. Chim. Fr. 3209 (1973).
20. J. LECOCQ and A. R. TODD. J. Chem. Soc. 2257 (1953).
21. J. E. LANCASTER. Spectrochim. Acta, Part A: **23A**, 1449 (1967).
22. M. P. WILLIAMSON, S. CASTELLANO, and C. E. GRIFFIN. J. Phys. Chem. **72**, 175 (1968).
23. W. ALTHOFF, M. FILD, H.-P. RIECK, and R. SCHMUTZLER. Chem. Ber. **111**, 1845 (1978).

Can. J. Chem. Downloaded from www.nrcresearchpress.com by 61.7.252.67 on 09/07/12
For personal use only.

Phenyl group as a probe in the ^1H nuclear magnetic resonance study of the conformations of quaternary heteroaromatic carbapenem antibiotics. Identification of the site of quaternization in -SCH_2- substituted nitrogen-containing heteroaromatic derivatives

VANGA S. RAO,[1] JEAN-PAUL DARIS, AND MARCEL MENARD
Bristol–Myers Pharmaceutical Group, 100 Industrial Boulevard, Candiac, P.Q., Canada J5R 1J1

Received December 9, 1987

VANGA S. RAO, JEAN-PAUL DARIS, and MARCEL MENARD. Can. J. Chem. **66**, 1546 (1988).

The phenyl group is shown as a useful probe in sensing the environment in the ^1H nuclear magnetic resonance conformational study of a variety of quaternary heteroaromatic carbapenem derivatives. The influence of the -SCH_2- substituent in determining the site of quaternization in nitrogen-containing heteroaromatic compounds is demonstrated through the acidity measurements of these methylene protons.

VANGA S. RAO, JEAN-PAUL DARIS et MARCEL MENARD. Can. J. Chem. **66**, 1546 (1988).

Au cours d'études conformationnelles, faites à l'aide de la résonance magnétique nucléaire du ^1H sur un certain nombre de dérivés carbapénem hétéro-aromatiques, on a démontré que le groupement phényle est une sonde sensible pour déceler l'environnement. Utilisant des mesures d'acidité des protons méthyléniques, on a démontré l'influence du substituant -SCH_2- sur le site de quaternisation de composés hétéro-atomiques contenant de l'azote.

[Traduit par la revue]

Introduction

Thienamycin, **1** (R = H), is an unusually potent β-lactam antibiotic isolated[2] from the fermentation broth of the soil microorganism *Streptomyces cattleya*. A major drawback of these β-lactams is their susceptibility to renal dehydropeptidase (DHP-I), an enzyme responsible for their metabolic inactivation in vivo (2). However, introduction of a β-methyl substituent at the C-1 position (R = CH_3) has resulted in an exceptional increase in stability to this devastating enzyme (3), presumably by way of partially blocking the carbonyl moiety of the β-lactam from being attacked by the serine OH group. Since the discovery of **1** (R = H), a large number of this carbapenem

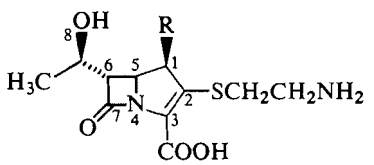

1

family have been synthesized by several research groups, in order to achieve better antibacterial activity and reduced toxic side effects.

The most desirable approach towards this goal is to evaluate the precise receptor binding site of these molecules. When this information is not easily attainable, then an understanding of the three-dimensional shape of these molecules becomes pivotal in the design and development of new and superior drugs.

Results and discussion

Although the bicyclic part of **1** is fairly rigid, the side chains at positions 2 and 6 can be seen as flexible and can adopt different rotameric states to a varying degree depending on the type of substituent. The present discussion is restricted to side-chain orientation at C-2. A number of quaternary carbapenem derivatives (4) of the type **2** have been synthesized in our laboratories with the aim of finding a better antibacterial agent with no or reduced toxicity.

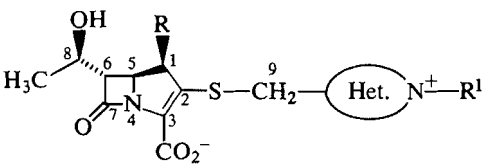

2

In an attempt to understand the results of biological screening of these compounds (4), the role of the methylene protons, flanked by the sulfur on one side and the positively charged heteroaromatic ring on the other side, has been studied by ^1H nmr spectroscopy. These protons are found to be acidic enough to be exchanged for the deuterium isotope in D_2O under mildly basic conditions. The origin of this acidity is discussed in a later section. Under controlled conditions the rate of exchange of these protons can be moderated to a measurable rate. Under these conditions the two diastereotopic protons of **10** are exchanged at different rates, as studied by ^1H nmr spectroscopy, implying that one of them is more acidic than the other. This may be attributed to a preferential rotameric distribution around the S—CH_2 bond, as depicted in **3**.

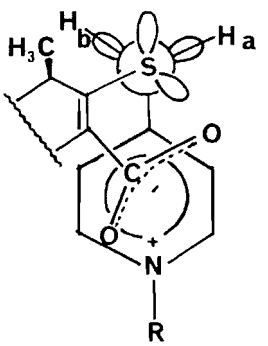

3 (Newman projection around S—CH_2 bond)

[1]Author to whom correspondence may be addressed.

[2]For the structure determination and absolute configuration of thienamycin, see ref. 1*a*. For a general review of carbapenems, see ref. 1*b*.

Can. J. Chem. Downloaded from www.nrcresearchpress.com by 61.7.252.67 on 09/07/12
For personal use only.

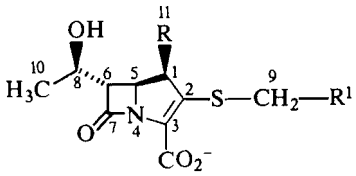

4 R = CH_3; R^1 = 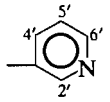 : NO

5 R = CH_3; R^1 = 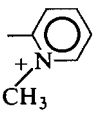 : YES

6 R = CH_3; R^1 = 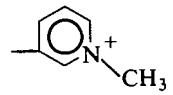 : NO

7 R = CH_3; R^1 = 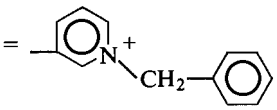 : NO

8 R = CH_3; R^1 = 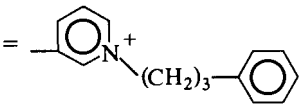 : NO

9 R = CH_3; R^1 = 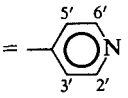 : NO

10 R = CH_3; R^1 = 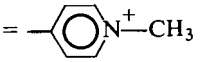 : YES

11 R = CH_3; R^1 = 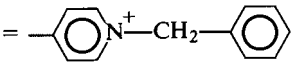 : YES

12 R = CH_3; R^1 = 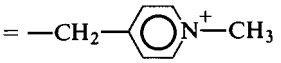 : NO

13 R = CH_3; R^1 = 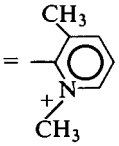 : NO

14 R = CH_3; R^1 = 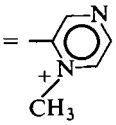 : YES

15 R = CH_3; R^1 = 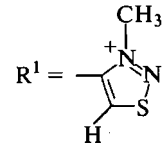 : YES

16 R = CH_3; R^1 = 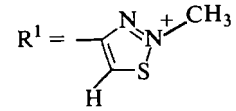 : NO

17 R = CH_3; R^1 = 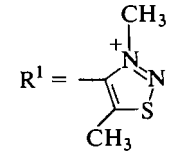 : NO

18 R = CH_3; R^1 = 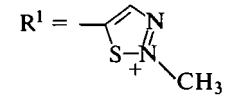 : YES

19 R = CH_3; R^1 = 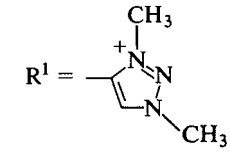 : NO

20 R = CH_3; R^1 = 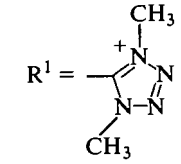 : YES

21 R = CH_3; R^1 = 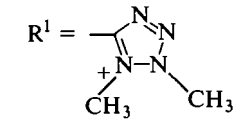 : YES

22 R = H; R^1 = 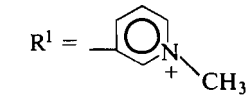 : NO

23 R = H; R^1 = 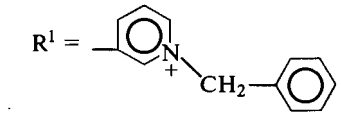 : NO

YES or NO denotes whether or not the methylene protons (SCH_2) exchange with the deuterium isotope in D_2O under basic conditions as described in the experimental section

CHART 1. Structures of zwitterionic compounds.

The *gauche* conformer around the S—CH_2 bond (**3**) places H_a doubly *gauche* to the sulfur lone pairs whereas H_b is *gauche* to only one lone pair. This, in principle, should allow H_a to be exchanged faster than H_b due to favorable "*gauche*" interactions (5) between the electron pairs of sulfur and the negative charge of the conjugate base (carbanion generated after removing H_a and (or) H_b by a suitable base). This conformation also allows a favorable secondary electrostatic stacking interaction between the oppositely charged pyridinium and the carboxylate moiety (**3**). To obtain experimental support for the existence of a folded (*gauche*) conformation, **3**, the pyridine nitrogen of **4** was quaternized with a benzyl group to give **7**, within which there exists a highly anisotropic probe, namely a phenyl moiety. The CH_2 group anchoring the pyridinium and the phenyl group gives just enough flexibility in this region to allow the phenyl group to stay in close proximity to the H-1 and H-5 protons of the β-lactam moiety (see **24**). A longer bridge ($(CH_2)_3$) as in **8** only makes the ends floppy, thus allowing the phenyl group to orient itself away from these protons in which case the magnitude of the phenyl anisotropic effect is expected to diminish.

Thus, it can be seen from Table 1 that the chemical shifts of

Can. J. Chem. Downloaded from www.nrcresearchpress.com by 61.7.252.67 on 09/07/12
For personal use only.

Can. J. Chem. Downloaded from www.nrcresearchpress.com by 61.7.252.67 on 09/07/12
For personal use only.

TABLE 1. Relevant ^{1}H nuclear magnetic resonance chemical shift (δ) data of some carbapenem derivatives

Compound	H-1 (AB)[a]		H-5	H-6	H-8	H-9 (AB)		CH_3 (10)	CH_3 (11)	$^+NCH_2X$	H-2′	H-3′	H-4′	H-5′	H-6
4	3.33		4.05	3.39	4.21	4.18	4.03	1.28	1.16	—	8.52	—	7.89	7.44	8.42
6	3.32		4.22	3.46	4.13	4.29	4.15	1.27	1.19	4.37	8.81	—	8.48	7.99	8.67
7	3.00		3.72	3.34	4.18	4.29	4.11	1.26	1.07	5.80	8.82	—	8.52	8.03	8.90
$\delta_7 - \delta_6$	−0.32		−0.5			0.0	−0.04								
8	3.27		4.05	3.42	4.11	4.24	4.07	1.24	1.18	4.63	8.77	—	8.43	7.90	8.65
9	3.28		4.02	3.39	4.21	4.17	4.00	1.27	1.15	—	8.47	7.47	—	7.47	8.47
10	3.29		4.09	3.46	4.21	4.35	4.16	1.27	1.19	4.34	8.68	7.98	—	7.98	8.68
11	3.22		4.04	3.35	4.20	4.39	4.16	1.26	1.06	5.77	8.81	8.00	—	8.00	8.81
$\delta_{11} - \delta_{10}$	−0.07		−0.05			0.04	0.0								
26	3.56		4.26	3.54	4.26	4.48	4.37	1.30	1.29	4.40	8.89	—	8.57	8.04	8.74
27	3.20		3.82	3.42	4.21	4.46	4.30	1.29	1.15	5.84	8.75	—	8.59	8.11	9.03
$\delta_{27} - \delta_{26}$	−0.36		−0.44			−0.02	−0.07								
28	3.51		4.16	3.50	4.12	4.41	4.28	1.27	1.26	4.67	8.82	—	8.50	7.95	8.73
29	3.49		4.19	3.50	4.24	4.54	4.40	1.29	1.25	4.36	8.74	8.06	—	8.06	8.74
30	3.44		4.14	3.44	4.19	4.53	4.37	1.27	1.16	5.79	8.87	8.06	—	8.06	8.87
$\delta_{30} - \delta_{29}$	−0.05		−0.05			−0.01	−0.03								
33	3.59		4.25	3.56	4.27	4.51	4.40	1.31	1.29	4.42	8.92	—	8.60	8.05	8.75
34	~3.20		3.82	3.43	4.21	4.43	4.30	1.28	1.14	5.84	8.75	—	8.59	8.10	9.00
$\delta_{34} - \delta_{33}$	−0.39		−0.43			−0.08	−0.10								
31	3.36	3.22	4.24	3.46	4.20	4.46	4.38	1.26	—	4.38	8.89	—	8.57	8.03	8.73
32	3.04	3.04	4.03	3.34	4.19	4.44	4.34	1.26	—	5.84	8.82	—	8.59	8.09	8.97
$\delta_{32} - \delta_{31}$	−0.32	−0.18	−0.21			−0.02	−0.04								
22	3.17	3.03	4.13	3.37	4.20	4.25	4.22	1.26	—	4.38	8.86	—	8.54	8.00	8.69
23	2.87	2.87	3.89	3.22	4.17	4.29	4.18	1.24	—	5.81	8.88	—	8.55	8.04	8.90
$\delta_{23} - \delta_{22}$	−0.30	−0.16	−0.24			0.04	−0.04								

[a](AB) refers to the AB (H-1,1′) part of an ABX spin system when R = H.

Can. J. Chem. Downloaded from www.nrcresearchpress.com by 61.7.252.67 on 09/07/12
For personal use only.

H-1 and H-5 of **7** are dramatically shifted upfield by 0.32 and 0.5 ppm, respectively, as compared to the H-1 and H-5 of **6**. This may be attributed to the through-space anisotropic effect of the phenyl group on these protons. As the rest of the chemical shifts (Table 1) are practically unaffected, particularly those attached to C-9 (AB), which forms a link between the positively charged heterocycle and the β-lactam moiety, it may be concluded that these upfield shifts do not arise because of through-bond (σ-skeleton) effects. The fact that the H-1 and H-5 protons are below the plane of the bicyclic ring and are most affected by quaternizing the pyridine ring with a benzyl group indicates a preferential underside folding of this group in the C-1 β-methyl series of compounds. In this conformation the phenyl moiety may be oriented appropriately to shield the H-1 and H-5 protons as depicted in **24**.

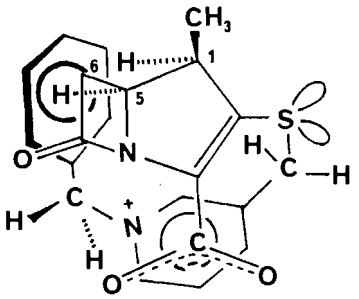

24 (6-hydroxyethyl group omitted for clarity)

In the case of the C-1 *non* β-methyl series, a comparison of the chemical shifts of compounds **22** and **23** indicates that the upfield shift effect of the phenyl anisotropy on one of the protons at C-1 and on H-5 is approximately half of that observed in the C-1 β-methyl series, thereby suggesting that both folded conformations (above and below) are significant in this series. Just how much of this particular conformer (**3** or **24**) contributes to the overall equilibrium mixture of conformers is difficult to assess without elaborate experimental and theoretical studies.

Furthermore, the pyridine ring was quaternized with a three-carbon chain at the end of which the same phenyl probe is present (**8**). As alluded to earlier, the increased number of bonds and in turn the increased rotational freedom is reflected in the magnitude of the phenyl anisotropic effect on the H-1 and H-5 protons. Thus the H-1 and H-5 chemical shifts are shifted upfield by only 0.05 and 0.17 ppm, respectively (Table 1; compare **6** and **8**).

The effect of changing the substitution pattern of the pyridine ring has also been examined. Compound **9** was quaternized with a benzyl group to give **11**, which differs from **7** only in its substitution pattern. In its folded conformation (**25**), it can be seen that the phenyl ring in **11** is unable to occupy an appropriate spatial position to exert its anisotropic effect on the H-1 and H-5 protons. In accordance with this expectation, the H-1 and H-5 protons of **11** are found to be affected to a negligible extent (0.07 and 0.05 ppm, Table 1) when compared to those of **10**. Thus the chemical shift data are consistent with the prominent role of *gauche* conformer around the S—CH_2 bond, which also allows a favorable interaction between the oppositely charged moieties in these zwitterionic derivatives.

The chemical shift changes observed for H-1 and H-5 protons due to the phenyl anisotropic effect in the allyl and methyl ester derivatives are similar to those in the corresponding zwitterionic

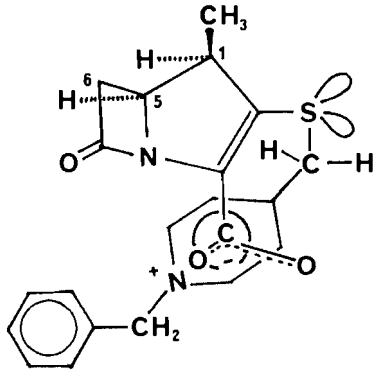

25 (6-hydroxyethyl group omitted for clarity)

compounds (Table 1, compare **6** and **7**, **26** and **27**, **33** and **34**). The shift changes for the H-1 and H-5 protons in the allyl and methyl ester derivatives are also similar. From these observations, it appears reasonable to rule out the possibility of any π-stacking interactions between the allyl group and the pyridinium ring. However, π interactions between the pyridinium nucleus and the electron-rich oxygen atoms of the ester seem quite possible and cannot be neglected. In conclusion, the data clearly show that there is an intrinsic preference for the *gauche* conformer around the S—CH_2 bond in these quaternized, heteroaromatic carbapenem derivatives.

Acidity of -SCH_2- protons

It was previously mentioned that the -SCH_2- protons in some compounds are acidic and can be exchanged for the deuterium isotope in D_2O under mildly basic conditions. It appears that they owe their acidity to some structural feature that allows the negative charge of the conjugate base to be stabilized by delocalization in such a way that the bond polarization terminates at the positive nitrogen atom. In corollary, by polarizing the —C=$\overset{+}{N}$—R bond, if the positive charge can be brought adjacent to the methylene carbon, then these protons become acidic. However, a few exceptions have been found and are discussed below. In the case of **13** (Chart 1) the non-acidic nature of the methylene protons can be rationalized by invoking a steric compression between sulfur/methyl/*N*-methyl/hydrogen, which can prevent the p-lobe of the incipient carbanion from being coplanar with the ring π-system necessary for effective delocalization as depicted below.

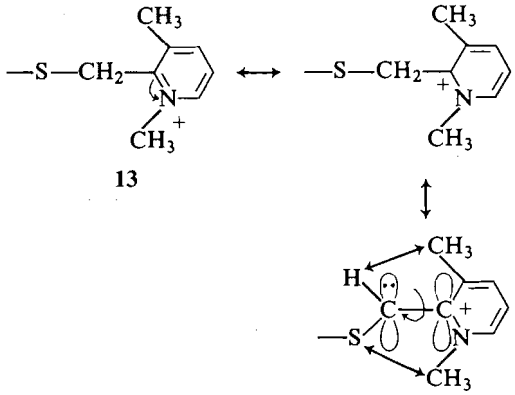

13

In another case the methylene protons of **15** (Chart 1) have been found to be exceptionally acidic. The reason for this may lie in the fact that the ring hydrogen (H-5′) is so acidic that it

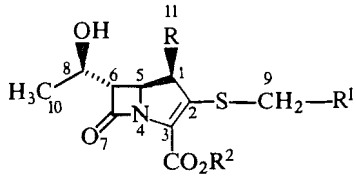

26 R = CH_3; R^1 = 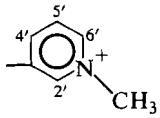 /TfO^-; R^2 = —CH_2CH=CH_2 : NO

27 R = CH_3; R^1 = 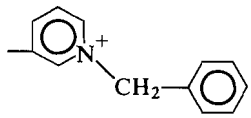 /Br^-; R^2 = —CH_2CH=CH_2 : NO

28 R = CH_3; R^1 = 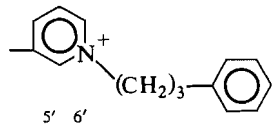 /TfO^-; R^2 = —CH_2CH=CH_2 : NO

29 R = CH_3; R^1 = 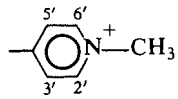 /TfO^-; R^2 = —CH_2CH=CH_2 : YES

30 R = CH_3; R^1 = 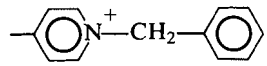 /Br^-; R^2 = —CH_2CH=CH_2 : YES

31 R = H; R^1 = 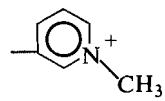 /TfO^-; R^2 = —CH_2CH=CH_2 : NO

32 R = H; R^1 = 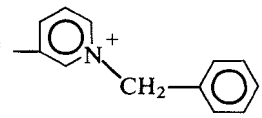 /Br^-; R^2 = —CH_2CH=CH_2 : NO

33 R = CH_3; R^1 = 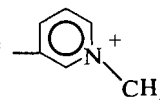 /Br^-; R^2 = —CH_3 : NO

34 R = CH_3; R^1 = 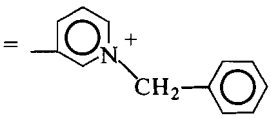 /Br^-; R^2 = —CH_3 : NO

YES or NO denotes whether or not the methylene protons (SCH_2) exchange with the deuterium isotope in D_2O under the basic conditions described in the experimental section

CHART 2. Structures of quaternary ester compounds.

exchanges rapidly for deuterium as soon as it is dissolved in D_2O. The negative charge generated at this position can initiate a transient ring opening and closing process with an end result of imparting unexpected acidic character to these protons, as shown below.[3]

When the H-5′ proton was replaced by a CH_3 group as in **17** (Chart 1), the methylene protons were found to be non-acidic. This lends strong support to the above scheme of events because an intermediate such as **35** cannot be generated from **17**. Moreover, there is literature precedence (7) for the ring opening

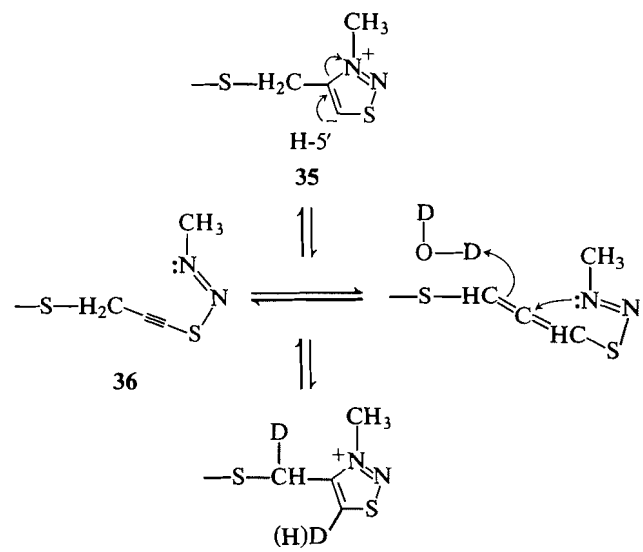

[3]Although acetylenic thioethers generally require a strong base to effect acetylene–allene interconversion, the unique structural features present in the acetylenic intermediate (**36**) may be responsible for the enhanced acidity of the methylene protons and, in turn, the facile acetylene–allene interconversion process. For some general information regarding interconversion of allene and alkyne, and rearrangements involving acetylenes, see ref. 6*a*; for heterosubstituted allenes, allenyl thioethers, etc., see ref. 6*b*.

Can. J. Chem. Downloaded from www.nrcresearchpress.com by 61.7.252.67 on 09/07/12
For personal use only.

of a quaternary tetrazole, involving a carbanion intermediate of the type **35**, and also the ring-opening processes are well known in many heterocyclic systems (8).

The results of the above acidity measurements can be helpful in the identification and the prediction of the site of quaternization in multi-nitrogen heteroaromatic rings, when they occur as part of a carbapenem derivative of the general structure **2**. That is, if the carbanion, generated after removing the proton from the -S—CH_2- moiety, can linearly conjugate with the ring π-system at the end of which there is an annular nitrogen atom, then that nitrogen atom is the one most likely to show increased affinity for an alkyl group and thus the preferred site of quaternization. Otherwise, the hetero atom in the ring is likely to direct the alkylation as illustrated below for both these cases.

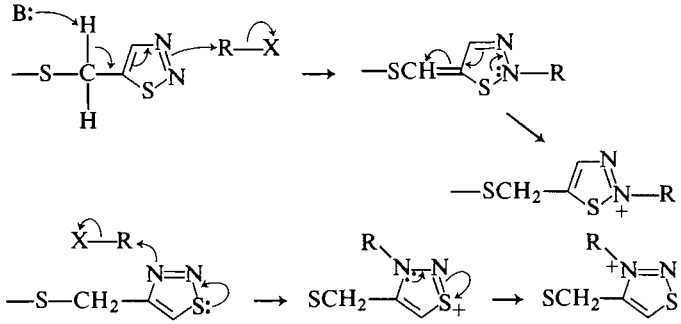

Finally, it may be pointed out that the methylene protons require simultaneous activation by sulfur and the positively charged heteroaromatic moiety (the nitrogen atom being in the proper location) for them to be acidic. Thus it has been found that the -SCH_2- protons of **9** (Chart 1), in which the pyridine ring is not quaternized, are not acidic; this is also the case for the methylene protons of the ethyl group of **37**, due to the lack of an adjacent sulfur atom.

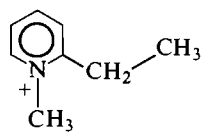

37

It may be concluded then that neighboring group participation by sulfur is crucial in stabilizing the positive charge, which in turn makes the SCH_2 protons acidic.

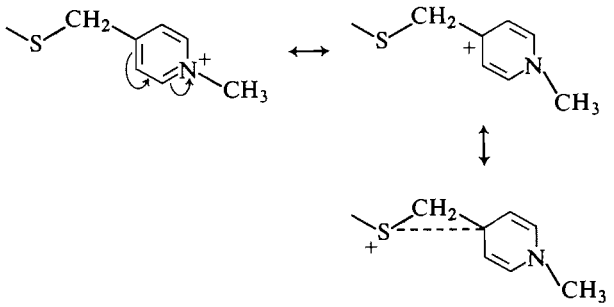

Experimental

Proton magnetic resonance spectra were recorded with a Bruker AC200SY instrument operating at 200 MHz. Chemical shifts (δ) are reported with reference to sodium 3-trimethylsilylproprionate-2,2,3,3-d_4 (TSP) in D_2O as solvent.

General procedure for the measurement of acidity of SCH_2 protons

In a typical experiment, the ^1H nmr spectrum of the compound (5 mg) is recorded in D_2O (~0.5 mL) to locate the SCH_2 protons. If these protons are not detectable due to severe overlap with other signals, then the spectrum may be recorded in DMSO-d_6. A second spectrum is recorded with the sample (~5 mg) in 0.5 mL of a solution of $KHCO_3$ in D_2O (2.5% w/v; pH 8.65). If the sample is scarce, after recording the first spectrum the sample may be mixed with ~8 equivalents of solid $KHCO_3$ and then the second spectrum is recorded. From these two spectra the evidence for the disappearance of the SCH_2 protons is obtained if these are exchangeable with the deuterium isotope in the solvent. If exchange rate measurements are necessary it is possible to spread the time required for complete exchange over a reasonable length (~2–3 h) by adding only ~1 equivalent of $KHCO_3$ and recording the spectra at regular intervals.

Acknowledgments

The authors are extremely grateful to their colleagues for making available a number of the compounds required in the study. The authors wish to thank Dr. M. Gorman and Dr. R. Partyka for their interest and encouragement, together with Professor B. Belleau and Dr. A. Martel for stimulating and very helpful discussions.

1. (*a*) G. Albers-Schonberg, K. Hoogsteen, R. W. Ratcliffe *et al.* J. Am. Chem. Soc. **100**, 6491 (1978); (*b*) R. W. Ratcliffe and G. Albers-Schonberg. *In* Chemistry and biology of β-lactam antibiotics. Vol. 2. *Edited by* R. B. Morin and M. Gorman. Academic Press, New York. 1982. Chap. 4.
2. H. Kropp, J. G. Sundelof, R. Hajdu, and F. M. Kahan. Antimicrob. Agents Chemother. **22**, 62 (1982).
3. D. H. Shih, F. Baker, L. Cama, and B. G. Christensen. Heterocycles, **21**, 29 (1984).
4. C. U. Kim. U.S. Patent No. 4644061. 1987; C. U. Kim, P. F. Misco, B. Y. Luh, and M. J. M. Hitchcock. J. Antibiot. **40**, 1707 (1987).
5. S. Oae (*Editor*). Organic chemistry of sulfur. Plenum Press, New York. 1977. p. 276, and references cited therein.
6. (*a*) S. Patai (*Editor*). The chemistry of the carbon–carbon triple bond. John Wiley and Sons, New York. 1978. pp. 85, 381, 395; (*b*) The chemistry of ketenes, allenes and related compounds. John Wiley and Sons, New York. 1980. pp. 392, 842, 851.
7. W. P. Norris and R. A. Henry. Tetrahedron Lett. 1213 (1965).
8. A. I. Meyers. Heterocycles in organic synthesis. John Wiley and Sons, New York. 1974.

Can. J. Chem. Downloaded from www.nrcresearchpress.com by 61.7.252.67 on 09/07/12
For personal use only.

The photochemistry of electron donor–acceptor (EDA) complexes in micellar solutions. I. The stilbene–methylviologen system

M. HAMITY AND R. H. LEMA

Universidad Nacional de Río Cuarto, Departamento de Química y Física, 5800 Río Cuarto, Córdoba, Argentina

Received August 14, 1987[1]

M. HAMITY and R. H. LEMA. Can. J. Chem. **66**, 1552 (1988).

The association constants for the electron donor–acceptor (EDA) complexes formed between both *cis*-stilbene (cS) and *trans*-stilbene (tS) as donors and methylviologen (MV^{+2}) as acceptor were determined in ethanol and micellar sodium dodecyl sulfate (SDS) solutions in the range of SDS concentration 0.05–0.1 M. The values obtained in micellar solutions were much higher than those in ethanol and were heavily dependent upon SDS concentration. This effect is due to an increase in the local concentration of the reactants in the micellar pseudophase. The tS fluorescence quenching by MV^{+2} was also studied in the same solvent media. In ethanol, the Stern–Volmer plot was found to be linear, with quenching constant (K_{SV}) similar to the association constant determined by the absorption method. In micellar solutions, although upward curvature of the Stern–Volmer plots was observed, a reaction scheme based on static quenching via ground state EDA complex is proposed, which explains the experimental results. Irradiation in the absorption band of the EDA complexes formed by tS or cS and MV^{+2} was carried out in ethanol and SDS solutions, in the absence of oxygen. Only *cis–trans* isomerization of cS in SDS solution was observed, with a quantum yield value of $\Phi_{cis} = 0.012$.

M. HAMITY et R. H. LEMA. Can. J. Chem. **66**, 1552 (1988).

Opérant dans l'éthanol ainsi que dans des solutions micellaires de dodécylsulfate de sodium (DSS) à des concentrations de DSS allant de 0,05 à 0,1 M, on a déterminé les constantes d'association des complexes donneur d'électron/accepteur (DEA) qui se forment entre les stilbènes *cis* et *trans* (Sc et St) agissant comme donneurs et le viologène de méthyle (VM^{+2}) agissant comme accepteur. Les valeurs obtenues en solutions micellaires sont beaucoup plus élevées que celles obtenues en solutions dans le méthanol et elles dépendent beaucoup de la concentration en DSS. Cet effet est dû à une augmentation de la concentration locale des réactifs dans la pseudo-phase micellaire. Opérant dans les mêmes solvants, on a aussi étudié le piégeage de la fluorescence du St par le VM^{+2}. Dans l'éthanol, on a observé que la courbe de Stern–Volmer est linéaire et que la constante de piégeage (K_{SV}) est semblable à la constante d'association déterminée par la méthode d'absorption. Dans les solutions micellaires, on a observé une courbure montante dans les courbes de Stern–Volmer; malgré cette observation, on propose un schéma réactionnel, basé sur un piégeage statique se produisant par le biais d'un complexe DEA dans son état fondamental, qui explique les résultats expérimentaux. Opérant en solution dans l'éthanol ou dans le DSS et en l'absence d'oxygène, on a effectué une irradiation de la bande d'adsorption des complexes DEA qui se forment entre le St ou le Sc et le VM^{+2}. En solution dans le DSS, on n'a observé que l'isomérisation *cis–trans* du Sc et le rendement quantique $\Phi_{cis} = 0{,}012$.

[Traduit par la revue]

Introduction

Photo-induced reactions of stilbenes have been the subject of a great quantity of experimental work (1). These photoprocesses have been carried out, in homogeneous solution, by means of straightforward excitation (2), triplet sensitization (3, 4), via radical cations (5) or exciplexes (6), and through the excitation of charge-transfer complexes formed by stilbenes and organic neutral molecules (7, 8). There have been, however, very few studies in microheterogeneous media (micelles, semiconductor particles, etc.), which present interesting properties that can be used to contribute to the knowledge of these photoreactions (9–11). Semiconductor particle photomediated *cis–trans* isomerization of stilbene was studied by Al-Ekabi and de Mayo (12). They found a photostationary state (>99% *trans* isomer) close to that corresponding to thermodynamic equilibrium and they proposed that isomerization was produced via a radical cation intermediate. Whitten and co-workers reported the synthesis of surfactant molecules that contain *trans*-stilbene incorporated both as a terminal and intrachain chromophore group. They studied the properties of these molecules as micellar fluorescence probes (13–15). Very slightly curved Stern–Volmer plots were determined by them for methylviologen quenching of the fluorescence of stilbene surfactants in 0.03 M SDS. They proposed a static quenching mechanism due to the occurrence of a ground state complex. They also attributed the slight deviation of linearity observed in these experiments to either the small influence of a dynamic process (13) or to neglecting the contribution of a term containing the complex concentration in the quencher concentration of the Stern–Volmer equation (14).

In this work, we have studied the *trans*-stilbene fluorescence quenching by methylviologen in ethanol and micellar solutions at several concentrations of sodium dodecyl sulfate. We have also studied, using absorption spectroscopy, the formation of ground-state charge-transfer (EDA) complexes by *cis*- and *trans*-stilbene and methylviologen in the same solvent media. We propose an alternative treatment of static quenching that satisfactorily explains our experimental data. We finally report some results on *cis–trans* isomerization of stilbene through the photolysis of EDA complexes with methylviologen, which to the best of our knowledge has not been studied in micellar systems. We are particularly interested in photoreactions of EDA complexes in microheterogeneous media. This work represents the beginning of such studies.

Experimental

Materials

Commercial *trans*-stilbene (Schuchardt Munchen) and *cis*-stilbene (Koch-Light) were used without further purification. Their purity grade was >99%, checked by glc.

Methylviologen, chloride was obtained from commercial Gramoxone solution by conventional techniques and purified as previously described (16).

[1]Revision received February 29, 1988.

Can. J. Chem. Downloaded from www.nrcresearchpress.com by 112.217.228.212 on 09/07/12
For personal use only.

Can. J. Chem. Downloaded from www.nrcresearchpress.com by 112.217.228.212 on 09/07/12
For personal use only.

Sodium dodecyl sulfate (SDS) (B.D.H.) was washed with diethyl ether and recrystallized from ethanol.

Absorption measurements

The ultraviolet–visible absorption measurements were performed with a Cary 17 spectrophotometer. Association of methylviologen (MV^{+2}) with both *cis*-stilbene (cS) and *trans*-stilbene (tS) in ethanol and SDS solutions was monitored by the absorption of the charge-transfer band. In all cases, the reference cell contained the same MV^{+2} concentration as the sample cell.

In micellar solutions, the MV^{+2} concentration was varied between 10^{-3} M and 10^{-2} M and stilbene concentration was kept constant at 3×10^{-4} M. The charge-transfer complex formation constants were determined through a Benesi–Hildebrand analysis and an iterative treatment of the data (17). Both methods yielded the same results.

In ethanolic solutions, for solubility reasons, the MV^{+2} concentration was kept constant (5×10^{-3} M) and the stilbene concentration was varied between 2×10^{-3} M and 2.5×10^{-2} M for tS and between 4×10^{-3} M and 4×10^{-2} M for cS. The iterative procedure was used to determine the association constants in ethanol.

Fluorescence measurements

The tS fluorescence quenching by MV^{+2} was monitored with an Aminco SPF 125 spectrofluorometer. The measured fluorescence intensities were corrected by the absorption of MV^{+2}.

Excitation wavelength was 330 nm in SDS solutions and 340 nm in ethanol, and emission intensity was measured at 355 nm in SDS solutions and 360 nm in ethanol.

Absolute isomerization quantum yields

Stilbene samples with and without MV^{+2}, in ethanol and micellar solutions, were degassed in a high vacuum line. The concentrations used were as follows: cS 4×10^{-2} M, tS 2×10^{-2} M in ethanol, and both stilbenes 6×10^{-4} M in 0.1 M SDS. MV^{+2} concentration was 5×10^{-3} M in all cases. Uranyl oxalate was used as actinometer.

The samples, in a merry-go-round apparatus, were irradiated at $\lambda >$ 430 nm with a Philips 1000-W quartz–halogen lamp as a light source and a Corning 3-72 filter. Temperature was maintained at 25 ± 0.1°C.

Stilbene concentrations were monitored by glc with a Varian 2800 chromatograph using an OV-101 on Chromosorb G H/P 100–120 mesh column. The samples in micellar solutions, after irradiation, were treated with $CaCl_2$ to precipitate SDS and then with CS_2, containing *n*-dodecane as external standard, to extract organic components and separate them from water-soluble MV^{+2} (18). Samples in ethanolic solution, after irradiation, were chromatographed, after adding *n*-dodecane as external standard.

Oxalate loss in ethanolic solutions was determined by titration with $KMnO_4$. During photolysis, the ampoules were open to the atmosphere.

Results and discussion

Determination of formation constants of EDA complexes

Stilbene and MV^{+2} solutions, when mixed, show an absorption band in a longer-wavelength region where neither S or MV^{+2} absorb (Fig. 1). This new band can be attributed to the occurrence of a ground-state EDA complex. The formation constants of these EDA complexes were determined in ethanol and micellar solutions at several SDS concentrations (Tables 1 and 2). The constants K_{BH} in micellar solutions are dependent on surfactant concentration. This trend is similar to that observed in micelle-catalyzed bimolecular reactions (19) and it has also been observed in the system naphthylamines–MV^{+2} in SDS (20).

Under our experimental conditions, the fraction of MV^{+2} bound to micelles is nearly unity (20), as is the case for stilbenes (21). The association of MV^{+2} with stilbene takes place in the micellar pseudophase, and therefore a volume change of the pseudophase could affect the equilibrium, thus changing the local concentration of reactants. The results can be analyzed by means of the following equations:

$$[1] \quad (S)_m + (MV^{+2})_m \overset{K_{ct}}{\rightleftharpoons} (S\ldots MV^{+2})_m$$

where the reactants are in the micellar pseudophase, K_{ct} is the

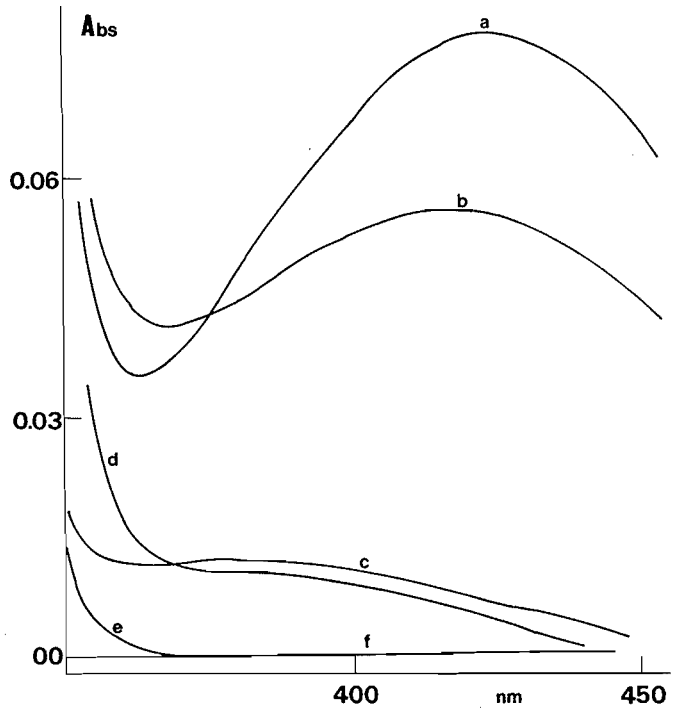

FIG. 1. Absorption bands of EDA complexes for the systems: (a) tS 3×10^{-4} M, MV^{+2} 10^{-2} M, in 0.1 M SDS; (b) tS 2×10^{-2} M, MV^{+2} 5×10^{-3} M, in ethanol; (c) cS 3×10^{-4} M, MV^{+2} 10^{-2} M, in 0.1 M SDS; (d) cS 4×10^{-2} M, MV^{+2} 5×10^{-3} M, in ethanol; (e) tS 3×10^{-4} M, in 0.1 M SDS; (f) baseline.

TABLE 1. Parameters of EDA complex for tS and MV^{+2}

Medium	K_{BH} (M^{-1})[a]	ε_c (M^{-1} cm^{-1})[a]	f_c[b]
SDS 0.10 M	303	406	0.9999
SDS 0.09 M	361	365	0.9999
SDS 0.08 M	382	383	0.9999
SDS 0.07 M	442	367	0.9998
SDS 0.06 M	582	380	0.9999
SDS 0.05 M	637	355	0.9999
Ethanol	14	40	0.9994

[a]Estimated error: 5%.
[b]Correlation coefficient.

TABLE 2. Parameters of EDA complex for cS and MV^{+2}

Medium	K_{BH} (M^{-1})[a]	ε_c (M^{-1} cm^{-1})[a]	f_c[b]
SDS 0.12 M	77	118	0.9984
SDS 0.10 M	93	118	0.9997
SDS 0.08 M	116	118	0.9994
SDS 0.06 M	160	118	0.9993
Ethanol	8	19	0.9984

[a]Estimated error: 5%.
[b]Correlation coefficient.

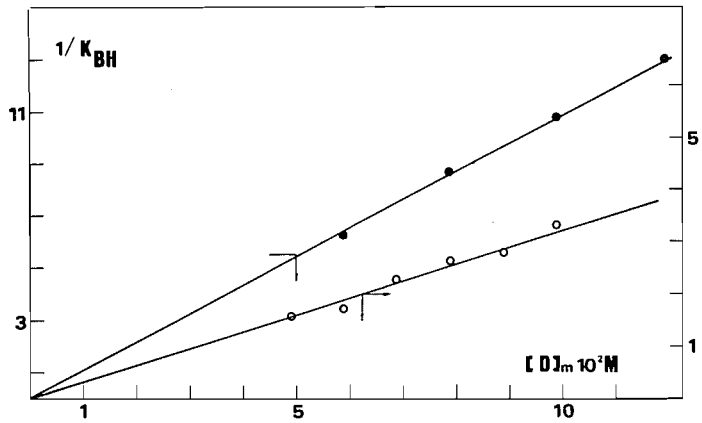

FIG. 2. Inverse of Benesi–Hildebrand formation constant as a function of micellized detergent concentration in SDS solutions, for (●) cS + MV^{+2}; (○) tS + MV^{+2}.

formation constant for the EDA complex $(S...MV^{+2})_m$, and the reaction occurs within the micelle and is not an intermicellar reaction. The concentration of any one of the reactants in the micellar pseudophase is

$$[2] \quad [R]_m = \frac{[R]_0 - [R]_w}{V[D]_m} \simeq \frac{[R]_0}{V[D]_m}$$

where $[R]_m$ is the concentration of the reactant in the micellar pseudophase; $[R]_0$ and $[R]_w$ are the analytical and water reactant concentrations, respectively, $[D]_m$ is the micellized detergent concentration ($[D]_{total}$ − cmc), and V is the molar volume of the micellized detergent (cmc is the abbreviation for critical micelle concentration).

Introducing the corresponding analytical concentrations in the equilibrium constant (K_{ct}) of reaction [1], by means of eq. [2] and assuming that Beer's law holds for the EDA complex, we have

$$[3] \quad \frac{[S]_0}{O.D.} = \frac{1}{\varepsilon_c} + \frac{1}{\varepsilon_c}\frac{V[D]_m}{K_{ct}}\frac{1}{[MV^{+2}]_0}$$

This is a Benesi–Hildebrand type equation, where

$$[4] \quad \frac{1}{K_{BH}} = \frac{V[D]_m}{K_{ct}}$$

O.D. is the optical density per cm, ε_c is the extinction coefficient for the complex, and $[S]_0$ and $[MV^{+2}]_0$ are the analytical concentrations of stilbene (*cis* or *trans*) and methylviologen, respectively. Equation [4] predicts the observed dependence of the formation constant for the EDA complex upon the detergent concentration. Plotting $(K_{BH})^{-1}$ vs. $[D]_m$, a straight line is obtained (Fig. 2) and K_{ct} can be calculated from the slope. The values given in Table 3 were determined using $V = 0.14\ M^{-1}$ (21) and cmc = 1×10^{-3} M. The latter is the appropriate value to use with the MV^{+2} concentration range in the present working conditions, since cmc for SDS changes with MV^{+2} concentration.[2]

The K_{ct} values determined by us are higher than those displayed by EDA complexes formed by stilbenes with moderately strong electron acceptors, such as the electron-poor alkenes ($K_{ct} \leq 1$) (1). We think that these high values are due to the ability of MV^{+2} to form a stable CT complex, since our

[2]F. H. Quina, personal communication.

TABLE 3. Formation constants for EDA complexes

System	Medium	K_{ct} (M^{-1})
tS + MV^{+1}	SDS	4.44
tS + MV^{+2}	Ethanol	14
cS + MV^{+2}	SDS	1.29
cS + MV^{+2}	Ethanol	8

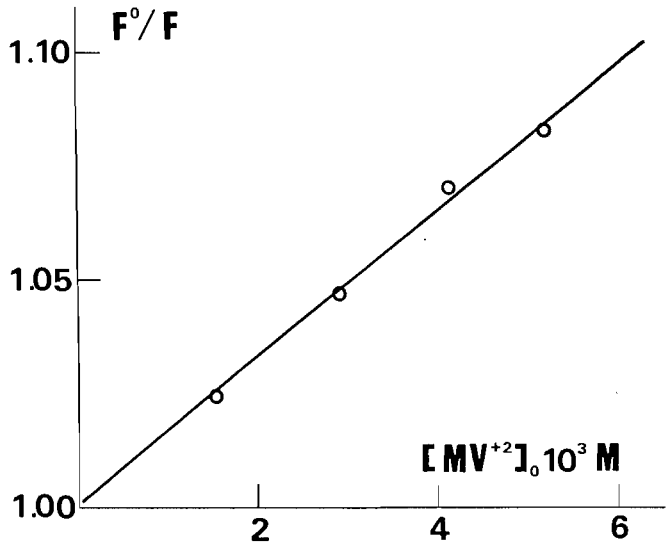

FIG. 3. Stern–Volmer plot for tS fluorescence quenching by MV^{+2} in ethanol; $[tS]_0 = 10^{-3}$ M.

values of K_{ct} are typical of complexes formed by MV^{+2} with electron donors ($2 \leq K_{ct} \leq 20$) (23).

As Table 3 shows, K_{ct} values for the complex $(tS...MV^{+2})$ are higher than those for the cS complex. This could be due to steric effects, which are magnified in SDS micelles. On the other hand, for a given complex, K_{ct} values in ethanol are higher than in SDS solutions. The difference in this case could be attributed to polarity effects, even when the band shift from ethanol to SDS (Fig. 1) indicates a small polarity difference between the two solvent media (24).

From Tables 1 and 2 it can be seen that the extinction coefficients of the complexes are nearly constant (376 ± 16 M^{-1} cm^{-1}) in SDS solutions. On the other hand, the extinction coefficients in ethanol are approximately one order of magnitude lower. This effect can be taken as indicative that micelles could diminish the random orientation of both molecules in the complex and lower the intermolecular distance, thus favouring orbital overlap and charge-transfer transition (25).

MV^{+2} quenching of tS fluorescence

Stern–Volmer plots for tS fluorescence quenching by MV^{+2} in ethanol are found to be linear (Fig. 3). The slope value (16 M^{-1}) is in agreement with that obtained by Russell and Whitten for a surfactant stilbene in acetonitrile (13) and with the K_{ct} value obtained in ethanol (Table 3). These facts strongly suggest that static quenching via a ground-state charge-transfer complex is the only quenching process occurring in this solvent.

In SDS micellar solutions, MV^{+2} quenching of tS fluorescence shows an upward curving of the Stern–Volmer plots (Fig. 4). This could be attributed to the simultaneous occurrence of both static and dynamic quenching. Nevertheless, taking into

Can. J. Chem. Downloaded from www.nrcresearchpress.com by 112.217.228.212 on 09/07/12
For personal use only.

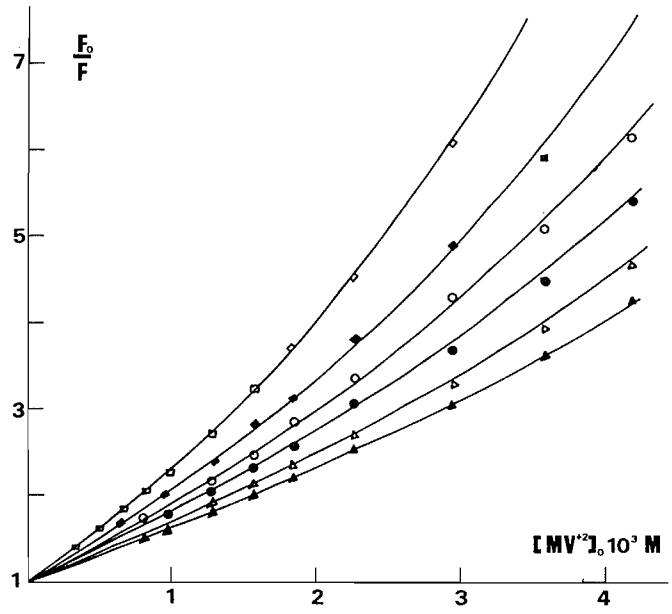

FIG. 4. Stern–Volmer plots for tS fluorescence quenching by MV^{+2} in micellar solutions of the following SDS concentrations: (□) 5×10^{-2} M; (■) 6×10^{-2} M; (○) 7×10^{-2} M; (●) 8×10^{-2} M; (△) 9×10^{-2} M; and (▲) 9.75×10^{-2} M. $r = [tS]_0/[M] = 0.03$.

account the short stilbene lifetime (approximately 0.1 ns) and the MV^{+2} concentration range, the value of the bimolecular quenching rate constant ought to be at least $k_q = 10^{12} \times M^{-1}\ s^{-1}$ for dynamic quenching to be appreciable. This is much higher than the value expected for a diffusion controlled process. Accordingly, we consider that the only process occurring in SDS micelles is static quenching. This could be a valid model assuming that emission is occurring only from micelles with fluorophore molecules that are free of quencher (case 1, Turro and co-workers (26)). According to Poisson statistics, in this case:

$$\ln \frac{F_0}{F} = \langle Q \rangle = \frac{[Q]_0}{[M]}$$

where [M] is the micelle concentration. A curving of the plots of $\ln F_0/F$ vs. $[MV^{+2}]_0$ is observed with our data. This is indicative that the above assumption is not valid in this case. Since quencher molecules entering a fluorophore-containing micelle are not 100% effective in quenching fluorescence, we assume that quenching is occurring only for quencher molecules bound to fluorophore molecules that form the charge-transfer complex. Emission can thus occur from micelles having MV^{+2} molecules, but not bound to tS molecules. With this assumption, we propose the following scheme to explain our experimental results:

$$[1a] \quad (tS)_m + (MV^{+2})_m \overset{K_{ct}}{\rightleftharpoons} (tS\ldots MV^{+2})_m$$

$$[1b] \quad K_{ct} = \frac{[(tS\ldots MV^{+2})_m]}{[(MV^{+2})_m]\{[(tS)_m]_0 - [(tS\ldots MV^{+2})_m]\}}$$

$$[5] \quad (tS)_m + h\nu \rightarrow {}^1(tS)_m^*$$

$$I_a = I_0(1 - 10^{-A})$$

$$[6] \quad {}^1(tS)_m^* \xrightarrow{k_f} (tS)_m + h\nu'$$

$$F = k_f[{}^1(tS)_m^*]$$

$$[7] \quad {}^1(tS)_m^* \xrightarrow{k_d} (tS)_m$$

$$\tau_0 = (k_f + k_d)^{-1}$$

where I_0, I_a, and F_0 are the incident, absorption, and emission light intensity; k_f and k_d are fluorescence and non-radiative rate constants, and A represents the tS absorbance at excitation wavelength.

Considering the stationary state for ${}^1(tS)_m^*$ and expanding in a power series the exponential $10^{-A} = \exp(-2.303\ A)$, neglecting terms of the third and higher order (since $A_0 = 0.3$), the ratio between fluorescence intensity in the absence and presence of quencher, respectively, becomes:

$$[8] \quad \frac{F_0}{F} = \frac{(A_0 - 1.15A_0^2)}{(A - 1.15A^2)} = \frac{[(tS)_m]_0 - 1.15\varepsilon l[(tS)_m]_0^2}{[(tS)_m] - 1.15\varepsilon l[(tS)_m]^2}$$

where A_0, $[(tS)_m]_0$ and A, $[(tS)_m]$ are tS absorbance and concentration in the absence and presence of quencher, respectively, and ε is the extinction coefficient of the tS.

Since $[(tS)_m] = [(tS)_m]_0 - [(tS\ldots MV^{+2})_m]$, we have

$$[9] \quad \frac{F_0}{F} = \frac{[(tS)_m]_0 - 1.15\varepsilon l[(tS)_m]_0^2}{[(tS)_m]_0 - [(tS\ldots MV^{+2})_m] - 1.15\varepsilon l\{[(tS)_m]_0^2 - B\}}$$

where

$$B = 2[(tS)_m]_0[(tS\ldots MV^{+2})_m] - [(tS\ldots MV^{+2})_m]^2$$

Since EDA complex concentration is lower than tS concentration, the term B inside the brackets can be neglected. Thus, after rearranging, eq. [9] becomes:

$$[10] \quad \frac{F_0 - F}{F_0} = \frac{[(tS\ldots MV^{+2})_m]}{[(tS)_m]_0\{1 - 1.15\varepsilon l[(tS)_m]_0\}}$$

Introducing in this equation the ratio $[(tS\ldots MV^{+2})_m]/[(tS)_m]_0$ from eq. [1b] and replacing $[(MV^{+2})_m]$ with $[MV^{+2}]_0$ from eq. [2], eq. [10] can be rewritten as:

$$[11] \quad \frac{F_0}{F_0 - F} = \{1 - 1.15\varepsilon l[(tS)_m]_0\} + \{1 - 1.15\varepsilon l[(tS)_m]_0\}\frac{V[D]_m}{K_{ct}[MV^{+2}]_0}$$

Two series of experiments were carried out, one in which $[(tS)_m]_0$ was kept constant and another keeping the ratio $r = [(tS)_m]_0/[M]$ at constant values of 0.03 and 0.3, respectively. In all cases, SDS concentration was varied between 0.05 and 0.1 M. Straight lines were obtained in all cases by plotting eq. [11] as shown in Fig. 5 for $r = 0.03$. Equation [11] yields an expression (slope/intercept = $V[D]_m/K_{ct}$) equivalent to eq. [4] and which is plotted in Fig. 5 (inset) for the ratio r of 0.03, giving, as in the rest of the cases, a straight line. From the slope the formation constant for the EDA complex is obtained ($K_{ct} = 7.2\ M^{-1}$, $r = 0.03$). Similar values of K_{ct} were determined for the different experiments and are comparable to those given in Table 3.

Equation [11] can be rewritten as:

$$[12] \quad \frac{F_0}{F} = \frac{W + Y_0[MV^{+2}]_0}{W - [MV^{+2}]_0(1 - Y_0)}$$

where Y_0 and W are the intercept and slope of eq. [11], respectively. Equation [12] satisfactorily fits the experimental

Can. J. Chem. Downloaded from www.nrcresearchpress.com by 112.217.228.212 on 09/07/12
For personal use only.

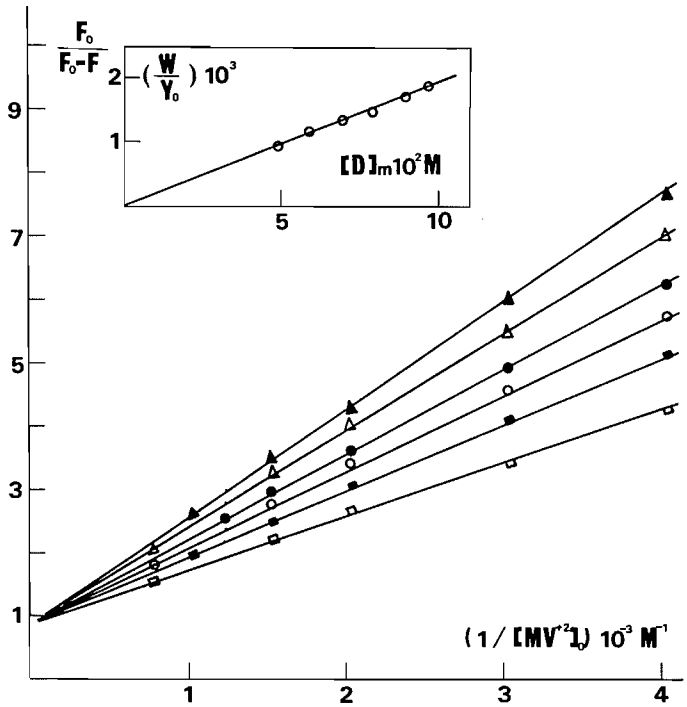

FIG. 5. Inverse of relative fluorescence intensity lowering as a function of inverse of quencher analytical concentration in micellar solutions of the following SDS concentrations: (□) 5×10^{-2} M; (■) 6×10^{-2} M; (○) 7×10^{-2} M; (●) 8×10^{-2} M; (△) 9×10^{-2} M; and (▲) 9.75×10^{-2} M. $r = [tS]_0/[M] = 0.03$. Inset: Ratio (slope/intercept) vs. micellized SDS concentration.

Stern–Volmer plots (Fig. 4, solid curves). Therefore we conclude that the only quenching process to occur is static quenching by formation of EDA complex in the micellar pseudophase. At low quencher concentrations, $[MV^{+2}]_0 (1 - Y_0) \ll W$ and the Stern–Volmer plots must be nearly linear, as observed for similar systems at lower MV^{+2} concentrations by Russell and Whitten (13, 14). They obtained a linear Stern–Volmer equation because they implicitly assumed $A_0 \ll 1$ (A_0 is tS absorbance before adding quencher), taking only the first-order term in the power series expansion for 10^{-A} in eq. [8]. This is equivalent to considering $Y_0 = 1$ in eq. [12], which thus yields a linear Stern–Volmer expression. Our reaction scheme satisfactorily explains the experimental results. This fact suggests that, in this particular system, micelles in which fluorophore and quencher are both present still yield emission if both molecules are not bound as an EDA complex. This, in turn, could be due to the existence of preferential sites inside the micelle. Each one of the reactants (tS and MV^{+2}) may be in two different sites, which are farther apart than the action sphere radius, so they do not interact to form an EDA complex. Another explanation may be that tS, being in equilibrium with the EDA complex, can fluoresce. This implies that the EDA complex formation rate constant is much lower than ($k_f + k_d$). We believe this latter to be the case, according to the reaction scheme presented.

Isomerization quantum yields

Stilbene isomerization, in the absence of oxygen, was studied under excitation of the EDA complex formed by cS and tS with MV^{+2} in ethanol and 0.1 M SDS. The same maximum irradiation time was used in all cases, but isomerization was observed only by photolysis of cS complex in SDS solution.

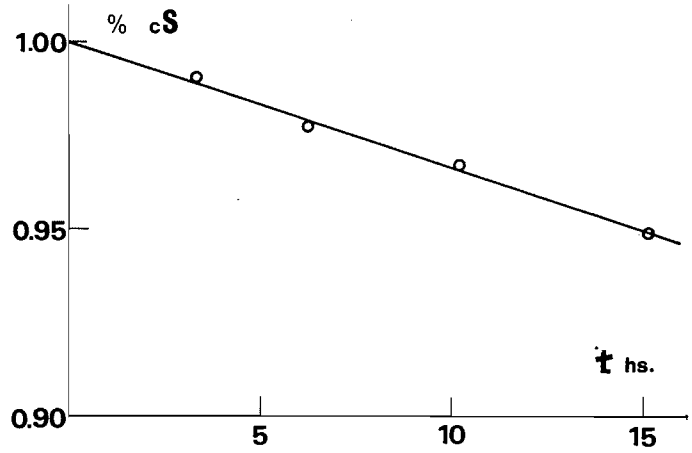

FIG. 6. Percentage of residual *cis*-stilbene as a function of irradiation time.

Quantum yield determination was made at low conversion (approximately 5%), thus not obtaining a photostationary state. Nevertheless, the lack of detectable isomerization of tS in SDS could indicate that the photostationary state that could be reached is almost completely on the side of the *trans* isomer.

Absolute quantum yield of isomerization (Φ_{cis}) was obtained through the equation:

$$[13] \quad \%cS = 100 - \frac{100\Phi_{cis} I_a}{[cS]_0} t$$

where %cS (= $[cS]/[cS]_0 \cdot 100$) is cS percentage remaining at time t, $[cS]_0$ is the analytical concentration of cS, and I_a is the light intensity absorbed by the EDA complex. The latter was determined by uranyl oxalate actinometry. Plotting eq. [13] (Fig. 6), the slope gives a value of $\Phi_{cis} = 0.012 \pm 0.002$.

The EDA complex photolysis to give stilbene isomerization products could occur either via the stilbene triplet state ($^3S^*$) or via the stilbene radical ($S^{+\cdot}$).

Isomerization of tS to cS by photolysis of charge-transfer complexes formed by tS with electron-poor alkenes has been proposed to occur via $^3tS^*$ (7, 27). Isomerization quantum yields for these systems show a strong dependence on solvent polarity and complex polarity (i.e., for tS/fumaronitrile complex $\Phi = 0.11$ in benzene, decreasing to $\Phi = 0.001$ in acetonitrile). The excited singlet state of the complex would lead either to $^3tS^*$ or to $tS^{+\cdot}$. Ion-pair formation from the excited complex is enhanced by increasing solvent polarity or exciplex polarity and so the isomerization quantum yield is lowered (27).

When isomerization is mediated by the stilbene radical cation, the formation of tS is heavily favoured (1, 5, 12). The $cS^{+\cdot}$ is believed to undergo rapid and essentially irreversible isomerization to $tS^{+\cdot}$ (1, 5).

In view of the above, we consider that our experimental observations are consistent with the intermediacy of the stilbene radical cation. This assumption can account for the lack of detectable isomerization in photolysis of the tS complex in both ethanolic and micellar solution, since the more stable $tS^{+\cdot}$ would not isomerize to $cS^{+\cdot}$. In the case of the cS complex, the lack of photoisomerization in ethanol could be due to ion-pair recombination in the solvent cage, which thus would inhibit subsequent isomerization from $cS^{+\cdot}$ to $tS^{+\cdot}$. Anionic micelles like SDS, however, could stabilize the intermediate $cS^{+\cdot}$, leading to the isomerization product tS. This stabilization effect

Can. J. Chem. Downloaded from www.nrcresearchpress.com by 112.217.228.212 on 09/07/12
For personal use only.

has already been observed for radical ions in micellar solutions (22). Micelles would thus play a catalytic role in the isomerization process. Even when the isomerization quantum yield in SDS, $\Phi_{cis} = 0.012$, is not high, comparison of this value with the near-zero value observed in homogeneous ethanolic solution indicates the occurrence of micellar catalysis.

Acknowledgments

We wish to thank CONICOR (Provincia de Córdoba) and CONICET (República Argentina) for financial support. We are gratefully indebted to M. V. Bohorquez (Indiana Radiation Laboratory, U.S.A.) for estimating the tS lifetime in SDS micelles.

1. F. D. Lewis. Adv. Photochem. **13**, 165 (1986).
2. G. Fischer, K. A. Muszkat, and E. Fischer. J. Chem. Soc. B, 1156 (1968).
3. D. R. Arnold and P. C. Wong. J. Am. Chem. Soc. **101**, 1894 (1979).
4. J. D. Simon and K. S. Peters. J. Am. Chem. Soc. **105**, 4875 (1983).
5. F. D. Lewis, J. R. Petisce, J. D. Oxman, and M. J. Nepras. J. Am. Chem. Soc. **107**, 203 (1985).
6. W. Hub, S. Schneider, F. Dorr, J. D. Oxman, and F. D. Lewis. J. Am. Chem. Soc. **106**, 701 (1984).
7. B. K. Adams and W. R. Cherry. J. Am. Chem. Soc. **103**, 6904 (1983).
8. J. L. Goodman and K. S. Peters. J. Am. Chem. Soc. **107**, 1441 (1985).
9. V. Ramamurthy. Indian Acad. Sci. (Chem. Sci.) **93**, 635 (1984).
10. P. Pichat. *In* Photoelectrochemistry, photocatalysis and photoreactions. *Edited by* M. Schiavello. A. Reidel Publ. Co., Dordrecht. 1985. p. 425.
11. J. K. Thomas. J. Phys. Chem. **91**, 270 (1987).
12. H. Al-Ekabi and P. de Mayo. J. Phys. Chem. **89**, 5815 (1985).
13. J. C. Russell and D. G. Whitten. J. Am. Chem. Soc. **103**, 3219 (1981).
14. J. C. Russell and D. G. Whitten. J. Am. Chem. Soc. **104**, 5937 (1982).
15. W. F. Mooney, P. E. Brown, J. C. Russell, S. B. Costa, L. G. Pedersen, and D. G. Whitten. J. Am. Chem. Soc. **106**, 5659 (1984).
16. L. Michaelis and E. S. Hill. J. Gen. Physiol. **16**, 859 (1933).
17. J. Anunziata, J. Singh, and J. J. Silber. Can. J. Chem. **59**, 1291 (1981).
18. D. A. Jaeger and R. E. Robertson. J. Org. Chem. **42**, 3298 (1977).
19. C. A. Bunton, G. Carichelli, Y. Ihara, and L. Sepulveda. J. Am. Chem. Soc. **101**, 2429 (1979).
20. S. G. Bertolotti, J. J. Cosa, H. E. Gsponer, M. Hamity, and C. M. Previtali. Can. J. Chem. **64**, 845 (1986).
21. M. Almgren, F. Grieser, and J. K. Thomas. J. Am. Chem. Soc. **101**, 279 (1979).
22. M. A. Fox. Adv. Photochem. **13**, 237 (1986).
23. B. G. White. Trans. Faraday Soc. **65**, 2000 (1969).
24. E. Blatt. J. Phys. Chem. **90**, 874 (1986).
25. K. M. C. Davis. *In* Molecular association. *Edited by* R. Foster. Academic Press, London. 1975. Chap. 3. p. 1.
26. A. Yekta, M. Aikawa, and N. J. Turro. Chem. Phys. Lett. **63**, 543 (1979).
27. F. D. Lewis and J. T. Simpson. J. Phys. Chem. **83**, 2015 (1979).

Can. J. Chem. Downloaded from www.nrcresearchpress.com by 112.217.228.212 on 09/07/12
For personal use only.

FOR ERRATA SEE V.66(11)1988 P.2963

Obtention de nouveaux squelettes diterpéniques lors de l'isomérisation d'époxydes diterpéniques sur alumine active

MARTINE TARAN[1] ET BERNARD DELMOND[2]

Laboratoire de chimie organique et organométallique, Unité associée n° 35 du Centre national de la recherche scientifique, Institut du Pin, Université de Bordeaux I, 351, cours de la Libération, 33405 Talence CEDEX, France

Reçu le 5 juin 1987[3]

MARTINE TARAN et BERNARD DELMOND. Can. J. Chem. **66**, 1558 (1988).

L'isomérisation d'époxydes diterpéniques sur alumine neutre active a permis de mettre en évidence des transpositions nouvelles du squelette diterpénique de base. Nous obtenons à partir de l'époxy-8,14β sandaracopimarate de méthyle des composés diterpéniques bicycliques par fragmentation de Grob, des dérivés à squelette cleistanthane par migration-1,2 du groupe vinyle, ainsi qu'un composé cycloditerpénique. Les dérivés époxy-7,8 et -8,9 de l'isopimarate de méthyle conduisent essentiellement à des hydroxy-oléfines provenant d'un mécanisme bifonctionnel acide–base à la surface de l'alumine.

MARTINE TARAN and BERNARD DELMOND. Can. J. Chem. **66**, 1558 (1988).

The isomerization of diterpene epoxides on active neutral alumina has established the existence of new rearrangements of the diterpene skeleton. Methyl 8,14β-epoxysandarcopimarate leads to bicyclic diterpene compounds by a Grob fragmentation, to derivatives of cleistanthane by a 1,2 migration of the vinyl substituent, as well as to one cycloditerpene compound. The 7,8 (or 8,9) derivatives of methyl isopimarate lead essentially to hydroxyolefins formed by a bifunctional acid–base mechanism at the alumina surface.

[Journal translation]

Can. J. Chem. Downloaded from www.nrcresearchpress.com by 112.217.228.212 on 09/07/12
For personal use only.

Il a été noté par divers auteurs (1–7) que, lors de la purification d'époxydes par chromatographie en phase liquide sur alumine ou sur silice, on constate parfois la perte totale de l'époxyde et l'obtention de produits d'isomérisation.

Ces observations ont par la suite été mises à profit pour analyser le comportement de certains époxydes terpéniques (8–13) vis-à-vis de ces supports solides.

Les conditions expérimentales sont très variées : agitation à température ambiante de l'époxyde en présence de support solide (8, 9), traitement prolongé à haute température (200–280°C) (14, 15), utilisant de quantités catalytiques du support solide à ébullition du toluène (16–21), dopage par la soude et les halogénures alcalins (13) ou divers autres réactifs (22).

Ayant observé au cours de travaux antérieurs (23) que certains époxydes diterpéniques s'isomérisaient partiellement au cours de leur séparation sur colonne d'alumine active, le protocole expérimental qui consiste à agiter l'époxyde en présence du support solide à température ambiante nous a semblé le plus approprié pour être appliqué aux époxydes diterpéniques.

Peu de travaux (24–26) ont à ce jour été entrepris concernant l'étude de la réactivité de tels époxydes vis-à-vis de l'alumine ou de la silice; les plus détaillés sont ceux d'ApSimon et Hall (26).

Nous décrivons dans ce mémoire le comportement vis-à-vis de l'alumine des époxy-8,14 sandaracopimarate de méthyle (**1** et **2**), et des époxy-7,8 (**3**, **4**) et -8,9 (**5**, **6**) isopimarate de méthyle.

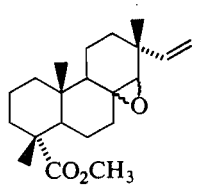

1 époxy-8,14β
2 époxy-8,14α

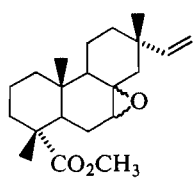

3 époxy-7,8β
4 époxy-7,8α

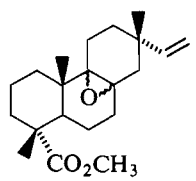

5 époxy-8,9β
6 époxy-8,9α

Chacun de ces époxydes en solution dans du cyclohexane est agité à température ambiante avec de l'alumine neutre active. La récupération des produits de la réaction est réalisée après filtration et lavage de l'alumine avec successivement de l'éther et un mélange éther/méthanol.

Résultats

1. *Époxy-8,14 sandaracopimarate de méthyle **1** et **2***

Le traitement de *l'époxy-8,14β sandaracopimarate de méthyle* **1** par de l'alumine neutre active dans les conditions standards précédemment définies conduit à l'obtention d'un mélange de composés carbonylés (18%) et de composés hydroxylés (56%).

La fraction constituée par les dérivés carbonylés se compose des cétones **7** (2%) (27) et **8** (11%) et de l'aldéhyde **9** (5%).

Les derivés carbonylés **8** et **9** sont des composés nouveaux, dont nous avons déterminé les structures au moyen de leurs caractéristiques physicochimiques.

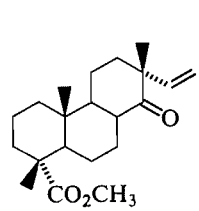

7

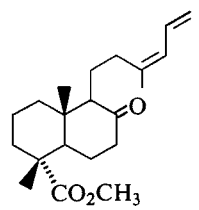

8

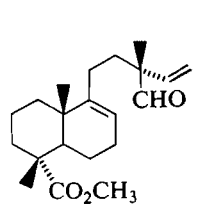

9

Dans le spectre de rmn ^1H du composé **8** on observe à champ faible un ensemble de signaux correspondant à 4 protons éthyléniques, dont l'analyse montre qu'il se compose d'un système ABX dû à un groupe vinyle (AB entre 4,89 et 5,20 ppm, X entre 6,27 et 6,69 ppm) et d'un proton éthylénique (H_m) résonnant sous forme d'un doublet (J = 11 Hz) à δ 5,89 ppm et couplé avec H_x.

Ces données sont compatibles avec la structure partielle suivante :

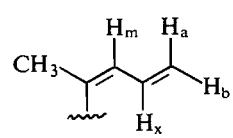

1. Unité d'enseignement et de recherche des sciences pharmaceutiques, Université de Bordeaux II.
2. Auteur à qui adresser toute correspondance.
3. Révision reçue le 8 février 1988.

TABLEAU 1. Attribution des déplacements chimiques (δ ppm) en rmn ^{13}C pour le composé **8**

	δ		Multiplicité observée	**8** attribution
	Composé modèle	Observé		
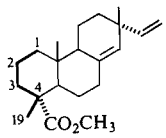 **A**	38,3 (C-1)	38,2	CH_2	C-1
	18,2 (C-2)	17,8	CH_2	C-2
	36,9 (C-3)	37,1	CH_2	C-3
	47,4 (C-4)	47,4	C	C-4
	17,0 (C-19)	16,6	CH_3	C-19
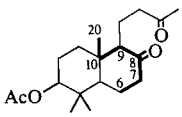 **B**	25,2 (C-6)	26,0	CH_2	C-6
	42,6 (C-7)	42,2	CH_2	C-7
	211,2 (C-8)	211,3	C	C-8
	62,7 (C-9)	62,9	CH	C-9
	42,1 (C-10)	41,7	C	C-10
	14,7 (C-20)	15,1	CH_3	C-20
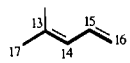 **C**	114,2 (C-16)	114,9	CH_2	C-16
	133,6 (C-15)	133,1	CH	C-15
	126,4 (C-14)	127,3	CH	C-14
	135,5 (C-13)	139,4	C	C-13
	25,9 (C-17)	23,5	CH_3	C-17

L'analyse des spectres de rmn ^{13}C de ce composé qui indique la présence de deux doubles liaisons (mono et trisubstituées) et d'un groupe cétonique permet d'envisager une structure bicyclique pour ce composé (28).

Nous avons pu préciser cette structure au moyen de la rmn ^{13}C en examinant les valeurs des déplacements chimiques observés pour chaque carbone ainsi que leur multiplicité avec ceux de trois composés modèles **A** (31), **B** (32) et **C** (tableau 1).

L'ensemble conjugué de ces données nous a donc permis de proposer la structure **8** pour ce dérivé carbonylé.

La configuration (*Z*) de la double liaison C13—C14 a été précisée au moyen de la rmn ^{13}C. Nous avons pu localiser à δ 23,5 ppm le groupe méthyle CH_3-17 porté par cette double liaison. Cette valeur est compatible avec une disposition *cis* entre ce groupe et l'hydrogène H-14 (29).

La spectrométrie de masse nous a également permis de confirmer la position de la chaîne latérale en C-9. La présence d'une fonction aldéhydique dans le composé **9** est déduite de l'analyse du spectre ir ($\nu_{C=O}$ 1710 cm^{-1}, ν_{C-H} 2720 cm^{-1}) et du spectre de rmn ^1H (singulet à δ 9,44 ppm).

Dans le spectre de rmn ^1H de ce composé on observe à champ faible, outre les signaux correspondant au système ABX caractéristique du groupe vinyle, un singulet élargi à δ 5,24 ppm attribuable à un proton éthylénique.

Ce composé étant particulièrement instable, l'étude par rmn ^{13}C a été réalisée sur l'alcool correspondant **10**:

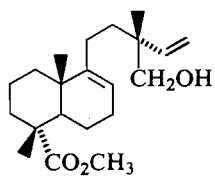

10

L'examen des spectres de rmn ^{13}C de ce composé confirme la nature primaire de l'alcool (triplet à δ 70,1 ppm), la présence d'une double liaison trisubstituée (singulet à δ 147,4, doublet à 119,2) et permet d'envisager une structure bicyclique pour ce composé, de même pour l'aldéhyde dont il dérive.

La spectrométrie de masse réalisée sur l'aldéhyde **9** nous a permis de positionner la double liaison en -8,9 et la chaîne latérale en C-9.

La fraction constituée par les composés hydroxylés se compose des hydroxy-oléfines **11** (43%) (23), **12** (2%), **13** (1%) et **14** (10%).

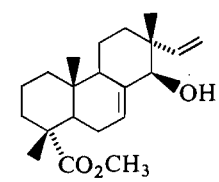

11

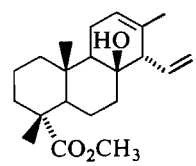

12

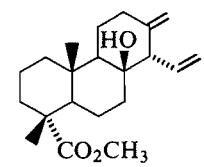

13

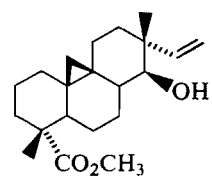

14

Le spectre de rmn ^1H du composé **12** révèle la présence d'une signal faiblement couplé à δ 1,62 ppm attribuable à un méthyle porté par une double liaison. On observe d'autre part à champ faible entre δ 4,92 et 5,80 ppm un ensemble de signaux correspondant à 4 protons ethyléniques se décomposant en un système ABX (—CH=CH_2) et en un proton éthylénique H_y résonnant vers δ 5,56 ppm. Une expérience de double irradiation montre que le proton H_x du système précédent est couplé (J = 9 Hz) avec un proton H_d résonnant sous la forme d'un doublet à 2,23 ppm. Ces données sont compatibles avec la structure partielle suivante **D**:

Can. J. Chem. Downloaded from www.nrcresearchpress.com by 112.217.228.212 on 09/07/12
For personal use only.

Can. J. Chem. Downloaded from www.nrcresearchpress.com by 112.217.228.212 on 09/07/12
For personal use only.

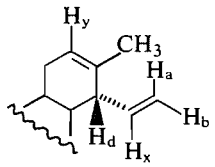

D

Les spectres de rmn ^{13}C du composé **12** indiquent la présence de deux doubles liaisons (mono et trisubstituée) et précisent la nature tertiaire de la fonction alcool (singulet à δ 72,5 ppm) que nous localisons en C-8, ce qui est confirmé par spectrométrie de masse.

Le spectre de rmn ^1H du composé hydroxylé **13** revèle à champ faible un multiplet (2H) à 4,82 ppm compatible avec la présence d'un méthylène exocyclique ($\rangle C{=}CH_2$) et des signaux entre δ 5,00 et 6,22 ppm correspondant au système vinylique (—CH=CH_2).

Par analogie avec le composé précédent, et d'après l'ensemble des données, nous proposons la structure **13** pour ce dérivé.

Dans le spectre de rmn ^1H du composé **14** on note comme principales caractéristiques : un singulet élargi à 3,20 ppm ($W_{1/2}$ = 4 Hz) correspondant à un proton en α d'un groupe hydroxyle et deux doublets à δ 0,11 et 0,92 ppm constituant un système AB (J = 4 Hz) attribuable à deux protons géminés situés sur un cycle cyclopropanique.

Nous observons d'autre part un effet significatif (blindage de 4,5 ppm) sur le déplacement chimique du CH_3-17, attribué à une interaction γ-*gauche* entre ce groupement méthyle et le groupe hydroxyle (30).

Ceci permet d'une part de localiser le groupe hydroxyle en C-14 et de proposer une configuration β pour celui-ci, par comparaison avec le composé **15**.

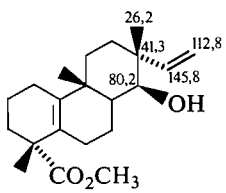

15

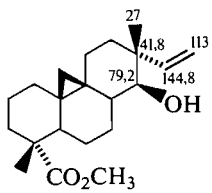

14

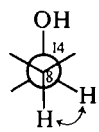

Nous avons pu noter d'autre part tant en rmn ^1H qu'en rmn ^{13}C l'absence de tout signal correspondant à la résonance du groupe méthyle CH_3-20, ce qui nous permet de localiser le pont cyclopropanique entre C-9 et C-10.

L'isomérisation de *l'époxy-8,14α sandaracopimarate de méthyle* **2** sur alumine active s'effectue avec un rendement de 84% en produits isolés après chromatographie. Il s'agit des composés carbonylés **7** (2%) et **9** (2%) obtenus et décrits précédemment et des composés hydroxylés **16** (20%) et **17** (60%).

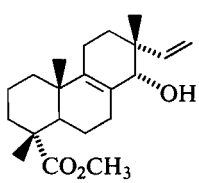

16

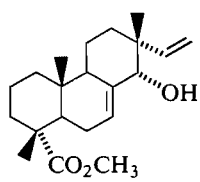

17

Le comportement de cet époxyde est tout à fait conforme aux résultats obtenus par ApSimon (26, 31).

2. *Époxy-7,8 isopimarate de méthyle* ***3*** *et* ***4***

Le traitement de *l'époxy-7,8β isopimarate de méthyle* **3** par l'alumine neutre active conduit à l'obtention d'un composé majeur, la cétone **18** (40%) (32), et à un mélange des composés hydroxylés **19** (4%) (32), **20** (5%) et **21** (8%).

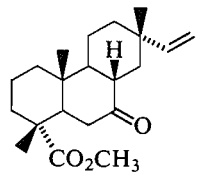

18

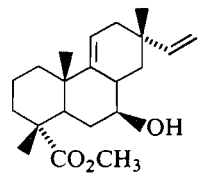

19

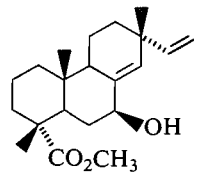

20

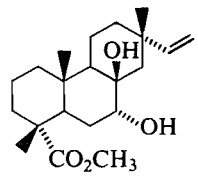

21

La structure du composé **20** et en particulier la stéréochimie du groupe hydroxyle en C-7 ont été précisées au moyen de la rmn ^{13}C par la comparaison des déplacements chimiques de ce composé avec ceux du sandaracopimarate de méthyle (3) et de son épimère **23** (23).

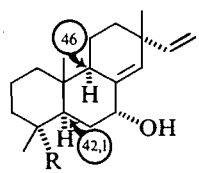

23

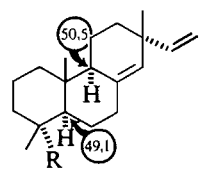

22

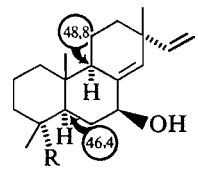

20

R = —CO_2CH_3

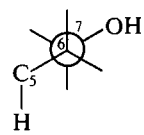

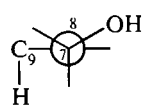

Nous observons en particulier sur les carbones C-5 et C-9 situés en γ par rapport au groupe hydroxyle des effets à champ fort plus faibles que ceux notés pour le composé épimère **23**. Cette tendance implique donc une interaction γ-*anti* entre le groupe hydroxyle et H-5 et H-9, ce qui nous permet d'attribuer une configuration β pour le groupe hydroxyle en C-7 dans l'alcool **20**.

Dans le spectre de rmn ^{13}C du composé hydroxylé **21** on note à δ 75 ppm la superposition de 2 signaux (CH et C) dus à deux carbones porteurs d'un groupe hydroxyle. La position de ces deux groupes hydroxyles et leur orientation respective ont été déduites de l'analyse des effets caractéristiques observés en rmn ^{13}C par comparaison avec le dihydroisopimarate de méthyle **24**, composé modèle.

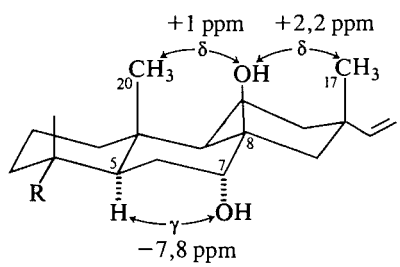

21

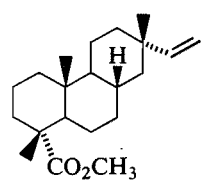

24

Can. J. Chem. Downloaded from www.nrcresearchpress.com by 112.217.228.212 on 09/07/12
For personal use only.

En effet nous observons :

(*i*) sur le carbone C-5 un effet à champ fort important (−7,8 ppm). Son amplitude est compatible avec une interaction γ-gauche entre H-5α et OH, ce qui implique une configuration α pour le groupe hydroxyle en C-7.

(*ii*) sur les carbones CH_3-17 et CH_3-20 des déblindages significatifs (+2,2 ppm et +1 ppm) qui découlent d'interactions δ *syn*-axiale entre ces carbones et le groupe hydroxyle en C-8, ce qui entraîne une configuration γ pour le groupe hydroxyle en C-8.

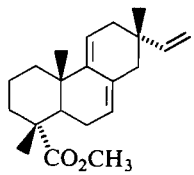

25

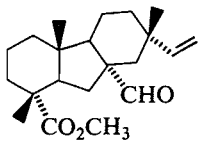

26

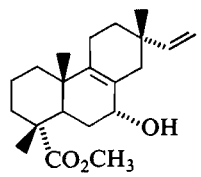

27

L'isomérisation de *l'époxy-7,8α isopimarate de méthyle* **4** par l'alumine neutre active conduit à un mélange constitué du triène **25** (2%), des dérivés carbonylés **18** (9%) et **26** (10%) et des hydroxy oléfines **23** (37%) et **27** (29%).

Les composés **25**, **18**, **26** et **23** ont été décrits dans un travail précédent (32). Le seul composé nouveau qui apparaît au cours de cette réaction est l'hydroxy-oléfine **27** dont la structure a pu être précisée au moyen de son analyse physicochimique.

3. *Époxy-8,9 isopimarate de méthyle* **5** *et* **6**

L'époxy-8,9β isopimarate de méthyle **5** est relativement stable vis-à-vis de l'alumine, puisque dans les conditions standards on récupère 30% d'époxyde n'ayant pas réagi. Les produits obtenus et identifiés au cours de cette réaction sont essentiellement le triène **25** (24%) et l'hydroxy-oléfine **28** (4%) (23, 33).

L'isomérisation de *l'époxy-8,9α isopimarate de méthyle* **6** conduit au triène **25** (24%) et à un mélange des hydroxy-oléfines **29** (28%) (4) et **30** (23%).

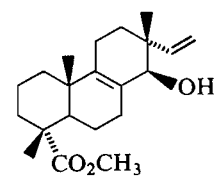

28

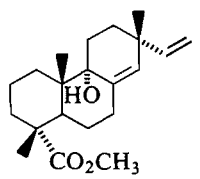

29

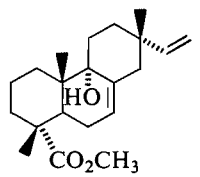

30

La nature tertiaire de l'hydroxy-oléfine **30** est précisée grâce à la rmn ^{13}C (singulet à δ 74,4 ppm). La présence d'une double liaison trisubstituée est également confirmée (singulet à δ 136,1 et doublet à δ 125,2 ppm).

Dans le spectre de rmn ^{13}C enregistré selon la technique de découplage «off resonance» à faible puissance, seulement deux des carbones tétrasubstitués sp^3 sont en position de couplage longue distance (^2J,^3J) avec des protons éthyléniques, ce qui est compatible avec la position de la double liaison en 7-8.

Nous avons pu préciser la configuration du groupe hydroxyle au moyen de la rmn ^{13}C, en comparant les valeurs des déplacements chimiques mesurés avec ceux de l'isopimarate de méthyle **31** (30).

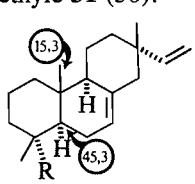

31

R = $-CO_2CH_3$

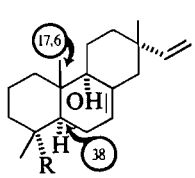

30

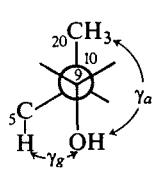

On observe deux effets significatifs : d'une part un effet à champ fort sur C-5 dû à une interaction γ-*gauche* H5/OH; et un effet à champ faible sur CH_3-20, dû à une disposition γ-*anti*, transmis par un hydroxyle tertiaire (7, 8).

Ces deux effets permettent donc de localiser le groupe hydroxyle en C-9 et de proposer une orientation α.

Discussion

La réactivité des époxydes vis-à-vis de l'alumine est attribuée à son caractère bipolaire (34–36) : elle possède à sa surface des sites électroaccepteurs de type acide de Lewis et des sites électrodonneurs.

L'obtention des différents composés fonctionnels met en jeu deux types d'intermédiaires (37) :

(*i*) la formation *d'alcools allyliques* qui s'explique par le caractère *bifonctionnel acide/base* du support.

(*ii*) le passage par une *espèce carbocationique* qui peut être responsable de l'obtention de *dérivés carbonylés* et de *diols*.

La plupart des composés que nous avons obtenus au cours de ces réactions peuvent s'expliquer en faisant intervenir ces deux types de mécanismes.

Ainsi, à partir de l'époxy-8,14β sandaracopimarate de méthyle **1**, on peut envisager l'intervention d'espèces carbocationiques.

Après adsorption de l'oxygène époxydique sur un site acide de l'alumine, l'ouverture du cycle époxydique peut conduire, selon le sens de la rupture à la formation de deux espèces carbocationiques.

(*i*) La rupture de la liaison C8—O conduit au carbocation **1***a* (schéma 1).

La migration de l'ion hydrure H-14α vers le carbone C-8 est à l'origine de la formation de la cétone **7** (voie 1).

La migration de l'hydrure H-9α pour stabiliser le carbocation en C-8 fait apparaître un carbocation tertiaire en C-9 **1***b* en position 1,3 par rapport à l'atome d'oxygène, disposition favorable à une réaction de Grob (38). Le carbocation **1***b* subit ainsi une fragmentation conduisant à l'aldéhyde éthylénique bicyclique **9** (voie 2).

(*ii*) La rupture de la liaison C14—O (schéma 2) fait apparaître un carbocation secondaire **1***c* qui peut se stabiliser par migration du groupe vinyle pour donner le carbocation tertiaire **1***d*.

Celui-ci peut évoluer soit par élimination 1,2 d'un atome d'hydrogène (H-12 ou H-17) conduisant alors aux alcools éthyléniques **12** et **13** (voie 1), soit par fragmentation de Grob à la formation de la cétone diénique **8** (voie 2).

Le mécanisme bifonctionnel acide–base, dans lequel nous avons une adsorption simultanée de l'oxygène époxydique sur un site acide situé à la surface du catalyseur et d'un hydrogène, convenablement disposé, sur un site basique permet d'expliquer la formation des composés hydroxylés **11** et **14** (schéma 3).

Ainsi, l'élimination de H-7 conduit au composé **11** (voie 1).

Par contre, si le site basique intervient au niveau des hydrogènes du méthyle angulaire C-20 on obtient selon un mécanisme concerté la formation d'un cycle cyclopropanique, par migration de H-9α et ouverture du noyau oxiranne pour aboutir à l'alcool **14** (voie 2).

Le mécanisme réactionnel que nous proposons pour expliquer la formation du dérivé cycloditerpénique **14** présente une certaine analogie avec celui qui intervient dans le schéma de biosynthèse du cycloarténol décrit par Goodwin et coll. (39).

L'époxy-8,14α sandaracopimarate de méthyle **2** est particulièrement sensible au contact de l'alumine. Cette instabilité

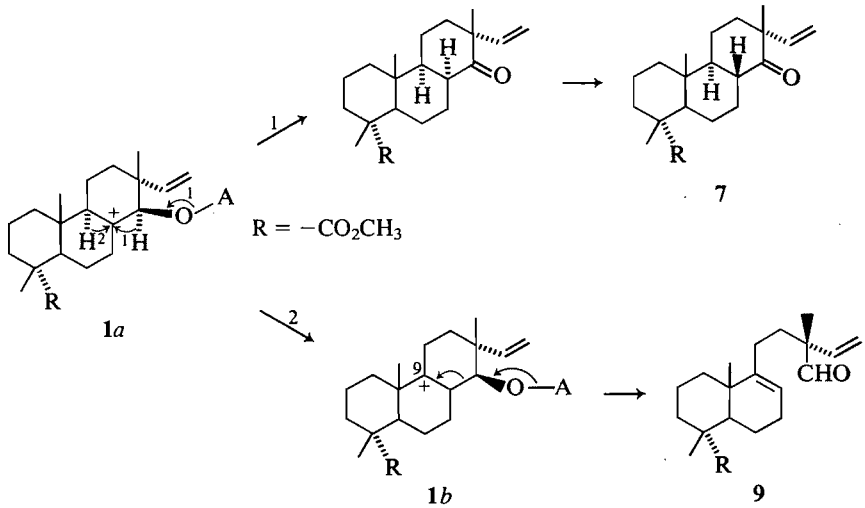

SCHÉMA 1

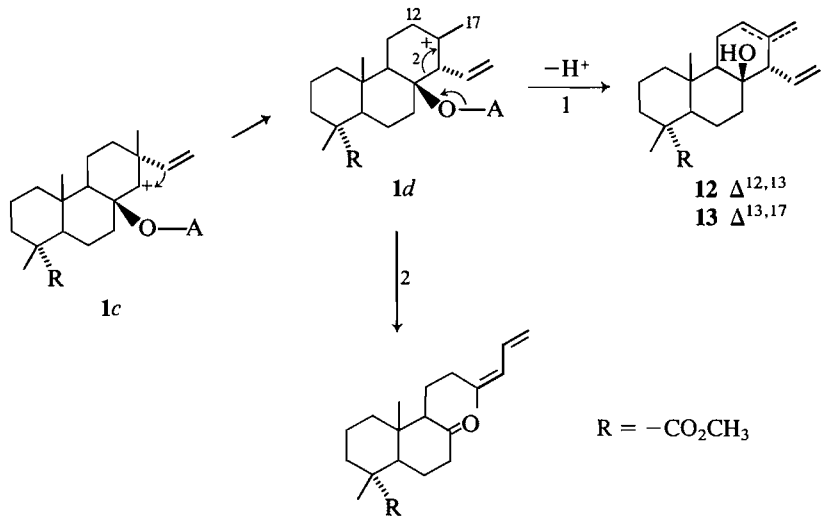

SCHÉMA 2

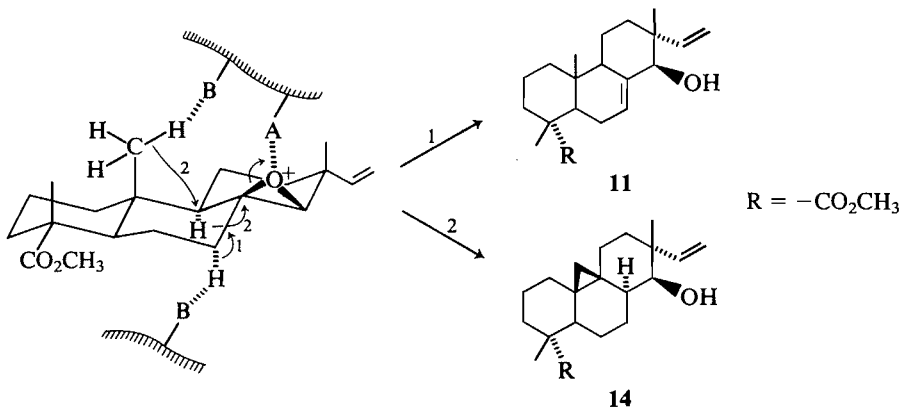

SCHÉMA 3

provient de la configuration du cycle époxydique qui entraîne une jonction de cycles B/C *cis*.

Nous obtenons essentiellement des alcools allyliques, **16** et **17**, dont on peut envisager la formation par une élimination 1,2 respectivement de H-9 et H-7.

À partir des époxy-7,8 isopimarates, la formation des dérivés carbonylés **18** et **26** peut s'expliquer par des mécanismes faisant intervenir des carbocations en C-8.

Ainsi à partir de l'isomère époxydique de configuration β, le carbocation en C-8 (schéma 4) formé par rupture de la liaison

Can. J. Chem. Downloaded from www.nrcresearchpress.com by 112.217.228.212 on 09/07/12
For personal use only.

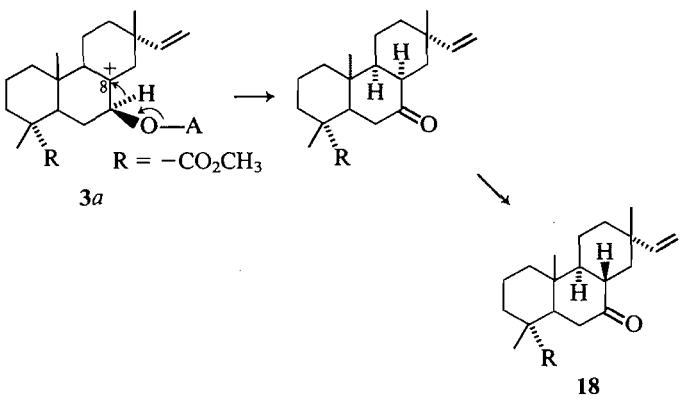

SCHÉMA 4

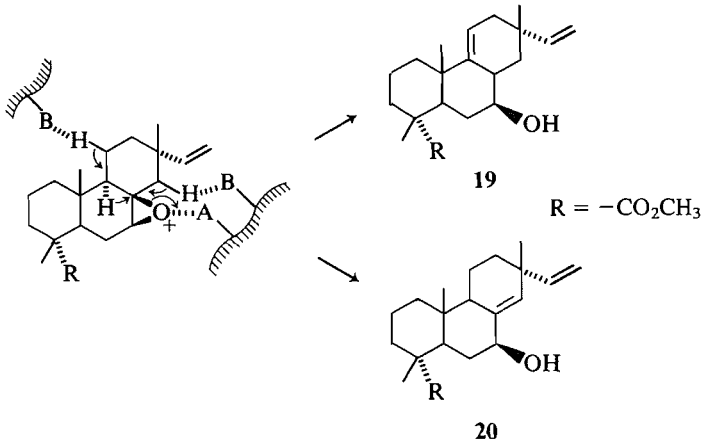

SCHÉMA 6

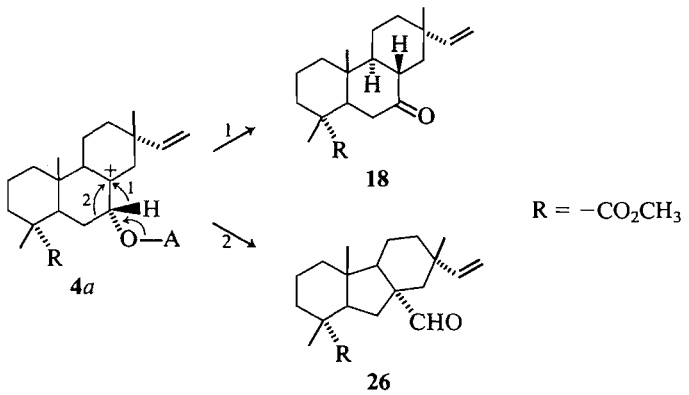

SCHÉMA 5

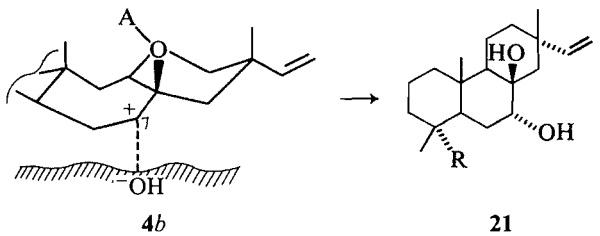

SCHÉMA 7

C8—O se stabilise par migration de H-7 vers C-8 conduisant ainsi à la cétone thermodynamiquement instable (jonction B/C *cis*), qui s'épimérise au contact de l'alumine, comme nous l'avons vérifié précédemment.

Par contre, à partir de l'isomère époxydique de configuration α (schéma 5) l'ouverture de la forme complexée conduit à l'intermédiaire carbocationique **4***a* en C-8 dans lequel les deux liaisons C6—C7 et C7—H occupent des positions favorables pour migrer vers C-8. On obtient alors les deux composés carbonylés **18** et **26**.

La mise en jeu d'un mécanisme bifonctionnel acide/base permet par contre d'expliquer la formation des hydroxy-oléfines **19** et **20** (schéma 6).

Il en est de même à partir de l'isomère époxydique de configuration α, l'élimination des hydrogènes H-14α et H-9α permettant d'expliquer la formation respective des alcools allyliques **23** et **27**.

Par contre, une autre possibilité d'évolution de l'époxyde β est l'ouverture avec la création d'un centre carbocationique en C-7 (schéma 7). On peut admettre que cet intermédiaire, éventuellement stabilisé par les sites basiques de l'alumine, subisse une attaque par une espèce nucléophile présente dans le milieu. Il a été montré (37) que 10% d'ions OH^- demeurent à la surface de l'alumine. L'attaque du côté opposé par la surface de l'alumine elle-même conduira donc au glycol *trans*.

En ce qui concerne les époxy-8,9 isopimarates **5** et **6**, nous n'avons pas observé la formation de dérivés carbonylés, contrairement aux réarrangements avec l'éthérate de trifluorure de bore (33). Nous mettons en évidence des hydroxy-oléfines dont la formation fait intervenir une élimination 1,2 selon un mécanisme bifonctionnel.

Conclusion

Les réactions d'isomérisation des époxydes diterpéniques en présence d'alumine neutre active nous ont permis de mettre en évidence des transpositions nouvelles du squelette diterpénique.

Partie expérimentale

Les points de fusion *F* (°C) non corrigés ont été pris avec l'appareil de Kofler. Les spectres ir ont été enregistrés au moyen d'un spectrographe SP 200 soit en film, soit en solution dans le tétrachlorure de carbone. Les spectres de rmn ^1H ont été enregistrés avec un appareil Bruker WH-90. Les échantillons sont étudiés en solution dans $CDCl_3$ avec pour référence interne le tétraméthylsilane; les déplacements chimiques sont exprimés en unités δ (ppm); les abréviations utilisées sont s (singulet), se (singulet élargi), d (doublet), t (triplet), q (quadruplet), m (massif complexe). Les spectres de rmn ^{13}C sont enregistrés en solution dans $CDCl_3$ sur un appareil Bruker WH-60 fonctionnant à 15,08 MHz, les déplacements chimiques sont exprimés en ppm par rapport au TMS. Les attributions des déplacements chimiques des carbones sont réalisées en utilisant les techniques de découplage large bande et «off resonance». Les spectres uv ont été enregistrés sur un appareil Beckman 25 en solution dans l'éthanol.

Isomérisation des époxydes diterpéniques sur alumine active

Mode opératoire type

Les époxydes diterpéniques sont obtenus par époxydation au moyen de l'acide paranitroperbenzoïque des hydrocarbures éthyléniques correspondants (23).

L'époxyde diterpénique (3 mmol) en solution dans 30 mL de cyclohexane anhydre (séché sur tamis moléculaire 4 Å) est mis à agiter en présence de 25 g d'alumine neutre active (grade I) à température ordinaire pendant 15 h. Après filtration, l'alumine est lavée successivement avec de l'éther puis un mélange éther/méthanol (1:1). L'ensemble des phases organiques est réuni et concentré sous vide. Le résidu est ensuite soumis à une analyse par chromatographie en phase liquide sur colonne d'alumine neutre désactivée (6% H_2O).

Isomérisation de l'époxy-8,14β sandaracopimarate de méthyle 1

L'isomérisation de 1,805 g d'époxy-8,14β sandaracopimarate de méthyle **1** sur alumine active conduit, après séparation par chromatographie en phase liquide, à des composés carbonylés (18%) et à

Can. J. Chem. Downloaded from www.nrcresearchpress.com by 112.217.228.212 on 09/07/12
For personal use only.

Can. J. Chem. Downloaded from www.nrcresearchpress.com by 112.217.228.212 on 09/07/12
For personal use only.

des composés hydroxylés (56%). L'élution avec le système éther de pétrole/éther (8:2) permet d'isoler :

L'aldéhyde ***9*** (90 mg) : ir (ν cm^{-1}) : 2720 (CH), 1710 (CO); rmn ^{1}H (90 MHz) δ : 1,01 (s, 3H), 1,20 (s, 6H), 3,69 (s, 3H), 5,24 (se, 1H), 5,04–5,37 (—CH=CH_2), 5,69–6,00 (—CH=CH$_2$), 9,64 (s, 1H); *m/z* (%) : 332 (M$^+$, 6), 161 (100). *Anal.* calc. pour $C_{21}H_{32}O_3$: C 75,90, H 9,64; trouvée : C 76,04, H 9,58.

La cétone ***8*** (195 mg) : F = 61°C (éthanol); ir (ν cm^{-1}) : 1710 (CO); uv (λ_{max}, EtOH) : 237 nm; rmn ^{1}H (90 MHz) δ : 0,74 (s, 3H), 1,20 (s, 3H), 1,75 (s, 3H), 3,72 (s, 3H), 5,89 (d, J = 11 Hz, 1H), 4,89–5,20 (—CH=CH_2), 6,27–6,69 (—CH=CH$_2$); rmn ^{13}C (ppm) δ : 15,1 (C-20), 16,6 (C-19), 17,8 (C-2), 19,7 (C-11), 23,5 (C-17), 26,0 (C-6), 37,2 (C-12), 37,3 (C-3), 38,2 (C-1), 41,7 (C-10), 42,2 (C-7), 47,4 (C-4), 48,6 (C-5), 52,1 (C-21), 62,9 (C-9), 114,9 (C-16), 127,3 (C-14), 133,1 (C-15), 139,4 (C-13), 178,9 (C-18), 211,3 (C-8); *m/z* (%) : 332 (M$^+$, 33), 223 (100). *Anal.* calc. pour $C_{21}H_{32}O_3$: C 75,90, H 9,64; trouvée : C 75,75, H 9,72.

La cétone 7 (37 mg) (27). L'élution avec le système benzène/éther (9:1) conduit à : *l'hydroxy-oléfine* ***13*** (15 mg); ir (ν cm^{-1}) : 3600 (OH); rmn ^{1}H (90 MHz) δ : 1,02 (s, 3H), 1,21 (s, 3H), 2,56 (d, J = 9 Hz, 1H), 3,68 (s, 3H), 4,82 (se, 2H), 5,00–5,22 (—CH=CH_2), 5,83–6,22 (—CH=CH$_2$); *m/z* (%) : 332 (M$^+$, 17), 223 (100).

L'hydroxy-oléfine ***12*** (44 mg) : ir (ν cm^{-1}) : 3600 (OH); rmn ^{1}H (90 MHz) δ : 1,10 (s, 3H), 1,24 (s, 3H), 1,62 (se, 3H), 2,23 (d, J = 9 Hz, 1H), 3,69 (s, 3H), 5,56 (m, 1H), 4,92–5,18 (—CH=CH_2), 5,40–5,80 (—CH=CH$_2$); rmn ^{13}C (ppm) δ : 15,1 (C-20), 16,7 (C-19), 22,1 (C-17), 36,3 (C-10), 46,6 (C-9 ou C-14), 47,4 (C-4), 50,2 (C-5), 51,6 (C-21), 59,8 (C-14 ou C-9), 72,5 (C-8), 116,9 (C-16), 121,3 (C-12), 132,2 (C-13), 138,1 (C-15), 179,3 (C-18); *m/z* (%) : 332 (M$^+$, 40), 223 (100). *Anal.* calc. pour $C_{21}H_{32}O_3$: C 75,90, H 9,64; trouvée : 75,46, H 9,74.

L'alcool cycloditerpénique ***14*** (124 mg) : ir (ν cm^{-1}) : 3600 cm^{-1}; rmn ^{1}H (90 MHz) δ : 0,11 (d, J = 4 Hz, 1H), 0,92 (d, J = 4 Hz, 1H), 1,07 (s, 3H), 1,17 (s, 3H), 3,20 (se, $W_{1/2}$ = 4 Hz, 1H), 3,67 (s, 3H), 4,93–5,19 (—CH=CH_2), 5,68–6,00 (—CH=CH$_2$); rmn ^{13}C (ppm) δ : 15,1 (C-19), 19,8 (C-9), 20,2 (C-10), 27,0 (C-17), 41,8 (C-13), 47,9 (C-4), 51,6 (C-21), 79,2 (C-14), 113,0 (C-16), 114,8 (C-15), 178,9 (C-18); *m/z* (%) : 332 (M$^+$, 11), 255 (100). *Anal.* calc. pour $C_{21}H_{32}O_3$: 75,90, H 9,64; trouvée : C 75,82, H 9,57.

L'hydroxy-oléfine ***11*** : (767 mg) (23); F = 94°C; ir (ν cm^{-1}) : 3580; rmn ^{1}H (90 MHz) δ : 0,85 (s, 3H), 0,90 (s, 3H), 1,28 (s, 3H), 3,64 (s, 3H), 3,77 (s, $W_{1/2}$ = 6–7 Hz, 1H), 5,80 (m, 1H), 4,99–5,22 (—CH=CH_2), 5,77–6,08 (—CH=CH$_2$); rmn ^{13}C (ppm) δ : 14,4 (C-17), 15,5 (C-20), 17,5 (C-19), 18,1 (C-2), 19,8 (C-11), 25,0 (C-6), 35,4 (C-10), 35,6 (C-12), 37,0 (C-3), 39,1 (C-1), 42,8 (C-13), 44,9 (C-5), 46,7 (C-4), 51,7 (C-9), 51,9 (C-21), 76,9 (C-14), 113,2 (C-16), 118,7 (C-7), 136,5 (C-8), 147,5 (C-15), 179,2 (C-18); *m/z* (%) : 332 (M$^+$, 49), 123 (100).

Réduction de l'aldéhyde ***9***

À 63 mg de l'aldéhyde **9** dissout dans 5 mL de méthanol, on ajoute à 0°C 57 mg de borohydrure de sodium. L'agitation est maintenue pendant 15 min à 0°C puis 3 h à température ordinaire. On ajoute alors 2 mL d'eau et on extrait avec de l'éther. La phase organique est ensuite séchée ($MgSO_4$) puis concentrée. On récupère alors 60 mg de l'alcool **10**; ir (ν cm^{-1}); 3580 (OH), 1720 (CO); rmn ^{1}H (90 MHz) δ : 0,99 (s, 3H), 1,01 (s, 3H), 1,18 (s, 3H), 3,36 (s, 2H), 3,62 (s, 3H), 5,18 (se, 1H), 4,91–5,22 (—CH=CH_2), 5,54–5,87 (—CH=CH$_2$); rmn ^{13}C (ppm) δ : 16,3 (C-19), 19,5 (C-20), 51,6 (C-21), 70,1 (CH_2OH), 114,5 (C-16), 119,2 (C-8), 143,9 (C-15), 147,4 (C-9), 179,1 (C-18); *m/z* (%) : 334 (M$^+$, 5), 161 (100).

Isomérisation de l'époxy-8,14α sandaracopimarate de méthyle ***2***

L'isomérisation de 942 mg d'époxy-8,14α sandaracopimarate de méthyle **2** sur alumine conduit par chromatographie sur colonne en phase liquide à l'aldéhyde **9** (24 mg) et à la cétone **7** (20 mg) élués avec le système de solvants d'éther de pétrole/éther (9:1).

L'élution avec le système éther de pétrole/éther (1:9) permet d'isoler *l'hydroxy-oléfine* ***16*** (190 mg); ir (ν cm^{-1}) : 3450; rmn ^{1}H (90 MHz) δ : 0,98 (s, 3H), 0,99 (s, 3H), 1,15 (s, 3H), 3,48 (s, $W_{1/2}$ = 4 Hz, 1H), 3,62 (s, 3H), 4,96–5,20 (—CH=CH_2), 5,77–6,08 (—CH=CH$_2$); *m/z* (%) : 332 (M$^+$, 18). *Anal.* calc. pour $C_{21}H_{32}O_3$: C 75,90, H 9,64; trouvée : C 75,68, H 9,70; et *l'hydroxy-oléfine* ***17*** (600 mg) (23, 31).

Isomérisation de l'époxy-7,8β isopimarate de méthyle ***3***

L'isomérisation de 1,98 g d'époxy-7,8β isopimarate de méthyle **3** sur alumine active conduit après séparation par chromatographie en phase liquide à divers composés.

L'élution avec le système de solvants éther de pétrole/éther (9:1) conduit à la *cétone* ***18*** (790 mg) (32). L'élution avec benzène/éther (9:1) permet d'isoler :

L'hydroxy-oléfine ***19*** (69 mg) (32).

L'hydroxy-oléfine ***20*** (99 mg); ir (ν cm^{-1}) : 3480 (OH), 1720 (CO); rmn ^{1}H (90 MHz) δ : 0,79 (s, 3H), 1,01 (s, 3H), 1,16 (s, 3H), 3,62 (s, 3H), 3,98 (m, $W_{1/2}$ = 20 Hz, 1H), 5,57 (se, 1H), 4,74–4,97 (—CH=CH_2), 5,60–5,90 (—CH=CH$_2$); rmn ^{13}C (ppm) δ : 15,5 (C-20), 17,0 (C-19), 18,2 (C-2), 18,6 (C-11), 26,3 (C-17), 34,2 (C-12), 34,9 (C-6), 37,1 (C-3), 37,1 (C-13), 38,0 (C-10), 38,2 (C-1), 46,4 (C-5), 47,4 (C-4), 48,8 (C-9), 52,0 (C-21), 71,9 (C-7), 110,8 (C-16), 126,2 (C-14), 138,9 (C-8), 148,6 (C-15), 179,2 (C-18); *m/z* (%) : 332 (M$^+$, 72), 123 (100). *Anal.* calc. pour $C_{21}H_{32}O_3$: C 75,90, H 9,64; trouvée : C 75,85, H 9,52.

Le diol ***21*** (157 mg); F = 121°C (éthanol/H_2O); ir (ν cm^{-1}) : 3550 (OH), 1720 (CO); rmn ^{1}H (90 MHz) δ : 1,02 (s, 3H), 1,18 (s, 3H), 1,22 (s, 3H), 3,40 (se, $W_{1/2}$ = 6 Hz, 1H), 3,63 (s, 3H), 4,72–4,97 (—CH=CH_2), 5,59–5,90 (—CH=CH$_2$); rmn ^{13}C (ppm) δ : 15,7 (C-20), 16,5 (C-19), 16,5 (C-11), 17,6 (C-3), 24,3 (C-17), 28,6 (C-6), 36,4 (C-13), 36,8 (C-10), 37,1 (C-3), 37,5 (C-12), 38,5 (C-1), 42,1 (C-5), 46,2 (C-14), 47,2 (C-4), 51,2 (C-9), 51,9 (C-21), 75,0 (C-8), 75,0 (C-7), 108,6 (C-16), 151,5 (C-15), 179,4 (C-18); *m/z* (%) : 350 (M$^+$, 7), 332 (100). *Anal.* calc. pour $C_{21}H_{34}O_4$: C 72,00, H 9,71; trouvée : C 71,92, H 9,59.

Isomérisation de l'époxy-7,8α isopimarate de méthyle ***4***

L'isomérisation de 2,533 g d'époxy-7,8α isopimarate de méthyle **4** sur alumine active nous a permis d'isoler par chromatographie en phase liquide en éluant avec le mélange benzène/éther (95:5) : *Le triène* ***25*** (43 mg) (32), *la cétone* ***18*** (235 mg) (32), *l'aldéhyde* ***26*** (260 mg) (32) et *l'hydroxy-oléfine* ***23*** (935 mg) composés précédemment obtenus et décrits.

L'hydroxy-oléfine ***27*** (737 mg) : ir (ν cm^{-1}) : 3550 (OH), 1720 (CO); rmn ^{1}H (90 MHz) δ : 0,91 (s, 3H), 0,94 (s, 3H), 1,16 (s, 3H), 3,62 (s, 3H), 3,68 (m, 1H), 4,80–5,02 (—CH=CH_2), 5,56–5,85 (—CH=CH$_2$); rmn ^{13}C (ppm) δ : 16,5 (C-19), 18,3 (C-2), 18,3 (C-20), 20,9 (C-11), 27,7 (C-17), 31,2 (C-6), 34,6 (C-12), 34,9 (C-13), 35,5 (C-1), 36,5 (C-3), 38,0 (C-10), 39,3 (C-14), 41,4 (C-5), 47,3 (C-4), 52,0 (C-21), 69,0 (C-7), 111,4 (C-16), 127,3 (C-8), 141,1 (C-9), 146,1 (C-15), 178,9 (C-18); *m/z* (%) : 332 (M$^+$, 21), 239 (100). *Anal.* calc. pour $C_{21}H_{32}O_3$: 75,90, H 9,64; trouvée : C 75,64, H 9,47.

Isomérisation de l'époxy-8,9β isopimarate de méthyle ***5***

L'isomérisation de 850 mg d'époxy-8,9β isopimarate de méthyle **5** n'est pas totale. On récupère par chromatographie en phase liquide en éluant avec le mélange éther de pétrole/éther (9:1) *le triène* ***25*** (192 mg) et l'époxyde (250 mg) n'ayant pas réagi.

L'élution avec benzène/éther (95:5) nous conduit à un mélange complexe à partir duquel nous isolons *l'hydroxy-oléfine* ***28*** (35 mg) (23).

Isomérisation de l'époxy-8,9α isopimarate de méthyle ***6***

L'isomérisation de 1,44 g d'époxy-8,9α isopimarate de méthyle **6** sur alumine active permet d'obtenir, après séparation par chromatographie en phase liquide en éluant avec le mélange benzène/éther (95:5), *le triène* ***25*** (300 mg), *l'hydroxy-oléfine* ***29*** (404 mg) (23) et *l'hydroxy-oléfine* ***30*** (332 mg) : ir (ν cm^{-1}) : 3550 (OH), 1720 (CO); rmn ^{1}H (90 MHz) δ : 0,82 (s, 3H), 0,97 (s, 3H), 1,24 (s, 3H), 3,58 (s, 3H), 5,36 (m, $W_{1/2}$ = 8–9 Hz, 1H), 4,73–4,98 (—CH=CH_2), 5,59–5,91 (—CH=CH$_2$); rmn ^{13}C (ppm) δ : 17,5 (C-19), 17,6 (C-20), 17,9 (C-2), 21,0 (C-17), 24,9 (C-6), 25,6 (C-11), 30,7 (C-12), 32,1 (C-1),

36,8 (C-3), 36,9 (C-13), 38,0 (C-5), 40,3 (C-10), 43,1 (C-14), 46,4 (C-4), 52,0 (C-21), 74,4 (C-9), 109,5 (C-16), 125,2 (C-7), 136,1 (C-8), 150,0 (C-15), 179,2 (C-18); *m/z* (%) : 332 (M^+, 2), 164 (100). *Anal.* calc. pour $C_{21}H_{32}O_3$: C 75,90, H 9,64; trouvée : C 75,81, H 9,58.

Remerciements

Nous remercions Messieurs M. Petraud et B. Barbe pour les spectres de rmn ^1H et rmn ^{13}C ainsi que Monsieur G. Bourgeois pour les spectres de masse (Centre d'études structurales et d'analyses des molécules organiques, Université de Bordeaux I).

1. V. Prelog, K. Schenker et H. H. Günthard. Helv. Chim. Acta, **35**, 1598 (1952).
2. G. Büchi, R. E. Erickson et N. Warabayashi. J. Am. Chem. Soc. **83**, 927 (1961).
3. I. E. Nigam et L. Levi. Can. J. Chem. **41**, 1726 (1962).
4. U. R. Nayak et Sukh Dev. Tetrahedron, **19**, 2293 (1963).
5. N. P. Damodaran et Sukh Dev. Tetrahedron Lett. 1941 (1963).
6. G. Berti, F. Bottari et A. Marsili. Tetrahedron Lett. 1 (1964).
7. I. C. Nigam et L. Levi. J. Org. Chem. **29**, 2803 (1964).
8. N. P. Damodaran et Sukh Dev. Tetrahedron, **24**, 4123 (1968).
9. V. S. Joshi, N. P. Damodaran et Sukh Dev. Tetrahedron, **24**, 5817 (1968).
10. T. S. Santhanakhrisnan, R. R. Sobti, U. R. Nayak et Sukh Dev. Tetrahedron, **26**, 657 (1970).
11. V. S. Joshi, N. P. Damodaran et Sukh Dev. Tetrahedron, **27**, 459 (1971); **27**, 475 (1971).
12. Luu Bang et G. Ourisson. Tetrahedron, **29**, 2097 (1973).
13. V. S. Joshi et Sukh Dev. Tetrahedron, **33**, 2955 (1977).
14. A. Kergomard et M. Th. Geneix. Bull. Soc. Chim. Fr. 390 (1958).
15. A. Kergomard et J. Philibert. Bull. Soc. Chim. Fr. 1381 (1959).
16. K. Arata et K. Tanabe. Chem. Lett. 321 (1976).
17. K. Arata, J. O. Bledsoe et K. Tanabe. Tetrahedron Lett. 3861 (1976).
18. K. Arata, S. Akutagawa et K. Tanabe. J. Catal. **41**, 173 (1976).
19. K. Arata, J. O. Bledsoe et K. Tanabe. J. Org. Chem. **43**, 1660 (1978).
20. K. Arata, J. O. Bledsoe et K. Tanabe. Bull. Chem. Soc. Jpn. **51**, 2289 (1978).
21. K. Arata et K. Tanabe. Chem. Lett. 1017 (1979).
22. G. H. Posner. Angew. Chem. Int. Ed. Engl. **90**, 527 (1978).
23. B. Papillaud, F. Tiffon, M. Taran, B. Arreguy-San Miguel et B. Delmond. Tetrahedron, **41**, 1845 (1985).
24. C. R. Enzell et B. R. Thomas. Acta Chem. Scand. **19**, 1875 (1965).
25. O. Tanaka, S. Mihashi, I. Yanagisawa, T. Nikaido et S. Shibata. Tetrahedron, **28**, 4523 (1972).
26. J. W. ApSimon et S. F. Hall. Can. J. Chem. **56**, 2156 (1978).
27. M. Taran et B. Delmond. Tetrahedron, **41**, 1859 (1985).
28. F. H. Wehrli et T. Wirthlin. Interpretation of carbon-13 NMR spectra. Heyden, London. 1976.
29. F. Bohlmann, R. Zeisberg et E. Klein. Org. Magn. Reson. **7**, 426 (1975).
30. B. Delmond, M. Taran, J. Valade, M. Petraud et B. Barbe. Org. Magn. Reson. **17**, 207 (1981).
31. J. W. ApSimon. J. Chem. Soc. Chem. Commun. 83 (1970).
32. M. Taran et B. Delmond. Tetrahedron, **41**, 4787 (1986).
33. M. Taran et B. Delmond. Tetrahedron, **42**, 4795 (1986).
34. S. E. Tung et E. Mininch. J. Catal. **3**, 229 (1964).
35. H. Pines et W. O. Haag. J. Am. Chem. Soc. **82**, 2471 (1960).
36. B. D. Flockart, C. Naccache, J. A. Scott et R. C. Pink. J. Chem. Soc. Chem. Commun. 238 (1965).
37. Sukh Dev. J. Sci. Ind. Res. **31**, 60 (1972).
38. C. A. Grob. Angew. Chem. Int. Ed. Engl. **8**, 535 (1969).
39. E. E. Rels, L. J. Goad et T. W. Goodwin. Biochem. J. **107**, 407 (1968).

Can. J. Chem. Downloaded from www.nrcresearchpress.com by 112.217.228.212 on 09/07/12
For personal use only.

Micellar catalysis of organic reactions. 22.[1] A comparison of the basic hydrolysis of benzodiazepinones in the presence of reactive counterion micelles and vesicles

TREVOR J. BROXTON,[2] XENIA SANGO, AND SALLYANNE WRIGHT
Department of Chemistry, La Trobe University, Bundoora Victoria, Australia 3083

Received October 26, 1987

TREVOR J. BROXTON, XENIA SANGO, and SALLYANNE WRIGHT. Can. J. Chem. **66**, 1566 (1988).

The basic hydrolysis of diazepam and several *N*-alkyl nitrazepam derivatives has been studied in the presence of reactive counterion micelles of cetyltrimethylammonium hydroxide (CTAOH) and vesicles of didodecyldimethylammonium hydroxide (DDAOH). In both surfactants, the rate of hydrolysis of all compounds was found to be dependent on the hydroxide concentration at constant surfactant concentration and this was interpreted as evidence for initial amide hydrolysis. The hydrolysis in CTAOH was inhibited by added salts in the order $Br^- < NO_3^- < SO_4^{2-}$. At concentrations above 3 m*M* surfactant, the rate of hydrolysis of each compound was similar in CTAOH and in DDAOH. At lower concentrations of CTAOH, however, the rate of hydrolysis was significantly lower than that in DDAOH. On the basis of this evidence, it was concluded that the cmc of CTAOH was between 2–3 m*M*, which is in good agreement with the value of 1.8 m*M* obtained by Zana from conductivity measurements. For diazepam, a mechanistic change is indicated on transfer from water to either micelles or vesicles and since vesicles are considered good models of biological membranes, this suggests that conclusions concerning the bioavailability of diazepam should not be based on studies in water but rather on studies in either micelles or vesicles.

TREVOR J. BROXTON, XENIA SANGO et SALLYANNE WRIGHT. Can. J. Chem. **66**, 1566 (1988).

Opérant en présence de micelles réactives d'hydroxyde de cétyltriméthylammonium (CTAOH) ou de vésicules d'hydroxyde de didodécyldiméthylammonium (DDAOH), on a étudié l'hydrolyse en milieu basique du diazépam de plusieurs dérivés nitrazépam *N*-alkylés. Dans chacun de ces agents de surface, on a trouvé que la vitesse d'hydrolyse de chacun des composés dépend de la concentration en ion hydroxyde, à concentration d'agent de surface constante; on interprète ces résultats en fonction d'une hydrolyse initiale de l'amide. Dans le CTAOH, l'hydrolyse est inhibée par l'addition de sels, dans l'ordre suivant : $Br < NO_3^- < SO_4^{2-}$. A des concentrations en agent de surface plus grandes que 3 m*M*, les vitesses d'hydrolyse de chacun des composés sont semblables dans le CTAOH et dans le DDAOH. Toutefois, à des concentrations plus faibles en CTAOH, la vitesse d'hydrolyse est beaucoup plus faible que dans le DDAOH. En se basant sur ces résultats, on en conclut que la cmc du CTAOH s'établit entre 2 et 3 m*M*; ceci est en bon accord avec la valeur de 1,8 m*M* qui a été obtenue par Zana à l'aide de mesures de conductivité. Pour le diazépam, la passage de l'eau à des micelles ou à des vésicules provoque un changement de mécanisme; puisque les vésicules sont considérées comme de bons modèles des membranes biologiques, il est suggéré que les conclusions concernant la bio-disponibilité du diazépam ne devraient pas être basées sur des études dans l'eau mais plutôt sur des études dans des micelles ou dans des vésicules.

[Traduit par la revue]

Can. J. Chem. Downloaded from www.nrcresearchpress.com by 112.217.228.212 on 09/07/12
For personal use only.

Introduction

Previous studies (1) of the basic hydrolysis of diazepam **1***a* in water and in micelles of cetyltrimethylammonium bromide (CTAB) have indicated a mechanistic change on transfer from water **1–3–4** to micelles **1–2–4**. On the other hand, for *N*-alkyl nitrazepam derivatives (**1***b–e*), hydrolysis is catalysed by micelles of CTAB but the mechanism (initial amide hydrolysis **1–2–4**) is the same in water and in the presence of micelles (Scheme 1).

Attempts to argue the biological relevance of these studies were hampered by the fact that micelles are poor models of biological membranes (2) because, although they have a polar exterior and a non-polar interior, they are composed of single chain surfactant molecules with only a single interface between the spherical aggregate and bulk water. Furthermore, micelles are dynamic species continually breaking up and reforming. Surfactant vesicles, on the other hand, are considered much better models of biological membranes (3) because, like membranes, they have a polar exterior and a non-polar interior and they are composed of double chain surfactant molecules arranged to form a bilayer.

For this reason, we have extended our studies to include the basic hydrolysis of benzodiazepinones in the presence of surfactant vesicles to determine if the mechanistic changes observed in micelles also occur in vesicles.

If similar behaviour is found in micelles and vesicles it should be reasonable to claim the biological relevance of our previous studies in micelles to reactions occurring in membranes. Vesicles formed from didodecyldimethylammonium hydroxide (DDAOH) are particularly suitable for this purpose. They are widely reported to form spontaneously on dissolving the solid (DDAOH) in water without the need for sonication or any other special treatment (4–6). Furthermore, the hydroxide ion required for basic hydrolysis of the substrate is provided by the reactive counterion surfactant.

To allow direct comparison between the vesicular studies and results obtained in micellar solution, the hydrolysis of substrates **1***a–e* was also studied in the presence of reactive counterion micelles of cetyltrimethylammonium hydroxide (CTAOH). The use of CTAOH rather than CTAB and NaOH avoids the added complication of competition between hydroxide and bromide ions for sites on the micellar surface. With both CTAOH and DDAOH, the only counterion present in solution is the hydroxide ion. We thus report our results for the first phase of hydrolysis of compounds **1***a–e* in CTAOH and in DDAOH in this paper.

[1]For Part 21, see ref. 12.

[2]Author to whom all correspondence should be addressed.

Printed in Canada / Imprimé au Canada

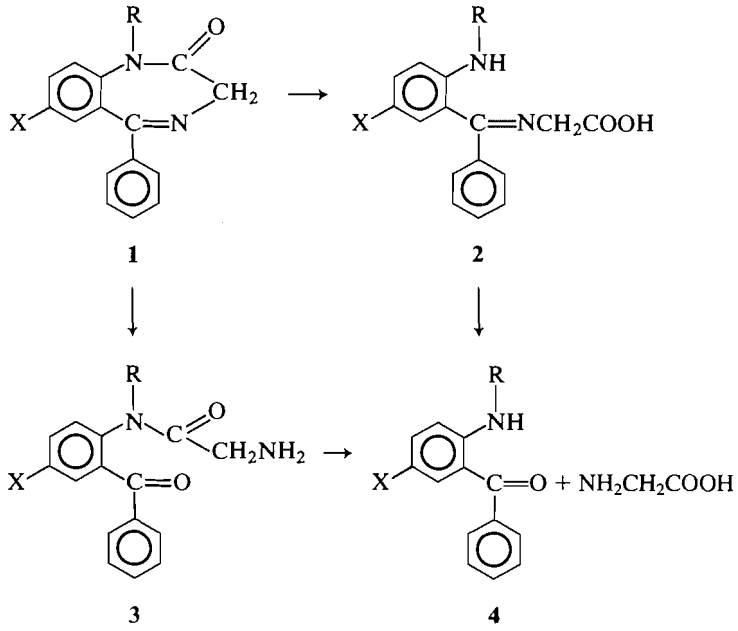

where a = X = Cl, R = CH_3
b = X = NO_2, R = CH_3
c = X = NO_2, R = $CH_2C_6H_5$
d = X = NO_2, R = —C_6H_{13}
e = X = NO_2, R = —$C_{12}H_{25}$

SCHEME 1

Results and discussion

Previous studies (1) of the basic hydrolysis of diazepam **1***a* and nimetazepam **1***b* in the presence of micelles of CTAB have shown a biphasic reaction. This has now also been observed for hydrolysis of these compounds in micelles of CTAOH and vesicles of DDAOH. For nimetazepam **1***b* and for other *N*-alkyl nitrazepam derivatives **1***c–e*, the first phase was characterized by an increase in absorbance at 385–390 nm and an isosbestic point at 340 nm. For diazepam **1***a*, however, the first phase was characterized by an increase in absorbance at 252 nm. This large difference in λ_{max} for the first phase of hydrolysis of compound **1***a* and for the other compounds **1***b–e*, is due to the production of a *p*-chloroaniline chromophore **2***a* from compound **1***a*, but a *p*-nitroaniline chromophore **2***b–e* from all of the other compounds.

Rate constants for the hydrolysis of diazepam **1***a* in micelles of CTAOH and in vesicles of DDAOH are in Table 1. In both surfactants, it can be seen that the rate of hydrolysis increased with detergent concentration. In principle, this may be due either to an increase in the concentration of hydroxide ion or to an increase in the CTA/DDA concentration resulting in an increased proportion of reaction in the surfactant aggregate. However, for both surfactants, it can be seen that the rate of hydrolysis of **1***a* increased as the surfactant concentration was increased at constant total hydroxide concentration (0.1 *M*) and as the concentration of added NaOH was increased at constant surfactant concentration (12 m*M*).

Since amide hydrolysis is first order in hydroxide concentration in surfactant aggregates (7) while azomethine hydrolysis is independent of hydroxide concentration, the above results are consistent with initial amide hydrolysis **1***a* → **2***a* in both surfactant systems.

Rate constants for the basic hydrolysis of *N*-alkyl nitrazepam derivatives **1***b–e* in CTAOH and in DDAOH are in Table 2.

For all compounds, the rate of hydrolysis increased with surfactant concentration. As for diazepam, it was found that the rate of basic hydrolysis of nimetazepam **1***b* increased with added NaOH at constant surfactant concentration (3 m*M*) and also increased with detergent concentration at constant total hydroxide concentration (5 m*M*).

Thus, we conclude that the hydrolysis of nitrazepam derivatives involves initial amide hydrolysis (mechanism **1**–**2**–**4**). However, on looking closely at the results for the different *N*-alkyl nitrazepam derivatives in DDAOH, we find that the dependence of DDAOH concentration in the range 1–5 m*M* varies from a 2.5-fold increase for compound **1***e* to a 6-fold increase for compound **1***b*.

This variation in rate dependence on DDAOH concentration for compounds **1***b–e* could arise from a number of different sources, including a different blend of concurrent amide hydrolysis (which is dependent on base concentration) and azomethine hydrolysis (which is independent of base concentration) for each compound, but we favour different orientational effects for substrates **1***b–e* in the surfactant aggregates as a possible explanation for these differences.[3] It is noteworthy that the compounds bearing the hydrophobic alkyl groups (**1***d* and *e*), which may anchor the benzodiazepinone nucleus into the surfactant aggregates, experience the smallest increase in rate as the concentration of DDAOH is increased, while compound **1***b*, which has only the methyl group at N-1, experiences a larger increase in rate.

The presence of the hydrophobic alkyl chains at N-1 in

[3]We thank a referee for suggesting this alternative explanation.

Can. J. Chem. Downloaded from www.nrcresearchpress.com by 112.217.228.212 on 09/07/12
For personal use only.

Can. J. Chem. Downloaded from www.nrcresearchpress.com by 112.217.228.212 on 09/07/12
For personal use only.

compounds **1***d* and **1***e* may result in the penetration of the amide group more deeply into the non-polar region of the aggregate where it is less sensitive to changes in the bulk solution. For the methyl compound (**1***b*), it is possible that the phenyl group on C-5 will be the anchoring group resulting in the amide moiety residing at the interface and being more sensitive to changes in bulk solution.

In the presence of a constant concentration of CTAOH (3 m*M*), the rate of hydrolysis of compound **1***b* also showed a slightly greater dependence on hydroxide concentration (2.12-fold as the total hydroxide concentration was increased from 4–12 m*M*) than that for compound **1***d* (1.7-fold increase).

Salt effects

In CTAOH the addition of salts (e.g., KBr, KNO_3, or K_2SO_4) resulted in decreased rates of hydrolysis. This inhibitory effect may be caused either by a reduction of the hydroxide ion concentration in the surfactant aggregate caused by a less favourable exchange constant or by the exclusion of the substrate from the surfactant aggregate. The inhibitory effect for 10 m*M* added salt in 5 m*M* CTAOH increased in the order $Br^- < NO_3^- < SO_4^{2-}$ for all *N*-alkyl nitrazepams studied. The magnitude of inhibition for each salt was less for the most hydrophobic substrate **1***e* than for the other compounds. For example, the addition of 10 m*M* KBr resulted in a decrease in rate to 19% of that in the absence of KBr for compound **1***e* (i.e., 81% inhibition), to between 12–15% of the rate in the absence of KBr for the other compounds **1***b–d* (i.e., 85–88% inhibition). Although these differences (between compounds **1***b–e*) are small, it is interesting to note that the most hydrophobic compound (**1***e*) is affected least. This may indicate that the inhibition is due to the exclusion of the substrate molecule from the surfactant aggregate, but further work would be necessary to prove this point. In DDAOH, the addition of 10 m*M* salt caused precipitation of the surfactant. Only 5 m*M* KBr could be added without causing precipitation. As expected, 5 m*M* KBr resulted in significant inhibition (72%) of the rate of hydrolysis of compound **1***c* over the concentration range 1–5 m*M* DDAOH. A similar result (76% inhibition) was achieved with 5 m*M* KBr in 5 m*M* CTAOH.

Comparison of CTAOH and DDAOH

The rate of hydrolysis at 30.4°C in CTAOH (5 m*M*) was slightly greater (2–26%) than that in DDAOH (5 m*M*) at 29.4°C for all *N*-alkyl nitrazepam derivatives studied. For diazepam, however, the rate of hydrolysis in CTAOH (10 m*M*) was 33% less than in DDAOH (10 m*M*) at the same temperature. At 5 m*M* surfactant concentration, the magnitude of inhibition of the hydrolysis of compound **1***c* by the addition of 5 m*M* KBr was similar in CTAOH (76%) and in DDAOH (72%). In both surfactants, the rate of hydrolysis of both diazepam **1***a* and nimetazepam **1***b* was dependent on the surfactant concentration (at constant total hydroxide concentration) and on the hydroxide concentration (at constant surfactant concentration).

One significant difference between reaction in CTAOH and in DDAOH was observed at low surfactant concentrations for the hydrolysis of compounds **1***b–e*. Using nimetazepam **1***b* as an example, the rates at 3 m*M* surfactant are similar: 32.4×10^{-3} s^{-1} CTAOH and 31.0×10^{-3} s^{-1} for DDAOH. However, at 2 m*M* and 1 m*M* surfactant, the rate in CTAOH is lower, 9.8×10^{-3} s^{-1} (2 m*M*) than for reaction in DDAOH, 1.8×10^{-2} s^{-1} (2 m*M*) (see Table 2). This can be explained by assuming that the cmc of CTAOH is between 1 and 2 m*M*, so that at 1 m*M* no micelles are present. Vesicles, on the other hand, are not lost on dilution (2, 3) and reaction in DDAOH was not retarded to the same extent when the concentration was reduced in this concentration range. In fact, a more gradual decrease in rate of hydrolysis of **1***b* was observed down to as low as 0.1 m*M* DDAOH. Thus, compound **1***b* is incorporated into surfactant aggregates at quite low concentrations and the behaviour in CTAOH is not due to the lack of solubilization so much as to the lack of micelles.

TABLE 1. Rate constants for the first phase of the basic hydrolysis of diazepam (**1***a*) at 68.8°C[a]

Surfactant/m*M*	NaOH/m*M*	$10^3 \times k_1$/s^{-1} for CTAOH	$10^3 \times k_1$/s^{-1} for DDAOH
3	—	—	0.898
4	—	1.24	1.16
5	—	—	1.82
8	—	2.08	—
10	—	2.15	3.19
12	—	2.54	3.03
16	—	3.36	3.81
20	—	3.62	6.00
50	—	8.18	9.64
100	—	13.5	—
At constant total hydroxide (0.1 *M*)			
0	100	0.378	0.378
1	99	4.56	—
2	98	8.51	—
3	97	10.8	—
4	96	12.4	14.7
8	92	15.1	22.5
12	88	15.9[b]	23.8
16	84	16.8	32.6
20	80	20.0	26.8
At constant surfactant (12 m*M*)			
12	20	4.57	5.68
12	40	8.54	9.01
12	80	13.8	20.2
12	100	15.4	28.4

[a]All followed at 252 nm.
[b]At 12 m*M* CTAB/100 m*M* NaOH, $k_1 = 9.69 \times 10^{-3}$ s^{-1}.

Reported values for the cmc of CTAOH vary considerably. Bunton and co-workers (8) comment that the cmc is not well defined but is approximately 10^{-3} M. Llamos and Zana quote a value of 1.8 m*M* obtained by a conductivity technique as being more reliable than the value of 0.8 m*M* obtained by the surface tension method (9). Furthermore, the 1.8 m*M* value from conductivity measurements obeys the logarithmic law usually found for the change of cmc with the number of carbon atoms (9). A value of 1.8 m*M* for the cmc of CTAOH fits in well with our observations, indicating differences in rates between CTAOH and DDAOH at 1 and 2 m*M* but not at 3 m*M* surfactant.

Comparison of CTAOH and CTAB/NaOH

For diazepam **1***a*, the rate of hydrolysis in 12 m*M* CTAOH and 88 m*M* NaOH (15.9×10^{-3} s^{-1}) was faster than in 12 m*M* CTAB and 0.1 *M* NaOH (9.69×10^{-3} s^{-1}) (same total concentration of hydroxide). The difference in rate is due to the combined effects of (*a*) the unfavourable exchange constants between hydroxide and bromide (not present in CTAOH) and (*b*) the different degrees of dissociation of micelles of CTAB ($\beta = 0.80$) and CTAOH ($\beta \approx 0.5$ between 4–10 m*M* CTAOH)

TABLE 2. Rate constants for the first phase of the basic hydrolysis of *N*-alkylnitrazepam derivatives **1***b–e*

(*a*) In DDAOH at 29.4°C

		$10^3 \times k_1/s^{-1}$ for			
[DDAOH]/m*M*	[Additive]/m*M*	*N*-Methyl (**1***b*)	*N*-Benzyl (**1***c*)	*N*-Hexyl (**1***d*)	*N*-Dodecyl (**1***e*)
0.1	—	0.055	—	—	—
0.2	—	0.108	—	—	—
0.3	—	0.599	—	—	—
0.4	—	1.16	—	—	—
0.5	—	2.20	—	—	—
1	—	8.45	26.1	6.08	4.72
2	—	18.0	50.4	8.89	7.39
3	—	31.0	68.9	13.5	9.17
4	—	42.6	78.8	15.9	11.1
5	—	51.1	96.7	18.5	11.9
At constant surfactant (3 m*M*)					
3	NaOH, 1 m*M*	36.0	—	—	—
3	NaOH, 3 m*M*	43.2	—	—	—
3	NaOH, 5 m*M*	51.3	—	—	—
3	NaOH, 7 m*M*	59.7	—	—	—
3	NaOH, 9 m*M*	63.2	—	—	—
At constant total hydroxide (5 m*M*)					
1	NaOH, 4 m*M*	19.8	—	—	—
2	NaOH, 3 m*M*	37.5	—	—	—
3	NaOH, 2 m*M*	45.5	—	—	—
4	NaOH, 1 m*M*	49.9	—	—	—
5	—	51.3	—	—	—
Salt effects					
1	KBr, 5 m*M*	—	2.00	—	—
2	KBr, 5 m*M*	—	5.49	—	—
3	KBr, 5 m*M*	—	10.7	—	—
4	KBr, 5 m*M*	—	17.3	—	—
5	KBr, 5 m*M*	—	27.6	—	—

(*b*) In CTAOH at 30.4°C

		$10^3 \times k_1/s^{-1}$			
[CTAOH]/m*M*	[Additive]/m*M*	*N*-Methyl (**1***b*)	*N*-Benzyl (**1***c*)	*N*-Hexyl (**1***d*)	*N*-Dodecyl (**1***e*)
1	—	0.52	2.85	1.0	0.5
2	—	9.8	40.4	8.7	5.5
3	—	32.4	85	18	9.9
4	—	44	105	22	11.2
5	—	52	119	25	14.5
At constant surfactant (3 m*M*)					
3	NaOH, 1 m*M*	32.3	—	24.8	—
3	NaOH, 3 m*M*	45.2	—	—	—
3	NaOH, 5 m*M*	54.6	—	36.7	—
3	NaOH, 7 m*M*	62.4	—	—	—
3	NaOH, 9 m*M*	68.7	—	43.0	—
At constant total hydroxide (5 m*M*)					
1	NaOH, 4 m*M*	6.45	—	—	—
2	NaOH, 3 m*M*	24.2	—	—	—
3	NaOH, 2 m*M*	44.2	—	—	—
4	NaOH, 1 m*M*	47.9	—	—	—
5	—	53.8	—	—	—
Salt effects					
5	KBr, 10 m*M*	7.64	14.8	3.4	2.7
5	KNO_3, 10 m*M*	6.1	10.4	2.3	2.03
5	K_2SO_4, 10 m*M* SO_4	1.57	3.72	0.86	0.77
5	KBr, 5 m*M*	—	28.3	—	—

Can. J. Chem. Downloaded from www.nrcresearchpress.com by 112.217.228.212 on 09/07/12
For personal use only.

(10). In other words, the reaction in CTAB/NaOH is inhibited by the salt effect of 12 m*M* NaBr. It is of interest that this inhibition of the hydrolysis of diazepam (**1***a*) by 12 m*M* NaBr (40%) is less than that observed for compounds (**1***b–e*) (81–88% inhibition by 10 m*M* KBr). It would be of interest to determine whether this difference is a function of the different counterion (Na^+ versus K^+) or whether it is a function of different substituents on the compounds studied (e.g., for **1***a*, X = Cl, while for **1***b–e*, X = NO_2).

The other difference observed between reaction in CTAB and in CTAOH concerns the shape of the rate/surfactant profile in each case. Whereas reactions with NaOH in CTAB typically show a maximum corresponding to the complete solubilization of the substrate into the micelle (12 m*M* CTAB in the case of diazepam (1)), reactions in CTAOH continue to increase in rate even after all the substrate is completely solubilized. The rate of hydrolysis of diazepam in CTAOH increased up to 100 m*M* CTAOH.

This behaviour has been observed previously for other reactions in CTAOH and explained by the variation of the fraction of head groups neutralized as the surfactant concentration is changed (10).

Conclusions

Since similar mechanistic effects have been observed for the basic hydrolysis of benzodiazepinones in micelles (CTAB and CTAOH) in vesicles (DDAOH) and since vesicles are considered to be good membrane mimics (3), it seems reasonable to conclude that any mechanistic changes observed on transfer from water to micelles have relevance to the corresponding reactions in biological membranes.

Specifically, the basic hydrolysis of diazepam in the presence of biological membranes probably occurs via initial amide hydrolysis, whereas reaction in water involves initial azomethine hydrolysis. Thus, conclusions concerning the bioavailability of diazepam should not be based on studies of hydrolysis carried out in water.

Experimental

Materials

Substrates **1***a–e* were available from previous studies (1, 11).

Solutions of CTAOH were prepared from CTAB (8) by treatment with excess Ag_2SO_4 in methanolic solution. The mixture was sonicated for 2 h and then the solution was filtered, additional Ag_2SO_4 added, and the mixture resonicated. The solution was then filtered and the methanol removed *in vacuo*. The resulting cetyltrimethylammonium sulfate (CTAS) was recrystallized from MeOH/Et_2O. An aqueous solution of CTAS was treated with an equivalent amount of $Ba(OH)_2$ under N_2 gas. The $BaSO_4$ was removed by filtration and centrifugation. The resulting CTAOH was shown to be free of bromide, barium, and sulfate ions by standard methods. Solutions of CTAOH were stored at 0°C under N_2 gas.

Solutions of DDAOH were prepared from didodecyldimethylammonium bromide DDAB in an analogous way. In the hydroxy dechlorination of 1-chloro-2,4-dinitrobenzene, the kinetic behaviour of DDAOH, prepared as described above, was shown to be identical to that reported by Bunton and co-workers (6) for DDAOH prepared by an ion exchange resin technique. The hydroxide concentration of both CTAOH and DDAOH was determined by quenching an aliquot of the surfactant in excess standard dilute HCl followed by back titration of the excess HCl with standard NaOH solution using phenolphthalein indicator. Identical results were obtained whether the analysis was carried out in the presence or absence of methanol.

Rate constants were obtained as described previously (1), except that all manipulations with either CTAOH or DDAOH were carried out under a CO_2-free, N_2 atmosphere.

Acknowledgement

We are pleased to acknowledge partial support for this project by the Australian Research Grants Scheme.

1. T. J. Broxton and S. Wright. J. Org. Chem. **51**, 2965 (1986).
2. J. H. Fendler. Chem. Brit. 1098 (1984).
3. J. H. Fendler. Acc. Chem. Res. **13**, 7 (1980).
4. J. E. Brady, D. F. Evans, B. Kachar, and B. W. Ninham. J. Am. Chem. Soc. **106**, 4279 (1984).
5. B. W. Ninham, D. F. Evans, and G. J. Wel. J. Phys. Chem. **87**, 5020 (1983).
6. A. Cipiciani, R. Germani, G. Savelli, and C. A. Bunton. Tetrahedron Lett. 3765 (1984).
7. T. J. Broxton, L. W. Deady, and N. W. Duddy. Aust. J. Chem. **31**, 1525 (1978).
8. C. A. Bunton, L. Gan, J. Moffatt, L. Romsted, and G. Savelli. J. Phys. Chem. **85**, 4118 (1981).
9. P. Llamos and R. Zana. J. Phys. Chem. **87**, 1289 (1983).
10. E. Rodenas and S. Vera. J. Phys. Chem. **89**, 513 (1985).
11. T. J. Broxton and S. R. Morrison. Aust. J. Chem. **38**, 1037 (1985).
12. T. J. Broxton, J. R. Christie, and S. M. Mannas. Aust. J. Chem. **41**, 325 (1988).

Can. J. Chem. Downloaded from www.nrcresearchpress.com by 112.217.228.212 on 09/07/12
For personal use only.

Cyclobutene photochemistry. Involvement of carbene intermediates in the photochemistry of alkylcyclobutenes

K. Brady Clark and William J. Leigh[1]

Department of Chemistry, McMaster University, Hamilton, Ont., Canada L8S 4M1

Received September 30, 1987

K. Brady Clark and William J. Leigh. Can. J. Chem. **66**, 1571 (1988).

The photochemistry of 1,3,3,4- and 1,3,4,4-tetramethylcyclobutene has been investigated in pentane solution with monochromatic far ultraviolet (185, 193, and 214 nm) light sources, as well as in methanol solution with 214-nm excitation. Photolysis of each of the two isomeric cyclobutene derivatives results in competitive electrocyclic ring opening (yielding mixtures of stereoisomeric dienes in each case), fragmentation to yield propyne and methyl-2-butene, and isomerization to the other cyclobutene isomer. Quantum yields for product formation with 185-nm excitation have been measured in each case by cyclooctene actinometry. The occurrence of the interconversion process is offered as evidence for the intermediacy of cyclopropyl carbenes in the photochemistry of simple cyclobutenes in solution. On the basis of the known chemistry of carbenes of this type, their intermediacy in cyclobutene photochemistry may account at least partially for the formation of the formal ($2\pi + 2\pi$) cycloreversion products from photolysis of simple cyclobutene derivatives.

K. Brady Clark et William J. Leigh. Can. J. Chem. **66**, 1571 (1988).

On a étudié la photochimie des triméthyl-1,3,3,4 (et -1,3,4,4) cyclobutènes dans le pentane avec des sources de lumière ultraviolette liontaine (183, 194 et 214 nm) ainsi qui dans le méthanol avec une excitation à 214 nm. La photolyse de chacun des deux dérivés cyclobutènes isomères conduit à une ouverture de cycle électrocyclique (conduisant dans chaque cas à des mélanges de diènes stéréoisomères) qui est en compétition avec une fragmentation conduisant au propyne et au méthyl-2 butène-2 et avec une isomérisation conduisant à l'autre isomère cyclobutène. Utilisant l'actinométrie du cyclooctène et opérant à 185 nm, on a mesuré les rendements quantiques pour la formation des produits. Le fait que l'on observe le processus d'interconversion est proposé comme preuve de la présence de carbènes cyclopropyles comme intermédiaires dans la photochimie des cyclobutènes simples, en solution. En se basant sur la chimie connue des carbènes de ce type, on peut supposer que leur présence comme intermédiaires peut expliquer, au moins en partie, la formation des produits de la cycloréversion formelle ($2\pi + 2\pi$) de la photolyse de dérivés cyclobutènes simples.

[Traduit par la revue]

Can. J. Chem. Downloaded from www.nrcresearchpress.com by 93.93.197.157 on 09/07/12
For personal use only.

Introduction

The photochemistry of simple cyclobutenes has, until recently (1), defied thorough investigation. While strained systems such as benzocyclobutenes (2) and Dewar aromatics (3) undergo the expected (4) electrocyclic ring opening (the latter adiabatically (3)), simpler systems bearing conjugating substituents are surprisingly stable toward irradiation. For example, 1,2-diphenylcyclobutene fluoresces with near unit efficiency (5, 6), and undergoes photofragmentation (yielding diphenylacetylene and ethylene) in hydrocarbons (6) or photosolvolysis in protic solvents (7) in relatively low yields. Simple unsubstituted or alkyl-substituted systems, which absorb only in the far ultraviolet, are more reactive, undergoing electrocyclic ring opening and photofragmentation with similar efficiencies (1, 8–10). While the use of far-uv photochemical techniques does allow investigation of the photochemistry of these simple systems in solution, stringent precautions must be taken to avoid problems associated with secondary photolysis of the primary photoproducts (1).

The photofragmentation process, yielding the corresponding alkyne and alkene (eq. [1]) by formal retro ($2\pi + 2\pi$) cycloaddition, is known to occur stereospecifically (8) and with fairly high efficiency in simple, alkyl-substituted systems (1, 8–10). An alternative mechanism to the concerted cycloreversion pathway for the formation of these products has recently been proposed (9, 10), and involves fragmentation of carbene intermediates formed by [1,2]-alkyl migration (ring contraction) in the excited singlet state(s) of the cyclobutene (eq. [2]).

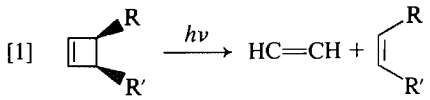

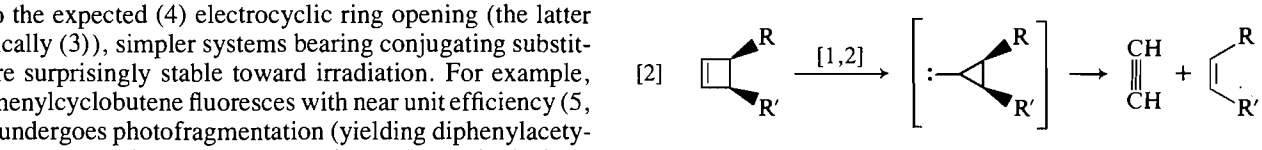

There is good precedent for such a suggestion. Cyclopropylmethylenes, generated by thermolysis or photolysis of the appropriate diazo compound or tosylhydrazone salt, are well known to undergo stereospecific fragmentation to the corresponding alkene and alkyne in high yield (11). Furthermore, the [1,2]-migration required for carbene formation from photolysis of cyclobutenes has ample precedent in alkene photochemistry (12), and this process has been attributed to the involvement of the $\pi,R(3s)$ Rydberg state. [1,2]-Hydrogen migrations are also common in alkene photochemistry (12, 13); in the case of cyclobutene, this would lead to cyclobutylidene, which is known to react predominantly by ring contraction to yield methylenecyclopropane (14; see also ref. 11*e*, pp. 42–44). Adam *et al.* have proposed the intermediacy of cyclobutylidene to explain the high yield of methylenecyclopropane observed from photolysis of cyclobutene itself in hydrocarbon solution with far-uv light (10).

We wish to report the results of a study that was designed to test for the involvement of cyclopropylmethylene intermediates in the direct photolysis of cyclobutenes by taking advantage of a second aspect of the known reactivity of these intermediates: ring expansion to cyclobutenes (11). We have investigated the photochemistry of two unsymmetrically substituted, isomeric

[1]Natural Sciences and Engineering Research Council of Canada University Research Fellow, 1983–1993. Author to whom correspondence may be addressed.

cyclobutene derivatives (**1** and **2**), on the premise that if ring contraction to cyclopropyl carbene intermediates occurs in these cases, it should be revealed by the interconversion of the two isomers (eq. [3]). Our results afford the first direct evidence for the formation of these intermediates in the photochemistry of simple cyclobutenes in solution.

[3] 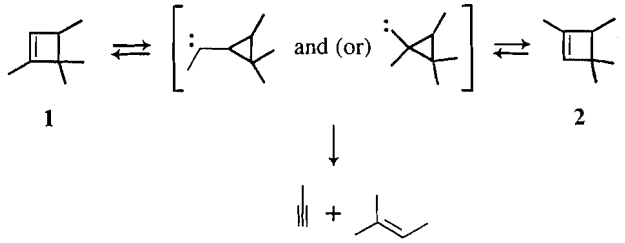

Results

The synthesis of 1,3,4,4- and 1,3,3,4-tetramethylcyclobutene (**1** and **2**, respectively) as a mixture of isomers was carried out by the route shown in eq. 4 (1). Compounds **1** and **2** were separated and purified by preparative gas chromatography (vpc), and their structures were assigned on the basis of their ir, mass, and 500-MHz ^1H and ^{13}C nmr spectra.

The isomers can be distinguished by the coupling between the two cyclobutene ring protons in the ^1H nmr spectra, since it is well established that in cyclobutene systems, vicinal (H1–H4 and H2–H3) interproton coupling is generally 1–2 Hz larger than allylic (H1–H3 and H2–H4) coupling (15). Thus, the isomer assigned as compound **1** has $J_{H2-H3} = 0.9$ Hz, while that assigned as **2** has $J_{H2-H4} < 0.2$ Hz (i.e., unresolvable).

[4] 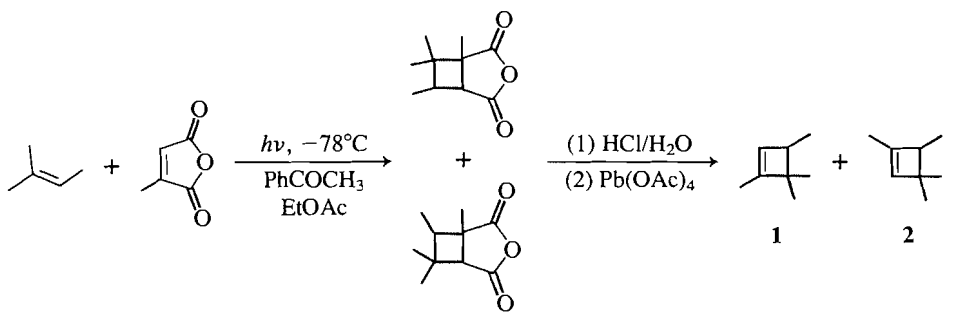

Further support for these structural assignments is obtained from the ^{13}C nmr spectra of the two isomers. First, the C2 chemical shift in **2** is shifted ca. 7 ppm downfield from its position in **1** due to the presence of the additional methyl group attached to C3 (16). Second, the undecoupled ^{13}C nmr spectra of the two isomers exhibit long-range $^{13}C-^1H$ coupling patterns that are also consistent with these assignments; the doublet splittings exhibited by the two highest field (quaternary) methyl groups in **1** and **2** as a result of long-range coupling with the ring hydrogens are particularly diagnostic. In the isomer assigned as **1**, only one of these carbons (that at 11.9 ppm) exhibits resolvable long-range coupling ($J \approx 1.3$ Hz), presumably with the ring hydrogen at C3. In the isomer assigned as **2**, the dominant quartet splittings of both of these carbons are further split into doublets, with $J \approx 1.0$ and 1.9 Hz, respectively. The assignment in this case is based upon the expectation that three-bond $^{13}C-^1H$ couplings (of which there should be three in **2** and one in **1**) should be better resolvable than four-bond couplings in compounds of this type (16).

Further corroborative attempts were made using proton nOe (nuclear Overhauser effect) difference spectroscopy, but these experiments were inconclusive; irradiation of only one of the methyl groups (that at 1.06 ppm in **1** and that at 1.08 ppm in **2**) resulted in significant nOe enhancement of any of the other proton resonances, and only the tertiary hydrogen (H3 in **1**; H4 in **2**) was affected.

The ultraviolet absorption spectra of **1** and **2** (not shown) in cyclohexane solution consist of single, featureless absorption bands with $\lambda_{max} = 192$ nm (ϵ 6700) in the case of **1**, and $\lambda_{max} = 193$ nm (ϵ 4960) in the case of **2**. In both spectra the absorption band tails out to ca. 215 nm and, while it is devoid of discernible fine structure, it is somewhat broader than the corresponding band in unsubstituted (at the double bond) homologs that we have studied (1, 17).[2]

Photolysis of **1** and **2** as deoxygenated, 0.02 M solutions in pentane or isopentane with a filtered (1, 18) low pressure mercury lamp (185 nm), the pulses of an argon fluoride excimer laser (193 nm), or an unfiltered Zn resonance lamp (214 nm) affords the product mixtures shown in eqs. [5] and [6], respectively. The dienes **3** and **4** were isolated by preparative vpc from 193-nm runs carried to ca. 40% conversion, and were identified on the basis of their ^1H nmr, ir, uv, and mass spectra, and by comparison to authentic samples (see experimental section). The formation of **3** from **1**, and **4** from **2**, affords

[5] 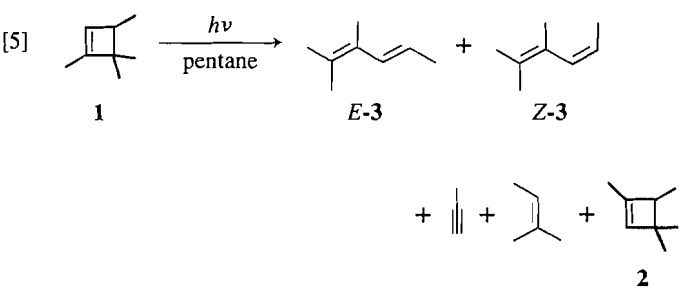

[6] 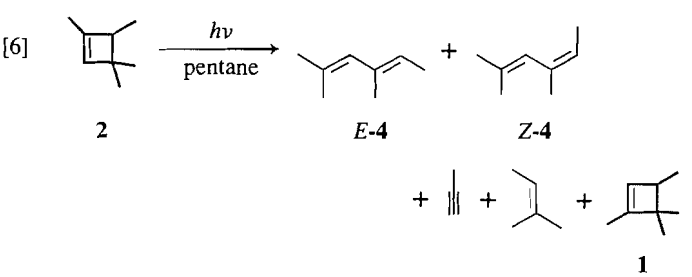

[2] W. J. Leigh, M. Pankratz, and K. B. Clark, to be published.

Can. J. Chem. Downloaded from www.nrcresearchpress.com by 93.93.197.157 on 09/07/12
For personal use only.

Can. J. Chem. Downloaded from www.nrcresearchpress.com by 93.93.197.157 on 09/07/12
For personal use only.

additional support for our structural assignments in the case of **1** and **2**.

The *E* and *Z* isomers of **3** were identified on the basis of their ^{1}H nmr spectra, and comparisons to the published spectra (19). Identification of *E*- and *Z*-**4** was not so straightforward. The ^{1}H nmr spectra of the two isomers exhibit substantially different chemical shifts for the four methyl groups; these allow a tentative assignment to be made on the basis of comparisons with the nmr spectra of the isomeric 3,4-dimethyl-2,4-hexadienes, whose identities have been previously assigned (20). The isomers have been more rigorously identified by uv photoelectron (pe) spectroscopy,[3] comparing the magnitude of the splitting between the two lowest energy bands in the pe spectra with calculated (MNDO) values. The magnitude of this splitting in simple cyclic and acyclic dienes varies dramatically with the dihedral angle defined by the four vinylogous carbons (ref. 22 and footnote 3). MNDO calculations carried out for *E*- and *Z*-**4** predict the most stable conformers to be twisted *s-cis* in both cases; the calculations for *E*-**4** predict a twist angle of 60.8° and a HOMO–SHOMO splitting of 1.1 eV, while those for *Z*-**4** predict a twist angle of 79° and a splitting of 0.5 eV. The uv photoelectron spectra of the two isomeric dienes from photolysis of **2** show splittings of ca. 0.7 and 1.3 eV, respectively, allowing the former to be identified as the *Z* isomer and the latter as the *E* isomer. The ultraviolet absorption spectra of the dienes thus identified as *E*-**4** (λ_{max} = 232 nm; ϵ 10 700) and *Z*-**4** (λ_{max} = 218 nm; ϵ 6300) are also consistent with their calculated geometries (23).

Propyne and methyl-2-butene were identified by gc–ms and by coinjection of authentic samples on at least two vpc columns.

Product yields were determined from the slopes of concentration vs. time plots, constructed for all products except propyne from vpc analyses of runs carried to <3% conversion. Figure 1 shows a typical plot, detailing the formation of **2**, *E*- and *Z*-**3**, and methyl-2-butene from 193-nm photolysis of **1**. Product quantum yields were determined by cyclooctene actinometry (24), using concentration vs. time plots from 185-nm runs (*n*-pentane solvent) carried to <3% conversion of starting material; these are collected in Table 1. No other products in addition to those shown in eq. [5] could be detected in the photolysate from **1** in yields greater than ca. 2% (our limits of detection). Photolysis of **2**, however, afforded three other minor products whose yields were too low (<5%) to enable isolation and identification.

Table 2 contains relative rates of diene and isomeric cyclobutene formation from photolysis of **1** and **2** in deoxygenated *n*-pentane or isopentane solution with the 185-, 193-, and 214-nm light sources, and in deoxygenated methanol solution with the 214-nm light source. No new products in addition to those observed in hydrocarbon solution with the 185-nm light source were found in any case. Photolyses of **1** and **2** were carried out in both *n*-pentane and isopentane solution with the 193-nm source, and yielded equivalent results for each compound in the two solvents.

We have demonstrated previously that the experimental conditions employed in these photolyses (monochromatic light sources, high substrate concentration, low conversion) are more than adequate to ensure that the products shown in eqs. [5] and [6] are indeed primary ones, and that secondary photolysis does not contribute to our results within our error limits. This can be considered rigorous in the case of the 185- and 193-nm photolyses, although in the 214-nm runs, it is likely that minor secondary photolysis of the diene products affects their relative (*E*/*Z*) yields to some extent (*vide supra*).

[3]N. H. Werstiuk, W. J. Leigh, and K. B. Clark, to be published.

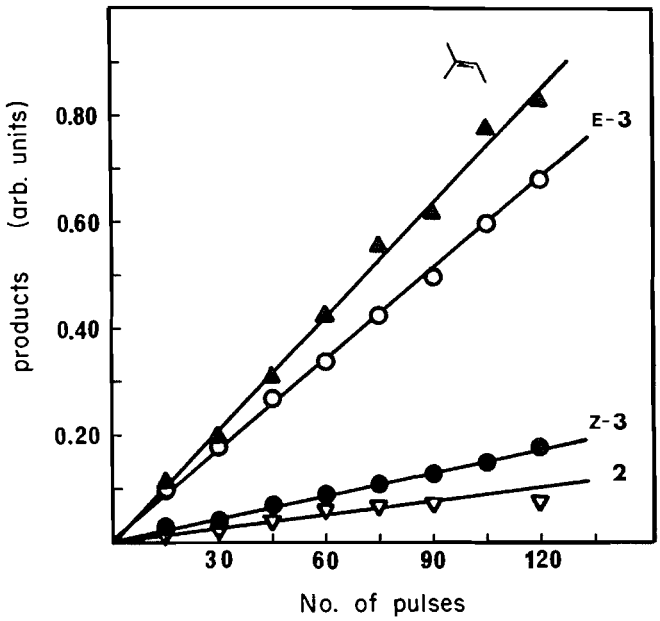

FIG. 1. Concentration versus dosage (time) plots for the formation of **2**, *E*- and *Z*-**3**, and methyl-2-butene from 193-nm photolysis of **1** in deoxygenated isopentane solution at 23°C.

TABLE 1. Product quantum yields from 185-nm photolysis of **1** and **2** in deoxygenated pentane solution[a]

Product	1	2
1	—	0.010 ± 0.003
2	0.015 ± 0.002	—
E-**3**	0.09 ± 0.01	—
Z-**3**	0.036 ± 0.002	—
E-**4**	—	0.096 ± 0.010
Z-**4**	—	0.030 ± 0.010
Methyl-2-butene	0.21 ± 0.02	0.092 ± 0.016

[a]Measured by cyclooctene actinometry (24), using a filtered (1, 18) low pressure mercury lamp.

Photostationary states for the direct *cis,trans*-photoisomerization of *E*- and *Z*-**3** were obtained by irradiation of deoxygenated, 0.003 M pentane solutions of the two diene isomers with 254-nm light until the compositions of the two solutions were identical. Similar experiments were carried out to determine photostationary states for isomerization of *E*- and *Z*-**4**. Quantum yield ratios, $\Phi_{Z\rightarrow E}/\Phi_{E\rightarrow Z}$, were then calculated for each isomeric diene pair from the photostationary state ratios and the extinction coefficients for absorption of the two diene isomers at the excitation wavelength (determined from the uv absorption spectra in pentane solution). These ratios are collected in Table 3.

Discussion

Direct photolysis of **1** and **2** in hydrocarbon solution with monochromatic far-ultraviolet light leads in both cases to fairly clean mixtures of five major products: the two geometric diene isomers from electrocyclic ring opening, methyl-2-butene and propyne from formal retrocycloaddition, and the other cyclobutene isomer resulting from **1**–**2** interconversion. The similari-

TABLE 2. Relative rates of product formation from 185-, 193-, and 214-nm photolysis of **1** and **2** in deoxygenated pentane and methanol solution[a]

Compound	Solvent	λ(nm)	Dienes		Methyl-2-butene	Isomer	Ring-opening/ fragmentation	E/Z
			E	Z				
			(**3**)			(**2**)		
	n-Pentane	185	5.4 ± 0.5	2.76 ± 0.12	12.0 ± 1.2	0.92 ± 0.12	0.6 ± 0.1	2.4 ± 0.4
	i-Pentane	193	5.4 ± 0.3	1.44 ± 0.04	7.2 ± 0.5	0.58 ± 0.02	1.0 ± 0.3	3.4 ± 0.6
1	*i*-Pentane	214	4.9 ± 0.4	1.49 ± 0.03	5.7 ± 1.0	0.55 ± 0.03	1.1 ± 0.3	3.0 ± 0.5
	Methanol	214	7.7 ± 0.5	2.2 ± 0.1	[b]	0.35 ± 0.17	—	3.2 ± 0.8
			(**4**)			(**1**)		
	n-Pentane	185	6.3 ± 0.5	2.0 ± 0.1	6.5 ± 0.8	0.64 ± 0.10	1.4 ± 0.2	3.2 ± 0.5
	i-Pentane	193	6.4 ± 0.1	1.86 ± 0.03	7.2 ± 1.3	0.3 ± 0.1	1.2 ± 0.2	3.4 ± 0.3
2	*n*-Pentane	214	5.2 ± 0.1	2.6 ± 0.2	10.0 ± 2.2	0.6 ± 0.2[c]	0.8 ± 0.3	2.0 ± 0.3
	Methanol	214	1.6 ± 0.1	0.84 ± 0.05	[b]	[b]	—	1.8 ± 0.2

[a]Rates were calculated from concentration vs. time plots for product formation (relative to internal standard). Errors were calculated using two standard deviations from these plots. The data are not corrected for differences in excitation source intensities.
[b]Not determined.
[c]Determined at ca. 4% conversion only.

TABLE 3. Photostationary states and quantum yield ratios for the direct *cis*, *trans* photoisomerization of *E*- and *Z*-**3** and *E*- and *Z*-**4**[a]

Diene	E/Z[b]	$\Phi_{Z\rightarrow E}/\Phi_{E\rightarrow Z}$[c]
3	0.25 ± 0.01	2.3 ± 0.1
4	0.36 ± 0.03	1.2 ± 0.1

[a]From photolysis of deoxygenated, 0.003 M pentane solutions with 254-nm light. The photostationary states were approached from both diene geometric isomers in each case.
[b]From the asymptotes in concentration vs. time plots (E/Z vs. t) for photolysis of each isomer.
[c]Calculated from the E/Z ratios of the 254-nm extinction coefficient ratios from the uv absorption spectra of the pure isomers (cyclohexane solution).

ties in the quantum yields for the ring-opening and fragmentation products (see Table 1) appear to be quite general in the photochemistry of simple cyclobutene derivatives, judging from the results of reported investigations of the photochemistry of bi- (1, 9) and tricyclic (8) systems, as well as those of other monocyclic derivatives (1, 10). Of special interest to this study, however, is the observation that interconversion of **1** and **2** occurs in significant amounts upon direct photolysis of either isomer in solution.

The formation of products consistent with the intermediacy of carbenes is a general feature of the photochemistry of simple alkenes in solution (12, 13). Generally, the intermediacy of carbenes in alkene photochemistry has been suggested by the similarities between the product mixtures obtained from alkene photolysis and those obtained when the carbenes are generated independently by photolysis or thermolysis of the corresponding diazo compound, diazirene, or tosylhydrazone salt. In addition, further support for carbene involvement has been provided by deuterium labelling studies (25) and intra- and intermolecular trapping with alcohols (13, 26). Usually, the distribution of carbene-derived products from alkene photolysis differs somewhat from that obtained when the carbene is generated by other means (13*a*,*b*), but it is well known that for a given multiplicity, carbene reactivity can vary markedly depending on the conditions of generation (11*e*, 14*a*).

The formation of carbene intermediates has been proposed to arise via [1,2]-alkyl or [1,2]-hydrogen migrations in the alkene $\pi,R(3s)$ Rydberg state (12), a species that presumably has some degree of radical cation character at the double bond. The Rydberg state assignment (as opposed to the π,π^* state, which leads to *cis*,*trans* isomerization, [1,3]-migrations, H_2 elimination (27), and hydrogen abstraction (12, 13)) has been made on the basis of several observations. P. J. Kropp and co-workers have shown that the yield of carbene-derived products from >200-nm photolysis of alkenes increases in importance with increasing alkyl substitution at the carbon–carbon bond (12), a trend that is mirrored in the progression to lower energy of the Rydberg state absorption (26) and fluorescence (29) bands in substituted alkenes in the gas phase. Related to this is the report that photolysis of 2,3-dimethyl-2-butene in hydrocarbon solution is strongly wavelength-dependent, with the yield of carbene-derived products increasing, at the expense of π,π^* derived products, with increasing excitation wavelength between 185 and 228 nm (30). The $\pi,R(3s)$ state is the lower energy one in this compound, according to gas phase uv absorption measurements (28). One question that remains to be answered in this area relates to the mechanism for population of the Rydberg state in solution phase photolyses, since the absorption coefficient for the $\pi,R(3s)$ transition is extremely weak in the condensed phase (27).

The photochemical interconversion of **1** and **2** observed in the present study, although it occurs in relatively minor amounts, provides convincing evidence for the formation of at least one common intermediate in the direct photolysis of these compounds. Other known alkene photoprocesses that could lead to cyclobutene products from **1** and **2**, such as [1,3]-hydrogen or -methyl migrations, clearly cannot interconvert the two isomers. For example, [1,3]-hydrogen migration (which might be considered the most likely alternative (12, 13)) is a degenerate rearrangement in the case of **1**, and [1,3]-methyl migration would afford the 1,2,3,4- (*cis* or *trans*) or 3,3,4,4-tetramethyl derivatives. While we cannot exclude the possibility that these products may indeed be formed in minor amounts, the main point to be made here is that single [1,3]-alkyl or -hydrogen migrations cannot account for the interconversion of **1** and **2**.

Can. J. Chem. Downloaded from www.nrcresearchpress.com by 93.93.197.157 on 09/07/12
For personal use only.

The most reasonable pathways for interconversion of **1** and **2** involve the intermediacy of one or both of the cyclopropyl carbenes shown in eq. [3], or the cyclobutylidenes formed via [1,2]-methyl or [1,2]-hydrogen migration, as shown in eq. [7].

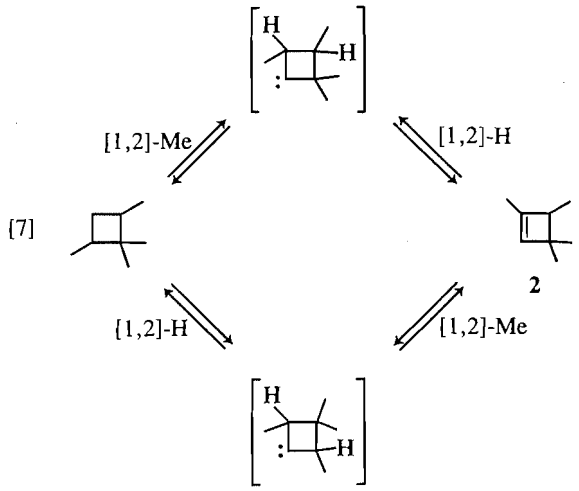

Cyclobutylidene has been proposed as an intermediate in the solution phase far-uv photochemistry of cyclobutene by Adam *et al.* (10), to explain the observed formation of methylcyclopropane in light yield. This carbene is indeed known to yield methylenecyclopropane, as well as minor amounts of cyclobutene, when it is generated independently from thermolysis or photolysis of diazo precursors (14). Several considerations lead us to favour the cyclopropylmethylene mechanism for the interconversion of **1** and **2**.

First, these intermediates may also account to some extent for the formation of propyne and methyl-2-butene (11), as was originally proposed (9, 10). It is clearly impossible to define this quantitatively since the extent to which the formally allowed, retro $(2\pi + 2\pi)$ cycloaddition pathway contributes to the formation of these products is indeterminable. In this regard, we note that fragmentation greatly outweighs isomer interconversion in the present cases, which is not the expected result if the behaviour of cyclopropyl carbenes generated from cyclobutene photolysis is assumed to be similar to that obtained when the carbene is generated directly from the diazo compound or diazo equivalent, unless fragmentation is derived largely from the $(2\pi + 2\pi)$ cycloreversion pathway. As noted above, however, the distribution of formally carbene-derived products from photolysis of alkenes in solution is usually quite different from that obtained when the carbenes are generated from other, more conventional, precursors.

Second, the interconversion of **1** and **2** by the cyclobutylidene pathway requires sequential [1,2]-Me/[1,2]-H or [1,2]-H/[1,2]-Me migrations (see eq. [7]). These combinations can be expected to be highly inefficient, since [1,2]-hydrogen migration usually predominates over [1,2]-methyl migration (when both are possible) in both alkene photochemistry (12, 13) and carbene chemistry (11*e*, 14*a*). It is possible, however, that these unfavourable combinations may be occurring as minor reactions competing only marginally with [1,2]-H/[1,2]-H migrations, which are identity reactions and hence undetectable.

Finally, the intermediacy of cyclobutylidenes in the photochemistry of **1** and **2** should be signalled by the formation of methylenecyclopropane derivatives to at least some extent. In the case of **1** at least, we have not observed the formation of any products in addition to those shown in eq. [5] in greater than ca. 2% yield, using several different sets of analytical conditions. We have obtained similar results from far-uv photolysis of a number of other simple mono- and bicyclic alkylcyclobutenes (1, 17); of the compounds that we have studied, only **5** (*vide infra*) affords a photoproduct of this type, and in very low yield. This contrasts the reported behaviour of cyclobutene itself (10), for reasons that we do not yet understand.

Our attempts to provide more conclusive evidence for carbene involvement by trapping the suspected intermediates with methanol have been unsuccessful, but this may be the simple result of exceedingly fast rates of unimolecular carbene rearrangement and (or) fragmentation. While methanol trapping of carbenes of this type has apparently not been investigated, it has been reported that trapping of triplet cyclopropylmethylenes by alkenes is relatively inefficient (even with high alkene concentrations); the singlet carbene (the suspected multiplicity in the present cases) could not be trapped at all(11*i*). The use of alkenes as potential carbene trapping agents in the photolysis of **1** and **2** is impractical because of their own competing absorption in the wavelength range necessary for our photolyses, and this would be prohibitive with the high alkene concentrations necessary for the experiment's possible success.

Photochemical electrocyclic ring opening of **1** and **2** can in each case proceed to yield both geometric isomers of the corresponding dienes by symmetry-allowed, disrotatory pathways. However, since the two diene isomers are also obtainable, in principle, by conrotatory (symmetry-forbidden) ring-opening pathways, the present study can afford no information regarding the preferred pathway for the photochemical ring opening of cyclobutene. In both cases, the *E*-diene isomer is clearly favoured over the *Z*-isomer, perhaps indicating some common preference for the least sterically demanding ring-opening pathway; i.e., that which avoids buttressing the 3- and 4-methyl groups as ring opening proceeds.

The situation is almost certainly more complicated than this, however. Our recent investigations of the photochemistry of bicyclo[4.2.0]oct-6-ene (**5**) and *cis*- and *trans*-3,4-dimethylcyclobutene (*c*- and *t*-**6**, respectively) showed clearly that, in general, photochemical ring opening of simple cyclobutenes proceeds non-stereospecifically to yield mixtures of all possible diene geometric isomers (1). The 185-nm photolysis of **5** yields a mixture of *cis,cis*- and *cis,trans*-1,3-cyclooctadiene that is consistent with the purely disrotatory, *adiabatic* excited-state ring-opening mechanism that theory predicts should be possible (31). However, the results of 185-nm photolyses of *c*- and *t*-**6**

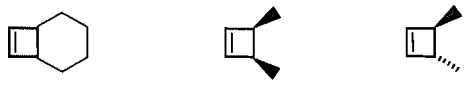

5 *c*-**6** *t*-**6**

(1), as well as more recent results (for other mono- and bicyclic derivatives and for **5** with longer wavelength excitation (17)), indicate that some portion of the formally forbidden diene isomer(s) *must* arise by the *conrotatory* ring-opening pathway. Whether this component is due to conrotatory opening on the same or a second excited-state surface, on the ground-state surface as a result of radiationless decay to hot vibrational levels, or some competition between (one or both of) these two pathways and adiabatic disrotatory ring opening remains to be determined. Comparison of the isomeric diene ratios obtained from photolysis of **1** and **2** (see Tables 1 and 2) with the quantum yield ratios for direct photoisomerization of the dienes (Table 3) verifies that the relative isomeric diene yields obtained from

Can. J. Chem. Downloaded from www.nrcresearchpress.com by 93.93.197.157 on 09/07/12
For personal use only.

Can. J. Chem. Downloaded from www.nrcresearchpress.com by 93.93.197.157 on 09/07/12
For personal use only.

cyclobutene photolysis are generally not defined by the decay characteristics of the diene singlet excited state (as obtained from the quantum yields for direct photoisomerization of the dienes).

The appearance of the solution phase uv absorption spectra of methyl-substituted monocyclic cyclobutenes (17) mirrors the trends found in substituted alkenes (28), suggesting that at least two excited states of similar energies are accessible in **1** and **2** under our conditions. Indeed, wavelength effects have been observed in the photochemistry of several of the simple cyclobutene derivatives that we have studied (1, 17). As the data in Table 2 show, however, the photochemistry of **1** and **2** is largely insensitive to changes in excitation wavelength. This might be expected if the various excited states accessible in the 185–214 nm region are approximately isoenergetic (21) or strongly coupled. While the *E*/*Z*-**4** ratio from photolysis of **2** does decrease significantly in the 214-nm photolysis compared to the shorter wavelength ones, it is likely that secondary diene photolysis affects the observed diene isomeric ratios to some degree at the longer wavelength. With cyclobutene absorption being fairly weak at 214 nm (while diene absorption is strong), secondary diene photolysis would probably not be discernible in the diene concentration vs. time plots.

Conclusions

In addition to undergoing electrocyclic ring opening and molecular fragmentation (formal retro $(2\pi + 2\pi)$ cycloaddition), the unsymmetrically substituted isomeric cyclobutene derivatives **1** and **2** are interconverted in low yields upon direct photolysis in solution with far-uv light. The photochemical interconversion of the two isomers provides direct evidence for the involvement of cyclopropyl carbene intermediates in the photochemistry of simple cyclobutenes in solution. These intermediates, formed by excited-state [1,2]-alkyl migration (ring contraction), might also account to some extent for the high yield of fragmentation products that is characteristic of the photochemistry of the chromophore.

Experimental

The ^{1}H nmr spectra were recorded on Varian EM390 (90 MHz) or Bruker AM500 (500 MHz) spectrometers in carbon tetrachloride (or deuteriochloroform where noted) and ^{13}C nmr spectra were recorded at 125.6 MHz on the Bruker AM500; all are reported in parts per million downfield from tetramethylsilane. Mass spectra were recorded on a VG7070 mass spectrometer interfaced with a Varian 3700 gas chromatograph, equipped with a 60 m × 0.25 mm DB-1 (Chromatograph Specialties, Inc.) fused silica capillary column. Exact masses were determined on a VGH ZABE mass spectrometer, and employed a mass of 12.000 000 for carbon. Ultraviolet absorption spectra were recorded in cyclohexane solution using a Perkin–Elmer Lambda 9 spectrometer equipped with a Model 3600 data station. Infrared spectra were recorded on a Perkin–Elmer 283 spectrometer as the neat liquids or in carbon tetrachloride or chloroform solution; spectra are reported in wavenumbers, calibrated using the 1601.9 cm^{-1} polystyrene absorption.

Analytical vpc separations were carried out using a Varian 3700 gas chromatograph (injector temperature = 80°C) equipped with a flame ionization detector, a Varian CDS101 or Hewlett–Packard HP-3393a integrator, and one of the following columns: (a) 1.0-μm SPB-1 wide-bore capillary (30 m × 0.75 mm i.d. borosilicate; Supelco, Inc.); or (b) 20% β,β-oxydipropionitrile (ODPN) on 80/100 Chromosorb PNAW (14 ft × 1/8 in. stainless steel; Supelco, Inc.). The detector response was calibrated for each photoproduct relative to an internal standard (*n*-octane or isooctane) by construction of working curves from a few standard solutions.

Semi-preparative vpc separations employed a Hewlett–Packard 5750B gas chromatograph equipped with a thermal conductivity detector (detector temperature = 160°C) and one of the following stainless steel columns: (c) 3.8% UC W892 on 80/100 Supelcoport (24 ft × 1/4 in.); or (d) 20% tris(cyanoethoxy)propane (TCEP) on Chromosorb 80/100 PNAW (12 ft × 1/4 in.).

n-Pentane (Baker Photrex), 2-methylbutane (Aldrich spectrophotometric), 2,2,4-trimethylpentane (isooctane; Baker Photrex), and *n*-octane (Polyscience, Quant grade) were used as received, as were citraconic anhydride, methyl-2-butene, 3-methyl-2-butanone; acetophenone, lead tetraacetate, and triphenylphosphine, all from Aldrich Chemical Co. Propyne was used as received from Canada Liquid Air, Inc. Methanol (Caledon HPLC) was distilled from magnesium methoxide. Mesityl oxide (Matheson, Coleman, and Bell) was bulb-to-bulb distilled and cyclooctene (Aldrich) was purified by vpc using column (c).

Compounds 1,3,4,4- (1) and 1,3,3,4-tetramethylcyclobutene (2)

Citraconic anhydride (15 g, 0.134 mol), methyl-2-butene (20.0 g, 0.286 mol), and acetophenone (5.15 g, 0.043 mol) were dissolved in ethyl acetate (500 mL) in a Pyrex immersion well equipped with a magnetic stirrer. The reaction mixture was cooled to ca. 5°C with an external ice–water bath and deoxygenated by bubbling dry nitrogen through the solution for approximately 30 min. The solution was then irradiated with a medium pressure mercury lamp (450 W, Hanovia), agitating constantly throughout the irradiation period with the magnetic stirrer as well as with a slow stream of dry nitrogen. After 11 h irradiation, nmr analysis of the crude photolysate revealed the disappearance of citraconic anhydride to be >95% complete. Evaporation of the solvent with a rotary evaporator afforded an orange-yellow oil, which was further distilled *in vacuo* (ca. 0.2 Torr; 1 Torr = 133.3 Pa) to remove acetophenone and unreacted anhydride.

A portion (12 g) of the orange, viscous oil that remained (17 g) was added to 12% aqueous hydrochloric acid (75 mL), stirred for ca. 10 h at room temperature, and then extracted with ether (3 × 50 mL). The extracts were washed with water (10 mL), saturated brine (10 mL), dried over anhydrous sodium sulfate, and then distilled to afford a light brown solid residue (11 g).

A portion (4.0 g, 0.019 mol) of the solid was added to pyridine (60 mL; distilled from barium oxide), the solution was placed in a 100-mL two-neck roundbottom flask connected to three sequential Dry Ice/acetone traps, and then saturated with oxygen. Lead tetraacetate (10.0 g, 0.023 mol) was added, a slight positive pressure of dry nitrogen was applied, and the mixture was placed in an oil bath (70°C). When gas evolution had subsided (ca. 10 min), the temperature of the oil bath was increased to 90°C and nitrogen was slowly bubbled through the reaction mixture over 24 h. The colourless liquid that had collected in the traps was dissolved in pentane (10 mL), washed with 5% aqueous hydrochloric acid (5 mL), water (5 mL), dried over anhydrous sodium sulfate, filtered, and concentrated by slow distillation. Vapor phase chromatographic analysis column (c) of the concentrated reaction mixure revealed the presence of two major products in a ca 1:1 ratio. These were collected by semipreparative vpc (column (c)); injector temperature = 120°C; detector temperature = 150°C; oven temperature = 70°C. Cyclobutenes **1** and **2** were obtained in >99% purity after further purification by vpc on column (d). Compound **1** eluted first from both vpc columns.

1,3,4,4-Tetramethylcyclobutene (1): ir (neat): 3036(s), 2951(s), 2866(s), 1641(m), 1436(s), 1361(s), 1328(m), 1284(m), 1214(m), 1140(w), 1071(w), 1027(s), 1000(s), 974(m), 871(w), 808(s); uv (cyclohexane) λ_{max}: 193 nm (ε 6700); ^{1}H nmr (500 MHz) δ: 0.93 (s, 3H), 0.96 (d, 3H, J = 7.1 Hz), 1.06 (s, 3H), 1.53 (m, 3H, J = 1.5 Hz), 2.30 (qd, 1H, J = 7.1, 0.9 Hz), 5.58 (dq, 1H, J = 0.9, 1.5 Hz); ^{13}C nmr δ: 11.36, 14.72, 20.08, 25.13, 44.47, 45.59, 128.74, 153.03; ms *m*/*e*(I): 110(55), 95(100), 93(9), 91(3), 81(13), 79(13), 77(6), 69(15), 67(85), 65(7), 55(79), 53(31), 41(69), 29(16), 27(10). *Exact Mass* calcd. for C_8H_{14}: 110.1116; found: 110.1100.

1,3,3,4-Tetramethylcyclobutene (2): ir (neat): 3026(s), 2950(s), 2910(s), 2866(s), 1626(m), 1436(s), 1363(s), 1326(m), 1282(m), 1211(m), 1121(w), 1091(m), 1051(m), 1022(m), 810(s); uv (cyclo-

Can. J. Chem. Downloaded from www.nrcresearchpress.com by 93.93.197.157 on 09/07/12
For personal use only.

hexane) λ_{max}: 192 nm (ϵ 4960); ^{1}H nmr (500 MHz) δ: 0.94 (d, 3H, J = 7.2 Hz), 0.96 (s, 3H), 1.08 (s, 3H), 1.57 (dd, 3H, J = 1.6, 1.2 Hz), 2.23 (qq, 1H, J = 7.2, 1.2 Hz), 5.66 (q, 1H, J = 1.6 Hz); ^{13}C nmr δ: 13.04, 13.89, 21.87, 27.27, 42.22, 48.70, 135.78, 146.71; ms m/e(I): 110(34), 95(100), 91(3), 81(11), 79(9), 77(7), 67(45), 65(5), 55(44), 53(17), 41(28), 39(16), 27(11). *Exact Mass* calcd for C_8H_{14}: 110.1116; found: 110.1100.

E-*2,3-dimethyl-2,4-hexadiene* (E-***3***)

Propyne (ca. 5 mL, 0.083 mol) was condensed in a Dry Ice/acetone trap and dissolved in anhydrous ether (70 mL) in a 100-mL three-neck roundbottom flask equipped with magnetic stirrer, Dry Ice condenser, addition funnel, thermometer, and gas inlet at −78°C. *n*-Butyllithium (36 mL of a 2 M hexane solution) was added dropwise with stirring under an argon atmosphere at a rate slow enough to ensure that the temperature of the reaction mixture did not rise above −50°C. The reaction mixture was stirred at −78°C for a further 1 h, and then neat 3-methyl-2-butanone (6.0 g, 0.071 mol) was added dropwise with stirring. The reaction mixture was allowed to warm to room temperature and then stirred for several hours. The mixture was then poured into a saturated aqueous ammonium chloride solution (30 mL) and extracted with ether (3 × 25 mL). The extracts were washed with water (10 mL), saturated brine (10 mL), and finally dried over anhydrous sodium sulfate. The filtered extracts were distilled to remove the solvent and then bulb-to-bulb distilled under vacuum (ca. 0.2 Torr) to yield a colourless liquid (5 g, 0.04 mol, 56%), identified as 4,5-dimethylhex-2-yn-4-ol (**7**) on the basis of its ^{1}H nmr, ir, and mass spectra, ir (neat): 3440(br s), 2970(s), 2920(s), 2880(s), 2250(w), 1460(m), 1445(m), 1365(s); ^{1}H nmr δ: 0.95 (dd, 6H), 1.35 (s, 3H), 1.80 (m, 4H); ms m/e(I) 126(1), 111(27), 108(13), 93(12), 84(31), 83(100), 82(17), 77(12), 67(15), 55(10). *Exact Mass* calcd. for $C_8H_{14}O$: 126.1045; found: 126.1038.

Alkynol **7** (2.7 g, 0.021 mol), Lindlar catalyst (0.08 g),and anhydrous ether (25 mL) were placed in a 100-mL two-neck roundbottom flask equipped with a reflux condenser and magnetic stirrer, and hydrogenated at 1 atm (101.3 kPa) for 7 h. The reaction mixture was filtered through Celite and the solvent was distilled, affording a colourless liquid that was identified at *Z*-4,5-dimethylhex-2-en-4-ol (**8**) on the basis of its ^{1}H nmr, ir, and mass spectra; ir (neat): 3480(br), 2960(s), 2932(m), 2870(m), 1610(w), 1460(m), 1368(m), 1258(m), 1089(m), 1016(m) 800(m); ^{1}H nmr (500 MHz) δ: 0.90 (d, 3H, J = 6.8 Hz), 0.91 (d, 3H, J = 6.9 Hz), 1.27 (s, 3H), 1.75 (septet, 1H, J = 6.9 Hz), 1.83 (dd, 3H, J = 7.2, 1.7 Hz), 5.37 (dq, 1H, J = 12.0, 1.7 Hz), 5.47 (dq, 1H, J = 12.0, 7.2 Hz). ms m/e(I): 128(1), 113(4), 111(15), 100(4), 87(17), 86(7), 85(100), 71(11), 69(47), 67(28), 65(4). *Exact Mass* calcd. for $C_8H_{16}O$: 128.1201; found: 128.1192.

Alkenol **8** (1.0 g, 0.0075 mmol), propionic anhydride (5 mL), and a small amount of iodine were placed in a 10 mL roundbottom flask equipped with a reflux condenser and magnetic stirrer (20). The mixture was stirred at ca. 120°C for 1 h. The flask was then cooled to room temperature, and the contents were poured into ether (ca. 15 mL). The solution was washed with saturated aqueous bicarbonate (3 × 25 mL), water (20 mL), dried over anhydrous sodium sulfate, and filtered. The solution was slowly distilled to remove the solvent, and the residue was then bulb-to-bulb distilled under vacuum (0.2 Torr) to yield a clear, colourless liquid. Vapor phase chromatographic analysis of the liquid (column (c)) showed it to contain one major product, which was separated with the same column by semi-preparative vpc (injector temperature = 120°C; detector temperature = 170°C; column temperature = 90°C). Diene *E*-**3** was obtained in >99% purity after further vpc purification (0.63 g, 70% yield from **9**); ir (neat): 3040(s), 2919(s), 2862(s), 1446(m), 1375(m), 1142(w), 1051(w), 1005(w), 956(s), 781(w); uv (cyclohexane) λ_{max}: 241 nm (ϵ = 21 250); ^{1}H nmr (500 MHz) δ: 1.69 (s, 3H), 1.74 (s, 3H), 1.77 (m, 6H) 5.47 (dq, 1H, J = 15.3, 6.8 Hz), 6.38 (d, 1H, J = 15.3 Hz); ms m/e(I): 110(58), 95(100), 81(13), 77(10), 67(49), 55(34), 53(16), 41(37), 39(28), 27(14). *Exact Mass* calcd. for C_8H_{14}: 110.1116; found: 110.1087.

Z-*2,3-Dimethyl-2,4-hexadiene* (Z-***3***) was synthesized by photolysis of a deoxygenated pentane (30 mL) solution of *E*-**3** (0.4 g, 0.0036 mol) in a Rayonet reactor fitted with 10 254-nm lamps. Irradiation of the solution for 5 h yielded a mixture of *E*- and *Z*-**3** along with one other minor product. The pentane was removed by slow distillation, and the photolysate was bulb-to-bulb distilled under vacuum (0.2 Torr). Diene *Z*-**3** was separated cleanly from the other components of the mixture by semi-preparative vpc (column (c)), and finally obtained in >99% purity after further vpc purification with the same column; ir (neat): 3004(s), 2920(s), 2863(s), 1444(m), 1405(w), 1372(m), 1156(w), 1124(w), 930(m), 735(m), 713(m); uv (cyclohexane) λ_{max}: 223 nm (ϵ 3500); ^{1}H nmr (500 MHz) δ: 1.52 (dd, 3H, J = 6.9, 11.8 Hz), 1.58 (s, 3H), 1.67 (s, 3H), 1.69 (s, 3H), 5.35 (dq, 1H, J = 11.1, 6.9 Hz), 5.80 (br d, 1H, J = 11.1 Hz); ms m/e(I): 110(75), 95(100), 81(14), 77(11), 67(55), 55(38), 53(20), 41(40), 39(28), 27(16). *Exact Mass* calcd. for C_8H_{14}: 110.1116; found: 110.1090.

E- *and* Z-*2,3-dimethyl-2,4-hexadiene* (***4***)

Sodium hydride (0.8 g, 0.033 mol) and dimethylsulfoxide (10 mL) were placed in a 100-mL, two-neck roundbottom flask equipped with a reflux condenser, magnetic stirrer, gas inlet, and addition funnel. The mixture was heated under a nitrogen atmosphere at 85°C until gas evolution ceased (ca. 45 min) and then cooled to room temperature. Ethyltriphenylphosphonium bromide (9.0 g, 0.023 mol) was dissolved in warm DMSO (30 mL) and added dropwise over 20 min. The orange-coloured mixture was stirred for a further 1 h at room temperature and neat mesityl oxide (2.3 g, 0.024 mol) was then added dropwise over 20 min. The resulting mixture was stirred for 15 h at room temperature, filtered through Celite, poured into water (50 mL), and extracted with pentane (5 × 25 mL). The extracts were washed with water (25 mL), saturated brine (15 mL), dried over anhydrous sodium sulfate, and filtered. Slow distillation to remove the solvent followed by bulb-to-bulb distillation of the residue at 0.2 Torr afforded a mixture of *E*- and *Z*-**4** as a colourless liquid. Dienes *E*- and *Z*-**4** (0.47 g, 0.0043 mol, 18%) were isolated as a mixture by semi-preparative vpc on column (c). Separation and further purification under the same conditions afforded the isomers in >99% purity.

E-*2,4-Dimethyl-2,4-hexadiene* (E-***4***): ir (neat): 3020(sh), 2967(s), 2922(s), 2862(s), 1656(w), 1445(s), 1374(m), 1182(w), 1052(w), 857(s), 772(w), 511(w); uv (cyclohexane) λ_{max}: 231 nm (ϵ 10 700); ^{1}H nmr (500 MHz, $CDCl_3$) δ: 1.65 (d, 3H, J = 6.9 Hz), 1.69 (s, 3H), 1.73 (s, 3H), 1.74 (s, 3H), 5.21 (q, 1H, J = 6.9 Hz), 5.61 (br s, 1H); ms m/e(I): 110(36), 95(100), 81(17), 77(13), 67(64), 55(59), 53(32), 41(53), 39(50), 27(34). *Exact Mass* calcd. for C_8H_{14}: 110.1116; found: 110.1088.

Z-*2,4-Dimethyl-2,4-hexadiene* (Z-***4***): ir (neat): 3020(sh), 2966(s), 2922(s), 2863(s), 2661(w), 1625(w), 1446(s), 1385(m), 1206(w), 1185(w), 1035(m), 824(m), 783(m), 554(w); uv (cyclohexane) λ_{max}: 217 nm (ϵ 6800); ^{1}H nmr (500 MHz, $CDCl_3$) δ: 1.48 (d, 3H, J = 6.8 Hz), 1.56 (s, 3H), 1.70 (br s, 3H), 1.76 (s, 3H), 5.26 (q,1H, J = 6.8 Hz), 5.54 (br s, 1H); ms m/e(I): 110(57), 95(100), 81(20), 77(21), 67(61), 55(43), 53(23), 41(35), 39(32), 27(19). *Exact Mass* calcd. for C_8H_{14}: 110.1116; found: 110.1087.

Photochemical experiments employed a 10-W Osram HNS 10W/U OZ low pressure mercury lamp in conjunction with a 25 × 3 mm LiF disc (Harshaw VUV) that had been irradiated with ca. 1.7 Mrad of γ-radiation from a ^{60}Co source (18), a 16-W Philips 93106E zinc resonance lamp, or the pulses (193 nm, ca. 10 ns, 20–100 mJ, 1-Hz repetition rate) from a Lumonics TE-861M excimer laser filled with an argon/fluorine/helium mixture. The low pressure mercury and Zn resonance lamps were surrounded by a metal case that incorporated a 1-in. port to contain the sample cell and filter (in the case of the Hg lamp). During 185-nm irradiations, the transmittance spectrum of the filter was monitored quite closely, as the transmittance at 254 nm tends to increase slowly with uv exposure (1, 18). A freshly prepared filter typically had an optical density of ca. 0.5 at 185-nm and ca. 5 at 254 nm. The lamps were given a 20-min warm-up period before each experiment and cooled with a stream of dry nitrogen.

Quantitative photolyses were carried out at ambient temperature (ca. 23°C) in 10 × 25 mm cylindrical Suprasil uv cells (Hellma). Preparative scale photolyses were carried out with the laser, in rectangular cells constructed from 10 × 20 mm rectangular Suprasil tubing (Vitro

Dynamics). In all cases, the sample was agitated during irradiation with a small magnetic stirrer. Solutions were deoxygenated before irradiation by bubbling dry nitrogen or argon through the cooled (to ca. 0°C) solutions for 5–15 min.

The products obtained from photolysis of **1** and **2** were identified by coinjecting photolysates carried to ca. 5% conversion with authentic samples on at least two vpc columns, and by comparison of the ^{1}H nmr spectra of isolated (from preparative runs carried to 30–40% conversion, by vpc with column (c), after concentration and bulb-to-bulb distillation) samples with those of the authentic samples.

Quantum yield determinations for 185-nm photolyses were carried out by cyclooctene actinometry (24), using approximately matched cells and alternately irradiating the substrate and actinometer solutions for identical, short periods of time.

Quantitative photolyses were monitored between 0.2 and 3% conversion, with aliquots being withdrawn at suitable time intervals for vpc analysis on columns (b) (for methyl-2-butene) and (a) (for all other products). Relative product yields were determined from the slopes of concentration versus time plots constructed for all components of the mixture relative to an internal standard. Relative detector responses were calibrated for all products using authentic samples. The concentration vs. time plots were linear in each case. Quantum yields were determined in similar fashion after calculating the light flux from the concentration vs. time plot for the formation of *trans*-cyclooctene from the *cis* isomer, whose photolysis was conducted concurrently with the substrate of interest as described above. A value of 0.32 was employed for the actinometric quantum yield (24).

The photostationary state for the direct photoisomerization of *E*- and *Z*-**3** at 254 nm was determined by irradiating deoxygenated, 0.003 M solutions of the two diene geometric isomers in 7 mm quartz tubes in a Rayonet reactor. Irradiation was continued, with periodic analysis by vpc (column (a)), until the photostationary state was reached. A similar procedure was employed for determination of the photostationary state for photoisomerization of *E*- and *Z*-**4**.

Acknowledgements

We thank the McMaster University Nuclear Reactor Facility for providing us with the LiF filters, Dr. D. Hughes (McMaster University) for acquiring the high field ^{1}H and ^{13}C nmr spectra, and the McMaster University Regional Mass Spectrometry Facility for the mass spectra and exact mass determinations. We acknowledge the financial support of this work by the Natural Sciences and Engineering Research Council of Canada.

1. K. B. Clark and W. J. Leigh. J. Am. Chem. Soc. **109**, 6086 (1987).
2. G. Quinkert, M. Finke, J. Palmowski, and W.-W. Wiersdorff. *Mol. Photochem*, **1**, 433 (1969).
3. (*a*) N. C. Yang, R. V. Carr, E. Li, J. K. McVey, and S. A. Rice. J. Am. Chem. Soc. **96**, 2297 (1974); (*b*) R. V. Carr, B. Kim, J. K. McVey, N. C. Yang, W. Gerhartz, and J. Michl. Chem. Phys Lett. **39**, 57 (1976).
4. (*a*) R. B. Woodward and R. Hoffmann. J. Am. Chem. Soc. **87**, 395 (1965); **87**, 2046 (1965); **87**, 2511 (1965); (*b*) The conservation of orbital symmetry. Verlag Chemie, Weinheim, W. Germany. 1970; (*c*) H. C. Longuet-Higgins and G. W. Abrahamson. J. Am. Chem. Soc. **87**, 2045 (1965).
5. C. D. DeBoer and R. H. Schlessinger. J. Am. Chem. Soc. **90**, 803 (1968).
6. G. Kaupp and M. Stark. Chem. Ber. **111**, 3608 (1978).
7. M. Sakuragi and M.Hasegawa. Chem. Lett. 29 (1974).
8. J. Saltiel and L.-S. Ng Lim. J. Am. Chem. Soc. **91**, 5405 (1969).
9. Y. Inoue, M. Sakae, and T.Hakushi. Chem. Lett. 1495 (1983).
10. W. Adam, T. Oppenlander, and G. Zang. J. Am. Chem. Soc. **107**, 3921 (1985).
11. (*a*) L. Friedman and H. Shechter. J. Am. Chem. Soc. **82**, 1002 (1960); (*b*) J. A. Smith, H. Shechter, J. Bayless, and L.Friedman. J. Am. Chem. Soc. **87**, 658 (1965); (*c*) W. Kirmse and K.-H. Pook. Chem. Ber. **98**, 4022 (1965); (*d*) W. Kirmse and G. Wachtershauser. Tetrahedron, **22**, 63 (1966); (*e*) M. Jones, Jr. and R. A. Moss. Carbenes. Vol. 1. Wiley, New York. 1973; (*f*) S. S. Olin and R. M. Venable. J. Chem. Soc. Chem. Commun. 104 (1974); 273 (1974); (*g*) J. A. Berson, W. Bauer, and M. M. Campbell. J. Am. Chem. Soc. **92**, 7515 (1970); (*h*) A. Guarino and A. P. Wolf. Tetrahedron Lett. 655 (1969); (*i*) R. R. Gallucci and M. Jones, Jr. J. Am. Chem. Soc. **98**, 7704 (1976).
12. P. J. Kropp. Org. Photochem. **4**, 1 (1979); and references cited therein.
13. (*a*) W. J. Leigh and R.Srinivasan. Acc. Chem. Res. **20**, 107 (1987); (*b*) W. Adam and T. Oppenlander. Angew. Chem. Int. Ed. Engl. **25**, 661 (1986); (*c*) M. G. Steinmetz. Org. Photochem. **8**, 1 (1987).
14. (*a*) W. Kirmse. Carbene chemistry. Academic Press, New York. 1971. pp. 473–475, and references cited therein; (*b*) U. H. Brinker and G.Schenker. J. Chem. Soc. Chem. Commun. 679 (1982).
15. (*a*) W.Hartmann, L. Schrader, and D.Wendisch. Chem. Ber. **106**, 1076 (1973); (*b*) W. H. Pirkle and L. H. McKendry. J. Am. Chem. Soc. **91**, 1179 (1969); (*c*) S. Masamune and K. Fukumoto. Tetrahedron Lett. 4647 (1965); (*d*) M. Barfield, R. J. Spear, and S. Sternhell. Chem. Rev. **76**, 593 (1976).
16. J. B. Stothers. Carbon-13 NMR spectroscopy. Academic Press, New York. 1972.
17. K. B. Clark. PhD thesis, McMaster University (1988).
18. (*a*) J. L. Weeks, S. Gordon, and G. M. A. C. Meaburn. Nature, **191**, 1186 (1961); (*b*) R. A. Holroyd and T. E. Pierce. J. Phys. Chem. **68**, 1392 (1964).
19. P. G. Gassman, T. J. Atkins, and F. J. Williams. J. Am. Chem. Soc. **93**, 1812 (1971).
20. W. Reeve and D. M. Reichel. J. Org. Chem. **37**, 68 (1972).
21. R. Srinivasan, T. H. Baum, K. H. Brown, J. A. Ors, L. S. White, A. R. Rossi, and G. A. Epling. J. Chem. Soc. Chem. Commun. 973 (1981).
22. N. H. Werstiuk and G. Timmins. Can. J. Chem. Accepted for publication.
23. M. E. Squillacote, T. C. Semple, and P. W. Mui. J. Am. Chem. Soc. **107**, 6842 (1985).
24. H.-P. Schuchmann, C. von Sonntag, and R. Srinivasan. J. Photochem. **15**, 159 (1981).
25. R. Srinivasan and K. H. Brown. J. Am. Chem. Soc. **100**, 4602 (1978).
26. T. R. Fields and P. J. Kropp. J. Am. Chem. Soc. **96**, 7559 (1974).
27. (*a*) W. J. Leigh and R.Srinivasan. J. Am. Chem. Soc. **104**, 4424 (1982); (*b*) Y. Inoue, T. Mukai, and T.Hakushi. Chem. Lett. 1725 (1984).
28. M. B. Robin. Higher excited states of polyatomic molecules. Vol. II. Academic Press, New York. 1975. Chap. 4.
29. F. Hirayama and S. Lipsky. J. Chem. Phys. **62**, 576 (1975).
30. Y. Inoue, T. Mukai, and T. Hakushi. Chem. Lett. 1665 (1983).
31. (*a*) D. Grimbert, G. Segal, and A. Devaquet. J. Am. Chem. Soc. **97**, 6629 (1975); (*b*) W. Th. A. M. Van der Lugt and L. J. Oosterhoff. J. Am. Chem. Soc. **91**, 6042 (1969); (*c*) D. Morihashi and O. Kikuchi. Theor. Chim. Acta, **67**, 293 (1985).

Can. J. Chem. Downloaded from www.nrcresearchpress.com by 93.93.197.157 on 09/07/12
For personal use only.

Surface photochemistry: Semiconductor mediated reactions of some saturated strained hydrocarbons[1]

N. Colin Baird, Anthony M. Draper, and Paul de Mayo

Photochemistry Unit, Department of Chemistry, The University of Western Ontario, London, Ont., Canada N6A 5B7

Received October 23, 1987

N. Colin Baird, Anthony M. Draper, and Paul de Mayo. Can. J. Chem. **66**, 1579 (1988).

Quadricyclane (**1**) and 1,8-bishomocubane (**2**) have been found to undergo valence isomerization to norbornadiene and tricyclo[4.2.2.$0^{2,5}$]deca-3,7-diene, respectively, on illuminated CdS and ZnO. An electron transfer mechanism is proposed. Quantum yield, solvent effects, the role of oxygen, and the quenching of the reaction were investigated, and were consistent with this interpretation. The thermal reaction of **1** on CdS was also suggested to be an electron transfer process involving, in this case, defects or trapped holes on the surface of the semiconductor. An examination of a series of strained hydrocarbons structurally related to **1** (tetracyclo[3.3.0.$0^{2,8}$.$0^{4,6}$]octane **3**, pentacyclo[4.3.0.$0^{2,4}$.$0^{3,8}$.$0^{5,7}$]nonane **4** and pentacyclo[4.4.0.$0^{2,4}$.$0^{3,8}$.$0^{5,7}$]decane **5**) resulted, largely, in a demonstration of the resistance of their respective radical cations to rearrangement prior to back electron transfer. Calculations by MNDO, in combination with a modified version of MM2, were used to explore the differences in the reactivity of the radical cations of **1**, **3**, **4**, **5**, and an interpretation is presented.

N. Colin Baird, Anthony M. Draper et Paul de Mayo. Can. J. Chem. **66**, 1579 (1988).

On a observé que, placés sur du CdS et du ZnO illuminés, le quadricyclane (**1**) et le bishomo-1,8 cubane (**2**) subissent des isomérisations de valence conduisant respectivement au norbornadiène et au tricyclo[4.2.2.$0^{2,5}$]décadiène-3,7. On propose un mécanisme par transfert électronique. On a examiné les rendements quantiques, les effets de solvants, le rôle de l'oxygène et le piégeage des réactions et les résultats sont en accord avec cette interprétation. On a suggéré que la réaction thermique du composé **1** déposé sur du CdS se produit aussi par un processus de transfert électronique impliquant, dans ce cas, les défauts de la surface du semiconducteur. Lorsqu'on a examiné les résultats obtenus avec une série d'hydrocarbures tendus dont la structure est reliée à celle du composé **1**, comme le tétracyclo[3.3.0.$0^{2,8}$.$0^{4,6}$]octane **3**, le pentacyclo[4.3.0.$0^{2,4}$.$0^{3,8}$.$0^{5,7}$]nonane **4** et le pentacyclo[4.4.0.$0^{2,4}$.$0^{3,8}$.$0^{5,7}$]nonane **5**, on a mis en évidence le fait que leurs radicaux cations respectifs résistent à une transposition avant le transfert électronique en retour. On a utilisé des calculs effectués par la méthode des MNDO en conjonction avec une version modifiée de MM2 pour examiner les différences de réactivité des radicaux cations des composés **1**, **3**, **4**, et **5** et on présente une interprétation.

[Traduit par la revue]

Introduction

Photocatalysis on powdered semiconductors has been, in recent years, an area of intensive study. Much of the interest has been concentrated on the splitting of water with the object of developing a solar energy storage system. Of late, semiconductors have also been used as photocatalysts for electron transfer in organic reactions, and there have been several reports of semiconductor photoinduced organic electron transfer reactions involving both oxidative (e.g., addition of oxygen (1)) and non-oxidative (e.g., dimerization (2–4) and isomerization (5–9)) processes. We now wish to report our findings for the semiconductor mediated reactions of a series of strained hydrocarbons: tetracyclo[3.2.0.$0^{2,7}$.$0^{4,6}$]heptane (quadricyclane) **1**, pentacyclo[4.4.0.$0^{2,5}$.$0^{3,8}$.$0^{5,7}$]decane (1,8-bishomocubane) **2**, tetracyclo[3.3.0.$0^{2,8}$.$0^{4,6}$]octane **3**, pentacyclo[4.3.0.$0^{2,4}$.$0^{3,8}$.$0^{5,7}$]nonane (norsnoutane) **4**, and pentacyclo[4.3.0.$0^{2,4}$.$0^{3,8}$.$0^{5,7}$]decane (snoutane) **5**.

Initial interest in electron transfer reactions of strained saturated hydrocarbons was sparked by the finding that many of these compounds have exceedingly low oxidation potentials (Table 1) (10). This led to several studies of the radical cation rearrangements of such compounds. For example, the valence isomerization of $\mathbf{1}^+$ to the radical cation of norbornadiene **6** has been studied under many conditions. The electron transfer may be initiated by organic sensitizers (11) and transition metal complexes (12) and also electrochemically (13). Uncertainty as to whether or not the radical cations of **1** and **6** were distinct entities (14) was settled in an elegant study by Roth and Schilling (15). They were able to show that the radical cations are distinct species and that $\mathbf{1}^+$ has a lifetime of at least a few nanoseconds before irreversible rearrangement to $\mathbf{6}^+$. Later, these conclusions were supported by extensive theoretical calculations (16, 17).

The electron transfer induced rearrangement of **2** had never been previously reported. However, there was strong presumptive evidence suggesting that $\mathbf{2}^+$ would rearrange to $\mathbf{7}^+$. On Rh(I) and Pd(II) complexes **2** was shown to yield **7** as the major product (18). Furthermore, substituted derivatives of **2** were shown to rearrange to the corresponding tricyclo[4.2.2.$0^{2,5}$]deca-3,7-diene by an electron transfer mechanism (5, 19). Roth and Schilling (20) have applied the CIDNP technique to gain insight into the structures of the $\mathbf{2}^+$ deriva-

Table 1. Oxidation potentials

Compound	$E^{ox}_{\frac{1}{2}}$ V vs. SCE
1	0.91
2	1.67[a]
3	~1.6[b]
4	1.54[a]
5	1.62[a]
1,2,4,5-Tetramethoxybenzene	0.81[c]
1,2,4-Trimethoxybenzene	1.34[d]
1,3,5-Trimethoxybenzene	1.35[d]

[a]0.1 M $LiClO_4$ in CH_3CN (10).
[b]Estimated from adiabatic IP (21).
[c]Reference 48.
[d]Reference 49.

[1]Publication No. 397 from the Photochemistry Unit, The University of Western Ontario.

Can. J. Chem. Downloaded from www.nrcresearchpress.com by 93.93.197.157 on 09/07/12
For personal use only.

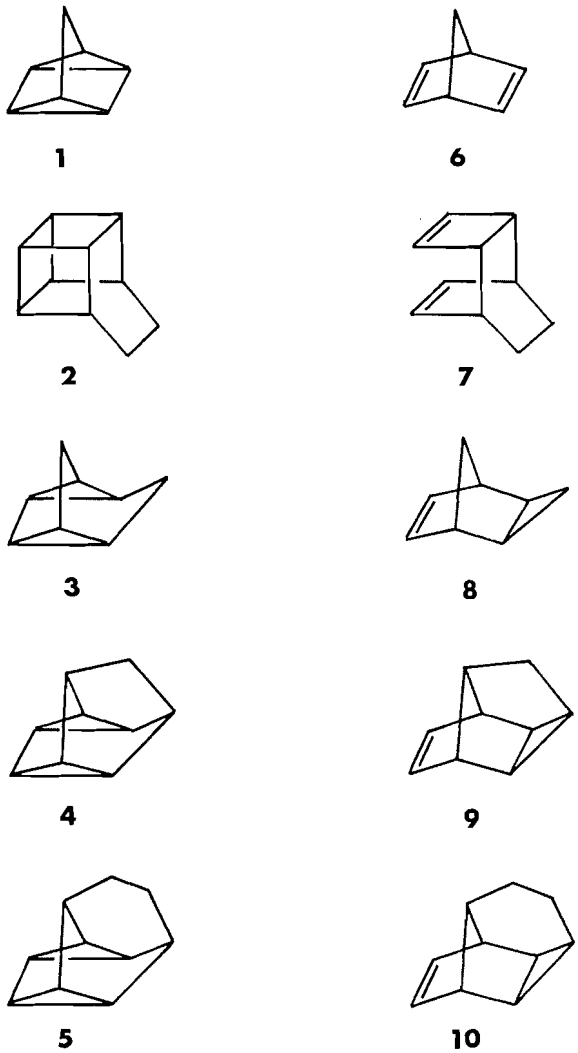

tives. They found that the rearrangement is, indeed, fast; however, they did observe an emission for one proton signal suggesting that this derivative of **7** has a discrete energy minimum.

The possible radical cation reactions of **3–5** had not yet been reported. Compounds **3–5** were known to quench the fluorescence of organic redox sensitizers (10, 12) through what is believed to be electron transfer to the fluorophore. If $\mathbf{3}^+$–$\mathbf{5}^+$ were to undergo an analogous rearrangement to that of $\mathbf{1}^+$, then the products would be **8–10**.

The semiconductors used in this work were ZnO and CdS, which have band gaps of 3.2 eV and 2.4 eV respectively. The positions of the valence bands, determined in acetonitrile (22), are 1.55 V for CdS and 2.4 V for ZnO. These values have been taken as being closest to those expected in the solvents used in experiments reported here. Thus, compounds **1–5**, having oxidation potentials less positive than the potential of the valence band of ZnO, fulfil the electrochemical requirements for electron transfer to illuminated ZnO. In the case of CdS, compound **1** has a suitable oxidation potential for electron donation to illuminated CdS while those of **2–5** are approximately isoenergetic with the photoinduced holes.[2]

By the virtue of these precedents, **1–5** seemed to be good candidates for electron transfer studies at illuminated semiconductors. Unanticipated results for the reactivity of $\mathbf{3}^+$–$\mathbf{5}^+$ led us to investigate these reactions further by calculations using MM2 and MNDO. A brief report of the conversion of **1** → **2** has been made (23).

Experimental

All solvents used for the semiconductor reactions were spec. grade from either Fisher, BDH, or Baker and were used as received. For the reaction of **1** on CdS, Aldrich Gold label 99.999% was used unless otherwise indicated. In all other reactions with CdS, "Fisher" CdS was used. The following saturated hydrocarbons were used as internal standards for gc analysis: *n*-heptane (Anachemia spectrograde C_7) for the reaction of **8**; cyclooctane (Aldrich, 99+% Gold Label, C_8) for the reactions of **1** and **2**; undecane (Aldrich, 99%, C_{11}) for the reactions of **9** and **10**. 1,2,4- and 1,3,5-trimethoxybenzene (Aldrich) were used as received: solutions were >99% pure as measured by analytical gc. 1,2,4,5-Tetramethoxybenzene was prepared as described by Bennington *et al.* (24) and was stored in the dark to prevent decomposition. Before a series of quenching experiments the 1,2,4,5-tetramethoxybenzene was sublimed. The material used in quenching experiments showed only one peak on analytical gc.

Procedure for irradiations

Two sizes of Pyrex vessels were used for semiconductor reactions: a 20 mm diameter base for 5-mL reaction volumes and a 11 mm diameter base for 1-mL reaction volumes. The base portion of the vessel was constructed from a test tube and was connected to either a B-10 joint (for reactions open to the atmosphere) or a 9-mm Fisher–Porter joint (for degassing).

All reaction vessels and magnetic stirbars were cleaned by sonication in an aqueous solution of Fisher FL-70 low foaming detergent. After sonication, the vessels were thoroughly rinsed with water followed by 1 × 10% NH_4OH; 5 × distilled H_2O; 2 × acetone; 2 × spec. grade CH_2Cl_2. The vessels were dried at 110°C overnight before use.

Semiconductor powders were weighed out and placed in a dry reaction vessel with a magnetic stirbar. The amount of semiconductor powder used was 10.0 ± 0.2 mg/mL of stock solution except in the reaction of **1** on CdS, where 10 mg/5 mL of stock solution was used: this was to maximize the difference between the thermal and light induced reactions. Stock solutions were prepared with known quantities of starting materials and internal standards. Reaction mixtures were sonicated for 4–5 min prior to, and stirred during, irradiation.

Degassed samples were evacuated prior to sonication to a residual pressure of $\leq 2 \times 10^{-5}$ Torr (1 Torr = 133.3 Pa) (three or more freeze/thaw cycles). Thermal reactions were wrapped in aluminium foil after sonication and stirred in a Braun Thermomix-1420 water bath at 40°C.

All irradiations, except for quantum yield determinations, were performed using a 1000-W Xenon lamp run at 880 W in either a PRA 301 or a PTI 02-A5001 lamp housing. A water-cooled water IR filter was used to remove infrared radiation. For all reactions an air-cooled Corning 0-52 filter was used to remove light ≤ 340 nm. The reaction vessel was held in the same position by a bracket to ensure reproducibility. The samples were cooled by compressed air and constantly stirred. The lamp output was periodically checked with a Scientech 364 power energy meter. However, for any given series of reactions a standard reaction was considered a more meaningful measure of the fluctuations in the light source. Irradiations of stock solution in the absence of semiconductor were performed to ensure that the semiconductor was required for reaction.

Reaction mixtures were open to the atmosphere via a condenser and were protected from atmospheric moisture by an anhydrous $CaSO_4$ drying tube. Unless specifically stated all samples were so treated except for the reaction of **1** on CdS where, contrariwise, all samples were degassed unless stated.

For the quantum yield determinations a PRA M303 150 W lamp was used with combined Corning 0-52 and 7-60 filters. This combination gave a window between 340 and 400 nm and transmitted light of energy

[2]The exact potentials of the holes or compounds are not known in the solvents used here. Furthermore, slightly endothermic electron transfers are known in homogeneous solution (22) and on CdS (7).

Can. J. Chem. Downloaded from www.nrcresearchpress.com by 93.93.197.157 on 09/07/12
For personal use only.

Can. J. Chem. Downloaded from www.nrcresearchpress.com by 93.93.197.157 on 09/07/12
For personal use only.

greater than the band gaps of both ZnO and CdS. Potassium ferrioxalate chemical actinometry was used to calibrate the light source. The reaction vessels were held in place using an aluminum block with a 1.0 × 1.5 cm window. All the light falling on the window was assumed to be adsorbed by the semiconductor.

All quantitative analysis of the semiconductor reactions was done on a Varian 3700 analytical gas chromatogram connected to a Hewlett Packard 3390A integrator. The semiconductor was removed by filtration through a short 1-cm Celite filter packed in a Pasteur pipette. Product analysis was based on the average of a minimum of two injections for each determination. For all reported yields the conservation of mass was > 95% relative to the internal standard.

Preparation of hydrocarbons

Quadricyclane (tetracyclo[3.2.0.0^{2,7}.0^{4,6}]heptane) 1: Quadricyclane was prepared from freshly distilled **6** (Aldrich) by triplet sensitization by irradiated acetophenone (25).**1** was filtered through a short (2 cm) silica column prior to use and samples of **1** used in reactions were typically 98.5% **1** and 1.1% **6**.

1,8-Bishomocubane (pentacyclo[4.4.0.0^{2,5}.0^{3,8}.0^{4,7}]decane) 2: 1,8-Bishomocubane was prepared as previously described (26), and before use was sublimed very slowly onto a Dry Ice/acetone cold finger (100 mg, 1 h, 30–40°C at 1 Torr). Samples used in semiconductor reactions were 98% **2** and 1.5% **7**.

Snoutane (pentacyclo[4.4.0.0^{2,5}.0^{3,8}.0^{5,7}]decane 5: Snoutane was prepared by intramolecular rearrangement of **2** on Ag^+ (27). The sample purity was only 90%; however, this was sufficient to test if reaction occurred on illuminated semiconductors or with organic redox sensitizers.

Tetracyclo[4.3.0.0^{2,4}.0^{3,7}]non-8-ene 9: The preparation of **9** was that of Freeman and Balls (28). The purified **9** (94%) was used for the preparation of **4**.

Norsnoutane (pentacyclo[4.3.0.0^{2,4}.0^{3,8}.0^{5,7}]nonane) 4: Norsnoutane was prepared by direct irradiation of **9** (28). The purity of **4** used in semiconductor experiments was 95% **4** and 2% **9**.

exo-*Tricyclo[3.2.1.0^{2,4}]oct-6-ene 8*: A Simmonds–Smith reaction on norbornadiene gave **8** (29). The ZnCu couple was prepared by Le Goff's method (30).

Tetracyclo[3.3.0.0^{2,8}.0^{4,6}]octane 3: Intramolecular rearrangement of **8** on $[Rh(CO)_2Cl_2]_2$ gave **3** (31). The purity of **3** used in semiconductor irradiations was 97%.

Calculations

The molecular mechanics calculations were performed using Allinger's MM2 program (32). The program was modified to MM2' IVANOV by introducing the new parameters for strained hydrocarbons published by Ōsawa and co-workers and by Ivanov (33).

The semiempirical calculations were performed using Dewar and Thiel's MNDO method and program (34). The MNDO method has been successfully used by Bauld *et al.* to study the reactivity of radical cations (45). Initial geometries of the neutral compounds were those of the MM2'IVANOV minimum energy conformation. The only deviation from standard procedures occurred during the geometry optimizations of $\mathbf{3}^+$ and $\mathbf{5}^+$. In this case the program had not converged after 6000 CPU seconds on a Cybernex computer. The heat of formation had not changed by more than 0.5 kcal mol^{-1} after the first 1000 s because, we suspected, the calculated minimum was shallow. The conditions for convergence were thus relaxed in order to obtain a detailed orbital description of the radical cations of **3** and **4**.

The routine used to calculate the reaction coordinates was the same for all three pathways. The reaction coordinates in Figs. 5–7 are graphed with respect to the C2—C4 distance. The left-hand side of Fig. 5 (for example) starts with **1** having a C2—C4 bond of 1.54 Å and a ΔH_f of 83 kcal mol^{-1} calculated using the MM2 minimized geometry. Removal of an electron from **1** generates $\mathbf{1}^+$ with a ΔH_f of 298 kcal mol^{-1}. The dashed line represents a vertical transition, i.e., the radical cation here has the same geometry as the neutral parent compound. The same type of vertical ionization of **6** is plotted at C2—C4 separation of 2.42 Å, which is the optimum distance in **6**. The carbon skeleton of the vertically generated radical cation was then allowed to relax to an energy minimum. The whole carbon skeleton was not optimized, merely those bond distances, bond angles, and dihedral angles that changed significantly in the rearrangement. For example, in the isomerization of **1** to **6** the C2—C4 distance and the ∡C2C3C4 change from 1.54 Å and 60.1° in **1** to 2.42 Å and 105.5° in **6**, respectively. Since these changes are significant, the corresponding parameters were optimized. On the other hand, the changes in the C6—C7 distance and in ∡C1C2C5 were only 0.03 Å and 1.9°, respectively; hence these parameters were not optimized. At this stage in the calculation the geometric parameters describing the hydrogens were taken to be those for the neutral parent compounds.

To follow the remainder of the reaction the C2C3C4 angle was frozen at appropriate points to produce the C2—C4 distances that appear in the figures. The transition state was approached from both sides. The points near the transition state were then recalculated allowing the geometric variables associated with the hydrogens to be optimized. This optimization is represented on the figures by the vertical drop in energy from the squares near the transition state to the blank dots.

Results

The conversion of **1** to **6** and **2** to **7** on CdS and ZnO is summarized in Tables 2 and 3 respectively.[3] Both systems were not reactive in the absence of semiconductor. However, **1** (but not **2**) on CdS gave a "dark", thermal, reaction. Table 2 shows the results with two CdS samples but, in fact, all seven CdS samples examined gave some dark reaction (see below). The products (**6** and **7**) were identified by comparison of their ^{1}Hmr spectra with those of authentic samples. The mass balance for the reactions was greater than 95% (as determined by gc analysis with an internal standard), i.e., in 1 h no oxidation products could be detected in the presence of air. No new peaks were detectable by glc. In the absence of oxygen both reactions on ZnO showed a decreased yield. However, on CdS, degassed samples of **1** showed an increased yield[3] and those of **2** showed no change in yield. In addition, **2** showed rapid conversion to **7** in homogeneous solution with 9,10-dicyanoanthracene as an electron transfer sensitizer.

The results of quantum yield determinations for both reactions are presented in Table 4, but that for the rearrangement of **1** on CdS was not determined since it was impossible to separate the thermal and photochemical contributions to reaction. The errors associated with the quantum yields in Table 4 were quite large owing to the small values obtained for Φ and the length of time required to obtain reasonable conversion, and which permitted dark reaction.

The solvent effect on the isomerization of **1** and on ZnO and CdS is given in Table 5. Relative yields are given, compared to that for the reaction in CH_2Cl_2. The reaction on ZnO proceeds more efficiently in CH_2Cl_2 and somewhat less efficiently in CH_2CN. However, in solvents more polar than CH_3CN or less polar than CH_2Cl_2 no reaction is observed. On CdS there is virtually no reaction in CH_3CN whereas the reaction is quite efficient in hydrocarbon solvents that are less polar than CH_2Cl_2.

The results of an examination of the thermal (dark) reaction of **1** with several different samples of CdS are given in Table 6, which includes several properties of each sample: purity, as stated by the supplier; surface area; and structure. There appears to be no correlation between surface area and reactivity except possibly within the same structure type. The most efficient

[3]As noted, this transformation was reported in a preliminary form (23). Subsequently and independently, Ikezawa and Kutal confirmed our observations (35).

TABLE 2. The conversion of quadricyclane to norbornadiene on CdS and ZnO

Semiconductor	[1] (mol L^{-1})	Time (h)	Thermal (% reaction) Aerated	Thermal (% reaction) Degassed	Photochemical (% reaction) Aerated	Photochemical (% reaction) Degassed
ZnO[a]	0.06	1	< 0.1		20	8.5
CdS[b]	0.10	2	1	2.2	2.6	13
CdS[c]	0.25	1	21		68	

[a]ZnO Fisher ≥ 99% ZnO.
[b]CdS Aldrich Gold label 99.999%.
[c]CdS Aldrich Gold label 99.99%.

TABLE 3. The conversion of bishomocubane to **7** on CdS and ZnO

Semiconductor	[2] (mol L^{-1})	Time (h)	Thermal (% reaction) Aerated	Thermal (% reaction) Degassed	Photochemical (% reaction) Aerated	Photochemical (% reaction) Degassed
CdS[a]	0.03	3	0	0	13	14
ZnO[b]	0.03	3	0		9	3.5
DCA[c]	0.03	4		0		95

[a]CdS Fisher ≥ 99% CdS.
[b]ZnO Fisher ≥ 99% ZnO.
[c]9,10-Dicyanoanthracene, 2 mg/5 mL CH_2Cl_2 irradiated with 450-W med. pressure Hg arc.

TABLE 4. Quantum yields for the reactions of **1** and **2**

Compound	Semiconductor	Φ
1	ZnO[a]	$1.5 \times 10^{-3} \pm 20\%$
2	ZnO[a]	$1.3 \times 10^{-3} \pm 20\%$
2	CdS[b]	$10^{-4} \pm 50\%$

[a]ZnO Fisher.
[b]CdS Fisher.

TABLE 5. Solvent effects on **1** → **6** isomerization

Solvent	ZnO[a]	CdS[b]
Dichloromethane	1	1
Carbon tetrachloride	0	< 0.07
Acetonitrile	0.75	< 0.07
Cyclohexane	0	0.73
Pentane	—	1.5
Methanol	0	—

[a]Aerated, ZnO Fisher.
[b]Degassed, CdS Aldrich > 99.999%.

TABLE 6. The relative efficiency of the thermal reaction of **1** on different CdS samples

CdS sample (lot number)	% Purity claimed	Surface area[a] ($m^2 g^{-1}$)	Structure[b]	Yield (%)
Fisher 792913	99	12	β	91.4
Aldrich 053087	98.8	7	β	64.4
Strem Ultrapure 16693-5	99.99	7.1	α + β	63.8
Strem Ultrapure 16027-51	99.99	44	Polytype	47.6
Strem NATL	99	32.4	Polytype	41.1
Fluka puriss 249326-684	99.999	1.4	α	5.6
Aldrich gold label 1721PJ	99 999	1.2	α	1.7

[a]Courtesy of Dr. M. Ilyas.
[b]Courtesy of Professor M. E. Fleet.

samples are those in the β (cubic) form, the slowest being in the α (hexagonal) form.

The quenching effects of added electron donors are shown in Figs. 1–4. The extent of quenching follows the oxidation potentials of the quencher, Table 1. The lines on the graphs are those obtained by curve fitting the data by a nonlinear least-squares treatment according to kinetics developed elsewhere (7, 36).

All attempts to rearrange **3–5** by photoinduced electron transfer using CdS, ZnO, TiO_2, and 9,10-dicyanoanthracene as sensitizers failed completely even when the reaction mixtures were irradiated for up to 20 h. Gas chromatographic (gc) analysis showed greater than 95% of the starting material remained.

The oxidation potentials of **3–5** are very close to that of bishomocubane, **2**. The values of k_q for the quenching of naphthalene for compounds **2**, **4**, and **5** is about the same (10). Both **1** and **2** have been shown to give radical cations that undergo subsequent reaction under conditions similar to those in which **3–5** were unchanged. It is not unreasonable to conclude,

Can. J. Chem. Downloaded from www.nrcresearchpress.com by 93.93.197.157 on 09/07/12
For personal use only.

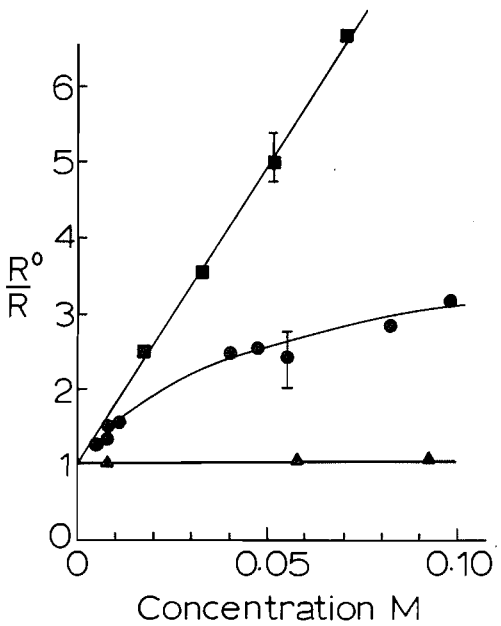

FIG. 1. Quenching of valence isomerization of **1–6** on CdS; (▲) 1,3,5-trimethoxybenzene, (●) 1,2,4-trimethoxybenzene, and (■) 1,2,4,5-tetramethoxybenzene.

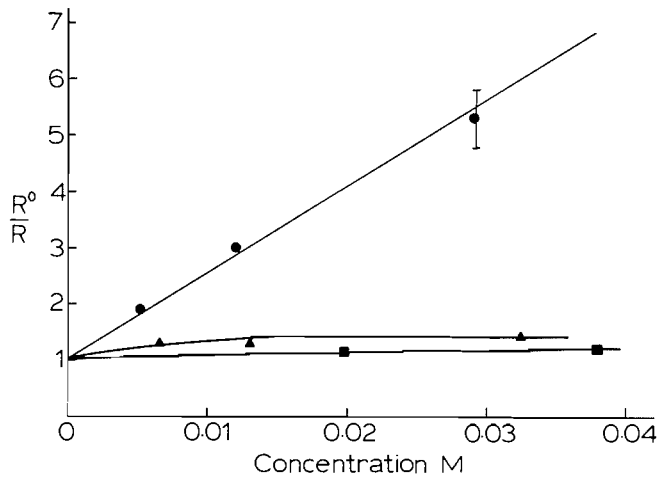

FIG. 2. Quenching of valence isomerization of **1–6** on ZnO; (●) 1,2,4,5-tetramethoxybenzene, (▲) digylme, (■) 1,2,4,5-trimethoxybenzene.

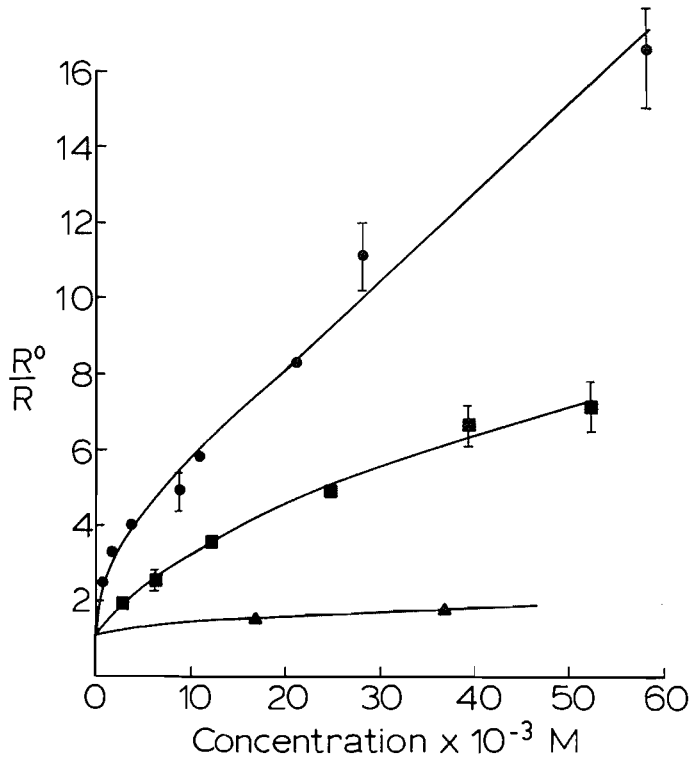

FIG. 3. Quenching of valence isomerization of **2–7** on CdS; (●) 1,2,4,5-tetramethoxybenzene, (■) 1,2,4-trimethoxybenzene, and (▲) 1,3,5-trimethoxybenzene.

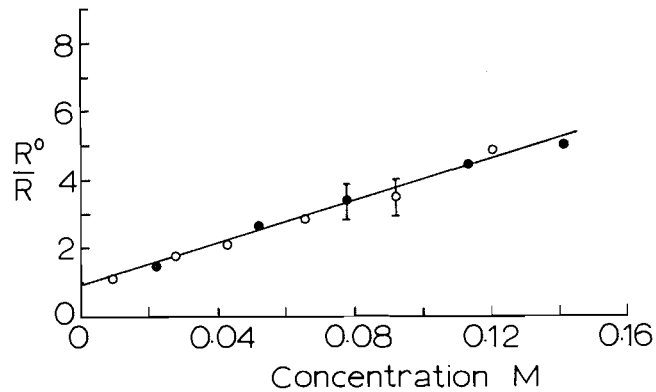

FIG. 4. Quenching of valence isomerization of **2–7** on ZnO; (○) 1,2,4,5-tetramethoxybenzene; (●) 1,2,4-trimethoxybenzene.

therefore, that under the conditions described, the radical cations of **3–5** were indeed being formed but that back electron transfer successfully competed with chemcal transformation.

One possible explanation for such a situation could be that cycloaddition was thermodynamically favoured over cyclorever-sion. In the case of the **3**/**8** radical cation interconversion this appeared to be true. In a study (21) that examined the exciplex fluorescence quenching of typical organic redox sensitizers by **8**, **8** was observed to give **3**. In the same study **3** was observed to quench the fluorescence of the sensitizers; however, no subsequent rearrangement was observed. It is also interesting to note that **8** was a very efficient quencher, quenching with rates comparable to those of **1**; however, the quantum yield for isomerization was an order of magnitude lower.

In experiments on CdS, ZnO, and TiO_2 **8** isomerized to give a small amount (< 1%) of **3** in 4 h,when illuminated with light of energy greater than the band gap of the semiconductor. The isomerization was accompanied by the formation (~4%) of unidentified high molecular weight compounds, possibly dimers or oxidation products. On extended irradiation (10 h) with semiconductors or DCA as sensitizers, **9** showed no indication of isomerization to **4**. In the case of semiconductor sensitized reaction systems there was some loss (~5%) of **9** with the consequent formation of a number of high molecular weight compounds.

The experimental data obtained for the radical cations of **3–5**, **8**, and **9** were largely a demonstration of their resistance to rearrangement. It was these observations that led us to enquire further, with the aid of MM2 and MNDO, into the factors that govern the reactivity of a radical cation.

The calculated heats of isomerization (i.e., the relative energies) of the neutral "closed" dicyclopropanes and their

Can. J. Chem. Downloaded from www.nrcresearchpress.com by 93.93.197.157 on 09/07/12
For personal use only.

TABLE 7. Heats of isomerization of the neutral compounds

Reaction	Theoretical method	Relative energy, ΔH_r (kcal mol^{-1})
1 → **6**	MNDO	− 15.9
	HF/STO-3G[a]	− 5.1
	HF/6-31G[a]	− 33.4
	MP2/6-31G[a]	− 38.2
	HF/6-31G*[a]	− 21.9
	MP2/6-31G*[a]	− 16.7
	Expt	− 22[b]
3 → **8**	MNDO	28.1
4 → **9**	MNDO	0.8

[a]Reference 17.
[b]Reference 37.

TABLE 8. Relative energies of radical cations

Reaction	Theoretical method	Relative energy, ΔH_r^+ (kcal mol^{-1})
$\mathbf{1}^+ \rightarrow \mathbf{6}^+$	MNDO	− 14
	MINDO/3[a]	+ 12
	HF/STO-3G[b]	− 2.2
	HF/6-31G[b]	− 22
	MP2/6-31G[b]	− 21
	HF/6-31G*[b]	− 12
	MP2/6-31G*[b]	− 11
	Expt[a,b]	− 9
$\mathbf{3}^+ \rightarrow \mathbf{8}^+$	MNDO	+ 9.0
$\mathbf{4}^+ \rightarrow \mathbf{9}^+$	MNDO	− 17

[a]Reference 17.
[b]Reference 16.

corresponding "open" olefins are listed in Table 7. The relative energy of **1** and **6** has been studied extensively, both theoretically and experimentally. The value of ΔH_r determined experimentally for **1** → **6** suggests that **1** lies at least 22 kcal mol^{-1} (37) above that of **6**. The theoretical values of ΔH_r closest to the experimental value were those obtained by higher level *ab initio* calculations, HF/6-31G* and MP2/6-31G* (17). MNDO (starting with MM2 minimum geometries) underestimates the difference in energy by 6 kcal mol^{-1}; however, its prediction is far superior to that of MINDO/3, which gives only a small difference in energy (16).

The relative energies calculated by MNDO suggest **3** is 28.1 kcal mol^{-1} more stable than **8**. There are no experimental values available for ΔH_r for the isomerization of **3** to **8**; however, thermolysis of **8** has been reported to give **3** at 200°C (38). This suggests that **3** may be thermodynamically more stable than **8** and supports the sign for the relative energy calculated by MNDO.

The relative energies of the radical cations are summarized in Table 8. Experimentally $\mathbf{6}^+$ is 9 kcal mol^{-1} lower in energy than is $\mathbf{1}^+$ (16, 17). The value calculated by MNDO is in the correct direction, but is 5 kcal mol^{-1} larger than the experimental value. This is quite acceptable considering that the MNDO calculation was not fully optimized (see above). The MNDO value is far superior to that of MINDO/3 which predicts $\mathbf{1}^+$ to be 12 kcal mol^{-1} more stable than $\mathbf{6}^+$. The calculated values of ΔH_r^+ closest to the experimental value are those obtained

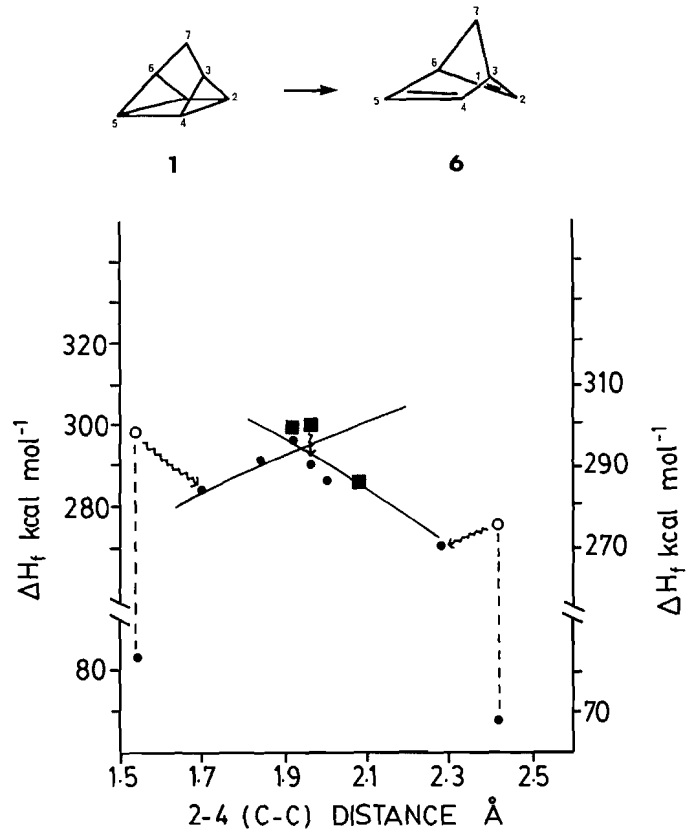

FIG. 5. Reaction coordinate for valence isomerization of **1**–**6**; (○) vertically generated radical cation, (■) hydrogens fixed.

using HF/6-31G* and MP2/6-31G* (17). The radical cation of **8** (MNDO) is 9 kcal mol^{-1} lower in energy than $\mathbf{3}^+$ (Table 8). The relative energy is in agreement with the experimentally observed direction of reaction. The calculated energy difference predicts $\mathbf{9}^+$ to be more stable than $\mathbf{4}^+$ by 17 kcal mol^{-1}. This suggests that if rearrangement were to occur it would be in the same direction as that of $\mathbf{1}^+$ to $\mathbf{6}^+$.

The reaction coordinates of the interconversions of $\mathbf{1}^+/\mathbf{6}^+$, $\mathbf{3}^+/\mathbf{8}^+$, and $\mathbf{4}^+/\mathbf{9}^+$ were investigated using MNDO (Figs. 5–7, respectively). Summarized in Table 9 are the activation energies for the reactions, calculated relative to the energy-minimized radical cations. The activation energies suggest that cycloreversion is favoured for $\mathbf{1}^+$ and $\mathbf{4}^+$. On the other hand, cycloaddition is favoured for $\mathbf{8}^+$ to give $\mathbf{3}^+$. Also listed in Table 10 is the approximate C2–C4 distance at the transition state. MNDO predicts the transition to be slightly on the side of the higher energy radical cation.

The calculated and experimental geometries of **1** and **6** are in good agreement with each other (Table 10). The structures are symmetric with respect to a plane that perpendicularly bisects the C1—C2 bond. This symmetry is also observed in the radical cations of **1** and **6** calculated by MNDO and *ab initio* methods. The agreement of the 6-31G (17) and MNDO geometries for the radical ion is very good, despite the approximations made in the MNDO calculation.

The geometries of **3**, **4**, **8**, and **9** calculated by MM2 also show symmetry with respect to a perpendicular plane that bisects the C1—C2 bond (Table 11). In radical cations $\mathbf{3}^+$ and $\mathbf{4}^+$ the symmetry with respect to this plane is lost according to MNDO calculations. The elongated C1—C7 bond of $\mathbf{3}^+$ was only obtained for the minimized radical cation.

Can. J. Chem. Downloaded from www.nrcresearchpress.com by 93.93.197.157 on 09/07/12
For personal use only.

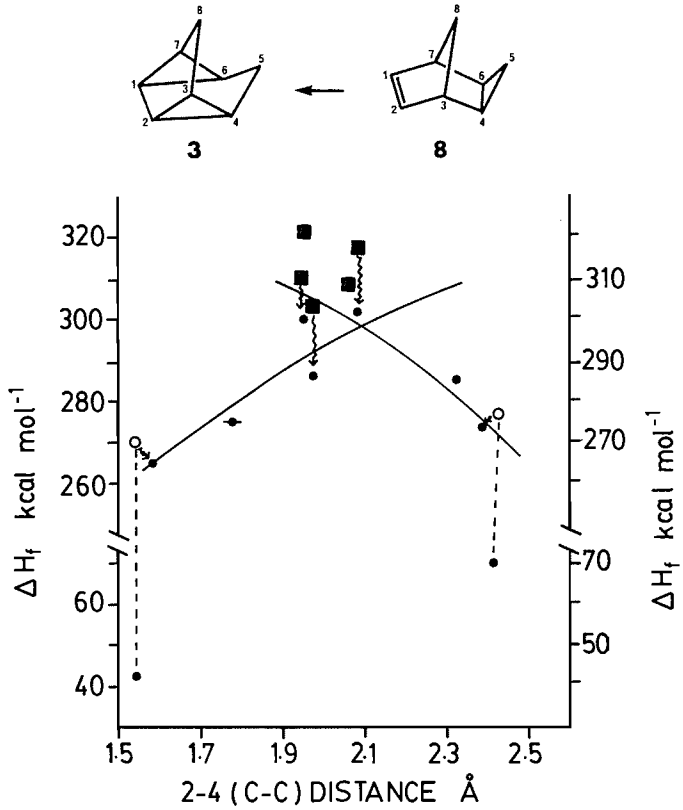

FIG. 6. Reaction coordinate for valence isomerization of **3**–**8**; (○) vertically generated radical cation (■) hydrogens fixed.

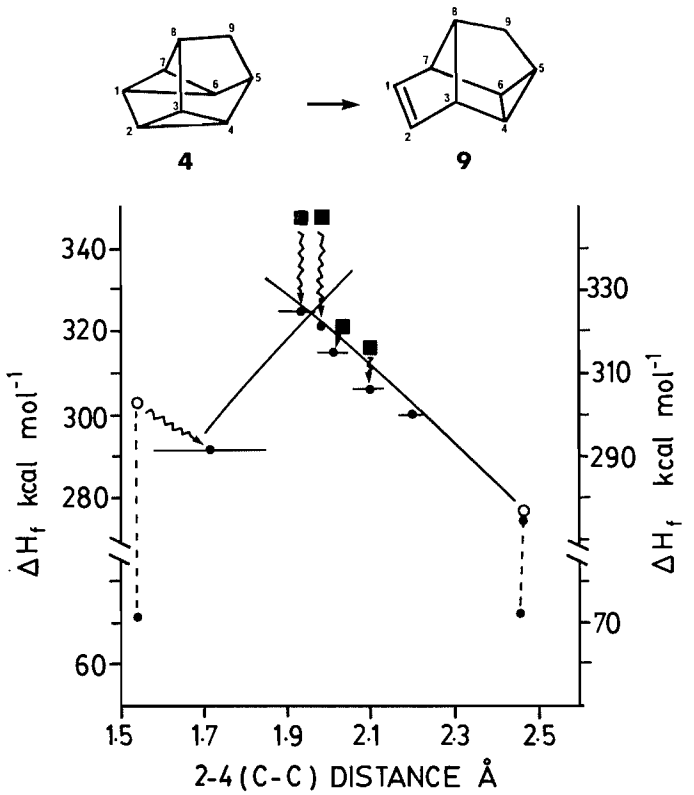

FIG. 7. Reaction coordinate for valence isomerization of **4**–**9**; (○) vertically generated radical cation, (■) hydrogens fixed.

TABLE 9. Activation energies for radical cation rearrangements and approximate C2–C4 distance at transition state

Reaction	$\Delta H^{\neq}$ (kcal mol^{-1})	C2–C4 distance at transition state (Å)
$\mathbf{1}^+ \rightarrow \mathbf{6}^+$	10	1.95
$\mathbf{6}^+ \rightarrow \mathbf{1}^+$	24	
$\mathbf{3}^+ \rightarrow \mathbf{8}^+$	33	2.10
$\mathbf{8}^+ \rightarrow \mathbf{3}^+$	25	
$\mathbf{4}^+ \rightarrow \mathbf{9}^+$	33	1.95
$\mathbf{9}^+ \rightarrow \mathbf{4}^+$	47	

TABLE 10. Geometries of **1** and **6** and their radical cations

Compound method	Geometric parameters $r_{1,2}$ (Å)	$r_{2,4}$ (Å)	$r_{1,6}$ (Å)	∡ 234°
1				
MM2IVANOV	1.54	1.53	1.50	60.1
6-31G[a]	1.55	1.52	1.52	60.0
Expt[b]	1.56	1.52	1.51	60.9
6				
MM2IVANOV	1.34	2.42	1.52	107.8
6-31G[a]	1.33	2.49	1.54	107.2
Expt[b]	1.34	2.47	1.53	107
$\mathbf{1}^+$				
MNDO	1.49	1.70	1.54	66.7
6-31G[a]	1.48	1.71	1.51	69.2
$\mathbf{6}^+$				
MNDO	1.40	2.28	1.52	97.9
6-31G[a]	1.37	2.29	1.53	96.9

[a]Reference 17.
[b]Reference 47.

TABLE 11. Geometries of **3**, **4**, **8**, **9**, and their radical cations

	Geometrical parameters[c] r_{12}	r_{24}	r_{46}	r_{16}	r_{17}	∡ 234	∡ 456
3[a]	1.54	1.51	2.46	1.51	1.54	60.2	108.9
4[a]	1.54	1.50	2.42	1.50	1.54	59.5	104.6
8[a]	1.34	2.43	1.54	2.43	1.52	105.4	60.4
9[a]	1.34	2.46	1.54	2.46	1.51	108.4	60.2
$\mathbf{3}^{+b}$	1.49	1.57	2.43	1.58	1.77	61.1	105.5
$\mathbf{4}^{+b}$	1.48	1.57	2.47	1.91	1.55	61.0	106.8
$\mathbf{8}^{+b}$	1.45	2.39	1.54	2.41	1.53	103.6	61.5
$\mathbf{9}^{+b}$	1.44	2.47	1.57	2.47	1.51	108.3	61.2

[a]MM2IVANOV.
[b]MNDO.
[c]Bond lengths in Å and angles in degrees.

This may have been because ∡C2C3C4 was fixed in order to move through the reaction coordinate. However, this was not the case for $\mathbf{4}^+$, yet as the reaction coordinate was followed, there were a number of points where MNDO predicts an asymmetric minimum geometry, as indicated by a horizontal bar through the point (Fig. 7: the bar signifies the difference in the C2—C4 and C1—C6 distances).

Can. J. Chem. Downloaded from www.nrcresearchpress.com by 93.93.197.157 on 09/07/12
For personal use only.

Can. J. Chem. Downloaded from www.nrcresearchpress.com by 93.93.197.157 on 09/07/12
For personal use only.

Discussion

The role of oxygen

In most semiconductor photocatalyzed processes so far examined, it has been found that oxygen enhances the rate of reaction (see refs. 1, 3–5 for some examples). Only in the valence isomerizations of **1**, **2**, and some geometric isomerizations (6, 9) has the presence of oxygen produced the reverse effect.[3] Molecular oxygen is usually believed to play a role in the stabilization of the e^-/h^+ pair, possibly by trapping the electron from the semiconductor conduction band to form adsorbed superoxide. Superoxide formation on the surface of CdS has been confirmed by spin trapping techniques (39).

An alternative or, perhaps, an additional rationale for the normally observed phenomenon (40) is that strongly adsorbed oxygen acts as an electron acceptor, thus causing a greater polarization in the space charge layer of the semiconductor and the layer of adsorbate than in its absence. This increases the electric field and, in turn, increases band bending. The charge separation of the e^-/h^+ pair is accelerated and the potentials of the conduction and valence bands are lowered. The accelerated charge separation improves the migration of the holes to the surface, thereby facilitating their interception.

Both rationales for the role of oxygen give an explanation for the decreased rates of reactions of **1** and **2** on ZnO in the absence of oxygen. However, on CdS an *increased* rate is observed. For the stilbene isomerization (6) the explanation suggested for this phenomenon was that the beneficial effects of oxygen were outweighed by a competing quenching process: the quenching of the radical ion by superoxide. It was also observed that, in a series of substituted stilbenes, as the polarity of the compound increased the effect of oxygen diminished. This was tentatively explained in terms of increasing adsorptive ability with increasing polarity, thus competitively decreasing the amount of molecular oxygen on the surface.

Quantum yields

In both reactions (**1**→**6**, **2**→**7**) a chain mechanism is thermodynamically possible.[4] The radical cation rearrangement of **1** has been suggested to proceed through a chain mechanism when it is catalyzed electrochemically (catalytic factors as high as 11 have been reported (13)) and also when photosensitized by metal complexes ($\Phi > 200$) (12), but the rearrangement apparently does not proceed by a chain mechanism when sensitized by organic redox sensitizers in nonpolar solvents (41). Under the latter conditions it is believed that the reaction proceeds through an exciplex. Since the reaction of **2** itself has not been previously studied, the only comparison that can be made is with that of the substituted derivatives of **2**: these are believed to proceed by a chain mechanism (19).

The quantum yield values for the reactions on CdS of **1** and **2** were found to be very small indeed (10^{-3}–10^{-4}): a chain mechanism seems unlikely.

Solvent effects

The relative efficiencies found for the reaction of **1** in different solvents (Table 5) are largely consistent with findings from other studies. The most extensive examination of solvent effects previously reported concerned phenyl vinyl ether dimerization (3). No correlation could be found between rates of reaction and dielectric constants or solvent polarity, but there was a general indication that solvents of moderate polarity gave higher conversions. This was taken to suggest the results were a consequence of competitive adsorption phenomena: these observations have been noted in other systems examined (4, 6, 8). The reaction of certain stilbenes (6) and that of **1** on CdS proceed quite well in hydrocarbon solvents. The low polarity solvents may allow more successful competition by **1** for the surface, whereas the more polar CH_2Cl_2 would stabilize charge and elute products more efficiently. This suggestion is consistent with the observed increase in conversion for less polar reactants (stilbene, **1**, and **2**). For more polar reactants the effect may diminish as desorption of products becomes more important.

The dark reaction

Initially trace impurities were believed to be responsible for the thermal (dark) reactivity of CdS. However, the reaction was quenched by electron transfer quenchers, which would suggest that the reaction was proceeding through formation of a radical cation. The generation of radical cations in the dark on CdS has been previously proposed in the thermal dimerization of phenyl vinyl ether (2) where it was concluded that the rate of the dark reaction depended on defects in the CdS samples (42). Luminescence in colloidal CdS has been attributed to the formation of cadmium vacancies, and the presence of cadmium vacancies acting as electron acceptors had been reported earlier and assigned an energy level of 0.7 eV above the valence band (43). It is thus possible that the dark reaction of **1** is a result of interception of trapped holes either associated with cadmium vacancies or interstitial sulfur (for examples, see ref. 12). The very low oxidation potential of **1** (0.91 V) would make it possible for **1** to intercept centres that lie in the forbidden gap. This could account for the lack of dark reactivity of compounds such as **2** on CdS since the oxidation potential of **2** would be below that of such centres, so inhibiting reaction. In addition, low purity samples would be expected to give higher conversion (as observed) because impurities would increase the number of donor–acceptor centres.

Quenching studies

"Electronic quenching" decreases product formation by electron donation to the reactant radical cation, the photogenerated hole, and (or) the product radical cation, in the case of a chain mechanism. A good electronic quencher should have an oxidation potential above (less positive than) that of the photoinduced holes and (or) that of the reactant. 1,2,4,5-Tetramethoxybenzene, TEMB, (Table 1) is thermodynamically suitable to quench exothermically the photoinduced holes of ZnO and CdS as well as $\mathbf{1}^+$ and $\mathbf{2}^+$. The addition of TEMB to the reactions of **1** and **2** on either CdS or ZnO substantially reduces product formation (Figs. 1–4 respectively). Also Fig. 1 shows the effect of adding diglyme as a surface adsorbate to the reaction of **1** on ZnO. Diglyme is a very poor quencher whereas TEMB is very effective. Since diglyme's oxidation potential lies below the holes of ZnO, this suggests that TEMB is indeed quenching by electron transfer and not by competitive adsorption.

In the reactions mediated by ZnO (Figs. 1 and 3), 1,2,4-trimethoxybenzene, 1,2,4-TMB, only quenches the formation of **7**. The oxidation potential of 1,2,4-TMB (Table 1) lies between that of the holes and that of **1**, hence 1,2,4-TMB may quench the holes but not $\mathbf{1}^+$. When 1,2,4-TMB intercepts a hole it generates 1,2,4-TMB^+, but the latter is able, in turn, to accept an electron from **1** ($\Delta eV \simeq 0.2$). The net effect is no quenching. In the reaction of **2** on ZnO, 1,2,4-TMB can quench both $\mathbf{2}^+$ and the photoexcited holes, as with TEMB, and the curves are superimposable.

[4]The $E_{\frac{1}{2}}^{ox}$ of **2** is 1.56 V vs. SCE (10) and the $E_{\frac{1}{2}}^{ox}$ of **5** is estimated at 1.7 V vs. SCE by comparison with related compounds (5).

Can. J. Chem. Downloaded from www.nrcresearchpress.com by 93.93.197.157 on 09/07/12
For personal use only.

The situation with CdS is a little more complex; here 1,2,4-TMB quenches both reactions. The quenching of the reaction of **1** is, however, considerably less than that of **2** and levels off at higher concentrations. The less efficient quenching and leveling off may be attributed to the interception of 1,2,4-TMB$^+$ by **1**, as on ZnO. The reason 1,2,4-TMB quenches **6** formation on CdS and not on ZnO is not fully understood. One possibility may be a shorter lifetime of the e^-/h^+ pair on CdS as compared to ZnO, and that quenching the hole on CdS by 1,2,4-TMB may be coupled to a fast electron recombination before interception by **1**.

Another substance was examined as a potential quencher: 1,3,5-trimethoxybenzene, 1,3,5-TMB. This showed virtually no quenching at those concentrations where the other quenchers were effective. In fact, 1,3,5-TMB has not yet displayed any significant quenching in CdS-mediated reactions This suggests that 1,3,5-TMB is a poor electron donor to the semiconductor and semiconductor generated radical cations. It is possible that the 0.2-eV difference between the holes and 1,3,5-TMB in CH_3CN solution may be significantly smaller in CH_2Cl_2 on the CdS surface.[2] However, the use of 1,3,5-TMB does demonstrate, because of its similar structure to the other methoxylated quenchers, that competitive adsorption plays a very minor role in quenching at these concentrations.

Calculations

Roth and Schilling have shown by the obtention of different nuclear spin polarization patterns for **1** and **6** that two different radical cations do, in fact, exist (15). This view is also supported by the photoelectron spectra (16, 44) and high level *ab initio* calculations (17). The electronic structures of the different radical ions are in agreement with expectations from simple molecular orbital models. The radical cation of **1** has one electron in a b_1 orbital and that of **6** has one electron in a b_2 orbital. The interconversion of $\mathbf{1}^+$ to $\mathbf{6}^+$ involves an orbital crossing as in the case of the neutral parent compound.

The results of the MNDO investigation reported here are in good agreement with these observations. Two distinct radical ions are predicted. The SOMO of $\mathbf{1}^+$ is a b_1 orbital and that of $\mathbf{6}^+$ is a b_2 orbital. The interconversion follows C_{2v} symmetry with orbital crossing of the SOMO and LUMO orbitals. Even if the initial geometry for $\mathbf{1}^+$ were given C_s symmetry, the MNDO program optimized the structure back to C_{2v} symmetry. This demonstrates that MNDO calculates a real minimum with C_{2v} symmetry and not just a shallow edge. Calculations at the STO-3G level predict a strongly distorted C_s symmetry structure for both radical cations; however, at the higher 6-31G level a symmetric structure is calculated for both radical cations (17). Removal of an electron from the b_1 orbital of **1** should result in the C1—C6 and C2—C4 bonds of **1** becoming less bonding (elongated) while the C1—C2 and C4—C6 bonds should become less antibonding (shorter). This idea suggests that $\mathbf{1}^+$ should relax to a geometry structurally closer to that of **6**, as suggested by Haselbach and co-workers for Type C radical cation rearrangements (44*b*). This process is predicted by MINDO/3 (16), 6-31G (17), and by the MNDO calculations reported here. The overall effect is to shorten the reaction coordinate. The same effect is observed from the other side of the reaction coordinate: $\mathbf{6}^+$ relaxes to a geometry structurally closer to **1**. MNDO calculates a shortening of the reaction coordinate from 0.89 to 0.58 Å due to this effect.

The relative energy of $\mathbf{1}^+$ and $\mathbf{6}^+$ is known experimentally to be approximately 9 kcal mol^{-1}. This energy difference is sufficient to account for the substantially different interconversion rates of $\mathbf{1}^+$ and $\mathbf{6}^+$, where, in fact, $\mathbf{1}^+$ is observed to rearrange irreversibly to $\mathbf{6}^+$. The MNDO calculated energy difference is in very good agreement with experiment considering that the structures could not be fully optimized. MNDO is superior to MINDO/3 in the treatment of such systems, since the latter failed to predict the correct order in energy for $\mathbf{1}^+$ and $\mathbf{6}^+$ (16).

The activation energy for the rearrangement of $\mathbf{1}^+$ and $\mathbf{6}^+$ was predicted to be approximately 10 kcal mol^{-1} by MNDO, which is considerably lower than the activation energy of 37.5 kcal mol^{-1} for the neutral parent compound. A value of 10 kcal mol^{-1} is still higher than expected for the reaction (4–5 kcal mol^{-1}) from the lifetime of only several nanoseconds predicted for $\mathbf{1}^+$ (16).

In summary, the MNDO calculations for the quadricyclane/norbornadiene system are in good agreement with the available experimental data and other theoretical calculations. Haselbach suggests the lowering of the activation energy for Type C processes can be attributed to: (*i*) the shorter reaction coordinate; (*ii*) involvement of only one electron; and (*iii*) the reduced energy gap between the SOMO and the LUMO as compared to that of the HOMO and LUMO of the parent compounds (45). The MNDO calculations show a reduction in the reaction coordinate of 40% for the reaction of the radical cations. Unfortunately no direct information about the relative energy levels of orbitals can be obtained for open shell molecules by MNDO. There is, however, an overall predicted 75% reduction in activation energy for the radical cation rearrangement.

The conversion of $\mathbf{8}^+ \rightarrow \mathbf{3}^+$ was observed to be approximately 10 times less efficient than that of $\mathbf{1}^+ \rightarrow \mathbf{6}^+$. The MNDO results are consistent with all the experimental information available. The observed direction of both the thermolysis and radical cation reactions can be attributed to overall exothermicity. The activation energy for the $\mathbf{8}^+ \rightarrow \mathbf{3}^+$ reaction is calculated to be 25 kcal mol^{-1} by MNDO. The MNDO calculations offer some explanation for the higher activation energy for the $\mathbf{8}^+ \rightarrow \mathbf{3}^+$ rearrangement compared to that of $\mathbf{1}^+ \rightarrow \mathbf{6}^+$. The shortening of the reaction coordinate for the radical cation reaction is only 16% for $\mathbf{8}^+ \rightarrow \mathbf{3}^+$ compared to the 40% for $\mathbf{1}^+ \rightarrow \mathbf{6}^+$. This is attributable to differences in the structures of the radical cations. MNDO calculates in the HOMO of **8** a contribution from both the double bond and the cyclopropane Walsh orbitals. This is very similar to the b_2 HOMO orbital of **6** where there are contributions from both double bonds. In **6**, these through-space interactions are maintained in the radical cation; however, in $\mathbf{8}^+$ the SOMO orbital is localized on the double bond.[5] As a result $\mathbf{8}^+$ shows virtually no relaxation toward $\mathbf{3}^+$. Furthermore, the structure of $\mathbf{3}^+$ is predicted to have an elongated C1—C7 bond. If this be the case, the correlation of the SOMO of $\mathbf{8}^+$ may be with a higher lying virtual orbital of $\mathbf{3}^+$. Correlation with higher orbitals leads to less stabilization and would result in a higher activation energy (46).

The last two compounds examined by MNDO calculations were **4** and **9**. MNDO predicts that $\mathbf{9}^+$ be more stable than $\mathbf{4}^+$ by 17 kcal mol^{-1}. This suggests that cycloreversion of $\mathbf{4}^+$ should proceed to $\mathbf{9}^+$. An activation energy of

[5]The disappearance of interactions between C1 and C2 and the Walsh orbitals is observed both in $\mathbf{8}^+$ and $\mathbf{9}^+$ and occurs even when the radical cations have the same geometry as the neutral parent compounds. The reason for this is not clear, however, since the through-space interactions for **2** are maintained in the radical cation of **6**.

33 kcal mol^{-1} was predicted for the interconversion of 4^+ to 9^+: this is 3.3 times that calculated for the isomerization of 1^+ to 6^+, and readily accounts for the lack of reaction observed. This high activation energy can be attributed to the nature of 4^+ and 9^+ as compared to 1^+ and 6^+. The overall picture for 4^+ and 9^+ is very similar to that for 3^+ and 8^+: the geometry of the minimized 9^+ is predicted to be similar to that of the neutral compound. The SOMO orbital is localized on C1 and C2 with no contributions from the Walsh orbitals of the cyclopropane. This leads to a slight elongation in the C1—C2 bond in 9^+ as compared to **9**; however, there is no shortening of the reaction coordinate along the C2—C4 distance, as occurs with the radical cations 6^+ and 8^+. An elongated C1—C6 bond is calculated for 4^+. The coefficients for the SOMO orbital localize the orbital on C1 and C6, unlike the SOMO of 1^+, which has b_2 symmetry. The predicted orbital correlation of the SOMO and LUMO orbitals may not be correct and higher virtual orbitals may be involved; this would also lead to a higher activation energy.

1. M. A. Fox. Acc. Chem. Res. **16**, 314 (1983).
2. M. Ilyas and P. de Mayo. J. Am. Chem. Soc. **107**, 5093 (1985).
3. A. M. Draper, M. Ilyas, P. de Mayo, and V. Ramamurthy. J. Am. Chem. Soc. **106**, 6222 (1984).
4. H. Al-Ekabi and P. de Mayo. Tetrahedron, **42**, 6277 (1986).
5. K. Okada, K. Hisamitsu, and T. Mukai. J. Chem. Soc. Chem. Commun. 941 (1980).
6. H. Al-Ekabi and P. de Mayo. J. Phys. Chem. **89**, 5815 (1985).
7. T. Hasegawa and P. de Mayo. Langmuir, **2**, 362 (1986).
8. H. Al-Ekabi and P. de Mayo. J. Phys. Chem. **90**, 4075 (1986).
9. S. Yanagida, K. Mizumoto, and C. Pac. J. Am. Chem. Soc. **108**, 657 (1986).
10. P. G. Gassman and R. Yamaguchi. Tetrahedron, **38**, 1113 (1982), and references therein.
11. (*a*) G. Jones II, S. H. Chiang, and P. T. Xuan. J. Photochem. **10**, 1(1970); (*b*) G. Jones II, W. Schwarz, and V. Malba. J. Phys. Chem. **86**, 2286 (1982).
12. (*a*) C. K. Kelley and C. Kutal. Organometallics, **4**, 1351 (1985); (*b*) N. Borsub and C. Kutal. J. Am. Chem. Soc. **106**, 4826 (1984).
13. K. Yasufuku and K. Takahashi. Tetrahedron Lett. **25**, 4893 (1984).
14. (*a*) E. Heilbronner and H. D. Martin. Helv. Chim. Acta, **55**, 1490 (1972); (*b*) G. N. Taylor. Chem. Phys. Lett. **10**, 355 (1971); (*c*) Z. Dolejsek, V. Hanus, and H. Prinzbach. Angew. Chem. **74**, 902 (1962).
15. (*a*) H. D. Roth, M. L. M. Schilling, and G. Jones II. J. Am. Chem. Soc. **103**, 1246 (1981); (*b*) H. D. Roth and M. L. M. Schilling. J. Am. Chem. Soc. **103**, 7210 (1981).
16. E. Haselbach, T. Bally, Z. Lanyjova, and P. Baertshi. Helv. Chim. Acta, **62**, 583 (1979).
17. K. Raghavachari, R. C. Haddon, and H. D. Roth. J. Am. Chem. Soc. **105**, 3110 (1983).
18. L. A. Paquette, R. A. Boggs, W. B. Farnham, and R. S. Beckley. J. Am. Chem. Soc. **97**, 1112 (1975).
19. T. Mukai, K. Sato, and Y. Yamashita. J. Am. Chem. Soc. **103**, 670 (1981).
20. H. D. Roth and M. L. M. Schilling. Tetrahedron Lett. **24**, 5815 (1983).
21. G. Jones II, S. H. Ching, W. C. Becker, and D. P. Greenberg. J. Chem. Soc. Chem. Commun. 681 (1980).
22. (*a*) P. A. Kohl and A. J. Bard. J. Am. Chem. Soc. **99**, 7531 (1977); (*b*) S. N. Frank and A. J. Bard. J. Am. Chem. Soc. **97**, 7427 (1975); (*c*) M. A. Fox. Adv. Photochem. **13**, 237 (1986).
23. A. M. Draper and P. de Mayo. Tetrahedron Lett. **27**, 6157 (1986).
24. F. Benington, R. D. Morin, and L. C. Clark. J. Org. Chem. **20**, 102 (1955).
25. C. D. Smith. Org. Synth. **51**, 133 (1971).
26. (*a*) P. K. Freeman, D. M. Balls, and D. J. Brown. J. Org. Chem. **33**, 2211 (1968); (*b*) G. Mehta, A. Srikrishna, and S. C. Suri. J. Org. Chem. **45**, 5375 (1980).
27. L. A. Paquette, R. S. Beckley, and W. B. Farnham. J. Am. Chem. Soc. **97**, 1089 (1975).
28. (*a*) P. K. Freeman and D. M. Balls. Tetrahedron Lett. 437 (1967); (*b*) P. K. Freeman and D. M. Balls. J. Org. Chem. **32**, 2354 (1967).
29. H. E. Simmons, E. P. Blanchard, and R. D. Smith. J. Am. Chem. Soc. **86**, 1347 (1964).
30. E. Le Goff. J. Org. Chem. **29**, 2048 (1964).
31. H. C. Volger, H. Hogeveen, and M. M. P. Gaasbeek. J. Am. Chem. Soc. **91**, 218 (1969).
32. N. L. Allinger and Y. H. Yuh. Quantum Chemistry Program Exchange, **12**, 395 (1980).
33. (*a*) C. Jaime and E. Ōsawa. Tetrahedron. **39**, 2769 (1983); (*b*) P. M. Ivanov and E. Ōsawa. J. Comput. Chem. **5**, 307 (1984); (*c*) E. Ōsawa, G. Szalontai, and A. Tsurumoto. J. Chem. Soc. Perkins Trans. 2, 1209 (1983); (*d*) P. M. Ivanov. J. Chem. Res. (M), 1173 (1985).
34. M. J. S. Dewar and W. Thiel. J. Am. Chem. Soc. **99**, 4899 (1977).
35. H. Ikezawa and C. Kutal. J. Org. Chem. **52**, 3299 (1987).
36. A. M. Draper. Ph.D. thesis, University of Western Ontario, London, Ont. 1987.
37. (*a*) D. S. Kabakoff, J. B. Bunzli, J. M. F. Oth, W. B. Hammond, and J. B. Berson. J. Am. Chem. Soc. **97**, 1510 (1975); (*b*) D. W. Rogers, L. S. Choi, R. S. Holmes, and N. L. Allinger. J. Phys. Chem. **84**, 1810 (1980); (*c*) W. V. Steele. J. Chem. Thermodyn. **10**, 919 (1978).
38. P. K. Freeman, D. G. Kuper, and V. N. Mallikarjuna Rao. Tetrahedron Lett. 3303 (1965).
39. (*a*) J. R. Harbour and M. L. Hair. J. Phys. Chem. **81**, 1791 (1977); (*b*) **83**, 652 (1979).
40. (*a*) A. J. Nozik. Ann. Rev. Phys. Chem. **29**, 189 (1978); (*b*) H. Gerischer and F. Willig. Top. Curr. Chem. **61**, 31 (1976).
41. (*a*) G. Jones II and W. G. Becker. Chem. Phys. Lett. **85**, 271 (1982); (*b*) G. Jones II, S. H. Chiang, W. G. Becker, and J. A. Welch. J. Phys. Chem. **86**, 2805 (1982).
42. (*a*) J. Woods and K. H. Nicholas. Brit. J. Appl. Phys. **15**, 1631 (1964); (*b*) **15**, 783 (1964); (*c*) J. J. Lamb, C. C. Klink, and D. L. Dexter. Phys. Rev. **103**, 1715 (1956); (*d*) J. J. Ramsden and M. Grätzel. J. Chem. Soc., Faraday Trans. 1, **80**, 919 (1984).
43. J. R. Brailsford and J. Wood. J. Phys. Chem. **1**, 1213 (1968).
44. (*a*) P. Bischof, J. A. Hashmall, E. Heilbronner, and V. Hornung. Helv. Chim. Acta, **52**, 1745 (1969); (*b*) H. D. Martin, C. Heller, E. Haselbach, and Z. Lanyjova. Helv. Chim. Acta, **57**, 465 (1974).
45. N. L. Bauld, D. J. Belleville, R. Rabon, R. Chelsky, and G. Green. J. Am. Chem. Soc. **105**, 2378 (1983).
46. F. A. Cotton. Chemical applications of group theory. Wiley–Interscience, New York. 1973.
47. (*a*) E. E. Burnell and P. Diehl. Can. J. Chem. **50**, 3566 (1972); (*b*) A. Yokozeki and K. Kuchitsu. Bull. Chem. Soc. Jpn. **44**, 2356 (1971); (*c*) K. Mizuno, T. Fukuyama, and K. Kuchitsu. Chem. Lett. 249 (1972).
48. A. Zweig, W. G. Hodgson, and W. H. Jura. J. Am. Chem. Soc. **86**, 4124 (1964).
49. H. Siegerman. *In* Techniques of chemistry. Vol. 5. Part 2. *Edited by* N. L. Weinberg. Wiley, New York. 1975. p. 792.

Can. J. Chem. Downloaded from www.nrcresearchpress.com by 93.93.197.157 on 09/07/12
For personal use only.

In-situ Fourier transform infrared spectroelectrochemical studies of the oxidation of some tetraphenylporphyrin complexes

A. Scott Hinman,[1] Brad J. Pavelich, and Karen McGarty

Department of Chemistry, The University of Calgary, Calgary, Alta., Canada T2N 1N4

Received August 10, 1987[2]

A. Scott Hinman, Brad J. Pavelich, and Karen McGarty. Can. J. Chem. **66**, 1589 (1988).

In-situ FTIR spectroelectrochemistry has been applied to determine difference spectra in the region 1800 to 1000 cm^{-1} associated with the oxidation of $TPPH_2$, TPPMg, TPPCu, TPPZn, TPPCo, TPPMnCl, and TPPFeCl. In all cases, formation of the π-cation radical results in two characteristic absorbance decreases near 1600 and 1485 cm^{-1}, and five characteristic absorbance increases near 1415, 1350, 1285, 1225, and 1005 cm^{-1}. Formation of the π-dication was observed for TPPZn, TPPMg, and TPPCo, and gave rise to a new absorbance increase near 1600 cm^{-1}, and a shift to higher frequency of bands in the 1200 to 1400 cm^{-1} region. Perchlorate coordination to oxidized TPPZn, TPPMg, and TPPCo gives rise to bands near 1140 and 1030 cm^{-1}.

A. Scott Hinman, Brad J. Pavelich, et Karen McGarty. Can. J. Chem. **66**, 1589 (1988).

On a utilisé la spectroélectrochimie FTIR *in situ* pour déterminer les différences spectrales, dans la région de 1800 à 1000 cm^{-1}, associées à l'oxydation des produits suivants: $TPPH_2$, TPPMg TPPCu, TPPCo, TPPMnCl, et TPPFeCl. Dans tous les cas, la formation du cation radical π provoque deux diminutions caractéristiques d'absorption près de 1600 et 1485 cm^{-1} ainsi que cinq augmentations caractéristiques d'absorption près de 1415, 1350, 1285, 1225 et 1005 cm^{-1}. On a observé la formation du dication π avec le TPPZn, le TPPMg et le TPPCo; elle donne lieu à une nouvelle augmentation de l'absorption près de 1600 cm^{-1} alors que les bandes de la région de 1200 à 1400 cm^{-1} sont déplacées vers des fréquences plus élevées. La coordination des TPPZn, TPPMg et TPPCo par le perchlorate donne lieu à l'apparition de nouvelles bandes près de 1140 et 1030 cm^{-1}.

[Traduit par la revue]

Introduction

In 1981, Goff, Reed, and co-workers (1) reported infrared spectra of a number of metallotetraphenylporphyrin π-cation radicals isolated from solution following one-electron oxidation of the neutral complexes. These all displayed strong absorbance in the vicinity of 1280 cm^{-1}. Since that time this band has been suggested (2) as the simplest of definitive criteria available for distinguishing between metal and porphyrin ring centered oxidation of tetraphenylporphyrin complexes. Other workers (3) have criticized the use of this band as a diagnostic criterion, and produced evidence suggesting that it could arise from occluded chlorocarbon solvent molecules in the crystalline cation radicals.

Our laboratory has recently reported (4, 5) the first applications of the recently developed (6) methodology of *in situ* Fourier transform infrared reflectance spectroelectrochemistry to studies of the anodic oxidation of metalloporphyrins. In this technique, infrared radiation passes through a thin layer of solution onto a polished electrode surface which reflects the incident beam back through the thin solution layer to a detector. Analysis of the energy spectra obtained prior to and following electrolysis affords a difference spectrum between oxidized and unoxidized forms of electroactive species within the thin layer cavity. Utilizing this technique, we were able to detect (4, 5), *in situ*, a strong absorbance at 1277 cm^{-1} due to the cation radical of tetraphenylporphinatozinc(II) (TPPZn) in 1,2-dichloroethane containing tetra-*n*-butylammonium perchlorate.

In the present study, we have extended our utilization of this technique to include a variety of other metal-TPP complexes as well as the free base, $TPPH_2$. Our intent was to provide further evidence concerning the validity of the 1280 cm^{-1} band as a diagnostic for identifying oxidation of the porphyrin ring as opposed to the metal center of the complex. Also, as the method is a difference technique, we anticipated that additional correlations, not readily apparent in comparisons of individual spectra of the oxidized and unoxidized complexes, might be observed. In a limited number of cases we have also been able to obtain spectral differences associated with two-electron oxidation of tetraphenylporphyrins to the π-dication. The discussions here are concerned with the use of *in situ* FTIR as an empirical tool for identifying the site of oxidation within the porphyrin complex, and no attempt has been made to interpret the data in terms of possible band assignments or structural differences between the porphyrin complexes.

Experimental

Porphyrins

The free-base tetraphenylporphine ($TPPH_2$) was used as received from Aldrich. TPPMg, TPPCu, TPPZn, TPPCo, and $TPPMnCH_3CO_2$ were prepared from the free base utilizing Adler's DMF method (7). TPPMnCl was prepared by dissolving 100 mg of $TPPMnCH_3CO_2$ in 150 mL of methanol to which 2 mL of 1 *M* aqueous HCl were then added. TPPMnCl was precipitated by the slow, dropwise addition of 200 mL of water, recovered by filtration, and dried *in vacuo* at 100°C. TPPFeCl was used as received from Porphyrin Products Inc., Logan, Utah.

Solvents and supporting electrolyte

Dibromomethane (Eastman) was shaken with activated alumina (Woelm N Super I) prior to use. Dichloromethane and 1,2-dichloroethane (Caledon D.I.G. grade) were purified as described in ref. 5. Tetra-*n*-butylammonium perchlorate (TBAP) from Fluka was recrystallized from an isopropanol/water mixture and dried *in vacuo* at 60°C.

Electrochemistry and in-situ *FTIR spectroelectrochemistry*

The cell and instrumentation employed for cyclic voltammetry were as described in ref. 5. The cell, optical arrangement, and instrumentation employed for *in situ* FTIR studies is described in detail in ref. 4. The cell utilizes a Pt mirror electrode and a CaF_2 window. The CaF_2 window allows observation of spectral features at frequencies higher than 980 cm^{-1}, although the signal-to-noise ratio is best above 1000 cm^{-1}.

[1]To whom correspondance should be addressed.

[2]Revision received February 26, 1988.

Can. J. Chem. Downloaded from www.nrcresearchpress.com by 61.7.252.67 on 09/07/12
For personal use only.

Can. J. Chem. Downloaded from www.nrcresearchpress.com by 61.7.252.67 on 09/07/12
For personal use only.

Porphyrin concentrations in all experiments were approximately 2 m*M*. Supporting electrolyte concentration was 0.2 *M*. Prior to carrying out the infrared experiments, cyclic voltammetry was run on the porphyrin solutions to establish appropriate oxidation potentials. The solutions were then transferred to the thin layer reflectance cell mounted in a Nicolet 5DX FTIR spectrometer. The *in-situ* FTIR cell has previously been demonstrated (4) to possess excellent characteristics for both thin-layer and conventional cyclic voltammetry. The use of a different cell to determine oxidation potentials in these experiments was simply a matter of convenience. As the electrochemical equipment is situated in a different laboratory from the FTIR spectrometer, this procedure minimized the amount of equipment shuttling required (potentiostat only), and obviated the need for readjustment of the optical configuration which would have been required were the cell, instead of the solution, transferred between the laboratories.

After the solutions were transferred, a set of 128 energy spectra were collected and averaged with the electrode potential held at a value, E_1, approximately 100 mV cathodic of the half-wave potential for the first oxidation of the porphyrin complex. The potential was then increased to a value, E_2, which, as judged from the cyclic voltammetry, would facilitate the desired oxidation without interference from any process (e.g. dication formation) occurring at higher potentials. A second set of 128 spectra were then collected and averaged. The resulting averaged spectrum obtained at E_2 was then ratioed against the background spectrum obtained at the base potential E_1. Taking the log and multiplying by -1 then affords the difference in absorbance, $\Delta A = A(E_2) - A(E_1)$, between the oxidized and unoxidized solutions as a function of infrared frequency. In this mode of data presentation, negative absorbance bands indicate a loss of vibrational intensity associated with species in solution prior to electrolysis, and are referred to as disappearance bands. Positive absorbance indicates increased or new vibrational intensity associated with electrolysis products, and are referred to as appearance bands.

Results and discussion

Our initial report (4) of *in-situ* FTIR characterization of the one-electron oxidation of TPPZn utilized 1,2-dichloroethane as the solvent. This solvent displays strong absorbance bands at 1450, 1429, 1315, 1286, and 1233 cm^{-1} in the spectral region focused on in this study (1800 to 1000 cm^{-1}). The 1286 cm^{-1} band, in particular, limits the optical throughput in the region of the reported 1280 cm^{-1} diagnostic band of tetraphenylporphyrin cation radicals. Extremely small thin-layer thicknesses (< 10 μm) and high porphyrin concentrations are required to allow observation of spectral features due to the porphyrin oxidation in regions of solvent overlap. Dichloromethane possesses only a single strong absorbance, at 1269 cm^{-1}, in the wavelength region of interest, and would thus appear to be preferable to dichloroethane. We have, in fact, had some success with this solvent, but its volatility (bp 38°C) makes it difficult to work with. Prolonged exposure of the electrode to infrared radiation frequently leads to partial vaporization of the solvent within the thin-layer cavity, resulting in a broad, strong disappearance feature around 1270 cm^{-1} in the difference spectra obtained.

The results presented here utilized dibromomethane as solvent with TBAP as supporting electrolyte, except in a few cases noted differently. This solvent is superior to either dichloroethane or dichloromethane for infrared studies. It possesses a single strong absorbance, at 1192 cm^{-1}, in the 1800 to 1000 cm^{-1} region, and is less volatile (bp = 97°C) than either. The relatively clean infrared spectrum of the solvent allows the use of longer thin layer thicknesses (approximately 50 μm) than in dichloroethane. This increases the absorbance due to solvates and, consequently, the overall quality of the spectra obtained through most of the 1800 to 1000 cm^{-1} region. The tradeoff in utilizing the longer pathlength is that solvent absorbance at 1192 cm^{-1}, as well as that due to supporting electrolyte perchlorate, at 1089 cm^{-1}, are high enough that most of the detector signal in a 10 to 20 cm^{-1} region about these frequencies results from stray light reflected off the front surface of the window, precluding the observation of bands associated with porphyrin oxidation in these spectral regions.

TABLE 1. Cyclic voltammetric half-wave potentials[a] for oxidation of tetraphenylporphyrin complexes

Complex	Half-wave potential		
	Metal oxidation	1st ring oxidation	2nd ring oxidation
$TPPH_2$		1.06	Irreversible
TPPMg		0.66	0.94
TPPZn		0.78	1.08
TPPCu		1.04	1.26[b]
TPPCo	0.78	0.97	1.15
TPPMnCl		1.15	Irreversible
TPPFeCl		1.16	1.39[b]

[a]All potentials in volts vs. aqueous SCE as determined in 1,2-dichoroethane/0.2 *M* TBAP for TPPZn, and dibromomethane/0.2 *M* TBAP for all other complexes.

[b]Anodic to cathodic peak current ratio less than unity at sweep rates below 20 mV s^{-1}.

The characteristics of dibromomethane as a solvent for the electrochemical oxidation of metallotetraphenylporphyrins appear similar in most regards to those of dichloromethane. With TBAP as supporting electrolyte, both solvents allow access of potentials up to +1.8 V vs. SCE. Also, the half-wave potentials observed for metalloporphyrin oxidations in dibromomethane are generally very close to those reported in the literature for oxidations in dichloromethane. The first one electron oxidation of TPPMnCl occurs at $E_{1/2}$ = 1.15 V vs. SCE in CH_2Br_2/TBAP (0.2 *M*), as compared to a reported value of 1.14 V vs. SCE in CH_2Cl_2/TBAP (0.1 *M*) (8). TPPFeCl undergoes two oxidations at 1.16 and 1.39 vs. SCE in CH_2Br_2/TBAP (0.2 *M*), as compared to reported values of 1.11 and 1.38 V vs. SCE in CH_2Cl_2/TBAP (0.1 *M*) (9). TPPCo undergoes three oxidations at 0.78, 0.97, and 1.15 V vs. SCE in CH_2Br_2/TBAP (0.2. *M*) as compared to reported values of 0.78, 0.97, and 1.16 V vs. SCE in CH_2Cl_2/TBAP (0.1 *M*) (10). These data suggest that liquid junction potentials associated with the use of the aqueous SCE are similar for both solvents.

TPP complexes in nonaqueous solution frequently undergo two successive one-electron oxidations (11). While the cyclic voltammetric behaviour of TPP complexes in CH_2Br_2 and CH_2Cl_2 appear similar in many regards, the stability of the second one-electron oxidation products of some of the compounds investigated is lower in the former solvent. While we have been able to observe reversible behaviour for the second one-electron oxidation of $TPPH_2$ in dry dichloromethane, this process is irreversible in dibromomethane, with no cathodic peak coupled to the oxidation for sweep rates up to 300 mV s^{-1}. Similarly, the anodic-to-cathodic peak current ratios for the second oxidation of TPPFeCl and TPPCu become less than unity at sweep rates below 20 mV s^{-1}, while maintaining a value of unity for similar experiments in CH_2Cl_2. The nature of this irreversibility has not been investigated.

Table 1 summarizes the half-wave potentials, as observed by cyclic voltammetry, associated with oxidation of the porphyrin

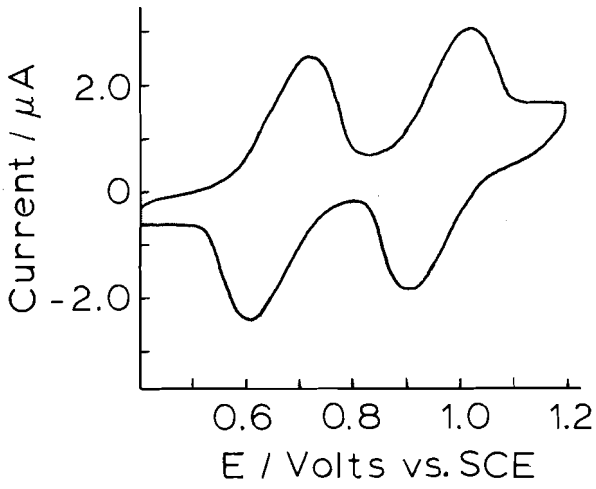

FIG. 1. Thin-layer voltammetry of 2.0 m*M* TPPMg in CH_2Br_2/TBAP (0.2 *M*) performed in the FTIR reflectance cell. Scan rate was 1.0 mV s^{-1}.

complexes utilized in this study. The oxidation products were stable ($i_{p,anodic}/i_{p,cathodic} = 1$) in all cases, except where noted otherwise. The assignment of the oxidation processes as ring centered in TPPMg, TPPZn, and $TPPH_2$ is unambiguous, as these complexes contain no oxidizable metal center. The assignment of oxidation site associated with the voltammetric waves for the other complexes is in accordance with their known behaviour in nonaqueous solution (11).

Figure 1 illustrates thin-layer voltammetry of TPPMg in CH_2Br_2/TBAP (0.2 *M*) in the same cell and under the same conditions used to collect the *in-situ* FTIR spectra reported below. The distortion from ideal symmetric thin layer behaviour is due to resistance-induced nonuniform potential distribution across the face of the working electrode (12). This distortion is more severe than we observed previously (4) for the oxidation of TPPZn in dichloroethane/TBAP, suggesting lower conductivity of the dibromomethane solutions. It is clearly not so severe, however, as to hinder our ability to carry out and resolve the successive oxidations of the complex. The resolution between successive oxidations associated with spectral data will, in fact, be better than that suggested by the voltammetry, as spectra are recorded after equilibrium conditions have been reached (ca. 90 s) at constant potential. Very little current flows and effects due to IR losses are minimized.

Figure 2*a* illustrates the difference spectrum associated with one-electron oxidation of TPPMg to the corresponding cation radical. The disappearance bands denoted 1D and 2D, and the appearance features denoted 1A–5A, are closely duplicated in difference spectra associated with cation radical formation in all complexes we have studied. The band positions and relative intensities, normalized to that of 3A, are summarized in Table 2. All of the bands reported in Table 2 were reproducibly observed in three successive experiments. Also, all bands are lost when the electrode potential is returned to the base value, indicating reversibility of the oxidations. Band 3A, occurring in the range 1276 to 1302 cm^{-1}, is always clearly evident as one of the strongest features in the spectrum, providing strong support for earlier reports (1, 2) of a 1280 cm^{-1} diagnostic band for TPP cation radicals.

Our results for TPPMnCl appear to contradict those of Spreer *et al.* (3). These workers reported that a band at 1280 cm^{-1} observed for the crystalline cation radical $TPPMnClSbCl_6 \cdot 4C_2H_2Cl_4$ was lost on prolonged exposure to vacuum, and suggested that the 1280 cm^{-1} band was due to the tetrachloroethane solvate molecules, rather than the cation radical. The *in-situ* difference spectrum in dibromomethane (Fig. 3) clearly shows the presence of a strong appearance band at 1286 cm^{-1}. CH_2Br_2 has no absorbance in this vicinity, so the band is not ascribable to solvent. This band was also clearly observable when dichloromethane or dichloroethane was the solvent.

The 1280 cm^{-1} band in the cation radicals occurs in a region where no significant absorbance due to the unoxidized porphyrin is observed. This facilitates its use as a diagnostic for ring oxidation in spectra of species isolated in the solid state. The additional bands observed in the difference spectra appear to provide a useful finger print for ring oxidation in *in-situ* studies, but are not likely to be as useful in interpreting single spectra of species isolated from solution. Bands 1D, 2D, 1A, 2A, and 5A all overlap with strong bands observed in the solid state spectra of the unoxidized porphyrins. Their observation in the difference spectra thus appears to result from a change in intensity of bands also present in the unoxidized species, rather from any new vibrational feature. Band 4A, in the region 1219 to 1239 cm^{-1}, occurs in a region where no major absorbance of the unoxidized porphyrins occur, and may be observable in solid state spectra of isolated cation radicals. Its intensity is much less than that of band 3A, however, and all of the unoxidized porphyrins examined display strong absorbance at approximately 1205 cm^{-1}, which could obscure this feature.

The difference spectrum associated with one-electron oxidation of TPPMg, Fig. 2*a*, also displays weak, broad appearance features at 1143 and 1034 cm^{-1}. Two such bands in the region above 1000 cm^{-1} are typical of coordinated perchlorate (13). We have previously shown (4, 5) that coordination of supporting electrolyte perchlorate accompanies the oxidation of TPPZn to the cation radical in dichloroethane, giving rise to appearance bands at 1137 and 1028 cm^{-1} in the *in-situ* difference spectrum. These bands were absent when the supporting electrolyte anion was tetrafluoroborate. Perchlorate coordination similarly appears to account for the 1143 and 1034 cm^{-1} bands accompanying the oxidation of TPPMg. Coordination of perchlorate is also indicated as accompanying the oxidation of the porphyrin ring in TPPCo (see below), but we were not able to reproducibly observe bands suggestive of perchlorate coordination to any of the other cation radicals investigated.

Figure 2*b* illustrates the difference spectrum observed on 2-electron oxidation of TPPMg to the π-dication. Not surprisingly, the bands due to coordinated perchlorate increase substantially, indicating that perchlorate complexation to the dication is more favourable than to the singly oxidized porphyrin. This increase in the extent of perchlorate complexation is also apparent when a second electron is removed from the porphyrin ring in TPPZn and TPPCo. With the π-dication species, in particular, it is possible that two perchlorate ions coordinate to yield a six-coordinate species. While the *in-situ* FTIR results do provide strong evidence that perchlorate complexation occurs, they do not provide unambiguous evidence as to the number of coordinating perchlorate ions involved.

In comparing Figs. 2*a* and 2*b*, it is evident that removal of a second electron from the porphyrin ring results in further changes in the vibrational spectrum of TPPMg. Appearance features at 1419, 1357, 1299, and 1226 cm^{-1} in Fig. 2*b* present a 4-band pattern reminiscent of that presented by bands 1A to

Can. J. Chem. Downloaded from www.nrcresearchpress.com by 61.7.252.67 on 09/07/12
For personal use only.

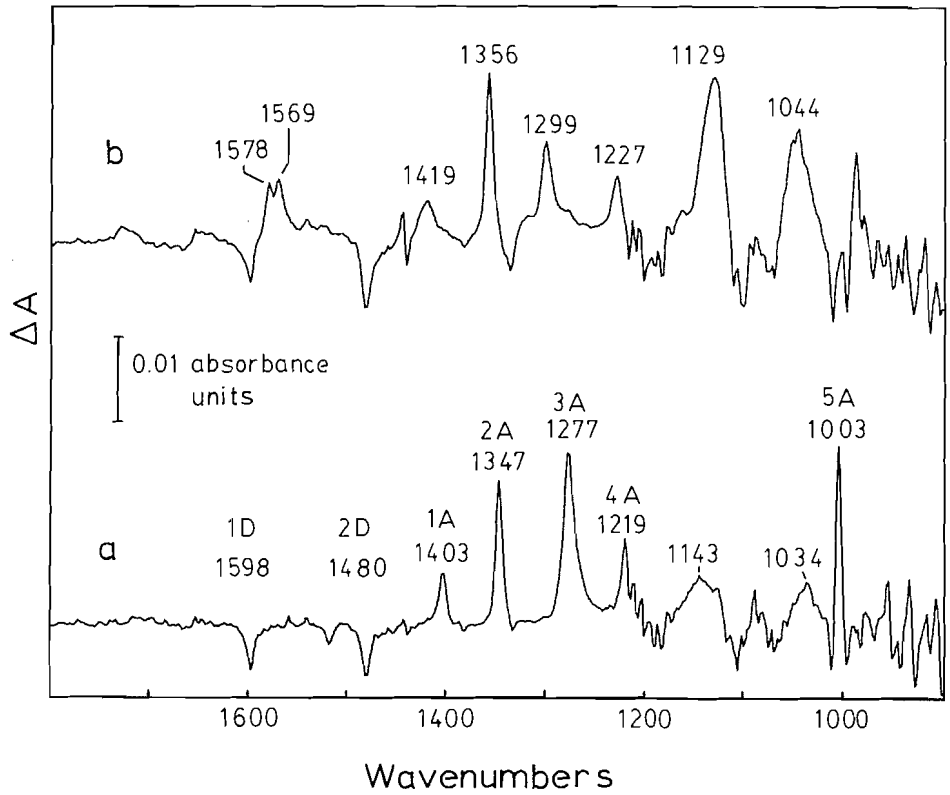

FIG. 2. *in-situ* FTIR difference spectrum for **1** (*a*) and **2** (*b*) electron oxidation of TPPMg in CH_2Br_2/0.2 *M* TBAP. In (*a*), $E_1 = 0.5$ V; $E_2 = 0.77$ V vs. SCE. In (*b*), $E_1 = 0.50$ V; $E_2 = 1.15$ V vs. SCE.

TABLE 2. Band positions (cm^{-1}) and normalized intensities[a,b] observed in difference spectra associated with one-electron oxidation for the porphyrin ring in TPP complexes

	Band position and normalized intensity						
Band	$TPPH_2$	TPPMg	TPPCu	TPPZn	TPPCo[d]	TPPMnCl	TPPFeCl
1D	1598 (0.29)	1598 (0.28)	1598 (0.23)	1598 (0.19)	1600 (0.22)	1598 (0.21)	1599 (0.12)
2D	1470 (0.40)	1480 (0.29)	1490 (0.24)	1487 (0.27)	1492 (0.16)	1492 (0.32)	1488 (0.12)
1A	1394 (0.40)	1403 (0.38)	1428 (0.38)	1408 (0.35)	1426 (0.60)	1430 (0.35)	1415 (0.15)
2A	1345 (1.21)	1347 (0.84)	1353 (1.00)	1346 (1.05)	1364 (0.76)	1348 (1.73)	1344 (1.12)
3A	1283 (1.00)	1277 (1.00)	1292 (1.00)	1277 (1.00)	1302 (1.00)	1286 (1.00)	1281 (1.00)
4A	1227 (0.42)	1219 (0.43)	1230 (0.09)	1222 (0.71)	1240 (0.13)	1223 (0.47)	1221 (0.18)
5A	[c]	1003 (1.13)	1002 (0.56)	1000 (0.67)	1008 (0.78)	1016 (0.58)	1012 (0.46)

[a]Measurements for TPPZn utilized 1,2-dichloroethane/0.2 *M* TBAP, all other measurements in dibromomethane/0.2 *M* TBAP.

[b]Normalized intensities (in parentheses) calculated by ratioing the observed absorbance to that of band 3A. See text for explanation of band designations.

[c]Corresponding band (see text) in the unoxidized porphyrin below the cutoff frequency of the CaF_2 window.

[d]Difference spectrum obtained by subtracting absorbance observed on one-electron oxidation (metal oxidation, see text) from that observed on two-electron oxidation.

Can. J. Chem. Downloaded from www.nrcresearchpress.com by 61.7.252.67 on 09/07/12
For personal use only.

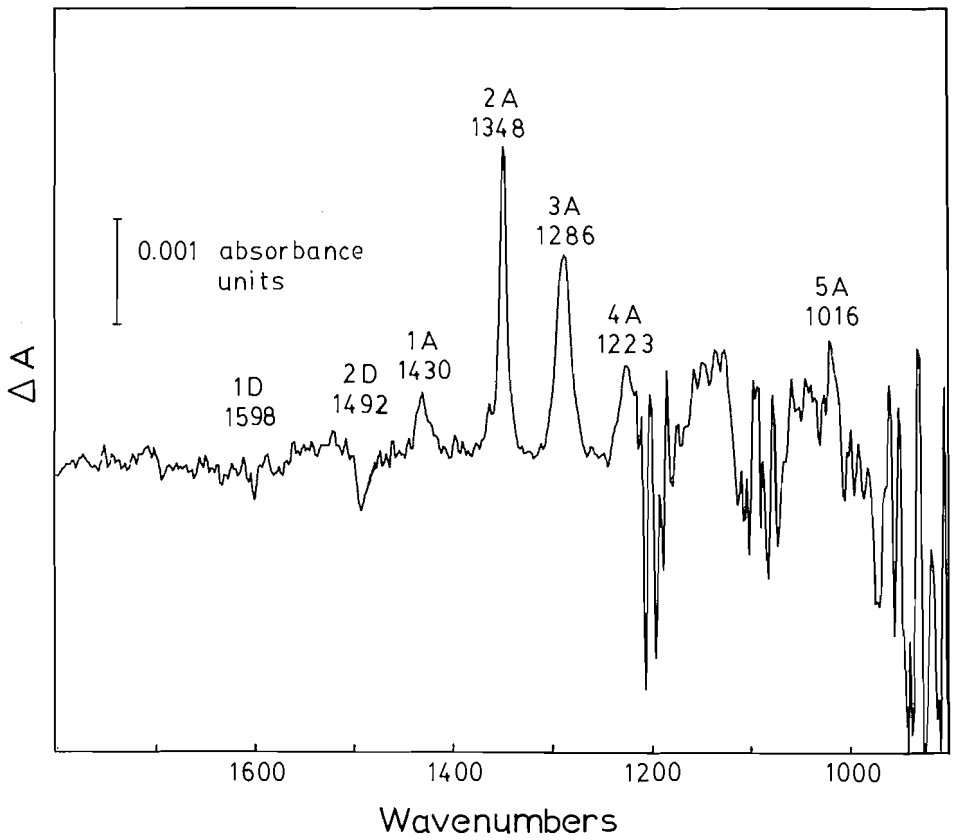

FIG. 3. *in-situ* FTIR difference spectrum for one-electron oxidation of TPPMnCl in CH_2Br_2/0.2 *M* TBAP. $E_1 = 0.95$ V; $E_2 = 1.20$ V vs. SCE. The lower absorbances in this figure as compared to figs. 2 and 5 should not be construed as an indication of lower molar absorptivity for bands of the TPPMnCl cation radical, as thin-layer cavity thickness and angle of incidence of the reflected infrared radiation were not rigorously controlled (see ref. 4).

Can. J. Chem. Downloaded from www.nrcresearchpress.com by 61.7.252.67 on 09/07/12
For personal use only.

4A in the spectrum of the singly oxidized species, but shifted to higher frequency. Also, two closely spaced appearance peaks at 1569 and 1578 cm^{-1} are observed, although it is not clear whether these represent two new vibrational features, or a single appearance band split by a less intense disappearance band. In particular, a high frequency shift of bands 2A and 3A and a new appearance feature near 1600 cm^{-1} appear to be typical of π-dication formation, as similar changes are observed on loss of two electrons from the porphyrin ring of TPPCo and TPPZn. In TPPCo, the π-dication spectra shows a strong appearance band at 1606 cm^{-1}, and bands 1A to 4A are observed at 1434, 1376, 1315, and 1242, respectively, as compared to 1426, 1365, 1302, and 1241 for the π-cation radical. Similarly, the π-dication derived from TPPZn shows a strong appearance feature at 1588 cm^{-1}, and bands 1A to 4A are observed at 1409, 1360, 1300, and 1222 as compared to 1408, 1346, 1277, and 1222 cm^{-1} in the π-cation radical. We have not attempted to obtain dication spectra of the other complexes utilized, as the voltammetric studies indicated that these would not be stable on the longer time scale (approximately 3 min) required for FTIR characterization.

TPPCo in CH_2Br_2/TBAP undergoes three successive one-electron oxidations, as is evident in the cyclic voltammetry of Fig. 4. The voltammetry is very similar to that observed by Kadish (11) in CH_2Cl_2/TBAP, in accordance with the above noted similarity of CH_2Br_2 and CH_2Cl_2 as solvents for metalloporphyrin oxidations. In that report, the first of the three evident oxidation processes was ascribed to metal oxidation, while the remaining two processes were assigned to loss of

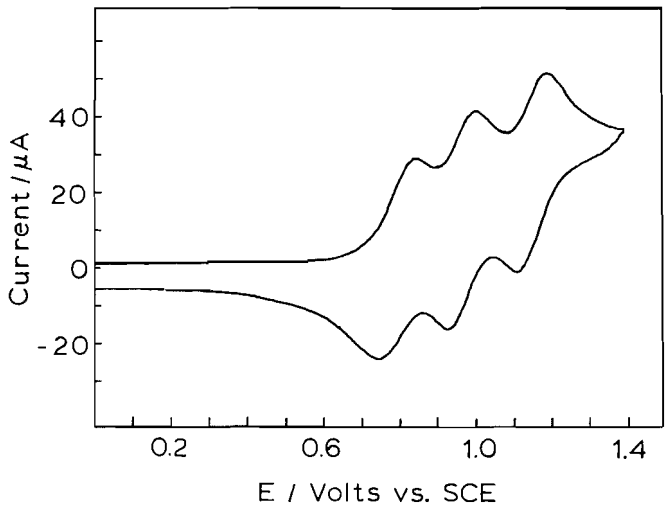

FIG. 4. Cyclic voltammetry of TPPCo in CH_2Br_2/0.2 *M* TBAP. Scan rate was 25 mV s^{-1}.

electrons from the porphyrin ring. Similarly, Gasyna *et al.* have considered that the first one-electron oxidation in CH_2Cl_2 is metal-centered based on magnetic circular dichroism measurements (14). The *in-situ* FTIR results confirm that this is also the correct assignment of the voltammetric waves in CH_2Br_2, and provide a comparison of vibrational changes due to oxidation of the metal center with those due to oxidation of the porphyrin ligand.

Figure 5 illustrates the *in-situ* FTIR spectroelectrochemistry

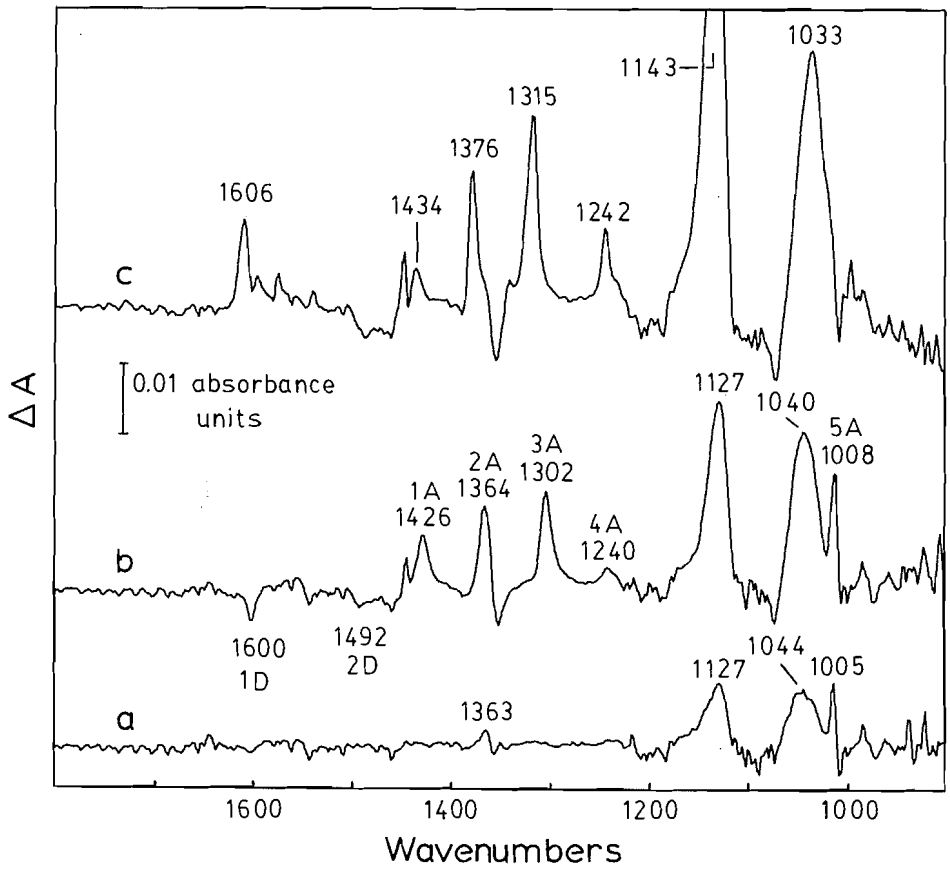

FIG. 5. *in-situ* FTIR difference spectra for **1** (*a*), **2** (*b*) and **3** (*c*) electron oxidation of TPPCo in CH_2Br_2/0.2 *M* TBAP. $E_1 = 0.65$ V vs. SCE for all spectra. $E_2 = 0.88$ (*a*); 1.08 (*b*); and 1.4 V vs. SCE (*c*).

associated with successive one-electron oxidation of TPPCo. In comparing Figs. 5*a* and *b* for one- and two-electron oxidation of TPPCo, it is evident that the porphyrin ligand vibrations in the region 1200 to 1700 cm^{-1} undergo very little perturbation on removal of one electron from the complex, while major perturbation of the ligand vibrations are observed on the loss of a second electron. It seems unreasonable to suggest that the porphyrin ligand vibrations would be more strongly affected by electron loss from the metal than from the ligand itself, and so these data force the conclusion that, at least under the conditions of these experiments, the first one-electron oxidation is metal-centered while the second electron derives from the porphyrin ring.

The difference spectrum associated with loss of the second electron from TPPCo, Fig. 5*b*, displays all of the appearance and disappearance bands which accompany the formation of the π-cation radicals of the other TPP complexes investigated. By way of contrast, the one-electron oxidation product, Fig. 5*a*, lacks any observable bands in the 1210 to 1310 cm^{-1} region where bands 3A and 4A would be anticipated for cation radical formation. The absence of any band near 1280 cm^{-1}, in particular, tends to confirm that the first oxidation of the Co(II) complex results in the formation of a Co(III) species.

The difference spectrum of Fig. 5*a* does indicate a sharp appearance feature at 1005 cm^{-1}, in the region where band 5A is anticipated for cation-radical formation, and a weaker appearance feature at 1363 cm^{-1}, in the region where band 2A is anticipated for ring oxidation. As was noted above, these bands are associated with an increase in the intensity of bands also present in the unoxidized complex. Increasing the charge on the metal center may thus result in the same type of perturbation responsible for the change in intensity of these bands as that due to removal of an electron from the porphyrin ring itself. The extent of the perturbation due to metal oxidation is much less than that due to ring oxidation, however, as evident in comparing Figs. 5*a* and 5*b*.

Also apparent in Fig. 5*a* are two strong bands at 1127 and 1044 cm^{-1}. As above, these are indicative of perchlorate coordination, and provide strong evidence that oxidation of the Co(II) center to Co(III) is accompanied by complexation of supporting electrolyte perchlorate.

The difference spectrum associated with removal of three electrons from TPPCo is illustrated in Fig. 5*c*. In comparing Fig. 5*b* and 5*c*, it is apparent that the third oxidation results in a shift of bands 2A and 3A to higher frequency and a new appearance band at 1606 cm^{-1}. As noted above, these changes are similar to those observed on formation of the π-dications of TPPMg and TPPZn, supporting the assignment of the third oxidation process as ring-centered.

It is also apparent in Fig. 5 that the extent of perchlorate complexation increases with the number of electrons removed from the porphyrin complex, as indicated by the increase in intensity of appearance bands near 1127 and 1040 cm^{-1}. TPPCo complexes with two axially bound ligands are well known. Thus, it is entirely feasible, particularly for the π-dication, that two perchlorates coordinate to yield an overall six-coordinate species. The splitting of these two bands also increases with oxidation state. The band positions are 1127 and 1044 cm^{-1} for

Can. J. Chem. Downloaded from www.nrcresearchpress.com by 61.7.252.67 on 09/07/12
For personal use only.

the Co(III) complex, 1127 and 1040 cm^{-1} for the π-cation radical, and 1131 and 1033 cm^{-1} for the π-dication. The extent of splitting may thus be correlated with the strength of perchlorate binding, although our data are as yet too limited to assess the usefulness of this criterion. The opposite trend, for instance, appears to hold for coordination of perchlorate to TPPMg cation-radical and dication, as evident in comparing Figs. 2*a* and 2*b*. The signal-to-noise ratio associated with the perchlorate bands at 1143 and 1034 cm^{-1} in Fig. 2*a* is too low to allow high precision in determination of the band positions, however.

It should be noted that, while the *in-situ* FTIR studies leave little doubt that the first oxidation of TPPCo under the conditions employed in this study is a metal-centered oxidation of Co(II) to Co(III), the one-electron oxidation product of TPPCo isolated with $SbCl_6^-$ as counterion has been characterized (15), on the basis of uv–vis and magnetic susceptibility data as well as an infrared band at 1290 cm^{-1}, as a π-cation radical containing Co(II). It has been demonstrated, however, that the site of oxidation in OEPCo(II) complexes (OEP = octaethylporphyrin) is highly dependent on the axial coordination environment of the metal center, and both OEPCo(III) and $OEP^{+\cdot}$Co(II) complexes are known (16). In the present case, the coordination of perchlorate, as clearly evident in the infrared data presented above, may be sufficiently more stabilizing to Co(III) than when $SbCl_6^-$ is present as counterion to direct loss of an electron from the metal center rather than the porphyrin ring. Coordination of trace water from the solvent is another possibility which, although there is no evidence to support it, cannot be ruled out as a contributing factor on the basis of our data. Coordination of water is believed to be important in determining the electron-transfer site in OEPCo(II) complexes (16).

Conclusions

The data presented above clearly supports previous workers' conclusions that infrared spectroscopy is a valuable tool for ascertaining the site of oxidation in TPP complexes (1, 2), and further demonstrate that such useful diagnostic evidence can be obtained *in situ* without isolation of the oxidized complexes. In addition to the obvious factor of convenience, *in-situ* characterization affords a difference spectrum in which small vibrational perturbations due to oxidation of the complexes are more likely to be observed than in single spectra of isolated species. The extra features observed in the difference spectra of this study indicate that the similarity of changes in vibrational structure accompanying oxidation of the porphyrin ring in TPP complexes goes beyond just the appearance of a band near 1280 cm^{-1}. Finally, *in-situ* FTIR spectroelectrochemistry provides evidence concerning coordination changes associated with the oxidation as they pertain in solution, rather than in the solid state. Such information cannot unambiguously be gleaned from spectra of isolated species.

Acknowledgements

The authors are grateful to the Natural Sciences and Engineering Research Council of Canada for financial support of this work.

1. E. T. Shimomura, M. A. Phillipi, H. M. Goff, W. F. Scholz, and C. A. Reed. J. Am. Chem. Soc. **103**, 6778 (1981).
2. P. Gans, G. Buisson, E. Duee, J. Marchon, B. S. Erler, W. F. Scholz, and C. A. Reed. J. Am. Chem. Soc. **108**, 1223 (1986).
3. L. O. Spreer, A. C. Maliyackel, S. Holbrook, J. W. Otvos, and M. Calvin. J. Am. Chem. Soc. **108**, 1949 (1986).
4. A. S. Hinman and B. J. Pavelich. Can J. Chem. **65**, 919 (1987).
5. A. S. Hinman, B. J. Pavelich, A. E. Kondo, and S. Pons. J. Electroanal. Chem. **234**, 145 (1987).
6. J. K. Foley and S. Pons. Anal. Chem. **57**, 945A (1985).
7. A. D. Adler, F. R. Longo, F. Kampas, and J. Kim. J. Inorg. Nucl. Chem. **32**, 2443 (1970).
8. S. L. Kelly and K. M. Kadish. Inorg. Chem. **21**, 3631 (1982).
9. M. A. Phillippi, E. T. Shimomura, and H. M. Goff. Inorg. Chem. **20**, 1322 (1981).
10. X. Q. Lin and K. M. Kadish. Anal. Chem. **57**, 1498 (1985).
11. K. M. Kadish. *In* Progress in inorganic chemistry. Vol. 34. *Edited by* S. J. Lippard. John Wiley. 1986. p. 435.
12. A. S. Hinman, S. Pons, and J. Cassidy. Electrochim. Acta. **30**, 89 (1985).
13. M. R. Rosenthal. J. Chem. Ed. **50**, 331 (1973).
14. Z. Gasyna, W. R. Browett, and M. J. Stillman. Inorg. Chem. **23**, 382 (1984).
15. W. F. Scholz, C. A. Reed, Y. J. Lee, W. R. Scheidt, and G. Lang. J. Am. Chem. Soc. **104**, 6791 (1982).
16. A. Salehi, W. A. Oertling, G. T. Babcock, and C. K. Chang. J. Am. Chem. Soc. **108**, 5630 (1986).

Can. J. Chem. Downloaded from www.nrcresearchpress.com by 61.7.252.67 on 09/07/12
For personal use only.

Études des propriétés adsorbantes des fibres d'amiante modifiées et de fibres proposées comme substitut à l'amiante par chromatographie en phase gazeuse

YVES LEFEBVRE, MARYSE LAMBERT, JALEH KHORAMI ET HUGUES MÉNARD[1]

Département de chimie, Université de Sherbrooke, Sherbrooke (Québec), Canada J1K 2R1

Reçu le 15 avril 1987[2]

YVES LEFEBVRE, MARYSE LAMBERT, JALEH KHORAMI et HUGUES MÉNARD. Can. J. Chem. **66**, 1596 (1988).

L'étude, par chromatographie en phase gazeuse, des tracés des isothermes d'adsorption du benzène sur les fibres d'amiante brutes et modifiées ainsi que sur des fibres proposées comme substitut à l'amiante, montre une différence marquée de comportement entre les différents adsorbants utilisés. La comparaison entre le pouvoir adsorbant des fibres d'amiante brutes, d'amiante phosphatées et d'amiante chauffées à 700°C, vis-à-vis de solutés ayant des groupements fonctionnels variables, a mis en évidence des phénomènes de physisorption et de chimisorption. La présence de groupements hydroxyles situés sur la surface des fibres d'amiante favorise l'adsorption de molécules organiques par la formation de liaisons hydrogènes.

YVES LEFEBVRE, MARYSE LAMBERT, JALEH KHORAMI, and HUGUES MÉNARD. Can. J. Chem. **66**, 1596 (1988).

A study, by vapor phase chromatography, of the adsorption isotherms of benzene on raw and modified asbestos fibers as well as on fibers proposed as substitutes for asbestos shows that there is a marked difference in the behaviour of the various fibers examined. A comparison of the adsorbing power of raw and phosphorylated asbestos fibers, as well as asbestos fibers heated to 700°C, has been made regarding their behaviour toward solutes bearing various functional groups, and it has shown the existence of physical adsorption as well as chemisorption. The presence of hydroxyl groups in the surface of the asbestos fibers favors the adsorption of organic molecules through hydrogen bonding.

[Journal translation]

Can. J. Chem. Downloaded from www.nrcresearchpress.com by 93.93.197.157 on 09/07/12
For personal use only.

Introduction

L'activité biologique des fibres d'amiante chrysotile est bien connue, et l'existence d'un effet synergique entre les fibres et les agents toxiques et (ou) cancérogènes a été démontrée par de nombreux chercheurs (1–3).

Parmi les facteurs responsables de l'activité biologique des fibres d'amiante chrysotile, la réactivité de la surface des fibres a été particulièrement soulignée. Plusieurs chercheurs ont entrepris leurs recherches dans le but de changer la composition chimique de la surface des fibres d'amiante (4, 5).

Parmi ces procédés, la phosphorylation des fibres, proposée et mise au point par Lalancette et Dunnigan (6), a connu beaucoup de succès. L'activité biologique de lamiante phosphaté est en effet diminuée de façon remarquable (7) et la réaction gaz–solide « $POCl_3$ vapeurs – amiante » permet la formation de polyphosphates qui encapsulent et obstruent les pores de ce minerai (8 et 9). Ménard *et al.* (10) ont également démontré que l'adsorption des hydrocarbures aromatiques polycycliques, en milieu liquide, sur l'amiante phosphaté est nettement diminuée.

Dans cette étude, nous présentons les mesures d'adsorption de différents hydrocarbures, avec groupements fonctionnels variables, sur l'amiante phosphaté, en utilisant la chromatographie en phase gazeuse. Ces résultats sont comparés avec ceux des fibres d'amiante brutes et chauffées à 700°C.

Nous avons aussi comparé les isothermes d'adsorption obtenus de l'amiante et de l'amiante modifié avec les isothermes de fibres synthétiques proposées comme substituts (par exemple Kevlar et carbone) (11) ainsi qu'avec un gel de silice utilisé comme support chromatographique de référence.

Partie expérimentale

Nous avons utilisé un chromatographe à gaz muni d'un détecteur à ionisation de flamme de la compagnie Perkin Elmer modèle 3920B pour mesurer les isothermes d'adsorption, en utilisant l'hélium comme gaz vecteur et nous avons éliminé les traces d'eau et le gaz carbonique avec un tamis moléculaire 13X.

Pour les injections, nous avons utilisé deux seringues Hamilton de 1 μL et de 10 μL. Le volume mort de la colonne est mesuré par injection de méthane.

Les tracés chromatographiques sont enregistrése via un intégrateur Hewlett Packard modèle 3390A.

Les isothermes d'adsorption sont mesurés à l'aide d'une série d'injections de benzène variant entre 0.1 et 5 μL, utilisant la méthode du maximum du pic. Les enthalpies isostériques d'adsorption sont obtenues en appliquant l'équation de Clausius–Clapeyron (12, 13) pour une série des isothermes obtenus à des températures variables.

Description des supports utilisés

1. L'amiante BC4-T provenant de la mine « British Canadian », a été défibrilé mécaniquement à l'aide d'un appareil B.O.P. (Ball Opener Penmen) et séché à 400°C.
2. L'amiante phosphaté a été préparé suivant les procédé de Lalancette et Dunnigan (6). Il faut noter que ces fibres ont été calcinées à 350°C après la réaction.
3. L'amiante traité thermiquement a été préparé par le chauffage de l'amiante à 700°C pendant 24 h.
4. Les fibres de carbone, Thornell grade VMA IIA. Ces fibres ont été broyées au mortier puis séchées à 400°C.
5. Les fibres de Kevlar, Dupont grade 6F-218, ont été séchées à 200°C, une température modérée pour éviter la décomposition thermique de ces fibres.
6. Le gel de silice, Merck, type 60, grade ART 9385, a été séchée à 300°C. La taille des particules se situe entre 40 et 63 μm.

Les traitements thermiques des supports entre 200 et 400°C éliminent les impuretés, comme l'eau sous forme moléculaire, éventuellement présentes sur la surface ou dans les pores des supports utilisés.

La liste des solutés utilisés en phase vapeur (gaz) dans ces études :

1. Benzène*	Fisher	Spectranalized A.C.S.
2. Cyclohexane	Fisher	Spectranalized A.C.S.
3. Hexane	Anachemia	Accusolv
4. Toluène	Anachemia	Accusolv
5. Tétrahydrofuranne	Anachemia	Accusolv
6. Acétonitrile	Anachemia	Accusolv
7. Dichlorométhane	Anachemia	Technique
8. Acétone	Shefford	Technique
9. Méthanol	Shefford	Technique

*Seul soluté utilisé pour les isothermes d'adsorption dans ce travail. Les autres solutés sont utilisés pour les mesures de volumes de retention.

1. Auteur à qui adresser toute correspondance.
2. Revision reçue le 23 février 1988.

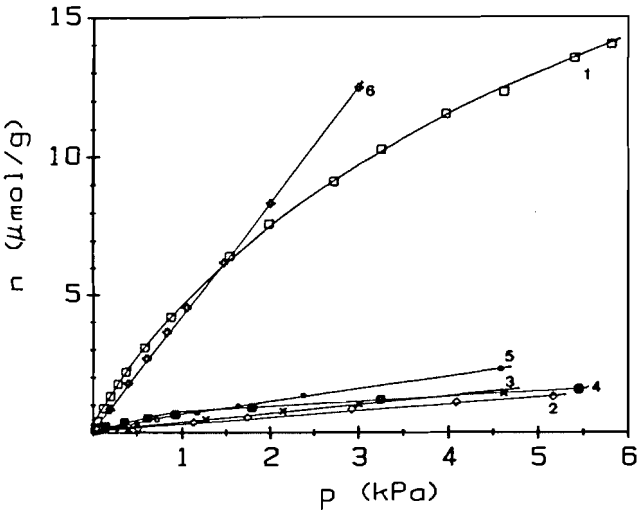

FIG. 1. Isotherme d'adsorption du benzène à 180°C exprimée avec la masse d'absorbant utilisée sur divers supports ; (1) amiante BC4-T, (2) amiante phosphaté, (3) amiante chauffé à 700°C, (4) fibre de carbone, (5) fibre Kevlar et (5) gel de silice.

Résultats et discussion

Isothermes d'adsorption du benzène

Les figures 1 et 2 représentent les isothermes d'adsorption du benzène sur les différents supports utilisés. Sur la figure 1, la quantité adsorbée *n* est exprimée par unité de poids de support utilisé, en fonction de la pression partielle de benzène en kPa. La quantité adsorbée peut être également exprimée par unité de surface de l'adsorbant (figure 2), en faisant intervenir les valeurs de surface spécifique mentionnées au tableau 1 ; cette représentation permet une meilleure interprétation de la réactivité de la surface ou des sites de surface. Nous pouvons observer sur la figure 2*a* que les fibres de carbone, qui sont actives biologiquement (14), possèdent la plus grande affinité pour le benzène.

L'adsorption du benzène sur les fibres de chrysotile brutes BC4-T est située en deuxième rang après les fibres de carbone ; cependant, les deux supports de l'amiante phosphaté et chauffé n'adsorbent que très peu de benzène et leurs isothermes d'adsorption sont situés dans le bas de l'échelle comme le Kevlar et la silice. La figure 2*b* montre une expansion sur l'axe *y* (ordonnée) pour mieux distinguer les isothermes d'adsorption des produits très peu adsorbants ; ce graphique nous montre aussi la linéarité de l'isotherme d'adsorption de la silice.

Pour obtenir la figure 3, nous avons appliqué le modèle de Langmuir (15) aux isothermes non-linéaires. Les tracés de p/Γ (ou Γ est la quantité adsorbée par unité de surface) en fonction de *p* montrent une adsorption en deux étapes mise en évidence par l'obtention de deux lignes brisées pour tous les adsorbants fibreux utilisés. Un isotherme de Langmuir typique ne donnerait qu'une seule droite. Un comportement similaire avait été observé par Contour *et al.* (16) dans le cas de l'adsorption de la diéthylaniline sur les fibres d'amiante chrysotile lors d'une étude par chromatographie en phase gazeuse. Dans un premier temps, l'adsorption se produit sur la surface externe des fibres. Un phénomène de condensation capillaire à l'intérieur des pores est reponsable de la deuxième étape de l'adsorption. Ce phénomène est souvent rencontré pour les adsorbants qui possèdent une large distribution de taille et de forme des pores.

L'isotherme d'adsorption de la silice étant linéaire (figures 1 et 2*b*), nous n'avons pas pu appliquer le modèle de Langmuir pour ce produit (14).

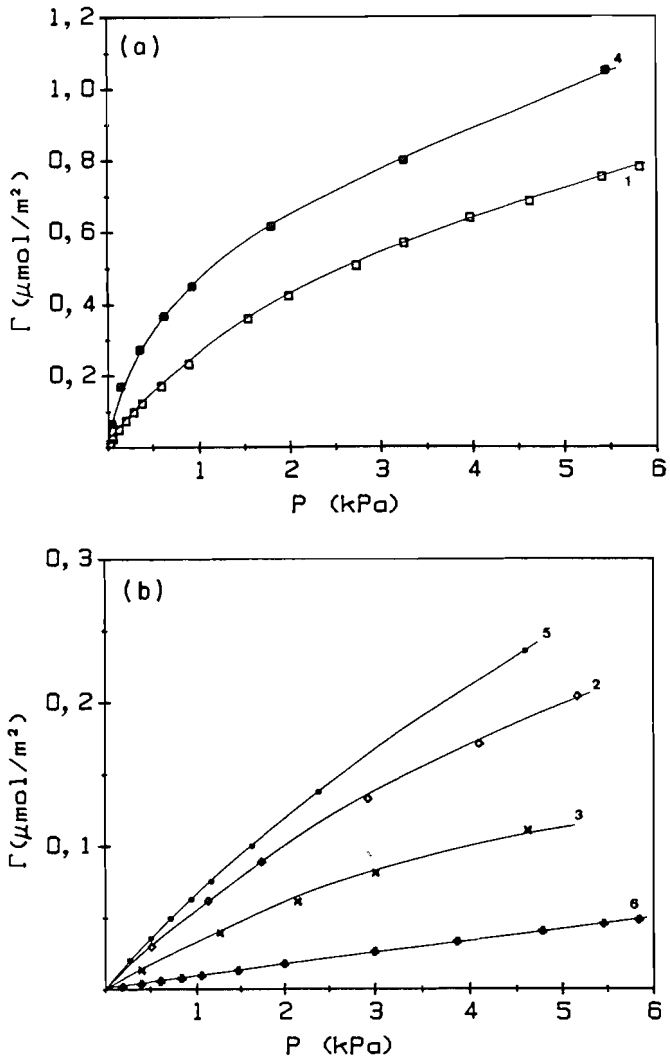

FIG. 2. Isotherme d'absorption du benzène à 180°C exprimée an excès de surface ; (1) amiante BC4-T et (4) fibre de carbone. (b) Isotherme d'absorption du benzène à 180°C exprimée en excès de surface, avec expansion en ordonnée ; (2) amiante phosphaté, (3) amiante chauffé à 700°C, (5) fibre Kevlar et (6) gel de silice.

TABLEAU 1. Surface spécifique (Σ) des adsorbants utilisés

Adsorbant	Σ (m^2/g)
Amiante BC4-T	18,0
Amiante phosphaté*	6,5
Amiante chauffé à 700°C	12,9
Silice	480
Fibre de carbone	1,5
Fibre Kevlar	9,8

*Contient 1,1% en poids de phosphore.

L'affinité de l'amiante chrysotile brut et modifié vis-à-vis les différents solutés

Dans un premier temps, les enthalpies isostériques moyennes d'adsorption (12) du benzène pour les trois échantillons de l'amiante BC4T brut, phosphaté et chauffé à 700°C, sont mesurées (tableau 2). Durant les expériences, nous avons constaté que nos mesures sont limitées en ce qui concerne les

Can. J. Chem. Downloaded from www.nrcresearchpress.com by 93.93.197.157 on 09/07/12
For personal use only.

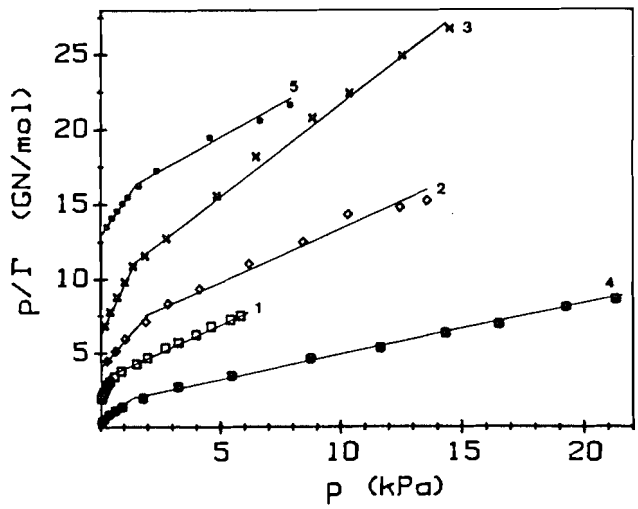

FIG. 3. Modèles théoretiques de Langmuir pour l'adsorption du benzène sur divers adsorbants; (1) amiante BC4-T (180°C), (2) amiante phosphaté (120°C), (3) amiante chauffé à 700°C (120°C), (4) fibre de carbone (180°C) et (5) fibre Kevlar (180°C).

TABLEAU 2. Enthalpies isostériques moyennes d'adsorption du benzène sur l'amiante et l'amiante modifié

Adsorbant	$-\Delta H$ (kJ/mol)	T (°C)
Amiante BC4-T	58 ± 1	210
Amiante phosphaté	50 ± 4	125
Amiante chauffé à 700°C	37 ± 2	150

échelles de température utilisées pour chaque support. Nous avons constaté que pour l'amiante BC4-T brut, le temps de retention mesurable se situe durant l'expérience entre 180 et 240°C, pour l'amiante phosphaté entre 90 et 140°C et pour l'amiante traité thermiquement entre 120 et 180°C. Le tableau 2 présente les isostériques moyennes d'adsorption du benzène sur les trois types d'amiante avant et après modification.

Néanmoins les enthalpies isostériques moyennes mesurées à la température moyenne pour chaque support, montrent une diminution de l'affinité de l'amiante après modification, surtout après traitement thermique à 700°C. Ceci provient probablement de la modification structurale intervenant à cette température (transformation chrysotile → forstérite).

Le tableau 3 illustre les volumes de rétention spécifiques mesurés sur l'amiante et l'amiante modifié, pour différents solutés ayant des groupements fonctionnels variables.

Nous pouvons constater que les volumes de retention spécifiques mesurés étant faibles pour le *n*-hexane et cyclohexane, nous n'avons pas pu observer une différence marquée entre les trois adsorbants. Cependant dans le cas du benzène et du toluène, une diminution marquée des volumes de rétention est observée. Pour les solutés ayant des groupements fonctionnels azotés et oxygénés, nous avons observé une adsorption significative pour les trois adsorbants de façon que dans plusieurs cas le pic chromatographique n'est même pas élué. Ce dernier peut être interprété comme une interaction très forte entre les trois supports et les groupements azotés et oxygénés des solutés et (ou) une chimisorption.

La diminution des volumes de rétention de l'amiante modifié

TABLEAU 3. Volumes de rétention spécifiques mesurés sur l'amiante et l'amiante modifié

	V(mL/g)		
	Support (température de la colonne)		
Soluté	Amiante BC4-T (180°C)	Amiante phosphaté (100°C)	Amiante chauffé à 700°C (100°C)
n-hexane	1,11	1,40	1,07
Cyclohexane	0,86	1,32	0,97
Dichlorométhane	1,89	0,64	0,95
Benzène	7,06	2,67	2,74
Toluène	19,44	5,85	6,67
Tétrahydrofuranne	11,47	N.E.*	N.E.*
Acétone	32,08	N.E.	N.E.
Méthanol	N.E.	N.E.	N.E.
Acétonitrile	N.E.	N.E.	N.E.

*Même résultat à 180°C.
N.E. Le pic chromatographique n'est pas élué.

(phosphaté et chauffé) vis-à-vis de benzène et toluène met en évidence l'intervention des groupements hydroxyles dans des liaisons hydrogènes par l'intermédiaire des électrons π de ces molécules. Il faut noter que dans le cas de l'amiante phosphaté, les groupements hydroxyles sont déjà engagés dans une intéraction entre $POCl_3$ et l'amiante et que la surface de l'amiante est encapsulée par les produits phosphatés formés. L'amiante chauffé à 700°C est presque complètement déhydroxylé et les groupements OH de la surface ont été expulsés sous forme d'eau à l'extérieur de la structure. L'interaction faible et la diminution légère de volumes de rétention dans le cas de dichlorométhane peut être reliée à la polarité de cette molécule. Pour le *n*-hexane et le cyclohexane l'absence des groupements fonctionnels et d'électrons π conduit à une affinité et une adsorption très faible entre ces solutés et les supports étudiés.

Conclusion

Les tracés des isothermes par chromatographie en phase gazeuse du benzène sur l'amiante brut et modifié montrent la grande affinité de l'amiante non traité pour le benzène et la probabilité de la formation des liaisons hydrogènes par l'intermédiaire des électrons π et les groupements hydroxyles. Nous avons aussi observé que les fibres de carbone actives biologiquement, adsorbent une quantité significative de benzène.

La comparaison des enthalpies isostériques moyennes d'adsorption du benzène sur l'amiante avant et après modification montre l'affinité accrue des fibres brutes pour le benzène et une diminution d'adsorption après modification surtout pour les fibres chauffées à 700°C.

La comparaison du pouvoir adsorbant des trois supports de l'amiante et l'amiante modifié vis-à-vis différents solutés organiques montre la possibilité de chimisorption par l'intermédiaire des groupements fonctionnels azotés ou oxygénés ainsi que la formation des liaisons hydrogènes entre les hydroxyles de l'amiante et les électrons π de ces molécules comme nous avons expliqué dans le cas de benzène.

Remerciements

Les auteurs remercient pour leur appui financier le Conseil national de recherches en sciences naturelles et en génie du

Can. J. Chem. Downloaded from www.nrcresearchpress.com by 93.93.197.157 on 09/07/12
For personal use only.

Canada, l'Institut de l'amiante et l'Institut en santé et sécurité au travail.

1. B. T. MOSSMAN et J. E. CRAIGHEAD. Environ. Res. **25**, 269 (1981).
2. E. G. HAMMOND, I. J. SELIKOFF et H. SEIDMAN. Ann. N.Y. Acad. Sci. **330**, 473 (1979).
3. H. SEIDMAN et I. J. SELIKOFF. Occup. Health saf. **46**, 197 (1982).
4. V. BOLIS, B. FUBINI et G. VENTURELLO. J. Therm. Anal. **28**, 249 (1983).
5. W. G. LIGHT et E. T. WEI. Nature, **265**, 537 (1977).
6. J. M. LALANCETTE et J. DUNNIGAN. Phosphated asbestos fibres and the process for preparing same. Brevet no 81103916.3, Bureau européen des brevets, La Haye, Pays-Bas. 1981.
7. F. M. KIMMERLE et P.-C. AITCIN. L'amiante chrysotile. Université de Sherbrooke, Sherbrooke (Québec). 1981. Chap. 1 et 8.
8. J. KHORAMI, L. NOEL et H. MENARD. Can. J. Chem. **65**, 1397 (1987).
9. J. KHORAMI, A. LEMIEUX et D. NADEAU. Can. J. Chem. **65**, 2268 (1987).
10. H. MENARD, L. NOEL, J. KHORAMI, J.-L. JOUVE et J. DUNNIGAN. Environ. Res. **40**, 84 (1986).
11. A. A. HOGSON. Alternatives to asbestos and asbestos products. Anjalena Publications Ltd., Angleterre. 1985. p. 56.
12. H. MENARD, Y. LEFEBVRE et J. KHORAMI. Talanta, **34**(6), 589 (1987).
13. J. R. CONDER et C. L. YOUNG. Physicochemical measurement by gas chromatography. Wiley, New York. Chap. 9. 1979.
14. R. D. ZUMWALDE et L. T. HARMISON. Carbon/graphite fibres: environmental exposures and potential health implications. Division of surveillance, hazard evaluations and field studies. NIOSH, U.S. department of health and human services, Cincinnati, OH. 1980.
15. A. W. ADAMSON. Physical chemistry of surfaces. 4^{e} ed. Wiley, New York. 1982. p. 521.
16. J. P. CONTOUR, I. GUERIN et G. MOUVIER. Stud. Environ. Sci. **1**, 255 (1978).

Can. J. Chem. Downloaded from www.nrcresearchpress.com by 93.93.197.157 on 09/07/12
For personal use only.

X-Ray structure determination of 1,2-anhydro-3,4:5,6-di-*O*-isopropylidene-1-*C*-nitro-D-mannitol

WALTER A. SZAREK,[1] GEORGE W. HAY, RAMESH K. SOOD, KONIA TROUTON, AND SUZANNE FORTIER
Department of Chemistry, Queen's University, Kingston, Ont., Canada K7L 3N6

Received October 13, 1987

WALTER A. SZAREK, GEORGE W. HAY, RAMESH K. SOOD, KONIA TROUTON, and SUZANNE FORTIER. Can. J. Chem. **66**, 1600 (1988).

The structure of the major product of the reaction of 1,2-dideoxy-3,4:5,6-di-*O*-isopropylidene-1-*C*-nitro-D-*arabino*-hex-1-enitol with 30% hydrogen peroxide and aqueous sodium hydrogencarbonate has been confirmed by X-ray crystallography to be that of 1,2-anhydro-3,4:5,6-di-*O*-isopropylidene-1-*C*-nitro-D-mannitol (*2*). The crystal structure of **2**, $C_{12}H_{19}NO_7$, is orthorhombic, $P2_12_12_1$, with cell dimensions $a = 10.269(3)$, $b = 15.115(7)$, $c = 9.295(8)$ Å, and $Z = 4$. The calculated density is $D_x = 1.336\ g\ cm^{-3}$. The structure was solved by direct methods and refined to a residual $R = 0.052$. The molecule has a $_2G^-$ conformation having bond lengths and angles in agreement with those observed in related structures, except for the C(1)—C(2), C(2)—C(3), and O(2N)—N bond distances which were found to be unusually small.

WALTER A. SZAREK, GEORGE W. HAY, RAMESH K. SOOD, KONIA TROUTON et SUZANNE FORTIER. Can. J. Chem. **66**, 1600 (1988).

Faisant appel à la diffraction des rayons-X, on a démontré que le produit principal de la réaction du didéoxy-1,3 di-*O*-isopropylidène-3,4:5,6 nitro-1-*C* D-*arabino*hexène-1 itol avec du peroxyde d'hydrogène à 30% et du carbonate acide de sodium aqueux est l'anhydro-1,2 di-*O*-isopropylidène-3,4:5,6 nitro-1-*C* D-mannitol (**2**). La structure cristalline du composé **2**, $C_{12}H_{19}NO_7$, est orthorhombique, $P2_12_12_1$, avec $a = 10{,}269(3)$, $b = 15{,}115(7)$ et $c = 9{,}295(8)$ Å et $Z = 4$. La densité calculée, D_x, est égale à $1{,}336\ g\ cm^{-3}$. On a résolu la structure par des méthodes directes et on l'a affinée jusqu'à une valeur résiduelle de $R = 0{,}052$. La molécule existe dans une conformation $_2G^-$ dont les longueurs des liaisons et les angles sont en accord avec ceux observés dans des structures semblables; on a toutefois observé que les longueurs des liaisons C(1)—C(2), C(2)—C(3) et O(2N)—N sont très courtes.

[Traduit par la revue]

Introduction

Syntheses of 2-deoxy-2-fluoro-D-glucose (1), or its ^{18}F-labeled analog (2), currently are of significant interest because of the application of the latter to the study of human metabolic processes by positron emission tomography (2). Recently, we reported (1) that 1,2-dideoxy-3,4:5,6-di-*O*-isopropylidene-1-*C*-nitro-D-*arabino*-hex-1-enitol (**1**) (3) reacted with 30% hydrogen peroxide and aqueous sodium hydrogencarbonate (4) to give a 1,2-anhydro derivative which, when treated with anhydrous potassium hydrogenfluoride, afforded a mixture of 2-deoxy-2-fluoro-3,4:5,6-di-*O*-isopropylidene-*aldehydo*-D-hexoses having the *gluco* and *manno* configurations in a ratio of approximately 4:1, respectively. Although this result, and other concurrent chemical evidence (1), strongly inferred that the 1,2-anhydro compound had the D-*manno* configuration (see **2**), there was some ambiguity[2] concerning the chirality of C(1) and C(2) which could not be resolved by the nmr data; the synthetic route, however, made the assignment of the absolute configurations of C(3)—C(5) completely unequivocal.

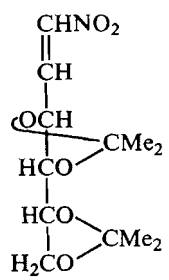

1

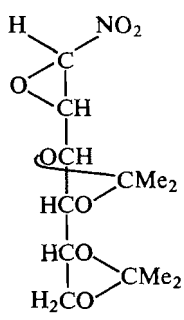

2

This problem has been solved by the determination of the crystal structure of the 1,2-anhydro compound described in ref. 1 by X-ray diffractometry. We present here the evidence which substantiates the structure of the 1,2-anhydro compound as **2**.

Results and discussion

The results of the X-ray diffraction studies (Tables 1–4) confirmed that the epoxidation (1, 4) of **1** afforded a product having a *manno* configuration. Although the X-ray data determined only the relative positions of the atoms, the certainty with respect to the chirality of C(3)—C(5) unambiguously established the absolute configuration as corresponding to D-*manno*, identical with that represented by structure **2** (see Fig. 1).

As expected, C(1) and C(2), which form part of an oxirane ring, have bond angles close to 60° and a bond distance (Table 3) similar to that reported (1.445(6) Å) (6) for the correspondent bond of 3,4-di-*O*-acetyl-1,2:5,6-dianhydrogalactitol. The remainder of the carbon atoms of the hexitol chain, each of which is involved in a 1,3-dioxolane ring, have bond angles (Table 3) which are nearly commensurate with those of DL (7), and the β (8) and K (9) forms of mannitol; the C(3)—C(4)—C(5) bond angle is ~1°[3] larger and the C(4)—C(5)—C(6) bond angle is ~1° smaller, relative to those compounds.

A salient feature of **2** in the crystalline state is the proximity of C(1), C(2), and C(3) (Table 3). The C(1)—C(2) bond distance (1.441(4) Å) is equal to that estimated (10) for tetrafluoroxirane. This is significantly shorter than the comparable bond of oxirane (1.462(3) Å) (11–13), (1*a*α, 2β, 2*a*β, 4α,

[1]Author to whom correspondence should be addressed.

[2]A similar uncertainty was reported by Baer and Madumelu (5) with respect to the configuration at C(6) of 5,6-anhydro-1,2-*O*-isopropylidene-6-nitro-α-D-glucofuranose.

[3]This angle is 2.6° larger than that reported (7) for DL-mannitol at −150°.

Can. J. Chem. Downloaded from www.nrcresearchpress.com by 61.7.252.67 on 09/07/12
For personal use only.

TABLE 1. Crystal data[a]

Parameter	Crystal data
Molecular formula	$C_{12}H_{19}NO_7$
Molecular weight	289.34
Space group; Z	$P2_12_12_1$; 4
Unit cell parameters (Å)	a = 10.269(3)
	b = 15.115(7)
	c = 9.295(8)
Volume (Å^3)	1442.81
Number of reflections used for the determination of unit cell parameters; 2θ range (deg)	25; 22–38
Density (calcd.) (g cm^{-3})	1.336
Number of measured reflections	1494
Number of observed reflections, $I \geqq 3\sigma(I)$	1112
2θ range scanned (deg)	1–50
μ (MoKα) (cm^{-1})	1.034
Crystal dimensions (mm)	0.40 × 0.10 × 0.10
Final R; R_w	0.052; 0.069
Largest shift/error in final least-squares cycle, Δ/σ	0.00
Maximum and minimum residual electron density in final difference Fourier map (e Å^{-3})	0.32; −0.37
Standard deviation of an observation of unit weight, S	2.589

[a]Estimated standard deviations are shown in parentheses.

TABLE 2. Final fractional coordinates and equivalent isotropic temperature factors with estimated standard deviation in parentheses

Atom	x	y	z	B_{eq} (Å^2)[a]
O(1)	0.2403(3)	−0.0133(2)	0.3139(3)	4.63
O(1N)	0.0251(4)	0.0055(3)	0.0271(4)	6.6
O(2N)	0.1041(5)	0.1062(3)	0.1626(5)	8.1
O(3)	0.3860(3)	−0.1628(2)	0.2058(3)	4.34
O(4)	0.5332(3)	−0.1704(2)	0.0234(3)	3.10
O(5)	0.5959(3)	0.0639(2)	0.0600(3)	3.97
O(6)	0.6190(3)	0.0578(2)	−0.1836(4)	4.50
N	0.1005(4)	0.0336(3)	0.1173(5)	4.60
C(1)	0.1934(4)	−0.0325(3)	0.1770(5)	3.56
C(2)	0.3287(4)	−0.0090(3)	0.1916(5)	3.63
C(3)	0.4355(4)	−0.0750(3)	0.1852(5)	3.28
C(4)	0.5014(4)	−0.0790(2)	0.0358(4)	2.69
C(5)	0.6261(4)	−0.0272(3)	0.0249(5)	3.03
C(6)	0.6783(4)	−0.0232(3)	−0.1288(6)	4.08
C(7)	0.4332(4)	−0.2190(3)	0.0942(5)	3.29
C(8)	0.4945(6)	−0.2998(3)	0.1595(6)	5.3
C(9)	0.3253(6)	−0.2390(5)	−0.0084(8)	6.6
C(10)	0.6161(5)	0.1178(3)	−0.0635(5)	3.85
C(11)	0.5011(6)	0.1759(4)	−0.0813(6)	5.6
C(12)	0.7438(5)	0.1675(4)	−0.0506(7)	5.9

[a]$B_{eq} = (4/3)\Sigma_i\Sigma_j\beta_{ij}(\boldsymbol{a}_i \cdot \boldsymbol{a}_j)$.

7α, 7aβ, 8β, 8aα)-octahydro-4,7-epoxy-2,8-methanooxireno[*h*][3]benzoxepin-3(4*H*)-one (1.462 Å) (14), and 1,2:5,6-dianhydrogalactitol (1.453(5) Å) (6), and is similar to that of methyl 3,4-anhydro-1,6-bis-*O*-(*p*-toluenesulfonyl)-β-D-tagatofuranoside (1.45(1) Å) (15). The C(2)—C(3) bond distance (1.484(4) Å) is 0.02 Å shorter than even the correspondent bond of 1-*O*-acetyl-2,3:4,5-di-*O*-isopropylidene-D-*erythro*-pent-1-enitol (16) which incorporates a nominally sp^2-hybridized carbon atom. The bond is similar in length to (although shorter than) some C—C bonds of certain isopropylidene substituents of carbohydrates (16–19), and is commensurate with the C(2)—C(3) bond of one molecule of dimorphic 3,4-di-*O*-acetyl-1,2:5,6-dianhydrogalactitol (1.484(5) Å) (6). To our knowledge, the only C—C bonds of carbohydrate chains which are shorter than the C(2)—C(3) bond of **2** (oxirane rings excepted) are the singular C(3)—C(4) bond of 1,4:1′,4′:3,6:3′,6′-tetraanhydro-5,5′-*O*-oxydiethylene-2,2′-*O*-[pyridine-2,6-diylbis(methylene)]-di-D-mannitol (1.474(5) Å) (20), and the C(2)—C(3) (1.475(2) Å) (21) and C(4)—C(5) (1.480(2) Å) bonds of 1,2:3,4:5,6-trianhydro-D-iditol (21).

The usual value for the length of a paraffinic C—C bond is 1.537 Å (22), and in carbohydrate rings the C(sp^3)—C(sp^3) bonds exhibit a normal range of 1.516–1.540 Å (23). It is well known that macrocyclic and acyclic polyethers (24–29) and macrocyclic thioethers (30) possess C—C bonds which are much shorter than those expected with tetrahedral carbons. Uncomplexed tetrathia-12-crown-4, pentathia-15-crown-5, and hexathia-18-crown-6 have C—C bond distances in the range 1.440–1.528 Å (30), and uncomplexed 18-crown-6 has been reported to have a mean C—C bond distance of 1.507 (24) to 1.519 Å (31), depending on the corrections applied for internal molecular motions; complexation with alkali metals results in further diminution of the C—C bond distances (32, 33), yet, except for the cesium complex (33), even those atypical bonds exceed the length of the C(2)—C(3) bond of **2**. With respect to those polyethers, it has been noted (24, 26, 27, 31) that inadequate treatment of thermal motion may lead to spurious values for bond lengths. However, even critical assessment of such data (31) afforded unusually small bond distances, which may be attributed (27) to inductive effects originating at adjacent polarized bonds.

In pyranoid systems the diminution of some acetal C—O bond lengths has been associated (34–38) with increased effective electronegativity of the exocyclic oxygen, and stereoelectronic effects involving the donation of electrons by the endocyclic oxygen to the anomeric carbon atom (34–37), thereby shortening the O—C(1) bond of the ring and lengthening the exocyclic C(1)—O bond. As well, it has been proposed (39) that elongation of acetal C—O bonds by hydrogen bonding may result in contraction of adjacent C—O and C—C bonds.

Can. J. Chem. Downloaded from www.nrcresearchpress.com by 61.7.252.67 on 09/07/12
For personal use only.

TABLE 3. Bond lengths (Å) and bond angles (deg) with estimated standard deviation in parentheses

Bond	Distance	Bond	Distance	Bond	Distance
O(1)—C(1)	1.388(4)	O(5)—C(5)	1.448(3)	C(4)—C(5)	1.504(4)
O(1)—C(2)	1.453(4)	O(5)—C(10)	1.420(4)	C(5)—C(6)	1.523(4)
O(1N)—N	1.216(4)	O(6)—C(6)	1.458(4)	C(7)—C(8)	1.501(5)
O(2N)—N	1.175(4)	O(6)—C(10)	1.436(4)	C(7)—C(9)	1.491(5)
O(3)—C(3)	1.434(4)	N—C(1)	1.488(4)	C(10)—C(11)	1.480(5)
O(3)—C(7)	1.423(3)	C(1)—C(2)	1.441(4)	C(10)—C(12)	1.517(5)
O(4)—C(4)	1.424(3)	C(2)—C(3)	1.484(4)		
O(4)—C(7)	1.422(3)	C(3)—C(4)	1.542(4)		

Bonds	Angle	Bonds	Angle	Bonds	Angle
C(1)—O(1)—C(2)	60.9(2)	O(1)—C(2)—C(3)	117.6(3)	O(3)—C(7)—O(4)	105.9(2)
C(3)—O(3)—C(7)	109.5(2)	C(1)—C(2)—C(3)	122.9(3)	O(3)—C(7)—C(8)	109.5(3)
C(4)—O(4)—C(7)	107.4(2)	O(3)—C(3)—C(2)	110.8(2)	O(3)—C(7)—C(9)	109.3(3)
C(5)—O(5)—C(10)	109.5(2)	O(3)—C(3)—C(4)	103.8(2)	O(4)—C(7)—C(8)	107.7(2)
C(6)—O(6)—C(10)	105.6(3)	C(2)—C(3)—C(4)	112.7(2)	O(4)—C(7)—C(9)	110.3(3)
O(1N)—N—O(2N)	126.3(3)	O(4)—C(4)—C(3)	102.2(2)	C(8)—C(7)—C(9)	113.8(3)
O(1N)—N—C(1)	115.4(3)	O(4)—C(4)—C(5)	107.7(2)	O(5)—C(10)—O(6)	105.4(2)
O(2N)—N—C(1)	118.3(3)	C(3)—C(4)—C(5)	114.4(2)	O(5)—C(10)—C(11)	108.3(3)
O(1)—C(1)—N	115.0(3)	O(5)—C(5)—C(4)	107.3(2)	O(5)—C(10)—C(12)	110.3(3)
O(1)—C(1)—C(2)	61.8(2)	O(5)—C(5)—C(6)	104.3(2)	O(6)—C(10)—C(11)	107.8(3)
N—C(1)—C(2)	119.2(3)	C(4)—C(5)—C(6)	112.5(3)	O(6)—C(10)—C(12)	110.9(3)
O(1)—C(2)—C(1)	57.3(2)	O(6)—C(6)—C(5)	102.2(2)	C(11)—C(10)—C(12)	113.9(3)

TABLE 4. Torsional angles (deg)

Bonds	Angles	Bonds	Angles
C(2)—O(1)—C(1)—N	−111.1(4)	O(1N)—N—C(1)—O(1)	−154.9(4)
C(1)—O(1)—C(2)—C(3)	−113.2(4)	O(1N)—N—C(1)—C(2)	134.8(4)
C(7)—O(3)—C(3)—C(2)	129.7(4)	O(2N)—N—C(1)—O(1)	23.4(6)
C(7)—O(3)—C(3)—C(4)	8.5(4)	O(2N)—N—C(1)—C(2)	−46.9(6)
C(3)—O(3)—C(7)—O(4)	12.1(4)	O(1)—C(1)—C(2)—C(3)	103.9(4)
C(3)—O(3)—C(7)—C(8)	127.9(4)	N—C(1)—C(2)—O(1)	104.5(4)
C(3)—O(3)—C(7)—C(9)	−106.7(4)	N—C(1)—C(2)—C(3)	−151.7(4)
C(7)—O(4)—C(4)—C(3)	34.0(4)	O(1)—C(2)—C(3)—O(3)	50.1(5)
C(7)—O(4)—C(4)—C(5)	154.8(3)	O(1)—C(2)—C(3)—C(4)	166.0(4)
C(4)—O(4)—C(7)—O(3)	−29.8(4)	C(1)—C(2)—C(3)—O(3)	−17.1(6)
C(4)—O(4)—C(7)—C(8)	−146.9(3)	C(1)—C(2)—C(3)—C(4)	98.8(5)
C(4)—O(4)—C(7)—C(9)	88.4(4)	O(3)—C(3)—C(4)—O(4)	−25.6(4)
C(10)—O(5)—C(5)—C(4)	−114.8(4)	O(3)—C(3)—C(4)—C(5)	141.7(3)
C(10)—O(5)—C(5)—C(6)	4.8(4)	C(2)—C(3)—C(4)—O(4)	−145.5(3)
C(5)—O(5)—C(10)—O(6)	17.4(4)	C(2)—C(3)—C(4)—C(5)	98.4(4)
C(5)—O(5)—C(10)—C(11)	132.5(4)	O(4)—C(4)—C(5)—O(5)	−171.3(3)
C(5)—O(5)—C(10)—C(12)	−102.3(4)	O(4)—C(4)—C(5)—C(6)	74.6(4)
C(10)—O(6)—C(6)—C(5)	35.7(4)	C(3)—C(4)—C(5)—O(5)	−58.4(4)
C(6)—O(6)—C(10)—O(5)	−33.7(4)	C(3)—C(4)—C(5)—C(6)	−172.6(3)
C(6)—O(6)—C(10)—C(11)	−149.2(4)	O(5)—C(5)—C(6)—O(6)	−24.5(4)
C(6)—O(6)—C(10)—C(12)	85.6(4)	C(4)—C(5)—C(6)—O(6)	91.5(4)

The effect of unsaturated (40–46) and electronegative (10, 13, 40, 45–52) substituents on the bond lengths of three-membered rings has been investigated extensively. In alicyclic systems π-accepting substituents (40, 42, 46) tend to shorten the distal bond and lengthen the vicinal bonds of the ring whereas fluoro, oxo, and methylene groups (43, 46, 48, 51, 52) exert the opposite effect. In heterocyclic systems the ring C—C bond length diminishes as the electronegativity of the hetero atom increases (refs. 11, 13, 50, but see ref. 53), or as fluorine is introduced into the oxirane ring (10, 49); the replacement of H by methyl increases the C—C bond distance (47). In both cyclopropane (48, 51, 52) and oxirane (10, 49) the introduction of vicinal fluorine atoms entrains a stereochemical effect which results in the (F)C—C(F) bond being shorter in the *trans* isomer. These results have been interpreted (10, 52) as being a consequence of enhanced electron delocalization in the *trans* isomer, based on consideration of the contributing molecular orbitals. In the course of CNDO/2 investigations (44, 45) of a large number of derivatives of oxirane, calculations of orbital hybridization (44) in oxiranemethanol indicated that the exocyclic C—C bond had 32% *s*-character whereas the ring C—C bond had 23%. If this hybridization were applicable to the

Can. J. Chem. Downloaded from www.nrcresearchpress.com by 61.7.252.67 on 09/07/12
For personal use only.

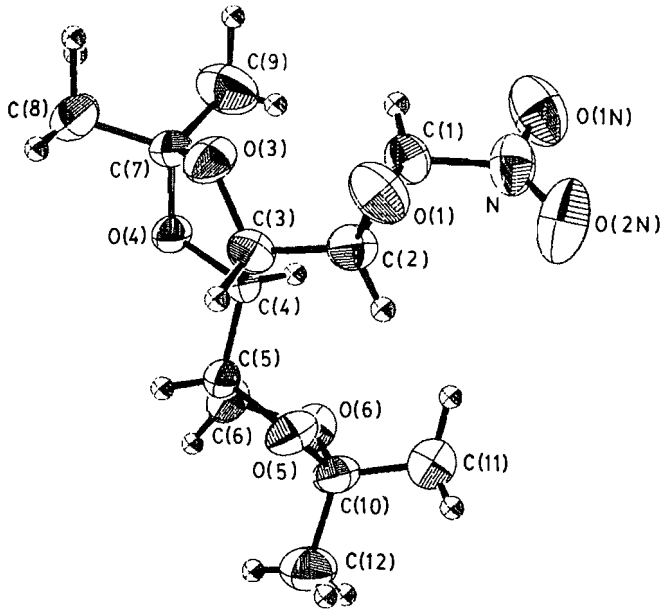

FIG. 1. The molecular structure of 1,2-anhydro-3,4:5,6-di-*O*-isopropylidene-1-*C*-nitro-D-mannitol (**2**).

C(2)—C(3) bond of **2** the contribution of such sp^2-hybridized atoms would afford a convenient explanation of its bond distance, which is intermediate to those of $\sigma(sp^2, sp^2)$ and $\sigma(sp^3, sp^3)$ molecular orbitals (22). However, in contrast to the cyclopropane ring (42), little conjugation has been detected (45) between the atoms of the oxirane ring and the π-electrons of substituents; with oxirane derivatives it was conjectured (45) that electron density distribution may be affected by intermolecular interactions. The ring C—C bond of tetracyanooxirane (41) is longer than that of oxirane and it was postulated (41) that this may be due to a weakening of the C—C bond by electron withdrawal. This may also be the case with nitrooxirane for which the C—C bond has been found (45) to be weaker than that of oxirane. Inasmuch as **2** incorporates an α-nitroepoxide and two 1,3-dioxolane rings, every carbon atom of the carbohydrate chain bears at least one strongly electronegative (54) substituent each of which possesses non-bonding or π-electrons, and the combination of factors contributing to the molecular dimensions may be very complex. Now that the molecular parameters of **2** have been established, the explanation for the proximity of C(1), C(2), and C(3) must await further theoretical studies.

The O(2N)—N bond distance (1.175(4) Å) is abnormally short and differs from the typical O(1N)—N bond distance (1.216(4) Å) by a factor greater than three times the estimated standard deviation. In an effort to explain this difference, a calculation of intermolecular atomic distances was performed; however, no close contact was evident.

The shape of **2** in the crystalline state (Fig. 1, Table 4) approximates the $_2G^-$ (55) sickle (56) conformation, although it is recognized that the carbon atoms of the sequence C(3)—C(4)—C(5)—C(6) are not coplanar: C(4) is +ac (57) with reference to C(1), C(5) is +ac to C(2), and C(6) is −ap to C(3); O(1) and O(3) are +sc (*gauche*), but O(4) and O(5) are −ap. The two acetal rings have very similar geometries, the O(3)—C(3)—C(4)—O(4) torsion angle being −25.6° (Table 4) and that for O(5)—C(5)—C(6)—O(6) being −24.5°; thus, each dioxolane ring is in a ^1E (58–60) conformation. This conformation of **2** agrees closely with that indicated by the ^{1}H-nmr data (1) for **2** in chloroform solution. It is noteworthy that, in the case of **2**, the value of $J_{1,2}$ (1) is not a useful criterion for determining the configurations of C(1) and C(2), although it is fully consistent with the assigned structure. The low (<1 Hz) value, which may be, in part, the consequence of the magnitude of the inductive effects, a phenomenon observed (61) with respect to ^3J values for *gauche* couplings in pyranoses, has been interpreted (5) as being indicative of a *trans* orientation. However, since both **2** and its *gluco* isomer exhibit the same value for $J_{1,2}$ (1), the configurations at those sites could be decided with certainty only on the basis of the X-ray data.

Experimental

Compound **2** was isolated (1) from ethyl acetate as colorless, orthorhombic crystals of space group $P2_12_12_1$. A single crystal, 0.40 × 0.10 × 0.10 mm, was selected for the collection of intensity data on an Enraf-Nonius CAD-4 diffractometer. The crystal data have been summarized in Table 1. The unit cell parameters were obtained by a least-squares analysis of 25-centered reflections in the range $22° < 2\theta < 38°$. The data were collected by the θ–2θ scan technique, with variable scanning rate, using graphite-monochromated MoK_α radiation. A total of 1483 unique reflections were measured in the range $1° < 2\theta < 50°$, of which 1110 having $I \geqq 3\sigma(I)$ were considered observed. Three standard reflections were measured every 7200 s of radiation time and showed no significant variation during the course of data collection. The intensities were corrected for Lorentz and polarization effects.

The structure was solved by direct methods using the program MULTAN80 (62). Difference Fourier map calculations revealed the positions of all hydrogen atoms (Table 2). Full-matrix, least-squares refinement was performed for a scale factor, and positional, and anisotropic thermal parameters of the non-hydrogen atoms. The hydrogen atoms were included in the calculations but were not refined; they were assigned isotropic thermal parameters equal in magnitude to those of the parent carbon atom. The function minimized was $\Sigma w||F_o| - |F_c||^2$ where $w = 1/\sigma^2(|F_o|)$. The refinement resulted in $R = 0.052$ and $R_w = 0.069$. The estimated standard deviation of an observation of unit weight was 2.589, the maximum shift to error ratio was 0.00, and the final difference Fourier synthesis was essentially featureless. The scattering factors used were those of Cromer and Waber (63). The anomalous dispersion coefficients were taken from the data of Cromer (64). The final atomic coordinates are given in Table 2. All calculations were performed on a PDP 11/23 computer using the structure determination package of Enraf-Nonius, SDP (65). The program ORTEP (66) was used for the preparation of the illustration (Fig. 1).[4]

Acknowledgement

We thank the Natural Sciences and Engineering Research Council of Canada for financial support of this work.

1. W. A. SZAREK, G. W. HAY, B. DOBOSZEWSKI, and M. M. PERLMUTTER. Carbohydr. Res. **155**, 107 (1986) and references therein.
2. J. S. FOWLER and A. P. WOLF. Appl. Radiat. Isot. **37**, 663 (1986) and references therein.
3. H. PAULSEN and M. BUDZIS. Chem. Ber. **107**, 1998 (1974).
4. H. H. BAER and W. RANK. Can. J. Chem. **49**, 3192 (1971).
5. H. H. BAER and C. B. MADUMELU. Can. J. Chem. **56**, 1177 (1978).
6. M. CSUGLER, K. SIMON, L. INSTITORIS, I. VIDRA, and I. CSÖREGH. Carbohydr. Res. **108**, 173 (1982).
7. J. A. KANTERS, G. ROELOFSEN, and D. SMITS. Acta Crystallogr. Sect. B, **33**, 3635 (1977).

[4]A complete set of tables of positional parameters, temperature factors, and observed and calculated structure factors may be purchased from the Depository of Unpublished Data, CISTI, National Research Council of Canada, Ottawa, Ont., Canada K1A 0S2.

Can. J. Chem. Downloaded from www.nrcresearchpress.com by 61.7.252.67 on 09/07/12
For personal use only.

8. H. M. BERMAN, G. A. JEFFREY, and R. D. ROSENSTEIN. Acta Crystallogr. Sect. B, **24**, 442 (1968).
9. H. S. KIM, G. A. JEFFREY, and R. D. ROSENSTEIN. Acta Crystallogr. Sect. B, **24**, 1449 (1968).
10. C. A. DEAKYNE, J. P. CRAVERO, and W. S. HOBSON. J. Phys. Chem. **88**, 5975 (1984).
11. G. L. CUNNINGHAM, A. W. BOYD, R. J. MYERS, W. D. GWINN, and W. I. LE VAN. J. Chem. Phys. **19**, 676 (1951).
12. T. E. TURNER and J. A. HOWE. J. Chem. Phys. **24**, 924 (1956).
13. C. HIROSE. Bull. Chem. Soc. Jpn. **47**, 1311 (1974).
14. T. T. STEVENSON, M. G. ESSIG, F. SHAFIZADEH, L. H. JENSEN, and R. E. STENKAMP. Carbohydr. Res. **118**, 261 (1983).
15. R. D. GUTHRIE, I. D. JENKINS, R. YAMASAKI, B. W. SKELTON, and A. H. WHITE. J. Chem. Soc. Perkin Trans. I, 2328 (1981).
16. A. DUCRUIX and C. PASCARD-BILLY. Acta Crystallogr. Sect. B, **33**, 1384 (1977).
17. A. AUBRY, J. PROTAS, B. DUCHAUSSOY, P. DE CESARE, and B. GROSS. Acta Crystallogr. Sect. B, **36**, 187 (1980).
18. V. J. JAMES and J. D. STEVENS. Carbohydr. Res. **82**, 167 (1980).
19. M. ARGENTINI, R. WEINREICH, R. OBERTI, and L. UGARETTI. J. Fluorine Chem. **32**, 239 (1986).
20. T. H. CRAWSHAW, J. F. STODDART, and D. J. WILLIAMS. Acta Crystallogr. Sect. C, **42**, 211 (1986).
21. P. KÖLL, J. KOPF, J. O. METZGER, W. SCHWARTING, and M. OELTING. Liebigs Ann. Chem. 199 (1987).
22. L. E. SUTTON (*Editor*). Tables of interatomic distances and configurations in molecules and ions. Supplement 1956–1959. The Chemical Society, London. 1965.
23. P. M. MATIAS and G. A. JEFFREY. Carbohydr. Res. **153**, 217 (1986).
24. J. D. DUNITZ, M. DOBLER, P. SEILER, and R. P. PHIZACKERLEY. Acta Crystallogr. Sect. B, **30**, 2733 (1974).
25. J. D. DUNITZ and P. SEILER. Acta Crystallogr. Sect. B, **30**, 2739 (1974).
26. M. J. BOVILL, D. J. CHADWICK, I. O. SUTHERLAND, and D. WATKIN. J. Chem. Soc. Perkin Trans. II, 1529 (1980).
27. R. HILGENFELD and W. SAENGER. Topics Current Chem. **101**, 1 (1982).
28. C. J. VAN STAVEREN, V. M. L. J. AARTS, P. D. J. GROOTENHUIS, J. VAN EERDEN, S. HARKEMA, and D. N. REINHOUDT. J. Am. Chem. Soc. **108**, 5271 (1986).
29. G. W. GOKEL, J. C. HERNANDEZ, A. M. VISCARIELLO, K. A. ARNOLD, C. F. CAMPANA, L. ECHEGOYEN, F. R. FRONCZEK, R. D. GANDOUR, C. R. MORGAN, J. E. TRAFTON, S. R. MILLER, C. MINGANTI, D. EIBAND, R. A. SCHULTZ, and M. TAMMINEN. J. Org. Chem. **52**, 2963 (1987).
30. R. E. WOLF, JR., J.-A. R. HARTMAN, J. M. E. STOREY, B. M. FOXMAN, and S. R. COOPER. J. Am. Chem. Soc. **109**, 4238 (1987) and references therein.
31. E. MAVERICK, P. SEILER, W. B. SCHWEIZER, and J. D. DUNITZ. Acta Crystallogr. Sect. B, **36**, 615 (1980).
32. M. DOBLER and R. P. PHIZACKERLEY. Acta Crystallogr. Sect. B, **30**, 2746 (1974).
33. M. DOBLER and R. P. PHIZACKERLEY. Acta Crystallogr. Sect. B, **30**, 2748 (1974).
34. G. A. JEFFREY, J. A. POPLE, and L. RADOM. Carbohydr. Res. **25**, 117 (1972).
35. F. H. ALLEN and A. J. KIRBY. J. Am. Chem. Soc. **106**, 6197 (1984).
36. A. J. BRIGGS, R. GLENN, P. G. JONES, A. J. KIRBY, and P. RAMASWAMY. J. Am. Chem. Soc. **106**, 6200 (1984).
37. P. G. JONES and A. J. KIRBY. J. Am. Chem. Soc. **106**, 6207 (1984).
38. B. FUCHS, L. SCHLEIFER, and E. TARTAKOVSKY. Nouv. J. Chim. **8**, 275 (1984).
39. T. S. CAMERON, R. E. CORDES, and T. B. GRINDLEY. Acta Crystallogr. Sect. B, **33**, 3718 (1977).
40. M. YU. LUKINA. Russ. Chem. Rev. **31**, 419 (1962) and references therein.
41. D. A. MATTHEWS, J. SWANSON, M. H. MUELLER, and G. D. STUCKY. J. Am. Chem. Soc. **93**, 5945 (1971).
42. R. E. PENN and J. E. BOGGS. J. Chem. Soc. Chem. Commun. 666 (1972).
43. C. A. DEAKYNE, L. C. ALLEN, and V. W. LAURIE. J. Am. Chem. Soc. **99**, 1343 (1977).
44. E. G. FURMAN and A. P. MELESHEVICH. Theor. Exp. Chem. **13**, 246 (1977).
45. E. G. FURMAN and A. P. MELESHEVICH. Theor. Exp. Chem. **14**, 84 (1978).
46. F. H. ALLEN. Acta Crystallogr. Sect. B, **36**, 81 (1980).
47. R. A. CRESWELL and R. H. SCHWENDEMAN. J. Mol. Spectrosc. **64**, 295 (1977).
48. C. A. DEAKYNE, L. C. ALLEN, and N. C. CRAIG. J. Am. Chem. Soc. **99**, 3895 (1977).
49. C. W. GILLIES. J. Mol. Spectrosc. **71**, 85 (1978).
50. C. A. KINGSBURY, D. L. DURHAM, and R. HUTTON. J. Org. Chem. **43**, 4696 (1978).
51. S. K. SENGUPTA, H. JUSTNES, C. W. GILLIES, and N. C. CRAIG. J. Am. Chem. Soc. **108**, 876 (1986).
52. H. JUSTNES, J. ZOZOM, C. W. GILLIES, S. K. SENGUPTA, and N. C. CRAIG. J. Am. Chem. Soc. **108**, 881 (1986).
53. M.-M. ROHMER and B. ROOS. J. Am. Chem. Soc. **97**, 2025 (1975).
54. S. MARRIOTT, W. F. REYNOLDS, R. W. TAFT, and R. D. TOPSOM. J. Org. Chem. **49**, 959 (1984); J. MULLAY. J. Am. Chem. Soc. **106**, 5842 (1984), **107**, 7271 (1985); S. G. BRATSCH. J. Chem. Ed. **62**, 101 (1985).
55. D. HORTON and J. D. WANDER. J. Org. Chem. **39**, 1859 (1974).
56. D. HORTON and J. D. WANDER. Carbohydr. Res. **10**, 279 (1969).
57. W. KLYNE and V. PRELOG. Experientia, **16**, 521 (1960).
58. K. S. PITZER and W. E. DONATH. J. Am. Chem. Soc. **81**, 3213 (1959).
59. L. D. HALL. Chem. Ind. (London), 950 (1963).
60. J. F. STODDART. Stereochemistry of carbohydrates. Wiley-Interscience, New York. 1971. pp. 97–102.
61. A. DE BRUYN and M. ANTEUNIS. Org. Magn. Reson. **8**, 228 (1976).
62. P. MAIN, S. J. FISKE, S. E. HULL, L. LESSINGER, G. GERMAIN, J. P. DECLERCQ, and M. M. WOOLFSON. MULTAN80. University of York, England, and University of Louvain, Belgium. 1980.
63. D. T. CROMER and J. T. WABER. *In* International tables for X-ray crystallography. Vol. IV. *Edited by* J. A. Ibers and W. C. Hamilton. Kynoch Press, Birmingham, England. 1974. Table 2.2B, pp. 99–101.
64. D. T. CROMER. *In* International tables for X-ray crystallography. Vol. IV. *Edited by* J. A. Ibers and W. C. Hamilton. Kynoch Press, Birmingham, England. 1974. Table 2.3.1, pp. 148–151.
65. B. A. FRENZ. Enraf-Nonius structure determination package. Enraf-Nonius, Delft, The Netherlands. 1974.
66. C. K. JOHNSON. ORTEP. Report ORNL-3794. Oak Ridge National Laboratory, Oak Ridge, TN. 1965.

Can. J. Chem. Downloaded from www.nrcresearchpress.com by 61.7.252.67 on 09/07/12
For personal use only.

Conductance behavior of some electrolytes in tetramethylurea

E. M. HANNA[1] AND A. A. TOSSONIAN
Department of Chemistry, University of Basrah, Basrah, Iraq

Received January 26, 1987[2]

E. M. HANNA and A. A. TOSSONIAN. Can. J. Chem. **66**, 1605 (1988).

Conductance investigations have been done at 25°C on tetramethylurea solutions containing NaI, KI, RbI, CsI, NH_4I, LiBr, NaBr, NH_4Br, or LiCl in the concentration range $2.0 \times 10^{-4} - 3.6 \times 10^{-3}$ *M*. The conductance data have been analyzed using the full equations of Pitts, Fuoss, and Lee–Wheaton for the conductivity of free ions. The best-fit values of Λ_0 are consistent with strong cation solvation and weak anion solvation by tetramethylurea. The K_A values indicate that these salts are associated electrolytes in this solvent.

E. M. HANNA et A. A. TOSSONIAN. Can. J. Chem. **66**, 1605 (1988).

Opérant à 25°C et à des concentrations allant de $2{,}0 \times 10^{-4}$ à $3{,}6 \times 10^{-3}$ *M*, on a déterminé la conductance de solutions de tétraméthylurée contenant les sels suivants : NaI, KI, RbI, CsI, NH_4I, LiBr, NH_4Br ou LiCl. On a analysé les données à l'aide des équations complètes de Pitts, Fuoss et Lee–Wheaton pour des ions libres. Les meilleurs ajustements de Λ_0 sont en accord avec une solvatation forte des cations et une solvatation faible des anions par la tétraméthylurée. Les valeurs des K_A indiquent que, dans ce solvant, ces sels sont des électrolytes associés.

[Traduit par la revue]

Introduction

Tetramethylurea (TMU) is a colourless mobile liquid, commercially available, and readily purified. It is a good solvent for a number of organic and inorganic compounds. Its physical properties at 25°C (mp, −1°C; bp, 176.5°C; density, 0.9616 g cm^{-3}; viscosity, 0.01402 P; and dielectric constant, 23.50) indicate it to be one of the interesting dipolar aprotic solvents. However, only a few studies have been done on the behavior and properties of salts in this solvent (1–6). Therefore, in this work conductance investigations were extended to more alkali metal salts to explore the influence of molecular structure, viscosity, and dielectric constant in determining properties of electrolytes in nonaqueous solvents.

Experimental

Solvent

The main impurity in nonaqueous solvents is water. Tetramethylurea purchased from Merck was purified by vacuum distillation at 0.4 mm Hg through a heated fractionating column. Only the middle 80% of the distillate was collected. Dry nitrogen was used in all transfers. The middle fraction from the first distillation was collected over 4A molecular sieves, decanted after 24 h, and then distilled over another quantity of molecular sieves from which the solvent was again freshly distilled before use. The specific conductivity of freshly distilled solvent was in the range $(2–4) \times 10^{-8}$ S cm^{-1}. Water content of the purified TMU by Karl Fischer titration was 0.001%.

A viscosity of 0.01402 ± 0.001 P was determined at 25°C with size 25 Ostwald type viscometer. With 50 cm^3 density bottle a density of 0.9616 ± 0.0002 g cm^{-3} was determined for TMU at 25°C. A dielectric constant of 23.50 ± 0.01 was determined for TMU with a Wissenschaftlich–Techniche–Workstalten dipole meter DMO1 using MFL3 cell. A Forma 2160 thermostat bath filled with water and maintained at 25.00 ± 0.01°C was used in the viscosity, density, and dielectric constant determinations. Our values of viscosity, 0.01402 P; density, 0.9616 g cm^{-3}; and dielectric constant, 23.50 are in good agreement with those reported by Barker and Caruso (1) (η, 0.01401; *d*, 0.9619; ϵ, 23.45) and Okpala *et al.* (7) (η, 0.01395; *d*, 0.9616; ϵ, 23.60).

Salts

Merck (proanalysis) potassium chloride was recrystallized three times from conductivity water, dried *in vacuo*, and fused in a platinum crucible. The sample was cooled and then grounded up into a fine powder. Immediately before use, samples were dried *in vacuo* at 120°C for 6 h. Merck (suprapur) lithium chloride; sodium, potassium, rubidium, cesium, and ammonium iodide; and lithium, sodium, and ammonium bromide were used as received. Before use, samples were heated *in vacuo* at 80°C for 8 h.

Apparatus

The same conductivity bridge, conductivity cell, oil bath, and dry box are described in detail elsewhere (8). As before, the conductivity cell was of the Marsh–Stokes type (9). Dry nitrogen was passed through a three-way tap to transfer the solution between vessel and storage flask. The cell was calibrated at 25°C using the Lind–Zwoleink–Fuoss (10) empirical equation for the molar conductivity of potassium chloride. The cell constant, obtained from three independent sets of measurements, was found to be 0.6554 ± 0.0003 cm^{-1}.

All transfers of solids and solutions were made inside the dry box. A 2% decone solution was used for cleaning. Apparatus were dried overnight at 120°C. The conductivity cell was dried with a stream of dry nitrogen while hot air was passed over its outside.

For each salt, two runs with different stock solutions were made. Successive additions of stock solution to the solvent in the conductivity cell were made using a 10 cm^3 syringe. It was found that 20 min were required to re-establish thermal equilibrium. All weights were corrected to vacuo.

Results and discussion

Table 1 gives the molar conductivities Λ in S cm^2 mol^{-1} and the molar concentrations *C* in mol dm^{-3} of the nine salts studied in TMU. The experimental results were analyzed with the computer programs used previously (8).

The equations used were in the form

$$[1] \quad \Lambda = \alpha[\Lambda_0 - f(\kappa,d)]$$

$$[2] \quad K_A = (1 - \alpha)/\alpha^2 C y^2$$

$$[3] \quad -\log y = A\alpha^{1/2}C^{1/2}/(1 + Bd\alpha^{1/2}C^{1/2})$$

The adjustable parameters were the molar conductivity at infinite dilution Λ_0, the association constant K_A, and the association distance *d* within which the oppositely charged ions are considered paired. The full equations of Pitts (11), Fuoss (12), and Lee–Wheaton (13) were used for the function $f(\kappa,d)$ in eq. [1]. The values of the best-fit parameters Λ_0, K_A, and *d*

[1]Present address: University of Baghdad, Women Education College, Department of Chemistry, Jadiriyah, Baghdad, Iraq.

[2]Revision received March 1, 1988.

Printed in Canada / Imprimé au Canada

Can. J. Chem. Downloaded from www.nrcresearchpress.com by 61.7.252.67 on 09/07/12
For personal use only.

Can. J. Chem. Downloaded from www.nrcresearchpress.com by 61.7.252.67 on 09/07/12
For personal use only.

TABLE 1. Conductance of some electrolytes in TMU at 25°C

10^4C	Λ	10^4C	Λ	10^4C	Λ	10^4C	Λ
			NaI				
4.0370	39.922	4.0470	39.921	6.4624	38.876	6.6645	38.800
9.4356	37.967	9.6358	37.816	11.9980	37.414	12.0752	37.200
15.1745	36.400	17.0853	36.000	20.1607	35.878	20.2607	35.421
23.1461	34.888	26.2153	34.323				
			KI				
2.0982	44.182	2.8715	43.558	4.2597	42.951	5.4229	42.278
6.2936	42.032	8.0495	41.300	8.4371	41.315	10.7764	40.566
12.0621	40.227	13.7885	39.978	14.2191	39.784	15.9572	39.560
16.8548	39.196	17.8878	39.158	18.7339	38.951	23.1773	38.294
			RbI				
4.2495	42.662	5.1566	42.412	6.4526	41.126	9.1522	40.168
9.2452	39.622	12.0081	38.458	13.3474	38.322	17.1985	36.529
18.1900	36.678	19.7464	35.766	22.5272	35.010	24.1888	35.022
27.8325	34.122						
			CsI				
2.2346	45.899	2.4336	45.870	3.6420	44.772	3.6460	44.767
4.9262	43.828	5.1129	43.769	6.1601	42.999	6.3601	43.028
7.1918	42.508	7.3918	42.314	8.7871	41.537	9.9287	41.084
10.1123	41.144						
			NH_4I				
4.6624	41.500	4.8020	41.444	6.9231	40.348	7.0124	40.126
8.9214	39.405	9.1024	39.212	12.1216	38.256	12.3434	38.024
14.5713	37.478	17.1935	36.719	17.4434	36.626	19.7039	36.079
20.1073	35.844	22.4108	35.449	24.8419	34.884		
			LiBr				
2.2604	39.711	8.0087	38.460	8.8821	38.212	11.9989	37.240
14.1713	36.666	18.6625	35.669	22.8124	34.900	25.6622	34.492
			NaBr				
3.3889	39.551	4.3080	38.588	9.0225	37.044	9.4114	35.028
12.5791	33.466	16.9067	31.709	20.3380	30.611	24.4379	29.571
24.4379	29.571	29.0269	28.546	35.3108	27.391		
			NH_4Br				
3.6464	43.597	3.9994	43.465	6.4464	42.338	6.5462	42.238
8.0044	41.724	11.8848	40.492	12.0041	40.416	16.4424	39.262
16.6589	39.150	17.8994	38.868	18.3141	38.800	21.424	38.351
			LiCl				
5.2989	28.588	6.1356	27.480	10.3714	27.539	13.9811	26.964
19.8522	26.212	25.7252	25.644	26.9853	24.115	30.0044	23.860
33.0215	23.668	36.4467	24.701				

as well as σ_Λ, the standard deviation of the individual points, are given in Table 2.

As previously observed (1, 3) the conductance of iodide solutions increased with time after the addition of iodide to solvent due to solute–solvent interactions. It was found that these solutions reached a maximum conductivity after about 20 min. Thus all conductance measurements were taken after 20 min after the addition of stock solution to the content of the cell. Similar conductivity–time behavior have been observed in acetonitrile (14), pyridine (15), benzonitrile (16), and phenol (17).

The data in Table 2 support previous observation (18) that Λ_0 values obtained from the three conductivity equations are in good agreement. As expected, the molar conductivity at infinite dilution of the cation increases as the size of the cation increases, which indicates that the effective size and cation–solvent interaction becomes smaller as the crystallographic radius increases.

Can. J. Chem. Downloaded from www.nrcresearchpress.com by 61.7.252.67 on 09/07/12
For personal use only.

TABLE 2. Values of parameters giving the best-fit for some 1:1 salts using different conductivity equations

Salt	Equation[a]	Λ_0 (S cm^2 mol^{-1})	K_A (mol^{-1} dm^3)	d (nm)	σ_Λ
NaI	P	43.30	75.0	0.69	0.050
	F	43.35	69.4	0.87	0.077
	LW	43.40	48.4	0.76	0.065
KI	P	46.32	59.4	0.67	0.081
	F	46.36	63.9	0.65	0.065
	LW	46.57	67.8	0.37	0.057
RbI	P	48.11	208.9	1.28	0.040
	F	48.11	217.7	1.50	0.042
	LW	48.13	200.3	1.23	0.040
CsI	P	49.45	212.8	1.90	0.041
	F	49.48	217.1	1.90	0.042
	LW	49.47	199.4	1.90	0.041
NH_4I	P	46.19	139.3	0.63	0.069
	F	46.26	148.9	0.68	0.068
	LW	46.38	153.3	0.63	0.067
LiCl	P	30.89	84.5	1.90	0.066
	F	30.92	92.2	1.90	0.054
	LW	30.91	73.4	1.90	0.035
LiBr	P	43.59	242.7	1.90	0.064
	F	43.49	249.0	0.77	0.044
	LW	43.93	228.3	0.55	0.074
NaBr	P	45.78	380.3	1.90	0.044
	F	45.77	331.2	0.20	0.062
	LW	45.77	362.7	0.67	0.045
NH_4Br	P	47.15	113.1	1.51	0.034
	F	47.17	120.1	1.64	0.034
	LW	47.18	103.7	1.48	0.034

[a]P, Pitts equation (1953); F, Fuoss equation (1978); LW, Lee–Wheaton equation (1978).

The calculated association constants in Table 2 show that all the salts studied to be associated in TMU at 25°C. With the exception of KI, the association constants of the alkali metal iodides and bromides increase as the cation size increases, consistent with the degree of solvation of cations by TMU.

For the sake of comparison, the conductivities of LiBr, NaBr, NaI, and RbI were measured in TMU at 25°C. Our best-fit values of Λ_0 and K_A are presented in Table 3 together with those obtained by Barker and Caruso (1, 3) so that a comparison between the two sets can be made. A perusal of Table 3 reveals that, with the exception of RbI, our values of Λ_0 are about one conductance unit lower than those obtained by Barker and Caruso (1, 3). This difference is probably due to the difference in the purity of the salts and the different methods of solvent purification used. It has been shown earlier (1, 3, 14–17) that the molar conductivity of iodine solutions increases with time as the solution ages. As can be seen from Table 3, there is a disagreement about the order of Λ_0. Our values of Λ_0 increase with increasing cationic size. Barker and Caruso found that $\Lambda_0(NaI) = \Lambda_0(RbI)$. However, there is an agreement about the order of K_A which increases with increasing size of the cation. This pattern of ionic association has also been reported in hexamethylphosphotriamide (8) and in propylene carbonate (18). A reverse order of association constants has been reported in other aprotic solvents (19, 20). Table 3 also shows that our K_A values are higher than those reported by Barker and Caruso, indicating that these salts are associated in TMU at 25°C. Barker and Caruso reported a negative K_A value for NaI and concluded that the salt is unassociated in this solvent. We believe that our K_A value is more reasonable and this salt, like other salts, is associated in TMU at 25°C.

Starting from $\lambda_0(Br^-) = 30.12$ S cm^2 mol^{-1} reported in the literature (2), as obtained from transference number measurements, the values of limiting molar ionic conductances of the ions listed in Table 4 were calculated. A perusal of Table 4 reveals that ammonium and alkali metal ions are arranged in the following order of their decreasing mobility $Cs^+ > Rb^+ > K^+ \sim NH_4^+ > Na^+ > Li^+$. Table 4 also shows that the observed order for anions $Br^- > I^- > Cl^-$ is in agreement with the previous observation (2) that solvation of anions by this solvent does not follow the general pattern.

Values of solvated radii r_s of the ions tabulated in Table 4 were calculated from the Stokes equation (21)

$$[4] \quad r_s = F^2/6\pi N\eta\lambda_0 = 0.82/\eta\lambda_0$$

Values of the effective ionic radii r_s^* listed in Table 4 were calculated replacing 6 by 4 in the denominator of eq. [4]. Table 4 shows that values of r_s^* are larger than r_s values for all the ions. For cations, values of λ_0 decrease as the crystallographic radii increase, indicating once again that solvation of the cations by negative and exposed end of the solvent dipole become less firm as cation size increases. It is clear from Table 4 that the differences between r_s^* and r_s for anions (except Cl^-) are less than those for cations, indicating that anion–solvent inter-

TABLE 3. Limiting molar conductance and association constant of some salts in TMU at 25°C

	Λ_0 (S cm^3 mol^{-1})				K_A (mol dm^{-3})			
	This work[a]			Refs. 1, 3	This work[a]			Refs. 1, 3
Salt	P	F	LW	FO	P	F	LW	FO
LiBr	43.59	43.49	43.93	44.43	242.7	249.0	228.3	15.6
NaBr	45.78	45.77	45.77	46.20	380.3	331.2	262.7	316.0
NaI	43.30	43.35	43.40	44.81	75.0	69.4	48.4	−1.4
RbI	48.11	48.11	48.13	44.81	208.9	217.7	200.3	9.7

[a]P, Pitts equation (1953); F, Fuoss equation (1978); LW, Lee–Wheaton equation (1978); FO, Fuoss Onsager equation (1957).

TABLE 4. Limiting molar ionic conductance of ions in TMU at 25°C

Ion	λ_0 (S cm^2 mol^{-1}) This work	Refs. 1, 3	Ref. 2	r_c	r_s	r_s^*
Li^+	13.29	14.13	14.47	0.60	4.40	6.60
Na^+	15.13	15.74	16.08	0.95	3.87	5.80
K^+	18.33	15.26	15.73	1.33	3.19	4.79
Rb^+	19.86	15.63	16.04	1.48	2.95	4.42
Cs^+	21.20	16.52	16.93	1.69	2.76	4.14
NH_4^+	18.11	17.57	18.01	1.44	3.23	4.84
Cl^-	17.61	—	—	1.81	3.32	4.92
Br^-	30.12	30.38	30.12	1.95	1.94	2.91
I^-	27.75	29.12	—	2.16	2.11	3.16

actions are weaker than cation–solvent interactions. This is consistent with aprotic nature of this solvent.

1. B. J. BARKER and J. A. CARUSO. J. Am. Chem. Soc. **93**, 1341 (1971); J. Phys. Chem. **77**, 1884 (1973).
2. R. C. PAUL, S. P. JOHAR, J. S. BANAIT, and S. P. NURULA. J. Phys. Chem. **80**, 351 (1976).
3. B. J. BARKER and J. A. CARUSO. Electrochim. Acta, **18**, 315 (1973).
4. S. P. JAUHAR, P. S. GURAYE, and S. P. NURULA. Indian J. Chem. **23**(A), 680 (1984).
5. D. M. MAHARAJH. Thermochim. Acta, **52**, 83 (1982).
6. D. M. MAHARAJH and A. GUISEPPI-ELIE. Thermochim. Acta, **87**, 225 (1985).
7. C. OKPALA, A. GUISEPPI-ELIE, and D. M. MAHARAJH. J. Chem. Eng. Data, **25**, 384 (1980).
8. E. M. HANNA and N. J. AL-SALIHI. J. Solution Chem. **7**, 539 (1979).
9. K. N. MARSH and R. H. STOKES. Aust. J. Chem. **17**, 740 (1964).
10. J. E. LIND, J. ZWOLENIK, and R. M. FUOSS. J. Am. Chem. Soc. **81**, 1559 (1959).
11. E. PITTS. Proc. R. Soc. (A), **217**, 43 (1953).
12. R. M. FUOSS. J. Phys. Chem. **82**, 2427 (1978).
13. W. H. LEE and R. J. WHEATON. J. Chem. Soc. Faraday Trans. **II**, **74**, 743 (1978).
14. G. J. JANZ and S. S. DANYLUK. J. Am. Chem. Soc. **81**, 3854 (1959).
15. L. F. AUDRIETH and E. J. BIRR. J. Am. Chem. Soc. **55**, 668 (1933).
16. G. H. JANZ, I. AHMAD, and H. V. VENKATASETTY. J. Phys. Chem. **68**, 889 (1964).
17. R. M. DOLBY and P. W. ROBERTSON. J. Chem. Soc. 1711 (1930).
18. E. M. HANNA and K. AL-SUDANI. J. Solution Chem. **16**, 115 (1987).
19. R. FERNANDEZ-PRINI and J. E. PRUE. Trans. Faraday Soc. **62**, 1257 (1966).
20. D. F. EVANS, C. ZAWOYSKI, and R. L. KAY. J. Phys. Chem. **69**, 3878 (1965).
21. R. A. ROBINSON and R. H. STOKES. Electrolyte solutions. 2nd rev. ed. Butterworths, London. 1965. p. 44.

Can. J. Chem. Downloaded from www.nrcresearchpress.com by 61.7.252.67 on 09/07/12
For personal use only.

A new form of hydroxyaluminum phthalocyanine by acid treatment. Characterization and photoactivity

LÊ H. DAO[1] AND GÉRARD PERRIER
INRS-Energie, Institut National de la Recherche Scientifique, Varennes (Qué.), Canada J0L 2P0

AND

KENNETH COLE
Institut de Génie des Matériaux, Boucherville (Qué.), Canada J4B 6Y4

Received December 8, 1987

LÊ H. DAO, GÉRARD PERRIER, and KENNETH COLE. Can. J. Chem. **66**, 1609 (1988).

A new polymorph of hydroxyaluminum phthalocyanine (PcAlOH) was obtained when PcAlOH thin film was exposed to aqueous acid solutions. The new polymorph, which is characterized by infrared, near-infrared, and visible absorption spectrometry and X-ray diffractometry, shows enhanced photoactivity in a photoelectrochemical solar cell device.

LÊ H. DAO, GÉRARD PERRIER et KENNETH COLE. Can. J. Chem. **66**, 1609 (1988).

Une nouvelle forme de phtalocyanine d'hydroxyaluminium (PcAlOH) a été obtenue quand on traite des films minces de PcAlOH avec des solutions aqueuses d'acides. Le nouveau polymorphe qui a été caractérisé par les spectroscopies infrarouge, infrarouge proche et visible, et par la diffraction aux rayons X, démontre une activité accrue lors de son utilisation dans une cellule solaire photoélectrochimique.

Can. J. Chem. Downloaded from www.nrcresearchpress.com by 61.7.252.67 on 09/07/12
For personal use only.

1. Introduction

Investigations on organic semiconductors continue with high activity in view of solar energy conversion. Metal-free phthalocyanine (Pc) and many of its metal derivatives have attracted attention mainly due to their stability and their high absorption in the visible region. They were used in Schottky barrier junctions with aluminum, chromium, or indium as rectifying contacts (1–10). Heterojunction photovoltaic cells of the type ZnO or CdS/Pc were shown to have efficiencies as high as 0.22% under AM2 illumination of 75 mW cm^{-2} (11–14). Phthalocyanines have also been studied in photoelectrochemical cells (15–17) and efficiencies of up to 7×10^{-2}% have been reported for *x*-Pc under white light irradiation (75 mW cm^{-2}) (18).

Phthalocyanines are known to exist in different polymorphic forms depending on their molecular stacking arrangements in the solid state (19). It has been shown that the strong interaction in structure has a remarkable influence on the crystal habits (20). In the case of the phthalocyanine compounds, the crystal habits are determined by π electronic interaction, which binds most strongly two neighbouring planar molecules in the crystal. The resulting intermolecular forces are relatively weak and slight differences in the way of superpositioning stacked molecules are possible. Many polymorphic forms are known; they are designated by the letters α, β, *x*, ϵ, and τ. The transformation of one form to an other one (dimorphic transformation) can be affected by several techniques including thermal (21) and organic solvent treatments (22–25), acid ball-milling (26), and inert solvent grinding (27). It has been shown that the metastable α-form of metal phthalocyanine is transformed into the stable β-form through various intermediate forms depending on the properties of organic solvents and that an *x*-form appears in the weak *n*-donor solvents such as ethanol, acetone, and carbon disulfide (22, 23). The dimorphic transformations have been studied by optical spectroscopy, X-ray and electron diffraction, and electron microscopy techniques (1–10, 28). It has been also demonstrated that the dimorphic transformation reorganizes the molecular arrangement within the solids and changes in the same time the optical, electrical, and photoconductivity properties of phthalocyanines (22–25). Thus the electrical conductivity of α-form phthalocyanine is three to five times higher than that of the β-form (29), and the *x*-form of phthalocyanine is substantially more photoactive than the α- and β-forms (30).

In this paper, we would like to report a new dimorphic transformation of hydroxyaluminum phthalocyanine which is induced by a treatment with aqueous acid solutions. The new polymorph, which is characterized by infrared, near-infrared, and visible absorption spectra and by X-ray diffraction, shows enhanced photoactivity in a photoelectrochemical solar cell device.

2. Experimental section

2.1 Materials

Hydroxyaluminum phthalocyanine (PcAlOH) was prepared as follows. Chloroaluminum phthalocyanine was first synthesized by heating *o*-phthalonitrile and aluminum chloride in quinoline (31). The product was filtered after cooling and washed with acetone and then ethanol in a Soxhlet extractor. The powder was heated in aqueous ammonia solution (30%) in the presence of pyridine for 12 h to give PcAlOH. The product was then washed by repeated solvent extraction techniques with acetone, ethanol, and chloroform (14).

The α-form PcAlOH powdered crystal can be obtained by vacuum sublimation (19) or by the following procedure, showing in both cases the same X-ray diffraction patterns. The blue solid compound was completely dissolved in concentrated sulfuric acid, resulting in a viscous dark-green paste. This paste was poured slowly into a large amount of ice cube and water, and vigorously stirred, yielding a blue precipitate of PcAlOH. After filtration and repeated washing with water, the blue solid was dispersed in a large volume of water, stirred for 3 h, and filtered. This treatment was repeated several times until the pH of the filtrate was neutral.

2.2 Procedure of treatment

The main process of the transformation of hydroxyaluminum phthalocyanine was investigated with thin films which were obtained by a vacuum-condensation method. A few milligrams of the pure α-PcAlOH solid were sublimed from a small crucible of boron nitride heated with a furnace of coiled tantalum and were condensed onto glass

[1]Author to whom correspondence should be addressed.

Can. J. Chem. Downloaded from www.nrcresearchpress.com by 61.7.252.67 on 09/07/12
For personal use only.

plates, quartz plates, CaF_2 plates, AgBr plates, or polished aluminum plates kept at room temperature. The pressure in the evaporator was about 5×10^{-6} Torr. The film thickness was determined by electronic absorption spectra and referred to a standard curve obtained by profilometry with a Sloan Dektak II. The film thickness was controlled in the range of 50–5000 Å (16). For the organic solvent treatment, thin films on glass plates were placed in the vapors of the liquids held at 60°C or directly dipped in the liquids for a few minutes at room temperature. For the acid treatment, the PcAlOH films on different substrates were dipped in a 2 wt.% aqueous solution of different acids (e.g. sulfuric acid, hydrochloric acid, trifluoroacetic acid, potassium hydrogen phthalic acid, and nitrophthalic acid) which was held at room temperature.

In order to trace the transformation of PcAlOH by the acid treatment, thin films on different substrates were successively taken out of the acid solutions, extensively washed with distilled water, dried in air at room temperature, and directly examined by different techniques. Absorption spectra were recorded with a LKB 4050 spectrometer, FT-IR spectra with a Nicolet 170SX and X-ray diffraction patterns with a Siemens diffractometer D500 using a CuK_α ($\lambda = 1.54$ Å) radiation.

The transformation of PcAlOH in organic solvents and aqueous acid solution was also followed by electronic absorption spectrometry. The films on glass plates were dipped in a solution hold inside the spectrometer and the absorption spectrum was recorded at different time intervals. For infrared measurements, PcAlOH was sublimed on CaF_2 and AgBr plates. The electronic absorption spectra were recorded first to determine the film thickness and the extent of the transformation. Then only the infrared spectra were recorded.

For X-ray diffraction measurements, PcAlOH was sublimed in the same time on polished aluminum plates and glass plates. The aluminum and glass plates were treated in the same condition. The glass plates were used as references for determining any transformation process of the film on the aluminum plates.

2.3 Electrochemical measurements

The tin oxide on glass (NESA) (PPG Industries, sheet resistance $r = 250\ \Omega$/square) electrodes were cleaned before sublimation by placing them in a detergent solution, followed by subsequent rinsing with water, distilled water, and methanol. An insulating polymer was used to define a 4-cm^2 surface area. The contact with the substrate electrode was made with a copper wire and silver conducting paint (GC Electronic). All chemicals and solvents used in this work were classified as high purity and used without further purification. They were dissolved in distilled water from a Corning Megapure water distillation system. All electrolytic solutions contained 0.1 *M* Na_2SO_4 and the pH was adjusted with hydrochloric acid. The optimized concentration (32) of the redox couple $[I_3^-] = 10^{-3}$, $[I^-] = 10^{-4}$ *M* was used.

A conventional three-electrode single-compartment cell was used for the electrochemical measurements, a saturated calomel electrode (SCE) as the reference and a platinum foil (8 cm^2) as the counter electrode. Electrolytic solutions were not deaerated and measurements were performed under ambient atmosphere. The working electrode was placed at about 2 mm from the cell window to minimize the light absorption by the solution. The organic film was always directly illuminated. The white light illumination source is a 300 W ELH tungsten halogen lamp of a Kodak Ektrographic slide projector, Model AF2. Monochromatic illumination was performed with a 650 W tungsten halogen and a Schoffel Instruments monochromator. All action spectra were converted for the same photon flux incident on the film at each wavelength (N_{max}), taking into account the measured light exponent, γ, at these energies. This parameter is found in eq. [1] (30):

$$[1] \quad J_\lambda = kI^\gamma$$

where k is a proportionality constant and I is the light intensity incident on the semiconductor. In the energy range used for the action spectra (from 30 to 260 mW cm^{-2}), γ was around 0.9 and did not depend on the wavelength. The corrected short-circuit photocurrent is then calculated using eq. [2]:

$$[2] \quad J_{\lambda\ \text{corrected}} = J_{\lambda\ \text{measured}}\left(\frac{N_{max}}{N_\lambda}\right)^\gamma$$

where N_{max} and N_λ are the numbers of maximum incident photons and incident photons for the considered wavelength, respectively ($N_{max} = 8.3 \times 10^{14}$ photons $cm^{-2}\ s^{-1}$). The light intensity was measured by a United Detector Technology detector equipped with a radiometric filter.

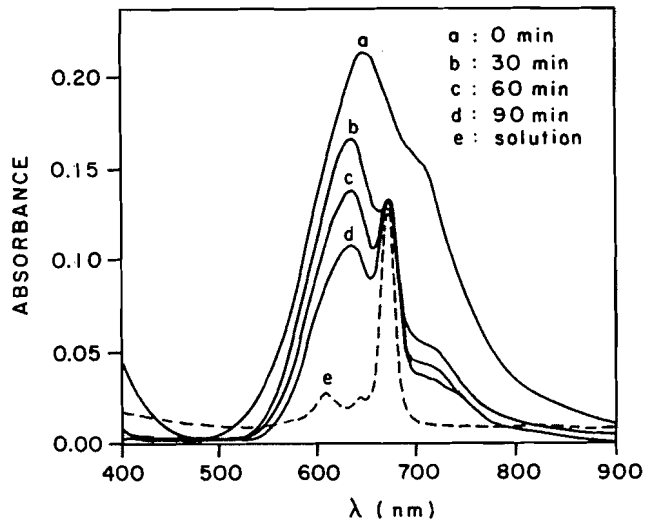

FIG. 1. Absorption spectra of PcAlOH: (*a*) solid thin film; (*b–d*) after different times of exposition to isopropanol vapour; and (*e*) solution in isopropanol.

All electrical measurements were performed in a Faraday cage. When used in the photogalvanic mode, the measurements were taken with a Keithley 616 electrometer; when used in the electrochemical and photoelectrochemical modes, the measurements were performed with a Model 362 potentiostat from Princeton Applied Research. The scanning rate was 2 mV s^{-1} for J–V measurements.

3. Results

3.1 Thin films absorption spectra

Visible absorption spectra were recorded for thin films of PcAlOH prepared by sublimation onto quartz and glass slides. Infrared spectra were recorded for similar films deposited onto calcium fluoride and silver bromide substrates.

The visible absorption spectra for thin films of PcAlOH on glass slide are shown in Figs. 1 and 2 (curve *a*). In the visible region the intense and broad Q band has a maximum at 640 nm with a shoulder at about 710 nm which are characteristic of the α-form. For comparison, the absorption spectra of PcAlOH dissolved in isopropanol is also shown in Fig. 1 (curve *e*). The relatively narrow Q band presented a maximum at 670 nm with shoulders at about 645 and 610 nm. When a thin film of PcAlOH (80 Å) was brought into contact with the isopropanol vapor at 55°C, a change of the absorption spectrum with time was observed (Fig. 1, curves *b* to *d*). A new absorption peak appears at 670 nm and increases with time, and this transformation is accompanied by the continual diminution of the 640 nm peak intensity. The variation is due probably to the transformation of the α-form to an amorphous phase and also to the slow dissolution of the solid film by the vapor of the alcohol. The observed spectrum could be, therefore, a combination of the PcAlOH solid thin film spectrum and the PcAlOH solution spectrum trapped in the thin film solid. Similar results were

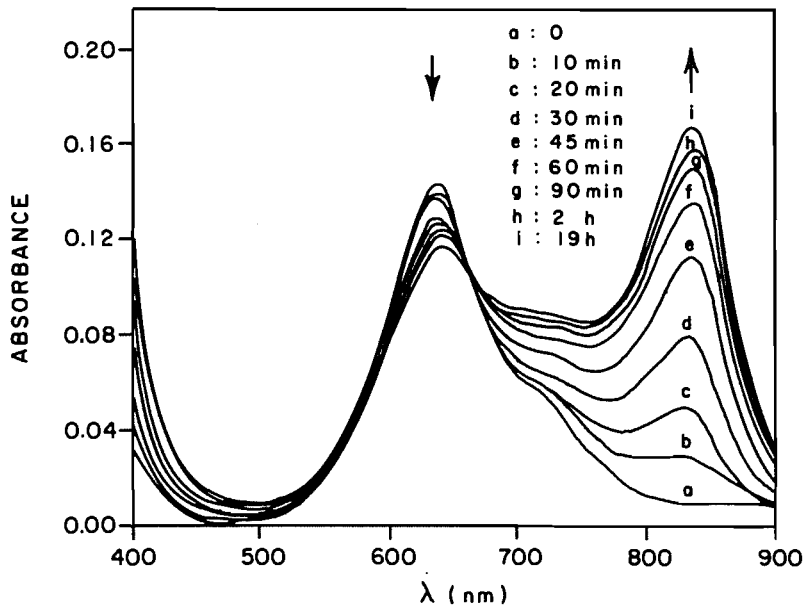

FIG. 2. Absorption spectra of PcAlOH thin film after different times of exposition to a 2 wt.% aqueous solution of potassium hydrogen phthalate.

observed when PcAlOH thin films on glass were dipped or exposed to the vapor of other organic solvents such as methanol, isopropanol, dichloromethane, and tetrahydrofuran. These results seem indicate that the α-form of PcAlOH is not transformed to an other polymorph form by a treatment with organic solvents as observed in the case of other metal phthalocyanines (22–25).

The absorption spectrum of PcAlOH thin films (60 Å) on a glass slide, when dipped in an aqueous potassium hydrogen phthalate (2 wt.%) at room temperature, changes drastically. A new and intense near-infrared absorption band appeared at 830 nm and this is accompanied by the diminution in the intensity of the peak absorption at 640 nm (Fig. 2). The visible spectra of the PcAlOH thin film dipped in a phthalate solution after various time at room temperature are depicted in Fig. 2. The new peak at 830 nm increased with time and this evolution is accompanied by a slow diminution of peak intensity at 640 nm. An isobestic point is observed at about 690 nm. The new peak at 830 nm is not due to the protonation of PcAlOH, because exhaustive washing of PcAlOH treated film with water showed the same absorption spectrum.

Similar results were observed when thin films of PcAlOH were dipped in other aqueous solutions of acids (Table 1).

The new form showing peak at 830 nm is tentatively called η-form.

The infrared absorption spectra of thin PcAlOH films (50 Å) evaporated on CaF_2 and AgBr substrates (showing only a Q-band at 640 nm, characteristic of the α-form) are shown in Figs. 3*a* and 4*a*, respectively. AgBr substrates were used to get information in the 1000–600 cm^{-1} region. After the samples have been dipped into a 2 wt.% aqueous solution of potassium hydrogen phthalate for 12 h, and the films extensively washed with water and allowed to dry in air, the infrared absorption spectra of the new form (showing absorption peak at 830 nm) changed drastically (Figs. 3*b* and 4*b*). Noticeable differences in the IR spectra were observed for the α-form and the η-form, particularly in the area of 1000 to 1200 cm^{-1}, where new peaks appeared at 1134, 1118, and 1065 cm^{-1} for the acid-treated films. A summary of the main absorption frequencies for the untreated (α-form) and acid-treated (η-form) films is given in Table 2.

TABLE 1. Effects of the acid treatment (12 h) on the absorption spectrum of PcAlOH films

Film thickness (Å)	Treatment by acids	Absorbance at 640 nm	Absorbance at 830 nm
140	(*1*) None	0.328	—
	(*2*) CF_3CO_2H	0.322	0.406
150	(*1*) None	0.341	—
	(*2*) 4-Nitrophthalic acid	0.241	0.300
130	(*1*) None	0.307	—
	(*2*) Potassium monophthalic acid	0.198	0.315
160	(*1*) None	0.353	—
	(*2*) HCl	0.300	0.855

3.2 X-ray diffraction

Figure 5 shows X-ray diffraction pattern for the sequential transformation of a thin PcAlOH film (50 Å). The α-form (Fig. 5*a*) was obtained by evaporation at 10^{-6} Torr on a polished aluminum plate. When exposed to an acid solution at room temperature, a new form η showing different X-ray diffraction pattern was obtained (Fig. 5*b*). These patterns show practically the same diffraction lines between $2\theta = 15$ to 30°. The main differences between *a* and *b* are the appearance of a new diffraction line at 12.1° and the disappearance of the line at 7.0°.

3.3 Photoactivity

The action spectra obtained for PcAlOH thin films (50 Å) with I_3^-/I^- redox couple before and after the treatment with trifluoroacetic acid are shown in Fig. 6. The photovoltaic effect occurs mainly at the interface PcAlOH and electrolyte. The photoresponse peaks coincide fairly well with the absorption

Can. J. Chem. Downloaded from www.nrcresearchpress.com by 61.7.252.67 on 09/07/12
For personal use only.

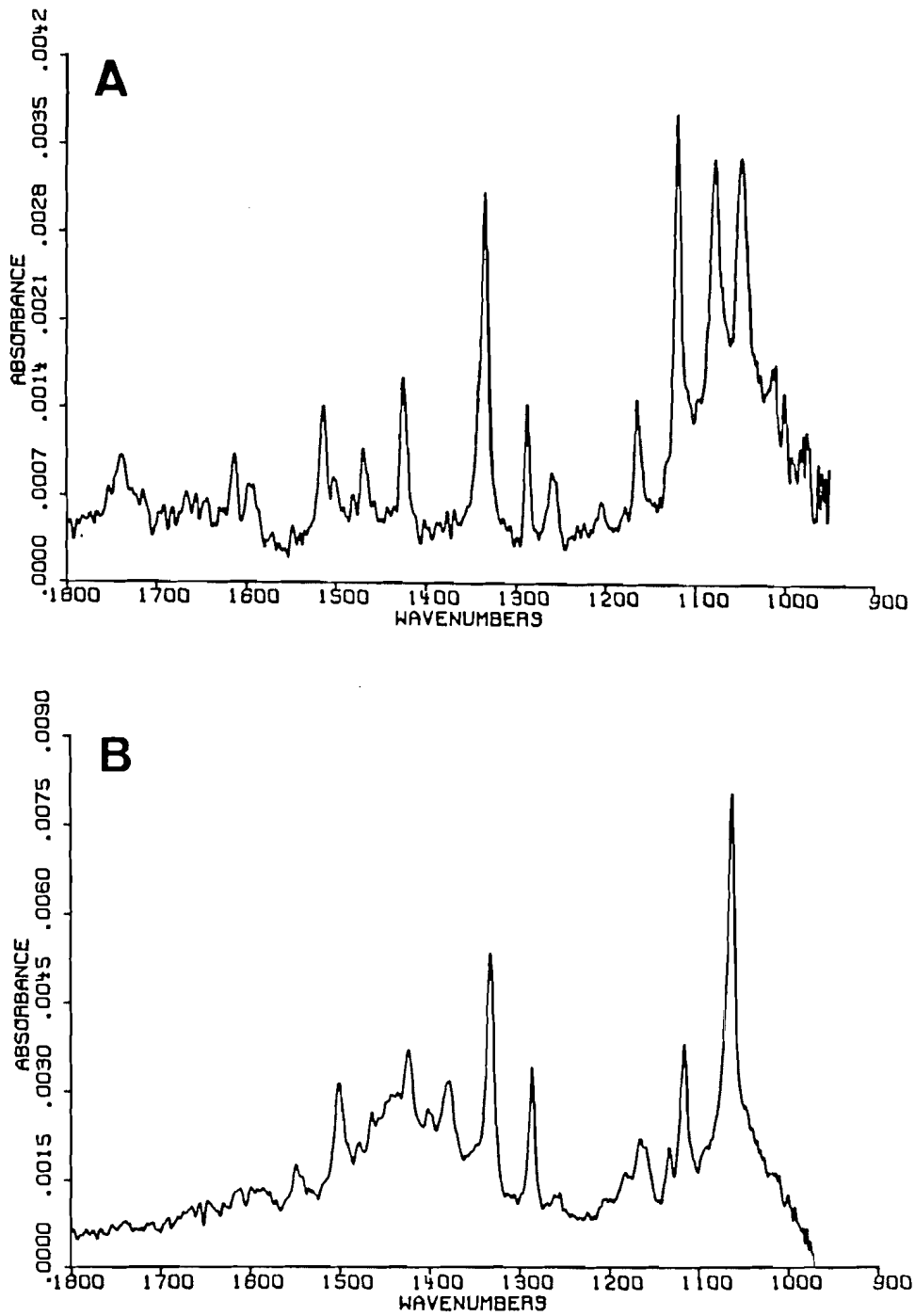

FIG. 3. Infrared spectra of PcAlOH thin film on CaF_2 plate before (*a*) and after (*b*) treatment with potassium hydrogen phthalate solution.

peaks (Fig. 7). The new polymorph which is very photoactive between 550–900 nm would permit the device to capture more light over a larger range of wavelengths and contributed to the improvement of its performance.

The current density – voltage (J–V) curves of a NESA/PcAlOH/I_3^-/I^-/Pt cell in the dark and under white light illumination of 10 mW cm^{-2} at pH = 1.0 are presented in Fig. 8. Curve *1* is for NESA in the dark, curves *2* and *3* are for untreated cells recorded in the dark and under illumination, respectively. (It took about 20 min to record curves *2* and *3*, so it is possible there are some dimorphic transformation induced by the electrolyte.) Curves *4* and *5* are for the trifluoroacetic acid treated cell in the dark and under illumination, respectively. Their photovoltaic properties are summarized in Table 3*A*. The acid-treated film shows an enhancement in the open-circuit voltage (V_{oc}) from 67 to 110 mV, the short-circuit photocurrent density (J) from 40 to 81 μA cm^{-2} and the fill factor (ff) from 0.41 to 0.58, resulting in an improvement of the conversion efficiency by a factor 5. The treatment by other acids gave similar results and for comparison, the photovoltaic

Can. J. Chem. Downloaded from www.nrcresearchpress.com by 61.7.252.67 on 09/07/12
For personal use only.

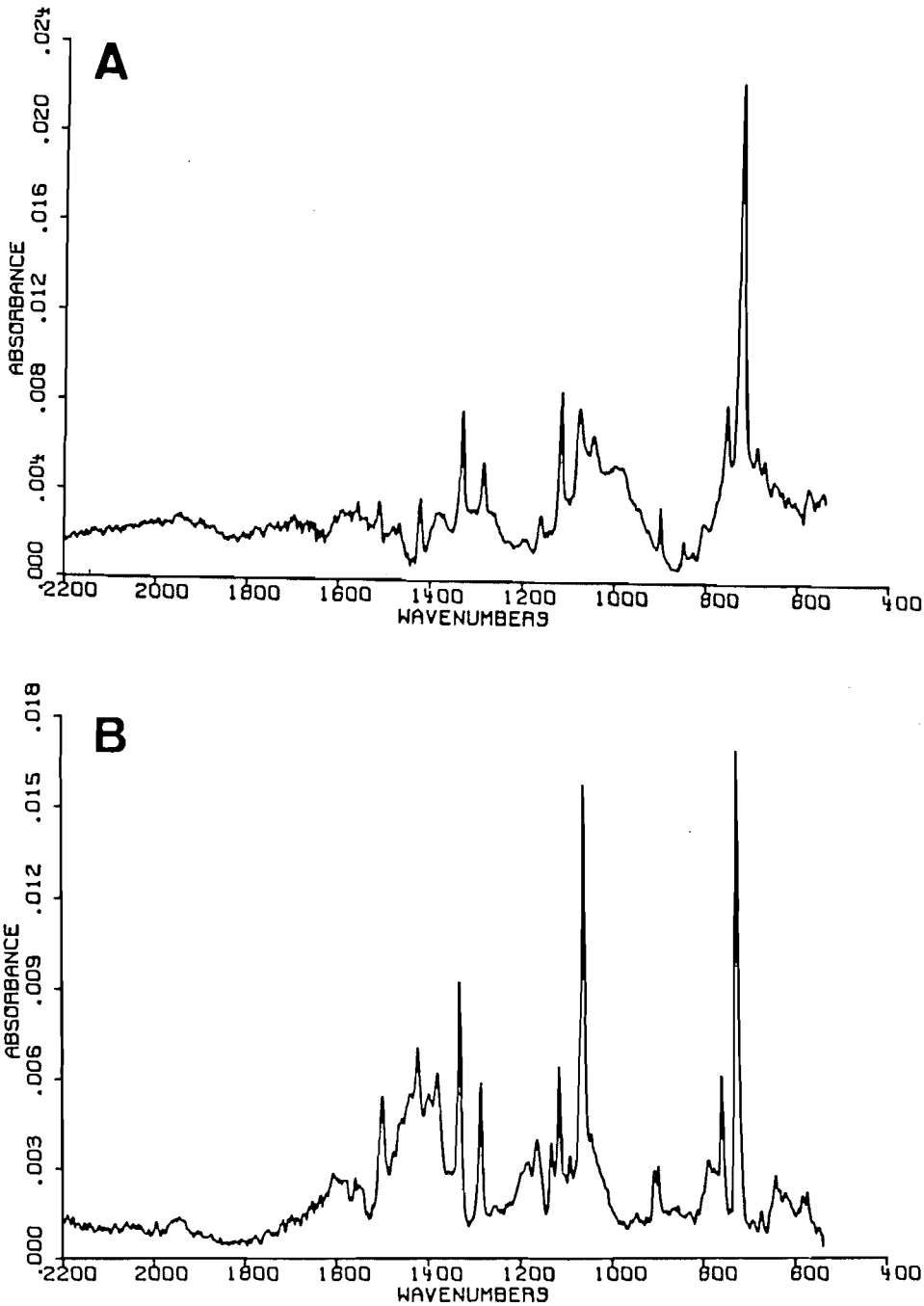

FIG. 4. Infrared spectra of PcAlOH thin film on AgBr plate before (*a*) and after (*b*) treatment with potassium hydrogen phthalate solution.

properties (15) of PcAlOH films treated with phthalic acid are shown in Table 3*B*. For I_3^-/I^- redox couple, lower pH usually gave higher conversion efficiency (32).

4. Discussion

Results of absorption spectra and X-ray diffraction indicate that the sublimed PcAlOH film exists in the α-form. Similar results are observed for ZnPc (23). Kobayashi *et al.* (22) have reported that the metastable α-form of metal phthalocyanine is transformed into the stable β-form through various intermediate forms (x, τ, ϵ) depending on the properties of the organic solvents and that an intermediate x-form appears in some solvents such as alcohols, acetone, ether, THF, $CHCl_3$. A schematic representation of the different molecular stacking for metallophthalocyanines can be found in reference (19). Hor and Loutfy (25) has observed a dimorphic transformation of PcMg (from the α-form to the x-form) induced by CH_2Cl_2 and THF, and an enhancement in photoactivity. No dimorphic transformation induced by organic solvents was observed for PcAlOH. But the metastable α-form of aluminum hydroxyphthalocyanine film can be transformed into a new form η by an acid treatment. The absorption spectrum of the new form is similar to the absorption spectra of the x-form of divalent metal phthalocyanine with absorption peaks at 640 and 830 nm. But the X-ray

Can. J. Chem. Downloaded from www.nrcresearchpress.com by 61.7.252.67 on 09/07/12
For personal use only.

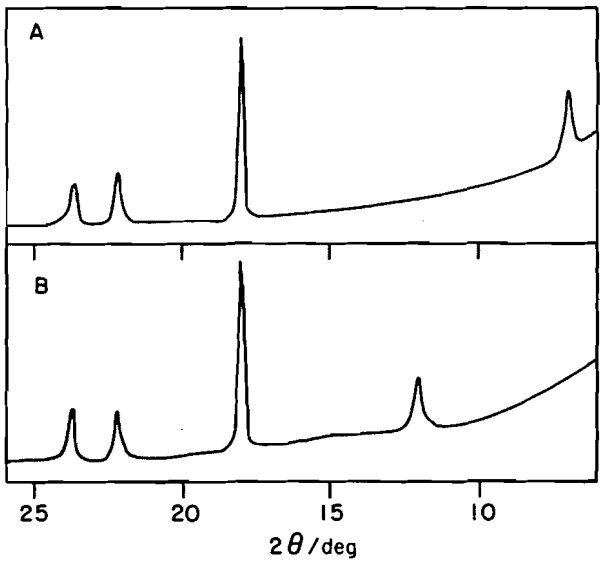

FIG. 5. X-ray diffraction patterns of PcAlOH thin film before (*a*) and after (*b*) treatment with potassium hydrogen phthalate solution.

diffraction pattern of the treated film is different from all X-ray diffractions of *x*-, τ-, or ϵ-forms described in the literature.

X-ray diffraction patterns of ZnPc films exposed to the vapor organic solvent show the transformation after 10 min of the α-form to the *x*-form which is completely transformed into the β-form after 120 min exposure (22). Based on the relation between the diffraction angle θ and the interplanetary distance *d*:

$$\sin\theta = \frac{\lambda}{2d}$$

with λ = 1.54 Å for Cu K_α, it was shown that the spacing *d* = 12.96 Å corresponds to the α-form, *d* = 12.54 and 9.48 Å to the β-forms and *d* = 11.4 Å to the *x*-form. For the untreated PcAlOH film, the spacing 12.78 Å corresponds probably to the α-form. For the treated films, the X-ray diffraction patterns show the spacing *d* = 7.31 Å for an unknown form η.

PcAlOH has a trivalent metal at centre and the OH group out of the macrocycle plane. Different dimeric structures are possible, with two Pc macrocycle planes parallel and the Al—OH oriented in the same direction (head-to-tail) or in the opposite direction (head-to-head or tail-to-tail). Similar results were observed for trivalent metal Pc's (21, 33–36). Thus, the X-ray structure determinations of single crystals of several vacuum-deposited thin film Pc's that have a trivalent or tetravalent metal at centre (e.g. PcGaCl, PcAlCl, PcInCl, PcVO) have shown that they have the tendency to aggregate in the solid state in either a cofacial stack (head-to-tail) or in various interleaved slipped stacks (head-to-head or tail-to-tail). It was proposed that the slipped configuration, in which the two Pc phases have more degree of movement than the α- or β-phases reported before for other Pc's (22, 23), is responsible for the strongly red-shifted visible absorbance spectra (33–36).

Infrared spectroscopy has been used by a number of authors as an indicator of crystallographic phase for phthalocyanines (23, 26, 37–40). The ir spectrum of the treated PcAlOH film

TABLE 2. Infrared absorption spectra of PcAlOH thin films

α-form	η-form
728	731
758	764
—	792
808	—
852	—
902	902
—	912
1051	—
—	1065
1080	—
1122	1118
	1134
1166	1167
1261	—
1289	1280
1336	1335
—	1380
1427	1425
1471	—
1502	1502
1514	—
1596	—
1613	—
1740	—
2919	2918

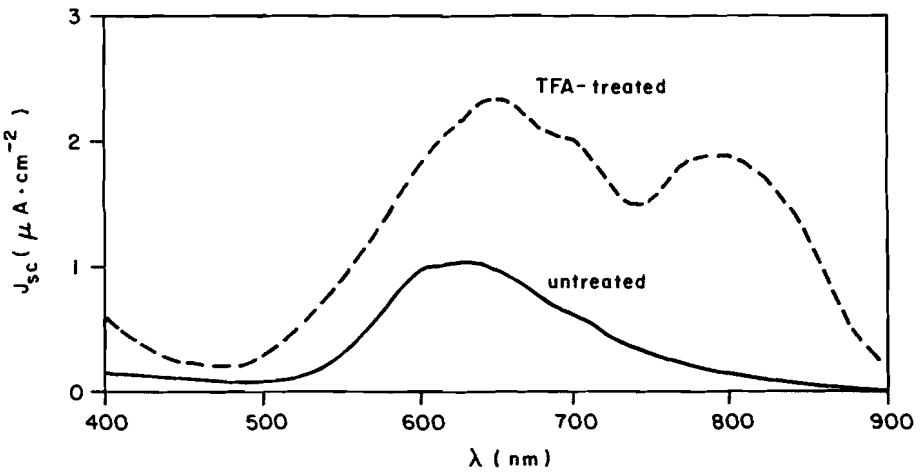

FIG. 6. Action spectra of a NESA/PcAlOH/I_3^-/I^-/Pt cell before (*a*) and after (*b*) treatment with trifluoroacetic acid.

Can. J. Chem. Downloaded from www.nrcresearchpress.com by 61.7.252.67 on 09/07/12
For personal use only.

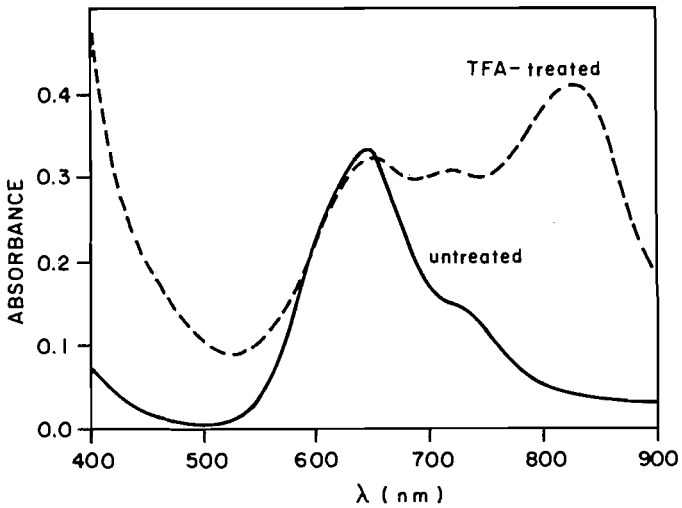

FIG. 7. Absorption spectra of PcAlOH thin film before (untreated) and after treatment with aqueous trifluoroacetic acid solution (TFA-treated).

is very different from that of the sublimed film. Besides the disappearance of peaks at 808, 852, 1261, 1471, 1514, 1596, 1613, and 1740 cm^{-1}, a change in the 1000–1100 cm^{-1} was observed, thus the two strong peaks at 1051 and 1080 cm^{-1} are replaced by a new peak at 1065 cm^{-1} for the treated PcAlOH film. The transformation from the α-form to the *x*-form for phthalocyanines induces modification principally in the absorption area of 700–800 cm^{-1} (37, 38), but rarely in the 1000–1100 cm^{-1} area.

It was also found that the treatment of other aluminum phthalocyanines such as chloroaluminum phthalocyanine or $PcAlOP(OH)_2OC_{16}H_{33}$ by acids gave the same effect, but free phthalocyanine is not converted. It seems that the aluminum metal has an effect on the transformation (32).

Spectroscopic studies and X-ray diffraction have shown the

TABLE 3. Open-circuit voltage, short-circuit current, fill factor, and conversion efficiency for a ITO/PcAlOH/I_3^-/I^-/Pt electrochemical cell under white light irradiation (10 mW cm^{-2}): effect of film thickness and acid treatment

pH	Thickness (Å)	Treatment	V_{oc} (mV)	J_{sc} (μA cm^{-2})	ff	η
		(*A*) Trifluoroacetic acid				
1.0	250	(*1*) Before	67	40	0.41	0.011
		(*2*) After	110	81	0.58	0.052
1.0	1110	(*1*) Before	88	33	0.34	0.010
		(*2*) After	123	62	0.54	0.041
		(*B*) Potassium monohydrogen phthalic acid (15)				
1.5	230	(*1*) Before	88	13.5	0.38	0.004
		(*2*) After	102	31.5	0.53	0.017
1.5	1850	(*1*) Before	59	14.0	0.34	0.003
		(*2*) After	98	33.5	0.52	0.017
1.5	600	(*2*) After	92	58.8	0.46	0.025
2.5	600	(*2*) After	104	21.3	0.77	0.016

transformation of α-PcAlOH to a new phase η by an acid treatment. The conversion mechanism and the crystallographic structure of the new form are not yet clear. One possible structure for η-form which collaborates well with spectroscopic and X-ray results is an interleaved arrangement involving four Pc planes with a tail-to-tail, head-to-head, tail-to-tail (PcAlOH..HOAlPc..PcAlOH..HOAlPc) stacking arrangement, slipping horizontally with respect to each other relatively to a *Z*-axis passing through the center of each Pc macrocycle in an *X*–*Y* parallel plane as suggested by Griffiths *et al.* for vanadyl phthalocyanine (21).

The enhancement of the photoactivity due to the dimorphic transformation of phthalocyanine films was already reported for

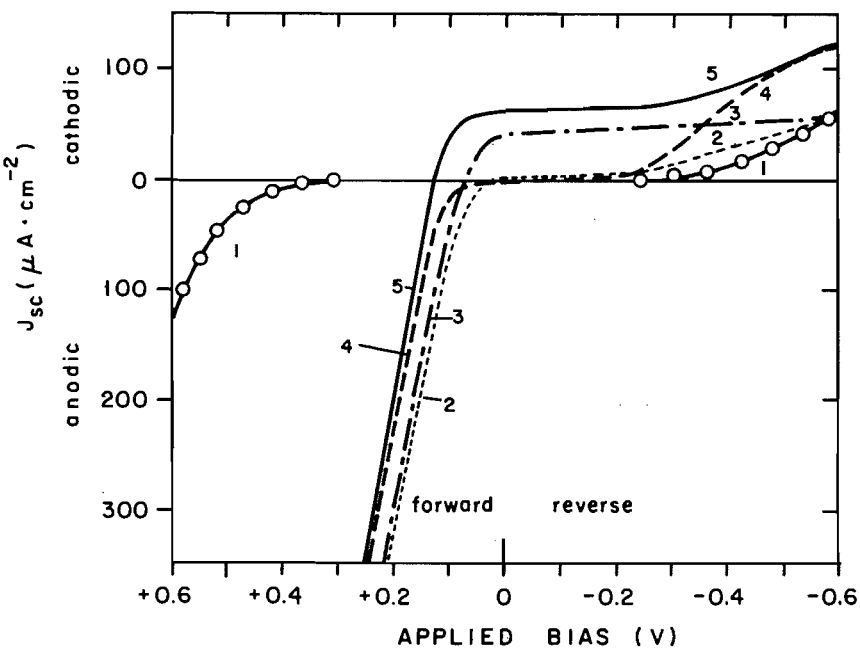

FIG. 8. *J*–*V* curves of a NESA/PcAlOH/I_3^-/I^-/Pt cell in the dark and under illumination (10 mW cm^{-2}): (*1*) NESA in the dark; (*2*) untreated in the dark; (*3*) untreated under illumination; (*4*) treated in the dark; (*5*) treated under illumination.

Can. J. Chem. Downloaded from www.nrcresearchpress.com by 61.7.252.67 on 09/07/12
For personal use only.

H_2Pc (20) and PcM (25) photovoltaic cells. In all cases, the improvement of the solar efficiency is only by a factor of 1.5. The enhancement in photoactivity of a PcAlOH treated with acid is more dramatic (factor up to 6) (Table 3). This is due mainly to a better quantum yield and an improvement of the junction rectifying behaviour of a NESA/PcAlOH/redox/Pt photoelectrochemical cells (15). The acid treatment broadens the absorption spectrum, modifies enormously the action spectra, and permits the device to capture more light over a larger range of wavelengths, contributing in part to the improvement of its performance. Better junction rectifying behavior was obtained for PcAlOH with the acid treatment. This is due to the decrease in the cell resistance by a factor of 4.2 (for I_3^-/I^-), an increase in J_{sc} and V_{oc}, and particularly an increase of ff (15). Values of ff up to 0.77 were obtained for a cell NESA/PcAlOH (600 Å)/I_3^-/I^-/Pt under 100 mW/cm^2 irradiation at pH 2.5 (15). This value is one of the highest observed for a photovoltaic organic cell.

5. Conclusion

A new polymorph η was obtained when thin films of the α-form of hydroxyaluminum phthalocyanine were dipped into aqueous acid solutions. The visible absorption spectrum of the new polymorph resembles that of the *x*-form for other metal phthalocyanines. However, the ir absorption spectrum and the X-ray diffraction patterns show absorption peaks and diffraction lines different from those observed for the middle energy polymorph (e.g. τ-, *x*-, or ϵ-forms). The structure of the *x*- or ϵ-forms has been assumed to have a dimeric structure of two neighboring, Pc macrocycle plane in a staggered configuration.

The new polymorph PcAlOH could have a similar structure but because of the trivalent nature of the Al metal, other configurations are possible as observed in the case of vanadyl phthalocyanine.

The photoactivity of the new PcAlOH polymorph induced by an acid treatment is substantially increased by a factor up to six. This is due mainly to a better quantum yield and an improvement of the function-rectifying behavior.

Acknowledgement

This work was supported by grants from the Natural Sciences and Engineering Research Council of Canada.

1. A. K. Ghosh, D. L. Morel, T. Feng, R. F. Shaw, and C. A. Rowe Jr. J. Appl. Phys. **45**, 230 (1974).
2. F. R. F. Fan and L. R. Faulkner. J. Chem. Phys. **69**, 3341 (1978).
3. R. O. Loutfy and J. H. Sharp. J. Chem. Phys. **71**, 1211 (1979).
4. G. A. Chamberlain and P. J. Cooney. Chem. Phys. Lett. **66**, 88 (1979).
5. M. Martin, J. J. André, and J. Simon. Nouv. J. Chim. **5**, 485 (1981).
6. S. Kanayama, N. Okuyama, and H. Yasunaga. Jpn. J. Appl. Phys. **20**, 141 (1981).
7. R. O. Loutfy, J. H. Sharp, C. K. Hsiao, and R. Ho. J. Appl. Phys. **52**, 5218 (1981).
8. W. J. Buttner, P. C. Rieke, and N. R. Armstrong. J. Am. Chem. Soc. **107**, 3738 (1985).
9. S. Kanayama, M. Hiroi, N. Okuyama, and H. Yasunaga. Jpn. J. Appl. Phys. **22**, 348 (1983).
10. R. O. Loutfy, C. K. Hsiao, and R. Ho. Can. J. Phys. **61**, 1416 (1983).
11. H. J. Wagner and R. O. Loutfy. J. Vac. Sci. Technol. **20**, 300 (1982).
12. R. O. Loutfy, Y. H. Shing, and D. K. Murti. Sol. Cells, **5**, 331 (1982).
13. A. M. Hor and R. O. Loutfy. Can. J. Chem. **61**, 901 (1983).
14. A. M. Hor, R. O. Loutfy, and C. K. Hsiao. Appl. Phys. Lett. **42**, 165 (1983).
15. G. Perrier and L. H. Dao. J. Electrochem. Soc. **134**, 1148 (1987).
16. G. Perrier and L. H. Dao. Can. J. Chem. **64**, 2431 (1986).
17. D. Bélanger, J. P. Dodelet, L. H. Dao, and B. A. Lombos. J. Phys. Chem. **88**, 4288 (1984).
18. R. O. Loutfy and L. F. McIntyre. Can. J. Chem. **61**, 72 (1983).
19. J. Simon and J. J. André. Molecular semiconductors, photoelectrical properties and solar cells. *Edited by* J. M. Lehn and C. W. Rees. Springer–Verlag, New York. 1985. pp. 73–147.
20. P. Hartman and W. G. Perdok. Acta Crystallogr. **8**, 49 (1955); **8**, 521 (1955); P. Hartman. Crystal growth: an introduction. North-Holland Publishers, Amsterdam. 1973. p. 358.
21. C. H. Griffiths, M. S. Walker, and P. Goldstein. Mol. Cryst. Liq. Cryst. **33**, 149 (1976).
22. T. Kobayashi, N. Uyeda, and F. Suto. J. Phys. Chem. **72**, 2446 (1968).
23. F. Iwatzu, T. Kobayashi, and N. Uyeda. J. Phys. Chem. **84**, 3223 (1980).
24. K. Y. Law. J. Phys. Chem. **89**, 2652 (1985).
25. A. M. Hor and R. O. Loutfy. Thin Solid Films, **106**, 291 (1983).
26. J. H. Sharp and M. Lardon. J. Phys. Chem. **72**, 3230 (1968).
27. S. Takano, T. Enokida, A. Kakata, and Y. Mori. Chem. Lett. 2037 (1984).
28. L. H. Dao and G. Perrier. Chem. Lett. 1259 (1986).
29. J. W. Weigl, J. Mammino, G. L. Whitaker, R. W. Radler, and J. F. Byrne. Current problems in electrophotography. *Edited by* W. I. Berg and K. Hauffe. de Gruyter, Berlin. 1972. p. 287.
30. H. Meier. Organic semiconductors. Verlag Chemie, Weinheim. 1974. p. 149.
31. J. P. Linsky, T. R. Paul, R. S. Nohr, and M. E. Kenney. Inorg. Chem. **19**, 3131 (1980).
32. G. Perrier. Ph.D. Thesis, INRS, Univ. of Québec, Canada. 1986.
33. T. J. Klofta, J. Danziger, P. Lee, J. Pankow, K. W. Nebesny, and N. R. Armstrong. J. Phys. Chem. **91**, 5646 (1987).
34. R. F. Ziolo, C. H. Griffiths, and J. M. Troup. J. Chem. Soc. Dalton Trans. 2300 (1900).
35. W. Hiller, J. Strähle, W. Kobel, and M. Hanack. Z. Kristallog. **159**, 173 (1982).
36. K. J. Wynne. Inorg. Chem. **23**, 4658 (1984).
37. T. J. Klofta, T. D. Sims, J. W. Pankow, J. Danziger, K. W. Nebesny, and N. R. Armstrong. J. Phys. Chem. **91**, 5651 (1987).
38. M. K. Debe. J. Appl. Phys. **55**, 3354 (1984).
39. J. H. Sharp and M. Abkowitz. J. Phys. Chem. **77**, 477 (1983).
40. K. Arishima, H. Hiratsuka, A. Tate, and T. Okada. Appl. Phys. Lett. **40**, 279 (1982).

Can. J. Chem. Downloaded from www.nrcresearchpress.com by 61.7.252.67 on 09/07/12
For personal use only.

The preparation and fungicidal activity of a series of thiazolyl- and isothiazolyl-diarylcarbinols

ALAN R. KATRITZKY[1] AND KATHLEEN S. LAURENZO
Department of Chemistry, University of Florida, Gainesville, FL 32611, U.S.A.

AND

DOUGLAS I. RELYEA
Uniroyal Chemical, Naugatuck, CT 06770, U.S.A.

Received September 29, 1987

ALAN R. KATRITZKY, KATHLEEN S. LAURENZO, and DOUGLAS I. RELYEA. Can. J. Chem. **66**, 1617 (1988).

(Isothiazol-5-yl)diarylcarbinols were prepared from 5-lithioisothiazole. (Thiazol-5-yl)diarylcarbinols were obtained via 5-lithio-2-bromothiazole or 5-lithio-2-trimethylsilylthiazole with subsequent removal of the 2-substituent. Corresponding 2-aminothiazol-5-ylcarbinols were made by protecting 2-aminothiazole as its bis(trimethylsilyl) derivative. Biological activities were compared to the calculated electron densities at the heterocyclic N-atoms.

ALAN R. KATRITZKY, KATHLEEN S. LAURENZO et DOUGLAS I. RELYEA. Can. J. Chem. **66**, 1617 (1988).

Des isothiazolyl-5 diarylcarbinols ont été préparés à partir de lithio-5 isothiazole. Des thiazolyl-5 diarylcarbinols ont été obtenus soit du bromo-2 lithio-5 thiazole soit du lithio-5 triméthylsilyl-2 thiazole suivi du clivage du groupement-2. La synthèse des amino-2 thiazolyl-5 carbinols correspondants a été effectuée en protégeant l'amino-2 thiazole sous forme de dérivé bis(triméthylsilyle). L'activité fongicide des produits a été comparée avec la densité électronique calculée de l'atome d'azote hétérocyclique.

Introduction

Azole fungicides inhibit a cytochrome P450 enzyme in the ergosterol biosynthetic pathway (1), responsible for the 14α-demethylation of 24-methylene-24,25-dihydrolanosterol, a precursor to ergosterol, which is an essential component of the fungal cell wall (1*c*). The general structural requirements, cf. **1**,

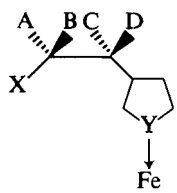

1

A, B, C, D = lipophilic backbone
X = polar group

for these inhibitors (1*d*) include a lipophilic backbone and polar group necessary for recognition and binding at the active site. Critical for enzyme inactivation is a nitrogen β to the ring fusion point, the unshared pair of electrons of which complex with the Fe^{III} of the heme prosthetic group in the active site of the enzyme, preventing binding of the natural substrate.

Most of the azole fungicides on the market today are based on imidazole (e.g., **2**) or on 1,2,4-triazole (e.g., **3**, **4**). The Eli Lilly inhibitor Triarimol (**5**) is a pyrimidine with structural features similar to the model demethylase inhibitors **1**–**4**. The aim of the present work was to explore other heterocyclic ring systems with a nitrogen in the β-position for fungicidal activity. We chose Triarimol (**5**) as our model because two obvious disconnections suggested convenient synthetic routes: the addition of a heterocyclic anion to a substituted benzophenone, or the addition of two moles of a Grignard reagent to a heterocyclic carboxylic ester or acid chloride.

We now report the synthesis and fungicidal activity of a series of thiazolyl- and isothiazolyl-diarylcarbinols.

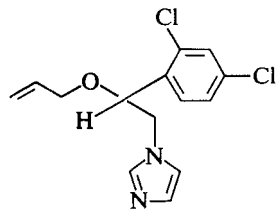

Imazalil
2

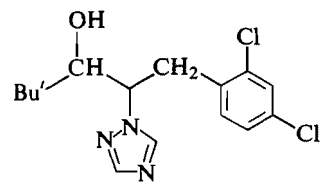

Diclobutrazol
3

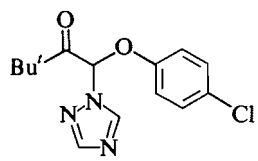

Triadimefon
4

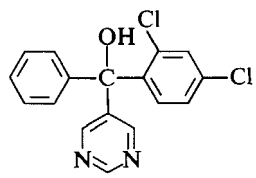

Triarimol
5

Results and discussion

Isothiazole compounds

Isothiazole is converted by *n*-butyllithium into isothiazol-5-yllithium (2), which has previously been added to various benzaldehydes affording secondary carbinols in low to moderate yields (3) and to one ketone (acetone) affording the corresponding tertiary carbinol in low yield (4).

In our hands, treatment of isothiazole with *n*-butyllithium at −78°C followed by benzophenone gave a trace of the desired product **6***a* (Table 1) (2%) but the major isolated product was benzhydrol. Addition of *n*-butyllithium to the isothiazole ring has been reported (2). We avoided this by using lithium diisopropylamide at ~ −70°C; reaction with 4,4′-dichlorobenzophenone then gave pure **6***b* in quantitative yield (Scheme 1).

This procedure was extended to a series of substituted benzophenones; reaction was sometimes complete after 2 h at −78°C; otherwise the temperature was allowed to rise to 0°C. After work-up, the products (Table 1) were purified by flash

[1]Author to whom correspondence may be addressed.

Printed in Canada / Imprimé au Canada

Can. J. Chem. Downloaded from www.nrcresearchpress.com by 93.93.197.157 on 09/07/12
For personal use only.

TABLE 1. Diaryl(isothiazol-5-yl)carbinols (**6**)

	R	R′	Yield (%)	Melting point (°C)	Analysis found %C	%H	%N	Molecular formula	Calculated %C	%H	%N
a	H	H	56[a]	121–123	72.25	5.00	4.89	$C_{16}H_{13}NOS$	71.88	4.90	5.24
b	4-Cl	4-Cl	100[b]	117–118	57.32	3.25	4.06	$C_{16}H_{11}Cl_2NOS$	57.16	3.30	4.17
c	4-Cl	H	81[a]	115–116	63.74	3.95	4.58	$C_{16}H_{12}ClNOS$	63.68	4.01	4.64
d	3,4-diCl	H	85[c]	90.5–91.5	57.34	3.24	4.12	$C_{16}H_{11}Cl_2NOS$	57.16	3.30	4.17
e	4-OCH_3	H	100[a]	Oil[d]	—	—	—	$C_{17}H_{15}NO_2S$	—	—	—
f	4-CF_3	H	93[a]	119.5–121	60.54	3.58	4.18	$C_{17}H_{12}F_3NOS$	60.89	3.61	4.18
g	2,4-diCl	H	81[c]	137–138	56.81	3.41	3.95	$C_{16}H_{11}Cl_2NOS$	57.14	3.30	4.17
h	2-Cl	H	78[c]	109–127	63.36	3.90	4.54	$C_{16}H_{12}ClNOS$	63.68	4.01	4.64

[a]Purified by flash chromatography (microcrystals, except *e*).
[b]No purification required.
[c]Purified by recrystallization from 2:1 hexane/ethanol (needles).
[d]*Mol. Wt.* calcd: 297.0823; found: 297.0824.

TABLE 2. The ^{13}C nmr chemical shifts and assignments[a] of diaryl(isothiazol-5-yl)carbinols (**6**): isothiazole ring carbons and α-carbons

Compound	C3	C4	C5	α-C
a	157.15	122.74	176.74	78.46
b	157.22	122.67	176.23	78.71
c	157.84	123.13	176.99	78.20
d	157.12	122.44	176.08	78.71
e	156.88	122.38	177.35	79.10
f	157.22	122.81	176.08	79.34
g	156.69	122.86	174.04	79.58
h	156.64	122.91	174.87	79.88

[a]**6***c* in DMSO; all others in $CDCl_3$.

chromatography and (or) recrystallization. The ^{13}C nmr chemical shifts and assignments are reported in Tables 2 and 3, and ^1H nmr data in Table 4.

Thiazole compounds

A sub-structure search of Chemical Abstracts from 1927 to 1986 revealed no otherwise unsubstituted thiazoles with a tertiary carbinol group in the 5-position. Direct lithiation of the thiazole nucleus normally affords the corresponding 2-lithio derivative (5); if the 2-position is blocked, lithiation can occur at the 5-position (5, 6). Blocking the 2-position with a removable group was previously used by Noyce and Fike (6) to prepare a secondary 2-chlorothiazol-5-ylcarbinol; the chloro substituent was removed with zinc and acetic acid.

2-Chlorothiazole, treated successively with *n*-butyllithium and 4,4′-dichlorobenzophenone, gave carbinol **7** (52%). Simple dehalogenation of the thiazole ring with Zn and acetic acid (reflux, 4 h) was unsuccessful, presumably due to the sensitivity of the triarylcarbinol group to acidic conditions.

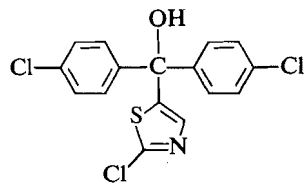

7

2-Halothiazoles are reported to undergo halogen–metal exchange with *n*-butyllithium (7). Carbinol **7**, on treatment with two equivalents of *n*-butyllithium at −78°C, followed by quenching with water, gave a mixture estimated by ^1H nmr to contain 50–60% of carbinol **9***b*. As 2-chlorothiazoles do not undergo this reaction as readily as 2-bromothiazoles (8), 2-bromo-5-lithiothiazole (unstable even in solution) was prepared by the controlled reaction of 2-bromothiazole and LDA (Scheme 2) and the benzophenone was added without delay. Complete reaction in about 15 min at −78°C gave diaryl-(2-bromothiazol-5-yl)carbinols (**8***a–f*) in good yields (Table 5), with structures confirmed by ^1H and ^{13}C nmr spectroscopy (Tables 6–8).

These yellow to light brown low-melting solids, though not analytically pure, were smoothly converted by treatment with two equivalents of *n*-butyllithium in THF at −78°C for 10–15 min, followed by water (Scheme 2), into the diaryl(thiazol-

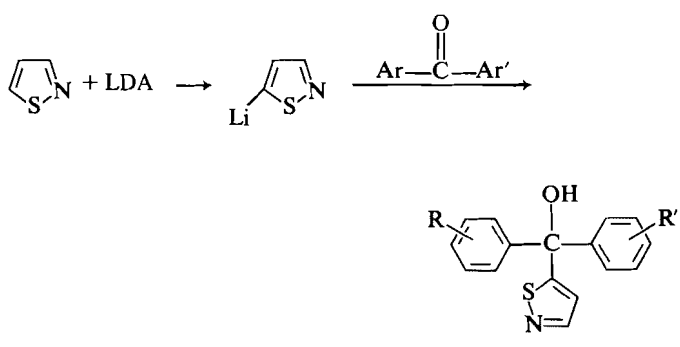

SCHEME 1

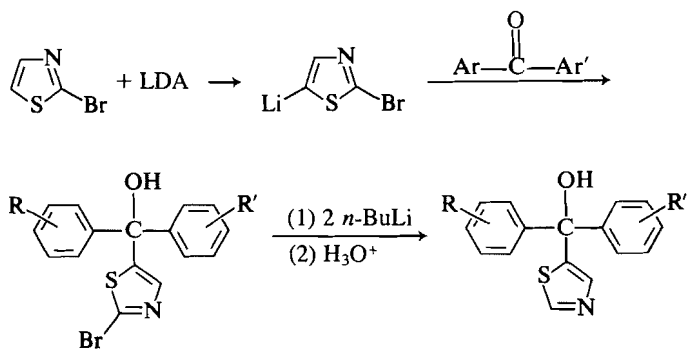

SCHEME 2

Can. J. Chem. Downloaded from www.nrcresearchpress.com by 93.93.197.157 on 09/07/12
For personal use only.

TABLE 3. The ^{13}C nmr chemical shifts and assignments of diaryl(isothiazol-5-yl)carbinols (**6**): aryl carbons

Compound	Ring	C1′	C2′	C3′	C4′	C5′	C6′
a	R = R′ = H	145.64	126.98	128.20	[a]	[b]	*c*
b	R = R′ = 4-Cl	143.67	128.37	[d]	134.07	[d]	[d]
c	R = 4-Cl	145.31	129.74	126.79	132.25	[b]	*c*
	R′ = H	145.89	128.00	[d]	127.57	[d]	[d]
d	R = 3,4-diCl	144.45	128.86	132.27	131.88	129.98	126.42
	R′ = H	145.77	126.81	128.32	[e]	[b]	*c*
e	R = 4-OCH_3[f]	137.87	128.22	113.21	158.83	[b]	*c*
	R′ = H	145.67	126.76	127.93	127.59	[b]	*c*
f	R = 4-CF_3[g]	149.33	125.13[h]	126.96	130.0[i]	[b]	*c*
	R′ = H	144.84	127.30	128.42	[e]	[b]	*c*
g	R = 2,4-diCl	140.16	134.60	130.47	133.05	126.52	130.86
	R′ = H	143.67	125.79	128.13	127.83	[b]	*c*
h	R = 2-Cl	141.53	132.37	129.49	129.69	126.42	132.25
	R′ = H	144.21	125.98	128.03	127.59	[b]	*c*

[a]Shoulder on C3′.
[b]Equivalent to C3′.
[c]Equivalent to C2′.
[d]A single large resonance was observed for C2′, 3′, 5′, and 6′.
[e]Resonance not observed.
[f]OCH_3: δ 54.98.
[g]CF_3: δ 123.92, J_{CF} = 272 Hz.
[h]J_{CF} = 3.66 Hz.
[i]J_{CF} = 33.0 Hz.

TABLE 4. The ^1H nmr chemical shifts and assignments of diaryl(isothiazol-5-yl)carbinols (**6**)

Compound	H3[a]	H4[a]	Aryl protons	OH[b]
a	8.14	6.91	7.29 (s, 10H)	4.51
b	8.2	6.8	7.2 (s, 8H)	3.5
c	8.5	7.05	7.45 (s, 9H)	3.3
d	8.5	7.05	7.2–7.6 (m, 8H)	2.4
e	8.5	6.9	7.0 (s, 2H)	2.5[c]
			7.3 (s, 2H)	
			7.5 (s, 5H)	
f	8.3	7.0	7.65 (s, 4H)	4.8
			7.45 (s, 5H)	
g	8.5	6.95	7.1–7.45 (m, 8H)	4.4
h	8.3	6.95	7.1–7.4 (m, 9H)	5.25

[a]s, 1H.
[b]Broad s.
[c]OCH_3: δ 3.85 (s, 3H).

TABLE 5. Diaryl-(2-bromothiazol-5-yl)carbinols (**8**)

Compound	R	R′	Yield (%)	Melting point (°C)
a	H	H	62	Oil
b	4-Cl	4-Cl	79	50–85
c	4-Cl	H	66	48–52
d	3,4-diCl	H	72	57–70
e	4-OCH_3	H	71	45–49
f	4-CF_3	H	72	Oil

5-yl)carbinols **9***a–f* (71–81%, Table 9). The structures of **9***a–f* were confirmed by ^1H and ^{13}C nmr spectroscopy (Tables 10–12).

Synthesis of 2-substituted thiazoles

Based on molecular orbital calculations and initial biological screening, we required thiazole compounds (**10**) with the 2,4-dichloro substitution pattern in the aryl rings, and electron-donating groups (e.g., methyl, methoxy, amino) at the 2-position of the thiazole ring. For the 2-amino compound **10***a*, 2-aminothiazole was protected as the *N,N*-bis(trimethylsilyl) derivative (9) by treating successively with two equivalents of *n*-butyllithium and two equivalents of trimethylsilyl chloride. Another equivalent of *n*-butyllithium, and then 2,4-dichlorobenzophenone, gave carbinol **10***a* (61%).

The reaction of 2-bromo-5-lithiothiazole with 2,4-dichlorobenzophenone failed, so carbinols **10***b* and *c* were prepared

TABLE 6. The ^{13}C nmr chemical shifts and assignments[a] of diaryl-(2-bromothiazol-5-yl)carbinols (**8**): thiazole ring carbons and α-carbons

Compound	C2	C4	C5	α-C
a	136.90	140.75	151.18	78.61
b	137.50	140.75	150.49	78.27
c	137.14	140.60	150.89	78.07
d	137.43	140.51	150.50	77.68
e	136.56	140.41	151.62	78.12
f	137.43	140.99	150.50	78.32

[a]In $CDCl_3$.

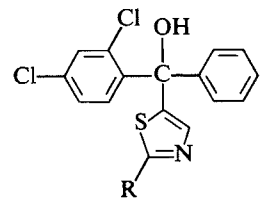

10
a: R = NH_2
b: R = H
c: R = CH_3
d: R = OCH_3

Can. J. Chem. Downloaded from www.nrcresearchpress.com by 93.93.197.157 on 09/07/12
For personal use only.

TABLE 7. The ^{13}C nmr chemical shifts and assignments of diaryl-(2-bromothiazol-5-yl)carbinols (**8**): aryl carbons

Compound	Ring	C1′	C2′	C3′	C4′	C5′	C6′
a	R = R′ = H	144.99	126.96	128.17	128.03	[a]	[b]
b	R = R′ = 4-Cl	140.75	128.52	128.32	134.32	[a]	[b]
c	R = 4-Cl	143.53	128.27[c]	[c]	133.88	[c]	[c]
	R′ = H	144.56	[c]	[c]	126.81	[c]	[c]
d	R = 3,4-diCl	143.97	129.83	132.37	132.02	128.86	126.42
	R′ = H	145.18	126.81	128.32	[d]	[a]	[b]
e	R = OCH_3[e]	137.24	128.27	113.31	158.93	[a]	[b]
	R′ = H	145.14	126.76	127.98	127.74	[a]	[b]
f	R = 4-CF_3[f]	148.79	126.96	125.27[g]	130.25[h]	[a]	[b]
	R′ = H	144.36	127.35	128.52	126.66	[a]	[b]

[a]Equivalent to C3′.
[b]Equivalent to C2′.
[c]A single large resonance was observed.
[d]Resonance not observed.
[e]OCH_3: δ 55.02.
[f]CF_3: δ 123.92; J_{CF} = 272 Hz.
[g]J_{CF} = 3.66 Hz.
[h]J_{CF} = 33.0 Hz.

TABLE 8. The ^1H nmr chemical shifts and assignments of diaryl-(2-bromothiazol-5-yl)carbinols (**8**)

Compound	H4[a]	Aryl protons	OH[b]
a	7.0	7.4 (s, 10H)	4.25
b	7.1	7.4 (s, 8H)	3.5
c	7.15	7.45 (s, 9H)	3.3
d	7.05	7.2–7.7 (m, 8H)	4.0
e	7.05	6.8–7.4 (dd + s, 9H)	3.8[c]
f	7.0	7.65 (s, 4H)	4.0
		7.4 (s, 5H)	

[a]s, 1H.
[b]Broad s.
[c]OH plus OCH_3: s, 4H.

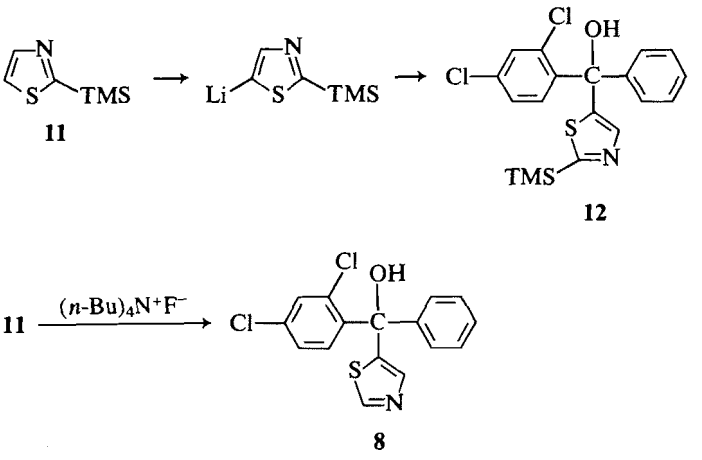

SCHEME 3

from 2-trimethylsilylthiazole (**11**) (10). Treatment of **11** with one equivalent of LDA followed by 2,4-dichlorobenzophenone gave the 2-trimethylsilyl-substituted carbinol **12** (Scheme 3) in which the thiazole ring is easily desilylated by silica gel (10). Tetrabutylammonium fluoride added directly to the ethereal solution of the crude product gave carbinol **10***b* (63%). Treatment of **10***b* with two equivalents of LDA followed by methyl iodide produced **10***c* (100%). The nmr spectral data for compounds **10***a–c* are included in Tables 9–12.

Chemical shift assignments

The ^{13}C chemical shifts of the heterocyclic ring carbons (Tables 2, 6, and 10) were assigned by comparison to literature values for the parent heterocycles (11, 12), and by APT (attached proton test) (13). An α,α-diarylcarbinol group substituted at C5 of isothiazole or 2-substituted thiazoles caused a downfield shift of ca. 28 ppm for C5. In the unsubstituted thiazole compounds (**9***b* and *f*) (Table 10), the signal for C5 was observed at δ 147.26 and 147.31, respectively, but for the other compounds **9** the signal for C5 is presumed to coincide with C1″ at δ 145–147; sometimes a shoulder can be detected.

The aryl ring carbons (Tables 3, 7, and 11) were assigned by APT and by comparison of shifts to those calculated by means of substituent parameters (11) using triphenylcarbinol as a model (14).

The ^1H nmr assignments (Tables 6, 9, and 12) are based on literature values for the ring protons in isothiazole (15) and thiazole (16); the ring protons in the 4-position were shielded by ca. 0.5 ppm compared to the parent heterocycles. For the unsubstituted thiazole compounds (**9**), this shift caused H4 (δ 7.9 in the parent ring) to be obscured by the aryl protons.

Biological evaluation

The compounds described in this paper were evaluated for control of the phytopathogenic fungi *Fusarium oxysporum*, *Botrytis cinerea*, *Alternaria solani*, *Cercospora arachidicola*, *Helminthosporium maydis*, *Sclerotinia sclerotiorum*, *Sclerotium rolfsii*, and *Phytophthora infestans* in in vitro tests at concentrations of 500 ppm and lower. In vivo tests were also conducted at 1000 ppm and lower with *Piricularia oryzae* on barley, *Erysiphe polygoni* on beans, *Erysiphe cichoracearum* on cucumber, *Erysiphe grammis* on barley, and *Uromyces phaseoli* on beans.

Control of phytopathogenic organisms is conveniently described by an efficacy value defined by

$$\text{efficacy} = \log\frac{\%\ \text{control}}{100} + \log\frac{10^6}{\text{concentration}}$$

Can. J. Chem. Downloaded from www.nrcresearchpress.com by 93.93.197.157 on 09/07/12
For personal use only.

TABLE 9. Diaryl(thiazole-5-yl)carbinols

Compound	R	R′	R″	Yield (%)	Melting point (°C)	Analysis found %C	%H	%N	Molecular formula	Calculated %C	%H	%N
7	4-Cl	4-Cl	Cl	52[a]	122.5–123.5	51.89	2.60	3.53	$C_{16}H_{10}Cl_3NOS$	51.84	2.72	3.78
9*a*	H	H	H	79[b](56)[c]	136–138	71.93	4.95	5.12	$C_{16}H_{13}NOS$	71.88	4.90	5.24
9*b*	4-Cl	4-Cl	H	71[b]	146.5–147	56.90	3.22	4.06	$C_{16}H_{11}Cl_2NOS$	57.16	3.30	4.17
9*c*	4-Cl	H	H	71[b]	127–128	63.44	3.94	4.52	$C_{16}H_{12}ClNOS$	63.68	4.01	4.64
9*d*	3,4-diCl	H	H	78[a]	143–144.5	57.66	3.44	3.97	$C_{16}H_{11}Cl_2NOS$	57.16	3.30	4.17
9*e*	4-OCH_3	H	H	72[a]	47–60	68.27	5.29	4.51	$C_{17}H_{15}NO_2S$	68.66	5.08	4.71
9*f*	4-CF_3	H	H	81[a]	147–148.5	60.36	3.29	4.10	$C_{17}H_{12}F_3NOS$	60.89	3.61	4.18
10*a*	2,4-diCl	H	NH_2	61[a]	87–115	54.80	3.62	7.30	$C_{16}H_{12}Cl_2N_2OS$	54.71	3.44	7.98
10*b*	2,4-diCl	H	H	63[a]	149–150	57.45	3.13	3.81	$C_{16}H_{11}Cl_2NOS$	57.16	3.30	4.17
10*c*	2,4-diCl	H	CH_3	100[a]	164–166	58.40	3.58	3.63	$C_{17}H_{13}Cl_2NOS$	58.30	3.74	4.00

[a]Purified by flash chromatography (microcrystals).
[b]Purified by recrystallization from 2:1 hexane/chloroform (needles).
[c]Second recrystallization.

TABLE 10. The ^{13}C nmr chemical shifts and assignments[a] of diaryl(thiazol-5-yl)carbinols: thiazole ring carbons and α-carbons

Compound	C2	C4	C5	α-C
7	153.06	139.35	148.63	77.87
9*a*	153.81	141.53	—	78.61
9*b*	154.76	141.65	147.26	76.59
9*c*	153.91	141.33	—	78.27
9*d*	154.33	141.51	—	76.74
9*e*	153.62	141.48	—	78.21
9*f*	154.67	141.65	147.31	77.13
10*a*	169.50	137.73	134.46	79.00
10*b*	154.20	142.55	—	79.14
10*c*	167.51	141.33	144.21	79.14[b]

[a]**9***b*, *d*, and *f* in DMSO; others in $CDCl_3$.
[b]2-CH_3: δ 19.20.

where concentration is measured in parts per million. Thus efficacy provides a single parameter in which large values reflect both high percent control and low concentration; for example, 90% control at 1000 ppm gives efficacy 2.95, 100% control at 50 ppm gives efficacy 4.30. Since control of less than 70% is generally not economically useful, efficacy is arbitrarily redefined as zero if percent control is less than 70% at the test concentration.

Certain members of both the isothiazole (**6**) and thiazole (**7**, **8**, **9**) series show significant fungicidal activity in both in vitro and in vivo testing (Table 13). For example, **6***c*, **6***g*, **8***e*, **9***a*, **9***b*, and **9***d* all control *Erysiphe polygoni* on beans at concentrations of 100 ppm or less. However, only compounds **6***g* and **9***d* might be described as having broad-spectrum activity and none are sufficiently potent for economic use.

In both the isothiazole and thiazole series there is no clearly evident effect on bioactivity by phenyl ring substituents that can be ascribed to electron release (**8***e* > **8***b*, but **9***e* ~ **9***b*) or lipophilicity (**6***b* < **6***c*, **8***b* ~ **8***c*, **9***b* > **9***c*). It does appear that the more active compounds from the standpoints of high activity and breadth of spectrum are the unsymmetrical dichloro analogs, perhaps because the molecular dipole promotes binding at the active site. Unsymmetric substitution is a frequent structural feature in fungicides of the ergosterol biosynthesis inhibitor class. Halogen at the 2-position of the thiazole ring appears to diminish activity (bromine, **8***b*) and narrow the spectrum (chlorine, **7**). This is consistent with expected steric and electronic effects on the heterocyclic nitrogen believed to bind with iron in the fungal enzyme.

Molecular orbital calculations

α,α-Diphenylmethyl substituted 5- and 6-membered nitrogen-containing heterocycles require a β-nitrogen for fungicidal activity (1*c*). A rough correlation exists[2] between biological activity and electron density at the β-nitrogen, calculated using the spectroscopic INDO program (17).

Thus, the 4-substituted pyridazine (activity = 4 on a 10-point scale) has a partial charge (−0.213) intermediate between those of the inactive 3-pyridazine compound (−0.060) and the compounds (pyridine, pyrimidine, pyrazine) with activity of 8–10 (−0.35 to −0.39). The five-membered rings (imidazole, 1,2,4-triazole) have slightly larger charges (−0.408, −0.411) than the six-membered rings though their activity is lower (activity = 6). Of the compounds in our synthetic program, the isothiazole and thiazole compounds had values in roughly the same range as the active six-membered ring compounds, but lower than the less active five-membered rings. The 1,2,3-thiadiazole compounds had far lower charges. In thiazole, the electron-withdrawing 2-chloro or 2-bromo substituent reduced the partial charge at the β-nitrogen relative to the unsubstituted ring, but thiazoles substituted with electron-releasing groups (amino, methyl, and methoxy) had enhanced partial charges at the β-nitrogen. These MO calculations suggest that thiadiazoles, oxazoles, and dioxazoles would not likely be active fungicides, and influenced our synthetic efforts.

Experimental

Melting points were determined on a Hoover capillary melting point apparatus and are uncorrected. The ^1H nmr spectra were obtained at 60 MHz on a Varian EM 360L nmr spectrometer, with TMS as internal standard. The ^{13}C nmr spectra were obtained on a JEOL FX-100 nmr spectrometer at 25 MHz, referenced to solvent (δ $CDCl_3$ = 77.0, δ DMSO-d_6 = 39.5). Low and high resolution mass spectra were obtained on an AEI MS30 mass spectrometer. Combustion analyses were performed on a Carlo Erba 1106 elemental analyzer.

Reagents were obtained from Aldrich with the exception of 2,4-dichlorobenzophenone, which was obtained from ICN Biochemicals.

[2]K. S. Laurenzo, Ph.D. dissertation, University of Florida, August, 1987.

Can. J. Chem. Downloaded from www.nrcresearchpress.com by 93.93.197.157 on 09/07/12
For personal use only.

TABLE 11. The ^{13}C nmr chemical shifts and assignments of diaryl(thiazol-5-yl)carbinols: aryl carbons

Compound	Ring	C1′	C2′	C3′	C4′	C5′	C6′
7	R = R′ = 4-diCl	143.01	128.54	128.32	134.36	[a]	[b]
9*a*	R = R′ = H	145.77	127.05	128.13	127.88	[a]	[b]
9*b*	R = R′ = 4-Cl	145.31	128.74	127.91	132.25	[a]	[b]
9*c*	R = 4-Cl	144.36	128.47	126.96	133.73	[a]	[b]
	R′ = H	145.37	128.22	[c]	128.08	[c]	[c]
9*d*	R = 3,4-diCl	145.60	128.64	130.98	130.35	129.71	127.08
	R′ = H	147.50	126.79	127.81	127.47	[a]	[b]
9*e*	R = 4-OCH_3[d]	138.21	128.42	113.31	159.03	[a]	[b]
	R′ = H	146.06	128.03	126.96	127.69	[a]	[b]
9*f*	R = 4-CF_3[e]	151.21	126.84	124.87[f]	127.91[g]	[a]	[b]
	R′ = H	146.04	127.66	128.01	127.57	[a]	[b]
10*a*	R = 2,4-diCl	141.04	133.44	130.95	133.15	[i]	131.29
	R′ = H	143.67	126.66	128.08	127.83	[a]	[b]
10*b*	R = 2,4-diCl	141.09	134.95	131.20	133.44	126.86	[h]
	R′ = H	144.01	126.57	128.42	128.22	[a]	[b]
10*c*	R = 2,4-diCl	141.19	134.80	131.15	133.44	126.76	131.25
	R′ = H	144.01	126.61	128.32	128.13	[a]	[b]

[a]Equivalent to C3′.
[b]Equivalent to C2′.
[c]A single large resonance was observed for C2′, 3′, 5′, and 6′.
[d]OCH_3: δ 55.17.
[e]CF_3: δ 124.2; J_{CF} = 272 Hz.
[f]J_{CF} = 3.66 Hz.
[g]J_{CF} = 31.7 Hz.
[h]C6′ and 3′ were superimposed.
[i]C5′ and C2″ were superimposed.

TABLE 12. The ^1H nmr chemical shifts and assignments of diaryl(thiazole-5-yl)carbinols

Compound	H2[a]	H4	Aryl protons	OH[b]
7	—	7.1	7.4 (s, 8H)	3.2
9*a*	8.8	[c]	7.45 (s, 11H)	4.75
9*b*	8.9	7.5	7.4 (s, 8H)	3.4
9*c*	8.7	[c]	7.4 (s, 10H)	5.1
9*d*	9.1	[c]	7.2–7.6 (m, 9H)	5.5
9*e*	8.8	[c]	7.3–7.5 (dd + s, 10H)	4.5[d]
9*f*	8.8	[c]	7.65 (s, 4H)	4.0
			7.45 (s, 6H)	
10*a*	—	6.5	7.3 (s, 2H)	4.8[f]
			7.5 (s, 6H)	
10*b*	8.9	[c]	6.9–7.6 (m, 9H)	4.55
10*c*	—	7.1	6.9–7.6 (m, 8H)	4.5[e]

[a]s, 1H.
[b]Broad s, 1H.
[c]H4 is obscured by the aryl protons.
[d]OCH_3: δ 3.9 (s, 3H).
[e]CH_3: δ 2.7 (s, 3H).
[f]NH_2: δ 5.4 (s, 2H).

THF and ether were distilled immediately before use from either CaH_2 or sodium/benzophenone under an argon atmosphere. Diisopropylamine was distilled from CaH_2 and stored over molecular sieves.

Geometric structures were obtained using the MNDO optimization procedure of Dewar and Thiel (18). At these geometries, wavefunctions and charge distributions were obtained using the INDO/S model of Zerner and others (17). Charge distributions were taken from a Mulliken population analysis using a deorthogonalized INDO wavefunction.

The following compounds were prepared by literature methods:

2-Propynal, 48% (crude), n_D = 1.4155 (lit. (19) 28–34% distilled, n_D = 1.4055); ^1H nmr ($CDCl_3$) δ: 3.63 (s, 1H, C≡C*H*), 9.37 (s, 1H, C(O)*H*); used without further purification.

cis-2-Propenal-3-thiosulfate, 48% (lit. (20) 65%); ^1H nmr (D_2O) δ: 6.5 (dd, 1H, H2), 7.85 (d, 1H, H3), 9.65 (bs, 1H, C(O)*H*).

Isothiazole, 41%, bp 113–114°C/760 Torr (1 Torr = 133.3 Pa) (lit. (20) 65%, bp 111–112°C/760 Torr); ^1H nmr ($CDCl_3$) δ: 7.4 (m, 1H, H4), 8.8 (m, 2H, H2 and H5); ^{13}C nmr ($CDCl_3$) δ: 156.34 (C3), 122.72 (C4), 147.08 (C5).

2-Chlorothiazole, 48%, bp 47°C/22 Torr (lit. (21) 70%, (22) bp 45°C/20 Torr); ^1H nmr ($CDCl_3$) δ: 7.4 (d, 1H, H5), 7.7 (d, 1H, H4); ^{13}C nmr ($CDCl_3$) δ: 151.32 (C2), 141.09 (C4), 121.01 (C5).

2-Bromothiazole, 65%, bp 65–68°C/20 Torr (lit. (21) 75%, (23) bp 70.5°C/20 Torr); ^1H nmr ($CDCl_3$) δ: 7.45 (m, 1H, H5), 7.6 (m, 1H, H4); ^{13}C nmr ($CDCl_3$) δ: 135.63 (C2), 142.60 (C4), 122.86 (C5).

2-Trimethylsilylthiazole, 55%, bp 70–72°C/22 Torr (lit. (10) 55%, bp 56–57°C/10 Torr); ^1H nmr ($CDCl_3$) δ: 8.25 (d, 1H, H4), 7.6 (d, 1H, H5), 0.45 (s, 9H, $(CH_3)_3$); ^{13}C nmr ($CDCl_3$) δ: 174.27 (C2), 145.66 (C4), 121.27 (C5), −1.04 ($(CH_3)_3$).

Bis(4-chlorophenyl)-(2-chlorothiazol-5-yl)carbinol

A solution of 2-chlorothiazole (3.0 g, 25.1 mmol) in ether (25 mL) and a solution of *n*-butyllithium (2.6 M, 10.6 mL, 27.6 mmol) were added simultaneously over a 45-min period to ether (30 mL) at −78°C. The somewhat brown solution was stirred an additional 2.5 h with gradual warming to −20°C. 4,4′-Dichlorobenzophenone (12.5 g, 50 mmol) in ether (50 mL) was added over 45 min. The temperature was allowed to rise to 0°C over 1 h, then held at room temperature an additional 30 min. Water (100 mL) was added and the aqueous phase was extracted with ether (2 × 100 mL). The combined organic phases were dried (Na_2SO_4) and the solvent was removed *in vacuo*. The crude product was purified by flash chromatography (230–400 mesh silica gel, 80:20 petroleum ether/diethyl ether) to give 4.85 g (52%) **7**, mp 122.5–123.5°C.

Diaryl(isothiazol-5-yl)carbinols: General synthetic procedure

Lithium diisopropylamide was prepared by the dropwise addition of *n*-butyllithium (2.6 M in hexanes, 1.27 mL, 3.3 mmol) to diisopropylamine (0.63 mL, 4.5 mmol) in THF (10 mL) at ≤ −70°C. The solution was allowed to warm gradually to 10°C, then cooled again to −78°C. Neat isothiazole (0.24 mL, 3.3 mmol) was added dropwise at such a rate that the temperature did not exceed −70°C. The resulting

Can. J. Chem. Downloaded from www.nrcresearchpress.com by 93.93.197.157 on 09/07/12
For personal use only.

TABLE 13. Maximum observed efficacy for experimental fungicides against various organisms

Compound	Species[a]											
	ALT	BAR	BMP	BMS	BOT	CMS	FUS	H.M.	PHY	RIC	SCM	SCO
6*a*	0.00	3.00	0.00	3.60	0.00	3.60	0.00	0.00	0.00	—	0.00	0.00
6*b*	0.00	0.00	0.00	0.00	0.00	0.00	0.00	0.00	3.24	—	0.00	0.00
6*c*	3.15	0.00	4.00	0.00	0.00	0.00	0.00	0.00	0.00	—	3.28	0.00
6*d*	0.00	—	—	—	0.00	—	0.00	0.00	0.00	—	3.16	3.85
6*g*	0.00	3.90	4.37	0.00	0.00	0.00	3.18	3.15	3.30	3.40	3.20	0.00
6*h*	3.20	—	—	—	3.30	—	0.00	0.00	0.00	—	3.30	4.57
7	0.00	0.00	0.00	0.00	4.65	—	0.00	0.00	0.00	—	0.00	4.70
8*b*	0.00	0.00	0.00	0.00	0.00	0.00	0.00	0.00	0.00	—	3.20	0.00
8*c*	0.00	0.00	0.00	0.00	3.26	0.00	0.00	0.00	0.00	—	0.00	0.00
8*d*	0.00	2.90	0.00	0.00	0.00	0.00	0.00	0.00	0.00	—	0.00	0.00
8*e*	0.00	3.37	4.50	0.00	0.00	3.51	0.00	0.00	0.00	—	0.00	0.00
9*a*	0.00	2.95	4.52	0.00	0.00	3.51	0.00	0.00	0.00	—	0.00	0.00
9*b*	0.00	3.51	4.00	0.00	0.00	0.00	0.00	0.00	0.00	—	3.26	0.00
9*c*	0.00	—	—	—	3.30	—	0.00	0.00	3.15	—	0.00	—
9*d*	0.00	2.90	4.52	0.00	0.00	0.00	3.18	3.15	3.23	—	0.00	0.00
9*e*	0.00	2.95	2.95	3.60	0.00	3.60	0.00	0.00	0.00	—	0.00	0.00

ALT = *Alternaria solani* (in vitro)
BAR = *Picicularia oryzae* on barley
BMP = *Erysiphe polygoni* on beans
BMS = *Erysiphe graminis* on barley
BOT = *Botrytis cinerea* (in vitro)
CMS = *Erysiphe cichoracearum* on cucumber
FUS = *Fusarium oxysporum* (in vitro)
H.M. = *Helminthosporium maydis* (in vitro)
PHY = *Phytophthora infestans* (in vitro)
RIC = *Piricularia oryzae* on rice
SCM = *Sclerotium rolfsii* (in vitro)
SCO = *Sclerotinia sclerotiorum* (in vitro)

Can. J. Chem. Downloaded from www.nrcresearchpress.com by 93.93.197.157 on 09/07/12
For personal use only.

flocculent white precipitate was stirred at −78°C for 2 h. A solution of the substituted benzophenone (3.0 mmol) in THF (10 mL) was added dropwise at ≤ −70°C, after which the reaction mixture was stirred at −78°C for 2 h. If the reaction was not complete (as evidenced by residual white precipitate and the presence of starting benzophenone in the tlc), the temperature was slowly allowed to rise to 0°C and held at this temperature until the reaction was complete. The clear light yellow solution was then poured into saturated NH_4Cl (50 mL) and extracted with ether (3 × 50 mL). The combined organic phases were dried (Na_2SO_4), filtered, and the solvent was evaporated *in vacuo*. The resulting yellow oil was placed under pump vacuum overnight, then purified by flash chromatography (230–400 mesh silica gel, 80:20 petroleum ether/diethyl ether). If necessary, the products were purified further by recrystallization from 2:1 hexane/ethanol (Table 1).

Diaryl-(2-bromothiazol-5-yl)carbinols: General synthetic procedure

Lithium diisopropylamide was prepared as described above from *n*-butyllithium (2.6 M in hexanes, 3.2 mL, 8.25 mmol) and diisopropylamine (1.59 mL, 11.25 mmol) in THF (20 mL). A solution of 2-bromothiazole (0.68 mL, 7.5 mmol) in THF (10 mL) was added dropwise without exceeding −75°C, as rapidly as possible at first, then more slowly toward the end of the addition. The total addition time was about 15–20 min. The rate of addition was critical; if too much time was taken or the temperature rose too high, considerable decomposition of the starting material occurred, as evidenced by the formation of a dark brown color. If all proceeded satisfactorily the reaction mixture at this point was yellow to light brown in color. After stirring 5 min at −78°C, a solution of the substituted benzophenone (7.5 mmol) in THF (10 mL) was added as rapidly as possible without exceeding −70°C. The light brown solution was stirred at −78°C for 15 min, then poured into saturated NH_4Cl (75 mL). The aqueous phase was extracted with ether (3 × 50 mL). The combined organic phases were dried over $MgSO_4$, filtered, and the solvent was removed *in vacuo*. The resulting brown oil was placed under pump vacuum overnight. The crude product was purified by flash chromatography (230–400 mesh silica gel, 80:20 petroleum ether/diethyl ether). The products are low-melting solids or semisolids (Table 2) that revert to oils on standing.

Diaryl(thiazol-5-yl)carbinols: General synthetic procedure

To a solution of the diaryl-(2-bromothiazol-5-yl)carbinol in THF (5–10 mL/mmol), was added dropwise a solution of *n*-butyllithium (2.6 M in hexanes, 2 equivalents plus a 10% excess) at ≤ −70°C. The reaction mixture was stirred at −78°C for 15 min, then poured into saturated NH_4Cl. The aqueous phase was extracted three times with an equal volume of ether. The combined organic phases were dried over $MgSO_4$, filtered, and the solvent was removed *in vacuo*. The crude products thus obtained were either solids or oils (Table 3). The solids were purified further by recrystallization from 2:1 hexane/chloroform, and the oils by flash chromatography (230–400 mesh silica gel, 1:1 petroleum ether/diethyl ether).

*(2,4-Dichlorophenyl)phenyl-(2-aminothiazol-5-yl)carbinol (**10**a)*

n-Butyllithium (3.2 mL, 2.5 M, 8 mmol) was added to a solution of 2-aminothiazole (0.40 g, 4 mmol) in THF (30 mL) at ≤ −70°C. The slightly cloudy light brown solution was stirred 1 h at −78°C, followed by the addition of chlorotrimethylsilane (1.01 mL, 8 mmol). The reaction mixture was allowed to slowly warm to −20°C, then cooled again to −78°C. *n*-Butyllithium (1.6 mL, 2.5 M, 4 mmol) was added at ≤ −70°C and the mixture was stirred for 15 min at −78°C. 2,4-Dichlorobenzophenone (1.0 g, 4 mmol) in THF (10 mL) was added at ≤ −65°C. The temperature was slowly allowed to warm to 0°C, then the mixture was stirred at room temperature overnight. The mixture was poured into saturated NH_4Cl (50 mL) and extracted with ether (3 × 50 mL). The combined ether phases were dried ($MgSO_4$), filtered, and evaporated to give 1.7 g brown oil. The crude product was purified by flash chromatography (230–400 mesh silica gel) using 50:50 petroleum ether/ethyl acetate (with 1% (v/v) triethylamine) until all other products were eluted, then pure ethyl acetate to elute the product (R_f = 0.41); yield 0.85 g (61%) **10***a*. The melting point (~87–115°C) was difficult to determine precisely due to the incorporation of air in the fluffy solid. The product could not be purified by recrystallization.

*(2,4-Dichlorophenyl)phenyl(thiazol-5-yl)carbinol (**10**b)*

A solution of lithium diisopropylamide was prepared from diisopropylamine (0.84 mL, 6 mmol) and *n*-butyllithium (2.0 mL, 2.5 M, 5 mmol) in THF (10 mL). The LDA solution was added to a solution of 2-trimethylsilylthiazole (**11**) (0.79 g, 5 mmol) in THF (40 mL) at $\leq -70°C$, then stirred at $-78°C$ for 2 h. A white precipitate formed. 2,4-Dichlorobenzophenone (1.26 g, 5 mmol) in THF (10 mL) was added and the temperature was slowly allowed to warm to 0°C, at which point the solution was clear. The reaction mixture was poured into saturated NH_4Cl (75 mL) and the aqueous phase was extracted with ether (3 × 50 mL). Tetrabutyl ammonium fluoride (5.5 mL, 1 M, 5.5 mmol) was added to the wet ether extract and the mixture was stirred overnight at room temperature. The ether phase was washed with water (50 mL), dried (Na_2SO_4), and evaporated to yield 1.7 g (100%) white solid. The crude product was purified by flash chromatography (230–400 mesh silica gel, 70:30 petroleum ether/ether) to give 1.05 g (63%) **10***b*, mp 149–150°C.

*(2,4-Dichlorophenyl)phenyl-(2-methylthiazol-5-yl)carbinol (**10**c)*

n-Butyllithium (1.2 mL, 2.5 M, 3 mmol) was added to a solution of (2,4-dichlorophenyl)phenyl(thiazol-5-yl)carbinol (**10***b*) (0.50 g, 1.5 mmol) in THF (15 mL) at $\leq -75°C$. The yellow solution was stirred 20 min at $-78°C$, followed by the addition of iodomethane (0.19 mL, 3 mmol). The reaction mixture was stirred for 45 min at $-78°C$; a white precipitate formed. The mixture was poured into saturated NH_4Cl (25 mL) and extracted with ether (3 × 25 mL). The combined ether phases were dried ($MgSO_4$), filtered, and evaporated to give 0.56 g yellowish solid. The crude product (0.42 g) was purified by flash chromatography (230–400 mesh silica gel, 50:50 petroleum ether/ether) to give 0.40 g (95% recovery, 100% overall yield) **10***c*, mp 164–166°C.

Acknowledgements

We thank Dr. John A. Minatelli for helpful discussions, Dr. Robert A. Davis and Mr. John Kasinkas for measurement of biological activity, and Uniroyal Chemical for financial support of K.S.L.

1. (*a*) N. N. RAGSDALE and H. D. SISLER. Biochem. Biophys. Res. Commun. **46**, 2048 (1972); (*b*) G. JAGER. *In* Pesticide chemistry—human welfare and the environment. Vol. 1. *Edited by* J. Miyamoto and P. C. Kearney. Pergamon Press, Oxford. 1982. pp. 55–66; (*c*) I. F. BROWN, JR., H. M. TAYLOR, and R. E. HACKLER. *In* Pesticide synthesis through rational approaches. *Edited by* P. S. Magee, G. K. Kohn, and J. J. Menn. ACS Symposium Series No. 255, Washington, DC. 1984. pp. 65–82; (*d*) A. F. MARCHINGTON. *In* Pesticide synthesis through rational approaches. *Edited by* P. S. Magee, G. K. Kohn, and J. J. Menn. ACS Symposium Series No. 255, Washington, DC. 1984. pp. 173–183; (*e*) P. GADHER, E. I. MERCER, B. C. BALDWIN, and T. E. WIGGINS. Pestic. Biochem. Physiol. **19**, 1 (1983).
2. M. P. L. CATON, D. H. JONES, R. SLACK, and K. R. H. WOOLRIDGE. J. Chem. Soc. 446 (1964).
3. (*a*) A. J. LAYTON and E. LUNT. J. Chem. Soc. (C), 611 (1968); (*b*) R. KALISH, E. BROGER, G. F. FIELD, T. ANTON, T. V. STEPPE, and L. H. STERNBACH. J. Heterocycl. Chem. **12**, 49 (1975); (*c*) M. J. ASHTON, A. ASHFORD, A. H. LOVELESS, D. RIDDELL, J. SALMON, and G. V. W. STEVENSON. J. Med. Chem. **27**, 1245 (1984).
4. D. S. NOYCE and B. B. SANDEL. J. Org. Chem. **40**, 3381 (1975).
5. J. V. METZGER. *In* Comprehensive heterocyclic chemistry. Vol. 6. *Edited by* A. R. Katritzky and C. W. Rees. Pergamon Press, Oxford. 1984. p. 261.
6. D. S. NOYCE and S. A. FIKE. J. Org. Chem. **38**, 3316 (1973).
7. J. V. METZGER. *In* The chemistry of heterocyclic compounds. Vol. 34. Thiazole and its derivatives. Part 1. *Edited by* A. Weissberger and E. C. Taylor. John Wiley and Sons, New York. 1979. p. 573.
8. R. G. JONES and H. GILMAN. Org. React. **6**, 339 (1951).
9. D. R. M. WALTON. J. Chem. Soc. (C), 1706 (1966).
10. A. MEDICI, P. PEDRINI, and A. DONDONI. J. Chem. Soc. Chem. Commun. 655 (1981).
11. G. C. LEVY, R. L. LICHTER, and G. L. NELSON. Carbon-13 nuclear magnetic resonance spectroscopy. 2nd ed. John Wiley and Sons, New York. 1980. pp. 110–112, 120.
12. R. FAURE, J.-P. GALY, E.-J. VINCENT, and J. ELGUERO. Can. J. Chem. **56**, 46 (1978).
13. (*a*) C. LE COCQ and J.-Y. LALLEMAND. J. Chem. Soc. Chem. Commun. 150 (1981); (*b*) S. L. PATT and J. N. SHOOLERY. J. Magn. Reson. **46**, 535 (1982).
14. (*a*) A. F. ANDREWS, R. K. MACKIE, and J. C. WALTON. J. Chem. Soc. Perkin Trans. 2, 96 (1980); (*b*) G. J. RAY, R. J. KURKLAND, and A. K. COLTER. Tetrahedron, **27**, 735 (1971).
15. D. L. PAIN, B. J. PEART, and K. R. H. WOOLRIDGE. *In* Comprehensive heterocyclic chemistry. Vol. 6. *Edited by* A. R. Katritzky and C. W. Rees. Pergamon Press, Oxford. 1984. pp. 136–137.
16. E. J. VINCENT, R. PHAN-TAN-LUU, J. METZGER, and J. SURZUR. Bull. Soc. Chim. Fr. 3524 (1966).
17. J. RIDLEY and M. C. ZERNER. (*a*) Theor. Chim. Acta, **32**, 111 (1973); (*b*) Theor. Chim. Acta, **42**, 223 (1976); (*c*) J. DEL BENE and H. H. JAFFE. J. Chem. Phys. **48**, 1807 (1968).
18. M. J. S. DEWAR and W. J. THIEL. J. Am. Chem. Soc. **99**, 4899 (1977).
19. J. C. SAUER. Org. Synth. Coll. Vol. IV, 1963. p. 813.
20. R. RAAP. Can. J. Chem. **44**, 1324 (1966).
21. K. GANAPATHI and A. VENKATARAMAN. Proc. Indian Acad. Sci. Sect. A, **22**, 362 (1945); Chem. Abstr. **40**, 4059 (1945).
22. G. VERNIN and J. METZGER. Bull. Soc. Chim. Fr. 2504 (1963).
23. R. HANDLEY, E. F. G. HERINGTON, M. AZZARO, and J. METZGER. Bull. Soc. Chim. Fr. **5**, 1904 (1963).

Can. J. Chem. Downloaded from www.nrcresearchpress.com by 93.93.197.157 on 09/07/12
For personal use only.

Heats of mixing of binary mixtures of pyridine base with *n*-alkane

TERESA KASPRZYCKA-GUTTMAN[1] AND JUAN H. VERA[2]
Department of Chemical Engineering, McGill University, Montreal, P.Q., Canada H3A 2A7

Received October 19, 1987

TERESA KASPRZYCKA-GUTTMAN and JUAN H. VERA. Can. J. Chem. **66**, 1625 (1988).

Heats of mixing of 2,4-lutidine and 2,4,6-collidine with *n*-alkanes were measured at 293.15 K using an isothermal dilution calorimeter. Experimental results were fitted with a Redlich–Kister polynomial. Experimental data and coefficients for the Redlich–Kister polynomials are reported.

TERESA KASPRZYCKA-GUTTMAN et JUAN H. VERA. Can. J. Chem. **66**, 1625 (1988).

Opérant à 293,15 K et utilisant un calorimètre à dilution isotherme, on a mesuré les chaleurs de mélange de la lutidine-2,4 et de la collidine-2,4,6 avec des *n*-alcanes. On a ajusté les résultats expérimentaux avec un polynôme de Redlich–Kister. On rapporte les données expérimentales et les coefficients des polynômes de Redlich–Kister.

[Traduit par la revue]

The literature provides no systematic studies of heats of mixing of binary systems comprising aromatic amines (pyridine bases) and *n*-alkanes. This study reports heats of mixing data for binary systems formed by 2,4-lutidine and 2,4,6-collidine with alkanes at 293.15 K.

Materials and apparatus

All the chemicals used in this work were 99 mol% pure as specified on their labels or certified by Aldrich Chemical Co. Their purity was verified by determinations of density and refractive indices, using a densimeter (Anton Paar K.G., Austria) and a precision refractometer (Bausch and Lomb Optical Company, USA), respectively. Their values are compared with literature data in Table 1 (1–3). All measurements of heats of mixing were carried out with a semicontinuous Van Ness type isothermal dilution calorimeter described in detail earlier (4, 5). The calorimeter was calibrated by determination of the excess heats of mixing of the system benzene–cyclohexane at 293.15 K. Our results were consistent with the literature data (6) within 1%. A maximum temperature deviation of 0.02 K with respect to the preset value may be present throughout the experiments.

Experimental results

The results of the measurements of heats of mixing for the systems: 2,4-lutidine + *n*-alkanes at 293.15 K are reported in Table 2, and those for the systems: 2,4,6-collidine + *n*-alkanes at the same temperature in Table 3. The data were fitted with the Redlich–Kister polynomial of the form:

$$[1] \quad H^M = x_1 x_2 [A + B(x_1 - x_2) + C(x_1 - x_2)^2]$$

TABLE 1. Densities and refractive indices component liquids at 293.15 K (1–3)

Compound	Densities		Refractive index	
	Obs.	Lit.	Obs.	Lit.
n-Hexane	0.65937	0.65934	1.37486	1.37484
n-Heptane	0.68793	0.68790	1.38765	1.38763
n-Octane	0.70252	0.70250	1.39743	1.39740
2,4-Lutidine	0.92685	0.92687	1.49905	1.49907
2,4,6-Collidine	0.91029	0.91027	1.50383	1.50385

[1]Present address: Department of Chemical Technology, University of Warsaw, Pasteura 1, 02-093 Warsaw, Poland.

[2]To whom correspondence should be addressed.

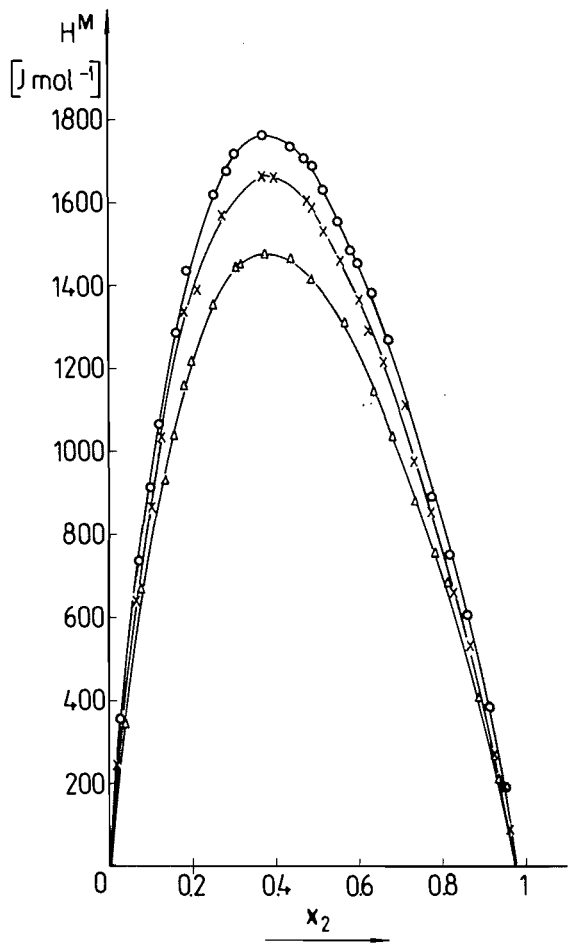

FIG. 1. Heats of mixing at 293.15 K for the binary systems: 2,4-lutidine (2) + *n*-hexane (1), Δ; 2,4-lutidine (2) + *n*-heptane (1), x; 2,4-lutidine (2) + *n*-octane (1), o.

where H^M = heat of mixing per mole of mixture (J/mol), A, B, C = coefficients of the Redlich–Kister polynomial (J/mol), and x = mole fraction. Subscript 1 is for *n*-alkanes and subscript 2 is for 2,4-lutidine, or 2,4,6-collidine. The parameters in eq. [1] and the standard deviation for all six binary systems are reported in Table 4.

Can. J. Chem. Downloaded from www.nrcresearchpress.com by 61.7.252.67 on 09/07/12
For personal use only.

TABLE 2. Experimental heats of mixing values for the binary systems 2,4-lutidine (2) + *n*-hexane (1), + *n*-heptane (1), + *n*-octane (1) at 293.15 K; H^M in J/mol

2,4-Lutidine + *n*-hexane		2,4-Lutidine + *n*-heptane		2,4-Lutidine + *n*-octane	
x_1	H^M	x_1	H^M	x_1	H^M
0.0405	350.11	0.0251	244.79	0.0343	355.10
0.0861	676.58	0.0731	646.59	0.0789	744.14
0.1320	937.68	0.1036	859.97	0.1018	914.38
0.1516	1030.66	0.1327	1035.57	0.1252	1069.10
0.1814	1152.55	0.1973	1336.88	0.1631	1281.14
0.2018	1223.27	0.2120	1389.85	0.1977	1436.43
0.2516	1356.45	0.2822	1572.74	0.2549	1621.52
0.3111	1450.86	0.3766	1663.06	0.2812	1679.76
0.3819	1487.14	0.4811	1602.53	0.3798	1770.43
0.4440	1463.80	0.4963	1582.52	0.4486	1737.30
0.4956	1412.72	0.5292	1530.98	0.4782	1703.36
0.5614	1313.74	0.5650	1463.21	0.4942	1681.63
0.6392	1157.33	0.6074	1369.02	0.5194	1639.15
0.6895	1037.41	0.6354	1299.43	0.5593	1561.50
0.7457	888.05	0.6672	1213.99	0.5887	1494.44
0.7922	752.72	0.7127	1081.06	0.6032	1459.78
0.8127	689.66	0.7463	975.54	0.6313	1385.19
0.8976	404.67	0.7837	851.33	0.6714	1270.78
0.9497	208.28	0.8354	668.53	0.7859	892.40
		0.8727	528.84	0.8236	752.92
		0.9393	262.76	0.8619	604.12
		0.9563	191.23	0.9146	386.54
		0.9813	83.17	0.9583	191.74

TABLE 3. Experimental heats of mixing values for the binary systems 2,4,6-collidine (2) + *n*-hexane (1), + *n*-heptane (1), + *n*-octane (1) at 293.15 K; H^M in J/mol

2,4,6-Collidine + *n*-hexane		2,4,6-Collidine + *n*-heptane		2,4,6-Collidine + *n*-octane	
x_i	H^M	x_i	H^M	x_i	H^M
0.0423	483.74	0.0241	334.41	0.0311	490.15
0.0541	601.87	0.0415	553.84	0.0521	778.09
0.0750	794.35	0.0510	666.09	0.0626	909.85
0.1214	1150.71	0.0615	784.17	0.0758	1064.48
0.1624	1392.58	0.0874	1049.67	0.1103	1414.17
0.1901	1521.69	0.1003	1168.80	0.1328	1602.96
0.2321	1670.81	0.1452	1520.50	0.1723	1867.32
0.2619	1746.28	0.1916	1790.85	0.2417	2155.58
0.2926	1800.79	0.2410	1988.32	0.2908	2249.73
0.3310	1839.73	0.2761	2077.29	0.3563	2267.77
0.3600	1850.23	0.3515	2159.58	0.4528	2137.43
0.4218	1827.28	0.4586	2066.24	0.5108	2000.97
0.4708	1773.23	0.5031	1975.31	0.5499	1893.27
0.5326	1670.11	0.5511	1852.02	0.5898	1774.00
0.5736	1584.44	0.6371	1581.81	0.6312	1642.57
0.6322	1442.48	0.6712	1461.27	0.6839	1465.96
0.6784	1316.26	0.7026	1344.87	0.7205	1337.36
0.7376	1136.85	0.7638	1104.89	0.7623	1183.54
0.8561	708.94	0.8026	944.27	0.7999	1037.16
0.8871	556.55	0.8386	789.20	0.8273	924.34
0.9199	404.80	0.8705	646.50	0.8618	733.65
0.9561	228.35	0.8998	510.53	0.9011	539.94
0.9600	156.67	0.9415	306.09	0.9425	330.48
		0.9708	157.27	0.9710	167.81

Can. J. Chem. Downloaded from www.nrcresearchpress.com by 61.7.252.67 on 09/07/12
For personal use only.

TABLE 4. Parameters for eq. [1], J/mol, at 293.15 K

Mixtures	A	B	C	$\delta(H^M)$*
2,4-Lutidine +				
n-hexane	5628.8	−2544.0	1260.2	0.46
n-heptane	6309.1	−2874.7	1069.1	0.004
n-octane	6689.3	−3141.3	1282.1	0.95
2,4,6-Collidine +				
n-hexane	6915.2	−3318.8	2372.0	0.003
n-heptane	7929.2	−4558.2	2153.6	0.53
n-octane	8114.9	−5053.4	3880.0	0.03

*δ is standard deviation.

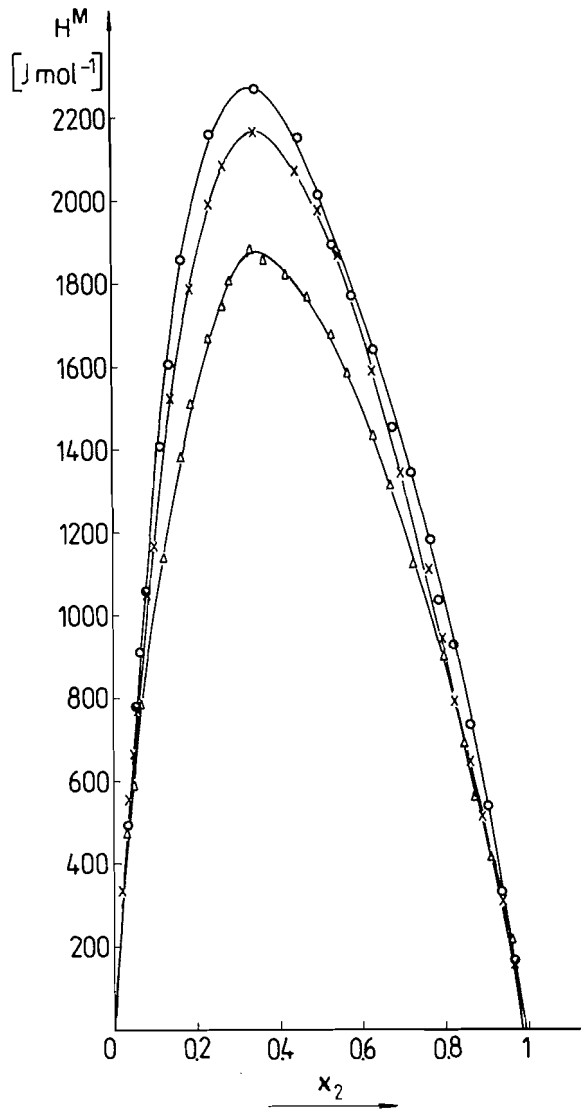

FIG. 2. Heats of mixing at 293.15 K for the binary systems: 2,4,6-collidine (2) + *n*-hexane (1), Δ; 2,4,6-collidine (2) + *n*-heptane (1), x; 2,4,6-collidine (2) + *n*-octane (1), o.

Discussion

Heats of mixing of the three binary systems 2,4-lutidine + *n*-hexane, + *n*-heptane, + *n*-octane, as a function of composition are shown in Fig. 1. Similarly, heats of mixing of the three binary mixtures 2,4,6-collidine + *n*-hexane, + *n*-heptane, + *n*-octane, as a function of composition, are shown in Fig. 2. All systems measured were found to be endothermal.

From the results of this work it is possible to see that in mixtures of pyridine bases with *n*-alkanes, it is the nature of the former that especially influences the heats of mixing values.

One of the factors responsible for the particular values of the heats of mixing seems to be the alkalinity of the pyridine base. According to Perrin (7), the pK_b values for pyridine bases are ($K_{b\ 2,4,6\text{-collidine}} = 7.5$) > ($K_{b\ 2,4\text{-lutidine}} = 6.7 = K_{b\ 2,6\text{-lutidine}}$) > ($K_{b\ \gamma\text{-picoline}} = 6$) > ($K_{b\ \alpha\text{-picoline}} = 5.9$) > ($K_{b\ \beta\text{-picoline}} = 5.7$) > ($K_{b\ \text{pyridine}} = 5.2$). At present we have not yet determined the heats of mixing for all mixtures of the above pyridine bases with hydrocarbons. However, the present results and previously reported values of heats of mixing for mixtures of pyridine with hydrocarbons (8–10), and of α-picoline with hydrocarbons (11) seem to indicate that the heats of mixing values at a given composition of the alkane increase with a rise of pK_b. However, in the case of 2,4- and 2,6-lutidine the pK_b values are virtually equal, whereas the respective values heats of mixing are different. This fact suggests that alkalinity is only one of the factors determining the heats of mixing values.

Acknowledgements

The authors are grateful to NSERC, Canada, for financial support and to University of Warsaw for granting a leave of absence to one of us (T.K.G.).

1. J. E. DESNOYERS and M. AREL. CAN. J. CHEM. **45**, 358 (1967).
2. A. E. POPE, H. D. PFLUG, B. DACRE, and G. C. BENSON. CAN. J. CHEM. **45**, 2665 (1967).
3. Selected values of properties of hydrocarbons and related compounds. American Petroleum Institute Research Project 44. Thermodynamics Research Center, Texas A & M, University College, Texas, Table 23-2. 31 October 1977.
4. J. E. SIMAN and J. H. VERA. CAN. J. CHEM. ENG. **57**, 355 (1979).
5. J. F. CHAMBLAIN. M. Eng. Thesis. McGill University. 1985.
6. R. V. MRAZEK and H. C. VAN NESS. AIChE J. **7**, 190 (1961).
7. D. D. PERRIN. Dissociation constants of organic bases in aqueous solutions. London, Butterworths. 1965.
8. H. WILCZURA, T. KASPRZYCKA-GUTTMAN, and S. RANDZIO. Bull. Acad. Pol. Sci. Ser. Chim. **34**, 483 (1986).
9. M. KIEFER and F. BECKER. Third International Conference on Chemical Thermodynamics, Section 5. Baden. 1973.
10. M. WOYCICKA. Pure Appl. Chem. **2**, 147 (1961).
11. J. C. MERLIN and A. AIT-KACI. Int. Data Ser. Selec. Data Mixtures Ser. A, 140 (1981).

Can. J. Chem. Downloaded from www.nrcresearchpress.com by 61.7.252.67 on 09/07/12
For personal use only.

Carcinogenic alkylation of nucleic acid bases. Solid state and solution studies of O^2-isopropyl-2′-deoxythymidine[1]

GEORGE I. BIRNBAUM

Division of Biological Sciences, National Research Council of Canada, Ottawa, Ont., Canada K1A 0R6

AND

KRISHAN L. SADANA, M. TAHIR RAZI, TERRY LEE, RUDY SEBASTIAN, GARRY W. BUCHKO, and FRANK E. HRUSKA

Department of Chemistry, University of Manitoba, Winnipeg, Man., Canada R3T 2N2

Received August 19, 1987

GEORGE I. BIRNBAUM, KRISHAN L. SADANA, M. TAHIR RAZI, TERRY LEE, RUDY SEBASTIAN, GARRY W. BUCHKO, and FRANK E. HRUSKA. Can. J. Chem. **66**, 1628 (1988).

O^2-Isopropyl-2′-deoxythymidine (i^{2}dT) crystallizes in the tetragonal space group $P4_32_12$, and the cell dimensions are $a = b =$ 8.7667(2), c = 37.1943(12) Å. X-ray intensity data were measured with a diffractometer, and the structure was solved by direct methods. Least-squares refinement, which included all hydrogen atoms, converged at R = 0.036 for 1780 observed reflections. In analogy with other *O*-alkylated bases, the exocyclic O2—C8 bond is *syn-periplanar* to the C2—N3 bond in the pyrimidine ring. Angular distortions in the base can be correlated with those observed in O^4-alkylated pyrimidines and O^6-alkylated guanines. The conformation of the glycosyl bond is *anti* with χ_{CN} = 27.1°. The furanose ring adopts a C2′ *endo* pucker and the conformation about C4′—C5′ is *gauche*$^+$. ^{1}H nmr data show that these conformations are also preferred in solution.

GEORGE I. BIRNBAUM, KRISHAN L. SADANA, M. TAHIR RAZI, TERRY LEE, RUDY SEBASTIAN, GARRY W. BUCHKO, et FRANK E. HRUSKA. Can. J. Chem. **66**, 1628 (1988).

La O^2-isopropyl désoxy-2′ thymidine (i^{2}dT) cristallise dans le groupe d'espace tétragonal $P4_32_12$ avec $a = b$ = 8,7667(2) et c = 37,1943(12) Å. On a mesuré les données relatives aux intensités de la diffraction des rayons-X à l'aide d'un diffractomètre et on a résolu la structure à l'aide de méthodes directes. Un affinement par le méthode des moindres carrés, impliquant tous les atomes d'hydrogène, converge à R = 0,036 pour 1780 réflexions observées. Par analogie avec d'autres bases *O*-alkylées, la liaison exocyclique O2—C8 est *syn-périplanaire* par rapport à la liaison C2—N3 du cycle pyrimidine. On peut établir une corrélation entre les distorsions angulaires et celles observées dans des pyrimidines alkylées en O^4 et des guanines alkylées en O^6. La conformation de la liaison glycosyle est *anti* et le χ_{CN} = 27,1°. Le cycle furannose adopte une conformation C2′ *endo* plissée et la conformation autour de la liaison C4′—C5′ est *gauche*$^+$. Les données obtenues par rmn du ^{1}H indiquent que ces conformations sont aussi les conformations privilégiées en solution.

[Traduit par la revue]

Introduction

The mutagenic and carcinogenic consequences of the *O*-alkylation of nucleic acid bases have been the focus of numerous studies. Following the work of Loveless (1), research centered on O^6-alkylated guanine (r^{6}G), but considerable interest has shifted to the O^2- and O^4-alkylated thymines (r^{2}T and r^{4}T) following their identification in DNA treated with the potent carcinogen ethylnitrosourea (2). *O*-Alkylation of guanine and thymine effects a keto-to-enol tautomeric shift, and an alteration in their hydrogen-bonding capacity which forms the basis for interpretation of the misincorporations observed during transcription and replication (3, 4). The biological significance of *O*-alkylation is evidenced by the existence of enzyme repair systems for these lesions (5–7). Information about the electronic and geometrical changes resulting from *O*-alkylation has been provided by the X-ray crystallographic studies of O^4-methyluridine (m^{4}U) (8), O^4-methyl-2′-deoxythymidine (m^{4}dT) (9), and O^4-ethyl-2′-deoxythymidine (e^{4}dT) (10), as well as for several O^6-alkylated purine nucleosides and analogues (11–13) (Scheme 1). These studies have shown that the *O*-alkyl groups favor the *syn-periplanar* conformation relative to the N3 (pyrimidine) and N1 (purine) atoms which would hinder the approach of a second base. However, the accessibility of alternate conformations (e.g. *anti-periplanar*) which could also be suitable for base pair formation remains open to investigation (4, 9, 10, 14, 15). A review of the biological significance of *O*-alkyl pyrimidines was published very recently by Singer (16).

Though the promutagenic properties of O^2-alkylthymines are of considerable interest (2, 3), no crystallographic data are available for this modified base. In the present work we report our X-ray crystallographic results for O^2-isopropyl-2′-deoxythymidine (i^{2}dT) and a comparison with m^{4}dT (9) and e^{4}dT (10). For comparison with solution structures, ^{1}H and ^{13}C nmr data are provided for i^{2}dT, as well as for m^{2}dT, e^{2}dT, m^{4}dT, e^{4}dT, and i^{4}dT. A mass spectrometric study of several O^2- and O^4-alkylated 2′-deoxythymidines has been presented (17).

Experimental

To obtain i^{2}dT and e^{2}dT, dT was converted to its 3′-acyl derivative by standard procedures (18) and then to the 2,5′-anhydronucleoside following Secrist (19), as described in earlier work (20). Reflux of the latter derivative (1 mmol) in 20 mL of methanolic sodium isopropoxide or sodium ethoxide afforded the unprotected i^{2}dT or e^{2}dT. To obtain i^{4}dT and e^{4}dT, the procedure of Divakar and Reese (21) was used to prepare the 4-(1,2,4-triazol-1-yl) intermediate of 3′,5′-acetyl protected dT. This intermediate was converted to i^{4}dT and e^{4}dT by treatment with the appropriate alcoholic sodium alkoxide. Following neutralization with IRC-50 resin, the three nucleosides were purified by silica gel chromatography. Compounds m^{2}dT and m^{4}dT were prepared earlier as described (20).

^{1}H nmr spectra of the nucleosides were obtained at 300.13 MHz on a Bruker AM300 spectrometer. Aqueous solutions (1–2 mg/mL; pH ~7; 300 K) were prepared and purified of paramagnetic ions as described elsewhere (22). TSP was used as the internal reference. Spec-

[1]NRC No. 28708.

Can. J. Chem. Downloaded from www.nrcresearchpress.com by 112.217.228.212 on 09/07/12
For personal use only.

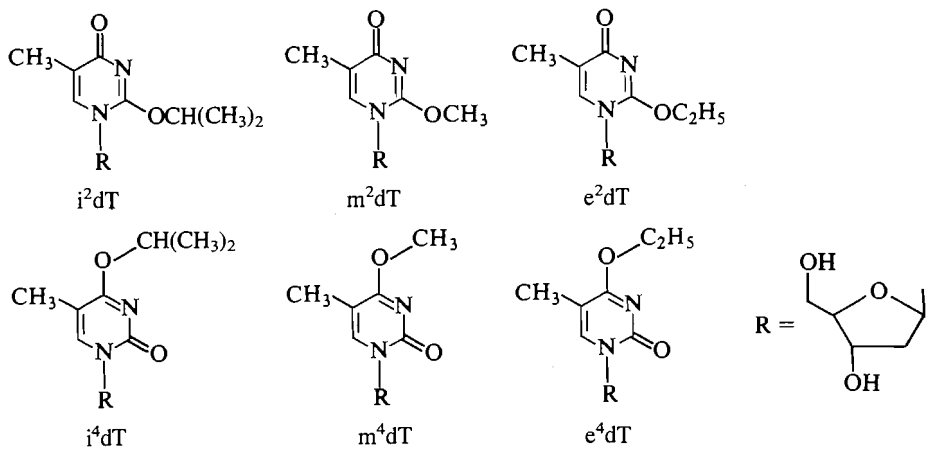

SCHEME 1

tral assignments followed earlier work (20, 22), and the analysis was carried out with NUMARIT (23). Proton decoupled ^{13}C nmr (75.5 MHz) spectra were obtained in 10 mm (od) tubes (5.5 mg/mL in D_2O; pH 5.4–8.0; 300 K; 1% dioxane for internal reference). Removal of paramagnetic ions and spectral assignments followed our earlier work (20, 22). Selective ^1H decoupling experiments confirmed our previous assignments (20) for the C1′ and C4′ atoms.

Colorless crystals were obtained from water. Precession photographs showed tetragonal symmetry and systematic absences corresponding to space groups $P4_12_12$ or $P4_32_12$. A crystal measuring 0.3 × 0.4 × 0.5 mm was mounted on an Enraf-Nonius CAD-4 diffractometer; it provided the following data:

$C_{13}H_{20}N_2O_5$ fw = 284.31

Tetragonal, $a = b = 8.7667(2)$, $c = 37.1943(12)$ Å, $V = 2858.53$ Å^3, $\rho_c = 1.32$ g cm^{-3}, $Z = 8$ (20°C; CuKα_1, $\lambda = 1.54056$ Å); $F(000) = 1216$, μ(CuKα) = 8.1 cm^{-1}.

The cell dimensions were determined from angular settings of 25 high-order ($47° < \theta < 59°$) reflections. Intensities were measured with Ni-filtered CuKα radiation, using $\omega/2\theta$ scans with variable ranges and speeds. Three standard reflections were monitored at frequent intervals; their intensities fluctuated by ±1%. A full octant with $2\theta \leq 152°$ was measured which included 3402 reflections. After averaging *hkl* and *khl* reflections, there were 1837 unique reflections of which 45 with $I < 3\sigma(I)$ were considered unobserved. The intensities were corrected for Lorentz and polarization factors; absorption corrections were considered unnecessary.

The structure was determined by direct methods with the aid of the computer program MULTAN78 (24). Assignment of the correct enantiomer established the space group as $P4_32_12$. Atomic parameters were refined by block-diagonal least squares. All 20 hydrogen atoms were refined with isotropic temperature parameters. The scattering factors were taken from the "International tables for X-ray crystallography" (25). Throughout the refinement the function $\Sigma w(|F_o| - |F_c|)^2$ was minimized and a factor of 0.8 was applied to all shifts. The following weighting scheme was used during the final stages: $w = w_1 \cdot w_2$, where $w_1 = 1$ for $|F_o| \leq 12$, $w_1 = 12/|F_o|$ for $|F_o| > 12$; and $w_2 = \sin^2\theta/0.7$ for $\sin^2\theta < 0.7$, $w_2 = 1$ for $\sin^2\theta \geq 0.7$. This scheme made the average value of $w(\Delta F^2)$ independent of $|F_o|$ and $\sin^2\theta$. The refinement converged to a conventional residual index $R = 0.036$ and a weighted index $R_w = 0.043$ for 1780 reflections (twelve strong, low-order reflections suffered from secondary extinction and were given zero weights). After the final least-squares cycle the average parameter shift equalled 0.1σ and the largest one 0.4σ. A final difference Fourier map showed no significant features. The atomic coordinates and equivalent isotropic temperature parameters of nonhydrogen atoms are listed in Table 1. Their anisotropic temperature parameters, hydrogen atom parameters, and a list of observed and calculated structure factors are available.[2]

TABLE 1. Final atomic parameters and their standard deviations[a]

Atom	x	y	z	U_{eq}
N1	3913(2)	5311(2)	54618(4)	345
C2	4875(2)	6511(2)	55103(4)	368
O2	5925(2)	6246(1)	57613(4)	491
N3	4777(2)	7803(2)	53415(4)	400
C4	3617(2)	8031(2)	50981(4)	351
O4	3556(2)	9257(1)	49325(4)	483
C5	2489(2)	6828(2)	50511(4)	366
C6	2686(2)	5518(2)	52338(4)	375
C7	1182(2)	7064(3)	47994(6)	527
C8	7093(3)	7420(2)	58245(6)	515
C9*R*	7569(3)	7208(3)	62118(7)	660
C9*S*	8345(4)	7222(5)	55619(9)	869
C1′	4170(2)	3846(2)	56529(4)	352
C2′	3405(2)	3757(2)	60204(4)	370
C3′	3239(2)	2033(2)	60638(4)	337
O3′	4619(2)	1348(2)	61838(4)	464
C4′	2972(2)	1484(2)	56765(4)	332
O4′	3511(2)	2690(1)	54460(3)	421
C5′	1331(2)	1130(2)	55826(5)	441
O5′	340(2)	2341(2)	56686(3)	575

[a]The z coordinates were multiplied by 10^5, the other parameters by 10^4.

Results and discussion

A stereoscopic view of i²dT, showing the overall conformation in the crystal and the atomic numbering scheme, is presented in Fig. 1. Note that the two methyl groups of the isopropyl group are diastereotopic due to the presence of the chiral centres in the sugar moiety; in Fig. 1, their carbon atoms are labelled C9*R* and C9*S* according to their *pro-R* or *pro-S* designation, respectively. Details of the conformation can be seen in the Newman projections (Fig. 2) and in Fig. 3 which also shows the bond lengths and bond angles.

[2]These tables may be purchased from the Depository of Unpublished Data, CISTI, National Research Council of Canada, Ottawa, Ont., Canada K1A 0S2.

Can. J. Chem. Downloaded from www.nrcresearchpress.com by 112.217.228.212 on 09/07/12
For personal use only.

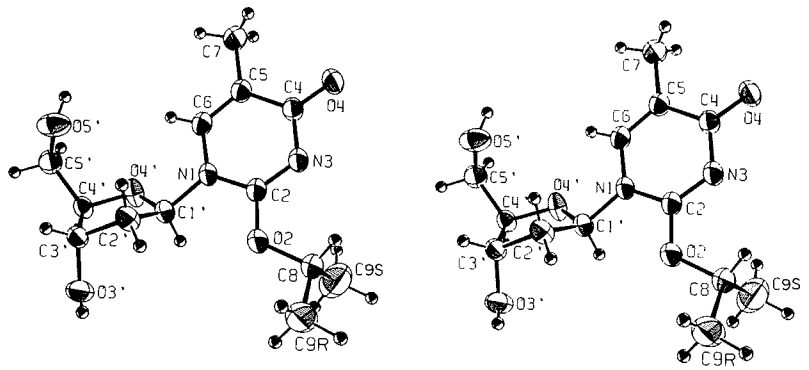

FIG. 1. Stereoscopic view of i^4dT; the ellipsoids correspond to 50% probability.

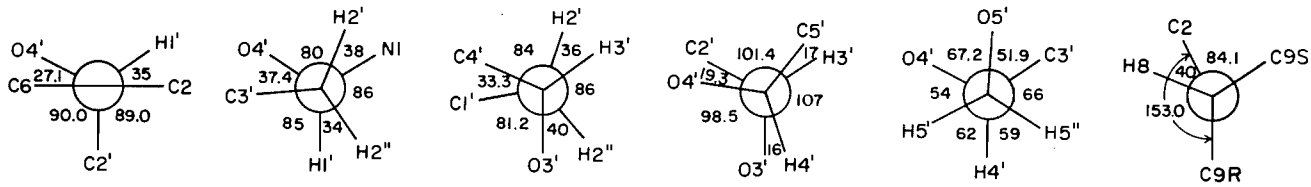

FIG. 2. Newman projections along (left to right) N1—C1′, C1′—C2′, C2′—C3′, C3′—C4′, C4′—C5′, and O2—C8.

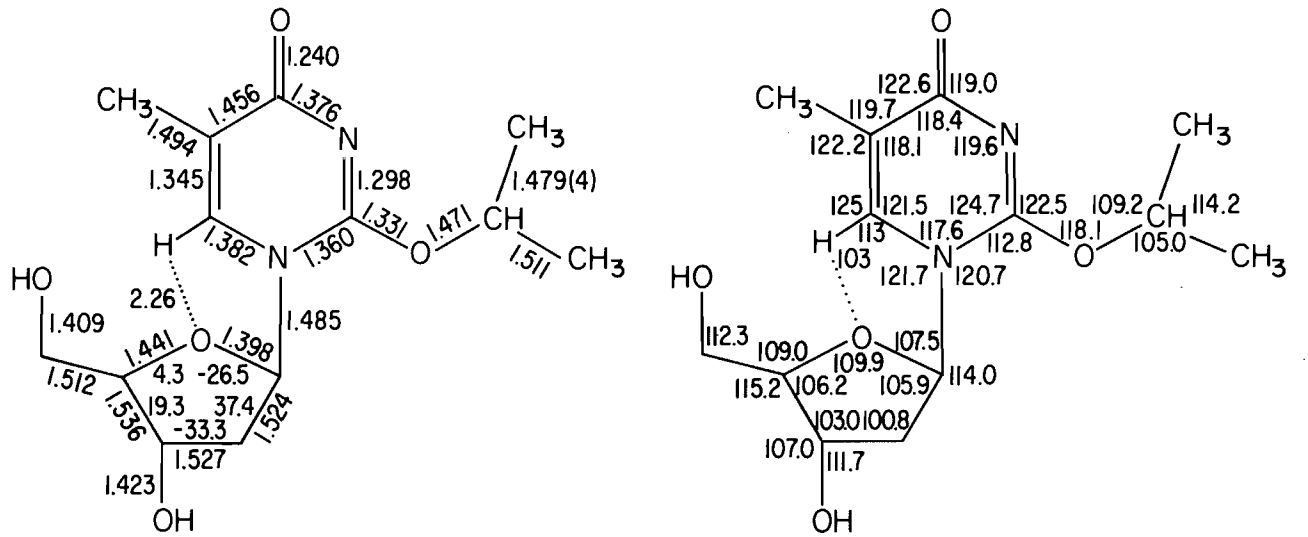

FIG. 3. Left, bond distances (Å) and endocyclic torsion angles (deg). Unless otherwise indicated, their estimated standard deviations (esd's) are 0.002–0.003 Å and 0.15–0.17°, respectively. Right, bond angles (deg); their esd's are 0.13–0.16°, except at C8 (0.2°).

Pyrimidine moiety

The pyrimidine ring is not exactly planar; N1 and C4 form the prows of a shallow boat. The absolute values of the endocyclic torsion angles are 0.4(3)° and 1.2(3)° at double bonds and 2.9(2)°–4.4(3)° at single bonds. While C8 is close to the mean plane of the ring, its methyl and hydrogen substituents are not.

As expected, the bond lengths differ significantly from average values in thymine residues (10). The conjugated system O2—C2=N3—C4=O4 created by O^2-alkylation can be compared to O4—C4=N3—C2=O2 in e^4dT, created by O^4-alkylation. We notice that C=N is 0.018 Å shorter in i^2dT, indicating a higher localization of electrons at this double bond. This can be explained by the cross-conjugated quinonoid system in i^2dT in which there is less delocalization than in the fully conjugated system in e^4dT.

Figure 4*a* facilitates further comparison of the effects of O^2- and O^4-alkylation on the bond angles of the pyrimidine ring; Fig. 4*b* provides similar data for the effect of O^6-alkylation on the bond angles of the guanine ring. In Fig. 4*a* the pyrimidine framework represents simultaneously an O^2-alkyl and O^4-alkyl thymine base. That is, we have rotated an i^2dT moiety about its N3—C6 axis and superimposed it on an r^4dT fragment so that their equivalent conjugated fragments, R(alkyl)—O4—C4—N3—C2=O2 and R—O2—C2—N3—C4=O4, are superimposed. (X represents the 5-methyl and sugar groups in r^4dT and i^2dT, respectively.) This approach facilitates comparison of corresponding positions in the ring, that is, those which are *ortho*, *meta*, and *para* to the *O*-alkylated carbon atom. The top number in Fig. 4*a* represents the difference in bond angle i^2dT − ⟨T⟩, where ⟨T⟩ is the average of six sets of literature values for the

Can. J. Chem. Downloaded from www.nrcresearchpress.com by 112.217.228.212 on 09/07/12
For personal use only.

Can. J. Chem. Downloaded from www.nrcresearchpress.com by 112.217.228.212 on 09/07/12
For personal use only.

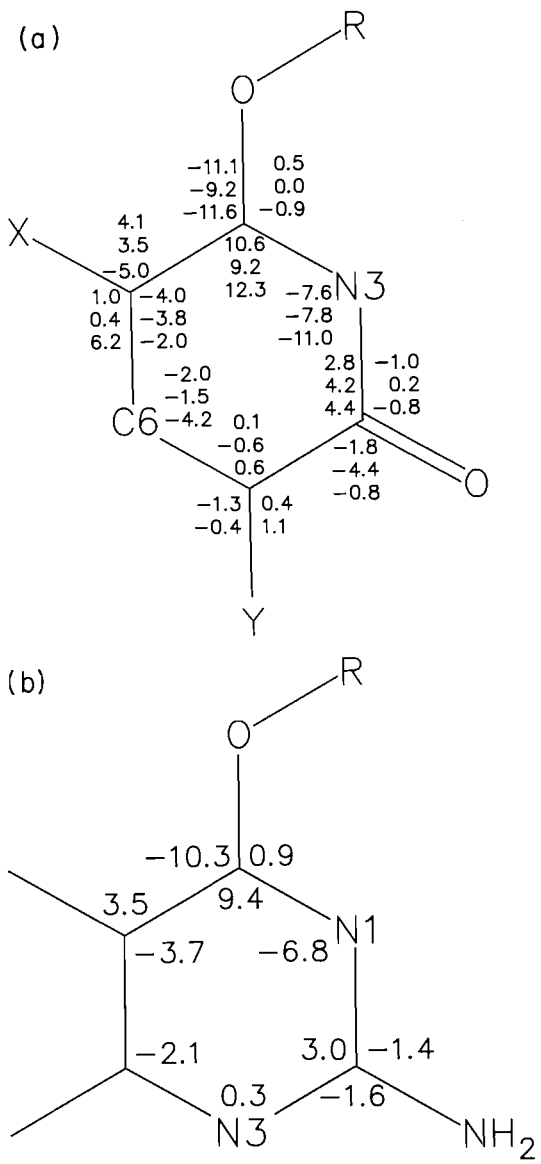

FIG. 4. Angular distortions caused by O^2- and O^4-alkylation of pyrimidine bases (*a*) and by O^6-alkylation of a guanine (*b*). The three values for each angle in (*a*) correspond to (top to bottom) $i^2dT - \langle T \rangle$, $r^4dT - \langle T \rangle$, and $\langle aU \rangle - \langle U \rangle$; the values in (*b*) correspond to $m^6G - \langle G \rangle$. See text for details.

thymine ring (10). The middle entry is $\langle r^4dT \rangle - \langle T \rangle$ where $\langle r^4dT \rangle$ is the average of the bond angles in m^4dT (9) and e^4dT (10). Since the formation of a 2,2′-anhydronucleoside mimics O^2-alkylation of a pyrimidine base, we also include $\langle aU \rangle - \langle U \rangle$ (lowest entry), where $\langle aU \rangle$ is the average of two sets of data for 2,2′-anhydrouridine (26, 27) and $\langle U \rangle$ the average of bond angles in a uracil base (28). Figure 4*b* provides $m^6G - \langle G \rangle$ data, the difference in bond angles for O^6-methylguanosine (12) and an average guanine base (28).

As can be seen, the distortions of the corresponding bond angles resulting from O^2- and O^4-alkylation are remarkably similar. For the most part, the bond angle changes effected by the formation of the 2,2′-anhydro link parallel those of O^2- and O^4-alkylation. Not surprisingly, the major differences are found at the exocyclic bond angles involving the N1—C1′ bond between sugar and base. Thus, in contrast with i^2dT and r^4dT, the C1′—N1—C2 angle of aU is compressed (−5.0°) whereas the C1′—N1—C6 angle is expanded (6.2°). These changes serve to diminish the C1′···O2 separation in aU relative to U.

The bond angle changes in the pyrimidine fragment of the guanine base produced by O^6-alkylation (Fig. 4*b*) are very similar to the changes at corresponding points of the thymine ring due to O^2- and O^4-alkylation. Thus the largest expansion (9.4°) occurs at the *O*-alkylated carbon (C6) whereas the largest compression (−10.3°) occurs at the exocyclic angle O6—C6—C5. This similarity is not unexpected since the tautomeric perturbations of the pyrimidine rings are identical for O^6- and O^4-alkylation.

Geometry of the isopropoxy group

The C2—O2—C8 bond angle is 118.8° which is similar to the magnitudes of the corresponding angle in m^2dT (9), e^4dT (10), and m^4U (8) (117.1°–118.4°); the corresponding angle in m^6G is smaller (116.4°) (12). The torsion angle in the N3—C2—O2—C8 fragment is −5.5°, placing the C8 atom in a *syn-periplanar* relation with the N3 atom. The C2—O2—C8—C9*R* and C2—O2—C8—C9*S* torsion angles are 153.0° and −84.1°, respectively. (C9*R* and C9*S* are the *pro-R* and *pro-S* methyl carbons of the isopropyl group.) The C9*S* methyl group flanks the pyrimidine on its 5′-face whereas the tertiary H8 hydrogen does so on its 3′-face. (We denote as 5′-, or 3′-, the face which points to the 5′-, or 3′-, end of a strand in a normal B–DNA molecule.) The C9*R* atom is directed away from the pyrimidine base, the situation which obtains for the methyl group of e^4dT. However, C9*R* is not coplanar with the base, but projects out slightly from the 3′-face. Relative to e^4dT, the O2—C8 bond of i^2dT has been rotated by 30° in order to avoid too short a contact between N3 and C9*S*. As it is, the distance between these atoms, 3.273(4) Å, is quite short.

Glycosyl bond

It has been known for some time that O^2-alkylation of pyrimidine nucleosides makes the glycosyl bond more susceptible to hydrolytic cleavage while O^4-alkylation has no measurable effect (20, 29). Therefore, it was of interest to determine whether the N1—C1′ bond in i^2dT is particularly weak (long). Our results show (Fig. 3) that this bond length (1.485 Å) is not significantly different from the corresponding one in m^4dT (1.478 Å) (9), e^4dT (1.493 Å) (10), and dT (1.480 Å) (30). Consequently, the relative facility with which the glycosyl bond is hydrolyzed must be due to the transition state rather than the ground state.

The conformation about the glycosyl bond is *anti* with χ_{CN} (C6—N1—C1′—O4′) = 27.1°, as it is m^4dT (40.6°), e^4dT (22.8°), and dT (39.1°).

Deoxyribose moiety

The bond lengths and bond angles of the sugar ring are normal (Fig. 3). The furanose ring adopts an *S*-type pucker (31) with a phase angle of pseudorotation (*P*) of 154.5° ($^2T_1$) and a maximum amplitude of pucker (τ_m) of 36.9°. *S*-Type puckers are also found in m^4dT (P = 133.8°; $_1T^2$; τ_m = 31.4°) (9) and the parent molecule dT (P = 187.5°; $_3T^2$; τ_m = 38.2°) (30). In contrast, e^4dT is in the *N*-range (P = 11.8°; $^3T_2$; τ_m = 36.5°) (10). The conformation about C4′—C5′ is *gauche*$^+$. This is also the case in m^4dT and e^4dT; in dT, on the other hand, it is *trans*.

Hydrogen bonding and packing

As shown in Fig. 3, there is an intramolecular C6—H···O4′ hydrogen bond. This unusual type of bond was first observed in 5-hydroxymethyl-2′-deoxyuridine (32). The H···O distance and C—H···O angle shown in the figure were calculated follow-

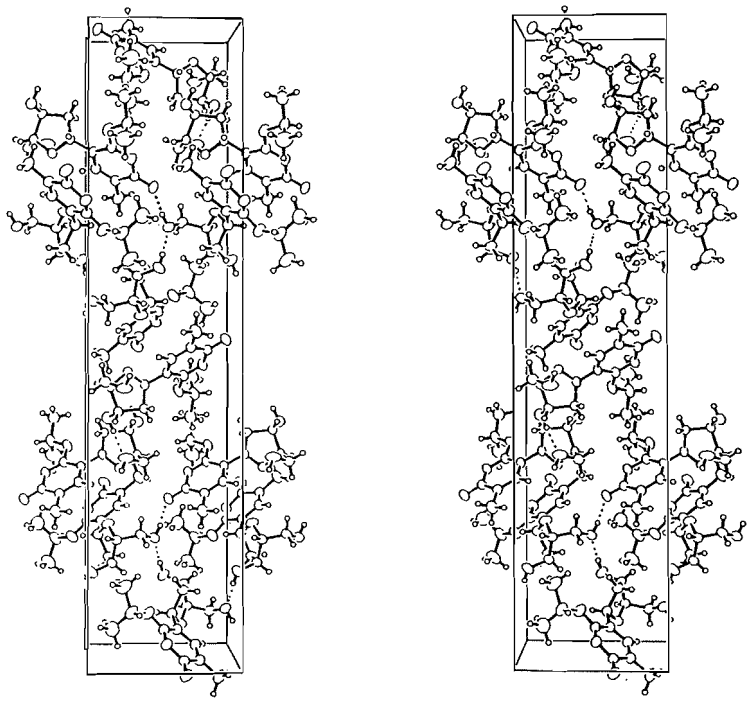

FIG. 5. Stereoscopic view of the molecular packing in the crystal. Dotted lines indicate hydrogen bonds.

ing the normalization of the C—H bond to its nominal value of 1.09 Å. They are well within the range of values previously observed in C—H···O bonds (33). In addition, there are two intermolecular hydrogen bonds: O3′—H···O5′ (at $1/2 + x$, $1/2 - y$, $5/4 - z$) and O5′—H···O4 (at y, x, $1 - z$). Their geometry is as follows: O3′···O5′ 2.742(2) Å, HO3′···O5′ 1.85(3) Å, HO3′···O5′$_{corr}$ 1.77Å (after normalizing O—H to 0.97 Å), O3′—H···O5′ 178(3)°; O5′···O4 2.652(2) Å, HO5′···O4 1.80(3) Å, HO5′···O4$_{corr}$ 1.70 Å, O5′—H···O4 168(3)°. The latter bond is quite strong, as one would expect on the basis of the "cooperative effect" (34). In contrast to the e^{4}dT structure, N3 does not act as a hydrogen bond acceptor. The packing of the molecules in the crystal is shown in Fig. 5. There are no significant stacking interactions.

^{1}H nmr analysis

With our previous studies (10, 20) we have a complete set of ^{1}H nmr data for the O^2- and O^4-methylated, -ethylated, and -isopropylated derivatives of dT. The sugar coupling constants (Table 2) are strikingly similar for the six molecules as well as for the parent dT, and indicate that these modifications have no significant influence on the sugar conformation in aqueous solution. Estimates based on $J(3'4')$ indicate a bias for the *S*-type pucker ($\%S = 60 \pm 4\%$) which is not unusual for pyrimidine 2′-deoxyribosides in solution. This is in line with the *S*-type pucker noted for m^{2}dT (9) and i^{2}dT, but contrasts with the $^3T_2$ pucker noted for e^{4}dT (10). The absence of any appreciable effect in solution of the bulky isopropyl group at the O2 position on the sugar ring is in line with a *syn-periplanar* conformation relative to N3.

The $J(4'5')$ and $J(4'5'')$ data (Table 2 and refs. 10 and 20) reveal little variation in the C4′—C5′ conformer distribution for dT and its *O*-alkyl derivatives, with average values of 49%, 38%, and 14% for the *gauche*$^+$, *trans*, and *gauche*$^-$ conformer populations, respectively. The overall similarity in the proton chemical shifts and coupling constants for the sugar protons suggests that O^2- and O^4-alkylation does not alter the *anti-syn* distribution of the *N*-glycosyl linkage.

TABLE 2. ^{1}H chemical shifts (δ) and coupling constants (J)[a,b]

Protons[c]	i^{2}dT	e^{2}dT	m^{2}dT	i^{4}dT	e^{4}dT	m^{4}dT
δ 1′	6.31	6.34	6.31	6.29	6.28	6.28
2′	2.41	2.43	2.42	2.32	2.32	2.32
2″	2.48	2.48	2.48	2.48	2.49	2.49
3′	4.46	4.47	4.47	4.46	4.46	4.46
4′	4.07	4.07	4.07	4.08	4.09	4.09
5′	3.87	3.87	3.87	3.87	3.87	3.88
5″	3.78	3.78	3.78	3.78	3.79	3.79
6	7.83	7.83	7.85	7.87	7.89	7.90
7[d]	1.95	1.95	1.95	1.97	1.99	1.99
8[d]	5.33	4.48	4.03	5.32	4.41	3.97
9[d]	1.40[e]	1.41	—	1.36	1.39	—
J 1′2′	6.4	6.4	6.4	6.6	6.6	6.5
1′2″	6.6	6.6	6.6	6.5	6.5	6.5
2′3′	6.6	6.6	6.6	6.7	6.7	6.6
2″3′	4.4	4.5	4.6	4.3	4.3	4.3
3′4′	4.2	4.4	4.2	4.1	4.0	4.3
4′5′	3.6	3.5	3.6	3.5	3.8	3.5
4′5″	5.3	5.2	5.1	5.2	5.1	5.1
67[d]	1.1	1.2	1.1	1.1	1.1	1.1
89[d]	6.2	7.1	—	6.2	7.1	—

[a]δ in ppm from TSP; *J* in Hz.

[b]Data at 300 MHz, 300 K: i^{2}dT, e^{2}dT, i^{4}dT, e^{4}dT; at 270 MHz, 294 K: m^{2}dT, m^{4}dT (ref. 20).

[c]Not included are $J(2'2'')$ (-14.1 ± 0.2 Hz) and $J(5'5'')$ (-12.5 ± 0.1 Hz).

[d]7: 5-methyl protons; 8 and 9: α- and β-protons of the *O*-alkyl group, respectively.

[e]A separation of 0.9 Hz is observed between the *pro-R* and *pro-S* methyl protons.

^{13}C nmr data

Table 3 provides ^{13}C chemical shift data (δ) at 75.5 MHz for

Can. J. Chem. Downloaded from www.nrcresearchpress.com by 112.217.228.212 on 09/07/12
For personal use only.

TABLE 3. ^{13}C chemical shifts[a] for 2′-deoxyribosides in aqueous solution

Carbons	dT	i²dT	e²dT	m²dT	i⁴dT	e⁴dT	m⁴dT
δ 2	153.0	3.7	4.2	4.7	5.9	5.8	5.8
4	167.8	8.6	8.6	8.5	4.4	4.9	5.3
5	112.7	4.6	4.9	5.0	−3.6	−4.0	−4.1
6	138.8	−1.1	−1.2	−1.1	2.6	2.8	2.9
7[b]	12.8	1.2	1.1	1.1	−0.2	−0.2	−0.3
1′	86.3	1.7	1.7	1.8	1.4	1.4	1.4
2′	39.8	1.0	0.8	0.8	1.0	1.0	1.0
3′	71.7	−0.3	−0.4	−0.4	−0.2	−0.2	−0.2
4′	87.8	0.5	0.4	0.5	0.3	0.3	0.3
5′	62.5	−0.2	−0.2	−0.2	−0.1	−0.1	−0.1
8[b]	—	75.9	67.4	57.4	73.1	65.6	56.1
9*R*[b]	—	22.083	14.6	—	22.15	14.6	—
9*S*[b]	—	22.151	—	—	22.15	—	—

[a]Data at 75.5 MHz measured relative to internal dioxane and converted to a TMS scale by addition of 67.86 ppm. The data for the r²dT and r⁴dT are relative to dT except for the *O*-alkyl carbons which are relative to TMS. A negative sign indicates a signal at high field of the reference.

[b]See footnote *d* in Table 2. The 9*R* and 9*S* assignment is arbitrary.

dT and its *O*-alkylated derivatives. Note that the δ values for dT are given relative to TMS, whereas those for the derivatives are given relative to dT (except for the *O*-alkyl carbons which are relative to TMS). Among the interesting trends are: (*1*) Corresponding δ values in the r²dT and r⁴dT series are similar, indicating that the tautomeric change effected by *O*-alkylation would account in each case for the δ changes relative to dT. (*2*) Alkylation at O2 and O4 causes a large deshielding of the alkoxylated carbon, C2 (3.7–4.7 ppm) and C4 (4.4–5.3 ppm), but the remaining carbonyl carbon, C4 or C2, is even more strongly deshielded. This is particularly evident in the r²dT series in which the effect at C4 is (on average) twice that at C2. (*3*) O^2-Alkylation causes a larger deshielding at the *para* C5 carbon than at C2. (*4*) In the r²dT and r⁴dT series, the alkoxylated carbon shifts upfield by about 0.4–0.5 ppm for each substitution of a methyl carbon at the C8 carbon; this can be attributed to a small γ-effect of methyl substitution (35).

Also interesting is the small chemical shift difference between C9*R* and C9*S* in i²dT (0.068 ppm; Table 3) which reflects the distereotopic relationship of the two methyl groups. (Distereotopic atoms will, in general, experience distinct magnetic shielding; see Jennings (36) and Tonelli *et al.* (37) for discussions of this phenomenon.) This relationship is also apparent in a small chemical shift difference of 0.9 Hz in their methyl protons (Table 2, footnote *e*). On the other hand, the two methyl groups in i⁴dT are also diastereotopic, but distinct resonances are not observed for them in either the ^{13}C or the ^1H nmr spectra. This is not surprising since the O^4-alkyl group is more distant from the chiral sugar moiety than the O^2-alkyl group; it is well known (36, 37) that the differential magnetic shielding of distereotopic atoms decreases rapidly with separation from chiral centres in a molecule.

Biological implications

In contrast to the e⁴dT structure (10), N3 does not act as a hydrogen bond acceptor. However, molecular models of i²dT suggest that the bulky isopropyl group may not prevent the base from pairing with either an adenine protonated at N1 (standard Watson–Crick geometry) or with a guanine (wobble base pair) (Fig. 6). With respect to the former we refer to the recent report by Hunter *et al.* (38), who found base pairing between a cytosine and an N1-protonated adenine in a double-helical dodecamer.

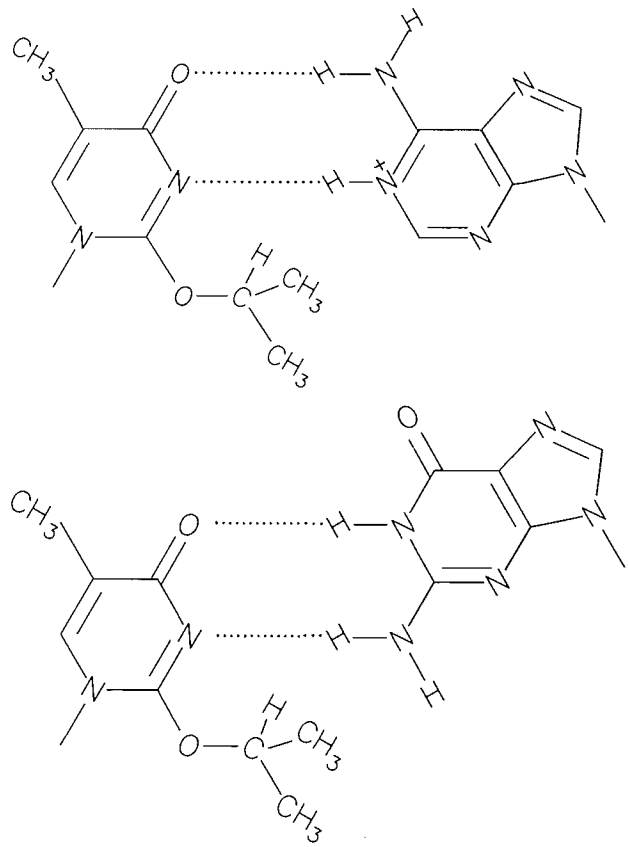

Fig. 6. Possible schemes of base pairing of i²dT with N1-protonated adenosine (top) and with guanosine (bottom).

The two schemes could account for the observed ambiguity of, for example, m²dT which can be incorporated opposite adenine by the Klenow fragment of DNA polymerase I, yet acts as dC upon replication (39). Analogous schemes could account for the recognition of O^2-ethyluridine as U or C in codon–anticodon binding (40).

Acknowledgements

K.L.S. and F.E.H. acknowledge NSERC for operating support (Grants A1549 and A6434). Apart from MULTAN78 (24),

Can. J. Chem. Downloaded from www.nrcresearchpress.com by 112.217.228.212 on 09/07/12
For personal use only.

all crystallographic computations were carried out with programs written by Ahmed *et al.* (41). Figures 1 and 5 were drawn with the ORTEP program of Johnson (42). We thank Dr. B. Singer for discussions.

1. A. Loveless. Nature (London), **223**, 206 (1969).
2. B. Singer. Nature (London), **264**, 333 (1976).
3. R. Saffhill, G. P. Margison, and P. J. O'Connor. Biochim. Biophys. Acta, **823**, 111 (1985).
4. A. Pohorille and G. H. Loew. Biophys. Chem. **22**, 37 (1985).
5. Z. Ahmmed and J. Laval. Biochem. Biophys. Res. Commun. **120**, 1 (1984).
6. R. Muller and M. Rajewsky. Z. Naturforsch. **38**c, 1023 (1983).
7. B. Demple, A. Jacobsson, M. Olsson, P. Robins, and T. Lindahl. J. Biol. Chem. **257**, 13776 (1982).
8. R. G. Brennan, G. G. Prive, W. J. P. Blonski, F. E. Hruska, and M. Sundaralingam. J. Am. Chem. Soc. **105**, 7737 (1983).
9. R. G. Brennan, D. Pyzalska, W. J. P. Blonski, F. E. Hruska, and M. Sundaralingam. Biochemistry, **25**, 1181 (1986).
10. G. I. Birnbaum, K. L. Sadana, W. J. P. Blonski, and F. E. Hruska. J. Am. Chem. Soc. **108**, 1671 (1986).
11. W. J. Cook, G. L. Gartland, and C. E. Bugg. Acta Crystallogr. Sect. B **36**, 2467 (1980).
12. R. Parthasarathy and S. M. Fridey. Carcinogenesis, **7**, 221 (1986).
13. T. Srikrishnan, R. Parthasarathy, N. C. De, and G. B. Chheda. Acta Crystallogr. Sect. C **39**, 1441 (1983).
14. J. W. Caldwell and P. A. Kollman. J. Biomol. Struct. Dyn. **3**, 57 (1986).
15. A. Psoda, B. Kierdaszuk, A. Pohorille, M. Geller, J. T. Kusmierek, and D. Shugar. Int. J. Quantum Chem. **20**, 543 (1981).
16. B. Singer. Cancer Res. **46**, 4879 (1986).
17. F. Lafortune, W. Ens, F. E. Hruska, K. L. Sadana, K. G. Standing, and J. B. Westmore. Int. J. Mass. Spectrom. Ion Processes, **78**, 179 (1987).
18. V. Amarnath and A. D. Broom. Chem. Rev. **77**, 183 (1977).
19. J. A. Secrist III. Carbohydr. Res. **42**, 379 (1975).
20. B. D. Allore, A. Queen, W. J. Blonski, and F. E. Hruska. Can. J. Chem. **61**, 2397 (1983).
21. K. J. Divakar and C. B. Reese. J. Chem. Soc. Perkin Trans. **1**, 1171 (1982).
22. F. E. Hruska and W. J. P. Blonski. Can. J. Chem. **60**, 3026 (1982).
23. A. R. Quirt and J. S. Martin. J. Magn. Reson. **5**, 318 (1971).
24. P. Main, S. E. Hull, L. Lessinger, G. Germain, J.-P. Declercq, and M. M. Woolfson. MULTAN78. University of York, England, and University of Louvain, Belgium. 1978.
25. International tables of X-ray crystallography. Vol. IV. Kynoch Press: Birmingham, England. 1974.
26. D. Suck and W. Saenger. Acta Crystallogr. Sect. B **29**, 1323 (1973).
27. L. T. J. Delbaere and M. N. G. James. Acta Crystallogr. Sect. B **29**, 2905 (1973).
28. R. Taylor and O. Kennard. J. Am. Chem. Soc. **104**, 3209 (1982).
29. B. Singer, M. Kroger, and M. Carrano. Biochemistry, **17**, 1246 (1978).
30. D. W. Young, P. Tollin, and H. R. Wilson. Acta Crystallogr. Sect. B **25**, 1423 (1969).
31. C. Altona and M. Sundaralingam. J. Am. Chem. Soc. **94**, 8205 (1972).
32. G. I. Birnbaum, R. Deslauriers, T.-S. Lin, G. T. Shiau, and W. H. Prusoff. J. Am. Chem. Soc. **102**, 4236 (1980).
33. R. Taylor and O. Kennard. J. Am. Chem. Soc. **104**, 5063 (1982).
34. G. A. Jeffrey and J. Mitra. Acta Crystallogr. Sect. B **39**, 469 (1983).
35. G. L. Levy and G. L. Nelson. *In* Carbon-13 nuclear magnetic resonance for organic chemists. Wiley Interscience, New York. 1972. p. 40.
36. W. B. Jennings. Chem. Rev. **75**, 307 (1975).
37. A. E. Tonelli, F. C. Schilling, and F. A. Bovey. J. Am. Chem. Soc. **106**, 1157 (1984).
38. W. N. Hunter, T. Brown, N. N. Anand, and O. Kennard. Nature (London), **320**, 552 (1986).
39. B. Singer, J. Sagi, and J. T. Kusmierek. Proc. Natl. Acad. Sci. U.S.A. **80**, 4884 (1983).
40. B. Singer, H. Fraenkel-Conrat, and J. T. Kusmierek. Proc. Natl. Acad. Sci. U.S.A. **75**, 1722 (1978).
41. F. R. Ahmed, S. R. Hall, M. E. Pippy, and C. P. Huber. J. Appl. Crystallogr. **6**, 309 (1973).
42. C. K. Johnson. ORTEP II Report ORNL-5138; Oak Ridge National Laboratory; Oak Ridge, TN. 1976.

Can. J. Chem. Downloaded from www.nrcresearchpress.com by 112.217.228.212 on 09/07/12
For personal use only.

Long-range $^{13}C,^{13}C$ spin–spin coupling constants in anisole and some derivatives

TED SCHAEFER AND GLENN H. PENNER
Department of Chemistry, University of Manitoba, Winnipeg, Man., Canada R3T 2N2

Received September 28, 1987

TED SCHAEFER and GLENN H. PENNER. Can. J. Chem. **66**, 1635 (1988).

^{13}C nuclear magnetic resonance chemical shifts and $^{n}J(^{13}C,^{13}C)$ are reported for anisole and 16 of its derivatives, all enriched with ^{13}C in the methoxyl group. $^{5}J(^{13}C,^{13}C)$ is directly proportional to $\sin^2\theta$, where θ is the angle by which the methoxy group twists about the C(1)—O bond. In acetone-d_6 solution, $^{5}J(C,C)$ is not observable for a number of 4-substituted anisoles, except for 1,4-dimethoxybenzene. For the latter, $^{5}J(C,C)$ is compatible with a twofold barrier of 19.3 ± 1.1 kJ/mol hindering rotation about the C(1)—O bond. However, it is unlikely that the barrier is purely twofold in nature. The observed $^{5}J(C,C)$ is also compatible with 10.5 and 6.0 kJ/mol for the twofold and fourfold components, respectively, implying a dynamical nuclear magnetic resonance barrier of less than 13 kJ/mol. While phase and solvent effects on the internal barrier in anisole are certainly substantial, it appears that a fourfold component must also be present. The apparent twofold barrier in 2,6-difluoroanisole is 5.4 ± 0.9 kJ/mol, based on $^{5}J(C,C)$ and $^{6}J(H\text{-}4,^{13}C)$. The latter coupling constant is also reported for 1,2,3-trimethoxybenzene and used to deduce its conformation. The θ dependence of $^{3}J(C,C)$ and $^{4}J(C,C)$ is briefly discussed for symmetrical anisole derivatives. Differential $^{13}C,^{13}C$ isotope shifts are reported for 1,4-dimethoxybenzene.

TED SCHAEFER et GLENN H. PENNER. Can. J. Chem. **66**, 1635 (1988).

On a déterminé les déplacements chimiques du ^{13}C ainsi que les constantes $^{n}J(^{13}C,^{13}C)$ pour l'anisole ainsi que 16 de ses dérivés, tous enrichis en ^{13}C dans le groupement méthoxyle. Les constantes de couplage $^{5}J(^{13}C,^{13}C)$ sont directement proportionnelles à $\sin^2\theta$, dans lequel θ est l'angle de torsion du groupement méthoxyle autour de la liaison C(1)—O. En solution dans l'acétone-d_6, on ne peut observer de constante $^{5}J(C,C)$ pour plusieurs dérivés de l'anisole substitués en position 4; la seule exception est le diméthoxy-1,4 benzène. Pour ce dernier, la valeur de la constante $^{5}J(C,C)$ suggère qu'il existe une barrière binaire à la rotation autour de la liaison C(1)—O de 19,3 ± 1,1 kJ/mol. Toutefois, il est peu probable que cette barrière soit uniquement de nature binaire. La valeur observée pour $^{5}J(C,C)$ est aussi compatible avec des composantes binaire et quaternaire respectivement de 10,5 et de 6,0 kJ/mol; ces données impliquent une barrière en résonance magnétique nucléaire dynamique inférieure à 13 kJ/mol. Alors que les effets de phase et de solvant sur la barrière interne de l'anisole sont certainement importants, il semble que la composante quaternaire doit certainement être présente. En se basant sur les constantes de $^{5}J(C,C)$ et $^{6}J(H\text{-}4,^{13}C)$, la barrière binaire apparente pour le difluoro-2,6 anisole est de 5,4 ± 0,9 kJ/mol. Cette dernière constante a aussi été observée avec le triméthoxy-1,2,3 benzène et on l'a utilisée pour déduire sa conformation. On discute brièvement du fait que, pour les dérivés symétriques de l'anisole, les constantes $^{3}J(C,C)$ et $^{4}J(C,C)$ varient avec θ. On rapporte aussi les déplacements isotopiques différentiels $^{13}C,^{13}C$ pour le diméthoxy-1,4 benzène.

[Traduit par la revue]

Introduction

The barrier to internal rotation about the C(1)—O bond in anisole in the liquid state is deduced from torsion frequencies as 25.3 kJ/mol and as 15.1 kJ/mol in the vapor on the assumption that it is twofold (1, 2). Because the conformation of lowest energy (3–5) has the carbon atom of the methyl group in the benzene plane, **1**, and because the ^{13}C nmr chemical shifts of

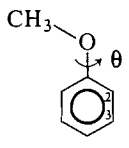

θ = 0° for planar anisole
θ = 180° for C-2, C-3
θ = 0° for C-5, C-6

1

C-2 and C-6 must differ by about 6 ppm (5–8), dynamic nmr measurements are indicated. At 120 K in dimethyl ether solution the resonance peaks of C-2 and C-6 are coincident and sharp, implying an internal rotational barrier of less than 19.7 kJ/mol (9). Spin-lattice relaxation measurements in the rotating frame suggest a barrier of less than 18.4 kJ/mol in the ether solution (9). Vibrational spectroscopy leads to a barrier of 48.1 kJ/mol in the solid anisole (10, 11). A recent exhaustive review is available (12).

The state dependence of the rotational motion about the C(1)—O bond is also suggested by *ab initio* molecular orbital calculations on the free molecule (13–18), which have the barrier as less than 8 kJ/mol, as do molecular mechanics computations (19). Microwave spectra (3) agree that **1** is the structure in the gas phase, while for 4-fluoroanisole such spectra (20) are consistent with a lower limit to the barrier of 4.6 kJ/mol. Photoelectron spectra of gaseous anisole imply an energy difference of 5.7 kJ/mol between planar and nonplanar forms of anisole (21). The long-range coupling constants between the ^{13}C nucleus in the methyl group and the ring protons of anisole in solution appear to be consistent with a relatively high barrier of more than 20 kJ/mol if it is assumed to be twofold (9). However, if a large fourfold component, V_4, is actually present, the long-range coupling constants are compatible with a smaller barrier. A V_2 of 11.0 kJ/mol and a V_4 of 10 kJ/mol, for example, yield a barrier of less than 16 kJ/mol and imply a $^{6}J(^{1}H,^{13}C)$ of 0.03 Hz, possibly compatible with a line width at half-height of 0.08 Hz in the ^{13}C multiplet (9). This negative evidence for a smaller barrier than 20 kJ/mol for anisole in solution is unsatisfactory.

It is conceivable that $^{6}J(^{1}H,^{13}C)$ is not simply proportional to $\sin^2\theta$ (see **1**), as has been assumed (9), although the methyl group replacement test (9, 22) does show $^{6}J(^{1}H,^{13}C)$ to be a σ–π coupling constant. Such a coupling mechanism is almost certainly consistent with a $\sin^2\theta$ behaviour (9, 23).

Another approach to the conformational behaviour of anisole involves the measurement of $^{n}J(^{13}C,^{13}C) \equiv {}^{n}J(C,C)$ in a set of compounds modelled to yield their θ dependence. Then, if the latter can be established, some independent conformational information may be accessible. This paper reports such measurements for a number of anisole derivatives, one of the ^{13}C nuclei in $^{n}J(C,C)$ being that at the methyl site.

Can. J. Chem. Downloaded from www.nrcresearchpress.com by 93.93.197.157 on 09/07/12
For personal use only.

Can. J. Chem. Downloaded from www.nrcresearchpress.com by 93.93.197.157 on 09/07/12
For personal use only.

TABLE 1. The ^{13}C nmr chemical shifts and $^{n}J(^{13}C,^{13}C)$ in anisole-α-^{13}C and some derivatives in acetone-d_6 solution at 300 K

Compound	δ_α	δ_1	δ_2	δ_3	δ_4	$(-)^2J$	$(+)^3J$	^4J	$(+)^5J$
Anisole[a]	55.32	160.68	114.67	130.22	121.25	2.32	4.12	(+)0.54	<0.03
α-CH_3[b]	63.75	160.01	115.21	130.28	121.12	2.19	3.90	(+)0.49	<0.05
4-OCH_3[c]	58.81	154.77	115.38	115.38	154.77	2.39	3.97	(+)0.41	0.074
4-F[d]	55.62	157.00	115.78	116.43	157.98	2.37	4.06	(+)0.45	<0.05
4-CH_3[e]	55.37	158.62	114.47	130.58	130.14	2.38	4.05	(+)0.49	<0.03
4-CHO[f]	56.06	165.53	115.13	132.47	131.20	2.39	4.19	(+)0.52	<0.03
3,5-diF[g]	56.45	163.06	98.76	164.67	96.56	2.33	4.31	(+)0.64	<0.05
3,5-diCl[h]	56.36	162.02	114.04	135.97	121.20	2.36	4.26	(+)0.62	<0.03
2,6-di-F[i,s]	62.17	137.44	156.92	113.17	124.09	3.00	1.70	(−)0.62	0.69
2,6-diCl[j]	60.90	153.21	129.96	130.14	126.12	3.57	1.58	(−)0.86	0.92
2,6-diCl-4-F[k]	61.11	150.21	130.49	117.16	158.62	3.60	1.53	(−)0.86	1.00
2,3,5,6-tetraCl[l]	61.24	155.50	128.09	132.63	127.22	3.59	1.55	(−)1.02	0.92
2,6-diBr[m]	60.72	154.81	118.6	133.59	127.46	3.60	1.62	(−)0.87	0.94
2,6-diBr-4-F[n]	61.04	152.16	118.68	120.72	159.08	3.62	1.60	(−)0.87	1.02
2,6-diBr-4-$COOCH_3$[o]	61.7	158.82	118.83	134.63	129.55	3.56	1.61	(−)0.85	0.92
2,6-diBr-4-CH_3[p]	60.80	152.72	118.11	134.07	138.03	3.63	1.61	(−)0.89	1.01
2,6-diCH_3[q,r]	60.73	—	130.67	129.58	124.52	—	1.38	(−)0.94	0.98

[a] 3 mol%.
[b] 1.8%; $^1J(C,C) = 39.0$ Hz.
[c] 3.0 mol%; $^6J(C,C) = 0.05$ Hz.
[d] 10 mol%; $^1J(C,F) = -235.92$, $^2J(C,F) = 23.21$, $^3J(C,F) = 8.05$, $^4J(C,F) = 1.97$, $^6J(C,F) = 0.11$; signs of $^{1,2,3,4}J(C,F)$ based on fluorobenzene (49).
[e] 1.5 mol%; $^5J(C,C) = 0.03$ Hz.
[f] 1.5 mol%; $^6J(C,C) = 0.05$ Hz.
[g] 1 mol%; $^1J(C,F) = -244.25$, $^2J(C,F) + {}^4J(C,F) = 29.09$, $^2J(C\text{-}4,F) = 26.41$, $^3J(C\text{-}1,F) = 13.93$, $^3J(C\text{-}5,F) = 16.06$ Hz.
[h] 3.5 mol%.
[i] 1.7 mol%; $^1J(C,F) = -246.74$, $^2J(C\text{-}2,F) + {}^4J(C\text{-}3,F) = 22.78$, $^2J(C\text{-}1,F) = 14.11$, $^3J(C\text{-}4,F) = 9.45$, $^4J(C\text{-}\alpha,F) = \pm 3.23$ Hz. Signs of $^nJ(C,F)$ within the rings are based on related molecules (50).
[j] 2.0 mol%.
[k] 4.6 mol%; $^1J(C,F) = -247.16$, $^2J(C,F) = 26.08$, $^3J(C,F) = 12.19$, $^4J(C,F) = 4.09$, $^6J(C,F) = 1.46$ Hz.
[l] 5.3 mol%.
[m] 10.0 mol%.
[n] 2.3 mol%; $^1J(C,F) = -249.25$, $^2J(C,F) = 25.6$, $^3J(C,F) = 10.96$, $^4J(C,F) = 3.86$, $^6J(C,F) = 1.48$ Hz.
[o] 4.0 mol%; $^6J(C,C) = (+)0.42$ Hz, $^8J(C,C) = 0.02$ Hz.
[p] 2.0 mol%; $^6J(C,C) = (-)0.35$ Hz.
[q] 1 mol%.
[r] $^6J(^1H,{}^{13}CH_3) = -0.62_2$ Hz.
[s] $^6J(^1H,{}^{13}CH_3) = -0.47_3$ Hz.

Can. J. Chem. Downloaded from www.nrcresearchpress.com by 93.93.197.157 on 09/07/12
For personal use only.

Experimental

Enrichment of ^{13}C at the methyl site of the anisoles used 4.0 mmol of the corresponding phenol. This was dissolved in 5 mL of dry acetone, to which were added 0.8 g of dry K_2CO_3. The mixture was stirred and this was followed by addition of $^{13}CH_3I$ (95 at.% or higher isotopic purity, from MSD Istopes) in 5 mL of dry acetone. This mixture was stirred overnight. Addition of water gave a cloudy suspension that was extracted with ether. The extract was dried over anhydrous $MgSO_4$, filtered, and rotary evaporated. The ^1H and ^{13}C nmr spectra were indisputably those of the desired products.

Solutions of the anisole derivatives in acetone-d_6, containing small amounts of tetramethylsilane (TMS), were transferred to 10-mm od nmr tubes for ^{13}C nmr experiments (a few ^{13}C nmr measurements were later done on 5-mm tubes when a dual $^1H/^{13}C$ probe became available). Samples for ^1H nmr measurements employed 5-mm od nmr tubes. The sample tubes were degassed by the freeze–pump–thaw procedure and were then flame sealed to provide symmetrical tops.

All nmr spectra were accumulated on an AM300 Bruker spectrometer at a probe temperature of 300 K. For proton decoupled ^{13}C nmr spectra, some 128–256 free induction decays were acquired, while for proton coupled ^{13}C spectra these ranged from 400 to 2800. Acquisition times ranged from 20 to 30 s. For example, a spectral width of 100 Hz was assigned to a 4 K data region in the computer, to give an acquisition time of 20.5 s. The ^1H nmr spectra were the results of 8–32 induction decays with acquisition times of up to 40 s. Some zero-filling to twice the original data size was employed when desirable. Small amounts of Gaussian multiplication were employed before transformation to the frequency domain. Line widths at half-height were typically 0.05–0.25 Hz in the ^1H and ^{13}C nmr spectra.

Spectral analyses used the locally modified computer program NUMARIT (24), coupled to a plotting routine. INDO MO FPT computations (25, 26) utilized geometries optimized at the STO-3G level of molecular orbital theory, the latter computations employing MONSTERGAUSS, GAUSSIAN 80, and GAUSSIAN 82 packages (27–29). All computations, including those for spectral analysis, used Amdahl 470/V8, 580/5850, or 5870 systems. Statistical analyses used the SAS nonlinear regression procedure, NLIN.

Results and discussion

Table 1 contains ^{13}C nmr chemical shifts and $^nJ(^{13}C,^{13}C) \equiv {}^nJ(C,C)$ for anisole and 16 of its derivatives. Note that one ^{13}C nucleus in $^nJ(C,C)$ is always that of the methyl group (methylene for an ethoxy side chain). The signs of $^nJ(C,C,)$ are assumed on the basis of the computations below and because of the known signs for related coupling constants. $^2J(C,C)$ was determined to be negative in 3,5-dichlorothioanisole-α-^{13}C in an experiment in this laboratory, and $^3J(C,C)$ was found as positive. This experiment succeeded because the methyl protons coupled weakly to the ^{13}C nuclei and hence signs relative to $^1J(H,C)$ could be found by partial decoupling experiments. Similarly, $^4J(C,C)$ and $^5J(C,C)$ in 2,6-dichlorothioanisole were negative and positive, respectively. It is reasonable to expect the same signs of $^nJ(C,C)$ in anisole derivatives, particularly because $^6J(H\text{-}4,^{13}C)$ values have very similar magnitudes at the extrema in the conformational angle in anisoles and thioanisoles (see below and ref. 30), and because $^6J(H\text{-}4,^{13}C)$ is negative in both types of compounds (9, 30); it is also negative in benzyl cyanide-8-^{13}C (31). Therefore, since $^5J(C,C)$ and $^6J(H,C,)$ are both transmitted via a $\sigma-\pi$ coupling mechanism and since the hyperfine coupling parameters, Q^C_{CH} and Q^H_{CH}, are of opposite sign (32, 33), it appears certain that $^5J(C,C)$ in anisole derivatives is positive. $^5J(H,C)$ in anisole derivatives is positive for large θ values (15). Combined with eq. [2], this means that $^4J(C,C)$ is negative for such molecules. It then appears inevitable that $^4J(C,C)$ is positive for a small θ, for example, in anisole.

Figure 1 displays some proton decoupled and proton coupled ^{13}C nmr spectra, illustrating the extraction of small coupling constants.

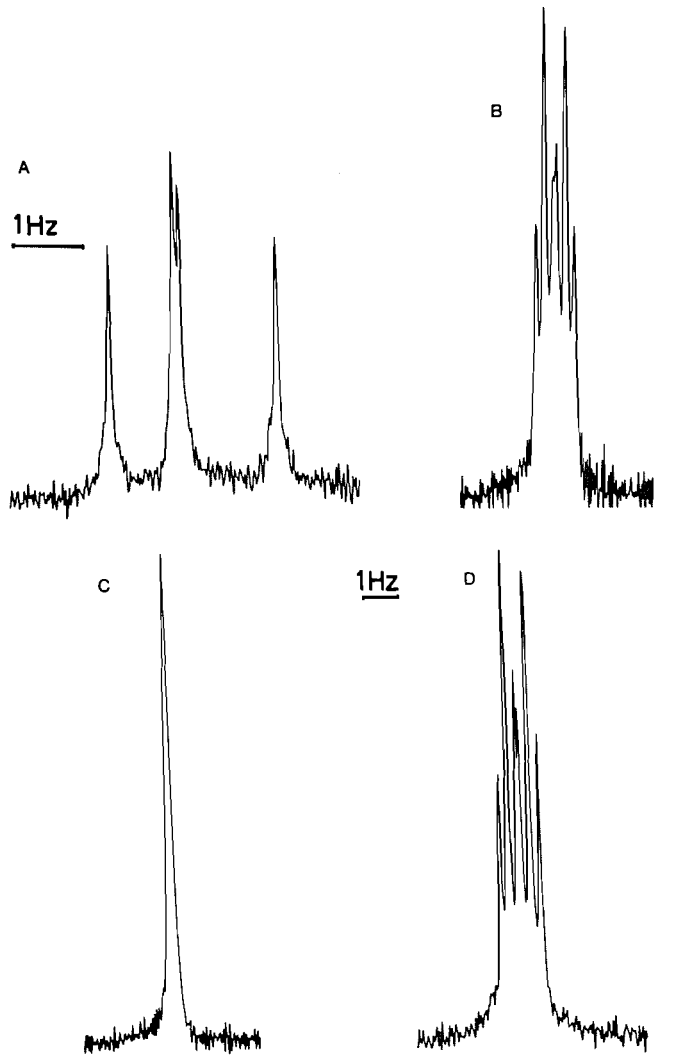

FIG. 1. In A the proton decoupled ^{13}C nmr spectrum of C-1 and C-4 is shown for 1,4-dimethoxybenzene as a 3.0 mol% solution in acetone-d_6 at 300 K and 75.486 MHz. One methoxy group is ^{13}C enriched. If it is attached at C-1, then the large splitting of 2.38 Hz is $^2J(C\text{-}1,C)$ and the small splitting of 0.065 Hz is $^5J(C\text{-}4,C)$. The latter splitting may be about 5% lower than the true $^5J(C\text{-}4,C)$ because of overlapping peaks. A differential isotope shift is present, the resonance frequency of C-1 being 0.23 Hz (3.0 ppb) lower than that of C-4. In B, part of the ^{13}C nmr spectrum of the 1-methoxy group in 2,6-dimethoxyanisole is shown at 300 K and as a 9.9 mol% solution in acetone-d_6. This natural abundance spectrum displays a $^5J(H\text{-}3,C)$ of 0.239(4) Hz and a $^6J(H\text{-}4,C)$ of (−)0.601(4) Hz. C displays the ^{13}C nmr spectrum of the flanking methoxy groups at positions C-2 and C-6. The single peak is not flat-topped, implying that coupling to the ring protons is rather small, probably less than 0.05 Hz. Note that the ^{13}C spectrum of the 1-methoxy group displays no evidence for coupling to methyl protons. In D, part of the ^{13}C nmr spectrum of the methoxy group in unenriched 2,6-dimethylanisole, as an 11 mol% solution in acetone-d_6 at 300 K, is shown under conditions in which the *ortho* methyl protons are being decoupled. The doublet of triplets arises from a $^5J(H\text{-}3,C) = {}^5J(H\text{-}5,C)$ of 0.263(7) Hz and a $^6J(H\text{-}4,C)$ of (−)0.622(4) Hz. In A the dispersion is greater than in B, C, and D, the lower scale being applicable to the latter.

INDO MO FPT computations

INDO MO FPT computations of $^nJ(C,C)$ in anisole as a function of the angle, θ, at intervals of 15°, gave numbers fitted

by eqs. [1]–[3]. The numbers in parentheses are standard deviations in the last significant figure. Equation [1] has the form of a Karplus relationship (34), although it is here written not in terms of cos θ and cos 2θ (trigonometric identities). While the actual values of the ^nJ(C,C) given by these equations are unlikely to be correct (9, 31, 35), the qualitative form is indicative of the empirical approach to follow in the use of ^nJ(C,C) for conformational deductions.

$$[1]\quad {}^3J(\mathrm{C,C})/\mathrm{Hz} = 1.92(3) - 0.76(4)\sin^2\theta + 1.47(4)\sin^2(\theta/2)$$

$$[2]\quad {}^4J(\mathrm{C,C})/\mathrm{Hz} = -0.15(1) - 1.45(2)\sin^2\theta + 0.36(2)\sin^2(\theta/2)$$

$$[3]\quad {}^5J(\mathrm{C,C})/\mathrm{Hz} = 0.00(0) + 1.53(1)\sin^2\theta$$

In an attempt to assess the intrinsic substituent effects on ^nJ(C,C), further computations were performed for the 4-fluoro, 2,6-difluoro, and 3,5-difluoro derivatives of anisole at intervales of 15° in θ. The STO-3G geometries were used as obtained by optimization procedures with the constraint that the carbon skeletons of the benzene rings remained as regular hexagons (our unpublished 6-31G MO geometry for anisole implies very small changes, less than 1°, in the internal ring angles). The fits to equations of the form $^nJ(\mathrm{C,C})/\mathrm{Hz} = A + B\sin^2\theta + C\sin^2(\theta/2)$ are summarized.

	^3J(C,C)	^4J(C,C)	^5J(C,C)
A: 4-F	1.86(4)	−0.17(2)	0.00(0)
3,5-diF	1.93(3)	−0.25(2)	−0.01(0)
2,6-diF	1.30(1)	−0.20(2)	0.00(1)
B: 4-F	−0.72(5)	−1.53(2)	1.61(1)
3,5-diF	−0.81(4)	−1.57(2)	1.49(1)
2,6-diF	−0.17(1)	−1.49(2)	1.51(1)
C: 4-F	1.59(5)	0.38(2)	—
3,5-diF	1.53(4)	0.63(2)	—
2,6-diF	1.66(2)	0.45(2)	—

Comparison with eqs. [1]–[3] indicates rather small intrinsic substituent effects except when the substituent is bonded to the carbon atom carrying the coupled nucleus.

^5J(C,C) as a conformational marker

^5J(C,C) is apparently a σ–π coupling, directly proportional to $\sin^2\theta$, just as ^6J(H,C) in anisole and involving the proton bonded to the *para* carbon nucleus of eq. [3] is very clearly a σ–π coupling (9).

The intrinsic perturbation of ^5J(C,C) by ring substituents, as distinct from their effect on $\langle\sin^2\theta\rangle$ and thereby on ^5J(C,C), is indicated as relatively small by the computations above. In 4-fluoroanisole, $^5J_{90}$ is computed to increase by 0.08 Hz or by 5.2% relative to anisole, whereas two *ortho* or *meta* fluorine substituents are calculated to decrease $^5J_{90}$ by only 0.02 Hz (1.3%) and 0.04 Hz (2.7%), respectively. Much of the increase in ^5J(C,C), from 0.94 Hz in 2,6-dibromoanisole to 1.02 Hz in 2,6-dibromo-4-fluoroanisole, is therefore plausibly attributable to an intrinsic perturbation by fluorine. However, fluorine is a weak π electron donor and is therefore expected also to cause a small increase in $\langle\sin^2\theta\rangle$. The apportionment of the 0.08 Hz between the two effects is problematical. The STO-3G MO barriers for anisole and 4-fluoroanisole imply an increase of 0.04 in $\langle\sin^2\theta\rangle$ for the latter, which would correspond to about 0.04 Hz in ^5J(C,C). However, the barriers in solution are certainly much larger than calculated for the free molecules and, of course, the change in $\langle\sin^2\theta\rangle$ caused by a 4-fluoro substituent in the presence of two *ortho* bromine substituents may well be different than in their absence.

Note, further, that ^5J(C,C) is 1.01 Hz in 2,6-dibromo-4-methylanisole. Because a methyl group is a weaker π electron donor than a fluorine substituent and because its intrinsic perturbation of $^6J_{90}$ is expected to be less than that by fluorine, this result emphasizes the difficulty of establishing an accurate value of $^5J_{90}$ in anisole itself and how it changes in the presence of ring substituents.

However, in the solid state, θ is given as 84° for 2,3,5,6-tetrachloro-1,4-dimethoxybenzene (36), corresponding to a $\sin^2\theta$ of 0.989. Kerr constants for solutions suggest θ as 90° when methyl, chlorine, or bromine substituents are placed in both *ortho* positions of anisole (37). For these substitution patterns, ^5J(C,C) lies between 0.92 and 0.98 Hz in Table 1. The latter value occurs for 2,6-dimethylanisole and the intrinsic perturbation of $^5J_{90}$ by the methyl groups is very likely rather small. It seems reasonable to write eq. [4] for anisole itself. Some of the other ^5J(C,C) values in Table 1 can then be discussed as follows.

$$[4]\quad {}^5J(\mathrm{C,C})/\mathrm{Hz} = (0.98 \pm 0.03)\langle\sin^2\theta\rangle$$

(i) 2,6-Difluoroanisole

The INDO MO FPT results imply a decrease of 1.3% in $^6J_{90}$ for this compound. Yet ^5J(C,C) is only 0.92 Hz in 2,6-dichloroanisole, so that $^6J_{90}$ could be as low as this in 2,6-difluoroanisole. For this value of $^6J_{90}$ and from the ^5J(C,C) of 0.69 Hz, there follow a $\langle\sin^2\theta\rangle$ of 0.75 and the conclusion that the perpendicular, with θ = 90°, is more stable than the planar conformation. The STO-3G MO computations, at 15° intervals of θ, agree with this conclusion and yield a twofold barrier of 6.9 ± 0.1 kJ/mol; a $\langle\sin^2\theta\rangle$ of 0.75 corresponds to one of 5.9 kJ/mol. If $^6J_{90}$ were as large as 0.98 Hz, then a twofold barrier of 4.5 kJ/mol would be deduced for the acetone-d_6 solution of 2,6-difluoroanisole. This value of $^6J_{90}$ cannot be unequivocally discarded but it should be noted that its use implies that the fluorine substituents do not intrinscally perturb $^6J_{90}$.

(ii) 1,4-Dimethoxybenzene

Of the *para* substituted anisoles in Table 1, only for 1,4-dimethoxybenzene is there a measurable value of ^5J(C,C). The methoxy group is a strong π electron donor and therefore the ^5J(C,C) of 0.07_4 Hz is consistent with the anticipated reduction of the barrier about the C_{sp^2}—O bond. Again, a $^6J_{90}$ is needed. In view of the INDO MO FPT calculations, an increase of less than 5% in $^6J_{90}$ from its value in eq. [4] can be assessed. A conservative estimate of 1.02 + 0.05 Hz leads to a $\langle\sin^2\theta\rangle$ of 0.072 ± 0.004 and thence to an apparent V_2 of 19.3 ± 1.1 kJ/mol. This result follows, as does that for 2,6-difluoroanisole above, from a hindered rotor model (38, 39) employing 31 free rotor basis functions.

Dielectric relaxation measurements on 1,4-dimethoxybenzene in tetrachloroethylene solution were compared with spin-lattice relaxation rates of the ^{13}C nuclei in the same solution (40). It was concluded that a twofold barrier of 22.2 ± 2.5 kJ/mol hindered the rotation about the C_{sp^2}—O bond. The following discussion of anisole shows the unlikelihood of a purely twofold barrier in both molecules.

(iii) Anisole

The ^5J(C,C) of less than 0.03 Hz strongly implies a $\langle\sin^2\theta\rangle$ of 0.03 or less. Were the internal barrier twofold, then its magnitude would be near 40 kJ/mol, easily ascertainable by previous experiments (9). The conclusion appears inescapable: a large fourfold component must be present in solution. For the free

Can. J. Chem. Downloaded from www.nrcresearchpress.com by 93.93.197.157 on 09/07/12
For personal use only.

Can. J. Chem. Downloaded from www.nrcresearchpress.com by 93.93.197.157 on 09/07/12
For personal use only.

molecule, our STO-3G and 4-21G MO computations imply that V_4/V_2 is 0.38; a 4-31G calculation (14) gives this ratio as 0.5 ± 0.1. If the latter ratio holds in solution, then a V_2 of 16.5 and a V_4 of 9.5 kJ/mol are consistent with a $\langle \sin^2 \theta \rangle$ of less than 0.03 and with a dynamic nmr barrier of about 19 kJ/mol. It seems natural that V_4 should also be present in 1,4-dimethoxybenzene, as predicted by MO computations (18). The $\langle \sin^2 \theta \rangle$ of 0.07 for the latter is also compatible with a V_2 of 10.5 and a V_4 of 6.0 kJ/mol.

In summary, the barrier to rotation about the C(1)—O bond in anisole and its *meta* and *para* substituted derivatives in acetone-d_6 solution is too large to yield an observable ^5J(C,C), except for the 4-methoxy substituent. It appears that the barrier in all these molecules in Table 1 must have a substantial fourfold component.

Remarks on ^{4}J(C,C), ^{3}J(C,C), and ^{2}J(C,C)

The INDO MO FPT computations imply a large negative ^4J(C,C) for values near 90° and a positive ^4J(C,C) at a θ of zero. For evenfold barriers, $\langle \sin^2 (\theta/2) \rangle$ is 0.5, so that the data in Table 1 can only yield a relationship between $\langle \sin^2 \theta \rangle$ and ^4J(C,C). Comparison of ^4J(C,C) for different *para* substituted anisoles shows that ^4J(C,C) decreases in magnitude as the π donating ability of the substituent increases, as expected if the coefficient of $\sin^2 \theta$ in eq. [2] is negative.

The INDO MO FPT results imply a large perturbation of ^3J(C,C) for 2,6-difluoroanisole and relatively small perturbations for 4-fluoro and 3,5-difluoroanisole. The term in $\sin^2 \theta$ is calculated to decrease from about −0.8 Hz to −0.2 Hz in the presence of two *ortho* fluorine substituents. Experimentally, ^3J(C,C) decreases substantially for large θ values, that is, for all *diortho* substituted molecules in Table 1. The data are consistent with an intrinsic increase in ^3J(C,C) caused by electronegative *ortho* substituents; compare 2,6-dimethyl and 2,6-dibromoanisole, for example. Athough a number of ^3J(C,C) values have been reported for benzene derivatives in which one of the coupled nuclei resides in a side chain (41), few are available for the β-position. In acetophenone, ^3J(C,C) is 8.4 Hz for the ^{13}C nucleus in the methyl group (42), whereas in phenylacetic acid ^3J(C,C) is 1.9 Hz for the ^{13}C nucleus in the carboxyl group (43). The latter molecule has a large preference (44) for a conformation in which the carboxyl group lies in a plane perpendicular to that of the benzene ring. The data in Table 1 cannot be used to establish that ^3J obeys a Karplus relationship, as implied by the computations, but are consistent with a minimum near θ = 90° and maxima at θ = 0° and 180°. The largest ^3J in Table 1 occurs for 3,5-difluoroanisole, for which our STO-3G MO computations yield a V_2 component that is 3.7 kJ/mol larger than that in the computed barrier of anisole. It is therefore this compound which is expected to display the smallest deviations from planarity.

The ^2J(C,C) values increase from 2.3 Hz in anisole to 3.6 Hz for the derivatives with large *ortho* substituents. The INDO MO FPT values suggest small intrinsic substituent effects and yield ^2J(C,C) as −5.1 Hz at θ = 0° and −5.6 Hz at θ = 90°.

^{6}J(^1H,$^{13}CH_3$) as a conformational indicator

In previous work, $^6J(^1\text{H},^{13}\text{CH}_3) \equiv {}^6J$(H,C) was assessed as a σ−π coupling constant, proportional to $\sin^2 \theta$. $^6J_{90}$(H,C) was taken as −0.63 ± 0.01 Hz (19).

No ^6J(H,C) is observable for anisole in acetone-d_6 or in a CS_2/C_6D_{12} mixture (9). In 2,6-dimethylanisole, we measure ^6J(H,C) as -0.62_2 Hz, compared to −0.602 Hz in the 2,6-dichloro derivative, both in acetone-d_6 solution. A previous value for the latter molecule is −0.603(5) Hz in benzene-d_6 solution (9). For 2,6-difluoroanisole, the present ^6J(H,C) is -0.47_3 Hz, corresponding to an apparent V_2 of 5.9 ± 0.4 kJ/mol.

In 2,6-dimethoxyanisole, which could not be prepared with ^{13}C enrichment in the 1-methoxy group by our methods, ^6J(H,C) is −0.60 Hz. This result implies an arcsin $\langle \sin^2 \theta \rangle^{\frac{1}{2}}$ of about 80° for the central methoxy moiety. Its flanking methoxy groups display no observable ^6J(H,C) in Figure 1 and are therefore confined to small θ values (no ^5J(H,C) is observed either, implying (9) that the O—C bonds point away from the central methoxy entity). In such a situation, one might have expected an internal barrier to rotation about the C(1)—O bond similar to that in 2,6-difluoroanisole rather than, as suggested by ^6J(H,C), to that in 2,6-dichloroanisole. It follows that the π electron donating properties of the two, roughly in-plane, methoxy groups (maximum conjugation) decrease the mobile bond order of the C(1)—O bond substantially more than do two flanking fluorine substituents. This conclusion seems reasonable.

The arcsin $\langle \sin^2 \theta \rangle^{\frac{1}{2}}$ value of about 80° compares with 82 ± 7° reported for a 1,2,3 arrangement of methoxy substituents in some crystal structures (16). It is also compatible with qualitative conclusions based on ^{13}C nmr chemical shifts and ^{13}C spin-lattice relaxation times (45, 46), as well as with the observed dipole moment in solution (47, 48). The perpendicular orientation of the 1-methoxy group is assumed in the interpretation of the photoelectron spectrum in the vapor (16).

Differential isotope shifts in 1,4-dimethoxybenzene

If the methoxy group enriched in ^{13}C is attached at C-1, then, in Gombler's notation (51), $^2\Delta^{13}\text{C}(^{13/12}\text{C}) - {}^5\Delta^{13}\text{C}(^{13/12}\text{C})$ is −3.0 ± 0.3 ppb (see Fig. 1A, where the centers of gravity of the C-1 and C-4 doublets are clearly not coincident). In other words, C-1 is more shielded than C-4, resonating at a lower frequency of 0.23 Hz at 75.486 MHz than C-4. Very few $^{13/12}$C isotope shifts on ^{13}C are known (52). In some monosubstituted benzenes (53), $^2\Delta^{13}\text{C}(^{13/12}\text{C})$ within the ring is always less than 4 ppb and $^3\Delta^{13}\text{C}(^{13/12}\text{C})$ is less than 1.2 ppb, perhaps implying that the number above for 1,4-dimethoxybenzene is mainly $^2\Delta$. For C-2 and C-3 in this molecule, $^3\Delta - {}^4\Delta$ is 2.3 ± 0.3 ppb.

Acknowledgements

We thank the Natural Sciences and Engineering Research Council of Canada for a grant-in-aid of research and the referees for cogent criticism.

1. G. Allen and S. Fewster. *In* Internal rotation in molecules. *Edited by* W. J. Orville-Thomas. J. Wiley & Sons, New York. 1974. Chap. 8.
2. N. L. Owen and R. E. Hester. Spectrochim. Acta, Part A, **25**, 343 (1969).
3. M. Onda, A. Toda, S. Mori, and I. Yamaguchi. J. Mol. Struct. **144**, 47 (1986).
4. D. G. Lister and N. L. Owen. J. Chem. Soc. Faraday Trans. 2, **69**, 1304 (1973).
5. H. M. Seip and R. Seip. Acta Chem. Scand. **27**, 4024 (1973).
6. E. T. Lippma, M. A. Alla, J. J. Pehk, and G. Engelhardt. J. Am. Chem. Soc. **100**, 1929 (1978).
7. J. S. Waugh, M. M. Maricq, and R. Cantor. J. Magn. Reson. **29**, 138 (1978).
8. G. R. Hays. J. Chem. Soc. Perkin Trans. 2, 1049 (1983).
9. T. Schaefer, R. Laatikainen, T. A. Wildman, J. Peeling, G. H. Penner, J. Baleja, and K. Marat. Can. J. Chem. **62**, 1592 (1984).
10. H. Tylli and H. Konschin. J. Mol. Struct. **42**, 7 (1977).
11. H. Tylli, H. Konschin, and C. Grundfelt-Forsius. J. Mol. Struct. **55**, 157 (1979).

12. H. KONSCHIN. Low-frequency Raman spectroscopy and STO-3G molecular orbital investigations of some hydroxy- and methoxy-substituted benzenes. Doctoral dissertation, University of Helsinki, 1985.
13. H. KONSCHIN, H. TYLLI, and C. GRUNDFELT-FORSIUS. J. Mol. Struct. **77**, 51 (1981).
14. M. KLESSINGER and A. ZYWIETZ. J. Mol. Struct. **90**, 341 (1982).
15. T. A. WILDMAN. Ph.D. thesis. University of Manitoba, 1982.
16. G. M. ANDERSON, P. A. KOLLMAN, L. N. DOMELSMITH, and K. N. HOUK. J. Am. Chem. Soc. **101**, 2344 (1979).
17. W. J. HEHRE, L. RADOM, and J. A. POPLE. J. Am. Chem. Soc. **94**, 1496 (1972).
18. T. SCHAEFER and G. H. PENNER. J. Mol. Struct. (Theochem), **152**, 179 (1987).
19. H. DODZIUK, H. v. VOITHENBERG, and N. L. ALLINGER. Tetrahedron, **38**, 2811 (1982).
20. D. G. LISTER. J. Mol. Struct. **68**, 33 (1980).
21. H. FRIEGE and M. KLESSINGER. Chem. Ber. **112**, 1614 (1979).
22. R. A. HOFFMAN. Mol. Phys. **1**, 326 (1958).
23. R. WASYLISHEN and T. SCHAEFER. Can. J. Chem. **50**, 1852 (1972).
24. J. S. MARTIN, A. R. QUIRT, and K. E. WORVILL. The NMR program library. Daresbury Laboratory, Daresbury, U.K.
25. J. A. POPLE, J. W. MCIVER, and N. S. OSTLUND. J. Chem. Phys. **49**, 2960 (1968).
26. P. DOBOSH and N. S. OSTLUND. QCPE, **11**, 281 (1975).
27. M. R. PETERSEN and R. A. POIRIER. MONSTERGAUSS. Department of Chemistry, University of Toronto, Toronto, Ontario. 1981.
28. J. S. BINKLEY, R. A. WHITESIDE, R. KRISHMAN, R. SEEGER, D. J. DEFREES, H. B. SCHLEGEL, S. TOPIOL, L. R. KAHN, and J. A. POPLE. GAUSSIAN 80. Program 406, QCPE.
29. J. S. BINKLEY, M. J. FRISCH, D. J. DEFREES, K. RAGHAVACHARI, R. A. WHITESIDE, H. B. SCHLEGEL, E. M. FLUDER, and J. A. Pople. GAUSSIAN 82. Department of Chemistry, Carnegie–Mellon University, Pittsburgh, PA.
30. T. SCHAEFER and J. D. BALEJA. Can. J. Chem. **64**, 1376 (1986).
31. T. SCHAEFER and G. H. PENNER. Can. J. Chem. **64**, 2013 (1986).
32. H. M. MCCONNELL and D. B. CHESNUT. J. Chem. Phys. **28**, 107 (1958).
33. M. KARPLUS and G. K. FRAENKEL. J. Chem. Phys. **35**, 1312 (1961).
34. M. KARPLUS. J. Am. Chem. Soc. **85**, 2870 (1963).
35. T. SCHAEFER, J. PEELING, and G. H. PENNER. Can. J. Chem. **61**, 2773 (1983).
36. M. W. WIECZOREK. Acta Crystallogr. Sect. B, **36**, 1515 (1980).
37. M. J. ARONEY, M. G. CORFIELD, and R. J. W. LEFÈVRE. J. Chem. Soc. London, 2954 (1964).
38. W. J. E. PARR and T. SCHAEFER. Acc. Chem. Res. **13**, 400 (1980).
39. P. B. AYSCOUGH, M. S. BRICE, and R. E. D. MCCLUNG. Mol. Phys. **20**, 41 (1971).
40. J. GOULON, D. CANET, M. EVANS, and G. J. DAVIES. Mol. Phys. **30**, 973 (1975).
41. J. L. MARSHALL. Carbon–carbon and carbon–proton nmr couplings. VCH Publishers, Deerfield Beach, FL. 1983.
42. J. L. MARSHALL, L. G. FAEHL, and R. KATTNER. Org. Magn. Reson. **12**, 163 (1979).
43. J. L. MARSHALL, L. G. FAEHL, and N. D. LEDFORD. Spectrosc. Lett. **9**, 877 (1976).
44. T. SCHAEFER, J. PEELING, G. H. PENNER, A. LEMIRE, and R. SEBASTIAN. CAN. J. CHEM. **63**, 24 (1985).
45. J. J. KNITTEL and A. MAKRIYANNIS. J. Med. Chem. **24**, 906 (1981).
46. A. MAKRIYANNIS and S. FESIK. J. Am. Chem. Soc. **104**, 6462 (1982).
47. O. EXNER and V. JEHLICKA. Collect. Czech. Chem. Commun. **48**, 1030 (1983).
48. H. LUMBROSO, CH. LIĠEOIS, L. TESTAFERRI, and M. TIECCO. J. Mol. Struct. **144**, 121 (1986).
49. W. S. BREY, L. W. JAQUES, and H. J. JAKOBSEN. Org. Magn. Reson. **12**, 243 (1979).
50. V. WRAY, L. ERNST, and E. LUSTIG. J. Magn. Reson. **27**, 1 (1977).
51. W. GOMBLER. J. Am. Chem. Soc. **104**, 6616 (1982).
52. P. E. HANSEN. Annu. Rep. NMR Spectrosc. **15**, 106 (1983).
53. V. WRAY, L. ERNST, T. LUND, and H. J. JAKOBSEN. J. Magn. Reson. **40**, 55 (1980).

Can. J. Chem. Downloaded from www.nrcresearchpress.com by 93.93.197.157 on 09/07/12
For personal use only.

Long-range coupling constants for α-^{13}C nuclei in phenyl-X-R (X = O,S,Se,Te) derivatives. Internal rotational information

TED SCHAEFER AND GLENN H. PENNER
Department of Chemistry, University of Manitoba, Winnipeg, Man., Canada R3T 2N2

Received December 4, 1987

TED SCHAEFER and GLENN H. PENNER. Can. J. Chem. **66**, 1641 (1988).

The long-range spin–spin coupling constant over six bonds between the ^{19}F nucleus and the ^{13}C nucleus in the side chain, ^6J(C,F), is reported for 4—F—C_6H_4—X—R, where X = O, S and R = CH_3, CH_2CH_3, $CH(CH_3)_2$ and $C(CH_3)_3$. ^6J(C,F) depends on $\sin^2\theta$, where θ is the angle by which the side chain twists out-of-plane about the C_{sp^2}—X bond. Expectation values of $\sin^2\theta$ are obtained from ^6J(C,F), yielding magnitudes of the apparent twofold barrier to rotation about the C_{sp2}—X bond. In these terms, the most stable conformation is that for θ = 0° for all compounds, with the exception of R = $C(CH_3)_3$ and of X = S, R = $CH(CH_3)_2$; there is effectively free rotation about the C_{sp^2}—S bond in isopropyl 4-fluorophenyl sulfide in acetone-d_6 solution. Good correlations exist between ^6J(C,F) and a number of other molecular properties, including certain differences of ionization potentials of the molecular orbitals in the ethers. In particular, the chemical shifts of C-4 are correlated with ^6J(C,F). Because ^5J(C,C), the coupling constant involving C-4, also depends on $\sin^2\theta$, it is measured for the methyl and ethyl selenides and tellurides, as are other ^{13}C,^{13}C couplings involving a ^{13}C nucleus in the side chain. The literature values for the ^{13}C nuclear magnetic resonance chemical shifts in alkyl phenyl selenides and tellurides can be related to θ preferences and also allow estimates of the extrema in ^5J(C,C). The resultant values of $\arcsin\langle\sin^2\theta\rangle^{1/2}$ for R = CH_3 are in good agreement with estimates of θ obtained from electron diffraction patterns, photoelectron spectra, and nuclear magnetic resonance in the nematic phase.

TED SCHAEFER et GLENN H. PENNER. Can. J. Chem. **66**, 1641 (1988).

On a déterminé les constantes de couplage spin–spin à longue distance, à travers six liaisons, entre le noyau de ^{19}F et le noyau de ^{13}C de la chaîne latérale, ^6J(C,F), des composés 4—F—C_6H_4—X—R, dans lesquels X = O ou S et R = CH_3, CH_2CH_3, $CH(CH_3)_2$ et $C(CH_3)_3$. Les valeurs des ^6J(C,F) varient avec le $\sin^2\theta$, dans lequel θ est l'angle entre le plan du noyau benzénique et la chaîne latérale. Les valeurs attendues de $\sin^2\theta$ sont obtenues à partir des valeurs des ^6J(C,F) et elles fournissent les amplitudes de la barrière binaire apparente pour la rotation autour de la liaison C_{sp^2}—X. Dans ces termes, la conformation la plus stable pour tous les composés, exceptés ceux pour lesquels R = $C(CH_3)_3$ ainsi que X = S et R = $CH(CH_3)_2$, est celle pour laquelle θ = 0°; en solution dans l'acétone-d_6, on observe de fait une rotation libre autour de la liaison C_{sp^2}—S du sulfure d'isopropyle et de fluoro-4 phényle. Il existe une bonne corrélation entre les valeurs de ^6J(C,F) et un certain nombre d'autres propriétés moléculaires, y compris certaines différences dans les potentiels d'ionisation des orbitales moléculaires des éthers. On peut établir, en particulier, une corrélation entre les déplacements chimiques en C-4 et les valeurs des ^6J(C,F). Puisque les valeurs de ^5J(C,C), les constantes de couplages impliquant le C-4, dépendent aussi de $\sin^2\theta$, on a mesuré cette constante pour les sélénures et les tellurures de méthyle ainsi que d'éthyle; on a aussi mesuré les constantes de couplage ^{13}C,^{13}C impliquant un noyau ^{13}C de la chaîne latérale. On peut établir une corrélation entre les préférences θ et les valeurs rapportées dans la littérature pour les déplacements chimiques en résonance moleculaire nucléaire du ^{13}C des sélénures et de tellurures d'alkyle et de phényle; à l'aide de ces déplacements chimiques, on peut aussi évaluer les extrêmes dans les valeurs des ^5J(C,C). Les valeurs résultantes pour $\arcsin\langle\sin^2\theta\rangle^{1/2}$, pour R = CH_3, sont en bon accord avec les évaluations obtenues pour θ à partir des patrons de diffraction, des spectres photoélectroniques et des spectres en résonance magnétique nucléaire dans une phase nématique.

[Traduit par la revue]

Introduction

The barriers to rotation about the C_{sp^2}—X bond in phenyl—X—R molecules (X = O, S, Se, Te; R = CH_3, CH_2CH_3, $CH(CH_3)_2$, $C(CH_3)_3$) are uncertain. The internal barrier in anisole is computed as consisting of twofold and fourfold components at the STO-3G level of *ab initio* molecular orbital theory, V_2 and V_4 being 5.6(4) and 2.1(4) kJ/mol, respectively (1, 2). A somewhat larger ratio of V_4/V_2 is approximated at the 4-31G level (3). A fully optimized STO-3G MO computation (4) has the planar conformer as 7.9 kJ/mol more stable than the orthogonal form. While microwave spectra (5) confirm the coplanar heavy atom conformation as the most stable (**1**, θ = 0°), they provide no information on the magnitude of the barrier; the microwave spectrum of 4-fluoroanisole places a lower limit of 4.5 kJ/mol on the height of the barrier (6). Molecular mechanics has this height as 7.9 kJ/mol (7) in anisole and the torsional frequency for motion about the C_{sp^2}—O bond yields 15.1 ± 0.3 kJ/mol on the assumption that the barrier is twofold in nature (8). The barrier height is phase dependent, reported as 48.2 ± 1.3 kJ/mol in the solid (9) and as 25.2 ± 0.3 kJ/mol (8) in the pure liquid (assumed twofold). Dynamic nmr experiments in ether solution imply a barrier height of less than 19.7 kJ/mol (10), while long-range coupling constants indicate the presence of a substantial fourfold component (10). Most experimental data (11–13) imply a rotational barrier in the gas phase of less than 10 kJ/mol.

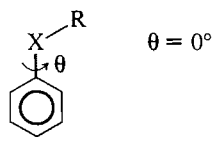

θ = 0°

1

Much less work has been reported on the conformational properties of other phenyl alkyl ethers. Photoelectron spectra (14) in the gas phase are best interpreted in terms of planar conformations for the ethyl and isopropyl compounds, but for the *tert*-butyl phenyl ether a nonplanar conformation is found. Similar conclusions follow from infrared absorption intensities in CCl_4 solution (15). At high temperatures the presence of a nonplanar conformer is detected for anisole and ethyl phenyl ether (14).

In chloroform solution (16), the ^{1}H and ^{13}C nmr chemical shifts and some of the spin–spin coupling constants between

Can. J. Chem. Downloaded from www.nrcresearchpress.com by 112.217.228.212 on 09/07/12
For personal use only.

Can. J. Chem. Downloaded from www.nrcresearchpress.com by 112.217.228.212 on 09/07/12
For personal use only.

nuclei within the phenyl group of phenyl alkyl ethers are sensitive to the nature of the alkyl group. For example, ^1J(H-4,C-4), the coupling constant between the *para* ^{1}H and ^{13}C nuclei, is relatively insensitive to the substitution of an ethyl or an isopropyl for a methyl group; a relatively large change in ^1J(H-4,C-4) is observed in the presence of a *tert*-butyl group. These studies (16) show, in agreement with the gas phase photoelectron spectra, that in solution the $2p-\pi$ conjugation is much smaller for R = *tert*-butyl than for R = CH_3, CH_2CH_3, and $CH(CH_3)_2$.

^{13}C nuclear magnetic resonance and photoelectron studies (17, 18) of alkyl phenyl sulfides (R = CH_3, CH_2CH_3, $C(CH_3)_3$) demonstrate that the degree of nonplanarity increases monotonically as the size of the alkyl group increases (19). The degree of nonplanarity is a compromise between the effects of $3p....\pi$ conjugation, tending to decrease θ, and steric interference between the alkyl group and the *ortho* C—H bonds, tending to increase θ. The chemical shift of C-4 of the *tert*-butyl derivative is the same as in benzene, consistent with a large average θ in this compound. The Kerr constant in cyclohexane solution (20) indicates a θ of 82 ± 11°C. In the 4-fluorophenyl derivative (21) the C-4 and ^{19}F chemical shifts are almost identical with the corresponding shifts in fluorobenzene, in line with the conclusions above. Attempts have also been made to relate the ^{13}C nmr shifts to the populations of the planar conformers of the alkyl phenyl sulfides (22).

The ^{1}H and ^{2}H nmr spectra of 4-chlorophenyl methyl selenide-α-d_3 dissolved in a liquid crystal are consistent with a θ near 40°, implying only a small barrier to rotation about the C_{sp^2}—Se bond (23). An electron diffraction pattern in the gas phase suggests a θ of 40 ± 13° (24). The Kerr effect in solution has θ as 32° (25). The ^{13}C nmr chemical shifts of neat alkyl phenyl selenides (26, 27) bear out the intuition that $p...\pi$ conjugation decreases in the order O > S > Se. Hence nonplanar conformations will be increasingly favored in that order. Photoelectron spectra (28) and electric dipole moments (29) are in apparent agreement with such a conclusion, although it has been stated (30) that ^{1}H and ^{13}C nmr spectra of C_6H_5XR (X = O, S, Se, Te) in CCl_4 solution do not contradict the hypothesis of planar conformations.

The $p...\pi$ conjugation in methyl phenyl telluride is even weaker than for the selenium compound (29) and photoelectron spectra are consistent (31) with a θ of at least 60°, implying that the perpendicular is possibly more stable than the planar conformer.[1]

This paper reports on another approach to the estimation of the internal rotational potentials about the C_{sp^2}—X bonds in some phenyl-X-R derivatives. This approach utilizes long-range ^{13}C,^{13}C spin–spin coupling constants, ^nJ(C,C), where one ^{13}C nucleus is situated in R, for X = Se, Te and R = CH_3, CH_2CH_3. For 4-fluorophenyl-X-R, where R = CH_3, CH_2CH_3, $CH(CH_3)_2$, $C(CH_3)_3$ and X = O, S, the coupling constant over six formal bonds, $^6J(^{13}C,^{19}F)$, is used to assess the mobility about the C_{sp^2}—X bond. Both ^5J(C,C) and ^6J(C,F) depend on the angle θ in a simple way.

Experimental

The synthesis of selenoanisole-α-^{13}C (methyl phenyl selenide) went as follows. About 0.1 g of sodium was added to 10 mL of absolute methanol, followed by addition of 2 mmol of selenophenol (benzeneselenol). Then 2.3 mmol of $^{13}CH_3I$ (95 at.%) was added while stirring. The solution was stirred for 15 min, after which time water was added, giving a cloudy suspension. The mixture was extracted with ether, the ether layer was dried over anhydrous $MgSO_4$, filtered, and rotary evaporated. Ethylation to give ethyl phenyl selenide employed 2.3 mmol of $CH_3{}^{13}CH_2I$.

The methyl phenyl telluride, enriched with ^{13}C at the methyl site, was made from diphenyl ditelluride, which was added to 5 mL of absolute methanol and 2 mL of benzene (dissolution in this solvent mixture was not quite complete). To this mixture, 0.5 g of $NaBH_4$ in 5 mL of 1 N sodium hydroxide was added dropwise. The undissolved telluride went into solution, which first became colorless and then slightly cloudy. At this time, 0.5 g of $^{13}CH_3I$ in about 1 mL of methanol was added, and the solution was stirred for 0.5 h and then poured over crushed ice. After addition of 10% HCl, the mixture was extracted with methylene chloride, dried over anhydrous $MgSO_4$, filtered, and evaporated to give a light brown liquid. Ethyl phenyl telluride was prepared similarly, using $CH_3{}^{13}CH_2I$.

The ethers and sulfides with R = CH_3, CH_2CH_3, $CH(CH_3)_2$ can be obtained by the standard method of reacting the phenol or thiophenol derivatives with the appropriate alkyl iodide in dry acetone as the solvent and in the presence of dry sodium carbonate.

The *tert*-butyl-4-fluorophenyl ether was made from 4-fluorophenol, which was added to absolute methanol containing sodium. Alkylation under these basic conditions was obtained by the addition of *tert*-butyl bromide.

The preparation of *tert*-butyl-4-fluorophenyl sulfide proceeded according to the literature (32). Ten grams of 80% H_2SO_4 in a 50-mL beaker was cooled in an ice bath. Then 1.5 g of *tert*-butyl alcohol was added dropwise while stirring, holding the temperature below 10°C. 4-Fluorothiophenol (1.3 g) was then added dropwise, stirring the while. The mixture was stirred overnight at room temperature. Addition of crushed ice to the mixture was followed by extraction with ether and rotary evaporation to yield a viscous liquid.

Solutions for nmr spectral work were prepared in acetone-d_6 or benzene-d_6 (see tables) and were transferred to 10 mm od nmr sample tubes, together with 10 drops of tetramethylsilane (TMS). The sample tubes were degassed by the freeze–pump–thaw procedure and were then flame sealed.

Most ^{13}C nmr spectra were taken at 75.486 MHz on a Bruker AM300 spectrometer at a probe temperature of 300 K under conditions of proton decoupling. Those for the sulfides employed a WH90 instrument at 22.63 MHz and 305 K. Typically, 128–256 free induction decays were accumulated. For example, a spectral width of 100 Hz was assigned to a 4K data region, using acquisition times of 20.5 s. Zero-filling to twice the original data region before Fourier transformation, and using a small amount of Gaussian multiplication, resulted in acceptable line shapes and peak widths at half-height usually lying between 0.05 and 0.25 Hz.

STO-3G MO computations (33) employed the computer program GAUSSIAN 82 (34).

Results and discussion

Table 1 presents ^{13}C nmr chemical shifts and ^nJ(C,C) for the selenides and tellurides, one ^{13}C nucleus being that in the methyl or methylene groups of the side chain. When observable, ^nJ(C,C) values were typically reproducible to 0.01 Hz. The signs of ^nJ(C,C), n = 2–5, are assumed on the basis of those determined for thioanisole derivatives (35) and also computed semiempirically.

^6J(C,F) values in the ethers and sulfides are given in Table 2. Although they are almost certain to be positive (10, 36–38), their sign has previously not been determined. Figure 1 demonstrates the sign determination of ^6J(C,F) in 4-fluoroanisole-α-^{13}C. ^nJ(C,F) values for ^{13}C nuclei within the benzene ring are available, as are the ^{13}C chemical shifts for the sulfides (21), and

[1]In all these experiments, the derived angle of twist, θ, about the C_{sp^2}—X bond is an average value but it is often unclear what this average is. The distribution among θ values depends, of course, on the temperature and the internal rotational potential.

TABLE 1. The ^{13}C nmr chemical shifts and $^{13}C,^{13}C$ coupling constants in Hz for some phenyl selenides and phenyl tellurides enriched in ^{13}C at the methyl or methylene sites

Parameter	$SeCH_3$[a]	$SeCH_2CH_3$[b]	$TeCH_3$[c]	$TeCH_2CH_3$[d]
$\delta(CH_3)$	15.01	15.73	−17.14	17.48
$\delta(CH_2)$		21.21		0.1
δ(C1)	132.82	131.71	112.95	112.16
δ(C2)	130.74	132.89	136.92	139.78
δ(C3)	129.85	129.34	129.26	129.30
δ(C4)	126.69	127.33	127.14	127.58
$^1J(^{13}C,C)$		35.79		36.0
$^2J(^{13}C,C\text{-}1)$	(−)1.51	(−)1.50	(−)1.10	(−)1.11
$^3J(^{13}C,C\text{-}2)$	(+)2.17	(+)1.62	(+)1.41	(+)1.06
$^4J(^{13}C,C\text{-}3)$	$(+)0.08_0$	$(-)0.11_4$	<0.05	<0.01
$^5J(^{13}C,C\text{-}4)$	(+)0.27	(+)0.38	(+)0.31	(+)0.37

[a]3.5 mol% in acetone-d_6.
[b]3.8 mol% in acetone-d_6.
[c]13.0 mol% in benzene-d_6.
[d]5.0 mol% in benzene-d_6.

TABLE 2. $^6J(^{13}C, ^{19}F)$ in Hz for some 4-fluorophenyl ethers and sulfides at 300 K and estimates of internal rotational barriers about the C_{sp^2}—O and C_{sp^2}—S bonds

	^6J(C,F)		$\sin^2\theta$		V_2	
R/X	O[a]	S[b]	O[c]	S[d]	O[e]	S
CH_3	0.11	0.47	0.07_3	0.31_6	19.4	4.0
CH_2CH_3	0.12	0.74	0.08_0	0.49_1	17.3	0.2
$CH(CH_3)_2$	0.27	0.92	0.18_0	0.61_4	8.7	−2.4[f]
$C(CH_3)_3$	1.04	1.38	0.69_3	0.92_3	−4.2[f]	−18.3[f]

[a]All samples were 50 mol% in acetone-d_6, except for R = $C(CH_3)_3$, which was 5 mol%.
[b]50 mol% in acetone-d_6.
[c]Based on $^6J_{90}$(C,F) as 1.50 Hz; see text.
[d]Based on $^6J_{90}$(C,F) as 1.50 Hz.
[e]These are *apparent* V_2 values, in kJ/mol. It is unlikely, in the phenyl ethers, that a twofold component alone adequately describes the internal motion; see text.
[f]Negative numbers indicate the perpendicular conformer as most stable.

are not reported here. ^{13}C nuclear magnetic resonance studies of alkyl phenyl ethers are also available (16).

The dependence of $^6J(C,F)$ in the ethers and sulfides

Previous experimental and theoretical investigations (10, 36, 37) of ^6J(C,F) in a variety of benzene derivatives are all consistent with a simple dependence of the form $^6J(C,F) = {}^6J_{90}\sin^2\theta$, where $^6J_{90}$ is the value for the perpendicular conformation of the side chain. In 2,6-dibromo-4-fluoroanisole, ^6J(C,F) is 1.48 Hz (37). Judging by crystallographic diffraction data for an anisole derivative, in which two *ortho* chlorine substituents cause θ to be 84° (39), it seems most likely that $^6J_{90}$ is no greater than 1.50 Hz. If this number is used for $^6J_{90}$, the expectation values of $\sin^2\theta$ in Table 2 apply. Apparent V_2 values in this table then follow on the basis of a hindered rotor model (40). They are only apparent values because the $\langle\sin^2\theta\rangle$ values are also compatible with various ratios, V_2/V_4.

STO-3G MO computations on 4-fluoroanisole (2) yield V_2 and V_4 as 4.5 ± 0.4 and 2.2 ± 0.4 kJ/mol, respectively. There is no doubt that the barrier in anisole itself is highly state dependent, ranging from 48.2 kJ/mol in the solid (9) to an apparent V_2 of 25.2 kJ/mol in the pure liquid (8) and one of 15.1 kJ/mol in the gas phase (8). The apparent V_2 of 19.4 kJ/mol based on ^6J(C,F) for 4-fluoroanisole in acetone-d_6 solution (Table 2) is sensible in these terms because the fluorine substituent will act to decrease the mobile bond order of the C_{sp^2}—O bond. However, it is most unlkely that the internal rotational potential in anisole or its *para* fluoro derivative is purely twofold (1–4). In fact, a $\langle\sin^2\theta\rangle$ of 0.07_3 for the fluorine derivative is also found for a V_2 of 11.1 and a V_4 of 4.5 kJ/mol, taking the theoretical ratio of these components as a guide. Such a ratio corresponds to a barrier magnitude of less than 12 kJ/mol, as would be measured in principle by dynamic nmr procedures, for example.

One may identify another possible ambiguity concerning ^6J(C,F). The OR group is a strong π electron donor when θ is zero. The hyperfine coupling parameter of ^{19}F in the aromatic C—F bond is probably a function of the C—F mobile bond order (41–43) and, in the presence of a *para* OR group, might vary with θ. Because ^6J(C,F) may also reflect variations in the mobile bond order, it is possible that $^6J_{90}$ as used here is an underestimate in the sense that, for nearly planar conformations, $\langle\sin^2\theta\rangle$ is actually smaller than the value used in the discussion above. In a study of ^5J(C,C) in anisole derivatives (35), it is estimated that $^5J_{90}$(C,C) is 0.98 Hz. Hence ^5J(C,C) in 4-fluoroanisole should be ^6J(C,F) (0.98/1.50) or 0.07 Hz. This coupling has not been resolved (35), it being estimated that $^5J(C,C) < 0.05$ Hz. It therefore seems possible or even probable that the apparent V_2 in Table 2 is a lower limit.[2]

What is fairly certain from the data in Table 2, however, is the marked destabilization of the planar conformation in *tert*-butyl 4-fluorophenyl ether. The discussion above implies that a $^6J_{90}$ of 1.50 Hz is most reliable for this compound (θ nearer 90°). Therefore the $\langle\sin^2\theta\rangle$ of 0.69 demonstrates that the perpendicular conformer is more stable than the planar conformer (a vanishing barrier or a purely fourfold barrier entails a $\langle\sin^2\theta\rangle$ of 0.5). It also seems certain that the other ethers in Table 2 have a planar conformation as the most stable in acetone-d_6 solution.

Of course, the 4-fluoro substitutent will destabilize the planar conformation by π electron donation, so that the present conclusions do not directly apply to the alkyl phenyl ethers themselves. It is interesting, therefore, to note eq. [1], in which ΔI^{γ}_{31} is

[2]The intrinsic perturbation of ^6J(C,F) by other ring substituents may be inferable from extensive studies of, say, ^6J(H,F) and ^5J(C,F) in a variety of toluene derivatives; such studies are underway.

Can. J. Chem. Downloaded from www.nrcresearchpress.com by 112.217.228.212 on 09/07/12
For personal use only.

Can. J. Chem. Downloaded from www.nrcresearchpress.com by 112.217.228.212 on 09/07/12
For personal use only.

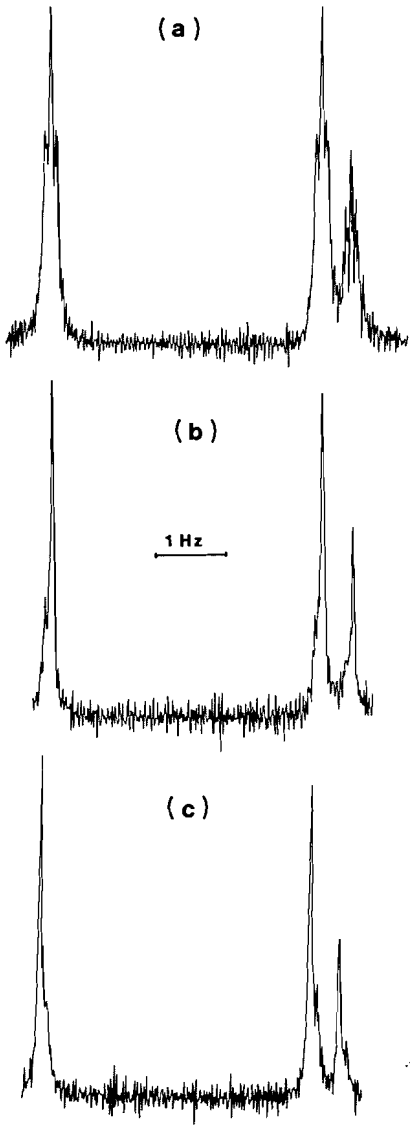

FIG. 1. In (a), part of the ^{19}F nmr spectrum of a 10 mol% solution of 4-fluoroanisole-α-^{13}C in acetone-d_6 is displayed at a probe temperature of 300 K and a spectrometer frequency of 282.363 MHz. The ^{19}F chemical shift is 38.45 ppm (deshielded) relative to internal C_6F_6. The digital resolution is 0.012 Hz/point. The ^{19}F spectrum evinces coupling interactions with all protons and with the ^{13}C nucleus of the methyl group. It is known that ^7J(H,F) is 0.083(1) Hz (46). The magnitude of ^6J(C,F) is 0.11 Hz, as measured from the proton decoupled ^{13}C nmr spectrum. These small coupling constants account for the fine structure of the bands in (a). In (b), the region of (a) is again displayed, but under conditions in which the low-frequency region of the methyl proton doublet is being irradiated. This irradiation causes partial decoupling (47) of the methyl protons, that is, for those molecules in which the ^{13}C nucleus has a given spin state, say $\frac{1}{2}$. A partial collapse of bands in (b) has occurred, so that intensity has accrued towards the right, that is, any quartet structure due to coupling with the methyl protons collapses in the low-frequency parts of the bands. In (c), the methyl protons are being irradiated at high frequency for the other spin state of ^{13}C, say $-\frac{1}{2}$. The high-frequency parts of the bands are collapsed. These $^{19}F\{^1H\}$ experiments show that ^1J(H,C)/^6J(C,F) is positive. It is known (48) that ^1J(H,C) is positive.

obtained from the photoelectron spectra of these ethers in the gas phase (14). ΔI^v_{31} represents the conjugative interaction between the oxygen lone pairs and the π electrons of the phenyl group. The correlation is significant at the 98% confidence level. It suggests that any perturbation of the conformational behaviour of the OR group by the fluorine substituent is proportional to the extent of $2p...\pi$ conjugation in the unsubstituted ethers and should therefore be least for the *tert*-butyl group. It also suggests that the qualitative nature of the internal rotational potential about the C_{sp^2}—O bond in the gas phase is not severely altered in solution, although, of course, the magnitudes of the *n*-fold components must increase in solution, as discussed above. Because ^6J(C,F) is proportional to $\sin^2\theta$, eq. [1] suggests that the conjugative interaction between the lone pairs on oxygen and the aromatic π orbitals also changes in this simple way with the conformational angle.

$$[1]\quad \Delta I^v_{31}/\text{eV} = 2.87 - 1.79\,{}^6J(\text{C,F}); \qquad r = 0.998$$

Equation [2] is also of some interest because it demonstrates a correlation between the one-bond $^1H,^{13}C$ coupling constant at C-4 in the phenyl groups of alkyl phenyl ethers as 1 molar solutions in $CDCl_3$ (16) and ^6J(C,F) in the corresponding 4-fluoro derivatives in acetone-d_6 solution. It is probable (44) that ^1J(H,C) is proportional to $-Q^H_{CH}$, a hyperfine interaction parameter that displays a much smaller variation (43) than that for ^{19}F in the C—F bond, possibly implying that ^6J(C,F) is a fairly reasonable indicator of the conformational properties of the OR group.

$$[2]\quad {}^1J(\text{H,C-4}) = 160.80 - 0.749\,{}^6J(\text{C,F}); \qquad r = 0.997$$

Turning to the sulfides in Table 2, it is noted that the SR is a much weaker π electron donor than the OR group. Consequently, it is likely that any intrinsic perturbation of ^6J(C,F) by conjugative interactions is much smaller for the sulfides. Furthermore, the barrier to internal rotation about the C_{sp^2}—S bond is therefore smaller than for the ethers; for thioanisole and 4-fluorothioanisole it is also computed as mainly twofold (2, 37).

In 2,6-dibromo-4-fluorothioanisole, ^6J(C,F) is 1.48 Hz (10), implying that $^6J_{90}$ is again about 1.50 Hz. On this basis, the $\langle\sin^2\theta\rangle$ and V_2 values follow as in Table 2. If the barriers for the larger alkyl groups are also mainly twofold, then there is essentially free rotation about the C_{sp^2}—S bond in the ethyl sulfide derivative, and for R = $CH(CH_3)_2$, $C(CH_3)_3$ the most stable conformation has θ as 90°. Our geometry-optimized STO-3G MO calculations on ethyl 4-fluorophenyl sulfide suggest that V_4 is about 10% of V_2, just as for the methyl compound (2), but essentially unaltered as to magnitudes: V_2 is calculated as 4.4(1) kJ/mol and V_4 as 0.5(1) kJ/mol. ^6J(C,F) is unequivocal in its indication of a much smaller barrier in the ethyl derivative in solution (Table 2).

A number of correlations between ^6J(C,F) and other conformationally dependent molecular properties exist for the sulfides. In eq. [3], σ°_R is related to the intensities of certain infrared bands (15) and is a measure of the resonance interaction between the substituent and the aromatic π system in CCl_4 solution. Again, in eq. [4] ^6J(C,F) correlates with the intensity of the ultraviolet band near 260 nm for these sulfides (18).

$$[3]\quad \sigma^\circ_R = -0.336 + 0.189\,{}^6J(\text{C,F})/\text{Hz}; \qquad r = 0.999$$

$$[4]\quad \varepsilon_{max} = (1.744 \times 10^4) - (1.143 - 10^4)\,{}^6J(\text{C,F})/\text{Hz}; \qquad r = 0.996$$

A very good correlation exists between the ^{13}C chemical shift of C-4 for the neat liquids (21) and ^6J(C,F) in acetone-d_6 solution for the four alkyl phenyl sulfides in Table 2, as in eq. [5]. This correlation is reasonable because δ(C-4) is most likely related to the electron density at C-4, and our computations of electron density, ρ, at C-4, using the STO-3G basis set on

TABLE 3. Conformational information about phenyl-X-R (X = S, Se, Te) derivatives from ^{13}C nmr chemical shifts and spin–spin coupling constants

	$\langle\sin^2\theta\rangle$				V_2[g]				arcsin $\langle\sin^2\theta\rangle^{\frac{1}{2}}$			
R	S(H)[a]	S(F)[d]	Se[e]	Te[f]	S(H)	S(F)	Se	Te	S(H)	S(F)	Se	Te
CH_3	0.26[b]	0.32	0.45	0.64	5.4	4.0	1.0	−2.9	31	34	42	53
CH_2CH_3	0.41[c]	0.49	0.5	0.73	1.9	0.2	−1.7	−5.2	40	44	50	58
$CH(CH_3)_2$	0.57[c]	0.61	0.69	0.76	1.4	2.4	−4.2	−6.2	49	51	56	61
$C(CH_3)_3$	0.93[c]	0.92	0.93	—	−18.8	−18.3	−18.8	—	74	74	74	—

[a]The alkyl phenyl sulfides.
[b]Based on ^6J(H,C) in ref. 37.
[c]Based on eq. [7] of the text and δ(C-4).
[d]The alkyl-4-fluorophenyl sulfides, using ^6J(C,F) in Table 2.
[e]Based on δ(C-4) values for the alkyl phenyl selenides (26) and eq. [7].
[f]Based on δ(C-4) values (49) and eq. [7], the value for R = $C(CH_3)_3$ being unknown.
[g]In kJ/mol, *apparent* V_2 values.

4-fluoroanisole, suggest a $\sin^2\theta$ dependence, eq. [6]:

[5] $^6J(C,F)/Hz = -70.23 + 0.439\,\delta(C\text{-}4) \qquad r = 0.999$

[6] $\rho(C\text{-}4) = 5.871 - 0.01036\sin^2\theta$

^6J(C,F) and δ(C-4) therefore go as $\sin^2\theta$.[3]

The selenides and tellurides

The conjugative interactions tending to decrease the angle θ are clearly weaker in the sulfides than in the ethers. Intuitively the strength of such interactions should fall off as O > S > Se > Te, partly because of the increase in the C_{sp^2}—X bond length, but also because of the increasing mismatch in the energies of the relevant orbitals for the heavier chalcogens.

^5J(C,C) in thioanisole and its derivatives has a $\sin^2\theta$ dependence (35). Were $^5J_{90}$(C,C) available, $\langle\sin^2\theta\rangle$ would follow for the selenides and tellurides in Table 1. The synthesis of the appropriate 2,6-disubstituted derivatives has not been achieved and hence $^5J_{90}$(C,C) is not available. However, the correlation represented by eq. [6] suggests the following procedure. δ(C-4) for the alkyl phenyl sulfides (19) is written as eq. [7], where 128.5 is the ^{13}C chemical shift of benzene (26). For thioanisole in solution, $\langle\cos^2\theta\rangle$ is 0.74 (37), yielding A as 5.4_1. In 4-fluorothioansole, of course, $\langle\cos^2\theta\rangle$ will be smaller than in thioanisole because of the π electron donation by the fluorine substituent. Equation [7] and the δ(C-4) of 128.1 ppm for *tert*-butyl phenyl sulfide yield $\langle\cos^2\theta\rangle$ as 0.074 and imply (Table 2) that the barrier in this compound is little different from that of the 4-fluorophenyl derivative. This conclusion is sensible in that the $p\ldots\pi$ conjugation in the former is already almost completely broken; the fluorine substituent will therefore have only a slight influence. The apparent V_2 values for the alkyl phenyl sulfides and their 4-fluorophenyl derivatives are entered in Table 3. Those for the latter are based on ^6J(C,F), while those for the former are based on the value for thioanisole (37) derived from ^6J(H,C) and the δ(C-4) values (19) using eq. [7].

[7] $\delta(C\text{-}4) = 128.5 - A\langle\cos^2\theta\rangle$

Turning to the selenides, it is striking that δ(C-4) is the same in 4-*tert*-butyl phenyl selenide (26) as in the corresponding sulfide (19). Therefore eq. [7] is appropriate for the selenides, and their chemical shifts (26) then yield the $\langle\sin^2\theta\rangle$ values in Table 3. The apparent V_2 values seem reasonable by comparison with the sulfides. It follows that $^5J_{90}$(C,C) is 0.62 ± 0.03 Hz for the selenides as compared to 0.91 Hz determined for $^5J_{90}$(C,C) in the sulfides. A smaller number is expected for the selenides because of the smaller σ–π interactions anticipated for the Se—C bond.

For the tellurides, in which R = CH_3, CH_2CH_3, and $CH(CH_3)_2$, δ(C-4) is larger (49) than for the corresponding selenides, indicating less $p\ldots\pi$ conjugation for tellurium. A rough correlation exists between δ(C-4) for these two series (r = 0.979, significant at the 85% confidence level) and gives an estimate of 127.9 for *tert*-butyl phenyl telluride, which has not been made. Now, if eq. [7] holds, then the $\langle\sin^2\theta\rangle$ values in Table 3 follow and imply that the most stable conformation has θ as 90° for all R. It also follows that $^5J_{90}$(C,C) for the tellurides is 0.50 ± 0.02 Hz, as derived from the $\langle\sin^2\theta\rangle$ values and ^5J(C,C) in Table 1. Thus $^5J_{90}$(C,C) is smaller for the tellurides than for the selenides.

Table 3 also contains estimates of arcsin $\langle\sin^2\theta\rangle^{\frac{1}{2}}$. These numbers are not strictly comparable with estimates of θ obtained by other methods. Nevertheless, it is noted that the present value of 42° for methyl phenyl selenide is close to the 40 ± 5° obtained for the 4-chlorophenyl derivative in solution in a liquid crystal (23) and the 40 ± 13° determined in the gas phase by electron diffraction methods (24). A photoelectron pattern for methyl phenyl telluride has θ as near 60° (31), whereas arcsin $\langle\sin^2\theta\rangle^{1/2}$ in Table 3 is 53°.

^{3}J(C,C) and ^{4}J(C,C) in the selenides and tellurides

Vicinal coupling constants often obey a Karplus equation (50), $^3J = A + B\cos\theta + C\cos 2\theta$, equivalent to $^3J = C + D\sin^2\theta + E\sin^2(\theta/2)$. For evenfolded barriers, $\langle\sin^2(\theta/2)\rangle$ is 0.5. The $\langle\sin^2\theta\rangle$ values in Table 3 and the ^3J(C,C) values in Table 1 yield $^3J(C,C)/Hz = -4.2\sin^2\theta + 4.1$ for the selenides and $^3J(C,C)/Hz = -3.9\sin^2\theta + 3.9$ for the tellurides, to be regarded as indicative only, of course. If the indicated signs of ^4J(C,C) in Table 1 for the selenium compounds are correct, then $^4J(C,C)/Hz = -1.49\sin^2\theta + 0.75$; the reliability of this formulation cannot be judged at present. ^4J(C,C) for the tellurides was not observed.

Acknowledgement

We are grateful to the Natural Sciences and Engineering Research Council of Canada for financial assistance, and to a referee for valuable criticism.

[3]A relationship between δ(C-4) and $\sin^2\theta$ has previously been assumed for some alkyl phenyl ketones (45).

Can. J. Chem. Downloaded from www.nrcresearchpress.com by 112.217.228.212 on 09/07/12
For personal use only.

1. T. A. WILDMAN. Ph.D. thesis. University of Manitoba, Winnipeg Man. 1982.
2. T. SCHAEFER and G. H. PENNER. J. Mol. Struct. (Theochem), **152**, 179 (1987).
3. M. KLESSINGER and A. ZYWIETZ. J. Mol. Struct. (Theochem), **90**, 341 (1982).
4. H. KONSCHIN. J. Mol. Struct. (Theochem), **105**, 213 (1983).
5. M. ONDA, A. TODA, S. MORI, and I. YAMAGUCHI. J. Mol. Struct. **144**, 47 (1986).
6. D. G. LISTER. J. Mol. Struct. **68**, 33 (1980).
7. H. DODZIUK, H. V. VOITHENBERG, and N. L. ALLINGER. Tetrahedron, **38**, 2811 (1982).
8. G. ALLEN and S. FEWSTER. *In* Internal rotation in molecules. *Edited by* W. J. Orville-Thomas. J. Wiley and Sons, New York. 1974. p. 275.
9. H. TYLLI and H. KONSCHIN. J. Mol. Struct. **42**, 7 (1977).
10. T. SCHAEFER, R. LAATIKAINEN, T. A. WILDMAN, J. PEELING, G. H. PENNER, J. BALEJA, and K. MARAT. Can. J. Chem. **62**, 1592 (1984).
11. H. M. SEIP and R. SEIP. Acta Chem. Scand. **27**, 4024 (1973).
12. M. KLESSINGER and P. RADEMACHER. Angew. Chem. **91**, 885 (1979).
13. G. M. ANDERSON, P. A. KOLLMAN, L. N. DOMELSMITH, and K. N. HOUK. J. Am. Chem. Soc. **101**, 2344 (1979).
14. H. FRIEGE and M. KLESSINGER. Chem. Ber. **112**, 1614 (1979).
15. A. R. KATRITZKY, R. F. PINZELLI, and R. D. Topsom. Tetrahedron, **28**, 3441 (1972).
16. L. B. KRIVDIN, G. A. KALABIN, and B. A. TROFIMOV. Izv. Akad. Nauk, Ser. Khim. 570 (1982).
17. A. MOHRAZ, W. JIAN-QI, E. HEILBRONNER, A. SOLLADIE-CAVALLO, and F. MATLOUBI-MOGHADAM. Helv. Chim. Acta, **64**, 97 (1981).
18. P. S. DEWAR, E. ERNSTBRUNNER, J. R. GILMORE, M. GODFREY, and J. M. MELLOR. Tetrahedron, **30**, 2455 (1974).
19. V. M. BZHEZOVSKII, G. A. KALABIN, I. A. ALIEV, V. I. DONSKIKH, and B. A. TROFIMOV. Izv. Akad, Nauk SSR, Ser. Khim. 1525 (1981).
20. M. J. ARONEY, W. P. MCPHERSON, and R. K. PIERENS. J. Mol. Struct. **69**, 289 (1980).
21. V. M. BZHEZOVSKII, V. A. PESTUNOVICH, G. A. KALABIN, I. A. ALIEV, B. A. TROFIMOV, I. D. KALIKHMAN, M. A. SHAKHGELDIEV, A. N. KULIEV, and M. G. VORONKOV. Izv. Akad. Nauk SSSR, Ser. Khim. 2004 (1976).
22. G. V. RATOVSKII, A. M. PANOV, V. I. GLUKHIKH, G. A. KALABIN, V. I. DMITRIEV, and I. A. ALIEV. Zh. Obshch. Khim. **51**, 1504 (1981).
23. A. G. AVENT, J. W. EMSLEY, M. LONGERI, S. G. MURRAY, and P. N. NICHOLSON. J. Chem. Soc. Perkin Trans. 2, 487 (1986).
24. N. M. ZARIPOV, A. V. GOLUBINSKII, G. A. CHMUTOVA, and L. V. VILKOV. Zh. Strukt. Khim. **19**, 894 1978).
25. A. N. VERESHCHAGIN, G. A. CHMUTOVA, G. YA. CHERYUKANOVA, and E. G. KATAEV. Izv. Akad. Nauk SSSR, Ser. Khim. 1244 (1973).
26. V. M. BZHEZOVSKII, G. A. KALABIN, G. A. CHMUTOVA, and B. A. TROFIMOV. Izv. Akad. Nauk SSR, Ser. Khim. 586 (1977).
27. G. A. KALABIN, D. F. KUSHNAREV, V. M. BZESOVSKY, and G. A. TSCHMUTOVA. Org. Magn. Reson. **12**, 598 (1979).
28. A. D. BAKER, G. H. ARMEN, and Y. GUANG-DI. J. Org. Chem. **46**, 4127 (1981).
29. H. LUMBROSO, CH. LIEGÓIS, N. DEREU, L. CHRISTIAENS, and A. LUXEN. J. Mol. Struct. **67**, 251 (1980).
30. G. LLABRÉS, M. BAIWIR, L. CHRISTIAENS, J. DENOEL, L. LAITEM, and J.-L. PIETTE. Can. J. Chem. **56**, 2008 (1978).
31. G. TSCHMUTOWA and H. BOCK. Z. Naturforsch. B: Anorg. Chem. Org. Chem. **31**, 1611 (1976).
32. V. N. IPATIEFF, H. PINES, and B. S. FRIEDMAN. J. Am. Chem. Soc. **60**, 2731 (1938).
33. W. J. HEHRE, L. RADOM, P. V. R. SCHLEYER, and J. A. POPLE. Ab initio molecular orbital theory. J. Wiley and Sons, New York. 1986.
34. J. S. BINKLEY, M. J. FRISCH, D. J. DEFREES, K. RAHGAVACHARI, R. A. WHITESIDE, H. B. SCHLEGEL, E. M. FLUDER, and J. A. POPLE. Department of Chemistry, Carnegie–Mellon University, Pittsburgh, PA.
35. G. H. PENNER. Ph.D thesis. University of Manitoba, Winnipeg, Man. 1987.
36. T. SCHAEFER, J. PEELING, G. H. PENNER, A. LEMIRE, and R. SEBASTIAN. Can. J. Chem. **63**, 24 (1985).
37. T. SCHAEFER and J. D. BALEJA. Can. J. Chem. **64**, 1376 (1986).
38. T. SCHAEFER, J. PEELING, and G. H. PENNER. Can. J. Chem. **64**, 2162 (1986).
39. M. W. WIECZOREK. Acta Crystallogr. Sect. B: Struct. Crystallogr. Cryst. Chem. **36**, 1515 (1980).
40. W. J. E. PARR and T. SCHAEFER. Acc. Chem. Res. **13**, 400 (1980).
41. D. R. EATON, A. D. JOSEY, R. E. BENSON, W. D. PHILLIPS, and T. L. CAIRNS. J. Am. Chem. Soc. **84**, 4100 (1962).
42. D. J. BLEARS, S. S. DANYLUK, and T. SCHAEFER. J. Chem. Phys. **47**, 5037 (1967).
43. J. R. BOLTON. *In* Radical ions. *Edited by* E. T. Kaiser and L. Kevan. Interscience, New York. 1968, pp. 9–26.
44. R. A. BERNHEIM and T. P. DAS. J. Chem. Phys. **33**, 1813 (1960).
45. K. S. DHAMI and J. B. STOTHERS. Tetrahedron Lett. 631 (1964).
46. T. SCHAEFER and R. SEBASTIAN. J. Magn. Reson. **73**, 541 (1987).
47. J. P. MAHER and D. F. EVANS. Proc. Chem. Soc. London, 208 (1961).
48. R. FREEMAN. J. Chem. Phys. **43**, 3087 (1965); A. D. BUCKINGHAM and K. A. MCLAUCHLAN. Proc. Chem. Soc. London, 144 (1963).
49. V. V. BAIROV, G. A. KALABIN, M. L. ALPERT, V. M. BZHEZOVSKII, I. D. SADEKOV, B. A. TROFIMOV, and V. I. MINKIN. Zh. Org. Khim. **14**, 622 (1978).
50. M. KARPLUS. J. Am. Chem. Soc. **85**, 2870 (1965).

Can. J. Chem. Downloaded from www.nrcresearchpress.com by 112.217.228.212 on 09/07/12
For personal use only.

Remarks on the internal motion in diphenyl ether. Fluorophenyl ethers

TED SCHAEFER, GLENN H. PENNER, CRAIG TAKEUCHI, AND POTLAKI TSEKI
Department of Chemistry, University of Manitoba, Winnipeg, Man., Canada R3T 2N2

Received January 13, 1988

TED SCHAEFER, GLENN H. PENNER, CRAIG TAKEUCHI, and POTLAKI TSEKI. Can. J. Chem. **66**, 1647 (1988).

The ^{13}C nuclear magnetic resonance chemical shifts and the $^{13}C,^{19}F$ spin–spin coupling constants are reported for 4,4′-difluorophenyl ether and 4-fluorophenyl phenyl ether in CS_2 and in acetone-d_6 solutions. An estimate of $^6J_{90}$, the extremum in the $\sigma-\pi$ coupling constant between the ^{19}F nucleus on one ring and the *ipso* ^{13}C nucleus on the other, is obtained from measurements on 2,6-dibromo-4-fluorophenyl phenyl ether. The ensuing estimates of $\langle\sin^2\theta\rangle$, the expectation values of $\sin^2\theta$ as obtained from $^6J(^{13}C,^{19}F)$, are compared with those obtained from STO-3G MO computations for diphenyl ether and its 4-fluoro derivatives. These computations give conformational energies at 30° intervals of the angles of twist about the two C—O bonds. In rough agreement with C-INDO computations, interconversion of the helical forms is calculated to occur most easily by the so-called one-ring flip mechanism; the barrier to interconversion is less than 1 kJ/mol in the ether and its 4-fluoro derivatives. It appears that the conformational behaviour of these derivatives is unaltered by passage from CS_2 to acetone solutions at 300 K. Furthermore, $\langle\sin^2\theta\rangle$ values from $^6J(^{13}C,^{19}F)$ in solution are very similar to those obtained from the computations on the free molecules. If this agreement is not accidental, then it may arise from a high degree of flexibility of the molecules in which, by a disrotatory or one-ring flip mechanism requiring a very low energy of activation, one helical or C_2 conformation can be converted to another. The other conformations have considerably higher energies and the solvents do not appear to lower these energies enough to favor their populations significantly at 300 K.

TED SCHAEFER, GLENN H. PENNER, CRAIG TAKEUCHI et POTLAKI TSEKI. Can. J. Chem. **66**, 1647 (1988).

Opérant en solutions dans le CS_2 ainsi que dans l'acétone-d_6, on a mesuré les déplacements chimiques en résonance magnétique nucléaire du ^{13}C ainsi que les constantes de couplage spin–spin $^{13}C,^{19}F$ de l'éther bis(difluoro-4,4′ phénylique) et de l'éther difluoro-4,4′ phényl phénylique. Utilisant des mesures effectuées sur l'éther dibromo-2,6 fluoro-4 phényl phénylique, on a évalué la constante $^6J_{90}$, l'extrême de la constante de couplage $\sigma-\pi$ entre le noyau de ^{19}F d'un cycle et le noyau ^{13}C *ipso* de l'autre. On a comparé les évaluations de $\langle\sin^2\theta\rangle$, les valeurs attendues pour $\sin^2\theta$ telles qu'obtenues à partir des constantes $^6J(^{13}C,^{19}F)$, avec celles obtenues à partir de calculs d'OM STO-3G effectués sur l'éther diphénylique ainsi que sur ses dérivés fluoro-4. Ces calculs conduisent à des énergies conformationnelles qui ont été évaluées à tous les 30° d'angle de torsion autour des deux liaisons C—O. En accord avec les résultats de calculs C-INDO, on a calculé que l'interconversion des formes hélicoïdales se produit principalement par le biais d'une mécanisme appelé inversion d'un cycle; dans le cas de l'ether et de ses dérivés fluoro-4, la barrière à l'interconversion est inférieure à 1 kJ/mol. Il semble que le comportement conformationnel de ces dérivés ne varie pas lorsque, à 300 K, on passe de solutions dans le CS_2 à des solutions dans l'acétone. De plus, les valeurs de $\langle\sin^2\theta\rangle$, obtenues à partir des constantes $^6J(^{13}C,^{19}F)$ en solution, ressemblent beaucoup à celles obtenues à partir de calculs sur des molécules libres. Si cet accord n'est pas accidentel, il pourrait alors découler d'un degré élevé de flexibilité des molécules qui, par un mécanisme disrotatoire ou un par un mécanisme d'inversion de cycle n'impliquant qu'une faible énergie d'activation, permettrait des conversions rapides entre les conformations hélicoïdales et C_2. Les énergies des autres conformations sont beaucoup plus élevées et les solvants ne semblent pas les abaisser suffisamment pour que, à 300 K, leurs populations soient importantes.

[Traduit par la revue]

Introduction

With some exceptions, a variety of experimental and theoretical approaches to the internal dynamics in diphenyl ether suggest that the molecule adopts a helical conformation in which ϕ_1 and ϕ_2 lie in the vicinity of 25–50°. These approaches have recently been reviewed (1, 2), so that a detailed recapitulation is not necessary here. The potential surface described by ϕ_1 and ϕ_2 is not available experimentally, although ^{13}C nmr spin-lattice relaxation times for a chloroform solution have been interpreted to mean that the barrier to internal rotation is 10.2 kJ/mol for the phenyl groups (2). This number is similar to the 10 kJ/mol estimated for the enthalpy of activation from dielectric relaxation studies on diphenyl ether dispersed in a polystyrene matrix (3). *Ab initio* computations of this surface seem not to be available. The semiempirical C-INDO method (4) appears to overcome the defects of the usual CNDO–INDO approaches to internal barriers in conjugated systems. Its recent application to diphenyl ether gave energies at 30° intervals for both ϕ_1 and ϕ_2 (1). So-called standard structural parameters were used in these calculations and a fixed C—O—C angle of 123° was assumed (1). The ensuing energy contours implied that **2** and not **3** was

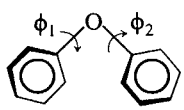

1

$\phi_1 = \phi_2 = 0°$
when phenyl groups are in the COC plane.

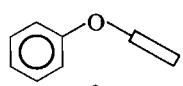

$\phi_1 = 0°$
$\phi_2 = 90°$ **2**

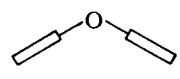

$\phi_1 = \phi_2 = 90°$ **3**

the transition state for interconversion of the helical forms **1**, the highest stability being calculated for $\phi_1 = \phi_2 = 35°$. Conformation **2** is reached by a disrotatory mechanism, the so-called one-ring flip (5, 6), while **3** is attained by a conrotatory mechanism or two-ring flip. A planar transition state would have a very high energy because of repulsive forces between *ortho* C—H bonds on neighbouring rings.

The C-INDO results indicated that **2** is only 1.4 kJ/mol less stable than **1**. In other words, the helical enantiomers can interconvert rather freely at ambient temperatures. Conformation **3** was computed as 8.0 kJ/mol less stable than **1**.

In Table 1 the computed STO-3G MO energies are presented. In our opinion this method of presentation is more easily com-

Can. J. Chem. Downloaded from www.nrcresearchpress.com by 61.7.252.67 on 09/07/12
For personal use only.

TABLE 1. The conformational energies in kJ/mol relative to $\phi_1 = \phi_2 = 45°$ for diphenyl ether from partially geometry-optimized STO-3G MO conputations[a]

	Computed STO-3G MO energies (kJ/mol)						
ϕ_2	ϕ_1:0	30	60	90	120	150	180
0	42.08[b]	26.14	4.38	0.69[c]	4.38	26.14	42.08
30	26.14	3.95[b]	0.12[c]	4.77	19.57	37.35	26.14
60	4.38	0.12[c]	4.60[d]	10.63	22.36	19.57	4.38
90	0.69[c]	4.77	10.63	11.30[d]	10.63	4.77	0.69[c]
120	4.38	19.57	22.36	10.63	4.60[d]	0.12[c]	4.38
150	26.14	37.35	19.57	4.77	0.12[c]	3.95[b]	26.14
180	42.08	26.14	4.38	0.69[c]	4.38	26.14	42.08[b]

[a]See structure **1** for definitions of the angle ϕ. If the COC plane lies in the plane of the page, then, as ϕ_1 and ϕ_2 increase somewhat from zero, the proximate *ortho* C—H bonds of the two rings have moved so that one lies above (ϕ_2), and one below (ϕ_1), the COC plane.

[b]The pathway for the high-energy, so-called zero-ring flip beginning at $\phi_1 = \phi_2 = 45°$.

[c]The pathway for the low-energy, so-called one-ring flip beginning at $\phi_1 = \phi_2 = 45°$ and having a barrier of 0.69 kJ/mol for interconversion.

[d]The pathway for the intermediate-energy, so-called two-ring flip having a barrier of 11.3 kJ/mol for interconversion.

prehended quantitatively than a contour diagram. The numbers were obtained by a geometry-optimization procedure in which all bond angles and lengths were allowed to vary, except that the carbon frameworks of the phenyl groups were constrained to remain as regular hexagons. At $\phi_1 = \phi_2 = 45°$, the energy is 42.08 kJ/mol lower than that of the planar form **1**. In qualitative agreement with the C-INDO computations, the $\phi_1 = 0°$, $\phi_2 = 90°$ conformer is found to be the transition state, calculated as only 0.7 kJ/mol above the minimum. The activation energy for interconversion via **3** is computed to be 11.3 kJ/mol, while that via the planar form is 42.1 kJ/mol. The one-ring flip is strongly favored over the two-ring flip mechanism for interconversion. Figure 1 gives the STO-3G MO structure at $\phi_1 = \phi_2 = 45°$.

No gas-phase experimental determinations of the conformational properties of diphenyl ether appear to be available. The C-INDO (1) and STO-3G MO computations both imply large amplitude motions about the C—O bonds at ambient temperatures. Apparently such motions are carried over into the liquid state, diphenyl ether displaying very short intramolecular dielectric relaxation times (3, 7); these are rather insensitive to the viscosity of the solution (8). Vibrational spectra in the solid and liquid phases are consistent with a helical (C_2) structure of diphenyl ether (1). The optical anisotropy (9) and the Kerr constant (10) of diphenyl ether are consistent with $\phi_1 = \phi_2 = 34–37°$. The large amplitudes of internal motion in diphenyl ether, indicated by the calculations and by the very short dielectric relaxation times, imply rather weak conjugation in this molecule (1). This suggestion is borne out by the ^{13}C chemical shifts of the *para* carbon-13 nuclei, which are sensitive to π electron density at the *para* site. The observed shifts (11, 12) imply an electron density much smaller than that in phenol or anisole and rather similar to that in fluorobenzene. In other words, the mobile bond order in the C—O bonds of diphenyl ether is much smaller than in phenol, leading to greater internal motional freedom.

Because of the paucity of experimental data on the internal motion in diphenyl ether, it seems worthwhile to add to these data. One conformational indicator, an angle dependent long-range nuclear spin–spin coupling constant, has not yet been used for diphenyl ether or its derivatives. By analogy to anisole

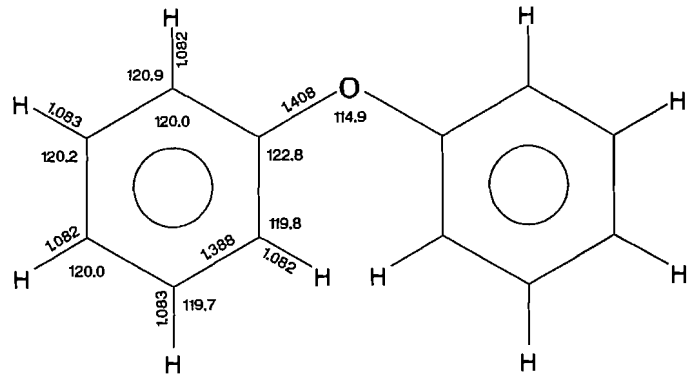

FIG. 1. The bond lengths and angles are given for the STO-3G MO structure of diphenyl ether at $\phi_1 = \phi_2 = 45°$ (see **1** in text). The geometry optimization procedure constrained the carbon skeletons of the phenyl groups to regular hexagons. This computed structure can serve as a basis for future computations with larger basis sets and for comparison with as yet unperformed experimental work on the structure of the free molecule. The COC angle seems particularly small in view of the 123° assumed in the C-INDO computations (1) and the values near 120° found from X-ray diffraction results (25, 26).

and its derivatives (13), a useful coupling constant would be $^6J_p(^1H,^{13}C) \equiv {}^6J(H,C)$ in diphenyl ether. This coupling constant is expected to be mediated by a $\sigma-\pi$ mechanism and to be proportional to $\sin^2\theta$ (see **4**). Its reliable measurement would

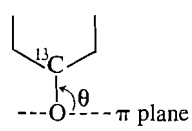

4

require ^{13}C enrichment at the C-1 site and the latter is beyond our resources. However, the corresponding $^6J(^{13}C, ^{19}F) \equiv {}^6J$ is also dependent on $\sin^2\theta$ in a variety of molecules, such as 4-fluoroanisole (13), 4-fluoroethylbenzene (14), and 4-fluorobiphenyl (15). In 4-fluorodiphenyl ether, for example, a fairly rigid planar conformation would then display a ^6J very near zero, while a rigid **3** should have the maximum coupling

Can. J. Chem. Downloaded from www.nrcresearchpress.com by 61.7.252.67 on 09/07/12
For personal use only.

TABLE 2. The ^{13}C nmr chemical shifts and $^{n}J(^{13}C,^{19}F)$ in Hz for some fluorophenyl ethers at 300 K

Parameter	4,4′-diF		4-F		2,6-diBr-4-F
δ_1	153.85[a]	154.33[b]	151.64[a]	154.46[b,d]	—
δ_2	120.16	120.80	116.44	116.89	119.45
δ_3	116.45	117.00	116.09	116.27	121.29
δ_4	159.16	159.46	157.65	159.61	160.08
$\delta_{4'}$	159.16	159.46	119.11	119.53	123.49
$\delta_{3'}$	116.45	117.00	129.86	130.68	130.68
$\delta_{2'}$	120.16	120.80	118.56	119.04	115.74
$\delta_{1'}$	153.85	154.33	157.98	158.55	157.50
^1J	−242.90[c]	−240.05	−239.3	−239.9	−250.79
^2J	23.27	23.51	23.18	23.06	25.90
^3J	8.02	8.37	7.78	7.92	10.99
^4J	2.63	2.49	2.31	1.98	—
^6J	0.57	0.57	0.61	0.62	1.25

[a]For a 10 mol% solution in CS_2, containing also 10 mol% C_6D_{12} and 0.5 mol% TMS.
[b]For a 10 mol% solution in acetone-d_6, containing 0.5 mol% TMS.
[c]The $^{13}C,^{19}F$ coupling constants are reproducible to within ±0.02 Hz.
[d]For 10 mol% solutions in CS_2(acetone-d_6) solutions, δ_1, δ_2, δ_3, and δ_4 for diphenyl ether are 157.31 (157.97), 118.86 (119.36), 129.55 (130.44). and 122.98 (123.87), respectively.

constant because $\sin^2\theta$ is near unity. At $\phi_1 = \phi_2 = 45°$, $\sin^2\theta$ is 0.5. If the maximum value of ^6J (that is, $^6J_{90}$) can be ascertained, then the measurement of ^6J in 4-fluorophenyl phenyl ether and in 4-fluorophenyl ether may well provide conformational insight.[1]

The presence of fluorine substituents can, in principle, alter the internal dynamics of the ether. Because fluorine is a weak π electron donor, it might be expected that the mobile bond orders at the C—O bonds will decrease further and hence that the internal motional freedom will increase beyond that in diphenyl ether itself. However, such an increase may be small because the conjugational extent in diphenyl ether is already rather small and because fluorine is not a strong donor. The variation of ^6J between the 4-fluorophenyl phenyl ether and the 4-fluorophenyl ether will proably indicate such conformational perturbations. The polarity of the solvent may alter the conformational equilibria.

Experimental

Diphenyl ether and 4-fluorophenyl ether came from Aldrich. The 2,6-dibromo-4-fluorophenyl phenyl ether was prepared as follows (16). A mixture of 4 g of diphenyl iodonium bromide (Aldrich), 0.44 g of NaOH, 60 mL of H_2O, and 2,6-dibromo-4-fluorophenol (Aldrich) was heated under reflux for 24 h. The extracted (ether) solution was washed with aqueous NaOH, dried with $MgSO_4$, and evaporated to yield a mixture of the desired product and iodobenzene (^1H nmr spectrum). The mixture was left open to the air for 3 days, after which a slightly yellow crystalline solid remained. It gave the correct molecular mass peak and a satisfactory ^1H nmr spectrum. The 4-fluorophenyl phenyl ether was prepared in a similar fashion.

The compounds were dissolved in acetone-d_6 or in a CS_2/C_6D_{12} solvent mixture to form approximately 10 mol% solutions. These were transferred to 5 mm od nmr sample tubes and were degassed by several freeze–pump–thaw cycles before flame sealing.

The ^{13}C nmr spectra were accumulated on a Bruker AM-300 FFT spectrometer at a probe temperature of 300 K by methods described previously (17).

[1]Note that it is the twist angle, ϕ, about the C—O bond belonging to the ring containing the fluorine nucleus, that defines the θ in $\sin^2\theta$. Thus, in 4-fluorophenyl phenyl ether, $\sin^2\theta$ is independent of the angle of twist about the C—O bond belonging to the phenyl group.

The STO-3G MO computations (18) utilized the computer program GAUSSIAN 82 (19) and were performed on an Amdahl 5870.

Results and discussion

Table 2 presents the ^{13}C nmr chemical shifts for diphenyl ether and three of its derivatives. For the latter, the $^{13}C,^{19}F$ spin–spin coupling constants are also given.

$^6J(^{13}C,^{19}F) \equiv {}^6J$ and $\langle\sin^2\theta\rangle$

In 2,6-dibromo-4-fluorophenyl phenyl ether, ^6J is 1.25(2) Hz (Table 2). This coupling constant arises from a $\sigma-\pi$ mechanism, going as $\sin^2\theta$, and is analogous to ^6J in 4-fluoroanisole (13). In the latter, two bromine substituents placed *ortho* to the methoxy group provide a measure of $^6J_{90}$. Now, in the diphenyl ether derivative above, both conformations **2** and **3** have θ as 90° if, in **2**, ϕ_2 defines the angle by which the $C_6H_2Br_2F$ group is rotated out of the COC plane (see **1**). In view of the computations for diphenyl ether, it appears sensible that this compound has its most stable conformation as **2**, in which the phenyl group lies in a plane perpendicular to the plane of the other, heavily substituted, phenyl group. Torsion about its own C—O bond by this phenyl group, that is, movement towards conformation **3**, does not cause θ to deviate from 90°. However, torsion about the other C—O bond decreases the value of θ. How large this reduction is, on average, is unknown. In the *ortho* dichloro and dibromo derivatives of anisole, the $\sigma-\pi$ couplings, $^6J(^1H,^{13}C)$, are very nearly equal (13), implying an average very near 90° at 300 K. Noting that the planar form of anisole, with θ as 0°, is very stable (13), it seems a reasonable surmise that $^6J_{90}$ in the phenyl ethers is very near 1.25 Hz.

It is also of interest that, in the crystal, 2-(3′-methyl-4′-nitrophenoxy)-1,3-diisopropylbenzene has a conformation analogous to **2** with θ being about 80° for the phenyl group bearing the isopropyl substituents (20), the latter having the methine C—H bonds pointing in the direction of the ether oxygen atom. Furthermore, rotation about the C—O bond of the isopropyl-substituted ring apparently has a free energy of activation at 203 K of 44.8 kJ/mol (21).

These data are consistent with the arguments above for the low-energy conformer as **2** in the dibromofluorophenyl phenyl

Can. J. Chem. Downloaded from www.nrcresearchpress.com by 61.7.252.67 on 09/07/12
For personal use only.

ether. In summary, torsion of the phenyl group about its own C—O axis to produce **3** is hindered by conjugational interactions of about 11 kJ/mol (Table 1), while torsion about the other C—O is opposed by steric repulsions between *ortho* C—H and C—Br bonds of the two phenyl groups. $^6J_{90}$ will be assumed to be 1.25(2) Hz (even a θ of 80° has $\sin^2\theta$ as 0.97).

On this assumption, the ^6J of 0.57(2) Hz in 4,4′-difluorophenyl ether in CS_2, as well as in acetone-d_6, solution implies a $\langle\sin^2\theta\rangle$ of 0.46 ± 0.02 at 300 K. At this temperature, the energies given in Table 1 for biphenyl yield $\langle\sin^2\theta\rangle$ as 0.49. Repetition of the STO-3G MO calculations for the same grid of θ values, but now for the difluorophenyl ether, yields a very similar set of conformational energies. The conformation with $\phi_1 = \phi_2 = 45°$ is now 42.8$_5$ kJ/mol more stable than the planar molecule, and the one-ring flip mechanism has a barrier of 0.9 kJ/mol. The expectation value of $\sin^2\theta$ is calculated as 0.50 at 300 K. The experimental results imply that the polar solvent, acetone-d_6, has not altered the conformational behaviour displayed in the nonpolar solvent, CS_2. Furthermore, these results are consistent with very small solvent effect on the conformational properties of the difluorophenyl ether, assuming that the STO-3G MO energies are reliable. Alternatively, the reasonable agreement between computation and experiment may be accidental.

Turning to 4-fluorophenyl phenyl ether, ^6J is 0.62(2) Hz in both solvent systems (Table 2), corresponding to a $\langle\sin^2\theta\rangle$ of 0.50 ± 0.02 at 300 K.

The STO-3G MO optimizations on this molecule have the barrier to interconversion by the one-ring flip mechanism as 0.6 kJ/mol, implying slightly larger torsion angles in the most stable conformation than in diphenyl ether or in 4,4′-difluorophenyl ether. The averaging procedure appropriate to the estimation of ^6J(C,F), which depends on rotations about only one C—O bond, yields the relevant $\langle\sin^2\theta\rangle$ as 0.494 at 300 K. Again, the computations for the free molecule agree with the experimental test in CS_2 and in acetone solutions.

The ^{13}C nmr chemical shifts

The solvent dependence of the ^{13}C nuclear screening for the fluorine derivatives of diphenyl ether is shared by the parent compound (footnote to Table 2). In view of the previous discussion, it is therefore reasonable that the decreased screening in the more polar solvent is attributable to a general solvent effect and not to conformational changes (the solvent dependence of ^nJ(C,F), $n = 1$–4, is reminiscent of that for ^3J(H,F) and ^4J(H,F) in other fluorobenzene derivatives (22); ^6J(C,F), in contrast, is solvent independent).

For a given solvent, the ^{13}C nmr chemical shifts of the unsubstituted phenyl groups in 4-fluorophenyl phenyl ether and in the bromine derivative are of some interest. Relative to diphenyl ether, $\delta_{4'}$ in the 4-fluorophenyl phenyl ether indicates a decreased screening of near 4 ppm, whereas the screening variations of the other ^{13}C nuclei in the phenyl moiety are very much smaller. It is commonly assumed that the nuclear screening at the *para* position is dominated by π electron (resonance) effects in benzene derivatives. Comparison of the chemical shifts for the 4,4′-difluorophenyl ether with those for the monofluoro compound suggests that the influence of the 4-fluoro substituent nine bonds removed in the latter arises mainly from a relay effect and not by a transfer of electron density between the two benzene rings. This suggestion was originally made on the basis of ^{19}F nmr chemical shifts (23).

The shielding of the ^{13}C nuclei in the phenyl group of 2,6-dibromo-4-fluorophenyl phenyl ether is consistent ($\delta_{4'}$ and $\delta_{1'}$) with somewhat increased electron donation from the oxygen atom, as expected for the conformation discussed above. The increase in shielding of nearly 4 ppm at C-2 and C-6 in the unsubstituted phenyl group has a precedent in 2,3,5,6-tetrachlorophenyl phenyl ether (12) and a similar deshielding occurs in 2,6-dimethylphenyl phenyl ether (24). These shift perturbations are intriguing because they are not understood.

Acknowledgments

We are grateful to the Natural Sciences and Engineering Research Council of Canada for financial assistance and to the referees for helpful criticism.

1. I. Baraldi, E. Gallinella, and F. Momicchioli. J. Chim. Phys. **83**, 653 (1986).
2. P. Dais. Magn. Reson. Chem. **25**, 141 (1987).
3. J. Chao, M. A. Desando, D. L. Gourlay, D. E. Orr, and S. Walker. J. Phys. Chem. **88**, 711 (1984).
4. F. Momicchioli, I. Baraldi, and M. C. Bruni. Chem. Phys. **70**, 161 (1982).
5. D. Gust and K. Mislow. J. Am. Chem. Soc. **95**, 1535 (1973).
6. D. Pitea and A. Ferrazza. J. Mol. Struct. **92**, 141 (1983).
7. D. M. Roberti, O. F. Kalman, and C. P. Smyth. J. Am. Chem. Soc. **82**, 3523 (1960).
8. C. P. Smyth. *In* Internal rotation in molecules. *Edited by* W. J. Orville-Thomas. Wiley, London. 1974. p. 49.
9. J.-P. Canselier and C. Clement. J. Chim. Phys. **76**, 699 (1979).
10. R. J. W. LeFèvre and J. D. Saxby. J. Chem. Soc. Part B, 1064 (1966).
11. J. B. Stothers. Carbon-13 nmr spectroscopy. Academic Press, New York. 1972. p. 197.
12. U. Edlund and A. Norström. Org. Magn. Reson. **9**, 196 (1977).
13. T. Schaefer, R. Laatikainen, T. A. Wildman, J. Peeling, G. H. Penner, J. Baleja, and K. Marat. Can. J. Chem. **62**, 1592 (1984).
14. T. Schaefer, J. Peeling, G. H. Penner, A. Lemire, and R. Sebastian. Can. J. Chem. **63**, 24 (1985).
15. T. Schaefer, J. Peeling, and G. H. Penner. Can. J. Chem. **64**, 2162 (1986).
16. J. R. Crowder, E. E. Glover, M. F. Grundon, and H. X. Kaempfen. J. Chem. Soc. 4578 (1963).
17. T. Schaefer, J. Peeling, and R. Sebastian. Can. J. Chem. **63**, 3219 (1985).
18. W. J. Hehre, R. F. Stewart, and J. A. Pople. J. Chem. Phys. **51**, 2657 (1969).
19. J. S. Binkley, M. J. Frisch, D. J. DeFrees, K. Raghavachara, R. A. Whiteside, H. B. Schlegel, E. M. Fluder, and J. A. Pople. GAUSSIAN 82. Department of Chemistry, Carnegie–Mellon University, Pittsburgh, PA.
20. E. A. H. Griffith, W. D. Chandler, and B. E. Robertson. Can. J. Chem. **50**, 2963 (1972).
21. J. J. Bergman and W. D. Chandler. Can. J. Chem. **50**, 353 (1972).
22. H. M. Hutton, B. Richardson, and T. Schaefer. Can. J. Chem. **45**, 1165 (1967).
23. I. R. Ager, L. Phillips, and S. J. Roberts. J. Chem. Soc. Perkin Trans. 2, 1988 (1972).
24. G. W. Buchanan, F. Montaudo, and P. Finocchiaro. Can. J. Chem. **52**, 767 (1974).
25. J. J. Bergman, E. A. H. Griffith, B. E. Robertson, and W. D. Chandler. Can. J. Chem. **51**, 162 (1972).
26. K. Gurtu, W. D. Chandler, and B. E. Robertson. Can. J. Chem. **53**, 2093 (1975).

Can. J. Chem. Downloaded from www.nrcresearchpress.com by 61.7.252.67 on 09/07/12
For personal use only.

Synthesis of a lactosamine-type trisaccharide: 6-(bromoacetamido)-hexyl 2-*O*-(4-*O*-β-D-galactopyranosyl-2- acetamido-2-deoxy-β-D-glucopyranosyl)-α-D-mannopyranoside, designed to affinity label the leukoagglutinin sugar binding site

HÉLÈNE AMMANN AND GILLES DUPUIS

Department of Biochemistry, Faculty of Medicine, University of Sherbrooke, Sherbrooke, P.Q., Canada J1H 5N4

Received December 8, 1987

HÉLÈNE AMMANN and GILLES DUPUIS. Can. J. Chem. **66**, 1651 (1988).

We describe the synthesis of a D-lactosamine-type trisaccharide, 6-(bromoacetamido)hexyl 2-*O*-(4-*O*-β-D-galactopyranosyl-2-acetamido-2-(deoxy-β-D-glucopyranosyl)-α-D-mannopyranoside (**18**), designed for affinity labeling the *Phaseolus vulgaris* leukoagglutinin sugar binding site. The trisaccharide derivative was obtained by condensation of 4-*O*-(2,3,4,6-tetra-*O*-acetyl-β-D-galactopyranosyl)-3,6-di-*O*-acetyl-2-deoxy-2-phthalimido-β-D-glucopyranosyl trichloroacetimidate (**8**) with 6-(*N*-benzyloxycarbonylamino)-hexyl 3,4,6-tri-*O*-benzyl-α-D-mannopyranoside (**13**). Removal of the protecting groups afforded 6-aminohexyl 2-*O*-(4-*O*-β-D-galactopyranosyl-2-acetamido-2-deoxy-β-D-glucopyranosyl)-α-D-mannopyranoside (**17**), which was converted into the corresponding bromoacetamido derivative by reaction with *N*-hydroxysuccinimido bromoacetate.

HÉLÈNE AMMANN et GILLES DUPUIS. Can. J. Chem. **66**, 1651 (1988).

Nous décrivons la synthèse d'un trisaccharide de type D-lactosamine, soit le *N*-bromométhylcarboxyamino-6 hexyl *O*-2-(*O*-4-β-D-galactopyranosyl acétamido-2 désoxy-2 β-D-glucopyranosyl)-α-D-mannopyranoside (**18**) qui est conçu pour marquer le site de reconnaissance des glucides chez la leucoagglutinine de *Phaseolus vulgaris*. Le trisaccharide a été obtenu par condensation du disaccharide trichloroacétimidate de *O*-4-(tétra-*O*-acétyl-2,3,4,6 β-D-galactopyranosyl) di-*O*-acétyl-3,6 désoxy-2 phtalimido-2 β-D-glucopyranosyle (**8**) avec le *N*-benzyloxycarbonylamino-6 hexyl tri-*O*-benzyl-3,4,6 α-D-mannopyranoside (**13**). L'enlèvement des groupements protecteurs a donné l'amino-6 hexyl *O*-2-(*O*-4-β-D-galactopyranosyl acétamido-2 désoxy-2 β-D-glucopyranosyl) α-D-mannopyranoside (**17**) qui a été converti en dérivé *N*-bromoacétamido par réaction avec le bromoacétate de *N*-hydroxysuccinimidyle.

Mammalian glycoproteins can be classified into two major categories according to the nature of the glycosidic bond involved in protein–carbohydrate linkage (1–3). For instance, the "mucin-type" glycoproteins are characterized by the presence of an *O*-glycosidic bond between the carbohydrate chain and serine or threonine residues of the polypeptide backbone. In the case of *N*-linked "serum-" and "surface-type" glycoproteins, the carbohydrate chains are covalently bound to asparagine residues located in the -Asn-X-Ser(Thr)- sequence (4, 5). These glycoproteins can be further divided into "high mannose" type (oligomannosidic type) and the "complex" and "hybrid" types (*N*-acetyl-D-lactosamine type) in accordance with the structure of the carbohydrate moiety.

Previous work by Cummings and Kornfeld (6), Kaifu and Osawa (7), and by Hammarström *et al.* (8) has established that leukoagglutinin, a mitogenic isolectin isolated from *Phaseolus vulgaris* (9), specifically recognizes the minimal trisaccharidic sequence 2-*O*-(4-*O*-β-D-galactopyranosyl-2-acetamido-2-deoxy -β-D-glucopyranosyl)-D-mannopyranose that is found in some *N*-type glycoproteins. The synthesis of this trisaccharide has previously been reported (7, 10). In addition, various saccharide derivatives substituted with a reactive alkyl or acyl chain designed to serve as photoaffinity labeling reagents or to establish covalent bonds with protein carriers have been prepared by a number of investigators (11–25). It was therefore of interest to prepare the trisaccharide **17** modified in a manner that allows its use as an affinity labeling reagent to probe the nature of the sugar binding site of leukoagglutinin.

We report the synthesis of the trisaccharide 2-*O*-(4-*O*-β-D-galactopyranosyl-2-acetamido-2-deoxy-β-D-glucopyranosyl)-α-D-mannopyranosyl derivative, modified at the C-1 position of the mannose moiety with an amino group-bearing side chain, which can be modified further in a number of ways to prepare various derivatives suitable for affinity labeling studies. We show one example of such a modification, by reporting the synthesis of the bromoacetyl derivative of trisaccharide **17**.

Results and discussion

The key intermediate in the synthesis of modified trisaccharide **18** was the known (26) D-lactosamine derivative 4-*O*-(2,3,4,6-tetra-*O*-acetyl-β-D-galactopyranosyl)-3,6-di-*O*-acetyl-2-deoxy-2-phthalimido-D-glucopyranose **7**. Grundler and Schmidt (26) have shown that conversion of **7** into the corresponding trichloroacetimidate **8** and reaction with suitably protected D-galactose derivatives possessing a free hydroxyl group at position C-3 give a high yield of the β-anomer, and it was anticipated that such a scheme could be applied for reaction of **8** with the D-mannose derivative **13**.

Compound **7** was prepared by Grundler and Schmidt (26) by selective deprotection of the C-1 position of *tert*-butyldimethylsilyl-4-*O*-(2,3,4,6-tetra-*O*-acetyl-β-D-galactopyranosyl)-3,6-di-*O*-acetyl-2-deoxy-2-phthalimido-β-D-glucopyranoside. We hypothesized that compound **7** could be obtained by a shorter route using a modification of the procedure described by Arnarp and Lönngren (10). Thus, peracetylated lactal **1** was obtained according to the procedure described by Haworth *et al.* (27), by reaction of 1-bromo peracetylated lactose with zinc in acetic acid. Azidonitration of **1** gave the same ratio of mixed crystalline azidonitrates **2**, **3**, and **4**, as described (10). The mixture was hydrogenated in the presence of a palladium catalyst, at atmospheric pressure. Anomers **5** and **6** (10) were converted into crystalline[1] **7**, by reaction with *N*-carbo-

[1]Compound **7** has been described by Grundler and Schmidt (26) as an amorphous powder. However, we succeeded in obtaining this intermediate as a crystalline product that possessed an ^{1}Hmr spectrum similar to that of the reported compound, except in the case of assignment of the aromatic protons. Grundler and Schmidt (26) reported values of 8.9–8.7 ppm, whereas we observed values of 7.9–7.7 ppm. This discrepancy between our findings and those reported may result from a typographical mistake, since our data are consistent with assignment values (9.7–7.7 ppm) reported by Grundler and Schmidt for other phthalimide derivatives of protected D-lactosamine.

Can. J. Chem. Downloaded from www.nrcresearchpress.com by 61.7.252.67 on 09/07/12
For personal use only.

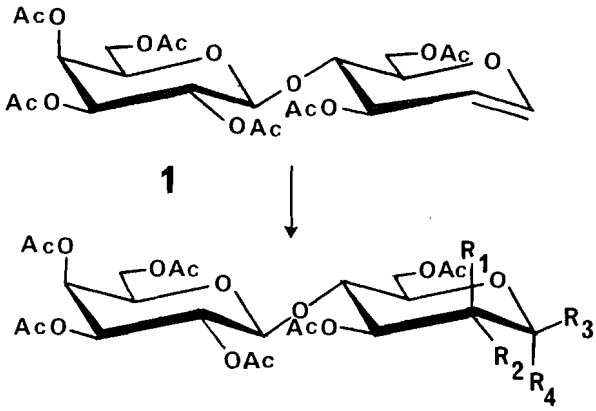

	R_1	R_2	R_3	R_4
2	N_3	H	H	ONO_2
3	H	N_3	H	ONO_2
4	H	N_3	ONO_2	H
5	H	NH_2	OH	H
6	H	NH_2	H	OH
7	H	NPht	OH	H
8	H	NPht	$OCNHCCl_3$	H

FIG. 1. Synthetic scheme for the preparation of the lactose derivatives used as intermediates for the synthesis of the trisaccharide described in this study. Lactal **1** was converted into the mixture of compounds **2**–**4** by azidonitration and the mixture of anomeric compounds **3** and **4** was hydrogenated to give **5** and **6**. Reaction with *N*-carboethoxyphthalimide gave **7**, which was converted into **8** by reaction with trichloroacetonitrile.

ethoxyphthalimide, under reflux of the solvent in the presence of a catalytic amount of triethylamine. We found these conditions to be superior to those described by Arnarp and Lönngren (10) for the protection of the primary amino group. At the same time, a free hydroxyl group at the C-1 position of the D-lactosamine derivative is obtained, and that allows for the planned conversion of **7** into the corresponding β-trichloroacetimidate derivative **8**.

Key intermediate **8** was essentially obtained as described (26). The D-lactosamine derivative **8** showed an ^{1}Hmr spectrum identical to that reported, but we observed a melting point of 174–175°C, as opposed to the reported 128°C (26).

Bundle and Josephson (28) have described the synthesis of a protected L-rhamnose derivative possessing a "linking arm" in the aglycon portion of the molecule. When one compares the structure of D-mannose to L-rhamnose, it is obvious that the two molecules possess identical equatorial/axial relative orientations of the substituents. It was thus expected that the sequence of reactions published by Bundle and Josephson could be applied to the synthesis of compound **13**. Furthermore, it was also expected that protection of the primary (C-6) alcohol of D-mannose by benzylation would not affect the general outline of the synthesis.

2,3,4,6-Tetra-*O*-acetyl-D-mannopyranosyl bromide **9** (29) was converted into 3,4,6-tri-*O*-acetyl-1,2-*O*-(methoxyethylidene)-β-D-mannopyranose **10** (30) by reaction of **9** with methanol using 2,6-lutidine as solvent. Compound **10** was crystalline and homogeneous by the usual criteria. Deacetylation of **10** by ammonolysis followed by treatment with benzyl bromide in the presence of sodium hydride afforded crystalline **11**, which was allowed to react with 6-(*N*-benzyloxycarbonyl)-aminohexanol to yield homogeneous compound **12**, after purification. It was found essential to use 1.1 equivalents of $HgBr_2$ instead of a catalytic amount of the mercuric salt to complete reaction of **11**. We consistently obtained a low yield of **12** (~30%). It is presumed that this results, in part, from the fact that methanol liberated during the reaction competes with the protected amino alcohol for reaction with **11**. Evidence for this side reaction was obtained by allowing **11** to react with methanol and analyzing the product of the reaction by tlc.

Selective removal of the acetyl protecting group at the C-2 position of intermediate **12** by treatment with a catalytic amount of sodium methoxide in methanol afforded D-mannose derivative **13** as an oil. Reaction of D-lactosamine derivative **8** with protected D-mannopyranoside intermediate **13** in the presence of one equivalent of boron trifluoroetherate (26) gave homogeneous protected trisaccharide **14**, with a 69% yield. Evidence that the glycosylation reaction gave the expected anomer is based on the work of Grundler and Schmidt (26) and on the characteristic signal of the anomeric proton (5.51 ppm, J = 8.5 Hz) observed by ^{1}Hmr.

Compound **14** was readily deacetylated by treatment with an ammonia-saturated methanol solution to give **15**, while treatment with hydrazine removed the phthalimido protecting group. The partially protected trisaccharide derivative was then *N*-acetylated, following the conditions described by Arnarp and Lönngren (10), to trisaccharide **16**. Product **16** was hydrogenated in the presence of colloidal palladium to give desired trisaccharide **17**.

Trisaccharide **17** possesses a versatile amino group that can be converted into a variety of derivatives, which in turn can serve for covalent modifications of *Phaseolus vulgaris* leukoagglutinin. For instance, acylation with a suitable aryl azido moiety will yield derivatives that can be used as probes for photoaffinity labeling studies (31). Alternatively, acylation by reaction with selected cyclic anhydrides affords derivatives that can be utilized as ligands for affinity chromatography purification of this lectin. Such compounds can further be converted into hydrazides that, in turn, can serve to generate the corresponding azides for affinity labeling studies. Leukoagglutinin affinity labeling reagents can also be obtained directly by conversion of the amino group of trisacharide **17** into a bromoacetamido derivative. Bromoacetamido compounds are highly reactive and have been used by Schoellman and Shaw (32) and by Ong *et al.* (33) to specifically inactivate proteolytic enzymes and by Givol and co-workers (34–36) to label the antigenic binding site of antibodies.

We therefore prepared the bromoacetyl derivative of trisaccharide **17** by reaction with *N*-oxysuccinimidyl 2-bromoacetate (37) in an aqueous tetrahydrofuran milieu. The desired sugar derivative **18** was obtained after purification by gel filtration. The ^{1}Hmr and ^{80}Br nmr analyses were consistent with the structure required. Further work is in progress to use derivative **18** for affinity labeling studies of the leukoagglutinin sugar binding site.

Materials and methods

Melting points were determined on a Büchi apparatus and are not corrected. Optical rotations were measured with a OLD 5 Carl Zeiss polarimeter. The nmr spectra were recorded at 250.13 MHz in the pulse Fourier-transformed mode on a Bruker WM-250 instrument. Unless otherwise indicated, samples were dissolved in deuterated chloroform. Chemical shifts are reported in ppm (δ) of the field relative to tetramethylsilane. Tentative signal assignments are based on values re-

Can. J. Chem. Downloaded from www.nrcresearchpress.com by 61.7.252.67 on 09/07/12
For personal use only.

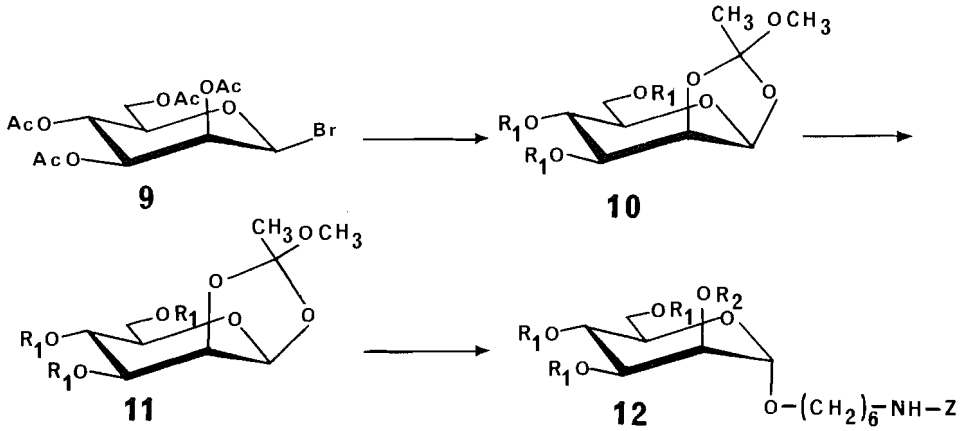

	R_1	R_2
10	Ac	
11	Bn	
12	Bn	Ac
13	Bn	H

Z: C_6H_5-CH_2-O-CO-

FIG. 2. Synthetic scheme to prepare the mannopyranosyl derivative intermediates used for the synthesis of the trisaccharide described in this study. Acetobromomannose **9** was converted into **10** by reaction with methanol in the presence of 2,6-lutidine. Deacetylation and treatment with benzyl bromide afforded **11**, which was allowed to react with 6-(*N*-benzyloxycarbonylamino)-hexanol to give **12**. Compound **13** was obtained by treatment of **12** with sodium methoxide.

ported in the literature (7, 10, 26, 28).[2] Thin-layer chromatographic analyses were performed on 0.5-mm-thick silica gel G (Sigma Chemical Co., St Louis, MO) coated plates. The systems used were I, ethyl acetate – petroleum ether (3:2); II: ethyl acetate – petroleum ether (1:1); III: ethyl acetate – light petroleum ether (2:1); IV: chloroform–methanol (7:1); V: 1-butanol – acetic acid – water (3:1:1). Sugar derivatives were detected by spraying 0.02 M ammonium molybdate and 0.025 M ceric(IV) sulfate in 10% sulfuric acid (38) and heating at 120°C. Column chromatography of intermediates was done by using silicic acid (Kieselgel 60 F_{254}, 70–230 mesh). Petroleum ether refers to the fraction boiling at 60–110°C, whereas light petroleum ether was the fraction boiling at 30–60°C. *N*-Carboethoxyphthalimide was recrystallized from ethanol. Zinc was activated by a 2-min treatment in 10% aqueous hydrogen chloride, washed with water to neutrality, and then with acetone (39). Sodium hydride was obtained as a 60% suspension in mineral oil. Prior to use, it was washed with the appropriate reaction solvent for 20 min, filtered, and resuspended in the same solvent. Evaporations were done with a rotary evaporator, at temperatures below 40°C.

6-(N-Benzyloxycarbonylamino)-hexanol)

The title compound was prepared by treating 6-aminohexanol (15 g, 128 mmol), dissolved in a mixture of tetrahydrofuran (150 mL) and water (45 mL), with benzylchloroformate (24 g, 141 mmol), which was added by portions at 4°C under vigorous stirring. The pH was maintained at 8–9 by addition of 1 N NaOH. After 30 min, the mixture was further stirred at room temperature for 30 min, while maintaining pH. The reaction mixture was extracted with diethyl ether and the organic phase was dried (Na_2SO_4) and evaporated. The desired compound was crystallized from diethyl ether – ethyl acetate – petroleum ether. Yield, 30.3 g (94%); mp 80–81°C. *Anal.* calcd. for $C_{14}H_{21}NO_3$ (251.3): C 66.91, H 8.42, N 5.57; found: C 66.21, H 8.56, N 5.42.

[2]Abbreviations used: Bn, benzyl; d, doublet; dd, doublet of doublets; hplc, high performance liquid chromatography; gal, galactopyranosyl; glc, glucopyranosyl; m, multiplet; man, mannopyranosyl; Ph, phenyl; Pht, phthaloyl; pyr, pyranosic (protons); q, quadruplet; s, singlet; t, triplet.

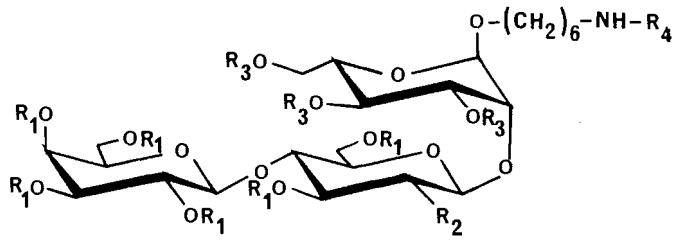

	R_1	R_2	R_3	R_4
14	Ac	NPht	Bn	Z
15	H	NPht	Bn	Z
16	H	NHAc	Bn	Z
17	H	NHAc	H	H
18	H	NHAc	H	$COCH_2Br$

FIG. 3. Synthetic route used for the synthesis of the trisaccharide **18**. Intermediate **14** was obtained by condensation of disaccharide **8** with protected mannose derivative **13**. Treatment of **14** with ammonia in methanol gave **15**, which was allowed to react with hydrazine and then acetylated to afford **16**. Hydrogenation gave **17**, which was converted into **18** by reaction with *N*-oxysuccinimidyl bromoacetate.

4-O-(2,3,4,6-Tetra-O-acetyl-β-D-galactopyranosyl)-3,6-di-O-acetyl-2-deoxy-2-phthalimido-D-glucopyranose (7)

The mixture of compounds **5** and **6** (10) (25 g) and *N*-carboethoxyphthalimide (19 g, 85 mmol) was dissolved in absolute ethanol (200 mL) and the solution was dried for a few minutes over molecular sieves. After 3 h of reflux of the solvent, no further change (tlc) was observed unless a few drops of triethylamine were added. Completion of the reaction occurred after 1.5 h. The solution was cooled at room temperature, filtered, and concentrated to dryness *in vacuo*. Purification by chromatography on silicic acid using ethyl acetate – petroleum ether – methanol (30:20:0.5) as eluent gave the desired product, which crystallized from methanol. Yield, 6 g; mp 138.5–140°C; R_f^{III}: 0.56; $[\alpha]_D^{24}$ +34° (*c* 1.1, chloroform) (lit. (26) $[\alpha]_D^{25}$

Can. J. Chem. Downloaded from www.nrcresearchpress.com by 61.7.252.67 on 09/07/12
For personal use only.

+39 (*c* 1.0, chloroform); ^{1}Hmr: 7.86–7.82 and 7.75–7.70 m (4H, Pht); 5.75 dd (1H, H-3); 5.64 dd (1H, H-1); 5.33 dd (1H, H-4′); 5.12 dd (1H, H-2′); 4.96 dd (1H, H-3′); 4.54 m ($2H_{pyr}$); 4.19–3.83 m ($7H_{pyr}$); 2.13, 2.12, 2.06, 2.03, 1.96, 1.90 s (18H, 6 CH_3-CO).

4-O-(2,3,4,6-Tetra-O-acetyl-β-D-galactopyranosyl)-3,6-di-O-acetyl-2-deoxy-2-phthalimido-β-D-glucopyranosyl trichloroacetimidate (8)

A solution of compound **7** (26) (2.0 g, 2.76 mmol) in distilled dichloromethane (15 mL) was added to a suspension of sodium hydride (70 mg, 1.75 mmol) in dichloromethane (20 mL). Trichloroacetonitrile (5.5 mL, 54.8 mmol) was added and the solution was stirred for 20 min at room temperature. The mixture was added at the top of a silicic acid column and elution was carried out with ethyl acetate – light petroleum ether (3:2). Compound **8** crystallized from ethyl acetate – light petroleum ether. Yield, 1.7 g (71%); mp 174.5–175°C; R_f^{III}: 0.80; ^{1}Hmr: 8.65 s (1H, NH); 7.84–7.81 and 7.72–7.69 m (4H, Pht); 6.61 d ($J_{1,2}$ = 7.8 Hz, 1H, H-1); 5.86 dd ($J_{3,2}$ = 10.6 Hz, $J_{3,4}$ = 8.5 Hz, 1H, H-3); 5.34 dd ($J_{4',3'}$ = 3.4 Hz, $J_{4',5'}$ = 1 Hz, 1H, H-4′); 5.13 dd ($J_{2',1'}$ = 7.8 Hz, $J_{2',3'}$ = 10.4 Hz, 1H, H-2′); 4.95 dd (1H, H-3′); 4.56–4.47 m ($3H_{pyr}$); 4.25–3.87 m ($6H_{pyr}$); 2.15, 2.14, 2.06, 2.05, 1.96, 1.93 s (18H, 6 CH_3-CO).

3,4,6-Tri-O-benzyl 1,2-O-(methoxyethylidene)-β-D-mannopyranose (11)

Compound **10** (30) (22 g, 61 mmol) dissolved in dry methanol (88 mL) and chloroform (0.5 mL) was treated with ammonia-saturated methanol (44 mL). The solution was stirred for 48 h at room temperature under an anhydrous atmosphere. After evaporation of the solvent, the residue was dried under high vacuum (P_2O_5) for 1 h. The oil (15 g) was dissolved in distilled *N,N*-dimethylformamide (90 mL) and added to a suspension of sodium hydride (9 g, 375 mmol) in *N,N*-dimethylformamide (145 mL). Benzyl bromide (33 mL, 286 mmol) was added dropwise over a 15-min period while maintaining the mixture at room temperature by cooling with a water bath. The mixture was stirred under anhydrous conditions for 18 h at which time dry methanol (30 mL) was added dropwise. After 1 h of stirring, the suspension was poured into water (300 mL) and the pH was brought to 8 with 1 N hydrogen chloride. The oil was extracted with ethyl acetate (4 × 100 mL), and the organic phase was washed with water (3 × 100 mL), dried (Na_2SO_4), and concentrated to dryness *in vacuo*. Crystallization from diethyl ether – petroleum ether gave compound **11**. Yield, 16 g (52%); mp 78–78.5°C; R_f^{II}: 0.79; $[\alpha]_D^{24}$: +26° (*c* 1.1, chloroform); ^{1}Hmr: 7.39–7.29 m (15H, 3Ph); 5.35 d ($J_{1,2}$ = 2.5 Hz, 1H, H-1); 4.92–4.57 m (7H, 3CH_2-Ph, H-3); 4.40 dd ($J_{2,3}$ = 4.0 Hz, 1H, H-2); 3.93 t ($J_{4,3}$ = $J_{4,5}$ = 9.4 Hz, 1H, H-4); 3.75–3.70 m (2H, H-6); 3.45 m (1H, H-5); 3.29 s (3H, CH_3-O); 1.74 s (3H, CH_3-C). *Anal.* calcd. for $C_{30}H_{34}O_7$ (506.6): C 71.13, H 6.76; found: C 70.47, H 6.76.

6-(N-Benzyloxycarbonylamino)-hexyl 2-O-acetyl-3,4,6-tri-O-benzyl-α-D-mannopyranoside (12)

Compound **11** (2 g, 3.95 mmol) was dissolved in dry distilled acetonitrile (22 mL), and 6-(*N*-benzyloxycarbonylamino)-hexanol (9.92 g, 39.5 mmol) and mercuric bromide (1.42 g, 3.95 mmol) were added simultaneously. After 70 min of reflux of the solvent, the mixture was filtered and evaporated. The residue was dissolved in chloroform (75 mL) and washed with water (2 × 25 mL). After drying (Na_2SO_4) and concentration, compound **12** was purified by chromatography on silicic acid using ethyl acetate – petroleum ether (9:41) as eluent. The product was obtained as an oil. Yield, 1.3 g (45%); R_f^{II}: 0.71; ^{1}Hmr: 7.38–7.25 and 7.18–7.13 m (20H, 4Ph); 5.36 dd (1H, $J_{2,1}$ = 1.8 Hz, $J_{2,3}$ = 3.3 Hz, H-2); 5.10 s (2H, COO-CH_2-Ph); 4.88–4.45 m (8H, H-1, H-3, 3CH_2Ph); 4.01–3.64 m (5H, $3H_{pyr}$, CH_2-O); 3.41–3.27 m (1H, H-5); 3.17 q (2H, CH_2-NH); 2.19 s (3H, CH_3-CO); 1.65–1.31 m (8H, $4CH_2$).

6-(N-Benzyloxycarbonylamino)-hexyl 3,4,6-tri-O-benzyl-α-D-mannopyranoside (13)

Compound **12** (1.3 g, 1.79 mmol) was treated with a catalytic amount of sodium in dry methanol (40 ml) for 4 h at room temperature. The pH was brought to 6 with acetic acid – methanol (1:1) and the mixture was filtered and concentrated to dryness *in vacuo*. The residue was dissolved in chloroform (50 mL) and washed with water (25 mL). The aqueous phase was extracted with chloroform (50 mL) and the combined organic phases were washed with water (25 mL). Evaporation of the dried (Na_2SO_4) chloroform solution gave an oil. Yield, 1.04 g (85%), R_f^{II}: 0.59; $[\alpha]_D^{24}$ +34° (*c* 1.1, chloroform); ^{1}Hmr: 7.34–7.21 and 7.15–7.12 m (20H, 4Ph); 5.06 s (2H, COOCH_2-Ph); 4.85 dd (1H, OH); 4.81–4.48 m (8H, $2H_{pyr}$, 3CH_2-Ph); 3.99 t (1H, H-2); 3.83–3.51 m (5H, $3H_{pyr}$, O-CH_2); 3.41–3.32 m (1H, H-5); 3.13 q (2H, CH_2-N); 1.48–1.29 m (8H, $4CH_2$). *Anal.* calcd. for $C_{41}H_{49}NO_8$ (683.8): C 72.01, H 7.22, N 2.05; found: C 72.09, H 7.37, N 1.98.

6-(N-Benzyloxycarbonylamino)-hexyl 2-O-[4-O-(2, 3, 4, 6-tetra-O-acetyl)-β-D-galactopyranosyl-(3, 6-di-O-acetyl)-2-deoxy-2-phthalimido-β-D-glucopyranosyl]-(3,4,6-tri-O-benyzl)-α-D-mannopyranoside (14)

Compounds **13** (730 mg, 1.067 mmol) and **8** (1.02 g, 1.175 mmol) were dissolved in distilled dichloromethane (36 mL). The solution was dried over molecular sieves for 10 min, cooled at −8°C, and boron trifluoride etherate was added (131 μL, 1.07 mmol). After 3.5 h under stirring, the mixture was washed with water (5 mL), 1 N sodium bicarbonate (3 × 5 mL), and water (2 × 5 mL). The organic phase was dried (Na_2SO_4), evaporated to dryness, and purified by chromatography on silicic acid using ethyl acetate – petroleum ether (15:35) as eluent. The product was obtained as an oil. Yield, 1.03 g (69% based on **13**); R_f^I: 0.57; $[\alpha]_D^{24}$ +3.4° (*c* 1.1, chloroform); ^{1}Hmr: 7.62–7.54 m (4H, Pht); 7.37–7.23 and 7.15–7.11 m (20H, 4Ph); 5.78 dd (1H, H-3_{glc}); 5.51 d ($J_{1,2}$ = 8.5 Hz; 1H, H-1_{glc}); 5.34 dd ($J_{4,3}$ = 3.8 Hz, $J_{4,5}$ = 1.2 Hz, 1H, H-4_{gal}); 5.14 dd ($J_{2,3}$ = 10.5 Hz, $J_{2,1}$ = 7 Hz, 1H, H-2_{gal}); 5.08 s (2H, COO-CH_2-Ph); 4.97 dd (1H, H-3_{gal}); 4.78–4.25 m (10H, $4H_{pyr}$, 3CH_2-Ph); 4.22–3.79 m (10H, $8H_{pyr}$, O-CH_2); 3.55–3.04 m (6H, $4H_{pyr}$, CH_2NH); 2.14, 2.07, 2.06, 2.03, 1.97, 1.91 s (18H, 6CH_3-CO); 1.48–1.19 m (8H, $4CH_2$). *Anal.* calcd. for $C_{73}H_{84}N_2O_{25}$ (1389.5): C 63.10, H 6.09, N 2.02; found: C 63.33, H 6.65, N 1.91.

6-(N-Benzyloxycarbonylamino)-hexyl 2-O-(4-O-β-D-galactopyranosyl-2-deoxy-2-phthalimido-β-D-glucopyranosyl)-3,4,6-tri-O-benzyl-α-D-mannopyranoside (15)

Compound **14** (1.00 g, 720 μmol) was dissolved in anhydrous methanol (15 mL). Deacetylation was accomplished in the presence of 15 mL of ammonia-saturated methanol for 40 h at room temperature. The mixture was concentrated to dryness. The residue (1.2 g) was purified by chromatography on silicic acid using chloroform–methanol (14:1) as eluent. The oil obtained consisted of two products. Yield, 0.57 g (70%); R_f^{IV}: 0.37 and 0.47; ^{1}Hmr (CD_3OD and DMSO-d_6): 7.83–7.75 m (4H, Pht); 7.39–7.20 and 7.13–7.06 m (20H, 4Ph); 5.22 d ($1H_{pyr}$); 4.96 s (2H, COO-CH_2-Ph); 4.74–3.18 m (28H, $20H_{pyr}$, 3CH_2Ph, O-CH_2); 2.93 m (2H, CH_2-N); 1.37–1.15 m (8H, $4CH_2$).

6-(N-Benzyloxycarbonylamino)-hexyl 2-O-(4-O-β-D-galactopyranosyl-2-acetamido-2-deoxy-β-D-glucopyranosyl)-3,4,6-tri-O-benzyl-α-D-mannopyranoside (16)

Compound **15** (0.32 g, 283 μmol) was dissolved in ethanol (30 mL) and 59.3 μL of hydrazine (1.7 mmol) was added. The solution was heated under reflux under a nitrogen atmosphere for 3 h. After cooling, the hydrazine was neutralized with glacial acetic acid (97.2 μL, 1.7 mmol). The mixture was concentrated and the residue was acetylated by treatment with 4 mL of acetic anhydride – pyridine (1:1) for 10 h at room temperature. The solution was then evaporated to dryness. Hydrazine by-products were eliminated by chromatography of the reaction mixture on a silicic acid column that was eluted with chloroform–methanol (7:1). Removal of the *O*-acetyl residues was accomplished by allowing the mixture of partially acetylated compounds, in methanol (10 mL), to react with ammonia-saturated methanol for 44 h at room temperature. After concentration to dryness *in vacuo*, the mixture (0.44 g) was purified by chromatography on a silicic acid column that was eluted with chloroform–methanol (14:1). Yield, 320 mg (92%); R_f^V: 0.24. The ^{1}Hmr (D_2O) spectrum of the crude product showed the

Can. J. Chem. Downloaded from www.nrcresearchpress.com by 61.7.252.67 on 09/07/12
For personal use only.

absence of signals corresponding to the phthalimido protons (7.9–7.8 ppm). A singlet at 1.83 ppm was attributed to CH_3-CO-NH.

6-Aminohexyl 2-O-(4-O-β-D-galactopyranosyl-2-acetamido-2-deoxy-β-D-glucopyranosyl)-α-D-mannopyranoside (17)

Compound **16** (320 mg, 306 μmol) was dissolved in 90% aqueous acetic acid (30 mL) and hydrogenated at 570 kPa over colloidal palladium (prepared by reduction of $PdCl_2$ with formic acid) for 26 h at room temperature. The catalyst was removed and the solution was lyophilized. The residue was purified on a Mono S column (Pharmacia Fine Chemicals, Montreal) using an hplc system (Waters Associates Inc., Milford, MA) in the following way. The trisaccharide derivative was dissolved in 2 mM acetic acid and injected at the top of the column equilibrated in water. Elution was done using triethylamine gradient concentrations of 1–100 mM. The desired product was located in the 55 mM triethylamine eluate (ninhydrin spot test). Yield, 183 mg (93%); R_f^V: 0.16; $[\alpha]_D^{24}$ −5.8° (*c* 1.0, H_2O); ^{1}Hmr (D_2O): 4.69 d ($J_{1,2}$ = 5.2 Hz, 1H, H-1_{man}); 4.38 dd ($J_{2,3}$ = 2.8 Hz, 1H, H-2_{man}); 4.26 d ($J_{1,2}$ = 7.9 Hz, 1H, H-1_{gal}); 3.85–3.29 m (19H, OCH_2, 17H_{pyr}); 2.79–2.71 m (2H, CH_2-N); 1.85 s (3H, CH_3-CO); 1.44–1.39 and 1.24–1.15 (8H, 4CH_2). The signal corresponding to H-1_{glc} was not observable due to interference of the HOD peak.

6-(Bromoacetamido)-hexyl 2-O-(4-O-β-D-galactopyranosyl-2-acetamido-2-deoxy-β-D-glucopyranosyl)-α-D-mannopyranoside (18)

Trisaccharide **17** (51 mg, 79 μmol) was dissolved in water (0.5 mL) and the pH was adjusted to 7–8 by addition of triethylamine (10% in tetrahydrofuran). *N*-Oxysuccinimidyl 2-bromoacetate (prepared by reaction with *N*-hydroxysuccinimide and 2-bromoacetic acid in the presence of *N*,*N*′-dicyclohexylcarbodiimide, mp 109–110°C) (23 mg, 99 μmol), dissolved in tetrahydrofuran (156 μL), was added in three portions. The pH was maintained at 7–8 by addition of dilute triethylamine. After 23 min, the reaction gave a negative ninhydrin test. The mixture was filtered and lyophilized. The dried powder was purified by gel filtration on a Bio Gel P-2 (Bio Rad, Richmond, CA) column equilibrated in water. Column elution was done with water. Lyophilization of the desired fractions afforded a white powder. Yield, 24.3 mg (62%); R_f^{IV}: 0.62; $[\alpha]_D^{24}$ +2.2° (*c* 1.0, H_2O); ^{1}Hmr (D_2O): 4.67 d ($J_{1,2}$ = 7.0 Hz, 1H, H-1_{man}); 4.41 s (2H, −CO-CH_2Br); 4.25 d ($J_{1,2}$ = 7.7 Hz, 1H, H-1_{gal}); 3.71–3.30 m (19H, 17H_{pyr}, OCH_2); 3.06 m (2H, CH_2-NH-$COCH_2$Br); 1.83 s (3H, CH_3-CO); 1.69–1.10 m (8H, 4CH_2). The presence of the bromide group was assessed by ^{80}Br nmr spectroscopy (67.55 MHz; reference, NaBr in D_2O), which showed a broad signal centred at 2.5 ppm.

Acknowledgements

The authors are indebted to the Medical Research Council of Canada for research support and for a Studentship (H.A.). We thank Mr. Serge Bérubé for his collaboration in determining the ^{1}Hmr spectra. We also thank Professor Jean Lessard for helpful discussions.

1. J. Montreuil. Adv. Carbohydr. Chem. Biochem. **37**, 157 (1980).
2. H. Schachter and D. Williams. Mucus in health and disease. *Edited by* E. N. Chantler, J. B. Elder, and M. Elstein. Plenum Press, New York. 1982. pp. 3–28.
3. R. Kornfeld and S. Kornfeld. Annu. Rev. Biochem. **54**, 631 (1985).
4. R. D. Marshall. Annu. Rev. Biochem. **41**, 673 (1972).
5. R. D. Marshall. Biochem. Soc. Symp. **40**, 17 (1974).
6. R. D. Cummings and S. Kornfeld. J. Biol. Chem. **257**, 11235 (1982).
7. R. Kaifu and T. Osawa. Carbohydr. Res. **52**, 179 (1976).
8. S. Hammarström, M.-L. Hammarstrom, G. Sundblad, J. Arnarp, and J. Lönngren. Proc. Natl. Acad. Sci. U.S.A. **79**, 1611 (1982).
9. V. Räsänen, T. H. Weber, and R. Gräsbeck. Eur. J. Biochem. **38**, 193 (1973).
10. J. Arnarp and J. Lönngren. J. Chem. Soc. Perkin Trans. 1, 2070 (1981).
11. K. Kawaguchi, M. Kuhlenschmidt, S. Roseman, and Y. C. Lee. J. Biol. Chem. **256**, 2230 (1984).
12. Y. C. Lee. Carbohydr. Res. **67**, 509 (1978).
13. M. Ramjeesingh and K. Kahlenberg. Can. J. Chem. **55**, 3717 (1977).
14. R. Barker, C.-K. Chiang, I. P. Trayer, and R. L. Hill. Methods Enzymol. **34**, 317 (1974).
15. M. A. Nashed. Carbohydr. Res. **123**, 241 (1983).
16. R. T. Lee and Y. C. Lee. Biochemistry, **19**, 156 (1980).
17. Y. C. Lee, C. P. Stowell, and M. J. Krantz. Biochemistry, **15**, 3956 (1976).
18. S. Chipowsky and Y. C. Lee. Carbohydr. Res. **31**, 339 (1973).
19. D. H. Buss and I. J. Goldstein. J. Chem. Soc. 1457 (1968).
20. R. T. Lee and Y. C. Lee. Carbohydr. Res. **34**, 151 (1974).
21. D. T. Connolly, S. Roseman, and Y. C. Lee. Carbohydr. Res. **87**, 227 (1980).
22. J. Dahmen, T. Frejd, G. Magnusson, G. Noori, and A.-S. Carlstrom. Carbohydr. Res. **129**, 63 (1984).
23. R. U. Lemieux, D. A. Baker, and D. R. Bundle. Can. J. Biochem. **55**, 507 (1977).
24. S. N. Husain, B. Gentile, R. R. Sauers, and A. Eichholz. Carbohydr. Res. **118**, 57 (1983).
25. R. T. Lee and Y. C. Lee. Biochemistry, **25**, 6835 (1986).
26. G. Grundler and R. R. Schmidt. Carbohydr. Res. **135**, 203 (1985).
27. W. N. Haworth, E. L. Hirst, M. M. T. Plant, and R. J. W. Reinolds. J. Chem. Soc. 2644 (1930).
28. D. R. Bundle and S. Josephson. Can. J. Chem. **57**, 662 (1979).
29. P. A. Levene and R. S. Tipson. J. Biol. Chem. **90**, 89 (1931).
30. J. K. Dale. J. Am. Chem. Soc. **46**, 1046 (1924).
31. H. Bayley. *In* Laboratory techniques in biochemistry and molecular biology. *Edited by* T. S. Work and R. H. Burdon. Elsevier, New York. 1983.
32. G. Schoellmann and E. Shaw. Biochemistry, **2**, 252 (1963).
33. E. B. Ong, E. Shaw, and G. Schoellmann. J. Biol. Chem. **240**, 694 (1965).
34. D. Givol. Contemp. Top. Mol. Immunol. **2**, 27 (1973).
35. P. H. Strausbauch, Y. Weinstein, M. Wilchek, S. Shaltiel, and D. Givol. Biochemistry, **10**, 4342 (1971).
36. M. J. Becker, D. Givol, and M. Wilchek. Immunol. Commun. **2**, 383 (1973).
37. P. Cuatrecasas, M. Wilchek, and C. B. An^{9}nsen. J. Biol. Chem. **244**, 4316 (1969).
38. R. Roy and H. J. Jennings. Carbohydr. Res. **112**, 63 (1983).
39. R. L. Frank and P. V. Smith. Org. Synth. Coll. Vol. **3**, 410 (1946).

Can. J. Chem. Downloaded from www.nrcresearchpress.com by 61.7.252.67 on 09/07/12
For personal use only.

The photochemistry of 8-cyano-2,3-benzobicyclo[4.2.0]octa-2,4,7-triene

CHRISTOPHER OWEN BENDER,[1] DOUGLAS DOLMAN, AND GAETANNE KATHRYN MURPHY[2]
Department of Chemistry, University of Lethbridge, Lethbridge, Alta., Canada T1K 3M4

Received January 15, 1988

CHRISTOPHER OWEN BENDER, DOUGLAS DOLMAN, and GAETANNE KATHRYN MURPHY. Can. J. Chem. **66**, 1656 (1988).

The direct irradiation of 6-cyanobenzocyclooctatetraene (**7**) led to 5- and 8-cyano-2,3-benzobicyclo[4.2.0]octa-2,4,7-triene (**9** and **8**), isolated in 21 and 63% yields, respectively. On triplet sensitized irradiation **8** gave 1- and 6-cyanobenzosemibullvalenes (**4** and **12**; Φ = 0.006 and 0.088, respectively) and naphthalene (Φ = 0.012). The direct irradiation of **8** yielded **12** (Φ = 0.050), naphthalene (Φ = 0.015), **7** (Φ = 0.007), 7-cyanobenzocyclooctatetraene (**13**; Φ = 0.007), and 5-cyano-7,8-benzotetracyclo[3.3.0.$0^{2,4}$.$0^{3,6}$]oct-7-ene (**14**; Φ = 0.004). Deuterium labelling studies suggest that **12** derives from Zimmerman di-π-methane rearrangement of **8**, and that photoproduct cyclooctatetraene **7** is not formed by simple electrocyclic opening of the cyclobutene ring of **8**.

CHRISTOPHER OWEN BENDER, DOUGLAS DOLMAN et GAETANNE KATHRYN MURPHY. Can. J. Chem. **66**, 1656 (1988).

La photolyse directe du cyano-6 benzocyclooctatetraène (**7**) conduit aux cyano-5 et -8 benzo-2,3 bicyclo[4.2.0]octatriènes-2,4,7 (**9** et **8**), avec des rendements de 21 and 63%, respectivement. Par irradiation sensibilizée, **8** conduit aux cyano-1 et -6 benzo semi-bullvalènes (**4** et **12**; Φ = 0,006 et 0,088, respectivement) et au naphtalène (Φ = 0,012). Par irradiation directe, **8** conduit à **12** (Φ = 0,050), au naphtalène (Φ = 0,015), à **7** (Φ = 0,007), au cyano-7 benzocyclooctatetraène (**13**; Φ = 0,007), et au cyano-5 benzo-7,8 tetracyclo[3.3.0.$0^{2,4}$.$0^{3,6}$]octène-7 (**14**; Φ = 0,004). Des études de marquages au deuterium suggèrent que **12** dérive d'une transposition di-π-méthane de Zimmerman, et que **7** ne se produit pas par un mécanisme qui comporte l'ouverture électrocyclique de l'anneau du cyclobutène de **8**.

Can. J. Chem. Downloaded from www.nrcresearchpress.com by 61.7.252.67 on 09/07/12
For personal use only.

Introduction

Semibullvalene derivatives are effective building blocks in the synthesis of a variety of cyclopentanoid natural products (1). Recently, we reported a new route to the semibullvalene (SB) ring system from the triplet sensitized photoisomerization of some 2,3-benzobicyclo[4.2.0]octa-2,4,7-trienes (viz., dienes **1** (2), **3**, and **5** (3)). A potential drawback to the general utility of this ring interconversion is a concurrent fragmentation process that produces naphthalene (and presumably acetylene) derivatives. Competition between these two reaction types is strongly dependent on the substituent location, and near extremes of the partitioning were found for the cyanolated derivatives **3** and **5**; **3** gave mostly SB **4**, while **5** yielded mainly naphthalene (note Scheme 1).

We have continued our studies aimed at delineating the product controlling features in 2,3-benzobicyclo[4.2.0]octa-2,4,7-trienes, and now report on the photochemistry of the 8-cyano derivative **8**. Diene **8** was selected for study since operation of the cleavage reaction would produce the same fragments (naphthalene and cyanoacetylene) found in the case of **5**. This study would therefore test the notion, discussed in our earlier paper (3), of correlation between the stability of the acetylene unit expelled and the preference for the fragmentation process in the reaction bifurcation.

Results

The desired diene **8** was obtained as the major (63%) product from the direct irradiation ($\lambda > 310$ nm) of the tail of the absorption band of the known 6-cyanobenzocyclooctatetraene (6-CN-BCOT; **7**) (cf. the preparation of dienes **1** (2), **3**, and **5** (3) from the corresponding BCOT's); the diene isomer **9** was the only other observable (gc and nmr monitoring) product (21%).

The structure of **8** was assigned on the basis of spectral data (see Experimental) and chemical evidence. Catalytic hydrogenation gave the tetrahydro derivative **10**, which was identical to the unique product from the hydrogenation of the known compound **11** (4). Additionally, it was found that **8** reverted almost quantitatively to BCOT **7** on heating (ca. 150°C for 3 h). Here we note that **1** (2), **3**, and **5** (3) also rearrange thermally to the corresponding BCOT's without fragmentation.

In contrast to the simplicity of the thermal behaviour of **8**, photolysis gave more complex reaction mixtures. Product structures, chemical yields (gc analysis), and quantum yields (Φ's) for the direct and sensitized irradiations of **8** are given in Scheme 2.

Of the photoproducts, only 5-cyano-7,8-benzotetracyclo-[3.3.0.$0^{2,4}$.$0^{3,6}$]oct-7-ene (**14**) and 6-cyanobenzotricyclo-[3.3.0.$0^{2,8}$]octa-3,6-diene (SB **12**) are new compounds. The structure of **14** was derived from spectral data alone. The mass spectrum is similar to that of **15** (3), and shows a strong molecular peak at *m/e* 179, and a major fragmentation peak at *m/e* 128, corresponding to naphthalene ion. In the ^{1}H nmr spectrum, the signals due to the non-aromatic protons approximate an AA'MXX' spin system (cf. **15** (3)), and the chemical shifts (δ 4.47 (H-1,6), δ 3.36 (H-4), and δ 2.25 (H-2,3)) are similar to those of the corresponding protons in **16** (5) (δ 3.85 (H-1,6), δ 2.94 (H-4), and δ 2.07 (H-2,3)); H-4 in both **14** and **16** occurs as a triplet, with $J_{4,2(3)}$ = 3.5 Hz. Finally, the plane of symmetry in **14** was confirmed by the proton decoupled ^{13}C nmr spectrum, which contained only eight resonances; the chemical shifts of the aliphatic ring carbons (δ 55.48 (C-1,6), δ 20.26 (C-2,3), δ 27.67 (C-4), and δ 55.48 (C-5)) correlate well with those reported (5) for **16** (δ 53.2 (C-1,6), δ 20.1 (C-2,3), δ 24.9 (C-4), and δ 64.5 (C-5)).

In the case of photoproduct **12**, the physical characterization was compromised by the facile polymerization of the semibullvalene upon solvent removal. Similar behaviour was observed with the isomeric vinyl cyano-substituted semibullvalene **6** (3). Persuasive evidence for structure **12** was, however, provided by nmr data and hydrogenation results. Details of the ^{1}H nmr spectrum of **12** are given in Table 1, along with those of the related semibullvalenes **6** (3) and **17** (6). Inspection of the data reveals that the proton chemical shifts for **12** fall within

[1]Author to whom correspondence may be addressed.
[2]Née Linders.

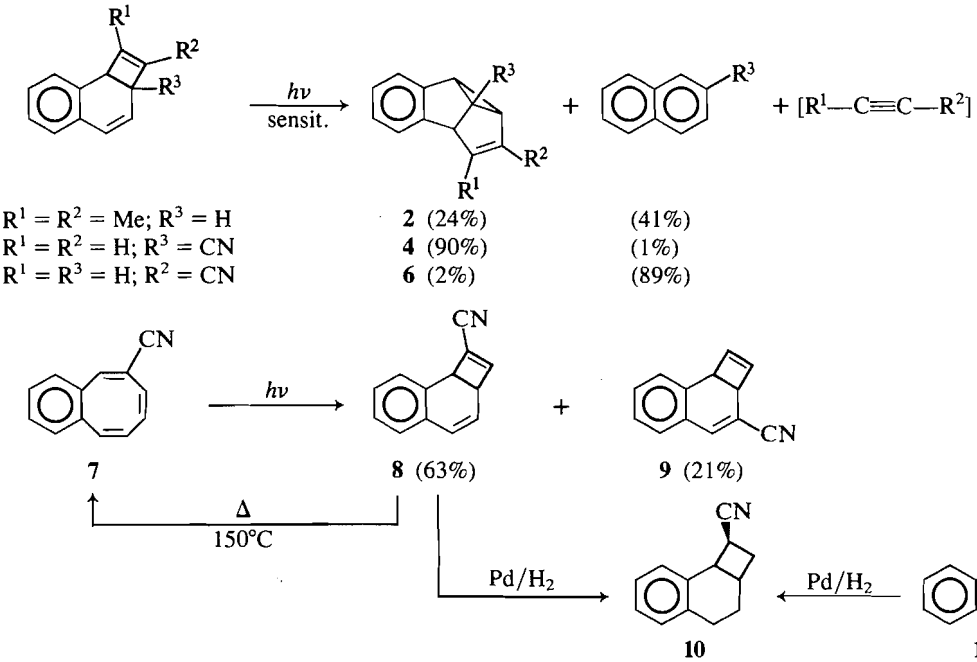

SCHEME 1

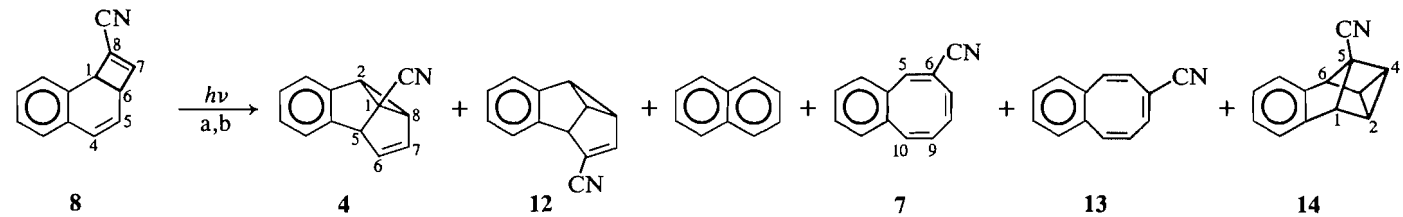

Chemical and quantum (Φ) yields	8	4	12	7	13	14
(a) Direct	—	55%(0.050)	15%(0.015)	8%(0.007)	8%(0.007)	5%(0.004)
(b) Sensitized	7%(0.006)	78%(0.088)	11%(0.012)	—	—	—

SCHEME 2

expected values; the 0.9-ppm downfield shift of H-7 in **12** relative to H-17 in **17** compares well with the reported chemical shift substituent constant of 0.8 ppm for the *cis* proton of acrylonitrile (7). Also, the coupling constants observed for **12** (see Table 1) are characteristic of the rigid benzosemibullvalene system (6).

Further support for structure **12** was provided by catalytic hydrogenation, which yielded three main products (4:1:1) by gc. The major product was isolated and identified as 6-cyano-3,4-benzotricyclo[3.3.0.$0^{2,8}$]oct-3-ene (**18**), a stable crystalline dihydro derivative of **12**. The characterization of **18** rests on comparison of its ^{1}H nmr spectrum with that of the closely related dihydro semibullvalene **19** (2). Details of the spectra are given in Table 2. Since $J_{5,6}$ = 5.0 Hz in **18** and **19**, the stereochemistry at C-6 is probably the same in both compounds, and opposite to that assigned to **20**, where $J_{5,6}$ = 0 Hz (8). Also in both **18** and **19**, $J_{5,7}$ = 1.5 Hz. This small coupling, previously overlooked by us in the case of **19** (2), is attributed to "W" coupling (9), which operates through the saturated and approximately coplanar H5—C5—C6—C7—H7 portion of the molecule (Dreiding Model).

Next, attention was turned to the possible involvement of

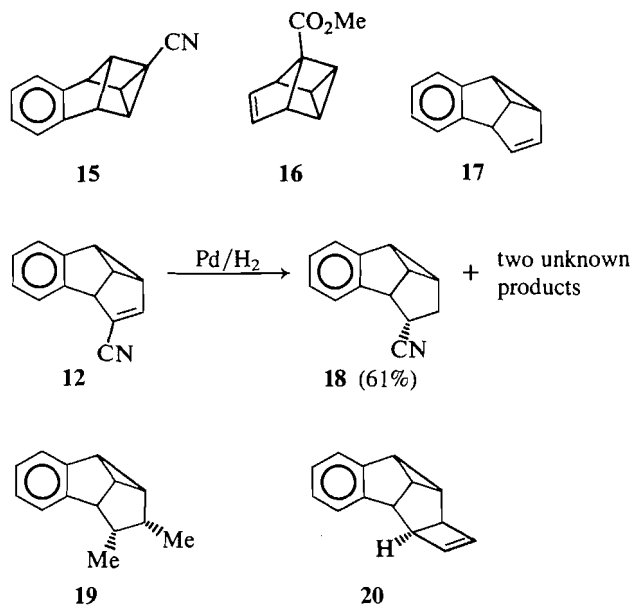

SCHEME 3

Can. J. Chem. Downloaded from www.nrcresearchpress.com by 61.7.252.67 on 09/07/12
For personal use only.

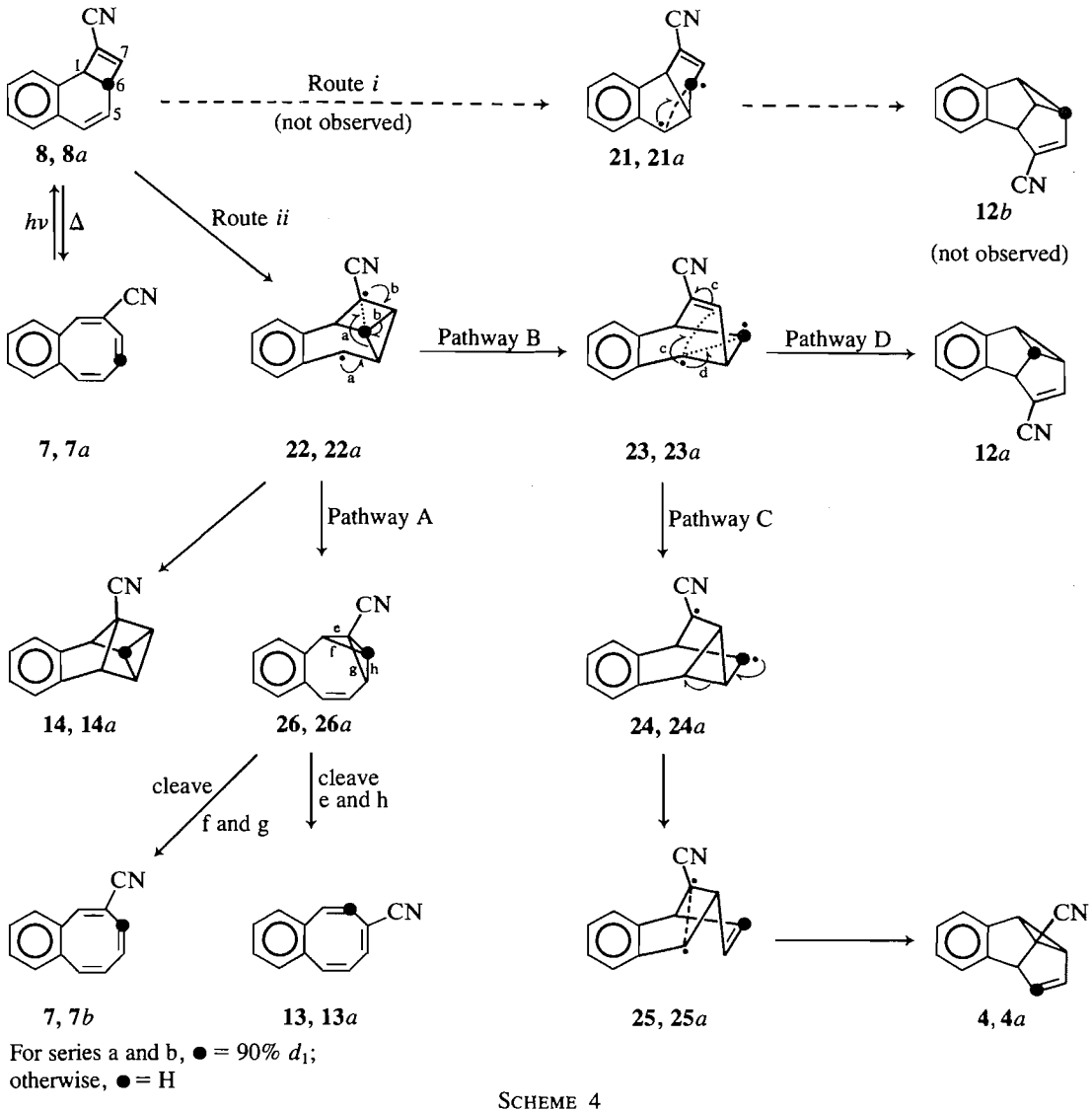

SCHEME 4

secondary photochemistry in the formation of the photoproducts given in Scheme 2. Separate irradiations of the product isomers **4**, **7**, **12**, and **14**, under the conditions employed for the starting diene **8**, showed that all were essentially unreactive on exposure to Pyrex filtered light, and were similarly resistant to photoisomerization on attempts at sensitization with Michler's ketone. In the case of photoproduct **13**, the absence of dienes **3** and **5** in photolysates of **8** indicate that COT **13** (3) also plays no part in secondary interconversions in the present study at the conversion levels used.

Mechanistic considerations

Although the formation of the major product, SB **12**, from the direct and sensitized irradiations of **8** can be readily interpreted in terms of a Zimmerman di-π-methane (DPM) rearrangement (10) with initial bridging between C-5 and C-7 (Scheme 4, route *ii*), there exists an attractive alternative mechanism which involves cleavage of the cyclobutene C1—C6 bond (Scheme 4, route *i*). This latter mechanism is appealing since it engenders immediate relief of ring strain (note structure **21**) while providing extensive stabilization of the radical centres. To distinguish between operation of these two possible mechanisms, irradiations of the deuterium labelled compound **8***a* were undertaken. Labelled diene **8***a* was obtained from the direct irradiation of the known (11) deuterated COT **7***a* (ca. 90% d_1 at C-8).

TABLE 1. The ^{1}H nmr data of semibullvalenes **6**, **12**, and **17**

	Description and signal positions, $\delta^{a,b}$		
Assignment	**12**	**6**	**17**
Aromatics	7.18–7.42 m	6.97–7.45 m	6.80–7.33 m
H-1	3.49 q	3.35 q	3.14 q
H-2	3.29 t	3.15 t	2.86 t
H-5	4.06 d	4.02 dd	3.81 dd
H-6	—	6.24 d	5.47 dd
H-7	6.01 d	—	5.08 dd
H-8	2.82 ddd	2.90 t	2.60 dt

[a]Run in $CDCl_3$ (**12**) or CCl_4 (**6** and **17**) solvent with TMS as internal standard.

[b]Coupling constants for **12** are: $J_{1,2} = J_{1,5} = J_{1,8} = 6$; $J_{2,8} = 7$, and $J_{7,8} = 2.5$ Hz; corresponding coupling constants for **6** and **17** are within 0.5 Hz.

The direct and sensitized photolysis of **8***a* led to SB product **12***a* with deuterium located exclusively at C-1, as determined by ^{1}H nmr analysis (integration results for **12***a* and for all subsequent labelled compounds are given in the Experimental).

Can. J. Chem. Downloaded from www.nrcresearchpress.com by 61.7.252.67 on 09/07/12
For personal use only.

TABLE 2. The ^{1}H nmr data of the ring-attached protons of the dihydrosemibullvalenes **18** and **19**

Assignment	Description and signal positions, $\delta^{a,b}$	
	18	**19**
Aromatics	7.17–7.30 m	6.90–7.21 m
H-1	2.90 br q	2.98 q
H-2	2.40 dd	2.25 d
H-5	3.73 dt	3.34 bt
H-6	3.32 ddd	2.83 m
H-7	2.27 m	2.52 m
H-7′	1.40 ddd	—
H-8	1.95 dq	2.01 q

[a]Run in $CDCl_3$ solvent with TMS as internal standard.
[b]Coupling constants for **18** are: $J_{1,2} = J_{1,8} = 6.5$; $J_{1,5} = J_{5,6} = 5.0$; $J_{2,8} = 7.5$; $J_{5,7} = 1.5$; $J_{6,7} = 8.5$; $J_{6,7'} = 10.5$; $J_{7,7'} = 13.5$; $J_{7,8} = 7$; and $J_{7',8'} = 2$ Hz; corresponding coupling constants for **19** are within 1.0 Hz.

Thus the DPM rearrangement (Scheme 4, route *ii*) alone accounts for the conversion of diene **8** to SB **12**.

The label locations in the other photoproducts derived from **8***a* were also examined, and proved to be intriguing in the cases of **4**, **7**, and **13**. Firstly, **4***a* is the minor SB product obtained from sensitization. A mechanism consistent with this observation is given in Scheme 4 (pathway C), and can be seen to involve a novel cyclopropyl ring closure of diradical **23***a*, to give the rearranged diradical **24***a*.

The second and by far the more surprising finding is that the 6-CN-BCOT product isolated from the direct irradiation of **8***a* is **7***b*, and not the label-isomer **7***a*. A possible rationale for the formation of COT **7***b* is given in Scheme 4 (pathway A), where the intermediacy of octavalene **26***a* is called upon. Here it is assumed that **26***a*, a member of the little known tricyclo[5.1.0.0^{2,8}]octa-3,5-diene ring system (12, 13), is thermally unstable under the photolysis conditions used. Operation of this mechanism not only accounts for the production of **7***b*, but also provides a convenient explanation for the formation of COT **13**, and it predicts the observed location of the deuterium label at C-6 in **13***a*. Furthermore, one would anticipate that intermediate **26** should generate more or less equal quantities of the COT's **7** and **13** by cleavage of alternate pairs of allylic (g or h) and benzylic (e or f) bonds. Inspection of the yields in Scheme 2 shows that the product ratio (**7**:**13**) is indeed 1:1.

Lastly with respect to the labelling studies, the thermolysis of **8***a* was carried out. This led to regeneration of the starting COT (**7***a*); no **7***b* could be detected by nmr integration.

Discussion

Diene **8** follows the general trend observed for derivatives **1**, **3**, and **5** of producing SB and naphthalene products upon triplet excitation. Unlike **5** (3), however, cleavage into the same fragments (naphthalene and cyanoacetylene) is seen to be a minor pathway (ca. <15%) in the case of **8**. Thus contrary to our previous suggestion (3), we now conclude that the stability of the acetylene unit expelled is not the controlling feature of the SB/naphthalene product bifurcation.

In the present case, the predominance of the SB **12** formation is attributed to the favorable stabilization (benzylic and cyano) afforded the radical centres in the initial DPM rearrangement intermediate **22** (see Scheme 4). The rearrangement is both singlet and triplet derived. Sensitization of **8** led to naphthalene and the SB's **4** and **12**, and is attributed to triplet (T_1) processes. The absence of SB **4** in direct irradiations of diene **8** implies that SB **12**, and its companion products formed from this mode of excitation, originate from S_1 alone. Thus **8** provides the second example of a 2,3-benzobicyclo[4.2.0]octa-2,4,7-triene that undergoes DPM rearrangement from both singlet and triplet excited states; diene **5** was the first (3). These observations are of interest, since DPM rearrangements in rigid systems show a general preference of triplet initiation (10).

Further to SB's **4** and **12**, it appears that their formation depends on the spin multiplicity of diradical **23**. For the singlet, it is assumed that the radical centres close to give SB **12**, while for the triplet, intersystem crossing and closure (→SB **12**) compete with rearrangement to the cyclopropyldicarbinyl diradical **24** and thence SB **4** formation. Precedence for this latter pathway (i.e., **24** → **25** → **4**) exists. Species like **24** are commonly invoked in barrelene photochemistry, and Zimmerman has studied product formations from the corresponding prototype diradical of **24** (i.e., **24** less the CN group). It was found that generation of the triplet species did indeed lead predominantly to benzosemibullvalene (14).

The tetracyclic compound **14** arises only from the S_1 state of **8**. Analogous $2\pi + 2\pi$ cycloaddition reactions occur in related dienes when the cyclobutenyl double bond is substituted with at least one good electron acceptor group. Thus the reaction is observed with **5** (3), 4,5-diphenyl-2,3-benzo- and 7-*tert*-butyl-8-methoxycarbonyl-bicyclo[4.2.0]octa-2,4,7-triene (15, 16), but not with **1** (2) nor with **3** (3).

The remaining minor singlet rearrangement products of **8** are the COT's **7** and **13**. Our interpretation of the coformation of these COT's via octavalene **26** (Scheme 4, pathway A) is tentative, but the recent observation of isomerization of parent octavalene to cyclooctatetraene in the ground state is consistent with the mechanism proposed here (12, 13). That COT **7** does not result from electrocyclic opening of the cyclobutene ring is noteworthy since such a process is formally allowed in the excited state. Evidently channelling of the excitation energy to the C1—C6 bond is avoided, as a consequence of the substitution pattern in **8**.

In conclusion, we note that all the photoisomerization products (from S_1 or T_1) of **8** can be accounted for by mechanisms involving the initial formation of the "Zimmerman-type" DPM diradical **22**. The present findings, together with those from our previous studies (2, 3), suggest that promotion of the SB formation in the triplet SB/naphthalene product bifurcation of 2,3-benzobicyclo[4.2.0]octa-2,4,7-trienes correlates with factors that generally enhance DPM reactivity, i.e., attachment of delocalizing substituents to the methane carbon (17) or the terminal vinyl carbons of the DPM moiety (11, 18).

Experimental

The nmr spectra were recorded on a Bruker 400-MHz or a Varian 60-MHz instrument, with TMS as internal standard. The chemical shifts are in δ units and the coupling constants (J) in Hz. The abbreviations br, s, d, t, q, and m refer to broad, singlet, doublet, triplet, quartet, and multiplet, respectively. The ir spectra were recorded on a Perkin–Elmer 337 spectrometer. The uv spectra were measured on either a Cary 15 or a Varian DMS 100S spectrometer; maxima are given in nm, with ε_{max} values in parentheses; sh = shoulder. Melting points are uncorrected. Elemental analyses were performed either by Galbraith Labs, Inc., Knoxville, TN, or by the

Can. J. Chem. Downloaded from www.nrcresearchpress.com by 61.7.252.67 on 09/07/12
For personal use only.

Can. J. Chem. Downloaded from www.nrcresearchpress.com by 61.7.252.67 on 09/07/12
For personal use only.

Analytical Services Lab, Department of Chemistry, the University of Alberta. Unless stated otherwise, column chromatography was carried out on Silica Gel 60 (Merck; 230–400 mesh) mixed with Sylvania 2282 phosphor and slurry packed into quartz columns permitting monitoring by a hand uv lamp, or on Lobar columns (Merck; size B, LiChroprep Si 60). Rotating (i.e., centrifugally accelerated) tlc separations were done on a Model 7924 Chromatotron (Harrison Research). The gc analyses were made on a Varian 3700 instrument (FID), coupled to a Varian CDS 111 computing integrator, and fitted with, unless otherwise stated, an SE-30 glass capillary column 30 m × 0.32 mm. For preparative gc separations, a Varian AP-90 instrument was used (0.25 in. × 8 ft of 7.5% SE-30 on DMCS 45/50; helium gas; 190°C). Cyclohexane solvent for photolyses was prepared by scrubbing with 20% fuming sulfuric acid, followed by washing with 10% aqueous sodium hydroxide, drying ($MgSO_4$), and finally distilling from calcium hydride. Michler's ketone sensitizer was crystallized and vacuum sublimed prior to use.

General procedures for preparative photolyses

The apparatus consisted of a 450-W Hanovia medium pressure mercury arc surrounded by a water-cooled quartz immersion well. The light was filtered through either a cylindrical Pyrex sleeve or an aqueous copper sulfate solution (250 g $CuSO_4$ in 1 L water; cut-off λ was 310 nm) contained in a concentric filter jacket (10-mm path length). Two types of sample cell were used. Cell A (200-mL sample volume) consisted of a cylindrical collar (Pyrex), which surrounded the aqueous filter jacket. The cell was fitted with gas inlet and exit ports, and sample solutions were purged with argon prior to, and during, irradiations. Cell B (35-mL sample volume) was a test-tube-like vessel (quartz), and sample solutions contained therein were deoxygenated, by flushing with argon, and sealed under a positive pressure; the solutions were magnetically stirred throughout the course of the irradiations.

Direct irradiation of cyclooctatetraene 7

A solution of 140.1 mg (0.78 mmol) of **7** (11) in 200 mL of cyclohexane was photolyzed at >310 nm for 20.5 h in Cell A. The photolysate analysed (nmr) for a diene photoproduct ratio (**8**:**9**) of 2.3:1. The photolysate was concentrated and the residue crystallized from 3 mL of hexane to give 98.3 mg (70%) of recovered COT **7**. The mother liquors were column chromatographed on Silica Gel 60 (2 cm × 45 cm; 2.5% ethyl acetate – cyclohexane) into two bands. The second band contained 17.7 mg (13%) of diene **8**, mp 69–71°C (from hexane); ir (KBr): 2220 (C≡N) cm^{-1}; uv (hexane): 261 sh (5 040), 267 (5 780), 274 sh (5 370), 290 sh (2 850), and 301 sh (730); nmr (400 MHz; $CDCl_3$): 7.17–7.28 (m, 3H, aromatics), 7.08 (m, 1H, aromatic), 6.77 (d, 1H, H-7, $J_{7,6}$ = 1.1), 6.37 (br d, 1H, H-4, $J_{4,5}$ = 10, $J_{4,6}$ = 1.5), 5.80 (dd, 1H, H-5, $J_{5,4}$ = 10, $J_{5,6}$ = 4.5), 4.37 (d, 1H, H-1, $J_{1,6}$ = 4.5), and 3.75 (br tt, 1H, H-6, $J_{6,1}$ = $J_{6,5}$ = 4.5, $J_{6,4}$ = $J_{6,7}$ = 1.3); spin decoupling experiments: irradiation of H-7 collapsed H-6 to a dt ($J_{6,1}$ = $J_{6,5}$ = 4.5, $J_{6,4}$ = 1.5); irradiation of H-4 collapsed H-5 to a d ($J_{5,6}$ = 4.5) and H-6 to a dt ($J_{6,1}$ = $J_{6,5}$ = 4.5, $J_{6,7}$ = 1.1); irradiation of H-5 modified H-6 and collapsed H-4 to a d ($J_{4,6}$ = 1.5); irradiation of H-1 modified H-6; irradiation of H-6 collapsed H-1 to an s, H-7 to an s, H-5 to a d ($J_{5,4}$ = 10). Mass spectrum showed molecular ion at m/e = 179.0733 (83%), 128 (base peak); $C_{13}H_9N$ requires 179.0734. *Anal.* calcd. for $C_{13}H_9N$: C 87.12, H 5.06, N 7.82; found: C 86.81, H 5.25, N 7.72.

The first band was rechromatographed three times on Silica Gel 60 (2 cm × 45 cm; 2% ether–cyclohexane); COT **7** was eluted first, followed by diene **9**. This procedure led to the isolation of 13.9 mg (10%) of COT **7** and 5.8 mg (4%) of diene **9**, mp 75–77°C (from hexane); ir (KBr): 2200 (C≡N) cm^{-1}; uv (hexane): 276 sh (8 500), 286.5 (12 200), 296.5 (12 600), 304 sh (9 400), and 318.5 (5 700); nmr (400 MHz; $CDCl_3$): 7.15–7.35 (m, 4H, aromatics), 6.99 (br s, 1H, H-4), 6.25 (br d, 1H, H-7, $J_{8,7}$ = 2.8), 6.13 (dd, 1H, H-8, $J_{8,1}$ = 1, $J_{7,8}$ = 2.8), 4.27 (d, 1H, H-1, $J_{1,6}$ = 4.5), and 3.82 (br d, 1H, H-6, $J_{6,1}$ = 4.5, $J_{6,4}$ = $J_{6,7}$ = 1); spin decoupling experiments: irradiation of H-4 modified H-6 to a dd ($J_{6,1}$ = 4.5, $J_{6,7}$ = 1); irradiation of H-7 collapsed H-8 to a d ($J_{8,1}$ = 1); irradiation of H-8 collapsed H-7 to a br s; irradiation of H-1 modified H-7 to a dd ($J_{7,6}$ = 1, $J_{8,7}$ = 2.8) and collapsed H-6 to a br s and H-8 to a d ($J_{7,8}$ = 2.8); irradiation of H-6 sharpened H-4 and H-7, and collapsed H-1 to a br s. Mass spectrum showed molecular ion at m/e = 179.0731 (93%), 153 (base peak).

Catalytic reduction of endo*-8-cyano-2,3-benzobicyclo[4.2.0]octa-2,4-diene (**11**)*

A stirred mixture of 41.8 mg (0.23 mmol) of **11** (4) and 6.0 mg of 10% Pd on C in 8 mL of ethyl acetate was hydrogenated at room temperature and pressure during 20 min. The catalyst was removed by filtration through Celite, and the solution concentrated. The residue was subjected to rotating tlc (silica gel; 2 mm thickness; 10% ethyl acetate – cyclohexane). Short path distillation (70°C/0.1 Torr; 1 Torr = 133.3 Pa) of the main band gave 32.4 mg (77%) of *endo*-8-cyano-2,3-benzobicyclo[4.2.0]oct-2-ene (**10**; gc purity >99%) as a colourless oil; ir (neat liquid): 2230 (C≡N) cm^{-1}; uv (hexane): 249 sh (120), 253 sh (175), 261 sh (280), 266 (375), and 273 (380); nmr (400 MHz; $CDCl_3$): 7.07–7.26 (m, 4H, aromatics), 3.82 (br t, 1H, H-1, $J_{1,6}$ ~ $J_{1,8}$ ~ 9, $J_{1,7'}$ ~ 2), 3.61 (dt, 1H, H-8, $J_{8,1}$ = 8, $J_{8,7}$ = $J_{8,7'}$ = 9), 2.92–3.03 (m, 2H, H-4′ and H-6), 2.76 (dt, 1H, H-4, $J_{4,5}$ = $J_{4,5'}$ = 4.5, $J_{4,4'}$ = 16), 2.53 (sym m, 1H, H-7′), 2.20 (dt, 1H, H-7, $J_{7,6}$ = $J_{7,8}$ = 8, $J_{7,7'}$ = 12), 1.79–1.86 and 1.66–1.75 (m and m, 2H, C-5 methylenes); spin decoupling experiments: irradiation of H-1 modified H-8 and the 2.92–3.03 m, and collapsed H-7′ to a dt ($J_{7,7'}$ = 12, $J_{7',6}$ = $J_{7',8}$ = 10.5); other decouplings confirmed the above assignments and coupling constants. Mass spectrum showed molecular ion at m/e = 183.1048 (6.5%), 130 (base peak); $C_{13}H_{13}N$ requires 183.1048.

Catalytic reduction of diene 8

A stirred mixture of 6.0 mg (0.034 mmol) of **8** and 2.1 mg of 10% Pd on C in 4 mL of ethyl acetate was hydrogenated at room temperature and pressure during 25 min. The catalyst was removed by filtration through Celite, and the solution concentrated. The residue was subjected to rotating tlc (silica gel; 2 mm thickness; 10% ethyl acetate – cyclohexane). Short path distillation (65°C/0.1 Torr) of the main band gave 5.4 mg (88%) of colourless oil identical (gc, ir, nmr) to **10**.

Thermolysis of diene 8

A solution of 15.2 mg (0.085 mmol) of **8** in 2 mL of *n*-nonane was refluxed (ca. 150°C) during 3 h. The thermolysis product (no naphthalene by gc) was column chromatographed on Silica Gel 60 (1 cm × 35 cm; 2% ether–cyclohexane). Crystallization of the main band from hexane gave 13.8 mg (91%) of COT **7**, mp 72–74°C (lit. (11) mp 73–74°C).

Direct irradiation of diene 8

A solution of 78.0 mg (0.44 mmol) of diene **8** and 6.7 mg of tetradecane (gc standard) in 35 mL of cyclohexane was photolyzed (Pyrex filter) for 12 h in cell B (45% conversion by gc). The photolysate composition analysed (gc and nmr) for 3.9 mg (7%) naphthalene, 1.6 mg (2%) tetracyclic **14**, 2.7 mg (3%) COT **13**, 2.7 mg (3%) COT **7**, 42.9 mg (55%) diene **8**, and 19.4 mg (25%) SB **12**. The photolysate was concentrated and the residue chromatographed on a Lobar column (4% ethyl acetate – cyclohexane). The first band eluted was naphthalene (identified by gc and nmr). The second band gave 2.2 mg (3%) of COT **7**, and the third band gave 2.1 mg (3%) of COT **13**, mp 100–102°C (from hexane; lit. (11) mp 102–103°C), identified by gc and nmr comparison with an authentic sample (11). The fourth band gave 39.7 mg (51%) of recovered diene **8**. The fifth band contained 1.2 mg (1.5%) of tetracyclic **14**, mp 95–97°C (from hexane); ir (KBr): 2230 (C≡N) cm^{-1}; uv (hexane): 253 (135), 258 (210), 264 (280), 266 (270), 271 (165), and 273 (250); ^1H nmr (400 MHz; $CDCl_3$): 7.20–7.25 (sym m, 4H, aromatics), 4.45–4.48 (sym m, 2H, H-1 and H-6), 3.36 (br t, 1H, H-4, $J_{4,2(3)}$ = 3.5, $J_{4,1(6)} \leq 0.3$), 2.24–2.27 (sym m, 2H, H-2 and H-3); spin decoupling experiments: irradiation of H-1,6 collapsed H-2,3 to a d ($J_{2(3),4}$ = 3.5) and H-4 to a sharp t ($J_{4,2(3)}$ = 3.5); irradiation of H-4 modified both H-1,6 and H-2,3; irradiation of H-2,3 collapsed both H-1,6 and H-4 to br singlets; ^{13}C nmr (100 MHz; ^1H decoupled; $CDCl_3$): 144.07 (C7 and C8), 127.24 and 122.04 (α- and β-aromatics), 117.63 (C≡N), 55.48 (C1 and C6), 50.99 (C5), 27.67 (C4), and 20.26 (C2 and C3) ppm. Mass spectrum showed molecular

Can. J. Chem. Downloaded from www.nrcresearchpress.com by 61.7.252.67 on 09/07/12
For personal use only.

ion at m/e = 179.0726 (69%), 128 (base peak); $C_{13}H_9N$ requires 179.0734. *Anal.* calcd. for $C_{13}H_9N$: C 87.12, H 5.06, N 7.82; found: C 87.24, H 5.17, N 7.63.

The seventh, and last, band contained SB **12** of gc purity >98% (note: SB **12** rapidly polymerizes when solvent free); details of the nmr data are given in Table 1; spin decoupling experiments: irradiation of H-7 collapsed H-8 to a dd ($J_{8,1}$ = 6, $J_{8,2}$ = 7); irradiation of H-5 collapsed H-1 to a t ($J_{1,2} = J_{1,8}$ = 6); irradiation of H-1 collapsed H-5 to an s, H-2 to a d ($J_{2,8}$ = 7), and H-8 to a dd ($J_{8,2}$ = 7, $J_{8,7}$ = 2.5); irradiation of H-2 modified H-1 and H-8; irradiation of H-8 collapsed H-7 to an s, H-1 to a t ($J_{1,2} = J_{1,5}$ = 6), and H-2 to a d ($J_{2,8}$ = 7).

Catalytic reduction of SB ***12***

A stirred mixture of ca. 49 mg (0.27 mmol) of **12**, 8.1 mg of 10% Pd on C, and 8.6 mg of tetradecane (gc standard) in 10 mL of ethyl acetate was hydrogenated at room temperature and pressure during 40 min (complete loss of starting material). The catalyst was removed by filtration through Celite, and the resulting solution, when analysed by gc, showed three major peaks of relative area 4(**18**):1(unknown):1(unknown). The solution was concentrated and the residue was chromatographed on a column of Silica Gel 60 (2 cm × 45 cm; 2% ether–cyclohexane). Crystallization of the main band from hexane gave 29.8 mg (61%) of colourless **18**, mp 106–108°C; ir (KBr): 2225 (C≡N) cm^{-1}; uv (hexane): 223 sh (4 600), 258 sh (240), 264 (400), 269 sh (550), 270 (600), and 278 (720); ^1H nmr (400 MHz; $CDCl_3$), see Table 2; spin decoupling experiments: irradiation of H-5 collapsed H-6 to a dd ($J_{6,7}$ = 8.5, $J_{6',7}$ = 10.5), H-1 to a br t ($J_{1,2} \sim J_{1,8} \sim$ 6.5), and H-7 to a ddd ($J_{7,6}$ = 8.5, $J_{7',7}$ = 13.5, $J_{7,8}$ = 7); irradiation of H-6 collapsed H-5 to a dd ($J_{5,1}$ = 5.0, $J_{5,7}$ = 1.5), H-7′ to a dd ($J_{7',7}$ = 13.5, $J_{7',8}$ = 2), and modified H-7; irradiation of H-1 collapsed H-5 to a d ($J_{5,6}$ = 5.0), H-2 to a d ($J_{2,8}$ = 7.5), and H-8 to a br dt ($J_{8,2} \sim J_{8,7} \sim$ 7.5, $J_{8,7'}$ = 2); irradiation of H-2 modified H-1 and H-8; irradiation of H-7 collapsed H-5 to a t ($J_{5,1} = J_{5,6}$ = 5.0), and modified H-6, H-8, and H-7′; irradiation of H-8 modified H-1, and collapsed H-2 to a d ($J_{2,1}$ = 6.5), H-7 to a ddd ($J_{7,6}$ = 8.5, $J_{7,7'}$ = 13.5, $J_{7,5}$ = 1.5), and H-7′ to a dd ($J_{7',6}$ = 10.5, $J_{7',7}$ = 13.5); irradiation of H-7′ modified H-6 and H-7, and collapsed H-8 to a br q ($J_{8,1} \sim J_{8,2} \sim J_{8,7} \sim$ 7). Mass spectrum showed molecular ion at m/e = 181.0890 (69%), 128 (base peak); $C_{13}H_{11}N$ requires 181.0892. *Anal.* calcd. for $C_{13}H_{11}N$: C 86.15, H 6.12, N 7.73; found: C 86.33, H 6.13, N 7.74.

Sensitized irradiation of diene ***8***

A solution of 38.2 mg (0.21 mmol) of diene **8**, 4.3 mg (0.02 mmol) of Michler's ketone, and 5.2 mg of tetradecane (gc standard) in 35 mL of cyclohexane was photolyzed (uranium glass filter) for 1.5 h in cell B (74% conversion by gc). The photolysate composition analysed (gc) for 2.3 mg (8%) naphthalene, 2.0 mg (6%) SB **4**, 9.9 mg (26%) diene **8**, and 22.1 mg (58%) SB **12**. The photolysate was concentrated and the residue chromatographed on Silica Gel 60 (2 cm × 45 cm; 4% ether–cyclohexane). The first band eluted was naphthalene (identified by gc and nmr) and the second band contained 8.6 mg (23%) of recovered diene **8**. The third band contained a mixture of SB **4** and SB **12**; a small sample of pure SB **12** (>98% by gc) was obtained from the tail end of the band. Preparative gc of the bulk of the third band on an S.E. 30 column eluted, firstly, 0.9 mg (2%) of SB **4**, identified by gc and nmr comparison with an authentic sample (11), followed by SB **12**, much of which polymerized in the collector. We have subsequently found that SB's **4** and **12** can be completely separated by column chromatography on silica gel impregnated with silver nitrate.

Quantum yield determinations

Quantum yields were performed on an apparatus previously described (19), which includes an optical bench arranged for beam splitting into ferrioxalate actinometer (20). Cyclohexane solutions (3 mL) of reactants (ca. (5–6.5) × 10^{-3} M) and sensitizer, if any (Michler's ketone, 0.57 × 10^{-3} M), were deoxygenated prior to irradiation by flushing with argon. A positive pressure of argon was maintained over the stirred solutions throughout the course of the irradiations. The quantum yields, given in Scheme 2, were obtained from several runs extrapolated to zero conversion. Product analyses were determined by gc (internal tetradecane standard) and by nmr. For the direct irradiations, light of wavelength 280 nm was used. For sensitized runs, the sensitizer absorbed >95% of the incident light (334 nm) employed.

Labelled COT ***7****a*

Deuterated COT ***7a*** (90% d_1 at C-8) was prepared as previously described (11); nmr (400 MHz; $CDCl_3$): 7.22–7.28 (m, 3.51H, H-5 + 2 aromatics + residual $CHCl_3$), 6.95–7.00 (m, 2.00H, 2 aromatics), 6.55 (d, 1.02H, H-10, $J_{10,9}$ = 11.5), 6.08 (dd, 0.07H, H-8, $J_{8,7}$ = 11, $J_{8,9}$ = 4), 6.04 (d, 1.00H, H-9, $J_{9,10}$ = 11.5), and 5.76 (br s, 0.97H, H-7). Integrations for ***7a*** and for all subsequent deuterium labelled compounds were normalized by assigning integer values to one or more aromatic proton signals, unless otherwise indicated; integration errors due to baseline undulations are estimated to be within ca. ±0.05H.

Labelled diene ***8****a from COT* ***7****a*

A solution of 238.9 mg (1.33 mmol) of COT ***7a*** (ca. 90% d_1 at C-8) in 200 mL of cyclohexane was photolyzed directly at >310 nm for 21 h in Cell A. The photolysate was worked up as in the case of the direct irradiation of COT **7** to give 33.3 mg (14%) of diene ***8a***; nmr (400 MHz; $CDCl_3$): 7.18–7.27 (m, 3.72H, 3 aromatics + residual $CHCl_3$), 7.08 (m, 1.00H, 1 aromatic), 6.78 (s, 0.98H, H-7), 6.38 (d, 1.00H, H-4, $J_{4,5}$ = 10), 5.80 (d, 1.00H, H-5, $J_{5,4}$ = 10), 4.36 (s, 1.00H, H-1), and 3.76 (m, 0.07H, H-6).

Thermolysis of labelled diene ***8****a*

A solution of 9.5 mg (0.053 mmol) of ***8a*** in 1 mL of *n*-nonane was refluxed (ca. 151°C) during 2.25 h. The thermolysis product was worked up as in the case of the thermolysis of nondeuterated diene to give 8.3 mg (87%) of COT ***7a***; nmr (400 MHz; $CDCl_3$): 7.22–7.28 (m, 3.53H, H-5 + 2 aromatics + residual $CHCl_3$), 6.95–7.00 (m, 2.00H, 2 aromatics), 6.55 (d, 1.00H, $J_{10,9}$ = 11.5), 6.08 (dd, 0.09H, H-8, $J_{8,7}$ = 11, $J_{8,9}$ = 4), 6.04 (d, 1.00H, H-9, $J_{9,10}$ = 11.5), and 5.76 (br s, 0.98H, H-7).

Direct irradiation of labelled diene ***8****a*

A solution of 30.3 mg (0.17 mmol) of diene ***8a*** and 6.0 mg of tetradecane (gc standard) in 35 mL of cyclohexane was photolyzed (Pyrex filter) for 10.3 h in cell B (46% conversion by gc). The photolysate, when worked up as in the case of the direct irradiation of unlabelled **8**, gave: 0.8 mg (3%) COT ***7b***, nmr (400 MHz; $CDCl_3$): 7.22–7.28 (m, 5.47H, H-5 + 2 aromatics + residual $CHCl_3$), 6.95–7.00 (m, 2.00H, 2 aromatics), 6.55 (d, 1.04H, H-10, $J_{10,9}$ = 11.5), 6.08 (m, 0.98H, H-8), 6.04 (dd, 1.00H, H-9, $J_{9,8}$ = 4, $J_{9,10}$ = 11.5), and 5.76 (d, 0.09H, H-7, $J_{7,8}$ = 11); 0.9 mg (3%) COT ***13a***, nmr (400 MHz; $CDCl_3$): 7.21–7.31 (m, 3.58H, 2 aromatics + residual $CHCl_3$), 6.95–7.05 (m, 2.00H, 2 aromatics), 6.75 and 6.73 (s and d, 1.99H, H-5 and H-10, $J_{10,9}$ = 11.5), 6.67 (d, 0.96H, H-8, $J_{8,9}$ = 4), 6.07 (dd, 1.00H, H-9, $J_{9,8}$ = 4, $J_{9,10}$ = 11.5), and 5.95 (d, 0.10H, H-6, $J_{6,5}$ = 11.5); 13.9 mg (46%) of recovered diene ***8a***, nmr (60 MHz; CCl_4): 6.93–7.48 (m, 4.00H, 4 aromatics), 6.77 (s, 0.95H, H-7), 6.43 (d, 0.95H, H-4, $J_{4,5}$ = 10), 5.83 (d, 1.00H, H-5, $J_{5,4}$ = 10), 4.46 (s, 1.03H, H-1), and 3.83 (m, 0.09H, H-6); ca. 0.5 mg (2%) of tetracyclic **14**-d_1, nmr (400 MHz; $CDCl_3$): 7.20–7.25 (m, 4.55H, 4 aromatics + residual $CHCl_3$), 4.45–4.48 (m, 2.00H, H-1 and H-6), 3.36 (d, 0.99H, H-4, $J_{4,3}$ = 3.5), 2.24–2.27 (t, 1.05H, H-2 and H-3, $J_{3,4} = J_{3,6}$ = 3.5); and 6.4 mg (21%, estimated by gc) of SB ***12a***, nmr (400 MHz; $CDCl_3$): 7.33 (m, 1.00H, 1 aromatic), 7.18–7.28 (m, 3.66H, 3 aromatics + residual $CHCl_3$), 6.01 (d, 0.98H, H-7, $J_{7,8}$ = 2.5), 4.06 (s, 1.03H, H-5), 3.49 (q, 0.08H, H-1, $J_{1,2} = J_{1,5} = J_{1,8}$ = 6), 3.29 (d, 1.03H, H-2, $J_{2,8}$ = 7), and 2.79 (dd, 0.98H, H-8, $J_{8,2}$ = 7, $J_{8,7}$ = 2.5).

Sensitized irradiation of labelled diene ***8****a*

A solution of 39.6 mg (0.22 mmol) of diene ***8a***, 4.3 mg (0.02 mmol) of Michler's ketone, and 5.4 mg of tetradecane (gc standard) in 35 mL of cyclohexane was photolyzed (uranium glass filter) for 1.5 h in cell B (76% conversion by gc). The photolysate, when worked up as in the case of the direct irradiation of unlabelled **8**, gave: 8.1 mg (20%) of recovered diene ***8a***, nmr (60 MHz; CCl_4): 6.77–7.48 (m, 4.00H, 4 aromatics), 6.77 (s, 1.01H, H-7), 6.43 (d, 1.06H, H-4, $J_{4,5}$ = 10),

5.83 (d, 0.99H, H-5, $J_{5,4}$ = 10), 4.46 (s, 0.97H, H-1), and 3.83 (m, 0.10H, H-6); 0.9 mg (2%) of SB **4***a*, nmr (400 MHz; $CDCl_3$): 7.38 (m, 1.05H, 1 aromatic), 7.20 (m, 2.01H, 2 aromatics), 7.10 (m, 0.94H, aromatic), 5.72 (m, 0.07H, H-6), 5.20 (d, 1.00H, H-7, $J_{7,8}$ = 2.5), 4.20 (s, 0.95H, H-5), 3.68 (d, 0.95H, H-2, $J_{2,8}$ = 7.5), 3.36 (dd, 0.99H, H-8, $J_{8,2}$ = 7.5, $J_{8,7}$ = 2.5); and SB **12***a*, nmr (400 MHz; $CDCl_3$): 7.33 (m, 1.00H, 1 aromatic), 7.18–7.28 (m, 3.20H, 3 aromatics + residual $CHCl_3$), 6.01 (d, 0.99H, H-7, $J_{7,8}$ = 2.5), 4.06 (s, 1.00H, H-5), 3.49 (q, 0.09H, H-1, $J_{1,2}$ = $J_{1,5}$ = $J_{1,8}$ = 6), 3.29 (d, 1.04H, H-2, $J_{2,8}$ = 7), and 2.79 (dd, 1.03H, H-8, $J_{8,2}$ = 7, $J_{8,7}$ = 2.5).

Acknowledgements

The authors thank the Spectroscopic Services Laboratory of the University of Alberta and the Agriculture Canada Research Station at Lethbridge for the 400-MHz nmr and mass spectra. Financial support from the Natural Sciences and Engineering Research Council of Canada is gratefully acknowledged.

1. (*a*) M. DEMUTH. Mod. Synth. Methods, **4**, 89 (1986); (*b*) Pure Appl. Chem. **58**, 1233 (1986); (*c*) M. DEMUTH and K. SCHAFFNER. Angew. Chem. Int. Ed. Engl. **21**, 820 (1982); (*d*) K. SCHAFFNER and M. DEMUTH. Mod. Synth. Methods, **4**, 61 (1986).
2. C. O. BENDER, I. M. CASSIS, D. DOLMAN, L. D. HEERZE, and F. L. SCHULTZ. Can. J. Chem. **62**, 2769 (1984).
3. C. O. BENDER, D. L. BENGTSON, D. DOLMAN, and S. F. O'SHEA. Can. J. Chem. **64**, 237 (1986).
4. R. M. BOWMAN, C. CALVO, J. J. MCCULLOUGH, R. C. MILLER, and I. SINGH. Can. J. Chem. **51**, 1060 (1973).
5. J. STAPERSMA, I. D. C. ROOD, and G. W. KLUMPP. Tetrahedron, **38**, 191 (1982).
6. H. E. ZIMMERMAN, R. S. GIVENS, and R. M. PAGNI. J. Am. Chem. Soc. **90**, 6096 (1968).
7. C. PASCUAL, J. MEIR, and W. SIMON. Helv. Chim. Acta, **49**, 164 (1966).
8. L. A. PAQUETTE, M. J. KUKLA, and J. C. STOWELL. J. Am. Chem. Soc. **94**, 4290 (1972).
9. J. B. LAMBERT, H. R. SHURVELL, L. VERBIT, R. G. COOKS, and G. H. STOUT. Organic structural analysis. MacMillan Publishing Co., Inc., New York. 1976. p. 75.
10. S. S. HIXSON, P. S. MARIANO, and H. E. ZIMMERMAN. Chem. Rev. **73**, 531 (1973).
11. C. O. BENDER, D. W. BROOKS, W. CHENG, D. DOLMAN, S. F. O'SHEA, and S. S. SHUGARMAN. Can. J. Chem. **56**, 3027 (1978).
12. M. CHRISTL and R. LANG. J. Am. Chem. Soc. **104**, 4494 (1982).
13. M. CHRISTL and R. LANG. Tetrahedron, **42**, 1585 (1986).
14. H. E. ZIMMERMAN, R. J. BOETTCHER, N. E. BUEHLER, G. E. KECK, and M. G. STEINMETZ. J. Am. Chem. Soc. **98**, 7680 (1976).
15. P. J. COLLIN and W. H. F. SASSE. Tetrahedron Lett. 1689 (1968).
16. Y. HANZAWA and L. A. PAQUETTE. Synthesis, 661 (1982).
17. (*a*) H. E. ZIMMERMAN and R. L. SWAFFORD. J. Org. Chem. **49**, 3069 (1984); (*b*) H. E. ZIMMERMAN and R. E. FACTOR. Tetrahedron, **37**, 125 (1981); (*c*) H. E. ZIMMERMAN, D. ARMESTO, M. G. AMEZUA, T. P. GANNETT, and R. P. JOHNSON. J. Am. Chem. Soc. **101**, 6367 (1979); (*d*) H. E. ZIMMERMAN, R. J. BOETTCHER, and W. BRAIG. J. Am. Chem. Soc. **95**, 2155 (1973).
18. (*a*) C. O. BENDER and S. F. O'SHEA. Can. J. Chem. **57**, 2804 (1979); (*b*) L. A. PAQUETTE, A. Y. KU, C. SANTIAGO, M. D. ROZENBOOM, and K. N. HOUK. J. Am. Chem. Soc. **101**, 5972 (1979); (*c*) L. A. PAQUETTE, E. BAY, A. Y. KU, N. G. RONDAN, and K. N. HOUK. J. Org. Chem. **47**, 422 (1982).
19. C. O. BENDER, D. L. BENGTSON, D. DOLMAN, D. E. L. HERLE, and S. F. O'SHEA. Can. J. Chem. **60**, 1942 (1982).
20. (*a*) C. G. HATCHARD and C. A. PARKER. Proc. R. Soc. London, Ser. A, **235**, 518 (1956); (*b*) W. D. BOWMAN and J. N. DEMAS. J. Phys. Chem. **80**, 2434 (1976).

Can. J. Chem. Downloaded from www.nrcresearchpress.com by 61.7.252.67 on 09/07/12
For personal use only.

Influence of alkylation of the amino group on the reactions of adenine with the methylmercury(II) cation

LUCIE GRENIER, JEAN-PIERRE CHARLAND, AND ANDRÉ L. BEAUCHAMP[1]

Département de Chimie, Université de Montréal, C.P. 6128, Succ. A, Montréal (Qué.), Canada H3C 3J7

Received December 24, 1987

LUCIE GRENIER, JEAN-PIERRE CHARLAND, and ANDRÉ L. BEAUCHAMP. Can. J. Chem. **66**, 1663 (1988).

Reaction of the CH_3Hg^+ cation with 6-dimethylamino- and 6-diethylaminopurine (HL) yielded compounds of the types $[(CH_3Hg)L]$, $[(CH_3Hg)_2L]X$ (X = NO_3, ClO_4), and $[(CH_3Hg)_2(HL)](NO_3)_2$. Metal binding to N(9) in $[(CH_3Hg)L]$ was deduced from the nmr spectra. The coordination sites in the other types of compounds were determined from X-ray diffraction studies on two complexes of 6-dimethylaminopurine. Crystals of $[(CH_3Hg)_2L]ClO_4$ are monoclinic, space group $P2_1/c$, a = 9.319(3) Å, b = 9.581(8) Å, c = 19.624(8) Å, β = 118.23(3)°, and Z = 4. The structure was refined on 1521 nonzero MoKα reflections to R = 0.040. $[(CH_3Hg)_2(HL)](NO_3)_2.H_2O$ belongs to the same space group, a = 11.012(3) Å, b = 23.669(7) Å, c = 6.748(4) Å, β = 95.25(4)°, Z = 4, 1781 MoKα reflections, R = 0.053. In both complexes, the CH_3Hg^+ groups are bound to the N(9) and N(3) sites of the purine ring. In the $[(CH_3Hg)_2L]^+$ cation, the lone pair of N(7) is free, whereas it is occupied by a proton in $[(CH_3Hg)_2(HL)]^{2+}$. The ^1H and ^{13}C nmr spectra show that the solid state structures are retained in DMSO solutions. The $^2J(^{199}Hg—^1H)$ coupling constants suggest that protonation on N(7) produces for N(9) and N(3) average decreases of basicity corresponding to ~3 pK units.

LUCIE GRENIER, JEAN-PIERRE CHARLAND et ANDRÉ L. BEAUCHAMP. Can. J. Chem. **66**, 1663 (1988).

La réaction du cation CH_3Hg^+ avec la diméthylamino-6 et la diéthylamino-6 purine (HL) conduit à des composés de type $[(CH_3Hg)L]$, $[(CH_3Hg)_2L]X$ (X = NO_3, ClO_4) et $[(CH_3Hg)_2(HL)](NO_3)_2$. Les spectres rmn indiquent que le métal se lie au site N(9) dans $[(CH_3Hg)L]$. Les sites de coordination dans les deux autres cas ont été déterminés par diffraction des rayons-X sur des composés de la diméthylamino-6 purine. Les cristaux de $[(CH_3Hg)_2L]ClO_4$ sont monocliniques, groupe spatial $P2_1/c$, a = 9,319(3) Å, b = 9,581(8) Å, c = 19,624(8) Å, β = 118,23(3)° et Z = 4. La structure a été affinée au moyen de 1521 réflexions MoKα observées, jusqu'à un facteur R de 0,040. $[(CH_3Hg)_2(HL)](NO_3)_2.H_2O$ appartient au même groupe spatial, a = 11,012(3) Å, b = 23,669(7) Å, c = 6,748(4) Å, β = 95,25(4)°, Z = 4, 1781 réflexions MoKα, R = 0,053. Dans les deux complexes, les groupes CH_3Hg^+ sont liés aux sites N(9) et N(3) du noyau purinique. Dans le cation $[(CH_3Hg)_2L]^+$, le doublet de N(7) est libre, tandis qu'il est occupé par un proton dans $[(CH_3Hg)_2(HL)]^{2+}$. Les résultats de rmn ^1H et ^{13}C montrent que les structures observées à l'état solide sont retenues en solution dans DMSO. Les constantes de couplage $^2J(^{199}Hg—^1H)$ indiquent que la protonation de N(7) entraîne pour N(9) et N(3) un abaissement moyen de basicité correspondant à ~3 unités de pK.

Introduction

Over the past few years, we have been conducting an in-depth study of the coordination of the uniligating CH_3Hg^+ cation with adenine and some of its derivatives, both in the solid state and in solution (1–3). It was found that CH_3Hg^+ and the proton are not introduced onto the adenine ring following the same order. Indeed, protons bind to the adeninate monoanion in the sequence N(9)—N(1)—N(7)—N(3) (4), whereas only three CH_3Hg^+ cations could be introduced, in the order N(9)—N(7)—N(3). Binding to N(1) was not observed with adenine.

We recently became interested in developing multidentate ligands that could induce the formation of metal–metal bonds, while retaining available coordination sites to accept other types of electrophilic moieties. Since ^1H and ^{13}C nmr results had revealed that the N(9)/N(7)-bonded $[(CH_3Hg)_2(adeninate)]^+$ cation is probably involved in a tautomeric equilibrium with an N(9)/N(3) form in DMSO (5), we felt that mild steric hindrance in the neighborhood of N(7) might cleanly displace reactivity to the N(9)/N(3) side of the ring. To test this assumption, adenine was dialkylated at the amino group and allowed to react with CH_3Hg^+. The marked differences displayed by these dialkylated ligands are discussed in the present paper.

Experimental

Preparation

6-Dimethylaminopurine (HDMAd) and 6-diethylaminopurine (HDEAd) were prepared from 6-chloropurine (Aldrich) according to Itaya, Matsumoto, and Ogawa (6). The aqueous CH_3HgOH (1 *M*) solutions were used as received from Aldrich. Solutions of CH_3HgClO_4 and CH_3HgNO_3 were prepared in our laboratory as described earlier (7). The microanalyses were carried out by Schwarzkopf Microanalytical Laboratories, New York.

The ^1H nmr spectra were obtained at ambient probe temperature with a Bruker WH-90 instrument. The ^{13}C spectra were recorded at 100.62 MHz with the Bruker WH-400 instrument of the Centre Régional de RMN Haut Champ located at the Université de Montréal. The solvent was DMSO-d_6 ("Silanor", Merck, Sharp & Dohme Canada) containing TMS as internal reference.

$[(CH_3Hg)(DMAd)]$

The ligand (164 mg, 1 mmol) was dissolved in boiling water (19 mL) and CH_3HgOH 1 *M* (1.0 mL, 1 mmol) was added. The mixture was left at room temperature for 2 days and a white powder was obtained. It was quickly washed with small amounts of cold water. Yield: 290 mg, 78%. *Anal.* calcd. for $C_8H_{11}HgN_5$: C 25.43, H 2.93, N 18.54, Hg 53.09; found: C 25.38, N 2.90, N 18.49, Hg 53.02.

$[(CH_3Hg)_2(DMAd)]ClO_4$

The ligand (164 mg, 1 mmol) was dissolved in boiling water (18 mL). To the hot solution were added 1.0 mL (1 mmol) 1 *M* CH_3HgClO_4 and 1.0 mL (1 mmol) 1 *M* CH_3HgOH. After 2 days at room temperature, colorless crystals were filtered and quickly washed with small amounts of cold water. Yield: 410 mg, 63%. The same compound was obtained in lower yield (42%) when 1 mmol of CH_3HgClO_4 was used without hydroxide. The crystalline sample was morphologically homogeneous and the structure analysis described hereafter was done on a crystal from this batch.

$[(CH_3Hg)_2(DMAd)]NO_3.H_2O$

The method above was used, replacing CH_3HgClO_4 by CH_3HgNO_3. Yield: 41%. *Anal.* calcd. for $C_9H_{16}Hg_2N_6O_4$: C 16.05, H 2.39, N 12.48, Hg 59.57; found: C 16.17, H 2.31, N 12.70, Hg 60.19.

[1]To whom all correspondence should be addressed.

Can. J. Chem. Downloaded from www.nrcresearchpress.com by 112.217.228.212 on 09/07/12
For personal use only.

Can. J. Chem. Downloaded from www.nrcresearchpress.com by 112.217.228.212 on 09/07/12
For personal use only.

[(CH$_3$Hg)$_2$(HDMAd)](NO$_3$)$_2$.H$_2$O

To a suspension of 163 mg (1 mmol) of ligand in acetonitrile (30 mL) were added 2.0 mL (2 mmol) of aqueous 1 *M* CH_3HgNO_3, whereupon a clear solution was obtained. After spontaneous evaporation of two thirds of the solvent at room temperature, a white precipitate was collected and quickly washed with cold acetonitrile. Yield: 450 mg, 63%. *Anal.* calcd. for $C_9H_{15}Hg_2N_7O_6$: C 15.05, H 2.10, N 13.65, Hg 55.84; found: C 15.48, H 2.26, N 13.53, Hg 55.37. The same compound was obtained in low yield (11%) from a mixture of 1 mmol (163 mg) of ligand dissolved in 30 mL of water, with 1.0 mL of concentrated HNO_3 and 2.0 mL (2 mmol) of 1 *M* CH_3HgNO_3. After spontaneous evaporation of 20 mL of solvent at room temperature, a fine colorless powder was obtained.

With 6-diethylaminopurine, similar compounds were obtained by starting with 1 mmol (191 mg). Yields and microanalytical results are given below.

[(CH$_3$Hg)(DEAd)]

Yield: 270 mg, 67%. *Anal.* calcd. for $C_{10}H_{15}HgN_5$: C 29.59, H 3.73, N 17.26, Hg 49.42; found: C 29.67, H 3.88, N 17.33, Hg 49.53.

[(CH$_3$Hg)$_2$(DEAd)]NO$_3$

Yield: 220 mg, 33%. *Anal.* calcd. for $C_{11}H_{18}Hg_2N_6O_3$: C 19.33, H 2.65, N 12.30, Hg 58.70; found: C 19.28, H 2.86, N 12.21, Hg 58.58.

[(CH$_3$Hg)$_2$(DEAd)]ClO$_4$

Yield: 297 mg, 39%. *Anal.* calcd. for $C_{11}H_{18}ClHg_2N_5O_4$: C 18.33, H 2.52, N 9.71, Cl 4.92, Hg 55.65; found: C 18.41, H 2.67, N 9.39, Cl 4.68, Hg 55.18.

[(CH$_3$Hg)$_2$(HDEAd)](NO$_3$)$_2$

Yield: 192 mg, 62%. *Anal.* calcd. for $C_{11}H_{19}Hg_2N_7O_6$: C 17.70, H 2.57, N 13.13, Hg 53.74; found: C 17.55, H 2.62, N 13.06, Hg 53.46.

X-ray diffraction work

Space group and initial cell dimensions for both compounds were determined from precession and cone-axis photographs. The $2/m$ Laue symmetry and systematic absences ($0k0$, $k \neq 2n$; $h0l$, $l \neq 2n$) uniquely defined space group $P2_1/c$. The intensity data were collected with an Enraf-Nonius CAD4 diffractometer, following the procedure described elsewhere (8). The data were corrected for the Lorentz effect, polarization, and absorption (Gaussian integration, grid 8 × 8 × 8). The structures were solved by the heavy-atom method and refined on $|F_o|$ by least-squares procedures. The mercury atoms were located from Patterson maps and the non-hydrogen atoms were subsequently found from difference Fourier (ΔF) maps phased on Hg. The non-hydrogen atoms were isotropically refined by full-matrix squares. The ring hydrogen atoms were fixed at idealized positions (C(N)—H = 0.95 Å, sp^2 hybridization, isotropic B = 4.0 Å^2). Their parameters were not refined, but the coordinates were recalculated after each least-squares cycle. The methyl hydrogens were not visible on the ΔF maps. In the last cycles, the non-hdyrogen atoms were anisotropically refined by block-diagonal least squares. Details for each structure are given below. The scattering curves used were from standard sources (9). The f' and f'' contributions to anomalous dispersion for Hg and Cl (10) were included in structure factor calculations.

[(CH$_3$Hg)$_2$(DMAd)]ClO$_4$

$C_9H_{14}ClHg_2N_5O_4$ fw = 692.88

Monoclinic, $P2_1/c$, a = 9.319(3) Å, b = 9.581(8) Å, c = 19.624(8) Å, β = 118.23(3)°, V = 1544 Å^3, D_{calcd} = 2.981 g cm^{-3}, D_{obs} (in $C_2H_2Br_4/CH_3I$) = 2.88(3) g cm^{-3}, Z = 4, λ(MoKα) = 0.71069 Å, μ(MoKα) = 200.6 cm^{-1}, crystal dimensions (0.54 × 0.26 × 0.15 mm), transmission range = 0.021–0.096, T = 293 K.

A set of 2020 independent hkl and $hk\bar{l}$ reflections within a sphere limited by 2θ = 45° was collected. The three standard reflections fluctuated within ±4.0% during data collection. On the basis of the criterion $I > 3\sigma(I)$, a set of 1521 reflections was retained for structure determination. Isotropic refinement of all non-hydrogen atoms converged to $R = \Sigma||F_o| - |F_c||/\Sigma|F_o| = 0.101$ and $R_w = [\Sigma w(|F_o| - |F_c|)^2/\Sigma w|F_o|^2]^{1/2} = 0.112$. Anisotropic refinement of the non-hydrogen atoms with hydrogens fixed converged at $R = 0.040$, $R_w = 0.050$, and a goodness-of-fit ratio of 1.97 and 190 parameters varied. The general background in the final ΔF map was lower than ±0.70 e Å^{-3}, and a few peaks in the range ±|0.7–1.3| e Å^{-3} were found near Hg.

TABLE 1. Refined coordinates (× 10^3, Cl × 10^4, Hg × 10^5) and equivalent isotropic temperature factors (×10^3)

Atom	x	y	z	U_{eq}
	[(CH$_3$Hg)$_2$(DMAd)]ClO$_4$			
Hg(3)	13417(8)	19565(7)	37446(4)	48
Hg(9)	14179(8)	33256(7)	53126(4)	48
Cl(1)	512(7)	4497(5)	6834(3)	68
O(1)	85(2)	542(2)	744(1)	121
O(2)	182(3)	369(3)	695(1)	217
O(3)	14(2)	518(2)	617(1)	127
O(4)	−77(4)	373(3)	678(2)	251
N(1)	−299(2)	−45(2)	303(1)	55
N(3)	−78(2)	110(1)	369(1)	48
N(6)	−475(2)	−121(1)	350(1)	53
N(7)	−261(2)	73(2)	493(1)	49
N(9)	−52(1)	191(1)	492(1)	43
C(2)	−176(2)	25(2)	310(1)	56
C(3)	341(2)	278(2)	380(1)	71
C(4)	−124(2)	118(2)	425(1)	44
C(5)	−254(2)	47(2)	425(1)	43
C(6)	−346(2)	−39(2)	361(1)	47
C(8)	−142(2)	158(2)	530(1)	54
C(9)	326(2)	479(2)	566(1)	72
C(61)	−548(2)	−116(2)	401(1)	63
C(62)	−557(3)	−203(2)	280(1)	75
	[(CH$_3$Hg)$_2$(HDMAd)](NO$_3$)$_2$.H$_2$O			
Hg(3)	35235(9)	45059(4)	17643(13)	56
Hg(9)	28869(8)	31698(4)	21291(12)	47
O(10)	669(2)	163(1)	409(3)	97
O(11)	816(1)	206(1)	571(2)	63
O(12)	827(2)	116(1)	523(3)	92
O(20)	280(2)	305(1)	638(3)	93
O(21)	395(2)	349(1)	850(2)	93
O(22)	306(2)	391(1)	604(2)	86
O(30)	443(2)	558(1)	160(2)	69
N(1)	725(2)	445(1)	431(2)	50
N(3)	522(1)	422(1)	321(2)	50
N(6)	876(2)	380(1)	523(3)	53
N(7)	656(2)	292(1)	445(2)	44
N(9)	475(1)	323(1)	323(2)	42
N(10)	771(2)	161(1)	494(2)	57
N(20)	324(2)	349(1)	699(3)	69
C(2)	618(2)	458(1)	357(3)	51
C(3)	184(2)	473(1)	38(4)	76
C(4)	552(2)	367(1)	351(3)	37
C(5)	668(2)	350(1)	426(3)	40
C(6)	760(2)	390(1)	467(3)	44
C(8)	544(2)	278(1)	382(3)	52
C(9)	110(2)	312(1)	107(4)	71
C(61)	925(2)	322(1)	557(4)	66
C(62)	969(2)	425(1)	551(5)	96

[(CH$_3$Hg)$_2$(HDMAd)](NO$_3$)$_2$.H$_2$O

$C_9H_{17}Hg_2N_7O_7$ fw = 736.46

Monoclinic, $P2_1/c$, a = 11.012(3) Å, b = 23.669(7) Å, c = 6.748(4) Å, β = 95.25(4)°, V = 1751 Å^3, D_{calcd} = 2.793 g cm^{-3},

D_{obs} (in $C_2H_2Br_4$–CH_3I) = 2.84(2) g cm^{-3}, Z = 4, λ(MoKα) = 0.71069 Å, μ(MoKα) = 175.5 cm^{-1}, crystal dimensions: 0.60 × 0.03 × 0.17 mm, transmission range: 0.040–0.596, T = 293 K.

A total of 3069 independent hkl and $hk\bar{l}$ reflections was collected ($2\theta_{max}$ = 50°), of which 1781 were above background ($I > 3.0\sigma(I)$). The standard reflections fluctuated within ±2.0% during data collection. Isotropic refinement led to R = 0.109 and R_w = 0.115. Anisotropic refinement converged for R = 0.053, R_w = 0.060 and a goodness-of-fit ratio of 2.11 for 226 parameters varied. The general background on the final ΔF map was below ±0.9 e Å^{-3}, and a few peaks in the range ± |0.9–1.9| e Å^{-3} were found near Hg.

The refined coordinates for both structures are listed in Table 1. The anisotropic temperature factors are provided in the supplementary material.[2]

Results and discussion

Reactions

The reaction of CH_3HgOH with the dialkylaminopurines (HL) yielded as the only product the neutral [(CH_3Hg)L] complex, in which the N(9)—H proton has been displaced by the CH_3Hg^+ cation and neutralized by the OH^- group. As in the case of adenine (2), all attempts to obtain 1:1 complexes without loss of the imidazole proton were unsuccessful. Adding HNO_3 or $HClO_4$ to a 1:1 mixture of the ligands with the corresponding CH_3Hg^+ salt led to the purinium salt [H_2L]X. When the reaction was conducted with CH_3HgNO_3 or CH_3HgClO_4 without adding acid, the 2:1 [$(CH_3Hg)_2$L]X compounds were obtained, one half of the ligand being used to accept the proton displaced by the methylmercury cation (equation [1]):

[1] $2CH_3HgX + 2HL \rightleftharpoons [(CH_3Hg)_2L]X + [H_2L]X$

Better yields were obtained from equimolar amounts of ligand, CH_3HgOH and CH_3HgX. In this respect, the dialkylaminopurines react like adenine (2).

Various attempts were made to prepare higher complexes, by using CH_3HgX:ligand ratios as high as 8. These mixtures invariably yielded the [$(CH_3Hg)_2$L]X complexes as the major products, indicating that in contrast with adenine, introducing a third CH_3Hg^+ group onto the ligand is difficult. With high metal-to-ligand ratios, a small amount of a compound whose analog with adenine had not been obtained, appeared in crystalline form and could be separated from the major powdery material. This compound was subsequently shown to be a 2:1 complex [$(CH_3Hg)_2$(HL)]$(NO_3)_2$ in which the ligand retained the imidazole proton, its formation being favored by the excess of acidic $CH_3HgOH_2^+$ ions ($pk_a \sim 4.6$) (11). The same compound was obtained in high yields by adding HNO_3 to a 2:1 CH_3HgX:ligand mixture in acetonitrile–water.

The structures of the two cationic compounds of dimethylaminopurine were determined by X-ray diffraction.

Crystal structures

The numbering scheme used for the complex cations in [$(CH_3Hg)_2$(DMAd)]ClO_4 and [$(CH_3Hg)_2$(HDMAd)]$(NO_3)_2.H_2O$ is shown in Fig. 1. In both compounds, the CH_3Hg^+ groups are bonded to the N(9) and N(3) sites of dimethylaminopurine. In the [$(CH_3Hg)_2$(DMAd)]$^+$ ion, the ligand is formally anionic, since the N(9)—H proton has been substituted by the metal. The N(7) position in [$(CH_3Hg)_2$(HDMAd)]$^{2+}$ is occupied by a proton, which can be regarded as having been transferred from N(9) to N(7) in a formally neutral purine ligand.

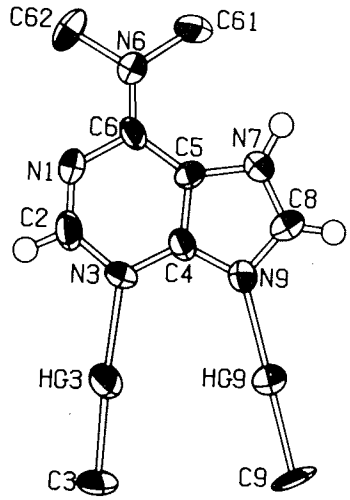

FIG. 1. ORTEP drawing of the complex cation in [$(CH_3Hg)_2$(HDMAd)]$(NO_3)_2.H_2O$. Ellipsoids correspond to 50% probability. The hydrogens are shown as spheres of arbitrary size. The same numbering scheme is used for [$(CH_3Hg)_2$(DMAd)]ClO_4, whose ORTEP drawing is given in the supplementary material.

Interatomic distances and bond angles are listed in Table 2. The four Hg—N and Hg—C distances, averaging 2.11 and 2.06 Å (σ = 0.02 Å), respectively, do not significantly differ from those reported for similar systems (2, 3). These two primary bonds define a roughly linear coordination about mercury: departure from the ideal 180° angle (≤3.7(8)°) is significant, but common for such compounds. The Hg...Hg separation is 3.315(1) Å for [$(CH_3Hg)_2$(DMAd)]$^+$ and 3.253(1) Å for [$(CH_3Hg)_2$(HDMAd)]$^{2+}$. This is higher than the sum of the van der Waals radii (3.0 Å) (12) and Hg...Hg contacts as short as 3.06 Å have been observed in cytosine complexes (7, 13). Positioning two CH_3Hg^+ groups side-by-side did not introduce severe constraints in normal coordination geometry, since the two Hg—N—C angles show no dramatic differences for any of the coordination sites. The greatest difference occurs for the N(9)-bound metal in [$(CH_3Hg)_2$(HDMAd)]$^{2+}$, where the C—N(9)—Hg(9) angles (123.5(11) and 132.7(13)°) indicate that binding is achieved in a direction only 5° off the normal lone pair orientation.

The bond lengths in the ligands are listed in Table 2. The large standard deviations in these heavy-atom structures mask any significant changes in distances that might result from complexation. For the [$(CH_3Hg)_2$(HDMAd)]$^{2+}$ ion, the C(5)—N(7)—C(8) and C(4)—C(5)—N(7) angles are respectively 4° greater and 7° smaller than those of a neutral adenine ring (14) and of the [$(CH_3Hg)_2$(DMAd)]$^+$ cation (Table 2). Taylor and Kennard (15) have shown for a broad sample of purines that protonation on a ring nitrogen produces on the internal C—N—C angle an increase of 4–6°, balanced by opposite changes on one or both adjacent N—C—C angles to keep the ring planar. The observed variations follow the pattern expected for N(7)-protonation, which has also been found for the

[2]The supplementary material includes lists of observed and calculated structure factor amplitudes, anisotropic temperature factors, fixed hydrogen coordinates, distances and angles in the anions, and details on the geometry of intermolecular interactions and on least-squares planes calculations for both structures. Complete set of data may be purchased from the Depository of Unpublished Data, CISTI, National Research Council of Canada, Ottawa, Ont., Canada K1A 0S2.

Can. J. Chem. Downloaded from www.nrcresearchpress.com by 112.217.228.212 on 09/07/12
For personal use only.

TABLE 2. Interatomic distances and bond angles

Bond	Distance (Å)	
	$[(CH_3Hg)_2(DMAd)]ClO_4$	$[(CH_3Hg)_2(HDMAd)](NO_3)_2.H_2O$
Hg(3)—C(3)	2.04(2)	2.07(2)
Hg(3)—N(3)	2.10(2)	2.14(2)
Hg(9)—C(9)	2.07(2)	2.04(2)
Hg(9)—N(9)	2.09(1)	2.12(2)
N(1)—C(2)	1.28(3)	1.27(3)
C(2)—N(3)	1.36(2)	1.36(3)
N(3)—C(4)	1.36(2)	1.35(2)
C(4)—C(5)	1.39(3)	1.39(3)
C(5)—C(6)	1.40(2)	1.40(3)
C(6)—N(1)	1.40(2)	1.37(2)
C(5)—N(7)	1.39(2)	1.39(2)
N(7)—C(8)	1.29(2)	1.31(3)
C(8)—N(9)	1.40(2)	1.35(3)
N(9)—C(4)	1.35(2)	1.35(2)
C(6)—N(6)	1.37(2)	1.32(3)
N(6)—C(61)	1.45(3)	1.49(3)
N(6)—C(62)	1.45(2)	1.48(3)
	Angle (deg)	
Bonds	$[(CH_3Hg)_2(DMAd)]ClO_4$	$[(CH_3Hg)_2(HDMAd)](NO_3)_2.H_2O$
C(2)—N(3)—Hg(3)	121.1(12)	121.0(13)
C(4)—N(3)—Hg(3)	126.0(11)	124.3(13)
N(3)—Hg(3)—C(3)	179.7(7)	176.3(8)
C(8)—N(9)—Hg(9)	125.6(11)	123.5(11)
C(4)—N(9)—Hg(9)	129.6(11)	132.7(13)
N(9)—Hg(9)—C(9)	177.3(7)	179.5(8)
C(6)—N(1)—C(2)	120.0(16)	122.2(17)
N(1)—C(2)—N(3)	127.9(17)	126.4(19)
C(2)—N(3)—C(4)	112.5(15)	113.6(16)
N(3)—C(4)—C(5)	125.6(15)	122.4(17)
C(4)—C(5)—C(6)	116.8(15)	120.1(17)
C(4)—C(5)—N(7)	110.4(14)	103.2(15)
C(5)—N(7)—C(8)	103.6(14)	108.4(16)
N(7)—C(8)—N(9)	114.6(16)	112.6(18)
C(8)—N(9)—C(4)	104.7(14)	103.9(16)
N(9)—C(4)—C(5)	106.5(14)	111.9(16)
C(5)—C(6)—N(1)	117.2(15)	114.9(17)
N(6)—C(6)—N(1)	116.0(15)	118.0(17)
N(6)—C(6)—C(5)	126.8(16)	126.9(18)
C(61)—N(6)—C(6)	122.4(15)	122.6(17)
C(62)—N(6)—C(6)	119.5(15)	123.3(18)
C(61)—N(6)—C(62)	117.6(16)	114.1(18)

Can. J. Chem. Downloaded from www.nrcresearchpress.com by 112.217.228.212 on 09/07/12
For personal use only.

adeninate ligand in the N(3)/N(9)-coordinated N(7)-protonated $Cu_2(adeninate)_4(ClO_4)_4.4H_2O$ compound (16). These angles, together with hydrogen-bonding (see packing pattern below), provide unambiguous proof for the presence of an acidic proton at N(7).

The purine system can be described as two planar units rings bent by 2° about the C(4)—C(5) bond. Maximum deviation of any ring atom from its own plane is 2σ (0.04 Å). Packing forces produce greater distortion in the substituents mainly for the CH_3Hg^+ groups. The NO_3^- ion is trigonal planar and the ClO_4^- ions is tetrahedral as expected. The mean distances are 1.23 Å (σ = 0.03 Å) for N—O and 1.37 Å (σ = 0.04 Å) for Cl—O. More details are given in the supplementary material.

The unit cell of $[(CH_3Hg)_2(DMAd)]ClO_4$ is shown in Fig. 2. Pairs of complex cations and ClO_4^- ions are clustered about crystallographic inversion centres and held together by eight Hg...O contacts. The six Hg(9)...O contacts are shorter than 3.07 Å (Table 3). Each Hg(3) atom participates in rather long 3.11(2) Å interactions with O(3). There are no particular contacts involving N(1) or N(7).

The packing pattern for $[(CH_3Hg)_2(HDMAd)](NO_3)_2.H_2O$ is shown in Fig. 3. The structure is stabilized by various Hg(9)–nitrate contacts (Table 3). Water molecule O(30), tightly held by Hg(3) at 2.74(1) Å, forms hydrogen bonds with two nitrate ions. O(11) is suitably oriented to be hydrogen-bonded with N(7)—H. The N(7)...O(11) distance of 2.77(2) Å

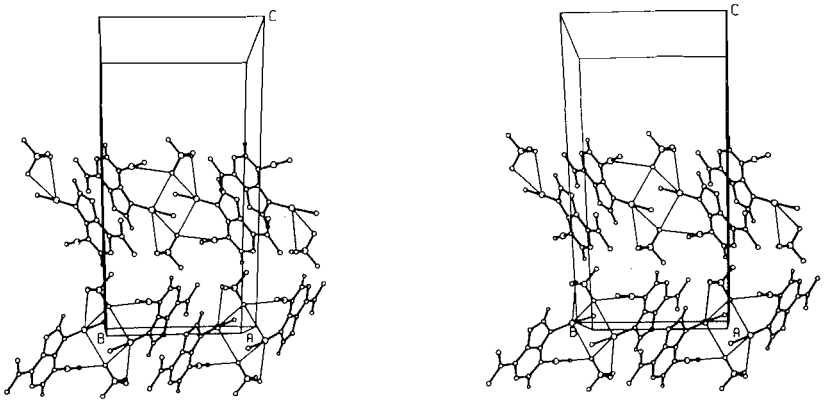

FIG. 2. Stereo view of the unit cell of $[(CH_3Hg)_2(DMAd)]ClO_4$. Thin lines represent Hg...O contacts.

TABLE 3. Selected intermolecular distances (A)[f]

Atoms	Distance
$[(CH_3Hg)_2(DMAd)]ClO_4$	
Hg(3)...O(3)[a]	3.11(2)
Hg(9)...O(2)	3.07(2)
Hg(9)...O(3)	3.05(2)
Hg(9)...O(3)[a]	2.94(2)
$[(CH_3Hg)_2(HDMAd)](NO_3)_2.H_2O$	
Hg(3)...O(30)	2.74(1)
Hg(9)...O(20)	2.89(2)
Hg(9)...O(22)	3.16(2)
Hg(9)...O(20)[b]	2.93(2)
Hg(9)...O(21)[c]	2.91(2)
N(7)—H...O(11)	2.77(2)
O(30)—H...O(21)[d]	2.84(2)
O(30)—H...O(10)[e]	2.79(2)

[a] $-x, 1-y, 1-z$.
[b] $x, \frac{1}{2}-y, z-\frac{1}{2}$.
[c] $x, y, z-1$.
[d] $1-x, 1-y, 1-z$.
[e] $1-x, \frac{1}{2}+y, \frac{1}{2}-z$.
[f] Angles given in the supplementary material.

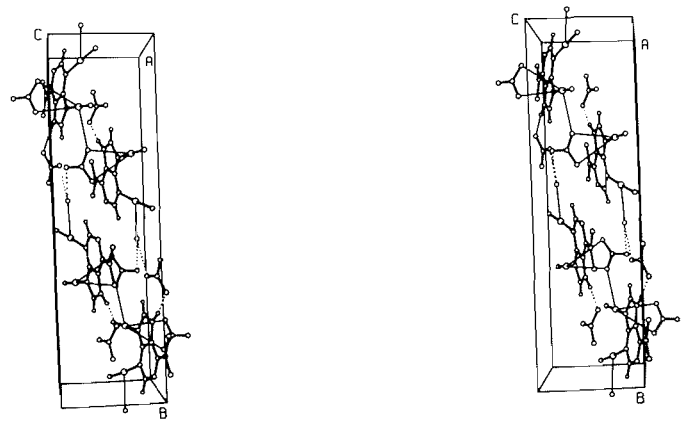

FIG. 3. Stereo view of the unit cell of $[(CH_3Hg)_2(HDMAd)](NO_3)_2.H_2O$. Thin lines correspond to Hg...O contacts and dashed lines to hydrogen bonds.

is much shorter than the sum of the van der Waals radii (3.05 Å) (12) and consistent only with strong hydrogen-bonding, thereby confirming that N(7) is protonated.

Nuclear magnetic resonance spectroscopy

The ^1H and ^{13}C nmr data for the two ligands and their three types of complexes are given in Tables 4 and 5, respectively. Our results for the free ligands are similar to those already reported (17–19).

Substitution of H(9) to yield the neutral $[(CH_3Hg)L]$ compounds induces upfield shifts of 0.28 ppm for H8 and 0.10 ppm for H2. In the ^{13}C spectrum, large downfield shifts are observed for C4 (5.7 ppm) and C8 (7.8 ppm). These displacements are similar to those observed upon formation of the corresponding adenine complex (1) and indicate that the neutral complex is N(9)-bonded here as well. The dialkylamino resonances are not appreciably affected in this case, but introducing a second CH_3Hg^+ group onto the ring generates a cationic species and induces downfield shifts of 0.1 ppm for the ^1H signals of the methyl protons in the dimethylamino compound and for the methylene protons in the other ligand. This second CH_3Hg^+ group shifts the H2 resonance by +0.31 ppm and the H8 resonance by +0.17 ppm from their respective positions for $[(CH_3Hg)L]$. This is consistent with coordination to N(3) for this second metal atom. In the ^{13}C spectra, the signal of the C(4) atom, adjacent to N(3), is shifted 5.8 ppm upfield, but the C(2) resonance does not move.

The $[(CH_3Hg)_2(HL)]^{2+}$ cations can be regarded as resulting from the protonation of $[(CH_3Hg)_2L]^+$. This proton does not greatly affect the dialkylamino resonances, but produces downfield shifts of 0.30 ppm for H8 and 0.10 ppm for H2. The ^{13}C signals appreciably displaced by protonation are those of the carbons adjacent to N(7), namely C(5) ($\Delta\delta \sim 2.5$ ppm) and C(8) ($\Delta\delta \sim 2$ ppm) (Table 5). This provides support for the presence of the acidic proton at the N(7) site as observed in the crystal structure. This proton does not produce independent ^1H signals, but broad peaks are found at ~6.7 ppm for the N(7)—H proton in exchange with those of the small amount of water present in the solvent.

The spectra of the complexes also contain a high-field signal for the mercury-bound methyl protons. Only one signal is observed for the 2:1 complexes, because these groups are in fast exchange. The ^1H signals undergo small downfield shifts as the number of CH_3Hg^+ groups increases, but they are not very informative. The ^2J coupling constants between the methyl

Can. J. Chem. Downloaded from www.nrcresearchpress.com by 112.217.228.212 on 09/07/12
For personal use only.

Can. J. Chem. Downloaded from www.nrcresearchpress.com by 112.217.228.212 on 09/07/12
For personal use only.

TABLE 4. ^{1}H nmr data[a]

(*a*) Dimethylaminopurine

Compound	δ H2	H8	CH_3(N6)	CH_3(Hg)	$^2J(^1H—^{199}Hg)$[b]
HDMAd	8.18	8.09	3.44	—	—
[(CH_3Hg)(DMAd)]	8.08	7.81	3.43	0.80	203
[$(CH_3Hg)_2$(DMAd)]X[c]	8.39	7.98	3.55	0.86	218
[$(CH_3Hg)_2$(HDMAd)]$(NO_3)_2$	8.49	8.32	3.51	0.87	232

(*b*) Diethylaminopurine

Compound	δ H2	H8	CH_2(N6)[d]	CH_3(N6)[d]	CH_3(Hg)	$^2J(^1H—^{199}Hg)$[b]
HDEAd	8.17	8.07	3.92	1.17	—	—
[(CH_3Hg)(DEAd)]	8.08	7.81	3.94	1.18	0.78	202
[$(CH_3Hg)_2$(DEAd)]X[c]	8.39	7.99	4.02	1.24	0.87	217
[$(CH_3Hg)_2$(HDEAd)]$(NO_3)_2$	8.50	8.26	4.01	1.26	0.89	233

[a] δ (ppm) vs. TMS in DMSO-d_6.
[b] In Hz.
[c] X = NO_3, ClO_4.
[d] ^3J of 6.9 Hz between CH_2 and CH_3 protons in all cases.

TABLE 5. ^{13}C nmr data[a]

Compound	δ C2	C4	C5	C6	C8	CH_3(N6)	CH_2(N6)	CH_3(Hg)
				Dimethylaminopurine				
HDMAd	151.76	151.23	118.95	154.29	137.74	37.84		
[(CH_3Hg)(DMAd)]	150.29	156.93	119.96	154.30	145.47	37.92		0.95
[$(CH_3Hg)_2$(DMAd)]X[b]	149.92	151.17	120.68	153.87	146.43	38.51		1.97
[$(CH_3Hg)_2$(HDMAd)]$(NO_3)_2$	149.11	—[d]	117.76	153.06	144.39	(38.80)[c]		1.03
				Diethylaminopurine				
HDEAd	151.93	151.13	118.50	153.07	137.92	13.54	42.26	
[(CH_3Hg)(DEAd)]	150.53	156.97	119.48	153.12	145.72	13.76	42.07	0.96
[$(CH_3Hg)_2$(DEAd)]X[b]	150.00	151.33	120.35	152.96	146.78	13.52	43.17	1.93
[$(CH_3Hg)_2$(HDEAd)]$(NO_3)_2$	149.20	—[d]	118.09	152.29	144.74	13.41	43.56	1.02

[a] δ (ppm) in DMSO-d_6 vs. TMS.
[b] X = NO_3, ClO_4.
[c] Possible interference with the residual solvent signal.
[d] Weak signal for this atom not detected due to low solubility.

protons and ^{199}Hg are more interesting, as they provide information on the nucleophilic character of the coordination site. Rabenstein (11) has noted that the $^2J(^1H—^{199}Hg)$ coupling constants and the formation constants K for a series of [(CH_3Hg)L] complexes obey the approximate equation $^2J = 249 - 5.09 \log K$. It happens that the [(CH_3Hg)L] formation constants and the protonation constants of the same ligands are not numerically very different for oxygen and nitrogen ligands, so that a similar relationship is loosely applicable to pK_a. This relationship is found to be surprisingly well followed in the present case. The neutral compound shows a ^2J value of 200 Hz, the same as the adenine analogue (1). When this ^2J value is placed into the above equation, a value of 9.2 is predicted for the pK_a of the site occupied by mercury. The pK_a of the imidazole proton of 6-dimethylaminopurine is 10.5 (20, 21). For the $[(CH_3Hg)_2L]^+$ cations, an average coupling constant of 217 Hz is obtained for the two CH_3Hg^+ groups. It corresponds to an average pK_a of 6.3. If the value of 9.2 is assumed for one of the CH_3Hg^+ groups, this would lead to a pK_a 3.4 for the other site. This is about 1 pK_a unit less basic than found for the formation of the H_2L^+ cations, which are however known to be protonated at the N(1) site (4). It is reasonable that N(3) be less nucleophilic than N(1).

For the protonated $[(CH_3Hg)_2(HL)]^{2+}$ ions, the coupling constant of 232 Hz corresponds to an average pK_a of 3.3 for the N(3) and N(9) sites of an N(7)-protonated molecule. This corresponds to a decrease of nucleophilicity of 3 pK_a units compared to the non-protonated form. Fast exchange of the

CH_3Hg^+ groups leading to averaged ^2J constants does not allow to determine whether this change of basicity is equally shared by the two coordination sites.

Conclusion

The reaction occurring in the first place between the CH_3Hg^+ ion and adenine is a substitution of the N(9)—H proton. The present work shows that alkylation of the 6-amino group does not affect this behavior. However, the second coordination takes place only at N(3) with the dialkylated derivatives, whereas for adenine, the N(9)/N(7) species is present in the solid state and represents the major tautomer in solution. Displacement of the reaction to the N(9)/N(3) region must be ascribed to the steric effect of the alkyl groups: not enough room is left for a CH_3Hg^+ ion to bind in a normal way to the N(7) lone pair, but the smaller H^+ ion can fit in this region without drastic steric hindrance.

Acknowledgments

We wish to thank M. J. Olivier who collected the X-ray data. The financial supports of the Natural Sciences and Engineering Research Council of Canada and the Ministère de l'Éducation du Québec are gratefully acknowledged.

1. J. P. CHARLAND, M. T. P. VIET, M. ST-JACQUES, and A. L. BEAUCHAMP. J. Am. Chem. Soc. **107**, 8202 (1985), and references therein.
2. L. PRIZANT, M. J. OLIVIER, R. RIVEST, and A. L. BEAUCHAMP. Can. J. Chem. **59**, 1311 (1981).
3. J. P. CHARLAND, J. F. BRITTEN, and A. L. BEAUCHAMP. Inorg. Chim. Acta, **124**, 161 (1986); R. SAVOIE, J. J. JUTIER, L. PRIZANT, and A. L. BEAUCHAMP. Spectrochim. Acta, **38A**, 561 (1982); J. HUBERT and A. L. BEAUCHAMP. Acta Crystallogr. **B36**, 2613 (1980); Can. J. Chem. **58**, 1439 (1980); J. P. CHARLAND and A. L. BEAUCHAMP. Croat. Chem. Acta, **57**, 679 (1984); L. PRIZANT, M. J. OLIVIER, R. RIVEST, and A. L. BEAUCHAMP. J. Am. Chem. Soc. **101**, 2765 (1979); Acta Crystallogr. **B38**, 88 (1982); A. L. BEAUCHAMP. J. Cryst. Mol. Struct. **10**, 149 (1980).
4. R. L. BENOIT and M. FRÉCHETTE. Can. J. Chem. **62**, 995 (1984).
5. J. P. CHARLAND and A. L. BEAUCHAMP. To be published.
6. T. ITAYA, H. MATSUMOTO, and K. OGAWA. Chem. Pharm. Bull. **28**, 1920 (1980).
7. L. PRIZANT, R. RIVEST, and A. L. BEAUCHAMP. Can. J. Chem. **59**, 2290 (1981).
8. F. BÉLANGER-GARIÉPY and A. L. BEAUCHAMP. J. Am. Chem. Soc. **102**, 3461 (1980).
9. D. T. CROMER and J. T. WABER. Acta Crystallogr. **18**, 104 (1965); R. F. STEWART, E. R. DAVIDSON, and W. T. SIMPSON. J. Chem. Phys. **42**, 3175 (1965).
10. D. T. CROMER. Acta Crystallogr. **18**, 17 (1965).
11. D. L. RABENSTEIN. Acc. Chem. Res. **11**, 100 (1978).
12. J. E. HUHEEY. Inorganic chemistry, principles of structure and reactivity. Harper and Row, New York. 1975. pp. 184, 185.
13. J. P. CHARLAND, M. SIMARD, and A. L. BEAUCHAMP. Inorg. Chim. Acta, **80**, L57 (1983).
14. R. TAYLOR and O. KENNARD. J. Am. Chem. Soc. **104**, 3209 (1982).
15. R. TAYLOR and O. KENNARD. J. Mol. Struct. **78**, 1 (1982).
16. A. TERZIS, A. L. BEAUCHAMP, and R. RIVEST. Inorg. Chem. **12**, 1166 (1973).
17. J. H. KECK, JR., R. A. SIMPSON, and J. L. WONG. J. Org. Chem. **43**, 2587 (1978).
18. W. O. COBURN, JR., M. C. THORPE, J. A. MONTGOMERY, and K. HEWSON. J. Org. Chem. **30**, 1114 (1965).
19. M. C. THORPE, W. C. COBURN, JR., and J. A. MONTGOMERY. J. Magn. Reson. **15**, 98 (1974).
20. S. F. MASON. J. Chem. Soc. 2071 (1954).
21. A. ALBERT. Synthetic procedures in nucleic acid chemistry. Vol. 2. *Edited by* W. W. Zorbach and R. S. Tipson. Wiley-Interscience, New York. 1973. pp. 28, 29.

Can. J. Chem. Downloaded from www.nrcresearchpress.com by 112.217.228.212 on 09/07/12
For personal use only.

Cerium(IV)-induced nitration of cinnamic acids. Novel remote electrophilic substitution

JOHN R. PETERSON,[1] HOANG D. DO, AND ANDREW J. DUNHAM
The Michael Faraday Laboratories, Department of Chemistry, Northern Illinois University, DeKalb, IL 60115, U.S.A.

Received July 24, 1987[2]

JOHN R. PETERSON, HOANG D. DO, and ANDREW J. DUNHAM. Can. J. Chem. **66**, 1670 (1988).

The treatment of (*E*)-3,4-dimethoxycinnamic acid with ceric ammonium nitrate in trifluoroacetic acid afforded (*E*)-1,2-dimethoxy-4-nitro-5-(2-nitroethenyl)benzene in 79% yield. The unusual ipso substitution of the carboxylic acid moiety by a nitro functional center illustrated a new reaction manifold of cerium(IV). Six cinnamic acids were examined to ascertain the generality of the transformation. The bidentate nitrato structure of the metal salt is believed to account for the nitrating ability of this system.

JOHN R. PETERSON, HOANG D. DO et ANDREW J. DUNHAM. Can. J. Chem. **66**, 1670 (1988).

La réaction de l'acide diméthoxy-3,4 cinnamique-(*E*) avec le nitrate d'ammonium cérique dans l'acide trifluoroacétique conduit au diméthoxy-1,2 nitro-4 (nitro-2 éthènyl)-4 benzène-(*E*), avec un rendement de 79%. La réaction ipso inhabituelle qui conduit à un remplacement de la portion acide carboxylique par un groupement nitro est une illustration d'un nouvel aspect des réactions variées du cérium(IV). Dans le but d'évaluer la généralité de cette réaction, on l'a appliqué à six acides cinnamiques. On croit que la structure bidentate du nitrato peut expliquer les qualités nitratantes de ce système.

[Traduit par la revue]

Introduction

The nitration of aromatic compounds has been an area of extensive investigation, and the nitronium ion (NO_2^+) has been well established as an electrophile for this reaction (1). Standard procedures for NO_2^+ generation have employed nitric acid directly or have produced nitric acid *in situ* by means of nitrate salts in protic media (2). Although transition metal salts could provide a synthetically attractive alternative to conventional procedures for benzenoid compound nitration, only a few reports describing the use of these reagents have appeared in the literature. Palladium(II) (3), zirconium(IV) (4), iron(III) (4), titanium(IV) (5), and most recently cerium(IV) nitrate (6) have effected nitration of aromatic compounds. The nature of the electrophilic agent in a metal induced nitration would be of interest, as the intermediacy of NO_2^+ would not be mandated. In conjunction with studies focused at the projected synthesis of podophyllotoxin, the reaction of methoxy substituted cinnamic acids with ceric ammonium nitrate (CAN) was investigated. We report herein the results obtained with this metal system, which led not only to nitration of the aromatic nucleus, but to novel ipso substitution of the carboxylic acid group by a nitro functional center as well.

Results and discussion

Attention will be first directed to the reaction of (*E*)-3,4-dimethoxycinnamic acid (**1**) with CAN, eq. [1]. This reaction,

[1] 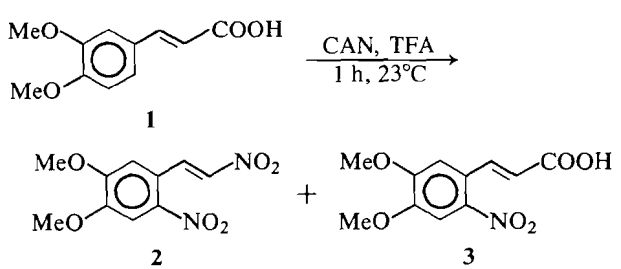

as well as the other discussed below, was conducted by magnetically stirring a mixture of CAN and the cinnamic acid in trifluoroacetic acid (TFA) for 1 h at 23°C. Product isolation was accomplished by medium pressure liquid chromatography (mplc) after esterification of the acidic product fraction. (*E*)-1,2-Dimethoxy-4-nitro-5-(2-nitroethenyl)benzene (**2**) and the methyl ester of (*E*)-4,5-dimethoxy-2-nitrocinnamic acid (**3**) were thereby obtained from **1** in 79 and 4% yields, respectively. The infrared spectrum of **2** was characterized by strong absorptions at 1570 and 1321 cm^{-1} for the nitro groups and a lack of absorption in the carbonyl region.

The formation of **2** provided incentive for further exploration of this novel remote and nuclear electrophilic substitution reaction. Dinitrostyrenes are synthetically versatile compounds, having been transformed into cinnolines (7), indoles (8), benzodiazepines (9), and amino substituted mescaline congeners (10). In addition, various analogues of **2** have been reported to exhibit fungicidal activity (11). A standard route to the dinitrostyrenes has been the condensation of nitromethane with nitrobenzaldehydes, with the latter prepared by an aromatic nitration reaction (7, 8). The procedure described in this paper provides a unique entry into this class of compounds, as both nitro groups are introduced into the molecule simultaneously.

Our results with other cinnamic acids are shown in Table 1. Nitrobenzaldehydes and nitrobenzoic acids were sometimes obtained in addition to the dinitrostyrene and nitrocinnamic acid (entries 2–4). The side-chain double-bond cleavage products were formed in the course of the reaction, rather than during the work-up or isolation steps, and could not be avoided. The regioselectivity of nuclear ring nitration could be rationalized for all of the products from the well-known *ortho,para*-directing effects of a methoxy substituent (12). Remote ipso substitution of a carboxylic acid moiety by a nitro group occurred when an electron-donating substituent was present at the 2- or 4-position of the aromatic ring with regard to the propenoic acid side chain (entries 1–4). Even (*E*)-3-methoxycinnamic acid (**18**) afforded a dinitrostyrene (**19**), albeit in low yield. In this case, electron donation by the methoxy group to the position α to the carboxylic acid was not possible through conjugation, and the major product isolated was (*E*)-3-methoxy-4-nitrocinnamic acid (**20**). Our efforts to achieve a material balance in the latter reaction were unsuccessful. Cinnamic acid (**21**) presented a limit to the nitrating ability of

[1]Author to whom correspondence may be addressed.
[2]Revision received February 26, 1988.

Printed in Canada / Imprimé au Canada

Can. J. Chem. Downloaded from www.nrcresearchpress.com by 61.7.252.67 on 09/07/12
For personal use only.

TABLE 1. Cerium(IV)-induced nitration of cinnamic acids[a]

Entry	Cinnamic acid	Products (% yield)			
1	**1**	**2** (79)	**3** (4)		
2	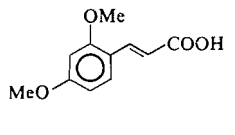 **4**	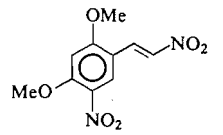 **5** (18)	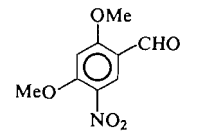 **6** (44)	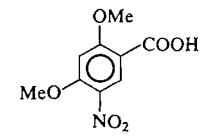 **7** (20)	
3	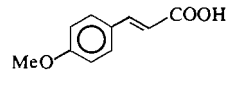 **8**	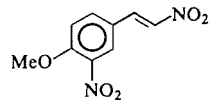 **9** (39)	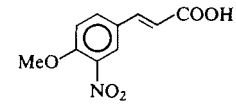 **10** (20)	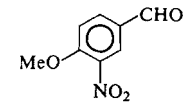 **11** (29)	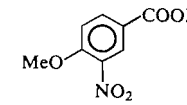 **12** (4)
4	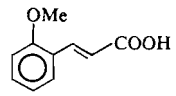 **13**	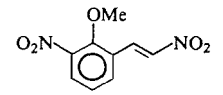 **14** (4)	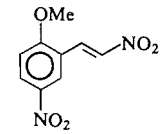 **15** (20)	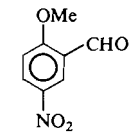 **16** (8)	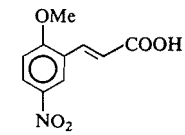 **17** (68)
5	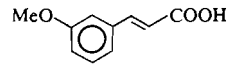 **18**	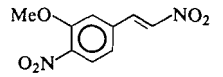 **19** (3)	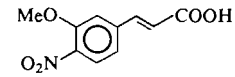 **20** (35)		
6	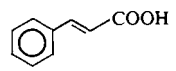 **21**	No reaction; 100% recovery			

[a]All experiments employed a trifluoroacetic acid solution of the cinnamic acid (0.33 M) and ceric ammonium nitrate (0.42 M). The reactions were stirred for 1 h at 23°C.

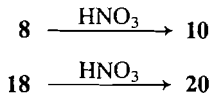

SCHEME 1

the CAN system with quantitative recovery of starting material realized. The electron-withdrawing character of the propenoic acid side chain in **21** even circumvented aromatic ring nitration.

Four experimental facts must be accounted for when the mechanism of remote ipso substitution of a carboxylic acid group by a nitro substituent is considered. First, Luff (13), Chakravarti *et al.* (14), and Rubenstein (15) have examined the reaction of nitric acid with methoxy substituted cinnamic acids, Scheme 1. The failure of NO_2^+ to produce a dinitrostyrene in their studies would only be consistent with the presence of a different nitrating species in the CAN system. Second, the CAN reaction was found to be very electrophilic in character; the reaction viability depended upon the presence of *ortho,para*-directing and ring-activating substituents on the cinnamic acid. Next, products that would be anticipated from solvolysis or nucleophilic capture of a carbocationic intermediate were not found in the CAN nitrations. Finally, the yield of dinitrostyrene was not improved when greater than 1.25 mole equivalents of CAN were employed in the reaction.

Sodium nitrate/TFA mixtures have found synthetic utility for the nitration of aromatic compounds (2). We have established that CAN was not serving simply as another nitrate anion source in the remote ipso substitution reaction. The key significance of the Ce(IV) ion in this system was demonstrated by the substitution of acetonitrile for TFA as the reaction medium. No reaction was observed when a cinnamic acid was subjected to powdered ammonium nitrate in acetonitrile; however, the inclusion of CAN in the reaction quickly afforded a nitrostyrene.

Aromatic compound nitration by nitrogen dioxide (NO_2) has been well documented (16). Two sets of experiments have demonstrated that NO_2 was not the electrophilic agent responsible for the chemistry reported in Table 1, even though NO_2 was occasionally liberated during the CAN nitrations. Very different results from those reported in Table 1 were obtained when the cinnamic acids were treated with dinitrogen tetroxide.[3] The reaction of **8** with dinitrogen tetroxide yielded not only **9**, **11**, and **12**, but in addition a similar product series, **22–24**, lacking a nitro substituent on the aromatic ring, eq. [2].

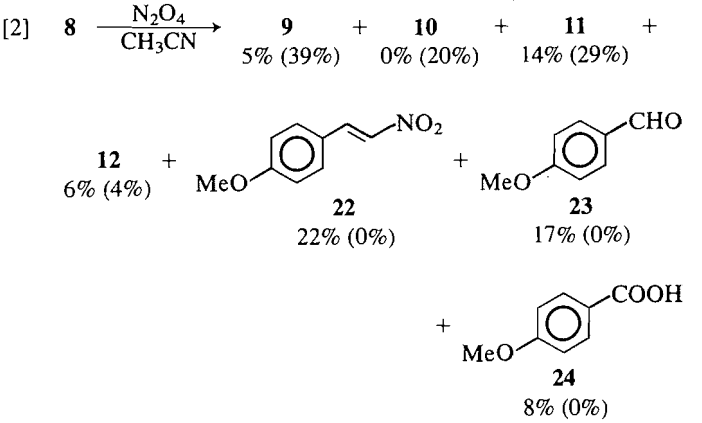

[3]The oxides of NO_2 and N_2O_4 exist in equilibrium (see ref. 17).

Can. J. Chem. Downloaded from www.nrcresearchpress.com by 61.7.252.67 on 09/07/12
For personal use only.

The latter were not observed when the TFA/CAN system was employed (product % yields for this system in parentheses). The absence of **10** in the product mixture of the dinitrogen tetroxide experiment and the large product composition variations between the two systems led to the conclusion that NO_2 was not the electrophilic species of the CAN/TFA system. Further evidence for this conclusion was obtained when the behavior of **21** with CAN in TFA and with dinitrogen tetroxide in acetonitrile was compared, eq. [3]. In CAN/TFA system, the

[3] **21** $\xrightarrow[CH_3CN]{N_2O_4}$ 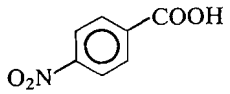

25

usual dark color of the reaction failed to develop even after 4 h at 23°C, and neither the evolution of NO_2 nor any exothermicity was observed over the course of the experiment. In contrast, the subjection of **21** to dinitrogen tetroxide in acetonitrile resulted in a vigorous reaction, raising the temperature to the boiling point of acetonitrile. 4-Nitrobenzoic acid (**25**) was isolated in 7% yield after esterification of the acidic fraction. Although unreacted **21** was not present in the product mixture, we were unsuccessful in isolating any other products in reasonably pure form.

Our proposed mechanism for a remote ipso substitution reaction utilizing **8** as the substrate and a simplified structure for CAN is shown in Scheme 2. Cerium(IV) nitrate serves as the electrophile for this transformation, obviating NO_2^+ or NO_2 generation. We suggest that the bidentate nitrato structure of this metal salt is fundamental to its nitrating ability (18). The nitrating capacity of isostructural metal nitrates has been noted by Addison and others (4, 5). The first step of the mechanism would be facilitated by methoxy substitution on the aromatic nucleus. In this regard, the failure of **21** to provide a nitrostyrene in the presence of CAN suggested that the first step of the mechanism could be rate determining. An electronic reorganization of zwitterion **26** would afford a Ce(IV) alkoxide and carbocation **27**. Decarboxylation of the latter would then deliver nitrostyrene **22**.

An alternative mechanism in which an aromatic radical cation would be formed by Ce(IV) oxidation of the cinnamic acid appears less likely to us.[4] Such a process would require the radical cation to selectively capture NO_2 or NO_2^- for dinitrostyrene formation. Our strongest evidence against an oxidative mechanism comes from an examination of the product composition for reactions in which a high material balance was achieved (Table 1, entries 3 and 4). The oxidation of certain aromatic substrates with CAN has been shown to yield side-chain and nuclear substitution products that arose by nucleophilic capture (benzyl nitrates) or solvolysis (benzyl and aryl acetates) of a carbocationic intermediate (19). Kochi *et al.* have likewise reported the formation of trifluoroacetoxylated products from aromatic substrates when the oxidation reaction was conducted in TFA (20). The absence of nitrate and trifluoroacetic containing products in our reaction mixtures makes an oxidative mechanism seem unreasonable. Dinctürk and Ridd previously put forth similar arguments against the generation of an aromatic radical cation in their nitrations of aromatic compounds with CAN (6*c*). As an additional point, the stoichiometry associated with remote ipso substitution of a nitro group for a carboxylic acid by an oxidative mechanism would require two cerium(IV) ions per aromatic molecule (6*b*). Our observation of optimal dinitrostyrene formation with 1.25 equivalents of CAN per equivalent of aromatic substrate would be consistent with the mechanism proposed in Scheme 2, but not with an oxidative process.[5]

Aromatic ring nitration with CAN in acetonitrile is likely to proceed by a mechanism similar to that shown in Scheme 2 (6). In the present studies, however, we are unable to ascribe a particular mechanism to the formation of the ring nitrated products. Nuclear ring nitration in TFA could have resulted either from electrophilic attack by CAN or NO_2^+.

In conclusion, the reaction of methoxy substituted cinnamic acids with CAN afforded dinitrostyrenes. A mechanism for the remote ipso substitution of a carboxylic acid group by a nitro substituent was presented where CAN served as the electrophilic agent. The bidentate nitrato structure of CAN is felt to be responsible for the nitrating ability of this system.

Experimental

Melting points were determined with a Mel-Temp apparatus and are uncorrected. Infrared spectra were recorded on a Sargent Welch 3-200 spectrophotometer employing either a thin film or KBr pellet technique. The nmr spectra were accumulated on an IBM WP-200 instrument at 200 MHz for proton and at 50 MHz for carbon. Chemical shifts were reported as parts per million downfield relative to tetramethylsilane in chloroform-*d*. Products were isolated by medium-pressure liquid chromatography (FMI pump, silica gel column, and a Gilson model 131 refractive index detector) utilizing ethyl acetate/hexane mixtures as eluents.

CAN, TFA, and **21** were obtained from Aldrich Chemical Co. and used without further purification. Cinnamic acids **1**, **4**, **8**, **13**, and **18** were prepared by the literature method (21). References after a compound name refer to literature physical data that matched the present values.

General procedure for cinnamic acid nitration by CAN in TFA

A 50-mL, round-bottomed flask equipped with a nitrogen inlet was charged with a cinnamic acid (1.68 mmol), TFA (6 mL), and CAN (1.16 g, 2.11 mmol). The reaction was magnetically stirred for 1 h at 23°C before diluting the dark brown mixture with water (25 mL). The aqueous mixture was extracted with chloroform (3 × 25 mL), and the combined extracts washed with saturated sodium bicarbonate solution (2 × 25 mL), dried (magnesium sulfate), and concentrated. Chromatography afforded the dinitrostyrenes and nitrobenzaldehydes.

Acidification (37% hydrochloric acid) of the sodium bicarbonate washes to approximately pH 1 and extraction with chloroform (3 × 20 mL) provided the acidic coproducts after solvent removal. Esterification was effected by refluxing a methanol (25 mL) solution of the carboxylic acids in the presence of 98% sulfuric acid (0.5 mL) for 3 h. The reaction mixture was cooled, diluted with water (30 mL), and extracted with chloroform (3 × 20 mL). The combined organic extracts were washed with saturated sodium bicarbonate solution (20 mL), dried (magnesium sulfate), concentrated, and chromatographed to deliver the methyl cinnamates and benzoates.

Structural data for compounds in Table 1

(E)-1,2-Dimethoxy-4-nitro-5-(2-nitroethenyl)benzene (2) (8)

Yield: 79%; mp 171–172°C (lit. mp 166–169°C); ir: 3120, 1570, 1532, 1497, 1321, 1283, 1225, 1067, 949, 872, 841, 795, 754 cm^{-1}; ^1H nmr δ: 8.61 (d, 1H, J = 13.35 Hz), 7.75 (s, 1H), 7.42 (d, 1H, J =

[4]The authors thank reviewer I for the helpful comments that were provided on this issue.

[5]This argument precludes the possible competitive oxidation of the dinitrostyrene when additional quantities of CAN were employed, which could have resulted in no improvement in product yield.

Can. J. Chem. Downloaded from www.nrcresearchpress.com by 61.7.252.67 on 09/07/12
For personal use only.

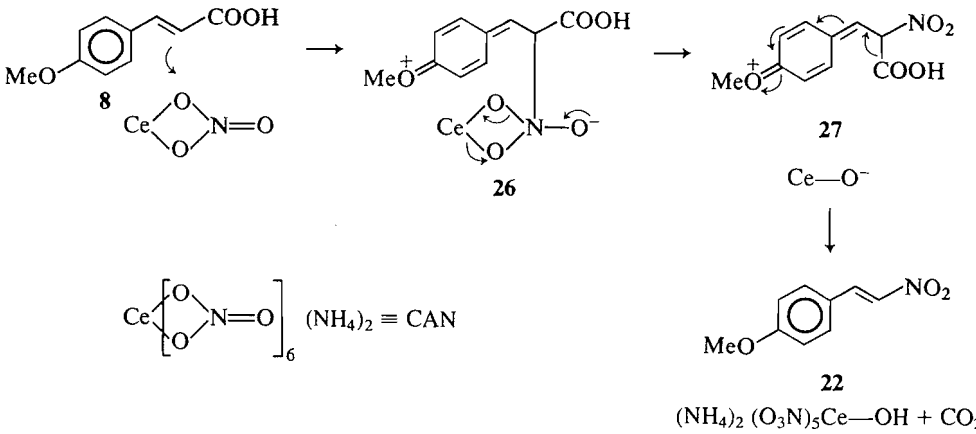

SCHEME 2

13.35 Hz), 6.92 (s, 1H), 4.04 (s, 3H), 4.02 (s, 3H); ^{13}C nmr δ: 153.54, 151.32, 141.81, 139.10, 135.87, 120.21, 110.32, 108.68, 56.74, 56.69. *Anal.* calcd. for $C_{10}H_{10}N_2O_6$: C 47.25, H 3.97, N 11.02; found: C 47.02, H 4.19, N 10.70.

*Methyl (E)-3-(4,5-dimethoxy-2-nitrophenyl)propenoate (**3**-Me ester) (22)*

Yield: 4%; mp 174–175°C (lit. mp 174–175°C); ir: 1705, 1524, 1435, 1333, 1283, 1259, 1223, 1061, 986, 874, 802, 756 cm^{-1}, ^{1}H nmr δ: 8.21 (d, 1H, J = 16.50 Hz), 7.62 (s, 1H), 6.92 (s, 1H), 6.30 (d, 1H, J = 16.50 Hz), 4.02 (s, 3H), 4.00 (s, 3H), 3.86 (s, 3H); ^{13}C nmr δ: 166.36, 153.29, 150.07, 140.92, 125.15, 121.63, 110.14, 108.11, 56.53, 51.83.

*(E)-1,5-Dimethoxy-2-nitro-4-(2-nitroethenyl)benzene (**5**) (23)*

Yield: 18%; mp 207–209°C (not recrystallized) (lit. mp 214°C); ir: 3040, 1615, 1560, 1520, 1500, 1400, 1350, 1325, 1305, 1290, 1225, 1205, 1095, 1010, 970, 840, 820 cm^{-1}, ^{1}H nmr δ: 8.19 (s, 1H), 8.03 (d, 1H, J = 13.52 Hz), 7.78 (d, 1H, J = 13.52 Hz), 6.58 (s, 1H), 4.08 (s, 6H); ^{13}C nmr δ: 163.69, 157.07, 138.34, 132.76, 130.31, 105.50, 96.47, 56.93, 56.62.

*2,4-Dimethoxy-5-nitrobenzaldehyde (**6**) (24)*

Yield: 44%; mp 182–185°C (not recrystallized) (lit. mp 188–189°C); ir: 3140, 1680, 1615, 1400, 1310, 1295, 1220, 1075, 1010, 925, 880, 840 cm^{-1}; ^{1}H nmr δ: 10.28 (s, 1H), 8.50 (s, 1H), 6.54 (s, 1H), 4.07 (s, 3H), 4.05 (s, 3H).

*Methyl 2,4-dimethoxy-5-nitrobenzoate (**7**-Me ester) (25)*

Yield: 20%; mp 145–147°C (lit. mp 147°C); ir: 3140, 2925, 2855, 1700, 1620, 1570, 1560, 1530, 1440, 1400, 1350, 1290, 1280, 1220, 1015, 825 cm^{-1}; ^{1}H nmr δ: 8.63 (s, 1H), 6.54 (s, 1H), 4.05 (s, 3H), 4.02 (s, 3H), 3.89 (s, 3H).

*(E)-1-Methoxy-2-nitro-4-(2-nitroethenyl)benzene (**9**) (26)*

Yield: 39%; mp 163–165°C (lit. mp 166°C); ir: 3109, 2920, 2847, 1688, 1611, 1534, 1454, 1437, 1348, 1279, 1184, 1088, 1009, 972, 822, 760, 675 cm^{-1}; ^{1}H nmr δ: 8.06 (d, 1H, J = 2.22 Hz), 7.96 (d, 1H, J = 13.68 Hz), 7.74 (dd, 1H, J = 8.79, 2.22 Hz), 7.55 (d, 1H, J = 13.68 Hz), 7.18 (d, 1H, J = 8.79 Hz), 4.04 (s, 3H); ^{13}C nmr δ: 160.32, 137.42, 136.16, 134.35, 126.06, 122.66, 116.11, 114.48, 56.96.

*Methyl (E)-3-(4-methoxy-3-nitrophenyl)propenoate (**10**-Me ester) (27)*

Yield: 20%; mp 128–130°C (lit. mp 130.0–130.5°C); ir: 2950, 1717, 1616, 1533, 1439, 1344, 1273, 1177, 1088, 1013, 822, 760, 673 cm^{-1}; ^{1}H nmr δ: 8.01 (d, 1H, J = 2.25 Hz), 7.83 (dd, 1H, J = 8.76, 2.25 Hz), 7.62 (d, 1H, J = 16.26 Hz), 7.12 (d, 1H, J = 8.76 Hz), 6.40 (d, 1H, J = 16.26 Hz), 4.00 (s, 3H), 3.82 (s, 3H).

*4-Methoxy-3-nitrobenzaldehyde (**11**) (28)*

Yield: 29%; mp 81–83°C (lit. 82–84°C); ir: 3117, 3069, 2997, 2922, 2853, 1690, 1611, 1528, 1446, 1354, 1279, 1206, 1159, 1080, 1007, 930, 820, 764, 719, 690, 598 cm^{-1}; ^{1}H nmr δ: 9.95 (s, 1H), 8.36 (d, 1H, J = 2.04 Hz), 8.10 (dd, 1H, J = 8.76, 2.04 Hz), 7.24 (d, 1H, J = 8.76 Hz), 4.08 (s, 3H).

*Methyl 4-methoxy-3-nitrobenzoate (**12**-Me ester) (29)*

Yield: 4%; mp 106–108°C (lit. mp 107.5–108.5°C); ir: 2920, 1715, 1616, 1526, 1435, 1341, 1277, 1186, 1011, 816, 754, 675 cm^{-1}; ^{1}H nmr δ: 8.55 (d, 1H, J = 2.20 Hz), 8.20 (dd, 1H, J = 8.76, 2.20 Hz), 7.16 (d, 1H, J = 8.76 Hz), 4.15 (s, 3H), 3.90 (s, 3H).

*(E)-2-Methoxy-1-nitro-3-(2-nitroethenyl)benzene (**14**) (11)*

Yield: 14%; mp 152–154°C (lit. mp 154°C) ir: 2920, 1692, 1636, 1603, 1528, 1424, 1346, 1277, 1250, 1088, 988, 847, 814, 754 cm^{-1}; ^{1}H nmr δ: 8.19 (d, 1H, J = 13.89 Hz), 7.95 (dd, 1H, J = 8.12, 1.60 Hz), 7.75 (d, 1H, J = 13.89 Hz), 7.74 (dd, 1H, J = 8.73, 1.60 Hz), 7.33 (t, 1H, J = 7.97 Hz), 3.99 (s, 3H); ^{13}C nmr δ: 157.62, 140.13, 133.82, 132.09, 128.82, 124.52, 123.80, 106.99, 63.52.

*(E)-1-Methoxy-4-nitro-2-(2-nitroethenyl)benzene (**15**) (30)*

Yield: 20%; mp 172–174°C (lit. mp 174–176°C); ir: 1600, 1570, 1480, 1325, 1275, 1190, 1140, 1095, 1000, 985, 960, 830, 780, 740, 620 cm^{-1}; ^{1}H nmr δ: 8.39 (br s, 1H), 8.36 (dd, 1H, J = 8.88, 2.84 Hz), 8.14 (d, 1H, J = 13.75 Hz), 7.87 (d, 1H, J = 13.75 Hz), 7.10 (d, 1H, J = 8.88 Hz), 4.10 (s, 3H); ^{13}C nmr δ: 163.33, 140.21, 132.64, 128.30, 127.12, 120.00, 111.57, 56.84.

*2-Methoxy-5-nitrobenzaldehyde (**16**) (31)*

Yield: 8%; mp 88–89°C (lit. mp 89–90°C); ir: 3075, 2922, 1686, 1609, 1586, 1522, 1487, 1429, 1398, 1341, 1275, 1176, 1074, 1015, 943, 916, 829, 750, 633 cm^{-1}; ^{1}H nmr δ: 10.46 (s, 1H), 8.71 (d, 1H, J = 2.91 Hz), 8.44 (dd, 1H, J = 9.19, 2.91 Hz), 7.12 (d, 1H, J = 9.19 Hz), 4.08 (s, 3H).

*Methyl (E)-3-(2-methoxy-5-nitrophenyl)propenoate (**17**-Me ester) (32)*

Yield: 68%; mp 159–161°C (lit. mp 163°C); ir: 1700, 1570, 1480, 1435, 1300, 1250, 1170, 1080, 1005, 915, 865, 820, 740 cm^{-1}; ^{1}H nmr δ: 8.41 (d, 1H, J = 2.75 Hz), 8.25 (dd, 1H, J = 9.18, 2.75 Hz), 7.95 (d, 1H, J = 16.21 Hz), 6.95 (d, 1H, J = 9.18 Hz), 6.61 (d, 1H, J = 16.21 Hz), 4.02 (s, 3H), 3.83 (s, 3H).

*(E)-2-Methoxy-1-nitro-4-(2-nitroethenyl)benzene (**19**)*[6]

Yield: 3%; mp 234–235°C; ir: 1591, 1549, 1485, 1443, 1341, 1273, 1123, 1042, 1018, 932, 883, 798, 777, 692 cm^{-1}; ^{1}H nmr δ: 8.60 (d, 1H, J = 13.27 Hz), 8.27 (d, 1H, J = 8.95 Hz), 7.83 (d, 1H, J = 2.62 Hz), 7.54 (dd, 1H, J = 8.95, 2.62 Hz), 7.35 (d, 1H, J = 13.27 Hz), 3.91 (s, 3H). *Anal.* calcd. for $C_9H_8N_2O_5$: C 48.22, H 3.60, N 12.50; found: C 48.54, H 3.75, N 12.47.

[6]Dinitrostyrene **19** was identified by spectral analysis and comparison of its melting point with that of the known other possible isomers, (*E*)-1-methoxy-2-nitro-3-(2-nitroethenyl)benzene (lit. (33) mp 155–157°C) and (*E*)-4-methoxy-1-nitro-2-(2-nitroethenyl)benzene (lit. (11) mp 103°C).

Can. J. Chem. Downloaded from www.nrcresearchpress.com by 61.7.252.67 on 09/07/12
For personal use only.

*(E)-Methyl 3-(3-methoxy-4-nitrophenyl)propenoate (**20**-Me ester) (13, 14)*

Yield: 35%; ir: 1711, 1587, 1506, 1435, 1337, 1271, 1233, 1084, 1036, 966, 847 cm^{-1}; ^1H nmr δ: 8.21 (d, 1H, J = 15.82 Hz), 8.14 (d, 1H, J = 10.01 Hz), 7.04–6.93 (m, 2H), 6.29 (d, 1H, J = 15.82 Hz), 3.92 (s, 3H), 3.83 (s, 3H). The product was further characterized by melting point of the acid (**20**), mp 218°C (lit. mp 218°C).

Nitration with dinitrogen tetroxide in acetonitrile

Dinitrogen tetroxide (2 mL) was added to a solution of **8** or **21** (5 mmol) in acetonitrile (30 mL). The reaction, which immediately evolved heat and became dark brown, was stirred for 1 h before work-up as described in the general synthetic procedure. Product isolation by mplc afforded **9** (5%), **11** (14%), **12** (6%), **22** (22%), **23** (17%), and **24** (8%) from the reaction of **8**. Similarly, **25** (7%) was obtained from the reaction of **21** with dinitrogen tetroxide.

Structure data for 22–25

*(E)-1-Methoxy-4-(2-nitroethenyl)benzene (**22**) (34)*: mp 87–88°C (lit. mp 88°C); ^1H nmr δ: 7.99 (d, 1H, J = 13.50 Hz), 7.46 (d, 2H, J = 9.00 Hz), 7.44 (d, 1H, J = 13.50 Hz), 6.99 (d, 2H, J = 9.00 Hz), 3.90 (s, 3H).

*4-Methoxybenzaldehyde (**23**) (35)*: ^1H nmr δ: 9.88 (s, 1H), 7.83 (d, 2H, J = 8.83 Hz), 7.00 (d, 2H, J = 8.83 Hz), 3.90 (s, 3H).

*Methyl 4-methoxybenzoate (**24**-Me ester) (36)*: mp 46–48°C (lit. mp 48°C); ir: 2925, 2855, 1720, 1605, 1510, 1460, 1435, 1280, 1255, 1170, 1115, 1100, 1030, 850, 770, 700 cm^{-1}; ^1H nmr δ: 7.99 (d, 2H, J = 8.75 Hz), 6.92 (d, 2H, J = 8.75 Hz), 3.89 (s, 3H), 3.87 (s, 3H).

*Methyl 4-nitrobenzoate (**25**-Me ester) (37)*: mp 93–95°C (lit. mp 94–96°C); ir: 3115, 1720, 1525, 1440, 1400, 1350, 1280, 1105, 875, 825, 720 cm^{-1}; ^1H nmr δ: 8.30 (d, 2H, J = 8.75 Hz), 8.21 (d, 2H, J = 8.75 Hz), 3.98 (s, 3H).

Acknowledgments

We are greatly indebted to the Donors of The Petroleum Research Fund, administered by the American Chemical Society, to the Milheim Foundation for Cancer Research (grant no. 87-32), and to the American Cancer Society, Illinois Division, Inc. (grant no. 87-53) for their generous support of this research. J.R.P. also wishes to acknowledge support from the Northern Illinois University Graduate School and Office of Sponsored Projects.

1. J. G. Hoggett, R. B. Moodie, J. R. Penton, and K. Schofield. *In* Nitration and aromatic reactivity. Cambridge University Press, London. 1971.
2. (*a*) U. A. Spitzer and R. Stewart. J. Org. Chem. **39**, 3936 (1974); (*b*) S. Uemura, A. Toshimitsu, and M. Okano. J. Chem. Soc. Perkin Trans. 1, 1076 (1978).
3. (*a*) T. Tisue and W. J. Downs. J. Chem. Soc. Chem. Commun. 410 (1969); (*b*) R. O. Norman, W. J. E. Parr, and C. B. Thomas. J. Chem. Soc. Perkin Trans. 1, 369 (1974).
4. R. G. Coombes and L. W. Russell. J. Chem. Soc. Perkin Trans. 1, 1751 (1974).
5. (*a*) C. C. Addison. Coordin. Chem. Rev. **1**, 58 (1966); (*b*) R. G. Coombes and L. W. Russell. J. Chem. Soc. Perkin Trans. 1, 830 (1974); (*c*) D. W. Amos, D. A. Baines, and G. W. Flewett. Tetrahedron Lett. 3191 (1973).
6. (*a*) G. I. Nikishin, E. P. Kaplan, and N. I. Kapustina. Izv. Akad. Nauk SSSR, Ser. Khim. 1434 (1975); (*b*) S. Dinctürk and J. H. Ridd. J. Chem. Soc. Perkin Trans. 2, 961 (1982); (*c*) J. Chem. Soc. Perkin Trans. 2, 965 (1982); (*d*) H. M. Chawla and R. S. Mittal. Indian J. Chem. Sect. B, **22B**, 751 (1983); (*e*) H. M. Chawla and R. S. Mittal. Synthesis, 70 (1985).
7. I. Baxter and G. A. Swan. J. Chem. Soc. (C), 468 (1968).
8. C. F. Huebner, H. A. Troxell, and D. C. Schroeder. J. Am. Chem. Soc. **75**, 5887 (1953).
9. (*a*) H. R. Rodriguez and G. Stevens. U.S. Patent 3 681 340 (1972); Chem. Abstr. **77**, 140178d (1972); (*b*) J. T. Suh and R. A. Schnettler. U.S. Patent 3 849 400 (1974); Chem. Abstr. **82**, 73041s (1975).
10. G. J. Kapadia and M. B. E. Fayez. J. Pharm. Sci. **59**, 1699 (1970).
11. G. S. Sidhu, P. B. Sattur, and S. J. Hasan. J. Sci. Ind. Res. Sect. C: **19**, 38 (1960).
12. F. A. Carey and R. J. Sundberg. *In* Advanced organic chemistry. Part B. Plenum, New York. 1984. pp. 489–503.
13. G. Luff. Chem. Ber. **22**, 291 (1889).
14. S. N. Chakravarti, K. Ganapati, and S. Aravamudhacti. J. Chem. Soc. 171 (1938).
15. L. Rubenstein. J. Chem. Soc. 648 (1926).
16. L. Eberson and F. Radner. Acc. Chem. Res. **20**, 53 (1987).
17. F. A. Cotton and G. Wilkinson. *In* Advanced inorganic chemistry. Wiley–Interscience, New York. 1980. p. 426.
18. T. A. Beineke and J. Delgandio. Inorg. Chem. **7**, 715 (1968).
19. (*a*) E. Baciocchi, S. Mei, and C. Rol. J. Org. Chem. **43**, 2919 (1978); (*b*) E. Baciocchi and C. Rol. Gazz. Chim. Ital. **113**, 727 (1983).
20. J. K. Kochi, R. T. Tang, and T. Bernath. J. Am. Chem. Soc. **95**, 7114 (1973).
21. J. Koo, M. S. Fish, G. N. Walker, and J. Blake. *In* Organic syntheses. Collect. Vol. 1. *Edited by* N. Rabjohn. Wiley, New York. 1963. p. 327.
22. Z. I. Kanevska, M. M. Shemyakin, and E. M. Bamdas-Shemyakina. Arch. Pharm. **272**, 770 (1934).
23. M. G. S. Rao, C. Srikantia, and M. S. Iyengar. Helv. Chim. Acta, **12**, 581 (1929).
24. M. G. S. Rao, C. Srikantia, and M. S. Iyengar. J. Chem. Soc. **127**, 556 (1925).
25. E. Spath and C. Schlosser. Ber. Dtsch. Chem. Ges. B: **64**, 2203 (1931).
26. M. Chibu, M. Abiko, and Y. Kawamura. Jpn. Patent 26 960 (1964); Chem. Abstr. **62**, 14569f (1965).
27. R. F. Heck. J. Am. Chem. Soc. **90**, 5518 (1968).
28. K. Shankaran and A. S. Rao. Synth. Commun. **10**, 573 (1980).
29. W. D. Chandler, W. MacFarlane-Smith, and R. Y. Moir. Can. J. Chem. **42**, 2549 (1964).
30. D. E. Norrall and F. Benington. J. Am. Chem. Soc. **60**, 2844 (1938).
31. A. Schnell. Chem. Ber. **17**, 1381 (1884).
32. B. B. Dey and K. K. Row. J. Chem. Soc. **125**, 554 (1924).
33. A. Kalir, D. Balderman, H. Edery, and G. Porath. Israel J. Chem. **5**, 129 (1967).
34. W. L. F. Armarego. J. Chem. Soc. C, 986 (1969).
35. Proton NMR collection. *In* Standard spectra. Sadtler Research Laboratories, Philadelphia. 1980. No. 126.
36. R. H. Cox. Spectrochim. Acta, Part A, **25**, 1189 (1969).
37. Proton NMR collection. *In* Standard spectra. Sadtler Research Laboratories, Philadelphia. 1980. No. 584.

Can. J. Chem. Downloaded from www.nrcresearchpress.com by 61.7.252.67 on 09/07/12
For personal use only.

The transformation of levopimaric acid into warburganal

WILLIAM A. AYER AND FRANCISCO X. TALAMAS
Department of Chemistry, University of Alberta, Edmonton, Alta., Canada T6G 2G2

Received January 8, 1988

WILLIAM A. AYER and FRANCISCO X. TALAMAS. Can. J. Chem. **66**, 1675 (1988).

The chiral resin acid levopimaric acid (**1**), isolated from pine oleoresin, is used as a starting material for the synthesis of (−)-warburganal (**2**). The synthesis proceeds via the endoperoxide of methyl levopimarate, which after ozonolysis, protection of the resulting aldehyde function, reduction, and treatment with sodium methoxide provides the tetranorditerpenoid **12***a*. The hemiacetal **12***a* is then transformed to a mixture of hemithioacetals. At this point the carbomethoxyl group at C-4 is reduced to a methyl group, and then a C-11, C-12 double bond is introduced. Ozonolysis followed by elimination of formic acid provides a mixture of olefins (**27**) that is hydroxylated at C-9. Removal of the protecting group then gives (−)-warburganal (**2**). The sequence requires 15 steps and the overall yield from levopimaric acid to warburganal is 2.7%.

WILLIAM A. AYER et FRANCISCO X. TALAMAS. Can. J. Chem. **66**, 1675 (1988).

L'acide lévopimarique (**1**), la résine chirale extraite de l'oléorésine du pin, est utilisé comme produit de départ pour la synthèse du (−)-warburganal (**2**). La synthèse implique la formation de l'endoperoxyde du lévopimarate de méthyle et son ozonolyse, la protection de l'aldéhyde qui en résulte, une réduction et un traitement par le méthylate de sodium qui fournit le tétranorditerpénoïde **12***a*. Cet hémiacétal **12***a* est ensuite transformé en un mélange d'hémithioacétals. À ce point, le groupement carbométhoxyle en C-4 est réduit en groupement méthyle et la double liaison en C-11, C-12 est alors introduite. Une ozonolyse, suivie d'une élimination d'acide formique, fournit un mélange des oléfines **27** qui est hydrolyse en C-9. L'élimination du groupement protecteur fournit alors le (−)-warburganal (**2**). La série de réactions implique 15 étapes et le rendement global de l'acide lévopimarique au warburganal est de 2,7%.

[Traduit par la revue]

The exudate of pine trees, called oleoresin, is rich in the so-called resin acids, one of the major acids being levopimaric acid (**1**). The isolation of levopimaric acid from the inexpensive oleoresin is straightforward (1) and thus **1** is an attractive chiral starting material for organic synthesis. In this report we describe the transformation of levopimaric acid into (−)-warburganal (**2**), a drimane class sesquiterpene that acts as an antifeedant towards both the African army worm (2) and certain fish (3). Warburganal, which has a hot taste to the human tongue (3, 4), also shows strong molluscicidial activity (5). The transformation of the resin acid abietic acid (**3**) to (−)-warburganal has been described previously (6), as have several total synthesis of (±)-warburganal (ref. 7 and references therein).

The first stage in the transformation was the removal of the five extra carbon atoms (C-12, C-13, and the isopropyl group) contained in the diterpene framework of levopimaric acid (**1**). Methyl levopimarate (**1***a*), prepared by treating **1** with diazomethane, was photooxygenated to give the known (8) crystalline endoperoxide **4** in 76% yield. The appearance of a high field methyl signal (δ 0.57) in the ^{1}H nmr spectrum of **4** is consistent with the α-orientation of the peroxide, since now the methyl group at C-10 is shielded by the C-13, C-14 double bond (9). Ozonolysis of **4**, followed by reductive work-up ($(CH_3)_2S$), provided the oily ketoaldehyde **5**, which was transformed to the crystalline dimethyl acetal **6** by treatment with trimethyl orthoformate in the presence of acid. The electron impact mass spectrum (eims) of **6** does not show a molecular ion, but the chemical ionization mass spectrum (cims) shows a prominent $(M + NH_4)^+$ peak and the ^{1}H nmr spectrum shows three methoxyl peaks and an acetal methine singlet δ 4.64.

Endoperoxides may be cleaved to γ-hydroxyketones by treatment with base (10). Since the hydrogen at C-12 is activated by the adjacent carbonyl group, compound **6** was smoothly transformed to oily yellow α-diketone **7** by treatment with triethylamine. The ir spectrum of **7** shows hydroxyl (3456 cm^{-1}) and carbonyl (1725 cm^{-1}) absorption. The ^{1}H nmr spectrum (most signals are doubled) indicates that **7** exists as a tautomeric mixture of the diketone (yellow color) and cyclic hemiacetal(s). Treatment of **7** with trimethyl orthoformate under acid catalysis gave the crystalline cyclic acetal **8**. The ^{1}H nmr spectrum of **8** shows an apparent quintet at δ 3.34 for the isopropyl methine (assignment confirmed by decoupling the methyl doublets at δ 1.09 and 1.14). The chemical shift of the methine proton is appropriate for a hydrogen α to a ketone rather than α to an acetal, indicating the formation of the five-membered cyclic acetal. Treatment of **8** with sodium methoxide in methanol-d_1 caused exchange of the methine hydrogen. The deuterated compound does not show the δ 3.34 signal in the ^{1}H nmr spectrum and shows the isopropyl methyls as singlets at δ 1.12 and 1.08, confirming structure **8**. Attempts to introduce an 11,12-double bond by elimination of the elements of methanol from **8** were unsuccessful.

Treatment of diketone **7** with acetic anhydride – triethylamine provided a mixture of enol acetates **9** and **10** in a ratio of about 1:1 (as determined by nmr). When diisopropylethylamine was used as the base (and solvent), **9** was the major component of the enol acetate mixture (ratio ca. 12:1). The enol acetates were separated by flash chromatography over silica gel. Compound **9** displays an alkenic hydrogen (doublet, J = 11 Hz, δ 6.45) and an isopropyl methine (δ 3.06). The stereochemistry of the double bond (Z) was assigned on the basis of the low field shift (δ 6.45) of the alkenic hydrogen in the nmr (11). Enol acetate **10** does not show an alkenic hydrogen in the nmr, but does show alkenic methyls (d 2.17 and d 1.76). With compound **9** in hand, we set out to remove the unneeded five carbons from the diterpene skeleton. However, the compound was resistant to oxidative cleavage (ozone, osmium tetroxide – sodium periodate (12, 13), potassium permanganate (14), ruthenium tetraoxide (15)) of the C—C double bond. In all cases **9** was recovered from the reaction mixture. This lack of reactivity is attributed to the conjugated nature of the double bond and to its hindered nature.

Can. J. Chem. Downloaded from www.nrcresearchpress.com by 93.93.197.157 on 09/07/12
For personal use only.

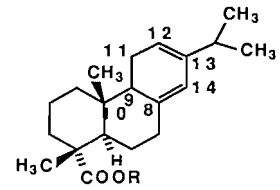

1 R = H
1*a* R = CH_3

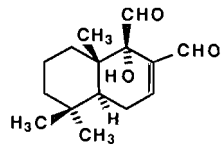

2

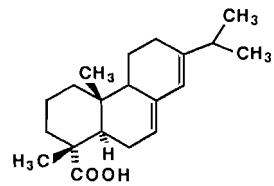

3

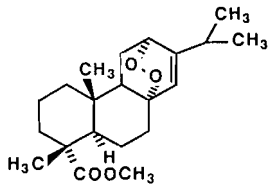

4

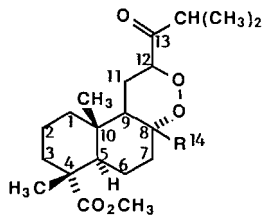

5 R = CHO
6 R = $CH(OCH_3)_2$
6*a* R = CH(-OCH_2CH_2O-)

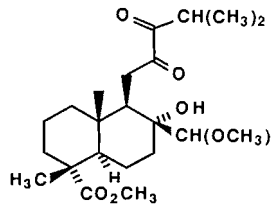

7

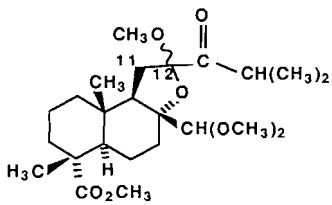

8

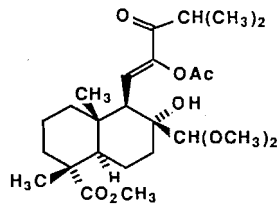

9

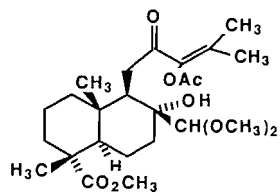

10

At this point we discovered a very useful reaction, which led to the removal of four of the unwanted carbon atoms. Reduction of the ketone function in the peroxide **6** provided a mixture of C-13 epimeric alcohols **11**. Treatment of the mixture **11** with sodium methoxide in methanol at room temperature brought about the fragmentation reaction, indicated by the arrows in **11**, to furnish the C-12 aldehyde, which was isolated as a mixture consisting mainly of the epimeric hemiacetals **12**. The ir spectrum of **12** shows hydroxyl (3480 cm^{-1}) and ester (1725 cm^{-1}) absorption. The ^1H nmr spectrum shows two hemiacetal methine hydrogens (δ 5.64 and 5.43) as well as a small signal for the aldehyde tautomer (δ 9.70). Acetylation of **12** gave a separable mixture of the acetal acetates **13***a* and **13***b*. The stereochemical assignments are made on the basis of ^1H nmr measurements. In one epimer (**13***a*) the C-12 hydrogen appears as a doublet (J = 5.5 Hz) while in the other (**13***b*), this signal is an apparent triplet (J's 5.5 Hz). Inspection of molecular models suggests that these observations are best accommodated as illustrated in Fig. 1. In **13***a* the dihedral angles are ca. 30° and 90° (J's 5.5 and 0 Hz) whereas in **13***b* they are ca. 30° and 150° (J's each 5.5 Hz). The base-catalyzed cleavage of **11** to give **12** finds analogy in the known reaction of epoxides with alkaline hydrogen peroxide (16).

The carbon skeleton of **12** closely resembles that of the drimanes except for the extra carbon at C-11. We felt that this carbon could be removed by oxidation of enol ether **14**, since the carbon–carbon double bond in **14** should be much more reactive than that in the enol acetate **9**. Attempts to dehydrate hemiacetal **12** under a variety of conditions ($POCl_3$, $SOCl_2$, tosyl isocyanate) gave complex mixtures of products. Attempted mesylation of **12** gave an unexpected result. The product was a separable mixture of the epimeric methyl acetals **15** containing a free C-14 aldehyde group. A similar result was obtained when **12** was treated with iodine in refluxing toluene or with *p*-toluenesulfonic acid in benzene at room temperature. The mass spectra of **15***a* and **15***b* both show base peaks at m/z 295 corresponding to $M^+ - CHO$. The ^1H nmr spectrum of **15***a* reveals the presence of only two methoxyl groups (δ 3.64 (ester), δ 3.39 (acetal)) and of aldehydic hydrogen (δ 9.82). The methine hydrogen at C-12 appears as an apparent triplet (δ 5.24, J's 5.0 Hz). The ^1H nmr spectrum of **15***b* gives a similar spectrum except that the C-12 methine hydrogen appears as a doublet (δ 5.31, J = 5.5 Hz). In both **15***a* and **15***b*, nuclear Overhauser enhancement (nOe) experiments confirmed the proximity of the aldehyde function to the angular methyl group. The formation of **15***a* may be rationalized as depicted in Scheme 1. Formation of ion **A** is followed by a methoxyl shift to give **B**. Ion **B** is then captured by a nucleophile (chloride ion in

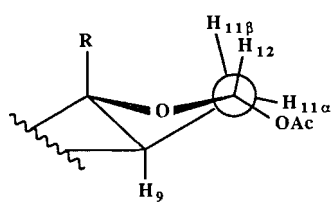

13*a*

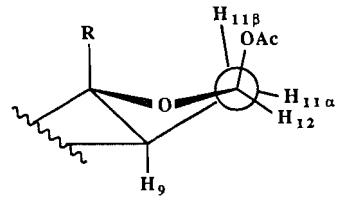

13*b*

FIG. 1. Newman projection along the C-12 to C-11 bond of acetates **13***a* and **13***b*.

Can. J. Chem. Downloaded from www.nrcresearchpress.com by 93.93.197.157 on 09/07/12
For personal use only.

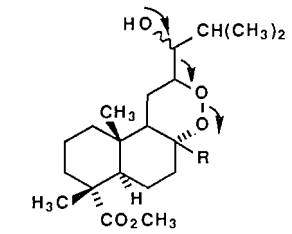

11 R = $CH(OCH_3)_2$

11*a* R = $CH(-OCH_2CH_2O-)$

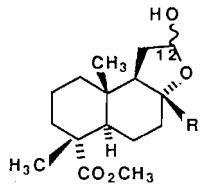

12 R = $CH(OCH_3)_2$

12*a* R = $CH(-OCH_2CH_2O-)$

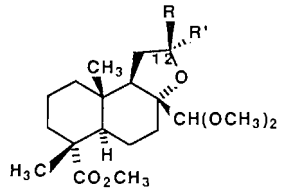

13*a* R = H, R' = OAc

13*b* R = OAc, R' = H

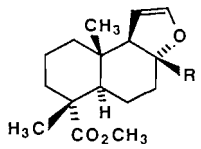

14 R = $CH(OCH_3)_2$

14*a* R = $CH(-OCH_2CH_2O-)$

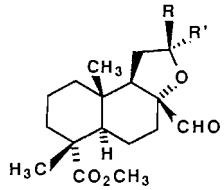

15*a* R = OCH_3, R' = H

15*b* R = H, R' = OCH_3

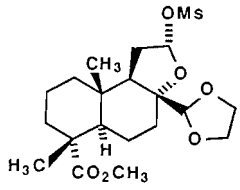

16

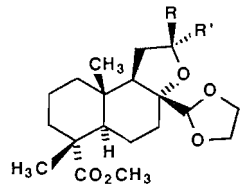

17*a* R = SPh, R' = H

17*b* R = H, R' = SPh

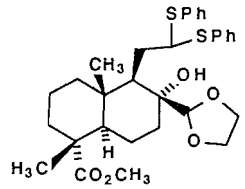

18

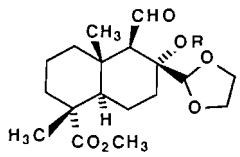

19 R = H

19*a* R = CHO

the case of the mesyl chloride reaction) to give an intermediate **C**, which is hydrolyzed to the aldehyde by traces of water or during work-up. The more stable cyclic acetal **15***b* is formed by acid-catalyzed epimerization of **15***a*.

At this stage we decided to protect the C-14 aldehyde function as the dioxolane derivative since we felt this would not interfere with operations at the cyclic hemiacetal center. It proved most convenient to introduce the dioxolane protecting group directly into the ozonolysis product **5**. The resulting **6***a* was then reduced with $NaBH_4$ and the resulting mixture of epimeric alcohols treated with sodium methoxide to give **12***a*. Treatment of **12***a* with methanesulfonyl chloride in the presence of triethylamine gave the mesylate **16**. The ^1H nmr spectrum shows only one methylsulfonate peak (δ 3.37) and the C-12 hydrogen appears as a doublet (δ 5.06, J = 5.8 Hz), indicating that only the α isomer is present. Attempts to form the enol ether **14***a* by treatment of **16** with 1,8-diazabicyclo[5.4.0]undec-7-ene (DBU) in refluxing toluene were unsuccessful.

The desired enol ether **14***a* was prepared in the following way. Treatment of hemiacetal **12***a* with thiophenol in the presence of trifluoroacetic acid (TFA) gave a mixture of the hemithioacetals **17***a* and **17***b* along with small amounts of the thioacetal **18**. The latter compound could be transformed into a mixture of **17***a* and **17***b* under acidic conditions (TFA–CH_2Cl_2). The epimeric hemithioacetals are separable by flash chromatography and are distinguished by their ^1H nmr spectra. The minor component **17***a* shows the signal for H-12 as a doublet of doublets (J's 9.0 and 6.5 Hz) at δ 5.54. Epimer **17***b* also shows this signal as a double doublet, but with smaller J values (8.0 and 1.5 Hz). In **17***a* one of the hydrogens of the dioxolane ring appears at especially low field (δ 4.31), presumably deshielded by the β substituent at C-12. The mixture of **17***a* and **17***b* was oxidized with one equivalent of *m*-chloroperbenzoic acid (*m*-CPBA) to yield the corresponding sulfoxides, which were heated in xylene in the presence of triethylphosphite (17) to give the acid-sensitive enol ether **14***a* in 65% yield from the hemithioacetals. The nmr spectra of **14***a* show olefinic hydrogens at δ 6.40 (H-12) and δ 5.17 (H-11) and olefinic carbons at δ 147.8 (C-12) and δ 101.7 (C-11), the remainder of the signals being consistent with the assigned structure.

Ozonolysis of **14***a* in dichloromethane–methanol and reductive work-up (dimethyl sulfide) gave the aldehyde **19** containing the desired drimane sesquiterpene skeleton. The ^1H nmr spectrum of **19** shows an aldehydic hydrogen as a doublet at δ 9.92 coupled (3 Hz) to another doublet at δ 2.17 (H-9).

With the desired carbon skeleton of warburganal in hand we were left with the problems of adjusting the ring B functionality and of transforming the C-4 carbomethoxyl into a methyl group. Since compound **19** would require protection of the aldehyde functionality, we decided to backtrack somewhat and use the mixture of hemithioacetals **17***a* and **17***b* as the point of introduction of the C-4 methyl group, since in these the projected ring B functionality is in a protected form. Most methods for the transformation of an ester group to a methyl group proceed through the intermediate alcohol or aldehyde. Reduction of the mixture **17** with lithium aluminum hydride gave the corresponding alcohols **20** in over 90% yield.

Can. J. Chem. Downloaded from www.nrcresearchpress.com by 93.93.197.157 on 09/07/12
For personal use only.

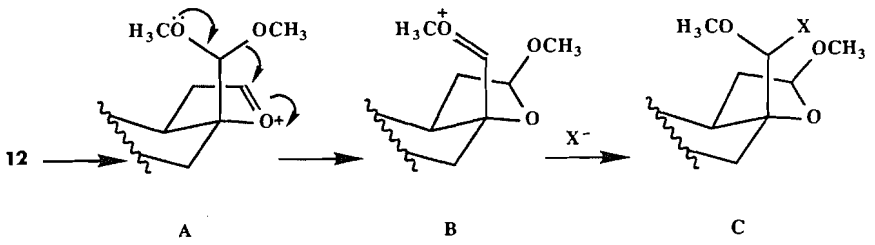

SCHEME 1

Oxidation of **20** with pyridinium chlorochromate (PCC) (18) gave the aldehydes **21**, which show aldehydic hydrogen singlets at δ 9.22 and 9.17 in the nmr. Treatment of the aldehydes under the conditions of the Huang-Minlon modification of the Wolff–Kishner reaction (19) gave a mixture of products in which alcohol **22** was the major component. The ir spectrum of **22** shows hydroxyl absorption (3565 cm^{-1}) and a characteristic (20) *gem*-dimethyl doublet (1387 and 1364 cm^{-1}). The ^1H nmr spectrum displays three quarternary methyl singlets and a methyl triplet. Presumably the thiophenol group is displaced by hydroxyl (or hydrazine) under the forcing conditions of this reaction, leading to reduction of the masked aldehyde at C-12 as well as the aldehyde at C-4. Aldehyde **21** was treated with *p*-toluenesulfonyl hydrazine (tosyl hydrazine) in refluxing ethanol to afford the tosylhydrazones **23**. Reduction of **23** with sodium borohydride gave a complex mixture of products, but treatment with bis(benzyloxy)borane followed by addition of sodium acetate (21) gave a separable mixture of the desired 4α-methyl compounds **24***a* and **24***b* in about 50% overall yield from the aldehydes **21**. The use of tetrabutylammonium acetate in place of sodium acetate (22) did not improve the yield. Similar results were obtained when catecholborane (23) was used instead of bis(benzoyloxy)borane. The ^1H nmr spectrum of **24***a* displays signals for three quaternary methyls and shows H-12 as a doublet of doublets at δ 5.56 (*J*'s 9.0 and 6.0 Hz). The ^{13}C nmr spectrum shows methyl signals at δ 33.4, 20.9, and 15.9. The chemical shift of the methyls is similar to those reported for natural products with the 4α,4β,10-trimethyldecalin system (24). The hemithioacetal **24***b* has spectroscopic (ir, ms, nmr) properties similar to those of **24***a* except that the coupling constants for H-12 are smaller (8.0 and 1.5 Hz). Because of the poor yields in the reduction step, other methods for effecting the carbomethoxyl to methyl transformation were investigated. Alcohols **20** were mesylated and the mesylates reduced with lithium triethylborohydride (superhydride) (25). The only products obtained were the alcohols **20**, the result of S—O cleavage. Similar results were obtained when the tosylates of **20** were reduced with superhydride, except that in this case about 25% of the product resulted from C—O cleavage. Recently it has been reported that 2-propanesulfonates of hindered alcohols give better yields of C—O cleavage than the corresponding mesylates or tosylates (26). Indeed, preparation of the 2-propanesulfonyl derivatives of **20** and reduction with superhydride in toluene (90°C) gave **24***a* and **24***b* in about 65% yield, a modest improvement over the tosylhydrazone route.

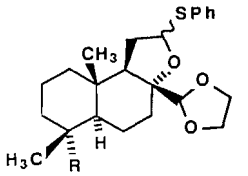

20 R = CH_2OH

21 R = CHO

23 R = CH=NNHTs

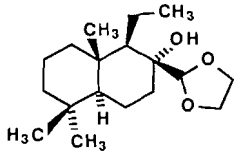

22

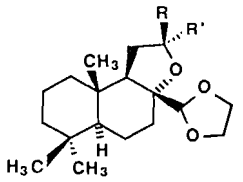

24*a* R = SPh, R' = H

24*b* R = H, R' = SPh

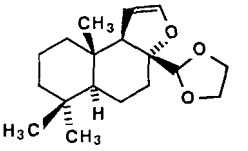

25

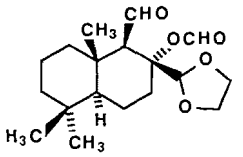

26

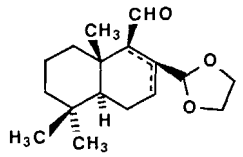

27

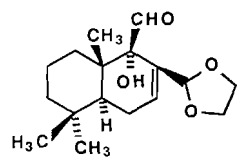

28

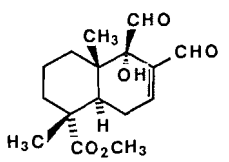

29

Can. J. Chem. Downloaded from www.nrcresearchpress.com by 93.93.197.157 on 09/07/12
For personal use only.

Can. J. Chem. Downloaded from www.nrcresearchpress.com by 93.93.197.157 on 09/07/12
For personal use only.

The hemithioacetals **24***a* and **24***b* were oxidized with *m*-CPBA to give the corresponding sulfoxides, which were heated in refluxing xylenes to afford the enol ether **25** in 65% yield. The ^{1}H nmr spectrum of **25** shows signals for three quaternary methyls and for enol ether hydrogens at δ 6.47 (H-11) and δ 5.39 (H-12). Earlier we had encountered difficulties in dehydrating alcohol **19** and had found that introduction of the ring B double bond was best achieved using the *O*-formyl derivative **19***a*, obtained when the ozonolysis of **14***a* was carried out in a nonprotic solvent. Accordingly, enol ether **25** was treated with ozone in ethyl acetate (−78°C), followed by trimethylphosphite, to give the *O*-formyl aldehyde **26**. The crude reaction product, which shows signals at δ 9.88 (aldehydic hydrogen) and δ 8.24 (*O*-formyl hydrogen), was treated with DBU in refluxing benzene to provide a mixture of unsaturated aldehydes **27**. The mixture **27** was not characterized but was immediately treated with potassium hydride in tetrahydrofuran followed by addition of the molybdenum peroxide reagent MoO_5·pyridine·HMPA (MoOPH) (27). The product, formed in about 60% yield from **25**, was compound **28**, the monoethylene acetal of warburganal (**2**). Compound **28** shows hydroxyl (3460 cm^{-1}) and aldehyde carbonyl (1724 cm^{-1}) absorption in the ir, and its ^{1}H nmr spectrum displays an aldehydic hydrogen (δ 9.85) and an alkenic hydrogen (δ 6.36, dd, *J*'s 5.0, 2.5 Hz). Removal of the dioxolane protecting group (*p*-TsOH–acetone) gave (−)-warburganal (**2**). The melting point (6, 28), specific rotation (6), and spectroscopic data (ir, nmr, ms (5, 7)) obtained for the synthetic material agree well with those reported.

During the course of our studies, the 4-carbomethoxy analog of warburganal, compound **29**, was prepared from the aldehyde **19***a* using the same sequence of reactions as for the transformation of aldehyde **26** to warburganal. The experimental details for this process have been recorded (33). Compound **29** has previously been prepared from abietic acid (6).

Experimental

All reactions were carried out under a positive pressure of an inert gas unless otherwise noted. Reactions requiring anhydrous conditions were performed in oven-dried glassware (115°C, 2 h), which was cooled in a desiccator, assembled, sealed with a rubber septum, and purged with an inert gas. Solvents were distilled before use for chromatography or extraction. Anhydrous solvents were distilled from appropriate drying agents: diethyl ether by distillation from a blue solution of sodium benzophenone ketyl; tetrahydrofuran (THF) by distillation from a blue solution of potassium benzophenone ketyl; dichloromethane, chloroform, toluene, pyridine, triethylamine, diisopropylamine, diisopropylethylamine, benzyl alcohol, oxalyl chloride, dimethyl sulfoxide (DMSO), dimethylformamide (DMF), and hexamethylphosphoric triamide (HMPA) by distillation from calcium hydride (the latter three under reduced pressure and stored over molecular sieves (3A) under nitrogen). Skellysolve B refers to Skelly Oil Company light petroleum, bp 62–70°C. The commercial solutions (Aldrich) of methyllithium in ether, *n*-butyllithium in THF, and phenyllithium in ether were titrated before use by the diphenylacetic acid method (29).

Flash chromatography was performed by using E. Merck silica gel 60 (230–400 ASTM mesh) according to the procedure of Still *et al.* (30). Analytical thin-layer chromatography (tlc) was carried out on aluminum sheets precoated (0.2-mm layer thickness) with silica gel 60 F_{254} (E. Merck, Darmstadt).

Melting points were recorded on a Fisher–Johns melting point apparatus and are uncorrected. Fourier transform infrared spectra were recorded on a Nicolet 7199 FT interferometer. Films for ir are "cast" by placing a drop of solution onto KBr plates and then allowing the solvent to evaporate. Ultraviolet spectra were recorded on a Hewlett Packard HP8450A diode array spectrometer coupled to a 7470A plotter.

Hydrogen nuclear magnetic resonance (^{1}H nmr) spectra were recorded on Bruker WP-80 (at 80 MHz), Varian HA-100 (at 100 MHz), Bruker WH-200 (at 200 MHz), Bruker WM-360 (at 360t MHz), or Bruker WH-400 (at 400 MHz) spectrometers in the specified deuterated solvent with tetramethylsilane (TMS) as an internal standard and measurements are reported in ppm downfield from TMS (δ). ^{13}C nuclear magnetic resonance (^{13}C nmr) spectra were measured on Bruker WH-200 (at 50.3 MHz) or Bruker WH-400 (at 100.6 MHz) spectrometers. For ^{13}C nmr, deuterochloroform ($CDCl_3$) was employed as the internal standard (assigned as 77.0 ppm downfield from TMS) and measurements are reported in ppm downfield from TMS (δ). Carbon-13 multiplicities were derived from gate decoupling spin echo experiments (31). In the assignments quoted terpenoid numbering, as in **1** and **5**, is used throughout.

High resolution electron impact mass spectra (hrms) were recorded on an A.E.I. MS-50 mass spectrometer coupled to a DS50 computer. Chemical ionization (ammonia as reagent gas) mass spectra (cims) and low resolution electron impact mass spectra (lrms) were obtained using an A.E.I. MS-9 mass spectrometer. Data are reported as *m/z* (relative intensity). Unless diagnostically significant, peaks with intensities less than 20% of the base peak are omitted. Optical rotations were determined on a Perkin Elmer model 141 polarimeter with a sodium lamp (589 nm) at room temperature. Combustion analyses were performed by the Microanalytical Laboratory of the University of Alberta.

*Levopimaric acid (**1**)*

Levopimaric acid was isolated from pine oleoresin (Naval Stores and Timber Production Laboratory, Olustee, Florida, U.S.A.) as described (1); mp 128°C; $[\alpha]_D$ −265° (*c* 6.6, MeOH).

*Methyl levopimarate (**1**a)*

An ethereal solution of diazomethane was added dropwise with stirring to a solution of levopimaric acid (5.092 g) in ether (200 mL) at 0°C until the yellow color persisted. The reaction mixture was dried (Na_2SO_4), and concentrated *in vacuo* to give **1***a* as a solid (5.230 g, 98%); mp 60–62°C; ^{1}H nmr (200 MHz, $CDCl_3$) δ: 5.5 (1H, d, 1.5 Hz, H-14), 5.11 (1H, t, 4 Hz, H-12), 3.65 (3H, s, C-18 OCH_3), 2.38–2.0 (5H, m), 1.91 (1H, dd, 12.75, 2.75 Hz, H-5), 1.84–1.38 (9H, m), 1.17 (3H, s, C-4 CH_3), 0.95 (6H, d, 7 Hz, CH_3-16,17), 0.89 (3H, s, C-10 CH_3); hrms, *m/z* calcd. for $C_{21}H_{32}O_2$ (M^+): 316.2394; found: 316.2402.

*Methyl 8α,12α-epidioxyabiet-13-enate (**4**) (8)*

A solution of methyl levopimarate (4.040 g) and rose bengal (50 mg) in 95% ethanol (240 mL) was irradiated with a 40-watt Luminate lamp while oxygen was bubbled through the solution. After 9 h the solvent was removed *in vacuo*. The residue was dissolved in ether (300 mL), washed with saturated $NaHCO_3$, water, brine, dried (Na_2SO_4), and concentrated to give a pink solid (4.350 g). Purification by flash chromatography, eluant Skellysolve B – ethyl acetate (85:15) gave the endoperoxide **4** as a solid (3.360 g, 76%). An analytical sample of the endoperoxide was obtained by recrystallization from Skellysolve B; mp 102°C (lit. (8) mp 100–101°C); $[\alpha]_D$ +82.6° (*c* 1.4, $CHCl_3$) (lit. (8) $[\alpha]_D$ +93.5°); ^{1}H nmr (400 MHz, $CDCl_3$) δ: 5.88 (1H, t, 1.5 Hz, H-14), 4.63 (1H, dt, 4.5, 1.5 Hz, H-12), 3.69 (3H, s), 2.51 (1H, quintet d, 7, 1.5 Hz, H-15), 2.25 (1H, ddd, 14, 9.5, 4.5 Hz, H-11α), 1.98 (1H, dd, 9, 5.5 Hz, H-9), 1.94–1.02 (12H, m), 1.14 (3H, s, C-4 CH_3), 1.12 (3H, d, 7 Hz, CH_3-16), 1.08 (3H, d, 7 Hz, CH_3-17), 0.57 (3H, s, C-10 CH_3); ^{13}C nmr ($CDCl_3$) δ: 178.8 (s, C-18), 149.1 (s, C-13), 124.7 (d, C-4), 76.9 (s, C-8), 74.7 (d, C-12), 51.9 (q, C-18 OCH_3), 50.2 (d), 49.3 (d), 47.1 (s, C-4), 36.9 (t), 36.8 (t), 36.3 (s), 32.2 (t), 31.1 (d, C-15), 25.1 (t), 21.7 (t), 20.4 (q, C-16), 20.2 (q, C-17), 17.1 (t), 16.6 (q), 15.2 (q); hrms, *m/z* calcd. for $C_{21}H_{32}O_4$ (M^+): 348.2292; found: 348.2300 (5), 316 (67), 146 (34), 121 (100), 105 (30).

Can. J. Chem. Downloaded from www.nrcresearchpress.com by 93.93.197.157 on 09/07/12
For personal use only.

*(1S,5R,6R,9R,12S,14R)-1,5-Dimethyl-10,11-dioxa-12-isopropylcarbonyl-9-formyl-5-methoxycarbonyltricyclo[8.4.0.0^{9,14}]tetradecane (**5**)*

A solution of the endoperoxide **4** (820 mg, 2.3 mmol) in dichloromethane–methanol (9:1, 100 mL) was cooled in a Dry Ice – acetone bath. Ozone was bubbled through the solution until the solution remained pale blue. Excess ozone was removed with N_2, then methyl sulfide (0.4 mL) was added to the solution. The reaction mixture was allowed to warm to room temperature and the solvent was removed. The residue was dissolved in ether, washed with water (2×), brine, dried (Na_2SO_4), and the solvent removed to give the ketoaldehyde **5** as an oil (860 mg, 98%). A sample was purified by flash chromatography (CH_2Cl_2–EtOAc, 98:2); $[\alpha]_D$ −183.5° (*c* 0.2, $CHCl_3$); ir ($CHCl_3$, cast): 2750, 1723 (br, vs), 1248 cm^{-1}; ^{1}H nmr (200 MHz, $CDCl_3$) δ: 9.77 (1H, s), 4.85 (1H, dd, 9, 4.5 Hz, H-12), 3.67 (3H, s), 2.85 (1H, quintet, 7 Hz, H-15), 2.13–1.21 (14H, m), 1.17 (3H, s, C-4 CH_3), 1.14 (3H, d, 7 Hz, CH_3-16), 1.07 (3H, d, 6.5 Hz, CH_3-17), 0.95 (3H, s, C-10 CH_3)); hrms, *m/z* calcd. for $C_{21}H_{32}O_6$ (M^+): 380.2190; found: 380.2199 (0.3), 352 (13), 281 (16), 164 (16), 263 (22), 203 (10), 121 (34), 71 (100). *Anal.* calcd. for $C_{21}H_{32}O_6$: C 66.33, H 8.48; found: C 66.35, H 8.59.

*(1S,5R,6R,9R,12S,14R)-1,5-Dimethyl-9-(dimethoxymethyl)-10,11-dioxa-12-isobutyryl-5-methoxycarbonyltricyclo[8.4.0.0^{9,14}]-tetradecane (**6**)*

A solution of the ketoaldehyde **5** (860 mg, 2.26 mmol) and *p*-toluenesulfonic acid (catalytic amount) in trimethyl orthoformate (10 mL) was stirred at room temperature for 20 h. The solution was diluted with ether, washed with saturated $NaHCO_3$, H_2O, brine, dried (Na_2SO_4), and evaporated to give **6** as a solid (930 mg). The crude product was recrystallized from ether to yield colorless needles (665 mg, 69%); mp 167–168°C; $[\alpha]_D$ −119° (*c* 0.75, $CHCl_3$); ir ($CHCl_3$, cast): 1722, 1248, 1128, 1068 cm^{-1}; ^{1}H nmr (200 MHz, $CDCl_3$) δ: 4.72 (1H, dd, 11, 3 Hz, H-12), 4.64 (1H, s, H-14), 3.67 (3H, s, C-18 OCH_3), 3.60 (3H, s, C-14 OCH_3), 3.46 (3H, s, C-14 OCH_3), 2.96 (1H, quintet, 7 Hz, H-15), 2.20–0.95 (14H, m), 1.17 (3H, s, C-4 CH_3), 1.10 (3H, d, 7 Hz, C-16), 1.08 (3H, d, 7 Hz, CH_3-17), 0.91 (3H, s, C-10 CH_3); hrms, *m/z* calcd. for $C_{19}H_{31}O_6$ ($M^+ - C_4H_7O$): 355.2112; found: 355.2121 (0.3), 263 (1.6), 121 (3), 81 (2), 75 (100); cims (NH_3): 444 (M^+ − 18, 100). *Anal.* calcd. for $C_{23}H_{38}O_7$: C 64.76, H 8.98; found: C 64.95, H 9.08.

*(1S,2R,3R,6R,7R)-1,7-Dimethyl-3-(dimethoxymethyl)-2-(2,3-dioxo-4-methylpentyl)-3-hydroxy-7-methoxycarbonylbicyclo[4.4.0]-decane (**7**)*

A solution of the peroxide **6** (107 mg, 0.25 mmol) and triethylamine (0.04 mL, 0.28 mmol) in chloroform (5 mL) was stirred for 48 h at room temperature. The resulting yellow solution was concentrated *in vacuo* to give **7** as an oil. The crude product was purified by flash column chromatography (Skellysolve B – acetone, 3:1) to give pure α-diketone **7** (103 mg, 96%); ir ($CHCl_3$, cast): 3456 (br), 1725, 1245, 1119, 1070 cm^{-1}; cims: 444 (M^+ + 18, 19), 426 (M^+, 10), 412 (100).

*(1S,5R,6R,9R,13R)-1,5-Dimethyl-9-(dimethoxymethyl)-11-isobutyryl-11-methoxy-5-methoxycarbonyl-10-oxatricyclo[7.4.0.0^{9,13}]-tetradecane (**8**)*

α-Diketone **7** (199.4 mg, 0.47 mmol), *d,l*-camphorsulfonic acid (catalytic amount), and trimethyl orthoformate (5 mL) were stirred for 12 h at room temperature. The solution was diluted with ether, washed with saturated $NaHCO_3$, H_2O, brine, dried (Na_2SO_4), and the solvent removed *in vacuo* to give a solid (179.5 mg). The solid was recrystallized from Skellysolve B to afford **8** as colorless needles (102 mg, 49%); mp 180–182°C; ir (CH_2Cl_2, cast): 1726, 1247, 1119, 1067, 1008, 955 cm^{-1}; ^{1}H nmr (400 MHz, $CDCl_3$) δ: 4.49 (1H, s, H-14), 3.70 (3H, s, C-18 OCH_3), 3.56 (3H, s), 3.34 (1H, quintet, 7 Hz, H-15), 3.26 (3H, s), 3.25 (3H, s), 2.46 (1H, dd, 15, 12 Hz, H-11β), 2.35 (1H, dt, 12, 3 Hz, H-7β), 2.07 (1H, dd, 15, 7 Hz, H-11α), 1.90 (1H, dd, 10, 3.5 Hz, H-5), 1.83 (1H, dd, 11, 5 Hz), 1.74 (1H, dd, 12, 7 Hz, H-9), 1.7–1.01 (8H, m), 1.19 (3H, s, C-4 CH_3), 1.14 (3H, d, 7 Hz, CH_3-16), 1.09 (3H, d, 7 Hz, CH_3-17), 0.92 (3H, s, C-10 CH_3); hrms, *m/z* calcd. for $C_{20}H_{33}O_6$ ($M^+ - C_4H_7O$): 369.2268; found: 369.2277 (37), 365 (18), 337 (23), 305 (20), 273 (27), 263 (32), 245 (53), 171 (15), 121 (15), 75 (100); cims (NH_3): 458 (M^+ + 18, 43), 426 (35), 409 (100). *Anal.* calcd. for $C_{24}H_{40}O_7$: C 65.43, H 9.15; found: C 65.34, H 9.20.

*(1S,5R,6R,9R,13R)-1,5-Dimethyl-9-(dimethoxymethyl)-11-(2-^{2}H)-isobutyryl-11-methoxy-5-methoxycarbonyl-10-oxatricyclo-[7.4.0.0^{9,13}]tetradecane (**8**-d$_1$)*

A small piece of metallic sodium was dissolved in methanol-d_1 (1 mL), then ketone **8** (8 mg) was added to the solution. After 12 h at room temperature the reaction was quenched with 1 drop H_2O, the solvent removed, and the residue dissolved in CH_2Cl_2. The organic extract was dried (Na_2SO_4), filtered, and evaporated under reduced pressure to yield a solid (7.5 mg). The solid was crystallized from Skellysolve B to give **8**-d_1 as white crystals; mp 179–180°C; ^{1}H nmr (400 MHz, $CDCl_3$) δ: 4.48 (1H, s, H-14), 3.68 (3H, s, C-18 OCH_3), 3.54 (3H, s), 3.25 (3H, s), 3.24 (3H, s), 2.45 (1H, dd, 14.5, 11.5 Hz, H-11β), 2.34 (1H, dt, 12.3 Hz, H-7β), 2.06 (1H, dd, 14.5, 7 Hz, H-11α), 1.89 (1H, dd, 10, 3.5 Hz, H-5), 1.82 (1H, dd, 11, 5 Hz), 1.73 (1H, dd, 11.5, 7 Hz, H-9), 1.70–1.20 (8H, m), 1.19 (3H, s, C-4 CH_3), 1.12 (3H, s, CH_3-16), 1.08 (3H, s, CH_3-17), 0.92 (3H, s, C-10 CH_3); cims (NH_3): 459 (M^+ + 18, 12), 427 (13), 410 (100).

*(1S,2R,3R,6R,7R)-2-Acetoxy-3-oxo-4-methylpent-1-enyl)-1,7-dimethyl-3-(dimethoxymethyl)-3-hydroxy-7-methoxycarbonylbicyclo[4.4.0]decane (**9**) and (1S,2R,3R,6R,7R)-1,7-dimethyl-3-(dimethoxymethyl)-3-hydroxy-7-methoxycarbonyl-2-(4-oxo-3-acetoxy-2-methylpent-2-enyl)-bicyclo[4.4.0]decane (**10**)*

The α-diketone **7** (187 mg), acetic anhydride (2 mL), and diisopropylethylamine (4 mL) were placed in a round-bottom flask fitted with a condenser. The two-phase reaction was refluxed under N_2 for 1.5 h. The reaction mixture was poured on ice and saturated $NaHCO_3$ and extracted with ether (3×). The organic extracts were combined, washed with 10% HCl (3×), saturated $NaHCO_3$ (2×), brine (2×), dried (Na_2SO_4), and concentrated *in vacuo* to give a dark yellow oil (198 mg). The crude product was purified by flash column chromatography (Skellysolve B – acetone, 4:1) to give **9** (145 mg), then **10** (11 mg). Compound **9**: ir ($CHCl_3$, cast): 3550, 1759, 1725, 1686, 1640, 1250, 1212 cm^{-1}; uv (MeOH) λ_{max}: 235 nm (ε 10 702); ^{1}H nmr (400 MHz, $CDCl_3$) δ: 6.45 (1H, d, 11 Hz, H-11), 4.48 (1H, s, H-14), 3.63 (3H, s, C-18 OCH_3), 3.43 (3H, s, C-14 OCH_3), 3.40 (3H, s, C-14 OCH_3), 3.06 (1H, quintet, 7 Hz, H-15), 2.58 (1H, br s, D_2O exchangeable), 2.56 (1H, d, 11 Hz, H-9), 2.22 (3H, s, $OCOCH_3$), 2.13 (1H, m), 1.86 (1H, m), 1.76–1.20 (9H, m), 1.16 (3H, d, 7 Hz, CH_3-16), 1.15 (3H, s, C-4 CH_3), 1.12 (3H, d, 7 Hz, CH_3-17), 1.01 (3H, s, C-10 CH_3); hrms, *m/z* calcd. for $C_{24}H_{36}O_7$ ($M^+ - CH_4O$): 436.2461; found: 436.2461 (2), 394 (36), 351 (4), 333 (3), 291 (6), 273 (7), 121 (100), 75 (10); cims (NH_3): 486 (M^+ + 18, 100). *Anal.* calcd. for $C_{25}H_{40}O_8$: C 64.08, H 8.60; found: C 64.37, H 8.63.

Compound **10**: ir ($CHCl_3$, cast): 3544 (br), 1754, 1723, 1695, 1625, 1249, 1211, 1128, 1068, 750 cm^{-1}; ^{1}H nmr (200 MHz, $CDCl_3$) δ: 4.36 (1H, s, H-14), 3.67 (3H, s, C-18 OCH_3), 3.60 (3H, s, C-14 OCH_3), 3.45 (3H, s, C-14 OCH_3), 3.06 (1H, dd, 20, 5 Hz), 2.41 (2H, m), 2.28 (3H, s, $OCOCH_3$), 2.17 (3H, s, CH_3-16), 2.12–1.96 (2H, m), 1.76 (3H, s, CH_3-17), 1.58–0.9 (10H, m), 1.12 (3H, s, C-4 CH_3), 0.84 (3H, s, C-10 CH_3); hrms, *m/z* calcd. for $C_{24}H_{36}O_7$ ($M^+ - CH_4O$): 436.2461; found: 436.2460 (7), 393 (37), 376 (22), 375 (11), 333 (25), 315 (34), 273 (18), 263 (21), 141 (15), 121 (23), 75 (100); cims (NH_3): 486 (M^+ + 18, 8), 437 (29), 405 (100).

*(1S,5R,6R,9R,12S,14R)-1,5-Dimethyl-9-(dimethoxymethyl)-10,11-dioxa-12-(1-hydroxy-2-methylpropyl)-5-methoxycarbonyltricyclo[8.4.6.0^{9,14}]tetradecane (**11**)*

Sodium borohydride (9.1 mg, 0.24 mmol) was added slowly over 15 min to a solution of the ketoperoxide **6** (102 mg, 0.24 mmol) in methanol–dichloromethane (4:1). After addition was completed, 1 drop of acetic acid was added, the reaction mixture stirred for 5 min, then the solvent removed *in vacuo*. The residue was partitioned between ether and water. The organic layer was washed with saturated

Can. J. Chem. Downloaded from www.nrcresearchpress.com by 93.93.197.157 on 09/07/12
For personal use only.

$NaHCO_3$ (2×), brine (2×), dried (Na_2SO_4), and concentrated to yield **11** as a solid (94 mg, 92%). A portion of the product was recrystallized from ether – Skellysolve B to give colorless needles, mp 134–135°C. The following data were obtained for the mixture of epimers **11**; ir (CH_2Cl_2, cast): 3537 (br), 1724, 1250, 1192, 1170, 1153, 1125, 1089 cm^{-1}; ^1H nmr (200 MHz, $CDCl_3$) δ: 4.61 (0.6H, s, H-14), 4.59 (0.4H, s, H-14), 4.36 (1H, m, H-12), 3.67 (3H, s, C-18 OCH_3), 3.62 (3H, s, C-14 OCH_3), 3.48 and 3.47 (3H, s, C-14 OCH_3), 3.35 (0.6H, dd, 11.5, 3 Hz, H-13), 3.12 (0.4H, dd, 8.5, 4.5 Hz, H-13), 2.66 (0.6H, br s, D_2O exchangeable), 2.41 (0.4H, br s, D_2O exchangeable), 2.41–2.17 (1H, m), 1.98–1.24 (14H, m), 1.18 (3H, s, C-4 CH_3), 1.03 (3H, d, 7 Hz, CH_3-16), 0.94 (3H, s, C-10 CH_3), 0.85 (3H, d, 7 Hz, CH_3-17); cims (NH_3): 446 (M^+ + 18, 53), 382 (100).

Hemiacetals ***12***

Metallic sodium (5 mg) was added to methanol (2 mL) and when the sodium was consumed the solution was added to compound **11** (20 mg) in methanol (2 mL). After 12 h at room temperature one drop of water was added, the solvent evaporated, and the residue dissolved in CH_2Cl_2. The organic layer was washed with H_2O, brine, dried (Na_2SO_4), and the solvent removed *in vacuo* to yield a solid (13.5 mg). A pure sample was obtained by recrystallization from Skellysolve B; mp 99–100°C; ir (CH_2Cl_2, cast): 3480 (br), 2760, 1725, 1248, 1121, 1070 cm^{-1}; ^1H nmr (200 MHz, $CDCl_3$) δ: 9.7 (0.15H, t, 2.5 Hz, H-12), 5.64 (0.15H, m, H-12), 5.43 (0.7H, m, H-12); cims (NH_3): 374 (M^+ + 18, 17), 356 (18), 310 (100).

*(1S,5R,6R,9R,11S,13R)-11-Acetoxy-1,5-dimethyl-9-(dimethoxymethyl)-5-methoxycarbonyl-10-oxatricyclo[7.4.0.0^{9,13}]tridecane (**13**a) and (1S,5R,6R,9R,11R,13R)-11-acetoxy-1,5-dimethyl-9-(dimethoxymethyl)-5-methoxycarbonyl-10-oxatricyclo[7.4.0.0^{9,13}]tridecane (**13**b)*

The hemiacetals **12** (10.8 mg) and acetic anhydride (10 drops) in triethylamine (2 mL) were stirred at room temperature for 36 h. The solution was poured into cold saturated $NaHCO_3$ and extracted with ether. The ether extract was washed with 10% HCl, saturated $NaHCO_3$, H_2O, brine, dried (Na_2SO_4), and evaporated to give a yellow oil. Purification by flash chromatography (Skellysolve B – ethyl acetate, 55:45) furnished the acetate **13***a* (6.8 mg, 57%) and the acetate **13***b* (1.6 mg, 14%), each as a colorless oil.

The acetone **13***a* has the following properties: ir (CH_2Cl_2, cast): 1744, 1729, 1241 cm^{-1}; ^1H nmr (200 MHz, $CDCl_3$) δ: 6.37 (1H, d, 5.5 Hz, H-12), 4.55 (1H, s, H-14), 3.7 (3H, s, C-18 OCH_3), 3.51 (3H, s, C-14 OCH_3), 3.38 (3H, s, C-14 OCH_3), 2.46 (1H, ddd, 14, 11.5, 5.5 Hz, H-11β), 2.35 (1H, m, H-7β), 2.07 (3H, s, $OCOCH_3$), 1.95 (1H, dd, 14, 7 Hz, H-11α), 1.54 (1H, dd, 11.5, 7 Hz, H-9), 1.91–1.21 (10H, m), 1.19 (3H, s, C-4 CH_3), 0.93 (3H, s, C-10 CH_3); cims (NH_3): 416 (M^+ + 18, 87).

The acetate **13***b* has the following properties: ir (CH_2Cl_2, cast): 1744, 1727, 1239, 1127, 1070, 969 cm^{-1}; ^1H nmr (200 MHz, $CDCl_3$) δ: 6.16 (1H, t, 5.5 Hz, H-12), 4.5 (1H, s, H-14), 3.65 (3H, s, C-18 OCH_3), 3.43 (3H, s, C-14 OCH_3), 3.37 (3H, s, C-14 OCH_3), 2.26 (1H, brd, 12, 3 Hz, H-7β), 2.20 (1H, ddd, 17, 11, 5.5 Hz, H-11β), 2.06 (3H, s, CH_3COO), 2.0 (1H, dt, 17, 5.5 Hz, H-11α), 1.85–1.18 (11H, m), 1.16 (3H, s, C-4 CH_3), 0.94 (3H, s, C-10 CH_3); cims (NH_3): 416 (M^+ + 18, 2).

*(1S,5R,6R,9R,11S,13R)-1,5-Dimethyl-9-formyl-5-methoxycarbonyl-11-methoxy-10-oxatricyclo[7.4.0.0.^{9,13}]tridecane (**15**a) and(1S,5R,6R,9R,11R,13R)-1,5-dimethyl-9-formyl-5-methoxycarbonyl-11-methoxy-10-oxatricyclo[7.4.0.0^{9,13}]tridecane (**15**b)*

Methanesulfonyl chloride (0.05 mL) was added to a solution of hemiacetal **12** (14.8 mg), triethylamine (0.1 mL), and CH_2Cl_2 (2 mL) at 0°C. After 4 h at 0°C the solution was warmed to room temperature and 1 drop of H_2O was added. The solution was stirred for 2 h, then poured onto H_2O and extracted with CH_2Cl_2 (2×). The extract was washed with H_2O, brine, dried (Na_2SO_4), and evaporated *in vacuo* to give a yellow oil. Purification by flash chromatography (Skellysolve B – ethyl acetate, 3:1) afforded the aldehyde **15***a* (6.2 mg), mp 109°C (from Skellysolve B); $[\alpha]_D$ −54.9° (*c* 0.41, $CHCl_3$); ir (CH_2Cl_2, cast): 2760, 1723, 1248 cm^{-1}; ^1H nmr (400 MHz, $CDCl_3$) δ: 9.82 (1H, d, 1.5 Hz, H-14), 5.24 (1H, t, 5 Hz, H-12 X portion of an ABCX system), 3.64 (3H, s, C-18 OCH_3), 3.39 (3H, s, C-12 OCH_3), 2.44 (1H, dt, 12, 3 Hz, H-7β), 2.24 (1H, complex, C portion of an ABCX system), 1.96 (2H, complex, AB portion of an ABCX system), 1.81 (1H, dd, 12.75, 2.75 Hz, H-5), 1.78–1.12 (9H, m), 1.1 (3H, s, C-4 CH_3), 0.82 (3H, s, C-10 CH_3); ^{13}C nmr ($CDCl_3$) δ: 198.1 (d, C-14), 178.7 (s, C-18), 107.0 (d, C-12), 85.3 (s, C-8), 61.1 (d, C-9), 56.2 (q, C-12 OCH_3), 51.9 (q, C-18 OCH_3), 50.9 (d, C-5), 46.8 (s, C-4), 38.2, 37.1, 36.1 (s, C-16), 31.2, 31.0, 22.5, 17.3 (t, C-2), 15.9 (q, CH_3), 15.4 (q, CH_3); hrms, *m/z* calcd. for $C_{17}H_{27}O_4$ (M^+ − CHO): 295.1902; found: 295.1910 (100), 231 (4), 203 (23), 121 (12); cims (NH_3): 342 (M^+ − 18, 20), 310 (100), 292 (10).

Nuclear Overhauser enhancement difference spectroscopy (nOeds) on the aldehyde gave the following results: presaturation of H-14 (δ 9.82): 7% (H-11β), 7% (C-4 CH_3), 17% (C-10 CH_3); presaturation of C-10 CH_3 (δ 0.82): 15% (H-14), 9.5% (H-11β), 20% (C-4 CH_3).

In some cases the aldehyde **15***b* was present as a minor component in the crude product. A pure sample was obtained by recrystallization from Skellysolve B; mp 90–91°C; ir (CH_2Cl_2, cast): 2740, 1725, 1247, 1172, 1102, 1002 cm^{-1}; ^1H nmr (400 MHz, $CDCl_3$) δ: 9.61 (1H, s, H-14), 5.31 (1H, d, 5.5 Hz, H-12), 3.67 (3H, s, C-18 OCH_3), 3.39 (3H, s, C-12 OCH_3), 2.37 (1H, complex, H-7β), 2.18 (1H, dd, 14, 6 Hz, H-11α), 2.06 (1H, ddd, 14.5, 12, 5.5 Hz, H-11β), 1.91 (1H, dd, 12.5, 3 Hz, H-5), 1.78 (1H, dd, 12, 6 Hz, H-9), 1.82–1.73 (1H, m), 1.69–1.21 (8H, m), 1.13 (3H, s, C-4 CH_3), 0.76 (3H, s, C-10 CH_3); ^{13}C nmr ($CDCl_3$) δ: 198.3 (d, C-14), 178.6 (s, C-18), 105.5 (d, C-12), 86.5 (s, C-8), 58.7 (d, C-9), 55.3 (q, C-12 OCH_3), 51.9 (q, C-18 OCH_3), 50.6 (d, C-5), 46.8 (s, C-4), 38.1 (t), 37.1 (t), 35.8 (s, C-10), 32.6 (t), 30.4 (t), 22.7 (t), 17.4 (t, C-2), 16.3 (q), 15.9 (q); hrms, *m/z* calcd. for $C_{17}H_{27}O_4$ (M^+ − CHO): 295.1902; found: 295.1911 (100), 265 (3), 203 (24), 185 (7), 159 (8), 121 (21).

Nuclear Overhauser enhancement difference spectroscopy gave the following results: presaturation of C-10 CH_3 (δ 0.76): 12% (H-14), 7.5% (H-11β), 15% (C-4 CH_3).

*(1S,5R,6R,9R,12S,14R)-1,5-Dimethyl-10,11-dioxa-9-ethylenedioxymethyl-12-isobutyryl-5-methoxycarbonyltricyclo[8.4.0.0.^{9,14}]tetradecane (**6**a)*

A solution of the crude aldehyde **5** (543 mg, 1.43 mmol), ethylene glycol (0.4 mL, 7.15 mmol), trimethyl orthoformate (0.78 mL, 7.15 mmol), and *p*-toluenesulfonic acid (40 mg) in dry benzene (6 mL) was stirred in an oil bath at 45°C under reduced pressure (160 Torr; 1 Torr = 133.3 Pa) for 10 h. The dimethyl acetal formed in the reaction was converted to the dioxolane by adding ethylene glycol (0.4 mL) and heating the solution at 80°C for 10 min at atmospheric pressure. The reaction mixture was diluted with CH_2Cl_2, washed with 10% HCl (2×), saturated $NaHCO_3$ (2×), brine, dried ($MgSO_4$), and concentrated *in vacuo* to yield an oil. Recrystallization from ether afforded the ketone **6***a* as white crystals (239 mg) and purification of the mother liquors by flash chromatography (dichloromethane – ethyl acetate, 9:1) gave further **6***a* (121 mg). The overall yield of the ketone from levopimaric acid is 49% when the reaction sequence is carried out without purification. Ketone **6***a* shows the following properties: $[\alpha]_D$ −133.3° (*c* 0.15, $CHCl_3$); ir (CH_2Cl_2, cast): 1722, 1713, 1245, 1171, 1147, 1042 cm^{-1}; ^1H nmr (400 MHz, $CDCl_3$) δ: 5.37 (1H, s, H-14), 4.80 (1H, dd, 11.5, 2.5 Hz, H-12), 4.20–3.84 (4H, complex), 3.68 (3H, s), 2.88 (1H, quintet, 7 Hz, H-15), 2.21 (1H, complex), 1.94 (1H, dt, 12.5, 3 Hz, H-7β), 1.9–0.83 (12H, m), 1.18 (3H, s, C-4 CH_3), 1.12 (3H, d, 7 Hz, CH_3-16), 1.06 (3H, d, 7 Hz, CH_3-17), 1.01 (3H, s, C-10 CH_3); ^{13}C nmr ($CDCl_3$) δ: 210.5 (s, C-13), 178.7 (s, C-18), 105.5 (d, C-14), 86.3 (d, C-12), 81.4 (s, C-8), 65.2 (t), 57.4 (d, C-9), 51.9 (q, C-18 OCH_3), 50.9 (d, C-5), 47.4 (s, C-4), 38.1 (t), 36.9 (t), 35.9 (s, C-10), 32.7 (t), 22.3 (t), 22.0 (t), 18.1 (q), 17.6 (t), 17.5 (q), 16.0 (q, two carbons); hrms, *m/z* calcd. for $C_{19}H_{29}O_6$ (M^+ − C_4H_7O): 353.1956; found: 353.1965 (1), 281 (1), 203 (1), 121 (3), 73 (100); cims (NH_3): 442 (M^+ + 18, 24), 424 (M^+, 3), 337 (100). *Anal.* calcd. for $C_{23}H_{36}O_7$: C 65.03, H 8.55; found: C 65.03, H 8.50.

*(1S,5R,6R,9R,12S,14R)-1,5-Dimethyl-10,11-dioxa-9-ethylenedioxymethyl-12-(1-hydroxy-2-methylpropyl)-5-methoxycarbonyltricyclo[8.4.0.0.^{9,14}]tetradecane (**11**a)*

Sodium borohydride (225 mg, 5.94 mmol) was added slowly to a stirred solution of ketone **6***a* (2.52 g, 5.94 mmol) in CH_2Cl_2–MeOH (20 mL, 1:1). After 15 min, addition was complete and the reaction was quenched by adding 3 drops of acetic acid. The solvent was removed under vacuum and the residue partitioned between ether and water. The ethereal layer was separated and washed with saturated $NaHCO_3$, H_2O, brine, dried ($MgSO_4$), and evaporated *in vacuo* to yield the epimeric alcohols **11***a* (2.40 g) as a solid. An analytical sample was obtained by recrystallization from Skellysolve B; mp 163.5–164.5°C; ir ($CHCl_3$, cast): 3520 (br), 1724, 1249, 1170, 1150, 1106, 1008 cm^{-1}; ^1H nmr (200 MHz, $CDCl_3$) δ: 5.28 (0.3H, s, H-14), 5.22 (0.7H, s, H-14), 4.34 (0.7H, dt, 11, 3 Hz, H-12), 4.29 (0.3H, ddd, 11, 5.5, 3 Hz, H-12), 3.3 (0.7H, dd, 8, 3 Hz, H-13), 3.18 (0.3H, t, 5.5 Hz, H-13), 2.31 (0.7H, s, D_2O exchangeable), 2.13 (0.3H, s, D_2O exchangeable); hrms, *m/z* calcd. for $C_{19}H_{29}O_6$ ($M^+ - C_4H_9O$): 353.1956; found: 353.1964 (0.3), 321 (1), 281 (2), 121 (3), 73 (100); cims (NH_3): 444 (M^+ + 18, 25), 426 (M^+, 1), 337 (100). *Anal.* calcd. for $C_{23}H_{38}O_7$: C 64.75, H 8.98; found: C 65.11, H 8.93.

*Hemiacetals **12**a*

A solution of the crude alcohols **11***a* (2.40 g) and sodium methoxide (321 mg) in methanol (30 mL) was stirred for 12 h at room temperature. Water (0.1 mL) was added and the solvent removed *in vacuo*. The residue was dissolved in CH_2Cl_2 and washed with H_2O, brine, dried ($MgSO_4$), and evaporated *in vacuo* to give the hemiacetals **12***a* (1.94 g) as a solid. An analytical sample was prepared by recrystallization from Skellysolve B – diisopropyl ether; mp 122–123°C; ir ($CHCl_3$, cast): 3428 (br), 2720, 1726 (br), 1249, 1172, 1142, 1119, 1070 cm^{-1}; ^1H nmr (200 MHz, $CDCl_3$) δ: 9.74 (0.2H, t, 2.5 Hz, H-12), 5.56 (0.4H, d, 6 Hz, H-12), 5.44 (0.4H, m, H-12), 5.19, 5.11, and 5.06 (1H, s, H-14); hrms, *m/z* calcd. for $C_{19}H_{30}O_6$: 354.2034; found: 354.2042 (3), 281 (66), 221 (27), 203 (21), 121 (26), 73 (100). *Anal.* calcd. for $C_{19}H_{30}O_6$: C 64.38, H 8.53; found: C 64.61, H 8.62.

*(1S,5R,6R,9R,11S,13R)-1,5-Dimethyl-9-ethylenedioxymethyl-11-methanesulfonyl-5-methoxycarbonyl-10-oxatricyclo[7.4.0.0.^{9,13}]tridecane (**16**)*

To a solution of hemiacetal **12***a* (10 mg, 0.028 mmol) and triethylamine (0.1 mL, 1.36 mmol) in CH_2Cl_2 in an ice-water bath (5°C) was added methanesulfonyl chloride (0.05 mL, 0.29 mmol). The solution was stirred for 2 h at 5°C, then poured onto cold H_2O and extracted twice with ether. The organic layer was washed with cold 10% HCl, saturated $NaHCO_3$, H_2O, brine, dried ($MgSO_4$), and evaporated *in vacuo* to give a yellow oil (8.9 mg). Purification by flash chromatography (Skellysolve B – acetone, 3:1) yielded **16** as a colorless oil (6 mg); ir (CH_2Cl_2, cast): 1726, 1358, 1335, 1247, 1150, 1143, 1122, 1100, 945 cm^{-1}; ^1H nmr (400 MHz, $CDCl_3$) δ: 5.18 (1H, s, H-14), 5.06 (1H, d, 5.75 Hz, H-12), 4.02–3.94 (2H, m), 3.9–3.78 (2H, m), 3.65 (3H, s, C-18 OCH_3), 3.37 (3H, s, C-12 OSO_2CH_3), 2.38 (1H, dt, 12, 3 Hz, H-7β), 2.34 (1H, ddd, 14.5, 11.5, 5.75 Hz, H-11β), 2.02 (1H, dd, 14.5, 6.75 Hz, H-11α), 1.92 (1H, dd, 11.5, 3 Hz, H-5), 1.81 (1H, dt, 13.5, 5 Hz), 1.94 (1H, dd, 11.5, 6.75 Hz, H-9), 1.78–1.21 (8H, m), 1.16 (3H, s, C-4 CH_3), 0.95 (3H, s, C-10 CH_3).

*(1S,5R,6R,9R,11R,13R)-1,5-Dimethyl-9-ethylenedioxymethyl-5-methoxycarbonyl-10-oxa-11-phenylthiotricyclo[7.4.0.0.^{9,13}]tridecane (**17**a), (1S,5R,6R,9R,11S,13R)-1,5-dimethyl-9-ethylenedioxymethyl-5-methoxycarbonyl-10-oxa-11-phenylthiotricyclo[7.4.0.0^{9,13}]tridecane (**17**b) and (1S,2R,3R,6R,7R)-1,7-dimethyl-2-[2,2′-bis(phenylthio)-ethyl]-3-ethylenedioxymethyl-3-hydroxy-7-methoxycarbonylbicyclo[4.4.0]decane (**18**)*

A solution of the crude hemiacetal **12***a* (2.04 g), thiophenol (1.22 mL), and trifluoroacetic acid (3 drops) in CH_2Cl_2 (25 mL) was stirred for 38 h at room temperature. The solution was diluted with CH_2Cl_2 and washed with 5% Na_2CO_3 (4×), brine, dried ($MgSO_4$), and evaporated *in vacuo* to yield the mixture of thioacetals as an oil. Purification by flash chromatography (Skellysolve B – acetone, 3:1) gave the hemithioacetals **17***a* and **17***b* (1.93 g, 72%) as an oil and the thioacetal **18** (0.19 g, 6%) as an oil.

Compounds **17***a* and **17***b* were separated by flash chromatography (Skellysolve B – ethyl acetate, 7:3). Compound **17***a*, obtained as an oil, shows the following properties: $[\alpha]_D$ +80.3° (*c* 0.11, $CHCl_3$), ir (CH_2Cl_2, cast): 3045, 1725, 1580 cm^{-1}; ^1H nmr (200 MHz, $CDCl_3$) δ: 7.48 (2H, dd, 8.5, 1.5 Hz, Ar-H), 7.32–7.12 (3H, m, Ar-H), 5.54 (1H, dd, 9, 6.5 Hz, H-12), 5.28 (1H, s, H-14), 4.39 (1H, complex), 4.10–3.71 (3H, complex), 3.67 (3H, s, C-18 OCH_3), 2.39 (1H, dd, 14.5, 11.5, 9 Hz, H-11β), 2.38 (1H, m, H-7β), 2.12 (1H, dt, 11.5, 6.5 Hz, H-11α), 1.91–1.28 (11H, m), 1.16 (3H, s, C-4 OCH_3), 1.02 (3H, s, C-10 CH_3); ^{13}C nmr ($CDCl_3$) δ: 178.7 (s, C-18), 138.1 (s), 129.7 (d, 2×), 128.8 (d, 2×), 126.0 (d), 105.3 (d, C-14), 89.3 (s, C-12), 84.2 (s, C-8), 66.5 (t), 64.9 (t), 61.8 (d, C-9), 51.9 (q, C-18 OCH_3), 51.8 (d, C-5), 47.0 (s, C-4), 39.1 (t), 37.2 (t), 36.3 (t), 35.8 (s, C-10), 31.3 (t), 23.2 (t), 17.5 (t), 16.2 (q), 15.8 (q); hrms, *m/z* calcd. for $C_{25}H_{34}O_5S$ (M^+): 446.2117; found: 446.2127 (2), 373 (51), 337 (100), 293 (21), 263 (39), 215 (18), 121 (17), 73 (85); cims (NH_3): 464 (M^+ + 18, 0.6), 354 (4), 337 (3). *Anal.* calcd. for $C_{25}H_{34}O_5S$: C 67.23, H 7.67; found: C 67.23, H 7.58.

Compound **17***b*, obtained as an oil, shows the following properties: $[\alpha]_D$ −81.3° (*c* 0.16, $CHCl_3$); ir (CH_2Cl_2, cast): 3045, 1725, 1580 cm^{-1}; ^1H nmr (200 MHz, $CDCl_3$) δ: 7.61–7.5 (2H, m, Ar-H), 7.42–7.28 (3H, m, Ar-H), 5.63 (1H, dd, 8, 1.5 Hz, H-12), 5.22 (1H, s, H-14), 4.08–3.80 (4H, m), 3.67 (3H, s, C-18 OCH_3), 2.72 (1H, ddd, 14.5, 11.5, 8 Hz, H-11β), 2.38 (1H, m, H-7β), 1.84 (1H, ddd, 11.5, 7, 1.5 Hz, H-11α), 1.76–1.22 (11H, m), 1.12 (3H, s, C-4 CH_3), 0.93 (3H, s, C-10 CH_3); ^{13}C nmr ($CDCl_3$) δ: 178.7 (s, C-18), 134.5 (s, Ar), 132.0 (d, Ar, 2×), 128.7 (d, Ar, 2×), 127.0 (d, Ar), 105.5 (d, C-14), 86.8 (d, C-12), 85.0 (s, C-8), 66.2 (t), 64.7 (t), 60.0 (d, C-9), 51.9 (q, C-18 OCH_3), 51.6 (d, C-5), 46.9 (s, C-4), 39.0 (t), 37.1 (t), 35.8 (t), 35.5 (s, C-10), 31.8 (t), 22.9 (t), 17.5 (t), 16.0 (q), 15.8 (q); hrms, *m/z* calcd. for $C_{25}H_{34}O_5S$ (M^+): 446.2117; found: 446.2127 (1), 373 (37), 337 (100), 293 (16), 263 (26), 215 (15), 121 (14), 73 (78); cims (NH_3): 464 (M^+ + 18, 8), 354 (15). *Anal.* calcd. for $C_{25}H_{34}O_5S$: C 67.23, H 7.67; found: C 67.14, H 7.74.

The thioacetal **18** shows the following properties: ir ($CHCl_3$, cast): 3512 (br), 3056, 1723, 1582 cm^{-1}; ^1H nmr (200 MHz, $CDCl_3$) δ: 7.54 (2H, dd, 8, 1.5 Hz, Ar-H), 7.46 (2H, dd, 8, 1.5 Hz, Ar-H), 7.36–7.19 (6H, m, Ar-H), 4.99 (1H, s, H-14), 4.96 (1H, dd, 9.5, 5.75 Hz, H-12), 3.87–3.66 (4H, m), 3.66 (3H, s, C-18 OCH_3), 2.83 (1H, ddd, 15.5, 6.75, 5.5 Hz, H-11), 2.51 (1H, s, D_2O exchangeable), 2.1 (1H, dd, 10, 3 Hz, H-5), 2.05 (1H, dd, 7, 2.75 Hz, H-9), 1.82 (1H, ddd, 15.5, 9.5, 2.75 Hz, H-11), 1.95–1.16 (10H, m), 1.1 (3H, s, C-4 CH_3), 0.83 (3H, s, C-10 CH_3).

A solution of the thioacetal **18** (189 mg) and trifluoroacetic acid (1 drop) in CH_2Cl_2 (2 mL) was stirred at room temperature for 78 h. The reaction was worked up and purified as described above to yield the hemithioacetals **17***a* and **17***b* (172 mg) as an oil. The overall yield from the ketoperoxide **6***a* is 75%.

*(1S,5R,6R,9R,13R)-1,5-Dimethyl-9-ethylenedioxymethyl-5-methoxycarbonyl-10-oxatricyclo[7.4.0.0.^{9,13}]tridec-11-ene (**14**a)*

A solution of *m*-chloroperbenzoic acid (188 mg) in CH_2Cl_2 (3 mL) was added to a cooled solution (ice bath) of hemithioacetals **17** (468 mg) in CH_2Cl_2 (8 mL). The solution was stirred for 15 min, then diluted with CH_2Cl_2, and washed with saturated $NaHCO_3$, brine, dried ($MgSO_4$), and evaporated *in vacuo* to give the corresponding sulfoxides (462 mg) as an oil.

A solution of the sulfoxides (462 mg) and triethylphosphite (0.89 mL) in 10 mL of xylenes was refluxed for 2½ h under nitrogen. The solvent was removed azeotropically with benzene in the rotary evaporator. The residue was purified by flash chromatography (Skellysolve B – ethyl acetate, 65:35) to give the enol ether **14***a* (225 mg, 65% overall yield) from the hemithioacetals) as a solid. An analytical sample was obtained by recrystallization from Skellysolve B – diisopropyl ether; mp 93–95°C; ir (CH_2Cl_2, cast): 3080, 1723, 1585, 1246 cm^{-1}; ^1H nmr (200 MHz, $CDCl_3$) δ: 6.4 (1H, t, 3.25 Hz, H-12), 5.31 (1H, s, H-14), 5.17 (1H, t, 2.5 Hz, H-11), 4.06–3.76 (4H, m), 3.67 (3H, s, C-18 OCH_3), 3.06 (1H, br s, H-9), 2.42 (1H, dt, 12,

Can. J. Chem. Downloaded from www.nrcresearchpress.com by 93.93.197.157 on 09/07/12
For personal use only.

Can. J. Chem. Downloaded from www.nrcresearchpress.com by 93.93.197.157 on 09/07/12
For personal use only.

3.25 Hz, H-7β), 1.91–1.18 (10H, m), 1.17 (3H, s, C-4 CH_3), 1.08 (3H, s, C-10 CH_3); ^{13}C nmr ($CDCl_3$) δ: 178.7 (s, C-18), 147.8 (d, C-12), 104.9 (d, C-14), 101.7 (d, C-11), 88.9 (s, C-8), 65.5 (t), 65.0 (t), 64.5 (d, C-9), 51.9 (q, C-18 OCH_3), 51.4 (d, C-5), 46.9 (s, C-4), 39.3 (t), 37.2 (t), 36.2 (s, C-10), 34.6 (t), 23.6 (t), 17.7 (t), 17.5 (q), 15.5 (q); hrms, *m/z* calcd. for $C_{19}H_{28}O_5$ (M^+): 336.1929; found: 336.1936 (0.2), 263 (22), 262 (12), 203 (30), 121 (11), 95 (10), 81 (39), 73 (100); cims (NH_3): 354 (M^+ + 18, 24), 337 (100). *Anal.* calcd. for $C_{19}H_{28}O_5$: C 67.83, H 8.39; found: C 67.55, H 8.28.

*12,12-Ethylenedioxy-8α-hydroxy-4α-methoxycarbonyldriman-11-al (**19**)*

A solution of the enol ether **14***a* (125 mg) in dichloromethane–methanol (10 mL, 1:1) was cooled in a Dry Ice – acetone bath. Ozone was bubbled through the solution until a pale blue color appeared. Excess ozone was removed with nitrogen. Methyl sulfide (0.06 mL) was added and the reaction mixture was allowed to warm to room temperature. The solvent was evaporated and the residue dissolved in CH_2Cl_2, washed with H_2O, brine, dried ($MgSO_4$), and evaporated *in vacuo* to give the β-hydroxyaldehyde **19** (124 mg, 98%) as a solid. An analytical sample was obtained by recrystallization from Skellysolve B – ethyl acetate; mp 120–121°C; $[\alpha]_D$ −52.8° (*c* 0.13, $CHCl_3$); ir (CH_2Cl_2, cast): 3505 (br), 2755, 1720, 1253 cm^{-1}; ^1H nmr (400 MHz, $CDCl_3$) δ: 9.92 (1H, d, 3 Hz, H-11), 5.26 (1H, s, H-12), 4.08–3.86 (4H, m), 3.68 (3H, s, C-13 OCH_3), 2.97 (1H, s, D_2O exchangeable), 2.17 (1H, d, 3 Hz, H-9), 2.15 (1H, dd, 10, 3 Hz, H-5), 1.99 (1H, br d, 13 Hz), 1.82–1.10 (9H, m), 1.29 (3H, s, C-10 CH_3), 1.19 (3H, s, C-4 CH_3); hrms, *m/z* calcd. for $C_{18}H_{18}O_6$ (M^+): 340.1878; found: 340.1885 (2), 322 (2), 295 (14), 267 (9), 207 (10), 121 (8), 73 (100); cims (NH_3): 358 (M^+ + 18, 100), 341 (M^+ + 1, 11). *Anal.* calcd. for $C_{18}H_{28}O_6$: C 63.51, H 8.29; found: C 63.13, H 8.27.

*(1S,5R,6R,9R,13R)-1,5-Dimethyl-9-ethylenedioxymethyl-5-hydroxymethyl-10-oxa-11-phenylthiotricyclo[7.4.0.0.^{9,13}]tridecane (**20**)*

A solution of **17***a* and **17***b* (849 mg) in THF (4 mL) was added slowly to a suspension of $LiAlH_4$ (144 mg) in THF (2 mL) cooled in an ice bath. The suspension was stirred for ½h at 5°C, then 1 h at room temperature. The excess $LiAlH_4$ was destroyed by careful addition of H_2O (0.15 mL), 15% NaOH (0.15 mL), H_2O (0.45 mL). The slurry was vigorously stirred until a fine solid formed, dried ($MgSO_4$), and filtered. The white solid was washed with ether (3×), and the solvent removed *in vacuo* to yield the epimeric mixture of alcohols **20** (730 mg, 92%) as a colorless oil; ir (CH_2Cl_2, cast): 3436 (br), 3050, 1580 cm^{-1}; ^1H nmr (200 MHz, $CDCl_3$) δ: 5.34 (0.2H, s, H-14), 5.25 (0.8H, s, H-14), 3.37 (1H, br d, 11 Hz, H-18), 3.11 (1H, br d, 11 Hz, H-18), 1.04 (0.6H, s, C-10 CH_3), 0.93 (2.4H, s, C-10 CH_3), 0.80 (0.6H, s, C-4 CH_3), 0.77 (2.4H, s, C-4 CH_3); hrms, *m/z* calcd. for $C_{24}H_{34}O_4S$ (M^+): 418.2168; found: 418.2177 (1), 345 (44), 309 (98), 265 (19), 247 (21), 235 (35), 217 (26), 110 (15), 73 (100).

*(1S,5R,6R,9R,13R)-1,5-Dimethyl-9-ethylenedioxymethyl-5-formyl-10-oxa-11-phenylthiotricyclo[7.4.0.0.^{9,13}]tridecane (**21**)*

A solution of the epimeric mixture of alcohols **20** (414 mg) in CH_2Cl_2 (5 mL) was added to a suspension of pyridinium chlorochromate (18) (373 mg) in CH_2Cl_2 (10 mL). The suspension was stirred for 1½h at room temperature, then diluted with ether (30 mL). The reaction mixture was decanted and the sticky oil washed with ether (3×) until it turned solid. The combined organic extracts were filtered through a pad of Florisil and evaporated to give aldehyde **21** (373 mg, 90%) as an oil. The ^1H nmr spectrum of the product shows signals for two epimers in a ratio of about 4:1. The mixture shows the following properties: ir (CH_2Cl_2, cast): 3050, 2680, 1723, 1580 cm^{-1}; ^1H nmr (200 MHz, $CDCl_3$) δ: 9.22, 9.17 (1H, s, H-18), 5.29, 5.19 (1H, s, H-14), 1.09, 1.05, 1.03, 0.94 (6H, s, C-4 and C-10 CH_3); hrms, *m/z* calcd. for $C_{24}H_{32}O_4S$ (M^+): 416.2012; found: 416.2021 (2), 343 (30), 307 (100), 233 (29), 73 (77).

*(1S,2R,3R,6S)-1,7,7-Trimethyl-2-ethyl-3-ethylenedioxymethyl-3-hydroxybicyclo[4.4.0]decane (**22**)*

A mixture of the aldehydes **21** (20 mg), ethanol (0.1 mL), 95% hydrazine (0.1 mL), and KOH (0.2 g) in ethylene glycol (2 mL) was placed in an oil bath and warmed slowly to 150°C under nitrogen. After 3 h at 150°C the condenser was replaced with a short distillation column and the temperature was increased to 210°C. The reaction mixture was stirred for 5 h at this temperature during which time a few drops of colorless liquid distilled off. The solution was cooled, diluted with H_2O, and extracted with ether. The combined extracts were washed with H_2O, brine, dried ($MgSO_4$), and evaporated *in vacuo* to give a complex mixture (12.8 mg) as an oil. Purification by flash chromatography (Skellysolve B – ethyl acetate 7:3) gave the alcohol **22** (1.2 mg) as an oil; ir (CH_2Cl_2, cast): 3565 (Br), 1387, 1364, 1340, 1118, 1059, 1045, 1020, 963, 947 cm^{-1}; ^1H nmr (400 MHz, $CDCl_3$) δ: 5.1 (1H, s, H-14), 4.13–3.85 (4H, m), 2.67 (1H, s, D_2O exchangeable), 2.23 (1H, dt, 11.5, 3 Hz, H-7β), 1.99 (1H, complex), 1.78–1.16 (12H, m), 1.01 (3H, t, 7.5 Hz, CH_3-12), 0.87 (6H, s), 0.81 (3H, s); hrms, *m/z* calcd. for $C_{15}H_{27}O$ (M^+ − $C_3H_5O_2$): 223.2055; found: 223.2062 (100), 205 (86), 137 (40), 123 (15), 109 (13), 99 (15), 95 (17), 83 (11), 73 (96); cims (NH_3): 314 (M^+ + 18, 100), 296 (M^+, 2), 279 (95), 235 (15), 217 (59).

(1S,5R,6R,9R,13R)-1,5-Dimethyl-9-ethylenedioxymethyl-5-formyl-10-oxa-11-phenylthiotricyclo[7.4.0.0.^{9,13}]tridecane p*-toluenesulfonyl hydrazone (**23**)*

A solution of the mixture of aldehydes **21** (96 mg) and *p*-tosylhydrazine (48 mg) in 98% ethanol (0.5 mL) was refluxed for 1 h under a nitrogen atmosphere. The reaction mixture was diluted with methanol and the solvent removed *in vacuo* to yield **23** (4:1 mixture of epimers) as a white solid showing the following properties: ir (CH_2Cl_2, cast): 3195, 3058, 1597, 1584, 1359, 1169, 1120, 1022, 814, 738, 696, 579, 549 cm^{-1}; ^1H nmr (400 MHz, $CDCl_3$) δ: 6.85, 6.81 (1H, s, H-18), 5.25, 5.16 (1H, s, H-14), 2.44 (3H, s, Ar-CH_3), 1.0, 0.97 (3H, s), 0.98, 0.89 (3H, s); hrms, *m/z* calcd. for $C_{28}H_{35}N_2O_3S_2$ (M^+ − $C_3H_5O_2$): 511.2079; found: 511.2089 (1), 327 (25), 291 (89), 217 (28), 109 (20), 91 (52), 73 (100).

*(1S,6S,9R,11R,13R)-9-Ethylenedioxymethyl-10-oxa-11-phenylthiotricyclo[7.4.0.0.^{9,13}]tridecane (**24**a) and (1S,6S,9R,11S,13R)-9-ethylenedioxymethyl-10-oxa-11-phenylthiotricyclo[7.4.0.0.^{9,13}]-tridecane (**24**b)*

A. From the tosylhydrazone 23

A flamed three-necked round-bottom flask was charged with benzoic acid (115.3 mg, 9.44 mmol) and chloroform (1.5 mL) in a nitrogen atmosphere. The solution was cooled in an ice bath. A 1 M BH_3–THF solution (0.47 mL, 0.47 mmol) was added slowly by syringe to the cool solution, and the mixture was stirred for ½h. A solution of the tosylhydrazone **23** (135 mg, 0.231 mmol) in chloroform (2.5 mL) was added to the hydride reagent and stirred for 1 h in the ice bath, then $NaOAc \cdot 3H_2O$ (64 mg, 0.47 mmol) was added and the ice bath removed. The solution was diluted with DMSO (2 mL), then refluxed for 1 h under a nitrogen atmosphere. The reaction mixture was diluted with CH_2Cl_2, washed with 5% Na_2CO_3 (3×), brine, dried ($MgSO_4$), and evaporated in the rotavaporator to yield an oil. Purification by flash chromatography (Skellysolve B – ethyl acetate, 85:15) afforded the β-hemithioacetal **24***a* and α-hemithioacetal **24***b* (43 mg, 46% from the aldehyde), each as an oil that solidified in the refrigerator.

The β-hemithioacetal **24***a* was recrystallized from methanol–acetone; mp 98.5–99.5°C; $[\alpha]_D$ +65° (*c* 0.21, $CHCl_3$); ir (CH_2Cl_2, cast): 3045, 1583, 1390, 1380 cm^{-1}; ^1H nmr (400 MHz, $CDCl_3$) δ: 7.5 (2H, dd, 8, 1.5 Hz, Ar-H), 7.34–7.26 (2H, m, Ar-H), 7.19 (1H, tt, 7.5, 1.5 Hz, Ar-H), 5.56 (1H, dd, 9, 6 Hz, H-12), 5.35 (1H, s, H-14), 4.40 (1H, complex), 4.08–3.76 (1H, complex), 2.44 (1H, m), 2.37 (1H, ddd, 14, 11.5, 9 Hz, H-11β), 2.15 (1H, dt, 11, 6 Hz, H-11α), 1.73 (1H, dd, 14, 6 Hz, H-9), 1.84–0.98 (10H, m), 0.98 (3H, s), 0.87 (3H, s), 0.84 (3H, s); ^{13}C nmr (100 MHz, $CDCl_3$) δ: 138.2 (s, Ar), 129.8 (d, Ar, 2×), 128.8 (d, Ar, 2×), 126.0 (d, Ar-C), 105.5 (d, C-14), 89.4 (d, C-12), 84.3 (s, C-8), 66.5 (t), 64.8 (t), 62.1 (d, C-9), 57.5 (d, C-5), 42.5 (t), 40.1 (t), 36.8 (t), 36.4 (s, C-10), 33.4 (q, C-18), 33.2 (s, C-4), 31.5 (t), 20.9 (q, C-19), 20.8 (t), 18.6 (t, C-2), 15.9 (q, C-20); hrms, *m/z* calcd. for $C_{24}H_{34}O_3S$ (M^+): 402.2219; found: 402.2228 (2), 329 (40), 293 (100), 219 (31), 149 (38), 73 (72). *Anal.* calcd. for $C_{24}H_{34}O_3S$: C 71.60, H 8.51; found: C 71.48, H 8.39.

A pure sample of the α-hemiacetal **24***b* was obtained by recrystallization from acetone; mp 123–124°C; $[\alpha]_D$ −96°C (*c* 0.32, $CHCl_3$);

ir (CH_2Cl_2, cast): 3045, 1580, 1396, 1379 cm^{-1}; ^1H nmr (400 MHz, $CDCl_3$) δ: 7.54 (2H, dd, 8, 1.5 Hz, Ar-H), 7.36–7.24 (3H, m, Ar-H), 5.6 (1H, dd, 8, 1.5 Hz, H-12), 5.26 (1H, s, H-14), 4.07–3.80 (4H, complex), 2.68 (1H, ddd, 14.5, 11.75, 8.5 Hz, H-11β), 2.4 (1H, dt, 12, 3 Hz, H-7β), 1.79 (1H, ddd, 12, 7, 1.5 Hz, H-11α), 1.74 (1H, ddd, 14, 6.5, 3 Hz), 1.48 (1H, dd, 14.5, 7 Hz, H-9), 1.67–0.78 (3H, m), 0.89 (3H, s), 0.84 (3H, s), 0.8 (3H, s); ^{13}C nmr ($CDCl_3$) δ: 132.7 (s, Ar), 132.5 (d, Ar, 2×), 128.6 (d, Ar, 2×), 127.0 (d, Ar), 105.7 (d, C-14), 86.5 (d, C-12), 85.2 (s, C-8), 66.2 (t), 64.7 (t), 60.2 (d, C-9), 56.3 (d, C-5), 42.5 (t), 39.9 (t), 36.2 (t), 36.2 (s, C-10), 33.4 (q, C-18), 33.1 (s, C-4), 32.1 (t), 20.9 (q, C-19), 20.7 (t), 18.5 (t, C-2), 15.8 (q, C-20); hrms, *m/z* calcd. for $C_{24}H_{34}O_3S$ (M^+): 402.2219; found: 402.2228 (1), 329 (24), 293 (100), 219 (20), 73 (69). *Anal.* calcd. for $C_{24}H_{34}O_3S$: C 71.60, H 8.51; found: C 71.44, H 8.45.

In a separate experiment, catecholborane (1 mL, 9 mmol) was added to a solution of the tosylhydrazone **23** (prepared as described above from the aldehyde **21** (110 mg) and tosylhydrazine (501 mg)) in $CHCl_3$ (7 mL) cooled in an ice bath. The solution was stirred for 1½ h at 5°C, quenched with $NaOAc \cdot 3H_2O$ (2.34 g), then warmed to room temperature. The slurry was diluted with DMSO (2 mL) and refluxed for 2 h under a nitrogen atmosphere. Work-up and purification as described above gave the epimeric mixture of hemithioacetals **24***a* and **24***b* (355 mg, 36% from the aldehyde) as an oil.

*B. From the isopropylsulfonates of **20***

2-Propanesulfonyl chloride (0.14 mL, prepared as described (31)) was added to a solution of the epimeric mixture of alcohols **20** (105 mg) and triethylamine (0.43 mL) in ether (4 mL), cooled in a Dry Ice – CCl_4 bath. The reaction mixture was kept at −20°C for 2 h, then poured onto a cool solution of $NaHCO_3$. The oily product was extracted with CH_2Cl_2, washed with 10% HCl, saturated $NaHCO_3$, brine, dried ($MgSO_4$), and evaporated to give an oil. Purification by flash chromatography (Skellysolve B – ethyl acetate, 3:2) afforded the isopropylsulfonates of alcohols **20** (112 mg) as a separable mixture of the C-12 epimers.

A 0.4 M solution of $LiEt_3BH$–THF (1.3 mL) was added to a solution of the isopropylsulfonates (68 mg) in toluene (1.5 mL). The reaction mixture was stirred in an oil bath (90°C) for 6 h, then cooled and a drop of H_2O added. The reaction mixture was diluted with ether, washed with $NaHCO_3$, H_2O, brine, dried ($MgSO_4$), and the solvent removed to give an oil (45 mg). Purification by flash chromatography (Skellysolve B – ethyl acetate, 85:15) afforded the hemithioacetals **24***a* and **24***b* (33.6 mg, 64%) as an oil that shows the same spectroscopic properties as above.

*(1S,6S,9R,13R)-9-Ethylenedioxymethyl-10-oxa-1,5,5-trimethyltricyclo[7.4.0.0.^{9,13}]tridec-11-ene (**25**)*

A solution of *m*-chloroperbenzoic acid (260 mg, 1.5 mmol) in CH_2Cl_2 (10 mL) was added to a cooled solution (ice bath) of the hemithioacetals **24***a* and **24***b* (606 mg, 1.5 mmol) in CH_2Cl_2 (10 mL). The reaction mixture was stirred for 15 min at 5°C, diluted with CH_2Cl_2, washed with saturated $NaHCO_3$, brine, dried, and the solvent evaporated *in vacuo* to give the sulfoxides (611 mg) as an oil. A solution of the crude sulfoxides and triethylphosphite (0.75 mL) in xylene (10 mL) was refluxed for 4 h under nitrogen. The solvent was removed azeotropically with benzene. The residue was purified by flash chromatography (Skellysolve B – ethyl acetate, 3:1) to give the enol ether **25** (287 mg, 65%) as a solid; ir (KBr): 3089, 1592, 1387, 1369 cm^{-1}; ^1H nmr (400 MHz, $CDCl_3$) δ: 6.47 (1H, t, 3.5 Hz, H-12), 5.39 (1H, s, H-14), 5.23 (1H, m, H-11), 4.12–3.82 (4H, complex), 3.02 (1H, br s, H-9), 2.51 (1H, dt, 12, 3 Hz, H-7β), 1.91–1.0 (10H, m), 1.05 (3H, s), 0.89 (3H, s), 0.84 (3H, s); ^{13}C nmr ($CDCl_3$) δ: 147.7 (d, C-11), 105.3 (d, C-14), 102.2 (d, C-12), 89.2 (s, C-8), 65.5 (t), 65.0 (t), 64.8 (d, C-9), 57.1 (d, C-5), 42.8 (t), 40.3 (t), 36.8 (s, C-10), 35.3 (t), 33.5 (q, CH_3-18), 33.2 (s, C-4), 21.4 (t), 20.7 (q, CH_3-19), 18.6 (t, C-2), 17.5 (q, CH_3-30); hrms, *m/z* calcd. for $C_{18}H_{28}O_3$ (M^+): 292.2031; found: 292.2038 (2), 219 (30), 125 (14), 81 (46), 73 (100).

*12,12-Ethylenedioxy-9α-hydroxydrim-7-en-11-al (**28**)*

A solution of the enol ether **25** (62.3 mg) in ethyl acetate (6 mL) was cooled in a Dry Ice – acetone bath. Ozone was bubbled through the solution until a pale blue color appeared. Excess ozone was removed with nitrogen. Triethylphosphite (0.1 mL) was added and the reaction mixture allowed to reach room temperature. The solvent was evaporated *in vacuo* and the residue left under vacuum for 2 h. The formate **26** was identified by its ^1H nmr spectrum (100 MHz, $CDCl_3$) δ: 9.88 (1H, d, 3 Hz, H-11), 8.24 (1H, s, OCHO), 5.51 (1H, s, H-14), 2.83 (1H, d, 3 Hz, H-9), 1.29 (3H, s, CH_3-15), 0.9 (3H, s), 0.85 (3H, s).

A solution of the crude formate **26** and DBU (0.063 mL) in dry benzene (3 mL) was refluxed under argon for 1½ h. The reaction mixture was diluted with ether, washed with 10% HCl, $NaHCO_3$, brine, dried ($MgSO_4$), and the ether evaporated *in vacuo* to give a mixture of unsaturated aldehydes **27** (50.4 mg). In a flame-dried three-neck, round-bottom flask, fitted with an L-shaped tube, a nitrogen line, and a septum, was placed a 35% KH emulsion (50 mg). The oil was removed with Skellysolve B, and THF (1 mL) was added. The flask was cooled in an ice bath, then the crude aldehydes in THF (1 mL) were added slowly to the slurry and the mixture stirred for 2 h at 5°C. Oxodiperoxymolybdenum(pyridine)-hexamethylphosphoramide (MoOPH, 118 mg, Aldrich Chemicals) was placed in the L-shaped tube and the flask was cooled in a Dry Ice – acetone bath. The MoOPH was added all at once, and the suspension stirred vigorously, then warmed slowly to −55°C (Dry Ice – acetonitrile) and stirred for 1 h. The bath was removed and the reaction was quenched with 10% Na_2SO_3 (1 mL) at 0°C. The two-phase solution was stirred until no change in color in the organic layer was observed. The two phases were separated and the aqueous layer was extracted with ether, washed with H_2O, brine, and dried ($MgSO_4$). The ether solution was filtered and evaporated *in vacuo* to yield the crude hydroxyaldehyde **28** (37.5 mg). Purification by flash chromatography (dichloromethane–acetone, 97:3) gave the hydroxyaldehyde **28** as a solid: ir (CH_2Cl_2, cast): 3460, 1713, 1387, 1362, 1111 cm^{-1}; ^1H nmr (400 MHz, $CDCl_3$) δ: 9.85 (1H, d, 1 Hz, H-11), 6.36 (1H, dd, 5, 2.5 Hz, H-7), 5.22 (1H, s, H-12), 3.9 (1H, d, 1 Hz, D_2O exchangeable), 3.99–3.85 (4H, m), 2.28 (1H, dt, 19, 5 Hz, H-6α), 2.11 (1H, ddd, 19, 12, 2.5 Hz, H-6β), 1.89 (1H, dd, 12, 4 Hz, H-5), 1.77 (1H, td, 13, 4.5 Hz), 1.53 (1H, dt, 13.5, 3 Hz), 1.49–1.0 (4H, m), 1.22 (3H, s), 0.97 (3H, s), 0.91 (3H, s); ^{13}C nmr ($CDCl_3$) δ: 203.5 (d, C-11), 136.6 (d, C-7), 134.2 (s, C-8), 106.1 (d, C-12), 77.9 (s, C-9), 64.8 (t), 64.5 (t), 41.6 (d, C-5), 41.5 (t), 41.4 (s, C-10), 33.1 (q, C-13), 33.0 (s, C-4), 31.9 (t), 24.3 (t), 22.2 (q, C-14), 18.0 (t, C-2), 17.2 (q, C-15); hrms, *m/z* calcd. for $C_{17}H_{26}O_4$ (M^+): 294.1824; found: 294.1831 (6), 276 (2), 266 (11), 265 (58), 221 (10), 109 (23), 73 (100).

*Warburganal (**2**)*

A solution of the crude hydroxyaldehyde **28** (37.5 mg) and a catalytic amount of *p*-toluenesulfonic acid in acetone (4 mL) was stirred at room temperature for 1 h. The reaction was quenched with saturated $NaHCO_3$ (1 drop), the solvent removed, and the residue diluted with CH_2Cl_2. The organic solution was washed with saturated $NaHCO_3$, brine, dried ($MgSO_4$), and evaporated *in vacuo* to give the crude product (30.4 mg) as an oil. Purification by flash chromatography (CH_2Cl_2–acetone, 97:3) gave an impure sample of polygodial (3.9 mg) and warburganal (**2**) (7.5 mg, 14% overall yield from the enol ether **25**) as a solid. Recrystallization from Skellysolve B provided material, mp 106–107°C (lit. (6) mp 107–108°C, (28) mp 106–107°C); $[\alpha]_D$ −243° (*c* 0.037, $CHCl_3$); (lit. (6) $[\alpha]_D$ −263°); ir (CH_2Cl_2, cast): 3479, 1720, 1682, 1638, 1360, 1357, 1129, 803 cm^{-1}; ^1H nmr (400 MHz, $CDCl_3$) δ: 9.76 (1H, d, 1 Hz, H-11), 9.43 (1H, s, H-12), 7.28 (1H, dd, 5, 2.5 Hz, H-7), 4.09 (1H, d, 1 Hz, D_2O exchangeable), 2.59 (1H, dt, 21.5, 5 Hz, H-6α), 2.35 (1H, ddd, 21.5, 12, 2.5 Hz, H-6β), 1.9 (1H, dd, 12, 5 Hz, H-5), 1.75–1.22 (6H, m), 1.1 (3H, s), 1.0 (3H, s), 0.95 (3H, s); ^{13}C nmr ($CDCl_3$) δ: 202.0 (d, C-12), 192.5 (d, C-11), 157.2 (d, C-7), 140.5 (s, C-8), 77.1 (s, C-9), 41.7 (d, C-5), 41.4 (s, C-10), 41.3 (t, C-3), 33.0 (s, C-4), 33.0 (q, C-13), 31.2 (t, C-1), 25.9 (t, C-6), 22.0 (q, C-14), 17.7 (t, C-2), 17.0 (q, C-15); hrms, *m/z* calcd. for $C_{15}H_{22}O_3$ (M^+): 250.1563; found: 250.1569 (8), 232 (7), 222 (31), 221 (92), 189 (18), 124 (43), 123 (20), 109 (100), 104 (41), 91 (26), 69 (42).

Acknowledgements

We wish to thank the Natural Sciences and Engineering

Can. J. Chem. Downloaded from www.nrcresearchpress.com by 93.93.197.157 on 09/07/12
For personal use only.

Research Council and the Alberta Heritage Foundation for Medical Research for financial support. Exploratory studies, including the initial preparation of diketone **7**, were carried out by Drs. L. M. Browne and A. Shariff, to whom we express our gratitude.

1. G. W. HEDRICK and W. D. LLOYD. Org. Synth. **45**, 64 (1965).
2. I. KUBO, Y. W. LEE, M. PETTEI, F. PILKIEWICZ, and K. NAKANISHI. J. Chem. Soc. Chem. Commun. 1013 (1976).
3. V. CAPRIOLI, G. CIMINO, R. COLLE, M. GAVAGNIN, G. SODANO, and A. SPINELLA. Jour. Nat. Prod. **50**, 146 (1987).
4. I. KUBO and I. GANJIAN. Experientia, **37**, 1063 (1981).
5. K. NAKANISHI and I. KUBO. Isr. J. Chem. **16**, 28 (1977).
6. H. NAKAI, O. OKAWARA, and M. OHNO. Tetrahedron Lett. **23**, 1087 (1982).
7. D. M. HOLLINSHEAD, S. C. HOWELL, S. V. LEY, M. MAHON, and N. M. RATCLIFFE. J. Chem. Soc. Perkin Trans. 1, 1579 (1983).
8. R. N. MOORE and R. V. LAWRENCE. J. Am. Chem. Soc. **80**, 1438 (1958).
9. W. A. AYER, C. E. MCDONALD, and J. B. STOTHERS. Can. J. Chem. **41**, 1113 (1963).
10. W. A. ADAM and I. ERDEN. J. Org. Chem. **43**, 2737 (1978).
11. L. M. JACKMAN and S. STERNHELL. Applications of nuclear magnetic resonance spectroscopy in organic chemistry. 2nd ed. Pergamon Press, New York. 1969. p. 184.
12. R. PAPPO, D. S. ALLEN, R. U. LEMIEUX, and W. S. JOHNSON. J. Org. Chem. **21**, 478 (1956).
13. J. S. BARAN. J. Org. Chem. **25**, 257 (1960).
14. H. C. SLATES and N. L. WENDLER. J. Am. Chem. Soc. **81**, 5472 (1959).
15. P. H. J. CARLSEN, T. KATSUKI, V. S. MARTIN, and K. B. SHARPLESS. J. Org. Chem. **46**, 3936 (1981).
16. Y. OGATA, V. SAWAKI, and H. SHIMIZU. J. Org. Chem. **43**, 1760 (1978).
17. I. AGER, D. H. R. BARTON, G. LUCENTE, and P. G. SAMMES. J. Chem. Soc. Chem. Commun. 601 (1972).
18. E. J. COREY and J. W. SUGGS. Tetrahedron Lett. 2647 (1975).
19. HUANG-MINLON. J. Am. Chem. Soc. **71**, 3301 (1949).
20. K. NAKANISHI and P. H. SOLOMON. Infrared absorption spectroscopy. 2nd ed. Holden–Day Inc., Oakland, CA. 1977. p. 16.
21. G. W. KABALKA and S. T. SUMMERS. J. Org. Chem. **46**, 1217 (1981).
22. G. W. KABALKA and J. H. CHANDLER. Synth. Commun. **9**, 275 (1979).
23. G. W. KABALKA and J. D. BAKER. J. Org. Chem. **40**, 1834 (1975).
24. F. W. WEHRLI and T. NISHIDA. Progress in the chemistry of organic natural products. Vol. 36. *Edited by* W. Herz, H. Grisebach, and G. W. Kirby. Springer-Verlag, New York. 1979. p. 59.
25. R. W. HOLDER and M. G. MATTURO. J. Org. Chem. **42**, 2166 (1977).
26. D. H. HUA, G. SINAI-ZINGDE, and S. VENKATARAMAN. J. Am. Chem. Soc. **107**, 4088 (1985).
27. E. VEDEJS, D. A. ENGLER, and J. E. TELSCHOW. J. Org. Chem. **43**, 188 (1978).
28. I. RAZMILIC, J. SIERRA, J. LOPEZ, and M. CORTES. Chem. Lett. 1113 (1985).
29. W. G. DOFROM and L. M. BACLAWSKI. J. Org. Chem. **41**, 1879 (1976).
30. W. C. STILL, M. KAHN, and A. MITRA. J. Org. Chem. **43**, 2923 (1978).
31. D. W. BROWN, T. T. NAKASHIMA, and D. L. RABENSTEIN. J. Magn. Reson. **45**, 302 (1981).
32. I. B. DOUGLASS and T. B. JOHNSON. J. Am. Chem. Soc. **60**, 1486 (1938).
33. F. X. TALAMAS. Ph.D. thesis, University of Alberta. 1987. pp. 128–142.

Can. J. Chem. Downloaded from www.nrcresearchpress.com by 93.93.197.157 on 09/07/12
For personal use only.

The reactions of simple dimethylallylamines with dimethyl acetylenedicarboxylate. Formation of 1-dimethylamino-2-allylmaleates via formal allyl transfer[1]

ADRIAN L. SCHWAN[2] AND JOHN WARKENTIN[3]

Department of Chemistry, McMaster University, 1280 Main Street West, Hamilton, Ont., Canada L8S 4M1

Received January 13, 1988

ADRIAN L. SCHWAN and JOHN WARKENTIN. Can. J. Chem. **66**, 1686 (1988).

Tertiary amines bearing two methyl groups and an allylic substituent (X) react with dimethyl acetylenedicarboxylate (DMAD) to afford the corresponding 1-dimethylamino-2-X′ maleates, in which X′ is the allylic isomer of X. The mechanism postulated involves reversible formation of a zwitterion by attack of the amine at an *sp*-carbon of DMAD. The zwitterion then undergoes intramolecular allyl transfer, through a 6-membered transition state. Evidence for a zwitterionic intermediate (quaternary ammonium allenolate) includes capture of the allenolate centre by intramolecular addition to a carbonyl group and by proton transfer from chloroform.

ADRIAN L. SCHWAN et JOHN WARKENTIN. Can. J. Chem. **66**, 1686 (1988).

Les amines tertiaires qui portent deux groupements méthyles et un substituant allylique (X) réagissent avec l'acétylènedicarboxylate de diméthyle (ADDM) pour fournir les maléates correspondants, diméthylamino-1 X′-2 maléates, dans lesquels le groupement X′ est l'isomère allylique de X. Le mécanisme postulé implique la formation réversible d'un zwitterion par l'attaque de l'amine sur le carbone-*sp* de l'ADDM. Le zwitterion subit alors un transfert allylique intramoléculaire par le biais d'un état de transition à six chaînons. Les données supportant l'hypothèse de l'existence d'un zwitterion comme intermédiaire (allènolate d'ammonium quaternaire) comportent la capture du centre allènolate par une addition intramoléculaire sur un groupement carbonyle ainsi qu'un transfert de proton à partir du chloroforme.

[Traduit par la revue]

Introduction

There are few publications concerning the reactions of tertiary amines with dimethyl acetylenedicarboxylate (DMAD), but those reports that do exist are rather interesting (1, 2). Whereas DMAD and primary or secondary amines usually give Michael adducts via a series of proton transfers after initial encounter, this possibility is precluded with tertiary amines, and other transformations must take place to give non-ionic products. Scheme 1 suggests that, in all cases, products result from initial formation of a zwitterion such as **1**.

Two main types of reactions are known to take place when **1** results from a tertiary amine. One involves the intramolecular abstraction of a proton by the anionic end of the zwitterion with subsequent migration of one or more bonds to restore the nitrogen atom to neutrality. Carrié and co-workers (3) used that chemistry in ring-opening reactions of diaziridines (Scheme 2). Other authors have suggested a similar deprotonation step to account for their observed products (4–8).

The second major reaction available to **1** is the intramolecular

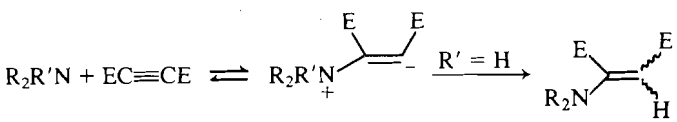

SCHEME 1

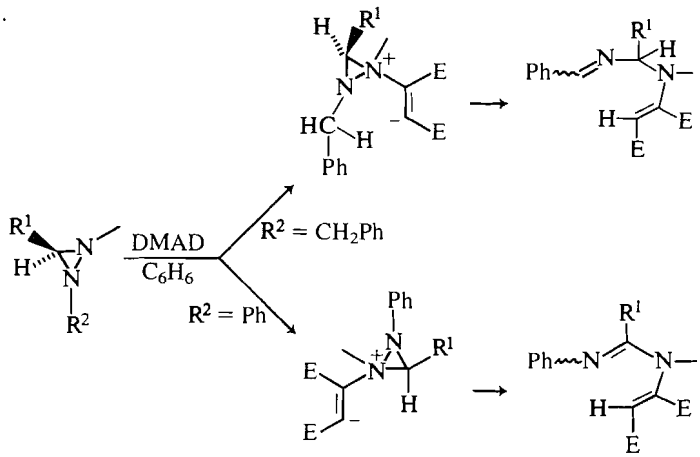

SCHEME 2

attack of the anionic end on a suitably situated electrophilic centre on one of the other groups attached to the nitrogen. Carbonyl groups have been shown to be appropriate electrophiles (7, 10).[4] The work of Hassner and co-workers (reaction [1]) provides an illustration of the attack on another

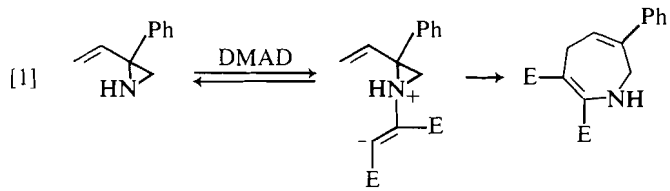

functionality (11). One of their proposals is that the ring opening depicted in reaction [1] is fast enough to preclude Michael adduct formation by proton transfer (11). Similar rearrangements have been demonstrated using propiolate esters (8, 12–15).

[1]Presented in part at the 70th Canadian Chemical Conference, Université Laval, Ste. Foy, Quebec, June, 1987.

[2]Holder of NSERC of Canada Postgraduate Scholarship, 1983–1987. Present address: State University of New York at Albany, Albany, NY 12222, U.S.A.

[3]Author to whom correspondence may be addressed.

[4]Also E. Winterfeldt, quoted in ref. 1.

Can. J. Chem. Downloaded from www.nrcresearchpress.com by 112.217.228.212 on 09/07/12
For personal use only.

Can. J. Chem. Downloaded from www.nrcresearchpress.com by 112.217.228.212 on 09/07/12
For personal use only.

The double bond migrations exemplified by reaction [1] are accompanied by a second simultaneous transformation that makes the overall rearrangement energetically favourable (8, 11–15). In some cases there is release of ring strain accompanying the double bond migration (11, 14, 15), while in other instances a suitably disposed methoxy group aids in the migration of the double bond and in the overall neutralization of the nucleophilic nitrogen (8, 12, 13) (reaction [2]).

[2] 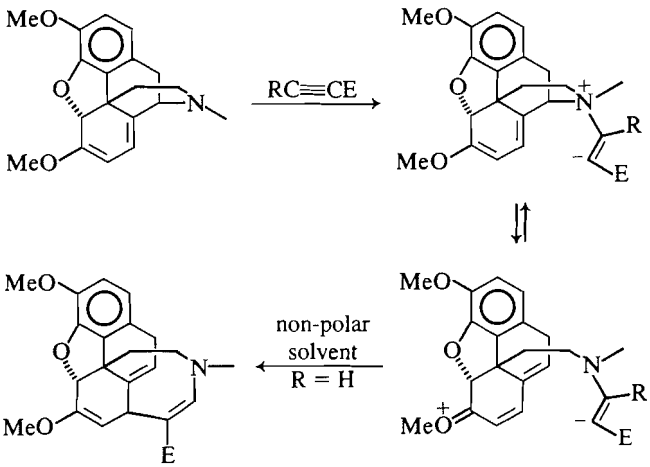

These transformations caught our attention and we wondered if the structurally specialized systems are necessary for the success of the reaction. This curiosity led us to investigate the chemistry of DMAD and simple dimethylallyl amines.

Results

Several dimethylallyl amines of the general structure **1** were synthesized. Refluxing these amines with one equivalent of DMAD in CH_3CN gave a series of 1-dimethylamino-2-allyl maleates **2** in all but two cases (**2***e*, **2***f*) (reaction [3]). These

[3] 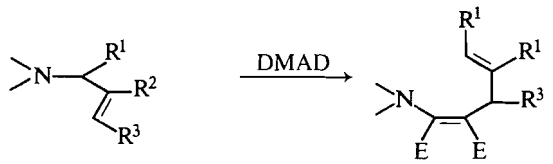

1

a $R^1 = R^2 = R^3 = H$
b $R^1 = CH_3$, $R^2 = R^3 = H$
c $R^1 = R^3 = H$, $R^2 = CH_3$
d $R^1 = R^3 = H$, $R^2 = Ph$
e $R^1 = R^3 = H$, $R^2 = Cl$
f $R^1 = R^3 = H$, $R^2 = Br$
g $R^1 = R^2 = H$, $R^3 = Me$

2 + 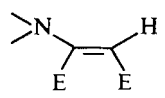

3

products were identified from their proton and carbon nmr data as well as from infrared and mass spectra. The maleate geometry was assigned with the aid of mechanistic arguments (see Discussion).

The geometry of the 2-butenyl moiety of **2***b* could not be assigned readily by measuring the coupling constants of the vinyl protons because a 500-MHz nmr instrument was incapable of separating the vinyl proton signals. Therefore a different criterion had to be employed. The ^{13}C nmr chemical shift of the methyl group of the 2-butenyl side chain was found to be 18.6 ppm. This correlates well with *trans*-2-butene and *trans*-2-octene whose sp^2-bonded methyl carbons resonate at 17.3 and 19 ppm respectively (16). The methyl signals of the *cis* analogs appear at 10.6 ppm (*cis*-2-butene) and 13 ppm (*cis*-2-octene) (16). Comparison to these data allowed us to assign the geometry of the 2-butenyl portion of **2***b* as *trans*.

Product **2***g* was obtained as an inseparable mixture of fumarate and maleate isomers. The ^1H nmr spectrometry indicated that the ratio was 3:1. The major isomer was assigned the fumarate geometry on the following basis. Dimethylamino groups have been shown to shield protons on substituents *cis* to them. That is, in instances where geometric isomers have been obtained and their ^1H nmr spectra have been recorded, the protons on substituents *cis* to the dimethylamino moiety resonated at higher field than those *trans* to the dimethylamino group (17, 18). The methine proton of the major isomer of the mixture (**2***g*) resonated at 3.47 ppm while the signal from the analogous proton of the minor isomer was found at 2.92 ppm. This is consistent with the dimethylamino group situated *cis* to the butenyl function of the minor isomer of **2***g*.

The other criterion for differentiating between the two isomers is the chemical shifts of the methoxyl protons of butenedioic esters. The signals of the methoxyl protons of methyl maleates are found slightly downfield from those of the fumarates (19–21). The methoxyl peaks in the ^1H nmr spectrum of the minor isomer of **2***g* were found at 3.61 and 3.72 ppm while those of the major isomer appeared at 3.56 and 3.69 ppm. These two criteria allow confident assignments to be made of the identities of the geometric isomers **2***g*.

A product common to all of the reaction mixtures is the previously synthesized dimethylamino maleate **3** (21). Facile separation of reaction components by column chromatography permitted determination of the yields of products **2** and **3** in each reaction (Table 1). The aminoallylation products **2**, obtained as oils, are all new compounds. A significant amount of coloured by-product remained at the top of the chromatography column in each case.

Benzyldimethylamine (**4**) was also treated with DMAD in CH_3CN but only dimethylamino maleate **3** and starting amine **4** were among the non-polar products recovered.

Some of the amines (**1***a–d*) were also treated with 1 equivalent of DMAD in $CHCl_3$ at room temperature. Reaction times extended from 1 day to 6 weeks. Yields from reactions in $CHCl_3$ were very dependent upon initial concentrations. More concentrated solutions gave increased yields of **3**, in most cases, and lower yields of **2** (Table 2).

Amines **1***a* and **1***c* reacted with DMAD in $CHCl_3$ to afford **5***a* and **5***c*, respectively, as additional non-polar products. Both were isolated in low yields. In both solvents, DMAD was usually the limiting reagent and yields were therefore based on the amount of amine consumed. Amines **1***c* and **1***d* were also treated with DMAD in CH_2Cl_2 but lower yields of **2** were obtained in these cases (15% **2***c*, 10% **2***d*).

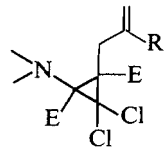

5*a* R = H
5*b* R = CH_3

Treatment of α-(dimethylaminomethyl)-isobutyrophenone (**6**) with DMAD in $CHCl_3$ gave heterocyclic alcohol **7** in 42% yield (reaction [4]). In deuteriochloroform, **7** (O—D) was

TABLE 1. Yields of products of reaction [3] run in CH_3CN

Amine	Initial concentration of amine and DMAD (M)	Duration[a] of reaction (h)	Yield of **2**[b] (%)	Yield of **3**[c] (%)
1*a*	0.200	14	37	22
1*a*	0.914	1.5	8	43
1*a*	0.008	20.5	54	21
1*b*	0.217	11.5	51	16
1*c*	0.217	9.5	44	30
1*d*	0.202	12	64	14
1*e*	0.201	34	0	31
1*f*	0.201	42	0	28
1*g*	0.212	5	43[d]	32

[a]Reactions may have been complete in a shorter time period.
[b]The product of allyl transfer from N to C.
[c]Dimethylamino maleate.
[d]Obtained as a mixture of 3 parts fumarate and 1 part maleate.

TABLE 2. Yields of products of reaction [3] run $CHCl_3$

Amine	Starting concentration of reactants (M)	Duration[a] of reaction (days)	Yield of **2**[b] (%)	Yield of **3**[c] (%)	Yield of **5**[d] (%)	Sum (**2** + **5**) (%)
1*a*	0.164	14	16	40	18	34
1*a*	0.165[e]	6	13	37[f]	4	17
1*b*	0.585	1	28	15	0	28
1*b*	0.069	4	52	28	0	52
1*c*	0.464	40	22	31	10	32
1*d*	0.434	21	46	34	0	46

[a]Reactions may have been complete in a shorter time period.
[b]The product of allyl transfer from N to C.
[c]Dimethylamino maleate.
[d]Dichlorocyclopropane species from attack of $:CCl_2$ on **2**.
[e]In $CDCl_3$.
[f]Vinyl position was 85–90% deuterated (estimated from ^1H nmr of the crude product).

[4]

6 **7**

formed. The rate of formation of the hydroxylated product in $CHCl_3$ was 1.9 times the rate of formation of the deuterated analog in $CDCl_3$.

Discussion

We believe that the double bond migration or allyl transfer proceeds via a zwitterionic intermediate (e.g., **8**) as proposed by several other authors (1, 2, 8, 11–15). We choose to depict the anionic end of **8** as an allenolate anion rather than a vinyl anion in accord with results of recent calculations by Grein and co-workers (reaction [5]) (22).[5]

[5] **1** + DMAD 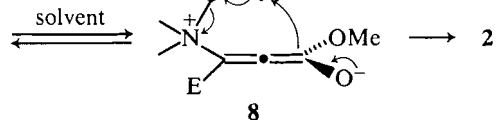

→ **2**

8

[5]Also F. Grein, personal communication.

Strong evidence for the intramolecularity of this reaction lies in the fact that more dilute chloroform solutions lead to cleaner reaction mixtures (Table 1). If **8** were to lead to **2** via an intermolecular route (i.e., bimolecular in **8**), then the yield of **2** would be expected to be lowered significantly by dilution due to the greater likelihood of competitive side reactions such as proton abstraction from chloroform. Amine **1***b* gave solely allyl transfer product **2***b* and none of its *cis* isomer **12**. This result also lends credence to the proposed intramolecular mechanism (Scheme 3). Scheme 3 shows conformations **8***b* and **8***b*′ leading to **2***b* and to **12** by intramolecular transfer. Both must be viewed as having the N—C (allyl) bond approximately eclipsing the allyl π orbital, to permit good overlap for formation of the new π bond that develops in the allyl fragment during its transfer. Examination of models suggests that **8***b* is less congested that **8***b*′ and that **2***b* should therefore be the preferred product. Bimolecular self-reaction of zwitterion **8***b* could also lead to **2***b*, after deallylation of intermediate **9**, or to **12** after deallylation of **10**. Models for the intermolecular transfer suggest a preference for **9** rather than **10** and therefore for product **2** rather than **12**. However, the geometric requirements for bimolecular reactions are more relaxed with respect to the preference for **9** over **10**. Moreover, it is highly unlikely that intermediate **9** is dequaternized efficiently to **2** whereas the isomeric **10** is not dequaternized efficiently to **12**. Since **12** is not formed, the suggested

Can. J. Chem. Downloaded from www.nrcresearchpress.com by 112.217.228.212 on 09/07/12
For personal use only.

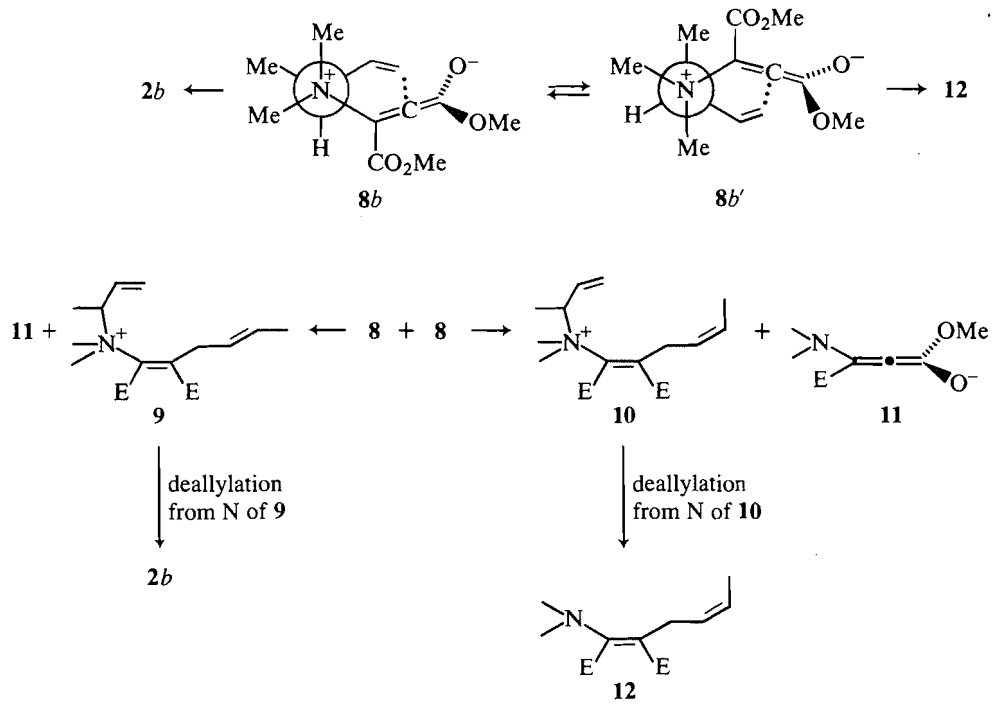

SCHEME 3

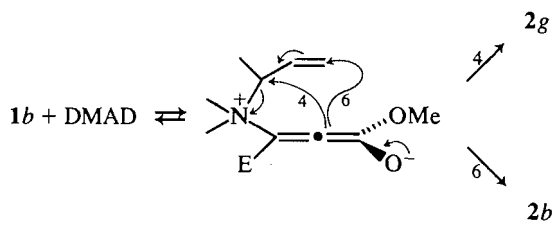

SCHEME 4

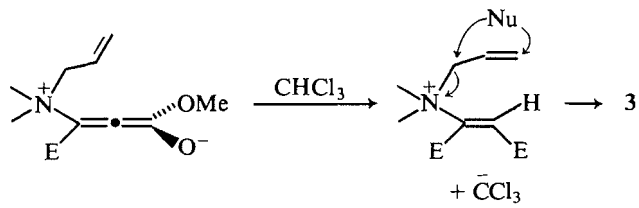

SCHEME 5

conclusion is that most (or all) of the allylic transfer occurs by an intramolecular mechanism. The only indication that intermolecular reactions, whatever they are, compete with intramolecular allyl transfer is the concentration dependence of the yields of **2** (Table 2).

The question as to whether there is a six-membered transition state or a four-membered transition state (Scheme 4) during the allyl transfer is also answered by analysis of the reaction products of amine **1***b* and DMAD. Maleate **2***b* was isolated whereas maleate **2***g* should have been the product of the allyl transfer if a four-membered transition state were involved. Also consistent with the proposed mechanism is the fact that **2***g* rather than **2***b* is the product when **1***g* is treated with DMAD.

Isomers **2***g* are the only allyl transfer products obtained as a mixture of fumarate and maleate esters. Presumably the additional steric bulk of the *sec*-butenyl substituent of **2***g* aids in the facile isomerization of the initial maleate product. The 3:1 isomer ratio was consistently present after work-up whether the reaction was carried out in CH_3CN for 1, 2, or 5.5 h, or in $CHCl_3$. The 3:1 ratio is probably the equilibrium composition.

The reaction proceeds more readily in CH_3CN than in $CHCl_3$ and the best conditions for the allyl transfer in $CHCl_3$ are dilute solution and low temperature. Consumption of starting materials may therefore take extended periods of time. A competing reaction in this solvent is deprotonation of $CHCl_3$ by the anionic end of the zwitterion (Scheme 5). The cation may then lose its allyl group to a nucleophile in solution, such as starting amine, via an S_N2 or S_N2' substitution with the aminomaleate as the leaving group. This would account for the significant amounts of **3** observed.

The lower average yields of **3** produced in CH_3CN as compared to those in $CHCl_3$ are probably attributable to the lower pK_a of $CHCl_3$ (24 (ref. 23)), compared to that of CH_3CN (31 (ref. 24)). We assume that the kinetic acidities of these solvents, which would be more suitable data for comparison, are different in the same sense.

The observation that the product resulting from deprotonation from the solvent (**3**) is the maleate rather than the fumarate deserves discussion. The maleate is more often obtained in a non-protic than in a protic solvent (25–27). Despite early recognition of this phenomenon, a satisfactory explanation has not been published. One theory is that the fumarate anion is formed initially and if there is no good proton transfer agent available (e.g., alcohol) it then inverts to the maleate anion, which undergoes subsequent reaction that may include deprotonation from $CHCl_3$ or CH_3CN (27, 28).

We postulate that the anion is allenic and has the option of adding an electrophile from either face of the enolate plane to give the maleate or the fumarate. A structure such as **13** depicts how maleate formation is preferred in $CHCl_3$. If the molecule of $CHCl_3$ to be deprotonated is situated "inside" the zwitterion, then it is between the ammonium and the allenyl moieties. This proximity to the ammonium nitrogen allows for a favourable coulombic interaction, which lowers the energy of the proton transfer transition state. The maleate geometry is a necessary result from alignment as in **13**. Formation of the fumarate ester

Can. J. Chem. Downloaded from www.nrcresearchpress.com by 112.217.228.212 on 09/07/12
For personal use only.

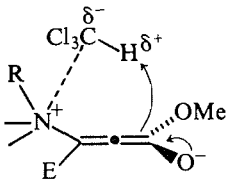

13

has no such intramolecular stabilizing effect available. A similar explanation can be involved for deprotonation from CH_3CN. This explanation for maleate formation is similar to that proposed when the two addends deposited across the acetylene originate from one molecule (26).

In alcohols, which have pK_a values much lower than that of $CHCl_3$, as well as better H-bonding ability, the deprotonation is presumably very fast and the need for minimizing the separation of paired ions is much reduced. Consequently the protonation step in alcohols is governed, at least in part, by thermodynamics, and the fumarate product predominates.

The presence of trichloromethyl anion accounts for the formation of cyclopropanes **5***a* and **5***c*. The anion loses chloride ion to generate dichlorocarbene, which adds to the more nucleophilic double bond of maleates **2***a* and **2***c* (29). The stereochemistry of **5***a* and **5***c* in assigned as *cis* (diester), based on the geometries of the precursors **2***a* and **2***c*. We are unsure of the reason why similar cyclopropanes, derived from **2***b* and **2***d*, were not obtained. The greater efficiency of allyl transfer in the phenyl-substituted case and the lower amount of **3** formed in the case of **2***b* suggest that deprotonation of $CHCl_3$, and hence formation of dichlorocarbene, is less important in cases **2***b* and **2***d* than it is in cases **2***a* and **2***c*.

Amines **1***e* and **1***f* did not undergo the allyl transfer reaction on treatment with DMAD. Their failure to do so cannot be attributed to steric effects because steric hindrance cannot be larger in those cases than it is in the case of **1***c*. Electronic effects of the halogen substituents (in **1***e*, **1***f*) should not be very important either, because those substituents are effectively at the centre of an allylic fragment in the transition structure. The failure of **2***b* and **2***d* to react with DMAD in the expected way is surprising.

The allyl transfer reaction of **8** may be a [3,3]-sigmatropic rearrangement to a new zwitterion with orthogonal π-systems, followed by rotation (Scheme 6). Some heteroatomic species that are known to undergo [3,3]-sigmatropic rearrangement are zwitterions (8, 11–15), ammonium ions (30), and neutral maleates (31, 32).

In our cases, since the solvent was obviously being deprotonated, as indicated by the products derived from dichlorocarbene, the reaction environment is probably of an alkaline nature. This does not, however, eliminate the possibility that a species such as **14** (formed by deprotonation of $CHCl_3$) is doing the [3,3]-sigmatropic rearrangement (Scheme 6). Deprotonation of **15** would then produce **2**. It follows that the addition of a weak acid such as benzoic acid to the reaction mixture should enhance the yield of allyl transfer product if the mechanism of Scheme 6 were correct. The presence of benzoic acid (0.05 equiv.) led to a reduced rather than enhanced yield of **2***a* from **1***a*. The benzoic acid experiment therefore does not support the mechanism in which [3,3]-sigmatropic rearrangement of ammonium ion **14** plays a major role. On the other hand, the much lower yields of **2***c* and **2***d* obtained when CH_2Cl_2 was substituted for $CHCl_3$ as the solvent suggests that proton transfer from the solvent *is* important. As it is, we can offer no explanation for the $CHCl_3$–CH_2Cl_2 solvent dependence.

Benzyldimethylamine (**4**) did not undergo the rearrangement. Presumably the disruption of aromaticity requires too much energy, although neutral maleates have been shown to overcome similar barriers and to undergo [3,3]-sigmatropic rearrangements (26, 27).

The formation of alcohol **7** during the treatment of **6** with DMAD is another example demonstrating the nucleophilicity of the anionic portion of zwitterions such as **1**. Scheme 7 illustrates a mechanism that fits the evidence acquired. As in the other cases, formation of zwitterion **16** should be reversible. The next steps, to form **17** and **18**, are also best described as reversible for the following reason. The observed isotope effect on the rate of formation of **7** in $CHCl_3$ ($CDCl_3$) is 1.9. If the step **17** → **18** were rate determining and irreversible then the isotope effect at room temperature would be expected to be considerably larger, be-

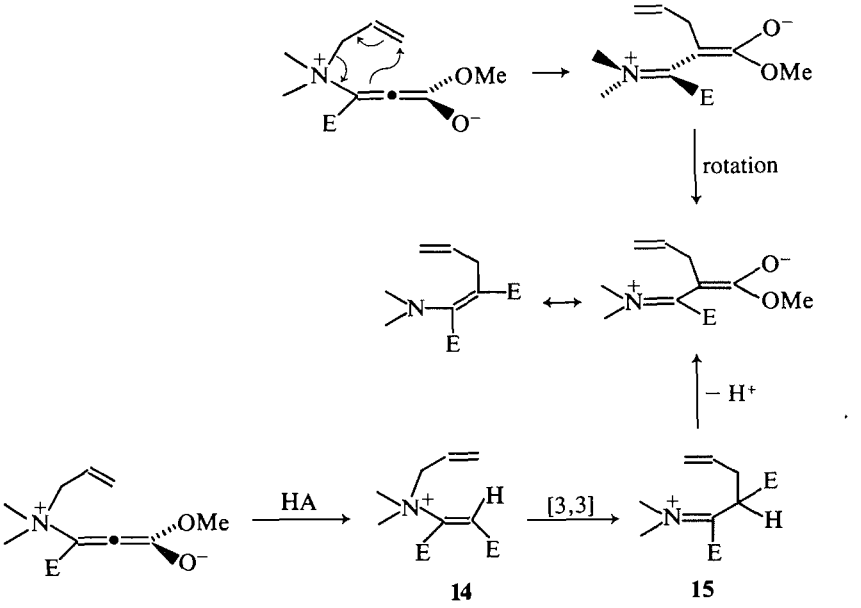

14 15

SCHEME 6

Can. J. Chem. Downloaded from www.nrcresearchpress.com by 112.217.228.212 on 09/07/12
For personal use only.

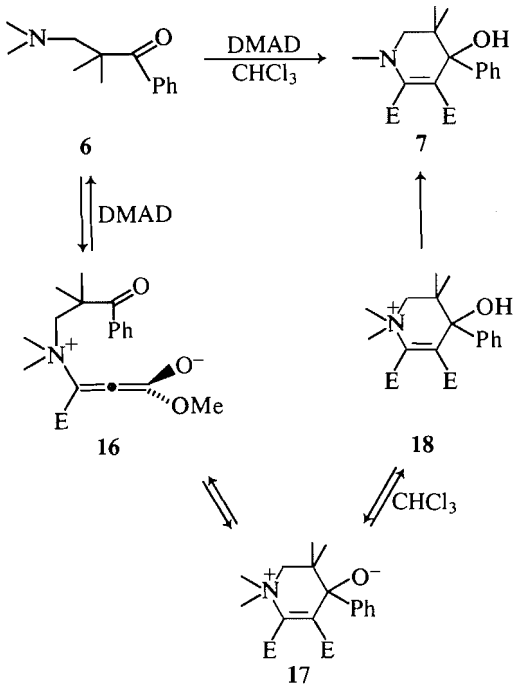

SCHEME 7

cause it would represent the primary kinetic isotope effect for proton transfer from carbon to oxygen. If that step is reversible, however, then the observed isotope effect represents an equilibrium isotope effect or a composite of kinetic and equilibrium isotope effects. If partial or total equilibration of **17** and **18** is granted, then the more likely equilibration of **17** with **16** follows.

Once ammonium ion **18** is formed, it can either be demethylated to give **7** or remain as a polar by-product. Trichloromethyl anion is not the demethylating agent since CH_3CCl_3 was not found in the reaction mixture. It is expected that chloride is not the demethylating agent either since ammonium chloride salts remain as such at room temperature rather than equilibrating with alkyl chlorides and amines. Therefore, the demethylating agent is probably starting amine and this would help to account for the low yield of non-polar products.

In summary, we have shown that a reaction that was previously applied to specialized systems can also be achieved in simple systems. The new products have potential in synthesis as highly functionalized dienophiles and dipolarophiles, either directly or after facile conversion to their respective *N*-phenylmaleimides (33). The formation of **7** illustrates the potential of the procedure for the synthesis of heterocycles.

Experimental

Melting points were determined on a Thomas Hoover capillary melting point apparatus and are uncorrected.

The ^1H nmr spectra were recorded on a Varian EM 390 or a Bruker AM 500 spectrometer. The ^{13}C nmr spectra were recorded on a Bruker WP 80/90, WH 250, or AM 500 spectrometer. Infrared spectra were obtained with a Perkin–Elmer model 283 instrument and were calibrated against the 1601.4 cm^{-1} band of polystyrene. Ultraviolet spectra were taken with a Hewlett–Packard model 8451/A diode array spectrophotometer. Analytical thin-layer chromatography was performed with plastic backed thin-layer neutral alumina plates (Merck Aluminiumoxid 60 F_{254}) of 0.2 mm thickness.

Chloroform was washed with H_2SO_4 and distilled from P_2O_5 before use. Methylene chloride was distilled from P_2O_5. Acetonitrile was dried by elution through a neutral Al_2O_3(I) column.

Allylamine, methallylamine, 40% aqueous dimethylamine, benzylamine, 3-chloro-1-butene, crotyl chloride, 2,3-dibromopropene, and 2,3-dichloropropene are all commercially available and were used as received. DMAD (Aldrich) was distilled under reduced pressure before use.

Amines **1***a* (34) and **1***f* (35) were prepared according to published procedures. Amines **1***c*, bp 81–83°C (lit. (36) bp 82–83.5°C), and **4**, bp 85°C (27 Torr; 1 Torr = 133.3 Pa), (lit. (36) bp 72–78°C (8 Torr)), were prepared from methallylamine and benzylamine, respectively, by using the Eschweiler–Clarke methodology employed for **1***a* (34).

1-Amino-2-butene and 3-amino-1-butene were prepared from their respective chlorides via the Gabriel synthesis (37). Amine **1***b* was then synthesized from 3-amino-1-butene via the Eschweiler–Clarke method (34), bp 87–88°C (lit. (38) bp 91°C). Similarly, **1***g* (90–95% pure) was prepared from 1-amino-2-butene, bp 95–96°C (lit. (39) bp 93°C). The impurity was found to be inert to DMAD.

Synthesis of amine ***1****c*

A 100-mL flask was charged with 8.92 g (0.080 mol) of 2,3-dichloropropene, 30 mL of 40% Me_2NH/H_2O, and 20 mL of MeOH. The solution was warmed at 60°C for 15 h. After cooling, 50 mL of 50% aqueous KOH was added and the solution was extracted with 2 × 40 mL of ether. The organic phases were combined and dried over KOH. After concentration (aspirator), the residue was dried once more over KOH and then distilled from KOH. The yield of **1***c* was 3.56 g (37%), bp 113–114°C (lit. (40) bp 119–120°C (755 Torr)).

Synthesis of amine ***1****d*

A 250-mL flask was charged with 100 mL of α-methylstyrene and 13.6 g (0.11 mol) of *tert*-butyl hypochlorite (Frinton). AIBN (0.25 g, 1.8 mmol) was added and the contents were warmed to 80°C for 4 h. After cooling, the contents were distilled under reduced pressure. The fractions collected above 70°C (6.5 Torr) were combined (≅ 20 mL) and dissolved in 170 mL of MeOH. The solution was stirred with ice cooling while 70 mL of 40% Me_2NH/H_2O was added dropwise over a period of 20 min. The ice bath was then removed and the contents were allowed to stir at room temperature for 16 h. The solution was then carefully added to 200 mL of ice-cooled aqueous HCl (6%). The aqueous solution was washed (3 × 70 mL) with ether and was then added dropwise to ice-cooled aqueous Na_2CO_3 (5%). After addition was complete, the solution was saturated with Na_2CO_3 and extracted (3 × 100 mL) with ether. The combined organic extracts were washed with brine and dried over $MgSO_4$.

After filtration and concentration, the residue was applied to an Al_2O_3(II) column and eluted with 10% ether in light petroleum. The only compound that was eluted was amine **1***d* (4.60 g, 27% yield overall); ^1H nmr (90 MHz, $CDCl_3$) δ: 2.24 (s, 6H), 3.27 (s, br, 2H), 5.19 (s, br, 1H), 5.42 (s, br, 1H), 7.24–7.60 (m, 5H); ^{13}C nmr (22.62 MHz, $CDCl_3$ at 77.20) δ: 145.35, 140.21, 128.27, 127.55, 126.27, 115.18, 64.52, 45.28; ms(ei) *m/z* (%): 161(30), 118(16), 115(15), 59(13), 58(100).

Reactions of DMAD with amines

In the general procedure the appropriate amine and one equivalent of DMAD were mixed together in a volume of solvent chosen to give the concentrations indicated in Tables 1 and 2. Air above the chloroform solutions was displaced with N_2 and the solutions were allowed to stand protected from light. The CH_3CN solutions were refluxed with a $CaCl_2$ drying tube attached to the condenser. When periodic ^1H nmr spectra of the mixtures indicated complete consumption of either reactant, the mixtures were worked up. Mixtures were separated as described below. Spectral data of all products of allyl transfer are in Tables 3–5.

Amine ***1****a and DMAD*

After removal of solvent (aspirator), the residue was applied to a column containing basic Al_2O_3(II). Elution with 50% ether in light petroleum provided three components from reactions with $CHCl_3$ as solvent and two components from reactions with CH_3CN as solvent. Product **5***a* was eluted first (R_f 0.79, 50:50 ether:petroleum) followed by **2***a* (R_f 0.41) and **3** (R_f 0.26), mp 80–80.5°C (petroleum ether –

Can. J. Chem. Downloaded from www.nrcresearchpress.com by 112.217.228.212 on 09/07/12
For personal use only.

TABLE 3. ^{1}H nuclear magnetic resonance data of allyl transfer products ($CDCl_3$, TMS)

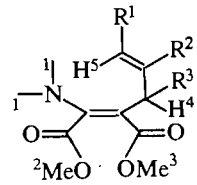

Compound	R^1	R^2	R^3	Chemical shifts (δ)[a]
2*a*[b]	H	H	H	2.92 (s, 6H, 1), 3.16 (dd, J = 7.0 and 1.5 Hz, 2H, R^3 and H^4), 3.69 (s, 3H, 2), 3.87 (s, 3H, 3), 4.96 (m, 2H, R^1 or H^5), 5.12 (m, 1H, R^1 or H^5), 5.71–6.22 (m, 1H, R^2)
2*b*[c]	CH_3	H	H	1.65 (dd, J = 6.0 and 1.5 Hz, 3H, R^1), 2.86 (s, 6H, 1), 3.07 (m, 2H, R^3 and H^4), 3.66 (s, 3H, 2), 3.82 (s, 3H, 3), 5.47 (m, 2H, R^2 and H^5)
2*c*[b]	H	CH_3	H	1.66 (s, 3H, R^2), 2.86 (s, 6H, 1), 3.05 (s, 2H, R^3 and H^4), 3.64 (s, 3H, 2), 3.83 (s, 3H, 3), 4.66 (s, br, 1H, R^1 or H^5), 4.78 (s, br, 1H, R^1 or H^5)
2*a*[b]	H	Ph	H	2.89 (s, 6H, 1), 3.54 (t, $J \cong$ 1.5 Hz, 2H, R^3 and H^4), 3.64 (s, 3H, 2) 3.88 (s, 3H, 3), 5.07 (s, br, 1H, R^1 or H^5), 5.47 (s, br, 1H, R^1 or H^5), 7.26–7.60 (m, 5H, R^2)
2*g*[c] (major isomer)	H	H	CH_3	1.21 (d, J = 7 Hz, 3H, R^3), 2.65 (s, 6H, 1), 3.47 (quint, J = 7 Hz, 1H, H^4), 3.56 (s, 3H, 2), 3.69 (s, 3H, 3), 4.87 (dt, J = 10.4 and 1.5 Hz, R^1 or H^5), 4.92 (dt, J = 17.2 and 1.5 Hz, R^1 or H^5), 5.92 (ddd, J = 17.2, 10.4, and 6.3 Hz, 1H, R^2)
2*g*[c] (minor isomer, maleate)	H	H	CH_3	1.13 (d, J = 7 Hz, 3H, R^3), 2.60 (s, 6H, 1), 2.92 (quint, J = 7 Hz, 1H, H^4), 3.61 (s, 3H, 2), 3.72 (s, 3H, 3), 4.83 (dt, J = 10.3 and 1.5 Hz, 1H, R^1 or H^5), 4.86 (dt, J = 17.2 and 1.5 Hz, 1H, R^1 or H^5)
3[b]	—	—	—	2.90 (s, 6H, 1), 3.64 (s, 3H, 2), 3.94 (s, 3H, 3), 4.60 (s, 1H)

[a]Chemical shifts are followed in brackets by the multiplicity symbol, the coupling constant(s) where appropriate, the relative integral, and the assignment according to the diagram at the head of the table.
[b]90 MHz.
[c]500 MHz.

Can. J. Chem. Downloaded from www.nrcresearchpress.com by 112.217.228.212 on 09/07/12
For personal use only.

acetone) (lit. (21) mp 83–84.5°C). Spectra of **5***a*: uv ($CHCl_3$) λ_{max} (log ε): 240 nm (3.13); ir (neat film), cm^{-1}: 1732 (v br) 1639, 1595 (br); ^{1}H nmr (500 MHz, $CDCl_3$) δ: 2.33 (s, 6H), 2.81 (dd, J = 8.0 and 13.8 Hz, 1H), 2.98 (dd, J = 6.2 and 13.8 Hz), 3.75 (s, 3H), 3.81 (s, 3H), 5.13 (dd, J = 10.3 and 1.3 Hz, 1H), 5.19 (dd, J = 17.1 and 1.3 Hz, 1H), 5.94 (m, 1H); ^{13}C nmr (62.90 MHz, $CDCl_3$ at 77.20) δ: 39.90, 40.87, 51.71, 52.76, 73.78, 118.94, 125.83, 133.06, 135.18, 166.18, 167.84; ms (ci, CH_4) m/z: 314(6), 312(23), 310(52), 308(18), 272(10), 270(52), 268(78), 254(8), 252(41), 250(63), 56(100); ms (ei, 70 eV) m/z: 272(14), 270(66), 268(100), 156(35), 150(32); ms (ei, high resolution) m/z calcd. for $C_9H_{12}NO_4{}^{35}Cl^{37}Cl$ ($M^+ - C_3H_5$): 270.0114; found: 270.0116; calcd. for $C_9H_{12}NO_4{}^{35}Cl_2$: 268.0143; found: 268.0139.

Amine ***1***b *and DMAD*

After removal of solvent, the residue was applied to a column containing basic Al_2O_3(II). Elution with 20% ether in petroleum provided first **2***b* (R_f 0.53, 50:50 ether–petroleum) followed by **3**.

Amine ***1***c *and DMAD*

After removal of solvent and application of the residue to a basic Al_2O_3(II) column, elution with 20% ether in light petroleum yielded **5***c* (from reaction in $CHCl_3$ solution only) (R_f 0.31, 20% ether). Increasing the ether component to 50% gave **2***c* (R_f 0.44, 50%) followed by **3**. Elution of the product mixture from reaction in CH_3CN was begun with 50% ether in light petroleum. Spectra of **5***c*: uv ($CHCl_3$) λ_{max} (log ε): 240 nm (3.14); ir (neat film), cm^{-1}: 1741, 1735, 1646, 1603; ^{1}H nmr (90 MHz, $CDCl_3$) δ: 1.81 (s, 3H), 2.42 (s, 6H), 2.91(ab q, J = 13.5 Hz, 2H), 3.76 (s, 3H), 3.82 (s, 3H), 4.96 (s, br, 2H); ^{13}C nmr (62.90 MHz, $CDCl_3$ at 77.20) δ: 24.26, 40.67, 41.26, 51.41, 52.61, 74.36, 117.32, 126.63, 135.40, 140.89, 166.44, 167.31; ms (ci, CH_4) m/z: 328(4), 326(10), 324(22), 322(12), 272(12), 270(60), 268(100), 266(28), 264(38), 170(58); ms (ei, 70 eV) m/z: 272(10), 270(65), 268(100), 266(40), 264(65), 170(18), 150(23); ms (ei, high resolution) m/z calcd. for $C_9H_{12}NO_4{}^{35}Cl^{37}Cl$: 270.0114; found: 270.0113; calcd. for $C_9H_{12}NO_4{}^{35}Cl_2$: 268.0143; found: 268.0132.

Amine ***1***d *and DMAD*

After removal of solvent and application of the residue to a basic Al_2O_3(II) column, elution with 40% ether in light petroleum gave **2***d* (R_f 0.43, 50% ether) followed by **3**.

Amines ***1***e *and* ***1***f *and DMAD*

Chromatography of the residue after concentration of the reaction mixture gave only **3**.

Amine ***1***g *and DMAD*

After concentration of the solution and application of the residue onto Al_2O_3(II), elution with 33% ether in light petroleum provided *cis* and *trans* **2***g* as an inseparable mixture (R_f 0.40, 33%) followed by **3**.

Amine ***4*** *and DMAD*

After complete consumption of DMAD, as revealed by ^{1}H nmr spectroscopy, chromatography yielded only **3** and starting amine **4**.

Reaction of ***6*** *with DMAD*

A reaction vessel was charged with 5 mL of dry $CHCl_3$, 0.341 g (1.66 mmol) of **6** (ref. 9), and 0.235 g (1.65 mmol) of DMAD. Air was displaced by passing N_2 briefly over the solution, which was allowed to

TABLE 4. ^{13}C nuclear magnetic resonance data of allyl transfer products

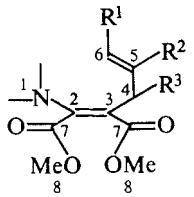

Compound	R_1	R_2	R_3	1	2	3	4	5	6	7	8	Other
2*a*[a]	H	H	H	42.63	153.99	102.90	31.91	137.17	115.10	169.80 167.43	52.49 51.57	—
2*b*[a]	CH_3	H	H	42.72	153.59	104.88	30.89	129.44	125.80	169.64 167.51	52.44 51.59	18.01 (Me)
2*c*[a]	H	CH_3	H	42.36	154.28	102.97	35.80	145.52	110.48	169.72 167.84	52.74 52.30	23.81 (Me)
2*d*[a]	H	Ph	H	41.94	154.25	101.52	33.34	147.43	112.53	169.62 167.35	52.40 51.53	141.46 128.15 (Ph) 125.69
2*g*[b] (major)	H	H	CH_3	43.34	151.02	119.94	37.16	141.41	113.51	168.51 166.82	51.98 51.15	19.09 (Me)
2*g*[b] (minor)	H	H	CH_3	42.35	147.36	113.06	39.23	141.96	112.40	167.98 167.10	52.03 50.82	19.09 (Me)
3[a]	—	—	—	39.65	155.23	84.35	—	—	—	168.11 166.06	52.79 50.62	—

[a]22.62 MHz, $CDCl_3$ ref. at δ 77.20
[b]125.62 MHz.

TABLE 5. Additional spectral data of allyl transfer products

Compound	Ultraviolet λ_{max}, $CHCl_3$ (log ε)	Mass spectra *m/z* (%)		High resolution	Infrared (neat film) (cm^{-1})			
2*a*	304 (3.88)	227(34) 195(16) 168(100) 152(25)	108(58) 72(19)	Observed: 227.1159 Calcd. for $C_{11}H_{17}NO_4$: 227.1158	3060 3045 2998 2986 2942	2890 2804 1735 1692 1575	1429 1385 1302 1248	1222 1195 1153 1082
2*b*	306 (3.85)	241(38) 209(22) 182(100) 166(29) 122(55)	72(12)	Observed: 241.1315 Calcd. for $C_{12}H_{19}NO_4$: 241.1315	3022 2992 2946 2916 2854	2814 1740 1696 1575 1432	1388 1302 1246 1226	1186 1157 1081
2*c*	304 (3.85)	241(81) 210(40) 200(46) 182(93) 166(38)	150(40) 123(51) 122(100) 108(50) 96(46)	Observed: 241.1317 Calcd. for $C_{12}H_{19}NO_4$: 241.1315	3078 2985 2948 2918 2862	2811 1739 1693 1575	1432 1385 1307 1248	1221 1202 1159 1084
2*d*	302 (3.81)	303(40) 244(35) 200(100) 184(29) 141(20) 118(26)	96(28)	Observed: 303.1469 Calcd. for $C_{17}H_{21}NO_4$: 303.1471	3049 3020 2989 2941 2852	1741 1695 1578 1433	1387 1309 1251 1207	1189 1158 1084
2*g* (3:1 mixtures of isomers)	312 (2.79)	241(18) 226(36) 209(20) 182(100) 166(40)	150(32) 122(52) 108(35) 72(21)	Observed: 241.1314 Calcd. for $C_{12}H_{19}NO_4$: 241.1315	3080 2997 2950 2908 2874	2845 2801 1740 (br) 1701 (br) 1572 (br)	1452 1433 1390 1325	1241 (v br) 1189 1132 1090
3	280 (4.22)	187(38) 156(40) 155(43) 128(100) 82(22)	72(37) 68(24)		3090 2992 2948 2798	1742 1684 1584 1434	1412 1371 1245 1192	1162 1130 1045

Can. J. Chem. Downloaded from www.nrcresearchpress.com by 112.217.228.212 on 09/07/12
For personal use only.

stand in the dark. After 21 days at room temperature the solution was concentrated and applied to a basic Al_2O_3(II) column. Elution with 10% ether in petroleum afforded unreacted amine (41 mg). By increasing the polarity gradually, **7** (mp 126–127°C, petroleum) was eluted (R_f 0.24, 25% EtOAc in petroleum). The yield was 42%, based on the amount of **6** consumed. Spectral data for **7**: uv (CH_3OH), λ_{max} (log ε): 292 nm (4.18); ir (neat film), cm^{-1}: 3402 (v br), 1746, 1696, 1652; ^1H nmr (90 MHZ, $CDCl_3$) δ: 0.67 (s, 3H), 1.20 (s, 3H), 2.93 (ab q, J = 13 Hz, 2H), 2.99 (s, 3H), 3.53 (s, 3H), 3.94 (s, 3H), 4.81 (s, br, 1H), 7.26–7.58 (m, 5H); ^{13}C nmr (22.62 MHz, $CDCl_3$ at 77.20) δ: 21.88, 22.77, 35.22, 40.27, 51.93, 52.75, 59.51, 77.37, 98.46, 127.31, 146.21, 149.78, 166.02, 167.74; ms (ei, 70 eV) m/z (%): 333(12), 302(14), 300(14), 276(25), 244(32), 218(22), 198(49), 186(40), 105(100), 77(23); ms (high resolution) m/z calcd. for $C_{18}H_{23}NO_5$: 333.1576; found: 333.1576.

Relative rates of reactions of ***6*** *with DMAD in $CHCl_3$ and in $CDCl_3$*

Solutions of DMAD and **6** (each 0.33 M) in $CHCl_3$ ($CDCl_3$) were degassed by means of three freeze–pump–thaw cycles at 0.05 Torr and sealed into nmr tubes. The tubes were kept at room temperature for 6 days, during which time changes were monitored by ^1H nmr spectroscopy. Product **7** was formed 1.9 times faster in $CHCl_3$ than in $CDCl_3$. Examination of the contents of the $CDCl_3$-containing tube by ^2H nmr spectroscopy (76.75 MHz) revealed a strong broad signal at δ 4.81, as well as the ^2H signal from the solvent. Addition of CH_3CCl_3 to the $CHCl_3$-containing tube led to a new singlet in the ^1H nmr spectrum.

NOTE ADDED IN PROOF: After this paper was accepted we became aware of recent, closely related work by Kandeel and Vernon (41).

Acknowledgements

This work was financed from a grant provided by the Natural Sciences and Engineering Research Council of Canada. The authors thank Dr. D. Hughes and Mr. B. Sayer for some of the nmr data and Dr. R. Smith and Messrs J. Capron and F. Ramelan for the mass spectra. They are indebted also to Professor F. Grein for information concerning the energy/geometry relationships of alleneolate anion systems.

1. E. WINTERFELDT. Agnew. Chem. Int. Ed. Engl. **6**, 423 (1967).
2. M. V. GEORGE, S. K. KHETAN, and R. K. GUPTA. Adv. Heterocycl. Chem. **19**, 279 (1976).
3. B. CARBONI, L. TOUPET, and R. CARRIÉ. Tetrahedron, **43**, 2293 (1987).
4. R. J. ALAIMO and D. G. FARNUM. Can. J. Chem. **43**, 700 (1965).
5. W. FUNKE. Chem. Ber. **102**, 3148 (1969).
6. E. WINTERFELDT and W. KROHN. Chem. Ber. **102**, 2336 (1969).
7. E. WINTERFELDT. Chem. Ber. **97**, 1952 (1964).
8. K. HAYAKAWA, I. FUJII, and K. KANEMATSU. J. Org. Chem. **48**, 166 (1983).
9. J. K. COWARD and T. C. BRUICE. J. Am. Chem. Soc. **91**, 5339 (1969).
10. E. WINTERFELDT and H. J. DILLINGER. Chem. Ber. **99**, 1558 (1966).
11. A. HASSNER, R. D'COSTA, A. T. MCPHAIL, and W. BUTLER. Tetrahedron Lett. 3691 (1981); A. HASSNER, W. CHAU, and R. D'COSTA. Isr. J. Chem. **22**, 76 (1982).
12. K. HAYAKAWA, S. MOTOHIRO, I. FUJII, and K. KANEMATSU. J. Am. Chem. Soc. **103**, 4605 (1981).
13. A. SINGH, S. ARCHER, K. HOOGSTEEN, and J. HIRSCHFELD. J. Org. Chem. **47**, 752 (1982); **48**, 173 (1983).
14. F.-A. KUNNG, J.-M. GU, S. CHAO, Y. CHEN, and P. S. MARIANO. J. ORG. CHEM. **48**, 4262 (1983).
15. S. CHAO, F.-A. KUNNG, J.-M. GU, H. L. AMMON, and P. S. MARIANO. J. Org. Chem. **49**, 2709 (1984).
16. J. B. STOTHERS. Carbon-13 nmr spectroscopy. Academic Press, New York. 1972. p. 81.
17. S. I. YAKIMOVICH and V. S. KHRUSTALEV. J. Org. Chem. USSR (Engl. Transl.), **12**, 957 (1976).
18. M. RIVIERE-BAUDET and J. SATGE. J. Organomet. Chem. **56**, 159 (1973).
19. W. E. NOLAND and C. K. LEE. J. Chem. Eng. Data, **26**, 91 (1981).
20. D. N. REINHOUDT, J. GEEVERS, W. P. TROMPENAARS, S. HARKEMA, and G. J. VAN HUMMEL. J. Org. Chem. **46**, 424 (1981).
21. R. HUISGEN, K. HERBIG, A. SIEGL, and H. HUBER. Chem. Ber. **99**, 2526 (1966).
22. J.-F. LAVALLEE, G. BERTHIAUME, P. DESLONGCHAMPS, and F. GREIN. Tetrahedron Lett. 5455 (1986).
23. A. C. LIN, Y. CHANG, D. B. DAHLBERG, and A. J. KRESGE. J. Am. Chem. Soc. **105**, 5380 (1983).
24. W. S. MATTHEWS, J. E. BARES, J. E. BARTMESS, F. G. BORDWELL, F. J. CORNFORTH, G. E. DRUCKER, Z. MARGOLIN, R. J. MCCALLUM, G. J. MCCOLLUM, and N. R. VANIER. J. Am. Chem. Soc. **97**, 7006 (1975).
25. S. I. MILLER and R. TANAKA. *In* Selective organic transformations. Vol. 1. *Edited by* B. S. Thyagaragan. Wiley–Interscience, New York. 1970. p. 143.
26. J. I. DICKSTEIN and S. I. MILLER. *In* The chemistry of the carbon–carbon triple bond. Part II. *Edited by* S. Patai. Wiley, New York. 1978. Chap. 19.
27. K. N. HOUK, R. W. STROZIER, M. D. ROZEBOOM, and S. NAGASE. J. Am. Chem. Soc. **104**, 323 (1982).
28. K. HERBIG, R. HUISGEN, and H. HUBER. Chem. Ber. **99**, 2546 (1966).
29. S. A. G. DE GRAAF and U. K. PANDIT. Tetrahedron, **29**, 2141 (1973).
30. P. S. MARIANO, D. DUNAWAY-MARIANO, and P. L. HUESMANN. J. ORG. CHEM. **44**, 125 (1979).
31. G. SCHMIDT and E. WINTERFELDT. Chem. Ber. **104**, 2483 (1971).
32. E. WINTERFELDT. Fortschr. Chem. Forsch. **16**, 75 (1970).
33. N. D. HEINDEL. J. Org. Chem. **35**, 3138 (1970).
34. R. W. JEMISON, T. LAIRD, W. D. OLLIS, and I. O. SUTHERLAND. J. Chem. Soc. Perkin Trans. I, 1436 (1980).
35. D. BAR, P. MARCINCAL, and A. MARCINCAL-LEFEBVRE. Bull. Soc. Chim. Fr. 2484 (1972).
36. A. C. COPE, T. T. FOSTER, and P. H. TOWLE. J. Am. Chem. Soc. **71**, 3929 (1949).
37. J. D. ROBERTS and R. H. MAZUR. J. Am. Chem. Soc. **73**, 2509 (1951).
38. W. G. YOUNG, R. A. CLEMENT, and C.-H. SHIH. J. Am. Chem. Soc. **77**, 3061 (1955).
39. M. LARCHEVEQUE, G. GUILLAUMET, T. CUVIGNY, and P. CAUBERE. Bull. Soc. Chim. Fr. 2275 (1975).
40. J. COUSSEAU and L. GOUIN. Bull. Soc. Chim. Fr. 244 (1976).
41. K. A. KANDEEL and J. M. VERSON. J. Chem. Soc. Perkin Trans. **1**, 2023 (1987).

Can. J. Chem. Downloaded from www.nrcresearchpress.com by 112.217.228.212 on 09/07/12
For personal use only.

Extraction of Zn(II), Cd(II), and Hg(II) by dodecyloligo(oxyethylene) carboxylic acids

JERZY STRZELBICKI[1] AND WITOLD CHAREWICZ
Institute of Inorganic Chemistry and Metallurgy of Rare Elements, Technical University of Wroclaw, 50-370 Wroclaw, Poland

AND

JORG BEGER AND LUTZ HINZ
Chemistry Section, Bergakademie Freiberg, 9200 Freiberg, GDR

Received November 23, 1987

JERZY STRZELBICKI, WITOLD CHAREWICZ, JORG BEGER, and LUTZ HINZ. Can. J. Chem. **66**, 1695 (1988).

The synthesis of a series of *n*-dodecyloligo(oxyethylene) carboxylic acids of general formula $C_{12}H_{25}(OCH_2CH_2)_nOCH_2COOH$ ($n = 0$ to 5) and application of these compounds for the separation of Zn(II), Cd(II), and Hg(II) in extraction are reported. Negligible extractability of the metal ions investigated was found using dodecyloxyacetic acid ($n = 0$) which indicated that complexation resulted from metal–cation interaction with oxygen atoms of the polyoxyethylene chain incorporated into the molecule of complexon. In extractions from aqueous solutions containing $ZnCl_2$, $CdCl_2$, $HgCl_2$, and NaOH (pH regulator), loading of the organic phases increased for extractants with more oxyethylene units. In particular, Hg(II) extractability and molecular structure of the extractant are related. The selectivity of extraction increased drastically if NaCl was added to the initial aqueous phase, as the extractabilities of Cd(II) and, particularly, Hg(II) declined while the extractability of Zn(II) remained high. Selectivity of extraction is produced by the complex chemical equilibria resulted from complexation of the metal cation by an alkyloligoether carboxylic acid in the organic phase and by Cl^- and OH^- anions in the aqueous phase. Thus, aqueous solution parameters greatly influence the efficiency and the selectivity of the extraction process and suitable experimental conditions are very important.

JERZY STRZELBICKI, WITOLD CHAREWICZ, JORG BEGER, et LUTZ HINZ. Can. J. Chem. **66**, 1695 (1988).

On a réalisé la synthèse d'une série d'acides *n*-dodécyloligo(oxyéthylène)carboxyliques de formule générale $C_{12}H_{25}(OCH_2CH_2)_nOCH_2COOH$ ($n = 0$ à 5) et on a examiné l'utilité de ces composés pour séparer et extraire les ions Zn(II), Cd(II) et Hg(II). La quantité d'ions métalliques extraite par l'acide dodécyloxyacétique ($n = 0$) est négligeable; ce résultat indique que la complexation est dûe aux interactions des ions métalliques avec les atomes d'oxygène de la chaîne polyoxyéthylène incorporée dans la molécule complexante. Lors d'extractions effectuées à partir de solutions aqueuses contenant du $ZnCl_2$, du $CdCl_2$, du $HgCl_2$ et du NaOH (pour régulariser le pH), les molécules complexantes contenant le plus grand nombre d'unités oxyméthylènes provoquent une augmentation de la concentration des ions extraits dans les phases organiques; on a pu mettre en évidence une relation entre la facilité d'extraction du Hg(II) et la structure moléculaire des molécules complexantes. La sélectivité des extractions augmente d'une façon drastique lorsqu'on ajoute du NaCl à la phase aqueuse initiale; dans ces conditions, la facilité d'extraction du Cd(II) et, en particulier, celle du Hg(II) diminuent alors que celle du Zn(II) demeure élevée. La sélectivité des extractions est le reflet d'équilibres chimiques complexes qui proviennent de la complexation des cations métalliques par un acide alkyloligoéther carboxylique dans la phase organique et par les anions Cl^- et OH^- dans la phase aqueuse. Ainsi, les paramètres de la solution aqueuse influencent beaucoup l'efficacité et la sélectivité du processus d'extraction; des conditions expérimentales appropriées sont donc très importantes.

[Traduit par la revue]

Introduction

Previously, single ion and competitive extraction of Co(II) and Ni(II) ions from ammonia–chloride aqueous solutions by highly lipophilic crown carboxylic acids was reported (1), and separation of Co(II) ammine cations from Ni(II) ammine cations was found possible. "Sandwich" type of extraction complexes of stoichiometry $M(CE)_2$ were postulated in which the metal ammine cation is located between two polyether rings of crown carboxylate anions (CE). The metal ammine cation interacts with the crown carboxylic acid forming hydrogen bonds between oxygen atoms of the polyether rings and hydrogen atoms of the ammine ligands. On the other hand, no detectable extraction of Co(II) and Ni(II) cations from their chloride solutions was found using these highly lipophilic crown carboxylic acids (1).

Further studies on Co(II) and Ni(II) ion extraction, using the highly lipophilic oligoether carboxylic acid $C_{12}H_{25}O(CH_2CH_2O)_4CH_2CO_2H$ (2), showed that the ligand exhibited higher selectivity toward Co(II) and Ni(II) ammine cations than crown carboxylic acids. Moreover, acyclic polyether carboxylic acid extracted Co(II) and Ni(II) cations efficiently from aqueous chloride solutions but selectivity of the process was low. This low selectivity could be explained in terms of similar physicochemical properties and sizes of Co(II) and Ni(II) cations.

To determine the relationship between the size of the extracted ion and the number of oxyethylene units incorporated into a molecule of an alkyloligo(oxyethylene) carboxylic acid, experiments were performed on competitive extraction of Zn(II), Cd(II), and Hg(II) by a series of dodecyloligo(oxyethylene) carboxylic acids **1**–**6** of the general formula $C_{12}H_{25}(OCH_2CH_2)_nOCH_2COOH$ ($n = 0$ to 5). Zn(II), Cd(II), and Hg(II) were chosen because their ionic diameters change gradually (3). Only competitive extraction experiments were conducted as it was found previously (4, 5) that results from single cation extractions often do not agree with results obtained in a competitive extraction in compatible systems.

The results of this investigation are reported in this paper.

Experimental

Apparatus

Concentrations of metals in aqueous and organic phases were determined radiometrically (^{65}Zn, ^{115m}Cd, and ^{203}Hg) with a Nuclear Data Inc. (Model 1200) multichannel gamma radiation spectrometer and a

[1]To whom all correspondence should be addressed.

Can. J. Chem. Downloaded from www.nrcresearchpress.com by 61.7.252.67 on 09/07/12
For personal use only.

TABLE 1. Physical properties, elemental analysis data, yields, and spectral data for *n*-dodecyloligo(oxyethylene) carboxylic acids

Compd No.	Melting point (°C) found, reported	Molecular formula, molecular weight	Elemental analysis theory/found C	Elemental analysis theory/found H	Yield, %	^{1}H nmr spectra (80 MHz), ppm[a]
1	47 46.3 (10)	$C_{14}H_{28}O_3$ 244.36	68.81 68.54	11.55 11.40	61	0.80 (t, 3H) 0.93–1.34 (m, 20H) 3.48 (t, 2H) 4.04 (s, 2H) 11.15 (s, 1H)
2	44	$C_{16}H_{32}O_4$ 288.42	66.63 66.75	11.18 11.18	43	0.83 (t, 3H) 1.00–1.75 (m, 20H) 3.35 (t, 2H) 3.48–3.75 (m, 4H) 4.03 (s, 2H) 10.88 (s, 1H)
3	35.5–36 37.3 (10)	$C_{18}H_{36}O_5$ 332.47	65.02 65.01	10.92 10.77	47	0.80 (t, 3H) 1.00–1.37 (m, 20H) 3.30 (t, 2H) 3.45 (s, 4H) 3.56 (s, 4H) 4.01 (s, 2H) 11.06 (s, 1H)
4	31.5–32.5	$C_{20}H_{40}O_6$ 376.52	63.79 63.69	10.71 10.70	62	0.81 (t, 3H) 1.02–1.75 (m, 20H) 3.33 (t, 2H) 3.38–3.75 (m, 12H) 4.01 (s, 2H) 10.18 (s, 1H)
5	30 28.2 (10)	$C_{22}H_{44}O_7$ 420.57	62.82 62.99	10.55 10.50	35	0.78 (t, 3H) 0.98–1.70 (m, 20H) 3.38 (t, 2H) 3.50–3.75 (m, 16H) 4.09 (s, 2H) 10.29 (s, 1H)
6	24–25	$C_{24}H_{48}O_8$ 464.62	62.04 61.99	10.41 10.65	25	0.79 (t, 3H) 0.98–1.53 (m, 20H) 3.30 (t, 2H) 3.35–3.62 (m, 20H) 3.98 (s, 2H) 10.04 (s, 1H)

[a]Measured in $CDCl_3$.

Canberra Industries (Model 7228) Ge/Li semiconductor probe. Measurements of the equilibrium pH in the aqueous phases were made with an ELPO (Model N-512) pH-meter and an Energopomiar (Model SAgP-209W) glass body combination electrode. ^{1}H nmr spectra were determined with a Tesla BC 487 nuclear magnetic resonance spectrometer. Melting points, which were corrected, were determined using a Carl Zeiss Jena micromelting point Boethius apparatus.

Reagents

Radioisotopes were from the Isotope Production and Reactor Center of the Institute of Atomic Energy, Swierk, Poland (^{65}Zn, ^{115m}Cd), and from the Central Institute of Nuclear Research, Dresden, GDR (^{203}Hg). Reagent grade sodium, hydrochloric acid, sulphuric acid, zinc chloride, cadmium chloride, mercury(II) chloride, sodium chloride, sodium hydroxide, sodium chloroacetate, diethylether, *n*-hexane, xylene, and chloroform were obtained from POCh (Gliwice, Poland). $ZnCl_2$, $CdCl_2$, and $HgCl_2$ were additionally dried at 120°C and then kept in a desiccator containing drying agent. 1-Dodecanol, 1-bromododecane, ethylene, diethylene, triethylene, and tetraethylene glycols were obtained from Fluka (GFR). Pentaethylene glycol was obtained from Aldrich (Milwaukee, WI, U.S.A.). The glycols were converted into the corresponding α-*n*-dodecyl-ω-hydroxy-oligo(oxyethylene)s according to published procedures (6–9).

Synthesis of n*-dodecyloligo(oxyethylene) carboxylic acids* ***1–6***

Xylene (500 mL) was heated over 1 mol (23 g) of metallic sodium until the mixture came to a boil. Thereafter, the mixture was slowly heated while being stirred vigorously and a white–grey suspension of sodium was obtained. The corresponding α-*n*-dodecyl-ω-hydroxy-oligo(oxyethylene) $C_{12}H_{25}$ $(OCH_2CH_2)_nOH$ (1 mol) was added dropwise to the suspension until a clear solution was obtained. Fine powdered sodium chloroacetate (1.1 mol = 128 g, 10% excess) was added in small portions to the solution. The reaction mixture was stirred at reflux for 16 h at a temperature of 110–130°C. After the reaction mixture cooled to room temperature, 100 mL of water and 100 mL of diethylether were added. The mixture was acidified with concentrated HCl (12 *M*) or H_2SO_4 (9 *M*). Phases were separated and the solvents (xylene and diethylether) were evaporated from the organic phase. The residue was dissolved in 100 mL of *n*-hexane and then the product, dodecyloligo(oxyethylene) carboxylic acid, was crystallized in a re-

Can. J. Chem. Downloaded from www.nrcresearchpress.com by 61.7.252.67 on 09/07/12
For personal use only.

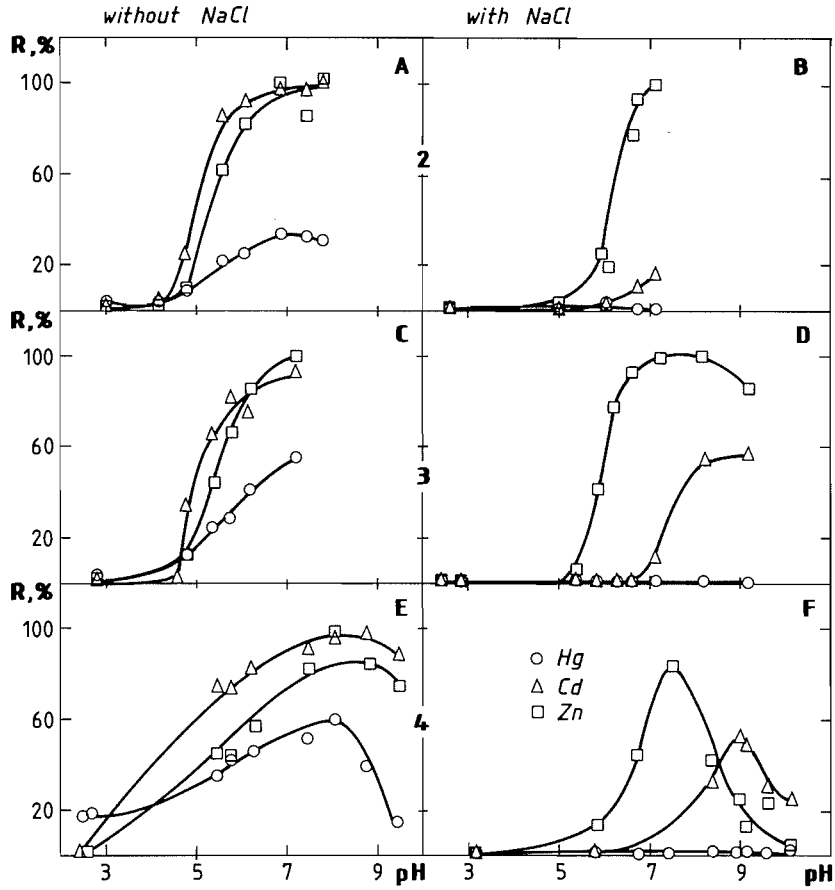

FIG. 1. Fraction of metals extracted (R) from aqueous solutions of 0.00167 M Zn(II), Cd(II), and Hg(II) chlorides (each) (A, C, E) and from aqueous solutions of 0.00167 M Zn(II), Cd(II), and Hg(II) chlorides (each), and 2.34 M NaCl (B, D, F) into 0.010 M solutions of n-dodecyloligo(oxyethylene) carboxylic acid in chloroform vs. the equilibrium pH of the aqueous phase.

frigerator (at about 4°C). Furthermore, recrystallization from n-hexane was repeated a few times. Before the last crystallization, the organic phase was dried over sodium sulphate and then n-hexane was evaporated *in vacuo*. Physical properties, elemental analysis data, yields, and spectral data for **1**–**6** are collected in Table 1.

$$C_{12}H_{25}(OCH_2CH_2)_nOCH_2COOH$$

$n = 0$, **1**;
$n = 1$, **2**;
$n = 2$, **3**;
$n = 3$, **4**;
$n = 4$, **5**;
$n = 5$, **6**.

Procedure

The extraction experiments were conducted at room temperature (19–21°C). The organic phase (5 mL) was a 0.010 M solution of an oligoether carboxylic acid in chloroform and the aqueous phase (5 mL) was a 0.00167 M solution of zinc, cadmium, and mercury chlorides (each) (labelled with ^{65}Zn, ^{115m}Cd, and ^{203}Hg radioisotopes) and NaOH (pH regulator). In the series of experiments, NaCl (at a concentration of 2.34 M) was added to the aqueous phases. Furthermore, a few experiments were done with each divalent metal chloride at a concentration of 0.000835 M and a NaCl concentration of 1.17 M in the initial aqueous phase.

Both organic and aqueous phases were placed in a separatory funnel and shaken vigorously for 15 min. Usually, the phases separated just after shaking was stopped (in particular, in the systems with acidic or neutral aqueous solution) or they could be separated by centrifuging for several minutes (15–20 min) if an emulsion appeared (usually in the systems with basic aqueous solution). However, most often with emulsions the phases were left in the separatory funnel for 18 h to allow them to separate. Samples (1.0 mL or 2.0 mL) of each phase were removed for the γ-spectrometric determination of metal concentrations. The metal concentrations were determined only in the clear organic and aqueous phases. Finally, the equilibrium pH of the aqueous phase was measured.

At the high equilibrium pH of the aqueous phase (usually a pH higher than 9), the emulsion formed was often so stable that the separation of the phases was impossible even by centrifuging. The results of the extraction experiments were presented only for those regions of equilibrium pH of the aqueous phase in which the organic and aqueous phases were separated and clear before metal concentrations were determined. Therefore the end of the extraction curves in the figures indicates pH values for which the emulsification process was too strong to continue the extraction experiments. Emulsions did not appear in the extraction systems with 0.000835 M solutions of divalent metal chlorides without NaCl addition.

In a few experiments, in the basic region of equilibrium pH, Zn(II) and/or Cd(II) hydroxide precipitation appeared in the systems. Because the metal concentrations were determined in the clear organic phase and the systems were fully equilibrated, the experimental data are included in the paper and they indicate concentrations of the metal complex soluble in chloroform.

Results and discussion

No divalent metal ions were transferred from the aqueous solutions containing NaCl at a concentration of 2.34 M into a chloroform solution of **1**. In the systems with an aqueous phase containing no addition of NaCl, tracer amounts of divalent metal

Can. J. Chem. Downloaded from www.nrcresearchpress.com by 61.7.252.67 on 09/07/12
For personal use only.

Can. J. Chem. Downloaded from www.nrcresearchpress.com by 61.7.252.67 on 09/07/12
For personal use only.

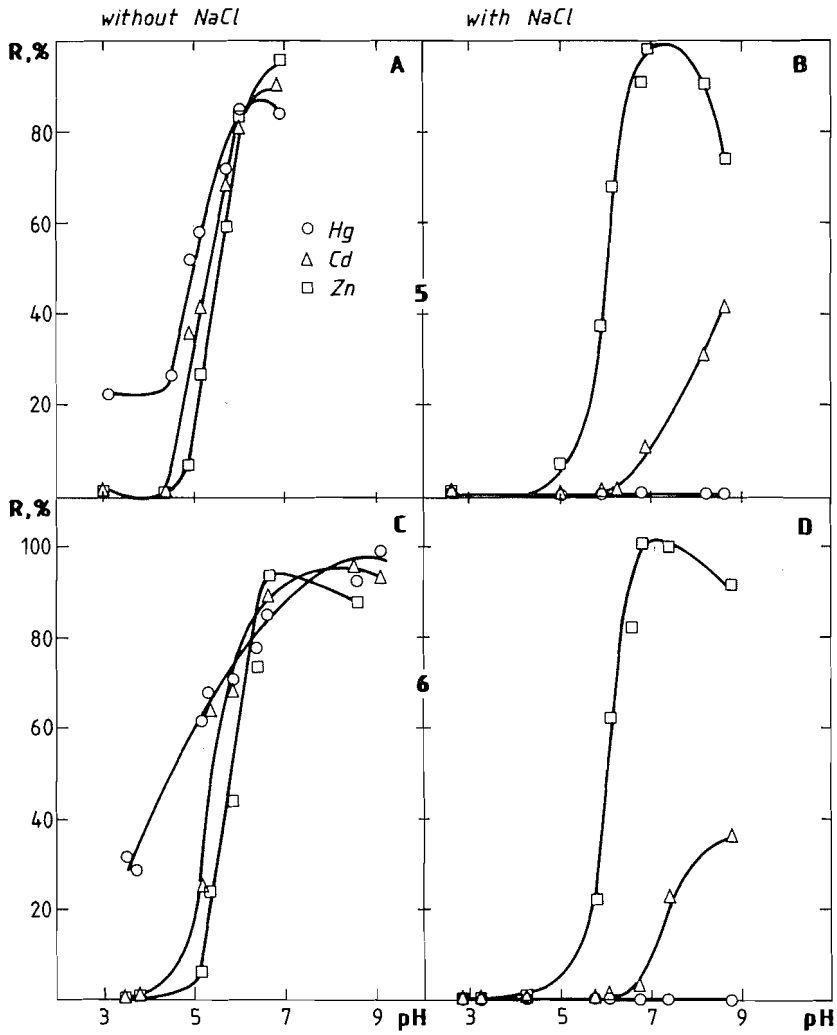

FIG. 2. Fraction of metals extracted (R) from aqueous solutions of 0.00167 M Zn(II), Cd(II), and Hg(II) chlorides (each) (A, C) and from aqueous solutions of 0.00167 M Zn(II), Cd(II), and Hg(II) chlorides (each) and 2.34 M NaCl (B, D) into 0.010 M solutions of *n*-dodecyloligo(oxyethylene) carboxylic acid in chloroform vs. equilibrium pH of the aqueous phase.

cations were extracted by **1** at the equilibrium pH of the aqueous phase above 9 (2% of Hg(II), 2.5% of Cd(II), and 1.2% of Zn(II)).

The results from the competitive extraction of Zn(II), Cd(II), and Hg(II) from 0.00167 M aqueous solutions of metal chlorides (each) into a 0.010 M solution of oligoether carboxylic acids **2**–**6** in chloroform are presented in Figs. 1 and 2. Two series of experiments were done. In the first one, the aqueous phase contained zinc, cadmium, and mercury chlorides and sodium hydroxide (the pH regulator) (Figs. 1*A*, *C*, *E* and 2*A*, *C*) while in the second one, sodium chloride was added to the initial aqueous phase at a concentration of 2.34 M (Figs. 1*B*, *D*, *F* and 2*B*, *D*). The sodium concentration in the initial aqueous solutions, which resulted from pH regulation using a NaOH solution, did not exceed 0.02 M (for the highest pH values).

Between the pH values 5 to 7, the extractability of divalent metal cations increased sharply with increasing equilibrium pH of the aqueous phase. A further increasing of the pH usually did not produce remarkable changes in the divalent metal cation extractability, but in some systems (Figs. 1*F* and 3*A*, *C*, *D*) extractability decreased sharply at pH > 8 and simultaneously the precipitation of Zn(II) and/or Cd(II) hydroxides appeared.

Extraction from a 0.00167 M *solution of divalent metal chlorides*

From solutions containing no addition of NaCl, extraction of Zn(II) and Cd(II) ions was very high and usually more than 90% of those cations were transported into the chloroform phase from the neutral and basic aqueous phase (Figs. 1*A*, *C*, *E*, and 2*A*, *C*). The extractability of Hg(II) increased with the increasing number of oxyethylene units incorporated into the molecule of extractant. The highest Hg(II) extractabilities were as follows: 33% using **2** (in the pH region 6.9 to 7.8), 57% using **3** (at pH 7.25), 60% using **4** (at pH 8.1), 85% using **5** (at pH 6.0), and 99.6% using **6** (at pH 9.2).

The correlation between the number of oxyethylene units incorporated into the molecule of an extractant and the extractability of Hg(II) indicates that an enlargement of the polyether portion in the acyclic polyether carboxylic acid may improve metal cation extractability. It seems that Hg(II) ions are too large (ionic diameters of Zn(II), Cd(II), and Hg(II) are 1.48, 1.94, and 2.20 Å, respectively (3)) to be strongly complexed by the short oligo(oxyethylene) portion of **2**–**4**. On the other hand, the interaction of the oxygens of the oxyethylene chain with Zn(II) ion was evidently very strong, because Zn(II) was extracted

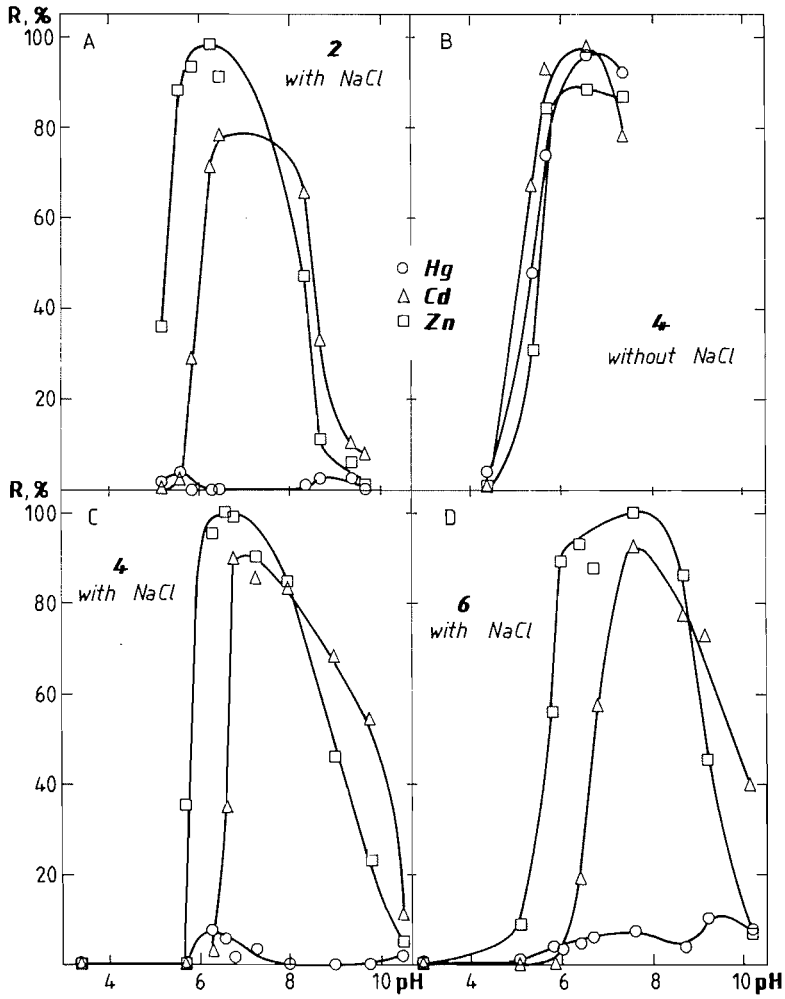

FIG. 3. Fraction of metals extracted (R) from aqueous solutions of 0.000835 M Zn(II), Cd(II), and Hg(II) chlorides (each) (B) and from aqueous solutions of 0.000835 M Zn(II), Cd(II), and Hg(II) chlorides (each) and 1.17 M NaCl (A, C, D) into 0.010 M solutions of n-dodecyloligo(oxyethylene) carboxylic acid in chloroform vs. equilibrium pH of the aqueous phase.

efficiently also by **2** (with only one oxyethylene unit incorporated into the molecule). The complexation of Zn(II), Cd(II), and Hg(II) ions are associated with the oxyethylene portion of the molecule because no extractability of the divalent cations by alkyloxyacetic acid **1** was observed. The interaction between a metal cation and a carboxylate anion is evidently not strong enough to produce metal extractability by itself. Thus, the carboxylic group is important mainly because after its deprotonization, an electroneutral metal extraction complex can be transferred into the organic phase without simultaneous transfer of an inorganic anion.

From the total divalent metal concentration in the best loaded organic phases (Table 2) it turns out that the most probable stoichiometry of the extraction complex is $M(II)(OE)_2$ (OE = an oligo(oxyethylene) carboxylate anion). This stoichiometry is anticipated also from electroneutrality of the complexes transferred into chloroform phase, taking into account that transfer of strongly hydrated Cl^- and OH^- anions into the low polar organic phase has low probability (5).

The stoichiometry of the extraction complexes was confirmed by additional experiments in which a 0.01 M chloroform solution of **5** was contacted with a 0.01 M aqueous solution of $ZnCl_2$, $CdCl_2$, or $HgCl_2$ in the single cation extraction. The metal concentrations in the organic phase after equilibration (pH 6.9) did not exceed 0.005 M (0.0047 M, 0.0044 M, and 0.0040 M for Zn(II), Cd(II), and Hg(II), respectively).

Extraction from a 0.00167 M *solution of divalent metal chlorides and 2.34* M *NaCl*

The selectivity of extraction of the divalent cations from a 2.34 M solution of NaCl improved remarkably. The extractability of Zn(II) remained very high (usually up to 100% of extraction from the neutral solution) but extractability of Cd(II) and, particularly, Hg(II) decreased sharply. The decrease of the extractability of Cd(II) and Hg(II) from a 2.34 M solution of NaCl resulted clearly from the formation of divalent metal chloride complexes. It is known that the stability of chloride complexes decreases in the order Hg(II) > Cd(II) > Zn(II) (11, 12). Under experimental conditions, the chloride complexes of Hg(II) are thermodynamically more stable than complexes of Hg(II) with oligoether carboxylic acids.

In some cases Zn(II) was efficiently separated from Cd(II) and Hg(II) in the systems with 2.34 M solutions of NaCl. Cd(II) and Hg(II) were not extracted by **3** in the pH region 2.5 to 6.6 while extractability of Zn(II) in that system at pH 6.6 was 93.5% (Fig. 1D). Cd(II) and Hg(II) were not extracted by **5** in the pH

Can. J. Chem. Downloaded from www.nrcresearchpress.com by 61.7.252.67 on 09/07/12
For personal use only.

TABLE 2. Total concentration of divalent metals in the highest loaded organic phases after extraction

Polyether carboxylic acid	Data taken from	Total M(II) concentration in organic phase, $M \times 10^3$
2	Fig. 1*A* at pH 6.9	3.88
3	Fig. 1*C* at pH 7.25	4.19
4	Fig. 1*E* at pH 8.1	4.29
5	Fig. 2*A* at pH 6.9	4.50
6	Fig. 2*C* at pH 9.1	4.86

region 2.6 to 6.8 while Zn(II) extractability at pH 6.8 was 92% (Fig. 2*B*). Similarly, neither Cd(II) nor Hg(II) were extracted by **6** in the pH region 2.95 to 6.6 while 82.5% of Zn(II) at pH 6.6 was extracted in that system.

Extraction from a 0.000835 M *solution of divalent metal chlorides*

The selectivity of extraction decreased markedly when the divalent metal chloride concentration in the initial aqueous phase was 0.000835 *M* (each). All three divalent cations were similarly extracted and almost no separation was achieved in the system containing no addition of NaCl (Fig. 3*B*). After NaCl was added into the aqueous phase at a concentration of 1.17 *M*, separation was somewhat improved, because extractability of Hg(II) decreased sharply. Moreover, due to the shift of the Cd(II) extraction curves into the more basic region than those of Zn(II), separation of those cations in the pH region from about 5 to 7 was also possible (Figs. 3*A*, *C*, *D*).

Above pH 8 in the systems with NaCl (Figs. 3*A*, *C*, *D*), the metal concentrations in the organic phase decreased sharply and precipitation of Zn(II) and/or Cd(II) hydroxide appeared. This phenomenon indicates that, under experimental conditions, metal hydroxides are more stable than metal – alkyloligo(oxyethylene) carboxylic acid complexes. It also indicates that the interaction of an alkyloligo(oxyethylene) carboxylic acid with Zn(II) and Cd(II) is very different from that with Co(II) and Ni(II). It has been reported previously (2) that in the system with **5**, the extractability of Co(II) and Ni(II) from their chloride aqueous solution increased with increasing pH, also in the basic region of pH. The different complexation of Zn(II), Cd(II), Co(II), and Ni(II) by alkyloligo(oxyethylene) carboxylic acids in the basic region of pH cannot be explained in terms of the different stability of metal hydroxides (stability of $M(OH)_2$ decreases in the order Zn(II) > Ni(II) > Co(II) > Cd(II) (13)) or the different ionic diameter of the metal ions (ionic diameter for Zn(II), Cd(II), Co(II), and Ni(II) is 1.48, 1.96, 1.48, and 1.44 Å, respectively (3)). Apparently, the accommodation of the ligand field of a polyether carboxylate and oxygen donor atoms of the polyoxyethylene chain to the field imposed by Ni(II) and Co(II) is much better than to the field imposed by Zn(II) and Cd(II).

Acknowledgements

We express our appreciation to Mrs. Aleksandra Kotecka of the IICMRE, Technical University of Wroclaw, who carried out most of the extraction experiments. J.S. would like to thank Mr. Larry Bratton of the Department of Chemistry and Biochemistry, Texas Tech University, for his help in improving the English in the manuscript.

1. J. STRZELBICKI, W. A. CHAREWICZ, and R. A. BARTSCH. J. Incl. Phenom. **6**, 57 (1988).
2. J. STRZELBICKI, W. CHAREWICZ, J. BEGER, and L. HINZ. Extraction of nickel and cobalt by ionizable polyethers. 6th International Symposium on High Purity Materials in Science and Technology — Preparation Characterization and Application of Well-Defined Materials. Dresden, GDR. May 1985. Poster Abstracts. pp. 144, 145.
3. C. S. G. PHILLIPS and R. J. P. WILLIAMS. Inorganic chemistry. Vol. I. Oxford University Press, New York and Oxford. 1965. p. 152.
4. J. STRZELBICKI and R. A. BARTSCH. Anal. Chem. **53**, 1894 (1981).
5. J. STRZELBICKI and R. A. BARTSCH. Anal. Chem. **53**, 2247 (1981).
6. T. GIBSON. J. Org. Chem. **45**, 1095 (1980).
7. W. GERHARDT. Monatsber. Deutsch. Akad. Wiss. Berlin. **9**, 922 (1967).
8. B. A. MULLEY. J. Chem. Soc. London. 2065 (1958).
9. B. A. GINGRAS and C. H. BAYLEY. Can. J. Chem. **35**, 599 (1957).
10. K. OGINO, T. ACHI, and Y. TABATA. Nippon Kagaku Kaishi. **9**, 1385 (1980).
11. L. G. SILLEN and A. E. MARTELL. Stability constants of metal ion complexes. Special Publication No. 17. The Chemical Society, Burlington House, London. 1964. pp. 61–65, 289–293.
12. L. G. SILLEN and A. E. MARTELL. Stability constants of metal ion complexes. Special Publication No. 25. The Chemical Society, Burlington House, London. 1971. pp. 26, 27, 179–182.
13. R. C. WEAST, M. J. ASTLE, and W. H. BEYER (*Editors*). CRC handbook of chemistry and physics. 65th ed. CRC Press, Inc., Boca Raton, FL. 1984–85. p. B-220.

Can. J. Chem. Downloaded from www.nrcresearchpress.com by 61.7.252.67 on 09/07/12
For personal use only.

A novel method of complete activation by carbonyldiimidazole: application to ester synthesis

ROBERT C. MORTON, DEV MANGROO, AND GERHARD E. GERBER[1]
Department of Biochemistry, McMaster University, Hamilton, Ont., Canada L8N 3Z5

Received October 13, 1987

ROBERT C. MORTON, DEV MANGROO, and GERHARD E. GERBER. Can. J. Chem. **66**, 1701 (1988).

The activation of carboxylic groups by carbonyldiimidazole (CDI) results in the presence of excess CDI; it is shown that this reacts rapidly with the target hydroxyl groups under acylation conditions, thus preventing the desired acylation even when an excess of reagent is present and resulting in poor yields. The methods described result in rapid, complete, and convenient removal of the excess CDI. This procedure thus permits the use of sufficient excess of CDI to effect complete activation of the acid to the imidazolide. The imidazolides prepared in this manner, when used in limiting amounts, can be quantitatively converted to esters or amides; when used in slight excess, these imidazolides result in the quantitative acylation of target groups.

ROBERT C. MORTON, DEV MANGROO et GERHARD E. GERBER. Can. J. Chem. **66**, 1701 (1988).

L'activation des groupements carboxyliques par le carbonyldiimidazole (CDI) fait qu'on se trouve toujours en présence d'un excès de CDI; on démontre que, dans des conditions conduisant à une acylation, celui-ci réagit rapidement avec les groupements hydroxyles des molécules cibles et que l'acylation désirée est empêchée, même lorsqu'un excès du réactif est présent, et que les rendements obtenus sont faibles. Les méthodes proposées permettent d'enlever rapidement, complètement et d'une façon simple l'excès de CDI. Ces méthodes permettent donc d'utiliser un excès suffisant de CDI pour effectuer une activation complète de l'acide en imidazolide. Lorsqu'on utilise des quantités limitantes des imidazolides ainsi préparés, on peut les transformer quantitativement en esters ou en amides; lorsqu'on les utilise avec un léger excès, ces imidazolides conduisent à une acylation complète des groupements cibles.

[Traduit par la revue]

Can. J. Chem. Downloaded from www.nrcresearchpress.com by 61.7.252.67 on 09/07/12
For personal use only.

Introduction

Carbonyldiimidazole (CDI), is a commonly used reagent for the activation of carboxylic acid groups and has been used for the preparation of affinity columns (1–5), the attachment of *t*-BOC amino acids to solid supports (6, 7), and in the preparation of fatty acyl CoA thioesters (8), phospholipids (9–16), and simple peptides (17–21). In general, the activation reaction consists of reacting the carboxylic acid with an excess of CDI in an anhydrous solvent such as tetrahydrofuran, chloroform, benzene, or dimethylformamide and the resulting activated acid is used as the acylating reagent without further purification.

We have adopted this method of activation for the preparation of esters of coenzyme A, phospholipids, and polar derivatives of hydrophobic proteins (23). However, in each case the reaction was variable and the yield of the desired products was often low. High performance liquid chromatographic (hplc) analysis of the acylation reaction, using DNP-prolylserinamide as a model compound, indicated that this was related to the presence of CDI during the acylation reaction.

Activation of the acid by one equivalent or only a slight excess of CDI results in a slow and incomplete reaction, leaving a residual amount of free CDI unless very long activation times are used. Activation by a substantial excess of CDI results in faster and complete activation but the excess CDI is still present. The activated acyl imidazolide is normally used directly without purification due to its sensitivity to hydrolysis, and thus the excess of CDI still present reacts with the target groups and thereby prevents their acylation.

We have developed a method of complete activation of the carboxylic acid by a substantial excess of CDI, which is subsequently removed selectively by incubation of the activation mixture with Sephadex LH-20 in dry benzene. The described activation procedure completely eliminates the side reaction with the activating agent and affords the desired acylation in excellent yield.

Experimental

General

Trimesic acid (1,3,5-benzenetricarboxylic acid), 1,1-carbonyldiimidazole (CDI), and ninhydrin were purchased from Sigma Chemical Co. Sephadex LH-20 was purchased from Pharmacia and triethylamine from Pierce.

Reagent grade dimethylformamide (DMF) was dried by the addition of 0.1 volume of dry benzene, removal of 0.2 volume under reduced pressure, and storage over 4 A molecular sieve and under nitrogen. All distillation was performed under nitrogen. Benzene was dried by refluxing for 4 h over calcium hydride, distilled, and stored over 4 A molecular sieve under nitrogen. Triethylamine was distilled from ninhydrin and stored over 4 A molecular sieve, under nitrogen and at 4°C in the dark.

Synthesis of DNP-prolylserinamide

DNP-proline was activated by the addition of 1.1 equivalents of CDI in dry THF as a 60 mM solution and incubated at room temperature for 1 h under nitrogen. To the reactive imidazolide derivative, 3 equivalents of the hydrochloride salt of serinamide were added as a freshly prepared 1.54 M aqueous solution in the presence of 1 equivalent of Bu_4NOH. After 12 h at room temperature, the reaction was diluted with a 0.5 volume of water and the DNP-peptide extracted into ethyl acetate. The peptide product was purified by preparative hplc on a reversed phase μ Bondapak C_{18} column, which was equilibrated and run isocratically with 1% aqueous acetic acid containing 10% methanol. The DNP-peptide was dried several times from anhydrous pyridine and then stored as a 25 mM solution in dry pyridine over molecular sieve and under nitrogen.

Synthesis of di(trimethylsilylethyl)trimesic acid (DT-TM acid)

All steps in the synthesis of the diprotected trimesic acid (DT-TM acid) were performed in a closed vessel under nitrogen and at room temperature. The triimidazolide derivative of trimesic acid was generated by the addition of 4.8 mmol of trimesic acid in 6 mL of anhydrous DMF, in approximately 1-mL aliquots, to a screw cap tube containing

[1]Author to whom correspondence may be addressed.

Can. J. Chem. Downloaded from www.nrcresearchpress.com by 61.7.252.67 on 09/07/12
For personal use only.

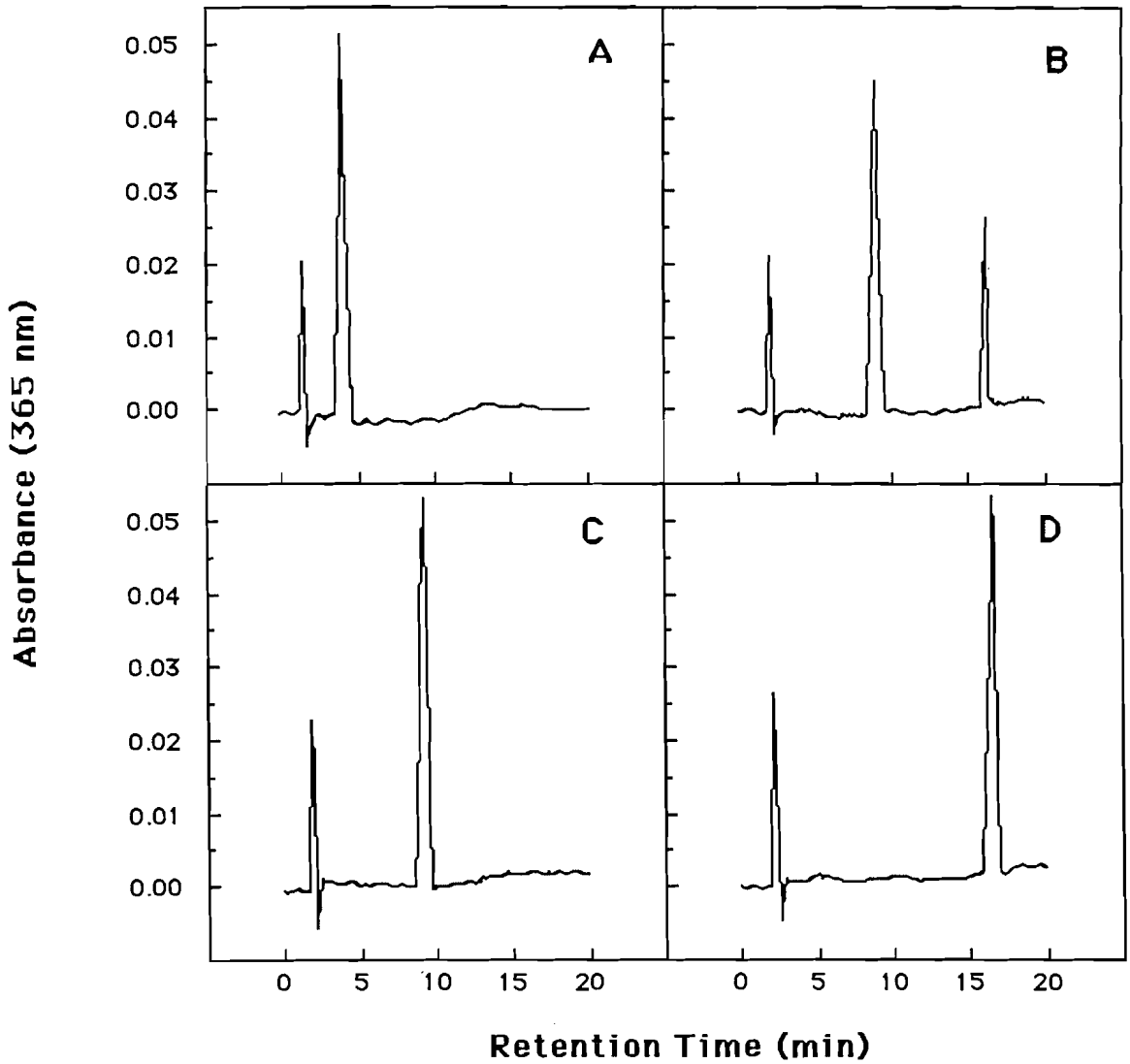

FIG. 1. Analysis of the reaction products by hplc. DT-TM imidazolide was prepared using 1.5 equiv. of CDI and incubated for 1 h with or without 4 equiv. of Sephadex LH-20 in dry benzene as described in the experimental section. The peptide DNP-prolylserinamide was subjected to standard acylation conditions using the following reagents: A. No reagent; B. 200 mM DT-TM imidazolide without Sephadex LH-20 pretreatment; C. 50 mM CDI; D. 200 mM DT-TM imidazolide pretreated with Sephadex LH-20. After 1 h, aliquots were diluted into aqueous DMF and subjected to hplc analysis as described in the experimental section.

2.33 g CDI (3 equivalents) in 4 mL of dry DMF. During the addition, the mixture was continuously vortexed. After 1 h, two equivalents of $Me_3SiCH_2CH_2OH$ were added and the reaction allowed to proceed overnight. Following dilution with an equal volume of dry DMF, the remaining imidazolides were hydrolyzed by the addition of 2 mL of 2.5 M aqueous NaOH. Three petroleum ether extractions completely removed the triester of TM acid. Acidification with HCl to pH 1 allowed the desired product, DT-TM acid, to be selectively extracted into diethyl ether/petroleum ether (1:9, v/v). The monoester of TM acid remained in the aqueous phase. The extracts containing DT-TM acid were pooled, and washed once with 0.1 N HCl and then once with 4 M NaCl. The solvent was evaporated under a stream of nitrogen and the product was repeatedly (3 times) dissolved in dry benzene and the solvent removed under reduced pressure. The DT-TM acid was a single peak on hplc analysis and had the expected nmr spectrum. The dried DT-TM acid was stored as a 0.2 M solution in dry benzene, over molecular sieve (4 A) and under nitrogen.

Determination of the capacity of Sephadex LH-20 for CDI

To a flamed Pyrex screw cap tube (13 × 100 mm) containing 40 mg of dry Sephadex LH-20 in 1.0 mL of dry benzene was added 6.9×10^{-4} mol of CDI (1.5 M in dry DMF). The tube was flushed with nitrogen, then mixed continuously at room temperature for 1 h. An aliquot (10 μL) of the reaction was diluted to 2 mL with dry benzene and the absorbance at 290 nm was measured to assess the extent of CDI removal. The extinction coefficient of CDI at 290 nm in benzene is 210. After maximal removal of CDI (66.6%) the capacity of Sephadex LH-20 for CDI was calculated to be 1.15×10^{-5} mol of hydroxyl groups per mg of dry Sephadex LH-20.

Preparation of acid imidazolides

The DT-TM acid (1 M in dry DMF) was transferred to a flamed Pyrex screw cap tube (10 × 100 mm) containing 1.5 equivalents of CDI (0.2 M) in 15% DMF/85% benzene under nitrogen. The reaction was allowed to proceed for 1 h; the imidazolide was then diluted with dry benzene to 40 mM, and transferred to another flamed Pyrex screw cap tube containing 4 equivalents of dry Sephadex LH-20. The tube was flushed with nitrogen and mixed continuously for 1 h; centrifugation removed the Sephadex LH-20 and removal of the solvent under reduced pressure afforded the imidazolide free of excess CDI.

Standard peptide acylation

DNP-prolylserinamide was routinely acylated at room temperature,

under nitrogen, as a 1 mM solution in anhydrous DMF in the presence of 200 mM DT-TM imidazolide and 1 M triethylamine. The extent of acylation of the DNP-peptide was determined by reverse phase hplc by diluting an aliquot of the reaction into aqueous DMF (10% water; v/v) and analyzing a portion using a 4.6 × 250 mm μBondapak C_{18} column equilibrated with 35% methanol in 10 mM sodium acetate, pH 4.4. The column was developed at 1 mL/min, while the methanol content of the eluent was increased to 100% over 15 min to afford a 10-min separation between the retention times of the starting peptide and the trimesylated product.

Results and discussion

Carbonyldiimidazole (CDI) has been used extensively (22) for the activation of carboxylic acid groups since it reacts quantitatively to produce the acid imidazolide. An excess of CDI is used to ensure complete activation of the acid since the purity of the commercially available CDI is variable due to its extreme sensitivity to water, and since any residual water in the solvents would result in some loss of CDI. It has been reported (8, 9–16) and we confirmed that the yields of desired acylation products is often poor. Consequently, we studied the acylation of the peptide DNP-prolylserinamide by an acid imidazolide: the dinitrophenyl group allows detection (365 nm) of peptide-related products produced during the acylation; the acid chosen for this study was the diprotected derivative of trimesic acid (DT-TM acid) developed by us for derivatization of proteins (23), since it could readily be detected spectrally during hplc analysis, as well as being available to us in tritiated form.

The products of the reaction of DT-TM imidazolide with DNP-prolylserinamide were analyzed by hplc as shown in Fig. 1. The peptide is essentially pure and runs as a single peak at 4.0 min (panel A), the peak observed at 1.2 min being due to solvent. Reaction of the peptide with acid activated with 1.5 equivalents of CDI resulted in complete loss of starting material and formation of two new products. The minor product (10%) eluting at 16.6 min (Fig. 1B) was determined to be the desired trimesylated peptide since it contained the DNP chromophore and the tritiated form of the DT-TM acid; the major product (90%) eluting at 9.1 min did not contain DT-TM acid (data not shown). A product eluting at the latter position is also generated when the peptide is incubated with CDI under acylation conditions (Fig. 1C) in the absence of DT-TM imidazolide. This product is presumed to be the imidazole-*N*-carboxylic ester of the peptide since the reaction between an alcohol and CDI to produce imidazole-*N*-carboxylic ester has been previously described (22) and since it contains the peptide but not the DT-TM acid. Although the imidazolide is present in twice the concentration of the excess CDI, the trimesylated product is obtained only in about 10% yield; this indicates that the CDI must react considerably faster than does the imidazolide under these conditions. It was therefore concluded that this side reaction with CDI was responsible for the poor yields of the desired acylated peptide.

The effect of excess CDI on the rate of acylation was assessed quantitatively using this system and the results are shown in Fig. 2. Acylation with DT-TM acid, that had been activated with 1.0 or 1.5 equivalents of CDI resulted in 60 and 10% acylation of the peptide respectively. Addition of freshly activated reagent to these samples resulted in no increase in the amount of acylated peptide formed; this is consistent with the observed loss (Fig. 1B) of starting peptide under these conditions and the excess CDI thus had irreversibly blocked the hydroxyl group of the peptide.

The acylation reaction must therefore be performed in the absence of CDI. The obvious route of activation of the carboxylic acid with only one equivalent of CDI still produced unsatisfactory results since this required exact titration of the reagents and anhydrous conditions; in addition, as the CDI is consumed, the activation becomes slow, resulting in incomplete activation and the resulting presence of residual CDI. A better alternative would be the complete activation of the acid with an excess of CDI followed by removal of the unreacted CDI. This selective removal of CDI without significant loss of the activated acid should be possible since the reactivity of the CDI seemed to be much higher. This was confirmed by determining the reactivities of CDI and DT-TM imidazolide towards methanol in benzene or DMF, as shown in Fig. 3. The extent of reaction of CDI and DT-TM imidazolide under these conditions was determined by monitoring the absorbance at 290 nm (CDI) and at 310 nm (DT-TM imidazolide) at the specified times. The reactivities of the two reactive compounds towards methanol were similar in DMF while in benzene the rate of reaction of CDI was approximately 175 times faster than that of the imidazolide. This higher reactivity of CDI in benzene should allow its selective reaction with hydroxyl groups without significant loss of the imidazolide. The reaction of the excess CDI with the solid phase hydroxylic support Sephadex LH-20 (3-hydroxypropyl derivative of Sephadex G-25) in benzene resulted in the removal of the generated reactive by-product, imidazolide-*N*-carboxylic ester, which became attached to the Sephadex LH-20. The time course of removal of CDI from solution is shown in Fig. 4. Complete removal of the excess CDI was achieved within 1 h after incubation with a 4-fold excess of Sephadex LH-20 per mole equiv-

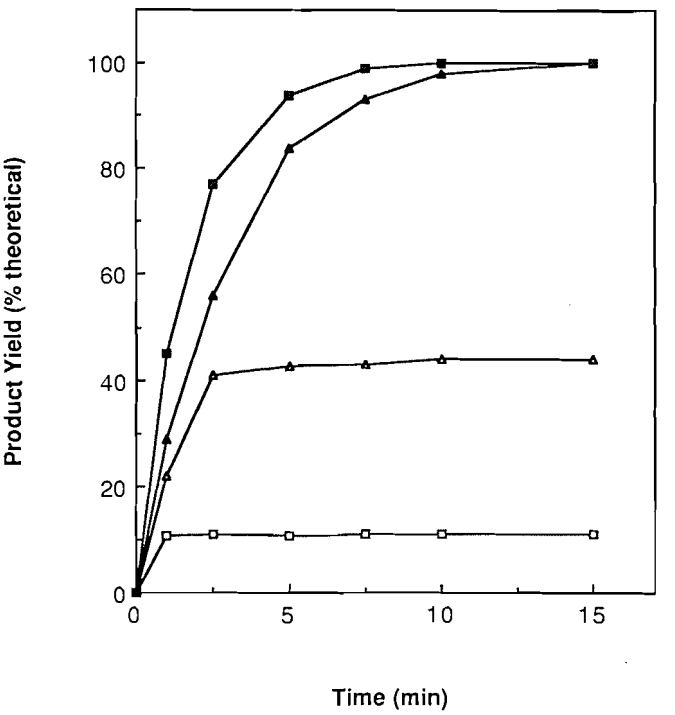

FIG. 2. Trimesylation time course for DNP-prolylserinamide with Sephadex LH-20 treated or untreated DT-TM imidazolide. DT-TM imidazolide was generated by activation with 1.5 equiv. (square) or 1.0 equiv. (triangle) of CDI and then incubated for 1 h with (■, ▲) or without (□, △) 4 equiv. of Sephadex LH-20 in dry benzene. The resulting reagents were then used to trimesylate DNP-prolylserinamide under the standard reaction conditions. At the times indicated, an aliquot was withdrawn, diluted into aqueous DMF, and subjected to hplc analysis as described in the experimental section.

Can. J. Chem. Downloaded from www.nrcresearchpress.com by 61.7.252.67 on 09/07/12
For personal use only.

TABLE 1. Formation of DT-TM imidazolide

Solvent	Molar ratio CDI to DT-TM acid	Molar ratio Et_3N to DT-TM acid	Number of equal portions of DT-TM acid	DT-TM anhydride (% theor)	DT-TM imidazolide (% theor)
DMF	1.5	0	1	8	84
	1.5	0	4	10	80
	1.5	2	1	20	60
	1.5	2	4	28	44
	3.0	0	2	6	88
	3.0	2	2	10	80
Benzene:DMF (3: 1)	1.5	0	1	0	100
	1.5	0	4	0	100

Diprotected trimesic (DT-TM) acid was activated by its addition to a solution of CDI under the conditions specified in the table. The activation was allowed to proceed at room temperature for a period of 1 h after the last addition of reagent. Cyclohexylamine (10 molar excess to CDI) was added and left for an additional 0.5 h. Aliquots of 100 nmol were analyzed by hplc at 280 nm on a Waters Bondpak C_{18} reversed phase column (0.46 × 25 cm) eluted with a methanol gradient from 20% to 100% over 10 min. The amount of DT-TM anhydride generated was determined from the amount of DT-TM acid formed due to addition of the cyclohexylamine; the amount of DT-TM imidazolide was calculated from the amount of DT-TM cyclohexylamide, corrected for the amount derived from the DT-TM anhydride.

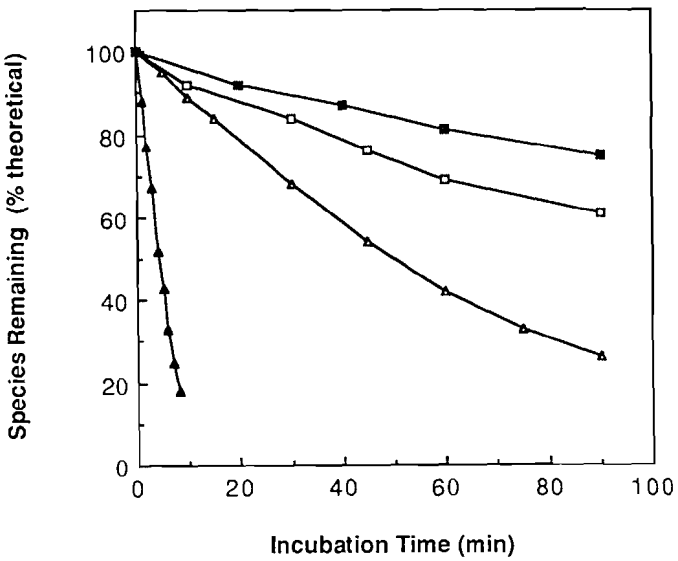

FIG. 3. Solvent effect on the reactivity of CDI and DT-TM imidazolide. Methanol was added to 6.7 mM solutions of CDI (triangle) and DT-TM imidazolide (square) to give a final methanol concentration of 100 mM. These reactions were performed in anhydrous DMF (△, □) or benzene (▲, ■) and the concentration of the activated species was monitored spectrally using a Varian Cary 210 spectrophotometer; a wavelength of 290 nm was used for CDI (ϵ_{290} = 210 M^{-1} cm^{-1}) and 310 nm for DT-TM imidazolide (ϵ_{310} = 280 M^{-1} cm^{-1}).

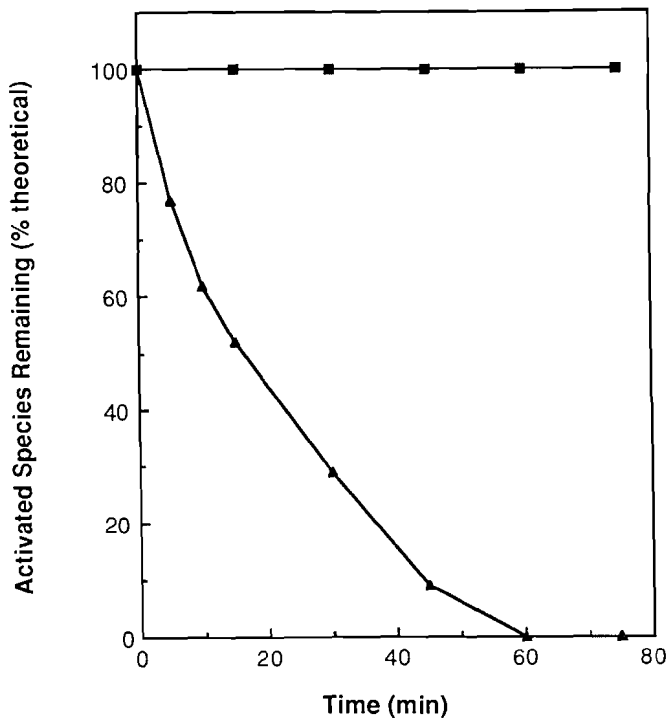

FIG. 4. Reaction of CDI and DT-TM imidazolide with Sephadex LH-20. Four equivalents of Sephadex LH-20 were added to a 20 mM solution of CDI (▲) and a 40 mM solution of DT-TM imidazolide (■) in anhydrous benzene. At the times indicated, an aliquot of the solution was diluted 20-fold with dry benzene and the activated species quantitated spectrally at 290 nm for CDI and 310 nm for DT-TM imidazolide.

alent of residual CDI, in the absence of base; under these conditions no loss of radioactive DT-TM imidazolide was observed. The capacity of Sephadex LH-20 for CDI was determined to be 1.15 × 10^{-5} mol/mg as described in the experimental section.

The time course of acylation of the peptide after removal of the excess CDI using this procedure is shown in Fig. 2. The reactions with DT-TM acid that had been activated with 1.0 or 1.5 equivalents CDI now both resulted in 100% reaction whereas in the absence of the LH-20 treatment this reagent had produced yields of 60 and 10% respectively. Analysis of the final product of this reaction by hplc is shown in Fig. 1D; a single product corresponding to the DT-TM peptide was observed, while the product corresponding to the CDI adduct was absent. It is thus clear that the treatment with Sephadex LH-20 completely removes the CDI, resulting in faster acylation rates, more complete reactions, and purer products.

In those cases where availability of the acylating agent is limiting, a side reaction that may account for low yields is the formation of anhydride during activation, since the maximum yield via the anhydride based on acid is reduced to one half of that via the imidazolide. Th extent of anhydride formation during the preparation of the DT-TM imidazolide derivative was determined by hplc. This analysis involved an indirect assay in

Can. J. Chem. Downloaded from www.nrcresearchpress.com by 61.7.252.67 on 09/07/12
For personal use only.

which DT-TM acid was activated as described in Table 1, followed by the addition of 10 equivalents of cyclohexylamine. Reaction of cyclohexylamine with DT-TM imidazolide formed the corresponding amide derivative, while reaction with DT-TM anhydride resulted in the formation of one equivalent of the amide derivative and one equivalent of DT-TM acid. This reaction mixture was analyzed by hplc, as described in the legend to Table 1, and monitored at 280 nm; the amount of free DT-TM acid generated afforded a quantitative assay of the amount of anhydride that had been formed.

The results in Table 1 clearly show that DMF is a relatively poor solvent for CDI activation of DT-TM acid, in all cases resulting in substantial formation of DT-TM anhydride. The presence of Et_3N during the activation was found to double the amount of DT-TM anhydride formed. Apparently the generation of the DT-TM carboxylate ion results in the nucleophilic attack on the DT-TM imidazolide, thereby forming the anhydride. Increasing the amount of CDI or the number of additions of DT-TM acid, in equal portions, was found to make little difference in reducing the anhydride formation. In the benzene/DMF mixture, the formation of DT-TM imidazolide was 100%, irrespective of the method of addition of the DT-TM acid (all at once or in four equal aliquots), and the activation reaction was found to be complete within 0.5 h. The activation of acids by CDI is thus best done in nonpolar solvents such as benzene in the absence of base, since more polar solvents or the presence of base result in anhydride formation.

We have systematically assessed the imidazolide approach of carboxylic acid activation and have solved several problems associated with this procedure: activation of the acid is best achieved in a nonpolar solvent in the absence of any base. Complete formation of the imidazolide is ensured by an excess of CDI with respect to the carboxylic acid. Any residual CDI can be entirely eliminated by a brief incubation with Sephadex LH-20 in dry benzene without any loss of the acid imidazolide. The resulting imidazolide can be quantitatively converted to an ester or amide without any side reactions.

Acknowledgements

This investigation was supported by grants to G. E. Gerber by the Medical Research Council of Canada. Robert C. Morton was the recipient of a Medical Research Council of Canada studentship.

1. G. S. Bethel, J. S. Ayers, W. S. Hancock, and M. T. W. Hearn. J. Biol. Chem. **254**, 2572 (1979).
2. M. T. W. Hearn, G. S. Bethel, J. S. Ayers, and W. S. Hancock. J. Chromatogr. **185**, 463 (1979).
3. M. T. W. Hearn, E. L. Harris, G. S. Bethel, W. S. Hancock, and J. A. Ayers. J. Chromatogr. **218**, 509 (1981).
4. G. S. Bethel, J. S. Ayers, M. T. W. Hearn, and W. S. Hancock. J. Chromatogr. **219**, 353 (1981).
5. G. S. Bethel, J. S. Ayers, M. T. W. Hearn, and W. S. Hancock. J. Chromatogr. **219**, 361 (1981).
6. H. C. Beyerman and R. A. Veld. Recl. Trav. Chim. Pays-Bas, **88**, 1019 (1969).
7. J. Stewart and J. D. Young. *In* Solid phase peptide synthesis. 2nd ed. Pierce Chemical Company, Rockford, IL. 1984. p. 72.
8. A. Kawaguchi, T. Yoshimura, and S. Okuda. J. Biochem. **89**, 337 (1981).
9. W. F. Boss, C. J. Kelley, and F. R. Landsberger. Anal. Biochem. **64**, 289 (1975).
10. T. G. Warner and A. A. Benson. J. Lipid Res. **18**, 548 (1977).
11. A. Hermetter and F. Paltauf. Chem. Phys. Lipids, **28**, 111 (1981).
12. A. Hermetter, F. Paltauf, and H. Hanser. Chem. Phys. Lipids, **30**, 35 (1982).
13. A. Hermetter and F. Paltauf. Chem. Phys. Lipids, **30**, 47 (1982).
14. A. Hermetter, H. Stutz, and F. Paltauf. Chem. Phys. Lipids, **32**, 145 (1983).
15. S. B. Farren, E. Summerman, and P. R. Cullis. Chem. Phys. Lipids, **34**, 279 (1984).
16. J. K. Longmuir, O. C. Martin, and R. E. Pagano. Chem. Phys. Lipids, **36**, 197 (1985).
17. G. W. Anderson and R. L. Paul. J. Am. Chem. Soc. **80**, 4423 (1958).
18. A. R. Ronzio and T. J. DeCino. Microchem. J. **4**, 531 (1960).
19. R. Paul and G. E. Anderson. J. Am. Chem. Soc. **82**, 4596 (1960).
20. R. Paul and G. E. Anderson. J. Org. Chem. **27**, 2094 (1962).
21. R. A. Lawrsen. Eur. J. Biochem. **20**, 89 (1971).
22. H. A. Staab. Angew. Chem. Int. Ed. Engl. **1**, 351 (1962).
23. R. C. Morton and G. E. Gerber. J. Biol. Chem. **263**, 7989 (1988).

Can. J. Chem. Downloaded from www.nrcresearchpress.com by 61.7.252.67 on 09/07/12
For personal use only.

Effect of solvent structure on electron reactivity: 2-propanol/water mixtures

YADOLLAH MAHAM AND GORDON R. FREEMAN
Chemistry Department, University of Alberta, Edmonton, Alta., Canada T6G 2G2

Received February 2, 1988

YADOLLAH MAHAM and GORDON R. FREEMAN. Can. J. Chem. **66**, 1706 (1988).

The reactivity of solvated electrons (e_s^-) with efficient (nitrobenzene, acetone) and inefficient (phenol, toluene) scavengers is affected greatly by the solvent composition in 2-propanol/water mixed solvents. 2-Propanol is the only secondary alcohol that is completely miscible with water. The variation of the nitrobenzene rate constant k_2 with solvent composition displays four viscosity zones, as in primary and tertiary alcohol/water mixtures. In zone (*c*), where the Stokes–Smoluchowski equation applies, the nitrobenzene k_2 values in the secondary alcohol/water mixtures are situated between those in the primary and tertiary alcohols, due to the relative values of the dielectric permittivity ϵ. The charge–dipole attraction energy varies as ϵ^{-1}.

The two water-rich zones (*c*) and (*d*) are characterized by a large change of viscosity η and a small change in e_s^- solvation energy (trap depth) E_r; here k_2 for all the scavengers correlates with the inverse of the viscosity. In the two alcohol-rich zones (*a*) and (*b*) the change of η is small but that of E_r is large; here k_2 of inefficient scavengers correlates with the inverse of E_r, due to the difficulty of electron transfer out of deeper traps. Activation energies E_2 and entropies $\Delta S_2^{\ddagger}$ also show composition zone behaviour. The value of $\Delta S_2^{\ddagger}$ is more negative for less efficient scavengers; E_2 varies less and does not correlate with reactivity or E_r. Electron transfer from solvent to inefficient scavenger is driven by solvent rearrangement around the reaction center, reflected in $\Delta S_2^{\ddagger}$.

YADOLLAH MAHAM et GORDON R. FREEMAN. Can. J. Chem. **66**, 1706 (1988).

La réactivité des électrons solvatés (e_s^-) avec des pièges efficaces (nitrobenzène ou acétone) ou inefficaces (phénol ou toluène) est fortement affectée par la composition des solvants mixtes propanol-2/eau. Le propanol-2 est le seul alcool secondaire qui soit complètement miscible avec l'eau. La variation de la constante de vitesse, k_2, du nitrobenzène en fonction de la composition du solvant présente quatre zones de viscosité, comme dans le cas des mélanges eau/alcools primaire ou tertiaire. Dans la zone (*c*), où l'équation de Stokes–Smoluchowski s'applique, les valeurs k_2 du nitrobenzène dans les mélanges alcool secondaire/eau se situent entre celles des alcools primaire et tertiaire; cette situation resulte des valeurs relatives des permitivités diélectriques ϵ. L'énergie d'attraction charge–dipôle varie en fonction de ϵ^{-1}.

Les zones (*c*) et (*d*), qui sont riches en eau, sont caractérisées par un changement important de la viscosité η et de faibles changements dans l'énergie de solvatation des e_s^- (profondeur de la trappe) E_r; dans ce cas, il existe une corrélation entre la valeur de k_2 pour tous les pièges et l'inverse de la viscosité. Dans les zones (*a*) et (*b*) riches en alcools, le changement dans la valeur de η est faible alors que celui de E_r est grand; dans ce cas, il existe une corrélation entre la valeur de k_2 pour les pièges inefficaces et l'inverse de E_r; cette corrélation est dûe à la difficulté d'effectuer une transfert d'électrons pour sortir des trappes plus profondes. Il existe aussi une corrélation entre les énergies (E_2) et les entropie $\Delta S_2^{\ddagger}$ d'activation et le comportement de la zone de composition. La valeur de $\Delta S_2^{\ddagger}$ est plus négative pour les pièges les moins efficaces; les valeurs de E_2 varient moins et elles ne présentent pas de corrélation avec la réactivité ou E_r. Le transfert d'électron du solvant vers un piège inefficace est facilité par une transposition du solvant autour du centre réactionnel et celui-ci se réflète dans la valeur du $\Delta S_2^{\ddagger}$.

[Traduit par la revue]

Can. J. Chem. Downloaded from www.nrcresearchpress.com by 112.217.228.212 on 09/07/12
For personal use only.

Introduction

The reactivities of solvated electrons with neutral solutes in primary (1, 2) and tertiary (3) alcohol/water mixed solvents are strongly dependent on solvent composition. Aqueous mixtures of the secondary alcohol 2-butanol have also been studied (4), but the alcohol is not completely miscible with water. A preliminary study with the completely miscible secondary alcohol, 2-propanol/water mixtures (5), had displayed complex behavior, but subsequent studies with other alcohols (1–4) indicated that a further study of 2-propanol/water was needed.

The static dielectric permittivity of the solvent has been shown to affect the rate of a nearly diffusion-controlled reaction of solvated electrons with a neutral, polar solute (4, 6). The same effect has now been observed in 2-propanol/water mixed solvents.

Experimental

Materials

2-Propanol (2-PrOH) was obtained from Aldrich Chemical Co. (99+%, spectroscopic grade, Gold Label). Nitrobenzene (99+%) and phenol (99+%) were from Aldrich. Acetone (99.9%) and toluene (99.8+%) were from Burdick and Jackson Labs.

Purification of 2-PrOH was as described in ref. 5. The water content was 0.2 mol% (Karl Fischer titration). The half-life of e_s^- after a 100-ns pulse of 1.9 MeV electrons ($\sim 2 \times 10^{16}$ eV/g) at 298 K was 15–17 μs.

The water was passed through a Nanopure II Barnstead ion exchanger. The half-life of e_s^- after a 100-ns pulse at 298 K was ~25 μs. In the mixed pure solvents the half-lives were as follows (mole fraction H_2O, μs): 0.10, 18 ± 3; 0.50, 30 ± 6; 0.74, 30 ± 5; 0.90, 37 ± 3; 0.97, 27 ± 3. The half-lives depend on solvent structure in a manner not yet determined.

Techniques

The methods of sample preparation (1) and irradiation (7, 8) were essentially the same as in the indicated references.

Results and discussion

Four solutes, with e_s^- rate constants in the range 10^7–10^4 m^3/mol s, were studied as a function of temperature. First-order decay constants k_1 were measured at four or five different scavenger concentrations in a given solvent. Second-order rate constants k_2 were obtained from the slopes of plots of k_1 against concentration (1). Arrhenius plots of k_2 for nitrobenzene, acetone, phenol, and toluene are given in Figs. 1–4, respectively.

The Arrhenius parameters A_2 (m^3/mol s) and E_2 (kJ/mol) are listed in Table 1, along with the entropy of activation $\Delta S_2^{\ddagger}$ (J/mol K).

[1] $k_2 = A_2 \exp(-E_2/RT)$

[2] $\Delta S_2^{\ddagger} = 19(\log A_2 - 9.8)$ at 298 K

The four solutes are discussed in two categories.

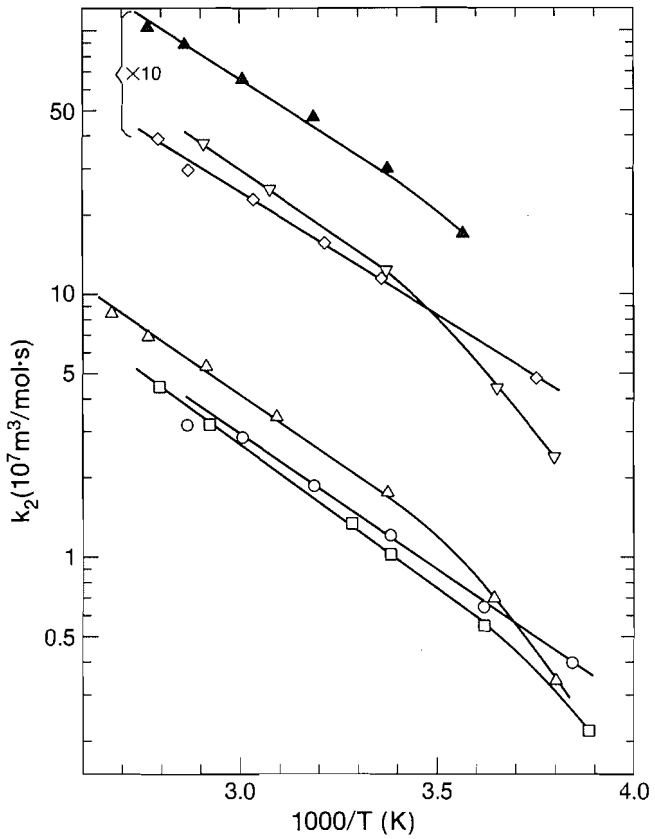

FIG. 1. Arrhenius plots of k_2(nitrobenzene) in 2-PrOH/water mixed solvents. x_{H_2O}: ○, 0; ◇, 10; □, 50; ▽, 74; △, 90; and ▲, 97.

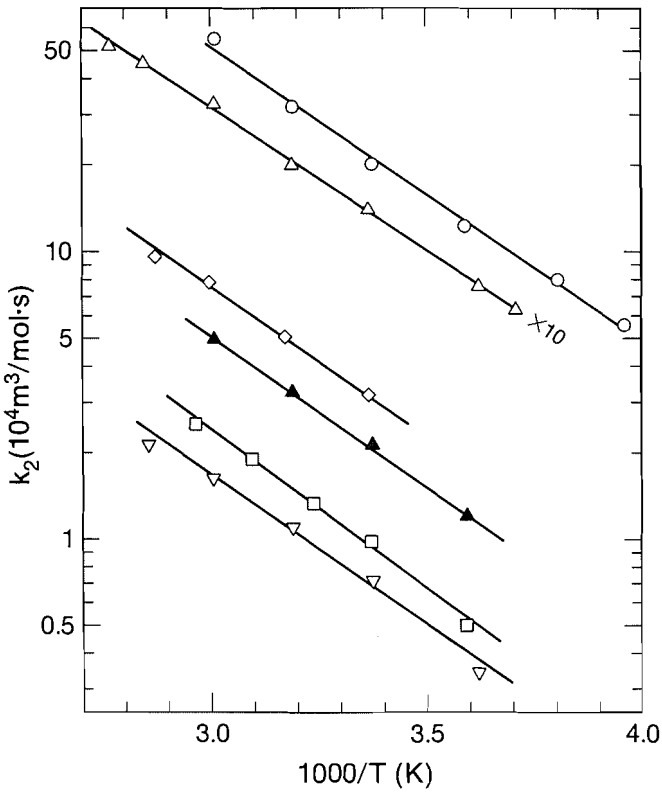

FIG. 3. Arrhenius plots of k_2(phenol) in 2-PrOH/water mixed solvents. x_{H_2O}: ○, 0; ◇, 10; □, 50; ▽, 74; △, 90; and ▲, 97.

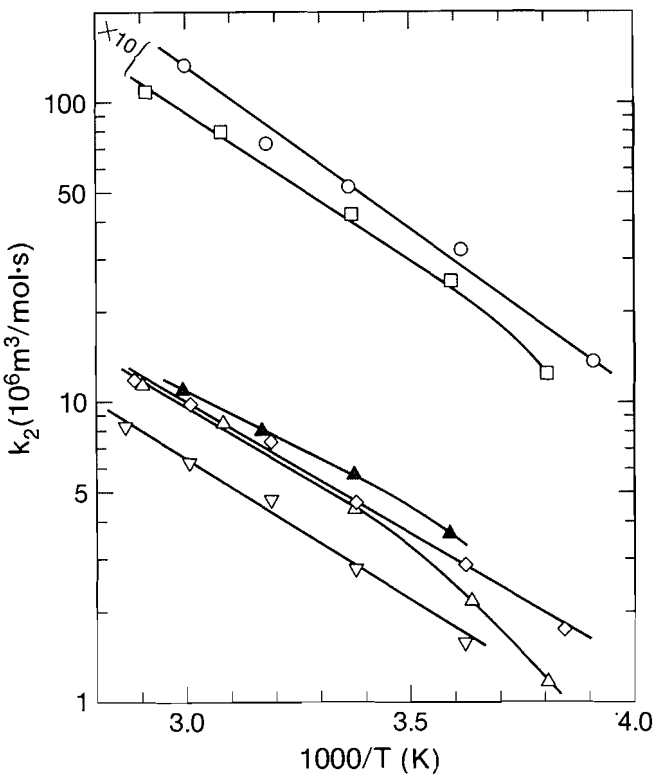

FIG. 2. Arrhenius plots of k_2(acetone) in 2-PrOH/water mixed solvents. x_{H_2O}: ○, 0; ◇, 10; □, 50; ▽, 74; △, 90; and ▲, 98.

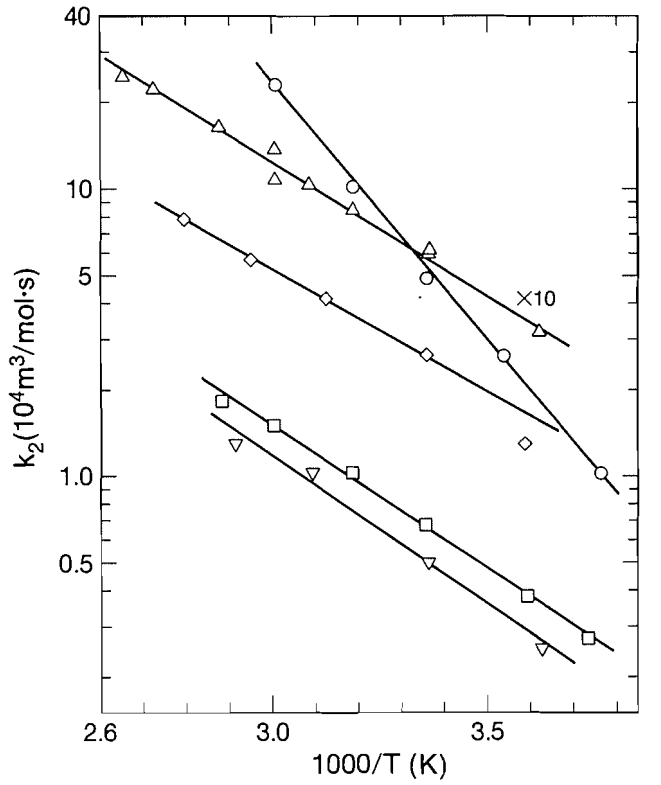

FIG. 4. Arrhenius plots of k_2(toluene) in 2-PrOH/water mixed solvents. x_{H_2O}: ○, 0; ◇, 10; □, 50; ▽, 74; △, 90; and ▲, 97.

Can. J. Chem. Downloaded from www.nrcresearchpress.com by 112.217.228.212 on 09/07/12
For personal use only.

TABLE 1. e_s^- reaction rate parameters in 2-PrOH/water at 298 K

				Nitrobenzene[h]					Acetone[i]			
x_{H_2O}	ϵ[a]	η[b]	E_r[c]	f[d]	k_2[d]	E_2[e]	log A_2[f]	$\Delta S_2^{\ddagger}$	k_2[d]	E_2[e]	log A_2[f]	$\Delta S_2^{\ddagger}$
0	18.0	2.08	1.08	1.64	127	20	10.6	14	54	21	10.4	+11
10	18.6	2.13	1.18	1.62	114	18	10.2	7	49	17	9.6	−3
50	22.2	2.68	1.36	1.51	110	21	10.7	17	41	19	10.0	+3
74	45.3	3.10	1.40	1.23	110	20	10.6	15	30	18	9.7	−3
80	55.7	3.03	1.40	1.19	135	20	10.7	17	—	—	—	—
90	59.0	2.42	1.40	1.18	180	20	10.7	18	43	17	9.6	−3
96	69.6	1.56	1.40	1.15	270	20	10.9	20	—	—	—	—
97	71.7	1.38	1.40	1.14	290	18	10.7	17	—	—	—	—
98	73.9	1.22	1.39	1.14	290	19	10.7	19	58	14	9.3	−10
99	76.2	1.02	1.38	1.13	360	18	10.7	16	—	—	—	—
100	78.5	0.89	1.37	1.13	380	17	10.6	16	77	13	9.1	−14

	Phenol[j]				Toluene[k]			
x_{H_2O}	k_2[d]	E_2[e]	log A_2[f]	$\Delta S_2^{\ddagger}$	k_2[d]	E_2[e]	log A_2[f]	$\Delta S_2^{\ddagger}$
0	2.2	20	8.8	−19	0.54	34	10.7	+18
10	0.32	20	8.0	−34	0.26	16	7.3	−48
50	0.098	21	7.7	−40	0.068	19	7.2	−50
74	0.072	20	7.4	−47	0.051	20	7.2	−50
90	0.14	19	7.5	−44	0.059	18	6.9	−56
97	0.215	20	7.8	−37	—	—	—	—
99	0.25	19	7.7	−40	—	—	—	—
100	0.27	19	7.8	−37	0.13	19	7.4	−45

[a]Static dielectric permittivity.
[b]Viscosity, mPa s.
[c]e_s^- trap depth, eV.
[d]10^5 m^3/mol s.
[e]kJ/mol.
[f]A_2 units m^3/mol s.
[g]J/mol K.
[h]Concentrations 0.007–0.09 mol/m^3.
[i]0.02–0.4 mol/m^3.
[j]0.3–18 mol/m^3.
[k]0.1–14 mol/m^3.
[l]Equation [4].

1. Efficient scavengers

The reaction of solvated electrons with nitrobenzene is nearly diffusion-controlled (4, 9). However, a plot of k_2(nitrobenzene) against solvent viscosity (10) at 298 K displays four zones of behaviour (Fig. 5), as did similar plots in other alcohol/water mixed solvents (3). The values from 1-PrOH/water (1) and *t*-BuOH/water (3) are included in Fig. 5 for comparison.

In the 2-PrOH/water mixtures the mole fractions of water in the four zones are (*a*) $0 \leq x_{H_2O} \leq 0.10$; (*b*) $0.10 \leq x_{H_2O} \leq 0.74$ (mixture with maximum viscosity η_{max}); (*c*) $0.74 \leq x_{H_2O} \leq 0.97$; (*d*) $0.97 \leq x_{H_2O} \leq 1.00$.

If the effective radii of e_s^- and nitrobenzene for diffusion (r_e and r_S, respectively) and for reaction (R_e and R_S) were constant in a given zone, one would expect to find $k_2 \propto \eta^{-1.0}$. This only occurs in zone (*c*). In the mixtures of each of the different alcohols with water, zone (*c*) extends from the mole fraction of maximum viscosity $x_{\eta_{max}}$ to $x_{H_2O} \approx 0.97$. The structure of the solvent about the reactants therefore remains relatively constant in zone (*c*). The values of k_2 in the secondary alcohol mixtures lie between those for the primary and tertiary alcohol/water mixtures. The values of ηk_2(nitrobenzene) in zone (*c*) at 298 K are 4.0, 4.2, and 4.7 (10^4 m^3 Pa/mol) for primary, secondary, and tertiary alcohol/water mixed solvents, respectively. This means that the Stokes–Smoluchowski term $(1/r_e + 1/r_s)(R_e +$

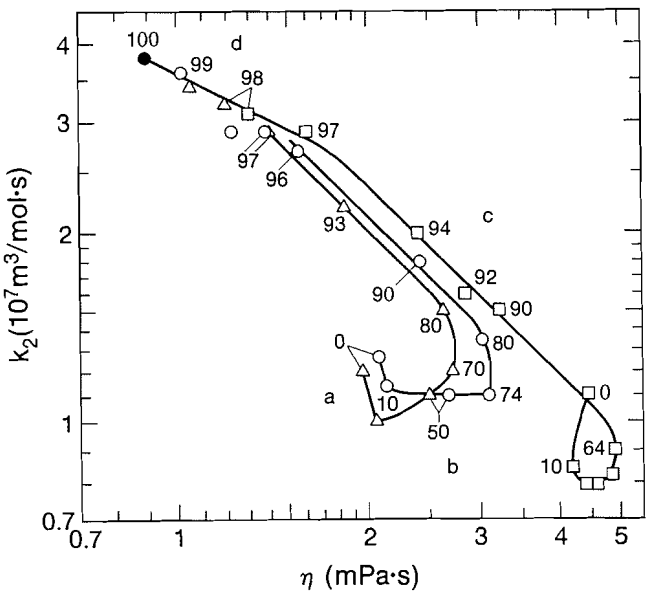

FIG. 5. k_2(nitrobenzene) at 298 K against viscosity of alcohol/water mixed solvents. ●, pure water; ○, 2-PrOH/water; △, 1-PrOH/water (1); □, *t*-BuOH/water (4). Numbers beside the points indicate mol% water. Zone (*c*) lines are drawn with slope −1.0.

Can. J. Chem. Downloaded from www.nrcresearchpress.com by 112.217.228.212 on 09/07/12
For personal use only.

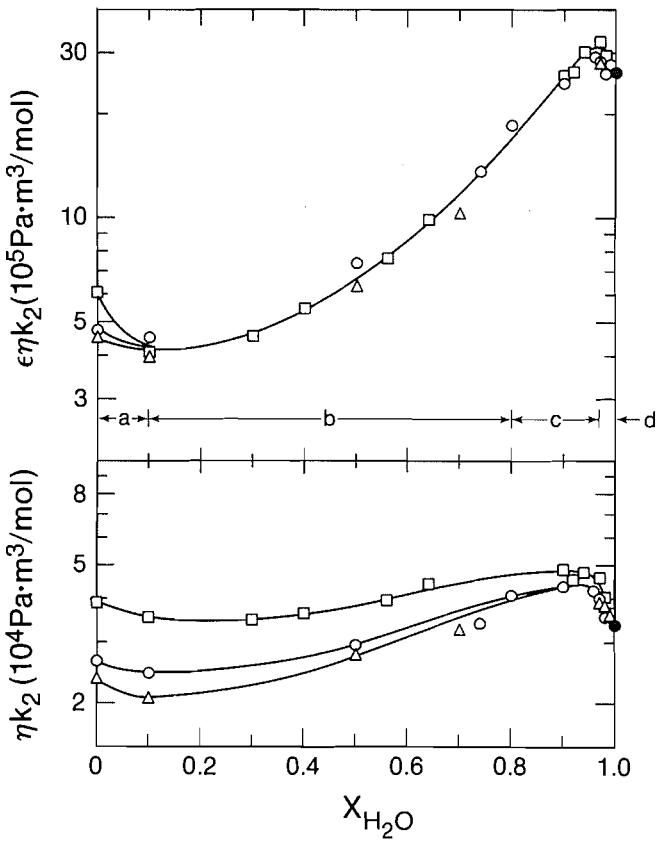

FIG. 6. Nitrobenzene rate constant normalized for viscosity, ηk_2, and for static dielectric permittivity and viscosity, $\epsilon\eta k_2$, at 298 K as a function of solvent composition. ○, 2-PrOH/water; △, 1-PrOH/water (ref. 1); □, *t*-BuOH/water (ref. 4); ●, pure water.

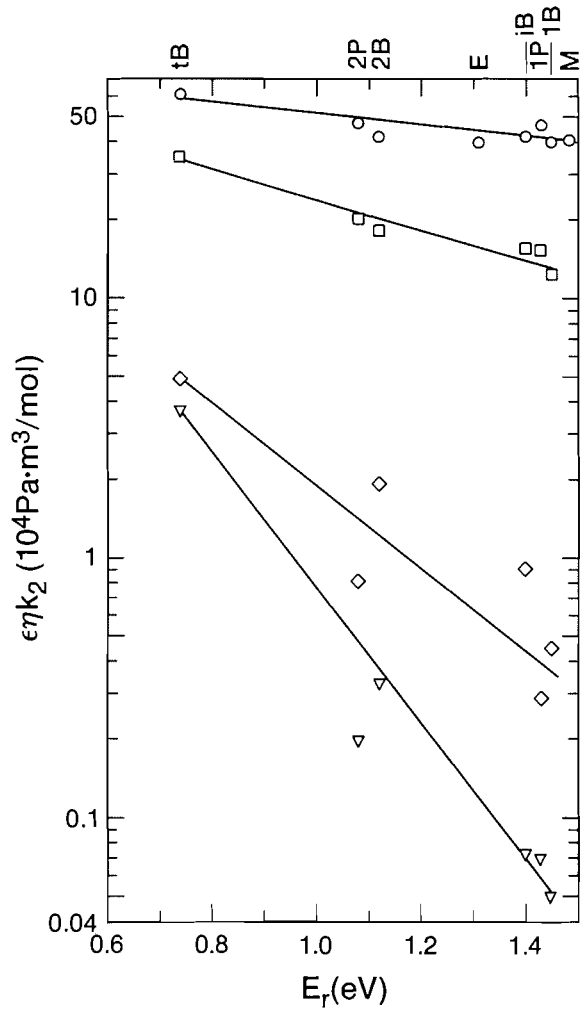

FIG. 7. Rate constant normalized for viscosity and static dielectric permittivity, $\epsilon\eta k_2$, as a function of trap depth E_r of e_s^- in pure alcohols at 298 K. Solutes: ○, nitrobenzene; □, acetone; ◇, phenol; and ▽, toluene. E_r values are from ref. 11; ϵ and η from ref. 10; k_2 in methanol (M) from ref. 12 at 292 K; k_2 in ethanol (E) from ref. 13; k_2 in 1-PrOH from ref. 1; k_2 in 1-BuOH from ref. 2; k_2 in *i*-BuOH and 2-BuOH from ref. 4.

R_s) increases in that order. The increase is partly attributed to an effective increase of $R = (R_e + R_S)$, due to the decreasing static dielectric permittivity ϵ of the solvents (10) and the attendant increase of charge–dipole attraction energy $U(R)$. This introduces a Debye factor f into the equation for a diffusion-controlled reaction (4, 6):

$$[3] \quad k_2 = 4\pi N_A(D_e + D_S)(R_e + R_S)f$$

where

$$[4] \quad f = \frac{U(R)}{k_B T} (\exp [U(R)/k_B T] - 1)^{-1}$$

and

$$[5] \quad U(R) = -M\xi/4\pi\epsilon_0\epsilon R^2$$

were $M = 1.4 \times 10^{-29}$ C m is the dipole amount of nitrobenzene, $\xi = 1.6 \times 10^{-19}$ C is the electron charge, and ϵ_0 is the permittivity of vacuum. The value of f increases with decreasing ϵ (Table 10).

In zone (*d*) k_2 decreases approximately as $\eta^{-0.5}$, so r or R does not remain constant. The behavior is similar for all of the alcohols.

On the lower-water-content side of the viscosity maximum, zones (*a*) and (*b*), there is no simple correlation between k_2 and viscosity (Fig. 5).

The dependence of k_2(nitrobenzene) on the static dielectric permittivity is demonstrated in Fig. 6. When the viscosity normalized ηk_2 is plotted against mole fraction of water in 1-PrOH, 2-PrOH, and *t*-BuOH, a separate curve is obtained for each alcohol. However, when normalized for static dielectric permittivity $\epsilon\eta k_2$, the data for the three alcohols fall on the same curve, except in zone (*a*).

The electron trap depth is for kinetic purposes represented by the optical absorption energy E_r, on the low energy side of the absorption maximum:

$$[6] \quad E_r = E_{Amax} - W_r$$

where E_{Amax} is the energy at maximum absorption and W_r is the width of the low energy side of the band at half height (11).

The electron trap depth changes greatly across zone (*a*), and the $\epsilon\eta k_2$ differences are attributed to that. The values of E_r in pure 1-PrOH, 2-PrOH, and *t*-BuOH are 1.43, 1.08, and 0.82 eV, respectively (11). The slight dependence of k_2 on E_r means that the reaction of e_s^- with nitrobenzene is not quite diffusion-controlled.

The dependence of $\epsilon\eta k_2$ on E_r in pure alcohol solvents (1, 4, 12, 13) is displayed in Fig 7 for solutes of different reactivity

Can. J. Chem. Downloaded from www.nrcresearchpress.com by 112.217.228.212 on 09/07/12
For personal use only.

Can. J. Chem. Downloaded from www.nrcresearchpress.com by 112.217.228.212 on 09/07/12
For personal use only.

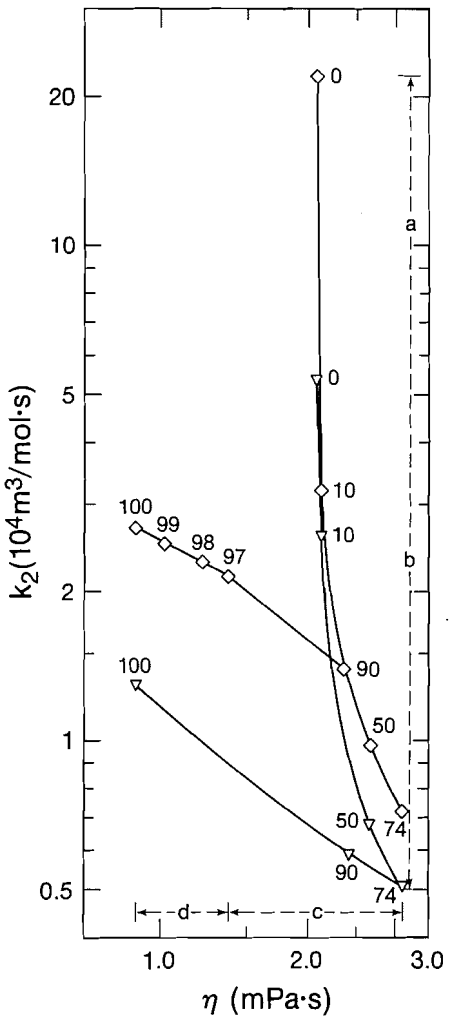

FIG. 8. Plot of k_2 vs. η for inefficient scavengers in 2-PrOH/water mixtures at 298 K. Solute: ◇, phenol; ▽, toluene.

with e_s^-. The slope of the line becomes more negative with decreasing reactivity. The limiting slope for a diffusion controlled reaction is presumed to be zero. Thus the nitrobenzene reaction is not quite diffusion controlled.

2. Inefficient scavengers

In zones (*a*) and (*b*), on the higher alcohol side of the composition of maximum viscosity, the values of k_2 for phenol and toluene decrease with increasing water content and do not correlate with solvent viscosity (Fig. 8). On the higher water side of the viscosity maximum the values of k_2 increase with water content and do correlate with viscosity (Fig. 8).

The decrease of k_2 in zones (*a*) and (*b*) for inefficient scavengers is caused by the increasing trap depth of the electrons, which makes it more difficult for the electron to jump from the solvent trap onto the solute molecule (1, 3, 14).

The encounter efficiency of the reaction is approximated by the ratio of k_2 for the inefficient scavenger to that for nitrobenzene, k_2/k_N. Semilog plots of k_2/k_N against E_r are shown in Fig. 9. The negative slopes reflect the increasing free energy of activation of the electron capture reactions as E_r increases (4).

[7] $e_s^- + S \rightleftharpoons [e_s^-, S]$

[8] $[e_s^-, S] \rightarrow$ *products*

and

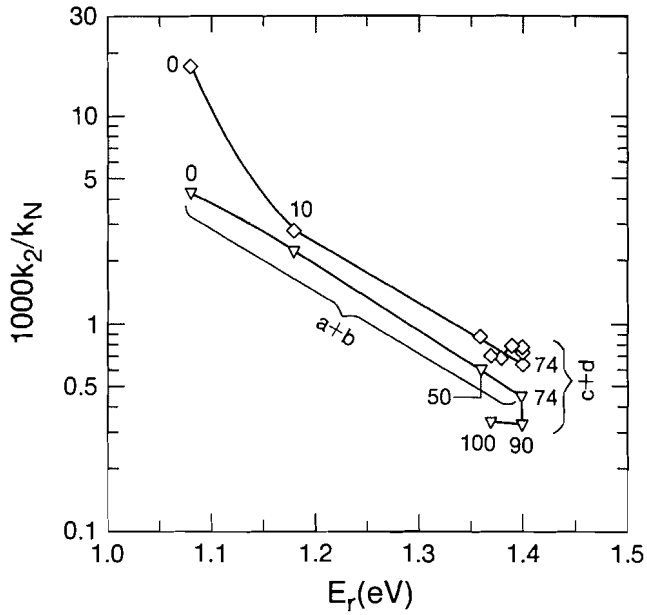

FIG. 9. Effect of optical absorption energy E_r on encounter efficiency k_2/k_N for inefficient scavengers in 2-PrOH/water mixtures. Solute: ◇, phenol; ▽, toluene. The numbers beside the points indicate mol% water.

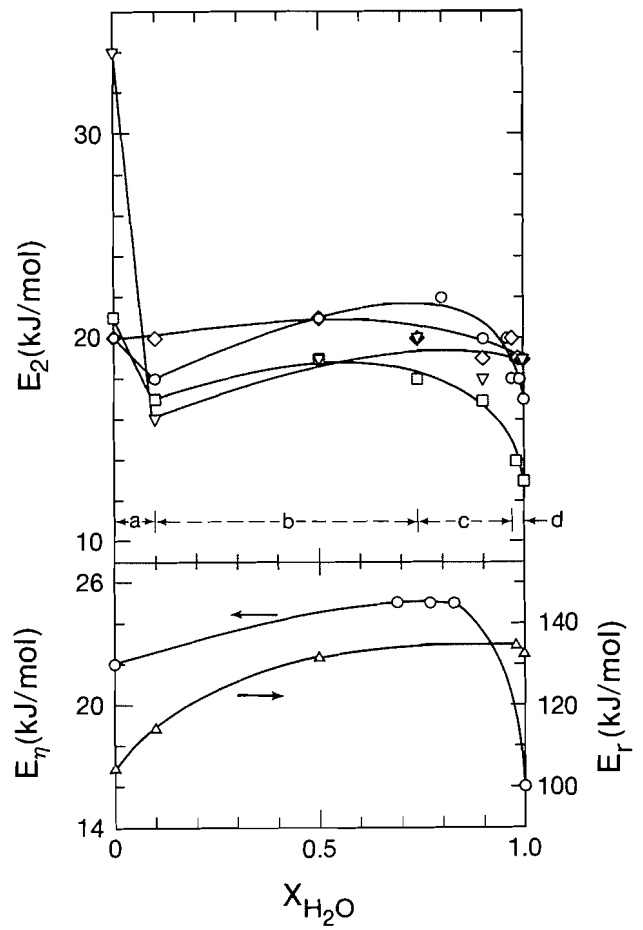

FIG. 10. Activation energy E_2 for (e_s^- + S) between T = 295 and 360 K in 2-PrOH/water mixtures against mole fraction water. Solute: ○, nitrobenzene; □, acetone; ◇, phenol; ▽, toluene. E_η (○) is the Arrhenius temperature coefficient for shear viscosity, calculated from data in ref. 15. E_r (△), ref. 11.

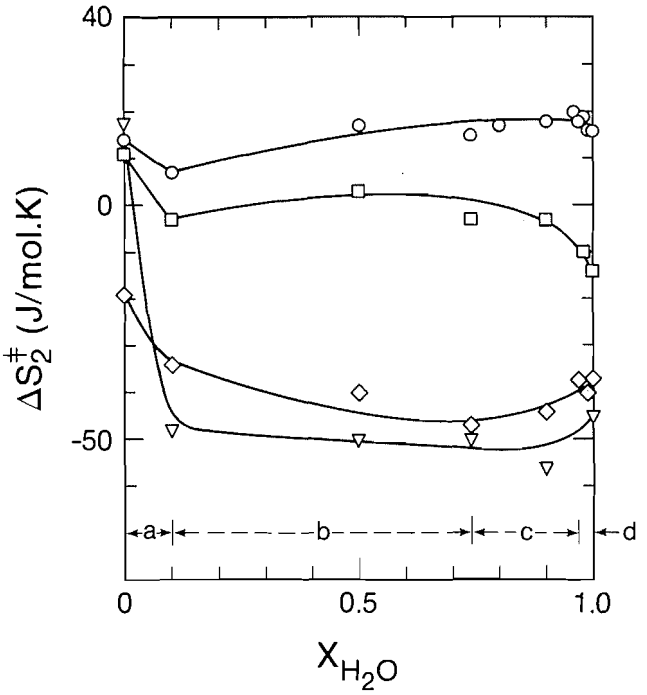

FIG. 11. Entroy of activation $\Delta S_2^{\ddagger}$ at 298 K for (e_s^- + S) against mol fraction water in 2-PrOH/water mixtures. Solute: ○, nitrobenzene; □, acetone; ◇, phenol; ▽, toluene.

[9] $$\ln (k_2/k_N) \approx -\Delta G_5^{\ddagger} 4 /RT$$

for inefficient scavengers.

3. Energies and entropies of activation

The activation energies E_2 of the e_s^- reactions in zones (*b*) – (*d*) follow trends similar to that of viscous flow E_η (15) (Fig. 10). In zone (*a*) the behavior of E_2 is different, as was that of $\epsilon\eta k_2$ (Fig. 6). The entropies of activation $\Delta S_2^{\ddagger}$ also indicate special behavior in zone (*a*) (Fig. 11).

Although there are not many points on the E_η curve in Fig. 10, the behavior is similar to that for 1-PrOH/water mixtures (10, 16). There is no special behavior of E_η in zone (*a*). The rapid decreases of E_2 and $\Delta S_2^{\ddagger}$ in zone (*a*) must be due to the changing solvation of the reactant pair.

The decrease of reactivity in the series nitrobenzene, acetone, phenol, toluene is associated mainly with a decrease in $\Delta S_2^{\ddagger}$ (Fig. 11). It does not correlate with E_2 (Fig. 10). Nor does E_2 correlate with E_r (Fig. 10). The entropy of activation is associated with rearrangement of solvent molecules around the reactant pair.

Acknowledgements

We thank the Natural Sciences and Engineering Research Council of Canada for financial assistance and the staff of the Radiation Research Center for technical assistance.

1. Y. MAHAM and G. R. FREEMAN. J. Phys. Chem. **89**, 4347 (1985).
2. Y. MAHAM and G. R. FREEMAN. J. Phys. Chem. **91**, 1561 (1987).
3. P. C. SENANAYAKE and G. R. FREEMAN. J. Phys. Chem. **91**, 2123 (1987).
4. P. C. SENANAYAKE and G. R. FREEMAN. J. Chem. Phys. **87**, 7007 (1987).
5. J. CYGLER and G. R. FREEMAN. Can. J. Chem. **62**, 1265 (1984).
6. Y. MAHAM and G. R. FREEMAN. J. Phys. Chem. **92**, 1506, (1988).
7. K. OKAZAKI and G. R. FREEMAN. Can. J. Chem. **56**, 2313 (1978).
8. F.-Y. JOU and G. R. FREEMAN. (*a*) Can. J. Chem. **54**, 693 (1976); (*b*) J. Phys. Chem. **81**, 909 (1977); (*c*) J. Phys. Chem. **83**, 1979 (1979).
9. G. L. BOLTON and G. R. FREEMAN. J. Am. Chem. Soc. **98**, 6825 (1976).
10. (*a*) J. TIMMERMANS. Physico-chemical constants of binary mixtures. Vol. 4. Wiley-Interscience, New York, 1960; (*b*) R. W. GALLANT. Physical properties of hydrocarbons. Vol. 1. Gulf Publishing, Houston, TX. 1968.
11. A. D. LEU, K. N. JHA, and G. R. FREEMAN. Can. J. Chem. **60**, 2342 (1982).
12. B. H. MILOSAVLJEVIC and O. I. MICIC. J. Phys. Chem. **82**, 1359 (1978).
13. F. BARAT, L. GILLES, B. HICKEL, and B. LESIGNE. J. Phys. Chem. **77**, 1711 (1973).
14. A. M. AFFANASIEV, K. OKAZAKI, and G. R. FREEMAN. J. Phys. Chem. **83**, 1244 (1979).
15. W. WEBER. Rheol. Acta, **14**, 1012 (1975).
16. T. ERDEY-GRÉUZ, E. KUGLER, and L. MAJTHENYI. Electrochim. Acta, **13**, 947 (1968).

Can. J. Chem. Downloaded from www.nrcresearchpress.com by 112.217.228.212 on 09/07/12
For personal use only.

Ambident reactivity in the reaction of phenoxide ion with 2-*N*-(2′,4′-dinitrophenyl)- and 2-*N*-(4′-nitrophenyl)-4,6-dinitrobenzotriazole 1-oxides, new superelectrophiles[1]

ERWIN BUNCEL[2] AND JULIAN M. DUST[3]

Department of Chemistry, Queen's University, Kingston, Ont., Canada K7L 3N6

Received October 20, 1987

ERWIN BUNCEL and JULIAN M. DUST. Can. J. Chem. **66**, 1712 (1988).

Reaction of the novel superelectrophiles 2-*N*-(2′,4′-dinitrophenyl)- and 2-*N*-(4′-nitrophenyl)-4,6-dinitrobenzotriazole 1-oxides, **3**, and **4**, possessing two electrophilic centres, with the ambident nucleophile potassium phenoxide in $(CD_3)_2SO$ was followed by 400 MHz ^1H nuclear magnetic resonance spectroscopy. A dichotomy in the reaction pathways has been observed. With MeO^-, attack at C-7 leads to reversible adduct formation, while attack at C-1′ results in irreversible N-2:C-1′ bond scission via the metastable C-1′ adduct. In contrast, the reaction of **3** and **4** with PhO^- proceeds by a two-pronged attack: formation of C-7 carbon-bonded phenoxide adducts via the *ortho* and *para* carbon sites, and oxygen-based cleavage products by attack at the C-1′ position, accompanied by N-2:C-1′ bond scission, in accord with the ambident reactivity of PhO^-. Significantly, in this case reaction of both C-7 and C-1′ is effectively irreversible. Moreover, the reaction of phenoxide with either **3** or **4** shows striking differences compared to the reaction of PhO^- with 2-*N*-(picryl)-4,6-dinitrobenzotriazole 1-oxide, **1**. Reaction of PhO^- with **1** resulted only in O-attack at C-1′ and N-2:C-1′ bond scission; there was no evidence for C-7 adduct formation via O- or C-attack. This marked difference in behaviour can be attributed to the decreased susceptibility to C-1′ attack exhibited by **3** and **4** as compared to **1** and arises from the successive removal of electron-withdrawing nitro groups from the 2-*N*-nitroaryl moiety in the series **1** → **3** → **4**. The reactions are discussed on the basis of selectivity considerations and an activation energy/reaction coordinate profile comparing the pathways for both C-attack at C-7 and O-attack at C-1′ as electrophilicity (delocalizability) is progressively modulated in the reaction series.

ERWIN BUNCEL et JULIAN M. DUST. Can. J. Chem. **66**, 1712 (1988).

Opérant dans le $(CD_3)_2SO$ et faisant appel à la résonance magnétique nucléaire du ^1H à 400 MHz, on a suivi l'évolution de la réaction des nouveaux super-électrophiles possédant deux sites de réaction, les oxydes-1 des *N*-2-(dinitro-2′,4′ phényl) et N-2-(nitro-4′ phényl) dinitro-4,6 benzotriazoles (**3** et **4**), avec le phénolate de potassium, un nucléophile possédant deux sites de réaction. On a observé une dichotomie dans les voies réactionnelles. Avec le MeO^-, l'attaque en C-7 conduit à la formation réversible d'un adduit alors que l'attaque en C-1′ conduit à une scission irréversible de la liaison N-2:C-1′ par le biais de l'adduit métastable C-1′. Par ailleurs, la réaction des composés **3** et **4** avec le PhO^- procède par une attaque sur deux fronts : la formation d'adduits phénolates liés en C-7 par le biais des sites carbonés en *ortho* et en *para* ainsi que la formation de produits de clivage contenant de l'oxygène, qui proviennent d'une attaque en position C-1′ accompagnée d'une scission de la liaison N-2:C-1′; ces résultats sont en accord avec la réactivité ambivalente du PhO^-. Il est important de noter que, dans ce cas, les réactions tant en C-7 qu'en C-1′ sont de fait irréversibles. De plus, la réaction du phénolate avec les composés soit **3** ou **4** présente des différences marquées par rapport à ce qui est observé lors de la réaction du PhO^- avec l'oxyde-1 du *N*-2-(picryl) dinitro-4,6 benzotriazole, **1**. La réaction du PhO^- avec le composé **1** ne conduit qu'à une attaque sur l'oxygène en C-1′ et à une scission de la liaison N-2:C-1′; on n'a pas obtenu de résultats suggérant qu'il y a formation d'un adduit en C-7 par le biais d'une attaque du O ou du C. Cette différence marquée de comportement peut être attribuée à une diminution de la susceptibilité à l'attaque en C-1′ qui est observée avec les composés **3** et **4**, par rapport au composé **1**, et qui provient de l'élimination successive (dans la portion *N*-2 nitroaryl de la série **1** → **3** → **4**) des groupements nitro qui possèdent un effet électro-attracteur. On discute des réactions en fonction de considérations de sélectivité et d'un profil d'énergie d'activation vs. les coordonnées de la réaction comparant les voies réactionnelles tant de l'attaque du C en C-7 que de l'attaque du O en C-1′ lorsque le caractère électrophile (possibilité de délocalisation) est progressivement modulé dans les séries de réactions.

[Traduit par la revue]

As part of our ongoing program of study concerning the interactions of normal and ambident nucleophiles with electron-deficient aromatic and heteroaromatic series (1–5), we have previously investigated the reactions of a wide variety of nucleophiles with 2-*N*-(picryl)-4,6-dinitrobenzotriazole 1-oxide (Pi-DNBT, **1**). Pi-DNBT was found to be a superelectrophile; on the basis of its reactivity with ethanethiol, **1** has been ranked between the conventional electrophile, 1,3,5-trinitrobenzene (TNB), and the superelectrophile, 4,6-dinitrobenzofuroxan (DNBF) (6), on a scale of increasing electrophilicity in Meisenheimer complex (anionic σ-adduct) formation (3).

Reaction of **1** with a wide range of nucleophiles results in

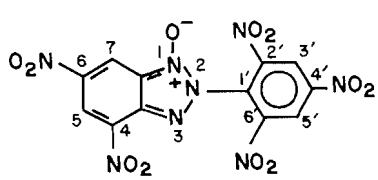

1

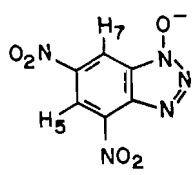

2

partition of the attack (Scheme 1): at C-7 (Path a) reaction generally yields an observable Meisenheimer adduct, or at C-1′ (Path b) forms a metastable adduct that rapidly decomposes to give displacement products (3–5).

Interestingly, while reaction of **1** with methoxide, for example, follows the two-pronged attack outlined in Scheme 1, the reaction with phenoxide is observed to occur solely at C-1′ to give rise to picryl phenyl ether (TNP) and the 4,6-dinitrobenzotriazole 1-oxyanion ($DNBT^-$, **2**) (3–5). This is

[1]Ambident nucleophilic reactivity in σ-complex formation, Part 8. For Part 7, see ref. 8.

[2]Author to whom correspondence may be addressed.

[3]Current address: Department of Chemistry, University of Alabama in Huntsville, Huntsville, AL 35899, U.S.A.

Can. J. Chem. Downloaded from www.nrcresearchpress.com by 61.7.252.67 on 09/07/12
For personal use only.

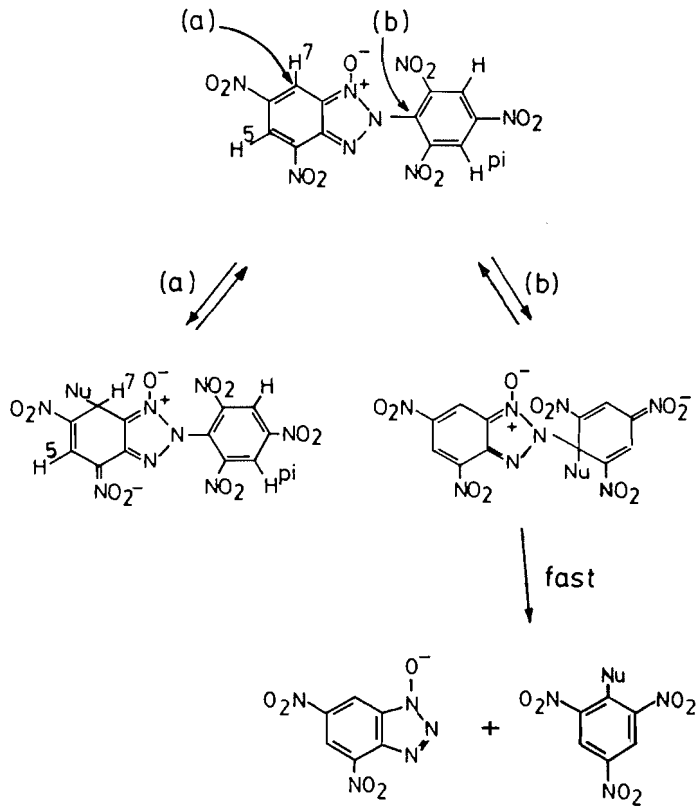

SCHEME 1

presumably the result of both facile formation of the metastable C-1′ oxygen-centered adduct and its rapid irreversible decomposition. The relative importance of these two factors depends upon the comparison made, i.e., O- versus C-attack, and C-7 versus C-1′ attack.

It is pertinent to the study that reaction of phenoxide with TNB (1, 2) or with DNBF (4) yields carbon-centered Meisenheimer adducts as the only spectrally observable species in these systems. In contrast, reaction of the sterically hindered 2,4,6-trimethylphenoxide with TNB leads to formation of a spectrally observable oxygen-centered Meisenheimer complex that eventually decomposes in favour of formation of 2,4,6-trimethylphenyl 3′,5′-dinitrophenyl ether, through loss of nitrite ion in a displacement (S_NAr) process involving free TNB present in the system at equilibrium (7).

Most recently we have examined the reaction of dopamine (3,4-dihydroxyphenylethylamine) with TNB (8). Dopamine is an interesting ambident nucleophile that may react via oxygen, carbon, or nitrogen centres, depending, at least partially, on the degree of ionization of the nucleophile. We have found, however, that reaction occurs to form initially a kinetically preferred nitrogen adduct, followed by formation of a thermodynamically more stable carbon-centered complex. No oxygen-centered complex was noted. Clearly, there is an order of thermodynamic stability of these complexes; carbon adducts are generally the most stable, oxygen adducts the least stable, and nitrogen-based complexes are of intermediate stability. Recent work by Terrier and co-workers (9), concerning the reactions of imidazolide and pyrrolide anions with TNB, confirms the relative order of stability of N- and C-bonded Meisenheimer complexes.

As part of our studies to delineate the stabilities of oxygen-centered Meisenheimer complexes formed by phenoxide ions relative to carbon-bonded adducts (1, 7, 8, 10), we have extended the study to the reactions of PhO^- with the newly prepared members of the 2-*N*-(nitroaryl)-4,6-dinitrobenzotriazole 1-oxide series of compounds: 2-*N*-(2′,4′-dinitrophenyl)-4,6-dinitrobenzotriazole 1-oxide and 2-*N*-(4′-nitrophenyl)-4,6-dinitrobenzotriazole 1-oxide (DNP-DNBT and NP-DNBT, **3** and **4**, respectively). Compounds **1**, **3**, and **4** represent a decreasing order of electron deficiency in the 2-*N*-nitroaryl ring, and consequently we expected that C-1′ attack (Scheme 1) would become increasingly disfavoured and, as a result, C-7 attack increasingly favoured in going from **1** → **3** → **4**. In turn, this would provide the opportunity for PhO^- to react at the anticipated superelectrophilic centre, C-7, via O- or C-attack, contrasting with the situation as regards **1**, where PhO^- reacts only at C-1′ as an O-nucleophile.

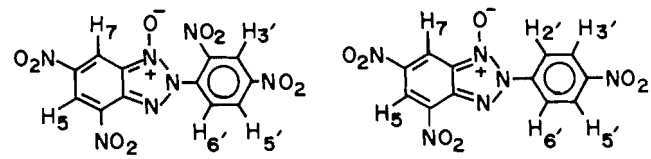

3 **4**

Results

The salient features of the reaction of potassium phenoxide with **3** and **4** in $(CD_3)_2SO$ solution are (*a*) formation of C-7 carbon-centered complexes, i.e., the C-7 *ortho* and *para* complexes, **5** and **6**, and (*b*) simultaneous formation of **2** and the respective nitroaryl phenyl ether. Moreover, there is evidence for the formation of a C-7 hydroxide adduct in the reaction with **3**.

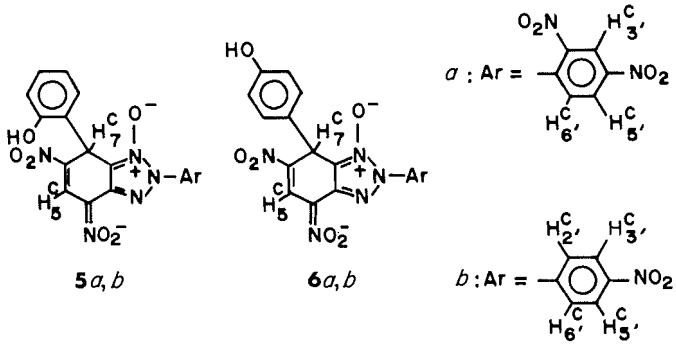

5*a*,*b* **6***a*,*b*

Thus, the reaction pathways comprise both O- and C-attack. O-attack is restricted to the C-1′ position and C-attack is restricted to the C-7 position; both are effectively irreversible processes.

The reactions were followed by 400 MHz ^1H nmr spectroscopy. All chemical shifts are listed in parts per million (ppm) and all coupling constants are given in units of hertz (Hz). $(CD_3)_2SO$ served as the solvent. To obtain quantitative information, a known amount of 1,4-dibromobenzene was added to each sample; integration of the dibromobenzene singlet and the peaks of the complexes permitted estimation of the concentrations of all identifiable species.

Reactions were undertaken with equimolar or excess (3 equiv.) KOPh. The potassium phenoxide was prepared separately and dissolved in $(CD)_3)_2SO$; the relevant quantity could be readily injected into the nmr tube to initiate the reaction.

Reaction of DNP-DNBT (3) with KOPh

The initial spectrum in the reaction of 1 equivalent of PhO^-

Can. J. Chem. Downloaded from www.nrcresearchpress.com by 61.7.252.67 on 09/07/12
For personal use only.

TABLE 1. The ^{1}H nmr spectral characteristics of the σ adducts (δ ppm, J in Hz in parentheses)

Substrate	Adduct	$H_7^{c,c}$	H_5^c	$H_{2'}^c$	$H_{3'}^c$	$H_{5'}^c$	$H_{6'}^c$	Ar*OH*[a]
3	**5***a*	5.575 (s)	8.723 (s)	—	8.793 (d, 2.28)	8.665[b] (d,d 2.28, 8.91)	8.033 (d, 8.91)	9.419 (s, OH)
3	**6***a*	5.294 (s)	8.748 (s)	—	8.808 (d, 2.25)	[d]	8.066 (d, 9.04)	9.311 (s, OH)
4	**5***b*	5.603 (s)	8.716 (s)	8.253	8.453	8.453 (A_2X_2 d,d, 8.98)	8.253	9.377 (s, OH)
4	**6***b*	5.330 (s)	8.748 (s)	[d]	[d]	[d]	[d]	9.321 (s, OH)

[a]The phenyl ring is not observed for any of the adducts.
[b]Partly obscured by peaks due to **2**.
[c]Superscript "c" refers to σ complex.
[d]Not observed, obscured by peaks due to phenoxide, **2**, and other species.

with **3** (initial concentration: ca. 0.020 M) contains broad signals for **3** with somewhat sharper resonances for the various reaction products. Even from this first spectrum (acquired within 3 min) peaks can be noted that are attributable to **2** and, by comparison with the authentic ether, to the 2,4-dinitrophenyl phenyl ether (DNP). The DNP peaks occur at 7.542 (2H, t, *meta*), 7.368 (1H, t, *para*), and 7.269 (2H, d, *ortho*) for the phenyl moiety of the ether, and at 7.146 (1H, d, J = 9.31, H_6), 8.463, 8.438 (1H, d,d, J = 9.31, 2.75, H_5), and 8.892 (1H, d, J = 2.75, H_3) for the 2,4-dinitrophenyl portion of the ether. Examination of the phenolic region also reveals resonances due to phenol at 7.149 (1H, t, *para*) and 6.740 (4H, m, *meta* and *ortho*), while a singlet at 9.335 ppm is ascribed to the phenolic hydroxyl.

With time the spectrum resolved further to reveal signals assignable to two separate carbon-centered phenoxide adducts of **3**. The larger set of signals appears at 5.575 (s), 8.723 (s), and 8.793 (d, J = 2.28), with an apparent doublet of doublets centered at 8.665 (d,d, J = 8.91, 2.28), as well as a doublet at 8.033 (J = 8.91). These resonances are ascribed to H_7^c, H_5^c, $H_{3'}^c$, $H_{5'}^c$, and $H_{6'}^c$, of a C-7 (*ortho*) DNP-DNBT·PhOH$^-$ adduct, formulated as **5***a*. The smaller set of signals is found at 5.294 (s), 8.748 (s), 8.808 (d, J = 2.25), and 8.066 (d, J = 9.04), and ascribed to H_7^c, H_5^c, $H_{3'}^c$, and $H_{6'}^c$, of another C-7 C-centered (*para*) DNP-DNBT·PhOH$^-$ adduct, **6***a*. (Superscript "c" indicates "complex".)

Several pertinent comments must be made concerning the assignment of the nmr spectra. First, in no spectrum could protons of the various phenyl moieties of the carbon adducts **5***a* and **6***a* be discerned, as a result of overlap of the signals with those due to phenol/phenoxide, **2**, etc. In fact, the spectrum is complex and, consequently, in the case of **5***a*, the doublet of doublets due to $H_{5'}^c$ is partially obscured by the resonances which correspond to **2** at 8.719 (d, J = 2.00, H_7) and 8.697 (d, J = 2.00, H_5). The assignment, therefore, partially rests upon the fact that the sp^3-bound protons of anionic σ-complexes are very sensitive to the nature of the attached group (11). Thus, the sp^3-bound protons of the *ortho* and *para* C-adducts of TNB are separated by 0.34 ppm, with the *ortho* C-adduct proton found farthest downfield (1, 2). In the present system ΔH_7^c for the **5***a*/**6***a* pair is 0.281 ppm. Furthermore, acidification does not affect the resonances due to **5***a* or **6***a*, in accord with the known stability of phenoxide-type carbon-bonded Meisenheimer adducts in mildly acidic media (1, 2).[4]

Equally important to the assignment is the presence of two singlets downfield at 9.419 and 9.311. The proximity of these singlets to that at 9.335, which was previously assigned to the OH of phenol, as well as the observed disappearance of the signals upon treatment with D_2O indicates that these peaks are also due to phenolic OH groups. The 9.419 peak has an integral equivalent to that for the H_7^c peak of the complex **5***a*, while the integral of the 9.311 peak corresponds to that for the H_7^c resonance of the complex **6***a*. Note that in structure **5***a* the phenolic OH group must be close to either the 6-NO_2 or the *N*-oxide function of the complex; internal hydrogen bonding could cause the 0.1-ppm downfield shift of the OH peak of the *ortho* C-bonded phenoxide complex, **5***a*, relative to the position of the OH peak of the *para* DNP-DNBT·PhOH$^-$ adduct, **6***a*.

Therefore, the chemical shifts of the H_7^c protons, the observed acid stability, and the presence of the phenolic OH groups all combine to confirm the assignment of the foregoing signals (Table 1) to the carbon-centered C-7 DNP-DNBT·PhOH$^-$ adducts, **5***a* and **6***a*. It is also significant to note that the ratio of the *ortho* adduct, **5***a*, to the *para* adduct, **6***a*, is 2:1.

Simultaneous with identification of the resonances due to the C-7 DNP-DNBT·PhOH$^-$ adducts, **5***a* and **6***a*, another set of signals is noted at 5.958 (d, J = 7.39), 6.079 (d, J = 7.00), and 8.131 (d, J = 7.00). Significantly, all of these signals disappear upon acidification of the solution. Although the chemical shift data are limited, it would appear that the signals are attributable to an O-centered adduct, since such adducts are known to be acid labile (13, 14). Comparison with the reaction of hydroxide with **3**[5] suggests that these signals belong to the C-7 DNP-DNBT·OH$^-$ adduct, formed by attack of hydroxide on the C-7 position. (Hydroxide would be generated by the equilibration of phenoxide with traces of water present in the $(CD_3)_2SO$ solvent.)

The behaviour of the DNP-DNBT/PhO$^-$ system under the condition of 3 equivalents of added phenoxide is very similar to that of the 1 equivalent case. Addition of KOPh results in an initial very broad, unresolved ^{1}H nmr spectrum. The first well-resolved spectrum is recorded after 1.5 h. This spectrum displays the signals for the DNP ether, **2**, PhO$^-$, and the two C-bonded phenoxide adducts, **5***a* and **6***a*. The signals for the substrate, **3**, are not observable. The C-7 bonded H_7^c peaks of **5***a* and **6***a* now appear at 5.644 and 5.331 ppm, respectively. The positions of the other signals of these complexes are unchanged by the modification of the medium. Such behaviour with

[4]See also ref. 11, pp. 433–435.

[5]E. Buncel and R. A. Manderville, unpublished work.

Can. J. Chem. Downloaded from www.nrcresearchpress.com by 61.7.252.67 on 09/07/12
For personal use only.

Can. J. Chem. Downloaded from www.nrcresearchpress.com by 61.7.252.67 on 09/07/12
For personal use only.

varying concentration ratios of PhO^- to substrate has been observed previously in related systems (*1b*). No evidence for formation of the C-7 DNP-DNBT·OH^- adduct is found in this case, which may be a result of the relatively long period of time required before a well-resolved nmr spectrum can be recorded. It is interesting to note that the integral ratio of the *ortho*-bonded carbon-based DNP-DNBT·$PhOH^-$ adduct, **5***a*, to the *para*-bonded counterpart, **6***a*, is almost 1:1 in this reaction system.

Reaction of NP-DNBT (4) with KOPh

The course followed in the reaction of **4** with PhO^- is superficially similar to that observed in the DNP-DNBT/PhO^- system. The initial spectrum (5 min) consists of broad resonances that resolve in later spectra. A resolved spectrum includes peaks for **4**, as well as resonances attributable to the C-7 *para* and *ortho*-C-bonded adducts of **4**, i.e., **6***b* and **5***b*, in the 1 equivalent reaction.

Thus, the more intense peaks of **5***b* appear at 5.603 (s, H_7^{ς}), with a pair of doublets at 8.253 and 8.453 (d,d, J = 8.98, $H_{2',6'}^{\varsigma}$, $H_{3',5'}^{\varsigma}$) and a singlet at 8.716 ppm (H_5^{ς}) with the phenolic OH resonance at 9.377 ppm. Note the similarity of the H_7^{ς} chemical shift of **5***b* as compared to **5***a*; given the known sensitivity of the sp^3-bound proton to the nature of the attached group (11), it is reasonable that H_7^{ς} for **5***a* appears at 5.575 while H_7^{ς} due to **5***b* appears at 5.603, a difference of only 0.028 ppm. This comparison demonstrates the internal consistency of the assignments in that the chemical shift of H_7^{ς} for the *ortho*-C-bonded adducts formed at C-7 of either substrate, **3** or **4**, should be similar.

The *para*-C-bonded NP-DNBT·$PhOH^-$ adduct, **6***b*, displays weaker bands situated at 5.330 (s, H_7^{ς}), 8.748 (s, H_5^{ς}), with the phenolic OH at 9.321 ppm. Although $H_{2',6'}^{\varsigma}$ and $H_{3',5'}^{\varsigma}$ are hidden from view, a doublet centered at 6.639 (J = 7.91 Hz) may be part of the A_2B_2 (or A_2X_2) spin system of the *para*-C phenoxy moiety.

Once again, the similarity in the chemical shifts for H_7^{ς} of **6***b* versus its analogue **6***a* is striking: 5.330 for the former as compared to 5.294 for the latter, a difference of only 0.036 ppm. The assignment is also confirmed by the ΔH_7^{ς} value for **6***b* as compared to **5***b*: 0.333 ppm. In the TNB/PhO^- system the corresponding difference in chemical shift was found to be 0.34 ppm (1, 2).

In accord with the results of the DNP-DNBT/PhO^- reaction, the integral ratio of **5***b* compared to **6***b* is almost exactly 2:1. Also in agreement with the assignments made, acidification does not diminish the signals attributed to **5***b* or **6***b* other than would be expected as a result of dilution, and addition of D_2O results in the disappearance of the singlets due to the phenolic hydroxyls.

The presence of the other product of N-2:C-1′ bond scission, the 4-nitrophenyl phenyl ether (PN), is inferred from the observation of **2** in the reaction mixture; the ether signals are presumably hidden by those of other species, such as phenoxide.

The results in the 3 equivalent experiment are comparable to the above. The starting material, **4**, is wholly consumed by the added KOPh but otherwise the course of the reaction is unchanged.

Discussion

Reaction pathways

The course of the reaction of phenoxide with either **3** or **4** shows striking differences compared to the reaction of PhO^- with Pi-DNBT, **1**. Reaction at C-1′ of either **3** or **4** occurs via the oxygen centre of the attacking PhO^- and leads to formation of

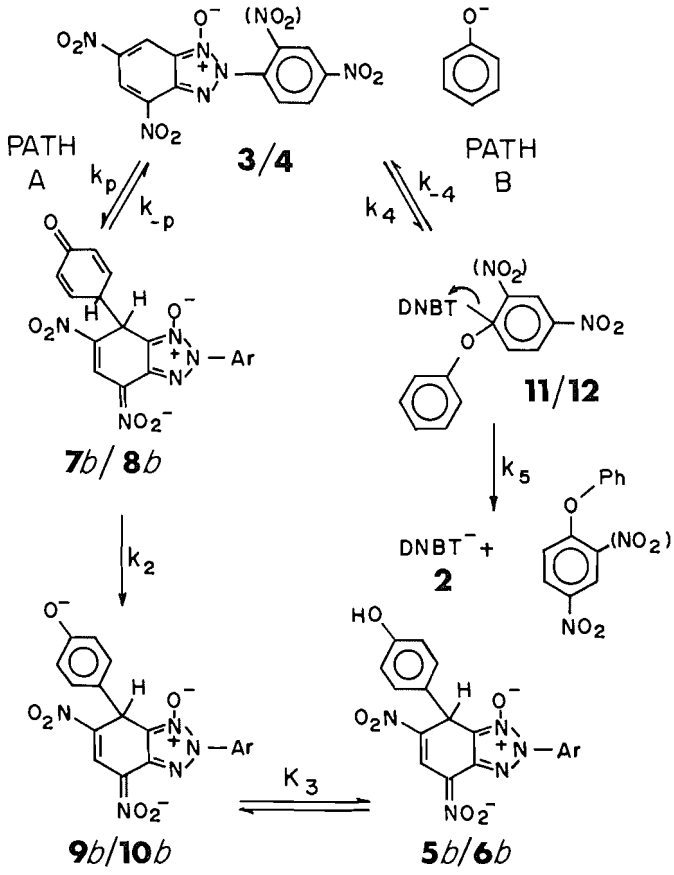

SCHEME 2

the N-2:C-1′ cleavage products: the nitroaryl phenyl ether and **2**. This behaviour is strictly comparable to that found for methoxide reacting with Pi-DNBT (Scheme 1). However, the nitroaryl phenyl ether does not react further with the added KOPh, contrasting with the Pi-DNBT/MeO^- system.

Concurrently, there is reaction of PhO^- at C-7 with both **3** and **4**, in which PhO^- behaves only as a C-nucleophile (Scheme 2). This contrasts with the behaviour observed in the Pi-DNBT/PhO^- system where reaction of PhO^- at C-7 is not detectable, either by C- or O-attack (4, 5).

In addition, **3** reacts with hydroxide, generated through equilibration of the added KOPh with water present in the solvent, to form the C-7 DNP-DNBT·OH^- adduct.[5]

Thus, the dichotomy inherent in the present results is clear: in attack at C-1′ PhO^- behaves solely as an oxygen-centered nucleophile, whereas in attack at C-7 PhO^- acts only as a carbon-centered nucleophile.

Selectivity considerations

It has previously been found useful to consider the reactions of **1** from a reactivity–selectivity point of view (4, 5). Since semiquantitative data could be obtained for these reactions from the comparative integrals for the internal standard, 1,4-dibromobenzene, and the species of interest, the percentage of each complex formed can be estimated for the 1 equivalent experiments (Table 2).

Before considering the selectivity of each of the substrates (**1**, **3**, **4**) with respect to the reaction with PhO^-, it is necessary first to consider the overall kinetics involved in these reactions.

Unlike the reaction of methoxide with **1**, reaction of PhO^- at C-7 of **3** or **4** occurs by an effectively irreversible process. Thus,

TABLE 2. The extent of adduct formation with **1**, **3**, and **4** (1 equiv. PhO^-)

Substrate	Time (min)[a]	% Adducts (total)	%C-7	%C-1′[b]	%C-7/%C-1′[c]
1	2.5	100	—	100	0
3	74	52.7[d]	33.9[e]	18.8	1.80
4	200	28.8	21.6[f]	7.2	3.00

[a]Broadness prevents an earlier estimate.
[b]% C-1′ = % **2** = % nitroaryl phenyl ether.
[c]Related to k_1/k_4.
[d]Percentage excludes the C-7 DNP-DNBT·OH^- adduct (7.5%).
[e]***5a*** makes up 22.6% of the 33.9%; ***5b*** makes up the remaining 11.3%.
[f]***6a*** makes up 14.4% of the 21.6%; ***6b*** makes up the remaining 7.2%.

reaction of PhO^- as a carbon-centered nucleophile would involve initial formation of a quinoidal intermediate, ***7b*** or ***7a***, which, in a second step, would undergo rearomatization with protonation to yield the observed C-adduct, ***5b*** or ***5a*** (Scheme 2). The presence of the hydroxyl groups of the attached phenoxyls of each adduct (***5a/5b***, ***6a/6b***) confirms the aromatic nature of the final, observed C-adduct.

The process may be written as occurring in three steps (Scheme 2). In the first step the quinoidal adduct is formed; this is characterized by a forward rate constant (k_p for the *para* adduct, ***7b***, and k_o for the *ortho* adduct, ***7a*** (not shown in Scheme 2)). The rearomatization step is associated with a forward rate constant k_2, and the protonation step is described by an equilibrium constant, K_3. The observations suggest that K_3 is large (as befits protonation of what is essentially a substituted phenoxide ion, i.e., $K_3 = 1/K_a$ (15)),[6] and that k_2 is larger than $k_p(k_o)$. The last conclusion follows from the lack of observation of the quinoidal adduct in this or in previous studies (1, 2, 4). It is possible that the reverse rate coefficients (k_{-p} and k_{-o}) may also be ignored, i.e., $k_2 \gg k_{-p}$. Under these circumstances the rate-determining step for this process would be characterized by the rate constant $k_p(k_o)$.

On the other hand, reaction at C-1′ via the oxygen centre of PhO^- also leads to formation of a metastable intermediate, in this case the C-1′ adduct. If formation of this species is assigned a rate constant k_4, and the rapid decomposition of the adduct a rate constant k_5, then the lack of observation of a C-1′ adduct in this and related systems (4, 5) suggests that k_4 should be viewed as the effective overall rate-determining rate constant for this process. Once again this derivation requires the assumption that $k_5 \gg k_{-4}$.

Thus, the overall rate expression is given by eq. [1]:

$$[1] \quad -d[\mathbf{3}]/dt = (k_p + k_o + k_4)[\mathbf{3}][PhO^-]$$

The derivation of eq. [1] ignores the process of C-7 adduct formation by HO^-.[5] A comparable equation can be derived for the reaction of **4** with PhO^- through replacement of [**3**] with [**4**] in eq. [1].

It is interesting to note that the 2:1 statistical ratio found for the C-adduct pairs ***5a/6a***, as well as ***5b/6b*** (Table 2), suggests that $k_p = k_o$ for **3** and **4**; i.e., the activation barrier associated with formation of ***7a*** and ***8a*** is equivalent to that for ***7b*** and ***8b*** formation, respectively.

To compare the overall tendencies for attack at C-7 as compared to C-1′ in both substrates, it is useful to substitute an overall C-7 rate constant, k_1, for the quantity ($k_p + k_o$) and replace [**3**] (or [**4**]) by the concentration of substrate, S, i.e.:

$$[2] \quad -d[S]/dt = (k_1 + k_4)[S][PhO^-]$$

The form of eq. [2] is that of competing second-order reactions (16) and comparison of the competing rate constants k_1 and k_4 gives insight into the relative electrophilicity and selectivity of C-7 versus C-1′.

In related systems (4, 5) it has been noted that the hallmark of a selective reaction is the observation of the C-7 adduct. Clearly, this will only be true in the case where the quantity of nucleophile is limited. Therefore, selectivity may be defined as the ratio of the rate constants for attack at C-7 and C-1′, i.e., k_1/k_4, where k_1 represents C-attack at C-7 by both the *para* and *ortho* positions of PhO^-, for the 1 equivalent reactions.

The data shown in Table 2 were obtained at somewhat different reaction times, owing to the initial broadness encountered in the reactions of **3** and **4** with PhO^-. However, the percentages of complexes formed may be used as a guide to the selectivities since the ratio of the products formed must be a reflection of the magnitudes of the ratio constants (k_1, k_4) involved.

In this regard, it is clear that **1** is a less selective electrophile than **3**, in the reaction with PhO^-. In the case of **1**, 100% of the reaction proceeds via Path B (Scheme 2) to yield the products derived solely from C-1′ O-attack, while in the case of the **3**, reaction is partitioned between C-7 attack via carbon (33.9%, both *para* and *ortho* adducts) and C-1′ attack via oxygen (18.8%). To the extent that the percentages of complexes formed reflect the magnitudes of the rate constants, the ratio k_1/k_4 would be 33.9/18.8 = 1.80.

Proceeding from **3** to **4**, the ratio of C-7 versus C-1′ attack increases; now the ratio (k_1/k_4) is 3.0. Thus by our definition **3** would be more selective than **4** and even more selective than **1**.

It is interesting to consider, as well, the overall reactivity of the substrates towards PhO^-. **1** reacts completely while for **3** the total percentage of complexes formed is only 52.7% (excluding the C-7 HO^- adduct). The percentage drops further for **4**, which, even after 200 min reaction time, yields only 28.8% of all complexes formed.

Equally interesting is the fact that the ratio of the *ortho* to the *para* C-adduct is 2:1 for both **3** and **4**, contrasting with the situation for TNB (1). This is the ratio predicted purely on a statistical basis. Clearly C-7 is a highly reactive and relatively unselective position in these systems.

Comparative energy profiles

While the trend in selectivity discussed above (see also Table 2) is a function of an increase in the relative magnitude of k_1, it is even more a result of a significant decrease in k_4. Hence, even though the percentage of the C-7 adduct formed increases from nil to 33.9% in going from **1** to **3** as substrate, the absolute percentage of C-7 complex formed actually drops to 21.6% for

[6]pK_a of PhOH in DMSO = 16.4; $1/K_a = 2.5 \times 10^{16}$ (ref. 15).

Can. J. Chem. Downloaded from www.nrcresearchpress.com by 61.7.252.67 on 09/07/12
For personal use only.

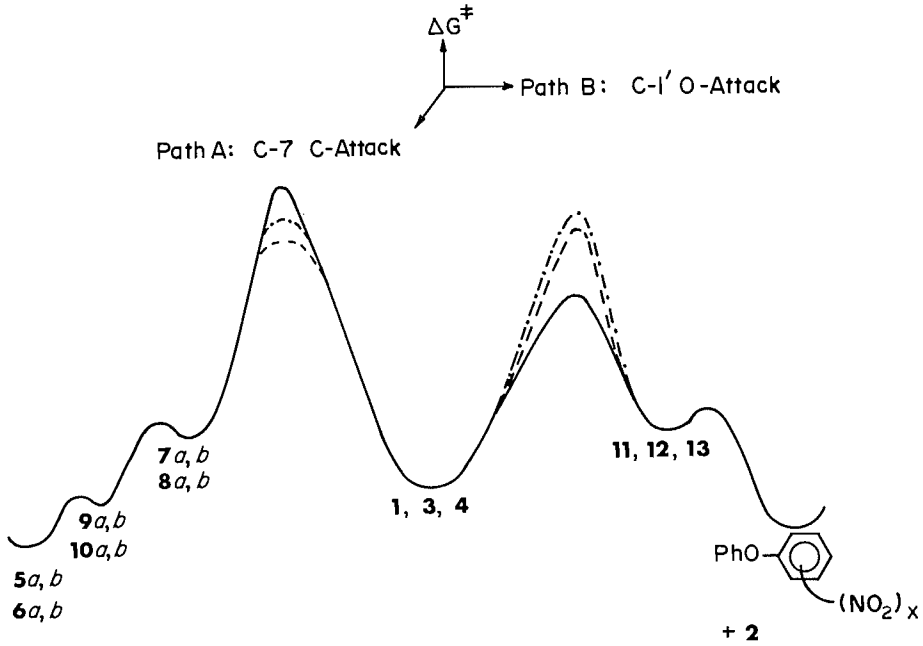

FIG. 1. Comparative activation energy – reaction coordinate profile: left-hand branch represents Path A (Scheme 2) and the right-hand branch represents Path B (Scheme 2). The energy profile for **1** (solid line) is compared with those for **3** (dashed line) and **4** (dot and dash line) in reaction with PhO^-. The C-1′ O-adducts formed from **1**, **3**, and **4** are labelled **13**, **11**, and **12** respectively; the other adducts are labelled as in the text.

4. This decrease in the actual percentage of C-7 NP-DBNT·$PhOH^-$ adduct(s) formed is offset by a larger decrease in the percentage of C-1′ adduct formation in going from **3** to **4** (18.8 to 7.2%, respectively).

These results can be illustrated by the energy/reaction coordinate profile shown in Fig. 1. The profile shows both Path A (left-hand branch), which involves C-attack at the C-7 position, and Path B (right-hand branch), which involves O-attack at the C-1′ position (Scheme 2). The requirement (17, 18) that reactivity–selectivity considerations apply to reactions that can be compared on the same energy profile is, therefore, met in the present system.

Path B shows that the activation barrier associated with O-attack at C-1′ increases substantially between **1** and **3** and less significantly between **3** and **4**. This is consistent with the semi-quantitative results (Table 2). The second activation barrier illustrated in Path B represents the decomposition of the C-1′ O-adduct to **2** and the nitroaryl phenyl ether. Since this step is not rate-determining it is not possible to ascertain any modification in the energetics involved as the substrate is changed from **1** to **3** and to **4**.

The increase in the activation barrier for rate-determining formation of the C-1′ adduct along the series (Path B) must be linked to the decrease in the nitro functions attached to the 2-*N*-nitroaryl ring. As the nitro groups are progressively removed the 2-*N*-nitroaryl ring becomes successively less able to delocalize the charge acquired upon formation of the C-1′ adduct. If the transition state associated with attack at C-1′ in Path B is relatively late (19), then the kinetic barrier for attack at C-1′ would change as shown in Fig. 1 as the substrate is changed. In other words, the factors that stabilize the C-1′ adducts would also be expected to stabilize a late, adduct-like transition state and, therefore, the rate of formation of the N-2:C-1′ cleavage products would decrease as the nitro groups attached to the 2-*N*-nitroaryl function are removed.

An alternative view would hold that reaction of PhO^- via oxygen at C-1′ proceeds through a relatively early transition state. If this is the case, then the decrease in reaction at C-1′ that accompanies removal of the nitro groups of the 2-*N*-nitroaryl moieties of the substrates may simply indicate a decrease in the positive charge density (and attendant electrophilicity) of the C-1′ position. We have previously pointed out that σ-complex formation may proceed through an early transition state (10) where the overall S_NAr process (20) involves reaction of a 1-X-2,4,6-trinitrobenzene in which X is a bulky substituent. This description may also apply to **3** and **4**, where DNBT is the bulky substituent.

Proceeding to Path A, the results listed in Table 2 also allow one to compare the energetics involved. While the kinetic barrier is shown to decrease for C-7 C-attack on **3** as compared to **1**, the barrier increases again for **4** as compared to **3**.

Apparently, removal of the nitro groups from the 2-*N*-nitroaryl ring leads to decreased reactivity at the C-7 position for **4** as compared to **3**. The effect of the distant 2-*N*-nitroaryl ring is likely to be inductive in nature and, therefore, dependent upon the proximity of the substituents to the C-7 reactive centre. Whether the 2-*N*-nitroaryl ring influences reactivity at the C-7 centre by modifying the electrophilicity (positive charge density) at the position (in an early transition state) or by modifying the ability to stabilize the final C-7 complex (in a late transition state) is not clear from the present results. In either case, a nitro group in the *para* position of the 2-*N*-nitroaryl moiety is not as effective as an *ortho* nitro group in affecting the reactivity of the C-7 position.

Electron transfer on the reaction pathway?

The broadness noted in the initial ^1H nmr spectrum is interesting, in light of the recent suggestion (21) that the reaction of picryl chloride with hydroxide proceeds via electron transfer. The central intermediate in the reaction is then a radical anion-radical pair. Such paramagnetic species are known to cause ^1H nmr spectral broadening (22) and such broadening has been

Can. J. Chem. Downloaded from www.nrcresearchpress.com by 61.7.252.67 on 09/07/12
For personal use only.

observed in other systems involving Meisenheimer adducts (23).

However, although the spectra are generally broad in the early stages of the reaction, the signals due to the substrates are broad even after the peaks due to the complexes have resolved. Furthermore, the C-7 HO^- adduct declines with time in favour of the cleavage products. It is noteworthy that the spectrum is sharp and well resolved at this point in the reaction. If the C-7 HO^- adduct or the other C-7 adducts result from an electron transfer process, then their decomposition should also proceed via an electron transfer process; the spectrum should hence remain broad until the C-7 HO^- adduct has decomposed.

These observations suggest that the initial broadness noted in the ^1H nmr spectra in the reactions is a consequence of a side reaction, probably involving free radicals, but is not the main pathway for formation of the Meisenheimer complexes reported here.

Conclusions

The present results represent the first comparison of irreversible oxygen- and carbon-centered attack involving Meisenheimer complex formation. Thus, C-attack by PhO^- at C-7 of the substrates **3** and **4** leads to initial formation of a quinoidal adduct; rearomatization to give adducts such as **5** and **6** is an effectively irreversible process. Similarly, O-attack at C-1′ is an effectively irreversible process in the systems since the C-1′ O-adduct decomposes rapidly and irreversibly to products of N-2:C-1′ bond scission.

The decrease in intrinsic stability of the C-1′ adducts and the transition state leading to them (or, alternatively, the decrease in electrophilicity of the C-1′ positions), for **3** and **4**, accounts for the observation of the C-7 adducts in these two cases. This result is in marked contrast to the reaction of **1** with PhO^- where neither O- nor C-bonded C-7 adducts are observed.

The statistical concentration ratio of the C-7 *ortho* and *para* C-adducts of both **3** and **4** emphasizes the highly electrophilic and relatively unselective nature of the C-7 site. Clearly **3** and **4** are superelectrophiles.

Experimental

Materials

$(CD_3)_2SO$ (Merck) was treated thrice sequentially with 4A molecular sieves prior to use. 1,4-Dibromobenzene (Eastman) was recrystallized twice from ethanol and dried *in vacuo* (<1 Torr; 1 Torr = 133.3 Pa). 2,4-Dinitrophenylhydrazine (BDH), 4-nitrophenylhydrazine (Aldrich), 2,4-dinitrochlorobenzene (Eastman), and tris(hydroxymethyl)aminoethane (Tris; Aldrich) were dried but otherwise used without purification. Nitration of 2,4-dinitrochlorobenzene afforded the picryl chloride used in the preparations below (24), mp 83°C (lit. (24) mp 83°C). Methanol was purified by reflux with and distillation from Mg turnings (25). Phenol was purified by recrystallization from petroleum ether. Potassium methoxide (ca. 4 M) was prepared from freshly cut potassium metal and dry methanol in a nitrogen-filled dry box. The potassium methoxide solution was then standardized against standard HCl, which had been standardized against weighed quantities of Tris (26). Potassium phenoxide was prepared from the purified phenol and standardized KOMe in MeOH in a dry box; excess MeOH was evaporated under a stream of nitrogen and the solid dried under vacuum, mp > 220°C (lit. (27) mp 285–289°C). The 400 MHz ^1H nmr spectrum displayed the following resonances (δ, ppm, $(CD_3)_2SO$): 5.910 (1H, t, *para*), 6.123 (2H, d, *ortho*), and 6.706 (2H, t, *meta*).

Preparation of 2-N-(2′,4′-dinitrophenyl)-4,6-dinitrobenzotriazole 1-oxide, 3

2,2′,4,4′,6-Pentanitrohydrazobenzene (PNH) was synthesized from picryl chloride and 2,4-dinitrophenylhydrazine by the procedure of Leeman and Grandmougin (28) in 88.6% yield, mp 220–223°C (lit. (28) mp 225°C (dec.)). The PNH (2.00 g, 0.0049 mol) was dissolved in concentrated H_2SO_4 (100 mL) in a beaker, and the solution was heated to 40°C and allowed to stir until a thin-layer chromatogram (silica, THF eluant) of the reaction mixture showed no remaining PNH (ca. 1.5 h). The mixture was cooled in ice and then poured into ice water. The yellow precipitate was collected by vacuum filtration and recrystallized from benzene and then from acetonitrile. Yield: 0.930 g, 48.6%; R_f (silica, THF eluant): 0.69; mp 254–256°C (dec.); uv–vis (CH_2Cl_2): 420.0 nm (log ε: 3.85), 340 (sh), 296.0 (log ε: 519); ^1H nmr (δ, ppm, $(CD_3)_2SO$; coupling constants are given in hertz): 8.368 (1H, d, $J_{5',6'}$ = 8.71, $H_{6'}$), 8.950 (1H, d,d, $J_{6',5'}$ = 8.71, $J_{3',5'}$ = 2.30, $H_{5'}$), 9.072 (1H, d, $J_{5',3'}$ = 2.30, $H_{3'}$), 9.091 (1H, d, $J_{5,7}$ = 1.90, H_5) and 9.363 (1H, d, $J_{7,5}$ = 1.90, H_7). *Anal.* calcd. for $C_{12}H_5N_7O_9$ (%): C 36.84, H 1.29, N 25.06; found (%): C 37.32, H 1.47, N 24.76.

Preparation of 2-N-(4′-nitrophenyl)-4,6-dinitrobenzotriazole 1-oxide, 4

2,4,4′,6-Tetranitrohydrazobenzene (TNH) was prepared from picryl chloride and 4-nitrophenylhydrazine (29) in quantitative yield, mp 213–215°C (lit. (12) mp 214–215°C). In the best of several attempts to cyclize the TNH, the hydrazobenzene (3.0 g; 0.0082 mol) was added to concentrated H_2SO_4 (100 mL) in a beaker at room temperature and the TNH solution was stirred for no more than 7 min and then poured into ice water. The tarry residue was collected by vacuum filtration. When crystallized (twice) from acetonitrile it yielded 0.307 g, 10.4%; R_f (silica, CH_2Cl_2 eluant): 0.57; (THF eluant): 0.72 (with streaking); mp 225–226°C; uv–vis (CH_2Cl_2): 424.0 nm (log ε: 3.85), 340 (sh), 316 (log ε: 4.41), 260 (log ε: 4.14); ^1H nmr (δ(ppm), $(CD_3)_2SO$): 8.489 (2H, d, $J_{2',6'-3',5'}$ = 9.18, $H_{2',6'}$), 8.591 (2H, d, $J_{3',5'-2',6'}$ = 9.18, $H_{3',5'}$), 9.059 (1H, d, $J_{5,7}$ = 1.90, H_5) and 9.293 (1H, d, $J_{7,5}$ = 1.90, H_7). *Anal.* calcd. for $C_{12}H_6N_6O_7$ (%): C 41.63, H 1.75, N 24.27; found (%): C 41.49, H 1.85, N 23.94.

^1H nuclear magnetic resonance experiments

The ^1H nmr experiments were carried out on a Bruker AM-400 spectrometer, operating at 400 MHz. Wilmad PP-507 nmr tubes were used in all experiments. The spectrometer was adjusted routinely as follows: spin rate, 25 rps; relaxation delay, 2.0 s; acquisition time, 2.982 s; pulse width, 5 μs (with a pulse angle of 45°); sweep width, 5500 Hz; 32 000 data points; temperature, ambient (21 ± 2°C). All stock solutions and the nmr tubes were capped with rubber septa and all tubes were swept out with N_2 prior to the injection of the reactants. All tubes were injected with a known volume of a stock 1,4-dibromobenzene (DBB) solution in $(CD_3)_2SO$, which acted as an internal integration standard. DMSO-d_5H served as the chemical shift standard.

A representative experiment: the reaction of DNP-DNBT (3) with equimolar KOPh

The DNP-DNBT stock solution (0.1329 M) was prepared by dissolution of a weighed quantity of **3** (0.2601 g, 6.649×10^{-5} mol) in $(CD_3)_2SO$ (0.50 mL). Dissolution of KOPh (0.1347 g, 0.001019 mol) in $(CD_3)_2SO$ (1.0 mL) afforded the phenoxide stock solution used (1.019 M). The initial spectrum was measured using an nmr tube that contained the substrate, 1,4-dibromobenzene, and $(CD_3)_2SO$ (75, 5, and 400 μL of the solutions, respectively). After the injection of 1 equiv. of KOPh (10 μL) to the substrate sample, the FID (16 transients) was collected within 3 min of the mixing of the reactants. In later spectra 64 transients per FID sufficed to obtain the spectra reported here. Final concentration of both reagents was ca. 0.020 M. Spectra were recorded at the following time intervals: 3, 20, 140, 232, 313, 386, 429, and finally 2730 min.

In a separate experiment, D_2O (2 drops) was added to the sample tube after the reaction was well advanced and the spectrum was acquired. Finally TFA (3 μL) was injected into the nmr tube and the spectrum again obtained.

Spectra were plotted from 4200 to 0 Hz and replotted from 3850 to 2050 Hz at a higher peak amplitude. Computer printouts of the chemical shifts (5 places) were obtained. The spectra were integrated.

Can. J. Chem. Downloaded from www.nrcresearchpress.com by 61.7.252.67 on 09/07/12
For personal use only.

Acknowledgments

Support of this research in the form of grants from the Natural Sciences and Engineering Research Council (E.B.) and an Ontario Graduate Scholarship (J.M.D.) is gratefully acknowledged.

1. (*a*) E. BUNCEL and J. G. K. WEBB. J. Am. Chem. Soc. **95**, 8470 (1973); (*b*) E. BUNCEL, A. JONCZYK, and J. G. K. WEBB. Can. J. Chem. **53**, 3761 (1975).
2. E. BUNCEL and W. EGGIMANN. Can. J. Chem. **54**, 2436 (1976).
3. R. A. RENFROW, M. J. STRAUSS, S. COHEN, and E. BUNCEL. Aust. J. Chem. **36**, 1843 (1983).
4. E. BUNCEL, R. A. RENFROW, and M. J. STRAUSS. J. Org. Chem. **52**, 488 (1987).
5. E. BUNCEL, J. M. DUST, K. T. PARK, R. A. RENFROW, and M. J. STRAUSS. *In* Nucleophilicity. *Edited by* J. M. Harris and S. P. McManus. Advances in Chemistry Series. Vol. 215. American Chemical Society, Washington, DC. 1987. p. 369.
6. (*a*) M. J. STRAUSS, A. DEFUSCO, and F. TERRIER. Tetrahedron Lett. **22**, 1945 (1981); (*b*) F. TERRIER, F. MILLOT, and W. P. NORRIS. J. Am. Chem. Soc. **98**, 5888 (1976); (*c*) W. P. NORRIS, R. J. SPEAR, and R. W. READ. Aust. J. Chem. **36**, 297 (1983).
7. E. BUNCEL, R. Y. MOIR, A. R. NORRIS, and A. P. CHATROUSSE. Can. J. Chem. **59**, 2470 (1981).
8. E. BUNCEL, J. M. DUST, R. A. MANDERVILLE, K. T. PARK, and I. ONYIDO. Bull. Chim. Soc. Fr. In press.
9. (*a*) F. TERRIER, F. DEBLEDS, J. C. HALLE, and M. P. SIMONNIN. Tetrahedron Lett. **23**, 4079 (1982); (*b*) M. P. SIMONNIN, J. C. HALLE, F. TERRIER, and M. J. POUET. Can. J. Chem. **63**, 866 (1985), and references therein.
10. E. BUNCEL, S. K. MURARKA, and A. R. NORRIS. Can. J. Chem. **62**, 534 (1984).
11. E. BUNCEL, M. R. CRAMPTON, M. J. STRAUSS, and F. TERRIER. Electron deficient aromatic and heteroaromatic-base interactions. The chemistry of anionic sigma complexes. Elsevier, Amsterdam. 1984. Chap. 2, Table 1, p. 23 and Table 11, p. 58.
12. A. G. GREEN and F. M. ROWE. J. Chem. Soc. 2443 (1912).
13. T. N. HALL and C. F. PORANSKI, JR. *In* The chemistry of the nitro and nitroso groups. Part 2. *Edited by* H. Feuer. Interscience, New York. 1970.
14. E. BUNCEL. *In* The chemistry of amino, nitro and nitroso compounds. Supplement F. *Edited by* S. Patai. Wiley, London. 1982.
15. I. M. KOLTHOFF, M. K. CHANTOONI, JR. and S. BLOWMICK. J. Am. Chem. Soc. **90**, 23 (1968).
16. A. A. FROST and R. G. PEARSON. Kinetics and mechanism. Wiley, New York. 1953. pp. 147–154.
17. E. BUNCEL and H. WILSON. J. Chem. Educ. **64**, 475 (1987).
18. (*a*) E. BUNCEL and C. CHUAQUI. J. Org. Chem. **45**, 2825 (1980); (*b*) E. BUNCEL, C. CHUAQUI, and H. WILSON. J. Org. Chem. **45**, 3621 (1980).
19. G. S. HAMMOND. J. Am. Chem. Soc. **59**, 96 (1955).
20. J. MILLER. Nucleophilic aromatic substitution. Elsevier, Amsterdam. 1968.
21. R. BACALOGLU, C. A. BUNTON, and G. CERICHELLI. J. Am. Chem. Soc. **109**, 621 (1987).
22. P. LASZLO and P. STANG. Organic spectroscopy: Principles and applications. Harper and Row, New York. 1971. p. 71.
23. V. F. STARICHENKO, V. A. RYABININ, and S. M. SHEIN. Zh. Strukt. Khim. **15**, 138 (1974).
24. P. F. FRANKLAND and F. H. GARNER. J. Soc. Chem. Ind. **39**, 257 (1921).
25. A. I. VOGEL. A textbook of practical organic chemistry. Longmans, London. 1948. p. 168.
26. T. H. WHITEHEAD. J. Chem. Educ. **36**, 297 (1959).
27. A. RODRIGUE, J. W. BOVENCAMP, B. V. LACROIX, and R. A. BANNARD. Can. J. Chem. **64**, 808 (1986).
28. H. LEEMAN and E. GRANDMOUGIN. Ber. Dtsch. Chem. Ges. **41**, 1295 (1908).
29. H. LEEMAN and E. GRANDMOUGIN. Ber. Dtsch. Chem. Ges. **41**, 1306 (1908).

Can. J. Chem. Downloaded from www.nrcresearchpress.com by 61.7.252.67 on 09/07/12
For personal use only.

Conductimetric studies of ionic association of tetraalkylammonium halides in iso-propanol + water mixtures at 25°C. Part II.

AIJAZ AHMAD ANSARI[1]
Department of Chemistry, Aligarh Muslim University, Aligarh-202002, India

AND

M. R. ISLAM
Department of Chemistry, Kashmir University, Srinagar, Kashmir (J & K), India

Received December 15, 1987

AIJAZ AHMAD ANSARI and M. R. ISLAM. Can. J. Chem. **66**, 1720 (1988).

Electrical conductivities of Me_4NBr, Et_4NBr, Pr_4NBr, Bu_4NBr, and Bu_4PBr have been measured in isopropanol + water (2-PrOH + H_2O) mixtures covering the approximate range of dielectric constant ($71.40 \geq D \geq 19.40$) at 25°C. The conductance data have been analysed by using the Fuoss-1978 (F78) conductance equation and the results compared with those obtained from the Fuoss–Onsager–Skinner (FOS) equation. The values of the limiting equivalent conductance, Λ_0, the association constant, K_A, and the distance of ion-size parameter (R or a_K^0) are computed from these data. A better fit of the conductance data was provided by the F78 equation. Ion–solvent interactions and effective sizes of tetraalkylammonium ions are also discussed in order to understand the magnitude of the ionic association. The overall association behaviour of these salts has been found to increase with decrease in dielectric constant of the medium.

AIJAZ AHMAD ANSARI et M. R. ISLAM. Can. J. Chem. **66**, 1720 (1988).

Opérant à 25°C, on a mesuré les conductivités électriques du Me_4NBr, du Et_4NBr, du Pr_4NBr, du Bu_4NBr et du Bu_4PBr dans des mélanges d'isopropanol/eau (PrOH-2 + H_2O) couvrant des constantes diélectriques de $71{,}40 \geq D \geq 19{,}40$. On a analysé les données de conductivité à l'aide de l'équation de conductance de Fuoss-1978 (F78) et on a comparé les résultats obtenus avec ceux auxquels conduit l'équation de Fuoss–Onsager–Skinner (FOS). Utilisant ces données, on a calculé les valeurs limites de la conductance équivalente, Λ_0, la constante d'association, K_A, ainsi que la distance ou le paramètre de la grosseur de l'ion (R ou a_K^0). Les données de conductance donnent un meilleur accord avec l'équation F78. Afin de comprendre l'amplitude de l'association ionique de ces sels, on discute aussi des interactions ion–solvant et des grosseurs effectives des ions tétraalkylammonium. On a trouvé que le comportement global de l'association de ces sels augmente avec une diminution de la constante diélectrique du milieu.

[Traduit par la revue]

Introduction

Extensive studies (1–6) on the electrical conductance of dilute electrolytic solutions have been made in aqueous, non-aqueous, and mixed organic solvents to examine the influence of dielectric constant on ionic-association and solute–solvent interactions. In addition, the anomalous physical proties of isopropanol + water mixtures have enabled several workers (7, 8) to interpret the unique structure of that solvent. Recently, it has been reported (9) that the isomeric isopropanol (2-PrOH) differs considerably from normal alcohols in undergoing protonation by solvated proton (H_3O^+) in water either as $(R'OH)_2^+H$ or as $(R'OH)_3^+H$, where R′ is an alkyl group. Conway and Bockris (10) have also proposed that in the tetrahedral structure of protonated alcohol, i.e. $(R'OH)_3^+H$, the alcohol chain becomes more bulky in the presence of water and thus the mobility of the alcohol-solvated proton becomes normal due to alignment of solvent molecules. Therefore, 2-PrOH appears to be a stronger base as well as a stronger hydrogen bond acceptor than any other lower alcohols. Furthermore, the conductance studies (6, 7) of alkali and tetraalkylammonium halides in various mixed solvent systems reveal that the association behaviour of specific ion–solvent interactions mainly depends on the nature, composition variation, and the structure of the solvents. It has been found that the association of electrolytes in solvents containing hydroxyl groups appears to increase with increasing proportion of alcohol and ionic size (2, 3) contrary to the predictions in the electrolytic theory. This has, however, been explained in terms of the multiple-step association process (11–13), i.e., the formation of solvent-separated ion-pairs, SSIP, and the formation of contact ion-pairs, CIP. Therefore, it would be of great interest to undertake the measurement of electrical conductances of tetramethyl-, tetraethyl-, tetrapropyl-, tetrabutyl-ammonium bromides (Me_4NBr, Et_4NBr, Pr_4NBr, and Bu_4NBr) and tetrabutylphosphonium bromide (Bu_4PBr) in 2-PrOH + H_2O mixtures in comparison with those in 1-PrOH + H_2O mixtures (14).

Experimental

Purified (7) and redistilled reagent grade 2-PrOH (BDH) with specific conductance, $(2–7) \times 10^{-8}\ \Omega^{-1}\ cm^{-1}$ was used immediately for the preparation of solvent mixtures with triply distilled water (specific conductance = $2.3 \times 10^{-6}\ \Omega^{-1}\ cm^{-1}$). The density and viscosity measurements of pure 2-PrOH and those of its aqueous mixtures (2-PrOH + H_2O) have been reported earlier (15). The dielectric constants of solvent mixtures used for analysis were taken from the literature (16). Me_4NBr, Et_4NBr, Pr_4NBr (Fluka, AG), Bu_4NBr (Estman, AG), and Bu_4PBr (Alfa, inorganic) were used as solute.

The conductivity measurements were done using an impedence bridge, 1608-A (General Radio & Co., USA), at a constant frequency of 1 kHz with an accuracy of ±0.05 to ±0.005%. The conductivity cell used was a four-necked flask with a 250 cm^3 capacity, and was equipped with a nitrogen inlet, a magnetic stirrer, and two platinized platinum electrodes. The cell (cell constant 0.995 cm^{-1}) was calibrated with aqueous KCl solution.

The solvent mixtures and solutions were prepared by weight under nitrogen atmosphere in a dry box just before conductivity measurements. Initially a known volume of concentrated electrolytic solution,

[1]To whom correspondence should be addressed.

Can. J. Chem. Downloaded from www.nrcresearchpress.com by 112.217.228.212 on 09/07/12
For personal use only.

Can. J. Chem. Downloaded from www.nrcresearchpress.com by 112.217.228.212 on 09/07/12
For personal use only.

$C_{max} = 2 \times D^3 \times 10^{-7}$ (17), was taken in the conductivity cell which was immersed in a thermostated liquid paraffin bath maintained at 25 ± 0.01°C. The solutions of desired concentrations were obtained by dilution and the conductance values recorded after attainment of thermal equilibrium. All the conductivity measurements were made in an atmosphere of pure and dry nitrogen. The reproducibility of the conductivity measurements was better than 0.05%.

Results and discussion

Analysis of conductance data

The molar conductivities, Λ (S cm^2 mol^{-1}), for dilute solutions of Me_4NBr, Et_4NBr, Pr_4NBr, Bu_4NBr, and Bu_4PBr in 2-PrOH + H_2O mixtures as a function of concentration, C (mol dm^{-3}), at 25°C are given in Table 1.

The concentration dependence of conductance data for all the salts have been first analysed in terms of F78 conductance equation (18, 19) based on the concept of diffusion-controlled steady state approach. The conductance equation used is of the form,

$$[1] \quad \Lambda = [1 - \alpha(1 - \gamma)][\Lambda_0(1 + \Delta X/X) + \Delta\Lambda_e]$$

where Λ_0 is the limiting equivalent conductance, the term $\Delta X/X$ represents the relaxation effect, $\Delta\Lambda_e$ the electrophoretic effect, γ denotes the fraction of solute present as free ions, and α is the contact pair parameter. Both ΔX and $\Delta\Lambda_e$ depend on the values of the diameter of Gurney cosphere, R, dielectric constant, and viscosity. The parameters and auxilliary variables are related by the following set of equations,

$$[2] \quad K_R = (1 - \alpha)(1 - \gamma)/C\gamma^2 f^2 = (4\pi NR^3/3000) \exp(\beta/R)$$

and

$$[3] \quad K_S = \alpha/(1 - \alpha) = \exp(-E_s/kT)$$

where K_R and K_S refer to the SSIP and CIP formation constants, respectively. The activity coefficient, f, and the difference in energy, E_s, between a pair in the states $r = R$ and $r = a$, where r is the centre-to-centre distance in the case of paired ions and α is the ionic diameter. On rearranging eq. [3] we get

$$[4] \quad (1 - \alpha) = 1/(1 + K_S)$$

Substitution of eq. [4] in eq. [2] gives the conductometric association constant, K_A

$$[5] \quad K_A = (1 - \gamma)/C\gamma^2 f^2 = K_R/(1 - \alpha) = K_R(1 + K_S)$$

The activity coefficient is given by

$$[6] \quad -\ln f = \beta\kappa/2(1 + \kappa R)$$

where $\beta = e^2/DkT$ and $\kappa^2 = 8\pi\beta\gamma n = \pi\beta NC\gamma/125$.

For this purpose the specially designed PARACOND (17) computer programme for the PARAmetric analysis of CONDuctance data for the symmetrical electrolytes have been used. Equations [1]–[6] have been used to find the values of conductance parameters, Λ_0, K_A, and R where $\gamma < 1$ and $K_A > 0.0$ which minimize the standard deviation, σ_Λ, calculated from the relation

$$[7] \quad \sigma_\Lambda = [\Sigma(\Lambda(obs) - \Lambda(cal))^2/N - 3]^{1/2}$$

Similarly, each set of conductance data was then analysed using the FOS equation (20).

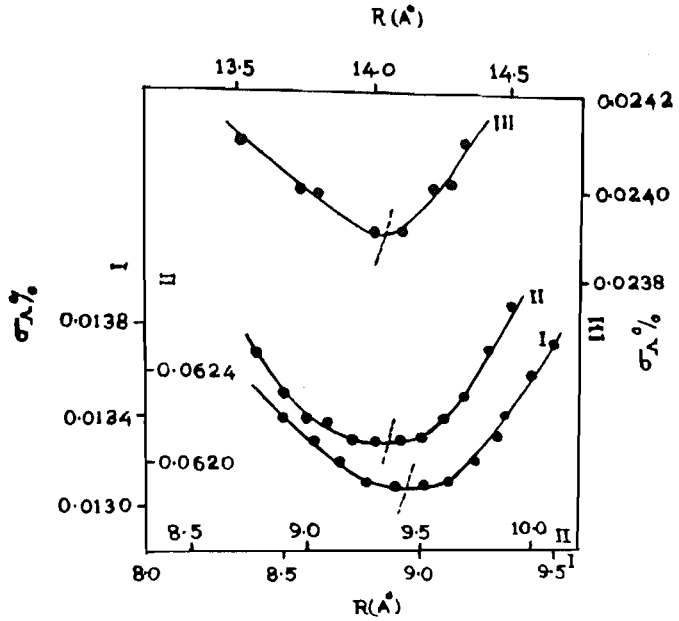

FIG. 1. Plots of σ_Λ% vs. R for Me_4NBr (*I*) in 20 wt.% Bu_4NBr (*II*) in 30 wt.% and Bu_4NBr (*III*) in 80 wt.% 2-PrOH.

$$[8] \quad \Lambda = \Lambda_0 - SC^{1/2} + EC \log(6E_1'C) + LC$$

for unassociated electrolyte while

$$[9] \quad \Lambda = \Lambda_0 - S(C\gamma)^{1/2} + EC\gamma \log(6E_1'C\gamma) + LC\gamma - K_A C\gamma f^2 \Lambda$$

for associated electrolyte. The terms appearing in eq. [8] and eq. [9] are those given by Fuoss (21). To solve eqs. [8] and [9] a similar computer programme developed by Kay *et al.* (2) was used.

The initial values of limiting equivalent conductance used in the Fuoss method of analysis have been obtained using the Shedlovsky's (22) method of extrapolation of the conductance data. The values of Λ_0 have been computed for each of the sequence of R values by minimizing the standard deviation, σ_Λ. The computed values of R depend on the dielectric constant of the medium (19). It is initially set equal to $a + d_s$ where a is sum of crystallographic radii and d_s is the diameter of a solvent molecule, when $a + d_s$ is greater than $\beta/2$. When $\beta/2$ is greater than $(a + d_s)$, R is set equal to $\beta/2$, and $\beta/2$ are used to find the value of R_{min} for each salt in order to obtain the final value of R. For mixture of higher dielectric constant ($D > 30$) the plots of σ_Λ% vs. R usually show a shallow minimum with R_{min} values ranging from 4 to 10 Å and for $D < 30$ rather sharp minimum is found in σ_Λ% vs. R plots (Fig. 1).

The computed values of the adjustable parameters Λ_0, K_A, K_R, K_S, and R from F78 and Λ_0, K_A, and a_K^0 from FOS conductance equations along with σ_Λ% (i.e. $\sigma_{min} \times 100/\Lambda_0$) which correspond to minimum standard deviations are listed in Tables 2 and 3, respectively. All calculations have been carried out on an VAX-11/780 computer.

Limiting equivalent conductance

The values of Λ_0 (Tables 2 and 3) obtained for all salts through the F78 equation are found to be almost close to those obtained by using the FOS equation within the limits of errors. An inspection of Tables 2 and 3 reveal an apparently normal behaviour of tetraalkylammonium salts in various solvent

TABLE 1. Molar conductivities, Λ (S cm^2 mol^{-1}) and molar concentrations, C (mol dm^{-3}), of Me_4NBr, Et_4NBr, Pr_4NBr, Bu_4NBr, and Bu_4PBr in 2-PrOH–H_2O mixtures at 25°C

Me4NBr		Et4NBr		Pr4NBr		Bu4NBr		Bu4PBr	
C/10⁻⁴	Λ	C/10⁻⁴	Λ	C/10⁻⁴	Λ	C/10⁻⁴	Λ	C/10⁻⁴	Λ
				10 W% 2-PrOH-H2O					
725.430	69.314	726.684	61.380	728.280	53.650	728.950	49.565	335.428	53.815
659.480	70.043	660.620	62.052	633.286	54.666	633.869	50.610	262.508	54.672
518.164	71.810	484.456	64.144	520.200	56.050	520.678	52.054	215.632	55.334
439.654	72.957	415.248	65.110	441.380	57.168	441.787	53.220	172.505	56.024
345.440	74.614	363.342	65.905	364.140	58.406	364.474	54.515	134.171	56.722
308.690	75.230	290.673	67.204	291.312	59.770	291.579	55.942	109.776	57.266
263.790	76.168	242.228	68.180	242.760	60.816	236.908	57.194	93.174	57.674
207.264	77.495	207.624	68.946	194.208	62.014	189.526	58.430	72.919	58.225
170.688	79.490	145.336	70.616	145.656	63.488	157.938	59.377	59.897	58.633
120.904	80.060	96.890	72.207	97.104	65.128	108.453	61.133	47.918	59.062
90.678	81.209	72.668	73.172	83.232	65.698	94.762	61.710		
72.542	81.996	58.134	73.840	72.828	66.170	78.969	62.397		
				20 W% 2-PrOH-H2O					
489.419	53.260	414.684	45.680	444.910	41.055	398.287	45.734	300.410	40.073
383.023	53.992	331.747	46.856	355.928	42.310	318.630	46.641	225.307	41.115
314.626	54.511	276.456	47.753	296.606	43.265	265.525	47.334	180.246	41.836
251.700	55.066	207.342	49.084	222.455	44.693	199.143	48.360	150.205	42.400
195.767	55.670	184.304	49.600	177.964	45.734	159.315	49.072	112.650	43.210
160.173	56.110	138.228	50.738	111.227	47.650	106.210	50.245	90.123	43.772
97.884	57.090	110.582	51.563	88.982	48.442	84.968	50.810	75.103	44.216
78.307	57.474	92.152	52.156	74.152	48.987	70.806	51.235	60.082	44.680
65.255	57.784	69.114	53.022	55.614	49.860	60.691	51.554	50.068	45.040
55.933	58.012	55.291	53.622	49.434	50.162	53.105	51.822	42.292	45.338
48.942	58.196	46.076	54.045	40.446	50.655	47.204	52.046		
		39.493	54.375	34.224	51.016				
				30 W% 2-PrOH-H2O					
286.035	41.712	301.912	35.672	348.017	33.124	314.742	31.545	199.486	31.231
223.853	42.765	241.529	36.540	272.360	34.026	246.319	32.490	156.119	32.392
183.879	43.559	201.274	37.215	223.725	34.715	202.334	33.382	128.241	33.294
147.103	44.410	172.520	37.750	178.980	35.447	161.867	34.240	102.592	34.236
114.414	45.284	134.183	38.560	139.206	36.202	125.896	35.144	89.768	34.775
93.611	45.917	109.786	39.169	113.896	36.767	103.006	35.816	71.815	35.618
79.454	46.406	89.411	39.742	96.671	37.200	87.428	36.330	55.413	36.510
62.181	47.066	69.974	40.366	75.656	37.786	68.422	37.036	43.366	37.258
51.077	47.546	57.478	40.818	62.146	38.221	56.204	37.544	35.623	37.786
40.862	48.033	45.983	41.270	49.716	38.673	44.963	38.075	28.498	38.334
35.754	48.264	40.235	41.522	43.502	38.932	39.343	38.370	24.936	38.635
28.603	48.710	32.188	41.916	34.900	39.314	31.474	38.824	19.948	39.091
				40 W% 2-PrOH-H2O					
231.078	35.458	208.650	31.940	192.786	28.834	226.440	27.462	226.163	26.933
180.843	36.313	166.920	32.537	150.876	29.592	177.213	28.220	176.997	27.651
148.550	36.973	139.100	32.982	115.671	30.385	135.864	28.996	145.390	28.195
118.840	37.652	104.325	33.660	99.147	30.810	101.898	29.776	116.312	28.762
92.431	38.365	83.460	34.136	86.754	31.153	90.576	30.070	81.418	29.594
75.625	38.876	61.822	34.712	69.403	31.698	74.107	30.552	62.823	30.125
64.188	39.270	48.383	35.155	53.553	32.265	62.900	30.920	49.165	30.590
46.215	39.992	39.743	35.462	41.910	32.760	49.226	31.417	32.309	31.274
38.513	40.260	31.794	35.774	32.131	33.223	37.740	31.889	22.616	31.753
21.007	41.324	24.728	36.116	24.098	33.674	28.305	32.350		

Can. J. Chem. Downloaded from www.nrcresearchpress.com by 112.217.228.212 on 09/07/12
For personal use only.

mixtures, i.e., Λ_0 decreases with increasing size of the tetraalkylammonium ions in the order $Me_4N^+ > Et_4N^+ > Pr_4N^+ > Bu_4N^+ \approx Bu_4P^+$ and with decreasing dielectric constant of the solvent mixtures. This is in agreement with the earlier findings (1–8, 11–14) in several pure and mixed solvents. However, the decrease in Λ_0 values with increasing proportion of 2-PrOH can also be explained on the basis of ion–solvent interactions, which increase with the increase in ionic size and hydrophobic solvation of cations following the order $Me_4N^+ < Et_4N^+ < Pr_4N^+ < Bu_4N^+ \approx Bu_4P^+$. As a result the mobilities of respective ions decrease in the reverse order. However, in any given solvent mixture the limiting equivalent conductance decreases in the order $Me_4NBr > Et_4NBr > Pr_4NBr > Bu_4NBr \approx Bu_4PBr$. It may also be noted that in the case of high dielectric medium ($71.40 \geq D \geq 49.70$) the extent of decrease in the Λ_0 values are significant due to higher mobility as compared to those in low dielectric constant medium ($42.50 \geq D \geq 20.30$).

Association constant and distance parameter

The values of K_A (Tables 2 and 3) for all the salts in 2-PrOH + H_2O mixtures computed through F78 equation are found to be larger than those obtained using the FOS equation. On the other hand, the K_A values obtained from FOS equation are negative or less than ten in the dielectric range ($71.40 \geq D \geq 49.70$) and it has been considered as non-associated but in the dielectric range

TABLE 1 (*concluded*)

Me4NBr		Et4NBr		Pr4NBr		Bu4NBr		Bu4PBr	
C/10⁻⁴	Λ	C/10⁻⁴	Λ	C/10⁻⁴	Λ	C/10⁻⁴	Λ	C/10⁻⁴	Λ
				50 W% 2-PrOH-H2O					
149.292	29.461	131.645	27.650	132.070	26.562	148.065	25.564	151.798	24.610
116.837	30.350	103.026	28.321	103.359	27.205	111.048	26.200	109.294	25.647
95.973	31.026	84.629	28.826	84.903	27.712	88.839	26.675	91.078	26.190
76.778	31.760	67.703	29.341	67.922	28.230	74.032	27.016	78.066	26.612
53.745	32.820	59.240	29.639	59.432	28.510	63.456	27.290	68.307	27.010
33.176	34.023	47.392	30.102	47.546	28.967	55.524	27.537	54.645	27.588
25.963	34.566	30.908	30.884	35.218	29.526	44.419	27.898	37.949	28.416
17.062	35.318	20.311	31.528	22.641	30.210	37.016	28.155	21.684	29.498
14.929	35.544	14.218	31.984	15.848	30.677	25.564	28.697	16.864	29.890
				12.678	30.930	14.806	29.252	13.797	30.166
				60 W% 2-PrOH-H2O					
73.672	27.996	71.691	24.034	71.356	25.296	72.874	22.584	75.356	23.156
58.938	28.620	53.768	24.970	53.517	26.070	54.655	23.405	56.517	24.004
49.115	29.132	43.014	25.670	42.813	26.628	43.724	24.010	45.213	24.595
36.836	29.840	35.845	26.185	35.678	27.048	36.437	24.456	37.677	25.074
24.557	30.734	26.884	26.952	26.758	27.659	27.327	25.114	28.257	25.746
19.646	31.170	21.507	27.494	21.406	28.088	21.862	25.577	22.605	26.230
15.716	31.522	16.130	28.120	15.856	28.586	18.218	25.933	15.699	26.915
13.097	31.856	10.753	28.863	12.409	28.955	12.145	26.594	11.303	27.439
9.823	32.276	9.217	29.110	9.514	29.316	9.109	26.995	9.419	27.682
7.858	32.540	8.065	29.305	7.135	29.630	7.287	27.270	7.064	28.040
				70 W% 2-PrOH-H2O					
43.215	23.214	36.795	25.280	34.451	22.321	30.550	21.530	34.939	23.220
33.820	23.950	28.797	26.155	26.961	23.137	23.908	22.355	26.205	24.175
27.781	24.512	23.655	26.760	22.147	23.735	19.639	22.976	17.469	25.386
22.225	25.090	18.924	27.445	17.717	24.379	15.712	23.645	13.102	26.170
19.446	25.426	14.719	28.131	15.503	24.746	11.456	24.514	10.482	26.714
9.663	26.934	11.519	28.754	12.919	25.210	8.966	25.110	9.172	27.022
7.938	27.282	9.462	29.212	9.302	25.970	7.365	25.532	7.337	27.502
6.350	27.650	7.569	29.650	7.752	26.346	5.892	26.010	6.114	27.828
5.556	27.832	6.624	29.915	6.644	26.658	4.124	26.614	4.586	28.320
4.445	28.136	5.298	30.310	5.168	27.090			3.668	28.644
				80 W% 2-PrOH-H2O					
25.704	23.066	23.030	24.014	20.430	23.244	23.326	21.451	21.404	21.061
20.563	23.936	18.424	24.652	15.989	23.873	18.255	22.155	16.053	21.898
17.136	24.622	15.353	25.157	12.258	24.514	13.996	22.876	12.843	22.507
12.852	25.674	11.515	25.882	9.194	25.130	10.497	23.598	10.702	22.972
10.282	26.420	9.212	26.405	7.355	25.566	8.397	24.110	9.173	23.362
8.568	27.008	7.677	26.780	5.675	26.038	6.479	24.640	8.027	23.660
6.705	27.710	6.008	27.269	4.441	26.410	5.071	25.098	6.421	24.140
5.508	28.240	4.935	27.602	3.648	26.688	4.165	25.426	5.351	24.502
4.406	28.776	3.455	28.155	2.554	27.133	3.332	25.748	4.013	25.010
3.856	29.092					2.916	25.933	3.211	25.365
				90 W% 2-PrOH-H2O					
13.501	21.660	15.416	21.804	15.953	21.014	13.897	20.582		
11.740	22.280	13.405	22.316	13.872	21.490	11.812	21.060		
9.644	23.114	11.858	22.785	12.272	21.915	10.271	21.466		
8.182	23.786	10.277	23.289	10.635	22.372	8.437	22.026		
6.750	24.556	8.809	23.820	9.116	22.880	7.158	22.446		
5.400	25.403	7.708	24.292	7.090	23.635	5.249	23.180		
4.500	26.045	6.348	24.917	6.381	23.944	4.725	23.424		
3.857	26.572	5.395	25.407	5.318	24.458	3.375	24.095		
		4.692	25.819	4.558	24.846				

(42.50 ≥ D ≥ 19.41) gives appreciably large values for those electrolytes which are associated. The overall values of association constant increase with a decrease in the solvent dielectric constant. However, the association constant obtained from F78 and FOS equations are an exponential function of the dielectric constant of the medium as is evident from the linear plots of log K_A vs. $1/D$ (Fig. 2). Therefore, this linearity of the plots suggest the applicability of the Bjerrum theories of ion association (28–30).

Further, the K_A values for all the salts in a given dielectric medium increases with increasing size of the ions in the dielectric range (71.40 ≥ D ≥ 28.70) in the order $Me_4N^+ < Et_4N^+ < Pr_4N^+ < Bu_4N^+ \approx Bu_4P^+$ as expected (23–27). However, this order does not carry over in the dielectric range (23.70 ≥ D ≥ 19.40), it becomes $Me_4N^+ > Et_4N^+ > Pr_4N^+ > Bu_4N^+ \approx Bu_4P^+$. This anomalous behaviour of K_A in the low dielectric medium may be ascribed to the predominant solvation of cations due to increasing the charge density with decreasing size. Consequently, it is evident from Table 2 that the overall values of the solvent-separated ion-pair (SSIP) formation constant, K_R, increases with a decrease in the dielectric constant of the medium as is the case with K_A but the contact

Can. J. Chem. Downloaded from www.nrcresearchpress.com by 112.217.228.212 on 09/07/12
For personal use only.

TABLE 2. Best-fit parameters for Me_4NBr, Et_4NBr, Pr_4NBr, Bu_4NBr, and Bu_4PBr in 2-PrOH–H_2O mixtures at 25°C, using the F78 conductance equation

Salt	Λ_0 (S cm^2 mol^{-1})	K_A (dm^3 mol^{-1})	K_S	K_R	R (Å)	σ_Λ%
			10 wt.% 2-PrOH (71.40)			
Me_4NBr	88.505 ± 0.019	6.86	1.88	2.38	6.60	0.028
Et_4NBr	79.357 ± 0.006	7.23	1.87	2.52	6.80	0.011
Pr_4NBr	72.598 ± 0.016	7.69	3.05	1.90	5.80	0.011
Bu_4NBr	69.335 ± 0.007	8.35	4.19	1.60	5.20	0.011
Bu_4PBr	63.035 ± 0.006	5.66	0.97	2.87	7.30	0.012
			20 wt.% 2-PrOH (64.10)			
Me_4NBr	61.417 ± 0.005	6.83	0.54	4.44	7.60	0.013
Et_4NBr	58.243 ± 0.006	9.85	3.00	2.46	6.20	0.013
Pr_4NBr	55.705 ± 0.005	9.22	1.45	3.76	6.80	0.012
Bu_4NBr	54.706 ± 0.008	11.35	4.11	2.22	7.90	0.024
Bu_4PBr	48.696 ± 0.005	10.96	1.58	4.23	8.40	0.013
			30 wt.% 2-PrOH (56.90)			
Me_4NBr	51.812 ± 0.008	11.37	3.42	2.57	5.60	0.021
Et_4NBr	44.954 ± 0.004	13.87	2.50	3.96	7.50	0.012
Pr_4NBr	43.821 ± 0.023	18.68	1.96	6.31	8.90	0.063
Bu_4NBr	42.124 ± 0.021	21.62	2.62	5.98	9.40	0.062
Bu_4PBr	42.161 ± 0.004	27.50	5.70	4.05	7.60	0.012
			40 wt.% 2-PrOH (49.70)			
Me_4NBr	42.300 ± 0.006	14.40	2.12	4.62	8.20	0.019
Et_4NBr	38.481 ± 0.006	16.51	1.71	5.50	8.40	0.020
Pr_4NBr	36.287 ± 0.005	21.20	2.70	5.70	8.60	0.015
Bu_4NBr	37.956 ± 0.005	29.94	3.79	6.96	8.24	0.013
Bu_4PBr	34.073 ± 0.004	24.75	2.10	6.69	9.20	0.014
			50 wt.% 2-PrOH (42.50)			
Me_4NBr	35.113 ± 0.005	20.29	2.68	5.50	8.24	0.015
Et_4NBr	34.092 ± 0.006	25.58	2.72	6.87	8.14	0.019
Pr_4NBr	32.880 ± 0.005	28.80	2.36	8.55	9.42	0.019
Bu_4NBr	32.496 ± 0.009	42.59	2.34	13.94	12.10	0.032
Bu_4PBr	31.142 ± 0.007	29.38	1.34	12.57	11.75	0.023
			60 wt.% 2-PrOH (35.30)			
Me_4NBr	34.596 ± 0.012	46.10	3.60	9.77	9.30	0.047
Et_4NBr	31.504 ± 0.005	56.40	2.80	14.82	11.30	0.021
Pr_4NBr	31.688 ± 0.003	72.89	5.08	11.99	9.80	0.014
Bu_4NBr	29.984 ± 0.006	82.36	4.32	15.47	11.60	0.022
Bu_4PBr	30.012 ± 0.005	66.46	3.71	14.12	12.20	0.021
			70 wt.% 2-PrOH (28.70)			
Me_4NBr	30.228 ± 0.005	113.65	4.81	19.55	10.88	0.022
Et_4NBr	33.013 ± 0.013	129.60	6.21	17.96	10.20	0.040
Pr_4NBr	29.746 ± 0.007	159.58	6.11	22.44	12.10	0.022
Bu_4NBr	29.127 ± 0.009	185.20	8.54	19.21	12.70	0.028
Bu_4PBr	30.836 ± 0.006	164.86	5.22	26.36	13.50	0.023
			80 wt.% 2-PrOH (23.70)			
Me_4NBr	32.661 ± 0.009	305.19	8.01	33.86	12.90	0.024
Et_4NBr	30.563 ± 0.007	195.68	4.08	38.55	14.30	0.020
Pr_4NBr	29.025 ± 0.005	184.01	4.05	36.44	13.70	0.018
Bu_4NBr	28.154 ± 0.006	222.22	5.17	36.11	13.60	0.024
Bu_4PBr	27.818 ± 0.004	236.32	6.56	31.27	14.50	0.017

Can. J. Chem. Downloaded from www.nrcresearchpress.com by 112.217.228.212 on 09/07/12
For personal use only.

TABLE 2 (*concluded*)

Salt	Λ_0 (S cm^2 mol^{-1})	K_A (dm^3 mol^{-1})	K_S	K_R	R (Å)	σ_Λ %
			90 wt.% 2-PrOH (20.30)			
Me_4NBr	32.460 ± 0.019	710.44	13.46	50.47	14.20	0.023
Et_4NBr	30.943 ± 0.014	506.02	8.70	52.09	14.62	0.025
Pr_4NBr	29.389 ± 0.014	495.05	5.86	72.20	16.70	0.023
Bu_4NBr	27.393 ± 0.017	398.20	6.08	56.20	15.60	0.036
			100 wt.% 2-PrOH (19.40)			
Me_4NBr	24.89 ± 0.010	2142.82	34.46	60.96	14.35	0.092
Et_4NBr	26.36 ± 0.020	1349.70	20.74	62.09	15.85	0.060
Pr_4NBr	23.33 ± 0.040	1127.59	16.29	65.20	16.50	0.116
Bu_4NBr	21.81 ± 0.050	1199.69	17.69	63.74	16.20	0.138

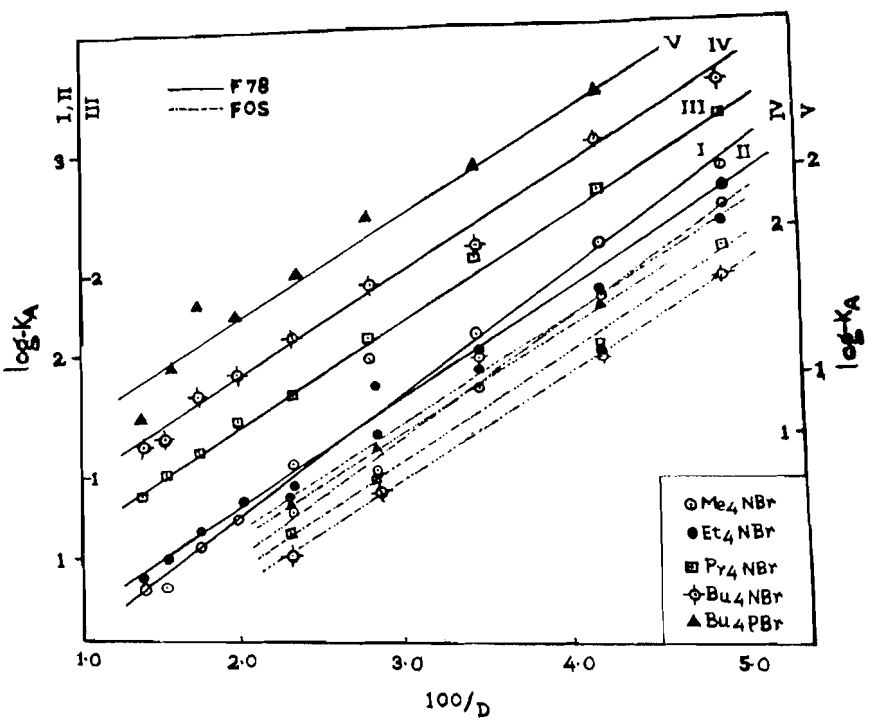

FIG. 2. Plots of log K_A vs. $100/D$.

ion-pair (CIP) formation constant K_S seems to be independent of such effects.

The values of distance or ion-size parameters (R or a_K^0), obtained from different theories of ion-association to predict the K_A values, are compared with the crystallographic radii of the salts under study. The values of a_K^0 (Table 3) obtained from the FOS equation in the dielectric range ($71.4 \geq D \geq 35.5$) are smaller than the crystallographic radii of the ion. We find the results difficult to understand. However, the F78 equation predicts meaningful values of R (Table 2), which are greater (31, 32) than the Bjerrum critical distance, q ($= e^2/2DkT$) while the a_K^0 is less than q. However, an increase in R with a decrease in the dielectric constant of the medium also indicates an increase in ionic association (18, 19), a behaviour that can be explained by the formation of the solvent-separated ion-pair (SSIP) and the contact ion-pair (CIP). For a contact ion-pair, $R = a$; and for SSIP, $R = a + d_s$, where d_s is the diameter of the solvent molecule and is equal to 3.20 to 4.60 Å. Therefore, the values of R show that the tetraalkylammonium halides do not form SSIP or CIP in 10 and 20 wt.% 2-PrOH. In the dielectric range ($56.90 \geq D \geq 19.40$), ion-pairs are formed, and are mostly SSIP. Consequently, it is difficult to draw any definite conclusion from the best-fit R values as they are particularly susceptible to the choice of conductance equation.

Can. J. Chem. Downloaded from www.nrcresearchpress.com by 112.217.228.212 on 09/07/12
For personal use only.

TABLE 3. Best-fit parameters for Me_4NBr, Et_4NBr, Pr_4NBr, Bu_4NBr, and Bu_4PBr in 2-PrOH–H_2O mixtures at 25°C, using the FOS conductance equation

Salt	Λ_0 (S cm^2 mol^{-1})	K_A (dm^3 mol^{-1})	a_K^0 (Å)	σ_Λ %
		10 wt.% 2-PrOH (71.40)		
Me_4NBr	88.32 ± 0.045	1.18	1.28	0.050
Et_4NBr	79.23 ± 0.023	1.38	1.98	0.028
Pr_4NBr	72.45 ± 0.034	2.91	2.24	0.046
Bu_4NBr	69.17 ± 0.043	4.54	3.06	0.060
Bu_4PBr	62.98 ± 0.013	−1.30	1.45	0.050
		20 wt.% 2-PrOH (64.10)		
Me_4NBr	61.34 ± 0.038	3.68	2.90	0.080
Et_4NBr	58.18 ± 0.013	4.02	2.45	0.022
Pr_4NBr	55.65 ± 0.012	2.24	2.52	0.022
Bu_4NBr	54.66 ± 0.023	6.19	2.78	0.040
Bu_4PBr	48.66 ± 0.015	0.94	2.36	0.030
		30 wt.% 2-PrOH (56.90)		
Me_4NBr	51.76 ± 0.015	5.10	2.69	0.030
Et_4NBr	44.90 ± 0.010	4.46	2.50	0.020
Pr_4NBr	43.75 ± 0.050	3.96	2.38	0.075
Bu_4NBr	42.07 ± 0.048	10.02	3.28	0.120
Bu_4PBr	42.13 ± 0.010	9.52	3.92	0.020
		40 wt.% 2-PrOH (49.70)		
Me_4NBr	41.75 ± 0.327	6.43	1.35	0.078
Et_4NBr	38.46 ± 0.014	4.94	2.48	0.022
Pr_4NBr	36.24 ± 0.012	7.93	2.90	0.020
Bu_4NBr	37.14 ± 0.014	12.80	3.48	0.032
Bu_4PBr	34.01 ± 0.015	5.05	2.58	0.030
		50 wt.% 2-PrOH (42.50)		
Me_4NBr	35.06 ± 0.006	7.02	2.80	0.030
Et_4NBr	34.06 ± 0.018	18.74	3.27	0.032
Pr_4NBr	32.84 ± 0.012	18.35	3.12	0.030
Bu_4NBr	32.45 ± 0.016	19.10	3.92	0.040
Bu_4PBr	31.08 ± 0.015	14.30	2.59	0.030
		60 wt.% 2-PrOH (35.30)		
Me_4NBr	34.59 ± 0.031	25.10	4.03	0.060
Et_4NBr	31.46 ± 0.009	28.27	3.79	0.022
Pr_4NBr	31.65 ± 0.009	35.30	4.67	0.023
Bu_4NBr	29.20 ± 0.012	40.10	4.10	0.032
Bu_4PBr	29.96 ± 0.010	33.57	4.38	0.030
		70 wt.% 2-PrOH (28.70)		
Me_4NBr	30.20 ± 0.015	66.80	5.20	0.035
Et_4NBr	32.93 ± 0.034	80.82	4.80	0.053
Pr_4NBr	29.70 ± 0.025	96.10	5.50	0.040
Bu_4NBr	29.09 ± 0.023	139.52	6.34	0.060
Bu_4PBr	30.83 ± 0.014	110.17	6.22	0.035
		80 wt.% 2-PrOH (23.70)		
Me_4NBr	32.58 ± 0.021	215.69	6.07	0.031
Et_4NBr	30.50 ± 0.015	106.21	5.55	0.040
Pr_4NBr	29.00 ± 0.015	92.82	5.76	0.030
Bu_4NBr	28.10 ± 0.006	127.60	5.59	0.020
Bu_4PBr	27.85 ± 0.012	161.65	6.46	0.030
		90 wt.% 2-PrOH (20.30)		
Me_4NBr	32.23 ± 0.052	537.73	6.33	0.030
Et_4NBr	30.89 ± 0.048	378.36	7.66	0.035
Pr_4NBr	29.32 ± 0.053	325.10	7.41	0.032
Bu_4NBr	27.24 ± 0.040	225.07	5.79	0.040

Can. J. Chem. Downloaded from www.nrcresearchpress.com by 112.217.228.212 on 09/07/12
For personal use only.

TABLE 3 (*concluded*)

Salt	Λ_0 (S cm^2 mol^{-1})	K_A (dm^3 mol^{-1})	a_K^0 (Å)	σ_Λ%
		100 wt.% 2-PrOH (19.40)		
Me_4NBr	24.48 ± 0.05	1791.75	7.33	0.02
Et_4NBr	26.16 ± 0.04	1102.67	6.69	0.01
Pr_4NBr	23.09 ± 0.01	857.44	6.99	0.01
Bu_4NBr	21.52 ± 0.03	891.89	6.74	0.02

Some generalizations, however, have been made about the R value obtained from the F78 equation as discussed.

Thus, in view of the above facts, it can be concluded that the F78 conductance equation gives significantly better fit parameters than the FOS equation; it also appears to be better suited for explaining all respects of conductance behaviour because it includes the solvated radii of the ions present in the solution.

Acknowledgements

We thank Professor R. M. Fuoss, Professor R. L. Kay for invaluable help in making his computer programmes available, and Professor M. T. Ahmad and Z. H. Engg. College, A.M.U., Aligarh, for providing the impedence bridge. We would also like to thank Professor N. Islam for his helpful discussion and the Chairman of the Department of Chemistry for providing the necessary facilities.

1. R. L. KAY and D. F. EVANS. J. Phys. Chem. (*a*) **69**, 4216 (1965); (*b*) **70**, 366 (1966); **70**, 2325 (1966).
2. R. L. KAY, C. S. ZAWOYSKI, and D. F. EVANS. J. Phys. Chem. **69**, 4208 (1965).
3. D. F. EVANS and P. GARDAM. J. Phys. Chem. (*a*) **72**, 3281 (1968); (*b*) **73**, 158 (1969).
4. B. J. BARKER and J. A. CARUSO. J. Phys. Chem. **77**, 1884 (1973).
5. J. THOMAS and D. F. EVANS. J. Phys. Chem. **74**, 3812 (1970).
6. J. F. COETZEE and G. P. CUNNINGHAM. J. Am. Chem. Soc. **87**, 2529 (1965).
7. S. M. A. MATESICH, J. A. NADAS, and D. F. EVANS. J. Phys. Chem. **74**, 4568 (1970).
8. T. L. BROADWATER and D. F. EVANS. J. Phys. Chem. **73**, 3985 (1969).
9. M. K. CANTOONI, JR. and I. M. KOTHOFF. J. Phys. Chem. **82**, 994 (1978).
10. B. E. CONWAY, J. O. M. BOCKRIS, and H. LINTON. J. Chem. Phys. **24**, 834 (1956).
11. M. GOFFREDI and T. SHEDLOVSKY. J. Phys. Chem. **71**, 2176 (1967); **71**, 2182 (1967).
12. W. H. LEE and R. J. WHEATON. J. Chem. Soc. Faraday Trans. II, **75**, 1128 (1979).
13. P. BERONIUS. Acta Chem. Scand. A, **34**, 309 (1980).
14. M. R. ISLAM and A. A. ANSARI. J. Electrochem. Soc. India. To be published.
15. M. R. ISLAM and A. A. ANSARI. Indian J. Chem. **21**A, 1057 (1982).
16. H. S. HARNED and B. B. OWEN. The physical chemistry of electrolytic solution. Reinhold Publishing Corporation, New York. 1958. p. 161.
17. R. M. FUOSS. PARACOND, Department of Chemistry, Yale University, New Haven, CT. 1978.
18. R. M. FUOSS. Proc. Natl. Acad. Sci. **75**, 16 (1978).
19. R. M. FUOSS. J. Phys. Chem. **82**, 2427 (1978).
20. R. M. FUOSS, L. ONSAGER, and J. F. SKINNER. J. Phys. Chem. **69**, 2581 (1965).
21. R. M. FUOSS and F. ACCASCINA. Electrolytic conductance. Interscience, New York. 1959.
22. T. SHEDLOVSKY. J. Am. Chem. Soc. **54**, 1411 (1932).
23. T. L. BROADWATER and R. L. KAY. J. Phys. Chem. **74**, 3802 (1970).
24. R. L. KAY and T. L. BROADWATER. Electrochim. Acta, **16**, 667 (1971).
25. R. L. KAY and T. L. BROADWATER. J. Solution Chem. **5**, 57 (1976).
26. L. BAHADUR and M. V. RAMANAMURTI. J. Chem. Soc. Faraday Trans. I, **76**, 1409 (1980).
27. R. L. KAY, T. VITUCCIO, C. S. ZAWOYSKY, and D. F. EVANS. J. Phys. Chem. **70**, 2336 (1966).
28. R. A. ROBINSON and R. H. STOKES. Electrolytic solution. Butterworths, London. 1970. p. 123.
29. J. C. JUSTICE. J. Phys. Chem. **79**, 454 (1975).
30. J. C. JUSTICE. Electrochim. Acta, **16**, 701 (1971).
31. E. REMARD and J. C. JUSTICE. J. Solution Chem. **3**, 633 (1974).
32. A. D. PETHYBRIDGE and S. S. TABA. J. Chem. Soc. Faraday Trans. I, **76**, 368 (1980).

Can. J. Chem. Downloaded from www.nrcresearchpress.com by 112.217.228.212 on 09/07/12
For personal use only.

Molecular emission and electronic structure of associated chlorophyll *a*

N. E. BINNIE, L. V. HALEY, T. A. MATTIOLI, D. L. THIBODEAU, W. WANG, AND J. A. KONINGSTEIN[1]
Department of Chemistry, Carleton University, Ottawa, Ont., Canada K1S 5B6

Received February 5, 1987[2]

N. E. BINNIE, L. V. HALEY, T. A. MATTIOLI, D. L. THIBODEAU, W. WANG, and J. A. KONINGSTEIN. Can. J. Chem. **66**, 1728 (1988).

We report the wavelength-selective Raman and fluorescence spectra of monomeric and aggregate species of chlorophyll *a* in solution. The excitation profile for the molecular emission of the various chlorophyll complexes permit the construction of part of the electronic energy level diagram. For a T-shaped dimeric chlorophyll *a*, pseudo-exciton splittings of 667 cm^{-1} in the Soret and 397 cm^{-1} in the Q_y bands are obtained.

N. E. BINNIE, L. V. HALEY, T. A. MATTIOLI, D. L. THIBODEAU, W. WANG et J. A. KONINGSTEIN. Can. J. Chem. **66**, 1728 (1988).

On a déterminé les spectres Raman et de fluorescence à longueurs d'onde sélective d'espèces monomères et sous forme d'agrégats de chlorophylle *a* en solution. A l'aide des profils d'excitation de l'émission moléculaire des complexes de diverses chlorophylles, on peut construire une partie du diagramme des niveaux d'énergie électronique. Pour une chlorophylle *a* dimère en forme de T, on a obtenu des séparations de 667 et de 397 cm^{-1} respectivement pour les bandes de Soret et de Q_y.

[Traduit par la revue]

1. Introduction

There are numerous reports in the literature which deal with spectroscopic and other properties of solutions which contain chlorophyll *a* (Chl*a*). Much attention has been paid to the interpretation of the absorption (1–4) and fluorescence (5–13) spectrum of this biologically interesting molecule. It is well known that monomers and aggregates of this and the bacteriochlorophyll molecule play an important role in the photophysical process in plants and bacteria. We discuss here spectral properties of the model compound Chl*a* *in vitro*. In particular, the spectra of aggregates of this compound could be of importance in the identification of the spectra of chlorophyll *in vivo* (14).

The principal features of the absorption spectrum of Chl*a* are the $Q_{y,x}$ ($S_{1,2} \leftarrow S_0$) and Soret bands ($S_{3,4} \leftarrow S_0$). They occur in the spectral regions of 600–720 nm and 400–450 nm, respectively. Compared to the position of these bands of the less concentrated solutions in non-polar solvents like carbon tetrachloride, benzene, or hexane, the positions are red-shifted in the more concentrated solutions. Furthermore, the bands broaden and the Q_y absorption band is split into two components. These spectral features in combination with thermodynamic data, have in the past been interpreted (1, 11–15, 35) in terms of the contribution to the absorption spectra of the aggregates. Also, large changes in the concentration of Chl*a* result in minor changes in the absorption spectrum (11, 16, 17). In addition, the absorption spectrum of some of the monomeric species is known but not that of the aggregates.

In recent publications (11–13) from this laboratory, information was presented leading to the assignment of the fluorescence spectrum of monomeric and aggregated Chl*a* in hexane. In dry hexane the fluorescence of the penta-coordinated monohydrate dominates over that of any other species in highly diluted solutions ($<10^{-6}$ *M*). For more concentrated solutions the fluorescence spectrum reveals the presence of an approximately T-shaped dimer (hereafter referred to as the dimer) where bonding occurs (16–20, 25, 26) between the keto group on ring V of one Chl*a* molecule (donor) to the Mg atom of another (acceptor). The macrocycles of the chlorophyll molecules are thought to be approximately perpendicular to each other, contrary to the geometry for another dimer (21) where the rings are parallel but translated with respect to each other. This dimer, composed of bacteriochlorophyll molecules, is found in the reaction center of certain bacteria (21). The structure of this dimer is stabilized through linkages of the cluster with a protein molecule. In contrast, such co-facial dimers are less stable in solution. They are thought to be a minority species in our solutions.

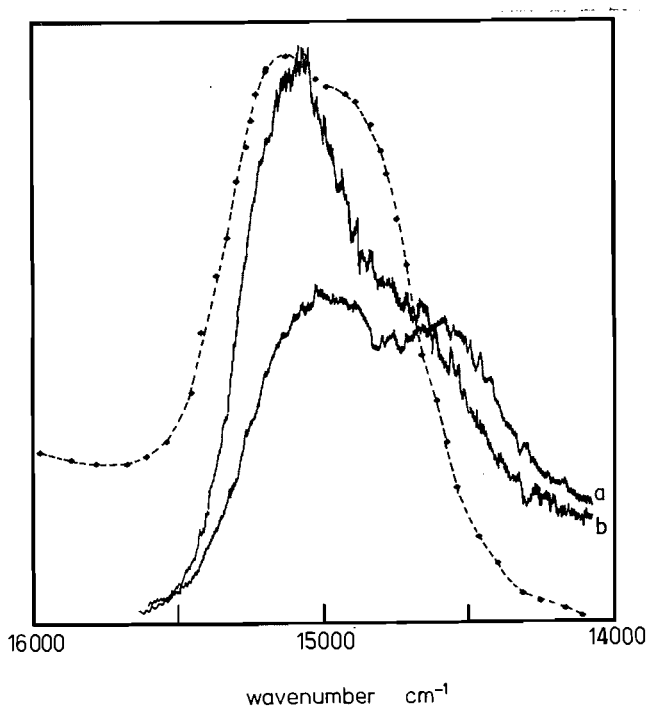

FIG. 1. Fluorescence of a 1×10^{-4} *M* solution of Chl*a* in hexane. (*a*) Cell thickness is 10 mm. (*b*) Same solution as in (*a*) with a cell thickness of 1 mm. Absorption spectrum (·-·-·-·) of this solution.

In the present work we report the results of fluorescence excitation and nanosecond resonance Raman measurements of solutions containing monomeric Chl*a* and the dimer. In addition to information which can be obtained from the absorption spectrum, the fluorescence excitation profiles for specific species

[1]Killam Fellow 1985–1987. Research supported by the Natural Sciences and Engineering Council of Canada.
[2]Revision received March 21, 1988.

Can. J. Chem. Downloaded from www.nrcresearchpress.com by 93.93.197.157 on 09/07/12
For personal use only.

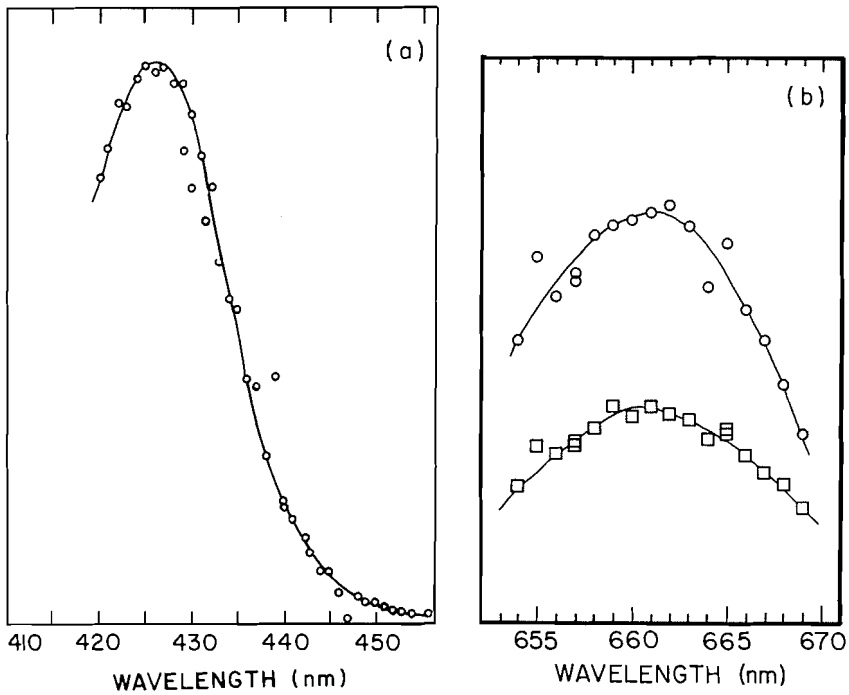

FIG. 2. Fluorescence excitation profiles of a $<10^{-6}$ *M* solution which contains the Chl*a* monohydrate. (*a*) Excitation profile in the range of 415–460 nm for the intensity of the emission at 664 nm. (*b*) Excitation profile between 653 and 670 nm detected at the shoulder of the 664 nm emission: 671 nm (○, upper curve) and 675 nm (—, lower curve).

Can. J. Chem. Downloaded from www.nrcresearchpress.com by 93.93.197.157 on 09/07/12
For personal use only.

and the resonance Raman excitation profiles can provide one with sufficient data to obtain the positions of energy levels lying in the Q and Soret bands of the species in solution.

II. Experimental

Chl*a* was extracted from fresh spinach according to the method of Omata and Murata (22) and purity established by standard techniques (23, 24). The pure Chl*a* wa stored in the dark in a nitrogen-purged dry box. Chl*a* was dried by codistillation sequentially three times with dry carbon tetrachloride (Baker Photorex) and two times with dry hexane (Caledon Labs. Inc., spectral grace) prior to preparation of a concentrated stock solution. All solvents were dried by passing through a column of neutral aluminum oxide (Woelm Activity 1, carried out in the nitrogen-purged dry box) and were then degassed.

Samples for fluorescence and Raman measurements were contained in either air-tight quartz optical cells fitted with Teflon stopcocks (fluorescence measurements) or a flowing cell technique was used ensuring that neither oxygen or water would enter the solutions (Raman measurements). The dilute 10^{-7}–10^{-6} *M* Chl*a* hexane solutions were prepared by dilution of the stock solution with degassed solvents of dried hexane (hereafter referred to only as hexane) or undried hexane (used as received) as specified in the text. The samples were equilibrated for a minimum of 1 h before use. The 10^{-5} and 10^{-4} *M* solutions were prepared using dried hexane.

Molecular emissions from solutions of chlorophyll dissolved in 2,4-lutidine were also studied. The solvent lutidine (Aldrich 97% pure) was successively distilled over KOH and BaO under reduced pressure. The dried solvents were kept over molecular sieves and purged with N_2 before use.

Pulsed laser fluorescence and Raman spectroscopy experiments were performed using a tunable dye laser pumped with a Nitrogen or Excimer laser (Lambda Physik Fl 2000 and M2000 or Lumonics models TE 430 and EPD 330), pulse FWHM of 5 and 10 ns, respectively. The emitted light was observed in the back scattering or reflection techniques in order to minimize self-absorption. Because both the incident light and emitted light were absorbed, the depth of the sample illumination was a critical parameter in the experiments. If the width of the sample was not adjusted with respect to increasing sample concentration, then reabsorption effects distorted the spectra. In Fig. 1 we show the fluorescence spectra of a 10^{-4} *M* Chl*a* solution in hexane where the sample was placd in a 10 mm cell (Fig. 1*a*) and a 1 mm cell (Fig. 1*b*). Superimposed on the data is the absorption spectrum of this solution. Self absorption is evident across the entire fluorescence spectrum. As a result of this observation, we chose a 1 mm cell for the 10^{-4} *M* solution, therefore minimizing the spectral distortion due to self absorption.

The light was dispersed by a Jobin-Yvon Ramanor HG2 spectrometer equipped with curved holographic ruled gratings. Spectra were recorded with a slit of 3–7 cm^{-1} and the radiation emerging frm the exit slit was detected by a RCA 31034 cooled photomultiplier tube. The pulsed signals were fed into a gated detection system (Stanford Research Associates) and the spectra were recorded on a stripchart recorder or processed with a computer. If not stated differently, fluorescence spectra were recorded with a gate of 3 ns at a point in time at which the intensity of the fluorescence signal has reached its maximum intensity. The Raman spectra were recorded with a similar gate but at a point in time (t_0) at which the laser pulse has reached its maximum intensity. Lifetimes were computer-calculated with a modified phase-plane method, and are estimated to contain an uncertainty of 0.5 ns.

Our spectroscopic studies in the past and present point to the fact that for equal concentration of dry Chl*a* in the solvents hexane, carbon tetrachloride, or benzene, the concentration of aggregates is higher in hexane. Hence, we chose to use hexane as the solvent to investigate the emission spectra of aggregates of Chl*a*.

III. Results and discussion

A. Fluorescence excitation spectra

Monomer

It is well known that fluorescence from monomeric species of Chl*a* is most conveniently studied if the large molecule is

Can. J. Chem. Downloaded from www.nrcresearchpress.com by 93.93.197.157 on 09/07/12
For personal use only.

dissolved in polar solvents. However, if dissolved in non-polar solvents the fluorescence as well as the absorption spectrum cannot be interpreted in terms of properties of a single species. We have shown in an earlier publication (13) that for solutions which are $<10^{-6}$ *M* Chl*a* in hexane, the fluorescence spectrum of the monohydrate which has a maximum intensity at 664 nm exceeds that of any other species. Shown in Figs. 2*a* and *b* are the excitation profiles of the Soret and Q_y absorption band systems which are characterized by maxima at 426 nm and 660–662 nm. The positions of these maxima coincide with the maxima of the Soret and Q_y absorption bands of the monohydrate in solution (13). Therefore there exists a correlation between the absorption spectrum and the fluorescence excitation profile for the red emission of the monohydrate. The observed decay time of this emission if excited at 436 nm is 6.2 ns.

Dimer

The results of a wavelength-selective fluorescence study of Chl*a* for concentrations $>10^{-6}$ *M* in hexane are presented in Figs. 3 and 4. These solutions contain, besides the monohydrate, various aggregates of Chl*a*. It is known that a chemical equilibrium exists between the species in solution (16, 17) as is evident by the appearance of red-shifted absorption features in both the Soret and Q_y spectral regions. In the solvents CCl_4 and hexane, vapour phase osmometry (35) data were directly attributed to species having an average aggregation number of approximately 2. Therefore we assume that in our hexane solutions, upon an increase in concentration of Chl*a*, the first species to exhibit fluorescence besides the monohydrate should be the dimer. Some information on the spectroscopic properties of this dimer has been discussed in earlier work (13). In the following discussion we present a comparison of molecular emission (fluorescence and Raman) and other data. These results, in particular the resonance Raman spectra, strongly support the existing picture of the chemical link betwen the two Chl*a* molecules of the dimer.

In Fig. 3 we show the wavelength-dependent fluorescence spectra of a solution which is 5×10^{-6} *M* and contains monohydrate species as well as dimers. If the solution is excited at 422 nm the emission of the monohydrate at 664 nm is clearly observed. The apparent shift in the 664 nm emission is due to the effect of reabsorption caused by an increase in the illuminated sample volume as the wavelength of the laser is scanned away from the intensity maximum of the Soret absorption band. Upon excitation between 430 and 457 nm the intensity of an emission at 686 ± 1 nm is detectable. Relative to the excitation profile of the monomer (Fig. 2*a*), that for the band at 686 nm has a maximum between 440 and 448 nm (Fig. 5) and we assign this fluorescence (13) to that of the dimer. The increase in concentration of the dimer with respect to that of the monomer is evident if the results in Figs. 3 and 4 are compared. The spectra shown in Fig. 4 of solutions which are 10^{-5} and 10^{-4} *M* are recorded from cells which are, respectively, 10 mm and 1 mm thick, therefore minimizing the relative effect of reabsorption of the fluorescences. The result of mimimizing the effect of reabsorption has permitted us to increase our accuracy so as to establish a reliable emission wavelength for each of the species. Preliminary experimental data for a 10^{-3} *M* solution suggest that the 686 nm emission band still dominates the spectra, indicating that the concentration of the dimer is still high in comparison to that of other species. In an earlier publication (13), a dicussion was given of the emission band assignments in the spectral region of 668–688 nm in terms of fluorescences originating in the acceptor and donor molecules of the dimer. In the present study we conclude that the donor emits at 686 ± 1 nm, and further evidence for this assignment will be given in section B.

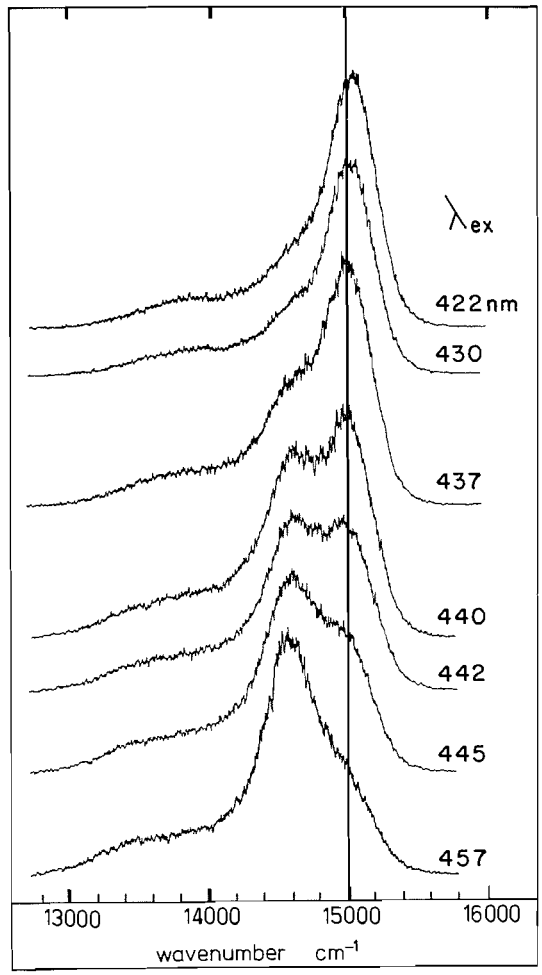

FIG. 3. Wavelength-selective fluorescence spectrum of a solution of 5×10^{-6} *M* Chl*a* Chl*a* in dry hexane. The vertical bar denotes the position of the fluorescence of the chlorophyll monohydrate molecule at 664 nm. Fluorescence from the donor at 686 nm (14577 cm^{-1}) is selectively excited with the laser wavelength of 457 nm.

B. Nanosecond resonance Raman spectra and excitation profiles

Raman spectra of Chl*a* in hexane, excited with pulsed (27–29) and cw laser radiation (30–32) have been reported in the literature. If excited with laser radiation tuned to the spectral region of the Soret band of Chl*a*, the intensity of the Raman spectrum is resonance enhanced. Spectra from solutions which are $>10^{-5}$ *M* in chlorophyll can be recorded with good signal/noise ratios. The solutions contain more than one species with overlapping Soret bands. The vibrational frequencies of normal modes of the different Chl*a* species are not far apart because the width and the shift of the Raman bands are similar. Hence, the resonance Raman excitation profile for the intensity of Raman bands may contain useful information on the position of electronic excited states. Of relevance here is the experimental result that the width of these profiles at resonance is ~ 100 cm^{-1} as compared to a ~ 1000 cm^{-1} width for absorption bands of the solutions.

In the present work we are mainly interested in the excitation spectra (see Fig. 5) of one of the most intense Raman bands of

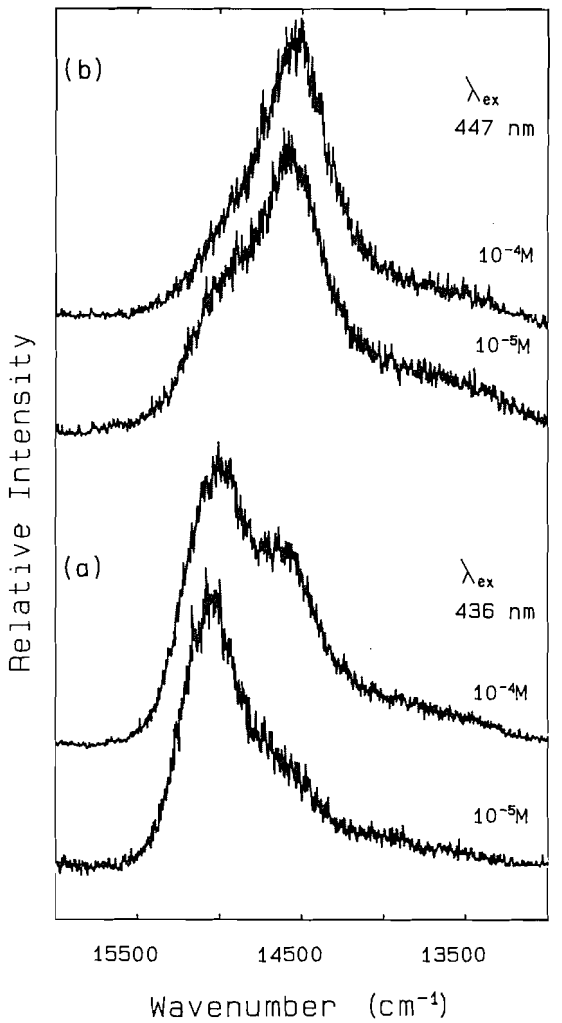

FIG. 4. Pulsed laser fluorescence excitation of Chl*a* in hexane. The spectra of the 10^{-5} *M* solution are obtained from a 10 mm cell, and those from the 10^{-4} *M* solution from a 1 mm cell.

Chl*a* in solution. The excitation profile was obtained by plotting the intensity ratio of the intense Raman band at approximately 1550 cm^{-1} of Chl*a* to that of a band of the solvent as a function of the wavelength of the pulsed laser radiation that induces the spectra. This Raman shift is primarily due to C—C stretching modes of the Chl*a* molecule and its position changes from species to species.

Monomer

When the Chl*a* is dissolved in lutidine, aggregation does not occur (32) and the penta-coordinated Chl*a* complex is the species present in a 10^{-4} *M* solution. The resonance Raman profile (not shown) for the intensity of the 1550 cm^{-1} band has a maximum between 430 and 445 nm which is close to the cross-over point of the Soret absorption band at 433 nm and the two-photon induced Stokes shifted fluorescence at 444 nm, see Fig. 6. The maximum at 439 nm is assigned to the position of the electronic origin for transitions between the S_3 and S_0 electronic surfaces of the chlorophyll–lutidine complex.

Dimer

The excitation profile for the Raman band at 1550 cm^{-1} in the spectral interval of 430–450 nm for 1×10^{-4} *M* Chl*a* in hexane is shown in Fig. 5. The main components in this solution are the monohydrate and the donor–acceptor dimer complex. In order to record these spectra, the intensity of the laser radiation at 435.2 nm was sufficiently high to produce effective population saturation of lower-lying nanosecond-lived excited states (S_1) of the monohydrate, and donor molecule as judged from Q_y fluorescence of these entities. From the pulsed laser intensity-dependent value of the sample transmission, it follows that the intensity of the $S_n \leftarrow S_1$ absorption at 435.5 nm is smaller than that of the transition at that wavelength which originates in the ground state (34). Hence we predict a smaller intensity enhancement for vibrational scattering in the electronic excited state at the ground state resonant wavelengths.

Also shown in Fig. 5 is the two-photon induced blue fluorescence from the 1×10^{-4} *M* solution and the excitation profile of the dimer fluorescence band at 686 nm. The width of the fluorescence band is ~2000 cm^{-1} as compared to 1000 cm^{-1} for the emission in the blue for monomeric chlorophyll in lutidine, see Fig. 6. The large width of the blue fluorescence band is due to contributions of emissions from the monohydrate, dimer, and perhaps even higher aggregates. The maximum intensity of the blue emission is at 455 nm and is assigned to emission of the dimer. This fluorescence originates in the S_3 level of the donor molecule. From the Raman excitation spectra we find that resonance with this state occurs if the laser is tuned to 448.2 nm, hence the S_3 state of the donor is near 22 300 cm^{-1}. This position is within experimental error equal to the cross-over point of the two-photon induced blue fluorescence and the contour of the excitation profile for the emission at 686 nm, see Fig. 5.

In order to assign the S_3 position of the acceptor molecule the following arguments are pertinent. The position of the Soret band for the monohydrate complex is at 426 nm. Although two-photon induced blue fluorescence from solutions containing this complex could not be detected, the Stokes shift for the penta-coordinated lutidine (see above) and other complexes (33, 34) is between 11 and 14 nm. We predict for the monohydrate complex an electronic orgin between 431 and 433 nm. The excitation profile of Fig. 5 shows maxima at 435.2 and 448.2 nm. However, a search for intensity increases in the excitation profile between 426 and 435.2 nm for a 10^{-4} *M* solution of Chl*a* in hexane was negative. The position of the Soret absorption band of this solution, which yields the excitation profile of Fig. 5 is at 430 nm, and the Soret band of the monohydrate was not detected. Assuming a Stokes shift similar to that of the monomer, an electronic origin of the acceptor would then be expected between 435 and 437 nm. Hence we assign the maximum of the profile at 435.2 nm to the position of an electronic origin (S_3) of the acceptor molecule, and that at 448.2 nm to an origin (S_3) of the donor. At the resonating wavelengths, the degree of enhancement of the Raman band intensities of the dimer is in agreement with the difference of the intensity of the absorption bands at 430 and 444 nm.

For the acceptor molecule, the assignment of the electronic origin is supported by wavelength-dependent intensity measurements of Raman bands at 1705 and 1655 cm^{-1}. The band at 1655 cm^{-1} is due to scattering from the Mg-bound C—O group on ring V of the donor chlorophyll molecule, while the band at 1705 cm^{-1} is the frequency of this mode for the free keto group of the acceptor molecule (30). Compared to the intensity of the band at 1655 cm^{-1} that of the band at 1705 cm^{-1} goes through a maximum if the wavelength of the laser is tuned to 404.9 nm. At this wavelength, resonance occurs with the vibronic side band due to the C=O vibration at 1705 cm^{-1} of the non-ligated keto group on ring V of the electronic surface having its origin at

Can. J. Chem. Downloaded from www.nrcresearchpress.com by 93.93.197.157 on 09/07/12
For personal use only.

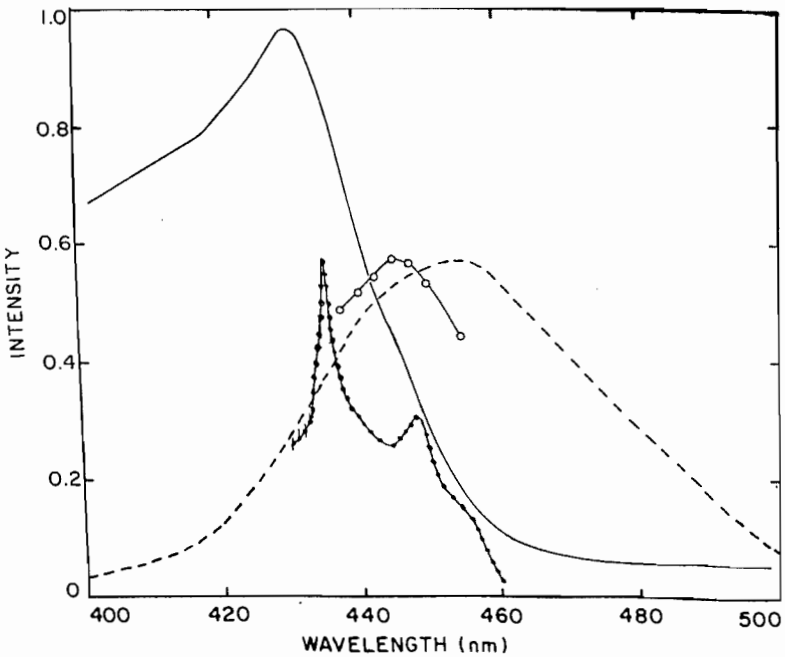

FIG. 5. Absorption (—) and two-photon induced fluorescence (----) of a solution in which the concentration of the dimeric complex dominates over that of other species. Also indicated is the excitation profile (-○-○) for the donor emission at 686 nm. The resonance Raman excitation profile (-●-●-●-) peaks at the position of electronic origins of the donor (448.2 nm) and acceptor molecule (435.2 nm).

TABLE 1. Spectroscopic data and electronic origins for Chl*a* complexes

Concentrations	Fluorescence	Absorption	Flourescence excitation profile	Assignment	Species
5×10^{-5} *M* in lutidine	444 nm	433 nm	—	S_4^{0-0}: 433 nm[b,c] S_3^{0-0}: 439 nm[b]	Chl*a* – lutidine (penta-coordinated)
	674 nm[a]	665.7 nm	—	$S_1(Q_y^{0-0})$: ~ 670 nm	
10^{-6} in hexane	—	426 nm	(427 ± 1 nm) of Fl 664	S_3^{0-0}: ~ 433 nm[d]	Chl*a*.H_2O (penta-coordinated)
	664 nm	659 nm	(661 ± 1 nm) of Fl 664	$S_1(Q_y^{0-0})$: ~ 662 nm	
10^{-4}–10^{-5} *M* in hexane	445 nm		(444 nm) of Fl 686	S_3^{0-0}: 448.2 nm[b]	Donor Chl*a*·H_2O
	~686 nm	~677 nm		$S_1(Q_y^{0-0})$: 682 nm	
	—	~430 nm		S_3^{0-0}: 435.2 nm[b]	Acceptor (Chl*a*), dimer $n = 2$
	667[d] nm	~662 nm		$S_1(Q_y^{0-0})$: 664 nm	

[a]2,4,6-Trimethylpyridine solution, from ref. 37.
[b]From resonance Raman excitation profile.
[c]Tentative assignment.
[d]Estimated-monohydrate absorption maximum and lutidine Stokes shift.

435.2 nm (22 978 cm^{-1}). Furthermore, the intensity of the 1705 cm^{-1} band is higher than that of the band at 1655 cm^{-1} if the spectrum is excited with radiation at 435.2 nm while the reverse occurs for radiation tuned to 448.2 nm. The spectral results and assignments are summarized in Table 1.

Finally, the spectral results presented above are used to determine the pseudo-exciton splitting in both the Q_y and Soret band systems. In the absence of resonance Raman data from the Q_y band system, the band origins were estimated from absorption and fluorescence measurements of the donor, and for the acceptor, we used the absorption data and an estimated Stokes shift for the fluorescence maximum (based on a similar Stokes shift as in lutidine). Origins are located at 664 and 682.5 nm for the acceptor and donor molecules, respectively. The splitting of the pseudo-exciton components is 397 cm^{-1}. As mentioned above, the resonance Raman excitation profile in the Soret band region yields the S_3 electronic origins of the donor and acceptor molecules directly. Here, the pseudo-exciton splitting is 667 cm^{-1}. For the complex mentioned above (T-shaped dimer in hexane), calculations utilizing an exciton formalism which includes the environmental effects (36) on the electronic states of the donor–acceptor complex revealed the fact that the contribution of the transition density – transition density interaction energy to the total splitting is small. This result is to be expected if the angle

Can. J. Chem. Downloaded from www.nrcresearchpress.com by 93.93.197.157 on 09/07/12
For personal use only.

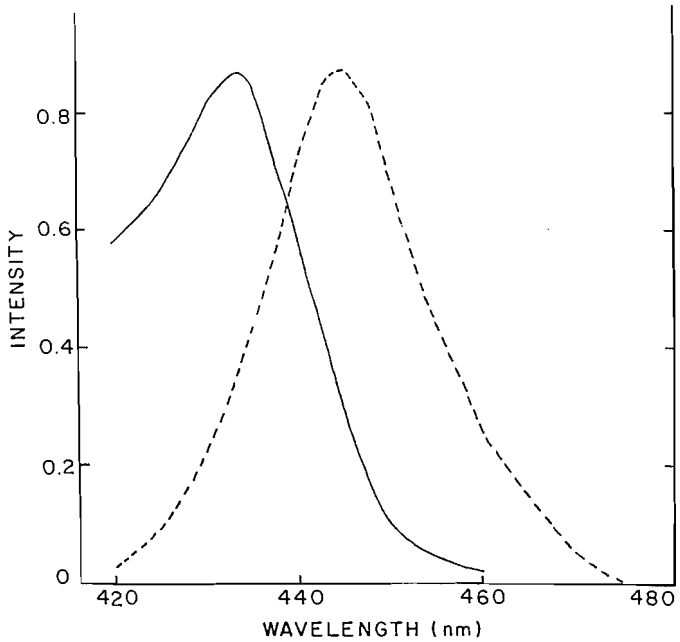

FIG. 6. Absorption (—), and two-photon induced blue fluorescence (---) of penta-coordinated Chl*a* in lutidine.

between the two macrocycles deviates significantly from zero. Future polarization studies will be undertaken to evaluate this angle.

1. K. SAUER, J. R. LINDSAY SMITH, and A. J. SCHULTZ. J. Am. Chem. Soc. **88**, 2681 (1966).
2. J. RABANI (*Editor*). Proceeding of the 4th Intl. Conf. on Photochemical Energy Conversion and Storage, Weizman Science Press of Israel, 1983.
3. F. K. FONG, V. J. KOESTER, and J. S. POELLES. J. Am. Chem. Soc. **98**, 6406 (1976).
4. G. P. GURINOVICH, A. N. SEVCHENKO, and K. N. SOLOVEV. Spectroscopy of chlorophyll and related compounds, A.E.C. Translation Series A.E.C.-tr-1968. p. 7199.
5. S. B. BROYDE and S. S. BRODY. J. Chem. Phys. **46**, 3334 (1967).
6. A. C. DE WILTON and J. A. KONINGSTEIN. Chem. Phys. Lett. **114**, 161 (1984).
7. J. BAUGHER, J. C. HINDMAN, and J. J. KATZ. Chem. Phys. Lett. **63**, 159 (1979).
8. M. J. YUEN, L. L. SHIPMAN, J. J. KATZ, and J. C. HINDMAN. Photochem. Photobiol. **36**, 211 (1982).
9. T. J. SCHAAFSMA. *In* Triplet state ODMR spectroscopy: techniques and applications to biophysical systems. *Edited by* R. H. Clarke. Wiley-Interscience, New York. 1982, p. 316 and references therein.
10. F. K. FONG, M. KUSUNOKI, L. GALLOWAY, T. G. MATTHEWS, F. E. LYTLE, A. J. HOFF, and F. A. BRINKMAN. J. Am. Chem. Soc. **104**, 2579 (1982).
11. A. C. DE WILTON, L. V. HALEY, and J. A. KONINGSTEIN. J. Phys. Chem. **88**, 1077 (1984).
12. A. C. DE WILTON. Ph.D. Thesis, Carleton University, Ottawa, Canada 1984.
13. N. E. BINNIE, L. V. HALEY, T. A. MATTIOLI, D. L. THIBODEAU, W. WANG, and J. A. KONINGSTEIN. J. Phys. Chem. **90**, 4939 (1986).
14. J. C. GOEDHEER. Ann. Rev. Plant Physiol. **23**, 87 (1972).
15. J. J. KATZ, L. L. SHIPMAN, T. M. COTTON, and T. R. JANSON. *In* The porphyrins, Vol. V, Academic Press, NY. 1978. pp. 401–482.
16. J. J. KATZ and J. R. NORRIS. Curr. Top. Bioene. 5, 41 (1973).
17. L. L. SHIPMAN, T. M. COTTON, J. R. NORRIS, and J. J. KATZ. J. Am. Chem. Soc. **98**, 8222 (1976).
18. R. P. H. KOOYMAN and T. J. SCHAAFSMA. J. Am. Chem. Soc. **106**, 551 (1982).
19. K. BALLSCHMITER and J. J. KATZ. J. Am. Chem. Soc. **91**, 2661 (1969).
20. C. HOUSSIER and K. SAUER. J. Am. Chem. Soc. **92**, 779 (1970).
21. J. DEISENHOFER, O. EPP, K. MIKI, R. HUBER, and H. MICHEL. J. Mol. Biol. **180**, 385 (1984).
22. T. OMATA and N. MURATA. Photochem. Photobiol. **31**, 183 (1980).
23. A. C. DE WILTON and J. A. KONINGSTEIN. J. Am. Chem. Soc. **106**, 5088 (1984).
24. W. A. SVEC. *In* The porphyrins, Vol. V. *Edited by* D. Dolphin. Academic Press, New York. 1978. pp. 341–399.
25. W. W. A. KELLER, B. A. ALBERS, E. STRAUSS, and K. MAIER-SCHWARTZ. J. Lumin. **31/32**, 892 (1984).
26. A. J. ALFANO, F. E. LYTLE, M. S. SHOWELL, and F. K. FONG. J. Chem. Phys. **82**, 758 (1985).
27. A. C. DE WILTON, L. V. HALEY, and J. A. KONINGSTEIN. Chem. Phys. Lett. **97**, 538 (1983).
28. A. C. DE WILTON, L. V. HALEY, and J. A. KONINGSTEIN. J. Raman Spectros. **14**, 288 (1983).
29. T. M. COTTON and P. P. VAN DUYNE. J. Am. Chem. Soc. **103**, 6020 (1981).
30. M. LUTZ. J. Raman Spectrosc. **2**, 497 (1974).
31. M. FUJIWARA and M. TASUMI. J. Phys. Chem. **90**, 250 (1986).
32. F. C. BELANGER and C. A. REBEIZ. Spectrochim. Acta, **40**A, 807 (1984).
33. A. C. DE WILTON and J. A. KONINGSTEIN. Chem. Phys. Lett. **114**, 161 (1985).
34. J. E. HUNT, J. J. KATZ, A. SVIRMICKAS, and J. C. HINDMAN. Chem. Phys. **82**, 413 (1983).
35. K. BALLSCHMITER, K. TRUESDELL, and J. J. KATZ. Bichem. Bin'hys. Acta, **184**, 604 (1969).
36. L. L. SHIPMAN, J. R. NORRIS, and J. J. KATZ. J. Phys. Chem. **80**, 877 (1976).
37. K. MAURING, I. RENGE, P. SAW, and R. AVARMA. Spectrochim. Acta, **43**A(4), 507 (1987).

Can. J. Chem. Downloaded from www.nrcresearchpress.com by 93.93.197.157 on 09/07/12
For personal use only.

Biosynthesis of the lupine alkaloids. II. Sparteine and lupanine

W. MAREK GOLEBIEWSKI[1] AND IAN D. SPENSER
Department of Chemistry, McMaster University, Hamilton, Ont., Canada, L8S 4M1

Received December 8, 1987

W. MAREK GOLEBIEWSKI and IAN D. SPENSER. Can. J. Chem. **66**, 1734 (1988).

Contrary to predictions based on earlier observations, it is now found that label from DL-[6-^{14}C]lysine and from [6-^{14}C]-Δ^1-piperideine does not enter the three C_5 segments of lupanine with equal efficiency. One of the C_5 segments is labelled at a significantly higher level than the other two C_5 segments, which show identical levels of labelling. A new biogenetic model is proposed, which is consistent with these new findings as well as with all other regio- and stereochemical evidence on the mode of incorporation of precursors that is available.

W. MAREK GOLEBIEWSKI et IAN D. SPENSER. Can. J. Chem. **66**, 1734 (1988).

Contrairement à ce qui a été prédit en se basant sur des observations antérieures, on a maintenant trouvé que le marqueur de la DL-[^{14}C-6]-lysine et celui e la [^{14}C-6]-Δ^1-pipéridéine ne sont pas incorporés des les trois segments en C_5 de la lupanine avec des efficacités identiques. L'un des segments en C_5 porte un taux de marquage beaucoup plus élevé que celui des deux autres segments en C_5 dont les niveaux de marquage sont identiques. On propose donc un nouveau modèle biogénétique qui est en accord avec ces nouvelles données ainsi qu'avec d'autres données disponibles sur les régio- ou stéréochimies du mode d'incorporation.

[Traduit par la revue]

Introduction

Recent investigations (1–5) employing ^{13}C- and ^{13}C,^{15}N-labelled substrates have confirmed and extended earlier results obtained with ^{14}C-labelled tracers (6–16) on the biosynthesis of the tetracyclic bisquinolizidine-type lupine alkaloids (e.g., (−)sparteine (1, 2, 5, 7, 9, 12) (**1**), (+)lupanine (3–6, 8, 10, 11, 13, 16) (**2**), (+)-13α-hydroxylupanine (4, 5, 8, 13, 14) (**3**), (−)multiflorine (12, 15) (**4**)), and have firmly established that

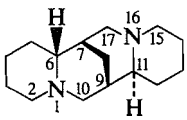

1

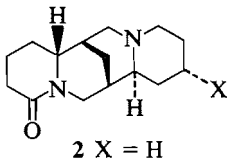

2 X = H
3 X = OH

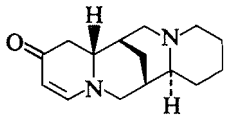

4

these alkaloids originate from three C_5 chains derived from lysine (9–13, 15) or, more specifically, from L-lysine (**5**) (16). Cadaverine (1–9, 11, 14, 15) (**6**), the decarboxylation product of lysine, is also a precursor and is, presumably, an intermediate (17) between lysine and the alkaloids.

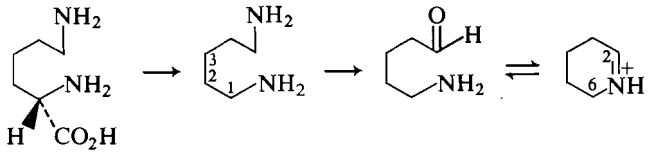

5 **6** **7** **8**

It is likely that the intact C_5 chain of cadaverine is utilized in the generation of a C_5 intermediate and that three molecules of this C_5 intermediate supply the three C_5 units, C-2,-3,-4,-5,-6, C-10,-9,-8,-7,-17, and C-15,-14,-13,-12,-11, of the alkaloids.

The two nitrogen atoms of the $C_{15}N_2$ skeleton of the alkaloids are also derived from lysine (9, 15) or cadaverine (1–4). Two C—N units, C-2,N-1 and C-15,N-16, of the alkaloids are derived from the NH_2CH_2- group of cadaverine, whereas the other four C—N bonds of the alkaloids are formed in the course of biosynthesis.

The evidence suggests that lysine, C_6N_2, via cadaverine, C_5N_2, supplies a C_5N intermediate from which the two C_5N chains of the alkaloids, N-1,C-2,-3,-4,-5,-6 and N-16,C-15,-14,-13,-12,-11, are derived *in toto*, and that the central C_5 unit of the alkaloids, C-10,-9,-8,-7,-17, is derived from the same C_5N intermediate with loss of nitrogen.

Incorporation studies with deuterium-labelled samples of lysine (3) and cadaverine (3, 18–21) into (−)sparteine (3, 18, 21) (**1**), (+)sparteine (19) (the enantiomer of **1**), (+)lupanine (3, 18, 20, 21) (**2**), and (+)-13α-hydroxylupanine (20, 21) (**3**) throw light on the mode of incorporation of the C_5N unit and define the stereochemistry of some of the steps in the biosynthetic sequence from lysine into cadaverine and thence into the alkaloids.

It is observed that deuterium is retained, *inter alia*, at C-2, C-10, and C-17 of sparteine, derived from one or the other of the enantiomers of [1-^{2}H]cadaverine (3, 18). 17-Oxosparteine (22, 23), 10-oxosparteine (23), lupanine (24, 25), or 1,2-dehydrosparteinium ion (26) cannot therefore be intermediates between cadaverine and sparteine, contrary to what had variously been suggested (22–26). Retention of deuterium at C-8 of lupanine (20, 21), 13α-hydroxylupanine (20, 21), and sparteine (21), derived from [3,3-$^2H_2$]cadaverine, disposes of a hypothetical biosynthetic sequence (22) that requires loss of hydrogen from C-8 of the alkaloids.

From the experiments with deuteriated cadaverine (3, 18, 19) it can be inferred that, on the route to the alkaloids, loss of one of the two amino groups of cadaverine is accompanied by removal of the *si*-hydrogen atom from the adjacent enantiotopic -CH_2- group. This is the hydrogen atom that is known to be lost in the course of the conversion of cadaverine into the corresponding aldehyde, 5-aminopentanal (**7**) (or rather the corresponding Schiff base, Δ^1-piperideine (**8**), into which 5-aminopentanal is spontaneously transformed (27)),[2] by oxidative deamination, catalyzed by diamine oxidase (27, 31) (EC 1.4.3.6), or by

[1]On leave from the Department of Chemistry, University of Warsaw, 02-093 Warsaw, Poland.

[2]The spontaneous pH-dependent conversion of 5-aminopentanal into Δ^1-piperideine, and thence into the corresponding dimer and trimers, has been the subject of detailed investigations (28, 29). These spontaneous conversions were not taken into account in a proposed biosynthetic model (22, 30), which has now been disproved (20, 21).

Can. J. Chem. Downloaded from www.nrcresearchpress.com by 112.217.228.212 on 09/07/12
For personal use only.

Can. J. Chem. Downloaded from www.nrcresearchpress.com by 112.217.228.212 on 09/07/12
For personal use only.

transamination, catalyzed by diamine aminotransferase (32–34) (EC 2.6.1.29).

The evidence would appear to point to 5-aminopentanal (**7**), or rather its cyclic Schiff base, Δ^1-piperideine (**8**), as the cadaverine-derived C_5N unit that serves as the intermediate in the biosynthesis of the lupine alkaloids and supplies the two C_5N chains that yield the C_5N units N-1,C-2,-3,-4,-5,-6 and N-16,C-15,-14,-13,-12,-11, as well as the C_5 chain that yields the central C_5 unit, C-10,-9,-8,-7,-17, of the alkaloids.

Indeed, label from [2-^{14}C]- and [6-^{14}C]-Δ^1-piperideine is incorporated into lupanine (23). Moreover, entry of label from these two tracers is regiospecific: Approximately one third of the activity of the intact lupanine from [6-^{14}C]-Δ^1-piperideine is located at each of C-2 and C-15, whereas C-11 and C-17 each bear ca. one third of the total label of the alkaloid when [2-^{14}C]-Δ^1-piperideine serves as the substrate. Furthermore, deuterium from [2-^{2}H]-Δ^1-piperideine is located at C-6, C-11, and at the α-site of C-17 of lupanine (3), and at no other carbon atom. This regiospecific incorporation of labelled Δ^1-piperideine into the C_5 unit, C-10,-9,-8,-7,-17, proves that derivation of this segment from the cadaverine-derived C_5N unit cannot proceed via a later intermediate with C_{2v} symmetry (such as glutardialdehyde (35)). Furthermore, the observed (3, 23) regiochemistry of the incorporation of label from [2-^{2}H]-, [2-^{14}C]-, and [6-^{14}C]-Δ^1-piperideine into the carbon atoms, C-10 and C-17, of the central C_5 unit disproves a biosynthetic model (36) that predicts a result opposite to that actually observed.

The alkaloids, derived from tracer experiments carried out over the past 25 years, show a consistent labelling pattern: Without exception, incorporation of label from the ^{14}C-labelled substrates, [2-^{14}C]lysine (9–13, 15) and [1-^{14}C]cadaverine (6–9, 11, 14, 15), led to $C_{15}N_2$ alkaloids that contained approximately one sixth of their total specific activity at each of the labelled carbon atoms that were assayed individually. [2-^{14}C]- and [6-^{14}C]-Δ^1-piperideine gave alkaloids containing approximately one third of their activity at such carbons (23). Similarly, without exception, incorporation of label from ^{13}C-labelled substrates, [1-^{13}C,1-^{15}N]cadaverine (1–4) and [1,2-$^{13}C_2$]cadaverine (5), yielded alkaloids approximately equally enriched at each of six sites. Correspondingly, equal enrichments were observed at the various ^{2}H-labelled sites within alkaloids derived from deuterium labelled substrates (3, 18).

Thus, in every case, precursor entered each of the three C_5 segments of the $C_{15}N_2$ alkaloids simultaneously, suggesting that elaboration of the $C_{15}N_2$ skeleton takes place either by modification of a trimeric intermediate formed in one step from the C_5N monomer, or by a multistep process in a closed system (e.g., on an enzyme surface) that does not permit exchange of intermediates. Either way, the experimental results do not yield information on the steps of the process from C_5N monomer to $C_{15}N_2$ product.

The tracer results now reported indicate that the equal distribution over six (or three) sites, hitherto observed, must have been the result of fortuitous experimental conditions.

The characteristic distribution of incorporation of label from DL-[6-^{14}C]lysine and [6-^{14}C]-Δ^1-piperideine, now observed, opens the way to the study of the intermediate steps between the C_5N monomer and the $C_{15}N_2$ alkaloids.

Methods and results

In 11 tracer experiments (expts. 7–17) samples of lysine, cadaverine, and Δ^1-piperideine, specifically labelled with radioactive (expts. 7–12) or stable isotopes (expts. 13–17) were administered by wick to intact plants of *Lupinus angustifolius*. The plants were kept in contact with tracer solution for 3–9 days and lupanine was then isolated. Details of these experiments are summarized in Table 1.

In six further experiments (expts. 1–6), details of which have been reported (37), samples of the same three substrates, labelled with radioactive (expt. 6) or stable isotopes (expts. 1–5), were administered to *Lupinus luteus*, from which labelled samples of lupinine and sparteine were isolated. These experiments have been fully described in the first paper of this series (37), which dealt with the biosynthesis of lupinine. The incorporation of label into samples of sparteine obtained in these experiments will be discussed in the present context.

The labelled compounds employed in the tracer experiments were obtained as follows: DL-[6-^{14}C]Lysine monohydrochloride (expts. 7–9) was a commercial product (CEA France); [2-^{14}C]-Δ^1-piperideine (expt. 10) and [6-^{14}C]-Δ^1-piperideine (expts. 11, 12) were prepared by oxidation of the correspondingly labelled DL-lysine (see Experimental).

DL-[6-^{13}C]Lysine (expt. 17) was synthesized by adaptation of a known method (38), in five steps from diethyl acetamidomalonate, acrolein, and potassium [^{13}C]cyanide (99 at .% ^{13}C) (see Experimental). The preparation of samples of DL-[2-^{2}H]lysine (27) (expts. 3, 16), [1-^{13}C,1-^{15}N]cadaverine (37) (expts. 5, 13), (*R*)-[1-^{2}H]cadaverine (27) (expts. 1, 14), and (*S*)-[1-^{2}H]-cadaverine (27) (expts. 2, 15) has been described.

After being kept in contact with tracer solution for several days, the plants were harvested and alkaloids were extracted by standard methods. *Lupinus luteus* yielded lupinine and (−)sparteine (37), *L. angustifolius* gave (+)lupanine and (+)-13α-hydroxylupanine (see Experimental).

The labelling pattern within the samples of lupanine (**2**) derived from the experiments with ^{14}C-labelled lysine (expts. 7–9, Table 2) and Δ^1-piperideine (expts. 10–12, Table 3) was determined by the degradation sequence shown in Scheme 1. Radioactivity at C-2 and C-17 of lupanine (**2**) was assayed directly (benzoic acid). Radioactivity at C-15 was determined as β-alanine (**17**) (C-15,14,13) and as γ-aminobutyric acid (**16**) (C-15,14,13,12), on the assumption that label from the precursors that were employed would be confined to carbon atoms of lupanine that are adjacent to nitrogen, and that other carbons would be unlabelled. Radioactivity at C-15 together with C-11 was determined as pipecolic acid (**15**) (C-9,11,12,13,14,15), on the basis of the same assumption. Thus, four of the six carbon atoms adjacent to nitrogen became accessible.

Lupanine derived from [6-^{14}C]lysine contained approximately one half of its label within pipecolic acid (C-11 plus C-15), and approximately one quarter of its label within β-alanine and γ-aminobutyrate (C-15). One eighth of the label was recovered from each of C-2 and C-17 (expts. 7–9, Table 2; Scheme 2).

Lupanine derived from [2-^{14}C]-Δ^1-piperideine contained approximately one third of its label (33%) within pipecolic acid (C-11 plus C-15) whereas β-alanine and γ-aminobutyrate (C-15) were essentially inactive. Somewhat less than one third (27%) was present at C-17, whereas C-2 was not labelled (expt. 10, Table 3; Scheme 2).

Lupanine derived from [6-^{14}C]-Δ^1-piperideine again contained one third or more of its label (32%, 42%) within pipecolic acid (C-11 plus C-15) as well as within β-alanine (33%, 39%) and γ-aminobutyrate (32%) (C-15) (expts. 11, 12, Table 3; Scheme 2).

The labelling pattern within the sample of lupanine derived from DL-[6-^{13}C]lysine (expt. 17, Fig. 1) and within the samples

TABLE 1. Experiments with *Lupinus angustifolius*

(*a*) Radioactive isotopes

Expt. no.	Substrate	Nominal total specific activity (mCi)	Nominal total specific activity (mCi/mmol)	Plant material: Dry weight (g)	Plant material: No. of plants	Lupanine (mg)	Lupanine diluted for degradation: Weight of added carrier (mg)	Lupanine diluted for degradation: Specific activity of diluted lupanine (dpm/mmol)
7	DL-[6-^{14}C]Lysine monohydrochloride[a]	0.1	48	31	12	30	470	4.9×10^4
8	DL-[6-^{14}C]Lysine monohydrochloride[a]	0.25	48	15	14	12	340	6.8×10^4
9	DL-[6-^{14}C]Lysine monohydrochloride[a]	0.3	48	9	30	18	320	5.4×10^4
10	[2-^{14}C]-Δ^1-Piperideine[b]	0.03	0.8[c]	4	12	8	350	1.0×10^5
11	[6-^{14}C]-Δ^1-Piperideine[b]	0.05	0.9[d]	16	13	15	650	4.8×10^5
12	[6-^{14}C]-Δ^1-Piperideine[b]	0.05	0.9[d]	12	19	14	600	1.8×10^5

(*b*) Stable isotopes

Expt. no.	Substrate	Weight fed (mg)	Enrichment (at.%)	Plant material: Fresh weight (g)	Plant material: No. of plants	Lupanine (mg)	Specific incorporation of substrate per C_5 unit of lupanine (%)
13	[1-^{13}C,1-^{15}N]Cadaverine dihydrochloride[b]	167	99, 99	126	75	69[e]	9.7
14	(*R*)-[1-^{2}H]Cadaverine dihydrochloride[b]	169	99		43	140	2.5
15	(*S*)-[1-^{2}H]Cadaverine dihydrochloride[b]	95	93	128	46	69	2.8
16	DL-[2-^{2}H]Lysine monohydrochloride[b]	500	95	64	100	110	2.3
17	DL-[6-^{13}C]Lysine monohydrochloride[b]	848	99	390	94	125	1.9

[a]CEA France.
[b]See Experimental.
[c]From DL-[2-^{14}C]lysine dihydrochloride, specific activity 4.7 mCi/mmol (New England Nuclear).
[d]From DL-[6-^{14}C]lysine monohydrochloride, specific activity 48 mCi/mmol (CEA France).
[e]13-Hydroxylupanine (30 mg) was also isolated from this experiment. Specific incorporation of cadaverine per C_5 unit, 3.2%.

TABLE 2. Distribution of activity from DL-[6-^{14}C]lysine in lupanine (Expts. 7–9)

	C-atoms of lupanine	Experiment 7: SA[a]	Experiment 7: RSA[b]	Experiment 8: SA[a]	Experiment 8: RSA[b]	Experiment 9: SA[a]	Experiment 9: RSA[b]
Lupanine perchlorate	All	4.93±0.11	100±2	6.84±0.08	100±1	5.36±0.07	100±1
17-Oxolupanine	All					5.51±0.08	103±2
17-Oxosparteine	All	4.79±0.05	97±2	6.92±0.08	101±2		
Benzoic acid (C-2) from lupanine	C-2	0.67±0.10	14±2	0.92±0.02	13±0.3		
Benzoic acid (C-17) from 17-oxosparteine	C-17	0.58±0.03	12±1	0.79±0.05	12±1		
Pipecolic acid	C-9, C-11–C-15					2.57±0.04	48±1
γ-Aminobutyric acid	C-12–C-15					1.38±0.03	26±1
β-alanine	C-13–C-15					1.34±0.02	25±1

[a]SA = specific activity (dpm/mmol) × 10^{-4}.
[b]RSA = relative specific activity (percent) (lupanine perchlorate = 100%).

Can. J. Chem. Downloaded from www.nrcresearchpress.com by 112.217.228.212 on 09/07/12
For personal use only.

TABLE 3. Distribution of activity from ^{14}C-labelled Δ^1-piperideine in lupanine (Expts. 10–12)

	C-atoms of lupanine	SA[a]	RSA[b]	SA[a]	RSA	SA[a]	RSA[b]
Precursor: [2-^{14}C]-Δ^1-piperideine (Expt. 10)							
Lupanine perchlorate	All	10.2±0.2	100±1			3.2±0.04[c]	100±1[b]
17-Oxosparteine	All	10.3±0.2	101±2	2.3±0.04[d]	100±2[e]		
Benzoic acid (C-2) from lupanine	C-2	0.14±0.01	1.4±0.1				
Benzoic acid (C-17) from 17-oxosparteine	C-17			0.6±0.03	27±1		
Pipecolic acid	C-9, C-11–C-15					1.05±0.03	33±1
γ-Aminobutyric acid	C-12–C-15					0.011±0.06	0.3±2
β-Alanine	C-13–C-15					0.011±0.022	0.3±0.7
Precursor: [6-^{14}C]-Δ^1-piperideine (Expt. 11)							
Lupanine perchlorate	All	48.2±0.4	100±1			22.8±0.1[c]	100±1
17-Oxolupanine	All					22.8±0.1	100±1
17-Oxosparteine	All	48.3±0.6	100±1	8.3±0.06[d]	100±1[e]		
Benzoic acid (C-2) from lupanine	C-2	13.0±0.2	27±1				
Benzoic acid (C-17) from 17-oxosparteine	C-17			0.18±0.02	2±0.2		
Pipecolic acid	C-9, C-11–C-15					7.4±0.2	32±1
γ-Aminobutyric acid	C-12–C-15					7.3±0.3	32±1
β-Alanine	C-13–C-15					7.6±0.08	33±0.4
Precursor: [6-^{14}C]-Δ^1-piperideine (Expt. 12)							
Lupanine perchlorate	All	18.3±0.2	100±1	4.7±0.04[c]	100±1	3.5±0.3[c]	100±1
17-Oxolupanine	All	18.5±0.2	101±2			3.5±0.03	100±1
Benzoic acid (C-2) from lupanine	C-2			1.5±0.01	32±0.4		
Pipecolic acid	C-9, C-11–C-15					1.5±0.02	42±1
β-Alanine	C-13–C-15	7.2±0.2	39±1				

[a]SA = specific activity (dpm/mmol) × 10^{-4}.
[b]RSA = relative specific activity (percent) (lupanine perchlorate = 100%).
[c]This sample was obtained by further dilution of the lupanine perchlorate with non-radioactive carrier.
[d]This sample was obtained by further dilution of the 17-oxosparteine with non-radioactive carrier.
[e]RSA = relative specific activity (percent) (17-oxosparteine = 100%).

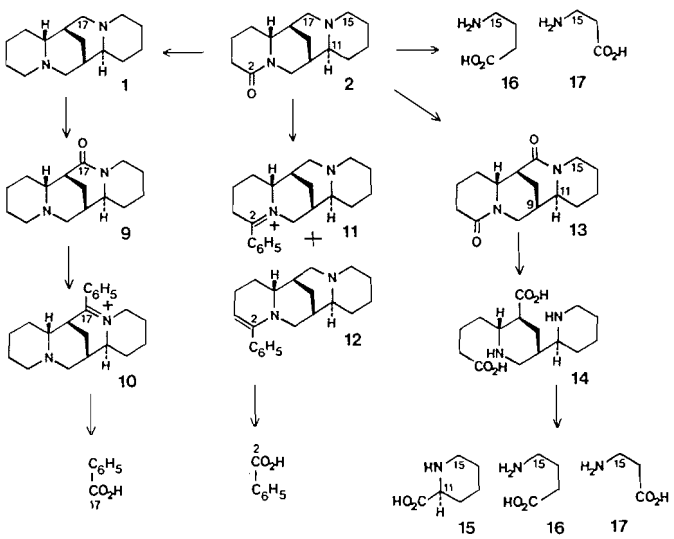

SCHEME. 1. Degradation of lupanine to determine labelling at C-2, C-11, C-15, and C-17.

of lupanine (expt. 13, Fig. 2), 13-hydroxylupanine (expt. 13, Fig. 3), and sparteine (expt. 5, Fig. 4) derived from [1-^{13}C, 1-^{15}N]cadaverine was determined by ^{13}C nmr spectroscopy. Spectra were recorded in the Fourier mode, at 20.15 MHz on a Bruker WP 80 spectrometer and at 125.8 MHz on a Bruker AM 500 spectrometer. Spectral assignments for sparteine, lupanine, and hydroxylupanine have been reported (39) [3].

The ^{13}C nmr spectrum of the sample of lupanine derived from DL-[6-^{13}C]lysine (Fig. 1) shows that the six carbon atoms adjacent to nitrogen, C-2, C-6, C-10, C-11, C-15, and C-17, but none of the other carbon atoms, are enriched in ^{13}C. Within experimental error the six carbon atoms are enriched to an equal extent. Similarly, the ^{13}C nmr spectra of the samples of lupanine (Fig. 2), 13α-hydroxylupanine (Fig. 3), and sparteine (Fig. 4), derived from [1-^{13}C,1-^{15}N]cadaverine, show enrichment at the same six carbon atoms. The enrichment at each of the six carbon atoms, calculated from the signal areas, was 1.9 ± 0.1% for the lupanine from DL-[6-^{13}C]lysine and 9.7 ± 0.5% for the lupa-

[3]The assignment of the two signals, C-5 and C-8, in the spectrum of lupanine, reported in ref. 39, must be reversed (5).

Can. J. Chem. Downloaded from www.nrcresearchpress.com by 112.217.228.212 on 09/07/12
For personal use only.

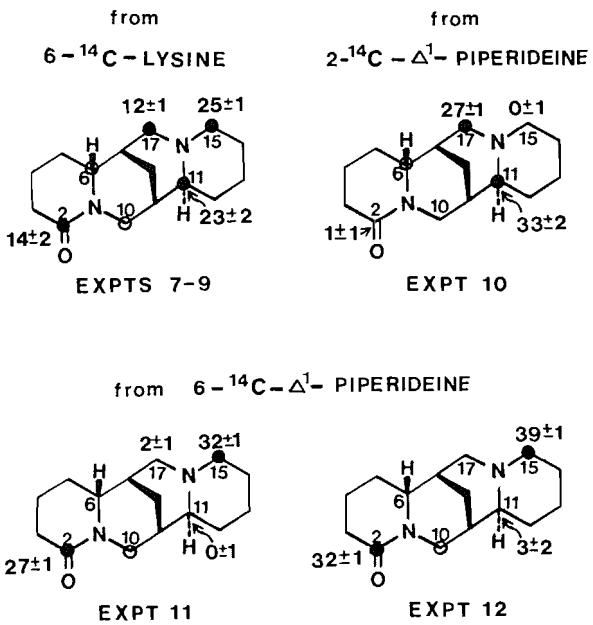

SCHEME. 2. Incorporation of label from [6-^{14}C]lysine and from [2-^{14}C]- and [6-^{14}C]-Δ^1-piperideine into lupanine.

nine, 3.2 ± 0.2% for the 13α-hydroxylupanine, and 50 ± 3% for the sparteine from [1-^{13}C,1-^{15}N]cadaverine.

In the spectrum of each of the three alkaloids, derived from [1-^{13}C,1-^{15}N]cadaverine, each of the signals due to two of the carbon atoms, C-6 and C-11, appears as a singlet, whereas each of the signals due to two carbon atoms, C-2 and C-15, appears as a doublet associated with a singlet of lower intensity, and each of the signals due to C-10 appears as a singlet associated with a well-resolved but much less intense doublet. The signals due to C-17 vary in appearance: In the spectra of lupanine (Fig. 2) and hydroxylupanine (Fig. 3), C-17 appears as a singlet whereas it appears as a singlet associated with a less intense doublet in the spectrum of sparteine (Fig. 4).

The distribution of deuterium within the samples of sparteine (expts. 1–4) and lupanine (expts. 14–16) derived from DL-[2-^{2}H]lysine (expts. 3, 16), from (*R*)-[1-^{2}H]cadaverine (expts. 1, 14), and (*S*)-[1-^{2}H]cadaverine (expts. 2, 15) and from [2-^{2}H]-Δ^1-piperideine (expt. 4) was determined by ^{2}H nmr spectroscopy. Spectral details and results of these experiments have been published (3).

Discussion

Feeding experiments with ^{13}C-labelled samples of lysine (see Fig. 1) and cadaverine (1–5), bearing enriched ^{13}C at one of the carbon atoms adjacent to nitrogen (Figs. 2–4), yielded ^{13}C-enriched $C_{15}N_2$ lupine alkaloids. The distribution of ^{13}C within these alkaloids, established by ^{13}C nmr spectroscopy, substantiates the inferences drawn from the results of the tracer experiments with correspondingly ^{14}C-labelled substrates (6–15), that label is evenly distributed over the six carbon atoms adjacent to the nitrogen atoms of the $C_{15}N_2$ lupine alkaloids.

Thus, each of carbon atoms C-2, C-6, C-10, C-11, C-15, and C-17 within lupanine derived from DL-[6-^{13}C]lysine (Fig. 1), from [1-^{13}C,1-^{15}N]cadaverine (3, 4), from [1,2-$^{13}C_2$]-cadaverine (5), and within 13α-hydroxylupanine (4, 5) and sparteine (1, 2, 5) derived from the latter two substrates, show equal ^{13}C enrichment (1–5), within the limits of detection.

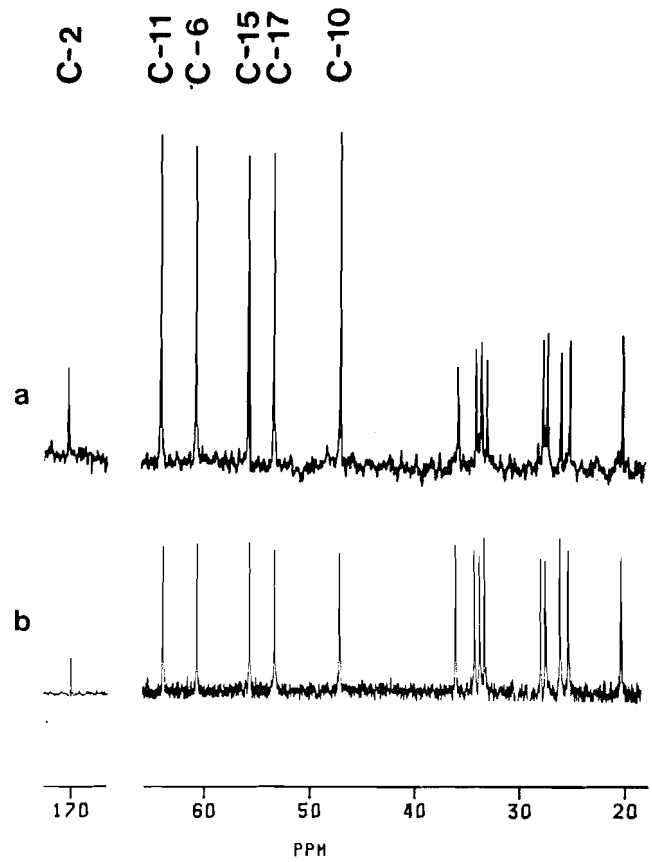

FIG. 1. (a) The 125.8-MHz ^{13}C nmr spectrum of (+)lupanine (**2**) derived from DL-[6-^{13}C]lysine; (b) natural abundance spectrum of (+)lupanine.

This distribution of label together with the evidence, presented in the introduction, on the retention of an intact C—N bond of cadaverine at N-1,C-2 and at N-16,C-15 of the alkaloids (1–4) and on the regiospecificity of entry of label from ^{14}C-labelled Δ^1-piperideine (23) leads to the inference that the $C_{15}N_2$ skeleton of the alkaloids is generated from three identical cadaverine-derived C_5N units, as shown in Scheme 3.

On the basis of the tracer evidence that was available 10 years ago we suggested (23) that equal distribution of label over the three C_5 segments of the $C_{15}N_2$ skeleton might be explained if the $C_{15}N_2$ alkaloids were derived from a trimer of Δ^1-piperideine. This biogenetic model also accounts for the stereochemistry of the alkaloids. The model is entirely consistent with the more recent results on the incorporation of ^{13}C and ^{13}C,^{15}N-labelled (1–5) and ^{2}H-labelled (3, 18–21) substrates, which are summarized in the introduction. These results define the regiochemistry and the prochirality of biosynthesis. Scheme 4 presents an updated version of the piperideine trimer model of biosynthesis. A cornerstone of this model is the equal incorporation of ^{14}C- or ^{13}C-label into the three C_5 segments of the alkaloids.

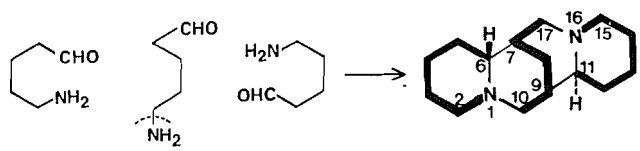

SCHEME. 3. Incorporation of three C_5N units into the bisquinolizidine skeleton.

Can. J. Chem. Downloaded from www.nrcresearchpress.com by 112.217.228.212 on 09/07/12
For personal use only.

Can. J. Chem. Downloaded from www.nrcresearchpress.com by 112.217.228.212 on 09/07/12
For personal use only.

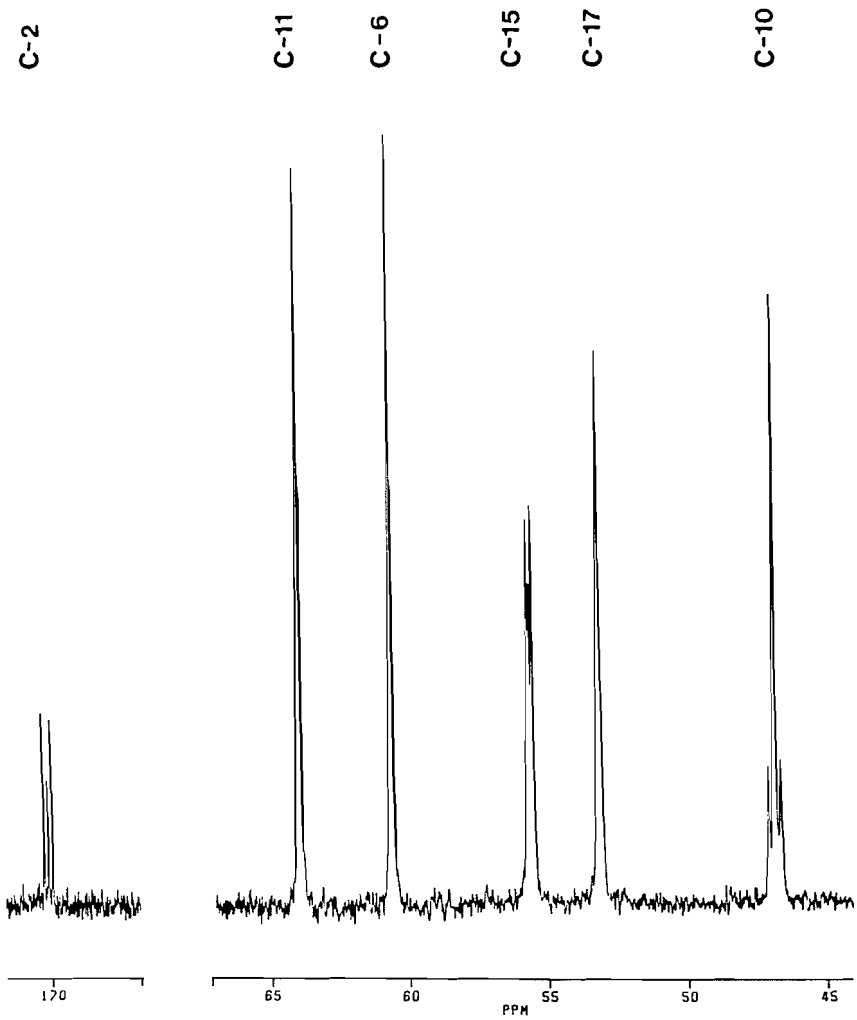

FIG. 2. Signals due to the ^{13}C-enriched carbon atoms in the 20.15-MHz ^{13}C nmr spectrum of (+)lupanine (**2**) derived from [1-^{13}C, 1-^{15}N]cadaverine.

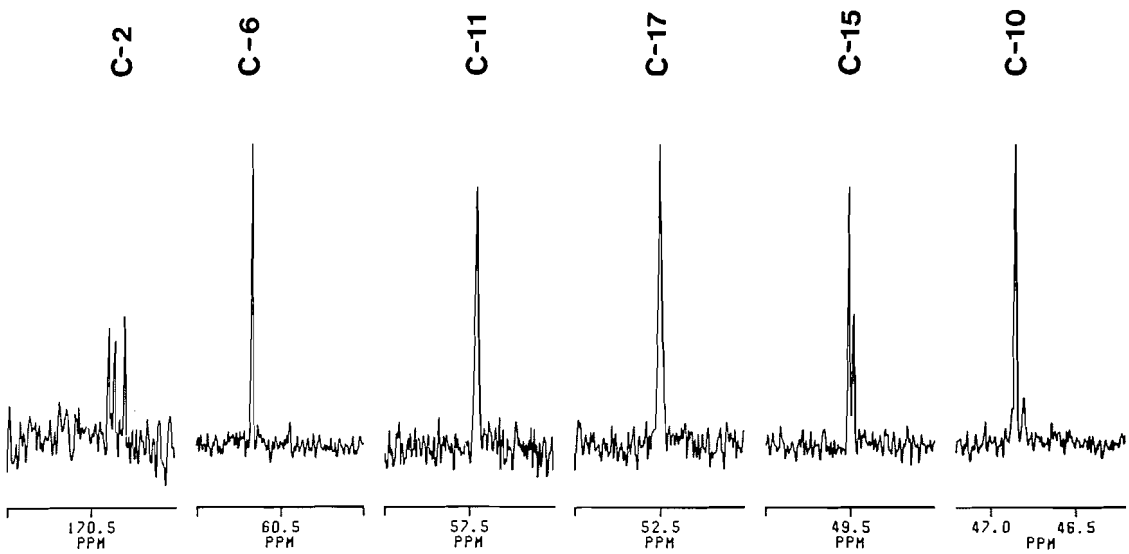

FIG. 3. Signals due to the ^{13}C-enriched carbon atoms in the 125.8-MHz ^{13}C nmr spectrum of 13α-hydroxylupanine (**3**) derived from [1-^{13}C,1-^{15}N]cadaverine.

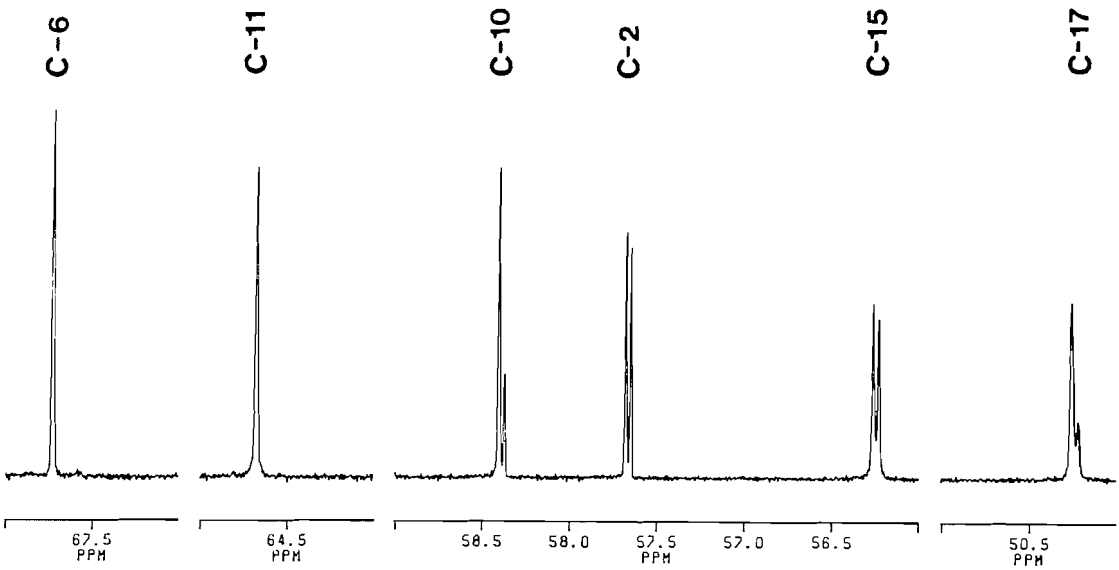

FIG. 4. Signals due to the ^{13}C-enriched carbon atoms in the 125.8-MHz ^{13}C nmr spectrum of (−)sparteine (**1**) derived from [1-^{13}C, 1-^{15}N]cadaverine.

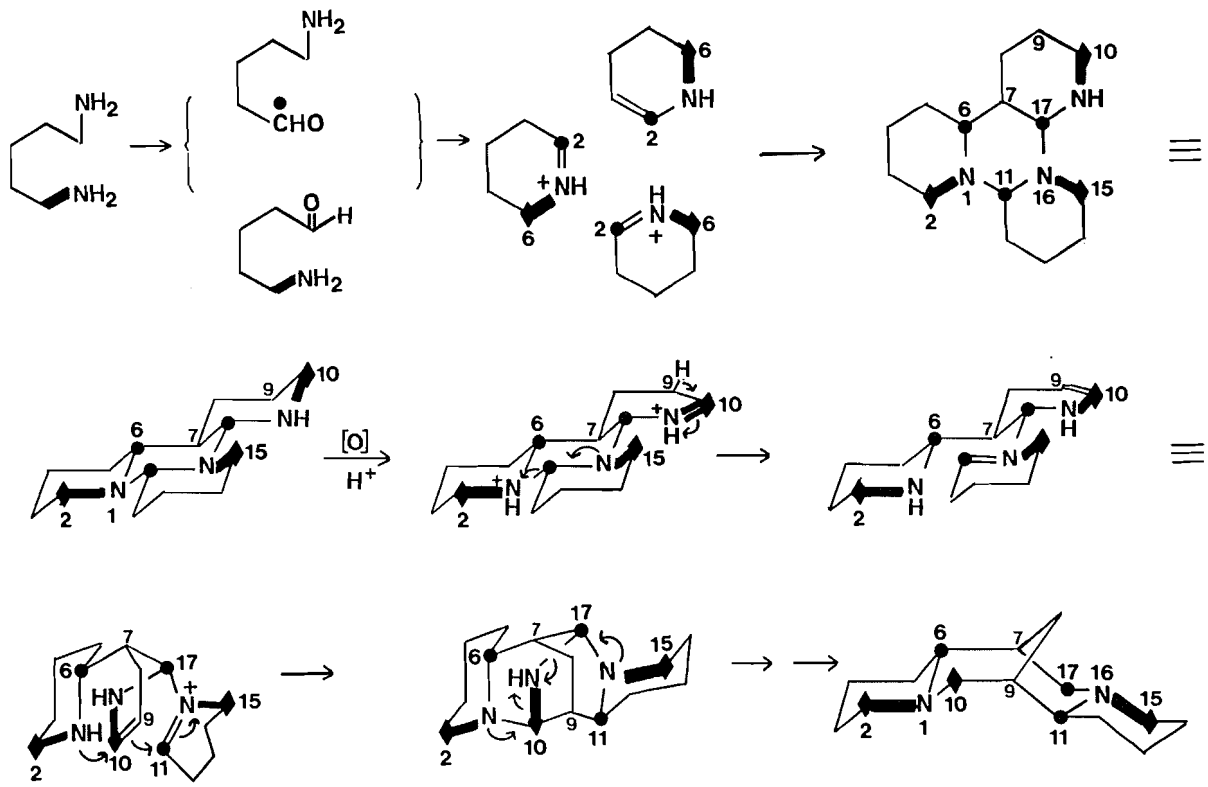

SCHEME. 4. The Δ^1-piperideine trimer model of sparteine biosynthesis, showing the predicted distribution of label from [1-^{13}C,1-^{15}N]cadaverine (■, ●) and from [2-^{14}C]- and [6-^{14}C]-Δ^1-piperideine (2 = ●, 6 = ◆).

The 20.15-MHz ^{13}C nmr spectrum (2) of the sample of sparteine, derived from [1-^{13}C,1-^{15}N]cadaverine, showed six signals that indicated ^{13}C enrichment. Two of these signals, those due to C-2 and C-15, appeared as doublets ($J_{^{13}C\text{-}2,^{15}N\text{-}1}$ 3.6 Hz, $J_{^{13}C\text{-}15,^{15}N\text{-}16}$ 3.9 Hz), proving intact incorporation of the ^{13}C–^{15}N moiety of the precursor into the two C—N units, C-2,N-1 and C-15,N-16 of the alkaloid. Central singlets were not detectable in these signals. This showed that every molecule containing ^{13}C at either of these sites also contains ^{15}N at the position adjacent to ^{13}C, and that in no case is ^{13}C, at either of these sites, contiguous with ^{14}N.

Two other signals, due to C-6 and C-11, appeared as singlets. This proved that ^{13}C at these sites is not intramolecularly contiguous with ^{15}N. This is as would be predicted if each of the

Can. J. Chem. Downloaded from www.nrcresearchpress.com by 112.217.228.212 on 09/07/12
For personal use only.

C_5N units of the alkaloids, N-1,C-2,-3,-4,-5,-6 and N-16,C-15,-14,-13,-12,-11, originated *in toto* from a cadaverine-derived C_5N unit, NH_2—CH_2—CH_2—CH_2—CH_2—CHO. [1-^{13}C,1-^{15}N]Cadaverine would yield either $^{15}NH_2$—$^{13}CH_2$—CH_2—CH_2—CH_2—CHO or NH_2—CH_2—CH_2—CH_2—CH_2—^{13}CHO. Thus, C-6 cannot be enriched in ^{13}C, in molecules in which N-1 is enriched in ^{15}N; and C-11 cannot be enriched in ^{13}C if N-16 is enriched in ^{15}N. The ^{13}C-enriched signals due to C-6 and C-11 must therefore appear as singlets, as was indeed observed. The last two ^{13}C-enriched signals, due to C-10 and C-17, were unresolved in the 20.15-MHz ^{13}C nmr spectrum (2). At 125.8 MHz (Fig. 4) each of these two signals is resolved into a pair of lines of relative signal area 3:1.

Each of these signals represents a singlet, relative area 1, due to ^{13}C adjacent to ^{14}N, superimposed on a doublet, relative area 1, due to ^{13}C adjacent to ^{15}N ($J_{^{13}C\text{-}10,^{15}N\text{-}1}$ 4.0 Hz, isotope shift −0.015 ppm; $J_{^{13}C\text{-}17,^{15}N\text{-}16}$ 4.4 Hz, isotope shift −0.015 ppm). This is the result that would be expected if sparteine were generated from a 1:1 mixture of natural abundance and highly ^{13}C,^{15}N-enriched C_5N precursor, and if a C_5N unit from this mix, destined to lose ^{15}N to become the central C_5 chain, C-10,-9,-8,-7,-17, of the alkaloid were to couple with each of the two other units from this mix that yield the two outer rings of the sparteine system.

The incorporation pattern of [1-^{13}C,1-^{15}N]cadaverine into sparteine, as revealed by high resolution nmr, is entirely consistent with and supports the Δ^1-piperideine trimer model of biosynthesis.

Close scrutiny of the ^{13}C nmr spectra of lupanine (Fig. 2) and 13α-hydroxylupanine (Fig. 3) reveals a somewhat different picture.

As in the case of sparteine (2) (Fig. 4), the signals due to C-6 and C-11 in the spectra of lupanine (3) (Fig. 2) and 13α-hydroxylupanine (Fig. 3) appear as enriched singlets. As in the case of sparteine, the signals due to C-2 and C-15 show that an intact ^{15}N–^{13}C unit of the precursor had entered the two sites, N-1,C-2 and N-16,C-15, of the alkaloids. However, whereas in the case of sparteine these two signals appeared as doublets (2), due to the high specific incorporation (ca. 50% per C_5 unit), in the present cases each of these signals appears as a doublet associated with a singlet (lupanine $J_{^{13}C\text{-}2,^{15}N\text{-}1}$ 11.9 Hz, isotope shift −0.02 ppm; $J_{^{13}C\text{-}15,^{15}N\text{-}16}$ 3.6 Hz, isotope shift −0.02 ppm; 13α-hydroxylupanine $J_{^{13}C\text{-}2,^{15}N\text{-}1}$ 12.7 Hz, isotope shift −0.02 ppm; $J_{^{13}C\text{-}15,^{15}N\text{-}16}$ 3.5 Hz, isotope shift −0.01 ppm). The doublet/singlet ratios (lupanine C-2 3.3; C-15 3.1; 13α-hydroxylupanine C-2 2.0; C-15 2.1) are consistent with the lower specific incorporation of enriched substrate into the products (9.7% and 3.2% per C_5 unit, respectively). It is important to note that, in each of the alkaloids, the doublet/singlet ratio at the two sites is equal within experimental error, as expected. This shows that the two outer rings originate from the same doubly enriched precursor. Yet, the spectrum indicates that there is an important difference between the interactions of the two outer rings with the central C_5 unit: Whereas the signal due to C-10 appears as a singlet associated with a doublet due to ^{13}C-10, ^{15}N-1 coupling (lupanine singlet/doublet ratio 2.4, $J_{^{13}C\text{-}10,^{15}N\text{-}1}$ 9.0 Hz, isotope shift −0.02 ppm; 13α-hydroxylupanine singlet/doublet ratio 2.5, $J_{^{13}C\text{-}10,^{15}N\text{-}1}$ 3.2 Hz, isotope shift −0.02 ppm), the signal due to C-17 appears, in each case, as a broad-based (4 Hz) singlet and does not show a resolved doublet. Similar observations have been reported by Rana and Robins (4). The differences in the appearance of the signals due to C-10 and C-17 may be due to differences in the coupling constants around N-1 and N-16 (ca. 12 and 3.5 Hz, respectively). However, it is conceivable that, since the enrichment within C-10 and C-17 is equal, the observed differences in the signals may indicate that N-16 is less enriched in ^{15}N than N-1.

It should be noted that in the sparteine, from the same substrate (1, 2) (Fig. 4), the observed singlet/doublet ratios shown by the signals due to C-10 and C-17 were identical (see above), indicating equal ^{15}N enrichment at N-1 and N-16.

It would thus appear that, whereas under the conditions of the sparteine experiments (1, 2) the efficiency of entry of label from [1-^{13}C,1-^{15}N]cadaverine into each of the two C_5N units and into the central C_5 unit of the alkaloid was the same, in the other experiments (3, 4) the efficiency of entry of label from the precursor into the C_5N unit, N-16,C-15,-14,-13,-12,-11, may not have been the same as that of its entry into the other two units.

As a corollary of unequal enrichment in ^{15}N at N-1 and N-16, one would expect to find that enrichment at C-2(≡ C-6) would be different from enrichment at C-15(≡ C-11). This prediction cannot be conclusively confirmed or controverted on the basis of the spectra that are at hand, because of the difficulties of obtaining accurate and reproducible quantitative values for the signal areas of the different signals in the ^{13}C nmr spectrum of a minute sample of compound containing enrichment at individual carbon atoms. At best, it can be said that the spectra that are available (3, 4) suggest the possibility that the $C_{15}N_2$ alkaloids that were generated in some of the experiments with [1-^{13}C,1-^{15}N]cadaverine contained different levels of isotopic enrichment in the two C_5N segments, N-1,C-2,-3,-4,-5,-6 and N-16,C-15,-14,-13,-12,-11.

Since other evidence, reviewed earlier, led to the inference that these two moieties, as well as the central C_5 chain of the alkaloids, originate from one and the same C_5N precursor, it follows that, in the course of construction of the $C_{15}N_2$ skeleton, at least one of the C_5N precursor units may have undergone endogenous carrier dilution at a level different from that suffered by the other two C_5N precursor units.

The suspicion, aroused on the basis of the ^{13}C nmr spectra, that one of the C_5 segments of the $C_{15}N_2$ alkaloids may contain isotopic enrichment at a level different from that of the other two C_5 segments, became certainty, on the basis of the results of tracer experiments with ^{14}C-labelled substrates. The distribution of label, established by controlled chemical degradations of lupanine samples derived from DL-[6-^{14}C]lysine in three separate experiments (expts. 7–9, Table 2, Scheme 2), differed dramatically from the equal labelling at six sites adjacent to nitrogen, expected on the basis of published work with DL-[2-^{14}C]lysine (10, 11, 13). One quarter of the total activity of the alkaloid was located at each of C-15 and C-11, so that the C_5N unit, N-16,C-15,-14,-13,-12,-11, accounted for half the activity within the lupanine molecule. The other half was distributed over the rest of the molecule, C-2 and C-17 each containing one eighth of the activity, with the other two eighths presumably distributed over C-6 and C-10 (Scheme 2).

Degradation of the samples of lupanine derived from [2-^{14}C]- and [6-^{14}C]-Δ^1-piperideine showed similar trends, in that in each case the C_5N moiety, N-16,C-15,-14,-13,-12,-11, contained somewhat higher labelling than the other two C_5 moieties. In one case (expt. 12, Table 3), approximately 40% of label was located at C-15, whereas C-2 and, presumably, C-10 each contained approximately 30% of label (Scheme 2).

Such a distribution of label can arise only if one of the three identical C_5N units, namely that which serves as the precursor of

Can. J. Chem. Downloaded from www.nrcresearchpress.com by 112.217.228.212 on 09/07/12
For personal use only.

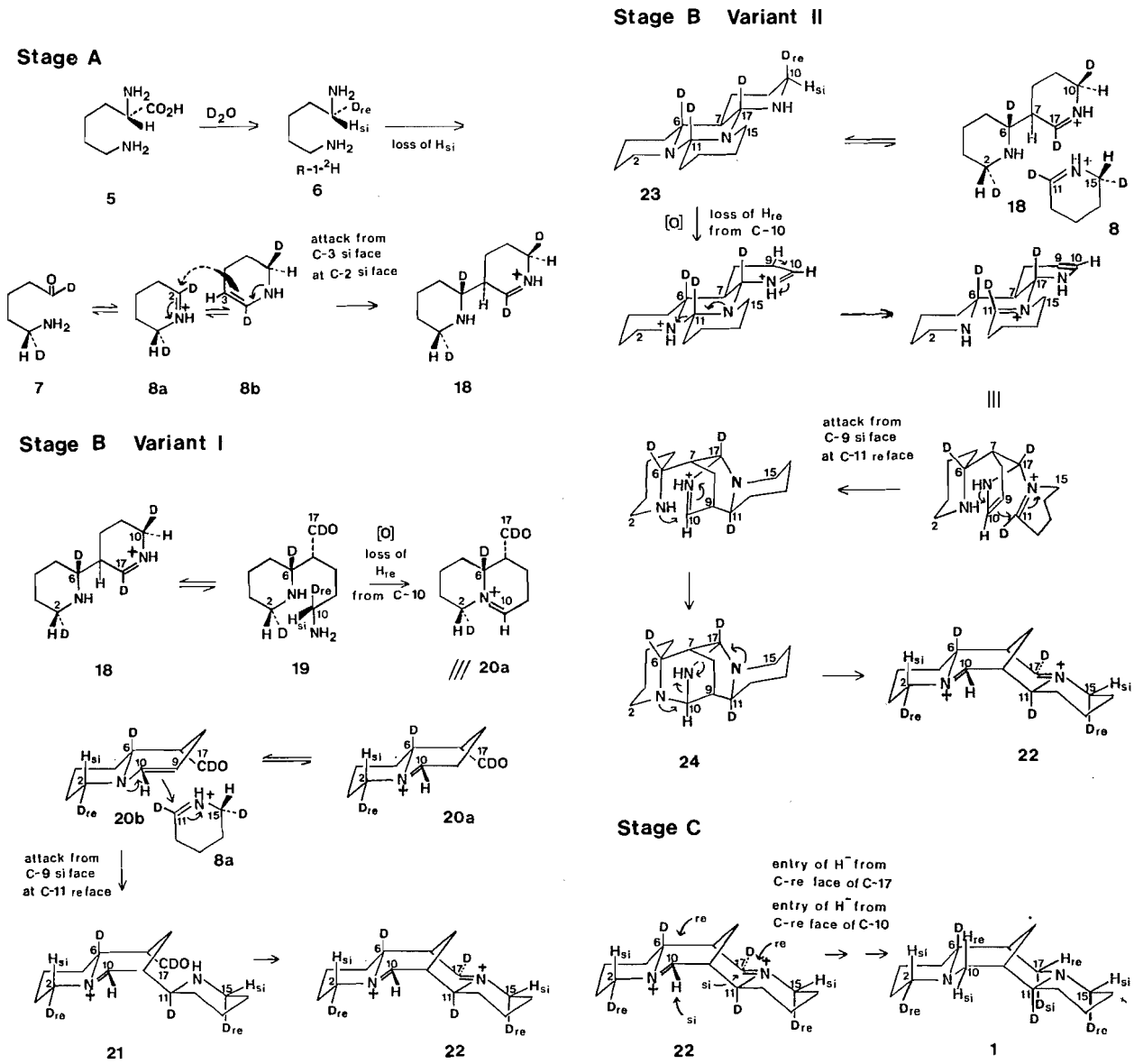

SCHEME. 5. Biosynthesis of sparteine from (*R*)-[1-^{2}H]cadaverine. Stage A: The initial steps. Stage B: Two variants, I and II, of the intermediate steps. Stage C: The final step. (a = acid, b = base).

the C_5N moiety N-16,C-15,-14,-13,-12,-11 of the alkaloids, suffers less endogenous carrier dilution on the route to the product than the two units that give rise to the rest of the bisquinolizidine system.

Clearly, a bisquinolizidine skeleton showing this distribution of label cannot be derived from a trimer of the C_5N precursor since trimerization of a labelled monomer would deliver equimolar quantities of label into each of the three subunits of the trimer.

Evidently the Δ^1-piperideine trimer model (23) of the biosynthesis of the $C_{15}N_2$ lupine alkaloids, as it stands (Scheme 4), cannot accommodate these new experimental findings, which indicate that two of the three C_5 units of the bisquinolizidine skeleton, C-2,-3,-4,-5,-6 and C-10,-9,-8,-7,-17, are invariably labelled at the same level, while the third C_5 unit, C-11,-12,-13,-14,-15, can carry label at a lower level (as may have been the case in some of the experiments with [^{13}C,^{15}N]cadaverine (3, 4)), at the same level (as in all the experiments with ^{14}C-labelled lysine and cadaverine, hitherto reported (6–15)) or at a higher level (as now observed with ^{14}C-labelled lysine and Δ^1-piperideine).

A modified biosynthetic model, which is consistent with the new findings and also accounts for the earlier observations on the regiospecificity of entry of label from ^{14}C-, ^{13}C-, ^{13}C,^{15}N-, and ^{2}H-labelled substrates (1–21, 23) and accommodates the evidence on the stereochemistry of biosynthesis derived from the incorporation of label from deuteriated substrates (3, 18–21), is presented in Schemes 5 and 6.

The two key intermediates of this model are the Δ^1-piperideine dimer, tetrahydroanabasine (**18**), and the bisquinolizidine derivative, 1,10;16,17-didehydrosparteinium ion (**22**).

The initial steps of the model (Stage A, Schemes 5 and 6), conversion of L-lysine (**5**) into tetrahydroanabasine (**18**) via cadaverine (**6**) and Δ^1-piperideine (**8**), in four stereochemically defined reactions, are identical with those of the route from L-lysine into the $C_{10}N$ lupine alkaloid lupinine, whose biosynthesis has been discussed in detail in the first paper of this series (37). The suggestion that tetrahydroanabasine may be an in-

Can. J. Chem. Downloaded from www.nrcresearchpress.com by 112.217.228.212 on 09/07/12
For personal use only.

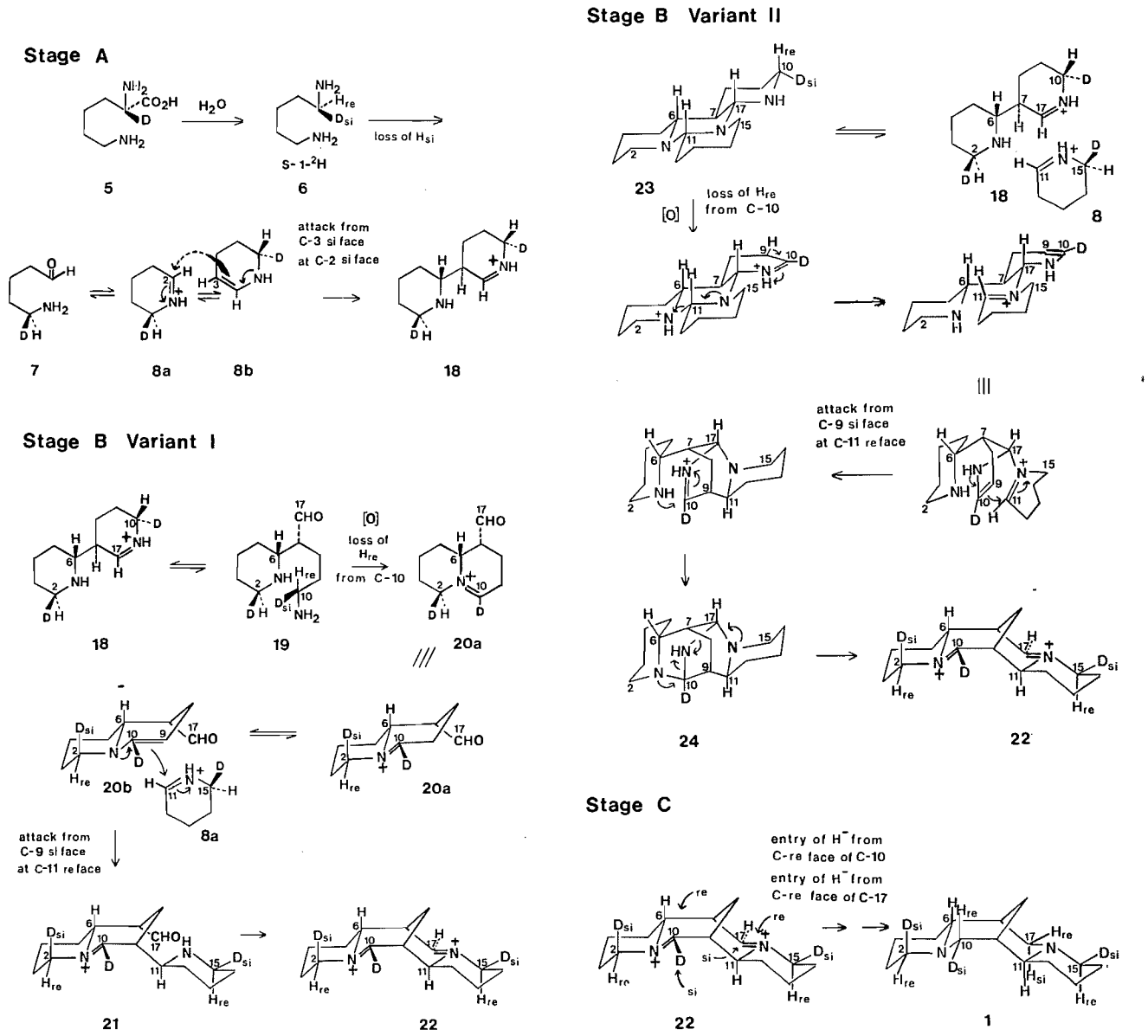

SCHEME. 6. Biosynthesis of sparteine from (*S*)-[1-^{2}H]cadaverine. Stage A: The initial steps. Stage B: Two variants, I and II, of the intermediate steps. Stage C: The final step. (a = acid, b = base).

termediate on the pathway to lupinine was first made by Schütte (40).

In the final steps of the proposed sequence (Stage C, Schemes 5 and 6) sparteine (**1**), lupanine (**2**), and other bisquinolizidine lupine alkaloids are generated from 1,10;16,17-didehydrosparteinium ion (**22**). This is the entity that we regard as the first intermediate containing the complete $C_{15}N_2$ skeleton.

The intermediate steps of the model (Stage B, Schemes 5 and 6) lead from tetrahydroanabasine (**18**) into the didehydrosparteinium ion (**22**). Two routes for this transformation must be considered. The major difference between these routes is the timing of the loss of nitrogen from the C_5N precursor unit that is destined to yield the central C_5 chain, C-10,-9,-8,-7,-17, of the bisquinolizidine skeleton.

In one case (variant I) nitrogen is eliminated from a tetrahydroanabasine-derived $C_{10}N_2$ intermediate (**19**). Further condensation with the additional C_5N unit takes place after nitrogen loss. Generation of the didehydrosparteinium ion (**22**) by this route can be schematically represented by the reaction sequence (*i*) $C_{10}N_2$ minus $N \rightarrow C_{10}N$; (*ii*) $C_{10}N$ plus $C_5N \rightarrow C_{15}N_2$. The key $C_{10}N$ intermediate (**20**) of this sequence not only serves as one of the building blocks of the bisquinolizidine lupine alkaloids but is also a precursor of the $C_{10}N$ lupine alkaloid, lupinine (37). The possible involvement of this key intermediate in the elaboration of the $C_{15}N_2$ lupine alkaloids was first suggested by Leete (41) (see ref. 23).

In the other case (variant II) the didehydrosparteinium ion (**22**) is generated by elimination of nitrogen from a $C_{15}N_3$ intermediate (**24**) that is formed after condensation of tetrahydroanabasine (**18**) with Δ^1-piperideine (**8**). This reaction sequence is schematically represented by (*i*) $C_{10}N_2$ plus $C_5N \rightarrow C_{15}N_3$; (*ii*) $C_{15}N_3$ minus $N \rightarrow C_{15}N_2$. This pathway implicates the conformationally favoured stereoisomer (**23**) of isotripiperideine (42) and is a modification of the Δ^1-piperideine trimer model (23) of lupine alkaloid biosynthesis (Scheme 4).

Both variants predict that the two C_5 chains, C-2,-3,-4,-5,-6 and C-10,-9,-8,-7,-17, of the alkaloids are derived from the two C_5 chains of tetrahydroanabasine (**18**). Since tetrahydroanaba-

Can. J. Chem. Downloaded from www.nrcresearchpress.com by 112.217.228.212 on 09/07/12
For personal use only.

Can. J. Chem. Downloaded from www.nrcresearchpress.com by 112.217.228.212 on 09/07/12
For personal use only.

sine is formed by dimerization of Δ^1-piperideine (**8**) it is a necessary consequence of its mode of formation that the two C_5 chains contain equimolar amounts of label, if generated from labelled Δ^1-piperideine, and that the four carbon atoms, C-2, -6, -10, and -17, of sparteine or lupanine are invariably equally labelled with ^{14}C or equally enriched in ^{13}C, when derived from appropriately ^{14}C- or ^{13}C-labelled lysine or cadaverine.

Both variants of Stage B, Schemes 5 and 6, predict that the C_5 chain, C-11,-12,-13,-14,-15, of the alkaloids is derived from the C_5 chain of a third Δ^1-piperideine unit that condenses with the previously formed C_{10} intermediate in a later separate step. Since, in the intact plant, the pool sizes of the C_{10} and the C_5 intermediates are not necessarily the same at the time of their condensation, conditions can therefore exist, in an experiment with labelled substrates, that can lead to the delivery into the C_5 chain, C-11,-12,-13,-14,-15, of a different concentration of label, higher or lower, than into the C_{10} unit, C-2,-3,-4,-5,-6;C-10,-9,-8,-7,-17.

In experiments with intact plants it would appear to be almost impossible to control the conditions that might lead to predictably different levels of enrichment in the C_{10} and C_5 segments of the product. It is likely, however, that in the case of the experiments with DL-[6-^{14}C]lysine (expts. 7–9) the high specific activity (48 mCi/mmol) and thus the minute quantity of the precursor that was administered (ca. 0.03, 0.07, 0.04 mg labelled lysine per plant administered in a single dose, then allowed to metabolize for 4 days) favoured discrimination of labelling in the two segments of lupanine. This must be compared with the results obtained when a much larger amount of precursor was administered, as in the experiment with DL-[6-^{13}C]lysine (expt. 17) (9 mg enriched lysine per plant, administered in 5 equal portions daily for 5 days, then allowed to metabolize for 4 more days) and in the experiments with DL-[2-^{14}C]lysine reported in the literature (9, 13, 15) (ca. 1–2 mg labelled lysine per plant, then incubated over 4 days). In these experiments equimolar labelling or enrichment was observed at each of the six labelled sites, presumably because the endogenous pools of the C_{10} and C_5 intermediates were swamped by the large amount of exogenous substrate that had been administered. On the other hand, in the experiments with [6-^{14}C]lysine (expts. 7–9) the tracer amounts of exogenous substrate that were administered evidently did not obliterate the differences in the pool sizes, of the C_{10} and the C_5 precursor, that existed endogenously. As a consequence, different levels of labelling at the sites of the C_{10} unit and those of the C_5 unit resulted.

This serendipitous observation opens the way to the next stage of the investigation of the biosynthesis of the $C_{15}N_2$ lupine alkaloids, a critical examination of the intermediate steps of the biosynthetic route.

Even though we currently tend to favour variant I of the model outlined in Stage B of Schemes 5 and 6, both variants, I and II, are consistent with the regiochemical and stereochemical evidence derived from incorporation experiments with intact plants, and must be tested. This work is in progress.

Experimental

Radioactive materials

DL-[2-^{14}C]Lysine and DL-[6-^{14}C]lysine were obtained from commercial sources (see Table 1).

Δ^1-Piperideine was obtained from DL-lysine by oxidation with *N*-bromosuccinimide (cf. ref. 43). *N*-Bromosuccinimide (40 mg, 0.22 mM) was added to a solution containing the radioactive lysine together with carrier DL-lysine monohydrochloride to make a total of 20 mg (0.11 mM) lysine monohydrochloride in 3 mL of water. The flask was rotated on a rotary evaporator under mild suction while immersed in a water bath at 40–50°C. When the solution had become colorless (ca. 20 min) it was basified with potassium carbonate (20% w/v, 2 mL) and extracted with chloroform (6 × 5 mL). The chloroform extract was washed with water, filtered, and evaporated to dryness. The oily residue (30 mg) was dissolved in dilute hydrochloric acid (0.25 M, 1 mL). Thin-layer chromatography (silica gel, 1-butanol:acetic acid:water, 2:1:1) showed the presence of Δ^1-piperideine (R_f 0.6) as the major component, together with traces of unchanged lysine (R_f 0.23). The radiochemical yield was approximately 50%.

In this manner DL-[6-^{14}C]lysine (total activity 0.1 mCi, specific activity 48 mCi/mmol, CEA France) was converted into [6-^{14}C]-Δ^1-piperideine (specific activity 0.9 mCi/mmol) (expts. 11, 12), and DL-[2-^{14}C]lysine (total activity 0.1 mCi, specific activity 4.7 mCi/mmol, New England Nuclear) was converted into [2-^{14}C]-Δ^1-piperideine (specific activity 0.8 mCi/mmol) (expt. 10).

Administration of radioactive tracers to L. angustifolius *and* L. luteus

Plants were grown from seed and used for tracer experiments 3–6 weeks after germination. Experiments with *L. angustifolius* were carried out in the greenhouse (expts. 7–11) or in the growth chambers (expt. 13). The tracer experiment with *L. luteus* (expt. 6) has been described (37). Tracer solution was administered to 12–30 plants by wick in a single dose. The plants were allowed to grow 3–5 days in contact with tracer. Details of the experiments with *L. angustifolius* are summarized in Table 1. Details of the experiments with *L. luteus* were reported previously (37).

^{13}C- and ^{2}H-enriched compounds

The preparation of [1-^{13}C,1-^{15}N]cadaverine (37) and of the ^{2}H-enriched samples of cadaverine (27), lysine (27), and Δ^1-piperideine (27) has been reported previously.

DL-*[6-^{13}C]Lysine monohydrochloride* (Scheme 7)

*Ethyl 2-acetylamino-2-ethoxycarbonyl-5-hydroxypentanoate (ref. 44) (**28**).* Diethyl acetamidomalonate (**26**) (10.9 g) was added to a suspension of freshly prepared sodium methoxide (from 18 mg sodium metal) in dry benzene (17 mL). The mixture was cooled and freshly distilled acrolein (**25**) (2.9 g) in dry benzene (4 mL) was added dropwise with stirring over 15 min. Stirring was continued for 2 h at room temperature. The mixture was then filtered and the filtrate evaporated. The crude aldehyde (**27**) so obtained was dissolved in ethanol (5 mL), triethylamine (5 mL) and freshly prepared Raney nickel catalyst (1 g) were added, and the mixture was shaken 24 h in a Parr hydrogenator (40–50 psi, 75°C; 1 psi = 6.9 kPa). The catalyst was centrifuged off, the supernatant solution was concentrated, and the oily residue was dissolved in ether (40 mL) and cooled (−5°C). The product (**28**) that separated was filtered off, washed with cold ether, and recrystallized from acetone/ether. Yield 5.5 g, mp. 80°C (lit. (44) mp 80–81°C); ^{1}H nmr ($CDCl_3$) δ: 7.1 (1H, s, NH), 4.2 (4H, q, *J* 7.5 Hz, CH_2CH_3), 3.6 (2H, t, *J* 6.9 Hz, H-5), 3.3 (1H, s, OH), 2.5–2.3 (2H, m, H-4), 1.5–1.2 (2H, m, H-3), 2.0 (3H, s, CH_3CO), 1.3 (6H, t, *J* 7.5 Hz, CH_3CH_2) ppm.

Ethyl O-p-*toluenesulfonyl-2-acetylamino-2-ethoxycarbonyl-5-hydroxypentanoate (**29**).* Tosyl chloride (6.42 g) was added in small portions to a solution of the alcohol (**28**) (4.63 g) in anhydrous pyridine (70 mL) at 0°C. The mixture was kept 20 h at 5°C and was then poured into a water/ice mixture, which was stirred 2 h. The white precipitate was filtered off, washed with water (3 × 50 mL), and dried *in vacuo* over anhydrous potassium hydroxide. The product (**29**) was recrystallized from methanol and was filtered off at 0°C. Yield 5.34 g, mp. 106.5–107°C; ^{1}H nmr (C_6D_6) δ: 7.7 (2H, d, *J* 8.4 Hz, H-2′,6′), 7.1 (2H, d, *J* 8.4 Hz, H-3′,5′), 6.7 (1H, s, NH), 4.1 (4H, q, *J* 7.2 Hz, -CH_2CH_3), 3.9 (2H, t, *J* 6.3 Hz, H-5), 2.5–2.3 (2H, m, H-4), 2.2 (3H, s, CH_3Ph), 1.7 (3H, s, CH_3CO), 1.7–1.4 (2H, m, H-3), 1.1 (6H, t, *J* 7.2 Hz, CH_2CH_3) ppm.

*Ethyl 2-acetylamino-2-ethoxycarbonyl-5-[^{13}C-cyano]pentanoate (**30**)* (cf. ref. 38). A solution of the above tosylate (**29**) (4.23 g) in

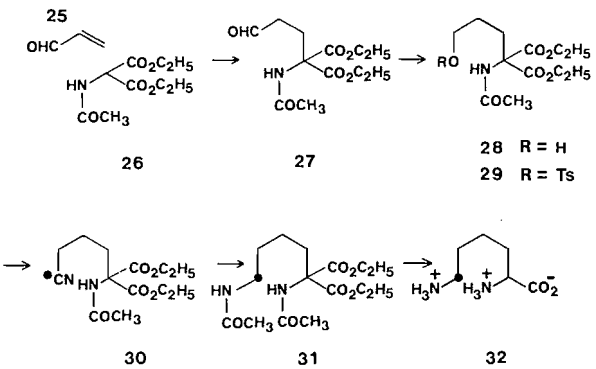

SCHEME. 7. Synthesis of [6-^{13}C]lysine (● denotes ^{13}C).

dimethyl sulfoxide (11 mL) was added dropwise at room temperature over 2 h to a stirred solution of potassium [^{13}C]cyanide (99 at.% ^{13}C, MSD Isotopes, Montreal) (680 mg) in dimethyl sulfoxide (15 mL) and water (2 mL). Stirring was continued for a further 21 h, at which time starting material was no longer present (tlc). The yellow solution was poured into water (150 mL) and the product was extracted into benzene (5 × 50 mL). The benzene extract was washed with saturated sodium chloride solution (6 × 50 mL), dried, and evaporated *in vacuo* to yield the nitrile (**30**) as a yellowish oil that crystallized on cooling (2.75 g). An analytical sample was obtained by recrystallization from ethanol/hexane at −44°C; mp 47–48°C. In an earlier report the substance failed to crystallize (38). Infrared (liquid film): 3360 (NH), 2220 (CN), 1742, 1190 (CO_2Et), 1665 (NCO) cm^{-1}; ^{1}H nmr $CDCl_3$) δ: 6.9 (1H, s, NH), 4.1 (4H, q, *J* 7.5 Hz, CH_2CH_3), 2.6–2.2 (4H, m, H-3,-5), 2.0 (3H, s, CH_3CO), 1.5 (2H, m, H-4), 1.3 (6H, t, *J* 7.5 Hz, CH_2CH_3); ^{13}C nmr δ; 169.5 ($COCH_3$), 167.7 (-CO_2-), 119.1 (CN), 66.1 (-OCH_2-), 58.3 (C-2), 31.7 (d, *J* 3.6 Hz, C-3), 23.0 (CH_3-CO), 19.5 (d, *J* 42 Hz, C-5), 15.6 (C-4), 14.0 (CH_3CH_2) ppm.

*Ethyl N,N′-diacetyl-2,6-diamino-2-ethoxycarbonyl[6-^{13}C]hexanoate (**31**).* Freshly prepared Raney-nickel catalyst (0.5 g) was added to a solution of the above nitrile (**30**) (2.68 g) in ethanol (absolute, 20 mL) and the mixture stirred 2 h at room temperature. The mixture was then centrifuged, the supernatant solution decanted, and the residue washed twice with ethanol. Solvent was removed *in vacuo*, and the residue dissolved in acetic anhydride (5 mL) and mixed with a suspension of Raney nickel (0.8 g) in acetic anhydride (15 mL). The mixture was shaken 3 h in a Parr hydrogenator (45–50 psi, 68°C internal temperature). The catalyst was centrifuged off and the supernatant solution evaporated to dryness. The product (**31**) was obtained as a yellow solid, which was recrystallized from ethanol. Yield 2.15 g, mp 133–135°C; ^{1}H nmr ($CDCl_3$) δ: 6.9 (1H, s, NH-2), 6.1 (1H, br, NH-6), 4.3 (4H, q, *J* 7 Hz), 3.1 (2H, dq, $J_{^{13}C,H-6}$ 147 Hz, $J_{H-5,H-6} = J_{H-6,NH}$ 6.6 Hz), 2.5–2.3 (2H, m, H-5), 2.0, 1.9 (2 × 3H, 2 × s, CH_3CON-2, CH_3CON-6), 1.5 (4H, m, H-3,-4), 1.3 (6H, t, *J* 7 Hz); ^{13}C nmr ($CDCl_3$) δ: 170.1, 169.1 (CON-6, CON-2), 168.0 (-CO_2-), 66.4 (-OCH_2-), 63.9 (C-2), 42.8 (C-3), 39.2 (C-6), 31.9 (d, *J* 4.1 Hz, C-4), 29.1 (d, *J* 36.3 Hz, C-5), 22.9, 21.0 (CH_3CON-2, CH_3CON-6), 13.5 (CH_3CH_2) ppm.

DL-*[6-^{13}C]Lysine monohydrochloride (**32**).* The diacetamide (**31**) (1.36 g) was refluxed 20 h in hydrochloric acid (4.8 M, 11.3 mL). The solution was evaporated to dryness, water was added, and the solution again evaporated and the residue dried *in vacuo*, yielding crystalline dihydrochloride of [6-^{13}C]lysine (0.88 g). This was dissolved in hot ethanol (10 mL) and the mixture was filtered. Pyridine (0.5 mL) in ethanol (1 mL) was added dropwise to the stirred solution. The monohydrochloride of [6-^{13}C]lysine crystallized and was washed with cold ethanol (absolute, 2 × 1 mL). Yield 0.66 g; ^{1}H nmr (D_2O) δ: 3.8 (1H, t, *J* 5.7 Hz, H-2), 3.2 (2H, dt, $J_{^{13}C,H-6}$ 127.8 Hz, $J_{H-6,H-5}$ 7.2 Hz), 2.1–1.4 (6H, m); ^{13}C nmr (D_2O) δ: 175.3 (C-1), 55.3 (C-2), 40.0 (C-6), 30.7 (d, *J* 4.9 Hz, C-3), 27.2 (d, *J* 35.5 Hz, C-5), 22.3 (C-4) ppm. For assignments see ref. 45.

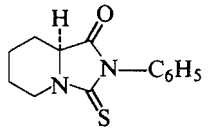

33

Administration of ^{13}C- and ^{2}H-enriched substrates to L. angustifolius *and* L. luteus

The plants used in these experiments were grown from seed and were used in feeding experiments 3–6 weeks after germination. The feeding experiments with *L. angustifolius* were carried out in the greenhouse (summer months, expts. 13, 16) or in the growth chambers (winter months, expts. 14, 15, 17). The experiments with *L. luteus* (expts. 1–5) have been described (37). Tracer solution was administered by wick over a period of 5 days, and the plants were then grown for a further period of 3–4 days before being harvested. Details of the experiments with *L. angustifolius* are summarized in Table 1. The experiments with *L. luteus* have been reported (37).

*Extraction of (+)sparteine (**1**) from* Lupinus luteus

This procedure has been described previously (37).

*Extraction of (+)lupanine (**2**) and (+)-13-hydroxylupanine (**3**) from* Lupinus angustifolius (cf. ref. 46)

In the experiments with radioactive substrates (expts. 7–12) the plant material was dried (2 days, 50°C) and ground. In a typical procedure (expt. 11) the ground plant material (16 g) was moistened with potassium carbonate solution (25% w/v, 25 mL); the mixture was allowed to stand 20 min and was then mixed with Kieselguhr G (Stahl) (16 g) and continuously extracted 5 h with methylene chloride. (In the experiments with substrates enriched with stable isotopes (expts. 13–17), the fresh plant material was macerated with methanol and extracted continuously for 7 h). The extract was evaporated to dryness, hydrochloric acid (1 M, 3 mL) was added, the mixture was shaken with ether (5 × 3 mL), and the extract discarded. The aqueous layer was filtered through Celite and the filtrate was further extracted with chloroform (4 × 3 mL), neutralized with potassium carbonate, made alkaline with potassium hydroxide solution (50% w/v, 1 mL), and extracted with methylene chloride (3 × 5 mL). The chloroform extract, containing acylated alkaloids, was dried over sodium sulfate and evaporated. The residue was dissolved in hydrochloric acid (4%, 3 mL), and reextracted with chloroform (3 × 2 mL). The aqueous layer was basified, and extracted with methylene chloride (3 × 2 mL).

The two methylene chloride extracts were combined, dried over sodium sulfate, and evaporated. The residue (50 mg) was dissolved in dilute hydrochloric acid (1 M, 4 mL). The solution was neutralized with potassium carbonate, basified with potassium hydroxide solution (50% w/v, 2 mL), and mixed with Kieselguhr G (Stahl) (7 g). The mixture was placed on a column (1.5 cm diameter) containing Kieselguhr (7 g) that had been mixed with potassium hydroxide solution (50% w/v, 2 mL). The column was washed with petroleum ether (30–60°C, 150 mL), which eluted the lupanine fraction (15 mg), then with ether (50 mL), which yielded the angustifoline fraction (1 mg), and finally with methylene chloride (150 mL), which yielded pure 13-hydroxylupanine (32 mg). Thin-layer chromatography (silica, hexane:ethyl acetate:diethylamine, 17.5:77.5:5) of the lupanine fraction showed that all radioactivity was present at the R_f value (0.65) corresponding to lupanine.

(+)Lupanine perchlorate

Crude lupanine from the radioactive feeding experiments was mixed with a solution of perchloric acid in methanol (10% v/v, 3 drops) yielding an immediate precipitate of the perchlorate. The radioactive product was diluted with inactive lupanine perchlorate as carrier and recrystallized from methanol. Melting point 213°C (lit. (47) mp. 211–212°C; (48) mp 209°C).

(+)Lupanine methiodide

Lupanine (23 mg) was dissolved in benzene (1 mL). Methyl iodide (0.5 mL) was added, and the solution was refluxed for 1 h and kept

Can. J. Chem. Downloaded from www.nrcresearchpress.com by 112.217.228.212 on 09/07/12
For personal use only.

overnight. The solution was evaporated and the residue triturated with benzene, filtered, and washed with benzene. The product was recrystallized from 2-propanol, yielding lupanine methiodide, melting point 274–275°C (lit. (48) mp 274°C for (−)lupanine methiodide).

Degradation of lupanine (Scheme 1)

Carbon-17 as benzoic acid (cf. refs. 13, 49)

Conversion of lupanine (2) perchlorate into sparteine (1) (cf. ref. 50). Lupanine perchlorate (128 mg) was dissolved in dilute hydrochloric acid (1.3 M, 8 mL); platinum oxide (140 mg) was added and the mixture shaken in a Parr hydrogenator for 15 h at 20 psi. The solution was filtered, the precipitate washed with water (3 × 1 mL), the aqueous filtrate basified with aqueous sodium hydroxide (10% w/v), and product extracted into ether (4 × 4 mL). The ether solution was dried (anhydrous potassium carbonate) and evaporated, yielding sparteine as a colorless oil whose ir spectrum was identical with that of an authentic specimen of sparteine.

Conversion of sparteine (1) into 17-oxosparteine (9) (cf. refs. 7, 50). Sparteine (64 mg) was dissolved in dilute hydrochloric acid (0.4 M, 1.2 mL); the solution was basified with diluted sodium hydroxide (10% w/v, 1.8 mL) and an aqueous solution of potassium ferricyanide (0.4 g in 1.5 mL) was added. The mixture was vigorously shaken for 40 min, acidified with dilute hydrochloric acid (4 M, 1 mL), and extracted with ether (3 × 3 mL). The ether extract was washed with dilute hydrochloric acid (1 M, 2 × 3 mL); the aqueous extract was basified with dilute sodium hydroxide (10% w/v, 3 mL) and extracted with ether (3 × 3 mL). The ether extract was dried (anhydrous potassium carbonate) and evaporated, yielding 17-oxosparteine (**9**) (60 mg) as an oil that crystallized on standing, and was recrystallized from petroleum ether (30–60°C). Melting point 83–84°C (lit. (7) mp 86–87°C; (50) mp 87°C).

Phenylation of 17-oxosparteine (9) (cf. refs. 13, 49). 17-Oxosparteine (55 mg) in anhydrous ether (1 mL) was added to a stirred suspension of phenyllithium in anhydrous ether, prepared from lithium (0.14 g) and bromobenzene (0.6 mL) in anhydrous ether (10 mL) in a nitrogen atmosphere. The mixture was refluxed 30 min, dry toluene (3 mL) was added, and the temperature of the oil bath was slowly raised to 100°C and so maintained for 1 h. The mixture was allowed to cool to room temperature overnight, anhydrous ether (5 mL) was added, unreacted lithium removed with a spatula, and the solution poured into dilute hydrochloric acid (4 M, 2 mL) and crushed ice. After being stirred for 15 min the solution was extracted with ether (3 × 5 mL), and the ether extract washed with dilute hydrochloric acid (M, 2 × 3 mL). The combined acid fractions were basified with solid sodium carbonate and extracted with chloroform (3 × 5 mL). The chloroform extract was washed with saturated sodium chloride solution, filtered, dried (anhydrous sodium carbonate), and evaporated. The product, presumably 17-phenyl-16,17-dehydrosparteinium hydroxide (**10**), was obtained as a yellow oil (53 mg); ir: 3070, 3030, 1675 (C=N$^+$), 1600, 1500, 750, 700 (phenyl) cm^{-1}; ^{1}H nmr ($CDCl_3$) δ: 8.0 (m, 1H (*para* H)), 7.5 (m, 2H (2 × *ortho* H)), 7.2 (m, 2H (2 × *meta* H)) ppm.

Benzoic acid from 17-phenyl-16,17-dehydrosparteinium hydroxide (10). Crude 17-phenyl-16,17-dehydrosparteinium hydroxide (53 mg) was dissolved in acetone (1 mL), water (8 mL) was added, the mixture was heated to remove acetone, and finely powdered potassium permanganate (0.4 g) was then added in small portions to the stirred suspension. The mixture was refluxed for 3 h with vigorous stirring, more potassium permanganate (0.4 g) was added, and refluxing continued for 3 h. Manganese dioxide was filtered off, the precipitate washed with water (3 × 1 mL), the filtrate extracted with ether, and the extract discarded. The aqueous layer was acidified with dilute sulfuric acid (1 M, 3 mL), decolorized by addition of sodium bisulfite, and extracted with ether (3 × 10 mL). Evaporation of the ether extract gave benzoic acid (13 mg), which was purified by sublimation at 40°C and 5 × 10^{-2} Torr (1 Torr = 133.3 Pa). Yield 7 mg, mp 121–121.5°C.

Carbon-2 as benzoic acid (cf. refs. 8, 13, 49)

Phenylation of lupanine (2) (cf. ref. 49). Lupanine perchlorate (95 mg) was dissolved in aqueous ammonia (0.880 ammonia:water, 1:2, 5 mL), and the solution stirred with benzene (5 mL) at room temperature. The benzene layer was separated, the aqueous layer extracted with chloroform (3 × 5 mL), and the combined chloroform solution was washed with sodium chloride solution, dried, and evaporated, yielding lupanine (65 mg) as a colorless oil. Phenylation was performed by a procedure similar to that described above for the phenylation of 17-oxosparteine. The product (73 mg), presumably 2-phenyl-1,2-dehydrosparteinium hydroxide (**11**) together with a little 2-phenyl-2,3-dehydrosparteine (**12**), was obtained as a glass; ir: 3070, 3030, 2820, 2775, 2740 (Bohlmann bands), 1680 (C=N$^+$), 1640 (HC=C), 1605, 1495, 750, 700 (phenyl) cm^{-1}; ^{1}H nmr ($CDCl_3$) δ: 7.4 (m, 5H) ppm.

Benzoic acid from 2-phenyl-1,2-dehydrosparteinium hydroxide (11). Benzoic acid (9 mg), mp 122°C, was obtained by permanganate oxidation of crude 2-phenyldehydrosparteinium hydroxide (73 mg) by a method similar to that described above for the oxidation of 17-phenyl-16,17-dehydrosparteinium hydroxide.

Carbon-15 (together with carbon-14,13 (and 12)) as β-alanine (17) and γ-aminobutyric acid (16) (by direct oxidation of lupanine (**2**))

Oxidation of lupanine perchlorate (cf. ref. 13). Lupanine perchlorate (200 mg) was dissolved in an ice-cooled mixture of concentrated sulfuric acid (1 mL) and water (1.6 mL). A solution of chromic oxide (1.2 g) in water (1 mL) was added with stirring. The mixture was heated (100°C) for 72 h with continuous stirring. Excess chromic acid was decomposed by addition of 2-propanol, water was added, and the solution continuously extracted for 20 h with ether to remove succinic acid and small amounts of other oxidation products. The acid layer was neutralized by addition of an excess of a hot saturated solution of barium hydroxide followed by solid carbon dioxide. The precipitate of barium sulfate and carbonate was centrifuged off and washed with hot water. The combined aqueous solution was filtered and evaporated. The residue was dissolved in water and applied to a column (1.2 × 10 cm) of Dowex 50 × 4 (H$^+$ form). Inorganic salts were eluted with water (100 mL), and the mixture of amino acids (mainly β-alanine and γ-aminobutyric acid) with pyridine (1 M, 100 mL). The pyridine eluate was evaporated to dryness, and the residue dissolved in water and applied to a second column (1.4 × 15 cm) of Dowex 50 × 4 (pyridinium form). The column was washed with water (100 mL) followed by pyridine (0.025 M, 150 mL and 0.050 M, 100 mL). Fractions of 3 mL were collected. β-Alanine (2 mg) emerged first, followed by γ-aminobutyric acid (0.4 mg). The amino acids were converted into the hydrochloride salts, which were then purified by sublimation at 90–100°C and 3 × 10^{-2} Torr. The sublimed salts were recrystallized from methanol–ether, yielding β-alanine hydrochloride, mp 120–121°C (lit. (51*a*) mp 123°C) and γ-aminobutyric acid hydrochloride, mp 133–135°C (lit. (51*b*) mp 135–136°C).

Carbons-11 and -15 (together with carbons-9, -12, -13, and -14) as pipecolic acid (15) (by stepwise oxidation of lupanine)

Conversion of lupanine (2) into 17-oxolupanine (13) (cf. ref. 50). Lupanine (150 mg) obtained from lupanine perchlorate (see above) was dissolved in dilute acetic acid (50% w/v, 3 mL). A solution of potassium permanganate (267 mg) in acetone (25 mL) was added dropwise over 30 min to the stirred solution and stirring continued 30 min. Manganese dioxide was filtered off, the precipitate washed with acetone, the acetone was evaporated, and the residue decolorized with a dilute solution of sodium bisulfite (5 mL). The product was extracted into chloroform (3 × 5 mL), the chloroform extract was washed first with cold dilute hydrochloric acid (1 M, 1 × 5 mL), then with sodium carbonate solution, and finally with water, and was then evaporated. 17-Oxolupanine (**13**) was obtained as a colorless oil (155 mg), which crystallized on standing and was recrystallized from acetone-ether; mp 153–155°C (lit. (52) mp 154°C).

Hydrolysis of 17-oxolupanine (13) (cf. ref. 53). 17-Oxolupanine (90 mg) was dissolved in concentrated hydrochloric acid (2 mL) and heated for 20 h in a sealed tube at 180°C. The solution was then extracted with benzene to remove traces of starting material. The solution was concentrated *in vacuo*, water was added, and the pH of the solution adjusted to pH 6.5 by addition of dilute sodium hydroxide. The solution was applied to a column (1.2 × 10 cm) of Dowex 50 × 4 (H$^+$ form).

Can. J. Chem. Downloaded from www.nrcresearchpress.com by 112.217.228.212 on 09/07/12
For personal use only.

Can. J. Chem. Downloaded from www.nrcresearchpress.com by 112.217.228.212 on 09/07/12
For personal use only.

The column was eluted with water, followed by 1 M ammonia. Evaporation of the ammonia solution gave the product, presumably **14**, as a slightly colored amorphous solid (50 mg) that was oxidized without further purification.

Oxidation of the hydrolysis product. The crude product (**14**) (40 mg) was dissolved in dilute sulfuric acid (20% v/v, 2 mL), the solution was cooled to 0°C and stirred, and chromium trioxide (200 mg) was added in small portions with vigorous stirring. The solution was then heated to 100°C and stirring was continued for 6 h. Excess chromic acid was decomposed by addition of 2-propanol, and the solution was diluted and extracted with ether (3 × 10 mL). The aqueous layer was neutralized by addition of saturated barium hydroxide solution, followed by solid carbon dioxide. The precipitate was centrifuged off and washed, the aqueous layer was filtered and concentrated, and the crude amino acid mixture, so obtained, was applied to a column (1.2 × 10 cm) of Dowex 50 × 4 (H^+ form). The column was washed with water, and pipecolic acid, together with a little starting material, was eluted with 1 M ammonia. The ammoniacal eluate was evaporated, yielding a residue (12 mg) that contained five components, including β-alanine, γ-aminobutyric acid, pipecolic acid, and some unchanged starting material. The residue was dissolved in methanol. The methanol solution was filtered and evaporated to dryness. The residue was sublimed at 2×10^{-2} Torr. β-Alanine and γ-aminobutyric acid both sublimed at approximately 150°C in low yield. Pipecolic acid sublimed at 200°C. The pipecolic acid, presumably *S*-pipecolic acid, was resublimed. Yield 1.5 mg (9%), mp 269–270°C (dec.) (lit. (51*c*) mp 270°C for (±) and *R*-; 259–260°C for *S*-pipecolic acid (*sic*!)).

To increase the yields of β-alanine and of γ-aminobutyric acid an improved separation procedure was devised. The crude amino acid mixture (70 mg) obtained by oxidation of the diamino acid (**14**) (200 mg) was applied to a column (1.2 × 12 cm) of Dowex 50 × 4 (pyridinium form). The column was washed with water and amino acids were then eluted with pyridine (0.025 M). The early fractions yielded a mixture of β-alanine and pipecolic acid (20.7 mg). Later fractions contained γ-aminobutyric acid (2.4 mg). β-Alanine and pipecolic acid were dissolved in aqueous pyridine (2:3 v/v, 2 mL) and the pH of the mixture was adjusted to pH 8.5 with potassium carbonate. Freshly distilled phenylisothiocyanate (0.25 mL) was added and the mixture heated for 3 h at 45°C and kept overnight at room temperature. The mixture was acidified with dilute hydrochloric acid with cooling and extracted with chloroform (3 × 2 mL). The extract was concentrated and the residue shaken with dilute sodium hydroxide. The aqueous layer containing the phenylthiourea derivatives was acidified with dilute hydrochloric acid and extracted with chloroform. The solvent was removed *in vacuo* and the oily residue was heated for 2 h at 40°C with methanolic hydrochloric acid (1.2 M, 2 mL) and left overnight at room temperature. Solvent was evaporated and the residue was diluted with water and extracted with chloroform. The solution was concentrated to dryness and the residue (21 mg) was applied to a silica gel column (2 g, 230–400 mesh BDH). The column was washed with hexane (4 mL) and then with a mixture of hexane:diethyl ether (2:1, 10 mL). The methyl ester of the phenylthiourea derivative of β-alanine ($PhNHC(=S)NHCH_2CH_2CO_2CH_3$) was eluted with hexane:diethyl ether (1:1); yield 7.9 mg, mp 54°C (after recrystallization from diethyl ether:hexane) (lit. (54) mp 66.5–67°C; ir: 1732, 1180 (-CO_2-), 3100–3000, 1600, 1530 (phenyl), 1500 (C=S), 3210–3320 (NH) cm^{-1}; ^1H nmr ($CDCl_3$) δ: 8.0 (bs, 1H, NH—Ph), 7.1–7.5 (m, 5H), 6.7 (1H, NH), 3.9 (m, 2H, CH_2—N, collapsed to a t, *J* 5.7 Hz, on shaking with D_2O), 3.6 (3H, s) 2.8 (2H, t, CH_2CO) ppm; ms *m/z*: 238 (36%, molecular ion), 207(9) 131(17), 93(100), 87(9). *Exact Mass* calcd. for $C_{11}H_{14}N_2O_2S$: 238.0776; found: 238.0779 (±0.0003).

A further elution with the same solvent system afforded the pipecolic acid condensation product (**33**) (5.8 mg), mp 161°C (from methanol) (lit. (55) mp 162–163°C); ms *m/z*: 246 (100%, molecular ion), 217(15), 135(46), 83(90), 81(58), 77(62), 55(56).

Acknowledgments

We are grateful to Professor Dr. M. Wiewiórowski, University of Poznan, for a gift of seeds of *Lupinus luteus* and *L. angustifolius*, to Thelma Leech, Greenhouse Supervisor, McMaster University, for providing facilities for our experiments, and to Brian G. Sayer, Department of Chemistry, for recording nmr spectra. This investigation was supported by a grant from the Natural Sciences and Engineering Research Council of Canada.

1. J. Rana and D. J. Robins. J. Chem. Soc. Chem. Commun. 1335 (1983); J. Chem. Soc. Perkin Trans. 1, 1133 (1986).
2. W. M. Golebiewski and I. D. Spenser. J. Chem. Soc. Chem. Commun. 1509 (1983).
3. W. M. Golebiewski and I. D. Spenser. J. Am. Chem. Soc. **106**, 7925 (1984).
4. J. Rana and D. J. Robins. J. Chem. Res. (S), 196 (1985).
5. D. J. Robins and G. N. Sheldrake. J. Chem. Res. (S), 256 (1987); J. Chem. Res. (M), 2101 (1987).
6. H. R. Schütte and C. Schäfer. Naturwissenschaften, **48**, 669 (1961).
7. H. R. Schütte, F. Bohlmann, and W. Reusche. Arch. Pharm. (Weinheim), **294**, 610 (1961).
8. H. R. Schütte, E. Nowacki, and C. Schäfer. Arch. Pharm. (Weinheim), **295**, 20 (1962).
9. H. R. Schütte, H. Hindorf, K. Mothes, and G. Hübner. Justus Liebigs Ann. Chem. **680**, 93 (1964).
10. E. Nowacki and R. U. Byerrum. Bull. Acad. Polon. Sci. Ser. Sci. Biol. **12**, 483 (1964).
11. E. Nowacki and R. U. Byerrum. Bull. Acad. Polon. Sci. Ser. Sci. Biol. **12**, 489 (1964).
12. E. Nowacki. Genet. Polon. **5**, 189 (1964).
13. H. R. Schütte and H. Hindorf. Justus Liebigs Ann. Chem. **685**, 187 (1965).
14. H. R. Schütte and D. Knöfel. Z. Pflanzenphysiol. **57**, 188 (1967).
15. H. R. Schütte and G. Seelig. Justus Liebigs Ann. Chem. **711**, 221 (1968).
16. E. Leistner and I. D. Spenser. Pol. J. Chem. **53**, 49 (1979).
17. H. R. Schütte and D. Knöfel. Z. Pflanzenphysiol. **59**, 80 (1968).
18. A. M. Fraser and D. J. Robins. J. Chem. Soc. Chem. Commun. 1477 (1984); J. Chem. Soc. Perkin Trans. 1, 105 (1987).
19. A. M. Fraser and D. J. Robins. J. Chem. Soc. Chem. Commun. 545 (1986).
20. T. Hemscheidt and I. D. Spenser. Can. J. Chem. **65**, 170 (1987).
21. D. J. Robins and G. N. Sheldrake. J. Chem. Res. (S), 159 (1987); J. Chem. Res. (M), 1427 (1987).
22. M. Wink, T. Hartmann, and H. M. Schiebel. Z. Naturforsch. C: Biosci. **34**, 704 (1979).
23. W. M. Golebiewski and I. D. Spenser. J. Am. Chem. Soc. **98**, 6726 (1976).
24. M. Wink, L. Witte, and T. Hartmann. Planta Med. **43**, 342 (1981).
25. M. Wink, T. Hartmann, L. Witte, and H. M. Schiebel. J. Nat. Prod. (Lloydia), **44**, 14 (1981).
26. Y. D. Cho, R. O. Martin, and N. J. Anderson. J. Am. Chem. Soc. **93**, 2087 (1971).
27. J. C. Richards and I. D. Spenser. Tetrahedron, **39**, 3549 (1983).
28. K. Hasse and H. Maisack. Biochem. Z. **327**, 296 (1955).
29. C. Schöpf, F. Braun, and A. Komzak. Chem. Ber. **89**, 1821 (1956).
30. A. D. Kinghorn and M. F. Balandrin. *In* Alkaloids: chemical and biological perspectives. Vol. 2. *Edited by* S. W. Pelletier. John Wiley, New York. 1984. pp. 118–122.
31. H. J. Gerdes and E. Leistner. Phytochemistry, **18**, 771 (1979).
32. K. Hasse and G. Schmid. Biochem. Z. **337**, 69 (1963).
33. K. Kim. J. Biol. Chem. **239**, 783 (1964).
34. K. Tanizawa, T. Yoshimura, Y. Asada, S. Sawada, H. Misono, and K. Soda. Biochemistry, **21**, 1104 (1982).

35. C. SCHÖPF, H. ARM, G. BENZ, and H. KRIMM. Naturwissenschaften, **38**, 186 (1951).
36. E. LEETE. *In* Biosynthesis (Specialist Periodical Reports), **7**, 110 (1984).
37. W. M. GOLEBIEWSKI and I. D. SPENSER. Can. J. Chem. **63**, 2707 (1985).
38. M. ROTHSTEIN and C. J. CLAUS. J. Am. Chem. Soc. **75**, 2981 (1953).
39. W. M. GOLEBIEWSKI and I. D. SPENSER. Can. J. Chem. **63**, 716 (1985).
40. H. R. SCHÜTTE. Arch. Pharm. (Weinheim), **293**, 1006 (1960).
41. E. LEETE. *In* Biogenesis of natural compounds. 2nd ed. *Edited by* P. Bernfeld. Pergamon Press, Oxford. 1963. p. 973.
42. H. KESSLER, H. MÖHRLE, and G. ZIMMERMANN. J. Org. Chem. **42**, 66 (1977).
43. R. N. GUPTA and I. D. SPENSER. Can. J. Chem. **47**, 445 (1969).
44. O. A. MOE and D. T. WARNER. J. Am. Chem. Soc. **70**, 2763 (1948).
45. E. LEETE. J. Nat. Prod. (Lloydia), **45**, 197 (1982).
46. M. D. BRATEK-WIEWIÓROWSKA, M. WIEWIÓROWSKI, I. REIFER, K. GOLANKIEWICZ, E. NOWACKI, W. BOCZOŃ, and M. DEZOR. Acta Biochim. Polon. **12**, 395 (1965).
47. J. F. COUCH. J. Am. Chem. Soc. **59**, 1469 (1937).
48. L. MARION and J. OUELLET. J. Am. Chem. Soc. **70**, 3076 (1948).
49. E. NOWACKI and D. NOWACKA. Rocz. Chem. **40**, 1435 (1966).
50. F. GALINOVSKY and E. STERN. Chem. Ber. **77**, 132 (1944).
51. Dictionary of organic compounds. 5th ed. Chapman and Hall, New York. 1982. (*a*) Vol. 1, A-02606; (*b*) Vol. 1, A-01169; (*c*) Vol. 5, P-01953.
52. O. E. EDWARDS, F. H. CLARKE, and B. DOUGLAS. Can. J. Chem. **32**, 235 (1954).
53. F. BOHLMANN, E. WINTERFELDT, and D. SCHUMANN. Chem. Ber. **93**, 1948 (1960).
54. A. F. MCKAY, D. L. GARMAISE, R. GAUDRY, H. A. BAKER, G. Y. PARIS, R. W. KAY, G. E. JUST, and R. SCHWARTZ. J. Am. Chem. Soc. **81**, 4328 (1959).
55. W. D. MARSHALL, T. T. NGUYEN, D. B. MACLEAN, and I. D. SPENSER. Can. J. Chem. **53**, 41 (1975).

Can. J. Chem. Downloaded from www.nrcresearchpress.com by 112.217.228.212 on 09/07/12
For personal use only.

Orientation of some disk-shaped solutes in nematic liquid crystals

C. T. YIM

Department of Chemistry, Dawson College, 350 Selby St., Westmount, P.Q., Canada H3Z 1W7

AND

D. F. R. GILSON

Department of Chemistry, McGill University, 801 Sherbrooke St. W., Montreal, P.Q., Canada H3A 2K6

Received December 9, 1987

C. T. YIM and D. F. R. GILSON. Can. J. Chem. **66**, 1749 (1988).

The solute orientation parameters for benzene, trichloro-, and tribromobenzene have been measured, as functions of temperature, in the nematic solvents EBBA and ZLI-1132. The potential functions for orientation were derived for the model based on short and long-range contributions to the potential, with the former dependent on either a function of molecular shape or of molecular volume. There is reasonable agreement between calculated and experimental solute order parameters in both cases, and the difference in solute order parameter in the two solvents arises mainly from the difference in solvent electric field gradient.

C. T. YIM et D. F. R. GILSON. Can. J. Chem. **66**, 1749 (1988).

Utilisant les solvants nématiques EBBA et ZLI-1132, on a mesuré les paramètres d'orientation de soluté du benzène et des trichloro- et tribromo-benzènes, en fonction de la température. On a obtenu les fonctions de potentiel du modèle en se basant sur les contributions au potentiel à courte ainsi qu'à longue distance; les premières dépendent soit de la forme soit du volume moléculaire. Dans chacun de ces cas, on observe une bonne concordance entre les paramètres calculés et les paramètres expérimentaux pour l'ordre des solutés; dans ces deux solvants, la différence dans le paramètre d'ordre du soluté provient principalement de la différence dans le gradient du champ électrique.

[Traduit par la revue]

Can. J. Chem. Downloaded from www.nrcresearchpress.com by 93.93.197.157 on 09/07/12
For personal use only.

Introduction

There have been numerous attempts to extend the original Maier–Saupe theory of nematic liquid crystals (1) to account for the orientation of a solute molecule dissolved in a nematic solvent, and, in particular, to relate this orientation to some molecular property of the solute. Recently, Burnell and co-workers (2–4) have proposed two approaches to this problem. The first is that the intermolecular forces responsible for the orientation of the solute arise from both short-range and long-range interactions, which depend upon the solute molecular size and shape and on the interaction of the solute molecular quadrupole moment with the electric field gradient in the solvent, respectively. The second theory (4) requires that a plot of the solute order parameter, S_2, versus that of the solvent, S_1, should yield a universal curve independent of concentration and temperature and related to the ratio of the magnitudes of the ordering potentials, which is interpreted in terms of a virtual transition temperature for the non-mesogenic solute.

As part of a program of studying the orientation of substituted benzene derivatives (5), we have measured the solute order parameters as functions of temperature in dilute solutions of benzene, 1,3,5-trichlorobenzene, and 1,3,5-tribromobenzene in the solvents EBBA and 1132, and these results have been used to examine factors affecting the short-range interactions.

Experimental

Solutes were obtained from commercial sources and used without further purification. EBBA was prepared by literature methods (6) and 1132 obtained from BDH Chemicals. Solutions were prepared at concentrations of 1 mol% for the trihalobenzenes and 2 mol% for benzene. Spectra were recorded on Varian XL-200 or XL-300 spectrometers without deuterium lock, and the temperatures were measured by the ethylene glycol shift. The molecular geometry for benzene was taken from the work of Lounila and Diehl (7), and for trichlorobenzene from ref. 8; the same structure was also adopted for the tribromo derivative. The solvent order parameters were obtained from dipolar splittings in the nmr spectrum of the pure solvent for EBBA (5), and from refractive index data for 1132 (9).

Results and discussion

For all three solutes, at similar reduced temperature, the solute orientation is always greater in 1132 than in EBBA, Fig. 1.

The orientation parameters can be calculated by solving integrals of the type

$$[1] \quad S_{ij} = \int (3 \cos\theta_i \cos\theta_j - \delta_{ij}) \exp(-U/k_B T)\, d\Omega/2Z$$

where $Z = \int \exp(-U/k_B T)\, d\Omega$.

For molecules with 3-fold (or higher) symmetry only one order parameter is required to describe the orientation, and the potential function, $U(\cos\theta)$, is given by eq. [2];

$$[2] \quad U(\cos\theta) = (3/2)\, A_{12} S_1 \cdot \cos^2\theta$$

where S_1 is the solvent order parameter and A_{12} describes the strength of the solute–solvent interaction. In dilute solution the solute–solute interaction can be ignored and A_{12} is assumed to contain the two contributions due to short and long-range interactions. For each solute/solvent pair, the constants can be determined by interpolation for the same temperatures at which the electric field gradients were measured (11, 12) and the short-range term can be obtained by subtracting the calculated long-range contribution from the experimental value for that temperature, and averaging the results.

To determine the long-range forces, which are given by $-(1/3)\,\Sigma Q_{ii} F_{ii}$, it is necessary to know the molecular quadrupole tensors and the electric field gradients. The molecular quadrupole moment is not a commonly available parameter, but values have been reported for these three compounds (13–16). In the case of benzene the values range from -18 to -33×10^{-40} C m^2, and the average of these has been used in the present work. The electric field gradients in EBBA and 1132 have been measured by Burnell and co-workers (11, 12) from an analysis of the quadrupole splittings in the deuterium nmr spectra of HD and D_2 dissolved in these two solvents. An interesting result of these studies is that the field gradients are of opposite sign, and,

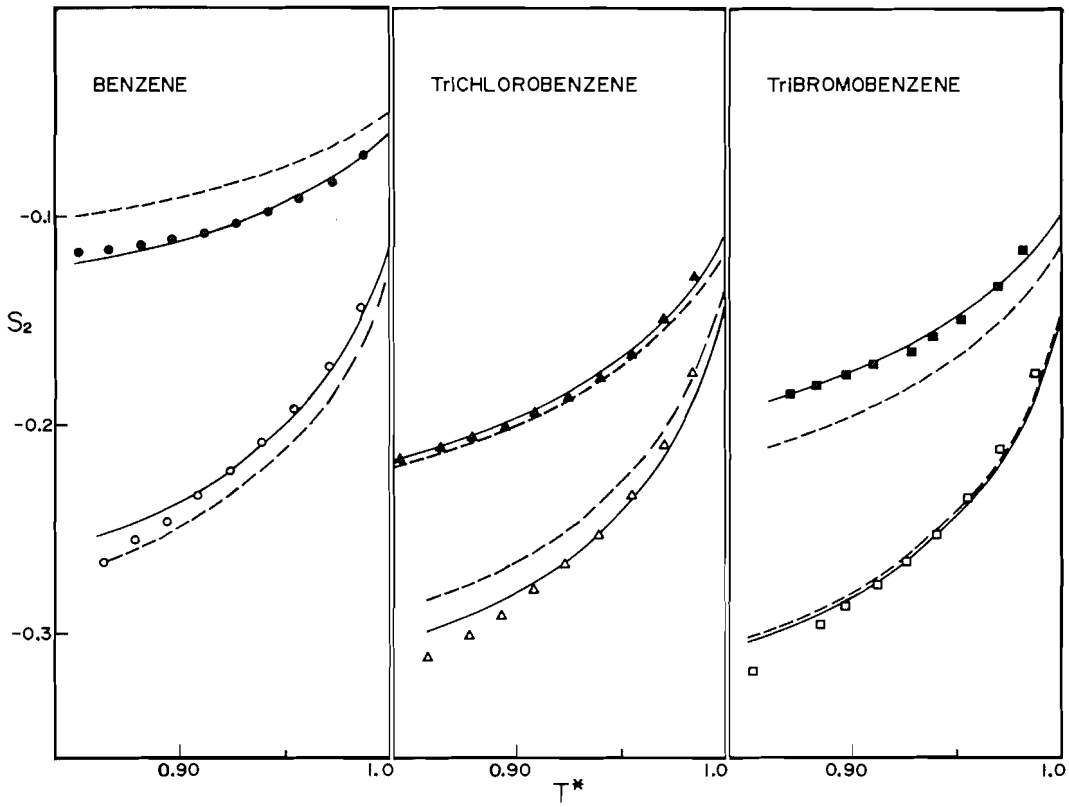

FIG. 1. Solute order parameters as functions of reduced temperature. The solid lines are calculated for the averaged experimental A_{12} values, and the dashed lines for the length model. Benzene/1132, ○; /EBBA, ●; trichlorobenzene/1132, △; /EBBA, ▲; tribromobenzene/1132, □; / EBBA, ■.

Can. J. Chem. Downloaded from www.nrcresearchpress.com by 93.93.197.157 on 09/07/12
For personal use only.

therefore, for a common solute molecule there should be an enhanced orientation in one solvent and a diminished orientation in the other, as observed in the present study. A consideration of the errors in the reported values of the quadrupole moment and the field gradients suggests that the uncertainty in both quantities may be 10%.

For the three solutes used in this study, the parameter A_{12} is not entirely independent of temperature and (or) the solvent order parameter, as it should be from eq. [2]. This can be seen in the plots, Fig. 2, of $A_{12}S_1/k_BT$ versus S_1/T, which should be straight lines with slopes A_{12}/k_B, but show a curvature as the temperature increases, with a downward deviation in EBBA and an upward deviation in 1132. It is assumed that the short-range interaction is given by a solvent dependent constant multiplied by some molecular property. Burnell and co-workers have proposed (2, 3) that it is linked to a function of the perimeter length of the molecule and a restoring force constant that results from the displacement of the liquid crystal molecules by the solute. In the present work we have examined two other functions. The first is based on molecular shape anisotropy, similar to eq. [3], and which has been used for molecules of lower symmetry (5).

$$[3] \quad A_{SR} = A_L(L_2 - (L_1 + L_3)/2)$$

where L_i is the molecular dimension, including the van der Waals radii,[1] along the ith axis.[2] The constant A_L has the dimension of force. The second approach assumes a short-range force dependent on molar volume, eq. [4],

$$[4] \quad A_{SR} = A_V V$$

[1]The van der Waals radii were taken from ref. 17.

[2]The axis system is chosen such that the 3-axis is perpendicular to the ring plane of the solute molecule.

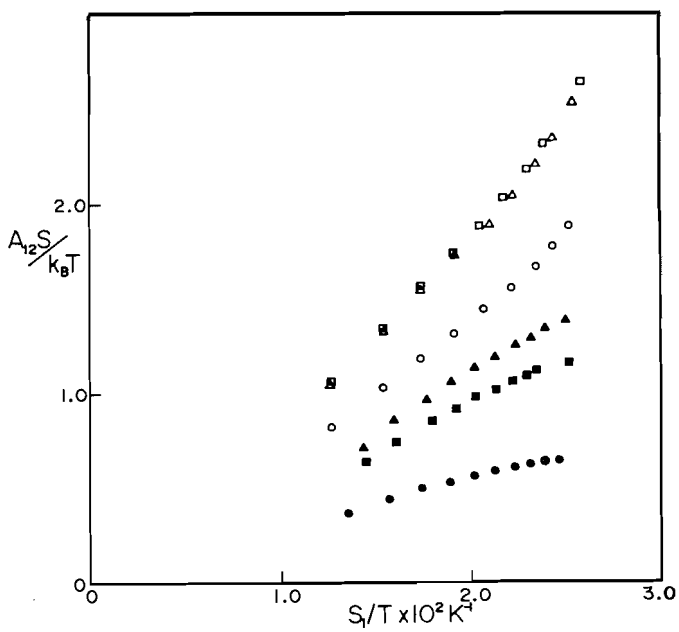

FIG. 2. Plots of $\{A_{12}S_1/k_BT\}$ versus S_1/T. Symbols as in Fig. 1.

and gives a constant, A_V, with dimensions of pressure, but, since the molecules have approximately the same thickness, this might be better interpreted as a function of cross-sectional area in the present case. Since the ratios of A_L or A_V for the same solute in different liquid crystal solvents should be independent of the solute, they have been constrained so that their ratio is constant. The calculated A_{12} values for the length, volume, and circumference models are compared with the experimental re-

TABLE 1. Potential constants for different models.[a] L, C, and V refer to the length, circumference, and volume[b] models, respectively

		A_{exp}	A_L	A_V	A_C
Benzene	1132	9.63	10.42	10.64	10.46
Trichlorobenzene	1132	12.61	11.51	11.23	11.37
Tribromobenzene	1132	12.73	12.67	12.71	12.79
Benzene	EBBA	3.84	3.06	3.24	3.09
Trichlorobenzene	EBBA	7.74	7.89	7.60	7.75
Tribromobenzene	EBBA	6.60	7.65	7.66	7.75
Root-mean-square error			0.77	0.86	0.83

[a] $\times 10^{21}$ J molecule^{-1}.
[b] The molar volume data, ref. 18, were measured for solutions in carbon tetrachloride at 25°C.

sults in Table 1. The rms errors between the calculated and experimental A_{12} values favour the model based upon the anisotropy in the molecular length, but the uncertainties in the various quantities are large, and there is not really any difference between any treatment. The calculated order parameters for the length model are compared with the experimental values in Fig. 1.

An obvious deficiency in all these models is that they do not explain the non-linearity of the plots in Fig. 2. This could be an indication that the two different contributions have a different temperature dependence, or it may be due to an incomplete function for the pseudopotential, the omission of higher rank terms (10) for instance, the assumption of constant volume, or it could be attributed to difficulties over the choice of values for the solvent order parameter, which were measured by different experimental methods and may not be comparable. It is possible that different solutes occupy, on the average, different regions of the liquid crystal solvent and are exposed to different order parameters.

The potential function in eq. [2] applies to the solvent itself (assuming uniaxial symmetry) and, according to the mean field approach of Maier and Saupe (1), the transition from the nematic to the isotropic phase occurs when the term $A_{11}/k_BTV = 4.54$, where V is the molar volume. This proportionality between A_{ii} and the transition temperature was used by Burnell and co-workers (4) to derive a virtual transition temperature at which the solute would exhibit a nematic-to-isotropic transition. Using the present results, although there was quite good agreement between the experimental points and theoretical curves in plots of solute versus solvent order parameters, there was little agreement between the virtual transition temperatures for the three solvents 1132, EBBA, and 5CB.

Acknowledgements

This work was supported by grants from the Natural Sciences and Engineering Research Council of Canada (to D.F.R.G.) and from Fonds pour la formation de chercheurs et l'aide à la recherche (Québec) (to C.T.Y.). We are grateful to Professor E. E. Burnell for details of his results prior to their publication.

1. W. MAIER and A. SAUPE. Z. Naturforsch. A: Astrophys. Phys. Phys. Chem. **14A**, 882 (1959).
2. A. J. VAN DER EST, M. Y. KOK, and E. E. BURNELL. Mol. Phys. **60**, 397 (1987).
3. A. WEAVER, A. J. VAN DER EST, J. C. T. RENDELL, G. L. HOATSON, G. S. BATES, and E. E. BURNELL. Liq. Cryst. **2**, 633 (1987).
4. G. S. BATES, E. E. BURNELL, G. L. HOATSON, P. PALFFY-MUHORAY, and A. WEAVER. Chem. Phys. Lett. **134**, 161 (1987).
5. C. T. YIM and D. F. R. GILSON. Can. J. Chem. **65**, 2513 (1987).
6. H. KELKER and B. SCHUERLE. Angew. Chem. Int. Ed. Engl. **8**, 884 (1969).
7. J. LOUNILA and P. DIEHL. Mol. Phys. **52**, 827 (1984).
8. A. ALMENNINGEN, I. HARGITTAI, J. BRUNVOLL, A. DOMENICANO, and S. SAMDAL. J. Mol. Struct. **116**, 199 (1984).
9. B. BAHADUR, R. K. SARNA, and V. G. BHIDE. Mol. Cryst. Liq. Cryst. **72**, 139 (1982).
10. J. W. EMSLEY, R. HASHIM, G. R. LUCKHURST, and G. L. SHILSTONE. Liq. Cryst. **1**, 437 (1986).
11. G. N. PATEY, E. E. BURNELL, J. G. SNYDERS, and C. A. DE LANGE. Chem. Phys. Lett. **99**, 271 (1983).
12. P. B. BARKER, A. J. VAN DER EST, E. E. BURNELL, G. N. PATEY, C. A. DE LANGE, and J. G. SNYDERS. Chem. Phys. Lett. **107**, 426 (1984).
13. R. L. SHOEMAKER and W. H. FLYGARE. J. Chem. Phys. **51**, 2988 (1969).
14. J. VRBANICH and G. D. L. RITCHIE. J. Chem. Soc. Faraday Trans. 2, **76**, 648 (1980).
15. M. R. BATTAGLIA, A. D. BUCKINGHAM, and J. H. WILLIAMS. Chem. Phys. Lett. **78**, 421 (1981).
16. G. D. L. RITCHIE. Chem. Phys. Lett. **93**, 410 (1982).
17. A. BONDI. J. Phys. Chem. **68**, 441 (1964).
18. F. SHAHIDI. Can. J. Chem. **61**, 1414 (1983).

Can. J. Chem. Downloaded from www.nrcresearchpress.com by 93.93.197.157 on 09/07/12
For personal use only.

Azapropellanes 5.[1] Synthesis of chiral (non-racemic) 2-methyl azapropellanes

JOHN M. MCINTOSH AND SAMUEL O. ACQUAAH[2]

Department of Chemistry and Biochemistry, University of Windsor, Windsor, Ont., Canada N9B 3P4

Received January 29, 1988

JOHN M. MCINTOSH and SAMUEL O. ACQUAAH. Can. J. Chem. **66**, 1752 (1988).

The preparation of *S*-(−)-6-methyl-2-piperidinone from *S*-alanine and *R*-(−)-5-methyl-2-pyrrolidinone from *S*-glutamic acid and their conversion into *S*-2-methyl-1-azoniatricyclo[4.4.4.$0^{1,6}$]tetradecane (**2***a*) and *R*-2-methyl-1-azoniatricyclo-[4.4.3.$0^{1,6}$]tridecane (**2***b*) with enantiomeric excesses of 95 and 92% respectively are described. The use of these compounds as phase-transfer catalysts did not lead to significant asymmetric induction.

JOHN M. MCINTOSH et SAMUEL O. ACQUAAH. Can. J. Chem. **66**, 1752 (1988).

On décrit la préparation de la *S*-(−)-méthyl-6 pipéridone-2 à partir de la *S*-alanine et de la *R*-(+)-méthyl-5 pyrrolidinone-2 à partir de l'acide *S*-glutamique ainsi que leur conversion en *S*-méthyl-2 azonia-1 tricyclo[4.4.4.$0^{1,6}$]tétradécane (**2***a*) et *R*-méthyl-2 azonia-1 tricyclo[4.4.3.$0^{1,6}$]tridécane (**2***b*) avec des excès d'énantiomères qui sont respectivement de 95 et 92%. Lorsqu'on a utilisé ces composés comme catalyseurs de transfert de phase, on n'a pas obtenu de quantités importantes d'induction asymétrique.

[Traduit par la revue]

The use of chiral catalysts in phase-transfer reactions for the preparation of enantiomerically enriched products has attracted continuing attention by many groups, With some very notable exceptions (1, 2), the results obtained have been disappointing. In most cases, the catalysts utilized have been derived by quaternization of readily available chiral amines. In general, catalysts derived by quaternization of amines such as norephedrine, in which the chirality resides exclusively in the carbon skeleton, have proven to be ineffective in inducing asymmetry whereas the use of quaternary derivatives of tertiary amines such as quinine, cinchonidine, etc. (2) has been much more successful. Some time ago we noted (3) that the latter type of catalyst possesses a chiral nitrogen atom in addition to asymmetry in the carbon skeleton, and we postulated a set of criteria for the structure of chiral phase-transfer catalysts that led to the selection of compounds of type **1** (azapropellanes) (Fig. 1) as possible candidates for investigation. The reasons for the choice of this type of molecule have been given elsewhere (3).

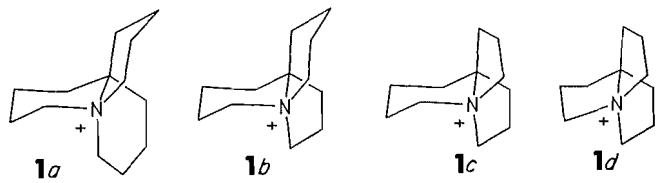

FIG. 1

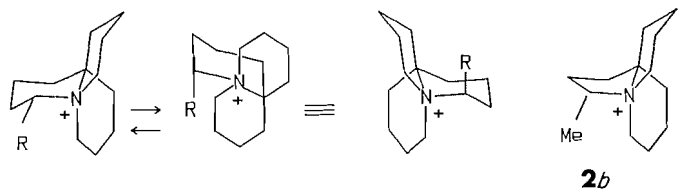

1*a* (R=H) **2***a* (R=Me)

FIG. 2

The use of synthetic materials as catalysts has the advantage that one can choose specific structures designed to demonstrate the result of structural changes and thus allow the correlation of structure with the extent of asymmetric induction. The disadvantage lies in the inability to use the chiral molecules provided by nature. Thus the synthesis of **1***a–d* was carried out and nmr experiments allowed the unambiguous conclusion that, while **1***a* is a chiral (C_3) molecule, the rapid rate of the chair–chair interconversion of all three rings, a process which converts **1***a* into its enantiomer (Fig. 2 R = H), does not give rise to an optically stable catalyst (4). This conclusion was independently reached by Alder and Arrowsmith (5). The rate of inversion of **1***b* and **1***c* is even faster, while the geometry of **1***d* does not render it chiral.

If one considers the geometry of **1***a* as it should influence the transition state of a phase-transfer reaction, the following points emerge. The anion X^- of the quaternary salt must, by virtue of the structure of **1***a*, be associated with *only one face* of the tetrahedral nitrogen atom. The choice of **1***a* was made to ensure this fact. This face of the nitrogen atom is surrounded by the three α-equatorial protons. The discrimination between the relative topicity relies on the very small hydrogen atoms. If one of these atoms is replaced by a larger group, two effects should be evident. First, the steric discrimination on the chiral face should be larger, and, more importantly, the rate of ring inversion should be dramatically reduced and the bias to the conformational equilibrium between the two (now diastereomeric) forms should be large, since one conformation must have an axial substituent that, models suggest, would be impossibly hindered (Fig. 2. R ≠ H).

In support of these ideas, the synthesis of **2***a* in racemic form was carried out (6) and nmr experiments indicated that the presence of the α-methyl group had indeed rendered **2***a* both conformationally stable and apparently existing in only one conformational form. The single substituent had frozen the conformation of not only the substituted ring, but the other two rings as well. Unfortunately, all attempts at resolving **2***a* into its optical antipodes failed. For this reason, the absolute asymmetric synthesis of **2***a* was attempted. This synthesis and the synthesis of **2***b* in a chiral form are the subject of this report.

Results and discussion

The syntheses of **2***a* and **2***b* were planned around one central point. It has been shown that pyrolysis of *N*-ω-carboxyalkyllactams with soda lime affords bicyclic iminium

[1]For part 4, see ref. 6.

[2]Taken in part from the Ph.D. dissertation of S. O. Acquaah, University of Windsor, February 1988.

Can. J. Chem. Downloaded from www.nrcresearchpress.com by 61.7.252.67 on 09/07/12
For personal use only.

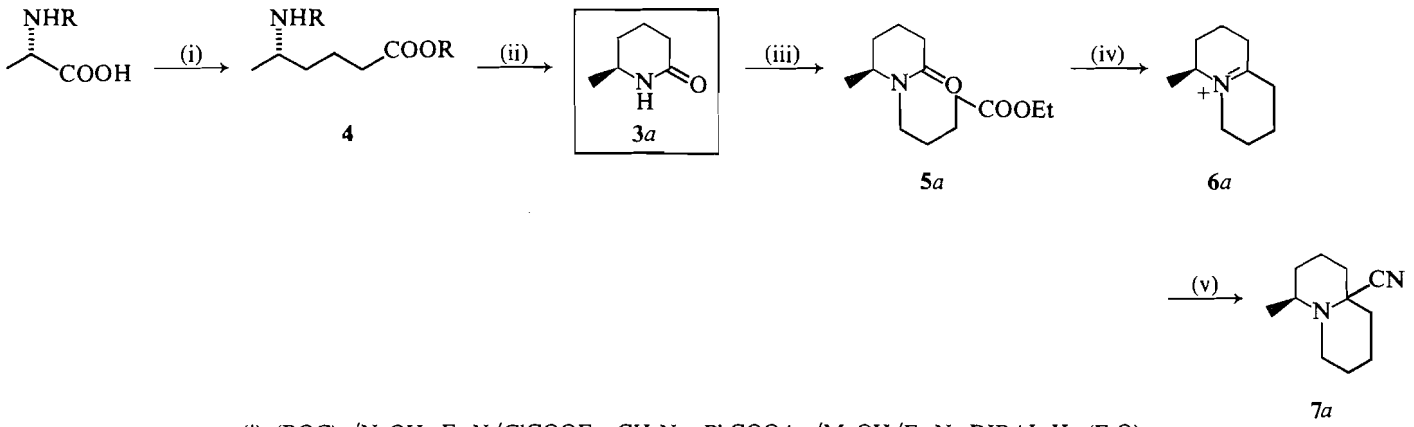

(i) $(BOC)_2$/NaOH; Et_3N/ClCOOEt; CH_2N_2; PhCOOAg/MeOH/Et_3N; DIBAL-H; $(EtO)_2$-P(O)CH_2COOEt/BuLi; H_2/Pd. (ii) TFA/CH_2Cl_2; heat. (iii) KH/Br$(CH_2)_4$COOEt. (iv) soda lime/ heat: $HClO_4$. (v) NaCN

SCHEME 1

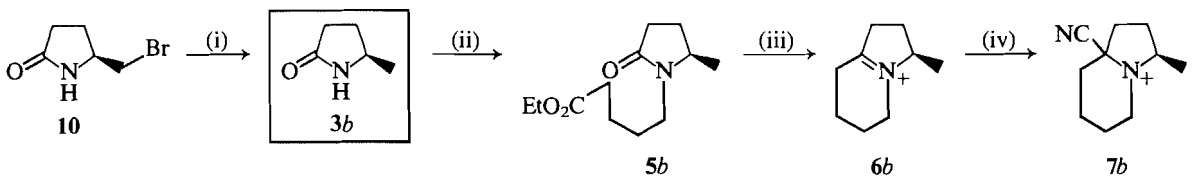

(i) H_2/Pd. (ii) KH/Br$(CH_2)_4$COOEt. (iii) soda lime/ heat: $HClO_4$. (iv) NaCN

SCHEME 2

salts in which the stereochemistry of the α-carbon is not disturbed (7). Since these iminium salts were the central intermediates in our synthesis of **1**, the preparation of **2***a* and **2***b* simplified to the preparation of lactams **3***a* (Scheme 1) and **3***b* (Scheme 2) in enantiomerically pure form. Lactam **3***b* is a known compound (8*a*), but its reported synthesis was not amenable to preparation on the scale we required and the absolute configuration of the (+) isomer has been the subject of conflicting reports (8). To establish the configuration unambiguously and provide amounts suitable for further synthetic operations, lactam **3***b* was prepared by reduction of the known (14) bromomethyl lactam **10** derived from *S*-glutamic acid. The sign of rotation of **4** was identical to that originally reported for the *S* isomer by Cervinka *et al.* (8*a*) and the *R*-isomer by Cervinka and others (8*b*, *c*). This synthesis confirms that the (+) isomer must have the *R* configuration. Using the highest rotation reported for **3***b*, the calculated enantiomeric excess for our preparation is 95%.

The synthesis of **3***a* (8*a*) was not as straightforward since chiral α-aminoadipic acid is not easily available (9). Attempts at homologating **3***b* or asymmetrically reducing the imine derived from (+) α-methylbenzyl amine and 5-oxohexanoic acid failed. The successful synthesis of **3***a* from *S*-alanine is outlined in Scheme 1. The overall yield was approximately 40% and the enantiomeric excess calculated on the basis of the highest previously reported rotation for **3***a* (8*a*) was 92%.

Alkylation of **3***a* or **3***b* with ethyl 5-bromopentanoate using potassium hydride (10) afforded **5***a* or **5***b*, which on pyrolysis over soda lime in the published manner (11) and treatment of the distillate with 70% perchloric acid gave **6***a* or **6***b*. Completion of the synthesis of **2***a* and **2***b* was achieved using the methodology applied to the synthesis of **1***a* (Scheme 3) (3*a*). The iminium perchlorate was alkylated using 4-phenoxybutylmagnesium bromide (3*a*) and the product was cleaved to the bromoamine hydrobromide with concentrated hydrobromic acid. Cyclization to the azapropellane was achieved by treating this material with an excess of silver oxide.

The yields of the Grignard products **8** were quite low and they appeared to be a mixture of stereoisomers based upon nmr data. However, the synthetic route was planned in such a way that the distinction between the stereoisomers is lost in the final cyclization. The physical and spectroscopic data for **2***a* are identical to those previously reported for the racemic material (6).

The molecular weight (FI ms), elemental analysis, and nmr data for **2***b* are fully consistent with the assigned structure. DEPT editing of the ^{13}C nmr spectrum confirms the presence of one CH_3, one CH, and one quaternary carbon. The normal ^{13}C nmr spectrum shows only nine resonances whose chemical shifts are consistent with those expected from a comparison with **1***b* (4). Either average values for the carbons in the two six-membered rings are being observed, or the difference between them is insufficient to be resolved at 75 MHz.

The conversion of lactams **3***a* and **3***b* to **2***a* and **2***b* respectively is expected to proceed without loss of optical integrity based on literature precedents (7). In an attempt to demonstrate this fact, the nmr of salt **2***b* was run in the presence of *S* (+)camphor-10-sulfonic acid. Although the methyl region was severely complicated by the presence of the signals due to the camphor moiety, no signals could be seen that could be attributed to a second diastereomer of **2***b*. The use of other chiral anions (e.g., mandelate) also failed to demonstrate the presence of a second diastereomer. Therefore, the best estimates of the optical purity of **2***a* and **2***b* are based on the known purity of lactams **3***a* and **3***b*

Can. J. Chem. Downloaded from www.nrcresearchpress.com by 61.7.252.67 on 09/07/12
For personal use only.

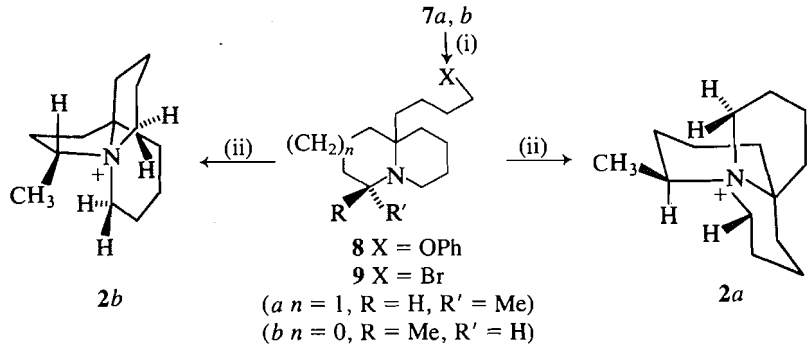

SCHEME 3

and are 92 and 95% respectively. Salts **1***a* and **1***b* have previously been shown to be effective phase-transfer catalysts (3*a*). To determine the effect of the asymmetry in the catalysts on phase-transfer reactions, two test reactions were performed. In both cyclopropanation of 2-chloroacrylonitrile (12) with diethylbromomalonate and allylation of 2-carbethoxycyclohexanone (13), excellent chemical yields of adducts were obtained. However, in each case, as measured by 300-MHz nmr in the presence of the chiral lanthanide shift reagent $Eu(hfc)_3$, the maximum amount of asymmetric induction that could be measured was <2%. In the case of the alkylation product, the reported optical rotation of the material with 6% e.e. was −8.2° and the induction in our reaction calculated on this basis is of similar magnitude.

The instances of high stereoselectivity in phase-transfer reactions reported to date have demonstrated the apparent desirability of a second, polar group critically situated to allow a coordinating group in the catalytic site. The high enantiomeric excesses obtained in the epoxidations using cinchona alkaloid-derived catalysts is lost upon acetylation (2*c*, *d*) and Colonna and co-workers have demonstrated the requirement for a β-hydroxy group in the catalyst for an asymmetric Darzen's condensation (1*c*). In addition, Dolling *et al.* (1*b*) have demonstrated the effect on asymmetric induction of changing a benzyl group to the more coordinatively unsaturated *p*-CF_3benzyl group. If molecules of the azapropellane type are to exhibit more stereoselective results, they should be modified to place such a coordinating group on the face of the nitrogen atom. However, we have no plans to pursue this avenue any further.

Experimental

All melting points and boiling points are uncorrected. Infrared spectra were run on a Perkin–Elmer model 180 instrument in chloroform solution or in the FT mode on a Nicolet 5 DX spectrometer as neat samples. The ^{1}H nmr spectra were run at 60 MHz on a Varian EM 360 spectrometer in chloroform-*d* with tetramethylsilane (TMS) as the internal standard. The data are presented in the format: chemical shift (multiplicity, number of protons, coupling constant). The ^{13}C nmr spectra were recorded at 22.64 MHz on a Bruker CXP 100 spectrometer. Gas chromatographic analyses were performed on a Varian model 3700 instrument using a 1.5 ft × 1/8 in. column packed with 5% OV-101 on Chromosorb W or a column packed with 20% SE30 on Chromosorb W. Mass spectra were run on a Varian MAT CH5 instrument in the field ionization (FI), field desorption (FD), or electron impact (EI) mode. Optical rotations were measured on a Perkin–Elmer model 241 polarimeter. Concentrations in g/100 mL of solvent are included following the measured optical rotations.

Microanalyses were done by Guelph Chemical Laboratories, Guelph, Ontario, and Galbraith Laboratories, Knoxville, Tennessee. For column chromatography, silica gel (Merck silica gel 60) 70–230 mesh was used. Reagent grade chemicals were used without further purification unless otherwise specified. Tetrahydrofuran or dimethoxyethane were dried with potassium and benzophenone and distilled under nitrogen. Diisopropyl amine was stored over potassium hydroxide. Methylene chloride, chloroform, and carbon tetrachloride were distilled from calcium hydride. Dimethyl formamide was distilled over barium oxide and stored over molecular sieves. For reactions that involved aqueous work-up, the drying agent was magnesium sulfate.

S-(+)-*6-Methyl-2-piperidinone* (*3*a)

L-Alanine was protected as the N-^{t}BOC derivative and converted via the mixed anhydride with ethyl chloroformate to the diazoketone by treatment with diazomethane (14*a*, *b*). The diazoketone (16 g, 0.08 mol) was dissolved in dry methanol (120 mL) and treated with a few drops of a solution of silver benzoate (1 g) in triethyl amine (11.6 mL). A vigorous reaction occurred with the evolution of nitrogen. When the reaction had subsided, the mixture was treated with charcoal, boiled for a few minutes, and then filtered. The solvent was removed and ether (150 mL) was added and the mixture was washed with dilute HCl, saturated $NaHCO_3$, and then brine. The solution was dried, the ether evaporated, and the residue chromatographed over silica gel using petroleum ether – ether (3:1) and crystallized in pentane to give the N-^{t}BOC derivative of (*S*)-3-aminobutanoic acid methyl ester in 75% yield, mp 42°C; $[\alpha]_D^{25}$ −24.4° (*c* 0.54, chloroform) (lit. (14*c*) mp 42°C; $[\alpha]_D^{25}$ −20.0° (*c* 0.54 chloroform)).

The ester (10 g, 0.046 mol) in ether (100 mL) was cooled to −78°C and reduced with DIBAL (90 mL of 1.5 M solution in toluene). The reaction was quenched at the same temperature by adding 6.5 mL of methanol. The solution was poured into a saturated solution of sodium potassium tartrate (Rochelle salt) (65 mL) and water (400 mL) at 0°C. After stirring for 1 h at this temperature, the mixture was filtered, the filtrate extracted with ether (2 × 100 mL), and the residue also extracted with ether (4 × 75 mL). The combined filtrates were dried and evaporated to give the aldehyde, which was used directly as follows. The residue in THF solution (50 mL) was added under nitrogen to a −78°C solution of the Wittig reagent prepared from *n*-BuLi (28.6 mL of 2.5 M solution in hexane) and triethyl phosphonoacetate (13.6 g, 0.06 mol) in THF (250 mL). After stirring for 2 h at −78°C, the reaction was quenched with water, extracted with ethyl acetate (3 × 100 mL), and dried. The solvents were removed and the residue chromatographed on silica gel using petroleum ether – ethyl acetate (9:1) as eluant to give the homologated olefinic ester, which was immediately dissolved in ethanol and reduced to **3***b* with hydrogen in the presence of 10% palladium on carbon. Filtration and evaporation of the solvent was followed by treatment of the residue with 1:1 trifluoroacetic acid in methylene chloride at 0°C for 30 min to remove the ^{t}BOC protecting group. Triethyl amine (1.1 equiv.) in methylene chloride was added and, after removal of the solvent, the residue was heated at 180°C for 1 h. Distillation at approximately 1 Torr pressure (1 Torr = 133.3 Pa) gave the lactam **3***a*, which immediately solidified; mp 80–81°C; $[\alpha]_D^{25}$ +25.6° (*c* 2.04, water) (lit. (8*a*) $[\alpha]_D^{25}$ +27.8° (*c* 2.03, water)); ^{1}H nmr: 7.30–6.80 (bs, 1H), 3.67–3.05 (m, 1H), 2.40–2.05 (m, 2H), 2.00–1.25 (m, 4H), 1.20–1.15 (d, 3H, J = 8 Hz).

Can. J. Chem. Downloaded from www.nrcresearchpress.com by 61.7.252.67 on 09/07/12
For personal use only.

Can. J. Chem. Downloaded from www.nrcresearchpress.com by 61.7.252.67 on 09/07/12
For personal use only.

(R)-*(+)-5-Methyl-2-pyrrolidinone* **3**b)

(*S*)-5-Bromomethyl-2-pyrrolidinone (**10**) (15) (8.8 g, 0.05 mol) in ethanol (150 mL) and triethylamine (5.06 g, 0.05 mol) was reduced with hydrogen in the presence of a catalytic amount of 10% palladium on carbon for 36 h at 1 atmosphere pressure (1 atm = 101.3 kPa) and ambient temperature. The mixture was filtered through Celite and the solvent evaporated. The residue was extracted with ether (3 × 100 mL), the ether evaporated, and the residue was distilled under reduced pressure to give 4.1 g (85%) of **3***b* as a colorless oil, bp 90°C (1.8 Torr); $[\alpha]_D^{25}$ +24.8 (*c* 0.9, water) (lit. (8*a*) $[\alpha]_D^{25}$ +26.6 (*c* 0.9, water)); ir: 3240, 2967, 2931, 1690, 1423, 1378, 1277 cm^{-1}; ^1H nmr: 1.17 (d, 3H, J = 7 Hz), 1.67 (m, 1H), 2.27 (m, 3H), 3.76 (m, 1H), 7.76 (bs, 1H); ^{13}C nmr: 178.4, 50.1, 30.6, 29.0, 22.0; ms (FI), m/z: 99.

(S)-N-*(4-Carbethoxybutyl)-6-methyl-2-piperidinone (5*a)

Potassium hydride (20 g of 35% by weight in mineral oil (0.16 mol)) was washed three times with pentane and dried under nitrogen. Dry 1,2-dimethoxyethane (DME) (100 mL) was added, followed by the dropwise addition of **3***a* (17 g, 0.15 mol) in 50 mL of DME. The mixture was stirred at room temperature for about 3 h. Ethyl 5-bromovalerate (17 g, 0.15 mol) in 50 mL of DME was added slowly and the mixture was stirred at room temperature for 8 h. The reaction was quenched with ethanol followed by a small amount of water and then filtered. The filtrate was concentrated and methylene chloride (100 mL) and water (50 mL) were added. The aqueous layer was separated and the organic layer washed with brine and dried. Removal of the solvent and distillation gave **5***a* as a colorless oil; ir: 3048, 2943, 2872, 1733, 1634, 1472, 1375, 1248, 1182 cm^{-1}; ^1H nmr: 1.20 (d, 3H, J = 7 Hz), 1.23 (t, 3H, J = 7 Hz), 1.43–2.10 (m, 8H), 2.10–2.53 (m, 4H), 2.67–3.17 (m, 1H), 3.27–3.57 (m, 2H), 4.13 (q, 2H, J = 7 Hz); ^{13}C nmr: 178.2, 169.5, 59.9, 51.8, 44.3, 33.7, 30.1, 27.0, 22.2, 19.8, 17.3, 14.0.

(R)-N-*(4-Carbethoxybutyl)-5-methyl-2-pyrrolidinone (5*b)

This compound was prepared in the same manner as described for **5***a* using (*R*)-5-methyl-2-pyrrolidinone (**3***b*). A colorless oil was obtained in 70% yield, bp 140–142°C (1 Torr); $[\alpha]_D^{25}$ +6.5° (*c* 2.0, ethanol); ir: 2967, 2934, 2870, 1733, 1687, 1417, 1375, 1251, 1184, 1156, 1098 cm^{-1}; ^1H nmr: 1.20 (d, 3H J = 7 Hz), 1.26 (t, 3H, J = 7 Hz), 1.56 (m, 5H), 2.23 (m, 5H), 2.93 (m, 1H), 3.60 (m, 2H), 4.13 (q, 2H, J = 7 Hz). *Anal.* calcd. for $C_{12}H_{21}NO_3$: C 63.39, H 9.31, N 6.16; found: C 63.65, H 9.68, N 6.35.

(S)-*4-Methyl-*$\Delta^{4,10}$*-dehydroquinolizidinium perchlorate (6*a)

Ester **5***a* (5 g, 0.02 mol) was mixed thoroughly with 10 g of soda lime and transferred to a flask that was fitted with a short-path distillation head. The system was purged with nitrogen and heated with a free flame until all the volatile material had distilled (head temperature ca. 180°C). The two-phase distillate was diluted with ether, the phases separated, and the aqueous phase extracted with ether. The combined ethereal phases were dried and evaporated to give the crude enamine, which was treated with sufficient 1:1 70% perchloric acid in ethanol to just render the solution acidic. The dried precipitated crystalline product (2.35 g, 45%) had mp 249–250°C (dec.). The racemic form has previously been reported (16). *Anal.* calcd. for $C_{10}H_{18}ClNO_4$: C 47.70, H 7.21, N 5.56; found: C 48.02, H 6.98, N 5.39.

*(3*R*)-3-Methyl-*$\Delta^{4,9}$*-dehydroindolizidinium perchlorate (6*b)

Using the procedure described for **6***a*, the enamine derived from **5***b* was obtained as a colorless oil in 65% yield. The perchlorate was obtained by treatment of a freshly prepared sample of the enamine in ethanol (20 mL) at 0°C with cold 70% perchloric acid. The precipitated salt was filtered and recrystallized from ethanol to give **6***b* in 45% overall yield from the lactam ester **5***b*, mp 215–218°C; ir: 1700 cm^{-1}; ^1H nmr: 1.46 (d, 3H, J = 7 Hz), 1.50–1.99 (m, 2H), 2.46–2.49 (m, 2H), 2.51–2.84 (m, 2H), 2.85–3.14 (m, 2H), 3.60 (m, 2H), 4.50 (m, 2H); ^{13}C nmr: 190.4, 68.9, 45.7, 37.4, 27.8, 26.5, 20.0, 17.8, 16.3. *Anal.* calcd. for $C_9H_{16}ClNO_4$: C 45.47, H 6.78, N 5.89; found: C 45.62, H 6.62, N 6.27.

*(4*S*,9a*R*) and (4*S*,9a*S*)-9a-(4-phenoxybutyl)-4-methylquinolizidine (8*a)

This was prepared from **6***a* as follows. The perchlorate was converted to the nitrile (**7***a*) in 70% yield using saturated sodium cyanide solution according to Leonard's procedure (17); ir (neat): 2360 cm^{-1}; ^1H nmr: 1.05 (d, 3H, J = 7 Hz), 1.0–1.80 (m, 12H), 2.15 (t, 1H), 2.35 (m, 1H), 3.12 (bd, 1H). The nitrile gave **8***a* in 40% yield upon refluxing with a THF solution of the Grignard reagent derived from 4-phenoxybutyl bromide (3*a*), followed by chromatography of the crude material on silica gel with ether as the eluant; ^1H nmr: 7.50–6.75 (m, 5H), 3.50 (t, 2H, J = 6 Hz), 2.75–2.05 (m, 4H), 2.10–1.00 (m, 20H).

This material was not purified further but carried on directly to the cyclization reaction.

*(3*R*,9*S*)/(3*R*,9*R*)-(4-Phenoxybutyl)-3-methylindolizidine (8*b)

In the same manner as described for **8***a*, nitrile **7***b* was prepared from perchlorate **6***b* in 78% yield, bp 80–84°C (4.5 Torr); $[\alpha]_D^{25}$ −62.3 (*c* 1.06, chloroform); ir: 2200 cm^{-1}; ^1H nmr: 1.12 (d, 3H, J = 6.1 Hz), 1.2–1.8 (m, 8H), 1.95–2.20 (m, 4H), 2.62 (m, 1H), 3.15 (bd, 1H, J = 10.5 Hz); ^{13}C nmr: 99.7, 98.0, 57.0, 45.7, 35.3, 34.6, 34.5, 28.9, 24.6, 21.4.

The Grignard product **8***b* was obtained from **7***b* in 45% yield, $[\alpha]_D^{25}$ −39.5° (*c* 1.5, chloroform); ir: 3010, 2930, 1600, 1585, 1490, 1465, 1450, 1290 cm^{-1}; ^1H nmr: 1.00–2.00 (m, 18H), 2.74–2.77 (m, 4H), 3.48 (t, 2H, J = 6 Hz), 6.71–7.42 (m, 5H); ^{13}C nmr: 160.3, 129.5, 120.7, 114.8, 67.9, 49.2, 35.5, 26.0, 20.5, 20.2. *Anal.* calcd. for $C_{19}H_{29}NO$: C 79.39, H 10.16, N 4.88; found: C 80.12, H 11.09, N 5.03.

2-Methyl-1-azoniatricyclo[4.4.4.$0^{1,6}$*]tetradecane iodide (2*a)

Using the procedure described below for the preparation of **2***b*, iodide **2***a* (X = I^-) was obtained in 20% yield from **8***a*: mp >300°C, $[\alpha]_D^{25}$ −14.9° (*c* 0.5, methanol). Spectroscopic data for the hydroxide salt were identical to the previously prepared racemic material (6) and the fdms gave a single peak at m/z = 208.

(R)-*2-Methyl-1-azoniatricyclo[4.4.3.*$0^{1,6}$*]tridecane bromide (2*b)

This was prepared by the procedure described in the literature (3*a*, 6). The ether **8***b* (0.25 g) was converted to the bromide **9***b* using concentrated hydrobromic acid, and the crude material, without any purification, was cyclized using silver oxide in water to give the hydroxide salt, which was neutralized with hydrobromic acid to give pure product (0.085 g) after recrystallization from methanol; mp >300°C; $[\alpha]_D^{25}$ −22.5° (*c* 1.0, methanol). Spectroscopic data were acquired on the trifluoroacetate salt. Although acceptable carbon analysis could not be obtained, the field desorption mass spectrum gave a single peak at the expected m/z = 194, the ^{13}C nmr showed the correct number of absorptions, and the ^1H nmr was entirely consistent with the assigned structure; ^1H nmr (D_2O): 1.35 (d, 3H, J = 6.5 Hz), 1.5–2.1 (m, 13H), 2.3–2.6 (m, 3H), 3.07 (m, 2H), 3.22 (ddd, 1H, J = 13.0, 13.0, 3.7 Hz), 3.78 (ddd, 1H, J = 13.4, 13.4, 3.5 Hz), 4.57 (m, 1H); ^{13}C nmr (D_2O): 73.5, 63.3, 52.5, 29.9, 26.8, 25.0, 19.1, 17.4, 12.1. *Anal.* calcd. for $C_{13}H_{24}NBr$: C 56.93, H 8.82, N 5.11; found: C 55.70, H 9.02, N 4.93.

General procedure for the phase-transfer cyclopropanation reactions (ref. 12)

To a mixture of toluene (20 mL) and 1 mL of 9.5 M aqueous sodium hydroxide was added the catalyst **2***a* or **2***b* (20 mg). The system was purged with nitrogen and cooled to 0°C in an ice bath. To this solution was added 0.01 mol of the α,β-unsaturated carbonyl compound (2-chloroacrylonitrile, acrolein, or methyl vinyl ketone) at 0°C with good stirring. The addition required 10 min and stirring was continued for 1 h at 0°C and a further 2 h at ambient temperature. The solution was diluted with water (20 mL), the layers separated, and the organic phase dried. The mixture was filtered, the solvent evaporated, and the catalyst removed by the addition of anhydrous ether and filtration of the turbid solution. The ether was evaporated and the residue chromatographed on silica gel with ether–hexane as eluant. The products were obtained in 60–75% yields and had spectra identical to those of authentic

material (12), and the specific rotations in various runs varied between 0.7 and 1.6°.

General procedure for phase-transfer alkylation reactions

A solution of ethyl 2-oxocyclohexanecarboxylate (0.005 mol) in toluene (20 mL), which contained 0.005 mol of the alkylating agent and the catalyst **2***a* or **2***b* (15 mg), was stirred vigorously in the presence of 4.5 mL of aqueous 2.5 M sodium hydroxide solution at room temperature overnight. The organic phase was separated and washed with water, and then with brine. The dried solution was filtered, evaporated, and the residue chromatographed over silica gel using ether–hexane as eluant. The products were obtained in 60–80% yields, showed specific rotations varying between 0.8 and 1.3°, and had spectra identical to those of authentic material (13).

Acknowledgments

The financial assistance of the Natural Sciences and Engineering Research Council of Canada in the form of operating grants and of the University of Windsor in the form of assistantships (to S.A.) is most gratefully acknowledged. We also wish to thank Dr. R. D. Bach of Wayne State University for the use of his polarimeter.

1. (*a*) S. COLONNA and R. E. ALBERTO. J. Chem. Soc. Perkin Trans. 1, 547 (1981); (*b*) U. DOLLING, P. DAVIS, and E. GRABOWSKI. J. Am. Chem. Soc. **106**, 116 (1984); (*c*) J. BALCELLS, S. COLONNA, and R. FORNASIER. Synthesis, 266 (1976).
2. (*a*) R. HELDER, J. C. HUMMELEN, R. W. P. M. LAANE, J. S. WIERING, and H. WYNBERG. Tetrahedron Lett. 1831 (1976); (*b*) H. WYNBERG and B. MARSMANN. J. Org. Chem. **45**, 158 (1980); (*c*) H. HEIMSTRA and H. WYNBERG. J. Am. Chem. Soc. **103**, 417 (1981); (*d*) H. WYNBERG and B. GREIJANUS. J. Chem. Soc. Chem. Commun. 625 (1978).
3. (*a*) J. M. MCINTOSH. Can. J. Chem. **58**, 2604 (1980); (*b*) Tetrahedron Lett. 403 (1979).
4. J. M. MCINTOSH. Tetrahedron, **38**, 261 (1982).
5. R. W. ALDER and R. J. ARROWSMITH. J. Chem. Res. 2301 (1980).
6. J. M. MCINTOSH. J. Org. Chem. **47**, 3777 (1982).
7. (*a*) I. MURAKOSHI, A. KUBO, J. SAITO, and J. HAGINIWA. Chem. Pharm. Bull. **12**, 747 (1964); (*b*) I. MURAKOSHI, K. TAKADA, and J. HAGINIWA. Chem. Abstr. **72**, 55217 (1970); (*c*) I. MURAKOSHI, S. YOSHIDA, and J. HAGINIWA. Chem. Abstr. **61**, 9465a (1964); (*d*) Chem Abstr. **61**, 9465c (1964); (*e*) I. MURAKOSHI, A. KUBO, J. SAITO, and J. HAGINIWA. Chem. Abstr. **70**, 47269 (1969).
8. (*a*) O. CERVINKA, A. FABRYOVA, and V. NOVAK. Collect Czech. Chem. Commun. **30**, 1742 (1965); (*b*) O. CERVINKA, L. HUB, F. SNATZKE, and G. SNATZKE. Collect. Czech. Chem. Commun. **38**, 897 (1973); (*c*) W. H. PIRKLE, R. M. ROBERTSON, and M. H. RYUN. J. Org. Chem. **49**, 2433 (1984).
9. (*a*) S. KONDO, K. MIYAZAKI, H. KODAMA, and H. HORIMOTO. Bull. Chem. Soc. Jpn. **54**, 1121 (1985); (*b*) K. RAMSAMY, R. K. OLSEN, and T. EMERY. Synthesis, 42 (1982).
10. R. W. ALDER, R. J. ARROWSMITH, C. J. BOOTHBY, E. HEILBRONNER, and Y. ZHONG-ZHI. J. Chem. Soc. Chem. Commun. 940 (1982).
11. (*a*) J. M. MCINTOSH, L. Z. PILLON, S. O. ACQUAAH, J. R. GREEN, and G. S. WHITE. Can. J. Chem. **61**, 2016 (1983); (*b*) S. MIYANO, T. SOMEHARA, M. NAKAO, and K. SUMOTO. Synthesis, 701 (1978); (*c*) S. MIYANO, S. FUJII, O. YAMOSHITA, N. TORAISHI, and K. SUMOTO. J. Org. Chem. **46**, 1737 (1982).
12. J. M. MCINTOSH and H. KHALIL. Can. J. Chem. **56**, 2134 (1978).
13. J. C. FIAUD. Tetrahedron Lett. 3495 (1975).
14. (*a*) B. PENKE, J. CZOMBOS, L. BALASPIRI, J. PETRES, and K. KOVACS. Helv. Chim. Acta, **53**, 1057 (1972); (*b*) P. L. BIRCH, A. EL OBEID, and M. AKHTAR. Arch. Biochem. Biophys. **148**, 447 (1972); (*c*) P. CASARA, C. DANZIN, B. METCALF, and M. JUNG. J. Chem. Soc. Perkin Trans. 1. 2201 (1985).
15. R. B. SILVERMAN and M. A. LEVY. J. Org. Chem. **45**, 815 (1980).
16. N. J. LEONARD, K. CONROW, and R. R. SAUNDERS. J. Am. Chem. Soc. **80**, 5185 (1958).
17. N. J. LEONARD and A. S. HAY. J. Am. Chem. Soc. **78**, 1984 (1956).

Can. J. Chem. Downloaded from www.nrcresearchpress.com by 61.7.252.67 on 09/07/12
For personal use only.

Anodic behaviour of limonene in low aqueous acetonitrile solutions of Cl^-

J. A. CARAM[1] AND M. E. MARTINS[2]

Instituto de Investigaciones Físico Químicas Teóricas y Aplicadas C.C. 16, Suc. 4, (1900) La Plata, Argentina

E. G. GROS[2]

Departamento de Química Orgánica, Facultad de Ciencias Exactas y Naturales, Universidad de Buenos Aires, Pabellón 2, Ciudad Universitaria, (1428) Buenos Aires, Argentina

AND

C. M. MARSCHOFF[3,4]

Departamento de Ingeniería Química, Facultad de Ingeniería, Universidad de Buenos Aires, Pabellón de Industrias, (1428) Buenos Aires, Argentina

Received June 4, 1987[5]

J. A. CARAM, M. E. MARTINS, E. G. GROS, and C. M. MARSCHOFF. Can. J. Chem. **66**, 1757 (1988).

The anodic behaviour of limonene on Pt electrodes was studied in LiCl solutions in acetonitrile with low water content. It was found that *cis*-6-acetamido-*p*-menth-1,8-diene is formed with acceptable yields. This compound is of interest as a potential intermediate for obtaining oxidation derivatives of limonene. Other products, among them the new compound 8-acetamido-2,4,8-trimethyl-4-chloromethyl-3-*aza*-bicyclo[3.3.1]non-2-ene, were identified. Reaction routes are proposed.

J. A. CARAM, M. E. MARTINS, E. G. GROS et C. M. MARSCHOFF. Can. J. Chem. **66**, 1757 (1988).

Le comportement anodique du limonène est étudié dans solutions de LiCl en acétonitrile avec minces quantités d'eau en employant électrodes de Pt. Le produit principal est le *cis*-6-acétamide-*p*-menth-1,8-diène, qui s'obtient spécifiquement. Ce dérivé peut etre utilisé pour la préparation de produits d'oxidation du limonène. D'autres produits, parmi lesquels le nouveau composé 8-acétamide-2,4,8-triméthyl-4-chlorométhyl-3-*aza*-bicycle[3.3.1]non-2-ène, ont été identifiés et les chemins de reaction qui abutissent a sa formation sont proposés.

Introduction

Some of the most valuable essential oils of monoterpenoid structure are those which have at least one oxygen-containing group in the otherwise unmodified hydrocarbon molecule. Examples of this are fairly abundant and, for reagent grade compounds, it can be mentioned that limonene (**1**) is priced at 0.61 dollars (U.S.) per g, while carvone (**2**), cineol (**3**), and *p*-menth-1-en-8-ol (**4**) costs are, respectively, 1.39, 1.04, and

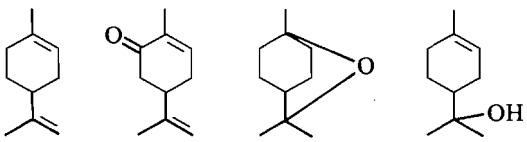

1 **2** **3** **4**

6.40 dollars per g (1). Consequently, significant efforts have been devoted to find synthetic paths for preparing derivatives of this type from the naturally abundant hydrocarbons on a cost-effective basis.

It is noteworthy that, in spite of a theoretically favourable scenario (high specificity needs for the oxidation reaction and relatively low production volume requirements), electrochemical processes have not been frequently considered as candidates to intervene in these syntheses. In fact, there are only a few published papers dealing with the electrochemical behaviour of terpenes and related molecules, and almost all of them correspond to different attempts at directly obtaining oxidation products.

Early work has shown (2–4) that anodic oxidation of monoterpenes in aqueous solutions is not very promising as a preparative technique because of the tendency of monoterpenes to polymerize on the electrode surface, a feature which comes from the fact that two independent double bonds are present in the hydrocarbon molecule. As a consequence of this limitation, some studies have been carried out on terpene oxidation in non-aqueous media, since it is expected that competition for electrode sites by the organic solvent might reduce the tendency to polymerization.

Thus, Shono and co-workers (5, 6) have studied the anodic behaviour of limonene and the pinenes in methanol and acetic acid, employing carbon electrodes, and Montiel *et al* (7) have recently worked on the oxidation of limonene in tetrahydrofurane–water mixtures. In the first case, methyl ethers (**5**) and acetates (**6**) were obtained with yields of *ca.* 30%, while the latter workers were able to produce dihydrocarvone (**7**) as well

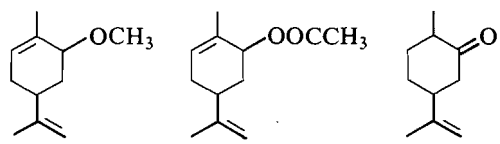

5 **6** **7**

as other ring oxidation products in unknown yields, but always at the expense of losing one of the double bonds.

In our laboratory, limonene oxidation on Pt electrodes in acetonitrile (AN) solutions has been studied (8) and, although potentiodynamic measurements led to the conclusion that anodic oxidation of the organic molecule takes place after homogeneous hydration of the double bonds, the existence of other, simultaneous, chemical reactions made the mixtures

[1]Supported by a fellowship of the Consejo Nacional de Investigaciones Científicas y Técnicas (CONICET).

[2]Member of the Carrera del Investigador (CONICET).

[3]Member of the Carrera del Investigador of the Comisión de Investigaciones Científicas de la Provincia de Buenos Aires.

[4]Author to whom correspondence should be addressed.

[5]Revision received March 18, 1988.

Printed in Canada / Imprimé au Canada

Can. J. Chem. Downloaded from www.nrcresearchpress.com by 112.217.228.212 on 09/07/12
For personal use only.

Can. J. Chem. Downloaded from www.nrcresearchpress.com by 112.217.228.212 on 09/07/12
For personal use only.

resulting from potentiostatic experiments too complex to be adequately resolved. Further work on the chemistry of limonene in AN acid solutions (9) showed that a completely non-electrochemical reaction also takes place, yielding a new type of iminium salt, 8-acetamido-2,4,4,8-tetramethyl-3-azaniumbicyclo[3.3.1]non-2-ene perchlorate (ATABNEP), which displays quite an unusual chemical behaviour for compounds of this kind (10). In this case, ATABNEP is very stable and does not undergo hydrolysis in acid media.

Taking into account the above-mentioned difficulties encountered in direct anodic oxidation efforts, it was thought worthwhile to explore the possibilities of electrochemically preparing molecules with other functional groups in the hydrocarbon ring which might serve as intermediates for obtaining the desired compounds. With this goal in mind, we decided to investigate the anodic behaviour of limonene in acetonitrile solutions containing Cl^- ions.

Experimental

AN (Carlo Erba p.a.) was purified as previously described (8) and *d*-limonene (Fluka, purum) was distilled under reduced pressure yielding a 98% purity compound. LiCl (Riedel de Haen p.a.) and $LiClO_4$ (Fluka, p.a.) were dried under vacuum at 100°C prior to use. Water content of the solvent was always below 0.05%.

Two types of electrochemical cell were employed depending on the kind of experiment performed. Thus, potentiodynamic measurements were carried out in a one-compartment cell, while preparative electrolyses at controlled potential conditions were done in a three-body cell of the type used before (8). In the latter case, the working electrode compartment included an auxiliary Pt wire electrode which was employed for obtaining voltammograms of the working solution at different times during electrolysis. The working electrode was, in all cases, a Pt wire (Johnson Mattey, Specpur) and the counterelectrode as well as the auxiliary electrode were made of platinized Pt. The reference electrode was Ag/Ag^+ 0.01 *M* in AN, with respect to which all potential data are referred. Purified nitrogen was bubbled into the cell prior to each experiment.

After every preparative electrolysis, the central compartment was drained and the solution transferred to an adequate vessel, where the solvent was evaporated at 25°C under vacuum. The resulting mixture was extracted with chloroform and the remaining solution dissolved in water. The organic phase was then washed with water and dried with anhydrous Na_2SO_4 and concentrated in 3–5 mL. The aqueous phase was treated with NaOH (0.5 *M*) and the resulting mixture extracted with chloroform.

Product analysis was performed by gas chromatography (GC) with a Hewlett-Packard 5830A gas chromatograph equipped with a FID detector and Hewlett-Packard 18850A terminal using glass columns (1.80 m × 2 mm i.d.) packed with 3% OV-225 on Chromosorb W-AW-DMCS. Gas chromatography – mass spectrometry (GC–MS) analyses were conducted with a Varian 1440 gas chromatograph coupled to a Varian-MAT CH7-A mass spectrometer interfaced to a Varian-MAT Data System 166 computer. Separation of compound **10** for ^{1}H-NMR analysis was achieved by high performance liquid chromatography (HPCL) employing reverse phase operation with a 10 micron silica-gel column (Altech C-18; 250 × 10 mm) and methanol–water (90:10) as developing solvent. Flow rate was 6 mL/min.

Results

Current–potential plots obtained with repetitive triangular potential sweeps for blank solutions and for one of the reaction media are shown in Fig. 1. It is seen from these data that the response of the AN–$LiClO_4$ and AN–$LiClO_4$–limonene systems are in good agreement with previous data (8, 11–14).

Preparative electrolysis was carried out with 0.02 *M* LiCl, 0.02 *M* limonene solutions in AN (0.1 *M* $LiClO_4$) at the

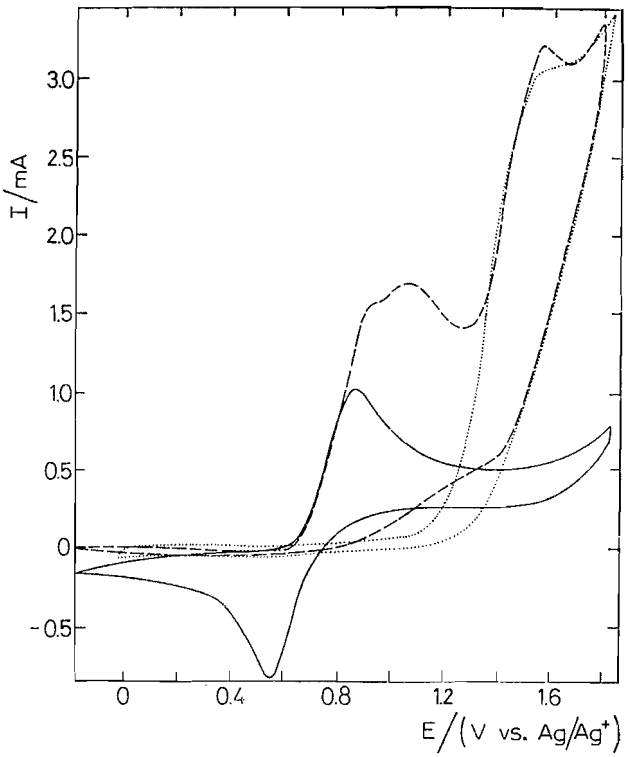

FIG. 1. Cyclic voltammograms of $LiClO_4$ 0.1 *M*, LiCl 0.02 *M* (—); $LiClO_4$ 0.1 *M*, limonene 0.02 *M* (·····); and $LiClO_4$ 0.1 *M*, LiCl 0.02 *M*, limonene 0.02 *M* (----) solutions in acetonitrile on Pt electrodes at 25°C. Scan rate 0.15 V/s.

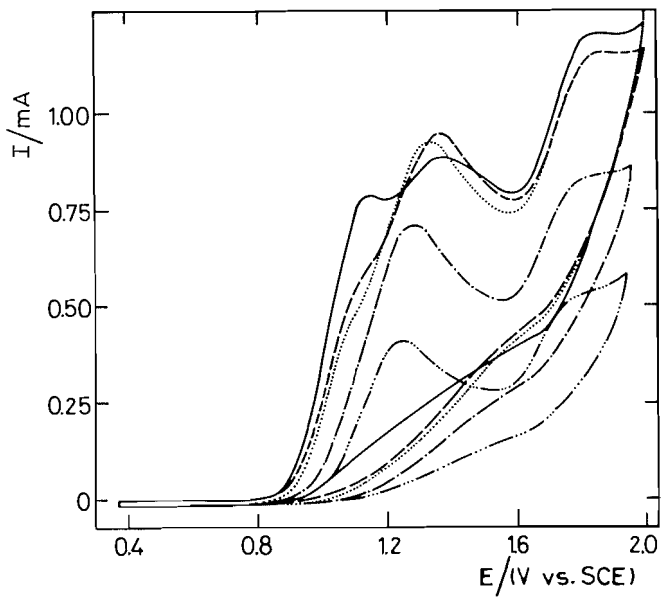

FIG. 2. Change in the voltammetric response of the working solution as electrolysis at 1.10 V vs. Ag/Ag^+ (or 1.55 V vs. SCE) proceeds. Solution composition: $LiClO_4$ 0.1 *M*, LiCl 0.02 *M*, limonene 0.02 *M*. Scan rate 0.050 V/s. (—) t = 0; (----) t = 147 min; (·····) t = 337 min; (-·-·-) t = 432 min; (-··-··) t = 547 min.

observed potential peaks, i.e., 0.95 and 1.10 V. The current–potential plots resulting under repetitive triangular potential sweeps at different times are shown in Fig. 2 for one of the experiments at 1.10 V. Very similar responses were obtained when the electrolysis potential was fixed at 0.95 V.

The chromatograms obtained are summarized in Tables 1–3.

Can. J. Chem. Downloaded from www.nrcresearchpress.com by 112.217.228.212 on 09/07/12
For personal use only.

TABLE 1. Chromatographic run for the chloroformic extract of an electrolysis at 0.95 V

Peak	Retention time (min)	Area (%)
1	1.98	14.55
2	2.27	15.11
3	2.67	3.21
4	3.84	46.86
5	15.73	5.06

TABLE 2. Chromatographic run for the chloroformic extract of an electrolysis at 1.10 V

Peak	Retention time (min)	Area (%)
1	1.98	8.54
2	2.18	5.94
3	2.66	2.56
4	3.83	46.84
5	8.73	5.28
6	12.93	4.27
7	15.19	2.14
8	15.73	7.77

TABLE 3. Chromatographic run for the aqueous extract of an electrolysis at 1.10 V after treatment with alkali and extraction with chloroform

Peak	Retention time (min)	Area (%)
9	19.08	67.76
10	24.25	10.72
11	24.75	9.26

TABLE 4. Identification of compounds corresponding to the chromatographic peaks

Peak number	Compound
1	8-Chloro-*p*-menth-1-ene (**8**)
2	1,2-dichloro-*p*-menth-8-ene (**9**)
3	Not detected by the GS–MS system
4	*cis*-6-Acetamido-*p*-menth-1,8-diene (**10**)
5	Not detected by the GC–MS system
6,7,8	Isomers of 1-acetamido-2-chloro-*p*-menth-8-ene (**11**)
9	8-acetamido-2,4,4,8-tetramethyl-3-*aza*-bicyclo[3.3.1] non-2-ene (ATABNE) (**12**)
10,11	Isomers of 8-acetamido-2,4,8-trimethyl-4-chloro methyl-3-*aza*-bicyclo[3.3.1]non-2-ene (**13**)

It must be mentioned that the chromatogram for the alkali extract of the electrolysis at 0.95 V is essentially the same than that shown in Table 3. Taking into account the results of mass spectroscopy experiments and, in some cases, ^{1}H-NMR spectra, chromatographic peaks were assigned as shown in Table 4.

Stereospecificity in the formation of **10** is confirmed by

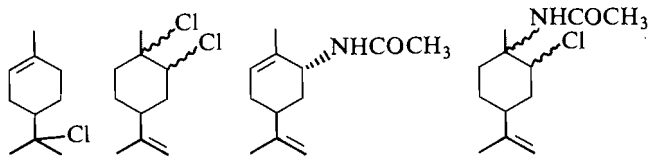

8 **9** **10** **11**

analysis of the ^{1}H-NMR spectrum, which is in good agreement with published data for the *cis*-form (15). The formation of this isomer is an interesting result, since chemical production of compound **10** leads, according to the reagent employed, either to specific production of the *trans* form or to a mixture of both isomers (15).

It must also be mentioned that compound **13** has not been

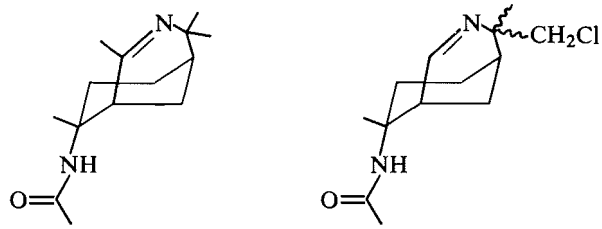

12 **13**

previously reported and, as far as we are aware, this is the first time it has been prepared.

An estimation of the different product yields was carried out by chromatographic analysis, using benzyl chloride as internal standard for the chloroformic extract and compound **12**, chemically prepared (10), for the alkaline extract. Faradic yields thus obtained are shown in Tables 5 and 6.

Also, repetitive triangular potential sweep experiment were performed at different reactant concentrations and varying sweep rates. Thus, Fig. 3 shows the voltammograms obtained when limonene concentration (C_L) is varied from 0 to 0.02 *M* at LiCl concentration (C_{Cl^-}) of 0.02 *M*. Figure 4 gives the resulting curves when C_{Cl^-} is varied at $C_L = 0.01$ *M*. Finally, experiments performed at different scan rates are shown in Fig. 5.

Discussion

When the above results are considered, the main product to be stressed is the quite high yield of compound **10**, which is just the limonene molecule with both double bonds preserved and an acetamido group in position 6. This product seems promising for further chemical attack to yield carvone or other oxidation derivatives of limonene, and work in this direction is being presently pursued.

From another point of view, it is of some interest to analyze the possible reaction paths and other characteristics of the processes taking place in the system under study. In this connection, the first consideration to be made regards the voltammograms in Fig. 1. It seems clear from these voltammograms that, in agreement with published data (11) and taking into account the results in Figs. 3 and 4, the peak at *ca.* 0.95 V can be assigned to the oxidation of Cl^-, with the reduction peak completely inhibited by further reaction with limonene. Also

Can. J. Chem. Downloaded from www.nrcresearchpress.com by 112.217.228.212 on 09/07/12
For personal use only.

TABLE 5. Faradic yields for the electrolysis at 0.95 V (organic phase only)

Product	Faradic yield (%)
8-Chloro-*p*-menth-1-ene	6.5
1,2-Dichloro-*p*-menth-8-ene	11
6-Acetamido-*p*-menth-1,8-diene	37
1-Acetamido-2-chloro-*p*-menth-8-ene	5.5

TABLE 6. Faradic yields for the electrolysis at 1.10 V (both phases considered)

Product	Faradic yield (%)
8-Chloro-*p*-menth-1-ene	2
1,2-Dichloro-*p*-menth-8-ene	2
6-Acetamido-*p*-menth-1,8-diene	16
8-Acetamido-2,4,4,8-tetramethyl-3-aza-bicyclo[3.3.1]-non-2-ene	2
1-Acetamido-2-chloro-*p*-menth-8-ene	4
8-Acetamido-2,4,8-trimethyl-4-chloromethyl-3-*aza*-bicyclo[3.3.1]non-2-ene	1

the large peak at 1.6 V must be assigned to limonene oxidation, with no direct bearing of the halogen on its behaviour (8, 14). The curves in Figs. 3 and 4 also show that the potential of the first peak is almost independent of limonene concentration in the anodic scan, while the cathodic peak potential varies with C_L and is rapidly inhibited by increasing concentration of the hydrocarbon. These figures also show that the peak at 1.1–1.15 V is only seen when both species, limonene and Cl^-, are present at significant concentrations and its potential depends on both C_L and C_{Cl^-}. Finally, Fig. 5 shows that the potential value for the first peak is very sensitive to scan rate, while the potential value for the second peak is almost independent of this parameter.

These results strongly suggest that the electrochemical step involved in the second peak occurs via an intermediate which is formed by a surface reaction between an oxidized halogen atom and a limonene-derived species, a proposal that is further supported by the fact that the potential of this peak is almost independent of scan rate.

This behaviour, and the necessity of having both species at significant concentrations, are understandable in terms of the well known fact that limonene, because of its two double bonds, is strongly adsorbed on Pt and shows a definite tendency to polymerize on the electrode surface. Thus, for low Cl^- ion concentration, adsorbed limonene molecules are stabilized, and attack by an adsorbed Cl· radical is difficult, while for larger anion concentrations, competition for the adsorption sites takes place and, hence, limonene is more prone to react.

On account of all this, and taking note of the nature of the obtained products, the following reaction paths, which because of the vicinity of both peaks are to some extent operative during electrolyses at 0.95 V and at 1.10 V, are proposed, with the common initial step:

[1] $Cl^- = Cl\cdot + e^-$

(a) Reaction route for compound ***10***

As it has been mentioned, the second peak observed in the cyclic voltammograms should be assigned to an anodic process

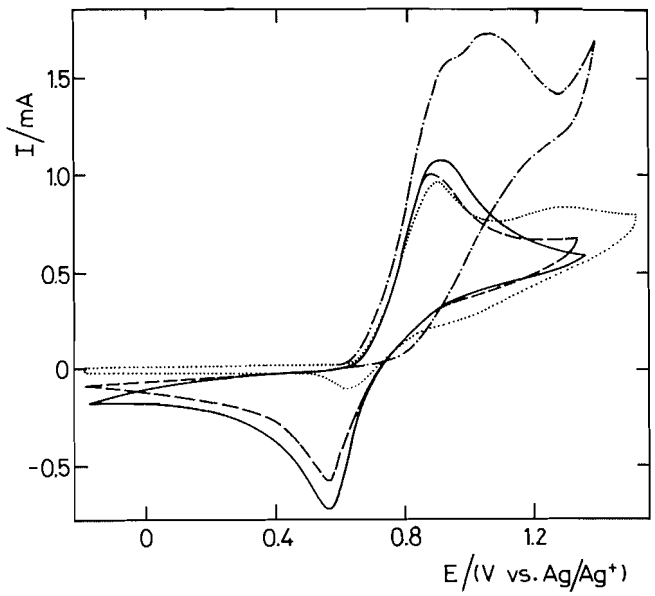

FIG. 3. Voltammetric response to varying limonene concentration. $LiClO_4$ 0.1 *M*, LiCl 0.02 *M*, limonene (—) = 0; (----) = 0.000425 *M*; (····) = 0.0018 *M*; (-.-.-.) = 0.0238 *M*. Scan rate 0.150 V/s.

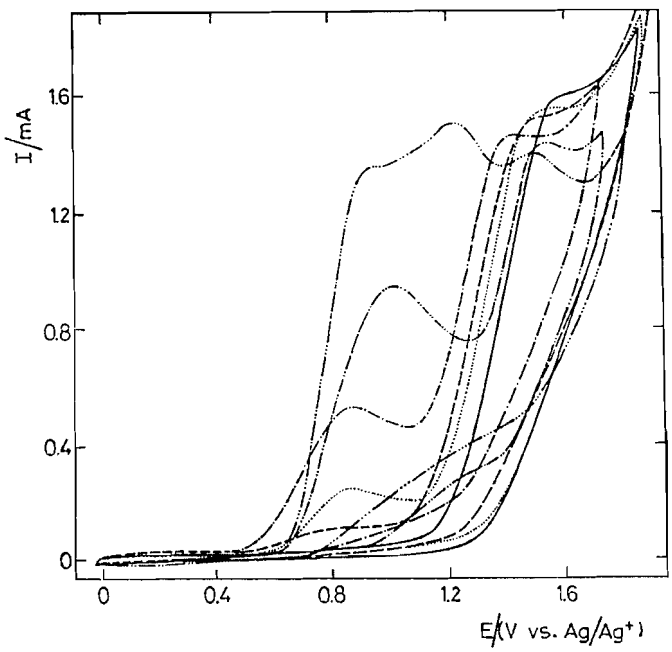

FIG. 4. Voltammetric response to varying Cl^- concentration. $LiClO_4$ 0.1 *M*, limonene 0.01 *M*, LiCl (—) = 0; (----) = 0.000395 *M*; (····) = 0.0018 *M*; (-.-.-.) = 0.0050 *M*; (-...-..) = 0.010 *M*; (-...-...) = 0.020 *M*. Scan rate 0.150 V/s.

involving a surface species formed from halogen atoms and limonene-derived species. Also, since **10** is the principal product, its formation should account for most of the charge involved in the process and for the fact that only rather small amounts of molecular chlorine are formed, thus giving a rationale to the low yields observed for products **8**, **9**, and **11**. These low yields should be compared with the rather high quantities obtained for equivalent compounds in the electrochemical chlorination of cyclohexene (16).

Thus, it is proposed that on the electrode surface an adsorbed Cl· radical produces the abstraction of an allylic proton from a

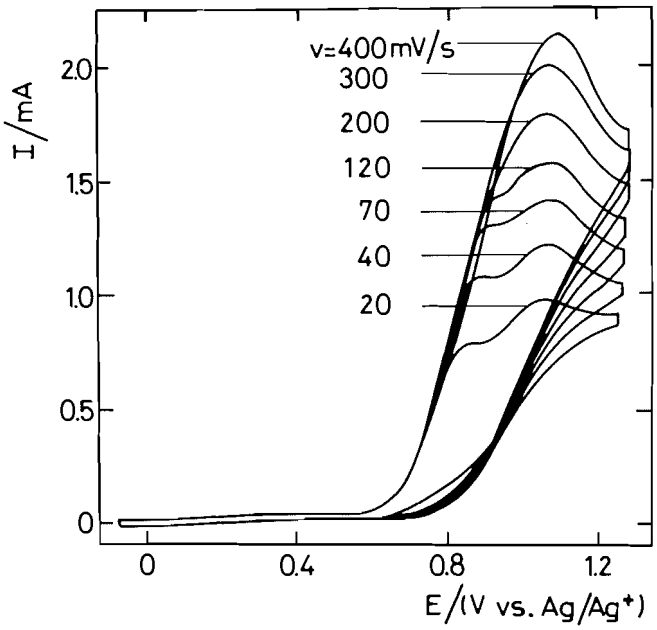

FIG. 5. Scan rate dependence of the voltammograms of the working solution.

neighbouring adsorbed limonene molecule:

[2] $Cl\cdot(ads) + (ads) = Cl^- + (ads) = Cl^- + H^+$

$+ (ads)$

followed by the electrochemical step:

[3] $(ads) = + e^-$

Finally, nucleophilic attack of the solvent gives the main product:

[4] $CH_3CN + H_2O +$ $= NHCOCH_3 + H^+$

(b) Reaction route for compounds ***9***, ***11***, *and* ***13***

It is generally admitted that electrochemical chlorination usually occurs by homogeneous reaction of molecular chlorine, generated *in situ*, with double bonds through formation of an halonium ion (16). In our case, however, the fact that the limonene molecule has two double bonds and the nature and yield of the resulting products points to a different path.

In this respect, it is to be first considered which are the steps leading from Cl^- ions in solution to molecular chlorine. Although the detailed mechanisms which operate in electrochemical generation of molecular chlorine continue to be an open field for basic research and depend on the nature of the electrode material as well as on the characteristics of the electrochemical medium, it seems safe (17) to state that the first process is the formation of adsorbed Cl· radicals, as indicated in eq. [1], followed by surface reactions involving one or two of these radicals and, perhaps, Cl^- ions or oxidized species which give adsorbed molecular chlorine:

[5] nCl·(ads) + X = Cl_2(ads) (n = 1,2)

which finally desorbs to give molecular chlorine in solution:

[6] $Cl_2(ads) = Cl_2(sol)$

However, if this sequence were completed in our case, and the halogenated derivatives formed by homogeneous reaction via halonium intermediates, products resulting from attack on both double bonds should be obtained with similar yields. This is not the case and, thus, it seems reasonable to propose that halonium ion formation takes place on the electrode surface, before molecular chlorine is desorbed:

[7] $Cl_2(ads) +$ $(ads) =$ $+ Cl^-$

or

[8] $Cl_2(ads) +$ $(ads) =$ $+ Cl^-$

Desorption of these ions is strongly favoured by the anodic potential and, hence, for the halonium ion generated on position 1 we have:

[9] $+ Cl^- =$

9

or

[10] $+ CH_3CN =$

followed by:

[11] $+ H_2O =$

11

By its hand, the halonium ion resulting from eq. [8] when reacting with the solvent follows the Ritter mechanism and yields an iminium salt (9):

Can. J. Chem. Downloaded from www.nrcresearchpress.com by 112.217.228.212 on 09/07/12
For personal use only.

[12] 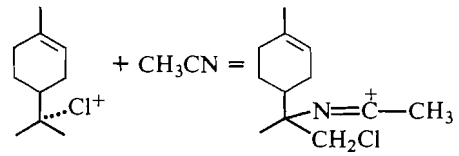

[13] 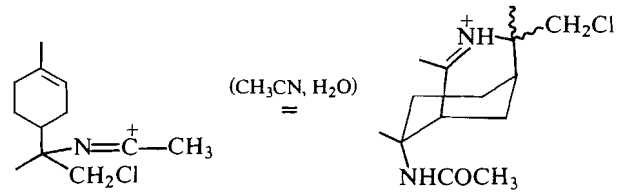

which is dissolved in water and, when treated with alkali gives the corresponding imine (10):

[14] 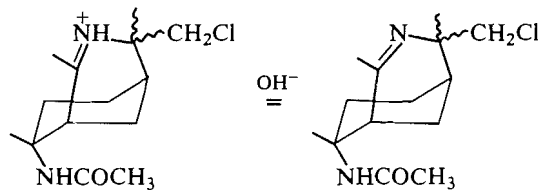

which is extracted by chloroform.

The absence of 8,9-dichloro compounds and the lower yields observed for compound **13** when compared to products **9** and **11** indicate that the concentration of halonium ions on position 1,2 is far larger than that of those obtained on position 8,9. This fact agrees well with our proposal since, for steric reasons, limonene adsorption should preferentially occur through the exocyclic double bond.

(c) Reaction routes for compounds 8 and 12

Formation of **8** can be explained in terms of the generation of a positive center in the limonene molecule, at position 8, due to the acidification produced when compound **10** is formed:

[15] 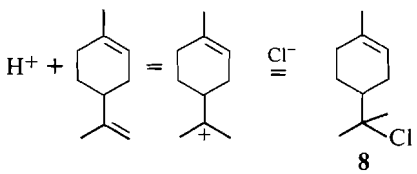

8

When the solvent is the nucleophile, ATABNEP is formed (9):

[16] 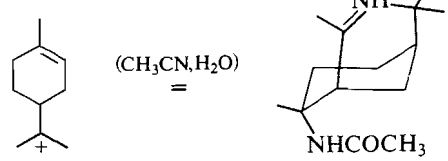

which, under alkali attack in the water phase, gives the imine, **12**, which is extracted in chloroform.

Acknowledgments

The authors gratefully acknowledge financial support to this work through a grant of the Comisión Investigaciones Científicas de la Provincia de Buenos Aires. Thanks are due to UMYMFOR (FCEN-CONICET) for chromatographic and spectroscopic determinations. Financial support from the Organization of American States is also recognized.

1. Catalog Handbook of Fine Chemicals, Aldrich Chemical Co., Milwaukee. 1984.
2. F. FICHTER and G. SCHETTY.Helv. Chim. Acta, **20**, 1304 (1937).
3. S. GLASSTONE and H. E. STANLEY. Trans. Electrochem. Soc. **97**, 327 (1947).
4. J. B. REDD and J. E. HAWKINS. J. Electrochem. Soc. **99**, 178 (1950).
5. T. SHONO and A. IKEDA. J. Am. Chem. Soc. **94**, 7892 (1972).
6. T. SHONO, A. IKEDA, J. HAYASHI, and S.HAKOZAKI. J. Am. Chem. Soc. **97**, 4261 (1975).
7. V. MONTIEL, M. LÓPEZ SEGURA, and A. ALDAZ. Electrochim. Acta, **29**, 1123 (1984).
8. M. Y. DUARTE, H. LANDERRECHE, C. M. MARSCHOFF, and M. E. MARTINS. Electrochim. Acta, **28**, 331 (1983).
9. J. A. CARAM, M. E. MARTINS, C. M. MARSCHOFF, L. F. R. CAFFERATA, and E. G. GROS. Z. Naturforsch. **39**b, 972 (1984).
10. J. A. CARAM, E. G. GROS, B. E. RIVERO, O. E. PIRO, and C. M. MARSCHOFF. To be published.
11. O. A. PETRII and I. G. KHOMCHENKO. Elektrokhimiya, **14**, 1435 (1978).
12. M. SZKLARCZYK and J. SOBKOWSKI. Electrochim. Acta, **25**, 159 (1980).
13. M. VERNIETTE, C. DAREMOND, and J. SIMONET. Electrochim. Acta, **23**, 929 (1978).
14. J. W. CARAM. Doctoral Thesis. Facultad de Ciencias Exactas y Naturales, Universidad de Buenos Aires. 1987.
15. I. Z. KABORÉ, Q. KHUONG-HUU and A. PANCRAZI. Tetrahedron, **34**, 2815 (1978).
16. J. P. POUILLEN, R. MINKO, M. VERNIETTE, and P. MARTINET. Electrochim. Acta, **24**, 1189 (1979).
17. S. TRASATTI. Electrochim. Acta, **32**, 369 (1987).

Appendix

Mass spectra of the identified peaks were as follows:

Peak 1 (compound **8**): m/z (%) 174(2.2), 172 (7.8), 136(44.9), 121(62.7), 95(60.1), 93(100), 81(33), 79(37), 77(26), 67(69), 68(63), 41(60).

Peak 2 (compound **9**): m/z (%) 173(0.7), 172 (4.1), 171(1.3), 170(9.6), 137(2.0), 136(8.1), 135(14.6), 134(16.4), 129(9.8), 127(30.4), 121(16.2), 119(29.1), 93(100), 91(51.5), 83(63.6), 79(30.0), 77(24.4), 68(29.0), 67(36.3), 41(80.3).

Peak 4 (compound **10**): m/z (%) 193(41.3), 178(4.2), 151(3.7), 150(9.4), 136(14.9), 134(33.1), 119(100), 110(21.5), 93(13.5), 81(22.1), 67(31.1), 43(36.3), 42(59.2), 41(53.8).

Peaks 6, 7, and 8 yield the same mass spectra which correspond to compound **11**: m/z (%) 229(1.5), 194(9.3), 193(15.9), 178(7.8), 172(4.8), 170(1.3), 150(20.4), 135(16.4), 134(44), 110(43.7), 93(49.4), 70(59.7), 60(100), 43(34.0).

Peak 9 (compound **12**) m/z (%) 236(37.0), 221(12.2), 177(35.3), 162(25.8), 150(29.1), 136(37.7), 122(82.4), 43(56.0), 42(100).

Peaks 10 and 11 yield the same mass spectra which correspond to compound **13**: m/z (%) 236(17.4), 235(100), 221(7.6), 213(4.3), 211(13.1), 176(39.4), 162(15.7), 136(42.7), 135(12.6), 134(22.5), 122(29.2), 43(39.4), 42(61.3), 41(28.0).

^{1}H-NMR spectrum of compound **10**:

Chemical shifts ($CDCl_3$, TMS): 1.65 (m, CH_3-1), 1.74 (m, CH_3-10), 1.97 (s, $COCH_3$), 4.72–4.76 (m, H-6 and CH_2-9), 5.4 (m, H-2).

Can. J. Chem. Downloaded from www.nrcresearchpress.com by 112.217.228.212 on 09/07/12
For personal use only.

Molecular structure of opiate alkaloids. Part II. Crystal structures of 4-methylhomobenzomorphan hydrobromide (I) and 4,12β-dimethylhomobenzomorphan (II)[1]

ANDRÉ G. MICHEL[2]
Laboratoire de chimie structurale, Université de Sherbrooke, Sherbrooke (Qué.), Canada J1K 2R1

GUY EVRARD AND BERNADETTE NORBERG
Facultés Universitaires Notre-Dame de la Paix, rue de Bruxelles, 61, B5000 Namur, Belgium

AND

EUGÈNE MILCHERT
Politechnika Szczecinska, Szczecin, Poland, 0422141, PS PL

Received September 18, 1987[3]

ANDRÉ G. MICHEL, GUY EVRARD, BERNADETTE NORBERG, and EUGÈNE MILCHERT. Can. J. Chem. **66**, 1763 (1988).

The two title compounds belong to the family homobenzomorphans. Their analgesic properties are comparable to morphine but without inducing physical dependence. This work presents the results of X-ray diffraction and NMR studies to elucidate the conformational properties particular to this class of compounds. More specifically, the spatial orientation of the nitrogen lone-pair are compared to those observed for other related molecules. The two molecules adopt the same L-shaped structure and the 16β-methyl substituent present in the second molecule does not modify this structure. Although very different in both structures, the intermolecular interactions do not alter the molecular conformation. The nitrogen lone pair is oriented away from the benzene ring and its orientation is conserved in solution, as proven by nmr studies. The main conclusions are that the seven-membered ring shows very specific conformational properties and that the lone-pair orientation is predictable, according to the position of the nitrogen in the ring. Finally, it is concluded that correlations between the nitrogen lone-pair orientation and the analgesic activity have to be reconsidered.

ANDRÉ G. MICHEL, GUY EVRARD, BERNADETTE NORBERG et EUGÈNE MILCHERT. Can. J. Chem. **66**, 1763 (1988).

Les deux composés faisant l'objet de cette étude, appartiennent à la famille des homobenzomorphanes. Leurs propriétés analgésiques se sont avérées très intéressantes sous deux aspects : ils conservent une activité proche de la morphine et d'autre part ne provoquent pas de dépendance physique. Le présent travail vise à mettre en évidence les propriétés conformationnelles caractéristiques de ces composés, en vue d'en expliquer les propriétés typiques en terme de conformations. Plus particulièrement, l'orientation de la paire libre de l'azote est comparée à celle que l'on observe dans d'autres composés analgésiques. Il apparaît que les deux molécules adoptent la forme en L caractéristique et que le groupe 16β-méthyl présent dans le composé **II**, n'induit aucune modification conformationnelle importante. Les interactions intermoléculaires sont également décrites; quoique très différentes d'une molécule à l'autre, elles n'induisent pas non plus de modification conformationnelle notoire. Le comportement de ces molécules en solution est aussi étudié. Il s'avère que ce type de molécule possédant un cycle C à 7 membres oriente la paire libre de l'azote de façon spécifique selon la position de l'atome d'azote dans le cycle. On doit également conclure que la corrélation entre cette orientation et l'activité analgésique de ces molécules doit être reconsidérée.

Introduction

The present work is part of a more general crystal and molecular structure study of opiate alkaloids. The first part was published earlier (1) and reported oripavine and thebaine structure determinations in order to analyse the geometrical properties of narcotic opioids; the influence of the 16β-aryl substitution adjacent to the N atom in the piperidinyl ring was also discussed.

The present paper deals with opiate alkaloids where the classical C ring has been changed for a seven-membered ring with the N atom at the second position. These compounds have been found to be very active as opioids: analgesic activity of title compounds were determined using optically resolved stereoisomers (2, 3). Surprisingly, it was reported that the optical resolution gave no effect on the analgesic activity of compound **I**. Nevertheless, the *levo* isomer of compound **II** was analgesically much more potent than the *dextro* isomer and equipotent with morphine (3).

In light of X-ray structure determination, we describe the configuration of the seven-membered ring integrated into the

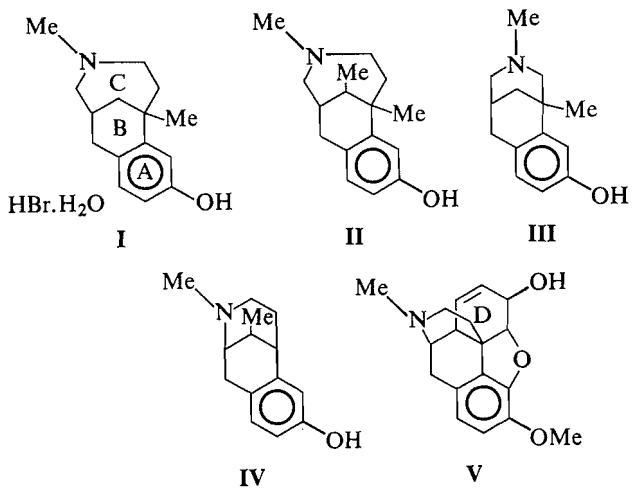

I, 1,4-dimethyl-11-hydroxy-2,3,4,5,6,7-hexahydro-1,6-1*H*-4-benzazonine hydrobromide
II, 1,4,14β-trimethyl-11-hydroxy-2,3,4,5,6,7-hexahydro-1,6-methano-1*H*-4-benzazonine
III, 1,3-dimethyl-1,2,3,4,5,6-hexahydro-1,5-methano-3-benzazocin-9-ol (10)
IV, 2,9β-dimethyl-6,7-benzomorphan (8)
V, codeine (7)

[1]Homobenzomorphan is a conventional designation for 10-hydroxy-4-methyl-2,3,4,5,6,7-hexahydro-1,6-methano-1*H*-4-benzazonine.

[2]To whom correspondence should be addressed.

[3]Revision received January 29, 1988.

Can. J. Chem. Downloaded from www.nrcresearchpress.com by 93.93.197.157 on 09/07/12
For personal use only.

Can. J. Chem. Downloaded from www.nrcresearchpress.com by 93.93.197.157 on 09/07/12
For personal use only.

TABLE 1. Crystallographic data

Parameter	Compound **I**	Compound **II**
Molecular formula	$C_{15}H_{21}NO \cdot HBr \cdot H_2O$	$C_{16}H_{23}NO$
Molecular weight	330.28	245.35
Unit cell	Orthorhombic	Orthorhombic
a (Å)	17.333 (2)	14.566 (1)
b	16.652 (1)	8.347 (1)
c	10.953 (1)	11.250 (1)
V (Å^3)	3161.354	1367.882
Z	8	4
d_{obs} (g cm^{-3})	1.38	1.19
Space group	Pbca	$Pna2_1$
Radiation, $K\bar{\alpha}$ (Å)	1.54178	1.54178
T (°C)	20	20
Crystal size (mm)	0.2 × 0.1 × 0.2	0.35 × 0.22 × 0.26

multi-ring system of homobenzomorphans. The nmr results suggest that the same conformations are also present in solution. After earlier statements on the importance of the nitrogen lone-pair orientation in the stereospecific opiate receptor (12), it was interesting to have an insight into the particular configuration of the seven-membered ring integrated into the multi-ring system of compounds **I** and **II**. It was hoped to correlate the above-mentioned differences in the analgesic activity with the presence of 12β-methyl group (C18 in the crystal numbering) in compound **II**.

Experimental

X-ray diffraction

The compounds have been synthesized (2) and supplied as racemic mixtures. Recrystallisation of compound **I** from MeOH–H_2O gave a crystalline mixture. On the basis of ref. 3, this mixture was expected to be the (+) and (+/−) bases. The crystal used for the X-ray analysis was from the (+) component. Subsequent photographic oscillation and Weissenberg films confirmed the assumption of a single stereoisomer, and a non-centrosymmetric space group was determined.

In case of compound **II**, the recrystallisation from MeOH–H_2O gave needles of the racemic mixture, confirmed by the determination of a centrosymmetric space group. For both compounds, the cell dimensions were refined with 25 reflections measured on the diffractometer. Independent reflections were collected on a Nonius, CAD-4 automatic diffractometer system. Table 1 gives the experimental conditions of the X-ray experiments.

Intensity data were corrected for Lorentz-polarization effects. No corrections were made for absorption or dispersion effects. Direct methods were applied to solve the structures using a MULTAN80 system of programs (4). The coordinates of all non-hydrogen atoms in the two compounds were determined from the best E-map. Further calculations were performed using SHELX (5). The positions of all hydrogen atoms were determined on an electron density difference Fourier map after initial refinement of non-hydrogen atoms. The final structures were refined by using full-matrix least squares with anisotropic temperature factors for non-hydrogen atoms and isotropic temperature factors for hydrogen atoms. The weighting scheme used in the least-squares refinement was $w = 1/[\sigma^2(F) + 0.001F^2]$. Table 2 gives the parameters concerning the refinements. Atomic parameters are given in Table 3.[4]

The high negative residual on the last difference Fourier synthesis for compound **I** appears in a region close to the water O(18) atom. This observation is to be correlated with a high equivalent B for this atom, reflecting an important level of disorder for the solvent molecule.

[4]Tables of anisotropic temperature factor tables, the structure factor tables, the atomic coordinates of the hydrogen atoms nmr ^{13}C chemical shifts may be purchased from the Depository of Unpublished Data, CISTI, National Research Council of Canada, Ottawa, Ont., Canada K1A 0S2.

TABLE 2. Experimental conditions for data collection and refinement

Parameter	Compound **I**	Compound **II**
$F(0,0,0)$	1376.0	536.0
μ (cm^{-1})	32.97	4.92
Scan range (deg)	0.6 + 0.3 tan θ	0.6 + 0.3 tan θ
Scan rate (deg min^{-1})	1 to 10	1 to 10
Aperture of the detector (mm)	2.5 + 0.5 tan θ	2.5 + 0.5 tan θ
2θ range (deg)	4–144	4–144
h, k, l ranges	$0 \leqslant h \leqslant 21$	$0 \leqslant h \leqslant 17$
	$0 \leqslant k \leqslant 20$	$0 \leqslant k \leqslant 10$
	$0 \leqslant l \leqslant 13$	$0 \leqslant l \leqslant 13$
Maximum fluctuation of standard reflection (%)	⩽2	⩽2
Number of reflections measured	3114	1417
Number of reflections observed	2145	1286
Threshold: $I \geqslant k\sigma(I)$, k =	2.5	2.5
$R = \Sigma\|\Delta F\|/\Sigma\|F_o\|$	0.031	0.037
$R_w = [\Sigma w \Delta F^2/\Sigma w(F_o)^2]^{1/2}$	0.045	0.041
$(\text{Displacement}/\sigma)_{max}$	0.26	0.19
$(\text{Displacement}/\sigma)_{average}$	0.00	0.07
Extreme fluctuations of residual electron density (e Å^{-3})	−0.51, 0.17	−0.16, 0.14

Nuclear magnetic resonance

Proton decoupled carbon-13 nuclear magnetic resonance measurements were performed on a BRUKER CXP200/ASPECT 2000 spectrometer. Chemical shift assignments were facilitated by T_1 measurements and selective decoupling experiments. Compound **II** was studied in $CDCl_3$ from 223 to 323 K and in DMSO-d_6 at 323 K whereas compound **I** was studied from 300 to 373 K in DMSO-d_6 and in D_2O/CD_3OH (1:3 v/v) at 273 K.

Results

Molecular structures

Figure 1 shows the stereoscopic view of the molecular structures for compounds **I** and **II**. The characteristic L-shape is clearly observable, and the methylation at C(10) does not induce significant changes in compound **II**. In both compounds, the N-methyl group is pseudo-equatorial with respect to the seven-membered ring C: as a consequence the nitrogen hydrogen in compound **I** and the nitrogen lone pair in compound **II** are oriented away from cycle A. In Fig. 1*a*, this orientation has been visualized by placing the proton on the nitrogen pointing towards the bromide ion. In the case of compound **II** represented in Fig. 1*b*, a symmetry-related O(1) atom has been used to illustrate the nitrogen lone pair orientation, involved in an intermolecular hydrogen bond in the crystal.

Figure 2 gives the numbering scheme used. Bond lengths, valence, and torsional angles are given in Tables 4, 5, and 6, respectively. Significant differences in bond lengths and angles are only observed for the seven-membered ring and especially the region of the N(14) atom. Nevertheless, in both compounds, the C ring appears to adopt a "crown" conformation. This can be quantitatively realised examining the seven torsional angles indicated in Table 6.

Crystal packing

In the crystal of compound **I**, the packing of the molecules is achieved by hydrogen bonds between atoms of Br, O, and N. Each water oxygen O(18) is bonded to two symmetry-related bromide ions. The water–bromide system constitutes endless

TABLE 3. Fractional coordinates ($\times 10^4$) and equivalent B^a for non-hydrogen atoms of compounds **I** and **II**

	Compound **I**					Compound **II**			
Atom	x/a	y/b	z/c	B_{eq}	Atom	x/a	y/b	z/c	B_{eq}
O(1)	6422(1)	4853(1)	4562(2)	5.83	O(1)	2674(1)	4466(2)	6151(1)	6.00
C(2)	5859(1)	4889(1)	3692(2)	4.52	C(2)	1806(1)	4411(2)	6967(3)	4.37
C(3)	5680(2)	5632(1)	3208(2)	5.24	C(3)	1369(2)	2939(3)	7063(3)	5.16
C(4)	5098(2)	5688(1)	2344(2)	4.97	C(4)	486(2)	2888(2)	7499(3)	5.18
C(5)	4712(1)	5016(1)	1905(2)	3.88	C(5)	13(1)	4242(2)	7883(3)	4.32
C(6)	4916(1)	4256(1)	2365(2)	3.51	C(6)	456(1)	5726(2)	7803(2)	3.85
C(7)	5483(1)	4208(1)	3264(2)	4.05	C(7)	1350(1)	5784(2)	7342(3)	4.24
C(8)	4073(1)	5122(1)	983(2)	4.39	C(8)	−956(2)	4092(3)	8366(3)	5.55
C(9)	3487(1)	4436(1)	1071(2)	4.15	C(9)	−1488(1)	5650(3)	8211(3)	4.78
C(10)	3932(1)	3649(1)	916(2)	4.05	C(10)	−924(2)	6975(3)	8799(3)	4.80
C(11)	4531(1)	3483(1)	1910(2)	3.72	C(11)	−5(1)	7309(2)	8165(3)	4.33
C(12)	4135(1)	3033(1)	2973(2)	4.07	C(12)	−128(1)	8335(2)	7042(3)	4.99
C(13)	3538(1)	3487(1)	3703(2)	4.36	C(13)	−653(2)	7604(3)	6009(3)	4.98
N(14)	2856(1)	3794(1)	2979(2)	3.97	N(14)	−1638(1)	7334(2)	6245(3)	4.33
C(15)	3039(1)	4543(1)	2267(2)	4.37	C(15)	−1788(2)	5831(2)	6894(3)	4.98
C(16)	5149(2)	2921(1)	1368(3)	4.97	C(16)	630(2)	8228(3)	9018(4)	7.01
C(17)	2202(1)	3953(2)	3833(3)	5.28	C(17)	−2113(2)	7175(3)	5094(3)	6.39
O(18)	6721(2)	1561(2)	480(3)	11.57	C(18)	−1510(2)	8475(3)	9072(3)	6.22
Br	2140(1)	2181(1)	1736(1)	7.24					

$^aB_{eq} = \frac{8\pi^2}{3}\sum_i\sum_j U_{ij}a_i^*a_j^*a_ia_j.$

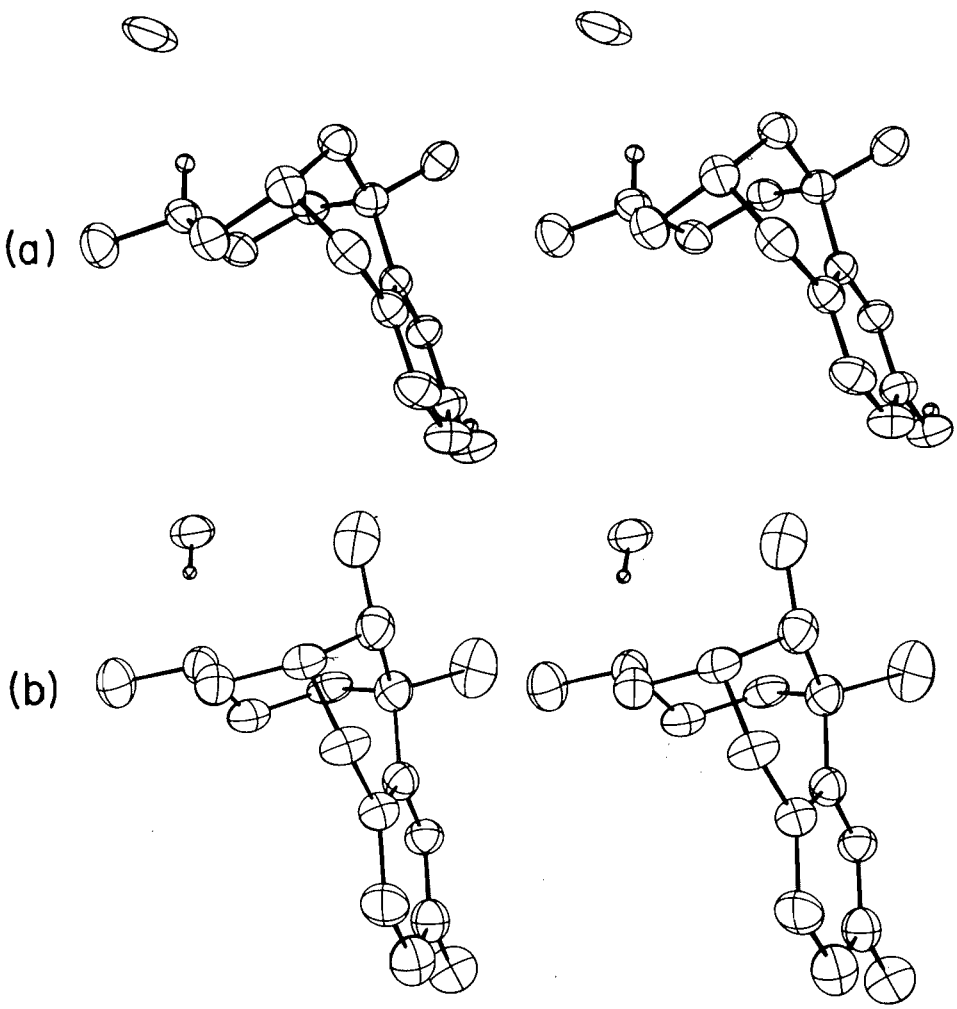

FIG. 1. Stereoscopic views of the N-protonated compound **I** with a facing Br atom (a), and the basic compound **II**, (b), with 50% probability ellipsoids for the non-hydrogen atoms.

Can. J. Chem. Downloaded from www.nrcresearchpress.com by 93.93.197.157 on 09/07/12
For personal use only.

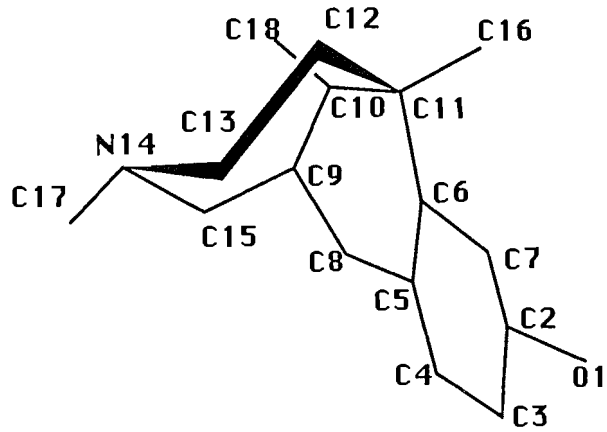

FIG. 2. Atom numbering scheme.

TABLE 4. Intramolecular distances (Å) for compounds **I** and **II** estimated standard deviations are indicated in parentheses

Bond	Distance (Å)	
	Compound **I**	Compound **II**
O(1)—C(2)	1.365(3)	1.364(2)
C(3)—C(2)	1.381(3)	1.388(3)
C(7)—C(2)	1.389(2)	1.390(3)
C(4)—C(3)	1.386(4)	1.377(4)
C(5)—C(4)	1.391(3)	1.392(3)
C(6)—C(5)	1.407(2)	1.399(2)
C(8)—C(5)	1.509(3)	1.517(3)
C(7)—C(6)	1.394(3)	1.403(2)
C(11)—C(6)	1.533(2)	1.537(3)
C(9)—C(8)	1.532(2)	1.524(4)
C(10)—C(9)	1.529(2)	1.528(4)
C(15)—C(9)	1.533(3)	1.552(5)
C(11)—C(10)	1.530(3)	1.542(4)
C(18)—C(10)		1.539(4)
C(12)—C(11)	1.546(3)	1.537(4)
C(16)—C(11)	1.541(3)	1.538(4)
C(13)—C(12)	1.511(3)	1.519(4)
N(14)—C(13)	1.513(3)	1.476(3)
C(15)—N(14)	1.505(3)	1.467(3)
C(17)—N(14)	1.493(3)	1.474(5)

chains oriented along the (b,c) diagonal. The molecules are connected to the water–bromide chains by two hydrogen bonds. The first one is formed between the phenolic O(1) as donor and O(18) water atom as acceptor. The second one involves a bromide ion as acceptor, sharing a proton with the basic nitrogen N(14) atom. The resulting extensive network of hydrogen bonds is shown in Fig. 3.

The packing in the crystal of compound **II** is mainly achieved by hydrogen bondings between the phenolic oxygen O(1) and a nitrogen atom N(15). The resulting head-to-tail system gives rise to infinite chains of molecules shown in Fig. 4. Hydroxyl hydrogen atoms H(1) have been included in the packing diagram. Van der Waals interactions assume the cohesion between the chains. Table 7 gives the hydrogen-bond distances and angles obtained for both compounds. The values obtained

TABLE 5. Intramolecular valence angles (deg) for compounds **I** and **II**, estimated standard deviations are indicated in parentheses

Bonds	Angle (deg)	
	Compound **I**	Compound **II**
O(1)—C(2)—C(3)	117.9(2)	119.0(2)
O(1)—C(2)—C(7)	122.3(2)	121.9(2)
C(3)—C(2)—C(7)	119.3(2)	119.1(2)
C(2)—C(3)—C(4)	119.1(2)	118.9(2)
C(3)—C(4)—C(5)	122.1(2)	123.2(2)
C(4)—C(5)—C(6)	118.7(2)	118.1(2)
C(4)—C(5)—C(8)	119.4(2)	120.2(2)
C(6)—C(5)—C(8)	121.9(1)	121.6(2)
C(5)—C(6)—C(7)	118.8(1)	118.8(2)
C(5)—C(6)—C(11)	121.9(2)	122.9(1)
C(7)—C(6)—C(11)	119.2(1)	118.3(1)
C(2)—C(7)—C(6)	121.5(2)	121.8(2)
C(5)—C(8)—C(9)	110.9(1)	111.2(2)
C(8)—C(9)—C(10)	107.3(1)	107.1(2)
C(8)—C(9)—C(15)	107.6(1)	109.6(2)
C(10)—C(9)—C(15)	116.7(1)	119.6(2)
C(9)—C(10)—C(11)	114.8(2)	113.4(2)
C(9)—C(10)—C(18)		112.4(2)
C(11)—C(10)—C(18)		114.8(2)
C(6)—C(11)—C(10)	112.0(1)	110.3(2)
C(6)—C(11)—C(12)	110.8(1)	108.2(2)
C(6)—C(11)—C(16)	109.4(2)	109.4(2)
C(10)—C(11)—C(12)	108.8(1)	112.3(2)
C(10)—C(11)—C(16)	107.9(2)	108.9(3)
C(12)—C(11)—C(16)	107.7(2)	107.8(2)
C(11)—C(12)—C(13)	117.4(1)	117.6(2)
C(12)—C(13)—N(14)	115.3(2)	114.4(3)
C(13)—N(14)—C(17)	109.0(2)	108.2(3)
C(13)—N(14)—C(15)	112.8(1)	111.4(2)
C(15)—N(14)—C(17)	109.7(2)	106.9(2)
N(14)—C(15)—C(9)	116.9(1)	121.1(2)

TABLE 6. Comparison of the torsional angles (deg) in rings B and C for compounds **I** and **II**

Bonds	Torsional angle (deg)	
	Compound **I**	Compound **II**
C(8)—C(5)—C(6)—C(11)	3.2(3)	−1.5(4)
C(6)—C(5)—C(8)—C(9)	25.4(2)	25.2(4)
C(5)—C(6)—C(11)—C(10)	0.9(3)	9.3(4)
C(5)—C(6)—C(11)—C(12)	−120.8(2)	−113.9(2)
C(5)—C(8)—C(9)—C(10)	−55.7(2)	−55.0(3)
C(5)—C(8)—C(9)—C(15)	70.7(2)	76.2(3)
C(8)—C(9)—C(10)—C(11)	63.0(2)	66.4(3)
*C(15)—C(9)—C(10)—C(11)	−57.9(2)	−59.0(3)
C(8)—C(9)—C(15)—N(14)	−140.3(2)	−131.8(2)
*C(10)—C(9)—C(15)—N(14)	−19.6(2)	−7.6(3)
C(9)—C(10)—C(11)—C(6)	−34.7(2)	−42.0(3)
*C(9)—C(10)—C(11)—C(12)	88.2(2)	78.7(3)
C(6)—C(11)—C(12)—C(13)	56.5(2)	55.8(2)
*C(10)—C(11)—C(12)—C(13)	−67.1(2)	−66.1(3)
*C(11)—C(12)—C(13)—N(14)	59.4(2)	67.3(2)
*C(12)—C(13)—N(14)—C(15)	−78.3(2)	−82.4(3)
*C(13)—N(14)—C(15)—C(9)	78.6(2)	69.8(3)
C(17)—N(14)—C(15)—C(9)	−159.8(2)	−172.2(2)

Can. J. Chem. Downloaded from www.nrcresearchpress.com by 93.93.197.157 on 09/07/12
For personal use only.

TABLE 7. Hydrogen-bond distances (Å) and angles (deg) between donor (D) and acceptor (A) atoms

Compound	D—H---A	∠ DHA (deg)	D---A (Å)	D—H (Å)	H---A (Å)
I	O(1)—H---O(18)	176.5 (12)	2.631 (5)	0.94 (3)	1.68 (4)
I	O(18)—H---Br	179.9 (12)	3.275 (4)	1.00 (4)	2.27 (1)
I	O(18)—H---Br	180.0 (12)	3.293 (4)	1.00 (4)	2.29 (4)
I	N(14)—H---Br	160.0 (13)	3.256 (2)	0.87 (2)	2.41 (1)
II	O(1)—H---N(15)	165.6 (13)	2.869 (2)	1.03 (2)	1.85 (2)

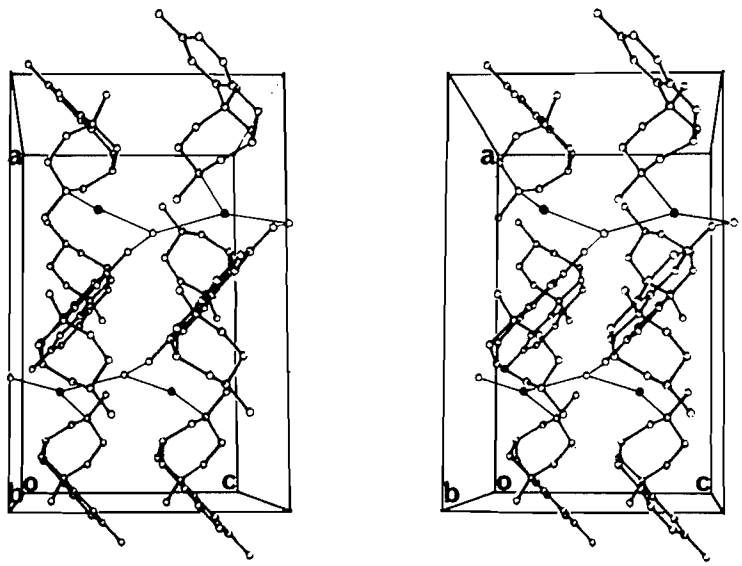

FIG. 3. Stereoscopic view of the cell content for compound **I**, showing the packing and the hydrogen-bonding network (thin lines). Filled circles indicate Br atoms.

Can. J. Chem. Downloaded from www.nrcresearchpress.com by 93.93.197.157 on 09/07/12
For personal use only.

for compound **I** may be compared to those of related 6,7-benzomorphan compounds published earlier (6). It is interesting to observe that the benzomorphan hydrobromide (6) and compound **I** of the present study adopt similar crystal packing. Values obtained for hydrogen-bond geometries (Table 7) are also very similar.

Molecular comparisons

Comparisons of the molecular conformations of compounds **I**, **II**, **III**, and **V** have been made using the molecular modelling system SYBYL (11). After introduction of the experimental atom coordinates of two molecules into the program, one molecule is subjected to translation and rigid rotation so that the homologous series of atoms of ring A coincide for the two molecules (FIT subprogram of SYBYL). The stereoviews of the resultant pairs of molecules are given in Fig. 5. As can be seen in Fig. 5(*a*), although packed in very different ways, molecular conformations of compounds **I** and **II** are very similar. Also, the presence of a 12β-methyl substituent in compound **II** does not induce important modifications on the molecular conformation. Significant differences may be observed on intramolecular bonds C(15)—N(14) and C(13)—N(14): see Table 4. The most different valence angles are C(8)—C(9)—C(15), C(10)—C(9)—C(15), C(6)—C(11)—C(12), C(10)—C(11)—C(12), and C(15)—N(14)—C(17) as can be seen in Table 5. Meanwhile, it must be pointed out that the nitrogen atom region of the molecule is mostly affected, as seen from the selected torsional angles given in Table 6.

Dynamic nuclear magnetic resonance analysis (DNMR)

The ^{13}C nmr chemical shifts of compound **I** (in $CDCl_3$) and compound **II** (in DMSO-d_6) have been recorded as a function of temperature. The small chemical shift changes are entirely consistent with solvent effects and within the temperature range studied show no evidence of conformational changes.

Discussion

Examining the stereoviews of molecular superpositions of various six-membered piperidyl and seven-membered C ring structures of opiates, it appears that several rules are emerging.

In the case of a piperidyl C ring, the conformation is always "chair". As a consequence and assuming that the N—CH_3 group will always be pseudo equatorial, the N lone pair will point away from the A ring if the N is in first position adjacent to the tertiary carbon. This was observed in compound **IV** (8) and can be seen for compound **V** in Fig. 5*c* and has been observed for all known morphine-like molecules (6, 9). If the nitrogen is moved to the second position, for the same chair conformations and the N—CH_3 equatorial, the lone-pair will point towards the A ring: see compound **III** (10) on Fig. 5*b*.

The same rules apply in the case of seven-membered C rings. In compounds **I** and **II**, the complete multi-ring structure adapts itself by modifying the B ring to accommodate the special C ring. This can be seen on superpositions 5*b* and 5*c*. For these structures, the "crown" conformation of the seven-membered ring observed in the present study for compounds **I** and **II**, appears to be very rigid and changes very little in solution. The

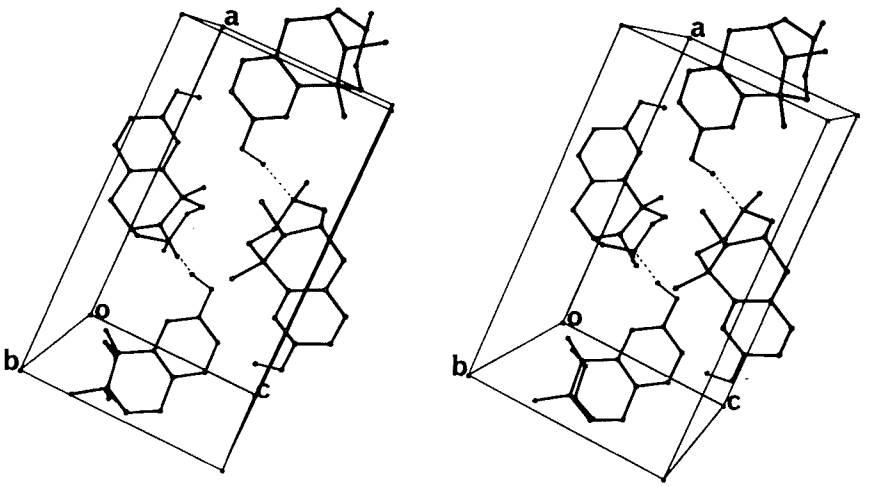

FIG. 4. Stereoscopic view of the cell content for compound **II** showing the packing and the hydrogen bond involving the hydroxyl group and bridging molecules into infinite chains.

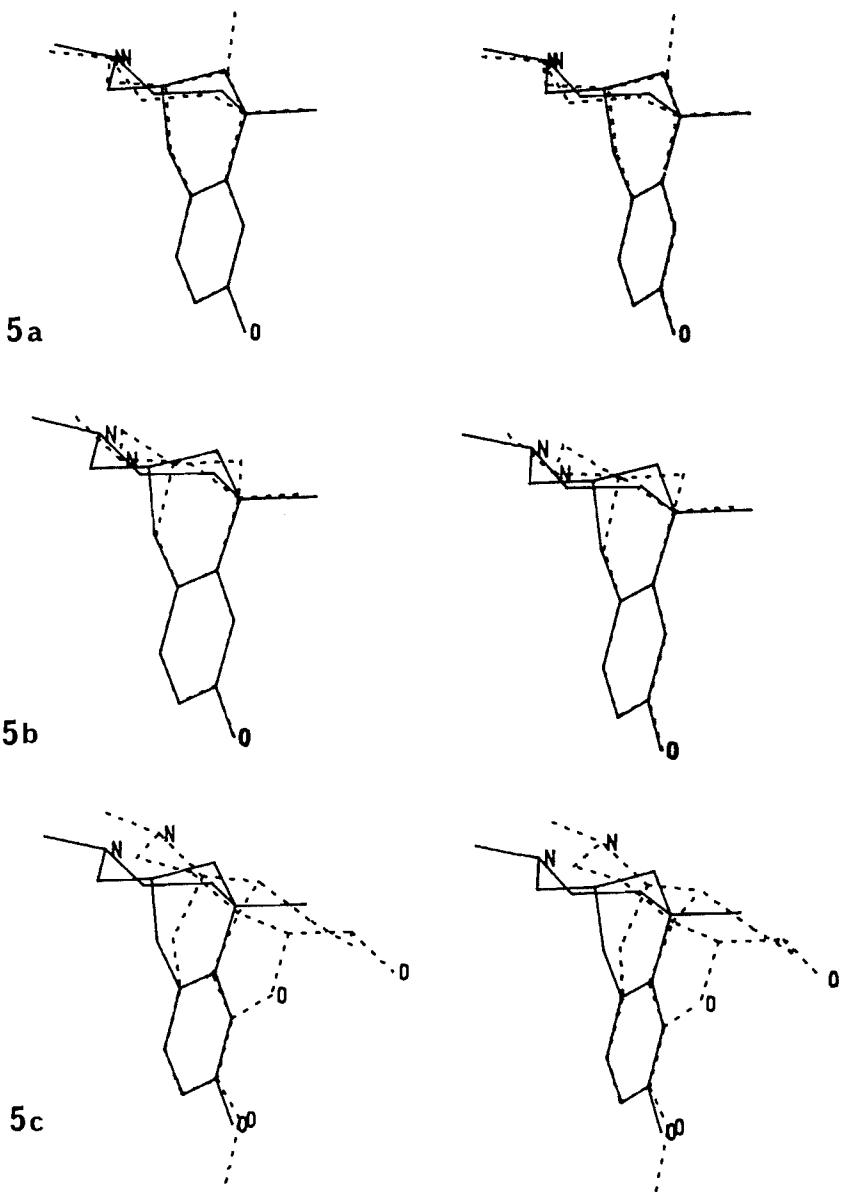

FIG. 5. Stereoviews of pairs of opiates after a least-squares superposition of pairs of homologous atoms in phenyl (A) moiety; (*a*) compound **I** and compound **II** (dotted lines); (*b*) compound **I** and compound **III** (dotted lines); (*c*) compound **I** and compound **IV** (dotted lines).

Can. J. Chem. Downloaded from www.nrcresearchpress.com by 93.93.197.157 on 09/07/12
For personal use only.

examination of this C ring shows that a nitrogen atom in a position adjacent to the tertiary carbon, would have its lone pair pointing towards the A ring in order to place the N—CH_3 in an equatorial position. If the nitrogen atom is moved to the second position, the lone pair will point away from the A ring, as shown by the structures of **I** and **II** and as observed in Fig. 5*a*.

From the present study it follows that the direction (away or toward the A ring) of the electron lone pair of the nitrogen atom in 6-piperidyl and seven-membered C-ring opioids is completely predictable: it depends on the position of the nitrogen atom in the C ring. For the wide variety of modified benzomorphanes synthesized (2), all compounds were shown to be active (2, 3) at various levels, regardless of the nitrogen atom position and hence lone pair orientation. Although a "black or white" answer was not observed, minor structural variations in benzomorphan opiates have been associated with drastic changes in the relative agonist or antagonist properties (14). Following these observations, in the particular case of compounds **I** and **II** the minor distortions observed in the C ring (Table 5 and Fig. 5*a*) have to be considered to account for different activities, the differentiation in the analgesic activity and stereospecificity could also be associated with the presence of the 12β-methyl (C18) group and the steric hindrance of a particular region of space, as invoked in the case of compound **IV** (8) and other benzomorphans.

Acknowledgements

Financial support by the Natural Scineces and Engineering Research Council of Canada (NSERC) is gratefully acknowledged. We are grateful to Professor B. Belleau for fruitful discussions and his help in obtaining the compounds.

1. A. G. MICHEL, G. EVRARD, B. NORBERG, and E. MILCHERT. Can. J. Chem. To be published.
2. S. SHIOTANI, T. KOMETANI, K. MITSUHASHI, T. NOZAWA, A. KUROBE, and O. FUTSUKAICHI. J. Med. Chem. **19**, 803 (1976).
3. S. SHIOTANI, T. KOMETANI, T. NOZAWA, A. KUROBE, and O. FUTSUKAICHI. J. Med. Chem. **22**, 1558 (1979).
4. P. MAIN, M. M. WOOLFSON, L. LESSINGER, G. GERMAIN, and J. P. DECLERCQ. MULTAN 78. A system of computer programs for the automatic solution of crystal structures from X-ray diffraction data. Univs. of York, England, and Louvain-la-Neuve, Belgium. 1978.
5. G. M. SHELDRICK. SHELX 76. Program for crystal structure determination. Univ. of Cambridge, England. 1976.
6. Y. G. GELDERS, C. J. DE RANTER, and A. R. AVERBEEK. Acta Crystallogr. Section B, **35**, 1111 (1979).
7. G. KARTHA, F. R. AHMED, and W. H. BARNES. Acta Crystallogr. **15**, 326 (1962).
8. T. G. COCHRAN and J. E. ABOLA. Acta Crystallogr. Section B, **31**, 919 (1975).
9. L. GYLBERT. Acta Crystallogr. Section B, **29**, 1630 (1973).
10. A. ITAI and Y. IITAKA. Acta Crystallogr. Section C, **41**, 222 (1985).
11. SYBYL Program Version 2. A system of computer programs for interaction molecule modeling and computer assisted drug design. Tripos Associates, St-Louis, MO. 1983.
12. B. BELLEAU, T. CONWAY, F. R. AHMED, and A. D. HARDY. J. Med. Chem. **17**, 907 (1974).
13. K. E. OPHEIM and B. M. COX. J. Med. Chem. **19**, 857 (1976).
14. C. B. PERT, S. H. SNYDER, and E. L. MAY. J. Pharm. Exp. Therap. **196**, 316 (1976).

Can. J. Chem. Downloaded from www.nrcresearchpress.com by 93.93.197.157 on 09/07/12
For personal use only.

Reactions between Co(II), 1,2-bis(diphenylphosphino)ethane, and $NaBH_3CN$ in the presence and absence of CO. The crystal structure of bis(cyanotrihydroborato)tetrakis(*N*,*N*-dimethylformamide)cobalt(II)

DAVID J. ELLIOT, SANNA HAUKILAHTI, DAVID G. HOLAH,[1] ALAN N. HUGHES, AND STANISLAW MACIASZEK
Department of Chemistry, Lakehead University, Thunder Bay, Ont., Canada P7B 5E1

AND

RICHARD J. BARTON, YAOGUANG LUO, AND BEVERLY E. ROBERTSON
Department of Chemistry, University of Regina, Regina, Sask., Canada S4S 0A2

Received November 2, 1987

DAVID J. ELLIOT, SANNA HAUKILAHTI, DAVID G. HOLAH, ALAN N. HUGHES, STANISLAW MACIASZEK, RICHARD J. BARTON, YAOGUANG LUO, and BEVERLY E. ROBERTSON. Can. J. Chem. **66**, 1770 (1988).

Reactions between Co(II), Diphos, and $NaBH_3CN$ lead to $Co(BH_3CN)_2(Diphos)_2$, **1**, or $[Co(BH_3CN)(Diphos)_2]X$, **2** (X = ClO_4 or BPh_4), and, in certain solvents, **2** reacts to produce $[Co(CN)(Diphos)_2](ClO_4)$. Compound **1** can be reversibly converted to $Co(BH_3CN)_2(DMF)_4$, **4**, via $Co(BH_3CN)_2(Diphos)(DMF)$. In addition, **1** reacts with CO to form the Co(I) and Co(III) compounds $[Co(Diphos)_2](CO)]X$ and $[Co(Diphos)_2(CN)_2]X$ (X = BH_3CN or BPh_4). Single crystal X-ray diffraction studies of **4** show that the compound crystallizes in the triclinic space group $P\bar{1}$, with unit cell parameters $a = 7.572(6)$, $b = 9.695(6)$, $c = 9.395(6)$ Å, $\alpha = 81.06(4)$, $\beta = 68.46(5)$, $\gamma = 68.19(5)°$, $V = 595.5$ Å^3, $Z = 1$, and $d_{calcd} = 1.202$ g cm^{-3}. The structure converged to a conventional *R* factor of 0.040 for 2841 observations and showed an octahedral arrangement of four O atoms from DMF molecules and two *trans* N-bound BH_3CN groups around the Co(II) center.

DAVID J. ELLIOT, SANNA HAUKILAHTI, DAVID G. HOLAH, ALAN N. HUGHES, STANISLAW MACIASZEK, RICHARD J. BARTON, YAOGUANG LUO et BEVERLY E. ROBERTSON. Can. J. Chem. **66**, 1770 (1988).

Les réactions de Co(II) avec le Diphos et le $NaBH_3CN$ conduisent aux composés $Co(BH_3CN)_2(Diphos)_2$, (**1**) ou $[Co(BH_3CN)(Diphos)_2]X$ (**2**) (X = ClO_4 ou BPh_4) et, dans certains solvants, le composé **2** réagit pour conduire à la formation de $[Co(CN)(Diphos)_2)](ClO_4)$. On peut transformer le composé **1** en composé **4** (le $Co(BH_3CN)_2(DMF)_4$) par le biais du $Co(BH_3CN)_2(Diphos)(DMF)$. De plus, le composé **1** réagit avec le CO pour conduire à la formation des composés Co(I) et Co(III) $[Co(Diphos)_2](CO)]X$ et $[Co(Diphos)_2(CN_2]X$ (X = BH_3CN ou BPh_4). Des études par diffraction des rayons-X sur des cristaux uniques du composé **4** démontrent qu'ils cristallisent dans le groupe d'espace triclinique $P\bar{1}$, avec des dimensions de maille de $a = 7{,}572(6)$, $b = 9{,}695(6)$, et $c = 9{,}395(6)$ Å, $\alpha = 81{,}06(4)$, $\beta = 68{,}46(5)$, et $\gamma = 68{,}19(5)°$, $V = 595{,}5$ Å^3, $Z = 1$ et $d_{calc} = 1{,}202$ g cm^{-3}. La structure converge vers un facteur *R* conventionnel de 0,040 pour 2841 observations et elle présente un arrangement octaédrique pour les quatre atomes d'oxygène des molécules de DMF alors que les deux groupements BH_3CN sont liés par l'azote dans des arrangements *trans* par rapport au Co(II) qui se trouve au centre.

[Traduit par la revue]

Introduction

We have been interested for some time in reactions between $NaBH_4$ (1), $NaBH_3CN$ (2,3) (or $NaBH_2(CN)_2$ (4)), and metal ions in the presence of phosphines, particularly with respect to the extent to which metal ion reduction occurs, the sequence of steps in the reduction, and the mode of coordination of the hydroborate grouping in those products in which it is present. Reactions involving $NaBH_4$ are often very fast and can lead to a very complex series of intermediates and products (1). We therefore felt that the introduction of a second π acceptor molecule, like CO, into these systems may significantly modify the course of events (5). This paper reports on reactions between (Co(II), $NaBH_3CN$, and $Ph_2PCH_2CH_2PPh_2$ (Diphos) in the presence of CO; the results obtained prompted a reinvestigation of the same system in the absence of CO (6).

Experimental

Materials

The hydrates of cobalt perchlorate, chloride, and bromide, and $NaBPh_4$ were obtained from Alfa Products; 1,2-bis(diphenylphosphino)ethane, Diphos, from Strem Chemicals, Inc.; $NaBH_3CN$ from Aldrich; and CO from Canadian Liquid Air.

All solvents were reagent grade and were purified by distillation before being degassed with oxygen-free, dry nitrogen and stored in a glove box.

Analyses and physical measurements

These were carried out as previously described (3).

Synthesis of the compounds

Unless otherwise specified, all synthetic work was carried out under nitrogen in a glove box. Yields were generally in the range of 50–80%. Although the $NaBH_3CN$ was stored under dry conditions, its reactivity was found to vary from sample to sample, especially with age. This did not, in general, change the outcome of the reactions.

Bis(cyanotrihydroborato)[1,2-bis(diphenylphosphino)ethane]-cobalt(II), $Co(BH_3CN)_2(Diphos)_2$ (1)

$Co(ClO_4)_2 \cdot 6H_2O$ (2.0 g, 5.5 mmol), dissolved in ethanol (15 mL), was mixed with Diphos (4.3 g, 10.8 mmol) in benzene (20 mL) to produce a bright yellow solid. A solution of $NaBH_3CN$ (1.7 g, 27 mmol) in ethanol (≈10 mL) was added dropwise, with stirring, over a 10-min period, and the stirring was continued for ≈3 h. The resulting yellow-orange solid was filtered off, washed with EtOH and benzene, and dried. It was recrystallized by dissolving it in the minimum amount of DMF, which produces a red solution, and adding ethanol. Crystallization took place overnight. Yield = 75%. μ_{eff}: 1.82 BM at 22°C; ir, ν_{BH}: 2310(s), 2250(sh); ν_{CN}: 2190 cm^{-1}; $^{31}P-\{^1H\}$ nmr (DMF), δ: −9.1(vb, see discussion). *Anal.* calcd. for $Co(BH_3CN)_2(Diphos)_2$: C 69.32, H 5.82, N 3.00; found: C 70.68, H 6.02, N 2.99.

The complex is much less soluble in CH_2Cl_2 than in DMF, but small amounts can be recrystallized from the former. *Anal.* calcd. for

[1]Author to whom correspondence may be addressed.

Can. J. Chem. Downloaded from www.nrcresearchpress.com by 112.217.228.212 on 09/07/12
For personal use only.

$Co(BH_3CN)_2(Diphos)_2 \cdot CH_2Cl_2$: C 64.74, H 5.53, N 2.75; found: C 65.02, H 5.46, N 2.78.

The compound is unstable if left in solvents for long periods. For example, in acetone, orange, green, and, finally, blue solutions are observed in sequence over a period of several days at room temperature. In DMF, unstable, blue crystals were isolated after several days. These showed the presence of Co—CN groups.

Bis(cyanotrihydroborato)tetrakis(N,N-dimethylformamide)cobalt(II), $Co(BH_3CN)_2(DMF)_4$ (4)

$Co(ClO_4)_2 \cdot 6H_2O$ (0.55 g, 1.5 mmol) in DMF (10 mL) was reacted with $NaBH_3CN$ (0.5 g, 8 mmol) in ethanol (10 mL). The reaction mixture turned pink and crystals were produced in high yield within 2–3 h on cooling. These were filtered off, washed with ether and dried under reduced pressure. The product is both soluble and stable in DMF. It slowly dissolves in CH_3CN to give a blue-violet solution, and turns violet immediately in CH_2Cl_2 and acetone. μ_{eff}: 5.10 BM at 22°C; ir, ν_{DMF}: 1650(vs. b), 1500(s), 1250(s), 1120(s), 860(s); ν_{BH}: 2370(sh), 2330(s), 2290(m), 2275(m); ν_{CN}: 2200(s), 2220(w); other peaks at 2150(w), 2100(w), 2030(w) 2010(w), 1985(w) cm^{-1}. Reflectance spectrum $^4T_{1g}(F) \rightarrow {}^4T_{2g}$ at 8330 cm^{-1}, $^4T_{1g}(F) \rightarrow {}^4T_{1g}(P)$ at 19 230 cm^{-1}. *Anal.* calcd. for $Co(BH_3CN)_2(DMF)_4$: C 39.01, H 7.95, N 19.50; found: C 38.92, H 7.95, N 19.65.

The same product is also formed by crystallizing **1** from DMF/ether over a period of ≈3 days at room temperature.

$Co(BD_3CN)_2(DMF)_4$

$CoCl_2 \cdot 6H_2O$[2] (0.12 g, 0.50 mmol) in DMF (5 mL) was treated with $NaBD_3CN$ (0.16 g, 2.5 mmol) in EtOH (5 mL). Et_2O (5 mL) was added and the solution produced crystals in ≈2 h when cooled; ir, ν_{BH}: 2330(w, residual); ν_{CN}: 2200(vs); ν_{BD}: 1760(s), 1775(sh), 1730(vw,sh); $\nu_{CO(DMF)}$: 1650(vs,b); other peaks at 2155(vw), 2100(vw), 2030(w), and 1970(vw) cm^{-1}.

Bis(cyanotrihydroborato)N,N-dimethylformamide-1,2-bis(diphenyl phosphino)ethanecobalt(II), $Co(BH_3CN)_2(Diphos)(DMF)$ (5)

$Co(BH_3CN)_2(Diphos)_2$ (0.19 g, 0.2 mmol) and $Co(BH_3CN)_2(DMF)_4$ (0.076 g, 0.18 mmol) were mixed in CH_3CN (≈20 mL). The reaction produced a clear red solution within a few minutes and this was stirred for ≈4 h. Concentration of this solution by a slow N_2 flow produced red crystals of the product in high yield. This product is soluble in DMF and CH_3CN, but turns green instantly in $CHCl_3$. μ_{eff}: 1.93 BM at 22°C; ir, ν_{BH}: 2330(s), 2280(m), 2255(m); ν_{CN}: 2200(s); ν_{CO}: 1650(s). *Anal.* calcd. for $Co(BH_3CN)_2(Diphos)(DMF)$: C 60.98, H 6.07, N 6.88; found: C 60.91, H 5.92, N 6.90.

Reactions of $Co(BH_3CN)_2(Diphos)(DMF)$, (5)

(i) With Diphos

Compound **5** was dissolved in DMF to which was added a slight excess of Diphos. Addition of ethanol produced yellow crystals of $Co(BH_3CN)_2(Diphos)_2$ over a 2-day period in the refrigerator. The composition of the product was confirmed by ir and CHN analyses.

(ii) With DMF

$Co(BH_3CN)_2(Diphos)(DMF)$ was dissolved in DMF. Addition of ether produced crystals of $Co(BH_3CN)_2(DMF)_4$.

Cyanotrihydroboratobis[1,2-bis(diphenylphosphino)ethane]cobalt(II) perchlorate or tetraphenylborate, $[Co(BH_3CN)(Diphos)_2]X$, $X = ClO_4$ or BPh_4 (2)

(a) $X = ClO_4$

A solution of $NaBH_3CN$ (0.31 g, 4.9 mmol) in ethanol (≈10 mL) was added dropwise over a 10-min period to a stirred mixture of $Co(ClO_4)_2 \cdot 6H_2O$ (0.90 g, ≈2.5 mmol) and Diphos (3.0 g, 7.5 mmol) in ethanol/toluene 6:1 (≈10 mL). The solution was stirred for 3 h after which an orange solid was filtered off, and recrystallized from a deep red CH_2Cl_2 solution by the addition of hexane. The complex may also be recrystallized from DMF/EtOH.

[2]It was found that when $Co(ClO_4)_2 \cdot 6H_2O$ was used in this reaction, more rapid D–H exchange took place and the resulting crystals contained little B–D.

Decomposition occurs if samples are left for long periods in solvents (see later); the compound is stable in air.

Other reaction conditions also lead to the same product. For example, reactions in which ratios of $Co(ClO_4)_2 \cdot 6H_2O$/Diphos/$NaBH_3CN$ of 1:3:6 or 1:2:5 are used, and which are filtered after ≈10 min of reaction time, also lead to this product, although some contamination with $Co(BH_3CN)_2(Diphos)_2$ may occur. The ready solubility of $[Co(BH_3CN)(Diphos)_2](ClO_4)$ in CH_2Cl_2 allows for its easy separation from the latter. μ_{eff}: 1.94 BM; ir, ν_{BH}: 2270(w,sh), 2310(s), 2360(w,sh); ν_{CN}: 2180(s); ν_{ClO_4}: 1100(vs,b). *Anal.* calcd. for $[Co(BH_3CN)(Diphos)_2](ClO_4)$: C 63.97, H 5.17, N 1.41; found: C 64.02, H 5.29, N 1.42.

(b) $X = BPh_4$

A slight excess of $NaBPh_4$ in ethanol was added to a solution of **2** ($X = ClO_4$) in acetone. An orange microcrystalline product was precipitated by the addition of ether or hexane. The complex was identified from its reflectance spectrum, which is identical with that of **2** ($X = ClO_4$), as is its ir spectrum (with the exception of ν_{ClO_4} at 1100 cm^{-1}).

Cyanobis[1,2-bis(diphenylphosphino)ethane]cobalt(II) perchlorate, $[Co(CN)(Diphos)_2](ClO_4)$ (3)

$[Co(BH_3CN)(Diphos)_2](ClO_4)$ was dissolved in acetone, producing a brown solution from which a dark brown crystalline solid was obtained by the addition of a small amount of hexane. The product was filtered off, washed with hexane, and dried under reduced pressure. The crystals do not redissolve completely in acetone. They are soluble in methylene chloride, but decomposition occurs within ≈20 min. μ_{eff} 1.80 BM; ir, ν_{CN}: 2098(s); ν_{ClO_4}: 1100(vs, vb). *Anal.* calcd. for $[Co(CN)(Diphos)_2](ClO_4)$: C 64.87, H 4.93, N 1.43; found: C 65.24, H 5.09, N 1.31.

The same product is formed when CH_2Cl_2 solutions of $[Co(BH_3CN)(Diphos)_2](ClO_4)$ are left for 3–4 days.

Carbonylbis[1,2-bis(diphenylphosphino)ethane]cobalt(I) cyanotrihydroborate or tetraphenylborate, $[Co(CO)(Diphos)_2]X$, $X = BH_3CN$ or BPh_4 (6)

(a) $X = BH_3CN$

CO was passed for 10 min into a green solution of $CoBr_2 \cdot 6H_2O$ (0.43 g, 1.3 mmol) and Diphos (1.0 g, 2.5 mmol) in EtOH/benzene (1:1, 15 mL) to which $NaBH_3CN$ (0.23 g, 3.7 mmol) in EtOH (5 mL) had been added over a 15-min period. The solution turned red and the small amount of a green solid that precipitated out was filtered off. Concentration of the filtrate by a slow N_2 stream produced yellow-orange crystals, which were filtered off, washed with hexane, and dried under vacuum; ir, ν_{BH}: 2310(s), 2280(sh); ν_{CN}: 2160; ν_{CO}: 1918 cm^{-1}; $^{31}P-\{^1H\}$ nmr (CH_2Cl_2), δ: 69.7(s). *Anal.* calcd. for $[Co(CO)(Diphos)_2](BH_3CN)$: C 70.22, H 5.57, N 1.52; found: C 70.10, H 5.63, N 1.65.

In an alternative synthesis, a solution of $Co(BH_3CN)_2(Diphos)_2$ in DMF/EtOH (1:1) was filtered after CO had been passed for 20 min. Addition of ether or hexane to the red filtrate produced orange crystals after several days at ≈0°C. The ^{31}P nmr and ir spectra were found to be the same as above, except that the presence of ethanol in the lattice is revealed by ν_{OH} 3350(w), 1670(m) cm^{-1} and by the ^1H nmr spectrum ($CDCl_3$) (EtOH at δ 1.25(t), 3.75(q); integration EtOH:Diphos ≈1:1).

(b) $X = BPh_4$

A slight excess of $NaBPh_4$ in ethanol was added to a solution of **6** ($X = BH_3CN$) in CH_2Cl_2. Addition of hexane produced a crystalline solid that exhibited ^{31}P nmr and ir spectra identical (with the exception of the BH_3CN ir absorptions) with those shown by **6** ($X = BH_3CN$).

Dicyanobis[1,2-bis(diphenylphosphino)ethane]cobalt(III) cyanotrihydroborate or tetraphenylborate, $[Co(CN)_2(Diphos)_2]X$, $X = BH_3CN$ or BPh_4 (7)

(a) $X = BH_3CN$

A suspension of $Co(BH_3CN)_2(Diphos)_2$ in CH_2Cl_2 was saturated with CO for ≈20 min. The undissolved starting material slowly dissolved over 24–48 h. Ether was added and the solution produced

Can. J. Chem. Downloaded from www.nrcresearchpress.com by 112.217.228.212 on 09/07/12
For personal use only.

yellow crystals. Similarly, a solution of $Co(BH_3CH)_2(Diphos)_2$ in DMF/EtOH (or the filtrate after this compound was recrystallized from DMF/EtOH) was saturated with CO for ≈40 min, filtered, and ether added to the filtrate. Several weeks in the freezer produced yellow crystals, which were filtered off, washed with ether, and dried under reduced pressure; ir, ν_{CN}: 2100(s); ν_{CN} (from BH_3CN): 2160(s); ν_{BH}: 2305(s), 2270(sh); ν_{OH} (from EtOH): 3300(b), 1665(m) cm^{-1}; $^{31}P-\{^1H\}$ nmr (DMF), δ: 55.8(s); ^1H nmr ($CDCl_3$) EtOH at δ: 1.25(t), 3.75(q); integration EtOH:Diphos 1:1. *Anal.* calcd. for $[Co(CN)_2(Diphos)_2](BH_3CN)\cdot 2EtOH$: C 66.86, H 5.95, N 3.97; found: C 66.50, H 5.79, N 4.00. The amount of ethanol varies from sample to sample. For example, good chemical analyses have also been obtained for this compound with only one EtOH molecule per Co atom.

(b) X = BPh_4

The yellow crystals obtained by the method described above were dissolved in $EtOH/CH_2Cl_2$ (1:1) to which an equal molar quantity of $NaBPh_4$ in EtOH was added. The bright yellow crystalline product that formed was filtered off, washed with EtOH, and dried under reduced pressure; ir, ν_{CN}: 2110 cm^{-1}. *Anal.* calcd. for $[Co(CN)_2(Diphos)_2](BPh_4)$: C 76.35, H 5.59, N 2.28; found: C 75.49, H 5.52, N 2.20.

X-ray structure determination of $Co(BH_3CN)_2(DMF)_4$

$C_{14}H_{34}CoN_6O_4$ fw = 431.02

Triclinic, space group $P\bar{1}$, $a = 7.572(6)$, $b = 9.695(6)$, $c = 9.395(6)$ Å, $\alpha = 81.06(4)$, $\beta = 68.46(5)$, $\gamma = 68.19(5)°$, $V = 595.5(6)$ Å^3, $T = 293(2)$ K, $Z = 1$, $D_x = 1.202$ g cm^{-3}, F(000) = 227, μ(MoKα) = 14.1 cm^{-1}, λ(MoKα) = 0.71069 Å.

A crystal with irregular shape, and dimension approximately 0.4 mm on a side, was mounted and sealed in a quartz capillary.

Unit-cell parameters were determined by least-square refinement on the positions of 72 reflections with $30 \leq 2\theta \leq 39°$. The density of the crystal was not determined. Intensities were measured with graphite-monochromated MoKα radiation on a modified Picker FACS-1 diffractometer, using the NRCC diffractometer control system (7). The θ–2θ scan technique, with profile analysis, was employed. Data were measured in the range of $3 \leq 2\theta \leq 60°$, using a scan speed of 2°/min and a scan width of $(0.7 + 0.692 \tan\theta)$ degrees. The intensities of three reference reflections, measured after every 47 reflections throughout the data collection, did not change significantly. A total of 3414 independent reflections were collected, of which 2841 were considered as observed with $I/\sigma(I) \geq 2.0$, and were used in the structure determination.

The data were corrected for the Lorentz effect and polarization. All calculations were carried out with the XTAL system of crystallographic programs (8). Scattering factors were taken from the XTAL system. A dispersion correction, taken from International Tables for X-ray Crystallography Vol. 4 (9), was applied to the scattering factor of the cobalt atom.

The average values of $|E|$, $|E^2-1|$, $|E^2-1|^2$, and $|E^2-1|^3$ were 0.879, 0.744, 0.961, and 2.212 respectively, clearly indicating a noncentrosymmetric space group. The structure was then solved by direct methods. An *E*-map gave 23 out of 27 non-hydrogen atoms. Subsequent electron density Fourier syntheses revealed all non-hydrogen atoms and the structure was refined on *F*. However, examination of the structure showed that it contained a center of symmetry at the Co atom.[3] The space group was changed to $P\bar{1}$ and refinement proceeded. All hydrogen atoms were found from a difference map. The non-hydrogen atoms were refined with anisotropic temperature factors and the hydrogen atoms with isotropic temperature factors. Weights were calculated as $\sigma^2(F)$ where $\sigma(F)$ is based on counting statistics and the excess of scatter in the standard reflections. The structure was refined using data not corrected for absorption, using data corrected for absorption based on a single psi scan assuming absorption in the quartz capillary, and using data corrected for absorption by the Gaussian integration method (10).[4] All three refinements gave identical coordinates and temperature factors within the esd's and nearly identical estimated standard deviations. The results reported here are for the final refinement. The absorption corrections (*A*) ranged from 0.823 to 0.865. Convergence was reached at $R = 0.036$, $R_w = 0.039$, and $S = 2.87$. The maximum residual electron density was 0.31 e Å^{-3}. The average and maximum shift/error were 0.004 and 0.070.[5]

Results and discussion

One of the first products obtained from $Co(II)/NaBH_3CN$/Diphos/CO reactions is a yellow-brown crystalline product, $Co(BH_3CN)_2(Diphos)_2$, **1**. This surprised us, since we had previously reported (6) that reactions between Co(II) (as the chloride), $NaBH_3CN$, and Diphos lead to the formation of Co(I), and it prompted us to reexamine the latter type of reaction using both $CoCl_2\cdot 6H_2O$ (6) and $Co(ClO_4)_2\cdot 6H_2O$ as the source of cobalt(II). In fact, starting with $Co(ClO_4)_2\cdot 6H_2O$, the product depends on the Co(II) : $NaBH_3CN$ ratio and the time of the reaction as outlined in Scheme 1. Thus, short reaction times and (or) smaller amounts of $NaBH_3CN$ lead to the formation of the dark brown $[Co(BH_3CN)(Diphos)_2]X$, **2** (X = ClO_4), which readily forms **2** (X = BPh_4) on addition of $NaBPh_4$ in ethanol. Solutions of **2** (X = ClO_4) in acetone or methylene chloride produce $[Co(CN)(Diphos)_2](ClO_4)$ **3**. The ir spectral data (see Experimental) support the presence of ionic ClO_4^-, N-bound BH_3CN^- in **2**, and the Co—CN group in **3**. No meaningful nmr data were obtained since the complexes are paramagnetic, $\mu_{eff} \approx 2.1$ BM, i.e., low spin d^7 systems.

Reflectance spectra of **2** and **3** are shown in Fig. 1. In CH_2Cl_2 solution, the peaks are in almost the same positions, i.e., ≈8500 cm^{-1}, ε 130 L M^{-1} cm^{-1} (with a shoulder at ≈6900 cm^{-1}) and 14 900, ε = 33 L M^{-1} cm^{-1}. Included in Fig. 1 for comparison is the reflectance spectrum of the low-spin distorted 5-coordinated species $CoH(BH_3CN)(PPh_3)_3$ (11). There are several published spectral studies on other closely related low-spin Co(II) compounds of the type $[CoX(P\cap P)_2]Y$. Representative examples are X = Br, P∩P = *cis*-1,2-bis-(diphenylphosphino)ethylene, Y = BPh_4 (12); P∩P = Diphos, X = Y = halide, X = halide, Y = BPh_4, ClO_4 (13); and P∩P = bis(diphenylphosphino)methane, X = halide, Y = ClO_4 (14). While there are some similarities between the spectra of all of these compounds, the agreement is not good and the differences may well reflect varying distortions in the molecules.

The same reactants under different conditions (Scheme 1), or reactions using $CoCl_2\cdot 6H_2O$ as the Co(II) source, all produce **1**, which was recrystallized from DMF–ethanol.

In the solid state, **1** has a magnetic moment of 1.82 BM. When freshly dissolved in DMF (i.e., such that there is insufficient time for the formation of **4**, see later) the ^{31}P nmr spectrum of **1** shows only an extremely broad (peak base from approximately δ −5 to δ +10) low intensity signal at δ −9.1. This is probably due to paramagnetically shifted and broadened ^{31}P resonances from coordinated Diphos since the signals for

[3]The realization that the structure was centrosymmetric occurred after the original manuscript was submitted. We wish to acknowledge that this most serious error was also noted by one of the referees.

[4]Absorption corrections were suggested by a referee.

[5]Supplementary material deposited: tables of atomic coordinates and temperature factors, bond lengths and angles, anisotropic temperature factors, and observed and calculated structure factors (24 pages). This material may be purchased from the Depository of Unpublished Data, CISTI, National Research Council of Canada, Ottawa, Ont., Canada K1A 0S2.

Can. J. Chem. Downloaded from www.nrcresearchpress.com by 112.217.228.212 on 09/07/12
For personal use only.

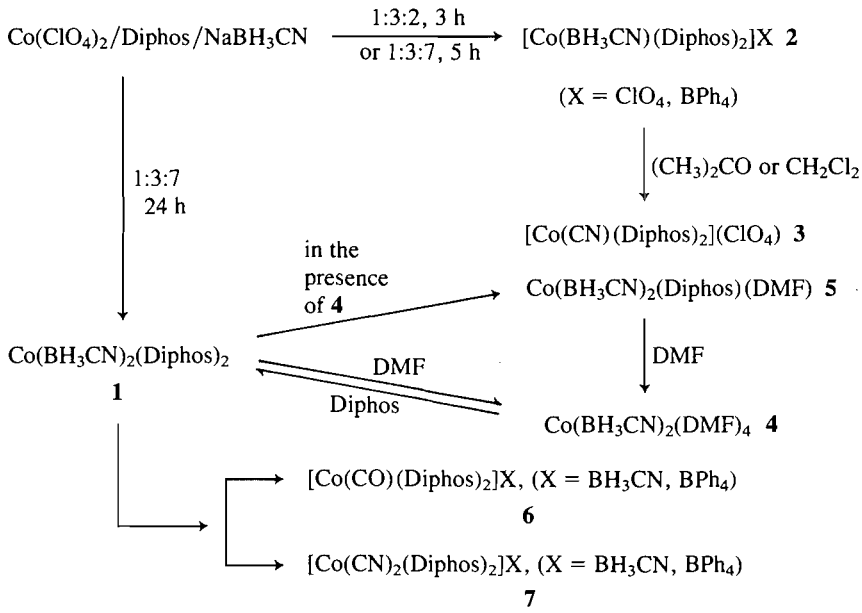

SCHEME 1

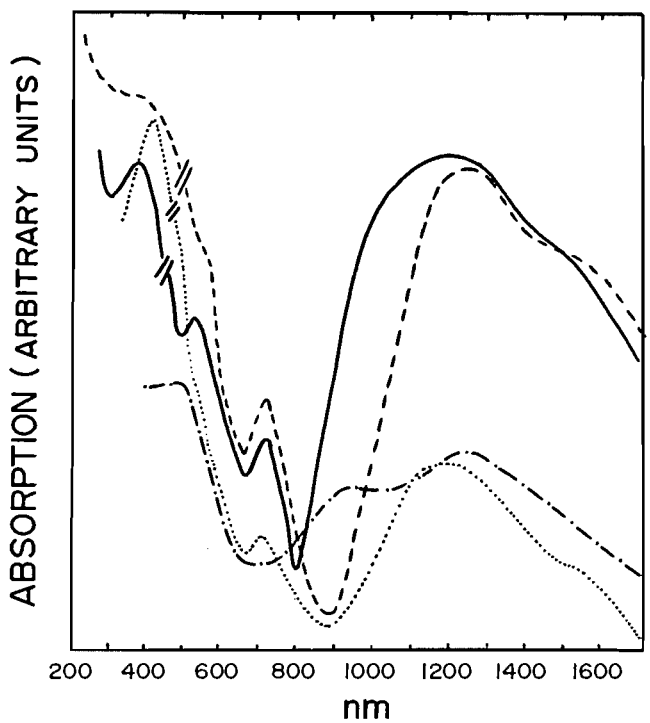

FIG. 1. Reflectance spectra. —— $[Co(CN)(Diphos)_2](ClO_4)$, **3**; ---- $[Co(BH_3CN)(Diphos)_2](ClO_4)$, **2**; ..... $[Co(BH_3CN)_2(Diphos)(DMF)$ **5**; —·— $[CoH(BH_3CN)(PPh_3)_3$.

free Diphos in these and solutions of other paramagnetic species, while shifted somewhat, remain comparatively sharp. The ir spectrum of **1** shows only a single ν_{CN} at 2190 cm^{-1}, which is close to ν_{CN} (2179 cm^{-1}) for $NaBH_3CN$. We have observed no reaction between solutions of **1** in DMF and $NaBPh_4$ in ethanol and, therefore, the two (ir-equivalent) BH_3CN groups appear to be coordinated to the cobalt. It therefore appears that **1** may be a low-spin 6-coordinated Co(II) compound of which very few examples have been characterized (15).

The reflectance spectrum of **1** shows a broad peak at ≈10 000 cm^{-1} with a shoulder at ≈18 000 cm^{-1}. In DMF, the main peak is at ≈8250 cm^{-1} ($\epsilon \approx 30\ L\ M\ cm^{-1}$) with the shoulder at ≈13 300 cm^{-1}. In CH_2Cl_2, the spectrum is essentially the same except that the additional peak occurs at 15 400 cm^{-1} ($\epsilon \approx 60\ L\ M^{-1}\ cm^{-1}$). There are some similarities between these spectra and those already reported for compounds believed to contain low-spin 6-coordinated Co(II), which have bands in the 7500–8000 cm^{-1} and 15 000–16 000 cm^{-1} regions.[6] Tentative assignments have been made.

Because of the potential importance of **1**, many (unsuccessful) attempts were made to grow crystals suitable for X-ray diffraction studies. Data were collected on a crystal obtained by the diffusion of ether into dilute solutions of **1** in DMF at 0°C. However, even though the yellow-brown colour of **1** persists for long periods in such solutions, the crystal was later shown to be **4**, $Co(BH_3CN)_2(DMF)_4$. The ir spectrum of **4** shows a strong peak at 2000 cm^{-1}, due to the coordinated CN group of BH_3CN, and a series of weak, but sharp, peaks of unknown origin at 2150, 2100, 2030, 2010, and 1985 cm^{-1}, which do not change significantly in the spectrum of the deuterated complex. There are also strong peaks, due to DMF, at 1650, 1500, 1250, 1120, and 860 cm^{-1}. Compound **4** is readily prepared in high yield simply by treating Co(II) perchlorate in DMF with $NaBH_3CN$. It reacts with Diphos to produce **1**. As expected, changing the four P atoms of **1** to four O atoms in **4** results in a spin state change, **4** having a magnetic moment of 5.1 BM, and an electronic spectrum typical of octahedral Co(II) compounds (see Experimental).

There is also a reaction between **1** and **4** that produces **5** according to:

$$Co(BH_3CN)_2(Diphos)_2 + Co(BH_3CN)_2(DMF)_4 \rightarrow 2\ Co(BH_3CN)_2(Diphos)(DMF) + 3\ DMF$$

Compound **5** is soluble in DMF (producing **4** over several days)

[6]See the references cited under ref. 2 in the paper by Hartman *et al.* (15).

Can. J. Chem. Downloaded from www.nrcresearchpress.com by 112.217.228.212 on 09/07/12
For personal use only.

TABLE 1. Fractional atomic coordinates with esd's in parentheses and thermal parameters ($Å^2 \times 10^2$) $U_{eq} = \frac{1}{3}\Sigma_i\Sigma_j U_{ij} a_i^* a_j^* \mathbf{a}_i \cdot \mathbf{a}_j$

Atom	x	y	z	U_{eq}
Co	0.5000	0.5000	0.5000	3.9
N(1)	0.7698(3)	0.3425(2)	0.3686(2)	5.3
C(1)	0.9136(3)	0.2592(2)	0.2933(2)	4.9
B(1)	1.1129(5)	0.1454(4)	0.1861(4)	6.8
O(11)	0.5802(2)	0.4208(2)	0.6972(2)	5.2
C(12)	0.6930(3)	0.4547(2)	0.7412(2)	4.6
N(13)	0.7446(3)	0.3947(2)	0.8622(2)	4.6
C(14)	0.6724(5)	0.2789(3)	0.9536(3)	6.2
C(15)	0.8791(5)	0.4390(4)	0.9096(4)	7.7
O(21)	0.3533(2)	0.3436(2)	0.5422(2)	5.1
C(22)	0.3859(3)	0.2311(2)	0.6255(2)	4.7
N(23)	0.3015(3)	0.1292(2)	0.6464(2)	4.7
C(24)	0.3415(5)	0.0015(3)	0.7494(3)	6.6
C(25)	0.1614(5)	0.1426(3)	0.5678(4)	6.6

TABLE 2. Bond lengths (Å) and angles (deg) with esd's in parentheses

Bond	Length (Å)
Co—N(1)	2.109(2)
Co—O(11)	2.104(2)
Co—O(21)	2.105(2)
N(1)—C(1)	1.138(2)
C(1)—B(1)	1.582(3)
O(11)—C(12)	1.232(4)
C(12)—N(13)	1.317(3)
N(13)—C(14)	1.452(4)
N(13)—C(15)	1.462(6)
O(21)—C(22)	1.241(3)
C(22)—N(23)	1.319(4)
N(23)—C(24)	1.458(3)
N(23)—C(25)	1.460(5)

Bonds	angle (deg)
N(1)—Co—O(11)	89.74(8)
N(1)—Co—O(21)	89.56(9)
O(11)—Co—O(21)	89.41(7)
Co—N(1)—C(1)	177.7(2)
N(1)—C(1)—B(1)	178.9(3)
Co—O(11)—C(12)	127.6(1)
O(11)—C(12)—N(13)	124.2(2)
C(12)—N(13)—C(14)	121.2(3)
C(12)—N(13)—C(15)	122.0(2)
C(14)—N(13)—C(15)	116.8(3)
Co—O(21)—C(22)	124.2(2)
O(21)—C(22)—N(23)	124.2(3)
C(22)—N(23)—C(24)	121.7(3)
C(22)—N(23)—C(25)	120.5(2)
C(24)—N(23)—C(25)	117.8(3)

and in CH_3CN but turns green instantly in $CHCl_3$. The ir spectrum clearly shows ν_{CN} at 2200 cm^{-1} and ν_{CO} of DMF at 1650 cm^{-1}. The single Diphos molecule in **5** is sufficient to cause a low-spin configuration, ($\mu_{eff} = 1.93$ BM) and the reflectance spectrum of **5** is identical with those of **2** and **3**. (Fig. 1).

X-ray crystallography shows that the Co(II) ion, which is

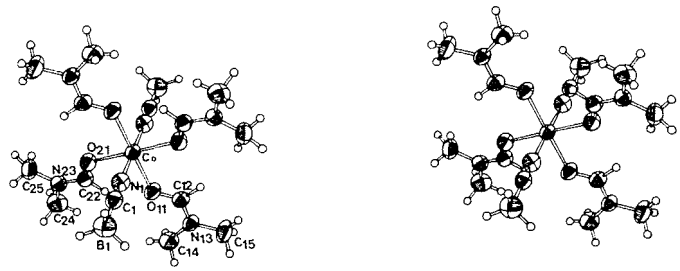

FIG. 2. Stereogram showing the molecular structure and labelling scheme for $Co(BH_3CN)_2(DMF)_4$.

located on a center of symmetry, is surrounded by two *trans*, N-bound BH_3CN groups and four O-bound DMF molecules in an almost perfect octahedron. Tables 1 and 2 list atomic coordinates and bond lengths and angles, and the stereogram in Fig. 2 shows the molecular structure with the atom labelling scheme. The two essentially identical Co—O bond lengths are almost equal to the Co—N bond length. The bond angles about the Co atom are very close to 90°.

The metal—N—C bond angles in coordinated BH_3CN complexes have been related to the positions of the ν_{CN} in ir spectra (16). In **4** the C—N bond length of 1.138(3) Å and the Co—N—C bond angle of 177.6(2)° account for the single ν_{CN} absorption at 2200 cm^{-1} and compare favourably with, for example, a ν_{CN} at 2210 cm^{-1} for a Cu—N—C angle of 175.6° in $(Me_2dien)Cu(BH_3CN)_2$ (16). The bond lengths and angles of the coordinated DMF molecules are similar to those found in other structures (17).

Since, as outlined in the above discussion, $NaBH_3CN$ alone seems unable to reduce Co(II)-Diphos mixtures, as observed with analogous Ni(II) systems (3), we have introduced CO into these reactions. This will increase the reductive nature of the conditions and the excellent π bonding properties of CO should help stabilize the resulting products. Two approaches have been followed: (*i*) saturating solutions of Co(II)-Diphos mixtures with CO before and after the addition of $NaBH_4$ or $NaBH_3CN$ and (*ii*) reactions of **1** with CO. The former has produced several new Co(O) complexes (18) along with $[Co(CO)(Diphos)_2]X$ ($X = BH_3CN$, BPh_4) **6**. This compound, **6** ($X = ClO_4$) has previously been characterized (5, 19), as have related Rh (20) and Ir (21) complexes. Compound **6** has also been obtained from reactions of **1** with CO, but what is perhaps more interesting is that when CO and solutions of **1** in either DMF–ethanol of CH_2Cl_2 are left for longer periods of time, the Co(III) complex **7**, $[Co(CN)_2(Diphos)_2](BH_3CN)$ is formed as the ethanol solvate (Scheme 1). This reacts with $NaBPh_4$ to form **7** ($X = BPh_4$).

The coordinated CN groups appear in ir spectra of **7** as a sharp signal at 2100 cm^{-1}, as observed previously in this cation (22) (prepared by the interaction of $Co(CN)_2(Diphos)_2$ with O_2). The ν_{CN} of BH_3CN^- occurs at 2160 cm^{-1}, i.e., at slightly lower energy than in $NaBH_3CN$, and this seems to be a general observation for a number of coordination compounds with ionic BH_3CN groups. In the ^{31}P nmr spectra of these complexes, a singlet at δ 55, consistent with chelating Diphos, is observed. Formation of Co(III) by oxidative addition of HX (X = H, halogens, etc.) is well known and the resulting Co(III) hydrido species have been extensively studied (2). However, it seems more likely in this case that disproportionation of a Co(II)-CO-Diphos species occurs to produce the Co(III) and Co(I)

Can. J. Chem. Downloaded from www.nrcresearchpress.com by 112.217.228.212 on 09/07/12
For personal use only.

compounds, which, overall, may be represented as:

$$2\,Co(BH_3CN)_2(Diphos)_2 \xrightarrow{CO} [Co(CN)_2(Diphos)_2]^+ + [Co(CO)(Diphos)_2](BH_3CN) + \text{borane (?)}$$

The effect of (mostly monodentate) phosphines on Co(II) disproportionation has been extensively discussed recently, and it is significant that all four of the bidentate phosphines included in this study (23) resulted in disproportionation. However, CO is clearly needed in the above reaction, as the available evidence suggests that **1** produces paramagnetic blue Co(II)—CN compounds when left in DMF (Experimental).

Acknowledgements

The authors thank the Natural Sciences and Engineering Research Council of Canada for financial support in the form of operating grants to D.G.H. and A.N.H. and to R.J.B. and B.E.R. We also thank the Lakehead University Senate Research Committee.

1. D. G. Holah, A. N. Hughes, S. Maciaszek, V. R. Magnuson, and K. O. Parker. Inorg. Chem. **24**, 3956 (1985).
2. D. J. Elliot, D. G. Holah, A. N. Hughes, S. I. Khan, and S. Maciaszek. Inorg. Chim. Acta, **96**, L29 (1985).
3. D. G. Holah, A. N. Hughes, and N. I. Khan. Can. J. Chem. **62**, 1016 (1984).
4. P. G. Egan, D. G. Holah, and K. W. Morse. Inorg. Chem. **23**, 2203 (1984); K. W. Morse, D. G. Holah, and M. Shimoi. Inorg. Chem. **25**, 3113 (1986).
5. C. Carriedo, P. Gomez-Sal, P. Royo, S. Martinez-Carrera, and S. Garcia-Blanco. J. Organomet. Chem. **301**, 79 (1986).
6. D. G. Holah, A. N. Hughes, B. C. Hui, and K. Wright. Can. J. Chem. **52**, 2990 (1974).
7. A. C. Larson and E.J. Gabe. Computing in crystallography. *Edited by* H. Shenk, K. Olthof-Hazekamp, H. van Konigsveld, and G. C. Bassi. Delft University Press, Delft, The Netherlands. 1978. pp. 81–89.
8. J. M. Stewart and S.R. Hall. Technical report TR-873.2. Computer Science Center, University of Maryland, College Park, MD. 1984.
9. International tables for X-ray crystallography. Vol. 4, Kynoch Press, New York, 1974. p. 149.
10. W. R. Busing and H. A. Levy. Acta Crystallogr. **10**, 180 (1957).
11. R. J. Barton, D. G. Holah, S. Hu, A. N. Hughes, S. I. Khan, and B. E. Robertson. Inorg Chem. **23**, 2391 (1984).
12. C. H. Sethulakshmi and P. T. Nlanoharan. Inorg. Chem. **20**, 2533 (1981).
13. W. DeW. Horrocks, Jr., G. R. Van Hecke, and D. DeW. Hall. Inorg. Chem. **6**, 694 (1967).
14. K. Chow and C. A. McAuliffe. Inorg. Chim. Acta, **14**, 121 (1975).
15. J. R. Hartman, E. J. Hintsa, and S. R. Cooper. J. Chem. Soc. Chem. Commun. 386 (1984), and references therein.
16. B. G. Segal and S. J. Lippard. Inorg. Chem. **13**, 822 (1974).
17. O. S. Filipenko, V. I. Ponomarev, and L. O. Atovmyan. Sov. J. Coord. Chem. (Engl. Transl.), **12**, 991 (1986); O. Baumgartner. Z. Kristallog. **174**, 253 (1986).
18. D. J. Elliot, D. G. Holah, and A. N. Hughes. Inorg. Chim. Acta. In press.
19. G. Pilloni, G. Zotti, and M. Martelli. Inorg. Chim. Acta, **13**, 213 (1975); C. F. Nobile, M. Rossi, and A. Sacco. Inorg. Chim. Acta, **5**, 698 (1971).
20. L. H. Pignolet, D. G. Doughty, S. C. Nowidki, and A. L. Casalnuovo. Inorg. Chem. **19**, 2172 (1980).
21. J. S. Miller and K. G. Caulton. J. Am. Chem. Soc. **97**, 1067 (1975).
22. P. Rigo, B. Longato, and G. Favero. Inorg. Chem. **11**, 300 (1972).
23. S. M. Socol and J. G. Verkade. Inorg. Chem. **25**, 2658 (1986).

Can. J. Chem. Downloaded from www.nrcresearchpress.com by 112.217.228.212 on 09/07/12
For personal use only.

A comparative electron spin resonance study of the selenothiadiazolyl radicals cyclo-$Se_{3-n}S_nN_2^+$ (n = 0–3)[1]

ED AWERE AND JACK PASSMORE
Chemistry Department, University of New Brunswick, Fredericton, N.B., Canada E38 6E2
KEITH F. PRESTON
Division of Chemistry, National Research Council of Canada, Ottawa, Ont., Canada K1A 0R6
AND
LESLIE H. SUTCLIFFE
Chemistry Department, Royal Holloway and Bedford New College, Egham, Surrey, England TW20 0EX

Received December 18, 1987

ED AWERE, JACK PASSMORE, KEITH F. PRESTON, and LESLIE H. SUTCLIFFE. Can. J. Chem. **66**, 1776 (1988).

Electron spin resonance spectra observed in dilute solutions of the hexafluoroarsenate salts of selenothiadiazolylium cations in polar solvents are ascribed to the parent cation radicals $\overline{SeNSeSeN}^+$, $\overline{SNSeSeN}^+$, $\overline{SNSeSN}^+$, and $\overline{SNSSN}^+$. The **g**- and nitrogen hyperfine tensors for the three selenium-containing species are entirely in line with the planar π-radical description deduced in earlier studies of trithiadiazolylium. Substantial increases in the *g*-shifts on substitution of sulphur by selenium result in broadening of the solution spectra and concomitant loss of nitrogen hyperfine structure. From measurements made in solid SO_2, the following principal tensor components were deduced for the new, Se-containing radicals: $\overline{SeNSeSeN}^+$: **g** = (1.9930, 2.0108, 2.1379), $\mathbf{a}_N(2)$ = (7.4, ≈0, ≈0) gauss, $\mathbf{a}_{Se}(2)$ = (180, 70, 43) gauss; $\overline{SNSeSeN}^+$: **g** = (1.9941, 2.0108, 2.1355), $\mathbf{a}_N(2)$ = (6.9, ≈0, ≈0) gauss, $\mathbf{a}_{Se}(2)$ = (180, 70, 45) gauss; $\overline{SNSeSN}^+$: **g** = (1.9957, 2.0086, 2.0736), $\mathbf{a}_N(2)$ = (8.3, ≈0, ≈0) gauss, $\mathbf{a}_{Se}$ = (198, 78, 75) gauss, where the values are given in the order *x*, *y*, *z*, *x* being the direction perpendicular to the radical plane.

ED AWERE, JACK PASSMORE, KEITH F. PRESTON et LESLIE H. SUTCLIFFE. Can. J. Chem. **66**, 1776 (1988).

Les spectres de résonance paramagnétique électronique de solutions diluées d'hexafluoroarsénates de cations sélénothiazolylium, dans des solvants polaires, sont attribués aux cations radicaux $\overline{SeNSeSeN}^+$, $\overline{SNSeSeN}^+$, $\overline{SNSeSN}^+$ et $\overline{SNSSN}^+$. Les tenseurs hyperfins-**g** et de l'azote des trois espèces contenant du sélénium correspondent complètement avec la description planaire d'un radical π qui a été déduite sur la base d'études antérieures sur le trithiadiazolylium. Les augmentations importantes des déplacements-*g* qui se produisent lors de la substitution du soufre par du sélénium conduisent à un élargissement des spectres en solution et à une perte concomitante de la structure hyperfine de l'azote. À l'aide de mesures faites dans du SO_2 à l'état solide, on a déduit les composantes principales des tenseurs pour les nouveaux radicaux contenant du Se : $\overline{SeNSeSeN}^+$: **g** = (1,9930; 2,0108 et 2,1379), $\mathbf{a}_N(2)$ = (7,4; ≈0; ≈0) gauss, $\mathbf{a}_{Se}(2)$ = (180; 70; 43) gauss; $\overline{SNSeSeN}^+$: **g** = (1,9941; 2,0108 et 2,1355), $\mathbf{a}_N(2)$ = (6,9; ≈0; ≈0) gauss, $\mathbf{a}_{Se}(2)$ = (180; 70; 45) gauss; $\overline{SNSeSN}^+$: **g** = (1,9957; 2,0086 et 2,0736), $\mathbf{a}_N(2)$ = (8,3; ≈0; ≈0) gauss, $\mathbf{a}_{Se}$ = (198; 78; 75) gauss dans lesquels les valeurs sont données dans l'ordre *x*, *y* et *z* et *x* est dans la direction perpendiculaire au plan du radical.

[Traduit par la revue]

Introduction

As an unsurpassed probe of unpaired electron spin density, the electron spin resonance spectrometer has provided a unique link between experimentalist and theoretician in the study of free-radical structures. Nowhere has this been more evident than in the interpretation of hyperfine splittings in conjugated organic π-radicals, and in particular, carbocyclic radicals (1). Delocalization of the unpaired electron confers stability upon many annulene radicals, and they are often "persistent" species. There is, of course, no a priori reason why resonance stabilization should be restricted to carbocyclics, although relatively few persistent inorganic cyclic radicals are known. Notable exceptions are provided by the cyclic sulphur and sulphur–nitrogen radicals (2). This dearth of persistent inorganic cyclic radicals is all the more surprising in view of the considerable number of known stable inorganic radicals, such as O_2, NO, NO_2, ClO_2, etc. A particularly simple and remarkably persistent inorganic radical, which is often a by-product of reactions of sulphur–nitrogen compounds in polar solvents, is the sulphur nitride cation $S_3N_2^+$ (3–8). Recent crystallographic and esr spectroscopic studies (6–9) have shown that this species is a planar π-radical having the structure shown in Fig. 1. As part of a programme of studies of this prototypal free radical and its derivatives, we report here the results of an esr investigation of certain selenium analogues.

Experimental

$Se_4(AsF_6)_2$ was prepared by the reaction of elemental selenium with an excess of AsF_5 containing a trace of bromine (10, 11).[2] S_4N_4 was prepared by a modification[3] of an established procedure (14). $Se_8(AsF_6)_2$ was obtained by a modification of the recipe of Gillespie and Ummat (15), and $SNAsF_6$ by the reaction of $S_3N_3Cl_3$ with three equivalents of $AgAsF_6$ (16). Deuteriosulphuric acid (99.5% isotopically pure), purchased from Aldrich, and sulphur dioxide from Matheson were used as received.

The reaction between $Se_4(AsF_6)_2$ and S_4N_4 was used to generate (17) the compound $(Se_2N_2S)_2(AsF_6)_2$. Although the portion of the products least soluble in SO_2 gave an elemental analysis appropriate for that formulation, esr spectra (see below) cast some doubt on the purity of the product. Accordingly, the product was treated further by

[1]NRCC No. 29001.

[2]Also, M. P. Murchie and J. Passmore. To be published.

[3]J. Passmore and M. N. S. Rao. Personal communication.

Printed in Canada / Imprimé au Canada

Can. J. Chem. Downloaded from www.nrcresearchpress.com by 61.7.252.67 on 09/07/12
For personal use only.

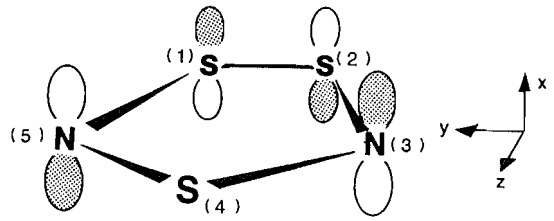

FIG. 1. The $^2A_2$ SOMO of $S_3N_2^+$.

oxidation with AsF_5 and a trace of bromine as a "facilitating agent" (10, 11).[2] The weights of products and reactants were consistent with a new formulation $(Se_2N_2S)(AsF_6)_2$, and an X-ray crystallographic structural determination confirmed the formation of the $Se_2N_2S^{2+}$ 6π doubly charged cation.[4] This compound $(Se_2N_2S)(AsF_6)_2$ constitutes sample A for the purposes of further discussion.

A solid sample containing crystals of $(Se/SSN_2S)_2(AsF_6)_2$, where Se/S denotes 50% occupancy by Se and S, was prepared from a reaction of $Se_8(AsF_6)_2$ and four equivalents of $NSAsF_6$ in SO_2 solution. The less soluble $Se_4(AsF_6)_2$ was precipitated from a supernatant liquid that yielded a mixture of yellow and black crystals upon removal of solvent. One of the black crystals was shown to be $(Se/SSeN_2S)_2(AsF_6)_2$ by single-crystal X-ray crystallography.[4] The black crystals were sorted from the yellow by hand in a dry-box, and these constituted sample B.

Minute quantities ($\approx$1 mg) of each of compounds A and B were transferred in turn to a 3-mm borosilicate esr tube under an atmosphere of dry nitrogen in a standard dry-box. Deuteriosulphuric acid was added at this stage or, alternatively, the tubes were capped and attached to a vacuum line for the addition of SO_2. After the addition of sufficient solvent to ensure complete dissolution of all the solid, the tubes were sealed under vacuum and transferred to the resonant microwave cavity of a Varian E-12 or a Bruker ESP 300 spectrometer. Temperature control in the esr cavity was achieved with liquid nitrogen, with a regulated flow of cold nitrogen, or with an Oxford Instruments' liquid helium cryostat. Microwave frequencies were measured with a Systron–Donner frequency counter and dc magnetic fields with a Cyclotron Corporation gaussmeter.

Results

Single, broad, featureless absorptions were the dominant features of the esr spectra (Fig. 2) of both A and B in liquid SO_2 or liquid D_2SO_4. The isotropic g-factor of A was larger than that of B, as was its linewidth. An additional weak feature of the solution spectra (Fig. 2) consisted of a 1:2:3:2:1 quintet with isotropic g, ^{14}N hyperfine coupling, and linewidth parameters characteristic of the radical $S_3N_2^+$ (7, 8). This radical was clearly present in traces only and its spectral intensity varied from sample to sample.

To minimize the extent of decomposition of the selenium-containing cations and reduce the complexity of the powder spectra, samples were dissolved in solvent in as short a time as possible, then frozen and kept in liquid nitrogen. In this manner, interference from the purely sulphur-containing species was essentially eliminated, and the powder spectra (Figs. 3, 4) are those of the selenium-containing radicals. Both powder spectra bear a close resemblance to the known spectrum of $S_3N_2^+$ (7, 8) with three distinct g-features, only one of which displayed a resolved hyperfine manifold due to interaction with two equivalent ^{14}N ($I = 1$) nuclei (Figs. 3, 4). For the purposes of comparison, a spectrum of $S_3N_2^+$ was generated by the reaction of $NS_2^+AsF_6^-$ with tetrahydrofuran vapour (19), followed by

[4]E. Awere, J. Passmore, and P. S. White. Unpublished results.

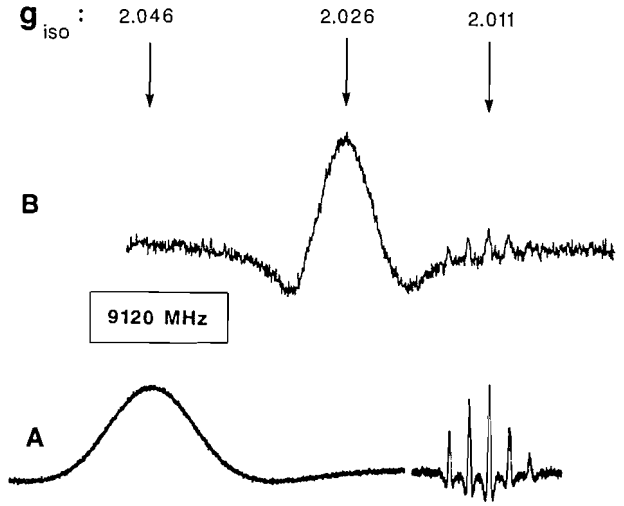

FIG. 2. Second-derivative esr spectra of samples A and B in liquid D_2SO_4 at 23°C. The high-field quintet is due to impurity $\overline{SNSSN}^+$ present in the samples.

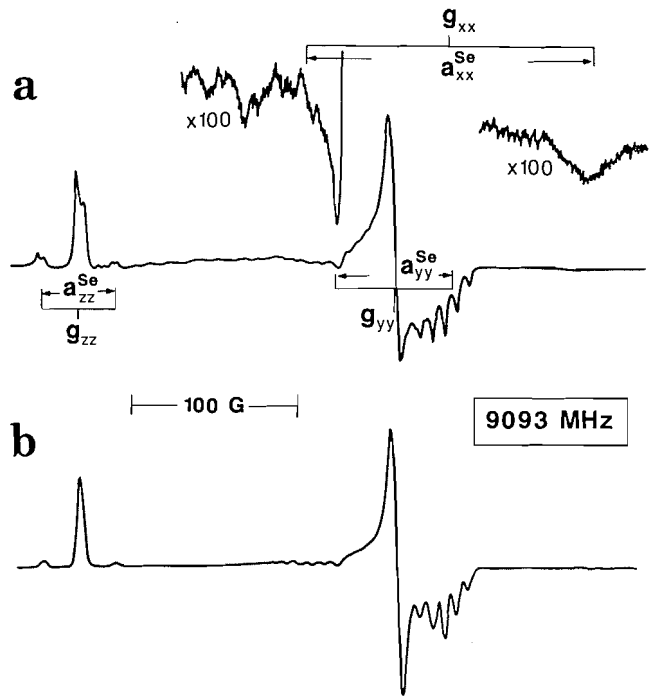

FIG. 3. First-derivative esr spectrum of A in solid SO_2 at 77 K (a) and simulation thereof (b) based on the parameters for $\overline{SeNSeSeN}^+$ given in Table 1.

dissolution in SO_2 or D_2SO_4. g-factors and ^{14}N hyperfine interactions were determined from the turning points of the powder spectra, and their values (Tables 1, 2) were confirmed by spectral simulation (20). Spectra in D_2SO_4 were considerably weaker than in SO_2, and a number of features, particularly those of $Se_3N_2^+$, were only detectable in the latter matrix.

The esr spectra were obtained in similar fashion from the portion of products of the reaction (17) between $Se_4(AsF_6)_2$ and S_4N_4 that was least soluble in SO_2 (see experimental section). However, these spectra were more complex than those obtained from either A or B, and closer inspection showed that they were due to a mixture of all four title radicals.

Can. J. Chem. Downloaded from www.nrcresearchpress.com by 61.7.252.67 on 09/07/12
For personal use only.

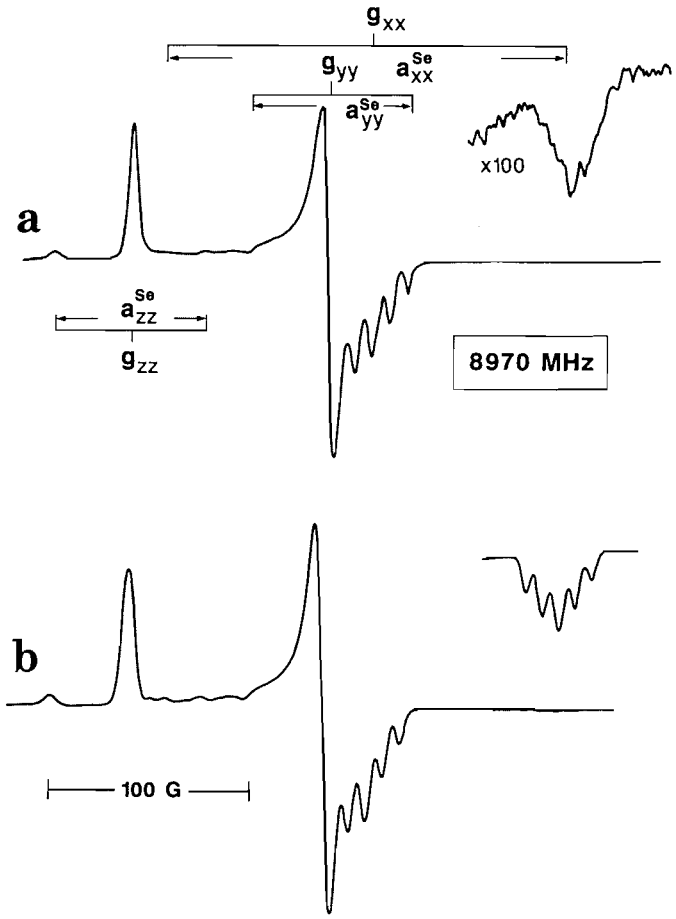

FIG. 4. First-derivative esr spectrum of B in solid SO_2 at 77 K (a) and simulation thereof (b) based on the parameters for $\overline{SNSeSN}^+$ given in Table 1.

TABLE 1. g- and hyperfine tensors[a] for selenothiadiazolylium radicals in SO_2 matrix at 77 K

g_{xx}	1.9930	1.9941	1.9957	2.0020
$a_{xx}(^{14}N)^a$	7.44	6.92	8.33	9.34
$a_{xx}(^{77}Se)^b$	180	180	198	
g_{yy}	2.0108	2.0108	2.0086	2.0082
$a_{yy}(^{14}N)^a$	≈0	≈0	≈0	≈0
$a_{yy}(^{77}Se)^b$	≈70	≈70	78	
g_{zz}	2.1379	2.1355	2.0736	2.0258
$a_{zz}(^{14}N)^a$	≈0	≈0	≈0	≈0
$a_{zz}(^{77}Se)^b$	43	45	75	
$\langle g \rangle$	2.0472	2.0468	2.0260	2.0120
g_{iso}	2.0464	2.0464	2.0255	2.0115
p–p width[c]	34	34	15	1

[a]Values in gauss.
[b]Hyperfine coupling, in gauss, ascribed to ^{77}Se at the 1,2 positions.
[c]Maximum-slope linewidth, in gauss, of isotropic spectrum.

Discussion

The striking similarity of the powder spectra of A and B to that of 1,2,4,3,5-trithiadiazolyl (7, 8) leaves little doubt that the carriers are all closely related free radicals. The spectra of A and B (Figs. 3, 4) were readily simulated (20) using parameters, given in Table 1, that closely resemble those of $S_3N_2^+$.

TABLE 2. g- and hyperfine tensors[a] for selenothiadiazolylium radicals in D_2SO_4 matrix at 77 K

				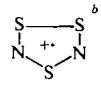 [b]
g_{xx}	n.m.[c]	1.9931	1.9953	2.0013
$a_{xx}(^{14}N)^a$	n.m.	7.28	8.00	9.18
$a_{xx}(^{77}Se)^d$	n.m.	≈180	≈200	
g_{yy}	n.m.	2.0124	2.0096	2.0062
$a_{yy}(^{14}N)^a$	n.m.	≈0	≈0	≈0
$a_{yy}(^{77}Se)^d$	n.m.	≈70	n.m.	
g_{zz}	2.1408	2.1369	2.0734	2.0250
$a_{zz}(^{14}N)^a$	≈0	≈0	≈0	≈0
$a_{zz}(^{77}Se)^d$	n.m.	50	74	
$\langle g \rangle$		2.0475	2.0261	2.0108
g_{iso}		2.0472	2.0262	2.0111
p–p width[e]		22	12	1

[a]Values in gauss.
[b]Data taken from ref. 8.
[c]Not measured because feature too weak or obscured.
[d]Hyperfine coupling, in gauss, ascribed to ^{77}Se in the 1,2 positions.
[e]Maximum-slope linewidth, in gauss, of isotropic spectrum.

Simulation did not, however, reproduce the "doublet" structure apparent in the g_{zz} and g_{xx} features of A (Fig. 3). This doubling of lines in the spectrum of A is due, we believe, to the presence of two very similar radicals, $\overline{SNSeSeN}^+$ and $\overline{SeNSeSeN}^+$, rather than to the occurrence of two distinct trapping sites for the same species. The formation of both radicals from A was somewhat surprising, and must be the result of complex reactions following the initial reduction of the dication $\overline{SNSeSeN}^{2+}$ in solution. Examination of crystals of A indicated the complete absence of paramagnetic impurities. The g-factors, discussed below, support our contention that the spectra obtained from A arose from a mixture of the two radicals. Furthermore, we note that the same doubling of lines occurred in D_2SO_4, and that multiple trapping sites were not observed for either $\overline{SNSSN}^+$ or $\overline{SNSeSN}^+$. We have considerable confidence, therefore, in our assignment of the spectrum of B to $\overline{SNSeSN}^+$ and that of A to a mixture of $\overline{SeNSeSeN}^+$ and $\overline{SNSeSeN}^+$. Trace amounts of $S_3N_2^+$ were also present (Fig. 2) in both cases. It should also be pointed out that one crystal of B was shown by X-ray crystallography[4] to be $\overline{SNSe/SSeN}^+$, with one position occupied by 50% Se and 50% S atoms. It is conceivable that the Se/S ratio is variable, and that the particular samples chosen for esr study had a larger percentage content of S than the crystal used for the X-ray structure determination.

The esr measurements on $S_3N_2^+$ in liquid, polycrystalline, and single-crystal samples have shown beyond any doubt that it has the planar C_{2v} geometry of Fig. 1 and an $^2A_2$ ground state (7–9). Experiment has shown that the two equivalent sulphur nuclei in that species make important $3p_x$ contributions to the SOMO, whereas the unique sulphur nucleus makes only a small, indirect contribution through spin polarization (7–9). Theoretical calculations at the Hückel level, summarized in Fig. 5 and Table 3, agree extremely well with the experimental findings, whereas INDO calculations overemphasize the polarization contribution at the unique atom (7). Accordingly, one would expect substitution of selenium for sulphur at the equivalent positions to exert a considerable influence on the electronic parameters, but much less so at the unique position.

Can. J. Chem. Downloaded from www.nrcresearchpress.com by 61.7.252.67 on 09/07/12
For personal use only.

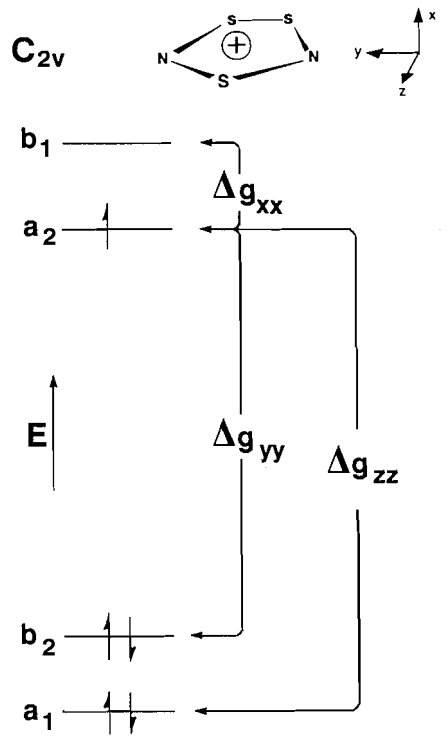

FIG. 5. Hückel energy level scheme for the upper molecular orbitals of $\overline{SNSSN}^+$ and symmetry-allowed g-shifts.

TABLE 3. Certain orbital energies and atomic-orbital coefficients from energy-optimized Hückel calculation for $S_3N_2^+$ in C_{2v} geometry

Orbital no.		12	13	14[a]	15
Designation		a_1	b_2	a_2	b_1
Energy[b]		−0.2912	−0.2584	−0.1010	−0.0709
	s	0.1203	0.0000	0.0000	0.0000
S(4)	p_x	0.0000	0.0000	0.0000	−0.6556
	p_y	0.0000	−0.1905	0.0000	0.0000
	p_z	0.2126	0.0000	0.0000	0.0000
	s	−0.2392	0.1395	0.0000	0.0000
N(3)	p_x	0.0000	0.0000	−0.3790	0.5039
	p_y	−0.3611	0.6363	0.0000	0.0000
	p_z	0.1172	−0.1541	0.0000	0.0000
	s	−0.2392	−0.1395	0.0000	0.0000
N(5)	p_x	0.0000	0.0000	0.3790	0.5039
	p_y	0.3611	0.6363	0.0000	0.0000
	p_z	0.1172	0.1541	0.0000	0.0000
	s	0.1801	−0.0922	0.0000	0.0000
S(1)	p_x	0.0000	0.0000	0.5969	−0.1767
	p_y	0.4806	0.1012	0.0000	0.0000
	p_z	0.0739	0.1223	0.0000	0.0000
	s	0.1801	0.0922	0.0000	0.0000
S(2)	p_x	0.0000	0.0000	−0.5969	−0.1767
	p_y	−0.4806	0.1012	0.0000	0.0000
	p_z	0.0739	−0.1223	0.0000	0.0000

[a]Half-filled orbital.
[b]Energy in hartrees.

This expectation is realized, for example, in the effect of selenium substitution on the principal g-values, particularly g_{zz} (Table 1).

The displacement of g from the free-spin value are determined by the relative disposition of ground and excited electronic states that are connected by the spin-orbit interaction operator, and by the size of the atomic spin-orbit coupling parameters. Δg values in the present instance are given by a simplification of the Stone formula (21):

$$\Delta g = \frac{2}{(E_0 - E_n)} \cdot (\Sigma \lambda_i c_{gi} c_{ei})(\Sigma c_{gi} c_{ei})$$

where c_{gi} and c_{ei} are p-atomic orbital coefficients of atom i in the ground- and excited-state wavefunctions connected by spin-orbit interaction, and E_0 and E_n are the energies of the ground and excited SOMOs. As we have shown elsewhere (9), the application of this formula to the Hückel molecular orbitals of $S_3N_2^+$ readily accounts for the observed ordering of the principal g-values with respect to the free-spin value, viz. $g_{zz} \gg g_{yy} > g_e > g_{xx}$. Since the spin-orbit coupling constants of ^{77}Se, ^{33}S, and ^{14}N are in the ratio of 22:5:1 (12), we may justifiably ignore the contributions of the nitrogen nuclei to the g-shifts of these radicals. If we furthermore assume that the excitation energy does not change significantly in the series of radicals, $\overline{SNSSN}^+$, $\overline{SNSeSN}^+$, $\overline{SNSeSeN}^+$, and ignore contributions from the unique S nucleus, we predict from the simplified Stone expression g-shifts in the ratio 1:2.7:4.4. For $H_0 /\!/ z$, the axis of greatest g-shift, the ratio of experimental shifts, 1:3.0:5.7, is in fair accord with this prediction. Along the other axes, the agreement with prediction is poor, but the anticipated trend is correct, i.e., increasing departure of g from the free-spin value with increasing selenium substitution. The substitution of the unique sulphur nucleus by selenium has very little effect on the spectral parameters of the radical, as shown by the comparison of the data for $\overline{SNSeSeN}^+$ and $\overline{SeNSeSeN}^+$ (Tables 1, 2). This weak influence is due to the absence of direct contributions from the unique atom to the SOMO. Nevertheless, further small increases in both Δg_{xx} and Δg_{zz} are observed upon replacement of the last sulphur atom by selenium.

TABLE 4. Estimated unpaired spin populations[a] of valence atomic s and p orbitals in selenothiadiazolyl radicals

$N_{3,5}$	s	0.4	0.4	0.4	0.5
	p_x	12.5	11.6	14.0	15.7
$S_{1,2}$	s				0.7
	p_x				42.0
$Se_{1,2}$	s	0.3	0.3	0.2	
	p_x	45.1	45.3	52.3	
S_4	s				0.2
	p_x				(−)13.8

[a]Percentage unpaired spin populations estimated using parameters of ref. 13 and experimental hyperfine tensors of Table 1 and ref. 8.

Turning now to the nuclear hyperfine interactions (Tables 1, 2), we note firstly the decrease in a_{xx} for the two equivalent ^{14}N nuclei as sulphur is replaced by selenium. This drift of unpaired spin away from the nitrogens is the anticipated result of replacing sulphur by the more electropositive selenium in an *antibonding* (Fig. 1) orbital. To place the effect on a more quantitative basis, we have converted (Table 4) the hyperfine couplings of Table 1 into unpaired spin populations of the

Can. J. Chem. Downloaded from www.nrcresearchpress.com by 61.7.252.67 on 09/07/12
For personal use only.

atomic s and p orbitals using theoretical one-electron parameters (13). In so doing, we have assumed that, as found experimentally for ^{33}S (8, 9), the signs of a_{yy} and a_{zz} for ^{77}Se are opposite to that of a_{xx}. Since the summed spin populations then exceed unity, we assume that the excess represents negative spin density on the unique S (or Se) nucleus, for which a coupling has not been observed or measured in this work. In the case of the $S_3N_2^+$ radical, hyperfine coupling to the unique sulphur nucleus has been measured (7–9), and the assumption of a negative spin density leads (Table 4) to an excellent spin count. With these assumptions, we see that the shift of unpaired spin indicated by the nitrogen hyperfine couplings is confirmed by the increased spin density at the equivalent selenium positions. In the case of the monoselenium radical, the lone selenium nucleus apparently gains spin at the expense of the nitrogen and remaining sulphur nuclei. Strictly speaking, this radical has lower symmetry (C_s) than the others and has geometrically inequivalent nitrogen nuclei. The ^{14}N manifold of $\overline{SNSeSN}^+$ did in fact differ from those of the other three radicals (Fig. 3), in that the inner three lines of the quintet had a width and asymmetry suggestive of an incompletely resolved hyperfine manifold due to inequivalent ^{14}N nuclei.

The disparity in linewidths of the liquid-phase spectra (Table 1) is a direct consequence of the increased g-anisotropy occasioned by selenium substitution. In the McConnell expression (18) for epr spectral linewidths in solution,

$$[T_2(m_I)]^{-1} = A + Bm_I + Cm_I^2$$

the coefficients A, B, C are proportional to the inner products of the anisotropic **g**- and hyperfine tensors, **g**:**g**, **g**:**a**, and **a**:**a**, respectively. The variation in linewidth across the ^{14}N manifold of $\overline{SNSSN}^+$ (7, 8) clearly indicates that the second term in this expression is an important one. If, in fact, it is the dominant term, we would anticipate a ratio of linewidths of 1:3:4:4 for the four species. If, on the other hand, the first term is dominant, we would expect a ratio of 1:11:39:41, which is very much in line with the observed ratio of linewidths (Tables 1, 2). We conclude, therefore, that the m_I-independent term makes the major contribution to the isotropic spectral linewidth. It is, of course, this strong dependence of linewidth on g-anisotropy which unfortunately obliterates the ^{14}N hyperfine structure of the selenium-containing radicals in solution.

All of the data presented here reinforce our original assignments of a C_{2v} geometry and an $^2A_2$ ground state (Fig. 1) to trithiadiazolyl. Furthermore, the trends observed in the spectral parameters upon substitution of sulphur by selenium conform very well to quantum theoretical expectations. The structure of this important class of simple inorganic cyclic free radicals is now firmly established.

Can. J. Chem. Downloaded from www.nrcresearchpress.com by 61.7.252.67 on 09/07/12
For personal use only.

Acknowledgements

The authors are indebted to Mr. R. Dutrisac for technical assistance. K.F.P. and L.H.S. wish to express thanks to NATO for the award of a travel grant.

1. J. E. WERTZ and J. R. BOLTON. Electron spin resonance: Elementary theory and practical applications. McGraw–Hill, New York. 1972. Chaps. 5 and 6.
2. H. FISCHER and K.-H. HELLWEGE (*Editors*). Magnetic properties of free radicals. Vol. 9. Springer, New York. 1977. Part a; H. FISCHER (*Editor*). Magnetic properties of free radicals. Vol. 17. Springer, New York. 1987. Part a.
3. D. CHAPMAN and A. G. MASSEY. Trans. Faraday Soc. **58**, 1291 (1962).
4. D. A. C. MCNEIL, M. MURRAY, and M. C. R. SYMONS. J. Chem. Soc. A, 1019 (1967).
5. S. A. LIPP, J. J. CHANG, and W. L. JOLLY. Inorg. Chem. **9**, 1970 (1970).
6. R. J. GILLESPIE, P. R. IRELAND, and J. E. VEKRIS. Can. J. Chem. **53**, 3147 (1975).
7. S. A. FAIRHURST, K. F. PRESTON, and L. H. SUTCLIFFE. Can. J. Chem. **62**, 1124 (1984).
8. S. A. FAIRHURST, K. M. JOHNSON, L. H. SUTCLIFFE, K. F. PRESTON, A. J. BANISTER, Z. V. HAUPTMAN, and J. PASSMORE. J. Chem. Soc. Dalton Trans. 1465 (1986).
9. K. F. PRESTON, J.-P. CHARLAND, and L. H. SUTCLIFFE. Can. J. Chem. **66**, 1299 (1988).
10. J. PASSMORE, G. SUTHERLAND, and P. S. WHITE. J. Chem. Soc. Chem. Commun. 330 (1980).
11. M. P. MURCHIE. Ph.D. thesis, University of New Brunswick, 1986.
12. J. R. MORTON, J. R. ROWLANDS, and D. H. WHIFFEN. National Physical Laboratory Report BPR13. Teddington, U.K. 1962.
13. J. R. MORTON and K. F. PRESTON. J. Magn. Reson. **30**, 577 (1978).
14. M. VILLENA-BLANCO and W. L. JOLLY. Inorg. Synth. **9**, 98 (1967).
15. R. J. GILLESPIE and P. K. UMMAT. Can. J. Chem. **48**, 1239 (1970).
16. A. APBLETT, A. J. BANISTER, D. BIRON, A. G. KENDRICK, J. PASSMORE, M. SCHRIVER, and M. STOJANAC. Inorg. Chem. **25**, 4451 (1986).
17. R. J. GILLESPIE, J. P. KENT, and J. F. SAWYER. Inorg. Chem. **20**, 4053 (1981).
18. H. M. MCCONNELL. J. Chem. Phys. **25**, 709 (1956).
19. S. A. FAIRHURST, A. HULME-LOWE, K. M. JOHNSTON, L. H. SUTCLIFFE, J. PASSMORE, and M. J. SCHRIVER. Magn. Reson. Chem. **23**, 828 (1985).
20. R. L. BELFORD and M. J. NILGES. Computer simulation of powder spectra. EPR Symposium, 21st. Rocky Mountain Conference, Denver, CO. August, 1979.
21. A. J. STONE. Proc. R. Soc. A, **271**, 424 (1963).

MP2 calculation of nuclear magnetic shielding constants involving gauge-invariant bases

EDOUARD C. VAUTHIER,[1] MICHEL COMEAU, SIMONE ODIOT,[1] AND SANDOR FLISZAR
Département de Chimie, Université de Montréal, C.P. 6128, Succ. A, Montreal (Qué.), Canada H3C 3J7

Received August 12, 1987

EDOUARD C. VAUTHIER, MICHEL COMEAU, SIMONE ODIOT, and SANDOR FLISZAR. Can. J. Chem. **66**, 1781 (1988).

Dia- and paramagnetic shielding constants of HF, NH_3, N_2, H_2O, and CO were calculated in the 4-31G, 4-31G*, and 6-31G** bases, using gauge-invariant atomic orbitals. Correlation effects were evaluated by 2nd-order perturbation theory: while the diamagnetic contributions are virtually unaffected by correlation, the paramagnetic parts (σ_p) are modified by ~10 ppm in the 6-31G** basis. With or without correlation, calculated σ_p values differ significantly from results obtained from measured spin-rotation constants. However, improvements in the basis set descriptions and inclusion of correlation yield chemical shift values for ^{15}N and ^{17}O converging toward their experimental counterparts obtained from conventional nuclear magnetic resonance spectroscopy.

EDOUARD C. VAUTHIER, MICHEL COMEAU, SIMONE ODIOT et SANDOR FLISZAR. Can. J. Chem. **66**, 1781 (1988).

Des orbitales atomiques gauge invariantes sont utilisées pour le calcul des constantes d'écran dia- et paramagnétiques des molécules HF, NH_3, N_2, H_2O et CO dans les bases 4-31G, 4-31G* et 6-31G**. L'effet de la corrélation électronique est évalué par perturbation au 2e ordre : celle-ci est pratiquement sans effet sur la partie diamagnétique mais modifie la partie paramagnétique (σ_p) d'environ 10 ppm dans la base 6-31G**. Les valeurs de σ_p avec et sans corrélation diffèrent sensiblement des valeurs déduites à partir de mesures de constantes spin-rotation. Par contre, une augmentation de base avec corrélation électronique fait converger les déplacements chimiques calculés pour ^{15}N et ^{17}O vers les valeurs expérimentales mesurées par voie traditionnelle.

Can. J. Chem. Downloaded from www.nrcresearchpress.com by 61.7.252.67 on 09/07/12
For personal use only.

Introduction

Ab initio calculations of magnetic shielding constants have been carried out using (*i*) the finite perturbation method (1–3), (*ii*) the coupled Hartree–Fock (CHF) approach (4–6), (*iii*) the IGLO formalism (7, 8), or (*iv*) a variant thereof (9). The first method has been applied either without (2) or with consideration of GIAO's (3, 10, 11), while the CHF approach has involved GIAO's (4, 5, 12–14) or GTO bases without gauge factors (15–17). The use of the latter in methods (*i*) and (*ii*) may be criticized since the vector potential, from which the magnetic field is derived, is determined only to within an arbitrary gradient; hence, an infinite basis is required to satisfy the special gauge invariance with respect to choice of the origin of the vector potential (18). In contrast, a gauge factor associated with each atomic orbital (GIAO) ensures this invariance with atomic orbital bases which are necessarily limited: the price to be paid is an increase in computer time because the presence of gauge factors requires evaluation of non-classical bielectronic integrals. Unfortunately, the use of GIAO's is not a panacea. Average deviations between calculated and experimental ^{13}C chemical shifts in alkanes and alkenes are ~8 ppm in the IGLO method (19) and ~5 ppm in semi-empirical (20, 21) and *ab initio* calculations (12). In short, there is room for improvement.

In order to improve numerical results, to save computer time, and to achieve an acceptable gauge invariance, GTO wave functions are expanded via configuration interaction (16, 17, 22) or a gauge factor is used with each molecular orbital. In the latter approach, the evaluation of non-classical bielectronic integrals is avoided by insertion of a completeness relation (8). The first alternative (16, 17, 22), however, leads to numerical results which are not entirely gauge invariant. In the HF molecule, for example, a translation of its molecular axes affects the calculated shielding of ^{19}F by 2 ppm (22). On the other hand, in comparison with calculations involving single determinants, the role of electron correlation appears to be important.

On these grounds it seems appropriate to ensure translational invariance with the use of gauge invariant (GIAO) orbitals and to consider correlation as well. To our knowledge, no formalism has yet been developed which would allow to retain correlation effects in gauge invariant calculations. In the present approach, electron correlation is treated by second-order perturbation theory (23), as indicated below.

Theory

The expression derived below for σ without correlation differs from that obtained in the traditional way using the GIAO basis. In the latter, $\vec{\sigma}$ is obtained by a double differentiation of $E(\vec{B},\vec{\mu}_M)$ after that a transformation $h|f_\nu\chi_\nu^0\rangle = f_\nu h_\nu|\chi_\nu^0\rangle$ is done leading to a diamagnetic term involving $\vec{r}_\nu\vec{r}_M/r_M^3$. It is possible to get the same diamagnetic term as Ramsey by following the Musher's approach (24) and developing the energy and ψ in term of $\vec{B}$ and $\vec{\mu}_M$. Let us shortly introduce our notations to go toward correlation, and improve the computation of bielectronic integrals with gauge factors in traditional CHF.

In the presence of a magnetic field $\vec{B}$ and a magnetic moment $\vec{\mu}_M$, the appropriate hamiltonian is

$$H_0(\vec{B},\vec{\mu}_M) = \sum_k \left[(1/2)(-i\hbar\vec{\nabla}_k + \frac{e}{c}\vec{A}_k)^2 + V_k \right]$$

$$\vec{A}_k = \frac{1}{2}\vec{B}\wedge\vec{r}_k + \frac{\vec{\mu}_M\wedge\vec{r}_{Mk}}{r_{Mk}^3}$$

Separating now the orders in $\vec{B}$ and $\vec{\mu}_M$, it follows that

$$H_0(\vec{B},\vec{\mu}_M) = H_0^0 + \vec{B}\sum_k\vec{h}^{10}(k) + \vec{\mu}_M\sum_k\vec{h}^{01}(k) + \vec{\mu}_M\sum_k\vec{\vec{h}}^{11}(k)\vec{B}$$

$$H_0(\vec{B},\vec{\mu}_M) = H_0^0 + \vec{B}\vec{H}_0^{10} + \vec{\mu}_M\vec{H}_0^{01} + \vec{\mu}_M\vec{\vec{H}}_0^{11}\vec{B}$$

with

[1]Visiting scientists. Permanent address: Département de Recherches Physiques, Université Pierre et Marie Curie (Paris V9), 4 place Jussieu, Tour 22, 75252 Paris Cedex 05, France.

$$\vec{H}_0^{10} = \sum_k \vec{h}^{10}(k) = \sum_k -\frac{ie\hbar}{2mc}\vec{r}_k \wedge \vec{\nabla}_k$$

$$\vec{H}_0^{01} = \sum_k \vec{h}^{01}(k) = \sum_k -\frac{ie\hbar}{mc}\frac{\vec{r}_{Mk} \wedge \vec{\nabla}_k}{r_{Mk}^3}$$

$$\vec{\vec{H}}_0^{11} = \sum_k \vec{\vec{h}}^{11}(k) = \sum_k \frac{e^2}{2c^2}\frac{\vec{r}_k\vec{r}_{Mk}\vec{\vec{1}} - r_k r_{Mk}}{r_{Mk}^3}$$

The wave function $\Psi_0(\vec{B},\vec{\mu}_M)$ of the ground state is described by a Slater determinant constructed from molecular orbitals having the form

$$\Phi_i(\vec{B},\vec{\mu}_M) = \sum_\mu C_{\mu i}(\vec{B},\vec{\mu}_M)\chi_\mu(\vec{B})$$

$$\chi_\mu(\vec{B}) = \chi_\mu^0 \exp\left(-\frac{ie}{\hbar c}\vec{A}_\mu.\vec{r}\right)$$

$$\vec{A}_\mu = \frac{1}{2}\vec{B} \wedge \vec{R}_\mu$$

Defining here

$$c_{\mu i}(\vec{B},\vec{\mu}_M) = c_{\mu i}^0 + i\vec{B}\ \mathrm{Im}\ \vec{x}_{\mu i}^{10} \ldots$$

$$\chi_\mu(\vec{B}) = \chi_\mu^0 - \frac{ie}{2\hbar c}\chi_\mu^0\vec{B}.\overrightarrow{R_\mu \wedge r}$$

we obtain the following expression for the molecular orbitals

$$\Phi_i(\vec{B},\vec{\mu}_M) = \Phi_i^0 + i\vec{B}\sum_\mu \vec{x}_{\mu i}^{10}\chi_\mu^0 - \frac{ie}{2\hbar c}\vec{B}\sum_\mu c_{\mu i}^0\overrightarrow{(R_\mu \wedge r)}\chi_\mu^0$$

The latter equation is conveniently rewritten in the following manner

$$\Phi_i(\vec{B},\vec{\mu}_M) = \Phi_i^0 + \vec{B}\vec{\Phi}_i^{10} + \vec{B}\vec{\Phi}_i^{10}(0)$$

where

$$\vec{\Phi}_i^{10} = i\sum_\mu \vec{x}_{\mu i}^{10}\chi_\mu^0$$

$$\vec{\Phi}_i^{10}(0) = -\frac{ie}{2\hbar c}\sum_\mu c_{\mu i}^0\overrightarrow{(R_\mu \wedge r)}\chi_\mu^0$$

At this point we turn our attention to the Schrödinger equation

$$H_0(\vec{B},\vec{\mu}_M)\Psi_0(\vec{B},\vec{\mu}_M) = E_0(\vec{B},\vec{\mu}_M)\Psi_0(\vec{B},\vec{\mu}_M)$$

and expand the wave function in terms of $\vec{B}$ and $\vec{\mu}$, i.e.,

$$\Psi_0(\vec{B},\vec{\mu}_M) = \Psi_0^0 + \vec{B}\vec{\Psi}_0^{10} + \vec{\mu}_M\vec{\Psi}_0^{01}$$

with energy

$$E_0(\vec{B},\vec{\mu}_M) = E_0^0 + \vec{B}\vec{E}_0^{10} + \vec{\mu}_M\vec{E}_0^{01} + \vec{\mu}_M\vec{\vec{E}}_0^{11}\vec{B}$$

Thus we arrive at Musher's formula

$$\vec{\vec{E}}_0^{11} = \langle\Psi_0^0|\vec{\vec{H}}_0^{11}|\Psi_0^0\rangle + 2\,\mathrm{Re}\langle\Psi_0^0|\vec{H}_0^{01}|\vec{\Psi}_0^{10}\rangle$$

which is instrumental in the derivation of the shielding tensor $\vec{\vec{\sigma}}$. Indeed, the second-order energy $\vec{\vec{E}}_0^{11}$ given in terms of molecular orbitals

$$\vec{\vec{E}}_0^{11} = 2\sum_{i=1}^n \langle\Phi_i^0|\vec{\vec{h}}^{11}|\Phi_i^0\rangle + 4\,\mathrm{Re}\sum_{i=1}^n \langle\Phi_i^0|\vec{h}^{01}|\vec{\Phi}_i^{10}\rangle + 4\,\mathrm{Re}\sum_{i=1}^n \langle\vec{\Phi}_i^0|\vec{h}^{01}|\vec{\Phi}_i^{10}(0)\rangle$$

leads directly to $\vec{\vec{\sigma}}$ in terms of atomic orbitals, i.e.,

$$[1]\quad {}^M\sigma_{\alpha\beta} = \frac{e^2}{2c^2}\sum_{\mu,\nu} P_{\mu\nu}^0\langle\chi_\mu^0\left|\frac{\vec{r}.\vec{r}_M\delta_{\alpha\beta} - r_\alpha r_{M\beta}}{r_M^3}\right|\chi_\nu^0\rangle + \frac{4}{c}\sum_{i=1}^{occ}\sum_{\mu,\nu}\mathrm{Im}\ x_{\nu i}^{10}(\beta)\, c_{\mu i}^0\langle\chi_\mu^0\left|\frac{l_{M\alpha}}{r_M^3}\right|\chi_\nu^0\rangle + \frac{e^2}{c^2}\sum_{\mu,\nu}P_{\mu\nu}^0\langle\chi_\mu^0\left|(R_\mu \wedge r)_\beta\frac{l_{M\alpha}}{r_M^3}\right|\chi_\nu^0\rangle$$

with $l_{M\alpha} = \overrightarrow{(r_M \wedge \nabla)}_\alpha$.

The imaginary coefficients, Im $x_{\nu i}^{10}(\beta)$, appearing in eq. [1] are calculated following the traditional coupled Hartree–Fock method with a separation of the orders in $\vec{B}$ and $\vec{\mu}_M$, and their projection, i.e.,

$$\mathrm{Im}\ \vec{x}_\nu^{10} = \sum_{l\neq i}^{basis}\vec{a}_{il}c_{\nu l}^0$$

The $\vec{a}_{il}$ coefficients are obtained by solving iteratively the equation

$$\vec{a}_{ji} = (\epsilon_j^0 - \epsilon_i^0)^{-1}\sum_{\mu,\nu} c_{\mu i}^0 c_{\nu j}^0(\vec{F}_{\mu\nu}^{10} - \epsilon_j^0\vec{S}_{\mu\nu}^{10})$$

for all i and j's. Moreover, letting

$$\sum_{\mu,\nu} c_{\mu i}^0 c_{\nu j}^0\vec{G}_{\mu\nu}^{10} = \sum_{\mu,\nu,\eta,\sigma}(\mu^0\nu^0|\eta^0\sigma^0)(c_{\mu i}^0 c_{\nu j}^0\vec{P}_{\eta\sigma}^{10} - \frac{1}{2}c_{\mu i}^0 c_{\sigma j}^0\vec{P}_{\eta\nu}^{10}) + \frac{e}{2hc}\sum_{\mu,\nu,\eta,\sigma}\left(\mu^0\nu^0\left|\frac{\overrightarrow{(R_\eta - R_\sigma)\wedge r_2}}{r_{12}}\right|\eta^0\sigma^0\right)\left(c_{\eta i}^0 c_{\sigma j}^0 P_{\mu\nu}^0 + c_{\mu i}^0 c_{\nu j}^0 P_{\eta\sigma}^0 - \frac{1}{2}\left(c_{\eta i}^0 c_{\nu j}^0 P_{\mu\sigma}^0 + c_{\mu i}^0 c_{\sigma j}^0 P_{\eta\nu}^0\right)\right)$$

where

$$\vec{P}_{\eta\sigma}^{10} = 2\sum_l^{occ}\sum_{i\neq l}^{basis}\vec{a}_{li}(c_{\sigma l}^0 c_{\eta i}^0 - c_{\eta l}^0 c_{\sigma i}^0)$$

calculations are *significantly simplified* because they involve evaluation of *only one type* of bielectronic integrals.

So far we have dealt exclusively with single determinantal wave functions. Consider now the second-order electronic correlation energy

$$E^{(2)}(\vec{B},\vec{\mu}_M) = \sum_{i\neq 0}\frac{\langle\Psi_0(\vec{B},\vec{\mu}_M)|H(\vec{B},\vec{\mu}_M)|\Psi_i(\vec{B},\vec{\mu}_M)\rangle^*\langle\Psi_0(\vec{B},\vec{\mu}_M)|H(\vec{B},\vec{\mu}_M)|\Psi_i(\vec{B},\vec{\mu}_M)\rangle}{W_0(\vec{B},\vec{\mu}_M) - W_i(\vec{B},\vec{\mu}_M)}$$

Can. J. Chem. Downloaded from www.nrcresearchpress.com by 61.7.252.67 on 09/07/12
For personal use only.

where the singlet diexcited states leading to 4,2,0 open shells are represented by $\Psi_i(\vec{B},\vec{\mu}_M)$. The corresponding Hartree–Fock energies are $W_i(\vec{B},\vec{\mu}_M)$. This correlation energy, expanded in terms of S^2 eigenfunctions, i.e.,

$$E^{(2)}(\vec{B},\vec{\mu}_M) = -2\sum_{i<j}\sum_{a<b}\frac{2(ib|ja)^*(ib|ja) + 2(ia|jb)^*(ia|jb) - (ia|jb)^*(ib|ja)}{\epsilon_a + \epsilon_b - \epsilon_i - \epsilon_j} - \frac{(ib|ja)^*(ia|jb)}{\epsilon_a + \epsilon_b - \epsilon_i - \epsilon_j}$$
$$- \sum_i\sum_{a<b}\frac{2(ia|ib)^*(ia|ib)}{\epsilon_a + \epsilon_b - \epsilon_i - \epsilon_i} - \sum_{i<j}\sum_a\frac{2(ia|ja)^*(ia|ja)}{\epsilon_a + \epsilon_a - \epsilon_i - \epsilon_j} - \sum_i\sum_a\frac{(ia|ia)^*(ia|ia)}{\epsilon_a + \epsilon_a - \epsilon_i - \epsilon_i}$$

is differentiated with respect to both $\vec{B}$ and $\vec{\mu}_M$. Thus we obtain the second-order Möller–Plesset correction, ${}^M\sigma_{\alpha\beta}(MP2)$, for the shielding tensor. The final result is

$${}^M\sigma_{\alpha\beta}(MP2) =$$
$$4\sum_{i<j}\sum_{a<b}(\epsilon_a^0 + \epsilon_b^0 - \epsilon_i^0 - \epsilon_j^0)^{-2}({}^M\epsilon_{a\alpha\beta}^{11} + {}^M\epsilon_{b\alpha\beta}^{11} - {}^M\epsilon_{i\alpha\beta}^{11} - {}^M\epsilon_{j\alpha\beta}^{11})((i^0b^0|j^0a^0)^2 + (i^0a^0|j^0b^0)^2 - (i^0a^0|j^0b^0)(i^0b^0|j^0a^0))$$
$$+ 2\sum_i\sum_{a<b}(\epsilon_a^0 + \epsilon_b^0 - \epsilon_i^0 - \epsilon_i^0)^{-2}({}^M\epsilon_{a\alpha\beta}^{11} + {}^M\epsilon_{b\alpha\beta}^{11} - {}^M\epsilon_{i\alpha\beta}^{11} - {}^M\epsilon_{i\alpha\beta}^{11})(i^0a^0|i^0b^0)^2$$
$$+ 2\sum_{i<j}\sum_a(\epsilon_a^0 + \epsilon_a^0 - \epsilon_i^0 - \epsilon_j^0)^{-2}({}^M\epsilon_{a\alpha\beta}^{11} + {}^M\epsilon_{a\alpha\beta}^{11} - {}^M\epsilon_{i\alpha\beta}^{11} - {}^M\epsilon_{j\alpha\beta}^{11})(i^0a^0|j^0a^0)^2$$
$$+ \sum_i\sum_a(\epsilon_a^0 + \epsilon_a^0 - \epsilon_i^0 - \epsilon_i^0)^{-2}({}^M\epsilon_{a\alpha\beta}^{11} + {}^M\epsilon_{a\alpha\beta}^{11} - {}^M\epsilon_{i\alpha\beta}^{11} - {}^M\epsilon_{i\alpha\beta}^{11})(i^0a^0|i^0a^0)^2$$

In this equation, it is

$${}^M\epsilon_{a\alpha\beta}^{11} = \left(\frac{\partial^2\epsilon_a(\vec{B},\vec{\mu}_M)}{\partial B_\beta\partial\mu_{M\alpha}}\right)_{\mu_{M\alpha}=B_\beta=0}$$

and, therefore,

$$\epsilon_{a\alpha\beta}^{11} = \frac{e^2}{2c^2}\sum_{\mu,\nu}c_{\mu a}^0c_{\nu a}^0\langle\chi_\mu^0\left|\frac{\vec{r}_\nu.\vec{r}_M\delta_{\alpha\beta} - r_{\nu\alpha}r_{M\beta}}{r_M^3}\right|\chi_\nu^0\rangle + \frac{e^2}{2c^2}\sum_{\mu,\nu}c_{\mu a}^0c_{\nu a}^0\langle\chi_\mu^0\left|((R_\mu - R_\nu)\wedge r)_\beta\frac{l_{M\alpha}}{r_M^3}\right|\chi_\nu^0\rangle$$
$$+ \frac{1}{c}\sum_{\mu,\nu}(c_{\mu a}^0\,\mathrm{Im}\,x_{\nu a}^{10}(\beta) - c_{\nu a}^0\,\mathrm{Im}\,x_{\mu a}^{10}(\beta))\langle\chi_\mu^0\left|\frac{l_{M\alpha}}{r_M^3}\right|\chi_\nu^0\rangle$$

Using here the equation

$$\langle\chi_\mu^0\left|\frac{\vec{R}_\nu.\vec{r}_M\delta_{\alpha\beta} - R_{\nu\alpha}r_{M\beta}}{r_M^3}\right|\chi_\nu^0\rangle = -\langle\chi_\nu^0\left|(R_\nu\wedge r)_\beta\frac{l_{M\alpha}}{r_M^3}\right|\chi_\mu^0\rangle - \langle\chi_\mu^0\left|(R_\nu\wedge r)_\beta\frac{l_{M\alpha}}{r_M^3}\right|\chi_\nu^0\rangle$$

which follows from the Hermitian property of the operator $l_{M\alpha}$, we deduce the final result given in eq. [2]

$$[2]\quad {}^M\epsilon_{a\alpha\beta}^{11} = \frac{e^2}{2c^2}\sum_{\mu,\nu}c_{\mu a}^0c_{\nu a}^0\langle\chi_\mu^0\left|\frac{\vec{r}.\vec{r}_M\delta_{\alpha\beta} - r_\alpha r_{M\beta}}{r_M^3}\right|\chi_\nu^0\rangle + \frac{e^2}{c^2}\sum_{\mu,\nu}c_{\mu a}^0c_{\nu a}^0\langle\chi_\mu^0\left|(R_\mu\wedge r)_\beta\frac{l_{M\alpha}}{r_M^3}\right|\chi_\nu^0\rangle$$
$$+ \frac{1}{c}\sum_{\mu,\nu}(c_{\mu a}^0\,\mathrm{Im}\,x_{\nu a}^{10}(\beta) - c_{\nu a}^0\,\mathrm{Im}\,x_{\mu a}^{10}(\beta))\langle\chi_\mu^0\left|\frac{l_{M\alpha}}{r_M^3}\right|\chi_\nu^0\rangle$$

Our diamagnetic term involving $1/c^2$ in eqs. [1] and [2] is the same as that obtained from a theory using a basis set without gauge factors and *thus depends on the origin defined for the molecular axes*. The other two terms in eqs. [1] and [2] represent the paramagnetic contribution. They differ, of course, from what would be obtained from a basis set without gauge factors. This is due to the presence in front of each AO of a gauge factor which introduces continually (i.e., for each AO) a gradient in the vector potential. As a consequence, we cannot compare our paramagnetic term to that determined from spin-rotation experiments, first because the latter corresponds to a fixed origin of the vector potential, defined either at the center of mass of the molecule or at the atom M of interest (25*b*) and, second, because our calculations involve a finite basis set. The use of an infinite basis set, of course, would lead to the paramagnetic term given by spin-rotation experiments whether or not we use gauge factors. Hence, tentatively we are inclined to judge the quality of our basis sets and of the correlation effects from a comparison between our calculated paramagnetic terms and those given by experiment.

Results

Using this approach, we have now calculated the average dia- and paramagnetic shielding constants of F, N, O in HF, NH_3, N_2, H_2O, and CO, locating the origin at the atom of interest. In each case, both the geometry and the basis sets (4-31G, 4-31G*, and 6-31G**) were carefully optimized. Our calculations are reported in Table 1 along with experimental results obtained from spin-rotation experiments. The agreement is only moderate for the reasons given earlier: while basis set and correlation effects, as revealed by second-order Möller–Plesset perturbation theory, are visibly significant in the evaluation of the paramagnetic terms, improvement in the basis sets and inclusion of correlation cannot be claimed to yield

Can. J. Chem. Downloaded from www.nrcresearchpress.com by 61.7.252.67 on 09/07/12
For personal use only.

TABLE 1. Average magnetic shielding constants (ppm)

Molecule	Shielding	Average magnetic shielding constant						
		4-31G	4-31G MP2	4-31G*	4-31G* MP2	6-31G**	6-31G** MP2	Experimental[a]
HF	$\bar{\sigma}_F^d$	481.9	481.7	482.0	481.6	482.3	481.8	
	$\bar{\sigma}_F^p$	−73.2	−70.5	−57.2	−35.8	−55.9	−45.9	−62.8 ± 0.3
	$\bar{\sigma}$					426.4	435.9	410 ± 6[b]
NH_3	$\bar{\sigma}_N^d$	354.4	354.2	353.9	353.7	354.4	354.0	
	$\bar{\sigma}_N^p$	−71.8	−61.8	−83.1	−80.1	−81.8	−72.9	−91; −90.06; −88.17
	$\bar{\sigma}$					272.6	281.1	264.5[c]
N_2	$\bar{\sigma}_N^d$	384.2	384.0	373.6	374.3	375.2	375.7	
	$\bar{\sigma}_N^p$	−487.2	−471.8	−449.7	−440.2	−447.4	−438.2	−485.8 ± 20[d]
	$\bar{\sigma}$					−72.2	−62.5	−101.3 ± 20; −61.6[c]
H_2O	$\bar{\sigma}_O^d$	415.8	415.5	415.9	415.5	416.4	415.9	
	$\bar{\sigma}_O^p$	−80.4	−83.7	−71.7	−46.0	−75.0	−84.8	
	$\bar{\sigma}$					341.4	331.1	334[e] ± 17.2
CO	$\bar{\sigma}_C^d$	325.9	325.9	326.3	327.1	326.4	327.5	
	$\bar{\sigma}_C^p$	−349.4	−335.7	−323.7	−310.7	−321.2	−296.9	−325.0 ± 1.0; −323.4 ± 1.6; −324.2 ± 0.9
	$\bar{\sigma}$					5.2	30.6	1.0 ± 1.2[f]
	$\bar{\sigma}_O^d$	443.8	443.2	443.2	442.7	444.0	443.6	
	$\bar{\sigma}_O^p$	−544.1	−607.4	−482.2	−496.0	−480.6	−494.9	−485.5 ± 17.2
	$\bar{\sigma}$					−36.6	−51.3	−42.3 ± 17.2[e]

[a]From spin rotation experiments: HF (25), NH_3 (26–28), N_2 (28), and CO (29–31, 34).
[b]Reference 25.
[c]Reference 32.
[d]Reference 28.
[e]Reference 31.
[f]Reference 34.

TABLE 2. Comparison between computed and experimental chemical shifts for NH_3 (from N_2) and CO (from H_2O), in ppm

Shift	Value							
	4-31G	4-31G MP2	4-31G*	4-31G* MP2	6-31G**	6-31G** MP2	Expl. *a*	Expl. *b*
$\delta_{N_2}^{NH_3}$	385.6	380.2	346.9	339.5	344.8	343.6	326.16 ± 0.08	330.9 ± 0.08
$\delta_{H_2O}^{CO}$	435.6	496.0	383.2	422.8	378.1	382.5	386.3 ± 1	394.4 ± 1

[a]The experimental values follow from conventional nmr measurements, in the gas phase at 300 K, reported in ref. 32 for NH_3/N_2 and in ref. 31 for CO/H_2O. In the liquid phase, at 300 K, the results are 307.0 for $\delta_{N_2}^{NH_3}$ (35) and 353.3 ppm for $\delta_{H_2O}^{CO}$ (31). For a discussion of the difference between gas phase and liquid phase results, see ref. 32.
[b]Experimental shift corrected of rovibronic effects. See text.

results converging toward their experimental counterparts. The most striking effects appear with a change of basis, and the best results are with the 6-31G** basis set. In this basis, inclusion of correlation worsens the calculation in nearly all cases. Our calculated values for the total shielding tensor $\bar{\sigma} = \sigma^d + \sigma^p$ at 0 K without MP2 at the 6-31G** level are only respectable in comparison with experimental values at 300 K, provided that these latter are carefully selected. A word of caution is in order, however, regarding this type of assessment involving data derived from spin-rotation experiments; a problem discussed in detail by Jameson and co-workers (32), and in our case for $\bar{\sigma}$ of N_2: for this molecule an old spin-rotation measurement gives $\sigma^p(N_2) = -485.8 \pm 20$ ppm leading to $\bar{\sigma}(N_2) = 384.5 - 485.8 = -101.3 \pm 20$ ppm, but Jameson gives $\bar{\sigma}(N_2) = -61.6$ ppm from an nmr measurement of the chemical shift between NH_3 and N_2 (32). On the other hand, using Huzinaga's extended basis Schindler and Kutzelnigg calculate a total shielding of nitrogen, namely, −108.4 ppm in N_2 (33) supporting the spin-rotation experimental value, but in contrast our computed $\bar{\sigma}$ value for N_2, namely, −72.2 ppm supports the value −61.6 ppm of Jameson and not the spin-rotation value -101.3 ± 20 ppm. Later we shall see also that our computed chemical shift $\delta_{N_2}^{NH_3}$ agrees with Jameson's experimental shift 326.16 ppm supporting also the experimental $\sigma^p(NH_3) = -90.06$ ppm.

Temporarily leaving the problems regarding the nitrogen shielding constants, let us briefly examine the results deduced for oxygen. For H_2O no direct spin-rotation data are available, but from nmr measurement of $\delta_{H_2O}^{CO} = 386.3 \pm 1$ ppm and assuming $\bar{\sigma} = -42.3 \pm 17.2$ for CO (31), a total shielding of 344.0 ± 17.2 ppm is deduced for H_2O at 300 K and finally 357.6 ± 17.2 ppm at 0 K (with the value 13.6 ppm for rovibronic corrections). Our computed 6-31G** values for $\sigma(H_2O) = 341.4$ ppm and $\sigma(CO) = -36.6$ ppm are in reasonable agreement with experimental values 357.6 ± 17.2 and -42.3 ± 17.2 ppm, respectively. For H_2O the total

Can. J. Chem. Downloaded from www.nrcresearchpress.com by 61.7.252.67 on 09/07/12
For personal use only.

shielding calculated by Schindler and Kutzelnigg is 327.4 (7) and −84.1 ppm for CO (33). As a consequence the difference between the CO and H_2O oxygen calculated in the Schindler approach amounts to 411.5 ppm, a value differing significantly from its nmr experimental counterpart 386.3 ± 1 (Table 2).

Inspection of Table 2 suggests that our calculated shift for NH_3 (from N_2), namely, 343.6 converges toward its experimental counterpart obtained from conventional gas phase nmr measurement; 326.16 (32) and not toward the shift deduced from spin-rotation data; 375 ± 25 and seems to confirm the conclusion of Jameson (32) concerning the imprecision for $\sigma^p(N_2)$ issued from spin rotation. Going from 4-31G to 6-31G** MP2 we gain 42 ppm toward the experimental shift for $\delta_{N_2}^{NH_3}$ and 53 ppm in the same direction for $\delta_{H_2O}^{CO}$. Admittedly the improvement appears to be relatively small for $\delta_{N_2}^{NH_3}$ since we are, still, 17 ppm removed from the experimental shift at 300 K. In fact we must take into account rovibronic corrections in comparing our computed chemical shift at the equilibrium geometry with the experimental counterpart at 300 K; recently Jameson and Osten have reported values for $\sigma(300\,K) - \sigma_e$ for a set of molecules: with Table 13 of ref. 36 and experimental values at 300 K (Table 2) we deduce $\delta_{H_2O}^{CO}(r_e) = \delta_{H_2O}^{CO}(300\,K) + 13.0 - 4.88 = 394.4 \pm 1$ and our computed 6-31G** MP2 value (382.5) is in disagreement by ≃11.9 ppm. For N_2 and NH_3 we get from the same reference $\delta_{N_2}^{NH_3}(r_e) = \delta_{N_2}^{NH_3}(300\,K) - 3.49 + 8.3 = 330.9$ ppm and our 6-31G** MP2 value (343.6) is imprecise by 12.6 ppm. Indeed Table 2 confirms the important roles of correlation and *basis set* in reproducing the nmr shift.

Nevertheless, no definite statement can be made as to how important correlation effects of nmr shielding constants in HF, NH_3, H_2O, N_2, CO may be. For theoretical reasons explained earlier concerning the use of an infinite basis set when gauge factors occur, it would become necessary to perform computations with a nearly saturated basis set: the 6-31G** basis is far from saturated and MP2 is partly compensating, in the wrong direction, for inadequacy of the basis: MP2 is not worth doing at this level. This conclusion is itself a worthwhile thing for other workers to know about. Improvement of the calculations start, *first*, with a search of a better basis set and secondly with higher corrections in the correlation: the theory outlined above can be extended to give MP4 corrections for the shielding tensor. Another way to improve numerical results would be to use the Xα theory without gauge factors reviewed in ref. 37 by incorporating an appropriate α.

Acknowledgements

We thank a referee for his most valuable suggestions; the France–Québec cooperation program and the Natural Sciences and Engineering Research Council of Canada for support, and the Centre de Calcul de l'Université de Montréal for computer time.

1. J. A. POPLE, J. W. MCIVER, and N. S. OSTLUND. J. Chem. Phys. **49**, 2960 (1968).
2. R. DITCHFIELD, D. P. MILLER, and J. A. POPLE. J. Chem. Phys. **53**, 613 (1970).
3. R. DITCHFIELD. Chem. Phys. Lett. **15**, 203 (1972).
4. R. DITCHFIELD. Mol. Phys. **27**, 789 (1974).
5. F. R. PRADO, C. GIESSNER-PRETTRE, B. PULLMAN, and J. P. DAUDEY. J. Am. Chem. Soc. **101**, 1737 (1973).
6. R. M. STEVENS, R. H. PITZER, and W. N. LIPSCOMB. J. Chem. Phys. **38**, 550 (1963).
7. M. SCHINDLER and W. KUTZELNIGG. J. Chem. Phys. **76**, 1919 (1982).
8. W. KUTZELNIGG. Isr. J. Chem. **19**, 193 (1980).
9. A. E. HANSEN and T. D. BOUMAN. J. Chem. Phys. **82**, 5035 (1985).
10. R. DITCHFIELD and P. D. ELLIS. Chem. Phys. Lett. **17**, 942 (1972).
11. G. BOUCEKKINE-YAKER, A. BOUCEKKINE, M. ZAUCER, and G. BERTHIER. Int. J. Quantum Chem. **23**, 365 (1985).
12. C. MCMICHAEL ROHLFING, L. C. ALLEN, and R. DITCHFIELD. Chem. Phys. **87**, 9 (1984).
13. C. MCMICHAEL ROHLFING, L. C. ALLEN, and R. DITCHFIELD. Chem. Phys. Lett. **86**, 380 (1982).
14. S. K. GARG and J. S. TSE. Chem. Phys. Lett. **92**, 150 (1982).
15. P. LAZZARETTI and R. ZANASI. J. Chem. Phys. **68**, 1523 (1978).
16. H. FUKUI. Int. J. Quantum Chem. **23**, 633 (1983).
17. H. FUKUI, K. MIURA, and F. TADA. J. Chem. Phys. **79**, 6112 (1983).
18. J. S. GRIFFITH. The theory of metal transition ions. Cambridge University Press. 1961.
19. M. SCHINDLER and W. KUTZELNIGG. J. Am. Chem. Soc. **105**, 1360 (1983).
20. E. C. VAUTHIER, S. ODIOT, and F. TONNARD. Can. J. Chem. **60**, 957 (1982).
21. E. C. VAUTHIER, S. FLISZAR, F. TONNARD, and S. ODIOT. Can. J. Chem. **61**, 1417 (1983).
22. M. IWAI and A. SAIKA. J. Chem. Phys. **77**, 1951 (1982).
23. C. MÖLLER and M. S. PLESSET. Phys. Rev. **46**, 618 (1934).
24. J. MUSHER. Advances in magnetic resonance. *Edited by* J. S. Waugh. **2**, Academic Press, New York, NY. 1966.
25. (*a*) D. K. HINDERMAN and C. D. CORNWELL. J. Chem. Phys. **48**, 4148 (1968); (*b*) W. H. FLYGARE. J. Chem. Phys. **41**, 793 (1964).
26. T. D. GIERKE and W. H. FLYGARE. J. Am. Chem. Soc. **94**, 7277 (1972).
27. S. G. KUKOLICH. J. Am. Chem. Soc. **97**, 5704 (1975).
28. J. F. HARRISON. J. Chem. Phys. **47**, 2990 (1967).
29. R. D. AMOS. Chem. Phys. Lett. **68**, 536 (1979).
30. I. OZIER, L. M. CRAPO, and N. F. RAMSEY. J. Chem. Phys. **49**, 2314 (1968).
31. R. E. WASYLISHEN, S. MOOIBROEK, and J. B. MACDONALD. J. Chem. Phys. **81**, 1057 (1984).
32. C. J. JAMESON, A. K. JAMESON, O. OPPUSUNGGU, S. WILLE, P. M. BURRELL, and J. MASON. J. Chem. Phys. **74**, 81 (1981).
33. M. SCHINDLER and W. KUTZELNIGG. Mol. Phys. **48**, 781 (1983).
34. A. K. JAMESON and C. J. JAMESON. Chem. Phys. Lett. **134**, 461 (1987); C. J. JAMESON. Nuclear magnetic resonance specialists reports. Vol. 16. The Royal Society of Chemistry, London. p. 1.
35. R. GRINTER and J. MASON. J. Chem. Soc. A, 2196 (1970).
36. C. J. JAMESON, H. JÖRG OSTEN. Annual Reports on NMR Spectroscopy. Vol. 17. Academic Press. 1986. p. 1.
37. H. FUKUI. Magn. Reson. Rev. **11**, 205 (1987).

Can. J. Chem. Downloaded from www.nrcresearchpress.com by 61.7.252.67 on 09/07/12
For personal use only.

Douglas M. Templeton. Acceleration of the mercury-induced aquation of bromopentammine Co(III) by naturally occurring glycosaminoglycans. Can. J. Chem. **65**, 2411 (1987).

Page 2414. In the eighth line from the bottom, column two, a rate constant is given as $k_{2,0} = (5.67 \pm 0.44) \times 10^4\ M^{-1}\ s^{-1}$. The correct value is simply $k_{2,0} = 5.67 \pm 0.44\ M^{-1}\ s^{-1}$.

Can. J. Chem. Downloaded from www.nrcresearchpress.com by 61.7.252.67 on 09/07/12
For personal use only.

Long-range formyl proton coupling constants of 4-X-phenyl formates (X = H,F,CH_3,NO_2) and 2,6-dichlorophenyl formate. Conformations in solution

TED SCHAEFER, RUDY SEBASTIAN, AND GLENN H. PENNER
Department of Chemistry, University of Manitoba, Winnipeg, Man., Canada R3T 2N2

Received November 9, 1987

This paper is dedicated to Professor Charles A. McDowell on the occasion of his 70th birthday

TED SCHAEFER, RUDY SEBASTIAN, and GLENN H. PENNER. Can. J. Chem. **66**, 1787 (1988).

The signs and magnitudes of the long-range coupling constants between the formyl and ring protons over five, six, seven, and eight bonds in phenyl formate and its 4-fluoro, 4-methyl, and 4-nitro derivatives are reported. These numbers are combined with CNDO/2 and INDO MO FPT computations of their conformational dependence and with STO-3G MO populational distributions to provide a description of the conformational behaviour of these molecules. The *Z* conformers, predominantly nonplanar and having the carbonyl group pointing towards the ring, appear to account for more than 95% of the molecules in CS_2 solution at 300 K. In polar solvents, significant populations of the *E* conformers are indicated by the long-range coupling constants. The long-range coupling constants for the formyl proton in 2,6-dichlorophenyl formate are consistent with geometry-optimized STO-3G MO computations, which imply that the *Z* conformation, with the aldehyde group lying near the plane perpendicular to the benzene plane, is again at least 95% abundant at 300 K. The proton chemical shifts are also consistent with these conclusions.

TED SCHAEFER, RUDY SEBASTIAN et GLENN H. PENNER. Can. J. Chem. **66**, 1787 (1988).

On a déterminé les signes et les amplitudes des constantes de couplage à longue distance entre les protons du groupement formyle et ceux du cycle à travers cinq, six, sept et huit liaisons du formate de phényle et de ses dérivés fluoro-4, méthyl-4 et nitro-4. On a combiné ces valeurs avec celles obtenues à l'aide de calculs d'OM CNDO/2 et INDO sur leur dépendance conformationnelle ainsi qu'avec celles de distributions de populations évaluées par des calculs d'OM STO-3G pour obtenir une description du comportement conformationnel de ces molécules. En solution dans le CS_2, à 300 K, il semble que 95% des molécules existent comme conformères *Z*, qui sont principalement non-planaires et dans lesquels le groupement carbonyle est orienté vers le cycle. Dans les solvants polaires, les constantes de couplage à longue distance indiquent qu'il existe une proportion importante de conformères *E*. Les constantes de couplage à longue distance pour le proton formyle du formate de dichloro-2,6 phényle sont en accord avec les calculs d'OM STO-3G optimisés pour la géométrie: ils indiquent que, à 300 K, la conformation *Z*, dans laquelle le groupement aldéhyde est pratiquement perpendiculaire au plan du benzéne, correspond à au moins 95% des molécules. Les déplacements chimiques du proton sont aussi en accord avec ces conclusions.

[Traduit par la revue]

Introduction

An early discussion of the conformational behaviour of phenyl formate suggested a nearly planar *Z* form, planar because of resonance stabilization, *Z* because of a favorable interaction between the C═O and O—C(1) dipoles and because of a

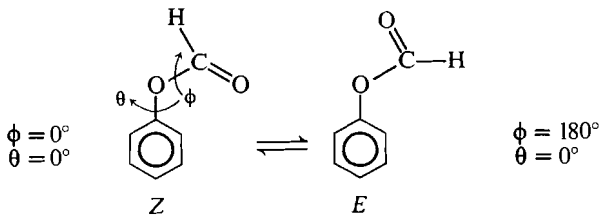

minimal repulsion between the lone-pair electrons on the two oxygen atoms (1). Consistent with the existence of only one conformer is the presence of only one carbonyl stretching band in both CS_2 and CH_3CN solutions (1).

A recent study of spin–spin coupling constants over six bonds between ^{19}F and ^{13}C nuclei in 4-F-phenyl esters concluded that ^6J(C,F) is consistent with severely nonplanar *Z* conformations (2*a*). Geometry-optimized STO-3G MO computations for a grid of θ and ϕ values implied that less than 3% of the most stable *E* conformer (at θ = 60°) would be present at 300 K. Rotation about the O—C(1) bond was computed to have a relatively low barrier and the expectation value of θ was predicted as 58° at 300 K and that of $\sin^2\theta$ as 0.68, in excellent agreement with the value (2*a*) obtained from ^6J(C,F).

Although ^6J(C,F) was consistent with a nonplanar *Z* conformer, it could not be shown that ^6J(C,F) would not also agree with a nonplanar *E* conformer (ϕ near 180° instead of 0°). A referee of that paper (2*a*) suggested the measurement of ^7J(H,F) in 4-fluorophenyl formate because this coupling constant might well be sensitive to the orientation of the aldehyde group.

It turns out that ^7J(H,F) is very small indeed. However, the coupling constants over five and six bonds between the aldehydic proton and the *ortho* and *meta* ring protons, when combined with CNDO/2 and INDO MO FPT computations, are informative about the nonplanarity of the molecule and appear to distinguish between *Z* and *E* conformers. This paper reports on the measurement of these parameters under very high resolution in phenyl formate and its 4-fluoro, 4-methyl, 4-nitro, and 2,6-dichloro derivatives.

Experimental

Phenyl formate and 4-nitrophenyl formate came from Aldrich, while the 4-fluorophenyl formate was synthesized in this laboratory (2*a*). The 4-methylphenyl formate and 2,6-dichlorophenyl formate were obtained in small amounts from the corresponding phenols by the procedure in the literature (2*b*), but reaction times were increased to 33 days. Samples for nmr analysis were prepared in a CS_2/C_6D_{12}/TMS mixture, containing 10 mol% of the deuterated cyclohexane and 0.5 mol% of tetramethylsilane. The phenyl formate sample had a concentration of 0.7 mol% and the sample containing the 4-nitro derivative was very dilute, certainly less than 0.7 mol%. A 5.0 mol% solution of 4-fluorophenyl formate in the solvent mixture above, containing a tiny amount of C_6F_6, was transferred to a 5 mm o.d. sample tube via a pipette containing a wad of cotton wool; the other samples were treated similarly. Degassing of the sample tubes by the freeze–

Can. J. Chem. Downloaded from www.nrcresearchpress.com by 112.217.228.212 on 09/07/12
For personal use only.

TABLE 1. The ^{1}H nmr spectral parameters at 300 K for phenyl formate, 4-fluorophenyl formate, 4-nitrophenyl formate, and 4-methylphenyl formate in CS_2 solution

Parameter	C_6H_5OCHO[a]	4-F-C_6H_4OCHO[b]	4-NO_2—C_6H_4OCHO[c]	4-CH_3—C_6H_4OCHO[i]
ν(CHO)[d]	2440.881(0)[e]	2424.215(1)	2463.841(1)	2431.585(1)
ν_2	2110.743(0)	2102.525(1)	2192.450(1)	2071.390(0)
ν_3	2188.551(0)	2083.056(1)	2462.328(1)	2122.878(0)
ν_4	2148.223(0)	13117.171(1)[f]	—	699.606(0)[j]
$^3J_{23}$	8.196(0)	8.938(1)	8.950(1)	8.282(1)
$^3J_{34}$	7.470(1)	7.869(1)	—	—
$^4J_{26}$	2.491(1)	3.098(1)	2.768(2)	2.585(1)
$^4J_{24}$	1.118(1)	4.448(1)	—	—
$^4J_{35}$	1.707(1)	2.950(1)	2.546(2)	2.255(1)
$^5J_{25}$	0.458(1)	0.346(1)	0.376(1)	0.430(0)
^5J(2,CHO)	+0.413(1)[g]	0.417(1)	0.433(1)	0.404(1)
^6J(3,CHO)	+0.081(1)[g]	0.063(1)	0.068(1)	0.074(1)
^7J(4,CHO)	+0.051(1)[g]	0.001(1)	—	(−)0.030(1)[k]
Calculated transitions	160	164[h]	64	512
Assigned transitions	155	154	62	429
Observed peaks	134	113	48	164
Largest difference	0.010	0.015	0.011	0.017
Root-mean-square deviation	0.003	0.004	0.005	0.005

[a]0.7 mol% in a CS_2 solution containing 10 mol% cyclohexane-d_{12} and 0.5 mol% tetramethylsilane.
[b]5.0 mol% in the CS_2/C_6D_{12}/TMS solvent mixture, containing a very small amount of C_6F_6.
[c]Less than 0.7 mol% in the CS_2/C_6D_{12}/TMS solvent mixture.
[d]In Hz at 300.135$_2$ MHz to high frequency of internal TMS.
[e]Numbers in parentheses are standard deviations in the last significant figure, as given by the NUMARIT analysis.
[f]In Hz at 282.363 MHz to high frequency of internal C_6F_6.
[g]From weak irradiation experiments, see Experimental and Fig. 1.
[h]The ^{1}H nmr peaks only; the ^{19}F nmr spectrum shows no evidence for coupling interactions with the aldehydic proton.
[i]1.25 mol% in the CS_2/C_6D_{12}/TMS solvent mixture.
[j]This is the chemical shift of the methyl protons. ^4J(H,CH_3) is −0.715(0) Hz and ^5J(H,CH_3) is 0.341(0) Hz.
[k]After correction of 15% for incomplete resolution of ^8J(CH,CH_3), the splitting observed being 0.026 Hz.

pump–thaw technique was followed by flame sealing to produce a symmetrical closure. Samples in other solvents were prepared in the same way.

The ^{1}H nmr spectra were accumulated at a probe temperature of 300 K on a Bruker AM300 spectrometer. The general procedure necessary to produce narrow peaks has been described previously (3). Peak widths at half-height of as little as 0.03 Hz or less were attainable.

The signs of the coupling constants between the aldehydic and ring protons in phenyl formate were found by weak irradiation (4) experiments. Simulations of double resonance spectra with the computer program DOR (5), as modified in this laboratory, confirmed the signs of the long-range coupling constants deduced by visual inspection.

Results and discussion

Spectral analyses and sign determinations

The ^{1}H nmr spectra were analyzed with the computer program NUMARIT (6), as reworked in this laboratory, and some of the ensuing spectral parameters appear in Table 1. There exist no significant correlations of those of the aldehyde proton with other spectral parameters. Figure 1 illustrates the sign determinations of ^5J, ^6J, and ^7J, the coupling constants between the aldehydic proton and the ring protons in phenyl formate. The aldehydic proton nmr spectrum is also shown for 4-fluorophenyl formate.

The long-range couplings to the aldehyde proton

One striking aspect of $^{5,6,7}J$ is their positive sign. Anisole, for example (7), displays alternating signs for $^{5,6,7}J$, as does thioanisole (8). In anisole, ^5J is negative as a consequence of a through-space or proximate interaction of the orbitals in the *ortho* C—H bond with those in the methyl group (9) in the stable planar form of this molecule. In phenyl formate, ^5J is +0.41 Hz, an immediate indication that the planar *E* form is not the predominant conformer. This indication is supported by our CNDO/2 and INDO MO FPT (10, 11) computations, which do predict a negative ^5J for the planar *E* conformation. These computations were performed for a grid of θ and φ values, namely, $0° \leq \theta \leq 90°$ in steps of 15°, together with $0° \leq \phi \leq 180°$ in steps of 30°. Note that $\theta = 0°$, $\phi = 0°$ defines the planar *Z* conformer, while $\theta = 0°$, $\phi° = 180°$ defines the planar *E* conformer.

Rather than tabulate some 500 computed coupling constants, Figs. 2 and 3 display the computed θ dependence of ^5J and ^6J. The curves are only drawn for the extremes of φ, that is, for $\phi = 0°$ (*Z* conformer) and $\phi = 180°$ (*E* conformer). Intermediate values of φ produce plots lying between these extremes.

The θ dependence of ^5J in Fig. 2 is perhaps unanticipated. Thus, in the *Z* conformation the largest value is calculated for an "anti-zigzag" arrangement of the intervening bonds at $\theta = 0°$. In the *E* conformation large and negative ^5J values occur at $\theta = 0°$, perhaps as anticipated because of probable through-space or proximate interactions between the orbitals in the *ortho* and aldehydic C—H bonds. Note also that for this conformation the CNDO/2 values for ^5J go effectively to zero at large values of θ, while the INDO numbers remain significantly negative throughout the range of θ.

Now, the geometry-optimized STO-3G MO energies of phenyl formate (2*a*) allow a calculation of the population distribution at 300 K, the temperature of the nmr experiments. It appears that 93.4% of the free molecules should exist in the *Z* conformation ($\phi = 0°$), another 4.2% in the conformation with $\phi = 30°$, and 2.1% as the pure *E* conformers ($\phi = 180°$). Combination of these populations and their θ distributions with the theoretical coupling constants yields ^5J as 0.374 and 0.286

Can. J. Chem. Downloaded from www.nrcresearchpress.com by 112.217.228.212 on 09/07/12
For personal use only.

Can. J. Chem. Downloaded from www.nrcresearchpress.com by 112.217.228.212 on 09/07/12
For personal use only.

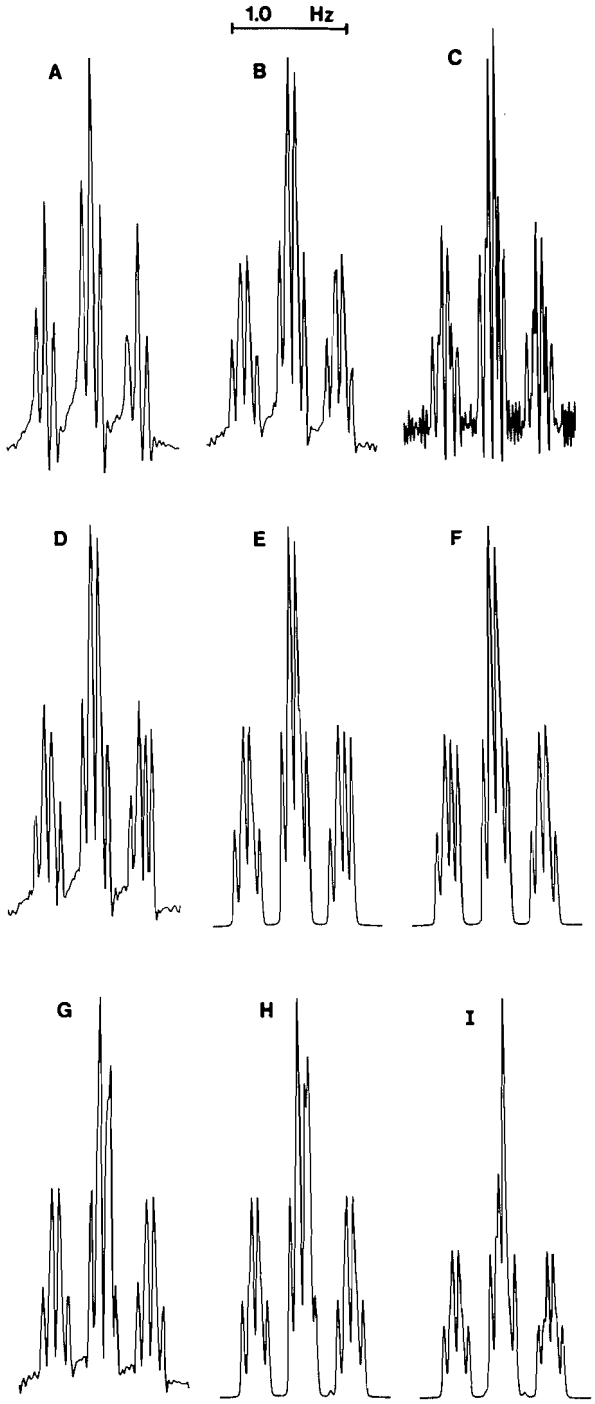

FIG. 1. In A the aldehydic proton nmr spectrum of 4-fluorophenyl formate is shown at 300 MHz and 300 K for a 5.0 mol% solution in a CS_2 solvent mixture (see Experimental). The linewidth at half-height is less than 0.03 Hz and no evidence for a coupling interaction with ^{19}F is present. In B the aldehyde proton of a 0.7 mol% solution of phenyl formate displays coupling interactions with all ring protons. In C severe resolution enhancement procedures show that the inner peaks of the apparent quartets in B can be further resolved. Of course, the ring proton nmr spectrum displays all the expected doublets and with clean resolution. In D the *para* ring protons are being weakly irradiated (low frequency region), demonstrating that ^5J(H-2,HCO) $\equiv$ ^5J, and ^6J(H-3,CHO) $\equiv$ ^6J are positive with respect to the positive coupling constants within the ring. In E the computed double resonance spectrum is displayed, assuming a B_2 field of 0.20 Hz and positive signs for ^5J and ^6J. The computed spectrum assumes peak widths of 0.025 Hz, causing fine structure of the inner bands (compare C). The important comparison with D should be made at the right of the spectra. In F the computed spectrum assumes a negative ^5J for the irradiation conditions in D. In G the *meta* proton region is being irradiated (low frequency region). The computed spectrum in H assumes ^5J and ^7J as positive, that in I has ^7J as negative. A complete series of experiments and simulations leaves no doubt that all couplings to the aldehyde proton are positive.

Hz with the INDO and CNDO/2 approaches, respectively. The populations with $\phi > 0°$ contribute -0.011 Hz to the value for the INDO numbers. According to Fig. 2, large populations of the *E* conformer would give rise to a negative ^5J, the observed value, however, being $+0.41$ Hz (Table 1) in the nonpolar solvent, CS_2. Because the conformational dependence of long-range coupling constants between side-chain nuclei and ring protons is usually computed correctly qualitatively and often quantitatively (9, 12–14), it is likely that the present results do indeed exclude significant populations of the *E* conformer. Previously, the ^6J(C,F) values in 4-fluorophenyl formate (2*a*) gave information about the θ but not the ϕ preferences.

Turning to ^6J, its computed dependence for the *Z* and *E* conformers is shown in Fig. 3. For the *Z* conformer, the INDO values are described by $^6J/\text{Hz} = -0.03 + 0.52 \sin^2(\theta/2)$ to within an average deviation of less than 0.005 Hz. This dependence is reminiscent of the σ electron component of $^5J(H,CH_3)$, involving the *meta* protons, in toluene (15, 16). It may also be noted that INDO values for coupling interactions of side chain nuclei with *meta* protons are usually overestimated (12, 17) although their conformational dependence is given correctly qualitatively. For example, in benzaldehyde the aldehyde proton coupling constant with the *meta* protons is computed as 0.90 Hz, whereas the CNDO/2 value is 0.46 Hz (17), much closer to the experimental value of 0.43 Hz (18). It is therefore not surprising that the INDO values of ^6J for phenyl formate correspond to a population-weighted average of 0.22_3 Hz, rather larger than the measured 0.08_1 Hz, but that the CNDO/2 numbers yield 0.10_5 Hz, perhaps in acceptable agreement with observation. Further, noting that the *E* conformer has computed ^6J values lying between -0.08 and $+0.04$ Hz (Fig. 3) for $0° \leq \theta \leq 180°$, it again appears that the observed ^6J in phenyl formate is consistent with the conformational conclusions above.

The theoretical values of ^7J are also most consistent with a *Z* conformation for phenyl formate in that they are computed as <-0.01 Hz in any *E* conformer. See a later section for a discussion.

According to the ^5J of 0.41_7 Hz for 4-fluorophenyl formate, the conformational distribution of phenyl formate is not significantly perturbed by the fluorine substituent. This indication is reasonable in view of the ^{13}C nmr chemical shifts of a series of 1,4-disubstituted benzene derivatives (19), from which it was concluded that the $OCOCH_3$ group (and presumably also the OCOH group) does not interact strongly with a *para* substituent. The reduction of ^6J by almost 0.02 Hz in 4-fluorophenyl formate (Table 1) is then attributable to an intrinsic perturbation by the nearby fluorine substituent.

This perturbation is slightly larger than in the 4-nitrophenyl formate,[1] in which, however, ^5J has increased to 0.43_3 Hz. The small increase (Table 1 and Fig. 2) is consistent with a small decrease of θ relative to the parent compound. In turn, this decrease would correspond to a small increase in the conjugative interaction of the OCOH moiety with the phenyl ring in the nitro derivative.

The OCOH group is expected to be a weak π electron donor

[1]A recent reference (28) to an unpublished X-ray structure of 4-nitrophenyl chloroformate has θ as 61° for the *Z* conformer.

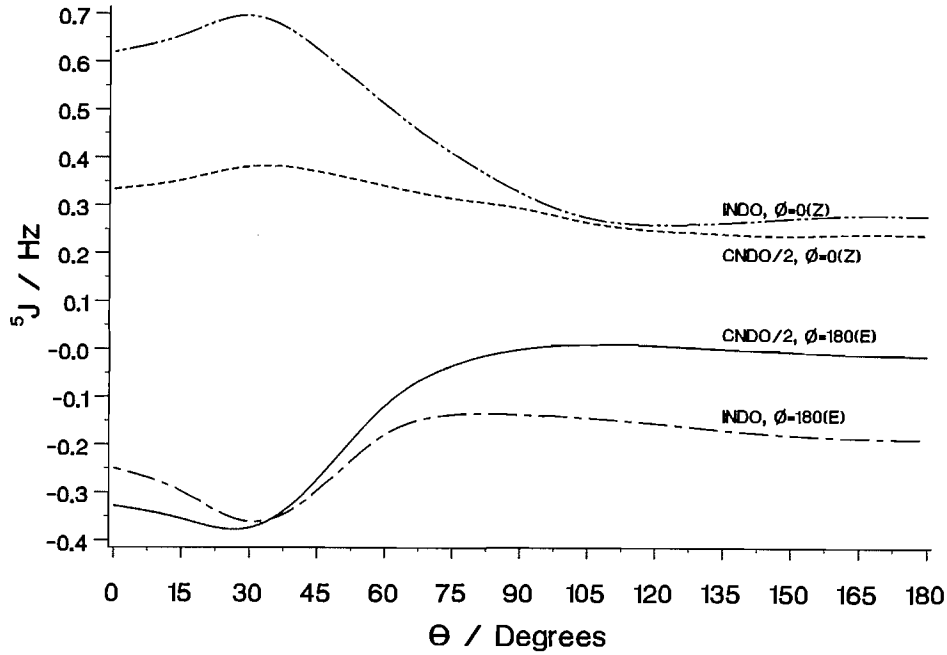

FIG. 2. The CNDO/2 and INDO MO FPT values of ^5J(aldehydic and *ortho* ring protons) are plotted as a function of θ for the *Z* and *E* conformations (see structural diagrams in the text) of phenyl formate. Note that $\theta = 0°$, $\phi = 0°$ defines the planar *Z* conformation. Rotation about the C(1)—O bond is described by θ. The planar *E* conformation has θ as 0° and φ as 180°. The computed numbers for $0° \leq \phi \leq 180°$ fall between the curves for $\phi = 0°$ and 180° shown in the figure.

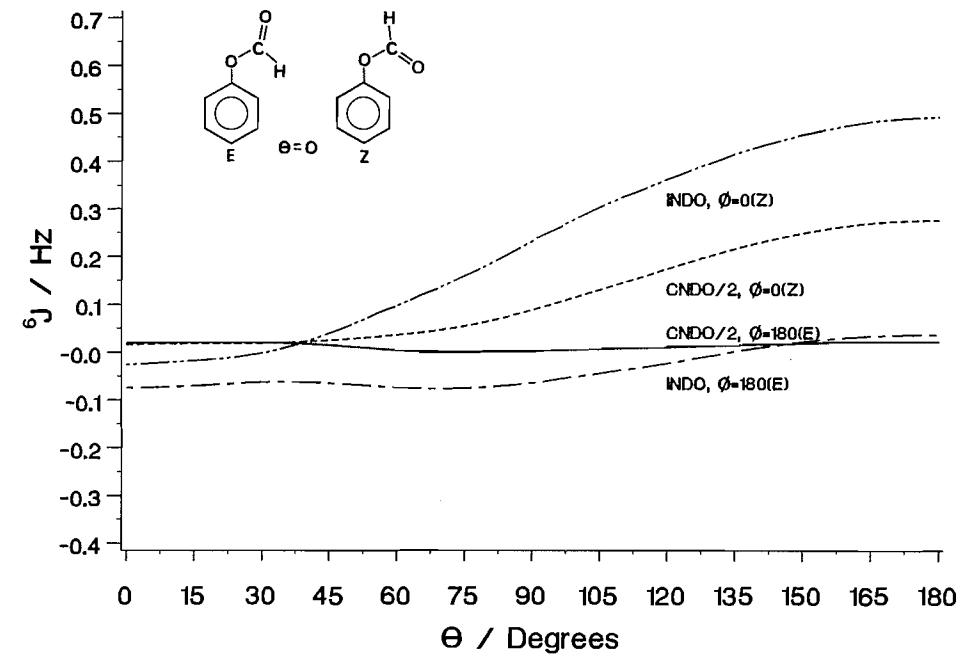

FIG. 3. Plots of the computed ^6J(aldehydic and ring protons) values are shown for the *E* and *Z* conformations of phenyl formate. See the structural diagrams in the text and the caption of Fig. 2 for further description. The top curve is described by the equation $^6J/\text{Hz} = -0.03 + 0.52 \sin^2(\theta/2)$.

(19), as is also suggested by the chemical shift of H-4 in phenyl formate in Table 1. In the same solvent system, the protons of benzene are less shielded by 0.06 ppm (16) than H-4 in phenyl formate. Comparison with the increased shielding of 0.21 ppm of H-4 in toluene (16), relative to benzene, indicates the weakness of the π electron donating abilities of the OCOH grouping in the neutral molecule.

Solvent effect on the conformational equilibrium

Apparently the dipole moment of phenyl formate is unavailable. The CNDO/2 values are 1.1 D for the planar *Z* conformer and 0.9 D if $\theta = 90°$. The STO-3G value is 0.8 D for both of these *Z* conformers. Theory therefore indicates a dipole moment of approximately 1 D for the *Z* form of phenyl formate. For the *E* conformer, the computed dipole moments are again roughly independent of θ, but are large, 3.7 D from the semiempirical computation and near 3 D from the *ab initio* calculation. Accordingly, a solvent perturbation of the gas phase conformational distribution is possible, particularly for a polar solvent, which should favor the *E* conformers as judged by an electrosta-

Can. J. Chem. Downloaded from www.nrcresearchpress.com by 112.217.228.212 on 09/07/12
For personal use only.

TABLE 2. Long-range coupling constants in Hz for the formyl proton in different solvents at 300 K

Solvent	^5J	^6J	^7J	Solvent	^5J	^6J	^7J
CS_2[a]	0.413(1)	0.081(1)	0.051(1)	CS_2[b]	0.404(1)	0.074(1)	—[c]
CD_2Cl_2[a]	0.373(0)	0.072(0)	0.045(1)	CD_3CN[b]	0.344(1)	0.061(1)	—[c]
$(CD_3)_2CO$[a]	0.349(1)	0.067(1)	0.041(1)	CS_2[d]	—	0.136(1)	−0.002(1)
CD_3CN[a]	0.349(1)	0.069(1)	0.041(1)	CD_3CN[d]	—	0.129(0)	−0.001(1)

[a]These numbers refer to phenyl formate. The concentrations were 1.0 mol% in CD_2Cl_2, $(CD_3)_2CO$, and CD_3CN, all containing also 0.5 mol% TMS. The rms deviations in the analyses of the ^1H nmr spectra in these three solvents were 0.002, 0.004, and 0.004, respectively.

[b]These numbers refer to 4-methylphenyl formate at 1.25 mol% in concentration.

[c]$^8J(OCH,CH_3)$ is ±0.030 Hz in CS_2 and ±0.020 Hz in CD_3CN.

[d]These numbers refer to 2,6-dichlorophenyl formate. $^7J(OCH,H)$ is unobservable, the formyl ^1H nmr peak widths at half-height being 0.014 Hz in CD_3CN and 0.025 Hz in CS_2 (the formyl proton is relatively far from other nuclear dipoles). The numbers given for ^7J come from the analytical fitting procedure and probably indicate rounding off results. The rms deviations in the analyses were 0.001 for both solutions.

Can. J. Chem. Downloaded from www.nrcresearchpress.com by 112.217.228.212 on 09/07/12
For personal use only.

tic model (20*a*). For alkyl formates there exists evidence for a solvent dependence of the energy difference between *Z* and *E* conformers (20*b*, 20*c*).

In Table 2 the long-range coupling constants for the formyl proton in phenyl formate are given for solutions in CD_2Cl_2, acetone-d_6, and CD_3CN. The dielectric constants of these solvents are near 9, 21, and 39, respectively. ^5J decreases from 0.413 Hz in CS_2 solution to 0.373 Hz in CD_2Cl_2 and then to 0.349 Hz in acetone-d_6 and CD_3CN. The plots in Fig. 1 imply increased populations of the *E* conformer in the more polar solutions. An approximate estimate of these populations can be had as follows. The population distribution obtained from the molecular orbital computations (2*a*) implies that 97.6% of the phenyl formate molecules effectively exist in the *Z* conformation at 300 K. On the assumption that this distribution holds in the nonpolar CS_2 solution and that ^5J_Z is 0.43 Hz while ^5J_E is −0.20 Hz (these ^5J values are the averages of the INDO MO FPT numbers at θ equal to 45° and 60°, such θ values representing almost isoenergetic conformers), it follows that the *Z* conformers constitute 91% of the total population in CD_2Cl_2 solution and 87% in acetone-d_6 and CD_3CN solutions. The above values of ^5J_Z and ^5J_E also reproduce the larger ^5J in CS_2 solution. Note, however, that these estimates of the conformer populations must be treated with circumspection; it is probably safe to conclude that significant amounts of the *E* conformer are present in the more polar solvents at 300 K. Confirmation of this conclusion by other methods would be useful.

^6J also decreases in the polar solvents (Tables 1 and 2), although the decrease is rather small. Nevertheless, the CNDO/2 computations, as used above in the discussion of ^6J in the CS_2 solution, agree that ^6J should decrease as the population of the *E* conformer rises. Thus, at θ > 45° the computed ^6J becomes less than 0.01 Hz for the *E* form of phenyl formate compared to about 0.1 Hz for the *Z* form. Decreases in ^5J and ^6J on passing from CS_2 to CD_3CN solutions also occur for 4-methylphenyl formate, the magnitudes of these decreases being the same as for phenyl formate.

The coupling constants, $^7J(H,H)$, $^8J(H,H)$, and $^7J(H,F)$

The INDO MO FPT values for $^7J(H,H)$ in the *Z* conformation of phenyl formate are reproduced precisely (to within an average deviation of 0.001 Hz for seven values) by $^7J(H,H)/Hz = -0.043 \sin^2\theta + 0.119 \cos^2\theta$. For the *E* conformation, the theoretical values are independent of θ to within 0.003 Hz and do not rise above 0.009 Hz. In the *Z* conformation, the C=O bond pointing towards the phenyl group, the theory therefore suggests a σ–π electron mechanism, going as $\sin^2\theta$ and involving subtle exchange interactions at the ester site, as well as a possible π electron mechanism, varying as $\cos^2\theta$. The latter mode of transmission of spin state information could conceivably involve the 2*p*...π conjugation at the C(1)—O bond, which would be most effective for θ = 0°. In that event, the mechanism would include the aromatic π electron system and transmission at the *para* C—H bond would depend on the usual spin polarization at that end of the coupling pathway. In toluene and *p*-xylene, $^6J(H,H) = -^7J(H,H)$ to within experimental error, consistent with the assumption that, for these molecules, the σ–π parameters of the aromatic C—H and the C—CH_3 bonds are equal in magnitude. It would follow that, in 4-methylphenyl formate, $^8J(H,H)$ should be equal to $-^7J(H,H)$ in phenyl formate (12, 18, 21, 22), assuming that the methyl substituent did not alter significantly the conformational behaviour of the ester linkage. This latter assumption is supported by the near equality of ^5J for the two compounds (Table 2), ^5J apparently being sensitive to conformation.

In fact, $^8J(H,H)$ is $\pm 0.03_0$ Hz in CS_2 solution, compared to 0.05_1 Hz for $^7J(H,H)$. This result implies that the term in $\cos^2\theta$ does not involve 2*p*...π conjugation at the C(1)—O bond. On the contrary, this term may represent a coupling via the σ electrons of the phenyl group and, in particular, probably does not involve π electron spin polarization at the *para* C—H bond. An approximate prediction of the σ–π electron component of $^7J(H,H)$, proportional to $\sin^2\theta$, can be had from the expectation value of $\sin^2\theta$ obtained from the MO computations. This value is 0.680 and yields −0.029 Hz for the σ–π component of $^7J(H,H)$, using the equation above, perhaps in fortuitous agreement with the measured value of $\pm 0.03_0$ Hz for $^8J(H,H)$ (footnote in Table 2). The $^8J(H,H)$ of $\pm 0.02_0$ Hz in CD_3CN solution is consistent with an increase in the *E* population, as deduced on the basis of ^5J and ^6J in a previous section.

The vanishing $^7J(H,F)$ in 4-fluorophenyl formate is now understandable. The ratio of the hyperfine parameters of the *para* C—H and C—F bonds is available from $^6J(H,H)$ and $^6J(H,F)$ in toluene (16) and 4-fluorotoluene (23). It is −1.92, the hyperfine parameters being of opposite sign for the two bonds and larger in magnitude for fluorine. The σ–π component of $^7J(H,F)$ is therefore -0.03_0 (−1.92) or 0.05_8 Hz. It follows that a σ electron component of near −0.06 Hz may exist for $^7J(H,F)$. Its existence could be tested if the carbonyl group could be held in the aromatic plane.

The discussion in the preceding paragraphs suggests that the theoretical value of the σ–π coupling magnitude in ^7J is correct. However, it does not follow that the theoretical coefficient of $\cos^2\theta$ is valid. In fact, the $^7J(H,H)$ of +0.05 Hz for phenyl formate in CS_2 solution indicates, together with the above expectation value of $\sin^2\theta$, that the multiplier of $\cos^2\theta$ should be 0.24_8 Hz.

It is interesting, therefore, that $^7J(H,H)$ in 2,6-dichlorophenyl

Can. J. Chem. Downloaded from www.nrcresearchpress.com by 112.217.228.212 on 09/07/12
For personal use only.

formate apparently vanishes (Table 2) in both CS_2 and CD_3CN solutions (the formyl ^1H nmr spectrum is a triplet with a linewidth of half-height of 0.014 Hz in the CD_3CN solution and is probably so small because there are no proximate magnetic dipoles of substantial magnitude). The modified relationship between $^7J(H,H)$ and $\sin^2\theta$, $^7J(H,H)/Hz = -0.04 \sin^2\theta + 0.25\cos^2\theta$, predicts $\langle\sin^2\theta\rangle$ as 0.85, which might, however, be as large as 0.90 in view of experimental error. This conclusion assumes the *Z* conformer as stable.

Our geometry-optimized STO 3G MO computations (24, 25), retaining the carbon atoms of the phenyl group in a plane but not as a regular hexagon, confirm the stability of the *Z* conformer. At $\theta = 90°$, this conformer is computed as 15.4 kJ/mol more stable than the *E* conformer. This stability is 4.5 kJ/mol larger than for phenyl formate at $\theta = 90°$. At a θ of 75°, the most stable computed conformer is twisted by 5.9° away from the pure *Z* form and is 0.96 kJ/mol less stable than the pure *Z* form for $\theta = 90°$. At a θ of 60°, the corresponding twist is 16.2° and this conformer, effectively *Z*, is 7.1 kJ/mol less stable than the pure *Z* conformer at a θ of 90°. At lower θ values the energy of the *Z* conformer rises rapidly and all *E* conformers are computed as not less than 15.3 kJ/mol higher in energy than the most stable *Z* conformer. Accordingly, the computations imply a $\langle\sin^2\theta\rangle$ of about 0.96 at 300 K, corresponding to a $^7J(H,H)$ of −0.03 Hz. This value does not agree with experiment, although it is indeed smaller in magnitude than measured in phenyl formate and has therefore changed in the qualitatively correct way. However, the INDO MO values of $^7J(H,H)$ are quite sensitive to the angle ϕ at θ values between 75° and 60°, dropping to −0.01 Hz at $\theta = 75°$, $\phi = 30°$ and becoming +0.02 Hz at $\theta = 60°$, $\phi = 30°$. In other words, not very large changes of the computed ϕ values for the stable conformers of 2,6-dichlorophenyl formate might well lead to the vanishing $^7J(H,H)$.

It is possible that intrinsic perturbations of $^7J(H,H)$ by the chlorine substituents are present, although $\sigma-\pi$ interactions involving the *para* proton and side-chain nuclei are insensitive to such perturbations in other systems (26). For θ near 90°, of course, $^7J(H,H)$ is indicated as a $\sigma-\pi$ coupling.

By way of contrast, $^6J(H,H)$ is probably significantly perturbed by the *ortho* chlorine substituents, judging by other systems. Thus, in toluene (15, 16) the coupling constant between the *meta* protons and those in the side chain increases significantly in the presence of two *ortho* fluorine substituents. The increase has been attributed to the perturbation of the electron component (16). A similar increase also appears to occur in benzaldehyde and its derivatives, as another example (18). The measured value of 0.13 Hz for $^6J(H,H)$ in 2,6-dichlorophenyl formate can be attributed partly to a substituent perturbation. Furthermore, the computed $^6J(H,H)$ for the *E* conformer of phenyl formate is always less than 0.01 Hz in magnitude (Fig. 2), so that $^6J(H,H)$ is consistent with a *Z* conformation for the 2,6-dichloro derivative, in agreement with the STO-3G MO computations.

The chemical shifts

The value of δ for the *para* proton of phenyl formate in the CS_2 solution mixture is 0.06 smaller than that of benzene under the same conditions. In 2,6-dichlorophenyl formate in this solvent mixture, δ_p is 7.11. Assuming additivity of substituent shifts, in the absence of two *meta* chlorine atoms δ_p would be 7.23 ppm. Comparison with the δ of 7.22 for benzene suggests, first, that conjugative π electron release by the ester group is effectively absent and, second, that the *Z* conformation is predominant in the dichloro derivative given that this is true for the parent molecule. However, this suggestion is plausible only, since the carbonyl group is known to possess a substantial diamagnetic anisotropy, which is ignored in this interpretation. Correction for shifts caused by the two chlorine substituents yields a δ of 7.28 for H-3 and H-5 in 2,6-dichloro phenyl formate, very near the 7.29 measured for phenyl formate (correction for an *ortho* chlorine is only 0.02 and for a *para* chlorine is −0.04). It is again plausible that the *Z* conformer is the stable one in 2,6-dichlorophenyl formate.

Perhaps more convincing, the δ values of the formyl proton in the two molecules differ by only 0.017 in the CS_2 solutions. The *E* conformer brings the formyl proton into the shielding region of the benzene magnetic dipole for $\theta > 60°$. From the model of Haigh and Mallion (27) it might be estimated that, at $\theta = 90°$, the formyl proton in the *E* conformer would be shielded by at least 0.25 ppm relative to the *Z* conformer. Large amounts of the *E* conformer are therefore contraindicated for the 2,6-dichloro derivative in CS_2 solution. In CD_3CN solution, the formyl proton in the latter molecule is more shielded, by 0.042 ppm, than in phenyl formate, again suggesting little difference in *Z*/*E* ratios for the two molecules. In summary, the proton chemical shifts are consistent with the arguments concerning the long-range coupling constants in previous sections.

In conclusion, a word of caution is in order. The minimal basis set used in the present work may turn out to be inadequate, although it is noted that substantially larger basis sets are sometimes in substantially poorer agreement with experimental internal barriers for benzene derivatives, for example, for benzaldehyde (29). On the other hand, for methyl formate surprisingly large basis sets and even corrections for electron correlation are necessary for a correct description of its conformational behaviour (30).

Acknowledgments

We are grateful to the Natural Sciences and Engineering Research Council of Canada for a grant in aid of research and to the referees for cogent remarks.

1. M. Ōki and H. Nakanishi. Bull. Chem. Soc. Jpn. **43**, 2558 (1970).
2. (*a*) T. Schaefer and G. H. Penner. Can. J. Chem. **65**, 2175 (1987); (*b*) W. Stevens and A. Van Es. Recl. Trav. Chim. Pays-Bas, **83**, 1287 (1964); **83**, 1294 (1964).
3. T. Schaefer, J. Peeling, and R. Sebastian. Can. J. Chem. **63**, 3219 (1985).
4. W. A. Anderson and R. Freeman. J. Chem. Phys. **37**, 85 (1962).
5. G. Govil and D. H. Whiffen. Mol. Phys. **12**, 449 (1967).
6. J. S. Martin, A. R. Quirt, and K. E. Worvill. The NMR program library, Daresbury Laboratory, Daresbury, U.K.
7. T. Schaefer and R. Sebastian. J. Magn. Reson. **73**, (1987).
8. T. Schaefer and J. D. Baleja. J. Magn. Reson. **60**, 131 (1984).
9. T. Schaefer and R. Laatikainen. Can. J. Chem. **61**, 224 (1983).
10. J. A. Pople, J. W. McIver, Jr., and N. S. Ostlund. J. Chem. Phys. **49**, 2960 (1968); **49**, 2965 (1968).
11. P. Dobosh and N. S. Ostlund. QCPE, **11**, 281 (1975).
12. R. Wasylishen and T. Schaefer. Can. J. Chem. **50**, 1852 (1972).
13. M. Barfield, C. J. Fallick, K. Hata, S. Sternhell, and P. W. Westerman. J. Am. Chem. Soc. **105**, 2178 (1983).
14. T. Schaefer, R. Laatikainen, T. A. Wildman, J. Peeling, G.

H. PENNER, J. BALEJA, and K. MARAT. Can. J. Chem. **62**, 1592 (1984).
15. T. SCHAEFER and R. LAATIKAINEN. Can. J. Chem. **61**, 2785 (1983).
16. T. SCHAEFER, R. SEBASTIAN, and G. H. PENNER. Can. J. Chem. **63**, 2597 (1985).
17. R. WASYLISHEN and T. SCHAEFER. Can. J. Chem. **49**, 3216 (1971).
18. T. SCHAEFER, J. PEELING, G. H. PENNER, A. LEMIRE, and R. LAATIKAINEN. Can. J. Chem. **64**, 1859 (1986).
19. R. T. C. BROWNLEE and M. SADEK. Aust. J. Chem. **34**, 1593 (1981).
20. (*a*) R. J. ABRAHAM AND E. BRETSCHNEIDER. *In* Internal rotation in molecules. *Edited by* W. J. Orville-Thomas. J. Wiley and Sons. New York. 1974. Chap 13; (*b*) H. WENNERSTRÖM, S. FORSÉN, and B. ROOS. J. Phys. Chem. **76**, 2430 (1972); (*c*) G. I. L. JONES and N. L. OWEN. J. Mol. Struct. **18**, 1 (1973).
21. R. A. HOFFMAN. Mol. Phys. **1**, 326 (1958).
22. C. J. MACDONALD and W. F. REYNOLDS. Can. J. Chem. **49**, 94 (1971).
23. R. WASYLISHEN and T. SCHAEFER. Can. J. Chem. **49**, 94 (1971).
24. W. J. HEHRE, R. F. STEWART, and J. A. POPLE. J. Chem. Phys. **51**, 2657 (1969); W. J. HEHRE, R. DITCHFIELD, R. F. STEWART, and J. A. POPLE. J. Chem. Phys. **52**, 2769 (1970).
25. J. S. BINKLEY, M. J. FRISCH, D. J. DEFREES, K. RAGHAVACHARA, R. A. WHITESIDE, H. B. SCHLEGEL, E. M. FLUDER, and J. A. POPLE. GAUSSIAN 82. Department of Chemistry, Carnegie–Mellon University, Pittsburgh, PA.
26. W. J. E. PARR and T. SCHAEFER. Acc. Chem. Res. **13**, 400 (1980).
27. C. W. HAIGH and R. B. MALLION. Prog. Nucl. Magn. Reson. Spectrosc. **13**, 303 (1979).
28. O. EXNER and P. FIEDLER. Collect. Czech. Chem. Commun. **52**, 970 (1987).
29. G. H. PENNER, P. GEORGE, and C. W. BOCK. J. Mol. Struct. (Theochem), **152**, 201 (1987).
30. K. B. WIBERG and K. E. LAIDIG. J. Am. Chem. Soc. **109**, 5935 (1987).

Can. J. Chem. Downloaded from www.nrcresearchpress.com by 112.217.228.212 on 09/07/12
For personal use only.

Enantiospecific synthesis of longiborneol and longifolene[1,2]

DAVID L. KUO AND THOMAS MONEY
Chemistry Department, University of British Columbia, 2036 Main Mall Vancouver, B.C., Canada V6T 1Y6

Received September 25, 1987

This paper is dedicated to Professor Charles A. McDowell on the occasion of his 70th birthday

DAVID L. KUO and THOMAS MONEY. Can. J. Chem. **66**, 1794 (1988).

A trimethylsilyl enol ether (**34**) derived from camphor (**1**) undergoes intramolecular Mukaiyama reaction to provide a tricyclic ketone (**36**) that can serve as a key intermediate in a new enantiospecific synthesis of longiborneol (**11**) and longifolene (**12**).

DAVID L. KUO et THOMAS MONEY. Can. J. Chem. **66**, 1794 (1988).

L'éther énolique triméthylsilylé (**34**) du camphre (**1**) subit une réaction intramoléculaire de Mukaiyama pour conduire à la cétone tricyclique (**36**) qui peut servir d'intermédiaire clé dans une nouvelle synthèse énantiospécifique du longibornéol (**11**) et du longifolène (**12**).

[Traduit par la revue]

Can. J. Chem. Downloaded from www.nrcresearchpress.com by 112.217.228.212 on 09/07/12
For personal use only.

(+)-Camphor (**1**), (+)-borneol (**2**), (+)-camphene (**3**) and tricyclene (**4**) (Scheme 1) represent a quartet of monoterpenoid compounds that are synthetically and, perhaps, biosynthetically related to each other. From a synthetic viewpoint (+)-camphor (**1**) can be regarded as the parent compound, which is readily converted to the other three members of the quartet by reduction, dehydration, and rearrangement reactions (cf. Scheme 1). As indicated in previous reports (1), a structural survey of sesquiterpenoids reveals the possibility of similar structural quartets in which each individual sesquiterpenoid can be regarded as the isoprenylog of camphor, borneol, camphene, or tricyclene. In this way one can recognise the possible occurrence of at least five structural quartets (Scheme 2) with (−)-campherenone (**6**), (+)-epicampherenone (**7**), (+)-copacamphor (**8**), (+)-ylangocamphor (**9**), and (+)-longicamphor (**10**) having the same synthetic relationship with other members of the quartet as camphor has with borneol, camphene, and tricyclene.

The synthetic strategy (Scheme 2) revealed by this structural analysis involves the initial conversion of (+)-camphor (**1**) or (−)-camphor (**5**) to the appropriate enantiomer of the "parent" sesquiterpenoid ketones, i.e., campherenone (**6**), epicampherenone (**7**), copacamphor (**8**), ylangocamphor (**9**), and longicamphor (**10**). The subsequent conversion of these compounds to other members of the quartet would then involve reduction, rearrangement, and cyclization reactions analogous to those used for the conversion of camphor to borneol, camphene, and tricyclene (cf. Scheme 1). On the basis of these speculative proposals previous investigations in our laboratory (1) established camphor as a chiral starting material in the enantiospecific synthesis of campherenone, campherenol, β-santalene, α-santalene, epicampherenone, isoepicampherenol, epi-β-santalene, sativene,[3] copaborneol, and copacamphene (cf. Scheme 2).

The use of this strategy for the synthesis of (+)-longiborneol (**11**),[3,4] (+)-longifolene (**12**),[3,4] and (+)-longicyclene (**13**)[4]

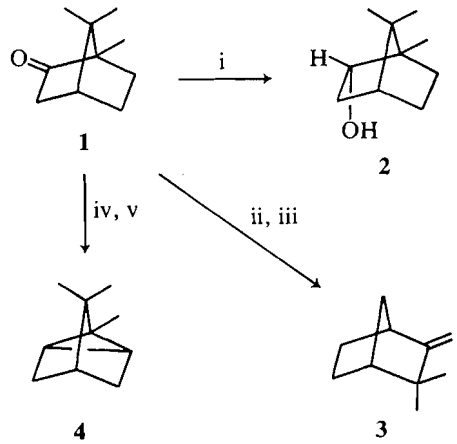

Reagents and conditions: i, Ca/NH_3; ii, $LiAH(OBu^t)_3$/THF; iii, TsCl/C_5H_5N; iv, NH_2NH_2/H^+; v, HgO/heat

SCHEME 1

(Scheme 2) requires a method for converting (+)-camphor (**1**) to (+)-longicamphor (**10**), and in our initial investigations we assumed that this could be accomplished by cyclization of (+)-campherenone (**20**) or an enol derivative of this compound. (+)-Campherenone (**20**) was synthesized from (+)-8-bromocamphor (**14**) (4)[5] by a reaction sequence (Scheme 3) that is less hazardous and more convenient than the one previously reported by us (1*b*). However, all our attempts to construct the longicamphor framework by cyclization of (+)-campherenone (**20**), campherenone hydrochloride (**21**), campherenone hydrochloride trimethylsilyl enol ether (**22**), or campherenone hydrochloride enol acetate (**23**) were unsuccessful (5) (cf. Experimental) and the only product isolated was dimer **24**. As a result, we turned our attention to the possibility of employing an intramolecular Mukaiyama reaction (6) to construct the longibornane framework. The bicyclic trimethylsilyl enol ether (**34**) required in this approach was synthesized from (+)-8-cyanocamphor ethylene ketal (**17**) (7) by the reaction sequence outlined in Scheme 4 and subsequently treated with titanium tetrachloride at −78°C for ~45 min to provide a mixture (~3:1) of diastereomeric tricyclic methoxyketones (**36***a*,*b*)[6] in ~85%

[1]Preliminary communication: ref. 8.

[2]An outline of this research was previewed at the 70th Canadian Chemical Conference, Quebec City, June 1987, and the 42nd ACS Northwest Regional Meeting, Western Washington University, Bellingham, WA, U.S.A., June 1987.

[3]Both enantiomers occur in nature and their synthesis would involve commercially available (+)- or (−)-camphor as a starting material.

[4]Several synthetic routes to racemic or optically active forms of longicamphor (2), longiborneol (2), longifolene (3), and longicyclene (2) have previously been reported.

[5]We have not been able to repeat the yield quoted in our original paper (4*a*), and now find that (+)-8-bromocamphor (**7**) can be prepared from (+)-camphor (**1**) in ~35% overall yield.

[6]Diastereomeric hydroxyethoxyketones (**35***a*, *b*) were obtained in ~75% yield when the enol trimethylsilyl ether (**33**) derived from **31** was treated in a similar way (cf. Scheme 5).

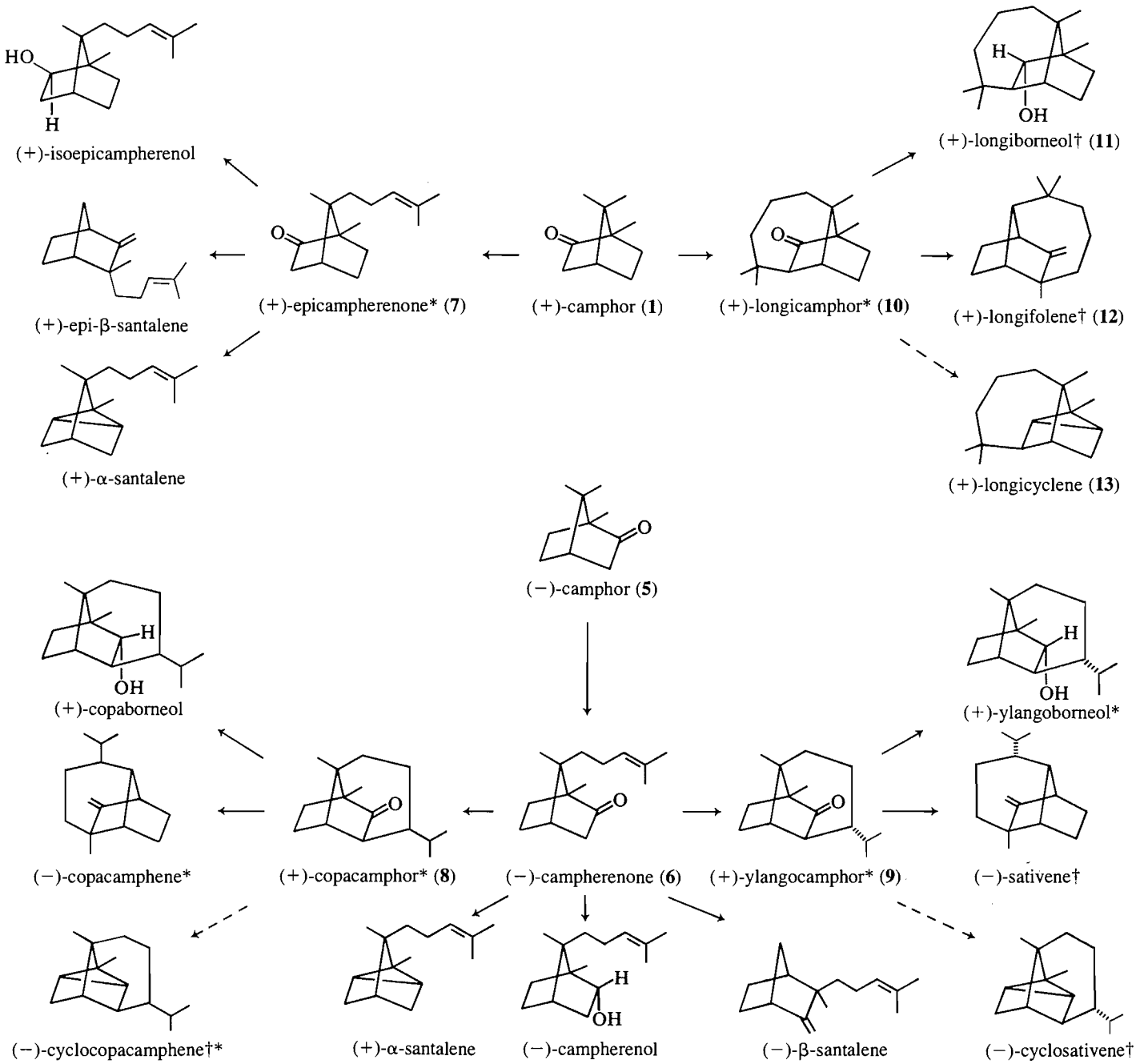

SCHEME 2

yield. The structure (**36***a*) of the major diastereomer produced in this intramolecular Mukaiyama reaction was subsequently confirmed by X-ray crystallographic analysis.[7]

At this stage in our investigations we considered the possibility of synthesizing isolongiborneol (**47**) from methoxy ketones **36***a*,*b* by a series of simple functional group transformations. For this purpose methoxyketones **36***a*,*b* were converted, in 91% yield, to the corresponding *exo*-alcohols **37***a*,*b* (Scheme 5) by reduction with lithium aluminum hydride. However, acetylation of **37***a*, *b* was only partially successful since the product was a mixture (~3:1) of (*R*)-methoxyalcohol **37***a* and (*S*)-methoxyacetate **38** (Scheme 5). The initial assignment of configuration to **37***a* was based on this acetylation experiment since a molecular model of **37***a* clearly indicates that the hydroxyl group in this compound is sterically hindered by the methoxyl group.

The difficulties encountered above prompted us to use an alternative approach, which involved initial reduction (Ca/NH_3) of methoxy ketones **36***a*,*b* to *endo*-alcohols **39***a*,*b* (Scheme 4). Subsequent acetylation, demethylation, and oxidation provided keto-acetates (**42**) in ~75% overall yield. Construction of the *gem*-dimethyl group was then accomplished by an efficient 3-step procedure (9) (methylenation, cyclopropanation, and hydrogenolysis) and, when this was coupled with reductive removal of the acetyl group, (+)-longiborneol (**11**) ($[\alpha]_D$ +15.8; *c* 0.54, $CHCl_3$) was obtained in ~70% overall yield. The capillary glc retention time and 400-MHz ^1H nmr spectrum of our synthetic material were identical with those of authentic longiborneol (11). In addition, the optical purity of synthetic

[7]S. J. Rettig and J. Trotter. Chemistry Department, University of British Columbia, Vancouver; unpublished results.

Can. J. Chem. Downloaded from www.nrcresearchpress.com by 112.217.228.212 on 09/07/12
For personal use only.

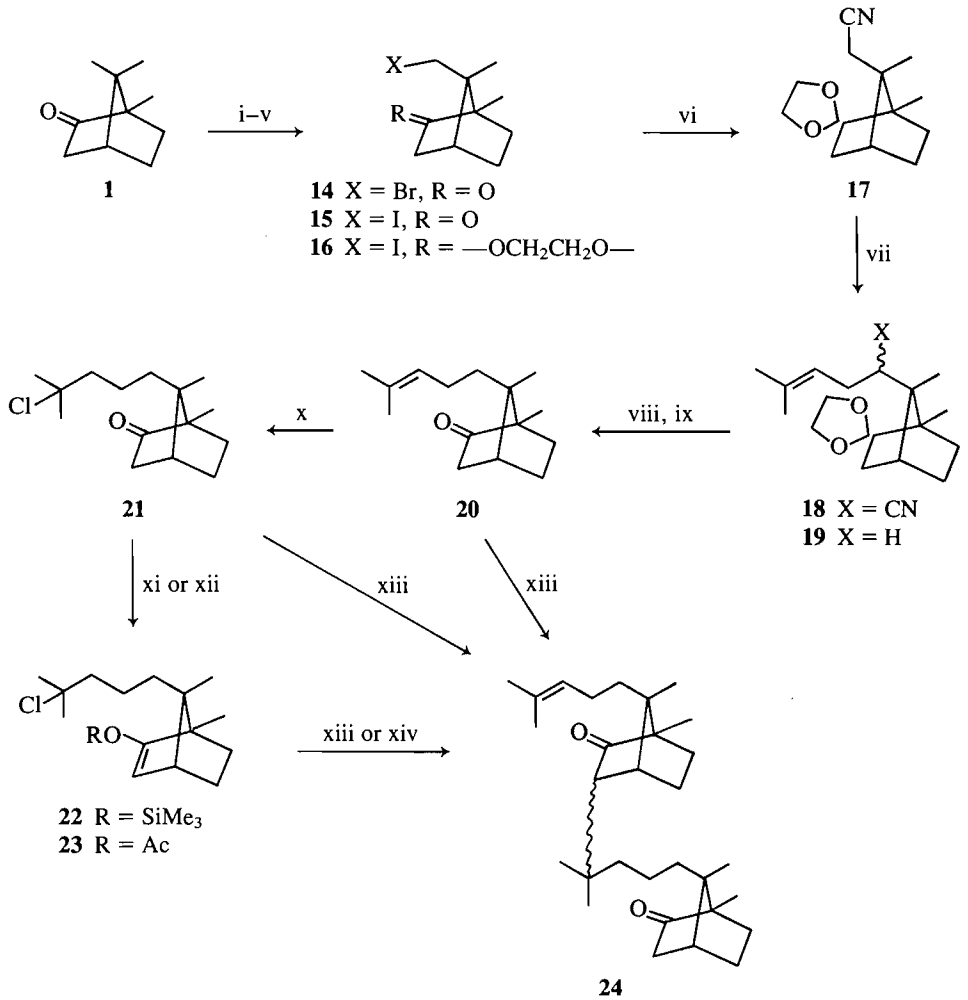

Reagents and conditions: i, Br_2, HBr, HOAc, 110°C; ii, Br_2, $ClSO_3H$; iii, Zn, HOAc, Et_2O, O°C; iv, KI, dimethyl sulphoxide (DMSO), 110°C, 40 h; v, Me_3SiCl, $HOCH_2CH_2OH$; vi, NaCN, DMSO, 70°C, 3 days; vii, LDA, THF, −78°C; $(CH_3)_2C{=}CHCH_2Br$; viii, K, HMPA, Et_2O, Bu'OH, 0°C; ix, HCl/acetone/H_2O; x, HCl(g), Et_2O; xi, LDA, THF/−78°C; Me_3SiCl; xii, BuLi, THF/25°C; Ac_2O/−50°C; xiii, $SnCl_4/CH_2Cl_2$; xiv, $TiCl_4$, CH_2Cl_2

SCHEME 3

(+)-longiborneol (**11**) was supported by the absence of diastereomeric signals in the ^1H nmr ^{19}F nmr, and ^{13}C nmr spectra of the corresponding MTPA ester (**46**) (12). Oxidation of (+)-longiborneol (**11**) with PCC in CH_2Cl_2 (13) gave (+)-longicamphor (**10**) (2), which was reduced with $LiAlH_4$ in THF to provide (+)-isolongiborneol (**45**). Subsequent treatment of (+)-isolongiborneol (**47**) with methanesulphonyl chloride in DMAP/pyridine at ~100°C resulted in Wagner–Meerwein rearrangement and formation of (+)-longifolene (**12**) (3*d*) ($[\alpha]_D$ +51.78; *c* 0.89, $CHCl_3$) in ~65% yield.

Experimental

Melting points (mp) were determined on a Kofler micro heating stage and are uncorrected. Infrared spectra were recorded on a Perkin–Elmer 137 spectrophotometer and optical rotations were made on a Perkin–Elmer 141 polarimeter. The ^1H nmr spectra were recorded on Bruker WH-400, Bruker WP-80, or Nicolet–Oxford H-270 instruments. Signal positions are given in delta (δ) with tetramethylsilane (TMS) as internal reference. The integrated areas and signal multiplicities are indicated in parentheses. Low resolution mass spectra were determined on a MAT CH-4 spectrometer and high resolution spectra were recorded on a Kratos MS-50 spectrometer. Gas–liquid chromatography was performed on a Hewlett–Packard model 5830A gas chromatograph with a 6 ft × 1/8 in. column (3% OV-17) or a Hewlett–Packard model 5830A gas chromatograph with a 12 m × 0.2 mm column (OV-1). Column chromatography was done using Merck silica gel 60 (230–400 mesh), and thin-layer chromatography (tlc) utilizing silica gel 1 B2-F (Baker-flex) sheets. Microanalyses were performed by Mr. P. Borda, Microanalytical Laboratory, University of British Columbia.

All reactions involving moisture sensitive reagents were performed under an atmosphere of dry argon using either oven or flame dried glassware. All reaction products were dried by allowing the solutions to stand over anhydrous magnesium sulphate. The solvents and reagents used were purified as follows: tetrahydrofuran was distilled from calcium hydride and then from lithium aluminum hydride (LAH). Diethyl ether was distilled from LAH and hexamethylphosphoramide (HMPA), benzene, methylene chloride, diisopropylamine, dimethyl sulphoxide (DMSO), and pyridine were distilled from calcium hydride. Methanol was obtained by distillation from magnesium methoxide. Petroleum ether (the hydrocarbon fraction of boiling range 30–60°C) was distilled prior to use.

(+)-3,3-Dibromocamphor

Bromine (292 mL, 5.7 mol) was added to (+)-camphor (**26**) (102 g, 0.67 mmol; Aldrich Chemical Co.) dissolved in glacial acetic acid (326

Can. J. Chem. Downloaded from www.nrcresearchpress.com by 112.217.228.212 on 09/07/12
For personal use only.

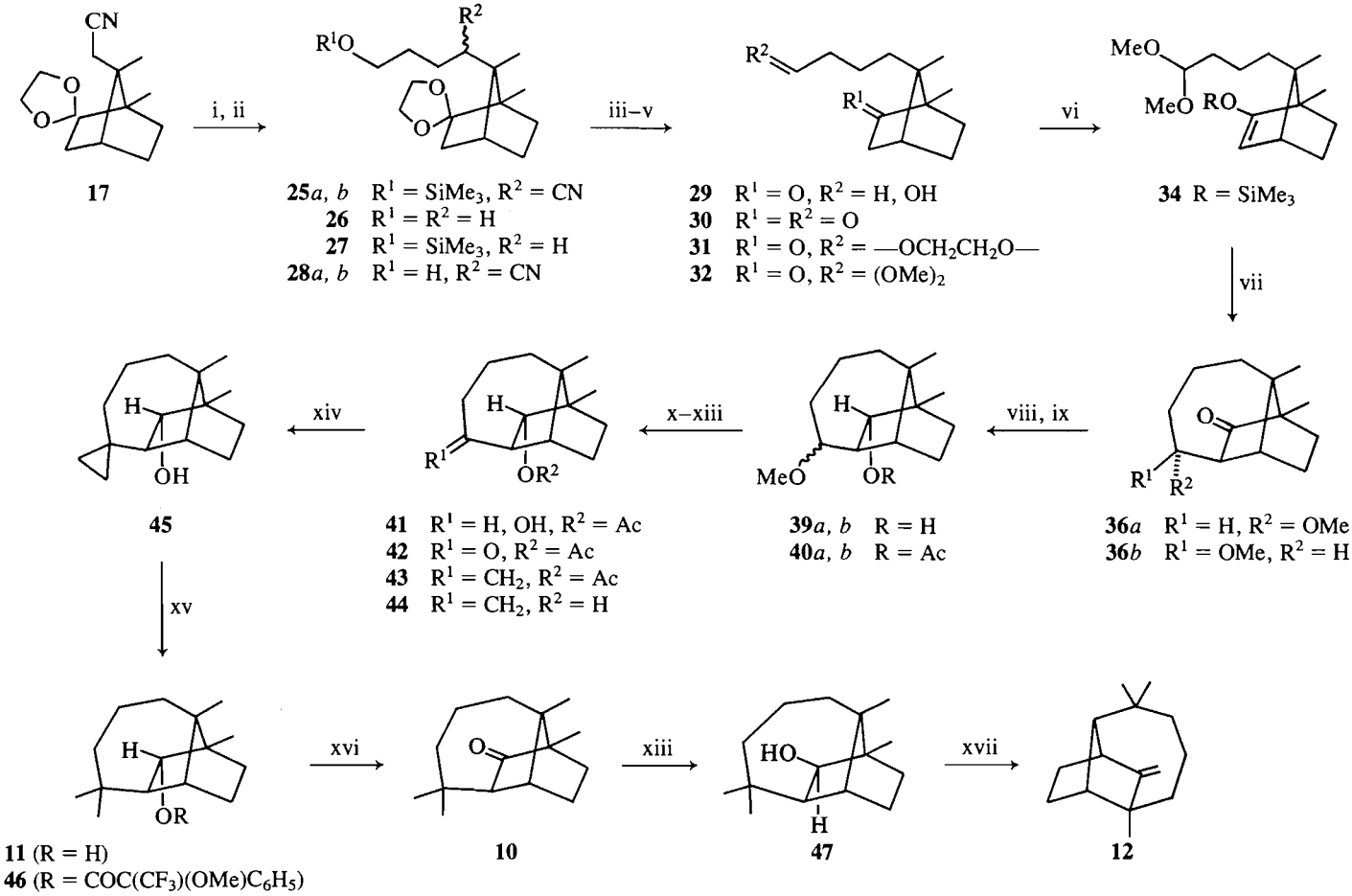

Reagents and conditions: i, lithium diisopropylamide (LDA), THF, −78°C; Bu^{t}Me$_2$SiOCH$_2$CH$_2$CH$_2$Br; ii, K, hexamethylphosphoramide (HMPA), Et$_2$O, Bu^{t}OH, 0°C; iii, HCl, Me$_2$CO; iv, PDC, CH$_2$Cl$_2$; v, HC(OMe)$_3$, CeCl$_3$, MeOH *or* *p*-TSA/C$_6$H$_6$/HOCH$_2$CH$_2$OH; vi, LDA, THF, −78°C; Me$_3$SiCl; vii, TiCl$_4$, CH$_2$CL$_2$, −78°C; viii, Ca/NH$_3$(l), Et$_2$O; ix, Ac$_2$O, DMAP, C$_5$H$_5$N; x, BBr$_3$, 15-crown-5, NaI, CH$_2$Cl$_2$; xi, PDC/CH$_2$Cl$_2$; xii, Ph$_3$MePBr, BuLi, −78 → 20°C; xiii, LiAlH$_4$, THF; xiv, Et$_2$Zn, CH$_2$I$_2$, PhMe; xv, H$_2$/Pt, HOAc, 2.5 atm; xvi, PCC, CH$_2$Cl$_2$; xvii, MeSO$_2$Cl, C$_5$H$_5$N, DMAP, 100°C, 16 h

SCHEME 4

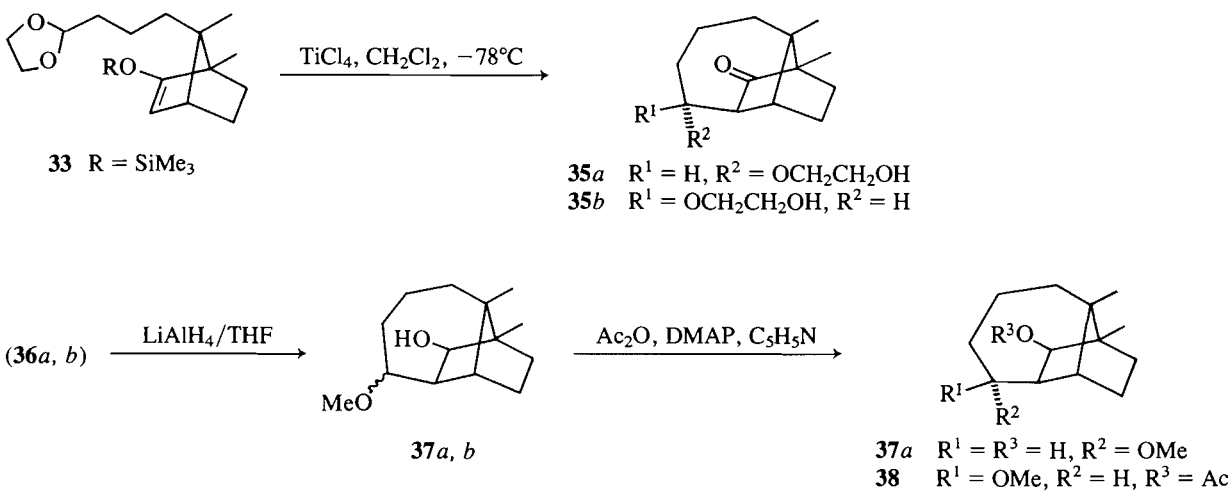

SCHEME 5

Can. J. Chem. Downloaded from www.nrcresearchpress.com by 112.217.228.212 on 09/07/12
For personal use only.

Can. J. Chem. Downloaded from www.nrcresearchpress.com by 112.217.228.212 on 09/07/12
For personal use only.

mL, 5.7 mol) and hydrogen bromide gas was bubbled through the reaction mixture for 1 h at 110°C. Stirring was continued at 110°C for 16 h in the dark and the reaction mixture was then poured into water and excess bromine destroyed with sodium bisulphite. The aqueous layer was extracted with ether and the combined organic extracts were washed with water, saturated sodium bicarbonate, saturated brine, and dried over $MgSO_4$. Removal of solvent gave a pale yellow oil, which solidified upon cooling in an ice bath. Crystallization from petroleum ether provided (+)-3,3-dibromocamphor (205 g, 99%); mp 60°C; $[\alpha]_D^{25}$ 37.1° (*c* 1.67, C_2H_5OH); ν_{max} (CCl_4): 2950, 1770 cm^{-1}; δ ($CDCl_3$, 80 MHz): 1.05 (s, 3H), 1.15 (s, 3H), 1.27 (s, 3H), 2.82 (d, 1H, J = 4 Hz, C_4H); *m/e* (relative intensity): 308/310/312(0.59/1.15/0.66, $M/M+2/M+4$), 284(1.43), 282(2.92), 280(1.09), 232(8.28), 230(7.97), 203(11.30), 201(11.73), 123(66.82), 107(44.10), 95(28.80), 91(32.45), 83(100.00). *Mol. Wt.* calcd. for $C_{10}H_{14}OBr_2$: 307.9411/309.9391/311.9370; found (high resolution mass spectrometry): 307.9418/309.9397/311.9375. *Anal.* calcd. for $C_{10}H_{14}OBr_2$: C 38.74, H 4.55; found: C 38.63, H 4.58.

*(+)-8-Bromocamphor (**14**) (4)*

A solution of (+)-3,3-dibromocamphor (19.7 g, 63.5 mmol) in bromine (3,3 mL, 63.5 mmol) was cooled in an ice-water bath while chlorosulphonic acid (25 mL, 372.7 mmol) was added dropwise. The ice bath was then removed and stirring was continued for 3.5 h before the reaction mixture was carefully poured into ice. Excess bromine was destroyed with sodium bisulphite and the aqueous solution was extracted with ether and worked up in the usual way to provide crude 3,3,8-tribromocamphor (24.2 g) as a viscous brown oil that was used in the next step without further purification.

Crude 3,3,8-tribromocamphor (300 g, 0.771 mol) was dissolved in glacial acetic acid (450 mL) and cooled by an ice-water bath. Zinc dust (75 g, 1.15 mol), was slowly added with *vigorous stirring*. The ice-water bath was then removed and stirring was continued for 4.5 h at room temperature. The reaction mixture was poured into ice-water containing sodium bicarbonate, and extracted with ether. The combined organic extract was washed with saturated sodium bicarbonate solution until neutral, then with water, and dried ($MgSO_4$). Removal of solvent gave a brown oil (190 g) that upon fractional distillation provided (+)-8-bromocamphor (**14**) (107 g, 60%) (4) as a colorless crystalline solid; bp 70–110°C (0.005 Torr; 1 Torr = 133.3 Pa). Sublimation followed by crystallization from petroleum ether (30–60°C) provided colorless crystals; mp 83–85°C; $[\alpha]_D^{25}$ +73.1° (*c* 1.17, C_2H_5OH); $[\alpha]_D^{25}$ +76.7° (*c* 1.24, $CHCl_3$); R_f 0.39 (petroleum ether:ether, 9:1); ν_{max} ($CHCl_3$): 2975, 1751 cm^{-1}; δ ($CDCl_3$, 400 MHz): 0.93 (s, 3H), 1.15 (s, 3H), 3.10, 3.17 (AB quartet, 2H, J_{AB} = 10 Hz); *m/e* (relative intensity): 230/232(3.57/2.79, $M/M+2$), 205(1.18), 188(1.93), 186(2.05), 175(1.07), 159(1.45), 151(5.36), 149(15.07), 109(28.36), 108(42.74), 107(46.55), 95(10.13). *Mol. Wt.* calcd. for $C_{10}H_{15}OBr$: 230.0306/232.0286; found: 230.0308/232.0290. *Anal.* calcd. for $C_{10}H_{15}OBr$: C 38.74, H 4.55; found: C 38.63, H 4.58.

(+)-8-Bromocamphor ethylene ketal

To a solution of (+)-8-bromocamphor (**14**) (9.8 g, 4.3 mmol) in dry ethylene glycol (140 mL, 354 mmol) under an argon atmosphere was added chlorotrimethylsilane (31 mL, 244 mmol) (18) and the reaction mixture stirred for 6 h at room temperature. Water (50 mL) was then added and work-up by extraction with ether gave a crude product that was purified by chromatography on silica gel (petroleum ether:ether, 15:1) to afford (+)-8-bromocamphor ethylene ketal (10.34 g, 88%) as a colorless oil; $[\alpha]_D^{25}$ +12.06° (*c* 1.02, $CHCl_3$); ν_{max} (film): 2981 cm^{-1}; δ ($CDCl_3$, 400 MHz): 0.82 (s, 3H), 1.06 (s, 3H), 3.70–4.00 (m, 4H, $ROCH_2CH_2OR$), 3.24, 4.22 (AB quartet, 2H, J_{AB} = 10 Hz); *m/e* (relative intensity): 275(1.59, M^+), 273(1.72), 197(1.27), 196(13.56), 195(100.00). *Mol. Wt.* calcd. for $C_{12}H_{19}O_2Br$: 275.0568; found: 275.0468. *Anal.* calcd. for $C_{12}H_{19}O_2Br$: C 52.38, H 6.96; found: C 52.60, H 6.93.

*(+)-8-Iodocamphor (**15**)*

Dry potassium iodide (31.2 g, 188 mmol) was added to a stirred solution of (+)-8-bromocamphor (**14**) (14.48 g, 63 mmol) in dry dimethyl sulphoxide (60 mL) and stirring continued at 110°C under an argon atmosphere for 40 h. The cooled reaction mixture was added to water (200 mL), extracted with ether, and worked up in the usual way to provide a crude product that was purified by column chromatography (silica gel, petroleum ether:ether, 15:1) to afford (+)-8-iodocamphor (**15**) (16.8 g, 95%) as a colorless oil; R_f 0.30 (pet. ether:ether, 9:1); $[\alpha]_D^{25}$ +72.14° (*c* 14.5, $CHCl_3$); ν_{max} (film): 2981, 1741 cm^{-1}; δ ($CDCl_3$, 270 MHz): 0.94 (s, 3H, CH_3), 1.12 (s, 3H, CH_3), 2.91, 3.00 (AB quartet, 2H, RCH_2I, J_{AB} = 10 Hz); *m/e* (relative intensity): 278(23.10, M^+), 277(1.90), 223(1.90), 182(3.3), 1.52(7.30), 151(50.00), 123(28.00), 109(69.40), 107(100.00). *Mol. Wt.* calcd. for $C_{10}H_{15}OI$: 278.0167; found: 278.0169. *Anal.* calcd. for $C_{10}H_{15}OI$: C 43.18, H 5.44, I 45.63; found: C 43.30, H 5.43, I 45.45.

*(+)-8-Iodocamphor ethylene ketal (**16**)*

Chlorotrimethylsilane (31 mL, 242 mmol) was added to a solution of (+)-8-iodocamphor (**15**) (16.8 g, 60.4 mmol) in dry ethylene glycol (80 mL) under an argon atmosphere and the reaction mixture stirred for 6 h at room temperature (18). Water (50 mL) was added and the mixture was extracted with ether and worked up in the usual way to provide, after column chromatography (silica gel, pet. ether:ether, 15:1), (+)-8-iodocamphor ethylene ketal (**16**) (18.2 g, 94%) as a colorless oil; R_f 0.63 (pet. ether:ether, 9:1); $[\alpha]_D^{25}$ +34.32° (*c* 0.7, $CHCl_3$); ν_{max} (film): 2973 cm^{-1}; δ ($CDCl_3$, 400 MHz): 0.82 (s, 3H, CH_3), 1.05 (s, 3H, CH_3), 3.04, 4.07 (AB quartet, 2H, ICH_2R, J_{AB} = 10 Hz), 3.74–3.98 (m, 4H, $ROCH_2CH_2OR$); *m/e* (relative intensity): 321(0.27, M^+-1), 304(0.22), 262(0.29), 221(0.59), 197(1.38), 196(13.41), 195(100.00). *Mol. Wt.* calcd. for $C_{12}H_{18}IO_2$ 321.0350; found: 321.0350. *Anal.* calcd. for $C_{12}H_{19}IO_2$: C 44.74, H 5.94; found: C 45.03, H 6.10.

*(+)-8-Cyanocamphor ethylene ketal (**17**) (7)*

(*a*) Dry sodium cyanide (9.0 g, 184 mmol) was added to a stirred solution of (+)-8-bromocamphor ethylene ketal (10.34 g, 37.6 mmol) in dry dimethyl sulphoxide (150 mL) and stirring continued at 60°C under an argon atmosphere for 7 days. After cooling, the reaction mixture was added to water (200 mL), extracted with ether, and worked up in the usual way. Column chromatography (silica gel, pet. ether: ether, 6:1) of the crude product gave (+)-8-cyanocamphor ethylene ketal (**17**) (4.5 g, 54%) as a colorless oil; R_f 0.48 (pet. ether:ether, 4:1); $[\alpha]_D^{25}$ +5.06° (*c* 2.35, C_2H_5OH); ν_{max} (film): 2950, 2250 cm^{-1}; δ ($CDCl_3$, 400 MHz): 0.85 (s, 3H, CH_3), 1.09 (s, 3H, CH_3), 2.30, 2.98 (AB quartet, 2H, $NCCH_2R$, J_{AB} = 16 Hz), 3.70–4.00 (m, 4H, $ROCH_2CH_2OR$); *m/e* (relative intensity): 221(1.07, M^+), 182(3.14), 181(24.80), 166(1.94), 140(1.30), 133(1.01), 127(1.76), 125(3.87), 113(11.7), 95(100.00). *Mol. Wt.* calcd. for $C_{13}H_{19}O_2N$: 221.1416; found: 221.1416. *Anal.* calcd. for $C_{13}H_{19}O_2N$: C 70.56, H 8.65, N 6.33; found: C 70.72, H 8.80, N 6.22.

(*b*) Dry sodium cyanide (1.46 g, 29.8 mmol) was added to a stirred solution of (+)-8-iodocamphor ethylene ketal (**16**) (2.4 g, 7.5 mmol) in dry dimethyl sulphoxide (35 mL) and stirring continued at 60°C under an argon atmosphere for 3 days. After cooling, the reaction mixture was poured onto water (50 mL), extracted with ether, and worked up in the usual way. Column chromatography (silica gel, pet. ether: ether, 6:1) of the crude product gave (+)-8-cyanocamphor ethylene ketal (**17**) (1.53 g, 92%) as a colorless oil.

*Cyanoketal (**18**)*

n-Butyllithium (1.6 M; hexane) (3.6 mL, 5.7 mmol) was added to a stirred solution of diisopropylamine (0.8 mL, 5.7 mmol) in dry tetrahydrofuran (8 mL) under an argon atmosphere at 0°C, and stirring was continued for 30 min. (+)-8-Cyanocamphor ethylene ketal (**17**) (1.0 g, 4.7 mmol) in dry tetrahydrofuran (23 mL) was added to this cooled solution at −78°C. Stirring was continued for 2 h before prenyl bromide (0.82 mL, 7.1 mmol) was introduced at −78°C. The reaction mixture was stirred for 10 h and worked up by adding water (10 mL) and extracting with ether. The combined organic layer was washed with saturated ammonium chloride solution, brine solution, and dried ($MgSO_4$). Removal of solvent followed by column chromatography (silica gel, pet. ether:ether, 10:1) provided a mixture of epimers of cyanoketal (**18**) (1.28 g, 95%) as a colorless oil; the ratio (6:1) of

Can. J. Chem. Downloaded from www.nrcresearchpress.com by 112.217.228.212 on 09/07/12
For personal use only.

epimers was determined from the proton integrations in the nmr spectrum; R_f 0.22 (pet. ether:ether, 9:1); ν_{max} (film): 2975, 2250 cm^{-1}; δ ($CDCl_3$ 400 MHz), ^1H nmr of the major diastereomer: 1.03 (s, 3H, CH_3), 1.1 (s, 3H, CH_3), 1.65 (s, 3H, CH_3), 1.75 (s, 3H, CH_3), 3.38 (dd, 1H, R^1R^2CHCN, J = 4 Hz, 12 Hz), 3.70–4.00 (m, 4H, ROC_2H_4OR), 5.24 (t, 1H, $(CH_3)_2C{:}CHR$, J = 8 Hz); *m/e* (relative intensity): 289(4.62, M^+), 181(17.79), 125(15.64), 107(1.10), 99(1.32), 96(7.46), 95(100.00). *Mol. Wt.* calcd. for $C_{18}H_{27}O_2N$: 289.2024; found: 289.2045. *Anal.* calcd. for $C_{18}H_{27}O_2H$: C 74.70, H 9.40, N 4.84; found: C 74.39, H 9.55, N 4.90.

(−)-Campherenone ethylene ketal (19)

To a solution of potassium (0.36 g, 92 mmol) in dry hexamethylphosphoramide (7 mL) (14) under an argon atmosphere at 25°C was added a solution of cyanoketal (**18**) epimers (1.33 g, 4.59 mmol) in anhydrous ether (7 mL), followed by *tert*-butanol (0.65 mL, 6.9 mmol). Stirring was continued for 12 h and the reaction mixture worked up by adding brine solution (10 mL) and extracting with ether. The combined organic extract was washed with brine solution and dried ($MgSO_4$). Removal of solvent gave a crude product that was purified by column chromatography (silica gel, pet. ether:ether, 10:1 to give (−)-campherenone ethylene ketal (**19**) (0.716 g, 78%) as a colorless oil; R_f 0.89 (pet. ether:ether, 9:1); $[\alpha]_D^{25}$ −14.48° (*c* 0.58, $CHCl_3$); ν_{max} (film): 2776, 1661 (weak) cm^{-1}; δ ($CDCl_3$, 400 MHz): 0.80 (s, 3H, CH_3), 0.88 (s, 3H, CH_3), 1.62 (s, 3H, CH_3), 1.69 (s, 3H, CH_3), 3.7–4.0 (m, 4H, ROC_2H_4OR). 5.15 (t, 1H, R, J = 8 Hz); *m/e* (relative intensity): 264(10.96, M^+), 221(2.67), 195(2.16), 187(2.74), 180(6.82), 165(4.44), 159(2.10), 155(2.29), 153(7.49), 149(2.00), 140(3.57), 135(6.66), 133(4.02), 125(100.00). *Mol. Wt.* calcd. for $C_{17}H_{28}O_2$: 264.2089; found: 264.2086. *Anal.* calcd. for $C_{17}H_{28}O_2$: C 77.22, H 10.67; found: C 77.50, H 10.70.

(+)-Campherenone (20)

(−)-Campherenone ethylene ketal (**19**) (0.52 g, 2.0 mmol) was dissolved in acetone (5 mL) and treated with hydrochloric acid solution (1 N, 3 mL) for 3 h at 25°C. Work-up in the usual way provided a crude product that was purified by column chromatography (silica gel, pet. ether:ether, 10:1) to provide (+)-campherenone (**20**) (0.42 g, 96%) as a colorless oil; R_f 0.50 (pet. ether:ether, 9:1); $[\alpha]_D^{25}$ +30.77° (*c* 2.78, $CHCl_3$) (lit. (1*a*) for (−)-campherenone, $[\alpha]_D^{23}$ −30.6° (*c* 10.7, $CHCl_3$)); ν_{max} (film): 2979, 1748 cm^{-1}, δ ($CDCl_3$, 400 MHz): 0.90 (s, 3H, CH_3), 0.98 (s, 3H, CH_3), 1.59 (s, 3H, CH_3), 1.67 (s, 3H, CH_3), 5.05 (t, 1H, $(CH_3)_2C{:}CHR$, J = 8 Hz); *m/e* (relative intensity): 220(19.06, M^+), 163(3.98), 137(6.83), 135(12.72), 121(12.77), 109(34.25), 95(29.54), 69(45.85). *Mol. Wt.* calcd. for $C_{15}H_{24}O$: 220.1827; found: 220.1827. *Anal.* calcd. for $C_{15}H_{24}O$: C 81.76, H 10.98; found: C 82.00, H 11.00.

(+)-Campherenone hydrochloride (21)

(+)-Campherenone (**20**) (0.29 g, 1.3 mmol) was dissolved in anhydrous ether (8 mL) and concentrated hydrochloric acid (3 mL, 13.0 mmol) was added slowly at 25°C. Stirring was continued for 8 h before water (10 mL) was added; the reaction mixture was extracted with ether and the combined organic layer washed with saturated sodium bicarbonate solution, water, and then dried ($MgSO_4$). Removal of solvent followed by chromatography of the crude product on silica gel (pet. ether:ether, 10:1) afforded (+)-campherenone hydrochloride (**21**) (0.32 g, 96%) as a colorless oil; R_f 0.38 (pet. ether:ether, 9:1); $[\alpha]_D^{25}$ +37.89° (*c* 0.47, $CHCl_3$); ν_{max} (film): 1741, 2964 cm^{-1}; δ ($CDCl_3$, 400 MHz): 0.9 (s, 3H, CH_3), 0.93 (s, 3H, CH_3), 1.55 (s, 6H, $R'RC{:}C(CH_3)_2$); *m/e* (relative intensity): 256(9.92, M^+), 221(10.05), 220(23.28), 177(8.38), 163(17.64), 151(10.79), 137(15.12), 135(19.63), 123(15.13), 111(39.54), 109(84.16), 108(26.88), 95(68.77), 81(100.00). *Mol. Wt.* calcd. for $C_{15}H_{25}OCl$: 256.1594; found: 256.1596. *Anal.* calcd. for $C_{15}H_{25}OCl$: C 70.15, H 9.81; found: C 69.90, H 10.09.

Campherenone hydrochloride enol trimethylsilylether (22)

Lithium diisopropylamide was generated by reacting *n*-butyllithium (1.6 M; hexane) (0.29 mL, 0.43 mmol) with diisopropylamine (0.06 mL, 0.43 mmol) in dry tetrahydrofuran (4 mL) at 0°C under an argon atmosphere for 30 min. A solution of (+)-campherenone hydrochloride (**21**) (91 mg, 0.36 mmol) in dry tetrahydrofuran (2 mL) was added to the reaction mixture at −78°C. After 2 h, freshly distilled chlorotrimethylsilane (0.067 mL, 0.53 mmol) was added and stirring was continued for 1 h at room temperature. The solvent was filtered through a column of Celite and evaporated to provide campherenone hydrochloride enol trimethylsilylether (**22**) (110 mg, 97%) as a colorless oil; ν_{max} (film): 2977, 1618 cm^{-1}; δ ($CDCl_3$, 80 MHz): 0.2 (s, 9H, $RSi(CH_3)_3$), 0.7 (s, 3H, CH_3), 0.85 (s, 3H, CH_3), 1.55 (s, 6H, $(CH_3)_2CClR$), 4.58 (d, 1H (TMSO)$RC{:}CHR'$, J = 4 Hz).

Campherenone hydrochloride enol acetate (23)

A solution of (+)-campherenone hydrochloride (**21**) (89 mg, 0.35 mmol) in dry tetrahydrofuran (5 mL) was treated at 25°C with *n*-butyllithium (1.6 M;hexane) (0.3 mL, 0.4 mmol) for 15 min. The enolate anion thus generated was cooled to −50°C and treated with dry acetic anhydride (0.06 mL, 0.6 mmol). After 15 min, the reaction mixture was warmed to 25°C and saturated sodium bicarbonate solution (5 mL) was added to quench excess acetic anhydride. The mixture was then extracted with pet. ether and the combined organic extracts washed with brine solution and dried ($MgSO_4$). After removal of solvent, the crude product was purified by column chromatography (silica gel, pet. ether:ether, 6:1) to provide campherenone hydrochloride enol acetate (**23**) (92 mg, 95%) as a colorless oil; R_f 0.65 (pet. ether:ether, 4:1); ν_{max} (film): 2980, 1760 cm^{-1}; δ ($CDCl_3$, 400 MHz): 0.78 (s, 3H, CH_3), 0.92 (s, 3H, CH_3), 1.56 (s, 3H, CH_3), 1.57 (s, 3H, CH_3), 2.15 (s, 3H, CH_3), 5.53 (d, 1H, (AcO)RC: CHR', J = 4 Hz); *m/e* (relative intensity): 298(3.20, M^+), 258(18.24), 256(54.65), 220(72.17), 192(16.48), 179(55.87), 177(21.46), 161(20.67), 149(16.13), 137(77.71), 135(75.24), 123(25.51), 110(100.00). *Mol Wt.* calcd. for $C_{17}H_{27}O_2Cl$: 298.1699; found: 298.1700.

Attempted cyclization of campherenone derivatives[8] *(5)*

(*a*) To a cooled (0°C), well-stirred solution of (+)-campherenone (**20**) (25 mg, 0.11 mmol) in dry methylene chloride (2 mL) under an argon atmosphere was added dropwise stannic chloride (0.003 mL, 0.02 mmol). After 24 h the reaction mixture was diluted with water (10 mL) and extracted with ether. The combined organic extract was washed with saturated sodium bicarbonate solution, water, and dried ($MgSO_4$). After removal of solvent, the crude product was purified by column chromatography (silica gel, pet. ether:ether, 5:1) to give campherenone dimer (**24**) (13 mg) as a colorless oil; R_f 0.1 (pet. ether:ether, 9:1); ν_{max} (film): 2986, 1736 cm^{-1}; δ ($CDCl_3$, 400 MHz), ^1H nmr of the major diastereomer: 0.81 (s, 6H, $(CH_3)_2$), 0.90 (s, 6H, $(CH_3)_2$), 0.93, 0.98 (s, s, 6H, $(CH_3)_2$), 162 (s, 3H, CH_3), 1.86 (s, 3H, CH_3), 5.00 (t, 1H, $(CH_3)_2C{:}CHR$, J = 8 Hz); *m/e* (relative intensity): 440(8.45, M^+), 277(5.94), 262(3.45), 233(3.16), 222(13.29), 220(16.75), 177(8.11), 149(11.70), 138(10.59), 135(13.10), 121(12.92), 109(41.22), 95(50.84). *Mol. Wt.* calcd. for $C_{30}H_{48}O_2$: 440.3654; found: 440.3650.

(*b*) Titanium tetrachloride (0.055mL, 0.50 mmol) was added dropwise to a cooled (−78°C), well-stirred solution of campherenone hydrochloride trimethylsilyl enol ether (**22**) (140 mg, 0.42 mmol) in dry methylene chloride (26 mL) under an argon atmosphere. After 12 h, the reaction mixture was diluted with water (10 mL) and extracted with ether. The combined organic extract was washed with saturated sodium bicarbonate solution, water, and dried ($MgSO_4$). After removal of solvent, the crude product was purified by column chromatography (silica gel, pet. ether:ether, 5:1) to give a mixture of epimers of campherenone dimer (**24**) (47 mg) and (+)-campherenone hydrochloride (**21**) (49 mg).

(*c*) To a cooled (0°C), well-stirred solution of dry stannic chloride (6.4 μL, 5.4×10^{-2} mmol) in dry methylene chloride (6 mL) was added dropwise a solution of (+)-campherenone hydrochloride (**21**) (68 mg, 0.27 mmol) in methylene chloride (8 mL), under an argon atmosphere. After 2 days, the reaction mixture was diluted with water (10 mL) and extracted with ether. The combined organic extract was

[8]We are grateful to Dr. Susan Piper for preliminary investigations in this area.

Can. J. Chem. Downloaded from www.nrcresearchpress.com by 112.217.228.212 on 09/07/12
For personal use only.

washed with saturated sodium bicarbonate solution, water, and dried ($MgSO_4$). After removal of solvent, the crude product was purified by column chromatography (silica gel, pet. ether:ether, 5:1) to give a mixture (3.5:1 by nmr) of epimers of campherenone dimer (**24**) (57 mg) as a colorless oil.

(*d*) To a cooled (0°C), well-stirred solution of campherenone hydrochloride enol acetate (**23**) (76 mg, 0.27 mmol) in dry methylene chloride (5 mL) under an argon atmosphere was added stannic chloride (6.4 μL, 5.4×10^{-2} mmol). After 16 h, the reaction mixture was diluted with water (10 mL) and extracted with ether. The combined organic extract was washed with saturated sodium bicarbonate solution, water, and dried ($MgSO_4$). After removal of solvent, the crude product was purified by column chromatography (silica gel; pet. ether:ether, 5:1) to give campherenone dimer (**24**) (20 mg) as a colorless oil.

tert-*Butyldimethylsilyltrifluoromethanesulfonate (TBDMS-triflate)*

Triflic acid (20.5 mL, 232 mmol) was added dropwise to freshly sublimed *tert*-butyldimethylsilyl chloride (35.0 g, 232 mmol) at room temperature and the resulting mixture heated at 60°C for 16 h. The product was then distilled from the reaction flask to afford TBDMS-triflate (56.0 g, 91%) as a colorless liquid (bp 65–67°C; 12 Torr).

3-Bromo-1-tert-*butyldimethylsilyloxypropane*

Freshly distilled TBDMS-triflate (13 g, 49 mmol) was added dropwise to a solution of 3-bromo-1-propanol (6.8 g, 49 mmol) and 2,6-lutidine (5.3 g, 49 mmol) in dry methylene chloride (35 mL) at 0°C under an argon atmosphere and stirring was continued for 4 h. The reaction mixture was added to water (50 mL) and extracted with methylene chloride. The combined organic extract was washed with hydrochloric acid (1 N), saturated ammonium chloride solution, water, and dried ($MgSO_4$). Upon removal of solvent under vacuum, the crude product was subjected to column chromatography (silica gel, pet. ether:ether, 9:1) to afford the 3-bromo-*tert*-butyldimethylsilyloxypropane (10 g, 85%) as a colorless oil; R_f 0.95 (pet. ether:ether, 9:1); ν_{max} (film): 2940 cm^{-1}; δ ($CDCl_3$, 270 MHz): 0.08 (s, 6H, $RSi(CH_3)_2$), 0.91 (s, 9H, $(CH_3)_3C$-SiR), 1.96–2.08 (m, 2H, $ROCH_2CH_2CH_2Br$), 3.5 (t, 2H, RCH_2OSi, J = 6 Hz), 3.72 (t, 2H, RCH_2Br, J = 6 Hz); *m/e* (relative intensity): 253/255(7.04/6.69, $M/M+2$), 213(1.38), 207(1.04), 205(1.02), 197(52.07), 195(53.40), 169(63.49), 167(66.12), 139(90.35), 137(89.69), 115(100.00).

*Ketal-nitrile (25*a,b*)*

n-Butyllithium (1.6 M; hexane) (31 mL, 31 mmol) was added to a stirred solution of diisopropylamine (4.4 mL, 31 mmol) in dry tetrahydrofuran (50 mL) under an argon atmosphere at 0°C and stirring was continued for 30 min. (+)-8-Cyanocamphor ethylene ketal (**17**) (5.7 g, 26 mmol) in dry tetrahydrofuran (20 mL) was added to this cooled solution at −78°C and stirring was continued for 2 h before a solution of 3-bromo-*tert*-butyldimethylsilyloxypropane (9.3 g, 39 mmol) in tetrahydrofuran (20 mL) was introduced at −78°C. The reaction mixture was stirred for 10 h and worked up by adding water (10 mL) and extracting with ether. The combined organic extract was washed with saturated ammonium chloride solution, brine solution, and dried ($MgSO_4$). After removal of solvent and column chromatography (silica gel, pet. ether:ether, 5:1) a mixture of (*R*)-ketal-nitrile (**25***a*)[9] and its epimer (**25***b*) (9.5 g, 94%) was obtained as a colorless oil. The ratio (6:1) of epimers (**25***a*:**25***b*) was determined by proton integrations in nmr; R_f 0.85 (pet. ether:ether, 1:1); ν_{max} (film): 2980, 2257 cm^{-1}; δ ($CDCl_3$, 400 MHz) (**25***a*): 0.55 (s, 6H, $RSi(CH_3)_2$), 0.89 (s, 9H, $(CH_3)_3CSiR$), 1.25 (s, 3H, CH_3), 1.75 (s, 3H, CH_3), 3.48 (m, 1H, R^1CHCNR^2), 3.58–3.98 (m, 6H, $ROCH_2CH_2OR$, and RCH_2OSi); *m/e* (relative intensity): 393(0.41, M^+), 378(1.14), 338(1.64), 336(26.30), 293(2.10), 292(9.14), 274(2.63), 265(1.35), 255(1.09), 181(39.71), 113(15.15), 95(100.00). *Mol. Wt.* calcd. for $C_{22}H_{39}O_3SiN$: 393.2699; found: 393.2707. *Anal.* calcd. for $C_{22}H_{39}O_3SiN$: C 67.13, H 10.00, N 3.56; found: C 67.10, H 10.12, N 3.78.

(−)-Hydroxy-ketal (26)

Potassium (0.14 g, 3.6 mmol) was added to dry hexamethylphosphoramide (6 mL) (14) under an argon atmosphere at 25°C and to the dark blue solution was added a solution of nitrile (**25***a*, *b*) (0.71 g, 1.8 mmol) in anhydrous ether (5 mL) and *tert*-butanol (0.25 mL, 2.7 mmol). Stirring was continued for 10 h and the reaction was worked up in the usual way after extraction with ether. The crude product was purified by column chromatography (silica gel, pet. ether:ether, 5:1) to afford (−)-hydroxy-ketal (**26**) (0.36 g, 83%) as a colorless oil; R_f 0.32 (pet. ether:ether, 1:1); $[\alpha]_D^{25}$ −14.67° (*c* 0.45, $CHCl_3$); ν_{max} (film); 2964, 3407 cm^{-1}; δ ($CDCl_3$, 400 MHz): 0.80 (s, 3H, CH_3), 0.85 (s, 3H, CH_3), 3.70–4.00 (m, 4H, $ROCH_2CH_2OR$), 3.66 (t, 2H, RCH_2OH, J = 6 Hz); *m/e* (relative intensity): 254(6.48 M^+), 224(1.79), 223(1.73), 199(2.26), 195(1.19), 181(11.72), 143(36.53), 135(13.37), 125(99.91), 99(40.70), 95(100.00). *Mol. Wt.* calcd. for $C_{15}H_{26}O_3$: 254.1882; found: 254.1879. *Anal.* calcd. for $C_{15}H_{26}O_3$: C 70.83, H 10.30; found: C 70.56, H 10.41.

A later fraction provided silyloxy-ketal (**27**) (11 mg) as a colorless oil; R_f 0.81 (pet. ether:ether, 1:1; $[\alpha]_D^{25}$ −6.88° (*c* 0.77, $CHCl_3$); ν_{max} (film): 2986 cm^{-1}; δ ($CDCl_3$, 400 MHz): 0.60 (s, 6H, $RSi(CH_3)_2$), 0.79 (s, 3H, CH_3), 0.84 (s, 3H, CH_3), 0.91 (s, 9H, $RSiC(CH_3)_3$), 3.62 (t, 2H, RCH_2OSi, J = 6 Hz), 3.71–3.96 (m, 4H, $ROCH_2CH_2OR$); *m/e* (relative intensity): 368(4.43, M^+), 353(2.31), 311(20.75), 268(11.83), 267(54.66), 257(24.87), 193(53.78), 181(14.99), 175(29.49), 125(74.92), 119(33.90), 95(100.00). *Mol. Wt.* calcd. for $C_{21}H_{40}O_3Si$: 368.2746; found: 368.2737. *Anal.* calcd. for $C_{21}H_{40}O_3Si$: C 68.42, H 10.94; found: C 68.71, H 10.88.

A final fraction provided a mixture of epimers of hydroxyketal-nitrile (**28***a*, *b*) (89 mg) as a colorless oil; R_f 0.26 (pet. ether:ether, 2:3); ν_{max} (film): 3420, 2970, 2248 cm^{-1}; δ ($CDCl_3$, 400 MHz): 1.03 (s, 3H, CH_3), 1.08 (s, 3H, CH_3), 3.46 (dd, 1H, R^1R^2CHCN, J = 10 Hz, 4 Hz), 3.70–4.00 (m, 6H, $ROCH_2CH_2OR$, and RCH_2OH); *m/e* (relative intensity): 279(0.48, M^+), 239(0.79), 182(4.47), 181(35.86), 144(2.02), 113(11.66), 95(100.00). *Mol. Wt.* calcd. for $C_{16}H_{25}O_3N$: 279.1834; found: 279.1819. *Anal.* calcd. for $C_{16}H_{25}O_3N$: C 68.79, H 9.02, N 5.01; found: C 68.70, H 9.00, N 4.90.

A further quantity of hydroxy-ketal (**26**) was obtained when tetra-*n*-butyl ammonium fluoride (100 mL, 1 M solution in tetrahydrofuran) was added to (−)-silyloxy-ketal (**27**) (10.5 g, 28.5 mmol) at 25°C under an argon atmosphere. Stirring was continued for 6 h before water (50 mL) was added. The reaction mixture was extracted with ether and the combined organic layer was washed with saturated sodium bicarbonate solution, brine solution, water, and dried ($MgSO_4$). Upon removal of solvent under vacuum, the crude product was purified by column chromatography (silica gel, pet. ether:ether, 5:1) to give the (−)-hydroxyketal (**26**) (7.0 g, 97%) as a colorless oil.

(+)-Hydroxyketone (29)

Hydroxyketal (**26**) (1.0 g, 3.9 mmol) was dissolved in acetone (20 mL), hydrochloric acid (1 N, 12 mL) was added dropwise, and the reaction mixture stirred at 25°C for 2 h. The reaction mixture was added to water (20 mL) and, following extraction with ether, was worked up in the usual way. The crude product was purified by column chromatography (silica gel, pet. ether:ether, 10:1) to afford (+)-hydroxyketone (**29**) (0.81 g, 99%) as a colorless oil; R_f 0.30 (pet. ether:ether, 7:2); $[\alpha]_D^{25}$ +41.88° (*c* 0.16, $CHCl_3$); ν_{max} (film): 3340, 2980, 1745 cm^{-1}; δ ($CDCl_3$, 400 MHz): 0.91 (s, 3H, CH_3), 0.97 (s, 3H, CH_3), 3.64 (t, 2H, RCH_2OH, J = 6 Hz); *m/e* (relative intensity): 210(22.98 M^+), 192(1.59), 177(1.63), 168(1.31), 167(2.08), 153(3.85), 151(9.99), 149(5.32), 138(18.55), 137(25.14), 135(17.70), 111(14.27), 110(15.16), 109(100.00). *Mol. Wt.* calcd. for $C_{13}H_{22}O_2$: 210.1620; found: 210.1615. *Anal.* calcd. for $C_{13}H_{22}O_2$: C 74.24, H 10.54; found: C 73.96, H 10.80.

[9]The (*R*)-stereoselectivity of this reaction was determined by X-ray crystallographic analysis[7] of the *p*-bromobenzoate derivative of hydroxyketalnitrile (**28***a*) derived from the major epimer (**25***a*). Stereoselective reactions at the C(8) or C(9) neopentyl position in camphor derivatives (15; also S. E. Piper, unpublished observations) and norcamphor derivatives (16) have been observed previously.

Can. J. Chem. Downloaded from www.nrcresearchpress.com by 112.217.228.212 on 09/07/12
For personal use only.

*(+)-Ketoaldehyde (**30**)*

A solution of (+)-hydroxyketone (**29**) (0.76 g, 3.6 mmol) and pyridinium dichromate (17) (2.7 g, 7.2 mmol) in dry methylene chloride (25 mL) was stirred at 25°C under an argon atmosphere for 10 h. The reaction mixture was then diluted with ether and filtered through a pad of silica gel. Removal of solvent gave a crude product that was purified by column chromatography (silica gel, pet. ether:ether, 4:1) to afford (+)-ketoaldehyde (**30**) (0.72 g, 96%) as a colorless oil; R_f 0.49 (pet. ether:ether, 2:7); $[\alpha]_D^{25}$ +27.46° (*c* 1.18, $CHCl_3$); ν_{max} (film): 2735 cm^{-1}; δ ($CDCl_3$; 400 MHz): 0.91 (s, 3H, CH_3), 0.98 (s, 3H, CH_3), 9.76 (t, 1H, RC*H*O, *J* = 1.5 Hz); *m/e* (relative intensity): 208(14.19, M^+), 180(6.03), 175(9.95), 162(6.56), 147(14.42), 137(24.96), 136(14.72), 135(24.90), 133(21.93), 109(57.16), 95(80.99), 81(100.00). *Mol. Wt.* calcd. for $C_{13}H_{20}O_2$: 208.1463; found: 208.1467. *Anal.* calcd. for $C_{13}H_{20}O_2$: C 74.96, H 9.68; found: C 74.89, H 9.73.

*Keto-acetal (**31**)*

A solution of (+)-keto-aldehyde (**30**) (38 mg, 0.18 mmol), ethylene glycol (0.013 mL, 0.23 mmol), and *p*-toluenesulfonic acid (catalytic amount) in benzene (5 mL) was refluxed in a Dean–Stark apparatus for 1.25 h. Water (20 mL) was added and the reaction mixture was extracted with ether and worked up in the usual way. Removal of solvent gave a crude product that was purified by column chromatography (silica gel, pet. ether:ether, 5:1) to provide keto-acetal (**31**) (40 mg, 89%) as a colorless oil; R_f 0.41 (pet. ether:ether, 1:1); ν_{max} (film): 1740, 2979 cm^{-1}; δ ($CDCl_3$, 400 MHz): 0.91 (s, 3H, CH_3), 0.97 (s, 3H, CH_3), 3.80–4.00 (m, 4H, ROCH_2CH_2OR), 4.84 (t, 1H, RC*H*(OR^1)$_2$, *J* = 4.5 Hz); *m/e* (relative intensity): 252(4.52, M^+), 238(1.24), 191(2.90), 190(6.89), 176(2.09), 175(7.39), 167(1.45), 164(1.18), 148(6.24), 99 (22.90), 95(15.37), 73(100.00). *Mol. Wt.* calcd. for $C_{15}H_{24}O_3$: 252.1725; found: 252.1722. *Anal.* calcd. for $C_{15}H_{24}O_3$: C 71.39, H 9.59; found: C 71.12, H 9.55.

*Trimethylsilyl enol ether (**33**)*

Lithium diisopropylamide was generated by reacting *n*-butyllithium (1.6 M; hexane) (1.35 mL, 2.03 mmol) with diisopropylamine (0.28 mL, 2.0 mmol) in dry tetrahydrofuran (5 mL) at 0°C under an argon atmosphere for 30 min. A solution of keto-acetal (**31**) (0.42 g, 1.7 mmol) in dry tetrahydrofuran (5 mL) was then added to this cooled reaction mixture at −78°C and, after 2 h, dry chlorotrimethylsilane (0.37 mL, 2.6 mmol) was introduced. Stirring was continued for 1 h while the temperature reached 25°C. The solvent was removed and a solution of the residue in ether was filtered through a pad of Celite and sand. Removal of ether provided trimethylsilyl enol ether (**33**) (0.54 g, 98%) as a colorless oil; ν_{max} (film): 2951, 1616 cm^{-1}; δ ($CDCl_3$, 80 MHz): 0.13 (s, 9H, RSi(CH_3)$_3$), 0.67 (s, 3H, CH_3), 0.81 (s, 3H, CH_3), 3.50–4.00 (m, 4H, ROCH_2CH_2OR), 4.54 (d, 1H, R^1C*H*:C(OR^2)R^3, *J* = 4 Hz), 4.79 (t, 1H, RC*H*(OR)$_2$, *J* = 4.5 Hz); *m/e* (relative intensity): 324(4.57, M^+), 281(1.22), 253(3.11), 252(5.29), 251(16.01), 209(8.96), 183(15.62), 99(9.51), 95(7.19), 73(100.00). *Anal.* calcd. for $C_{18}H_{32}O_3Si$: C 66.62, H 9.94; found: C 66.68, H 9.88.

*Hydroxyethoxy-ketones (**35**a,b)*

To a solution of trimethylsilyl enol ether (**33**) (0.13 g, 0.41 mmol) in dry methylene chloride (25 mL) under an argon atmosphere was added titanium tetrachloride (0.050 mL, 0.48 mmol) at −78°C and stirring continued for 20 min. Saturated sodium bicarbonate solution (10 mL) was added at −78°C and, after warming, the reaction mixture was extracted with ether, and the combined organic layer was washed with saturated sodium bicarbonate solution, brine solution, water, and dried ($MgSO_4$). Removal of solvent gave a crude product that was purified by column chromatography (silica gel, pet. ether:ether, 4:1) to afford a mixture of epimers of hydroxyethoxy-ketones (**35***a,b*) (78 mg, 78%) as a colorless oil. The ratio (1.2:1) of epimers (**35***a*:**35***b*) was determined from proton integration in the nmr spectrum.

35*a*: R_f 0.22 (pet. ether:ether, 3:7), ν_{max} (film): 3457, 1734, 2950 cm^{-1}; δ ($CDCl_3$, 270 MHz): 0.92 (s, 3H, CH_3), 0.97 (s, 3H, CH_3), 2.48 (d, 1H, α*H*, *J* = 6 Hz), 3.60–3.70 (m, 4H, ROCH_2CH_2OR), 3.70–3.80 (m, 1H, R^2C*H*OR); *m/e* (relative intensity): 252(2.83, M^+), 234(1.16), 222(3.18), 209(2.27), 207(3.44), 192(3.38), 191(6.92), 190(9.91), 179(1.99), 177(1.36), 175(6.70), 173(6.07), 164(3.60), 163(18.33), 147(59.08), 137(10.70), 135(29.86), 134(26.63), 132(23.22), 107(22.40), 95(27.14). *Mol. Wt.* calcd. for $C_{15}H_{24}O_3$: 252.1725; found: 252.1725.

35*b*: R_f 0.28 (pet. ether:ether, 3:7); ν_{max} (film): 3457, 2950, 1734, cm^{-1}; δ ($CDCl_3$, 270 MHz); 0.92 (s, 3H, CH_3), 2.30–2.40 (m, 2H, C-3H, C-4H). 3.50–3.75 (m, 4H, ROCH_2CH_2OR), 3.76–3.86 (m, 1H, R^2C*H*OR); *m/e* (relative intensity): 252(35.14, M^+), 234(3.92), 224(1.18), 222(6.04), 209(4.46), 208(5.97), 107(31.69), 191(22.41), 190(70.93), 175(40.28), 163(47.37), 162(41.74), 161(19.93), 149(13.83), 148(27.41), 147(100.00). *Mol. Wt.* calcd. for $C_{15}H_{24}O_3$: 252.1725; found: 252.1721.

*(+)-Dimethoxyketone (**32**)*

(+)-Ketoaldehyde (**30**) (0.64 g, 3.1 mmol) was treated with a methanolic solution of cerium trichloride heptahydrate (0.4 M, 6.7 mL) and trimethyl orthoformate (2.3 mL, 21 mmol) (19). Stirring was continued at 25°C for 2 h before sodium bicarbonate solution (5%, 20 mL) was added and the reaction mixture extracted with ether and worked up as usual. The crude product was purified by column chromatography (silica gel, pet. ether:ether, 1:1) to give (+)-dimethoxyketone (**32**) (0.63 g, 83%) as a colorless oil; R_f 0.72 (pet. ether:ether, 2:7); $[\alpha]_D^{25}$ +32.14° (*c* 0.98, $CHCl_3$); ν_{max} (film): 2960, 1742, 1121 cm^{-1}; δ ($CDCl_3$, 270 MHz): 0.90 (s, 3H, CH_3), 0.95 (s, 3H, CH_3), 3.30 (s, 6H, RCH(OCH_3)$_2$), 4.33 (t, 1H, RC*H*(OCH_3)$_2$, *J* = 4 Hz); *m/e* (relative intensity): 254(0.98, M^+), 224(2.28), 223(13.72), 222(19.48), 207(3.88), 191(15.27), 190(22.66), 175(14.94), 162(10.42), 149(11.38), 148(16.51), 147(18.45), 75(100.00). *Mol. Wt.* calcd. for $C_{15}H_{26}O_3$: 254.188; found: 254.188. *Anal.* calcd. for $C_{15}H_{26}O_3$: C 70.83, H 10.30; found: C 71.12, H 10.26.

*(+)-Trimethylsilyl enol ether (**34**)*

Lithium diisopropylamide was generated by adding *n*-butyllithium (1.6 M; hexane) (2.4 mL, 3.6 mmol) to diisopropylamine (0.50 mL, 3.6 mmol) in dry tetrahydrofuran (10 mL) at 0°C under an argon atmosphere for 30 min. A solution of (+)-dimethoxyketone (**32**) (0.74 g, 2.9 mmol) in dry tetrahydrofuran (10 mL) was then introduced to this cooled reaction mixture at −78°C. After 2 h, freshly distilled chlorotrimethylsilane (0.56 mL, 4.4 mmol) was added and stirring was continued for 1 h while the temperature warmed slowly to 25°C. The solvent was removed and a pentane solution of the crude product was filtered through a column of Celite and sand. Removal of solvent provided (+)-trimethylsilyl enol ether (**34**) (0.96 g, 100%) as a colorless oil; $[\alpha]_D^{25}$ +1.64° (*c* 0.61, $CHCl_3$); ν_{max} (film): 1620, 2975 cm^{-1}; δ ($CDCl_3$, 270 MHz): 0.18 (s, 9H, RSi(CH_3)$_3$), 0.69 (s, 3H, CH_3), 0.84 (s, 3H, CH_3), 3.28 (d, 6H, RHC(OCH_3)$_2$, *J* = 2.0 Hz), 4.31 (t, 1H, RC*H*(OCH_3)$_2$, *J* = 4 Hz), 4.51 (d, 1H, R^3CH:CR^1R^2, *J* = 3.5 Hz); *m/e* (relative intensity): 326(1.35, M^+), 312(1.57), 311(6.78), 296(2.18), 295(7.68), 294(15.95), 251(8.93), 209(18.98), 208(17.12), 182(28.59), 75(100.00). *Mol. Wt.* calcd. for $C_{18}H_{34}O_3Si$: 326.2277; found: 326.2271. *Anal.* calcd. for $C_{18}H_{34}O_3Si$: C 66.21, H 10.50; found: C 66.32, H 10.63.

(R)- *and* (S)-*methoxyketones (**36**a, b)*

To a solution of (+)-trimethylsilyl enol ether (**34**) (0.58 g, 1.8 mmol) in dry methylene chloride (40 mL) under an argon atmosphere was added titanium tetrachloride (0.23 mL, 2.1 mmol) at −78°C for 45 min. Saturated sodium bicarbonate solution (10 mL) was added at −78°C and the reaction mixture extracted with ether and worked up as usual. The crude product was purified by column chromatography (silica gel, pet. ether:ether, 1:1) to provide (*S*)-methoxyketone (**36***b*) (83 mg, 21%) as a colorless oil, followed by (*R*)-methoxyketone (**36***a*) (260 mg, 66%) as a white solid. Crystallization from petane provided **36***a* as colorless prisms; mp 40°C; R_f 0.64 (pet. ether:ether, 2:7); $[\alpha]_D^{25}$ +91.47° (*c* 0.34, $CHCl_3$); ν_{max} ($CHCl_3$): 2951, 1741, 1100 cm^{-1}; δ ($CDCl_3$, 400 MHz): 0.91 (s, 3H, CH_3), 0.97 (s, 3H, CH_3), 2.45 (d, 1H, αH, *J* = 6 Hz), 3.42 (s, 3H, $ROCH_3$), 3.65 (dd, 1H,

Can. J. Chem. Downloaded from www.nrcresearchpress.com by 112.217.228.212 on 09/07/12
For personal use only.

R^2CHOMe, J = 6 Hz, 4 Hz); m/e (relative intensity): 222(17.97, M^+), 207(3.55), 193(4.92), 192(26.43), 191(3.36), 190(15.42), 179(5.00), 177(10.90), 175(18.41), 163(32.46), 162(20.50), 148(20.06), 147(59.54), 135(18.88), 134(35.93), 107(67.70), 95(88.00), 71(100.00). *Mol. Wt.* calcd. for $C_{14}H_{22}O_2$: 222.1619; found: 222.1619. *Anal.* calcd. for $C_{14}H_{22}O_2$: C 75.63, H 9.97; found: C 75.43, H 9.87.

*Methoxyketone (**36**b)*: R_f 0.87 (pet. ether:ether, 2:7); $[\alpha]_D^{25}$ +72.74° (*c* 1.7, $CHCl_3$); ν_{max} (film): 2951, 1741, 1100 cm^{-1}; δ ($CDCl_3$, 400 MHz): 0.92 (s, 3H, CH_3, 0.94 (s, 3H, CH_3), 2.38 (d, 1H, αH, J = 2 Hz), 3.35 (s, 3H, R-ROCH_3), 3.68 (ddd, 1H, R^2CHOMe, J = 11 Hz, 7 Hz, 2 Hz); m/e (relative intensity): 222(21.19, M^+), 211(15.16), 190(26.33), 175(23.85), 162(22.15), 149(43.87), 147(59.02), 135(31.41), 121(33.18), 109(57.20), 107(61.96), 105(47.21), 95(100.00). *Mol. Wt.* calcd. for $C_{14}H_{22}O_2$: 222.1620; found: 222.1635. *Anal.* calcd. for $C_{14}H_{22}O_2$: C 75.63, H 9.97; found: C 75.80, H 9.99.

*Methoxyalcohols (**37**a,b)*

To a cold (0°C), stirred solution of lithium aluminum hydride (73 mg, 1.9 mmol) in dry tetrahydrofuran (20 mL) under an argon atmosphere was added a solution of a mixture of epimers of methoxyketones (***36****a, b*) (0.43 g, 1.9 mmol) in dry tetrahydrofuran (5 mL). Stirring was continued for 2 h and, after dilution with water (10 mL), the reaction mixture was extracted with ether and worked up in the usual way. The crude product was purified by column chromatography (silica gel, pet. ether:ether, 10:1) to give a mixture of methoxyalcohols (***37****a, b*) (0.39 g, 91%) as a colorless oil; ν_{max} (film): 3500, 2950, 1080 cm^{-1}; δ ($CDCl_3$, 80 MHz): 0.83 (s, 3H, CH_3), 0.99 (s, 3H, CH_3), 3.41 (s, 3H, $R^1R^2CHOCH_3$), 3.50–3.70 (m, 1H, R^1R^2CHOMe), 3.94 (d, 1H, R^2CHOH, J = 8 Hz); m/e (relative intensity): 224 (not observed, M^+), 223(0.42), 222(3.64), 207(1.49), 206(6.61), 192(17.11), 177(15.99), 174(19.08), 161(19.82), 159(35.01), 149(24.77), 147(21.16), 133(23.89), 131(29.39), 121(32.34), 119(35.44), 105(54.75), 109(67.04), 95(100.00). *Mol. Wt.* calcd. for $C_{14}H_{24}O_2$: 224.1776; found: 224.1775. *Anal.* calcd. for $C_{14}H_{24}O_2$: C 74.95, H 10.78; found: C 74.89, H 10.72.

(S)-*Methoxyacetate (**38**)*

Dry acetic anhydride (0.12 g, 1.2 mmol) was added to a solution of a mixture of epimeric methoxyalcohols (***37****a, b*) (0.13 g, 0.59 mmol) and 4-dimethylaminopyridine (15 mg, 0.12 mmol) in dry pyridine (5 mL) at 25°C under an argon atmosphere. Stirring was continued for 12 h and the reaction mixture was diluted with water (10 mL) and extracted with ether. Removal of solvent gave a crude product that was purified by column chromatography (silica gel, pet. ether:ether, 5:1) to afford (*S*)-methoxyacetate (**38**) (29 mg) and (*R*)-methoxyalcohol (***37****a*) (89 mg), as colorless oils. *Acetate (**38**)*: R_f 0.70 (pet. ether:ether, 3:2); ν_{max} (film): 2975, 1740 cm^{-1}; δ ($CDCl_3$, 80 MHz): 0.85 (s, 3H, CH_3), 0.88 (s, 3H, CH_3), 2.12 (s, 3H, ROCOCH_3), 3.10–3.25 (m, 1H, R^1R^2CHOMe), 3.30 (s, 3H, ROCH_3), 4.95 (d, 1H, R^2CHOAc, J = 9 Hz); m/e (relative intensity): 266 (not observed, M^+), 251(0.39), 224(1.03), 219(1.87), 207(10.27), 206(36.74), 191(12.80), 175(17.25), 174(53.01), 163(15.71), 161(10.21), 160(16.52), 159(100.00). *Mol. Wt.* calcd. for $C_{16}H_{26}O_3$: 266.1882; found: 266.1873. *Anal.* calcd. for $C_{16}H_{26}O_3$: C 72.14, H 9.84; found: C 72.20, H 9.84.

Methoxy-endo-*alcohols (**39**a,b)*

Calcium (0.84 g, 21 mmol) was treated with dry liquid ammonia (80 mL) at −78°C for 5 min under an argon atmosphere and a solution of methoxyketones (***36****a, b*) (0.72 g, 3.2 mmol) in dry ether (6 mL) was then added. The reaction mixture was stirred at reflux for 30 min and dry 1-propanol (3 mL) was added. Care was taken at all times to exclude water from the system. When the blue color was discharged the reaction mixture was diluted with water and extracted with ether. Removal of solvent gave a crude product that was purified by column chromatography (silica gel, pet. ether:ether, 5:1) to give a mixture of epimeric methoxy-*endo*-alcohols (***39****a, b*) (0.71 g, 98%) as a colorless oil; R_f 0.30 (pet. ether:ether, 1:1); ν_{max} (film): 3492, 2967 cm^{-1}; δ ($CDCl_3$, 400 MHz): 0.80 (s, 3H, CH_3), 0.97 (s, 3H, CH_3), 3.38 (s, 3H, $ROCH_3$), 3.50–3.60 (m, 1H, R^2CHOMe), 3.92 (d, 1H, R^2CHOH, J = 8 Hz); m/e (relative intensity): 224(0.88 M^+), 206(2.67), 193(2.62), 192(20.37), 191(2.08), 177(23.86), 174(15.05), 161(25.57), 159(23.92), 108(32.75), 107(76.42), 95(100.00). *Mol. Wt.* calcd. for $C_{14}H_{24}O_2$: 224.1776; found: 224.1776. *Anal.* calcd. for $C_{14}H_{24}O_2$: C 74.95, H: 10.78; found: C 74.73, H 10.68.

Methoxy-endo-*acetates (**40**a,b)*

Dry acetic anhydride (7.3 mL, 77 mmol) was added to a solution of epimeric methoxy-*endo*-alcohols (***39****a, b*) (5.8 g, 26 mmol) and 4-dimethylaminopyridine (9.4 g, 77 mmol) in dry pyridine (150 mL) at 25°C under an argon atmosphere. Stirring was continued for 5 h before water (50 mL) was added and the reaction mixture worked up by extraction with ether. Removal of solvent gave a crude product that was purified by column chromatography (silica gel, pet. ether:ether, 5:1) to provide a mixture of epimeric methoxy-*endo*-acetates (***40****a,b*) (6.1 g, 89%) as a colorless oil; R_f 0.58 (pet. ether:ether, 1:1); ν_{max} (film): 2947, 1741 cm^{-1}; δ ($CDCl_3$, 400 MHz): 0.82 (s, 3H, CH_3), 0.85 (s, 3H, CH_3), 2.06 (s, 3H, $ROCOCH_3$), 3.25 (s, 3H, $ROCH_3$), 3.25–3.34 (m, 1H, R^2CHOMe), 5.30 (dd, 1H, R^2CHOAc, J = 5 Hz, 2 Hz); m/e (relative intensity): 266 (not observed, M^+), 251(1.28), 236(7.53), 224(17.37), 207(34.09), 206(44.09), 174(82.19), 159(66.33), 119(55.74), 107(79.07), 105(64.97), 95(91.52), 91(77.33), 83(71.54), 79(82.81), 71(100.00). *Mol. Wt.* calcd. for $C_{16}H_{26}O_3$: 266.1881: found: 266.1873. *Anal.* calcd. for $C_{16}H_{26}O_3$: C 72.14, H 9.84; found: C 72.11, H 9.90.

*Hydroxyacetates (**41**a,b)*

To a well-stirred solution of a mixture of epimeric methoxy-*endo*-acetates (***40****a, b*) (2.0 g, 7.5 mmol) in dry methylene chloride (10 mL) at −30°C under an argon atmosphere was added 15-crown-5 (0.30 M, 8.9 mL) saturated with dry sodium iodide in dry methylene chloride, followed by the addition of boron tribromide (1.25 M, 1.54 mL) in dry methylene chloride (10). Stirring was continued for 4 h and the reaction worked up by dilution with saturated sodium bicarbonate solution (20 mL) followed by extraction with methylene chloride. The combined organic extract was washed with saturated sodium bicarbonate solution, hydrochloric acid solution (1 N), saturated sodium bisulphite solution, water, and dried ($MgSO_4$). Removal of solvent gave a crude product that was purified by column chromatography (silica gel, pet. ether:ether, 5:1) to yield a mixture of epimeric hydroxyacetates (***41****a, b*) (1.7 g, 89%) as a colorless oil; R_f 0.29 (pet. ether:ether, 1:1); ν_{max} (film): 3467, 2967, 1717 cm^{-1}; δ ($CDCl_3$, 400 MHz): 0.88 (s, 3H, CH_3), 0.89 (s, 3H, CH_3), 2.01 (s, 3H, $ROCOCH_3$), 3.33 (d, 1H, R^2CHOH, J = 12 Hz, exchangeable with D_2O), 3.53–3.60 (m, 1H, R^2CHOH), 4.74 (dd, 1H, R^2CHOAc, J = 4.5 Hz, 1.5 Hz); m/e (relative intensity): 252(0.59, M^+), 250(1.38), 210(1.87), 209(1.23), 208(7.09), 207(3.85), 206(1.95), 193(10.50), 192(49.20), 190(12.69), 174(53.74), 159(63.13), 121(100.00). *Mol. Wt.* calcd. for $C_{15}H_{24}O_3$: 252.1725; found: 252.1731. *Anal.* calcd. for $C_{15}H_{24}O_3$: C 71.39, H 9.59; found: C 71.62, H 9.60.

*(+)-Ketoacetate (**42**)*

A solution of epimeric hydroxyacetates (***41****a, b*) (90 mg, 0.35 mmol) and pyridinium dichromate (0.40 g, 1.1 mmol) (17) in dry methylene chloride (10 mL) was stirred at 60°C under an argon atmosphere for 10 h. The reaction mixture was then diluted with ether and filtered through a pad of silica gel. Removal of solvent gave a crude product that was purified by column chromatography (silica gel, pet. ether:ether, 10:0) to give (+)-ketoacetate (**42**) (85 mg, 95%) as a white solid, which was recrystallized from pentane as colorless prisms; mp 77–79°C; R_f 0.48 (pet. ether:ether, 1:1); $[\alpha]_D^{25}$ +101.38° (*c* 0.65, $CHCl_3$); ν_{max} ($CHCl_3$); 2969, 1717, 1699 cm^{-1}; δ ($CDCl_3$, 400 MHz): 0.94 (s, 3H, CH_3), 0.98 (s, 3H, CH_3), 2.07 (s, 3H, R-OCOCH_3), 5.05 (dd, 1H, R^2CHOAc, J = 4.5 Hz, 1.5 Hz); m/e (relative intensity): 250(23.95 M^+), 208(32.63), 207(54.57), 191(18.76), 190(100). *Mol. Wt.* calcd. for $C_{15}H_{22}O_3$: 250.1569; found: 250.1572. *Anal.* calcd. for $C_{15}H_{22}O_3$: C 71.97, H 8.86; found: C72.06, H 8.85).

Can. J. Chem. Downloaded from www.nrcresearchpress.com by 112.217.228.212 on 09/07/12
For personal use only.

*(+)-Ene-acetate (**43**)*

Methyltriphenylphosphonium bromide (1.5 g, 4.2 mmol) was suspended in dry tetrahydrofuran (20 mL) under an argon atmosphere and cooled to −78°C. *n*-Butyllithium (3.2 mL, 4.2 mmol; 1.3 M solution in hexane) was added and, after 10 min, the cold bath was removed and the reaction mixture was stirred for 1 h. During this time all the solid disappeared and the solution became dark orange. A solution of (+)-ketoacetate (**42**) (0.70 g, 2.8 mmol) in dry tetrahydrofuran (10 mL) was then introduced. Stirring was continued for 1 h and the reaction mixture was then diluted with water (10 mL) and extracted with petroleum ether. Removal of solvent gave a crude product that was purified by column chromatography (silica gel, pet. ether:ether, 15:1) to provide (+)-eneacetate (**43**) (0.59 g, 85%) as a colorless oil; R_f 0.94 (pet. ether:ether, 1:1); $[\alpha]_D^{25}$ +18.25° (*c* 0.16, $CHCl_3$); ν_{max} (film): 2960, 1738, 1640, 885 cm^{-1}; δ ($CDCl_3$, 270 MHz): 0.82 (s, 3H, CH_3), 0.88 (s, 3H, CH_3), 2.05 (s, 3H, $ROCOCH_3$), 4.55 (s, 1H, $R^1R^2C{:}CHH$), 4.57 (s, 1H, $R^1R^2C{:}CHH$), 5.12 (dd, 1H, R^2CHOAc, *J* = 4.5 Hz, 2Hz); *m/e* (relative intensity): 248 (not observed, M^+), 247(0.10), 239(2.37), 207(2.41), 206(7.15), 205(4.22), 191(12.70), 188(67.71), 173(48.65), 160(44.53), 145(43.12), 131(50.61), 121(40.23), 108(42.28), 107(64.47), 95(67.81), 93(82.49), 91(100.00). *Anal.* calcd. for $C_{16}H_{24}O_2$: C 77.38, H 9.74; found: C 77.56, H 9.69.

*(+)-Hydroxyalkene (**44**)*

To a cold (0°C) stirred solution of lithium aluminum hydride (11 mg, 0.28 mmol) in dry tetrahydrofuran (1 mL) under an argon atmosphere was added a solution of (+)-alkene-acetate (**43**) (68 mg, 0.28 mmol) in dry tetrahydrofuran (3 mL). Stirring was continued for 2 h and the reaction mixture worked up by careful addition of water (10 mL) followed by extraction with ether. Removal of solvent gave a crude product that was purified by column chromatography (silica gel, pet. ether:ether, 10:1) to give (+)-hydroxyalkene (**44**) (56 mg, 99.6%) as a colorless oil; R_f 0.67 (pet. ether:ether, 1:1); $[\alpha]_D^{25}$ +64.0° (*c* 0.5, $CHCl_3$); ν_{max} (film): 3375, 2950, 1640, 885 cm^{-1}; δ ($CDCl_3$, 270 MHz): 0.89 (s, 3H, CH_3), 0.90 (s, 3H, CH_3), 3.91 (dd, 1H, R^2CHOH, *J* = 4.5 Hz, 2 Hz), 4.62 (s, 1H, $R^1R^2C{:}CHH$), 4.67 (s, 1H, $R^1R^2C{:}CHH$); *m/e* (relative intensity): 206(9.49, M^+), 204(2.33), 191(38.86), 188(31.18), 173(30.30), 163(22.28), 161(23.24), 146(39.62), 136(69.60), 132(29.02), 123(25.04), 121(85.72), 109(40.53), 108(66.91), 107(100.00). *Mol. Wt.* calcd. for $C_{14}H_{22}O$: 206.1672; found: 206.1671. *Anal.* calcd. for $C_{14}H_{22}O$: C 81.49, H 10.75; found: C 81.27, H 10.60.

*(+)-Tetracyclic alcohol (**45**)*

To a well-stirred, heated (60°C) solution of (+)-hydroxyalkene (**44**) (0.42 g, 2.0 mmol) in dry toluene (5 mL) was added successively a solution of diethylzinc (1.4 mL, 2.8 mmol, 25% w/v) in toluene and methylene iodide (0.23 mL, 2.8 mmol). A stream of dry air was passed through the reaction mixture for 3.5 h. After acidification with hydrogen chloride solution (1 N) the reaction mixture was extracted with ether and worked up as usual. Removal of solvent gave a crude product that was purified by column chromatography (silica gel, pet. ether:ether, 10:1) to afford (+)-tetracyclic alcohol (**45**) (0.45 g, 99%) as a white solid, which was recrystallized from pentane as colorless prisms; mp 109–111°C; $[\alpha]_D^{25}$ +31.61° (*c* 0.31, $CHCl_3$); R_f 0.21 (pet. ether:ether, 8:2); ν_{max} ($CHCl_3$): 3643, 3010, 2965 cm^{-1}; δ ($CDCl_3$, 400 MHz): 0.20–0.28 (m, 2H, $R^1R^2CCH_2CH_2$), 0.40–0.53 (m, 2H, $R^1R^2CCH_2CH_2$), 0.88 (s, 3H, CH_3), 4.03 (dd, 1H, R^1R^2CHOH, *J* = 4 Hz, 2 Hz); *m/e* (relative intensity): 220(2.89, M^+), 205(8.42), 203(1.53), 202(5.91), 189(15.12), 187(18.89), 177(11.05), 161(10.28), 159(13.34), 149(19.21), 147(16.05), 146(12.20), 145(18.79), 135(29.88), 121(45.17), 119(33.75), 107(81.32), 105(54.84), 95(81.66), 93(91.26), 91(96.66), 79(100.00). *Mol. Wt.* calcd. for $C_{15}H_{24}O$: 220.1827; found: 220.1821. *Anal.* calcd. for $C_{15}H_{24}O$: C 81.76, H 10.98; found: C 81.89, H 10.88.

*(+)-Longiborneol (**11**)*

To a solution of (+)-tetracyclic alcohol (**45**) (380 mg, 1.72 mmol) in glacial acetic acid (3 mL) was added platinum oxide (16 mg, 0.07 mmol). The resultant suspension was stirred with hydrogen under pressure (2.7 atm; 1 atm = 101.3 kPa) at room temperature for 12 h. Saturated sodium bicarbonate solution was added until the mixture was neutral and the aqueous slurry was extracted with ether. The combined organic layer was washed with hydrochloric acid (1 N), brine solution, and dried ($MgSO_4$). Removal of solvent yielded a crude product that was subjected to column chromatography (silica gel, pet. ether:ether, 5:1) to provide (+)-longiborneol (**11**) (0.383 g, 100%), which crystallized from pentane as colorless prisms; mp 105–107°C (lit. (10, 11) mp for (−)-longiborneol, 106–107°C); R_f 0.41 (pet. ether:ether, 4:1); $[\alpha]_D^{25}$ +15.83° (*c* 0.54, $CHCl_3$) (lit. (10, 11) for (−)-longiborneol, $[\alpha]_D^{25}$ −16.3° (*c* 0.66, $CHCl_3$)); ν_{max} ($CHCl_3$): 3643, 2943 cm^{-1}; δ ($CDCl_3$, 400 MHz): 0.84 (s, 3H, CH_3), 0.87 (s, 3H, CH_3), 0.94 (s, 6H, CH_3, CH_3), 3.77 (dd, 1H, R^2CHOH, *J* = 5 Hz, 2 Hz); *m/e* (relative intensity): 222(7.36, M^+), 208(4.52), 207(28.42), 204(50.55), 189(59.98), 161(25.91), 133(26.52), 121(26.36), 119(81.13), 109(58.59), 95(100.00). *Mol. Wt.* calcd. for $C_{15}H_{26}O$: 222.1983; found: 222.1979. *Anal.* calcd. for $C_{15}H_{26}O$: C 81.02, H 11.79; found: C 81.16, H 11.69.

*Longiborneol MTPA ester (**46**)*

To a stirred solution of (+)-longiborneol (**11**) (15 mg, 0.067 mmol) in dry carbon tetrachloride (0.5 mL) and pyridine (2 mL) was added *R*-(+)-α-methoxy-α-trifluoromethylphenylacetyl chloride (+)-MTPA-chloride; 26 mg, 0.10 mmol) at 25°C under an argon atmosphere. After 20 h, the solution was diluted and extracted with ether and the combined organic layer was washed with hydrochloric acid solution (1 N), brine solution, and dried ($MgSO_4$). Removal of solvent gave a crude product that was purified by column chromatography (silica gel; petroleum ether:ether, 10:1) to yield pure longiborneol MTPA ester (**46**) (28 mg, 95%) as a white solid. Crystallization from pentane afforded **46** as colorless prisms; mp 89–91°C; R_f 0.88 (petroleum ether:ether, 4:1); ν_{max} ($CHCl_3$): 1750 cm^{-1}; δ ($CDCl_3$, 400 MHz): 0.80 (s, 3H, CH_3), 0.81 (s, 3H, CH_3), 0.83 (s, 3H, CH_3), 0.94 (s, 3H, CH_3), 3.57 (q, 3H, R-OCH_3, *J* = 1.2 Hz), 5.41 (dd, 1H, $R^1R^2CHOR^3$, *J* = 5 Hz, 2 Hz), 7.36–7.44 (m, 3H, RC_6H_5), 7.58–7.66 (m, 2H, RC_6H_5); ^{13}C nmr ($CDCl_3$, 100.6 MHz): 22.237, 26.979, 30.035, 33.297, 35.201, 40.685, 50.626, 52.000, 60.597 (quarternary and methylene carbons); 13.210, 22.279, 28.798, 29.402, 44.019, 55.463, 60.597, 23.990 (methyl and methine carbons); 83.772 (RCF_3), 125.383, 127.456, 128.215, 129.450 (aromatic carbons), 166 (carbonyl carbon); ^{19}F nmr ($CDCl_3$, 254 MHz): singlet at δ 5.08 in the resolution-enhanced, proton-decoupled spectrum; *m/e* (relative intensity): 220(1.20), 205(49.10), 189(58.40), 95(100.00). *Mol. Wt.* calcd. for $C_{25}H_{33}O_3F_3$; 438.2381; found: 438.2377. *Anal.* calcd. for $C_{25}H_{33}O_3F_3$, C 68.47, H 7.59; found: C 68.44, H 7.69.

*(+)-Longicamphor (**10**)*

Pyridinium chlorochromate (0.51 g, 2.4 mmol) (13) was suspended in dry methylene chloride (2 mL), and a solution of (+)-longiborneol (**11**) (0.35 g, 1.6 mmol) in dry methylene chloride (4 mL) was added rapidly at room temperature. After 3 h under argon the black reaction mixture was diluted with ether and filtered through a pad of silica gel. Removal of the solvent provided a crude product that was purified by column chromatography (silica gel, pet. ether) to afford (+)-longicamphor (**10**) (0.29 g, 85%) as a colorless oil; R_f 0.87 (pet. ether:ether, 4:1); $[\alpha]_D^{25}$ +18.92° (*c* 0.74, C_2H_5OH); ν_{max} (film): 2971, 1739 cm^{-1}; δ ($CDCl_3$, 400 MHz): 0.89 (s, 3H, CH_3), 0.92 (s, 3H, CH_3), 1.00 (s, 3H, CH_3), 1.07 (s, 3H, CH_3); *m/e* (relative intensity): 220(100.00, M^+), 206(7.00), 205(28.40), 178(12.60), 177(86.70), 163(19.90), 150(20.10), 149(25.70), 137(34.70), 136(43.50), 135(34.80), 124(52.90), 95(95.40). *Mol. Wt.* calcd. for $C_{15}H_{24}O$: 720.1827; found: 220.1826. *Anal.* calcd. for $C_{15}H_{24}O$: C 81.76, H 10.98; found: C 81.67, H 11.00.

*(+)-Isolongiborneol (**47**)*

Lithium aluminum hydride (22 mg, 0.59 mmol) was suspended in dry tetrahydrofuran (2 mL) at 0°C, and a solution of (+)-longicamphor (**10**) (130 mg, 0.59 mmol) in dry tetrahydrofuran (1.5 mL) was added slowly. The reaction mixture was stirred at 0°C under an argon

atmosphere for 3 h and, after dilution with water (10 mL), extracted with ether. The combined organic layer was washed with hydrochloric acid solution (1 N), brine, water, and dried ($MgSO_4$). After removal of solvent the crude product was purified by column chromatography (silica gel, pet. ether) to yield (+)-isolongiborneol (**47**) (0.12 g, 92%) as a colorless oil; R_f 0.94 (pet. ether:ether, 9:1); $[\alpha]_D^{25}$ +45.8° (*c* 0.69, $CHCl_3$); ν_{max} (film): 3436, 2965 cm^{-1}; δ ($CDCl_3$, 400 MHz): 0.80 (s, 3H, CH_3), 0.94 (s, 3H, CH_3), 0.98 (s, 3H, CH_3), 1.12 (s, 3H, CH_3), 3.84 (dd, 1H, R^2CHOH, J = 8 Hz, 4 Hz); *m/e* (relative intensity): 222(4.50, M^+), 221(1.80), 220(5.30), 219(2.20), 208(3.80), 207(17.10), 205(11.30), 204(48.10), 189(34.40), 161(24.70), 137(31.10), 133(35.90), 119(100.00). *Mol. Wt.* calcd. for $C_{15}H_{26}O$: 222.1984; found: 222.1987. *Anal.* calcd. for $C_{15}H_{26}O$: C 81.02, H 11.79; found: C 81.28, H 11.80.

(+)-Longifolene (12)

(+)-Longiisoborneol (**47**) (0.12 g, 0.54 mmol) was treated with methanesulphonyl chloride (0.085 mL, 1.1 mmol) and 4-dimethylaminopyridine (30 mg, 0.25 mmol) in dry pyridine (1 mL) and stirred at 105°C under an argon atmosphere for 16 h. After dilution with water (10 mL) and extraction with ether, the combined organic layer was washed with hydrochloric acid solution (1 N), saturated sodium bicarbonate solution, water, and dried ($MgSO_4$). Removal of solvent provided a crude product that was purified by column chromatography (silica gel, pet. ether) to give (+)-longifolene (**12**) (73 mg, 66%) as a colorless oil; R_f 0.91 (pet. ether:ether, 10:0); $[\alpha]_D^{25}$ +51.77° (*c* 1.07, $CHCl_3$) (lit. (3*d*) $[\alpha]_D^{19}$ +51.5° (*c* 0.35)); ν_{max} (film): 2964, 1661, 871 cm^{-1}; δ ($CDCl_3$, 400 MHz): 0.90 (s, 3H, CH_3), 0.95 (s, 3H, CH_3), 1.00 (s, 3H, CH_3), 4.50 (s, 1H, RC:C*H*H), 4.75 (s, 1H, RC:CH*H*); *m/e* (relative intensity): 204(47.60 M^+), 203(15.40), 190(11.80), 189(63.20), 175(27.20), 163(19.60), 162(18.40), 161(76.00), 133(56.70), 121(59.00), 119(66.20), 109(65.20), 108(55.00), 107(86.50), 95(96.60), 91(100.00). *Mol. Wt.* calcd. for $C_{15}H_{14}$: 204.1878; found: 204.1877. *Anal.* calcd. for $C_{15}H_{24}$: C 88.16, H 11.84; found: C 87.94, H 11.72.

Acknowledgments

We are grateful to the Natural Sciences and Engineering Research Council of Canada, Ottawa, for financial support of this research and to Professor S. C. Welch (University of Houston) and Professor N. H. Anderson (University of Washington) for samples of longiborneol and nmr spectra.

1. (*a*) C. R. Eck, G. L. Hodgson, D. F. MacSweeney, R. W. Mills, and T. Money. J. Chem. Soc. Perkin Trans. 1, 1938 (1974); (*b*) G. L. Hodgson, D. F. MacSweeney, and T. Money. J. Chem. Soc. Perkin Trans. 1, 2113 (1973).
2. S. C. Welch and R. L. Walters. Synth. Commun. **3**, 15 (1973); **3**, 419 (1973); J. Org. Chem. **39**, 2665 (1974).
3. (*a*) E. J. Corey, M. Ohno, R. B. Mitra, and P. A. Vatakencherry. J. Am. Chem. Soc. **86**, 478 (1964); (*b*) J. E. McMurry and S. J. Isser. J. Am. Chem. Soc. **94**, 7132 (1972); (*c*) R. A. Volkman, G. C. Andrews, and W. S. Johnson. J. Am. Chem. Soc. **97**, 4777 (1975); (*d*) W. Oppolzer and T. Godel. J. Am. Chem. Soc. **100**, 2538 (1978); Helv. Chim. Acta, **67**, 1154 (1984); (*e*) A. G. Schultz and S. Puig. J. Org. Chem. **50**, 915 (1985).
4. (*a*) C. R. Eck, R. W. Mills, and T. Money. J. Chem. Soc. Perkin Trans. 1, 251 (1975); (*b*) P. Cachia, N. Darby, C. R. Eck, and T. Money. J. Chem. Soc. Perkin Trans. 1, 359 (1976); (*c*) W. M. Dadson and T. Money. J. Chem. Soc. Chem. Commun. 112 (1982).
5. (*a*) M. T. Reetz. Angew. Chem. Int. Ed. Engl. **21**, 96 (1982), and references cited; (*b*) T. H. Chan, I. Paterson, and J. Pinsonnault. Tetrahedron Lett. 4183 (1977).
6. T. Mukaiyama. Org. React. **28**, 203 (1982), and references cited; P. Brownbridge. Synthesis, 1 (1983); 85 (1983); G. S. Cockerill and P. Kocienski. J. Chem. Soc. Chem. Commun. 705 (1983), and references cited to intramolecular Mukaiyama reaction; T. H. Chan and M. A. Brook. Tetrahedron Lett. **26**, 2943 (1985); G. Mehta and V. P. Pathak. J. Chem. Soc. Chem. Commun. 876 (1987); J. H. Hutchinson, G. Pattenden, and P. L. Meyers. Tetrahedron Lett. **28**, 1313 (1987).
7. P. Cachia, N. Darby, T. C. W. Mak, T. Money, and J. Trotter. Can. J. Chem. **58**, 1172 (1980).
8. D. L. Kuo and T. Money. J. Chem. Soc. Chem. Commun. 1691 (1986).
9. (*a*) M. T. Reetz, J. Westermann, and S.-H. Kyung. Chem. Ber. **118**, 1050 (1985), and references cited: (*b*) J. Furukawa, N. Kawabata, and J. Nishimura. Tetrahedron, **24**, 53 (1968); S. Miyano and H. Hashimoto. Chem. Commun. 1418 (1971); B. M. Trost and H. Hiemstra. J. Am. Chem. Soc. **104**, 886 (1982), and references cited.
10. H. Niwa, T. Hida, and K. Yamada. Tetrahedron Lett. **22**, 4239 (1981).
11. H. Erdtman and B. R. Thomas. Chem. Ind. 384 (1955); K. Doi and T. Shibuya. Phytochemistry, **11**, 1174 (1972); S. C. Bisarya and S. Dev. Tetrahedron Lett. 3751 (1964); S. Akiyoshi, H. Erdtmann, and T. Kubota. Tetrahydron, **9**, 237 (1960).
12. (*a*) J. A. Dale and H. S. Mosher. J. Am. Chem. Soc. **95**, 512 (1973); (*b*) N. Kalyanam and D. A. Lightner. Tetrahedron Lett. 415 (1979); (*c*) S. Yamaguchi. Asymmetric synthesis. Vol. 1. *Edited by* J. D. Morrison. Academic Press, New York. 1983. pp. 125–152; (*d*) S. Yamaguchi, F. Yasuhara, and K. Kabuto. Tetrahedron, **32**, 1363 (1976).
13. E. J. Corey and J. W. Suggs. Tetrahedron Lett. 2647 (1975); E. J. Corey and D. L. Boger. Tetrahedron Lett. 2461 (1978).
14. T. Cuvigny, M. Larcheveque, and H. Normant. Bull. Soc. Chim. Fr. 1174 (1973); M. Larcheveque and T. Cuvigny. Tetrahedron Lett. 3851 (1975); A. Debal, T. Cuvigny, and M. Larcheveque. Synthesis, 391 (1976); D. Heissler and J.-J. Riehl. Tetrahedron Lett. **21**, 4711 (1980); T. Ohsawa, T. Kobayashi, Y. Mizuguchi, T. Saitoh, and T. Oishi. Tetrahedron Lett. **26**, 6103 (1985).
15. (*a*) N. Lamb. Ph. D. thesis, U.B.C., Vancouver, 1979; (*b*) P. Cachia. Ph. D. thesis, U.B.C., Vancouver, 1980; (*c*) D. Kuo. Ph. D. thesis, U.B.C., Vancouver, 1987.
16. (*a*) P. A. Grieco., T. Tagikawa, S. L. Bongers, and H. Tanaka. J. Am. Chem. Soc. **102**, 7587 (1980); (*b*) G. Majetich, P. A. Grieco, S. Rogers, M. G. Erman, and D. A. Langs. J. Org. Chem. **46**, 209 (1981).
17. E. J. Corey and G. Schmidt. Tetrahedron Lett. 399 (1979).
18. T. H. Chan, M. A. Brook, and T. Chaly. Synthesis, 203 (1983).
19. A. L. Gemal and J.-L. Luche. J. Org. Chem. **44**, 4187 (1979).

Can. J. Chem. Downloaded from www.nrcresearchpress.com by 112.217.228.212 on 09/07/12
For personal use only.

7-Diethylamino-3-((4′-iodoacetylamino)phenyl)-4-methylcoumarin, a fluorescent probe of the hydrophobic cleft in the tropomyosin coiled coil

LESLIE D. BURTNICK[1] AND ANITA RACIC

Department of Chemistry, University of British Columbia, Vancouver, B.C., Canada V6T 1Y6

Received September 25, 1987

This paper is dedicated to Professor Charles A. McDowell on the occasion of his 70th birthday

LESLIE D. BURTNICK and ANITA RACIC. Can. J. Chem. **66**, 1805 (1988).

A sulfhydryl-specific fluorescent reagent, 7-diethylamino-3-((4′-iodoacetylamino)phenyl)-4-methylcoumarin (DCIA) was used to label cysteine residues on tropomyosin (TM) from rabbit cardiac and rabbit skeletal muscles. The emission maximum at 486 nm, the high degree of fluorescence polarization, and the limited accessibility of the bound probe to quenching by iodide suggest that the probe is bound in the hydrophobic cleft between polypeptide chains of the TM coiled coil, as well as being bound covalently at a cysteine residue. The labelled TMs retain their abilities to bind F-actin and are able to interact with deoxyribonuclease I. They, however, show a reduced tendency to aggregate into filaments in low ionic strength solutions.

LESLIE D. BURTNICK et ANITA RACIC. Can. J. Chem. **66**, 1805 (1988).

On a utilisé un réactif fluorescent spécifique aux groupements sulfhydriles, la diéthylamino-7 ((iodo-4′acétylamino)phényl)-3 méthyl-4 coumarine (DCIA), pour marquer les résidus de cysteine de la tropomyosine (TM) des muscles cardiaques et du squellette du lapin. L'émission maximale à 486 nm, le haut degré de polarisation de la fluorescence et l'accessibilité limitée de la sonde liée à un piégeage par l'iode suggère que la sonde est liée, d'une part, à la portion hydrophobe que l'on retrouve entre les chaînes polypeptidiques de l'enroulement de la TM et, d'autre part, à un résidu de cystéine par une liaison covalente. Les TM marquées conservant la possibilité de se lier à la F-actine et elles sont capables d'interagir avec la désoxyribonucléase I. Toutefois, leur tendance à former des filaments par aggrégats, dans des solutions de faible force ionique, est réduite.

[Traduit par la revue]

Introduction

Tropomyosin (TM) in striated muscle binds along the length of the F-actin filaments and, with troponin, confers calcium sensitivity to the interaction between actin and myosin (reviewed in ref. 1). The TM molecule consists of two α-helical polypeptide chains, each of molecular mass 33 kDa. The chains run parallel to each other, are in register, and are wound around each other to form a rod-like coiled coil having a cross-sectional diameter of about 2 nm and a length of 40 nm (reviewed in ref. 2). In low ionic strength solutions, adjacent TM molecules aggregate in a head-to-tail manner to form filaments. This interaction involves an 8 or 9 residue overlap between the NH_2-terminal and COOH-terminal ends of adjacent molecules (3). An increase in ionic strength leads to depolymerization of the filaments.

Rabbit skeletal muscle contains two types of TM chain, α and β, which are combined into molecular species αα and αβ in equal proportions (4, 5). Rabbit cardiac muscle TM contains only αα-TM. The α and β chains have identical lengths of 284 amino acid residues but exhibit 39 differences in sequence. Of particular interest for this study is that the α chain contains a single cysteine residue at position 190 in the sequence, while the β chain contains two cysteines, Cys-36 and Cys-190 (6).

The coiled coil structure of TM is stabilized to a large extent by the presence of a hydrophobic core in the region where the two helical chains come into contact. Since two turns of an α-helix contain 7 amino acid residues, a 2-stranded helical coiled coil can be stabilized by hydrophobic residues at positions 2 and 5 of a repeating heptad sequence $(X\text{-}N\text{-}X\text{-}X\text{-}N\text{-}X\text{-}X)_n$, where N is a nonpolar residue (7). This pattern is closely followed by TM sequences from both muscle and non-muscle sources (8). Both Cys-36 and Cys-190 are located at position 2 in the repeating heptad pattern and, so, are located in the hydrophobic cleft between the adjacent chains in a TM molecule. This explains their limited accessibility to sulfhydryl-reactive reagents in native TM.

We have labelled both cardiac and skeletal muscle TMs with a sulfhydryl-specific fluorescent reagent, 7-diethylamino-3-((4′-iodoacetylamino)phenyl)-4-methylcoumarin (DCIA) to obtain the respective products DCIA-C-TM and DCIA-S-TM. Both exhibit a bright blue fluorescence on excitation with ultraviolet light. The fluorescence properties of the bound probes provide information about the structure of TM and on its interactions with two other proteins, actin and deoxyribonuclease I (DNAase I).

Results and discussion

When the labelling reaction was performed in 5 M guanidine hydrochloride, typical degrees of labelling of cardiac and skeletal muscle TMs were 0.9 and 1.2 DCIA labels per molecule, respectively. The products, DCIA-C-TM and DCIA-S-TM, were highly fluorescent, with emission maxima at 486 nm on excitation at 365 nm (Fig. 1). When subjected to polyacrylamide gel electrophoresis in the presence of sodium dodecyl sulfate, the fluorescent bands moved to positions that could be identified as α and β chains of TM after staining with Coomassie Brilliant Blue and comparison with the migration patterns of unlabelled TM. The general similarity in shape of the emission spectra for the two DCIA-TMs suggests that the environments of the labels on Cys-190 and Cys-36 are similar.

Emission spectra for the protein-bound DCIA more closely resemble that for DCIA in *N*,*N*-dimethylformamide than for DCIA in water (Fig. 2), suggesting that the labels are in rather hydrophobic environments. As both Cys-36 and Cys-190 are in position 2 of the repeating heptad model for a coiled coil protein, it may be that the aromatic ring system of the label is partly buried in the hydrophobic cleft between the two TM chains that form the coiled coil. Evidence to support this suggestion comes

[1]Author to whom correspondence may be addressed.

Can. J. Chem. Downloaded from www.nrcresearchpress.com by 112.217.228.212 on 09/07/12
For personal use only.

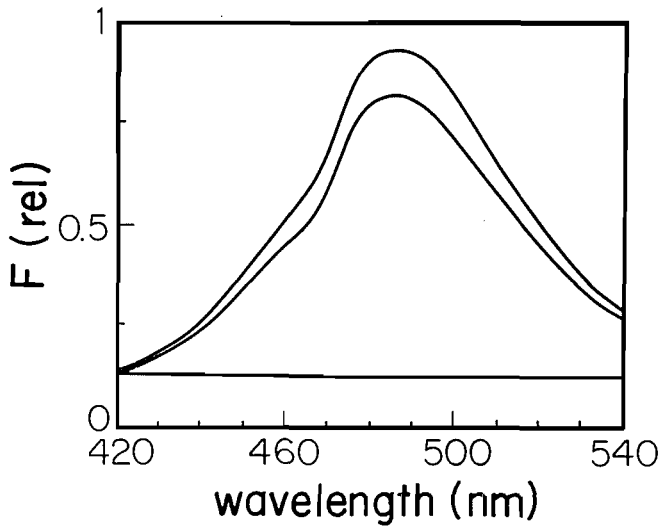

FIG. 1. Fluorescence emission spectra. Upper curve, DCIA-S-TM, 0.8 mg/mL, 1.1 DCIA per protein molecule. Lower curve, DCIA-C-TM, 0.8 mg/mL, 0.9 DCIA per protein molecule. Baseline, unlabelled S-TM, 0.8 mg/mL. Solvent was 0.3 M KCl, 10 mM Tris-HCl, pH 8.0. Excitation was at 365 nm.

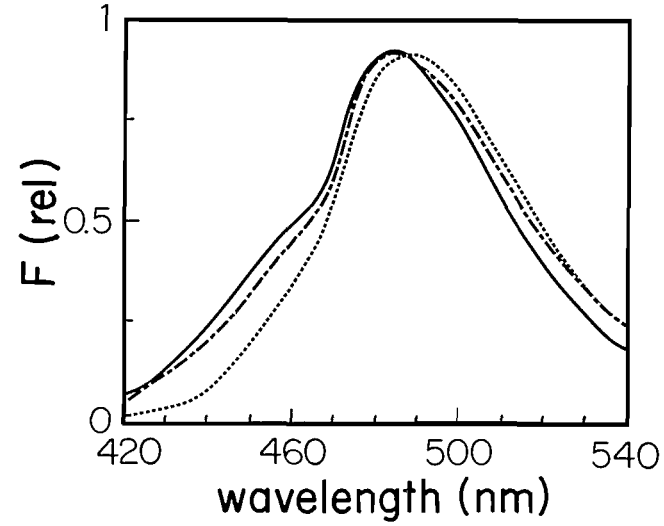

FIG. 2. Emission spectra of DCIA in various environments. Solid line, 43 ng/mL DCIA in *N*,*N*-dimethylformamide. Dashed line, 1.1 mg/mL DCIA-C-TM in 5 mM Tris-HCl, pH 8.0. Dotted line, 8.5 μg/mL DCIA in water. Excitation was at 365 nm. Photomultiplier gain settings were adjusted so that maximal emission intensities were the same for all 3 samples.

from fluorescence quenching experiments using iodide as a quencher. Stern–Volmer plots demonstrate that fluorescence from DCIA-C-TM and DCIA-S-TM is much less affected by iodide quenching than is the fluorescence of a DCIA adduct of 2-mercaptoethanol (Fig. 3). A small difference in slopes of the plots for DCIA-C-TM and DCIA-S-TM is apparent. K_{sv} = 0.523 ± 0.017 M^{-1} for DCIA-C-TM and K_{sv} = 0.384 ± 0.013 M^{-1} for DCIA-S-TM. This may be the result of subtle conformational differences in the environments of Cys-36 (present in S-TM but not in C-TM) or may be the result of different quenching efficiencies at the two sites that arise due to differences in charge of residues adjacent to the Cys at each position. In the presence of 5 M guanidine hydrochloride, the slopes of Stern–Volmer plots for the DCIA-TMs increase by more than

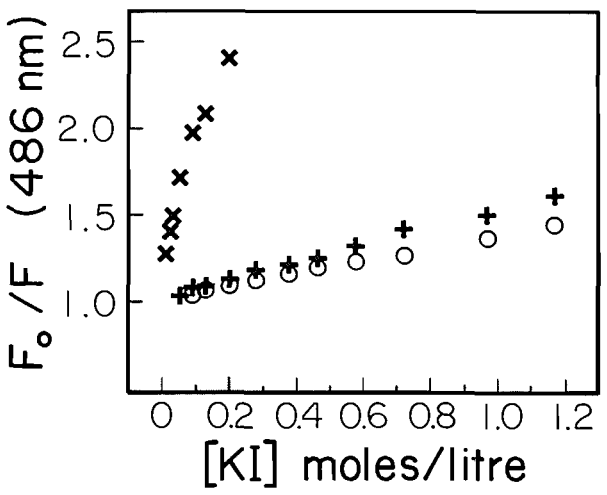

FIG. 3. Quenching of DCIA fluorescence by iodide. Stern–Volmer plot shows iodide quenching of an adduct of DCIA and 2-mercaptoethanol (X), of DCIA-C-TM (+), and of DCIA-S-TM (○). Initial protein concentrations were 0.02 mg/mL. Solvent was 0.3 M KCl, 50 mM Tris-HCl, 1 mM $MgCl_2$, pH 8.0. Aliquots of 3 M KI were added to the samples. Dilution and ionic strength effects were corrected for by adding appropriate volumes of 3 M KCl to control samples.

5-fold, reflecting the greater exposure of the probe to iodide quenching on the denatured proteins.

Fluorescence polarization values at room temperature are high for both DCIA-TMs, typically $p = 0.38 \pm 0.02$. Such high values indicate that during the fluorescence lifetime of the DCIA probe (about 3 ns (9)), rotational motions of the probe are severely hindered. Therefore, the probe is rigidly attached to the large and slow-tumbling (calculated to be on the microsecond time scale (10)) TM molecule. This need not be expected *a priori* as the label is attached through a single covalent bond about which rotations might be expected to occur on a time scale comparable to or more rapid than that of the fluorescence lifetime of the probe. The high polarization value is further evidence that the DCIA is involved in hydrophobic interactions with the TM molecule, such interactions acting with the covalent bond to limit the rotational freedom of the probe.

Muscle TMs interact in an end-to-end manner in low ionic strength solutions (11). We studied the behaviour of DCIA-TMs in solutions of ionic strength ranging up to 0.6 M and did not observe any changes in fluorescence emission intensity or spectral shape. Polarization values were not affected by ionic strength. The viscosities of DCIA-TM solutions were higher in low than in high ionic strength solutions, indicating that some end-to-end interactions were taking place (Fig. 4); however, these interactions clearly were impaired relative to those in unlabelled S-TM. It has been reported elsewhere that labelling at Cys-190 on muscle TM affects the polymerizability of the molecule (12). A similar effect seems to be occurring in the present case.

To ensure that the reduced end-to-end polymerization of DCIA-TMs is not the result of a general loss of structure in the protein, we checked whether the labelled TMs are able to bind F-actin. DCIA-C-TM and DCIA-S-TM cosediment with F-actin when solutions of the proteins are centrifuged at 100 000 × g and the pellets examined by sodium dodecyl sulfate polyacrylamide gel electrophoresis. Bands corresponding to the TMs can be detected due to their fluorescence prior to staining with Coomassie Brilliant Blue. The binding of actin results in an increased

Can. J. Chem. Downloaded from www.nrcresearchpress.com by 112.217.228.212 on 09/07/12
For personal use only.

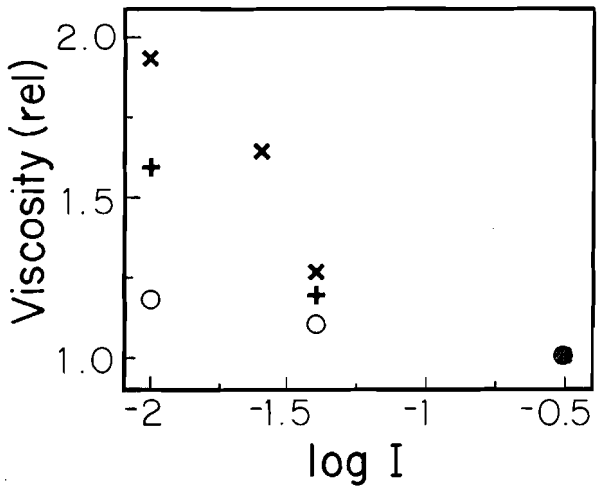

FIG. 4. Relative viscosity measurements. Unlabelled S-TM (X), DCIA-C-TM (+) (0.9 DCIA per protein molecule), and DCIA-S-TM (O) (1.3 DCIA per protein molecule) at 0.8 mg/mL in 10 mM Tris-HCl, pH 8.0, with added KCl as indicated.

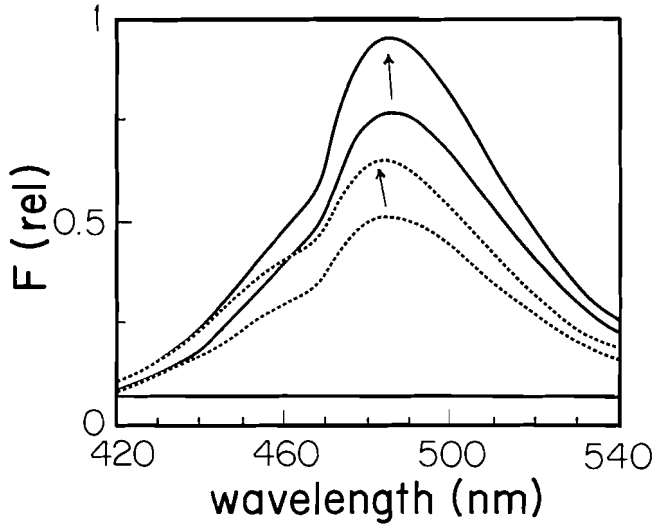

FIG. 5. Effects of actin on emission spectra. Solid lines are for DCIA-S-TM (1.2 DCIA per protein molecule) and dashed lines are for DCIA-C-TM (0.9 DCIA per protein molecule). Four samples were prepared, two containing DCIA-C-TM and two containing DCIA-S-TM. Actin was added to one of each of the DCIA-TM solutions and an equal volume of actin dialysate was added to its control. Final concentration of DCIA-TM in each solution was 0.51 mg/mL. Final concentration of actin, where present, was 2.4 mg/mL. Final buffer composition was 133 mM KCl, 22 mM Tris-HCl, 0.4 mM $MgCl_2$, pH 8.0. Arrows indicate the effects of the added actin to TM at a mole ratio of 7.3 to 1, after waiting for 30 min to ensure that the actin was fully polymerized.

intensity and a blue shift in the emission of the DCIA probe (Fig. 5), suggesting that it has moved into a more hydrophobic environment, possibly being partly covered by F-actin itself. These effects can be titrated with actin and reach plateau values at actin to tropomyosin mole ratios near seven. The binding of DCIA-TM to the extended F-actin filaments does not change the polarization value for DCIA-TM. This might be because the polarization is very high even prior to the binding of actin to TM, to which the DCIA is bound. Any increase in rigidity of the bound probe due to its indirect attachment to the large F-actin system might give only a marginal increase in polarization.

Deoxyribonuclease I (DNAase I) has been shown to bind to TM and has been shown to depolymerize TM filaments (13). The presence of DNAase I in DCIA-TM solutions did not alter fluorescence emission intensities or wavelengths of maximal emission. But evidence for interaction of DCIA-TM with DNAase I was obtained by observation of a consistent decrease of polarization value from 0.38 ± 0.02 to 0.26 ± 0.02 in solutions containing equimolar DNAase I and TM. Interaction with DNAase I introduces a greater freedom of motion into the environment of the bound DCIA on both DCIA-S-TM and DCIA-C-TM in both low ionic strength solutions (5 mM Tris-HCl, pH 8.0) and at higher ionic strengths (at 0.3 and 0.6 M KCl in 5 mM Tris-HCl, pH 8.0). As minor structural changes near Cys-190 are known to affect end-to-end interactions of TM, it may be that it is this loosening up of the coiled coil structure in response to the binding of DNAase I that leads to its depolymerizing activity on TM.

Experimental

Tropomyosin was prepared from frozen rabbit hearts and from frozen rabbit back and leg muscle (Pel-Freez Biologicals, Inc.) according to Smillie (14). Actin was prepared from rabbit skeletal muscle powder as described by Spudich and Watt (15). Bovine pancreatic DNAase I was purchased from Calbiochem. All proteins were greater than 95% pure as judged by polyacrylamide gel electrophoresis in the presence of sodium dodecyl sulfate (SDS) (16).

Concentrations of unlabelled proteins in solution were determined spectrophotometrically using molar absorption coefficients at 277 nm of 21 780 M^{-1} cm^{-1} for TM (17), at 280 nm of 38 130 M^{-1} cm^{-1} for DNAase I (18), and at 290 nm of 26 230 M^{-1} cm^{-1} for G-actin (19). Concentrations of DCIA-labelled TM (DCIA-S-TM and DCIA-C-TM) in solution were determined according to Bradford (20), using unlabelled TM to prepare standard curves. The concentration of label in solutions of DCIA-TM was estimated spectrophotometrically using a molar absorption coefficient at 387 nm of 29 700 M^{-1} cm^{-1} (21).

Initial attempts to react TM with DCIA (Molecular Probes) in nondenaturing buffers of the type used to label a reactive cysteine on platelet TM with *N*-(1-pyrenyl)iodoacetamide (22) gave insignificant degrees of labelling. Significant yields of labelled product required, first, the prereduction of the cysteine residues on TM (4). Subsequently, about 20 mg of TM was dissolved in 5 M guanidine hydrochloride, 1 M KCl, 20 mM Mops-KOH, 1 mM EDTA, pH 7.0. Then 25 mg of DCIA dissolved in 0.4 mL of *N*,*N*-dimethylformamide was added dropwise and the mixture allowed to incubate at room temperature for 4 h. Excess dithiothreitol (DDT) was added to quench the reaction. The samples were clarified by centrifugation and then dialysed extensively against 10 mM Tris-HCl, 1 mM DTT, pH 8.0, prior to being studied further.

Viscosity measurements were conducted in a thermostatted water bath held at 27°C using a Cannon–Manning semimicro viscosimeter. Solutions of TM and DCIA-TM (1.00 mL of 0.80 mg/mL solutions) were used in each case. The flow time for water in this viscosimeter was about 2 min.

Fluorescence measurements were performed with an instrument constructed in this laboratory (23). Excitation was performed using a 200-W Hg arc lamp (Osram) through a Spex Micromate monochromator with a Schott UG11 black glass filter at its exit port. Excitation was at 365 nm with a bandpass of 12 nm. Emission was detected with an EMI 9558 QB photomultiplier tube after passage of the emitted light through a 1-cm path of a 2 M $NaNO_2$ solution, which cuts off light of wavelengths shorter than 400 nm, and a Spex double monochromator equipped with a wavelength drive mechanism. Emission bandwidths were 10 nm. The data were digitized and stored using an Apple IIe computer. The data presented have not been corrected for instrumental response.

Fluorescence polarization, $p = (I_{\parallel} - I_{\perp})/(I_{\parallel} + I_{\perp})$, was determined by incorporating uv-polarizing filters (Polacoat) and a photoelastic light modulator (Hinds International) into the fluorimeter as described

Can. J. Chem. Downloaded from www.nrcresearchpress.com by 112.217.228.212 on 09/07/12
For personal use only.

by Ehrenberg (24). The instrument was calibrated for polarization measurements using fluorescein in 95% glycerol at 10°C.

Fluorescence quenching experiments were analysed using the Stern–Volmer equation (25), $F_0/F = 1 + K_{sv}$ [Q], where F is the measured fluorescence intensity at a particular wavelength, F_0 is the fluorescence intensity in the absence of quencher, K_{sv} is the Stern–Volmer quenching constant, measured from the slope of a graph of F_0/F against [Q], the concentration of quenching agent in the solution. $K_{sv} = \tau_0 k_q$, where τ_0 is the fluorescence lifetime of the probe in the absence of quencher and k_q is the bimolecular rate constant for collisions between the fluorescent chromophore and the quenching agent.

Acknowledgements

This work was supported by grants from the British Columbia Heart Foundation and the Natural Sciences and Engineering Research Council of Canada.

1. W. D. McCubbin and C. M. Kay. Acc. Chem. Res. **13**, 185 (1980).
2. L. B. Smillie. Trends Biochem. Sci. **4**, 151 (1979).
3. A. S. Mak and L. B. Smillie. Biochem. Biophys. Res. Commun. **101**, 208 (1981).
4. S. S. Lehrer. Proc. Natl. Acad. Sci. U.S.A. **72**, 3377 (1975).
5. E. Eisenberg and W. W. Keilley. J. Biol. Chem. **249**, 4742 (1974).
6. A. S. Mak, L. B. Smillie, and G. R. Stewart. J. Biol. Chem. **255**, 3647 (1980).
7. R. S. Hodges, A. K. Saund, P. C. S. Chong, S. A. St.-Pierre, and R. E. Reid. J. Biol. Chem. **256**, 1214 (1981).
8. G. P. Côté. Mol. Cell. Biochem. **57**, 127 (1983).
9. K. J. Angelides and T. J. Nutter. J. Biol. Chem. **258**, 11948 (1983).
10. S. Hvidt, J. D. Ferry, D. L. Roelke, and M. L. Greaser. Macromolecules, **16**, 740 (1983).
11. W. D. McCubbin and C. M. Kay. Can. J. Biochem. **47**, 411 (1969).
12. Y. Ishii and S. S. Lehrer. Biochemistry, **24**, 6631 (1985).
13. M. R. Payne, H. Badoyannis, and S. E. Rudnick. Biochim. Biophys. Acta, **883**, 454 (1986).
14. L. B. Smillie. Methods Enzymol. **85**, 234 (1982).
15. J. A. Spudich and S. Watt. J. Biol. Chem. **246**, 4688 (1971).
16. U. K. Laemmli. Nature (London), **227**, 680 (1970).
17. A. Holtzer, R. Clark, and S. Lowey. Biochemistry, **4**, 2401 (1965).
18. S. E. Hitchcock, L. Carlsson, and U. Lindberg. Cell, **7**, 531 (1976).
19. D. J. Gordon, Y.-Z. Yang, and E. D. Korn. J. Biol. Chem. **251**, 7474 (1976).
20. M. Bradford. Anal. Biochem. **72**, 248 (1975).
21. T. O. Sippel. J. Histochem. Cytochem. **29**, 1377 (1981).
22. L. D. Burtnick, D. I. H. Stewart, I. D. Clark, and L. B. Smillie. Biochemistry, **25**, 3875 (1986).
23. L. D. Burtnick. Arch. Biochem. Biophys. **216**, 81 (1982).
24. B. Ehrenberg. Ph.D. thesis, Weizmann Institue of Science, Rehovot, Israel (1976).
25. O. Stern and M. Volmer. Phys. Z. **20**, 183 (1919).

Can. J. Chem. Downloaded from www.nrcresearchpress.com by 112.217.228.212 on 09/07/12
For personal use only.

Main group (IIIA or 13) complexes of benzohydroxamic acid and the crystal structure of tris(benzohydroxamato)indium(III)

CAREY A. MATSUBA, STEVEN J. RETTIG,[1] AND CHRIS ORVIG[1]

Department of Chemistry, University of British Columbia, 2036 Main Mall, Vancouver, B.C., Canada V6T 1Y6

Received November 25, 1987

This paper is dedicated to Professor Charles A. McDowell on the occasion of his 70th birthday

CAREY A. MATSUBA, STEVEN J. RETTIG, and CHRIS ORVIG. Can. J. Chem. **66**, 1809 (1988).

A series of tris(benzohydroxamato)metal(III) complexes has been prepared and characterized wherein the metals are aluminum, gallium, and indium. The complexes are synthesized in high yield from aqueous solution. The indium complex, as its ethanol solvate $In(C_7H_6NO_2)_3 \cdot C_2H_5OH$, has been studied by single crystal X-ray diffraction. The crystals are monoclinic with a = 11.091(2), b = 18.065(3), c = 12.861(2) Å, β = 105.55(1)°, Z = 4, and space group $P2_1/n$. The structure was solved by Patterson and Fourier methods and was refined by full-matrix least-squares procedures to R = 0.038 and R_w = 0.037 for 2579 reflections with $I \geq 3\sigma(I)$. Bond lengths and angles in the compound were normal, although there is a strong In—O(C) interaction; the arrangement of the three ligands is *mer*. There is extensive hydrogen bonding involving all possible donors. All three complexes have been studied by mass spectrometry, and by infrared and nuclear magnetic resonance (^1H, ^{27}Al) spectroscopies. Parallel studies have been attempted with acetohydroxamic acid.

CAREY A. MATSUBA, STEVEN J. RETTIG et CHRIS ORVIG. Can. J. Chem. **66**, 1809 (1988).

On a préparé et caractérisé une série de complexes de tris(benzohydroxamato)métal(III) dans lesquels les métaux sont l'aluminium, le gallium et l'indium. On a synthétisé ces complexes avec d'excellents rendements, à partir de solutions aqueuses. Utilisant la diffraction des rayons-X sur un cristal unique, on a étudié le complexe d'indium, solvaté par l'éthanol, $In(C_7H_6NO_2)_3 \cdot C_2H_5OH$. Les cristaux sont monocliniques avec a = 11,091(2), b = 18,065(3) et c = 12,861(2) Å, β = 105,55(1)°, Z = 4 et groupe d'espace $P2_1/n$. On a résolu la structure par les méthodes de Fourier et Patterson et on l'a affinée par la méthode des moindres carrés jusqu'à des valeurs respectives de R et R_w de 0,038 et 0,037 pour 2579 réflexions avec $I \geq 3\sigma(I)$. Les longueurs des liaisons et les angles de ce composé sont normaux, même s'il existe une forte interaction In—O(C); l'arrangement des trois ligands est *mer*. On retrouve beaucoup de liaisons hydrogènes avec tous les donneurs possibles. On a étudié les trois complexes par spectrométrie de masse, par infrarouge et par la résonance magnétique nucléaire du ^1H et du ^{27}Al. On a essayé de réaliser des études parallèles avec l'acide acétohydroxamique.

[Traduit par la revue]

Introduction

As part of a project to examine lipophilic, neutral, water soluble complexes of aluminum, gallium, and other trivalent non-transition metals, we have become interested in a variety of oxygen donor, bidentate, monobasic ligands for these ions in aqueous solution (1–6).[2] Recently, we have prepared several pyrone (**1**) complexes (1, 2), some of which have found use in the study of aluminum neurotoxicity, as well as a family of 3-hydroxy-2-methyl-4-pyridinone complexes (3, 5), which form extensively hydrogen bonded arrays and which have very high overall formation constants for the group IIIA (or group 13) metal ions. In an effort to extend this work, we have examined acetohydroxamic and benzohydroxamic (**2**) acids, both of which form simple tris(ligand) metal species.

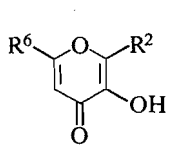

1

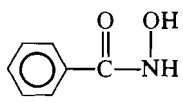

2

The hydroxamates are well-known binders of M(III) (8) and have been used as gravimetric reagents for them for many years (9). Hydroxamates are also used as binding groups in several siderophores, naturally occurring chelators for ferric ion (10). There has been interest in the substitution into hydroxamate siderophores and the simple hydroxamates of paramagnetic Fe^{3+} with diamagnetic Al^{3+} or Ga^{3+} for solution studies by nmr (11),[3] and for mechanistic work (13).

Herein we report our studies of these complexes using various physical techniques including single crystal X-ray crystallography. While this study was in progress, the structure of the gallium benzohydroxamate complex appeared (14).

Experimental

Materials and methods

Most procedures and materials were as previously described (2, 4). Benzohydroxamic acid (Hbz; from Aldrich) and acetohydroxamic acid (Hah; from Sigma) were used as received. The ^1H nmr spectra were recorded in d_6-DMSO using a Bruker HXS 270 spectrometer at 270 MHz. The ^{27}Al nmr spectra were obtained with a Varian XL 300 spectrometer operating at 78.16 MHz in either water or methanol. Melting points are uncorrected. Al and Ga were analyzed gravimetrically with 8-hydroxyquinoline (15). All the metal complexes of bz^- were prepared in a similar manner and the synthesis is presented only for $Al(bz)_3$.

Tris(benzohydroxamato)aluminum(III) monohydrate, $Al(bz)_3 \cdot H_2O$

Hbz (1.070 g, 7.80 mmol) was dissolved in 75 mL water with stirring at 50°C. A solution of $Al(NO_3)_3 \cdot 9H_2O$ (0.962 g, 2.56 mmol) in 25 mL water was added and the pH dropped to 1.7. Dropwise addition of 2 N NaOH initially resulted in precipitation of a white solid, which redissolved upon further stirring. As the pH was raised to 8, a white solid appeared and this was isolated by filtration and washed with cold water. The product was dried overnight *in vacuo* at 90°C to yield 0.99 g

[1]Authors to whom correspondence may be addressed.

[2]Also, C. A. Matsuba, W. O. Nelson, S. J. Rettig, and C. Orvig. Submitted for publication.

[3]References 14 and 26 contain many references to Ga and Al substitution for Fe.

Can. J. Chem. Downloaded from www.nrcresearchpress.com by 112.217.228.212 on 09/07/12
For personal use only.

Can. J. Chem. Downloaded from www.nrcresearchpress.com by 112.217.228.212 on 09/07/12
For personal use only.

(89%) of the monohydrate, mp 270°C (dec.). Recrystallization was from 1:1:6 methanol:water:acetone. Infrared (KBr, all very strong): 3600–2700 cm^{-1} (ν(OH), ν(NH), ν(CH)); 1605, 1530 (amide I and II); 925 ν(NO)); ^1H nmr δ: 12.7 (br s, ~1H, NH), 7.79 (d, 2H, ring *ortho* CH), 7.49 (m, 3H, ring *meta* and *para* CH), 3.33 (br s, H_2O); ^{27}Al nmr (CH_3OH) δ: 37 ($W_{1/2}$ = 550 Hz); FAB mass spectrum, *m/e*: 299 (ML_2^+); 436 (HML_3^+). *Anal.* calcd. for $C_{21}H_{20}AlN_3O_7$: C 55.63, H 4.45, Al 5.95, N 9.27; found: C 55.21, H 4.23, Al 6.19, N 9.26.

Tris(benzohydroxamato)gallium(III), Ga(bz)$_3$

(This complex was reported by a similar preparation as a monohydrate monoethanolate while this work was underway). Hbz (0.990 g, 7.22 mmol) and $Ga(NO_3)_3 \cdot 9H_2O$ (0.990 g, 2.37 mmol) were used. The resulting product was dried overnight *in vacuo* at 90°C to yield 0.97 g (86%), mp 240°C (dec.). Recrystallization was from 3:1 acetone:water. Infrared (KBr, all very strong): 3600–2700 cm^{-1} (ν(OH), ν(NH), ν(CH)); 1600, 1520 (amide I and II); 920 (ν(NO)); ^1H nmr δ: 12.8 (br s, ~1H, NH), 7.78 (d, 2H, ring *ortho* CH), 7.49 (m, 3H, ring *meta* and *para* CH), 3.3 (br s, H_2O); FAB mass spectrum, *m/e*: 341, 343 (ML_2^+); 478, 480 (HML_3^+); 820 (broad envelope for $M_2L_5^+$). *Anal.* calcd. for $C_{21}H_{18}GaN_3O_6$: C 52.76, H 3.79, Ga 14.58, N 8.79; found: C 52.38, H 3.77, Ga 14.66, N 8.81.

Tris(benzohydroxamato)indium(III), In(bz)$_3$

Hbz (0.746 g, 5.44 mmol) and $In(NO_3)_3 \cdot 5H_2O$ (0.687 g, 1.76 mmol) were used. The resulting product was dried overnight *in vacuo* at 90°C to yield 0.865 g (94%), mp 250°C (dec.). X-ray quality crystals were grown from a concentrated warm ethanolic solution. Infrared (KBr, all very strong): 3600–2700 cm^{-1} (ν(OH), ν(NH), ν(CH)); 1600, 1520 (amide I and II); 915 (ν(NO)); ^1H nmr δ: 7.82 (d, 2H, ring *ortho* CH), 7.49 (m, 3H, ring *meta* and *para* CH). A mass spectrum could not be determined by any of EI, FAB, or DCI. *Anal.* calcd. for $C_{21}H_{18}InN_3O_6$: C 48.21, H 3.47, N 8.03; found: C 48.42, H 3.55, N 8.03.

The M(bz)$_3$ complexes are soluble in methanol, ethanol, acetone, acetonitrile, DMSO, and slightly soluble in isopropanol. Several unsuccessful attempts were made to prepare pure tris(acetohydroxamato) complexes because these are very water soluble; however, the samples were always contaminated with a salt (e.g., $NaNO_3$, if a metal nitrate was neutralized in the synthesis with NaOH).

X-ray crystallographic analysis of tris(benzohydroxamato)indium(III) ethanol solvate

A crystal 0.32 × 0.32 × 0.40 mm in size, with the faces {010} and {101} developed, was mounted in a general orientation. Unit cell parameters were refined by least squares on 2 sin θ/λ values for 25 reflections (2θ = 20–26°) measured on an Enraf–Nonius CAD4-F diffractometer with Mo-K_α radiation ($\lambda(K_{\alpha 1})$ = 0.70930, $\lambda(K_{\alpha 2})$ = 0.71359 Å). Crystal data at 21°C are

$C_{21}H_{18}InN_3O_6 \cdot C_2H_6O$ f.w. = 569.28

Monoclinic, a = 11.091(2), b = 18.065(3), c 12.861(2) Å, β = 105.55(1)°, V = 2482.5(7) $Å^3$, Z = 4, ρ_c = 1.523 mg m^{-3}, $F(000)$ = 1152, $\mu(Mo - K_\alpha)$ = 9.80 cm^{-1}. Absent reflections: $0k0$, k odd, and $h0l$, $h + l$ odd, uniquely indicate the space group $P2_1/n$.

Intensities were measured with graphite-monochromated Mo − K_α radiation. An ω–2θ scan at 1.1–10.0° min^{-1} over a range of (0.75 + 0.35 tan θ)° in ω (extended by 25% on both sides for background measurement) was employed. Data were measured to 2θ = 55°. The data were corrected for Lorentz polarization and absorption (analytical method), transmission factors ranging from 0.730 to 0.760.[4] Of the 5656 independent reflections measured, 2579 had intensities greater than or equal to 3σ(I) above background where $\sigma^2(I) = S + 2B + (0.04(S - B))^2$ with S = scan count and B = normalized background count.

The structure was solved by Patterson and Fourier methods. The position of the indium atom was determined from the Patterson function while the coordinates of the remaining non-hydrogen atoms were determined from a subsequent difference Fourier map. The non-hydrogen atoms were refined with anisotropic thermal parameters and the hydrogen atoms were fixed in idealized positions (staggered methyl, C(sp^3)—H = 0.98, C(sp^2)—H = 0.97, N—H = 0.92 Å, $U_H \propto U_{\text{bonded atom}}$). The hydroxyl proton position was taken from a difference Fourier map and was not refined. Neutral atom scattering factors and anomalous scattering corrections for In were taken from ref. 16. The weighting scheme $w = 1/\sigma^2(F)$, where $\sigma^2(F)$ is derived from the previously defined $\sigma^2(I)$, gave uniform values of $w(|F_o| - |F_c|)^2$ over ranges of both $|F_o|$ and sin θ/λ and was employed in the final stages of full-matrix refinement (307 variables). Reflections with $I < 3\sigma(I)$ were not included in the refinement. Convergence was reached at R = 0.038 and R_w = 0.037 for 2579 reflections with $I \geq 3\sigma(I)$. The function minimized was $\Sigma w(|F_o| - |F_c|)^2$, $R = \Sigma||F_o| - |F_c||/\Sigma|F_o|$, and $R_w = (\Sigma w(|F_o| - |F_c|)^2/\Sigma w|F_o|^2)^{1/2}$.

On the final cycle of refinement the mean and maximum parameter shifts corresponded to 0.002 and 0.027 σ, respectively. The mean error in an observation of unit weight was 1.249. Final coordinates and equivalent isotropic thermal parameters (U_{eq} = 1/3 trace of diagonalized U) are given in Table 1. Bond lengths and angles appear in Tables

TABLE 1. Final positional (fractional × 10^4, In × 10^5) and isotropic thermal parameters ($U \times 10^3$ $Å^2$) with estimated standard deviations in parentheses

Atom	x	y	z	U_{eq}
In	46678(4)	29941(2)	51519(3)	34
O(1)	2949(3)	2630(2)	4053(3)	44
O(2)	3255(4)	3208(2)	5992(3)	49
O(3)	6026(3)	2968(2)	6688(3)	42
O(4)	5293(3)	1853(2)	5340(3)	43
O(5)	4708(4)	4171(2)	5023(3)	47
O(6)	5803(4)	3201(2)	4055(3)	48
O(7)	−34(5)	1791(3)	3456(4)	85
N(1)	1999(4)	2682(3)	4554(4)	48
N(2)	6505(4)	2274(3)	6906(4)	37
N(3)	5577(5)	4374(3)	4492(4)	45
C(1)	2168(5)	2981(4)	5492(5)	43
C(2)	6116(5)	1735(3)	6212(5)	36
C(3)	6102(6)	3882(4)	4025(5)	43
C(4)	1132(5)	3051(4)	6004(5)	52
C(5)	−112(6)	3026(5)	5416(5)	74
C(6)	−1040(7)	3102(6)	5945(8)	96
C(7)	−751(8)	3222(4)	7026(8)	82
C(8)	485(8)	3245(4)	7617(6)	75
C(9)	1423(6)	3164(4)	7105(6)	60
C(10)	6661(5)	983(3)	6457(5)	38
C(11)	7352(7)	770(4)	7465(6)	74
C(12)	7782(8)	44(5)	7648(7)	85
C(13)	7526(7)	−458(4)	6829(8)	70
C(14)	6847(9)	−242(4)	5854(7)	90
C(15)	6417(7)	461(4)	5659(6)	67
C(16)	7069(6)	4123(4)	3511(6)	56
C(17)	7834(8)	4721(5)	3875(8)	87
C(18)	8765(10)	4918(5)	3381(10)	116
C(19)	8908(11)	4497(7)	2158(11)	127
C(20)	8197(13)	3893(7)	2193(10)	158
C(21)	7259(9)	3710(5)	2676(8)	105
C(22)	−400(10)	1085(8)	3720(10)	152
C(23)	−796(17)	1065(10)	4649(14)	232

[4]The computer programs used include locally written programs for data processing and locally modified versions of the following: MULTAN 80, multisolution program by P. Main, S. J. Fiske, S. E. Hull, L. Lessinger, G. Germain, J. P. Declercq, and M. M. Woolfson; AGNOST, absorption corrections, by J. A. Ibers; ORFLS, full-matrix least squares, and ORFFE, function and errors, by W. R. Busing, K. O. Martin, and H. A. Levy; FORDAP, Patterson and Fourier syntheses, by A. Zalkin; and ORTEP II, illustrations, by C. K. Johnson.

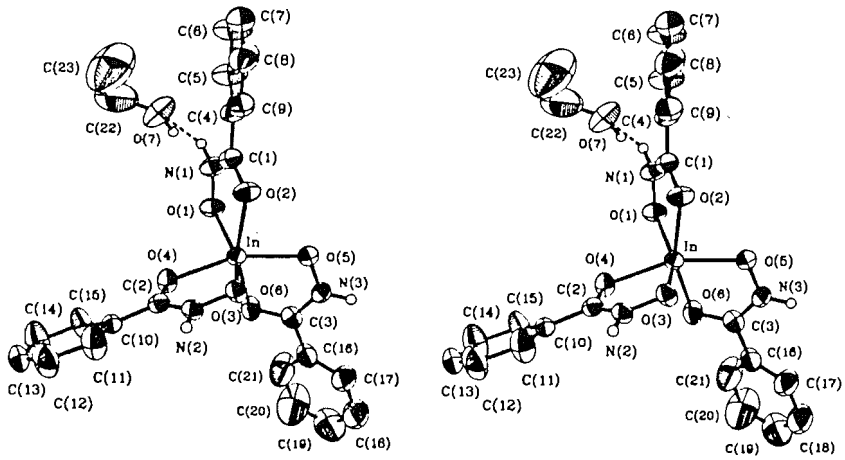

FIG. 1. Stereoview of the asymmetric unit of $In(bz)_3 \cdot EtOH$. 50% probability thermal ellipsoids are shown for the non-hydrogen atoms.

TABLE 2. Bond lengths (Å) with estimated standard deviations in parentheses

Bond	Length (Å)	Bond	Length (Å)
In—O(1)	2.150(4)	C(4)—C(5)	1.385(8)
In—O(2)	2.164(4)	C(4)—C(9)	1.381(9)
In—O(3)	2.141(3)	C(5)—C(6)	1.383(9)
In—O(4)	2.167(4)	C(6)—C(7)	1.358(11)
In—O(5)	2.134(4)	C(7)—C(8)	1.379(11)
In—O(6)	2.161(4)	C(8)—C(9)	1.380(9)
O(1)—N(1)	1.378(6)	C(10)—C(11)	1.373(8)
O(2)—C(1)	1.272(6)	C(10)—C(15)	1.366(8)
O(3)—N(2)	1.361(6)	C(11)—C(12)	1.394(9)
O(4)—C(2)	1.260(6)	C(12)—C(13)	1.361(10)
O(5)—N(3)	1.372(6)	C(13)—C(14)	1.336(10)
O(6)—C(3)	1.277(7)	C(14)—C(15)	1.356(10)
O(7)—C(22)	1.408(14)	C(16)—C(17)	1.376(10)
N(1)—C(1)	1.289(7)	C(16)—C(21)	1.370(10)
N(2)—C(2)	1.313(7)	C(17)—C(18)	1.395(10)
N(3)—C(3)	1.296(7)	C(18)—C(19)	1.388(14)
C(1)—C(4)	1.474(7)	C(19)—C(20)	1.346(14)
C(2)—C(10)	1.487(8)	C(20)—C(21)	1.387(12)
C(3)—C(16)	1.469(8)	C(22)—C(23)	1.38(2)

2 and 3, respectively. Intra-annular torsion angles for the five-membered chelate rings, hydrogen atom parameters, anisotropic thermal parameters, a complete listing of torsion angles (Tables 4–7), and measured and calculated structure factor amplitudes (Table 8) have been placed in the Depository of Unpublished Data.[5]

Results and discussion

The benzohydroxamato complexes of Al, Ga, and In can be easily synthesized from aqueous solution; however, their aqueous solubility is very low. It proved impossible to isolate pure samples of the acetohydroxamato complexes although the ^{27}Al and ^{1}H nmr and FAB mass spectra were measurable and supported the tris(ligand)metal(III) formulation. The ^{27}Al nmr spectrum of $Al(ah)_3$ at pH 6 was consistent (36 ppm, $W_{1/2} \approx 400$ Hz) with that in the literature (11). The ^{27}Al nmr spectrum of $Al(bz)_3$ in methanol has a broader line ($W_{1/2} \approx 550$ Hz) in the same chemical shift range (37 ppm), consistent with a significantly larger size complex (three phenyl substituents vs. three methyls) and with the somewhat decreased viscosity of MeOH vs. H_2O, but the same hydroxamate-based AlO_6 nucleus.

The ir and nmr spectra are completely consistent with the formulation of complexes containing bound ligands, and they show the characteristic changes in frequency and chemical shifts to lower and higher values, respectively. The ν(NO) stretch moves from 900 in Hbz to ~920 cm^{-1} in the complexes, suggesting some delocalization of the ketone double bond into the chelate ring. Some possible M–O stretches are observed in the low energy region (<600 cm^{-1}); however, assigning these with any certainty is difficult. Notable also are the shifts of the N-H proton in the benzohydroxamato complexes to ~13 ppm from 9.6 in the free acid. The FAB mass spectra of the Al and Ga complexes of both acids showed most of the expected (2) ML_2^+, HML_3^+, and $M_2L_5^+$ peaks.

The asymmetric unit of $In(bz)_3 \cdot EtOH$ is shown in Fig. 1. The crystal structure (Fig. 2) consists of tris(benzohydroxamato)indium(III) and ethanol molecules, linked by an extensive hydrogen bonding network that incorporates all available hydrogen bond donors (O(7)—H(O7)···O(3) ($x - 1/2, 1/2 - y, z - 1/2$), N(1)—H(N1)···O(7) ($x, y, z$), N(2)—H(N2)···O(1) ($1/2 + x, 1/2 - y, 1/2 + z$), and N(3)—H(N3)···O(5) ($1 - x, 1 - y, 1 - z$); H···O = 1.87, 1.95, 1.95, 1.99 Å; (N/O)···O = 2.859(6), 2.822(7), 2.801(6), 2.738(6) Å; (N/O)—H···O = 160, 158, 153, 137°; respectively). The coordination about the indium atom is *mer*-octahedral, distorted by the small bite (17) of the chelating ligand (mean intraligand O···O = 2.637(7) Å, mean In—O = 2.153, normalized bite b = O···O/M—O = 1.22). This contrasts directly with the *fac* geometry found for the Ga analogue (14).

As observed previously in structures of Ga^{3+} (14), Sn^{4+} (18–21), Fe^{3+} (22–27), Cr^{3+} (28), and Zn^{2+} (29) hydroxamates, the M—O(N) bonds are shorter than the M—O(C) bonds ({In—O(C)} − {In—O(N)} = 0.014, 0.026, 0.027 Å for the three ligands). Correction for differences in effective ionic radii (30) shows that the hydroxamate moiety makes a stronger chelate with In^{3+} than with Sn^{4+}, in which complexes the Sn—O bonds are relatively much longer, especially Sn—O(C) (18–21). The corrected bond lengths for the Ga structure (14), however, are very similar to those in our In complex. In the latter the In bond to the O—N (In—O(1)), which is hydrogen bonded to the ethanol molecule, is notably longer than the other two.

[5]Materials mentioned in the text may be purchased from the Depository of Unpublished Data, CISTI, National Research Council of Canada, Ottawa, Ont., Canada, K1A 0S2.

Can. J. Chem. Downloaded from www.nrcresearchpress.com by 112.217.228.212 on 09/07/12
For personal use only.

TABLE 3. Bond angles (deg) with estimated standard deviations in parentheses

Bonds	Angle (deg)	Bonds	Angle (deg)
O(1)—In—O(2)	75.5(1)	N(2)—C(2)—C(10)	119.5(5)
O(1)—In—O(3)	151.8(2)	O(6)—C(3)—N(3)	119.7(6)
O(1)—In—O(4)	89.0(1)	O(6)—C(3)—C(16)	121.7(6)
O(1)—In—O(5)	106.7(2)	N(3)—C(3)—C(16)	118.5(6)
O(1)—In—O(6)	101.1(2)	C(1)—C(4)—C(5)	122.4(6)
O(2)—In—O(3)	88.1(1)	C(1)—C(4)—C(9)	118.4(5)
O(2)—In—O(4)	111.5(2)	C(5)—C(4)—C(9)	119.3(6)
O(2)—In—O(5)	83.9(2)	C(4)—C(5)—C(6)	119.5(7)
O(2)—In—O(6)	157.3(1)	C(5)—C(6)—C(7)	121.1(7)
O(3)—In—O(4)	75.6(1)	C(6)—C(7)—C(8)	119.7(7)
O(3)—In—O(5)	94.0(2)	C(7)—C(8)—C(9)	119.9(7)
O(3)—In—O(6)	102.6(1)	C(4)—C(9)—C(8)	120.4(7)
O(4)—In—O(5)	160.6(2)	C(2)—C(10)—C(11)	123.3(6)
O(4)—In—O(6)	90.7(2)	C(2)—C(10)—C(15)	118.9(5)
O(5)—In—O(6)	75.5(2)	C(11)—C(10)—C(15)	117.6(6)
In—O(1)—N(1)	109.0(3)	C(10)—C(11)—C(12)	120.2(7)
In—O(2)—C(1)	113.9(4)	C(11)—C(12)—C(13)	120.3(7)
In—O(3)—N(2)	110.5(3)	C(12)—C(13)—C(14)	118.7(7)
In—O(4)—C(2)	113.2(4)	C(13)—C(14)—C(15)	122.0(7)
In—O(5)—N(3)	109.7(3)	C(10)—C(15)—C(14)	121.2(6)
In—O(6)—C(3)	112.8(4)	C(3)—C(16)—C(17)	122.5(7)
O(1)—N(1)—C(1)	122.0(5)	C(3)—C(16)—C(21)	118.4(7)
O(3)—N(2)—C(2)	120.2(4)	C(17)—C(16)—C(21)	118.9(7)
O(5)—N(3)—C(3)	120.6(5)	C(16)—C(17)—C(18)	120.6(8)
O(2)—C(1)—N(1)	119.3(5)	C(17)—C(18)—C(19)	118.8(9)
O(2)—C(1)—C(4)	119.5(6)	C(18)—C(19)—C(20)	120.6(9)
N(1)—C(1)—C(4)	121.2(5)	C(19)—C(20)—C(21)	120.1(9)
O(4)—C(2)—N(2)	120.5(5)	C(16)—C(21)—C(20)	120.9(9)
O(4)—C(2)—C(10)	120.0(5)	O(7)—C(22)—C(23)	114.3(14)

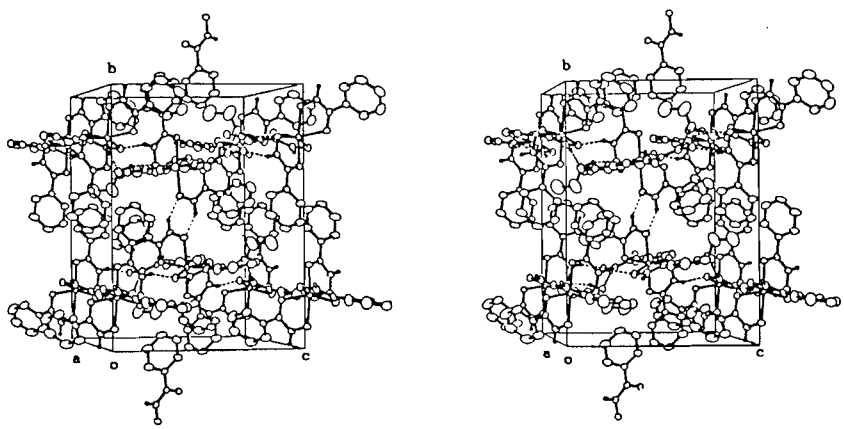

FIG. 2. Stereoview of the unit cell of $In(bz)_3 \cdot EtOH$. Broken lines indicate hydrogen bonds.

In the ferric ion structures, a similarly corrected comparison shows a weaker M—O(C) interaction, but a comparable M—O(N) bond (22–27). $Ga(bz)_3$ (14) and $Cr(bz)_3$ (28) are the only structurally characterized metal hydroxamates to have the difference between M—O(C) and M—O(N) as small as it is in the present structure (0.014, 0.022, 0.039 Å); in the Cr complex, this was ascribed to a crystal-field effect (28) that is not available to Ga or $In(bz)_3$. The usual difference between M—O(C) and M—O(N) is 0.05–0.11 Å (14, 18–27, 29). Because all possible hydrogen bond donors in the $In(bz)_3$ structure are so utilized (e.g., the N—H), there is likely an addition of electron density to the N—O, causing this bond to be anomalously short relative to other values. An alternative explanation might be an increased double bond character to C—N, making the chelate ring more delocalized; however, the observed bond distances support the former rather than the latter argument.

The average In—O distance of 2.153 Å in $In(bz)_3$, with five-membered chelate rings, is slightly longer than the average In—O distance of 2.133 Å observed for six-coordinate indium 1,3-diketonate complexes (7, 31–33) containing six-membered chelate rings. The internal geometry of the benzohydroxamate ligands is normal (12, 14, 18–29). The chelate ring containing N(2) is planar within experimental error while the two others are significantly nonplanar, the maximum deviations from the mean plane being 0.042(4) and 0.083(4) Å for the rings containing N(1) and N(3), respectively. The dihedral angles between the

Can. J. Chem. Downloaded from www.nrcresearchpress.com by 112.217.228.212 on 09/07/12
For personal use only.

chelate ring and the associated phenyl mean planes are 17.3, 12.7, and 33.6° for the N(1), N(2), and N(3) ligands.

The general affinity for trivalent metal ions that one would suspect from the presence of hydroxamate groups in the siderophores extends to Al and In of the group IIIA metals; bz^- forms a strong chelate with In^{3+} (demonstrated by the relatively short In—O(C) bonds found in the structure of $In(bz)_3$). The extensive hydrogen bonding found in this structure is in keeping with the pattern that we have seen (3, 5) in other neutral tris(ligand) complexes of these main group metal ions wherein every possible hydrogen bond donor is involved in this type of interaction.

Acknowledgements

The authors acknowledge support from the Natural Sciences and Engineering Research Council of Canada and from the British Columbia Health Care Research Foundation in the form of operating grants. C.O. thanks NSERC for a University Research Fellowship, as well as an Undergraduate Student Research Award to C.A.M. We also thank Professor J. Trotter for the use of his crystallographic facilities, and Prof. C. A. McDowell for his continuing interest in our work.

1. M. M. FINNEGAN, S. J. RETTIG, and C. ORVIG. J. Am. Chem. Soc. **108**, 5033 (1986).
2. M. M. FINNEGAN, T. G. LUTZ, W. O. NELSON, A. SMITH, and C. ORVIG. Inorg. Chem. **26**, 2171 (1987).
3. W. O. NELSON, S. J. RETTIG, and C. ORVIG. J. Am. Chem. Soc. **109**, 4121 (1987).
4. W. O. NELSON, T. B. KARPISHIN, S. J. RETTIG, and C. ORVIG. Can. J. Chem. **66**, 123 (1988).
5. W. O. NELSON, T. B. KARPISHIN, S. J. RETTIG, and C. ORVIG. Inorg. Chem. **27**, 1045 (1988).
6. W. O. NELSON, T. G. LUTZ, and C. ORVIG. Submitted for publication.
7. G. J. PALENIK and K. R. DYMOCK. Acta Crystallogr. Sect. B: Struct. Crystallogr. Cryst. Chem. **36**, 2059 (1980).
8. B. CHATTERJEE. Coord. Chem. Rev. **26**, 281 (1978).
9. (*a*) S. C. SHOME. Analyst (London), **75**, 27 (1950); (*b*) M. D. PALMIERI AND J. S. FRITZ. Anal. Chem. **59**, 2226 (1987).
10. K. N. RAYMOND, G. MULLER, and B. F. MATZANKE. Top. Curr. Chem. **123**, 49 (1984).
11. M. LLINAS and A. DE MARCO. J. Am. Chem. Soc. **102**, 2226 (1980).
12. B. H. BRACHER and R. W. H. SMALL. Acta Crystallogr. Sect. B: Struct. Crystallogr. Cryst. Chem. **26**, 1705 (1970).
13. J. M. GARRISON and A. L. CRUMBLISS. Inorg. Chim. Acta, **138**, 61 (1987); Inorg. Chem. **26**, 3660 (1987).
14. B. A. BORGIAS, S. J. BARCLAY, and K. N. RAYMOND. J. Coord. Chem. **15**, 109 (1986).
15. W. RIEMAN, J. D. NEUSS, and B. NAIMANN. Quantitative analysis: a theoretical approach. McGraw–Hill, New York. 1951. pp. 369–370.
16. International tables for X-ray crystallography. Vol. IV. Kynoch Press, Birmingham. 1974. pp. 99–102 and 149.
17. D. L. KEPERT. Prog. Inorg. Chem. **23**, 1 (1977).
18. T. J. KING and P. G. HARRISON. J. Chem. Soc. Chem. Commun. 815 (1972).
19. P. G. HARRISON and T. J. KING. J. Chem. Soc. Dalton Trans. 2298 (1974).
20. P. G. HARRISON, T. J. KING, and J. A. RICHARDS. J. Chem. Soc. Dalton Trans. 826 (1975).
21. P. G. HARRISON, T. J. KING, and J. A. RICHARDS. J. Chem. Soc. Dalton Trans. 1414 (1976).
22. A. ZALKIN, J. D. FORRESTER, and D. H. TEMPLETON. J. Am. Chem. Soc. **88**, 1810 (1966).
23. H. J. LINDNER and S. GOTTLICHER. Acta Crystallogr. Sect. B: Struct. Crystallogr. Cryst. Chem. **24**, 832 (1969).
24. D. VAN DER HELM and M. POLING. J. Am. Chem. Soc. **98**, 86 (1976).
25. M. B. HOSSAIN, D. L. ENG-WILMOT, R. A. LOGHRY, and D. VAN DER HELM. J. Am. Chem. Soc. **102**, 5766 (1980).
26. D. VAN DER HELM, J. R. BAKER, D. L. ENG-WILMOT, M. B. HOSSAIN, and R. A. LOGHRY. J. Am. Chem. Soc. **102**, 4224 (1980).
27. D. VAN DER HELM, J. R. BAKER, R. A. LOGHRY, and J. D. EKSTRAND. Acta Crystallogr. Sect. B: Struct. Crystallogr. Cryst. Chem. **37**, 323 (1981).
28. K. ABU-DARI, J. D. EKSTRAND, D. P. FREYBERG, and K. N. RAYMOND. Inorg. Chem. **18**, 108 (1979).
29. S. GOTTLICHER and P. O. OCHSENREITER. Chem. Ber. **107**, 391 (1974).
30. R. D. SHANNON. Acta Crystallogr. Sect. A: Cryst. Phys. Diffr. Theor. Gen. Crystallogr. **32**, 751 (1976).
31. J. G. CONTRERAS, F. W. B EINSTEIN, and D. G. TUCK. Can. J. Chem. **52**, 3793 (1972).
32. H. SOLING. Acta Chem. Scand. Ser. A: **A30**, 163 (1976).
33. J. G. RODRIGUEZ, F. H. CANO, and S. GARCIA-BLANCO. Cryst. Struct. Commun. **8**, 53 (1979).

Can. J. Chem. Downloaded from www.nrcresearchpress.com by 112.217.228.212 on 09/07/12
For personal use only.

The solution conformation of the synthetic tubulin fragment Ac-tubulin-α(430–441)-amide based on two-dimensional ROESY experiments

ALBIN OTTER AND GEORGE KOTOVYCH[1]

Department of Chemistry, University of Alberta, Edmonton, Alta., Canada T6G 2G2

Received January 18, 1988

This paper is dedicated to Professor Charles A. McDowell on the occasion of his 70th birthday

ALBIN OTTER and GEORGE KOTOVYCH. Can. J. Chem. **66**, 1814 (1988).

Ac-tubulin-α(430–441)-amide, a synthetic fragment of tubulin, has been studied by 300-MHz ^{1}H nuclear magnetic resonance spectroscopy in 80% CD_3OH/20% D_2O solution at neutral pH. The results, based on two-dimensional phase-sensitive techniques such as COSY, RELAY, and ROESY, reveal that the dodecapeptide exists in a non-random conformation. The conformation can be described as an α helix for the N-terminal five residues, followed by an extended section. The extended part exhibits a significant change in the nuclear Overhauser enhancement (nOe) pattern between units number 9 and 10. Together with long-range nOe data this can be attributed to a folding back that allows the close proximity of the C-terminal half of the extended chain and amino acids 3 to 5 of the α-helical turn. The existence of an α helix is in good agreement with previously published circular dichroism data.

ALBIN OTTER et GEORGE KOTOVYCH. Can. J. Chem. **66**, 1814 (1988).

Opérant à un pH neutre, dans des solutions contenant 80% de CD_3OH et 20% de D_2O et faisant appel à la résonance magnétique nucléaire du ^{1}H à 300 MHz, on a étudié l'Ac-tubuline-α(430–441)-amide, un fragment de la tubuline obtenu par synthèse. Les résultats, qui sont basés sur des techniques bidimensionnelles, sensibles à la phase, comme la spectroscopie de corrélation (COSY), relais (RELAY) et la spectroscopie d'effet Overhauser relais (ROESY), indiquent que le dodécapeptide existe dans une conformation qui n'est pas statistique. On peut décrire la conformation des cinq résidus du terminus-N comme celle d'une hélice α; cette portion serait suivie par une section linéaire. On observe un changement important dans la présentation de l'effet Overhauser nucléaire entre les unités n° 9 et 10 de la section linéaire. Ces données ainsi que celles relatives à l'effet Overhauser nucléaire à distance peuvent être attribuées à un repli de la chaîne qui permet à la portion du terminus-C de la chaîne linéaire de se rapprocher des acides aminés n° 3 et 5 de la portion α-hélicoïdale. L'existence d'une hélice α est en bon accord avec les données de dichroïsme circulaire publiées antérieurement.

[Traduit par la revue]

Introduction

Microtubules are formed by reversible polymerization of the protein tubulin along with several "microtubule associated proteins". Substances affecting assembly and maintenance of microtubules therefore serve important roles in nerve function regulation, as microtubules transport chemicals from the cell bodies of neurones along the axons to the nerve terminal locality (1). Enzymes needed to synthesize various neurotransmitters from their amino acid precursors are among the substances transported.

Recent studies (2–4) have shown that a 4-kDa peptide fragment, resulting from limited proteolysis of tubulin with subtilisin, is essential for the interactions of microtubule associated proteins as well as for the self-assembly of tubulin into microtubules. A subdomain, believed to be important for the activity of the 4-kDa fragment, has been synthesized (5) as a protected peptide, containing 12 amino acids: *N*-acetyl-Lys^1-Asp^2-Tyr^3-Glu^4-Glu^5-Val^6-Gly^7-Val^8-Asp^9-Ser^{10}-Val^{11}-Glu^{12}-NH_2 (*N*-acetyl-tubulin-α(430–441)-amide). The circular dichroism (cd) spectrum of this peptide has been published recently (6), indicating a completely unstructured and somewhat aggregated behavior in water, but the presence of an α helix to the extent of 30% in methanol/water (80:20, v/v) mixtures was observed. The use of mixed solvents to induce secondary structure in various peptides has recently been reported (6–9). Although the exact reasons for the secondary structure-inducing properties of mixed solvents are not known, it appears that a change in viscosity plays an important role. For 80% methanol/20% water, as used in the present study, the kinematic viscosity of the binary liquid is very close to its maximum (10, 11), thus reducing the mobility of the peptide dissolved in the solvent mixture.

With the ultimate aim of understanding the role of the tubulin fragment in the self-assembly of tubulin into microtubules and its interactions with neurotransmitters (4, 6), we began to study the solution conformation of the isolated dodecapeptide. Small proteins and peptides are conveniently studied at the molecular level by nuclear magnetic resonance (nmr) spectroscopy (12, 13). However, the observation of nuclear Overhauser effects (nOe), using conventional methods, often fails for molecules of the size of the tubulin fragment, irrespective of the internuclear distances involved, because the tumbling rate for these solutes is close to that at which the maximum possible nOe passes through zero (14). Consequently, sequential assignments along the peptide backbone and the observation of interproton distances revealing secondary structure are impossible. By using the rotating frame nOe experiment (15, 16), this problem could be completely overcome. From Fig. 1, where the maximum observable nOe is depicted as a function of correlation time and spectrometer frequency, it can be seen clearly that the obtainable rotating frame Overhauser effects (rOe) are considerably stronger than the nOe's over a wide range of correlation time/spectrometer frequency combinations. Our results, based on phase-sensitive COSY (17, 18) and ROESY experiments, confirm the cd studies and localize the α turn in the N-terminal half of the molecule, whereas the C-termal end is found to be in an approximately extended conformation. This result is of particular interest given the fact that binding studies (6) reveal the N-terminal half to be actively involved in intermolecular interactions.

[1]Author to whom correspondence may be addressed.

Can. J. Chem. Downloaded from www.nrcresearchpress.com by 112.217.228.212 on 09/07/12
For personal use only.

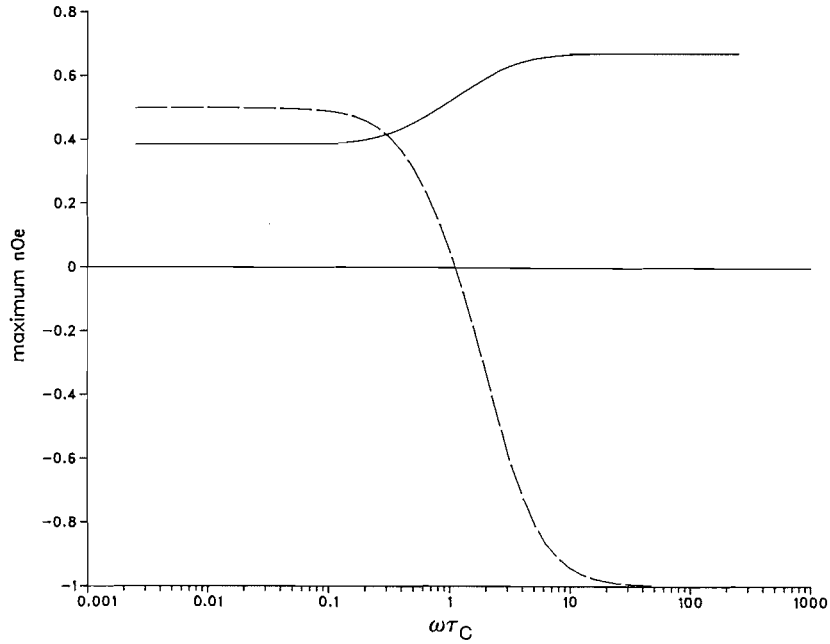

FIG. 1. The maximum $^1H-^1H$ nuclear Overhauser enhancement (nOe) as a function of spectrometer frequency ω times the correlation time τ_c. The solid line represents the fit for a ROESY experiment (15) whereas the dotted line represents the NOESY experiment (13).

Experimental

Ac-tubulin-α(430–441)-amide was synthesized and purified following standard procedures (5). The nmr samples were prepared by dissolving the solid material in 0.5 mL H_2O and the pH was adjusted to 7.1. The sample was then freeze-dried and redissolved in 0.45 mL of a CD_3OH/D_2O (80:20, v/v) mixture (CD_3OH from MSD Isotopes, number MD-67, 99.9% D enriched). Before sealing, argon was bubbled through the sample for ca. 15 min. The final concentration was 8 mM. In the same manner two 5-mM samples, one at pH 7.2 and one at pH 6.7, were prepared as well. Slight changes in pH were helpful in eliminating some spectral overlap in the NH region due to some very small (<0.05 ppm) chemical shift changes. It is also noteworthy that the change in concentration did not have any measurable influence on the spectra, indicating that no aggregation was present.

All nmr experiments were carried out on a Bruker AM 300 nmr spectrometer, which was modified to perform spin-locking at a field of 2.5 kHz at ambient temperature (297 ± 1 Hz). Data acquisition and data processing were controlled by an Aspect 3000 computer equipped with an array processor using Bruker 1987 DISNMR software. The chemical shifts are reported relative to the undeuterated fraction of the methyl group of CD_3OH at 3.30 ppm with respect to TMS.

A sweep width of 2650 Hz and 8K (zero-filled to 16K) data points were used to record one-dimensional spectra (Fig. 2). A total of 600 scans were accumulated to obtain a good signal-to-noise ratio for the relatively low-intensity NH protons even after resolution enhancement. Typically, the FID was multiplied by a Gaussian function (line broadening factors up to −5 Hz) before Fourier transformation. Both solvent signals (OH group and undeuterated fraction of CD_3OH at 3.30 ppm) were presaturated during a 2.4-s relaxation delay by changing the decoupler frequency every 0.2 s. To account for the big difference in intensity between the two solvent peaks, the OH signal was presaturated twice as long as that of the methyl group. The effect of presaturation on the exchangeable protons was carefully monitored and no wipe-out due to saturation transfer was observed.

The parameters used in the two-dimensional nmr techniques (12, 19) are summarized in Table 1. The COSY (17) and the ROESY (15, 16) experiments were carried out in the phase-sensitive mode using time-proportional phase increments (18) whereas the relayed coherence transfer spectrum (RELAY) (20, 21) was recorded in the absolute value mode. Solvent suppression was carried out in the same way as described for the one-dimensional spectra. In addition, irradiation of the OH signal was continued at all times aside from data acquisition (22). The phase-sensitive spectra were first phased using the second FID to determine the phase constants, which were then applied to all spectra in the t_2 domain. In addition, the ROESY experiment required a basic 90° phase correction in t_1. The resulting 2D matrices were displayed and slight phase adjustments in both dimensions were usually necessary to obtain the best possible data representation. Concerning the ROESY experiment, a few more remarks are appropriate. This experiment often suffers from spurious resonances due to magnetization transfer between scalar coupled spins (23, 24). Under the selected experimental conditions (25), the resulting two-dimensional spectrum was almost free of any such peaks, which are easily identified by their phase being the same as the diagonal signals (real rOe cross-peaks have opposite signs with respect to the diagonal peaks). Some baseline distortions, however, were present, especially around intense peaks such as the residual solvent signals and methyl groups. As suggested by other authors (26), we treated the spectra in both dimensions with the Bruker ABS baseline correction routine, which eliminated this problem almost completely (using a polynomial fitting of fifth degree to the baseline).

Results

The spectral analysis of the dodecapeptide is based on the results of various two-dimensional nmr experiments suitable for structure elucidations of peptides (13). First, a phase-sensitive COSY spectrum (18) was recorded, the contour plot of which is shown in Fig. 3. The so-called "fingerprint" region (27) reveals $NH-H_\alpha$ connectivities, and $NH-H_\alpha$ coupling constants can be determined to an accuracy of about 0.6 Hz as the digital resolution along the F_2 axis is 1.2 Hz. Figure 3 illustrates the power of phase-sensitive COSY spectra in the region around 8.35 ppm where the coupling constants can be determined unambiguously, whereas in the one-dimensional spectrum this is impossible. Further valuable information could be obtained from the relayed COSY experiment (20, 21), providing cross-peaks between spins that are not mutually coupled but belong to

Can. J. Chem. Downloaded from www.nrcresearchpress.com by 112.217.228.212 on 09/07/12
For personal use only.

Can. J. Chem. Downloaded from www.nrcresearchpress.com by 112.217.228.212 on 09/07/12
For personal use only.

TABLE 1. Summary of 2D experimental parameters[a]

Parameter	Unit	COSYPH[b]	RELAY	ROESYPH[b]
Sweep width F2	Hz	2400	2400	2500
Sweep width F1	Hz	1200	1200	1250
Matrix size (F1 × F2) before zero-filling	—	512 × 1K	256 × 1K	280 × 1K
Matrix size (F1 × F2) after zero-filling	—	1K × 4K	1K × 4K	1K × 2K
Evolution time:				
initial value	μs	1	1	1
increment	ms	0.21	0.41	0.20
Number of scans (dummy scans)		48(2)	112(2)	96(2)
Acquisition time	s	0.21	0.21	0.20
Relaxation delay	s	1.8	1.8	1.8
Other delays	ms	—	80[c]	125[d]
Window functions for 2D FT (F1/F2)	—	S/S	S/S	S/S
Shifts of window function in fractions of π (F1/F2)	—	4/8	6/8	3/4

[a]All spectra were recorded at 297 K at concentrations between 5 and 8 mM.
[b]The phase-sensitive spectra were first phased using the second FID and then, after Fourier transformation, the phase was optimized in both dimensions by an additional phase correction applied to the entire 2D spectrum. The ROESY spectrum was baseline corrected in F1 and F2 by means of a Bruker ABS baseline correction.
[c]Coherence transfer time.
[d]Spin-locking time at an average rf field strength of 2.5 kHz.

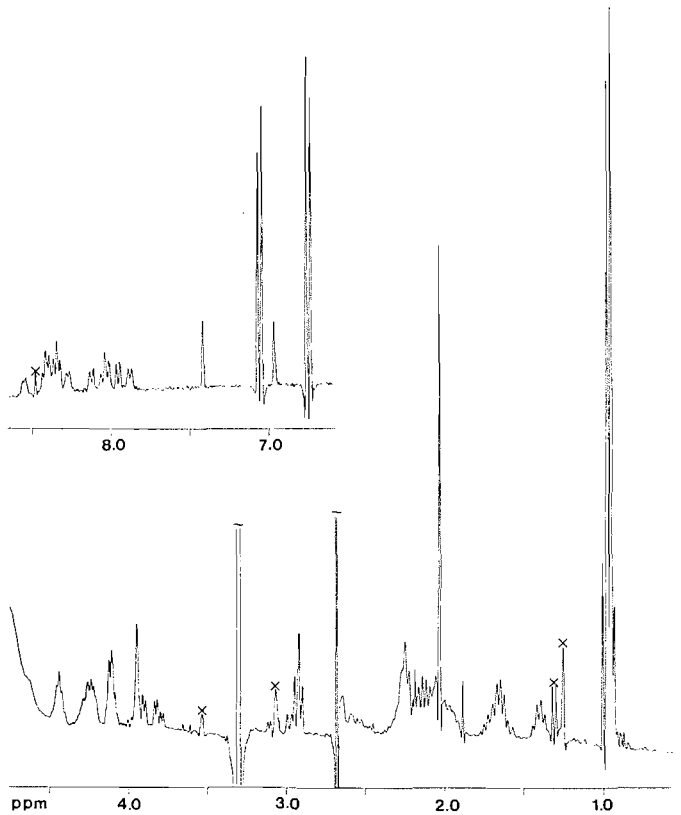

FIG. 2. The 300-MHz ^1H spectrum of Ac-tubulin-α(430–441)-amide recorded at 5.0 mM concentration in CD_3OH/D_2O (80:20), 297 K, pH 6.7. The inset depicts the region of the exchangeable and aromatic protons, the lower trace shows the range from the H_α protons to the H_γ's of the valines. Impurities and ^{13}C satellites of the solvent are denoted with an X.

the same spin system. In particular, the three valine moieties could be easily distinguished from other amino acids and from each other (through NH–H_β cross-peaks). Combining the results of the COSY and RELAY experiments, all resonances of the peptide could be assigned to individual amino acids. However, as there are many amino acids of the same kind, for example three Glu and three Val, the sequential assignment remained undefined. This problem could be overcome by recording the phase-sensitive rotating frame nOe spectrum (ROESY, 15, 16), which provides distance information based on the nuclear Overhauser effect (14). Under the selected experimental conditions (see experimental section), the two-dimensional spectrum (Fig. 4) provided a large number of cross-peaks of remarkably strong intensity. In addition, our experiments were essentially free of often-reported artifacts such as spurious resonances due to COSY and Hartmann–Hahn-type transfers (23, 24). Furthermore, we wish to point out that ROESY spectra recorded with longer spin-locking times produced cross-peaks of lower intensities. Consequently, 125 ms must be close to optimum for the system under investigation. Based on the observation of NH–H_α cross-peaks between adjacent amino acids, the sequential assignment could be easily achieved. The results are summarized in Table 2 and in Fig. 5. Besides the (i)–$(i + 1)$ interactions, some long-range effects were observed as well, indicating clearly that the molecule does not exist in a stretched conformation. This is in perfect agreement with the results of a temperature dependence study of the amide protons between 282 and 302 K. The values for the changes in chemical shifts as a function of temperature were found to be between 3.5 and approximately 7.0 ppb/K (6). The latter value is typical for protons that are not hydrogen bonded or otherwise shielded from interactions with the solvent, but the former value is borderline and some shielding cannot be excluded (28). Therefore, we conclude that weak hydrogen

Can. J. Chem. Downloaded from www.nrcresearchpress.com by 112.217.228.212 on 09/07/12
For personal use only.

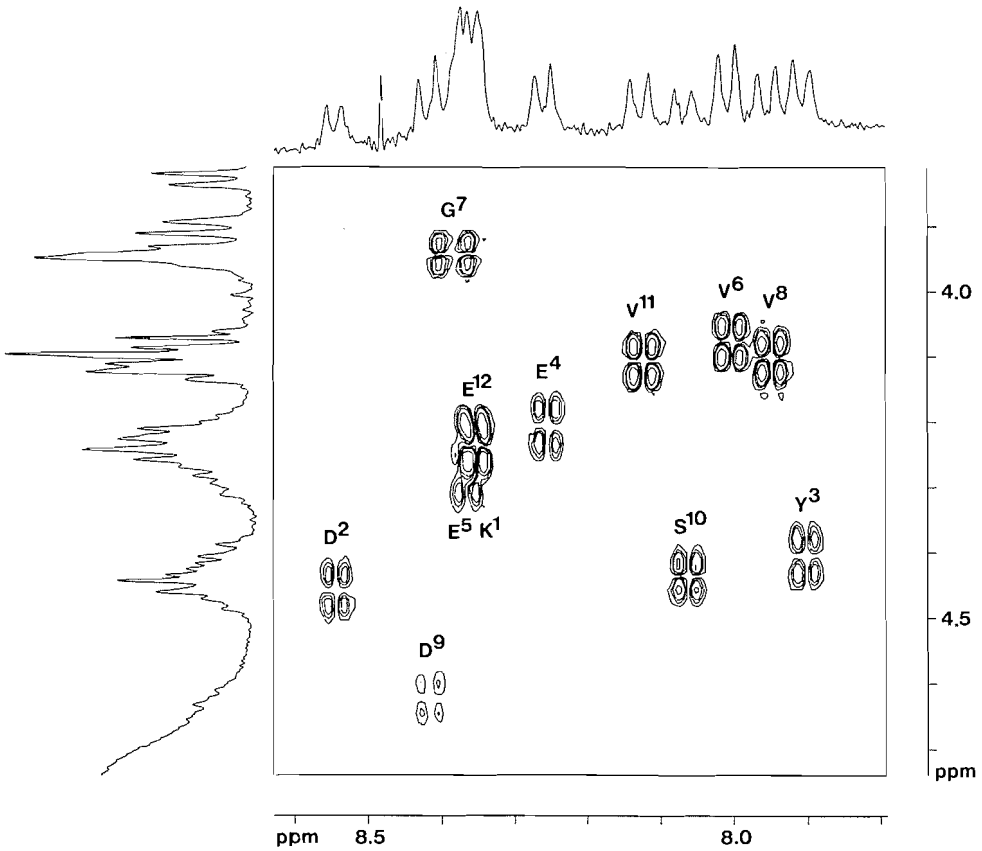

FIG. 3. Two-dimensional contour plot of a 300-MHz phase-sensitive COSY experiment of Ac-tubulin-α(430–441)-amide recorded at 8 mM, pH 7.1, in the same solvent as described in Fig. 2. Only the fingerprint region and the corresponding one-dimensional spectra are shown. The digital resolution along the F2 axis is 1.2 Hz. Positive and negative levels are plotted without distinction and the spectrum is unsymmetrized.

TABLE 2. ^{1}H chemical shifts[a] and coupling constants[b] of Ac-tubulin-α(430–441)-amide[c]

Unique residue	NH	H_α	H_β	H_γ	H_δ	Others	J_{NH-H_α}
K^{1d}	8.38	4.27	1.70, 1.64	1.39	1.66, 1.61	H_ε: 2.92	7.0
D^2	8.55	4.45	2.60, 2.49	—	—	—	5.0
Y^3	7.88	4.42	3.07, 2.95	—	—	H2/H6: 7.06 H3/H5: 6.75	6.5
E^4	8.27	4.22	2.08, 2.03	2.23	—	—	5.5
E^5	8.36	4.29	2.06, 2.02	2.26	—	—	7.1
V^6	8.03	4.09	2.11	0.97	—	—	7.0
G^7	8.38	3.95	—	—	—	—	5.9/5.9
V^8	7.96	4.11	2.13	0.97	—	—	7.2
D^9	8.42	4.62	2.65	—	—	—	7.0
S^{10}	8.05	4.43	3.92, 3.81	—	—	—	8.0
V^{11}	8.13	4.11	2.16	0.95	—	—	7.5
E^{12e}	8.36	4.23	2.03, 1.93	2.25	—	—	6.7

[a]Chemical shifts in ppm relative to methyl group of CD_3OH (3.30 ppm downfield from TMS).
[b]Coupling constants in Hz.
[c]Concentration 5 mM in CD_3OH/D_2O (80:20, v/v), pH 6.7, 297 K.
[d]Data for N-acetyl: 2.02 ppm.
[e]C-terminal NH_2 group: 7.44, 6.97 ppm.

bonds are present between C=O(Lys^1) and NH(Glu^5) and between NH(Glu^4) and C=O(Ser^{10}) as well as some shielding due to the conformation of the peptide. It must be said clearly that these effects are of relatively weak nature. This was confirmed by a proton–deuterium exchange experiment where at room temperature all NH protons exchanged completely within 5 min from dissolving the peptide in the deuterated solvent mixture. Given the small size of the peptide, this effect was not surprising and confirmed that no strong interactions are present.

Discussion

The combination of nuclear Overhauser enhancements and NH–H_α coupling constants allows an almost complete defini-

Can. J. Chem. Downloaded from www.nrcresearchpress.com by 112.217.228.212 on 09/07/12
For personal use only.

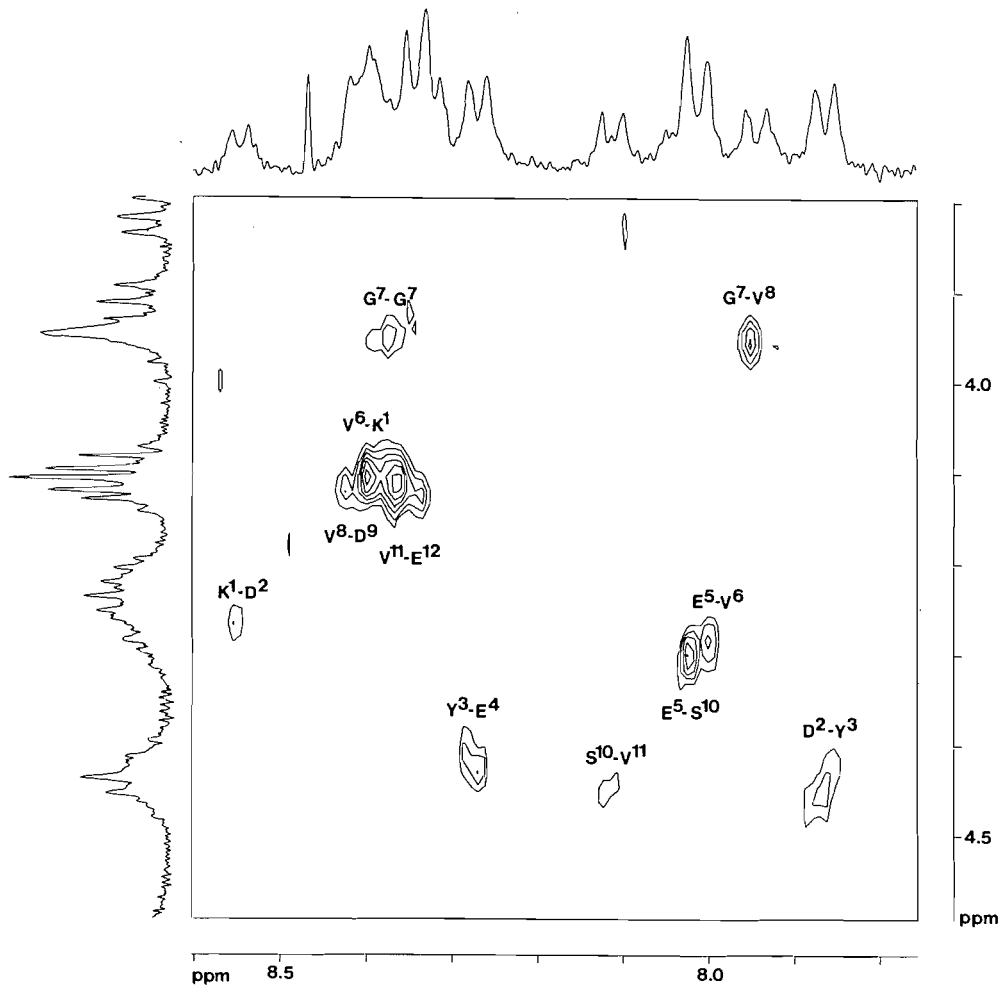

FIG. 4. NH–H_α region of a 300-MHz phase-sensitive ROESY experiment of Ac-tubulin-α(430–441)-amide recorded at 5 mM, pH 7.2, in the same solvent as described in Fig. 2. The spin-locking time was 125 ms. The contour levels are equidistant, separated by 500 vertical display units, and the cross-peaks are of opposite sign with respect to the diagonal peaks. No symmetrization, but ABS baseline correction in both dimensions.

tion of the torsion angles (29) in the peptide backbone, thereby establishing the peptide's conformation.

We consider first the torsion angle ϕ, describing the rotation about the N—C_α bond. ϕ is related to the dihedral angle θ, which itself is related to the observed coupling constants (30) by the Karplus equation (31). Although various sets of constants exist for this equation (32), a narrow limit for θ is found using different sets of Karplus constants (13, 33). By the very nature of the ϕ/θ relationship, two ϕ values result from each θ (J, respectively) value, and the selection of the correct value has to be based on additional (usually nOe) information. The values we found for ϕ are all well within the generally observed range (34) for peptides. The Ψ angles cannot be derived from proton nmr coupling data (35) but they can be estimated satisfactorily from the intensities of $H_\alpha(i)$–NH(i + 1) nOe's. As can be seen in Fig. 4, the nOe cross-peaks are of quite different strength and some, e.g., $H_\alpha(E^4)$–NH(E^5) are missing altogether. Assuming *trans* peptide bonds (ω = 180°), the existence of the above-mentioned nOe's requires the C_α—$H_\alpha(i)$ bond to be approximately *trans* to the carbonyl group (i + 1), which is equivalent to an angle Ψ of +120°. In the cases where a strong nOe cross-peak is observed, we therefore assume Ψ to be +120°, whereas in the cases of weaker, but still clearly observable, effects we allow at least ±60° deviation from this value. Where no nuclear Overhauser enhancement was recorded, values of Ψ = −60° (C_α—$H_\alpha(i)$ *cis* to C=O (i + 1)) and, again, deviations of ±60° have to be considered. Of course, in the latter case, the angle remains undefined over a relatively wide range, and only additional long-range nOe's can provide further information. Finally, the peptide bond angle ω has to be discussed. It is generally found to be either 180° (*trans*) or 0° (*cis*), due to the partial double bond character, with the former value being strongly preferred. Not surprisingly, as there are no proline units present in the investigated peptide, we did not find any spectroscopic indication of *cis* peptide bonds, thus ω = 180° throughout the peptide. Concerning side-chain rotamer populations (33), clearly resolved H_α–H_β coupling constants are a prerequisite. For the vast majority of amino acids these could not be resolved because of spectral overlapping and therefore an unambiguous analysis was impossible. However, when analyzing the nOe's along the side chains, it appears that many of them have considerably reduced mobility but not necessarily fixed conformations.

Summarizing the spectroscopic results (coupling constants, sequential and long-range nOe's, temperature dependence of the NH protons), the conformation is considerably different in the N-terminal half of the peptide from the C-terminal section. Based on extensive molecular modeling using CPK models

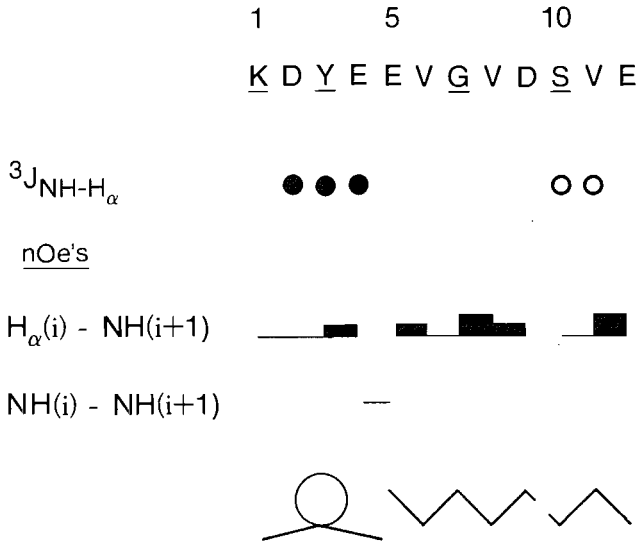

FIG. 5. The amino acid sequence of Ac-tubulin-α(430–441)-amide with unique residues underlined. For the ^3J coupling constants the symbols are used in the following way: filled circles for values of 5.0–6.5 Hz, open circles for values ≥7.5 Hz. The sequential nOe's are indicated by lines and the strength of the effect is depicted by the height of the bar (differentiation between weak, medium, and strong only). For long-range nOe's see text. The secondary structure is schematically described at the bottom. A zigzag line indicates an extended chain (interrupted by a kink between residues number 9 and 10) and the helical region is drawn as such.

as well as computer models (36), we propose the following conformation for the tubulin fragment: An α-helical turn for the first five units (Lys^1 to Glu^5) followed by an approximately extended section (Val^6 to Glu^{12}) with a kink between Asp^9 and Ser^{10}. Due to this kink the amino acids Ser^{10} to Val^{11} are folded back towards the Tyr^3 to Gln^5 moieties, which are part of the α helix. This folded tertiary structure is stabilized by at least one hydrogen bond, most likely between NH(Glu^4) and C=O(Ser^{10}). The helical region is characterized by small coupling constants and weak $H_\alpha(i)$–NH(i + 1) nOe effects, as well as an NH(i)–NH(i + 1) nOe. The low temperature dependence of NH(Gln^5) and a strong nOe between NH(Lys^1) and $H_\alpha(Val^6)$ provide further evidence for this conformation. The extended part of the peptide exhibits typical coupling constant data around 7 Hz and typical $H_\alpha(i)$–NH(i + 1) nOe's. The pattern of nOe interactions is, however, interrupted several times. First, the effect is small between Val^6 and Gly^7 and, secondly, no nOe is observed between $H_\alpha(Asp^9)$ and NH(Ser^{10}). The folded structure is further corroborated by clearly observable nOe's between $H_\alpha(Gln^5)$ and NH(Ser^{10}) and between $H_{meta}(Tyr^3)$ and $H_\gamma(Val^{11})$. Furthermore, NH(Glu^4) and to a somewhat smaller extent NH(Ser^{10}) are less temperature dependent than the other amide protons, indicating hydrogen bonding or at least some shielding from solvent interactions. In summary, the conformation is consistent with all nmr data and confirms the previously published cd results (6). Nevertheless, the consistency of all data does not imply the existence of one fixed conformation, which thermodynamic considerations render unlikely (37), but rather a strong preference for one particular conformation.

Conclusion

All spectroscopic data obtained on the Ac-tubulin-α(430–441)-amide consistently indicate a non-random conformation under the given experimental conditions (CD_3OH/D_2O (80:20) solvent mixture, neutral pH, ambient temperature). The first five residues, Lys^1 to Glu^5, form one complete α-helical turn, followed by an extended conformation with a distinct fold-back due to a kink between residues Asp^9 and Ser^{10}. This creates close proximity of the C-terminal end of the molecule with several of the amino acids involved in the α helix as evidenced by long-range nOe effects. The nmr results confirm cd measurements predicting 30% α helix.

Acknowledgements

We thank Prof. J. M. Stewart, and Eunice J. York at the University of Colorado, Denver, for providing the peptide, Prof. P. G. Scott, Department of Oral Biology, University of Alberta, Edmonton, for valuable discussions, Prof. R. R. Ernst, ETH Zurich, for a preprint of ref. 26, and Dr. H. Beierbeck for computing Fig. 1. The technical assistance of Mr. Glenn Bigam is acknowledged in connection with hardware modifications for the ROESY experiment. Generous financial support by the Alberta Heritage Foundation for Medical Research, the Natural Sciences and Engineering Research Council of Canada, and the University of Alberta is gratefully acknowledged.

1. R. B. MACCIONI. Molecular cytology of microtubules. Servicio Editorial Universidad del Pais Vasco, Leioa, Spain. 1986.
2. L. SERRANO, J. AVILA, and R. B. MACCIONI. Biochemistry, **23**, 4675 (1984).
3. L. SERRANO, J. DE LA TORRE, R. B. MACCIONI, and J. AVILA. Proc. Natl. Acad. Sci. U.S.A. **81**, 5989 (1984).
4. R. B. MACCIONI, J. R. CANN, and J. M. STEWART. Eur. J. Biochem. **154**, 427 (1986).
5. J. M. STEWART and J. D. YOUNG. Solid phase peptide synthesis. Pierce Chemical Co., Rockford, IL. 1985.
6. M. SUGIURA, R. B. MACCIONI, J. R. CANN, E. J. YORK, J. M. STEWART, and G. KOTOVYCH. J. Biomol. Struct. Dyn. **4**, 1105 (1987).
7. G. M. CLORE, S. R. MARTIN, and A. M. GRONENBORN. J. Mol. Biol. **191**, 553 (1986).
8. O. LICHTARGE, O. JARDETZKY, and C. H. LI. Biochemistry, **26**, 5916 (1987).
9. A. OTTER, P. G. SCOTT, and G. KOTOVYCH. Biochemistry, **27**, 3560 (1988).
10. K. NODA, M. OHASHI, and K. ISHIDA. J. Chem. Eng. Data, **27**, 326 (1982).
11. M. DIZECHI and E. MARSCHALL. J. Chem. Eng. Data, **27**, 358 (1982).
12. R. R. ERNST, G. BODENHAUSEN, and A. WOKAUN. Principles of NMR in one and two dimensions. Oxford Science Publishers, Oxford, England. 1987.
13. K. WÜTHRICH. NMR of proteins and nucleic acids. Wiley–Interscience, New York. 1986.
14. J. H. NOGGLE and R. E. SHIRMER. The nuclear Overhauser effect. Academic Press, New York. 1971.
15. A. A. BOTHNER-BY, R. L. STEPHENS, J. LEE, C. D. WARREN, and R. W. JEANLOZ. J. Am. Chem. Soc. **106**, 811 (1984).
16. A. BAX and D. G. DAVIS. J. Magn. Reson. **63**, 207 (1985).
17. W. P. AUE, E. BARTHOLDI, and R. R. ERNST. J. Chem. Phys. **64**, 2229 (1976).
18. D. MARION and K. WÜTHRICH. Biochem. Biophys. Res. Commun. **113**, 967 (1983).
19. R. BENN and H. GÜNTHER. Angew. Chem. Int. Ed. Engl. **22**, 350 (1983).
20. G. EICH, G. BODENHAUSEN, and R. R. ERNST. J. Am. Chem. Soc. **104**, 3731 (1982).
21. P. H. BOLTON and G. BODENHAUSEN. Chem. Phys. Lett. **89**, 139 (1982).

Can. J. Chem. Downloaded from www.nrcresearchpress.com by 112.217.228.212 on 09/07/12
For personal use only.

22. G. WIDER, R. V. HOSUR, and K. WÜTHRICH. J. Magn. Reson. **52**, 130 (1983).
23. D. MARION. FEBS Lett. **192**, 99 (1985).
24. D. NEUHAUS and J. KEELER. J. Magn. Reson. **68**, 568 (1986).
25. H. KESSLER, CH. GRIESINGER, R. KERSSEBAUM, K. WAGNER, and R. R. ERNST. J. Am. Chem. Soc. **109**, 607 (1987).
26. CH. GRIESINGER and R. R. ERNST. J. Magn. Reson. **75**, 261 (1987).
27. G. WIDER, S. MACURA, A. KUMAR, and R. R. ERNST. J. Magn. Reson. **56**, 207 (1984).
28. V. J. HRUBY. Chem. Biochem. Amino Acids, Pept. Proteins, **3**, 1 (1974).
29. IUPAC–IUB Commission on Biochemical Nomenclature. Biochemistry, **9**, 3471 (1970).
30. A. PARDI, M. BILLETER, and K. WÜTHRICH. J. Mol. Biol. **180**, 741 (1984).
31. M. J. KARPLUS. J. Am. Chem. Soc. **85**, 2870 (1963).
32. E. L. BECKER, H. E. BLEICH, A. R. DAY, R. J. FREER, J. A. GLASEL, and J. A. VISINTAINER. Biochemistry, **18**, 4656 (1979).
33. O. JARDETZKY and G. C. K. ROBERTS. NMR in molecular biology. Academic Press, New York. 1981.
34. J. RICHARDSON. Adv. Protein Chem. **34**, 167 (1981).
35. V. F. BYSTROV. Prog. Nucl. Magn. Reson. Spectrosc. **10**, 41 (1976).
36. J. G. HENKEL and F. H. CLARKE. Molecular graphics on the IBM PC microcomputer. Academic Press, Orlando, FL. 1986.
37. T. E. CREIGHTON. Proteins. W. H. Freeman and Company, New York. 1984.

Can. J. Chem. Downloaded from www.nrcresearchpress.com by 112.217.228.212 on 09/07/12
For personal use only.

Anisotropy of indirect spin–spin coupling constants from nuclear magnetic resonance powder patterns of rigid solids. $^1J(^{31}P,^{199}Hg)$ in $[HgP(o\text{-tolyl})_3(NO_3)_2]_2$

GLENN H. PENNER, WILLIAM P. POWER, AND RODERICK E. WASYLISHEN[1]
Department of Chemistry, Dalhousie University, Halifax, N.S., Canada B3H 4J3

Received March 15, 1988

This paper is dedicated to Professor Charles A. McDowell on the occasion of his 70th birthday

GLENN H. PENNER, WILLIAM P. POWER, and RODERICK E. WASYLISHEN. Can. J. Chem. **66**, 1821 (1988).

The anisotropy of the indirect $^{31}P,^{199}Hg$ spin–spin coupling constant, ΔJ, in solid $[HgP(o\text{-tolyl})_3(NO_3)_2]_2$ is obtained from an analysis of the ^{31}P nuclear magnetic resonance powder pattern. The value of ΔJ, 5170 ± 250 Hz, is large and indicates that mechanisms other than the Fermi contact mechanism are important for this spin–spin coupling. The powder spectrum also indicates that the absolute sign of $^1J(^{31}P,^{199}Hg)$ is positive.

GLENN H. PENNER, WILLIAM P. POWER et RODERICK E. WASYLISHEN. Can. J. Chem. **66**, 1821 (1988).

En se basant sur une analyse du spectre en résonance magnétique nucléaire de poudre du ^{31}P du $[HgP(o\text{-tolyl})_3)(NO_3)_2]_2$, on a pu déterminer l'anisotropie de la constante de couplage spin–spin indirecte $^{31}P,^{199}Hg$, ΔJ. La valeur observée pour le ΔJ, 5170 ± 250 Hz, est importante et elle indique que des mécanismes autres que le mécanisme de contact de Fermi jouent un rôle important dans ce couplage spin–spin. Le spectre de poudre indique aussi que la valeur absolue de la constante $^1J(^{31}P,^{199}Hg)$ est positive.

[Traduit par la revue]

Can. J. Chem. Downloaded from www.nrcresearchpress.com by 112.217.228.212 on 09/07/12
For personal use only.

The anisotropy of nuclear magnetic shielding has been extensively studied, particularly for the lighter isotopes (e.g., ^1H, ^3C, and ^{31}P), and tabulations of the principal components of shielding tensors for nuclei in many molecules can be found in the literature (1–8). In comparison there are few reliable data on the anisotropy of indirect spin–spin coupling tensors, ΔJ (9–12). The experimental determination of indirect coupling anisotropies is complicated because it is generally difficult to separate the anisotropy of the indirect spin–spin coupling from the direct dipolar coupling, D (9–12). Also, both theory (13–15) and experiment (9–12, 16–23) indicate that the anisotropy of the indirect coupling is usually small, particularly when the coupling involves only nuclei of low atomic number; this complicates any effort to separate ΔJ and D.

Experimentally the anisotropy of J is determined from the nmr study of oriented molecules in liquid crystalline solvents (9–12) and from nmr studies of solid powders (16–20) or single crystals (21–23). Liquid crystal studies have been most popular; however, the analysis of data is often not straightforward due to complications introduced by solvent and vibrational effects (9–12). The results from single crystal studies are the most reliable, but such studies are tedious and require a large single crystal, which is often unavailable. In the present study we demonstrate that the anisotropy in the indirect coupling between two spins A and X can be readily determined from a *powder* spectrum of A if the isotropic value of the indirect coupling is sufficiently large that the subspectra, which result from the X spin Zeeman states, $m = +1/2$ and $m = -1/2$, are completely separated. This requirement is satisfied when one analyzes the ^{31}P nmr spectrum of a powder sample of $[HgP(o\text{-tolyl})_3(NO_3)_2]_2$. The spectrum, Fig. 1, was obtained with high power proton decoupling and cross polarization on a Bruker MSL-200 (B_0 = 4.70 T). The central feature in the spectrum results from ^{31}P nuclei that are directly bonded to magnetically inactive Hg nuclei while the high and low frequency subspectra result from ^{31}P nuclei directly bonded to ^{199}Hg ($I = 1/2$, natural abundance 16.84%). The central feature in the spectrum indicates that the ^{31}P shielding anisotropy is approximately axially symmetric, $\Delta\sigma = \sigma_\parallel - \sigma_\perp = -38.3$ ppm. The isotropic value of each subspectrum was determined from a ^{31}P nmr spectrum obtained with magic angle sample spinning (frequencies indicated by arrows in Fig. 1). The isotropic frequencies of each of these subspectra are separated by the isotropic value of the indirect spin–spin coupling constant, $J(^{31}P,^{199}Hg)_{iso}$, 9660 Hz. If one assumes that the J tensor is axially symmetric and $J_\parallel$ is coincident with $\sigma_\parallel$ and the ^{31}P–^{199}Hg dipolar vector, the two subspectra can be analyzed following the theory of VanderHart and Gutowsky (24). Using the same general equations as these authors but working in Hz instead of angular frequency units, the frequency spread of each subspectrum about ν_{iso} is given by eq. [1]

$$[1]\quad \Delta\nu_m = (3\cos^2\theta - 1)K_m - (J_{iso})m$$

where m is $\pm 1/2$ and refers to the spin state of the ^{199}Hg in this particular example, J_{iso} is the isotropic spin–spin coupling constant, $J_{iso} = (1/3)(J_\parallel + 2J_\perp)$, θ is the angle between the ^{31}P–^{199}Hg dipolar vector and the applied magnetic field, B_0, and K_m is defined by eq. [2].

$$[2]\quad K_m = \beta + Dm - (\Delta J/3)m$$

In eq. [2],

$$\beta = (1/3)(\nu_\parallel - \nu_\perp) = 1033 \text{ Hz}$$

and is one-third the chemical shielding anisotropy in Hz;

$$D = \left(\frac{\mu_0}{4\pi}\right)\left(\frac{\gamma_P\gamma_{Hg}}{r^3_{P-Hg}}\right)\left(\frac{\hbar}{2\pi}\right)$$

and is the direct dipolar coupling constant, 634 Hz (see discussion below); and $\Delta J = J_\parallel - J_\perp$ is the anisotropy of the indirect spin–spin coupling constant. Taking the shoulder and discontinuity of the high frequency subspectrum as 8300 and 3550 Hz respectively and the corresponding values for the low frequency subspectrum as −3600 and −5050 Hz respectively, substitution of β, D, and J_{iso} into eqs. [1] and [2] leads to the following conclusions:

1. The absolute sign of $J(^{31}P,^{199}Hg)$ is positive (i.e., the high

[1]Author to whom all correspondence may be addressed.

Can. J. Chem. Downloaded from www.nrcresearchpress.com by 112.217.228.212 on 09/07/12
For personal use only.

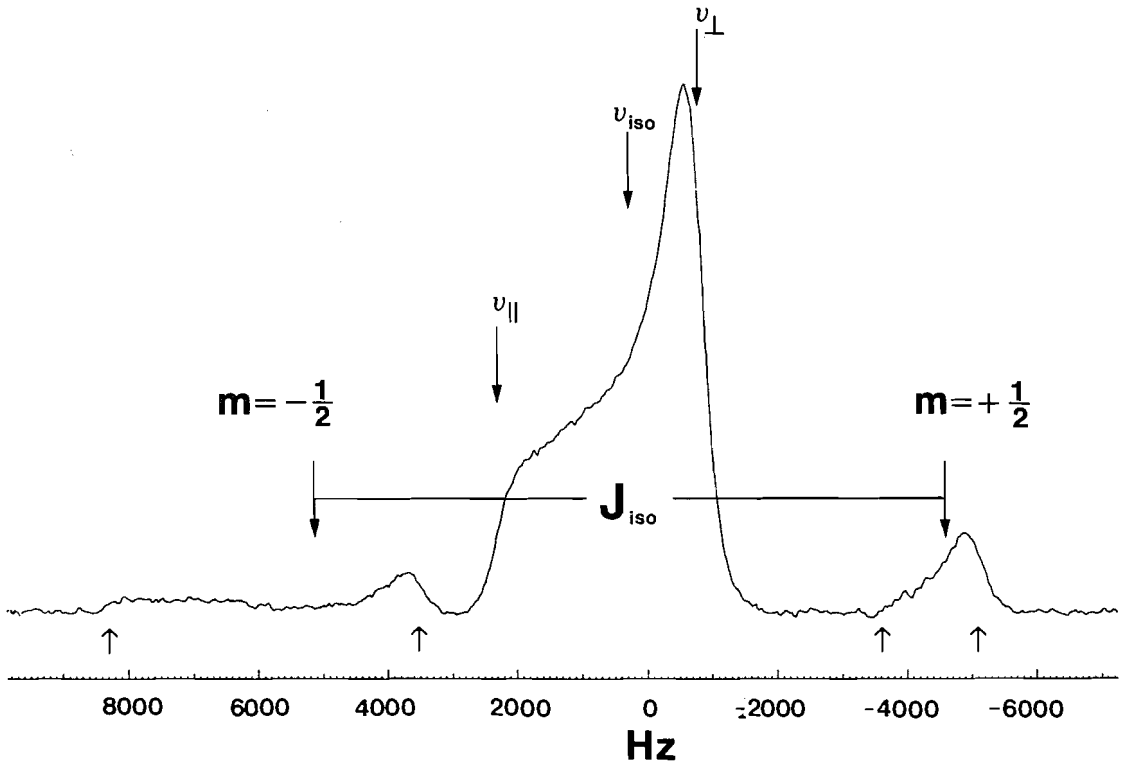

FIG. 1. The ^{31}P nmr spectrum of a stationary solid powder sample of $[HgP(o\text{-tolyl})_3(NO_3)_2]_2$ obtained at 80.962 MHz. All frequencies are relative to the ^{31}P resonance of solid $NH_4H_2PO_4$. The isotropic chemical shift of solid $[HgP(o\text{-tolyl})_3(NO_3)_2]_2$ relative to $NH_4H_2PO_4$ is 3.6 ppm. The arrows (pointing up) beneath the spectrum indicate the positions of the shoulders and discontinuities of the $m = \pm 1/2$ subspectra.

frequency subspectrum is to be associated with $m = -1/2$); this is in agreement with conclusions deduced from the relative sign determinations based on double resonance experiments in other compounds containing P—Hg bonds (25, 26).

2. The value of ΔJ is 5170 Hz; thus $J_\parallel = 13{,}110$ Hz and $J_\perp = 7940$ Hz. The error in these values is estimated to be ±250 Hz. The implication of this substantial anisotropy in J(P,Hg) is that mechanisms other than the Fermi contact mechanism must play an important role in the transfer of spin information between these two nuclei (11–13, 27).

In solving eq. [1] and [2] for ΔJ we used $D = 634$ Hz; this value was calculated from γ_P, γ_{Hg}, and taking $r_{P—Hg}$ as 240 pm. Although diffraction data are unavailable for $[HgP(o\text{-tolyl})_3(NO_3)_2]_2$ they are available for the related compounds, $[HgP(\text{mesityl})_3(NO_3)_2]_2$ (28), $[HgPCy_3(NO_3)_2]_2$ (29), and $[HgP(o\text{-tolyl})_3(OAc)_2]_2$ (30). In all three compounds $r_{P—Hg} = 240 \pm 3$ pm. Also in each of these compounds the X-ray data indicate that mercury forms three strong bonds, the P—Hg bond and two Hg—O bonds with an essentially trigonal planar arrangement; however, each mercury is further associated with three oxygen atoms giving an overall mercury coordination number of 6. The complex, $[HgP(o\text{-tolyl})_3(NO_3)_2]_2$ was prepared as described in ref. 31.

To anticipate how sensitive the observed spectrum is to the requirement that the dipolar vector be colinear with $\sigma_\parallel$ we have written a general computer program based on the relations outlined by Valentine *et al.* (32), but generalized to include indirect spin–spin coupling. Qualitatively the line-shape simulations indicate substantial asymmetry (i.e., non-axial powder patterns) in both subspectra as the angle between $r_{P—Hg}$ and σ_{11} ($\sigma_{11} = \sigma_\parallel$ for axial symmetry) deviates significantly from zero. We feel the assumption of $r_{P—Hg}$ being colinear with $J_\parallel$ and J being axially symmetric is reasonable on the basis of the single crystal results of Tutunjian and Waugh (22, 23). They found that the J(P,P) tensors in tetraethyldiphosphine disulfide and in tetrabutyldiphosphine disulfide are essentially axially symmetric. Axial symmetry of the indirect coupling tensor is intuitively reasonable when two nuclei are essentially σ bonded.

It is of interest to point out that the ^{31}P chemical shielding anisotropy in $[HgP(o\text{-tolyl})_3(NO_3)_2]_2$, −38.3 ppm, is substantially smaller than the values reported for the three inequivalent phosphorus nuclei of chlorotris(triphenylphosphine) rhodium(I) (33), the only other metal phosphine for which such data are available. Also, the three shielding tensors in the latter compound are not axially symmetric. The implication is that ^{31}P shielding tensors observed in metal-phosphine complexes are very sensitive to subtle changes in electronic and molecular structure and in principle much more informative than isotropic chemical shifts.

In conclusion, our results indicate that it should be possible to obtain accurate values of $\Delta^1J(^{31}P,^{199}Hg)$ from ^{31}P nmr powder patterns, particularly when the mercury-199 satellites are completely isolated from the central uncoupled ^{31}P nmr spectrum. Detailed investigations of related compounds are presently underway in our laboratory.

Acknowledgements

We wish to thank the Natural Sciences and Engineering Research Council of Canada for financial support. G. H. Penner is the holder of a Killam Postdoctoral Fellowship.

1. M. MEHRING. Principles of high resolution NMR in solids. 2nd ed. Springer-Verlag, New York. 1983.
2. H. W. SPIESS. *In* NMR basic principles and progress. Vol. 15.

Edited by P. Diehl, E. Fluck, and R. Kosfeld. Springer-Verlag, New York. 1978. p. 55.
3. U. HAEBERLEN. Adv. Magn. Reson. Supplement 1. *Edited by* J. S. Waugh. Academic Press, New York. 1976. p. 1.
4. W. S. VEEMAN. Prog. Nucl. Magn. Reson. Spectrosc. **16**, 193 (1984).
5. T. M. DUNCAN. J. Phys. Chem. Ref. Data, **16**, 125 (1987).
6. J. MASON. *In* Multinuclear NMR. *Edited by* J. Mason. Plenum Press, New York. 1987. p. 335.
7. J. B. ROBERT and L. WIESENFELD. *In* Phosphorus-31 NMR spectroscopy in stereochemical analysis, organic compounds and metal complexes. *Edited by* J. G. Verkade and L. D. Quin. VCH Publishers, Inc., New York. 1987. p. 151.
8. C. J. JAMESON. *In* Nuclear Magnetic Resonance, Specialist Periodical Reports. Vol. 16. Senior Reporter, G. A. Webb. The Royal Society of Chemistry, London. 1987. p. 1, and earlier volumes.
9. J. LOUNILA and J. JOKISAARI. Prog. Nucl. Magn. Reson. Spectrosc. **15**, 249 (1982).
10. J. JOKISAARI, Y. HILTUNEN, and J. LOUNILA. J. Chem. Phys. **85**, 3198 (1986).
11. J. B. ROBERT and L. WIESENFELD. Phys. Rep. **86**, 363 (1982).
12. C. J. JAMESON. *In* Multinuclear NMR. *Edited by* J. Mason. Plenum Press, New York. 1987. p. 89.
13. J. KOWALEWSKI. *In* Annual reports in NMR spectroscopy. Vol. 12. *Edited by* G. A. Webb. Academic Press, London. 1982. p. 163.
14. P. PYYKKÖ and L. WIESENFELD. Mol. Phys. **43**, 557 (1981).
15. J. C. FACELLI and M. BARFIELD. J. Magn. Reson. **59**, 452 (1984).
16. A. R. GRIMMER, R. PETER, and E. FECHNER. Z. Chem. **18**, 109 (1978).
17. R. BALZ, M. HALLER, W. E. HERTLER, O. LUTZ, A. NOLLE, and R. SCHAFITEL. J. Magn. Reson. **40**, 9 (1980).
18. K. W. ZILM and D. M. GRANT. J. Am. Chem. Soc. **103**, 2913 (1981).
19. R. K. HARRIS, K. J. PACKER, and A. M. THAYER. J. Magn. Reson. **62**, 284 (1985).
20. U. HAUBENREISSER, U. STERNBERG, and A.-R. GRIMMER. Mol. Phys. **60**, 151 (1987).
21. A. NOLLE. Z. Phys. B: Condens. Matter, **34**, 175 (1979).
22. P. N. TUTUNJIAN and J. S. WAUGH. J. Chem. Phys. **76**, 1223 (1982).
23. P. N. TUTUNJIAN and J. S. WAUGH. J. Magn. Reson. **49**, 155 (1982).
24. D. L. VANDERHART and H. S. GUTOWSKY. J. Chem. Phys. **49**, 261 (1968).
25. W. MCFARLANE and D. S. RYCROFT. J. Chem. Soc. Faraday Trans. 2, **70**, 377 (1974).
26. P. L. GOGGIN, R. J. GOODFELLOW, D. M. MCEWAN, A. J. GRIFFITHS, and K. KESSLER. J. Chem. Soc. J. Chem. Res. (M), 2315 (1979).
27. (*a*) A. D. BUCKINGHAM and I. LOVE. J. Magn. Reson. **2**, 338 (1970); (*b*) A. D. BUCKINGHAM and P. PYYKKÖ. Mol. Phys. **46**, 177 (1982).
28. E. C. ALYEA, S. A. DIAS, G. FERGUSON, and M. PARVEZ. Inorg. Chim. Acta, **37**, 45 (1979).
29. E. C. ALYEA, S. A. DIAS, G. FERGUSON, and A. J. RESTIVO. Inorg. Chem. **16**, 2329 (1977).
30. E. C. ALYEA, S. A. DIAS, G. FERGUSON, M. A. KHAN, and P. J. ROBERTS. Inorg. Chem. **18**, 2433 (1979).
31. E. C. ALYEA, S. A. DIAS, R. G. GOEL, W. O. OGINI, P. PILON, and D. W. MEEK. Inorg. Chem. **17**, 1697 (1978).
32. K. G. VALENTINE, A. L. ROCKWELL, L. M. GLERASCH, and S. J. OPELLA. J. Magn. Reson. **73**, 519 (1987).
33. A. NAITO, D. L. SASTRY, and C. A. MCDOWELL. Chem. Phys. Lett. **115**, 19 (1985).

Can. J. Chem. Downloaded from www.nrcresearchpress.com by 112.217.228.212 on 09/07/12
For personal use only.

First observation and analysis of the $0_u^+(^1D)$ ion-pair state of Br_2 by optical–optical double resonance

TAKASHI ISHIWATA, OSAMU NAKAMURA, KINICHI OBI, AND IKUZO TANAKA

Department of Chemistry, Tokyo Institute of Technology, Ohokayama, Meguro, Tokyo 152, Japan

Received November 27, 1987

This paper is dedicated to Professor Charles A. McDowell on the occasion of his 70th birthday

TAKASHI ISHIWATA, OSAMU NAKAMURA, KINICHI OBI, and IKUZO TANAKA. Can. J. Chem. **66**, 1824 (1988).

The technique of optical–optical double resonance has been applied to a study of the $0_u^+(^1D)$ ion-pair state of Br_2. Two pulsed dye lasers excite the molecules from the ground state to the $0_u^+(^1D)$ ion-pair state stepwise through the $B^3\Pi(0_u^+)$ state in the pump-probe scheme: $0_u^+(^1D) \leftarrow (2h\nu_2)$–$B^3\Pi(0_u^+) \leftarrow (h\nu_1)$–$X^1\Sigma_g^+$. The $0_u^+(^1D)$–$X^1\Sigma_g^+$ emission identified at around 215 nm is used to detect the double resonance signals when the probe laser frequency (ν_2) is scanned by fixing the pump laser frequency (ν_1) to appropriate $B^3\Pi(0_u^+)$–$X^1\Sigma_g^+$ transitions. The emission spectra are resolved to establish the absolute vibrational numbering of the ion-pair state in terms of the Franck–Condon calculations. The Dunham coefficients of the $0_u^+(^1D)$ state obtained in a global least-squares fit analysis of 377 transitions ($0 \leqq v' \leqq 8$, $6 \leqq J' \leqq 100$) are $Y_{00} = 57929.724(24)$, $Y_{10} = 212.227(23)$, $Y_{20} = -1.5683(56)$, $Y_{30} = 1.606(40) \times 10^{-2}$, $Y_{01} = 0.0465652(89)$, $Y_{11} = -4.500(36) \times 10^{-4}$, $Y_{21} = 1.133(41) \times 10^{-5}$, and $Y_{02} = -9.37(94) \times 10^{-9}$ for $^{79}Br_2$ isotope species (all in cm^{-1} with 3σ in parentheses).

TAKASHI ISHIWATA, OSAMU NAKAMURA, KINICHI OBI et IKUZO TANAKA. Can. J. Chem. **66**, 1824 (1988).

On a utilisé la technique de la double résonance optique–optique pour étudier l'état de la paire ionique $0_u^+(^1D)$ du Br_2. Deux lasers à colorant pulsés excitent les molécules de leur état fondamental à l'état de paire ionique $0_u^+(^1D)$, en procédant par étape par le biais de l'état $B^3\Pi(0_u^+)$, dans le schéma de la pompe-sonde : $0_u^+(^1D) \leftarrow (2h\nu_2)$–$B^3\Pi(0_u^+) \leftarrow (h\nu_1)$–$X^1\Sigma_g^+$. On a utilisé l'émission $0_u^+(^1D)$–$X^1\Sigma_g^+$ qui est observée autour de 215 nm pour détecter les signaux de double résonance; à cette fin, on a balayé la fréquence du laser-sonde (ν_2) alors que la fréquence du laser-pompe (ν_1) était fixée aux transitions $B^3\Pi(0_u^+)$–$X^1\Sigma_g^+$ appropriées. On a résolu le spectre d'émission pour établir le nombre absolu de vibrations, dans l'état de la paire ionique, en fonction de calculs de Franck–Condon. Les coefficients de Dunham de l'état $O_u^+(^1D)$ des espèces isotopiques du $^{79}Br_2$ (tous en cm^{-1}, avec les valeurs de 3σ inscrites entre parenthèses), qui ont été obtenus en appliquant la méthode des moindres carrés à 377 transitions ($0 \leqq v' \leqq 8$, $6 \leqq J' \leqq 100$), sont $Y_{00} = 57929{,}724(24)$, $Y_{10} = 212{,}227(23)$, $Y_{20} = -1{,}5683(56)$, $Y_{30} = 1{,}606(40) \times 10^{-2}$, $Y_{01} = 0{,}0465652(89)$, $Y_{11} = -4{,}500(36) \times 10^{-4}$. $Y_{21} = 1{,}133(41) \times 10^{-5}$ et $Y_{02} = -9{,}37(94) \times 10^{-9}$.

[Traduit par la revue]

I. Introduction

In spite of many studies on the spectroscopy of halogen molecules over the past 50 years (see, for example, ref. 1), there remain a number of problems that should be solved. Some of the questions most frequently mentioned are concerned with the interpretation of ultraviolet emission spectra observed in a discharge. Until recently this problem received little attention, largely because of the difficulty of making reliable measurements and assignments on the congested bands.

In the last several years, we have carried out a program of studies on the Br_2 molecule by optical–optical double resonance (OODR) spectroscopy to investigate the role of ion-pair states in ultraviolet emission (2–4).[1] The method has the quite attractive advantage of studying ion-pair states with regard to symmetrical selection rules and the Franck–Condon principle. For example, ion-pair states correlating with $Br^-(^1S) + Br^+(^3P, ^1D, ^1S)$ can be combined stepwise with the ground state either through the $B^3\Pi(0_u^+)$ state or the $A^3\Pi(1_u)$ state, according to the selection rule $\Delta\Omega = 0$ for parallel-type transitions between ion-pair and valence states. Furthermore, the parity selection rule for multiphoton transition is different from that for one-photon transition. We can observe ion-pair states with either g or u symmetry, depending on whether the total number of photons is even or odd, respectively. The stepwise process exploits the changing Franck–Condon factors during molecular excitation. A considerable range of vibrational levels in ion-pair states is accessed through the different pump transitions. The double resonance method has the capability of state selection, giving simple and easily assignable spectra. The results provide a reliable data base for ion-pair states with regard to the energy levels, potential curves, and related features. The emission spectra of ion-pair states observed in the double resonance experiments are quite helpful in sorting out the congested spectra observed in a discharge, by avoiding the simultaneous formation of many kinds of excited states.

In this paper we present the results of the optical–optical double resonance study on the $0_u^+(^1D)$ ion-pair state of Br_2 correlating with $Br^-(^1S) + Br^+(^1D)$ at the dissociation limit. Monoisotopic $^{79}Br_2$ was used throughout the experiments to exclude spectral congestion problems as much as possible, since natural Br_2 contains three isotope species of comparable abundance. Using a J selected (1 + 2) photon double resonance $0_u^+(^1D) \leftarrow (2h\nu_2) - B^3\Pi(0_u^+) \leftarrow (h\nu_1) - X^1\Sigma_g^+$, the $0_u^+(^1D)$ ion-pair state occurs in the spectrum as vibrational progressions consisting of O, Q, and S branches according to the selection rule of $\Delta J = 0, \pm 2$ in the 0_u^+–0_u^+ coherent two-photon transition. The energy levels of the $0_u^+(^1D)$ state were analyzed on the vibrational levels of $v' = 0$ through $v' = 8$ and a set of molecular constants was given in a Dunham-type expression. Analysis of the emission shows that the $0_u^+(^1D)$–$X^1\Sigma_g^+$ transition is responsible for the 220-nm emission in a discharge (5).

II. Experimental

The experimental set-up used in this work is similar to that described previously (3*d*). The double resonance excitation of Br_2 was carried out by two tunable dye lasers pumped by the divided outputs of a XeCl excimer laser. A pump laser was tuned to appropriate transitions of the $B^3\Pi(0_u^+)$–$X^1\Sigma_g^+$ system in the visible region, which assignments were

[1]Also, T. Ishiwata, T. Hara, K. Obi, and I. Tanaka, to be published, and T. Ishiwata, K. Obi, and I. Tanaka, to be published.

Printed in Canada / Imprimé au Canada

Can. J. Chem. Downloaded from www.nrcresearchpress.com by 112.217.228.212 on 09/07/12
For personal use only.

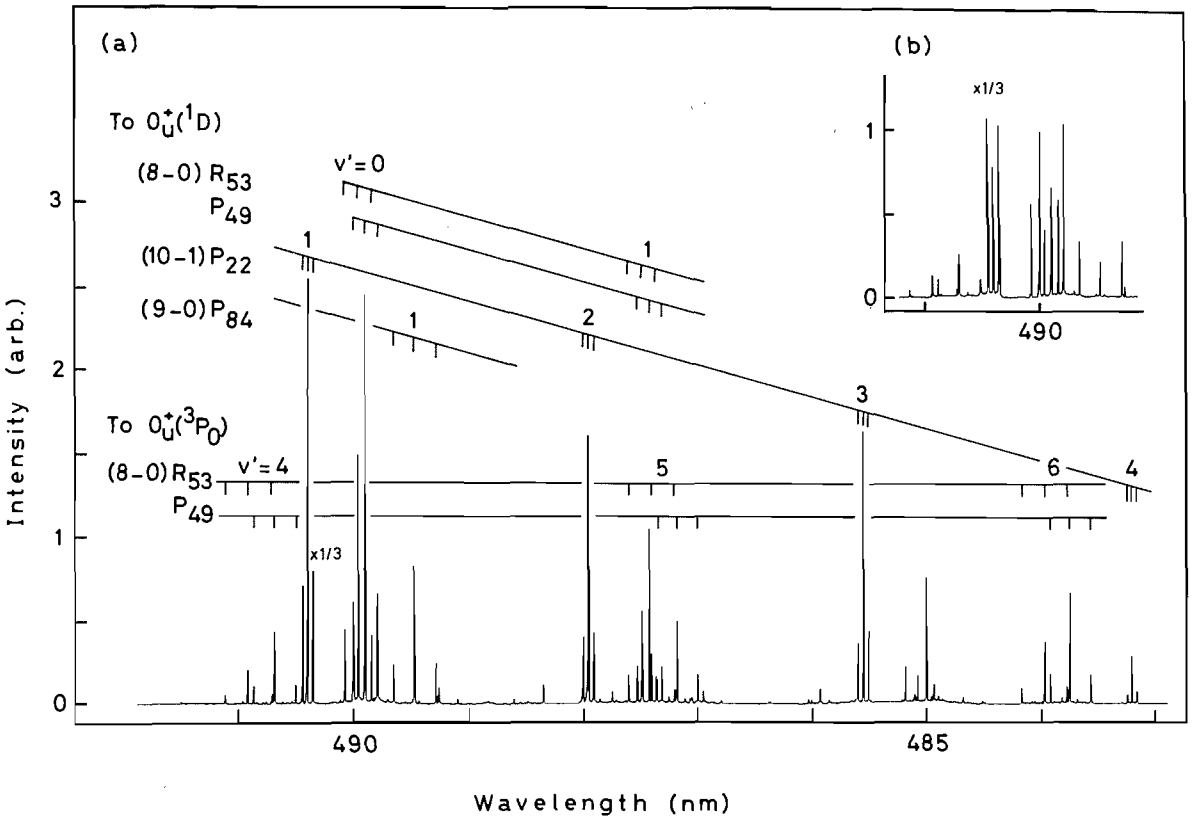

FIG. 1. An OODR excitation spectrum of $^{79}Br_2$ according to the excitation scheme, $0_u^+(^1D)$–$B^3\Pi(0_u^+)$–$X^1\Sigma_g^+$. The spectrum was obtained by fixing the pump laser to the (8–0) P_{49} and R_{53}, (9–0) P_{84}, and (10–1) P_{22} transitions of the $B^3\Pi(0_u^+)$–$X^1\Sigma_g^+$ system. The probe laser was scanned to probe the $0_u^+(^1D)$ state in a coherent two-photon transition from the $B^3\Pi(0_u^+)$ state under low resolution by monitoring the ultraviolet emission at 220 nm with a spectral slit width of 30 nm. The pump and probe lasers were operated with vertical polarization in spectrum (a), while the polarization of the probe laser was changed to circular with maintaining the pump laser vertical polarization in spectrum (b).

made on the basis of published data (6). For fixing the pump frequency, a probe laser was scanned in the visible to observe the transitions to the $0_u^+(^1D)$ state by coherent two-photon absorption. The double resonance transitions were then monitored by ultraviolet emission of the $0_u^+(^1D)$–$X^1\Sigma_g^+$ system through a monochromator and the photomultiplier signals were averaged by a boxcar integrator.

The pump and probe laser beams were carefully aligned to focus on the same spot from opposite directions. The two dye lasers produced pulses with an energy of 3–5 mJ/pulse at a repetition rate of 10 Hz. The laser bandwidth was 0.04 cm^{-1} in the case of operating with an "étalon" tuning element, and 0.3 cm^{-1} without an étalon. The output beams of the two dye lasers were vertically polarized in normal experiments. We examined the anisotropic character of a two-photon transition from the $B^3\Pi(0_u^+)$ state by changing the polarization angle of the probe laser beam. The optical components used for these studies consisted of a polarizer, a double Fresnel rhomb, and a single Fresnel rhomb. The amount of polarization retardation was changed by rotating the double Fresnel rhomb and was determined by the relative angle between the optically active planes of the double Fresnel rhomb and the single Fresnel rhomb.

III. Results and discussion

A. *Optical–optical double resonance transition*

Figure 1 represents a typical example of spectra observed in the double resonance experiments of Br_2. The pump laser frequency (ν_1) was adjusted to a photon energy of 16969.0 cm^{-1}, which is in resonance with the (8–0) P_{49} and R_{53}, (9–0) P_{84}, and (10–1) P_{22} transitions of the $B^3\Pi(0_u^+)$–$X^1\Sigma_g^+$ system within the bandwidth of the pump laser (~0.3 cm^{-1}). We monitored the ultraviolet emission at 220 nm with a spectral slit width of 30 nm. Spectrum (a) was recorded under low resolution by scanning the probe laser in the 492–483 nm range. There was no time delay between two laser pulses of 15-ns duration. Under the experimental condition of a sample pressure of 2 Torr (1 Torr = 133.3 Pa), the rotational relaxation is negligible in the intermediate $B^3\Pi(0_u^+)$ state. The double resonance spectra, therefore, are quite simple; two 0_u^+–0_u^+ systems originate from the different (1 + 2) photon excitation schemes.

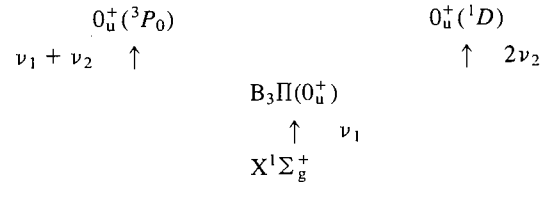

Type II: $\nu_1 + (\nu_1 + \nu_2)$ Type I: $\nu_1 + (2\nu_2)$

The first is the transition to the $0_u^+(^3P_0)$ state, correlating with the ionic state of $Br^-(^1S) + Br^+(^3P_0)$ at the dissociation limit (3*a*, 3*b*). This state is known to lie in the 53 000 cm^{-1} range, whose emission terminating in the ground state has been identified as the transition around 248 nm. Our previous publication (3*b*) shows that the double resonance transition to the $0_u^+(^3P_0)$ state occurs in the (1 + 2) photon sequence of the type II transition $\nu_1 + (\nu_1 + \nu_2)$: the pump laser excites the $B^3\Pi(0_u^+)$–$X^1\Sigma_g^+$ transition while the pump and probe laser

Can. J. Chem. Downloaded from www.nrcresearchpress.com by 112.217.228.212 on 09/07/12
For personal use only.

Can. J. Chem. Downloaded from www.nrcresearchpress.com by 112.217.228.212 on 09/07/12
For personal use only.

pulses combine to execute the second step of the $0_u^+(^3P_0)$–$B^3\Pi(0_u^+)$ transition, due to the temporal overlap of two laser pulses. Since the line positions of the $0_u^+(^3P_0)$–$B^3\Pi(0_u^+)$ system can be tabulated from the published data (*3b*) within an accuracy of about 2 cm^{-1}, we have no real difficulty in the assignments. For example, Fig. 1(a) shows the double resonance signals through the (8–0) P_{49} and R_{53} transitions of the $B^3\Pi(0_u^+)$–$X^1\Sigma_g^+$ system. The vibrational progression with ~150 cm^{-1} intervals can be unequivocally assigned to the transitions terminating on the $v' = 4$–6 levels of the $0_u^+(^3P_0)$ state. Furthermore, the bands observed are J selected transitions, showing band structures consisting of O, Q, and S branches in accordance with the selection rule of the 0_u^+–0_u^+ transition $\Delta J = 0, \pm 2$.

The second is the transition to the $0_u^+(^1D)$ ion-pair state, which will be discussed in this paper. This state lies in the 58 000 cm^{-1} range and shows the $0_u^+(^1D)$–$X^1\Sigma_g^+$ emission around 215 nm. In view of the quadratic dependence of fluorescence signals on the probe laser power, the double resonance transition is predicted to proceed in the type I transition $\nu_1 + (2\nu_2)$, where the coherent $0_u^+(^1D)$–$B^3\Pi(0_u^+)$ two-photon transition is executed by the probe laser alone. This assignment of the two-photon excitation mechanism is confirmed by comparing the observed polarization effect on line intensities with the theoretical prediction.

B. Polarization effect

According to the theoretical treatment of McClain and Harris (*7*), the 0_u^+, 1_u, and 2_u states can be combined with the $B^3\Pi(0_u^+)$ state by a coherent two-photon transition of identical photons. The rotational selection rules are as follows.

[1] $\Delta J = 0, \pm 2$ for the 0^+–0^+ transition

[2] $\Delta J = 0, \pm 1, \pm 2$ for the 1–0^+ and 2–0^+ transitions

The strengths of a coherent two-photon transition (δ) then depend on (*i*) a factor specified by J'' and J', analogous to the Hönl–London factor for a one-photon transition, (*ii*) an intrinsic factor characteristic of the particular vibronic transition, and (*iii*) a factor dependent on the polarization vector of two photons absorbed simultaneously. In the case of the 0^+–0^+ transition, the ratio of the absorption of the linearly polarized light to the circularly polarized light holds the relation

[3] $\delta_{ll}/\delta_{cc} = 2/3$

for the O and S branches, where subscripts l and c designate linearly and circularly polarized photons, respectively. The transition strength for the Q branch depends on the character of the two-photon transition and the polarization ratio is predicted to follow the relation

[4] $\delta_{ll}/\delta_{cc} = (2/3)\{1 + 5(\mu_I^2/\mu_S^2)\}$

for high J, where μ_I and μ_S denote the transition dipole factors given by $\mu_I = (2a + b)$ and $\mu_S = (a - b)$ in terms of Cartesian tensor components of the 0^+–0^+ two-photon transition:

[5] $$\begin{pmatrix} a & 0 & 0 \\ 0 & a & 0 \\ 0 & 0 & b \end{pmatrix}$$

The polarization ratio in eq. [4] thus ranges from infinity (no Q branch in the excitation by circular polarized photons), for the case $\mu_S = 0$, to 14 for only perpendicular transitions involved in the two-photon process, and to 4 for only parallel transitions involved. On the other hand, the ratios of transition strengths (δ_{ll}/δ_{cc}) are predicted to be 2/3 for all branches of the 1–0^+ and 2–0^+ transitions.

We have measured the polarization character of the two-photon transition. Figure 1(b) shows a small portion of the spectrum where the polarization of the probe laser was changed from (a) vertical to (b) circular while maintaining the pump laser in the vertical polarization. Since double resonance excitation helps to resolve the rotational structure reasonably well, polarization effects on single rotational transitions are straightforward.

In the type I transition, the essential features are (*i*) the intensity ratios between the O, Q, and S lines are approximately 1:4:1 in spectrum (a), while their ratios change to about 3:2:3 in spectrum (b), and (*ii*) the O and S branches increase in intensity by ~50% by changing the polarization of the probe laser from linear to circular, while the Q branch drastically loses intensity by ~75%.

[6] $\delta_{ll}/\delta_{cc} = 0.68 \pm 0.07$ for O and S branches

[7] $\delta_{ll}/\delta_{cc} = 4.2 \pm 0.6$ for Q branches

This behavior is obviously characteristic of the $0_u^+(^1D)$–$B^3\Pi(0_u^+)$ transition executed by two identical photons, as predicted in eqs. [3] and [4]. The observed ratio of eq. [7] indicates that the parallel-type transition is executed in the two-photon process according to the theoretical prediction expressed in eqs. [4] and [5]: $a/b \sim 0$. The view is quite reasonable. The valence–ion-pair transitions are of the charge transfer type, whose transition moments lie along the internuclear axis.

In the type II transition, where the $0_u^+(^3P_0)$–$B^3\Pi(0_u^+)$ transition occurs by the combination of pump and probe lasers, the intensity pattern of O, Q, and S branches is close to the 1:3:1 ratios in spectrum (a), and changes to approximately 1:2:1 in spectrum (b). The polarization ratios for the transition strengths are $\delta_{lc}/\delta_{ll} \sim 0.9$ for the O and S branches and ~0.6 for the Q branches, which agree with our previous results (*3b*).

C. Emission

Figure 2 represents two examples of the emission spectra showing the $0_u^+(^1D)$–$X^1\Sigma_g^+$ system. The spectra were obtained by tuning the probe laser frequency to the Q branch involved in the first members of the vibrational progression in Fig. 1(a); (a) (8–0) P_{49} and (b) (10–1) P_{22} transitions of the $B^3\Pi(0_u^+)$–$X^1\Sigma_u^+$ system. The molecular parameters of the higher vibrational levels of the ground state were reported for the ^{79}Br–^{81}Br species (*8*). We adjusted these constants to $^{79}Br_2$ to allow for the isotope difference and the assignments of the vibrational progressions are shown in Fig. 2. The absolute wavelength positions of the expected P and R doublets in the $0_u^+(^1D)$–$X^1\Sigma_g^+$ system agreed with the observations within a spectral slit width of 2 Å. The transition obviously terminates at the high vibrational levels of the ground state, since the internuclear distance of the ion-pair state (typically $r_e = 3.2$ Å) is much longer than that of the ground state ($r_e = 2.281$ Å). The low v' level of the ion-pair state thus displays in emission a band system whose intensity distribution is modulated according to the probability distribution of the upper vibrational wavefunction: the $v' = 0$ level shows a single intensity maximum in an envelope of the emission spectrum, $v' = 1$ shows double maxima, and so on.

Can. J. Chem. Downloaded from www.nrcresearchpress.com by 112.217.228.212 on 09/07/12
For personal use only.

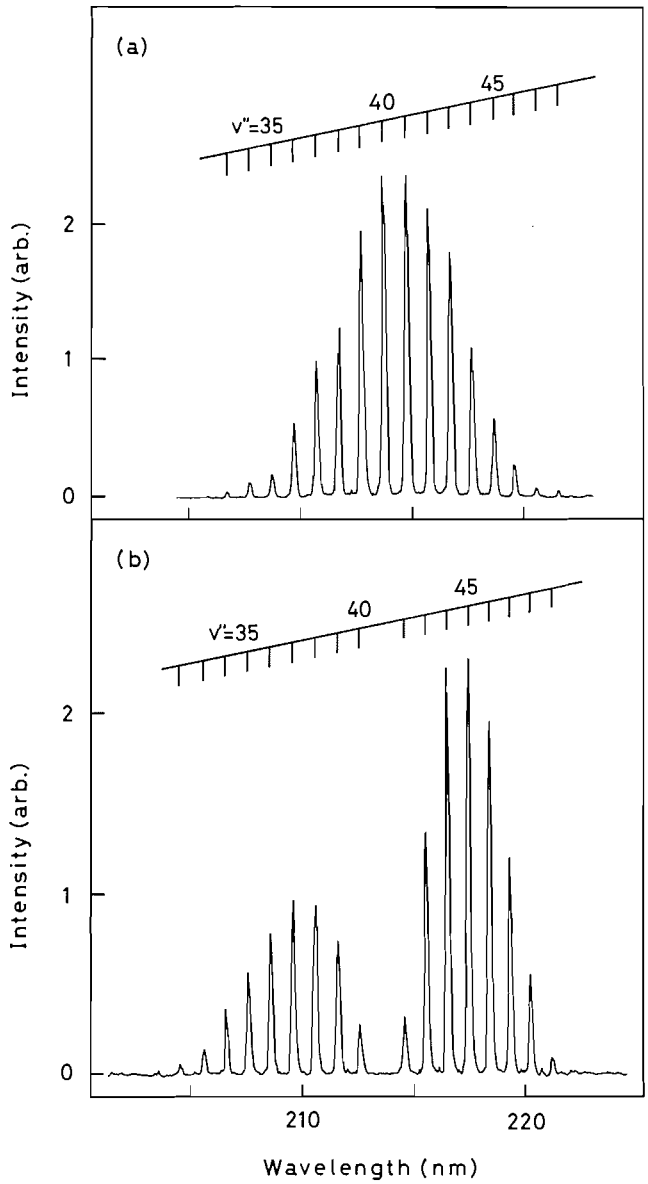

FIG. 2. The emission spectra of the $0_u^+(^1D)$–$X^1\Sigma_g^+$ system of Br_2. The excitation scheme is

$$0_u^+(^1D) \xleftarrow{2h\nu_2} B^3\Pi(0_u^+) \xleftarrow{h\nu_1} X^1\Sigma_g^+$$

(a) (0–8) Q_{48} (8–0) P_{49}

(b) (1–10) Q_{21} (10–1) P_{22}

Calculated Franck–Condon factors are as follows:

Scheme	$v' = 30$	31	32	33	34	35	36	37	38	38	40
(a)			1	3	7	16	31	54	83	114	139
(b)	1	2	6	13	25	43	64	79	77	56	23

Scheme	$v' = 41$	42	43	44	45	46	47	48	49	50
(a)	149	139	112	77	44	21	7	2		
(b)	0	13	60	115	144	129	87	43	15	3

The spectra in Fig. 2 are, therefore, predicted to originate from (a) $v' = 0$ and (b) $v' = 1$ levels of the $0_u^+(^1D)$ ion-pair state, and the use of isotopes is eventually not necessary for the absolute vibrational numbering of the double resonance spectrum shown in Fig. 1(a).

D. Analysis

The transitions from a J-selected level of the $B^3\Pi(0_u^+)$ state to the $0_u^+(^1D)$ state were measured by installing the intra-cavity étalon in the probe laser. The probe laser frequency was calibrated by reference to the absorption spectrum of $^{130}Te_2$ (9), recorded simultaneously. A typical result is shown in Fig. 3. The spectral position of the OODR signal could be determined within an estimated accuracy of $0.02\,cm^{-1}$. Table 1 summarizes the double resonance transitions observed in the experiments. The raw data include 377 transitions in the range of $0 \leqq v' \leqq 8$ and $6 \leqq J' \leqq 100$. Even though the range of the rotational levels probed in the $0_u^+(^1D)$ ion-pair state is not uniform for each vibrational level and does not cover all rotational levels, there remains no serious gap in the rotational distribution and we could not find any traces of local perturbation. As an example, a Fortrat diagram of the (0–8) $0_u^+(^1D)$–$B^3\Pi(0_u^+)$ transition is shown in Fig. 4. The measurements were continued for high J levels until the data were sufficient to determine the centrifugal distortion.

In the energy level analysis of the $0_u^+(^1D)$ ion-pair state, we converted the probe laser frequencies (ν_2) to the energies of the ion-pair state ($T_{v,J}$) relative to the potential minimum of the $X^1\Sigma_g^+$ ground state by the relation

$$[8] \quad T_{v,J} = T_{v^*,J^*}(B) + 2h\nu_2$$

where $\Delta J = J^* - J = 0, \pm 2$ corresponding to the rotational selection rule of the coherent $0_u^+(^1D)$–$B^3\Pi(0_u^+)$ two-photon transition. The term value of the $B^3\Pi(0_u^+)$ state, $T_{v^*,J^*}(B)$, from which the two-photon transition originated, could be calculated from the molecular constants given by Barrow *et al.* (6). The term values of the $0_u^+(^1D)$ state were then submitted to a global least-squares fit to the Dunham-type expansion

$$[9] \quad T_{v,J} = \Sigma_{n,k} Y_{n,k}(v + 1/2)^n J^k (J + 1)^k$$

The fitting requires eight parameters as listed in Table 2. The standard deviation of the fit is $0.0466\,cm^{-1}$ and the molecular parameters in Table 2 can regenerate all $0_u^+(^1D)$ term values within the range of $0.15\,cm^{-1}$.

The molecular constants in Table 2 were used to construct an RKR (Rydberg–Klein–Rees) potential curve of the $0_u^+(^1D)$ state. The RKR turning points for the observed vibrational levels are given in Table 3. We then calculated the Franck–Condon factors (FCF) between the $0_u^+(^1D)$ and $X^1\Sigma_g^+$ states to confirm the intensity distribution of the emission spectra in Fig. 2.[2] Calculations were made of the effective potentials for the corresponding J levels, including the centrifugal term; $U_J(r) = U_0(r) + J(J + 1)h/(8\pi^2 c\mu r^2)$. As shown in the caption of Fig. 2, the Franck–Condon factor calculations support our observations in terms of the intensity pattern, making the absolute v numbering of the $0_u^+(^1D)$ state unequivocal. However, there exist slight discrepancies in the intensity distribution of the spectra in Fig. 2: the maxima predicted at $v'' = 41$ for $v' = 0$ and $v'' = 45$ for $v' = 1$ shift to shorter

[2]We used the Hougen version of the RKR and FCF program originally written by Zare *et al.* (11).

TABLE 1

Pump		Probe transition (cm^{-1})		
		O	Q	S
(8-0)P_7	v=0		20415.972	20416.674
P_{10}	v=0	20414.964	20415.761	20416.712
R_{11}	v=0	20414.409	20415.463	20416.725
R_{14}	v=0	20413.704	20415.104	20416.637
P_{17}	v=0	20413.547	20414.974	20416.576
R_{21}	v=0	20411.963	20413.981	20416.148
P_{23}	v=0	20411.971	20413.974	20416.138
R_{27}	v=0	20410.113	20412.630	20415.366
P_{28}	v=0	20410.420	20412.898	20415.503
R_{32}	v=0	20408.316	20411.337	20414.483
P_{35}	v=0	20407.935	20411.033	20414.323
R_{39}	v=0	20405.467	20409.065	20412.951
P_{42}	v=0	20405.025	20408.775	20412.694
R_{46}	v=0	20402.199	20406.515	20410.986
P_{49}	v=0	20401.685	20406.104	20410.670
	1	505.804	510.154	514.706
R_{53}	v=0	20398.527	20403.490	20408.633
	1	502.497	507.418	512.511
P_{56}	v=0	20397.988	20403.040	20408.256
R_{60}	v=0	20394.492	20400.090	20405.880
P_{63}	v=0	20393.896	20399.566	20405.436
R_{67}	v=0	20390.063	20396.291	20402.709
P_{70}	v=0	20389.396	20395.729	20402.291
R_{74}	v=0	20385.261	20392.138	20399.195
P_{77}	v=0	20384.540	20391.490	20398.667
R_{81}	v=0		20387.583	20395.288
P_{84}	v=0	20379.300	20386.917	20394.711
(9-0)P_{10}	v=1	20451.625	20452.412	20453.350
R_{14}	v=1	20450.445	20451.767	20453.272
P_{19}	v=1	20449.745	20451.358	20453.142
R_{23}	v=1	20448.106	20450.269	20452.607
P_{27}	v=1	20447.501	20449.864	20452.358
R_{31}	v=1	20445.469	20448.358	20451.437
P_{36}	v=1	20444.339	20447.505	20450.841
R_{40}	v=1	20441.867	20445.579	20449.467
P_{43}	v=1	20441.425	20445.232	20449.208
R_{47}	v=1	20438.628	20422.961	20447.484
R_{60}	v=1	20431.564	20437.104	20442.829
P_{69}	v=1	20427.207	20433.380	20439.766
P_{76}	v=1	20422.495	20429.323	20436.339
P_{83}	v=1	20417.443	20424.906	20432.562
P_{84}	v=1	20416.699	20424.225	20431.982
R_{87}	v=1		20420.855	20429.054
R_{92}	v=1	20408.831	20417.296	20425.915
R_{97}	v=1	20404.616	20413.541	20422.625
(10-0)P_{15}	v=6	20885.952	20887.128	20888.506
	7	982.260	983.445	984.801
R_{19}	v=6	20884.434	20886.153	20888.047
	7	980.680	982.399	984.314
P_{22}	v=1	20383.092	20384.974	20387.033
	2	486.125	487.965	490.024
	3	587.650	589.543	591.561
P_{30}	v=1	20380.776	20383.391	20386.184
	2	483.692	486.294	489.077
	3	585.191	587.801	590.540
	6	881.490	883.985	886.693
	7	977.717	980.195	982.870
R_{33}	v=1	20379.081	20382.148	20385.424
R_{42}	v=1	20375.571	20379.456	20383.533
	2	478.294	482.138	486.175
	3	579.592	583.432	587.440
	5		781.881	785.812
	6	875.414	879.161	883.087
	7	971.482	975.191	979.108

Pump		Probe transition (cm^{-1})		
		O	O	S
(10-0)R_{62}	v=1	20356.622	20371.342	20377.302
	2	467.937	473.611	479.489
	3	568.929	574.537	580.346
	6	863.628	869.130	874.836
	7	959.400	964.846	970.509
R_{75}	v=1	20357.685	20364.577	20371.687
	2	459.673		
	3	560.273	567.051	574.013
	5	757.447	764.113	771.012
	6	854.138	860.768	867.579
	7	949.635	956.231	962.982
(12-0)P_{47}	v=2	20352.140	20356.240	20360.619
	3	453.404	457.516	461.788
R_{64}	v=2	20343.413	20349.273	20355.313
	3	444.310	450.115	456.092
R_{81}	v=2	20333.838	20341.223	20348.777
	3	434.245	441.560	449.102
	7	823.027	830.109	837.456
R_{87}	v=3	20430.297	20438.156	20446.208
(13-1)P_{51}	v=2	20350.537	20355.023	20359.696
	3	451.696	456.150	460.789
	4	551.508	555.936	560.546
	6	747.149	751.514	756.073
	7	843.154	847.502	852.015
(13-1)P_{18}	v=3	20402.596	20404.076	20405.755
	4	502.760	504.228	505.907
	5	601.568	603.037	604.676
	6	699.094	700.533	702.175
R_{41}	v=4	20495.409	20499.130	20503.023
	5	594.007	597.696	601.549
	6	691.325	694.943	
P_{55}	v=3	20390.749	20395.543	20400.520
	4	490.454	495.237	500.166
	5	588.863	593.622	
	8	876.693	881.330	886.174
R_{68}	v=4	20483.023	20489.151	
R_{67}	v=4	20483.563	20489.580	
(14-1)R_{25}	v=4	20442.721	20444.984	20447.441
	5	541.447	543.717	546.137
	6	638.928	641.168	643.586
R_{48}	v=4	20435.378	20439.721	20444.223
	5	533.845	538.181	542.651
P_{67}	v=4	20428.093	20433.942	20439.978
	5	526.270	532.038	538.052
R_{78}	v=4	20421.555	20428.581	20435.756
	5	519.424	526.388	533.488
(15-0)P_{33}	v=8	20772.655	20775.413	20778.314
R_{36}	v=8	20771.092	20774.265	20777.639
P_{50}	v=8	20766.684	20770.877	20775.276
P_{61}	v=8	20761.881	20767.047	20772.382
P_{68}	v=8	20758.474	20764.244	20770.203
R_{78}	v=8	20752.057	20759.865	20765.837
(16-0)R_{17}	v=8	20722.225	20723.727	20725.422
P_{23}	v=8	20721.377	20723.232	20725.297
R_{26}	v=8	20720.218	20722.522	20725.005
P_{35}	v=8	20718.349	20721.280	20724.355
R_{38}	v=8	20716.853	20720.191	20723.714
P_{44}	v=8	20715.573	20719.272	
R_{47}	v=8	20713.841	20717.955	
P_{50}	v=8	20713.484	20717.690	20722.063
R_{53}	v=8	20711.579	20716.234	20721.053
(17-0)P_{14}	v=8		20724.185	20725.422
P_{20}	v=8	20670.121	20671.736	20673.522
R_{23}	v=8	20669.166	20671.180	20673.409
P_{33}	v=8	20667.329	20670.044	20672.957
R_{36}	v=8	20665.966	20669.182	20672.532

Can. J. Chem. Downloaded from www.nrcresearchpress.com by 112.217.228.212 on 09/07/12
For personal use only.

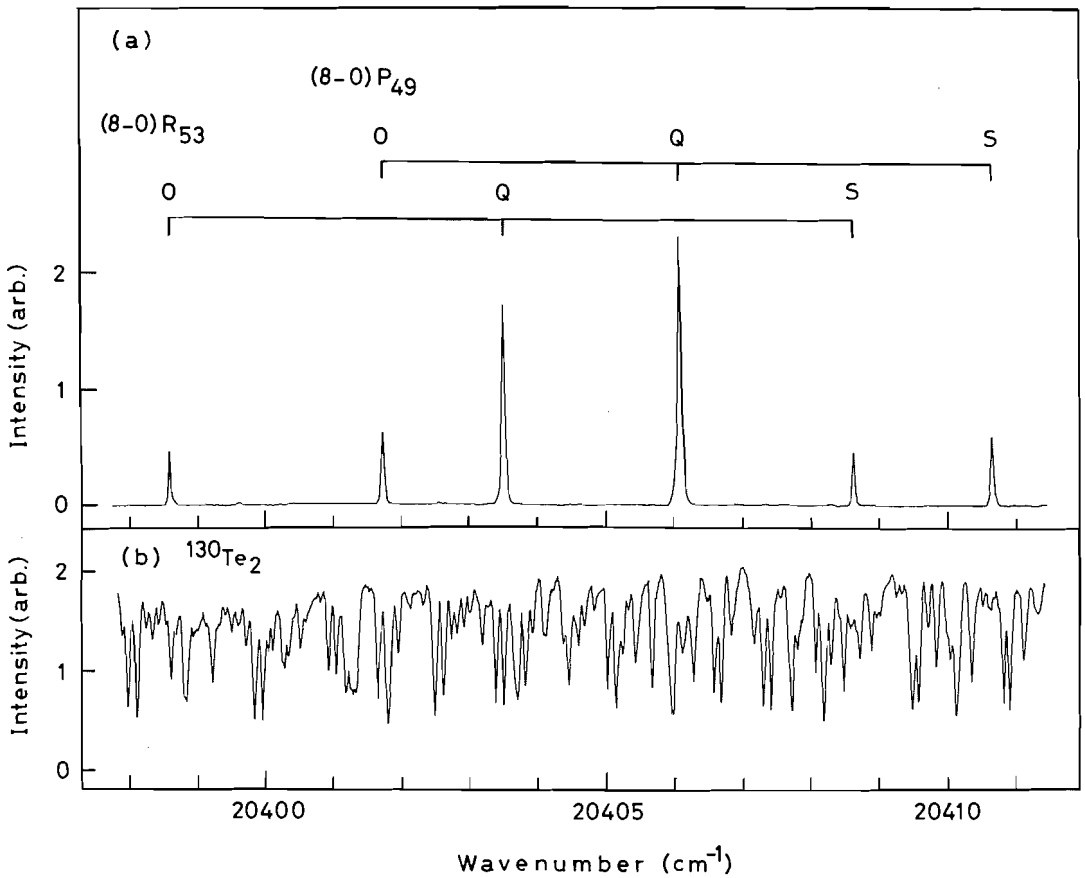

FIG. 3. (a) The double resonance spectrum of the (0–8) $0_u^+(^1D)$–$B^3\Pi(0_u^+)$ transition taken under high resolution in the vicinity of 490 nm shown in Fig. 1. Two rotational multiplets consisting of O, Q, and S branches reflect the transitions through the (8–0) P_{49} and R_{53} transitions of the $B^3\Pi(0_u^+)$–$X^1\Sigma_g^+$ system according to the selection rule of $\Delta J = 0, \pm 2$. (b) The absorption spectrum of $^{130}Te_2$ used for the laser frequency calibration.

wavelengths in the observations. The situation is quite similar to the $0_u^+(^3P_2)$–$X^1\Sigma_g^+$ system (3*d*), because the molecular constants used to calculate the RKR potential of the ground state would be not accurate enough to reproduce the potential in a long range.

E. Ion-pair state of Br_2

Table 4 lists the ion-pair states of Br_2 known to date according to their ionic correlations at the dissociation limit expected in the empirical model (5). The ion-pair states have similar vibrational frequencies close to 150 cm^{-1}, bond lengths $r_e = 3.2$ Å, and, because of the predominance of the coulombic attraction in their potential functions, they have relatively large dissociation energies of ~35 000 cm^{-1}. To the extent that these states reflect the intervals in the various Br^+ ions, there are six states (0_u^+, 1_u, 2_u, 0_g^+, 1_g, $2_g(^3P_2)$) around 49 000 cm^{-1}, six (0_u^-, 1_u, 0_g^-, $1_g(^3P_1)$, and 0_u^+, $0_g^+(^3P_0)$) around 52 000 cm^{-1}, six (0_u^+, 1_u, 2_u, 0_g^+, 1_g, $2_g(^1D)$) around 60 000 cm^{-1}, and two (0_u^+, $0_g^+(^1S)$) considerably higher (17).[3]

Among the 12 states correlating with $Br^-(^1S) + Br^+(^3P)$, it is surprising that only the 0_g^+ and $2_g(^3P_2)$ states have been analyzed through the emission spectra observed in the discharge (12, 15). Double resonance methods have been used to fill this gap and elucidated the 11 ion-pair states except for the $2_g(^3P_2)$ state. The $\Omega = 0^+$ and 1 states have been characterized with reasonable accuracy either through the $B^3\Pi(0_u^+)$ or $A^3\Pi(1_u)$ state as an intermediate using (1 + 1) photon excitation for g states and (1 + 2) excitation for u states (2–4, 13, 14). However, the spectroscopic data for the $2_u(^3P_2)$ and $0_u^-(^3P_1)$ states are quite fragmentary, since these excited states have only been seen as extra lines through the heterogeneous interaction with $\Omega = 0^+$ and 1 ion-pair states correlating with the same ionic

TABLE 2. Molecular parameters of the $0_u^+(^1D)$ ion-pair state

Parameter	Value
Y_{00}	57929.724(24)[a]
Y_{10}	212.227(23)
Y_{20}	−1.5683(56)
Y_{30}	$1.606(40) \times 10^{-2}$
Y_{01}	0.0465652(89)
Y_{11}	$-4.500(36) \times 10^{-4}$
Y_{21}	$1.133(41) \times 10^{-5}$
Y_{02}	$-9.37(94) \times 10^{-9}$[b]

[a]Effective for $v = 0$–8. 3σ in parentheses.
[b]Y_{02}(calcd.) $= -4Y_{01}^3/Y_{10}^2 = -9.0 \times 10^{-9}$ cm^{-1}.

[3]The terms of Br^+ are, in order of energy, $^3P_2$ (ground state), $^3P_1$ (3139 cm^{-1}), $^3P_0$ (3840 cm^{-1}), ^1D (11 409 cm^{-1}), and ^1S (not measured).

Can. J. Chem. Downloaded from www.nrcresearchpress.com by 112.217.228.212 on 09/07/12
For personal use only.

TABLE 3. RKR turning points for the $0_u^+(^1D)$ ion-pair state of Br_2

v	G_v[a] (cm^{-1})	B_v[a] (cm^{-1})	Turning point (Å)[b] r_{min}	r_{max}
0	105.72	0.046343	2.971	3.098
1	314.87	0.045916	2.934	3.156
2	521.02	0.045510	2.912	3.200
3	724.27	0.045129	2.895	3.238
4	924.73	0.044770	2.880	3.272
5	1122.48	0.044329	2.868	3.303
6	1316.63	0.044119	2.857	3.333
7	1510.26	0.043828	2.847	3.361
8	1700.48	0.043559	2.838	3.387

[a]Calculated value from the constants in Table 2.
[b]r_e = 3.029 Å.

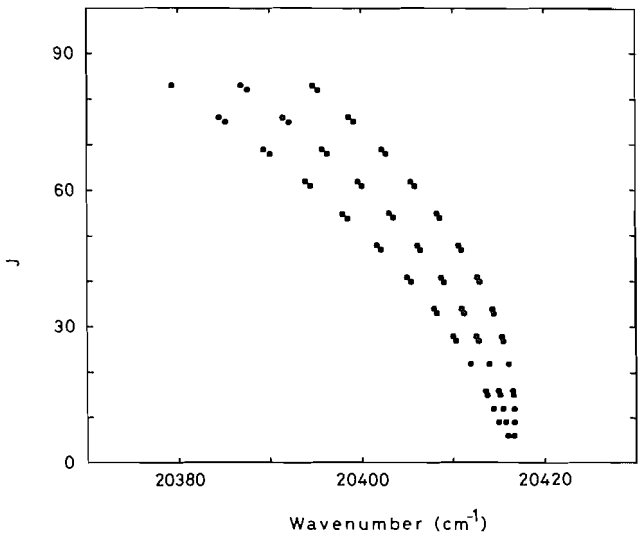

FIG. 4. A Fortrat diagram of the (0–8) $0_u^+(^1D)$–$B^3\Pi(0_u^+)$ transition.

asymptotes: 0_u^+–1_u–$2_u(^3P_2)$ and 0_u^-–$1_u(^3P_1)$.[1] Furthermore, the position of the $0_g^-(^3P_1)$ state has been only predicted from the Ω-type splitting constants of the $1_g(^3P_1)$ state, on the basis of the pure precession approximation of the 1_g–$0_g^-(^3P_1)$ interaction (4*b*). The direct approach to the $\Omega = 0^-$ and 2 ion-pair states is mainly limited by the $\Delta\Omega = 0$ selection rule of the valence–ion-pair transitions originating from their primary transition moments parallel to the internuclear axis.

Among the six states correlating with $Br^-(^1S) + Br^+(^1D)$, the $0_u^+(^1D)$ state is the first one identified spectroscopically. This state is anomalous among the ion-pair states. (*i*) The dissociation energy of ~38 000 cm^{-1} is ~3000 cm^{-1} larger than the average of the ion-pair states correlating with $Br^-(^1S) + Br^+(^3P)$. (*ii*) The vibrational frequency of the $0_u^+(^1D)$ state is 40–70% higher than those of other ion-pair states and the equilibrium internuclear distance is 0.15–0.3 Å shorter. These facts indicate that a covalent character results from the configuration interaction with Rydberg states. The lowest vibrational level of the $0_u^+(^1D)$ state shows the emission spectrum around 215 nm. According to Tellinghuisen *et al.* (5), the 220-nm band had a discrete structure and persisted at high Ar pressure in the discharge. This band obviously corresponds to the $0_u^+(^1D)$–$X^1\Sigma_g^+$ system described in this work. The red shift of the emission peak by ~5 nm is not surprising. In ion-pair states the vibrational relaxation competes with the fast cascade to lower excited states by collisions. The thermalization might be inefficient in the high-lying ion-pair state and the overlap of the emission bands from the unthermalized vibrational levels is expected to show a red-shifted band structure.

Tellinghuisen *et al.* (see Table 1 in ref. 5) also showed evidence of at least five other electronic transitions in addition

TABLE 4. Electronic states of Br_2

	T_e (cm^{-1})	ω_e (cm^{-1})	r_e (Å)	Emission	Dissociation limit	Reference
0_u^+	57929.7	212.2	3.03	To X 215 nm	$Br^-(^1S) + Br^+(^1D)$	This work
0_u^+	53899.5	155.8	3.28	X 248 nm	$Br^-(^1S) + Br^+(^3P_0)$	3*b*
0_g^+	53101.7	152.8	3.17	B 281 nm		2*b*
0_u^-	53479.8[a]	148.6	3.35		$Br^-(^1S) + Br^+(^3P_1)$	
1_u	53257.6[a]	164.2	3.27			
1_g	52641.5	153.9	3.17	A 265 nm		4*b*
0_g^-	(52000)[b]					4*b*
2_u	50452.7[a]	147.9	3.35		$Br^-(^1S) + Br^+(^3P_2)$	
1_u	50212.0[a]	125.7	3.26			3*d*, 11
0_u^+	49928.4[a]	134.5	3.18	X 270 nm		3*d*, 11
0_g^+	49778.5	150.8	3.20	B 311 nm		2*a*, 12, 13
1_g	49390.4	151.7	3.18	A 291 nm		4*a*, 14
2_g	(48930)[c]	150.9	3.17	A′ 292 nm		15
$B^3\Pi(0_u^+)$	15902.5	167.6	2.68			6
$A^3\Pi(1_u)$	13905	153	2.70			16
$A'^3\Pi(2_u)$	(13220)[c]	165.2	2.68			15
$X^1\Sigma_g^+$	0	325.3	2.28			6

[a]Unpublished results; see footnote 1.
[b]Crude estimate from the Ω-type splitting constant of the $1_g(^3P_1)$ state in terms of the pure precession model.
[c]Through the analysis of the $2_g(^3P_2)$–$A'^3\Pi(2_u)$ emission, their potential curves are well characterized. However, there is no other state combining with these excited states, and their absolute positions are still ambiguous (±100 cm^{-1}).

Can. J. Chem. Downloaded from www.nrcresearchpress.com by 112.217.228.212 on 09/07/12
For personal use only.

to the $2_g(^3P_2)$–$A'^3\Pi(2_u)$ and $0_g^+(^3P_2)$–$B^3\Pi(0_u^+)$ systems in the 200–300 nm region. As to the 227 and 237-nm bands, spectroscopic data are not available to specify the assignment on the data base listed in Table 4. Assuming that the discrete 227-nm band originates from the ion-pair state having $r_e \sim 3.2$ Å, its energy is estimated to be 59 000 or 61 500 cm^{-1}, according to whether the transition terminates on either the $A^3\Pi(1_u)$ or the $A'^3\Pi(2_u)$ state, or on the $B^3\Pi(0_u^+)$ state. For the 237-nm band, the energy of the upper state decreases by ~2000 cm^{-1}. These energies lie in the region for the states correlating with $Br^-(^1S) + Br^+(^1D)$. The 251 and 265-nm bands are definitely assigned to the $0_u^+(^3P_0)$–$X^1\Sigma_g^+$ and $1_g(^3P_1)$–$A^3\Pi(1_u)$ systems, respectively. The 276-nm band is close to the $0_u^+(^3P_2)$–$X^1\Sigma_g^+$ system in the wavelength. However, we can expect the transition of the $0_g^-(^3P_1)$ ion-pair state to terminate at the 0_u^- state that correlates with the two ground-state atoms ($Br_{3/2}$) around 276 nm, by analogy with the emission spectrum of I_2. Tellinghuisen and co-workers reported the 0_g^-–0_u^- system around 288 nm as the second most intense transition in the high-pressure emission spectrum of I_2 (18). The energy levels of the ion-pair states correlating with the second ionic states of $I^-(^1S) + I^+(^3P_{1,0})$ are somewhat different from those of Br_2: the $0_g^+(^3P_0)$, $0_g^-(^3P_1)$, $0_u^+(^3P_0)$, and $1_g(^3P_1)$ states of I_2 are located in the 47 000 cm^{-1} region in order of energy. The other two states $0_u^-(^3P_1)$ and $1_u(^3P_1)$ are not observed in the experiment and are expected, from theoretical prediction,[4] to lie much higher. Since the $0_g^-(^3P_1)$ ion-pair state of Br_2 lies lowest in the second cluster of the states correlating with $Br^-(^1S) + Br^+(^3P_{1,0})$, we could not neglect the possibility that the $0_g^-(^3P_1)$–0_u^- emission overlaps with the $0_u^+(^3P_2)$–$X^1\Sigma_g^+$ system. The high-lying states correlating with the same asymptote are expected to be collisionally converted to the $0_g^-(^3P_1)$ state.

Finally, Brand and Hoy (19) have recently discussed the r-dependent homogeneous interaction of the $0_u^+(^1D)$ state with the $0_u^+(^3P_0)$ state of I_2. The interaction matrix is suggested to be small at r_e, but increases rapidly as r decreases. Their potential functions are consequently distorted at small r, making the principal constants anomalous. In Br_2, the effects might also be responsible for the large anharmonicity of the potential function observed at the lower vibrational levels of the $0_u^+(^1D)$ state: the ratio Y_{20}/Y_{10} (or Y_{11}/Y_{01}) $\sim 1 \times 10^{-2}$ is larger than those of other ion-pair states ($\sim 3 \times 10^{-3}$) by a factor of 3. This problem will be addressed in future.

[4]R. L. Jaffe. Private communication cited in ref. 19*b*.

1. K. P. Huber and G. Herzberg. Molecular spectra and molecular structure. I. Constants of diatomic molecules. Van Nostrand–Reinhold, New York. 1978.
2. (*a*) T. Ishiwata, A. Tokunaga, T. Shinzawa, and I. Tanaka. Bull. Chem. Soc. Jpn. **57**, 1317 (1984); (*b*) T. Ishiwata, H. Ohtoshi, and I. Tanaka. J. Chem. Phys. **81**, 2300 (1984).
3. (*a*) T. Ishiwata, T. Shinzawa, A. Tokunaga, and I. Tanaka. Chem. Phys. Lett. **101**, 350 (1983); (*b*) T. Shinzawa, A. Tokunaga, T. Ishiwata, I. Tanaka, K. Kasatani, M. Kawasaki, and H. Sato. J. Chem. Phys. **80**, 5909 (1984); (*c*) T. Ishiwata, A. Tokunaga, T. Shinzawa, and I. Tanaka. Bull. Chem. Soc. Jpn. **57**, 1469 (1984); (*d*) T. Ishiwata, A. Tokunaga, T. Shinzawa, and I. Tanaka. J. Mol. Spectrosc. **108**, 314 (1984).
4. (*a*) T. Ishiwata, T. Hara, K. Obi, and I. Tanaka. J. Chem. Phys. **87**, 2513 (1987); (*b*) T. Ishiwata, K. Obi, and I. Tanaka. J. Mol. Spectrosc. In press.
5. J. Tellinghuisen, P. Berwanger, J. G. Ashmore, and K. S. Viswanathan. Chem. Phys. Lett. **84**, 528 (1981).
6. R. F. Brown, T. C. Clark, J. A. Coxon, and K. K. Yee. J. Mol. Spectrosc. **51**, 428 (1974).
7. W. M. McClain and R. A. Harris. *In* Excited states. Vol. 3. *Edited by* E. C. Lim. Academic Press, New York. 1977. p. 1.
8. P. Ventateswarlu, V. S. Sarma, and J. Tellinghuisen. J. Mol. Spectrosc. **100**, 143 (1983).
9. J. Cariou and P. Luc. Atlas du spectre d'absorption de la molécule de tellure. Partie 2. CNRS, Paris. 1980.
10. R. N. Zare, A. L. Schmeltekopf, W. J. Harrop, and D. L. Albritton. J. Mol. Spectrosc. **46**, 37 (1973).
11. A. R. Hoy. J. Mol. Spectrosc. **115**, 232 (1986).
12. P. Berwanger, K. S. Viswanathan, and J. Tellinghuisen. J. Mol. Spectrosc. **91**, 275 (1982).
13. J. C. D. Brand, U. D. Deshpande, A. R. Hoy, and S. M. Jaywant. J. Mol. Spectrosc. **100**, 143 (1983).
14. J. C. D. Brand, A. R. Hoy, S. M. Jaywant, and A. W. Taylor. J. Mol. Spectrosc. **123**, 84 (1987).
15. A. Sur and J. Tellinghuisen. J. Mol. Spectrosc. **88**, 323 (1981).
16. J. A. Coxon. J. Mol. Spectrosc. **41**, 548 (1972).
17. C. E. Moore. Atomic energy levels. Natl. Stand. Ref. Data Ser. (U.S. Natl. Bur. Stand.) **35**, Vol. II. 1971. p. 161.
18. (*a*) A. L. Guy, K. S. Viswanathan, A. Sur, and J. Tellinghuisen. Chem. Phys. Lett. **73**, 582 (1980); (*b*) K. S. Viswanathan and J. Tellinghuisen. J. Mol. Spectrosc. **101**, 285 (1983).
19. A. R. Hoy and J. C. D. Brand. Chem. Phys. **109**, 109 (1986).

Can. J. Chem. Downloaded from www.nrcresearchpress.com by 112.217.228.212 on 09/07/12
For personal use only.

Two independent isotope effects and their magnetic field dependences in the photoreduction of menadione in deuterium labeled SDS micellar solutions. A spin trapping study

MASAHARU OKAZAKI,[1] KAZUMI TORIYAMA,[1] KEICHI NUNOME, HACHIZO MUTO, AND TAKESHI SHIGA[2]

Department of Radiation Chemistry, Government Industrial Research Institute, Nagoya, Hirate, Kita, Nagoya, Japan, 462

Received November 9, 1987

This paper is dedicated to Professor Charles A. McDowell on the occasion of his 70th birthday

MASAHARU OKAZAKI, KAZUMI TORIYAMA, KEICHI NUNOME, HACHIZO MUTO, and TAKESHI SHIGA. Can. J. Chem. **66**, 1832 (1988).

Spin adduct yields in the photoreduction of menadione (2-methylnaphthoquinone) in isotope labeled micellar solutions were measured as functions of the external magnetic field. As surfactants, ordinary SDS, perdeuteriated SDS, and a mixture of the two were employed. In a mixed micellar solution, a normal isotope effect on the spin adduct yield was observed. On the other hand, in the pure micellar solutions with each of the former two surfactants, a reversed isotope effect was observed. These two apparent isotope effects depend on the external magnetic field and were separated into two independent isotope effects: one is the primary isotope effect on the hydrogen abstraction step and the other is the secondary magnetic isotope effect on the intersystem crossing step of the intermediate radical pair.

MASAHARU OKAZAKI, KAZUMI TORIYAMA, KEICHI NUNOME, HACHIZO MUTO et TAKESHI SHIGA. Can. J. Chem. **66**, 1832 (1988).

On a mesuré l'influence du champ magnétique externe sur les rendements d'adduits de spin qui se forment lors de la photoréduction de la ménadione (méthyl-2 naphtoquinone) dans des solutions micellaires marquées par des isotopes. On a utilisé du DSS ordinaire, du DSS perdeutéré et un mélange des deux agents de surface. Dans une solution micellaire mixte, on a observé un effet isotopique normal sur le rendement en adduit de spin. Par ailleurs, dans des solutions micellaires contenant chacun des deux autres agents de surface à l'état pur (ordinaire ou perdeutéré), on a observé un effet isotopique inverse. Ces deux effets isotopiques apparemment inverses dépendent du champ magnétique externe et on a pu les séparer en deux effets isotopiques indépendants : l'un est l'effet isotopique primaire impliqué dans l'étape de l'enlèvement de l'hydrogène et l'autre est l'effet isotopique magnétique secondaire impliqué dans l'étape de croisement de la paire de radicaux intermédiaires.

[Traduit par la revue]

Introduction

The isotope effect in organic chemistry (1) has been widely studied not only because the effect has its own relevance in chemistry but it also gives detailed information about chemical reaction mechanisms. As well, it may give a method for isotope enrichment. Included in those studies, the isotope effect in hydrogen abstraction reactions has been studied extensively and the mechanism developed (2–5). In addition, it was recently found that reactions that involve a radical pair as the intermediate show another type of isotope effect, i.e., the "magnetic isotope effect" (6–9). In these cases, it is very important to observe these isotope effects separately to deduce relevant results from them.

In a series of our previous studies (10–13), using the spin trapping technique (14, 15) and a flow apparatus, we developed a method to probe radical pair interactions that induce the magnetic field dependence of chemical reactions. Because the magnetic field effect is usually considered to be aroused through magnetic interaction between the intermediate radicals (16), an isotope effect can be expected in a reaction involving isotopes with different nuclear magnetisms. Because our method is quite sensitive to the magnetic field effect on chemical reactions (12), a new insight into the mechanism of isotope effects can be expected in such chemical reactions.

In this study, we observed the isotope effect on the yield of a spin trapping reaction during the photoreduction of menadione (2-methylnaphthoquinone) (17) in micellar solutions with each of ordinary SDS (SDS(H)), perdeuteriated SDS (SDS(D)), and a mixture of the two. The spin adduct with SDS(D) radical could be clearly distinguished spectroscopically by esr from that with the H-species. In the micellar solution of SDS(D) the spin adduct yield was about twice as large as that in SDS(H) micellar solution (reversed D/H isotope effect). On the other hand, in a mixed micellar solution with SDS(D) and SDS(H) at a molar ratio of 1:1, the yield of the spin adduct with the D-species was much smaller than that with the H-species (normal D/H isotope effect). The mechanism is studied by analysis of the magnetic field dependence of these isotope effects.

Experimental

Menadione (2-methylnaphthoquinone) was purchased from Wako Pure Chemicals (Osaka, Japan) as a guaranteed grade reagent, sodium dodecylsulphate (SDS) for electrophoresis from Nakarai Chemicals (Kyoto, Japan), and perdeuteriated SDS from MSD isotopes (Montreal, Canada). All these chemicals were used as received. Perdeuteriodimethylnitrosobenzenesulfonate (DMNS) was kindly supplied by Drs. Ryusei Konaka and Shigeru Sakata at Shionogi Pharmaceuticals (18). The extent of deuteriation of SDS(D) was larger than 98% as checked by mass spectrometry.

Menadione was dissolved at the concentration of 0.1 mM in a 0.1 M SDS micellar solution (buffered at pH 7.4 with 0.1 M phosphates) with a spin trap of DMNS (1 mM), and the solution was charged in a quartz flat cell using a flow apparatus and then photolysed with uv light (Ushio UH500D mercury lamp) filtered with a 5-cm water filter and a uv cut-off filter (Toshiba UV-31, <310 nm cut). The esr spectra were recorded with a Varian E-12 spectrometer at room temperature (ca. 25°C). Each component esr signal from the spin adduct of SDS(H) radical and SDS(D) radical in a composite spectrum was separated by computer simulation. The signal intensity was estimated by double integration of the first derivative spectrum. Zero magnetic field was achieved by canceling the residual field with a Helmholtz coil, which

[1]Author to whom correspondence may be addressed.

[2]Department of Physiology, Medical School, Ehime University, Shigenobu, Onsen-gun, Ehime, Japan, 791-02.

Can. J. Chem. Downloaded from www.nrcresearchpress.com by 112.217.228.212 on 09/07/12
For personal use only.

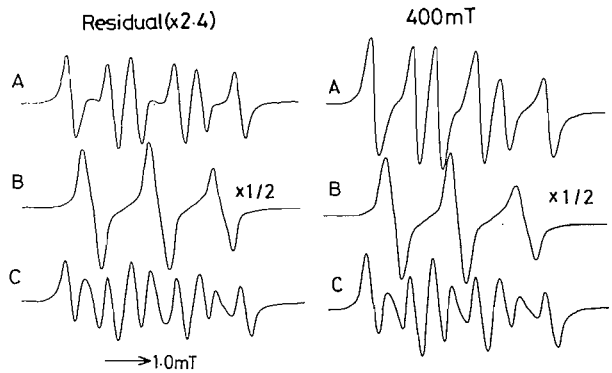

FIG. 1. Electron spin resonance spectra of the spin adducts in the photoreduction of menadione (0.1 mM) in SDS (0.1 M in 0.1 M phosphate buffer at pH 7.4) micellar solutions at residual magnetic field (left) and at 400 mT (right). The relative gain for the spectra at the residual field was 2.4 times as large as that for the spectra at 400 mT; (a) in SDS(H) micellar solution, (b) in SDS(D) micellar solution, and (c) in the mixed micellar solution of SDS(H) and SDS(D) at the molar ratio of 1:1. The microwave power was 5 mW, the modulation frequency and amplitude were 100 kHz and 0.2 mT, respectively.

was placed outside a Varian standard rectangular cavity. The detailed procedure has been described elsewhere (10).

Results

Figure 1 shows the esr spectra of the spin adducts of SDS radical accumulated during the photoreduction of menadione at the residual magnetic field (ca. 3.5 mT, right) and at 400 mT (left) (a) in the SDS(H) (ordinary SDS) micellar solution, (b) in the SDS(D) (perdeuteriated SDS) micellar solution, and (c) in the micellar solution with a 1:1 mixture of SDS(H) and SDS(D). The amplifier gain for the spectra at the residual field was set 2.4 times as large as that for the spectra at 400 mT. The sextet signal of spectra A has been assigned to the spin adduct of SDS radical (10), which is produced by hydrogen abstraction from the alkyl chain of the SDS molecule by the excited triplet menadione. The triplet signal of spectra B should be from the spin adduct of deuteriated SDS radical. We hereafter use the terms SDS(H) radical and SDS(D) radical for these SDS radicals from SDS(H) and SDS(D) molecules, respectively. At the residual magnetic field, the spin adduct concentration for the pure SDS(H) system was about half that for the pure SDS(D) system. On the other hand, in the mixed micellar system the concentration of the SDS(H) radical adduct was about twice that of the SDS(D) radical adduct. At 400 mT, both of the radical adducts increased greatly compared with those at the residual field. However, comparing the spectra C at the two magnetic fields, it is noticed that the increase of the SDS(H) radical adduct with the increase of the magnetic field is considerably larger than that of the SDS(D) radical adduct.

Figure 2 shows the magnetic field effect on the spin adduct yield for the photoreduction of menadione in each of the micellar solutions with pure SDS(H), pure SDS(D), and the mixed (at the ratio of 1:1) SDS. Here we define an index for the extent of the isotope effect:

$$[1] \quad \text{I.E.} = [T(\text{H})/C^0(\text{H})]/[T(\text{D})/C^0(\text{D})]$$

Where, T(H) and C^0(H) are the product yield of the SDS(H) radical adduct and the initial concentration of SDS(H), respectively. T(D) and C^0(D) are defined in the same way for the SDS(D) system. Therefore, the relation I.E. = 1.0 corresponds to the null isotope effect.

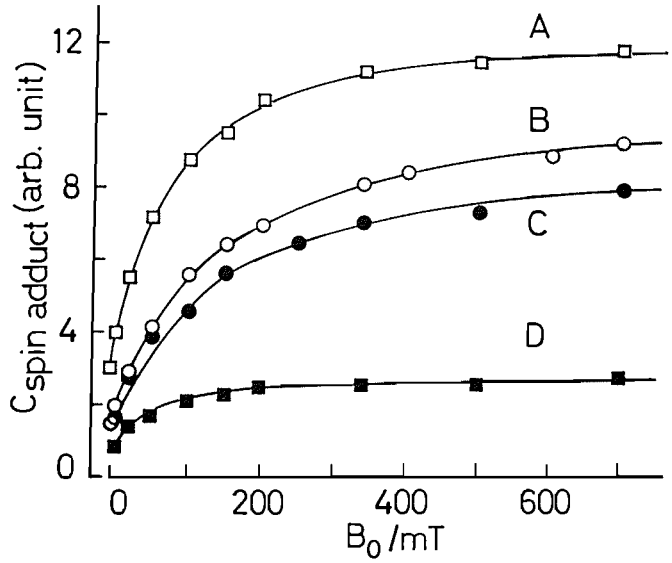

FIG. 2. Magnetic field dependences of spin adduct yields in the photoreduction of menadione in SDS micellar solutions: A, spin adduct of SDS(D) radical in an SDS(D) micellar solution; B, that of SDS(H) radical in an SDS(H) micellar solution; C and D, those of SDS(H) radical and SDS(D) radical, respectively, in the mixed (1:1) micellar solution. In the case of the pure micellar solutions, spin adduct yields were also obtained at zero magnetic field (<0.1 mT).

From the results shown in Fig. 2, we deduce the following results:

(*i*) In the pure systems, the SDS(H) system gave a much smaller spin adduct yield at all fields compared with the SDS(D) system. At higher fields, however, the I.E. value for the pure systems seems to approach unity with increasing magnetic field (0.5 at zero field to 0.78 at 700 mT).

(*ii*) In the mixed system, the spin adduct yield for the SDS(H) radical was much larger than that for the SDS(D) radical at all magnetic fields. The I.E. value increased from 2.0 (at the residual field) to 2.9 (at 700 mT) with increasing magnetic field. Even if the mole fraction of SDS(H) was decreased to half the original value, the decrease in the spin adduct yield of SDS(H) radical was only about 15% at 400 mT.

(*iii*) The magnetic field dependence (Δ spin adduct yield/ΔB_0) for the deuteriated system at higher field than 400 mT was small, in contrast to that for the non-deuteriated system.

Discussion

The reaction mechanism for the present system has been well elucidated in previous studies (10, 12, 19) and is shown below:

$$[2] \quad \text{MD} \rightarrow {}^1\text{MD}^* \rightarrow {}^3\text{MD}^*$$

$$[3] \quad {}^3\text{MD}^* + \text{SDS} \xrightarrow{k_{ABS}} {}^3(\text{MDH}\cdot\ \cdot\text{SDS})$$

$$[4] \quad {}^3(\text{MDH}\cdot\ \cdot\text{SDS}) \xrightarrow{k_{ISC}} {}^1(\text{MDH}\cdot\ \cdot\text{SDS})$$

$$\downarrow k_E \qquad\qquad \searrow k_p$$

$$[5] \quad \text{SDS}\cdot + \text{MDH}\cdot \qquad\qquad \text{singlet product}$$

$$[6] \quad \text{SDS}\cdot + \text{TNO} \xrightarrow{k_{TR}} \text{T(SDS)NO}\cdot$$

Menadione (MD) is promoted to its excited singlet state (^{1}MD*) by uv light and is transferred to its lowest triplet state (^{3}MD*; eq. [2]). ^{3}MD* abstracts a hydrogen from one of the surround-

Can. J. Chem. Downloaded from www.nrcresearchpress.com by 112.217.228.212 on 09/07/12
For personal use only.

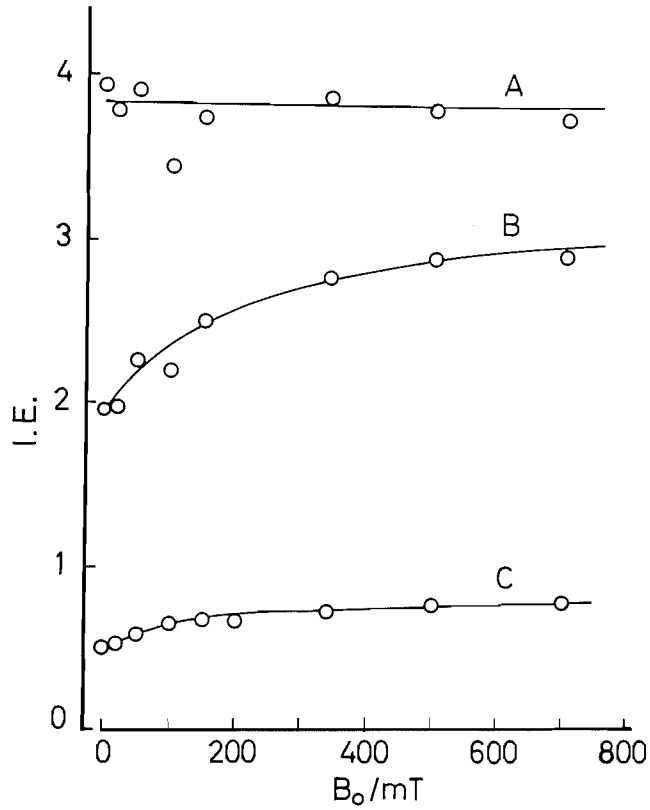

FIG. 3. Magnetic field dependence of the isotope effect (for hydrogen in the alkyl group of SDS molecule) in the photoreduction of menadione in SDS micellar solutions detected with the spin trapping technique. A: the primary isotope effect; B: the apparent isotope effect for the mixed micellar solution; C: the secondary magnetic isotope effect. I.E. is defined in eq. [1].

ing SDS molecules at the rate k_{ABS} (eq. [3]). The triplet radical pair ^{3}(MDH· ·SDS), composed of the SDS radical and the semiquinone radical from menadione, decays either to produce escaped radicals (SDS· and MDH·, eq. [4]) or to be converted to the singlet radical pair ^{1}(MDH· ·SDS), which then reacts to produce cage (singlet) products (eqs. [4], [5]). A water soluble spin trap (TNO), DMNS in the present case, may trap an escaped SDS radical outside the micelle (9) and a stable spin adduct (T(SDS)NO·), which can be detected by the esr technique, is formed (eq. [6]). (The semiquinone radical is not very reactive to the spin trap under the present experimental conditions.) The rate of interconversion between the two states of the radical pair (eq. [4]) is modified by the external magnetic field, which therefore modifies the yield of reaction product.

There are several possible stages in the reaction path from which the deuterium isotope effects originate: 1. hydrogen abstraction stage [k_{ABS}, eq. [3]]; 2. intersystem crossing process of the radical pair [k_{ISC}, eq. [4]]; 3. collapse of the radical pair [k_E, eq. [5]]; and 4. cage product formation [k_P, eq. [5]]. As is evidenced by the small exchange interaction (13), the magnetic interaction between the members of the radical pair is very small in the micelle. Besides, although a very small isotope effect for the solubility of SDS radical in the micelle may be expected, the isotope effects shown in Fig. 3 are far above the expected effect due to the solubility difference. Thus, an observable isotope effect is not expected for the escaping stage of the SDS radical. As for the cage product formation stage, since no deuterium nuclei exist at the reaction center, which consists of the oxygen nucleus of the semiquinone radical and the carbon nucleus of the SDS alkyl radical in our case, only a small β-deuterium secondary isotope effect may be expected. Moreover, it is usually assumed that k_P is much larger than k_{ISC}, as has been confirmed by the computer simulation of the product yield detected esr (PY-ESR) spectrum of this system in the previous study (11). Therefore, this stage should also not be the origin of our isotope effects. Consequently, we conclude that the isotope effects observed in this study come from the first two stages, the hydrogen abstraction stage and the intersystem crossing stage.

The most interesting fact found in the present study is the reversal of direction of the isotope effect when the reaction proceeds in pure micellar solutions instead of the mixed micellar solution. This can be explained, assuming that the two isotope effects mentioned above coexist and work in the opposite direction to each other in the spin adduct yield.

The product of the rate constant of the hydrogen abstraction (10^6–10^9 M^{-1} s^{-1}) (20) by the local concentration of SDS (>1 M) exceeds by far the spontaneous decay rate of the triplet menadione (~10^4 s^{-1}) (ref. 18, Chap. 9). Therefore, even if there is an isotope effect in the rate constant of the hydrogen abstraction, each photo-excited quinone may abstract just one hydrogen atom from an SDS molecule within its lifetime. Thus, in the pure micellar solutions, the final yields of the spin adducts are determined in the stages after the hydrogen abstraction, i.e., the intersystem crossing process of the radical pair.

On the other hand, in the mixed micellar solution those two isotope effects mentioned above must coexist, because the excited quinone may preferably abstract hydrogen from SDS(H) instead of deuteron from SDS(D). By analyzing the difference between the yields of the spin adducts in the pure micellar solutions and that in the mixed micellar solution, we can obtain the isotope effect that occurred in the hydrogen abstraction stage. We call this isotope effect the primary isotope effect, and the other the secondary magnetic isotope effect. Using the simple reaction scheme shown in eqs. [2]–[6], we obtain the following representations for I.E. (see eq. [1]) values:

$$[7]\quad \text{I.E.(primary)} = k_{ABS}(H)/k_{ABS}(D)$$

for the primary isotope effect, and

$$[8]\quad \text{I.E.(magnetic)} = [k_E(H) + k_{ISC}(H)]/[k_E(D) + k_{ISC}(D)]$$

for the secondary magnetic isotope effect.

Figure 3 shows the isotope effects in this system, which are calculated based on the fact that the primary isotope effect and the secondary magnetic isotope effect are independent of each other. As mentioned above, the secondary magnetic isotope effect (curve C) can be calculated from the yields in the pure micellar solutions (Fig. 2, open circles and open squares) with eq. [1]. Curve B represents the apparent isotope effect in the mixed micellar solution. The primary isotope effect (curve A) can be obtained as the ratios between the latter values (on curve C) and the former values (on curve B). Curve A shows that the primary isotope effect is independent of the magnetic field, as was a priori postulated. The difference in the zero point stretching energy between the C—H bond and the C—D bond is around 1100 cal/mol (5). Therefore the maximum isotope effect at 25°C is calculated as 6.4, assuming a loose potential along the reaction coordinate around the activated complex and a negligible tunneling effect (2). This value is not far from the experimental value.

The increase of the secondary magnetic isotope effect with

Can. J. Chem. Downloaded from www.nrcresearchpress.com by 112.217.228.212 on 09/07/12
For personal use only.

increase of the magnetic field in the pure system is due to the steady increase in the spin adduct yield of the SDS(H) radical at high fields, which is far beyond the hyperfine field. Since only S_0–T_0 mixing in the radical pair is allowed at these fields, this steady increase in the spin adduct yield should be due to the magnetic relaxation between $T_{\pm 1}$ and T_0 or S_0 (21, 22). Here, S_n and T_n represent the singlet and the triplet states (with magnetic quantum number n) of the radical pair, respectively. Because the hyperfine interactions in the SDS(D) radical are about 1/6.5 of those in the SDS(H) radical, the relaxation rate of the electron spin in the SDS(D) radical is much smaller than that in the SDS(H) radical. This fact accords with the smaller increase in the spin adduct yield of the SDS(D) system at high field over 300 mT. Although the relaxation mechanism for the magnetic field effect on chemical reactions has been proposed (22), especially for these micellar systems (23), only limited supporting evidence has been given so far. Our observation, that there is a larger magnetic field dependence in spin adduct yield for the SDS(H) system than for the SDS(D) system at high fields (e.g., >300 mT), is clear evidence for the relaxation mechanism.

The magnetic field dependence in spin adduct yield for the corresponding pure micellar solution was the same as that for the mixed micellar solution (e.g., closed circles vs. open circles in Fig. 2). Therefore, the two isotope effects, the primary and the secondary magnetic, should be independent. This fact indicates that little radical center migration among the SDS molecules (half of them are deuteriated) occurs during the period of intersystem crossing in the radical pair, because radical center migration between SDS(D) radical and SDS(H) molecule, and vice versa, interferes with the intersystem crossing process and this interference would have made the magnetic field dependences of the two spin adduct yields similar to each other.

Conclusion

Two independent isotope effects in the photoreduction of menadione in deuterium labeled SDS micellar solutions were obtained using the spin trapping technique. Those isotope effects are attributed to the stages of hydrogen abstraction of triplet menadione from the SDS molecule and intersystem crossing in the transient radical pair.

The primary isotope effect was independent of the magnetic field but the secondary magnetic isotope effect was very much dependent on the magnetic field. This latter magnetic field dependence was attributed to the difference in magnetic interactions in the radical pairs.

It is suggested that it is very important to pay attention to the secondary magnetic isotope effect, which was about 0.5 at zero field in the present system, in the analysis of isotope effects in reactions, such as hydrogen abstraction.

Acknowledgments

The gift of DMNS from Drs. S. Sakata and R. Konaka of Shionogi Research Laboratory, Shionogi Pharmaceuticals, is gratefully acknowledged. Sincere thanks should also go to Drs. K. Iseda and S. Fujii of our institute for the measurements of mass spectra of deuteriated SDS.

1. E. BUNCEL and C. C. LEE (*Editors*). Isotopes in organic chemistry. Elsevier, Amsterdam. 1984.
2. J. BIGELEISEN. J. Chem. Phys. **17**, 675 (1949).
3. P. GRAY, A. A. HEROD, and A. JONES. Chem. Rev. **71**, 247 (1971).
4. G. BRUNTON, D. GILLER, L. R. C. BARCLAY, and K. U. INGOLD. J. Am. Chem. Soc. **98**, 6803 (1976).
5. A. T. DROEGE and F. P. TULLY. J. Phys. Chem. **90**, 5937 (1986), and references therein.
6. A. L. BUCHACHENKO, E. M. GALIMOV, V. V. ERSHOV, G. A. NIKIFOROV, and A. D. PERSHIN. Dokl. Phys. Chem. (Engl. Transl.) **228**, 451 (1976).
7. R. Z. SAGDEEV, T. V. LESHINA, M. A. KAMKHA, O. I. BELCHENKO, and YU. N. MOLIN. Chem. Phys. Lett. **48**, 89 (1977).
8. N. J. TURRO and B. KRAEUTLER. Acc. Chem. Res. **13**, 369 (1980).
9. L. STERNA, D. RONIS, S. WOLFE, and A. PINES. J. Chem. Phys. **73**, 5493 (1980).
10. M. OKAZAKI, S. SAKATA, R. KONAKA, and T. SHIGA. J. Am. Chem. Soc. **107**, 7214 (1985).
11. M. OKAZAKI and T. SHIGA. Nature (London), **323**, 240 (1986).
12. M. OKAZAKI, S. SAKATA, R. KONAKA, and T. SHIGA. J. Phys. Chem. **91**, 1131 (1987).
13. M. OKAZAKI, S. SAKATA, R. KONAKA, and T. SHIGA. J. Chem. Phys. **86**, 6792 (1987).
14. E. G. JANZEN. Acc. Chem. Res. **4**, 31 (1971).
15. E. G. JANZEN. *In* Free radicals in biology. Vol. 4. *Edited by* W. F. Pryor. Academic Press, New York. 1980. pp. 115–154.
16. YU. N. MOLIN (*Editor*). Spin polarization and magnetic effect in radical reactions. Elsevier, Amsterdam. 1984.
17. Y. TANIMOTO, K. SHIMIZU, and M. ITOH. Chem. Phys. Lett. **112**, 217 (1984).
18. R. KONAKA and S. SAKATA. Chem. Lett. 411 (1982).
19. Y. SAKAGUCHI and H. HAYASHI. J. Phys. Chem. **88**, 1437 (1984).
20. N. J. TURRO. Modern molecular photochemistry. Benjamin, Menlo Park, CA. 1978. Chap. 10.
21. H. HAYASHI and S. NAGAKURA. Bull. Chem. Soc. Jpn. **57**, 322 (1984).
22. B. BROCKLEHURST. J. Chem. Soc. Faraday Trans. 2, **72**, 1869 (1978).

Can. J. Chem. Downloaded from www.nrcresearchpress.com by 112.217.228.212 on 09/07/12
For personal use only.

Synthesis and structural characterization of *N,N'*-diarylpiperazine *N,N'*-dioxide tetrahydrates (aryl = *o*-tolyl, *p*-tolyl, *p*-chlorophenyl)

CHUN-KIU KWOK AND THOMAS C. W. MAK[1]

Department of Chemistry, The Chinese University of Hong Kong, Shatin, New Territories, Hong Kong

Received September 29, 1987

This paper is dedicated to Professor Charles A. McDowell on the occasion of his seventieth birthday

CHUN-KIU KWOK and THOMAS C. W. MAK. Can. J. Chem. **66**, 1836 (1988).

The synthesis and X-ray structure determination of *N,N'*-di(*o*-tolyl)piperazine *N,N'*-dioxide tetrahydrate, **I**, *N,N'*-di(*p*-tolyl)piperazine *N,N'*-dioxide tetrahydrate, **II**, and *N,N'*-di(*p*-chlorophenyl)piperazine *N,N'*-dioxide tetrahydrate, **III**, are described. Compound **I** crystallizes in space group $P\bar{1}$ with $a = 7.778(1)$, $b = 7.915(2)$, $c = 8.919(2)$ Å, $\alpha = 106.25(2)$, $\beta = 99.56(1)$, $\gamma = 108.80(2)°$, and $Z = 1$. Compound **II** crystallizes in space group $P\bar{1}$ with $a = 6.558(1)$, $b = 7.134(2)$, $c = 11.610(3)$ Å; $\alpha = 73.23(2)$, $\beta = 78.08(2)$, $\gamma = 72.67(2)°$, and $Z = 1$. Compound **III** crystallizes in space group $P2_1/c$ with $a = 9.159(3)$, $b = 12.390(4)$, $c = 8.339(4)$ Å, $\beta = 97.38(3)°$, and $Z = 2$. The structures of **I–III** were solved by the direct method and refined to $R = 0.049$ (1749 observed Mo$K\alpha$ reflections), 0.055 (2651 observed reflections), and 0.035 (1827 observed reflections), respectively. In each case, the *N,N'*-dioxide molecule occupies a site of symmetry $\bar{1}$. The piperazine ring takes the chair form, with two N—O bonds oriented axially in a *trans* configuration. The structures are characterized by strong hydrogen bonding between the water molecules, as well as between the *N*-oxide groups and water molecules, giving rise to puckered layers composed of various combinations of edge-sharing four-membered, six-membered, ten-membered, and twelve-membered rings. The aryl rings, which protrude on both sides of each puckered layer, constitute hydrophobic regions separating the hydrophilic layers in the crystal packing.

CHUN-KIU KWOK and THOMAS C. W. MAK. Can. J. Chem. **66**, 1836 (1988).

On décrit la synthèse et la détermination de la structure, à l'aide de la diffraction aux rayons-X, des tétrahydrates des *N,N'*-dioxydes des *N,N'*-di(*o*-tolyl) pipérazine (**I**), des *N,N'*-di(*p*-tolyl) pipérazine (**II**) et des *N,N'*-di(*p*-chlorophenyl) pipérazine (**III**). Le composé **I** cristallise dans le groupe d'espace $P\bar{1}$, avec $a = 7{,}778(1)$, $b = 7{,}915(2)$ et $c = 8{,}919(2)$ Å, $\alpha = 106{,}25(2)$, $\beta = 99{,}56(1)$ et $\gamma = 108{,}80(2)°$ et $Z = 1$. Le composé **II** cristallise dans le groupe d'espace $P\bar{1}$, avec $a = 6{,}558(1)$, $b = 7{,}134(2)$ et $c = 11{,}610(3)$ Å, $\alpha = 73{,}23(2)$, $\beta = 78{,}08(2)$ et $\gamma = 72{,}67(2)°$ et $Z = 1$. Le composé **III** cristallise dans le groupe d'espace $P2_1/c$, avec $a = 9{,}159(3)$, $b = 12{,}390(4)$ et $c = 8{,}339(4)$ A, $\beta = 97{,}38(3)°$ et $Z = 2$. Les structures des composés **I**, **II** et **III** ont été résolues par la méthode directe et on les a affinées jusqu'à des valeurs respectives de $R = 0{,}049$ (pour 1749 réflexions du MoKα qui ont été observées), 0,055 (2651 réflexions observées) et 0,035 (pour 1827 réflexions observées). Dans chacun des cas, la molécule de *N,N'*-dioxyde occupe un site de symétrie $\bar{1}$. Le noyau pipérazine se trouve dans une conformation chaise; deux des liaisons N—O sont orientées d'une façon axiale, dans une configuration *trans*. Les structures sont caractérisées par de fortes liaisons hydrogènes entre les molécules d'eau ainsi qu'entre les groupements *N*-oxydes et les molécules d'eau; ces interactions donnent lieu à la formation de couches plissées composées de diverses combinaisons de cycles à quatre, à six, à dix et à douze chaînons qui se partagent des arêtes. Les noyaux aryles, qui font saillie sur les deux côtés de chacune des couches, forment des régions hydrophobes qui séparent les couches hydrophiles de l'entassement du cristal.

[Traduit par la revue]

Introduction

Many aspects of the chemistry of amine *N*-oxides, such as their synthetic chemistry, spectroscopic properties, and chemical reactivities have been subjected to numerous studies (1–3). In many instances (4–6), amine *N*-oxides crystallized from aqueous alcoholic solutions or water are in the form of hydrates. However, a systematic structural study of this class of hydrated compounds has rarely been attempted. A research program on the structural chemistry of polycyclic tertiary amine *N*-oxides has been pursued in our laboratory. A series of preparative and X-ray crystallographic studies on the adducts of hexamethylenetetramine *N*-oxide (HMTO) have shown that all these structures involve hydrogen bonding between the terminal O atom of the N → O dative bond and the proton donor molecule(s) (7–10). We now report the synthesis and structural characterization of a series of heterocyclic tertiary amine *N,N'*-dioxide hydrates, namely *N,N'*-di(*o*-tolyl)piperazine *N,N'*-dioxide tetrahydrate, **I**, *N,N'*-di(*p*-tolyl)piperazine *N,N'*-dioxide tetrahydrate, **II**, and *N,N'*-di(*p*-chlorophenyl)piperazine *N,N'*-dioxide tetrahydrate, **III**. These structures are to be compared to the three-dimensional networks found in the related hydrate inclusion compounds *N,N'*-diphenylpiperazine *N,N'*-dioxide octahydrate, **IV** (11), and *N,N'*-dicyclohexylpiperazine *N,N'*-dioxide octahydrate, **V** (12), which have been established recently via X-ray crystallography.

[1]To whom correspondence should be addressed.

Experimental

All reagents or solvents used are general purpose grade. Proton nmr spectra were recorded on a Bruker Cryospec WM250 (250 MHz) spectrometer. Deuterated methanol was used as solvent and δ (ppm) was measured with TMS as an internal standard. Mass spectra were recorded on a VG Micromass 7070F spectrometer. Solid-state ir spectra were recorded on a Beckman AccuLab 1 spectrometer, and KBr discs were prepared according to the standard procedure (13).

Synthetic procedures

(a) N,N'-*Diarylpiperazine*

The heterocyclic amines were prepared according to the procedure of Morera (14). Heating a mixture of arylamine and dibromoethane (1.35:1 in mole ratio) at 130–140°C for several hours gave the corresponding *N,N'*-diarylpiperazine (*N,N'*-di(*o*-tolyl)piperazine, 4 h; *N,N'*-di(*p*-tolyl)piperazine, 5 h; *N,N'*-di(*p*-chlorophenyl)piperazine, 3 h). The *N,N'*-diarylpiperazines were liberated by the addition of an excess amount of 10% NaOH and purified by recrystallization in xylene. The individual yields are 13.0, 33.7, and 42.0%, respectively.

Can. J. Chem. Downloaded from www.nrcresearchpress.com by 112.217.228.212 on 09/07/12
For personal use only.

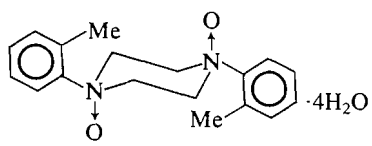

I

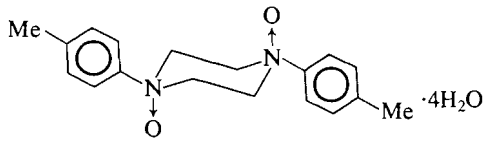

II

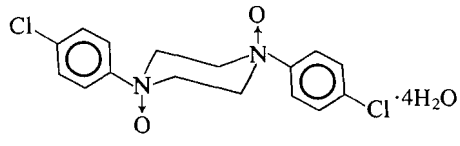

III

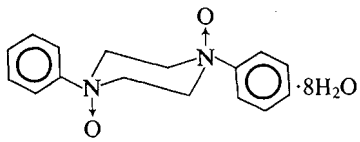

IV

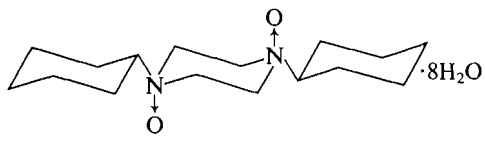

V

(b) N,N′-*Diarylpiperazine* N,N′-*dioxide tetrahydrate*

The oxidation of each *N,N′*-diarylpiperazine to the corresponding *N,N′*-dioxide was effected by the procedure of Bennett and Glynn (15). *N,N′*-Diarylpiperazine (4.0 g) was dissolved in a mixture of glacial acetic acid and 30% hydrogen peroxide. The mole ratio of *N,N′*-diarylpiperazine:acetic acid:hydrogen peroxide was 1:24.0:12.6. The mixture was kept at 50–70°C for about 16 h. The excess hydrogen peroxide was removed by the addition of an equal volume of acetic acid to the reaction mixture, which was then evaporated to dryness at ~60°C under reduced pressure. The above process was repeated three times. Trace amounts of acetic acid remaining in the "residue" were removed by placing it in a desiccator charged with sodium hydroxide pellets for several days. The "residue" was dissolved in water, and after several further recrystallizations at ~60°C, *N,N′*-diarylpiperazine *N,N′*-dioxide tetrahydrate was obtained as well-formed crystals. In the case of **I**, crystals of good quality were obtained from the evaporation of an aqueous solution in a desiccator containing silica gel placed in a refrigerator.

Spectral data

I: ^{1}H nmr (ppm): 2.94 (s, 6H), 3.60 (d, 4H, J = 8 Hz), 5.08 (d, 4H, J = 9 Hz), 7.43 (s, 6H$_{arom}$), 8.20 (m, 2H$_{arom}$). Infrared (KBr, cm^{-1}): 3095–3345 (s, br), 2795 (sh), 1672 (s), 1470 (s), 1428 (s), 1394 (sh), 1368 (sh), 1280 (m), 1268 (s), 1168 (s), 1098 (m), 1056 (m), 1015 (m), 968 (s), 765 (br). Mass spectroscopy, *m/e*: 282.0 (8.7%), 266.1 (13.3%), 251.1 (11.6%), 146.1 (60.9%), 133.1 (27.9%), 132.0 (64.6%), 119.0 (62.0%), 118.0 (100%), 105.1 (9.6%), 91.0 (83.9%).

II: ^{1}H nmr: 2.42 (s, 6H), 3.24 (d, 4H, J = 8 Hz), 5.13 (d, 4H, J = 9 Hz), 7.35 (d, 4H$_{arom}$, J = 8 Hz), 8.08 (d, 4H$_{arom}$, J = 8 Hz). Infrared (KBr, cm^{-1}): 3062–3352 (s, br), 2860 (sh), 1680 (m), 1498 (m), 1442 (m), 1368 (sh), 1275 (m), 1188 (m), 1010 (m), 980 (s), 805 (s). Mass spectroscopy, *m/e*: 298.0 (2.5%), 282.0 (17.4%), 266.0 (53.4%), 251.0 (27.3%), 224.0 (1.9%), 146.0 (57.7%), 133.0 (28.2%), 132.0 (19.0%), 119.0 (100%), 118.0 (55.3%), 105.1 (30.9%), 91.0 (80.0%).

III: ^{1}H nmr: 3.28 (d, 4H, J = 9 Hz), 5.12 (d, 4H, J = 9 Hz), 7.55 (d, 4H$_{arom}$, J = 13 Hz), 8.15 (d, 4H$_{arom}$, J = 13 Hz). Infrared (KBr, cm^{-1}): 3032–3480 (s, br), 2880 (m), 1680 (s), 1482 (s), 1438 (m), 1402 (m), 1368 (m), 1295 (m), 1278 (m), 1155 (m), 1092 (s), 1008 (s), 980 (s), 930 (m), 672–830 (s, br). Mass spectroscopy, *m/e*: 322.0 (18.1%), 306.1 (66.8%), 291.1 (21.5%), 166.1 (42.6%), 153.1 (26.3%), 152.1 (11.3%), 139.0 (100%), 138.0 (66.8%), 125.1 (32.1%), 111.0 (53.0%).

X-ray crystallographic analysis

Densities were measured by flotation in *n*-hexane/carbon tetrachloride. All three compounds were handled in the same manner. A single crystal was cut to a suitable size and attached directly to a glass fiber with epoxy glue. Determination of the crystal class and orientation matrix on a Nicolet R3m diffractometer using Mo$K\alpha$ radiation was performed according to established procedures (16). Accurate unit-cell dimensions were derived from a least-squares fit of the refined angular settings of 21 high-angle reflections. Intensity data were collected at 22°C following established procedures in

TABLE 1. The assignment of the ir spectra of *N,N′*-diarylpiperazine *N,N′*-dioxide tetrahydrates, **I–III**

Assignment	Frequency* (cm^{-1})		
	I	**II**	**III**
Antisymmetric and symmetric O—H stretching	3095–3345br,s	3062–3352br,s	3030–3480br,s
CH stretching in —CH$_3$ and —CH$_2$—	2795sh	2860sh	2880m
H$_2$O bending	1672s	1680m	1680m
CH$_2$ deformation	1470s, 1428s	1498m, 1442m	1482s, 1438m
CH$_2$ bending	1394sh, 1368sh	1368sh	1402m, 1368m
C—N stretching	1280m, 1268m, 1168s	1275m, 1188m	1295m, 1278m, 1155m
Ring vibration	1098m, 1056m, 1015m	1010m	1092br, 1008s, 930m
N—O stretching	968s	980s	980s
CH (phenyl ring) out-of-plane deformation	765br	805s	672–830s,br
C—Cl stretching			672s,br

*s = strong, m = medium, w = weak, sh = shoulder, br = broad.

Can. J. Chem. Downloaded from www.nrcresearchpress.com by 112.217.228.212 on 09/07/12
For personal use only.

TABLE 2. The assignment of the nmr spectra of hydrated *N,N'*-diarylpiperazine *N,N'*-dioxides, I–III

Piperazine	Chemical shift (ppm)	Multiplicity	Assignment
I	2.94	Singlet	H of methyl group
	3.60	Doublet	H of piperazine ring
	5.08	Doublet	H of piperazine ring
	7.43	Singlet	H of phenyl ring
	8.20	Multiplet	H of phenyl ring
II	2.42	Singlet	H of methyl group
	3.24	Doublet	H of piperazine ring
	5.13	Doublet	H of piperazine ring
	7.35	Doublet	H of phenyl ring
	8.08	Doublet	H of phenyl ring
III	3.28	Doublet	H of piperazine ring
	5.12	Doublet	H of piperazine ring
	7.55	Doublet	H of phenyl ring
	8.15	Doublet	H of phenyl ring

our laboratory (17–18). The crystal remained stable throughout the diffraction experiment as two standard reflections monitored every 125 data measurements showed only random fluctuations within ±1% of their mean values. The raw intensities were processed with the learnt-profile procedure (19), and application of absorption corrections were based on a pseudo-ellipsoidal fit to azimuthal scans of selected strong reflections over a range of 2θ values. The statistical distribution of the normalized structure factors was consistent with that expected for a centrosymmetric space group. The crystal data are summarized in Table 3.

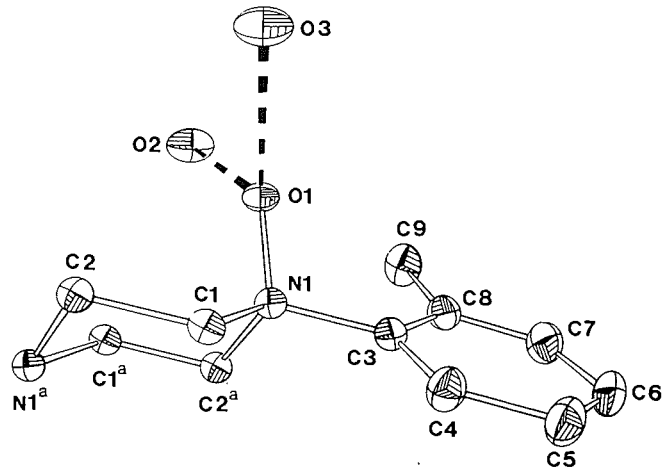

FIG. 1. Numbering of atoms in the asymmetric unit of **I**. The thermal ellipsoids are drawn at the 25% probability level.

Structure solutions were achieved by direct phase determination guided by negative quartets (20). All non-hydrogen atoms were varied anisotropically in structure refinement. The aromatic, methylene, and methyl H atoms were generated geometrically (C—H bond length fixed at 0.96 Å) and assigned isotropic thermal parameters. Water H atoms, some of which exhibited two-fold disorder (only in compound **I**), were located from successive difference Fourier maps; they were assigned isotropic temperature factors and held stationary in subsequent least-squares cycles. Computations were performed on a Data General Corporation Nova 3/12 minicomputer using the SHELXTL program package (21). Analytic expressions of neutral-atom scattering factors were employed, and anomalous dispersion corrections were

TABLE 3. Crystal data of hydrated *N,N'*-diarylpiperazine *N,N'*-dioxides

Parameter	Value		
	I	**II**	**III**
Space group	$P\bar{1}$ (No. 2)	$P\bar{1}$ (No. 2)	$P2_1/c$ (No. 14)
Cell constants			
a, Å	7.778(1)	6.558(1)	9.159(3)
b, Å	7.915(2)	7.134(2)	12.390(4)
c, Å	8.919(2)	11.610(3)	8.339(4)
α, deg	106.25(2)	73.23(2)	90
β, deg	99.56(1)	78.08(2)	97.38(3)
γ, deg	108.80(2)	72.67(2)	90
V, Å^3	478.8(2)	492.1(2)	938.5(6)
Density (calculated), g cm^{-3}	1.29	1.25	1.46
Density (measured), g cm^{-3}	1.270	1.28	1.395
Z	1	1	2
F(000)	200	200	424
Linear absorption coefficient, cm^{-1}	0.90	0.87	3.75
Crystal size, mm	0.36 × 0.32 × 0.20	0.50 × 0.42 × 0.36	0.40 × 0.28 × 0.20
Mean μr	0.013	0.025	0.066
Transmission factors	0.852 to 0.945	0.927 to 0.946	0.831 to 0.859
$2\theta_{max}$, deg	55	65	56
Unique data measured	2112	3190	2286
Observed data with $\|F\| > 3\sigma(\|F_o\|)$, n	1749	2651	1827
Number of variables, p	121	121	118
$R = \Sigma\|\|F_o\| - \|F_c\|\|/\Sigma\|F_o\|$	0.049	0.055	0.035
Weighting scheme, g in $w = [\sigma^2(F_o) + g\|F_o\|^2]^{-1}$	0.0006	0.0018	0.0003
$wR = [\Sigma w(\|F_o\| - \|F_c\|)^2/\Sigma w\|F_o\|^2]^{1/2}$	0.061	0.083	0.045
$S = [\Sigma w(\|F_o\| - \|F_c\|)^2/(n - p)]^{1/2}$	1.716	1.531	1.696
Residual extrema in final difference map, e Å^{-3}	+0.29 to −0.29	+0.35 to −0.27	+0.25 to −0.27

Can. J. Chem. Downloaded from www.nrcresearchpress.com by 112.217.228.212 on 09/07/12
For personal use only.

Can. J. Chem. Downloaded from www.nrcresearchpress.com by 112.217.228.212 on 09/07/12
For personal use only.

TABLE 4. Atomic coordinates ($\times 10^4$) and equivalent isotropic temperature factor* (Å^2 $\times$ 10^3) for the non-hydrogen atoms in the asymmetric unit of *N,N'*-di(*o*-tolyl)piperazine *N,N'*-dioxide tetrahydrate (**I**)

Atom	*x*	*y*	*z*	U_{eq}
N,N'-Dioxide				
O(1)	2566(1)	2674(1)	1256(1)	30(1)
N(1)	1167(2)	1400(2)	1666(1)	26(1)
C(1)	−744(2)	1292(2)	826(2)	27(1)
C(2)	−1096(2)	612(2)	−995(2)	27(1)
C(3)	1565(2)	2036(2)	3499(2)	30(1)
C(4)	178(2)	2377(3)	4198(2)	41(1)
C(5)	498(3)	2924(3)	5875(2)	51(1)
C(6)	2195(3)	3189(3)	6844(2)	54(1)
C(7)	3567(3)	2874(3)	6140(2)	51(1)
C(8)	3329(2)	2317(2)	4467(2)	37(1)
C(9)	5001(3)	2118(3)	3897(2)	51(1)
Water molecules				
O(2)	5213(2)	1771(2)	−156(2)	54(1)
O(3)	1905(2)	5719(2)	938(2)	51(1)

*U_{eq} defined as 1/3 of the trace of the orthogonalized **U** matrix.

TABLE 5. Atomic coordinates ($\times 10^4$) and equivalent isotropic temperature factor* (Å^2 $\times$ 10^3) for the non-hydrogen atoms in the asymmetric unit of *N,N'*-di(*p*-tolyl)piperazine *N,N'*-dioxide tetrahydrate (**II**)

Atom	*x*	*y*	*z*	U_{eq}
N,N'-Dioxide				
O(1)	2902(1)	508(1)	−1218(1)	38(1)
N(1)	763(1)	674(1)	−1295(1)	32(1)
C(1)	−676(2)	2131(2)	−563(1)	33(1)
C(2)	−264(2)	1373(2)	747(1)	33(1)
C(3)	319(2)	1372(2)	−2589(1)	35(1)
C(4)	2048(2)	1370(2)	−3504(1)	46(1)
C(5)	1651(3)	1985(2)	−4704(1)	53(1)
C(6)	−408(3)	2582(2)	−5008(1)	50(1)
C(7)	−2110(3)	2547(3)	−4071(1)	53(1)
C(8)	−1768(2)	1936(2)	−2859(1)	47(1)
C(9)	−812(4)	3253(3)	−6319(1)	67(1)
Water molecules				
O(2)	4027(2)	2966(2)	1519(1)	65(1)
O(3)	3654(2)	3990(2)	−979(1)	59(1)

*U_{eq} defined as 1/3 of the trace of the orthogonalized **U** matrix.

incorporated (22). Blocked-cascade least-squares refinement (23) converged to the *R* indices listed in Table 3. Numbering of the atoms in the asymmetric unit of **I** is shown in Fig. 1, **II** in Fig. 5, and **III** in Fig. 9, respectively. The refined atomic parameters of **I**–**III** are given in Tables 4–6, respectively.

Results and discussion

Although some of the *N,N'*-diarylpiperazines have been characterized previously by their nmr and mass spectra (24–26), a thorough investigation of the spectral properties of their corresponding hydrated *N,N'*-dioxides has not been available. The assignment of the ir spectra shown in Table 1 was done with reference to that of piperazine (27, 28) and the scheme proposed in the literature (29, 30). The assignment of the nmr spectra is

TABLE 6. Atomic coordinates ($\times 10^4$) and equivalent isotropic temperature factor* (Å^2 $\times$ 10^3) for the non-hydrogen atoms in the asymmetric unit of *N,N'*-di(*p*-tolyl)piperazine *N,N'*-dioxide tetrahydrate (**III**)

Atom	*x*	*y*	*z*	U_{eq}
N,N'-Dioxide				
O(1)	4672(1)	1613(1)	949(1)	31(1)
N(1)	3869(1)	841(1)	−10(1)	27(1)
C(1)	4653(2)	613(1)	−1468(2)	28(1)
C(2)	6188(2)	197(1)	−936(2)	28(1)
C(3)	2328(2)	1224(1)	−579(2)	28(1)
C(4)	1892(2)	2229(1)	−97(2)	35(1)
C(5)	509(2)	2614(1)	−700(2)	39(1)
C(6)	−418(2)	1978(1)	−1737(2)	34(1)
C(7)	−8(2)	958(1)	−2183(2)	36(1)
C(8)	1385(2)	577(1)	−1598(2)	34(1)
Cl(1)	−2129(1)	2487(1)	−2552(1)	47(1)
Water molecules				
O(2)	4962(1)	3524(1)	−701(2)	41(1)
O(3)	2683(1)	4994(1)	−177(2)	51(1)

*U_{eq} defined as 1/3 of the trace of the orthogonalized **U** matrix.

shown in Table 2; crystal data of the compounds are shown in Table 3.

An interesting difference between the nmr spectra of the *N,N'*-dioxides and their parent piperazines is the splitting of the peaks of the heterocyclic ring protons. A previous nmr study of *N,N'*-diphenylpiperazine has shown that ring inversion is so rapid that resolution of the peaks of equatorial and axial protons is impossible even at −100°C (25). An AA'BB' or AA'XX' pattern is expected to be observed in the nmr spectra of *N,N'*-disubstituted piperazines when the ring proton interconversion has been "frozen out" (25, 31*a*). In fact, from the 250 MHz spectra recorded here, it is seen that the protons of the piperazine rings in all three *N,N'*-dioxides showed "two doublets". An "AX pattern" rather than a AA'BB' or AA'XX' pattern was observed. In fact, a well-defined AA'BB' or AA'XX' pattern was not observed even at −100°C in piperazine (25). A somewhat similar "two doublets" pattern has been reported in a synthesized spectrum of the ring protons of piperazine at −100°C in ethanol–methylene chloride using $\nu_0\delta_{ae}$ = 9.6 Hz taken from the 100 MHz results (25).

A common feature of the ir spectra of the hydrated *N,N'*-diarylpiperazine *N,N'*-dioxides is the presence of strong and broad peaks of antisymmetric and symmetric O—H stretching in the 3600–3000 cm^{-1} range. The aromatic C—H stretching peak is masked by these O—H stretching frequencies and therefore not observable. The N—O stretching mode generally occurs as a strong peak in the region of 970–950 cm^{-1} for aliphatic amine *N*-oxide (31*b*). Hence a common strong peak at 980 cm^{-1} in the ir spectra of **II** and **III**, and at 968 cm^{-1} in **I**, may be attributed to N—O stretching. A slight shift in the frequency of the vibration mode in **I** may be due to steric interaction between the *o*-methyl and *N*-oxide groups.

The major fragmentation paths for the parent piperazines of **II** and **III** have been proposed (26). Similar major fragmentation paths for the hydrated *N,N'*-diarylpiperazine *N,N'*-dioxide is proposed in Scheme 1. Peaks corresponding to radical ions of the monoxides of **I**–**III** and the dioxide of **II** can be observed. After the two N—O bonds in each *N,N'*-dioxide molecule have

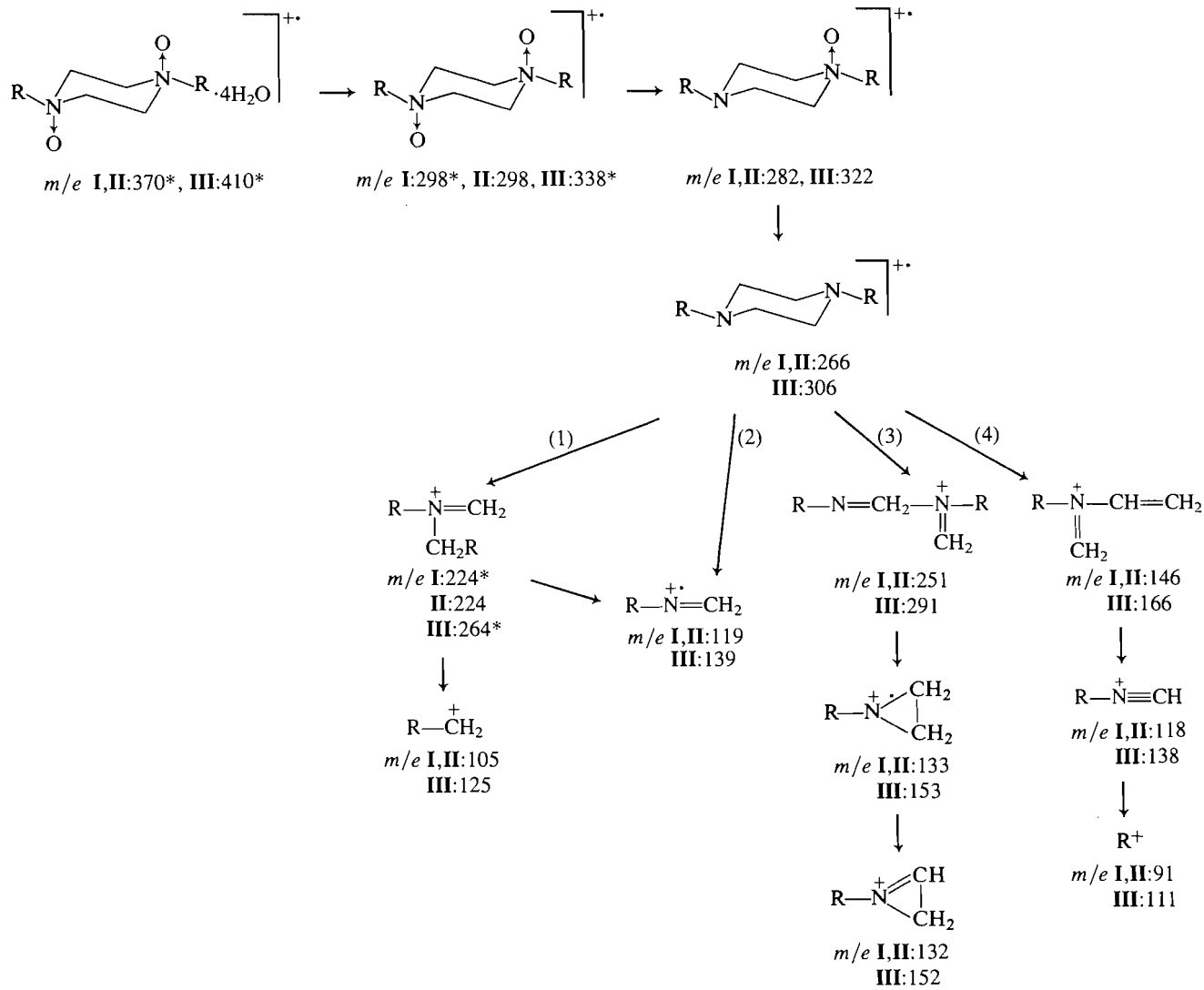

*Unobservable

SCHEME 1

been cleaved in the early stages, the subsequent fragmentation process is expected to be the same as that of the corresponding piperazine.

Description of the structures

In the crystal structures of **I–III**, the *N,N'*-dioxide molecule of each compound occupies a site of symmetry $\bar{1}$, with two N—O bonds oriented axially in a *trans* configuration; measured bond distances and angles are given in Tables 7–9. The measured N—O bond lengths of **I–III** and some related amine *N*-oxide derivatives are tabulated in Table 10. According to these data, the N—O bond length in **II** and **III** are nearly identical within the limits of experimental error, and are also in good agreement with the corresponding values in trimethylamine oxide dihydrate (1.398(1) Å) (33) and in the 1:3 molecular complex of triethylenediamine *N,N'*-dioxide with water (1.395(8) Å) (37). The apparent deviation of the N—O bond length of **I** (1.402(2) Å) from the norm may be due to steric repulsion between the *o*-methyl group and the N—O bond.

The phenyl rings are nearly coplanar with the two N—O bonds in **II** and **III**, but not in **I**, as shown by the torsion angles in Table 11. In fact, the *o*-methyl group in **I** is nearly "midway" between the N(1)—O(1) and N(1)—C(1) bonds. The relative orientation of the phenyl rings with respect to the N—O bonds in **I** is a consequence of steric repulsion between the *o*-methyl groups and the piperazine ring and/or the neighbouring N—O bonds.

The crystal structure of the hydrated *N,N'*-dioxide studied here are characterized by strong hydrogen bonding between the water molecules, as well as between the *N*-oxide groups and water molecules, giving rise to puckered layers composed of various combinations of edge-sharing four-membered, six-membered, ten-membered, and twelve-membered rings. The oxygen atom in each *N*-oxide group in **I–III** forms only two acceptor hydrogen bonds with two neighbouring water molecules. In contrast to this, the oxygen atom forms three acceptor hydrogen bonds with neighbouring donor molecules in some *N*-oxide adducts, e.g. $O \leftarrow N(CH_2CH_2)_3N \rightarrow O.3H_2O$ (37), $(CH_2)_6N_4O.(NH_2)_2CS$ (9), and $(CH_2)_6N_4O.H_2O_2.H_2O$ (8). The hydrogen bonding features of hydrated *N,N'*-dioxides **I–III** are described in the following sections.

(a) N,N'-*Di*(o-*tolyl*)*piperazine* N,N'-*dioxide tetrahydrate*, ***I***

In the crystal structure of **I**, the water molecules and oxygen atoms of the *N*-oxide groups are interconnected to generate a

Can. J. Chem. Downloaded from www.nrcresearchpress.com by 112.217.228.212 on 09/07/12
For personal use only.

TABLE 7. Bond distances (Å), bond angles (deg), and selected torsion angles (deg) in *N*,*N*′-di(*o*-tolyl)piperazine-*N*,*N*′-dioxide tetrahydrate (**I**)

Bond	Distance	Bond	Distance
O(1)—N(1)	1.402(2)	N(1)—C(1)	1.513(2)
N(1)—C(3)	1.514(2)	N(1)—C(2)[a]	1.515(2)
C(1)—C(2)	1.507(2)	C(3)—C(8)	1.408(2)
C(3)—C(4)	1.384(3)	C(5)—C(6)	1.369(3)
C(4)—C(5)	1.388(3)	C(7)—C(8)	1.393(3)
C(6)—C(7)	1.379(3)	O(1)...O(2)	2.765(4)
C(8)—C(9)	1.510(3)	O(2)...O(3)[b]	2.808(5)
O(1)...O(3)	2.699(4)	O(3)...O(3)[d]	2.827(5)
O(2)...O(2)[c]	2.813(5)		

Angle	Value	Angle	Value
O(1)—N(1)—C(1)	108.3(1)	O(1)—N(1)—C(3)	109.7(1)
C(1)—N(1)—C(3)	112.9(1)	O(1)—N(1)—C(2)[a]	111.0(1)
C(1)—N(1)—C(2)[a]	105.2(1)	C(3)—N(1)—C(2)[a]	109.7(1)
N(1)—C(1)—C(2)	111.0(1)	C(1)—C(2)—N(1)[a]	111.6(1)
N(1)—C(3)—C(4)	119.2(1)	N(1)—C(3)—C(8)	119.9(2)
C(4)—C(3)—C(8)	120.9(1)	C(3)—C(4)—C(5)	120.6(2)
C(4)—C(5)—C(6)	119.6(2)	C(5)—C(6)—C(7)	119.5(2)
C(6)—C(7)—C(8)	123.1(2)	C(3)—C(8)—C(7)	116.2(2)
C(3)—C(8)—C(9)	127.2(2)	C(7)—C(8)—C(9)	116.6(2)
N(1)—O(1)...O(2)	124.5(3)	N(1)—O(1)...O(3)	115.8(3)
O(2)...O(1)...O(3)	116.8(3)	O(1)...O(2)...O(3)[b]	125.8(4)
O(1)...O(2)...O(2)[c]	102.3(4)	O(3)[b]...O(2)...O(2)[c]	130.4(4)
O(1)...O(3)...O(2)[b]	114.1(4)	O(1)...O(3)...O(3)[d]	106.2(4)
O(2)[b]...O(3)...O(3)[d]	120.5(4)		

Torsion angle	Value	Torsion angle	Value
O(1)—N(1)—C(1)—C(2)	59.6(1)	C(3)—N(1)—C(1)—C(2)	−178.7(1)
O(1)—N(1)—C(3)—C(4)	124.6(2)	C(1)—N(1)—C(3)—C(8)	−176.3(1)
C(8)—C(3)—C(4)—C(5)	0.0(3)	C(4)—C(3)—C(8)—C(7)	1.1(3)
C(3)—C(4)—C(5)—C(6)	−0.7(3)	C(6)—C(7)—C(8)—C(9)	177.3(2)
O(1)—N(1)—C(3)—C(8)	−55.3(2)	C(4)—C(3)—C(8)—C(9)	−177.6(2)
C(4)—C(5)—C(6)—C(7)	0.2(3)	C(6)—C(7)—C(8)—C(3)	−1.6(3)
N(1)—C(3)—C(8)—C(9)	2.3(3)	C(5)—C(6)—C(7)—C(8)	1.0(3)

*Symmetry transformations: *a*, $-x, -y, -z$; *b*, $1-x, 1-y, -z$; *c*, $1-x, -y, -z$; *d*, $-x, 1-y, -z$; *e*, $-1+x, y, z$; *f*, $x, -1+y, z$.

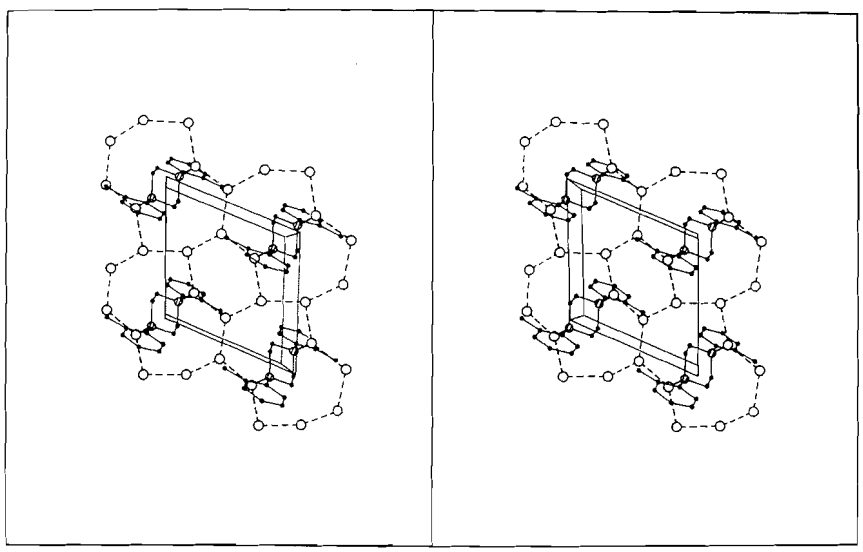

FIG. 2. Stereodrawing showing a puckered layer in the crystal structure of **I**. The origin of the unit cell lies at the lower left corner, with *a* pointing from left to right at a slant, *b* upwards, and *c* towards the reader. The hydrogen bonds are represented by broken lines.

Can. J. Chem. Downloaded from www.nrcresearchpress.com by 112.217.228.212 on 09/07/12
For personal use only.

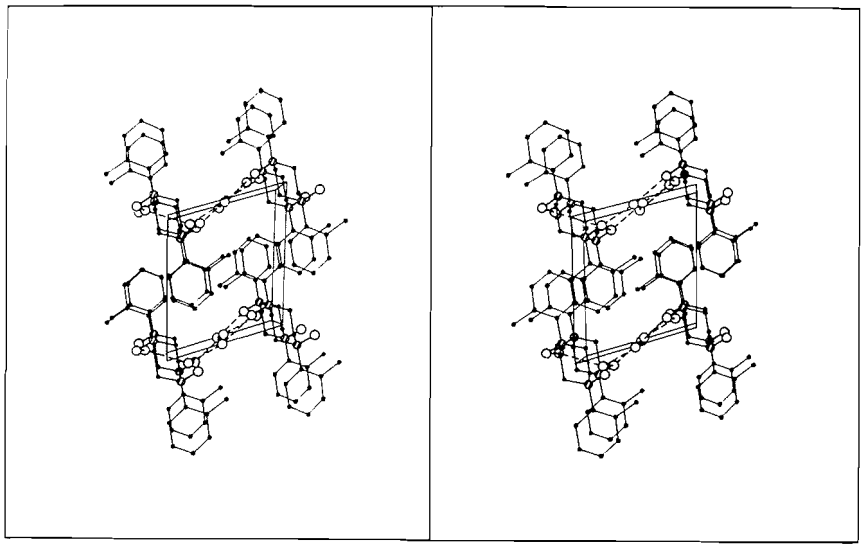

FIG. 3. Stereodrawing of the crystal structure of **I**. The origin of the unit cell lies at the lower left corner, with *a* pointing towards the reader, *b* from left to right at a slant, and *c* upwards. The hydrogen bonds are represented by broken lines.

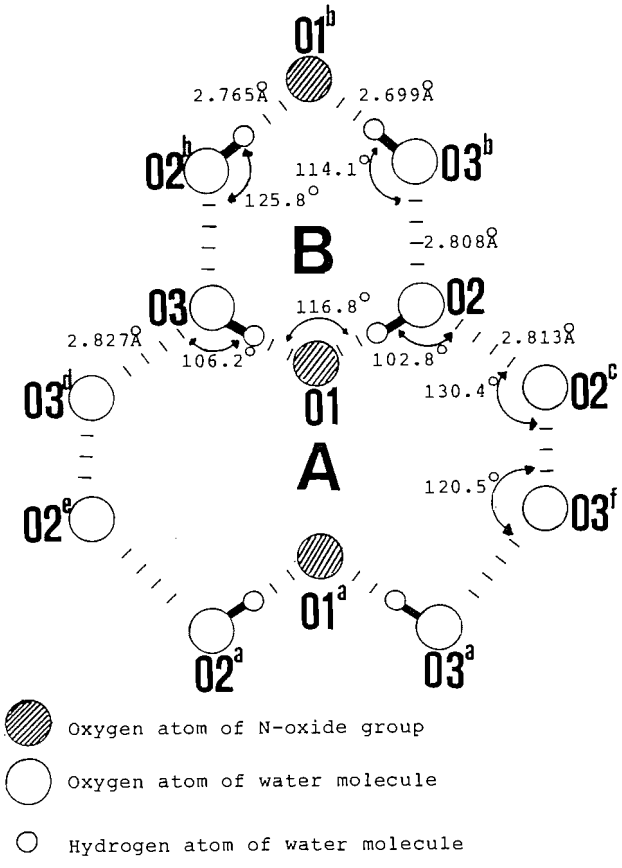

FIG. 4. Geometry of the six-membered and ten-membered hydrogen-bonded rings of a puckered layer in **I**. Symmetry transformations are as given in Table 7.

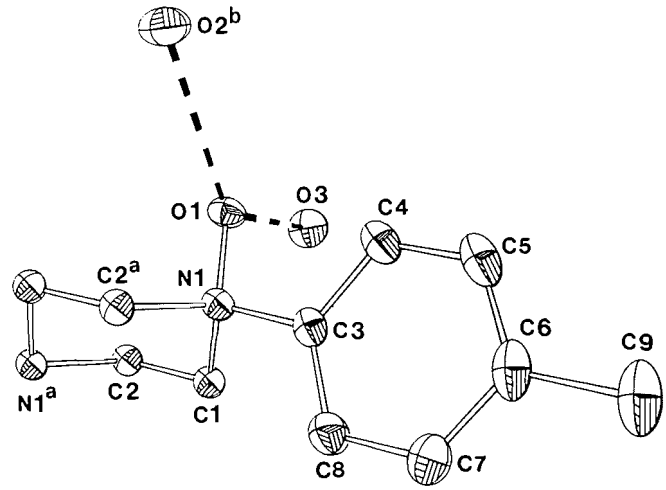

FIG. 5. Numbering of atoms in the asymmetric unit of **II**. The thermal ellipsoids are drawn at the 25% probability level.

puckered layer parallel to the *ab* plane (Fig. 2). There is no cross-linking between two adjacent puckered layers (Fig. 3). The *N*,*N*′-dioxide molecule is surrounded by a ten-membered hydrogen-bonded ring (type *A*, Fig. 4) of oxygen atoms, including those of its two *N*-oxide groups. The aromatic rings thus point in opposite directions above and below the mean plane of ring *A*. Edge-sharing of such ten-membered rings in a puckered layer generates other six-membered hydrogen-bonded rings (type *B*, Fig. 4). The water protons which are not involved in hydrogen bonding with the *N*-oxide groups are two-fold disordered.

(b) N,N′-*Di*(p-*tolyl*)*piperazine* N,N′-*dioxide tetrahydrate,* ***II***

In the crystal structure of **II**, a ribbon-like arrangement of centrosymmetric four- and six-membered hydrogen-bonded rings extends parallel to the *b* axis (Fig. 6). A similar ribbon-like arrangement has been observed in the crystal structure of bis(tetrahydropicolinato)copper(II) octahydrate (40). The six-membered, chair-like ring is formed by four water molecules and the *N*-oxide groups of two adjacent *N*,*N*′-dioxide molecules. The four-membered ring is formed by linking the edges of two adjacent six-membered rings. Adjacent ribbons are cross-linked by the *N*,*N*′-di(*p*-tolyl)piperazine moieties lying between them, thereby giving rise to a composite layer parallel to the *ab* plane. In the resulting crystal structure, only van der Waals interaction exists between neighboring composite layers (Fig. 7). All water protons in **II** are completely ordered: each water molecule forms an acceptor hydrogen bond with an

Can. J. Chem. Downloaded from www.nrcresearchpress.com by 112.217.228.212 on 09/07/12
For personal use only.

TABLE 8. Bond distances (Å), bond angles (deg), and selected torsion angles (deg) in *N*,*N*′-di(*p*-tolyl)piperazine *N*,*N*′-dioxide tetrahydrate (**II**)*

Bond	Distance	Bond	Distance
O(1)—N(1)	1.392(1)	N(1)—C(1)	1.512(1)
N(1)—C(3)	1.501(2)	N(1)—C(2)[a]	1.519(2)
C(1)—C(2)	1.513(2)	C(2)—N(1)[a]	1.519(2)
C(3)—C(4)	1.383(2)	C(3)—C(8)	1.382(2)
C(4)—C(5)	1.390(2)	C(5)—C(6)	1.377(3)
C(6)—C(7)	1.389(2)	C(6)—C(9)	1.512(2)
C(7)—C(8)	1.383(2)	O(1)...O(3)	2.771(3)
O(1)...O(2)[b]	2.749(3)	O(2)...O(3)	2.822(4)
O(2)...O(3)[c]	2.865(4)		

Angle	Value	Angle	Value
O(1)—N(1)—C(1)	108.7(1)	O(1)—N(1)—C(3)	111.3(1)
C(1)—N(1)—C(3)	110.7(1)	O(1)—N(1)—C(2)[a]	109.6(1)
C(1)—N(1)—C(2)[a]	108.0(1)	C(3)—N(1)—C(2)[a]	108.5(1)
N(1)—C(1)—C(2)	110.1(1)	C(1)—C(2)—N(1)[a]	110.3(1)
N(1)—C(3)—C(4)	118.6(1)	N(1)—C(3)—C(8)	120.5(1)
C(4)—C(3)—C(8)	120.9(1)	C(3)—C(4)—C(5)	118.9(1)
C(4)—C(5)—C(6)	121.9(1)	C(5)—C(6)—C(7)	117.9(1)
C(5)—C(6)—C(9)	121.3(1)	C(7)—C(6)—C(9)	120.8(2)
C(6)—C(7)—C(8)	121.6(2)	C(3)—C(8)—C(7)	118.8(1)
N(1)—O(1)...O(3)	114.3(3)	N(1)—O(1)...O(2)[b]	119.2(3)
O(3)...O(1)...O(2)[b]	126.3(4)	O(3)...O(2)...O(1)[b]	89.0(4)
O(3)...O(2)...O(3)[c]	87.3(4)	O(1)...O(3)...O(2)	101.1(4)
O(3)[c]...O(2)...O(1)[b]	105.2(4)	O(1)...O(3)...O(2)[c]	154.5(4)

Torsion angle	Value	Torsion angle	Value
O(1)—N(1)—C(1)—C(2)	−59.3(1)	C(2)[a]—N(1)—C(1)—C(2)	59.6(1)
C(9)—C(6)—C(7)—C(8)	−179.9(2)	C(2)[a]—N(1)—C(3)—C(8)	69.4(1)
C(3)—N(1)—C(1)—C(2)	178.1(1)	C(5)—C(6)—C(7)—C(8)	0.2(3)
C(1)—N(1)—C(3)—C(4)	133.4(1)	O(1)—N(1)—C(3)—C(4)	12.3(2)
N(1)—C(1)—C(2)—N(1)[a]	−61.0(1)	C(8)—C(3)—C(4)—C(5)	1.3(2)
C(6)—C(7)—C(8)—C(3)	0.6(3)	C(3)—C(4)—C(5)—C(6)	−0.4(3)
C(1)—N(1)—C(3)—C(8)	−48.9(2)	O(1)—N(1)—C(3)—C(8)	−169.6(1)
C(4)—C(3)—C(8)—C(7)	−1.4(2)	N(1)—C(3)—C(4)—C(5)	179.0(1)
C(4)—C(5)—C(6)—C(7)	−0.3(3)	C(4)—C(5)—C(6)—C(9)	179.8(2)
C(2)[a]—N(1)—C(3)—C(4)	−108.3(1)	N(1)—C(3)—C(8)—C(7)	−179.1(1)

*Symmetry transformations: *a*, $-x, -y, -z$; *b*, $1-x, -y, -z$; *c*, $1-x, 1-y, -z$.

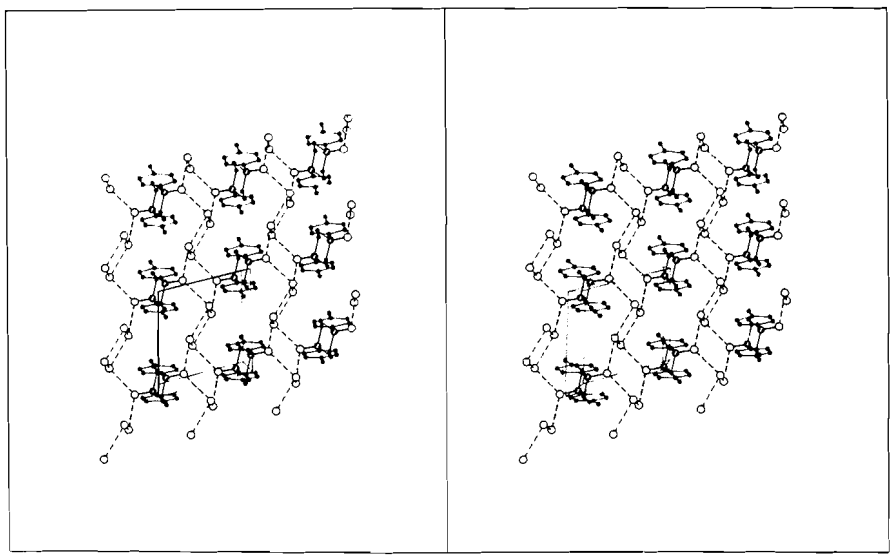

FIG. 6. Stereodrawing showing a composite layer in the crystal structure of **II**. The origin of the unit cell lies at the lower left corner, with *a* pointing from left to right at a slant, *b* upwards, and *c* towards the reader. The hydrogen bonds are represented by broken lines.

Can. J. Chem. Downloaded from www.nrcresearchpress.com by 112.217.228.212 on 09/07/12
For personal use only.

TABLE 9. Bond distances (Å) and bond angles (deg) in *N,N'*-di(*p*-chlorophenyl)piperazine *N,N'*-dioxide tetrahydrate (**III**)*

Bond	Distance	Bond	Distance
O(1)—N(1)	1.395(1)	N(1)—C(1)	1.516(2)
N(1)—C(3)	1.506(2)	N(1)—C(2)[a]	1.514(2)
C(1)—C(2)	1.510(2)	C(2)—N(1)[a]	1.514(2)
C(3)—C(4)	1.384(2)	C(3)—C(8)	1.386(2)
C(4)—C(5)	1.386(2)	C(5)—C(6)	1.379(2)
C(6)—C(7)	1.383(2)	C(6)—Cl(1)	1.744(2)
C(7)—C(8)	1.388(2)	O(1)...O(2)	2.767(3)
O(1)...O(2)[c]	2.778(3)	O(2)...O(3)	2.846(4)
O(2)...O(3)[b]	2.856(4)	O(2)...O(1)[d]	2.778(4)

Angle	Value	Angle	Value
O(1)—N(1)—C(1)	108.6(1)	O(1)—N(1)—C(3)	111.6(1)
C(1)—N(1)—C(3)	109.1(1)	O(1)—N(1)—C(2)[a]	109.6(1)
C(1)—N(1)—C(2)[a]	108.2(1)	C(3)—N(1)—C(2)[a]	109.8(1)
N(1)—C(1)—C(2)	110.3(1)	C(1)—C(2)—N(1)[a]	110.5(1)
N(1)—C(3)—C(4)	119.1(1)	N(1)—C(3)—C(8)	119.7(1)
C(4)—C(3)—C(8)	121.2(1)	C(3)—C(4)—C(5)	119.3(1)
C(4)—C(5)—C(6)	119.5(2)	C(5)—C(6)—C(7)	121.6(1)
C(5)—C(6)—Cl(1)	119.2(1)	C(7)—C(6)—Cl(1)	119.2(1)
C(6)—C(7)—C(8)	119.0(1)	C(3)—C(8)—C(7)	119.4(1)
N(1)—O(1)...O(2)	112.3(3)	N(1)—O(1)...O(2)[c]	120.7(3)
O(2)...O(1)...O(2)[c]	123.3(4)	O(1)...O(2)...O(3)	110.6(4)
O(1)...O(2)...O(3)[b]	122.7(4)	O(1)...O(2)...O(1)[d]	116.4(4)
O(3)...O(2)...O(3)[b]	95.4(4)	O(3)...O(2)...O(1)[d]	102.5(4)
O(3)[b]...O(2)...O(1)[d]	105.6(4)		

*Symmetry transformations: *a*, $1-x, -y, -z$; *b*, $1-x, 1-y, -z$; *c*, $x, \frac{1}{2}-y, \frac{1}{2}+z$; *d*, $x, \frac{1}{2}-y, -\frac{1}{2}+z$; *e*, $1-x, -\frac{1}{2}+y, -\frac{1}{2}-z$; *f*, $x, -1+y, z$.

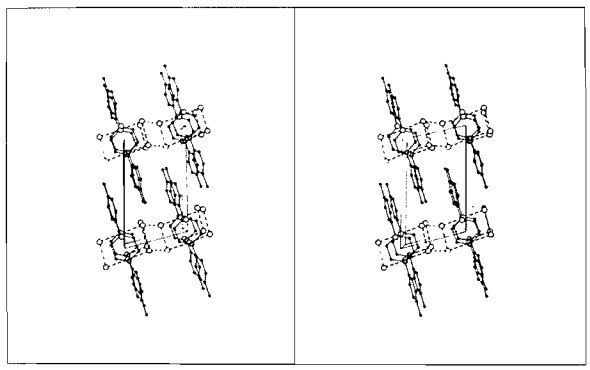

FIG. 7. Stereodrawing of the crystal structure of **II**. The origin of the unit cell lies at the lower left corner, with *a* pointing towards the reader, *b* from left to right at a slant, and *c* upwards. The hydrogen bonds are represented by broken lines.

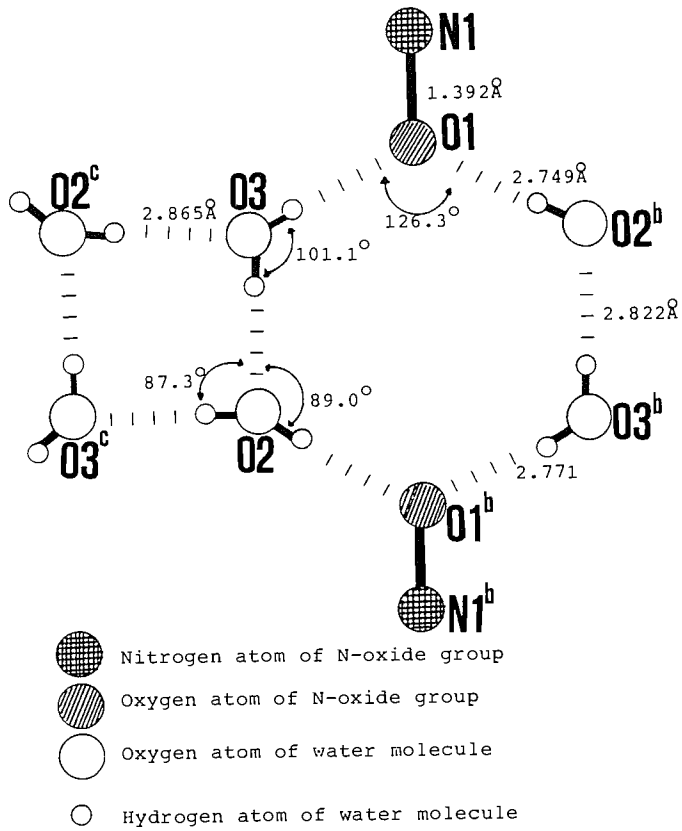

FIG. 8. The four- and six-membered rings of the ribbon in **II**. Symmetry transformations are as given in Table 8.

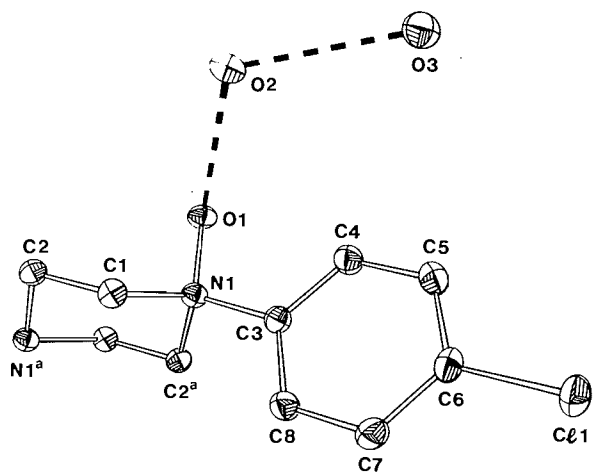

FIG. 9. Numbering of atoms in the asymmetric unit of **III**. The thermal ellipsoids are drawn at the 25% probability level.

adjacent water molecule and two donor hydrogen bonds with a second water molecule and a *N*-oxide group. Within each hydrogen-bonded four-membered ring, the protons are therefore arranged in a cyclic manner (Fig. 8).

(c) N,N'-*Di*(p-*chlorophenyl)piperazine* N,N'-*dioxide tetrahydrate,* ***III***

The crystal structure of **III** is also characterized by a network of hydrogen bonds in the pattern of a puckered layer. Four water molecules form a centrosymmetric four-membered hydrogen-bonded ring. The *N,N'*-dioxide molecule in the center of unit cell is surrounded by a twelve-membered, fourteen-atom hydrogen-bonded ring incorporating a couple of four-membered rings (Figs. 10 and 11). The *N,N'*-di(*p*-chlorophenyl)piperazine moiety constitutes a bridge between O(1) and O(1)[a]. Edge-sharing of these fourteen-atom hydrogen bonded rings generates a puckered layer parallel to the *bc* plane (Fig. 10). No cross-linking occurs between any pair of adjacent puckered layers. The hydrogen atoms of all the water molecules, just like those in **II**, are completely ordered. Unlike the case in **II**, the

Can. J. Chem. Downloaded from www.nrcresearchpress.com by 112.217.228.212 on 09/07/12
For personal use only.

TABLE 10. The N—O bond lengths in **I–III** and some related amine derivatives

Compound	N—O bond length (Å)	References
N,*N*′-Di(*o*-tolyl)piperazine *N*,*N*′-dioxide tetrahydrate, **I**	1.402(2)	This work
N,*N*′-Di(*p*-tolyl)piperazine *N*,*N*′-dioxide tetrahydrate, **II**	1.392(2)	This work
N,*N*′-Di(*p*-chlorophenyl)piperazine *N*,*N*′-dioxide tetrahydrate, **III**	1.395(1)	This work
N,*N*′-Diphenylpiperazine *N*,*N*′-dioxide octahydrate	1.387(2)	11
N,*N*′-Dicyclohexylpiperazine *N*,*N*′-dioxide octahydrate	1.392(1)	12
Me_3NO	1.388(5)	32
$Me_3NO.2H_2O$	1.398(1)	33
$Me_3NO.HCl$	1.425(11)	34, 35
$(CH_2)_6N_4O$	1.363(6)	36
$(CH_2)_6N_4O.H_2O_2.H_2O$	1.376(6)	8
$ON(CH_2CH_2)_3NO.3H_2O$	1.395(8)	37
NH_2OH	1.453(3)	38
$(NH_3OH)Cl$	1.411(2)	39

TABLE 11. Principal structural features of hydrated *N*,*N*′-disubstituted piperazine *N*,*N*′-dioxides

	Value				
piper$R_2O_2.nH_2O$	**I**	**II**	**III**	**IV**	**V**
R	*o*-Tolyl	*p*-Tolyl	*p*-Chlorophenyl	Phenyl	Cyclohexyl
n	4	4	4	8	8
Space group	$P\bar{1}$	$P\bar{1}$	$P2_1/c$	*Pnma*	$C2/m$
Site symmetry of piperR_2O_2	$\bar{1}$	$\bar{1}$	$\bar{1}$	*m*	2/*m*
Crystal structure	Layer	Composite layer	Layer	3-D network	3-D network
Water proton ordering	Partial	Complete	Complete	Partial	Partial
Hydrogen-bonded rings found*	[6], [10]	[4], [6]	[4], [12]	[4], [5], [6], [14]	[4], [5], [6], [8]
O(1)—N(1)—C(3)—C(4) torsion angle (deg)†	124.6(2)	12.3(2)	−1.1(2)	0	
References	This work	This work	This work	11	12

*The number of oxygen atoms in a hydrogen-bonded ring is enclosed in square brackets. The 12-membered ring in **III** is composed of 14 atoms and has two double bridges.

†This angle describes the orientation of the aryl ring with respect to the central piperazine *N*,*N*′-dioxide moiety (see Fig. 1).

Can. J. Chem. Downloaded from www.nrcresearchpress.com by 112.217.228.212 on 09/07/12
For personal use only.

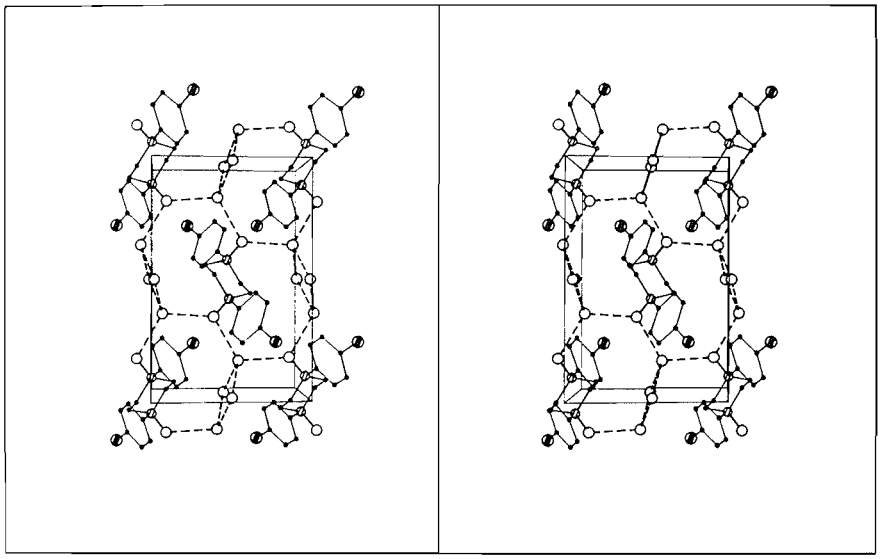

FIG. 10. Stereodrawing showing a puckered layer in the crystal structure of **III**. The origin of the unit cell lies at the lower left corner, with *a* pointing towards the reader, *b* downwards, and *c* from left to right. The hydrogen bonds are represented by broken lines.

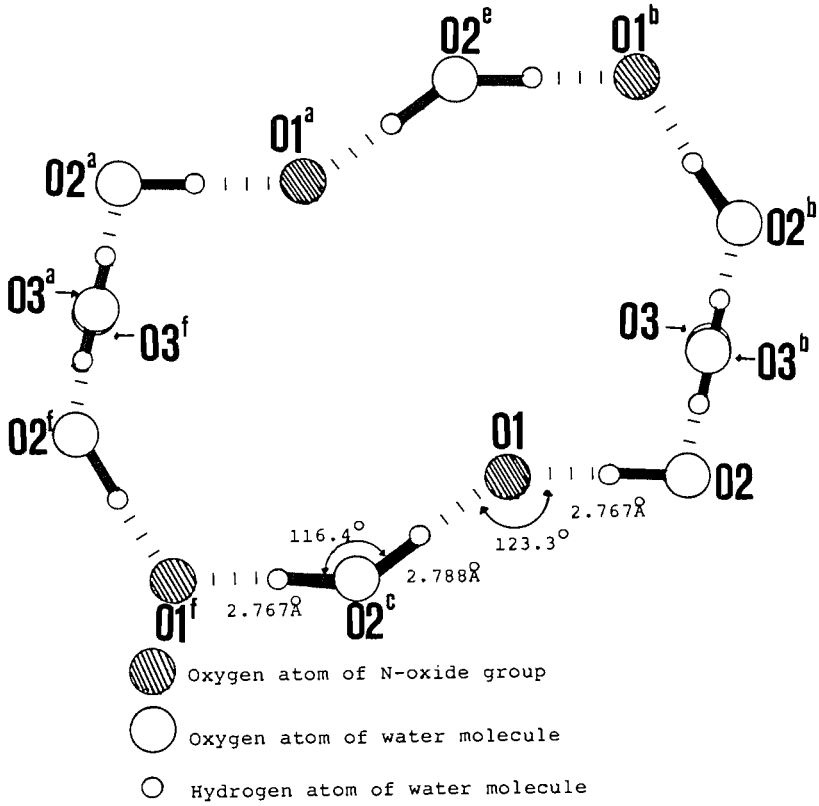

FIG. 11. The twelve-membered, fourteen-atom ring in **III**. Symmetry transformations are as given in Table 9.

water molecule O(2) (Fig. 12) forms only donor hydrogen bonds to two adjacent *N*-oxide groups and acceptor hydrogen bonds to a pair of neighboring water molecules which are members of the same four-membered ring. The water molecule O(3) is not involved in acceptor hydrogen bonding, so that O(2) and O(3) are four- and two-coordinated, respectively (Fig. 12).

(d) Effect of substitution in the phenyl ring

According to the results tabulated in Table 11, it readily follows that the more symmetric the *N*-substituted group, the higher the symmetry of the site which is occupied by the *N,N'*-dioxide molecule. Substitution in the phenyl ring has the effect of decreasing the hydration number (the number of water

Can. J. Chem. Downloaded from www.nrcresearchpress.com by 112.217.228.212 on 09/07/12
For personal use only.

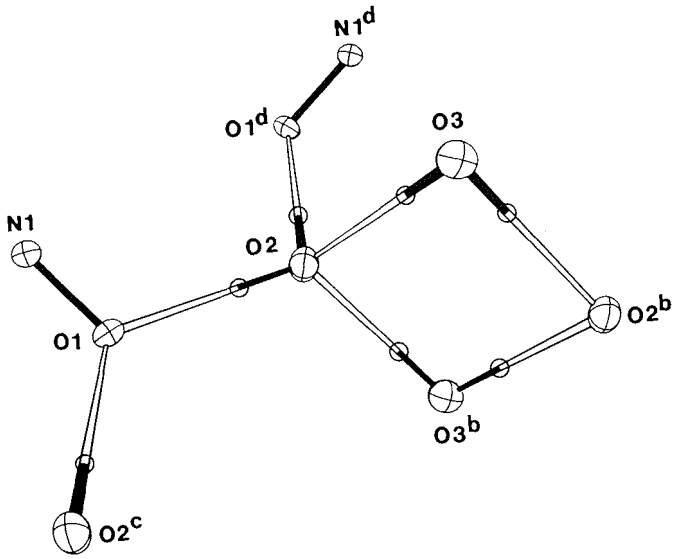

FIG. 12. Details of hydrogen bonding environment about the oxygen atoms in **III**. The proton positions are represented by small circles, and symmetry transformations are as given in Table 9.

molecules per *N,N'*-dioxide molecule in the stoichiometric formula) and consequently the complexity of the crystal lattice. In contrast to the three-dimensional networks observed in the crystal structures of **IV** (11) and **V** (12), all three hydrated *N,N'*-dioxides studied here comprise hydrogen-bonded puckered layers separated by hydrophobic regions which accommodate the protruding aryl rings.

1. A. R. KATRITZKY and J. M. LAGOWSKI. Chemistry of heterocyclic N-oxides. Academic Press, London. 1971.
2. C. OCHIAI. Aromatic amine oxide. Elsevier, Amsterdam. 1967.
3. R. A. ABRAMOVITCH and J. G. SAHA. Adv. Heterocycl. Chem. **6**, 299 (1966).
4. R. BOSCH, G. JUNG, and W. WINTER. Acta Crystallogr. C, **39**, 1089 (1983).
5. E. MAIA and S. PEREZ. Acta Crystallogr. B, **38**, 849 (1982).
6. H. CHANZY, E. MAIA, and S. PEREZ. Acta Crystallogr. B, **38**, 852 (1982).
7. Y. S. LAM and T. C. W. MAK. Acta Crystallogr. B, **34**, 1915 (1978).
8. Y. S. LAM and T. C. W. MAK. Acta Crystallogr. B, **34**, 1732 (1978).
9. P. Y. YU and T. C. W. MAK. Acta Crystallogr. B, **34**, 3053 (1978).
10. J. TROTTER and T. C. W. MAK. Acta Crystallogr. B, **35**, 2367 (1919).
11. C.-K. KWOK and T. C. W. MAK. J. Cryst. Spectrosc. Res. In press.
12. C.-K. KWOK and T. C. W. MAK. J. Incl. Phenom. In press.
13. W. KEMP. Organic spectroscopy. Macmillan, London. 1979. p. 34.
14. E. S. MORERA. Quin. Ind. **71**, 303 (1929); Chem. Abstr. **24**, 1644 (1930).
15. G. M. BENNETT and E. GLYNN. J. Chem. Soc. 211 (1950).
16. R. A. SPARKS. *In* Crystallographic computing techniques. *Edited by* F. R. Ahmed. Munksgaard, Copenhagen. 1976. p. 452.
17. F. TODA, K. TANAKA, S. NAGAMATSU, and T. C. W. MAK. Isr. J. Chem. **25**, 346 (1985).
18. F. TODA, K. TANAKA, and T. C. W. MAK. J. Incl. Phenom. **3**, 225 (1985).
19. R. DIAMOND. Acta Crystallogr. A, **25**, 43 (1969).
20. G. T. DETITTA, J. W. EDMONDS, D. A. LANGS, and H. HAUPTMAN. Acta Crystallogr. A, **31**, 472 (1975).
21. G. M. SHELDRICK. Computational crystallography. *Edited by* D. Sayre. Oxford University Press, New York. 1982. p. 506.
22. International tables for X-ray crystallography. Vol. IV. Kynoch Press, Birmingham. 1974. pp. 55, 99, 149.
23. J. W. SCHILLING. Crystallographic computing. *Edited by* F. R. Ahmed. Munksgaard, Copenhagen. 1976. p. 201.
24. P. CAUBIRE and N. DEROZIER. Bull. Soc. Chim. Fr. 1737 (1969).
25. R. G. LETT, L. PETRAKIS, A. F. ELLIS, and R. K. JENSEN. J. Phys. Chem. **74**, 2816 (1970).
26. F. YAMADA, Y. FUJIMOTO, and T. NISHIYUMA. Bull. Chem. Soc. Jpn. **45**, 280 (1972).
27. P. J. HENDRA and D. B. POWELL. J. Chem. Soc. 5105 (1960).
28. P. J. HENDRA and D. B. POWELL. Spectra. Acta, **18**, 299 (1962).
29. J. B. LAMBERT, H. F. SHURVELL, L. VERBIT, R. G. COOKS, and G. H. STOUT. Organic structural analysis. Macmillan, New York. 1976. pp. 37–64.
30. W. KEMP. Organic spectroscopy. Macmillan, London. 1979. p. 34.
31. J. B. LAMBERT, H. F. SHURVELL, L. VERBIT, R. G. COOKS, and G. H. STOUT. Organic structural analysis. Macmillan, New York. 1976. (*a*) pp. 81–82; (*b*) pp. 274–279.
32. A. CARON, G. J. PALENIK, E. GOLDISH, and J. DONOHUE. Acta Crystallogr. **17**, 102 (1964).
33. T. C. W. MAK. J. Mol. Struct. In press.
34. P. C. RÉRAT. Acta Crystallogr. **13**, 63 (1960).
35. A. CARON and J. DONOHUE. Acta Crystallogr. **15**, 1052 (1962).
36. T. C. W. MAK, M. F. C. LADD, and D. C. POVEY. J. Chem. Soc. Perkin Trans. 2, 593 (1979).
37. P. K. HON and T. C. W. MAK. J. Cryst. Spectrosc. Res. **17**, 419 (1987).
38. S. TSUNEKAWA. J. Phys. Soc. Jpn. **33**, 167 (1972).
39. K.-L. SHI, R.-Q. WANG, and T. C. W. MAK. J. Mol. Struct. **160**, 109 (1987).
40. Y. YORKOVSKY, M. KAPON, and Z. DORI. Inorg. Chim. Acta, **124**, 149 (1986).

Can. J. Chem. Downloaded from www.nrcresearchpress.com by 112.217.228.212 on 09/07/12
For personal use only.

Molecular motion in the crystalline donor–acceptor complex trimethylamine–trifluoroborane as studied by proton and fluorine magnetic resonance

YUKIKO N. CHIHARA, NOBUO NAKAMURA, AND HIDEAKI CHIHARA

Department of Chemistry, Faculty of Science, Osaka University, Toyonaka, 560, Japan

Received November 13, 1987

This paper is dedicated to Professor Charles A. McDowell on the occasion of his 70th birthday

YUKIKO N. CHIHARA, NOBUO NAKAMURA, and HIDEAKI CHIHARA. Can. J. Chem. **66**, 1848 (1988).

The proton and fluorine second moments and the spin-lattice relaxation times T_1 (at 25.75 MHz) were measured in the solid complex trimethylamine–trifluoroborane from 53 to 300 K. There is a cross-relaxation effect between ^1H and ^{19}F below 120 K. Their T_1 minima near 140 K led to activation energies of 10.6 and 11.1 kJ mol^{-1} for the reorientation of the methyl and the trifluoride groups, respectively. An additional minimum observed in the T_1 of protons at about 240 K was attributed to the reorientation of the trimethylamine group about the N—B bond with an activation energy of 25.0 kJ mol^{-1}. A comparison of these potential parameters with those in other trimethylamine complexes led to a notion that the activation energies for the reorientation of the $(CH_3)_3N$ group in the trimethylamine–trifluoroborane complex are mainly governed by the intramolecular steric effect.

YUKIKO N. CHIHARA, NOBUO NAKAMURA et HIDEAKI CHIHARA. Can. J. Chem. **66**, 1848 (1988).

Opérant à des températures allant de 53 à 300 K, on a mesuré les moments secondaires ainsi que les temps de relaxation spin-réseau, T_1, à 25,75 MHz, du complexe solide triméthylamine/trifluoroborane. À des températures inférieures à 120 K, il existe un effet de relaxation croisée entre le ^1H et le ^{19}F. Près de 140 K, leurs T_1 minima conduisent à des énergies d'activation respectives de 10,6 et 11,1 kJ mol^{-1} pour les réorientations des groupements méthyle et trifluorure. Dans le T_1 du proton, on a observé un autre minimum autour de 240 K; on l'a attribué à une réorientation du groupement triméthylamine autour de la liaison N—B; son énergie d'activation serait de 25,0 kJ mol^{-1}. Lorsqu'on compare les paramètres de ces potentiels avec ceux observés dans d'autres complexes de la triméthylamine, on en déduit que les énergies d'activation pour la réorientation du groupement $(CH_3)_3N$ du complexe triméthylamine–trifluoroborane sont principalement déterminées par l'effet stérique intramoléculaire.

[Traduit par la revue]

Trimethylamine (TMA) forms donor–acceptor complex compounds with a variety of electron accepting materials (1). Some of these complexes have threefold symmetry and different types of intramolecular degrees of freedom. Moreover, some undergo a phase transition or transitions in their crystalline state (2–4) but the nature of the phase transitions has not yet been clarified. To understand the mechanism of phase transition(s) as well as the intricate inter- or intramolecular interactions in the crystals of these molecular complexes, studies are necessary both of the dynamical properties of molecules and of the crystal lattices in relation to detailed structural studies.

The 1:1 complex compound between TMA and trifluoroborane (TFB) is a typical example of such a complex. It has a molecular threefold symmetry axis and three intramolecular rotational degrees of freedom, and can undergo two different rotations as a whole, i.e., the rotations about the molecular symmetry axis and about the two short axes. The molecule has a large dipole moment (5.76 D) (5) and the crystal belongs to a rhombohedral space group with three TMB·TFB complexes per unit cell (6). This compound does not undergo any phase transition between 77 K and its melting point and therefore is a good specimen for examining molecular motion in detail without interruption by the discontinuities of a phase transition.

This paper presents the results of proton and fluorine nuclear magnetic resonance and relaxation measurements below room temperature. The molecular modes are assigned and the cross-relaxation effect between the proton and fluorine is discussed. The origin of the activation processes and the possible mechanism of phase transitions in trimethylamine complexes will be considered.

Experimental

TMA–TFB was synthesized according to a method reported in the literature (7); a saturated aqueous solution of KOH was added to trimethylamine hydrochloride from a commercial source and gaseous TMA thus generated was introduced into an ether solution of vacuum-distilled BF_3·OEt. The $(CH_3)_3N·BF_3$ precipitate was recrystallized from a dry benzene solution and purified by vacuum sublimation, twice, at 60–70°C: mp 420 K (literature (5) mp 419–419.5 K). *Anal.* calcd.: C 28.39, H 7.15, N 11.04%; found: C 28.43, H 7.38, N 10.69%. No phase transition was detected by differential thermal analysis between 77 K and the melting point.

The linewidths and the second moments of ^1H and ^{19}F resonances for a powdered specimen were measured by a Robinson-type spectrometer at 11.25 MHz from 53 K to room temperature. The spin-lattice relaxation times T_1 were measured at 25.75 MHz between 77 and 330 K by 180°–90° pulse sequences with a home-built pulsed spectrometer. The details of the apparatus have been described elsewhere (8). The temperature was measured by Chromel-P–Constantan thermocouples with an accuracy of ±0.5 K.

Results and discussion

Second moment

Previous measurements of the linewidths and the second moments of both ^1H and ^{19}F down to 68 K did not reach the rigid-lattice values (9, 10). We therefore extended the temperature region of the continuous-wave experiments down to 53 K. The results indicate that the second moment of ^1H reaches an almost flat plateau below 60 K at (31 ± 1) G^2. On the other hand, the second moment of ^{19}F increases sharply from (7.3 ± 0.2) G^2 at 85 K to (19 ± 1) G^2 at 60 K. Our second moment values of both ^1H and ^{19}F agree with the previous results (9, 10) above 85 K.

A rigorous calculation of the second moments was performed by Yim and Gilson (9) on the basis of various models for the molecular rotational states. Our model calculation using the structural data (6) with the assumption that the methyl groups in TMA assume a tetrahedral bond arrangement with a C—H bond length, 0.109 nm, leads to results consistent with those of ref. 9

Can. J. Chem. Downloaded from www.nrcresearchpress.com by 112.217.228.212 on 09/07/12
For personal use only.

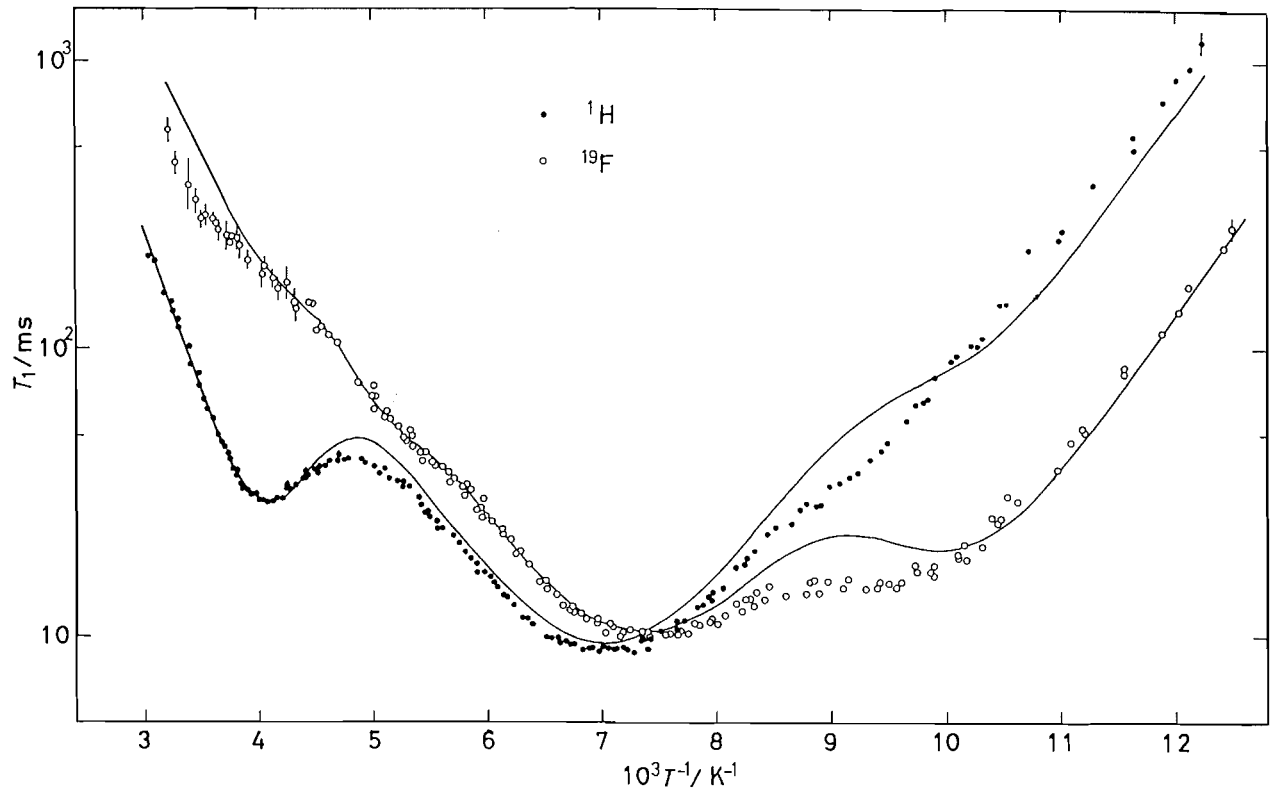

FIG. 1. The spin-lattice relaxation times for ^{1}H(●) and ^{19}F(○) at 25.75 MHz; the estimated experimental errors are shown by vertical lines. Calculated relaxation times are given by solid lines (see in text).

except for the rigid lattice value of the ^{19}F second moment: our value was 20.0 G^2 whereas that of ref. 9 is 25.9 G^2; the latter seems to be too large. Although some discrepancy can be recognized between our calculated second moment values and those in ref. 9, our analysis of the experimental second moments led to the same assignment of the molecular motion as given in ref. 9: i.e., the large change in the second moments of both ^{1}H and ^{19}F below about 90 K is caused by the simultaneous excitation of the reorientation or rotation of the methyl groups about the C—N bonds (C_3 rotation) and the reorientation of the BF_3 group about the N—B bond (C_F rotation), and another change of the proton second moment between 100 and 150 K is brought about by the reorientation of the TMA group about the N—B bond (C_3' rotation) in addition to C_3 and C_F rotations. The overall molecular tumbling is not seen even above 300 K.

Temperature dependence of T_1

To determine the activation parameters for each of the above-mentioned internal rotational modes, we measured the spin-lattice relaxation times T_1 of both ^{1}H and ^{19}F between 77 K and room temperature. The results are shown in Fig. 1. The experimental errors in T_1 are depicted by vertical bars. The recovery of the magnetization was nearly exponential for both nuclei over the whole temperature range of the measurements.

The T_1 of ^{19}F decreases almost linearly on heating from 77 K, with a flat part between about 110 K and 120 K, reaches a broad minimum of 10 ms at about 130 K, and then turns to increase.

The T_1 curve of ^{1}H is more complex: it shows only a slight change in curvature between 110 and 120 K, and has a major, broad minimum (8.8 ms) at 140 K. There is another minimum at about 240 K, the value of which is 30 ms.

Analysis of T_1 *data in terms of motional model*

We now attempt to rationalize the measured temperature dependences of proton and fluorine T_1 in the light of the general understanding of the molecular motion outlined above. The proton and fluorine relaxation rates $(T_1^H)^{-1}$ and $(T_1^F)^{-1}$ are expressed, respectively, by

$$[1]\quad (T_1^H)^{-1} = (T_1^{HH})^{-1}_{\text{intra Me}} + (T_1^{HH})^{-1}_{\text{inter Me}} + (T_1^{HH})^{-1}_{\text{intermol}} + (T_1^{HF})^{-1} + (T_1^{HB})^{-1}$$

$$[2]\quad (T_1^F)^{-1} = (T_1^{FF})^{-1}_{\text{intra BF}_3} + (T_1^{FF})_{\text{inter}} + (T_1^{FH})^{-1} + (T_1^{FB})^{-1}$$

where $(T_1^{HH})^{-1}_{\text{intra Me}}$ represents the relaxation rate due to fluctuations of the dipolar interaction between the protons within a methyl group. Other notation will then be self-explanatory.

In the presence of C_3 and C_3' rotations of the TMA group, the relaxation rate $(T_1^{HH})^{-1}_{\text{intra Me}}$ of the powdered specimen is given (3*b*, 4) by

$$[3]\quad (T_1^{HH})^{-1}_{\text{intra Me}} = K(r_{HH})\{8B_H(\tau_3) + 19B_H(\tau_e) + 8B_H)\tau_3')\}$$

$$[4]\quad K(r_{HH}) = r_H^4\hbar^2/60r_{HH}^6$$

$$[5]\quad B(\tau) = \tau/(1 + \omega_0^2\tau^2) + 4\tau/(1 + 4\omega_0^2\tau^2)$$

where r_{HH} is the interproton distance in a methyl group, ω_0 the Larmor frequency, τ_3 and τ_3' are the correlation times of the C_3 and C_3' rotations, respectively, and

$$\tau_e^{-1} = \tau_3^{-1} + \tau_3'^{-1}$$

Here we assume that there is no coupling between the two kinds of molecular rotational modes.

We learned above that the C_3' rotation becomes more excited at higher temperatures than does the C_3 reorientation, so that the relation $\tau_3 \ll \tau_3'$ holds over the whole temperature range of

Can. J. Chem. Downloaded from www.nrcresearchpress.com by 112.217.228.212 on 09/07/12
For personal use only.

Can. J. Chem. Downloaded from www.nrcresearchpress.com by 112.217.228.212 on 09/07/12
For personal use only.

the T_1 measurements. Thus, we can put $\tau_3' = \infty$ and eq. [3] is reduced below about 200 K to

$$[6] \quad (T_1^{HH})^{-1}_{\text{intra Me}} = 27K(r_{HH})B(\tau_3)$$

The strength of the dipolar interaction $K(r_{HH})$ is calculated using the molecular geometry of the TMA group (6) as

$$[7] \quad (T_1^{HH})^{-1}_{\text{intra Me}} = 7.79 \times 10^9 B(\tau_3)$$

Below about 200 K where the C_3' rotation is essentially frozen, it is difficult to evaluate the contribution of the dipolar interaction between different methyl groups in a molecule and the intermolecular proton–proton interaction. We put, therefore,

$$[8] \quad (T_1^{HH})^{-1}_{\text{inter Me}} + (T_1^{HH})^{-1}_{\text{intermol}} = A \cdot B_H(\tau_3)$$

where the factor A is left as an adjustable parameter.

The shoulders on the T_1 curve of both ^{1}H and ^{19}F below 120 K are caused by the cross-relaxation between protons and fluorines sitting on the reorienting methyl and BF_3 groups. In the presence of the cross-relaxation between ^{1}H and ^{19}F, the recovery of the magnetization of each spin is described (11–14) by

$$dM_H/dt = -(T_1^{HH})^{-1}_{cr}(M_H - M_H^0) - (T_1^{HF})^{-1}_{cr}(M_F - M_F^0)$$

$$dM_F/dt = -(T_1^{FH})^{-1}_{cr}(M_H - M_H^0) - (T_1^{FF})^{-1}_{cr}(M_F - M_F^0)$$

where M_H and M_H^0 represent the magnetization of ^{1}H at a time t and at thermal equilibrium, respectively, under the influence of the fluorine spins, and $(T_1^{HH})^{-1}_{cr}$ is the diagonal matrix element of the cross-relaxation matrix of the system of interacting protons and fluorines. Other symbols will be obvious. Although explicit expressions of $(T_1^{ik})^{-1}_{cr}$, where i, k = H or F, have been given in the literature (12, 13), it is hardly possible to apply them directly to our system involving simultaneously reorienting methyl and BF_3 groups. Therefore, we use a formulation which relates the relaxation matrix to the second moments (12, 14):

$$[9a] \quad (T_1^{HH})^{-1}_{cr} = aM_2^H(F)D(\tau_e') = B \cdot D(\tau_e')$$

$$[9b] \quad (T_1^{HF})^{-1}_{cr} = (T_1^{FH})^{-1}_{cr} = aM_2^H(F)\{-\tau_e'/(1 + \Delta^2\tau_e'^2) + 6\tau_e'/(1 + 4\omega_0^2\tau_e'^2)\}$$

and

$$[9c] \quad (T_1^{FF})^{-1}_{cr} = aM_2^F(H)D(\tau_e') = C \cdot D(\tau_e')$$

where

$$[10] \quad D(\tau) = \tau/(1 + \Delta^2\tau^2) + 3\tau/(1 + \omega_0^2\tau^2) + 6\tau/(1 + 4\omega_0^2\tau^2)$$

and

$$\Delta = \omega_H - \omega_F$$

$$\tau_e'^{-1} = \tau_3^{-1} + \tau_F^{-1}$$

$M_2^H(F)$ is the fluorine contribution to the proton second moment and τ_F the correlation time for the C_F rotation. We use the approximation that $\omega_0 = (\omega_H + \omega_F)/2$. The factors a, B, and C obviously depend on the relative location of protons and fluorines. As we mentioned in a preceding section, the recovery of the magnetizations of both ^{1}H and ^{19}F is nearly exponential so that only $(T_1^{HH})_{cr}$ and $(T_1^{FF})_{cr}$ can be deduced from the observed T_1, and we cannot evaluate $(T_1^{HF})_{cr}$ in eq. [9b].

The relaxation rate $(T_1^{FF})^{-1}$ due to the dipolar interaction within a BF_3 group is given by

$$[11] \quad (T_1^{FF})^{-1}_{\text{intra } BF_3} = 27K(r_{FF})B(\tau_F) = 1.66 \times 10^9 B(\tau_F)$$

the numerical value for $K(r_{FF})$ being obtained by the use of the crystal data (6). The fluorine relaxation that arises from fluorines on neighboring molecules is assumed to be small and is ignored.

The ^{19}F cross-relaxation rate by ^{10}B and ^{11}B within a BF_3 group is approximated (13) by

$$[12] \quad (T_1^{FB})^{-1} = C(^{10}B)T_1^{-1}(F\text{-}^{10}B) + C(^{11}B)T_1^{-1}(F\text{-}^{11}B)$$

where

$$T_1^{-1}(F\text{-}X) = (1/10)r_F^2 r_X^2 \hbar^2 r_{FX}^{-6} S_X(S_X + 1)f(\xi)D(\tau_F, X)$$

$X = {}^{10}B$ or ^{11}B

and $f(\xi) = 4\sin^2\xi\cos^2\xi + \sin^4\xi$ with ξ as the angle between the internuclear vector r_{BF} and the external magnetic field. S_X and $C(X)$ are the spin number and the natural abundance, respectively, of the two isotopes, ^{10}B or ^{11}B. $D(\tau_F, X)$ represents the same quantity as in eq. [9] except that Δ and $2\omega_0$ are replaced by $\omega_F - \omega_X$ and $\omega_F + \omega_X$, respectively. Using structural data, the intra-BF_3 relaxation rate is calculated to be

$$[13] \quad (T_1^{BF})^{-1} = 0.22 \times 10^9 D(\tau_F, {}^{10}B) + 2.67 \times 10^9 D(\tau_F, {}^{11}B)$$

Finally, the relaxation rate $(T_1^{HB})^{-1}$ is ignored.

The minimum in T_1 of ^{1}H at 240 K is due to the onset of the C_3' rotation, i.e., the reorientation of the TMA group about the N—B bond. The contribution of this motion to the proton relaxation rate is approximated by

$$[14] \quad (T_1^{HH})_{C_3'}{}^{-1} = 81K(r^*)B(\tau_3')$$

where r^* is the distance between the centers of gravity of the three protons in individual methyl groups in the molecule. We calculated the factor $81K(r^*)$ to be $3.32 \times 10^9\ s^{-2}$ using the assumed geometry of TMA. The cross-relaxation rate of ^{19}F due to C_3' rotation is given by eq. [9c], with τ_e' substituted by τ_3' and C by another adjustable parameter D, i.e.,

$$[15] \quad (T_1^{FF})_{cr,C_3'}{}^{-1} = D \cdot D(\tau_3')$$

Fitting of calculation to experimental T_1

Using eqs. [6]–[15] and adjusting the parameters A, B, C, and D, we attempted to fit the theoretical relaxation rates of ^{1}H and ^{19}F of eqs. [1] and [2], respectively, to the experimental ones using a personal computer. Here we assumed an Arrhenius-type activation process

$$[16] \quad \tau_i = \tau_i^0 \exp(E_i/RT)$$

for each of the three reorientational modes. The best fit to the experimental T_1 was obtained with $A = 3.9 \times 10^9$, $B = 0.13 \times 10^9$, $C = 0.85 \times 10^9$, and $D = 0.10 \times 10^9$ (in s^{-2}). The

TABLE 1. Activation parameters in $(CH_3)_3N \cdot BF_3$

Motion	E_a/kJ mol^{-1}	τ_c^0/s
C_3 rotation	10.6 ± 0.1	$(5.14 \pm 0.55) \times 10^{-13}$
C_F rotation	11.1 ± 0.2	$(3.12 \pm 0.59) \times 10^{-13}$
C_3' rotation	25.0 ± 0.2	$(1.91 \pm 0.16) \times 10^{-14}$

TABLE 2. Activation parameters in TMA complexes

Substance	Motion[a]	E_a/kJ mol^{-1}	τ_c^0/s	References
TMA	C_3	24.1	—	23
TMA·I_2	C_3	14.2	2.9×10^{-12}	16
TMA·ICl	C_3	18.0	1.9×10^{-12}	16
TMA·Br_2	$C_3 + C_3'$	19.7	3.0×10^{-13}	16
TMA·BH_3	C_3	14.0	8.6×10^{-14}	3*b*
	C_3'	28.2	7.3×10^{-15}	3*b*
	$C_3 + C_3' + C_X$	25.5	1.3×10^{-14}	3*c*
	iso[b]	134	—	3*c*
TMA·BF_3	C_3	10.6	5.14×10^{-13}	
	C_3'	25.0	1.91×10^{-14}	Present work
	C_X	11.1	3.12×10^{-13}	
TMA·BCl_3	C_3	11.3	1.7×10^{-12}	
	C_3'	56.8	1.2×10^{-17}	16
TMA·BBr_3	C_3	12.1	4.4×10^{-13}	
		13.3	1.1×10^{-12}	16
	C_3'	60.6	6.1×10^{-17}	
TMA·GaH_3	C_X	3.6	—	4
	$(C_3 + C_3')$	21	—	

[a] C_3, C_3', C_X, and iso denote the C_3, C_3', and threefold reorientation of the acceptor molecule, and the isotropic reorientation of the molecule, respectively.
[b] One of the two inequivalent molecular sites.

activation parameters for the three reorientations are listed in Table 1 and the calculated relaxation times T_1^F and T_1^H are reproduced in Fig. 1 by the solid and the broken lines.

As can be seen in Fig. 1, the agreement between the experimental and the theoretical relaxation times for both ^1H and ^{19}F is satisfactory over the whole temperature region of the measurements except in the range between 100 and 120 K. The poor agreement in this region is probably due to the neglect of the off-diagonal elements in the cross-relaxation matrix. The second moment data lead to $A = 1.21 \times 10^9$, $B = 0.198 \times 10^9$, $C = 0.595 \times 10^9$, and $D = 0.342 \times 10^9$ (in s^{-2}). Calculation of T_1 with these parameters does not give satisfactory fitting to the experiment, implying that the estimation of the intergroup as well as the intermolecular dipolar interaction is very difficult for a complex molecule in which a number of different types of motions are simultaneously excited.

Activation energies for TMA complexes

The activation parameters for TMA and a variety of its complex compounds are compared in Table 2. One can see from this table that the activation energies E_a for the C_3 rotation in the TMA complexes of BX_3 (X = H, F, Cl, and Br) fall in the range 10–13 kJ mol^{-1}, which is rather low for the activation energies of methyl reorientation. These values are comparable with those for the less hindered methyl rotation in *tert*-butyl groups in $(CH_3)_3CNH_3^+$ ions (15). The other complexes, especially the strong complexes of TMA with halogens, give higher activation energies for the C_3 rotation. Ang and Dunell attempted to correlate the activation energy for the C_3 rotation to an expected structural change in $(CH_3)_3N$ due to charge transfer to an electron acceptor (16). Their attempts were not promising because of a lack of precise molecular structural data for most of the TMA complexes. Now we find that the activation energy for the C_3 rotation increases with an increase in the electron affinity (17) of the acceptor in the series of BF_3, Cl_2, Br_2, ICl, and I_2, or, for BX_3-type acceptor molecules, with an increase in the electron-withdrawing power introduced by Eames and Hoffman (18). Since these two quantities are measures of the strength of the acceptor species, this fact suggests that the methyl rotational barrier in the TMA donor molecule goes up as the acceptor strength increases.

As to the C_3' rotation, the activation energies of the complexes with BCl_3 and BBr_3 are about twice as high as those of BH_3 and BF_3. The TMA component in the former two complexes is significantly distorted in the unit cells belonging to the space group $P2_1/m$ (19) and so the high barriers can be ascribed to asymmetric intermolecular rotational potentials.

It is worth pointing out that the activation energy for the rotation of BF_3 group about the N—B bond in TMA–BF_3 is comparable to that for the methyl reorientation. This fact is analogous to the experimental observation that the activation energy of the BH_3 reorientation is indistinguishable from that of C_3 rotation in TMA–BH_3 (3*a*). Furthermore, the activation energies for the C_3' rotation are nearly the same in these two complexes. Hence we can conclude that TMA–BF_3 and TMA–BH_3 show similar dynamical behavior except that the latter undergoes two phase transitions immediately below its melting point whereas the former has no phase changes in the solid state. If the phase transitions in TMA–BH_3 and its analogues are associated with the overall molecular tumbling as suggested in ref. 3*a*, the cause of the phase transitions in these substances may be systematically understood on the basis of the size, shape, and the magnitude of the molecular electric dipole moment, which together determine the molecular packing (20–22).

Acknowledgment

The present work was partially supported by Grant-in-Aid for Scientific Research No. 61430006 from the Ministry of Education, Science and Culture.

1. J. YARWOOD (*Editor*). Spectroscopy and structure of molecular complexes. Plenum Press, London. 1973.

Can. J. Chem. Downloaded from www.nrcresearchpress.com by 112.217.228.212 on 09/07/12
For personal use only.

2. H. SUGA, K. NAKATSUKA, and S. SEKI. Bull. Chem. Soc. Jpn. **31**, 792 (1958).
3. (*a*) T. T. ANG and B. A. DUNELL. J. Chem. Soc. Faraday Trans. 2, **70**, 17 (1974); (*b*) Can. J. Chem. **54**, 1087 (1978); (*c*) E. C. REYNHARDT. J. Phys. C: **19**, 1823 (1986).
4. M. B. DUNN and C. A. MCDOWELL. Mol. Phys. **24**, 969 (1972).
5. G. M. PHILLIPS, J. S. HUNTER, and L. E. SUTTON. J. Chem. Soc. 146 (1945).
6. S. GELLER and J. L. HOARD. Acta Crystallogr. **4**, 399 (1951).
7. R. L. AMSTER and R. C. TAYLOR. Spectrochim. Acta, **20**, 1487 (1964).
8. T. EGUCHI, G. SODA, and H. CHIHARA. J. Magn. Reson. **23**, 55 (1975).
9. C. T. YIM and D. F. R. GILSON. Can. J. Chem. **48**, 515 (1970).
10. B. A. DUNELL, C. A. FYFE, C. A. MCDOWELL, and J. RIPMEESTER. Trans. Faraday Soc. **65**, 1153 (1969).
11. A. ABRAGAM. The principles of nuclear magnetism. Oxford Univ. Press, London. 1961.
12. R. BLINC and G. LAHAJNAR. J. Chem. Phys. **47**, 4146 (1967).
13. P. S. ALLEN. J. Phys. C: **6**, 3174 (1973).
14. D. E. O'REILLY, E. M. PETERSON, and T. TSANG. Phys. Rev. **160**, 160 (1967).
15. C. I. RATCLIFFE and B. A. DUNELL. J. Chem. Soc. Faraday Trans. 2, **73**, 493 (1977).
16. T. T. ANG and B. A. DUNELL. Can. J. Chem. **52**, 1840 (1974).
17. H. O. PRITCHARD. Chem. Rev. **52**, 529 (1953); W. B. PERSON. J. Chem. Phys. **38**, 109 (1963).
18. T. B. EAMES and B. M. HOFFMAN. J. Am. Chem. Soc. **93**, 3141 (1971).
19. P. H. CLIPPARD, J. C. HANSON, and R. C. TAYLOR. J. Cryst. Mol. Struct. **1**, 363 (1971).
20. T. TUNEYOSHI, N. NAKAMURA, and H. CHIHARA. J. Magn. Reson. **27**, 191 (1977).
21. N. N. GREENWOOD and R. L. MARTIN. Q. Rev. **8**, 1 (1954).
22. M. STAMMLER. J. Inorg. Nucl. Chem. **29**, 2203 (1967).
23. A. W. KHANZADA and C. A. MCDOWELL. J. Magn. Reson. **27**, 483 (1977).

Can. J. Chem. Downloaded from www.nrcresearchpress.com by 112.217.228.212 on 09/07/12
For personal use only.

Photoelectrochemical water splitting by tandem type and heterojunction amorphous silicon electrodes

YUICHI SAKAI, SATOSHI SUGAHARA, MICHIO MATSUMURA, YOSHIHIRO NAKATO, AND HIROSHI TSUBOMURA

Laboratory for Chemical Conversion of Solar Energy and Department of Chemistry, Faculty of Engineering Science, Osaka University, Toyonaka, Osaka 560, Japan

Received January 6, 1988

This paper is dedicated to Professor Charles A. McDowell on the occasion of his 70th birthday

YUICHI SAKAI, SATOSHI SUGAHARA, MICHIO MATSUMURA, YOSHIHIRO NAKATO, and HIROSHI TSUBOMURA. Can. J. Chem. **66**, 1853 (1988).

The tandem type hydrogenated amorphous silicon (a-Si) electrode having an [n–i–p–n–i–p] structure and a similar tandem a-Si electrode having [n–i–p–n–i–p–n] layers deposited on p-type crystalline Si showed cathodic photocurrents accompanied by hydrogen evolution starting at potentials 1.67 and 2.08 V, respectively, more positive than the thermodynamic hydrogen evolution potential in a sulfuric acid solution. These electrodes, when connected to an RuO_2 counterelectrode, caused sustained water splitting without external bias, giving solar-to-chemical conversion efficiencies of 1.98% and 2.93%, respectively, under simulated AM 1, 100 mW cm^{-2} solar radiation. These efficiencies are critically compared with the efficiency of another type of solar photoelectrolysis of water, namely, the electrolysis of water by the electrical output from solid-state solar cells.

YUICHI SAKAI, SATOSHI SUGAHARA, MICHIO MATSUMURA, YOSHIHIRO NAKATO et HIROSHI TSUBOMURA. Can. J. Chem. **66**, 1853 (1988).

L'électrode (a-Si) de silicium amorphe hydrogéné de type tandem possédant une structure [n–i–p–n–i–p] et une électrode similaire tandem a-Si sur laquelle des conches [n–i–p–n–i–p–n] ont été déposés sur du Si cristallin de type-p présentent des photo-conrants cathodiques qui sont accompagnés d'une évolution d'hydrogène à partir de potentiels respectifs de 1,67 et 2,08 V; ces potentiels sont plus positifs que le potentiel thermodynamique d'évolution d'hydrogène dans une solution d'acide sulfurique. Lorsqu'on connecte ces électrodes avec une contre-électrode de RuO_2, il se produit une décomposition continue de l'eau sans influence externe et, lorsqu'on opère dans des conditions simulée de radiation solaire AM 1, 100 mW cm^{-2}, on obtient des efficacités de conversion solaire à chimique de respectivement 1,98 et 2,93%. On compare ces efficacités d'une façon critique a celle obtenue dans un autre type de photo-électrolyse solaire de l'eau, soit lors de l'électrolyse de l'eau par un apport électrique provenant de cellules solaires à l'état solide.

[Traduit par la revue]

Introduction

Semiconductor photoelectrochemical (PEC) cells have been attracting keen interest in relation to their capability to convert solar energy into either electrical or chemical energy. As a photoelectric converter, energy conversion efficiencies as high as those of the solid-state solar cells have been reported (1–4). Solar-to-chemical conversion, which is a unique property of the PEC cells, has also been progressively improved. We reported efficiencies of 10.2% and 10.8% based on the Gibbs free energy change in the solution for the decomposition of hydrogen iodide into hydrogen and iodine with PEC cells equipped with either a platinum (Pt) coated n^+–p junction single crystalline Si electrode having a matt-textured surface (5) or a heterojunction Si electrode having an (n-type amorphous Si/p-type crystalline Si) structure (6).

Water splitting is an important type of photochemical reaction for the solar-to-chemical conversion, having the merit that water is a very abundant material and electric energy can be obtained efficiently by the reverse reaction using the technologically established fuel cells. Many studies have been made on water photolysis using the PEC cells, starting from the well known work of Fujishima and Honda (7), who used n-type titanium dioxide as a photoanode. Some trials followed using strontium titanate (8) and other oxide semiconductors (9). These materials are chemically strong but have a fatal drawback in that their band gaps are too large and they convert only the ultraviolet portion, less than 3% of the total solar energy. Some years ago, we reported (10) that n-type strontium titanate doped with ruthenium or other metal ions absorb a considerable part of visible light and decompose water without the aid of external electrical bias. The quantum efficiency of the photocurrent obtained at wavelengths between 400 and 500 nm is as high as 2%.

We have been investigating the properties of platinized hydrogenated amorphous silicon (a-Si) electrodes used in PEC cells. In our previous paper (11), we studied hydrogen evolution by PEC cells equipped with a-Si electrodes having n–i–p and n–i–p–n–i–p structures (i stands for an intrinsic a-Si layer). The n–i–p electrode caused hydrogen evolution at a potential 0.8 V more positive than the thermodynamic hydrogen evolution potential. This shift was higher than that of a crystalline silicon electrode, though still insufficient for water splitting. The n–i–p–n–i–p electrode caused hydrogen generation at about 1.6 V more positive, and water was decomposed in a PEC cell equipped with this electrode and a Pt counterelectrode with an energy conversion efficiency of about 0.25%. For the purpose of further improving the efficiency of water splitting we investigated tandem type a-Si electrodes having [n–i–p–n–i–p a-Si] and [n–i–p–n–i–p–n a-Si/p-type crystalline Si] structures.

Experimental

Hydrogenated amorphous silicon (a-Si) films were deposited on stainless steel or other substrates by the plasma decomposition of hydrogen-diluted monosilane (10 vol%) in an RF (13.56 MHz), capacitance-coupled glow discharge, with a gas flow rate of 50–60 sccm and a gas pressure of 2 Torr. The substrate temperature was kept at 200–230°C during deposition and the input RF power was 2 W. The p- and n-layers were made using hydrogen-diluted diborane (0.1 vol%) and hydrogen-diluted phosphine (0.05 vol%) as doping gases, respectively. For the deposition of n-layers, the input RF power was raised to 25–30 W so as to make the layer microcrystalline (μc-Si).

Printed in Canada / Imprimé au Canada

Can. J. Chem. Downloaded from www.nrcresearchpress.com by 112.217.228.212 on 09/07/12
For personal use only.

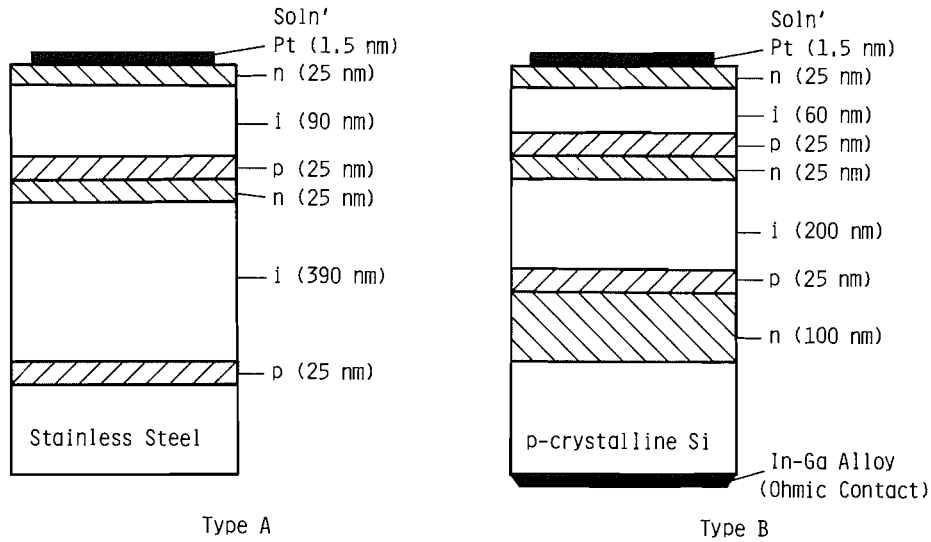

FIG. 1. Structures of a-Si PEC electrodes.

Two types of a-Si electrodes, Types A and B, were fabricated whose structures are shown in Fig. 1. For the Type A electrode, a stainless steel plate which was mirror finished by electrochemical buffing (Hitachi Zosen Corp., 0.5 mm thick), was used as the substrate and a-Si was deposited on it successively as shown in Fig. 1. For the Type B electrode, an n-type μc-Si layer (100 nm) was deposited on a wafer of single crystal p-type Si (denoted as p-c-Si) to make an n–p heterojunction and a-Si layers were deposited on it successively as shown in Fig. 1. The p-c-Si wafers, obtained from Shin-Etsu Handotai Co., Ltd., were cut perpendicular to the ⟨111⟩ axis and had a resistivity of 0.1–0.15 Ω cm. After these electrodes were prepared, their surfaces were coated with a 1.5 nm thick Pt layer by electron-beam evaporation to catalize the hydrogen evolution, then heat-treated at 330°C for 10 min in vacuum. All specimens had an active cell area of 10 to 20 mm^2.

Electrochemical measurements were made by use of a three electrode cell consisting of an a-Si electrode, a Pt counterelectrode and a saturated calomel electrode (SCE). The 0.5 mol dm^{-3} sulfuric acid used as the electrolyte solution was bubbled with high purity nitrogen gas and magnetically stirred during the measurements. A solar simulator (AM 1, 100 mW cm^{-2}) of Wacom Co., Ltd., was used as the light source. Water splitting was performed in a PEC cell consisting of an a-Si electrode directly connected to an RuO_2 counterelectrode. The RuO_2 electrode was prepared by wetting a titanium plate with an aqueous solution of 0.01 mol dm^{-3} $RuCl_3$ and 20% HCl, drying at 90°C for 10 min in an oven, and putting into a preheated furnace at 350°C for 10 min. This procedure was repeated eight times and the plate was heated at 500°C for 1 h in air.

Solid-state photocells were also fabricated. These have a structure similar to Type B except that an ITO (indium tin oxide, 70 nm) layer was deposited on the surface by electron-beam evaporation instead of the Pt layer.

Results and discussion

The hydrogen evolving cathodic current in a Type A electrode under illumination in an aqueous solution of 0.5 mol dm^{-3} sulfuric acid (Fig. 2) starts at +1.43 V vs. SCE, which is 1.67 V more positive than the normal onset potential of hydrogen evolution in a Pt electrode. The i–V curve is given by the dotted line in Fig. 2. Since the open-circuit photovoltage (V_{oc}) of a-Si solar cells having a p–i–n unit is ca. 0.8 V, the observed shift in the potential can be understood as the sum of the photovoltages generated in each of the two p–i–n units. The hatched area in Fig. 2(*A*) gives the maximum electrical energy saved for the reduction of water using this photoelectrode. This area divided by the light intensity is called the bias-assisted energy conversion efficiency (η_1).

The photovoltage of a p–i–n unit, ca. 0.8 V, is an intrinsic property of this unit and no further increase in photovoltage in such a tandem type a-Si photoelectrode is expected. Therefore, an improvement of the electrode performance is expected to be attained only by an effort to increase the photocurrent density, in other words, by minimizing undesirable loss of light intensity in the various layers of the electrode. Firstly, the uppermost Pt layer is indispensable for decreasing the overvoltage of the electrode reaction. The thickness adopted, 1.5 nm, is enough for this purpose and causes minimal light absorption. Secondly, it is desirable to make the p- and n-layers as thin as possible in order to reduce light absorption in these layers, since the charge carriers are produced only in the two i-layers. However, when these layers become too thin, the minority carriers in these layers are completely depleted and the photovoltages in the p–i–n units drop (12, 13). Finally, the thickness of the two i-layers should be controlled so as to make the rates of carrier production in the two layers equal and maintain the continuity of the photocurrents. The thicknesses of the various layers of the Type A cell as given in Fig. 1 have been settled as a result of optimizing all the conditions described above and the best value of the bias-assisted energy conversion efficiency (η_1) obtained was 3.56%.

The i–V curve for the anodic oxidation of water in an RuO_2 electrode is given by the broken lines in Fig. 2, showing the onset of anodic current at +1.15 V vs. SCE in an aqueous solution of 0.5 mol dm^{-3} sulfuric acid. Compared with this, the onset potential for the hydrogen evolution in the Type A electrode is about 0.28 V more positive. This suggests that water splitting can occur by connecting these two electrodes. In fact, a PEC cell consisting of the Type A electrode and an RuO_2 counterelectrode immersed in a 0.5 mol dm^{-3} H_2SO_4 solution and directly connected with each other generated a photocurrent of 1.61 mA cm^{-2} under simulated solar illumination (AM 1, 100 mW cm^{-2}). The conversion efficiency η_2 for water splitting, defined as the product of the photocurrent density and the thermodynamic decomposition potential of water, 1.23 V, divided by the incident light energy, 100 mW cm^{-2}, is calculated to be 1.98% from the current density given above.

The solar-to-chemical conversion efficiency η_2 defined above

Can. J. Chem. Downloaded from www.nrcresearchpress.com by 112.217.228.212 on 09/07/12
For personal use only.

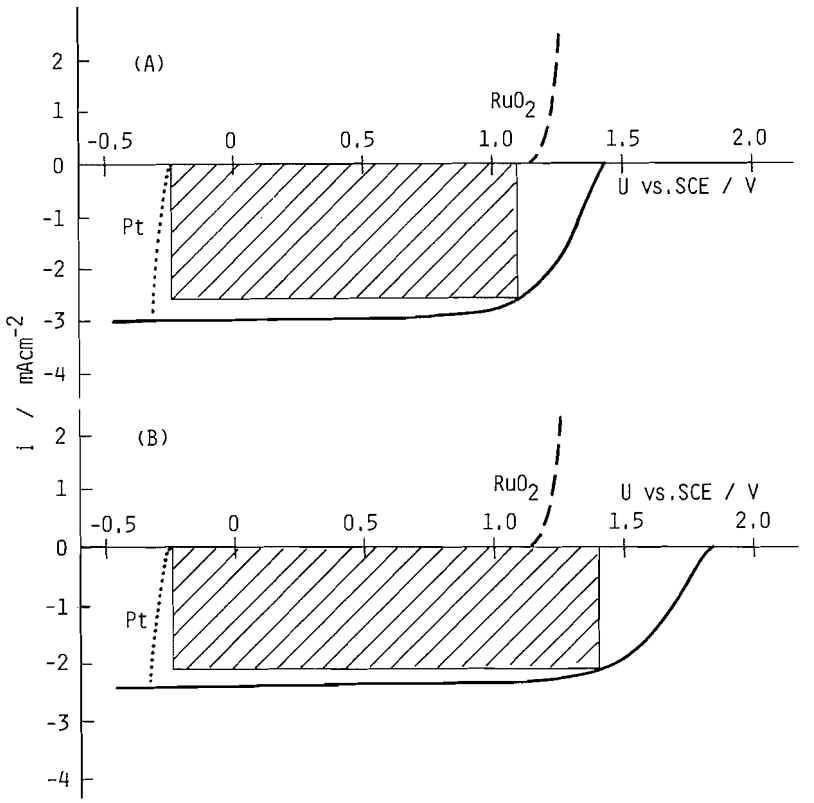

FIG. 2. The i–V curves for a Type A electrode (A) and a Type B electrode (B) in a 0.5 mol dm^{-3} sulfuric acid solution under simulated solar radiation of AM 1, 100 mW cm^{-2} (solid lines), and those in the dark for a RuO_2 and a Pt electrodes. The hatched areas give the electrical energy saved for the water splitting by Type A and Type B electrodes.

corresponds more strictly to the efficiency of converting solar energy into real storable chemical energy. The values of η_2 obtained have been considerably lower than the bias-assisted energy conversion efficiency designated as η_1. This arises mainly from the fact that the onset potential for the photocathodic current in the Type A electrode is barely more positive than the onset potential for the anodic current of the RuO_2 electrode, making the photocurrent weak. In order to raise η_2, therefore, a slight enhancement of the photovoltage is desirable. Although it is expected that the photovoltage will become as high as 2.4 V by stacking the p–i–n unit three times, the triply-stacked cell actually generates only 1.96 V. In such an electrode, an anodic dark current begins to flow at about +1.5 V vs. SCE, increasing as the electrode potential gets more positive, thus lowering the photovoltage output of the electrode. The dark current is thought to arise from the electrochemical reaction between the stainless steel substrate and the electrolyte solution penetrating through the pinholes existing in the a-Si films to the stainless steel surface (11, 14).

We have taken a different approach to the improvement of the photovoltage by constructing an electrode having a Pt/n–i–p–n–i–p–n a-Si/p–c-Si structure which we call Type B (Fig. 1). Since c-Si has a narrow bandgap, 1.1 eV, it absorbs light at wavelengths longer than the light absorbed by the a-Si film deposited on it, thus improving the energy conversion efficiency. In this electrode, anodic dark current was not observed even at a potential of +1.8 V vs. SCE, conceivably because the points on the c-Si surface in contact with the pinholes existing in the a-Si film are passivated by the reaction with the solution. The i–V curves for the Type B cell in an aqueous solution of 0.5 mol dm^{-3} H_2SO_4 are shown in Fig. 2(B). The hydrogen evolving cathodic photocurrent has an onset at +1.84 V vs. SCE, which is 2.08 V more positive than that at a Pt electrode. It is concluded, therefore, that a photovoltage output of 0.4 to 0.5 V arises at the n–a-Si/p–c-Si heterojunction. By connecting this electrode directly with an RuO_2 counterelectrode, a photocurrent of 2.38 mA cm^{-2} was obtained under simulated solar illumination (AM 1, 100 mW cm^{-2}), indicating that water is decomposed at a solar-to-chemical conversion efficiency (η_2) of 2.93%. For bias-assisted water splitting, a 3.47% efficiency (η_1) was obtained from the hatched area of Fig. 2(B). Higher energy conversion efficiencies will be realized by optimizing the thickness of the i-layers included in the Type B electrode.

The photocurrent in a cell having a Type B electrode and an RuO_2 counterelectrode did not decay under AM 1 illumination for 1 h, but it declined to half the initial value after 55 h. This decline is presumably due to the contamination of the Pt electrode surface by chemical impurities existing in the solution because the durability was found to be better the purer the solution used in the PEC cell.

For the purpose of comparison, we investigated the electrolysis of water by use of the electric power generated by the solid-state solar cell having an ITO/n–i–p–n–i–p–n a-Si/p–c-Si structure, prepared under exactly the same condition as the Type B electrode. In the water splitting experiment, the electrical output of the solid-state solar cell (0.15 cm^2) is supplied to a Pt electrode (2 cm^2) and an RuO_2 electrode (2.5 cm^2) immersed in an aqueous solution of 0.5 mol dm^{-3} sulfuric acid. The electrolysis of water by the solid-state solar cell proceeded at a current density of 2.62 mA cm^{-2} under simulated solar illumination (AM 1, 100 mW cm^{-2}) and the

Can. J. Chem. Downloaded from www.nrcresearchpress.com by 112.217.228.212 on 09/07/12
For personal use only.

solar-to-chemical conversion efficiency for water splitting was 3.23%, a little higher than that in the PEC cell having a Type B electrode. The higher photocurrent for the solid-state solar cell arises mainly from the low reflectivity at the surface, the ITO layer acting as an anti-reflection coating. On the other hand, the photovoltage in the PEC cell was a little higher than that of the solid-state solar cell. This is thought to occur by the very small anodic dark current in the PEC electrode at potentials near the photocurrent onset.

Approximately one third of the solid-state photocells prepared by us showed large dark currents due probably to the penetration of the deposited ITO into the pinholes of the a-Si films. The energy conversion efficiencies of such photocells were very low. On the contrary, none of the PEC cells using the multi-layer a-Si electrode prepared in the same apparatus showed leakage currents of a significant order. This result can be explained by the fact that in a PEC cell the electrodes are separated by the electrolyte solution and no current flows between them unless the chemical components of the solution react on the electrodes. For the case of the Type B electrode, the leakage current is also stopped by the passivated c-Si substrate exposed to the solution through the pinholes. These results indicate that the pinholes in a-Si layers are less hazardous when used in a PEC cell than in a solid photocell; an advantage of a PEC cell over the solid-state photocells, especially for large area solar cells.

Recently, Bockris *et al.* (15) reported 8.2% efficiency for water splitting under sun light using an n–GaAs/KOH/p–InP PEC cell. However, an a-Si electrode can be constructed at much lower cost and is thus expected to be more advantageous.

1. B. A. PARKINSON, A. HELLER, and B. MILLER. J. Electrochem. Soc. **126**, 954 (1979).
2. J. F. GIBBONS, G. W. COGAN, C. M. GRONET, and N. S. LEWIS. Appl. Phys. Lett. **45**, 1095 (1984).
3. R. TENNE and A. WOLD. Appl. Phys. Lett. **47**, 707 (1985).
4. J. REICHMAN, B. R. THACKER, and J. M. OLSON. Nature, **316**, 51 (1985).
5. K. UEDA, Y. NAKATO, and H. TSUBOMURA. Sol. Energy Mater. **17**, 37 (1988).
6. K. UEDA, Y. NAKATO, H. SAKAMOTO, Y. SAKAI, M. MATSUMURA, and H. TSUBOMURA. Chem. Lett. 747 (1987).
7. A. FUJISHIMA and K. HONDA. Nature, **238**, 37 (1972).
8. M. S. WRIGHTON, A. B. ELLIS, P. T. WOLCZANSKI, D. L. MORSE, H. B. ABRAHAMSON, and D. S. GINLEY. J. Am. Chem. Soc. **98**, 2774 (1976).
9. H. P. MARUSKA and A. K. GHOSH. Sol. Energy, **20**, 443 (1978).
10. M. MATSUMURA, M. HIRAMOTO, and H. TSUBOMURA. J. Electrochem. Soc. **130**, 326 (1983).
11. M. MATSUMURA, Y. SAKAI, S. SUGAHARA, Y. NAKATO, and H. TSUBOMURA. Sol. Energy Mater. **13**, 57 (1986).
12. Y. KUWANO, T. FUKATSU, T. IMAI, M. OHNISHI, H. NISHIWAKI, and S. TSUDA. Jpn. J. Appl. Phys. **20**, Suppl. **20**-2, 163 (1982).
13. Y. SAKAI, M. MATSUMURA, Y. NAKATO, and H. TSUBOMURA. J. Appl. Phys. **62**, 3424 (1987).
14. Y. SAKAI, S. YAE, M. MATSUMURA, Y. NAKATO, and H. TSUBOMURA. Sol. Energy Mater. **17**, 89 (1988).
15. R. C. KAINTHLA, B. ZELENAY, and J. O'M. BOCKRIS. J. Electrochem. Soc. **134**, 841 (1987).

Can. J. Chem. Downloaded from www.nrcresearchpress.com by 112.217.228.212 on 09/07/12
For personal use only.

Spatial intensity distributions of vacuum ultraviolet photon beams measured by thermoluminescent image films

NOBUYUKI KIKUKAWA[1] AND TSUTOMU MAKITA[2]

Department of Chemistry, Faculty of Science, Kyoto University, Kyoto, 606 Japan

Received January 5, 1988

This paper is dedicated to Professor Charles A. McDowell on the occasion of his 70th birthday

NOBUYUKI KIKUKAWA and TSUTOMU MAKITA. Can. J. Chem. **66**, 1857 (1988).

The thermoluminescent phosphor, calcium sulfate activated by manganese, was found to be a suitable material for imaging films to record the spatial distributions and reflections of vacuum ultraviolet (vuv) photon beams used for high-resolution photoelectron spectrometers. He I 584 Å photons radiated in a microwave discharge tube were collimated through capillary tubes, and the phosphor films were placed at the position of the photoionization chamber. When the irradiated phosphor films were heated up to 200°C in a darkroom, faint green glow images were observable on the phosphor films and these images were recorded by photographic films. When the films were placed 118 mm from the exit of the collimating capillary tube, the photon beam images were almost circular, about 4.5 mm in diameter. The photon distribution in the collimated beam was interpreted with the aid of computer simulation. The experimental results revealed that the reflections of vuv photons at planes of various kinds were almost specular if the surface was clean and smooth and the glancing angles were small.

NOBUYUKI KIKUKAWA et TSUTOMU MAKITA. Can. J. Chem. **66**, 1857 (1988).

On a trouvé que le sulfate de calcium activé par le manganèse, un produit phosphorescent et thermoluminescent, est un produit utile pour faire des films desquels on peut tirer des images permettant d'enregistrer les distributions spatiales et les réflexions des faisceaux de photons ultraviolet sous vide (uvv) qui sont utilisés dans les spectromètres photoélectroniques à haute résolution. On a dirigé les photons du He I 584 Å qui proviennent d'une radiation dans un tube à décharge à micro-ondes vers des tubes capillaires servant de collimateur et on a placé les films phosphorescents à la place de la chambre à photoionisation. Lorsque les films phosphorescents irradiés ont été chauffés à 200°C, dans un chambre noire, on a pu observer de faibles lueurs d'images vertes que l'on a enregistré images sur des films photographiques. Lorsqu'on place les films à 118 mm de la sortie du tube capillaire agissant comme collimateur, les images du faisceau de photons sont pratiquement circulaires, avec un diamètre d'environ 4,5 mm. On a interprété la distribution des photons dans le faisceau qui a passé au collimateur en faisant appel à une simulation par ordinateur. Les résultats expérimentaux suggèrent que les réflexions des photons (uvv) sur divers types de plans sont pratiquement spéculaires si la surface est lisse et propre et que les angles de percement sont faibles.

[Traduit par la revue]

Can. J. Chem. Downloaded from www.nrcresearchpress.com by 112.217.228.212 on 09/07/12
For personal use only.

Introduction

Vacuum ultraviolet (vuv) radiation is indispensable for photoionization studies and photoelectron spectroscopy. For instance, high energy photons, He I 584 Å, are radiated conveniently by the microwave discharge of low pressure helium gas flowing in a source tube (1). The radiation is collimated through capillary tubes between the discharge tube and the ionization chamber, which contains target molecules. The capillary tubes are necessary to maintain the pressure differential of helium gas between the discharge tube and the ionization chamber. Furthermore, for the He I 584 Å radiation, no material can be used as an efficient window between them.

The size and the intensity distribution of collimated vuv photon beams are one of the fundamental design factors for the ionization chamber of high-resolution photoelectron spectrometers (2). Schumann-type plates are not feasible for imaging, because of their sensitivity to visible radiation from the discharge tube.

Lyman (3) reported that a thermoluminescent phosphor was sensitive to photon beams of wavelengths from 1300 to 140 Å. The phosphor was mainly calcium sulfate containing a few percent of manganese sulfate. Lyman found that atmospheric air was almost transparent to radiation of 1300–1100 Å, but that it absorbed radiation of 2000–1300 Å and of wavelengths shorter than 1100 Å. Watanabe investigated the properties of the manganese-activated $CaSO_4$ phosphor in detail (4) in connection with its use as a detector of extreme ultraviolet radiation. These thermoluminescent plates were flown in rockets, exposed to the sunlight at an altitude level between 82 and 128 km, and recovered for dosimetry (5).

Image plates made of thermoluminescent phosphor are convenient devices to record the dimensions and intensity distributions of vuv photon beams, for instance, He I 584 Å. Because the plates are not sensitive to light of wavelength longer than 1340 Å, they can be handled under room light. The faint green glow images of the thermoluminescent plates have to be detected in the darkroom. This paper reports on the spatial distributions and reflections of He I 584 Å photon beams for a high-resolution photoelectron spectrometer.

Experimental

Figure 1 is the schematic diagram of a He I 584 Å light source assembly combined with the thermoluminescent image film on copper plate, helium gas flow regulation system, and microwave power supply. Figure 2 is a detailed diagram of the light source to show the quartz discharge tube, capillary tubes I and II of Pyrex glass, and the differential pumping. Helium gas was introduced from a cylinder through pressure-reducing valves and a needle valve. The microwave generator was type MR-1S of Ito Electro-Medical and Chemical Instruments Mfg. Co., Tokyo (2450 MHz and 200 watts maximum). The cooking electronic range was, with some modifications, suitable for the microwave generator. The microwave cavity at the discharge tube was a cavity of type 5 as described by Fehsenfeld, Evenson, and Broida (7). The photon beam was mainly He I 584 Å, with weak contaminations such as H I Ly α 1216 Å. The intensity of 1216 Å photons was found to be reduced remarkably when the helium gas was

[1]Present address, National Research Institute for Pollution and Resources, Tsukuba, Ibaraki, 305 Japan.

[2]Present address, Notre Dame Women's College, Chemistry Institute, Kyoto, 606 Japan.

Can. J. Chem. Downloaded from www.nrcresearchpress.com by 112.217.228.212 on 09/07/12
For personal use only.

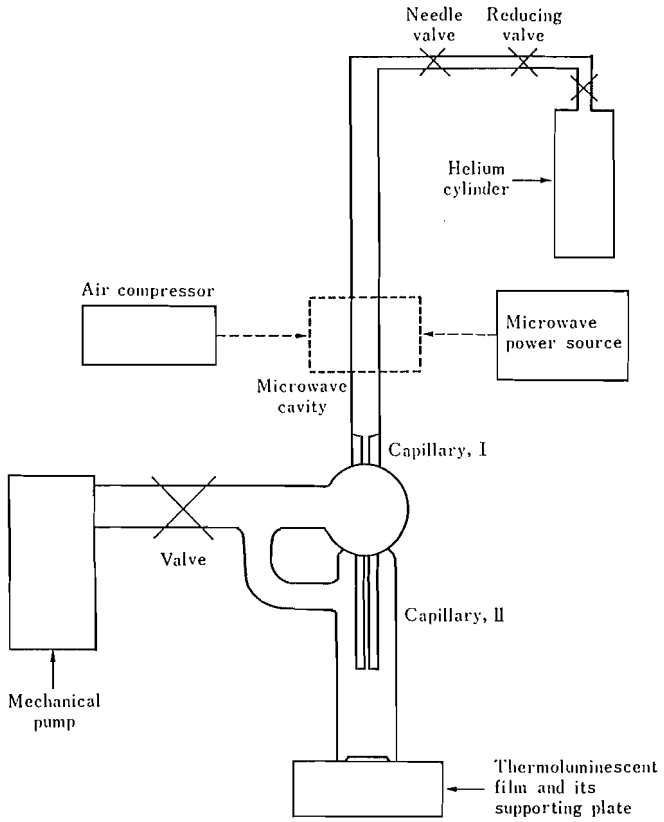

FIG. 1. Schematic diagram of vacuum ultraviolet light source assembly with thermoluminescent imaging film and helium gas flow system.

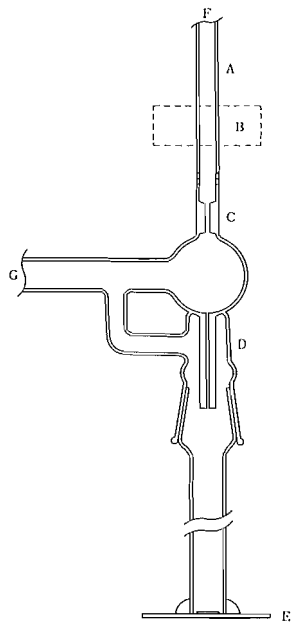

FIG. 2. Detailed diagram of the light source. A; Quartz tube, 8 mm i.d. B; Microwave cavity, Fehsenfeld–Evenson–Broida type (7). C; Capillary I, 1.0 mm i.d., 10 mm length, Pyrex glass. D; Capillary II, 0.5 mm i.d., 35 mm length. E; Thermoluminescent imaging film on copper plate, 20 × 50 × 1 mm. Distance between E and the end of D is 118 mm. F; From helium cylinder, through pressure reducing valves, a needle valve, and U-shaped copper tube cooled in liquid nitrogen. G; To mechanical pump.

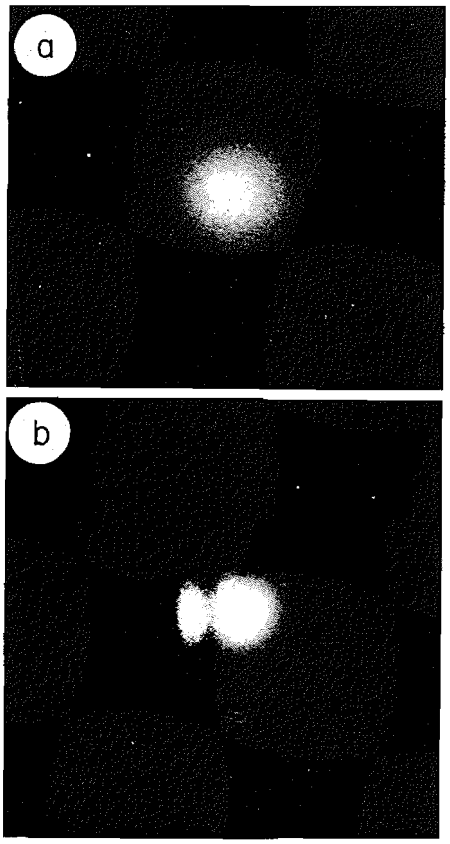

FIG. 3. Photographic picture of glowing images. (a) Image of collimated photon beam falling directly on the phosphor film. (b) Images of split photon beam on the identical phosphor film, see Fig. 8.

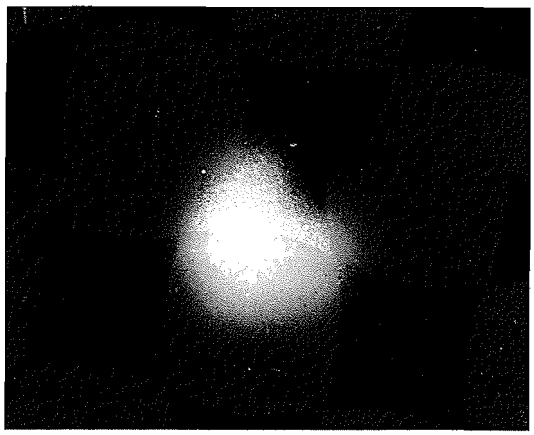

FIG. 4. Picture recorded on photographic film in contact with glowing phosphor film, without photographic lens. To give reference exposures on identical phosphor film, each quarter of the circular film was irradiated with a broad flux of photons for different time intervals (see text).

supplied through a U-shaped copper tube, which was cooled in liquid nitrogen.

Three different procedures to make the phosphor were tried, as described by the reports of Lyman (3), Watanabe (4), and Novotný *et al.* (6). These three kinds of the phosphor were exposed to He I 584 Å photon beams under similar conditions. The intensities of thermoluminescent green glow images were compared visually in a darkroom;

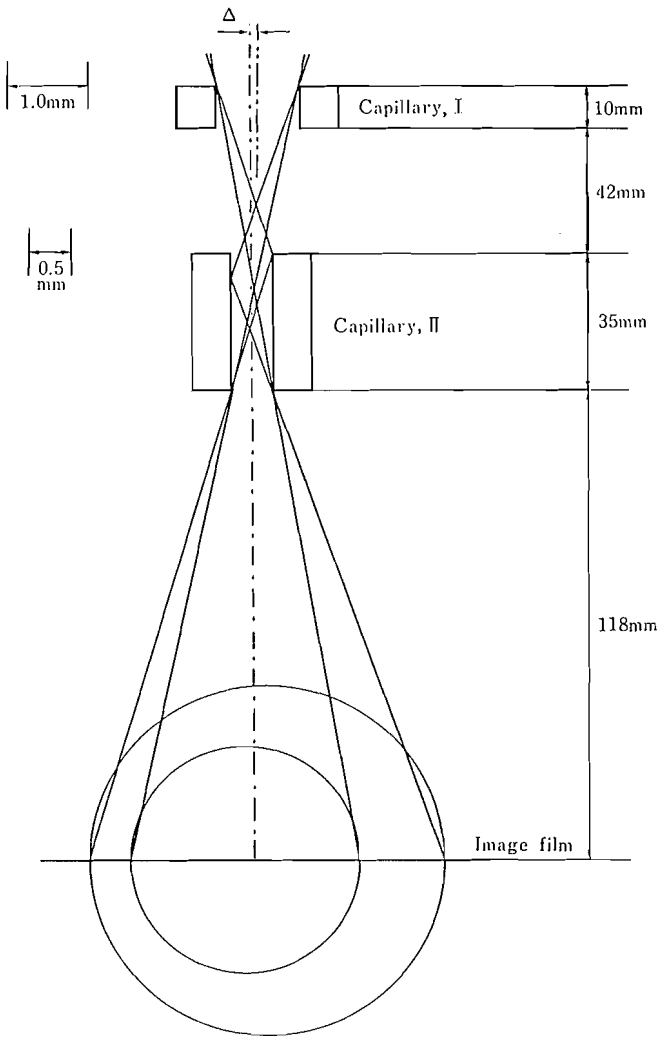

FIG. 5. Schematic diagram of the spatial distribution of a collimated photon beam. The horizontal scale is expanded 20-fold compared to the vertical scale. Axes of capillary I and II are assumed to be parallel but slightly shifted. The two circles on the imaging film correspond to the limits of the photon trajectories; (a), no reflection and (b) single reflection in capillary II.

the phosphor made following Watanabe (4) was found to be the brightest, and was used throughout with slight modifications as follows. Approximately 8.8 g of $CaSO_4 \cdot 2H_2O$ was mixed with 0.12 g of $MnSO_4$ in 60 mL of concentrated sulfuric acid and a small amount of water. The slurry was left at room temperature for 72 h. Most of the liquid part was then removed by decantation. The excess sulfuric acid was vaporized at 250°C, and the residual mixture was heated to red heat in a porcelain crucible for 90 min. After cooling, the mixture was ground to fine powder, and was suspended in a dilute benzene solution of Dow Corning high vacuum silicone grease. One drop of the suspension was sufficient to make a thin film of 10 mm diameter on a copper plate, 20 × 50 × 1 mm. Such imaging films were strong enough for repetitive exposures to intense vuv photon beams and heatings up to 200°C for thermoluminescence.

The imaging film on a copper plate that had been exposed to the photon beam was heated by a tape heater in the darkroom, and the thermoluminescent glowing image was photographed using Polaroid type 107 film in a model 180 camera. Close-up lenses, Cannon 240 and 450, were attached to the camera. Figure 3*a* is an example of the glow image. It was possible to record the glowing images on a Kodak Tri-X film directly without photographic lens. The Tri-X films were sandwiched between thin glass plates, and were placed on the glowing

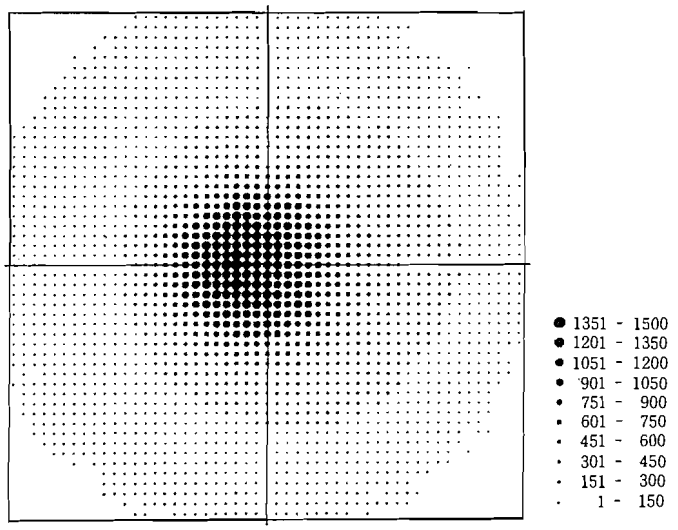

FIG. 6. Number of photons arriving at each 0.1 × 0.1 mm meshed area on phosphor film, computer simulation for 500 000 photons. Symbols (right) correspond to the intensities listed.

film and exposed for less than 3 s. Figure 4 is an example of Tri-X film images. High temperatures from the tape heater had no effect on the Tri-X film.

When the collimated photon beam was directed around the edge of a plane surface, some of the photons can proceed directly to the phosphor film, while the remainder reflect on the surface and may proceed to another position on the same film. Figure 5 is a schematic diagram to show the trajectories of photons to the phosphor film and the positions of the points of arrival at the film for the split photon beams. Figure 3*b* is an example of the split images on the same phosphor film. The relative intensities of the split beams can be determined by comparing the glowing intensities of the two images. The relative attenuation factors for photon beams reflected on the surface were determined as a function of the incident angles, assuming that the incident angle and reflection angle were equal.

Results and discussion

The slurry of fine powder of the phosphor was painted on a copper plate to make the thermoluminescent film, 10 mm diameter, about 10 mg/cm^2 in thickness. The films were stable in the atmosphere for many months. They were irradiated by He I 584 Å photons for up to 160 min. The output power of the microwave generator was usually 50 watts. The copper plate was dismounted from the light source and transferred to a darkroom within 5 min of irradiation to inspect the thermoluminescent image. Before heating the film, it was necessary to wait for 10 min for vision to adjust in the darkroom. The temperature of the film was then increased to 200°C in 15 min. The faint thermoluminescent glow image was observable for the first 5-min period and then faded out. When the irradiated films were exposed under room light for 2 min, there was no appreciable effect on the subsequent intensity of the glow image. When the films were left under room light for 90 h, the glow intensity decreased to one sixth of that of the control films kept in the darkroom. Spatial distribution of the collimated vuv photon beam was determined by measuring the size of the thermoluminescent image of the phosphor film. Figure 3*a* is an example of the images. This shows that the He I 584 Å photon beams are collimated within a 4.5 mm diameter, 118 mm from the exit of capillary II. The ionization chambers for photoionization studies were customarily placed ca. 100 mm from

Can. J. Chem. Downloaded from www.nrcresearchpress.com by 112.217.228.212 on 09/07/12
For personal use only.

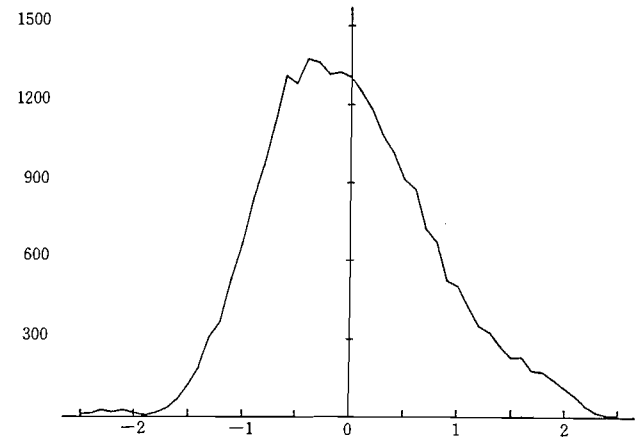

FIG. 7. Intensity distribution profile of photons along the horizontal central meshes in Fig. 6.

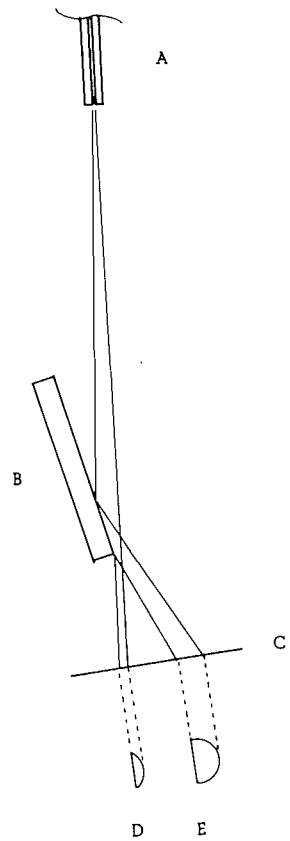

FIG. 8. Schematic geometry for split photon beam images. A, Capillary II. B, Reflecting plate. C, Phosphor film. D, Image of direct beam. E, Image of reflected beam.

the light sources. The divergence of the collimated photon beam was estimated to be 2.2° or 9×10^{-4} steradians. The resolution of the image film was better than 0.1 mm.

Close examination of the 4.5-mm circular image of Fig. 3*a* revealed that the image consisted of two overlapping but not concentric circles, one bright inside and one faint outside. The intensity of the inner bright circle was about three times that of the faint one. Figure 5 is a schematic diagram of the spatial distribution of a collimated photon beam. It is suggested that the two circles, as well as the separation of their centers, resulted from reflections of the photons on the inside surfaces of the capillaries when the central axes of the capillaries were made parallel but their centres were shifted slightly, indicated as Δ in Fig. 5. The ratio of the diameters of the two circles in these theoretical considerations is similar to the experimentally determined ratio (Fig. 3*a*). Reflections of photons at the inside wall of capillary II were assumed to be specular. The slight shift of the two centers of the circles could be explained schematically via a corresponding shift of the two capillaries.

TABLE 1. Results on the estimated intensity attenuation factors of a He I 584 Å photon beam due to specular reflections at various conditions of the reflecting plates

Material of the plate	Surface conditioning	Glancing angle (°)	Intensity ratio, reflected/impinging
Glass	Cleaned, in ethanol	7	1
Glass	Cleaned	10	1
Glass	Cleaned	15	0.5
Glass	Covered with thin layer of silicone oil	10	0.7
LiF crystal	Cleaned	17	0.7
LiF crystal	Cleaned	45	0.3*
LiF crystal	Cleaned	65	0.2*
LiF crystal	Covered with colloidal graphite	17	0.0
Copper	Sandpapered	12	<0.2
Copper	Amalgamated	10	0.5

*Split beams were detected by two different films.

A preliminary computer simulation study was carried out using a Toshiba ACOS 600 S on the trajectories of the collimating photons through the collimating system. Figures 6 and 7 are examples of the results for 500 000 photons. It was assumed that, (*i*) each photon started at a random point on the circular plane at the entrance to capillary I, (*ii*) the starting direction of the photon is also random, and (*iii*) some photons can emerge from the exit circular plane of capillary II without reflection, some after a single specular reflection, and some after two specular reflections. The numbers of photons arriving at each 0.1×0.1 mm meshed area on the plane of the film are shown as various kinds of dots in Fig. 6. Figure 7 is the intensity distribution profile along the horizontal central line in Fig. 6.[3]

The collimated vuv photon beam source for high-resolution photoelectron spectrometers (2) was designed on the assumption that all reflections of photons at the inside surface of capillary tubes were specular without intensity attenuation when the glancing angles were small. The following considerations refer to this assumption.

Figure 3*b* is an example of split photon beam images, one transmitted directly to a phosphor film, and the other reflected from near the edge of a plate to the same phosphor film. The geometry used is described in Fig. 8.

The relative intensities of the photon beams were estimated by comparing with the glow images of the reference beams, as described below. Figure 4 is an example of the glow image. The phosphor film of Fig. 4 was circular, about 10 mm diameter, and one half part of the circle was covered with a thin plate of lithium fluoride while the film was irradiated by a large-diameter flux of

[3]Tables of supplementary material may be purchased from the Depository of Unpublished Data, CISTI, National Research Council of Canada, Ottawa, Ont., Canada K1A 0S2.

Can. J. Chem. Downloaded from www.nrcresearchpress.com by 112.217.228.212 on 09/07/12
For personal use only.

He I 584 Å photons for 5 min. Then, a different half part of the circle, which was displaced by 90° from the previously irradiated half of the film, was covered with the LiF plate and irradiation continued for 10 min. Each quarter of the circular phosphor film was thus irradiated at different time intervals by this procedure, the relative exposures being 0, 5, 10, and 15 min in this case. It was realized that visual observation was more accurate than photographic recording, to estimate the relative size and intensities of the faint glow images of the phosphor film. Therefore, photographic records (Figs. 3*a*, 3*b*, and 4) are given only for illustration. Table 1 is a summary of the experimental results on the intensity ratio of the specularily reflected photon beam to the impinging photon beam upon various kinds of plate, as investigated via the arrangement of Fig. 8 and the above calibration procedure. It is thereby well established that vuv photon reflections are mainly specular at clean and smooth planes if the glancing angles are less than 10°.

Acknowledgements

This work was supported in part by a Grant-in-Aid from the Ministry of Education, Science and Culture, Japan. One of the authors (T.M.) is very grateful to Professor C. A. McDowell and Professor D. C. Frost, University of British Columbia, for their encouragement during this research. The authors are indebted to Dr. N. Itada, Kyoto National Hospital, for helpful discussions.

1. M. I. Al-Joboury and D. W. Turner. J. Chem. Soc. 5141 (1963).
2. G. R. Branton, D. C. Frost, T. Makita, C. A. McDowell, and I. A. Stenhous. J. Chem. Phys. **52**, 802 (1970).
3. T. Lyman. Phys. Rev. **48**, 149 (1935).
4. K. Watanabe. Phys. Rev. **83**, 785 (1951).
5. R. Tousey, K. Watanabe, and J. D. Purcell. Phys. Rev. **83**, 792 (1951).
6. J. Novotoneý, Z. Spurný, and M. Binová. J. Phys. Chem. Solids, **31**, 1412 (1970).
7. F. C. Fehsenfeld, K. M. Evenson, and H. P. Broida. Rev. Sci. Instrum. **36**, 294 (1965).

Can. J. Chem. Downloaded from www.nrcresearchpress.com by 112.217.228.212 on 09/07/12
For personal use only.

^1H and ^{14}N ENDOR spectra of *tert*-butylphenylnitroxide

JUN YAMAUCHI AND YASUO DEGUCHI

College of Liberal Arts and Sciences, Kyoto University, Kyoto 606, Japan

Received December 23, 1987

This paper is dedicated to Professor Charles A. McDowell on the occasion of his seventieth birthday

JUN YAMAUCHI and YASUO DEGUCHI. Can. J. Chem. **66**, 1862 (1988).

^1H and ^{14}N ENDOR spectra of *tert*-butylphenylnitroxide were observed in ethylbenzene solution. The experimental conditions for detecting optimum ^1H and ^{14}N ENDOR lines were quite different. The ^1H hyperfine coupling constants and their signs are discussed from the viewpoints of molecular orbital calculations, general triple resonance, CRISP (cross relaxation intensity sequence pattern) method, and steric hindrance. In view of the large anisotropic hyperfine interaction between the nitrogen and the unpaired electron, detection of ^{14}N ENDOR in nitroxide radicals is rather difficult, so that a TM_{110} mode cavity was utilized in this experiment. The observed ^{14}N hyperfine coupling constant 11.86 G at −80°C is one of the smallest values observed to date for nitroxide radicals.

JUN YAMAUCHI et YASUO DEGUCHI. Can. J. Chem. **66**, 1862 (1988).

Opérant en solution dans l'éthylbenzène, on a déterminé les spectres ENDOR ^1H et ^{14}N du nitroxyde de *tert*-butyle et de phényle. Les conditions expérimentales permettant des détections optimales des raies ENDOR du ^1H et du ^{14}N sont très différentes. On discute des constantes et des signes du couplage hyperfin du ^1H à l'aide de calculs d'orbitales moléculaires, de la résonance générale triple, de la méthode CRISP (patron de la séquence des intensités de la relaxation croisée) et de l'empêchement stérique. A cause de l'interaction anisotropique hyperfine importante qui existe entre l'azote et l'électron qui n'est pas apparié, la détection des spectres ENDOR du ^{14}N, dans les radicaux nitroxydes, est plutôt difficile; pour cette expérience, on a donc utilisé un mode de cavité TM_{110}. La constante de couplage hyperfin observé pour le ^{14}N, à −80°C, est égale à 11,86 G et elle est l'une des plus faibles valeurs observées à date pour des radicaux nitroxydes.

[Traduit par la revue]

Introduction

Electron nuclear double resonance (ENDOR) is the most useful technique for establishing detailed proton hyperfine coupling constants in complicated electron spin resonance (ESR) spectra (1). The specific relaxation of protons in the ENDOR spectroscopy has been investigated extensively and their ENDOR spectra are well understood on the basis of Freed's theory (2). To obtain more information on the molecular structures of free radicals, the ENDOR method has been extended to nuclei other than protons.

Nitrogen nuclei, for example, sometimes participate in electronic π-system and have large unpaired electron distributions. In addition, the nitrogen nuclei have a quadrupole moment, the parameters of which are sometimes sensitive to the charge distribution on the nitrogen atoms. On the other hand, protons are further away from the electronic π-system, giving indirect information about the π-system. Thus, both ^1H and ^{14}N data are desirable for the discussion of the molecular structures and magnetic properties of radicals.

There are, however, several experimental problems in detecting ENDOR signals of the nuclei other than protons (3). The major difficulty compared to the detection of proton signals is a decreased ENDOR enhancement in such systems, resulting in quite different experimental conditions for optimum ENDOR observations.

ENDOR work on ^{14}N began with the first observation of its signal by Leniart *et al.* in 1970 (4). Since then a number of studies have been published on many kinds of nitroxides or other nitrogen-containing radicals, including a few anion radicals. Recently Janzen *et al.* have reported a conformational study of alkyl and aryl spin adducts using α-phenyl-*N*-*tert*-butylnitrone (PBN), which produces stable nitroxide radicals. They have reviewed work on the various types of nitroxide radicals as studied by ENDOR (5).

In this paper we present ^1H and ^{14}N spectra of *tert*-butylphenylnitroxide (BPNO), which is similar to the spin adducts of PBN. The ENDOR spectra of BPNO were first observed by Ishizu *et al.* (6). The hyperfine coupling constants due to the protons were compared between ESR and ENDOR, and some experimental conditions for optimum ENDOR observations were discussed. However, ^{14}N ENDOR signals could not be detected in their study.

In our experiment, a TM_{110} mode cavity was used, instead of the TE_{011} mode used in the previous work. Möbius *et al.* have developed the TM_{110} mode cavity for an easy access to a triple resonance spectroscopy. Its structure and several advantages were described elsewhere (2). The TM_{110} mode cavity allows one to apply a higher radiofrequency power than the TE_{011} mode one. This advantage was fully utilized for ^{14}N ENDOR observations of di-*tert*-butylnitroxide (DBNO) (7) and for ^1H ENDOR study of some cation radicals (8).

We could observe ^{14}N ENDOR of BPNO among the ^1H lines at the temperature between −20 and −80°C. The observed ^{14}N hyperfine coupling constant A_N = 11.86 G (1 G = 10^{-4} T) at −80°C is among the smaller values found for nitroxide radicals studied to date.

Experimental

Sample

tert-Butylphenylnitroxide was synthesized as follows. Nitrosobenzene and *tert*-butylmagnesium chloride were reacted through the Grignard reaction. *tert*-Butylphenylhydroxylamine thus obtained was oxidized by silver oxide *in vacuo*. Similar preparative methods have been reported elsewhere (9).

ENDOR measurement

The ENDOR spectrometer has been described in detail elsewhere (10). Ethylbenzene was used as solvent and the temperature was varied between −10 and −100°C. Other typical experimental conditions were as follows: microwave power, 70–90 mW, radiofrequency power, 150 W.

General triple resonance (GTR) measurement

In addition to the ENDOR apparatus described in the literature (10), a signal generator (National VP-8179B10) for pumping radiofrequency

Can. J. Chem. Downloaded from www.nrcresearchpress.com by 112.217.228.212 on 09/07/12
For personal use only.

TABLE 1. Hyperfine coupling constants of *tert*-butylphenylnitroxide in Gauss

	$A_{H(para)}$	$A_{H(ortho)}$	$A_{H(meta)}$	$A_{H(t\text{-}Bu)}$	A_N	Conditions	Reference
ENDOR	−2.132	−2.132	0.860	−0.10	11.950	−70°C ethylbenzene	This work
ENDOR	2.29	2.29	0.94	0.092*	—	−100°C toluene *Ethyl alcohol	6
ESR	2.09	2.09	0.89	—	12.08	−100°C toluene	6
MO	−2.337	−2.673	1.286	—	10.996	Twisted angle 0°	This work
MO	−1.704	−2.015	1.048	—	11.630	Twisted angle 30°	This work

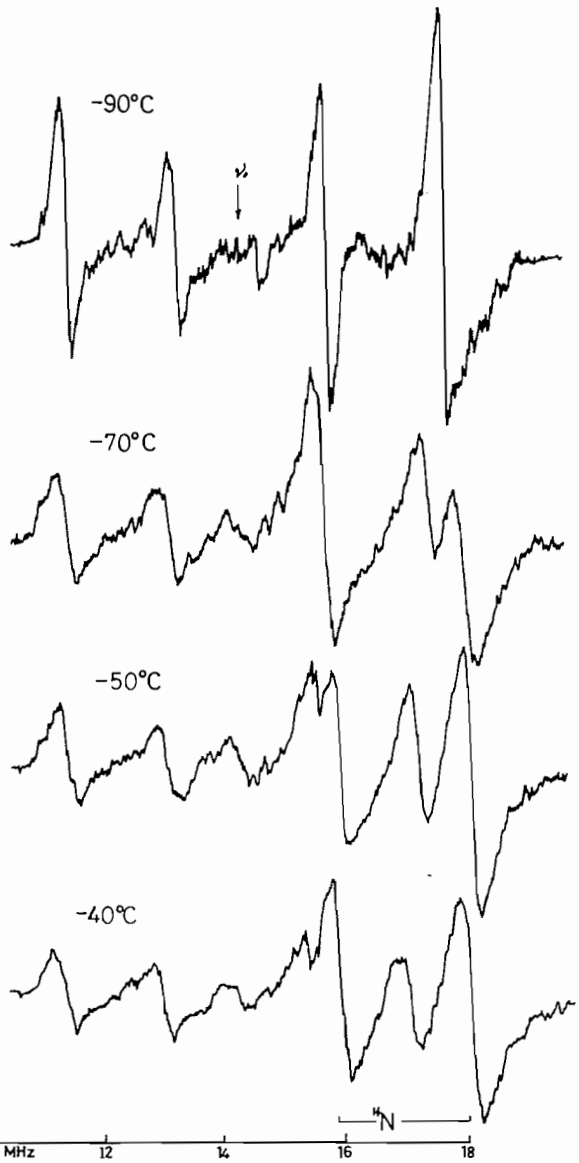

FIG. 1. Temperature-dependent ENDOR spectra of *tert*-butylphenylnitroxide. ν_0 indicates the free proton frequency.

and a power splitter/combiner (Mini Circuit PSC-2-1) for signal mixer were used to determine the signs of the hyperfine coupling constants (11).

Results

The ^1H absorptions were easily observed at the lowest temperature. Even in the higher temperature regions, the ^1H signals were not difficult to detect. ^{14}N lines, however, were sometimes not present and the ENDOR lines of the *tert*-butyl protons appeared as a weaker single line centered at the free proton frequency. ^1H absorptions are essentially similar to those observed by Ishizu *et al.* (6).

The temperature dependence of the ^1H and ^{14}N ENDOR spectra is shown in Fig. 1, indicating overlapped ^1H and ^{14}N signals. At the lowest temperature (−90°C) in Fig. 1, ^{14}N signals can not be identified, but the absorption line of ^1H at the highest frequency is rather broad. On increasing the temperature, a pair of the ^{14}N lines with $2\nu_n$ separation started to appear and grew in intensity in contrast to the decreasing ^1H signals.

The analyzed coupling constants are summarized in Table 1, where the results of molecular orbital (MO) calculations (McLachlan's method) are also listed for comparison. The same MO parameters as in the previous papers (10, 12) were employed. The theoretical hyperfine coupling constants were calculated with the aid of the McConnell relation between the spin density and hyperfine coupling constant, where a proportionality constant of $|Q| = 27.3$ G was used (10).

Discussion

^1H hyperfine coupling constants

According to the MO calculation, the spin density at the *meta*-position is less than half as compared to the *para*- or *ortho*-positions. Therefore, the larger ^1H hyperfine coupling constant is assigned to the *para*- and *ortho*-protons on the phenyl ring. Thus, the agreement between experiment and theory is excellent, although a certain amount of non-planarity was assumed in the MO calculations as discussed later.

It is also predicted by McLachlan's method that the *meta*-position has a negative spin density. This was ascertained by the GTR measurement. Figures 2(*b*) and 2(*c*) show the GTR spectra at −90°C obtained when the ^1H lines were pumped at *b* and *c* depicted in Fig. 2(*a*), respectively. In Fig. 2(*b*) the low frequency absorption of the outer pair lines is enhanced by the pumping, whereas the high frequency absorption of the inner pair lines is increased. On the other hand, the situation is completely reversed in Fig. 2(*c*). These facts imply opposite signs between the protons assigned to the outer and inner pair lines. If one assumes the positive spin density at the *para*- and *ortho*-positions as is predicted by McLachlan's method, a negative sign for the spin density at the *meta*-position can be deduced. Such a negative spin density in nitroxide radicals was first demonstrated for diphenylnitroxide (DPNO) by GTR spectroscopy (11). The positive and negative signs on the two phenyl rings of DPNO are the same as those on the phenyl ring of BPNO.

The relative signs of the hyperfine coupling constants can also be determined by comparing the relative intensity changes within each of the nitrogen and proton doublets as different branches of the nitrogen triplet are saturated. This method is called CRISP (cross relaxation intensity sequence pattern) (5).

Can. J. Chem. Downloaded from www.nrcresearchpress.com by 112.217.228.212 on 09/07/12
For personal use only.

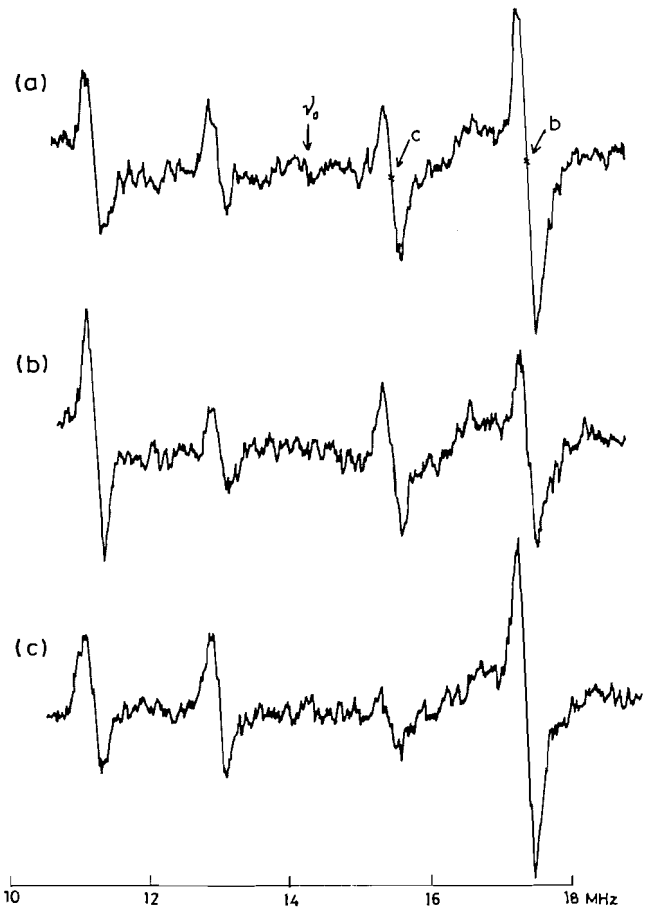

FIG. 2. GTR spectra of *tert*-butylphenylnitroxide at −90°C. The pumping radiofrequency was applied at either *b* or *c*, which is depicted in Fig. 2(*a*).

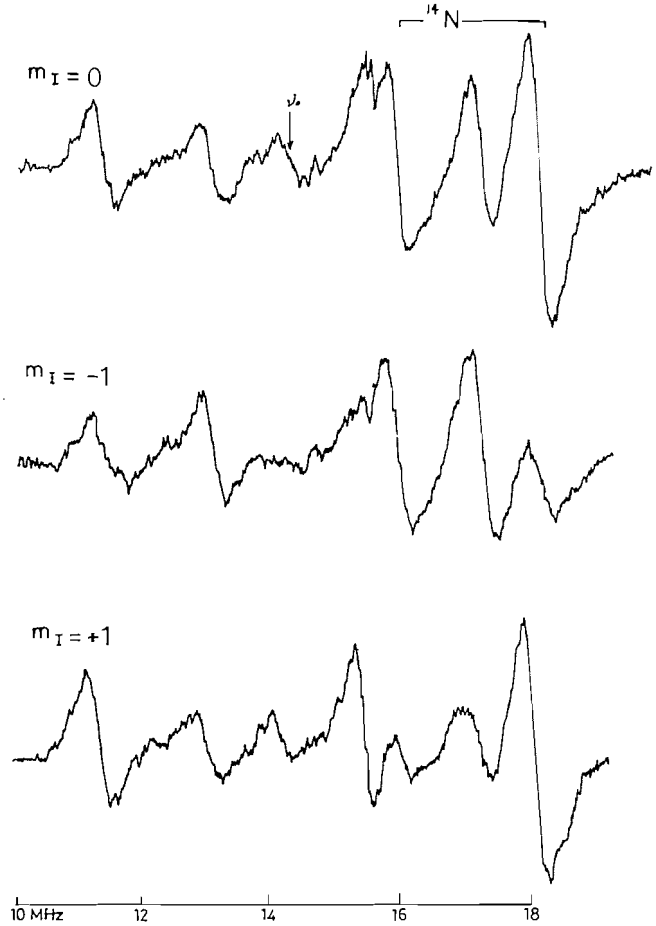

FIG. 3. ENDOR spectral changes by monitoring the ESR of the nitrogen triplet hyperfine lines, $m_I = 0$, $m_I = -1$, and $m_I = +1$. ν_0 indicates the free proton frequency.

Some examples were reported for aminoxyl spin adducts (13) and DBNO (14). From this method the same relative signs as those determined by the GTR measurement are found as shown in Fig. 3. Since those spectra were taken under the optimum conditions for the ^{14}N observation, the ^{1}H signal intensities are rather weak. Nevertheless, these intensity changes are clear. When one compares the intensity changes between $m_I = 0$ and $m_I = -1$ in the two absorption lines of each of the two ^{1}H pairs at the low frequency side, the outer peak decreases, while the inner one increases in the $m_I = 1$ spectrum. These changes actually occur in opposite directions on the ^{1}H counterparts at the high frequency side, although all of these are not necessarily apparent because of the overlapping of the ^{1}H and ^{14}N ENDOR lines in the high frequency region. These experimental data definitely indicate the opposite signs between these two kinds of ^{1}H hyperfine coupling constants.

The CRISP effect should be observed on the *tert*-butyl protons near the free proton frequency. Although the spectra in Fig. 3 are not best resolved for the proton nuclei, the spectral changes of the *tert*-butyl protons are the same as was observed in DBNO (14). Therefore, one can conclude the sign of the *tert*-butyl hyperfine coupling constant is the same as that of the *para*- and *ortho*-protons, that is, negative. This result is compatible with the sign determined from the NMR Knight shift studies which have been carried out for DBNO (15) and nitroxides containing *tert*-butyl group (16). ^{14}N ENDOR spectral dependency on the $m_I = 1, 0$, and -1 will be discussed in the following section.

^{14}N ENDOR spectra

Strong ENDOR lines were observed among the ^{1}H ENDOR lines in rather high temperature regions (Fig. 1). Their intensity reaches a maximum around −50°C, whereas the intensity of the ^{1}H lines still grows even below −90°C as shown in Fig. 4. For detecting optimum ^{14}N ENDOR lines, different experimental conditions were necessary; for example, the lower concentration of the radical solution, the higher radiofrequency power, and the higher temperature. Therefore, in other conditions one may get stronger ^{1}H and weaker ^{14}N lines at the same temperature. In view of these facts, Fig. 4 is not necessarily definitive, but one might conclude that ^{14}N ENDOR lines appear at rather higher temperature than the ^{1}H lines do. This observation would be related to the different anisotropic hyperfine interactions of these nuclei. In general, the calculated ENDOR signal can be expressed by τ_R and $\mathrm{Tr}\{A'^2\}$ on certain assumptions, where τ_R is the rotational correlation time of the molecule and $\mathrm{Tr}\{A'^2\}$ is the trace of the squared anisotropic part of the electron–nuclear dipolar interaction (17). The anisotropic ^{14}N hyperfine interaction $\mathrm{Tr}\{A'^2\}$ for nitroxide radicals such as DPNO is $\mathrm{Tr}\{A'^2\} = 2200\ \mathrm{MHz}^2$ (18), whereas that of the ^{1}H which is attached to the benzene ring is about 30 MHz^2 (18). Therefore, the ^{14}N has larger $\mathrm{Tr}\{A'^2\}$ by at least a factor of 70. This difference explains the behavior in Fig. 4. Here a comment may be necessary for the observation of ^{14}N ENDOR of DBNO (7). Judging from its small molecular size compared to BPNO, DBNO seems to have a short rotational correlation time τ_R

Can. J. Chem. Downloaded from www.nrcresearchpress.com by 112.217.228.212 on 09/07/12
For personal use only.

Can. J. Chem. Downloaded from www.nrcresearchpress.com by 112.217.228.212 on 09/07/12
For personal use only.

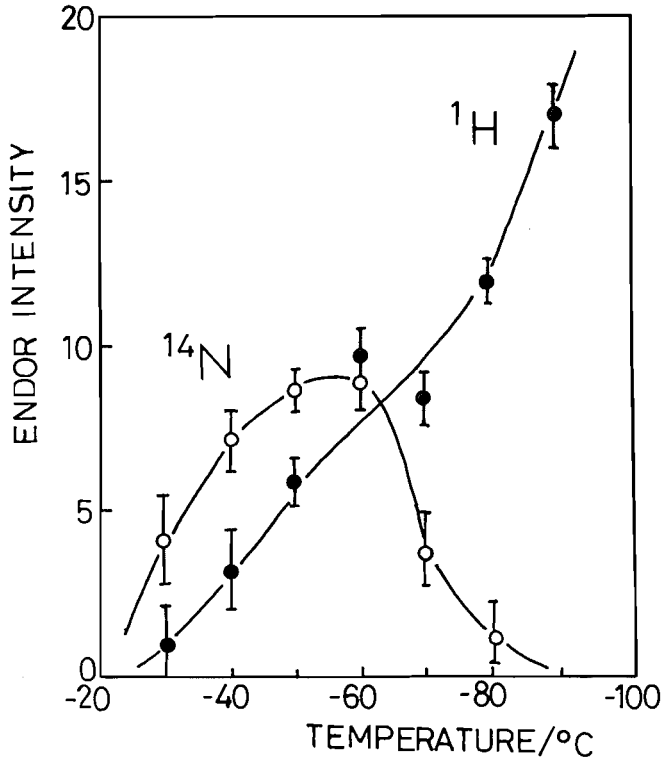

FIG. 4. Temperature dependence of the ENDOR intensities of the ^{1}H and ^{14}N absorption lines.

at a given temperature. Then even though its anisotropic ^{14}N hyperfine coupling constant is the same order, its optimum temperature for the ^{14}N ENDOR will be decreased as is the case of DBNO (7).

Figure 3 shows the spectral change in the ^{14}N ENDOR depending on the ESR monitoring as well as in the ^{1}H ENDOR. For instance, when the ESR line of the ^{14}N spin quantum number $m_I = 1$ (low field line) is saturated, the ^{14}N ENDOR line at the high frequency side is enhanced. In the case of $m_I = -1$ the relative intensity of the ^{14}N lines is also varied. This is the cross relaxation effect which was first pointed out in the first ^{14}N ENDOR observation (4). Furthermore, the detailed analysis of the absorption frequency indicates a slight deviation of the distance between the paired ^{14}N lines from $2\nu_n$, where ν_n is the ^{14}N nuclear magnetic resonance frequency at this ESR magnetic field. In this experiment ν_n was calculated to be 1.022 MHz. When observing the $m_I = -1$ ESR line, the high frequency ENDOR line is shifted up by c, where c is the second order shift of the energy levels due to the ^{14}N hyperfine interaction. For the $m_I = 0$ ESR the distance between the paired ^{14}N ENDOR lines $\Delta\nu$ is equal to $2\nu_n + 2c$, which was found to be 2.156 MHz. The second order shift $c = 0.056$ MHz was obtained, which is compared to the calculated value of 0.059 MHz using the ^{14}N isotropic hyperfine coupling $A_N = 11.86$ G.[1]

The ^{14}N hyperfine coupling constant $A_N = 11.86$ G at -80°C, is among the smaller values found in ENDOR observations of nitroxide radicals. Although the nuclear magnetic moment of ^{14}N is smaller by a factor of 14 than that of ^{1}H, one can observe strong ^{14}N ENDOR intensity. This is due to the enhancement of the radiofrequency at the nucleus over the applied radiofrequency through a large hyperfine interaction between the ^{14}N nucleus and the unpaired electron. In view of this radiofrequency enhancement effect by the hyperfine interaction, the lower the hyperfine coupling constant is, the more difficult its detection becomes. Our observation is, at present, a lower-limit case for the nitroxide radicals. Thus, the easy application of the radiofrequency power in the ENDOR study is indispensable, so that, in the ^{14}N ENDOR observation, the TM_{110} mode cavity seems to have a great advantage over TE type cavities.

There are a few examples of the observation of smaller ^{14}N hyperfine coupling constants in other systems. For example, an electrolytically prepared nitrobenzene anion radical showed ^{14}N ENDOR of $A_N = 9.64$ G (17) and a pyrazine anion radical in liquid ammonia exhibited much smaller value $A_N = 7.25$ G (19). In the neutral free radical, 1,1-diphenyl-2-picrylhydrazyl, $A_N = 7.95$ G was also observed (20). The reason why it is difficult to observe the ^{14}N ENDOR for the nitroxide radicals can not be explained at present. Taking into account that the anisotropic hyperfine interaction $\mathrm{Tr}\{A'^2\}$ is similar, the following situation might be possible; the anion radicals are surrounded by some cation species through a strong electrostatic interaction, resulting in a slow rotational correlation time. Actually ESR saturation was easily achieved for both anion radicals. Furthermore, it seems that, in the case of the nitroxide radicals, the oxygen atom attached to the nitrogen plays a specifically important role in the ENDOR relaxation mechanism.

Steric distortion

The effect of a steric repulsion around the N—O group was discussed and the molecular conformation around the N—O bond was proposed in several nitroxide radicals produced by spin trapping (5, 21). In these cases the conformation of the α and β carbons was deduced. In BPNO the bulky *tert*-butyl group and the phenyl ring are sterically hindered and the coplanarity between the phenyl ring and the N—O group might be influenced. One of the methods considering such a reduced electronic π-system is a MO treatment of the distorted overlap of $2p_z$ π-orbitals on the nitrogen and the carbon atoms connected with each other. This conformational change reduces the population of the unpaired electron on the phenyl ring, implying smaller hyperfine coupling constants. The results in Table 1 were obtained assuming an angle of 30° between the N and C $2p_z$ π-orbitals. These values agree well with the observed ones rather than in non-distorted case. This twist angle of 30° for BPNO seems to be reasonable, if one considers DPNO case where the N—C bond is twisted by 22.5°, that is, two benzene rings have a dihedral angle of 45° (12).

Acknowledgement

The authors express their sincere thanks to Mr. K. Okada for synthesizing the sample and observing the ENDOR and GTR spectra.

1. L. KEVAN and D. L. KISPERT. Electron spin double resonance spectroscopy. John Wiley and Sons, New York. 1976.
2. M. M. DORIO and J. H. FREED. Multiple electron resonance spectroscopy. Plenum Press, New York. 1979.
3. M. PLATO, W. LUBITZ, and K. MÖBIUS. J. Phys. Chem. **85**, 1202 (1981).
4. D. S. LENIART, J. C. VEDRINE, and J. S. HYDE. Chem. Phys. Lett. **6**, 637 (1970).
5. E. G. JANZEN, U. M. OEHLER, D. L. HAIRE, and Y. KOTAKE. J. Am. Chem. Soc. **108**, 6858 (1986).

[1]Correctly the second order shift must be averaged for the three principal comonents of the anisotropic ^{14}N hyperfine tensor.

6. K. ISHIZU, H. NAGAI, K. MUKAI, M. KOHNO, and T. YAMAMOTO. Chem. Lett. 1261 (1973).
7. J. YAMAUCHI and Y. DEGUCHI. Chem. Lett. 257 (1983).
8. J. LOPEZ, J. YAMAUCHI, K. OKADA, and Y. DEGUCHI. Bull. Chem. Soc. Jpn. **57**, 673 (1984).
9. G. CHAPELET-LETOURNEUX, H. LEMAIRE, and A. RASSAT. Bull. Soc. Chim. Fr. 444 (1965); A. CALDER, A. R. FORRESTER, P. G. JAMES, and G. R. LUCKHURST. J. Am. Chem. Soc. **91**, 3727 (1969).
10. J. YAMAUCHI, K. OKADA, and Y. DEGUCHI. Bull. Chem. Soc. Jpn. **60**, 483 (1987).
11. Y. DEGUCHI, K. OKADA, J. YAMAUCHI, and K. FUJII. Chem. Lett. 1161 (1983).
12. J. YAMAUCHI, H. NISHIGUCHI, K. MUKAI, Y. DEGUCHI, and H. TAKAKI. Bull. Chem. Soc. Jpn. **40**, 2512 (1967).
13. E. G. JANZEN and U. M. OEHLER. Chem. Lett. 1233 (1984).
14. J. YAMAUCHI and Y. DEGUCHI. Chem. Lett. 111 (1985).
15. R. W. KREILICK. J. Chem. Phys. **45**, 1922 (1966).
16. A. CALDER, A. R. FORRESTER, J. W. EMSLEY, G. R. LUCKHURST, and R. A. STOREY. Mol. Phys. **18**, 481 (1970).
17. F. LENDZIAN, M. PLATO, and K. MÖBIUS. J. Magn. Res. **44**, 20 (1981).
18. Y. DEGUCHI. Bull. Chem. Soc. Jpn. **34**, 910 (1961); T. S. LIN. J. Chem. Phys. **57**, 910 (1972).
19. W. LUBITZ and T. NYROENEN. J. Magn. Res. **41**, 17 (1980).
20. R. BIEHL, K. MÖBIUS, S. E. O'CONNOR, R. I. WALTER, and H. ZIMMERMANN. J. Phys. Chem. **83**, 3449 (1979).
21. Y. KOTAKE and K. KUWATA. Can. J. Chem. **60**, 1610 (1982).

Can. J. Chem. Downloaded from www.nrcresearchpress.com by 112.217.228.212 on 09/07/12
For personal use only.

Design of novel mesomorphic compounds methyl-substituted *N,N'*-dialkanoyl-1,3-benzenediamines

HIROMITSU KAWADA, YOSHIO MATSUNAGA,[1] TAKUMI TAKAMURA, AND MASAHIRO TERADA
Department of Chemistry, Faculty of Science, Hokkaido University, Sapporo 060, Japan

Received December 5, 1987

This paper is dedicated to Professor Charles A. McDowell on the occasion of his 70th birthday

HIROMITSU KAWADA, YOSHIO MATSUNAGA, TAKUMI TAKAMURA, and MASAHIRO TERADA. Can. J. Chem. **66**, 1867 (1988).

Calorimetric, X-ray diffraction, and broad-line proton nuclear magnetic resonance studies on the thermal behaviour of *N,N'*-dialkanoyl-1,3-benzenediamines carrying one, two, three, and four methyl groups disclosed that the enthalpy change at the transition to an isotropic liquid can be considerably diminished by this substitution and that various mesomorphic states can be obtained by this approach. Thus, the 2-methyl compounds with decanoyl to octadecanoyl groups exhibit hexagonal disordered columnar phases. Furthermore, the enthalpy changes in the 2,4,6-trimethyl compounds with octanoyl to octadecanoyl groups are so much reduced that their mesophases are nematic in type. On the other hand, the viscous birefringent fluids formed by the 4-methyl, 2,4-dimethyl, 4,6-dimethyl, and 2,4,5,6-tetramethyl compounds give X-ray diffraction patterns indicating highly ordered structures.

HIROMITSU KAWADA, YOSHIO MATSUNAGA, TAKUMI TAKAMURA et MASAHIRO TERADA. Can. J. Chem. **66**, 1867 (1988).

Des études par calorimétrie, par diffraction des rayons-X et par résonance magnétique nucléaire du ^1H à bandes larges sur le comportement thermique de *N,N'*-dialcanoyl benzènediamines-1,3 portant un, deux, trois ou quatre groupements méthyles ont montré que le changement d'enthalpie, lors de la transition vers un liquide isotrope, peut diminuer beaucoup par cette substitution et que divers états mésomorphes peuvent ainsi être obtenus. Ainsi, les composés méthyl-2 des groupements allant de décanoyle à octadécanoyle se présentent sous des phases en forme de colonnes hexagonales désordonnées. De plus, les changements d'enthalpies dans les composés triméthyl-2,4,6 des groupements allant d'octanoyle à octadécanoyle sont tellement réduits que leurs mésophases sont du type nématique. Par ailleurs, les fluides visqueux biréfringents, qui sont formés par les composés méthyl-4, diméthyl-2,4, diméthyl-4,6 et tétraméthyl-2,4,5,6, présentent des patrons de diffraction des rayons-X qui indiquent la présence de structures hautement ordonnées.

[Traduit par la revue]

Introduction

As reported in our previous paper, both the substituents $CONHC_nH_{2n+1}$ and $NHCOC_nH_{2n+1}$ are efficient in promoting the thermal stability of mesophases (1). We have examined the thermal behaviour of benzene derivatives carrying the two former substituents and could show that not only the 1,4-derivatives but also the 1,3-analogues are promising as parent compounds in the search for novel mesomorphic derivatives (2). In other words, the compounds in these two series melt with rather small enthalpy changes.

As a first approach towards designing mesomorphic compounds, we introduced an extra $CONHC_nH_{2n+1}$ group to the 5-position in the 1,3-disubstituted benzene molecule. This modification led us to the discovery of novel discogenic compounds: *N,N',N''*-trialkyl-1,3,5-benzenetricarboxamides (2, 3). In this paper, we describe our efforts to obtain mesomorphic compounds by the methyl substitution of *N,N'*-dialkanoyl-1,3-benzenediamine molecules. This substituent is expected to modify the intermolecular cohesion by increasing the intermolecular separation and the molecular polarizability, and to change the anisotropy of the intermolecular forces, which is the primary factor in the formation of liquid crystals.

Experimental

Materials

Acyl chlorides, unsubstituted 1,3-benzenediamine, and 2-methyl- and 4-methyl-1,3-benzenediamines were commercially available. 2,4-Dimethyl- and 4,6-dimethyl-1,3-benzenediamines were obtained by the reduction of the precursory dinitro compounds acquired from commercial sources. 1,3-Dinitro-2,4,6-trimethylbenzene was synthesized with good yield by adding mesitylene, drop by drop, to fuming nitric acid cooled in an ice-water bath (4). Tin and hydrochloric acid then were used to prepare 2,4,6-trimethyl-1,3-benzenediamine. Nitration of 1,2,3,4-tetramethylbenzene was carried out following the method proposed by Smith for the preparation of dinitrodurene (5). The product was reduced to the diamine with stannous chloride and concentrated hydrochloric acid. The final step of our synthesis was the acylation of these 1,3-benzendiamines. The results of elemental analysis were in accord with the composition of the desired compounds. For example, *Anal.* calcd. for $C_6H(CH_3)_3(NHCOC_5H_{11})_2$: C 72.79, H 9.89, N 8.08%; found: C 72.79, H 9.85, N 8.06%. *Anal.* calcd. for $C_6(CH_3)_4(NHCOC_{15}H_{31})_2$: C 78.69, H 11.95, N 4.37%; found: C 78.57, H 11.91, N 4.33%.

Measurements

Calorimetric, X-ray, and nmr measurements were made as described in our previous papers (6, 7).

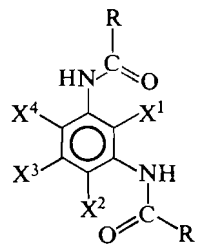

$R = C_nH_{2n+1}$

1: $X^1 = X^2 = X^3 = X^4 = H$
2: $X^1 = CH_3$, $X^2 = X^3 = X^4 = H$
3: $X^1 = H$, $X^2 = CH_3$, $X^3 = X^4 = H$
4: $X^1 = X^2 = CH_3$, $X^3 = X^4 = H$
5: $X^1 = H$, $X^2 = CH_3$, $X^3 = H$, $X^4 = CH_3$
6: $X^1 = X^2 = CH_3$, $X^3 = H$, $X^4 = CH_3$
7: $X^1 = X^2 = X^3 = X^4 = CH_3$

[1]Author to whom correspondence may be addressed.

Can. J. Chem. Downloaded from www.nrcresearchpress.com by 112.217.228.212 on 09/07/12
For personal use only.

TABLE 1. Transition temperatures (°C) and enthalpy changes (kJ mol^{-1}) of compounds **1**[a]

n[b]	Solid–solid	Solid–liquid
11	67 (5) 102 (8)	136 (53)
13	95 (17)	136 (63)
15	101 (26)	133 (71)
17	100 (21)	130 (81)

[a]The latter quantities are in parentheses.
[b]The number of carbon atoms in the alkyl group.

TABLE 2. Transition temperatures (°C) and enthalpy changes (kJ mol^{-1}) of compounds **2**[a]

n[b]	K	M		I
7	·	213 (47)		·
8	·	206 (45)		·
9	·	200 (13)	· 205 (33)	·
10	·	191 (16)	· 203 (31)	·
11	·	179 (19)	· 202 (30)	·
13	·	168 (22)	· 201 (26)	·
15	·	161 (24)	· 200 (28)	·
17	·	156 (21)	· 199 (26)	·

[a]The latter quantities are in parentheses.
[b]The number of carbon atoms in the alkyl group.

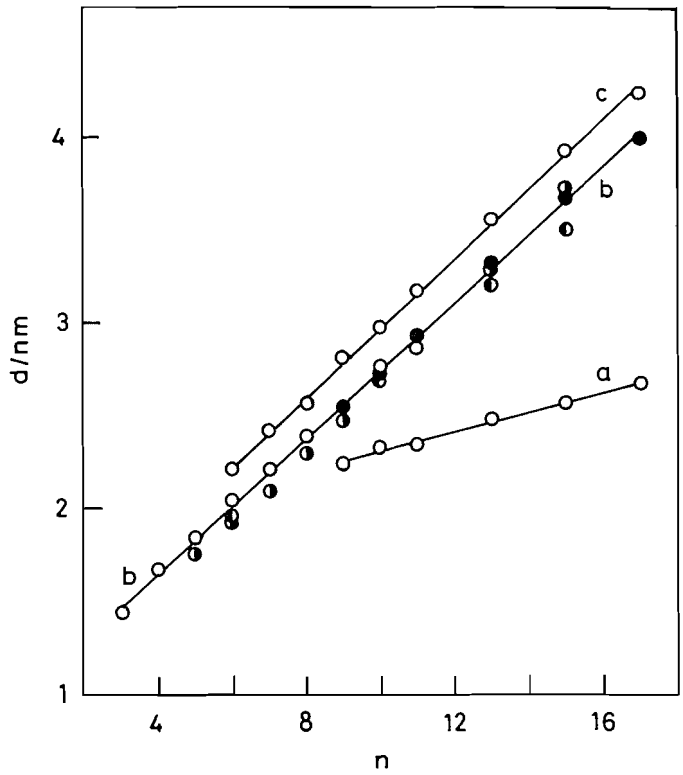

FIG. 1. Plots of the longest spacings in mesophases against the number of carbon atoms in the alkyl group. (a) Compounds **2**; (b) compounds **3** (●), compounds **5** (◑), compounds **6** (○), and compounds **7** (◐); and (c) compounds **4**.

Results

Unsubstituted compounds 1

As summarized in Table 1, these compounds exhibit a solid–solid transition around 100°C and are transformed into isotropic liquids above 130°C. The enthalpy change upon melting ranges from 53 to 81 kJ mol^{-1}. These values are markedly larger than those of the *N,N'*-dialkyl-1,3-benzenedicarboxamides reported before (2). For example, the dodecyl derivative in the latter series melts with an enthalpy change of 36 kJ mol^{-1} and the octadecyl derivative with a change of 54 kJ mol^{-1}. In this sense, the present series does not seem to provide better parent compounds. However, 1,3-benzenediamines carrying various substituents are easily obtainable. If the introduction of such substituents is an effective approach to mesomorphic compounds, compounds **1** may have a great advantage over the *N,N'*-dialkyl-1,3-benzenedicarboxamides.

2-Methyl compounds 2

The thermal properties are presented in Table 2. Here, K, M, and I denote crystal, mesophase, and isotropic liquid, respectively. The enthalpy of melting given by the nonanoyl derivative is 45 kJ mol^{-1} and seems to compare well with those of compounds **1** even though the corresponding homologous member was not examined. However, the melting point is considerably raised by the substitution. When the alkanoyl group is lengthened by a methylene unit, the melting process occurs in two steps. A transition located at 200°C is accompanied by an enthalpy change of 13 kJ mol^{-1}, and the other transition at 205°C by 33 kJ mol^{-1}. The separation between these two transition temperatures is enlarged by the increase in alkyl chain length. When $n = 17$, the high-temperature phase occupies a range as wide as 43°C. In contrast to compounds **1**, the enthalpy change at the transition into an isotropic liquid decreases as the series is ascended. As a result of these different tendencies, the value of the octadecanoyl derivative is merely one third of the corresponding value in series **1** and is small enough that one may consider the high-temperature phase as a mesophase. Indeed, the specimen flows between glass plates if gently pressed. It must be added that the isotropic liquid can be supercooled by 4–9°C.

The X-ray diffraction pattern of the liquid crystals spread in the form of a thin film over an aluminum holder consists of two major peaks. The inner sharp peak gives a spacing that increases linearly from 2.25 nm for the decanoyl derivative to 2.68 nm for the octadecanoyl derivative (see line a in Fig. 1). No peak assignable to the second-order reflection is detectable. The outer peak is diffuse and gives a spacing of 0.46 nm throughout the series. This feature is consistent with both unstructured smectic and hexagonal disordered columnar phases. An examination of the liquid crystals prepared while carefully avoiding the orientational influence of the sample holder revealed the presence of an additional weak peak, the spacing of which is about $1/\sqrt{3}$ times that given by the inner sharp peak. Such a ratio is characteristic of a hexagonal lattice; therefore, the structure must be columnar. The longest spacing is assigned to the first-order 100 reflection and the other one to the 110 reflection. The spacing of 0.46 nm must be the average stacking distance between the molecular planes in a column and is in agreement with those reported for similar discotic phases (7, 8).

As is shown by curve a in Fig. 2, the second moment of the broad-line proton nmr spectrum (the mean-square width of the resonance line), $\langle \Delta H^2 \rangle$, of the octadecanoyl derivative decreases gradually around the melting point of 156°C from about 4.5 to 0.1 G^2 ($G = 10^{-4}$ T). The latter value is of the same

Can. J. Chem. Downloaded from www.nrcresearchpress.com by 112.217.228.212 on 09/07/12
For personal use only.

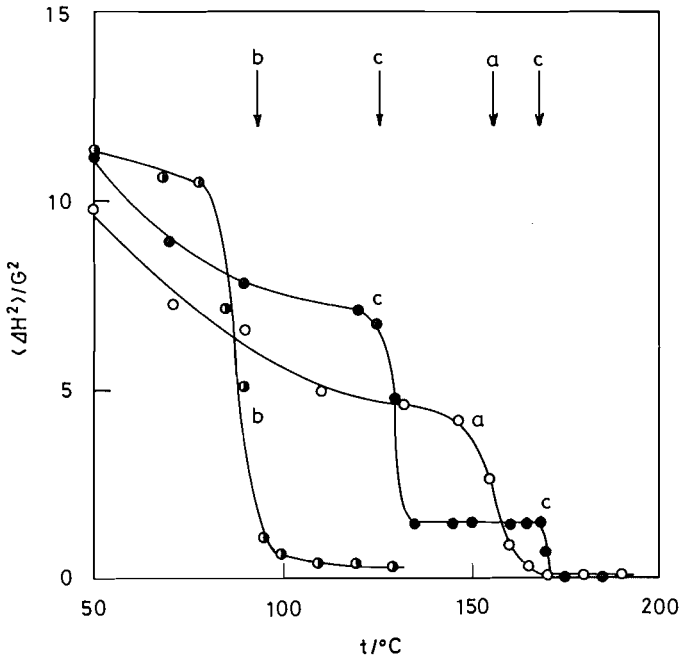

FIG. 2. Second moments of the broad-line proton nmr spectrum of (a) compound **2**, $n = 17$, (b) compound **5**, $n = 15$, and (c) compound **6**, $n = 9$. The vertical arrows indicate the transition temperatures determined by calorimetry.

TABLE 3. Transition temperatures (°C) and enthalpy changes (kJ mol^{-1}) of compounds **3**[a]

n[b]	K	M	I
7	·	171 (30)	·
8	·	163 (28)	·
9	·	114–132 (6) · 162 (26)	·
10	·	96–145 (13) · 159 (26)	·
11	·	115–133 (11) · 159 (27)	·
13	·	117–145 (16) · 152 (30)	·
15	·	118–139 (20) · 148 (30)	·
17	·	111–138 (24) · 144 (32)	·

[a]The latter quantities are in parentheses.
[b]The number of carbon atoms in the alkyl group.

order as those shown by the mesophase of *N,N'*-dialkanoyl-2,3,5,6-tetrakis(alkanoyloxy)-1,4-benzenediamines (7).

4-Methyl compounds 3

The enthalpy change at the transition to an isotropic liquid in this series is essentially the same as that observed for the previous series (see Table 3). It must be noted that the value increases as the alkyl chain length increases. This trend is opposite to that observed in series **2**. Morever, the transition temperature is lower by 43–55°C. The appearance of a mesophase in the process of cooling at a rate of 5 K min^{-1} is delayed by 3–4°C. The endothermic peak overlaps with peak(s) due to solid–solid transition(s); therefore, the total enthalpy changes and the corresponding temperature range are presented in Table 3.

The high-temperature phases found with the decanoyl to octadecanoyl derivatives are viscous fluids. The undecanoyl derivative and higher members give a common X-ray diffraction pattern composed of four sharp and two broad peaks. The sharp peak at the lowest Bragg angle is accompanied by its second- and third-order reflections. The spacing is markedly longer than that shown by the corresponding member in series **2** (see line b in Fig. 1). Two broad peaks that overlap with each other have maxima at 0.42 and 0.46 nm, respectively, regardless of the alkyl chain length. The former peak is relatively narrow compared with the latter. Another somewhat sharper peak, which is not so broad as the aforementioned one, gives a spacing of 0.72–0.73 nm. This spacing is also independent of the alkyl chain length. Thus, the mesophase is certainly more structured than that of compounds **2**. The second moments, which are as large as 0.9 G^2 and are observed just below the clearing point for the decanoyl and octadecanoyl derivatives, are in support of the above conclusion.

TABLE 4. Transition temperatures (°C) and enthalpy changes (kJ mol^{-1}) of compounds **4**[a]

n[b]	K	M	I
5	·	218 (29)	·
6	·	122–139 (8) · 206 (26)	·
7	·	125–148 (11) · 197 (25)	·
8	·	125–139 (17) · 189 (23)	·
9	·	114–129 (14) · 181 (22)	·
10	·	124–139 (21) · 178 (24)	·
11	·	118–131 (23) · 172 (23)	·
13	·	119 (21) · 163 (24)	·
15	·	122 (25) · 155 (26)	·
17	·	113–128 (18) · 149 (25)	·

[a]The latter quantities are in parentheses.
[b]The number of carbon atoms in the alkyl group.

2,4-Dimethyl compounds 4

Table 4 gives the transition temperatures and associated enthalpy changes of compounds **4**. The clearing points are a little higher than those of compounds **3**. The isotropic liquids may be supercooled by 3–14°C, when cooled at a rate of 5 K min^{-1}. The enthalpy changes are in the range of 22–29 kJ mol^{-1} and exhibit no marked trend with alkyl chain length. The X-ray diffraction patterns of the undecanoyl derivative and higher members are similar to those described for compounds **3**. The spacing defined by the inner sharp peak is the longest, though the difference is small, among those of the compounds examined (see line c in Fig. 1). The peak is accompanied by its second- and third-order reflections in most cases. The following spacings are independent of the alkyl chain length: 0.38, 0.45, and 0.64 nm. The distance between the molecular cores in a column, 0.38 nm, is only slightly longer than 0.366 nm found in the hexamethylbenzene crystals (9). Therefore, the phase is almost certainly ordered in a column. This proposition is strongly supported by a rather large second moment, 1.5 G^2, measured for the mesophase of the octadecanoyl derivative. Finally, it may be added that the hexanoyl derivative, which shows no additional transition, gives a viscous fluid near 218°C.

4,6-Dimethyl compounds 5

The thermal properties are summarized in Table 5. Both the clearing point and the associated enthalpy change are reduced compared with those of compounds **3**. In particular, the enthalpy change given by the highest homologous member is less than one half that of the corresponding member in the latter series. Nevertheless, the innermost sharp peak in the X-ray diffraction pattern gives a spacing close to that given by

Can. J. Chem. Downloaded from www.nrcresearchpress.com by 112.217.228.212 on 09/07/12
For personal use only.

TABLE 5. Transition temperatures (°C) and enthalpy changes (kJ mol^{-1}) of compounds **5**[a]

n[b]	K	M	I
5	·	216 (27)	·
6	·	207 (24)	·
7	·	96 (19) · 195 (22)	·
8	·	87 (17) · 182 (19)	·
9	·	97 (28) · 170 (16)	·
10	·	67 (21) · 163 (15)	·
11	·	70 (24) · 156 (15)	·
13	·	86 (33) · 147 (14)	·
15	·	93 (42) · 135 (14)	·
17	·	88 (44) · 130 (14)	·

[a]The latter quantities are in parentheses.
[b]The number of carbon atoms in the alkyl group.

TABLE 7. Transition temperatures (°C) and enthalpy changes (kJ mol^{-1}) of compounds **7**[a]

n[b]	K	M	I
4	·	279 (40)	·
5	·	181 (3) · 266 (31)	·
6	·	151 (6) · 262 (29)	·
7	·	137 (9) · 252 (26)	·
8	·	123 (11) · 244 (26)	·
9	·	121 (13) · 234 (24)	·
10	·	119 (14) · 226 (23)	·
11	·	117 (16) · 222 (23)	·
13	·	122 (18) · 216 (25)	·
15	·	123 (19) · 206 (29)	·

[a]The latter quantities are in parentheses.
[b]The number of carbon atoms in the alkyl group.

TABLE 6. Transition temperatures (°C) and enthalpy changes (kJ mol^{-1}) of compounds **6**[a]

n[b]	K	M_1	M_2	I
2	·	295 (38)		·
3	·	249 (17) ·	255 (14)	·
4	·	214 (17) ·	247 (17)	·
5	·	158–174 (15) ·	240 (15)	·
6	·	152–168 (21) ·	232 (13)	·
7	·	127–158 (22) ·	215 (8) · 223 (3)	·
8	·	136 (31) ·	188 (5) · 217 (2)	·
9	·	126 (33) ·	168 (5) · 211 (2)	·
10	·	130 (40) ·	148 (5) · 203 (2)	·
11	·	121 (40) ·	139 (5) · 199 (2)	·
13	·	108 (73)	· 187 (1)	·
15	·	109 (79)	· 176 (0.9)	·
17	·	113–129 (45)	· 168 (0.7)	·

[a]The latter quantities are in parentheses.
[b]The number of carbon atoms in the alkyl group.

compounds **3**. Its second- and third-order reflections, and broad and sharp peaks giving spacings of 0.46 and 0.82 nm, respectively, are observable for the dodecanoyl derivative and higher members. The absence of a spacing shorter than 0.46 nm suggests that the mesophase is less ordered than those of compounds **3** and **4**. An nmr study on the hexadecanoyl derivative gives a second moment of 0.3 G^2 for the mesophase, as is shown by curve b in Fig. 2. Some eight weak peaks appear in the broad-peak region of the undecanoyl derivative and they become stronger in the lower members. In the case of the octanoyl derivative, the following peaks are detected in the above-mentioned range: 0.36, 0.39, 0.41, 0.45, 0.51, 0.53, 0.57, and 0.75 nm. Thus, the small enthalpy change at the clearing point in the lower members of the present series does not necessarily mean a highly disordered structure of the mesophase.

2,4,6-Trimethyl compounds **6**

The calorimetric data of the trimethyl compounds are given in Table 6. In this series, two kinds of mesophases are found for the octanoyl to dodecanoyl derivatives. They are denoted by M_1 and M_2 in the table. The first mesophase is observed starting with the butyryl derivative. It must be noted that the enthalpy change by the M_1–I or M_1–M_2 transition is much larger than that by the M_2–I transition. Both the former and the latter values decrease as the series is ascended. The M_2–I transition occurs at the same temperature in the processes of heating and cooling, whereas the M_1–M_2 and M_1–I transitions show detectable, often considerable, supercooling. Schlieren texture is adopted by the M_2 phase. This phase is nematic in type as the X-ray diffraction pattern of unoriented specimens consists of two diffuse peaks only. As the mesophases exhibited by the 2-methyl compounds are undoubtedly columnar, the M_2 phase is likely to be nematic discotic. The phase denoted by M_1 gives a diffraction pattern composed of a number of sharp peaks. The longest spacings in this phase for the butyryl to dodecanoyl derivatives are in the range given by the relatively less-disordered phases (see line b in Fig. 1). The second moment of the decanoyl derivative decreases from about 7 to 1.5 G^2 at the melting point and from the latter value to about 0.01 G^2 at the M_1–M_2 transition temperature. The value shown by the M_2 phase is only one tenth of the moment observed for the hexagonal disordered columnar phase of compounds **2** (compare curves a and c in Fig. 2).

2,4,5,6-Tetramethyl compounds **7**

A mesophase is exhibited by the hexanoyl to hexadecanoyl derivatives. The temperature range is 83–85°C for these end members but 121°C for the nonanoyl derivative. As is seen in Table 7, the enthalpy change at the clearing point is as large as those given by compounds **3**, **4**, and **5**. The values exhibit a minimum around the undecanoyl and dodecanoyl derivatives. It may be noted that the enthalpy change at the melting point is markedly smaller than that at the clearing point.

The X-ray diffraction pattern recorded for the mesophase of the hexadecanoyl derivative shows a sharp peak, giving a spacing of 3.51 nm and its second- and third-order reflections. Rather sharp peaks with spacings of 0.40, 0.45, and 0.74 nm, respectively, are located on a broad peak, the maximum of which is near 0.46 nm. Consequently, the whole pattern bears a close similarity to those of the mesophases exhibited by compounds **3**, **4**, **5**, and **6**. Moreover, the longest spacings given by the corresponding members in these series, except **4**, almost agree with each other, as is shown by line b in Fig. 1. The diffraction pattern becomes more complicated as the series is descended. Namely, a few extra peaks are detected between 0.46 and 0.73 nm for the decanoyl derivative and the lower members. A drop of the second moment from about 5.5 to 2.0 G^2 is observed at the melting point of the tetradecanoyl derivative.

Can. J. Chem. Downloaded from www.nrcresearchpress.com by 112.217.228.212 on 09/07/12
For personal use only.

Can. J. Chem. Downloaded from www.nrcresearchpress.com by 112.217.228.212 on 09/07/12
For personal use only.

Discussion

As mentioned earlier, substituents may produce opposing effects on the intermolecular cohesion. Moreover, these effects may be susceptible to interaction between the substituents, especially when the intramolecular crowding is extensive. Naturally, the effect on the thermal properties of the introduction of a single methyl group into the *N,N'*-dialkanoyl-1,3-benzenediamine molecule is quite large. In particular, the group at the 2-position is so effective that the resulting phase is disordered columnar. This finding indicates that a hexagonal phase may be formed by changing the molecular orientation around the columnar axis even if the molecular shape is virtually that of *m*-disubstituted benzene. The spacing d_{100} is a little longer than that found for the similar phase of *N,N'*-dialkanoyl-2,3,5,6-tetrakis(alkanoyloxy)-1,4-benzenediamine described in our previous paper (7). For example, the tetradecanoyl derivative in the present series gives 2.48 nm and the corresponding member in the hexasubstituted benzene series gives 2.29 nm. Therefore, the chains in compounds **2** are less disordered. The difference is clearly manifested by the thermal properties and broad-line proton nmr spectra of the mesophases. While the hexadecanoyl derivative in the series **2** gives an enthalpy change at the clearing point of 28 kJ mol^{-1}, the corresponding hexasubstituted benzene gives a change of 18 kJ mol^{-1}. Furthermore, the octadecanoyl derivative exhibits a moment three times that given by the hexadecanoyl derivative in the latter series.

The general features of the X-ray diffraction pattern given by the 4-methyl compounds bear some resemblance to that reported by Levelut for the hexagonal ordered columnar phase of hexakis(pentyloxy)triphenylene (10). In addition to the reflections related to the distance between the neighboring columns, the following three were noted by Levelut: 0.359, 0.45, and 1.3 nm. The first spacing was assigned to the distance between the parallel molecules in a column, the second to the mean distance between the alkyl chains in the liquid-like order, and the last to the pitch of the helicoidal stacking of the molecular cores. In the present compounds, the spacing of 0.42 nm seems too long to be the well-defined distance between the parallel molecules in a column. As is suggested by the diffuseness of the peak, the stacking may be, to some extent, disordered. The pattern of compounds **3** has no reflection comparable with 1.3 nm but it shows a spacing of 0.72–0.73 nm. On the basis of the above observations, one might say that the 4-methyl group is less effective in producing mesophase than the 2-methyl group; however, this is true only for the monomethyl compounds.

The change in mesomorphic behaviour by introduction of an additional methyl group to the 2-methyl compound is striking. The X-ray diffraction pattern and the second moment indicate an increase of order in the structure of the mesophase. On the other hand, the mesophase of the 4,6-dimethyl compounds is less ordered than that of the 4-methyl compounds. Summing up all the available evidence, the mesophases of the above-mentioned four series may be in various stages between hexagonal disordered and ordered columnar structures and appear to be disordered in the following order: 2-methyl > 4,6-dimethyl > 4-methyl > 2,4-dimethyl.

Since the 2-methyl and 4-methyl compounds are displaced in the above order by the introduction of the second methyl group, the thermal behaviour of the 2,4,6-trimethyl compounds does not seem predictable. As a matter of fact, the M_1 phases observed with the dodecanoyl derivative and the lower members are as structured as the mesophases of the corresponding 4-methyl compounds. On the other hand, the M_2 phases exhibited by the octanoyl derivative and the higher members are nematic. The presence of four methyl groups in a molecule is not favourable to the formation of a highly disordered mesophase, as evidenced by the spacing as short as 0.40 nm and the second moment as large as 2 G^2.

Methyl-substituted *N,N'*-dialkanoyl-1,2- and -1,4-benzenediamines have been also studied in our laboratory and will be the subjects of the forthcoming papers.

Acknowledgement

This work was supported by a Grant-in-Aid for Scientific Research No. 60470001 from the Ministry of Education, Science, and Culture.

1. E. Chino, Y. Matsunaga, and M. Suzuki. Bull. Chem. Soc. Jpn. **57**, 2371 (1984).
2. Y. Matsunaga, N. Miyajima, Y. Nakayasu, S. Sakai, and M. Yonenaga. Bull. Chem. Soc. Jpn. **61**, 207 (1988).
3. Y. Matsunaga, Y. Nakayasu, S. Sakai, and M. Yonenaga. Mol. Cryst. Liq. Cryst. **141**, 327 (1986).
4. R. Fittig. Ann. **141**, 133 (1867).
5. L. I. Smith. Org. Synth. Coll. Vol. II, 254 (1943).
6. Y. Matsunaga and M. Terada. Mol. Cryst. Liq. Cryst. **141**, 321 (1986).
7. Y. Kobayashi and Y. Matsunaga. Bull. Chem. Soc. Jpn. **60**, 3515 (1987).
8. S. Chandrasekhar, B. K. Sadashiva, K. A. Suresh, N. V. Madhusudana, S. Kumar, R. Shashidar, and G. Venkatech. J. Phys. (Paris), **40**, C3-120 (1979).
9. L. O. Brockway and J. M. Robertson. J. Chem. Soc. 1324 (1939).
10. A. M. Levelut. J. Phys. (Paris), **40**, L-81 (1979).

Cation mobility in gaseous, critical, and liquid deuterated methanes

M. Antonio Floriano, Norman Gee, and Gordon R. Freeman
Chemistry Department, University of Alberta, Edmonton, Alta., Canada T6G 2G2

Received October 28, 1987

This paper is dedicated to Professor Charles A. McDowell on the occasion of his seventieth birthday

M. Antonio Floriano, Norman Gee, and Gordon R. Freeman. Can. J. Chem. **66**, 1872 (1988).

Cation mobilities μ have been measured in the deuterated methanes CH_xD_{4-x} (x = 0–4) at field strengths $E/n < 4 \times 10^{-21}$ V m^2/molecule, $92 \leq T/K \leq 598$ and $0.025 \leq n/10^{26}$ molecules m$^{-3} \leq 171$. The mobility in the equilibrium fluids was the same at a given number density n for all five methanes. In the liquid the mobility decreased as the critical region was approached. Changes in $n\mu$ in the nonsaturated gases reflected changes in clustering, which was favored at lower T or higher n. The Arrhenius temperature coefficients of ion mobilities at constant gas density near the vapor/liquid coexistence curve nearly equalled those of electron mobilities at similar experimental conditions. The ion mobility in the saturated gas was determined mainly by density and in the liquid by the viscosity.

M. Antonio Floriano, Norman Gee et Gordon R. Freeman. Can. J. Chem. **66**, 1872 (1988).

On a mesuré les mobilités (μ) des cations dans les méthanes deutérés (CH_xD_{4-x}) (x = 0 à 4), à des forces de champs (E/n) < 4×10^{-21} V m^2/molécule, $92 \leq T$ (K) ≤ 598 et $0{,}025 \leq n$ (10^{26} molécules m^{-3}) ≤ 171. Pour chacun des cinq méthanes et pour une densité donnée, on observe toujours la même mobilité dans les fluides en équilibre. Dans le liquide, la mobilité diminue lorsqu'on approche de la région critique. Les changements observés dans les $n\mu$ des gaz qui ne sont pas saturés sont le reflet de changements dans la formation d'agrégats; ces formations sont favorisées par l'abaissement de T ou l'augmentation de n. Les coefficients de température d'Arrhénius pour les mobilités ioniques à densité de gaz constante, près de la courbe de coexistence vapeur/liquide, sont presqu'égaux à ceux des mobilités électroniques dans des conditions semblables. Pour expliquer la mobilité ionique dans le gaz saturé, on a principalement fait appel à la densité alors que la viscosité a été utilisées dans le liquide.

[Traduit par la revue]

Introduction

Cation transport in hydrocarbon fluids undergoes a mechanism transition as the fluid density is decreased from that of a normal liquid, through the critical fluid, to that of a normal gas (1–3). In normal liquids the mobility μ is determined by the fluid viscosity η and in normal gases at densities $n <$ 10^{26} molecule/m^3 by n. A transition from viscosity to density control occurred at $0.6 \lesssim \eta/\eta_c \lesssim 3$ corresponding to $0.5 \lesssim$ $n/n_c \lesssim 1.9$ (subscript c denotes critical fluid property). In this work we extend our study of cation transport to the series of deuterated methanes CH_xD_{4-x} at densities $0.01 \leq$ $n/10^{27}$ molecule m$^{-3} \leq 17$.

Experimental

The suppliers, chemical and isotopic purities, and further purification of the deuterated methanes are given in ref. 4. A schematic of the cooling (4) and heating (5) set ups, and of the low pressure gas (5), dense gas (6) and liquid (7) conductance cells are given in the cited references. In the near critical region some measurements were obtained with the modified high pressure cell described in ref. 5. The separations l between the electrodes were measured to ± 0.01 mm.

Physical properties of the fluids and sources for them are listed in ref. 4. Determination of the fluid density is described in ref. 8. Along the coexistence curve the density was obtained from the measured temperature, using literature tables of density against temperature (9–11). The tables were for CH_4 and CD_4, but when plotted as n against T/T_c the two sets agreed within 0.8% (4), so we assumed that n of CH_3D, CH_2D_2, and CHD_3 would be the same as in CH_4 and CD_4 at the same T/T_c. Thermocouples used to monitor the temperature at three or four points at the top, plate area and bottom of the cells had been calibrated to 0.1 K at $T <$ 373 K (8). The reliability of the recorded temperature was determined by the spread between thermocouple readings, <0.1 K at room temperature and at near T_c, and $< \pm 0.025$ K elsewhere. Outside the calibrated range the spread in thermocouple readings was less than the manufacturer's stated uncertainty for uncalibrated type t special thermocouples. This uncertainty, ± 0.5 K at 450 K increasing to ± 1.2 K at 550 K (12), set the uncertainty limit in recorded T at $T >$ 373 K.

The generation of the cations with a 100 or 300 ns pulse of X-rays from a van de Graaff accelerator, a signal amplifier, data collection procedure, and an example current–time signal are described in ref. 3*a*. The initial spike in the current–time signal corresponds to electrons, which have mobilities $\sim 10^4$ times larger than those of the ions and are removed first. The samples had been purified to study electron mobilities, so capture by impurities to form negative ions was negligible (4, 8). The signal ramp therefore corresponded to cations.

At each applied voltage V the time required for the radiation-induced current to decay linearly back to the baseline was determined (Fig. 1 of ref. 3*a*) to give the drift time t_d. The mobility was then obtained from $\mu = l^2/t_dV$. Both positive and negative applied voltages were used and the results averaged to give μ at V.

Results and discussion

A. Field independence

The mobility was measured typically at fields $0.01 < E/n$ (Td) < 0.1 in the liquids and $0.1 < E/n$ (Td) < 1 in the gases (Td = 10^{-21} V m^2/molecule). Some values in the liquid phase were measured at E/n as low as 0.002 Td and some gas phase μ values were measured at E/n up to 28 Td. No field dependence was found. The value of μ reported at each (n,T) in Figs. 1 and 2 was the average of >10 measurements, half with positive and half with negative applied polarity; the average deviation of the measured values from the reported μ at V (Figs. 1, 2) was <2%.

The mobility was constant up to 28 Td because these fields were less than the threshold $(E/n)_{thr}$ required to heat the cation energy distribution. In gases two conditions have been used to define $(E/n)_{thr}$: the field where (*a*) the cation drift velocity $v_d \equiv \mu \times E$ approaches v_{mol} the random velocity of the molecules (13*a*, 14); (*b*) v_d approaches c_0 the speed of sound in the fluid (15). These conditions apply to electrons as well as cations (14, 16) and give

Can. J. Chem. Downloaded from www.nrcresearchpress.com by 112.217.228.212 on 09/07/12
For personal use only.

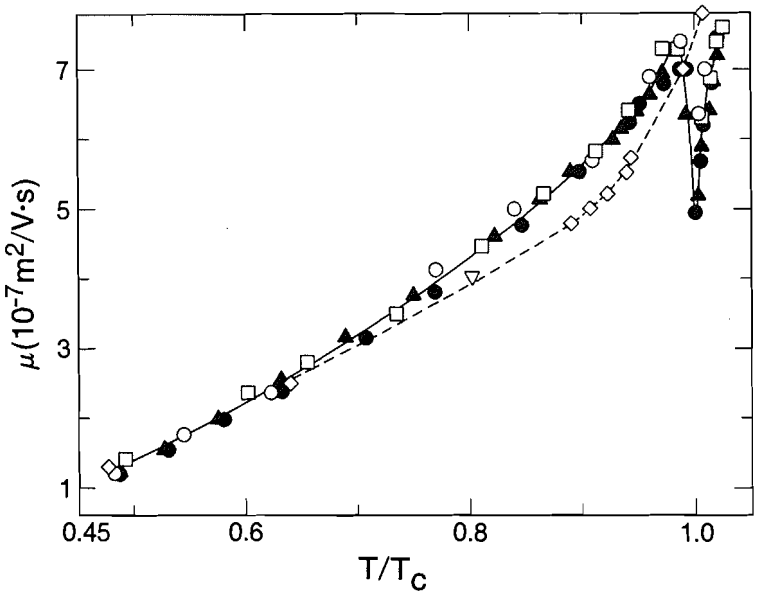

FIG. 1. Cation mobility as a function of reduced temperature T/T_c in liquids and supercritical fluids of (symbol, T_c/K (4)): CH_4 (○, ◇, 190.6), CH_2D_2 (□, 189.2), CHD_3 (▲, 189.0), CD_4 (●, 189.2). Present work except ◇ (1*a*). Lines are visual guides.

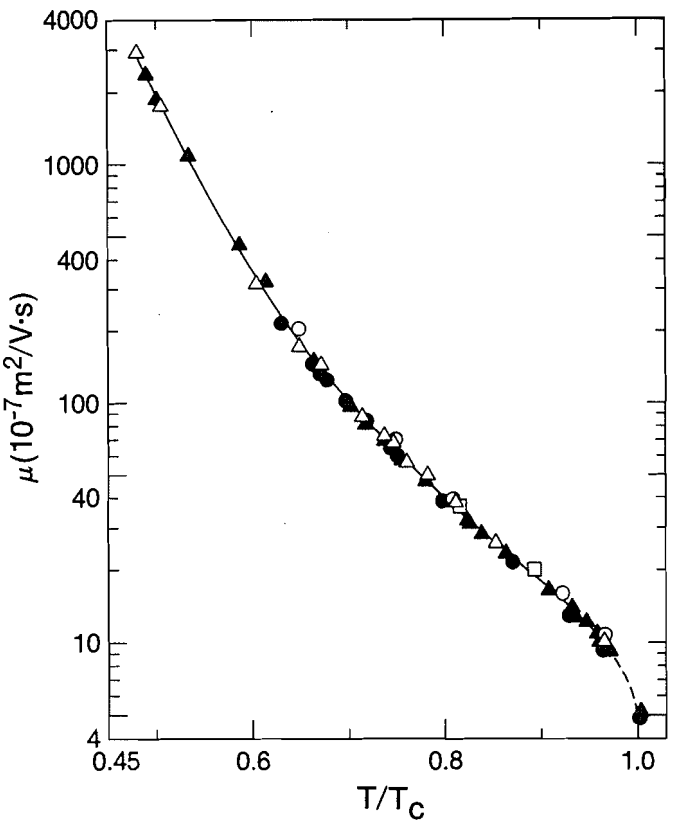

FIG. 2. Cation mobility in saturated vapors as a function of temperature T/T_c. Symbols as Fig. 1, with CH_3D (△, T_c = 191.1 K).

[1] $(E/n)_{thr} = v_{mol}/n\mu$

or

[2] $(E/n)_{thr} = c_0/n\mu$

The two limits are nearly the same in gases (3*b*, 13). For example, in the hydrocarbon series ethane to *n*-decane, $c_0 \approx 0.7\, v_{mol}$ (3*b*). Using n and c_0 from ref. 11, eq. [2] indicates that $(E/n)_{thr}$ would be 94 Td in CH_4 gas (Fig. 2) at $T/T_c = 0.648$ ($n = 1.54 \times 10^{26}$ molecules/m^3, $c_0 = 296$ m/s). Likewise in CH_4 liquid (Fig. 1) at $T/T_c = 0.987$ (8.6×10^{27} molecules/m^3, 324 m/s) $(E/n)_{thr} = 51$ Td, and at $T/T_c = 0.483$ (17.0×10^{27} molecules/m^3, 1510 m/s) $(E/n)_{thr} = 740$ Td. As c_0 in the other CH_xD_{4-x} would only differ from c_0 in CH_4 by the ratio of square root of the molecular masses, $(E/n)_{thr}$ in all of these methanes would be similar at the same T/T_c. Hence the μ values in Figs. 1 and 2 were all obtained at $E/n \ll (E/n)_{thr}$ and are those of thermal cations.

B. Effect of temperature in nonsaturated gases

In gases at low n and very low ion mole fraction, $n\mu$ at a given T is independent of n (13*b*). Thus the temperature coefficient of $n\mu$ is also independent of n at low n (Fig. 3). At high n the temperature coefficient increases (Fig. 3) and the value of $n\mu$ at a given T decreases at low T (Fig. 4). At ~100 K the upper limit of density independence in methane is $n \approx 6 \times 10^{25}$ molecules/m^3 (Fig. 3), which is larger than the limits for larger alkanes at a similar temperature (3*b*).

In methane radiolysis the initial ions are mainly CH_4^+ and CH_3^+ which rapidly react at $n \approx 10^{24}$ molecules/m^3 to form other ions, mainly CH_5^+ and $C_3H_7^+$ (17–19). At higher densities the ions can cluster, for example (17*a*)

[3] $CH_5^+ + CH_4 \rightleftharpoons CH_5^+(CH_4)$

[4] $CH_5^+(CH_4)_{m-1} + CH_4 \rightleftharpoons CH_5^+(CH_4)_m$

The extent of clustering is temperature dependent, with equilibrium constants represented by

[5] $$K_{eq,m} = \frac{[CH_5^+(CH_4)_m]}{[CH_5^+(CH_4)_{m-1}][CH_4]}$$

Using values of the equilibrium constants from ref. 17*a*, we estimate that at $n = 3 \times 10^{25}$ molecules/m^3 the dominant value of m is 5 at 100 K, 2 at 200 K, 1 at 300 K, and zero (unclustered) at $T > 500$ K. The $C_3H_7^+$ likewise clusters with CH_4 molecules,

Can. J. Chem. Downloaded from www.nrcresearchpress.com by 112.217.228.212 on 09/07/12
For personal use only.

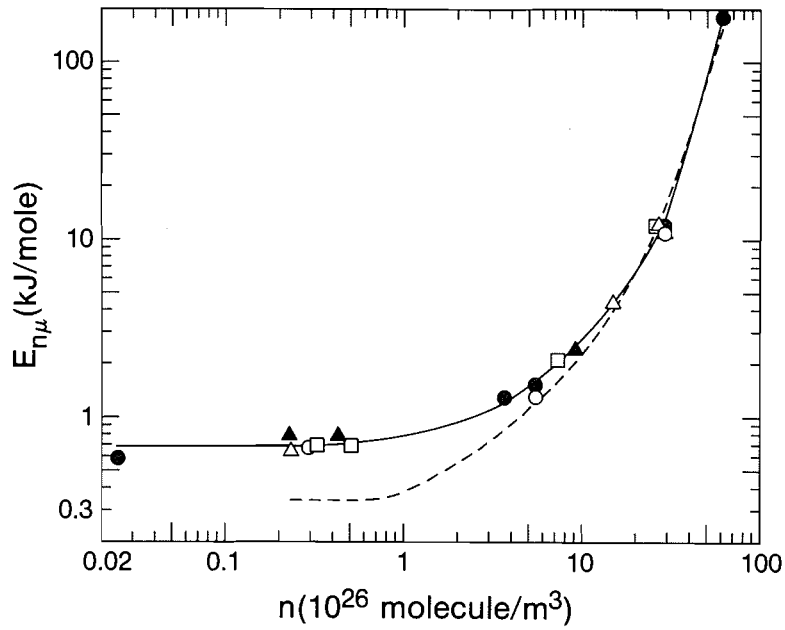

FIG. 3. Arrhenius temperature coefficients $E_{n\mu}$ (eq. [8]) near the vapor/liquid coexistence region. Symbols as in Figs. 1 and 2. The solid line is empirical. The dashed line represents $E_{n\mu}$ for electron mobilities measured at similar conditions, ref. 8.

although to a smaller extent than CH_5^+ (17). The decrease of $n\mu$ with increasing n at a given T (Fig. 4) is attributed to clustering about the ions.

The value of $n\mu$ is related to the average ion–molecule momentum transfer cross section σ_{av} (20):

$$[6] \quad n\mu = \frac{3e}{4M_r\langle v\rangle\sigma_{av}}$$

where M_r is the ion–molecule reduced mass, e is the protonic charge, $\langle v\rangle$ is the average velocity of the ions relative to the molecules and for a Maxwellian distribution (thermal ions) is $(8k_BT/\pi M_r)^{1/2}$, where k_B is Boltzmann's constant. Equation [6] is derivable from eq. [5-3-8] of ref. 13*c*. Clustering increases both M_r and σ_{av}, so $n\mu$ decreases.

At 300 K $n\mu$ of CH_5^+ in CH_4 was $(6.7 \pm 0.5)10^{21}$ molecules/m V s, and of $C_3H_7^+$ was $(6.1 \pm 0.7)10^{21}$ molecules/m V s (19). For two ions at the same temperature, eq. [6] gives

$$[7] \quad (n\mu)_2 = (n\mu)_1[(M_r)_1/(M_r)_2]^{1/2}[(\sigma_{av})_1/\sigma_{av})_2]$$

Assuming σ_{av} of $CH_5^+(CH_4)$ in CH_4 was similar to or greater than that of CH_5^+, $n\mu[CH_5^+(CH_4)] \leq (0.87 \times 6.7 \pm 0.5)10^{21} = (5.8 \times 0.5)10^{21}$ molecules/m V s. Our $n\mu = 5.4 \times 10^{21}$ at 2.95×10^{25} molecules/m^3 (Fig. 4) is hence consistent with the cations being a mixture of $C_3H_7^+$ and $CH_5^+(CH_4)$.

At lower temperatures and higher densities the cations in CH_4 became further clustered and $n\mu$ decreased. At 180 K increased clustering occurred at $n > 1 \times 10^{26}$ molecules/m^3. At low T and high n, the temperature dependence of $n\mu$ at constant n was large. In terms of an Arrhenius model,

$$[8] \quad n\mu = A \exp(-E_{n\mu}/k_BT)$$

where A is the pre-exponential factor. The temperature coefficient $E_{n\mu}$ near the vapor/liquid coexistence region was 1.3 kJ/mol at 5.5×10^{26} molecules/m^3, and 11 kJ/mol at 2.9×10^{27} molecule/m^3. The low density limit of $E_{n\mu}$ displayed in Fig. 3 does

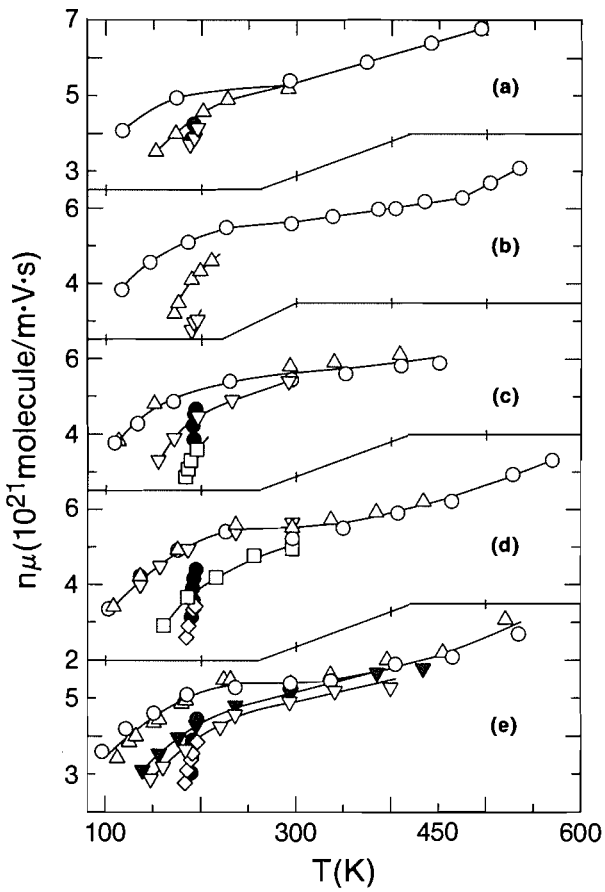

FIG. 4. Plot of density-normalized mobility against T in constant density gas at ($n/10^{26}$ molecules m^{-3}): (*a*) CH_4, ○ (0.295), △ (5.5), ▽ (29.0), ● (61); (*b*) CH_3D, ○ (0.235), △ (15.0), ▽ (27.0); (*c*) CH_2D_2, ○ (0.330), △ (0.61), ▽ (7.3); □ (26.0), ● (61); (*d*) CHD_3, ○ (0.230), △ (0.43), ▽ (1.22), □ (9.3), ◇ (29.1), ● (61); (*e*) CD_4, ○ (0.025), △ (0.56), ▼ (3.70), ▽ (5.5), ◇ (29.0), ● (61).

Can. J. Chem. Downloaded from www.nrcresearchpress.com by 112.217.228.212 on 09/07/12
For personal use only.

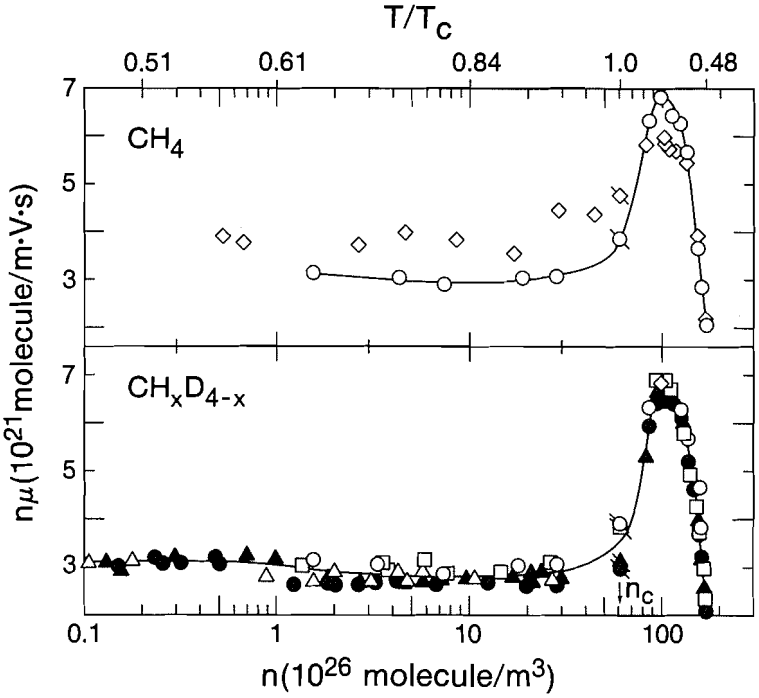

FIG. 5. Density-normalized mobility as functions of density and T/T_c. Symbols as in Figs. 1 and 2. ◇, T_c + 1.4 K; ○, T_c + 0.6 K; □, T_c + 1.3 K; ▲, T_c + 0.5 K; ●, T_c + 0.1 K. T_c = 190.6 K for CH_4.

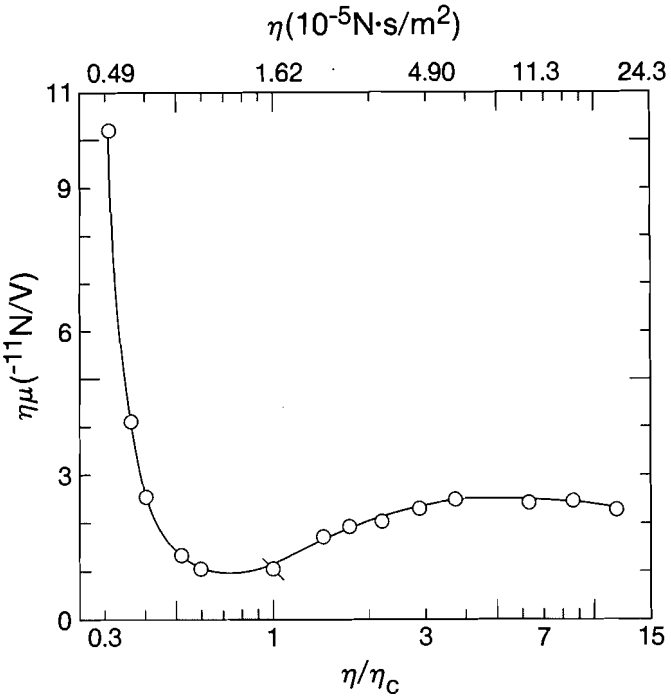

FIG. 6. Viscosity normalized mobility as a function of η/η_c in CH_4. ○, $\eta\mu$ at T_c + 0.6 K. $\eta_c = (1.62 \pm 0.03) \times 10^{-5}$ N s/m^2, refs. 21 and 22.

not correspond to an Arrhenius activation process and is merely shown for comparison with the temperature coefficients at higher densities. At the lowest densities the temperature coefficient of $n\mu$ corresponds to the velocity dependence of σ_{av} and the temperature dependence of $\langle v \rangle$.

The values of $n\mu$ and their temperature and density dependences in the deuterated methanes (Fig. 4*b–e*) were similar to those in CH_4 (Fig. 4*a*). Presumably the cations in the deuterated methanes are clustered like those in CH_4. The difference between $n\mu$ at different n was smaller at higher T, but at n_c the value of $n\mu$ increased above that at lower n. Arrhenius energies determined from [8] fall on a single curve (Fig. 3). Furthermore, at $>10^{26}$ molecules/m^3 these $E_{n\mu}$ values are similar to those obtained from electron mobilities and eq. [8] (8). The fluid compressibility and density fluctuations decrease as the gases are heated away from the liquid coexistence region; this affects the cation and electron mobilities in a similar way.

C. Saturated fluids

The effect of temperature on μ in the saturated fluids (Figs. 1 and 2) can be explained as previously (1–3): in the gas the mobility is dominated by density and in the liquid by viscosity.

The density effect is shown in Fig. 5. Earlier values for CH_4 (1*b*) indicated a smaller density dependence (top portion of Fig. 5), perhaps due to temperature inhomogeneities in the sample. Part of the difference might also be due to the different method used to obtain the time of flight t_d.

The values of $n\mu$ are the same, within the experimental uncertainty, in all the isotopic isomers of methane (Fig. 5, lower portion). At $n < 1 \times 10^{26}$ molecules/m^3, $n\mu$ is constant. At $n > 1 \times 10^{26}$ molecules/m^3, $n\mu$ decreases slightly due to increased clustering, then at $n > 50 \times 10^{26}$ molecules/m^3 $n\mu$ increases due to destructive interference of the long range interactions of the cation with more than one molecule at a time (2). At $n > 100 \times 10^{26}$ molecules/m^3, $n\mu$ decreases due to transition into the viscosity limited regime of transport.

A plot of the mobility normalized for the fluid viscosity, $\eta\mu$, against reduced viscosity η/η_c displays a nearly constant value of $\eta\mu$ at $\eta/\eta_c \geq 2$ (Fig. 6; liquid η ref. 23, gas ref. 22, η_c refs. 21 and 22). This is the viscosity limited regime; $n = 100 \times 10^{26}$ molecules/m^3 for the liquid under its vapor pressure

Can. J. Chem. Downloaded from www.nrcresearchpress.com by 112.217.228.212 on 09/07/12
For personal use only.

corresponds to $\eta/\eta_c = 1.73$. The rapid increase of $\eta\mu$ at $\eta/\eta_c < 0.5$ corresponds to the density-limited regime of transport. The transition region is $0.5 < \eta/\eta_c < 1.7$, which corresponds to $0.2 < n/n_c < 1.7$. The behavior is similar for cations in other hydrocarbon gases and liquids, including ethene, ethane, and *n*-hexane (1*b*).

In the viscosity-limited regime the effective Stokes' radius R_s of the ions is

$$[9] \quad R_s = e/6\pi\eta\mu = 8.5 \times 10^{-21}/\eta\mu \quad \text{in SI}$$

For methane ions in methane, $\eta\mu \approx 2.4 \times 10^{-11}$ N/V at $3 \leq \eta/\eta_c \leq 12$, which corresponds to $R_s = 3.5 \times 10^{-10}$ m. This is nearly twice the molecular radius 2.0×10^{-10} m obtained from gas phase viscosity and diffusion measurements (24). The greater effective radius of the ion for transport is due to the attractive charge-induced–dipole interaction and the resulting electrostriction of the fluid about the ion.

At $\eta/\eta_c \gtrsim 10$ there is a tendancy for $\eta\mu$ to decrease slightly (1*b*). This decrease might be the source of discrepancy between earlier reports that cation mobility in liquid alkanes varies as η^{-x} with $x = 1.5$ (25) or 1.2 ± 0.1 (7). The reported value of x would depend on the range of η/η_c investigated (1).

Acknowledgements

We thank the staff of the Radiation Research Center for maintaining the experimental apparatus, and the Natural Sciences and Engineering Research Council of Canada for financial assistance.

1. N. Gee and G. R. Freeman. Can. J. Chem. (*a*) **58**, 1490 (1980); (*b*) **59**, 2988 (1981).
2. N. Gee, S. S.-S. Huang, T. Wada, and G. R. Freeman. J. Chem. Phys. **77**, 1411 (1982).
3. N. Gee, M. A. Floriano, and G. R. Freeman. (*a*) Z. Naturforsch. **39**a, 1225 (1984); (*b*) Can. J. Chem. **64**, 2423 (1986).
4. M. A. Floriano and G. R. Freeman. J. Chem. Phys. **85**, 1603 (1986).
5. M. A. Floriano, N. Gee, and G. R. Freeman. J. Chem. Phys. **84**, 6799 (1986).
6. T. Wada and G. R. Freeman. Phys. Rev. Lett. **42**, 715 (1978).
7. J.-P. Dodelet and G. R. Freeman. Can. J. Chem. **55**, 2264 (1977).
8. M. A. Floriano, N. Gee, and G. R. Freeman. J. Chem. Phys. **87**, 4829 (1987).
9. A. F. Grigor. Ph.D. Thesis, Pennsylvania State University. 1966.
10. R. D. Goodwin. The thermophysical properties of methane from 90 to 500 K at pressures up to 700 bar. National Bur. Stand. Tech. Note 653. U.S. GPO, Washington DC. 1974.
11. S. Angus, B. Armstrong, and K. M. de Reuck (*Editors*). International thermodynamic tables for the fluid state – 5: Methane, IUPAC Chemical Data Series, No. 16. Pergamon, Oxford. 1978.
12. Thermoelectric Co. Catalog, 6th ed. Saddlebrook, NJ. 1974. p. 10.
13. E. W. McDaniel and E. A. Mason. The mobility and diffusion of ions in gases. J. Wiley, New York. 1973. (*a*) Eq. (5-2-15), p. 123; (*b*) p. 4-6; (*c*) p. 140.
14. R. E. Robson and E. A. Mason. Phys. Rev. A, **25**, 2411 (1982).
15. B. V. Paranjape. Phys. Rev. A, **21**, 405 (1980).
16. S. S.-S. Huang and G. R. Freeman. J. Chem. Phys. **68**, 1355 (1978).
17. K. Hiraoka and P. Kebarle. (*a*) J. Am. Chem. Soc. **97**, 4179 (1975); (*b*) J. Chem. Phys. **63**, 394 (1975).
18. D. P. Ridge and J. L. Beauchamp. J. Chem. Phys. **64**, 2735 (1976).
19. M. Saporoschenko. Int. J. Mass Spectros. Ion Phys. **42**, 285 (1982).
20. N. Gee and G. R. Freeman. Can. J. Chem. **61**, 1644 (1983).
21. Y. S. Touloukian, S. C. Saxena, and P. Petermans. Viscosity, thermophysical properties of matter. Vol. II. IFI/Plenum, New York. 1975. p. 186.
22. N. B. Vargaftik. Tables on the thermophysical properties of liquids and gases. 2nd ed. J. Wiley, Halsted Press. 1975. p. 222.
23. W. M. Haynes. Physica, **70**, 410 (1973).
24. J. O. Hirschfelder, C. F. Curtiss, and R. B. Bird. Molecular theory of gases and liquids. Wiley, New York. 1954. p. 545.
25. I. Adamczewski. Ionization, conductivity and breakdown in dielectric liquids. Taylor and Francis, London. 1969. Chapt. 2.

Can. J. Chem. Downloaded from www.nrcresearchpress.com by 112.217.228.212 on 09/07/12
For personal use only.

Investigation of electron correlation effects in the inner-valence photoelectron spectra of argon and xenon using synchrotron radiation at high resolution

C. E. BRION AND A. O. BAWAGAN

Department of Chemistry, University of British Columbia, Vancouver, B.C., Canada V6T 1Y6

AND

K. H. TAN

Canadian Synchrotron Radiation Facility, Synchrotron Radiation Center, University of Wisconsin, Stoughton, WI 53589, U.S.A.

Received December 14, 1987

This paper is dedicated to Professor Charles A. McDowell on the occasion of his seventieth birthday

C. E. BRION, A. O. BAWAGAN, and K. H. TAN. Can. J. Chem. **66**, 1877 (1988).

High-resolution, magic angle photoelectron spectra have been obtained for the Ar 3*s* and Xe 5*s* inner-valence regions using photon energies in the range 60–170 eV. Measurements were made using monochromatized synchrotron radiation from the Canadian Synchrotron Radiation Facility at the new 1-GeV storage ring at the University of Wisconsin. The binding energy spectra show detailed and complex structures due to electron correlation (many-body) effects. Relative satellite intensities are compared with the results of recent configuration-interaction calculations. Additional binding energy spectra obtained at much higher resolution (0.16 eV fwhm) than any previous published work show extremely detailed satellite structure consistent with information from recent high resolution fluorescence studies for argon. The newly revealed satellite structure provides further insight into existing differences between calculated and measured satellite intensities. In the case of the Ar 3*s* spectrum, very close agreement is predicted between the measured intensities and those calculated by CI methods when the previously unresolved satellite structure is taken into account. These new spectral observations also provide information and perspective relevant to recent controversies in the literature concerning intensities and mechanisms in photoelectron and electron momentum spectroscopies.

C. E. BRION, A. O. BAWAGAN et K. H. TAN. Can. J. Chem. **66**, 1877 (1988).

Utilisant des énergies photoniques allant de 60 à 170 eV, on a déterminé les spectres photoélectroniques à haute résolution, à l'angle magique, des régions de valence interne 3*s* du Ar et 5*s* du Xe. On a effectué les mesures à l'aide d'une radiation synchrotron monochromatique provenant du laboratoire canadien de radiation synchrotron installé dans l'anneau d'emmagasinage de 1 GeV, à l'Université du Wisconsin. Les spectres d'énergie de liaison présentent des structures détaillées et complexes à cause des effets de corrélation électronique (à plusieurs corps). On a comparé les intensités relatives des satellites avec les résultats de calculs récents relatifs aux interactions de configuration. Des spectres additionnels d'énergie de liaison, obtenus à une résolution beaucoup plus grande (0,16 eV fwhm) que celles utilisées antérieurement, présentent une structure satellite extrêmement détaillée qui est en accord avec l'information obtenue à partir d'études récentes de fluorescence à haute résolution effectuées sur l'argon. La nouvelle structure satellite observée fournit une connaissance plus profonde sur les différences qui existent entre les intensités satellites calculées et mesurées. Dans le cas du spectre du Ar 3*s*, alors qu'on prend en considération la structure satellite qui n'avait pas été résolue antérieurement, on observe une excellente corrélation entre les intensités mesurées et celles calculées par les méthodes des IC. Ces nouvelles observations spectrales fournissent aussi de l'information et une perspective qui présentent de l'intérêt en relation avec les récentes controverses qui ont surgies dans la littérature concernant les intensités et les mécanismes des spectroscopies photoélectronique et du moment électronique.

[Traduit par la revue]

Introduction

Photoelectron spectroscopy (PES) using vacuum ultraviolet radiation has provided detailed insight into valence-shell photoionization processes and the electronic structure of free atoms and molecules. Early HeI PES studies of the outer-valence *np* photoionization of the noble gases by Al-Joboury and Turner (1, 2), and also the elegant photoelectron studies of Ar, Kr, and Xe by Frost, McDowell, and Vroom (3), using a spherical grid retarding spectrometer were seminal in the rise and development of ultraviolet PES. Today PES is a precise tool not only for the study of fundamental processes in photoionization, but also for the investigation of electron correlation effects as well as the detailed evaluation of quantum mechanical calculations of ionization energies and cross-sections. *Outer-valence* (*np*) photoionization of noble gases is well described by a single-particle (independent-particle) model, i.e., electron-correlation effects do not appear to play a major role in the ionization process. As such, *np* photoionization results in a single process in which the only splitting in the PES spectrum of each noble gas is the doublet ($^2P_{3/2,1/2}$) due to spin–orbit interaction (1–3).

In contrast to the situation for the outer-valence region of noble gases and other species, it is now increasingly well known that ionization of *inner-valence* electrons in many atoms and molecules is, in most cases, accompanied by significant many-body (electron-correlation) effects, leading to extensive splitting of the ionization strength into a manifold consisting of many final ion states (satellites). In simple terms, this means that (outside of spin–orbit effects) there is often more than one peak per orbital in the binding energy spectrum, particularly in the inner-valence region. In this situation it is obvious that spectral interpretations based on simple (i.e., independent particle) atomic or molecular orbital theory will be erroneous. Early experiments using binary (e,2e) spectroscopy (4) and X-ray photoelectron spectroscopy (XPS) (5, 6) at modest energy resolution clearly showed the existence of such satellite structures in the inner-valence (*ns*) ionization spectra of noble gases. Similar early experimental observations reported for

Can. J. Chem. Downloaded from www.nrcresearchpress.com by 112.217.228.212 on 09/07/12
For personal use only.

Can. J. Chem. Downloaded from www.nrcresearchpress.com by 112.217.228.212 on 09/07/12
For personal use only.

molecules using binary (e, 2e) (now usually referred to as EMS or Electron Momentum Spectroscopy) (7–9) and dipole (e, 2e) spectroscopy (7, 10, 11) were supported by the many-body Green's function calculations of Cederbaum and co-workers (12–14).

The more detailed investigation of the inner-valence binding energy region by photoelectron spectroscopy at high resolution remained largely uninvestigated from an experimental standpoint for a long time, since it is energetically inaccessible using HeI radiation (21.22 eV). This situation has changed over the past decade with the growing availability of monochromatized synchrotron radiation, which provides light of tunable energy throughout the vacuum UV and soft X-ray regions of the electromagnetic spectrum (10 eV up to at least several hundred eV, depending on the monochromator). In particular, the energies and intensities of the rich satellite structure resulting from the photoionization of the inner-valence (*ns*) electrons in the noble gases should provide, in principle, a precise and detailed "test-bed" for quantum mechanical treatments of the role of electron-correlation effects in photoionization processes.

The earlier observations of satellite structures in the *ns* ionization spectra of the noble gases were followed in the period up to early 1986 by further photon (15–20) and electron (21–24) impact experiments at generally rather modest energy resolution, as well as a series of theoretical investigations (25–37) (for a discussion of these and other relevant studies, see refs. 19 and 20). As a result of the different findings and conclusions in these various experimental and theoretical studies, a growing controversy developed in the period up to mid-1986. Sharp differences of opinion and interpretation were published (19, 20, 25, 27, 28–31, 36, 38) with particular regard to the various different observed and calculated satellite intensity distributions as well as the comparison between PES and EMS mechanisms (39, 40), particularly in the case of the Ar 3*s* spectrum. Further experimental and theoretical debate on this issue has continued up to the present date (41–47). It became increasingly clear that much of the controversy and confusion was probably arising because of the likely existence of many unresolved satellite lines belonging to different symmetry manifolds in the respective Ar 3*s* and Xe 5*s* spectra. Since all experiments up to early 1986 were carried out at low and often rather different energy resolutions, the presence of any such unresolved satellites could well be a major contributing reason for the different spectral envelopes observed in the various published results. In addition, when comparing the results of these various experiments with theory, the fact that in most cases the calculations only include the major symmetry manifolds and, more importantly, are "resolutionless" was generally overlooked by most authors, although some consideration of the effects of resolution on spectral envelopes and interpreted peak heights was given in our earlier publications (20, 41).

In mid-1986 we obtained significantly higher-resolution PES spectra for Ar 3*s* and Xe 5*s* photoionization (42) by taking advantage of the higher photon flux available on the Canadian Synchrotron Radiation Facility (CSRF) at the new 1-GeV Storage Ring (formerly known as ALADDIN) at the University of Wisconsin. These results show many more satellite lines than had been resolved in any of the earlier-reported spectra (5, 6, 15–24). A preliminary communication of the new high-resolution Ar 3*s* results, including a comparison with measurements by XPS and electron momentum spectroscopy, has recently been published (41). Concurrently, Schmidt and co-workers in West Germany (43, 44) reported Ar 3*s* PES spectra of similar quality. We now report full details of the energies and intensities in these high-resolution binding energy spectra for Ar 3*s*, as well as similar results for Xe 5*s* photoionization. A comparison is also made with calculated satellite intensities (25–33, 37, 44, 45) as well as with very recent Al Kα XPS studies of Ar 3*s* (46). In addition, we make an initial report of new Ar 3*s* and Xe 5*s* binding-energy spectra at even higher resolution (0.16 eV fwhm and 0.19 eV fwhm, respectively) that have been obtained very recently at CSRF. These binding-energy spectra, which are at significantly higher resolution than any previously published work using PES or EMS, reveal even further detailed satellite structure, providing new insight into the existing discrepancies and controversies between theory and experiment. The new highest-resolution Ar 3*s* results obtained with PES are consistent with the very recent high-resolution fluorescence studies of argon using broad-band synchrotron radiation as reported by Samson, Chung, and Lee (47).

Experimental

PES measurements were made on the Canadian Synchrotron Radiation Facility (CSRF) at the new 1-GeV storage ring located at the Synchrotron Radiation Center at the University of Wisconsin. Photoelectron spectra for argon were obtained using a Leybold-Heraeus LHS-11 hemispherical, magic-angle spectrometer over the binding-energy range 26–48 eV, and at photon energies in the range 60–170 eV. The CSRF facility has been described earlier in some detail (48–50). In the case of xenon the binding energy range was 22–38 eV, and photon energies were in the range 80–140 eV. Polarized synchrotron radiation from the 1-GeV storage ring, dispersed using a Mark IV Grasshopper monochromator (49), was directed into the collision chamber of the photoelectron spectrometer. The high light flux of the 1-GeV storage ring facilitated the measurement of photoelectron spectra at significantly higher energy resolution and at higher photon energies than in our earlier work (19, 20), which was carried out using the older, less intense, Tantalus I storage ring. At lower photon energies, where the monochromator energy band pass is narrow, an electron spectrometer pass energy of 50 eV used in the electron spectrometer gave an overall energy resolution as good as 0.3 eV fwhm. Above $h\nu$ = 120 eV the overall spectral resolution is less good since the pass energy was increased to 100 eV to be more compatible with the larger energy band-pass of the Grasshopper monochromator. Under these conditions the transmission efficiency of the analyzer input lens system is effectively constant (48) over the electron kinetic energy ranges involved for the Ar 3*s* and Xe 5*s* spectra. For the highest-resolution spectra (~0.16 eV fwhm) the analyzer pass energy was lowered to 25 eV (contributing ~0.1 eV to the overall resolution) and the monochromator band pass was further narrowed to contribute about 0.1 eV at a photon energy of 80 eV. Under these conditions the overall energy resolution is as good as ~0.15 eV fwhm, but the analyzer transmission efficiency varies slowly (dropping by ~30%) over the range of the binding-energy spectrum, and therefore highly accurate relative intensities of satellite lines cannot be obtained at present from the highest resolution spectra. Nevertheless the trend of relative peak intensities should be semi-quantitative. Experiments are in hand to determine the transmission function of the analyzer at lower pass energies, corresponding to the highest-resolution conditions, so that the spectral intensities may be corrected appropriately. The absolute binding energy scale has been established by assigning a value of 29.235 eV to the Ar $3s3p^6(^2S)$ primary hole state, and 23.397 eV to the Xe $5s5p^6(^2S)$ hole state using optical emission data (51). Argon and xenon gases were taken from Matheson lecture bottles of both high purity (99.995%) and research grade (99.9995%) for each gas so as to carefully check for impurities.

Results and discussion

1. Ar 3s spectrum

Figure 1 shows typical Ar 3*s* photoelectron spectra measured

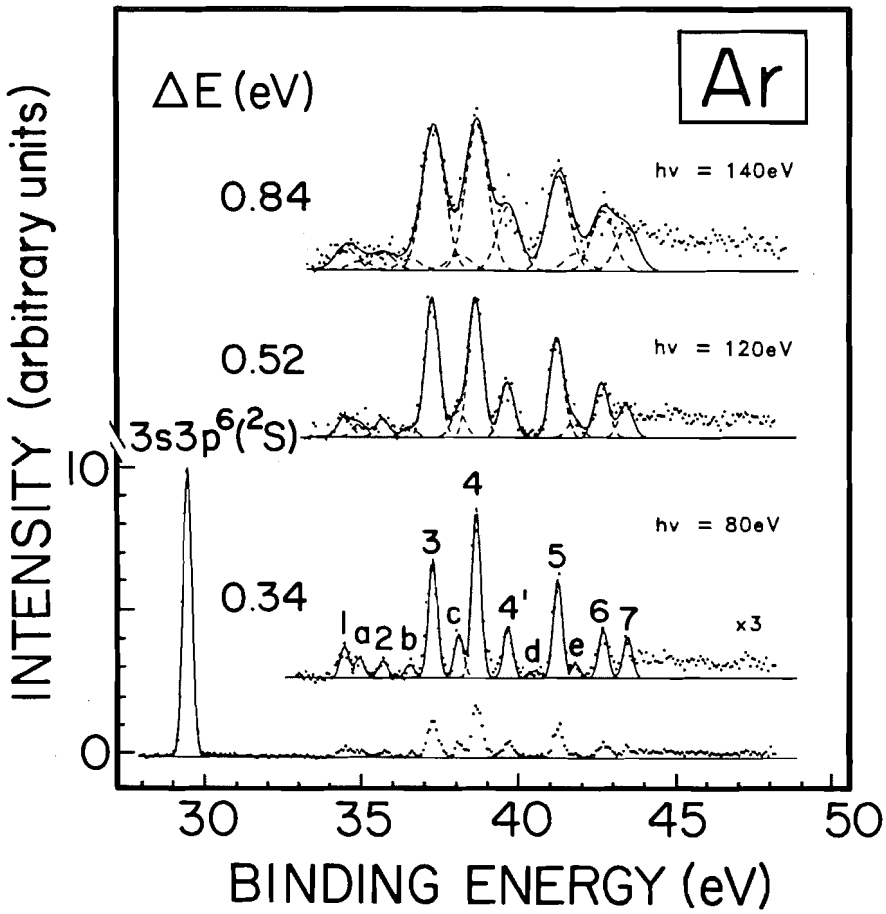

FIG. 1. Photoelectron spectra as a function of photon energy in the inner-valence ($3s$) binding-energy region of argon.

at photon energies of 80, 120, and 140 eV at combined analyzer/monochromator band-passes as good as 0.34 eV fwhm. Spectra were obtained at a series of photon energies in the range 60–170 eV. Gaussian peaks have been fitted to the satellite spectrum using widths determined by the $3s3p^6(^2S)$ hole state. The spectra shown in Fig. 1 are considerably better resolved than those in earlier published work (15, 17–23) and show many satellite lines not previously resolved. Results similar to those shown in Fig. 1 have also recently been reported by Schmidt and co-workers (43, 44). Considering the $h\nu$ = 80 eV spectrum (Fig. 1), at least three peaks (c, 4 and 4')[1] are seen to contribute to the single peak observed in earlier low-resolution work (5, 15, 17–23) at 38.6 eV and assigned to the dominant configuration $3s^23p^43d(^2S)$. Clearly all earlier comments and conclusions (6, 19, 20, 25–31, 38, 44, 46) based on comparisons of peak intensities, particularly at 38.6 eV, in low-energy-resolution PES (5, 15–20) and EMS (21–23) binding-energy spectra, may be incorrect due to effects from the more complex satellite structure now revealed. In addition to the main $3s3p^6(^2S)$ hole state[2] at 29.30 eV, at least 12 higher-binding-energy satellite lines are seen, with possibly a further line (d) being present. The states indicated by a, c, d, and e have not been observed until our earlier preliminary report (41) except in the concurrent work of Schmidt and co-workers (43, 44).

The intensities of the satellite lines relative to the height of the main $3s3p^6(^2S)$ line are given in Table 1 and are in close agreement with those also recently reported by Kossman *et al.* (44). Peaks 4, 5, 6, and 7 may be identified with Ar II states having dominant configurations $3s^23p^4(^1D)nd(^2S)$, n = 3–6. This dominant satellite series has been the subject of much theoretical work, of which the more recent CI calculations (relative intensities) of Smid and Hansen (30) and Kossman *et al.* (44) appear to show the best agreement (41, 44) with experiment. Figure 2 shows a comparison between the relative intensities in the spectrum obtained at $h\nu$ = 80 eV in the present work and the relative intensity predictions of the CI calculations of Smid and Hansen (30) for the $nd(^2S)$ series only, for $h\nu$ = 77.2 eV. The calculations (30) include the photon-energy dependence. For this comparison the experimental energy positions were used for both the experiment and the calculations. The calculated intensities have been convoluted with a Gaussian peak shape corresponding to the experimental resolution, as given by the main $3s$ line at 29.24 eV. The peaks in the experimental spectrum at the energies corresponding to the $nd(^2S)$ series have been shaded for ease of comparison and it can be seen that there is quite good general agreement between theory and the measured spectrum. A more detailed and quantitative comparison with theory is given in Fig. 3 in graphical form. The relative satellite intensities for the $nd(^2S)$

[1]The labelling system follows that of earlier papers (18, 41, 46) to facilitate comparison (note that peak b in the present work has been designated as 3' earlier (18, 46)). Newly resolved states are indicated by lower case letters a, c, d, etc.

[2]Note that the single particle configurations as used in ref. 51 and elsewhere to designate states are only an approximation and at best represent the dominant configuration in a CI description.

Can. J. Chem. Downloaded from www.nrcresearchpress.com by 112.217.228.212 on 09/07/12
For personal use only.

TABLE 1. Peak energies and relative intensities (%) in the Ar 3*s* binding energy spectrum as a function of photon energy

Photon energy (eV)	fwhm* (eV)	Peak number, peak energy, and relative intensity (%)‡												
		$3s^{-1}$ 29.24†	1 34.34	a 34.82	2 35.57	b 36.42	3 37.17	c 38.00	4 38.56	4′ 39.57	5 41.17	e 41.74	6 42.63	7 43.41
60	0.30	100	4(3)	5(3)	1(3)	1(3)	14(3)	4(3)	19(3)	7(3)	12(3)	3(3)	7(3)	5(3)
70	0.32	100	4(3)	3(3)	3(3)	3(3)	16(3)	4(3)	19(3)	6(3)	13(3)	3(3)	7(3)	5(3)
80	0.34	100	4(1)	2(1)	2(1)	1(1)	14(1)	5(1)	19(1)	6(1)	11(1)	1(1)	6(1)	5(1)
90	0.36	100	3(2)	2(2)	2(2)	1(2)	15(2)	4(2)	17(2)	6(2)	12(2)	2(2)	6(2)	4(2)
100	0.39	100	3(2)	2(2)	3(2)	2(2)	18(2)	4(2)	18(2)	6(2)	12(2)	2(2)	8(2)	4(2)
110	0.45	100	3(2)	2(2)	2(2)	2(2)	16(2)	3(2)	18(2)	6(2)	12(2)	1(2)	6(2)	4(2)
120	0.52	100	2(1)	2(1)	2(1)	1(1)	16(1)	3(1)	16(1)	7(1)	12(1)	2(1)	6(1)	4(1)
130	0.76	100	2(1)	1(1)	2(1)	1(1)	17(1)	1(1)	16(1)	7(1)	12(1)	2(1)	5(1)	4(1)
140	0.84	100	3(1)	1(1)	2(1)	1(1)	17(1)	2(1)	17(1)	7(1)	12(1)	1(1)	7(1)	5(1)
150	0.94	100	1(2)	1(2)	2(2)	<1	16(2)	1(2)	15(2)	6(2)	9(2)	<1	5(2)	4(2)
160	1.08	100	3(2)	<1	3(2)	<1	17(2)	<1	17(2)	7(2)	12(2)	<1	6(2)	6(2)
170	1.16	100	2(4)	<1	2(4)	<1	16(4)	<1	15(4)	8(4)	10(4)	<1	4(4)	3(4)

*Width of $3s3p^6(^2S)$ peak used for peak fitting.
†Optical value (29.235 eV) (51); note PES data give a value of 29.30 eV (15, 18).
‡Uncertainties shown in parentheses.

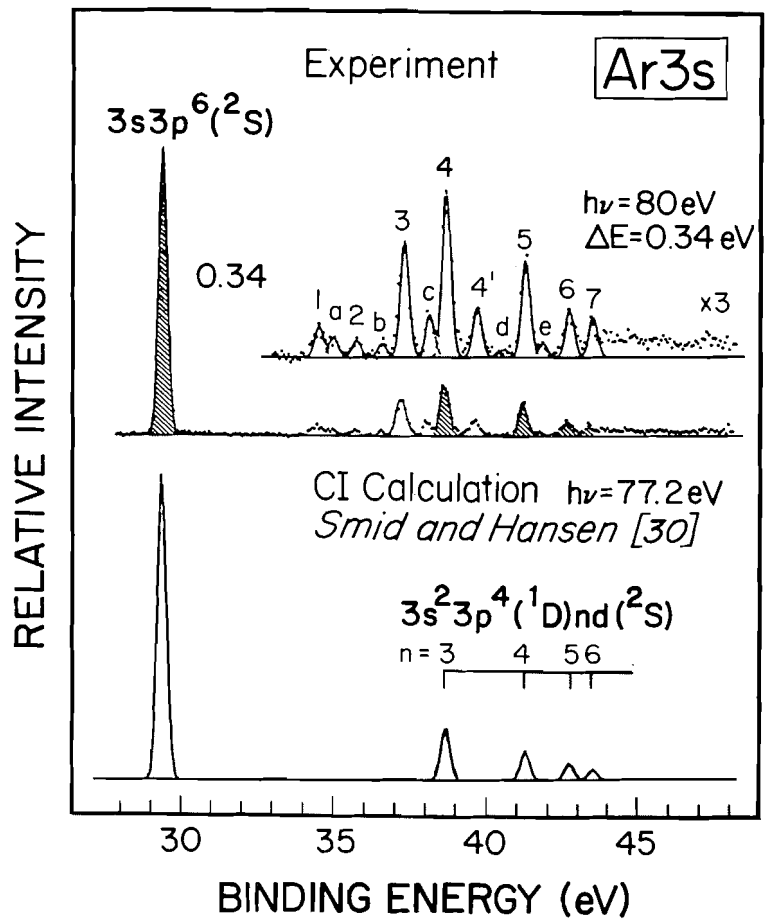

FIG. 2. Comparison of experimental PES spectrum ($h\nu$ = 80 eV, ΔE = 0.34 eV fwhm) with the calculated intensities of the $3s^23p^4(^1D)nd(^2S)$ series of argon reported for $h\nu$ = 77.2 eV by Smid and Hansen (30). The calculated spectrum has been convoluted with a Gaussian function (0.34 eV fwhm) and the transition energies are set at the experimental values. The corresponding peaks in the experimental spectrum have been shaded for ease of identification with the calculation.

Can. J. Chem. Downloaded from www.nrcresearchpress.com by 112.217.228.212 on 09/07/12
For personal use only.

Can. J. Chem. Downloaded from www.nrcresearchpress.com by 112.217.228.212 on 09/07/12
For personal use only.

series, measured in the present work (solid circles) and in the work of Kossman *et al.* (44) (open circles), are shown together with the results of CI calculations of Smid and Hansen (30) and Kossman *et al.* (44) (plus signs, mean of velocity and length calculations) and also the values calculated by Dyall and Larkins (32, 33) (solid triangles) at $h\nu$ = 151 eV. Also shown on Fig. 3 are experimental data points from magic-angle PES measurements (open squares) by Adam *et al.* (15, 18) at 58.3 and 77.2 eV, and 90° XPS measurements (open diamonds) by Spears *et al.* (5) at 151 eV. It can be seen that in general there is reasonable agreement between theory and experiment, for both the magnitudes and the trends of the relative cross-sections with a particularly noticeable decrease in relative intensity with increase in photon energy in the case of peak 4.

It is of further interest to consider the trend of relative satellite intensities over a much wider range of photon energies, and in particular to include the XPS data obtained at high photon energies (5, 46). In addition, results from electron-momentum spectroscopy (EMS) (or binary (e,2e) spectroscopy, as it has been earlier known) are expected to yield the true spectroscopic factors (at sufficiently high energy resolution) since there is no photon-energy-dependent dipole matrix element in the cross-section expression (38–40). Thus, as has been discussed earlier (7, 19, 20, 38–41), it is to be expected that EMS and very-high energy XPS will give similar values for relative satellite intensities within the same symmetry manifold, provided that the energy resolutions are comparable and that initial state correlation effects are negligible (39–41). As has also been discussed earlier (20, 39–41), it should be remembered that XPS and EMS sample very different electron momenta, and therefore very different regions of the wave function. In the context of the above considerations, various data (PES, XPS, and theory) have been plotted on Fig. 4 for the relative intensity of the $3s^2 3p^4(^1D)3d(^2S)$ main satellite line (peak 4 of Figs. 1 and 2) as a function of energy over the photon-energy range 60–1487 eV. An inverse energy scale has been used so that infinite photon energy can be represented (i.e. the high-energy photon limit). The EMS data point of Leung and Brion (22), with the intensity re-evaluated using the new spectral information for Ar 3*s* as discussed in ref. 41, is shown on the left-hand axis, together with the pole-strength calculation (CI2, basis 2) of Mitroy *et al.* (37). It is clear that the common trend of the measured and calculated data at low photon energy (shown by the dotted line) is not followed by experiment at high photon energy (>1200 eV), even though such a trend is predicted by the calculations of Smid and Hansen (30) and Dyall and Larkins (32, 33). The earlier XPS measurement by Spears *et al.* (5) at 1487 eV is in good agreement with the recent much higher-quality measurements of Svensson *et al.* (46). It should be noted, however, that both XPS measurements were made at an ejection angle of 90° and not at the magic angle, but not withstanding this the *relative* satellite intensity should be little affected since both states involved are in the same symmetry manifold (38–41) and variations in β are not usually considered to be significant. As discussed earlier (41), however, it should be noted that relativistic and multipole effects (52, 53) may well be important in calculations corresponding to XPS energies above the kilovolt range. The EMS data point (22), reinterpreted (41) allowing for the previously undetected nearby satellite lines (see Fig. 1), seems to be in the region of what would be projected for the high-energy photon limit, in keeping with earlier expectations (7, 19, 20, 39). A final confirmatory

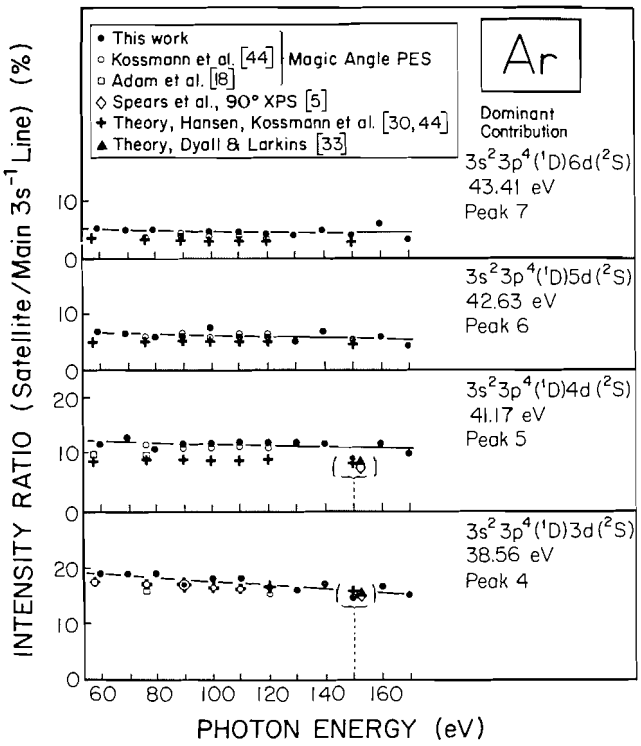

FIG. 3. Variation of measured and calculated relative intensities with photon energy for selected satellites in the Ar 3*s* binding-energy spectrum.

test of these preliminary findings must await further XPS and EMS measurements at much higher energy resolution, comparable at least with that in the high-resolution PES data of Fig. 1. The pole strength (spectroscopic factor) calculation by Mitroy *et al.* shown on Fig. 4 is the most sophisticated (CI2, basis 2) of three calculations reported (37), and corresponds quite well with the reinterpreted EMS data (41). A new CI calculation of spectroscopic factors by Hibbert and Hansen (54) shows good agreement with the measured XPS values (5, 46) at $h\nu$ = 1487 eV, but poorer agreement with the earlier CI calculations by Smid and Hansen (30) and Dyall and Larkins (32, 33). The XPS value at $h\nu$ = 1254 eV reported earlier by Spears *et al.* (5) is quite low relative to the $h\nu$ = 1487 eV measurement and the trend of the other data. Further XPS measurements at this energy and also at even higher photon energies and at better resolution would be informative.

From the data in Fig. 4 and a consideration of the high-resolution Ar 3*s* spectra (see Fig. 1 and refs. 41–44), it is clear that the earlier interpretations of the variation of relative intensities both in our own work (19, 20) and in other publications (28–31, 38), based on lower-resolution PES and EMS spectra, are probably erroneous due to the unrecognized presence of previously unresolved neighboring satellite states. Similarly the recent assessment of our earlier work (see Fig. 3 of ref. 19) by Kossman *et al.* in Fig. 4 of ref. 44 is not meaningful in view of the newly available Ar 3*s* spectroscopic data (41, 43, 44).

A more detailed examination of the relative-intensity data in Fig. 3, however, shows that, despite the overall quite good agreement, the CI calculations (30, 44) are lower in all cases than the presently reported measured relative intensities, with a particularly large discrepancy (~30%) existing for peak 5

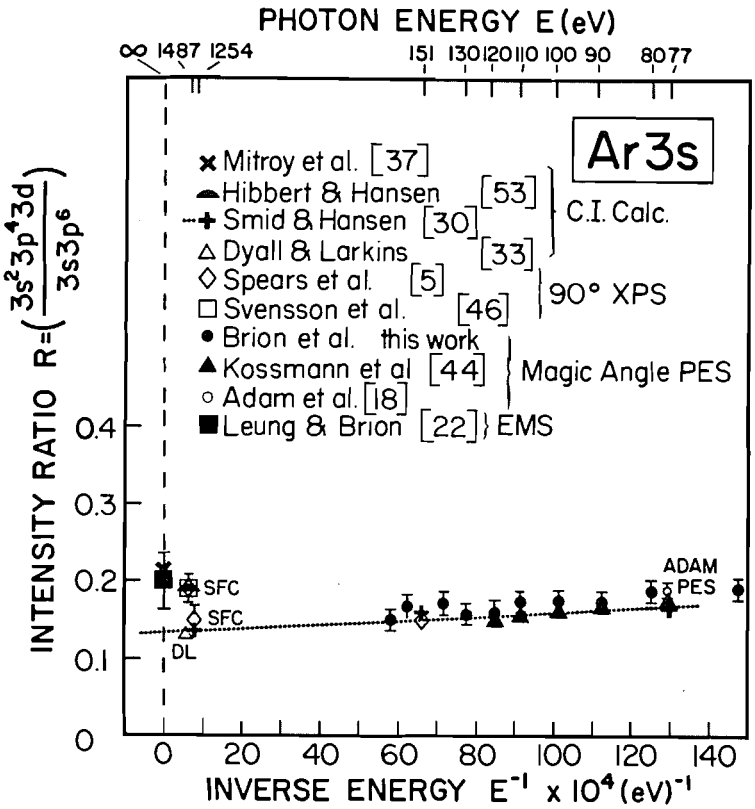

FIG. 4. Comparison of measured (PES, XPS, and EMS) and calculated relative intensities of the satellite peak at 38.56 eV (containing mainly $3s^23p^4(^1D)3d(^2S)$) as a function of energy. Note the non-linear and inverse energy scales on the top and bottom of the figure, respectively.

(dominant configuration $3s^23p^4(^1D)4d(^2S)$). Reasons for these appreciable discrepancies may include any or all of the following: (*i*) inaccuracy of the CI calculations; (*ii*) errors in the measurements; e.g., uncertainties in the electron transmission efficiency and/or non-magic-angle effects involving the polarization direction (53); (*iii*) the presence of yet further unresolved satellite lines of different symmetries contributing to the measured peaks (Figs. 1 and 2) nominally assigned (41–44) to the $3s^23p^4nd(^2S)$ series. Most states are expected on the basis of optical emission data (51); and (*iv*) breakdown of the Dipole Approximation and the plane wave treatment of the ionized electron.

In order to further investigate the differences between theory and experiment with regard to item *3* above, the Ar 3*s* binding energy spectrum has recently been obtained at very high resolution (0.16 eV fwhm) by lowering the electron analyzer pass energy and narrowing the slits in the Grasshopper monochromator. A typical spectrum obtained under these conditions at $h\nu = 80$ eV is shown in Fig. 5. These new data, at significantly higher resolution than any previously published PES spectra, exhibit very detailed satellite structure. In addition to a number of readily observed new peaks, several partially resolved shoulders, notably on peaks 3, c, 4, 4′, 5, and 6 are also apparent. The energies corresponding to the peaks and shoulders in Fig. 5 are listed in Table 2. For ease of identification and comparison with previous spectra, the same notation as was used earlier (18, 41–44, 46) has been used for the corresponding peaks, whereas newly observed peaks and shoulders are denoted by asterisks (*). At the low analyzer pass energy used, the electron transmission efficiency varies slowly over the range of kinetic energies involved in the higher-resolution spectrum of Fig. 5. As such, until this transmission function can be accurately determined (see experimental section), no highly accurate relative intensities can be derived from the spectrum. Nevertheless, the detailed spectroscopy and qualitative relative-intensity considerations provide helpful insight into the discrepancies observed in comparisons of intensities between theory and experiment (see Fig. 3) for the constant transmission, lower-resolution spectra (Figs. 1 and 2). In particular, peaks 4, 5, 6, and 7 (Fig. 5), which were assigned earlier exclusively to $n = 3$, 4, 5, and 6 of the main satellite series $3s^23p^4(^1D)nd(^2S)$, each show additional structure that was not evident in the lower-resolution spectrum (Figs. 1 and 2). Specifically, as indicated by the shaded areas on Fig. 5, peak 4 shows a high-energy unresolved shoulder (estimated as ~10% of peak 4) and peak 5 shows a low-energy shoulder and an extra peak on the high-energy side (~20% and 10% of peak 5, respectively). In addition, small extra peaks are now seen on either side of each of peaks 6 and 7. An examination of Fig. 3 shows that in each case (peaks 4, 5, 6, and 7) the calculated relative intensities are below those measured under the existing medium-energy resolution (41–44) conditions. These discrepancies in Fig. 3 for $n = 3$ and 4 (i.e. peaks 4 and 5) correspond closely to the estimated extra areas (10% and 30%, respectively, see above) attributable to the previously unresolved satellites in the vicinity of peaks 4 and 5. Application of these corrections would lead to much better agreement between experiment and the CI calculations (30, 44) for the relative intensities of the satellite peaks in the $3s^23p^4(^1D)nd(^2S)$ series. In a similar fashion it can be seen that improved agreement would also exist between theory and experiment for $n = 5$ and 6 (i.e. peaks 6 and 7) when contributions from newly observed neighbouring

Can. J. Chem. Downloaded from www.nrcresearchpress.com by 112.217.228.212 on 09/07/12
For personal use only.

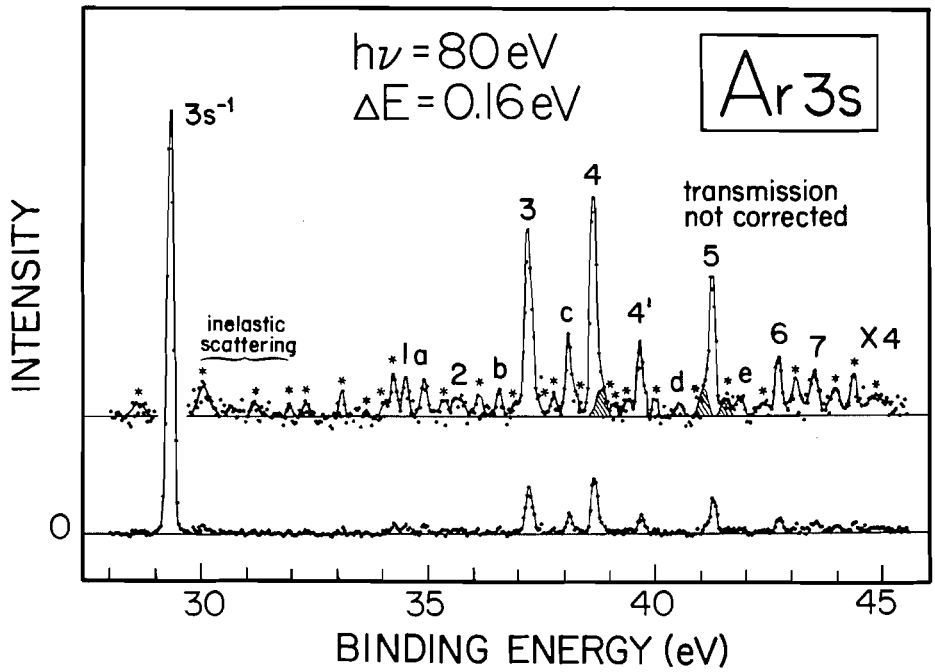

FIG. 5. Ar 3*s* binding-energy spectrum at high resolution (0.16 eV fwhm) and $h\nu$ = 80 eV. See Table 2 for details. The shaded peaks show contributions to peaks 4 and 5 in the lower-resolution spectrum in Fig. 1 from other newly observed satellites. Peaks at 29.95 and 31.10 eV are due to inelastic scattering. Note that the intensities in these spectra have not been corrected for the slowly varying electron-transmission efficiency (see text).

TABLE 2. Energies of features in the Ar 3*s* photoelectron spectrum at high resolution

Peak† designation	Peak energy (eV) This work (±0.04) PES ($h\nu$ = 80 eV)	Peak energy (eV) Threshold PES Ref. 56	Peak† designation	Peak energy (eV) This work (±0.04) PES ($h\nu$ = 80 eV)	Peak energy (eV) Threshold PES Ref. 56§
*	28.6	—	*(sh)	37.33	37.42
$3s^{-1}$	29.235‡	29.24	*	37.69	—
*(is)	29.95	—	c	38.01	38.03
*(is)	31.10	—	*(sh)	38.17	(38.3)
*	31.86	—	4	38.56	38.59
*	32.21	32.17	*(sh)	38.80	38.90
	—	32.47	*	39.08	—
	—	32.88	*	39.32	39.35
*	33.05	33.00	4′	39.60	39.61
*	33.56	33.54	*	39.91	40.03
	—	33.78	d	40.47	(40.5)
*(sh)	34.00	34.04	*(sh)	40.99	(40.9)
*	34.16	34.20	5	41.15	41.16
1	34.44	34.39	*	41.50	—
a	34.83	34.91	e	41.74	(41.7)
*	35.27	35.28	*	42.30	—
2	35.59	35.51	6	42.65	—
*	36.02	36.00	*	43.01	—
b(3′)	36.50	36.51	7	43.45	—
*(sh)	36.86	36.90	*	43.88	—
3	37.14	37.11	*	44.32	—
	—	37.23	*	44.80	—

† * indicates newly observed peak or shoulder *(sh), see Fig. 5; *(is) signifies inelastic scattering.

‡ Value from optical emission (51) used to calibrate energy scale.

§ Values shown in parentheses have been estimated for additional peaks present in the threshold spectrum but not identified in ref. 56.

Can. J. Chem. Downloaded from www.nrcresearchpress.com by 112.217.228.212 on 09/07/12
For personal use only.

Can. J. Chem. Downloaded from www.nrcresearchpress.com by 112.217.228.212 on 09/07/12
For personal use only.

peaks in the more-detailed high-resolution spectra (Fig. 5) are considered. It should be noted that there have been a variety of different CI calculations by Hansen and co-workers (28–31, 54) and it is not necessarily clear which are considered to be the most accurate for either relative intensities or energies. Further improvement in the accuracy of the calculated energies is desirable (for example, see ref. 54). However, it should be noted that the very recent many-body perturbation calculations of argon satellite intensities by Wijesundera and Kelly (55) give intensities in close agreement with the results of Smid and Hansen in ref. 30.

Two other very recent spectroscopic studies provide information relevant to the newly reported high-resolution Ar 3*s* PES spectrum shown in Fig. 5. Firstly Becker *et al.* (56) have reported very high-resolution-threshold and near-threshold PES spectra of argon by sweeping the photon energy through the binding-energy range 29–44 eV. Although the resolution varies with binding energy (0.09–0.2 eV) and, as expected, the intensities are very different in the threshold region (56), similar fine structure to that seen in the present work is observed between 32 and 42 eV (see Table 2). Also of interest are the high-resolution Ar 3*s* fluorescence spectra, excited by broad-band undispersed synchrotron radiation, recently reported by Samson, Chung, and Lee (47). In these studies the photon resolution for the emission resulting from decay of the Ar II excited states is in the range 0.05–0.10 eV fwhm. Fluorescence is observed (47) from all the states of Ar II observed above 32 eV and up to 43 eV in the PES spectrum in Fig. 5 except for those for which the emission transitions are forbidden (i.e. $p \rightarrow p$). The final states corresponding to many of these optically forbidden transitions can, however, be seen in the threshold PES spectrum (56). The fluorescence spectra of Ar reported by Samson *et al.* (47), and particularly the higher-resolution second-order spectra, clearly show features that correspond to the "extra" contributions (see above discussion) to peaks 4, 5, 6, and 7 of the intermediate-resolution PES spectrum (41–44) referred to above (see Fig. 1) and which are revealed in the new high-resolution spectrum in Fig. 5. A discussion of possible identities for the peaks obtained below 32.2 eV in the Ar spectrum, together with similar peaks in the case of Xe, is given in Section 3 below.

2. Xe 5s spectrum

Figure 6 shows the Xe 5*s* binding-energy spectrum at $h\nu$ = 90 eV, at an energy resolution of 0.35 eV fwhm and over the binding energy range 23–37 eV. Similar spectra were obtained over the photon energy range 80–130 eV. At somewhat lower photon energies the binding-energy spectra are complicated by resonance Auger effects (57, 58). The spectra are considerably better resolved than earlier published work using PES at similar photon energies (16, 17) or XPS (5, 6) with the peaks a, b, c, d, e, f, g, h, and i not having been resolved previously. Fahlman *et al.* (59, 60) have also reported Xe 5*s* PES spectra at quite good energy resolution, and also obtained angular distribution information over the photon-energy range 28.5–74.8 eV, which includes the region of the Xe 5*s* cooper minimum. Suzer and Hush (61) have reported high-resolution HeII ($h\nu$ = 40.8 eV) PES spectra of Xe up to a binding energy of 28 eV.

Possible assignments of the Xe 5*s* binding-energy spectrum have been discussed by Hansen and Persson (25–27, 45) and also by Dyall and Larkins (32, 33) in several papers reporting CI calculations. Of these, the calculations of refs. 27 and 45 show the best agreement with experiment for relative satellite

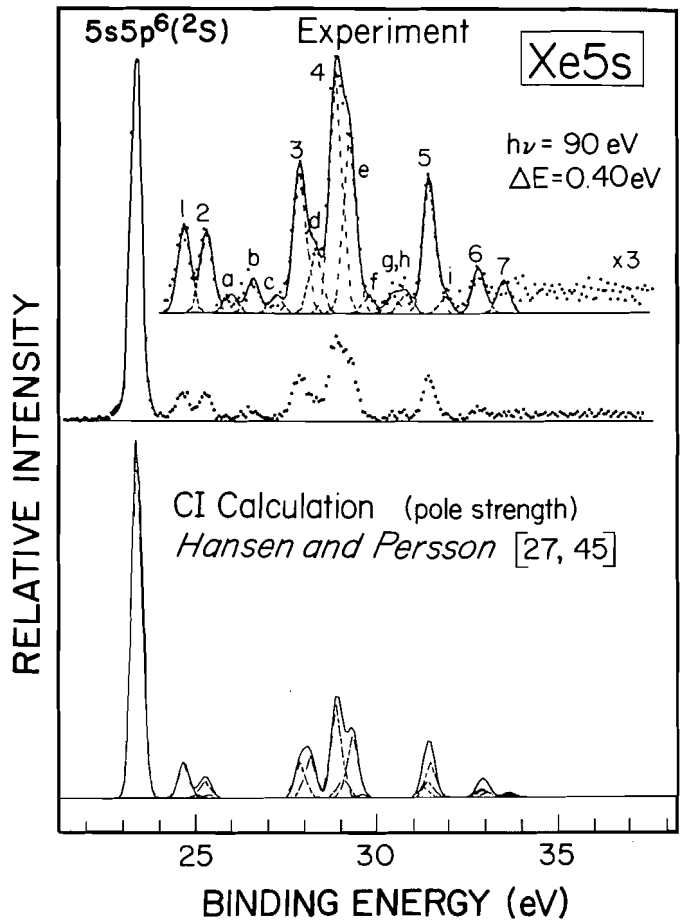

FIG. 6. Comparison of experimental Xe 5*s* PES spectrum ($h\nu$ = 90 eV, ΔE = 0.40 eV fwhm) with the calculated intensities (pole strengths or relative spectroscopic factors, without photon-energy dependence) of the Xe 5*s* satellites reported by Hansen and Persson (27, 45). The calculated spectrum has been convoluted with a Gaussian function (0.40 eV fwhm). The transition energies in the calculated spectrum are assigned from optical work as shown in refs. 27 and 45.

intensities. Figure 6 shows a theoretical spectrum obtained using the intensities as calculated by Hansen and Persson using CI methods (27, 45) and convoluted with the experimental energy resolution (0.34 eV). Unlike the case of the Ar 3*s* CI calculations (30), the xenon calculations (27, 45) included a wide range of final ion states and not just those of the principal series (i.e. not just those of $5s^25p^4(^1D)ns(^2S)$ symmetry). It can be seen from Fig. 6 that good general quantitative agreement exists between theory and experiment. Since the intensities from the CI calculations (27, 45) are not given as a function of photon energy, it is assumed that they are simply pole strengths (i.e. relative spectroscopic factors).

By fitting the peak energies of Fig. 6 (upper spectrum) to binding energy spectra of xenon obtained at higher photon energies (80–130 eV) and using an individual peak width (resolution) determined by the main line at 23.397 eV at each photon energy, we have obtained information on the variation of satellite peak intensities relative to that of the main line ($5s5p^6(^2S)$) and the results are shown in Fig. 7 and Table 3. It can be seen that while the intensity of lines 1, 2, and h are reasonably constant, the relative intensities of lines b, 3, 4, g, 5, 6, and 7 increase slowly with increase in photon energy. This latter situation for xenon is contrary to the behavior observed for

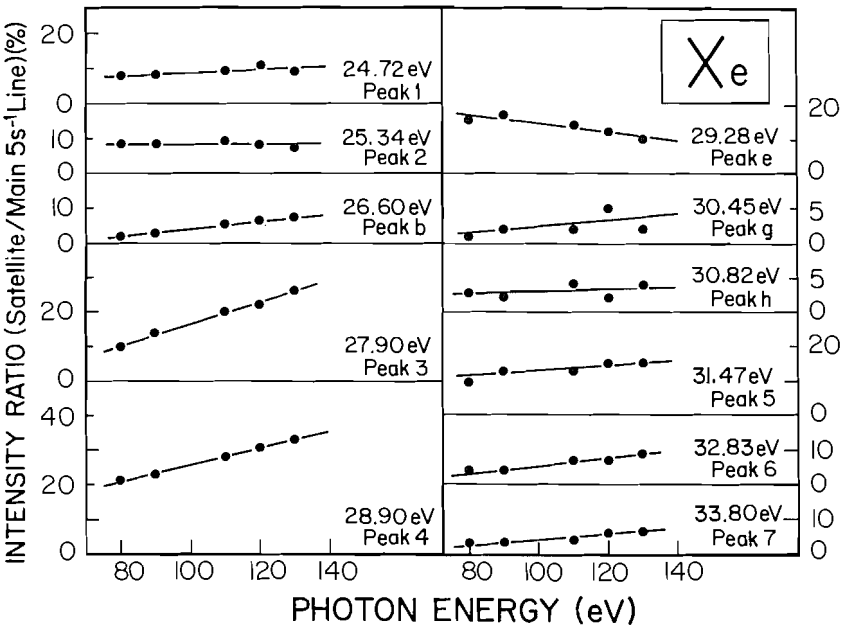

FIG. 7. Variation of measured relative intensities with photon energy for satellites in the Xe 5*s* spectrum.

TABLE 3. Peak energies and relative intensities (%) in the Xe 5*s* binding energy spectrum as a function of photon energy

Photon energy (eV)	fwhm* (eV)	Peak number†, peak energy (eV), and relative intensity (%)‡											
		$5s^{-1}$ 23.40§	1 24.72	2 25.34	b 26.60	3 27.90	4 28.90	e 29.28	g 30.45	h 30.82	5 31.47	6 32.83	7 33.80
80	0.34	100	8(1)	8(1)	2(1)	10(1)	21(2)	15(2)	1(1)	3(1)	10(1)	4(1)	3(1)
90	0.40	100	8(1)	8(1)	3(1)	14(2)	23(2)	17(2)	2(1)	2(1)	13(1)	4(1)	3(1)
110	0.66	100	9(1)	9(1)	5(1)	20(2)	28(2)	14(2)	2(1)	4(1)	13(2)	7(1)	4(1)
120	0.73	100	11(1)	8(1)	6(1)	22(2)	31(2)	12(2)	5(1)	2(1)	15(2)	7(1)	6(1)
130	0.77	100	9(2)	7(2)	7(2)	26(5)	33(5)	10(2)	2(2)	4(2)	15(4)	9(2)	6(2)

†See Figs. 6 and 7. Relative intensities for peaks a, c, d, f, and i are approximately 1, 1, 6, 1, and 1, respectively, at 80 eV but were not obtained at higher photon energies.
‡% of main $5s^{-1}$ line, uncertainties shown in parentheses.
§Based on optical value of 23.397 eV (51).
*Width of main $5s^{-1}$ line used for fitting satellites.

the ^2S lines of argon at intermediate photon energies (see Fig. 3 and refs. 41 and 44) and is contrary to predictions from theory (30). In contrast to the behavior for the other peaks (Fig. 7), the relative intensity of line e decreases with increase in photon energy according to the present measurements. The overall increase in total satellite intensity in the Xe 5*s* spectrum is consistent with the trend of earlier findings based on much-lower-resolution spectra (20).

A consideration of the CI calculations (27, 45) and optical emission data (51) suggests that further (unresolved) fine structure is expected to be contributing to the Xe 5*s* spectrum shown in Fig. 6. Figure 8 shows a very recently obtained Xe 5*s* PES spectrum ($h\nu$ = 95 eV) at significantly higher resolution (~0.19 eV fwhm) than any other previously reported work (6, 16) except the low-photon-energy data of Suzer and Hush (61), which is only over a very limited binding energy range. The spectrum shows a great deal of additional resolved structure compared to the situation in the experimental spectrum shown in Fig. 6. As in the case of the very-high-resolution Ar 3*s* spectrum (Fig. 5), the electron transmission efficiency is slowly varying over the spectral range due to the low analyzer pass energies involved. Therefore the relative intensities are only semi-quantitative in Fig. 8. The energies of the spectral features in Fig. 8 are given in Table 4 together with low-photon-energy, high-resolution PES data (59–61). From a comparison of the presently obtained higher-resolution Xe spectra (Fig. 8) with the data in Figs. 6 and 7, it is quite clear that many of the peaks contain contributions from more than one state (see particularly peaks 2, 3, 4, and 5). A detailed quantitative investigation of the relative satellite intensities in the Xe 5*s* spectrum must await transmission-corrected high-resolution spectra of preferably even higher resolution than that shown in Fig. 8.

3. *Peaks at low binding energy in the Ar 3s and Xe 5s high-resolution spectra*

In the present work, several peaks have been observed below 32.2 eV in the Ar^+ spectrum (Fig. 5, Table 2) and below the main $5s^{-1}$ peak at 23.397 eV in the Xe^+ spectrum (Fig. 8, Table 4). The identity of these structures is of some speculation and interest. The lowest excited state of Ar^+, above the main $3s^{-1}$ line, is listed as being at 32.18 eV according to the tables of atomic-energy levels (from optical emission) published by

Can. J. Chem. Downloaded from www.nrcresearchpress.com by 112.217.228.212 on 09/07/12
For personal use only.

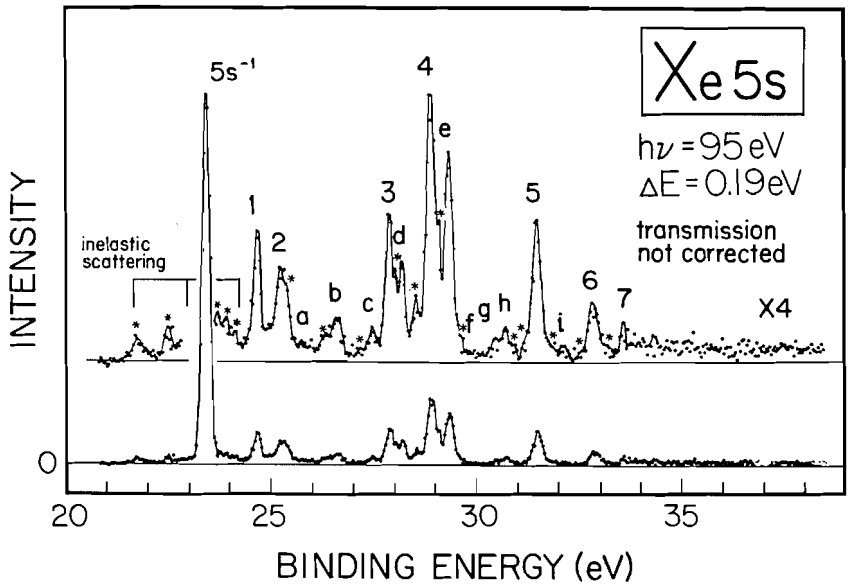

FIG. 8. Xe 5*s* binding-energy spectrum at high resolution (0.16 eV fwhm) and $h\nu = 95$ eV. See Table 4 for details. Peaks at 21.73 and 24.1 eV are due to inelastic scattering. Note that the intensities in these spectra have not been corrected for the slowly varying electron-transmission efficiency (see text).

Moore (51). However, at least four low-intensity peaks are observed below this energy in the present work, in addition to the $3s^{-1}$ line in Ar. Of these four peaks, one is at ~28.6 eV, below the main $3s^{-1}$ line at 29.235 eV. In the case of Xe, Moore's tables (51) list no state of Xe^+ below the main $5s^{-1}$ line. These "extra" peaks may be attributable to any of the following possible processes. (*i*) Photoelectron peaks from impurity gases of which the most likely is N_2. However, high-resolution inner-valence PES spectra of N_2 (62) show no sufficiently sharp peaks in the binding energy regions in question. Two independent samples of each of Ar and Xe were used (high purity (99.995%) and research grade (99.9995%)). The "extra" peaks persisted in the spectra with both samples; (*ii*) Auger lines from higher-order radiation passing through the monochromator. This explanation has been advanced by Fahlman *et al.* (59) to account for two lines observed at ~22.6 and 24.67 eV in PES spectra of Xe at $h\nu = 33$ eV. The fact that these lines are also present at the same binding energy (but different kinetic energy) in the present work at $h\nu = 95$ eV and also in other Xe PES spectra at photon energies in the range 85–120 eV (63) suggests that these lines are not due to Auger effects. Auger lines should appear at constant electron kinetic energy as the photon energy is varied. The "extra" lines in Ar (Table 2, Fig. 5) at ~28.6 eV and 29.95 eV are present in separate spectra at $h\nu = 80$ and 100 eV, and are thus also probably not due to Auger transitions. Other features in the binding-energy range 30–32 eV are extremely weak and no definite conclusion can be stated at present. (*iii*) Reflections and background effects from the electron analyzer may be causing spurious signals. (*iv*) The peaks may be due to inelastic scattering processes, e.g. $3p^{-1}$ (or $5p^{-1}$) primary photoelectrons that have excited a neutral Ar (or Xe) atom in the collision chamber before analysis. For argon (Fig. 5) structures in the region 29.9–31.3 eV could be due to $3p^{-1}$ photoelectrons, which have subsequently undergone inelastic scattering, leading to the $3s^2 3p^5 5s$ and $3s^2 3p^5 6s$ manifolds of argon. Similarly in xenon, features in the ranges 21.6–21.9, 22.7–23.1, and 24.0–24.1 eV could be due to $5p^{-1}$ photoelectrons that leave Xe excited in the $5s^2 5p^5 6s$, and $5s^2 5p^5 7s$ manifolds. Pressure-dependent studies could identify such processes. (*v*) The peaks may arise from many-body (electron correlation) effects and therefore intrinsically belong to the Ar 3*s* or Xe 5*s* satellite spectra.

In connection with the last possibility, i.e. many-body effects, it should be noted that the levels listed by Moore (51) are all assigned on the basis of the independent particle model and are designated as single-particle excited-state configurations. However, in reality the listed configurations may, at best, correspond to dominant configurations occurring in a CI description of the final states in question (32, 33). In a many-body approach such as the Green's function calculations for molecules by Cederbaum *et al.* (12, 14), many final-state poles from ionization of a given ground-state orbital are frequently found scattered throughout the inner-valence region. Of these, some are often found to occur at energies *below* that of the first single-particle excitation (i.e., the lowest "shake-up" state) above the predicted single-particle ground ionic state (this would correspond approximately to the so-called $3s^{-1}$ and $5s^{-1}$ states of Ar^+ and Xe^+, respectively). In some cases, many-body ionization peaks have even been predicted and observed (64–66) *below* the energy expected for the single-particle ground ionic state (i.e. "shake-down"). In other cases (12–14, 65), there is not even a clearly identifiable "parent" ion peak in the inner-valence region. Such many-body descriptions are at present apparently more highly developed for molecules than for atoms.

It is possible that some of the previously unobserved low-intensity peaks observed in the vicinity of the main Ar $3s^{-1}$ and Xe $5s^{-1}$ lines are ionization lines due to many-body effects. Such lines would probably not have been observed in previous photoelectron studies due to their low intensity and the lower energy resolution used in earlier work. The small structures at 28.6, 31.86, and 37.69 eV in the argon spectrum (Fig. 5) and at 22.52, 23.7, and 23.95 eV in the xenon spectrum (Fig. 8) may be due to many-body effects since they do not correspond to expected optical or inelastic scattering processes. The present

Can. J. Chem. Downloaded from www.nrcresearchpress.com by 112.217.228.212 on 09/07/12
For personal use only.

TABLE 4. Energies of features in the Xe 5*s* photoelectron spectrum at high resolution

Peak† designation	Peak energy (eV) This work (±0.04 eV) PES ($h\nu$ = 95 eV)	Fahlman *et al.* PES ($h\nu$ = 33 eV) ref. 59	Suzer and Hush PES ($h\nu$ = 40.8 eV) ref. 61
*(is)	21.73	(~21.6)§‖	
*	22.52	(~22.6)§	
$5s^{-1}$	23.397‡	23.397	23.394
*	23.7		
*	23.95	23.9	23.93
*	24.1		
1	24.67	24.67	
2	25.30	25.33	25.28
a	25.42		
*	25.78	26.36	26.37
b	26.65	26.8	26.63
			26.88
*(sh)	27.17		
c	27.49	27.58	27.54
3	27.88		27.93
*(sh)	28.04	28.1	
d	28.20		28.24
*	28.56		
4	28.92	28.9	
*(sh)	29.11		
e	29.35	29.37	
*(sh)	29.59		
f	29.87		
g	30.50		
h	30.74	30.7	
*(sh)	30.98		
*(sh)	31.22		
5	31.50	31.4	
*(sh)	31.77		
i	32.13		
*(sh)	32.61	32.6	
6	32.85		
*(sh)	33.20		
7	33.60		
*	34.35		

†The * indicates newly resolved peak or shoulder *(sh), see Fig. 8; *(is) signifies inelastic scattering.
‡Value from optical emission (51), used to calibrate energy scale.
§Present in spectrum but not identified in ref. 59.
‖Also seen in ref. 6.

work suggests that a search for low-intensity, low-energy, ionization poles in atomic many-body Green's functions or CI calculations, as well as further experimental investigations as a function of pressure, may prove fruitful.

Conclusions

High-resolution PES spectra of Ar 3*s* as a function of photon energy yield satellite relative intensities that are in general quite well reproduced by previously published CI calculations. Agreement between theory and experiment is further improved when account is taken of additional overlapping satellite peaks revealed by new very-high-resolution Ar 3*s* PES spectra. A similar level of agreement between theory and experiment is also obtained for the general features of the intensity distribution in the Xe 5*s* satellite spectrum. The new very-high-resolution PES spectra of Ar 3*s* and Xe 5*s* reveal significantly more detailed satellite spectra than have been observed previously. Even higher-resolution spectra for Xe 5*s* will be required in the future.

Finally a consideration of the extremely complex spectroscopy in the presently reported Ar 3*s* and Xe 5*s* PES binding energy spectra at very high resolution reveals a number of newly observed peaks, including some below the main $3s^{-1}$ and $5s^{-1}$ lines, which may be due to many-body (electron-correlation) effects. These high-resolution spectra also indicate that great care should be taken in the interpretation of much-lower-resolution spectra obtained by PES and particularly EMS (i.e. binary (e,2e) spectroscopy). In particular, detailed interpretations of recently obtained (low-resolution) EMS binding-energy spectra of Ar 3*s* (67, 68) and Xe 5*s* (67, 69) have been based on the assumption of much simpler manifolds of satellite states than are observed in the present PES work. Even a simple reinterpretation of the EMS Ar 3*s* spectrum, using more states, yields very different conclusions (41). While there are well-

Can. J. Chem. Downloaded from www.nrcresearchpress.com by 112.217.228.212 on 09/07/12
For personal use only.

known different considerations (7, 38–41, 70) in EMS and PES spectroscopies, particularly with regard to the different spatial regions of the wavefunctions that are sampled and also the photon-energy-dependent dipole matrix element in photoionization, final confirmation of the assignments and intensities must await the measurement of EMS binding-energy spectra as a function of momentum, at high *momentum* resolution and with at least as high an energy resolution as that used in the PES spectra shown in Figs. 5 and 8. At present the highest-resolution EMS noble-gas spectra that have been reported are the results for argon 3*s* (0.6 eV fwhm for Ar 3*s* and 0.06 eV fwhm in the Ar 3*p* regions respectively) by Williams (71), and for Xe 5*s* (1.0 eV fwhm for Xe 5*s* and 5*p*) by Hood *et al.* (72). While the Ar 3*s* work (71) is at somewhat higher resolution than other EMS work (21–23, 67, 68), relatively few data points were obtained in the spectral regions of interest. A comparison of both the present high-resolution PES spectra (0.16 eV fwhm), and earlier PES work for Ar 3*s* with the EMS work of Williams (71) at low resolution (~0.6 eV fwhm) also indicates that much higher-resolution EMS work is needed before definite conclusions regarding intensities and assignments can be reached. By the same token, similar high-resolution EMS measurements will also be needed before definitive statements can be made as to similarities (or differences) in spectroscopic factors in EMS and PES (allowing for photon-energy variation). Therefore speculations made in the case of atoms (19, 20, 25–31, 38, 40, 41, 54) and also recently for molecules (73–75) as to the viability of the approximations and reaction model (21) presently used in the EMS (binary (e, 2e) spectroscopy) that are based on a comparison between resolutionless calculations, medium-resolution PES, and lower-resolution EMS spectra, are premature. In the meantime, the present very-high-resolution PES results provide new and more detailed information that gives further insight into electron correlation effects and helps to clarify and explain much of the existing confusion and controversy concerning satellite relative intensities in both theoretical and experimental studies of Ar 3*s* and Xe 5*s* ionization.

Can. J. Chem. Downloaded from www.nrcresearchpress.com by 112.217.228.212 on 09/07/12
For personal use only.

Acknowledgments

Financial support for this work was provided by the Natural Sciences and Engineering Research Council of Canada and also the Natural Research Council of Canada. The advice and assistance of the Synchrotron Radiation Center staff at the 1-GeV ring is gratefully acknowledged. We would like to thank Professor J. A. R. Samson for helpful discussions and for making the fluorescence results available to us prior to publication.

1. D. W. Turner and M. I. Al-Joboury. J. Chem. Phys. **37**, 3007 (1962).
2. M. I. Al-Joboury and D. W. Turner. J. Chem. Soc. 5141 (1963).
3. D. C. Frost, C. A. McDowell, and D. A. Vroom. Proc. R. Soc. A, **296**, 566 (1967).
4. E. Weigold, S. T. Hood, and P. J. O. Teubner. Phys. Rev. Lett. **30**, 457 (1973).
5. D. P. Spears, H. J. Fishbeck, and T. A. Carlson. Phys. Rev. A**9**, 1603 (1974).
6. U. Gelius. J. Electron Spectrosc. **5**, 985 (1974).
7. J. P. D. Cook, M. G. White, C. E. Brion, W. Domcke, J. Schirmer, and L. S. Cederbaum. J. Electron Spectrosc. **22**, 261 (1981).
8. A. Hamnett, S. T. Hood, and C. E. Brion. J. Electron Spectrosc. **11**, 263 (1977).
9. J. P. D. Cook, C. E. Brion, and A. Hamnett. Chem. Phys. **45**, 1 (1980).
10. C. E. Brion, J. P. D. Cook, and K. H. Tan. Chem. Phys. Lett. **59**, 241 (1978).
11. A. Hamnett, W. Stoll, and C. E. Brion. J. Electron Spectrosc. **8**, 367 (1976).
12. L. S. Cederbaum and W. Domcke. Adv. Chem. Phys. **36**, 205 (1977).
13. W. von Niessen, J. Schirmer, and L. S. Cederbaum. Comput. Phys. Rep. **1**, 57 (1984).
14. L. S. Cederbaum, W. Domcke, J. Schirmer, and W. von Niessen. Adv. Chem. Phys. **65**, 115 (1986).
15. M. Y. Adam, F. Wuilleumier, S. Krummacher, V. Schmidt, and W. Melhorn. J. Phys. B, **11**, L413 (1978).
16. M. Y. Adam, F. Wuilleumier, N. Sandner, V. Schmidt, and G. Wendin. J. Phys. (Paris) **38**, 129 (1978).
17. M. Y. Adam, F. Wuilleumier, S. Krummacher, N. Sandner, V. Schmidt, and W. Melhorn. J. Electron Spectrosc. **15**, 211 (1979).
18. M. Y. Adam, P. Morin, and G. Wendin. Phys. Rev. A, **31**, 1426 (1985).
19. C. E. Brion, K. H. Tan, and G. M. Bancroft. Phys. Rev. Lett. **56**, 584 (1986).
20. C. E. Brion and K. H. Tan. Aust. J. Phys. **39**, 565 (1986).
21. E. Weigold and I. E. McCarthy. Adv. At. Mol. Phys. **14**, 127 (1978) and references therein.
22. K. T. Leung and C. E. Brion. Chem. Phys. **82**, 87 (1983).
23. I. E. McCarthy and E. Weigold. Phys. Rev. A, **31**, 160 (1985).
24. J. P. D. Cook, I. E. McCarthy, and E. Weigold. Phys. Rev. A, **33**, 211 (1986).
25. J. E. Hansen. Comments At. Mol. Phys. **12**, 197 (1982).
26. J. E. Hansen and W. Persson. Phys. Rev. A, **18**, 1459 (1978).
27. J. E. Hansen and W. Persson. Phys. Rev. A, **30**, 1565 (1984).
28. H. Smid and J. E. Hansen. J. Phys. B, **14**, L811 (1981).
29. H. Smid and J. E. Hansen. J. Phys. B, **16**, 3339 (1983).
30. H. Smid and J. E. Hansen. Phys. Rev. Lett. **52**, 2138 (1984).
31. H. Smid and J. E. Hansen. J. Phys. B, **18**, L97 (1985).
32. K. G. Dyall and F. P. Larkins. J. Phys. B, **15**, 203 (1982).
33. K. G. Dyall and F. P. Larkins. J. Phys. B, **15**, 219 (1982).
34. R. L. Martin, P. Kowalczyk, and D. A. Shirley. J. Chem. Phys. **68**, 3829 (1978).
35. G. Wendin. Phys. Scr. **16**, 296 (1977).
36. M. Ya. Amusia and A. S. Kheifets. J. Phys. B, **18**, L679 (1985).
37. J. Mitroy, K. Amos, and I. Morrison. J. Phys. B, **17**, 1659 (1984).
38. J. Mitroy, I. E. McCarthy, and E. Weigold. J. Phys. B, **18**, L91 (1985).
39. I. E. McCarthy. J. Electron Spectrosc. **36**, 37 (1985).
40. I. E. McCarthy. Aust. J. Phys. **39**, 587 (1986).
41. C. E. Brion, A. O. Bawagan, and K. H. Tan. Chem. Phys. Lett. **134**, 76 (1987).
42. C. E. Brion, A. O. Bawagan, and K. H. Tan. Abstracts of Contributed Papers, XV International Conference on the Physics of Electronic and Atomic Collisions. *Edited by* J. Geddes *et al.*, Belfast. July 1987. Brighton, U.K.
43. V. Schmidt. J. Phys. D, **2**, 275 (1986).
44. H. Kossman, B. Krässig, V. Schmidt, and J. E. Hansen. Phys. Rev. Lett. **58**, 1620 (1987).
45. J. W. Hansen and W. Persson. Phys. Scr. **36**, 302 (1987).
46. S. Svensson, K. Helenlund, and U. Gelius. Phys. Rev. Lett. **58**, 1624 (1987).
47. J. A. R. Samson, Y. Chung, and E. M. Lee. Phys. Lett. A, **127**, 171 (1988).
48. B. Yates, K. H. Tan, L. L. Coatsworth, and G. M. Bancroft. Phys. Rev. A, **31**, 1529 (1985); **32**, 1219 (1985).
49. K. H. Tan, G. M. Bancroft, L. L. Coatsworth, and B. W. Yates. Can. J. Phys. **60**, 131 (1982).

50. G. M. BANCROFT, K. H. TAN, and J. D. BOZEK. Physics in Canada, July 1987. pp. 113–120.
51. C. E. MOORE. Atomic Energy Levels, U.S. Nat. Bur. Stan. NBS Circular No. 467. 1949.
52. A. RON, R. H. PRATT, and H. K. TSENG. Chem. Phys. Lett. **47**, 377 (1977).
53. J. A. R. SAMSON. *In* Handbuch der Physik, Vol. 31. Corpuscles in radiation and matter I. *Edited by* W. Mehlhorn. Springer, Berlin. 1982. p. 156.
54. A. HIBBERT and J. E. HANSEN. J. Phys. B, **20**, L245 (1987).
55. W. WIJESUNDERA and H. P. KELLY. Phys. Rev. A, **36**, 4539 (1987).
56. U. BECKER, B. LANGER, H. G. KERKHOFF, M. KUPSCH, D. SZOSTAK, R. WEHLITZ, P. A. HEIMANN, S. H. LIU, D. W. LINDLE, T. A. FERRETT, and D. A. SHIRLEY. Phys. Rev. Lett. **60**, 1490 (1988); P. A. HEIMANN. Ph.D. Thesis, University of California. 1987.
57. U. BECKER, T. PRESCHER, E. SCHMIDT, B. SONNTAG, and H. E. WETZEL. Phys. Rev. A, **33**, 3891 (1986).
58. S. SOUTHWORTH, U. BECKER, C. M. TRUESDALE, P. H. KOBRIN, D. W. LINDLE, S. OWAKI, and D. A. SHIRLEY. Phys. Rev. A, **28**, 261 (1983).
59. A. FAHLMAN, M. O. KRAUSE, T. CARLSON, and A. SVENSSON. Phys. Rev. **30**, 812 (1984).
60. A. FAHLMAN, M. O. KRAUSE, and T. CARLSON. J. Phys. B, **17**, L217 (1984).
61. S. SUZER and N. S. HUSH. J. Phys. B, **10**, L705 (1977).
62. S. KRUMMACHER, V. SCHMIDT, and F. WUILLEUMIER. J. Phys. B, **13**, 3993 (1980).
63. C. E. BRION, A. O. BAWAGAN, and K. H. TAN. Unpublished work.
64. A. O. BAWAGAN, C. E. BRION, E. R. DAVIDSON, and D. FELLER. Chem. Phys. **113**, 19 (1987).
65. A. HAMNETT, S. T. HOOD, and C. E. BRION. J. Electron Spectrosc. **11**, 268 (1977).
66. J. P. D. COOK, C. E. BRION, and A. HAMNETT. Chem. Phys. **45**, 1 (1980).
67. I. E. MCCARTHY and E. WEIGOLD. Rept. Prog. Phys. **51**, 299 (1988).
68. R. PASCUAL, I. E. MCCARTHY, and E. WEIGOLD. To be published.
69. R. PASCUAL, I. E. MCCARTHY, and E. WEIGOLD. To be published.
70. M. YA. AMUSIA and A. S. KHEIFETS. J. Phys. B, **18**, L679 (1985).
71. J. F. WILLIAMS. J. Phys. B, **11**, 2015 (1978).
72. S. T. HOOD, A. HAMNETT, and C. E. BRION. J. Electron Spectrosc. **11**, 205 (1977).
73. M. Y. ADAM. Chem. Phys. Lett. **128**, 280 (1986).
74. M. Y. ADAM, C. CAULETTI, and M. N. PIANCASTELLI. J. Electron Spectrosc. **42**, 1 (1987).
75. M. N. PIANCASTELLI, C. CAULETTI, and M. Y. ADAM. J. Chem. Phys. **87**, 1982 (1987).

Can. J. Chem. Downloaded from www.nrcresearchpress.com by 112.217.228.212 on 09/07/12
For personal use only.

Ab initio studies on 1,2-oxathietane, *Z* and *E* 3,4-dimethyl-1,2-oxathietane, and their products of formal [σ2s + σ2a] cycloreversion

ALI NAGHIPUR AND J. WILLIAM LOWN[1]
Department of Chemistry, University of Alberta, Edmonton, Alta., Canada T6G 2G2

DULI C. JAIN
York College of City University of New York, Jamaica, NY 11451, U.S.A.

AND

ANNE-MARIE SAPSE[1]
John Jay College of City University of New York, 445 West 59 Street, New York, NY 10019, U.S.A. and Rockefeller University, New York, NY 10021, U.S.A.

Received July 14, 1987

This paper is dedicated to Professor Charles A. McDowell on the occasion of his 70th birthday

ALI NAGHIPUR, J. WILLIAM LOWN, DULI C. JAIN, and ANNE-MARIE SAPSE. Can. J. Chem. **66**, 1890 (1988).

Ab initio calculations at the level of 3-21G* SCF and MP3/3-21G* have been performed on the novel heterocycle 1,2-oxathietane and the formal [σ2s + σ2a] cycloreversion products. Hartree–Fock calculations have been performed for the *E* and *Z* 3,4-dimethyl-1,2-oxathietanes and their corresponding cycloreversion products. The calculations afford fully geometry optimized conformations, energies, net atomic charges, and HOMO values for the heterocycles. 1,2-Oxathietane is found to be close in energy to the sum of energies of either pair of its cycloreversion products. The most plausible mechanism of cycloreversion features the formation of ground state formaldehyde and thioformaldehyde via a biradical intermediate. This result is in accord with the lack of detection of chemiluminescence with the 1,2-oxathietanes, in contrast to the 1,2-dioxetanes.

ALI NAGHIPUR, J. WILLIAM LOWN, DULI C. JAIN et ANNE-MARIE SAPSE. Can. J. Chem. **66**, 1890 (1988).

Opérant au niveau 3-21G* en champs auto-cohérents et au niveau MP3/3-21G*, on a effectué des calculs *ab initio* sur le nouvel hétérocycle oxathiéthane-1,2 et sur les produits formels de sa cycloréversion [σ2s + σ2a]. On a aussi effectué des calculs de Hartree–Fock sur les isomères (*E*)- et (*Z*)- des diméthyl-3,4 oxathiéthanes-1,2 ainsi que sur leurs produits correspondants de cycloréversion. Les calculs permettent d'obtenir les conformations complètement optimisées pour la géométrie, les énergies, les charges atomiques nettes ainsi que les valeurs des OMHO des hétérocycles. On a trouvé que l'énergie de l'oxathiéthane-1,2 se rapproche de la somme des énergies de l'une ou l'autre paire de ses produits de réversion. Le mécanisme le plus plausible de la cycloréversion implique la formation, via un intermédiaire biradicalaire, de formaldéhyde et de thioformaldéhyde dans leur état fondamental. Ce résultat est en accord avec le fait qu'avec les oxathiéthanes-1,2, par opposition avec ce qui est observé avec les dioxéthanes-1,2, on n'observe pas de chimiluminescence.

[Traduit par la revue]

Introduction

Experimental studies of the decomposition of antileukemic 1-[2-[(2-chloroethyl)sulfinyl]ethyl-3-cyclohexyl-1-nitrosourea and its alkyl substituted analogues have provided evidence for the intermediacy of novel 1,2-oxathietanes (1–3). These compounds are of interest due to analogy with 1,2-dioxetanes, which are of significance in bioluminescence and chemiluminescence reactions. The extensively studied 1,2-dioxetanes (4–6) have been observed to induce pyrimidine dimers in DNA (7–9) and to effect interstrand cross-linking and local denaturation of DNA (10). Therefore it is of theoretical and biological interest to investigate the possibility for 1,2-oxathietane to undergo similar types of reactions. In contrast to 1,2-dioxetane, to our knowledge, there is only one preliminary theoretical treatment of 1,2-oxathietane reported (11) that did not employ full *ab initio* methods nor did it treat the experimentally observed formal [σ2s + σ2a] cycloreversion to identifiable products (1–3).

Decomposition of 1-[2-[(2-chloroethyl)sulfinyl]ethyl-2-d_2]-3-cyclohexyl-1-nitrosourea **1***b* (Fig. 1) under physiological conditions affords formaldehyde and thioformaldehyde-d_2-hydrate with no label scrambling in accord with formation of a 1,2-oxathietane species **4** and **5** rather than the symmetrical thiirane S-oxide intermediates **6** and **7** (1, 2). In addition, similar aqueous decomposition of 1-[2-[(2-chloroethyl)sulfinyl-^{18}O]-1,1-dimethyl]-3-cyclohexyl-1-nitrosourea (**1***c*-^{18}O) affords acetone-^{18}O and thioformaldehyde hydrate among the volatile products (Fig. 1) (1, 2). Thus the reaction proceeds by intramolecular transfer of ^{18}O via the four-membered 1,2-oxathietanium intermediate **4**.

Subsequently 3,3,4,4-tetramethyl-1,2-oxathietane **5***e* proved to be isolable and was demonstrated to undergo spontaneous formal [σ2s + σ2a] cycloreversions primarily to acetone and thioacetone (which was trapped with a variety of dienes) and, to a much lesser extent, to 2,3-dimethylbut-2-ene **9***a* and sulfur monoxide (2). No detectable chemiluminescence occurs in these reactions (1–3) in contrast to the case of 1,2-dioxetanes (4–6). Therefore the present work focuses on the energetics of the cycloreversion reactions of 1,2-oxathietane and certain stereoisomeric derivatives. The purpose of the calculations is to provide theoretical support for the experimental findings, which, as mentioned above, do not include the observation of chemiluminescence.

It had been observed experimentally that, depending on the substitution pattern of the precursor sulfinylnitrosoureas, rearrangements of the intermediate 1,2-oxathietane may supervene over the cycloreversions (1–3) (see Fig. 1, example **1***d*, and structures **10**–**12**, Fig. 2). Therefore another objective of the calculations was to determine the effects of alkyl substitution on the stability and reactivity of this novel heterocycle.

[1]Authors to whom correspondence may be addressed.

Can. J. Chem. Downloaded from www.nrcresearchpress.com by 112.217.228.212 on 09/07/12
For personal use only.

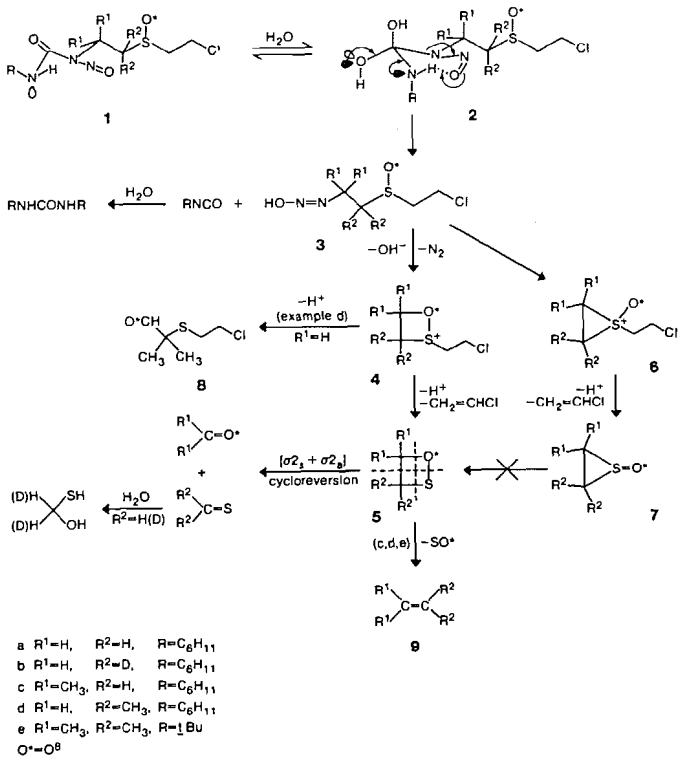

FIG. 1. Fragmentation products for decomposition of sulfinyl-(2-chloroethyl)nitrosoureas in aqueous potassium phosphate buffer at pH 7.0 and 37°C.

Calculations were performed at the SCF and MP3/3-21G* levels on the parent 1,2-oxathietane and at the Hartree–Fock SCF level for *E* and *Z* 3,4-dimethyl-1,2-oxathietanes.

Methods and results

Self consistent field (SCF) *ab initio* calculations were made, with full geometry optimization of the principal conformers, of the energies and net atomic charges of the heterocycles and their products of cycloreversion. The *ab initio* calculations at the Hartree–Fock level were performed on the heterocycles and subsystems using the 3-21G* Gaussian basis set, as implemented in the Gaussian-82 program (12). The geometry optimization was performed using the Berny optimization technique (13). SCF calculations with split valence or larger basis sets are known to usually predict accurate geometries (12, 14). 1,2-Oxathietane **13** (Fig. 3), in addition to its decomposition products SO, C_2H_6, H_2CO, and H_2CS, has been

TABLE 1. Optimized geometries of structures **13**, **14**, and **15** at 3-21G* level (Å and degrees)

Structure	13	14	15
SO	1.708	1.707	1.706
CO	1.477	1.479	1.480
CS	1.830	1.834	1.836
C3C4	1.559	1.561	1.572
C3H3 = C4H4	1.077	1.080	1.079
C4OS	95.5	95.4	95.6
C3SO	79.9	79.9	80.1
C4C3H3	113.8	111.7	111.4
C3C4H4	114.4	112.5	111.0
C3C6	—	1.529	1.529
C4C5	—	1.513	1.513
C6H6 = C5H5	—	1.084	1.083
C3C6H6 = C4C5H5	—	110.3	110.4
Dihedral angles			
C6C3C4O	—	116.8	−117.4
C5C4C3S	—	−116.8	117.4
H4C4C3S	—	−113.9	112.9
H3C3C4O	—	−113.9	−112.9
H6C6C3C4	—	69.6	54.3
H5C5C4C3	—	68.2	67.7

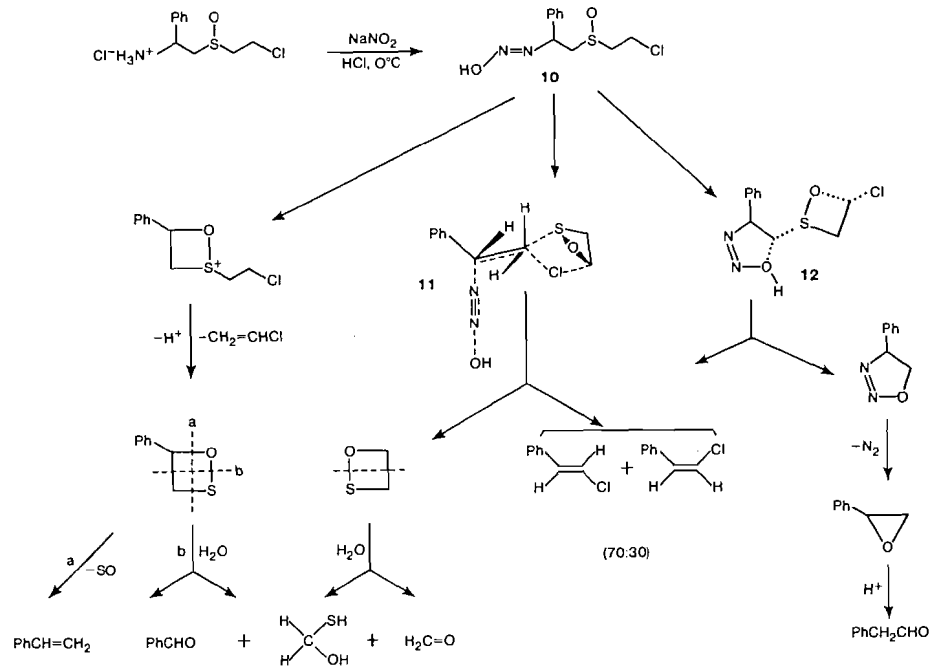

FIG. 2. Fragmentation pathways for decomposition of sulfinyl-(2-chloroethyl) substituted diazonium ions illustrating alternative reactions involving 1,2-oxathietanes.

Can. J. Chem. Downloaded from www.nrcresearchpress.com by 112.217.228.212 on 09/07/12
For personal use only.

Can. J. Chem. Downloaded from www.nrcresearchpress.com by 112.217.228.212 on 09/07/12
For personal use only.

TABLE 2. Energies of 1,2-oxathietane **13** and its alternative cycloreversion products (au)

Species	3-21G*	MP3/3-21G*
SO	−470.0747	−470.3043
Singlet SO	−470.0094	—
C_2H_4	−77.6010	−77.7970
H_2CO	−113.2218	−113.4369
H_2CS	−434.4465	−434.6780
1,2-Oxathietane	−547.6752	−548.1119

TABLE 3. 3-21G* Energies of *Z* and *E* 3,4-dimethyl-1,2-oxathietane and their alternative cycloreversion products (au)

Z-2-butene	−115.2420
E-2-butene	−115.2406
CH_3HCO	−152.0552
CH_3HCS	−473.2748
Z-3,4-dimethyl-1,2-oxathietane **14**	−625.3268
E-3,4-dimethyl-1,2-oxathietane **15**	−625.3243

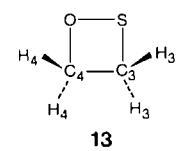

13

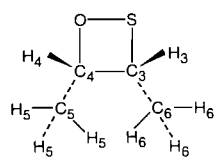

14

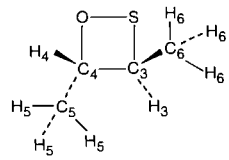

15

FIG. 3. Structures and numbering of 1,2-oxathietanes employed in the *ab initio* calculations.

completely geometry optimized. The resulting geometrical parameters are summarized in Table 1.

Since the heterocycles contain sulfur, the inclusion of *d* orbitals is particularly necessary for a good theoretical description. Goddard (15) has compared the results of the 3-21G* basis set with those of larger basis sets and has found that the 3-21G* basis set affords a good description. For example, the SO bond length in 1,2-oxathietane is found to be 1.708 Å, in good agreement with the known value of 1.7 Å for the SO single bond.

The optimized geometries have been used to perform single point MP3/3-21G* calculations, to estimate the correlation energies of the systems and to assess their influence on the stability of the heterocycle. The Hartree–Fock energies and the MP3/3-21G* energies are shown in Table 2. Table 3 shows the Hartree–Fock 3-21G* energies for structures **14** and **15** (Fig. 3) as well as for acetaldehyde, thioacetaldehyde, and *E* and *Z* 2-butenes. The differences between the energies of the cycloreversion products are shown in Table 4. Table 5 shows the net atomic charges on the atoms of the three heterocycles while Table 6 lists the basis set composition of 1,2-oxathietane HOMO (Highest Occupied Molecular Orbital).

TABLE 4. Energy differences (kcal/mol)

	3-21G*	MP3/3-31G*
E(**13**) − [E(SO) + $E(C_2H_4)$]	0.3	−6.65
E(**13**) − [$E(H_2CO)$ + $E(H_2CS)$]	−4.3	1.9
E(**14**) − [$E(Z((CH_3)_2C_2H_2))$ + E(SO)]	−6.3	—
E(**14**) − [$E(CH_3CHS)$ + $E(CH_3CHO)$]	2.0	—
E(**15**) − [$E(E((CH_3)_2C_2H_2))$ + E(SO)]	−5.9	—
E(**15**) − [$E(CH_3CHS)$ + $E(CH_3CHO)$]	4.6	—

TABLE 5. Net atomic charges (eu)

		3,4-Dimethyl-1,2-oxathietane	
1,2-Oxathietane		*Z*	*E*
S	0.428	0.429	0.429
O	−0.636	−0.637	−0.638
C3	−0.669	−0.501	−0.500
C4	0.095	0.076	0.079
H3	0.252	0.254	0.256
H4	0.234	0.235	0.238
C5	—	−0.591	−0.599
C6	—	−0.580	−0.588
H5	—	0.200	0.201
H6	—	0.212	0.228

TABLE 6. Atomic participation in the HOMO for 1,2-oxathietane*

E		−0.3319
S	$2p_z$	0.238
	$3p_z$	−0.522
		−0.508
O	$2p_z$	0.264
		0.341
C3	$2p_z$	0.084
		0.024
C4	$2p_z$	−0.055
		0.032

*p_z is perpendicular to the molecule's plane.

Discussion

The SO molecule is a triplet in its ground state. From Tables 2 and 4, it can be seen that the energy of the 1,2-oxathietane, at both the Hartree–Fock level and the MP3/3-21G* level of calculation, is within a few kcal/mol of the sum of energies of either SO + C_2H_4 or H_2CO + H_2CS, with the former energy being slightly lower and the latter energy being slightly higher than that of the heterocycle. Correlation energy inclusion at the MP3 level reverses the trend, while keeping the differences small. The *Z* 3,4-dimethyl-1,2-oxathietane **14** is found to be slightly more stable than the *E* isomer **15** by less than 1 kcal/mol. Both heterocycles are more stable than the combination of SO + $(CH_3)_2C_2H_2$ but somewhat less stable than the combined acetaldehyde and thioacetaldehyde. The differences remain around a few kcal/mol. The heterocycles are singlets, and therefore the concerted decomposition into SO + C_2H_4 cannot occur with the direct formation of triplet SO. The SO thus obtained would have to be a singlet, which shows, as

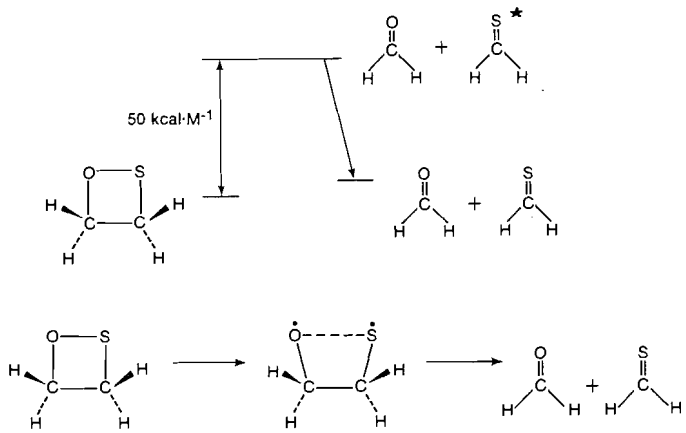

FIG. 4. (a) Hypothetical ($\sigma 2s + \sigma 2a$] cycloreversion of 1,2-oxathietane to carbonyl and thiocarbonyl fragments. (b) Proposed cleavage of 1,2-oxathietane via a biradical intermediate.

mentioned above, the decomposition to occur mainly via the formation of H_2CS and H_2CO (1, 2). Initial calculations of ΔE_{ST} for SO, using RHF for the singlet and UHF for the triplet at the 3-21G* computational level, give an estimate of ca. 40 kcal/mol. At a higher computational level, namely MP3/6-31G*, the value becomes 28 kcal/mol. This may be compared with the value of 25.3 kcal/mol by a previous SCF calculation, which is near the Hartree–Fock limit (16), and more recent calculations by the CEPA-PNO method that predict a value of 23.7 kcal/mol (17). It was concluded that, as in the case of O_2, the CEPA method seems to overestimate the correlation contribution to ΔE_{ST} (17). The experimental value of ΔE_{ST} for SO is 17.6 kcal/mol (18, 19).

Thus the calculations are in general agreement with the experiments.

Similarly, if the C—C and S—O bonds were to break simultaneously, one of the resulting products would be in an excited state, to obey the symmetry rules (20). Even though in our system the symmetry of 1,2-dioxetane is removed, the same rules apply, as shown by Woodward and Hoffmann (20), i.e., when the symmetry is removed by a small change (such as replacing a hydrogen by a methyl or, in this case, an oxygen by a sulfur). This refers mainly to the reaction proceeding in the absence of a triplet biradical, so the differences in spin effects between O and S should not be important). Indeed, the σ and σ^* bonds of the heterocycle are formed from the $\pi_1 + \pi_2$, $\pi_1^* + \pi_2^*$, $\pi_1 - \pi_2$, $\pi_1^* - \pi_2^*$ orbitals of the formaldehyde and thioformaldehyde molecules, so upon concomitant breakage of the two σ bonds, one of the products must be in an excited state. However, the excited states of both H_2CS and H_2CO lie high above the ground state, with 80.6 kcal/mol for the singlet excited state of H_2CO and with the triplet close to it (lower by a few kcal/mol) (21). The photoelectron spectrum of monomeric thioformaldehyde was recently reported and shows ionizations at 9.36, 11.87, 14.02, and 15 eV (22, 23). Thus H_2CS has been found theoretically and experimentally to feature a singlet excited state 46 kcal/mol above the ground state and a triplet state only 6 kcal/mol lower in energy (21). If the decomposition were to occur in this direction, the reaction would proceed as indicated in Fig. 4a. Such a reaction would feature an activation energy of 50 kcal/mol or more, since the transition state energy would probably be greater than the energy of the excited state. Therefore this reaction path cannot explain the experimentally observed high instability of the 1,2-oxathietane system (1–3).

Theoretical calculations on the dimethyl substituted 1,2-oxathietanes, at the Hartree–Fock level, lead to similar conclusions for decomposition of these compounds. It therefore appears plausible that the 1,2-oxathietane decomposes via a biradical mechanism into ground state formaldehyde and ground state thioformaldehyde according to Fig. 4b. This is in agreement with the fact that chemiluminescence is not observed experimentally (1–3). In the case of 1,2-dioxetane, however, chemiluminescence has been observed experimentally and different studies suggest that 1,2-dioxetane does indeed decompose into a ground state formaldehyde molecule and an excited state one, which can be a singlet or a triplet. The difference between 1,2-dioxetane and 1,2-oxathietane can be attributed to the difference in their stabilities. Indeed, while 1,2-oxathietane is close in energy to its decomposition products, 1,2-dioxetane has been found in this work, with 3-21G* (SCF) calculations, to show an energy higher by 40 kcal/mol than the sum of the energies of two formaldehyde molecules in the ground state. Using a larger basis set, Goddard (8) finds the number to be 50 kcal/mol. This result predicts that the energy difference between 1,2-dioxetane and the sum of energies of one formaldehyde molecule in its ground state and the other molecule in the excited state is only about 30 kcal/mol and, therefore, thermally it can decompose with accompanying chemiluminescence. Indeed, Kopecky *et al.* (4) have found an energy of activation for the thermolysis of dioxetane in the vicinity of 25 kcal/mol. Similar results have been found in other studies (5, 6). Goddard estimates the energy of the 1,2-dioxetane biradical to be higher by 16 kcal/mol than that of the heterocycle, averaging over eight singlet biradical states, via 6VB-CI calculations (8). Goddard also finds a state for the biradical of 1,2-dioxetane ($^1(4\pi)$) that correlates with the ground state products. This state is 3 kcal/mol below the lowest energy state ($^1(2\pi)$). Performing UHF calculations on a triplet state biradical that features a frozen SO bond of 2.3 Å and a CC bond of 1.54 Å, and optimizing the other parameters, using the 3-21G basis set, we find an energy lower than that of 1,2-oxathietane. When correlation energy is included, via MP3/3-21G calculations, the energy of the biradical becomes higher than that of the heterocycle by 25 kcal/mol.

Using single-point calculations with the 3-21G* basis set (optimization could not be performed due to convergence problems) the biradical exceeds the heterocycle in energy by ca. 7 kcal/mol. When the MP3/3-21G* is used, the difference becomes ca. 36 kcal/mol, still lower than the 40 kcal/mol required by the excitation of H_2CS. The value of 7 kcal/mol, which has to be viewed as an approximation, gives an indication that the transition state via a biradical might not require a large activation energy.

At the 3-21G level, performing complete optimization on both ground state and biradical (with the exception of the SO bond frozen at 2.3 Å and the CC bond maintained at 1.54 Å for the biradical), the energies of the two species are about equal. Introducing the correlation energy changes the results somewhat, with MP3/3-21G calculations showing the biradical higher in energy than the ground state by 25 kcal/mol. The MP3/3-21G* results increase this value to 37 kcal/mol. However, the value still remains smaller than the 45 kcal/mol found for the excited state of H_2CS. The values given above are close to the energy of activation for the thermolysis of dioxetane.

In conclusion, it is plausible that 1,2-oxathietanes decompose into ground state formaldehyde and thioformaldehyde via a biradical reaction, while 1,2-dioxetane has been shown in other

Can. J. Chem. Downloaded from www.nrcresearchpress.com by 112.217.228.212 on 09/07/12
For personal use only.

studies to decompose into a ground state formaldehyde and an excited state formaldehyde. Even if the decomposition were to occur with the formation of excited state thioformaldehyde, chemiluminescence would probably not be observed because of the small value of the excitation energy as compared to formaldehyde. As shown by Goddard (15), higher excited states of thioformaldehyde would be necessary to afford photochemical reactions.

Acknowledgements

This investigation was supported by grants (to J.W.L.) 1 R01 CA21488-11 awarded by the National Cancer Institute, DHHS, and A-2305 from NSERC, and (to A.-M.-S.) grant no. 666275 from the City University of New York. The authors wish to thank the City University of New York for computer time and Drs. R. Osman and W. A. Goddard III for helpful suggestions.

1. J. W. Lown and R. R. Koganty. J. Am. Chem. Soc. **105**, 126 (1983).
2. J. W. Lown and R. R. Koganty. J. Am. Chem. Soc. **108**, 3811 (1986).
3. J. W. Lown, R. R. Koganty, and A. Naghipur. J. Org. Chem. **51**, 2116 (1986).
4. K. R. Kopecky, J. E. Filby, C. Mumford, P. A. Lockwood, and J. Ding. Can. J. Chem. **53**, 1103 (1975).
5. T. Wilson, D. R. Golan, M. S. Harris, and W. L. Baumstark. J. Am. Chem. Soc. **98**, 1086 (1976).
6. W. H. Richardson, F. C. Montgomery, M. E. Yelvington, and H. E. O'Neal. J. Am. Chem. Soc. **96**, 7525 (1974).
7. A. A. Lamola, M. Gueron, T. Yamane, J. Eisinger, and R. G. Shulmass. J. Chem. Phys. **47**, 2210 (1967).
8. L. B. Harding and W. A. Goddard. J. Am. Chem. Soc. **99**, 4520 (1977).
9. A. A. Lamola. Biochem. Biophys. Rees. Commun. **43**, 893 (1971).
10. J. W. Lown, R. R. Koganty, and K. R. Kopecky. Photobiochem. Photobiophys. **12**, 295 (1986).
11. J. P. Snyder and L. Carlsen. J. Am. Chem. Soc. **99**, 2931 (1977).
12. J. S. Binkley, M. J. Frisch, D. J. Defrees, K. Raghavachari, R. A. Whiteside, H. B. Schlegel, E. M. Fluder, and J. A. Pople. Gaussian 82, Carnegie–Mellon University, Pittsburgh, PA. 1982.
13. H. B. Schlegel. J. Comput. Chem. **3**, 214 (1982).
14. W. J. Hehre, R. F. Stewart, and J. A. Pople. J. Chem. Phys. **81**, 2657 (1969).
15. J. D. Goddard. Can. J. Chem. **63**, 1910 (1985).
16. S. Green. Adv. Chem. Phys. **25**, 179 (1974).
17. V. Staemmler and R. Jaquet. Theor. Chim. Acta (Berlin), **59**, 501 (1981).
18. K. P. Huber and G. Herzberg. Molecular spectra and molecular structure IV. Constants of diatomic molecules. van Nostrand–Reinhold, New York. 1979.
19. W. C. Swope, Y.-P. Lee, and H. F. Schaefer. J. Chem. Phys. **71**, 3761 (1979).
20. R. B. Woodward and R. Hoffmann. The Conservation of Orbital Symmetry. Verlag Chemie, Weinheim, FRG. 1970.
21. S. A. Pope, I. H. Hillier, and M. F. Guest. J. Am. Chem. Soc. **107**, 3789 (1985).
22. Y. Vallee and J.-L. Ripoll. Can. J. Chem. **65**, 290 (1987).
23. M. Ohsaku. Bull. Chem. Soc. Jpn. **47**, 965 (1974).

Can. J. Chem. Downloaded from www.nrcresearchpress.com by 112.217.228.212 on 09/07/12
For personal use only.

N-14 ENDOR study of micellar solutions of sodium dodecylsulfate using small spin probes

YASHIGE KOTAKE AND EDWARD G. JANZEN
Guelph–Waterloo Centre for Graduate Work in Chemistry, Department of Chemistry and Biochemistry, University of Guelph, Guelph, Ont., Canada N1G 2W1

Received September 28, 1987

This paper is dedicated to Professor Charles A. McDowell on the occasion of his 70th birthday

YASHIGE KOTAKE and EDWARD G. JANZEN. Can. J. Chem. **66**, 1895 (1988).

ENDOR (electron nuclear double resonance) spectroscopy has been applied to the study of the state of solubilization of small nitroxide spin probes in micelles produced in sodium dodecylsulfate solution. The intensity ratio of the pair of N-14 ENDOR lines observed by fixing the field on the low-field ESR (electron spin resonance) line was monitored as a measure of the motion of spin probes. Neutral spin probes, when solubilized in micelles, show a discontinuous change of ENDOR spectral parameters such as hyperfine splitting constant and peak intensity ratio. Above the critical micelle concentration, the spectrum features change only gradually as the number of solubilized probes is increased. Spin probes in micelles appear to experience environments that are less polar than those met in aqueous solutions. However, the solubilized state is stable and is insensitive to changes in the concentration of the amphiphile. An anionic spin probe, Fremy's salt, shows no indication of interaction with the micelles. The applicability of the use of ENDOR peak intensities for the study of spin probe motion is discussed.

YASHIGE KOTAKE et EDWARD G. JANZEN. Can. J. Chem. **66**, 1895 (1988).

On a utilisé la spectroscopie ENDOR pour étudier l'état de solubilisation de petites sondes de spin nitroxydes dans des micelles produites dans une solution de dodécylsulfate de sodium. Dans le but de mesurer le mouvement des sondes de spin, on a déterminé les rapports des intensités des paires des raies ENDOR N-14 en fixant le champ sur la raie de résonance paramagnétique électronique (rpe) à bas champ. Lorsque des sondes de spin neutres sont solubilisées dans les micelles, elles présentent un changement discontinue des paramètres spectraux ENDOR, tels la constante de couplage hyperfin ainsi que le rapport de l'intensité des raies. Au-dessus de la concentration critique en micelles, les caractéristiques spectrales ne changent que graduellement avec une augmentation du nombre de sondes solubilisées. Il semble que les sondes de spin dans les micelles sont soumises à des environnements qui sont moins polaires que ceux rencontrés dans des solutions aqueuses. Toutefois, l'état solubilisé est stable et n'est pas sensible aux changements de concentration de l'amphiphile. Une sonde de spin anionique, le sel de Fremy, ne semble pas avoir d'interactions avec les micelles. On discute de la possibilité d'utiliser les intensités des bandes en spectroscopie ENDOR pour étudier le mouvement des sondes de spin.

[Traduit par la revue]

Can. J. Chem. Downloaded from www.nrcresearchpress.com by 112.217.228.212 on 09/07/12
For personal use only.

Introduction

The structure of micelles has been examined by using various spectroscopic techniques; however, a definitive answer has still not been given as to whether the molecules in the structure are loose and disordered or tightly aligned (1, 2). Very few techniques are applicable to determine the structure of micelles directly (3). Thus molecular probe methods play a major role in this field since different conclusions can sometimes be reached depending on the technique used. The ESR (electron spin resonance) spin-probing or spin-labelling method is one of these techniques (4, 5) used in monitoring the state of solubilization of solutes in micelles. Usually a stable nitroxide radical is dissolved in the micellar solution and both the magnitude of the N-14 hyperfine splitting (hfs) as well as the linewidth of an ESR line is measured as a function of the concentration of the amphiphilic compound. From these parameters the polarity and microviscosity of the micellar solution that surrounds the molecular probe can be estimated. Various spin probes have already been used in ionic micelles (6).

Comparison of ESR and ENDOR

A general feature of investigations in ionic micelles seems to be the observation of a distinct change in the N-14 hfs and the linewidth of the ESR peaks in passing through the critical micelle concentration (cmc) (see, for example, early work by Waggoner *et al.* (7)). Although numerous combinations of spin probes and amphiphiles have been investigated, sometimes the change observed is not clear enough to tell whether there is in fact a change in these parameters at the cmc point. This uncertainty may arise from a basic limitation in the resolution of the lines in the ESR spectrum of the spin probe. Because the magnitude of the proton hfs in the probe is comparable to the intrinsic linewidth and is dependent on the kind of probe used, analysis of these results can be complicated (8). In addition, the proton hfs itself is likely to change upon probe incorporation into the micelle.

These difficulties could in principle be avoided by using electron nuclear double resonance spectroscopy (ENDOR) since the determination of the N-14 hfs of the spin probes is straightforward and both the intensity and the linewidth of N-14 ENDOR spectra are not directly influenced by the presence of proton hfs. Recent ENDOR studies of solubilized radicals in inverse micelles have shown that ENDOR spectroscopy of micellar systems is feasible (9, 10).

Objective

The aim of this study is to test the applicability of the ENDOR method for investigating the solubilizing state of small spin probes. In this connection the sensitivity of the intensity ratio of the N-14 ENDOR lines to the viscosity of the medium incorporating the spin probe will be tested. Four different water-soluble nitroxides are examined as a function of sodium dodecylsulfate concentration in water:

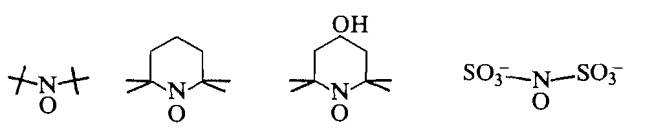

DTBN TEMPO TEMPOL PADS
(peroxylaminedisulfonate)

Can. J. Chem. Downloaded from www.nrcresearchpress.com by 112.217.228.212 on 09/07/12
For personal use only.

Experimental

Electrophoresis grade sodium dodecylsulfate (SDS) was obtained from BIO-RAD Laboratories and used as supplied. DTBN (di-*tert*-butyl nitroxide), TEMPO (2,2,4,4-tetramethylpiperidine-1-oxyl), and TEMPOL (2,2,4,4-tetramethylpiperidin-4-ol-1-oxyl) were purchased from Aldrich and used without further purification. Fremy's salt was synthesized in these laboratories as the dimer (11).

Solutions containing 5×10^{-4} M of spin probe and known amounts of SDS were made up in doubly distilled Millipore treated water. Sample cells for ESR and ENDOR experiments were made from 1 mm id and 2 mm od Pyrex tubes attached to a solvent-container arm. The solutions were thoroughly degassed by the freeze–pump–thaw method and the cells sealed under vacuum. A Bruker ER200 ESR spectrometer with an ENDOR accessory was used. The temperature in the cavity was controlled by use of the Bruker VT4110 controller. The actual temperature of the sample was checked by use of a copper–constantan thermocouple during radiowave and microwave irradiation. The accuracy of the temperature measurement was ±1 K.

ENDOR spectra for the determination of the N-14 hfs were obtained by setting the external field on the center line of the N-hfs triplet in the ESR spectrum. For the measurement of the ratio of the ENDOR doublet intensity, N-14 ENDOR spectra were observed by fixing the field on the low-field ESR line because the intensity of this line is normally greater than that from the high-field ESR line. ENDOR spectra were obtained by applying 100 mW (−3 db) microwave power and 150 W (−3 db) rf power. The depth of the frequency modulation of rf was 100 kHz. The precision in the measured value of RDI was ±0.03.

The viscosity of aqueous glycerol solutions was measured by the use of an Ubbelohde-type viscometer in a thermostat. The temperature of the thermostat was controlled to within 0.2 K.

Results and discussion

The ratio of the ENDOR doublet intensity

The ENDOR spectrum of DTBN in water at 296 K is shown in Fig. 1. Both the proton and N-14 signals can be seen in the same spectrum at this temperature. The peak due to the 18 magnetically equivalent γ-hydrogens at the NMR frequency ν_p = 14.5 MHz (X) of the free proton is not resolved into a doublet under these conditions. The N-14 signal is composed of a relatively large doublet centered at ν_N = 1.1 MHz. The high-frequency peak (H) is located at $\nu_N + a_N/2 = 25.2$ MHz. The low-frequency peak (L) of the doublet extends beyond zero MHz and is "reflected back" to a position that is $a_N/2 - \nu_N = 23.0$ MHz. Hence the halfway point between the peaks of the N-14 doublet is $a_N/2 = 24.1$ MHz.

The relative intensities of the N-14 doublet will vary depending on the choice of the ESR line saturated. Thus, when the $M_I = 1$ line (high-field line) of the ESR N-14 triplet is saturated the intensity of line (L) exceeds that of line (H), whereas when the $M_I = -1$ line (low-field line) is saturated the intensity of line (L) is less than that of line (H). The difference in intensities is known to be based on unequal cross-relaxation times (12, 13).

We define the Ratio of the ENDOR Doublet Intensity (RDI) as the ratio of the low-frequency peak (L) intensity to the high-frequency peak (H) intensity, using the height from maximum to minimum of the first-derivative trace.

The relationship between RDI and the rotational correlation time τ_R can be calculated from theory available in the literature (14–16). Six energy levels are assumed for one nucleus of $I = 1$ and one electron spin. The nuclear quadrupole interaction, the coherence effect, and the spin-exchange interaction are neglected. The electron-nuclear dipolar and spin-rotational interactions are assumed to be the cause of electron spin relaxation. Thus electron-spin relaxation rate W_e is expressed as:

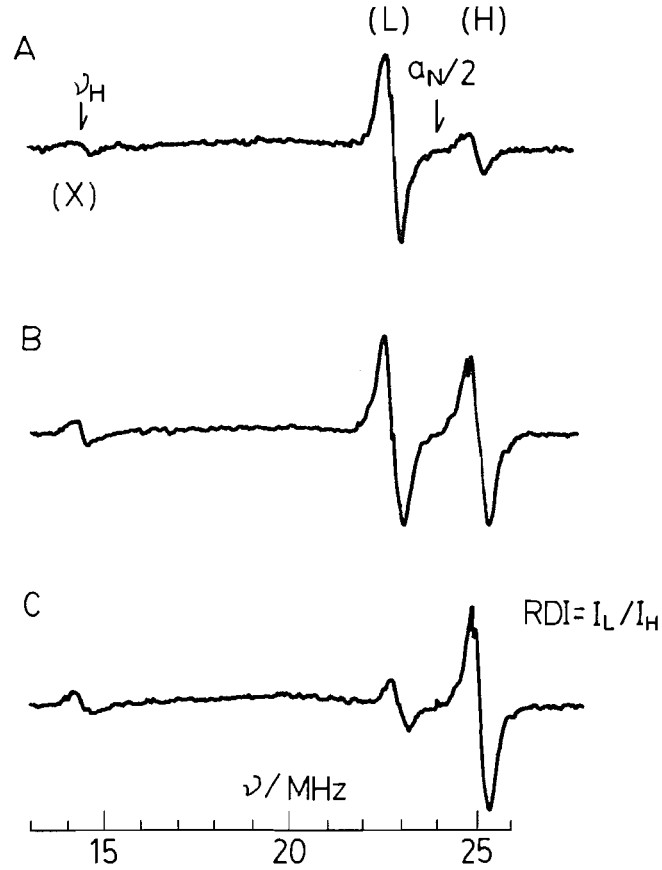

FIG. 1. ENDOR spectrum of 5×10^{-4} M DTBN in water at 296 K. A: the field is fixed at the $M_I = 1$ line (high-field ESR line). (X) denotes the proton ENDOR line and (L) and (H) denote the low and high frequency N-14 ENDOR lines, respectively. B: the field is fixed at the $M_I = 0$ line (center ESR line). C: the field is fixed at the $M_I = -1$ line (low-field ESR line). RDI is defined as I_L/I_H, where I_L and I_H denote the intensity of lines (L) and (H), respectively, in the spectrum C. The spikes on lines L and H are artifacts of the spectrometer, which appear at the even frequencies. The microwave frequency is 9.57 GHz. The rf frequency at $a_N/2 = 24.1$ MHz.

[1] $$W_e = W_{END} + W_{SR}$$

where W_{END} and W_{SR} denote relaxation rates induced by the electron-nuclear dipolar interaction and the spin-rotation interaction, respectively. If one assumes isotropic rotational diffusion (16),

[2] $$W_{END} = (1/40)(A_i' : A_i')\tau_R/(1 + \omega_e^2\tau_R^2)$$

[3] $$W_{SR} = \Sigma(g_i - g_e)^2/2\tau_R$$

where $A_i' : A_i'$ is the inner product of the dipolar tensor of N-hfs, g_i is the principal value of the g-tensor, and g_e, ω_e, and ω_n denote the free-electron g-value, and electron and nuclear Larmor frequencies, respectively. For the nuclear spin and cross-relaxations, it is assumed that the electron–nuclear dipolar interaction is the only mechanism. Thus the nuclear relaxation rate W_n and the cross-relaxation rates W_{x1} and W_{x2} are expressed as:

[4] $$W_n = (1/40)(A_i' : A_i')\tau_R/(1 + \omega_n^2\tau_R)$$

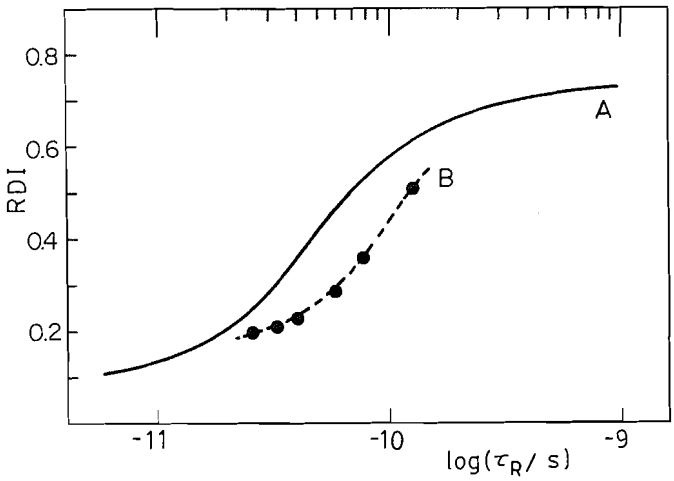

FIG. 2. A: Calculated N-14 ENDOR RDI as a function of the rotational correlation time τ_R. The method of calculation is specified in the text. Parameters used in eqs. [1]–[6] are taken from ref. 17. B: The plot of observed RDI in aqueous glycerol vs. τ_R calculated from observed viscosity in aqueous glycerol. The molecular radius is assumed to be 0.3 nm.

[5] $W_{x1} = 2W_{END}/3$

[6] $W_{x2} = 4W_{END}$

The ESR parameters required for the calculation of the electron-nuclear dipolar and spin-rotational relaxation times were taken to be those of DTBN (17). The transition probability matrix was constructed and the ENDOR enhancement was calculated from saturation factors by using a double cofactor method (14, 15). The low-field ESR line was chosen to be the observed ESR transition. The ENDOR enhancement factors were calculated with each of the two nuclear transitions saturated. The calculation was performed with the assumption that both electron and nuclear transitions are at just-resonance and that the nuclear transition is under complete saturation. The ratio of the two calculated enhancement factors can be plotted as a function of τ_R as shown in Fig. 2. The plot shows that the RDI increases smoothly with increase in correlation time. Thus the experimentally available values for RDI for DTBN in solution where N-14 ENDOR spectra can be obtained are directly related to τ_R.

If RDI for 5×10^{-4} M DTBN is plotted against the content of glycerol in water at various temperatures, the curves shown in Fig. 3 are obtained. From such plots one can find the microscopic viscosity in an unknown sample using aqueous glycerol as a reference. τ_R of DTBN in aqueous glycerol can be calculated based on the Stokes–Einstein equation by using the viscosity and molecular radius of the probe. Thus the dependence of observed RDI on τ_R is obtained and is plotted in Fig. 2.

To use RDI as a measure of τ_R it is essential to establish the condition under which no factors other than the diffusion of individual molecules influences the ratio. In Fig. 4 the dependence of RDI on the concentration of DTBN in water is shown at three different temperatures. At concentrations above 5×10^{-4} M DTBN, increase in concentration enhances the difference in the ENDOR doublet intensities. However, below this concentration the RDI approaches a constant value. Thus at 5×10^{-4} M the effect of spin–spin exchange on the RDI is apparently negligible.

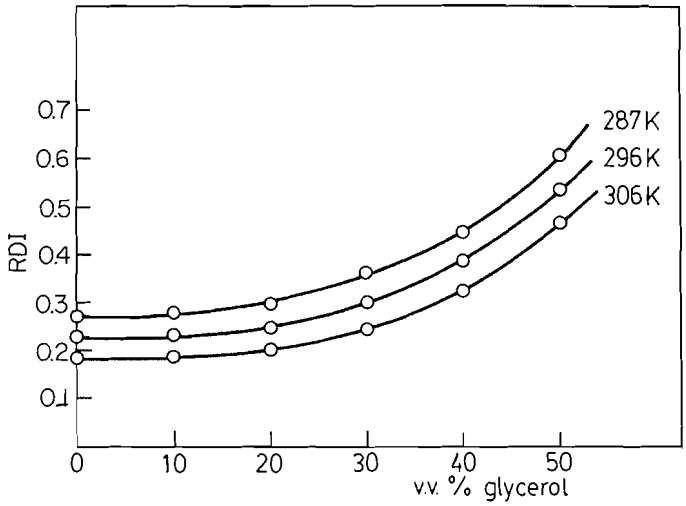

FIG. 3. The dependence of the N-14 ENDOR RDI on the glycerol content (v.v. denotes volume percent) in aqueous solutions of DTBN at various temperatures.

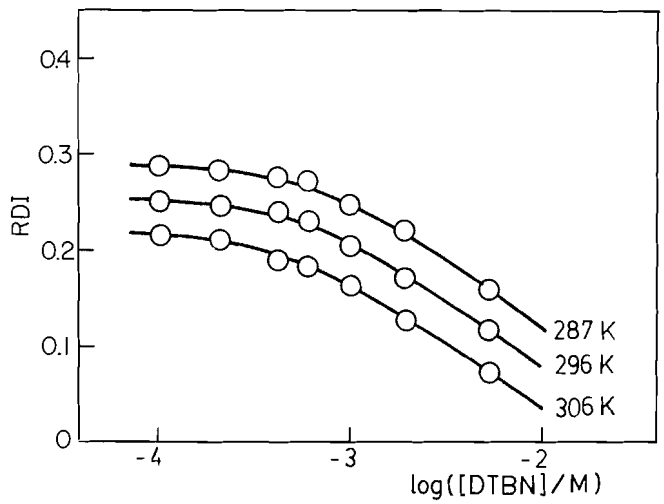

FIG. 4. The dependence of the N-14 ENDOR RDI of DTBN on the concentration of DTBN in water at various temperatures.

ENDOR RDI at SDS concentrations near micellization: DTBN

The ENDOR spectra of DTBN at several different concentrations of SDS from 0 to 0.1 M SDS in water were obtained at 296 K. The N-14 doublets only are plotted in Fig. 5. At relatively low and high concentrations (far from the SDS cmc) the doublets give fairly constant but different RDI values (Fig. 6). An abrupt change occurs between 0.02 and 0.03 M SDS, which is at a higher concentration than the reported cmc for SDS (18), namely 8.6×10^{-3} M. The discrepancy probably occurs because the number of micelle aggregates is much less than the number of probe molecules near the cmc.

Inspection of Fig. 5 reveals that the N-14 doublet moves to lower frequency in the range 0.02–0.03 M SDS, as the SDS concentration is increased. This corresponds to a decrease in the N-14 hfs. Figure 6 shows that the abrupt change in N-14 hfs corresponds to the sharp change in RDI values. Thus DTBN is completely solubilized in the SDS micelles at concentrations well above the cmc (19). The rotational correlation times calculated from Fig. 2 increase from 2.2×10^{-11} to $4.2 \times$

Can. J. Chem. Downloaded from www.nrcresearchpress.com by 112.217.228.212 on 09/07/12
For personal use only.

Can. J. Chem. Downloaded from www.nrcresearchpress.com by 112.217.228.212 on 09/07/12
For personal use only.

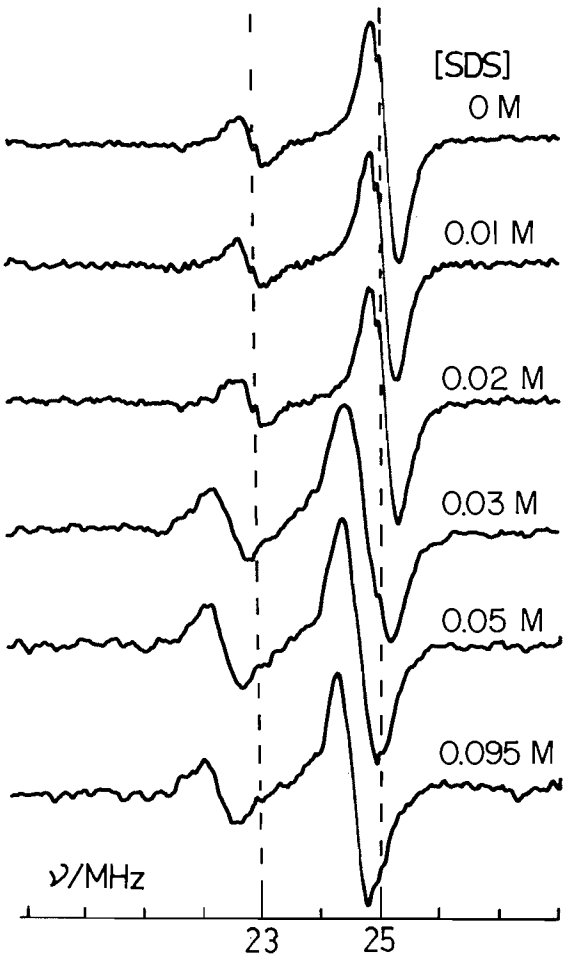

FIG. 5. N-14 ENDOR spectra of aqueous solutions of 5×10^{-4} M DTBN as a function of the concentration of SDS at 296 K. The magnetic field was fixed on lower field line of N-hfs.

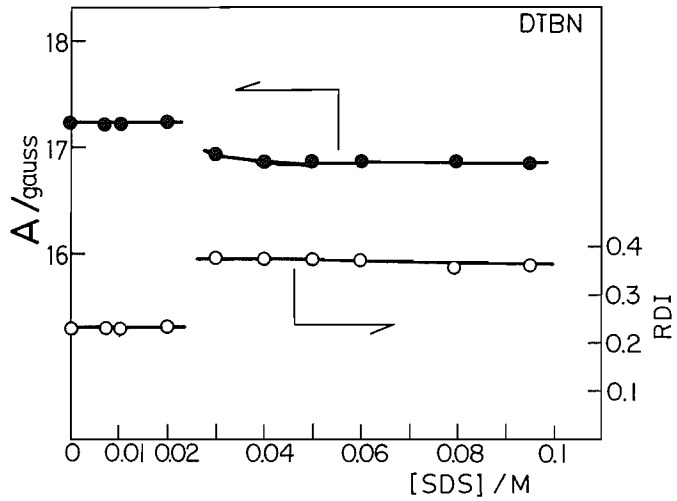

FIG. 6. The dependence of the N-14 hfs and the ENDOR RDI of 5×10^{-4} M DTBN in SDS aqueous solution as a function of the concentration of SDS at 296 K.

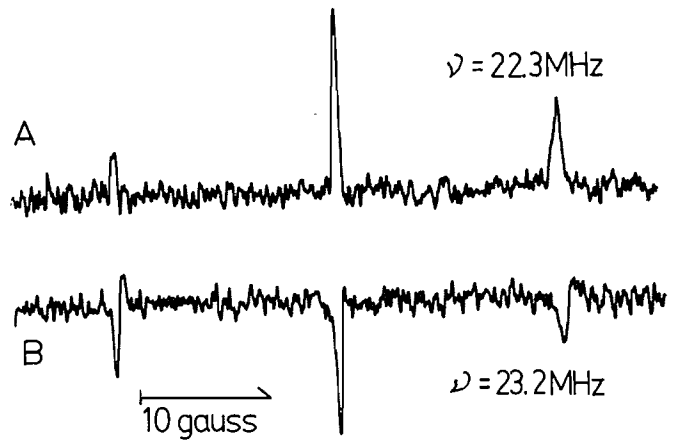

FIG. 7. ENDOR induced ESR spectra of DTBN in 3×10^{-2} M SDS aqueous solution taken by fixing the rf: (A) at 22.3 MHz, (B) at 23.2 MHz. These correspond to the ESR spectra of solubilized (less polar region) and free (more polar region) DTBN molecules, respectively.

10^{-11} s upon micellization. The microviscosities are 1.0 and 2.0 cP for the aqueous and micellar environment, respectively.

The spectra around the region of the cmc need further comment. The ENDOR doublet lines clearly have larger linewidths in the region of 3×10^{-2} to 5×10^{-2} M SDS than at SDS concentrations above and below this range. This is due to the coexistence of two DTBN spectra with different N-14 hfs (19). Although the two different ENDOR doublets could not be resolved under these conditions, the existence of such overlapping spectra could be ascertained by inspection of an ENDOR-induced ESR spectrum (20) of DTBN at 3×10^{-2} M SDS (Fig. 7). From this experiment the values $a_N = 17.2$ and 16.8 gauss were determined. These coupling constants agree well with the values obtained at pre and post cmc of DTBN in SDS.

Thus ENDOR spectroscopy confirms the generally accepted picture that DTBN is incorporated into SDS micelles around the cmc but that the average environment of the DTBN in the micelle is extremely polar and only slightly less polar than water itself (19). The existence of two locations for DTBN is also confirmed at concentrations of SDS near the cmc. The coexistence of these different DTBN molecules persists until all are dissolved in the micelles. The exchange rate between these two DTBN is slow on the ESR time scale (less than 10^{-6} s).

TEMPO

The N-14 hfs and RDI for TEMPO in water containing increasing amounts of SDS at 296 K are plotted in Fig. 8. Although the change in the RDI with increase in SDS concentration is abrupt (between 0.03 and 0.035 M SDS) the difference is not large. The change in N-14 hfs at this concentration range is also relatively small (0.2 gauss). If one applies the calculated results of RDI for DTBN, the change in the rotational correlation time is found to range from 2.3×10^{-11} to 4.2×10^{-11} s. The microviscosity changes from 1.1 to 1.9 cP. The broadness of the ENDOR doublet near the cmc again indicates the presence of two nitroxide species for which the polarity of the environment is different. In all aspects investigated, DTBN and TEMPO appear to behave essentially the same when dissolved in solutions containing increasing amounts of SDS.

TEMPOL

The ENDOR spectra of TEMPOL in water containing

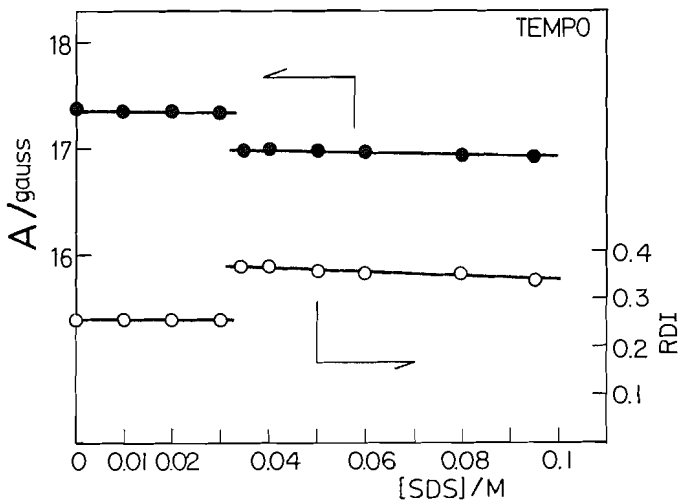

FIG. 8. The dependence of the hfs and ENDOR RDI of 5×10^{-4} M TEMPO in SDS aqueous solution as a function of the concentration of SDS at 296 K.

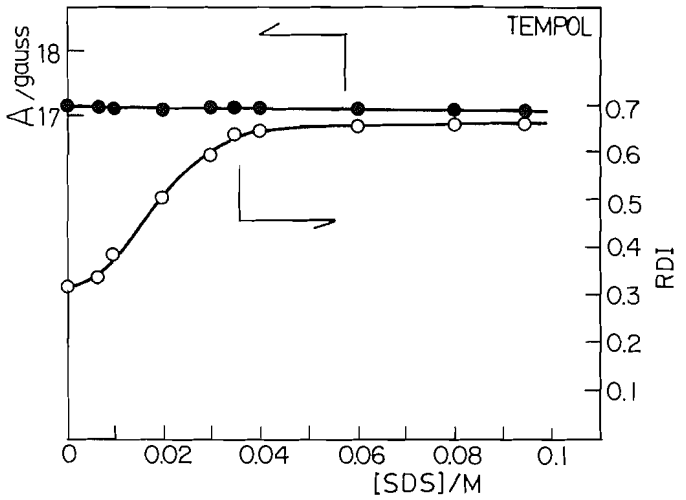

FIG. 10. The dependence of the N-14 hfs and ENDOR RDI of TEMPOL in SDS aqueous solution as a function of the concentration of SDS at 296 K.

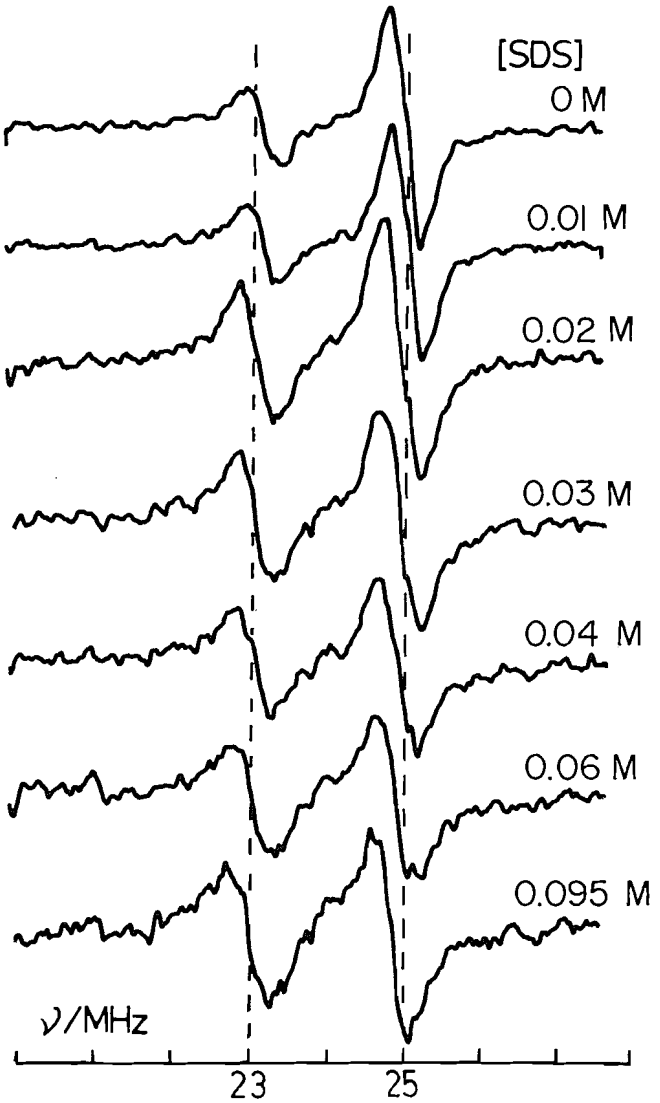

FIG. 9. N-14 ENDOR spectra of 5×10^{-4} M aqueous solution of TEMPOL as a function of the concentration of SDS at 296 K.

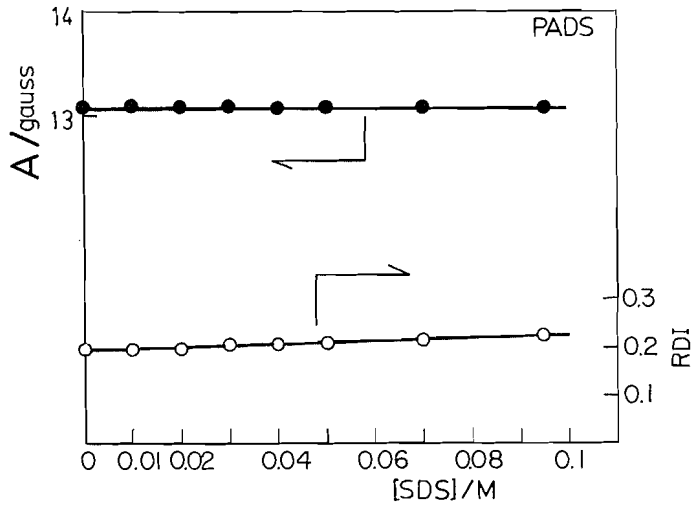

FIG. 11. The dependence of the N-14 hfs and ENDOR RDI of 5×10^{-4} M PADS in SDS aqueous solution as a function of the concentration of SDS at 296 K.

increasing amounts of SDS at 296 K are shown in Fig. 9 (N-14 ENDOR doublet only). The plots of the RDI and N-14 hfs are given in Fig. 10. Although an almost continuous change in the RDI is observed with increase in SDS concentration, the N-14 hfs does not change from the value in water. Thus the ENDOR spectra reveal a restriction in motion for the probe in spite of the fact that the environment for TEMPOL remains as polar as water. The rotational correlation times are found to be 2.3×10^{-11} and 1.0×10^{-10} s for aqueous and micellar phases, respectively. The change in microviscosity is estimated to be from 1.3 to >4.5 cP. After the concentration of SDS exceeds 5×10^{-2} M no more change in RDI occurs, indicating that all TEMPOL molecules are associated with SDS micelles.

PADS (Fremy's salt)

The values for RDI and N-14 hfs of PADS are plotted against SDS concentration in Fig. 11. While the change in the RDI is very small (about 5% from 10^{-2} to 10^{-1} M SDS) and well within the change in bulk viscosity of the solution, the N-14 hfs

Can. J. Chem. Downloaded from www.nrcresearchpress.com by 112.217.228.212 on 09/07/12
For personal use only.

does not change at all. Because there is no abrupt change in the RDI at any concentration it must be concluded that PADS does not associate with SDS micelles.

Evaluation of the ENDOR method

The estimation of the intrinsic ESR linewidth, which is hidden in the inhomogeneous linewidth due to proton hfs, has been a problem in spin labeling and spin probing methods. We have shown that N-14 ENDOR spectroscopy can determine both the hfs and the rotational correlation time of the nitroxide spin probe irrespective of the ESR linewidth. The ENDOR approach is much simpler than the ESR spin probing method since the latter requires a correction of the residual linewidth due to small unresolved proton hfs. The evaluation of the rotational correlation time, however, has the same degree of uncertainty as the ESR linewidth method because both methods assume the correct choice of effective relaxation processes.

Overlap of spectra from two species near the cmc region occurs in ENDOR as well as in ESR spectroscopy. However, we have shown that resolution of the spectrum is possible in some cases by using ENDOR-induced ESR spectroscopy.

The broadening of the ESR lines observed near the cmc region has been previously attributed to the site exchange of the probe between the aqueous and micellar phases (7). However, our ENDOR study in SDS gives no indication of such exchange.

Acknowledgement

We are grateful to the Natural Sciences and Engineering Research Council of Canada for continuing support and a grant for the purchase of the ENDOR spectrometer.

1. M. F. MENGER. Acc. Chem. Res. **12**, 111 (1979).
2. M. F. MENGER and D. W. DOLL. J. Am. Chem. Soc. **106**, 1109 (1984).
3. S. C. H. CHEN. Ann. Rev. Phys. Chem. **37**, 351 (1986).
4. L. J. BERLINER (*Editor*). Spin labeling. Theory and applications. Academic Press, New York. 1976.
5. L. J. BERLINER (*Editor*). Spin labeling II. Theory and applications. Academic Press, New York. 1979.
6. M. F. OTTAVIANI, P. BAGLIONI, and G. J. MARTINI. J. Phys. Chem. **87**, 3146 (1983), and references therein; P. BAGLIONI, E. FERRONI, G. MARTINI, and M. F. OTTAVIANI. J. Phys. Chem. **88**, 5107 (1984); P. BAGLIONI, M. F. OTTAVIANI, and G. MARTINI. J. Phys. Chem. **90**, 5878 (1986).
7. A. S. WAGGONER, A. D. KEITH, and O. H. GRIFFITH. J. Phys. Chem. **72**, 4129 (1968).
8. G. POGGI and C. S. JOHNSON, JR. J. Magn. Reson. **3**, 436 (1970).
9. E. G. JANZEN, Y. KOTAKE, G. A. COULTER, and U. M. OEHLER. Chem. Phys. Lett. **126**, 205 (1986).
10. N. BRETZ, I. MASTALSKY, M. ELSNER, and H. KURRECK. Angew. Chem. **99**, 357 (1987); Angew. Chem. Int. Ed. Engl. **26**, 345 (1987).
11. F. RASCHIG. Ann. **241**, 223 (1887).
12. D. S. LENIART, J. C. VERDINE, and J. S. HYDE. Chem. Phys. Lett. **6**, 637 (1967).
13. J. YAMAUCHI and Y. DEGUCHI. Chem. Lett. 111 (1985).
14. J. H. FREED. J. Phys. Chem. **71**, 38 (1967).
15. J. H. FREED. *In* Multiple electron resonance spectroscopy. *Edited by* M. M. Dorio and J. H. Freed. Plenum Press, New York. 1979.
16. M. PLATO, W. LUBITZ, and K. MOBIUS. J. Phys. Chem. **85**, 1202 (1981).
17. L. J. LIBERTINI and O. H. GRIFFITH. J. Chem. Phys. **53**, 1359 (1970).
18. H. C. EVANS. J. Chem. Soc. 579 (1956).
19. N. M. ATHERTON and S. J. STRACH. J. Chem. Soc. Faraday Trans. 2, **68**, 374 (1972).
20. J. S. HYDE. J. Chem. Phys. **43**, 1806 (1965).

Can. J. Chem. Downloaded from www.nrcresearchpress.com by 112.217.228.212 on 09/07/12
For personal use only.

An EPR/ENDOR study of aminoxyls (nitroxides) capable of intramolecular bonding: hydroxyalkyl radical spin adducts of nitrones[1]

D. Larry Haire, Yashige Kotake, and Edward G. Janzen[2]

Department of Chemistry and Biochemistry, Guelph–Waterloo Centre for Graduate Work in Chemistry, Guelph, Ont., Canada N1G 2W1

Received October 9, 1987

This paper is dedicated to Professor Charles A. McDowell on the occasion of his 70th birthday

D. Larry Haire, Yashige Kotake, and Edward G. Janzen. Can. J. Chem. **66**, 1901 (1988).

A comparison of the effect of solvent and ^{13}C labeling (of the radical addend) on the EPR (electron paramagnetic resonance) spectra of hydroxyalkyl vs. alkyl radical adducts of α-phenyl-*N*-*tert*-butyl nitrone (PBN) and 5,5-dimethyl-1-pyrroline-1-oxide (DMPO) has been investigated. The solution ENDOR spectra in toluene and in ethanol are the first examples studied of aminoxyls with hydroxyl substituents in close proximity to the free radical centre. Diastereomeric mixtures of hydroxyalkyl radical adducts are clearly resolved by ENDOR spectroscopy. Conformations of these radicals have been assigned based on the ^1H and ^{13}C hyperfine splittings (HFS's) and by differential optimum ENDOR temperatures. Definitive assignments of carbon-centered radical adducts of DMPO and PBN are shown to be feasible by monitoring the β-^{13}C HFS's of the radical addend. Long-range γ-H HFS's from the added radical group can be observed when the deuterated spin trap PBN-d_{14} is used. The production of ^{13}C labeled hydroxyalkyl adducts of nitrones (e.g., DMPO–$^{13}CH_2OH$, from the reaction of hydroxyl radicals with added $^{13}CH_3OH$) is shown to be useful as an improved EPR spectroscopic method for the verification of the presence of hydroxyl radicals.

D. Larry Haire, Yashige Kotake et Edward G. Janzen. Can. J. Chem. **66**, 1901 (1988).

On a effectué une étude comparative de l'effet de solvant et du marquage au ^{13}C (du radical qui s'ajoute) sur les spectres en résonance paramagnétique électronique d'adduits alkylés vs. hydroxy-alkylés de l'α-phényl *N*-*tert*-butyl nitrone (PBN) et de l'oxyde de la diméthyl-5,5 pyrroline (DMPO). Les spectres ENDOR, en solutions dans le toluène et dans l'éthanol, sont les premiers exemples de spectres de radicaux aminoxyles portant des substituants hydroxyles à proximité du centre radicalaire. La spectroscopie ENDOR permet de résoudre sans ambiguïté les mélanges diastéréomères des adduits radicalaires hydroxy-alkylés. On a attribué les conformations de ces radicaux en se basant sur les couplages hyperfins du ^1H et du ^{13}C et sur les températures différentielles ENDOR optimales. On a démontré que, si on détermine les couplages hyperfins du β-^{13}C du radical ajouté, il est possible de faire des attributions définitives des adduits, du DMPO ainsi que du PBN, qui portent des centres radicalaires sur le carbone. Lorsqu'on utilise le piège à spin PBN-d_{14}, on peut observer les couplages hyperfins du γ-H à longue distance du groupement radicalaire qui a été ajouté. On a démontré que la formation d'adduits hydroxy-alkylés des nitrones qui sont marquées au ^{13}C (par exemple, le DMPO–$^{13}CH_2OH$ qui provient de la réaction de radicaux hydroxyles avec du $^{13}CH_3OH$ ajouté) est une méthode en résonance paramagnétique électronique améliorée pour la vérification de la présence de radicaux hydroxyles.

[Traduit par la revue]

Can. J. Chem. Downloaded from www.nrcresearchpress.com by 112.217.228.212 on 09/07/12
For personal use only.

Introduction

Hydroxyalkyl radicals are difficult to detect in solution without special EPR spectroscopic techniques.[3] Transient radicals such as these, however, may be detected and identified by virtue of their reaction with nitrones (the spin trapping reaction) (for general reviews on EPR spin trapping and ancillary techniques such as spectral simulation, see ref. 2), which yields persistent aminoxyl adducts whose EPR parameters (nitrogen and β-hydrogen hyperfine splittings) (HFS's) as well as g values) in principle are unique for the radical trapped.

There has been previous interest in hydroxyalkyl radical adducts (e.g., $\dot{C}H_2OH$) produced from two widely used nitrone

[1] $RX\cdot + -CH=\overset{+}{N}(O^-)- \longrightarrow -CH(RX)-N(O\cdot)-$

Transient radical — Nitrone spin trap — Aminoxyl (nitroxide) spin adduct

spin traps, α-phenyl-*N*-*tert*-butyl nitrone (PBN) (**1**) (for the hydroxymethyl adduct of PBN, see ref. 3), and 5,5-dimethyl-1-pyrroline-*N*-oxide (DMPO) (**2**),[4] as well as from the C-nitroso spin trap, 2-nitroso-2-methylpropane (MNP) (**3**) (see ref. 5

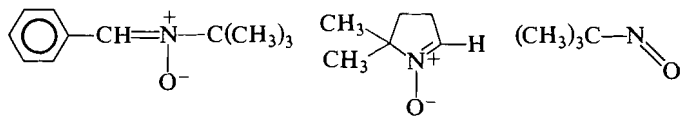

PBN (**1**) DMPO (**2**) MNP (**3**)

for the hydroxymethyl adduct). These adducts and higher analogues (e.g., those originating from ethanol and larger alcohols, glycerols, and sugars, etc.) have been generated mainly by radiolysis, photolysis, and even by sonolysis.

[1]This work was presented in part at the 70th Meeting of the Chemical Institute of Canada in Quebec City, June 7–11, 1987.

[2]Author to whom correspondence may be addressed.

[3]Kinetic EPR techniques (i.e., with short, strong pulses of UV radiation) have recently been used to detect the $\cdot CH_2OH$ radical in solution (1*a*). The $\cdot CH_2OH$ radical can also be detected in solution using a special EPR "flow cell" apparatus (1*b*), and has also been detected directly by EPR (e.g., during photolysis of the anticancer drug, Bleomycin) using matrix isolation techniques (at 77 K) (1*c*). Other hydroxyalkyl radicals (e.g., from X-irradiated saccharides such as glucose and derivatives) may be analyzed by EPR and ENDOR in the solid state (at 12 K) (1*d*).

[4]For the hydroxymethyl adduct of the aliphatic cyclic nitrone, 5,5-dimethyl-1-pyrroline-*N*-oxide (DMPO), see refs. 4*a*–*e*), and for the 2-hydroxypropyl adduct of the aliphatic acyclic nitrone, *tert*-butyl nitrone (BN), see ref. 4*f*).

Can. J. Chem. Downloaded from www.nrcresearchpress.com by 112.217.228.212 on 09/07/12
For personal use only.

An interesting recent development has been the use of nitrones to detect hydroxyalkyl radicals in biological systems. Specifically, hydroxyalkyl radicals have been observed in rat liver microsomal systems (*6a,b*)[5] treated with alcohols, suggesting that these reactive intermediates may be implicated in the toxicological effects of ethanol (e.g., liver damage) such as lipid peroxidation and related processes. The autoxidation of sugars under physiological conditions also apparently yields hydroxyalkyl radicals (*6i,j*).

Another interesting recent sidelight deals indirectly with the trapping of hydroxyl radicals. Since it is known that hydroxyl adducts of nitrones may in certain circumstances arise from artifactual reactions (2, 7) it has been suggested (*2c*, *5b*)[6] that the detection of hydroxyalkyl adducts might serve as a diagnostic check:

[2] $HO\cdot + R_2CHOH \rightarrow H_2O + R_2\dot{C}OH$

Hydroxyl radical — Added alcohol — Hydroxyalkyl radical

Objective

In the present study we have searched for methods to better characterize some carbon-centered adducts of nitrones (e.g., hydroxyalkyl vs. alkyl). To probe the radical structures in more detail high resolution techniques including Electron Nuclear Double Resonance (ENDOR) spectroscopy as well as the implementation of deuterated spin traps have been explored. Also the effects of solvent, temperature, and ^{13}C labeling (of the radical addend) on the EPR and ENDOR spectra have been investigated.

Radical formation and spin trapping chemistry

Hydrogen atom abstraction from alcohols by photoexcited benzophenone to form hydroxyalkyl radicals is a well-known process (8). Subsequent trapping by a nitrone leads to a hydroxyalkyl adduct (**4**). It is noteworthy that photoexcited nitrones may also act as hydrogen atom abstractors (*6h*).

[3] $PhCOPh^* + R_2CHOH \rightarrow PhC\dot{H}Ph + R_2\dot{C}OH$

[4] 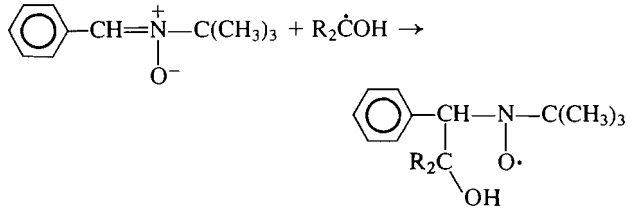

PBN–$COHR_2$ (**4**)
R = H, alkyl or aryl

ENDOR spectroscopy

Solution ENDOR spectroscopy has proven to be a valuable tool for gleaning detailed structural and environmental information about aminoxyl spin probes, spin labels, and spin adducts.[7] One advantage of ENDOR over EPR spectroscopy is the ability of the former to detect very small HFS's (e.g., in long-range hyperfine splittings, or small differences in HFS's such as those in radical mixtures).

Experimental

The hydroxyalkyl adducts in organic solvents were generally prepared according to previously described methods (*3e*) except that 5-mL alcohol solutions of 50 mM nitrone and 50 mM benzophenone were used. Photolysis of the deoxygenated alcohol solutions was accomplished using a low pressure 75 W xenon lamp (Oriel model 6137). The irradiation period was approximately 15 min. The hydroxyalkyl adducts in aqueous solutions were prepared by photolysis of aqueous solutions containing 50 mM nitrone, 50 mM hydrogen peroxide, and 50 mM alcohol. The PBN-d_{14} and DMPO alkyl adducts were prepared by the anion (RMgI) addition/quenching with water/and oxidation sequence referred to in ref. *10b*.[8] Typically, 2-mL solutions containing ~2 mg of nitrone and ~0.1 mL of 2 M Grignard reagent were used. Samples were deoxygenated by 4 freeze–pump–thaw cycles and sealed off on a vacuum line before spectral analysis.

EPR and ENDOR spectra were recorded with a Bruker ER-200D EPR spectrometer (ST 4102 and EN 801 X-band cavities, respectively) and Bruker ER-140 (Aspect 2000) data system. The ENDOR spectra were obtained with an E-N A-300 amplifier with 12.5 kHz radio-frequency modulation. The EPR spectral centre field was generally around 3400 gauss. Thus the centres (ν_H and ν_N) for the ^1H and ^{14}N ENDOR doublets (i.e., the ^1H and ^{14}N NMR frequencies) are 14.47 and 1.046 MHz, respectively. The sample temperature was controlled by a Bruker ER 4111 VT unit. Spectra were simulated with Oehler and Janzen's BASIC program (*2e*). (Note: line 485 should read MT = MT + MK(I4).) The *g* values were calculated as previously described (*3e*, *2f*) using Fremy's salt (sodium peroxylamine disulfonate in saturated aqueous $NaHCO_3$) as the internal standard (g = 2.00550, a^N = 13.091 gauss).

Solvent exchange was accomplished by the following procedure. The bulk of the solvent was removed by purging with N_2 (g). The final traces of solvent were pumped off using a vacuum line. The new solvent was introduced and dried (Na_2SO_4).

The nitrones α-phenyl-*N*-*tert*-butyl nitrone (PBN) and 5,5-dimethyl-1-pyrroline-*N*-oxide (DMPO) are commercially available (Aldrich and Sigma). The ^2H and ^{13}C methanol, ^2H and ^{13}C iodomethane, as well as benzaldehyde-carbonyl ^{13}C were obtained from MSD Isotopes.

Results and discussion

PBN–CH_2OH vs. PBN–CH_3

Radical conformations

Listed in Table 1 is a comparison of the HFS's of the two prototypical aminoxyls PBN–CH_2OH and PBN–CH_3. The solvents are listed in order of increasing solvent polarity, according to the solvent polarity parameter $E_{T(30)}$ (11). PBN–CH_2OH should have the capability for intramolecular H-bonding whereas PBN–CH_3 should not. The corresponding EPR spectra are shown in Figs. 1–6. Small amounts of the alkoxyl adduct (PBN–OCH_3, a^N = 14.5, a_β^H = 2.8 gauss in methanol) (*3a,d,k*) are also present in some of the EPR spectra (Figs. 1–3).

On the basis of the magnitudes of both the β-^1H and β-^{13}C HFS's (both of which exhibit a dihedral angle dependence (12) with respect to the aminoxyl *p*-orbital) PBN–CH_3 likely adopts the time-average conformation shown below (**5**) (*10b*). The proposed conformation for PBN–CH_2OH (**6**) can be compared to **5** by counterclockwise rotation of the frontal carbon about the C—N bond. A larger β-H, smaller β-^{13}C (radical addend), and larger β-^{13}C (phenyl) HFS should result, and this is what is observed.

The β-^{13}C radical addend HFS for PBN–CH_2OH (2.26 gauss in toluene) is relatively small compared to PBN–CH_3 (3.11 gauss)

[5]For radical adducts of PBN, DMPO, and MNP more complex than hydroxymethyl, see refs. *6a–m*.

[6]See ref. *2c* for reviews on EPR spin trapping in biological systems.

[7]For a detailed description of ENDOR spectroscopy, see ref. 9. For some recent ENDOR spectroscopic studies of aminoxyl (nitroxide) radicals, see ref. 10.

[8]This reference contains a mini-review on the ENDOR spectroscopy of aminoxyls to ~1985.

TABLE 1. EPR hyperfine splitting constants for PBN–$^{13}CH_2OH$ vs. PBN–$^{13}CH_3$ in various solvents at 300 K[a–d]

Solvent	$E_{T(30)}$	Radical	a^N	a_β^H	a_γ^H	a_β^{13C} (radical addend)	a_β^{13C} (phenyl)	g value
Tetramethylsilane	30.7	$^{\bullet}CH_2OH$	14.75	6.54	—	—	—	2.00594
Tetramethylsilane	30.7	$^{\bullet}CH_3$	14.63	3.70	0.48	—	—	2.00605
Toluene	33.8	$^{\bullet}CH_2OH$	14.92	6.69	0.31	2.26	11.3	2.00598
Toluene	33.8	$^{\bullet}CH_3$	14.81	3.58	0.45	3.11	10.6	2.00600
Acetonitrile	46.7	$^{\bullet}CH_2OH$	15.42	3.77	—	—	—	2.00582
Acetonitrile	46.7	$^{\bullet}CH_3$	15.79	3.80	0.42	—	—	2.00572
Methanol	55.5	$^{\bullet}CH_2OH$	15.28	3.65	—	3.23	—	2.00588
Methanol	55.5	$^{\bullet}CH_3$	15.55	3.89	0.44	3.52	10.3	2.00576
Water	63.1	$^{\bullet}CH_2OH$	15.96	3.87	—	3.85	—	2.00564
Water	63.1	$^{\bullet}CH_3$	16.49	3.56	0.34	4.60	9.7	2.00559

[a]The HFS's are in gauss; — indicates that this value is not available.
[b]For the $E_{T(30)}$ solvent polarity scale (kcal/mol) see ref. 11.
[c]The β-^{13}C (phenyl) HFS's were assigned as described in ref. 10*b*.
[d]The HFS's (in benzene, $E_{T(30)}$ = 34.8) of two other β-^{13}C (radical addend) labeled adducts: PBN–$^{13}CCl_3$, a^N = 13.88, a_β^H = 1.61, a_β^{13C} (CCl_3 = 9.67 gauss, g = 2.00631 (ref. 13); PBN–$^{13}C(O)C_6H_5$, a^N = 14.30, a_β^H = 4.54, a_β^{13C} (carbonyl) = 6.09 gauss (from benzaldehyde-carbonyl ^{13}C and *tert*-butoxyl radicals, unpublished data)).

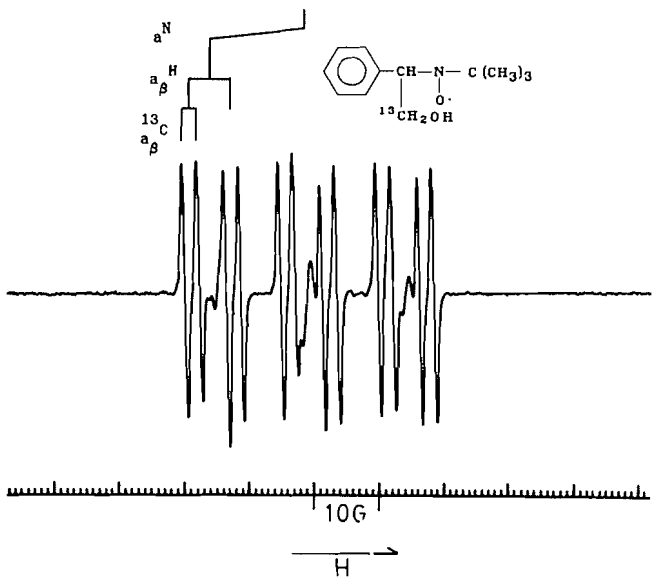

FIG. 1. EPR spectrum of PBN–$^{13}CH_2OH$ in toluene at 300 K.

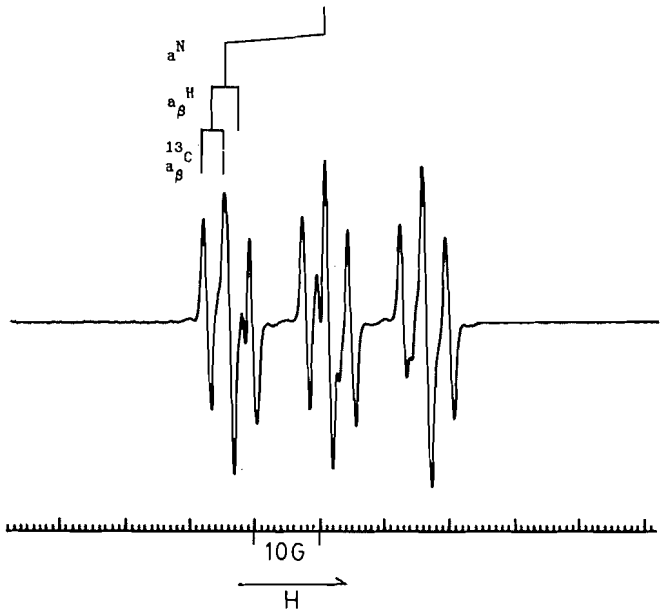

FIG. 2. EPR spectrum of PBN–$^{13}CH_2OH$ in methanol at 300 K.

as well as other PBN adducts such as PBN–$C(O)C_6H_5$ (6.09 gauss) and PBN-CCl_3 (9.67 gauss). In addition, PBN–CH_2OH exhibits larger β-H and β-^{13}C (phenyl) HFS's compared to PBN–CH_3 (6.69 vs. 3.58, and 11.3 vs. 10.6 gauss, respectively).

A reasonable explanation for this conformational preference (i.e., **6** vs. **5**) is the possibility of intramolecular H-bonding between the CH_2OH substituent and the aminoxyl function.[9] Significant π-attraction between the phenyl and aminoxyl groups (10*b*) may also assist in the intramolecular H-bonding interaction by swinging the CH_2OH group closer to the aminoxyl group.

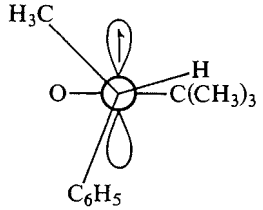

PBN—CH_3
(**5**)

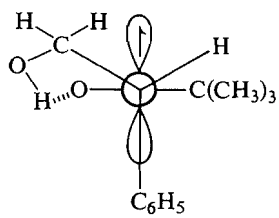

PBN—CH_2OH
(**6**)

EPR solvent effects

As the solvent polarity is increased (e.g., from tetramethylsilane to toluene) the nitrogen HFS's for both PBN–CH_2OH and PBN–CH_3 increase (Table 1). This effect is attributed to the stabilization of the polar resonance structure (**8**) with the unpaired electron on the nitrogen atom.[10] This effect is much

[9]The notion of H-bonding has been invoked before: ref. 4*f*; for a related system (hydroxyalkyl adducts of nitromethane radical anion) see ref. 14.

[10]The trend of increase in nitrogen HFS with increase in solvent polarity is well documented, for example, ref. 15*a*, with aminoxyl (nitroxide) spin probes, and 15*b*, with aminoxyl spin adducts.

Can. J. Chem. Downloaded from www.nrcresearchpress.com by 112.217.228.212 on 09/07/12
For personal use only.

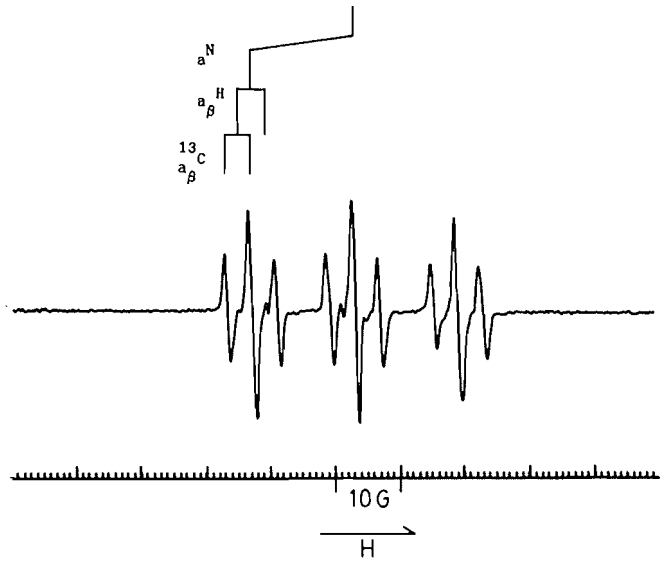

FIG. 3. EPR spectrum of PBN–$^{13}CH_2OH$ in water at 300 K.

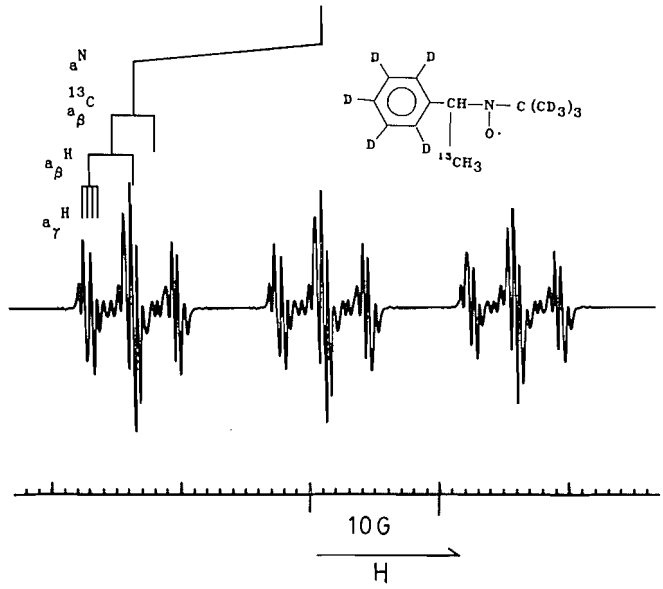

FIG. 4. EPR spectrum of PBN-d_{14}–$^{13}CH_3$ in toluene at 300 K.

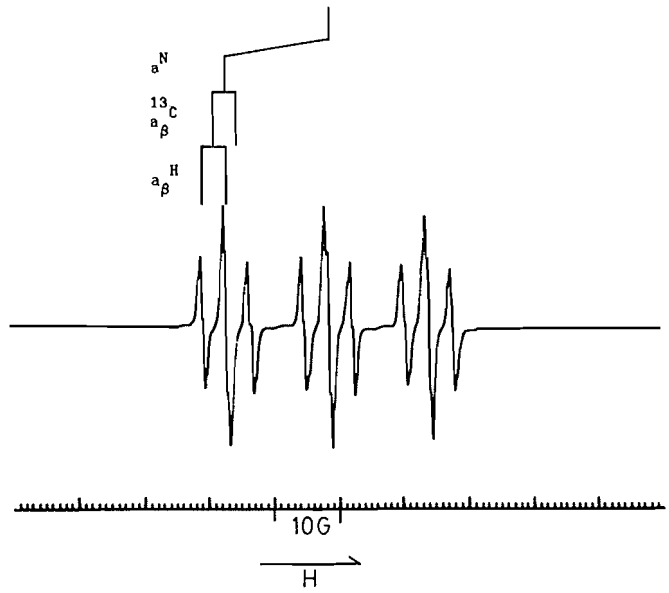

FIG. 5. EPR spectrum of PBN-d_{14}–$^{13}CH_3$ in methanol at 300 K.

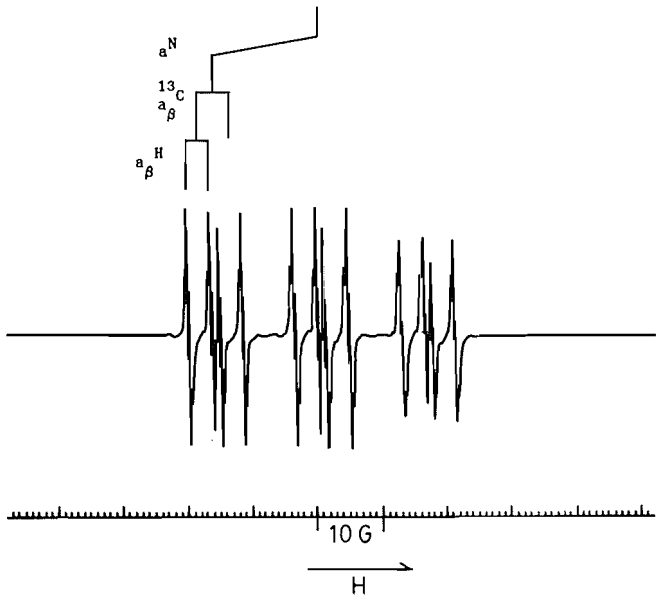

FIG. 6. EPR spectrum of PBN-d_{14}–$^{13}CH_3$ in water at 300 K.

more pronounced for both adducts as even more polar solvents are introduced (e.g., acetonitrile, methanol, and water).

In nonpolar solvents (e.g., TMS, toluene, etc.) the PBN–CH_2OH adduct exhibits an unusually large β-H HFS (~6.7 gauss). When this adduct is placed in polar solvents (e.g., acetonitrile, methanol, etc.) a remarkable phenomenon occurs. Despite the increase in nitrogen HFS (14.9 to 15.3 gauss) the β-H HFS undergoes a substantial *decrease* in magnitude (~6.7 to ~3.7 gauss). The β-^{13}C (CH_2OH) and β-^{13}C (phenyl) HFS's also show sensitivity to change in polarity of solvents. These data suggest that replacing a nonpolar with a polar solvent causes the disruption of the intramolecularly H-bonded structure (**6**) via the intervention of intermolecular H-bonding between the polar solvent molecules and the aminoxyl group. Further solvent effects are observed as a more polar solvent is introduced but these effects are comparatively smaller.

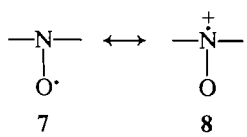

7 **8**

EPR/ENDOR temperature effects

In Table 2 (Figs. 7 and 8) it is clear that the β-hydrogen HFS of PBN–CH_2OH increases with decrease in temperature. This result suggests that the H-bonding interaction between the hydroxymethyl and aminoxyl groups becomes stronger at lower temperatures.

A striking feature of the ENDOR spectra of PBN–CH_2OH is the observation of a β-H doublet at a relatively high ENDOR temperature (300 K, Fig. 8A). The optimum intensity for an ENDOR response obtained at a given rotational correlation time (τ_R) is determined by the EPR parameters of the radical and its

Can. J. Chem. Downloaded from www.nrcresearchpress.com by 112.217.228.212 on 09/07/12
For personal use only.

TABLE 2. EPR and ENDOR hyperfine splittings (HFS's) for PBN–CH_2OH in toluene at various temperatures[a,b]

Temperature (K)	Experiment	a^N	a^H_β	a^H_γ (radical addend)
300	EPR	14.92	6.69	0.31
300	ENDOR	14.99	6.65	—
240	ENDOR	15.04	6.89	0.35
200	EPR	14.90	7.00	—
200	ENDOR	15.03	7.01	—

[a]The HFS's are gauss; — indicates that this value is not available. Conversion of gauss to MHz is multiplication by 2.81.

[b]The γ-H HFS of 0.31 gauss due to *one* of the diastereotopic methylene H's (CH_2OH) is visible by both EPR and ENDOR when PBN-d_{14} is used (assignment confirmed by comparison with the CD_2OH analogue). The second methylene γ-H HFS is too small (i.e., <0.1 gauss) to be readily resolved. No HFS from the hydroxyl-H could be resolved (checked by D_2O exchange).

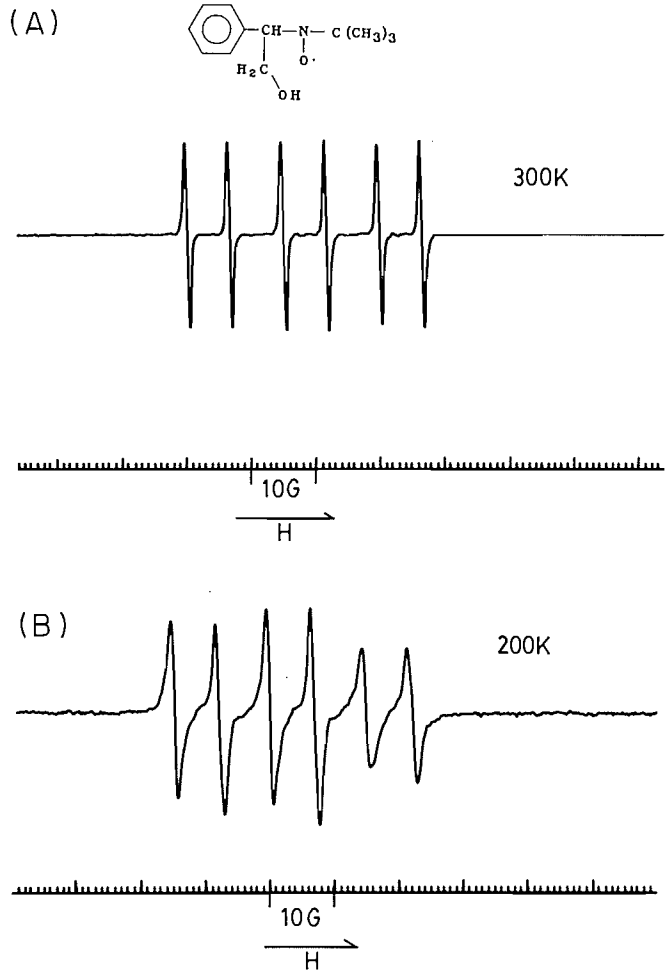

FIG. 7. EPR spectra of PBN–CH_2OH in toluene at (A) 300 and (B) 200 K, respectively.

nucleus.[11] Since τ_R is dependent upon the effective volume of the tumbling radical (V_{EFF}) (eq. [5]), an increase in V_{EFF} raises the optimum ENDOR temperature.

[5] $\tau_R = V_{EFF}(\eta/kT)$

[11]For a more detailed relationship between τ_R and the optimum ENDOR conditions see Equation 13 in ref. 16.

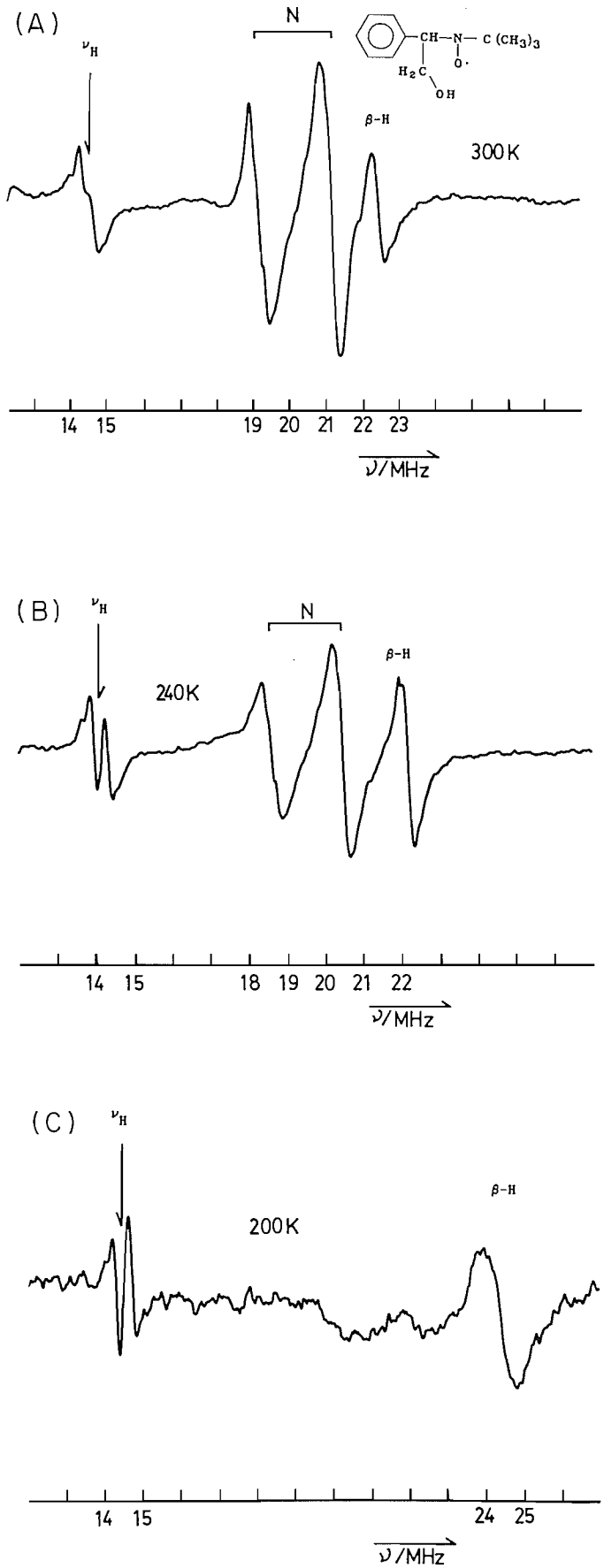

FIG. 8. ENDOR spectra of PBN–CH_2OH in toluene at (A) 300, (B) 240, and (C) 200 K, respectively (13–28 MHz region).

Can. J. Chem. Downloaded from www.nrcresearchpress.com by 112.217.228.212 on 09/07/12
For personal use only.

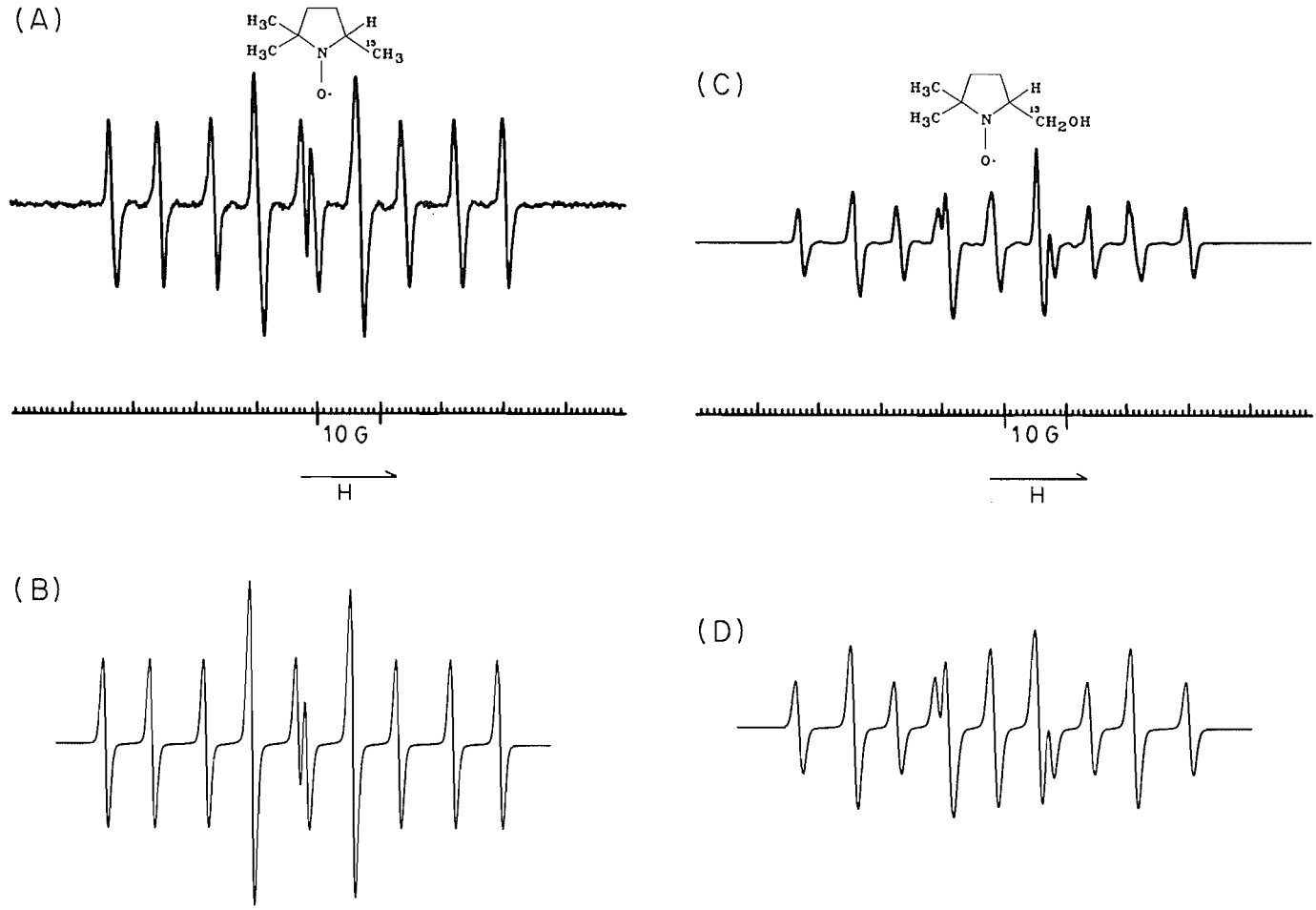

FIG. 9. (A) EPR spectrum of DMPO–$^{13}CH_3$ in water at 300 K. (B) Computer simulation of the above spectrum using the following parameters: $a^N = 16.35$, $a_\beta^H = 23.71$, $a_\beta{}^{13C} = 7.63$ gauss, linewidth = 1.2 gauss, lineshape = 0.3 Lorentzian. (C) EPR spectrum of a mixture of DMPO–$^{13}CH_3$ and DMPO–OH in water. (D) Computer simulation of the above mixture spectrum using the following parameters: DMPO–$^{13}CH_2OH$: $a^N = 15.92$, $a_\beta^H = 22.56$, $a_\beta{}^{13C} = 8.81$ gauss, linewidth = 1.2 gauss, lineshape = 0.3 Lorentzian. DMPO–OH: $a^N = 15.01$, $a_\beta^H = 15.01$ gauss, linewidth = 1.2 gauss, lineshape = 0.3 Lorentzian. The spectral centre for DMPO–OH is 0.1 gauss to the left of that for DMPO–$^{13}CH_2OH$. The DMPO–$^{13}CH_2OH$/DMPO–OH ratio (from the double integrated areas under the EPR spectra) = 2.6:1.

where V_{EFF} is the effective tumbling volume of the radical, η is the viscosity of the solvent, T is the absolute temperature, and k is the Boltzmann constant. This ENDOR result lends further support for the existence of the H-bonded chelate structure (**6**) because an increase in molecular volume (due to chelation) is expected to raise the optimum ^1H ENDOR temperature.

DMPO–CH_2OH vs. DMPO–CH_3

Radical conformations

The nitrogen HFS for DMPO–CH_2OH in toluene is considerably larger (~0.5 gauss) than the value for DMPO–CH_3 (Fig. 9, Table 3). This fact points to an increased contribution of the polar aminoxyl resonance form, **8**. The β-hydrogen and β-^{13}C (CH_2OH) HFS's are expected to be correspondingly larger for DMPO–CH_2OH vs. DMPO–CH_3 because β-nuclei HFS's are proportional to the nitrogen HFS (12). With this taken into account the conformation of DMPO–CH_2OH may well be quite similar to that of DMPO–CH_3 (**9**). In contrast to PBN–CH_2OH there is no abrupt change in the β-hydrogen of β-^{13}C (CH_2OH) HFS's of DMPO–CH_2OH when a nonpolar solvent (e.g., toluene) is replaced by a relatively polar and

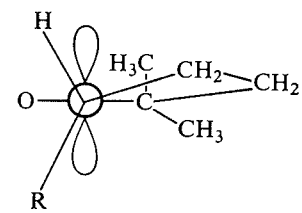

DMPO–R

(**9**)

R = CH_2OH or CH_3

hydrogen-bonding solvent such as methanol. Therefore the conformation of DMPO–CH_2OH probably does not change very much with solvent polarity. Perhaps this is due to the restricted rotation of the CH_2OH group as a result of the rigidity imposed by the pyrrolidine ring structure.

Unequivocal EPR assignment of hydroxyalkyl and other carbon-centered radical adducts of DMPO

Along with the numerous reports on hydroxyalkyl adducts of DMPO (2, 4, 6*d*,*g*,*h*,*i*) there have been some studies proposing that other carbon-centered radicals (e.g., methyl (17*a*–*k*), ethyl

Can. J. Chem. Downloaded from www.nrcresearchpress.com by 112.217.228.212 on 09/07/12
For personal use only.

TABLE 3. EPR hyperfine splitting constants (HFS's) for DMPO–$^{13}CH_2OH$ and DMPO–$^{13}CH_3$ in toluene, methanol, and water at 300 K[a]

Solvent	Radical	a^N	a_β^H	$a_\beta{}^{13}C$ (radical addend)	a_{other}	g value	Reference
Toluene	$^{\bullet}CH_2OH$	14.71	21.66	7.49	—	2.00570	This work
Toluene	$^{\bullet}CH_3$	14.25	20.64	6.65	—	2.00588	This work
Toluene	$^{\bullet}OH$	12.10	13.75	—	—	—	26
Methanol	$^{\bullet}CH_2OH$	15.19	21.38	8.42	—	2.00563	This work
Methanol	$^{\bullet}CH_3$	15.28	21.84	7.14	—	2.00560	This work
Water	$^{\bullet}CH_2OH$	15.92	22.56	8.81	—	2.00549	This work
Water	$^{\bullet}CH_3$	16.35	23.71	7.63	—	2.00539	This work
Water	$^{\bullet}$DMPO-yl	~16	~22	—	—	—	24
Water	$^{\bullet}OH$	15.01	15.01	—	$a_\beta{}^{17}O = 4.66$	2.00558[b]	27

[a]The HFS's are in gauss; — indicates that this value is not available.
[b]This work.

(18*a*,*b*), 2-propyl (18*a*), 2-cyano-2-propyl (18*c*), cyclopentadienyl (19), phenyl and substituted phenyl (18*c*, 20*a*–*d*), nitrobenzyl (21), uracil derived (22), and others of unspecific structure (18*a*, 23*a*–*d*) are also trapped by DMPO. Although many of these structural assignments are likely correct (e.g., the structure of DMPO–phenyl was confirmed by mass spectroscopy (20*c*), distinguishing alkyl, aryl, hydroxyalkyl, etc. adducts in general is difficult because the EPR parameters are so similar (2). For example, the HFS's for DMPO–CH_2OH and DMPO–CH_3 in methanol (Table 3) are essentially equivalent ($a^N \sim 15.2$, $a_\beta \sim 21.6 \pm 0.2$ gauss). An additional complication is the possible appearance of a carbon-centered adduct (DMPO–DMPO-yl) (24) produced by hydrogen atom abstraction of the pseudo-allylic position of the nitrone (**10**).

We have found that the β-^{13}C (radical addend) HFS's for alkyl, hydroxyalkyl (Table 3, Figs. 9A–D), as well as halomethyl adducts[12] are large (~6–16 gauss) and distinctive for the radical trapped. Thus, ^{13}C labeling is a viable strategy for verifying the structures of carbon-centered adducts of DMPO (4, 17–23).

^{13}C labeled hydroxyalkyl adducts as markers for hydroxyl radicals

Hydroxyl radical detection in biological systems by spin trapping with DMPO is of considerable interest even though potential artifactual reactions (2, 7) do exist.[13] The use of ^{17}O labeled reagents to produce β-^{17}O labeled spin adducts (spin = 5/2) (27) has shed some light on the various mechanisms of hydroxyl adduct formation but these methods cannot be applied routinely due to expense. Lai and Piette (5*b*), and Rosen (2*c*) have advocated the formation of hydroxyalkyl adducts (from added alcohol) as a useful safeguard against artifacts during the detection of hydroxyl radicals. We suggest that a ^{13}C labeled alcohol be used to guard against possible confusion with DMPO–DMPO-yl (**10**). Furthermore, it would appear that an

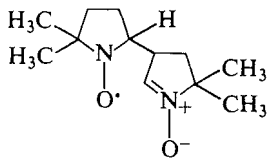

DMPO–DMPO-yl (**10**)

alcohol such as $^{13}CH_3OH$ would be preferred over ethanol because EPR spectra derived from the latter would be complicated by the presence of diastereomers (see PBN–$CHOHCH_3$ in the subsequent section).

Alternatively, dimethylsulfoxide (DMSO) as a detector of hydroxyl radicals is possible, but complications from the addition of hydroxide followed by oxidation should not be overlooked (29). Another possible indicator for hydroxyl is sodium formate (preferably $NaH^{13}CO_2$) because spin adduct spectra of CO_2^- (3*b*) are very similar to those of acyl spin adducts from nitrone hydrolysis (30).

PBN-CHOHCH$_3$

Radical conformation and stereochemistry

Formation of the hydroxyethyl adduct of PBN (**11**) creates an

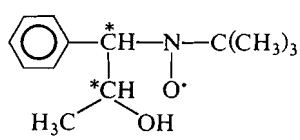

11

adduct with two asymmetric centres and therefore a diastereomeric mixture of aminoxyl radicals.

The EPR and ENDOR parameters for PBN–$CHOHCH_3$ are collected in Table 4. The EPR spectra of PBN–$CHOHCH_3$ in toluene at 300 K (Fig. 10A) as well as at 200 K (Fig. 10B) exhibit distinct asymmetry due to diastereomers that may have the following *cis*/*trans* structures (**12**) and (**13**):

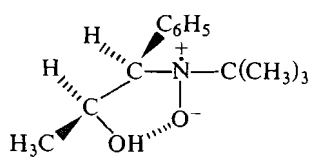

cis
(**12**)

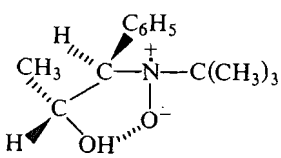

trans
(**13**)

[12]Weakly polar carbon-centred adducts of DMPO (e.g., DMPO–hydroxyalkyls) exhibit EPR spectra (e.g., a^N and $a_\beta{}^H$ HFS's) that are quite similar to ordinary carbon-centred adducts; however, strongly polar adducts (e.g., DMPO–CCl_3) show quite distinctive patterns: (a) for DMPO–$^{13}CCl_3$ in benzene, $a^N = 13.17$, $a_\beta{}^H = 15.28$, $a_\beta{}^{13}C(CCl_3) = 16.34$ gauss (E. G. Janzen and R. A. Towner, manuscript in preparation, 1987), and (b) for DMPO–CCl_3 in water, $a^N \sim a_\beta{}^H \sim 14.6$ gauss (see ref. 25).

[13]The hyperfine splittings (HFS's) of DMPO–OH are quite sensitive to solvent effects (ref. 26).

Can. J. Chem. Downloaded from www.nrcresearchpress.com by 112.217.228.212 on 09/07/12
For personal use only.

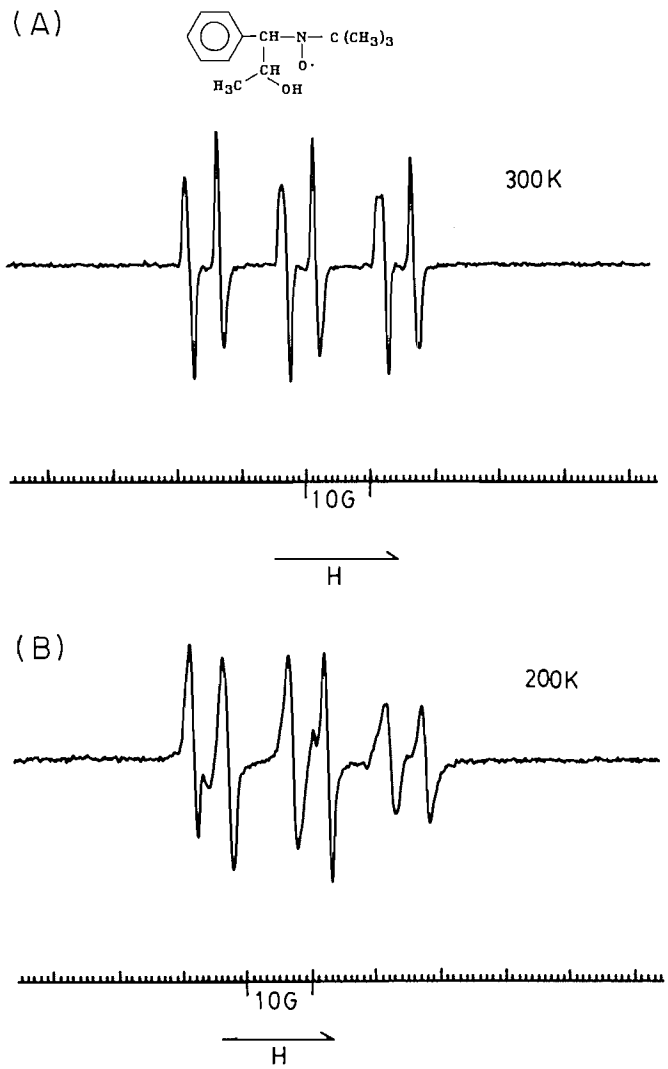

FIG. 10. EPR spectra of PBN–$CHOHCH_3$ in toluene at (A) 300 and (B) 200 K, respectively.

Unlike the hydroxymethyl adduct, the ENDOR spectrum of PBN–$CHOHCH_3$ at 300 K (compare Fig. 8A with Fig. 11A) shows only the aminoxyl nitrogen doublet. This may be an indication of a weaker H-bonding interaction, perhaps due to increased steric hindrance in the hydroxyethyl adduct. The ENDOR spectrum of PBN–$CHOHCH_3$ at 240 K (Fig. 11B) and 200 K (Fig. 11C), however, clearly demonstrates the superiority of ENDOR vs. EPR (cf. Figs. 7A and 7B) for resolving radical mixtures of diastereomers. In toluene at 210 K the larger β-H ENDOR peak (~6.4 gauss) is approximately twice as intense as the smaller one (~5.3 gauss) while at 190 K the converse is true (cf. Figs. 11A–C for the temperature dependence of the diastereomeric ENDOR peaks). Using arguments developed in the preceding section for PBN–CH_2OH, the PBN–$CHOHCH_3$ adduct with the larger β-H is assigned to the *cis* isomer (**12**) since it should have the larger effective tumbling volume (V_{EFF}) and hence higher optimum ENDOR temperature. The species with the smaller β-H is therefore attributed to the *trans* isomer (**13**).

Solvent effects

At 300 K (Fig. 12A) as well as at 200 K (Fig. 12B) PBN–$CHOHCH_3$ in ethanol does not show any significant EPR spectral differences due to the diastereomeric species.

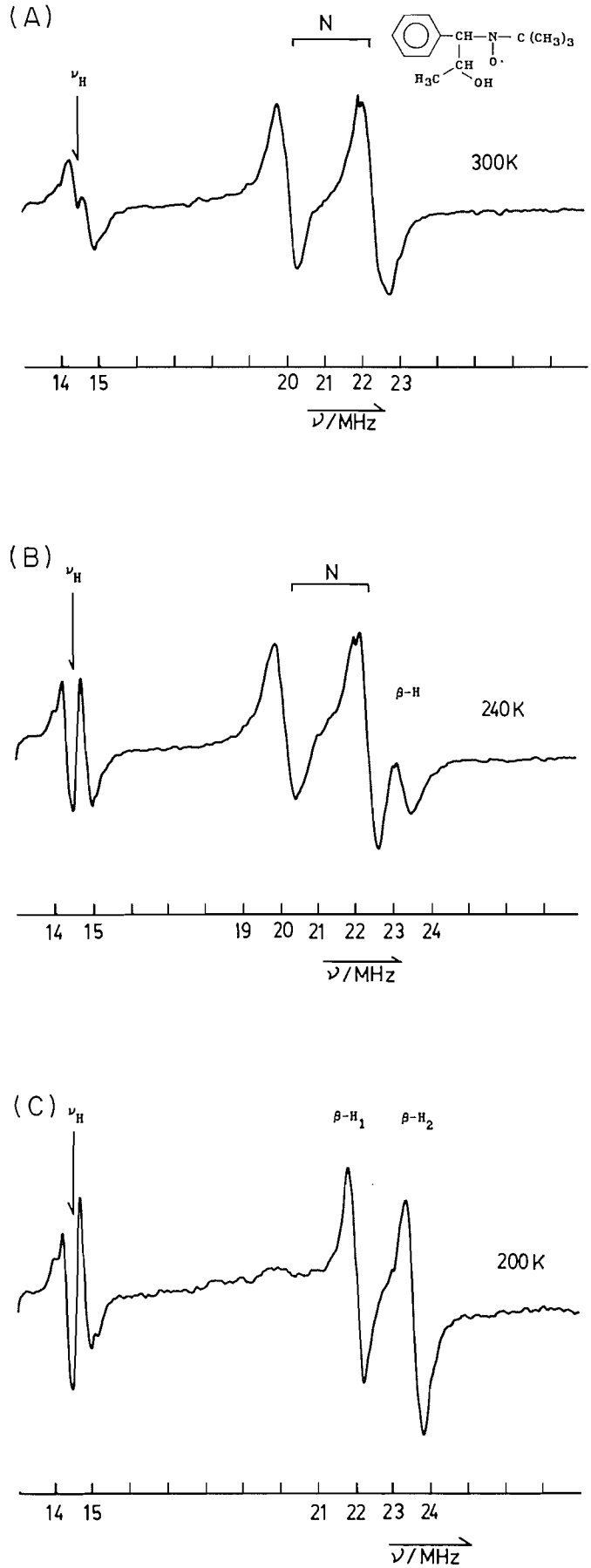

FIG. 11. ENDOR spectra of PBN–$CHOHCH_3$ in toluene at (A) 300, (B) 240, and (C) 200 K, respectively (13–28 MHz region).

Can. J. Chem. Downloaded from www.nrcresearchpress.com by 112.217.228.212 on 09/07/12
For personal use only.

TABLE 4. EPR and ENDOR hyperfine splitting constants (HFS's) for PBN–$CHOHCH_3$ in toluene and ethanol at various temperatures[a–d]

Solvent	Temperature (K)	Experiment	a^N	$a_\beta^{H_1}$ [b]	$a_\beta^{H_2}$ [b]	g value
Toluene	300	EPR	14.8	4.5	5.1	2.00583
Toluene	300	ENDOR	15.16	—	—	—
Toluene	240	ENDOR	15.20	5.56	6.20	—
Toluene	200	EPR	15.28	5.4	(avg.)[c]	—
Toluene	200	ENDOR	—	5.33	6.41	—
Ethanol	300	EPR	15.18	3.56	(avg.)[c]	—
Ethanol	200	EPR	~14.9	~3.1	(avg.)	—
Ethanol	200	ENDOR	—	2.44	2.88	—
Ethanol	210	ENDOR	—	2.65	3.08	—

[a]The HFS's are in gauss; — indicates that this value is not available. Conversion of gauss to MHz is multiplication by 2.81.
[b]These β-H HFS's are diastereomeric (cf. refs. 3*c* and 3*e*).
[c]The notation "avg." indicates an unresolved average value for the diastereomeric β-H HFS's.
[d]These HFS's are only approximate values due to the highly immobilized nature of the spin adduct in this solvent.

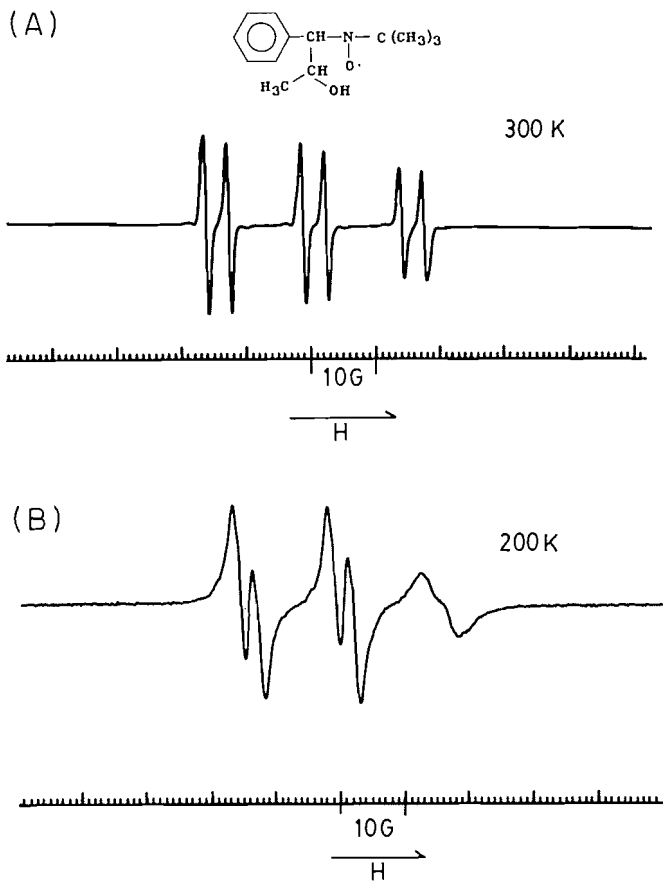

FIG. 12. EPR spectra of PBN–$CHOHCH_3$ in ethanol at (A) 300 and (B) 200 K, respectively.

Compared to toluene solution at 300 K, where the average β-H HFS for PBN–$CHOHCH_3$ is 4.8 gauss, the β-H HFS decreases markedly (to ~3.6 gauss) in ethanol whereas the nitrogen HFS remains quite similar (Table 4). As with the hydroxymethyl adduct discussed earlier, these phenomena are interpreted as due to the interruption of intramolecular H-bonding by alcohol solvent molecules. The ENDOR spectra at 200 K (Figs. 13A and 13B) exhibit a β-H HFS of about 3 gauss, which is assigned to the hydroxyethyl adduct.

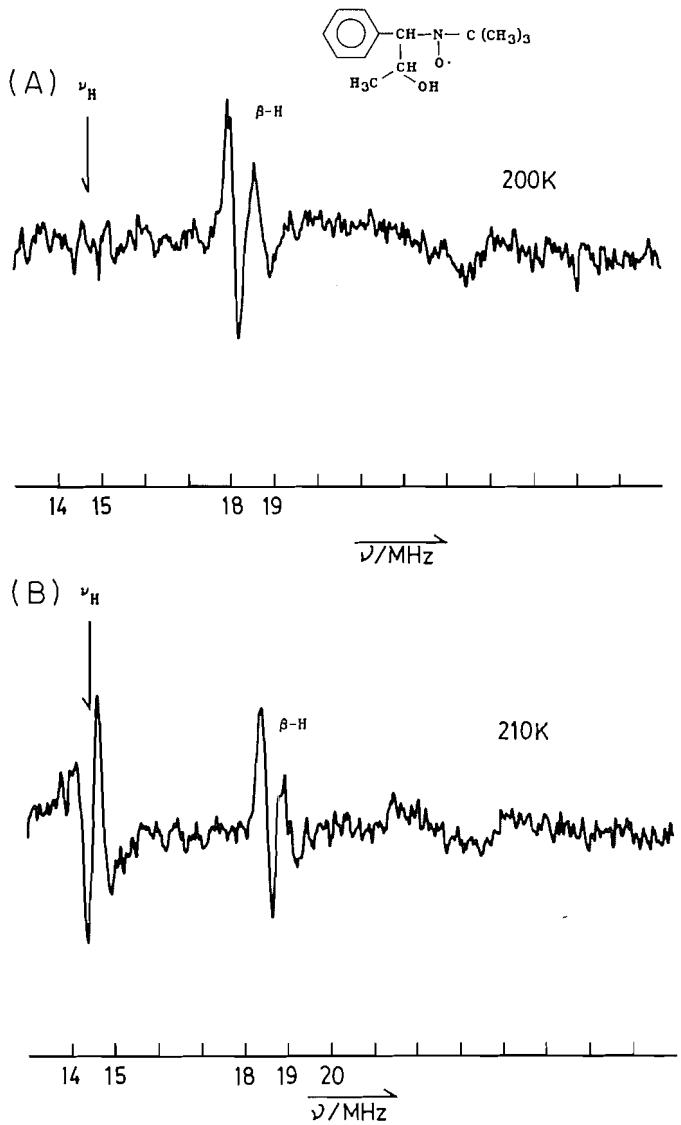

FIG. 13. ENDOR spectra of PBN–$CHOHCH_3$ in ethanol at (A) 200 and (B) 210 K, respectively. The smaller β-H ENDOR peak around 2.6 gauss is attributed to some alkoxyl adduct impurity, PBN–OCH_2CH_3 (a^N = 14.1, a_β^H = 2.8 gauss by EPR at 200 K).

Can. J. Chem. Downloaded from www.nrcresearchpress.com by 112.217.228.212 on 09/07/12
For personal use only.

Can. J. Chem. Downloaded from www.nrcresearchpress.com by 112.217.228.212 on 09/07/12
For personal use only.

Conclusions

From the solvent, temperature, and ^{13}C labeling effects on the EPR and ENDOR spectra of hydroxyalkyl aminoxyls it is apparent that the conformations of these free radicals may be strongly influenced by H-bonding interactions. In addition we have demonstrated the superiority of ENDOR spectroscopy (vs. EPR) for the spectral resolution of mixtures of diastereomeric radicals (28).[14] Utilization of a deuterated nitrone spin trap (e.g., PBN-d_{14}) reveals long-range γ-H HFS's from the added radical (e.g., $^{\bullet}CH_2OH$ or $^{\bullet}CH_3$), which serve to distinguish and identify the actual radical trapped. We have also illustrated the utility of ^{13}C labeled carbon-centred radical adducts of DMPO for conformational analysis as well as for proving the structure of the trapped radical.

Acknowledgements

We gratefully acknowledge the continuing support of the Natural Sciences and Engineering Research Council of Canada (NSERC).

1. (*a*) H. Fischer and H. Paul. Acc. Chem. Res. **20**, 200 (1987), and references cited therein; (*b*) R. Livingston and H. Zeldes. J. Chem. Phys. **44**, 1245 (1966), and references cited therein; (*c*) W. E. Antholine, T. Sarna, R. C. Sealy, B. Kalyanaraman, G. D. Shields, and D. H. Petering. Photochem. Photobiol. **41**, 393 (1985); (*d*) K. P. Madden and W. A. Bernard. J. Chem. Phys. **72**, 31 (1980).
2. (*a*) E. G. Janzen. Acc. Chem. Res. **4**, 31 (1971); (*b*) M. J. Perkins. *In* Advances in physical organic chemistry. Vol. 17. *Edited by* V. Gold and D. Bethell. Academic Press, New York. 1980. pp. 1–64; (*c*) G. M. Rosen. Adv. Free Radical Biol. Med. **1**, 345 (1985), and references cited therein; (*d*) G. R. Buettner. Free Radical Biol. Med. **3**, 259 (1987); (*e*) U. M. Oehler and E. G. Janzen. Can. J. Chem. **60**, 1542 (1982); (*f*) J. Q. Adams and J. R. Thomas. J. Chem. Phys. **39**, 1904 (1963).
3. (*a*) A. Halpern. Chem. Phys. Lett. **38**, 505 (1984); (*b*) B. Aurian-Blajeni, M. Halmann, and J. Manassen. Photochem. Photobiol. **35**, 157 (1982); (*c*) Y. Kotake and K. Kuwata. Bull. Chem. Soc. Jpn. **55**, 3686 (1982); (*d*) D. Rehorek. Acta Chim. Acad. Sci. Hung. **101**, 395 (1979); (*e*) Y. Kotake, K. Kuwata, and E. G. Janzen. J. Phys. Chem. **83**, 3024 (1979); (*f*) D. Rehorek. A. Allorg. Allg. Chem. **443**, 255 (1978); (*g*) A. N. Saprin and L. H. Piette. Arch. Biochem. Biophys. **180**, 480 (1977); (*h*) S. Schlick and L. Kevan. Chem. Phys. Lett. **48**, 505 (1976); (*i*) E. G. Janzen, D. E. Nutter, Jr., and C. A. Evans. J. Phys. Chem. **79**, 1983 (1975); (*j*) S. W. Mao and L. Kevan. Chem. Phys. Lett. **24**, 505 (1974); (*k*) A. Ledwith, P. J. Russell, and L. H. Sutcliffe. Proc. R. Soc. London, A: **332**, 151 (1973); (*l*) A. L. Bluhm and J. Weinstein. J. Org. Chem. **37**, 1748 (1972).
4. (*a*) A. J. Carmichael, M. M. Mossoba, P. Riesz, and I. Rosenthal. Photochem. Photobiophys. **10**, 13 (1985); (*b*) Y. Kirino, T. Ohkuma, and T. Kwan. Chem. Pharm. Bull. **29**, 29 (1981); (*c*) P. R. Marriott, M. J. Perkins, and D. Griller. Can. J. Chem. **58**, 803 (1980); (*d*) F. P. Sargent and E. M. Gardy. Can. J. Chem. **54**, 275 (1976); (*e*) E. G. Janzen and J. I.-P. Liu. J. Magn. Reson. **9**, 510 (1973); (*f*) E. G. Janzen and I. G. Lopp. J. Magn. Reson. **76**, 107 (1972).
5. (*a*) I. Rosenthal, M. M. Mossoba, and P. Riesz. J. Magn. Reson. **47**, 200 (1982); (*b*) C.-S. Lai and L. H. Piette. Tetrahedron Lett. **9**, 775 (1979); (*c*) F. P. Sargent and E. M. Gardy. J. Phys. Chem. **80**, 854 (1976); (*d*) J. A. Wargon and F. Williams. J. Am. Chem. Soc. **94**, 7917 (1972); (*e*) I. H. Leaver and G. C. Ramsey. Tetrahedron, **25**, 5669 (1969).
6. (*a*) E. Albano, A. Tomasi, L. Goria-Gatti, G. Poli, V. Vannini, and M. U. Dianzani. Free Radical Res. Commun. **3**, 243 (1987); (*b*) L. A. Reinke, E. K. Lai, C. M. DuBose, and P. B. McCay. Proc. Natl. Acad. Sci. U.S.A. In press; (*c*) J. J. Raffi, P. B. Vincent, J.-P.-L. Angel, C. M. Battesti, and C. L. Thiery. J. Chem. Soc. Faraday Trans. 1, **83**, 225 (1987); (*d*) B. K. Sinha, Y. Singh, and G. Krishna. Biochem. Biophys. Res. Commun. **15**, 583 (1986); (*e*) T.-M. Chiu, A. Siemiarczuk, S. K. Wong, and J. R. Bolton. J. Phys. Chem. **89**, 2243 (1985); (*f*) H. Baumann, H.-J. Timpe, V. E. Zubarev, N. V. Fok, and M. Y. Melnikov. J. Photochem. **30**, 487 (1985); (*g*) H. Baumann, H.-J. Timpe, V. E. Zubarev, N. V. Fok, M. Y. Melnikov, and Y. W. Raskasovskij. J. Prakt. Chem. **327**, 749 (1985); (*h*) M. Faraggi, A. Carmichael, and P. Riesz. Int. J. Radiat. Biol. Relat. Stud. Phys. Chem. Med. **46**, 703 (1984); (*i*) P. J. Thornalley and A. Stern. Carbohydrate Res. 191 (1984); (*j*) P. J. Thornalley, S. Wolf, J. Crabbe, and A. Stern. Biochim. Biophys. Acta, **797**, 286 (1984); (*k*) M. Kuwabara, Z.-Y. Zhang, O. Inanami, and G. Yoshii. Radiat. Phys. Chem. **21**, 451 (1983); (*l*) M. Kuwabara, Z.-Y. Zhang, O. Inanami, and G. Yoshii. Radiat. Phys. Chem. **24**, 217 (1984); (*m*) M. Kuwabara, Y. Lion, and P. Riesz. Int. J. Radiat. Biol. Relat. Stud. Phys. Chem. Med. **39**, 451 (1981).
7. (*a*) E. G. Janzen, L. T. Jandrisits, and D. L. Barber. Free Radical Res. Commun. **4**, 115 (1987); (*b*) H. Chandra and M. C. R. Symons. J. Chem. Soc. Chem. Commun. 1301 (1986); (*c*) D. Rehorek, C. M. DuBose, and E. G. Janzen. Inorg. Chim. Acta, **83**, L7-L8 (1984); (*d*) S. F. Chew, J. R. Bolton, R. G. Brown, and G. Porter. J. Phys. Chem. **84**, 1909 (1980).
8. C. Walling and M. J. Gibian. J. Am. Chem. Soc. **86**, 3902 (1964).
9. K. Möbius, M. Plato, and W. Lubitz. Phys. Rep. **87**, 171 (1982).
10. (*a*) M. Brustolon, A. L. Maniero, U. Segre, and L. Greci. J. Chem. Soc. Faraday Trans. 1, **83**, 69 (1987); (*b*) E. G. Janzen, U. M. Oehler, D. L. Haire, and Y. Kotake. J. Am. Chem. Soc. **108**, 6858 (1986); (*c*) E. G. Janzen and Y. Kotake. J. Magn. Reson. **69**, 567 (1986); (*d*) E. G. Janzen, Y. Kotake, G. A. Coulter, and U. M. Oehler. Chem. Phys. Lett. **126**, 205 (1986); (*e*) J. C. Evans, S. K. Jackson, C. C. Rowlands, and M. D. Barratt. Biochim. Biophys. Acta, **835**, 421 (1985).
11. C. Reichart and E. Harbusch-Görnert. Liebigs Ann. Chem. 721 (1983).
12. (*a*) E. G. Janzen. Can. J. Chem. **62**, 1653 (1984); (*b*) P. Riesz and S. Rustgi. Radiat. Phys. Chem. **13**, 21 (1979); (*c*) C. Heller and H. M. McConnell. J. Chem. Phys. **32**, 1535 (1960).
13. E. G. Janzen, R. A. Towner, and D. L. Haire. Free Radical Res. Commun. **3**, 357 (1987).
14. B. C. Gilbert and M. Trenwith. J. Chem. Soc. Perkin Trans. 2, 1834 (1973).
15. (*a*) A. H. Reddoch and S. Konishi. J. Chem. Phys. **70**, 2121 (1979); (*b*) E. G. Janzen, U. M. Oehler, and J. P. Bergsma. Can. J. Chem. **60**, 2725 (1982).
16. M. Plato, W. Lubitz, and K. Möbius. J. Phys. Chem. **85**, 1202 (1981).
17. (*a*) B. E. Britigan, M. S. Cohen, and G. M. Rosen. J. Leukocyte Biol. **41**, 349 (1987); (*b*) D. J. Hassett, B. E. Britigan, T. Svendsen, G. M. Rosen, and M. S. Cohen. J. Biol. Chem. **262**, 13404 (1987); (*c*) J. L. Zweier, L. Gianni, J. Muindi, and C. E. Myers. Biochem. Biophys. Acta, **884**, 326 (1986); (*d*) M. J. Turner III and G. M. Rosen. J. Med. Chem. **29**, 2439 (1986); (*e*) B. E. Britigan, G. M. Rosen, Y. Chai, and M. S. Cohen. J. Biol. Chem. **261**, 4426 (1986); (*f*) O. Augusto, M. J. M. Alves, W. Colli, L. S. Filardi, and A. Brener. Biochem. Biophys. Res. Commun. **135**, 1029 (1986); (*g*) B. D. Hilton, R. Misra, and J. L. Zweier. Biochemistry, **25**, 5533 (1986); (*h*) O. Augusto, C. L. W. Weingrill, S. Schreirer, and H. Amemiya. Arch. Biochem. Biophys. **244**, 147 (1986); (*i*) M. M. Mossoba and P. L.

[14]For the first report on the resolution of enantiomeric radicals (phenoxyls) in chiral solvents by ENDOR spectroscopy, see ref. 31.

GUTTIEREZ. Biochem. Biophys. Res. Commun. **132**, 445 (1985); (*j*) B. KALYANARAMAN, R. C. SEALY, and B. K. SINHA. Biochem. Biophys. Acta, **799**, 270 (1984); (*k*) E. FINKELSTEIN, G. M. ROSEN, and E. J. RAUCKMAN. Mol. Pharmacol. **21**, 262 (1982).

18. (*a*) B. K. SINHA. J. Biol. Chem. **258**, 796 (1983); (*b*) O. AUGUSTO, P. R. ORTIZ DE MONTELLANO, and A. QUINTANILHA. Biochem. Biophys. Res. Commun. **101**, 1324 (1981); (*c*) P. BARKER, A. L. J. BECKWITH, W. R. CHERRY, and R. HUIE. J. Chem. Soc. Perkin Trans. 2, 1147 (1985).
19. P. J. BARKER, S. R. STOBART, and P. R. WEST. J. Chem. Soc. Perkin Trans. 2, 127 (1986).
20. (*a*) D. F. CHURCH. J. Org. Chem. **51**, 1138 (1986); (*b*) O. AUGUSTO, K. L. KUNZE, and P. R. ORTIZ DE MONTELLANO. J. Biol. Chem. **257**, 6231 (1982); (*c*) H. A. O. HILL and P. J. THORNALLEY. Febs. Lett. **125**, 235 (1981); (*d*) C. F. CHIGNELL, B. KALYANARAMAN, R. H. SIK, and R. P. MASON. Photochem. Photobiol. **34**, 147 (1981).
21. S. N. J. MORENO, J. SCHREIBER, and R. P. MASON. J. Biol. Chem. **261**, 7811 (1986).
22. W. R. HEDRICK, M. D. WEBB, and J. D. ZIMBRICK. Int. J. Radiat. Biol. Relat. Stud. Phys. Chem. Med. **41**, 435 (1982).
23. (*a*) B. G. TAFFE, N. TAKAHASHI, T. W. KENSLER, and R. P. MASON. J. Biol. Chem. **262**, 12143 (1987); (*b*) B. PILAS, C. C. FELIX, T. SARNA, and B. KALYANARAMAN. Photochem. Photobiol. **44**, 689 (1986); (*c*) W. H. KOCH and M. R. CHEDEKEL. Photochem. Photobiol. **44**, 703 (1986); (*d*) B. H. STOCK, J. SCHREIBER, C. GUENAT, R. P. MASON, J. R. BEND, and T. ELING. J. Biol. Chem. **261**, 15915 (1986); (*e*) C. H. KENNEDY, W. A. PRYOR, G. W. WINTON, and D. F. CHURCH. Biochem. Biophys. Res. Commun. **141**, 1123 (1986).
24. (*a*) B. KALYANARAMAN, E. G. JANZEN, and R. P. MASON. J. Biol. Chem. **260**, 4003 (1984); (*b*) E. FINKELSTEIN, G. M. ROSEN, and E. G. RAUCKMAN. Arch. Biochem. Biophys. **200**, 1 (1980).
25. G. M. ROSEN and E. J. RAUCKMAN. Toxicol. Lett. **10**, 337 (1982).
26. B. KALYANARAMAN, C. MOTTLEY, and R. P. MASON. J. Biochem. Biophys. Methods, **9**, 27 (1984).
27. C. MOTTLEY, H. D. CONNOR, and R. P. MASON. Biochem. Biophys. Res. Commun. **141**, 622 (1986).
28. Y. KOTAKE and K. KUWATA. Can. J. Chem. **60**, 1610 (1982), and references cited therein.
29. I. ROSENTHAL, M. M. MOSSOBA, and P. RIESZ. Can. J. Chem. **60**, 1486 (1982).
30. S. TERO-KUBOTA, Y. IKEGAMI, T. KUROKAWA, R. SASAKI, K. SUGIOKA, and M. NAKANO. Biochem. Biophys. Res. Commun. **108**, 1025 (1982).
31. H. B. STEGMANN, H. WENDEL, H. DAO-BA, P. SHULER, and K. SCHEFFLER. Angew. Chem. Intl. Ed. Engl. **25**, 1007 (1986).

Can. J. Chem. Downloaded from www.nrcresearchpress.com by 112.217.228.212 on 09/07/12
For personal use only.

The complementary use of factor analysis and spectral deconvolution in a study of the CD_3COOD–D_2O system

JESSE B. NG,[1] B. PETELENZ,[2] AND H. F. SHURVELL[3]

Department of Chemistry, Queen's University, Kingston, Ont., Canada K7L 3N6

Received October 14, 1987

This paper is dedicated to Professor Charles A. McDowell on the occasion of his seventieth birthday

JESSE B. NG, B. PETELENZ, and H. F. SHURVELL. Can. J. Chem. **66**, 1912 (1988).

The carbonyl stretching region of fully deuterated acetic acid CD_3COOD in D_2O has been studied by means of Raman spectroscopy. The number of linearly independent spectral components was determined to be four by factor analysis. Fourier self-deconvolution of the spectra revealed another major component band which was assigned to an overtone and/or combination vibration of the acid monomer. The overall band envelope was fitted with five Gauss–Lorentz functions using a non-linear least squares procedure. The abnormally high intensity of the band assigned to the overtone/combination is discussed in terms of Fermi resonance.

JESSE B. NG, B. PETELENZ et H. F. SHURVELL. Can. J. Chem. **66**, 1912 (1988).

Faisant appel à la spectroscopie Raman et opérant dans le D_2O, on a étudié la région de l'élongation du carbonyle de l'acide acétique complètement deutéré, CD_3COOD. Utilisant l'analyse factorielle, on a déterminé que le nombre de composantes spectrales linéairement indépendantes est égal à quatre. Une auto-déconvolution de Fourier effectuée sur le spectre a permis de mettre en évidence une autre bande composante majeure qui a été attribuée à une harmonique et/ou à une vibration de combinaison de l'acide monomère. Utilisant une procédure non-linéaire des moindres carrés, on a fait concorder l'enveloppe globale des bandes avec cinq fonctions de Gauss–Lorentz. Pour expliquer le fait que l'intensité de la bande attribuée à l'harmonique/combinaison est anormalement élevée on fait appel à la résonance de Fermi.

[Traduit par la revue]

Can. J. Chem. Downloaded from www.nrcresearchpress.com by 112.217.228.212 on 09/07/12
For personal use only.

Introduction

The complexity of the carbonyl stretching region (1500–1900 cm^{-1}) in the system CH_3COOH–H_2O (1) prompted an examination of the fully deuterated species, CD_3COOD in D_2O. Results of a previous communication (2) suggested a model system in which, at high concentrations monomeric, dimeric, and polymeric species coexist. The validity of the argument was reinforced by the application of factor analysis (3, 4) to the spectra of CH_3COOH–H_2O mixtures in the carbonyl stretching region (1). The number of contributing components (NC) was found to be 5, including the bending mode of H_2O which occurs at ca. 1610 cm^{-1}.

Substitution of deuterium for hydrogen in both acid and water molecules was expected to simplify the analysis of the spectrum since the carbonyl band envelope in CD_3COOD (1450–1800 cm^{-1}) is well separated from the methyl deformation modes which shift from 1433 cm^{-1} ($\delta_a CH_3$) and 1366 cm^{-1} ($\delta_s CH_3$) to 1042 cm^{-1} ($\delta_a CD_3$) and 1090 cm^{-1} ($\delta_s CD_3$) (5), as well as from the DOD bending mode of D_2O at 1190 cm^{-1}. Thus, according to the previously assumed model (1, 2), no more than four components should appear in the spectrum. However, the inspection of the C=O stretching region of the fully deuterated acetic acid indicates the existence of two well-resolved peaks, the larger of which is accompanied by *three* and not two shoulders.

To complete the study and elucidate this somewhat unexpected behaviour, we applied factor analysis to the fully deuterated system and, independently, we have made use of spectral deconvolution (6–9), where part or all of the intrinsic lineshape function is deconvolved from a spectrum of overlapping bands. In essence, deconvolution yields information not obtainable by factor analysis, namely, the maximum number of bands that should be fitted to a contour. Deconvolution enhances the original band resolution by narrowing the spectral lines, so that the deconvolved spectra allow a reliable initial estimate of band positions, relative intensities and bandwidths, and make band-fitting less ambiguous.

Experimental

Acetic acid-d_4 (99.5 atom% D) was supplied by MSD Isotopes (Merck-Frosst Canada Inc.). Solutions were made up by weight in the range 5.3 to 17.5 mol L^{-1} (M) using D_2O (98 atom% D) purchased from the same company. To minimize exchange with atmospheric moisture, all operations including weighings and cell-filling manipulations were performed in a drybox under a nitrogen atmosphere. A drying agent, P_2O_5, was constantly present in the box. Prior to experimental operations, the relative humidity inside the box was monitored and it never exceeded 30%.

Raman spectra of the pure acid were recorded directly from the unopened vial. A survey spectrum of glacial CD_3COOD between 200 and 3000 cm^{-1} is shown in Fig. 1. The scanning range for the solutions was 780–1880 cm^{-1}. The spectra were calibrated using emission lines from a Ne lamp. The band intensity in the carbonyl stretching region was normalized by division by the area of the C—C stretching fundamental at ca. 799 cm^{-1}. Details of the Raman experiment have been published elsewhere (1).

Computations

Factor analysis

To determine the number of components which contribute to the overall band intensity in the C=O stretching region, a set of Raman spectra was subjected to factor analysis using the program CHISQ (4). Spectra of ten solutions (NS = 10) in the concentration range 14.2 to 17.5 M, each collected in the carbonyl stretching region (1450–1800 cm^{-1}) and digitized at 450 data points (NW = 450), were used to build the experimental intensity matrix, **I**, of dimension NS × NW. The elements of the Raman intensity matrix are given as

[1]Present address: Department of Chemistry, University of British Columbia, Vancouver, B.C., Canada V6T 1Y6.

[2]On leave from Institute of Nuclear Physics, 31-342 Cracow, Poland.

[3]To whom all correspondence should be addressed.

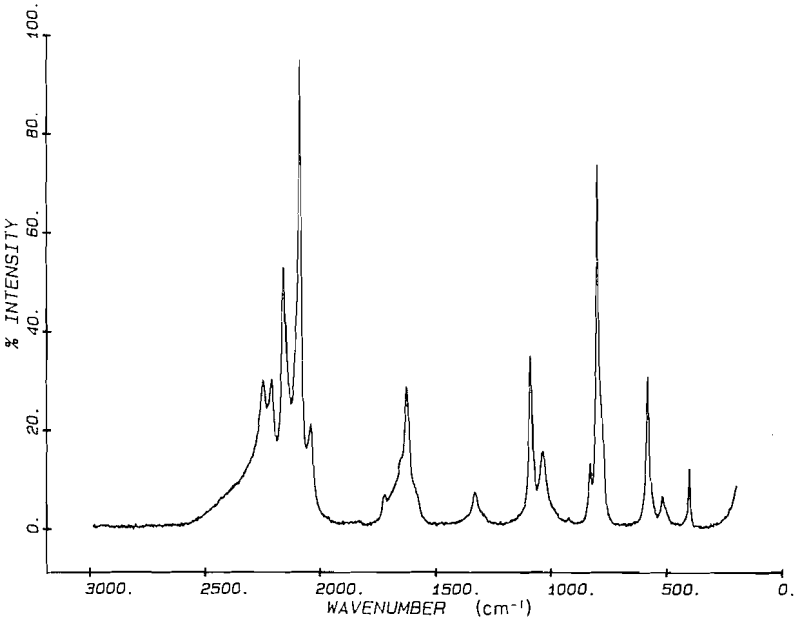

FIG. 1. Survey Raman spectrum of CD_3COOD.

$$[1] \quad I_{ij} = \sum_{k=1}^{NC} J_{ik} C_{kj}$$

where J_{ik} is the molar scattering coefficient of the kth component at the ith wavenumber and C_{kj} is the concentration of kth component in jth solution.

It can be shown that the number of components in the spectrum, N_C, is equal to the rank of the square matrix $\mathbf{Q} = \mathbf{I}^T\mathbf{I}$, which in turn is equal to the number of non-zero eigenvalues of $\mathbf{Q}$. However, the matrix $\mathbf{I}$ and the related matrices are obtained from experimental data which always contain an experimental error. Also, the diagonalization procedure introduces its own errors. Therefore, N_C must be determined according to a number of statistical criteria (3, 4) which, taken together, distinguish the genuine non-zero eigenvalues from statistical fluctuations. Linearly dependent factors do not appear as individual components in the result, which sometimes can be a limitation of the method.

Deconvolution

A measured spectrum $E(\tilde{\nu})$ can be expressed as a convolution of a "true" (i.e. involving only natural linewidths) spectrum $E'(\tilde{\nu})$ and an instrumental function $G(\tilde{\nu})$ (6–9).

$$[2] \quad E(\tilde{\nu}) = \int_{-\infty}^{+\infty} G(\tilde{\nu}')E'(\tilde{\nu} - \tilde{\nu}')\mathrm{d}\tilde{\nu}' \equiv G(\tilde{\nu}) * E'(\tilde{\nu})$$

This spectrum is related to its interferogram (which is actually the measured quantity in Fourier transform instruments) by the following relationships (7):

$$[3] \quad E(\tilde{\nu}) = \int_{-\infty}^{+\infty} I(x) \exp(i2\pi\tilde{\nu}x)\mathrm{d}x = \mathcal{F}\{I(x)\}$$

$$[4] \quad I(\tilde{\nu}) = \int_{-\infty}^{+\infty} E(\tilde{\nu}) \exp(-i2\pi\tilde{\nu}x)\mathrm{d}\tilde{\nu} = \mathcal{F}^{-1}\{E(\tilde{\nu})\}$$

where $\mathcal{F}\{\ \}$ denotes the Fourier transform and $\mathcal{F}^{-1}\{\ \}$ its inverse. The units used here are wavenumbers for $\tilde{\nu}$ and centimeters for x, but frequency and time or energy and time can be used as well. By applying the inverse Fourier transform to both sides of eq. [2] one obtains:

$$[5] \quad I(x) = \mathcal{F}^{-1}\{G(\tilde{\nu})\} \cdot I'(x)$$

In the distance domain the convolution operation is replaced by multiplication, so, the interferogram of the true spectrum can be obtained simply by dividing the transform of the experimental spectrum by that of the instrumental function

$$[6] \quad I'(x) = \frac{1}{\mathcal{F}^{-1}\{G(\tilde{\nu})\}} \cdot I(x)$$

By transforming $I'(x)$ back to the wavenumber domain the true spectrum should be in principle obtained, but in general, the function $G(\tilde{\nu})$ is not known explicitly and the deconvolution must be performed on a trial-and-error basis. Adjustment of the function $G(\tilde{\nu})$ is based on the fact that a Lorentz spectral line transforms into an exponentially decaying cosine, whereas a Gauss line yields a cosine damped with another Gaussian function. The broader are the bands the more rapidly decay their transforms. Appropriate choice of the function $G(\tilde{\nu})$ results in enhancing the features of the original spectrum: in the deconvolved spectrum all bands become narrower and many shoulders appear as separate peaks.

Fourier transforms can also be used to smooth the spectra. Noise in the wavenumber domain transforms into noise which becomes a predominant feature of the interferogram past the point $x = L$ at which the cosine is damped practically to zero. Noise can be filtered by multiplying the interferogram $I'(x)$ by a function which is nonzero for $0 < x < L$ and zero elsewhere. Various filtering functions have been suggested and discussed in the literature (10). Both deconvolving and smoothing operations can be performed simultaneously and in such a way they are incorporated in the computation program used in this work (11).

Results and discussion

General

The substitution of D for H in CH_3COOH and D_2O for H_2O results in a separation of the carbonyl band envelope from the

Can. J. Chem. Downloaded from www.nrcresearchpress.com by 112.217.228.212 on 09/07/12
For personal use only.

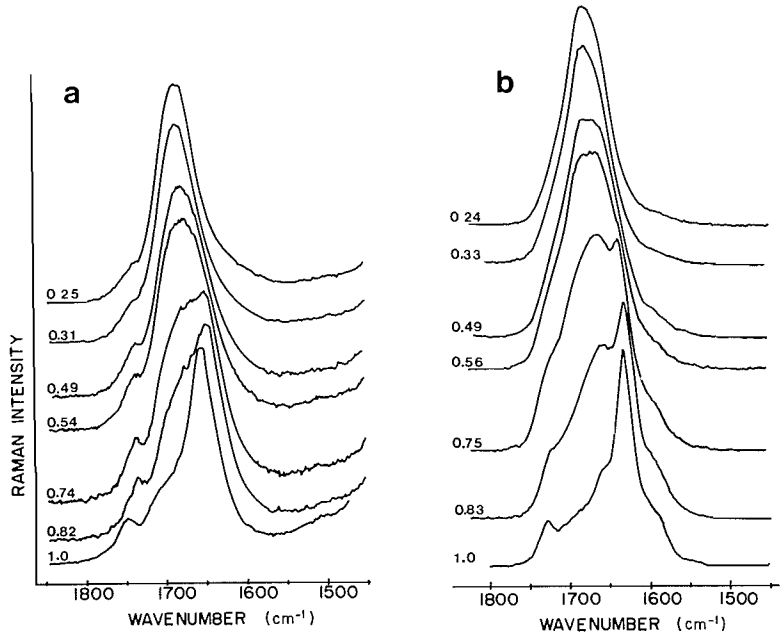

FIG. 2. Variation of the C=O stretching profiles of acetic acid upon dilution; (*a*) $CH_3COOH-H_2O$, (*b*) $CD_3COOD-D_2O$. Intensity units are arbitrary. Mole fraction of the acid is quoted at each curve.

methyl deformation modes and the water bending mode (2, 5). The variation of the band profile of the carbonyl stretching region of CD_3COOD (1450–1800 cm^{-1}) in solutions of different concentrations is shown in Fig. 2*b*. In comparison with the corresponding band envelope in CH_3COOH (Fig. 2*a*), the following observations can be made. The maxima in both profiles shift to higher frequencies on dilution. However, at similar mole fractions of acid ($x_{CD_3COOD} = 0.75$, $x_{CH_3COOH} = 0.74$), the shoulder on the high frequency side of the contour at ~1722 cm^{-1} is not as pronounced in the $CD_3COOD-D_2O$ system. In addition, there is a broad maximum centered at ~1660 cm^{-1} which is not visible in the $CH_3COOH-H_2O$ system.

Factor analysis

The results of factor analysis on the CD_3COOD solutions are shown in Tables 1 and 2. The standard errors in the first four eigenvalues are much less than the eigenvalues themselves, whereas the error in the fifth eigenvalue is larger. This clearly indicates the presence of four components.

The estimate of the experimental error (i.e. the ratio of standard deviation $\sqrt{N}$ to the average number of photon counts N in the peak (12)) is in the range 0.0061 to 0.0075. An examination of Table 1 indicates that for the third eigenvalue ($m = 3$) the calculated value of the residual standard deviation (RSD) is 0.006228 which lies in the above range. This criterion suggests NC = 3 for the system.

The difference in the imbedded error (IE) values (3) for $m = 4$ and $m = 5$ (0.000284) is much smaller than for $m = 3$ and $m = 4$ (0.001919). A minimum in the factor indicator function (IND) (3) also occurs for $m = 4$.

The expectation values of χ_4^2 (2676) and χ_5^2 (2225) indicate that four factors are significant, because the calculated value of χ_4^2 (2894) is much closer to its expectation value than is the calculated value of χ_5^2 (1684) (Table 2).

A regenerated data point is classified as a misfit if its deviation from the observed value is three or more times greater than the standard deviation σ. The smallest value of m, for which the regenerated data matrix has a negligible number of residual errors greater than 3σ is taken to be NC (3, 4). The experimental data matrix (Table 2) contains 4500 data points. With three eigenvectors, 172 regenerated data points are greater than 3σ, but with four, only 18 are greater. This is negligible compared to

TABLE 1. Factor analysis of solutions of CD_3COOD in D_2O

m	Eigenvalue (λ)	Std. error in λ	Res. Std. dev. (RSD)	Imbedded error (IE)	Factor Ind. Fcn. IND × 10^5
1	102.199997	0.031836	0.048295	0.015272	59.6
2	9.123996	0.024716	0.017349	0.007758	27.1
3	1.174958	0.031104	0.006228	0.003411	12.7
4	0.148568	0.025179	0.002360	0.001492	6.55
5	0.011850	0.022496	0.001708	0.001208	6.83
6	0.005857	0.032358	0.001267	0.000981	7.92
7	0.003299	0.021664	0.000930	0.000777	10.3
8	0.002075	0.032916	0.000630	0.000563	15.7
9	0.001242	0.041144	0.000340	0.000322	34.0
10	0.000546	0.026890	—	—	—

TABLE 2. Factor analysis for CD_3COOD in D_2O. Estimation of χ^2 and distribution of misfit

m	χ^2 expected	χ^2 calculated	3σ misfit
1	4 041	502 188	2 209
2	3 584	63 220	1 452
3	3 129	8 610	172
4	2 676	2 893	18
5	2 225	1 684	9
6	1 776	1 366	6
7	1 329	958	3
8	884	434	1
9	441	223	2
10	0	0	0

Can. J. Chem. Downloaded from www.nrcresearchpress.com by 112.217.228.212 on 09/07/12
For personal use only.

TABLE 3. Band assignment for pure CH_3COOH and CD_3COOD in $\nu_{C=O}$ region

Band no.	Frequency (cm^{-1}) CH_3COOH	Frequency (cm^{-1}) CD_3COOD	Assignment $\nu_{C=O}$ of
1	1760	1725[a]	End group of linear dimer or polymer
2	1710	1691[a], 1665[a]	Monomer, in Fermi resonance with overtone/combination vibration
3	1662	1639[a]	Cyclic dimer
4	1637	1601[a]	Hydrogen bonded carbonyl of linear dimer or polymer ("inner group")

[a]Average frequencies obtained from band fitting (present work).

TABLE 4. Band positions in the C=O stretching region of CD_3COOD, obtained from the fitting procedure

Conc. %w/w	x_{DAc}[a]	Frequency (cm^{-1}) End	Monomer	Overtone	Dimer	Polymer
94	0.83	1724.9	1682.7	1659.8	1632.0	1596.3
91	0.75	1729.6	1689.4	1663.1	1638.3	1599.8
80	0.56	1727.7	1691.3	1662.7	1637.1	1603.5
75	0.49	1723.2	1691.3	1662.5	1635.8	1603.4
70	0.42	1724.5	1693.5	1666.0	1639.0	1601.1
60	0.33	1721.5	1693.4	1668.8	1644.3	1606.8
50	0.24	1722.6	1693.5	1668.1	1640.2	1595.5
30	0.12	1725.0	1691.0	1666.2	1641.5	1598.4
	Average $\pm\sigma$	1724.5 2.42	1690.8 3.57	1664.6 3.11	1638.6 3.74	1600.6 3.87

[a]x_{DAc} is the mole fraction of CD_3COOD in D_2O.

the total number of points. The results of five criteria indicate that the factor space is four-dimensional, while only one criterion suggests three dimensions. Therefore, we conclude that the number of independent components contributing to the C=O stretching band envelope is four.

Band contour analysis

Figures 2*a* and 2*b* show that, on dilution, the carbonyl band envelope rapidly changes into a featureless profile. At this stage, there is no indication that the profile comprises anything else but the four bands revealed by factor analysis. Such an assumption agrees with our earlier discussion (1, 2, 13) of several associated forms of acetic acid coexisting in the solution. The dominant contribution of the cyclic dimer in pure liquid acetic acid was confirmed recently by means of neutron diffraction spectroscopy (14). Without contradicting this or the earlier assignment (5), four Raman bands in this region can be assigned to the C=O stretching of the monomer, that of the cyclic dimer (only one mode being Raman active), and two vibrations of the chain-like structures, representing stretching of their "inner" and end C=O groups.

The number of bands, revealed by factor analysis, is one of the most important input data for the band fitting procedure (15). Earlier work (5) gave quite reliable values for the positions of some contributing bands. To refine initial estimates for the positions of all contributing bands as well as for their intensities and widths, the band contour at every concentration was deconvolved using the technique developed recently by Moffatt *et al.* (11). For moderately dilute solutions of CD_3COOD in D_2O characterized by broad featureless bands in the C=O stretching region, this procedure revealed a *fifth* component in this region. Selected deconvolved spectra are shown in Fig. 3*a* alongside the corresponding band resolved spectra (Fig. 3*b*).

The C=O stretching frequencies of the normal and fully deuterated acetic acids, obtained from the band fitting are compared in Table 3. Table 3 shows that all C=O stretching modes of CD_3COOD exhibit a noticeable red shift with respect to those of the non-deuterated molecule. The magnitude of the shift is ~25–35 cm^{-1}. The shift of ~30 cm^{-1} for the monomer would result in a band near 1680 cm^{-1}. Such a band was not observed. Instead, two bands were detected in the immediate neighbourhood of the predicted frequency. We tentatively assigned the higher frequency peak (~1690 cm^{-1}) to the monomer. We will temporarily denote the lower frequency band (~1660 cm^{-1}) as *A*.

Deconvolution also revealed some additional bands in the Raman spectra of deuterated acetic acid at the highest concentrations (91–100%). The band at ~1600 cm^{-1} (assigned to the "inner C=O group" of the polymer) splits into two bands at ~1595 cm^{-1} and ~1605 cm^{-1}, while the monomer band (~1690 cm^{-1}) splits into two at ~1685 and ~1705 cm^{-1}. These extra bands are visible only in the most concentrated solutions.

To avoid unnecessary complication of the model, we performed band fitting of the C=O stretching manifold assuming only five components for the whole concentration range, i.e., we neglected the weak bands near 1605 cm^{-1} and 1705 cm^{-1}, revealed by deconvolution for high acid concentrations. This

Can. J. Chem. Downloaded from www.nrcresearchpress.com by 112.217.228.212 on 09/07/12
For personal use only.

Can. J. Chem. Downloaded from www.nrcresearchpress.com by 112.217.228.212 on 09/07/12
For personal use only.

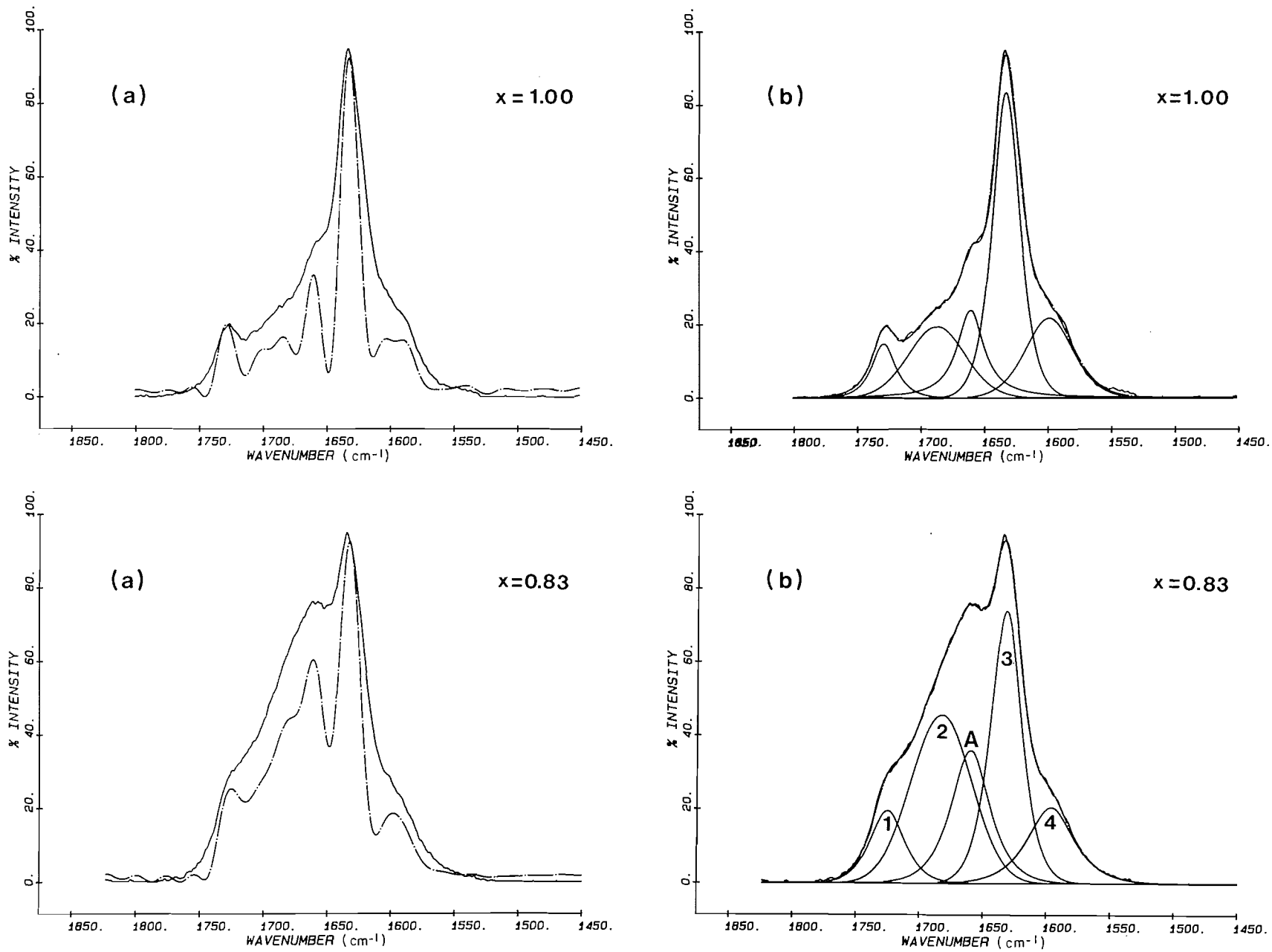

FIG. 3. (*a*) Deconvolved Raman spectra of CD_3COOD in C═O stretching region. Solid line: experimental spectrum. Broken line: deconvolved spectrum. Deconvolved bandwidth 26 cm^{-1}, narrowing factor $k = 1.5$, Lorentz fraction 0.6, Gauss fraction 0.4. (*b*) Corresponding fitted spectra. Solid line: experimental spectrum and its fitted components. Broken line: fitted envelope (practically overlapping with the experimental one). Band numbers: *1*, "end group"; *2*, monomer; *A*, overtone; *3*, dimer; *4*, "inner group". Arbitrary intensity units in all spectra.

Can. J. Chem. Downloaded from www.nrcresearchpress.com by 112.217.228.212 on 09/07/12
For personal use only.

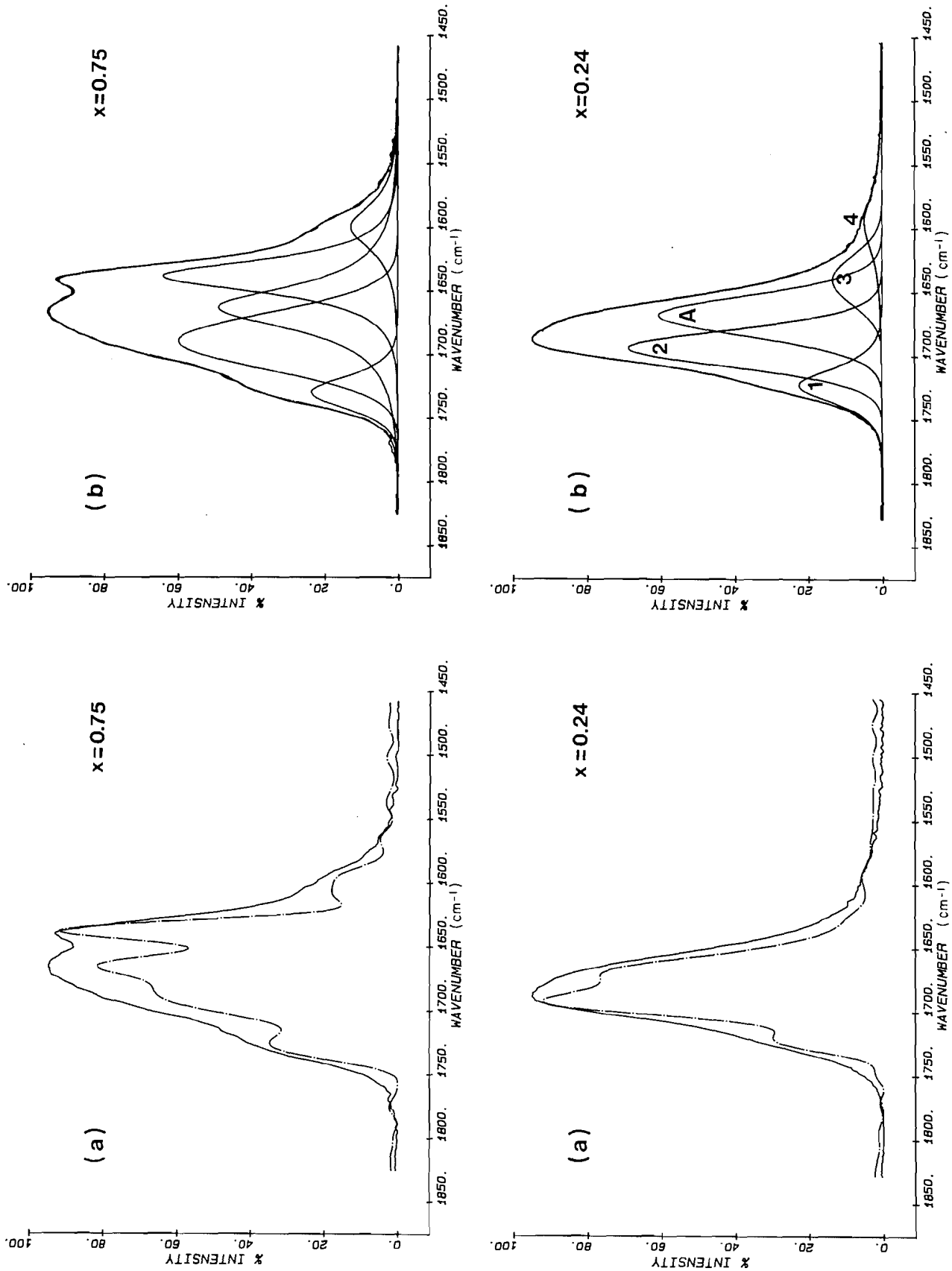

FIG. 3 (*concluded*)

Can. J. Chem. Downloaded from www.nrcresearchpress.com by 112.217.228.212 on 09/07/12
For personal use only.

assumption seems justified in view of the small intensity of these bands but, of course, it does introduce some error into the calculated band parameters.

The positions of the fitted bands are listed in Table 4. The regularities we noticed are the following:

1. Positions of the three middle bands in the range of study shift slightly (6–10 cm^{-1}) to higher frequencies with the increasing content of D_2O in the system. Positions of the two remaining bands fluctuate within ± 4 cm^{-1} without any regularity.

2. The intensity of the band attributed to the dimer decreases with dilution whereas that of the monomer increases.

3. The intensity of band *A* remains close to that of the monomer band and follows the same trend with dilution, being approximately proportional to the intensity of the monomer band. This behaviour explains why band *A* could not be detected by factor analysis as a separate component.

Band *A* has no counterpart in the spectrum of non-deuterated acetic acid (1, 2, 5) and the assumption that it is due to an overtone or combination mode seems natural. Normally in the Raman effect, the intensities of overtones or combinations are very weak so that they are hardly discernible unless enhanced by Fermi resonance (16). This seems to be just the case of band *A*.

The fact that band *A* grows significantly with dilution indicates that it is due to the monomer. For the assignment of band *A*, several combination modes of the monomer are possible. If the symmetry of the acetic acid monomer is C_s, then the combination $\nu_5 + \nu_{12}$ ($1280 + 386 = 1666$ cm^{-1}) would have the same symmetry (A') as the C=O and intensity borrowing through Fermi resonance could occur (the assignment of the monomer fundamentals is taken from ref. 17).

If the local symmetry of the monomer is in fact C_1 then two other combinations could contribute to the intensity of band *A*. These are $\nu_5 + \nu_{17}$ ($1280 + 408 = 1688$ cm^{-1}) and $\nu_{10} + \nu_{15}$ ($747 + 919 = 1666$ cm^{-1}). The lower symmetry in solution could be due to interaction with surrounding molecules or the fact that the barrier to rotation of the CD_3 group in CD_3COOD is low (1.96 kJ mol^{-1}) (18).

The intensity of band *A* in some of the deconvolved spectra (Fig. 3*a*) may appear unreasonably high. However, overlap with neighbouring bands (Fig. 3*b*) accounts for some of the intensity. In addition, an overtone of the dimer ($2 \times 832 = 1664$ cm^{-1}) might also contribute to the height of band *A*, especially in higher concentrations.

The additional bands observed in the deconvolved spectra of the most concentrated solutions must be interpreted cautiously, mainly because of their low intensity and relatively high noise. The conjecture that they are overtones of the dimer (predominant species) seems justified, at least for the low frequency band. There can be two symmetry-allowed combinations or overtones of the dimer: at 1598 cm^{-1} (2νC—C, 2×799 cm^{-1}) and at 1600 cm^{-1} (γCCO + $\delta_a CD_3$, $510 + 1090$ cm^{-1}).

The band near 1705 cm^{-1} can not be explained in this way. Most probably, it is the antisymmetric component of the C=O stretching of the dimer (B_u symmetry species). The transition is symmetry-allowed (and observed) in the infrared (5, 19) but forbidden in Raman. Symmetry perturbation in the concentrated liquid could give it a non-zero intensity so that it appears as a weak band in Raman spectrum.

Conclusions

The present study of fully deuterated acetic acid has revealed previously unreported components of its Raman spectrum in the C=O stretching region. Complementary use of factor analysis, deconvolution, and band resolution has led to detection of a strong overtone/combination band. The behaviour of this band upon dilution of the acid has been studied and it is concluded that the band is due to the monomer. Most probably, it involves more than one combination of monomer fundamentals. Several other new bands detected by deconvolution have been assigned to the dimer.

Acknowledgments

Financial support for this work was provided by the Natural Sciences and Engineering Research Council of Canada and Queen's University. We would like to thank Drs. R. N. Jones and D. Moffatt for supplying a copy of their deconvolution program.

1. J. B. Ng and H. F. Shurvell. J. Phys. Chem. **91**, 496 (1987).
2. J. B. Ng and H. F. Shurvell. Can. J. Spectrosc. **30**, 149 (1985).
3. E. R. Malinowski and D. G. Howery. *In* Factor analysis in chemistry. Wiley, New York. 1980.
4. J. T. Bulmer and H. F. Shurvell. *In* Vibrational spectra and structure. Vol. 6. *Edited by* J. R. Durig. Elsevier, Amsterdam. 1977. pp. 91–172.
5. M. Haurie and A. Novak. J. Chim. Phys. **62**, 146 (1965).
6. A. G. Marshall. *In* Fourier, Hadamard, and Hilbert transforms in chemistry. *Edited by* A. G. Marshall. Plenum Press, New York and London. 1982. pp. 1–43.
7. J. K. Kauppinen, D. J. Moffatt, H. H. Mantsch, and D. G. Cameron. Appl. Spectrosc. **35**, 271 (1981).
8. J. K. Kauppinen, D. J. Moffatt, H. H. Mantsch, and D. G. Cameron. Anal. Chem. **53**, 1454 (1981).
9. D. G. Cameron and D. J. Moffatt. J. Test. Eval. **12**, 78 (1984).
10. J. P. Lee and M. B. Comisarow. Appl. Spectrosc. **41**, 93 (1987).
11. D. J. Moffatt, J. K. Kauppinen, D. G. Cameron, H. H. Mantsch, and R. N. Jones. *In* NRC (Canada) Bull. 1986. No. 18.
12. S. Brandt. *In* Statistical and computational methods in data analysis. North Holland. 1976. p. 49 ff.
13. J. T. Bulmer and H. F. Shurvell. J. Phys. Chem. **77**, 256 (1973).
14. H. Bertagnolli. Chem. Phys. Lett. **93**, 287 (1982).
15. R. N. Jones and J. Pitha. *In* NRC (Canada) Bull. 1968. No. 12.
16. G. Herzberg. *In* Infrared and Raman spectra of polyatomic molecules. Vol. II. Van Nostrand-Reinhold, New York. 1945. p. 215.
17. R. Meyer, T.-K. Ha, H. Frei, and Hs. H. Günthard. Chem. Phys. **9**, 393 (1975).
18. L. C. Krisher and E. Saegebarth. J. Chem. Phys. **54**, 4553 (1971); W. J. Tabor. J. Chem. Phys. **27**, 974 (1957).
19. M. Ovaska. J. Phys. Chem. **88**, 5981 (1984).

The core binding energies of some gaseous aromatic carboxylic acids and their relationship to profon affinities and gas phase acidities

B. H. McQUAIDE AND M. S. BANNA
Department of Chemistry, Vanderbilt University, Nashville, TN 37235, U.S.A.

Received September 21, 1987

This paper is dedicated to Professor Charles A. McDowell on the occasion of his 70th birthday

B. H. McQUAIDE and M. S. BANNA. Can. J. Chem. **66**, 1919 (1988).

The C1*s* and O1*s* core binding energies of gaseous benzoic, phthalic, isophthalic, and terephthalic acids have been measured by X-ray photoelectron spectroscopy. The π-donor relaxation energies associated with the carbonyl oxygen ionization in these systems have been found to be around 2 eV, close to the value for acetic acid. Comparison of the O1*s* binding energies in phenol and benzoic acid with the gas phase acidities shows that the increased acidity of benzoic acid is attributable mostly to initial-state inductive effects. A number of O1*s* – proton affinity correlations have been used to predict proton affinities for these acids. It is found that benzoic acid is the strongest base and the weakest acid.

B. H. McQUAIDE et M. S. BANNA. Can. J. Chem. **66**, 1919 (1988).

Faisant appel à la spectroscopie photoélectronique des rayons-X, on a mesuré les énergies de liaison des noyaux C 1*s* et O 1*s* des acides benzoïque, phtalique, isophtalique et téréphtalique, à l'état gazeux. On a trouvé que les énergies de relaxation de donneur-π, associées avec l'ionisation de l'oxygène du carbonyle de ces systèmes, est d'environ 2 eV; cette valeur est proche de celle observée avec l'acide acétique. Une comparaison des énergies de liaison O 1*s* du phénol et de l'acide benzoïque avec leurs acidités en phase gazeuse démontre que l'acidité accrue de l'acide benzoïque est principalement dûe à des effets inductifs dans l'état initial. On a utilisé un certain nombre de corrélations O 1*s*/affinité protonique pour prédire les affinités protoniques de ces acides. On a trouvé que l'acide benzoïque est la base la plus forte et l'acide le plus faible.

[Traduit par la revue]

Can. J. Chem. Downloaded from www.nrcresearchpress.com by 112.217.228.212 on 09/07/12
For personal use only.

Introduction

Although carboxylic acids have been studied rather extensively by X-ray photoelectron spectroscopy (XPS) (1–3) there are to date no available core binding energy data on aromatic acids. The reason is primarily the lack of volatility of these species. We have therefore undertaken a study of gaseous benzoic, phthalic, isophthalic, and terephthalic acids to make possible comparisons between aliphatic and aromatic acids.

A number of studies in recent years have exploited the basic similarity between core ionization and proton affinity, which is $-\Delta H$ of the process

[1] $B + H^+ \rightarrow BH^+$

The correlations established between gas phase PA's and core E_B's for a large variety of compounds (1–7) stem from the fact that both processes have to do with the ability of a molecule to accept a positive charge. The contributions to these two quantities can be broken down into a ground-state effect (which includes inductive contributions) and a final-state relaxation effect dependent on the polarizability of the surrounding molecule. Previous studies (8, 9) have established the following relationships:

[2] $\Delta E_B = \Delta V - \Delta R$

[3] $\Delta PA = -\Delta V + \Delta R$

where V is the electrostatic potential energy at the proton site or the site of core ionization and R is the relaxation energy. The quantities are expressed relative to some reference compound.

The enthalpy change of the reaction

[4] $HA \rightarrow H^+ + A^-$

is called the heat of deprotonation (10) and is a measure of acid strength. Thus this quantity is the PA of the anion. For gas phase acidities, A, we have (3, 8)

[5] $\Delta A = -\Delta V - \Delta R$

It can therefore be seen that combining eqs. [2] and [5] can yield ΔV and ΔR. Furthermore, eqs. [2] and [3] suggest a correlation between E_B and PA. These results will be used in the present work to calculate a number of interesting quantities.

Experimental

Samples were heated to 100–120°C to obtain sufficient vapor pressure. In the O1*s* region, two peaks were observed in each case, corresponding to the carbonyl and hydroxyl oxygens. For each acid the low binding energy peak was ~10% weaker than the other; this can be seen in Fig. 1 displaying the core spectra of benzoic acid. We argue in the following section that it corresponds to the carbonyl oxygen. In the C1*s* region, several peaks would be expected as a result of the presence of different types of carbons. For example, benzoic acid would be expected to give rise to five different peaks. However, our resolution was insufficient to differentiate between the various ring carbons (see Fig. 1). We have therefore treated each C1*s* spectrum as consisting of only two peaks, arising from the carboxyl and ring carbons. Thus we obtain only an average of the benzene ring carbon binding energies.

To obtain binding energies (b.e.), a calibrant gas was bled simultaneously with the acid under study. For C1*s*, carbon dioxide is a suitable reference (b.e. = 297.71 eV) (11). Carbon monoxide was also used in the case of benzoic acid (b.e. = 296.20 eV) (11). The oxygen 1*s* binding energies were referenced to the O1*s* of CO (542.55 eV) (11) for benzoic acid and to the NeKLL $^1D_2$ Auger peak (kinetic energy = 804.50 eV) (12) for the remaining acids. When an Auger peak is used for binding energy calibration, it is also necessary to know the photon energy. AlKα X-rays were used throughout this study, with an energy of 1486.582 eV (11).

Experimental problems encountered include relatively poor statistics as a result of complications arising from evaporating an insulator onto the electron optical elements of the spectrometer, insufficient resolution to clearly deconvolute the various peaks, and the overlap between the carboxyl carbon peak and the weak shake-up peaks associated with the ring carbons that lie at lower binding energy (see Fig. 1). Thus the errors associated with our measured binding energies are somewhat larger than normally possible with conventional XPS.

In the case of phthalic acid, the possibility arises that the acid may be converted to the anhydride upon heating (13). This was ruled out,

TABLE 1. Binding energies (eV)[a] of acids

	C1*s* (carbonyl)	C1*s* (ring)	ΔC1*s*	O1*s* (hydroxyl)	O1*s* (carbonyl)	ΔO1*s*
Isophthalic	295.2	291.0	4.21(10)	540.1	538.0	2.05(10)
Terephthalic	295.2	291.0	4.25(8)	540.1	538.1	2.05(8)
Phthalic	295.1	291.1	4.06(6)	540.0	538.1	1.90(10)
Benzoic	295.0	290.75(5)	4.25	539.79(7)	537.73(7)	2.06(9)

[a]All binding energies without indicated uncertainties are probably accurate to ±0.15 eV.

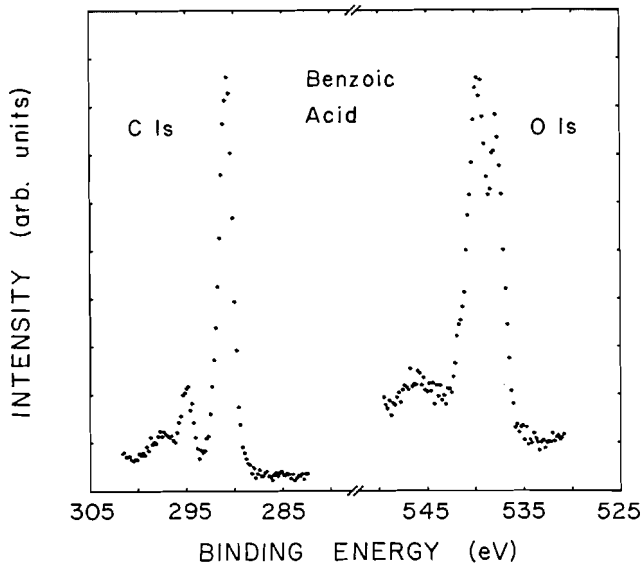

FIG. 1. The core spectra of benzoic acid obtained with AlKα radiation.

however, because the O1*s* spectrum obtained was very similar to those obtained for the other phthalic acids, where anhydride formation is not possible. In the case of the anhydride, two peaks with a relative intensity close to 2:1 would be expected.

Core binding energies

Our results are shown in Table 1. As expected, the core binding energies of the ring carbons are higher than in benzene (290.40 eV), which can be attributed to the presence of the carboxyl groups. For the same reason, the ring binding energies are somewhat higher in the dicarboxylic acids than in benzoic acid; otherwise, there appears to be little change among the phthalic acids, within the limits of accuracy of our measurements. The electron-withdrawing effect of the oxygens is manifested in higher binding energies for the carboxyl carbons, the binding energies being over 4 eV greater than those of the ring carbons.

As expected, two main peaks have been obtained in the O1*s* region. The lower binding energy peak must be due to the carbonyl oxygen because it is the more negative of the two oxygens. Previous workers have also pointed out that molecular orbital calculations (14) on formic acid bear this out. Furthermore, Carroll *et al.* (6) and subsequently Mills *et al.* (1) proved experimentally that the keto oxygen has the lower binding energy, by studying dimethyl carbonate where the higher binding energy peak was found to be twice as intense as the lower binding energy peak.

In connection with the O1*s* region, it is interesting to note that Siegbahn *et al.* (15) obtained only one broad peak for the O1*s* of solid phthalic acid. This suggests that the separation between the two types of oxygen narrows in the solid, probably because of hydrogen bonding. Our gas phase results point to *intra*molecular hydrogen bonding since the O1*s* splitting in phthalic acid is smaller than in any of the other acids studied (see Table 1).

Again, as observed for C1*s*, the O1*s* binding energies appear to change little in going from one dicarboxylic acid to another. The addition of a second carboxyl group definitely raises the binding energy, however. This may tentatively be attributed to the electron-withdrawing tendency of each carboxyl group, resulting in a "depletion" of the ring electrons and less electron withdrawal per substituent group, and hence higher C1*s* and O1*s* binding energies.

The splittings between the two types of oxygen fall outside the 1.3–1.8 eV range found by Mills *et al.* (1) for a number of aliphatic acids and esters.

The π donor relaxation energy in carbonyl oxygen ionization

Jolly and Schaaf (16) compared the oxygen and carbon 1*s* binding energies of a number of carbonyl compounds. They noted a lack of correlation between the two, and attributed this to differences in the π-donor abilities of the groups attached to the carbonyl groups resulting in differing relaxation energies associated with oxygen ionization. Replacing core-ionized oxygen by its "equivalent core" F^+, Jolly and Schaaf pointed out the importance of the resonance structure on the right below:

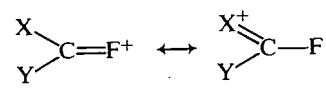

From the carbonyl O1*s* and C1*s* binding energies we measured in this work we can evaluate the π-donor relaxation energies starting with the equation

[6] $E_B(O) = 333.5 + 0.7E_B(C)$

which Jolly and Schaaf (16) obtained for compounds where no π-donor relaxation occurs. Thus using our C1*s* binding energies we can calculate a hypothetical O1*s* binding energy for each acid, and the difference from the experimental one gives the desired relaxation energy. Our results are given in Table 2, and are around 2 eV in each case. For comparison we have included the π-donor relaxation energy calculated (16) for acetic acid. Interestingly, replacement of the methyl group by a benzene ring results in little change in the π-donor relaxation energy.

In connection with charge delocalization upon core ionization we also wish to point out the conclusions of Smith and Thomas (3). They found that there is a correlation between the carboxyl carbon ionization energy and both the carbonyl (slope of 0.90 (7)) and ether (slope of 1.04 (9)) oxygen 1*s* binding energies. Their explanation for this close coupling between each pair of binding energies is that the positive charge is delocalized over the entire carboxyl group whether ionization occurs on the

Can. J. Chem. Downloaded from www.nrcresearchpress.com by 112.217.228.212 on 09/07/12
For personal use only.

TABLE 2. π-Donor relaxation energies in the carbonyl O1s ionization of some acids

Acid	Relaxation energy (eV)[a]
Benzoic	2.3(1)
Phthalic	2.0(2)
Isophthalic	2.1(2)
Terephthalic	2.0(2)
Acetic	2.1(1)

[a]Calculated as the difference between the experimental carbonyl O1s binding energy and the value predicted by eq. [6].

oxygen or the carbon. Smith and Thomas (3) gave resonance structures that support this conclusion. Furthermore, semi-empirical CNDO/2 calculations also supported the validity of their explanation. It is interesting to see how close our binding energies are to the correlation lines determined by Smith and Thomas. From their Fig. 3 it is clear that the carbonyl O1s binding energies correlate very well with C1s, but the hydroxyl O1s binding energies lie considerably above the correlation line. This is perhaps not surprising since relaxation (and hence charge delocalization) is more efficient for the carboxyl O1s than for the ether O1s ionization, given the possibility of π-donor relaxation in the former case. Thus charge delocalization over the entire carboxyl group may be somewhat hindered for ether O1s ionization, resulting in poor correlation with C1s ionization where the presence of the ring means rather efficient charge dispersal following ionization.

Core binding energies and gas phase acidities

From the discussion given in the Introduction it is clear that the heats of deprotonation can be coupled with binding energies to yield ΔV and ΔR. These two quantities are of interest because they correspond to the initial (inductive) and final (relaxation) effects, respectively, and thus provide insight into the underlying causes for the changes in acid strength as well as binding energies. To our knowledge, of the acids considered in this work only benzoic acid has an experimentally known gas phase acidity and heat of deprotonation. Cumming and Kebarle (17) reported a ΔH^0_D of 349.8 kcal/mol. Recently Siggel and Thomas (9) established that, in contradiction to the commonly held notion that the stronger acidity of organic acids compared to alcohols is due to resonance stabilization of the anion of the acid, the difference in acidities is caused largely by the *initial-state* charge distribution, which leads to a less attractive potential at the proton in acids than in alcohols. Using eqs. [2] and [5], we can test the applicability of the conclusions of Siggel and Thomas to phenol versus benzoic acid. This is done in Table 3, from which it is clear that $\Delta R \cong 0$ and hence the added acid strength of benzoic acid is indeed due almost entirely to initial-state effects.

Note that if we had started with the conclusions of Siggel and Thomas (9), which they supported with quantum mechanical calculations, a very good value for the acidity of benzoic acid could have been obtained from our binding energy. This shows the usefulness of core binding energies in deriving gas phase acidities. We can extend the conclusions of Siggel and Thomas somewhat and assume that $\Delta R \cong 0$ in going from phenol to, say, isophthalic acid. With this assumption, the known O1s binding energies for the two species, and the known heat of deprotonation of phenol, a ΔH^0_D for isophthalic acid can be obtained. The value of 14.3 eV (the analysis is given in Table 4) is probably a lower limit to the acid strength since some added relaxation might be expected in the phthalic acids as a result of their larger size. This would increase the acidity.

TABLE 3. Comparison of the properties of phenol and benzoic acid (eV)

	Phenol	Benzoic acid
E_B(O1s)	539.23(5)[a]	539.79(7)
ΔE_B	0.00	0.56(9)
ΔH^0_D[b]	15.17(9)	14.69(9)
ΔA	0.00	−0.48(13)
ΔV	0.00	0.52(16)
ΔR	0.00	−0.04(16)

[a]From ref. 9.
[b]Heat of deprotonation at 300 K from ref. 17.

TABLE 4. Comparison between phenol and dicarboxylic acids (eV)

	Phenol	Acid
E_B(O1s)	539.23(5)[a]	540.10(15)
ΔE_B	0.00	0.87(16)
ΔH^0_D	15.17(9)[b]	
ΔA	0.00	−0.87(16)[c]
ΔR	0.00	~0.00[d]
ΔV	0.00	0.87(16)[e]

[a]From ref. 9.
[b]Heat of deprotonation from ref. 17.
[c]Obtained by assuming $\Delta R = 0$.
[d]Assumed from the conclusions of Siggel and Thomas (9).
[e]Follows from taking $\Delta R = 0$.

Core binding energies and proton affinities

Previous studies (1, 6) have established that the carbonyl oxygen in carboxylic acids is the site of protonation. This is based on the fact that the keto O1s binding energies correlate better with the measured PA's than do the hydroxyl O1s binding energies. Previous workers have established a number of O1s–PA correlations. Unfortunately, the correlations do not agree with one another partly because of discrepancies in the experimental PA's used and, in some cases, in the binding energies. Here we use three different correlations to derive PA's for benzoic acid and the phthalic acids. Mills *et al.* (1) found the following empirical relationship.

$$[7]\quad PA = PA(H_2O) + 23.05[E_B(O1s,H_2O) - E_B(O1s,X)] - 7\ \text{kcal}$$

where the PA's are in kcal/mol and the binding energies are in eV. Using a PA for water of 166.5 kcal/mol from the tabulation of Lias *et al.* (18) and 539.90 eV (11) for the O1s binding energy in water, we calculate the PA's shown in column 2 of Table 5.

Benoit and Harrison (2) obtained the following correlation for carbonyl compounds:

$$[8]\quad PA = -0.843E_B(O1s) + 462.0$$

Using this equation we calculate the PA's shown in column 3 of Table 5.

Finally, the correlation of Smith and Thomas (3) (see Fig. 1

Can. J. Chem. Downloaded from www.nrcresearchpress.com by 112.217.228.212 on 09/07/12
For personal use only.

TABLE 5. Proton affinities (kcal/mol)

Acid	PA[a]	PA[b]	PA[c]
Benzoic	210	200	199
Phthalic	201	193	193
Isophthalic	203	195	195
Terephthalic	201	193	193

[a]From the correlation of Mills *et al.* (1). Uncertainty is ±5 kcal/mol.
[b]From the correlation of Benoit and Harrison (2). Uncertainty is ±3 kcal/mol.
[c]From the correlation of Smith and Thomas (3). Uncertainty is ±3 kcal/mol.

in their paper) yields the PA's given in column 4. This last set is probably the most accurate since it was obtained from a careful correlation between O1*s* and PA. All three sets are in reasonable agreement with one another, however, which is encouraging. In this connection we also note the correlation of Buschek *et al.* (19), which yields PA's in good agreement with those from the correlation of Smith and Thomas (3). This is not surprising since the O1*s* binding energies used in their least-squares fit were taken from ref. 3.

Conclusions

The aromatic acids constitute an interesting series for study with XPS. As demonstrated by other workers for related species, notably the aliphatic acids, the combination of binding energies and gas phase acidities allows for a more complete understanding of both processes. In particular, we have shown that the added acid strength of benzoic acid over phenol is attributable to initial-state effects rather than final-state charge delocalization. This conclusion serves to extend recent findings (9). We have also exploited existing proton affinity – binding energy correlations to extract PA values for the acids under study. Our finding that benzoic acid is a stronger base/weaker acid than the dicarboxylic acids is in accordance with the general rule relating to the effect of substituents on acidity and basicity, namely that electron-withdrawing groups (the carboxyl group in this case) are acid strengthening and base weakening while the opposite is true for electron-releasing groups (20).

Similar studies on involatile species, which are currently beyond the reach of the techniques used to measure PA's but are now within the domain of high temperature XPS, are clearly desirable and will be attempted in the near future.

Can. J. Chem. Downloaded from www.nrcresearchpress.com by 112.217.228.212 on 09/07/12
For personal use only.

Acknowledgements

It is a pleasure to thank Professor T. Darrah Thomas for his comments. This work was funded by the National Science Foundation Grand No. CHE-839476 and the Vanderbilt University Research Council and Natural Science Committee.

1. B. E. MILLS, R. L. MARTIN, and D. A. SHIRLEY. J. Am. Chem. Soc. **98**, 2380 (1976).
2. F. M. BENOIT and A. G. HARRISON. J. Am. Chem. Soc. **99**, 3980 (1977).
3. S. R. SMITH and T. D. THOMAS. J. Am. Chem. Soc. **100**, 5459 (1978).
4. R. L. MARTIN and D. A. SHIRLEY. J. Am. Chem. Soc. **96**, 5299 (1974).
5. D. W. DAVIS and J. W. RABALAIS. J. Am. Chem. Soc. **96**, 5305 (1974).
6. T. X. CARROLL, S. R. SMITH, and T. D. THOMAS. J. Am. Chem. Soc. **97**, 659 (1975).
7. R. G. CAVELL and D. A. ALLISON. J. Am. Chem. Soc. **99**, 4203 (1977).
8. D. W. DAVIS and D. A. SHIRLEY. J. Am. Chem. Soc. **98**, 7898 (1976).
9. M. R. SIGGEL and T. D. THOMAS. J. Am. Chem. Soc. **108**, 4360 (1986).
10. C. R. MOYLAN and J. I. BRAUMAN. Ann. Rev. Phys. Chem. **34**, 187 (1983).
11. T. D. THOMAS and R. W. SHAW, JR. J. Electron Spectrosc. **5**, 1081 (1974).
12. M. O. KRAUSE. *In* Synchrotron radiation research. *Edited by* H. Winick. Plenum, New York. 1980.
13. T. W. G. SOLOMONS. Organic chemistry. Wiley, New York. 1980.
14. L. C. SNYDER and H. BASCH. Molecular wave functions and properties. Wiley, New York. 1972.
15. K. SIEGBAHN, C. NORDLING, A. FAHLMAN, R. NORDBERG, K. HAMRIN, J. HEDMAN, G. JOHANSSON, T. BERGMARK, S.-E. KARLSSON, I. LINDGREN, and B. LINDBERG. ESCA—Atomic, molecular and solid state structure studied by means of electron spectroscopy. Uppsala, Sweden. 1967. p. 78.
16. W. L. JOLLY and T. F. SCHAAF. J. Am. Chem. Soc. **98**, 3178 (1976).
17. J. B. CUMMING and P. KEBARLE. Can. J. Chem. **56**, 1 (1978).
18. S. G. LIAS, J. F. LIEBMAN, and R. D. LEVIN. J. Phys. Chem. Ref. Data, **13**, 695 (1984).
19. J. M. BUSCHEK, F. S. JORGENSEN, and R. S. BROWN. J. Am. Chem. Soc. **104**, 5019 (1982).
20. A. PROSS and L. RADOM. Prog. Phys. Org. Chem. **13**, 1 (1981).

The radial charge distribution and the shell structure of atoms and ions

ALFRED M. SIMAS
Departamento de Quimica Fundamental, Universidade Federal de Pernambuco, 50000 – Recife, PE, Brasil

AND

ROBIN P. SAGAR, ANDREW C. T. KU, AND VEDENE H. SMITH, JR.
Department of Chemistry, Queen's University, Kingston, Ont., Canada K7L 3N6

Received January 28, 1988

This paper is dedicated to Professor Charles A. McDowell on the occasion of his seventieth birthday

ALFREDO M. SIMAS, ROBIN P. SAGAR, ANDREW C. T. KU, and VEDENE H. SMITH, JR. Can. J. Chem. **66**, 1923 (1988).

The radial charge distribution, $D(r)$, for the neutral atoms, hydrogen through uranium, and the singly positive ions, helium through barium and lutetium through radium, are computed from the non-relativistic SCF wavefunctions of Clementi and Roetti and McLean and McLean. The radial charge distribution is examined to see how effective it is for the determination of the shell structure of an atom or an ion with the results indicating that the maxima are the topological features of $D(r)$ most indicative of shells. At most five shells are apparent based on the criterion that the maxima in $D(r)$ correspond to the shells. The positions of the maxima in $D(r)$ are shown to correlate well with the shell radii from the Bohr–Schrödinger theory of an atom. The small deviations are consistent with the shielding of the outer electrons from the nucleus, by the inner electrons. Furthermore, it is shown that the effects of shielding are more pronounced on the values of the radial distribution function at the extremal points. The spherically averaged charge density, $\bar{\rho}(r)$, is seen to be monotonically decreasing for all these ground states, a result which extends the previously known range of atomic systems for which this is true.

ALFREDO M. SIMAS, ROBIN P. SAGAR, ANDREW C. T. KU et VEDENE H. SMITH, JR. Can. J. Chem. **66**, 1923 (1988).

Utilisant les fonctions d'ondes auto-cohérentes qui ne sont pas relativistes de Clementi et Roetti ainsi que de McLean et McLean, on a calculé les distributions des charges radiales, $D(r)$, des atomes neutres, de l'hydrogène à l'uranium, ainsi que des ions monovalents positifs, de l'hélium au baryum et du lutétium au radium. On a étudié les distributions relatives des charges afin d'évaluer si elles sont efficaces pour déterminer la structure des couches d'un atome ou d'un ion; les résultats indiquent que les maxima sont les caractéristiques topologiques de $D(r)$ qui donnent le plus d'indications sur les couches. On a démontré qu'il existe une bonne corrélation entre les positions des maxima des $D(r)$ et les rayons des couches obtenus par la théorie de Bohr-Schrödinger d'un atome. Les petites déviations sont en accord avec le fait que les électrons des couches intérieurs provoquent un blindage du noyau par rapport aux électrons extérieurs. De plus, on a démontré que les effets de blindage sont plus prononcés sur les valeurs des points extrèmes de la fonction de distribution radiale. On observe que la densité de charge moyenne pour la sphère, $\bar{\rho}(r)$, diminue d'une façon monotone pour tous les états fondamentaux; ce résultat prolonge le domaine des systèmes atomiques pour lesquels cette conclusion peut s'appliquer.

[Traduit par la revue]

Can. J. Chem. Downloaded from www.nrcresearchpress.com by 112.217.228.212 on 09/07/12
For personal use only.

Introduction

Of the concepts familiar to chemists, the charge density $\rho(\boldsymbol{r})$ of atoms and molecules is perhaps one of the most widely used as it allows the interpretation of chemical phenomena in a convenient, easily visualized, framework. Indeed, empirical concepts closely connected to the charge density such as bond lengths, angles, atomic radii, Van der Waals radii, electronegativity, etc. (1) have evolved to the extent that they now form an intrinsic part of the vocabulary of a chemist. Besides, $\rho(\boldsymbol{r})$ is experimentally accessible via X-ray Rayleigh scattering to within a phase factor (2).

The spin-traced one-electron charge density, $\rho(\boldsymbol{r})$, is defined as

$$[1]\quad \rho(\boldsymbol{r}_1) = N\int \Psi^*(y_1, \ldots, y_N)\Psi(y_1, \ldots, y_N)\mathrm{d}\sigma_1 \mathrm{d}y_2 \ldots \mathrm{d}y_N$$

where $\Psi(y_1, \ldots, y_N)$ is the position space normalized wavefunction for the N-electron atomic system, the asterisk denotes complex conjugation, and $y_m = (\boldsymbol{r}_m, \sigma_m)$ is the combined position, $\boldsymbol{r}_m$, and spin, σ_m, coordinates of the mth electron. Thus, $\rho(\boldsymbol{r})\mathrm{d}\boldsymbol{r}$ is the probability of finding an electron in a volume element $\mathrm{d}\boldsymbol{r}$ at a point $\boldsymbol{r}$ in position space.

The natural system of coordinates to be used in the atomic case is the spherical polar one centred at the atomic nucleus. The physically meaningful charge density is spherical because an ensemble average must be taken over degenerate states. Thus we shall study the spherical average, $\bar{\rho}(r)$, of the charge density, i.e.

$$[2]\quad \bar{\rho}(r) = \frac{1}{4\pi}\int \rho(\boldsymbol{r})\mathrm{d}\Omega_r = \frac{1}{4\pi}\int_0^{2\pi} \mathrm{d}\phi_r \int_0^{\pi} \sin\theta_r \,\mathrm{d}\theta_r \rho(\boldsymbol{r})$$

Both $\rho(\boldsymbol{r})$ and $\bar{\rho}(r)$ are normalized to the number of electrons, i.e.

$$[3]\quad N = \int \rho(\boldsymbol{r})\mathrm{d}\boldsymbol{r} = \int_0^{\infty} 4\pi\bar{\rho}(r)r^2\mathrm{d}r = \int_0^{\infty} D(r)\mathrm{d}r$$

with the definition of $\bar{\rho}(r)$ being the probability density of finding an electron at a radius r from the nucleus. $D(r) = 4\pi r^2\bar{\rho}(r)$ is the radial charge distribution which represents the probability density of finding an electron at a distance between r and $r + \mathrm{d}r$ from the origin of the coordinate system.

Although a complete formal proof is unavailable, numerical evidence has suggested that the spherically averaged charge density $\bar{\rho}(r)$ is monotonically decreasing for the ground state of an atom (3). Furthermore, the Hoffmann-Ostenhofs (4) have shown within the infinite nuclear-mass approximation that the atomic $\bar{\rho}(r)$ is indeed a convex monotonically decreasing function outside a sphere whose radius depends on the ionization energy and the electron–nucleus attraction.

Within a neighborhood of the nucleus, $\bar{\rho}(r)$ is monotonically decreasing as can be seen from its McLaurin expansion

Can. J. Chem. Downloaded from www.nrcresearchpress.com by 112.217.228.212 on 09/07/12
For personal use only.

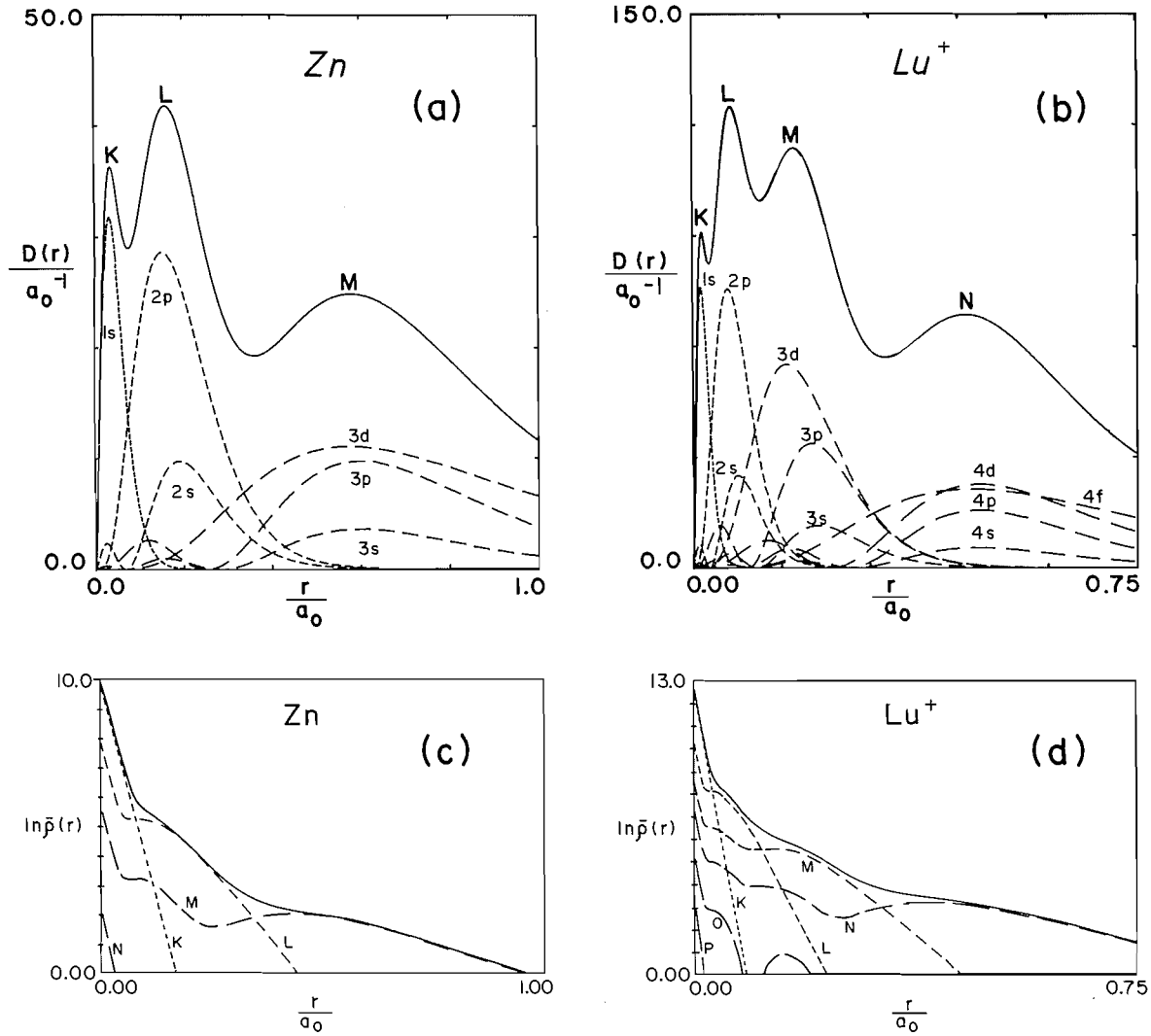

FIG. 1. Orbital (dotted lines) and the total (solid line) contributions to (*a*) $D(r)$ of the zinc atom ($Z = 30$); (*b*) $D(r)$ of the lutetium positive ion ($Z = 71$); (*c*) $\ln\bar{\rho}(r)$ of the zinc atom; (*d*) $\ln\bar{\rho}(r)$ of the lutetium ion. Note that in (*c*) and (*d*) those orbitals having the same principal quantum number have been grouped according to their corresponding shells.

[4] $$\bar{\rho}(r) = \bar{\rho}(0)[1 - 2Z\,\mathrm{Cen}\,r] + O(r^2)$$

where Cen is the electron nuclear cusp ratio (5)

[5] $$\mathrm{Cen} = \lim_{r\to 0} \bar{\rho}'(r)/2Z\bar{\rho}(r)$$

In sharp contrast to $\bar{\rho}(r)$, $D(r)$ vanishes at the origin and displays a number of maxima and minima (6). The values of r where $D(r)$ is a maximum or minimum are those that satisfy $D'(r) = 0$. Hence, by differentiation we obtain

[6] $$D'(r) = 4\pi r\left[2\bar{\rho}(r) + \frac{r\,d\bar{\rho}(r)}{dr}\right]$$

By solving this differential equation, $D'(r)$ is zero, for r not equal to zero, if $\bar{\rho}(r)$ possesses the functional form of r^{-2}. The topology of $D(r)$ suggests that the maxima and minima in $D(r)$ are the result of the increasing surface area ($4\pi r^2$) of the sphere. That is, if the rate of decay of $\bar{\rho}(r)$ is slower than r^{-2} then $D(r)$ is an increasing function. Conversely, if the damping effect in $\bar{\rho}(r)$ is stronger than r^{-2}, $D(r)$ is a decreasing function.

The relationship of the topology of $\bar{\rho}(r)$ to the shell structure in $D(r)$ was first examined by Wang and Parr (7) who examined plots of $\ln\bar{\rho}(r)$ versus r together with the respective $D(r)$ plots. Figure 1 contains $D(r)$ plots for Zn and Lu^+ together with their respective $\ln\bar{\rho}(r)$ plots. As was found by Wang and Parr, $\bar{\rho}(r)$ can be represented as a continuous piecewise exponential function of r with "as many different exponential regions as there are principal quantum numbers". The transition from one exponential region to the next occurs in an interval which roughly coincides with the corresponding minimum in the $D(r)$ plot as can be readily seen from Fig. 1.

If the charge density is constructed from a wavefunction in a Slater basis set, each Slater-type function (STF) whose radial part $R(r)$ is $Cr^{n-1}e^{-\zeta r}$ where C is the normalization coefficient and n is the principal quantum number, will lead to a $D(r)$ that peaks only at $r = n/\zeta$. Hence, due to the similarity of their radial parts, orbitals possessing the same principal quantum number lead to $D(r)$ contributions that peak generally in the same region (Fig. 1); the difference being in the cross-terms that arise in the multiplication of two STF's. In fact, knowledge of how the shell structure reveals itself through $D(r)$ has been utilized in the interpretation of beam-foil excitation processes (8–12).

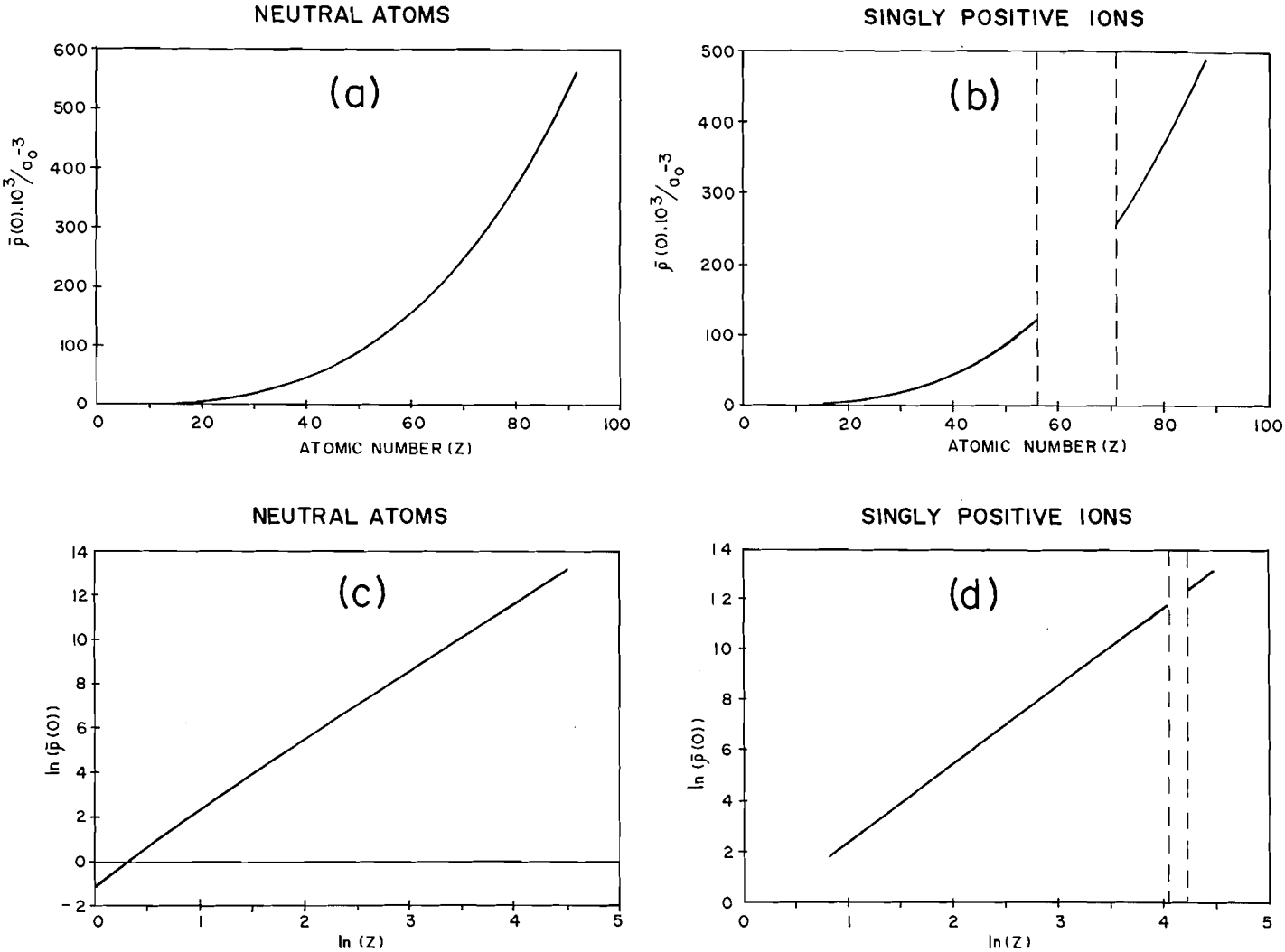

FIG. 2. A study of $\bar{\rho}(0)$ for the neutral atoms ($1 \leq Z \leq 92$) and the singly positive ions ($2 \leq Z \leq 57$, $70 \leq Z \leq 92$). (*a*) $\bar{\rho}(0)$ vs. Z for the neutral atoms; (*b*) $\bar{\rho}(0)$ vs. Z for the singly positive ions; (*c*) $\ln \bar{\rho}(0)$ vs. $\ln Z$ for the neutral atoms; (*d*) $\ln \bar{\rho}(0)$ vs. $\ln Z$ for the singly positive ions. Note that the gap $57 \leq Z \leq 70$ in (*b*) and (*d*) is due to the unavailability of wavefunctions for the ions with open *f*-shells.

Results and discussion

The values of the spherically averaged charge density $\bar{\rho}(r)$ and the radial charge distribution $D(r)$ were computed for the neutral atoms hydrogen to uranium and singly positive ions helium to barium and lutetium to radium from the non-relativistic SCF wavefunctions of Clementi and Roetti (13) and McLean and McLean (14). Published wavefunctions for the singly positive ions with open *f*-shells were not available.

The spherically averaged charge density, $\bar{\rho}(r)$, was found to be monotonically decreasing for the ground states of all the studied atomic and ionic cases (i.e. no local maxima or minima were observed).

Figures 2(*a*) and 2(*b*) contain plots of $\bar{\rho}(0)$ vs. Z for the atoms and the ions, respectively, and are meant to illustrate how $\bar{\rho}(0)$, the only extremal point in $\bar{\rho}(r)$, varies as a function of the atomic number Z (5). In Figs. 2(*c*) and (*d*) plots of $\ln \bar{\rho}(0)$ vs. $\ln Z$ are presented for the atoms and the ions, respectively.

Only orbitals possessing *s*-type symmetry will contribute to the spherically averaged charge density, at the origin, $\bar{\rho}(0)$. Since only the 1*s* Slater type functions are non-zero at the origin, we shall assume that one of these dominates the behaviour of $\bar{\rho}(0)$. For $\bar{\rho}(r)$ of such a 1*s* orbital which, according to Slater's rules (15), is subject to minimal screening, the value of $\bar{\rho}(0)$ is $2Z^3/\pi$. A plot of $\ln \rho(0)$ vs. $\ln Z$ would thus yield

$$[7] \quad \ln \bar{\rho}(0) \approx 3 \ln Z + \ln\left(\frac{2}{\pi}\right)$$

Therefore one would expect that if our assumption that the unscreened 1*s* function dominates $\bar{\rho}(0)$ is correct, the curves in Figs. 2(*c*) and (*d*) should have slopes equal to 3 and intercepts[1] equal to $\ln(2/\pi)$.

In Figs. 1(*a*) and (*b*) the $D(r)$ plots for the atom Zn ($Z = 30$) and the singly positive ion Lu^+ ($Z = 71$) are disassembled in terms of orbital contributions to the total function. These plots illustrate that orbitals having the same principal quantum number will peak in generally the same region, with the higher angular momentum orbitals peaking at smaller values of r, as

[1]The curve in Fig. 2(*c*) has a slope of 3.11 and an intercept of −0.768 while that in Fig. 2(*d*) has a slope of 3.20 and an intercept of −0.931.

Can. J. Chem. Downloaded from www.nrcresearchpress.com by 112.217.228.212 on 09/07/12
For personal use only.

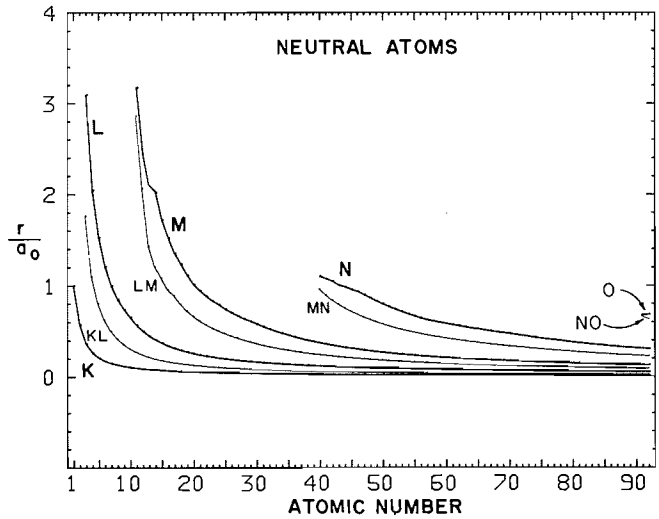

FIG. 3. Values of r_{max} (heavy lines, single letters) and r_{min} (thin lines, double letters) corresponding to the value of r at which the radial charge distribution is, respectively, a maximum or minimum for the neutral atoms hydrogen to uranium, as a function of the atomic number Z.

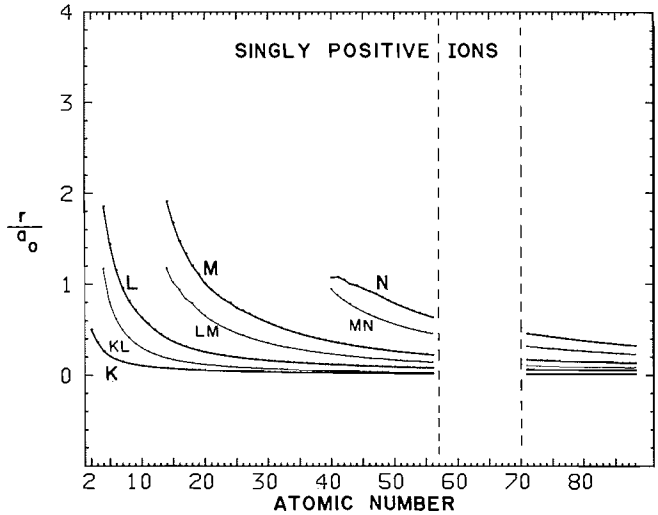

FIG. 4. Values of r_{max} (heavy lines, single letters) and r_{min} (thin lines, double letters) corresponding to the value of r at which the radial charge distribution is respectively a maximum or minimum for the singly positive ions, from helium to barium and lutetium to radium, as a function of the atomic number Z. Note that the gap $57 \leq Z \leq 70$ is due to the unavailability of wavefunctions for the ions with open f-shells.

compared to orbitals with smaller angular momenta. If a "shell" is defined as the region in r where orbital contributions to $D(r)$ of the same principal quantum number will peak, we can infer from Figs. 1(a) and (b) that the maxima in $D(r)$ correspond to these "shells", with the maximum at the smallest r corresponding in order to the K shell, and subsequent maxima corresponding to the L, M, shells etc. The minima in $D(r)$ which have been the subject of previous studies (16) are the consequence of a combination of the orbital contributions to $D(r)$ of the preceding maximum decaying and the orbital contributions to $D(r)$ of the succeeding maximum increasing and as such can be seen to be the region between two shells, i.e. an intershell valley. Figures 1(a) and (b) indicate that as the distance from the nucleus increases, the maxima become broad and shallow and sometimes difficult to discern. For the case of the lutetium ion (Fig. 1(b)), the outer shells are not even apparent.

Adopting a convention that has been used elsewhere (17), r_{max}, r_{min} shall be used to denote the values of r at which $D(r)$ is a maximum or minimum respectively, while D_{max}, D_{min} will correspond to $D(r_{max})$ and $D(r_{min})$, respectively. By inserting a third axis, Z, perpendicular to the plot in Fig. 1(a) and through its origin, and using it to mark the atomic number in ascending order, we confine all the $D(r)$ plots for the atoms to a single three dimensional figure. Furthermore, by connecting the r_{max}, r_{min} values of a particular shell or intershell valley and projecting these curves into the r–Z plane, one is able to observe the effect of atomic number on the positions of the extrema of $D(r)$. Figures 3 and 4 convey this information for the atoms and ions, respectively, with the single letters denoting the shells, and the double letters denoting an intershell region which lies between the shells corresponding to the two letters. Subsequently if the values of $D(r)$ at the extremal points are connected by straight lines and the resulting curves projected onto the D–Z plane from the hypothetical 3-D figure for a particular shell or intershell, one is able to observe the effect of atomic number on the values of $D(r)$ at the shell peaks and the intershell valley regions for the atoms and the ions (Figs. 5 and 6). It should be noted that the connections in Figs. 3–6 are meant only to guide the eye and should not convey the impression that the curves are continuous in Z.

Figures 3 and 4 can best be understood in terms of the Bohr theory of an atom which specifies shells (all electrons with the same principal quantum number n) with orbit radii equal to $(n^2/Z)a_0$. This expression can be used to account for the roughly first order hyperbolic plots present in Figs. 3 and 4 with the functional form suggesting that any deviations from a first order hyperbola must be due to either n, the principal quantum number, or to Z, the atomic number. The deviations resulting from Z should be the result of shielding of the outer electrons from the nucleus by the inner electrons. This means that the outer electrons are in a field resulting from an effective nuclear charge of $Z - S$ where S is an empirically defined shielding parameter (15).

To examine the nature of the deviations, the inverses, i.e. r_{max}^{-1}, r_{min}^{-1} of Figs. 3 and 4 were plotted and presented in Figs. 7 and 8. These latter curves being of the approximate form Z/n^2 show marked linearity with no obvious deviations, in contrast to Figs. 3 and 4 which do exhibit some deviations. Since any deviations due to shielding would mean a perturbation which would affect the atomic number, the expression from the Bohr theory for the radius of the nth shell becomes $n^2/(Z - S)a_0$ or $n^2/Z(1 - S/Z)a_0$. The latter expression implies that the deviations are larger at smaller Z, a result which is in accord with the shapes of the curves in Figs. 3 and 4. Thus the deviations are mainly a result of shielding as was previously reported (6). It should be noted here that the marked linearity in Figs. 7 and 8 is due to the fact that any shielding apparent in Figs. 3 and 4 will only affect the intercepts and not the slopes of the various curves. This can be seen by considering the corresponding expression for the reciprocal radius, namely $(Z - S)n^{-2}a_0^{-1}$.

Tables 1 and 2 contain the data obtained from a linear least-squares regression analysis of the r_{max}^{-1} curves for the shells in Figs. 7 and 8 and the slopes and intercepts obtained by analytical derivation from the highest angular momentum hydrogenic function of a particular shell. The highest angular

Can. J. Chem. Downloaded from www.nrcresearchpress.com by 112.217.228.212 on 09/07/12
For personal use only.

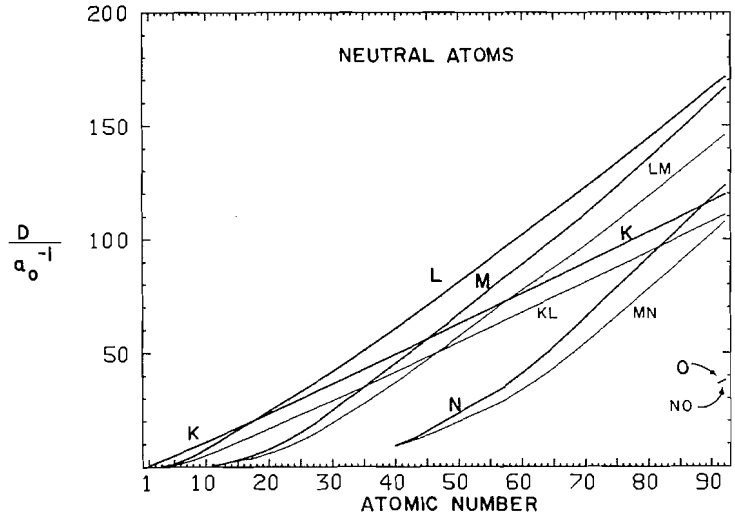

FIG. 5. Values of D_{max} (thicker lines, single letters) and D_{min} (thinner lines, double letters). These quantities correspond to the values of the radial charge distribution at the maxima and minima respectively, for the neutral atoms as a function of the atomic number Z.

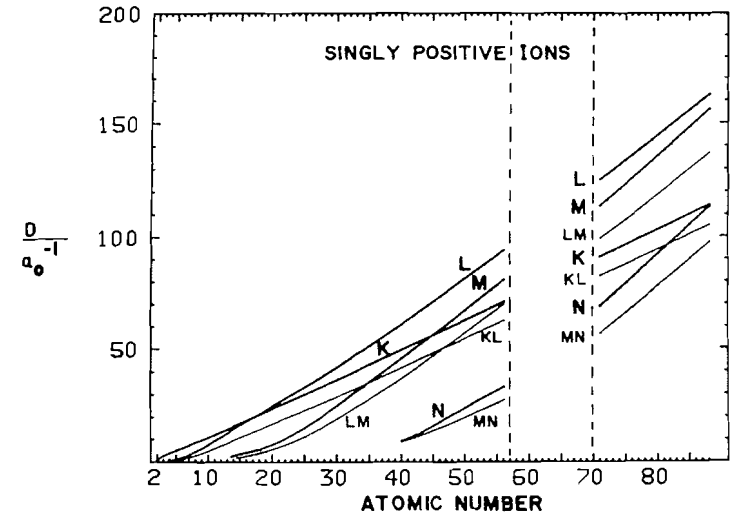

FIG. 6. Values of D_{max} (thicker lines, single letters) and D_{min} (thinner lines, double letters). These quantities correspond to the value of the radial charge distribution at the maxima and the minima respectively for the singly positive ions, as a function of the atomic number Z. Note that the gap $57 \leq Z \leq 70$ is due to the unavailability of wavefunctions for the ions with open f-shells.

momentum hydrogenic function of each shell has been used in this study in the assumption that these functions are the most descriptive of the trends in D_{max}, D_{min}, r_{max}, r_{min} for a particular shell, due to their higher occupation numbers in comparison with the lower angular momentum orbitals for most of the elements. Consider for example the neon atom. This atom possesses an electronic configuration in which the L shell is completely filled, i.e. $2s^2 2p^6$. For all the atoms beyond neon in the periodic table, the behaviour of the L shell would most likely be governed by the $2p$ orbitals since their occupation would always be three times that of the $2s$ orbital.

The slope was determined analytically from the highest angular momentum hydrogenic function of the particular shell by using its functional form to construct $D(r)$, which was then differentiated with respect to r, and the resulting equation set equal to zero to find r_{max}. Since this equation for r_{max} is Z dependent, the inverse, r_{max}^{-1} is also Z dependent with the coefficient of the equation for r_{max}^{-1} as a function of Z being referred to as the "analytically derived slope", A_D. The intercept was calculated by assuming a functional form $A_D(Z - S)$ where A_D is the "analytically derived slope", Z is the atomic number and S is an empirically defined shielding constant that was calculated via the use of Slater's rules (15). The intercept which shall be referred to as the "analytically derived intercept", B_D is thus seen to be the product of the "analytically derived slope", A_D, and the shielding parameter, S.

On comparison of the analytically derived slope, A_D, with the slope from the fitting, A_F one can see that there is an overall trend towards similarity between the two quantities, thereby substantiating the validity of the Bohr theory of an atom within this particular framework. On the other hand, the "analytically derived intercept", B_D bears no resemblance to the intercept from the fitting, B_F, a result which supports the fact that the effects of shielding on the position of the extrema in $D(r)$ are small.

A linear least-squares analysis was performed on the slopes determined from the fitting in Figs. 7 and 8 (A_F in Tables 1 and 2) against the inverse of the principal quantum number squared,

Can. J. Chem. Downloaded from www.nrcresearchpress.com by 112.217.228.212 on 09/07/12
For personal use only.

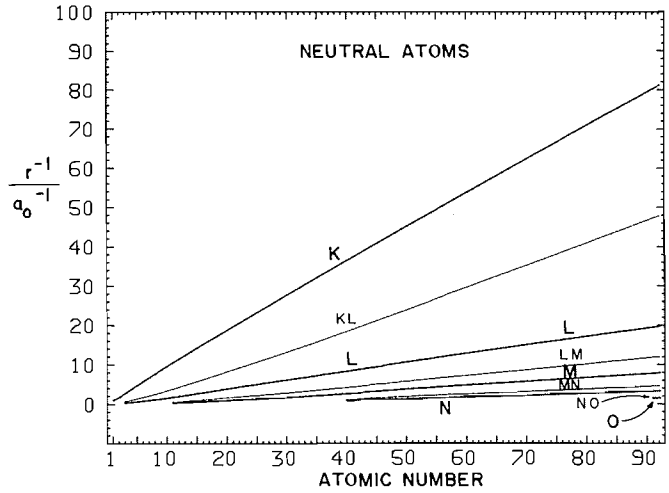

FIG. 7. Values of r_{max}^{-1} (heavy lines, single letters) and r_{min}^{-1} (thin lines, double letters) corresponding to the values of r^{-1} at which the radial charge distribution is respectively a maximum or minimum, for the neutral atoms hydrogen to uranium, as a function of atomic number Z.

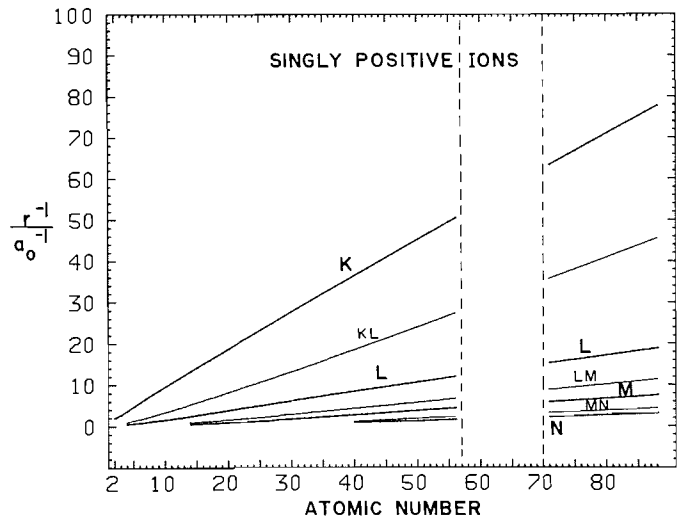

FIG. 8. Values of r_{max}^{-1} (heavy lines, single letters) and r_{min}^{-1} (thin lines, double letters) corresponding to the values of r^{-1} at which the radial charge distribution is respectively a maximum or minimum for the singly positive ions, as a function of atomic number Z. Note that the gap $57 \leq Z \leq 70$ is due to the unavailability of wavefunctions for the ions with open f-shells.

for the atoms and the ions respectively. The resulting equation obtained for the atoms was $A_F = 0.8977/n^2 - 0.01741$. The ions yielded the result $A_F = 0.8807/n^2 - 0.003611$. The fact that these intercepts are close to zero and that the slopes are close to unity for both the atoms and the ions further validates the correlation with the prediction from the Bohr theory.

Figures 5 and 6 show plots of D_{max} vs. Z of the shell and intershell regions for the atoms and the singly positive ions, respectively. These plots show regions of curvature as well as regions of linearity, with the regions of linearity occurring at higher values of Z. The curves are seen to be steadily increasing with Z, and as such are a consequence of the normalization of the wavefunction since as the atomic number increases, the particular extrema will move closer to the nucleus, and the value

TABLE 1. The slopes and intercepts obtained by the use of the outermost hydrogenic orbital pertaining to a particular shell, and also the slopes and intercepts obtained from a linear least-squares analysis of the data points for the curves in Fig. 7 corresponding to the shells of the neutral atoms[a]

	Value			
Parameter	K	L	M	N
A_D	1.00	0.250	0.110	0.0600
A_F	0.876	0.221	0.096	0.046
B_D	−0.300	−1.04	−2.33	−3.03
B_F	−1.13	−0.485	−1.03	−1.04
R^2	0.9974	0.9998	0.9983	0.9961

[a]The following definitions have been used: A_D, the slope determined from the largest angular momentum hydrogenic orbital of the particular shell; A_F, the slope determined from the linear least-squares fitting of the data points; B_D, the intercept determined from the largest angular momentum hydrogenic orbital of the particular shell with the use of Slater shielding parameters; B_F, the intercept determined from the linear least-squares fitting of the data points; R^2, the square of the correlation coefficient obtained from the fitting procedure of the data points.

TABLE 2. The slopes and intercepts obtained by the use of the outermost hydrogenic orbital pertaining to a particular shell, and also the slopes and intercepts obtained from a linear least-squares analysis of the data points for the curves in Fig. 8 corresponding to the shells of the neutral atoms[a]

	Value			
Parameter	K	L	M	N
A_D	1.00	0.250	0.110	0.0600
A_F	0.876	0.221	0.0970	0.0450
B_D	−0.300	−1.04	−2.33	−3.03
B_F	−1.16	−0.491	−1.07	−0.990
R^2	0.9997	0.9998	0.9984	0.9974

[a]The same definitions have been used as in Table 1.

of the function at the extrema will become larger in order for the normalization conditions to be obeyed. The various curves are also seen to intersect which is a consequence of shielding, as without shielding all the intercepts would be zero, with the plots diverging as a consequence of different slopes.

Tables 3 and 4 contain the parameters obtained from a linear least-squares regression analysis of the D_{max} curves for the shells in Figs. 5 and 6, and the slopes and intercepts obtained from analytical derivation using the highest angular momentum hydrogenic function of a particular shell.

The slope from the highest angular momentum hydrogenic function of a particular shell was obtained by substituting the value of r_{max} previously obtained from the same hydrogenic function into the expression for $D(r)$ derived for this particular hydrogenic function. The resulting equation is Z dependent with the coefficient being referred to as the "analytically derived slope", A_D'. The intercept, B_D', similar to the case of the r_{max}^{-1} studies was calculated by assuming the functional form $M(Z - S)$, and therefore is the product of the "analytically derived slope", A_D', and the shielding parameter, S.

The results suggest that there is no agreement between the "analytically derived slope", A_D', and the fitted slope, A_F', but there is in general good correlation between the "analytically derived intercepts" and the fitted intercepts, B_D' and B_F', in

Can. J. Chem. Downloaded from www.nrcresearchpress.com by 112.217.228.212 on 09/07/12
For personal use only.

TABLE 3. The slopes and intercepts obtained by the use of the outermost hydrogenic orbital pertaining to a particular shell, and also the slopes and intercepts obtained from a linear least-squares analysis of the data points for the curves in Fig. 5 corresponding to the shells of the neutral atoms[a]

Parameter	Value			
	K	L	M	N
A_D'	6.80	2.46	1.35	0.220
A_F'	1.32	1.97	2.13	2.27
B_D'	−2.04	−10.2	−28.3	−11.1
B_F'	−2.66	−14.8	−36.2	−90.3
R^2	0.9997	0.9971	0.9939	0.9894

[a]The following definitions have been used: A_D', the slope determined from the largest angular momentum hydrogenic orbital of the particular shell; A_F', the slope determined from the linear least-squares fitting of the data points; B_D', the intercept determined from the largest angular momentum hydrogenic orbital of the particular shell with the use of Slater shielding parameters; B_F', the intercept determined from the linear least-squares fitting of the data points; R^2, the square of the correlation coefficient obtained from the fitting procedure of the data points.

TABLE 4. The slopes and intercepts obtained by the use of the outermost hydrogenic orbital pertaining to a particular shell, and also the slopes and intercepts obtained from a linear least-squares analysis of the data points for the curves in Fig. 6 corresponding to the shells of the neutral atoms[a]

Parameter	Value			
	K	L	M	N
A_D'	6.80	2.46	1.35	0.220
A_F'	1.32	1.97	2.15	2.22
B_D'	−2.04	−10.2	−28.3	−11.1
B_F'	−2.69	−14.9	−37.5	−85.5
R^2	0.9997	0.9973	0.9957	0.9942

[a]The same definitions have been used as in Table 3.

sharp contrast to the r_{max}^{-1} studies. Thus the effects of shielding are seen to be more evident in the D_{max} case, while the r_{max}^{-1} studies indicate a good correlation with the Bohr theory of an atom.

The D_{max}, D_{min} plots have some interesting features that should be noted. The N shell is unique since it exhibits three distinct regions of linearity in contrast to the two regions observed with other shells and intershells. This is a consequence of the filling of the $4f$ orbitals as this region starts with Ce ($Z = 58$) precisely where the $4f$ orbitals begin to be occupied.

Figure 9 contains the radial charge distribution for the neutral atom uranium ($Z = 92$) in order to show the presence of a fifth maximum, in contrast to what was previously reported (6) to be a broad shoulder via computation from a relativistic SCF wavefunction (with local exchange). This result raises interesting questions into the nature of the wavefunctions used and the possibility of the appearance or disappearance of more shells with the use of more highly accurate wavefunctions and the effects of electron correlation and relativity.

Conclusions

The present examination of the radial charge distribution function, $D(r)$, shows that at most five shells are revealed in

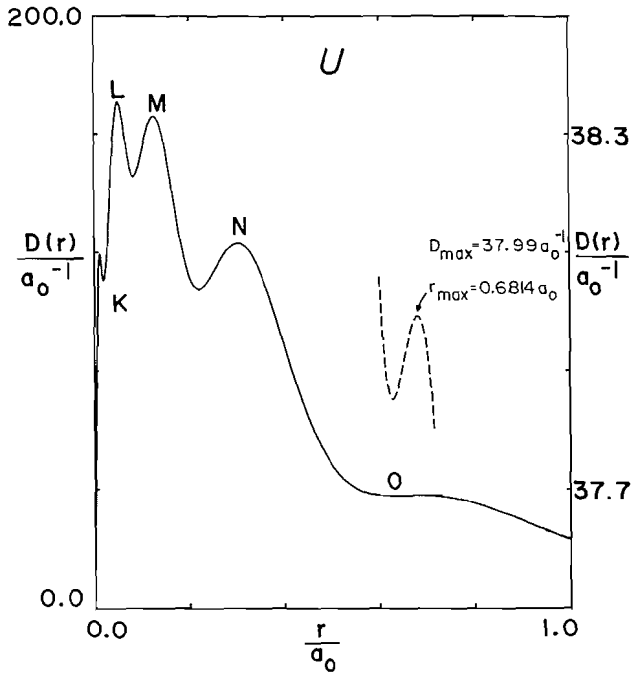

FIG. 9. Radial charge distribution of the neutral atom U ($Z = 92$) computed from the non-relativistic SCF wavefunction of McLean and McLean. The dashed curve corresponds to the scale on the right hand side in order to clearly show the maximum indicative of the O shell.

$D(r)$ based on the criterion that the maxima of $D(r)$ are the topological features most indicative of shells. Furthermore, the maxima exhibit strong correlations with that expected from the independent particle model (Bohr-hydrogenic theory). Any deviations from the Bohr theory were attributed to the effects of electronic shielding.

The spherically averaged charge density, $\bar{\rho}(r)$, was shown to be monotonically decaying for the ground states of all the studied atomic and ionic cases. This extends the previously known (3) upper limit for the range of atoms for which this is true from $Z = 36$ to $Z = 92$. For the first time, $\bar{\rho}(r)$ for the singly positive atomic ions was shown to have the same behaviour.

Acknowledgements

Support of this research by the Conselho Nacional de Desenvolvimento Cientifico e Technologico (CNPq), Brasil, and by the Natural Sciences and Engineering Research Council of Canada (NSERCC) is gratefully acknowledged.

1. L. PAULING. The nature of the chemical bond. 3rd ed. Cornell University, New York. 1960.
2. P. COPPENS and M. B. HALL. Electron distributions and the chemical bond. Plenum, New York. 1982.
3. H. WEINSTEIN, P. POLITZER, and S. SREBRENIK. Theoret. Chim. Acta, Berl. **38**, 159 (1975); G. SPERBER. Int. J. Quantum Chem. **5**, 189 (1971).
4. M. HOFFMAN-OSTENHOF and T. HOFFMAN-OSTENHOF. Phys. Rev. A**16**, 1782 (1977).
5. W. M. WESTGATE, A. D. BYRNE, V. H. SMITH, JR., and A. M. SIMAS. Can. J. Phys. **64**, 1351 (1986) and references therein.
6. J. T. WABER and D. T. CROMER. J. Chem. Phys. **42**, 4116 (1965).
7. W. P. WANG and R. G. PARR. Phys. Rev. A**16**, 891 (1977).
8. E. VEJE. Phys. Rev. A**14**, 2077 (1976).
9. A. LINGAREL, S. MANNERVIK, B. JELENKOVIC, and E. VEJE. Z. Phys. A**301**, 1 (1981).

Can. J. Chem. Downloaded from www.nrcresearchpress.com by 112.217.228.212 on 09/07/12
For personal use only.

10. A. LINGAREL, S. MANNERVIK, B. JELENKOVIC, and E. VEJE. Nucl. Instr. Meth. **202**, 59 (1982).
11. A. LINGAREL, S. MANNERVIK, B. JELENKOVIC, and E. VEJE. Nucl. Instr. Meth. **202**, 59 (1982).
12. E. VEJE. Phys. Rev. B**28**, 5029 (1983).
13. E. CLEMENTI and C. ROETTI. Atom. Data Nucl. Data Tables, **14**, 177 (1974).
14. A. D. MCLEAN and R. S. MCLEAN. Atom. Data Nucl. Data Tables, **26**, 197 (1981).
15. J. C. SLATER. Quantum theory of atomic structure. McGraw-Hill, New York. 1960. Vol. I. Phys. Rev. **36**, 57 (1930).
16. R. J. BOYD. J. Chem. Phys. **66**, 356 (1977) and references therein.
17. A. M. SIMAS, W. W. WESTGATE, and V. H. SMITH, JR. J. Chem. Phys. **80**, 2636 (1984).

Can. J. Chem. Downloaded from www.nrcresearchpress.com by 112.217.228.212 on 09/07/12
For personal use only.

Light-induced reversible ionization of tetramethylphenylenediamine in an inorganic polymer of *n*-butyl orthotitanate

HISASHI UEDA[1] AND MASAHIRO KAISE

National Chemical Laboratory for Industry, Tsukuba Research Center, Higashi, Tsukubashi, Ibaraki 305, Japan

Received November 23, 1987

This paper is dedicated to Professor Charles A. McDowell on the occasion of his 70th birthday

HISASHI UEDA and MASAHIRO KAISE. Can. J. Chem. **66**, 1931 (1988).

n-Butyl orthotitanate, BT, polymerized in tetrahydrofuran, if irradiated by visible light, gives a new electron spin resonance absorption that is not found before irradiation. In the present work, three different polymers of BT were synthesized by adding tetramethyl phenylenediamine (TMPD), dimethyl phenylenediamine (DMPD), or phenylenediamine (PD), to the solution of BT. The polymers thus prepared were tested to see if they give a new esr signal when irradiated by visible light. The polymer to which 1 mol% of TMPD was added gave $TMPD^{\bullet+}$ when irradiated by visible light, but the $TMPD^{\bullet+}$ signal decayed after the irradiation was discontinued. This change, therefore, is reversible. The resonant position of every hyperfine splitting line of the $TMPD^{\bullet+}$ found in this polymer coincided with that of $TMPD^{\bullet+}$ in solution, but the relative intensity ratios and the line width of each line depended on the nuclear spin quantum number of the coupling nuclei. This can be interpreted by the restricted rotational motion of $TMPD^{\bullet+}$ in the polymer matrix. The contribution of the non-diagonal term to the spin relaxation time would explain this phenomenon. In the case of the polymer to which DMPD was added, a small amount of $DMPD^{\bullet+}$ seemed to be formed, but no radical was detected in the case of the polymer to which PD was added.

HISASHI UEDA et MASAHIRO KAISE. Can. J. Chem. **66**, 1931 (1988).

Lorsqu'on soumet des solutions d'orthotitanate de *n*-butyle (TB) dans le tétrahydrofuranne à une irradiation par de la lumière visible, il se produit une polymérisation qui donne naissance à une absorption en résonance paramagnétique électronique qui n'est pas observée avant l'irradiation. Dans le présent travail, on a synthétisé trois polymères différents du TB; pour y parvenir, on a ajouté de la tétraméthyl phénylènediamine (TMPD), de la diméthyl phénylènediamine (DMPD) ou de la phénylènediamine (PD) à la solution de TB. On a vérifié si les polymères ainsi préparés donnent naissance à un nouveau signal rpe lorsqu'ils sont soumis à une irradiation par de la lumière visible. Lorsqu'on le soumet à une irradiation par de la lumière visible, le polymère auquel on a ajouté 1 mol% de TMPD donne l'ion radical $TMPD^{\bullet+}$; toutefois, ce signal disparaît lorsqu'on discontinue l'irradiation. Ce changement est donc réversible. La position de résonance de chacune des raies du $TMPD^{\bullet+}$ de ce polymère coïncide avec celle du $TMPD^{\bullet+}$ en solution; toutefois, les rapports des intensités relatives ainsi que les largueurs de chacune des raies dépendent du nombre quantique du spin nucléaire des noyaux qui se couplent. On interprète ces résultats en fonction d'une restriction au mouvement rotationnel du $TMPD^{\bullet+}$ dans la matrice de polymère. La contribution du terme non-diagonal au temps de relaxation de spin explique ce phénomène. Dans le cas du polymère auquel on a ajouté du DMPD, il semble se former une faible quantité de $DMPD^{\bullet+}$; toutefois, on n'a pas détecté de radicaux dans le cas du polymère auquel on a ajouté de la PD.

[Traduit par la revue]

Introduction

The demand for synthetic polymers has been changing in recent times. In addition to requirements of mechanical strength, thermal stability, and corrosion resistivity, new optical properties are being requested of the polymers (1). To find these types of polymers, the present authors have investigated, by the esr method (2), the light response of inorganic polymers containing titanium or zirconium. Bradley *et al.* studied the polymerization of titanium alkoxides and the structure of these products (3, 4). According to Bradley, there are five types of polymerization patterns and the chain growth can proceed in four possible directions (5). Boyd studied the hydrolysis-type polymerization of titanium alkoxides (6). Thus the polymers formed from titanium alkoxides can show diversity in their structures. The present authors have tried to polymerize titanium alkoxides in tetrahydrofuran (THF); a slower polymerization rate should be possible in THF because of its smaller dielectric constant compared to that of water. In THF, the alkoxyl groups will be eliminated as R_2O, leaving considerable amounts of the -Ti(RO)- type of group in the polymer molecule, which would give rise to paramagnetism in the molecule. The esr results have indicated that this actually happens (2). In the present work, tetramethyl phenylenediamine (TMPD), dimethyl phenylenediamine (DMPD), or phenylenediamine (PD) was added to the titanium butoxide/THF solution and the three polymers produced were tested to see if they show visible-light-induced esr spectra.

So far as the present authors know, inorganic polymers in which unpaired spins are intentionally created have rarely been synthesized. Therefore, esr observation of the light-induced change in this type of polymer was not made previous to the attempt of one of the present authors (Ueda and co-workers, ref. 2). The novelty in the present paper lies in the esr detection of the light-induced reversible electric charge flow from the bulk of the inorganic polymer synthesized by addition of aromatic diamine to the diamine.

Experimental

The TMPD/polymer was prepared by the following method: 6.3 g of $Ti(OBu)_4$ (*n*-butyl orthotitanate, BT) was dissolved in THF. To this solution an 0.18 mM equivalent of TMPD·2HCl and 2.0 g of silica gel, crushed immediately before use and to 100 mesh, were added. A Pyrex container, made from a 500-mL beaker by cutting off the beak part to cover it tightly with a glass plate, was used as the reactor. After covering the container with a watch glass it was placed in the middle of a circle of light from a 30-W fluorescent lamp. After 50 h, the watch glass was removed to evaporate the solvent. In some 20 h the THF was evaporated away, yielding colored solid polymer. The yield was ca. 38% based on the amount of $Ti(OBu)_4$ used. If the reaction

$$Ti(OBu)_4 \rightarrow \text{-Ti(=O)—O-} + 2Bu_2O$$

[1]Author to whom correspondence may be addressed.

Can. J. Chem. Downloaded from www.nrcresearchpress.com by 112.217.228.212 on 09/07/12
For personal use only.

goes to completion, the yield should be 23.5%. If TMPD was not added, the polymer yield experimentally obtained was ca. 29%. Therefore, the elimination of Bu_2O was somewhat inhibited by the addition of TMPD. Since the silica gel added had been crushed finer than 100 mesh, most of the silica gel powder was separated from the polymer particles by a sieve. Both polymer and silica gel portions thus prepared were washed with 1:4 acetic acid/water, 1:4 formic acid/water, and 1:1 aqueous ammonium solution, and were then dried. The esr measurements were made with this sample. The preparation of the PD/polymer system was attempted using an identical procedure. However, it was impossible to obtain a polymer in this case. No increment of the viscosity of the solution was observed. It may be possible that the polymerization of BT was hindered by PD. Instead of PD, PC·2HCl was used in the same procedure. No viscosity increment was observed in this case, either. Considering these facts, another attempt to obtain the PD/polymer system was made. After polymerizing $Ti(OBu)_4$ to the extent at which gelation can be observed, a THF solution of 0.18 mM PD was added. After 20 h, the PD/polymer system was obtained. Let this polymer be called "post-addition PD polymer."

The DMPD/polymer system was also prepared. The amount of DMPD in this case was also 0.18 mM to 6.3 g of $Ti(OBu)_4$. The addition of DMPD at the beginning of the polymerization failed as in the case of PD. The use of the HCl salt also failed. Therefore, a THF solution of DMPD was added to the gelated solution of $Ti(OBu)_4$/THF. After 20 h, the DMPD/polymer system was obtained. Let this polymer be called "post-addition DMPD polymer."

The light-induced esr signal detection system consisted of a halogen lamp (Iwasaki Electric JCR 100 V 150 W), a light guide cable (Sumita Optics SLS-150), and an esr spectrometer (JEOL ME3X). The illuminated light contained light components having wave lengths ranging from 700 to 400 nm. Microwave power output at the Gunn diode oscillator was 1 mW. No power saturation of the spectrum was observed below 5 mW. A magnetic field modulation frequency of 100 kHz was used and the amplitude of the modulation width was 0.08 mT. A time constant of 0.1 s was used when sweeping the entire magnetic field range of 10 mT in 5 min. g-Factor determination was made by using a cavity resonator-type wave meter and 1,1-diphenyl-2-picryl hydrazyl (g = 2.0036) and Mn^{2+}/MgO standard samples (8.69-mT interval between 3rd and 4th hfs lines).

Results

In Fig. 1 the esr spectra of the polymer part (solid line) and the silica gel part (dotted line) of samples washed with 1:4 aqueous formic acid and illuminated for 10 min with visible light are shown. The silica gel part gives relatively well-separated hfs lines. This is due to the lower concentration of the paramagnetic species in the silica gel part. We conclude that the nature of the paramagnetic species is not different in these two samples. In Fig. 2 the experimental esr spectrum E (the same as the dotted curve in Fig. 1) and the simulated spectrum S are compared. The SA spectrum was obtained by assuming a line width of 0.120 mT, Lorentz functional form, and hfs coupling constants of 0.699 mT for N, 0.197 mT for H of the benzene ring, and 0.676 mT for the CH_3 protons (7). The experimental curve E seems to contain a structureless component, which may be due to a peak with a very large line width. Then SB was calculated using 1.2 mT as the line width. The S spectrum was calculated as S = (24·SB + SA)/25. The experimental curve has different line widths if one looks at the lower field side and the higher field side. This phenomenon may be due to restricted rotational motion of the $TMPD^{\cdot+}$ cation in the polymer (8–10). The anisotropy in the hfs tensor cannot be ignored with respect to the spin relaxation time and, as a result, the line width depends on the spin quantum numbers, m, of the proton system or

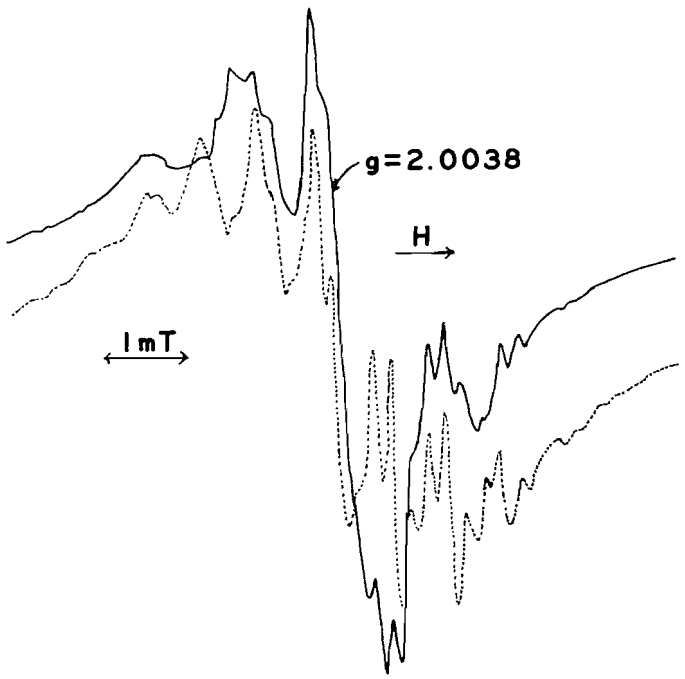

FIG. 1. The esr spectra of $Ti(OBu)_4$/TMPD/silica gel polymer. The solid curve was obtained from the polymer part. The dotted curve was obtained from the sample composed mainly of silica gel.

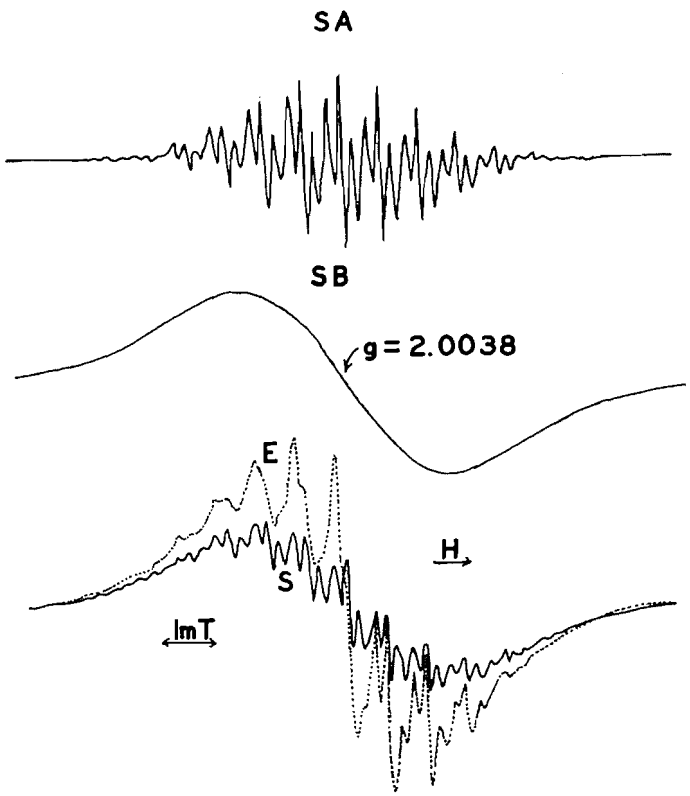

FIG. 2. The silica gel part of the esr spectrum (E) and the simulated ESR spectrum of $TMPD^{\cdot+}$; SA, SB, and S. For esr parameters of the simulation, refer to the text.

Can. J. Chem. Downloaded from www.nrcresearchpress.com by 112.217.228.212 on 09/07/12
For personal use only.

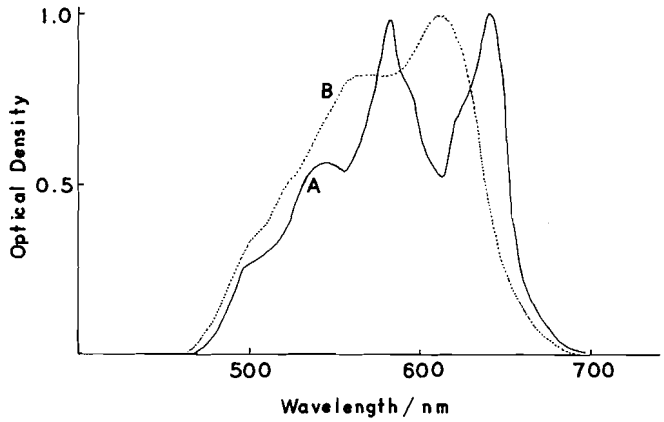

FIG. 3. The diffuse reflectance spectrum (B) of the silica gel part and the transmittance spectrum (A) of $TMPD^{\cdot+}$ trapped in CCl_4 at 77 K (A).

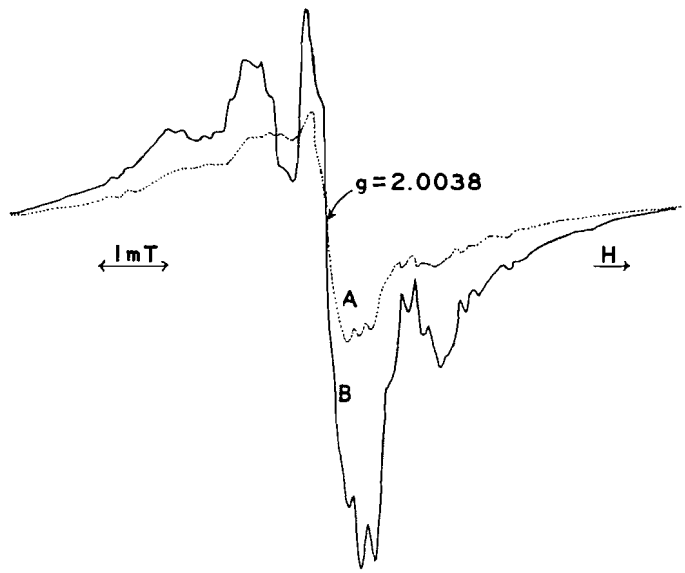

FIG. 4. The esr spectra of the polymer part of the reaction system ($Ti(OBu)_4$/TMPD/silica gel). The intensity depends on the light intensity. A was obtained from the sample kept in the darkness. B was obtained after 11 min of illumination.

the nitrogen nuclei system. The intensity ratio may also be dependent on m values (11). The simulated curve S is not constructed upon these considerations. However, it will be seen in Fig. 2 that the resonance positions of the E and S spectra coincide exactly. Therefore, it can be said that $TMPD^{\cdot+}$ is formed in the polymer of $Ti(OBu)_4$ by visible light. In Fig. 3 the reflectance spectrum of a sample of the silica gel part is shown. The spectrum B is the entire spectrum less the base-line spectrum. A is the transmittance spectrum of $TMPD^{\cdot+}$ stabilized in CCl_4 at 77 K (12). Though A and B do not coincide well, the absorption region seems to be the same. It would be proper to say that these two spectra are both due to $TMPD^{\cdot+}$ but they reflect the difference in the matrix environments in which they are stabilized. Figure 4 shows the intensity increment in the esr of the polymer part when illuminated by light. A indicates the spectrum before light illumination and B indicates the spectrum obtained by the sweep of 8.5–13.5 min after beginning the light illumination. As the A spectrum is from $TMPD^{\cdot+}$, it

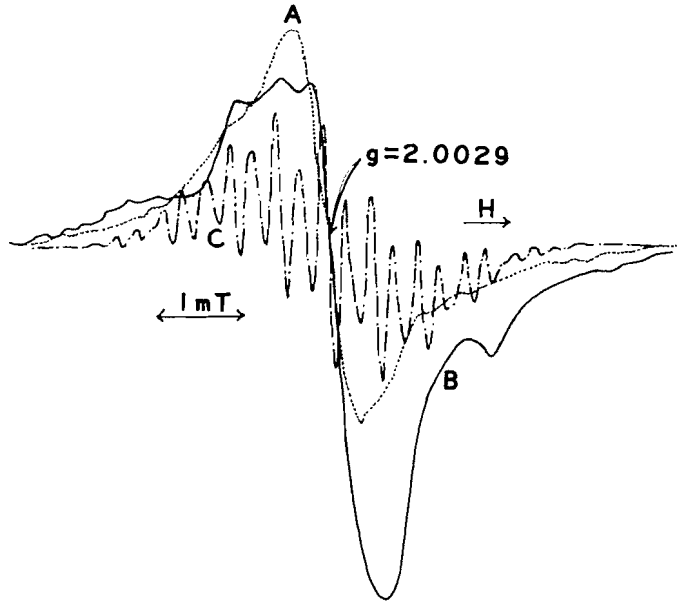

FIG. 5. The esr spectra of the polymer of $Ti(OBu)_4$ containing PD that was added at the latter stage of the polymerization. A was observed before light illumination. B was observed after 13.5 min of illumination. C is a simulated spectrum of $PD^{\cdot+}$; for esr parameters of simulation, refer to the text.

is concluded that $TMPD^{\cdot+}$ increases when illuminated and decreases when the light is turned off. This change could be repeated many times and, therefore, can be concluded to be reversible. Figure 5 indicates the esr spectra of the post-addition PD polymer kept in darkness (A) and under light illumination (B). The simulation parameters for curve C were 0.120 mT as line width, 0.211 mT as the coupling constant for C_6H_6 protons, 0.575 mT for the NH_2 protons, and 0.513 mT for N (14, 15). Figure 6 shows the esr spectra of post-addition DMPD polymer. A shows the spectrum without light illumination and B shows the spectrum 14.4 min after beginning light illumination. C is the simulated spectrum of $DMPD^{\cdot+}$ using a line width of 0.120 mT and coupling constants of 0.167 mT for two of the benzene protons (NMe_2 side) and 0.111 mT for another benzene proton (NH_2 side). The other coupling constants were 0.469 mT for NH_2 protons, 0.739 mT for CH_3 protons, 0.453 mT for the NH_2 nitrogen nucleus, and 0.719 mT for the NMe_2 nitrogen nucleus, respectively (16).

Figure 7 shows the reflectance spectra of the polymer that gave the esr spectra in Fig. 5. The reflectance spectrum of the silica gel part of the polymerization mixture and the transmittance spectrum of $PD^{\cdot+}$ reported by Nakayama and Suzuki (13) are also shown. It will be judged, by the comparison of these two spectra, that $PD^{\cdot+}$ does not exist in the present polymer mixture. Figure 8 indicates the reflectance spectra of the polymer that gave the esr spectra of Fig. 6, labelled "Polymer" in the figure. The spectrum of the silica gel part is labelled "SiG Polymer." The transmittance spectrum of Nakayama and Suzuki (13) is also shown. The comparison of these spectra may suggest that $DMPD^{\cdot+}$ is not formed in the present polymer mixture.

While TMPD forms a stable cation, TCNQ (tetracyano quinodimethane) is known to form either a stable anion or to function as an acceptor molecule. For this reason, an attempt was made to prepare a polymer mixture in which TCNQ was

Can. J. Chem. Downloaded from www.nrcresearchpress.com by 112.217.228.212 on 09/07/12
For personal use only.

Can. J. Chem. Downloaded from www.nrcresearchpress.com by 112.217.228.212 on 09/07/12
For personal use only.

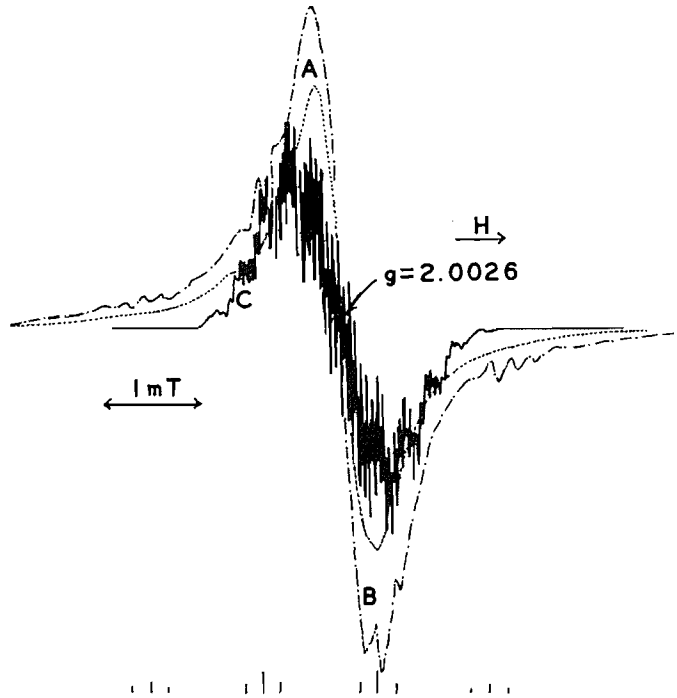

FIG. 6. The esr spectra of the $Ti(OBu)_4$ polymer to which DMPD was added at the latter stage of the polymerization. A was obtained before light illumination, B was obtained 14.4 min after beginning light illumination. The stick spectrum indicates the hf line positions due to the interaction with the $-CH_2CH_3$ group. C is a simulated spectrum of $DMPD^{\bullet+}$; for esr simulation parameters, refer to the text.

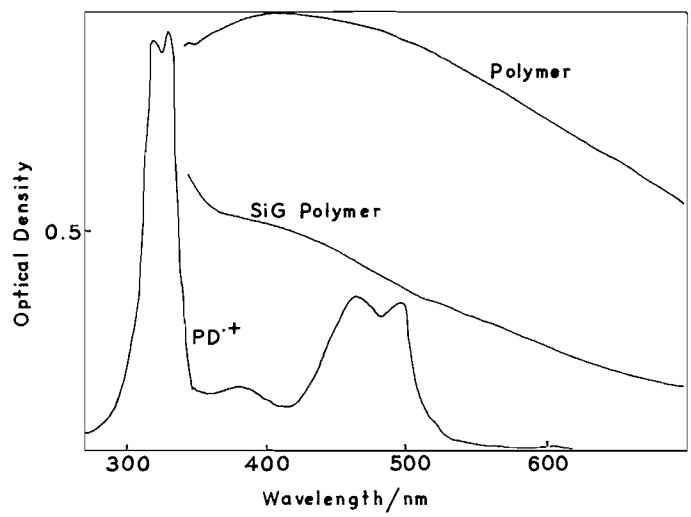

FIG. 7. The reflectance spectra of the polymer samples to which PD was added. The $PD^{\bullet+}$ curve is the transmittance spectrum of $PD^{\bullet+}$ in ref. 9, transformed to the wavelength-linear scale.

dissolved in $Ti(OBu)_4$ polymerization solution. It was expected that this polymer mixture might give the $TCNQ^{\bullet-}$ anion radical upon irradiation by visible light. The polymer mixture was washed with CCl_4 and then an esr spectrum was observed. The visible light response was strong, but there was little evidence of the formation of $TCNQ^{\bullet-}$. The observed spectra are shown in Fig. 9. The spectrum A was obtained from the sample stored in a dark place. The spectrum B was obtained after illuminating the sample for 40 min with visible light. The spectrum B is

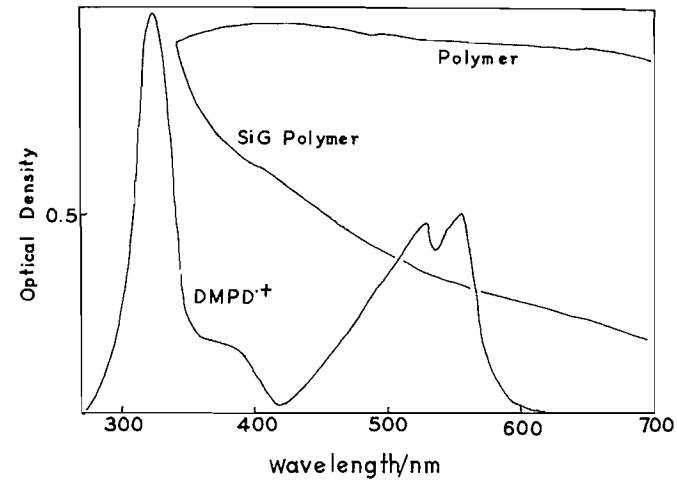

FIG. 8. The reflectance spectra of the polymer samples to which DMPD was added. The $DMPD^{\bullet+}$ curve is the transmittance spectrum of $DMPD^{\bullet+}$ in ref. 9, transformed to the wavelength-linear scale.

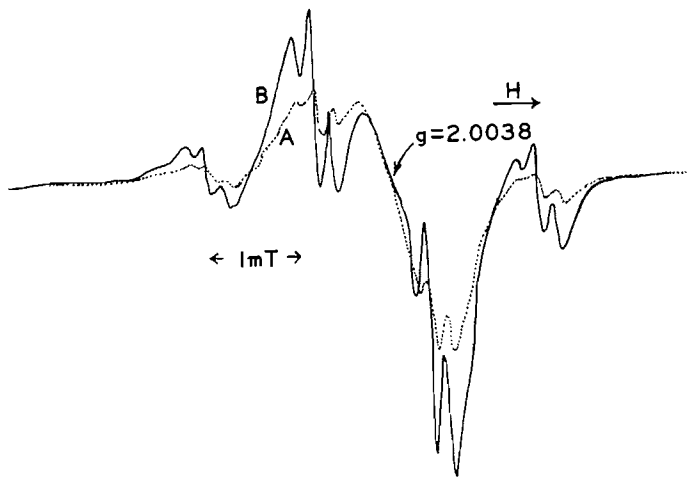

FIG. 9. The esr spectra obtained for the illumination of the polymer of $Ti(OBu)_4$ containing 1 mol% of TCNQ. A was obtained after keeping the sample in the darkness. B was obtained after illuminating the sample with visible light for 40 min. Illumination was maintained during the measurement.

composed of a broad component and an hfs component, only the latter being intensified with light. Neither A nor B can be ascribed to $TCNQ^{\bullet-}$.

Discussion

In the present work, silica gel powder was used as the initiating agent of the polymerization. Fluorescent light was used to maintain the polymerization reaction. The products obtained under the above conditions have been found to give the most light-sensitive polymer (2). The types of polymerization reaction and the structure of the reaction products have already been discussed (3–6). However, the preparation of the free-radical-type polymer in organic solvents has been carried out for the first time by the present authors. The polymer obtained in this manner is amorphous, chemical composition being approximately equal to TiO_2, and has many -Ti(=O)—O- units. In addition, some alkoxyl groups are left in the molecule (2). However, relatively less is known about the electronic states of the molecule and the behavior of the electrons photo-excited by illumination.

In the case of the polymer of $Ti(OBu)_4$ having no additive, a new esr signal is observed upon illumination with visible light (2). The spectrum is similar to the hfs component in Fig. 9. In this case, therefore,

$$\text{Polymer}\cdot \rightarrow \text{Polymer}'\cdot$$

may represent the conformation change of the radical polymer. In "Polymer·" no hfs due to $-CH_2CH_3$ is observed but in "Polymer′·" hfs due to $-CH_2CH_3$ is observed. In the case of the polymer to which TMPD is added,

$$:\text{TMPD}\text{---}\text{Polymer}\cdot \rightarrow \cdot\text{TMPD}^{+}\text{---}\text{Polymer}:^{-}$$

seems to explain the change that has occurred. A transient polarization caused by light illumination gives $TMPD^{\cdot+}$. On the contrary, when TCNQ is added, no $TCNQ^{\cdot-}$ is observed. This can be explained by the relatively large electronegativity of the polymer. In the case of $Ti(OBu)_4$ polymer to which Mn^{2+} is added, a decrease in the intensity of the esr spectrum of Mn^{2+} is observed (2). In this case,

$$Mn^{2+}\text{---}\text{Polymer}\cdot \rightarrow Mn^{3+}\text{---}\text{Polymer}:^{-}$$

is taking place. This phenomenon can also be explained by the shift of electron from Mn^{2+} to the polymer part.

The results obtained in this work can be summarized as follows. If a small amount of TMPD is added to the solution of $Ti(OBu)_4$, a $Ti(OBu)_4$ polymer with which TMPD is combined is formed. On light illumination, a polarization-type light excitation occurs, giving $TMPD^{\cdot+}-\text{Polymer}^{-}$. If kept in darkness, this polarization reverts to the original unpolarized state. In the polymer to which TMPD is added, the positive charge trapped on the polymer side can be used as an information carrier or the energy carrier of the incident light to the polymer; the light-to-electron conversion efficiency is desired to be as high as possible. Such efficiency will be improved by the presence of $TMPD^{\cdot+}$ because less chance of recombination may be expected.

In the case of PD, no presence of $PD^{\cdot+}$ was observed from the reflectance spectra, Fig. 7. However, a light-excited esr spectrum was observed, as in Fig. 5. Though some structure in the esr spectrum is found, it is not similar to the hfs of $PD^{\cdot+}$ (14, 15) or to the simulated spectrum, Fig. 5C. As $PD^{\cdot+}$ is reactive, it will only be observed while it is generated in the sample system placed in the microwave cavity. The analysis of Fig. 5B is, therefore, not easy.

In the case of DMPD, the formation of $DMPD^{\cdot+}$ cannot be concluded from the reflectance spectra in Fig. 8. Light-excited esr is found, cf. Fig. 6. The hfs in Fig. 6B is due to the coupling with the $-CH_2CH_3$ group. Since there is no analysable information except $-CH_2CH_3$ coupling, it is not possible to prove the presence of $DMPD^{\cdot+}$. According to Yao *et al.* (16), who generated $DMPD^{\cdot+}$ by an electrolytic method, the esr of $DMPD^{\cdot+}$ has many hfs lines because there are six different hfs constants, which give 1701 lines if well resolved. If each line has a line width of 0.12 mT, the entire spectrum may look like a structureless smooth spectrum. The simulated spectrum, Fig. 6C, has fine structures that may become smoothed in an experimental spectrum. If one looks at the total width of the spectrum only, B and C of Fig. 6 may be regarded as "similar" spectra. For this reason, the formation of $DMPD^{\cdot+}$ may be postulated.

1. M. IRIE. Molecular models of photoresponsiveness. *Edited by* G. Montagnoli and B. F. Erlanger. Plenum Press, New York. 1983. p. 291.
2. M. YONEMURA, T. SEKINE, and H. UEDA. Chem. Lett. 487 (1986); T. SEKINE, M. YONEMURA, and H. UEDA. Nippon Kagaku Kaishi, 605 (1985); H. UEDA, M. YONEMURA, and T. SEKINE. J. Mater. Sci. **22**, 3349 (1987).
3. D. C. BRADLEY, R. GAZE, and W. WARDLAW. J. Chem. Soc. 721 (1955); 3977 (1955); 469 (1957).
4. D. C. BRADLEY and H. HOLOWAY. Can. J. Chem. **40**, 1176 (1962).
5. D. C. BRADLEY. Coord. Chem. Rev. **2**, 299 (1967).
6. T. BOYD. J. Polym. Sci. **7**, 591 (1962).
7. J. R. BOLTON, A. CARRINGTON, and J. DOS SANTOS-VEIGA. Mol. Phys. **5**, 615 (1962).
8. H. M. MCCONNELL. J. Chem. Phys. **25**, 709 (1956).
9. D. KIVELSON. J. Chem. Phys. **33**, 1094 (1960).
10. G. E. PAKE. Paramagnetic resonance. W. A. Benjamin, Inc., New York. 1962. p. 111.
11. A. ABRAGAM and B. BLEANEY. Electron paramagnetic resonance of transition ions. Dover Publ. Inc., New York. 1986. p. 186.
12. T. SHIDA and W. H. HAMILL. J. Chem. Phys. **44**, 2369 (1966).
13. S. NAKAYAMA and K. SUZUKI. Bull. Chem. Soc. Jpn. **46**, 3694 (1973).
14. M. T. MELCHIOR and A. H. MAKI. J. Chem. Phys. **34**, 471 (1961).
15. L. H. PIETTE, P. LUDWIG, and R. N. ADAMS. Anal. Chem. **34**, 916 (1962).
16. T. YAO, S. MUSHA, and M. MUNEMORI. Chem. Lett. 939 (1974).

Can. J. Chem. Downloaded from www.nrcresearchpress.com by 112.217.228.212 on 09/07/12
For personal use only.

Laser-induced fluorescence study of the reactions of Ca with CH_3I and CF_3I in a molecular beam – gas apparatus[1]

GUO-ZHONG HE, JUE WANG, R. S. TSE,[2] AND NAN-QUAN LOU
Dalian Institute of Chemical Physics, Academia Sinica, Dalian, China

Received November 17, 1987

This paper is dedicated to Professor Charles A. McDowell on the occasion of his seventieth birthday

GHO-ZHONG HE, JUE WANG, R. S. TSE, and NAN-QUAN LOU. Can. J. Chem. **66**, 1936 (1988).

Energy partitioning of the CaI product from the Ca + CH_3I [1] and Ca + CF_3I [2] reactions was studied by laser-induced fluorescence. Product vibrational state distributions were obtained. It was also found that 19% and 16% of the exoergicity resides, respectively, in vibrational and rotational excitations of the CaI product from reaction [1], and 40% and 12%, respectively, from reaction [2]. The results are discussed in the context of various models, and product recoil momentum distributions have been estimated.

GHO-ZHONG HE, JUE WANG, R. S. TSE et NAN-QUAN LOU. Can. J. Chem. **66**, 1936 (1988).

Utilisant de la fluorescence induite au laser, on a étudié l'énergie de partition du produit CaI obtenu par les réactions Ca + CH_3I [1] et Ca + CF_3I [2]. On a obtenu les distributions des états vibrationnels des produits. On a aussi trouvé que 19% et 16% de l'«exoergicité» se retrouvent respectivement dans les excitations vibrationnelles et rotationnelles du produit CaI obtenu par la réaction [1] et 40% et 12% respectivement pour la réaction [2]. On discute des résultats dans le contexte de divers modèles et on a évalué les distributions de moments de recul des produits.

[Traduit par la revue]

Introduction

One of the major areas of interest in molecular dynamics is the study of the distribution of available energy to internal states of nascent reaction products by molecular beam techniques as well as by the laser-induced fluorescence (LIF) method.

In the past decade or so, the exoergic reactions of alkalis or alkaline earth metal atoms with iodides, CH_3I and CF_3I in particular, have received extensive interest since the first such experiments by Herschbach *et al.* (1). For example, Berstein *et al.* (2) paid special attention to the prototype "rebound" reaction K + $CH_3I \rightarrow$ KI + CH_3. For the corresponding K + $CF_3I \rightarrow$ KI + CF_3 reaction, the "dual mode" mechanism was first postulated by Brooks *et al.* (3). Subsequently Zare *et al.* (4, 5) reported the vibrational states analysis of unrelaxed BaI from the reaction Ba + CF_3I using the LIF method. In addition, Lin *et al.* (6) deduced BaI recoil energy distributions and angular distributions for the Ba + CH_3I, Ca + CH_3I, and Ba + CF_3I reactions using a molecular beam apparatus. In this paper we present a beam–gas experiment on the exothermic reactions:

[1] Ca + $CH_3I \rightarrow$ CaI + CH_3

[2] Ca + $CF_3I \rightarrow$ CaI + CF_3

for which the vibrational populations of the nascent product CaI were probed by means of LIF.

Experimental

The beam–gas apparatus employed is shown schematically in Fig. 1. A calcium beam effuses from an orifice (0.8 mm) on the top of a cylindrical crucible, is heated to 1050 K by thermal radiation from a sleeved graphite resistively heated tube, and passes through a slit (2.5 mm) into the scattering chamber which is filled with CH_3I (or CF_3I) at a pressure of (1–20) × 10^{-5} Torr. The pulsed laser beam from a Nd:YAG laser-pumped tunable dye laser (Quanta Ray DCR-1 and PDL) intersects the Ca beam perpendicularly in the center of the scattering chamber.

The dye laser wavelength was scanned to generate an excitation spectrum for the $A^2\Pi$–$X^2\Sigma^+$ band system of the CaI product. The linewidth of the dye laser beam was about 0.2 Å. The fluorescence was detected by a photomultiplier (R943). A PAR model 162/163 boxcar integrator was used to amplify and average the fluorescence signals. The output of the boxcar was fed to a stripchart recorder.

Results and discussions

A. Excitation spectra

The laser excitation spectrum of the CaI $A^2\Pi_{3/2}$–$X^2\Sigma^+$ band system in the region 6337–6395 Å was used to determine the internal state distribution of the reaction products. Figure 2 shows the variation of total fluorescence intensity with excitation wavelength for the CaI $\Delta V = 0$ sequence of the Ca + CH_3I and Ca + CF_3I reactions.

The CaI $A^2\Pi_{3/2}$–$X^2\Sigma^+$ transition belongs to the $^2\Pi(a)$–$^2\Sigma$ case. Neglecting the Λ-type doubling in the $^2\Pi$ state and the spin doubling in the $^2\Sigma$ state, one can obtain the formulas for the branches $P_2(J)$, $Q_2(J)$, $P_{21}(J)$, $R_2(J)$, $Q_{21}(J)$, and $R_{21}(J)$ (7).

In the CaI $A^2\Pi_{3/2}$–$X^2\Sigma^+$ band system, bands are formed in the Q_2 and P_{21} branches at almost the same frequency and value of J (7):

$$J_{\text{head}}^{Q_2+P_{21}} = \frac{(2B'' - B_{\text{eff}}^{(2)})}{2(B_{\text{eff}}^{(2)} - B'')}$$

Bands in the P_2 branch occur at

$$J_{\text{head}}^{P_2} = \frac{(B_{\text{eff}}^{(2)} + 2B'')}{2(B_{\text{eff}}^{(2)} - B'')}$$

The (0,0) band of the $A^2\Pi_{3/2}$–$X^2\Sigma^+$ transition occurs at $J_{\text{head}}^{Q_2+P_{21}} = 34$ and $J_{\text{head}}^{P_2} = 104$. Therefore, the presence of the P_2 branch implies that high rotational levels are appreciably populated.

For reaction [1], the CaI vibrational population peaks at $V = 2$. The presence of the P_2 heads of the (0,0), (1,1), (2,2), (3,3), and (4,4) bands indicates that substantial rotational excitation of the product CaI occurs.

[1]A preliminary report of this work was presented at the IXth International Symposium on Gas Kinetics, Bordeaux, 1986.

[2]Visiting scientist from the Department of Chemistry, the University of Hong Kong, Pokfulam Road, Hong Kong.

Printed in Canada / Imprimé au Canada

Can. J. Chem. Downloaded from www.nrcresearchpress.com by 112.217.228.212 on 09/07/12
For personal use only.

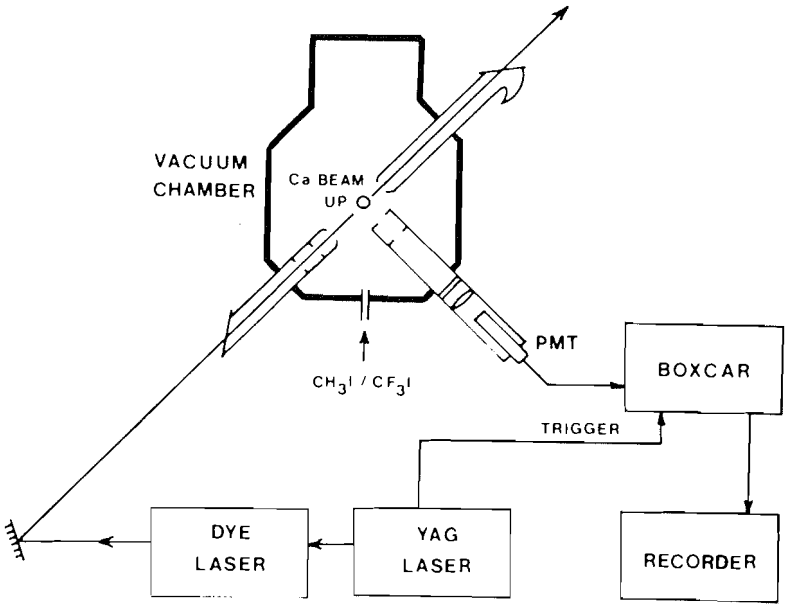

FIG. 1. Schematic diagram of the apparatus.

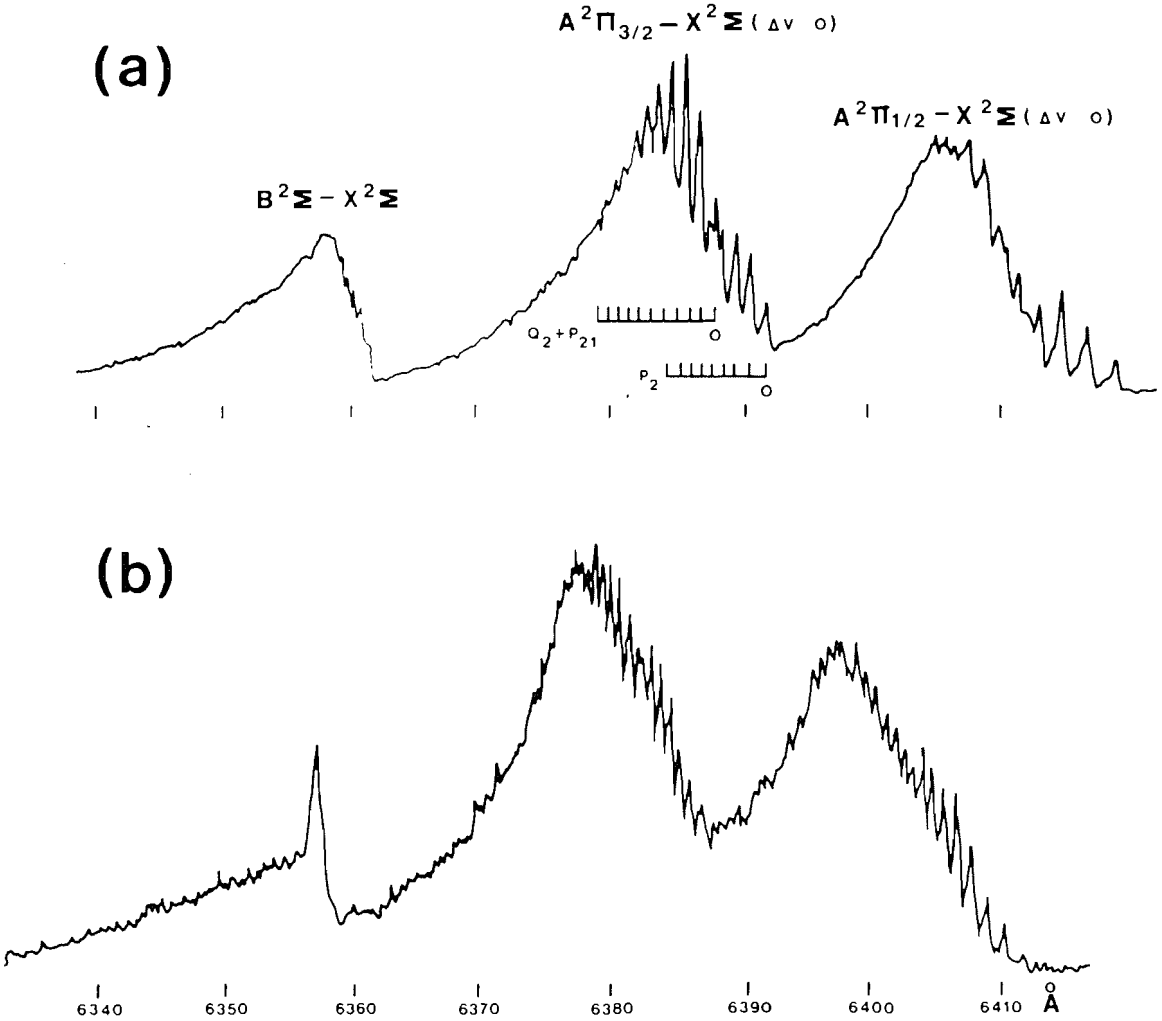

FIG. 2. LIF excitation spectra of CaI from (*a*) Ca + CH_3I and (*b*) Ca + CF_3I.

Can. J. Chem. Downloaded from www.nrcresearchpress.com by 112.217.228.212 on 09/07/12
For personal use only.

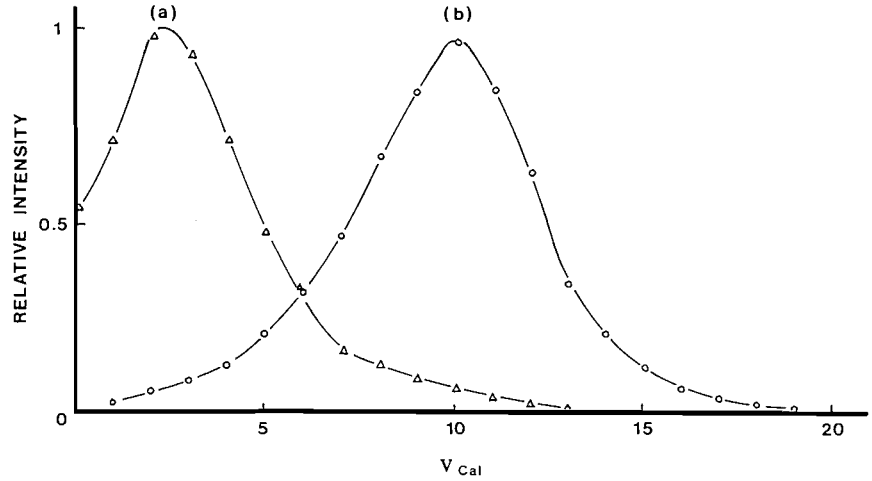

FIG. 3. Vibrational state distributions of CaI formed in the reactions (*a*) Ca + CH_3I and (*b*) Ca + CF_3I.

For reaction [2], no P_2 heads of the above bands are observed, but instead the P_2 heads of (8,8), (9,9), (10,10), (11,11) bands were present and the peak of CaI vibrational population is located at $V = 10$.

B. Computer simulation of the excitation spectrum

In order to make the quantitative estimations of the vibrational and rotational energy distributions from the excitation spectrum, computer simulation was carried out. A calculated excitation spectrum was constructed by assuming a population for the vibrational and rotational states and by convoluting it with the laser bandwidth function. The formula used for calculating the total fluorescence is as follows (8):

$$I(\nu_1) \propto \sum_{V'J'V''J''} \rho(\nu_1) N_{V''} \times P(J|V) \times Q_{V''V''} \frac{S_{J''J''}}{(2J'' + 1)}$$

where ν_1 is the transition frequency; $\rho(\nu_1)$ is the laser intensity; $Q_{V''V''}$ and $S_{J''J''}$ are the Franck–Condon (F–C) factor and the rotational line strength of the excitation transition, respectively; $N_{V''}$ is the vibrational population of the CaI ground state. The rotational population $P(J|V)$ is expressed as

$$P(J|V) = C_V \times P^0(J|V) \exp(-f_R \times \theta_R^V/(1 - f_V))$$

where C_V is a normalization factor, f_V, f_R are the fractions of total available energy going to diatomic product vibration and rotation, respectively, and θ_R^V is an adjustible parameter. The "prior" distribution $P^0(J|V)$ is given as (9):

$$P^0(J|V) = (2J + 1) \times (1 - f_V - f_R)$$

where we assume that the concomitant product CH_3 (or CF_3) is a nonlinear rotor in harmonic oscillations in six vibrational modes.

The laser intensity $\rho(\nu_1)$ is assumed to be proportional to $f_D(\nu_1)$, the Gaussian line profile, where (10)

$$f_D(\nu_1) = \frac{2 \ln \sqrt{2}}{\sqrt{\pi} \times \Delta\nu_D} \exp\left[-\left(\frac{2(\nu - \nu_0)}{\Delta\nu_D}\right)^2 \ln 2 \right]$$

and $\Delta\nu_D = 0.2$ Å, the laser linewidth.

The calculated vibrational population distributions $N_{V''}$ of the CaI ground state are plotted as a function of vibrational quantum number for reaction [1] and reaction [2] in Fig. 3.

Table 1 lists the spectroscopic constants used. Reisner *et al.* (11) determined these constants for CaI from spectra of the (0,0) and (1,1) bands. However, the vibrational levels observed in the experiments reported here are much higher. In order to have a satisfactory fit to the experimental data, some of the constants had to be modified a little for use in the simulation. Both the constants reported in ref. 11 and the constants actually used in the simulation are listed in Table 1. The F–C factors calculated from the R.K.R. method are listed in Table 2.

TABLE 1. Spectroscopic constants (in cm^{-1}) used in the simulation of CaI LIF excitation spectra

	A		*X* from ref. 11 and used in this work
State	From ref. 11	Used in this work	
T_e	15624.67	15624.67	0
W_e	241.19	241.32	238.75
W_eX_e	0.53	0.665	0.62789
B_e	0.07046	0.07022	0.0693254
α_e	0.000215	0.000262	0.000264
A_e	45.8968	45.8968	

The total available energy, E_{tot} for CaI product excitation has been calculated as follows (R = CH_3 or CF_3):

$$E_{tot} = D_0^0(\text{Ca—I}) - D_0^0(\text{I—R}) + E_{int}(\text{RI}) + E_t(\text{reactants})$$

The translational energies of the reactants are evaluated according to

$$E_t = (3/2)\mu(kT_1/M_1 + kT_1/M_2)$$

where M and T are respectively the molecular weight and the thermal distribution temperature of the reagents, subscripts 1 and 2 denote respectively the Ca atom and the CH_3I (or CF_3I) molecule, μ is the reduced mass of the reagents, k is the Boltzmann constant. The internal energy of the reagents E_{int} equals $(3/2)RT$, neglecting the vibrational excitation of CH_3I (or CF_3I). The bond dissociation energies are $D_0^0(\text{Ca—I}) = 68$ kcal/mol, $D_0^0(\text{I—CH}_3) = 56$ kcal/mol, and $D_0^0(\text{I—CF}_3) = 53$ kcal/mol.

Using the above values, computer simulations of the observed LIF spectra reveal that the average values $\langle f_V \rangle$ and $\langle f_R \rangle$ are 19% and 16% for reaction [1], 40% and 12% for reaction [2],

Can. J. Chem. Downloaded from www.nrcresearchpress.com by 112.217.228.212 on 09/07/12
For personal use only.

TABLE 2. Frank–Condon factors used in the simulation of CaI LIF excitation spectrum

V	F–C
0	0.90
1	0.83
2	0.77
3	0.71
4	0.66
5	0.61
6	0.57
7	0.51
8	0.47
9	0.43
10	0.39
11	0.35
12	0.32
13	0.29
14	0.26
15	0.23
16	0.21

TABLE 3. $\langle f_V \rangle$ for the reactions Ba (or Ca) + CH_3(or CF_3)I

	$\langle f_V \rangle$	
M	CH_3I	CF_3I
Ba	41%[a]	69%[a]
Ca	19%	40%

[a]From ref. 12.

respectively. The $\langle f_V \rangle$ values for the four reactions Ca(or Ba) + CH_3(or CF_3)I are compared in Table 3. $\langle f_V \rangle$ increases as the atomic mass of the alkaline earth metal atoms increases. $\langle f_V \rangle$ also increases as CH_3I changes to CF_3I.

C. Comparison between the reactions Ca + CH_3I and K + CH_3I

Originally, Herschbach (13) proposed a simple model — the impulsive photodissociation (IP) model — to describe the alkali atom + alkyl iodide reaction. He proposed that all particles had come essentially to rest before the electron jumped, whereupon repulsive energy of magnitude R was abruptly released between the iodine atom and the adjacent carbon atom. Now, we can use this model to describe the alkaline earth atom + CH_3I reaction and make a comparison between this reaction and the KI + CH_3I reaction.

Let M denote the metal atom. The product recoil momentum p_{MI}, recoil velocity u_{MI}, and relative translational energy E'_{tr} are determined from momentum conservation:

$$p_{MI} = m_{MI}u_{MI} = (2\mu_{I,CH_3}R)^{1/2} = (2\mu_{MI,CH_3}E'_{tr})^{1/2}$$

$$p'_{MI} = p_{MI}/h = 0.725(\mu_{MI,CH_3}E'_{tr})^{1/2}\ \text{Å}^{-1}$$

where R = EA(I) − D(I—CH_3) − EA(CH_3I), and μ_{I,CH_3} denotes the reduced mass of I and CH_3.

At the impulsive limit, $m_{MI}u_{MI}$ will not depend on the mass of M but only on the reduced mass of I and CH_3 and the repulsive energy. Using the data of the vibrational energy distribution of the product CaI of the Ca + CH_3I reaction

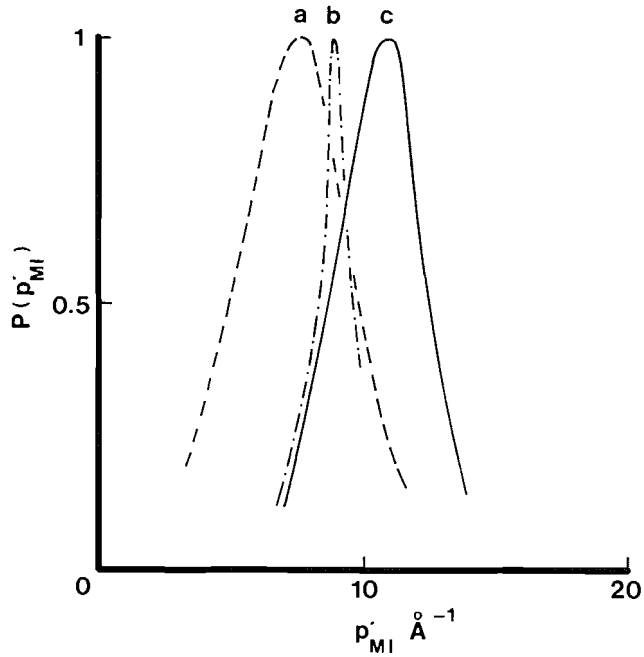

FIG. 4. Product recoil momentum distribution for the Ca (or K) + CH_3I reaction. (*a*) Ca + CH_3I (6), (*b*) Ca + CH_3I (this work), (*c*) K + CH_3I (13).

obtained here, and the following energy relationship

$$E'_{tr} = E_{tot} - E'_R(\text{CaI}) - E'_{int}(CH_3) - E_V'(\text{CaI})$$

where E'_R(CaI) = 1.6 kcal/mol, $E'_{int}(CH_3)$ = 0.9 kcal/mol, and E_{tot} = 15.4 kcal/mol, we can then obtain the distribution $P(p'_{MI})$ and find that the peak of $P(p'_{CaI})$ lies at about $p'_{CaI} = 8\ \text{Å}^{-1}$.

For comparison, we can use the E'_{tr} data from Lin *et al.* (6) to calculate $P(p'_{CaI})$ of the Ca + CH_3I reaction and take Hershbach's data of $P(p'_{KI})$ for the reaction K + CH_3I (13). It turns out that the peak of $P(p'_{CaI})$ lies (6) at 7.5 Å^{-1}, in good agreement with the present value but the peak of $P(p'_{KI})$ lies at about 11 Å^{-1}; note that the Ca and K masses are not very different. These values are shown in Fig. 4.

D. The Ba(or Ca) + CH_3I reactions

Herm's group reported (6) measurements of angular distributions of reactive scattering from crossed beam reactions between alkaline earth Ba or Ca atoms and CH_3I. Their results showed that the BaI(or CaI) + CH_3 products from Ba(or Ca) + CH_3I scattered predominantly backward in the center-of-mass system. The BaI product angular distribution was broader than that of CaI. Using Hershbach's IP model, we can obtain the peak positions of the $P(p'_{MI})$ values. These lie at 8.5 and 7.5 Å^{-1} for BaI and CaI, respectively. The relative atomic mass of the attacking alkaline earth atom in these reactions varies from 137 to 40, and the reactive exoergicity varies from 18.6 kcal/mol for Ba + CH_3I to 12 kcal/mol for Ca + CH_3I, yet the shape and position of product momentum distribution are hardly changed, as shown in Fig. 5.

E. The reactions Ca + CH_3I(or CF_3I) → CaI + CH_3(or CF_3)

In the Ca + CH_3I reaction, for example, the repulsive energy release is a normal result of the electron-jump process. This repulsion arises because the electron from the metal atom Ca enters a strongly antibonding orbital with a node between the carbon atom and the iodine ion which is ejected. We expect that

Can. J. Chem. Downloaded from www.nrcresearchpress.com by 112.217.228.212 on 09/07/12
For personal use only.

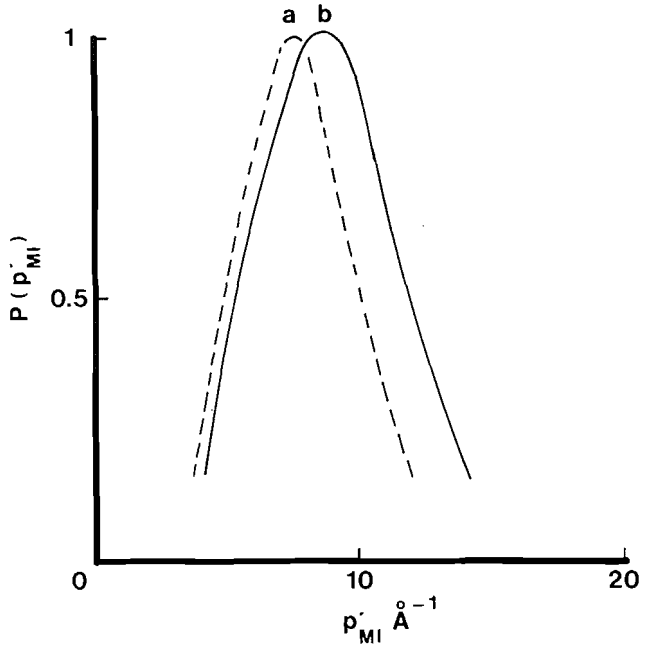

FIG. 5. Product recoil momentum distribution for the Ca (or Ba) + CH_3I reaction. (*a*) Ca + CH_3I (6), (*b*) Ba + CH_3I (6).

the repulsive energy of magnitude R is abruptly released between the iodine atom and the carbon atom. If we use the DIPR (direct interaction with product repulsion) model, postulated by Kuntz *et al.* (14), to describe the reactions studied here, the fractions of energy going into various CaI modes can be calculated for different values of R.

For simplicity, let A, B, C denote respectively the Ca atom, the iodine ion, and the alkyl group (or CF_3). Suppose a decaying force, $F(t)$, acts along the original direction of the B—C axis and decreases monotonically to zero. Then

$$F(t) = \pm ma \exp(-ct)$$

where m is the mass of CH_3 (or CF_3); a the acceleration of CH_3 (or CF_3) due to the force F at $t = 0$; and c is a constant which controls the rate of attenuation of the force on CH_3 (or CF_3). Then, the model can be made to take into account an attractive force between Ca and I atoms using an appropriate adjustment in the constant c. Table 4 shows the results of such calculation. The measured values are certainly within the range of calculated values.

F. Surprisal analysis

Dynamical properties for the present reactions may be deduced through a surprisal plot (9). The surprisal $I_n(V|E)$ is represented as $I(V|E) = \ln[P(V|E)/P_n^0(V|E)]$. Here $P(V|E)$ and $P_n^0(V|E)$ are the experimental probability and prior probability of producing CaI in the V vibrational state when the total available energy is E. One might get information concerning internal excitation of the CH_3 (or CF_3) radical employing four types of prior distribution. The product CH_3 (or CF_3) radical is assumed to be a structureless atom in model 1, a nonlinear rotor without vibrational excitation in model 2, a harmonic oscillator with six vibrational modes without rotation in model 3; and a nonlinear rotor in harmonic oscillation with six vibrational modes in model 4. The prior distribution

TABLE 4. Results of DIPR model calculations[a]

(*a*) For Ca + $CH_3I \rightarrow$ CaI + CH_3, $g/c = 10^{-6}$

R (eV)	$\langle f_V \rangle$	$\langle f_T \rangle$	$\langle f_R \rangle$
0.5	0.165	0.735	0.10
0.4	0.192	0.703	0.105
0.3	0.262	0.573	0.164

(*b*) For Ca + $CF_3I \rightarrow$ CaI + CF_3, $g/c = 8.3 \times 10^{-6}$

R (eV)	$\langle f_V \rangle$	$\langle f_T \rangle$	$\langle f_R \rangle$
0.5	0.273	0.624	0.102
0.4	0.356	0.524	0.119
0.3	0.459	0.419	0.122

[a] $g = a/c$ is the change in the x component of the velocity of CH_3 (or CF_3) due to the repulsive force $F(t)$ operating from $t = 0$ to $t = \infty$. $\langle f_T \rangle$ is the fraction of total available energy going to product relative translational energy. Please refer to discussion section E for definitions of a and c.

$P_n^0(V|E)$ for these four models are:

Model 1: $P_1^0(V|E) \propto (E - E_V)^{1.5}$

Model 2: $P_2^0(V|E) \propto (E - E_V)^3$

Model 3: $P_3^0(V|E) \propto (E - E_V)^{7.5}$

Model 4: $P_4^0(V|E) \propto (E - E_V)^9$

The surprisal plots of $I_n(V)$ vs. V ($n = 1, 2, 3, 4$) of these four models show that the I_3 and I_4 plots are almost linear functions of V, but the I_1 and I_2 plots are obviously nonlinear. This feature implies that the vibrational excitation of CH_3 (or CF_3) plays an important role in the dynamics.

G. Rotational excitation of the product CaI

We have obtained some information about the rotational excitation of the product CaI, as mentioned above. Now we can make a simple estimate of the fraction of exoergicity going into product rotational excitation by considering angular momentum conservation when the Ca atom approaches the I atom end of the ICH_3 molecule. For the reaction Ca + $CH_3I \rightarrow$ CaI + CH_3, the reduced masses of pre- and post-collision of this reaction system are $\mu = 31.2$ and $\mu = 13.8$, respectively. A crude estimate of the upper limit of the rotational energy of the product CaI can be made by supposing that this reaction belongs to the H + HL → HH + L mass combination, where H denotes the heavy atom and L denotes the light atom. Then, the reactants' orbital angular momentum L is equal to the product angular momentum, and $L = J$, where $L = \mu_{Ca,CH_3I} V_{rel} I_b$ ($= 15 \times 10^{-26}$ g cm^2/s). The rotational inertia of CaI, I_b, is about 4×10^{-38} g cm^2. The rotational energy

$$E_R' = J'^2/(2I_b) = L^2/(2I_b)$$

works out to be 0.17 eV, which is about 22% of the total available energy, in rough agreement with the measured values.

1. D. R. HERSCHBACH. Faraday Discuss. Chem. Soc. **33**, 149 (1962).
2. R. B. BERSTEIN and A. M. RULIS. Faraday Discuss. Chem. Soc. **55**, 293 (1973).
3. P. R. BROOKS. Faraday Discuss. Chem. Soc. **55**, 299 (1973).

Can. J. Chem. Downloaded from www.nrcresearchpress.com by 112.217.228.212 on 09/07/12
For personal use only.

4. G. P. SMITH, J. C. WHITEHEAD, and R. N. ZARE. J. Chem. Phys. **67**, 1912 (1977).
5. J. ALLISON, M. A. JOHNSON, and R. N. ZARE. Faraday Discuss. Chem. Soc. **67**, 124 (1979).
6. S. M. LIN, C. A. MIMS, and R. R. HERM. J. Phys. Chem. **77**, 569 (1973).
7. G. HERZBERG. Molecular spectra and molecular structure. Vol. 1. Spectra of diatomic molecules. van Nostrand. 1950. pp. 257–264.
8. W. SCHMIDT, A. SIEGEL, and A. SCHULTZ. Chem. Phys. **16**, 161 (1976).
9. T. MUNAKATA, Y. MATSUMI, and T. KASUYA. J. Chem. Phys. **79**, 1698 (1983).
10. W. DEMTRÖDER. Laser spectroscopy. Basic concepts and instrumentation. Springer-Verlag. 1982.
11. D. E. REISNER, P. F. BERNATH, and R. W. FIELD. J. Mol. Spectrosc. **89**, 107 (1981).
12. M. R. LEVY. Prog. Reaction Kinet. **10**, 1 (1979).
13. D. R. HERSCHBACH. Faraday Discuss. Chem. Soc. **55**, 233 (1973).
14. P. J. KUNTZ, M. H. MOK, and J. C. POLANYI. J. Chem. Phys. **50**, 4623 (1969).

Can. J. Chem. Downloaded from www.nrcresearchpress.com by 112.217.228.212 on 09/07/12
For personal use only.

High-resolution solid-state NMR investigation of the nature of the interaction between organic substrates and the zeolite ZSM-5 lattice

C. A. FYFE,[1] H. STROBL, H. GIES, AND G. T. KOKOTAILO

Department of Chemistry, University of British Columbia, Vancouver, B.C., Canada V6T 1Y6

Received March 11, 1988

This paper is dedicated to Professor Charles A. McDowell on the occasion of his seventieth birthday

C. A. FYFE, H. STROBL, H. GIES, and G. T. KOKOTAILO. Can. J. Chem. **66**, 1942 (1988).

The compounds *p*-xylene, *p*-chlorotoluene, and *p*-dichlorobenzene induce essentially identical changes in the ^{29}Si MAS NMR spectrum of zeolite ZSM-5, indicating that the major contribution to the induced phase change of the lattice structure in these cases is the size and shape of the sorbed organic molecules. Based on these results, *p*-dichlorobenzene may be used as a model system in future diffraction studies of the sorbate/lattice structure greatly facilitating these investigations.

C. A. FYFE, H. STROBL, H. GIES, et G. T. KOKOTAILO. Can. J. Chem. **66**, 1942 (1988).

Les changements induits par le *p*-xylène, le *p*-chlorotoluène et le *p*-dichlorobenzène dans les spectres rmn MAS du ^{29}Si du zéolite ZSM-5 sont essentiellement les mêmes; ces résultats indiquent que, dans ces cas, la contribution majeure au changement de phase induit dans la structure de réseau provient de la grosseur et de la forme des molécules organiques qui sont adsorbées. Sur la base de ces résultats, le *p*-dichlorobenzène peut être utilisé comme système modèle dans de futures études de diffraction de la structure du sorbate/réseau; cette possibilité facilitera beaucoup ces études.

[Traduit par la revue]

Can. J. Chem. Downloaded from www.nrcresearchpress.com by 112.217.228.212 on 09/07/12
For personal use only.

Introduction

Zeolites are porous aluminosilicates widely used in industrial applications as catalysts, ion exchange resins, and molecular sieves (1, 2). Formally, they can be represented as being derived from silica (SiO_2) by the replacement of SiO_4^{4-} tetrahedra by AlO_4^{5-} tetrahedra and described by the general oxide formula [1].

[1] $M_X(AlO_2)_X(SiO_2)_Y \cdot nH_2O$

Because of the difference in atomic charge between Al and Si, extra-lattice cations (M) must be present to preserve electrical neutrality, a single positive charge being needed for each (AlO_2) unit present. In general, these cations may be ion exchanged and in addition, water of hydration is usually present inside the lattice structure.

The size and shape selectivities of zeolites come from their unique framework structures, in general formed from open arrangements of the AlO_4^{5-} and SiO_4^{4-} tetrahedra linked through common oxygen atoms (the Al and Si atoms are often referred to as T atoms), giving lattice structures often containing both channels and cavities or cages which give a selectivity in the sorption of different organic molecules.

Although many of the lattice structures of zeolites have a high degree of symmetry, there are severe problems in their determination by diffraction techniques, even in the absence of organic sorbates. Thus, although they are highly crystalline materials, they are usually microcrystalline with particle dimensions of the order of microns, often precluding the use of single-crystal X-ray diffraction techniques and less informative powder diffraction data must be used.[2] Further complicating the situation is the fact that Si and Al are adjacent in the periodic table and have almost identical X-ray scattering factors, making it difficult to distinguish them, particularly if their distribution throughout the lattice is not ordered as is most often the case.

In recent years, high-resolution solid-state NMR has developed as a complementary technique to diffraction studies for the investigation of zeolite lattice structures (4). In low Si/Al ratio materials, ^{29}Si MAS NMR spectra are obtained which reflect the local environments around the silicon nuclei, yield the relative proportions of the five possible local orderings Si[4Al], Si[3Al,Si], Si[2Al,2Si], Si[Al,3Si], and Si[4Si] which are present and hence the distribution, on average, of silicon and aluminum throughout the lattice structure (4, 5).

In completely siliceous systems, only the Si[4Si] local environment is present and the spectra now exhibit very sharp resonances whose numbers and relative intensities reflect directly the numbers and relative intensities of the crystallographically inequivalent sites in the unit cell (6). These spectra are very sensitive probes of the degree and nature of the local ordering present and complement the diffraction-derived information on the long range periodicity of the lattice. They have been used to probe the uniqueness of zeolite structures, the effect of distortions from ideal symmetry, and the effects of temperature and sorbed organic molecules. In general, they are more sensitive to small changes in structure than the diffraction data which reflects the long range periodicity of the lattice although the latter technique must ultimately be used for direct structure determination. Particular attention has been paid to the changes in lattice structure induced by the presence of organic molecules and/or elevated temperatures for zeolite ZSM-5 (7).

ZSM-5, Fig. 1*B*, is the best known of a whole family of lattice structures based on the pentasil unit (Fig. 1*A*), and has unique and highly selective sorptive and catalytic properties (8). By preparing a very highly crystalline (as judged by NMR and XRD data), very highly siliceous sample of ZSM-5 and careful optimization of the experimental parameters of the MAS NMR experiment we have recently obtained ultra-high resolution ^{29}Si MAS NMR spectra in which 21 or 22 of the 24 lattice sites in the monoclinic room temperature form can be resolved, unambiguously confirming the proposed structure (9). Using this material we have recently confirmed and quantified earlier observations that elevated temperatures and sorbed organic molecules or combinations of these induce a change in the lattice structure

[1]Author to whom correspondence should be addressed.

[2]Recent work using a synchrotron X-ray source may make it possible to work with much smaller crystals although no published structures are available to date (3).

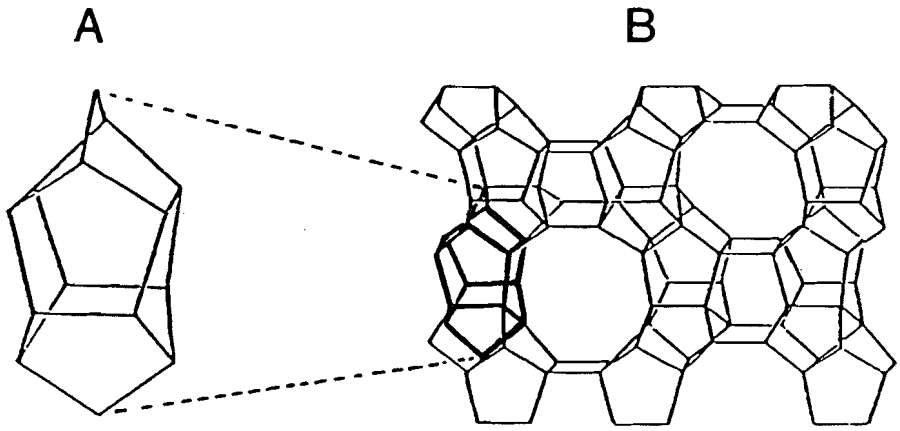

FIG. 1. (*A*) The pentasil building unit; (*B*) lattice structure of zeolite ZSM-5 (after ref. 8).

from monoclinic to a higher symmetry orthorhombic form. In the cases of *p*-xylene and acetylacetone, complete phase diagrams could be obtained by the NMR technique (10).

In the present work, we further investigate these changes for a series of carefully selected organic sorbates in an attempt to determine the nature of the sorbate/lattice interactions which induce the change in structure. In addition, it was hoped that the work would provide an optimal model system for both single-crystal and powder synchroton X-ray diffraction studies of the sorbate/lattice combination which would subsequently yield the geometric relationship for the guest molecule and host lattice directly, of considerable interest for the catalytic and sieving properties of this system. The present paper provides the justification for these investigations.

Experimental

High resolution ^{29}Si solid state MAS NMR spectra were obtained at 79.6 MHz using Bruker WH400 and MSL400 spectrometers with a home-built MAS NMR probe. Samples of *ca.* 400 μL volume were spun at 3.5 kHz in 9 mm o.d. cylindrical Torlon spinners in a modified version of the stator design of Wind. Temperatures are considered accurate to within ±2°C. There was no improvement in resolution when proton decoupling was used and all the spectra presented were recorded without decoupling. Powder XRD patterns were obtained using a Phillips powder X-ray diffractometer. The sample of XSM-5 was synthesized by conventional hydrothermal techniques and dealuminated as previously described (6).

Results and discussion

Figure 2 shows the effect of several different sorbed organic molecules on the ^{29}Si MAS NMR spectrum of zeolite ZSM-5. The spectrum of ZSM-5 with no sorbed organic (Fig. 2*A*) exhibits extremely high resolution ($\Delta V_{1/2} < 0{\cdot}1$ ppm) indicating that the sample is both very highly siliceous and very highly ordered. The spectrum can be deconvoluted in terms of 24 resonances of equal intensity, of which 22 are clearly resolved, confirming in general the proposed monoclinic symmetry with 24 T sites in the unit cell. In general, this high resolution is maintained in the presence of sorbed organic molecules, indicating that the highly crystalline nature of the sample is preserved. The spectra reflect a discrete change to new structures where 12 T sites are observed in the case of *p*-xylene characteristic of orthorhombic symmetry but where 24 T sites are still present for other sorbates (acetylacetone, pyridine). At elevated temperatures, 12 T sites are observed for all of the sorbates, indicating

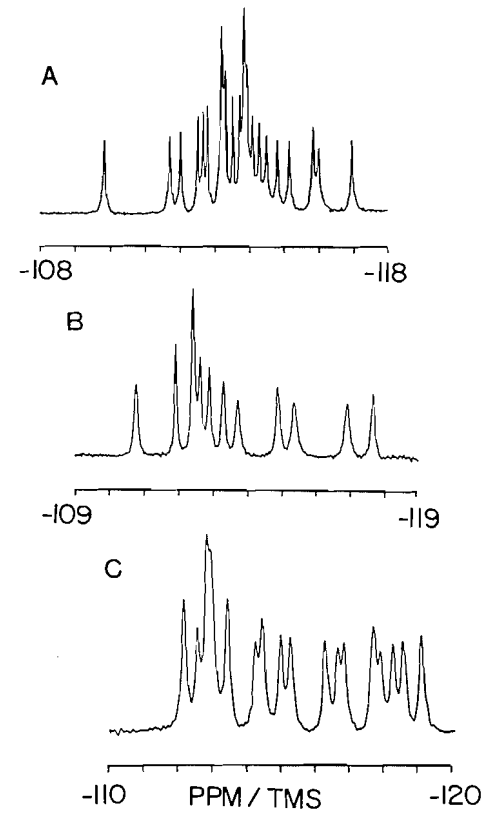

FIG. 2. ^{29}Si MAS NMR spectra obtained at 79.6 MHz of highly siliceous ZSM-5; (*A*) without sorbed organic; (*B*) with 10 μL p-xylene/250 mg zeolite; (*C*) with 35 μL pyridine/250 mg zeolite.

orthorhombic symmetry at least on the NMR timescale which, in this case, since it would involve averaging of chemical shifts would be at kHz frequencies. That the spectra reflect changes in the lattice is confirmed by powder X-ray diffraction measurements which detect changes in the lattice dimensions and, in some cases, changes in the lattice symmetry. The changes in the ^{29}Si MAS NMR spectra are quite reproducible and reversible on removal of the sorbate. More importantly, as can be seen from Fig. 2, they reflect in a unique way the *nature* of the organic molecule present, different sorbates giving quite different and characteristic spectra. ^{29}Si MAS NMR shifts are known to be affected by the local geometry of the Si atom, but it is also

Can. J. Chem. Downloaded from www.nrcresearchpress.com by 112.217.228.212 on 09/07/12
For personal use only.

possible that there are effects due to specific electronic interactions, dipolar interactions, or changes in local dielectric. The sieving properties of zeolites are most often discussed in terms of the size and shape of the organic molecules but this may not be directly reflected in the ^{29}Si MAS NMR spectra.

We have attempted to check this by investigating a series of organic sorbates of identical shape and size but differing in other chemical and physical properties. Thus, there is considerable evidence from physical organic chemistry that methyl groups and chlorine atoms have identical steric effects and this substitution can be used to eliminate this factor while probing other (mainly electronic) effects in reaction processes. In the present work, we have used this substitution to generate a series of organic sorbates of identical size and shape but differing in other properties to see if they produced the same changes in the ^{29}Si MAS NMR spectra. The molecules chosen for study were *p*-xylene **1**, *p*-chlorotoluene **2**, and *p*-dichlorobenzene **3**.

Figure 3 shows the limiting spectra obtained from the three sorbates, which in all three cases was reached at a loading of approximately 10 μL per 250 mg of zeolite. The similarity between all the spectra is remarkable, clearly indicating that the size/shape characteristics of the organic molecule are the main factors involved in the sorbate/lattice interactions. The fact that **2**, which has a net dipole, yields an identical spectrum to **1** and **3** which do not, indicates that this property is not an important factor in the interaction for these systems. In addition, all three spectra are characteristic of the orthorhombic form perhaps suggesting that the spectra reflect the lattice symmetry rather than that of the aggregate of the lattice plus the sorbed organics as **2** has lower molecular symmetry than the others.

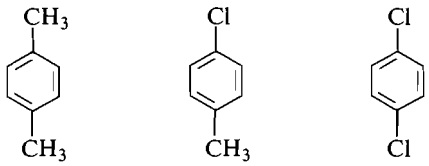

1 **2** **3**

The similarities are even more striking when the detailed behaviour of the systems in terms of concentration and temperature is investigated. Figure 4 shows the complete three-dimensional phase diagrams for both *p*-xylene and *p*-dichlorobenzene where the "in-plane" axes are changes in temperature and concentration while the vertical axis indicates the percentage of orthorhombic form present for a given combination of temperature and sorbate concentration. Thus the curve from left to right at the front of the diagrams shows the effect of adding increasing amounts of organic sorbate at ambient temperature (293 K) which is to induce a smooth change from monoclinic to orthorhombic symmetry. At intermediate concentrations both forms are present and the sharpness of all of the resonances indicates that crystallinity is maintained throughout the whole sample at all times. The other curves indicated from left to right delineate this transition at different temperatures. The second set of curves, from front to back of the diagram, describe the transition as a function of temperature at a fixed concentration of organic sorbate. The behaviour in both cases is identical in all important aspects, confirming the nature of the interaction as being primarily based on the size and shape of the organic molecule and presumably involving mainly Van der Waals interactions. It should be noted that the above molecules contain no strong donor base sites such as the aza-nitrogen in pyridine or the hydroxyl group in phenol and can not be used to

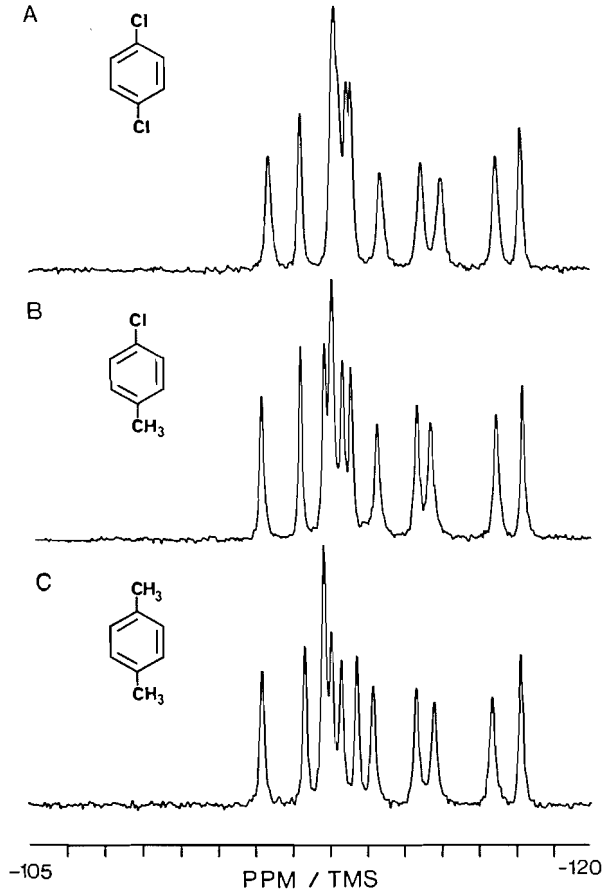

FIG. 3. ^{29}Si MAS NMR spectra obtained at 79.6 MHz of highly siliceous ZSM-5 with (*A*) *p*-xylene (10 μL/250 mg zeolite); (*B*) *p*-chlorotoluene (10 μL/250 mg zeolite); (*C*) *p*-dichlorobenzene (10 mg/250 mg zeolite).

evaluate the possible involvement of such functionalities in specific bonding interactions. However, the above conclusions should apply to all hydrocarbon systems, the most common sorbates in the use of zeolites as catalysts.

These NMR results are confirmed by the powder X-ray diffraction patterns of the systems. Diffraction occurs at exactly the same 2θ values in both cases, indicating that the lattice dimensions are identical, but there are large differences in the intensities of the reflections due to contributions from the different (more or less ordered) organic sorbates. It should be noted that the existence of these intensity differences implies a degree of ordering of the sorbates, as disordered guests would only contribute to the diffuse scattering. Although the powder X-ray data are less sensitive to the details of the interactions, they must ultimately be used to provide the structural arrangement between the guest molecules and the host lattice. In this regard, the case of *p*-dichlorobenzene **3** is particularly important. Using the NMR data to provide the justification that *p*-dichlorobenzene is a good model system for the case of *p*-xylene **1**, structural refinements may be carried out on the former system. Because of the large number of electrons present in the chlorine atoms, these will make a major contribution to the diffraction and will be much easier to locate within the lattice. We are currently engaged in a refinement of this structure using synchrotron-based powder x-ray diffraction data and feel that the resulting locations of the organic molecules will reflect those of *p*-xylene

Can. J. Chem. Downloaded from www.nrcresearchpress.com by 112.217.228.212 on 09/07/12
For personal use only.

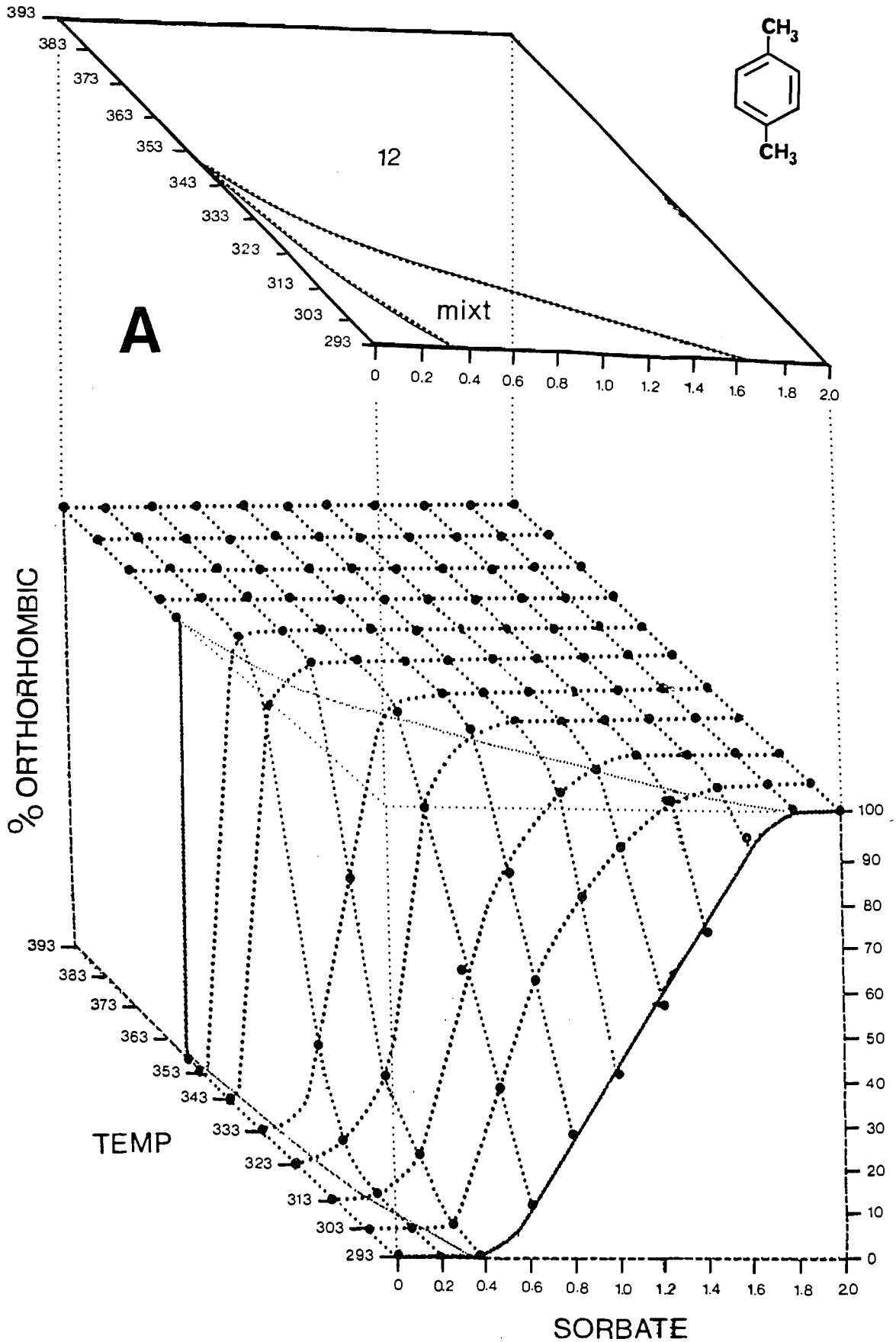

FIG. 4. Complete phase diagrams for highly siliceous ZSM-5 showing the percentage of orthorhombic form present at various temperatures and sorbate concentrations for (*A*) *p*-xylene (after ref. 9*b*); (*B*) *p*-dichlorobenzene. The concentrations of sorbate are expressed in terms of the number of molecules per unit cell so that the two diagrams can be compared directly.

Can. J. Chem. Downloaded from www.nrcresearchpress.com by 112.217.228.212 on 09/07/12
For personal use only.

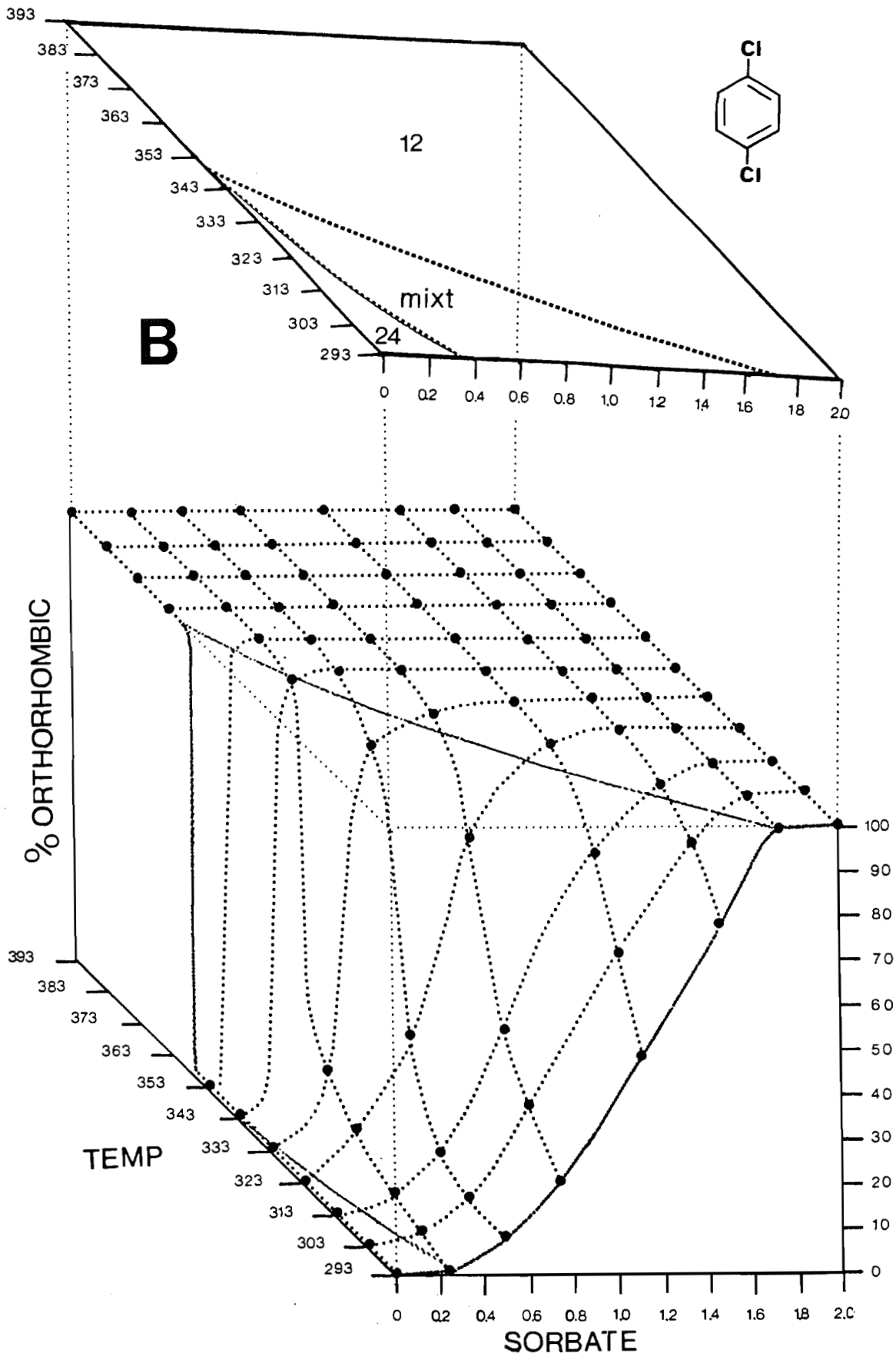

FIG. 4. (*concluded*)

Can. J. Chem. Downloaded from www.nrcresearchpress.com by 112.217.228.212 on 09/07/12
For personal use only.

and provide a starting point for refinement of existing synchrotron data on this system (10).

Further substitutions of this type in these systems may be contemplated, for example, α,ω-dichloro and other hydrocarbons for the corresponding aliphatics, chlorobenzene for toluene etc. In all cases, structural refinements should be greatly facilitated by the increased contribution to the diffraction data by the chlorine atoms. Such studies are currently in progress.

Acknowledgements

The authors acknowledge the financial assistance of the Natural Sciences and Engineering Research Council (NSERC) of Canada in the form of operating and equipment grants (C.A.F.) and a Graduate Scholarship (H.S.). H.G. and G.T.K. acknowledges the financial assistance of the Alexander von Hombolt Foundation.

1. D. W. BRECK. Zeolite molecular sieves. Wiley-Interscience, New York. 1974.
2. (*a*) R. M. BARRER. Zeolites and clay minerals as sorbents and molecular sieves. Academic Press, New York. (*b*) J. A. RABO (*Editor*). Zeolite chemistry and catalysis. ACS Monograph 171. 1976
3. P. EIESENBERGER, J. M. NEWSAM, M. E. LOENOWICA, and D. E. W. VAUGHAN. Nature, **309**, 45 (1984).
4. (*a*) C. A. FYFE, J. M. THOMAS, J. KLINOWSKI, and G. C. GOBBI. Angew. Chem. Intl. Ed. **22**, 259 (1983); (*b*) C. A. FYFE, G. T. KOKOTAILO, G. J. KENNEDY, G. C. GOBBI, C. T. DESCHUTTER, R. S. OZUBKO, and W. J. MURPHY. New directions in chemical analysis. *Edited by* B. L. Shapiro. Texas A & M University Press. 1985. pp. 25–55; (*c*) G. ENGELHARDT and D. MICHEL. High resolution solid state NMR of zeolites and related systems. John Wiley and Sons. To be published.
5. (*a*) E. LIPPMAA, M. MAGI, A. SAMOSON, M. TARMAK, and G. ENGELHARDT. J. Am. Chem. Soc. **103**, 4992 (1981); (*b*) E. LIPPMAA, M. MAGI, A. SAMOSON, G. ENGELHARDT, and A. R. GRIMMEL. J. Am. Chem. Soc. **102**, 4889 (1980).
6. (*a*) C. A. FYFE, G. C. GOBBI, W. J. MURPHY, R. S. OZUBKO, and D. A. SLACK. Chem. Lett. 1547 (1983); (*b*) C. A. FYFE, G. C. GOBBI, W. J. MURPHY, R. S. OZUBKO, and D. A. SLACK. J. Am. Chem. Soc. **106**, 4435 (1984); (*c*) J. M. THOMAS. J. Mol. catal. **27**, 59 (1984).
7. (*a*) C. A. FYFE, G. J. KENNEDY, C. T. DESCHUTTER, and G. T. KOKOTAILO. J. Chem. Soc. Chem. Commun. 541 (1984); (*b*) G. W. WEST. Aust. J. Chem. **37**, 455 (1984); (*c*) C. A. FYFE, G. T. KOKOTAILO, G. J. KENNEDY, J. R. LYERLA, and W. W. FLEMING. J. Chem. Soc. Chem. Commun. 740 (1985); (*d*) P. G. HAY, H. JAEGER, and G. W. WEST. J. Chem. Soc. Chem. Commun. **89**, 1070 (1985).
8. G. T. KOKOTAILO, S. L. LAWTON, D. H. OLSON, and W. M. MEIER, **272**, 437 (1978).
9. (*a*) C. A. FYFE, J. H. O'BRIEN, and H. STROBL. Nature, **363**, 6110 (1987); (*b*) C. A. FYFE, H. STROBL, G. T. KOKOTAILO, G. J. KENNEDY, and G. E. BARLOW. J. Am. Chem. Soc. **110**, 3373 (1988).
10. C. A. Fyfe, D. E. Cox, and G. T. KOKOTAILO. To be published.

Can. J. Chem. Downloaded from www.nrcresearchpress.com by 112.217.228.212 on 09/07/12
For personal use only.

Conjugate symmetry of molecular systems and determination of their conformations

JEAN MARUANI[1]

Laboratoire de chimie physique, Université Paris-VI et Centre national de la recherche scientifique, 11, rue Pierre et Marie Curie, 75005 Paris, France

AND

ALEJANDRO TORO-LABBÉ

Departamento de Quimica, Universidad de Chile, Santiago, Chile

Received November 19, 1987

This paper is dedicated to Professor Charles A. McDowell on the occasion of his 70th birthday

JEAN MARUANI and ALEJANDRO TORO-LABBÉ. Can. J. Chem. **66**, 1948 (1988).

In nonrigid molecules and molecular aggregates, the dependence of a property on conformation may be expressed in the form of a limited expansion in terms of appropriate harmonics. The use of the conjugate symmetry of the molecular groups to reduce such an expansion may have several advantages: (*i*) it helps decrease, sometimes drastically, the time required to calculate the conformational dependence of the considered property; (*ii*) it provides a parameterized functional form that can be used by experimentalists to rationalize their results. The symmetry rules that define the distinct non-zero harmonics are determined by a set of indices that depend on both the form and type of the property (scalar, polar, axial, tensorial; aggregate, mononuclear, binuclear) and the nature of the isodynamic operations characterizing the system. We have applied Altmann's isodynamic groups to the analysis of Wigner's harmonic expansions of dynamical, electric, and magnetic properties of various molecular structures: binary molecular associations, quasi-atoms in molecular fields, rigid molecules in crystal lattices, and non-rigid molecules involving one to three rotors. A few examples are given to illustrate these considerations.

JEAN MARUANI et ALEJANDRO TORO-LABBÉ. Can. J. Chem. **66**, 1948 (1988).

Dans les molécules non-rigides et les agrégats moléculaires, la dépendance d'une propriété à l'égard de la conformation peut s'exprimer sous la forme d'un développement limité en fonction d'harmoniques appropriées. L'utilisation de la symétrie conjuguée des groupes moléculaires pour réduire un tel développement peut avoir plusieurs avantages : (*i*) aider à diminuer, parfois considérablement, le temps nécessaire au calcul de la dépendance conformationnelle de la propriété considérée; (*ii*) fournir une forme fonctionnelle paramétrisée utilisable par les expérimentateurs pour rationaliser leurs résultats. Les règles de symétrie qui définissent les harmoniques non-nulles distinctes sont déterminées par un jeu d'indices qui dépendent à la fois de la forme et du type de la propriété (scalaire, polaire, axiale, tensorielle; globale, mononucléaire, binucléaire) et de la nature des opérations isodynamiques qui caractérisent le système. Nous avons appliqué les groupes isodynamiques d'Altmann à l'analyse des développements harmoniques de Wigner de propriétés dynamiques, électriques et magnétiques de diverses structures moléculaires : associations moléculaires binaires, quasi-atomes dans des champs moléculaires, molécules rigides dans des réseaux cristallins, et molécules non-rigides comportant de un à trois rotateurs. Quelques exemples sont fournis pour illustrer ces considérations.

Can. J. Chem. Downloaded from www.nrcresearchpress.com by 112.217.228.212 on 09/07/12
For personal use only.

1. Introduction

In the study of the structure and dynamics of molecular systems such as nonrigid molecules, molecular aggregates, or molecules embedded in crystals, one must often consider the conformational dependence of physical properties of the whole system. These properties can be classified in different ways. On the one hand, they may be scalar (i.e., invariant under all overall rotations), or polar (i.e., transforming as the translation vector X, Y, Z), or axial (i.e., transforming as the rotation vector R_x, R_y, R_z), or, more generally, tensorial (e.g., representable by a second-rank tensor). On the other hand, the properties may be of an aggregate type (i.e., characterizing the molecular system as a whole), or of a mononuclear type (i.e., defining the interaction of a particular nucleus with the electronic distribution), or of a binuclear type (i.e., defining the interaction between two particular nuclei through the electronic distribution).

The basic example of a scalar aggregate property is the total energy, E, a small part of which, V, usually depends on the conformation of the system (ref. 1). Examples of vectorial aggregate properties are intermolecular forces $\boldsymbol{F}$ and torques $\boldsymbol{G}$ (refs. 2), electric dipole moments $\boldsymbol{\mu}$, and chiral properties $\boldsymbol{\gamma}$. Examples of tensorial aggregate properties are the electric quadrupole moment $\boldsymbol{\theta}$, electric polarizability tensor $\boldsymbol{\alpha}$, spectroscopic splitting tensor $\mathbf{g}$ (if the system possesses a total electronic spin $S \geq \frac{1}{2}$) and spin–spin coupling tensor $\mathbf{D}$ (if $S \geq 1$). Examples of tensorial mononuclear properties are chemical shifts $\boldsymbol{\sigma}_i$ (for nuclei with effective spins $I_i \geq \frac{1}{2}$), quadrupole couplings $\mathbf{Q}_i$ (for nuclei with $I_i \geq 1$), and hyperfine couplings $\mathbf{c}_i$ (when both S and $I_i \geq \frac{1}{2}$). Magnetic internuclear interactions $\mathbf{J}_{ij}$ (when both I_i and $I_j \geq \frac{1}{2}$) illustrate tensorial binuclear properties. The theoretical interpretation of these properties can be found in, for example, refs. 3–5. Scalar (aggregate, mononuclear, or binuclear) properties are obtained when taking the traces of non-traceless tensors: e.g., α, g, σ_i, c_i, J_{ij}.

In the Born–Oppenheimer approximation, one defines conformational variables as internal coordinates relating the equilibrium positions of nuclei of the system. For a diatomic (such as HF) there is only one stretching variable, the interatomic distance (or bond length) ρ. For a triatomic (such as H_2O) there is, in addition to the two stretching variables, ρ_1 and ρ_2, a bending variable, the planar bond angle ψ (which equals π for a linear triatomic). For a tetratomic there may be, in addition to the three stretching variables, either (as in NH_3) three bending variables, or (as in H_2O_2) two bending and one twisting variable, the dihedral torsion angle α (which equals 0 for a planar tetratomic). In general, for an N-atomic system, there are $3N - 6$ conformational variables, including $n \leq N - 3$ torsion angles. Nonrigidity is defined as a set of features resulting from the

[1]Author to whom correspondence may be addressed.

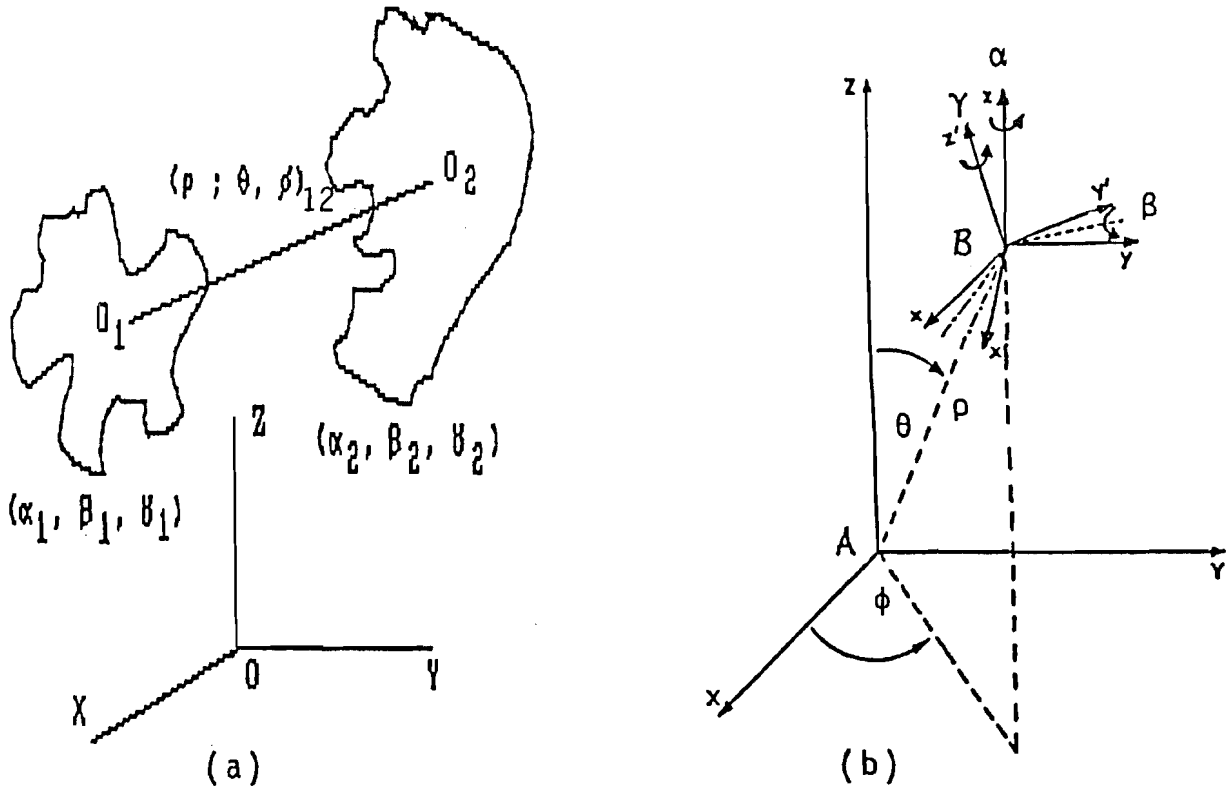

FIG. 1. (a) Two cluster components O_1 and O_2 referred to the cluster frame $OXYZ$: $\boldsymbol{R}_{12} \equiv (\rho; \theta, \phi)_{12}$ and $\boldsymbol{\Omega}_i \equiv (\alpha_i, \beta_i, \gamma_i)$. (b) A molecular pair A: B with the frame of B referred to that of A.

existence of several equilibrium conformations with different values for the conformational variables, and separated by significant but surmountable potential-energy barriers (refs. 6–10); the extent to which a barrier is significant or surmountable is determined by the time scale of the experimental procedure.

For nonrigid molecules, a switch from one stable conformation to the other may be defined by a change of a stretching variable, as in the double-well hydrogen-bonded complex H_2O:HF (ref. 11), or of a bending variable, as in the inversion of the ammonia molecule, or of a twisting variable, as in the internal rotation of ethane, or of several such variables, as in the internal motions of the pyramidal double-rotor dimethylamine. For molecular aggregates made up of rigid components (O_1, O_2, etc.), one may define a change of overall conformation by a change of the positions ($\boldsymbol{R}_{12}$, etc.) and orientations ($\boldsymbol{\Omega}_1$, $\boldsymbol{\Omega}_2$, etc.) of the constitutive parts relative to a reference frame $OXYZ$ (Fig. 1a, refs. 2). For a molecular pair A:B, one may use as conformational variables the relative position vector $\boldsymbol{R} \equiv (\rho; \theta, \phi)$ and relative orientation angles $\boldsymbol{\Omega} - (\alpha, \beta, \gamma)$ (Fig. 1b). If one of the molecules is much smaller than and not too close to the other, it may be treated as a quasi-atom in a molecular field, and the conformational variables reduce to $\boldsymbol{R}$. On the other hand, if a rigid molecule is embedded at the center of a lattice site (Fig. 2a), its interaction with the lattice depends only upon its orientational variables $\boldsymbol{\Omega}$ (Fig. 2b).

The dependence of a property on the conformational variables may belong to a variety of types. In favourable cases, a general procedure to obtain quasi-analytic forms is to use limited series expansions. For example, small variations of stretching variables can be accounted for by using Taylor series expansions, thus providing the well-known harmonic and anharmonic vibrational potentials around equilibrium positions. On the other hand, large variations of angular variables can be accounted for by using harmonic series expansions. For example, any property of a molecular pair can be written, in the frame defined in Fig. 1b (refs. 12):

$$[1] \quad A(\boldsymbol{R}, \boldsymbol{\Omega}) = \sum_{L,M} \sum_{l,m,m'} A_{Ll}^{Mmm'}(\rho) Y_L^M(\theta, \phi) D_l^{mm'}(\alpha, \beta, \gamma)$$

where Y_L^M and $D_1^{mm'}$ are the usual and generalized (Wigner rotation matrices) spherical harmonics (ref. 13).

The simplified case of a quasi-atom in a molecular field is quite similar to that of an ion in a crystal field (ref. 14), and requires the reduced expansion:

$$[2] \quad A(\boldsymbol{R}) = \sum_{L,M} A_L^M(\rho) Y_L^M(\theta, \phi)$$

In the particular case of a rigid molecule embedded at the center of a crystal site (refs. 15), the expansion [1] reduces to

$$[3] \quad A(\boldsymbol{\Omega}) = \sum_{l,m,m'} A_l^{mm'} D_l^{mm'}(\alpha, \beta, \gamma)$$

In the still simpler case of a system consisting of a rotating top bonded to a reference frame, one can replace the Wigner harmonics by Fourier harmonics (refs. 16):

$$[4] \quad A(\alpha) = \sum_{m=-\infty}^{+\infty} A_m \exp(-im\alpha) = \sum_{m=0}^{\infty} (A_m^{\,c} \cos m\alpha + A_m^{\,s} \sin m\alpha)$$

For an n-rotor molecule, this expansion can be generalized as follows (refs. 17):

Can. J. Chem. Downloaded from www.nrcresearchpress.com by 112.217.228.212 on 09/07/12
For personal use only.

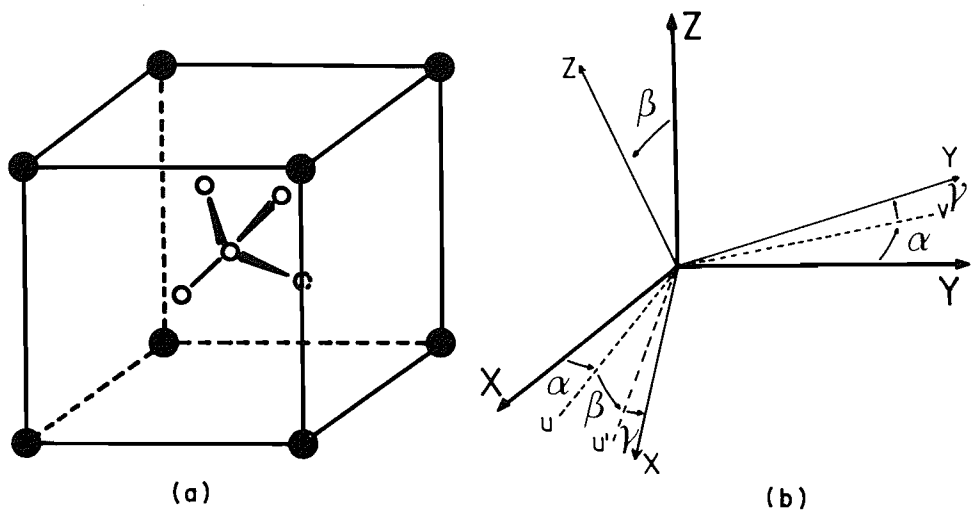

FIG. 2. (a) A rigid molecule embedded in a lattice site. (b) The Euler angles α, β, γ defining the relative orientation of the molecule axes *Oxyz* with respect to the site axes *OXYZ*.

$$[5]\quad A(\alpha_1,\ldots,\alpha_n) = \sum_{m_1,\ldots,m_n=-\infty}^{+\infty} A_{m_1\ldots m_n} \exp -i(m_1\alpha_1 + \ldots + m_n\alpha_n)$$

When a relative reorientation of the molecular groups constituting a system can be performed without bringing about important changes in the nuclear configuration and electronic distribution of the system elements, the dependence of most properties on the angular variables can be described with the first few significant terms of the harmonic expansion. Symmetry considerations can yield further reductions in the number of necessary harmonics: the selection rules that define the independent nonzero coefficients are determined by a set of symmetry indices, which depend on both the form of the property and the nature of the isodynamic operations characterizing the system.

The use of the conjugate symmetry of a molecular system to reduce the harmonic expansions of its physical properties affords a double advantage: (*i*) it helps reduce, sometimes drastically, the time required to compute the conformational dependence of the investigated property; (*ii*) it provides a parameterized functional form that can be used by experimentalists to rationalize their results. If the property is the energy, the hypersurface minima can be more easily derived and the stable conformations thus obtained. If the property is some spectroscopic parameter depending on the conformational variables, comparison of measured values with computed dependences can lead to these variables.

In this paper we review some applications of these considerations that we made to molecular pairs (ref. 12*b*), molecules in crystals (ref. 15*c*), and double-rotor molecules (refs. 17), using the formalism of isodynamic groups with illustrative quantum calculations.

2. Molecular pairs

The study of molecular interactions is usually a difficult task, because of the number of independent variables to be considered. The investigation of interaction potential-energy hypersurfaces is usually confined to a few variables, selected using physical intuition. A large amount of theoretical work has been devoted to hydrogen-bond complexes and proton-transfer systems, assuming a few symmetric conformations of the molecular pair. Using the formalism outlined above, we have considered a more extended set of conformations for the complex H_2O:HF and derived the lowest five dimensional minima defining the most stable conformations.

The harmonic expansion for a molecular pair is given by eq. [1], where the considered property, the interaction potential V, being real implies particular relations between the complex coefficients $V_{Ll}^{Mmm'}$. With an appropriate choice of the coordinate system, M is even and m is zero, because H_2O and HF possess C_2 and C_∞ symmetry axes, respectively. Equation [1] then becomes:

$$[6]\quad V(\boldsymbol{R},\boldsymbol{\Omega}) = \sum_{L,M}\sum_{l,m'} V_{Ll}^{Mm'}(\rho) Y_L^M(\theta,\phi) Y_l^{m'}(\beta,\gamma)$$

where the expansion coefficients satisfy the additional relations: $V_{Ll}^{Mm'} = V_{Ll}^{-Mm'} = (-1)^{m'} V_{Ll}^{M-m'}$, because both H_2O and HF possess σ_v symmetry planes.

One can obtain various cross-sections of this hypersurface by freezing some of the variables. For instance, if the motion of HF is confined to the plane bisecting H_2O, the above expansion reduces to the double Fourier series ($\phi = \gamma = 0$):

$$[7]\quad V(\rho,\theta,\beta) = \sum_{j,k} [V_{jk}^{cc}(\rho)\cos j\theta \cos k\beta + V_{jk}^{ss}(\rho)\sin j\theta \sin k\beta]$$

where the coefficients V_{jk}^{cs} and V_{jk}^{sc} are annihilated due to the double-switch isodynamic operation **V** (ref. 17*a*) illustrated in Fig. 3a: $\mathbf{V}\, V(\rho,\theta,\phi) \equiv V(\rho,-\theta,-\beta) = V(\rho,\theta,\beta)$. Figure 3*b* displays two energy contributions to this hypersurface cross-section, calculated with the optimized distance $\tilde{\rho} = 2.17$ Å.

Additional semiempirical and *ab initio* calculations have shown indeed (ref. 12*b*) that both azimuthal angles ϕ and γ are actually 0, though the dependence of V upon γ is very small. The calculations have also shown that around the stable conformations of the complex, which can be seen in Fig. 3b (left), the dispersion energy (Fig. 3b (right)) and the basis-set superposition error of the *ab initio* calculation (ref. 12*b*) nearly compensate each other. The minima of the surface $V(\tilde{\rho},\theta,\beta)$ (Fig. 3b) appear rather flat, so that the equilibrium values of the conformational angles, listed in Table 1, should be considered as defining the average conformation of a quite floppy supermolecule, quasi-free to distort within a few tens of degrees. This may give particular significance to the smaller values of θ and β

Can. J. Chem. Downloaded from www.nrcresearchpress.com by 112.217.228.212 on 09/07/12
For personal use only.

Can. J. Chem. Downloaded from www.nrcresearchpress.com by 112.217.228.212 on 09/07/12
For personal use only.

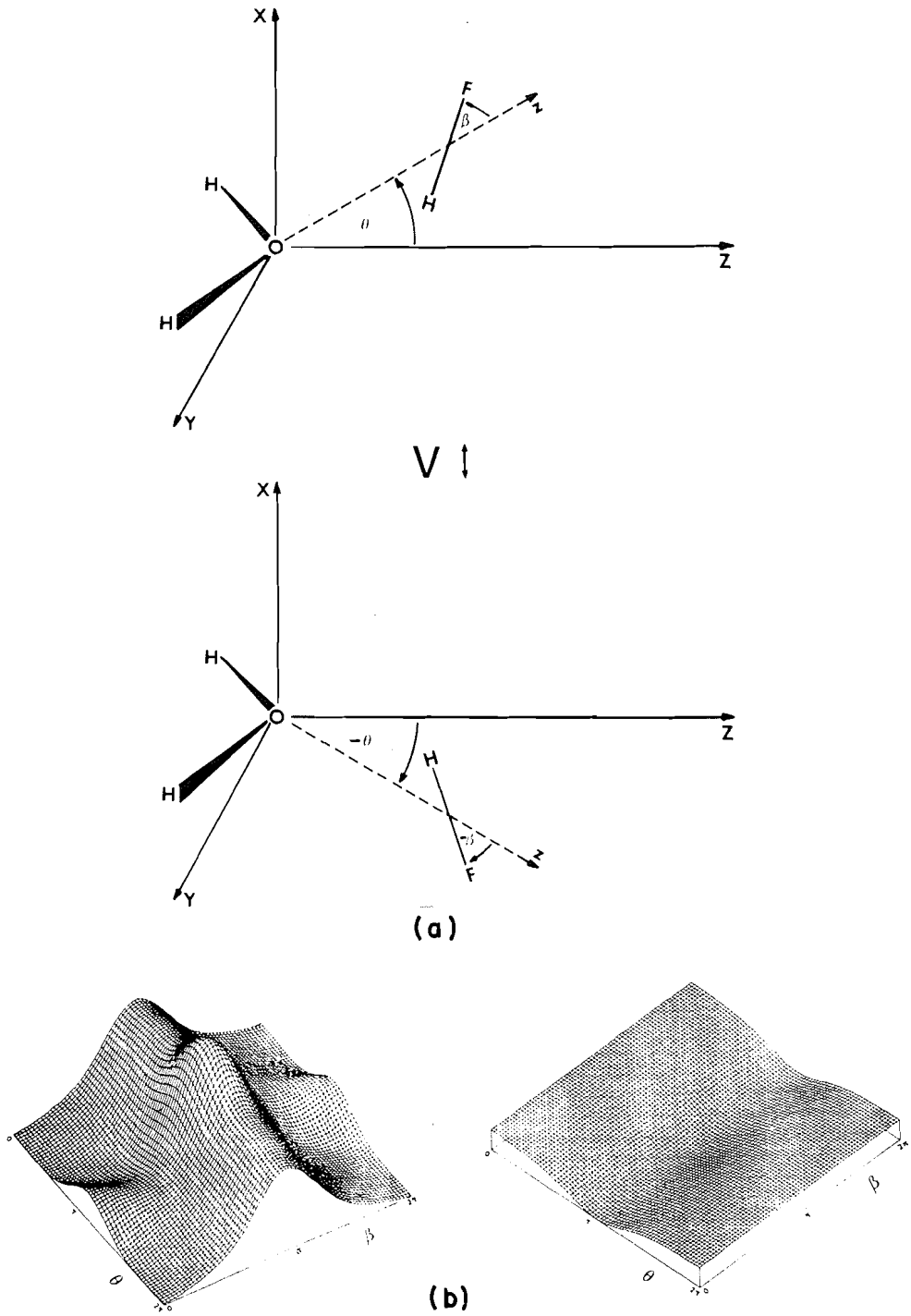

FIG. 3. (a) The complex H_2O: HF with HF confined to the σ_v plane of H_2O ($\phi = \gamma = 0$): conformations (θ, β) and ($-\theta$, $-\beta$), which can be superimposed through an Euclidean displacement, are related by the double-switch isodynamic operation V. (b) Cross-sections of the interaction potential-energy hypersurface for the case shown in (a), calculated with the optimized distance $\rho = 2.16$ Å: left, conformation-dependent part of the SCF energy obtained using STO / 4-21G*; right, dispersion-energy contribution calculated using Claverie's semiempirical formula (ref. 12*b*) (right scale is twice left scale).

deduced from microwave spectroscopy (ref. 12*c*), also listed in Table 1. In conclusion, we can represent the complex H_2O:HF as a floppy bent-pyramidal chelate, the H_2O lone pairs acting as attractors for the H of HF whose fluorine also bends towards the hydrogens of water.

3. Molecular crystals

A variety of crystals have lattice nodes occupied by neutral or ionic atoms or quasi-spherical molecules making up unit cells of some particular symmetry, housing at their center rigid molecules of the same or another symmetry (Fig. 2a). In such cases the symmetry of a property dependent on the orientation of the molecule with respect to the cell is completely determined by the symmetries of both molecule and cell. Such properties are usually expanded in terms of Wigner harmonics in the form given by eq. [3] (refs. 15). For most rigid molecules embedded

TABLE 1. Theoretical and experimental values of structural variables and physical properties of the complex H_2O:HF (from ref. 12*b*)

	$\tilde{\rho}$/Å	$\tilde{\theta}$	$\tilde{\beta}$	$\tilde{\phi}$	$\tilde{\gamma}$	ΔV/kJ mol^{-1}	$\tilde{\mu}$/debye
CNDO/2	1.87	82.1°	12.5°	0°	0°	4.10	3.27
STO/4-21G*	2.17	67.3°	8.3°	0°	0°	5.56	3.85
Microwave spectroscopy	2.20	46±8°		0°	0°	1.51±0.84	3.80

in regular crystals, the relative-orientation variables (α, β, γ) (Fig. 2b) can be separated from the internal molecular variables as well as from the phonon crystal variables, due to the large differences observed between the corresponding motion frequencies. Properties of interest include the molecule–site energy and torque, the orientational distribution and correlation functions, and any property that may be of interest in the interpretation of scattering or spectroscopic data, such as high-resolution vibration–rotation or pure rotation spectra for molecules trapped in crystals, or orientational statics and dynamics for molecular crystals studied by neutron or X-ray scattering.

We have given (ref. 15*c*) an overall description of how the symmetry properties of a composite system (SM) made up of a rigid molecule (M) and a crystal site (S) can be determined and yield significant, and sometimes drastic, reductions in the Wigner harmonic expansions of the various properties. Using the group theoretical approach initially proposed for nonrigid molecules by Longuet-Higgins (ref. 6), Miller and Decius (ref. 15*a*) have determined the complete groups for molecules of arbitrary symmetry embedded in sites of any symmetry. Alternatively, we have used the group theoretical approach initially proposed by Altmann (refs. 7) to determine the isodynamic groups ($\mathbf{I_{SM}}$) for molecules of arbitrary symmetry ($\mathbf{G_M}$) centered at sites of any symmetry ($\mathbf{G_S}$).

In the following we shall first summarize our results concerning the operator structure of the isodynamic groups $\mathbf{I_{SM}}$ in terms of the symmetry operations of the point groups $\mathbf{G_M}$ and $\mathbf{G_S}$, then recall the selection rules associated with the isodynamic operations of $\mathbf{I_{SM}}$, and finally indicate how reduced symmetry-adapted expansions can be derived from these selection rules.

3.1. Isodynamic groups

Among all symmetry operations, Altmann (refs. 7) distinguishes those which reduce to changes of the laboratory or system axes, leaving the electronic Hamiltonian invariant, and the internal motions of the system, which leave the nuclear Hamiltonian unaltered. He calls these latter operations "isodynamic" (ref. 7*b*) because they transform a conformation having broken symmetry into an isoenergetic conformation having the same symmetry. The isodynamic group made up of these operations can be written as the semidirect product of two further groups (ref. 7*d*):

$$[8] \quad \boldsymbol{I}^{\sim} = \boldsymbol{I}^{\sim}_{\mathbf{r}} \wedge \boldsymbol{I}^{\sim}_{\mathbf{d}}$$

where $\boldsymbol{I}^{\sim}_{\mathbf{r}}$ is the group of internal rearrangements that transfer a set of atoms from one equilibrium position onto another, and $\boldsymbol{I}^{\sim}_{\mathbf{d}}$ is the group of restricted distorsions that leave the equilibrium positions of all atoms unchanged.

We shall consider only those motions of a rigid molecule with respect to a crystal site that leave the centers of mass coincident. The 34 possible point groups $\mathbf{G_M}$ and 7 possible point groups $\mathbf{G_S}$ may involve symmetry centers, axes, and planes and, whenever possible, the reference axes of M (O*xyz*) and of S (O*XYZ*) will be chosen in relation with symmetry elements of M and of S (Fig. 2). If M or S has a symmetry center, this latter coincides with the center of mass and is taken as the origin of the axes.

Assume S possesses an n-fold principal axis and M an n'-fold principal axis, these two axes making an angle β (Fig. 2b). If $E(\alpha,\beta,\gamma)$ is the total energy of the composite system, an isodynamic rotation of M around C_n is defined by

$$[9] \quad C_n^q E(\alpha,\beta,\gamma) = E(\alpha + q\cdot 2\pi/n, \beta, \gamma)$$

and an isodynamic rotation of M around $C'_{n'}$ by

$$[10] \quad C'^{q'}_{n'} E(\alpha,\beta,\gamma) = E(\alpha, \beta, \gamma + q'\cdot 2\pi/n')$$

The first operation generates the isodynamic cyclic group $\boldsymbol{C}_n^{\sim}$ and the second operation the isodynamic cyclic group $\boldsymbol{C'}_{\mathbf{n'}}^{\sim}$. If S and M also possess twofold axes orthogonal to their principal axis, one can define the additional isodynamic operations:

$$[11] \quad {}^{\circ}C_2 E(\alpha,\beta,\gamma) = E(-\alpha, \pi - \beta, \gamma + \pi)$$

$$[12] \quad {}^{\circ}C'_2 E(\alpha,\beta,\gamma) = E(\alpha + \pi, \pi - \beta, -\gamma)$$

These two sets of isodynamic operations generate the respective isodynamic groups ${}^{\circ}\boldsymbol{C}_2^{\sim}$ and ${}^{\circ}\boldsymbol{C'}_2^{\sim}$. $\boldsymbol{T}$ and $\boldsymbol{O}$ cubic groups also involve diagonal threefold axes, which similarly induce the isodynamic groups ${}^{a}\boldsymbol{C}_3^{\sim}$ and ${}^{a}\boldsymbol{C'}_3^{\sim}$.

As a consequence of Altmann's representation of symmetry point groups as semidirect products (ref. 7*a*), the full isodynamic groups $\boldsymbol{R}_{\mathbf{M}}^{\sim}$ and $\boldsymbol{R}_{\mathbf{S}}^{\sim}$ generated by all proper rotations in $\mathbf{G_M}$ and $\mathbf{G_S}$ can then be written:

$$[13] \quad \begin{aligned} &\boldsymbol{C}_n^{\sim}(n = 1, 2, 3, 4, 6), \qquad \boldsymbol{D}_n^{\sim} = \boldsymbol{C}_n^{\sim} \wedge {}^{\circ}\boldsymbol{C}_2^{\sim} \\ &\boldsymbol{T}^{\sim} = \boldsymbol{D}_2^{\sim} \wedge {}^{a}\boldsymbol{C}_3^{\sim}, \qquad \boldsymbol{O}^{\sim} = \boldsymbol{D}_2^{\sim} \wedge {}^{a}\boldsymbol{D}_3^{\sim} \end{aligned}$$

for $\boldsymbol{R}_{\mathbf{S}}^{\sim}$, and similar (primed) expressions for $\boldsymbol{R}_{\mathbf{M}}^{\sim}$. The direct product of the site and molecule proper-rotation subgroups generates the isodynamic group of internal rearrangements defined in eq. [8]:

$$[14] \quad \boldsymbol{I}^{\sim}_{\mathbf{r}} = \boldsymbol{R}_{\mathbf{S}}^{\sim} * \boldsymbol{R}_{\mathbf{M}}^{\sim}$$

Whereas isodynamic internal rotations can be defined for the composite system whenever any one of the system components possesses proper-rotation symmetries, isodynamic operations resulting from rotation-reflections, reflections, and inversions can be defined only if both molecule and site possess improper-rotation symmetries. Since, according to Altmann (ref. 7*a*), improper point groups can be written as a direct or semidirect product of a proper point group with either $\boldsymbol{C}_i$ or $\boldsymbol{C}_s$, all isodynamic operations will be some product of an isodynamic operation of the first kind, considered above, with an isodynamic operation of the second kind, which we now consider.

Starting from a conformation in which the reference σ_v and σ'_v planes coincide ($\alpha = \gamma = 0$, $\beta \neq 0$), it can be seen (Fig. 2b) that the two distorted conformations (α,β,γ) and $(-\alpha, \beta, -\gamma)$ are connected by the isodynamic operation:

Can. J. Chem. Downloaded from www.nrcresearchpress.com by 112.217.228.212 on 09/07/12
For personal use only.

TABLE 2. Structure of the isodynamic groups of a site–molecule system for a site and a molecule of any symmetry point group. In D_{nh}, n = 2, 4, 94 6. The case of infinite n' is formally included in $C'_{n'v}$ and $D'_{n'h}$ (from ref. 15c)

M \ S	C_i (b)	C_{3v} (c)	C_{2h} (b)	D_{nh} (b)	O_h (b)
(a) $C'_{n'}$	$(\mathbb{C}_{n'}\mathbb{X}\mathbb{C}_1)^{\sim}$	$(\mathbb{C}_{n'}\mathbb{X}\mathbb{C}_3)^{\sim}$	$(\mathbb{C}_{n'}\mathbb{X}\mathbb{C}_2)^{\sim}$	$(\mathbb{C}_{n'}\mathbb{X}\mathbb{D}_n)^{\sim}$	$(\mathbb{C}_{n'}\mathbb{X}\mathbb{O})^{\sim}$
(a) $D'_{n'}$	$(\mathbb{D}_{n'}\mathbb{X}\mathbb{C}_1)^{\sim}$	$(\mathbb{D}_{n'}\mathbb{X}\mathbb{C}_3)^{\sim}$	$(\mathbb{D}_{n'}\mathbb{X}\mathbb{C}_2)^{\sim}$	$(\mathbb{D}_{n'}\mathbb{X}\mathbb{D}_n)^{\sim}$	$(\mathbb{D}_{n'}\mathbb{X}\mathbb{O})^{\sim}$
(a) T'	$(\mathbb{T}'\mathbb{X}\mathbb{C}_1)^{\sim}$	$(\mathbb{T}'\mathbb{X}\mathbb{C}_3)^{\sim}$	$(\mathbb{T}'\mathbb{X}\mathbb{C}_2)^{\sim}$	$(\mathbb{T}'\mathbb{X}\mathbb{D}_n)^{\sim}$	$(\mathbb{T}'\mathbb{X}\mathbb{O})^{\sim}$
(a) O'	$(\mathbb{O}'\mathbb{X}\mathbb{C}_1)^{\sim}$	$(\mathbb{O}'\mathbb{X}\mathbb{C}_3)^{\sim}$	$(\mathbb{O}'\mathbb{X}\mathbb{C}_2)^{\sim}$	$(\mathbb{O}'\mathbb{X}\mathbb{D}_n)^{\sim}$	$(\mathbb{O}'\mathbb{X}\mathbb{O})^{\sim}$
(d) S'_4	$(\mathbb{C}'_4\mathbb{X}\mathbb{C}_1)^{\sim}$	$(\mathbb{C}'_4\mathbb{X}\mathbb{C}_3)^{\sim}$	$(\mathbb{C}'_4\mathbb{X}\mathbb{C}_2)^{\sim}$	$(\mathbb{C}'_4\mathbb{X}\mathbb{D}_n)^{\sim}$	$(\mathbb{C}'_4\mathbb{X}\mathbb{O})^{\sim}$
(b) $S'^{\text{odd}}_{2n'}$	$(\mathbb{C}_{n'}\mathbb{X}\mathbb{C}_1)^{\sim}$	$(\mathbb{C}_{n'}\mathbb{X}\mathbb{C}_3)^{\sim\wedge\mathbb{V}_v^{\sim}}$	$(\mathbb{C}_{n'}\mathbb{X}\mathbb{C}_2)^{\sim}$	$(\mathbb{C}_{n'}\mathbb{X}\mathbb{D}_n)^{\sim}$	$(\mathbb{C}_{n'}\mathbb{X}\mathbb{O})^{\sim}$
(b) $C'^{\text{even}}_{n'h}$	$(\mathbb{C}_{n'}\mathbb{X}\mathbb{C}_1)^{\sim}$	$(\mathbb{C}_{n'}\mathbb{X}\mathbb{C}_3)^{\sim\wedge\mathbb{J}_v^{\sim}}$	$(\mathbb{C}_{n'}\mathbb{X}\mathbb{C}_2)^{\sim}$	$(\mathbb{C}_{n'}\mathbb{X}\mathbb{D}_n)^{\sim}$	$(\mathbb{C}_{n'}\mathbb{X}\mathbb{O})^{\sim}$
(c) $C'^{\text{odd}}_{n'h}$	$(\mathbb{C}_{n'}\mathbb{X}\mathbb{C}_1)^{\sim\wedge\mathbb{J}_h'^{\sim}}$	$(\mathbb{C}_{n'}\mathbb{X}\mathbb{C}_3)^{\sim\wedge\mathbb{V}_v^{\sim}}$	$(\mathbb{C}_{n'}\mathbb{X}\mathbb{C}_2)^{\sim\wedge\mathbb{J}_h'^{\sim}}$	$(\mathbb{C}_{n'}\mathbb{X}\mathbb{D}_n)^{\sim\wedge\mathbb{J}_h'^{\sim}}$	$(\mathbb{C}_{n'}\mathbb{X}\mathbb{O})^{\sim\wedge\mathbb{J}_h'^{\sim}}$
(c) $C'_{n'v}$	$(\mathbb{C}_{n'}\mathbb{X}\mathbb{C}_1)^{\sim\wedge\mathbb{J}_v'^{\sim}}$	$(\mathbb{C}_{n'}\mathbb{X}\mathbb{C}_3)^{\sim\wedge\mathbb{V}_v^{\sim}}$	$(\mathbb{C}_{n'}\mathbb{X}\mathbb{C}_2)^{\sim\wedge\mathbb{J}_v'^{\sim}}$	$(\mathbb{C}_{n'}\mathbb{X}\mathbb{D}_n)^{\sim\wedge\mathbb{J}_v'^{\sim}}$	$(\mathbb{C}_{n'}\mathbb{X}\mathbb{O})^{\sim\wedge\mathbb{J}_v'^{\sim}}$
(c) D'_{2d}	$(\mathbb{D}'_2\mathbb{X}\mathbb{C}_1)^{\sim\wedge\mathbb{J}_v'^{\sim}}$	$(\mathbb{D}'_2\mathbb{X}\mathbb{C}_3)^{\sim\wedge\mathbb{V}_v^{\sim}}$	$(\mathbb{D}'_2\mathbb{X}\mathbb{C}_2)^{\sim\wedge\mathbb{J}_v'^{\sim}}$	$(\mathbb{D}'_2\mathbb{X}\mathbb{D}_n)^{\sim\wedge\mathbb{J}_v'^{\sim}}$	$(\mathbb{D}'_2\mathbb{X}\mathbb{O})^{\sim\wedge\mathbb{J}_v'^{\sim}}$
(b) D'_{3d}	$(\mathbb{D}'_3\mathbb{X}\mathbb{C}_1)^{\sim}$	$(\mathbb{D}'_3\mathbb{X}\mathbb{C}_3)^{\sim\wedge\mathbb{J}_v^{\sim}}$	$(\mathbb{D}'_3\mathbb{X}\mathbb{C}_2)^{\sim}$	$(\mathbb{D}'_3\mathbb{X}\mathbb{D}_n)^{\sim}$	$(\mathbb{D}'_3\mathbb{X}\mathbb{O})^{\sim}$
(c) T'_d	$(\mathbb{T}'\mathbb{X}\mathbb{C}_1)^{\sim\wedge\mathbb{J}_v'^{\sim}}$	$(\mathbb{T}'\mathbb{X}\mathbb{C}_3)^{\sim\wedge\mathbb{V}_v^{\sim}}$	$(\mathbb{T}'\mathbb{X}\mathbb{C}_2)^{\sim\wedge\mathbb{J}_v'^{\sim}}$	$(\mathbb{T}'\mathbb{X}\mathbb{D}_n)^{\sim\wedge\mathbb{J}_v'^{\sim}}$	$(\mathbb{T}'\mathbb{X}\mathbb{O})^{\sim\wedge\mathbb{J}_v'^{\sim}}$
(b) D'^{even}_{nh}	$(\mathbb{D}_{n'}\mathbb{X}\mathbb{C}_1)^{\sim}$	$(\mathbb{D}_{n'}\mathbb{X}\mathbb{C}_3)^{\sim\wedge\mathbb{J}_v^{\sim}}$	$(\mathbb{D}_{n'}\mathbb{X}\mathbb{C}_2)^{\sim}$	$(\mathbb{D}_{n'}\mathbb{X}\mathbb{D}_n)^{\sim}$	$(\mathbb{D}_{n'}\mathbb{X}\mathbb{O})^{\sim}$
(c) D'_{3h}	$(\mathbb{D}'_3\mathbb{X}\mathbb{C}_1)^{\sim\wedge\mathbb{J}_v'^{\sim}}$	$(\mathbb{D}'_3\mathbb{X}\mathbb{C}_3)^{\sim\wedge\mathbb{V}_v^{\sim}}$	$(\mathbb{D}'_3\mathbb{X}\mathbb{C}_2)^{\sim\wedge\mathbb{J}_v'^{\sim}}$	$(\mathbb{D}'_3\mathbb{X}\mathbb{D}_n)^{\sim\wedge\mathbb{J}_v'^{\sim}}$	$(\mathbb{D}'_3\mathbb{X}\mathbb{O})^{\sim\wedge\mathbb{J}_v'^{\sim}}$
(b) T'_h	$(\mathbb{T}'\mathbb{X}\mathbb{C}_1)^{\sim}$	$(\mathbb{T}'\mathbb{X}\mathbb{C}_3)^{\sim\wedge\mathbb{J}_v^{\sim}}$	$(\mathbb{T}'\mathbb{X}\mathbb{C}_2)^{\sim}$	$(\mathbb{T}'\mathbb{X}\mathbb{D}_n)^{\sim}$	$(\mathbb{T}'\mathbb{X}\mathbb{O})^{\sim}$
(b) O'_h	$(\mathbb{O}'\mathbb{X}\mathbb{C}_1)^{\sim}$	$(\mathbb{O}'\mathbb{X}\mathbb{C}_3)^{\sim\wedge\mathbb{J}_v^{\sim}}$	$(\mathbb{O}'\mathbb{X}\mathbb{C}_2)^{\sim}$	$(\mathbb{O}'\mathbb{X}\mathbb{D}_n)^{\sim}$	$(\mathbb{O}'\mathbb{X}\mathbb{O})^{\sim}$

[15] $\boldsymbol{V}_v E(\alpha,\beta,\gamma) = E(-\alpha, \beta, -\gamma)$

One can similarly define, with a σ_v and a σ'_h plane, the isodynamic operation:

[16] $\boldsymbol{V}_h E(\alpha,\beta,\gamma) = E(\pi - \alpha, \pi - \beta, \gamma)$

These two isodynamic operations generate the respective groups $\boldsymbol{V}_v^{\sim}$ and $\boldsymbol{V}_h^{\sim}$. One could similarly define isodynamic groups $\boldsymbol{H}_v^{\sim}$ and $\boldsymbol{H}_h^{\sim}$. From the properties of the inversion it results that only the combinations of I with reflections through either σ_v or σ_h planes in either M (primed) or S (unprimed) produce isodynamic operations:

[17] $\boldsymbol{I}_v E(\alpha,\beta,\gamma) = E(\pi - \alpha, \pi - \beta, \gamma + \pi)$

[18] $\boldsymbol{I}_h E(\alpha,\beta,\gamma) = E(\alpha + \pi, \beta, \gamma)$

and similar relations for $\boldsymbol{I}'_v$ and $\boldsymbol{I}'_h$ with the roles of α and γ interchanged. These four idempotent operations generate the respective isodynamic groups $\boldsymbol{I}_v^{\sim}, \boldsymbol{I}_h^{\sim}, \boldsymbol{I}'_v{}^{\sim}, \boldsymbol{I}'_h{}^{\sim}$.

According to Altmann's classification (ref. 7a), there are 11 molecular point groups of type (a), $\boldsymbol{R}_{\mathbf{M}}$, 11 of type (b), $\boldsymbol{R}_{\mathbf{M}} \times \boldsymbol{C}_i$, 9 of type (c), $\boldsymbol{R}_{\mathbf{M}} \wedge \boldsymbol{C}_s$, and 3 unclassified (d) ($\boldsymbol{S}'_4$, $\boldsymbol{C}'_{\infty v}$, $\boldsymbol{D}'_{\infty h}$); for a lattice site, only 7 out of these 34 point groups are possible: 6 of type (b), $\boldsymbol{R}_{\mathbf{S}} \times \boldsymbol{C}_i$, and 1 of type (c), $\boldsymbol{R}_{\mathbf{S}} \wedge \boldsymbol{C}_s$ (C_{3v}). The isodynamic group of restricted distorsions $\boldsymbol{I}^{\sim}_{\mathbf{d}}$ defined in eq. [8] is generated by the factors of $\boldsymbol{R}_{\mathbf{M}}$ and $\boldsymbol{R}_{\mathbf{S}}$ in the molecule and site point groups and can be shown to be one of the isodynamic groups introduced in eqs. [15]–[18]. We have gathered in Table 2 the structures of the complete isodynamic groups $\boldsymbol{I}^{\sim}$ for all possible combinations of molecule and site point groups (ref. 15c).

3.2. Selection rules

From the action of the isodynamic operations considered above on Wigner harmonics making up series expansions (ref. 13), one can derive explicit relations between the expansion coefficients of a given property (ref. 15c). The symmetry-adapted expansion of a molecule–site property transforming as an irreducible representation Γ of the isodynamic group $\boldsymbol{I}^{\sim}$ can be obtained by applying to its Wigner harmonic expansion, given by eq. [3], the corresponding projection operator:

TABLE 3. Relations between the coefficients of the harmonic expansions induced by the various isodynamic operations. In the relations occurring for cubic groups $\cos {}^2\eta_a = 1/3$ (from ref. 15c)

$\mathbb{C}_n^{\sim}$: $A_1{}^{mm'} = (-1)^{2m/n} A_1{}^{mm'} = 0$ unless $m = kn$

$\mathbb{C}_{n'}^{r'\sim}$: $A_1{}^{mm'} = (-1)^{2m'/n'} A_1{}^{mm'} = 0$ unless $m' = k'n'$ ($m' = 0$ if $n' = \infty$)

$^{\circ}\mathbb{C}_2^{\sim}$: $A_1{}^{mm'} = (-1)^l A_1^{-mm'}$

$^{\circ}\mathbb{C}_2'^{\sim}$: $A_1{}^{mm'} = (-1)^l A_1^{\pi - m'}$

$^{a}\mathbb{C}_3^{\sim}$: $A_1{}^{mm'} = \sum (-1)^{(m+3r')/4 - r/3} d_1{}^{m\pi}(\eta_a) d_1{}^{\pi r'}(\eta_a) A_1{}^{r'm'}$

$^{a}\mathbb{C}_3'^{\sim}$: $A_1{}^{mm'} = \sum_{r,r'} (-1)^{(m'+3r)/4 - r'/3} d_1{}^{\epsilon' m'}(\eta_a) d_1{}^{\pi r'}(\eta_a) A_1{}^{m\epsilon}$

$\mathbb{V}_v^{\sim}$: $A_1{}^{mm'} = (-1)^{m-m'} A_1^{-m-m'}$

$\mathbb{H}_v^{\sim}$: $A_1{}^{mm'} = (-1)^{m+m'} A_1{}^{mm'}$

$\mathbb{V}_h^{\sim}$: $A_1{}^{mm'} = (-1)^{l+m+m'} A_1^{-mm'}$

$\mathbb{H}_h^{\sim}$: $A_1{}^{mm'} = (-1)^{l+m+m'} A_1^{m-m'}$

$\mathbb{J}_v^{\sim}$: $A_1{}^{mm'} = (-1)^{l+m} A_1^{-mm'}$

$\mathbb{J}_h^{\sim}$: $A_1{}^{mm'} = (-1)^m A_1{}^{mm'}$

$\mathbb{J}_v'^{\sim}$: $A_1{}^{mm'} = (-1)^{l-m'} A_1{}^{m-m'}$

$\mathbb{J}_h'^{\sim}$: $A_1{}^{mm'} = (-1)^{m'} A_1{}^{mm'}$

[19] $\boldsymbol{O}^{\Gamma} = (1/h) \sum_{i=1}^{h} \chi_i{}^{\Gamma} \boldsymbol{O}_i$

where h is the dimension of $\boldsymbol{I}^{\sim}$ and $\chi_i{}^{\Gamma}$ is the character corresponding to the isodynamic operator $\boldsymbol{O}_i$ in the irreducible representation Γ. The selection rules are obtained by stating, for each operator $\boldsymbol{O}_i$ in $\boldsymbol{O}^{\Gamma}$, that

[20] $\boldsymbol{O}_i A(\Omega) = A(\Omega)$

and by using the relations expressing the effects of the isodynamic operations on Wigner harmonics to compare the coefficients of the corresponding terms on both sides of eq. [20]. The selection rules corresponding to the various isodynamic operations are gathered in Table 3. Other rules can be obtained by combining the relations given in the table.

3.3. Reduced symmetry-adapted expansions

Our basic interest is in the conformational dependences of the various properties of a rigid molecule embedded in a crystal site. The fact that a property is of an aggregate, mononuclear, or binuclear type determines the effective isodynamic group $\boldsymbol{I}^{\sim}$ to

Can. J. Chem. Downloaded from www.nrcresearchpress.com by 112.217.228.212 on 09/07/12
For personal use only.

Can. J. Chem. Downloaded from www.nrcresearchpress.com by 112.217.228.212 on 09/07/12
For personal use only.

which the operators $\boldsymbol{O}_i$ in eq. [19] belong, whereas the fact that a property is scalar, vectorial, or tensorial determines the irreducible representation Γ to which the characters χ_i^{Γ} belong.

For an aggregate property A, the effective isodynamic group $\tilde{\boldsymbol{I}}(A)$ is the full isodynamic group determined in Section 3.1. For a mononuclear property M_i or S_i (depending on the location of the nucleus, in the molecule or in the site), the effective isodynamic group $\tilde{\boldsymbol{I}}(M_i)$ or $\tilde{\boldsymbol{I}}(S_i)$ is the same as that of A but for a system in which the symmetry of M or that of S has been reduced by singling out nucleus i. For a binuclear property one must distinguish the cases B_{ij}, C_{ij}, and D_{ij}, where nuclei i and j are both on M, shared between M and S, and both on S, respectively. In all three cases the effective isodynamic group is the same as that of A but for a system in which nuclei i and j have been singled out.

For a scalar property A, the relevant irreducible representation Γ_A is the totally symmetric representation of $\tilde{\boldsymbol{I}}(A)$, all characters of which are equal to 1. For a vectorial or tensorial property $\boldsymbol{A}$, one must consider the components of the representative vector or tensor on reference axes of the perturbed molecule related to the isodynamic operations defined by eqs. [15] and [16]: y for $\boldsymbol{V}_v$, z for $\boldsymbol{V}_h$, x orthogonal to these both. For all operators belonging to the rotational subgroup $\tilde{\boldsymbol{I}}_r$, the characters remain equal to 1 for all components of all vectors and tensors. For those operators belonging to the deflectional subgroup $\tilde{\boldsymbol{I}}_d$, the characters change their sign if the axis along which the component is measured is related (for polar vectors) or unrelated (for axial vectors) to the corresponding operation. For tensorial properties the diagonal components transform like scalars and the off-diagonal components like axial vectors.

It may be of interest to evaluate the numbers of independent non-zero coefficients remaining in eq. [3], up to a certain order, after applying the projection operator given by eq. [19], for a particular type of property. In Table 4 (ref. 15*c*) we have displayed such numbers for all combinations of site and molecule noncubic point groups.

TABLE 4. Numbers of independent non-zero coef cients up to the order $l = 6$ for scalar aggregate properties (from ref. 15*c*)

M \ S	C_i	C_{3v}	C_{2h}	D_{2h}	D_{4h}	D_{6h}
C_1'	455	155	231	119	59	41
C_2'	231	64	109	63	33	23
C_3'	155	55	79	41	21	15
C_4'	115	39	59	31	17	11
C_6'	75	27	39	21	11	9
D_2'	118	40	63	35	19	14
D_3'	81	28	43	24	13	10
D_4'	61	21	33	19	11	8
D_6'	41	15	23	14	8	7
S_2'	455	155	231	119	59	41
S_4'	115	43	59	31	17	11
S_6'	155	55	79	41	21	15
C_{2v}'	231	43	63	35	19	14
C_{3v}'	155	31	43	24	13	10
C_{4v}'	115	23	33	19	11	8
C_{6v}'	75	17	23	14	8	7
$C_{\infty v}'$	49	12	16	10	6	5
D_{2d}'	118	27	63	35	18	14
D_{3d}'	81	10	43	24	13	10
C_{1h}'	455	93	119	63	33	23
C_{2h}'	231	43	119	63	33	23
C_{3h}'	155	28	39	21	11	9
C_{4h}'	115	21	59	31	17	11
C_{6h}'	75	15	39	21	11	9
D_{2h}'	118	24	63	35	17	14
D_{3h}'	81	20	23	14	8	7
D_{4h}'	61	13	33	17	11	8
D_{6h}'	41	10	23	14	8	7
$D_{\infty h}'$	28	7	16	10	6	5

4. Double-rotor molecules

We have investigated single-rotor molecules (refs. 16), double-rotor molecules of linear, bent-planar, and *gauche* types (refs. 17), and triple-rotor molecules of some simple types (ref. 10, pp. 291–314),[2] for which the relevant expansions are given by eqs. [4] and [5]. We shall summarize the general results derived for double-rotor molecules (refs. 17*a*, *b*), and then illustrate the interest of these considerations in the case of the hyperfine couplings of hydrocarbon radicals (refs. 16*c*, 17*c*).

4.1. General considerations

We call a double-rotor molecule a structure consisting of a rigid frame (R), at least two-dimensional (with its bonds), bearing two rotating tops (R′ and R″). Such a molecule can be (*i*) linear (L) when the rotor axes are collinear, as in *para*-xylene; (*ii*) bent-planar (B) when these axes (whether they are parallel or not, and whether the bonded frame is planar or not) lie in the same plane, as in *ortho*- and *meta*-xylenes, dimethyl ether, dimethylamine, propane, or *cis*- and *trans*-dimethylethylenes; (*iii*) *gauche* (G) when the two axes are skew, as in *trans*-1,2-dimethylcyclopropane. It can be seen by inspection that the maximal symmetry of the bonded frame is D_{nh}, C_{2v}, or C_2 in the L, B, or G case, respectively.

We first consider the most symmetrical case (L) and, as before, deduce the Altmann group of the nonrigid structure from the symmetry properties of its constitutive parts. We define the principal axis of the molecule as the common axis of both rotors and the frame, and measure the rotation angles of R′ and R″, α' and α'', counterclockwise when viewed from R.

If R′ possesses an n'-fold axis, R″ an n''-fold axis, and R an n-fold axis (all these axes being collinear), isodynamic rotations of R′, R″, and R can be defined in the following way:

$$[21]\quad \boldsymbol{C}_{n'}^{p'}E(\alpha', \alpha'') = E(\alpha' + p'\cdot 2\pi/n', \alpha'')$$

$$[22]\quad \boldsymbol{C}_{n''}^{p''}E(\alpha', \alpha'') = E(\alpha', \alpha'' + p''\cdot 2\pi/n'')$$

$$[23]\quad \boldsymbol{C}_{n}^{p}E(\alpha', \alpha'') = E(\alpha' + p\cdot 2\pi/n, \alpha'' - p\cdot 2\pi/n)$$

The direct product of the corresponding cyclic groups constitutes the isodynamic subgroup $\tilde{\boldsymbol{I}}_r$:

$$[24]\quad \tilde{\boldsymbol{I}}_r = \boldsymbol{C}_{n'}\tilde{} * \boldsymbol{C}_{n''}\tilde{} * \boldsymbol{C}_{n}\tilde{}$$

The most symmetrical situation is that of a linear double-rotor molecule having in addition (*i*) "equivalent" tops (as in *para*-xylene) and (*ii*) σ_v planes in both rotors and the frame. In such a case one can define the additional (concerted) isodynamic operations, respectively called double switch, angle exchange, and switch exchange (ref. 17*a*):

[2]Also, J-Ph. Caniparoli and J. Maruani. Unpublished results.

[25] $VE(\alpha', \alpha'') = E(-\alpha', -\alpha'')$

[26] $WE(\alpha', \alpha'') = E(\alpha'', \alpha')$

[27] $UE(\alpha', \alpha'') = E(-\alpha'', -\alpha')$

The direct product of any two of the three corresponding binary groups constitutes the isodynamic subgroup $\mathbf{I}^{\sim}_{d}$, e.g.:

[28] $I^{\sim}_{d} = V^{\sim} * W^{\sim}$

The complete isodynamic group is again given by eq. [8]. For less symmetric L-type molecules, two or three of the operations [25]–[27] may be absent. For bent-planar molecules, the operation [23] never exists. For *gauche* molecules, the operations [25] and [27] also disappear. One may then characterize double-rotor molecules by the following symmetry labels (ref. 17*a*):

[29] $L(n', n'', n; v, w, u)$;

$$B(n', n''; v, w, u); \qquad G(n', n''; w)$$

where the numerical indices n', n'', and n are the orders of the bond symmetry axes and v, w, and u are logical indices taking on the value $(+-)$ 1 or 0 depending on whether or not the corresponding isodynamic operation exists. Once the symmetry label characterizing a particular property in a given molecule is known, it is easy to simplify the corresponding double Fourier series expansion (eqs. [4] and [5]), the harmonic coefficients of which obey various selection rules following from the invariance of the property under the operations defined by the symmetry indices (ref. 17*a*).

4.2. Hyperfine couplings

The hyperfine couplings of organic radicals can yield detailed information on their nuclear arrangement and electronic distribution when one knows the dependence of the couplings on the parameters. An important class of organic radicals have their spin density concentrated on a π-type molecular orbital, which may be essentially a single atomic orbital (as in methyl, ethyl, and *n*-propyl) or made up of several $2p^z$ orbitals centered on carbon or hetero atoms (as in nitroxide, hydrazyl, and conjugated radicals). The isotropic hyperfine splitting constants are scalar mononuclear properties and, therefore, their symmetry indices depend on the particular position of the labelling nucleus i in the system.

Let us consider, for instance, the radical *n*-propyl, where (with the above conventions) $R \in \boldsymbol{C}_{2v}$, $R' \in \boldsymbol{C}'_{2v}$, and $R'' \in \boldsymbol{C}''_{3v}$. The symmetry labels of the conformational potential V and of the hyperfine couplings for the α, β, and γ positions are therefore, respectively,

$$B(2, 3; 0, 1, 0);$$

$$B_{\alpha}(1, 3; 0, 1, 0); \; B_{\beta}(2, 3; 0, 0, 0); \; B_{\gamma}(2, 1; 0, 1, 0)$$

We have used the corresponding symmetry-adapted Fourier series expansions to fit the conformational variations calculated using various theoretical approaches. In particular, we have shown that the following approximate formula can be derived from this analysis (ref. 17*c*):

[30] $c_{\gamma}(\alpha', \alpha'') = \rho^{\pi}_{c_{\alpha}}[A + B\cos^2\alpha' \times (1 + a\cos\alpha'' + b\cos 2\alpha'')]$

and have compared the shape of this dependence with those experimental results in which measured couplings corresponding to known conformations were available. The parameter values derived from quasi-localized *ab initio* numerical results are $A = -0.2$ G; $B = 1.1$ G; $a = 1.8$, and $b = 1.3$ (standard deviation $\sigma = 0.1$). For the α and β couplings we have discussed the range of validity of the usual McConnell's relations (ref. 16*c*).

5. Conclusions

We have shown how the harmonic expansions of the physical properties of molecular systems can be symmetry-adapted using isodynamic operations, and how the resulting expressions can be used to determine the conformations. We have given examples of this procedure for molecular pairs and for double-rotor molecules and a general outline of it for molecular crystals. Other examples would include a small molecule interacting with a large aggregate or with a regular surface. In this latter case, one could either assimilate the rigid molecule M and surface site S to the two rotors of a (linear, bent planar, or *gauche*) supermolecule, as in Part 4, if S and M belong to symmetry groups C_{nv} and $C'_{n'v}$; or consider a surface site of symmetry C_{nv} and rigid molecule of any symmetry and build tables similar to Tables 2 and 3 of Part 3, if the center of M is on the axis of S; or, more generally, use a formalism derived from that of the molecular pair used in Part 2.

Acknowledgements

Parts of the work reviewed in this paper have benefited from discussions with Professor R. M. Pick (Paris) and Professor Y. G. Smeyers (Madrid), whose contributions are acknowledged.

1. W. J. ORVILLE-THOMAS (*Editor*). Internal rotation in molecules. Wiley, New York. 1974.
2. (*a*) A. J. STONE. Mol. Phys. **36**, 241 (1978); (*b*) W. A. STEELE. Mol. Phys. **39**, 1411 (1980); (*c*) W. J. BRIELS. J. Chem. Phys. **73**, 1850 (1980).
3. D. W. DAVIES. The theory of electric and magnetic properties of molecules. Wiley, New York. 1967.
4. R. E. MOSS. Advanced molecular quantum mechanics. Chapman and Hall, London. 1975.
5. J. MARUANI. *In* Electron and magnetization densities in molecules and crystals. *Edited by* P. Becker. Plenum Press, New York. 1980. pp. 633–692.
6. H. C. LONGUET-HIGGINS. Mol. Phys. **6**, 445 (1963).
7. S. L. ALTMANN. (*a*) Philos. Trans. R. Soc. London, A: **255**, 216 (1962); (*b*) Proc. R. Soc. London, A: **298**, 184 (1967); (*c*) Mol. Phys. **21**, 587 (1971); (*d*) Induced representations in crystals and molecules. Academic Press, New York. 1977.
8. (*a*) A. BAUDER, R. MEYER, and Hs. H. GÜNTHARD. Mol. Phys. **28**, 1305 (1974); (*b*) H. FREI, A. BAUDER, and Hs. H. GÜNTHARD. Top. Curr. Chem. **81**, 1 (1979); (*c*) Mol. Phys. **43**, 785 (1981).
9. G. S. EZRA. (*a*) Mol. Phys. **38**, 863 (1979); (*b*) Symmetry properties of molecules. Springer, Berlin. 1982.
10. J. MARUANI and J. SERRE (*Editors*). Symmetries and properties of nonrigid molecules. Elsevier, Amsterdam. 1983.
11. P. SCHUSTER, W. JAKUBETZ, G. BEIER, W. MEYER, and B. M. RODE. *In* Chemical and biochemical reactivity. *Edited by* E. D. Bergman and B. Pullman. Reidel, Dordrecht. 1974. pp. 257–282.
12. (*a*) G. A. STEVENS. Physica, **44**, 387 (1969); (*b*) A. TORO-LABBÉ and J. MARUANI. Mol. Phys. **51**, 323 (1984); (*c*) A. C. LEGON and D. J. MILLEN. Faraday Disc. Chem. Soc. **73**, 71 (1982).
13. (*a*) M. E. ROSE. Elementary theory of angular momentum. Wiley, New York. 1957; (*b*) A. R. EDMONDS. Angular momentum in quantum mechanics. University Press, Princeton, NJ. 1960. Chap. 4.

Can. J. Chem. Downloaded from www.nrcresearchpress.com by 112.217.228.212 on 09/07/12
For personal use only.

14. H. WATANABE. Operator methods in ligand field theory. Prentice Hall, Englewood Cliffs, NJ. 1966.
15. (*a*) R. E. MILLEN and J. C. DECIUS. J. Chem. Phys. **59**, 4871 (1973); (*b*) M. YVINEC and R. M. PICK. J. Phys. **41**, 1045 (1980); (*c*) A. TORO-LABBÉ and J. MARUANI. *In* Structure and dynamics of molecular systems. Vol. II. *Edited by* R. Daudel *et al.* Reidel, Dordrecht. 1986. pp. 35–56.
16. (*a*) J. MARUANI. Mol. Phys. **30**, 1685 (1975); (*b*) J. MARUANI, A. HERNANDEZ-LAGUNA, and Y. G. SMEYERS. J. Chem. Phys. **63**, 4515 (1975); (*c*) J. MARUANI, A. HERNANDEZ-LAGUNA, and D. BAHIER. J. Mol. Struct. **92**, 303 (1983).
17. (*a*) J. MARUANI, Y. G. SMEYERS, and A. HERNANDEZ-LAGUNA. J. Chem. Phys. **76**, 3123 (1982); erratum: J. Chem. Phys. **81**, 1519 (1984); (*b*) A. TORO-LABBÉ and J. MARUANI. Int. J. Quantum Chem. **22**, 115 (1982); (*c*) A. TORO-LABBÉ and J. MARUANI. J. Magn. Reson. **61**, 254 (1985).

Can. J. Chem. Downloaded from www.nrcresearchpress.com by 112.217.228.212 on 09/07/12
For personal use only.

Electron spin resonance spin-trapping study of peroxidation of human low density lipoprotein

DUBRAVKA KRILOV[1]
School of Medicine, University of Zagreb, Zagreb, Croatia, Yugoslavia

GRETA PIFAT
Ruđer Bošković Institute, Zagreb, Croatia, Yugoslavia

AND

JANKO N. HERAK
Department of Pharmacy and Biochemistry, University of Zagreb, A. Kovačića 1, 41001 Zagreb, Croatia, Yugoslavia

Received December 18, 1987

This paper is dedicated to Professor Charles A. McDowell on the occasion of his 70th birthday

DUBRAVKA KRILOV, GRETA PIFAT, and JANKO N. HERAK. Can. J. Chem. **66**, 1957 (1988).

The electron spin resonance spin-trapping method has been used for detection of radicals in human low density lipoprotein (LDL) solution saturated with oxygen. The trapped radicals could be detected after about a day in an antioxidant-free solution. Two types of radicals are formed and stabilized in the lipid domain of LDL. The nature of the trapped radicals remains unclear: kinetic considerations suggest the trapped radicals to be of the LO· type, while the spectroscopic parameters are in favour of L· type radicals.

DUBRAVKA KRILOV, GRETA PIFAT, et JANKO N. HERAK. Can. J. Chem. **66**, 1957 (1988).

On a fait appel à la méthode de piégeage des spin par résonance paramagnétique électronique pour détecter des radicaux dans des solutions de LDL humaines, saturées par de l'oxygène. Utilisant une solution ne contenant pas d'antioxydant, on a pu détecter les radicaux piégés après environ une journée. Dans le domaine des lipides des LDL, il se forme deux types de radicaux stabilisés. La nature des radicaux piégés n'est toutefois pas bien définie : des considérations cinétiques suggèrent que les radicaux piégés sont du type LO·; toutefois, les paramètres spectroscopiques favorisent plutôt des radicaux du type L·.

[Traduit par la revue]

Introduction

Low density lipoprotein (LDL) forms a distinct class of plasma lipoproteins. LDL plays a major role in supplying cells with cholesterol. A major step on the metabolic pathway of LDL is a receptor-mediated uptake by cells (1). Certain chemical modifications of LDL, such as ε-amino groups of lysine residues of the protein moiety (apo B) of LDL, abolish its binding to the LDL receptor (2). However, LDL thus modified can be recognized by the "scavenger" or acetyl-LDL receptor on the membranes of macrophages (3, 4). An important group of chemicals found capable of modifying the receptor binding properties of LDL are the lipid peroxidation products, malonaldehyde (5, 6) and 4-hydroxynonenal (7). Studies in several laboratories have shown that cultured endothelial cells or smooth muscle cells can also modify LDL so that it can be recognized by the acetyl-LDL receptor (8–11). This modification by cells involves peroxidation of LDL, resulting in drastic alterations of both lipid and protein components. Among other changes, a substantial increase of electrophoretic mobility, fragmentation of apoprotein B, hydrolysis of phosphatidyl choline, and loss of esterified cholesterol have been detected (10, 12, 13). Most of the "biologically" activated alterations could be mimicked by exposure of LDL to oxidative conditions in a cell-free medium (12–15). It has been generally accepted that free radicals initiate the peroxidation and the subsequent changes. The conclusion is mostly based on the fact that the peroxidation and the peroxidation-induced alterations of LDL can be inhibited by the addition of free radical scavengers (10, 13). Moreover, the effect of superoxide dismutase (SOD) on the modification of LDL undoubtedly proves the involvement of superoxide, $O_2^{\cdot-}$, (10, 11, 16–19).

In the present study we offer direct evidence, by electron spin resonance (esr), of the involvement of free radicals in the peroxidation of LDL. The esr spin-trapping method has been found to be very suitable for such purposes (20–22). With the use of this method it is possible not only to detect the presence of free radicals but possibly also to learn about the structure and location of the radical in a supramolecular structure like LDL. One of the aims of this study is also to see whether the initial stage of LDL peroxidation, i.e., radical formation, takes place only in the lipid domain of LDL or also on the protein.

Methods

Chemicals

Phenyl-*N*-*tert*-butyl nitrone (PBN) was purchased from Aldrich. Other chemicals used were analytical grade, also available from commercial sources (Sigma, Merck, Aldrich). All chemicals were used without further purification.

Lipoprotein isolation

Low density lipoprotein was prepared from freshly drawn (<24 h) human plasma from normolipidemic individuals. To the plasma, taken from many different donors, 20 μM butylated hydroxytoluene (BHT) was added. Plasma solvent density was adjusted to 1.050 g/cm^3 with a high density salt solution of KBr in 0.1 M Tris buffer, pH 7.50, containing 0.9% NaCl, 1 g/L EDTA, and 50 mg/L chloramphenicol. The supernatant was removed after centrifugation (23) for 24 h at about 40 000 rpm, at 4°C in a Beckman ultracentrifuge using a titanium T50 or T40 rotor. The pooled supernatants were adjusted to density 1.020 g/cm^3 in the same buffer with the same inhibitors. Recentrifuged as before, LDL was collected in the infranatant. LDL solutions were concentrated by N_2 pressure dialysis to concentrations of about 3–4 mg/mL. The final concentration of LDL was determined gravimetri-

[1]Author to whom correspondence may be adressed.

Can. J. Chem. Downloaded from www.nrcresearchpress.com by 112.217.228.212 on 09/07/12
For personal use only.

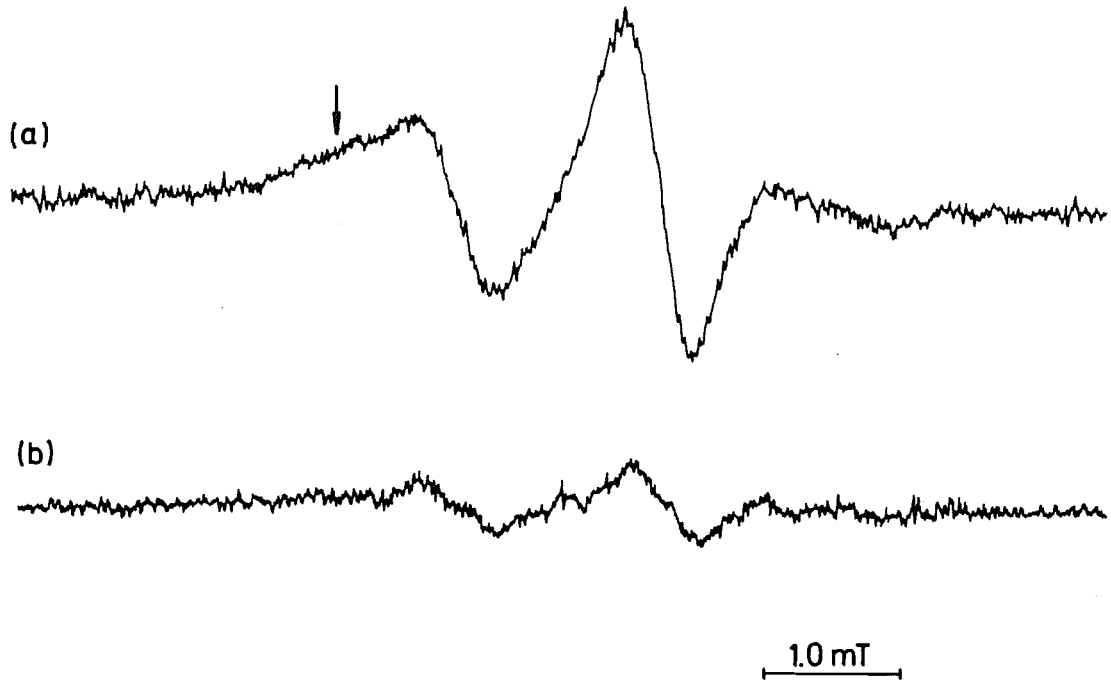

FIG. 1. Electron spin resonance spectra of PBN-trapped free radicals in oxygenated antioxidant-free LDL solution, recorded 3 days after removal of the antioxidants from the solution: (a) LDL in oxygen-saturated solution; (b) LDL in atmosphere after purging with N_2. The arrow indicates the presence of an extra broadening of the signal. The spectrometer settings: microwave power 20 mW, mod. amplitude 1 G, gain 1×10^5.

cally. The delipidation of LDL was performed by several extractions with chloroform:methanol (2:1, v/v) and once with diethyl ether at 4°C (24). The lipid fraction was left in the chloroform–methanol mixture and the protein fraction was kept in the buffer solution. The lipoprotein preparations were checked for purity by agarose gel electrophoresis.

Oxidation and electron spin resonance measurements

Before the oxidation, LDL preparations were dialyzed at 4°C for 24 h against six changes of at least 100 volumes of dialysate – 0.05 M Tris buffer adjusted to pH 7.4.

Phenyl-*N*-*tert*-butyl nitrone (PBN), used in this study as a spin trap, was dissolved in 0.05 M Tris buffer to the final concentration of 0.1 M. The oxidation of LDL solution was carried out in a similar way to that reported by Schuh *et al.* (12). The LDL solution in the dialysis bag was immersed in the PBN – Tris buffer and flushed with O_2 for at least 6 h before the esr measurements were made. Oxidation was carried out at room temperature.

The control LDL sample in the PBN – Tris buffer was flushed with nitrogen for half an hour and left at room temperature in the presence of air. The esr measurements were carried out with a Varian E-109 X-band spectrometer. The sample was placed in an aqueous sample flat cell. The measurements were made at room temperature, except when mentioned otherwise.

Results

Nitroxide esr spectra were quite regularly observed in all LDL samples with the spin trap (PBN), in which no antioxidants (EDTA or BHT) or other radical scavengers were present. If the LDL samples were exposed to the saturated oxygen solution, as described in the previous section, the esr signals recorded after several days were quite strong, as illustrated in Fig. 1a. In some samples the esr signals appeared after dialysis for only 6 h against the O_2-saturated buffer. In other cases it was necessary to wait for a day or longer for the signals to appear. However, it was essentially the same signal in all the samples. The esr spectrum contains a single major spectral component, and possibly a second minor component as suggested by subtle changes in the low-field portion of the spectrum. The esr spectrum of the control LDL sample (Fig. 1b) is essentially the same but of lower intensity.

The pattern changes upon prolonged storage of the sample at room temperature, as illustrated by the upper spectrum in Fig. 2. The sharper lines become even sharper and split into doublets. Under such conditions the broad line on the low-field side, indicated in Fig. 1, is repeatedly much better expressed. When the temperature is raised to about 40°C (lower tracing in Fig. 2), the sharper spectrum becomes even stronger and better resolved, and the broader component diminishes. This behaviour is not completely reversible; after lowering the temperature back to 20°C, the spectra are qualitatively the same, but the overall concentration of the radicals is increased.

After the radicals represented by the top curve in Fig. 1 had been developed, we made a separation of the three fractions of the oxidized LDL sample: water (buffer) fraction, LDL lipid fraction in the chloroform–methanol mixture, and apoprotein fraction in the buffer solution. Figure 3 shows the esr spectra recorded for the three fractions. It is seen that the stabilized radicals are associated only with the lipid fraction of LDL.

Discussion

It has been shown that free radicals are spontaneously formed in human plasma low density lipoprotein (LDL) exposed to molecular oxygen. The radicals are stabilized in the lipid domain of LDL, as demonstrated in Fig. 3. The esr lines are quite broad, indicating restricted motion of the trapped radical.

The radicals are the products of lipid peroxidation. Lipid peroxidation is an autooxidative process, initiated by abstraction of a weakly bonded allylic hydrogen by some strong oxidant (7, 22, 25–27). The initiators are oxidants like the hydroxyl radical (·OH), perhydroxyl radical (HO_2·), a chelated ion–oxygen complex ($Fe^{2+}O$ or $Fe^{2+}O_2$), or a triplet excited state of a photosensitizing dye. We do not see an obvious source of any of the above initiators in our system. However, even a small

Can. J. Chem. Downloaded from www.nrcresearchpress.com by 112.217.228.212 on 09/07/12
For personal use only.

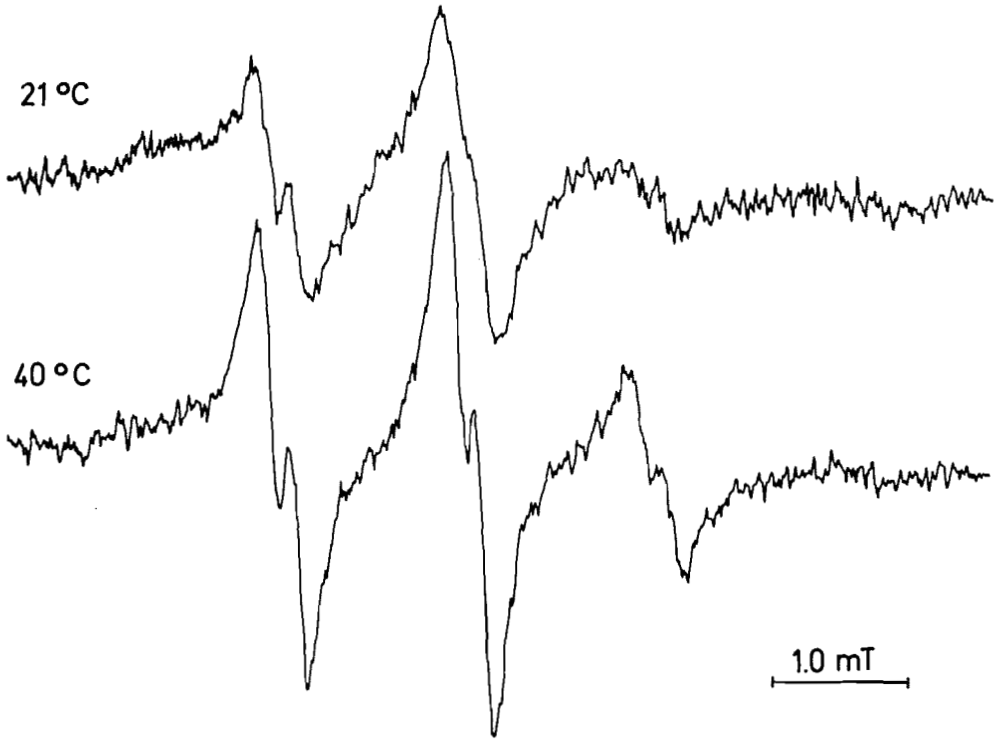

FIG. 2. Temperature dependence of the peroxidized LDL esr spectra, recorded 7 days after initiation of oxidation. The arrow indicates the existence of an additional broad signal. Other conditions the same as in Fig. 1.

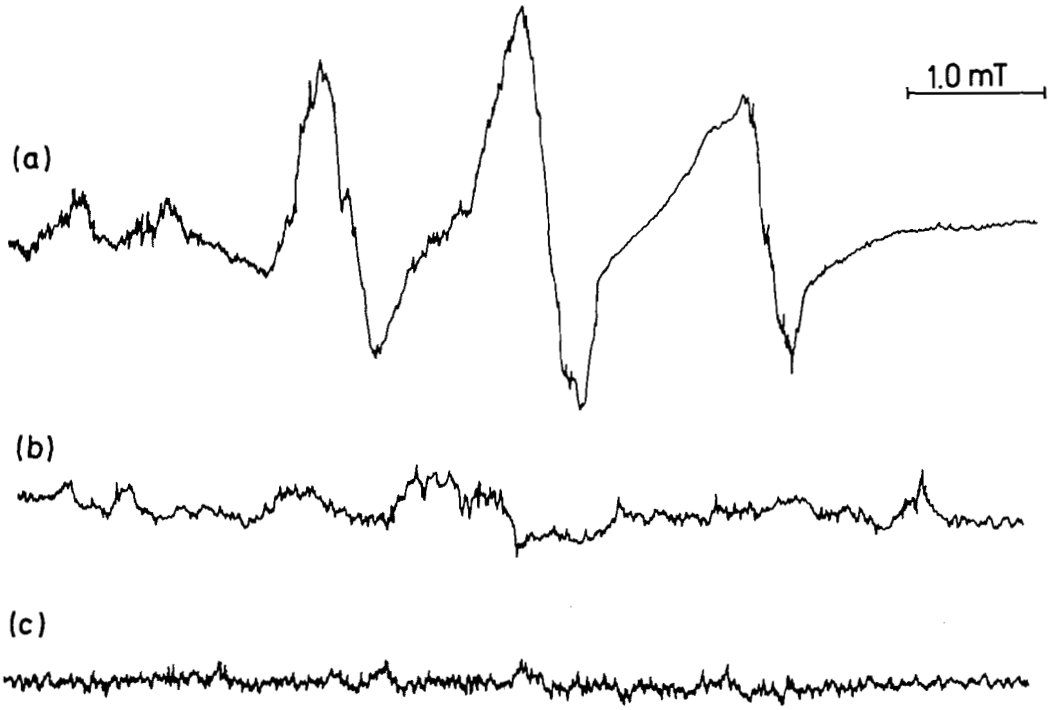

FIG. 3. Electron spin resonance spectra of three separate fractions of the oxygenized LDL sample: (a) the lipid fraction in the chloroform–methanol mixture; (b) the protein fraction in the buffer solution; (c) the buffer. Other conditions the same as in Fig. 1.

concentration of photosensitive dyes may be enough to initiate a slow process of lipid peroxidation. Alternatively, a small concentration of the transition metal ions, particularly Fe(II), might initiate oxygen radical production. The possible initiation given most attention is the perferryl ion, a complex between Fe(II) and O_2, or of Fe(III) and $O_2^{\cdot-}$:

$$[1] \quad Fe(II) + O_2 \rightarrow [Fe(II)O_2]^{2+} \leftrightarrows [Fe(III)O_2^{\cdot-}]^{2+}$$

This might be the source of the superoxide radical. Disproportionation of this species produces H_2O_2, which on reacting with $O_2^{\cdot-}$ via the Haber–Weiss reaction might produce the reactive hydroxyl radical:

Can. J. Chem. Downloaded from www.nrcresearchpress.com by 112.217.228.212 on 09/07/12
For personal use only.

[2] $H_2O_2 + Fe(II) \leftrightarrows OH^- + \dot{O}H + Fe(III)$

In our preparations the chelated metal ions are expected to be practically completely removed by extensive dialysis. However, the metal ions might be bound to some places in the LDL interior and the formation of the initiating oxygen radicals might be site specific (19, 27). Obviously, the process of initiation of lipid peroxidation in LDL requires further study.

Whatever the initiator, it is believed that the primary radical is a lipid alkyl radical L·. The next step is the reaction if L· with the spin trap or with O_2:

[3] $L\cdot + PBN \rightarrow \dot{L}$ (PBN)

[4] $L\cdot + O_2 \rightarrow LOO\cdot$

The competition between these two reactions is probably on the side of reaction [4]; i.e., the rate constant for reaction [3] is about 10^5–10^6 M^{-1} s^{-1} and that for reaction [4] about 10^9–10^{10} M^{-1} s^{-1} (28).

The difference in the rate constants of four orders of magnitude more than compensates for the large difference in concentrations of the competing reactants (3×10^{-4} M for O_2 and 10^{-1} M for PBN). Moreover, it is probable that in the lipid fraction, where the radicals are formed, concentration of O_2 is even higher. PBN is expected to be distributed between the bulk aqueous phase and the LDL lipid domain (29).

The peroxy radical may initiate further peroxidation of other lipids via the oxy radical, which may ultimately be trapped:

[5] $LOO\cdot + L'H \rightarrow LOOH + L'\cdot$

[6] $LOOH + E\,(\text{reduction}) \rightarrow LO\cdot + OH^-$

On the other hand, LOO· may be directly trapped, but is unstable (30) and may degrade to LO(PBN) (28). Thus, we do expect to find LO· radicals.

Unfortunately, because of the significant line broadening, the spectroscopic parameters of the trapped radicals in the present study cannot be determined with certainty. Our best estimate for the parameters for the radical represented in Fig. 2 is $a_N = 14.7$ G and $a_H = 2.6$ G. These parameters are closer to the values assigned to L· or L'· ($a_N = 14.4$ G, $a_H = 3.25$ G) than to LO· ($a_N = 13.8$ G, $a_H = 2.0$ G) trapped by PBN (28). It is possible that we observe a mixture of the two.

The two different spectra in our study may also mean two different environments for the same radical. Since the broader triplet spectrum could not be analysed in any detail, we presently have no further information to substantiate such an idea.

Our finding that primary radicals are formed in the lipid domain in LDL is in agreement with the conclusions of other authors. It has been quite generally agreed that the lipid peroxidation products are those species which form secondary damage by reacting with the apoprotein and altering the properties of LDL (10, 11, 13, 15, 18, 19, 25, 31). Induced cytotoxicity (16) is only one manifestation of the altered LDL structure.

Acknowledgements

We are grateful to Dr. M. Popović for carrying out delipidization of the LDL samples. This work was supported by The Scientific Council of Croatia and The Department of Health and Human Services through funds made available by the Yugoslav – U.S. Joint Board on Scientific and Technical Cooperation.

1. J. L. Goldstein and M. S. Brown. Ann. Rev. Biochem. **46**, 897 (1977).
2. K. H. Weisgraber, T. L. Innerarity, and R. W. Mahley. J. Biol. Chem. **253**, 9053 (1978).
3. J. L. Goldstein, Y. K. Ho, S. K. Basu, and M. S. Brown. Proc. Natl. Acad. Sci. U.S.A. **76**, 333 (1979).
4. M. S. Brown, S. K. Basu, J. R. Falck, Y. K. Ho, and J. L. Goldstein. J. Supramol. Struct. **13**, 67 (1980).
5. M. A. Fogelman, I. Shechter, J. Seager, M. Hokom, J. S. Child, and P. A. Edwards. Proc. Natl. Acad. Sci. U.S.A. **77**, 2214 (1980).
6. M. E. Haberland, M. A. Fogelman, and P. A. Edwards. Proc. Natl. Acad. Sci. U.S.A. **79**, 1712 (1982).
7. W. Jessup, G. Jürgens, J. Lang, H. Esterbauer, and R. T. Dean. Biochem. J. **234**, 245 (1986).
8. T. Henriksen, E. M. Mahoney, and D. Steinberg. Proc. Natl. Acad. Sci. U.S.A. **78**, 6499 (1981).
9. T. Henriksen, E. M. Mahoney, and D. Steinberg. Arteriosclerosis, **3**, 149 (1983).
10. D. W. Morel, P. E. Dicorleto, and G. M. Chisolm. Arteriosclerosis, **4**, 357 (1984).
11. J. W. Heinecke, L. Baker, H. Rosen, and A. Chait. J. Clin. Invest. **77**, 757 (1986).
12. J. Schuh, G. F. Fairclaugh, and R. H. Haschemeyer. Proc. Natl. Acad. Sci. U.S.A. **75**, 3173 (1978).
13. U. P. Steinbrecher, S. Parthasaraty, D. S. Leake, J. L. Witztum, and D. Steinberg. Proc. Natl. Acad. Sci. U.S.A. **81**, 3883 (1984).
14. R. Y. Ball, J. P. Bindmann, K. L. H. Carpenter, and M. Mitchinson. Atherosclerosis, **60**, 173 (1986).
15. H. Esterbauer, G. Jürgens, O. Quehenberger, and E. Koller. J. Lipid Res. **28**, 495 (1987).
16. D. W. Morel, J. R. Hessler, and G. M. Chisolm. J. Lipid Res. **24**, 1070 (1983).
17. A. W. Girotti. J. Free Radicals Biol. Med. **1**, 87 (1985).
18. K. Hiramatsu, H. Rosen, J. W. Heinecke, S. Wolfbauer, and A. Chait. Arteriosclerosis, **7**, 55 (1987).
19. J. W. Heinecke. J. Free Radicals Biol. Med. **3**, 65 (1987).
20. A. N. Saprin and L. H. Piette. Arch. Biochem. Biophys. **180**, 480 (1977).
21. E. G. Janzen. *In* Free radicals in biology. Vol. IV. Academic Press, New York. 1980. pp. 115–154.
22. K. M. Schaich and D. C. Borg. *In* Autoxidation in food and biological systems. *Edited by* M. G. Simic and M. Karel. Plenum Press, New York. 1980. pp. 45–69.
23. G. Pifat, J. Brnjas-Kraljević, J. N. Herak, G. Jürgens, and A. Holasek. Int. J. Biol. Macromol. **3**, 281 (1981).
24. M. D. Curry, W. J. McConathy, P. Alaupović, J. H. Ledford, and M. Popović. Biochim. Biophys. Acta, **439**, 413 (1976).
25. M. K. Logani and R. E. Davies. Lipids, **15**, 485 (1980).
26. E. N. Frankel. Progr. Lipid Res. **19**, 1 (1980).
27. S. Goldstein and G. Czapski. J. Free Radicals Biol. Med. **2**, 3 (1986).
28. P. B. McCay, E. K. Lai, J. L. Poyer, C. M. Dubose, and E. G. Janzen. J. Biol. Chem. **259**, 2135 (1984).
29. E. G. Janzen and G. A. Coulter. J. Am. Chem. Soc. **106**, 1962 (1984).
30. J. A. Howard and J. C. Tait. Can. J. Chem. **56**, 176 (1978).
31. U. P. Steinbrecher. J. Biol. Chem. **262**, 3603 (1987).

Can. J. Chem. Downloaded from www.nrcresearchpress.com by 112.217.228.212 on 09/07/12
For personal use only.

^{1}H nuclear magnetic resonance, differential scanning calorimetry, and electrical conductivity studies on the phase transitions of pentylammonium chloride and the cationic self-diffusion in its rotator phase

SHIGEHIKO IWAI, RYUICHI IKEDA, AND DAIYU NAKAMURA
Department of Chemistry, Faculty of Science, Nagoya University, Chikusa, Nagoya 464, Japan

Received December 29, 1987

This paper is dedicated to Professor Charles A. McDowell on the occasion of his seventieth birthday

SHIGEHIKO IWAI, RYUICHI IKEDA, and DAIYU NAKAMURA. Can. J. Chem. **66**, 1961 (1988).

Measurements of ^{1}H nmr, differential thermal analysis, and differential scanning calorimetry have revealed that solid pentylammonium chloride, cooled rapidly from room temperature, forms a mixture of the stable and metastable low-temperature phases below the phase transition temperature, T_{tr} (238 K). The sample annealed just below T_{tr} for 3 h was shown to consist of a single stable phase down to about 100 K, indicating the existence of a time-consuming phase transition taking place successively just below the normal transition. In the rotator phase obtainable above T_{tr} (257 K), ^{1}H nmr studies proved the presence of axial rotation of the whole cation about the long axis, similar to *n*-paraffins in their rotator phase. Above room temperature, the onset of the translational self-diffusion of the cations within 2D planes in the layer structure of the rotator phase was detected by measuring the temperature dependence of electrical conductivity as well as ^{1}H T_1 and $T_{1\rho}$. 2D self-diffusion constants and diffusional correlation times evaluated from the electrical conductivity observed between room and the melting temperatures indicate that the 2D cationic diffusion near the melting point is as fast as 3D self-diffusion in usual plastic crystals. Cationic motions in the two different rotator phases α and α′ are compared.

SHIGEHIKO IWAI, RYUICHI IKEDA, et DAIYU NAKAMURA. Can. J. Chem. **66**, 1961 (1988).

Des mesures de rmn du ^{1}H, d'analyse thermique différentielle et de calorimétrie à balayage différentielle ont révélé que le chlorure de pentylammonium solide, refroidi rapidement de la température ambiante à des températures inférieures à la température de transition, T_{tr} (238 K), forme un mélange de phases stables et métastables à basse température. On a montré qu'un échantillon recuit juste endessous de la T_{tr} pour trois heures consiste en une seule phase stable jusqu'à environ 100 K; ces résultats suggèrent qu'il se produit une transition de phase lente juste endessous de la transition normale. Dans la phase rotatrice qu'on peut obtenir au-dessus de la T_{tr} (257 K), les études par rmn du ^{1}H ont mis en évidence la présence d'une rotation axiale de l'ensemble du cation autour de l'axe allongé, comme on en observe avec le *n*-paraffines dans leur phase rotatrice. Au-dessus de la température ambiante, faisant appel à des mesures de dépendance de la conductivité électrique en fonction de la température ainsi que des T_1 et $T_{1\rho}$ on a détecté le début d'une auto-diffusion de translation à l'intérieur des plans bidimensionnels de la structure de la couche rotatrice. Les constantes d'auto-diffusion bidimensionnelles et les temps de corrélation de diffusion, qui ont été évalués à partir de la conductivité électrique observée entre les températures ambiante et de fusion, indiquent que la diffusion bidimensionnelle des cations près du point de fusion est aussi rapide que l'auto-diffusion tridimensionnelle dans les cristaux plastiques habituels. On a comparé les mouvements des cations dans les deux phases rotatrices différentes α et α′.
[Traduit par la revue]

Introduction

It has been reported that some *n*-alkylammonium halides have a smectic mesophase around room temperature (1–4), in which cations and anions are stacked alternately to form two-dimensional layers in the crystals. The orientations of the cations are dynamically disordered about their long axes which are perpendicular to the layer. The arrangement and the motion of the alkyl chains in this phase are quite similar to those in the rotator phase of the *n*-paraffins (5) obtainable in the temperature region below their melting point. Therefore, we call, hereinafter, this phase the rotator phase.

We have shown in the previous paper (6) that propylammonium chloride, $CH_3{\cdot}[CH_2]_2{\cdot}NH_3Cl$ [abbreviated to (pra)Cl] forms a rotator phase (α) around room temperature and transforms into another rotator phase (α′) at 406 K with a different ionic arrangement although the crystallographic unit cells of both phases have the same space group $P4/nmm$ as shown in Fig. 1. The α′-phase forms a bilayer structure where the nonpolar ends of two kinds of crystallographically inequivalent cations are packed head-to-head similar to the lamellar structure of liquid crystals. It has been revealed by the measurements of ^{1}H nmr and electrical conductivity in the α′-phase (6) that the cations perform translational self-diffusion at almost the same rate as that in plastic crystals (7, 8), whereas this motion is almost negligible in the α-phase, in spite of its quite similar layer structure.

In pentylammonium chloride, $CH_3{\cdot}[CH_2]_4{\cdot}NH_3Cl$ (hereafter abbreviated to (pna)Cl), the room-temperature phase (abbreviated to RTP) is also a rotator phase (9), being isomorphous with that of α′ of (pra)Cl as shown in Fig. 1. This phase can be heated without any solid–solid phase transition up to its melting point expected around 500 K (1). One of the purposes of the present study is to examine whether or not cationic rapid self-diffusion can be observed for (pna)Cl even at room temperature.

Southard *et al.* (9) measured the heat capacity of this salt and found two phase transitions at 222 and 246.5 K, and the appearance of some unusual thermal behavior at low temperatures. They reported that, when the sample was rapidly cooled to 90 K, a metastable phase was obtained and was slowly transformed on heating into a stable phase above 165 K. Consequently, they concluded that the transition observed at 222 K is that between the metastable and stable phases. On the other hand, Tsau and Gilson (1) have measured differential scanning calorimetry (DSC) of this compound and observed only one transition of 259 K when the sample was heated from 150 K. This transition temperature (T_{tr}) is different from either of the above two T_{tr}

Can. J. Chem. Downloaded from www.nrcresearchpress.com by 112.217.228.212 on 09/07/12
For personal use only.

Can. J. Chem. Downloaded from www.nrcresearchpress.com by 112.217.228.212 on 09/07/12
For personal use only.

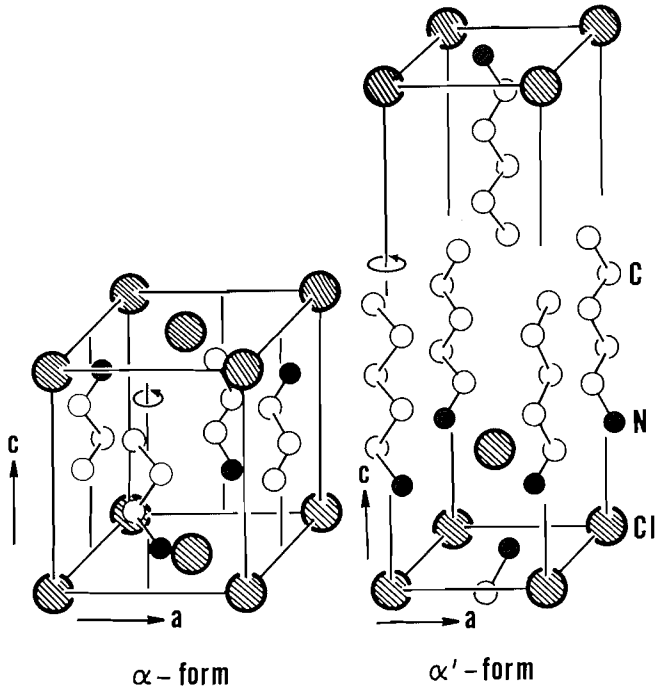

FIG. 1. The arrangement of heavy atoms in the unit cells of rotator phases α (propylammonium chloride) and α′ (pentylammonium chloride). The orientations of all cations are dynamically disordered about their long axes.

determined by Southard *et al.* (9). Furthermore, the transition enthalpy measured by DSC turned out to be several times larger than those of the old study (9).

Since the disagreement between these thermal studies seems to be arising from the possible coexistence of the stable and metastable phases at low temperatures, the preparation of a single phase and the measurement of its thermal behavior are indispensable to solve the present problem. In the present study, we have tried to reveal the feature of the cationic motions existing in the rotator phase of (pna)Cl and, at the same time, to clarify the relationship between the stable and metastable phases from the measurements of ^{1}H nmr, differential thermal analysis (DTA), DSC, and electrical conductivity.

Experimental

Pentylammonium chloride was prepared by neutralizing an ethanol solution of pentylamine (purity 99% from Nakarai Chemicals Co.) with hydrochloric acid. The crude crystals obtained by evaporating the solvent were recrystallized twice from a mixed solvent of ethanol and ether. Transparent thin plate crystals were obtained. Since this compound is hygroscopic, the purified sample, dried in a vacuum desiccator over phosphorus pentaoxide for a week, was finally dried in glass ampoules for nmr and DTA measurements by warming to 110°C for about 3 h under high vacuum. Then, the ampoules were sealed after putting in a small amount of dry nitrogen gas. For the DSC measurements, the dry sample was sealed in aluminum sample containers in a glove bag filled with dry nitrogen gas.

Second moments (M_2) of ^{1}H nmr absorptions were measured in the temperature range 100–450 K using a JEOL JNM-MW-40S wide line nmr spectrometer. ^{1}H spin–lattice relaxation times in the laboratory and rotating frame, T_1 and $T_{1\rho}$, respectively, were measured by use of pulsed spectrometers reported elsewhere (10–12). The inversion-recovery method was employed to measure T_1 at Larmor frequencies of 10.5, 11.5, and 20.0 MHz. $T_{1\rho}$ was determined at 32.5 MHz under a spin-locking rf field of 7.4 G. DTA was performed in a temperature range between 100 K and its mp using the apparatus already reported (13). In all of these measurements, a copper–constantan thermocouple was used to determine the sample temperature with an accuracy of ±1 K.

The measurements of DSC were carried out by use of a Perkin-Elmer DSC-1B calorimeter with a scanning rate of 5 K min^{-1}. The phase transition of succinonitrile at 233 K (14) and the melting of indium (15) were employed as calibration standards for determining enthalpy changes at phase transitions at low temperatures and mp, respectively.

Electrical conductivity was measured with an apparatus reported elsewhere (16) by applying an a.c. voltage of 1 kHz to the powdered sample formed as a disk of 1 cm diameter and about 1 mm thickness under a pressure of about 200 MPa. Graphite electrodes made by pressing finely powdered graphite were used.

Results

DTA curves recorded with a scanning rate of 2–3 K min^{-1} are shown in Fig. 2. When the sample was cooled from room temperature, exothermic anomalies were observed at 238 and 211 K. When the sample was warmed from about 100 K, two endothermic anomalies, one very weak and the other strong, were recorded at 238 and 256 K, respectively. With further heating of the sample, a strong and sharp heat absorption due to the melting was observed at 503 K. It was noticed that the anomaly observed at 238 K on the cooling runs was accompanied by another anomaly on the low-temperature side. When the scanning rate was decreased, the intensity of the low-temperature anomaly relative to the high-temperature one was increased. This result suggests that a phase transition taking a long time to be completed occurs just below the high-temperature transition with decreasing temperature. Then, we kept the sample temperature at 237 K for about 3 h just after passing the peak of the anomaly starting at 238 K. During this annealing process at the constant temperature, a gradual exothermic anomaly extending over about 3 h was observed as shown in Fig. 2*b*. When the sample was cooled after this annealing, no heat anomaly was recorded down to about 100 K, although various cooling rates were tried. On heating this sample from about 100 K, only a sharp endothermic anomaly was observed at 257 K, without any anomaly at 238 K, as depicted in Fig. 2*b*. Hereafter the sample annealed under the above condition will be called simply "the annealed sample".

Transition enthalpies determined on the warming runs of the DSC measurement for the sample cooled by three different methods are shown in Table 1 together with the reported data of the heat capacity studied by Southard *et al.*, (9) as well as those of DSC by Tsau and Gilson (1). The heat anomaly observed at 238 K on warming the sample in the DTA measurements could not be observed in our DSC experiments. This is probably because the DSC sample of 7 mg was too small to exhibit any measurable signal as compared with the DTA sample (about 0.2 g).

Temperature dependences of ^{1}H M_2 measured with increasing temperature from about 100 to 450 K are shown in Fig. 3 for the samples cooled in different ways, namely, the annealed sample and the sample cooled rapidly at a rate of about 20 K min^{-1} from room temperature to about 100 K. Hereafter, we call the sample cooled at this rate "the quenched sample". On heating the samples from about 100 K, the M_2 values of both annealed and quenched samples decreased gradually, but the former gave 3–4 G^2 higher M_2 values than those of the latter up to about 200 K, above which temperature both gave rise to about the same values at various temperatures up to 255 K. A sudden M_2 decrease from 13 to 3 G^2 was observed in both samples at 255 K, a temperature which agrees well with T_{tr} (257 K) deter-

TABLE 1. Phase transition temperatures (T_{tr}) and melting temperature measured by differential thermal analysis (DTA) along with transition enthalpies (ΔH) and entropies (ΔS) determined by differential scanning calorimetry (DSC) for *n*-pentylammonium chloride

	T_{tr}/K	Cooling condition from room temperature (DTA)	ΔH/kJ mol^{-1}	ΔS/J K^{-1} mol^{-1}	Cooling condition from room temperature (DSC)
Heating[a]	238	Cooled to ca. 100 K (2–3 K min^{-1})			
	256[b]		9.3	36	Cooled to 200 K(20 K min^{-1})
	256[b]		8.4	33	Cooled to 200 K(5 K min^{-1})
	257[b]	Annealed at 237 K for 3h, then cooled to ca. 100 K at 2–3 K min^{-1}	8.5	33	Annealed at 233 K for 2 h
	503[b]	(melting point)	10.0	20	
Cooling[a]	238				
	~211				
Heating[c]	259[d]		6.23	24.1	Cooled to 120 K (6 K min^{-1})
Cooling[c]	239[d]		2.59	10.9	
	217[d]		1.93	8.9	
Heating[e]	221.5[f]		1.184	5.35	Quenched to 165 K
	246.5[f]		0.134	0.545	
	222[f]		0.901	4.06	Annealed at 195 K for more than one month
	246.5[f]		2.377	9.64	

[a]Measured at a scanning rate of 2–3 K min^{-1}.
[b]The same T_{tr} was also measured by DSC.
[c]DSC data appeared in ref. 4, scanned at a rate of 6 K min^{-1}.
[d]T_{tr} determined by DSC.
[e]Data of heat capacity measurement reported in ref. 9.
[f]T_{tr} determined by heat capacity measurement.

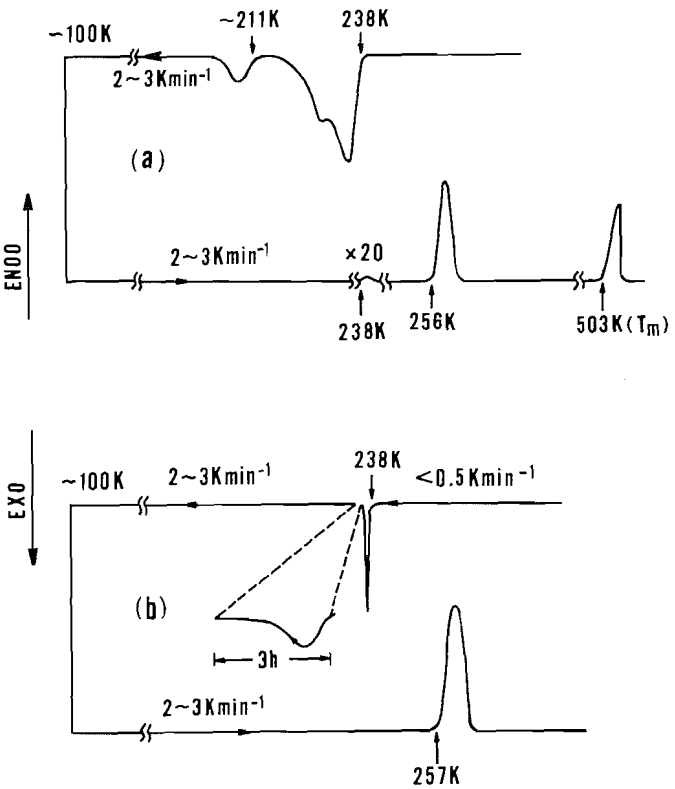

FIG. 2. DTA curves recorded for pentylammonium chloride. (*a*) Cooled with a constant rate down to about 100 K, and then heated up to the melting temperature (T_m). (*b*) In the course of cooling from room temperature, the sample temperature was kept constant at 237 K for 3 h while a broad exothermic anomaly was observed.

mined by DTA. The annealed sample showed a plateau of 23.5 G^2 between about 150 and 180 K. Above T_{tr} (257 K), M_2 decreased gradually with increasing temperature and reached 0.8 G^2 at 450 K.

Figure 4 shows the temperature dependence of ^{1}H T_1 measured at a Larmor frequency of 20 MHz in a temperature range between 100 K and room temperature for the annealed and quenched samples. Data are also shown in Fig. 4 for the annealed sample measured at 11.5 MHz in a narrow temperature range below T_{tr} (257 K). The annealed sample exhibited a T_1 minimum of 58 ms at about 140 K. With increasing temperature, T_1 showed a maximum value of about 400 ms around 220 K and then decreased up to T_{tr} (257 K). Above this T_{tr}, T_1 increased steeply with increasing temperature. Below T_{tr} (257 K), each run gave rise to a slightly different T_1 value and a constant value could not be determined at each temperature although the samples annealed for a longer time up to 7 h were used. This is the reason why the plotted values in Fig. 4 vary widely at low temperatures.

For the quenched sample, we have observed nonexponential behavior of T_1 below T_{tr} (257 K), which is unexplainable by a single relaxation process. We tentatively divided the observed inversion-recovery curve of the ^{1}H magnetization into two T_1 components because the presence of two different crystalline phases is expected from the DTA measurements. The intensity ratio of the short T_1 component to the long one was roughly estimated as $1/2 \sim 1/3$ in the whole temperature range below T_{tr} (257 K). As shown in Fig. 4, the T_1 values of the long component agree reasonably well with those for the annealed sample. The short T_1 values could not be determined accurately because this component gave a low intensity signal and it showed different T_1 values at each cooling run.

Can. J. Chem. Downloaded from www.nrcresearchpress.com by 112.217.228.212 on 09/07/12
For personal use only.

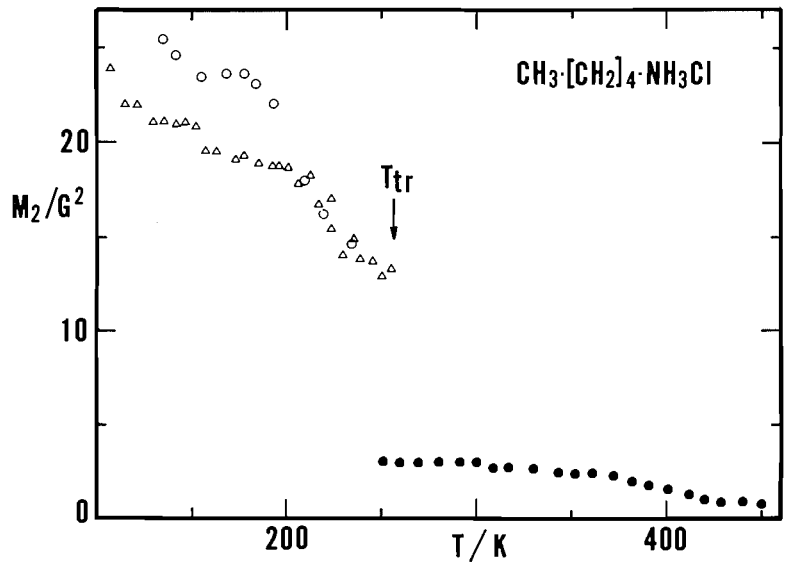

FIG. 3. Temperature dependences of ^{1}H nmr second moment (M_2) of pentylammonium chloride. Values in the room-temperature phase above the phase transition temperature (T_{tr}) are shown by ●. Those in the low-temperature phase below T_{tr} are given by △ and ○ for the quenched and annealed samples, respectively.

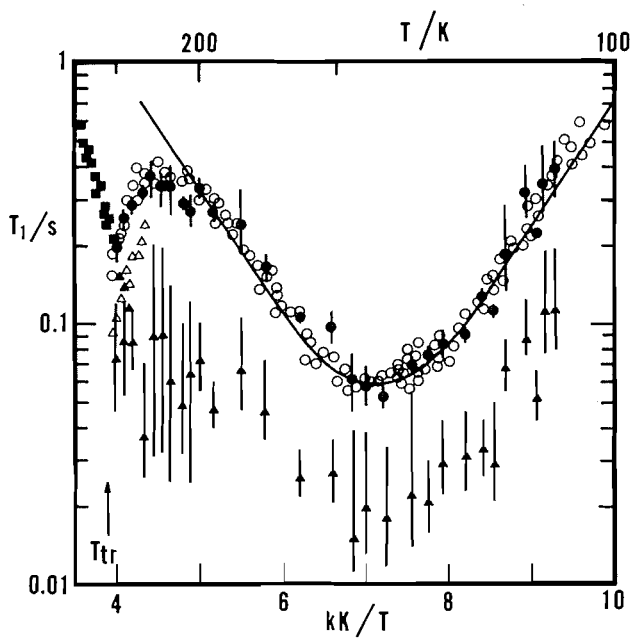

FIG. 4. Temperature dependences of ^{1}H nmr spin–lattice relaxation time T_1 in the room-temperature phase observed at 20 MHz (■), and the low-temperature phase for the annealed sample at 20 MHz (○) and 11.5 MHz (△). The quenched sample showed two T_1 values indicated by ● (long) and ▲ (short). The vertical line shows the extent of uncertainty for each T_1 value determined. The solid line is the best-fitted theoretical values.

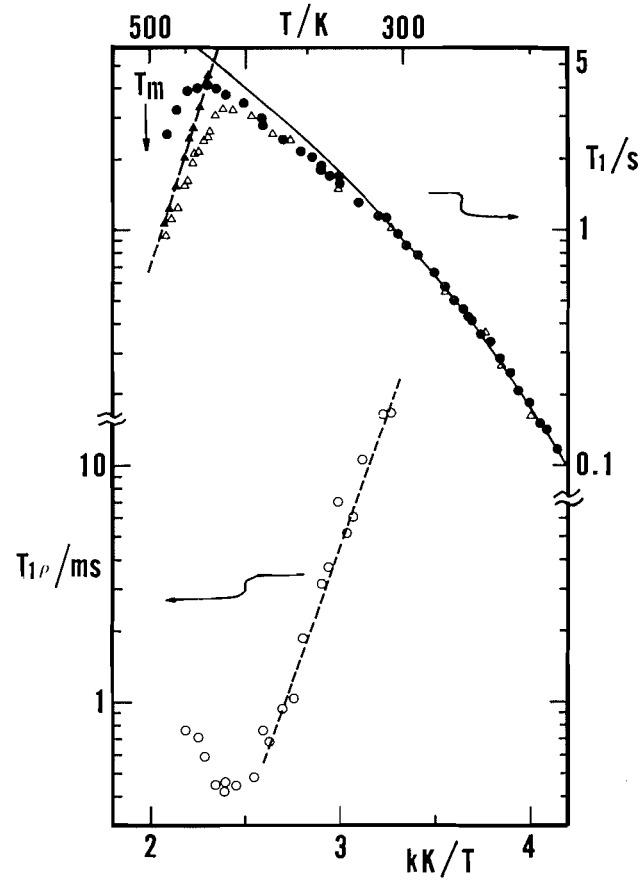

FIG. 5. ^{1}H nmr spin–lattice relaxation times in the laboratory frame T_1 and the rotating frame $T_{1\rho}$ for the room-temperature phase (rotator phase). T_1 values observed at 20 and 10.5 MHz are shown by ● and △, respectively, while $T_{1\rho}$ values at spin-locking field of 7.4 G are given by ○. T_1 observed at 10.5 MHz ($T_{1\,obs}$) was divided into two components $T_{1\,rot}$ (solid line) and $T_{1\,diff}$ (▲) which are expressed by $T_{1\,obs}^{-1} = T_{1\,rot}^{-1} + T_{1\,diff}^{-1}$. $T_{1\,diff}$ and $T_{1\rho}$ in the slow-motion limit were approximated by the dashed lines, whose slopes gave the activation energies of the cationic self-diffusion.

Figure 5 shows the temperature dependences of T_1 observed for RTP between T_{tr} (257 K) and its mp at the Larmor frequencies of 20 and 10.5 MHz, and $T_{1\rho}$ at an rf field of 7.4 G. In this phase, T_1 increased with increasing temperature and exhibited a maximum of 4.2 s around 440 K in the measurement at 20 MHz. Above this temperature, T_1 decreased rapidly up to mp. On the other hand, $T_{1\rho}$ yielded a minimum of 0.43 ms around 415 K.

The temperature dependence of electrical conductivity σ for RTP is shown in Fig. 6. The conductivity value of the order of

Can. J. Chem. Downloaded from www.nrcresearchpress.com by 112.217.228.212 on 09/07/12
For personal use only.

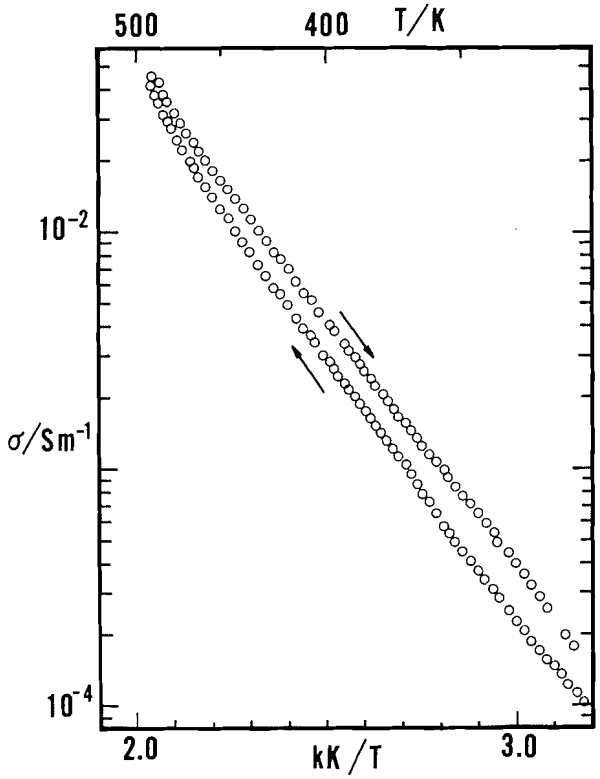

FIG. 6. The temperature dependence of electrical conductivities (σ) in the room-temperature phase (rotator phase) measured at 1 kHz. Arrows indicate the direction of the temperature change during the measurements.

10^{-5} S m^{-1} at room temperature, increased continuously with increasing temperature to that of the order of 10^{-2} S m^{-1} above 440 K. Near the mp σ increased more steeply with temperature than in the lower temperature range, and, on cooling from the neighborhood of the mp, it gave slightly higher values than those obtained for the heating runs. This thermal hysteresis seems to be due to the deformation of the sample by increasing the temperature, since the sample is fixed by the graphite electrodes. Such deformation is expected because slight plasticity of the crystals was observed even at room temperature when we tried to grind the crystal in a mortar. The plastic flow of the crystals could also be observed when a pellet was formed from the powder sample by applying pressure. A completely transparent pellet was prepared by a pressure of about 200 MPa at room temperature.

Discussion

Phase transitions

As shown in Fig. 2 and Table 1, a phase transition was always observed at 257 K in our DTA and DSC measurements performed at various scanning rates. This T_{tr} agrees well with that of 259 K reported by Tsau and Gilson (1), although it disagrees with either of two T_{tr}'s of 222 and 246.5 K observed in the heat capacity study (9). Since this transition at 257 K was observed for the annealed sample, it can be regarded as the transition between the low-temperature stable phase (abbreviated hereafter to LTSP) and RTP.

The experimental result that an exothermic DTA curve was recorded when the sample temperature was kept constant just after passing the exothermic peak starting at 238 K on the cooling runs indicates that the high temperature peak corresponds to the phase transition from RTP to a metastable phase, which transforms very slowly into LTSP. The exothermic anomaly superimposed on the low-temperature side of the peak starting at 238 K showed in Fig. 2*a* is attributable to this transition to LTSP partially occurring. Accordingly, the anomalies observed at 211 and 238 K on cooling and heating, respectively, are considered to be due to a transition between metastable phases, because these peaks disappeared in the measurements of the annealed sample. These results imply that unannealed samples consist of a mixture of LTSP and LTMP below T_{tr} (257 K).

With these interpretations of our DTA results, the two phase transitions reported by Southard *et al.* (9) at 222 and 246.5 K would correspond to those at 238 and 257 K on the heating runs in our measurements, respectively.

The fact that almost the same entropy change for the transition at 257 K was obtained for the samples cooled at the three different rates in our DSC measurement indicates that the entropy difference between LTSP and LTMP is not large and/or LTMP is contained only in a small amount in the quenched sample. It is noted that this transition entropy amounting to 33 J K^{-1} mol^{-1} is much larger than the melting entropy of 20 J K^{-1} mol^{-1}. The same reversed relationship of the transition entropies has been also found in *n*-butylammonium bromide (17) and iodide (18) for the transition from the low-temperature phase to the rotator one isomorphous with RTP of the present salt. This unusual relationship is well known in the plastic crystals, in which isotropic reorientations and translational self-diffusion of globular molecules are observed to take place quite frequently (7, 8). Accordingly, RTP can be expected to be in a highly dynamically-disordered state.

Second moments of ^1H nmr absorptions

Theoretical values of M_2 for (pna)Cl in five different motional states of the cations were calculated by use of Van Vleck's method (19). We employed the same bond angles and distances as those used in our M_2 calculation of *n*-butylammonium bromide (17) and iodide (18). *Trans* conformation of the alkyl chain was also assumed. Inter-ionic contributions to M_2 were roughly estimated using the lattice parameters in RTP reported by Southard *et al.* (9). The results of these M_2 calculations are summarized in Table 2, where the 180° chain flip means the reorientation of the cation by 180° about the chain axis, and the chain rotation is the reorientation jumps of cations among more than two orientations about the same axis.

The M_2 plateau of 23 G^2 exhibited by the annealed sample around 160 K agrees well with the calculated value for the model involving the reorienting CH_3 groups about their C_3 axes. On the other hand, the quenched sample yielded M_2 smaller than this plateau value by about 4 G^2 in the same temperature range. This implies that the quenched sample includes crystals in which the cations perform motions averaging magnetic dipolar interactions other than the CH_3 reorientation. Both annealed and quenched samples showed almost the same M_2 of 13 G^2 at the temperatures just below T_{tr} (257 K). This value is much smaller than the calculated M_2 for the cations with the CH_3 and NH_3^+ groups reorienting about their C_3 axes, but it is rather close to the theoretical value for the cations performing the 180° flip in addition to the above motions. This suggests that some kind of whole-cationic motions which inevitably result in disordered structures of the crystal take place even in the low temperature phases.

The small M_2 of 3 G^2 observed above T_{tr} (257 K) indicates the

Can. J. Chem. Downloaded from www.nrcresearchpress.com by 112.217.228.212 on 09/07/12
For personal use only.

TABLE 2. Calculated second moments (M_2/G^2) of pentylammonium chloride at various motional states of the cations

Contribution	Rigid lattice	CH_3 rot	$(CH_3 + NH_3^+)$ rot	$(CH_3 + NH_3^+)$ rot +cation 180° flip	$(CH_3 + NH_3^+$ +cationic axial) rot
Intra-ionic	23.1	19.0	13.7	10.2	4.0
Inter-ionic	~6.3	~5.1	~4.4	~2.5	~1.9
Total	29.4	24.1	18.1	12.7	5.9

onset of uniaxial rotation of cations about the long axis. According to Southard *et al.* (9), the tetragonal unit cell of RTP has the atomic arrangements as shown in Fig. 1. In this structure, the authors concluded that the cations, with respect to their orientation about their long axis pointing along the *c*-axis, are dynamically disordered in good agreement with the present M_2 analysis. The observed M_2 values in RTP, especially at high temperatures, however, are much smaller than the calculated value for the uniaxial rotation model. This result requires other kinds of dynamical positional disorders of the protons. As conceivable motions of the cations, we can envisage for example, partial conformational disorder of the alkyl chain, rotational and translational modes of lattice vibrations with large amplitudes, and self-diffusion of the cations, that is, cationic translational jumps to the vacant nearest neighbor lattice sites.

Spin–lattice relaxation times

Low-temperature stable phase (LTSP)

Since no detectable non-exponential T_1 behavior was seen for the annealed sample below T_{tr} (257 K), this sample can be regarded as almost pure LTSP including no significant amount of LTMP. The T_1 curve with a minimum observed for the annealed sample below about 200 K can be attributed to magnetic dipolar relaxation due to molecular motions, which is usually analyzed by the BPP theory (20). When T_1 is influenced by a single motional process, this theory predicts a T_1 curve expressed as

$$[1] \quad T_1^{-1} = C[\tau/(1 + \omega^2\tau^2) + 4\tau/(1 + 4\omega^2\tau^2)]$$

where C, τ, and ω denote the motional constant, the correlation time of the motion, and the angular Larmor frequency, respectively. We assume an Arrhenius type relationship between τ and the activation energy E_a of the motion written as

$$[2] \quad \tau = \tau_0 \exp(E_a/RT)$$

where τ_0 is the correlation time in the limit of infinite temperature. Equations [1] and [2] were fitted to the observed data by the least-squares method. The best-fitted calculated T_1 curve is shown in Fig. 4. The parameters, C, τ_0, and E_a determined are given in Table 3. The T_1 minimum can be attributed to the CH_3 reorientation about the C_3 axis by referring to the M_2 analysis in LTSP. In fact, the fitted motional constant C agrees well with the theoretical value of 1.67×10^9 s^{-2} for the CH_3 reorientation which was calculated using the equation given by (6)

$$[3] \quad C = \tfrac{3}{14}\tfrac{9}{20}\gamma^4\hbar^2 r^{-6}$$

where γ is the gyromagnetic ratio of the proton and the interprotonic distance r in a CH_3 group was evaluated by use of the geometry employed in the M_2 calculation. The fact that the observed T_1 curve could be explained well by a single BPP equation implies the following. The CH_3 groups are placed in such a homogeneous crystal field that no distribution of the correlation time (21) or non-exponential T_1 behavior can be observed. In the low-temperature phases of *n*-propyl- and *n*-butylammonium bromides (6, 17), corresponding to LTSP of the present salt, however, we have observed unusual T_1 curves explainable by considering distributions of τ. This suggests the presence of microscopic inhomogeneity for the atomic arrangements in these materials.

TABLE 3. Activation energies (E_a), pre-exponential factors (τ_0), motional constant (C), and motional modes of pentylammonium ions

Phase	E_a/kJ mol^{-1}	τ_0/s	$C/10^9$ s^{-2}	Motion mode
LTSP	9.5±1	1.2×10^{-12}	1.5(1.67)[d]	CH_3 rot
	28±2			NH_3^+ rot
RTP	6±1[a]	3×10^{-15}[b] (125±10 K)[c]	(1.38)[e]	Whole cationic rotation
	50±4			T_1 } 2 D self-
	44±2			$T_{1\rho}$ } diffusion

[a] E_{aR} in text.
[b] τ_{0R} in text.
[c] Fitted value of T_0 (see text).
[d] The value in parentheses is the theoretical value.
[e] Assumed value.

The T_1 decrease observed above 200 K with increasing temperature is attributable to another molecular motion because a clear frequency dependence of T_1 was observed. The estimated activation energy for this motion from the slope of the log T_1 vs. T^{-1} plot is 28 ± 2 kJ mol^{-1}. The mode of this motion seems to be assigned to the NH_3^+ reorientation about the C—N bond because similar decreases of T_1 due to the NH_3^+ reorientation were observed in the same temperature range in *n*-butylammonium halides (17, 18).

Low-temperature metastable phase (LTMP)

The experimental result that T_1 for the long and major component in the two component values, separated from the observed free induction decay signals for the quenched sample, agrees well with that of LTSP indicates that the quenched sample consists mostly of LTSP. The short T_1 component regarded as a single component, can be assigned to LTMP. Since the T_1 values of the short component could not be determined accurately, it is difficult to discuss quantitatively its temperature dependence. The broad T_1 minimum of the short component appearing around 140 K seems to be partly contributed from the CH_3 reorientation. The T_1 values shorter than those in LTSP observed over the whole temperature range below T_{tr} (257 K) imply that other motional processes including such as those relating to the whole cationic motions also contribute to the relaxation, suggesting the presence of a more disordered atomic arrangement in LTMP than those in LTSP.

Room-temperature phase (RTP)

In this phase, T_1 increased with temperature and no frequency dependence of T_1 was observed up to ca. 400 K. It is noted that the gradient of the log T_1 vs. T^{-1} curve decreases with increasing

Can. J. Chem. Downloaded from www.nrcresearchpress.com by 112.217.228.212 on 09/07/12
For personal use only.

Can. J. Chem. Downloaded from www.nrcresearchpress.com by 112.217.228.212 on 09/07/12
For personal use only.

temperature. This is unexplainable in terms of the usual Arrhenius type excitation given by eq. [2]. Unusual T_1 curves similar to the above have been observed in the supercooled liquid state of glass-forming substances such as glycerol (22, 23), in which the correlation time τ_R of molecular reorientation can be given as

$$[4] \quad \tau_R = \tau_{R0} \exp [E_{aR}/R(T-T_0)]$$

where τ_{R0} and E_{aR} are defined for the molecular reorientation in a similar way as done for τ_0 and E_a in eq. [2], respectively. T_0 is a reference temperature supposed to exist near the glass transition temperature. In a previous study on (pra)Cl and (pra)Br (6), we have observed the T_1 behavior quite similar to that of the present salt in the room temperature phases having the crystalline unit cell with the same space group as that in RTP of the present salt. In these tetragonal phases containing cations with highly disordered orientations about their long axes, it is possible for the present salt to form an orientational glass at low temperatures. We performed a curve fitting calculation for the T_1 values observed in RTP up to 350 K using eqs. [1] and [4]. In this calculation, the motional constant C in eq. [1] was roughly evaluated using the equation given by (24)

$$[5] \quad C = \tfrac{2}{3}\gamma^2 \Delta M_2$$

where ΔM_2 is the M_2 reduction due to the onset of the cationic motion at room temperature. Since we have no information about the mode of this motion, we assumed ΔM_2 due to this motion to be equal to the difference between the calculated M_2 for the axial rotation of cations given in Table 2 and the observed M_2 just above T_{tr} (257 K), namely, $\Delta M_2 = (5.9 - 3.0)$ G^2. The best-fitted T_1 curve determined by inspection is shown in Fig. 5. The most probable values of the unknown parameters, E_{aR}, τ_{R0}, and T_0 are given in Table 3. The E_{aR} value of 6 kJ mol^{-1} obtained in the present calculation is very close to those of 6.4 and 4.8 kJ mol^{-1} experimentally obtained for the axial rotation of the cations in (pra)Cl and (pra)Br, respectively. The small activation energies indicate quite free whole-cationic rotation taking place already at room temperature.

With increasing temperature the T_1 decrease observed above about 400 K is attributable to the existence of a magnetic dipolar mechanism due to a new cationic motion because a frequency dependence of T_1 was observed. This new motion can be considered as the translational self-diffusion of the cation in the crystal by the reason given in the following section, although several other motions can be expected to occur. The T_1 data observed at 10.5 MHz above 400 K can be separated into two components given by

$$[6] \quad T_1^{-1} = T_{1\,\mathrm{diff}}^{-1} + T_{1\,\mathrm{rot}}^{-1}$$

where $T_{1\,\mathrm{diff}}$ and $T_{1\,\mathrm{rot}}$ are spin–lattice relaxation times due to the cationic self-diffusion and the whole-cationic uniaxial rotation, respectively. The whole-cationic uniaxial rotation is, as already described above, due to the relaxation mechanism involving the non-Arrhenius type correlation time. We estimated $T_{1\,\mathrm{rot}}$ by extrapolating the fitted non-Arrhenius T_1 curve to the higher temperature range. The $T_{1\,\mathrm{diff}}$ values determined by substituting $T_{1\,\mathrm{rot}}$ and T_1 observed at 10.5 MHz into eq. [6] are exhibited in Fig. 5.

Since RTP has the layer structure as shown in Fig. 1, it is highly probable that cationic self-diffusion within each layer occurs more frequently than that in the direction perpendicular to the layer. In such 2D diffusion, it has been reported (25, 26) that the relaxation times are expressed differently from the usual BPP equations (20). It can be shown, however, that the T_1 expression becomes almost the same as that for the BPP equation in the limit of slow motion, $\omega\tau_D \gg 1$ where τ_D is the correlation time of the self-diffusion of the cation (27, 28). Therefore, the activation energy for self-diffusion, evaluated from the slope of the log $T_{1\,\mathrm{diff}}$ vs. T^{-1} plot became 50 ± 4 kJ mol^{-1}.

The observed $T_{1\rho}$ minimum can also be assigned to cationic 2D self-diffusion by taking into account the general relationship between T_1 and $T_{1\rho}$ curves. We evaluated the activation energy as 44 ± 2 kJ mol^{-1} from the slope of the log $T_{1\rho}$ vs. T^{-1} plots observed for the low temperature side of the minimum in a similar manner to the analysis of T_1. This activation energy is close to that obtained from the T_1 data, supporting the suggestion that the same motional process contributes to both T_1 and $T_{1\rho}$. The activation energy for the cationic self-diffusion in (pra)Cl has been determined as about 40 kJ mol^{-1} (6) in a crystal with the layer structure isomorphous with RTP of the present salt. The fact that this value is a little smaller than that of the present salt is attributable to the differences in the size and mass of the two cations.

Electrical conductivity

The ionic conductivity in RTP having the layer structure is expected to be anisotropic. In other words, the conductivity within the layer and perpendicular to the cationic long axis ($\sigma_\perp$) is considered to be different from that in the direction parallel to this axis ($\sigma_\parallel$). For the powder sample, the observed conductivity can be expressed as

$$[7] \quad \sigma = (1/3)\sigma_\parallel + (2/3)\sigma_\perp$$

Here, we assume that the translational jumps of the ions within the layer take place much more frequently than those in the direction perpendicular to the layer, as already assumed in the analysis of the $T_{1\rho}$ data. Then we have

$$[8] \quad \sigma \simeq (2/3)\sigma_\perp$$

The self-diffusion constant $D_\perp$ in the direction perpendicular to the cationic long axis can be written, using the Nernst–Einstein equation as

$$[9] \quad D_\perp = \frac{3\sigma\lambda kT}{2(Ze)^2 N}$$

where λ, Ze, and N denote the spatial correlation factor, the electric charge of the diffusing ion and the number of the diffusing ions in a unit volume, respectively. For the monovacancy diffusion model within a 2D square lattice, λ has been calculated as 0.46694 (29). The temperature dependence of $D_\perp$, obtained by substituting the observed σ values into eq. [9], is shown in Fig. 7. Between room temperature and about 460 K, the plot of log $D_\perp$ vs. T^{-1} showed a linear relationship, indicating that a single Arrhenius-type activation process of diffusion accounts for most of the observed conductivity. From the slope of the log $D_\perp$ vs. T^{-1} plot, the activation energy was determined to be 46 ± 2 kJ mol^{-1}. This value agrees well with 44 and 50 kJ mol^{-1} obtained for cationic self-diffusion from the T_σ and T_1 data, respectively. Accordingly, it is concluded that the conductivity is determined by the cationic self-diffusion.

For 2D self-diffusion, the diffusion constant can be approximately related to the correlation time τ_D of the 2D self-diffusion by the equation (27, 30):

$$[10] \quad D_\perp = d^2/4\tau_D$$

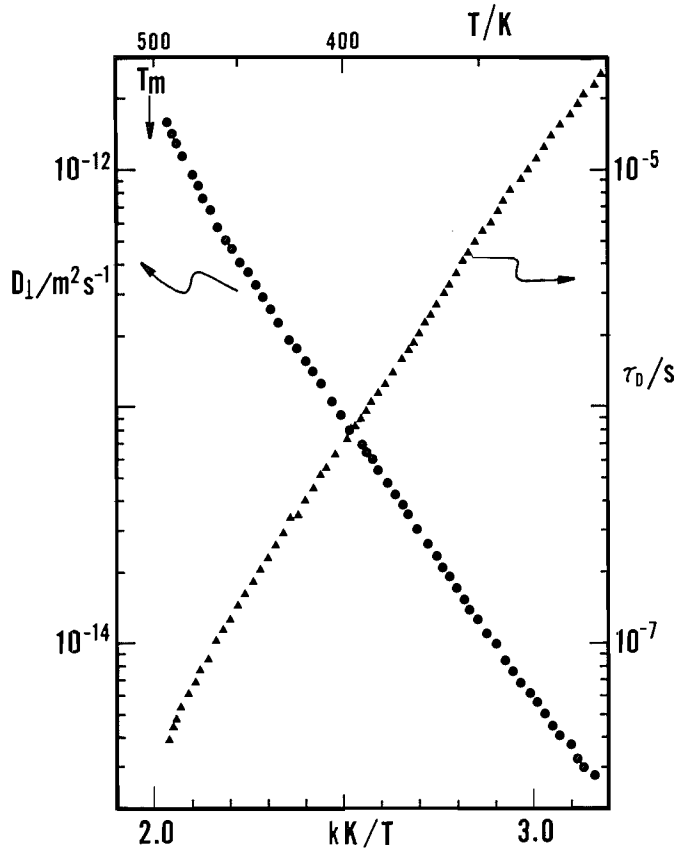

FIG. 7. The 2D diffusion constant $D_\perp$ and diffusion correlation time τ_D of pentylammonium cations in the room-temperature phase (rotator phase).

where d is the nearest jump distance. In the present monovacancy model, the cations can jump only to the nearest vacant lattice site of the cation. Then d can be taken as the length of the a axis in the tetragonal unit cell, reported as 5.01 Å at room temperature (2). The τ_D values evaluated by substituting $D_\perp$ into eq. [10] are shown in Fig. 7. Very short τ_D values of the order of 10^{-8} s were obtained above 460 K.

These short correlation times are of the same order of magnitude as those for the 3D self-diffusion observed in "ionic plastic crystals" such as the highest-temperature solid phases of methylammonium nitrate (16) and perchlorate (31). It has been reported also in the plastic phases of molecular crystals (7, 8) that diffusion correlation times are shortened to the order of 10^{-7} -10^{-8} s in the neighborhood of the respective melting temperatures. These results indicate that RTP of the present salt contains a high concentration of lattice defects at higher temperatures as is the case with the plastic crystals. In fact, marked plasticity of the crystals was definitely observed even at room temperature, as mentioned above. This free translational motion of cations can be considered as one of the origins of the large entropy change observed at the phase transition from LTSP to RTP. It should be noted, however, that this disorder with respect to the occupation of the lattice sites as well as the orientational disorder about the cationic long axis, observed in the present salt, takes place within layers. In each layer the rod-like cations, with partially deformed structures due to the conformational disorder, still do not gain the freedom of isotropic diffusion and isotropic reorientation that occur in the plastic crystals as well as in "the ionic plastic crystals."

Cationic motions in the rotator phases (α and α′)

It is interesting to compare the cationic motions found in RTP (α′-phase) of (pna)Cl and those in the room-temperature phase (α) and the high-temperature phase (α′) of (pra)Cl already reported (6). In (pra)Cl, the α′-phase can be obtained in a narrow temperature range of about 30 K just below its mp of 436 K, although it may be supercooled down to about 350 K. In (pna)Cl, on the other hand, the α′-phase is stable in a much wider temperature range, 257–503 K. Accordingly, we are interested in whether or not the high mobility of the cations in the α′-phase, which was observed only in the neighborhood of mp for (pra)Cl, exists in the isomorphous phase of (pna)Cl down to room temperature.

It is noted in the experimental results that surprisingly good agreement could be seen in the T_1 and M_2 values of these two salts observed in the temperature range (about 360–435 K) where both salts are in the α′-phase. This implies that the motional states of cations in these two salts are almost the same in the α′-phase. The fact that (pna)Cl in the α′-phase exhibited a constant M_2 of about 3 G^2 around room temperature shows a marked contrast to a large M_2 of 5.5 G^2 observed in the α-phase of (pra)Cl in the same temperature range. This indicates that the α′-phase has a much more disordered arrangement of cations than the α-phase even though comparison was made at the same temperatures.

An interesting result is that the non-Arrhenius type T_1 curve observed in the α-phase of (pra)Cl and (pra)Br (6) was also detected in (pna)Cl but in its α′-phase. At the present stage, we cannot explain definitely this unusual T_1 behavior, although it seems likely as described before that the orientational disorder of the cations about the long axis present in both phases is closely related to this phenomenon.

The electrical conductivity measurements can indicate another interesting difference between the cationic motions of the two salts. The conductivity in the α′-phase of (pra)Cl was just one order of magnitude higher than that in the same phase of (pna)Cl measured at the same temperatures. This result is attributable to the differences in the size and mass of the two cations, and hence supports our conclusion that the observed conductivity is due almost entirely to the cationic self-diffusion. On the other hand, the conductivity in the α-phase of (pra)Cl observed around room temperature was smaller by three orders of magnitude than that in the α′-phase of (pna)Cl measured at the same temperatures. We can conclude from these results that, in the α′-phase, not only the whole-cationic uniaxial reorientation, but also their translational self-diffusion takes place quite readily even at room temperature.

From the above discussion of the two kinds of rotator phases, α and α′, we can propose the possible cationic arrangements of these phases. In the α-phase, which can be found around room temperature in (pra)Cl and also in methylammonium bromide (32) and iodide (33) the only allowed whole-cationic motion is the uniaxial reorientation about the long axis. In other words, there is only a single kind of dynamical disorder involving the cations. This means that the cations, having an average structure like a rigid rod are packed regularly with their axes parallel to the crystallographic c axis between the layers made of the anions. On the other hand, the α′-phase formed by n-alkylammonium chlorides with alkyl chains longer than C_3 (2) is expected to contain a more disordered arrangement of cations around or above room temperature.

Of motions responsible for the above disorder, we have shown the presence of the rapid 2D translational jumps of the

Can. J. Chem. Downloaded from www.nrcresearchpress.com by 112.217.228.212 on 09/07/12
For personal use only.

cations. Other possible motions are partial conformational disorder of the alkyl chains, and large amplitude lattice vibrations such as precessional motions of cations with fixed polar ends. These motions strongly disturb the regular arrangement of the cationic axes parallel to each other. Accordingly, the long axes of the cations can be said to be directed along the *c* axis only when they are statistically averaged, although the cations are placed in a highly symmetrical crystal field made by the anions.

Acknowledgments

The authors are particularly indebted to Mr. K. Kawase and Dr. K. Toriyama at the Government Industrial Research Institute of Nagoya for carrying out DSC experiments.

1. J. TSAU and D. F. R. GILSON. J. Phys. Chem. **72**, 4082 (1968).
2. R. W. G. WYCKOFF. Crystal structures. 2nd ed. Vol. 5. Interscience Publishers, New York. 1966. Chap. XIVA.
3. V. BUSICO, P. CERNICCHIARO, P. CORRADINI, and M. VACATELLO. J. Phys. Chem. **87**, 1631 (1983).
4. J. TSAU and D. F. R. GILSON. Can. J. Chem. **51**, 1990 (1973).
5. A. MÜLLER. Proc. R. Soc. London, Ser. A, **138**, 514 (1932).
6. S. FUKADA, H. YAMAMOTO, R. IKEDA, and D. NAKAMURA. J. Chem. Soc. Faraday Trans. 1, **83**, 3207 (1987).
7. J. N. SHERWOOD (*Editor*). The plastically crystalline state. John-Wiley and Sons, Chichester. 1979.
8. J. M. CHEZEAU and J. H. STRANGE. Phys. Rep. **53**, 1 (1979).
9. J. C. SOUTHARD, R. T. MILNER, and S. B. HENDRICKS. J. Chem. Phys. **1**, 95 (1933).
10. L. S. PRABHUMIRASHI, R. IKEDA, and D. NAKAMURA. Ber. Bunsenges. Phys. Chem. **85**, 1142 (1981).
11. S. GIMA, Y. FURUKAWA, R. IKEDA, and D. NAKAMURA. J. Mol. Struct. **111**, 189 (1983).
12. H. ISHIDA, R. IKEDA, and D. NAKAMURA. Ber. Bunsenges. Phys. Chem. **90**, 598 (1986).
13. Y. KUME, R. IKEDA, and D. NAKAMURA. J. Magn. Reson. **33**, 331 (1979).
14. C. A. WULFF and E. F. WESTRUM, JR. J. Phys. Chem. **67**, 2376 (1963).
15. F. D. ROSSINI, D. D. WAGMAN, W. H. EVANS, S. LEVINE, and I. JAFFE. Selected values of chemical thermodynamic properties. Part I. Natl. Bur. Stand. (US) Circ. 500-I, U.S. Government Printing Office, Washington. 1961.
16. H. ISHIDA, R. IKEDA, and D. NAKAMURA. J. Chem. Soc. Faraday Trans. 2, **81**, 963 (1985).
17. S. FUKADA, R. IKEDA, and D. NAKAMURA. Bull. Chem. Soc. Jpn. **57**, 2802 (1984).
18. S. FUKADA, R. IKEDA, and D. NAKAMURA. Z. Naturforsch. **40***a*, 347 (1985).
19. J. H. VAN VLECK. Phys. Rev. **74**, 1168 (1948).
20. A. ABRAGAM. The principles of nuclear magnetism. Oxford University Press, Oxford. 1961. Chap. VIII.
21. T. M. CONNOR. Trans. Faraday Soc. **60**, 1574 (1964).
22. M. WOLFE and J. JONAS. J. Chem. Phys. **71**, 3252 (1979).
23. P. L. KUHN and M. S. CONRADI. J. Chem. Phys. **77**, 1771 (1982).
24. G. SODA and H. CHIHARA. J. Phys. Soc. Jpn. **36**, 954 (1974).
25. A. AVOGADRO and M. VILLA. J. Chem. Phys. **66**, 2359 (1977).
26. J. TABONY and J.-P. KORB. Mol. Phys. **56**, 1281 (1985).
27. M. VILFAN and S. ŽUMER. Phys. Rev. **21***A*, 672 (1980).
28. U. RÖDER, W. MÜLLER-WARMUTH, H. W. SPIESS, and R. SCHÖLLHORN. J. Chem. Phys. **77**, 4627 (1982).
29. K. COMPAAN and Y. HAVEN. Trans. Faraday Soc. **52**, 786 (1956); **54**, 1498 (1958).
30. S. ŽUMER and M. VILFAN. Phys. Rev. **17***A*, 424 (1978).
31. H. ISHIDA, R. IKEDA, and D. NAKAMURA. Bull. Chem. Soc. Jpn. **60**, 467 (1987).
32. H. ISHIDA, R. IKEDA, and D. NAKAMURA. J. Phys. Chem. **86**, 1003 (1982).
33. H. ISHIDA, R. IKEDA, and D. NAKAMURA. Bull. Chem. Soc. Jpn. **59**, 915 (1986).

Can. J. Chem. Downloaded from www.nrcresearchpress.com by 112.217.228.212 on 09/07/12
For personal use only.

Applications of enzymes in the synthesis and hydrolytic study of 2-deoxy-α-D-glucopyranosyl phosphate

M. DAVID PERCIVAL AND STEPHEN G. WITHERS[1]

Department of Chemistry, University of British Columbia, Vancouver, B.C., Canada V6T 1Y6

Received January 28, 1988

This paper is dedicated to Professor Charles A. McDowell on the occasion of his 70th birthday.

M. DAVID PERCIVAL and STEPHEN G. WITHERS. Can. J. Chem. **66**, 1970 (1988).

The labile sugar phosphate 2-deoxy-α-D-glucopyranosyl phosphate has been synthesized enzymically in a two-step process from 2-deoxy-D-glucose-6-phosphate via an intermediate uridine 5′-diphospho-2-deoxy-D-glucose. Rate constants for acid-catalysed (1 M $HClO_4$) hydrolysis at several temperatures were determined by using an enzymic assay to measure remaining substrate. The values obtained were consistent with that anticipated on the basis of known hydrolysis rates for alkyl- and aryl-2-deoxy-D-glucopyranosides.

M. DAVID PERCIVAL et STEPHEN G. WITHERS. Can. J. Chem. **66**, 1970 (1988).

Utilisant le phosphate-6 du désoxy-2 α-D-glucose comme produit de départ et faisant appel à une méthode enzymatique impliquant deux étapes et le diphospho-5′ désoxy-2 D-glucose uridine comme intermédiaire, on a synthétisé le phosphate du désoxy-2 α-D-glucopyrannosyle, un phosphate labile de sucre. Utilisant une méthode enzymatique pour mesurer la quantité de substrat qui n'a pas réagi et opérant à diverses températures, on en a mesuré les constantes de vitesse d'hydrolyse catalysée par les acides (1 M de $HClO_4$). Les valeurs obtenues sont en accord avec celles que l'on peut attendre sur la base des vitesses connues d'hydrolyse des désoxy-2 D-glucopyrannosides d'alkyles et d'aryles.

[Traduit par la revue]

Introduction

Kinetic studies with deoxy- and deoxyfluoro-sugar substrates can provide useful insight (1, 2) into the mechanisms of both enzymic and nonenzymic reactions. The importance of charged intermediates in both enzymic and nonenzymic reactions can be probed as can also the importance of hydrogen bonding in the enzyme-catalyzed reaction. As part of our studies on the catalytic mechanism of the enzyme glycogen phosphorylase we have synthesized a series of deoxy and deoxyfluoro analogues of α-D-glucopyranosyl phosphate and determined rates of both their enzymic breakdown and acid-catalyzed hydrolysis. The synthesis of all the deoxyfluoro- and three of the deoxy-α-D-glucopyranosyl phosphates was relatively readily achieved via MacDonald (3) phosphorylation of the corresponding peracetylated sugars. However, despite claims (4) of a successful synthesis of 2-deoxy-α-D-glucopyranosyl phosphate by this procedure, we were unable to prepare this material at a satisfactory level of purity. These problems stem largely from its hydrolytic instability. We therefore elected to synthesize this compound by an alternate route, using a combination of three enzymes in a two-step synthesis. This paper describes the enzymic synthesis and purification of 2-deoxy-α-D-glucopyranosyl phosphate. It also describes a novel enzymic method for measurement of rates of acid-catalyzed hydrolysis of this extremely labile glycosyl ester.

Results and discussion

Synthesis of the title compound by direct MacDonald phosphorylation of 1,3,4,6-tetra-*O*-acetyl-2-deoxy-β-D-glucopyranose proved unsuccessful despite a number of attempts under varying conditions. Equally unsuccessful were attempts to add phosphoric acid across the double bond of 3,4,6-tri-*O*-acetyl-D-glucal. In each case the initial phosphorylation mix was saponified with 1 M LiOH to deprotect the sugar products as well as to remove excess phosphoric acid as its insoluble lithium salt, and reaction mixtures were assayed by ^{31}P nmr. A mixture of phosphate esters was detected in each case and all attempts to isolate the desired 2-deoxy-α-D-glucopyranosyl phosphate were unsuccessful.

A viable alternative approach to this synthesis, involving reactions performed under mild, neutral conditions, appeared to be an enzymic synthesis, based upon observations of others (5) of the ability of 2-deoxy-D-glucose to be converted into its uridine-diphospho derivative in partially purified tissue homogenates. The approach employed was necessarily a two-step synthesis since the direct conversion of 2-deoxy-D-glucose-6-phosphate to 2-deoxy-α-D-glucopyranosyl phosphate, achieved by phosphoglucomutase (6), is energetically unfavourable and would result in, at best, 5% yields of the desired compound and a very tricky separation.

In the first step (Scheme 1a), commercially available 2-deoxy-D-glucose-6-phosphate (Sigma Chemical Co.) was converted into uridine diphospho-2-deoxy-D-glucose by the combined actions of phosphoglucomutase and uridine diphosphoglucose pyrophosphorylase. This reaction was pulled to completion by inclusion of inorganic pyrophosphatase in the reaction mixture to remove product pyrophosphate. Progress of the reaction was monitored by the appearance of acid-labile phosphate, the product uridine diphospho-2-deoxy-D-glucose being readily distinguished by its pair of phosphate resonances ($\delta = 8.50$, $\delta = 10.53$). Since this crude mixture contained large quantities of phosphate, which would be difficult to separate from the desired product by anion exchange chromatography, it was treated with LiOH to pH 13 to precipitate the phosphate as its lithium salt, which was then removed by filtration. An additional advantage of this step is that it removes any uridine diphosphoglucose arising from the glucose 1,6-diphosphate added to activate phosphoglucomutase, or from contaminating glucose-6-phosphate, since at high pH values, uridine diphosphoglucose decomposes (7) via intramolecular attack of the sugar 2-hydroxyl on its phosphate moiety, producing uridine 5′-monophosphate and α-D-glucopyranosyl-1,2-cyclic phos-

[1]Author to whom correspondence may be addressed.

Can. J. Chem. Downloaded from www.nrcresearchpress.com by 112.217.228.212 on 09/07/12
For personal use only.

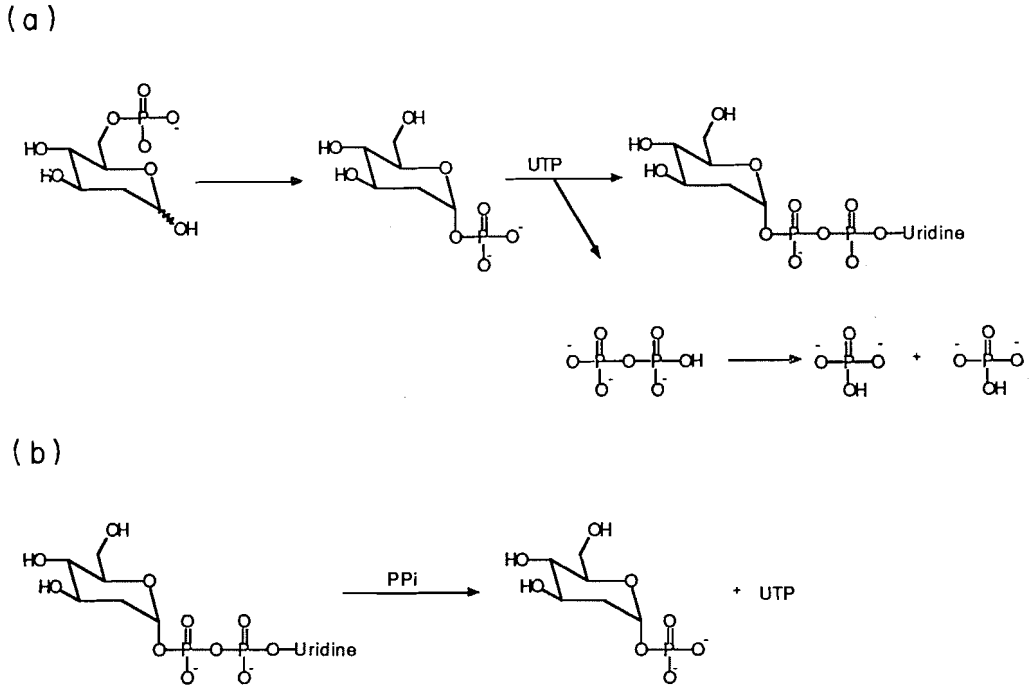

SCHEME 1. The enzymic synthesis of 2-deoxy-α-D-glucopyranosyl phosphate. (a) Conversion of 2-deoxy-D-glucose-6-phosphate to uridine-5′-diphospho-α-2-deoxy-D-glucose. (b) Conversion of uridine-5′-diphospho-α-2-deoxy-D-glucose to 2-deoxy-α-D-glucopyranosyl phosphate. Conditions as in Materials and Methods.

Can. J. Chem. Downloaded from www.nrcresearchpress.com by 112.217.228.212 on 09/07/12
For personal use only.

phate. Such a decomposition is clearly impossible for the 2-deoxy derivative. After neutralization of the mixture it was purified by gradient elution from a DE52-cellulose anion exchange column. Product elution was monitored by ultraviolet spectroscopy and by the appearance of acid-labile phosphate.

Purified uridine diphospho-2-deoxy-D-glucose was then again treated with uridine diphosphoglucose pyrophosphorylase and a large excess of pyrophosphate to drive the reaction backwards towards optimal production of 2-deoxy-α-D-glucopyranosyl phosphate as shown in Scheme 1b. Reaction progress was monitored by ^{31}P nmr, and the product purified by gradient elution from a DE52 anion exchange column. Repeated freeze-drying of the product fractions gave the desired product, which was characterized by ^{31}P and ^{1}H nmr, but proved too unstable to provide a satisfactory microanalysis.

Acid-catalysed hydrolysis rate

On the basis of previously determined (8) relative rates of acid-catalyzed hydrolysis of phenyl β-D-glucopyranoside and its 2-deoxy analogue, the half-life of 2-deoxy-α-D-glucopyranosyl phosphate under the conditions used to study other hydrolyses of glycopyranosyl phosphates (1 M $HClO_4$, 25°C) was estimated to be approximately 5 s, i.e., too rapid for simple measurement. On that basis it was decided to measure rates of hydrolysis at lower temperatures (0–8°C) and to extrapolate to a value at 25°C. Reaction progress had previously (1) been monitored via appearance of phosphate. However, in this case, even the modified phosphate assay (9), which had previously proved suitable for analysis of phosphate levels in the presence of acid-labile phosphate esters, proved unsuitable, since there was very substantial hydrolysis of the 2-deoxy derivative during the 15-s exposure to acid prior to addition of the reducing agent.

A novel method for measuring the extent of hydrolysis as a function of time was therefore developed, based upon a sensitive enzymic method for estimating the concentration of remaining *substrate* under neutral conditions. This assay was performed by removing aliquots of the acidic reaction mixture and immediately quenching them in strongly buffered reaction mixtures containing excess phosphoglucomutase, glucose-6-phosphate dehydrogenase, nicotinamide adenine dinucleotide (NAD), and other necessary cofactors. Under these conditions, the aliquot was instantly neutralized, halting acid-catalyzed hydrolysis, and remaining substrate rapidly converted to 2-deoxy-D-glucose-6-phosphate, since phosphoglucomutase operates very efficiently on 2-deoxy derivatives (6).[2] This stable phosphate ester was then slowly converted, over 20–30 min, to 2-deoxy-D-gluconic acid-6-phosphate by glucose-6-phosphate dehydrogenase, with concomitant stoichiometric conversion of NAD to its reduced form, NADH. This process could be followed by uv/visible spectroscopy at 340 nm, the quantity of 2-deoxy-α-D-glucopyranosyl phosphate remaining in each aliquot being readily determined from the total change in absorbance at 340 nm. In this manner, the time course of acid-catalyzed (1 M $HClO_4$) hydrolysis was determined at temperatures of 0, 4, and 9°C and the kinetics of hydrolysis found to be accurately first order over two half-lives in each case. The rate constants measured are presented in Table 1, along with that value calculated by extrapolation of the data to 25°C using an Arrhenius plot. Comparison of the value obtained with that (1) for hydrolysis of α-D-glucopyranosyl phosphate under these conditions (4.1×10^{-5} s^{-1}) reveals that the 2-deoxy derivative is hydrolyzed some 2680 times more rapidly than the parent compound. This compares very favourably with the relative ratio of 2200:1 observed (8) for the acid-catalyzed

[2]Also, M. D. Percival and S. G. Withers. Unpublished results.

TABLE 1. First-order rate constants for acid-catalysed hydrolysis[a] of 2-deoxy-α-D-glucopyranosyl phosphate

Temperature (°C)	Rate constant (s^{-1})
0	0.007
4	0.01
8	0.015
25[b]	0.11

[a]Hydrolysis was performed in 1 M $HClO_4$ as described in Methods.

[b]Value obtained from extrapolation of previous data using an Arrhenius plot.

hydrolysis rates of phenyl 2-deoxy-β-D-glucopyranoside and phenyl β-D-glucopyranoside and with the relative ratios of 2090:1 calculated (11) for the corresponding methyl glycosides. It does not, however, agree with the relative hydrolysis rates of 9:1 claimed by other authors (12) for acid-catalyzed hydrolysis of the title compound and its parent sugar. However, it is also difficult to reconcile the rate constant claimed (12) for acid-catalyzed hydrolysis of α-D-glucopyranosyl phosphate in that publication with other published values (13–15).

The high rate of acid-catalysed hydrolysis for such 2-deoxy glucosides and glycosyl esters is consistent with the generally accepted mechanism (11) of this reaction, involving an oxocarbonium ion intermediate. The replacement of the hydroxyl at C-2 by more electronegative substituents such as fluorine or chlorine has been shown previously (1, 16) to result in decreased reaction rates due to inductive destabilization of the oxocarbonium-ionlike transition states. Conversely, replacement by the relatively less electronegative hydrogen is expected to result in higher reaction rates.

Experimental

All buffer chemicals, substrates, and enzymes were obtained from Sigma Chemical Company and were used as supplied. The nmr studies were performed on a Varian XL 300 nmr spectrometer. The ^{31}P nmr chemical shifts are referenced relative to orthophosphoric acid and ^{19}F nmr chemical shifts relative to $CFCl_3$.

Uridine-5′-diphospho-2-deoxy-α-D-glucopyranose (1)

To a solution of 100 mM Tris buffer (20 mL), pH 7.6, containing 30 mM magnesium chloride was added uridine-5′-triphosphate (0.168 g, 0.274 mmol), 2-deoxy-D-glucose-6-phosphate (0.070 g, 0.228 mmol), α-D-glucose-1,6-diphosphate (0.1 μmol), and bovine serum albumin (0.15 mg/mL). After readjustment of the pH to 7.6, phosphoglucomutase (100 units), uridine-5′-diphosphoglucose pyrophosphorylase (25 units), and inorganic pyrophosphatase (10 units) were added and the reaction incubated at 25°C. The course of the reaction was monitored by the appearance of inorganic phosphate using the Fiske–SubbaRow method. After 6 days the solution was diluted with water to 150 mL and the pH adjusted to 8.0. The mixture was chromatographed at 4°C on a DE52 cellulose column (1.8 × 30 cm) that had been previously equilibrated with 30 mM ammonium bicarbonate. After washing with 200 mL water, the product was eluted with a gradient of 0–0.2 M ammonium bicarbonate at a flow rate of 2 mL/min in a total volume of 2 L. The desired product was the first uv active peak, eluting at 60–70 mM salt, a concentration characteristic of dianions. After repeated freeze-drying to remove the volatile buffer, inorganic phosphate, which coeluted with the product, was precipitated by addition of 2 M lithium hydroxide to pH 13. The precipitated lithium phosphate was removed by filtration through Celite. The pH of the filtrate was readjusted to pH 7.6 by addition of Dowex 50 W-X8H^+ resin; ^{31}P nmr (121.4 MHz, D_2O) δ: 8.5 (d, $J_{P,P}$ 21Hz), 10.53 (d, $J_{P,P}$ 21 Hz).

2-Deoxy-α-D-glucopyranosyl [bis(ammonium)phosphate] (2)

The solution of **1** was added to 100 mM Tris (20 mL), pH 7.6, containing 30 mM magnesium chloride, sodium pyrophosphate (1.0 g, 225 mmol), and bovine serum albumin (0.15 mg/mL). Uridine-5′-diphosphoglucose pyrophosphorylase (25 units) was added and the solution incubated at 25°C. The course of the reaction was monitored by ^{31}P nmr. After 3 days the inorganic phosphate was removed as described above, the pH readjusted to 8.0, and the mixture chromatographed on a DE52 cellulose column (2.8 × 40 cm) exactly as described previously. The product was identified by the presence of phosphate according to the method of Bartlett (10), and the buffer removed by repeated freeze-drying to yield a white foam; ^{31}P nmr (121.4 MHz, D_2O) δ: 1.28 (dd, $J_{P,1}$ 6.8, $J_{P,2}$ 2.0 Hz); ^1H nmr (300 MHz, D_2O) δ: 5.55 (m, $J_{1,P}$ 7 Hz, 1H, H-1), 4.1–3.2 (m, 5H, H-3,4,5,6,6′), 2.15 (dd, $J_{2eq,2ax}$ 12, $J_{2eq,3}$ 5 Hz, 1H, H_{2eq}) 1.65 (m, $J_{2ax,2eq}$ 12, $J_{2ax,3}$ 12 Hz, 1H, H_{2ax}).

Acknowledgements

The authors acknowledge grant support from the Natural Sciences and Engineering Research Council of Canada.

1. S. G. WITHERS, D. J. MACLENNAN, and I. P. STREET. Carbohydr. Res. **154**, 127 (1986).
2. E. M. BESSELL, A. B. FOSTER, and J. H. WESTWOOD. Biochem. J. **128**, 199 (1972).
3. J. L. MACDONALD. Methods Carbohydr. Chem. **6**, 389 (1972).
4. N. M. SHIBAEV, YU. YU. KUSOV, SH. KUCHAR, and N. K. KOCHETKOV. Izv. Akad. Nauk SSSR, Ser. Khim. **4**, 922 (1973).
5. R. T. SCHWARZ and M. F. G. SCHMIDT. Eur. J. Biochem. **62**, 181 (1976).
6. W. J. RAY, JR. and A. S. MILDVAN. Biochemistry, **9**, 3886 (1970).
7. A. C. PALADINI and L. F. LELOIR. J. Biol. Chem. **51**, 426 (1952).
8. T. MEGA and Y. MATSUSHIMA. J. Biochem. (Tokyo), **94**, 1637 (1983).
9. E. S. BAGINSKI, P. P. FOA, and B. ZAK. Clin. Chim. Acta. **15**, 155 (1967).
10. G. R. BARTLETT. J. Biol. Chem. **234**, 46 (1959).
11. B. CAPON. Chem. Rev. **69**, 407 (1969).
12. J. ZAMOCKY, J. ZEMEK, S. KUCAR, and V. SOUKUPOVA. Collect. Czech. Chem. Commun. **42**, 1379 (1977).
13. C. A. BUNTON, D. R. LLEWELLYN, K. G. OLDHAM, and C. A. VERNON. J. Chem. Soc. C, 3574 (1958).
14. C. A. BUNTON and E. HUMERES. J. Org. Chem. **34**, 573 (1969).
15. J. V. O'CONNOR and R. BARKER. Carbohydr. Res. **73**, 227 (1979).
16. E. BUNCEL and P. R. BRADLEY. Can. J. Chem. **45**, 515 (1967).

Can. J. Chem. Downloaded from www.nrcresearchpress.com by 112.217.228.212 on 09/07/12
For personal use only.

Phase transitions in adamantane derivatives: 2-chloroadamantane

RALPH M. PAROLI, NANCY T. KAWAI, IAN S. BUTLER,[1] AND DENIS F. R. GILSON[1]
Department of Chemistry, McGill University, 801 Sherbrooke St. West, Montreal (P.Q.), Canada H3A 2K6

Received November 27, 1987

This paper is dedicated to Professor Charles A. McDowell on the occasion of his seventieth birthday

RALPH M. PAROLI, NANCY T. KAWAI, IAN S. BUTLER, and DENIS F. R. GILSON. Can. J. Chem. **66**, 1973 (1988).

The phase transition behaviour of 2-chloroadamantane, 2-$C_{10}H_{15}Cl$, has been investigated by differential scanning calorimetry (DSC), and FT-IR and Raman spectroscopy. Two transitions were detected by both DSC and vibrational spectroscopy at 231 and 178 K, on cooling, and at 242 and 227 K, on heating. The measured enthalpies were 8.3 kJ mol^{-1} for the first transition (phase I → phase II), and 0.47 kJ mol^{-1} for the second (phase II → phase III). The entropies were 35 and 2.3 J K^{-1} mol^{-1}, respectively. These are similar to those observed for other 2-substituted adamantanes, but significantly different from those for 1-substituted derivatives. The large hystereses observed for the two transitions are independent of the DSC scanning rate and are characteristic of first-order phase transitions. The dramatic differences observed in the vibrational spectra of phases I and II provide clear evidence of an order–disorder transition at about 235 K.

RALPH M. PAROLI, NANCY T. KAWAI, IAN S. BUTLER, et DENIS F. R. GILSON. Can. J. Chem. **66**, 1973 (1988).

Utilisant la calorimétrie différentiel programmé (CDP) ainsi que la spectroscopie Raman et IR par TF, on a étudié le comportement du chloro-2 adamantane, 2-$C_{10}H_{15}Cl$, lors de sa transition de phase. Les trois méthodes ont permis de détecté deux transitions, soit à 231 et 178 K lors du refroidissement et 242 et 227 K lors du chauffage. On a évalué que l'enthalpie de la première transition (phase I → phase II) est de 8,3 kJ mol^{-1} et de 0,47 kJ mol^{-1} pour la deuxième (phase II → phase III). Les entropies sont respectivement de 35 et de 2,3 J K^{-1} mol^{-1}. Ces valeurs sont semblables à celles qui ont été observées pour d'autres adamantanes substitués en position 2; toutefois, elles diffèrent beaucoup des valeurs observées avec dérivés en position 1. Les hysterisis importantes que l'on observe pour chacune des deux transitions sont indépendantes du taux de balayage du CDP et sont caractéristiques de transitions de phase du premier ordre. Les différences dramatiques que l'on observe dans les spectres vibrationnels des phases I et II fournissent des preuves nonambigues que la transition à 235 K en est une d'ordre/désordre.
[Traduit par la revue]

Introduction

Molecular solids with high vapour pressures and melting points, and low entropies of fusion (<20 J K^{-1} mol^{-1}) are often referred to as "plastic crystals" (1–4). These materials are generally soft, colourless, transparent solids that are difficult to fracture or pulverize. Solid–solid phase transitions occur from an ordered to a disordered structure in which the molecules rotate about one or more of their axes in the crystal lattice. Furthermore, since the phase transitions are often strongly exothermic, these materials are currently receiving considerable attention as passive thermal storage systems (5–8).

The cage hydrocarbon, adamantane ($C_{10}H_{16}$), is one of the best known "plastic crystals" and its properties have been widely studied (9). The order–disorder transitions in 1-substituted adamantanes ($C_{10}H_{15}R$; R = 1-COOH (10), 1-$NH_3^+Cl^-$ (11), 1-CN (12), 1-Cl (16), 1-Br (16)) have been examined. Little work has been done on 2-substituted derivatives (13, 17, 18), and as part of a study of the phase-transition behaviour of adamantane derivatives, we report here the results of an investigation of the order–disorder transitions in 2-chloroadamantane, 2-$C_{10}H_{15}Cl$, by differential scanning calorimetry (DSC), and variable-temperature FT-IR and Raman spectroscopy.

Experimental

2-Chloroadamantane (Alfa Products) were purified immediately prior to use by slow vacuum sublimation (21°C, 10^{-3} Torr). Infrared spectra were recorded on an Analect AQS-18 FT-IR spectrometer equipped with a triglycine sulfate (TGS) detector. Raman spectra were obtained using an Instruments S.A. spectrometer with a Jobin-Yvon U-1000 1.0-m double monochromator that was interfaced to a Columbia Commandor microcomputer. The 514.532-nm line of a Spectra-Physics model 164, 5-W argon-ion laser was used to excite the Raman spectra; the laser power was 300 mW at the sample. The resolution for both the IR and Raman measurements was about 2 cm^{-1}. The Raman studies were done on samples sealed in glass capillary tubes which were mounted on to the cold finger of a cryostat using indium foil as the conducting junction. For the IR analysis, several sampling techniques were attempted: KBr pellets, diffuse reflectance, sublimation on to KBr windows, and pressing into a thin layer film. Since similar spectra were obtained in each case (including the large hystereses observed in phase transition temperatures), the KBr pellet technique was used as it proved to be the most convenient method. The effect of KBr pelleting on phase transitions has been studied previously and it was found that it only increases the degree of the hysteresis at a phase transition (14). Variable-temperature FT-IR and Raman spectra were recorded with the aid of a Cryodyne Cryocooler model 21 (Cryogenics Technology, Inc.) and a silicon-diode temperature sensor attached to a Cryophysics model 4025 controller (range 400–4 K). The sample temperatures remained essentially constant (±0.5 K).

Differential scanning calorimetric experiments were performed on a Perkin-Elmer DSC-7 calorimeter. The temperature and enthalpy calibrations were based on the phase and melting transitions of cyclohexane (Aldrich Chemical Co. "gold" grade). The sample weights were typically 5–10 mg, and the samples were hermetically sealed in aluminium pans. The phase transition temperatures and enthalpies did not show any dependence on scan rate (2.5 and 5 K min^{-1}).

Results and discussion

Two phase transitions (phase I → phase II → phase III) were detected by diffential scanning calorimetry. The transition temperatures were 231 and 178 K (on cooling) and 242 and 227 K (on heating) with enthalpies of 8.3 kJ mol^{-1} for the first transition and 0.47 kJ mol^{-1} for the second. Although large hystereses are observed (10 K for the first transition and 50 K for

[1]Authors to whom correspondence should be addressed.

Can. J. Chem. Downloaded from www.nrcresearchpress.com by 112.217.228.212 on 09/07/12
For personal use only.

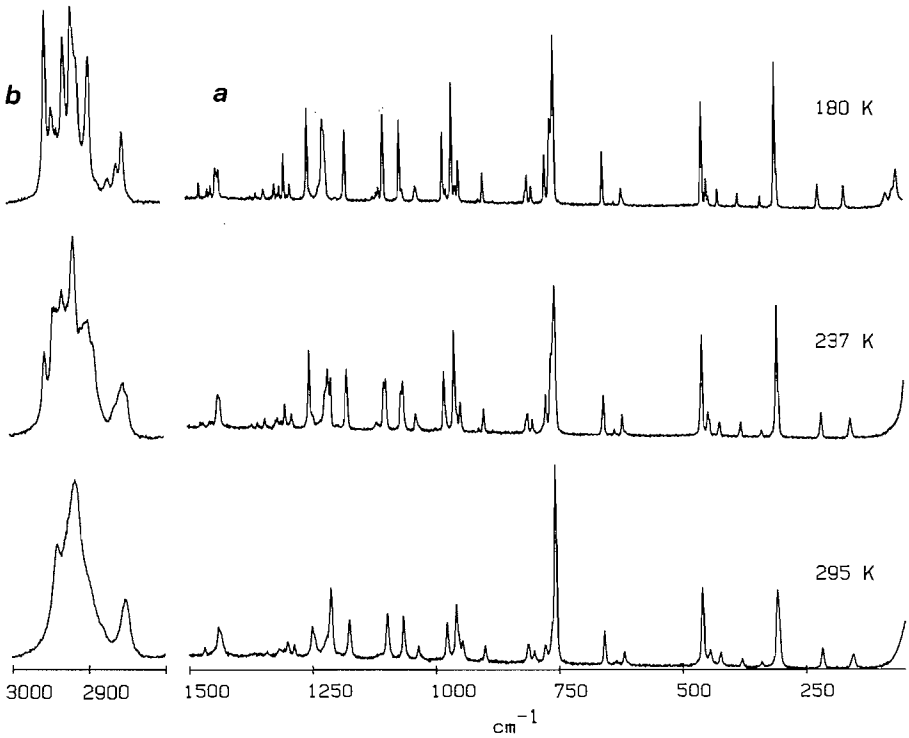

FIG. 1. Raman spectra on heating of phases I, II, and III of 2-$C_{10}H_{15}Cl$ in the (*b*) 3000–2800 and (*a*) 1500–50 cm^{-1} regions. Slits: 300 μm. Acquisition: 1 s pt^{-1}, 1 cm^{-1} step. Intensity: counts. Laser line: 514.532 nm, power 300 mW.

the second), 2-chloroadamantane did not exhibit any memory effects, i.e., the phase transition temperatures and enthalpies were not dependent on the previous thermal history of the sample. The hystereses are characteristic of first-order transitions. Rapid quenching, cycling at 20 K min^{-1}, did not reveal any exotherms on heating, hence no glassy state was formed. The entropies of transitions are 35 and 2.3 J K^{-1} mol^{-1} for the first and second phase transition, respectively. The entropy of the first phase transition is much larger than that of adamantane itself (15) and of various 1-substituted halo-derivatives which have entropies less than 25 J K^{-1} mol^{-1} (16), but is similar to the entropies of 2-bromoadamantane (17) and adamantanone (18) which are greater than 35 J K^{-1} mol^{-1}. Although the 2-derivatives (except 2-adamantanone) have lower symmetry (C_s), they still exhibit plastically crystalline behaviour (unpublished data).

The Guthrie and McCullough equation (19) for the interpretation of entropies of transition in plastic crystals is

$$[1] \quad \Delta S_{tr} = R \ln (N_1/N_2)$$

where N_1/N_2 is the ratio of the number of distinguishable positions on going from the ordered (N_2) to the disordered (N_1) phase. For the phase I → phase II transition the ratio is 70, while the second transition (phase II → phase III) only has a ratio of orientations slightly greater than one. This is an unreasonably large number of distinguishable orientations. Clark and coworkers (15, 16) have examined the entropies of transition for several cage hydrocarbons and proposed an empirical equation involving an excess entropy, which depends upon the temperature range of the disordered phase, eq. [2].

$$[2] \quad \Delta S_{tr} = R \ln(N_1/N_2) + 10.3 + 45 \exp \{- [0.0183(T_m - T_{tr})]\}$$

where $10.3 + 45 \exp \{- [0.0183(T_m - T_{tr})]\}$ is the excess entropy and $(T_m - T_{tr})$ is the temperature range of the plastically crystalline phase. There are two transitions in 2-chloroadamantane, and since phase II is probably partially disordered, the total entropy change between ordered and disordered structures is given by the sum of the two transition entropies, plus a small, negligible term for the heat capacity. Assuming that phase I is face-centered-cubic (fcc), which is typical for these materials, then there are 24 possible orientations for a molecule with C_s symmetry in the fcc lattice. Using eq. [2], with $T_m = 458$ K and $T_{tr} = 202.5$ K (the average of the heating and cooling transition temperatures), the calculated total entropy is 37.1 J K^{-1} mol^{-1}. This agrees very well with the experimental value of 37.3 J K^{-1} mol^{-1}. These results imply that there is a change in the unit cell dimensions that is accompanied by a decrease in volume only for the first phase transition.

Another method to probe phase transitions is by vibrational spectroscopy. The isolated 2-chloroadamantane molecule has C_s symmetry for which 72 normal modes of vibration are predicted (40A' and 32A''). Since the A' and A'' modes are both Raman and IR active, 72 peaks should be observed in both the Raman and the IR spectra.

The Raman and IR spectra of phases I–III are shown in Figs. 1*a*, *b* and 2*a*, *b*; the measured peak positions and the proposed vibrational assignments are given in Table 1. These assignments are based on literature values for various adamantane derivatives (20–22) and on Raman spectra of 2-$C_{10}H_{15}Cl$ in CCl_4 and CS_2 solution. Only 58 bands out of a possible 72 have been clearly identified, probably as a result of the overlapping of peaks. Even amongst those observed it is possible that some may be combinations and/or overtones.

Many interesting changes were observed in the Raman spectra as the sample was cooled and then heated between 298 and

Can. J. Chem. Downloaded from www.nrcresearchpress.com by 112.217.228.212 on 09/07/12
For personal use only.

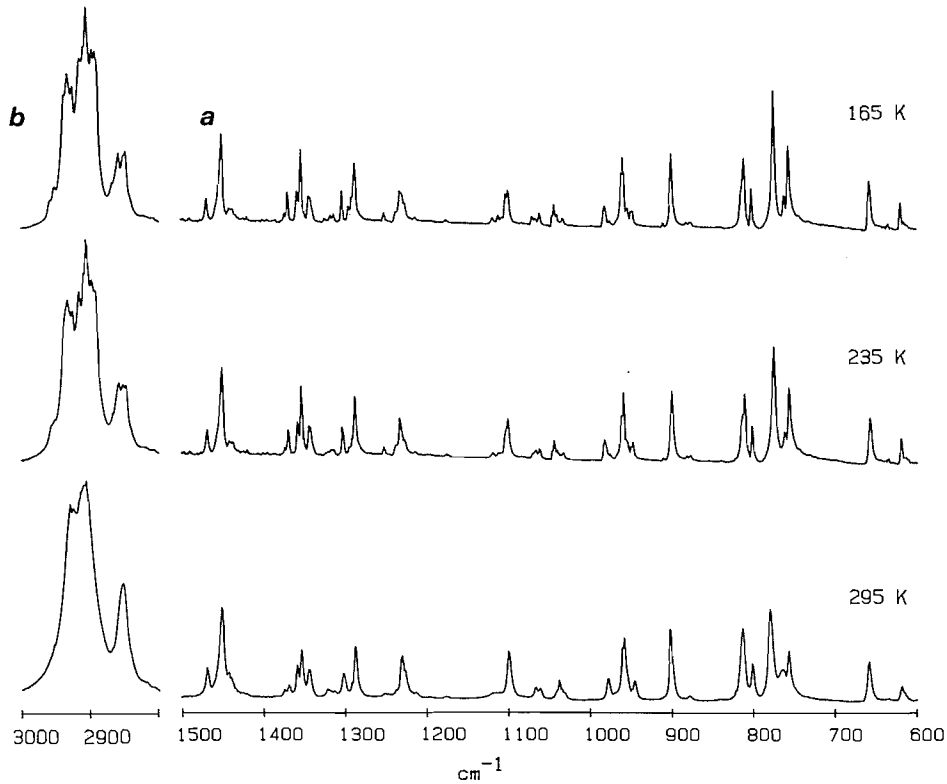

FIG. 2. IR spectra (in KBr) on heating of phases I, II, and III of 2-$C_{10}H_{15}Cl$ in the (*b*) 3000–2800 and (*a*) 1500–50 cm^{-1} regions. Intensity: absorbance units. Resolution: 2 cm^{-1}.

150 K. Consider the lattice region (100–20 cm^{-1}) shown in Fig. 3; the tail extending to 100 cm^{-1} in phase I is featureless. However, in phase II some weak features develop at ~60 and 80 cm^{-1}, and in phase III some very distinctive peaks appear. These results corroborate those of the DSC measurements, i.e., phase I is the completely disordered phase since it exhibits a total absence of lattice modes. The weak, broad peaks observed in this region for phase II indicate that it is orientationally disordered, while the sharp peaks in phase III show that it is a completely ordered phase.

In Fig. 3, the changes that occur in the Raman for the C—C—Cl bending mode are shown. In phase I, the peak appears at 156 cm^{-1}. As the sample is cooled down towards the first transition (phase I → phase II), the peak width narrows and the peak shifts to slightly higher wavenumber (159 cm^{-1}) once in phase II. However, on going from phase II to phase III, a new peak appears at 167 cm^{-1} and the 159 cm^{-1} peak decreases in intensity. The 167 cm^{-1} peak eventually shifts to 169 cm^{-1} and becomes a sharp singlet for phase III, while the peak at 159 cm^{-1} disappears completely.

The symmetric C—C stretching mode (Fig. 1*a*) also undergoes distinct changes as the sample proceeds from phase I to phase III. In the plastic phase, the peak occurs as a singlet at 760 cm^{-1} with a smaller peak at 780 cm^{-1}. In phase II, the 760 cm^{-1} peak is split into a doublet at 757 and 764 cm^{-1}. Moreover, the 780 cm^{-1} peak sharpens and increases in intensity moving finally to 775 cm^{-1}. Little change occurs as the sample progresses from phase II to phase III. Since this spectral region is solely due to C—C stretching, i.e., cage skeletal stretching, the observed changes must result from a change in crystal structure.

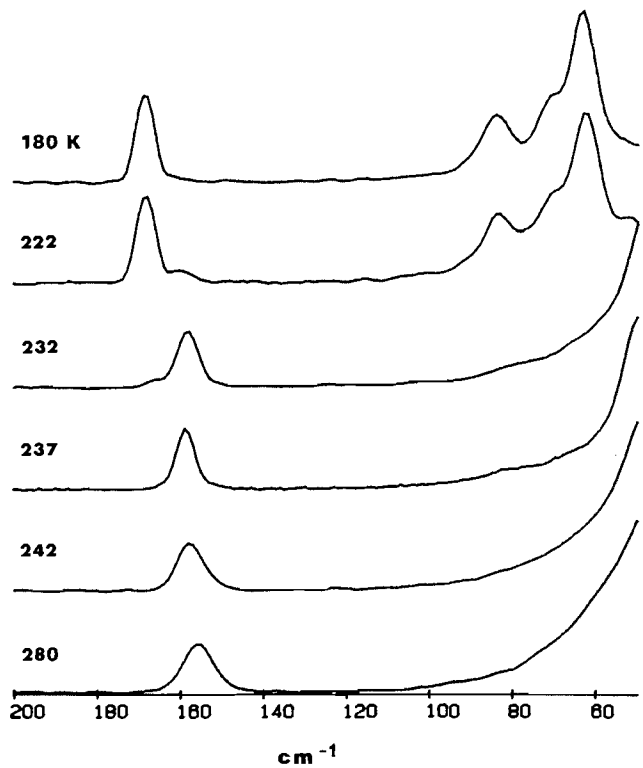

FIG. 3. Low frequency region of the Raman spectra of 2-$C_{10}H_{15}Cl$ on heating (180–280 K). Slits: 300 μm. Acquisition: 1 s pt^{-1}, 1 cm^{-1} step. Intensity: counts. Laser line: 514.532 nm, power 300 mW.

Can. J. Chem. Downloaded from www.nrcresearchpress.com by 112.217.228.212 on 09/07/12
For personal use only.

Can. J. Chem. Downloaded from www.nrcresearchpress.com by 112.217.228.212 on 09/07/12
For personal use only.

TABLE 1. Vibrational data (cm^{-1}) for 2-chloroadamantane

	Phase I (295 K)		Phase II (237 K)		Phase III (180 K)		
Solution[a]	Raman	IR	Raman	IR	Raman	IR	Assignments
			2956s	2959w		2960w	
				2952sh		2953s	
					2950vs	2951m	A'
2940s, pol	2941s		2943s		2942m		CH str.
			2939s	2938s		2939v	
			2934s	2933s	2935sh	2935vs	
		2930s				2930vs	
		2926s	2926sh	2926s	2926s	2928vs	
2918s	2918vs	2916sh	2918vs	2917s	2915vs	2913vs	A''
		2910sh		2910s	2909sh		CH_2 anti-
		2906vs		2906vs		2905vs	symmetric
		2903sh	2903sh				str.
			2899s	2899s		2896s	
			2891s	2895sh	2894vs	2890s	
						2871sh	
			2865sh	2867sh	2868m	2867m	A''
			2858sh	2859s	2857m	2859s	CH_2
2852m	2853m	2853s	2854m	2853s	2850m	2851s	symmetric
			2848m	2849s		2847s	str.
		2660w		2667w		2665w	
			1474w		1474w		A'
1471w,pol	1470w	1468w	1469vw	1469w		1469w	
			1456vw		1457vw		CH_2
			1454vw		1450vw		
		1450m		1451m		1451m	
1443m,pol	1441m	1442w	1438m	1442br,w	1440m	1441br,w	Def.
	1435sh		1435sh		1435w		
		1374w		1374vw		1373vw	
		1368w		1370w		1370w	
1356w		1358w	1359vw	1358w	1359w	1358w	A''
		1353m		1353m		1353m	
1345w	1344vw	1343w	1344vw	1343w	1344vw	1344w	CH_2 wag
		1321w	1321vw	1321w	1322w	1323br,w	and
						1320br,w	CCH def.
1319w	1319w		1319vw	1316w	1319vw	1318w	
		1313w	1310vw		1312w		
1304w	1302w	1301m	1304w	1302m	1303m	1303m	
			1294sh	1295vw	1295vw	1295w	A'
1290w,pol	1289w	1290sh	1290w	1291sh	1290w	1290vw	CC str.
		1287m		1287m		1287m	
1252w	1252m	1251w	1255s	1251w	1256s	1251w	A''
		1234sh		1236sh		1237sh	C—C str.
		1230m		1231w		1232w	CH_2 def.
	1228sh	1226sh	1220sh	1225sh	1223s	1225sh	
1215s	1214s		1218m		1221sh		A''
		1212vw	1211m	1213vw		1213vw	CH_2 twist
1178m	1177m	1175vw	1179m	1175vw	1179m	1175vw	and
1123w	1123w		1118w	118vw,br		1118br,vw	CCH def.
		1114w,br			1115vw		
			1112sh		1112w	1111sh	CCH def.
				1108vw		1107vw	
			1103m	1104sh	1102s	1102sh	
1101m	1100m	1099m	1098m	1100w		1100w	A''
						1070vw	CCH
1068m	1067m	1066w	1068w	1066w	1069s	1066vw	def.
		1061w	1063m	1061w	1063sh	1061w	
		1040sh		1045sh		1045sh	CCH def.
		1038w		1043w		1043w	
1039w,pol	1037w	1035sh	1039w	1037vw	1036w	1039br,w	A'
		1032sh		1032vw		1032vw	CCH def.

TABLE 1. Vibrational data (cm^{-1}) for 2-chloroadamantane

	Phase I (295 K)		Phase II (237 K)		Phase III (180 K)		
Solution[a]	Raman	IR	Raman	IR	Raman	IR	Assignments
			982m	982w	982m	982w	
980m	979m	978w	976sh	979sh			A''
				975vw	975w	975vw	
		960sh		960sh		960sh	CH_2 rock
961m	960m	958m	961s	958m	963s	958m	
	955sh		955sh		955w	953w	and
948m	947m	949sh	949w	950sh	949m	950sh	
		945w		946w		947w	CCC bend
	910sh		911vw	910vw	911vw	909vw	
903m	902w	901m	901w	900m	900w	899m	and
		878vw		880vw		881vw	
				876vw		876vw	CC str.
		822sh					
815w	815w	813m	813w	814w	811w	814sh	
				810m		810m	
803w,pol	803w	801w	802w	801w	802w	801w	A'
781vw,pol	780w	779m	775m	774m	775m	774m	
	764sh	764br,w	764s	761w	762s	761w	C—C str.
760vs,pol	760vs	756m	757vs	756m	757vs	756m	and
660m	660m	659m	658m	657m	658m	657m	C—C—C
	637vw	635vw	636vw	634vw	634vw	634vw	bending
621w	620w	619w	620w	618w	620w	617w	
				614br,vw		614br,vw	
	462s	462m	459s	462m	458s	462m	C—Cl
	446w	445w	446w	445w	448w	445w	str.
			443sh		442vw		
	425w		424w		425w		
380w	381w		381w		385w		A''
340w	341vw		338vw		339vw		skeletal
309m	309s		308s		309s		modes
			303sh		305sh		
220w	218w		218w		222w		
157w	156w		159w				C—C—Cl
					169w		str.
					84w		
					62sh		
					29w		

[a]In CCl_4 and CS_2 solutions

The C—C stretching and CH_2 twisting modes at 1067 cm^{-1} and the C—C—H deformation and CH_2 wag at 1100 cm^{-1} alternate between singlets and doublets as the sample goes from phase I to phase III. The doublets in phase I collapse to singlets in phase II which then split into doublets in phase III. Since the C—C and CH_2 modes contribute to the two bands, it is not surprising that the bands are sensitive to crystal structure (C—C) as well as to orientational (CH_2) changes. The same is true for the 3000–2800 cm^{-1} (symmetric and asymmetric CH stretching) region, which also undergoes dramatic changes as the sample transforms from phase I to phase III (Fig. 1*b*).

Figures 2*a* and *b* show variable temperature FT-IR spectra obtained for 2-chloroadamantane. As expected for a C_s symmetry molecule, all the changes parallel those observed in the Raman spectra. Again, phase III contains many sharp, well-resolved peaks indicating an ordered phase, whereas phase I has mostly broad, featureless bands implying a high degree of disorder. The 765 cm^{-1} peak is broad but well resolved in phase I. As the sample approaches phase II, the peak decreases in intensity until the transition to phase II in reached, at which point the peak becomes a shoulder. In phase III, the band reappears as a sharp, well-defined peak. The major differences between the IR and Raman data are that the effects observed in IR are gradual, as would be expected when using a KBr matrix (14), whereas in the Raman they are sudden. Moreover, some IR peaks are not observed in the Raman spectra, probably due to narrower peaks and better signal-to-noise ratio available for FT-IR.

Based on the vibrational splittings observed in phases II and III, the ordered phases have at least two molecules per unit cell.

Acknowledgements

This research was generally supported by scholarships (R.M.P., N.T.K.) and grants (I.S.B., D.F.R.G.) from NSERC (Canada) and FCAR (Quebec). R.M.P. also wishes to thank McGill University for the award of a Special Graduate Faculty Fellowship. The McGill University Department of Chemical Engineering is thanked for the use of their DSC instrument.

Can. J. Chem. Downloaded from www.nrcresearchpress.com by 112.217.228.212 on 09/07/12
For personal use only.

1. J. N. SHERWOOD (*Editor*). The plastically crystalline state (orientationally disordered crystals). J. Wiley and Sons, Inc., Chichester. 1979.
2. N. G. PARSONAGE and L. A. K. STAVELEY. Disorder in crystals. Clarendon Press, Oxford. 1978.
3. G. P. JOHARI and R. K. CHAN. Can. Chem. Ed. **10**, 8 (1975).
4. G. P. JOHARI and R. K. CHAN. Can. Chem. Ed. **10**, 10 (1975).
5. Chem. Eng. News, 30 (April 1984).
6. Chem. Week, 22 (August 1984).
7. Chem. Eng. News, 15 (October 1986).
8. T. L. VIGO and C. M. FROST. Text. Res. J. 737 (December 1985).
9. R. C. FORT JR. Adamantane: the chemistry of diamond molecules. Marcel Dekker, Inc., New York. 1976.
10. P. D. HARVEY, D. F. R. GILSON, and I. S. BUTLER. J. Phys. Chem. **90**, 136 (1986).
11. P. D. HARVEY, D. F. R. GILSON, and I. S. BUTLER. J. Phys. Chem. **91**, 1267 (1987).
12. J. L. SAUVAJOL, M. BEE, and J. P. AMOUREUX. Mol. Phys. **46**, 811 (1982).
13. G. H. WAHL, R. L. GREENE, and J. BORDNER. J. Chem. Soc. Chem. Commun. 927 (1973).
14. R. M. CORN, V. L. SHANNON, R. G. SNYDER, and H. L. STRAUSS. J. Phys. Chem. **81**, Pt. I, 5231 (1984).
15. T. CLARK, M. A. MCKERVEY, H. MACKLE, and J. J. ROONEY. J. Chem. Soc. Faraday Trans. **I**, **70**, 1279 (1974).
16. T. CLARK, T. M. KNOX, H. MACKLE, and M. A. MCKERVEY. J. Chem. Soc. Faraday Trans. **I**, **73**, 1224 (1977).
17. K. HARA, Y. KATOU, and J. OSUGI. Bull. Chem. Soc. Jpn. **54**, 687 (1981).
18. I. S. BUTLER, H. B. R. COLE, D. F. R. GILSON, P. D. HARVEY, and J. D. MCFARLANE. J. Chem. Soc. Faraday Trans. II, **82**, 535 (1986).
19. G. B. GUTHRIE and J. P. MCCULLOUGH. J. Phys. Chem. Solids, **18**, 53 (1961).
20. E. N. GRISHNA, I. V. ALEKSANDROV, Y. M. SOLOBODIN, and R. R. KOSTIKOV. Z. Prikl. Spektrosk. **32**, 664 (1980).
21. R. T. BAILEY. Spectrochim. Acta, **27**A, 1447 (1971).
22. T. E. JENKINS and J. LEWIS. Spectrochim. Acta. **36**A, 259 (1980).

Can. J. Chem. Downloaded from www.nrcresearchpress.com by 112.217.228.212 on 09/07/12
For personal use only.

Residence-time of muonium at micelles: Effect of added micelles on the reactivity of muonium towards ionic solutes in water

KRISHNAN VENKATESWARAN, MARY V. BARNABAS, BILL W. NG,[1] AND DAVID C. WALKER
Chemistry Department and TRIUMF, University of British Columbia, Vancouver, B.C., Canada V6T 1Y6

Received November 15, 1987

This paper is dedicated to Professor Charles A. McDowell on the occasion of his 70th birthday

KRISHNAN VENKATESWARAN, MARY V. BARNABAS, BILL W. NG, and DAVID C. WALKER. Can. J. Chem. **66**, 1979 (1988).

The effective rate constant for the reaction of muonium with NO_3^-, $S_2O_3^{2-}$, and Tl^+ ions in water is altered by the addition of micelles. There is a decrease when the charge on the micelle is the same as that of the solute and an increase when their charges are opposite. From the magnitude of the effect a mean residence-time for muonium of 2 ns has been deduced for dodecyl sulphate micelles. This suggests there is barely any preferred localization, because 2 ns is smaller, even, than the expected diffusion time if the micelle core is as viscous as reported. This use of muonium atoms to probe the dynamics of micelles seems to support the view that there are regions of low microviscosity and considerable water penetration within the micellar structure.

KRISHNAN VENKATESWARAN, MARY V. BARNABAS, BILL W. NG et DAVID C. WALKER. Can. J. Chem. **66**, 1979 (1988).

La constante de vitesse effective de la réaction du muonium avec les ions NO_3^-, $S_2O_3^{2-}$ et Tl^+ dans l'eau est modifiée par l'addition de micelles. Il se produit une diminution lorsque la charge de la micelle est la même que celle du soluté et une augmentation lorsque leurs charges sont opposées. En se basant sur l'amplitude de l'effet, on a pu déduire un temps moyen de résidence du muonium de 2 ns pour les micelles de sulfate de dodécyle. Ceci suggère que la localisation préférentielle existe à peine puisque 2 ns est un temps qui est plus court que le temps attendu de diffusion si le coeur de la micelle est aussi visqueux qu'on l'a rapporté. L'utilisation d'atomes de muonium pour étudier la dynamique des micelles semble apporter un support à l'hypothèse selencounters a micelle, then it will be isolated from the reactive species in ton laquelle il y a beaucoup de pénétration par l'eau et beaucoup de régions comportant de faibles microviscosités à l'intérieur de la structure des micelles.

[Traduit par la revue]

Can. J. Chem. Downloaded from www.nrcresearchpress.com by 112.217.228.212 on 09/07/12
For personal use only.

Introduction

It was recently demonstrated that colossal enhancements can occur in the reactivity of muonium towards organic solutes when the solutes are incorporated in the lipid phase of dilute micelles in water (1). The simplest explanation for such enhancements lies with the possibility that muonium atoms *also* localize preferentially at the micellar phase because, if mutual confinement of both reactants occurred, there would be a "concentrating effect" that would naturally lead to an equivalent increase in the observed pseudo first-order rate constant. But muonium is a free thermalized neutral atom (2), and there are no obvious reasons why this light isotope of hydrogen (3, 4) should prefer the organic phase when initially formed in the bulk aqueous phase.

The experiments reported here were designed to look directly at the degree of localization of muonium at micelles, simply by observing the effect of added "empty" micelles on the rate of muonium reactions with ionic solutes taking place in water.

Experimental

Muonium atoms (μ^+e^-, chemical symbol Mu) form at the end of some muon tracks when energetic positive muons (from pion decays) are injected into water. They are observed in transverse magnetic fields by the muon spin rotation technique (μSR) (4, 5). Chemical reaction rate contants of Mu are then evaluated from the spin precession signals (as in Fig. 1) as the relaxation constant (λ) of the "triplet" muonium signal oscillating at the Larmor frequency of 1.39 MHz G^{-1}. A MINUIT χ^2-minimization fit of the muon lifetime histogram to eq. [1] gives λ as one of the fitted parameters. (In eq. [1], N_t is the number of counts in the histogram corresponding to time t; N_0 a normalization factor; τ the mean muon lifetime; A_M and A_D, λ_M and λ_D, and ϕ_M and ϕ_D are the asymmetries, frequencies, and initial phases of the "muonium atoms" and "diamagnetic muon components", respectively; and B is the time-independent background signal.) λ is related to a bimolecular chemical rate constant of Mu (k_M) through eq. [2], where λ is the observed value with solute present at concentration [S] and λ_O is the background value in the same medium, including micelle, but with [S] = 0. A narrow observational time-window of 0.3–4 μs is imposed by the μSR technique, because it is a nuclear physics technique based on the intrinsic decay of the muon (τ = 2.2 μs). Therefore, all solutions to be studied must have their muonium chemical lifetimes carefully selected so that λ falls in the limited range of $3 \times 10^6 - 2.5 \times 10^5$ s^{-1}. This precludes the possibility of studying broad concentration dependencies as one would normally like to undertake in a complete kinetic analysis. Furthermore, the micelle concentrations are restricted to $\leq 10^{-2}$ M because, with 50–80 surfactant molecules per micelle, the rate of reaction of muonium with surfactant, or its inseparable impurities, forces the "background" relaxation rate (λ_0) too close to λ for reasonable accuracy. In fact, hydrogen atoms cannot be studied at all under these conditions because of their much greater reactivity towards the surfactants (6).

$$[1]\quad N_t = N_0 \exp(-t/\tau)[1 + A_M \exp(-\lambda t)\cos(\omega_M t + \phi_M) + A_D \cos(\omega_D t + \phi_D)] + B$$

$$[2]\quad k_M = (\lambda - \lambda_0)/[S] = \Delta\lambda/[S]$$

The presence of added micelles creates a second phase, a microenvironment separated from the bulk aqueous phase (7, 8). If Mu preferentially localizes for its entire lifetime (~2 μs) as soon as it encounters a micelle, then it will be isolated from the reactive species in these systems (NO_3^-, $S_2O_3^{2-}$, and Tl^+ ions) because they are in the water. Under such conditions the "trapped" Mu would exhibit a decay constant characteristic of the micelle. To analyse for this the muonium fraction of eq. [1], the A_M term, was replaced by eq. [3] (9), with two independent exponentials for the two fractions of the Mu ensemble. A test target for this two-component modification of eq. [1] was constructed partly of aqueous NO_3^- solution (10^{-3} M where $\lambda = 1.8 \times 10^6$ s^{-1}) and partly of crystalline quartz ($\lambda \approx 0.3 \times 10^6$ s^{-1}) (10). A portion of the beam struck the quartz crystal and the muonium atoms formed therein were long-lived, being unable to react with the nitrate.

$$[3]\quad [A_{M_1}\exp(-\lambda_1 t) + A_{M_2}\exp(-\lambda_2 t)]\cos(\omega_M t + \phi_M)$$

[1]Present address: Chemistry Department, Winona State University, Winona, MN 55987, USA.

TABLE 1. Parameters used to establish the concentrations required for the experiments

Solute	$k_M / 10^{10} M^{-1} s^{-1}$	[solute] / $10^{-3} M$ (to give $\Delta\lambda \approx 1.5 \times 10^6 s^{-1}$)
NO_3^-	0.15	1.0
$S_2O_3^{2}$	2.60	0.07
Tl^+	0.08	2.0
Na^+, SO_4^{2-}, Br^-	<0.0001	

Micelle	Charge	Critical micelle concentration / M	A^a	R_C / nm[b]	R_M / nm[b]	$[mic]_{min}$ / M[c]
SDDS	−	8.1×10^{-3}	62	1.7	2.1	1.3×10^{-4}
DDTAB	+	1.5×10^{-2}	60	1.7	2.1	3.0×10^{-4}
pEO	0	6.0×10^{-5}	50	1.7	3.2	1.2×10^{-6}

[a] A is the aggregation number.
[b] R_C is the micelle's core radius and R_M the total radius (ref. 7).
[c] Taken as the micelle concentration when half the surfactant molecules are in micelles as calculated from $[mic] = ([surf] - CMC)/A$.

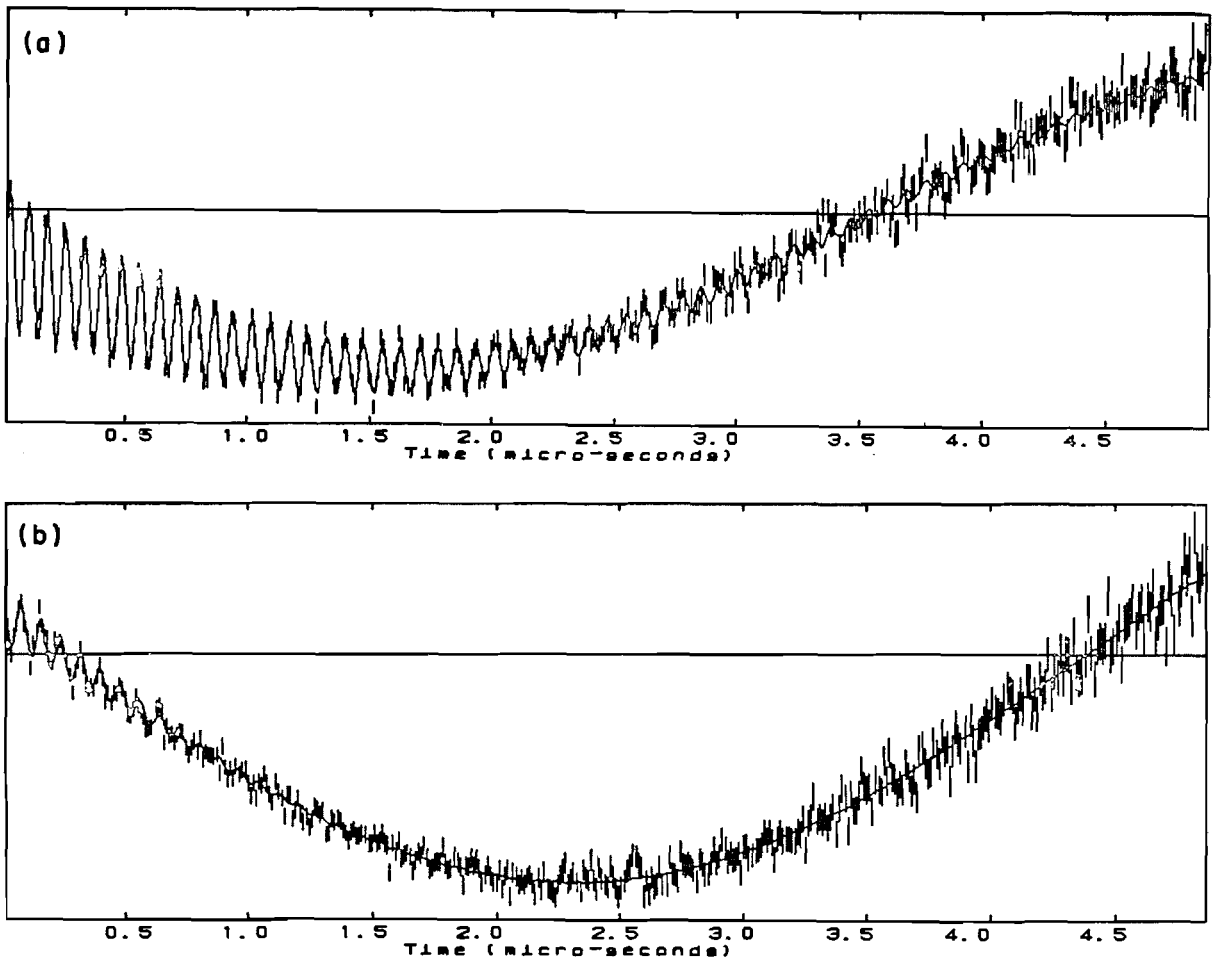

FIG. 1. (a) Asymmetry plot (A vs. t) for the quartz/NO_3^- solution artificial two-phase system. The solid line was obtained for the parameters in the text using the two-muonium function of eq. [3]. (b) Asymmetry plot for $[NO_3^-] = 0.7 \times 10^{-3}$ M and $[mic] = 10 \times 10^{-3}$ M. The line is the same as the usual one-component fit since $A_{M_2} = 0$.

Aqueous solutions were made from triply distilled water and reagent grade chemicals. They were thoroughly deoxygenated by bubbling with pure N_2. The μSR equipment on beamline M20 at the TRIUMF cyclotron was used. $NaNO_3$, $Na_2S_2O_3$, and $TlSO_4$ were used as reactive solutes for Mu, and the micelles were sodium dodecylsulphate (SDDS), dodecyltrimethylammonium bromide (DDTAB), and polyoxy(23)ethylenedodecanol (pEO). These ionic solutes were selected for their known values of k_M and matched appropriately with the charge on the micelle. Relevant k_M values and micelle properties are provided in Table 1. The concentration of the solute in water was always taken so that $\lambda \approx 1.5 \times 10^6$ s^{-1}, its most sensitive region. Micelles were added and the change in λ determined.

Can. J. Chem. Downloaded from www.nrcresearchpress.com by 112.217.228.212 on 09/07/12
For personal use only.

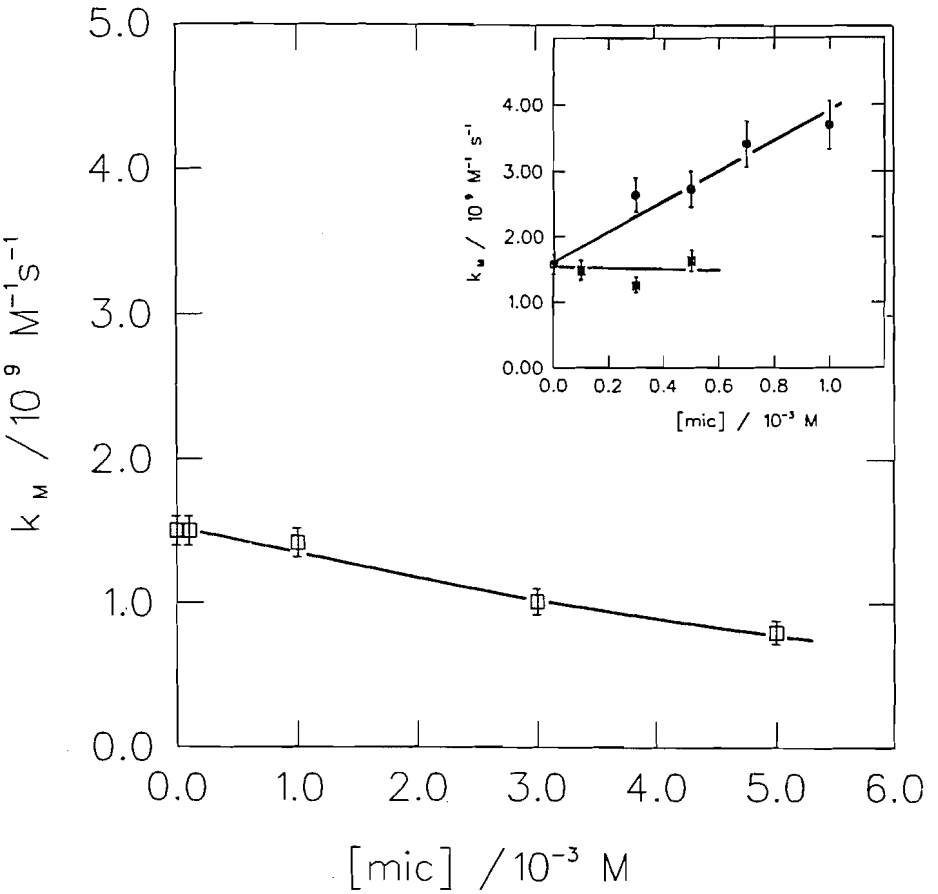

FIG. 2. Plot of k_M versus concentration of added micelles for NO_3^- solutions with [S] = 1×10^{-3} M (□) for SDDS, (●) for DDTAB, (⊠) for pEO micelles.

Results

The effect of adding micelles to 1.0×10^{-3} M NO_3^- solutions can be seen in Fig. 2. When the anionic micelle SDDS was added the observed muonium rate constant was reduced. With five times as many micelles as solutes the rate was essentially halved. On the other hand, a cationic micelle (DDTAB) increased the observed rate (doubling it approximately in a one-to-one mixture), while the neutral micelle (pEO) had no observable effect. These data are presented as k_M values determined from eq. [2]. Unfortunately pEO and DDTAB cannot be taken to higher concentrations because of their background corrections (λ_0). Similar effects, which depend primarily on the relative charge of solute and micelle, can be seen for other solutes. Table 2 shows data obtained for $S_2O_3^{2-}$ (which reacts with Mu at the diffusion-limited rate (10)) and for Tl^+ (which oxidizes Mu relatively inefficiently (10)).

The two-component overall muonium relaxation (eq. [3]) was found to apply well to the artificial two-phase system consisting of one-third quartz and two-thirds aqueous NO_3^- at 10^{-3} M. The asymmetry plot (after τ and B of eq. [1] were removed (4)) is shown in Fig. 1 (a). The best reduced χ^2 values are $A_{M_1} = 0.019$ with $\lambda_1 = 1.8 \times 10^6$ s^{-1} and $A_{M_2} = 0.033$ with $\lambda_2 = 3.5 \times 10^5$ s^{-1}. This is about what was expected since the muonium yield in quartz is 3.5 times larger than in water (10) but only one-third of the muon beam stopped in the quartz. These data verify that if the Mu ensemble is rapidly subdivided into two isolated fractions then the double-exponential fit of eq. [3] identifies it. However, for all the micelle solutions this two-component fit gives $A_{M_2} = 0$, regardless of how one tries to drive it with different limits on λ_1 and λ_2. An example is shown as Fig. 1 (b). It means that the regular fitting equation (eq. [1]) applies to micelle solutions, and, therefore, that *all* muonium atoms have access to the same decay channels.

We also report here that the data points of some of the occupied-micelle solutions studied previously (1) were subjected to eq. [3] incorporated in eq. [1]. In an aqueous solution containing styrene at 7.5×10^{-6} M and micelles at 1.5×10^{-5} M the best fit always gave $A_{M_2} = 0$. In this system the solute (styrene) was strongly localized in the micelle core without a significant chance of relocating during the 2-μs period corresponding to the muon lifetime. There are twice as many micelles as solutes in the solution, so about 61% of the micelles, based on Poisson distributions (11, 12), would be unoccupied, and about 8% would contain two styrene molecules. So, again, the failure of the analysis to see any fractionation of the Mu ensemble strongly implies that they localize at micelles for periods much shorter than their chemical lifetimes.

Discussion

These data show that muonium's effective rate of reaction towards a solute was decreased by adding a micelle of the same charge as the solute, increased by a micelle of the opposite charge, and barely affected when the micelle was neutral. Millimolar concentrations of micelles were needed to alter the chemical lifetime of muonium significantly.

In these experiments most muonium atoms were created

Can. J. Chem. Downloaded from www.nrcresearchpress.com by 112.217.228.212 on 09/07/12
For personal use only.

TABLE 2. Effect of added micelles on k_M: representative data from Fig. 2 for NO_3^-, and data for $S_2O_3^{2-}$ and Tl^+ with SDDS micelles

Solute	Concentration / 10^{-3} M	Micelle	Concentration / 10^{-3} M	$\Delta\lambda^a$ / 10^6 s^{-1}	$k_M{}^b$ / 10^9 M^{-1} s^{-1}
NO_3^-	1.0	—	0	1.50(10)	1.5
NO_3^-	1.0	SDDS	5.0	0.80(10)	0.80
NO_3^-	1.0	DDTAB	1.0	3.70(30)	3.7
NO_3^-	1.0	pEO	0.1	1.50(10)	1.5
$S_2O_3^{2-}$	0.05	—	0	1.32(10)	26.5
$S_2O_3^{2-}$	0.10	SDDS	0.2	2.40(20)	24.0
$S_2O_3^{2-}$	0.10	SDDS	0.5	1.95(20)	19.5
$S_2O_3^{2-}$	0.10	SDDS	1.0	1.95(20)	19.5
Tl^+	0.4	—	0	0.30(10)	0.75
Tl^+	0.8	SDDS	0.33	1.20(10)	1.5
Tl^+	0.4	SDDS	0.20	0.80(10)	2.0
Tl^+	0.4	SDDS	0.50	1.25(10)	3.2

[a]Observed.
[b]Calculated from eq. [2] for each solution.

initially in the aqueous phase, because water was by far the major constituent, but on encountering a micelle during its random diffusion Mu could localize there. ("Localization" will be used here to mean that Mu spends a greater fraction of its time in the micelle than the volume fraction of that phase in the whole solution. It does not take account of the different diffusion coefficients in the two phases.) The distributions of the ionic solutes are also influenced by the micelles, being preferentially caught in the ion atmospheres when of opposite charge and specifically excluded when of the same charge. The enhanced rate when the solute is localized is consistent with Mu also being localized, especially if the "fjord-like" character of micelles is appropriate (7, 13, 14) where there is considerable water penetration. However, it is impossible to use these enhancement data quantitatively without knowing in detail about the mutual localization and local structure. Instead the discussion will focus on the decreased rates.

Four possibilities present themselves regarding the localization of Mu: (a) it may be confined exclusively to the aqueous phase, (b) treat micellar and aqueous phases alike (no localization), (c) localize "permanently" (a microsecond or so here) in the micelle phase, or (d) localize to a limited extent at the micelle. Possibility (a) can be discarded, because enhancements in Mu rates have been observed for many organic solutes (1) that are themselves fully localized in micelles. (b) can be ruled out, because there would have been almost no effect, and what little there was would have been in the opposite sense to that seen, because the solutes of opposite charge to the micelles would have been "bunched" around them, thereby reducing the effective concentration of solute as seen by a randomly diffusing Mu. (c) can also be discarded, because the rate did not drop to almost zero in the highest concentration NO_3^-/SDDS case, for instance, whereas Mu would have had the chance to react with NO_3^- only prior to its first localization with a micelle at 5×10^{-3} M. Furthermore, any such permanent disbursement of Mu into the micelle phase would have led to a two-component muonium fit, as with the quartz/NO_3^- experiment. This leaves possibility (d), a limited degree of localization.

In quantitative terms there are three approaches: (*i*) estimate the localization time from the failure to observe two separate Mu components, (*ii*) calculate the residence time from the extended lifetime of Mu divided by the total number of encounters it makes with micelles, and (*iii*) propose a kinetic model. Approach (*i*) can only give an upper limit and is not very useful because of the difficulty in actually evaluating the point at which separation would be evident. One can assert only that less than half the muonium atoms spent less than half their lifetimes localized. This puts an upper limit of ≈250 ns on the mean residence time (T_R). A lower limit of T_R can be deduced from the time Mu would take to traverse an equal volume of water using $T_R > \bar{d}^2/2D$, where D is its diffusion coefficient in water ($\approx 7 \times 10^{-5}$ cm^2 s^{-1} (15), taking it to be the same as H (10)) and $\sqrt{\bar{d}^2}$ is the mean diffusion distance (≈ micelle radius). For SDDS (r = 1.7 nm) this gives $T_R > 0.21$ ns, so we have $0.21 < T_R < 250$ ns.

The second approach (*ii*) is to calculate T_R from the changed Mu lifetime ($\Delta\lambda_{(mic)}^{-1} - \Delta\lambda_{(s)}^{-1}$) for a reaction of given efficiency ($k_M/k_{(diff)}$) due to the relative number of encounters with micelle and solute for solute-to-micelle ratios in concentration ([S]/[mic]) and radii ($r_{(s)}/r_{(mic)}$) according to eq. [4]. Based on the most sensitive NO_3^-/SDDS data (lines 1 and 2 of Table 2, extremes of Fig. 2) we have the Mu lifetime increasing from 670 to 1250 ns, with a concentration ratio of 1:5, for species whose radii ratio is ≈1:5, and for a reaction that occurs about once per 13 encounters ($k_M = 1.5 \times 10^9$ M^{-1} s^{-1} for NO_3^- whereas the diffusion controlled limit, $k_{(diff)}$, for Mu with ions in aqueous solution averages to 2×10^{10} M^{-1} s^{-1} (10)). These values yield $T_R = (1250 - 670)(1/13)(1/5)(1/5) = 1.8$ ns. Let us take T_R = 2 ± 1 ns in view of the uncertainty in the $r_{(s)}/r_{(mic)}$ factor (an effective encounter radius for NO_3^- of 0.3 nm has been assumed).

$$[4] \quad T_R = (\Delta\lambda_{(mic)}^{-1} - \Delta\lambda_{(s)}^{-1})(k_M/k_{diff})([S]/[mic])(r_{(s)}/r_{(mic)})$$

For approach (*iii*), the following mechanism is proposed:

$$Mu_{(aq)} + em \underset{k_e}{\overset{k_d}{\rightleftharpoons}} Mu_{(em)}$$

$$Mu_{(aq)} + S_{(aq)} \xrightarrow{k_M} P_1$$

$$Mu_{(aq)/(em)} \xrightarrow{\lambda_0} P_2$$

Can. J. Chem. Downloaded from www.nrcresearchpress.com by 112.217.228.212 on 09/07/12
For personal use only.

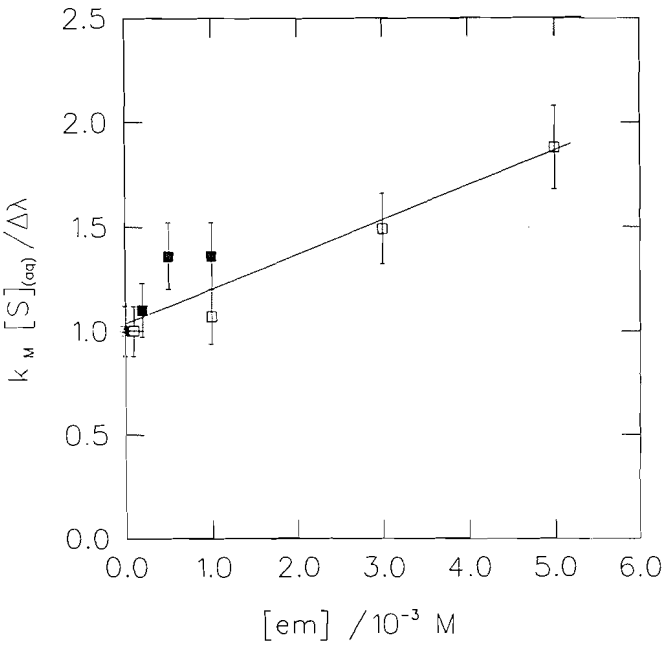

FIG. 3. $k_M[S]_{(aq)}/\Delta\lambda$ plotted against concentration of unoccupied SDDS micelles ([em]). (□) for NO_3^- as solute, (■) $S_2O_3^{2-}$ as solute.

where "em" represents an empty (unoccupied) micelle. In μSR experiments no distinction is possible between Mu in different phases, and because of (*i*) above, eq. [5] applies.

$$[5] \quad -d[Mu]/dt = \lambda([Mu_{(em)}] + [Mu_{(aq)}])$$

Since (*ii*) above has indicated that the Mu residence time (T_R) is very much shorter than the chemical lifetime (λ^{-1}), an analysis that leads to eq. [6], based on pre-equilibrium approximations, is appropriate. This can be rearranged to eq. [7], and the plot of the left-hand side against [em] is shown in Fig. 3 for the NO_3^-/SDDS data. A good straight line is obtained with slope equal to 175 ± 39 M^{-1}. The more limited $S_2O_3^{2-}$/SDDS data are also included, thereby giving an overall least-squares fit of 167 ± 37 M^{-1}. Since this equals k_d/k_e, an estimation of k_d must be made. Based on eq. [8], (since the micelle is much larger and more sluggish than Mu (10)), one gets $k_d = 8.8 \times 10^{10}$ M^{-1} s^{-1} using data already given. (This agrees well with the factor of ≈5 taken for radii ratios since $k_{(diff)}$ for small molecules is 2×10^{10} M^{-1} s^{-1}). Therefore, k_e is deduced to be 5.3×10^8 s^{-1} and T_R, its inverse, equals 1.9 ns. Everything points to a mean residence time for Mu at an empty SDDS micelle of 2 ns.

$$[6] \quad \Delta\lambda = k_M[S]_{(aq)}k_e/(k_d[em]_{(aq)} + k_e)$$

$$[7] \quad k_M[S]_{(aq)}/\Delta\lambda = 1 + k_d[em]/k_e$$

$$[8] \quad k_d = r_{(mic)}D_{(Mu)}(4\pi N_A 10^{-3})$$

This is much too short a localization time for "confined diffusion" to be responsible for the colossal enhancements that have been seen for some Mu reactions taking place inside micelles (1). The natural concentrating effect due to the water-to-micelle volume ratio evidently pertains only for 2 ns; therefore, the total number of encounters falls far short of that required to explain the 10^4-fold enhancements (1).

In fact, this 2 ns is probably no longer than the extended time scale caused by Mu having to traverse the more viscous phase of a micelle's interior. In this case localization has not occurred; the muonium atom has merely been slowed down by the changed microviscosity.

Pursuing this point further: if we assume Mu follows the Stokes–Einstein relationship inside micelles, as it does in water (10), then eq. [9] applies, where η is the local viscosity and $R_{(Mu)}$ is the effective radius of Mu. Even on taking the minimum value for the latter, namely the Bohr radius of 0.053 nm, one calculates T_R = 10 ns for η = 30 cP (which is reported to be the internal viscosity, from fluorescence studies based on the mobility of pyrene (16)). In other words, the expected diffusion time is at least fivefold larger than the observed residence time. Or, put the other way, using T_R = 2 ns in eq. [9], one gets an effective viscosity of only 6 cP. Since we know Mu penetrates the central core of micelles, because it reacts readily with organic solutes such as styrene localized there, our T_R value suggests that there is considerable water penetration into micelles and a large viscosity gradient across them. Coupled with this is the possibility that the hydrocarbon tails are more randomly oriented than hitherto supposed. The value of η = 6 cP presumably represents the mean microviscosity sensed by the track of a muonium atom; 6 cP lies squarely between that of pure water (0.30 cP) or dodecane (0.43 cP) on the one hand, and the viscous intertwining (30 cP) of surfactants in micelles as seen by a large organic molecule such as pyrene (16) on the other.

$$[9] \quad T_R = 3\pi d^2 R_{(Mu)}\eta / k_B T$$

Acknowledgements

The assistance of Dr. J. M. Stadlbauer, Zhennan Wu, and the staff of the μSR group at TRIUMF is very much appreciated. Funds for these experiments came from NSERC of Canada. The continuous support of this research program by the Directors of TRIUMF and the Heads of the Department of Chemistry over the years is gratefully acknowledged.

1. K. VENKATESWARAN, M. V. BARNABAS, Z. WU, J. M. STADLBAUER, B. W. NG, and D. C. WALKER. Chem. Phys. Lett. **143**, 313 (1988).
2. Y. C. JEAN, J. H. BREWER, D. G. FLEMING, D. M. GARNER, and D. C. WALKER. Hyperfine Interact. **6**, 409 (1979).
3. V. W. HUGHES. Annu. Rev. Nucl. Sci. **16**, 445 (1966).
4. J. H. BREWER and K. M. CROWE. Annu. Rev. Nucl. Part. Sci., **28**, 239 (1978).
5. A. SCHENCK. Muon spin rotation spectroscopy. Adam Hilger, Bristol and Boston. 1985.
6. K. M. BANSAL, L. K. PATTERSON, E. J. FENDLER, and J. H. FENDLER. Int. J. Radiat. Phys. Chem. **3**, 321 (1971).
7. J. H. FENDLER. Membrane mimetic chemistry. Wiley–Interscience, New York. 1982.
8. J. K. THOMAS. Acc. Chem. Res. **10**, 133 (1977).
9. K. VENKATESWARAN and I. D. REID. TRIUMF 'DIMUO' μSR MINUIT fitting program.
10. D. C. WALKER. Muon and muonium chemistry. Cambridge University Press, Cambridge. 1983.
11. K. KALYANASUNDARAM. Chem. Soc. Rev. **7**, 453 (1978).
12. N. J. TURRO, M. GRATZEL, and A. M. BRAUN. Angew. Chem. Int. Ed. Engl. **19**, 675 (1980).
13. F. M. MENGER, J. M. JERKUNICA, and J. C. JOHNSTON. J. Am. Chem. Soc. **100**, 4676 (1978).
14. F. M. MENGER and B. J. BOYER. J. Am. Chem. Soc. **102**, 5936 (1980).
15. V. A. BENDERSKII and A. G. KRIVENKO. High Energy Chem. (Engl. Transl.) **14**, 303 (1980).
16. M. GRATZEL and J. K. THOMAS. J. Am. Chem. Soc. **95**, 6885 (1973).

Can. J. Chem. Downloaded from www.nrcresearchpress.com by 112.217.228.212 on 09/07/12
For personal use only.

Electron spin resonance and electron spin echo spectroscopic studies of Cu^{2+} sites in synthetic cancrinite zeolites

P. RAGHUNATHAN[1] AND L. KEVAN[2]

Department of Chemistry, University of Houston, Houston, TX 77004, U.S.A.

Received December 12, 1987

This paper is dedicated to Professor Charles A. McDowell on the occasion of his 70th birthday

P. RAGHUNATHAN and L. KEVAN. Can. J. Chem. **66**, 1984 (1988).

Electron spin resonance (ESR) and electron spin echo modulation (ESEM) studies of Cu^{2+} sites introduced by ion exchange are reported in two types of synthetic cancrinite zeolites, one of them a more hydrated sample, $Na_6Al_6Si_6O_{24}\cdot 8H_2O$ (denoted C1), and the other a less hydrated sample with entrained calcium carbonate, $Na_6Al_6Si_6O_{24}\cdot CaCO_3\cdot 8H_2O$ (denoted C2). ESR spectra reveal that C1 activated at 100°C contains Cu^{2+} sites of tetrahedral symmetry with $g_\parallel = 2.442$, $g_\perp = 2.068$, $A_\parallel = 83 \times 10^{-4}$ cm^{-1}, and $A_\perp = 18 \times 10^{-4}$ cm^{-1} while at a higher activation temperature of 400°C Cu^{2+} sites with a different symmetry are produced corresponding to $g_\parallel = 2.400$, $g_\perp = 2.081$, and $A_\parallel = 138 \times 10^{-4}$ cm^{-1}. C2 activated at 100°C contains almost exclusively Cu^{2+} sites of trigonal symmetry with $g_\parallel = 2.340$, $g_\perp = 2.040$, $A_\parallel = 147 \times 10^{-4}$ cm^{-1}, and $A_\perp = 35 \times 10^{-4}$ cm^{-1}. Two- and three-pulse ESEM experiments at 4 K give ^{2}D and ^{27}Al modulation patterns that corroborate these ESR assignments. Possible locations of the Cu^{2+} sites in the C1 and C2 structures are proposed.

P. RAGHUNATHAN et L. KEVAN. Can. J. Chem. **66**, 1984 (1988).

On a effectué des études par résonance paramagnétique électronique (rpe) et par modulation écho paramagnétique électronique (mepe) sur des sites Cu^{2+} introduits par échange d'ions dans deux types de zéolites cancrinite de synthèse; l'un est un échantillon plus hydraté, $Na_6Al_6Si_6O_{24}\cdot 8H_2O$ (dénommé C1) et l'autre est un échantillon moins hydraté contenant du carbonate de calcium entrainé, $Na_6Al_6Si_6O_{24}\cdot CaCO_3\cdot 8H_2O$ (dénommé C2). Les spectres rpe révèlent que l'échantillon C1, activé à 100°C, contient des sites Cu^{2+} de symétrie tétraédrique avec $g_\parallel = 2{,}442$, $g_\perp = 2{,}068$, $A_\parallel = 83 \times 10^{-4}$ cm^{-1} et $A_\perp = 18 \times 10^{-4}$ cm^{-1}; par ailleurs, lorsque cet échantillon est activé à une température plus élevée comme 400°C, il y a production de sites Cu^{2+} de symétrie différente correspondant à $g_\parallel = 2{,}400$, $g_\perp = 2{,}081$ et $A_\parallel = 138 \times 10^{-4}$ cm^{-1}. L'échantillon C2 activé à 100°C contient presqu'exclusivement des sites Cu^{2+} de symétrie trigonale avec $g_\parallel = 2{,}340$, $g_\perp = 2{,}040$, $A_\parallel = 147 \times 10^{-4}$ cm^{-1} et $A_\perp = 35 \times 10^{-4}$ cm^{-1}. Des expériences de mepe, effectuées à 4 K, produisent des patrons de modulation ^{2}D et ^{27}Al qui corroborent les attributions faites sur la base de la rpe. On propose des attributions de sites pour les Cu^{2+} dans les structures des échantillons C1 et C2.

[Traduit par la revue]

Introduction

Zeolite frameworks are important catalyst supports by virtue of their having structural reaction sites that provide the basis for shape-selective catalysis. A variety of Cu^{2+}-doped zeolites such as zeolite-X (1), zeolite-A (2), zeolite-Y (3), and zeolite H-rho (4) have been recently studied by electron spin resonance (ESR) and electron spin echo modulation (ESEM) spectroscopies (5). In the present work, we extend these investigations to Cu^{2+} exchanged into cancrinite, $Na_6[(AlO_2)_6\ (SiO_2)_6]$, a generic framework structure belonging to the felspathoid family of zeolites. Recent studies have shown that the cancrinite structure provides a very efficient matrix trap for a variety of interesting free radicals (6–8).

The unit cell of cancrinite is hexagonal, belonging to the space group $P6_3$ ($a = 12.5$–12.7 Å, $c = 5.1$–5.2 Å) (9, 10), and comprises an undecahedral building unit called the "cancrinite cage", which is made up of five 6-rings and six 4-rings. These cages are linked in columns parallel to the c-axis, six linked columns defining a 12-sided tubular channel along the c-axis. The resultant compact structure is of lower symmetry than the A- and X-zeolites, and the pore sizes are somewhat smaller. We consider two synthetic cancrinites, namely, the "free" cancrinite, $Na_6Al_6Si_6O_{24}\cdot 8H_2O$ (denoted C1), and the calcium carbonate-entrained cancrinite, $Na_6Al_6Si_6O_{24}\cdot CaCO_3\cdot 2H_2O$ (denoted C2).

Experimental

The two cancrinite specimens were prepared according to the well-established hydrothermal procedures of Barrer *et al.* (11–13). In a typical preparation of the carbonate-entrained cancrinite C2, 2 g of high-purity, iron-free kaolinite, $Al_2O_3\cdot SiO_2\cdot 2H_2O$ (E. Merck, Darmstadt) was reacted for 1 week at 80°C with 200 mL of 4 M NaOH containing an excess of dissolved Na_2CO_3 in a sealed Teflon container. For preparing the carbonate-free hydrate structure C1, $CaCO_3$ was left out of the above reaction mixture and a small amount of silica gel was added to the mixture being digested at 80°C, to prevent the formation of the sodalite hydrate structure (14). The crystal structures were identified by comparing the indexed X-ray powder diffraction patterns with the literature values (11, 15).

Variable amounts of Cu^{2+} were exchanged into the two cancrinite frameworks by the slow addition of 4, 6, or 8 mL of 10^{-3} M $Cu(NO_3)_2$ solution to a slurry of 1 g of the dried cancrinite in 100 mL of triple-distilled water. By this procedure, about 0.3–0.5 mol% of the Na^+ and Ca^{2+} ions in the original structure are replaced by Cu^{2+}.

Thermal activation of the cancrinite was made under two conditions, (*i*) a "mild" activation by evacuation at 100°C for ~6 h, and (*ii*) a "high-temperature" activation by evacuation at 400°C for 12 h, followed by exposure of the sample to flowing O_2 to reoxidize any zero- or monovalent copper formed and a He gas flush before sealing the sample.

D_2O exchange with the water molecules in the cancrinites was accomplished by repeated soaking of 0.25 g of the activated samples in 2 mL of 99.9 mol% pure D_2O. The deuterated as well as undeuterated samples were sealed in 3 mm o.d. Suprasil quartz tubes for the ESR and ESEM experiments.

All the ESR spectra were recorded at X-band (~9 GHz) on a Varian E-4 spectrometer. Two- and three-pulse ESEM spectra were recorded at 4 K on a home-built spectrometer interfaced to a Nicolet 1280

[1]Permanent address: Department of Chemistry, Indian Institute of Technology, Kanpur 208016, India.

[2]Author to whom correspondence may be addressed.

Printed in Canada / Imprimé au Canada

Can. J. Chem. Downloaded from www.nrcresearchpress.com by 112.217.228.212 on 09/07/12
For personal use only.

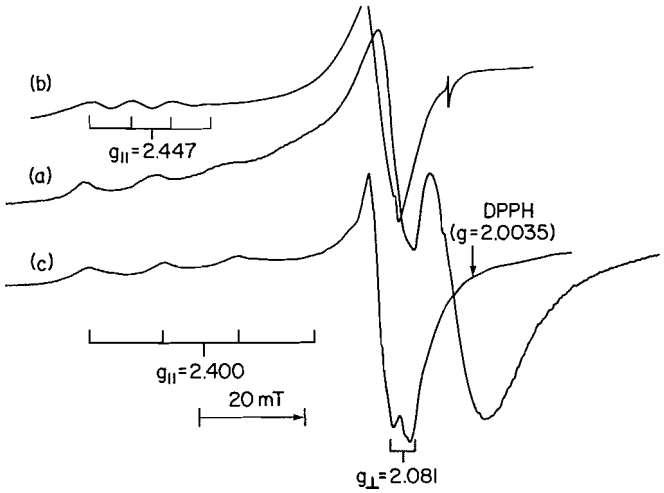

FIG. 1. ESR spectra of Cu^{2+} in the cancrinite C1 at 77 K: (a) freshly prepared sample, (b) 100°C activation, (c) 400°C activation.

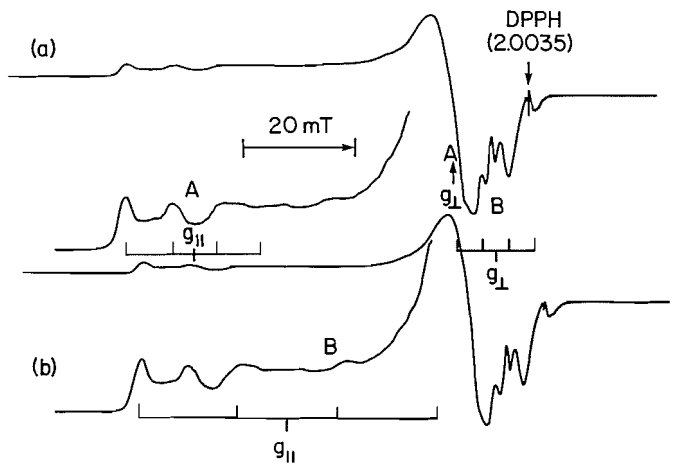

FIG. 2. ESR spectra of 0.3 mol% Cu^{2+} in cancrinite C2 after 100°C activation: (a) room temperature spectrum, (b) spectrum at 77 K.

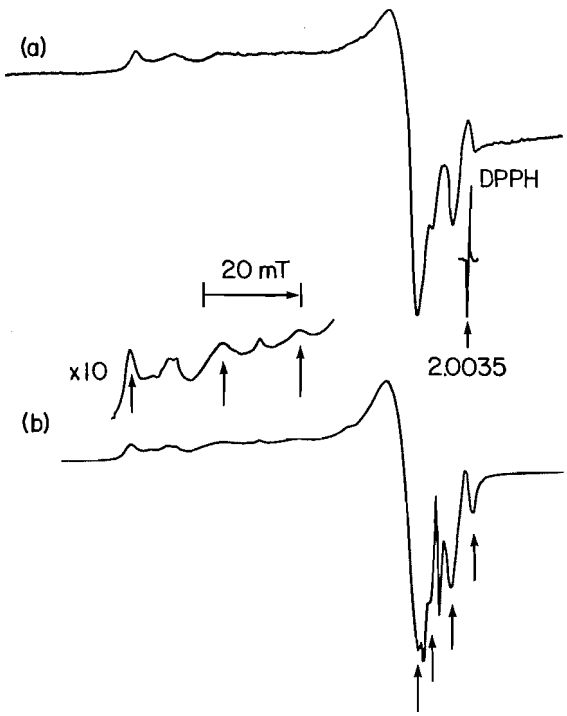

FIG. 3. ESR spectra of Cu^{2+} in cancrinite C2 at 77 K after 400°C activation: (a) 0.3 mol% of Cu^{2+}, (b) 0.5 mol% Cu^{2+}. Arrows in (b) denote the dominant spectral features of Cu^{2+}(B).

computer with 293B pulse programmer. Three-pulse stimulated echoes were recorded as a function of time T between the second and third pulses to observe modulation from both ^{2}D and ^{27}Al. To observe deuterium modulation without interference from Al modulation, the time τ between the first and second pulses was selected to be 0.27 μs, which suppresses Al modulation at the magnetic field used. To record ^{27}Al modulation, τ was set at 0.4 s. To suppress any two-pulse interferences in the three-pulse spin echo envelope at times $T = \tau$ and $T = 2\tau$, as well as to correct for baseline drifts, a phase-cycling procedure was employed (16).

ESEM spectral simulations were performed on the basis of the spherical averaging model (17) discussed in previous publications (5, 18, 19). The simulation procedure compares experimental ESEM spectra with the calculated ones to give "best fit" values for the electron–nucleus distance, R, the number of interacting nuclei, N, and the isotropic hyperfine interaction A_{iso}. All calculated ESEM spectra were multiplied by a decay function (nonlinear least squares fitted to the experimental decay) of the form exp $(a_0 + a_1T + a_2T^2 + a_3T^3)$ to account for the magnetic relaxation.

Results

A. ESR spectra

The room temperature ESR spectrum of freshly prepared C1 cancrinite gives a broad isotropic line centered around $g = 2.159$, which is identified to arise from a hexa-hydrated complex (19) undergoing motional tumbling in the tubular cancrinite channel. As the sample is cooled to 77 K the rotational freedom becomes partially hindered and the resulting ESR spectrum becomes axially symmetric as shown in Fig. 1 (a). Mild dehydration at 100°C destroys this hexa-hydrated species and the Cu^{2+} then becomes coordinated to the zeolite framework. The resulting spectrum is now axially symmetric as shown in Fig. 1 (b). This spectrum yields values of $g_{\|} = 2.442$, $g_{\perp} = 2.068$, $A_{\|} = 83 \times 10^{-4}$ cm^{-1}, and $A_{\perp} = 18 \times 10^{-4}$ cm^{-1}, which are strikingly reminiscent of a variety of examples in the literature where Cu^{2+} is in tetrahedral coordination (20, 21). This point will be further discussed in the light of our ESE results for C1.

Following activation at the higher temperature of 400°C, C1 yields the ESR spectrum shown in Fig. 1 (c). Samples of C1 containing other Cu^{2+} concentrations, activated at 400°C, also yield spectra of similar intensity and resolution. From Fig. 1 (c) we find that the ESR parameters characterizing this site are $g_{\|} = 2.400$, $A_{\|} = 138 \times 10^{-4}$ cm^{-1}, and $g_{\perp} = 2.081$ with unresolved $A_{\perp}$ features. These values suggest a square-pyramidally coordinated Cu^{2+}. Such a coordination of Cu^{2+} to the four oxygens of one of the four-rings of the cancrinite structure is possible.

In Figs. 2 and 3 are given the ESR spectra of the low- and high-temperature activated forms of the carbonate-containing structure C2. The most characteristic feature here is that the two differently activated C2 samples show two sets of g values indicative of two Cu^{2+} species. Figure 2(a) is the room temperature ESR spectrum of C2 doped with 0.3 mol% Cu^{2+} after 100°C activation. The spectral analysis for one species, Cu^{2+}(A), gives $g_{\|} = 2.442$, $g_{\perp} = 2.090$, and $A_{\|} = 90 \times 10^{-4}$ cm^{-1}, which are typical of tetrahedrally coordinated Cu^{2+}. Analysis for the other species, Cu^{2+}(B), gives $g_{\|} = 2.340$, $A_{\|} = 147 \times 10^{-4}$ cm^{-1}, $g_{\perp} = 2.040$, and $A_{\perp} = 35 \times 10^{-4}$ cm^{-1}.

Can. J. Chem. Downloaded from www.nrcresearchpress.com by 112.217.228.212 on 09/07/12
For personal use only.

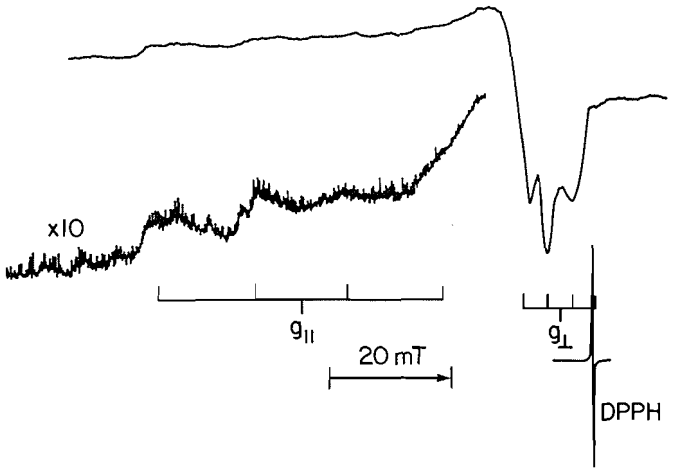

FIG. 4. ESR spectrum at 77 K of 0.3 mol% Cu in cancrinite C2 rehydrated after 400°C activation.

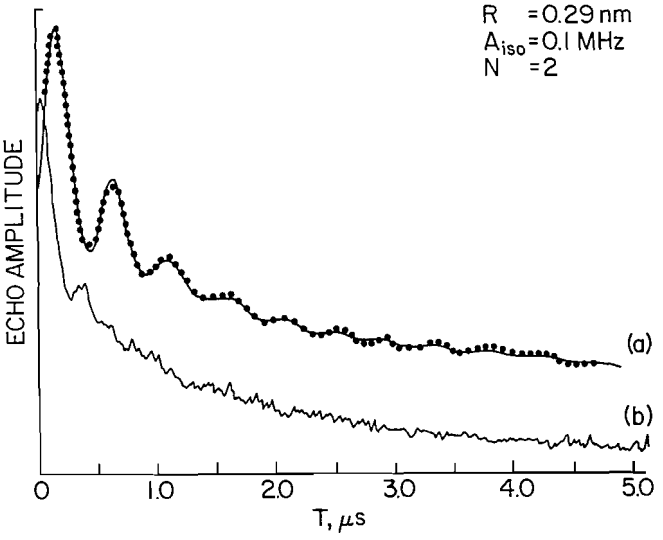

FIG. 5. Three-pulse ESEM spectra of Cu^{2+} in 100°C activated cancrinite C1: (a) Upper curve: experimental ^2D modulation at 4 K and 319 mT (———) and the simulation (····). The decay function used is exp $(2.465 - 0.753\ T + 0.181\ T^2 - 0.017\ T^3)$; (b) Lower curve: experimental ^{27}Al modulation at 4 K and 319 mT.

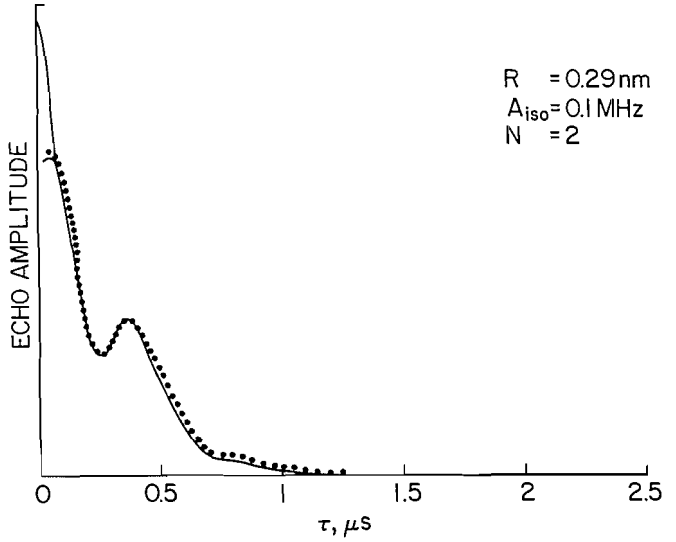

FIG. 6. Two-pulse ESEM spectrum of Cu^{2+} in 100°C activated cancrinite C1 at 4 K and 319 mT: (———) experimental spectrum, showing ^2D modulation, (····) simulation using the decay function exp $(-0.183 + 1.031\ \tau - 8.11\ \tau^2 + 2.81\ \tau^3)$.

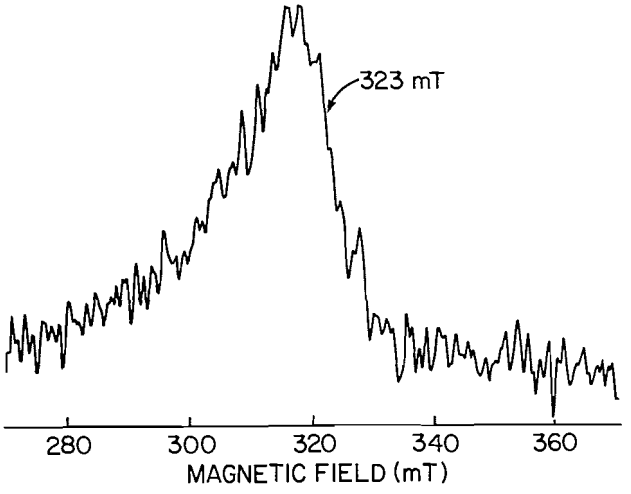

FIG. 7. Field-swept two-pulse ESE spectrum of Cu^{2+} in 100°C activated cancrinite C2 at 4 K, using $\tau = 0.58$ μs. Each field point was incremented after a delay of 193 ms, and the echo was accumulated 10 times during each increment.

Neither the anisotropy nor the g and A parameters of the above sites change when the ESR is recorded at 77 K, as shown in Fig. 2(b). However, after the 400°C activation of C2 the ESR lines of Cu^{2+}(B) become more prominent, as shown in Fig. 3(a). When the ESR spectrum is recorded at 77 K after 400°C activation of the C2 specimen with the highest Cu^{2+} concentration (0.5 mol%), the Cu^{2+}(B) is preponderant, while much weaker spectral features corresponding to Cu^{2+}(A) are barely discernible (see Fig. 3(b)).

On rehydrating the 400°C activated C2, an ESR spectrum corresponding mainly to Cu^{2+}(B) is obtained, as shown in Fig. 4. Long periods of exposure of the above activated samples to flowing oxygen did not change the above observations.

B. ESEM spectra

The three-pulse ^2D and ^{27}Al modulated ESEM spectra of a 100°C activated C1 sample after D_2O exchange are shown in Fig. 5. It is clearly seen that the ^2D modulation is much deeper than the ^{27}Al modulation. The best-fit simulation of the three-pulse deuterium modulated echo, showed by the dotted curve in Fig. 5, yields the result that the Cu^{2+} is interacting with two ($N = 2$) equivalent deuteriums (one water molecule), with a Cu^{2+}–$D(D_2O)$ distance of $R = 0.29$ nm and a small isotropic hyperfine constant A_{iso}. Assuming tetrahedral orbitals on the oxygen, this distance corresponds to a Cu—O bond length of 0.22 nm, which is a value typically observed in aluminosilicates. The shallow ^{27}Al modulation implies that the Cu^{2+} is displaced from a framework window that contains several aluminums.

These three-pulse simulation parameters are confirmed by a two-pulse ESEM spectrum for which simulation gives the same parameters as shown in Fig. 6.

The ESEM spectra of the 100°C activated carbonate-containing specimen C2 were next examined. To determine the magnetic field value for an optimum echo response, a field-swept two-pulse spin echo spectrum was first run on C2, with τ

Can. J. Chem. Downloaded from www.nrcresearchpress.com by 112.217.228.212 on 09/07/12
For personal use only.

TABLE 1. ESR parameters for Cu^{2+} in tetrahedral coordination in various lattices

Lattice	T (K)	$g_{\parallel}$	$g_{\perp}$	$A_{\parallel} \times 10^{-4}$ (cm^{-1})	$A_{\perp} \times 10^{-4}$ (cm^{-1})	Reference
$Na_6Al_6Si_6O_{24}\cdot 8H_2O$	77	2.442[a]	2.068[a]	83[b]	18	This work
$(NH_4)_{12}$–A zeolite	77	2.474	2.100	104	—	20
K_{12}–A zeolite	77	2.479	2.090	100	29	20
Cs_7K_5–A zeolite	77	2.478	2.091	100	—	20
Cs_7Na_5–A zeolite	77	2.488	2.100	97	33	20
Beryl($Be_3Al_2Si_6O_{18}$)	77	2.359	2.091	126	16	22
K_{12}–ZK4 zeolite	77	2.479	2.129	100	—	21

[a]Estimated error ±0.005.
[b]Estimated error ±1 cm^{-1}.

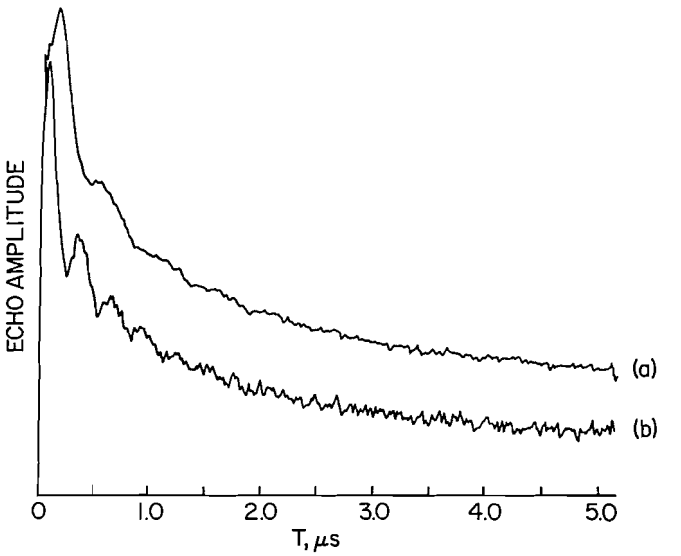

FIG. 8. Experimental three-pulse ESEM spectra of Cu^{2+} in 100°C activated cancrinite C2 at 4 K and 323.3 mT. (a) ^2D modulation, (b) ^{27}Al modulation.

set at 0.56 μs to suppress the ^{27}Al modulation. The magnetic field was swept over 100 mT. Each field point (512 per 100 mT) was incremented after a delay of 193 ms, and the echo was accumulated 100 times during each increment. The field-swept echo profile is presented in Fig. 7, and is seen to peak at 320 mT (a smilar field-sweep profile run for C1 peaked at 317 mT). Consequently, a field value of 323.3 mT (indicated by an arrow in Fig. 7) was chosen as the best setting for obtaining ESEM data for C2.

Figure 8 shows experimental three-pulse ^2D and ^{27}Al spin echo modulation results for C2. In contrast to C1 (Fig. 5) it is seen that the ^{27}Al modulation is deeper and the ^2D modulation is more shallow. Two observations may be made immediately. Firstly, the deeper Al modulation suggests that Cu^{2+} is closer to a framework Al in C2 if the ^{27}Al quadrupole interaction is not significantly changed. Secondly, although the deuterium-modulated echo was too weak to reliably simulate, one may interpret the weak ^2D modulation as suggesting that the Cu^{2+}–D distance is larger than in the C1 lattice.

Discussion

Our ESR and ESEM results for Cu^{2+} in 100°C activated C1 together establish that the active Cu^{2+} sites have tetrahedral symmetry. Although tetrahedral Cu^{2+} sites are somewhat less common than distorted octahedral Cu^{2+} sites, their preferential

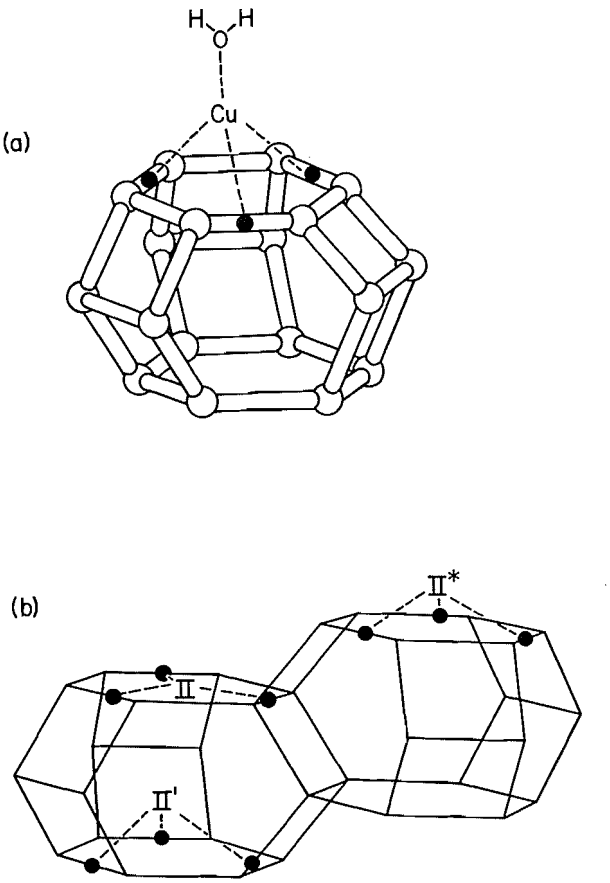

FIG. 9. Proposed sites for Cu^{2+} in the cancrinite framework: (a) tetrahedral site in C1, (b) trigonal sites II* and II′ in C2. The dark circles represent oxygen positions.

formation has been reported in a number of host structures where spatial constraints dominate (20, 21). Table 1 summarizes selected literature data on this point. It is proposed that this Cu^{2+} site in cancrinite C1 is situated as shown in Fig. 9 (a), where the Cu^{2+} ion is near a six-ring bonded to three oxygens of the ring and is located at a site *outside* the undecahedral cancrinite cage in the cancrinite channel. The fourth coordination position is a water molecule in the open cancrinite channel. This structure is consistent with the observed ESR parameters, and the cancrinite channel location can account for the shallow ^{27}Al modulation observed in the ESEM spectrum.

Such a Cu^{2+} site, which remains exposed in the cancrinite channel, should be easily accessible to adsorbate molecules. It is

Can. J. Chem. Downloaded from www.nrcresearchpress.com by 112.217.228.212 on 09/07/12
For personal use only.

TABLE 2. ESR parameters for trigonally coordinated Cu^{2+} in zeolite frameworks

Zeolite	Treatment	T (K)	$g_{\parallel}$	$g_{\perp}$	$A_{\parallel} \times 10^{-4}$ (cm^{-1})	$A_{\perp} \times 10^{-4}$ (cm^{-1})
Cancrinite C2	Evacuated at 400°C	77	2.340[a]	2.040[a]	147[b]	35[b]
K_{12}–A zeolite[c]	Evacuated at 400°C	77	2.391	2.065	133	—
K_{10}–ZK4(1)[c]	Evacuated at 400°C	77	2.357	—	154	—
K8–ZK4(2)[c]	Evacuated at 400°C	77	2.357	—	154	—

[a]Estimated error ±0.005.
[b]Estimated ±1 cm^{-1}.
[c]Reference 21.

suggested, therefore, that Cu^{2+} doped in the C1 structure is likely to be a potentially good catalytic site.

In the case of the carbonate-entrained cancrinite C2, it is significant that rehydration after 400°C activation gives exclusively the spectrum corresponding to the Cu^{2+}(B) species leaving the g and hyperfine parameters unaltered. It may be rationalized that high-temperature activation produces a Cu^{2+} species that is trigonally bound to three framework oxygens in a six-ring. Trigonal sites with similar g and A values have been characterized recently in Cu^{2+}-doped K-ZK4 zeolite (21). A comparison of the ESR parameters for species Cu^{2+}(B) in C2 with those reported for Cu^{2+} in trigonal sites of K-ZK4 is presented in Table 2.

The proposed Cu^{2+} sites in C2 are shown in Fig. 9 (b). Site II is trigonally coordinated at the center of a six-ring, and sites II* and II′ are displaced along the trigonal axis towards the cancrinite channel and into the cancrinite cage, respectively. Since there are two water molecules in the unit cell of cancrinite C2 at room temperature, a water molecule can coordinate with Cu^{2+} at II* to give the tetrahedral site, which is detected as species Cu^{2+}(A). Cu^{2+}(B) is suggested to be located in a trigonal site II or II′. Upon high-temperature activation most of the water is lost, and the Cu^{2+} ions originally at II* move into II or II′ to give trigonal sites. The somewhat stronger ^{27}Al modulation observed for Cu^{2+}(B) in C2 seems consistent with site II, which is within 0.3 nm of three framework Al atoms in a six-ring.

The weak deuterium modulation observed for C2 may be explained by the presence of distant hydroxyl (-OD) groups weakly interacting with Cu^{2+} sites but not directly coordinated to Cu^{2+}. It is known that hydroxyl groups capable of interacting with cation sites are generated during high-temperature activation of Ca^{2+}-containing zeolites (22–24). The presence of Ca^{2+} in the carbonate-entrained cancrinite may also generate hydroxyl groups, which can weakly interact with Cu^{2+}. It appears that "molecular" water is absent in high-temperature activated C2. In previous free-radical entrapment studies (6–8) in C2 cancrinite it has been suggested that the matrix is "water free".

Conclusions

ESR studies of two types of Cu^{2+}-doped cancrinite, one being more hydrated (C1) and the other being less hydrated with entrained carbonate (C2), reveal that upon activation C1 contains Cu^{2+} sites of tetrahedral symmetry while C2 contains mainly Cu^{2+} sites of trigonal symmetry. Two- and three-pulse ESEM studies show ^{2}D and ^{27}Al modulation patterns that corroborate the ESR assignments for the coordination symmetry of the Cu^{2+} sites in these two types of cancrinite.

Acknowledgments

This work was supported by the Texas Advanced Technology Research Program and the National Science Foundation (CHM-8514108). We thank J.S. Yu for assistance in sample preparation and D. Brown for assistance in the ESEM experiments.

1. T. ICHIKAWA and L. KEVAN. J. Am. Chem. Soc. **105**, 402 (1983).
2. (*a*) M. NARAYANA and L. KEVAN. J. Chem. Phys. **75**, 3269 (1981); (*b*) T. ICHIKAWA and L. KEVAN. J. Chem. Soc. Faraday Trans. 1, **77**, 2567 (1981).
3. T. ICHIKAWA and L. KEVAN. J. Phys. Chem. **87**, 4433 (1983).
4. M. W. ANDERSON and L. KEVAN. J. Phys. Chem. **90**, 6452 (1986).
5. L. KEVAN. Acc. Chem. Res. **20**, 1 (1987).
6. P. RAGHUNATHAN and S. K. SUR. J. Phys. Chem **87**, 3383 (1983).
7. P. RAGHUNATHAN and S. K. SUR. Proc. Indian Acad. Sci. **92**, 597 (1983).
8. P. RAGHUNATHAN and S. K. SUR. J. Am. Chem. Soc. **106**, 8014 (1984).
9. O. ZARCHOW. Z. Kristallogr. **122**, 407 (1965).
10. J. V. SMITH. *In* Zeolite chemistry and catalysis. *Edited by* J. A. Rabo. American Chemical Society, Washington, DC 1976. chap. 1.
11. R. M. BARRER and J. F. COLE. J. Chem. Soc. A, 1516 (1970).
12. R. M. BARRER, J. F. COLE, and H. STICHER. J. Chem. Soc. A, 2475 (1968).
13. R. M. BARRER. Hydrothermal chemistry of zeolites. Academic Press, New York, NY. 1982.
14. R. M. BARRER and E. A. D. WHITE. J. Chem. Soc. 1561 (1962).
15. W. L. ROBERTS, G. R. RAPP, and J. WEBER. Encyclopedia of minerals. Von Nostrand, New York, NY. 1974.
16. J. M. FAUTH, A. SCHWEIGER, L. BRAUNSCHWEILER, J. FORRER, and R. R. ERNST. J. Magn. Reson. **66**, 74 (1986).
17. L. KEVAN, M. K. BOWMAN, P. A. NARAYANA, R. K. BOECKMAN, V. F. YUDANOV, and YU.D. TSVETKOV. J. Chem. Phys. **63**, 409 (1975).
18. A. A. SHUBIN and S. A. DIKHANOV. J. Magn. Reson. **52**, 1. (1983).
19. J. C. CONESA and J. SORIA. J. Chem. Soc. Faraday Trans. 1, **75**, 406 (1979).
20. M. NARAYANA and L. KEVAN. J. Phys. C. **16**, 361 (1983).
21. M. W. ANDERSON and L. KEVAN. J. Phys. Chem. **90**, 3206 (1986).
22. V. P. SOLNTSEV, A. S. LEBEDEV, V. S. PAVLYUCHENKO, and V. A. KLYKIN. Sov. Phys.-Solid State (Engl. Transl.), **18**, 805 (1976).
23. M. L. COSTENOBLE, W. J. MORTIER, and J. B. UTTERHOEVEN. J. Chem. Soc. Faraday Trans 1, **74**, 466 (1978).
24. E. DEMPSEY and D. H. OLSON. J. Phys. Chem. **74**, 305 (1970).

Can. J. Chem. Downloaded from www.nrcresearchpress.com by 112.217.228.212 on 09/07/12
For personal use only.

Magnetic field effects upon photochemistry of bichromophoric chain molecules containing nitroaromatic and arylamino moieties: Elucidation of reaction mechanism and control of reaction yields

RYOICHI NAKAGAKI[1]
Institute for Molecular Science, Myodaiji, Okazaki, Japan 444

KIYOSHI MUTAI
College of Arts and Sciences, The University of Tokyo, Komaba, Meguro, Tokyo, Japan 153

MITSUO HIRAMATSU
Hamamatsu Photonics K. K., Ichino-cho, Hamamatsu, Japan 435

HIDEYUKI TUKADA
College of Arts and Sciences, The University of Tokyo, Komaba, Meguro, Tokyo, Japan 153

AND

SABURO NAKAKURA
Institute for Molecular Science, Myodaiji, Okazaki, Japan 444

Received November 13, 1987

This paper is dedicated to Professor Charles A. McDowell on the occasion of his 70th birthday

RYOICHI NAKAGAKI, KIYOSHI MUTAI, MITSUO HIRAMATSU, HIDEYUKI TUKADA, and SABURO NAKAKURA. Can. J. Chem. **66**, 1989 (1988).

The photochemistry of bichromophoric species containing nitroaromatic and arylamino moieties has been studied in the presence and absence of an external magnetic field. Photolysis products are an unsubstituted arylamine, a nitrosoaromatic species (Product 1), and a nitroaromatic compound (Product 2). On application of the magnetic field, the formation yield for Product 1 decreases and that for Product 2 correspondingly increases, whereas the consumption of the starting material and the release of the unsubstituted arylamine are independent of the magnetic field. Analysis of the magnetic field effects shows that the hyperfine coupling mechanism predominates and that the photoreaction takes place in the triplet manifold of the nitroaromatic moiety. Application of the magnetic field may cause an appreciable change in the relative yield of cage and escape products, i.e., the branching ratio of competitive processes.

RYOICHI NAKAGAKI, KIYOSHI MUTAI, MITSUO HIRAMATSU, HIDEYUKI TUKADA et SABURO NAKAKURA. Can. J. Chem. **66**, 1989 (1988).

On a etudié les effets du champ magnétique sur la photochimie des espèces bichromophoriques qui contiennent un groupement arylaminé et un noyau nitroaromatique. Les produits de photolyse sont l'amine aromatique nonsubstituée, le composé aromatique nitrosé (Produit 1), et le composé aromatique nitré (Produit 2). Sous un champ magnétique, le rendement du Produit 1 est diminué et celui de Produit 2 est augmenté, tandis que la consommation de l'espèce de départ ou la libération de l'amine aromatique nonsubstituée ne dépend pas de l'intensité du champ magnétique. De l'analyse des effets du champ magnétique, il résulte que le mécanisme du couplage hyperfin prédomine et la réaction photochimique a lieu dans un état triplet du noyau nitroaromatique. L'application du champ magnétique peut causer un changement manifeste dans la proportion des deux produits photochimiques de la réaction concurrente, c.-à-d., le produit de cage et celui de fuite.

1. Introduction

In our previous papers, we have shown that the photochemical behaviour of some bifunctional chain molecules, A-$(CH_2)_n$-D (A = nitroaromatic electron acceptor and D = arylamino electron donor) critically depends on excitation photon density (1), methylene chain length, n (2), and magnetic field strength (3, 4). Theoretical considerations given in our earlier publications (5, 6) predict that the magnetic field effect on cage product formation is quite opposite to that on escape product formation, when the same radical pair precursor is commonly involved as a reaction intermediate. Namely, when the cage product yield decreases, the escape product yield correspondingly increases and vice versa, irrespective of the factor governing the singlet–triplet transition (the hyperfine coupling or the Zeeman mechanism) or the precursor spin multiplicity. Therefore, it is possible by applying an external magnetic field to control the branching ratio between the cage and escape products formed through the common radical pair (or biradical) intermediate. The present paper is concerned with the magnetic field effects on the photodecomposition yield of bichromophoric species containing the 4-nitro-1-naphthoxyl moiety as an electron acceptor.

2. Experimental

2.1 General

Electronic absorption spectra were measured on a Hitachi U-3200 spectrophotometer. The ^1H nmr spectra were recorded on a Varian EM-390 spectrometer with CD_3Cl as solvent. An electromagnet (Tokin SEE-9G) was used. The magnetic field strength was monitored with a Densijiki Kogyo GM-1220 gaussmeter, and the residual field was 0.08 mT.

2.2 Material

Compounds **1**–**4**, the bifunctional species examined in this work, are shown in Chart 1. The following commercially available chemicals were used for intermolecular model photoreactions and identification

[1]Author to whom correspondence may be addressed.

Printed in Canada / Imprimé au Canada

Can. J. Chem. Downloaded from www.nrcresearchpress.com by 112.217.228.212 on 09/07/12
For personal use only.

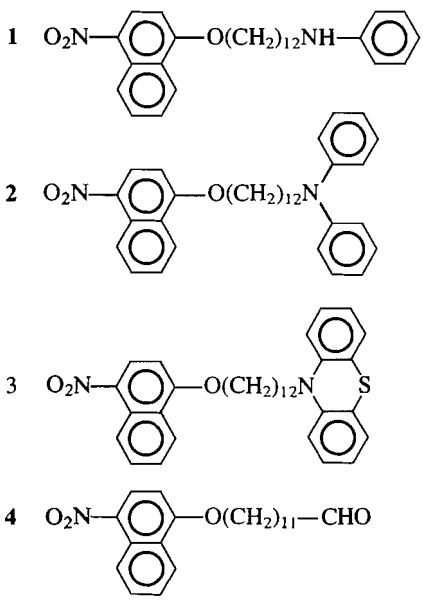

CHART 1

of photoproducts: 1-methoxy-4-nitronaphthalene (Aldrich), 10-methylphenothiazine (Eastman Kodak), phenothiazine, *N*-methylaniline, aniline, *N*-benzylaniline, benzaldehyde, and diphenylamine (Tokyo Kasei). 1-Methoxy-4-nitrosonaphthalene was prepared by procedures in the literature (7). γ-Cyclodextrin was purchased from Tokyo Kasei. The solvents listed below were used for steady-state photolysis and chromatographic analysis: acetonitrile, benzene, ethyl acetate (AcOEt), tetrahydrofuran (THF), *N*,*N*-dimethylformamide (DMF), and water. These were all of spectro or hplc grade.

12-(4-Nitro-1-naphthoxy)dodecyl bromide

A mixture of 1.37 g (10 mmol) of 4-nitro-1-naphthol, 3.94 g (12 mmol) of 1,12-dibromododecane, 1.38 g (10 mmol) of potassium carbonate, 0.3 g of tetrabutylammonium bromide, and 30 mL of water was heated overnight with stirring at 110°C. After the usual work-up, chromatography of the reaction mixture using a silica gel column with hexane–benzene (2:1) as eluent gave 1.96 g (45% yield) of pale yellow crystals, mp 71–72°C (EtOH); ^{1}H nmr δ: 1.33 (s, br, 16H, $-(CH_2)_8$), 1.65–2.1 (m, 4H, $2CH_2$), 3.37 (t, 2H, CH_2Br), 4.19 (t, 2H, CH_2O), 6.72 (d, 1H, Ar-2), 7.35–7.7 (m, 2H, Ar-6,7), 8.34 (two d, 2H, Ar-3,8), 8.74 (dd, 1H, Ar-5). *Anal.* calcd. for $C_{22}H_{30}NO_3Br$: C 60.55, H 6.93, N 3.21; found: C 60.42, H 7.11, N 3.25.

N-*[12-(4-Nitro-1-naphthoxy)dodecyl]aniline (1)*

A mixture of 405 mg (0.93 mmol) of 12-(4-nitro-1-naphthoxy)dodecyl bromide and 1.5 mL of aniline was heated at 90–95°C for 2 h. After the usual work-up and chromatography using a column (activated alumina) with hexane–benzene (1:1) as eluent, 322 mg (77%) of the amine was isolated as yellow crystals, mp 81.5–82°C; ^{1}H nmr δ: 1.32 (s, br, 16H, $-(CH_2)_8$), 1.4–2.1 (m, 4H, $2CH_2$), 3.06 (t, 2H, CH_2N), ca. 3.5 (s, br, 1H, NH), 4.17 (t, 2H, CH_2O), 6.45–6.7 and 7.0–7.25 (m, 5H, C_6H_5N), 6.72 (d, 1H, Ar-2), 7.4–7.8 (m, 2H, Ar-6,7), ca. 8.3 (two d, 2H, Ar-3,8), 8.71 (dd, 1H, Ar-5). *Anal.* calcd. for $C_{28}H_{36}N_2O_3$: C 74.97, H 8.08, N 6.24; found: C 74.85, H 8.22, N 6.23.

N-*(12-Bromododecyl)diphenylamine*

To a stirred solution of 1.69 g (10 mmol) of diphenylamine in 15 mL of dry DMF was added in one portion 0.44 g (11 mmol) of sodium hydride (60% dispersion in mineral oil) under nitrogen. After 30 min of stirring, 4.26 g (13 mmol) of 1,12-dibromododecane in 5 mL of dry DMF was added in one portion and stirring was continued for 2 h at room temperature and then for 1 h at ca. 50°C. After cooling the reaction mixture, the solvent was removed under reduced pressure, and the residue was triturated with chloroform. The extract was dried over magnesium sulfate and filtered. The solvent was removed, and the remaining liquid mass was charged on a column (activated alumina) and eluted with hexane–benzene (4:1). A crude eluate (1.36 g) containing ca. 15% of 1,12-bis(diphenylamino)dodecane was obtained; colorless liquid; ^{1}H nmr δ: 1.30 (s, br, 16H, $-(CH_2)_8$), 1.4–2.1 (m, 4H, $2CH_2$), 3.39 (t, 2H, CH_2Br), 3.66 (t, 2H, CH_2N), 6.7–7.3 (m, 10H, $2C_6H_5$).

N-*[12-(4-Nitro-1-naphthoxy)dodecyl]diphenylamine (2)*

A mixture of 1.25 g (3 mmol) of *N*-(12-bromododecyl)diphenylamine, further purified by hplc, 0.57 g (3 mmol) of 4-nitro-1-naphthol, 0.60 g (1.8 mmol) of cesium carbonate, and 10 mL of 2-methoxyethanol was heated at 120°C with stirring for 5 h. After cooling, the solvent was removed under reduced pressure, and the residue was triturated with chloroform. The extract was dried with magnesium sulfate and filtered. The remaining liquid mass was chromatographed on a silica gel column with benzene–dichloromethane (1:1) as eluent. The fraction (1.08 g) containing **2** was further purified by hplc. Yield 0.99 g (63%), mp 60–61°C (EtOH); ^{1}H nmr δ: 1.31 (s, br, 16H, $-(CH_2)_8$), 1.4–2.1 (m, 4H, $2CH_2$), 3.65 (t, 2H, CH_2N), 4.22 (t, 2H, CH_2O), 6.74 (d, 1H, Ar-2), 6.8–7.35 (m, 10H, $2C_6H_5$), 7.35–7.8 (m, 2H, Ar-6,7), ca. 8.35 (two d, 2H, Ar-3,8), 8.77 (dd, 1H, Ar-5). *Anal.* calcd. for $C_{34}H_{40}N_2O_3$: C 73.62, H 6.90, N 5.05; found: C 73.42, H 6.95, N 4.92.

10-(12-Bromododecyl)phenothiazine

This compound was prepared from 1,12-dibromododecane and phenothiazine, in a similar method to that applied to *N*-(12-bromododecyl)diphenylamine, as a crude liquid; ^{1}H nmr δ: 1.30 (s, br, 16H, $-(CH_2)_8$), 1.65–2.1 (m, 4H, $2CH_2$), 3.34 (t, 2H, CH_2Br), 3.76 (t, 2H, CH_2O), 6.7–7.2 (m, 8H, $N(C_6H_4)_2S$).

10-[12-(4-Nitro-1-naphthoxy)dodecyl]phenothiazine (3)

A mixture of 1.63 g (2.97 mmol) of 10-(12-bromododecyl)phenothiazine, 0.56 g (3 mmol) of 4-nitro-1-naphthol, 0.40 g (3 mmol) of potassium carbonate, 0.2 g of tetrabutylammonium bromide, and 15 mL of water was heated at 100°C for 40 h. After the usual work-up, chromatography using a column (silica gel) with hexane–benzene (1:1) as eluent gave 0.78 g (47% in yield) of **3** as pale yellow crystals, mp 82–83°C (EtOH–benzene); ^{1}H nmr δ: 1.28 (s, br, 16H, $-(CH_2)_8$), 1.4–2.1 (m, 4H, $2CH_2$), 3.77 (t, 2H, CH_2N), 4.15 (t, 2H, CH_2O), 6.6–7.2 (m, 9H, $N(C_6H_4)_2S$ and Ar-2), 7.35–7.75 (m, 2H, Ar-6,7), ca. 8.3 (two d, 2H, Ar-3,8), 8.74 (dd, 1H, Ar-5). *Anal.* calcd. for $C_{34}H_{38}N_2O_3$: C 77.83, H 7.68, N 5.34; found: C 77.68, H 7.55, N 5.25.

12-(4-Nitro-1-naphthoxy)-1-dodecanol

This compound was obtained from 12-bromo-1-dodecanol and 4-nitro-1-naphthol (70% yield), in a similar procedure to that used for the preparation of 12-(4-nitro-1-naphthoxy)dodecyl bromide, as yellow crystals, mp 85.5–86.5°C (EtOH); ^{1}H nmr δ: 1.30 (s, br, 16H, $-(CH_2)_8$), 1.7–2.1 (m, 4H, $2CH_2$), 3.57 (m, 2H, CH_2OH), 4.13 (t, 3H, CH_2OAr and OH), 6.62 (d, 1H, Ar-2), 7.2–7.8 (m, 2H, Ar-6,7), ca. 8.24 (two d, 2H, Ar-3,8), 8.66 (dd, 1H, Ar-5). *Anal.* calcd. for $C_{22}H_{31}NO_4$: C 70.75, H 8.37, N 3.75; found: C 70.83, H 8.53, N 3.80.

12-(4-Nitro-1-naphthoxy)dodecanal (4)

The alcohol was oxidized by chromium(III) oxide–pyridine complex as described by Collins *et al.* (8). Yield 84%, yellow crystals, mp 83–84°C (*n*-hexane–benzene); ^{1}H mr δ: 1.33 (s, br, 16H, $-(CH_2)_8$), 1.6–2.1 (m, 2H, CH_2CH_2OAr), 2.40 (dt, 2H, CH_2CHO), 4.19 (t, 2H, CH_2OAr), 6.73 (d, 1H, Ar-2), 7.35–7.8 (m, 2H, Ar-6,7), ca. 8.3 (two d, 2H, Ar-3,8), 8.68 (dd, 1H, Ar-5), 9.74 (t, 1H, CHO). *Anal.* calcd. for $C_{22}H_{29}NO_4$; C 71.13, H 7.87, N 3.77; found: 71.13, H 8.05, N 3.82.

2.3 Photolysis and chromatographic analysis

The concentration of the bichromophoric species was 1.2×10^{-4} M in all solvents unless otherwise indicated. Sample solutions were deaerated by several freeze–pump–thaw cycles and then sealed under vacuum before irradiation. The sample solution in a quartz cell of 1-cm path length was irradiated with uv light from an Ushio 500-W Xe arc filtered through an appropriate combination of coloured glass filters. For example, the combination of Hoya U-340 and Toshiba UV-35 shows a transmittance maximum at 363 nm with a 23-nm bandwidth

Can. J. Chem. Downloaded from www.nrcresearchpress.com by 112.217.228.212 on 09/07/12
For personal use only.

Can. J. Chem. Downloaded from www.nrcresearchpress.com by 112.217.228.212 on 09/07/12
For personal use only.

(full-width at half maximum), which enables the selective excitation of the acceptor moiety. The Xe arc intensity was monitored by a photosensor with a beam splitter (Toshiba glass filter UV-25). The accumulation of output signal from the sensor for a constant period indicated that the light intensity fluctuation was less than 0.6%. The quartz cuvette containing the sample solution was placed between the pole pieces of the electromagnet during photolysis at room temperature.

Reaction mixtures were analyzed by a Waters Model 510 high performance liquid chromatograph (hplc) equipped with a Waters Model 481 LC spectrophotometer. Reversed- and normal-phase columns were used for the hplc analysis of photoproducts in polar and nonpolar solvents, respectively. The photo-induced absorbance change or integrated intensity of a chromatographic peak due to a photoproduct was used for determining the reaction yield ratio Φ^H/Φ^0 where Φ^H and Φ^0 refer to the yields in the presence and absence of an external magnetic field, respectively. The relative yield was determined as an average value for six to eight separate measurements. Absorption spectra of labile photoproducts were measured by the lc–uv method, i.e., by the combined use of the Waters hplc and a spectrophotometer fitted with a diode array detector (Union Giken MCPD-350PC). The formation of nitrosoaromatic species was properly confirmed by the lc–uv method, although it could not be isolated from reaction mixtures in a conventional manner.

3. Results and discussion

3.1 Identification of photoproducts in intermolecular model photoreactions

To obtain preliminary information about the photolysis of **1–3**, we have studied intermolecular photoreactions between 1-methoxy-4-nitronaphthalene (MNN) and the model donor compounds. The intermolecular photoreaction products from MNN and *N*-methylaniline were identified as 1-methoxy-4-nitrosonaphthalene and aniline by means of hplc, when acetonitrile or benzene was employed as a solvent. When 10-methylphenothiazine was used instead of *N*-methylaniline, unsubstituted phenothiazine was detected in the reaction mixture. The formation of benzaldehyde was confirmed by an hplc analysis of the intermolecular photoreaction involving MNN and *N*-benzylaniline. Thus, the intermolecular photochemistry may be summarized as a redox reaction where deoxygenation of the nitro moiety is associated with oxidation of the methylene group adjacent to the arylamino nitrogen. Some of the intermolecular reactions are described in Scheme 1.

3.2 Characterization of reaction products in intramolecular photochemistry of 1–3

By analogy with the intermolecular model photoreactions mentioned above, it is anticipated that an oxidative *N*-dealkylation of the donor moiety takes place in the intramolecular photochemistry of **1–3**. Steady-state photolysis of **1–3** in benzene yields two major products and one minor product. A product analysis by hplc revealed that one of the major ones is an

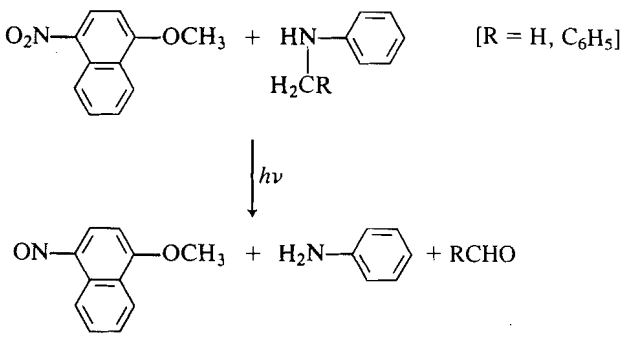

SCHEME 1

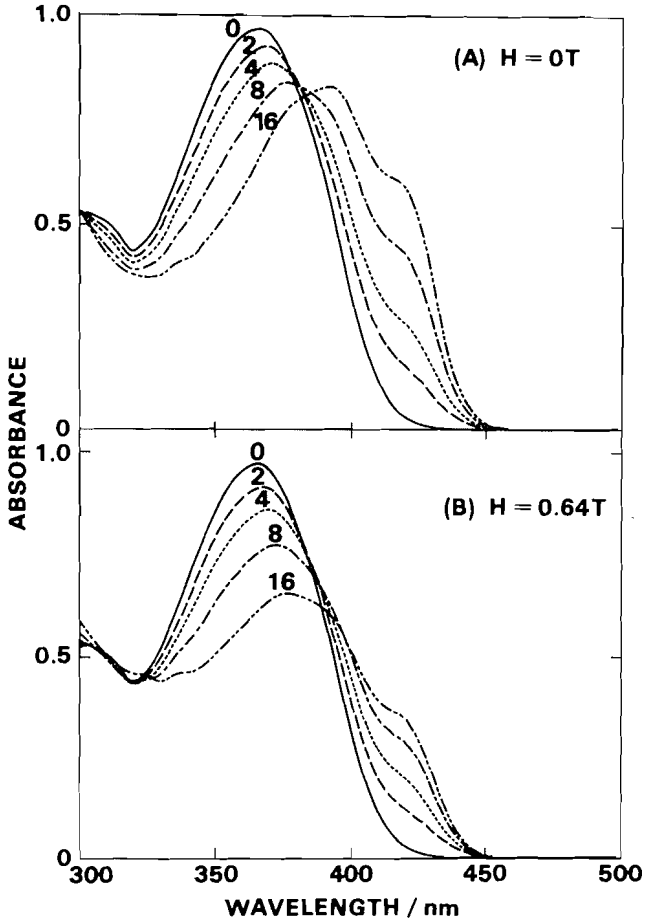

FIG. 1. Photoreaction of **1** in benzene as detected by uv-absorption spectroscopy (A) in the absence and (B) in the presence of an external magnetic field (0.64 T). The number refers to the irradiation time in min. Excitation source: 500-W Xe arc with coloured glass filters, Hoya U-340, Toshiba UV-25, and Toshiba UV-35.

unsubstituted aromatic amine, namely, aniline, diphenylamine, and phenothiazine, in photolysis of **1**, **2**, and **3**, respectively. The major products other than the arylamine (referred to hereafter as Product 1) and the minor product (referred to hereafter as Product 2) were commonly detected with reaction mixtures produced by photolysis of **1–3**.

The photoreaction of **1** in benzene was monitored by uv-absorption spectroscopy (see Fig. 1). Spectral changes observed in the region longer than 350 nm can be ascribed mainly to the disappearance of a 4-nitro-1-naphthoxyl chromophore and the appearance of the 4-nitroso-1-naphthoxyl group. Similar spectral changes have been observed for photoreactions of **2** and **3** in benzene, except for an absorption tail in the shorter wavelength region due to the donor moiety.

Aromatic chromophores in Product 1 and Product 2 were identified by comparison of their absorption spectra recorded by the lc–uv method with reference spectra for the authentic model compounds. The lc–uv spectrum of Product 1 shows an absorption maximum at 393 nm and is very similar to that of 1-methoxy-4-nitrosonaphthalene (see Fig. 2). Therefore, it is concluded that Product 1 contains a 4-nitroso-1-naphthoxyl group. The absorption band due to this chromophore in Product 1 is clearly seen in the spectrum recorded after 16-min irradiation in the absence of the magnetic field (see Fig. 1). In the same manner, the minor photoproduct was found to have a 4-nitro-1-

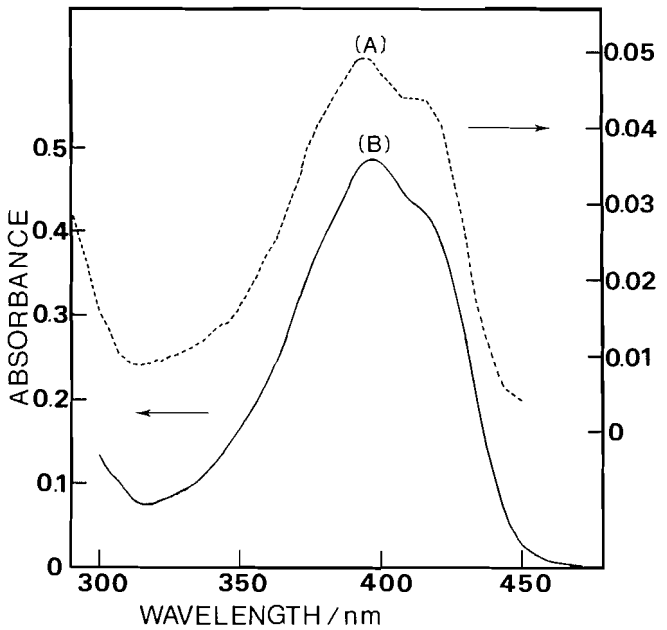

FIG. 2. Absorption spectra of Product 1 (A) and 1-methoxy-4-nitronaphthalene (B). (A): recorded by the lc–uv method for the reaction mixture obtained by 24-min photolysis of **1** in benzene with the concentration of 2.4×10^{-4} M. Excitation source, the same as that in Fig. 1. Normal-phase column, Merck Lichrosorb Si 60 (10 μm). (B): measured in benzene–acetonitrile mixed solvent (4:1) with the concentration of 4.7×10^{-5} M.

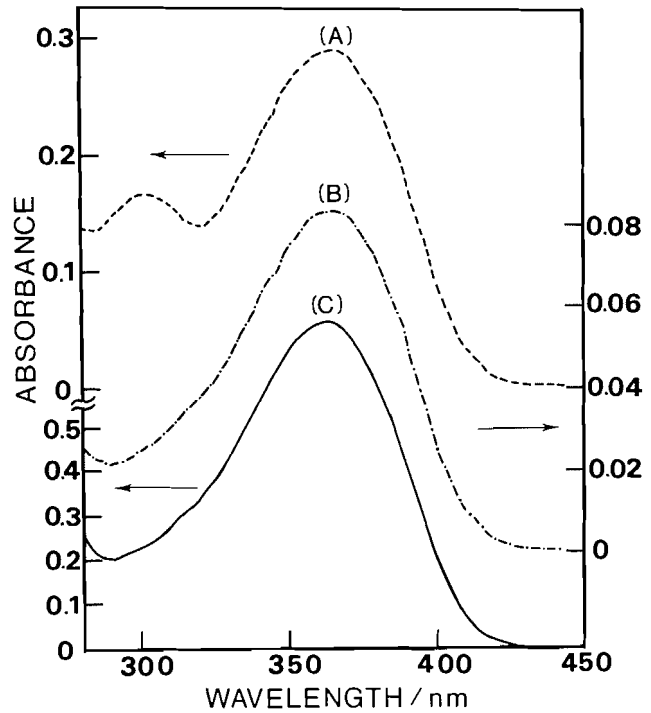

FIG. 3. Absorption spectra of **1** (A), Product 2 (B), and 1-methoxy-4-nitronaphthalene (C). (A) and (B): recorded by the lc–uv method for the reaction mixture obtained by 24-min irradiation of **1** in benzene. Experimental conditions are the same as those in Fig. 2. (C): MNN in benzene with the concentration of 9.5×10^{-5} M.

naphthoxyl chromophore (see Fig. 3). The lc–uv spectra indicate that neither Product 1 nor Product 2 has an arylamino moiety. From these findings, the photoractions of **1–3** in benzene can be characterized as follows:

$$4\text{-}O_2N\text{-}C_{10}H_6\text{-}1\text{-}O(CH_2)_{12}\text{-(Donor)} \xrightarrow{h\nu}$$

$$4\text{-}ON\text{-}C_{10}H_6\text{-}1\text{-}OR^1\text{(major)} + 4\text{-}O_2N\text{-}C_{10}H_6\text{-}1\text{-}OR^2\text{(minor)} + \text{H-(Donor)}$$

where (Donor) = NHC_6H_5, $N(C_6H_5)_2$, and $N{=}(C_6H_4)_2{=}S$.

In the photochemistry of **2** or **3** in benzene, the formation yield of Product 2 is much less than that in the photoreaction of **1**. Hence, ^1H nmr spectroscopy of the photoproducts of **2** or **3** in C_6D_6 may provide information about the structure of the side chain in Product 1, R^1. The observed nmr spectra show new signals attributable to the formyl methylene group, CH_2CHO, i.e., methylene protons at $\delta = 1.92$ ppm and aldehyde proton at $\delta = 9.31$ ppm.[2] This indicates that the terminal group in R^1 is CH_2CHO and suggests $R^1 = (CH_2)_{11}CHO$. The signals due to the formyl methylene group have been observed in the nmr spectra of the reaction mixture obtained by photolysis of 4-O_2N-C_6H_4-1-$O(CH_2)_{12}$-NHC_6H_5 (2). Product 2 is identified as **4** by an hplc analysis, i.e., from the agreement of the retention time and lc–uv spectra. It is concluded that R^2 is also $(CH_2)_{11}CHO$.

There was no indication of thermal reactions of **1–3** in solutions kept in the dark for 24 h at room temperature.

3.3 Magnetic field effects on the photochemistry of 1

3.3.1 Qualitative interpretation

Magnetic field effects on the photochemistry of **1** in benzene have been investigated by means of spectrophotometry. The observed results are given in Figs. 1 and 4. Figure 1 shows that the intensity of the absorption band peaking around 393 nm is reduced in the presence of the external magnetic field (0.64 T). This band is due to the 4-nitroso-1-naphthoxyl chromophore, and therefore the yield of Product 1 decreases on application of the magnetic field. Figure 4 illustrates two chromatograms recorded for the reaction mixtures obtained after 16-min irradiation of **1** in the presence and absence of the field. The peak intensity due to Product 1 decreases in the presence of the magnetic field, while that due to Product 2 increases.

Table 1 summarizes the magnetic field effects on photochemistry of **1**. We can see from this table that application of the external magnetic field (0.64 T) causes an appreciable change in the formation yields of Product 1 and Product 2, whereas neither the disappearance of **1** nor aniline formation is dependent on the magnetic field strength.

The magnetic field effects obtained in the present study suggest an intramolecular radical pair (biradical) in which two unpaired electrons are weakly coupled (3, 5, 6). The spin state of the reaction intermediate and the factor controlling the singlet–triplet mixing can be determined from analysis of the observed results on the basis of theoretical treatment of magnetic field effects upon chemical reactions via a radical pair (5, 6). The nitrosoaromatic species have been identified as cage products derived from the parent nitroaromatic compounds (3). Therefore, the following two cases can account for the observed magnetic field effects on the cage product formation: (*i*) a singlet biradical precursor is formed and the Zeeman mechanism is of dominant importance; (*ii*) a triplet biradical precursor is produced and the hyperfine coupling (HFC) mechanism predominates. The latter possibility is more likely, because the excited singlet state of the 4-nitro-1-naphthoxyl moiety undergoes a

[2]K. Mutai, H. Tukada, and R. Nakagaki. Unpublished results.

Can. J. Chem. Downloaded from www.nrcresearchpress.com by 112.217.228.212 on 09/07/12
For personal use only.

TABLE 1. Magnetic field effects on photochemical processes of **1**

Solvent	Disappearance of **1**[a]	Formation[b] Aniline	Product 1	Product 2
Benzene	0.96±0.04 (10)	1.03±0.05	0.71±0.03	1.92±0.16
CH_3CN	1.00±0.02 (30)	0.98±0.03	0.80±0.04	1.34±0.09
AcOEt			0.71±0.06[c]	
THF			0.84±0.04[c]	
DMF / H_2O[d]	(25)		0.80±0.10	1.68±0.11
DMF / H_2O / γ-CD[e]	(25)		0.68±0.07	1.63±0.11

[a]Determined by hplc as $[I(0)-I^H]/[I(0)-I^0]$, where $I(0)$ denotes the peak area in the chromatogram recorded before uv irradiation, and I^H and I^0 refer to the peak area in the chromatogram recorded after photolysis in the presence and absence, respectively, of an external magnetic field (0.64 T). The quoted uncertainty represents the standard deviation. The values in parentheses indicate the percentage consumption of **1**.

[b]Determined by hplc as I^H/I^0, unless otherwise indicated.

[c]Determined by analysis of absorbance increase at 420 nm.

[d]DMF–water mixed solvent (80:20 by volume ratio).

[e]DMF–water mixed solvent (80:20 by volume ratio) containing 6.9×10^{-3} M of γ-cyclodextrin.

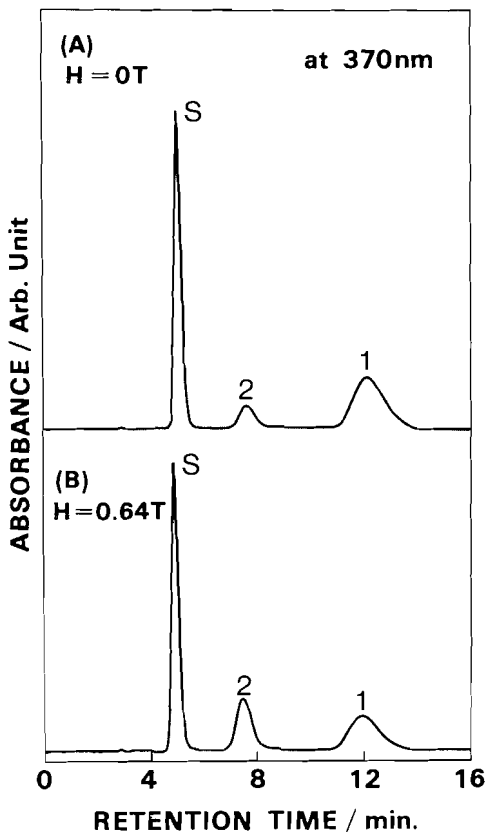

FIG. 4. Chromatograms recorded by monitoring absorbance at 370 nm for the reaction mixture obtained by 16-min irradiation of **1** in benzene (A) in the absence of (B) in the presence of an external magnetic field (0.64 T). Excitation source, the same as that in Fig. 1. S, starting material; 1, Product 1; and 2, Product 2. Normal-phase column, Merck Lichrosorb Si 60 (10 μm).

very rapid intersystem crossing (ISC) to the excited triplet state (10) and the initially prepared biradical must be of the triplet spin multiplicity. This conclusion is in accordance with the fact that the photo-redox reactions of 4-O_2N-C_6H_4-1-$O(CH_2)_{12}$-NHC_6H_5 (3) and related nitro compounds (11) occur mainly through the excited triplet state.

Figure 5 illustrates a reaction scheme proposed for the photochemistry of **1**. Since the HFC mechanism is of dominant importance, the ISC rate between ^{3}BR and ^{1}BR in Fig. 5 lowers in the presence of an external magnetic field (5, 6). The decrease in the ISC rate gives rise to the increase in the formation yield for escape products derived from the triplet precursor under the magnetic field. Therefore, Product 2 is identified as an escape product that may be formed through an intermolecular redox reaction. Because aniline is formed through both the cage and escape processes, its yield is insensitive to the magnetic field. Magnetic field effects on the consumption of **1** are hardly discernible from the experimental error.

3.3.2 Kinetic analysis

The observed magnetic field effects can be reasonably analyzed by a simple kinetic model based on the reaction scheme in Fig. 5. We measured magnetic field effects on the relative formation yield with changing field strength. Figure 6 shows the observed dependence of Φ^H/Φ^0 on H for Product 1 and Product 2 in the photochemistry of **1** in benzene. Since the relative yield becomes constant in the range higher than 0.5 T, the Zeeman mechanism is of no importance in the present case (5, 6). To analyze the magnetic field dependence of Φ^H/Φ^0, the following two kinetic parameters are introduced into the reaction scheme of Fig. 5: $K_{ISC}(X)$ for the ISC rate between ^{3}BR and ^{1}BR in the presence of the magnetic field of X T, and K_{esc} for the rate of escape process for ^{3}BR. The dependence of cage and escape product formations on H is described by eqs. [1] and [2], respectively[3]:

$$[1]\quad (\Phi^H/\Phi^0)_{cage} = K_{ISC}(H)\{K_{ISC}(0) + K_{esc}\}/K_{ISC}(0)\{K_{ISC}(H) + K_{esc}\}$$

$$[2]\quad (\Phi^H/\Phi^0)_{escape} = \{K_{ISC}(0) + K_{esc}\}/\{K_{ISC}(H) + K_{esc}\}$$

From the relative yield values for the cage and escape products given in Fig. 6, $Q(H) = (\Phi^H/\Phi^0)_{cage}/(\Phi^H/\Phi^0)_{escape} =$

[3]These equations were derived on the following assumptions: (*i*) Photostationary conditions are satisfied, i.e., $d[^3BR]/dt = d[^1BR]/dt = 0$. (*ii*) The cage process yielding Product 1 is much more rapid than other processes occurring from ^{1}BR, e.g., the ISC going back from ^{1}BR to ^{3}BR. Namely, K(cage product formation) $\gg K_{ISC}(X)$. (*iii*) The external magnetic field has no effects on K(cage product formation) or K_{esc}. The second assumption has usually been employed for the analysis of radical pair reactions involving triplet precursors: e.g., ref. 12.

Can. J. Chem. Downloaded from www.nrcresearchpress.com by 112.217.228.212 on 09/07/12
For personal use only.

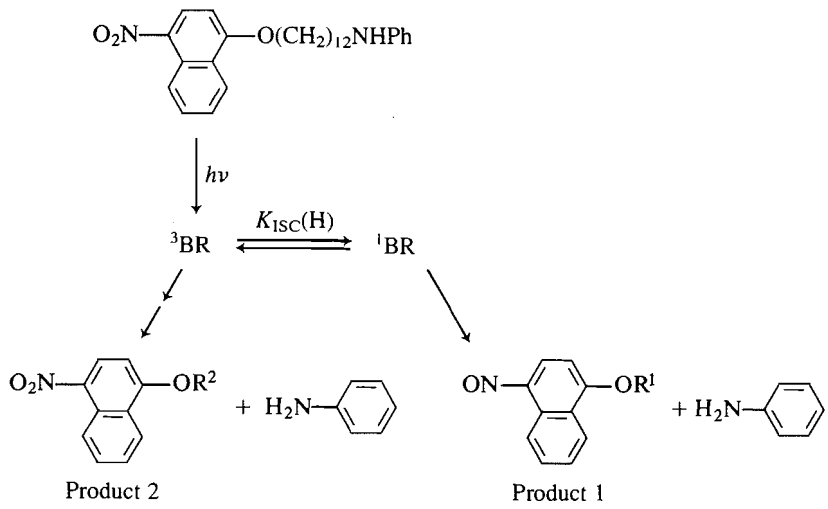

FIG. 5. Reaction scheme for the photochemistry of **1**. BR represents a biradical reaction intermediate. Superscripts 1 and 3 indicate the spin multiplicity.

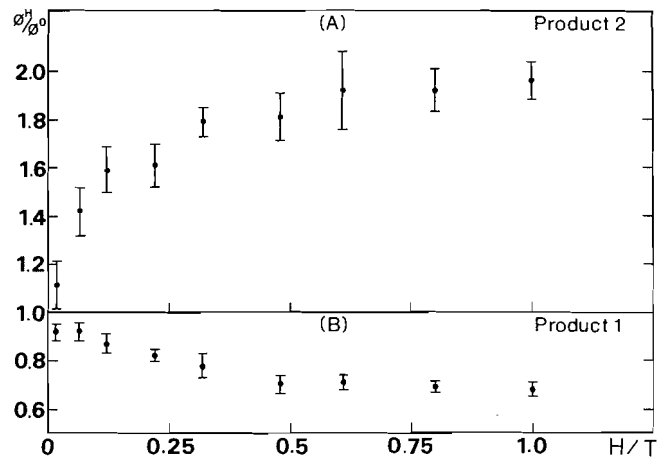

FIG. 6. Dependence of the relative yield, Φ^H/Φ^0 on the field strength, H, for photochemistry of **1** in benzene. The error bar represents the standard deviation. The relative yield was determined by hplc at 10% disappearance of **1**. Excitation source, the same as that in Fig. 1.

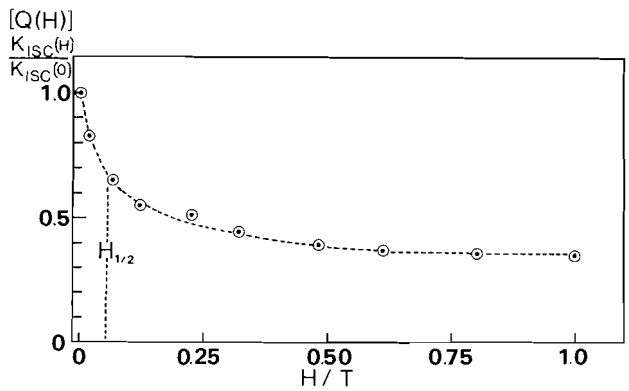

FIG. 7. Dependence of $Q(H) = K_{ISC}(H)/K_{ISC}(0)$ on the field strength, H.

$K_{ISC}(H)/K_{ISC}(0)$ was plotted in Fig. 7 as a function of the magnetic field strength, H. A magnetic field effect parameter, $H_{1/2}$, is defined as the field strength at which half the magnetic field effect in the saturation region is observed (13). The $H_{1/2}$ value was determined to be 55 mT from the plot of $Q(H)$ vs. H in Fig. 7 according to the relation, $Q(H_{1/2}) = [Q(0\ T) + Q(>0.5\ T)]/2 = [1 + Q(>0.5\ T)]/2$. The magnitude of this value is slightly larger than that usually observed in the magnetic field effects due to the HFC mechanism for the intramolecular photoreaction of polymethylene-linked chain molecules (14, 15), e.g., 20 mT for (1-pyrenyl)-$(CH_2)_{12}$-4-C_6H_4-1-$N(CH_3)_2$ (14). Consequently, there may be some contribution from other mechanisms, e.g., the relaxation mechanism (16).

3.4 Solvent effects and reaction mechanism of photochemistry of 1

The magnetic field effects upon the photochemistry of **1** have been studied in several solvents. We can see from the results in Table 1 that the effects have no systematic dependence on solvent polarity. However, the magnetic field effects on nitrosoaromatic formation depend appreciably on the irradiation time, especially in acetonitrile and tetrahydrofuran. This is due to the disappearance of the primary nitrosoaromatic product through a secondary process (3). Figure 8 shows that the formation yield of Product 2 becomes larger than that of Product 1 on prolonged photolysis of **1** in CH_3CN in the presence of a high magnetic field (0.64 T). On the other hand, the relation [Product 1] > [Product 2] holds when the consumption of **1** is low (see Table 2). Therefore, it is desirable to compare solvent effects on the relative yield, Φ^H/Φ^0, when the consumption of the starting material is still low (less than 40%). Benzene and ethyl acetate are much better than more polar solvents in that the secondary reaction is relatively slow.

In view of the rather low ionization potentials for *N*-alkylanilines (17), e.g., 7.65 eV for *N*-methylaniline, it is reasonable to assume photo-induced charge separation in polar media such as acetonitrile. Hence, the charge-separated biradical $A^{\cdot}$-$(CH_2)_n$-D^{+} formed by an electron transfer from the donor to the excited acceptor group can reasonably explain the observed magnetic field effects. In fact, the transient absorption due to the charge-separated biradical was recorded by laser photolysis of 4-O_2N-C_6H_4-1-$O(CH_2)_{12}$-NHC_6H_5 in acetonitrile (2). Magnetic field effects were observed for higher homologues with long methylene chains 4-O_2N-C_6H_4-1-$O(CH_2)_n$-NHC_6H_5 ($n \geq 8$) in CH_3CN and interpreted in terms of a change in the ISC

Can. J. Chem. Downloaded from www.nrcresearchpress.com by 112.217.228.212 on 09/07/12
For personal use only.

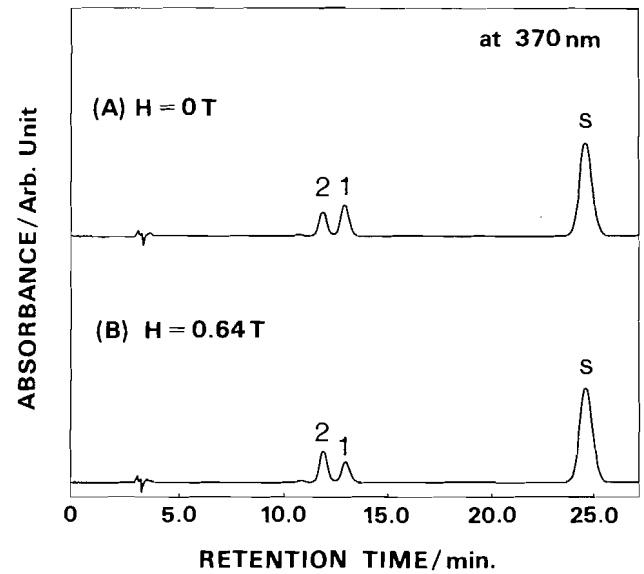

FIG. 8. Chromatograms recorded by monitoring absorbance at 370 nm for the reaction mixture obtained after 20-min irradiation of **1** in acetonitrile in the absence (A) and in the presence (B) of an external magnetic field (0.64 T). Radiation source: 500-W Xe arc with Toshiba glass filters, UV-D33S, UV-25, UV-35. S, starting material; 1, Product 1; and 2, Product 2. Both products have almost the same magnitude of molar extinction coefficient at 370 nm. Consumption of **1** = 69%. Reversed-phase column: Chemcopak, Chemcosorb 7-ODS-L (7 μm).

TABLE 2. Magnetic field effects on branching ratio in competitive photoreactions of **1**

Solvent	R_b(0 T)[a]	R_b(0.64 T)[a]	(%)[b]
Benzene	0.21±0.02	0.58±0.08	10
Benzene	0.17±0.02	0.59±0.07	35
CH_3CN	0.36±0.03	0.60±0.08	30
CH_3CN	0.66±0.06	1.23±0.12	69
DMF/H_2O[c]	0.51±0.04	1.06±0.11	25
DMF/H_2O/γ-CD[d]	0.62±0.04	1.49±0.15	25

[a] R_b = Φ (Product 2)/Φ (Product 1).
[b] Consumption of **1** in percentage.
[c] DMF–water mixed solvent (80:20 by volume ratio).
[d] DMF–water mixed solvent (80:20 by volume ratio containing 6.9×10^{-3} M of γ-cyclodextrin.

rate due to the HFC mechanism for the charge-separated biradical (3).

On the other hand, in nonpolar solvents, e.g., benzene, it is very unlikely that the charge-separated biradical is involved as a reaction intermediate, because solvation energy for a highly polar species is very small in solvents with low dielectric constants (18). By analogy with the intermolecular photo-redox reaction involving *N*-methylaniline and excited *m*-chloronitrobenzene (19), hydrogen abstraction from the alkyl chain by the nitro group is likely as a photochemical primary process in benzene. The charge-separated biradical formed after photoexcitation in benzene can be characterized as an exciplex or a contact ion pair (18) and, therefore, the interradical distance must be very small. The observation of pronounced magnetic field effects suggests a large separation (≥1 nm) between the two unpaired electrons (3, 15). It is reasonable to assume a neutral biradical as a reaction intermediate in benzene.

TABLE 3. Magnetic field effects on product formation of **1–3** in benzene[a]

Compound	Arylamine	Product 1	Product 2
1		0.71±0.03	1.92±0.16
2		0.88±0.03	1.37±0.10
3	1.01±0.04	0.91±0.06	[b]

[a] Determined by hplc as I^H/I^0 (H = 0.64 T). The quoted uncertainty represents the standard deviation.
[b] The precise determination was impossible, because the formation yield for Product 2 was very low.

A biradical intermediate in the reaction scheme of Fig. 5 may be the charge-separated species in CH_3CN and the neutral type of HA-$(CH_2)_{n-1}$-ĊHD in C_6H_6.

*3.5 Magnetic field effects on the competitive processes in photochemistry of **1***

A parameter for two competing reactions, R_b is defined as a yield ratio, R_b = Φ(escape product)/Φ(cage product). The value of R_b can be estimated from hplc data, namely, (*i*) measurement of chromatograms by monitoring absorbance at a particular wavelength, λ nm, and (*ii*) comparison of the integrated intensity of two peaks due to both products, on the assumption concerning the molar extinction coefficient at λ nm that ε(Product 2)/ε(Product 1) = ε(4-methoxy-1-nitronaphthalene)/ε(4-methoxy-1-nitrosonaphthalene). Table 2 lists the R_b values for photoreaction of **1**. The R_b value is sensitive to reaction environments, e.g., presence of γ-cyclodextrin (γ-CD). The escape product is considerably enhanced on addition of γ-CD, which suggests that the inclusion complexation of the donor and (or) the acceptor moieties by γ-CD depresses the intramolecular cage process forming Product 1.[4] The R_b value also increases on prolonged irradiation, because the denominator of R_b is reduced by the secondary decomposition of the primary cage product. On addition of γ-CD or on continuing photolysis for a long time, Product 2 becomes dominant over Product 1 under the magnetic field of 0.64 T (see Fig. 8). This fact implies that the magnetic field effect can be used for controlling chemical reactions that occur via a biradical or radical pair intermediate.

*3.6 Comparison of photochemistry of **1–3***

A photoreaction mechanism of **2** or **3** is closely related to that of **1** in Fig. 5, since they commonly undergo photo-induced oxidative *N*-dealkylation. Tables 3 and 4 list the magnetic field effects on photoproduct formation and on the competitive processes of **1–3** in benzene, respectively. On going from **1** to **3**, the magnitude of magnetic field effects on product formation shows a decreasing tendency and the R_b value is greatly diminished. These two findings can be explained in terms of eq. [1]. When the rate of escape process, K_{esc}, becomes negligibly small in comparison with $K_{ISC}(X)$, the relative yield, $(\Phi^H/\Phi^0)_{cage}$ approaches 1 as the limiting value. (Substitution of 0 for K_{esc} in eq. [1] gives $(\Phi^H/\Phi^0)_{cage}$ = 1.) Photochemistry of **3** can be classified as an example closest to this extreme case among **1–3**. There is an interesting correlation between the R_b values and the ionization potential of the donor moiety, IP(D) (see Table 6). When the electron-donating ability is increased, the cage product is formed more efficiently than the escape product.

[4] An inclusion complex formation has been known for an aqueous DMF solution: see ref. 20.

Can. J. Chem. Downloaded from www.nrcresearchpress.com by 112.217.228.212 on 09/07/12
For personal use only.

TABLE 4. Magnetic field effects on competitive processes in photochemistry of **1**–**3**[a]

Compound	R_b(0 T)	R_b(0.64 T)	IP(D) / eV
1	0.21±0.02	0.58±0.08	7.65[b]
2	0.10±0.02	0.16±0.04	7.44[c]
3	<0.04[d]	<0.04[d]	7.15[e]

[a] $R_b = \Phi$ (Product 2) / Φ (Product 1) determined based on the hplc data.
[b] A value for *N*-methylaniline taken from ref. 17.
[c] A value for *N*-methyldiphenylamine given in ref. 21.
[d] Since the Product 2 yield is too low to determine the R_b value precisely, the upper limit was estimated from the sensitivity of hplc analysis.
[e] A value for 10-methylphenothiazine reported in ref. 9.

4. Concluding remarks

The results reported in this work, as well as those presented in previous papers (3–6, 15, 16), show that the spin dynamics of radical pairs play one of the most important roles in the magnetic field effects on chemical processes or "spin chemistry". Although magnetic fields (≤1 T) generated by an ordinary electromagnet can cause rather small Zeeman splittings in a radical pair intermediate with triplet spin multiplicity, the relative ISC rate $K_{ISC}(H)/K_{ISC}(0)$ may change from 1 to ca. 1/3 in the case of magnetic field effects due to the HFC mechanism. Thus, magnetic field effects on radical reactions provide us with useful tools for elucidating the reaction mechanism (dynamical behaviour of the radical pair, spin states of biradical precursors, etc.), for controlling reaction rates and product yields, and for selecting reaction pathways.

Acknowledgements

This work was supported by the Joint Study Program (1986–1987) of the Institute for Molecular Science. We thank Professor Y. Tanimoto of Kanazawa University for his valuable comments and enlightening discussions.

1. K. YOKOYAMA, J. NAKAMURA, T. KOBAYASHI, and S. NAGAKURA. Bull. Chem. Soc. Jpn. **53**, 3474 (1980).
2. R. NAKAGAKI, M. HIRAMATSU, K. MUTAI, and S. NAGAKURA. Chem. Phys. Lett. **121**, 262 (1985).
3. R. NAKAGAKI, M. HIRAMATSU, K. MUTAI, Y. TANIMOTO, and S. NAGAKURA. Chem. Phys. Lett. **134**, 171 (1987).
4. M. HIRAMATSU, R. NAKAGAKI, Y. TANIMOTO, K. MUTAI, H. TUKADA, and S. NAGAKURA. Chem. Phys. Lett. **142**, 413 (1987).
5. H. HAYASHI and S. NAGAKURA. Bull. Chem. Soc. Jpn. **51**, 2862 (1978).
6. Y. SAKAGUCHI, H. HAYASHI, and S. NAGAKURA. Bull. Chem. Soc. Jpn. **53**, 39 (1980).
7. A. SCHORS, A. KRAAIJEVELD, and E. HAVINGA. Recl. Trav. Chim. Pays-Bas, **74**, 1243 (1955).
8. J. C. COLLINS, W. W. HESS, and F. J. FRANK. Tetrahedron Lett. 3363 (1968).
9. L. N. DOMELSMITH, L. L. MUNCHAUSEN, and K. N. HOUK. J. Am. Chem. Soc. **99**, 6506 (1977).
10. N. J. BUNCE, S. R. CATER, J. C. SCAIANO, and L. JOHNSTON. J. Org. Chem. **52**, 4214 (1987).
11. P. WAN and K. YATES. Can. J. Chem. **64**, 2076 (1986), and references cited therein; Y. L. Chow. *In* The chemistry of the amino, nitro, and nitroso compounds and their derivatives. *Edited by* S. Patai. Wiley, New York. 1982. Chap. 6.
12. Y. TANIMOTO, H. UDAGAWA, Y. KATSUDA, and M. ITOH. J. Phys. Chem. **87**, 3976 (1983); M. B. ZIMMT, C. DOUBLEDAY, JR., I. R. GOULD, and N. J. TURRO. J. Am. Chem. Soc. **107**, 6724 (1985); N. J. TURRO, C.-C. CHENG, P. WAN, C.-J. CHUNG, and W. MAHLER. J. Phys. Chem. **89**, 1567 (1985); M. OKAZAKI, S. SAKATA, R. KONAKA, and T. SHIGA. J. Phys. Chem. **91**, 1131 (1987); Y. Tanimoto and M. ITOH. *In* Studies in organic chemistry. Vol. 30. *Edited by* M. Kobayashi. Elsevier, Amsterdam. 1987. pp. 254–264, and references cited therein.
13. A. WELLER, F. NOLTING, and H. STAERK. Chem. Phys. Lett. **96**, 24 (1983).
14. H. STAERK, W. KÜNLE, R. TREICHEL, and A. WELLER. Chem. Phys. Lett. **118**, 19 (1985).
15. Y. TANIMOTO, N. OKADA, M. ITOH, K. IWAI, K. SUGIOKA, F. TAKEMURA, R. NAKAGAKI, and S. NAGAKURA. Chem. Phys. Lett. **136**, 42 (1987).
16. H. HAYASHI and S. NAGAKURA. Bull. Chem. Soc. Jpn. **57**, 322 (1984).
17. J. P. MAIER and D. W. TURNER. J. Chem. Soc. Faraday Trans. 2, **69**, 521 (1973).
18. A. WELLER. Z. Phys. Chem. NF (Wiesbaden), **133**, 93 (1983).
19. I. SAITO, M. TAKAMI, and T. MATSUURA. Tetrahedron Lett. 661 (1974).
20. B. SIEGEL and R. BRESLOW. J. Am. Chem. Soc. **97**, 6869 (1975).
21. H. J. HAINK, J. E. ADAMS, and J. R. HUBER. Ber. Bunsen-ges. Phys. Chem. **78**, 436 (1974).

Can. J. Chem. Downloaded from www.nrcresearchpress.com by 112.217.228.212 on 09/07/12
For personal use only.

Molybdenum–tin and molybdenum–copper complexes derived from the molybdenum tricarbonyl anions, $LMo(CO)_3^-$ (where L = $HBpz_3$ or $HBpz''_3$; pz = pyrazolyl, $N_2C_3H_3$; and pz″ = 3,5-dimethylpyrazolyl, $N_2C_5H_7$)

YAN-YUN LIU, ARTHUR MAR, STEVEN J. RETTIG, ALAN STORR,[1] AND JAMES TROTTER[1]

Department of Chemistry, University of British Columbia, 2036 Main Mall, Vancouver, B.C., Canada V6T 1Y6

Received December 18, 1987

This paper is dedicated to Professor Charles A. McDowell on the occasion of his seventieth birthday

YAN-YUN LIU, ARTHUR MAR, STEVEN J. RETTIG, ALAN STORR, and JAMES TROTTER. Can. J. Chem. **66**, 1997 (1988).

The pyrazolylborate molybdenum tricarbonyl anions, $(HBpz_3)Mo(CO)_3^-$ and $(HBpz''_3)Mo(CO)_3^-$, have been utilized to prepare a number of heteronuclear bimetallic species containing Mo—Sn and Mo—Cu bonds. Crystals of [hydrotris(1-pyrazolyl)borato-*N*,*N*,*N*](triphenylstannyl)tricarbonylmolybdenum are monoclinic, a = 17.570(2), b = 14.077(2), c = 12.180(1) Å, β = 96.985(8)°, Z = 4, space group $P2_1/n$, those of [hydrotris(1-3,5-dimethylpyrazolyl)borato-*N*,*N*,*N*](chlorodimethylstannyl)tricarbonylmolybdenum are monoclinic, a = 11.044(3), b = 12.061(2), c = 20.218(4) Å, β = 100.43(1)°, Z = 4, space group $P2_1/c$, and those of [hydrotris(1-pyrazolyl)borato-*N*,*N*,*N*]tricarbonylmolybdenum(*N*,*N*,*N*′,*N*′-tetramethylethylenediamine)copper dichloromethane solvate are orthorhombic, a = 19.027(2), b = 16.995(2), c = 16.136(2) Å, Z = 8, space group *Pbca*. The structures were solved by conventional heavy atom methods and refined by full-matrix least-squares procedures to R = 0.044, 0.042, and 0.059 for 2084, 2502, and 1891 reflections, respectively. The two tin structures have a 3:3:1 capped octahedral structure with Mo—Sn bonds of 2.864(1) and 2.823(1) Å. The copper complex has a 3:4 piano stool arrangement of ligands about Mo with a Mo—Cu bond of 2.639(2) Å, two semibridging carbonyl ligands, and one terminal carbonyl ligand.

YAN-YUN LIU, ARTHUR MAR, STEVEN J. RETTIG, ALAN STORR et JAMES TROTTER. Can. J. Chem. **66**, 1997 (1988).

On a utilisé les anions pyrazolylborate de molybdène tricarbonyle, $(HBpz_3)Mo(CO)_3^-$ et $(HBpz''_3)Mo(CO)_3^-$, pour préparer un certain nombre d'espèces bimétalliques hétéronucléaires contenant des liaisons Mo—Sn et Mo—Cu. Les cristaux de l'[hydrotris(pyrazolyl-1)borato-*N*,*N*,*N*](triphénylstannyl)tricarbonylmolybdène sont monocliniques avec a = 17,570(2), b = 14,077(2) et c = 12,180(1) Å, β = 96,985(8)°, Z = 4 et groupe d'espace $P2_1/n$, ceux de l'[hydrotris(diméthyl-3,5 pyrazolyl-1)borato-*N*,*N*,*N*](chlorodiméthylstannyl)tricarbonylmolybdène sont monocliniques avec a = 11,044(3), b = 12,061(2) et c = 20,218(4) Å, β = 100,43(1)°, Z = 4 et groupe d'espace $P2_1/c$, et ceux de l'[hydrotris(pyrazolyl-1)borato-*N*,*N*,*N*]tricarbonylmolybdène(*N*,*N*,*N*′,*N*′-tétraméthyléthylènediame)cuivre solvaté par du dichlorométhane sont orthorhombiques avec a = 19,027(2), b = 16,995(2), c = 16,136(2) Å, Z = 8 et groupe d'espace *Pbca*. On a résolu ces structures par les méthodes conventionnelles aux atomes lourds et on les a affinées par la méthode des moindres carrés (matrice entière) jusqu'à des valeurs de R de 0,044, 0,042 et 0,059 respectivement pour 2084, 2502 et 1891 réflexions. Les deux structures contenant de l'étain possèdent des structures octaédriques cappées 3:3:1 avec des liaisons Mo—Sn de 2,864(1) et 2,823(1) Å. Le complexe de cuivre possède un arrangement des ligands autour du Mo qui prend la forme d'un banc de piano 3:4 avec une liaison Mo—Cu de 2,639(2) Å, deux ligands carbonyle agissant comme ponts et un ligand carbonyle terminal.

[Traduit par la revue]

Introduction

Earlier reports (1, 2) have detailed our findings on the complexation of the anion $(MeGapz_3)Mo(CO)_3^-$ with Rh, Cu, and Sn containing moieties. Structural studies revealed a novel 3:3:1 arrangement of the ligating atoms about the Mo centre, and carbonyl groups in a variety of bonding modes. In one of these reports (2), the pyrazolyl-borate containing complex, $(HBpz_3)Mo(CO)_3Rh(PPh_3)_2$, was described. The present paper describes the general utility of the pyrazolyl borate molybdenum tricarbonyl anions, $LMo(CO)_3^-$, in the synthesis of mixed metal complexes containing Mo—Cu and Mo—Sn bonds, and presents X-ray structural results for three of the complexes prepared.

Experimental

Starting materials

Air-sensitive materials were handled in a nitrogen atmosphere. Tetrahydrofuran (THF), benzene, CH_2Cl_2, and hexane were dried by refluxing over Na/benzophenone, potassium, CaH_2, and $CaSO_4$, respectively, followed by distillation. $[Cu(PPh_3)Cl]_4$ (3), $(MeCN)_3Mo(CO)_3$ (4), $K^+HBpz_3^-$ (5), and $K^+HBpz''_3$ (5) were prepared by literature methods. Me_3SnCl (Aldrich Chemicals), Ph_3SnCl (Alpha Chemicals), and Me_2SnCl_2 (PCA Chemicals) were used as supplied. $Me_2NCH_2CH_2NMe_2$ (tmed) was dried over CaH_2 and distilled before use.

Synthesis of $K^+LMo(CO)_3^-$ ligands (L= $HBpz_3$ or $HBpz''_3$)

A solution of the K^+L^- ligand (~0.4 mmol per 100 mL THF) was added to an equimolar amount of $(MeCN)_3Mo(CO)_3$ in the same solvent. The initial yellow coloration of the molybdenum complex in THF changed to an amber color on addition of the ligand solution. The reaction mixture was stirred for ~2 days to ensure complete formation of the $K^+LMo(CO)_3^-$ species as evidenced by ir measurements. The resulting solution was then reacted directly with equimolar amounts of the various tin and copper compounds as described below.

Synthesis of $(HBpz_3)Mo(CO)_3SnPh_3$

A solution of $K^+(HBpz_3)Mo(CO)_3^-$ in THF was prepared as described above and Ph_3SnCl (1.584 g, 4.11 mmol) in THF was added to this salt solution. The resulting reaction mixture was stirred for ~2 days after which the solvent was removed *in vacuo*. The dark yellow residue was extracted with CH_2Cl_2 and filtered. An equal amount of hexane was added to the filtrate and the mixed solvents allowed to evaporate slowly. Yellow crystals of the product in ~50% yield were obtained. Pertinent physical data for this complex are presented in Table 1. The mass spectrum of the complex displayed the parent ion signal, P^+, together with prominent signals due to the ions $(P - CO)^+$, $(P - 2CO)^+$, and $(P - 3CO)^+$.

The $(HBpz_3)Mo(CO)_3SnMe_3$ and the two complexes, $LMo(CO)_3$-

[1]Authors to whom correspondence should be addressed.

Can. J. Chem. Downloaded from www.nrcresearchpress.com by 112.217.228.212 on 09/07/12
For personal use only.

Can. J. Chem. Downloaded from www.nrcresearchpress.com by 112.217.228.212 on 09/07/12
For personal use only.

TABLE 1. Physical data for the complexes $LMo(CO)_3$"M"

L	"M"	Analysis calcd/found C	H	N	IR data (cm^{-1}) Nujol ν_{BH}	ν_{CO}	^1H nmr pz-H^4	pz-H^5	pz-H^3	Sn-R	Other
$HBpz_3$	$SnPh_3$	48.49 48.23	3.37 3.46	11.31 11.17	2480w	1988w 1896vs 1882vs	[b] 4.36t	2.14d	2.02d	2.76m 1.72m	—
$HBpz_3$	$SnMe_3\frac{1}{2}C_6H_6$	36.28 36.27	3.69 3.70	14.10 13.85	2490w	2015w 1980w 1865vs	[b] 4.28t	2.76d	2.27d	9.14s[c]	—
$HBpz_3$	$SnMe_2Cl$	29.12 29.18	2.77 2.98	14.56 14.29	2500w	1993w 1908s 1885s	[b]A 4.38t B 4.34t	obscured 2.88d	2.32d 2.51d	8.91s[c] 8.99s[c] 9.14s	—
$HB(3,5diMepz)_3$	$SnMe_2Cl$	36.32 36.23	4.24 4.33	12.71 12.72	2560w	2005m 1910vs 1880vs	[a] 3.89s	7.49s	7.64s	8.72s[c]	—
$HBpz_3$	$CuPPh_3$	50.12 49.56	3.49 3.70	11.69 11.49	2480w	1915m 1893m 1805vs	[b] 4.24t	2.82d	2.14d		2.99m 2.39m PPh_3
$HBpz_3$	$Cu(TMED)\frac{1}{2}CH_2Cl_2$	36.12 36.13	4.39 4.46	18.22 18.34	2500w	1895s (CH_2Cl_2) 1772s ~1750s,sh	[b] 4.13t	2.54d	1.98d		7.73s NMe 5.70s CH_2Cl_2
$HB(3,5diMepz)_3$	Cu(TMED)	43.89 44.12	5.79 5.80	17.07 16.92	2530w	1885s (CH_2Cl_2) 1770s ~1750s,sh	[a] 4.29s	7.46s	7.59s		7.43s NMe

[a]Spectrum in d_6-acetone (τ_{actone} = 7.89 ppm).
[b]Spectrum in d_6-benzene ($\tau_{C_6H_6}$ = 2.84 ppm).
[c]$J_{^{119}Sn-Me} \approx J_{^{117}Sn-Me} \approx 50$ Hz, $J_{HCCH} \approx 2$ Hz for pz protons. w = weak, m = medium, s = strong, vs = very strong, sh = shoulder; t = triplet, d = doublet, s = singlet, m = multiplet; A, 3:3:1 isomer; B, 3:4 isomer (see ref. 1).

TABLE 2. Crystallographic data[a]

Compound	$(HBpz_3)Mo(CO)_3SnPh_3$	$(HBpz''_3)Mo(CO)_3SnMe_2Cl$	$(HBpz_3)Mo(CO)_3Cu(tmed)\cdot(1/2)CH_2Cl_2$
Formula	$C_{30}H_{25}BMoN_6O_3Sn$	$C_{20}H_{28}BClMoN_6O_3Sn$	$C_{18}H_{26}BCuMoN_8O_3\cdot(1/2)CH_2Cl_2$
fw	743.01	661.37	615.22
Crystal system	Monoclinic	Monoclinic	Orthorhombic
Space group	$P2_1/n$	$P2_1/c$	$Pbcn$
a (Å)	17.570(2)	11.044(3)	19.027(2)
b (Å)	14.077(2)	12.061(2)	16.995(2)
c (Å)	12.180(1)	20.218(4)	16.136(2)
β (deg)	96.985(8)	100.43(1)	—
V (Å^3)	2990.0(6)	2648.6(9)	5217.7(9)
Z	4	4	8
ρ_c (g/cm^3)	1.650	1.659	1.566
$F(000)$	1472	1312	2488
μ (cm^{-1})	12.88	15.41	14.24
Crystal dimensions (mm)	0.07 × 0.07 × 0.51	0.21 × 0.30 × 0.38	0.28 × 0.30 × 0.30
Transmission factors	0.886–0.930	0.686–0.746	0.663–0.705
Scan type	ω–2θ	ω–2θ	ω–2θ
Scan range (deg in ω)	0.55 + 0.35 tan θ	0.57 + 0.35 tan θ	0.60 + 0.35 tan θ
Scan speed (deg/min)	0.7–6.7	0.7–6.7	0.9–10.0
Data collected	$\pm h, +k, +l$	$\pm h, +k, +l$	$+h, +k, +l$
$2\theta_{max}$ (deg)	50	55	55
Crystal decay	Negligible	Negligible	10.8%
Unique reflections	5235	6057	5965
Reflections with $I \geq n\sigma(I)$	2084 ($n = 1$)	2502 ($n = 2.5$)	1891 ($n = 1.5$)
Number of variables	379	298	312
R	0.044	0.042	0.059
R_w	0.037	0.039	0.046
S	1.157	1.290	1.395
Mean Δ/σ (final cycle)	0.01	0.01	0.01
Max Δ/σ (final cycle)	0.07	0.07	0.45
Residual density (e/Å^3)	1.2	1.1	0.8

[a]Temperature 295 K, Enraf-Nonius CAD4-F diffractometer, graphite monochromatized Mo-K_α radiation ($\lambda_{K\alpha 1}$ = 0.70930, $\lambda_{K\alpha 2}$ = 0.71359 Å), takeoff angle 2.7°, aperture (2.0 + tan θ) × 4.00 mm at a distance of 173 mm from the crystal, scan range extended by 25% on both sides for background measurement, $\sigma^2(I) = C + 2B + [0.04(C - B)]^2$ (C = scan count, B = normalized background count), function minimized: $\Sigma w(|F_o| - |F_c|)^2$ where $w = 1/\sigma^2(F)$, $R = \Sigma||F_o| - |F_c||/\Sigma|F_o|$, $R_w = (\Sigma w(|F_o| - |F_c|)^2/\Sigma w|F_o|^2)^{1/2}$, $S = (\Sigma w(|F_o| - |F_c|)^2/(m - n))^{1/2}$. Values given for R, R_w, and S are based on those reflections with $I \geq n\sigma(I)$.

$SnMe_2Cl$, were prepared similarly. Table 1 lists selected physical data for these complexes. The X-ray structure analyses of the $(HBpz_3)Mo(CO)_3SnPh_3$ and $(HBpz''_3)Mo(CO)_3SnMe_2Cl$ compounds are described below.

Synthesis of $(HBpz_3)Mo(CO)_3CuPPh_3$

A solution of $K^+(HBpz_3)Mo(CO)_3^-$ in THF was added to a one-quarter molar amount of the tetramer $[Cu(PPh_3)Cl]_4$ (0.596 g, 1.65 mmol) in the same solvent. The reaction mixture was stirred for ~2 days after which the solvent was removed under vacuum. The residue was extracted with CH_2Cl_2, filtered, and hexane added. On slow evaporation of the mixed solvents, a yellow solid product was deposited in ~50% yield. Physical data for the complex are collected in Table 1.

Synthesis of $LMo(CO)_3Cu(tmed)$ complexes (L = $HBpz_3$ or $HBpz''_3$, tmed = N,N,N′,N′-tetramethylethylenediamine)

In a typical reaction the $K^+LMo(CO)_3^-$ salt (1–2 mmol) in ~200 mL THF was added to equimolar amounts of CuI and tmed in the same solvent. The reaction mixture was stirred for several hours and the solvent then removed under vacuum. The residue was extracted with CH_2Cl_2 and the mixture filtered. Slow evaporation of the solvent from the filtrate gave yellow orange crystals of the desired complexes. The crystal structure of the complex $(HBpz_3)Mo(CO)_3Cu(tmed)\cdot(1/2)CH_2Cl_2$ is described below. Physical data for both complexes are given in Table 1.

Spectra

The ir spectra were recorded on a Perkin-Elmer 598 spectrometer. The ^1H nmr spectra were recorded on Bruker WP-80 or Nicolet-Oxford H270 MHz instruments using FT techniques.

X-ray crystallographic analyses

Crystallographic data for $(HBpz_3)Mo(CO)_3SnPh_3$, $(HBpz''_3)Mo(CO)_3SnMe_2Cl$, and $(HBpz_3)Mo(CO)_3Cu(tmed)\cdot(1/2)CH_2Cl_2$ appear in Table 2. Unit-cell parameters were refined by least-squares on 2 sin θ/λ values for 25 reflections (2θ = 20–29, 14–23, and 20–29°, respectively) measured with Mo-$K\alpha_1$ radiation. The intensities of three standard reflections, measured each hour of X-ray exposure time, showed only small random variations for the two Sn compounds, and a uniform decay of 10.8% for $(HBpz_3)Mo(CO)_3Cu(tmed)\cdot(1/2)CH_2Cl_2$ (likely a result of surface decomposition). Data were corrected for Lp, absorption (numerical integration), and decay (where appropriate).[2]

All three data sets showed a relatively small number of reflections having significant intensity. High-angle washout is a contributing factor, very few reflections with $2\theta > 40°$ being classified as observed. The high-angle data were collected and retained in order to maximize the numbers of reflections used in the refinements at the expense of the overall fractions of significant data. This problem was particularly serious for $(HBpz_3)Mo(CO)_3Cu(tmed)\cdot(1/2)CH_2Cl_2$ where inter-

[2]The computer programs used include locally written programs for data processing and locally modified versions of the following: AGNOST, absorption corrections, by J. A. Ibers; ORFLS, full-matrix least-squares, and ORFFE, function and errors, by W. R. Busing, K. O. Martin, and H. A. Levy; FORDAP, Patterson and Fourier syntheses, by A. Zalkin; ORTEP II, illustrations by C. K. Johnson.

Can. J. Chem. Downloaded from www.nrcresearchpress.com by 112.217.228.212 on 09/07/12
For personal use only.

TABLE 3. Final positional (fractional × 10^4, Sn, Mo and Cu × 10^5) and isotropic thermal parameters (U × 10^3 Å^2) with estimated standard deviations in parentheses

Atom	x	y	z	U_{eq}
		$(HBpz_3)Mo(CO)_3SnPh_3$		
Sn	43142(4)	28017(6)	25076(6)	35
Mo	43321(5)	23128(7)	47934(7)	30
O(1)	2702(5)	2986(7)	3815(7)	72
O(2)	5488(6)	3963(7)	4577(7)	69
O(3)	4931(5)	577(6)	3534(7)	65
N(1)	5277(5)	1778(6)	6010(8)	38
N(2)	5157(6)	1571(7)	7063(9)	51
N(3)	3670(5)	1205(7)	5559(8)	42
N(4)	3792(6)	1039(7)	6678(9)	45
N(5)	4069(5)	3130(7)	6248(8)	42
N(6)	4101(5)	2706(8)	7282(7)	48
C(1)	3308(6)	2757(9)	4101(8)	39
C(2)	5039(7)	3367(10)	4582(10)	46
C(3)	4679(7)	1252(9)	3902(9)	45
C(4)	6010(7)	1610(9)	5938(10)	52
C(5)	6380(8)	1308(10)	6906(14)	71
C(6)	5841(9)	1304(9)	7628(11)	60
C(7)	3147(8)	575(10)	5157(10)	57
C(8)	2920(8)	7(10)	5983(13)	70
C(9)	3334(9)	318(10)	6916(12)	65
C(10)	3892(7)	4036(9)	6421(11)	51
C(11)	3798(9)	4192(10)	7527(13)	70
C(12)	3937(8)	3339(11)	8018(10)	61
C(13)	5367(7)	2445(8)	1887(9)	44
C(14)	5412(8)	1634(10)	1231(11)	64
C(15)	6101(13)	1395(12)	853(12)	90
C(16)	6722(10)	1937(18)	1111(15)	102
C(17)	6707(9)	2736(15)	1760(13)	95
C(18)	6016(8)	2973(10)	2132(11)	70
C(19)	3468(6)	2057(8)	1424(8)	34
C(20)	3336(8)	1077(10)	1481(12)	63
C(21)	2863(8)	610(9)	698(13)	60
C(22)	2469(7)	1080(12)	−168(13)	67
C(23)	2567(7)	2049(12)	−243(11)	67
C(24)	3047(7)	2523(7)	547(10)	45
C(25)	4145(6)	4267(9)	2130(9)	40
C(26)	3863(8)	4929(10)	2804(11)	63
C(27)	3727(9)	5868(11)	2536(12)	71
C(28)	3855(8)	6150(10)	1486(14)	69
C(29)	4099(8)	5521(11)	746(10)	58
C(30)	4256(7)	4612(9)	1100(10)	54
B	4362(11)	1663(11)	7416(13)	56
		$(HBpz''_3)Mo(CO)_3SnMe_2Cl$		
Sn	18621(6)	50860(5)	37097(3)	50
Mo	20828(7)	27867(5)	39631(3)	33
Cl	3158(3)	5582(2)	2925(1)	81
O(1)	619(7)	3901(5)	4971(3)	74
O(2)	761(7)	3241(5)	2486(3)	79
O(3)	4717(6)	3849(5)	4208(3)	77
N(1)	2980(6)	1476(5)	3434(3)	39
N(2)	2780(6)	394(5)	3575(3)	37
N(3)	2915(6)	1820(5)	4874(3)	35
N(4)	2966(6)	679(5)	4821(3)	35
N(5)	580(6)	1518(5)	3913(3)	38
N(6)	890(6)	443(5)	4088(3)	36
C(1)	1161(8)	3553(6)	4580(4)	46
C(2)	1254(8)	3150(6)	3043(5)	46
C(3)	3720(9)	3538(7)	4110(4)	45
C(4)	3528(8)	1466(7)	2889(4)	48
C(5)	3646(9)	387(7)	2684(4)	52

TABLE 3 (*concluded*)

Atom	x	y	z	U_{eq}
C(6)	3193(8)	−274(6)	3117(4)	42
C(7)	3537(7)	2076(6)	5489(4)	36
C(8)	3966(7)	1130(7)	5822(4)	41
C(9)	3610(7)	256(7)	5399(4)	40
C(10)	−647(8)	1562(7)	3764(4)	44
C(11)	−1116(8)	511(8)	3853(4)	53
C(12)	−138(8)	−167(7)	4048(4)	39
C(13)	3926(11)	2501(8)	2584(5)	83
C(14)	3038(8)	−1506(7)	3123(4)	55
C(15)	3686(9)	3241(8)	5738(4)	63
C(16)	3857(8)	−976(7)	5494(4)	53
C(17)	−1357(8)	2613(8)	3575(5)	70
C(18)	−138(8)	−1376(7)	4224(4)	57
C(19)	2570(9)	6120(7)	4546(5)	68
C(20)	106(10)	5639(8)	3202(5)	91
B	2238(9)	90(8)	4209(5)	40
		$(HBpz_3)Mo(CO)_3Cu(tmed)\cdot(1/2)CH_2Cl_2$[a]		
Mo	35753(5)	33236(5)	43709(5)	39
Cu	49311(7)	31194(8)	46396(8)	60
O(1)	3277(4)	1832(5)	5401(5)	81
O(2)	4354(5)	3913(6)	5954(6)	92
O(3)	4490(5)	2172(6)	3327(5)	94
N(1)	3734(5)	4420(5)	3596(5)	49
N(2)	3163(5)	4797(5)	3254(6)	48
N(3)	2753(5)	3084(6)	3405(5)	50
N(4)	2346(5)	3664(6)	3089(6)	52
N(5)	2684(5)	4047(5)	4874(7)	54
N(6)	2290(5)	4512(5)	4361(7)	60
N(7)	5956(4)	3377(7)	4302(7)	64
N(8)	5395(6)	2216(6)	5453(7)	77
C(1)	3377(5)	2404(7)	5001(7)	55
C(2)	4122(6)	3670(7)	5331(8)	61
C(3)	4210(6)	2646(7)	3766(7)	57
C(4)	4287(6)	4837(8)	3363(7)	58
C(5)	4099(7)	5456(8)	2882(8)	74
C(6)	3386(8)	5425(7)	2831(7)	68
C(7)	2583(7)	2437(8)	3003(8)	59
C(8)	2057(7)	2585(8)	2438(8)	75
C(9)	1916(6)	3370(8)	2499(8)	65
C(10)	2461(8)	4209(8)	5646(8)	71
C(11)	1950(8)	4767(9)	5629(10)	91
C(12)	1850(6)	4942(8)	4821(11)	76
C(13)	6345(8)	2698(10)	4599(12)	121
C(14)	6148(8)	2382(11)	5396(11)	122
C(15)	6188(7)	4106(10)	4676(9)	114
C(16)	6082(6)	3424(9)	3412(9)	106
C(17)	5216(8)	1440(8)	5126(9)	106
C(18)	5188(7)	2257(8)	6314(9)	98
B	2420(8)	4491(8)	3412(10)	59
Cl	5153(10)	31(7)	3245(7)	295
Cl′	4299(13)	313(24)	2617(35)	290
C(19)	5000	672(13)	2500	266

[a]Occupancy factors: Cl, 0.76, Cl′, 0.24.

molecular cavities are occupied by disordered solvent molecules. The molecular structures themselves, which contain large groups of coplanar atoms, contribute to this problem, resulting in a small number of very intense reflections and large numbers of weak reflections.

All three structures were solved by conventional heavy-atom methods, the coordinates of the heavy atoms being determined from the Patterson functions and those of the remaining non-hydrogen atoms from subsequent difference Fourier syntheses. The dichloromethane molecule in $(HBpz_3)Mo(CO)_3Cu(tmed).(1/2)CH_2Cl_2$ was found to be

Can. J. Chem. Downloaded from www.nrcresearchpress.com by 112.217.228.212 on 09/07/12
For personal use only.

Can. J. Chem. Downloaded from www.nrcresearchpress.com by 112.217.228.212 on 09/07/12
For personal use only.

TABLE 4. Bond lengths (Å) with estimated standard deviations in parentheses

Bond	Length (Å)	Bond	Length (Å)
	$(HBpz_3)Mo(CO)_3SnPh_3$		
Sn—Mo	2.8644(11)	C(4)—C(5)	1.34(2)
Sn—C(13)	2.142(11)	C(5)—C(6)	1.37(2)
Sn—C(19)	2.139(11)	C(7)—C(8)	1.38(2)
Sn—C(25)	2.126(12)	C(8)—C(9)	1.35(2)
Mo—N(1)	2.219(9)	C(10)—C(11)	1.40(2)
Mo—N(3)	2.218(9)	C(11)—C(12)	1.35(2)
Mo—N(5)	2.208(9)	C(13)—C(14)	1.401(15)
Mo—C(1)	1.992(11)	C(13)—C(18)	1.36(2)
Mo—C(2)	1.972(14)	C(14)—C(15)	1.39(2)
Mo—C(3)	1.985(14)	C(15)—C(16)	1.34(2)
O(1)—C(1)	1.127(11)	C(16)—C(17)	1.38(2)
O(2)—C(2)	1.152(13)	C(17)—C(18)	1.39(2)
O(3)—C(3)	1.161(13)	C(19)—C(20)	1.401(15)
N(1)—N(2)	1.356(12)	C(19)—C(24)	1.388(14)
N(1)—C(4)	1.322(13)	C(20)—C(21)	1.36(2)
N(2)—C(6)	1.363(14)	C(21)—C(22)	1.36(2)
N(2)—B	1.52(2)	C(22)—C(23)	1.38(2)
N(3)—N(4)	1.374(12)	C(23)—C(24)	1.37(2)
N(3)—C(7)	1.327(13)	C(25)—C(26)	1.37(2)
N(4)—C(9)	1.348(15)	C(25)—C(30)	1.381(15)
N(4)—B	1.54(2)	C(26)—C(27)	1.37(2)
N(5)—N(6)	1.389(11)	C(27)—C(28)	1.38(2)
N(5)—C(10)	1.335(13)	C(28)—C(29)	1.37(2)
N(6)—C(12)	1.321(14)	C(29)—C(30)	1.37(2)
N(6)—B	1.54(2)		
	$(HBpz''_3)Mo(CO)_3SnMe_2Cl$		
Sn—Mo	2.8227(9)	N(4)—C(9)	1.353(9)
Sn—Cl	2.398(3)	N(4)—B	1.523(11)
Sn—C(19)	2.133(9)	N(5)—N(6)	1.371(8)
Sn—C(20)	2.130(10)	N(5)—C(10)	1.334(9)
Mo—N(1)	2.238(6)	N(6)—C(12)	1.342(9)
Mo—N(3)	2.232(6)	N(6)—B	1.526(11)
Mo—N(5)	2.247(6)	C(4)—C(5)	1.379(11)
Mo—C(1)	1.977(9)	C(4)—C(13)	1.493(11)
Mo—C(2)	1.969(9)	C(5)—C(6)	1.346(11)
Mo—C(3)	1.996(10)	C(6)—C(14)	1.497(11)
O(1)—C(1)	1.152(9)	C(7)—C(8)	1.366(10)
O(2)—C(2)	1.163(9)	C(7)—C(15)	1.491(11)
O(3)—C(3)	1.147(9)	C(8)—C(9)	1.370(10)
N(1)—N(2)	1.362(8)	C(9)—C(16)	1.517(11)
N(1)—C(4)	1.350(9)	C(10)—C(11)	1.393(11)
N(2)—C(6)	1.366(9)	C(10)—C(17)	1.503(11)
N(2)—B	1.553(11)	C(11)—C(12)	1.356(11)
N(3)—N(4)	1.383(8)	C(12)—C(18)	1.501(11)
N(3)—C(7)	1.344(8)		
	$(HBpz_3)Mo(CO)_3Cu(tmed)\cdot(1/2)CH_2Cl_2$		
Mo—Cu	2.639(2)	N(4)—C(9)	1.351(12)
Mo—N(1)	2.264(9)	N(4)—B	1.506(15)
Mo—N(3)	2.245(9)	N(5)—N(6)	1.369(11)
Mo—N(5)	2.246(9)	N(5)—C(10)	1.345(13)
Mo—C(1)	1.902(13)	N(6)—C(12)	1.336(13)
Mo—C(2)	1.957(13)	N(6)—B	1.55(2)
Mo—C(3)	1.933(13)	N(7)—C(13)	1.45(2)
Cu—N(7)	2.071(9)	N(7)—C(15)	1.45(2)
Cu—N(8)	2.205(10)	N(7)—C(16)	1.458(14)
Cu—C(2)	2.119(12)	N(8)—C(14)	1.46(2)
Cu—C(3)	2.125(11)	N(8)—C(17)	1.460(15)
O(1)—C(1)	1.182(11)	N(8)—C(18)	1.446(15)
O(2)—C(2)	1.173(12)	C(4)—C(5)	1.355(15)

TABLE 4. (*concluded*)

Bond	Length (Å)	Bond	Length (Å)
O(3)—C(3)	1.198(12)	C(5)—C(6)	1.36(2)
N(1)—N(2)	1.375(10)	C(7)—C(8)	1.377(15)
N(1)—C(4)	1.324(12)	C(8)—C(9)	1.365(14)
N(2)—C(6)	1.336(13)	C(10)—C(11)	1.36(2)
N(2)—B	1.528(15)	C(11)—C(12)	1.35(2)
N(3)—N(4)	1.354(10)	C(13)—C(14)	1.44(2)
N(3)—C(7)	1.317(13)		

disordered about a crystallographic twofold axis. The single Cl atom in the asymmetric unit was found to occupy two different positions, related to one another by a 90° rotation about the twofold axis. The site occupancy factors for the two Cl positions were initially estimated from relative Fourier peak heights and subsequently adjusted to give equal equivalent isotropic thermal parameters for the two partially occupied sites. Non-hydrogen atoms were refined with anisotropic thermal parameters and hydrogen atoms were fixed in idealized positions (methyl group orientations based on observed positions, $C(sp^3)$—H = 0.98, $C(sp^2)$—H = 0.97, B—H = 1.08 Å, $U_H \propto U_{\text{bonded atom}}$). Neutral atom scattering factors and anomalous scattering corrections (Sn, Mo, Cu, and Cl) were taken from ref. 6. Final positional and equivalent isotropic thermal parameters (U_{eq} = (1/3) trace of diagonalized U) for the non-hydrogen atoms appear in Table 3. Bond lengths and bond angles are given in Tables 4 and 5, respectively. Calculated hydrogen atom parameters, anisotropic thermal parameters, complete lists of torsion angles, intra-annular torsion angles (Tables 6–9), and measured and calculated structure factor amplitudes have been placed in the Depository of Unpublished Data.[3]

Results and discussion

The ability of the tricarbonyl anion, $(MeGapz_3)Mo(CO)_3^-$, to form complexes with both transition metal and main group metal moieties in which heteronuclear metal–metal bonds are featured has been demonstrated in earlier publications (1, 2). The analogous tricarbonyl anions $(HBpz_3)Mo(CO)_3^-$ and $(HBpz''_3)Mo(CO)_3^-$ have now been utilized to synthesize a series of Mo—Cu and Mo—Sn complexes. The study was of interest to determine whether the incorporation of the $HBpz_3^-$ ligand in place of the $MeGapz_3^-$ ligand would have any effect on the geometry of the mixed metal complexes prepared. The cone angle (see Fig. 1) for $HBpz_3$ has been estimated to be ~180° (7–9), but unlike the 3:3:1 structures observed for a number of $(MeGapz_3)Mo(CO)_3X$ compounds (1, 2), only the 3:4 piano stool structure has been observed for $(HBpz_3)Mo(CO)_3X$ systems (10), an arrangement which is however ubiquitous in $CpMoL_4$ complexes. It has been pointed out, however, that the barrier for interconversion of ligands in the basal plane of the 3:4 structure is much lower in the $HBpz_3$ complexes than in the Cp complexes and further that the 3:3:1 isomers of $(HBpz_3)Mo(CO)_3X$ are viable intermediates in the observed fluxional processes (10). The cone angle for the $MeGapz_3^-$ ligand has been estimated to be ~180° from our structural data on "$(MeGapz_3)Mo$" systems (1, 2) (the longer Ga—N distance compared to the B—N distance being compensated for by a smaller N—Ga—N angle of ~100° *vis-à-vis* an N—B—N angle of ~108°), and thus any structural differences in the $(HBpz_3)Mo(CO)_3$"M" complexes would be attributable to

[3]Supplementary material mentioned in the text may be purchased from the Depository of Unpublished Data, CISTI, National Research Council of Canada, Ottawa, Ont., Canada K1A 0S2.

Can. J. Chem. Downloaded from www.nrcresearchpress.com by 112.217.228.212 on 09/07/12
For personal use only.

TABLE 5. Bond angles (deg) with estimated standard deviations in parentheses

Bonds	Angle (deg)	Bonds	Angle (deg)
	$(HBpz_3)Mo(CO)_3SnPh_3$		
Mo—Sn—C(13)	112.3(3)	N(5)—N(6)—C(12)	109.6(11)
Mo—Sn—C(19)	114.0(3)	N(5)—N(6)—B	119.0(10)
Mo—Sn—C(25)	115.3(3)	C(12)—N(6)—B	131.2(12)
C(13)—Sn—C(19)	103.5(4)	Mo—C(1)—O(1)	172.6(9)
C(13)—Sn—C(25)	104.8(4)	Mo—C(2)—O(2)	172.4(11)
C(19)—Sn—C(25)	105.9(4)	Mo—C(3)—O(3)	169.7(10)
Sn—Mo—N(1)	130.5(3)	N(1)—C(4)—C(5)	111.6(13)
Sn—Mo—N(3)	129.3(3)	C(4)—C(5)—C(6)	105.4(13)
Sn—Mo—N(5)	132.5(3)	N(2)—C(6)—C(5)	108.1(12)
Sn—Mo—C(1)	67.1(3)	N(3)—C(7)—C(8)	111.5(12)
Sn—Mo—C(2)	68.0(4)	C(7)—C(8)—C(9)	104.6(12)
Sn—Mo—C(3)	67.5(3)	N(4)—C(9)—C(8)	109.9(12)
N(1)—Mo—N(3)	82.5(3)	N(5)—C(10)—C(11)	111.1(12)
N(1)—Mo—N(5)	81.6(3)	C(10)—C(11)—C(12)	104.5(12)
N(1)—Mo—C(1)	162.4(4)	N(6)—C(12)—C(11)	110.1(12)
N(1)—Mo—C(2)	84.9(4)	Sn—C(13)—C(14)	120.2(9)
N(1)—Mo—C(3)	81.7(4)	Sn—C(13)—C(18)	122.0(10)
N(3)—Mo—N(5)	81.8(3)	C(14)—C(13)—C(18)	117.7(11)
N(3)—Mo—C(1)	84.6(4)	C(13)—C(14)—C(15)	119.9(14)
N(3)—Mo—C(2)	162.7(4)	C(14)—C(15)—C(16)	120(2)
N(3)—Mo—C(3)	85.0(4)	C(15)—C(16)—C(17)	122(2)
N(5)—Mo—C(1)	84.8(4)	C(16)—C(17)—C(18)	118(2)
N(5)—Mo—C(2)	84.8(4)	C(13)—C(18)—C(17)	122.6(15)
N(5)—Mo—C(3)	159.9(4)	Sn—C(19)—C(20)	123.9(9)
C(1)—Mo—C(2)	105.0(5)	Sn—C(19)—C(24)	120.6(8)
C(1)—Mo—C(3)	109.0(5)	C(20)—C(19)—C(24)	115.4(11)
C(2)—Mo—C(3)	104.8(5)	C(19)—C(20)—C(21)	122.2(12)
Mo—N(1)—N(2)	120.9(8)	C(20)—C(21)—C(22)	121.3(13)
Mo—N(1)—C(4)	132.2(9)	C(21)—C(22)—C(23)	118.5(13)
N(2)—N(1)—C(4)	106.9(10)	C(22)—C(23)—C(24)	120.4(13)
N(1)—N(2)—C(6)	107.9(10)	C(19)—C(24)—C(23)	122.2(11)
N(1)—N(2)—B	120.4(10)	Sn—C(25)—C(26)	125.5(9)
C(6)—N(2)—B	131.8(12)	Sn—C(25)—C(30)	120.4(9)
Mo—N(3)—N(4)	120.7(8)	C(26)—C(25)—C(30)	113.9(11)
Mo—N(3)—C(7)	133.6(9)	C(25)—C(26)—C(27)	125.1(13)
N(4)—N(3)—C(7)	105.6(10)	C(26)—C(27)—C(28)	116.9(13)
N(3)—N(4)—C(9)	108.4(11)	C(27)—C(28)—C(29)	121.4(13)
N(3)—N(4)—B	119.7(10)	C(28)—C(29)—C(30)	117.8(12)
C(9)—N(4)—B	131.9(12)	C(25)—C(30)—C(29)	124.7(12)
Mo—N(5)—N(6)	120.9(7)	N(2)—B—N(4)	110.0(12)
Mo—N(5)—C(10)	134.4(8)	N(2)—B—N(6)	108.9(12)
N(6)—N(5)—C(10)	104.6(10)	N(4)—B—N(6)	108.5(12)
	$(HBpz''_3)Mo(CO)_3SnMe_2Cl$		
Mo—Sn—Cl	108.84(7)	N(3)—N(4)—C(9)	109.3(6)
Mo—Sn—C(19)	115.0(2)	N(3)—N(4)—B	120.3(6)
Mo—Sn—C(20)	115.8(3)	C(9)—N(4)—B	130.0(7)
Cl—Sn—C(19)	101.7(3)	Mo—N(5)—N(6)	119.0(5)
Cl—Sn—C(20)	101.7(3)	Mo—N(5)—C(10)	134.0(6)
C(19)—Sn—C(20)	111.7(4)	N(6)—N(5)—C(10)	107.0(6)
Sn—Mo—N(1)	129.7(2)	N(5)—N(6)—C(12)	109.5(6)
Sn—Mo—N(3)	132.2(2)	N(5)—N(6)—B	119.7(7)
Sn—Mo—N(5)	128.5(2)	C(12)—N(6)—B	130.3(7)
Sn—Mo—C(1)	67.5(2)	Mo—C(1)—O(1)	173.2(7)
Sn—Mo—C(2)	66.4(2)	Mo—C(2)—O(2)	172.6(7)
Sn—Mo—C(3)	68.1(2)	Mo—C(3)—O(3)	172.1(8)
N(1)—Mo—N(3)	82.8(2)	N(1)—C(4)—C(5)	109.5(7)
N(1)—Mo—N(5)	83.4(2)	N(1)—C(4)—C(13)	122.6(8)
N(1)—Mo—C(1)	162.8(3)	C(5)—C(4)—C(13)	127.9(8)
N(1)—Mo—C(2)	82.9(3)	C(4)—C(5)—C(6)	107.3(7)
N(1)—Mo—C(3)	85.7(3)	N(2)—C(6)—C(5)	107.5(7)

TABLE 5 (*concluded*)

Bonds	Angle (deg)	Bonds	Angle (deg)
N(3)—Mo—N(5)	82.6(2)	N(2)—C(6)—C(14)	121.9(8)
N(3)—Mo—C(1)	84.6(3)	C(5)—C(6)—C(14)	130.5(8)
N(3)—Mo—C(2)	161.4(3)	N(3)—C(7)—C(8)	109.8(7)
N(3)—Mo—C(3)	83.5(3)	N(3)—C(7)—C(15)	122.4(7)
N(5)—Mo—C(1)	83.5(3)	C(8)—C(7)—C(15)	127.8(7)
N(5)—Mo—C(2)	84.0(3)	C(7)—C(8)—C(9)	107.5(7)
N(5)—Mo—C(3)	163.3(3)	N(4)—C(9)—C(8)	107.3(7)
C(1)—Mo—C(2)	106.7(3)	N(4)—C(9)—C(16)	122.2(7)
C(1)—Mo—C(3)	104.5(4)	C(8)—C(9)—C(16)	130.5(8)
C(2)—Mo—C(3)	107.1(3)	N(5)—C(10)—C(11)	108.7(7)
Mo—N(1)—N(2)	118.3(5)	N(5)—C(10)—C(17)	123.5(8)
Mo—N(1)—C(4)	134.4(6)	C(11)—C(10)—C(17)	127.7(8)
N(2)—N(1)—C(4)	106.0(6)	C(10)—C(11)—C(12)	106.9(7)
N(1)—N(2)—C(6)	109.7(6)	N(6)—C(12)—C(11)	107.9(7)
N(1)—N(2)—B	120.0(6)	N(6)—C(12)—C(18)	123.7(8)
C(6)—N(2)—B	130.2(7)	C(11)—C(12)—C(18)	128.4(8)
Mo—N(3)—N(4)	118.2(4)	N(2)—B—N(4)	109.6(7)
Mo—N(3)—C(7)	135.1(5)	N(2)—B—N(6)	108.2(6)
N(4)—N(3)—C(7)	106.3(6)	N(4)—B—N(6)	110.9(7)
	$(HBpz_3)Mo(CO)_3Cu(tmed)\cdot(1/2)CH_2Cl_2$		
Cu—Mo—N(1)	94.0(2)	N(3)—N(4)—B	119.7(10)
Cu—Mo—N(3)	140.5(2)	C(9)—N(4)—B	130.2(12)
Cu—Mo—N(5)	138.6(3)	Mo—N(5)—N(6)	120.7(8)
Cu—Mo—C(1)	89.9(3)	Mo—N(5)—C(10)	133.3(10)
Cu—Mo—C(2)	52.4(3)	N(6)—N(5)—C(10)	105.6(10)
Cu—Mo—C(3)	52.7(3)	N(5)—N(6)—C(12)	108.9(11)
N(1)—Mo—N(3)	81.9(3)	N(5)—N(6)—B	119.8(10)
N(1)—Mo—N(5)	81.4(3)	C(12)—N(6)—B	131.3(13)
N(1)—Mo—C(1)	176.1(4)	Cu—N(7)—C(13)	103.0(9)
N(1)—Mo—C(2)	96.9(4)	Cu—N(7)—C(15)	111.0(8)
N(1)—Mo—C(3)	97.4(4)	Cu—N(7)—C(16)	115.2(8)
N(3)—Mo—N(5)	79.9(3)	C(13)—N(7)—C(15)	112.8(11)
N(3)—Mo—C(1)	94.8(4)	C(13)—N(7)—C(16)	106.5(12)
N(3)—Mo—C(2)	167.0(4)	C(15)—N(7)—C(16)	108.3(12)
N(3)—Mo—C(3)	88.6(4)	Cu—N(8)—C(14)	102.7(9)
N(5)—Mo—C(1)	96.1(4)	Cu—N(8)—C(17)	108.7(8)
N(5)—Mo—C(2)	87.2(4)	Cu—N(8)—C(18)	115.4(8)
N(5)—Mo—C(3)	168.5(4)	C(14)—N(8)—C(17)	112.3(12)
C(1)—Mo—C(2)	85.9(5)	C(14)—N(8)—C(18)	108.5(12)
C(1)—Mo—C(3)	84.5(5)	C(17)—N(8)—C(18)	109.1(11)
C(2)—Mo—C(3)	104.3(5)	Mo—C(1)—O(1)	177.8(10)
Mo—Cu—N(7)	148.1(3)	Mo—C(2)—Cu	80.6(5)
Mo—Cu—N(8)	125.5(3)	Mo—C(2)—O(2)	169.9(10)
Mo—Cu—C(2)	47.0(4)	Cu—C(2)—O(2)	109.5(9)
Mo—Cu—C(3)	46.3(3)	Mo—C(3)—Cu	81.0(5)
N(7)—Cu—N(8)	85.8(4)	Mo—C(3)—O(3)	167.7(11)
N(7)—Cu—C(2)	136.8(5)	Cu—C(3)—O(3)	111.1(9)
N(7)—Cu—C(3)	120.9(5)	N(1)—C(4)—C(5)	111.6(12)
N(8)—Cu—C(2)	106.6(5)	C(4)—C(5)—C(6)	105.5(12)
N(8)—Cu—C(3)	112.9(4)	N(2)—C(6)—C(5)	108.4(12)
C(2)—Cu—C(3)	92.7(5)	N(3)—C(7)—C(8)	110.7(12)
Mo—N(1)—N(2)	120.0(7)	C(7)—C(8)—C(9)	105.8(12)
Mo—N(1)—C(4)	134.7(9)	N(4)—C(9)—C(8)	107.1(11)
N(2)—N(1)—C(4)	105.4(9)	N(5)—C(10)—C(11)	110.5(13)
N(1)—N(2)—C(6)	109.1(10)	C(10)—C(11)—C(12)	105.9(13)
N(1)—N(2)—B	120.4(9)	N(6)—C(12)—C(11)	109.1(13)
C(6)—N(2)—B	130.6(11)	N(7)—C(13)—C(14)	117.2(14)
Mo—N(3)—N(4)	121.9(7)	N(8)—C(14)—C(13)	112.5(14)
Mo—N(3)—C(7)	131.7(9)	N(2)—B—N(4)	110.2(11)
N(4)—N(3)—C(7)	106.3(9)	N(2)—B—N(6)	107.7(11)
N(3)—N(4)—C(9)	110.0(9)	N(4)—B—N(6)	110.4(10)

Can. J. Chem. Downloaded from www.nrcresearchpress.com by 112.217.228.212 on 09/07/12
For personal use only.

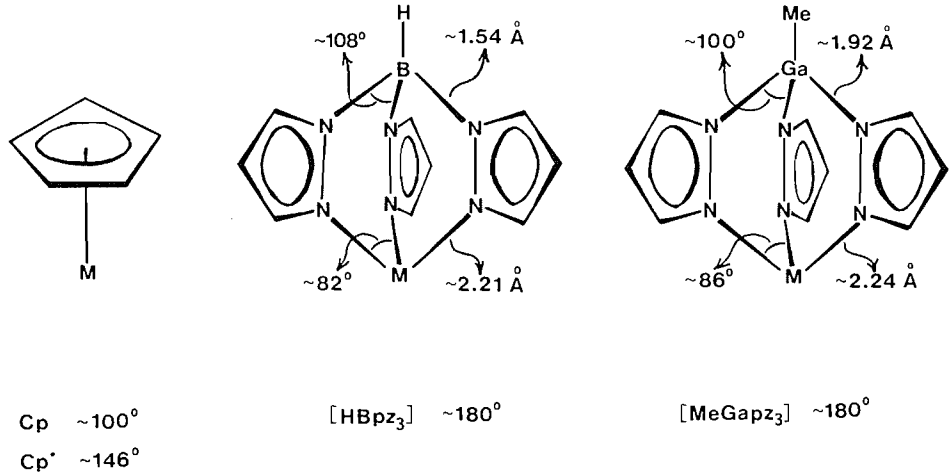

FIG. 1. Cone angles for the Cp, $HBpz_3$, and $MeGapz_3$ ligands.

electronic effects of substituting B for Ga in the compounds. Conversely, if similar 3:3:1 structures were observed with the boron analogs, then these would be a vindication of earlier arguments that the 3:3:1 arrangement represents a stable minimum in the potential energy surface for such $(HBpz_3)Mo(CO)_3X$ complexes (10, 11).

With the incorporation of the much more sterically demanding ligand $HBpz''_3{}^-$ (cone angle ~225° (7, 9)) in the molybdenum tricarbonyl anion, $(HBpz''_3)Mo(CO)_3{}^-$, it was anticipated that a crowded Mo centre might lead to different reactivity patterns. Precedents in the literature include the extensive chemistry of the $(HBpz''_3)Mo(NO)(X)_2$ (X = halogen), complexes (12), the oxo-molybdenum(V) complexes $(HBpz''_3)MoO(X)(Y)$, (X, Y = Cl^-, NCS^-, OR^-, SR^-, etc.) (13), and the efficient C—H activation properties of the $(HBpz''_3)Rh(CO)_2$ compound (14), all these examples relying on the steric properties the tris(3,5-dimethylpyrazolyl)borate ligand for their unique behavior.

The reaction of the $LMo(CO)_3{}^-$ anions (L = $HBpz_3$ or $HBpz''_3$) with organotin chlorides led to the yellow–orange crystalline products listed in Table 1. The complexes are moderately air-stable in the solid state but solutions deteriorate on exposure to air. A comparison with the analogous series of compounds involving the $CpMo(CO)_3{}^-$ ion (15) reveals that both series of compounds display only terminal ν_{CO} bands in their ir spectra, indicative of a Mo—Sn bond devoid of any bridging CO interactions. In the case of the cyclopentadienyl complexes three strong ν_{CO} bands were observed in each case, whereas the four compounds reported here show different patterns. Three of the complexes display two ν_{CO} bands much stronger than the third ν_{CO} band while the fourth complex exhibits one strong and two weak ν_{CO} bands. Structural differences between the two sets of complexes must be responsible and evidence presented below establishes a 3:3:1 structure for the "$LMo(CO)_3Sn$" complexes rather than the 3:4 structure suggested for the "$CpMo(CO)_3Sn$" compounds (15).

The ^1H nmr spectra of the $(HBpz_3)Mo(CO)_3SnMe_3$ and $(HBpz_3)Mo(CO)_3SnPh_3$ complexes indicate equivalent pyrazolyl rings in the compounds and are consistent with a 3:3:1 arrangement of ligating atoms about the Mo centre. This arrangement has been definitively established for the "$SnPh_3$" derivative by X-ray crystallography (see below). The two "$SnMe_2Cl$" compounds (Table 1) are of interest in that only the $(HBpz_3)Mo(CO)_3SnMe_2Cl$ derivative shows the presence of isomers in its ^1H nmr spectrum, a phenomenon observed and discussed for the analogous $(MeGapz_3)Mo(CO)_3SnMe_2Cl$ complex (1). The less symmetrical isomer B (3:4 piano stool) again disappears with time and produces isomer A (3:3:1 structure). The $(HBpz''_3)Mo(CO)_3SnMe_2Cl$ compound, by contrast, gave only one set of signals in its ^1H nmr spectrum, corresponding to the symmetrical 3:3:1 arrangement. This complex gave crystals suitable for X-ray analysis and the solid state structure reported below confirms our predictions of the molecular arrangement and provides a further example of the steric influence of the 3,5-methyl groups substituted on the pyrazolyl rings.

The reaction of the $(HBpz_3)Mo(CO)_3{}^-$ ion with the $[Cu(PPh_3)Cl]_4$ compound gave the Mo—Cu complex, $(HBpz_3)Mo(CO)_3Cu(PPh_3)$ in good yield, with properties similar to those described previously for the compound $(MeGapz_3)Mo(CO)_3Cu(PPh_3)$ (see Table 1 and ref. 2) and consequently we assign the 3:3:1 structure to the present system. The reactions of the $LMo(CO)_3{}^-$ ions with equimolar amounts of CuI and tmed (tmed = tetramethylethylenediamine) were investigated for two reasons. Firstly, would the tmed ligand chelate the copper centre as in the $CpMo(CO)_3Cu(tmed)$ derivative (16), or would the steric bulk of the pyrazolyl borate ligands prevent this, and secondly, if the latter, would the 3:3:1 or 3:4 structure about the Mo centre prevail. The complexes isolated showed, in their solution ^1H nmr, both the equivalence of the three pyrazolyl rings in the structure and also the equivalence of the "NMe_2" groups of the tmed ligand. The X-ray crystal structure of the $(HBpz_3)Mo(CO)_3Cu(tmed)$ complex shown in Fig. 2 clearly indicates a bidentate chelating tmed ligand and two semibridging carbonyl groups with one strictly terminal CO ligand. This arrangement is very comparable to both the $CpMo(CO)_3Cu(tmed)$ (16) mentioned above and also to the $CpW(CO)_3Cu(PPh_3)_2$ structures reported by Carlton *et al.* (17). The three strong bands in the solution ir spectra of the $LMo(CO)_3Cu(tmed)$ complexes are also similar to those reported for the above complexes. The solution ^1H nmr of the present compound can only be explained if fluxional processes are operative. A rotation of the $HBpz_3$ or $HBpz''_3$ moieties about the B···Mo axis might afford a rationale for the equivalence of the pyrazolyl rings but, in addition,

Can. J. Chem. Downloaded from www.nrcresearchpress.com by 112.217.228.212 on 09/07/12
For personal use only.

Can. J. Chem. Downloaded from www.nrcresearchpress.com by 112.217.228.212 on 09/07/12
For personal use only.

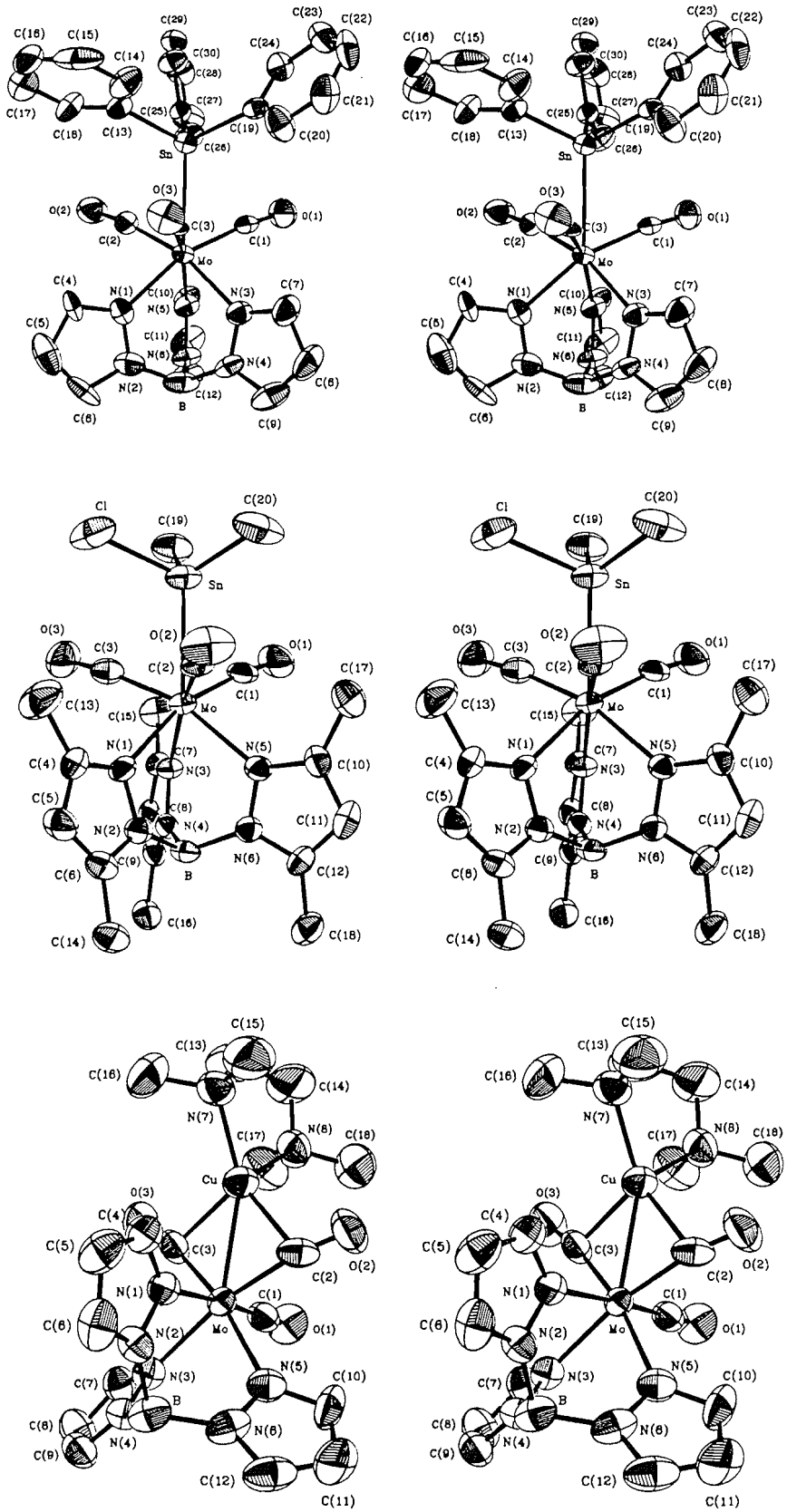

FIG. 2. Stereoscopic views of the $(HBpz_3)Mo(CO)_3SnPh_3$, $(HBpz''_3)Mo(CO)_3SnMe_2Cl$, and $(HBpz_3)Mo(CO)_3Cu(tmed)$ molecules; 50% probability thermal ellipsoids are shown for the non-hydrogen atoms. Hydrogen atoms have been omitted for the sake of clarity.

a rapid exchange of bridging and terminal CO groups, or a rotation of the tmed ligand, is necessary to explain the singlet observed for the "NMe_2" groups in the spectrum.

The structures of the $(HBpz_3)Mo(CO)_3SnPh_3$, $(HBpz''_3)Mo(CO)_3SnMe_2Cl$, and $(HBpz_3)Mo(CO)_3Cu(tmed)$ molecules are shown in Fig. 2. The two tin complexes have a 3:3:1 capped octahedral arrangement of ligands about the Mo atom as observed for the gallium analog $(MeGapz_3)Mo(CO)_3SnPh_3$ (1). The Mo—Sn, mean Mo—N, and mean Mo—C(O) distances are 2.864(1), 2.215, and 1.983 Å for $(HBpz_3)Mo(CO)_3SnPh_3$; 2.823(1), 2.239, and 1.981 Å for $(HBpz''_3)Mo(CO)_3SnMe_2Cl$; and 2.8579(3), 2.242, and 1.987 Å for $(MeGapz_3)Mo(CO)_3SnPh_3$. The major structural difference between the two "$SnPh_3$" complexes can be seen in the Mo—N distances and the N—Mo—N angles, the former being shorter (see above) and the latter being smaller for the "$HBpz_3$" compound than for the "$MeGapz_3$" analog (means of 82.0 and 86.0°, respectively). The reduced steric demands of the $SnMe_2Cl$ ligand relative to $SnPh_3$ are probably responsible for the significantly shorter Mo—Sn bond in $(HBpz''_3)Mo(CO)_3SnMe_2Cl$. Inspection of Fig. 2 shows that the sterically demanding $HBpz''_3$ ligand effectively imposes the 3:3:1 geometry, consistent with the observation of only one structural isomer of $(HBpz''_3)Mo(CO)_3SnMe_2Cl$ in solution (see above). The longer Mo—N distances in $(HBpz''_3)Mo(CO)_3SnMe_2Cl$, when compared with $(HBpz_3)Mo(CO)_3SnPh_3$, reflect both the electronic differences between the $HBpz_3$ and $HBpz''_3$ ligands and the stronger Mo—Sn interaction in the $SnMe_2Cl$ complex. The average C—O distances and M—C—O angles, 1.147 Å and 171.6° for $(HBpz_3)Mo(CO)_3SnPh_3$ and 1.154 Å and 172.6° for $(HBpz''_3)Mo(CO)_3SnMe_2Cl$, are as expected for terminal carbonyl ligands. In both of the tin complexes the slight nonlinearity of the Mo—C—O units represents a bending away from the capping Sn atom, as noted earlier for $(MeGapz_3)Mo(CO)_3SnPh_3$ (1).

The structure of $(HBpz_3)Mo(CO)_3Cu(tmed)$ features a Mo—Cu bond (2.639(2) Å), one terminal CO ligand (Mo—C = 1.90(1) Å, Mo—C—O = 178(1)°), and two semibridging CO ligands (Mo—C = 1.96(1) and 1.93(1) Å, Cu—C = 2.12(1) and 2.13(1) Å, Mo—C—O = 170(1) and 168(1)°, Cu—C—O = 109.5(9) and 111.1(9)°, Mo—C—Cu = 80.6(5) and 81.0(5)°). The complex has a 3:4 piano stool structure similar to those reported for $CpMo(CO)_3Cu(tmed)$ (16), $CpW(CO)_3Cu(PPh_3)_2$ (17), and $(MeGapz_3)Mo(CO)_3Rh(PPh_3)_3$ (2). Unlike the asymmetric $M(CO)_2M'$ units observed for the above-mentioned molecules, that in $(HBpz_3)Mo(CO)_3Cu(tmed)$ is symmetric with respect to the Cu atom. The CuN_2C_2 moiety in $(HBpz_3)Mo(CO)_3Cu(tmed)$ has an irregular tetrahedral geometry with equal Cu—C distances and significantly different Cu—N distances (2.07(1) and 2.20(1) Å), while the corresponding moiety in $CpMo(CO)_3Cu(tmed)$ has a distorted square planar geometry with effectively equal Cu—N distances (2.130(2) and 2.139(6) Å) and significantly different Cu—C distances (2.185(3) and 2.415(6) Å). The shorter Mo—Cu bond in the Cp compound (2.592 Å) is compensated for by a stronger interaction of the Cu atom with the semibridging CO ligands in the $HBpz_3$ complex. The Mo—N distance *trans* to the terminal CO ligand (2.264(9) Å) is longer than those *trans* to the semibridging carbonyls (2.245(9) and 2.246(9) Å), but the difference is not statistically significant.

Acknowledgments

We thank the Natural Sciences and Engineering Research Council of Canada for financial support and the University of British Columbia Computing Centre for assistance.

1. E. C. Onyiriuka, S. J. Rettig, and A. Storr. Can. J. Chem. **64**, 321 (1986).
2. G. A. Banta, B. M. Louie, E. C. Onyiriuka, S. J. Rettig, and A. Storr. Can. J. Chem. **64**, 373 (1986).
3. G. Costa, E. Reisenhofer, and L. Stefani. J. Inorg. Nucl. Chem. **27**, 2581 (1965).
4. D. P. Tate, W. R. Knipple, and J. M. Augl. Inorg. Chem. **1**, 433 (1962).
5. S. Trofimenko. Inorg. Synth. **XII**, 102 (1970).
6. International tables for X-ray crystallography. Vol. IV. Kynoch Press, Birmingham. 1974. pp. 99–102 and 149.
7. E. Frauendorfer and H. Brunner. J. Organomet. Chem. **240**, 371 (1982).
8. M. D. Curtis, K. Shiu, W. M. Butler, and J. C. Huffman. J. Am. Chem. Soc. **108**, 3335 (1986).
9. S. Trofimenko, J. C. Calabrese, and J. S. Thompson. Inorg. Chem. **26**, 1507 (1987).
10. M. D. Curtis and K. Shiu. Inorg. Chem. **24**, 1213 (1985).
11. P. Kubacek, R. Hoffman, and Z. Halvas. Organometallics, **1**, 180 (1982).
12. J. McCleverty. J. Chem. Soc. Rev. **12**, 331 (1983).
13. W. E. Cleland, K. M. Barnhart, K. Yamanouchi, D. Collison, F. E. Mabbs, R. B. Ortega, and J. H. Enemark. Inorg. Chem. **26**, 1017 (1987).
14. C. K. Ghosh and W. A. G. Graham. J. Am. Chem. Soc. **109**, 4726 (1987).
15. H. R. H. Patil and W. A. G. Graham. Inorg. Chem. **5**, 1401 (1966).
16. G. Doyle, K. A. Eriksen, and D. Van Engen. Organometallics, **4**, 2201 (1985).
17. L. Carlton, W. E. Lindsell, K. J. McCullough, and P. N. Preston. J. Chem. Soc. Dalton Trans. 1693 (1984).

Can. J. Chem. Downloaded from www.nrcresearchpress.com by 112.217.228.212 on 09/07/12
For personal use only.

Structural studies of organoboron compounds. XXXI.[1] (3-Benzoyl-(+)-camphorato)diphenylboron

WILLIAM R. CULLEN, STEVEN J. RETTIG, JAMES TROTTER, AND EUGENE B. WICKENHEISER
Department of Chemistry, University of British Columbia, 2036 Main Mall, Vancouver, B.C., Canada V6T 1Y6

Received December 4, 1987

This paper is dedicated to Professor Charles A. McDowell on the occasion of his seventieth birthday

WILLIAM R. CULLEN, STEVEN J. RETTIG, JAMES TROTTER, and EUGENE B. WICKENHEISER. Can. J. Chem. **66**, 2007 (1988).

Details of the synthesis and physical properties of the title compound are reported along with a new preparation of 3-benzoyl-(+)-camphor. Crystals of (3-benzoyl-(+)-camphorato)diphenylboron are triclinic, a = 9.0362(3), b = 9.4679(3), c = 14.2731(7) Å, α = 101.920(3), β = 100.086(3), γ = 93.251(3)°, Z = 2, space group $P\bar{1}$. The structure was solved by non-routine application of direct methods and was refined by full-matrix least-squares procedures to R = 0.036 and R_w = 0.039 for 4094 reflections with $I \geq 3\sigma(I)$. The unit-cell contains two crystallographically independent molecules, related to one another in the crystal lattice by a pseudo-inversion centre, and having the same configuration but different conformations. The structure analysis shows that the chiral, anionic, 1,3-diketonate ligand derived from 3-benzoyl-(+)-camphor is not symmetrically delocalized like most related ligands, resulting in significantly different O—B bond lengths. Bond lengths (corrected for libration) include: O—B = 1.514(4), 1.522(4); 1.568(4) and 1.567(4) Å; C—B = 1.594(5)–1.616(5) Å.

WILLIAM R. CULLEN, STEVEN J. RETTIG, JAMES TROTTER et EUGENE B. WICKENHEISER. Can. J. Chem. **66**, 2007 (1988).

On rapporte les détails de la synthèse et les propriétés du composé mentionné dans le titre ainsi qu'une nouvelle préparation du (+)-benzoyl-3 camphre. Les cristaux du ((+)-benzoyl-3 camphrato)diphénylbore sont tricliniques, avec a = 9,0362(3), b = 9,4679(3) et c = 14,2731(7) Å, α = 101,920(3), β = 100,086(3) et γ = 93,251(3)°, Z = 2 et groupe d'espace $P\bar{1}$. On a résolu la structure par une application qui n'est pas de routine des méthodes directes et on l'a affinée par la méthode des moindres carrés (matrice entière) jusqu'à des valeurs de R = 0,036 et R_w = 0,039 pour 4094 réflexions avec $I \geq 3\sigma(I)$. La maille contient deux molécules qui sont indépendantes d'un point de vue cristallographique, qui sont reliées entre elles dans le réseau cristallin par un centre de pseudo-inversion et qui possèdent la même configuration mais des conformations différentes. L'analyse de structure démontre que le ligand dicétonate-1,3, qui est chiral, anionique et dérivé du (+)-benzoyl-3 camphre, n'est pas délocalisé d'une manière symétrique comme c'est le cas avec la plupart des ligands apparentés; il en résulte que les longueurs des liaisons O—B sont très différentes. Parmi les longueurs de liaison observées et corrigées pour la libration, on note : O—B = 1,514(4), 1,522(4); 1,568(4) et 1,567(4) Å; C—B = 1,594(5)–1,616(5) Å.

[Traduit par la revue]

Introduction

Rhodium(I) complexes of 3-benzoyl-(+)-camphor have been found to be useful as homogeneous hydrogenation catalysts for the reduction of olefins. The catalytic species can be prepared *in situ* by the addition of the sodium salt of 3-benzoyl-(+)-camphor to a solution of bis(ethylene)rhodium(I) chloride dimer, or may be generated from the (3-benzoyl-(+)-camphorato)bis(ethylene)rhodium(I) complex, under an atmosphere of hydrogen in the presence of an olefinic substrate (1). The related diphenylboron chelate, (3-benzoyl-(+)-camphorato)diphenylboron, has now been synthesized, and an X-ray crystallographic analysis undertaken, to provide accurate geometrical parameters for the coordinated 3-benzoyl-(+)-camphorate ligand and also as part a continuing structural investigation of organoboron compounds.

Experimental

Preparation of 3-benzoyl-(+)-camphor, 4

A solution of lithium diisopropylamide was prepared by adding butyllithium (22.6 mL of 1.6 *M* solution in hexane, 36 mmol) to a solution of diisopropylamine (5.1 mL, 36 mmol) in 80 mL of dry diethyl ether. After 2 h, (+)-camphor (**1**, 5.0 g, 33 mmol) was added and the mixture was stirred overnight. The solution was cooled to 0°C and ethyl benzoate (6.2 mL, 43 mmol) was added dropwise. After 4 h the ether was removed by reduced pressure and the pinkish solid was washed with dry hexane. The solid was hydrolyzed with 25 mL of 20% HCl and the product extracted with diethyl ether. The ether extracts were dried over magnesium sulfate. Removal of the ether by reduced pressure yielded 3.4 g (40%) of 3-benzoyl-(+)-camphor, **4**. Melting point 83°C (lit. 84°C (2)). *Anal.* calcd. for $C_{17}H_{20}O_2$: C 79.65, H 7.86; found: C 79.90, H 7.88. Infrared (KBr, all strong): 1668, 1617 cm^{-1} (CO); 1600 (C=C).

Preparation of (3-benzoyl-(+)-camphorato)diphenylboron, 6

The sodium salt of 3-benzoyl-(+)-camphor, **5**, was prepared by the addition of sodium hydride (94 mg, 3.9 mmol) to a solution of 3-benzoyl-(+)-camphor (1.0 g, 3.9 mmol) in 30 mL of anhydrous diethyl ether. The mixture was stirred for 1 h at room temperature. A solution of diphenylborinic acid, prepared by the acid hydrolysis (40 mL, 0.1 *M* HCl) of (2-aminoethanolato)diphenylboron (0.88 g, 3.9 mmol) and extraction with diethyl ether (4 × 25 mL), was added dropwise to a solution of the sodium salt of 3-benzoyl-(+)-camphor and the mixture was stirred overnight. The solution was filtered, concentrated to 40 mL, and refrigerated to afford 1.2 g (73%) of yellow crystals. Melting point 167°C. *Anal.* calcd. for $C_{29}H_{29}BO_2$: C 82.86, H 6.95; found: C 82.60, H 6.94. Infrared (KBr, all strong): 1601, 1511 cm^{-1} (CO), 1597, 1501, 1483 (C=C). ^1H nmr (C_6D_6, 25°C, 300 MHz): δ 0.43 (s, 6H, unresolved $C(8)H_3$ and $C(10)H_3$), 0.93 (s, 3H, $C(9)H_3$), 1.10 (m, 2H, $C(5)H_2$), 1.32, 1.55 (m, 2H, $C(6)H_2$), 2.60 (m, 1H, C(4)H), 7.00–8.00 (m, 15H, aromatic protons). The multiplets due to the camphor protons were poorly resolved and accurate coupling constants were not obtained. The electron ionization mass spectrum showed the presence of a molecular ion peak as well as peaks due to the loss of a phenyl group, and peaks due to the presence of benzoylcamphor and diphenylboron ions.

The ir spectra were recorded on a Pye Unicam SP 1100 spectrophotometer, the ^1H nmr spectrum on a Varian XL-300, and the mass spectrum on a Kratos AES M50 spectrometer at 150°C and 70 eV.

X-ray crystallographic analysis

A crystal bounded by the six faces (followed by their distances in

[1]Part XXX: ref. 23.

Can. J. Chem. Downloaded from www.nrcresearchpress.com by 112.217.228.212 on 09/07/12
For personal use only.

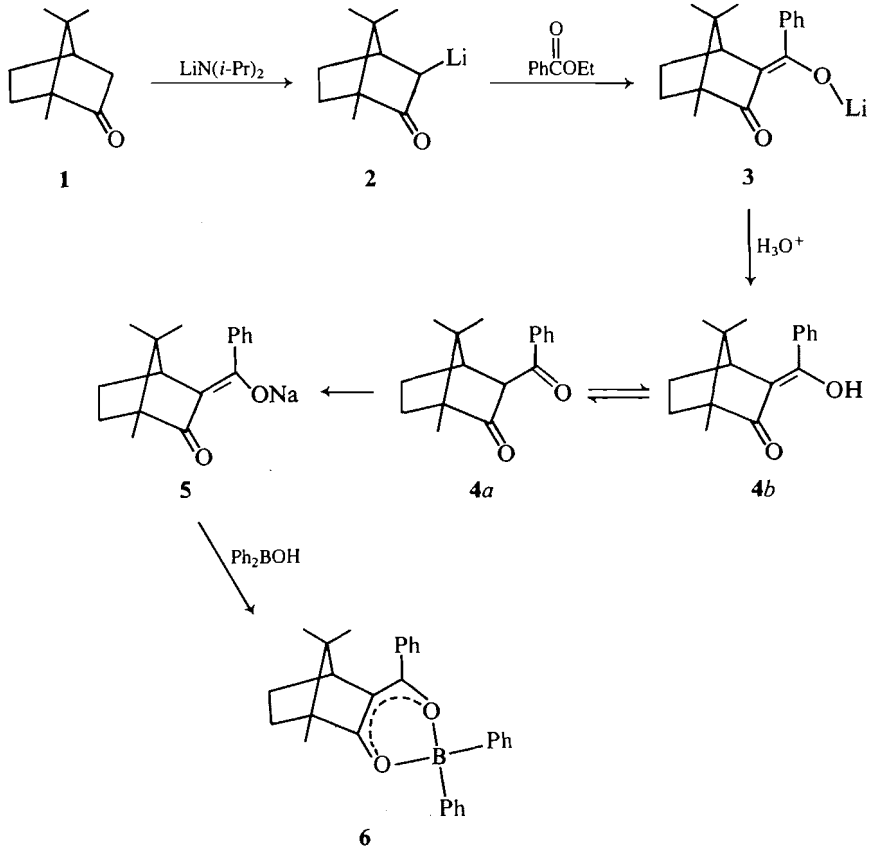

1 2 3 5 4a 4b 6

mm from a common origin): {0 1 1}, 0.22, {1 0 0}, 0.15, (0 1 −2), 0.26, and (0 −1 1), 0.26, was mounted in a general orientation. Unit-cell parameters were refined by least-squares on 2 sin θ/λ values for 25 reflections (2θ = 76–95°) measured on a diffractometer with Cu-$K\alpha$ radiation ($\lambda(K\alpha_1)$ = 1.540562, $\lambda(K\alpha_2)$ = 1.544390 Å). Crystal data at 22°C are as follows:

$C_{29}H_{29}BO_2$ f.w. = 420.36

Triclinic, a = 9.0362(3), b = 9.4679(3), c = 14.2731(7) Å, α = 101.920(3), β = 100.086(3), γ = 93.251(3)°, V = 1170.85(8) Å^3, Z = 2, ρ_c = 1.192 Mg m^{-3}, $F(000)$ = 448, μ(Cu-$K\alpha$) = 5.27 cm^{-1}. Absent reflections: none, space group $P1$ (C_1^1, No. 1, Buerger reduced cell).

Intensities were measured with nickel-filtered Cu-$K\alpha$ radiation on an Enraf-Nonius CAD4-F diffractometer. An ω-2θ scan at 1.2–10.0° min^{-1} over a range of (0.75 + 0.14 tan θ) degrees in ω (extended by 25% on both sides for background measurement) was employed. Data were measured to 2θ = 150°. The intensities of three check reflections, measured every 4000 s throughout the data collection, showed only small random variations. After data reduction,[2] an absorption correction was applied using the Gaussian integration method (3, 4). Transmission factors ranged from 0.768 to 0.864 for 96 integration points. Of the 4804 independent reflections measured, 4094 (85.2%) had intensities greater than or equal to $3\sigma(I)$ above background where $\sigma^2(I) = S + 2B + (0.04(S - B))^2$ with S = scan count and B = normalized background count.

Since the molecule is chiral it must crystallize in the noncentrosymmetric (and chiral) space group $P1$, thus there are two crystallographically independent molecules in the asymmetric unit. Attempts to solve the structure by direct methods in the space group $P1$ were not successful. The E-statistics were consistent with a centrosymmetric structure, implying that the two molecules in the unit-cell are related to one another by a pseudo-inversion centre. The structure was solved by direct methods in the centrosymmetric space group $P\bar{1}$, the coordinates of 24 of the 32 non-hydrogen atoms of the molecule (the three phenyl rings and the six-membered heterocyclic ring) being determined from an E-map. The refinement was then continued in $P1$, the coordinates of the second molecule being generated by inversion through the point (0, ½, ½) followed by a small translation to avoid a singular matrix. The positions of the remaining non-hydrogen atoms were determined from subsequent difference Fourier syntheses. In the final stages of refinement the non-hydrogen atoms were refined with anisotropic thermal parameters and the hydrogen atoms were fixed in idealized positions (methyl groups staggered, C(sp^2) = 0.97, C(sp^3)—H = 0.98 Å, $U_H \propto U_{\text{bonded atom}}$). Scattering factors for all atoms and anomalous scattering corrections for O, N, and C were taken from ref. 5. The weighting scheme $w = 1/\sigma^2(F)$, where $\sigma^2(F)$ is derived from the previously defined $\sigma^2(I)$, gave uniform average values of $w(|F_o| - |F_c|)^2$ over ranges of both $|F_o|$ and sin θ/λ and was employed in the final stages of full-matrix refinement of 575 variables. Reflections with $I < 3\sigma(I)$ were not included in the refinement. An isotropic Type I extinction correction (Thornley–Nelmes definition of mosaic anisotropy with a Lorentzian distribution) was applied (6–8). The final value of g was 0.53(2) × 10^4. Convergence was reached at R = 0.036 and R_w = 0.039 for 4094 reflections with $I \geq 3\sigma(I)$. A parallel refinement of the mirror-image structure resulted in R and R_w ratios of 1.006, in agreement with the known absolute configuration of the starting material. The function minimized was $\Sigma w(|F_o| - |F_c|)^2$, $R = \Sigma||F_o| - |F_c||/\Sigma|F_o|$ and $R_w = (\Sigma w(|F_o| - |F_c|)^2/\Sigma w|F_o|^2)^{1/2}$.

On the final cycle of refinement the mean and maximum parameter shifts corresponded to 0.03 and 0.16σ, respectively. The mean error in an observation of unit weight was 1.234. A final difference

[2]The computer programs used include locally written programs for data processing and locally modified versions of the following: MULTAN 80, multisolution program by P. Main, S. J. Fiske, S. E. Hull, L. Lessinger, G. Germain, J. P. Declercq, and M. M. Woolfson; AGNOST, absorption corrections, by J. A. Ibers; ORFLS, full-matrix least-squares, and ORFFE, function and errors, by W. R. Busing, K. O. Martin, and H. A. Levy; FORDAP, Patterson and Fourier syntheses, by A. Zalkin; ORTEP II, illustrations, by C. K. Johnson.

Can. J. Chem. Downloaded from www.nrcresearchpress.com by 112.217.228.212 on 09/07/12
For personal use only.

Can. J. Chem. Downloaded from www.nrcresearchpress.com by 112.217.228.212 on 09/07/12
For personal use only.

map showed maximum fluctuations of −0.24 to +0.15 e Å^{-3}. The final positional and thermal parameters appear in Tables 1 and 6,[3] respectively.

The ellipsoids of thermal motion for the non-hydrogen atoms are shown in Fig. 1. The thermal motion has been analysed in terms of the rigid-body modes of translation, libration, and screw motion (9). The rms standard error in the temperature factors σU_{ij} (derived from the least-squares analysis) is 0.0023 Å^2. Analysis of the entire molecules indicated significant independent motion of the phenyl rings. Each molecule was broken down into four structural subunits (PhC(11), 2 PhB, and the 14-atom fragment consisting of the polycyclic skeleton and attached methyl carbons), which were separately analysed (rms ΔU_{ij} = 0.0019–0.0033, average 0.0024 Å^2). The appropriate bond distances have been corrected for libration (9, 10), using shape parameters q^2 of 0.08 for all atoms involved. Corrected bond lengths appear in Table 2 along with the uncorrected values; corrected bond angles do not differ by more than 1σ from the uncorrected values given in Table 3. Intra-annular torsion angles defining the conformations of chelate and other rings are listed in Table 4. Calculated hydrogen coordinates and thermal parameters (Table 5), a complete listing of torsion angles (Table 7), and measured and calculated structure factors have been placed in the Depository of Unpublished Data.[3]

Results and discussion

The crystal structure of (3-benzoyl-(+)-camphorato)diphenylboron, **6**, consists of well-separated molecules. The shortest intermolecular contacts between non-hydrogen atoms are O(1)···C(8′) ($x - 1, y, z$) = 3.510(5) Å and C(27)···C(27′) ($x - 2, y + 1, z$) = 3.516(5) Å. The two crystallographically independent molecules (Fig. 1) are related to one another in the crystal lattice by a pseudo-inversion centre at approximately (0, ½, ½), only the atoms of the chiral (+)-camphor moieties deviating significantly from this pseudosymmetry. Since the atoms of the six-membered heterocyclic rings are related by the pseudo-inversion centre, the two molecules have different conformations. This can be seen clearly in Fig. 1 where the molecules are both viewed in approximately the same direction with respect to the (+)-camphor moieties. The six-membered C_3O_2B rings in the unprimed and primed molecules have, respectively, *exo-* and *endo-B*-envelope conformations (see Table 4), similar to those observed for the acetylacetone complexes of "Ar_2B", where Ar = Ph (11) and *p*-tolyl (12), and the related compound (salicylaldehydato)diphenylboron (13). Bond lengths and angles in the two crystallographically independent molecules of **6**, presented side-by-side in Tables 2 and 3, are generally equal within experimental error. Significant differences between bond angles, in particular at C(1) and C(4), are probably the result of packing effects.

Unlike the fully delocalized and symmetric 1,3-diketonate moieties observed in the acetylacetone complexes of "Ar_2B" (11, 12) and in (benzoylacetonato)difluoroboron (14), those observed in **6** show a small but statistically significant bond length alternation within the O(1)—C(2)—C(3)—C(11)—O(2) fragments. The O(1)—C(2) (average 1.288 Å) and C(3)—C(11) (1.379 Å) bonds are significantly shorter than O(2)—C(11) (1.322 Å) and C(2)—C(3) (1.404 Å), respectively, indicating a significant O(1)=C(2)—C(3)=C(11)—O(2) contribution to the molecular structure. The ν_{CO} values for **6** (see Experimental section) are consistent with these findings. The average O—C and C—C distances[4] in these fragments (1.305 and 1.391 Å,

[3]Supplementary material mentioned in the text may be purchased from the Depository of Unpublished Data, CISTI, National Research Council of Canada, Ottawa, Ont., Canada K1A 0S2.

[4]Libration corrected bond lengths (esd's assumed equal to those of the uncorrected values) are employed in the discussion and are compared with similarly treated (9) distances unless otherwise stated.

TABLE 1. Final positional (fractional × 10^4) and isotropic thermal parameters (U × 10^3 Å^2) with estimated standard deviations in parentheses*

Atom	x	y	z	U_{eq}
O(1)	944	7446	6534	49
O(2)	−675(3)	7048(3)	7716(2)	49
C(1)	2707(5)	5587(4)	6201(3)	52
C(2)	1536(5)	6310(4)	6712(3)	44
C(3)	1157(5)	5506(4)	7371(3)	47
C(4)	2166(5)	4265(4)	7285(3)	57
C(5)	1527(6)	3233(4)	6295(3)	74
C(6)	1849(5)	4148(4)	5558(3)	69
C(7)	3598(5)	5036(4)	7084(3)	57
C(8)	4383(5)	6256(5)	7932(4)	77
C(9)	4790(5)	4016(5)	6799(4)	86
C(10)	3543(6)	6500(5)	5667(4)	71
C(11)	−60(5)	5842(4)	7806(3)	45
C(12)	−802(5)	4968(4)	8359(3)	46
C(13)	−736(6)	3473(5)	8217(3)	61
C(14)	−1473(6)	2687(5)	8745(4)	73
C(15)	−2245(6)	3361(5)	9418(4)	69
C(16)	−2321(5)	4847(5)	9570(3)	63
C(17)	−1615(5)	5647(4)	9041(3)	54
C(18)	1341(5)	9238(4)	8167(3)	46
C(19)	1347(5)	9372(5)	9155(3)	59
C(20)	2424(6)	10275(5)	9863(3)	75
C(21)	3527(6)	11093(5)	9616(4)	76
C(22)	3536(6)	11016(5)	8642(4)	82
C(23)	2460(6)	10108(5)	7936(4)	68
C(24)	−1200(5)	9059(4)	6823(3)	46
C(25)	−2608(5)	9117(5)	7079(3)	63
C(26)	−3693(5)	9923(6)	6667(4)	76
C(27)	−3379(6)	10683(5)	6000(4)	71
C(28)	−2008(6)	10638(5)	5721(4)	67
C(29)	−931(5)	9848(4)	6135(3)	57
B	88(5)	8209(5)	7333(3)	45
O(1′)	8981(3)	2573(2)	3417(2)	50
O(2′)	10662(3)	2919(3)	2263(2)	49
C(1′)	7039(5)	4296(5)	3554(3)	62
C(2′)	8335(5)	3644(4)	3154(3)	49
C(3′)	8693(5)	4367(4)	2453(3)	44
C(4′)	7553(5)	5477(4)	2387(3)	55
C(5′)	6043(5)	4566(5)	1887(3)	75
C(6′)	5716(5)	3721(5)	2662(4)	82
C(7′)	7367(5)	5894(4)	3465(3)	63
C(8′)	8796(7)	6672(5)	4157(4)	90
C(9′)	6072(7)	6838(5)	3639(4)	102
C(10′)	6802(7)	3978(6)	4517(4)	98
C(11′)	9987(5)	4064(4)	2096(3)	45
C(12′)	10797(5)	4959(4)	1573(3)	46
C(13′)	10806(6)	6463(5)	1771(3)	63
C(14′)	11560(6)	7263(5)	1278(4)	77
C(15′)	12328(5)	6587(5)	583(4)	75
C(16′)	12324(5)	5104(5)	372(3)	66
C(17′)	11565(5)	4288(5)	874(3)	54
C(18′)	8675(5)	719(4)	1823(3)	48
C(19′)	8668(5)	544(5)	839(3)	62
C(20′)	7586(7)	−373(6)	133(3)	77
C(21′)	6477(6)	−1159(5)	394(4)	77
C(22′)	6455(6)	−1027(6)	1368(4)	80
C(23′)	7515(6)	−104(5)	2061(4)	68
C(24′)	11184(5)	1005(4)	3229(3)	44
C(25′)	12613(5)	975(5)	3011(4)	65
C(26′)	13704(6)	229(6)	3465(4)	81
C(27′)	13397(6)	−477(5)	4159(4)	69
C(28′)	12008(6)	−456(5)	4395(4)	77
C(29′)	10922(5)	279(5)	3938(3)	69
B′	9899(5)	1777(5)	2671(3)	45

*U_{eq} = (1/3) trace of diagonalized U.

Can. J. Chem. Downloaded from www.nrcresearchpress.com by 112.217.228.212 on 09/07/12
For personal use only.

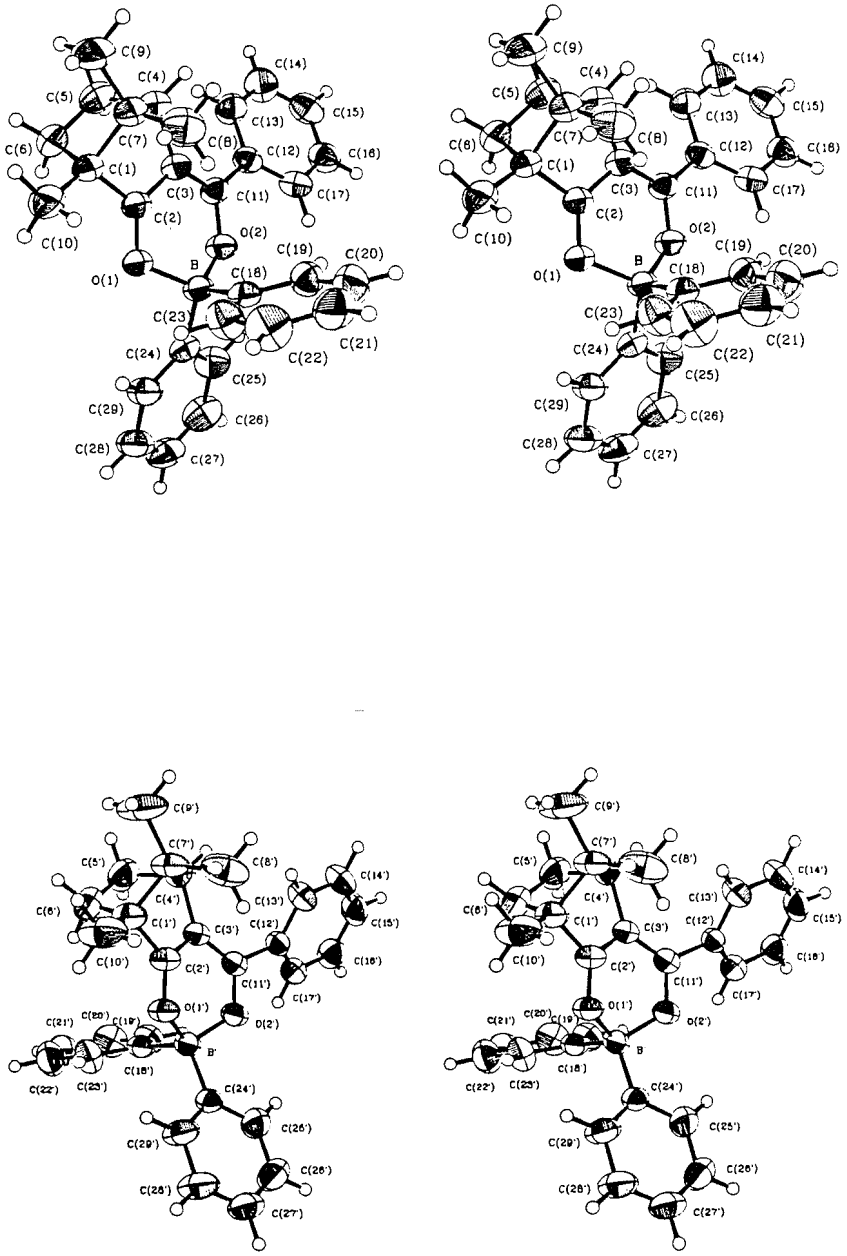

FIG. 1. Stereoscopic views of the two independent (3-benzoyl-(+)-camphorato)diphenyboron molecules; 50% probability thermal ellipsoids are shown for the non-hydrogen atoms. Hydrogen atoms have been assigned arbitrary thermal parameters for the sake of clarity.

respectively) may be compared with corresponding average values of 1.288–1.304 and 1.367(uncorr)–1.389 Å in the above-mentioned boron complexes (11, 12, 14), and with average uncorrected values of 1.274 and 1.391 Å observed for metal complexes of acetylacetone (15). The longer C—O distances observed for the boron complexes, when compared with the transition metal complexes, are consistent with the more covalent nature of the O—B interaction. The asymmetry of the 1,3-diketonate moiety in **6** leads to a significant difference between the two O—B bond lengths, those involving O(2) (average 1.518 Å) being about 0.05 Å shorter than those involving O(1) (1.568 Å). Transition metal complexes of 3-benzoyl-(+)-camphor would also be expected to show a significant difference between the two M—O bonds. A difference of 0.022 Å between the chemically equivalent O—B bonds in $(p\text{-tolyl})_2$B(acac) has been noted (12) while the O—B bonds in both crystal forms of Ph_2B(acac) are equal within experimental error. The asymmetric chelation observed for this chiral 1,3-diketonate ligand may play an important role in the catalytic properties of the Rh(I) complex mentioned in the Introduction.

The average O—B and C—B distances are 1.541 and 1.611 Å for the unprimed molecule and 1.545 and 1.605 Å for the primed molecule. These values are similar to the corresponding averages of 1.543 and 1.605 Å, and 1.533 and 1.607 Å observed for the two crystal forms of Ph_2B(acac) (11). Corresponding uncorrected values of 1.542 and 1.630 Å have been reported for $(p\text{-tolyl})_2$B(acac) (12). It has been shown that,

TABLE 2. Bond lengths (Å) with estimated standard deviations in parentheses

Bond	Length		Bond	Length	
	Uncorr.	Corr.		Uncorr.	Corr.
O(1)—C(2)	1.280(4)	1.284	O(1′)—C(2′)	1.288(4)	1.292
O(1)—B	1.566(4)	1.568	O(1′)—B′	1.561(5)	1.567
O(2)—C(11)	1.318(4)	1.322	O(2′)—C(11′)	1.317(4)	1.321
O(2)—B	1.509(4)	1.514	O(2′)—B′	1.517(4)	1.522
C(1)—C(2)	1.505(5)	1.510	C(1′)—C(2′)	1.500(5)	1.507
C(1)—C(6)	1.555(5)	1.562	C(1′)—C(6′)	1.566(6)	1.577
C(1)—C(7)	1.572(5)	1.579	C(1′)—C(7′)	1.561(5)	1.568
C(1)—C(10)	1.516(5)	1.520	C(1′)—C(10′)	1.514(5)	1.519
C(2)—C(3)	1.400(5)	1.405	C(2′)—C(3′)	1.395(5)	1.402
C(3)—C(4)	1.526(5)	1.531	C(3′)—C(4′)	1.518(4)	1.523
C(3)—C(11)	1.376(5)	1.378	C(3′)—C(11′)	1.377(5)	1.379
C(4)—C(5)	1.537(5)	1.544	C(4′)—C(5′)	1.545(5)	1.555
C(4)—C(7)	1.548(5)	1.555	C(4′)—C(7′)	1.549(5)	1.559
C(5)—C(6)	1.548(5)	1.553	C(5′)—C(6′)	1.550(5)	1.557
C(7)—C(8)	1.527(5)	1.534	C(7′)—C(8′)	1.526(6)	1.535
C(7)—C(9)	1.539(5)	1.542	C(7′)—C(9′)	1.536(5)	1.541
C(11)—C(12)	1.466(5)	1.470	C(11′)—C(12′)	1.481(5)	1.485
C(12)—C(13)	1.393(5)	1.402	C(12′)—C(13′)	1.393(5)	1.403
C(12)—C(17)	1.396(5)	1.403	C(12′)—C(17′)	1.383(5)	1.391
C(13)—C(14)	1.385(5)	1.388	C(13′)—C(14′)	1.364(6)	1.369
C(14)—C(15)	1.359(6)	1.367	C(14′)—C(15′)	1.380(6)	1.388
C(15)—C(16)	1.387(5)	1.396	C(15′)—C(16′)	1.373(6)	1.384
C(16)—C(17)	1.379(5)	1.382	C(16′)—C(17′)	1.387(5)	1.392
C(18)—C(19)	1.388(5)	1.402	C(18′)—C(19′)	1.379(5)	1.393
C(18)—C(23)	1.394(5)	1.406	C(18′)—C(23′)	1.400(5)	1.410
C(18)—B	1.604(5)	1.609	C(18′)—B′	1.612(5)	1.616
C(19)—C(20)	1.380(6)	1.385	C(19′)—C(20′)	1.387(6)	1.391
C(20)—C(21)	1.366(6)	1.377	C(20′)—C(21′)	1.363(6)	1.373
C(21)—C(22)	1.379(6)	1.394	C(21′)—C(22′)	1.373(7)	1.388
C(22)—C(23)	1.379(6)	1.384	C(22′)—C(23′)	1.369(6)	1.373
C(24)—C(25)	1.385(5)	1.397	C(24′)—C(25′)	1.381(5)	1.400
C(24)—C(29)	1.396(5)	1.407	C(24′)—C(29′)	1.380(5)	1.393
C(24)—B	1.607(5)	1.612	C(24′)—B′	1.590(5)	1.594
C(25)—C(26)	1.400(6)	1.404	C(25′)—C(26′)	1.392(6)	1.396
C(26)—C(27)	1.364(6)	1.374	C(26′)—C(27′)	1.361(6)	1.373
C(27)—C(28)	1.367(6)	1.379	C(27′)—C(28′)	1.356(6)	1.377
C(28)—C(29)	1.385(5)	1.389	C(28′)—C(29′)	1.383(5)	1.387

Can. J. Chem. Downloaded from www.nrcresearchpress.com by 112.217.228.212 on 09/07/12
For personal use only.

for a given chelate ring size, the sum of libration-corrected bond distances involving boron is essentially constant for *O,O*-chelates of diphenylboron (16). As a result, the average corrected O—B distance is a good indicator of the overall binding strength of the ligand with respect to the Ph_2B moiety. In order to compare structures for which libration corrections were either inappropriate, or were not made, with those for which the corrections were made, the ratio of the average C—B and O—B bond distances is a suitable parameter. The advantage of this parameter is that it is essentially the same whether it is calculated with corrected or uncorrected bond lengths. These C—B/O—B ratios for the ten structurally characterized *O,O*-chelates of diphenylboron containing six-membered chelate rings (11, 12, 17–21, this work) range from 1.039 to 1.088 with an average value of 1.058. The larger the value of this parameter, the stronger the O—B binding is in the molecule. The values of 1.039 and 1.045 for the two independent molecules of **6**, along with similar values of 1.040 and 1.048 for the two forms of Ph_2B(acac) (11) and 1.046 for (salicylaldehydato)diphenylboron (13) represent the weakest overall ligand binding observed for this type of compound. The differences between the average bond length ratios for the two molecules of **6** and also between the two crystal forms of Ph_2B(acac) are indicative of the extent to which packing forces, intramolecular steric effects, and resulting conformational differences can influence the molecular geometry.

Five of the six independent phenyl rings in the structure are planar within experimental error, while the other (containing C(18)) shows a statistically, but not chemically, significant deviation from planarity (maximum deviation from the mean plane 0.010(4) Å). The phenyl rings show the expected substituent-induced geometric distortions (22). The sp^2-hybridized C(3) atoms in both molecules are significantly displaced from the planes defined by their substituent atoms (C(3) by 0.070(4) Å and C(3′) by 0.059(4) Å), presumably a result of ring strain in the polycyclic ring system.

TABLE 3. Bond angles (deg) with estimated standard deviations in parentheses

Bonds	Angle (deg)	Bonds	Angle (deg)
C(2)—O(1)—B	114.4(3)	C(2′)—O(1′)—B′	113.9(3)
C(11)—O(2)—B	122.0(3)	C(11′)—O(2′)—B′	121.2(3)
C(2)—C(1)—C(6)	104.1(3)	C(2′)—C(1′)—C(6′)	100.5(3)
C(2)—C(1)—C(7)	97.8(3)	C(2′)—C(1′)—C(7′)	99.5(3)
C(2)—C(1)—C(10)	116.0(3)	C(2′)—C(1′)—C(10′)	116.2(3)
C(6)—C(1)—C(7)	101.2(3)	C(6′)—C(1′)—C(7′)	101.4(3)
C(6)—C(1)—C(10)	115.1(3)	C(6′)—C(1′)—C(10′)	116.1(4)
C(7)—C(1)—C(10)	119.9(3)	C(7′)—C(1′)—C(10′)	120.1(3)
O(1)—C(2)—C(1)	124.7(3)	O(1′)—C(2′)—C(1′)	124.5(3)
O(1)—C(2)—C(3)	126.0(3)	O(1′)—C(2′)—C(3′)	126.4(3)
C(1)—C(2)—C(3)	109.3(3)	C(1′)—C(2′)—C(3′)	109.1(3)
C(2)—C(3)—C(4)	104.5(3)	C(2′)—C(3′)—C(4′)	105.2(3)
C(2)—C(3)—C(11)	118.9(3)	C(2′)—C(3′)—C(11′)	117.9(3)
C(4)—C(3)—C(11)	135.9(3)	C(4′)—C(3′)—C(11′)	136.4(3)
C(3)—C(4)—C(5)	106.1(3)	C(3′)—C(4′)—C(5′)	104.4(3)
C(3)—C(4)—C(7)	100.5(3)	C(3′)—C(4′)—C(7′)	100.4(3)
C(5)—C(4)—C(7)	102.5(3)	C(5′)—C(4′)—C(7′)	102.3(3)
C(4)—C(5)—C(6)	102.7(3)	C(4′)—C(5′)—C(6′)	102.9(3)
C(1)—C(6)—C(5)	104.6(3)	C(1′)—C(6′)—C(5′)	104.4(3)
C(1)—C(7)—C(4)	93.8(3)	C(1′)—C(7′)—C(4′)	94.6(3)
C(1)—C(7)—C(8)	113.7(3)	C(1′)—C(7′)—C(8′)	113.2(3)
C(1)—C(7)—C(9)	113.4(3)	C(1′)—C(7′)—C(9′)	113.8(3)
C(4)—C(7)—C(8)	113.6(3)	C(4′)—C(7′)—C(8′)	113.4(3)
C(4)—C(7)—C(9)	114.4(3)	C(4′)—C(7′)—C(9′)	114.4(3)
C(8)—C(7)—C(9)	107.7(3)	C(8′)—C(7′)—C(9′)	107.4(4)
O(2)—C(11)—C(3)	118.8(3)	O(2′)—C(11′)—C(3′)	119.4(3)
O(2)—C(11)—C(12)	114.6(3)	O(2′)—C(11′)—C(12′)	114.0(3)
C(3)—C(11)—C(12)	126.6(3)	C(3′)—C(11′)—C(12′)	126.5(3)
C(11)—C(12)—C(13)	122.1(3)	C(11′)—C(12′)—C(13′)	121.5(3)
C(11)—C(12)—C(17)	119.1(3)	C(11′)—C(12′)—C(17′)	119.3(3)
C(13)—C(12)—C(17)	118.8(3)	C(13′)—C(12′)—C(17′)	119.2(3)
C(12)—C(13)—C(14)	120.1(4)	C(12′)—C(13′)—C(14′)	120.4(4)
C(13)—C(14)—C(15)	120.7(4)	C(13′)—C(14′)—C(15′)	120.2(4)
C(14)—C(15)—C(16)	120.0(4)	C(14′)—C(15′)—C(16′)	120.4(4)
C(15)—C(16)—C(17)	120.2(4)	C(15′)—C(16′)—C(17′)	119.6(4)
C(12)—C(17)—C(16)	120.2(3)	C(12′)—C(17′)—C(16′)	120.3(3)
C(19)—C(18)—C(23)	115.8(3)	C(19′)—C(18′)—C(23′)	115.2(4)
C(19)—C(18)—B	122.7(3)	C(19′)—C(18′)—B′	124.4(3)
C(23)—C(18)—B	121.4(3)	C(23′)—C(18′)—B′	120.4(3)
C(18)—C(19)—C(20)	121.9(4)	C(18′)—C(19′)—C(20′)	122.5(4)
C(19)—C(20)—C(21)	121.0(4)	C(19′)—C(20′)—C(21′)	120.5(4)
C(20)—C(21)—C(22)	118.7(4)	C(20′)—C(21′)—C(22′)	118.7(4)
C(21)—C(22)—C(23)	120.1(4)	C(21′)—C(22′)—C(23′)	120.4(4)
C(18)—C(23)—C(22)	122.4(4)	C(18′)—C(23′)—C(22′)	122.6(4)
C(25)—C(24)—C(29)	116.2(3)	C(25′)—C(24′)—C(29′)	115.9(3)
C(25)—C(24)—B	122.0(3)	C(25′)—C(24′)—B′	122.1(3)
C(29)—C(24)—B	121.7(3)	C(29′)—C(24′)—B′	122.0(3)
C(24)—C(25)—C(26)	121.5(4)	C(24′)—C(25′)—C(26′)	121.7(4)
C(25)—C(26)—C(27)	120.2(4)	C(25′)—C(26′)—C(27′)	120.5(4)
C(26)—C(27)—C(28)	119.8(4)	C(26′)—C(27′)—C(28′)	119.1(4)
C(27)—C(28)—C(29)	119.8(4)	C(27′)—C(28′)—C(29′)	120.3(4)
C(24)—C(29)—C(28)	122.3(4)	C(24′)—C(29′)—C(28′)	122.5(4)
O(1)—B—O(2)	108.0(3)	O(1′)—B′—O(2′)	107.6(3)
O(1)—B—C(18)	106.4(3)	O(1′)—B′—C(18′)	105.8(3)
O(1)—B—C(24)	108.3(3)	O(1′)—B′—C(24′)	109.1(3)
O(2)—B—C(18)	111.8(3)	O(2′)—B′—C(18′)	110.4(3)
O(2)—B—C(24)	108.1(3)	O(2′)—B′—C(24′)	107.9(3)
C(18)—B—C(24)	114.1(3)	C(18′)—B′—C(24′)	115.8(3)

Can. J. Chem. Downloaded from www.nrcresearchpress.com by 112.217.228.212 on 09/07/12
For personal use only.

TABLE 4. Intra-annular torsion angles (deg), standard deviations in parentheses

Atoms	Torsion angle	
	Unprimed	Primed
B—O(1)—C(2)—C(3)	18.3(5)	−18.3(5)
C(2)—O(1)—B—O(2)	−36.2(4)	38.1(4)
B—O(2)—C(11)—C(3)	−12.7(5)	11.6(5)
C(11)—O(2)—B—O(1)	35.1(4)	−36.5(4)
O(1)—C(2)—C(3)—C(11)	7.3(6)	−9.9(6)
C(2)—C(3)—C(11)—O(2)	−10.9(5)	13.9(5)
C(6)—C(1)—C(2)—C(3)	68.0(3)	71.9(4)
C(2)—C(1)—C(6)—C(5)	−68.6(3)	−70.1(4)
C(1)—C(2)—C(3)—C(4)	1.6(4)	−1.8(4)
C(2)—C(3)—C(4)—C(5)	−72.5(4)	−70.7(4)
C(3)—C(4)—C(5)—C(6)	67.4(4)	67.2(4)
C(4)—C(5)—C(6)—C(1)	2.5(4)	2.8(4)
C(7)—C(1)—C(2)—C(3)	−35.7(4)	−31.7(4)
C(2)—C(1)—C(7)—C(4)	52.7(3)	49.9(3)
C(1)—C(2)—C(3)—C(4)	1.6(4)	−1.8(4)
C(2)—C(3)—C(4)—C(7)	33.9(3)	35.0(4)
C(3)—C(4)—C(7)—C(1)	−53.2(3)	−51.7(3)
C(7)—C(1)—C(6)—C(5)	32.5(3)	32.0(4)
C(6)—C(1)—C(7)—C(4)	−53.3(3)	−52.9(3)
C(7)—C(4)—C(5)—C(6)	−37.5(3)	−37.1(3)
C(5)—C(4)—C(7)—C(1)	56.1(3)	55.7(3)
C(4)—C(5)—C(6)—C(1)	2.5(4)	2.8(4)

Can. J. Chem. Downloaded from www.nrcresearchpress.com by 112.217.228.212 on 09/07/12
For personal use only.

Acknowledgments

We thank the Natural Sciences and Engineering Research Council of Canada for financial support and the University of British Columbia Computing Centre for assistance.

1. W. R. CULLEN and E. B. WICKENHEISER. 194th Am. Chem. Soc. National Meeting. New Orleans, LA. Aug. 30 – Sept. 4, 1987.
2. E. JOSEPHY and F. RADT (*Editors*). Elsevier's encyclopaedia of organic chemistry. Vol. 12A. Series III. Elsevier Publishing Co., New York. 1948.
3. P. COPPENS, L. LEISEROWITZ, and D. RABINOVICH. Acta Crystallogr. **18**, 1035 (1965).
4. W. R. BUSING and H. A. LEVY. Acta Crystallogr. **22**, 457 (1967).
5. International tables for X-ray crystallography. Vol. IV. Kynoch Press, Birmingham. 1974. pp. 99–102 and 149.
6. P. J. BECKER and P. COPPENS. Acta Crystallogr. Sect. A, **30**, 129 (1974); **30**, 148 (1974); **31**, 417 (1975).
7. P. COPPENS and W. C. HAMILTON. Acta Crystallogr. Sect. A, **26**, 71 (1970).
8. F. R. THORNLEY and R. J. NELMES. Acta Crystallogr. Sect. A, **30**, 748 (1974).
9. V. SCHOMAKER and K. N. TRUEBLOOD. Acta Crystallogr. Sect. B, **24**, 63 (1968).
10. D. W. J. CRUICKSHANK. Acta Crystallogr. **9**, 747 (1956); **9**, 754 (1956); **14**, 896 (1961).
11. S. J. RETTIG and J. TROTTER. Can. J. Chem. **60**, 2957 (1982).
12. R. BOESE, R. KOSTER, and M. YALPANI. Chem. Ber. **118**, 670 (1985).
13. S. J. RETTIG and J. TROTTER. Can. J. Chem. **54**, 1168 (1976).
14. A. W. HANSON and E. W. MACAULAY. Acta Crystallogr. Sect. B, **28**, 1961 (1972).
15. E. C. LINGAFELTER and R. L. BRAUN. J. Am. Chem. Soc. **88**, 2951 (1966).
16. C. ORVIG, S. J. RETTIG, and J. TROTTER. Can. J. Chem. **65**, 590 (1987).
17. B. A. ARBUZOV, O. A. ERASTOV, G. N. NIKONOV, A. A. ESPENBETOV, A. I. YANOVSKII, and YU. T. STRUCHKOV. Izv. Akad. Nauk. SSSR, Ser. Khim. 1545 (1981).
18. J. C. JANSEN, M. VERHAGE, and H. VAN KONINGSVELD. Cryst. Struct. Commun. **11**, 305 (1982).
19. W. KLIEGEL, H.-W. MOTZKUS, S. J. RETTIG, and J. TROTTER. Can. J. Chem. **63**, 3516 (1985).
20. W. KLIEGEL, H.-W. MOTZKUS, D. NANNINGA, S. J. RETTIG, and J. TROTTER. Can. J. Chem. **64**, 507 (1986).
21. W. KLIEGEL, S. J. RETTIG, and J. TROTTER. Can. J. Chem. **66**, 1091 (1988).
22. A. DOMENICANO, P. MURRAY-RUST, and A. VACIAGO. Acta Crystallogr. Sect. B, **39**, 457 (1983), and references therein.
23. H. AMT, W. KLIEGEL, S. J. RETTIG, and J. TROTTER. Can. J. Chem. **66**, 1117 (1988).

Proton spin–lattice relaxation in a solid protein *Streptomyces* subtilisin inhibitor. Enhancement of segmental motions by adsorbed water

K. AKASAKA, K. TAKEGOSHI,[1] AND T. TERAO
Department of Chemistry, Faculty of Science, Kyoto University, Kyoto 606, Japan

AND

S. GANAPATHY[2]
Department of Chemistry, The University of British Columbia, Vancouver, B.C., Canada V6T 1Y6

Received January 4, 1988

This paper is dedicated to Professor Charles A. McDowell on the occasion of his seventieth birthday

K. AKASAKA, K. TAKEGOSHI, T. TERAO, and S. GANAPATHY. Can. J. Chem. **66**, 2014 (1988).

Proton spin–lattice relaxation times (T_1) were measured on a protein *Streptomyces* subtilisin inhibitor, in the solid state, in the presence and the absence of adsorbed ^2H_2O in the temperature range between −170 and 100°C at 30 and 60 MHz. In both samples, a common relaxation process is attributed to the methyl group rotations of amino acid side chains which show minimum values of T_1 of 0.11 s at −105°C at 30 MHz and 0.23 s at −80°C at 60 MHz. In the presence of adsorbed ^2H_2O, another, effective relaxation process was found above 0°C, showing a minimum value of T_1 of 0.12 s at about 80°C at 60 MHz. The latter relaxation process was attributed to internal motions of exposed peptide segments, a large part of which is located in the crucial enzyme-binding region of the inhibitor.

K. AKASAKA, K. TAKEGOSHI, T. TERAO et S. GANAPATHY. Can. J. Chem. **66**, 2014 (1988).

Opérant dans un intervalle de température allant de −170 à 100°C, on a mesuré les temps de relaxation spin–réseau de la protéine *Streptomyces*, un inhibiteur de la subtilisine, à l'état solide, à 30 et à 60 MHz en présence et en l'absence de ^2H_2O adsorbée. Dans les deux cas, on attribue à la rotation du méthyle des chaines latérales des acides aminés, un processus commun de relaxation qui a des valeurs de T_1 de 0,11 s à −105°C à 30 MHz et de 0,23 s à −80°C à 60 MHz. On a trouvé un autre processus effectif de relaxation au-dessus de 0°C avec une valeur minimum de T_1 de 0,2 s à environ 80°C à 60 MHz. On attribue ce dernier processus de relaxation à des mouvements internes des segments de peptides exposés dont une grande partie se situe dans la zone cruciale d'encrage de l'enzyme de l'inhibiteur.

[Traduit par la revue]

Streptomyces subtilisin inhibitor (SSI) is a dimeric globular protein made up of two identical subunits of 113 amino acids (molecular weight 23 000 as dimer) (Fig. 1) (1). SSI inhibits a wide variety of proteases of subtilisin family, e.g., subtilisin BPN′ as well as those of chymotrypsin family, e.g., *Streptomyces griseus* proteases A and B (1). Unlike the trypsin inhibitors, SSI has a relatively long, enzyme-binding peptide segment consisting of about ten amino acid residues (Arg 65-Tyr 75) which are well exposed on the surface of the protein (1, 2). Moreover, a part of this segment, i.e., Arg 65-Met 70, is apparently flexible, as in the X-ray diffraction analysis the electron density corresponding to a part of the peptide segment is extremely low (1, 2) (see Fig. 1). This portion, however, rigidifies upon binding to the enzyme, as its electron density becomes very clear in the SSI–subtilisin BPN′ complex (1, 3). It has been suggested by one of the present authors that this flexibility is to make SSI capable of binding to a wide variety of target enzymes (4). It is in this connection that a special interest lies in the mobility of the surface segments of SSI.

In this report, we applied ^1H NMR spin–lattice relaxation measurements for the detection of internal motions of SSI in the solid state. The great advantage of measuring spin relaxation times in solids is that only the internal motions affect spin relaxation, whereas in solution one needs to take the overall rotation of the molecule into account in the analysis of relaxation data. Our results clearly indicated that in addition to the well-known methyl group rotations, there are other motions in the protein attributable to the exposed segments. The latter motions were found to be greatly enhanced when the dry protein sample was allowed to equilibrate with the water vapor.

Materials and methods

Lyophilized powders of SSI were obtained in high purity according to the previously described procedure (5). A fully dry sample of SSI was prepared by evacuating the lyophilized protein powder on a vacuum line at 25°C to approximately 10^{-3} mm Hg and sealed in an NMR sample tube. A hydrated sample was prepared by equilibrating the dry sample with the ^2H_2O vapor for a long enough time (17 h) at 25°C, and then sealed in an NMR sample tube. Proton longitudinal relaxation times were measured on a Bruker BKR 322S spectrometer operating at 30 MHz and on a home-built spectrometer operating at 60 MHz (59.525 MHz) using either the saturation recovery or the inversion recovery pulse sequence. The ^2H_2O content of the sample was measured on a JEOL GX-61D NMR spectrometer operating at 61 MHz.

Results

At all temperatures of measurement, the time dependence of magnetization of protons obeyed single exponential functions, giving single relaxation times T_1. This indicates that possible differences in spin–lattice relaxation rate among different protons are fully averaged out by extensive spin diffusion, as normally expected in solid.

Figure 2 shows the plots of T_1 values obtained for the dry sample of SSI at 30 and 60 MHz in the temperature range between −170 and 100°C. At the lower temperature side of the plot, the T_1 value decreases with increasing temperature, while at the higher temperature side, it increases with temperature until it reaches maxima at about 0°C. Clearly, minimum values of T_1 occur approximately at −80°C at 60 MHz ($T_{1\,\min}$ =

[1]Present address: Foundation of Material Science and Technology of Japan, 3-11-1 Kami-Soshigaya, Setagayaku, Tokyo.

[2]Present address: National Chemical Laboratory, Pune 411008, India.

Printed in Canada / Imprimé au Canada

Can. J. Chem. Downloaded from www.nrcresearchpress.com by 112.217.228.212 on 09/07/12
For personal use only.

Can. J. Chem. Downloaded from www.nrcresearchpress.com by 112.217.228.212 on 09/07/12
For personal use only.

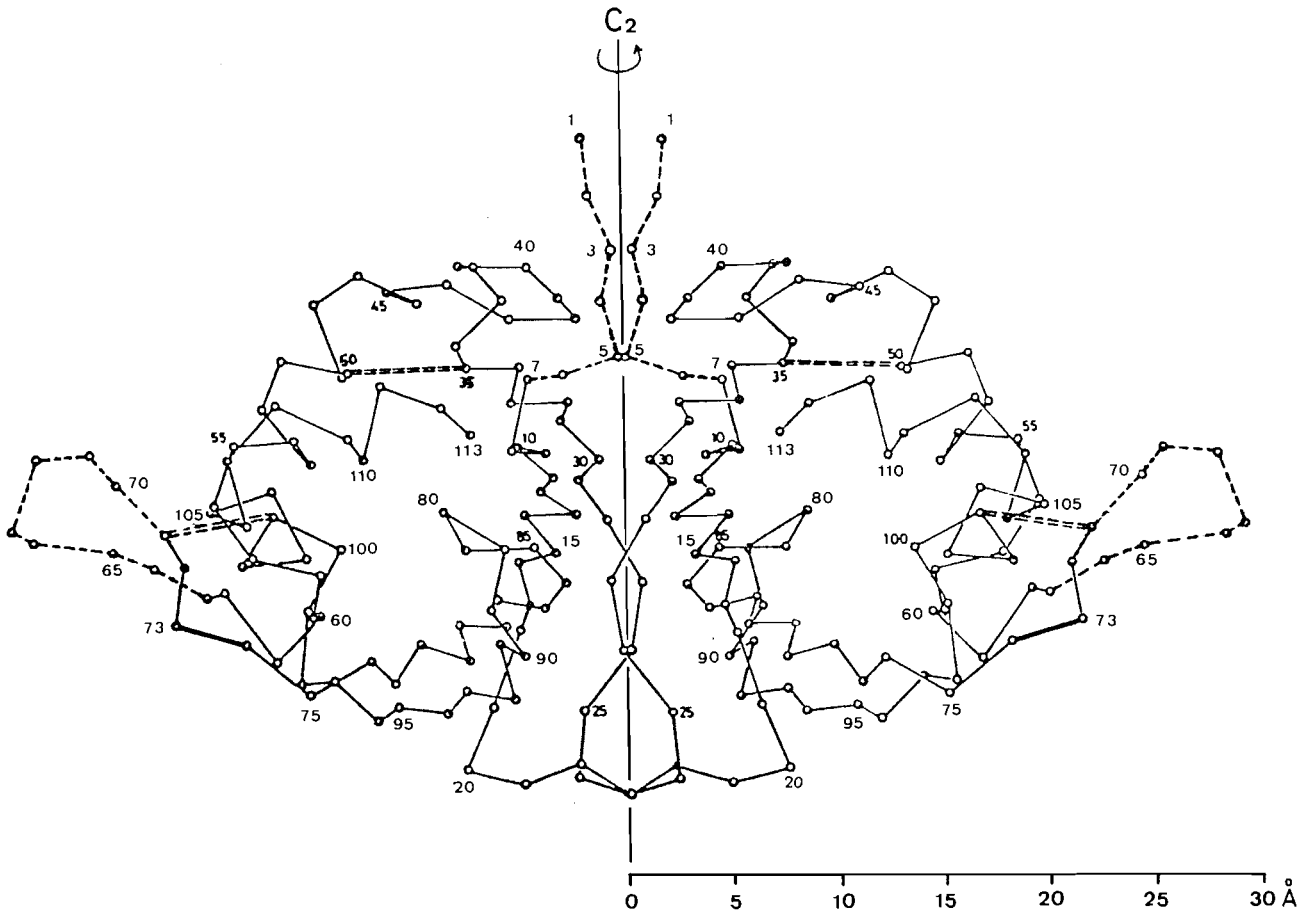

FIG. 1. The crystal structure of *Streptomyces* subtilisin inhibitor (after ref. 2). Two identical subunits are mutually related by a two-fold (C_2) axis. -○-, α-carbon backbone; ----, disulfide bridge. The dotted lines indicate where the electron density is dim or missing.

0.23 s) and at −105°C at 30 MHz ($T_{1\,\mathrm{min}} = 0.11$ s), indicating that there is a well-defined relaxation process (relaxation process I) in the temperature range between −170 and 0°C.

The experimental data could be fitted reasonably well for both frequencies by a Kubo–Tomita expression for longitudinal relaxation times (T_1) of protons (6), i.e.,

$$[1]\quad T_1^{-1} = C[\tau_c(1 + \omega^2\tau_c^2)^{-1} + 4\tau_c(1 + 4\omega^2\tau_c^2)^{-1}]$$

In this expression, the proton–proton dipolar interaction is assumed to fluctuate with the correlation time

$$[2]\quad \tau_c = \tau_0 \exp(E_a/RT)$$

in which a single set of parameters $C = 0.115 \pm 0.007 \times 10^{10}\,\mathrm{s}^{-2}$, $E_a = 1.14 \pm 0.07$ kcal/mol, and $\tau_0 = 0.653 \pm 0.152 \times 10^{-10}$ s are used for both frequencies (Fig. 2, solid lines).

Above 0°C T_1 values again show slight decrease with temperature (Fig. 2). This observation suggests that there may be another type of relaxation process (relaxation process II) in addition to the one observed at low temperature. This relaxation process was found to be greatly enhanced by introducing humidity to the protein sample. Ten hours after breaking the vacuum seal in the laboratory atmosphere at room temperature, T_1 decreased from 0.32 to 0.20 s at 30 MHz. When the sample was further exposed to an atmosphere saturated with water (^1H_2O) vapor for 30 min, T_1 further decreased to 0.083 s. These observations indicate that relaxation process II is strongly dependent on the adsorbed water. However, it was not clear

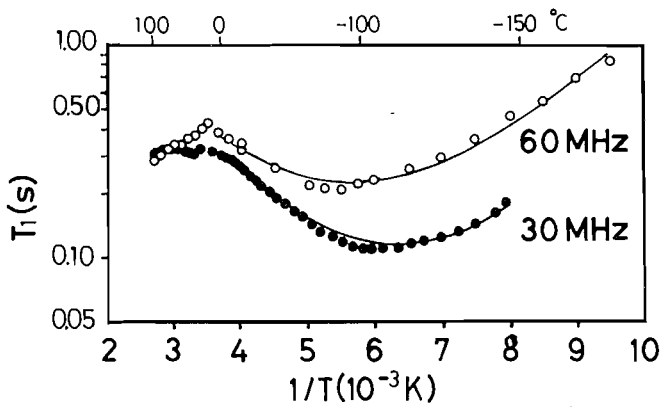

FIG. 2. The temperature dependence of the apparent ^1H spin–lattice relaxation times of *Streptomyces* subtilisin inhibitor in the dehydrated solid state, measured at 30 MHz (-●-) and at 60 MHz (-○-).

from the above experiment alone whether the protons of the adsorbed water molecules (^1H_2O) themselves act as relaxation sinks for the protons of the protein by way of spin diffusion among the protons or the adsorbed water protons induce new internal motions in the protein that have been largely quenched in the absence of adsorbed water.

In order to distinguish between the two cases, relaxation times were measured of solid protein samples equilibrated with a ^2H_2O vapor rather than with a ^1H_2O vapor. The water (^2H_2O)

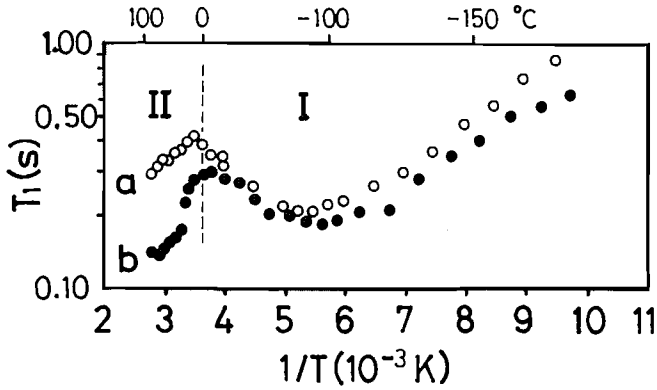

FIG. 3. The temperature dependence of the apparent ^1H spin–lattice relaxation times of *Streptomyces* subtilisin inhibitor measured at 60 MHz. (*a*) In dehydrated solid state (-○-) and (*b*) in hydrated solid state after exposure to the ^2H_2O vapor (-●-).

content in the ^2H_2O vapor-equilibrated sample was determined by dissolving it in a ^2H-depleted water and measuring the intensity of the ^2H_2O resonance in the high resolution ^2H NMR spectrum. The adsorption of ^2H_2O vapor by the dried protein was rapid, leading to a nearly final water (^2H_2O) content of approximately 50% of the total weight (protein plus water) within 10 h, which corresponds to about 1300 deuterons/subunit of SSI. The fraction of ^1H_2O within the water layer should be small, at most 5% even if all the labile protons of the protein after exchange with ^2H_2O remained adsorbed by the protein, and would give negligible contribution to the proton relaxation. On the other hand, cross relaxation caused by the flip–flop of the spins cannot take place effectively between the protons and the deuterons owing to a large difference in Larmor frequency of the two nuclei. Fluctuating dipolar field at the proton Larmor frequency produced by the deuterons of the mobile water molecules on the surface of the protein can still be a cause for relaxation of the protein protons. However, this contribution would not be appreciable, because of the small gyromagnetic ratio of the deuteron. After all, the bound ^2H_2O molecules would not themselves act as effective relaxation sinks for protons. Significant relaxation enhancement of the protons should arise only when the bound ^2H_2O molecules newly induced certain internal motions in the protein, which then would act as relaxation sinks.

Figure 3 compares T_1 values at 60 MHz of the solid SSI sample which had been equilibrated with a ^2H_2O vapor (-●-) with the T_1 values of the dry sample (-○-) at various temperatures. Clearly, the high temperature relaxation process (process II) was markedly enhanced by equilibrating the dry sample with the ^2H_2O vapor ($T_{1\,min} = 0.12$ s). The fact that the longitudinal magnetization in this sample also obeyed a single exponential function of time indicates that T_1's are averaged over all the protons by spin diffusion via proton–proton dipolar coupling. These observations clearly indicate that certain internal motions induced by the adsorbed water molecules act as new relaxation sinks in relaxation process II. In addition, a slight decrease in T_1 in the low temperature relaxation process (process I) is also noted in Fig. 3, which will be discussed later.

Discussion

Relaxation process I

The reasonable fit of relaxation process I to the Kubo–Tomita expression indicates that this relaxation process is due to a well-defined internal motion of the protein. The low activation energy (1.14 kcal/mol), together with C and τ_0 values, is analogous to the cases found in several other proteins by Andrew *et al.* (7). Through comparison of proton relaxation data of proteins with the corresponding data of polypeptides, they showed that the motion responsible for this relaxation process is mainly rotation of the methyl groups of amino acid side chains about their three-fold axes.

The subunit of SSI consists of 113 amino acids and contains 73 methyl groups, i.e., it has 219 methyl protons against 735 protons for the entire subunit when the proton content of the hydrogen atoms is 100% (1). The average values of the $T_{1\,min}$ for the methyl proton itself would therefore be 0.033 and 0.069 s for 30 and 60 MHz, respectively, should the protons other than the methyl protons make negligible contribution to the relaxation. These values may be compared with the $T_{1\,min}$ values calculated for the case when rotations of all the methyl groups of SSI were identical, using eq. [1] with $C = C_0 \times (219/735)$, where C_0 is the value of C for an isolated methyl group and is taken to be $0.8 \times 10^{10}\,s^{-2}$ (7). They are 0.053 and 0.10 s for 30 and 60 MHz, respectively. The difference between the experimental and the calculated $T_{1\,min}$ values would largely be explained by taking into consideration the distribution of temperatures of $T_{1\,min}$ for methyl groups of different amino acid residues (8).

A slight decrease in the observed T_1 values when the dry sample is equilibrated with ^2H_2O vapor can be explained reasonably well if one takes into account the fact that certain labile protons are replaced easily with deuterons (1). The percentage of replacement by deuterons in the present case can be estimated to be 10%, corresponding to approximately 70 protons/subunit, from the relative decrease of T_1.

Relaxation process II

The water content in the water vapor-equilibrated sample (approximately 50%) is comparable to that in the single crystal of SSI (about 45%). It is highly conceivable that, upon hydration in the ^2H_2O vapor-equilibrated powder sample, SSI largely regains its native conformation similar to that found in the single crystal, where ample segmental motions set in. The slight presence of relaxation process II in the dry sample (Fig. 2) could be either due to intrinsic motions that are present even in the absence of adsorbed water or due to a trace of water (^1H_2O) that could not be completely removed by evacuation.

The T_1 value for ^2H_2O vapor-equilibrated sample at 80°C (0.12 s at 60 MHz, Fig. 3) would have been as long as 1.9 s if only relaxation process I were present. It is noteworthy that $T_{1\,min}$ for relaxation process II is even shorter than the $T_{1\,min}$ for relaxation process I (0.23 s at 60 MHz at −105°C, Fig. 3), indicating that relaxation process II can be more efficient than in relaxation process I in SSI. Gaspar *et al.* (9) also found leveling off of T_{1D} (proton dipolar relaxation time) above 260 K in solid lysozyme, which they tentatively attributed to the effect of backbone and side chain motions. However, no such effect was found in their T_1 values.

The existence of the strong relaxation process at high temperature (relaxation process II) seems to be characteristic of SSI, and its origin must be sought in the unique structure of SSI (1, 2). SSI has unusually long exposed, peptide segment which acts as the binding segment towards the protease, i.e., Arg 65-Tyr 75 (3). In the absence of the protease, a part of this segment seems to be flexible, as they give only a dim electron density in the electron density map (1, 2). In addition, it has an *N*-terminal segment (residues 1–5) whose electron density is

Can. J. Chem. Downloaded from www.nrcresearchpress.com by 112.217.228.212 on 09/07/12
For personal use only.

completely missing (2) (see Fig. 1). Recent ^{1}H NMR studies in solution proved that the entire *N*-terminal segment undergoes rapid segmental motions of 10^{-9} s order (10–12).

Our present result (Fig. 3) indicates that even in solid, segmental motions with correlation times of similar magnitude take place in solid. We would not attempt to analyze the data of Fig. 3 (relaxation process II) quantitatively, because of the obvious complexity of the motions involved. However, their average value should be of the order of reciprocal Larmor frequency, i.e. ca 3×10^{-9} s at the temperature of $T_{1\,min}$ (80°C).

It has been often anticipated, but has been directly proved in very few cases, that the missing electron density in the X-ray crystallographic analysis be due to segmental motions of that part of the protein. Some direct proofs for the existence of internal motions in solids have been obtained by NMR investigations (7–9), but these have been restricted, in most cases, to those of the methyl group rotation. The present work not only demonstrated that segmental motions are present in the solid protein, but also that they occur predominantly in the hydrated state. The presence of ample segmental motions in SSI seems to be particularly important in view of the anticipation that segmental flexibility in the enzyme-binding region, particularly that of Arg 65 through Met 70, is a key to facilitate its binding with a variety of structurally different proteases (4, 11).

Conclusion

Although it has been generally accepted that in proteins proton spin relaxation is mainly dominated by methyl group rotations, the result of the present study has clearly indicated that other motions can be more important in causing spin relaxation. Since these motions were shown to be quenched in samples which had been vacuum-dried, they are likely to arise from surface segments that are mobilized by the adsorbed water molecules. Thus the water molecules appear to play essential roles in freeing those frozen segments on the surface and thereby bringing the protein in normal function.

Acknowledgements

We thank Professor K. Gonda of Tokyo Denki University for valuable suggestions and discussions on the measurement of the bound water in proteins. This work was supported in part by a grant-in-aid from the Ministry of Education, Science, and Culture #61430027.

1. K. Hiromi, K. Akasaka, Y. Mitsui, B. Tonomura, and S. Murao (*Editors*). Protein protease inhibitor – the case of *Streptomyces* subtilisin inhibitor (SSI). Elsevier Science Publishers. 1985.
2. Y. Mitsui, Y. Satow, Y. Watanabe, and Y. Iitaka. J. Mol. Biol. **131**, 697 (1979).
3. S. Hirono, H. Akagawa, Y. Iitaka, and Y. Mitsui. J. Mol. Biol. **178**, 389 (1984).
4. K. Akasaka. *In* Steric aspects of biomolecular interactions. *Edited by* G. Naray-Szabo and K. Simon. CRC Press, Florida. 1987. pp. 145–157.
5. S. Sato and S. Murao. Agr. Biol. Chem. **37**, 1067 (1972).
6. R. Kubo and K. Tomita. J. Phys. Soc. Jpn. **9**, 888 (1954).
7. E. R. Andrew, D. J. Bryant, and E. M. Cashell. Chem. Phys. Lett. **69**, 551 (1980).
8. E. R. Andrew, W. S. Hinshaw, M. G. Hutchins, and R. O. I. Sjöblom. Mol. Phys. **31**, 1479 (1976); **34**, 1695 (1977).
9. R. Gapser, Jr., E. R. Andrew, D. J. Bryant, and E. M. Cashell. Chem. Phys. Lett. **86**, 327 (1982).
10. K. Akasaka, S. Fujii, and H. Hatano. J. Biochem. **92**, 591 (1982).
11. K. Akasaka. J. Magn. Reson. **51**, 14 (1983).
12. K. Akasaka. Int. J. Peptide Protein Res. **25**, 547 (1987).

Can. J. Chem. Downloaded from www.nrcresearchpress.com by 112.217.228.212 on 09/07/12
For personal use only.

The ion–molecule reactivity of the positive muon molecular ions $HeMu^+$ and $NeMu^+$

D. J. ARSENEAU, D. G. FLEMING, M. SENBA, I. D. REID, AND D. M. GARNER
TRIUMF and Department of Chemistry, University of British Columbia, Vancouver, B.C., Canada V6T 1Y6

Received March 24, 1988

This paper is dedicated to Professor Charles A. McDowell on the occasion of his 70th birthday

D. J. ARSENEAU, D. G. FLEMING, M. SENBA, I. D. REID, and D. M. GARNER. Can. J. Chem. **66**, 2018 (1988).

Thermal (300 K) ion–molecule reaction rates are measured, using the μSR (muon spin rotation) technique, for the muonated rare gas molecular ions $HeMu^+$ and $NeMu^+$ reacting with NO, O_2, N_2O, NH_3, CF_4, C_2H_4, TMS, and CH_3NO_2. In almost every case (excepting O_2), both charge transfer (k_e) and muon transfer (k_μ) contribute to the reaction rate. Reaction is believed to occur from ro-vibrational excited states, $[HeMu^+]^*$ and $[NeMu^+]^*$, due to the poor efficiency of He and Ne moderators for collisional deactivation. The total experimental rate constants, $k_{exp} = k_\mu + k_e$, are generally in excellent agreement with total capture rates predicted by the simple ADO theory, regardless of the degree of internal excitation. Comparisons with literature values for corresponding protonated ion reaction rates with O_2 and C_2H_4 reveal little or no isotope effect, although it is noted that these reactions are dominated by proton transfer, in contrast to the μSR results.

D. J. ARSENEAU, D. G. FLEMING, M. SENBA, I. D. REID et D. M. GARNER. Can. J. Chem. **66**, 2018 (1988).

Utilisant la technique du μSR, on a mesuré les vitesses thermiques (300 K) de réactions ions–molécules des ions moléculaires de gaz rares muonées ($HeMu^+$ et $NeMu^+$) avec le NO, le O_2, le N_2O, le NH_3, le CF_4, le C_2H_4, le TMS et le CH_3NO. Dans pratiquement chacun des cas (excepté avec le O_2), le transfért de charge (k_e) ainsi que le transfert de muon (k_μ) contribuent à la vitesse de la réaction. On croit que la réaction se produit à partir d'états excités ro-vibrationnels, $[HeMu^+]^*$ et $[NeMu^+]^*$, qui sont dûs à la mauvaise efficacité des modérateurs He et Ne dans la désactivation par collision. En général, les constantes de vitesse expérimentales totales, $k_{exp} = k_\mu + k_e$, sont en excellent accord avec les vitesses totales de capture qu'on peut prédire en se basant uniquement sur la théorie ADO, sans tenir compte du degré d'excitation interne. En se basant sur une comparaison avec des valeurs de la littérature concernant les vitesses de réaction correspondantes des ions protonés avec le O_2 et le C_2H_4, on peut en déduire qu'il n'y a que peu ou pas d'effet isotopique; on tire ces conclusions même si, par opposition avec les résultats de μSR, on note que ces réactions sont dominées par des transferts de proton.

[Traduit par la revue]

Introduction

There is currently widespread interest in a variety of both experimental and theoretical studies of gas phase molecular ions and ion–molecule reactivity (1), centered on the formation of molecular ion complexes (2, 3) and the effect of ro-vibrational excitation on reactivity (4–6), including now some detailed studies of the quenching process itself (5, 6). On the theoretical side (7–10), ion–molecule reactions are more amenable to a quantitative understanding than are atom–molecule reactions because ion–molecule reactivity is usually dominated by the long range (induced or permanent) electric dipole interaction. This attraction captures the reactants and holds them together until they can react, regardless of the details of the reaction. Sometimes though, short range "chemical" forces may be important, particularly in the case of open-shell ions where reactivity may be facilitated by the formation of long-lived molecular ion complexes (2, 3, 11), but this should not be the case for reactions of very simple molecular ions such as the protonated rare gases HeH^+ and NeH^+ (12–14).

In an earlier paper (15) we reported preliminary observations on the reactivity of the positive muon analog of protonated neon, $NeMu^+$. The present paper extends that work considerably to include results on both $NeMu^+$ and $HeMu^+$ ions reacting with a variety of molecules of widely differing polarizabilities and dipole moments. Like their proton counterparts, $HeMu^+$ and $NeMu^+$ represent the simplest molecular ions, being essentially point charges as well as closed electron shell systems: the best choice for comparisons with theoretical calculations of reactivity based entirely on ion–molecule capture. To date, relatively few experimental data have been reported on the reactivity of the corresponding protonated ions (12–14), almost no work at all on NeH^+, and very little in general on molecules with non-zero dipole moments (14). The present paper on the muonated rare gases extends this data base considerably, particularly in the area of charge transfer reactions.

Most measurements of thermal ion–molecule rate constants have been obtained with flowing afterglow (FA), (selected ion) drift tubes (SIFT), or ion cyclotron resonance (ICR) techniques, at pressures in the range from about 1 to 10^{-6} Torr (1 Torr = 133.3 Pa). Such low pressures leave open the possibility that reported rate constants for some "binary" collisions may in fact be due to termolecular processes (11, 16). Just the opposite limit is provided by the present μSR study of molecular ions, which are observed typically at pressures $\gtrsim$1 atm (1 atm = 101.3 kPa). A general comparison of rate constants for protonated molecules with those for their positive muon analogs could reveal the importance, if any, of total pressure in determining ion–molecule reactivity.

Another reason for the present study was the possibility that the very light μ^+, being only 1/9 as massive as a proton, might reveal interesting behaviour due to quantum tunneling, raised vibrational zero point energies, or more widely spaced ro-vibrational excitation energies. In fact this paper deals with a subset of a larger program, including also investigation of quenching processes (17).

Experimental technique

This paper is concerned with molecular ions containing a positive muon, μ^+. To a chemist, a μ^+ is just a light proton, especially since it forms an atom called muonium, denoted Mu, which is just like hydrogen but with 1/9 the mass. Muons and muonium are studied by the technique of μSR wherever muons are available in quantity, notably at meson facilities such as TRIUMF, where the present experiments were performed. The

Can. J. Chem. Downloaded from www.nrcresearchpress.com by 112.217.228.212 on 09/07/12
For personal use only.

Can. J. Chem. Downloaded from www.nrcresearchpress.com by 112.217.228.212 on 09/07/12
For personal use only.

subject of μSR is well discussed elsewhere (18, 19), so only some main features will be briefly mentioned here.

Positive muons are produced 100% longitudinally spin polarized and have kinetic energies of ≳2.5 MeV as they enter the gas target in our experiment. This polarization is maintained as the μ^+ slows down in a moderator gas, although there can be appreciable loss through cyclic charge exchange ($\mu^+ + M \rightleftharpoons Mu + M^+$) at lower moderator pressures (19, 20). Depending on the moderator, M, the muon thermalizes within about 20 ns in a paramagnetic Mu atom, in some larger parmagnetic species (though not in these experiments), or in one of many diamagnetic species.

Regardless of its environment, the positive muon decays with a mean life $\tau_\mu = 2.2$ μs, emitting a positron preferentially along its spin axis ($\mu^+ \rightarrow e^+ \nu_e \bar{\nu}_\mu$), which is detected in the experiment by plastic scintillators. In a transverse magnetic field, muons in different magnetic environments precess with different Larmor frequencies, so their asymmetric positron decay patterns also precess, giving rise to a muon spin rotation (μSR) signal, in analogy with NMR and ESR spectroscopies (18). Like these other techniques, μSR can distinguish between paramagnetic environments and diamagnetic ones but, unlike the situation in NMR, muons in different diamagnetic environments (bare muons, molecular ions, neutral molecules) cannot easily be resolved; the frequency resolution of μSR is limited to ~0.5 MHz by the short muon lifetime.

In the present study, molecular ions are the only reasonable possibility for the observed diamagnetic signals (15), an example of which is shown in Fig. 1 for ~10 ppm NH_3 in He. As is clear from this figure, the precessing decay asymmetry, $A(t)$, undergoes a two-component relaxation, which is fitted to the equation

$$[1] \quad A(t) = (A_f e^{-\lambda_f t} + A_s e^{-\lambda_s t}) \cos(\omega_D t + \phi_D)$$

where A_f and λ_f represent the initial amplitudes and relaxation rates ($\lambda = 1/T_2$) for the fast-relaxing component of the signal, while A_s and λ_s apply to the slow- or non-relaxing component. All parameters apply to muons in diamagnetic environments, precessing with Larmor frequency ω_D, and initial phase ϕ_D. The total initial amplitude is indicative of processes that occur during the slowing down of the μ^+ in the gas, whereas λ corresponds to interactions of the μ^+ ensemble with its environment after thermalization; in μSR as in NMR, (T_2) relaxation is due to loss of phase coherence in the time ensemble of precessing muons. In the present study, this is a result of the formation of a paramagnetic species, either the Mu atom itself via charge exchange, or a radical ion via a muon transfer process. The first case is actually much more common and accounts for the fast-relaxing component, as will be discussed below.

The moderator gases used in this experiment (He and Ne) were of UHP grade and were further purified by passing them through a trap filled with molecular sieve and cooled by liquid nitrogen. The reactant gases were generally of research grade (>99% pure) and were used without further treatment. However, the low concentrations of reactant gases used (≲100 ppm) indicates that impurities in the moderator are of far more concern than reactant impurities.

The target vessel was a 200-litre aluminum cylinder with a thin Kapton beam entrance window at one end. The large volume is necessary because the low stopping power of helium would allow muons to reach the walls of a smaller vessel, giving rise to unwanted diamagnetic signals. Even with such a large vessel, however, the slight wall signals present in some data made subsequent analysis very difficult. The target was placed between a pair of 1.5 m diameter Helmholtz coils providing a magnetic field of ~300 gauss, and two sets of scintillation counters to detect decay positrons plus a thin counter placed before the entrance window to detect incoming muons. These provided, respectively, the "stop" and "start" signals to a high frequency time-digitizer, which maintained a histogram of decay times used to extract the signal of interest (Fig. 1).

Results and kinetic model

We have measured μSR spectra for reactants "X" = NO, NH_3, N_2O, C_2H_4, O_2, CF_4, CH_3NO_2, and $(CH_3)_4Si$ (TMS) in He and Ne gas at or above 1 atm pressure. All exhibit spectra similar to that shown in Fig. 1, with a two-component relaxation. This observation of both slow (λ_s) and fast (λ_f) relaxations indicates that there are two groups of muons in diamagnetic environments. However, rather than being distributed between these groups initially, we contend that all the initial diamagnetic signal comes from a single muonated molecular ion species formed in a ro-vibrationally excited state during the slowing down process (15), with muons subsequently entering differing environments through competing reactions. Specifically, in gas M = He or Ne, the diamagnetic $[MMu^+]^*$ reacts with the dopant, X, by charge (electron) transfer with rate constant k_e, yielding muonium, or by muon transfer with rate constant k_μ, to form diamagnetic XMu^+ according to the kinetic scheme

$$[2] \quad [MMu^+]^* + X \xrightarrow{k_e} Mu + X^+ + M$$
$$[MMu^+]^* + X \xrightarrow{k_\mu} XMu^+ + M$$
$$[MMu^+]^* + M \xrightarrow{k_q} MMu^+$$

where a third reaction channel is included to account for reactions with the moderator, with rate constant $k_q[M]$, indentified as quenching of excited MMu^+.

In a μSR experiment, as mentioned earlier, relaxation of the experimental signal is due to spin dephasing, which, in the majority of cases, is accomplished only via the electron transfer reaction forming Mu in the kinetic scheme above. Since the ground state binding energies of $HeMu^+$ and $NeMu^+$ are approximately 1.5 and 1.8 eV respectively (21), charge transfer between a ground state ion and most reactants is endothermic, indicating that the molecular ion must react from a ro-vibrationally excited state, $[MMu^+]^*$. The importance of including a quenching channel is indicated by the data to be discussed and is expected also from current studies on the effect of vibrational excitation on ion–molecule reactivity (4–6).

As only a few million muons are used per experiment, and only one muon at a time is permitted in the target, the X and M species are in vast excess, allowing a straightforward analysis to give the concentration at time t of all diamagnetic species of the reaction scheme [2] as

$$[3] \quad [D]_t = [MMu^+]^*_0 \left(\frac{k_e[X]}{\lambda} e^{-\lambda t} + \frac{k_\mu[X] + k_q[M]}{\lambda} \right)$$

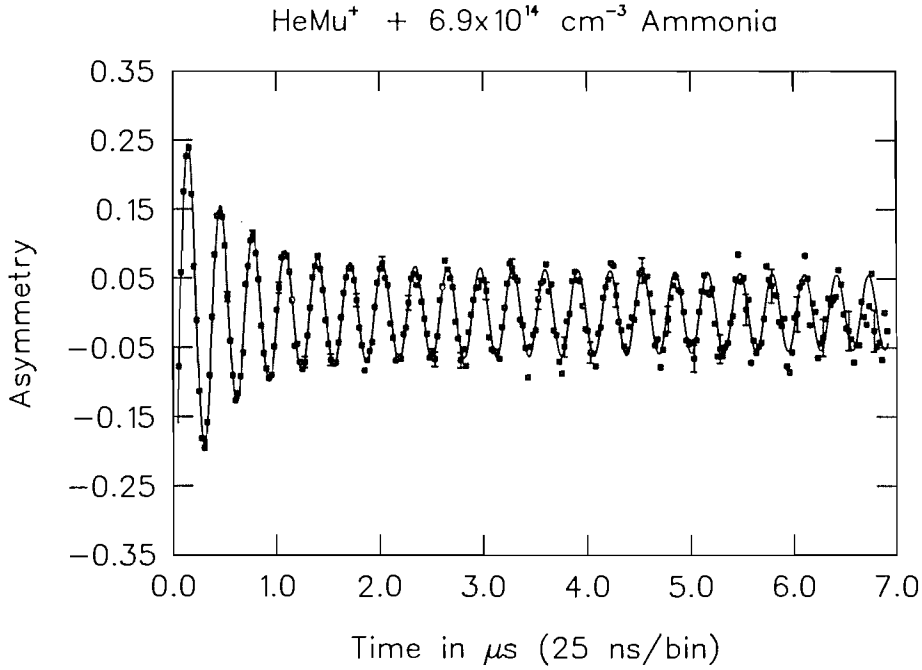

FIG. 1. A μSR "asymmetry" plot for ~10 ppm NH_3 added to He at 2280 Torr total pressure. The solid curve is a χ^2 fit of eq. [1] to the data, revealing the existence of two components: a quickly relaxing one and a very slowly relaxing one. The fast relaxation is due to charge exchange from a ro-vibrational excited state of a $[HeMu^+]^*$ molecular ion.

where λ is identified with the experimental λ_f and is given by $\lambda_f = (k_e + k_\mu)[X] + k_q[M]$. Thus a plot of λ_f vs. [X] gives a straight line with slope $k_e + k_\mu$ and intercept $k_q[M]$, which is indeed the case for all the gases investigated, as illustrated by Fig. 2, which shows the experimental values of λ_f for the reaction of $HeMu^+$ with nitromethane. Experimental values for $k_{exp} = k_e + k_\mu$ as well as values for k_q are listed in Table 1.

It may be noted that the rate constant for the reaction of NH_3 with $NeMu^+$ is much larger than that reported by us in ref. 15. At that time, the values reported for both X = CH_4 and NH_3 were based on earlier data of ref. 22, which were measured at much lower fields (~70 G) than used for the present measurements. Consequently, the two-component relaxations now observed were not resolved, leading to erroneously small ion–molecule relaxation rates in the case of NH_3. With improved apparatus and technique, the experimental errors in Table 1 are typically 10%, which are as good as or better than typical errors reported for related studies of ion–molecule reactivity (12–14).

Note that eq. [3] predicts a slow relaxation rate of exactly zero, but in fact there was always a finite slow relaxation observed, even in pure He or Ne. While this rate was usually ~0.05 μs^{-1}, commensurate with the inhomogeneity of the applied magnetic field, it was sometimes as high as 0.15 μs^{-1}. Such values for λ_s are indicative of additional relaxation processes affecting the products of muon transfer reactions, XMu^+ (15). They do not, however, interfere with the interpretation of λ_f and so will be ignored for the remainder of this paper.

Besides giving an interpretation for the relaxation λ_f, eq. [3] also shows that the ratio of the measured amplitudes from eq. [1] is $A_s/A_f = (k_\mu[X] + k_q[M])/k_e[X]$, indicating that a plot of A_s/A_f vs. $1/[X]$ should give a straight line with slope $k_q[M]/k_e$ and intercept k_μ/k_e. Such a plot for X = CF_4 is shown in Fig. 3, and the results of fitting such lines to the measured amplitudes are listed in Table 1 under the heading k_μ/k_e. This method of

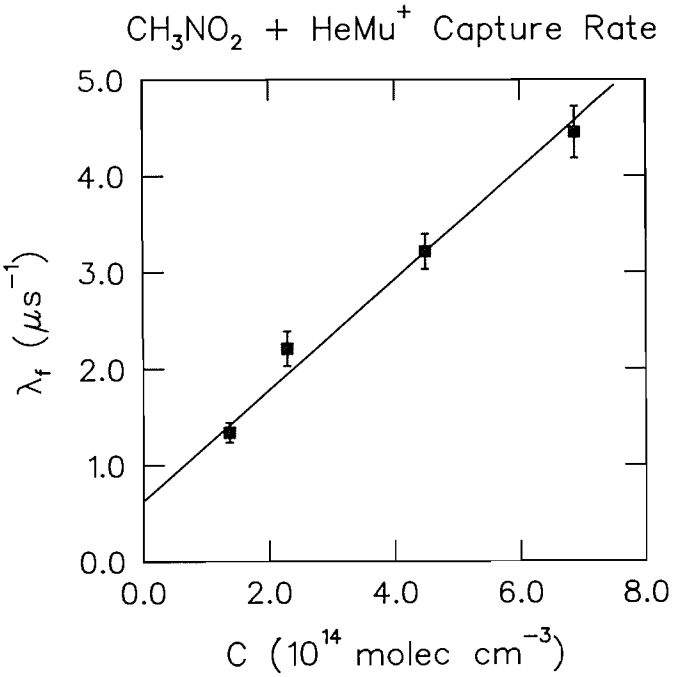

FIG. 2. A typical plot of the observed relaxation rate λ_f in nitromethane-doped helium vs. the concentration C of CH_3NO_2. The slope of the line gives the experimental capture rate constant $k_c = k_e + k_\mu$ for charge (k_e) and muon (k_μ) transfer reactions of the $[HeMu^+]^*$ molecular ion.

determining the relative importance of muon transfer and charge transfer fails in the case of X = NO in the present study, since the $NOMu^+$ ion formed is itself paramagnetic and leads to depolarization just as does the Mu formed by the electron transfer reaction. Thus, even though the amplitudes seem to indicate a value for $k_\mu/k_e = 0$, muon transfer may be quite prevalent in this particular case.

Can. J. Chem. Downloaded from www.nrcresearchpress.com by 112.217.228.212 on 09/07/12
For personal use only.

TABLE 1. Experimental results for the $[HeMu^+]^*$ and $[NeMu^+]^*$ + X reactions

Ion	X	I.P.[a]	ΔE[b]	k_{exp}[c]	k_q[c]	k_μ/k_e
$HeMu^+$						
	H_2	15.4	3.4[d]	0.0[e]	—	—
	NO	9.2	−2.9	14.6±0.3	2.6±0.5	−0.004±0.005
	N_2O	12.9	0.9	20.0±1.8	9.9±3.7	1.05±0.06
	NH_3	10.2	−1.8	34.7±1.3	0.8±0.9	0.14±0.02
	CH_3NO_2	11.1	−0.9	57.5±4.4	8.4±1.8	1.3±0.2
	TMS	9.9	−2.1	31.1±2.3	5.2±1.7	0.573±0.036
	CF_4	~13.0	~1.0	16.2±1.4	6.6±5.0	1.28±0.12
	C_2H_4[f]	10.5	−1.5	25.1±1.7	−2.1±2.2	1.09±0.05
$NeMu^+$						
	H_2	15.4	3.7[d]	0.0[e]	—	—
	NO	9.2	−2.6	9.2±0.4	1.4±2.0	0.012±0.009
	N_2O	12.9	1.2	11.3±1.1	12.±3.1	0.93±0.06
	O_2	12.1	0.35	6.4±0.4	2.4±1.3	0.030±0.016
	NH_3	10.2	−1.5	26.2±2.1	—	—
	CH_3NO_2	11.1	−0.6	41.6±4.1	−1.5±5.8	1.17±0.10
	TMS	9.9	−1.9	16.3±2.4	10.±7.	0.69±0.07
	CF_4	~13.0	~1.3	6.6±0.5	14.±4.7	0.390±0.031
	C_2H_4	10.5	−1.2	19.9±3.5	11.±8.	1.63±0.16

[a]First ionization points, in eV, taken from CRC Handbook of Chemistry and Physics, 1975 ed. Table E-74, except for CF_4, which was not given and was estimated from trends in the chloromethanes.
[b]Reaction endothermicities in eV; a negative value means that the reaction $MMu^+ + X \rightarrow M + Mu + X^+$ is exothermic from the *ground state* of the molecular ion.
[c]Experimental results from fits of eq. [1] to the data; k_{exp} in units of 10^{-10} cm^3 molec^{-1} s^{-1} and k_q in units of 10^{-15} cm^3 atom^{-1} s^{-1}.
[d]Charge exchange is endothermic for the bare μ^+.
[e]No relaxing component observed.
[f]Measured at a temperature of 125°C; all other measurements were made at room temperature, ~20°C.

Discussion and comparison with theory

What is not made clear in the kinetic scheme of [2] is that both charge transfer and muon transfer proceed from a single reaction in which the molecule, X, is captured by the molecular ion, MMu^+. For the case where the capture reaction is the limiting rate, the capture rate constant is given by $k_c = k_\mu + k_e$, which is exactly k_{exp} of the previous section. The capture rate is amenable to theoretical analysis (7–10), of which the most elementary treatment gives the Langevin rate constant (23), which is determined solely by the charge – induced dipole interaction and has the form

$$[4] \quad k_L = 2\pi q\sqrt{\frac{\alpha}{\mu}}$$

where α is the isotropic polarizability of the atom or molecule and μ is the reduced mass of the colliding pair. If the neutral molecule also possesses a permanent dipole moment, μ_D, the orientation of the dipole towards the charge adds a second term to the rate constant, the sum of both terms being conveniently written as

$$[5] \quad k_{ADO} = k_L\left(1 + c\mu_D\sqrt{\frac{2}{\alpha\pi k_B T}}\right)$$

where c is a "locking constant," frequently interpreted as some average orientation of the dipole, after the Average Dipole Orientation (ADO) theory of Su and Bowers (10). Although the ADO theory has been criticized for not taking angular momentum conservation properly into account (8, 9), it has been remarkably successful over the years at describing a wide variety of reactions in ion–molecule chemistry (1). Angular momentum conservation has been taken into account in an approximate way in the AADO version of the theory (8–10), which tends to increase the basic ADO rate constants by about 10%.

There have since been other, more advanced, treatments, including the classical derivations of Sakimoto and of Bates (9), in which total angular momentum transfer has been taken into account in a self consistent way, as well as TST (7) and trajectory calculations (24) of ion–molecule collision rates. In addition to these classical or semiclassical treatments, there are recent quantum calculations due to Clary (8), which, like the ADO and the AADO calculations, are based on a capture approximation (ACSA) with the potential again being dominated by the long range dipolar interaction. As pointed out by Troe (7), Clary's treatment is formally akin to a TST approach. Indeed, Troe's statistical theory in its high pressure limit and Clary's ACSA calculation give very similar results for ion–molecule reactivity, both agreeing with the simple ADO prediction of Su and Bowers at room temperature. That is the crucial point: while at low temperatures there can be marked differences between the different theories cited above, they give essentially the same results as the simpler ADO treatment at room temperature. Therefore, in this paper, our room temperature experimental capture rates are compared with ADO predictions. In a later publication we shall present results on the temperature dependence of these rates (17). In regard to comparisons with ADO, it is worth emphasizing that the theoretical ADO capture rate gives only the maximum possible (classical) rate, and subsequent reaction pathways may appreciably alter chemical reactivity with the result that k_{exp} may be considerably different from the theoretical maximum; the general expectation, then, is for $k_{exp} \leq k_{ADO}$.

Can. J. Chem. Downloaded from www.nrcresearchpress.com by 112.217.228.212 on 09/07/12
For personal use only.

TABLE 2. Comparison of experimental[a] and theoretical[b] rate constants for $[HeMu^+]^*$ and $[NeMu^+]^* + X$

X	α[c]	μ_D[d]	$[HeMu^+]^*$ k_{exp}	$[HeMu^+]^*$ k_{ADO}	$[NeMu^+]^*$ k_{exp}	$[NeMu^+]^*$ k_{ADO}
TMS	11.9	0.00	31.1±2.3	41.0	16.3±2.4	20.0
CF_4	~5.0[e]	0.00	16.2±1.4	~26.4	6.6±0.5	~12.9
C_2H_4	4.22	0.00	25.1±1.7[f]	25.5	19.9±3.5	14.0
O_2	1.60	0.00	—	15.6	6.4±0.4	8.4
NO	1.77	0.16	14.6±0.3	16.7	9.2±0.4	9.1
N_2O	3.00	0.17	20.0±1.8	21.1	11.3±1.1	11.0
NH_3	2.22	1.48	34.7±1.3	35.4	26.2±2.1	21.2
CH_3NO_2	4.94	3.50	57.5±4.4	67.8	41.6±4.1	34.1

[a]Experimental values taken from Table 1; all rate constants in units of 10^{-10} cm^3 molec^{-1} s^{-1}.
[b]Theoretical values calculated from eq. [5].
[c]Isotropic polarizabilities in Å^3, taken from several sources, including those in those in refs. 26 and 27; in some cases calculated from refractive indices using the Clausius–Mosotti equation.
[d]Electric dipole moments in debyes, taken from several sources, including those in ref. 27.
[e]Value for CF_4 not known to us and is therefore estimated from trends in the chloromethanes; likely uncertainty ~ ±30%.
[f]Measured at a temperature of 125°C; all other measurements were made at room temperature, ~20°C.

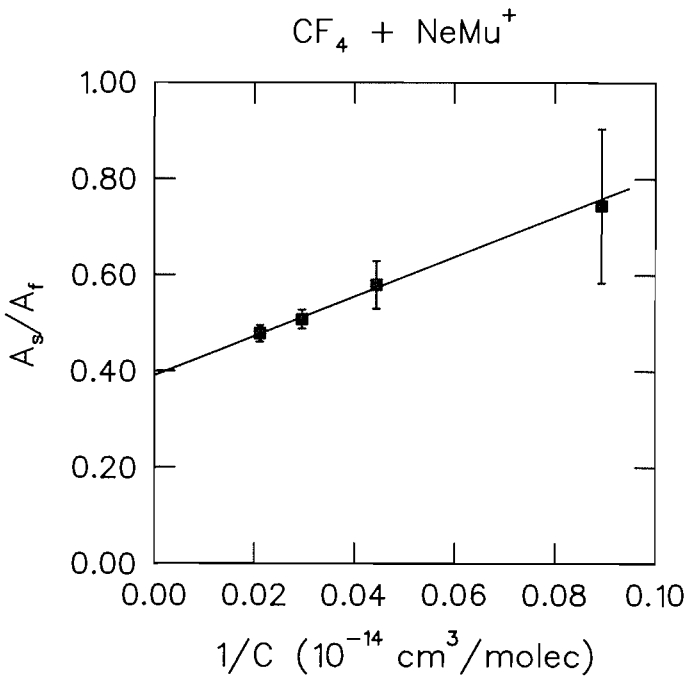

FIG. 3. A typical plot of the ratio of the observed amplitudes for the slow (A_s) and fast (A_f) relaxing components of the signal for CF_4 in 800 Torr neon vs. the inverse of the concentration of added CF_4. The slope of the line is related to a rate constant for quenching $[NeMu^+]^*$ and the intercept gives the ratio of rate constants for muon transfer to charge transfer, k_μ/k_e.

Table 2 shows the comparison between the experimental rate constants ($k_c = k_{exp} = k_e + k_\mu$) for $HeMu^+$ and $NeMu^+ + X$ taken from Table 1 with the values calculated from the polarizabilities and dipole moments (also listed in Table 2) using the ADO (or Langevin) theory of eqs. [4] and [5]. The entries in Table 2 are consistent with what is qualitatively expected based on current understanding of ion–molecule reactions. In every case the $[HeMu^+]^*$ reacts faster than $[NeMu^+]^*$, as expected from the reduced mass dependence of eq. [5]. The magnitudes of the polarizability α and the dipole moment μ_D of the target molecule seem to be the most important factors in determining the reactivity of these muon ions; e.g., TMS, with the largest polarizability, gives the fastest reaction rate among molecules with zero dipole moment, whereas CH_3NO_2, with the largest dipole moment (and also a large polarizability), gives the largest reaction rate seen. This dependence seems to be far more important generally than the ~1 eV variation in ionization potential, and thus in reaction exothermicity, between different reactant molecules.

The fact that the μSR results shown in Table 2 generally agree well with the ADO predictions means that the ion–molecule reactivity for these rare gas molecular ions is indeed dominated by the classical orbiting (dipole) radius and that other processes must play only a minor role. This conclusion is consistent with a wide body of other ion–molecule reactions (at 300 K) where the remarkable level of agreement frequently found between experiment and the ADO prediction is now well established (1, 8–10, 14). This level of agreement also verifies that the initial diamagnetic state in the present experiments is a $NeMu^+$ or $HeMu^+$ ion; were the initial ion a bare μ^+, for example, the measured rates would be faster by about a factor of 6 (He) to 13 (Ne) due to the lighter mass, and there would not be the observed consistent difference between He and Ne moderators.

Although the rate we measure experimentally is the overall capture rate, the presence of the charge transfer reaction is essential for the observation of any depolarization and, thus, for the measurement of the capture rate. Examination of the reaction exothermicities listed in Table 1, however, makes it clear that charge transfer occurs in cases where it is energetically disallowed for a ground state $NeMu^+$ or $HeMu^+$, namely O_2, N_2O, and CF_4, while it does not occur in the case of H_2 where charge exchange is endothermic even for a bare μ^+. This confirms the availability of extra excitation energy necessary for the reaction, which we have ascribed earlier to ro-vibrational excitation of $[HeMu^+]^*$ and $[NeMu^+]^*$. It can be noted that we have assumed charge exchange at thermal energies leads to a three-body final state (eq. [2]), which is favoured by phase space arguments, but a two-body final state formed by $[MMu^+]^* + X \rightarrow Mu + XM^+$ might also be possible: this could provide another source of reaction exothermicity, since XM^+ can be expected to be bound by a few electron volts (25). On the

Can. J. Chem. Downloaded from www.nrcresearchpress.com by 112.217.228.212 on 09/07/12
For personal use only.

TABLE 3. The rate constants k_c, k_μ, and k_e for $[HeMu^+]^*$ and $[NeMu^+]^*$ + X compared with available proton data

		Muonated ions				Protonated ions		
	X	k_c[a]	k_e	k_μ		k_c	k_e	k_p
$HeMu^+$					HeH^+			
	NO	14.6±0.3	14.7±0.4	−0.05±0.07				
	N_2O	20.0±1.8	9.8±0.9	10.2±1.0				
	O_2	~12[b]	~12	~0		11±2[c]	0	11
	NH_3	34.7±1.3	30.3±1.3	4.4±0.6				
	CH_3NO_2	57.5±4.4	25.0±2.9	32.5±3.3				
	TMS	31.1±2.3	19.8±1.5	11.3±1.0				
	CF_4	16.2±1.4	7.1±0.7	9.1±0.9				
	C_2H_4	25.1±1.7[d]	12.0±0.8	13.1±0.9		28±5[e]	15	13
$NeMu^+$					NeH^+			
	NO	9.2±0.4	9.1±0.4	0.11±0.08				
	N_2O	11.3±1.1	5.8±0.6	5.5±0.6				
	O_2	6.4±0.4	6.2±0.4	0.19±0.10				
	CH_3NO_2	41.6±4.1	19.2±2.1	22.4±2.4				
	TMS	16.3±2.4	9.6±1.5	6.6±1.0				
	CF_4	6.6±0.5	4.74±0.35	1.85±0.17				
	C_2H_4	19.9±3.5	7.6±1.4	12.3±2.2		18±4[e]	8	10

[a]The capture rate constant, taken from Table 1 k_{exp}; all rate constants have units of 10^{-10} cm^3 molec^{-1} s^{-1}.
[b]Reaction rate not measured, but estimated by scaling the $NeMu^+$ result according to the mass dependence of eq. [5].
[c]Results of Bohme and co-workers (12).
[d]Measured at a temperature of 125°C; all other measurements were made at room temperature, ~20°C.
[e]Results of Smith and Futrell (13).

Can. J. Chem. Downloaded from www.nrcresearchpress.com by 112.217.228.212 on 09/07/12
For personal use only.

other hand, the existence of this reaction channel is not indicated by results from the corresponding protonated ion studies (12–14), where the observation of charge exchange is the rare exception.

In regard to quenching of the excited states, we may expect that values of k_q[M] be independent of X. While this appears not to be the case at first glance from the values in Table 1, it should be noted that a large error in the intercept (~0.3 μs) can result from a relatively small error in the slope, making it particularly difficult to establish the value of small intercepts. Allowing for an error of this magnitude, one can indeed conclude that k_q is constant for essentially all X in Table 1 with an average value of $\bar{k}_q = (2.8 \pm 0.4) \times 10^{-15}$ cm^3 atom^{-1} s^{-1}, consistent with what would be expected for quenching by He and Ne (5, 6). The model we have used of a single excited state and a single quenching reaction is undoubtedly an oversimplification. For the more realistic case with a number of excitation levels it is quite reasonable to expect that different reactants, sensitive to different levels of excitation, would yield different values for "k_q". In the extreme case of a reactant such as NO, which can react with a ground state MMu^+ ion by either charge exchange or muon transfer, the measured k_q should be zero (i.e., quenching should have no effect.) The values tend to support this, but the scatter in the k_q values makes any conclusion uncertain. It is not entirely clear that our measured intercepts *are* due to quenching. Small concentrations of impurities that react predominantly via muon transfer would account for the observed values, and for their nonreproducibility. The meaning of the intercepts for λ_f must be left an open question.

As noted above, charge exchange is rarely seen in studies of the reactivity of protonated ions; proton transfer is the overwhelmingly dominant reaction channel. The present study of muonated ions indicates that both electron and muon (proton) transfer are prevalent. Using the ratios of k_μ/k_e listed in Table 1, as determined from the experimental amplitudes, values for k_μ and k_e were calculated, and are shown in Table 3 with relevant proton ion results from the literature. Such corresponding studies are few, as is made apparent by the sparseness of those columns in Table 3. Only the tandem ICR work of Smith and Futrell (13) has been sensitive to both charge exchange and proton transfer but, unfortunately, only their results for C_2H_4, reacting with HeH^+ and NeH^+, are comparable with the muonated ion results reported herein. Nevertheless, the agreement is exemplary: both the proton/muon transfer rates and the charge transfer rates are in agreement. While a difference in the charge transfer rates was not expected, some isotope effect on the proton/muon transfer rate could have been. The other protonated ion study cited in Table 3, due to Bohme and co-workers (12), measured the proton transfer rate constant for $O_2 + HeH^+$. Unfortunately, we have only measured the reaction of $O_2 + NeMu^+$ and have had to estimate a rate constant for the $O_2 + HeMu^+$ reaction from that result based on the difference in reduced mass. Even with the uncertainty due to this method, however, one feature is striking: Bohme observed only proton transfer while we saw *no* muon transfer, only charge exchange. While this may be due to differences between the $HeMu^+$ and $NeMu^+$ ions, it is more probably a result of differences in excitation; the muon ion results involve excited $NeMu^+$ while the proton ion results are for ground state ions, for which the charge exchange reaction is endothermic. The good agreement between the present work and both sets of proton ion data, considering the vastly different pressure regimes utilized, indicates that total pressure plays a negligible role in ion–molecule reactivity, in contrast to the suggestions of ref. 16. While these comparisons are useful, the relative lack of data for the corresponding

reactions of the HeH^+ and NeH^+ ions frustrates the potentially important broad comparisons that could otherwise be made with the present μSR results.

As noted, the present report is a subset of a larger body of data (17) for the formation, quenching, and ion–molecule reactivity of the muonated rare gases $[HeMu^+]^*$, $[NeMu^+]^*$, as well as $[ArMu^+]^*$, although fast relaxations are rarely seen in Ar. Some reactants are characterized by curved kinetic plots, pointing to more complex kinetic schemes than the one utilized here. Others, such as CH_4, give no fast relaxation when charge exchange is energetically allowed, indicating a dominant muon transfer channel. While, generally, agreement with the ADO theory remains good for this wider data set, there are notable exceptions that are still under consideration and will be discussed in a later paper. We have also measured temperature dependent reaction rates of $[NeMu^+]^*$ and $[HeMu^+]^*$ with a variety of reactants over the range ~100–500 K. In some cases there is good agreement with the ADO predictions, but others, such as $C_2H_4F_2$, react much faster than expected at lower temperatures. This work will also be reported in due course.

Acknowledgements

One of us (D. G. Fleming) would like to thank the Canada Council for the award of a Killam Research Fellowship for 1987–1989. The continued financial support of the Natural Sciences and Engineering Research Council of Canada is also gratefully acknowledged.

1. N. G. Adams and D. Smith; W. Lindinger and D. Smith. *In* Reactions of small transient species: kinetics and energetics. *Edited by* A. Fontijn and M. A. A. Clyne. Academic Press, London. 1983. Chaps. 6, 7.
2. P. R. Kemper, L. M. Bass, and M. T. Bowers. J. Phys. Chem. **89**, 1105 (1985); P. R. Kemper and M. T. Bowers. Int. J. Chem. Kinet. **11**, 707 (1984).
3. E. E. Ferguson, D. Smith, and N. G. Adams. J. Chem. Phys. **81**, 742 (1984); E. E. Ferguson, N. G. Adams, D. Smith, and E. Alge. J. Chem. Phys. **80**, 6095 (1984); E. E. Ferguson, D. Smith, and N. G. Adams. Int. J. Mass Spectrom. Ion Phys. **57**, 243 (1984).
3. E. E. Ferguson, D. Smith, and N. G. Adams. J. Chem. Phys. **81**, 742 (1984); E. E. Ferguson *et al.* J. Chem. Phys. **80**, 6095 (1984); E. E. Ferguson *et al.* Int. J. Mass Spectrom. Ion Phys. **57**, 243 (1984).
4. K. Tanaka, T. Kato, and I. Koyano. J. Chem. Phys. **84**, 750 (1986); I. Kusunoki and T. Ishikawa. J. Chem. Phys. **82**, 499 (1985).
5. I. Dotan, S. E. Barlow, and E. E. Ferguson. Chem. Phys. Lett. **121**, 38 (1985); M. Durup-Ferguson, H. Bohringer, D. W. Fahey, F. C. Fehsenfeld, and E. E. Ferguson. J. Chem. Phys. **81**, 2657 (1984).
6. E. E. Ferguson. J. Phys. Chem. **90**, 731 (1986).
7. J. Troe. Chem. Phys. Lett. **122**, 425 (1985); F. Celli, G. Weddle, and D. P. Ridge. Chem. Phys. Lett. **73**, 801 (1980).
8. D. C. Clary. Mol. Phys. **54**, 605 (1985); D. C. Clary, D. Smith, and N. G. Adams. Chem. Phys. Lett. **119**, 320 (1985).
9. K. Sakimoto. Chem. Phys. Lett. **85**, 273 (1984); D. R. Bates. Chem. Phys. Lett. **111**, 428 (1984).
10. T. Su and M. T. Bowers. *In* Gas phase ion chemistry. Vol. I. *Edited by* M. T. Bowers. Academic Press, New York. 1979. p. 83; T. Su and M. T. Bowers. Int. J. Mass Spectrom. Ion Phys. **17**, 211 (1975); **12**, 347 (1973).
11. J. Barassin, C. Reynaud, and A. Barassin. Chem. Phys. Lett. **123**, 191 (1986); H. Bohringer. Chem. Phys. Lett. **122**, 185 (1985); N. G. Adams, D. Smith, and E. E. Ferguson. Int. J. Mass Spectrom. Ion Phys. **67**, 67 (1985).
12. G. I. MacKay, H. I. Schiff, and D. K. Bohme. Can. J. Chem. **59**, 1771 (1981); D. K. Bohme, G. I. MacKay, and H. I. Schiff. J. Chem. Phys. **73**, 4976 (1980).
13. R. D. Smith and J. H. Futrell. Int. J. Mass Spectrom. Ion Phys. **20**, 33 (1976); **20**, 43 (1976); **20**, 59 (1976); **20**, 71 (1976).
14. V. G. Anicich and W. T. Huntress, Jr. A survey of bimolecular ion–molecule reactions. J.P.L. Report, Calif. Inst. of Technology, Pasadena, CA. Jan. 1986.
15. D. G. Fleming, R. J. Mikula, M. Senba, D. M. Garner, and D. J. Arseneau. Chem. Phys. **82**, 75 (1983).
16. A. A. Viggiano. J. Chem. Phys. **84**, 244 (1986); D. R. Bates. J. Chem. Phys. **83**, 4448 (1985); R. Patrick and D. M. Golden. J. Chem. Phys. **82**, 75 (1985); P. A. M. van Koppen, M. F. Jarrold, M. T. Bowers, L. M. Bass, and K. R. Jennings. J. Chem. Phys. **81**, 288 (1984).
17. D. J. Arseneau. Ph.D. thesis, Univ. of British Columbia, in progress.
18. R. H. Heffner and D. G. Fleming. Phys. Today, Dec. 1984. p. 30.
19. D. G. Fleming, R. J. Mikula, and D. M. Garner. Phys. Rev. A: **26**, 2527 (1982); D. G. Fleming. Proc. of XIIth ICPEAC, North Holland Press, Amsterdam. *Edited by* S. Datz. 1983. p. 297; D. G. Fleming, R. J. Mikula, and D. M. Garner. Hyperfine Interact. **9**, 207 (1979).
20. D. G. Fleming and M. Senba. Atomic physics with positrons. *Edited by* J. W. Humbertson and E. A. G. Armour. Plenum Press, London. 1987. p. 343; R. E. Turner and M. Senba. J. Chem. Phys. **84**, 3776 (1986).
21. P. G. Fournier and R. J. Le Roy. Chem. Phys. Lett. **110**, 487 (1984); P. G. Fournier and B. Lassier-Govers. J. Phys. Lett. **43**, L483 (1983).
22. R. J. Mikula. Ph.D. thesis, Univ. of British Columbia, 1981; R. J. Mikula, D. G. Fleming, and D. M. Garner. Hyperfine Interact. **6**, 379 (1979).
23. G. Gioumousis and D. P. Stevenson. J. Chem. Phys. **29**, 294 (1958).
24. P. K. Bhowmik and T. Su. J. Chem. Phys. **84**, 1432 (1986); T. Su and W. J. Chesnavich. J. Chem. Phys. **76**, 5183 (1982); W. J. Chesnavich, T. Su, and M. T. Bowers. J. Chem. Phys. **72**, 2644 (1980).
25. K. K. Huber and G. Herzberg. Constants of diatomic molecules. Van Nostrand Press, Princeton, NJ. 1979.
26. S. Y. Liu and C. E. Dykstra. Chem. Phys. Lett. **119**, 407 (1985); M. Gupta and S. Bhattacharyja. J. Chem. Soc. Faraday Trans. **80**, 1405 (1984); D. M. Bishop and A. Cartier. Chem. Phys. Lett. **95**, 250 (1983).
27. P. W. Atkins. Physical chemistry. 2nd ed. W. H. Freeman, 1982. p. 773; R. S. Berry, S. A. Rice, and J. Ross. Physical chemistry. John Wiley and Sons, New York. 1980. pp. 410, 411; R. C. Weast (*Editor*). Handbook of chemistry and physics. 55th ed. CRC Press, Cleveland, OH. 1975. Tables C75, E63, and E220.

Can. J. Chem. Downloaded from www.nrcresearchpress.com by 112.217.228.212 on 09/07/12
For personal use only.

Photolysis of, and the reactions of H-atoms with, isopropanethiol

W. W. LAM, T. YOKOTA, I. SAFARIK, AND O. P. STRAUSZ[1]

Department of Chemistry, University of Alberta, Edmonton, Alta., Canada T6G 2G2

Received November 27, 1987

This paper is dedicated to Professor Charles A. McDowell on the occasion of his seventieth birthday

W. W. LAM, T. YOKOTA, I. SAFARIK, and O. P. STRAUSZ. Can. J. Chem. **66**, 2025 (1988).

Detailed investigation of the photolysis of i-C_3H_7SH has been carried out in the absence and presence of the inert gas, n-C_4H_{10}. A mechanism consisting of three primary photochemical steps: i-$C_3H_7SH \xrightarrow{[1]} i$-$C_3H_7S$ + H, $\phi_1 = 0.93 \pm 0.02$; i-$C_3H_7SH \xrightarrow{[2]} i$-$C_3H_7$ + SH, $\phi_2 = 0.057 \pm 0.024$; i-$C_3H_7SH \xrightarrow{[3]} H_2S + C_3H_6$, $\phi_3 = 0.009 \pm 0.001$; six hot reaction steps and seven thermal reaction steps adequately explains all the experimental observations. As in the case of hot H* atoms both the H-atom abstraction, H + i-$C_3H_7SH \xrightarrow{[7]} H_2 + i$-$C_3H_7S$, and the SH-displacement, H + i-$C_3H_7SH \xrightarrow{[8]} H_2S + i$-$C_3H_7$, reactions occur with thermalized H-atoms, with the rate constant ratio $k_7/k_8 = 19.2 \pm 4.3$ at 25°C. The Arrhenius expressions have been determined over the temperature range 25–145°C, to be: $k_7 = (4.0 \pm 0.7) \times 10^{12} \exp[(-1066 \pm 43)/RT]$ and $k_8 = (2.8 \pm 0.6) \times 10^{12} \exp[(-2597 \pm 114)/RT]$ cm^3 mol^{-1} s^{-1}. It was found that the overall mechanism for the photolytic decomposition of i-C_3H_7SH is analogous to that established for C_2H_5SH in previous investigations.

W. W. LAM, T. YOKOTA, I. SAFARIK et O. P. STRAUSZ. Can. J. Chem. **66**, 2025 (1988).

Opérant en présence et en l'absence du gaz inerte n-C_4H_{10}, on a effectué une étude détaillée de la photolyse du i-C_3H_7SH. On peut expliquer toutes les observations expérimentales en faisant appel à trois étapes photochimiques primaires : i-$C_3H_7SH \xrightarrow{[1]} i$-$C_3H_7S$ + H, $\phi_1 = 0{,}93 \pm 0{,}02$; i-$C_3H_7SH \xrightarrow{[2]} i$-$C_3H_7$ + SH, $\phi_2 = 0{,}057 \pm 0{,}024$; i-$C_3H_7SH \xrightarrow{[3]} C_3H_6 + H_2S$, $\phi_3 = 0{,}009 \pm 0{,}001$; à six étapes réactionnelles chaudes et à sept étapes réactionnelles thermiques. Comme on l'a observé avec les atomes de H*, les atomes de H thermalisés donnent aussi lieu à des réactions d'abstraction d'atomes de H, i-C_3H_7SH + H $\xrightarrow{[7]} i$-$C_3H_7S + H_2$ ainsi qu'à des réactions de substitution des SH, i-C_3H_7SH + H $\xrightarrow{[8]} i$-$C_3H_7 + H_2S$ à 25°C, le rapport des constantes de vitesse $k_7/k_8 = 19{,}2 \pm 4{,}3$. Aux températures allant de 25 à 145°C, on a déterminé que les expressions d'Arrhénius doivent être représentées par les expressions $k_7 = (4{,}0 \pm 0{,}7) \times 10^{12} \exp[(-1066 + 43)/RT]$ et $k_8 = (2{,}8 \pm 0{,}6) \times 10^{12} \exp[(2597 \pm 114)/RT]$ cm^3 mol^{-1} s^{-1}. On a trouvé que le mécanisme global de la décomposition photolytique du i-C_3H_7SH est analogue à celui qui avait été proposé antérieurement pour le C_2H_5SH.

[Traduit par la revue]

Introduction

The gas-phase photolytic decomposition of simple alkane thiols has already been utilized for generating hydrogen atoms and thiyl radicals long ago (1, 2). Their formation was explained by simple S—H cleavage

$$RSH + h\nu \rightarrow RS + H$$

which was followed by

$$H + RSH \rightarrow H_2 + RS$$

$$2RS \rightarrow R_2S_2$$

In later studies H_2S (3, 4), alkane, and the corresponding alkene (5–9) were also detected as photolysis products indicating a more complicated mechanism.

Systematic in depth studies of the gas-phase photolysis of C_2H_5SH by the research groups of Steer and Knight (5, 6), White *et al.* (7, 8), and Lam *et al.* (9) revealed that the formation and the distribution of all the photolysis products can be accounted for by three primary photochemical reactions:

$$C_2H_5SH + h\nu\ (254\ nm) \rightarrow H^* + C_2H_5S$$
$$\rightarrow HS + C_2H_5^*$$
$$\rightarrow H_2S + C_2H_4$$

It has also been proven that H atoms and C_2H_5 radicals are formed with substantial excess energy and enter into hot reactions

$$C_2H_5^* \rightarrow C_2H_4 + H$$
$$C_2H_5^* + C_2H_5SH \rightarrow C_2H_6 + C_2H_5S$$
$$C_2H_5^* + M \rightarrow C_2H_5 + M$$
$$H^* + C_2H_5SH \rightarrow H_2 + C_2H_5S$$
$$\rightarrow H_2S + C_2H_5$$
$$H^* + M \rightarrow H + M$$

Finally the following thermal reactions complete the mechanism:

$$C_2H_5 + C_2H_5SH \rightarrow C_2H_6 + C_2H_5S$$
$$H + C_2H_5SH \rightarrow H_2 + C_2H_5S$$
$$\rightarrow H_2S + C_2H_5$$
$$HS + C_2H_5S \rightarrow C_2H_5SSH$$
$$2C_2H_5SSH \rightarrow 2C_2H_5SH + S_2(wall)$$
$$C_2H_5S + C_2H_5S \rightarrow C_2H_5SSC_2H_5$$
$$\rightarrow C_2H_4S + C_2H_5SH$$

In our systematic studies of the photolysis of simple alkane thiols we have investigated the photolysis of isopropanethiol. Nothing has yet been reported on the mechanism of the photolysis of isopropanethiol in the literature and we hoped to reveal the effect, if any, of the methyl substitution on the primary or secondary reactions. The results of our investigations are summarized in this paper.

[1]Author to whom all correspondence is to be addressed.

Can. J. Chem. Downloaded from www.nrcresearchpress.com by 112.217.228.212 on 09/07/12
For personal use only.

TABLE 1. Average product quantum yields in the photolysis of pure i-C_3H_7SH and C_2H_5SH[a]

Substrate	$\phi(H_2)$	ϕ(alkane)[b]	$\phi(H_2S)$	ϕ(alkene)[b]	ϕ(disulfide)[b]
i-C_3H_7SH	0.80 ± 0.03	0.21 ± 0.02	0.24 ± 0.02	0.042 ± 0.004	0.81 ± 0.07
C_2H_5SH	0.77 ± 0.02	0.22 ± 0.02	0.24 ± 0.03	0.030 ± 0.005	0.92 ± 0.05

[a]From ref. 9.
[b]Alkane = C_3H_8 or C_2H_6; alkene = C_3H_6 or C_2H_4; disulfide = $(i\text{-}C_3H_7)_2S_2$ or $C_2H_5SSC_2H_5$.

Experimental

Experiments were carried out in a grease-free conventional high vacuum system. The light source was a medium-pressure Hg lamp (Hanovia, Type SH, model 45078) equipped with a 253.7 nm interference filter (Baird Atomic). A cylindrical quartz reaction vessel, 5 × 10 cm, was employed and was enclosed in an aluminum block furnace heated by two pencil heaters. A 4-in. focal length quartz lens was placed between the lamp and the reaction vessel to collimate the light. The sample storage bulb was surrounded by a small temperature-controlled metallic jacket which could be cooled by tap water between experiments. The entire reaction system was fitted inside a thermostatted box and the temperature was monitored by standard Fe–constantan thermocouples. Reagent pressures were measured with a MKS Baratron absolute pressure gauge for 0–100 Torr and an absolute pressure Bourdon gauge (Matheson) for pressures greater than 100 Torr.

Research-grade i-C_3H_7SH (Aldrich) was purified by distillation in two stages at −88.5 and −95°C. The middle portion from the latter was retained and stored in the sample reservoir after purity test by GC/MS. Research-grade n-C_4H_{10} (Phillips), 99.97%, was used without further purification.

After a 60 min photolysis, H_2 was passed over traps at −196 and −210°C and was measured in a gas buret while H_2S, C_3H_6, C_3H_8, and $(i\text{-}C_3H_7)_2S_2$ were condensed at −196°C. H_2S, C_3H_6, and C_3H_8 were distilled at −95°C and analysed on a 6-ft Porapak Q:QS (1:1), 80/100 mesh, 6 mm o.d. glass column at 59°C. $(i\text{-}C_3H_7)_2S_2$ was analysed on a 6-ft, 12% tricresylphosphate, WAW–DMCS, 80/100 mesh column at 80°C.

When n-C_4H_{10} was present in the reaction mixture, the products condensable at −196°C were distilled in two stages at −117°C, for H_2S, C_3H_6, and C_3H_8. n-C_4H_{10} and substrate i-C_3H_7SH were distilled at −95°C.

Chemical actinometry was performed using H_2S as the actinometer on a separate set-up along an optical bench. The optical train consisted of a medium-pressure Hg lamp (Hanovia), a 1-cm aperture, a 253.7 nm interference filter (Baird Atomic), a quartz lens, a 5 × 10 cm, cylindrical quartz reaction vessel, a 5 × 10 cm, cylindrical quartz actinometer vessel, a monochromator (Bausch & Lomb; gratings = 2 700 grooves mm^{-1}), and a photocell connected to a readout meter, in this order. The aperture was employed to obtain better collimation of the light. The products from the reaction vessel were analyzed in the same manner as those in the main experiments. H_2 produced in the actinometry vessel was collected and measured in a gas buret while unreacted H_2S was kept in a trap at −196°C.

Results

The gas phase UV absorption spectrum of i-C_3H_7SH is a broad band in the 220–260 nm range with maximum absorbance located near 225 nm. The extinction coefficient at 254 nm is about 4.17×10^{-3} $Torr^{-1}$ cm^{-1} at 298 K, after the background for reflection by the quartz cell is taken into account.

In the photolysis total product conversion was maintained low, at 2–6%, in order to minimize secondary absorption by H_2S and $(i\text{-}C_3H_7)_2S_2$. Under these circumstances over 95% of the incident light was absorbed by i-C_3H_7SH.

H_2S actinometry

The absorbed light intensity in the reaction cell was determined experimentally by H_2S actinometry. The absorbed light intensity in the actinometric cell is equal to the rate of H_2 production since $\phi(H_2) = 1.00$ in the photolysis of H_2S (10–12).

From the results of the actinometric measurements the average value for $[R(H_2) + R(C_3H_8)]/I_a$ was found to be 1.01 ± 0.04. Therefore, the absorbed light intensity in the reaction cell, I_a, is equal to $0.99[R(H_2) + R(C_3H_8)]$. All the quantum yields obtained from the photolysis of i-C_3H_7SH were calculated by the relation $\phi_i = R_i/I_a$, where R_i (i = H_2, C_3H_8, H_2S, C_3H_6, and $(i\text{-}C_3H_7)_2S_2$) is the rate of product formation.

Photolysis of pure isopropanethiol

The major photolysis products were H_2 and $(i\text{-}C_3H_7)_2S_2$, while the minor products were C_3H_8, H_2S, and C_3H_6. The dark reaction runs at 25 and 145°C did not produce any measurable products, thus, i-C_3H_7SH is thermally stable within this temperature range. It was also observed that increasing reaction times up to 120 min did not affect the quantum yields. The quantum yields of these products from 60-min photolysis were observed to be independent of the substrate pressure in the range 5–50 Torr. The values of the product quantum yields averaged over the entire pressure range studied are listed in Table 1. The product yields of the photolysis of pure C_2H_5SH from our previous studies are also given in this table for comparison.

Photolysis of isopropanethiol with added thermalizer, n-C_4H_{10}

The effects of added thermalizer, n-C_4H_{10}, on the product quantum yields were investigated in this series of experiments. The pressure of i-C_3H_7SH was kept constant at 20 Torr while the pressure of n-C_4H_{10} was varied between 28 and 400 Torr. It was observed that with increasing pressure of the thermalizer $\phi(H_2)$ and $\phi[(i\text{-}C_3H_7)_2S_2]$ increased gradually along with a concomitant decline in the values of $\phi(C_3H_8)$, $\phi(H_2S)$, and $\phi(C_3H_6)$, but the sum of $R(H_2)$ and $R(C_3H_8)$ remained invariant at $(8.6 \pm 0.5) \times 10^{-2}$ μmol min^{-1}. The quantum yields of all products reach limiting values at approximately a fifteenfold excess of n-C_4H_{10} pressures over i-C_3H_7SH, that is, at a n-C_4H_{10} pressure of ≥300 Torr. This is shown in Table 2, along with the experimental product quantum yield at different n-C_4H_{10} pressures.

The photolysis of i-C_3H_7SH with added thermalizer, n-C_4H_{10}, was repeated at higher temperatures, 65, 105, and 145°C. Although the product quantum yields varied with increasing temperature, the effect of increasing n-C_4H_{10} pressure on these quantum yields was the same at each temperature as that observed at 25°C. With increasing temperature $\phi(H_2)$ and $\phi[(i\text{-}C_3H_7)_2S_2]$ decrease, while $\phi(C_3H_8)$, $\phi(H_2S)$, and $\phi(C_3H_6)$ increase, but the sum, $R(H_2)$ and $R(C_3H_8)$, remains invariant. The product quantum yields obtained at the

Can. J. Chem. Downloaded from www.nrcresearchpress.com by 112.217.228.212 on 09/07/12
For personal use only.

TABLE 2. Product quantum yields in the photolysis of i-C_3H_7SH with added thermalizer, n-C_4H_{10},[a] T = 25°C

$P(n\text{-}C_4H_{10})$ (Torr)	$[R(H_2) + R(C_3H_8)]$[b] (10^{-2} μmol min^{-1}) (±0.2)[c]	$\phi(H_2)$ (±0.02)	$\phi(C_3H_8)$ (±0.02)	$\phi(H_2S)$ (±0.02)	$\phi(C_3H_6)$ (±0.003)	$\phi[(i\text{-}C_3H_7)_2S_2)]$ (±0.07)
0	9.0[d]	0.80	0.21	0.24	0.042	0.81
28	8.48 (2)[e]	0.838	0.172	0.193	0.0211	0.887
35	8.92 (2)	0.840	0.171	0.183	0.0206	0.860
50	8.57 (2)	0.838	0.172	0.173	0.0182	0.793
70	8.71 (2)	0.851	0.159	0.168	0.0145	0.870
100	8.91 (3)	0.850	0.160	0.157	0.0126	0.840
150	8.76 (2)	0.859	0.151	0.153	0.0102	0.889
200	8.27 (2)	0.872	0.138	0.138	0.0097	0.855
250	8.38 (2)	0.878	0.133	0.129	0.0100	0.870
300	8.29 (2)	0.875	0.135	0.135	0.0097	0.890
350	8.41 (2)	0.887	0.123	0.129	0.0094	0.876
400	8.56 (3)	0.877	0.133	0.131	0.0087	0.896

[a] $P(i\text{-}C_3H_7SH)$ = 20.0 Torr; T = 25°C; photolysis time = 60 min; $I_a = 0.99[R(H_2) + R(C_3H_8)]$.
[b] Average $[R(H_2) + R(C_3H_8)] = (8.6 \pm 0.5) \times 10^{-2}$ μmol min^{-1}.
[c] Standard error.
[d] See results from Table 1.
[e] Number of experiments.

TABLE 3. Effect of temperature on product quantum yields[a] at high n-C_4H_{10} pressure limits[b]

Temperature (°C)	$[R(H_2) + R(C_3H_8)]$[c] (10^{-2} μmol min^{-1})	$\phi(H_2)$	$\phi(C_3H_8)$	$\phi(H_2S)$	$\phi(C_3H_6)$	$\phi[(i\text{-}C_3H_7)_2S_2)]$
25	8.6±0.3[d]	0.88±0.01	0.11±0.01	0.13±0.01	0.009±0.001	0.89±0.02
65	9.1±0.2	0.84±0.01	0.15±0.01	0.18±0.01	0.010±0.001	0.88±0.04
105	9.0±0.2	0.83±0.01	0.17±0.01	0.19±0.01	0.010±0.001	0.83±0.03
145	8.9±0.1	0.82±0.01	0.18±0.01	0.21±0.02	0.011±0.001	0.81±0.04

[a] Each quantum yield value is the average of 5–8 experimental points: photolysis time = 60 min; $I_a = 0.99[R(H_2) + R(C_3H_8)]$.
[b] $P(i\text{-}C_3H_7SH)$ = 20.0–28.1 Torr or $[i\text{-}C_3H_7SH] = 1.04 \times 10^{-3}$ M. $P(n\text{-}C_4H_{10})$ = 300–560 Torr or $[n\text{-}C_4H_{10}] = (1.61\text{–}2.15) \times 10^{-}$ M.
[c] Average of a minimum of 20 experimental values.
[d] Standard error.

high n-C_4H_{10} pressure limit, 300–560 Torr, and at different temperatures are summarized in Table 3.

Discussion

Reaction mechanism

Because the photolysis products for i-C_3H_7SH and their dependence on the pressure and temperature are quite similar to those observed in the photolysis of C_2H_5SH, a reaction mechanism analogous to that established for C_2H_5SH (9) can also be postulated for i-C_3H_7SH.

The primary photochemical reactions are:

[1] $i\text{-}C_3H_7SH + h\nu\ (254\ nm) \rightarrow H^* + i\text{-}C_3H_7S$

[2] $\rightarrow HS + i\text{-}C_3H_7^{\ddagger}$

[3] $\rightarrow H_2S + C_3H_6$

These are followed by hot H* atom and i-$C_3H_7^{\ddagger}$ radical reactions:

[4]* $i\text{-}C_3H_7^{\ddagger} \rightarrow C_3H_6 + H$

[5]* $i\text{-}C_3H_7^{\ddagger} + i\text{-}C_3H_7SH \rightarrow C_3H_8 + i\text{-}C_3H_7S$

[6]* $i\text{-}C_3H_7^{\ddagger} + M \rightarrow i\text{-}C_3H_7 + M$

[7]* $H^* + i\text{-}C_3H_7SH \rightarrow H_2 + i\text{-}C_3H_7S$

[8]* $\rightarrow H_2S + i\text{-}C_3H_7$

[9]* $H^* + M \rightarrow H + M$

and the thermal reactions are as follows, in parallel with that established for C_2H_5SH:

[5] $i\text{-}C_3H_7 + i\text{-}C_3H_7SH \rightarrow C_3H_8 + i\text{-}C_3H_7S$

[7] $H + i\text{-}C_3H_7SH \rightarrow H_2 + i\text{-}C_3H_7S$

[8] $\rightarrow H_2S + i\text{-}C_3H_7$

[10] $HS + i\text{-}C_3H_7S \rightarrow i\text{-}C_3H_7SSH$

[11] $2i\text{-}C_3H_7SSH \rightarrow 2i\text{-}C_3H_7SH + S_2(wall)$

[12] $2i\text{-}C_3H_7S \rightarrow (i\text{-}C_3H_7)_2S_2$

[13] $\rightarrow i\text{-}C_3H_7SH + (CH_3)_2CS$

The reaction enthalpies for [1], [2], and [3] are the same as those for the analogous reactions with C_2H_5SH; namely, 88, 70, and 18 kcal mol^{-1}, respectively. The photon energy at 254 nm is equal to 113 kcal Einstein^{-1}, thus the hot H* atoms are formed in the primary step [1] with excess energy of 25 kcal mol^{-1}. The excess energy distribution for the second primary step [2] has not been studied. However, because of the great number of vibrational degrees of freedom in the i-C_3H_7 radical we expect a

Can. J. Chem. Downloaded from www.nrcresearchpress.com by 112.217.228.212 on 09/07/12
For personal use only.

Can. J. Chem. Downloaded from www.nrcresearchpress.com by 112.217.228.212 on 09/07/12
For personal use only.

greater part of the 43 kcal mol^{-1} excess energy to be localized on it. The thermal energy for the i-$C_3H_7^*$ radical is estimated from $0.5(sRT)$ (13) (where $s = 24$, the number of effective oscillators) to be 8–11 kcal mol^{-1} in the temperature range 25–145°C, thus raising its total excess energy to about 51 kcal mol^{-1}.

The unimolecular decomposition of i-$C_3H_7^*$ into H + C_3H_6 has a reaction enthalpy of 36–39 kcal mol^{-1}, estimated from available thermochemical data (14, 15). The critical energy for [4]* is given by Benson and O'Neal (16) to be about 41 kcal mol^{-1}. This is about 10 kcal mol^{-1} less than the assumed excess energy of the i-$C_3H_7^*$ radical, so its decomposition in reaction [4]* is energetically feasible. Unfortunately, no computations of the unimolecular rate constant and its energy dependence were carried out for i-C_3H_7 radicals. However, Rabinovitch and Setser (17) have calculated $k_4^* \approx 10^8$ s^{-1} for n-propyl radicals carrying an active energy content of ~10 kcal mol^{-1} above the critical energy. Thus, it can be postulated that the rate constant for Reaction [4]* will also be $\leq 10^8$ s^{-1} for isopropyl radicals.

The addition reaction, which is the reverse of Reaction [4]*,

[14] $H + C_3H_6 \rightarrow i\text{-}C_3H_7^*$

is known to have an activation energy of ~1.6 kcal mol^{-1} (18, 19). The alternative competitive reaction, which is the addition of H at the non-terminal carbon,

[15] $H + C_3H_6 \rightarrow n\text{-}C_3H_7^*$

requires a higher activation energy of about 4 kcal mol^{-1} (19) and is of relatively minor importance at ~5% (20–22). Cvetanovic and co-workers (20, 21) have reported that over 95% of the i-$C_3H_7^*$ radicals formed from [14] invariably dissociate back to the reactants at low, 20 Torr, C_3H_6 pressures. This is in contrast to hot n-C_3H_7 radicals, which dissociate predominantly into a methyl radical and ethylene:

[16] $n\text{-}C_3H_7^* \rightarrow CH_3 + C_2H_4$

We can conclude from the above that the major secondary source of C_3H_6 is reaction [4]*. On the other hand, the amount of C_3H_6 lost in [15] and [16] cannot be significant since the rate of step [15] is very small at low conversions and C_2H_4 was not found in the products. Other possible source of C_3H_6 is the disproportionation reaction of i-C_3H_7 radicals

[17] $2\,i\text{-}C_3H_7 \rightarrow C_3H_6 + C_3H_8$

for which the rate constant ratio for the disproportionation to combination reaction,

[18] $2\,i\text{-}C_3H_7 \rightarrow C_6H_{14}$

k_{17}/k_{18}, has been determined to be 0.60 ± 0.01 (23). However, [17] cannot be important, since no 2,3-dimethylbutane was found in the products.

The collisional deactivating molecules for the quenching of hot H* and i-$C_3H_7^*$ radicals in reactions [6]* and [9]*, may be either i-C_3H_7SH or n-C_4H_{10}. The possibility of extra H_2 being produced by the hot H* atom reactions with n-C_4H_{10} was ruled out because of the several orders of magnitude difference between the rate constants, $k(H + RSH) = 1.23 \times 10^{12}$ cm^3 mol^{-1} s^{-1} (24) and $k(H + n\text{-}C_4H_{10}) = 2.82 \times 10^8$ cm^3 mol^{-1} s^{-1} (25). Since alkanes absorb only in the vacuum UV region, below 200 nm (26), H atoms from direct photolysis of n-C_4H_{10} can also be excluded.

The scatter in $\phi[(i\text{-}C_3H_7)_2S_2]$ is observed to be more than that in $\phi(H_2S)$. This may be due to the increased difficulty in measuring the heavier isopropyldisulfide product quantitatively, and also to the reactions of thiyl radicals with Hg,

$$2\,i\text{-}C_3H_7S + Hg \rightarrow (i\text{-}C_3H_7S)_2Hg$$

$$(i\text{-}C_3H_7S)_2Hg \rightarrow (i\text{-}C_3H_7)_2S_2 + Hg$$

$$(i\text{-}C_3H_7S)_2Hg \rightarrow (i\text{-}C_3H_7)_2S + HgS$$

The following quantum yield expressions have been derived from the steady-state treatment of the proposed mechanism.

$$[19]\quad \phi(C_3H_6) = \phi_3 + \frac{k_4^*\phi_2}{k_4^* + k_5^*[i] + k_6^*[M]}$$

$$[20]\quad \phi(H_2) = \frac{k_7\phi_1}{k_7 + k_8} - \frac{(k_7k_8^* - k_7^*k_8)\phi_1[i]}{(k_7 + k_8)\{(k_7^* + k_8^*)[i] + k_9^*[M]\}} + \frac{k_4^*k_7\phi_2}{(k_7 + k_8)(k_4^* + k_5^*[i] + k_6^*[M])}$$

$$[21]\quad \phi(C_3H_8) = \frac{k_8\phi_1}{k_7 + k_8} + \phi_2 + \frac{(k_7k_8^* - k_7^*k_8)\phi_1[i]}{(k_7 + k_8)\{(k_7^* + k_8^*)[i] + k_9^*[M]\}} - \frac{k_4^*k_7\phi_2}{(k_7 + k_8)(k_4^* + k_5^*[i] + k_6^*[M])}$$

$$[22]\quad \phi(H_2S) = \frac{k_8\phi_1}{k_7 + k_8} + \phi_3 + \frac{(k_7k_8^* - k_7^*k_8)\phi_1[i]}{(k_7 + k_8)\{(k_7^* + k_8^*)[i] + k_9^*[M]\}} + \frac{k_4^*k_8\phi_2}{(k_7 + k_8)(k_4^* + k_5^*[i] + k_6^*[M])}$$

$$[23]\quad \phi[(i\text{-}C_3H_7)_2S_2] = \frac{k_{12}\phi_1}{k_{12} + k_{13}}$$

where ϕ_1, ϕ_2, and ϕ_3 are the quantum yields associated with the three primary photochemical reactions, [1]–[3]. M is the collisional deactivating molecule for hot H* and i-$C_3H_7^*$ radicals and may be either i-C_3H_7SH or n-C_4H_{10} molecules. The expressions for $k_6^*[M]$ and $k_9^*[M]$ are $k_{6i}^*[i] + k_{6n}^*[n]$ and $k_{9i}^*[i] + k_{9n}^*[n]$, respectively. [i] is the concentration or pressure of i-C_3H_7SH and [n] is that of added n-C_4H_{10}.

Quantum efficiencies of primary photochemical steps: quantum yield of C_3H_6

The effect of n-C_4H_{10} pressure on $\phi(C_3H_6)$ is shown in Fig. 1 at 25, 65, 105, and 145°C. At each temperature $\phi(C_3H_6)$ decreases very rapidly with increasing n-C_4H_{10} pressure and approaches a constant value at high pressures. This behavior indicates the existence of two different sources of C_3H_6. One is the pressure dependent unimolecular decomposition of hot i-$C_3H_7^*$ radicals to H and C_3H_6, the other is the primary photochemical step [3]. The unimolecular decomposition is completely suppressed at high n-C_4H_{10} pressures, therefore the high pressure limit of $\phi(C_3H_6)$ gives the quantum yield of reaction [3].

Equation [19] derived for $\phi(C_3H_6)$ consists of a constant and a pressure-dependent term reflecting the existence of the two different sources. ϕ_3 can be determined from its modified form:

$$[24]\quad [\phi(C_3H_6) - \phi_3]^{-1} = (1 + \alpha P_i)/\phi_2 + \beta P_n/\phi_2$$

Can. J. Chem. Downloaded from www.nrcresearchpress.com by 112.217.228.212 on 09/07/12
For personal use only.

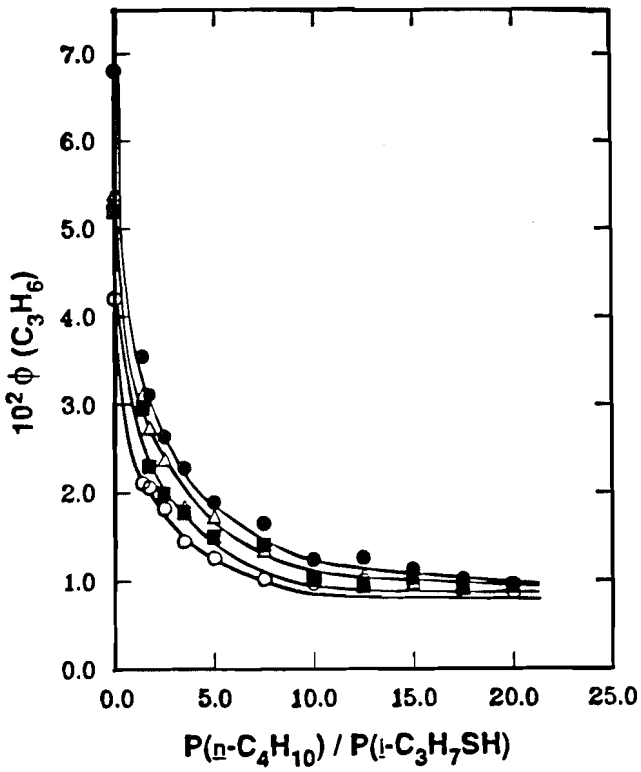

FIG. 1. Plots of quantum yield of C_3H_6 as a function of $P(n\text{-}C_4H_{10})/P(i\text{-}C_3H_7SH)$. ○, 25°C; ■, 65°C; △, 105°C; ●, 145°C.

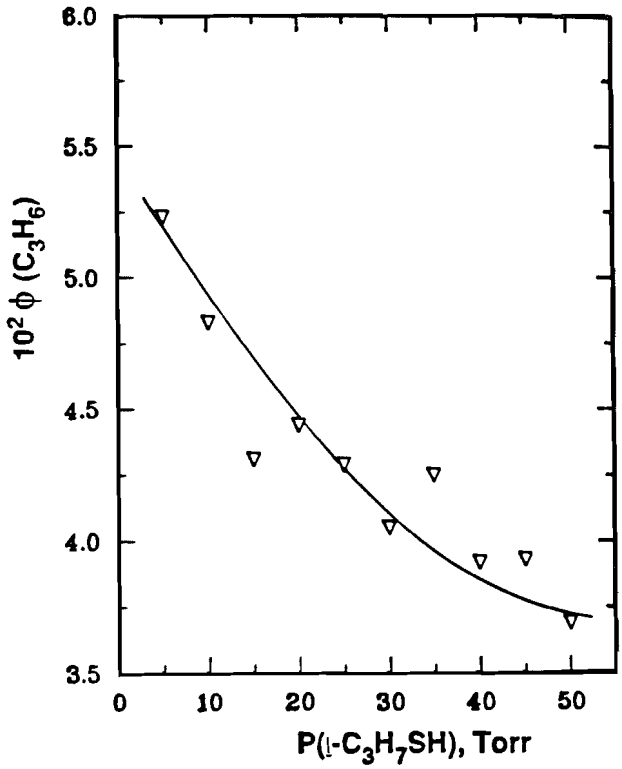

FIG. 2. Quantum yield ϕC_3H_6 versus $i\text{-}C_3H_7SH$ pressure.

where $\alpha = (k_5^* + k_{6i}^*)/k_4^*$, $\beta = k_{6n}^*/k_4^*$ and $[\phi(C_3H_6) - \phi_3]^{-1}$ is a linear function of P_n at constant P_i.

The linear correlation coefficient for eq. [24] was calculated, in the first approximation, for ten values of ϕ_3, ranging from 0.0081 to 0.0090. The results show that the highest correlation coefficient value is located at $\phi_3 = 0.0083$, which corresponds closely to the average experimental value $\phi(C_3H_6) = 0.009$ in the high (300–400 Torr) $n\text{-}C_4H_{10}$ pressure region at 25°C, Fig. 1.

Equation [24] becomes a linear function of P_i in the absence of thermalizer, i.e. $P_n = 0$,

$$[25]\quad [\phi(C_3H_6) - \phi_3]^{-1} = 1/\phi_2 + \alpha P_i/\phi_2$$

The plot of $\phi(C_3H_6)$ versus $P(i\text{-}C_3H_7SH)$ using a much expanded ordinate scale, Fig. 2, illustrates the marginal pressure dependence of $\phi(C_3H_6)$ on $P(i\text{-}C_3H_7SH)$. The values for $[\phi(C_3H_6) - \phi_3]^{-1}$ at $P_n = 0$ were calculated using $\phi_3 = 0.009$ and were plotted against $i\text{-}C_3H_7SH$ pressure in Fig. 3. The following linear relation was derived by the LMS method, for the condition $P_n = 0$;

$$[26]\quad [\phi(C_3H_6) - \phi_3]^{-1} = (23.5 \pm 0.9) + (0.24 \pm 0.03)P_i$$

Combining this equation with eq. [25], ϕ_2 and α were determined to be 0.043 ± 0.002 and $(1.03 \pm 0.14) \times 10^{-2}\,\text{Torr}^{-1}$, respectively.

The values of ϕ_2 at higher temperatures may now be determined from the intercepts of eq. [24]. The variations of $[\phi(C_3H_6) - \phi_3]^{-1}$ with pressure and temperature are plotted in Fig. 4, from which the derived intercepts are listed in Table 4. From the intercepts α appears to be little affected by temperature; the experimental observations (Table 3) show that changes in ϕ_3 up to 145°C are within experimental error. The derived values of ϕ_2 and subsequently ϕ_1 ($\phi_1 + \phi_2 + \phi_3 = 1.0$), are listed in Table 5. A slight increase in ϕ_2 (0.043–0.074) and consequently a decrease in ϕ_1 (0.95–0.92) are observed with increasing temperature. However, this variation is still within the experimental error. As a result, the quantum efficiencies of the primary photochemical reactions can be considered to be

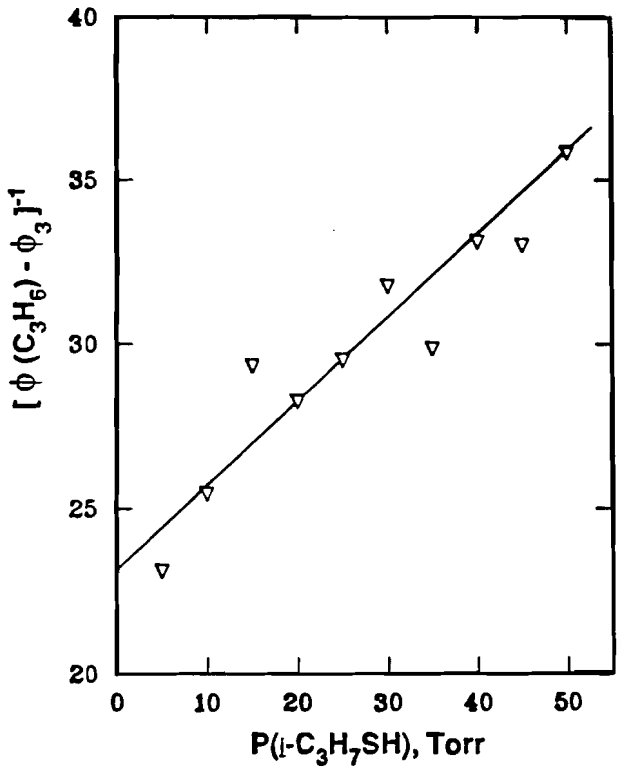

FIG. 3. $[\phi(C_3H_6) - \phi_3]^{-1}$ versus $i\text{-}C_3H_7SH$ pressure. The best fitted value of $\phi_3 = 0.009$ was used.

Can. J. Chem. Downloaded from www.nrcresearchpress.com by 112.217.228.212 on 09/07/12
For personal use only.

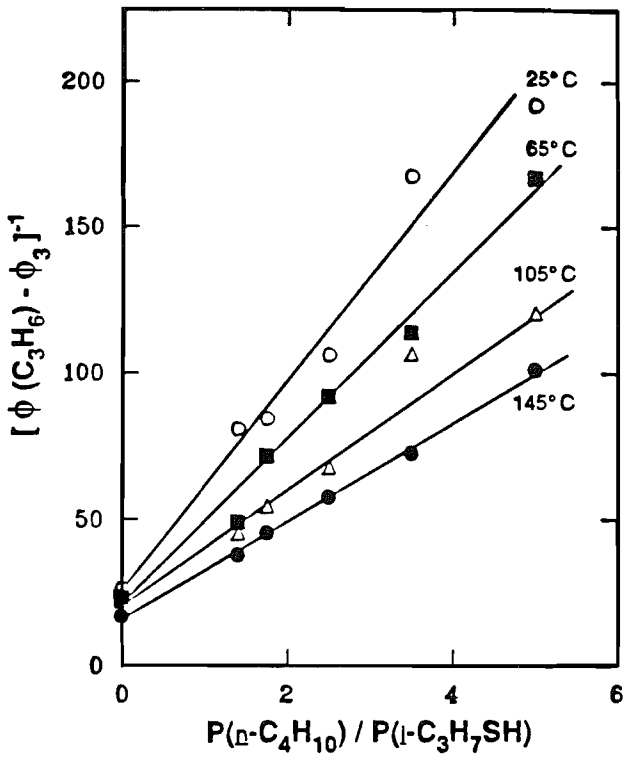

FIG. 4. Plots of $[\phi(C_3H_6) - \phi_3]^{-1}$ as a function of $P(n\text{-}C_4H_{10})/P(i\text{-}C_3H_7SH)$. The best fitted value of $\phi_3 = 0.009$ was used.

TABLE 4. Intercepts of the plots in Fig. 4

Temperature (°C)	$P(i\text{-}C_3H_7SH)$ (Torr)	Intercept[a]	Correlation coefficient
25	20.0	28 ± 8[b]	0.99287
65	22.7	26 ± 7	0.98510
105	25.4	19 ± 6	0.98278
145	28.1	17 ± 2	0.99834

[a]Intercept = $(1 + \alpha P_i)/\phi_2$; $\alpha = (k_5^* + k_{6i}^*)/k_4^*$, in units of $Torr^{-1}$.
[b]Standard error.

TABLE 5. Quantum yields for the primary photochemical processes

Temperature (°C)	ϕ_1	ϕ_2	ϕ_3
25	0.948 ± 0.012[a]	0.043 ± 0.012	0.009[b] ± 0.001
65	0.944 ± 0.013	0.047 ± 0.013	0.009 ± 0.001
105	0.926 ± 0.015	0.065 ± 0.015	0.009 ± 0.001
145	0.917 ± 0.009	0.074 ± 0.009	0.009 ± 0.001
Average:	0.93 ± 0.02	0.057 ± 0.024	0.009 ± 0.001

[a]Standard error.
[b]Assumed to be constant.

independent of temperatures within an experimental error of ±3%. The average values for ϕ_1, ϕ_2, and ϕ_3 from this work are then 0.93 ± 0.02, 0.057 ± 0.024, and 0.009 ± 0.001, respectively. When compared with the values obtained for C_2H_5SH (9), ϕ_1 is slightly lower, 0.96 ± 0.01, and ϕ_2 is higher, 0.029 ± 0.010, while ϕ_3 is almost the same, 0.010 ± 0.001, within experimental error. The similar ϕ-values are due to the same (S—H) and (C—S) bond energies for both C_2H_5SH and $i\text{-}C_3H_7SH$.

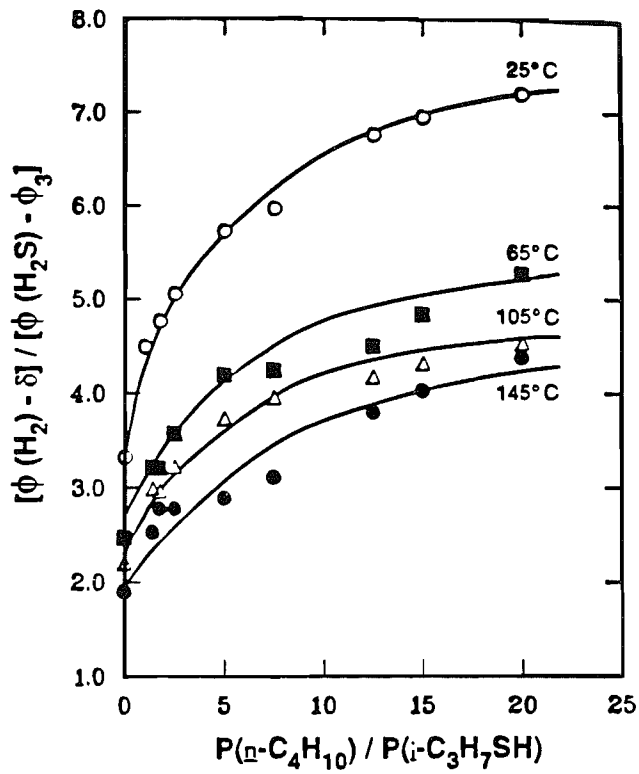

FIG. 5. Plots of $[\phi(H_2) - \delta]/[\phi(H_2S) - \phi_3]$ as a function of $P(n\text{-}C_4H_{10})/P(i\text{-}C_3H_7SH)$.

Hydrogen atom reactions with isopropanethiol: quantum yields of H_2 and H_2S

The variations of the H_2 and H_2S yields with pressure and temperature provide information on the relative rates of the hot and thermalized H-atom reactions with $i\text{-}C_3H_7SH$; [7]*, [7], [8]*, and [8]. The total $\phi(H_2S)$ comprises the H_2S formed in [8]* and [8] and in the molecular primary step [3], for which $\phi_3 = 0.009$. The H_2S yield contributed by the hot and thermalized H-atom reactions with $i\text{-}C_3H_7SH$, [8]* and [8], is thus $[\phi(H_2S) - \phi_3]$. The total $\phi(H_2)$ comes from reactions [7]* and [7], and from the unimolecular decomposition, [4]*. The contribution from [4]* is equal to the difference between the total C_3H_6 yield and that from the primary molecular step [3]. Thus, the H_2 yield from the hot and thermalized H-atom reactions with $i\text{-}C_3H_7SH$, [7]* and [7] is given by $[\phi(H_2) - \delta]$, where δ is the correction factor, $[\phi(C_3H_6) - \phi_3]$.

The variations of the ratio $[\phi(H_2) - \delta]/[\phi(H_2S) - \phi_3]$ with $n\text{-}C_4H_{10}$ pressure and temperature are plotted in Fig. 5. It is found that at each temperature $[\phi(H_2) - \delta]/[\phi(H_2S) - \phi_3]$ increases with increasing thermalizer pressure, indicating that thermalization of the H atoms favours the H-abstraction reaction, i.e. the displacement reaction [8] has a higher activation energy than the H-abstraction reaction [7]. Also, $[\phi(H_2) - \delta]/[\phi(H_2S) - \phi_3]$ decreases with increasing temperature, indicating that the rate of the displacement reaction increases faster than the H-abstraction reaction at higher temperatures, as expected.

Relative rate parameters for the H-atom reactions: quantum yields of H_2 and C_3H_8

The relative rate parameters for the thermalized H-atom reactions, [7] and [8], are determined from the H_2 and C_3H_8 yields. The quantum yield expressions for H_2 and C_3H_8 are given by eqs. [20] and [21], respectively. The plots of $\phi(H_2)$

Can. J. Chem. Downloaded from www.nrcresearchpress.com by 112.217.228.212 on 09/07/12
For personal use only.

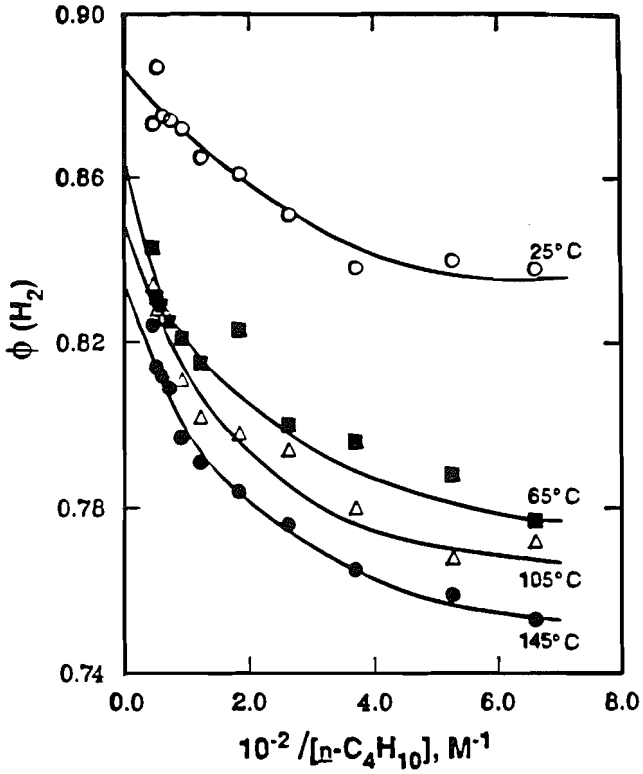

FIG. 6. Plots of $\phi(H_2)$ as a function of the reciprocal of n-C_4H_{10} concentration at $[i\text{-}C_3H_7SH] = 1.04 \times 10^{-3}\,M$.

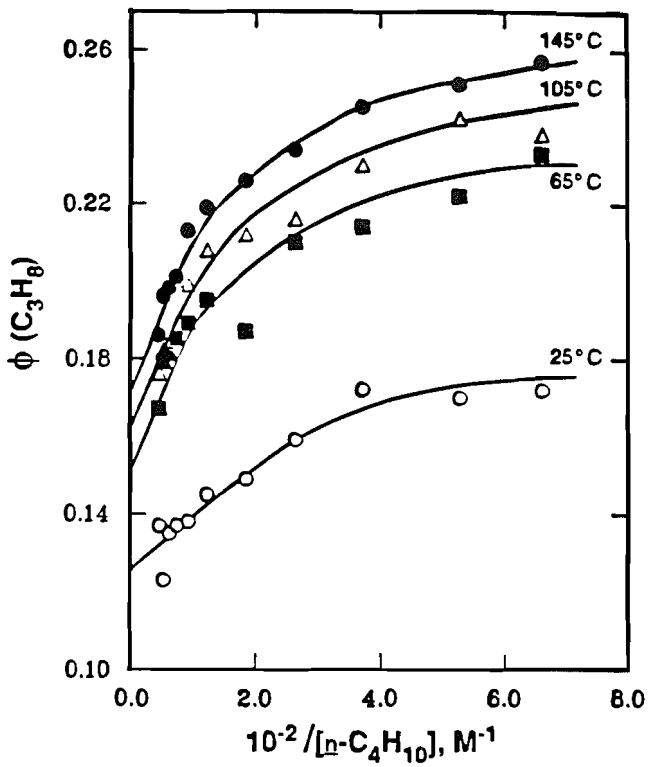

FIG. 7. Plots of $\phi(C_3H_8)$ as a function of the reciprocal of n-C_4H_{10} concentration at $[i\text{-}C_3H_7SH] = 1.04 \times 10^{-3}\,M$.

and $\phi(C_3H_8)$ against inverse n-C_4H_{10} concentration at each temperature are shown in Figs. 6 and 7. The variation with pressure observed in these plots can be correlated with the pressure-dependent terms in eqs. [20] and [21],

$$\frac{(k_7k_8^* - k_7^*k_8)\phi_1[\mathrm{i}]}{(k_7 + k_8)\{(k_7^* + k_8^*)[\mathrm{i}] + k_9^*[\mathrm{M}]\}}$$

and

$$\frac{k_4^*k_7\phi_2}{(k_7 + k_8)(k_4^* + k_5^*[\mathrm{i}] + k_6^*[\mathrm{M}])}$$

When $[n\text{-}C_4H_{10}]$ is large, deactivation of hot radicals by i-C_3H_7SH can be neglected and $k_9^*[\mathrm{M}]$ and $k_6^*[\mathrm{M}]$ become $k_{9\mathrm{n}}^*[\mathrm{n}]$ and $k_{6\mathrm{n}}^*[\mathrm{n}]$, respectively. Also, for the condition $P_\mathrm{n} \gg P_\mathrm{i}$, the terms $\{(k_7^* + k_8^*)[\mathrm{i}]\}$ and $\{k_4^* + k_5^*[\mathrm{i}]\}$ may be neglected from the pressure-dependent terms. After substituting for $k_9^*[\mathrm{M}]$ and $k_6^*[\mathrm{M}]$ and rearranging, the following linear relations are obtained for the high n-C_4H_{10} pressure condition;

$$[27]\quad \phi(H_2) = \frac{k_7\phi_1}{k_7 + k_8} - \frac{(k_7k_8^* - k_7^*k_8)k_{6\mathrm{n}}^*\phi_1[\mathrm{i}] - k_4^*k_7k_{9\mathrm{n}}^*\phi_2}{(k_7 + k_8)k_{6\mathrm{n}}^*k_{9\mathrm{n}}^*[\mathrm{n}]}$$

$$[28]\quad \phi(C_3H_8) = \frac{k_8\phi_1}{k_7 + k_8} + \phi_2 + \frac{(k_7k_8^* - k_7^*k_8)k_{6\mathrm{n}}^*\phi_1[\mathrm{i}] - k_4^*k_7k_{9\mathrm{n}}^*\phi_2}{(k_7 + k_8)k_{6\mathrm{n}}^*k_{9\mathrm{n}}^*[\mathrm{n}]}$$

The linear behaviour of $\phi(H_2)$ and $\phi(C_3H_8)$ at high n-C_4H_{10} pressures is illustrated in Figs. 6 and 7 for $P_\mathrm{n} > 100$ Torr, or $[n\text{-}C_4H_{10}]^{-1} < 0.02\,M^{-1}$. The intercepts of the linear portions of these plots are listed in Table 6 and are defined by [27] and [28] to be

$$[29]\quad \phi(H_2, P_\mathrm{n} \to \infty) = \frac{k_7\phi_1}{k_7 + k_8}$$

$$[30]\quad \phi(C_3H_8, P_\mathrm{n} \to \infty) = \frac{k_8\phi_1}{k_7 + k_8} + \phi_2$$

TABLE 6. Intercepts of the plots in Figs. 6 and 7[a]

Temperature (°C)	$P(i\text{-}C_3H_7SH)$ (Torr)	Intercepts	
		H_2	C_3H_8
25	20.0	0.884±0.003	0.125±0.005
65	22.7	0.866±0.007	0.144±0.009
105	24.7	0.852±0.005	0.158±0.007
145	28.1	0.838±0.005	0.172±0.007

[a]Linear region from $[n\text{-}C_4H_{10}]^{-1} < 0.02\,M^{-1}$ or $P(n\text{-}C_4H_{10}) > 100$ Torr.

From the intercepts and the derived values of ϕ_1 and ϕ_2 (Table 5), the rate constant ratio, k_7/k_8, may be calculated at each temperature. Their values are listed in Table 7, along with another set of values for k_7/k_8 which were derived directly from the experimental H_2 and C_3H_8 yields at high total pressures (Table 3). It is observed that the latter set of k_7/k_8 values are lower than the former. This difference may be due to the fact that the experimental H_2 and C_3H_8 values have not yet reached the true limiting yields at 300–400 Torr.

The Arrhenius plot for the thermalized H-atom reactions [7] and [8], shown in Fig. 8, is constructed using the kinetically derived values of k_7/k_8 in Table 7. The Arrhenius expression from the plot is given by,

$$[31]\quad \ln k_7/k_8 = (0.35 \pm 0.10) + (770 \pm 36)/T$$

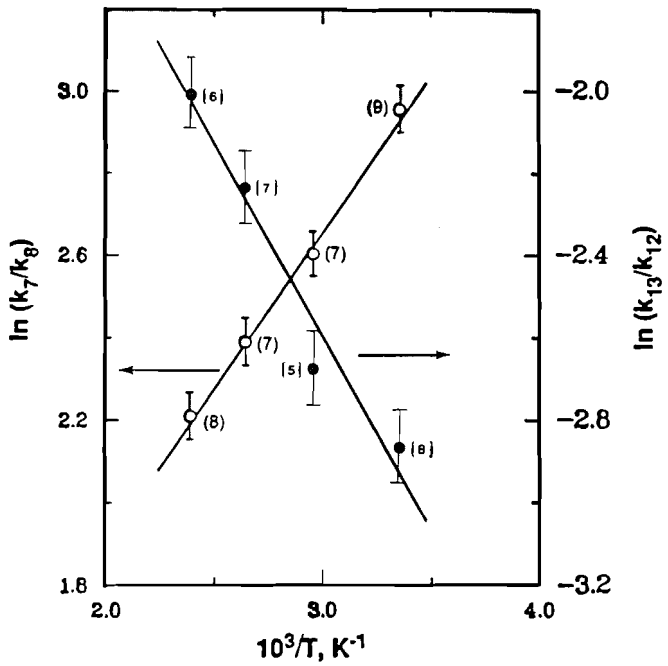

FIG. 8. Plots of ln k_7/k_8 and ln k_{13}/k_{12} versus the reciprocal of temperature. Figure in bracket indicates number of experiments.

TABLE 7. Temperature dependence of k_7/k_8 and k_{13}/k_{12}

Temperature (°C)	$(k_7/k_8)^a$	$(k_7/k_8)^b$	$(k_{13}/k_{12})^c$
25	19.2±4.3[d]	17.6±2.0	0.045±0.049
65	13.5±2.8	9.33±0.90	0.057±0.050
105	10.9±3.1	8.30±0.39	0.120±0.043
145	9.1±2.7	7.45±0.47	0.148±0.060

[a]Calculated by substituting into eq. [29] the intercept values from Table 6.
[b]Calculated by substituting into eq. [29] the experimental $\phi(H_2)$ yields at high n-C_4H_{10} pressures, Table 3.
[c]Calculated from the photolysis of i-C_3H_7SH with added n-C_4H_{10} at the high pressure limit.
[d]Standard error.

From eq. [31], the activation energy difference, $(E_7 - E_8) = -1.53 \pm 0.07$ kcal mol^{-1}, is slightly higher than that obtained for the H-atom reactions with C_2H_5SH (9), where $(E_7 - E_8) = -1.310 \pm 0.025$ kcal mol^{-1}. The ratio of the pre-exponential factors, A_7/A_8, derived from [31] is equal to 1.43 ± 0.06. Absolute rate parameters for k_7 and k_8 cannot be derived at this time due to the lack of available data in the literature. However, since the (S—H) bond strengths in C_2H_5SH and i-C_3H_7SH are the same, the rate constant, k_7, i-C_3H_7SH should be the same as, or close to the rate constant of the analogous reaction derived for C_2H_5SH (9):

$$[32] \quad k_7 \text{ (cm}^3 \text{ mol}^{-1} \text{ s}^{-1}) = (3.98 \pm 0.72) \times 10^{12} \exp [(-1066 \pm 43)/RT]$$

From this, the rate constant, k_8, for i-C_3H_7SH is then determined to be:

$$[33] \quad k_8 \text{ (cm}^3 \text{ mol}^{-1} \text{ s}^{-1}) = (2.78 \pm 0.56) \times 10^{12} \exp [(-2597 \pm 114)/RT]$$

The experimental entropy of activation, $S^{\ddagger}$, calculated from the A factor of k_8 is −27.6 eu for the standard state of 1 atm.

TABLE 8. Derived values of $\dfrac{k_7\phi_2{}^a}{(k_7 + k_8)(1 + \alpha P_i)}$

$P(i\text{-}C_3H_7SH)$ (Torr)	$\dfrac{k_7\phi_2}{(k_7 + k_8)(1 + \alpha P_i)}$
5	0.0540
10	0.0537
20	0.0532
30	0.0527
40	0.0521
50	0.0516

[a]T = 25°C, (k_7/k_8) = 19.2, ϕ_2 = 0.043, $\alpha = 1.03 \times 10^{-3}$ Torr^{-1}.

This value is similar to those obtained for the H + CH_3SCH_3 (27) and the H + $C_2H_5SC_2H_5$ (28) reactions, −24.1 and −22.1 eu, respectively, suggesting transition states with similar structures. Using Benson's method (29) for a transition state which involves an initial interaction between the H atom and the non-bonding 3p orbital of the sulfur atom:

$$H + i\text{-}C_3H_7SH \rightarrow [i\text{-}C_3H_7 \cdots \underset{\vdots}{\underset{H}{S}}\text{—}H]^{\ddagger} \rightarrow i\text{-}C_3H_7 + H_2S$$

we will obtain

$$\Delta S^{\ddagger} = S_0^{\ddagger} - S_0(i\text{-}C_3H_7SH) - S_0(H)$$
$$= S_0(i\text{-}C_3H_7SH) + R \ln 2 + x - S_0(i\text{-}C_3H_7SH) - S_0(H)$$
$$= 1.4 + x - 27.4 = -26.0 + x$$
$$x = -1.6 \text{ eu}$$

This low value for the vibrational contribution to $\Delta S^{\ddagger}$ indicates a very tight structure for the activated complex.

In the photolysis of pure i-C_3H_7SH, i.e. $P_n = 0$, the resulting expressions for H_2 and C_3H_8 yields are simplified from [20] and [21] as follows;

$$[34] \quad \phi(H_2) = \frac{k_7\phi_1}{k_7 + k_8} - \frac{(k_7k_8^{\ddagger} - k_7^{\ddagger}k_8)\phi_1}{(k_7 + k_8)(k_7^{\ddagger} + k_8^{\ddagger} + k_{9i}^{\ddagger})} + \frac{k_7\phi_2}{(k_7 + k_8)(1 + \alpha P_i)}$$

$$[35] \quad \phi(C_3H_8) = \frac{k_8\phi_1}{k_7 + k_8} + \phi_2 + \frac{(k_7k_8^{\ddagger} - k_7^{\ddagger}k_8)\phi_1}{(k_7 + k_8)(k_7^{\ddagger} + k_8^{\ddagger} + k_{9i}^{\ddagger})} - \frac{k_7\phi_2}{(k_7 + k_8)(1 + \alpha P_i)}$$

where α is the rate constant ratio, earlier derived to be $(k_5^{\ddagger} + k_{6i}^{\ddagger})/k_4^{\ddagger} \approx 1.03 \times 10^{-3}$ Torr^{-1}. The last term in both of the H_2 and C_3H_8 expressions indicates that $\phi(H_2, P_n = 0)$ and $\phi(C_3H_8, P_n = 0)$ are inverse functions of P_i. However, the predicted pressure dependence is not apparent and $\phi(H_2)$ and $\phi(C_3H_8)$ are approximately constant at 0.80 ± 0.01 and 0.21 ± 0.01, at 25°C, in the i-C_3H_7SH pressure range 5–50 Torr, Table 1. Thus, the magnitude of any changes in the pressure term in [34] and [35] is likely to be relatively small and should fall within the range of the experimental error. This prediction is again verified by evaluating the pressure term, using the already derived values of ϕ_2, α, and k_7/k_8. As shown in Table 8, this pressure term decreases with increasing i-C_3H_7SH pressure, and the net change is indeed small, being only 0.002 on going

Can. J. Chem. Downloaded from www.nrcresearchpress.com by 112.217.228.212 on 09/07/12
For personal use only.

from 5 to 50 Torr. Therefore, increasing the i-C_3H_7SH pressure has negligible effects on $\phi(H_2)$ and $\phi(C_3H_8)$, and the pressure terms in [34] and [35] can be considered to be constant, indicating that i-C_3H_7SH is not an efficient deactivator.

Disproportionation–combination of thiyl radicals: quantum yield of (i-C_3H_7)$_2S_2$

The quantum yield expression for the formation of $(i\text{-}C_3H_7)_2S_2$,

$$[23] \quad \phi[(i\text{-}C_3H_7)_2S_2] = \frac{k_{12}\phi_1}{k_{12} + k_{13}}$$

predicts that $\phi[(i\text{-}C_3H_7)_2S_2]$ and ϕ_1 are equal to each other if no disproportionation of i-C_3H_7S radicals occurs,

$$[13] \quad 2i\text{-}C_3H_7S \rightarrow i\text{-}C_3H_7SH + C_3H_6S$$

However, the observation that $\phi[(i\text{-}C_3H_7)_2S_2]$ is less than ϕ_1 indicates that reaction [13] occurs in competition with the combination reaction,

$$[12] \quad 2i\text{-}C_3H_7S \rightarrow (i\text{-}C_3H_7)_2S_2$$

The products of disproportionation are the thiol substrate, i-C_3H_7SH, and the aliphatic thioketone, thioacetone. The latter is known to be unstable, although it can be isolated in the monomeric thione form as well as in the tautomeric enethiol form (30). Since, however, $\phi(i\text{-}C_3H_7)_2S_2$ is only slightly less than $\phi(H_2)$, from Tables 1–3, the disproportionation of i-C_3H_7S radicals should be a relatively minor reaction, in comparison with the combination reaction.

Equation [23] predicts no pressure dependence for $(i\text{-}C_3H_7)_2S_2$. This is verified by the $\phi[(i\text{-}C_3H_7)_2S_2]$ values obtained both in the absence and presence of n-C_4H_{10} (Tables 1 and 2). The disproportionation–combination ratio, k_{13}/k_{12}, is derived from [23] to be;

$$[36] \quad \frac{k_{13}}{k_{12}} = \frac{\phi_1}{\phi[(i\text{-}C_3H_7)_2S_2]} - 1$$

Their values, calculated from Table 4, are listed in Table 7. k_{13}/k_{12} increases with temperature, however, this increase must be viewed with caution since large errors are associated with the calculated k_{13}/k_{12} values due to the scatter in the measured yields of $(i\text{-}C_3H_7)_2S_2$. The Arrhenius plot, Fig. 8, is constructed using the high pressure values of the disproportionation–combination steps [13] and [12], respectively. The following rate expression is derived:

$$[37] \quad \ln k_{13}/k_{12} = (1.30 \pm 0.72) - (1339 \pm 251)/T$$

from which $(E_{13} - E_{12}) = 2.65 \pm 0.50$ kcal mol^{-1} and $A_{13}/A_{12} = 3.6 \pm 1.1$. Since the recombination step [12] requires negligible activation energy, E_{13} is therefore estimated to be ~2.65 kcal mol^{-1} and is smaller than that determined for the disproportionation of C_2H_5S radicals, 3.12 kcal mol^{-1} (9).

Conclusion

Our results show that the most important primary step in the photolysis of i-C_3H_7SH is the cleavage of the S—H bond forming hot H-atoms, with a quantum yield of 0.93 ± 0.02. The quantum yields of the two other primary steps, the cleavage of the C—S bond and the molecular formation of H_2S are substantially lower, 0.057 ± 0.024 and 0.009 ± 0.001, respectively. Subsequently, the hot H* atoms react either in a H-atom abstraction or a SH-displacement reaction with the substrate. Both the H-atom abstraction and the SH-displacement occur also with thermalized H-atoms, with the average rate constant ratio $k_7/k_8 = 19.2 \pm 4.3$ at 25°C. The proposed overall mechanism explains satisfactorily not only the formation and distribution of the products but also the observed pressure and temperature effects. It was found that methyl substitution did not have any noticeable effect on any mechanistic aspects of the photolytic decomposition of simple alkane thiols.

Acknowledgments

The authors thank NSERC for continuing financial support.

1. T. Inaba and B. de B. Darwent. J. Phys. Chem. **64**, 1431 (1960).
2. R. R. Kuntz. J. Phys. Chem. **71**, 3343 (1967).
3. R. P. Steer, B. L. Kalra, and A. R. Knight. J. Phys. Chem. **71**, 783 (1967).
4. B. G. Dzantiev, A. V. Shishkov, and M. S. Unukovich. Khim. Vys. Energii, **3**, 111 (1969).
5. R. P. Steer and A. R. Knight. Can. J. Chem. **46**, 2878 (1968).
6. R. P. Steer and A. R. Knigth. Can. J. Chem. **47**, 1335 (1969).
7. G. P. Sturm, Jr. and J. M. White. J. Phys. Chem. **72**, 3679 (1968).
8. L. Bridges, G. L. Hemphill, and J. M. White. J. Phys. Chem. **76**, 2668 (1972).
9. W. W. Lam, T. Yokota, I. Safarik, and O. P. Strausz. J. Photochem. To be published.
10. B. de B. Darwent and R. Roberts. Proc. R. Soc. London, A**216**, 344 (1953).
11. R. G. Gann and J. Dubrin. J. Chem. Phys. **47**, 1867 (1967).
12. L. E. Compton, J. L. Gole, and R. M. Martin. J. Phys. Chem. **73**, 1158 (1969).
13. W. B. DeMore and S. W. Benson. *In* Advances in photochemistry. Vol. 2. *Edited by* W. A. Noyes, G. S. Hammond, and J. N. Pitts, Jr. Wiley, New York, NY. 1964.
14. R. Hiatt and S. W. Benson. Int. J. Chem. Kinet. **4**, 151 (1972).
15. W. Tsang. Int. J. Chem. Kinet. **10**, 821 (1978).
16. S. W. Benson and H. E. O'Neal. Natl. Stand. Ref. Data Ser. U.S. Natl. Bur. Stand. No. 21 (1971).
17. B. S. Rabinovitch and D. W. Setser. *In* Advances in photochemistry. Vol. 3. *Edited by* W. A. Noyes, G. S. Hammond, and J. N. Pitts, Jr. Wiley, New York, NY. 1964.
18. G. W. Harris and J. N. Pitts, Jr. J. Chem. Phys. **77**, 3994 (1982).
19. T. Watanabe, T. Kyogoku, S. Tsunashima, S. Sato, and S. Nagase. Bull. Chem. Soc. Jpn. **55**, 3720 (1982).
20. G. R. Woolley and R. J. Cvetanovic. J. Chem. Phys. **50**, 4705 (1969).
21. R. J. Cvetanovic and L. C. Doyle. J. Chem. Phys. **50**, 4705 (1969).
22. H. G. Wagner and R. Zellner. Ber. Bunsenges Phys. Chem. **76**, 518 (1972).
23. P. Arrowsmith. J. Chem. Soc. Faraday Trans. I, **74**, 3016 (1978).
24. P. H. Wine, J. M. Nicovich, A. J. Hynes, and J. R. Wells. J. Phys. Chem. **90**, 4033 (1986).
25. R. R. Baldwin and R. W. Walker. Faraday Trans. 1, **75**, 140 (1979).
26. J. G. Calvert and J. N. Pitts, Jr. Photochemistry. Wiley, New York, NY. 1966.
27. W. L. Hase and H. B. Schlegal. J. Phys. Chem. **86**, 3901 (1982).
28. M. M. Ekenchi, I. Safarik, and O. P. Strausz. Can. J. Chem. **59**, 3226 (1981).
29. S. W. Benson. Thermochemical kinetics. 2nd ed. Wiley, New York, NY. 1976.
30. R. Mayer. *In* Organic chemistry of sulfur. *Edited by* S. Oae. Plenum Press, New York, NY. 1977.

Can. J. Chem. Downloaded from www.nrcresearchpress.com by 112.217.228.212 on 09/07/12
For personal use only.

Ab initio molecular orbital studies of the potential energy curves for the low lying triplet states of Be_2 and Be_3

RATNAKAR K. GOSAVI AND OTTO P. STRAUSZ[1]

Department of Chemistry, University of Alberta, Edmonton, Alta., Canada T6G 2G2

Received November 30, 1987

This paper is dedicated to Professor Charles A. McDowell on the occasion of his seventieth birthday

RATNAKAR K. GOSAVI and OTTO P. STRAUSZ. Can. J. Chem. **66**, 2034 (1988).

Ab initio calculations with uniform quality gaussian basis set were carried out at the RHF-SCF and CI level on the potential energy curves of the low lying triplet states of Be_2 and Be_3. The lowest excited state, the $^3\Sigma_u^+$ state of Be_2 is 26.0 kcal/mol higher in energy than the ground $^1\Sigma_g^+$ state, and 39.4 kcal/mol lower than the separated Be($^1S_0$) + Be(^3P) atoms, with the *s*, *p*, *d* basis set. The next higher triplet state, the $^3\Pi_g$, is only 8.7 kcal/mol above the lowest $^3\Sigma_u^+$ state. The $^3\Sigma_g^-$ and $^3\Pi_u$ states lie comparatively much higher than the $^3\Sigma_u^+$ state. All the triplet state potential curves have a bonding nature. The lowest triplet state $^3\Sigma_u^+$ in Be_3 with $D_{\infty h}$ symmetry lies ~15 kcal/mol above the ground $^1A_1'$ state, and 48.2 kcal/mol lower than the separated atoms, 2Be($^1S_0$) + Be(^3P). The $^3\Sigma_u^+$ state has 1,3-diradical character and in all the higher triplet states α spin electrons are delocalized among the three Be atoms. The next higher triplet state $^3\Pi_u$ is 7.7 kcal/mol above the lowest $^3\Sigma_u^+$ state. The $^3\Sigma_g^-$ and $^3\Pi_g$ states lie much higher than the $^3\Sigma_u^+$ and $^3\Pi_u$ states. Like the triplet states of Be_2, all Be_3 triplet states have a bonding nature. Reaction path studies on the Be(^3P) energy transfer reactions, Be($^1S_0$) + Be(^3P) ⇄ Be_2($^3\Sigma_u^+$, $^3\Pi_g$) and Be_2($^1\Sigma_g^+$) + Be(^3P) → Be_2($^3\Sigma_u^+$) + Be($^1S_0$), show that these reactions do not feature any activation energy barrier.

RATNAKAR K. GOSAVI et OTTO P. STRAUSZ. Can. J. Chem. **66**, 2034 (1988).

On a réalisé des calculs *ab initio*, avec un ensemble de base de Gauss de qualité uniforme, au niveaux RHF-SCF et IC sur les courbes d'énergie potentielle des états triplets inférieurs du Be_2 et du Be_3. Dans l'état de plus faible excitation, l'énergie de l'état $^3\Sigma_u^+$ du Be_2 est de 26,0 kcal/mol supérieure à celle de l'état fondamental $^1\Sigma_g^+$ et de 39,4 kcal/mol inférieure à celle des atomes séparés Be($^1S_0$) + Be(^3P) avec l'ensemble de base *s*, *p*, *d*. L'état triplet suivant de plus haute énergie $^3\Pi_g$ n'est que de 8,7 kcal/mol plus élevé que l'état le plus faible $^3\Sigma_u^+$. Les états $^3\Sigma_g^-$ et $^3\Pi_u$ sont comparativement plus fortement liés que l'état $^3\Sigma_u^+$. Toutes les courbes de potentiel de l'état triplet sont de nature liante. L'énergie de l'état triplet le plus faible $^3\Sigma_u^+$ du Be_3 de symmétrie $D_{\infty h}$ est d'environ 15 kcal/mol au-dessus de celle de l'état fondamental $^1A_1'$ et de 48,2 kcal/mol inférieure à celle des atomes séparés Be($^1S_0$) + Be(^3P). L'état $^3\Sigma_u^+$ a un caractère de diradical-1,3 et les spins électroniques des états triplets supérieurs α sont délocalisés sur les trois atomes de Be. L'énergie de l'état triplet suivant le plus élevé $^3\Sigma_u$ est de 7,7 kcal/mol supérieure à celle de l'état le plus faible $^3\Sigma_u^+$. Les états $^3\Sigma_g^-$ et $^3\Pi_g$ sont plus fortement liés que les états $^3\Sigma_u^+$ et $^3\Pi_u$. Les états triplets du Be_3 sont de nature liante comme les états triplets du Be_2. L'étude du processus réactionnel des réactions de transfert d'énergie du Be(^3P) : Be($^1S_0$) + Be(^3P) ⇄ Be_2($^3\Sigma_u^+$, $^3\Pi_g$) et Be_2($^1\Sigma_g^+$) + Be(^3P) → Be_2($^3\Sigma_u^+$) + Be($^1S_0$) montre que ces réactions ne caractérisent aucune barrière d'énergie d'activation.

[Traduit par la revue]

Introduction

The electronic structure and properties of small metal clusters have gained considerable attention on account of their theoretical and experimental interest, as useful models for crystals (1–3), point defects (4), catalysis (5–7), and chemisorption (8–13). Among the various metal clusters that have been investigated theoretically, probably beryllium clusters of varying size have been studied most extensively (14–21). The smallest system, Be_2, has been used as a model in theoretical studies since 1931 (22, 23). The potential energy curve of the ground state of Be_2 has been the subject of a number of theoretical investigations (14–18) but in spite of the large number of calculations with various degrees of sophistication, it was only recently that reliable calculations on the potential energy curve for the ground state of Be_2 have been reported (14, 16, 17). The calculated values of R_e = 2.51 Å (16), 2.50 Å (17) and D_e = 2.23–2.34 kcal/mol (14), 2.04 ± 0.2 kcal/mol (17) are in good agreement with the experimentally determined values of R_e = 2.465 Å, and D_e = 2.29 kcal/mol (24–26).

Recently the Be atom has been used as a model in the molecular orbital studies of metal atom reactions with unsaturated hydrocarbons (27, 28) and with the hydrogen molecule (29). The reactions of Be(^3P) atoms have also been utilized in *ab initio* MO studies for the elucidation of the mechanism of electronic energy transfer reactions (28–30). As a simple model of Be(^3P) atom reactions, we studied the reaction of Be(^3P) with Be($^1S_0$) and Be_2($^1\Sigma_g^+$) giving rise to triplet Be_2 and Be_3, respectively. Even though a large number of theoretical studies with varying degrees of sophistication have been carried out on the ground state potential energy curve of Be_2 and Be_3, only relatively few studies on the excited states of Be_2 and Be_3 have been reported in the literature. The first study reported on the excited states of Be_2 by Furry and Bartlett (23) using the Heitler–London valence bond method indicated that the triplet state potential curves were repulsive for small values of internuclear distances and for larger separations, the method behaved erratically. Fraga and Ransil (31) calculated the potential energy curves for the lowest lying excited Σ states at the SCF level with best limited STO basis set. The low-lying electronic excited states of the Be_2 molecule have also been examined by Bender and Davidson (32) with the MO SCF CI method using a basis set of elliptical orbitals. Molecular binding energy curves for the low-lying states were also studied using the local spin-density functional formalism (33). Whiteside *et al.* (18) reported the optimized Be—Be distance for the $^3\Sigma_u^+$ state of Be_2 and Be_3 at the UHF-SCF level and total energy at the UHF-SCF and UMP4 (SDQ) level.

In our Be(^3P) reaction studies here we report the potential energy curves of the low-lying triplet states of Be_2 and Be_3 and

[1]Author to whom all correspondence is to be addressed.

Can. J. Chem. Downloaded from www.nrcresearchpress.com by 112.217.228.212 on 09/07/12
For personal use only.

Can. J. Chem. Downloaded from www.nrcresearchpress.com by 112.217.228.212 on 09/07/12
For personal use only.

the reaction paths for the processes $Be(^1S_0) + Be(^3P) \rightleftarrows Be_2(^3\Sigma_u^+, {}^3\Pi_g)$ and $Be_2(^1\Sigma_g^+) + Be(^3P) \rightarrow Be_3(^3\Sigma_u^+) \rightarrow Be_2(^3\Sigma_u^+) + Be(^1S_0)$.

Methods

The uniform quality gaussian basis set of $10s$, $5p$ were contracted according to a "2.5 zeta" (double zeta for the core and triple zeta for the valence shell) contraction scheme reported earlier (34). A single set of 6, d polarization function with $\alpha_d = 0.255$ was added to the s, p basis set. Molecular parameters were optimized at the RHF-SCF level by the energy gradient method and by the stepwise method, fitting the parabola for the minimum energy at the CI level. CI calculations including all singly and doubly excited configurations (CISD) with respect to the SCF configuration were done using the direct CI method (35). Davidson's formula (36) was applied to the CI results to estimate the correction for the quadruple excitation (CISDQ). All electrons and all orbitals were used in the CI calculations of the Be atom and Be_2 with s, p basis set. In the s, p, d basis set CI computations of Be_2, four δ virtual orbitals were kept frozen, and in the Be atom, two d virtual orbitals were kept frozen.

In the case of the triplet states of Be_3, the three lowest occupied orbitals corresponding to $1s$ core orbitals were kept doubly occupied and frozen, and only the lowest $15\sigma + 12\pi$ orbitals were used in CI calculations. Correspondingly, to calculate relative energies with respect to separated entities the total CI energies of $Be(^1S_0)$ and $Be(^3P)$ were recalculated with only $5s$ and $4p$ orbitals and the lowest occupied orbital corresponding to the $1s$ core orbital was kept doubly occupied and frozen. All computations were carried out employing the modified version of the GAUSSIAN 80 Program (37), the MONSTERGAUSS Program (38).

Results and discussion

Triplet states of Be_2

Total energies calculated at the RHF-SCF and CI level for Be, $^1S_0$ and ^3P states are given in Table 1. The optimized Be—Be distance for the four lowest triplet electronic states of Be_2, $^3\Sigma_u^+$, $^3\Pi_g$, $^3\Sigma_g^-$, and $^3\Pi_u$ with electronic configuration, total energy, and relative energies with respect to the separated $Be(^1S_0) + Be(^3P)$ atoms, are summarized in Table 2. The corresponding potential energy curves with s, p basis set at the CISD level are plotted in Fig. 1. For comparison the ground state, $^1\Sigma_g^+$, potential energy curve is calculated at the same level as the triplet states and is also plotted in Fig. 1. As expected with simple molecular orbital methods the ground $^1\Sigma_g^+$ state turns out to be repulsive, but the most sophisticated calculations predict a weak binding energy of ≈ 2 kcal/mol (14, 16, 17). Recent experimental results from gas phase, laser-induced fluorescence spectral studies of Be_2 also predict a binding energy of ≈ 2 kcal/mol (24–26). Since the ground $^1\Sigma_g^+$ state of Be_2 has the electronic configuration $(1\sigma_g)^2(1\sigma_u)^2(2\sigma_g)^2(2\sigma_u)^2$, featuring two bonding and two antibonding electrons, the binding energy expected is very small. Electronic excitation by promoting one electron from the highest occupied antibonding $2\sigma_u$ orbital to the low-lying unoccupied $3\sigma_g$ or $^1\pi_u$ bonding orbital will produce more strongly bonded low-lying excited states of Be_2 with respect to the corresponding separated atoms. This has been deduced from spectroscopic constants and lifetime calculations for the low-lying excited states, obtained in gas phase laser induced fluorescence studies of Be_2 (24–26). Similar conclusions were also arrived at in the theoretical

TABLE 1. Total energy (au) of Be

Level of calculation	Total energy $Be(^1S_0)$	Total energy $Be(^3P)$
$10s,5p$ basis set		
RHF-SCF	−14.572109	−14.510522
CISD	−14.629300	−14.526252
CISDQ	−14.634574	−14.526297
$10s,5p,1d$ basis set		
RHF-SCF	−14.572113	−14.512144
CISD	−14.630171	−14.530836
	(−14.629966)[a]	(−14.530835)
CISDQ	−14.635295	−14.530946
	(−14.635158)	(−14.530945)

[a]Values in parentheses are with two "d" virtual orbitals kept frozen in CI calculations.

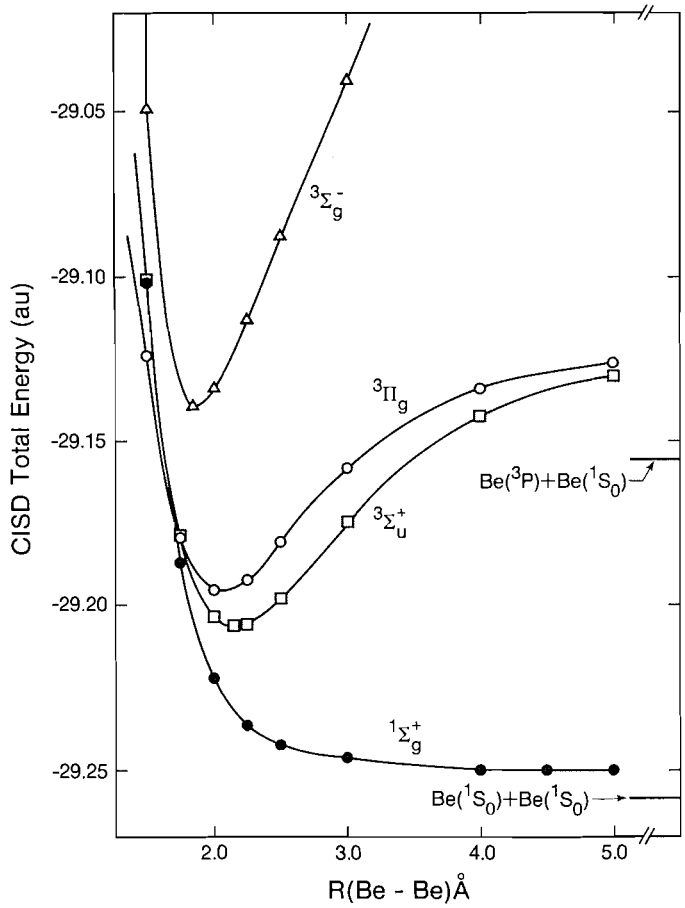

FIG. 1. Low lying triplet states potential energy curves of Be_2, with $10s$, $5p$ basis set at the CISD level.

calculations reported earlier on Be_2 (31–33). The lowest triplet state, $^3\Sigma_u^+$ has a diradical structure. At the RHF-SCF level, this state lies below the ground singlet state, $^1\Sigma_g^+$. This is mainly the consequence of the neglect of correlation energy, which is larger for the singlet than the triplet state. Inclusion of the correlation energy by CI calculations predict the correct order of the potential energy curves which can be seen in Fig. 1. The lowest triplet state, $^3\Sigma_u^+$, is 36.8 kcal/mol higher in energy than

TABLE 2. Optimized Be—Be distance, total and relative energies of low lying triplet states of Be_2

Electronic configuration[a]	State	Level of calculation	R(Be—Be) (Å)	Total energy (au)	Relative energy[b] (kcal/mol)
			$10s,5p$ basis set		
$..(2\sigma_g)^2(2\sigma_u)^1(3\sigma_g)^1$	$^3\Sigma_u^+$	RHF-SCF	2.147	−29.142956	−37.85
		CISD	2.161	−29.206720	−32.11
		CISDQ	2.161	−29.210449	−31.11
			$10s,5p,1d$ basis set		
		RHF-SCF	2.151	−29.145232	−38.26
		CISD	2.144	−29.223777	−39.52
		CISDQ	2.144	−29.228897	−39.40
			$10s,5p$ basis set		
$..(2\sigma_g)^2(2\sigma_u)^1(1\pi_u)^1$	$^3\Pi_g$	RHF-SCF	2.024	−29.108904	−16.49
		CISD	2.081	−29.195200	−24.88
		CISDQ	2.081	−29.203414	−26.70
			$10s,5p,1d$ basis set		
		RHF-SCF	2.022	−29.110997	−16.78
		CISD	2.022	−29.206014	−28.37
		CISDQ	2.066	−29.215077	−30.73
			$10s,5p$ basis set		
$..(2\sigma_g)^2(1\pi_u)^1(2\pi_u)^1$	$^3\Sigma_g^-$	RHF-SCF	1.790	−29.061645	+13.17
		CISD	1.847	−29.138862	+10.47
		CISDQ	1.847	−29.145105	+9.89
			$10s,5p,1d$ basis set		
		RHF-SCF	1.785	−29.063762	+12.86
		CISD	1.835	−29.150458	+6.49
		CISDQ	1.835	−29.157704	+1.94
			$10s,5p$ basis set		
$..(2\sigma_g)^2(1\pi_u)^1(3\sigma_g)^1$	$^3\Pi_u$	RHF-SCF	1.902	−29.036374	+29.03
		CISD	1.950	−29.124140	+19.71
		CISDQ	2.009	−29.137896	+14.42

[a]Valence electrons only, core is $(1\sigma_g)^2(1\sigma_u)^2$.
[b]Relative energy with respect to separated Be($^1S_0$) + Be(^3P) atoms, $\Delta E = E^3[Be_2] - E[Be(^1S_0) + Be(^3P)]$.

the ground state $^1\Sigma_g^+$ (in the present case the $^1\Sigma_g^+$ state total energy is taken as twice the total energy of Be($^1S_0$)), with the s, p basis set. Inclusion of the d polarization function brings this energy down to 26.0 kcal/mol. The next triplet state, $^3\Pi_g$, is very close to the $^3\Sigma_u^+$ state, with only 4.4 kcal/mol (with s, p basis set and 8.7 kcal/mol with s, p, d basis set at the CISDQ level) higher in energy. Single reference CI calculations at larger atomic separations (≥4 Å) does not give the complete representation of the state as seen by the coefficient of the root configuration ($C_0 \leq 0.90$). Thus, for the correct shape of the potential energy curve at larger separations ($R > 4$ Å) multi-reference CI calculations would be required. However, in the present studies this region was of no particular importance. The effect of addition of the d polarization function on the optimized Be—Be distance was not significant, Table 2, and inclusion of correlation energy by CI calculations slightly increased the optimized Be—Be distance in all cases, except in the case of s, p, d basis set calculations of the $^3\Sigma_u^+$ state, where it had a slightly decreasing effect on the computed distance. The optimized Be—Be distance in the $^3\Sigma_u^+$ state (2.144–2.161 Å) is close to the experimental value of 2.16 Å for the $^1\Sigma_u^+$ state (24, 26). Thus far triplet states of Be_2 have not been observed experimentally. The earlier reported optimized Be—Be distance of 2.182 Å for the $^3\Sigma_u^+$ state by STO basis set (31) and 2.20 Å by spin density functional calculations (33) are slightly longer than our optimized value. The recent UHF/6-31G optimized (18) value of 2.155 Å is close to the present optimized value. The Be—Be distance in the $^3\Pi_g$ state is slightly shorter than in the $^3\Sigma_u^+$ state (Table 2), and similar to the earlier reported optimized value of 2.03 Å (33). The optimized Be—Be distance in the $^3\Sigma_g^-$ state is much shorter than in the $^3\Sigma_u^+$ and $^3\Pi_g$ states (Table 2) and similar to the earlier reported value of 1.79 Å (33). The $^3\Pi_u$ state optimized Be—Be distance at the RHF-SCF level is close to the optimized distance of the $^3\Pi_g$ state (Table 2). The Be_2 $^3\Sigma_u^+$ state is 37.9 kcal/mol lower in energy at the RHF-SCF level with s, p basis set, than the separated Be($^1S_0$) and Be(^3P) atoms, which at the CISDQ level reduces to 31.1 kcal/mol.

These values are similar to the UHF/6-31G (39.8 kcal/mol) and UMP4(SDQ)/6-31G (33.5 kcal/mol) results reported by

Can. J. Chem. Downloaded from www.nrcresearchpress.com by 112.217.228.212 on 09/07/12
For personal use only.

Can. J. Chem. Downloaded from www.nrcresearchpress.com by 112.217.228.212 on 09/07/12
For personal use only.

Whiteside *et al.* (18). Addition of the *d* polarization function does not bring about a significant change in the relative energy (38.3 kcal/mol) at the SCF level. Inclusion of correlation energy by CI calculations at the *s*, *p* basis set at CISDQ level, however, decreases the relative energy compared to the SCF value. On the other hand, with the *s*, *p*, *d* basis set, the relative energy increases slightly to 39.4 kcal/mol as a result of CI calculations at the CISDQ level (Table 2). In the next higher-lying $^3\Pi_g$ state, the inclusion of correlation energy increases the relative energy by 10 kcal/mol with the *s*, *p* basis set, and 14 kcal/mol with the *s*, *p*, *d* basis set. The $^3\Pi_g$ state is 30.7 kcal/mol more stable than the separated Be($^1S_0$) + Be(^3P) atoms. A similar trend is observed in the $^3\Sigma_g^-$ and $^3\Pi_u$ state relative energies. These triplet states are slightly higher in energy than the separated Be($^1S_0$) + Be(^3P), and dissociate to higher excited Be atoms. The $^3\Sigma_u^+$, $^3\Pi_g$, and $^3\Sigma_g^-$ states potential energy curves have a bonding character. At shorter Be—Be distances ($\leq$1.5 Å) all three triplet states collapse into a single state.

Triplet states of Be_3

The ground state Be_3($^1A_1'$) with equilateral triangle (D_{3h}) has been studied in detail in recent years (14, 15, 18, 39, 40). The potential energy curve according to Whiteside *et al.* (18) at the RHF/6-31G level shows a shallow minimum of 0.5 kcal/mol at 4.706 Å with a close in maximum around 3.0 Å and a second minimum at 2.244 Å with an energy 1.6 kcal/mol above that of the three separated Be($^1S_0$) atoms. Addition of *d* functions (6-31G*) lowered this minimum by 3.3 kcal/mol at the optimized distance of 2.234 Å. Inclusion of correlation energy by MP_2, MP_3, MP_4(SDQ) level with 6-31G* basis set yielded binding energies of 24.7, 19.5, and 13.1 kcal/mol, respectively. This poor convergence of the perturbation series for the binding energy is associated with the isolated atoms rather than the Be_3 molecule. Whiteside *et al.* (18) estimate their best value at the CCD level, predicting 6.0 kcal/mol for the binding energy. Pacchioni and Koutecky (39) have also calculated the dissociation energy of 7.1 kcal/mol with 4*s*, 2*p*, 1*d* basis set at the MRSD CI level, for the distance of 2.223 Å. The most accurate results for the $^1A_1'$ ground state of Be_3, reported recently by Harrison and Handy (14), show that Be_3 is bound only at the full CI level of accuracy at 2.233 Å with 22–25 kcal/mol binding energy.

The closed shell $^1\Sigma_g^+$ and low lying $^3\Sigma_u^+$ and $^3\Sigma_g^-$ excited states for the linear ($D_{\infty h}$) structure have been studied by Whiteside *et al.* (18). The STO-3G basis set SCF level results predicted that the $^3\Sigma_u^+$ state has the lowest energy followed by the $^1A_1'$, $^1\Sigma_g^+$, and $^3\Sigma_g^+$ states. Their UHF/6-31G and UHF/6-31G* results also predicted that the $^3\Sigma_u^+$ state is lower than the $^1A_1'$ ground state, similar to that of Be_2. On inclusion of correlation energy by UMP computations, this order was reversed. Pacchioni and Koutecky (39) have also studied the $^1\Sigma_g^+$ and $^3\Sigma_u^+$ states with 4*s*, 2*p* and 4*s*, 2*p*, 1*d* basis set by an *ab initio* pseudopotential method followed by MRD CI calculations. The computed potential curves closely resembled those of diatomic Be, and the $^1\Sigma_g^+$ state was predicted to have a slight bonding character.

We studied the potential energy curves for the low-lying triplet states of Be_3, both at the RHF-SCF and limited CI levels, with linear $D_{\infty h}$ symmetry. The Be—Be distance for the lowest $^3\Sigma_u^+$ state has been optimized at the RHF-SCF, CISD and CISDQ level with both *s*, *p* and *s*, *p*, *d* basis set, whereas for the higher, $^3\Pi_u$, $^3\Sigma_g^+$, and $^3\Pi_g$ states, only the *s*, *p* basis set was used. The computed optimized Be—Be distance, with total and relative energies are given in Table 3. Relative energies were also calculated both with respect to separated atoms [2 × Be($^1S_0$) + Be(^3P)] and at 6.0 Å Be—Be separation. The corresponding potential energy curves with *s*, *p* basis set at the CISDQ level are plotted in Fig. 2. For comparison, the ground state equilateral triangle, D_{3h} symmetry $^1A_1'$ potential energy curve was also calculated at the same level as the triplet states and plotted in Fig. 2. Computed net atomic charges and atomic spin densities are summarized in Table 4. As predicted earlier (18), at the SCF level, the $^1A_1'$ potential energy curve goes through a local minimum at 2.240 Å, which is 3.7 kcal/mol higher in energy than the separated Be($^1S_0$) atoms, and a maximum around 2.75 Å, with 6.1 kcal/mol above the separated Be($^1S_0$) atoms, which disappears at the CI level calculations. At the present level of calculations the $^1A_1'$ ground state does not show much bonding. At the SCF level, the stability of the $^3\Sigma_u^+$ state is exaggerated and is predicted to be 25.6 kcal/mol more than the $^1A_1'$ ground state, which is due to the neglect of correlation energy. Inclusion of correlation energy, even with limited CI calculations gave the correct order of potential energy curves, Fig. 2. The lowest triplet state, $^3\Sigma_u^+$, lies ~15 kcal/mol above the ground $^1A_1'$ state. At the RHF-SCF level with *s*, *p* basis set, calculations showed that the $^3\Sigma_u^+$ state is the most stable triplet state being 64.3 kcal/mol lower in energy than the separated atoms, which is close to the earlier reported value of 68.3 kcal/mol with UHF/6-31G (18), and the optimized Be—Be distance of 2.161 Å is also similar to the UHF/6-31G optimized value of 2.172 Å (18). Addition of the *d* polarization function did not change much either the optimized Be—Be distance or the relative energy (Table 3). Inclusion of correlation energy slightly increased the bond distance and the relative energy with respect to the separated atoms. Values of relative energies with respect to the 6.00 Å distance of separation are much smaller than the values calculated by the separated atom values. This may be due to a poor convergence of the correlation energy in the separated atoms. Thus, if we take the 6.00 Å distance value as the lower limit, the $^3\Sigma_u^+$ state is 47.1 kcal/mol lower than the separated atoms at the CISDQ level computations with *s*, *p* basis set and 48.2 kcal/mol with the *s*, *p*, *d* basis set. From the calculated atomic spin density values (Table 4) and the localized molecular orbital (LMO) analysis, in its $^3\Sigma_u^+$ state the Be_3 molecule has a diradical character having one α spin electron on each of its terminal Be atoms.

The next lowest triplet state, the $^3\Pi_u$ state obtained by the promotion of an electron to the $1\pi_u$ orbital from $3\sigma_u$, is 36.8 kcal/mol higher in energy at the SCF level, than the $^3\Sigma_u^+$ state. With inclusion of correlation energy this value reduces to 7.7 kcal/mol at the CISDQ level, and lies 39.4 kcal/mol lower than the separated atoms at 6.00 Å separation. The optimized Be—Be distance of the $^3\Pi_u$ state is slightly shorter (~0.06 Å) than in the $^3\Sigma_u^+$ state. Computed atomic spin densities and the LMO analysis showed that the two α spin electrons are delocalized among the three Be atoms, with slightly more concentration at the central Be atom. Interaction between the three atoms takes place near 2.50 Å separation, above this distance the LMO analysis shows that all three atoms are separated. The lowest $^3\Sigma_u^+$ and $^3\Pi_u$ states dissociate to two Be($^1S_0$) and one Be(^3P), whereas the higher $^3\Sigma_g^-$ and $^3\Pi_g$ states dissociate to higher excited states. Both the $^3\Sigma_g^-$ and $^3\Pi_g$ states lie much higher than the low-lying $^3\Sigma_u^+$ and $^3\Pi_u$ states. The $^3\Sigma_g^-$ state is 51.1 kcal/mol at the SCF level (30.4 kcal/mol at CISDQ) and $^3\Pi_g$ state 61.1 kcal/mol at the SCF level

Can. J. Chem. Downloaded from www.nrcresearchpress.com by 112.217.228.212 on 09/07/12
For personal use only.

TABLE 3. Optimized Be—Be distance, total and relative energies of low lying triplet states of Be_3

Electronic configuration[a]	State	Level of calculation	R(Be—Be) (Å)	Total energy (au)	ΔE^b (kcal/mol)
$D_{\infty h}$					
			$10s,5p$ basis set		
$...(3\sigma_g)^2(2\sigma_u)^2(4\sigma_g)^1(3\sigma_u)^1$	$^3\Sigma_u^+$	RHF-SCF	2.161	−43.757168	−64.28 (−64.29)[c]
		CISD	2.202	−43.807205	−69.03 (−50.41)
		CISDQ	2.211	−43.812028	−70.77 (−47.11)
			$10s,5p,1d$ basis set		
		RHF-SCF	2.164	−43.760347	−65.25 (−65.26)
		CISD	2.203	−43.810353	−69.96 (−51.46)
		CISDQ	2.214	−43.815136	−71.68 (−48.15)
			$10s,5p$ basis set		
$...(3\sigma_g)^2(2\sigma_u)^2(4\sigma_g)^1(1\pi_u)^1$	$^3\Pi_u$	RHF-SCF	2.097	−43.698572	−27.51 (−27.48)
		CISD	2.155[d]	−43.785703	−55.53 (−36.87)
		CISDQ	2.155	−43.799801	−63.10 (−39.40)
$...(3\sigma_g)^2(2\sigma_u)^2(1\pi_u)^1(2\pi_u)^1$	$^3\Sigma_g^-$	RHF-SCF	1.937	−43.675740	−13.18 (−123.07)
		CISD	1.937[d]	−43.752318	−34.58 (−125.70)
		CISDQ	2.020	−43.763544	−40.35 (−126.31)
$...(3\sigma_g)^2(2\sigma_u)^2(1\pi_u)^1(3\sigma_u)^1$	$^3\Pi_g$	RHF-SCF	2.023	−43.659877	−3.22 (−113.18)
		CISD	2.023[d]	−43.744482	−29.67 (−120.84)
		CISDQ	2.115	−43.766091	−41.95 (−127.61)
$C_{\infty v}$					
$...(4\sigma)^2(5\sigma)^2(6\sigma)^1(1\pi)^1$	$^3\Pi$	RHF-SCF	2.123[e] 2.027[f]	−43.717752	−39.54 (−39.53)
		CISD	2.155[e] 2.130[f]	−43.781819	−53.10 (−34.31)
		CISDQ		−43.792652	−58.62 (−34.76)

[a]Valence electrons only, core is $(1\sigma_g)^2(1\sigma_u)^2(2\sigma_g)^2$.
[b]Relative energy with respect to separated atoms, $\Delta E = E^3[Be_3] - E[Be(^3P) + 2Be(^1S_0)]$.
[c]Relative energy with respect to (Be—Be) distance of 6.0 Å.
[d]Geometry not reoptimized.
[e]$R(Be_1—Be_2)$.
[f]$R(Be_1—Be_3)$ (Fig. 3).

(28.8 kcal/mol at CISDQ) higher than the lowest $^3\Sigma_u^+$ state. At the SCF level the $^3\Pi_g$ state is higher than the $^3\Sigma_g^-$ state; the inclusion of correlation energy brings the $^3\Pi_g$ state slightly lower than the $^3\Sigma_g^-$ state (~1.6 kcal/mol). Optimized Be—Be distances (Table 3) for these states are slightly shorter than the $^3\Sigma_u^+$ and $^3\Pi_u$ states. Computed atomic spin densities (Table 4) and LMO analysis showed that in both cases the α spin electrons are delocalized among the three Be atoms, slightly concentrating more at the central Be atom. Relative energies with respect to separated atoms at 6.00 Å separations and $2Be(^1S_0)$ + $Be(^3P)$ are given in Table 3 for comparison purposes. Computed net atomic charges calculated by the Mulliken population analysis (Table 4) show that the central Be atom has more negative charge than the terminal Be atoms in all the triplet states studied.

Be(^{3}P) reaction paths

The reaction, $Be(^3P)$ + $Be(^1S_0)$ can produce the Be_2 molecule in the $^3\Sigma_u^+$ and $^3\Pi_g$ states, both being more stable than the separated atoms, the $^3\Sigma_u^+$ state, by 39.4 kcal/mol, and the $^3\Pi_g$ state by 30.7 kcal/mol at the CISDQ level with s,p,d basis set. It is also important to note that there is no activation energy barrier for either of these reactions. We have also studied the $Be(^3P)$ reaction with the ground state $Be_2(^1\Sigma_g^+)$, producing triplet Be_3 molecules in two states, namely $^3\Sigma_u^+$ and $^3\Pi_u$. Both of these states are more stable than the separated entities by 47.1 and 39.4 kcal/mol, respectively, relative to the 6.0 Å separation. We calculated the total energies both at the SCF and CI levels with the s,p basis set, as a function of the $Be_1—Be_3$ distance along both the $^3\Sigma$ and $^3\Pi$ reaction paths. The $Be_1—Be_2$ distance was optimized for each $Be_1—Be_3$ distance. Cross sections of each of the resulting potential energy surfaces for the $^3\Sigma$ and $^3\Pi$ states at the CISDQ level are plotted in Fig. 3. Along the $^3\Sigma$ path, until the $Be_1—Be_3$ distance reaches 4.00 Å, all three Be atoms remain separated and around 3.75 Å the energy transfer from $Be(^3P)$ to $Be_2(^1\Sigma_g^+)$ takes place giving $Be(^1S_0)$ and $Be_2(^3\Sigma_u^+)$. From here the reaction can go in two directions to yield either $Be_2(^3\Sigma_u^+)$ and $Be(^1S_0)$, or if the $Be_1—Be_3$ distance decreases, this will form $Be_3(^3\Sigma_u^+)$, along the surface below 3.75 Å distance. At the SCF level for the $Be_2(^1\Sigma_g^+)$ + $Be(^3P)$ → $Be_2(^3\Sigma_u^+)$ + $Be(^1S_0)$ reaction path calculations predict a small activation energy barrier of 0.7 kcal/mol around 4.00 Å, which, however, disappears at the CI level. Along the $^3\Pi$ reaction path all three Be atoms remain separated until the $Be_1—Be_3$ distance reaches 3.00 Å. Below this distance, one of the α spin electrons is

Can. J. Chem. Downloaded from www.nrcresearchpress.com by 112.217.228.212 on 09/07/12
For personal use only.

TABLE 4. Net atomic charges and atomic spin densities of triplet Be_3[a]

	Net atomic charge		Atomic spin density	
State	Be_t	Be_c	Be_t	Be_c
$D_{\infty h}$				
$^3\Sigma_u^+$	0.118	−0.236	0.958	0.084
$^3\Pi_u$	0.152	−0.303	0.596	0.808
$^3\Sigma_g^-$	0.158	−0.316	0.476	1.048
$^3\Pi_g$	0.157	−0.315	0.635	0.730

	Net atomic charge			Atomic spin density		
$C_{\infty v}$	Be_2	Be_1	Be_3	Be_2	Be_1	Be_3
$^3\Pi$	0.198	−0.152	−0.046	0.948	0.375	0.677

[a]Be_t, terminal Be atoms; Be_c, central Be atom.

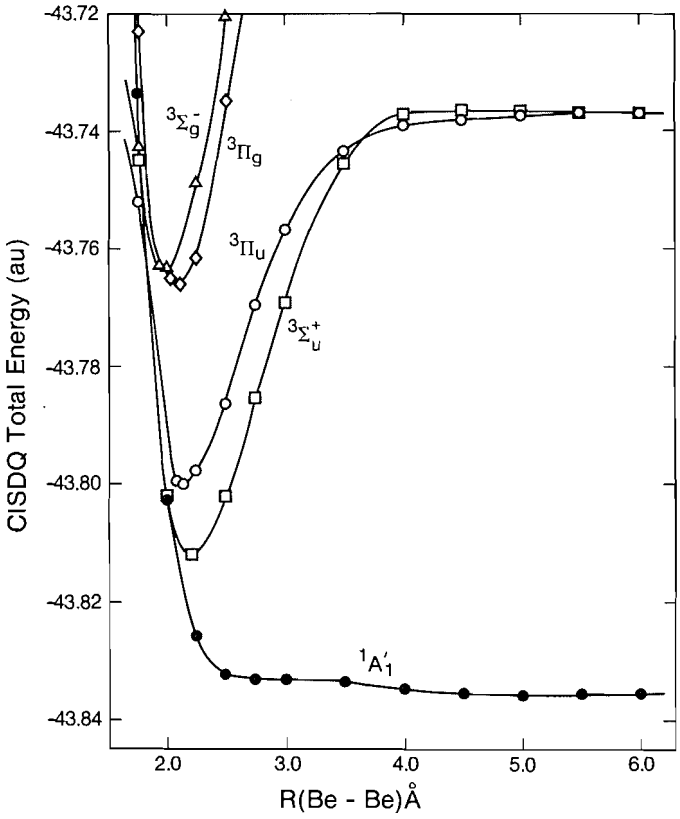

FIG. 2. Low lying triplet states potential energy curves of Be_3, with 10*s*, 5*p* basis set at the CISDQ level.

localized on the terminal Be_3 atom and the other α spin electron is delocalized between Be_1 and Be_2. Around a value of 2.0 Å for the distance of Be_1—Be_3, these electrons are switched, one localizing on Be_2 and the other delocalizing between Be_1 and Be_3. The fully optimized $^3\Pi$ state (with $C_{\infty v}$ symmetry) at the RHF-SCF level (Table 3) is 12.0 kcal/mol lower than the $^3\Pi_u$ (with $D_{\infty h}$ symmetry).

RHF-SCF geometry optimization of localized structures **I** and **II** with one short and one long bond length ($^3\Pi$, $C_{\infty v}$)

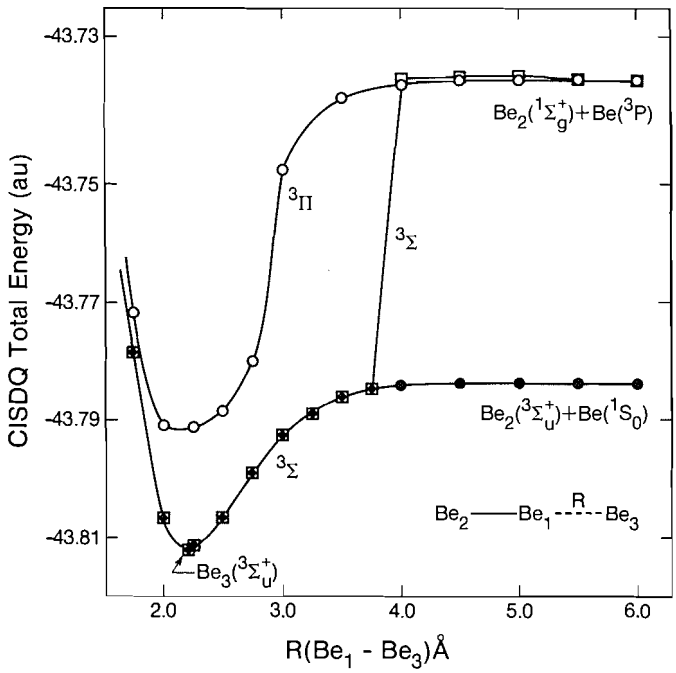

FIG. 3. $^3\Sigma$ and $^3\Pi$ Potential energy surface for the reaction of $Be_2(^1\Sigma_g^+)$ + Be(^3P) → $Be_3(^3\Sigma_u^+)$ → $Be_2(^3\Sigma_u^+)$ + Be($^1S_0$), with 10*s*, 5*p* basis set at the CISDQ level.

overestimates the stability relative to the delocalized structure **III** with intermediate equal bond lengths ($^3\Pi_u$, $D_{\infty h}$).

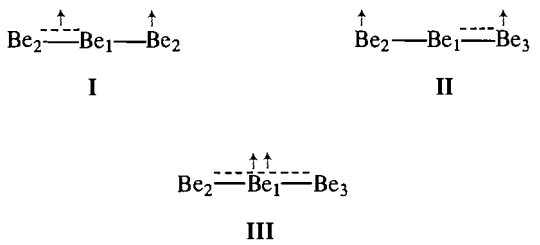

This type of symmetry dilemma has been observed for allyl and other carbon free radicals and is described in the literature (41–44), and the problem has been shown to be resolvable by inclusion of the correlation energy. The results of the CI computations predict the $^3\Pi_u$ state to be 4.5 kcal/mol lower in energy than the $^3\Pi$ state. The $^3\Pi$ reaction path does not show any activation energy barrier either at the SCF or at the CI level. This surface crosses over to the lowest $^3\Sigma$ or $^3\Sigma_u^+$ state at the early part of the reaction (~4.0 Å) or at shorter distances below 1.75 Å (Figs. 2 and 3). The $^3\Sigma$ reaction path for the $Be_3(^3\Sigma_u^+)$ → $Be_2(^3\Sigma_u^+)$ + Be($^1S_0$) was also computed at the SCF and CI level with *s*, *p* basis set as a function of $R(Be_1—Be_3)$ (Fig. 3). The $Be_3(^3\Sigma_u^+)$ state is 17.8 kcal/mol (at the CISDQ level) lower than that of $Be_2(^3\Sigma_u^+)$ + Be($^1S_0$) at 6.00 Å separation. Beyond 3.00 Å separation between Be_1 and Be_3, $Be_2(^3\Sigma_u^+)$ and Be($^1S_0$) remain as separated entities, with α spin electrons on Be_1 and Be_2. At the distance of 3.00 Å and below, the α electrons are localized on Be_2 and Be_3 and follow the $^3\Sigma$ path to the minimum at the $Be_3(^3\Sigma_u^+)$ state. At the SCF level there is a small energy barrier of 1.5 kcal/mol around 3.25 Å distance of Be_1—Be_3, for the reaction of $Be_2(^3\Sigma_u^+)$ + Be($^1S_0$) → $Be_3(^3\Sigma_u^+)$, which disappears at the CI level.

Thus, the energy transfer reaction of Be(^3P) to $Be_2(^1\Sigma_g^+)$ giving $Be_2(^3\Sigma_u^+)$ and Be($^1S_0$) suddenly goes through to the $^3\Sigma$

surface without any activation energy near 3.75 Å separation, or it can go through the $^3\Sigma$ path to form $Be_3(^3\Sigma_u^+)$ and dissociate without any activation energy barrier to $Be_2(^3\Sigma_u^+)$ and $Be(^1S_0)$. $Be_2(^1\Sigma_g^+)$ + $Be(^3P)$ can also give rise to the $Be_3(^3\Pi_u)$ state along the $^3\Pi$ reaction path, which in turn crosses over to the lowest $^3\Sigma_u^+$ state in the early stage of the reaction or at shorter distances in the molecular compression region ($R \geq 1.75$ Å) which subsequently can dissociate to give $Be_2(^3\Sigma_u^+)$ + $Be(^1S_0)$.

Acknowledgement

The authors thank the Natural Sciences and Engineering Research Council of Canada for continuing financial support.

1. S. Goldstein, L. A. Curtiss, and R. N. Euwema. J. Phys. C**9**, 4131 (1976).
2. W. H. Fink. J. Chem. Phys. **69**, 3325 (1978).
3. J. Wood. Chem. Phys. Lett. **50**, 129 (1977).
4. H. Stoll and H. Preuss. Phys. Stat. Sol. **64**B, 103 (1974).
5. R. van Hardeveld and F. Hartog. Adv. Catal. **22**, 75 (1972).
6. J. H. Sinfelt. J. Catal. **29**, 308 (1973).
7. M. Lelental. J. Catal. **32**, 429 (1974).
8. C. W. Bauschlicher, Jr., D. H. Liskow, C. F. Bender, and H. F. Schaefer III. J. Chem. Phys. **62**, 4815 (1975).
9. C. W. Bauschlicher, Jr., C. F. Bender, H. F. Schaefer III, and P. S. Bagus. Chem. Phys. **15**, 227 (1976).
10. A. B. Kunz, D. J. Mickish, and P. W. Deutch. Solid State Commun. **13**, 35 (1975).
11. P. S. Bagus, H. F. Schaefer III, and C. W. Bauschlicher, Jr. J. Chem. Phys. **78**, 1390 (1983).
12. B. N. Cox and C. W. Bauschlicher, Jr. Surface Sci. **102**, 295 (1981).
13. R. P. Messmer. Surface Sci. **106**, 225 (1981).
14. R. J. Harrison and N. C. Handy. Chem. Phys. Lett. **123**, 321 (1986); and references therein.
15. M. Bulski and G. Chalasinski. Chem. Phys. Lett. **128**, 25 (1986); and references therein.
16. R. J. Harrison and N. C. Handy. Chem. Phys. Lett. **98**, 97 (1983).
17. B. H. Lengsfield, A. D. McLean, M. Yoshimine, and B. Liu. J. Chem. Phys. **79**, 1891 (1983).
18. R. A. Whiteside, R. Krishnan, J. A. Pople, M. Krogh-Jespersen, P. von R. Schleyer, and G. Wenke. J. Comp. Chem. **1**, 307 (1980).
19. P. S. Bagus, C. J. Nelin, and C. W. Bauschlicher, Jr. Surface Sci. **156**, 615 (1985).
20. W. C. Ermler, C. W. Kern, R. M. Pitzer, and N. W. Winter. J. Chem. Phys. **84**, 3937 (1986).
21. C. W. Bauschlicher, Jr., and L. G. M. Pettersson. J. Chem. Phys. **84**, 2226 (1986); Chem. Phys. Lett. **130**, 111 (1986).
22. J. H. Bartlett, Jr. and W. H. Furry. Phys. Rev. **38**, 1615 (1931).
23. W. H. Furry and J. H. Bartlett, Jr. Phys. Rev. **39**, 210 (1932).
24. V. E. Bondybey and J. H. English. J. Chem. Phys. **80**, 568 (1980).
25. V. E. Bondybey. Chem. Phys. Lett. **109**, 436 (1984).
26. V. E. Bondybey. Science, **227**, 125 (1985).
27. W. C. Swope and H. F. Schaefer III. J. Am. Chem. Soc. **98**, 7962 (1976).
28. R. K. Gosavi, O. P. Strausz, F. Bernardi, A. Kapur, and P. G. Mezey. J. Phys. Chem. **91**, 283 (1987).
29. R. A. Poirier, M. R. Peterson, and M. Menzinger. J. Chem. Phys. **78**, 4592 (1983).
30. R. K. Gosavi and O. P. Strausz. To be published.
31. S. Fraga and B. J. Ransil. J. Chem. Phys. **35**, 669 (1961).
32. C. F. Bender and E. R. Davidson. J. Chem. Phys. **47**, 4972 (1967).
33. R. O. Jones. J. Chem. Phys. **71**, 1300 (1979).
34. P. G. Mezey, F. Bernardi, I. G. Csizmadia, and O. P. Strausz. Chem. Phys. Lett. **59**, 117 (1978).
35. N. C. Handy, J. D. Goddard, and H. F. Schaefer III. J. Chem. Phys. **71**, 426 (1979).
36. S. R. Langhoff and E. R. Davidson. Int. J. Quantum Chem. **8**, 61 (1974).
37. J. S. Binkley, R. A. Whiteside, R. Krishnan, R. Seeger, D. J. DeFrees, H. B. Schlegel, S. Topiol, L. R. Khan, and J. A. Pople. GAUSSIAN 80, QCPE. 406 (1981).
38. M. R. Peterson and R. A. Poirier. MONSTERGAUSS 81, Department of Chemistry, University of Toronto, Toronto, Ontario, Canada. 1981.
39. G. Pacchioni and J. Koutecky. Chem. Phys. **71**, 181 (1982).
40. K. D. Jordan and J. Simons. J. Chem. Phys. **67**, 4027 (1977).
41. R. K. Gosavi, I. Safarik, and O. P. Strausz. Can. J. Chem. **63**, 1689 (1985) and references therein.
42. N. C. Baird, R. R. Gupta, and K. F. Taylor. J. Am. Chem. Soc. **101**, 4531 (1979).
43. J. Paldus and A. Veillard. Chem. Phys. Lett. **50**, 6 (1977); Mol. Phys. **35**, 445 (1978).
44. O. Kikuchi. Chem. Phys. Lett. **72**, 487 (1980).

Can. J. Chem. Downloaded from www.nrcresearchpress.com by 112.217.228.212 on 09/07/12
For personal use only.

Ab initio calculations on tetramethoxymethane

R. J. McEachern, J. A. Weil, and P. G. Mezey
Department of Chemistry, University of Saskatchewan, Saskatoon, Sask., Canada S7N 0W0

Received September 27, 1987

This paper is dedicated to Professor Charles A. McDowell on the occasion of his 70th birthday

R. J. McEachern, J. A. Weil, and P. G. Mezey. Can. J. Chem. **66**, 2041 (1988).

Minimal basis set *ab initio* SCF-MO calculations were performed on the 21-atom system of tetramethoxymethane (tetramethyl orthocarbonate). The geometric configuration of this model was optimized in two conformations, one having quasi-S_4 symmetry and the other D_{2d} symmetry. The S_4 conformation was found to be 8 kJ mol^{-1} lower in energy than the D_{2d} conformation, at the STO-3G level. The calculated energy difference is consistent with the recently measured geometric configuration of crystalline tetrabenzyl orthocarbonate. The calculated values of the bond lengths and angles were compared to the results of an electron diffraction study of the methyl species, and agree well with experiment. The theoretical electric dipole moment was calculated to be 0.01 D.

R. J. McEachern, J. A. Weil et P. G. Mezey. Can. J. Chem. **66**, 2041 (1988).

Utilisant un ensemble de base minimal, on a effectué des calculs d'OM *ab initio* en champ auto-cohérent sur le système à 21 atomes du tétraméthoxyméthane (orthocarbonate de tétraméthyle). On a optimisé la configuration géométrique de ce modèle dans deux conformations, l'une possédant une symétrie quasi-S_4 et l'autre de symétrie D_{2d}. Au niveau STO-3G, on a trouvé que l'énergie de la conformation S_4 est 8 kJ mol^{-1} plus faible que celle de la conformation D_{2d}. La différence d'énergie calculée est en accord avec la configuration géométrique mesurée récemment pour l'orthocarbonate de tétrabenzyle à l'état cristallin. On a comparé les valeurs calculées pour les longueurs et les angles de liaison avec les données expérimentales obtenues par diffraction électronique sur l'espèce méthylée et elles sont en bon accord avec les expériences. On a calculé que le moment dipolaire électrique est de 0,01 D.

[Traduit par la revue]

Can. J. Chem. Downloaded from www.nrcresearchpress.com by 112.217.228.212 on 09/07/12
For personal use only.

1. Introduction

Study of molecules in which a carbon atom has four oxygens as nearest neighbors, the so-called orthocarbonates, has been rather neglected. In particular, relatively little is known about molecules of type $C(OR)_4$, where R is an organic group. The simplest member of this family, tetramethoxymethane (tetramethyl orthocarbonate), $C(OCH_3)_4$, was first synthesized (1) in 1927, and has been employed in organic synthesis, particularly for the preparation of spiro-orthocarbonates (2, 3). However, despite this utility, the structure of this molecule has not been determined by X-ray diffraction, and spectroscopic studies have resulted in disagreement over its structure (4, 5). There are two low-energy conformations of the tetramethoxymethane model that must be considered (4): one has S_4 symmetry, while the other has D_{2d} symmetry. We retain this nomenclature even though the optimized S_4 conformation was found to have slight deviations from S_4 symmetry, and should be described as quasi-S_4 (see Results and Discussion). Both conformations of the tetramethoxymethane molecule can be visualized as having a (close to) tetrahedral arrangement of oxygen atoms around the central carbon atom, with the methyl groups placed so that the $C(OC)_4$ portion of the molecule has the appropriate (S_4 or D_{2d}) symmetry (see Fig. 1). The methyl groups each have a staggered conformation with respect to the C(central)—O bond. Mijlhoff *et al.* (6) did an electron diffraction study on tetramethoxymethane, and found that only the S_4 structure is present in the gas phase, with the molecule flattened so as to be oblate with respect to the S_4 axis. The central C—O bonds were found to be shorter than the peripheral C—O bonds; the relative lengths of the C—O bonds are important since this information provides insight into the anomeric effect (7–9), which is an important phenomenon in carbohydrate chemistry.

The present theoretical study was initiated to gain insight into the properties of orthocarbonates, since tetrabenzyl orthocarbonate has recently been synthesized in our laboratory, is crystalline, and has been shown[1] by X-ray diffraction to have central symmetry very close to S_4. *Ab initio* calculations on tetramethoxymethane serve as a tool to gain insight into the controversial and complex problem regarding the relative stability of the S_4 and D_{2d} conformations of this molecule. Other properties, such as bond lengths and the electric dipole moment, have been calculated herein and compared to experiment. Our study of tetramethoxymethane was also done because it is a useful model for simulation of a hypothetical carbon impurity in α-quartz[2] and in other silicates. In particular, the absence of reports in the literature of the occurrence of carbon

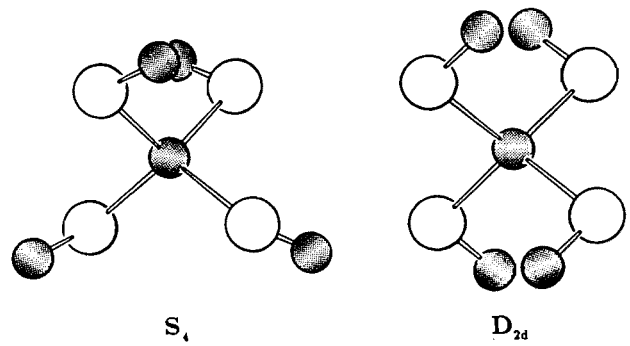

FIG. 1. The S_4 and D_{2d} conformations of the $C(OCH_3)_4$ model. The carbon and oxygen atoms are denoted by shaded and clear circles respectively. For clarity, the methyl protons are not shown. In the S_4 conformation, the S_4 axis lies vertically in the plane of the paper while, for the D_{2d} conformation, the S_4 axis lies horizontally in the plane of the paper; in both cases the axis threads the central carbon atom.

[1] D. R. Latimer, J. W. Quail, J. A. Weil, and W. T. Robinson. To be published.

[2] P. S. Rao, R. J. McEachern, and J. A. Weil. To be published.

Can. J. Chem. Downloaded from www.nrcresearchpress.com by 112.217.228.212 on 09/07/12
For personal use only.

TABLE 1. Cartesian coordinates (in Å) of the optimized geometric configurations of the $C(OCH_3)_4$ model

	S_4			D_{2d}		
Atom	x	y	z	x	y	z
C(0)	0.0000	0.0000	0.0000	0.0000	0.0000	0.0000
O(1)	0.0000	−0.7937	1.1879	0.7893	0.7886	0.8946
O(2)	0.0000	−0.7937	−1.1879	0.7893	−0.7886	−0.8946
O(3)	1.1872	0.7949	0.0000	−0.7883	0.7882	−0.8953
O(4)	−1.1872	0.7950	0.0000	−0.7883	−0.7882	0.8953
C(1)	−1.1971	−1.5805	1.2982	1.6698	1.6699	0.1755
C(2)	1.1968	−1.5805	−1.2984	1.6698	−1.6699	−0.1755
C(3)	1.2999	1.5773	1.1995	−1.6691	1.6790	−0.1786
C(4)	−1.2999	1.5773	−1.1995	−1.6691	−1.6790	0.1786
H(1)	−1.3699	−2.1885	0.4060	1.1246	2.3718	−0.4606
H(2)	−2.0791	−0.9588	1.4721	2.2253	2.2349	0.9252
H(3)	−1.0592	−2.2437	2.1541	2.3796	1.1243	−0.4513
H(4)	1.3697	−2.1886	−0.4064	1.1246	−2.3718	0.4606
H(5)	2.0789	−0.9590	−1.4724	2.2253	−2.2349	−0.9252
H(6)	1.0588	−2.2436	−2.1544	2.3797	−1.1243	0.4513
H(7)	0.4015	2.1721	1.3854	−1.1240	2.3731	0.4573
H(8)	1.4924	0.9541	2.0767	−2.2236	2.2352	−0.9296
H(9)	2.1452	2.2526	1.0554	−2.3807	1.1268	0.4476
H(10)	−0.4015	2.1721	−1.3854	−1.1240	−2.3731	−0.4573
H(11)	−1.4924	0.9541	−2.0767	−2.2236	−2.2352	0.9296
H(12)	−2.1451	2.2526	−1.0554	−2.3807	−1.1268	−0.4476

(in contradistinction to germanium) substituted for silicon merits investigation.

1.1 Models

The model used throughout this study has been the 21-atom cluster $C(OCH_3)_4$. Different conformations (S_4 and D_{2d}) of this model were considered by varying the starting configuration of the model; the two catchment regions on the energy hypersurface proved to be well separated, and there was no computational problem with conformations switching between the two regions in the process of geometry optimization.

1.2 Calculations

The calculations reported herein were performed using the program Gaussian 82 (12) on a VAX 8600/8650 computer cluster. The large size of the models and the need for geometry optimization constrained our choices for basis sets. In this study, the STO-3G minimal basis set (13–15) was used, and all calculations were carried out within the restricted Hartree–Fock (RHF) framework. No explicit symmetry restrictions were placed on the models in this study, i.e., all bond lengths and angles were allowed to vary independently. Optimizations were continued until the forces acting on all bond lengths and angles were reduced to less than 0.00045 hartree bohr^{-1} or hartree radian^{-1} respectively.

2. Results

The optimized Cartesian coordinates of the two conformations of the $C(OCH_3)_4$ system are given in Table 1. A diagram of the optimized configuration of the S_4 conformation of the $C(OCH_3)_4$ molecule is shown in Fig. 2. The net atomic charges on the optimized geometry of the S_4 conformation of the $C(OCH_3)_4$ molecule (obtained by Mulliken population analysis) are listed in Table 2. The energy differences between each of the models optimized in this study are presented in Table 3. The optimizations include those with methyl group rotation

TABLE 2. Net atomic charges q (in units of $|e|$) for the optimized S_4 conformation of the $C(OCH_3)_4$ model, as calculated by the Mulliken procedure

Atom	q
C(central)	+0.463
O	−0.265
C (peripheral)	−0.068
H	+(0.070 → 0.075)

TABLE 3. Total energy E_t (in hartree cluster^{-1}), and energy ΔE (in kJ mol^{-1}) relative to the lowest-energy S_4 conformation, for various conformations of the $C(OCH_3)_4$ model

Conformation symmetry	Methyl group rotation[a] (degrees)	E_t	ΔE
S_4	0[b]	−489.416175	1.0
S_4	8[c]	−489.416545	0.0
S_4	30[b]	−489.412642	10.3
S_4	60[b]	−489.407631	23.4
D_{2d}	0[d]	−489.413650	7.6
D_{2d}	30[b]	−489.411228	14.0
D_{2d}	60[b]	−489.407408	24.0

[a]Methyl group rotation is measured as the deviation from the antiperiplanar conformation, which is obtained when the dihedral H—C(peripheral)—O—C(central) angle is 180°. The positive direction is taken as counterclockwise, when viewed from the methyl group.

[b]Calculation was for a single geometric configuration using the program Monstergauss (26).

[c]S_4 conformation subjected to complete geometry optimization using Gaussian 82. The average deviation from the antiperiplanar conformation was 8°; however, there were slight deviations from S_4 symmetry, and the actual deviation varied for individual methyl groups from 7° to 10°.

[d]The complete geometry optimization of the D_{2d} conformation proved to have a 0° methyl group rotation.

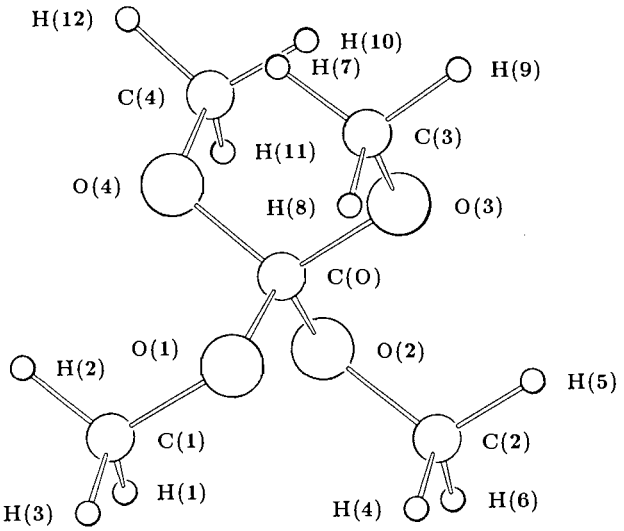

FIG. 2. The optimized S_4 conformation of the $C(OCH_3)_4$ model. The cluster shown here is enantiomorphic to the one shown in Fig. 1.

restricted (to 0, 30, or 60°) as well as complete geometry optimizations on both the S_4 and D_{2d} conformations.

3. Discussion

The results of this *ab initio* study support the view that the S_4 conformation is the most stable for the $C(OCH_3)_4$ molecule; the STO-3G calculations indicate that the energy difference between the two conformations is 8 kJ mol^{-1}. Among the factors that may be responsible for the conformation S_4 having lower energy than D_{2d}, increased repulsion between lone pairs (5) and unfavorable electric dipole–dipole interactions (16, 17) may be the most important. The calculated energy difference between the two conformations of tetramethoxymethane is somewhat larger than the estimate of 4.1 kJ mol^{-1} by Ypenburg and Gerding (4), but considerably smaller than the estimated value of 25.1 kJ mol^{-1} suggested by Mijlhoff *et al.* (6), based on a study of methanediol (18). The sizable difference (18.5 kJ mol^{-1}) may indicate that methanediol is not an appropriate model for tetramethoxymethane. It is known that although the STO-3G basis set generally predicts geometries reasonably well, it is usually less accurate with respect to energies. An *ab initio* study of similar compounds $X(OH)_4$, where X = C or Si, showed that the STO-3G basis set predicted energy differences between the S_4 and D_{2d} conformations that are appreciably too low as compared to the 6-31G* (19, 20) basis set values (21).

It should be noted that the optimized geometry of the S_4 model did not in fact show exact S_4 symmetry. Rather, there were small deviations from symmetry, particularly in the methyl groups, which reduced the formal symmetry to C_1. To see if the deviations from S_4 are significant, the model was reoptimized with S_4 imposed. The latter was found to be 4.1 kJ mol^{-1} higher in energy than the unconstrained model, with the STO-3G basis set. The difference in energy is small but significant, so that we feel that the symmetry of this model could appropriately be called quasi-S_4. The occurrence of slight deviations from S_4 symmetry encountered in this study is supported by the infrared spectrum of tetramethoxymethane (5).

Comparison of the net atomic charge data in Table 2 with the results of an *ab initio* study (22) of $(HO)_2Si(OSiH_3)_2$ illustrates clearly the more electronegative character of carbon as compared to silicon.

TABLE 4. Bond lengths (in Å) and angles (in degrees) for the two conformations of $C(OCH_3)_4$. Experimental values are from ref. 6. Values in parentheses represent the range (±) for parameters where there were slight deviations from symmetry for the theoretical results. For the experimental results, the values in parentheses are the estimated standard deviations

Parameter	D_{2d} (theor.)	S_4 (theor.)	S_4 (expt.)
r C—O (central)	1.429	1.429	1.396(3)
r C—O (peripheral)	1.438	1.437	1.423(3)
r C—H	1.092(2)	1.092(2)	1.114(3)
∠C—O—C	111.2	111.6	113.9(4)
∠O—C—O (sym)[a]	102.6	112.4	114.6(5)
∠O—C—O (non-sym)[a]	113.0	108.0	106.9(5)
∠O—C—H	110(4)	110(4)	112(1)
Methoxy torsion[b]	0.1	±4(2)[d]	+3(1)[e]
Methyl torsion[c]	0.3	∓8(2)[c,d]	+45(2)[e]

[a]For both conformations, there was a distortion of the CO_4 tetrahedron such that two types of O—C—O bond angles were formed: two (equivalent) O—C—O angles bisected by the symmetry axis ("O—C—O sym"), and the four other O—C—O angles ("O—C—O non-sym").

[b]Methoxy torsion is given as the deviation from the antiperiplanar configuration for the two pairs of methoxy groups related by two-fold symmetry along the S_4 or C_2 axis.

[c]Methyl torsion is given as the deviation from the antiperiplanar configuration for any one of the C(0)—O—C—H dihedral angles. Methyl group deviations from symmetry were reported using the range indicated in parentheses.

[d]For the methoxy carbon atom pairs (1,2) and (3,4) respectively (see Fig. 1).

[e]Results had been reported as deviations from the eclipsed periplanar configuration, and were converted to deviations from the antiperiplanar configuration.

We estimate that the energy barrier for simultaneous rotation of all four methyl groups in $C(OCH_3)_4$ is approximately 23 kJ mol^{-1}. From this, one may deduce that the barrier for rotation of a single methyl group is approximately 6 kJ mol^{-1}. It is recognized that this result is fairly crude, since the various methyl groups will interact with each other. Therefore, a calculation was done in which a single methyl group was rotated by 60° from the optimized configuration; with the STO-3G basis, the energy barrier was found to be 7.2 kJ mol^{-1}. This energy barrier for the rotation of the methyl groups is low enough to be consistent with the observed proton nmr spectra of this compound, which indicate that the methyl groups are not in different environments (23).

The data presented in Table 4 indicate that there is quite good agreement of the theoretically calculated optimum bond lengths and angles with the results of the electron diffraction study. The calculated values of the C—O bond lengths (average for the two types) are 0.024 Å longer than the experimental values. It is a well-known fact that the STO-3G basis set tends to produce theoretical bond lengths that are somewhat too large (24), so that the (small) difference between calculated and experimental values is not surprising. Other calculations on a similar model, $C(OH)_4$, showed that a change from the STO-3G to the 6-31G basis set caused a decrease of 0.036 Å in the C—O bond length.[3] Thus it seems reasonable to conclude that the major source of error in the present calculations is the basis set limitation. Mijlhoff *et al.* (6) noted that the central C—O bond lengths were 0.03 Å shorter than the peripheral C—O bond lengths; the results of our *ab initio* calculation confirm their findings with regard to the relative magnitude of the C—O bond lengths. The shortening of the central C—O bonds is consistent with the model of charge delocalization of oxygen lone-pair

Can. J. Chem. Downloaded from www.nrcresearchpress.com by 112.217.228.212 on 09/07/12
For personal use only.

Can. J. Chem. Downloaded from www.nrcresearchpress.com by 112.217.228.212 on 09/07/12
For personal use only.

electrons, proposed by Romers *et al.* (7) as a possible explanation of the anomeric effect. Essentially, this model states that, for a given O(j)—C(0)—O(i)—R fragment (Fig. 2), charge delocalization will occur when the O(j)—C(0)—O(i)—R dihedral angle is in the range 90 ± 30°. When the dihedral angle is in this range, the alignment of orbitals is advantageous, so that there is delocalization of electrons from the (essentially) p-type lone-pair orbital on O(i) into one of the C(0) $2p$ orbitals (partially emptied by the electronegative substituent O(j)). The delocalization of the O(i) lone pair thus gives the C(0)—O(i) bond some degree of double-bond character. This study is thus consistent with earlier works on similar models (18, 25) in supporting the theory of charge delocalization of oxygen lone-pair electrons. It should be noted, however, that work[3] on the $C(OH)_4$ model suggests that charge delocalization is not a major factor in the energy differences between the various conformations of this model.

The value 1.092 ± 0.002 Å determined in the C—H bond length calculation is 0.022 Å shorter than the experimental value. It is uncommon for the STO-3G basis set to predict bond lengths that are too short, but such results have been observed before (27). The agreement between theoretical and experimental results is within the range (0.03 Å) typically found for molecules consisting of first-row elements when using STO-3G (27). For acetaldehyde and methanol (28), the experimental results are in the range 1.09–1.10 Å.

The calculated distortion of the CO_4 tetrahedron (the structure is flattened in the direction of the S_4 axis) is in good agreement with the electron diffraction study. There are many possible qualitative explanations as to why the tetramethoxymethane model distorts in the manner it does; among these are repulsion between lone pairs on oxygen atoms (5), electric dipole interactions (29), and delocalization of lone pairs (as described above); probably a combination of all the above factors is responsible for the distortion. It should be noted that distortion of the CO_4 tetrahedron, in a manner similar to that seen in this model, was observed in the $C(OH)_4$ model with various basis sets.[2,3]

The electric dipole moment of the S_4 conformation of the $C(OCH_3)_4$ model was calculated to be 0.01 debye. The calculated dipole moment is consistent with the one available gas-phase measurement (<0.3 D), which is rather old and probably only represents an upper limit on the dipole moment of this molecule (30). Measurements of the dipole moment of $C(OCH_3)_4$ in the liquid phase were generally found to be in the range 0.7–0.9 D (10, 11, 16, 23). Whereas dipole moments calculated with basis sets of modest size are in general rather unreliable, the poor agreement between the calculated dipole moment and the experimental values determined in the liquid phase presumably is at least partly due to distortion of the $C(OCH_3)_4$ molecule by interaction with the solvent.

4. Conclusions

The results of *ab initio* calculations on a fully geometry-optimized model of $C(OCH_3)_4$ have been reported, using the STO-3G basis set for optimization. There is good agreement between the calculated and experimentally determined values of bond lengths and angles. The calculations provide support for the lone-pair delocalization model (25) since the calculated central C—O bonds are shorter than the peripheral C—O bonds. The results of the present study support the view that the quasi-S_4 conformation of the $C(OCH_3)_4$ molecule is more stable than the D_{2d} conformation; our results show that the theoretical energy difference is 8 kJ mol^{-1} with the STO-3G basis set.

[3]R. J. McEachern and J. A. Weil. To be published.

5. Acknowledgements

This work was done under the auspices of the Natural Sciences and Engineering Research Council of Canada. We would like to thank Dr. P. S. Rao for his assistance with this project.

1. H. v. Hartel. Ber. Dtsch. Chem. Ges. **60**B, 1841 (1927).
2. T. Endo and M. Okawara. Synthesis, **10**, 837 (1984).
3. S. Kirchmeyer, A. Mertens, M. Arvanaghi, and G. A. Olah. Synthesis, **6**, 498 (1983).
4. J. W. Ypenburg and H. Gerding. Recl. Trav. Chim. Pays-Bas, **391**, 1245 (1972).
5. H. Lee and J. K. Wilmshurst. Spectrochim. Acta, Part A: **23A**, 347 (1967).
6. F. C. Mijlhoff, H. J. Geise, and E. J. M. v. Schaick. J. Mol. Struct. **20**, 393 (1974).
7. C. Romers, C. Altona, H. R. Buys, and E. Havinga. Top. Stereochem. **4**, 39 (1969).
8. H. Booth and R. U. Lemieux. Can. J. Chem. **49**, 777 (1971).
9. R. U. Lemieux. Molecular rearrangements. Vol. 2. *Edited by* P. de Mayo. Interscience, New York, NY. 1964.
10. L. Ebert and H. v. Hartel. Naturwissenschaften, **15**, 669 (1927).
11. B. A. Arbuzov and T. G. Shavsha. Dokl. Akad. Nauk S.S.S.R. **68**, 515 (1949).
12. J. S. Binkley, M. J. Frisch, D. J. Defrees, K. Raghavachari, R. A. Whiteside, H. B. Schlegel, E. Fluder, and J. A. Pople. Gaussian 82, Revision H version. Carnegie–Mellon University, Pittsburgh, PA. 1985.
13. W. J. Hehre, R. F. Stewart, and J. A. Pople. J. Chem. Phys. **51**, 2657 (1969).
14. W. J. Hehre, R. Ditchfield, R. F. Stewart, and J. A. Pople. J. Chem. Phys. **52**, 2769 (1970).
15. R. F. Stewart. J. Chem. Phys. **52**, 431 (1970).
16. C. W. N. Cumper and R. F. Rossiter. J. Phys. Chem. **76**, 525 (1972).
17. J. T. Edward. Chem. Ind. (London), 1102 (1955).
18. G. A. Jeffrey, J. A. Pople, and L. Radom. Carbohydr. Res. **25**, 117 (1972).
19. P. C. Hariharan and J. A. Pople. Theor. Chim. Acta, **28**, 213 (1973).
20. J. D. Dill and J. A. Pople. J. Chem. Phys. **62**, 2921 (1975).
21. R. J. McEachern. M.Sc. thesis (1987). University of Saskatchewan, Saskatoon, Sask.
22. M. J. Mombourquette, J. A. Weil, and P. G. Mezey. Can. J. Phys. **62**, 21 (1984).
23. C. W. N. Cumper, A. Melnikoff, and A. I. Vogel. J. Chem. Soc. A: 323 (1966).
24. W. A. Lathan, L. A. Curtiss, W. J. Hehre, J. B. Lisle, and J. A. Pople. Prog. Phys. Org. Chem. **11**, 175 (1974).
25. J.-M. Lehn, G. Wipff, and H.-B. Buergi. Helv. Chim. Acta, **57**, 493 (1974).
26. J. S. Binkley, R. A. Whiteside, P. C. Hariharan, R. Seeger, J. A. Pople, W. J. Hehre, and M. D. Newton. Quantum Chemistry Program Exchange, Program 368. Indiana University, Bloomington, IN. The Monstergauss version was produced by R. Poirier and M. Peterson. The DEC version of Monstergauss was made by R. E. Kari of Laurentian University, Sudbury, Ontario. Adaptation for the DEC-2060 was by A. Kapur.
27. J. A. Pople. Applications of electronic structure theory. *Edited by* H. F. Schaefer III. Plenum, New York, NY. 1977.
28. R. C. Weast (*Editor*). CRC handbook of chemistry and physics. CRC Press, Cleveland, OH. 1974.
29. L. Radom, W. J. Hehre, and J. A. Pople. J. Am. Chem. Soc. **94**, 2371 (1972).
30. O. Fuchs. Z. Phys. **63**, 824 (1930).

Ionic rearrangements and domain growth near antiferroelectric transitions: EPR study of $NH_4H_2AsO_4$, $ND_4D_2AsO_4$, $NH_4H_2PO_4$, and $ND_4D_2PO_4$[1]

N. S. DALAL
Chemistry Department, West Virginia University, Morgantown, WV 26506, U.S.A.

AND

A. H. REDDOCH
Division of Physics, National Research Council, Ottawa, Ont., Canada K1A 0R6

Received January 29, 1988

This paper is dedicated to Professor Charles A. McDowell on the occasion of his 70th birthday

N. S. DALAL and A. H. REDDOCH. Can. J. Chem. **66**, 2045 (1988).

Using electron paramagnetic resonance spectroscopy we have measured the temperature dependence of ionic rearrangements and domain nucleation around the antiferroelectric transition temperature T_c of $NH_4H_2AsO_4$, $ND_4D_2AsO_4$, $NH_4H_2PO_4$, and $ND_4D_2PO_4$. CrO_4^{3-} radicals, produced by γ-irradiation of K_2CrO_4-doped samples, were used as microscopic probes because their charge, size, and symmetry match those of the host anions. The use of high deuteration level and "monodomain" samples prepared by temperature cycling was found to be crucial in the signal assignment and line-shape analysis. The results show that as a sample approaches T_c from $T > T_c$, the hydrogen-bonded protons slow down anomalously, much more slowly than expected for Arrhenius behaviour. Simultaneously, the lattices develop "clusters" of antiferroelectrically ordered molecules. These clusters eventually ($T \ll T_c$) expand to occupy the whole lattice and thus complete the lattice ordering. The probe selection and sample preparation methodology discussed and the microscopic details of the ionic rearrangements reported appear to be highly significant for further studies of these phase transitions.

N. S. DALAL et A. H. REDDOCH. Can. J. Chem. **66**, 2045 (1988).

Utilisant la spectroscopie en résonance paramagnétique électronique, on a mesuré les réarrangements ioniques et la nucléation de domaine en fonction de la température qui se produit près de la température de transition antiferroélectrique, T_c, du $NH_4H_2AsO_4$, du $ND_4D_2AsO_4$, du $NH_4H_2PO_4$ et du $ND_4D_2PO_4$. Des radicaux CrO_4^{3-}, produits par l'action d'irradiations-γ sur des échantillons dopés au K_2CrO_4, ont été utilisés comme sondes microscopiques parce que leur charge, leur grosseur et leur symétrie sont comparables à celles des anions hôtes. Pour l'attribution des signaux et pour l'analyse de la forme des raies, il est crucial d'utiliser des échantillons à «domaines uniques» qui ont été préparés par des cycles de température et qui contiennent des niveaux élevés de deutération. Lorsque la température d'un échantillon approche de T_c, on observe que les protons liés par des ponts hydrogènes sont anormalement ralentis, beaucoup plus que ce que l'équation d'Arrhénius nous laisserait prévoir. En même temps, les réseaux forment des «agrégats» de molécules qui sont ordonnés d'un point de vue antiferroélectrique. Lorsque $T \ll T_c$, ces agrégats prennent de l'expansion et complètent sa mise en ordre. La méthode de sélection de la sonde ainsi que la méthodologie de préparation d'échantillons qui est discutée et les détails microscopiques des réarrangements ioniques rapportés semblent très significatifs pour des études ultérieures de ces transitions de phase.

[Traduit par la revue]

Can. J. Chem. Downloaded from www.nrcresearchpress.com by 112.217.228.212 on 09/07/12
For personal use only.

Introduction

We report here probably the first observation via electron paramagnetic resonance (EPR) spectroscopy of atomic fluctuations and the growth of antiferroelectrically ordered domains in several disordered paraelectric lattices in the vicinity of their paraelectric–antiferroelectric phase transitions. As is well known (1), a paraelectric–antiferroelectric transition is defined to take place at a temperature (T_c) below which each molecule in the unit cell acquires an electric dipole moment oriented such that the net dipole moment of the unit cell is zero. The nature of interactions that lead to the antiferroelectric ordering is not yet understood (1) and is a topic of current activity (for recent reviews, see ref. 2), even after four decades of study (2, 3). We have now investigated the four KH_2PO_4-type of hydrogen-bonded antiferroelectrics: $NH_4H_2AsO_4$ (ADA), $ND_4D_2AsO_4$ (DADA), $NH_4H_2PO_4$ (ADP), and $ND_4D_2PO_4$ (DADP), where the letters inside the brackets form the commonly used abbreviations for the corresponding compound. The results obtained (see ref. 4 for a preliminary account) bear on the microscopic picture of an antiferroelectric sample as it approaches the phase transition ($2d$), and suggest guidelines for choosing a paramagnetic probe for studying atomic fluctuations in KH_2PO_4-type of ferroelectrics, antiferroelectrics, and perhaps other chemical systems.

Since all four compounds studied are normally diamagnetic, CrO_4^{3-} radicals (5), substituting for AsO_4^{3-} or PO_4^{3-} ions, were used as microscopic paramagnetic probes. CrO_4^{3-} was chosen over AsO_4^{4-} and SeO_4^{3-}, the two other probes used widely for such studies (2), because of the charge and symmetry requirements: an ideal probe must have approximately the same electronic charge, overall size, and symmetry as those of the substituted units in the host lattice. AsO_4^{4-}, formed (2) via γ-irradiation of an arsenate, has an extra negative charge compared to the substituted units (AsO_4^{3-} or PO_4^{3-}). This excess charge alters the electrostatic interactions in the vicinity of the AsO_4^{4-} center. Hence the motional fluctuations observed via this probe will not be expected to be the same as those of AsO_4^{3-} or PO_4^{3-} units in the unperturbed lattice. Of course SeO_4^{3-} has the same charge as the PO_4^{3-} or AsO_4^{3-} units, but electron nuclear double resonance (ENDOR) measurements have shown (6) that the disposition of the hydrogen-bonded protons around the SeO_4^{3-} center, and hence its observed site symmetry (D_{2d}) is quite different from that (7) (C_s) of a PO_4^{3-} unit below T_c. On the other hand, CrO_4^{3-} has the same charge and approximate size as a PO_4^{3-} or AsO_4^{3-} unit, and recent ENDOR studies have shown (8) that its proton arrangement and

[1]Issued as NRCC No. 29069.

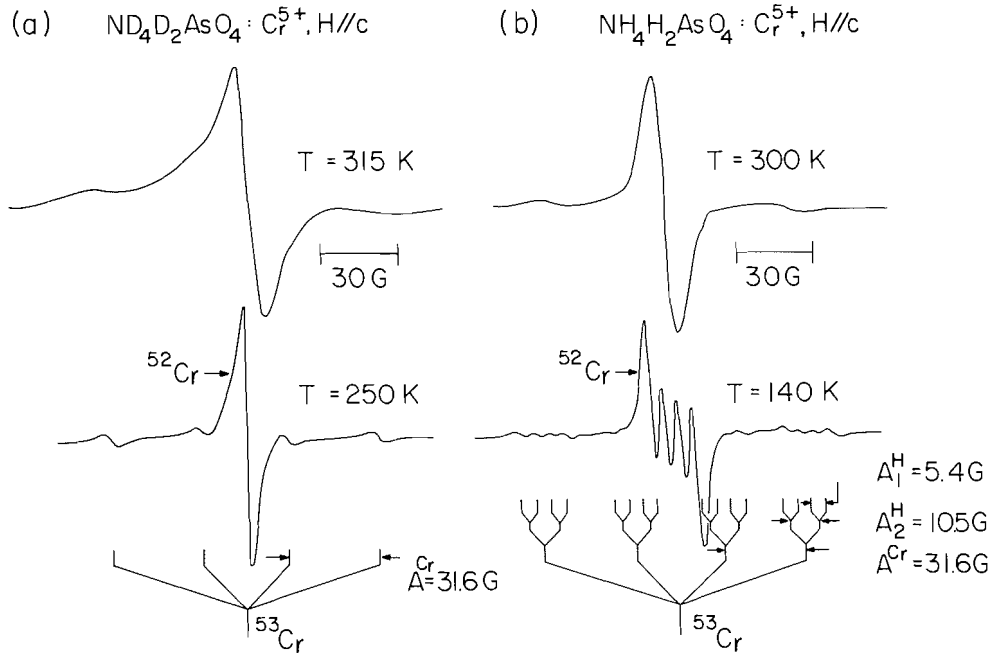

FIG. 1. EPR spectra of the CrO_4^{3-} center for H//c: (a) DADA, T = 315 K, paraelectric phase, and T = 250 K, antiferroelectric phase; (b) ADA, T = 300 K, paraelectric phase, and T = 140 K, antiferroelectric phase.

hence site symmetry approximate those of a host antiferroelectric lattice. We note that other probes such as Hg^+ ($6s^1$) also meet (9) the charge and symmetry requirements for these lattices, but those probes yield motional information on the cations, rather than the PO_4^{3-} or AsO_4^{3-} units. A fuller understanding of the role of the various chemical units in triggering the phase transition would benefit from motional and structural data obtained via the use of probes specific to different sites in the lattice.

After our initial study (4), Müller and Berlinger (10) reported an EPR study of CrO_4^{3-} in ADA and partially (~75%) deuterated ADA, as did Gaillard and Gloux (8) on the proton ENDOR of CrO_4^{3-} in ADA. The present work supplements the ENDOR study by employing specially prepared (monodomain) samples. Also, the present work includes ADP and DADP and focuses on the dynamical effects near T_c, not contained in the earlier work (8, 10).

Experimental

The single crystals used in this work were grown from aqueous solutions doped with ~1 mol% of K_2CrO_4 and γ-irradiated to a dose of about 1 Mrad at room temperature (4). Important differences from the earlier studies (8, 10) are (*a*) the growth of high isotopic purity (~99%) DADA and DADP crystals by vacuum line synthesis to obtain narrower EPR signals than before, since the earlier study (10) used only ~75% deuterated samples; (*b*) the annealing of samples at ~50°C to reduce the number of unwanted paramagnetic centers, which would interfere with the CrO_4^{3-} signals; (*c*) the growth of an essentially monodomain crystal in which the number of EPR signals was half that in a normal, polydomain crystal, thereby helping the assignment of signals to a given site and domain; and (*d*) the more detailed study of the angular and temperature dependence of the EPR spectra than before (10).

The EPR measurements were made at 9.5 GHz with the aid of a proton resonance fluxmeter and a frequency counter to read the fluxmeter and the microwave frequencies. The sample temperature was controlled to an accuracy of ±0.1 K.

Results and discussion

Characterization of the CrO_4^{3-} center

In all four cases the EPR spectra consist of strong central lines flanked by weak satellites. Typical spectra for ADA and DADA are shown in Fig. 1; those for ADP and DADP are very similar. From the intensity and the spin multiplicity considerations the central (strong) component can be identified with that from the ^{52}Cr (I = 0) isotope and the four satellites can be described in terms of the g tensor and the hyperfine interaction of the unpaired electron with the ^{53}Cr (I = 3/2) isotope. Figure 2 shows the angular dependence of the ^{52}Cr lines in the three crystallographic planes of DADA; those for the other compounds are essentially similar.

The paraelectric phase spectra (shown by the dashed lines) can be described by the spin Hamiltonian,

$$\mathcal{H} = \beta_e[g_\parallel H_z S_z + g_\perp (H_x S_x + H_y S_y)] + A_\parallel S_z I_z + A_\perp [S_x I_x + S_y I_y]$$

where the z direction coincides with the crystalline c-axis. The values of $g_\parallel$, $g_\perp$, $A_\parallel$, and $A_\perp$ obtained by fitting the experimental data are given in Table 1, wherein the results for other, related crystals (5, 11) are also included. The g and A parameters for ADA, DADA, ADP, and DADP compare well with those for KD_2AsO_4 and KD_2PO_4, implying that the CrO_4^{3-} centers have indeed substituted for the parent PO_4^{3-} or AsO_4^{3-} units. For all compounds, $g_\parallel < g_\perp$ and $A_\parallel > A_\perp$, implying (12) that the ground state of CrO_4^{3-} in all of these compounds uses mainly the Cr(V) $d_{x^2-y^2}$ orbital. Using the Maki–McGarvey (12) relationship between $g_\parallel$, $g_\perp$, $A_\parallel$, $A_\perp$ and the coefficients of $d_{x^2-y^2}$ and d_{z^2} in the wave function for CrO_4^{3-}, we find that the ground state has approximately 90% $d_{x^2-y^2}$ character, which is nearly the same as for Cr(V) in K_3CrO_8 (13).

A striking similarity is found also between the g-tensor results in the low temperature phases of the ammonium and the potassium salts. Detailed studies of the angular variation of the ^{52}Cr components of the CrO_4^{3-} center in all four ammonium compounds show that all have nearly identical variation. Figure 2 shows the results for DADA. A least-squares fitting of the lines in the three crystallographic planes yielded 16 tensors with nearly equal rms error of ~0.5 G. However, measurements in

Can. J. Chem. Downloaded from www.nrcresearchpress.com by 112.217.228.212 on 09/07/12
For personal use only.

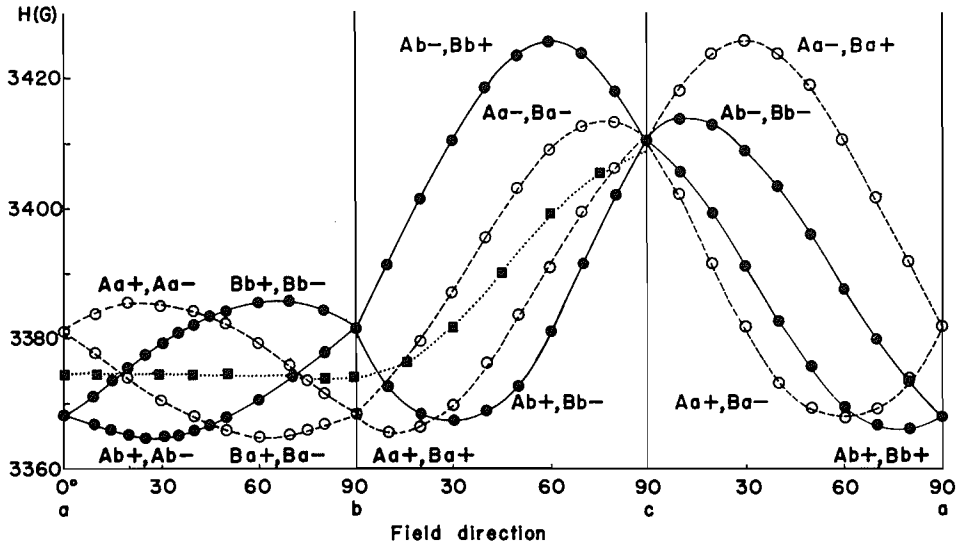

FIG. 2. Angular dependence of the central ($I = 0$) transitions for CrO_4^{3-} in DADA. The solid and the dashed lines belong to the different domains of polarization. The assignment of the lines to the various domains and sites has been made with the help of the monodomain samples and the symmetry analysis as explained in the text. The angular dependence in the paraelectric phase is that shown by the dotted lines.

the [1 1 0] (fourth) plane reduced them to a set of eight, which is the number expected from the crystal symmetry considerations, to be discussed in more detail in the next section. The g-tensor components for one of the eight tensors are given in Table 2, the other tensors being obtainable from this set by applying the crystal symmetry elements. The results for KD_2AsO_4 (DKDA) are also included therein, the comparison confirming the similarity between the ammonium and the potassium salts.

Further confirmation of the identification came from the analysis of the proton superhyperfine structure (shfs). Figure 3 shows the angular dependence of the shfs splitting from the two protons closest to the CrO_4^{3-} center in ADP. The high resolution necessary to obtain Fig. 3 was possible because of the use of the "monodomain" samples. The coupling constants obtained are in essential agreement with the ENDOR study of ADA by Gaillard and Gloux (8). The major outcome of the monodomain results is that they confirm the assignment of the ENDOR signals to the various antiferroelectric domains, which is not possible with the normal (polydomain) ADA crystals used in the ENDOR study (8), and that the proton shfs and hence the proton configuration around the CrO_4^{3-} center in ADP and ADA are essentially identical.

The finding of $d_{x^2-y^2}$ as the ground state of CrO_4^{3-} in the phosphates and arsenates is interesting, since the ground state of CrO_4^{3-} in nearly all other cases is found to be d_{z^2}, as discussed by Greenblatt (14). In fact, ligand field theory predicts (11, 12) that if the CrO_4^{3-} tetrahedron is compressed along the tetragonal distortion axis, then the ground state of Cr(V) would be d_{z^2} rather than $d_{x^2-y^2}$. The PO_4^{3-} and the AsO_4^{3-} tetrahedra in the compounds studied here are compressed (by ~2%) along the tetragonal (c)-direction. If some of these ions are substituted by CrO_4^{3-}, then the latter are also expected to be similarly compressed. Thus the observed $d_{x^2-y^2}$ ground state is in contradiction to the simple ligand field approach and differs from that (d_{z^2}) found in Li_3PO_4, Li_3AsO_4, and many other hosts (14). In an effort to reconcile these results, Müller and Berlinger (15) have suggested that electrostatic interaction of the hydrogen bonds (in these hosts) with the unpaired electron of CrO_4^{3-} stabilizes the $d_{x^2-y^2}$ as compared to d_{z^2}. However, we have recently carried out (13) detailed studies of the isoelectronic peroxy ion CrO_8^{3-} in K_3CrO_8, which of course has no hydrogen, and where the CrO_8^{3-} ion is similarly compressed. The ground state of the Cr(V) in K_3CrO_8 is also found to be $d_{x^2-y^2}$. Thus it is not clear why CrO_4^{3-} has $d_{x^2-y^2}$ as the ground state here and any further theoretical work to explain this discrepancy would be most welcome.

TABLE 1. Spin Hamiltonian parameters for the CrO_4^{3-} radical stabilized in the paraelectric phase of the KDP-type crystals. The error limits on $g_\parallel$ and $g_\perp$ are ±0.0005. The $A_\parallel$ and $A_\perp$ are in units of gauss, the ∥ direction is along the crystal c-axis

Host	T(K)	$g_\parallel$	$g_\perp$	$A_\parallel$	$A_\perp$
$NH_4H_2AsO_4$	300	1.9561	1.9740	27.5±0.5	10±4
$ND_4D_2AsO_4$	310	1.9563	1.9749	28.2±0.5	10±4
$NH_4H_2PO_4$	300	1.9560	1.9740	27.5±0.5	10±4
$ND_4D_2PO_4$	300	1.9558	1.9752	28 ±0.5	10±4
KH_2AsO_4	300	1.9559	1.9758	29 ±1	10±4
KD_2AsO_4	300	1.9560	1.9756	28.6±0.5	10±4
KH_2PO_4	300	1.9560	1.9759	29 ±1	10±4
KD_2PO_4	300	1.9561	1.9758	28.5±0.5	10±4

TABLE 2. The g tensors for CrO_4^{3-} in DKDA and DADA in their low temperature phases. θ and ϕ are the polar and the azimuthal angles in the crystallographic abc (tetragonal) system

Tensor component	DKDA ferro	DADA antiferro
g_{xx}	1.98234±26	1.98213±22
g_{yy}	1.97944±64	1.97954±11
g_{zz}	1.94386±36	1.94477± 7
θ_x	−34.4±4.6	−35.5±1.4
ϕ_x	82.4±3.3	83.0±0.9
θ_y	50.4±6.6	51.0±1.9
ϕ_y	124.3±1.2	121.4±0.3
θ_z	66.5±1.1	66.8±0.8
ϕ_z	35.8±0.5	32.45±0.13

Domain and site assignment

To be able to utilize the CrO_4^{3-} center as a probe of the phase

Can. J. Chem. Downloaded from www.nrcresearchpress.com by 112.217.228.212 on 09/07/12
For personal use only.

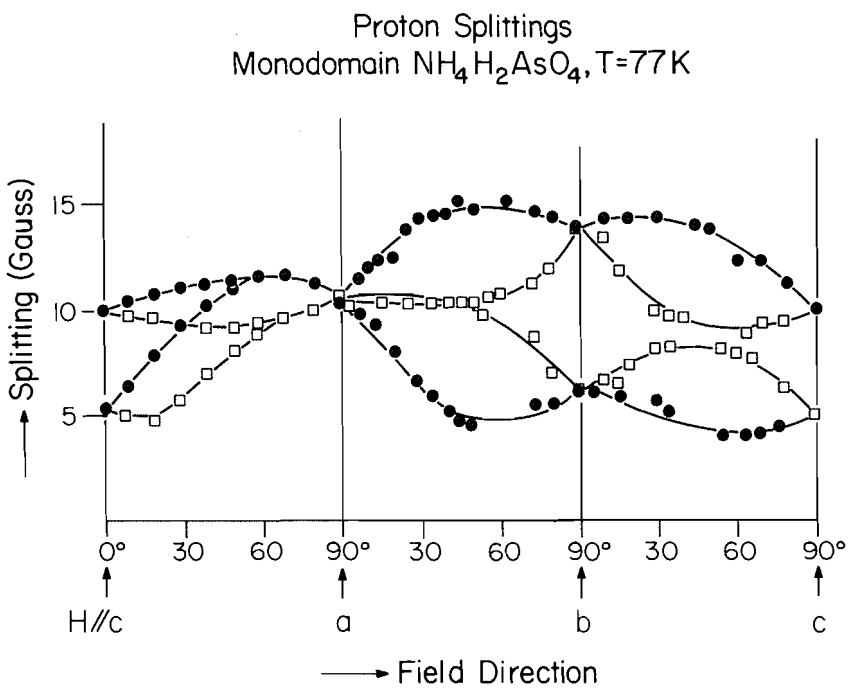

FIG. 3. Angular dependence of the proton superhyperfine (shfs) tensors for the close protons in the antiferroelectric phase of ADA. The use of monodomain samples was found to be essential for these measurements.

transition, it was important to be able to assign the observed signals to the various sites and domains in the crystal. Failure to do so in an earlier study (15) had led to erroneous interpretation of the motional correlation times for DKDA, as has been shown elsewhere (5).

The assignment was achieved by using the data on crystal symmetry (7). All of the four ammonium compounds crystallize in the space group $I\bar{4}2d$, which changes to $P2_12_12_1$ below T_c. There are two rotationally distinct crystallographic sites, say A and B, and each may be imbedded in domains with local polarization in the + or − directions along the a or b axes. These combinations yield 8 possible tensors, which may be labelled $Aa+$, $Bb-$, etc. in the notation of Dalal *et al.* (5). The crystallographic symmetry $P2_12_12_1$ implies twofold screw axes parallel to each crystallographic axis. In addition, the two domains can be related by introducing glide planes 110 and $1\bar{1}0$, which occur in the higher temperature structure. The application of these symmetry elements leads to the assignments indicated in Fig. 2.

These assignments predict that a domain effect, in the form of different line intensities, may be expected in the ab, bc, and ac planes but not in the 110 and $1\bar{1}0$ planes. This prediction was in complete agreement with the results on the monodomain crystals. It also supports the earlier assignment (5) of the domain structure for KD_2AsO_4 and KD_2PO_4.

The facts that the CrO_4^{3-} EPR shows the domain effect and that the effect conforms to the above analysis suggest that the Cr centers are coupled to the antiferroelectric domains, and can thus be used as sensitive probes of the long-range order that sets in around and below T_c.

Temperature dependence of the EPR spectra: evidence for dynamic clusters

Striking changes in line shapes and positions were observed near T_c in the EPR spectra of the CrO_4^{3-} centers in ADA, DADA, ADP, and DADP. The changes were reversible with a hysteresis of 2 K. Figure 4 shows the spectra for ADA and DADA. Similar effects were observed for ADP and DADP. The temperature dependence of g_c, the component of the g tensor along the c-axis, is shown in Fig. 5. A sudden change in g_c can be seen to occur at T_c in all three compounds. Similar changes were noted in the ^{53}Cr hyperfine couplings, as shown in Fig. 6. Even more interesting was the observation that in the temperature interval of about 5° around T_c, the observed line shape was a superposition of the signals characteristic of those from the high temperature, labeled P, and the low temperature phase, labeled A. The assignment of the P and the A-type signals to paraelectric and antiferroelectric phases respectively was achieved through detailed angular variation studies, such as shown in Fig. 2. As the temperature is lowered through T_c, the P-type signals are rapidly replaced by the A-type signals, although no line broadening or shifting is observed. It is seen that the position of the P signals is *not* that expected from a rapid averaging of all the A-type signals. This conclusion is evident from Fig. 5, and more clearly from Fig. 2 where the dashed line shows the angular dependence of the P-type signals.

These results disagree with those of Müller and Berlinger (10) who concluded that for ADA and DADA the high temperature spectra are the "averages" of the low temperature ones. Müller also used this result as a basis for concluding that the CrO_4^{3-} is a Halperin–Varma center, defined (10, 15, 16) as an impurity that has an activated motion of its own, not related to the intrinsic host fluctuations. Our results thus do not support this conclusion either.

The temperature dependence of the intensity of the A-type signals for ADA is shown in Fig. 7. Similar results were observed for DADA. To correlate the intensity of the A-type signals with the long-range order in this material, the dielectric loss and the EPR signal changes were simultaneously measured for several samples. This was achieved by using a standard EPR spectrometer but employing a dual-sample microwave cavity, containing the ADA sample in one part and a paramagnetic

Can. J. Chem. Downloaded from www.nrcresearchpress.com by 112.217.228.212 on 09/07/12
For personal use only.

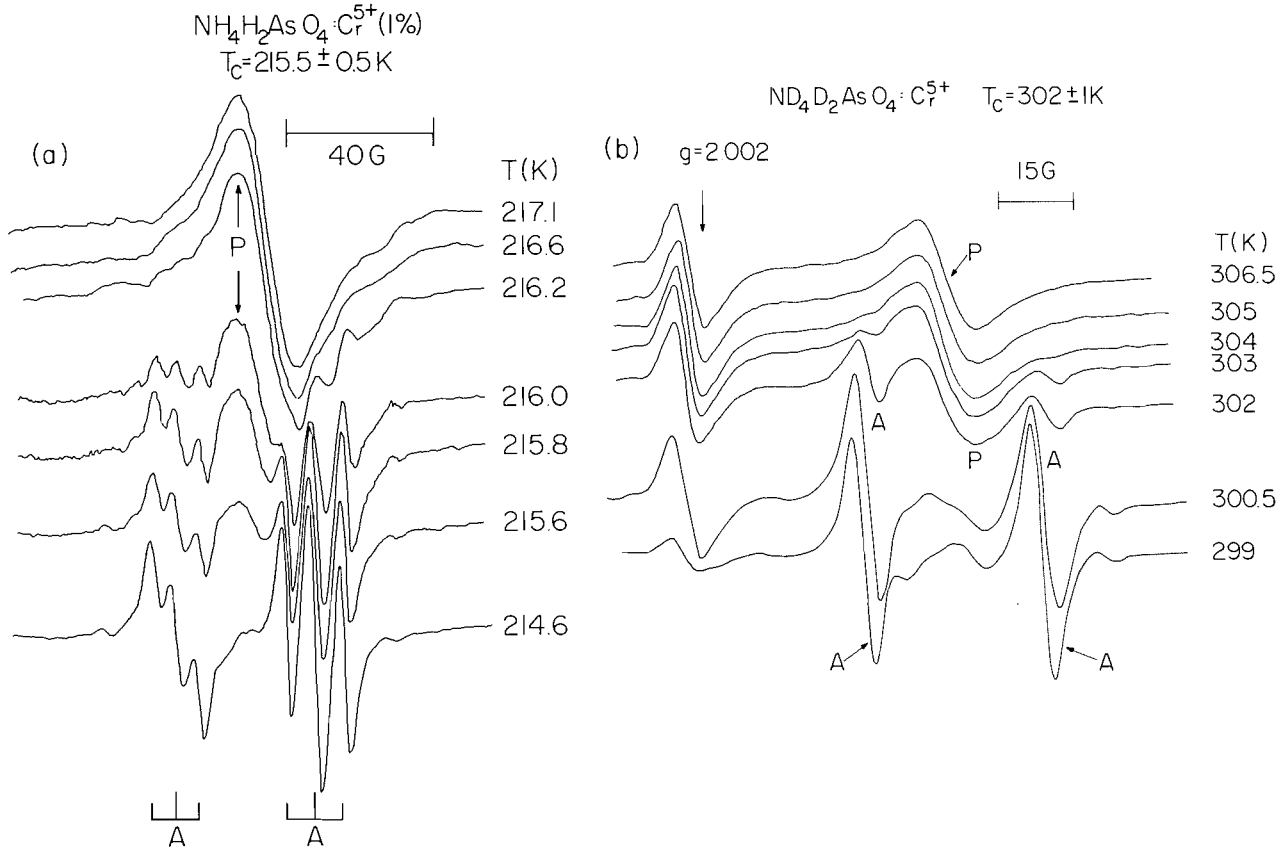

FIG. 4. Temperature dependence of some typical spectra in the *ac* plane of (a) ADA and (b) DADA. The labels "P" and "A" refer to the paraelectric and the antiferroelectric phase respectively.

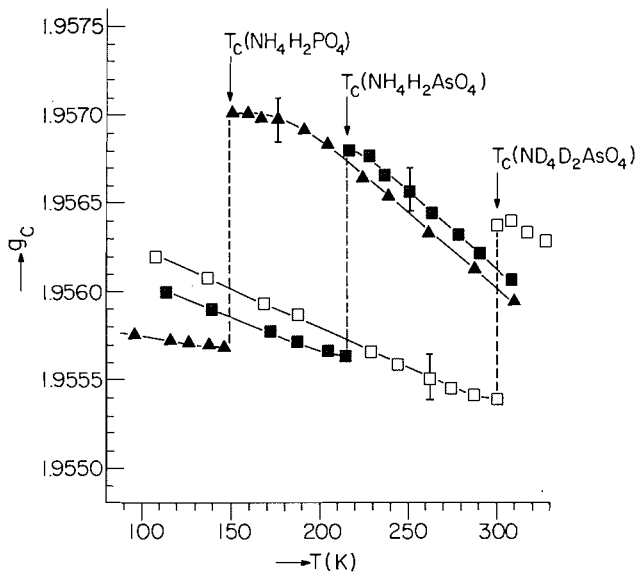

FIG. 5. Temperature dependence of g_c for ADP, ADA, and DADA.

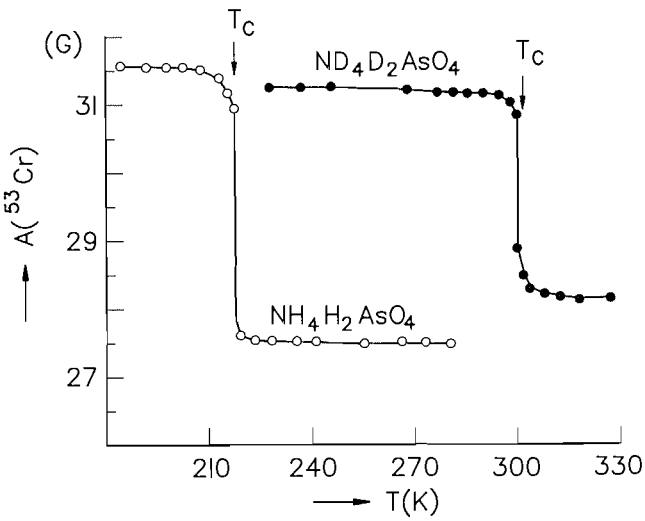

FIG. 6. Temperature dependence of the ^{53}Cr splitting for H//c in ADA and DADA.

reference salt ($CuSO_4 \cdot 5H_2O$) in the other. The latter was maintained at room temperature. The dielectric response of the sample was studied by following the change in the Q-factor of the microwave cavity, as monitored by observing the change in the intensity of the EPR signal from the reference salt. The dielectric loss and the CrO_4^{3-} signals could be studied independently at a given temperature. Alternatively, for a given magnetic field H_0, the dielectric loss could be recorded as a function of the sample temperature. Such a plot for ADA is shown in Fig. 8. The temperature dependence of the static dielectric constant was also measured with a capacitance bridge, as discussed elsewhere (17). Excellent quantitative agreement was found between the static and the microwave dielectric measurements. In particular, a thermal hysteresis of about 2° was found for the dielectric as well as the CrO_4^{3-} EPR measurements (17).

The role of the inhomogeneity in the sample temperature, arising from thermal gradients in the gas flow system, in causing

Can. J. Chem. Downloaded from www.nrcresearchpress.com by 112.217.228.212 on 09/07/12
For personal use only.

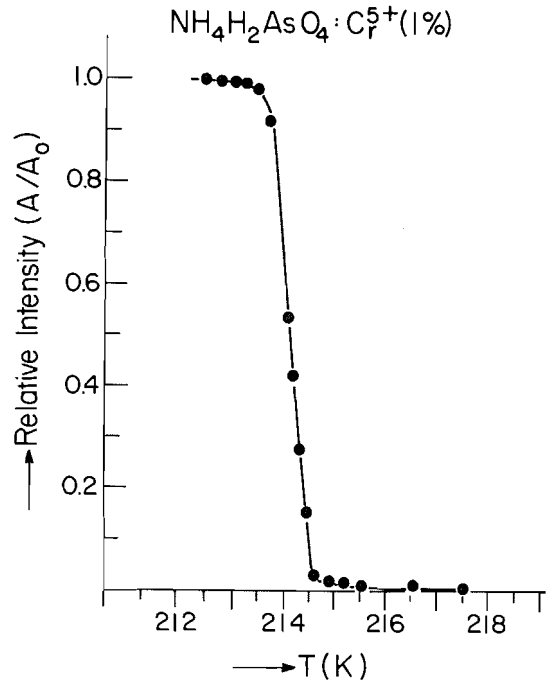

FIG. 7. Temperature dependence of the intensity of the A-type signals in ADA. A_0 is the intensity well below T_c.

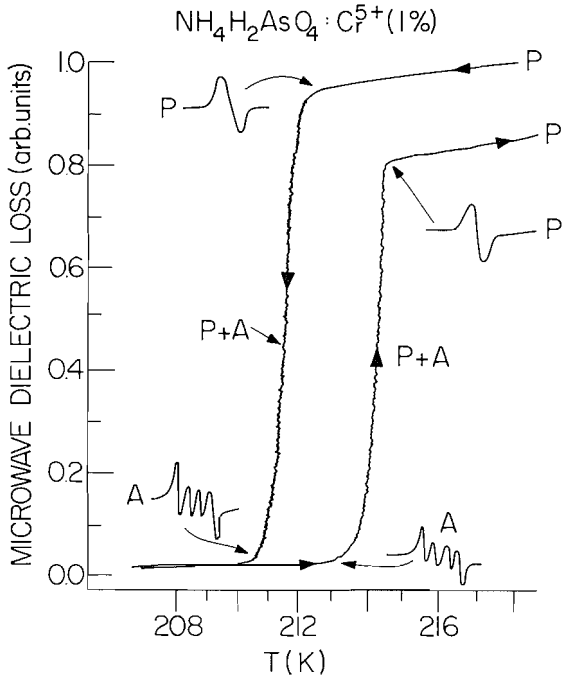

FIG. 8. Temperature variation of the dielectric loss (L) at 9.5 GHz for ADA. A sharp change in the dielectric loss is seen to occur at T_c and a hysteresis of $\sim 2.6 \pm 0.2$ K is noted. The microwave dielectric loss measurements agree with the static dielectric constant measurements.

the observed coexistence of the high temperature and the low temperature spectra was checked by reducing the sample size. No significant effect of the sample size on the spectral coexistence was observed. In addition, runs made with temperature sensors above and below the crystal indicate that the inhomogeneity does not exceed 0.1 K, a value smaller than the coexistence range. We thus conclude that the spectral coexistence is inherently related to the sample behavior near the phase transition, although the presence of the paramagnetic probe might cause some (perhaps small) perturbation.

The detection of A-type signals above T_c, the rapid growth of these signals as T approaches T_c (from $T > T_c$), and the fact that these are the only signals well below T_c imply the following picture of a lattice undergoing antiferroelectric transition. As $T \rightarrow T_c + 3°$ from above, molecular "islands" are formed in the "sea" of the paraelectric host lattice. The symmetry of molecules in these islands corresponds to that of the low-temperature (antiferroelectric) phase. As $T \rightarrow T_c$, these islands rapidly grow in size, and below $T_c - 3°$ they grow to occupy the whole crystal, thus setting up the long-range ordered domains in the whole sample.

The detection of the ordered regions above T_c is analogous to the ^{75}As NQR-perturbed NMR results (18) for $T > T_c$ in the ferroelectric KH_2AsO_4. The present study, however, constitutes the first detection of the "ordered clusters" in the paraelectric phases of the antiferroelectric compounds, and thus shows that the ferroelectric and the antiferroelectric phase changes involve essentially similar macroscopic transformations near T_c. Moreover, the corresponding NQR (nuclear quadrupole resonance) detection cannot be made for the phosphates, since ^{31}P has no quadrupole moment. There is no such restriction on EPR.

Proton dynamics in ADP and ADA

To measure the changes in the motion of the protons near T_c, the temperature dependence of the proton shfs was investigated for ADP and ADA. Figure 9 shows the temperature dependence for ADP, H//c. It is seen that well above T_c, the shfs is a 1:4:6:4:1 quintet, indicative of equal coupling to the four H-bond protons surrounding the CrO_4^{3-} probe. As $T \rightarrow T_c$, the motion of the protons slows down on the EPR time scale and the spectra change to a 1:1:1:1 quartet, showing that the CrO_4^{3-} has lost its $\bar{4}$ symmetry, that the four H-bond protons are now chemically distinct, and that the couplings of two of the protons are too small to be resolved by EPR. These two protons can thus be labeled as the "far" protons and the other two protons, causing the quartet of lines, are the "close" protons. The measured close proton couplings are $a_1 = 11.3$ and $a_2 = 6.1$ G and the far proton couplings were taken as $a_3 = -1.6$ and $a_4 = -1.0$ G for H//c, in accordance with the ENDOR measurements on ADA (8). The relative magnitudes and signs of (a_1, a_2) and (a_3, a_4) were also deduced from our observation that the high-temperature quintet was $(16 \pm 1)\%$ narrower than the low-temperature quartet as measured by the distance between the centers of the outermost lines. This conclusion follows because the width of the quintet is $a_1 + a_2 + a_3 + a_4$ while that of the quartet is $a_1 + a_2$. Thus $a_3 + a_4$ must have the sign opposite to that of $a_1 + a_2$. It may be noted here that while this relative sign information is implicit in the ENDOR data (8), the ENDOR results were obtained at 1.4 K and on ADA. The procedure used here gives the signs for ADP and ADA at the temperatures of interest to this study.

The temperature-dependent spectra were analyzed by employing the modified Bloch equations for a 4-site exchange process, as discussed previously (5). The actual calculated spectra are shown in Fig. 9. These are the results of adjusting the parameters τ and T_2, where τ is the correlation time for the protonic motion and T_2 is the inverse linewidth parameter. The agreement between the calculated and the observed spectra (also shown in Fig. 9) was found to be good except in the vicinity of T_c, perhaps due to the superposition of the high temperature and the low temperature spectra.

Can. J. Chem. Downloaded from www.nrcresearchpress.com by 112.217.228.212 on 09/07/12
For personal use only.

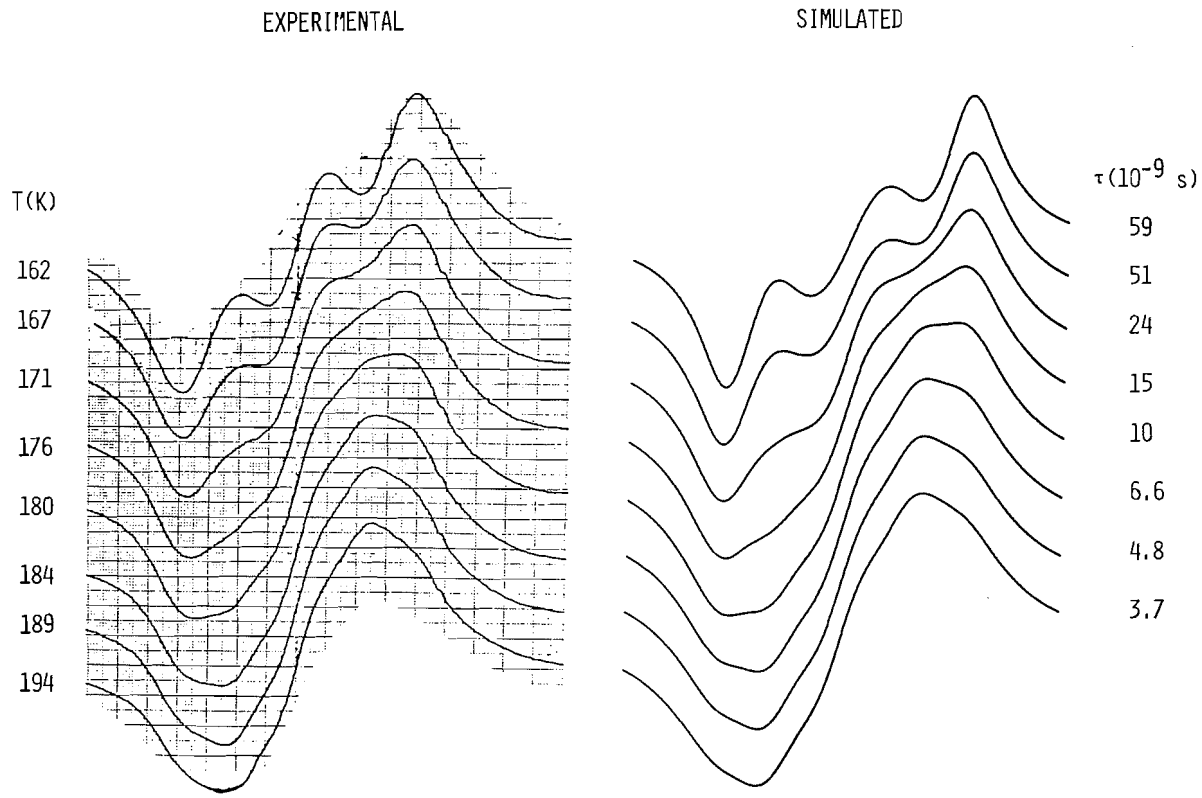

FIG. 9. Temperature dependence of proton superhyperfine splittings for CrO_4^{3-} in ADP, H//c: left, observed, and right, computer simulated.

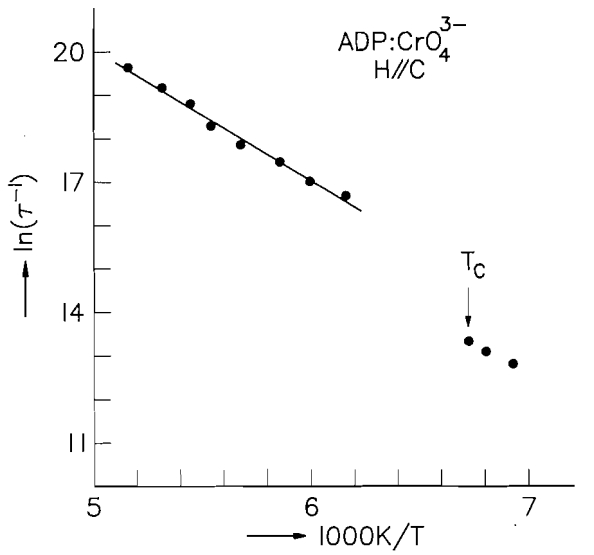

FIG. 10. Temperature dependence of the correlation time (τ) for the motion of protons around the CrO_4^{3-} center in ADP, H//c.

The derived values of τ are plotted as a function of temperature in Fig. 10. It is seen that τ varies rapidly in this temperature range with a larger increase at T_c. The average value of the slope, i.e., the Arrhenius activation energy, and the preexponential factors are (0.27 ± 0.05) eV and 2.2×10^{-16} s for $T > T_c$ and (0.23 ± 0.05) eV and 4.1×10^{-14} s for $T < T_c$, respectively, for ADP.

Unfortunately, it was not possible to obtain more values of τ close to T_c. Thus the nature of the non-Arrhenius behavior remains unclear. Non-Arrhenius behavior has been reported previously for AsO_4^{3-} in ADA (19) and KDA (19) (KH_2AsO_4), CrO_4^{3-} in KDP (20) (KH_2PO_4), and SeO_4^{3-} in KDP (21, 22)[2] but this has been far from T_c. Where results were obtained close to T_c no distinct unusual behavior was evident. However proton spin-lattice relaxation times (23) for NH_4^+ in $NH_4H_2PO_4$ show a sharp discontinuity at T_c reflecting a first-order phase transition. It may be that the present measurements for the hydrogen-bonded protons arise from similar effects.

Finally, the temperature dependence of the proton shfs in ADA is shown in Fig. 11. It was noted that here the quintet–quartet transition takes place within 2° of T_c (~216 K), and in the same region where the high and the low temperature spectra coexist, and the proton dynamics could be observed over only a few degrees. However, a comparison of the observed spectra with the calculated spectra shows that for ADA, $\tau = 5 \times 10^{-7}$ s at 218 K, which is of the same order of magnitude as that for ADP near T_c, thereby showing the similarity in the microscopic behavior of ADP and ADA near T_c.

Conclusions

This study establishes the following:

(a) CrO_4^{3-} can serve as sensitive probes of the antiferroelectric order in $NH_4H_2AsO_4$, $NH_4H_2PO_4$, and their deuterated analogs. Earlier failure (2) to observe similar changes via EPR of AsO_4^{4-} and SeO_4^{3-} can be ascribed to the fact that these probes do not have the same charge and site symmetry as those of the units they replace (PO_4^{3-} or AsO_4^{3-}). This important point does not seem to have been emphasized and (or) demon-

[2]This paper (22) also discussed the results for SeO_4^{3-} in KDP, but the activation data near T_c, as reported in ref. 21 could not be verified: R. Blinc, private communication.

Can. J. Chem. Downloaded from www.nrcresearchpress.com by 112.217.228.212 on 09/07/12
For personal use only.

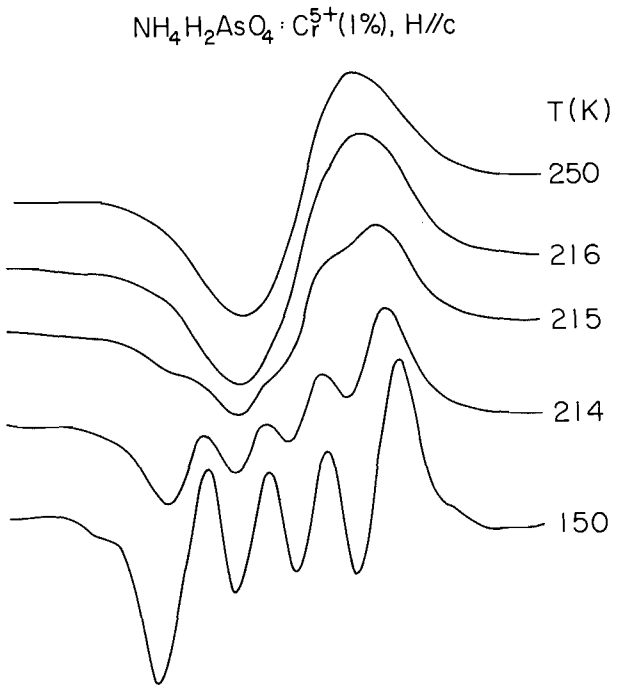

FIG. 11. Temperature dependence of the proton superhyperfine splittings for CrO_4^{3-} in ADA, H//c.

strated earlier, as also the use of monodomain antiferroelectric samples.[3]

(b) As the temperature is lowered to approach T_c, the paraelectric phase lattice starts to develop clusters of molecules that exhibit the symmetry and dynamics of the antiferroelectric phase. These clusters then grow rapidly below T_c and fill the whole lattice, leading to the antiferroelectric order in the sample.

(c) The motion of the hydrogen bonds around CrO_4^{3-} shows a strong deviation from Arrhenius behavior near T_c. Such behavior in the activation energy has been observed (23) for the NH_4^+ motion by NMR, ^1H T_1 measurements. The corresponding ^{31}P data would be important to obtain, since their comparison with the Cr EPR would show how faithful the CrO_4^{3-} probe is in representing the PO_4^{3-} unit. These results can provide experimental data for recent theoretical models (22) of the motion of paramagnetic probes in lattices undergoing order–disorder transitions.

(d) An important corollary from the above results is that the SeO_4^{3-} center should detect critical effects near T_c of the corresponding ferroelectric compounds (such as KH_2PO_4 and KD_2PO_4) but CrO_4^{3-} and AsO_4^{4-} should not, as pointed out here in the introduction. Of course, CrO_4^{3-} and AsO_4^{4-} do not show (2) marked changes near T_c of the ferroelectrics. Some evidence for changes in the EPR of SeO_4^{3-} in KH_2PO_4 has been reported (21) but the extensive proton superhyperfine structure makes the results hard to interpret. KD_2PO_4:SeO_4^{3-} could be a much better example, in particular because externally applied electric fields could be used to verify that the clusters observed above T_c do indeed represent a long-range order within the cluster, and are not due to a frozen molecular motion of the probe. Such experiments are in progress in our laboratory[4] and elsewhere (25)[5] as are also efforts to study the effects of applied pressure in the antiferroelectric case since there an electric field will have little or no effect.

(e) The ground state of CrO_4^{3-} has been found to derive mainly (~90%) from the Cr $d_{x^2-y^2}$ orbital, rather than the d_{z^2} orbital expected from a ligand field theoretical approach. Further theoretical calculations to explain this discrepancy would be helpful to understand the stabilization process of new paramagnetic probes.

1. M. E. LINES and A. M. GLASS. Principles and applications of ferroelectrics and related materials. Clarendon Press, Oxford. 1977.
2. (*a*) R. BLINC. *In* Magnetic resonance of phase transitions. *Edited by* C. P. Poole, Jr., H. Farach, and F. J. Owen. Academic Press, New York. 1979. Chap. V; (*b*) G. J. ADRIAENSSENS. J. Magn. Reson. **25**, 511 (1977); (*c*) K. A. MÜLLER. *In* Dynamical critical phenomena and related topics. *Edited by* C. P. Enz. Springer Verlag, Berlin–Heidelberg–New York. 1979. p. 210; (*d*) A. D. BRUCE and R. A. COWLEY. Adv. Phys. **29**, 219 (1980); (*e*) N. S. DALAL. Adv. Magn. Reson. **10**, 119 (1982); (*f*) R. BLINC and B. ZEKS. Ferroelectrics, **72**, 193 (1987).
3. (*a*) C. C. STEPHENSON and J. G. HOOLEY. J. Am. Chem. Soc. **66**, 1397 (1944); (*b*) C. C. STEPHENSON and A. C. ZETTLEMOYER. J. Am. Chem. Soc. **66**, 1402 (1944).
4. N. S. DALAL and A. H. REDDOCH. Sixth International Symposium on Magnetic Resonance, Banff, Alberta, Canada 1977. Symposium Abstracts. p. 241.
5. N. S. DALAL, A. H. REDDOCH, and D. J. NORTHCOTT. Chem. Phys. Lett. **58**, 553 (1978).
6. N. S. DALAL, J. A. HEBDEN, D. E. KENNEDY, and C. A. MCDOWELL. J. Chem. Phys. **66**, 4425 (1977).
7. R. J. KEELING and R. PEPINSKY. Z. Kristallogr. **106**, 236 (1955).
8. J. GAILLARD and P. GLOUX. J. Phys. Lett. **39**, 961 (1978).
9. N. S. DALAL, D. NETTAR, and P. GRANDINETTI. J. Am. Chem. Soc. **104**, 2054 (1982).
10. K. A. MÜLLER and W. BERLINGER. Z. Phys. B: Condens. Matter Quanta, **31**, 151 (1978).
11. K. A. MÜLLER, N. S. DALAL, and W. BERLINGER. Phys. Rev. Lett. **36**, 1504 (1976).
12. B. R. MCGARVEY. *In* Electron paramagnetic resonance of transition ions. *Edited by* T. F. Yen. Academic Press, New York. 1968. p. 1.
13. N. S. DALAL, J. M. MILLAR, M. S. JAGADEESH, and M. S. SEEHRA. J. Chem. Phys. **74**, 1916 (1981).
14. M. GREENBLATT. J. Chem. Educ. **57**, 546 (1980).
15. K. A. MÜLLER and W. BERLINGER. Phys. Rev. Lett. **37**, 916 (1976).
16. B. I. HALPERIN and C. M. VARMA. Phys. Rev. B: Solid State, **14**, 4030 (1976).
17. S. R. GOUGH, J. A. RIPMEESTER, N. S. DALAL, and A. H. REDDOCH. J. Phys. Chem. **83**, 664 (1979).
18. R. BLINC and J. L. BJORKSTAM. Phys. Rev. Lett. **23**, 788 (1969).

[3]While the exact mechanism that causes the samples to be monodomain is not understood, the samples can be prepared by a rapid crystallization over a few hours, as against a few days for normal crystal growth of these compounds. It was also observed that temperature cycling of the samples through T_c enhances the monodomain character. Further studies are in progress to understand the mechanism of this intriguing (and spectroscopically useful) phenomenon.

[4]A preliminary report of the observation of ferroelectric clusters in paraelectric KD_2PO_4 via electric field effects on the EPR of SeO_4^{3-} was presented at the Fifth International Meeting on Ferroelectricity, College Park, Pennsylvania (1981). See ref. 24.

[5]Those authors report on the coexistence of high-temperature and low-temperature spectra of SeO_4^{3-} in KD_2PO_4. However, electric field effects were not studied.

Can. J. Chem. Downloaded from www.nrcresearchpress.com by 112.217.228.212 on 09/07/12
For personal use only.

19. N. S. DALAL and C. A. MCDOWELL. Phys. Rev. B: Solid State, **5**, 1074 (1972).
20. N. S. DALAL, R. BLINC, P. PRELOVSEK, and A. H. REDDOCH. Solid State Commun. **43**, 887 (1982).
21. K. HUKUDA and Y. NAKAGAWA. J. Phys. Soc. Jpn. **44**, 1588 (1978).
22. G. M. RIBEIRO, L. V. GONZAGA, A. S. CHAVES, R. GAZZINELLI, R. BLINC, P. CEVC, P. PRELOVSEK, and N. I. SILKIN. Phys. Rev. B: Condens. Matter, **25**, 311 (1982).
23. J. A. RIPMEESTER and N. S. DALAL. Phys. Rev. B: Condens. Matter, **18**, 3739 (1978).
24. N. S. DALAL. (*a*) Ferroelectrics, **39**, 1060 (1981); (*b*) J. Am. Chem. Soc. **104**, 551 (1982).
25. K. HUKUDA, Y. TSUOURA, and S. AKAHOSHI. J. Phys. Soc. Jpn. **51**, 7 (1982).

Can. J. Chem. Downloaded from www.nrcresearchpress.com by 112.217.228.212 on 09/07/12
For personal use only.

LEED crystallographic studies for the chemisorption of oxygen on the (100) surface of copper

H. C. ZENG, R. A. MCFARLANE, R. N. S. SODHI, AND K. A. R. MITCHELL

Department of Chemistry, University of British Columbia, 2036 Main Mall, Vancouver, B.C., Canada V6T 1Y6

Received January 16, 1988

This paper is dedicated to Professor Charles A. McDowell on the occasion of his seventieth birthday

H. C. ZENG, R. A. MCFARLANE, R. N. S. SODHI, and K. A. R. MITCHELL. Can. J. Chem. **66**, 2054 (1988).

Intensity analyses with low-energy electron diffraction (LEED) are reported for surface structures obtained by adsorbing submonolayer amounts of oxygen on the (100) surface of copper. It is found for chemisorption on the four-coordinate hollow sites that the correspondence between experimental and calculated intensity-versus-energy curves, for 10 diffracted beams, is slightly better for coplanar adsorption than for adsorption about 0.75 Å above the surface (the latter model is essentially as proposed previously by both SEXAFS and photoelectron diffraction). Nevertheless, in neither of these contrasting situations is the agreement sufficient to conclude that the structural analysis is complete. Evidence is presented that nearly coplanar chemisorption, in combination with a missing row model, can accommodate a number of structural features for this system, including the existence of the $(2\sqrt{2} \times \sqrt{2})45°$–O phase, beam splittings resulting from antiphase domain boundaries, and the structural analogy noted in other studies between the $(2\sqrt{2} \times \sqrt{2})45°$–O phase and the stepped nature of the (410) copper surface which can form by faceting in oxygen. Considerations of O–Cu surface bond lengths, guided by those in bulk Cu_2O, suggest that additional lateral relaxations are likely in the topmost copper layer. This study provides no support for the O chemisorption occurring in tetrahedral-type sites.

H. C. ZENG, R. A. MCFARLANE, R. N. S. SODHI, et K. A. R. MITCHELL. Can. J. Chem. **66**, 2054 (1988).

On a effectué les analyses d'intensité de diffractions électronique de basse énergie (DEBE) pour des structures de surface obtenues par l'adsorption de quantités ne correspondant pas à des monocouches d'oxygène sur la surface (100) du cuivre. Pour la chemisorption sur les sites vides de coordination-4, examinée à l'aide de 10 faisceaux de diffraction, on a trouvé que la correspondance entre les courbes expérimentales et les courbes calculées de l'intensité vs l'énergie est légèrement meilleure pour l'adsorption coplanaire que pour l'adsorption à environ 0,75 Å au-dessus de la surface (ce dernier modèle est essentiellement celui qui avait été proposé antérieurement tant par SEXAFS que par diffraction électronique). Toutefois, ni l'une ni l'autre de ces situations pourtant très différentes ne conduit à une concordance suffisante pour conclure que l'analyse de structure est complète. On présente des données suggérant que de la chemisorption coplanaire, combinée avec un modèle impliquant une couche manquante, peut accommoder un certain nombre de caractéristiques de structure de ce système, y compris l'existence de la phase $(2\sqrt{2} \times \sqrt{2})45°$–O ainsi que la nature en escalier de la surface (410) du cuivre qui peut se former lorsqu'elle est facettée dans de l'oxygène. Des considérations concernant les longueurs des liaisons Cu–O de surface, basées sur celles que l'on retrouve dans du Cu_2O, suggèrent que les relaxations latérales additionnelles sont probables dans la couche supérieure du cuivre. Cette étude ne fournit accun support pour l'hypothèse selon laquelle la chemisorption des O se fait sur des sites de type tétraédriques.

[Traduit par la revue]

Can. J. Chem. Downloaded from www.nrcresearchpress.com by 112.217.228.212 on 09/07/12
For personal use only.

Introduction

It is a special pleasure to contribute to this issue honouring Professor C. A. McDowell, particularly since he provided much encouragement to the setting up of our surface science laboratory in 1975. That same year Professor McDowell organized a Faraday Discussion Meeting titled "Electron Spectroscopy of Solids and Surfaces", and a perusal of the presentations at that meeting (1) shows several associated with the chemisorption of oxygen on the (100) surface of copper. Over the years this system has been subjected to numerous investigations, especially for the chemisorption phases which are designated as $(\sqrt{2} \times \sqrt{2})45°$ (or $c(2 \times 2)$) and $(2\sqrt{2} \times \sqrt{2})45°$ according to the diffraction patterns observed with low-energy electron diffraction (LEED).[1] These phases are often reported to form sequentially, with increasing oxygen coverage, prior to the onset of bulk oxide formation (3, 4). However, another view of the chemisorption regime is that the $(2\sqrt{2} \times \sqrt{2})45°$ structure is always the stable form, and $c(2 \times 2)$ patterns are only observed when the ordering is insufficient to establish measurable intensities for the quarter-order beams (5).

Information on the chemisorption phases has been provided by a range of techniques including LEED (5–14), X-ray photoelectron spectroscopy (XPS) (15), work function measurements (10, 11), ion scattering (16, 17), secondary ion mass spectrometry (18), high-resolution electron energy loss spectroscopy (19, 20), photoelectron diffraction (21), and surface extended X-ray absorption fine structure (SEXAFS) (22). Several studies have suggested that oxygen penetrates below the top copper layer, especially for the $(2\sqrt{2} \times \sqrt{2})45°$ surface (6, 8, 10, 11) but other evidence has pointed to the $(\sqrt{2} \times \sqrt{2})45°$ and $(2\sqrt{2} \times \sqrt{2})45°$ surfaces as having related structures (12, 21). Attempts at quantitative structural analyses have not yet supported the model of oxygen penetration; nevertheless the structural models reported are wide-ranging. For example, determinations by SEXAFS (22) and photoelectron diffraction (21) indicate that O atoms adsorb close to 0.7 and 0.8 Å, respectively, above hollow sites of four-fold coordination (hereafter referred to as 4*f* sites), whereas an analysis with angular resolved XPS suggests O is coplanar with the topmost metal layer (15). Some preliminary support for a nearly-coplanar structure was provided by LEED (12), although an earlier study, in combination with ion scattering measurements, proposed that bridge bonding may occur (13, 16), a view that received indirect support from observations of beam splitting associated with antiphase domain boundaries (14).

Methods such as SEXAFS, photoelectron diffraction, and angular resolved XPS apparently emphasise the immediate

[1]The notations conventionally used in surface crystallography were introduced by Wood (2).

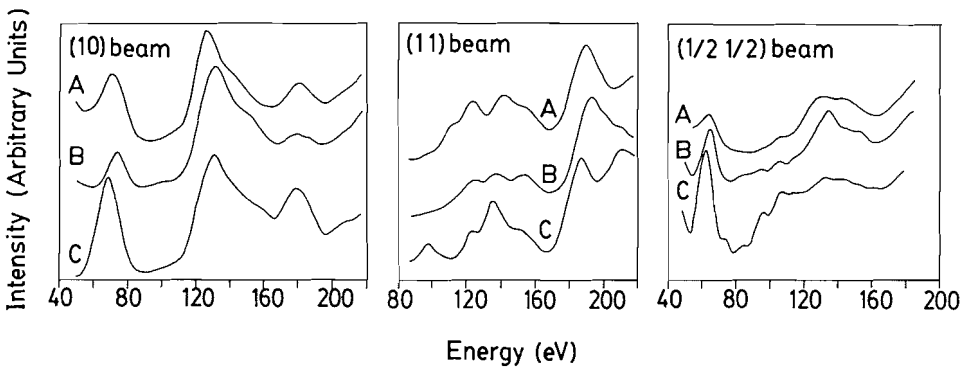

FIG. 1. Comparisons of $I(E)$ curves for the (1,0), (1,1), and (1/2,1/2) beams measured at normal incidence from the three surfaces Cu(100)–($\sqrt{2} \times \sqrt{2}$)45°–N (curves designated A), Cu(100)–($\sqrt{2} \times \sqrt{2}$)45°–O (curves designated B) and Cu(100)–($2\sqrt{2} \times \sqrt{2}$)45°–O (curves designated C).

neighbourhood of the adsorbate, while giving only limited information about any relaxations or reconstructions of the metal surface. By contrast, the latter contributions can perhaps be assessed more directly with LEED, and this provides a motivation for our undertaking the current work. A LEED crystallographic analysis involves measuring intensity-versus-energy ($I(E)$) curves for the set of diffracted beams which emerge from the surface, and making comparisons with the corresponding curves calculated for various structural models. The surface geometry is then determined by the conditions for which the calculated curves give the best match to the set of experimental $I(E)$ curves (23–25).

New LEED crystallographic analyses have been undertaken for the oxygen on Cu(100) system with the hope of clarifying some conflicting information which has emerged recently for this surface. This paper also addresses some associated points. The first relates to the tendency for oxygen to form the ($2\sqrt{2} \times \sqrt{2}$)45° structure on Cu(100), and this suggests that there should be some emphasis on those structural models which can naturally generate this particular translational symmetry. A second point, which also distinguishes this surface from the corresponding structure formed on Ni(100), concerns the tendency for the Cu(100) surface to roughen in the presence of oxygen (26), and ultimately to form (410) facets (27). In this regard, a structural similarity has been noted between the ($2\sqrt{2} \times \sqrt{2}$)45° superstructure formed by oxygen on Cu(100) and the stepped nature of the (410) surface (28, 29).

Experimental

The sample preparation, cleaning procedures, and analysis chamber used in this work were the same as those detailed in an earlier LEED study from this laboratory for the clean (311) surface of copper (30). The prepared Cu(100) surface, which showed a sharp (1 × 1) LEED pattern after cleaning and annealing, was exposed to reagent grade oxygen with continued pumping according to two alternative procedures which were used to form structures which manifests ($\sqrt{2} \times \sqrt{2}$)45° LEED patterns. The first procedure involved exposing the clean surface to 1×10^{-6} Torr of oxygen for 5 min while heating the surface to 300°C, followed by annealing at the same temperature for a further 5 min. In the second procedure the adsorption was done at room temperature for 5 min, while exposing the surface to 8×10^{-6} Torr of oxygen activated with the ion gun at 200 V, followed by a short anneal at 400°C. Most often this latter procedure gave the sharpest ($\sqrt{2} \times \sqrt{2}$)45° LEED patterns. LEED patterns corresponding to two orthogonal domains of ($2\sqrt{2} \times \sqrt{2}$)45°-type formed on exposing to oxygen at the above pressures for longer times, typically around 8 min, although there could be some variability in the conditions that gave the ($2\sqrt{2} \times \sqrt{2}$)45° patterns in particular cases.

Diffracted beam $I(E)$ curves were measured with a video LEED analyser (31) as detailed in a previous paper from this laboratory (32). For the Cu(100)–($\sqrt{2} \times \sqrt{2}$)45°–O surface structure, a total of 10 independent $I(E)$ curves were measured over the energy range 50–220 eV for the beams (1,0), (1,1), (1/2,1/2) at normal incidence, (0,0), (1,0), (0,1), (−1,1), (1/2,1/2), (−1/2,1/2), (1/2,3/2) at an off-normal direction where the polar angle is 15° and the azimuthal direction is [01$\bar{1}$] with respect to the crystal axes (i.e. the LEED pattern shows reflection symmetry about the [10] line). Corresponding data have also been measured from a Cu(100)–($2\sqrt{2} \times \sqrt{2}$)45°–O surface structure. Some comparisons are shown in Fig. 1 between these $I(E)$ curves measured at normal incidence and those similarly measured from the Cu(100)–($\sqrt{2} \times \sqrt{2}$)45°–N surface structure (33).

Calculations

Methods used

The LEED intensity calculations were made with the multiple scattering programs provided by Van Hove and Tong (34), and the procedures used are similar to those described in our recent structural analysis for the Cu(100)–($\sqrt{2} \times \sqrt{2}$)45°–N surface (33). The potential in each structural model was approximated with the muffin-tin form, and the scatterings of individual atoms were summed to give the layer scatterings. Layers were then stacked to form each structural model considered, the method for combining the layers being dependent on the interlayer spacings involved (23, 25). Briefly, layers were combined with the renormalised forward scattering method when interlayer spacings are 0.9 Å or greater, the full matrix inversion procedure was used to form "composite" layers where spacings are less than 0.6 Å, and the layer-doubling method was applied in intermediate situations (34).

The atomic potential in the substrate was characterized by phase shifts (up to $\ell = 7$) derived from a band structure potential for copper (35), and the real part of the constant potential (V_{or}) between the muffin-tin spheres was initially set at −10.0 eV for both the surface layer and the bulk. However values of V_{or} could be effectively refined later during the comparisons of experimental and calculated beam intensities. The oxygen phase shifts used were those derived by Demuth *et al.* (36) from a superposition potential, and the imaginary part (V_{oi}) of the potential between all atomic spheres was kept constant at −5.0 eV. The Debye temperatures were taken as 343 and 684 K for copper and oxygen, respectively. Appropriate domain averag-

Can. J. Chem. Downloaded from www.nrcresearchpress.com by 112.217.228.212 on 09/07/12
For personal use only.

Can. J. Chem. Downloaded from www.nrcresearchpress.com by 112.217.228.212 on 09/07/12
For personal use only.

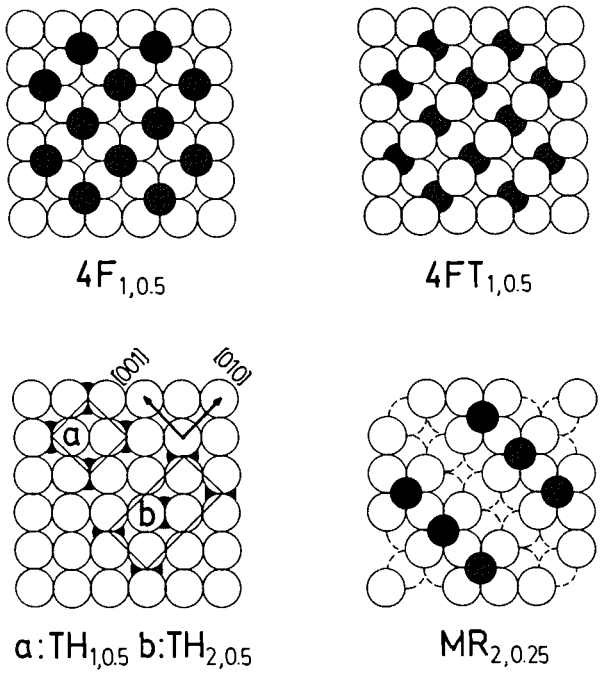

FIG. 2. Schematic indications of some models discussed in text. The dark filled circles represent oxygen atoms and the open circles formed by continuous and dashed lines correspond to copper atoms respectively in the topmost layer and the second layer of the ideal clean metal surface.

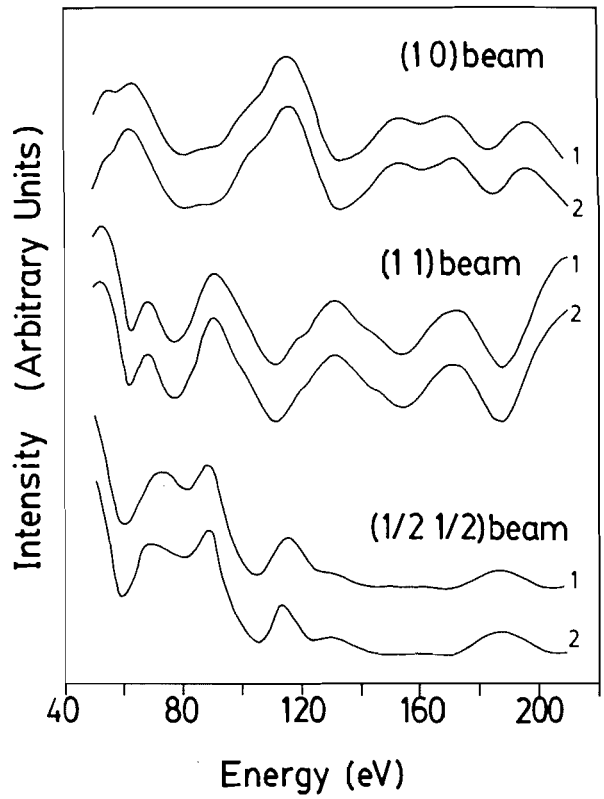

FIG. 3. Comparison of $I(E)$ curves at normal incidence for the (1,0), (1,1), and (1/2,1/2) beams calculated for the O on Cu(100) models designated $TH_{1,0.5}$ (curves identified by 1) and $TH_{2,0.5}$ (curves identified by 2) with d_{O-Cu} = 1.05 Å.

ing was done to the calculated $I(E)$ curves prior to comparing with those from experiment.

Models investigated

Figure 1 indicates that the $I(E)$ curves measured for the Cu(100)–$(\sqrt{2} \times \sqrt{2})45°$–O and Cu(100)–$(2\sqrt{2} \times \sqrt{2})45°$–O surfaces are relatively similar to those measured previously for Cu(100)–$(\sqrt{2} \times \sqrt{2})45°$–N (33). Further, since O and N have similar scattering factors (37), these three surfaces are likely to have structural features in common. The models considered for the $(\sqrt{2} \times \sqrt{2})45°$–O surface therefore start from the premiss that, as for N, adsorbed O atoms occupy 4f hollow sites. From this starting point other models can be produced involving lateral and vertical relaxations of copper atoms, as well as missing rows of copper atoms as indicated in Fig. 2. Missing-row models merit consideration since they can naturally yield $(2\sqrt{2} \times \sqrt{2})45°$ structures, and their involvement may help the rearrangement to the stepped Cu(410) surface formed during faceting. In addition, because oxygen atoms in crystalline Cu_2O and CuO are surrounded tetrahedrally by four copper atoms (38), other models are considered where O atoms occupy tetrahedral holes between the first and second layers of the Cu(100) surface, as well as relaxed models with distorted tetrahedral holes for the O atoms. Consideration is not given here to models with mixed 4f and bridge-site adsorption, as proposed by Onuferko and Woodruff (13), because they are not strongly supported by the $I(E)$ curves calculated in that work.

The basic structures considered in this study are distinguished by designations of the types $X_{n,m}$. In this notation, X identifies the type of model and is represented by 4F for O adsorption in regular 4f hollow sites, by TH for adsorption in tetrahedral holes between the first and second copper layers, by MR when O adsorbs in 4f sites but with missing rows of copper atoms, and by 4FT when the 4F structure with O initially coplanar with the neighbouring copper atoms is subjected to a tetrahedral-type distortion. The subscript n has a value 1,2 for the $(\sqrt{2} \times \sqrt{2})45°$, $(2\sqrt{2} \times \sqrt{2})45°$ structures respectively, while m indicates the O coverage as a fraction of a monolayer (i.e. ratio of number of O atoms to number of Cu atoms in the top layer for the ideal metal surface). Finally, a prime is added to the model designation (e.g. TH′) when additional lateral relaxations are included for the copper atoms in the vicinity of the surface. These relaxations act to increase the neighbouring O–Cu bond lengths. For example, for the models designated MR′, half the atoms in the top copper layer are laterally displaced perpendicular to the line of the missing row; similarly for the TH′ models copper atoms in the top two layers are displaced in the [010] and [001] directions. The specific models examined in this work are detailed in Table 1; the headings d_{O-Cu} and d_{Cu-Cu} are respectively the topmost O–Cu interlayer spacing and the first Cu–Cu spacing.

Results and discussion

Initial comparisons of experiment and calculation

Comparisons of $I(E)$ curves measured from Cu(100)–$(\sqrt{2} \times \sqrt{2})45°$–O, for normal incidence, with those calculated for the range of models considered for tetrahedral hole adsorption (i.e. the models TH and TH′ in Table 1) showed no reasonable levels of correspondence as assessed both by visual inspection and by use of the reliability index (R_p) introduced by Pendry (39). Therefore this model does not appear relevant to this chemisorption system, an observation which is in general agreement with the previous observations (3, 4) that bulk oxide formation occurs at much higher oxygen exposures than considered here. Nevertheless Fig. 3 reports $I(E)$ curves calculated for the $TH_{1,0.5}$ and $TH_{2,0.5}$ models, with a constant

TABLE 1. Models investigated with multiple scattering calculations

Type	d_{O-Cu} (Å)	d_{Cu-Cu} (Å)	Cu atom lateral shift (Å)
$4F_{1,0.5}$	−0.20 (0.20) 0.40 0.60 (0.10) 1.50	1.51 (0.15) 2.41 1.81	
$4F_{1.1.0}$	0.00 (0_1)* 0.55 (0.10) 0.95 (0_2)*	1.81 (0.10) 2.01	
$4FT_{1,0.5}$	0.15, 0.30, 0.45, 0.70	1.51 (0.15) 2.41	
$TH_{1,0.5}$	1.00 (0.05) 1.30	2.00 (0.10) 2.60	
$TH_{2,0.5}$	1.00 (0.05) 1.30	2.00 (0.10) 2.60	
$TH'_{1,0.5}$	0.90 (0.10) 1.30 0.90 (0.10) 1.20	1.80 (0.20) 2.60 1.80 (0.20) 2.40	0.29 0.37
$MR_{2,0.25}$	0.00	1.66 (0.075) 2.11	
$MR_{2,0.5}$	0.00	1.66 (0.075) 2.11	
$MR'_{2,0.25}$	0.00	1.66 (0.075) 2.11	0.26

*This model has 1/2 monolayer each of inequivalent O atoms designated O_1 and O_2.

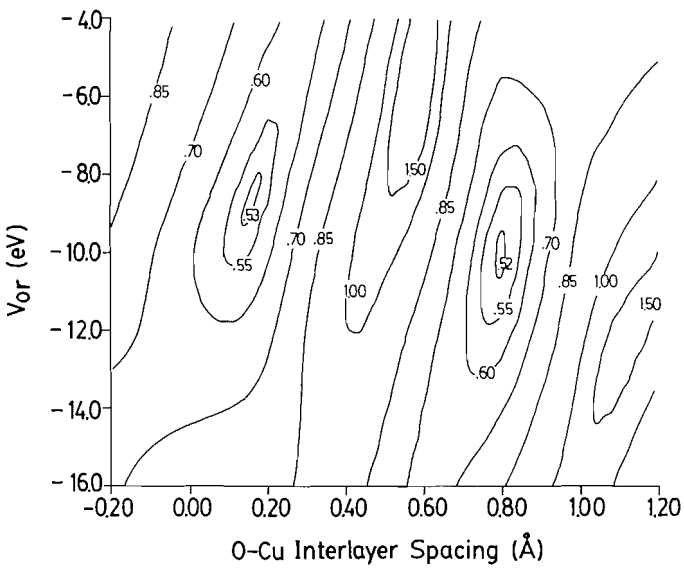

FIG. 4. Contour plot of R_p versus V_{or} and the O–Cu interlayer spacing for normal incidence data and $4F_{1,0.5}$ models of O on Cu(100). All neighbouring Cu–Cu interlayer spacings in the calculations equal 1.81 Å.

local geometry, using the approach applied previously for the CO on Pd(100) system (40). The close similarity of the curves for each beam designation reinforces arguments of Yang *et al.* (12) regarding the stability of $I(E)$ curves for corresponding beams when the local coordination is constant but the overall translational symmetry varies. The original observations of this behaviour emphasized the constancy of $I(E)$ curves for fractional-order beams, but in this case it is clear that the curves for corresponding integral beams are also closely similar.

The reliability index R_p is defined (39) so that the closer the correspondence between the sets of $I(E)$ curves being compared the smaller its value. Figure 4 shows for the $4F_{1,0.5}$ model type a contour plot of R_p versus V_{or} and d_{O-Cu}, the topmost O–Cu interlayer spacing, for the normal incidence data when the first Cu–Cu spacing (d_{Cu-Cu}) is held at the bulk value (1.81 Å). Two local minima are apparent with almost equal values. For one the oxygen atoms are held close to coplanarity with the topmost copper layer, while for the other the adsorbed atoms are about 0.75 Å above the 4f sites. Interestingly these two minima occur for conditions similar to the conclusions, noted in the Introduction, from studies with angular resolved XPS (O close to coplanar) and with photoelectron diffraction and SEXAFS (O close to 0.75 Å above surface). Nevertheless the comparison in Fig. 4 is not sufficient for distinguishing these two situations, one reason being that with coplanarity some vertical relaxation in the topmost Cu–Cu spacing would likely occur. Accordingly the contour plot of R_p in Fig. 5, made for the normal incidence data with O nearly coplanar with the topmost copper layer, suggests that the optimal value of d_{Cu-Cu} is close to 1.84 Å. The contour plot of R_p shown in Fig. 6 is calculated for both normal and off-normal incidence data with O held between 0.7 and 1.5 Å above the 4f sites. In this case R_p is minimized with d_{O-Cu} equal to 0.85 Å. Figure 7 compares some representative $I(E)$ curves from experiment, for both normal and off-normal incidence, with those calculated for three $4F_{1,0.5}$ models, namely: (*i*) d_{O-Cu} = 0.0, d_{Cu-Cu} = 1.88 Å; (*ii*) d_{O-Cu} = 0.7 Å, d_{Cu-Cu} = 1.81 Å; (*iii*) d_{O-Cu} = 0.9 Å, d_{Cu-Cu} = 1.81 Å. The minimum value of R_p calculated for the coplanar model for all 10 beams is 0.69; the corresponding values for models (*ii*) and (*iii*) are 0.76 and 0.75, respectively. Insofar as the best agreement between the experimental and calculated $I(E)$ curves corresponds to the smallest value of R_p, the coplanar model appears favoured. A similar conclusion may be reached from a visual comparison of the individual $I(E)$ curves shown in Fig. 7, although the correspondence remains far from ideal. We also made multiple-scattering calculations for one-monolayer ($\sqrt{2} \times \sqrt{2}$)45° models in which all the O atoms are held in 4f sites, but where half are coplanar with the topmost copper layer while the other half are held between 0.55 and 0.95 Å above the surface. These calculations showed much lower levels of correspondence with the experimental $I(E)$ curves, than those in Fig. 7, and so it seems safe to discount this type of inequivalent O adsorption.

Comparisons of ($\sqrt{2} \times \sqrt{2}$)45°–O and ($2\sqrt{2} \times \sqrt{2}$)45°–O structures

Overall the corresponding $I(E)$ curves measured in this work for the ($\sqrt{2} \times \sqrt{2}$)45°–O and ($2\sqrt{2} \times \sqrt{2}$)45°–O structures are quite similar (Fig. 1), and there is a broad agreement, at least

Can. J. Chem. Downloaded from www.nrcresearchpress.com by 112.217.228.212 on 09/07/12
For personal use only.

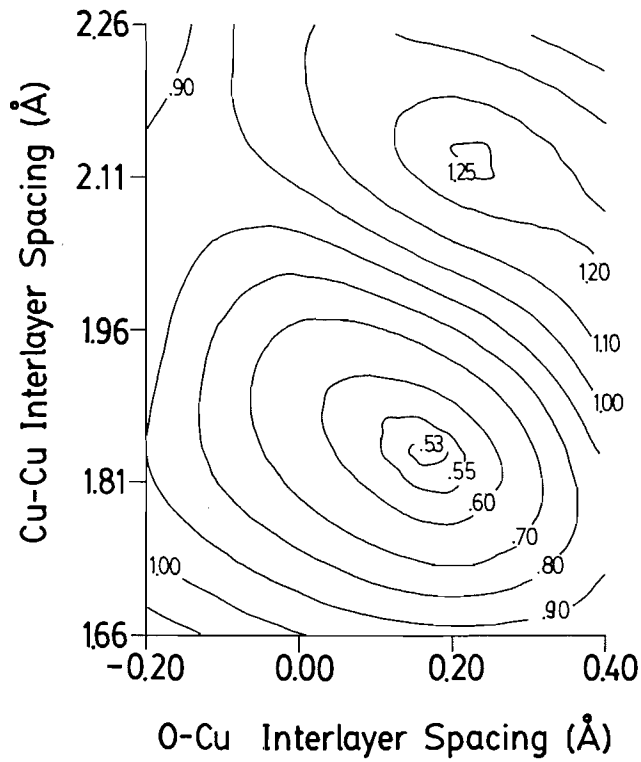

FIG. 5. Contour plot of R_p versus the topmost Cu–Cu interlayer spacing and the O–Cu interlayer spacing for normal incidence data and $4F_{1,0.5}$ models of O on Cu(100). V_{or} is fixed equal to −8.0 eV for these comparisons.

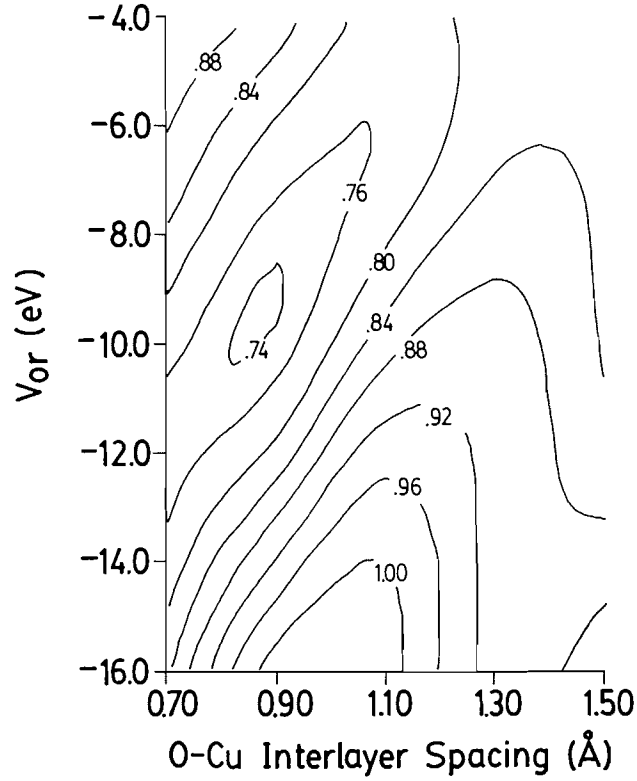

FIG. 6. Contour plot of R_p versus V_{or} and the O–Cu interlayer spacing for ten beams measured and for $4F_{1,0.5}$ models of O on Cu(100). All neighbouring Cu–Cu interlayer spacings in the calculations equal 1.81 Å.

in peak positions, with curves reported previously by Onuferko and Woodruff (13) and by Yang *et al.* (12). Certainly there is some variation in relative intensities, but we find such variations ourselves when making measurements from independently prepared surfaces which show a particular type of LEED pattern. Onuferko and Woodruff reported the existence of identical $I(E)$ curves from surfaces with the different translational symmetries, an observation that could be taken to support the contention of Mayer *et al.* (5) that only one structure, of $(2\sqrt{2} \times \sqrt{2})45°$ type, is produced throughout the oxygen exposure regime. Yang *et al.* (12), in contrast, report very similar $I(E)$ curves for the (1/2,1/2) beam, but somewhat different (1,0) and (1,1) beams, a situation similar to that found in the present work. Some evolution of $I(E)$ curves occurs with increasing coverage, particularly for the integral beams, although this appears more as a second-order effect.

The general similarity in peak positions for the half-order beams with changing translational symmetry (or perhaps just increasing surface order) suggests, in concert with the views of Yang *et al.* (12), that the environment of the chemisorbed O is essentially constant with the evolution (a conclusion that has also been reached from the photoelectron diffraction studies (21)). Whatever the initial situation, there is no doubt that ultimately chemisorbed O forms the $(2\sqrt{2} \times \sqrt{2})45°$ structure on Cu(100), and therefore it is important that consideration be given to structural models with this translational symmetry. Nevertheless, while emphasizing the basic aspects of the surface structures, as we do in this paper, and while recognizing that there is a general similarity in the $I(E)$ curves calculated for related $(\sqrt{2} \times \sqrt{2})45°$ and $(2\sqrt{2} \times \sqrt{2})45°$ models (e.g. Fig. 3), $I(E)$ curves measured from $(\sqrt{2} \times \sqrt{2})45°$ LEED patterns are compared here with $I(E)$ curves calculated for structural models with both types of translational symmetries.

Analysis of bond lengths

The contour plot in Fig. 5 suggests that the correspondence between experimental and calculated $I(E)$ curves is optimized with $d_{O-Cu} = 0.17$ Å and $d_{Cu-Cu} = 1.84$ Å. In this situation each O is bonded to one Cu atom (directly below) at 2.01 Å and the four Cu atoms at 1.81 Å, with the average of the five O–Cu bond lengths equalling 1.85 Å. This appears quite inconsistent with the structure of bulk CuO (38), for which each O is bonded to four Cu atoms in a distorted tetrahedral arrangement at an average distance of 1.92 Å. Even for the structure of bulk Cu_2O (38), in which the metal oxidation state is lower and therefore is more likely to be relevant to the low-coverage chemisorption situation, each O is bonded tetrahedrally to four Cu atoms at 1.85 Å. With the Brown–Altermatt expression (41)

$$[1] \quad r = r_o - 0.85 \log s$$

as used in an earlier report from this laboratory (42), the O–Cu distance for a unit bond valence (r_o) equals 1.59 Å. Therefore, when O (valency $v = 2$) is bonded to 5 neighbours ($n = 5$), the average bond valence is $s = v/n = 0.4$ and the corresponding average O–Cu bond distance is estimated to equal 1.93 Å. This suggests that further relaxations beyond those considered above may occur in the surface region for O on Cu(100) to make the average of the local O–Cu distances greater than 1.85 Å and closer to 1.93 Å.

The analysis in Fig. 5 uses just three beams and therefore the data base is insufficient to assert at this point whether the d_{O-Cu} spacing is really 0.17 Å as opposed, for example, to a smaller

Can. J. Chem. Downloaded from www.nrcresearchpress.com by 112.217.228.212 on 09/07/12
For personal use only.

Can. J. Chem. Downloaded from www.nrcresearchpress.com by 112.217.228.212 on 09/07/12
For personal use only.

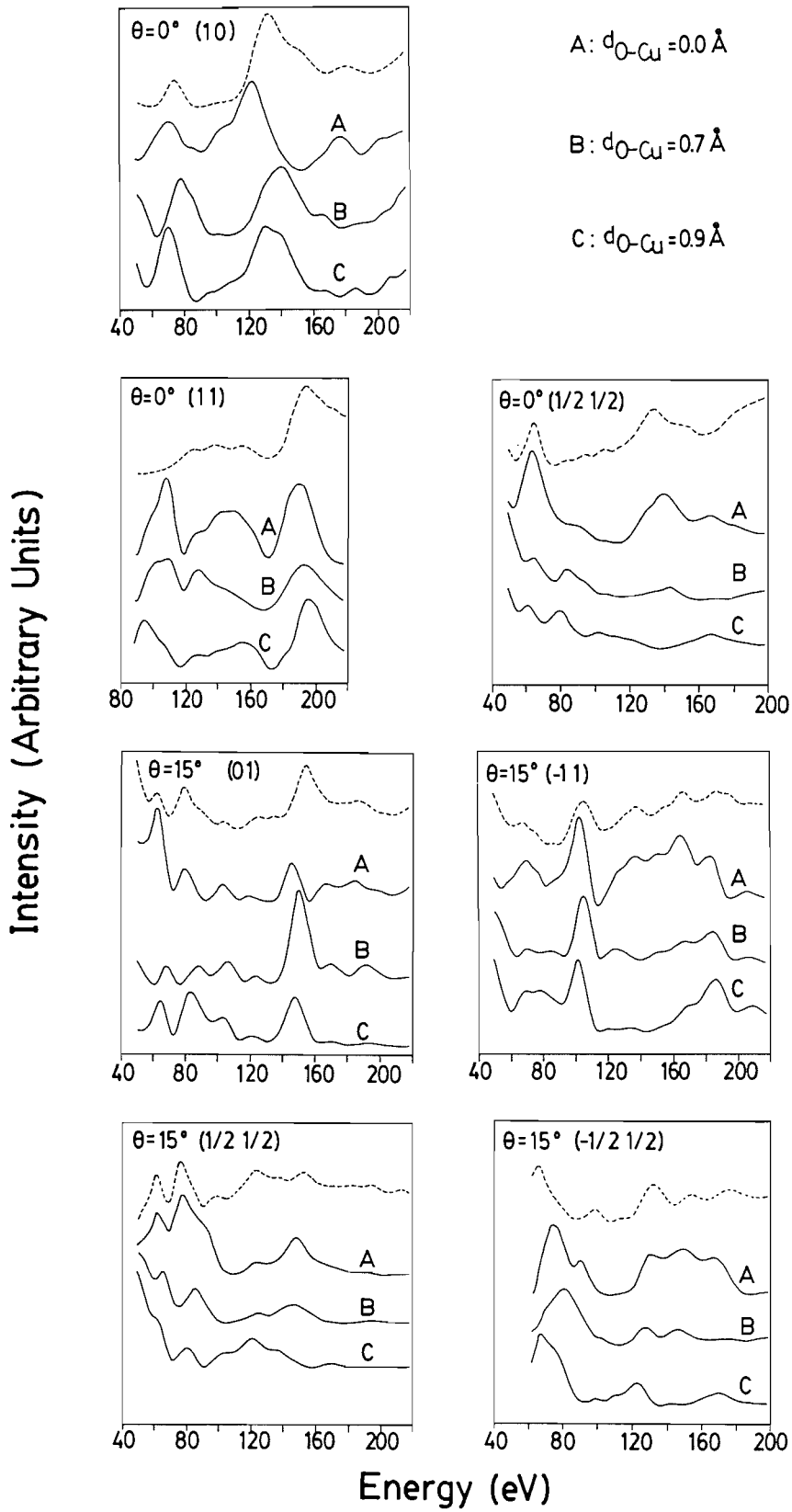

FIG. 7. Comparison of representative experimental $I(E)$ curves (dashed) from Cu(100)–($\sqrt{2} \times \sqrt{2}$)45°–O with those calculated for three 4F models: (*i*) $d_{O-Cu} = 0.0$, $d_{Cu-Cu} = 1.88$ Å (curves designated A); (*ii*) $d_{O-Cu} = 0.7$ Å, $d_{Cu-Cu} = 1.81$ Å (curves designated B); (*iii*) $d_{O-Cu} = 0.9$ Å, $d_{Cu-Cu} = 1.81$ Å (curves designated C). For these comparisons V_{or} is kept at the initial value of -10.0 eV.

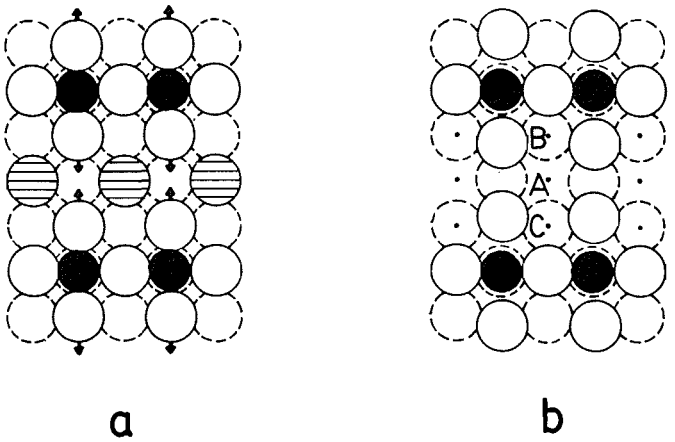

FIG. 8. Schematic illustration of formation of missing-row model of Cu(100) surface for 1/4 monolayer coverage of O atoms represented by dark filled circles. (*a*) With O atoms in coplanar 4f sites, some top layer Cu atoms are displaced laterally (indicated by arrows) and the Cu atoms represented by hatched circles are displaced to form the missing row. (*b*) Shows top layer and second layer Cu atoms after forming the missing row, and identifies sites designated A, B, C for further possible O chemisorption.

value. Since this paper aims just to assess the broader aspects of this surface structure, the current discussion will consider models with the chemisorbed O atoms coplanar with the topmost copper layer (this increases the layer symmetry with a consequent reduction in computing cost). Given the basic coplanar 4F model as a starting point, the average O–Cu bond distance may in principle be increased by vertical and lateral relaxations, either individually or in combination.

Variations on coplanar models

The 4FT model derives from the coplanar 4F model by having, for each O atom, two diagonally-related Cu atoms displaced vertically upwards while the other two are displaced downwards by the same amount (Fig. 2). This allows the O–Cu bond length to increase, although the rearrangement for the topmost metal structure can be substantial for only a small increase in the adsorbate bond length. For example, with the Cu atoms vertically displaced by 0.3 Å, the O–Cu distance increases by less than 0.03 Å. As judged both by R_p and visual comparisons, the $I(E)$ curves calculated for the 4FT models showed no improved correspondence with the experimental $I(E)$ curves relative to the situation for the coplanar 4F model. Therefore the 4FT models are not considered further in this paper.

In general with O chemisorption in coplanar 4f sites, lateral relaxations of the Cu atoms can provide an efficient route to increasing the average O–Cu bond length, although that may occur at the expense of strain in the metal structure. An exception is if the lateral relaxations are accompanied by removal of rows of Cu atoms. Missing row (MR) models have been postulated in other examples of O chemisorption, including that on the (110) surface of copper (43), and Fig. 8 outlines a possible scheme for the Cu(100) surface starting with a 1/4 monolayer coverage. The MR model shown naturally develops the $(2\sqrt{2} \times \sqrt{2})45°$ translational symmetry for the O chemisorption structure.

Missing row models

Figure 9 shows $I(E)$ curves calculated for normal incidence for some MR models, and it also allows comparisons with curves calculated for the corresponding coplanar 4F model. In all these models, the O atoms are in coplanar 4f sites and the topmost Cu–Cu interlayer spacings are fixed at 1.88 Å. Following the behaviour established in Fig. 3, and in other studies (12, 44), the $I(E)$ curves calculated for the $4F_{1,0.5}$ model are expected to be essentially identical to the corresponding model of $4F_{2,0.25}$ type. Then Fig. 9 indicates the trends in peak shapes and positions in calculated $I(E)$ curves on adding a missing row ($MR_{2,0.25}$), and on making two further independent changes, namely doubling the surface coverage, as in $MR_{2,0.5}$ where the extra O atom per unit mesh occupies the coplanar site A (Fig. 8), and introducing a lateral shift to the topmost copper layer ($MR'_{2,0.25}$). These changes can effect an improvement in the comparison with the experimental $I(E)$ curves, although some changes are quite subtle. For the (1,0) beam, the basic shape of the calculated $I(E)$ curves is relatively constant, although there is a systematic shift towards more favourable peak positions as the changes in surface structure are made (i.e. calculated peaks shift to higher energies). More substantial changes are found in the (1,1) and (1/2,1/2) beams.

Overall the best correspondence found so far is for the $MR'_{2,0.25}$ model, although no claim can be made that this corresponds to the actual surface structure. More detailed investigations are needed, in part because a systematic variation of geometrical parameters in the calculations has not yet been made. Also there is still a significant discrepancy between calculation and experiment for the (1,1) beam with regard to the strong peak which is calculated at around 110 eV. This peak is found in all curves calculated so far (including for models with O held close to 0.75 Å above the 4f site), but it is absent in curves measured from surfaces which show $(\sqrt{2} \times \sqrt{2})45°$ LEED patterns. By contrast, measurements from the $(2\sqrt{2} \times \sqrt{2})45°$ structure (Fig. 1) show a smaller peak at around 100 eV, although so far it remains unclear whether this discrepancy is one that can be primarily related to disorder at the surface, or whether it indicates that substantial changes in the basic structure are still needed. The trends in Fig. 9 suggest that an improved correspondence with the experimental $I(E)$ curves may occur for $MR'_{2,0.5}$ models with a larger lateral shift than the value of 0.26 Å used. That this lateral shift (Fig. 8) could be larger is suggested by the following considerations. With the O atoms in coplanar 4f sites, and with the value of d_{Cu-Cu} equal to 1.88 Å, there are two O–Cu distances at 1.81 Å and one at 1.88 Å. Equation [1] then requires the other two O–Cu distances to equal 2.15 Å in order that the sum of bond valences to the chemisorbed species equals the conventional valency. This corresponds to a lateral shift of 0.34 Å.

Some further points may be noted for the missing row model. First, other adsorption sites are available for oxygen, as indicated in Fig. 8 where three such sites are labelled A, B, and C. Presumably any energetic penalty in forming the missing rows can be counterbalanced by the extra possibilities for Cu–O bond formation. Most probably sites of the A type would fill first beyond the 1/4 monolayer coverage situation. Then, with eq. [1] and the assumptions above, such O atoms are predicted to chemisorb at about 0.65 Å above the *second* copper layer, assuming both that the interlayer spacing between the second and third copper layers equals the bulk value, and that there are no lateral relaxations at the second copper layer. Such an environment is noticeably closer to that reported from SEXAFS and photoelectron diffraction, although we have not yet had the opportunity to make the LEED intensity calculations for this more complicated model. Superficially this model

Can. J. Chem. Downloaded from www.nrcresearchpress.com by 112.217.228.212 on 09/07/12
For personal use only.

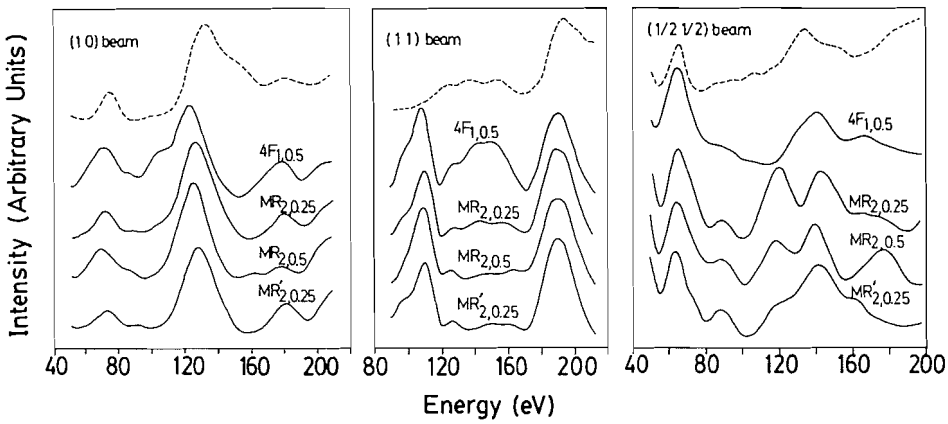

FIG. 9. $I(E)$ curves measured at normal incidence for the (1,0), (1,1), and (1/2,1/2) beams from Cu(100)–$(\sqrt{2} \times \sqrt{2})45°$–O (shown as dashed lines) and compared with calculated curves for the four models designated $4F_{1,0.5}$, $MR_{2,0.25}$, $MR_{2,0.5}$, $MR'_{2,0.25}$. In each model O is held in coplanar 4f sites and the topmost Cu–Cu interlayer spacing equals 1.88 Å (all other Cu–Cu interlayer spacings are fixed at 1.81 Å).

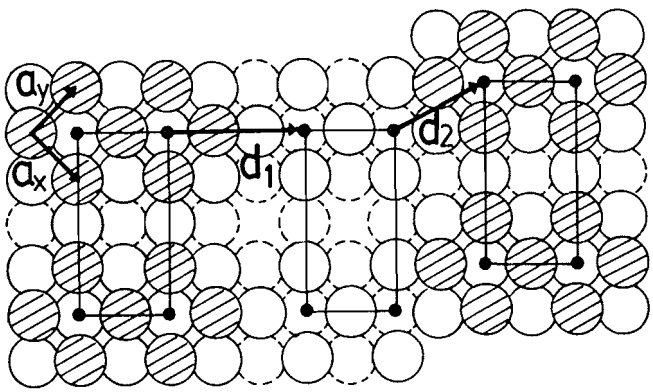

FIG. 10. Illustration of two types of antiphase boundaries with the missing row model. The parallel vectors shown satisfy $\boldsymbol{d}_1 = (3/2)\boldsymbol{a}_x + (3/2)\boldsymbol{a}_y$ and $\boldsymbol{d}_2 = (1/2)\boldsymbol{a}_x + (3/2)\boldsymbol{a}_y$. The dots represent oxygen atoms, and the first, second and third copper layers are represented by hatched circles, open continuous circles and dashed circles, respectively.

appears consistent with the reports that oxygen ultimately incorporates below the first copper layer (10, 11, 45).

If O can additionally adsorb in the sites of types B and C then the $(2\sqrt{2} \times \sqrt{2})45°$ translational symmetry could be maintained over the complete range of coverage from quarter monolayer to one monolayer. Further, with two copper layers involved in the ideal structure, antiphase domain boundaries can occur across atomic steps, as indicated by the examples in Fig. 10. Beam splittings, as a result of antiphase scattering, are determined by the parallel component of the vector which links related positions across the domain boundary (i.e. of the type $\boldsymbol{d} = d_x\boldsymbol{a}_x + d_y\boldsymbol{a}_y$ shown in Fig. 10). The (hk) beam is split according to the antiphase scattering mechanism, in directions perpendicular to the domain boundaries, whenever

$$hd_x + kd_y = (1/2)(2n + 1)$$

for n integral (46). Several domain boundaries are possible, but Fig. 10 shows the two different types of vector $\boldsymbol{d}$ that can occur. With these, the missing row model predicts splittings for the beams (1/2,1/2) and (1,0), but not (1,1), as reported by Richter and Gerhardt (14). However, the present analysis does not follow these other authors in concluding that the splittings reported indicate that the O chemisorption occurs on bridge sites.

Concluding remarks

This paper should be seen as a progress report of current LEED crystallographic investigations for the O on Cu(100) surface structure. A new feature introduced here concerns the proposal that a missing row model may be able to accommodate many observations reported previously for this system. With further possible surface relaxations, this structure may be more complicated than has previously been considered. A full resolution of the structural details for the $(2\sqrt{2} \times \sqrt{2})45°$ models could be aided by a combined investigation with other techniques including high-energy ion scattering and scanning tunneling microscopy. Disorder contributions apparently significantly affect this system. Frequently 1/4 order beams could not be detected on our conventional LEED screen, but we have no basis to disagree with the report of Mayer *et al.* (5) that, with appropriate ordering, $(2\sqrt{2} \times \sqrt{2})45°$ diffraction patterns always dominate. Nevertheless we do note that with the missing row model the $(2\sqrt{2} \times \sqrt{2})45°$ translational symmetry could be maintained over a range of O coverage. Incidentally, although they did not explicitly consider the missing row model, Boulliard and Sotto (29) proposed a 3/4 monolayer structure for the Cu(100)–$(2\sqrt{2} \times \sqrt{2})45°$–O surface which is closely analogous to the model in Fig. 8 with additional O adsorption on sites of types B and C. Whether there could be some change over of O adsorption sites between 1/2 and 3/4 monolayer coverage is a topic for further surface structural investigation.

Acknowledgement

We gratefully acknowledge the support of this research provided by the Natural Sciences and Engineering Research Council of Canada.

1. Electron spectroscopy of solids and surfaces. Faraday Discussions Chemical Society (London), no 60 (1975).
2. E. A. WOOD. J. Appl. Phys. **35**, 1306 (1964).
3. M. J. BRAITHWAITE, R. W. JOYNER, and M. W. ROBERTS. ref. 1, p. 89.
4 D. T. LING, J. N. MILLER, P. A. PIANETTA, D. L. WEISSMAN, I. LINDAU, and W. E. SPICER. J. Vac. Sci. Technol. **15**, 495 (1978).
5. R. MAYER, C. S. ZHANG, and K. G. LYNN. Phys. Rev. B**33**, 8899 (1986).
6. R. N. LEE and H. E. FARNSWORTH. Surf. Sci. **3**, 461 (1965).
7. G. ERTL. Surf Sci. **6**, 208 (1967).

Can. J. Chem. Downloaded from www.nrcresearchpress.com by 112.217.228.212 on 09/07/12
For personal use only.

8. G. W. SIMMONS, D. F. MITCHELL, and K. R. LAWLESS. Surf. Sci. **8**, 130 (1967).
9. A. OUSTRY, L. LAFOURCADE, and A. ESCAUT. Surf. Sci. **40**, 545 (1973).
10. P. HOFMANN, R. UNWIN, W. WYROBISCH, and A. M. BRADSHAW. Surf. Sci. **72**, 635 (1978).
11. C. BENNDORF, B. EGERT, G. KELLER, H. SEIDEL, and F. THIEME. J. Phys. Chem. Solids, **40**, 877 (1979).
12. W. S. YANG, F. JONA, and P. M. MARCUS. Phys. Rev. B**27**, 1394 (1983).
13. J. H. ONUFERKO and D. P. WOODRUFF. Surf. Sci. **95**, 555 (1980).
14. H. RICHTER and U. GERHARDT. Phys. Rev. Lett. **51**, 1570 (1983).
15. S. KONO, S. M. GOLDBERG, N. F. T. HALL, and C. S. FADLEY. Phys. Rev. B**22**, 6085 (1980).
16. D. J. GODFREY and D. P. WOODRUFF. Surf. Sci. **105**, 459 (1981).
17. TH. M. HUPKENS. Nucl. Instrum. Methods Phys. Res. B**9**, 277 (1985); B**9**, 285 (1985).
18. S. P. HOLLAND, B. J. GARRISON, and N. WINOGRAD. Phys. Rev. Lett. **43**, 220 (1979).
19. B. A. SEXTON. Surf. Sci. **88**, 299 (1979).
20. M. H. MOHAMED and L. L. KESMODEL. Surf. Sci. **185**, L467 (1987).
21. J. G. TOBIN, L. E. KLEBANOFF, D. H. ROSENBLATT, R. F. DAVIS, E. UMBACH, A. G. BACA, and D. A. SHIRLEY. Phys. Rev. B**26**, 7076 (1982).
22. U. DÖBLER, K. BABERSCHKE, J. STÖHR, and D. A. OUTKA. Phys. Rev. B**31**, 2532 (1985).
23. J. B. PENDRY. Low energy electron diffraction. Academic Press, New York. 1974.
24. L. J. CLARKE. Surface crystallography. John Wiley, London. 1985.
25. M. A. VAN HOVE, W. H. WEINBERG, and C.-M. CHAN. Low-energy electron diffraction. Springer-Verlag, Berlin. 1986.
26. S. M. THURGATE and P. J. JENNINGS. Surf. Sci. **131**, 309 (1983).
27. E. LEGRAND-BONNYNS and A. PONSLET. Surf. Sci. **53**, 675 (1975).
28. K. A. THOMPSON and C. S. FADLEY. Surf. Sci. **146**, 281 (1984).
29. J. C. BOULLIARD and M. P. SOTTO. Surf. Sci. **182**, 200 (1987).
30. W. T. MOORE, R. W. STREATER, D. C. FROST, and K. A. R. MITCHELL. Solid State Commun. **24**, 139 (1977).
31. P. C. WONG, M. Y. ZHOU, K. C. HUI, and K. A. R. MITCHELL. Surf. Sci. **163**, 172 (1985).
32. H. C. ZENG, R. N. S. SODHI, and K. A. R. MITCHELL. Surf. Sci. **177**, 329 (1986).
33. H. C. ZENG, R. N. S. SODHI, and K. A. R. MITCHELL. Surf. Sci. **188**, 599 (1987).
34. M. A. VAN HOVE and S. Y. TONG. Surface crystallography by LEED. Springer, Berlin. 1979.
35. V. L. MORUZZI, J. F. JANAK, and A. R. WILLIAMS. Calculations of electronic properties of metals. Plenum, New York. 1978.
36. J. E. DEMUTH, D. W. JEPSEN, and P. M. MARCUS. Surf. Sci. **45**, 733 (1974).
37. F. JONA, K. O. LEGG, H. D. SHIH, D. W. JEPSEN, and P. M. MARCUS. Phys. Rev. Lett. **40**, 1466 (1978).
38. R. W. G. WYCKOFF. Crystal structures. Vol. 1. Interscience, New York. 1960.
39. J. B. PENDRY. J. Phys. C**13**, 937 (1980).
40. R. J. BEHM, K. CHRISTMANN, G. ERTL, and M. A. VAN HOVE. J. Chem. Phys. **73**, 2984 (1980).
41. I. D. BROWN and D. ALTERMATT. Acta Crystallogr. B**41**, 244 (1985).
42. K. A. R. MITCHELL, S. A. SCHLATTER, and R. N. S. SODHI. Can. J. Chem. **64**, 1435 (1986).
43. K. BABERSCHKE, U. DÖBLER, L. WENZEL, D. ARVANITIS, A. BARATOFF, and K. H. RIEDER. Phys. Rev. B**33**, 5910 (1986).
44. K. C. HUI and K. A. R. MITCHELL. Can. J. Phys. **63**, 1377 (1985).
45. F. H. P. M. HABRAKEN, C. M. A. M. MESTERS, and G. A. BOOTSMA. Surf. Sci. **97**, 264 (1980).
46. P. J. ESTRUP and E. G. MCRAE. Surf. Sci. **25**, 1 (1971).

Can. J. Chem. Downloaded from www.nrcresearchpress.com by 112.217.228.212 on 09/07/12
For personal use only.

Durene-capped porphyrins: synthesis and characterization

TILAK P. WIJESEKERA, SHANTHA DAVID, JOHN B. PAINE III, BRIAN R. JAMES, AND DAVID DOLPHIN
Department of Chemistry, University of British Columbia, 2036 Main Mall, Vancouver, B.C., Canada V6T 1Y6

Received November 29, 1987

This paper is dedicated to Professor Charles A. McDowell on the occasion of his 70th birthday

TILAK P. WIJESEKERA, SHANTHA DAVID, JOHN B. PAINE III, BRIAN R. JAMES, and DAVID DOLPHIN. Can. J. Chem. **66**, 2063 (1988).

The synthesis of porphyrins having a fully hydrophobic cavity capped by a durene moiety is described. The size of the cavity is adjusted by varying the number of methylene $-(CH_2)_n-$ groups linking the tetramethylphenylene cap with the diametrically opposite β-positions of the porphyrin. Bis(chloromethyl)durene (**1**) was first converted to durene-bisalkanoic acids **11** (n = 4), **13** (n = 5), and **18** (n = 7) using standard chain extension methods. The diacid chlorides were then used to acylate two equivalents of a β-unsubstituted pyrrole to give a chain-linked bispyrrole. Each pyrrole, following appropriate manipulation of the α substituents, was condensed with an α-unsubstituted pyrrole and the resulting chain-linked dipyrromethane dimer was cyclized *intramolecularly* under high dilution to give the capped porphyrin **34** (n = 4, 5, or 7).

TILAK P. WIJESEKERA, SHANTHA DAVID, JOHN B. PAINE III, BRIAN R. JAMES et DAVID DOLPHIN. Can. J. Chem. **66**, 2063 (1988).

On décrit la synthèse de porphyrines portant une cavité complètement hydrophobe et qui sont cappées par une portion de durène. On ajuste la grandeur de la cavité en faisant varier le nombre de groupements méthylènes $-(CH_2)_n-$ reliant le tétraméthylphénylène servant de cap avec les positions β diamétralement opposées de la porphyrine. Dans la première étape, on transforme le bis(chlorométhyl)durène (**1**) en acides durène-bis-alcanoïques (**11**, n = 4; **13**, n = 5 et **18**, n = 7) en utilisant des méthodes standards pour l'extension de la chaîne. On utilise alors les chlorures de diacides pour acyler deux équivalents d'un pyrrole substitué en position β afin d'obtenir un bispyrrole lié par une chaîne. Après une manipulation appropriée des substituants en α, on a condensé chacun des pyrroles avec un pyrrole substitué en α et, utilisant la technique des grandes dilutions, on a ensuite procédé à une cyclisation *intramoléculaire* du dipyrrométhane lié par une chaîne qui en résulte afin d'obtenir la porphyrine cappée désirée (**34**, n = 4, 5 ou 7).

[Traduit par la revue]

Introduction

Synthetic heme models all necessarily incorporate an active site comparable to that of deoxymyoglobin that has an iron(II) atom coordinated to the four nitrogen atoms of a porphyrin dianion and an axial imidazole. The use of simple ferrous porphyrins as models for reversible oxygen-carrying hemoproteins has been thwarted for two main reasons. First, the addition of a nitrogen-donor base to four coordinate ferrous porphyrins in solution usually leads to a six-coordinate complex incapable of binding oxygen (1). Second, coordination of oxygen to the five coordinate species at room temperature leads rapidly and irreversibly to the formation of bridged oxo-iron(III) species (2, 3). Autoxidation of the iron centre proceeds via the initial formation of a monomeric iron-dioxygen adduct, followed by the reaction with a second iron(II) porphyrin unit (4).

Attempts to achieve reversible dioxygen binding at ambient temperature gave rise to model designs incorporating steric bulk on one face of the porphyrin. This not only retards the ligation of the nitrogenous base at the sixth site, thus facilitating dioxygen binding, but also prevents "dimerization" of the initially formed dioxygen adduct which leads to oxidation of the metal centre. The best known sterically hindered porphyrins are the "picket-fence" (5) and "pocket" (6) porphyrins of Collman *et al.*, the "capped" (7) porphyrins of Baldwin and co-workers, and the "cyclophane hemes" (8) of Traylor *et al.* Model systems with steric hindrances on both faces of the porphyrin (the "basket-handle" porphyrins (9) of Momenteau *et al.*), as well as those with protective structures on one and appended imidazole on the other face have also been prepared (10, 11). This area has recently been reviewed (12) and a survey of the synthesis and structure of these systems has been presented (13).

Two basic synthetic strategies have been used to obtain these hindered porphyrins. The first involves the condensation of a benzaldehyde derivative with pyrrole in a manner analogous to the synthesis of *meso*-tetraphenylporphyrin (14). The protective structure is introduced either by the modification of an appropriate *ortho*-substituent on the phenyl group (5, 6) or by carrying it in the aldehyde component prior to condensation with pyrrole (7, 9, 10). The second and the more widely used strategy is to condense, via ester or amide linkages, a diagonally β-disubstituted porphyrin with a terminally bifunctional molecule carrying the required protective structure (8, 11).

Differentiation between CO and O_2 in model systems arises from electronic, polar, and steric effects (12). Porphyrins synthesized by the above methods are limited in the size of the cavity produced and, in addition, do not provide a truly hydrophobic environment for small molecule binding. The durene-capped porphyrins described here provide a simple reference series where the influence of the distal steric effects on CO and O_2 binding may be evaluated in the absence of stabilizing electronic or polar interactions (12). An early attempt at the preparation of such a hydrophobic system resulted in a very low yield for the cyclization step due to the use of rigid and unreactive dipyrromethene precursors (15). However, the synthetic route originally developed by some of us to construct permanently deformed porphyrins (16–18), which utilizes more flexible and reactive dipyrromethane intermediates, appeared ideally suited for the synthesis of sterically hindered porphyrins having small fully hydrophobic cavities.

A preliminary communication outlining the synthesis of the durene-capped parent porphyrin and the crystallographic characterization of a chloroiron(III) derivative has appeared (19).

Results and discussion

The bis(chloromethyl)durene (**1**) was used as starting material for the introduction of the tetramethylphenylene protecting

Can. J. Chem. Downloaded from www.nrcresearchpress.com by 112.217.228.212 on 09/07/12
For personal use only.

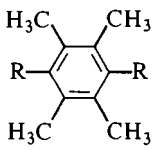

1 R: CH_2Cl $\xrightarrow[NaOEt/EtOH]{CH_2(CO_2Et)_2}$ **2** R: $CH_2CH(CO_2Et)_2$ $\xrightarrow[b.\ HCl]{a.\ Aq.\ KOH}$ **3** R: $CH_2CH(CO_2H)_2$

3 R: $CH_2CH(CO_2H)_2$ $\xrightarrow[\Delta]{Quinoline}$ **4** R: $CH_2CH_2CO_2H$ $\xrightarrow{B_2H_6}$

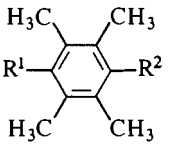

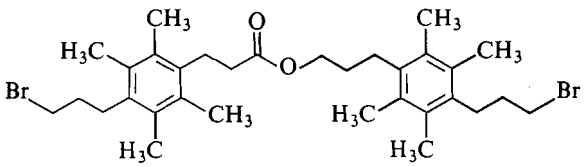

$\xleftarrow{Aq.\ HBr}$ **5** $R^1 = R^2 = CH_2CH_2CH_2OH$
6 $R^1 = CH_2CH_2CH_2OH$
$R^2 = CH_2CH_2CO_2H$

7

+

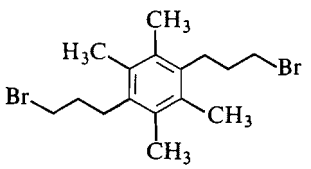

8

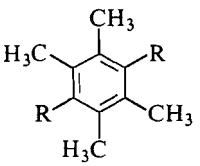

4 R: $CH_2CH_2CO_2H$ $\xrightarrow{EtOH/H_2SO_4}$ **9** R: $CH_2CH_2CO_2Et$ $\xrightarrow{B_2H_6}$ **5** R: $CH_2CH_2CH_2OH$

5 R: $CH_2CH_2CH_2OH$ $\xrightarrow{Aq.HBr}$ **8** R: $CH_2CH_2CH_2Br$ $\xrightarrow{KCN}$ **10** R: $CH_2CH_2CH_2CN$

10 R: $CH_2CH_2CH_2CN$ $\xrightarrow[b.\ HCl]{a.\ KOH/EtOH}$ **11** R: $CH_2CH_2CH_2CO_2H$

8 R: $CH_2CH_2CH_2Br$ $\xrightarrow[b.\ Aq.\ KOH\ \ c.\ HCl]{a.\ CH_2(CO_2Et)_2/NaOEt}$ **12** R: $CH_2CH_2CH_2CH(CO_2H)_2$ $\xrightarrow[\Delta]{Quinoline}$ **13**

13 R: $CH_2CH_2CH_2CH_2CO_2H$ $\xrightarrow{EtOH/H_2SO_4}$ **14** R: $CH_2CH_2CH_2CH_2CO_2Et$ $\xrightarrow{B_2H_6}$ **15**

15 R: $CH_2CH_2CH_2CH_2CH_2OH$ $\xrightarrow{Aq.\ HBr}$ **16** R: $CH_2CH_2CH_2CH_2CH_2Br$ $\xrightarrow[b.\ Aq.\ KOH\ \ c.\ HCl]{a.\ CH_2(CO_2Et)_2/NaOEt}$ **17**

17 R: $CH_2CH_2CH_2CH_2CH_2CH(CO_2H)_2$ $\xrightarrow[\Delta]{Quinoline}$ **18** R: $CH_2CH_2CH_2CH_2CH_2CH_2CO_2H$

SCHEME 1

group for the porphyrin. The synthetic strategy involved the elaboration of **1** into durene bisalkanoic acids (Scheme 1; **11**, **13**, and **18**), which could be employed to acylate, simultaneously, two β-unsubstituted pyrroles. Such chain-linked bispyrroles could then be transformed efficiently into the durene-capped porphyrins using the chemistry perfected for the synthesis of deformed porphyrins (16–18).

It was uncertain as to how reactive compound **1** might be, given a significant potential for steric hindrance by the *ortho*-methyl groups. However, in absolute ethanol containing excess sodium ethoxide and diethyl malonate, bis(chloromethyl)durene reacted rapidly and exothermically to give durene-bismethylene malonic ester (**2**) nearly quantitatively. Compound **2** could be isolated as a crystalline solid by aqueous dilution of the reaction mixture. However, we found it convenient to saponify the tetra ester *in situ*, by the addition of water and further alkali. The resulting durene-bismethylene malonic acid (**3**) was isolated by acidification of the reaction mixture. Its decarboxylation to the

Can. J. Chem. Downloaded from www.nrcresearchpress.com by 112.217.228.212 on 09/07/12
For personal use only.

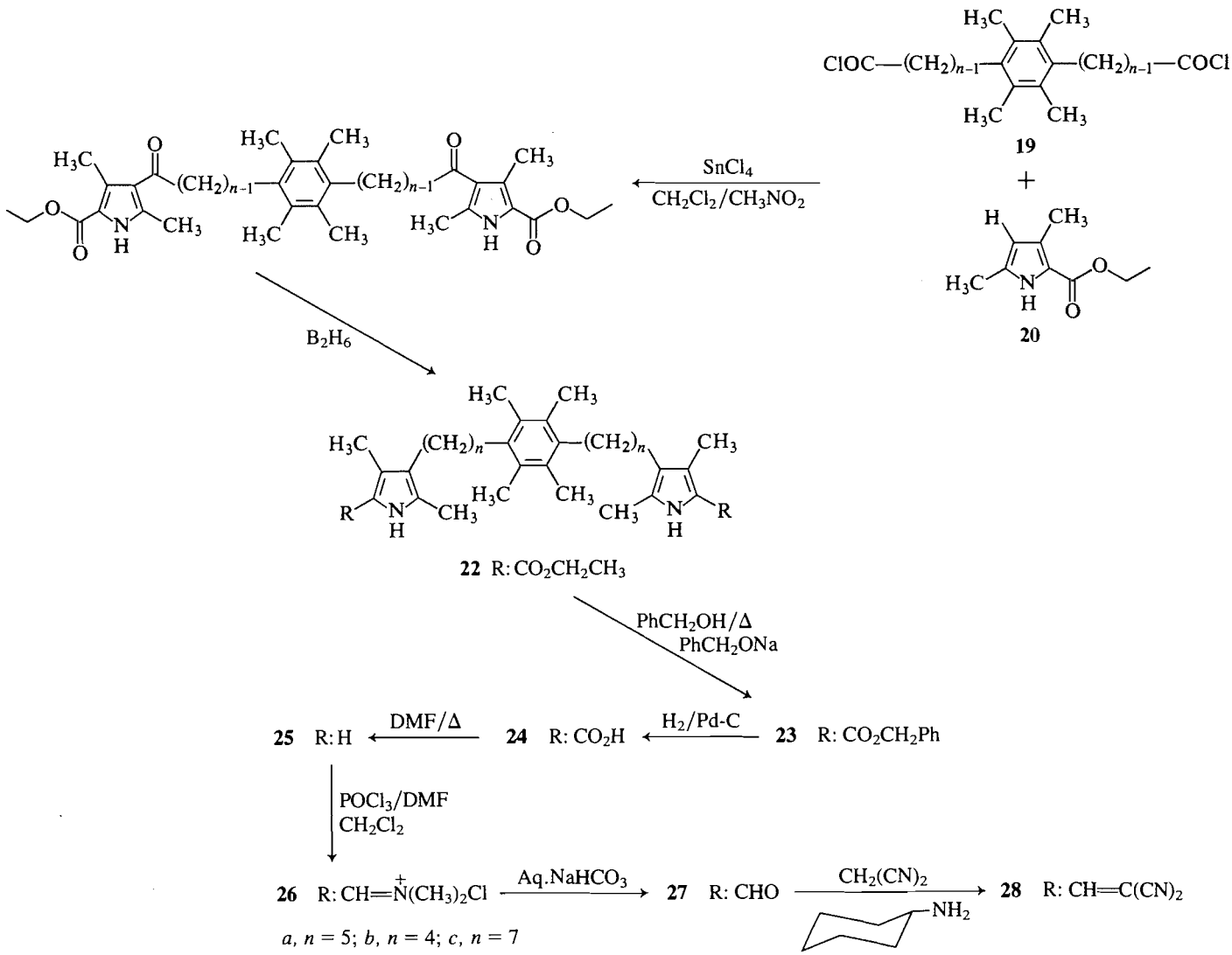

SCHEME 2

durene-bispropanoic acid (**4**) was initially effected by the addition of **3** to boiling quinoline, but *N*,*N*-diethylformamide was subsequently found to be an equally effective solvent.

Although diborane reduction of the diacid **4** was effective on a small scale, solubility problems were encountered upon scale-up, which led to incomplete reduction of the carboxyl groups, thus producing, in addition to the bis(hydroxypropyl)-durene (**5**), the monohydroxypropylmonocarboxyethyldurene (**6**). The use of this incompletely reduced material in the subsequent bromination reaction with 48% aqueous HBr led to the formation of an ester-linked durene dimer **7** as a significant by-product that was difficult to separate from the desired bis(bromopropyl)durene (**8**). However, these problems were avoided by prior esterification of the diacid **4**, which improved the solubility of both the starting material and intermediates of the diborane reduction. The bis(hydroxypropyl)durene (**5**) isolated in greater than 95% yield was converted to the bis(bromopropyl)durene (**8**) in over 90% yield. Had these problems been anticipated in the diborane reduction of **4**, the tetramethyl ester could have been isolated and its direct conversion to the diester **9** attempted. Decarbalkoxylations of similar geminal diesters have been reported by Krapcho *et al.* (20).

To generate the durene-bisbutanoic acid (**11**), bis(bromopropyl)durene (**8**) was reacted with KCN in ethanol and the resulting durene-bisbutyronitrile **10** hydrolyzed with alkali. The bispentanoic acid **13** and the bisheptanoic acid **18** were prepared by similar malonate syntheses and functional group modifications as shown in Scheme 1.

Examination of space-filling models suggested that two five-carbon chains would allow a durene moiety to be held close to the macrocycle, without significant deformation of the porphyrin core. It was to this species that we first directed our efforts (series a). The reaction sequence was then repeated using the bisbutanoic acid **11** (series b) and the bisheptanoic acid **18** (series c). The experimental methods and yields for all the intermediates in both series b and c were entirely comparable and are provided as supplementary material.[1]

The subsequent synthetic strategy involved the intramolecular cyclization of the chain-linked 5′-unsubstituted-5-formyldipyrromethane dimers. Only two basic pyrroles were used in this synthesis. 2-Ethoxycarbonyl-3,5-dimethylpyrrole (**20**) was pre-

[1]This material may be purchased from the Depository of Unpublished Material, CISTI, National Research Council of Canada, Ottawa, Ont., Canada K1A 0S2.

Can. J. Chem. Downloaded from www.nrcresearchpress.com by 112.217.228.212 on 09/07/12
For personal use only.

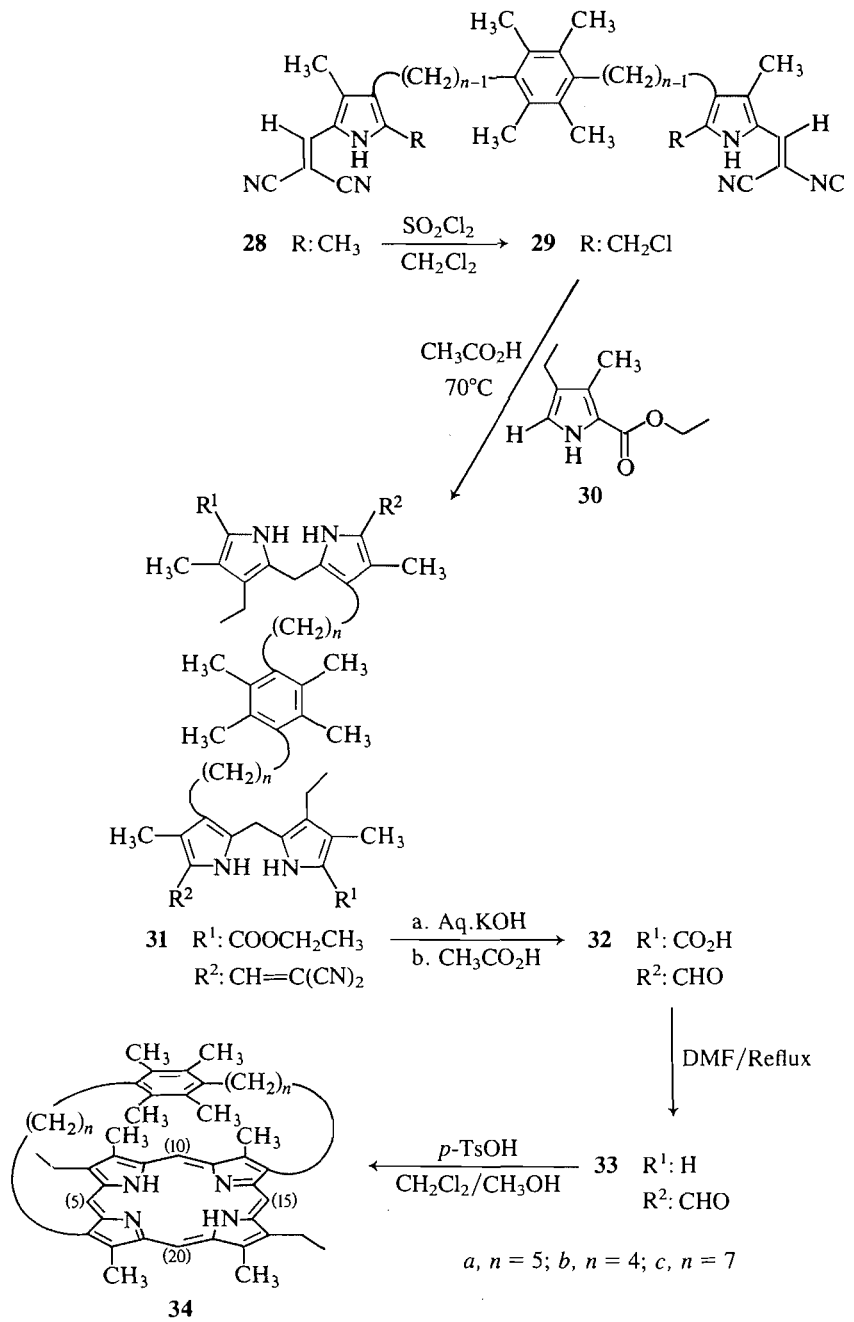

SCHEME 3

pared by the reductive condensation (21) of diethyloximinomalonate with 2,4-pentanedione in the presence of zinc and acetic acid. The other pyrrole, 2-ethoxycarbonyl-4-ethyl-3-methylpyrrole (**30**), was prepared by improved procedures (16) of standard degradations (22) of 2-ethoxycarbonyl-4-ethyl-3,5-dimethylpyrrole.

The synthesis of the durene-capped porphyrin was initiated by the acylation of the pyrrole **20** with the diacid chloride **19** in methylene chloride – nitromethane using stannic chloride as catalyst (Scheme 2). The resulting durene-bisoxoalkylidene pyrrole **21** was subjected to the usual diborane reduction, to convert the ketonic carbonyl to methylene groups. For ease of manipulation, the bispyrrole ethyl ester **22** was transbenzylated (18) to give the bispyrrole benzyl ester **23**, which was then transformed into the synthetically useful bisformylpyrrole **27** by standard methods (18). The benzyl ester **23** was cleaved by catalytic hydrogenation in tetrahydrofuran and, after removal of the catalyst and the solvent, the acid **24** was decarboxylated in refluxing dimethylformamide. Vilsmeier formylation with phosphorus oxychloride was effected in dimethylformamide without isolation of the bis α-free pyrrole **25**, and the resulting iminium salt **26** was hydrolyzed in aqueous bicarbonate to produce the formylpyrrole **27**. This was converted to its dicyanovinyl (23) derivative **28** primarily for the purpose of protecting the formyl group during the subsequent oxidation of the α-methyl group. This also served as a method of purification by chromatography, which was essential at this stage since none of the intermediates **24**–**27** was isolated.

Modification of the α-methyl groups of **28** to monochloromethyl groups was now required in order to condense them with the α-unsubstituted pyrrole **30** to produce the dipyrromethane dimers (Scheme 3). The possibility that the durene-methyl

Can. J. Chem. Downloaded from www.nrcresearchpress.com by 112.217.228.212 on 09/07/12
For personal use only.

Can. J. Chem. Downloaded from www.nrcresearchpress.com by 112.217.228.212 on 09/07/12
For personal use only.

groups might compete with the pyrrole α-methyl groups for the oxidant, sulfuryl chloride, made this reaction the most crucial step in the entire reaction sequence. However, in practice, sulfuryl chloride reacted exclusively with the pyrrole α-methyl groups, and the chloromethyl derivative **29** so produced gave the desired dipyrromethane dimer **31** in the excellent yield of ca. 90% overall for two reactions. The deprotection of the formyl groups and the saponification of the esters of **31** were effected in a single step using aqueous alkali. The 5-carboxy-5′-formyldipyrromethane dimer **32** was subsequently decarboxylated in refluxing dimethylformamide (monitored by the disappearance of the uv absorpion band at λ_{max} = 280 nm), but the product **33** was not isolated. Instead, the solution was concentrated *in vacuo*, diluted with methylene chloride, and most of the remaining dimethylformamide removed by extraction with water. The dried methylene chloride solution of the 5′-unsubstituted-5-formyldipyrromethane dimer **33** was added (by means of a syringe pump) to a solution of *p*-toluenesulfonic acid in methanol/methylene chloride to effect the intramolecular cyclization. The monomeric capped porphyrin **34** was the only porphyrin present in the reaction mixture and was isolated and purified by chromatography. The overall yield for the decarboxylation–cyclization reactions was dependent on the purity of the starting material **32**. In the pentamethylene series (n = 5), the yield of the porphyrin **34***a* varied from 22 to 31% while the tetramethylene and heptamethylene series produced the porphyrins **34***b* and **34***c* in 11–16% and 9–13% yield, respectively.

The ^{1}H nmr spectra of **34***a–c* exhibit significant upfield shifts for the durene methyl and chain -CH_2- resonances, resulting from the shielding effect of the porphyrin diamagnetic ring current. The durene methyl protons, usually observed at δ 2.2, are shifted, for example for **34***c*, to δ −0.20 ppm, and the chain -CH_2- resonances for **34***a–c* are spread over the range δ = +4 to −2 ppm.

The porphyrin methine protons appear as two singlets in the ^{1}H nmr, because of the asymmetry introduced into the molecule by the strap. A significant nuclear Overhauser effect was observed in the upfield methine resonance on irradiation of either the CH_2 resonance of the ethyl groups or the chain CH_2 at the porphyrin terminus. This allows for an unambiguous assignment of the upfield resonance to the 5- and 15-methine protons.

Work describing the formation of Fe(III) and Fe(II) derivatives of these durene-capped porphyrins and some data on the binding of amines, isocyanides, CO, and O_2 to the latter have already been published (12, 24). Further details on these systems (25) will be published elsewhere.

Experimental

The nmr spectra were obtained in the indicated solvents, using a Varian HA-100 or XL-100 instrument for proton (5-mm tube) or a Varian CFT-20 (at 25.2 MHz) or Bruker WH-400 (at 100.6 MHz) instrument for carbon-13 (10-mm tube). Melting points were obtained using a Thomas Hoover Unimelt oil bath/capillary tube or a Thomas Kofler Micro Hot Stage apparatus, and are uncorrected. Microanalyses were performed by P. Borda of this department. Reagents were employed as obtained, unless otherwise noted.

1,4-Bis(2,2-dicarboxyethyl)-2,3,5,6-tetramethylbenzene (3)

Freshly cut metallic Na (12.85 g, 0.56 mol) was dissolved under N_2, in anhydrous ethanol (600 mL) in a 2-L Erlenmeyer flask. Diethyl malonate (152 mL, 160.4 g, 1.0 mol) was stirred in followed by 1,4-bis(chloromethyl)-2,3,5,6-tetramethylbenzene (bis(chloromethyl)-durene) (**1**) (57.8 g, 0.25 mol), which was washed down with another 50 mL of anhydrous ethanol. The mixture was refluxed on a stirrer hot plate for 0.5 h; the starting material dissolved on reaction, with precipitation of NaCl.

Ethanol (approximately 200 mL) was distilled off, the reaction mixture cooled to room temperature, and a solution of KOH (200 g, 3.04 mol) in water (400 mL) added. Distillation of ethanol was continued until the temperature reached 100°C, more water (ca. 1 L) added until all of the solid dissolved, and the solution reheated to boiling. This was treated, dropwise, with concentrated HCl (ca. 300 mL). The white solid that precipitated out was collected by filtration, washed well with water, and dried in air to give 86.8 g (94.9%) of analytically pure material, mp 278.0–280.0°C (dec.); ^{1}H nmr (δ, DMSO-d_6): 2.13 (s, 12H, durene -CH_3), 3.13–3.22 (m, 4H, side-chain 1,1′-CH_2), 3.22–3.33 (m, 2H, -C*H*(CO_2H)$_2$); ms *m/e*: 278 (72) (*M*−2 CO_2), 219 (100), 205 (54). *Anal.* calcd. for $C_{18}H_{22}O_8$: C 59.01, H 6.05; found: C 58.95, H 5.92.

1,4-bis(2-carboxyethyl)-2,3,5,6-tetramethylbenzene (4)

Durene-bismethylenemalonic acid **3** (86.5 g; 0.24 mol) was added in portions to boiling quinoline (150 mL) over 20 min. The resulting thick mixture was heated until gas evolution ceased and then poured into 6 M HCl (400 mL). The product that crystallized out was collected by filtration and washed well with water under suction.

The crude solid was purified by dissolving in hot saturated aqueous $NaHCO_3$, filtering through Celite, and reprecipitating with concentrated HCl. Yield, 62.9 g (94.7%); mp 284.0– 286.0°C; ^{1}H nmr (δ, DMSO-d_6): 2.13 (s, 12H, durene CH_3), 2.06–2.39 (m, 4H, side-chain 2,2′-CH_2), 2.72–3.02 (m, 4H, side-chain 1,1′-CH_2). *Anal.* calcd. for $C_{16}H_{22}O_4$: C 69.04, H 7.97; found: C 68.48, H 7.93.

1,4-Bis(2-ethoxycarbonylethyl)-2,3,5,6-tetramethylbenzene (9)

1,4-Bis(2-carboxyethyl)-2,3,5,6-tetramethylbenzene(**4**) (158.9 g, 0.57 mol) was esterified with ethanol (400 mL) and concentrated H_2SO_4 (27 mL) using toluene (200 mL) to azeotrope out the water (Dean–Stark trap). Yield, 170.5 g (89.4%); mp: 118.5–120.0°C; ^{1}H nmr (δ, $CDCl_3$): 1.25 (t, 6H, J = 7 Hz, -OCH_2CH_3), 2.18 (s, 12H, durene CH_3), 2.28–2.50 (m, 4H, side-chain 2,2′-CH_2), 2.90–3.12 (m, 4H, side-chain 1,1′-CH_2), 4.14 (q, 4H, J = 7 Hz, -OCH_2CH_3); ^{13}C nmr (δ, $CDCl_3$): 173.10 (C=O), 135.25 (2C, durene 1,4), 132.39 (4C, durene 2,3,5,6), 60.41 (2C, -OCH_2CH_3), 34.21 (2C, side-chain 2,2′), 26.15 (2C, side-chain 1,1′), 16.30 (4C, durene CH_3), 14.28 (2C, OCH_2CH_3); ms m/*e*: 334 (M^+, 86), 289 (16), 247 (100), 233 (38). *Anal.* calcd. for $C_{20}H_{30}O_4$: C 71.82, H 9.04; found: C 72.10, H 9.11.

1,4-Bis(3-hydroxypropyl)-2,3,5,6-tetramethylbenzene (5)

1,4-Bis(2-ethoxycarbonylethyl)-2,3,5,6-tetramethylbenzene **9** (16.7 g, 0.05 mol) dissolved in dry THF (200 mL) was treated under N_2 with $NaBH_4$ (8.5 g, 0.22 mol), followed by $BF_3 \cdot Et_2O$ (45 mL, 0.36 mol). The reaction was monitored by tlc and, on completion, the excess diborane was destroyed with acetic acid (50 mL) and water (100 mL). The solvent was evaporated under reduced pressure causing the product to separate out as a white solid. More water (300 mL) was added and the solid was collected by filtration. The crude product was recrystallized by dissolving in warm ethanol (350 mL) and reprecipitating with water. Two crops of the recrystallized bis(hydroxypropyl)durene amounted to 11.2 g, an overall yield of 89.6%; mp 158.0–159.5°C; ^{1}H nmr (δ $CDCl_3$): 1.50 (s, 2H,-OH), 1.58–1.94 (m, 4H, side-chain 2,2′-CH_2), 2.26 (s, 12H, durene CH_3), 2.66–2.90 (m, 4H, side-chain 1,1′-CH_2), 3.78 (t, 4H, -C*H*$_2$OH); ^{13}C nmr (δ, $CDCl_3$): 136.16 (2C, durene 1,4), 132.23 (4C, durene 2,3,5,6), 63.14 (2C, CH_2OH), 32.82 (2C, side-chain 1,1′), 26.96 (2C, side-chain 2,2′), 16.38 (4C, durene CH_3); ms *m/e*: 250 (M^+, 87), 205 (94), 191 (47), 161 (63), 147 (100). *Anal.* calcd. for $C_{16}H_{26}O_2$: C 76.75, H 10.47; found: C 77.02, H 10.64.

1,4-Bis(3-bromopropyl)-2,3,5,6-tetramethylbenzene (8)

1,4-Bis(3-hydroxypropyl)-2,3,5,6-tetramethylbenzene (**5**) (7.5 g, 0.03 mol) and 48% aqueous HBr (24 mL) were heated at reflux under N_2. The starting material did not dissolve, but turned into a pale yellow oil, resulting in an overall emulsion. Thin-layer chromatographic

Can. J. Chem. Downloaded from www.nrcresearchpress.com by 112.217.228.212 on 09/07/12
For personal use only.

analysis of the reaction mixture after 30 min indicated that the reaction was complete.

The solution was cooled to room temperature, CH_2Cl_2 (100 mL) added, and the acid extracted out with saturated aqueous $NaHCO_3$ (2 × 30 mL) and water (30 mL). The organic layer was dried (Na_2SO_4) and evaporated *in vacuo* after adding CH_3OH. The product crystallized out as silvery white needles, yield 9.4 g (83.3%). The mother liquors were concentrated to give a second crop of 0.90 g (7.9%), mp 113.0–114.0°C; ^1H nmr (δ, $CDCl_3$): 1.84–2.10 (m, 4H, side-chain 2,2′-CH_2), 2.17 (s, 12H, durene CH_3), 2.68–2.92 (m, 4H, side-chain 1,1′-CH_2), 3.45 (t, 4H, J = 6.5 Hz, CH_2Br); ^{13}C nmr (δ, $CDCl_3$): 135.39 (2C, durene 1,4), 132.33 (4C, durene 2,3,5,6), 33.92 (CH_2Br), 32.69 (2C, side-chain 1,1′), 29.37 (2C, side-chain 2,2′), 16.44 (4C, durene-CH_3); ms *m/e*: 374–376–378 (M^+), 267–269 (30–30), 173 (15), 161 (26), 145 (27). *Anal.* calcd. for $C_{16}H_{24}Br_2$: C 51.09, H 6.43, Br 42.48; found: C 50.95, H 6.49, Br 42.28.

*1,4-Bis(3-cyanopropyl)-2,3,5,6-tetramethylbenzene (**10**)*

1,4-Bis(3-bromopropyl)-2,3,5,6-tetramethylbenzene (**8**) (20.0 g, 0.05 mol), KCN (13.0 g, 0.20 mol), and ethanol (250 mL) were refluxed under N_2 for 4 h. Water (300 mL) was then added to the cooled solution causing crystallization of the product, which was filtered off and washed with more water. Yield: 13.0 g (97%); mp 139.0–141.5°C; ^1H nmr (δ, $CDCl_3$): 1.57–2.05 (m, 4H, side-chain 2,2′-CH_2), 2.29 (s, 12H, durene CH_3), 2.48 (t, 4H, J = 7 Hz, side-chain 1,1′-CH_2), 2.72–3.00 (m, 4H, CH_2CN); ^{13}C nmr (δ, $CDCl_3$): 135.07 (2C, durene 1,4), 132.39 (4C, durene 2,3,5,6), 119.57 (2C, CN), 29.60 (2C, side-chain 1,1′), 25.37 (2C, side-chain 2,2′), 17.33 (2C, side-chain 3,3′), 16.44 (4C, durene CH_3); ms *m/e*: 268 (M^+, 90), 214 (100), 200 (60). *Anal.* calcd. for $C_{18}H_{24}N_2$: C 80.55, H 9.01, N 10.44; found: C 80.46, H 9.06, N 10.15.

*1,4-Bis(3-carboxypropyl)-2,3,5,6-tetramethylbenzene (**11**)*

1,4-Bis(3-cyanopropyl)-2,3,5,6-tetramethylbenzene (**10**) (12.5 g, 0.047 mol), KOH (21 g, 0.38 mol), and ethanol (250 mL) were refluxed under N_2 until the evolution of NH_3 (g) ceased (ca. 5 h). The ethanol was distilled off and replaced with water. The resulting clear solution was refluxed for another 1 h. The solution was cooled, carefully acidified with concentrated HCl, and the white diacid product was collected and washed with water to give 14.1 g (98%), mp 265.0–267.0°C; ^1H nmr (δ, 10% TFA/$CDCl_3$): 1.60–2.10 (m, 4H, side-chain 2,2′-CH_2), 2.32 (s, 12H, durene CH_3), 2.48–2.97 (m, 8H, side-chain 1,1′,3,3′-CH_2);ms *m/e*: 306 (M^+, 40), 233 (100), 219 (30). *Anal.* calcd. for $C_{18}H_{26}O_4$: C 70.56, H 8.55; found: C 70.86, H 8.53.

*1,4-Bis(4,4-dicarboxybutyl)-2,3,5,6-tetramethylbenzene (**12**)*

The bis(bromopropyl)durene **8** (15 g, 40 mmol) was treated with diethyl malonate (25 mL, 26.4 g, 165 mmol) and Na (2.4 g, 104 mmol) in anhydrous ethanol (200 mL) in a manner analogous to that described for the preparation of **3**. The tetraethyl ester so obtained was saponified *in situ* using KOH and acidified with concentrated HCl to give 15.9 g (94.9%) of the desired product, mp 193.5–195.0°C (dec.); ^1H nmr (δ, DMSO-d_6): 1.14–1.98 (m, 8H, side-chain 2,2′,3,3′-CH_2), 2.07 (s, 12H, durene CH_3), 2.38–2.74 (m, 4H, side-chain 1,1′-CH_2), 3.25 (t, 2H, J = 7 Hz, C*H*(CO_2H)$_2$); ms *m/e*: 334 ($M-2CO_2$, 20), 247 (100), 147 (70). *Anal.* calcd. for $C_{22}H_{30}O_8$: C 62.55, H 7.16; found: C 62.32, H 7.20.

*1,4-Bis(4-carboxybutyl)-2,3,5,6-tetramethylbenzene (**13**)*

1,4-Bis(4,4-dicarboxybutyl)-2,3,5,6-tetramethylbenzene (**12**) (15.5 g, 36.7 mmol) was decarboxylated in boiling quinoline (50 mL) and purified as described for the bismalonic acid (**3**). Yield 11.6 g (94.6%), mp 210.0–211.0°C; ^1H nmr (δ, DMSO-d_6): 1.10–1.82 (m, 8H, side-chain 2,2′, 3,3′-CH_2), 2.13, 2.06–2.38 (s, m, 16H, durene CH_3, side-chain 4,4′-CH_2), 2.42–2.76 (m, 4H, side-chain 1,1′-CH_2); ms *m/e*: 334 (M^+, 30), 247 (100), 233 (20), 147 (50).

*1,4-Bis(4-ethoxycarbonylbutyl)-2,3,5,6-tetramethylbenzene (**14**)*

The dicarboxylic acid **13** (37.5 g, 110 mmol) was esterified as described for the diacid **4** to produce the diester **14** in 95% yield, mp 55.0–56.0°C; ^1H nmr (δ, $CDCl_3$): 1.25 (t, J = 7 Hz, 6H, OCH_2CH_3), 1.35–1.95 (m, 8H, side-chain 2,2′,3,3′-CH_2), 2.20 (s, 12H, durene CH_3), 2.25–2.80 (m, 8H, side-chain 1,1′4,4′-CH_2), 4.13 (q, 4H, J = 7 Hz, OCH_2CH_3); ^{13}C nmr (δ, $CDCl_3$): 173.54 (C=O), 136.65 (2C, durene 1,4), 131.95 (4C, durene 2,3,5,6), 60.14 (2C, OCH_2CH_3), 34.24 (2C, side-chain 4.4′), 30.36 (2C, side-chain 3,3′), 29.37 (2C, side-chain 2,2′), 25.49 (2C, side-chain 1,1′), 16.28 (durene CH_3), 14.23 (OCH_2CH_3); ms *m/e*: 390 (M^+, 40), 275 (50), 129 (100). *Anal.* calcd. for $C_{24}H_{38}O_4$: C 73.81, H 9.81; found: C 73.89, H 9.89.

*1,4-Bis(5-hydroxypentyl)-2,3,5,6-tetramethylbenzene (**15**)*

The diethyl ester **14** (41.0 g, 0.1 M) was reduced by diborane as described for the analogous compound **9** to give 32.1 g (99%) of **15**, mp 109.5–111.0°C; ^1H nmr (δ, $CDCl_3$): 1.35–1.80 (m, 14H, OH and side-chain 2,2′,3,3′,4,4′-CH_2) 2.27 (s, 12H, durene CH_3), 2.50–2.88 (m, 4H, side-chain 1,1′-CH_2), 3.71 (t, 4H, CH_2OH); ^{13}C nmr (δ, $CDCl_3$): 136.71 (2C, durene 1,4), 131.90 (4C, durene 2,3,5,6), 62.85 (2C, CH_2OH), 32.66 (2C, side-chain 1,1′), 30.71 (2C, side-chain 2,2′), 29.73 (2C, side-chain 3,3′), 26.37 (2C, side-chain 4,4′), 16.34 (durene CH_3); ms *m/e*: 306 (M^+, 80), 233 (100), 161 (20), 147 (30). *Anal.* calcd. for $C_{20}H_{34}O_2$: C 78.38, H 11.18; found: C 78.47, H 11.40.

*1,4-Bis(5-bromopentyl)-2,3,5,6-tetramethylbenzene (**16**)*

The bis(hydroxypentyl)durene **15** (31,6 g, 100 mmol) was brominated as described for **5** to give 38.3 g (86%) of the dibromo compound **16**, mp 100–102.0°C; ^1H nmr (δ, $CDCl_3$): 1.40–1.65 (m, 8H, side-chain 2,2′,3,3′-CH_2), 1.75–2.07 (m, 4H, side-chain 4,4′-CH_2), 2.20 (s, 12H, durene CH_3), 2.50–2.85 (m, 4H, side-chain 1,1′-CH_2), 3.43 (t, 4H, -CH_2Br); ^{13}C nmr (δ, $CDCl_3$): 136.58 (2C, durene 1,4), 131.98 (4C, durene 2,3,5,6), 33.69 (2C, CH_2Br), 32.71 (2C, side-chain 1,1′), 30.60 (2C, side-chain 2,2′), 29.07 (2C, side-chain 3,3′), 28.79 (2C, side-chain 4,4′), 16.37 (durene -CH_3); ms *m/e*: 430–432–434 (M^+, 55), 295–297 (100); *Anal.* calcd. for $C_{20}H_{32}Br_2$: C 55.70, H 7.46, Br 36.97; found: C 55.82, H 7.45, Br 36.76.

*1,4-Bis(6,6-dicarboxyhexyl)-2,3,5,6-tetramethylbenzene (**17**)*

This compound was prepared in 96% overall yield, starting from the bis(bromopentyl)durene **16** (37.3 g, 86 mmol) in the manner described for the preparation of the analogous compound **12**, mp 160.5–162.5°C (dec.); ^1H nmr (δ, 10% TFA/$CDCl_3$): 1.35 (br, 12H, side-chain 2,2′,3,3′,4,4′-CH_2), 1.58–1.93 (m, 4H, side-chain 5,5′-CH_2), 2.12 (s, 12H, durene CH_3), 2.33–2.73 (m, 4H, side-chain 1,1′-CH_2), 2.97 (t, 2H, J = 7 Hz, C*H*($COOH$)$_2$); ms *m/e*: 390 ($M-2CO_2$, 45), 275 (100).

*1,4-Bis(6-carboxyhexyl)-2,3,5,6-tetramethylbenzene (**18**)*

The bismalonic acid **17** was decarboxylated in refluxing diethylformamide to give the diacid **18** in near quantitative yield, mp 147–149.0°C (dec.); ^1H nmr (δ, 10% TFA/$CDCl_3$): 1.35 (br, 16H, side-chain 2,2′,3,3′,4,4′,5,5′-CH_2), 2.13 (s, 12H, durene CH_3), 2.20 (bs, 4H, side-chain 6,6′-CH_2), 2.35–2.70 (m, 4H, side-chain 1,1′-CH_2); ms *m/e*: 390 (M^+, 30), 275(30), 161(60), 147(50). *Anal.* calcd. for $C_{24}H_{38}O_4$: C 73.81, H 9.81; found: C 73.77, H 9.72.

Chain-linked bispyrroles

*1,4-Bis[5-(5-ethoxycarbonyl-2,4-dimethylpyrrol-3-yl)-5-oxopentyl]-2,3,5,6-tetramethylbenzene (**21**a)*

Durene-bispentanoic acid (**13**) (16.7 g, 0.05 mol) and $SOCl_2$ (23.8 g, 0.2 mol) were refluxed on a steam bath until the mixture was homogeneous and gas evolution had ceased (ca. 30 min). The excess $SOCl_2$ was removed by evaporation *in vacuo* and by codistillation with CCl_4 (4 × 30 mL). The resulting crude diacid chloride (**19***a*) and 2-ethoxycarbonyl-3,5-dimethylpyrrole (**20**) (18.0 g, 0.11 mol) were dissolved in CH_2Cl_2 (175 mL); CH_3NO_2 (100 mL) and anhydrous $SnCl_4$ (38.9 g, 0.15 mol) were added dropwise at room temperature under moisture-exclusion conditions.

After being stirred for 1 h, the reaction mixture was poured into water (300 mL) acidified with concentrated HCl (10 mL), stirred for 15 min, and filtered to collect the solid product (18.3 g, 57.9%). Evaporation *in vacuo* of the organic phase from the filtrate afforded a second crop of 2.7 g (8.5%).

An analytical sample was obtained by adding ethanol to a concentrat-

Can. J. Chem. Downloaded from www.nrcresearchpress.com by 112.217.228.212 on 09/07/12
For personal use only.

ed solution of the crude solid in CH_2Cl_2 and minimum trifluoroacetic acid; mp 207.5–209.0°C; ^{1}H nmr (δ, 10%, TFA/$CDCl_3$): 1.46, 1.38–2.10 (t, br, 14H, OCH_2CH_3, chain 2,2′,3,3′-CH_2), 2.24 (s, 12H, durene CH_3), 2.39 (s, 6H, pyrrole 4-CH_3), 2.42 (s, 6H, pyrrole 2-CH_3), 2.58–2.85 (m, 4H, chain 1,1′-CH_2), 2.96 (t, 4H, J = 7.5 Hz, chain 4,4′-CH_2), 4.47 (q, 4H, J = 7 Hz, OCH_2CH_3), 10.20 (bs, 2H, NH); ^{13}C nmr (δ, 10% TFA/$CDCl_3$): 204.11 (2C, ketonic C=O), 164.25 (2C, ester C=O), 142.50 (2C, pyrrole 2), 136.59 (2C, durene 1,4), 132.37 (6C, pyrrole 4, durene 2,3,5,6), 123.03 (2C, pyrrole 3), 118.61 (2C, pyrrole 5), 62.57 (2C, -OCH_2CH_3), 42.27 (2C, chain 4,4′), 30.62, 29.88 (4C, chain 1,1′,2,2′), 26.12 (2C, chain 3,3′), 16.41 (4C, durene CH_3), 15.44 (2C, pyrrole 2-CH_3), 14.26 (2C, -OCH_2CH_3), 13.03 (2C, pyrrole 4-CH_3); ms m/*e*: (M^+, 19), 209 (100), 194 (71), 148 (62). *Anal.* calcd. for $C_{38}H_{52}N_2O_6$: C 72.12, H 8.28, N 4.43; found: C 72.10, H 8.08, N 4.63.

*1,4-Bis[5-(5-ethoxycarbonyl-2,4-dimethylpyrrol-3-yl)pentyl]-2,3,5,6-tetramethylbenzene (**22**a)*

The diketone **21***a* (17 g, 0.027 mol) and $NaBH_4$ (3 g, 0.079 mol) were suspended in dry THF (400 mL) under N_2 and treated dropwise (ice-bath) with $BF_3{\cdot}Et_2O$ (14 mL, 0.11 mol). When tlc examination showed the absence of starting material or intermediates (more $NaBH_4$ and $BF_3{\cdot}Et_2O$ were added if necessary), the reaction mixture was quenched by careful dropwise addition of glacial acetic acid (100 mL). Water (1.5 L) was added causing the separation of the product, which was filtered and washed with water. The solid was redissolved by heating in THF (500 mL), the undissolved impurities were removed by filtration, and the filtrate was then diluted with CH_3OH and concentrated *in vacuo* to give 14.3 g (88.3%) of a white powdery solid, in two crops, mp 198.0–199.0°C; ^{1}H nmr (δ, $CDCl_3$): 1.35, 1.32–1.62 (t, br, 18H, OCH_2CH_3, chain 2,2′,3,3′4,4′-CH_2), 2.20, 2.22, 2.28, 2.24–2.50 (s,s,s,m, 28H, pyrrole 2-CH_3, durene CH_3, pyrrole 4-CH_3, chain 5,5′-CH_2), 2.50–2.80 (m, 4H, chain 1,1′-CH_2), 4.32 (q, 4H, J = 7 Hz, OCH_2CH_3), 8.73 (bs, 2H, NH); ms m/*e*: 688 (M^+, 62), 558 (29), 180 (100), 134 (90). *Anal.* calcd. for $C_{38}H_{56}N_2O_4$: C 75.46, H 9.33, N 4.63; found: C 75.18, H 9.32, N 4.72.

*1,4-Bis[5-(5-benzyloxycarbonyl-2,4-dimethylpyrrol-3-yl)pentyl]-2,3,5,6-tetramethylbenzene (**23**a)*

The diethyl ester **22***a* (13.1 g, 21.5 mmol) and benzyl alcohol (125 mL) (redistilled from K_2CO_3 at 1 atm) were heated to boiling under N_2, and a fresh solution of Na in dry benzyl alcohol was added in ca. 1-mL portions until the exchange was complete. The hot solution was quenched by pouring (cautiously) into a solution of acetic acid (25 mL) in CH_3OH (500 mL) when the solid product appeared immediately. Water (400 mL) was stirred in, the mixture was allowed to stand for 5 min, and the solid filtered and washed with 50% aqueous CH_3OH. Yield 15.5 g (98.1%). A sample was recrystallized from THF–CH_3OH for analysis; mp 171.0–172.0°C; ^{1}H nmr (δ, $CDCl_3$): 1.46 (br, 12H, chain 2,2′,3,3′,4,4′,-CH_2), 2.19, 2.22, 2.30, 2.22–2.50 (s,s,s,m, 28H, pyrrole 2-CH_3, durene CH_3, pyrrole 4-CH_3, chain 5,5′-CH_2), 2.50–2.78 (m, 4H, chain 1,1′-CH_2), 5.31 (s, 4H, $OCH_2C_6H_5$), 7.30–7.52 (m, 10H, C_6H_5), 8.60 (bs, 2H, NH); ^{13}C nmr (δ, 10% TFA/$CDCl_3$): 164.53 (2C, C=O), 137.17 (2C, durene 1,4), 135.81 (2C, benzene 1), 134.25 (2C, pyrrole 2), 132.35 (4C, durene 2,3,5,6), 131.03 (2C, pyrrole 4), 128.91, 128.69, 128.39 (10C, benzene 2,3,4,5,6), 123.96 (2C, pyrrole 3), 115.57 (2C, pyrrole 5), 67.37 (2C, -$OCH_2C_6H_5$), 30.96, 30.82, 30.24, 30.07 (8C, chain, 1,1′,2,2′,3,3′,4,4′), 24.20 (2C, chain 5,5′), 16.49 (4C, durene CH_3), 11.69, 11.34 (4C, pyrrole 2-CH_3, 4-CH_3); ms m/*e*: 728 (M^+, 88), 620 (36), 242 (32), 108 (100), 91 (68). *Anal.* calcd. for $C_{48}H_{60}N_2O_4$: C 79.08, H 8.30, N 3.84; found: C 78.91, H 8.47, N 3.83.

*1,4-Bis[5-(5-formyl-2,4-dimethylpyrrol-3-yl)pentyl]-2,3,5,6-tetramethylbenzene (**27**a)*

This compound was prepared from the foregoing dibenzyl ester **23***a* in three steps without the isolation and characterization of the intermediates.

(*i*) *Debenzylation*. The dibenzyl ester **23***a* (10.0 g, 13.8 mmol) and 10% Pd/C (0.9 g) were stirred under H_2 (1 atm, room temperature), in THF (250 mL) containing triethylamine (5 drops). When the H_2 uptake ceased (ca. 3 h), the solution was checked by tlc for the absence of starting material and the catalyst was filtered. The solvent was then removed *in vacuo* below 40°C, affording the crude biscarboxypyrrole as a pale yellow solid.

(*ii*) *Decarboxylation*. The above yellow solid was dissolved in DMF (100 mL) and refluxed under N_2 until the uv absorption maximum at 284 nm was reduced to a minor shoulder (ca. 2.5 h).

(*iii*) *Formylation*. The decarboxylation mixture above was added dropwise to an ice-cooled solution of the Vilsmeier reagent (prepared by adding $POCl_3$ (30 mL) in CH_2Cl_2 (10 mL) to DMF (25 mL) in CH_2Cl_2 (80 mL)); the reaction mixture was stirred for 30 min, when the CH_2Cl_2 was removed *in vacuo* and the remaining solution poured onto crushed ice (500 g).

Solid $NaHCO_3$ was added cautiously (with effervescence) until the solution was weakly basic. The solution was heated on a steam bath (further bicarbonate being added if the solution became acidic) until the remaining CH_2Cl_2 evaporated, and a clear brown single-phase solution was formed (pH should remain around 8).

The solution was suction filtered to remove minor insoluble tars, the volume adjusted to ca. 1 L with water, and heating continued for a further 30–60 min. The bisformylpyrrole **27***a* separated out as a grey solid and was filtered, washed with water, and dried to give 7.1 g. The crude solid was reacted with malonitrile to afford the bisdicyanovinylpyrrole **28***a* (*vide infra*). After purification by chromatography, a sample of this was deprotected with KOH in aqueous propanol to produce **27***a* for analysis; mp 233.0–234.0°C; ^{1}H nmr (δ, $CDCl_3$): 1.46 (br, 12H, 2,2′,3,3′,4,4′-CH_2), 2.20 (s, 12H, durene CH_3), 2.22, 2.26 (s,s 12H, pyrrole 2,4-CH_3), 2.30–2.43 (m, 4H, 5,5′-CH_2), 2.56–2.69 (m, 4H, 1,1′-CH_2), 8.99 (bs, 2H, NH), 9.44 (s, 2H, CHO); ms m/*e*: 516 (M^+, 42), 488 (33), 473 (18), 136 (100), 108 (76). *Anal.* calcd. for $C_{34}H_{48}N_2O_2$: C 79.02, H 9.36, N, 5.42; found: C 78.87, H 9.47, N 5.43.

*1,4-Bis{5-[5-(2,2-dicyanovinyl)-2,4-dimethylpyrrol-3-yl]pentyl}-2,3,5,6-tetramethylbenzene (**28**a)*

The crude bisformylpyrrole **27***a* (6.5 g) and malononitrile (2.0 g, 30.3 mmol) were refluxed in toluene (300 mL) in the presence of cyclohexylamine (2 mL). Thin-layer chromatographic analysis of the reaction mixture indicated the completion of the reaction in 2 h. Toluene was evaporated *in vacuo*, CH_3OH added, and the crude product isolated in two crops. The combined solid was chromatographed on silica (activity I, 150 g) using CH_2Cl_2 initially, and 0.2–0.5% CH_3OH in CH_2Cl_2 later, for elution. The yellow solution was concentrated *in vacuo* and the bisdicyanovinylpyrrole crystallized out analytically pure, as a lemon yellow solid (4.82 g, 62.6% overall from the bisbenzyl ester **23***a*) by the addition of CH_3OH; mp 228.5–229.5°C; ^{1}H nmr (δ, $CDCl_3$): 1.44 (br, 12H, chain 2,2′,3,3′,4,4′-CH_2), 2.13 (s, 6H, pyrrole 4-CH_3), 2.20 (s, 12H, durene CH_3), 2.31 (s, 6H, pyrrole 2-CH_3), 2.34–2.45 (m, 4H, chain 5,5′-CH_2), 2.56–2.69 (m, 4H, chain 1,1′-CH_2), 7.28 (s, 2H, C(*H*)=$C(CN)_2$), 9.29 (bs, 2H, NH); ^{13}C nmr (δ, 10% TFA/$CDCl_3$): 145.09 (2C, pyrrole 2), 140.97 (2C, *C*(H)=$C(CN)_2$), 138.80 (2C, pyrrole 4), 136.85 (2C, durene 1,4), 132.19 (4C, durene 2,3,5,6), 126.94 (2C, pyrrole 3), 125.04 (2C, pyrrole 5), 117.24 (2C, C≡N), 116.29 (2C, C≡N), 58.77 (2C, C(H)=*C*$(CN)_2$), 30.83 (2C, chain 1,1′), 30.11 (6C, chain 2,2′,3,3′,4,4′), 24.04 (2C, chain 5,5′), 16.45 (4C, durene CH_3), 12.59 (2C, pyrrole 2-CH_3), 9.81 (2C, pyrrole 4-CH_3); ms m/*e*: 612 (M^+, 94), 597 (12), 226 (17), 184 (100). *Anal.* calcd. for $C_{40}H_{48}N_6$: C 78.39, H 7.89, N 13.71: found: C 78.49, H 7.77, N 13.63.

*1,4-Bis{5-[2-(5-ethoxycarbonyl-3-ethyl-4-methylpyrrol-2-yl)methyl]-5-(2,2-dicyanovinyl)-4-methylpyrrol-3-yl]pentyl}-2,3,5,6-tetramethylbenzene (**31**a)*

(*i*) *Monochlorination of the α-methyl substituents*. The bisdicyanovinylpyrrole **28***a* (1.23 g, 2.01 mmol) in dry CH_2Cl_2 (180 mL) was treated dropwise, at room temperature, with 20 mL of a stock solution of SO_2Cl_2 (2.85 g, 21.1 mmol; redistilled) in CH_2Cl_2 (100 mL). The solvent was carefully displaced with anhydrous diethyl ether, causing

Can. J. Chem. Downloaded from www.nrcresearchpress.com by 112.217.228.212 on 09/07/12
For personal use only.

the bischloromethyl derivative **29***a* to crystallize as a lemon yellow powdery solid. This was collected by filtration, washed with 10% CH_2Cl_2 in ether, air dried, and used in the following reaction without further purification.

(*ii*) *Formation of the bisdipyrromethane*. The above bischloromethyl derivative **29***a* and 2-ethoxycarbonyl-4-ethyl-3-methylpyrrole **30** (1.2 g, 6.6 mmol) were warmed (water bath) in glacial acetic acid (600 mL), under N_2 to 80°C. The yellow starting material dissolved with reaction and the solution turned orange-red. Thin-layer chromatographic analysis indicated that the reaction was complete in 1 h.

The solution was cooled to room temperature, concentrated to ca. 25 mL *in vacuo*, CH_3OH (100 mL) was added, and it was allowed to stand overnight under refrigeration. The product crystallized as a dark yellow solid, which was collected by filtration and washed with CH_3OH; yield 1.74 g (89.2%). An analytical sample was recrystallized from CH_2Cl_2–CH_3OH, mp 186.0–190.0°C; ^{1}H nmr (δ, $CDCl_3$): 1.02 (t, 6H, J = 7.5 Hz, 3′-CH_2CH_3), 1.32 (t, 6H, J = 7 Hz, -OCH_2CH_3), 1.44 (br, 12H, chain 2,2′,3,3′,4,4′-CH_2), 2.13 (s, 6H, pyrrole 4-CH_3), 2.20 (s, 12H, durene CH_3), 2.26 (s, 6H, pyrrole 4′-CH_3), 2.33–2.48 (m, 8H, 4′-CH_2CH_3, chain 5,5′-CH_2), 2.56–2.69 (m, 4H, chain 1,1′-CH_2), 3.94 (s, 4H, *meso* CH_2), 4.23 (q, 4H, J = 7 Hz, OCH_2CH_3), 7.28 (s, 2H, C(*H*)=$C(CN)_2$), 8.75 (br, 2H, 1′-NH), 9.17 (br, 2H, 1–NH); ^{13}C nmr (δ, 10% TFA/$CDCl_3$): 164.74 (2C, C=O), 142.93 (2C, *C*(H)=$C(CN)_2$), 141.89 (2C, pyrrole 2), 138.78 (2C, pyrrole 4), 136.89 (2C, durene 1,4), 132.21 (4C, durene 2,3,5,6), 129.82, 128.98, 126.51, 126.11 (8C, pyrrole 3,2′,3′,4′), 125.19 (2C, pyrrole 5), 118.09 (2C, pyrrole 5′), 116.75 (2C, C≡N), 115.67 (2C, C≡N), 61.97 (2C, -OCH_2CH_3), 60.99 (2C, C(H)=*C*$(CN)_2$), 30.82 (2C, chain 1,1′), 30.19, 29.97 (4C, 2C, chain 2,2′,3,3′,4,4′), 24.20 (4C, *meso* CH_2, chain 5,5′), 17.44 (2C, pyrrole 3′-*C*H_2CH_3), 16.42 (4C, durene CH_3), 15.29 (2C, pyrrole 3′-CH_2CH_3), 14.24 (2C, -OCH_2CH_3), 10.85 (2C, pyrrole 4′-CH_3), 9.76 (2C, pyrrole 4-CH_3); ms *m/e*: 970 (0.2), 924 (1.6), 878 (2.6), 745 (26). *Anal.* calcd. for $C_{60}H_{74}N_8O_4$: C 74.20, H 7.68, N 11.54; found: C 73.99, H 7.51, N 11.60.

*1,4-Bis{5-[2-[(5-carboxy-3-ethyl-4-methylpyrrol-2-yl)methyl]-5-formyl-4-methylpyrrol-3-yl]pentyl}-2,3,5,6-tetramethylbenzene (**32**a)*

The dimeric dicyanovinyl dipyrromethane ester **31***a* (1.21 g, 1.25 mmol) was suspended in a solution of KOH (7.5 g) in water (100 mL) and the mixture heated under N_2. At reflux, *n*-propanol (60 mL) was added; the yellow starting material dissolved promptly giving a pale brown solution. Reflux was continued and the reaction was monitored by uv–visible spectroscopy. The starting material absorbed strongly at 407 nm, and moderately at 275 nm, while the product absorbed strongly at 270 nm and 320 nm. Propanol was then boiled off while replenishing with water (total volume 300 mL) until the reflux temperature reached 100°C. The solution was cooled to room temperature under N_2, acidified with acetic acid, and the product isolated and dried to give 1.01 g (99%) of analytically pure material, mp 158.0–160.0°C (dec.); ^{1}H nmr (δ, DMSO-d_6): 0.84 (t, 6H, 3′-CH_2-CH_3), 1.32 (br, 12H, chain 2,2′,3,3′,4,4′-CH_2), 1.96–2.44 (m, br, 36H, durene CH_3, pyrrole 2,4-CH_3, chain 1,1′,5,5′-CH_2, 3′-CH_2CH_3), 3.78 (br, 4H, *meso* CH_2), 9.48 (s, 2H, CHO), 10.94 (bs, 2H, 1-NH), 11.48 (bs, 2H, 1′-NH); ms *m/e*: 818 (M^+, 5), 816 (15), 730 (40). *Anal.* calcd. for $C_{50}H_{66}N_4O_6$: C 73.32, H 8.12, N 6.84; found: C 73.28, H 8.22, N 6.80.

*7,17-Diethyl-2,8,12,18-tetramethyl-3,13-[2,3,5,6-tetramethylphenylene-1,4-bis(pentamethylene)]porphyrin (**34**a)*

(*i*) *Decarboxylation*. The chain-linked bisdipyrromethane **32***a* (901 mg; 1.1 mmol) was decarboxylated in refluxing DMF (100 mL) under N_2. The reaction was monitored by uv spectroscopy; the absorption band at 280 nm decayed relative to the band at 320 nm and the reaction was complete in 2–2.5 h.

The solution was cooled under N_2, concentrated *in vacuo* to approximately 50 mL, and diluted with CH_2Cl_2 (200 mL). This was washed with water (3 × 60 mL) to remove most of the remaining DMF, dried (Na_2SO_4), filtered, and diluted to 500 mL with CH_2Cl_2 in preparation for the next step.

(*ii*) *Intramolecule 2 + 2 coupling*. The cyclization was carried out in two 2-L Erlenmeyer flasks (covered with aluminum foil to exclude light) each containing *p*-toluenesulfonic acid (4.0 g) in CH_3OH (25 mL) – CH_2Cl_2 (600 mL). The CH_2Cl_2 solution from the above decarboxylation step was added to the catalyst solution by means of a syringe pump; the entire addition was complete in 6 days.

The reddish violet solution was concentrated *in vacuo* to approximately 150 mL, extracted with saturated aqueous $NaHCO_3$ (3 × 50 mL) to remove the acid catalyst, and then taken to dryness *in vacuo*. The residue was taken up in minimal CH_2Cl_2 and chromatographed as described below.

(*iii*) *Chromatographic purification of porphyrin*. The crude porphyrin was initially chromatographed on silica gel (Woelm, act. I, 70–150 mesh, 100 g) using CH_2Cl_2 to elute most of the nonfluorescent impurities. The porphyrin was eluted with 2% CH_3OH in CH_2Cl_2 and rechromatographed on activity IV silica gel (35 g). The impurities were removed with CH_2Cl_2 and the porphyrin was eluted cleanly using 1% CH_3OH in CH_2Cl_2, and crystallized from CH_3OH to give a yield of 239 mg (31.4% overall for decarboxylation–cyclization). Typically, the yield varied between 22 and 31% and appeared to depend to a large extent on the particular sample of the starting material **32***a*; mp 273.0–274.5°. Visible spectrum (CH_2Cl_2), λ_{max}(nm) (log ε): 400.7 (5.16), 500.8 (4.04), 537.0 (3.98), 569.8 (3.76), 623.9 (3.64); ^{1}H nmr (δ, $CDCl_3$): 9.94 (s, 2H, 10-H and 20-H), 9.86 (s, 2H, 5-H and 15-H), 4.09 (m, 6H, CH_2CH_3 and one proton each at chain termini), 3.84 (m, 2H, one proton each at chain termini), 3.64 (s, 6H, CH_3), 3.48 (s, 6H, CH_3), 1.90, 1.87 (t, m, 10H, CH_2CH_3 and four chain protons), 1.40 (t, 4H, chain-durene termini), 0.91 (m, 2H, chain protons), 0.69 (m, 2H, chain protons), 0.41 (s, 12H, durene CH_3), −1.06 (m, 4H, chain protons), −3.81 (bs, 2H, N–H); ^{13}C nmr (δ, 10% TFA/$CDCl_3$): 146.07, 143.08, 142.90, 142.71, 141.25, 140.31, 139.17 (16C, α- and β-pyrrolic carbons), 134.79 (2C, durene 1,4), 130.25 (4C, durene 2,3,5,6), 99.87, 98.91 (4C, *meso* 5,10,15,20), 30.80, 29.46, 27.20 (10C, chain carbons), 20.16 (2C, CH_2CH_3), 16.67 (2C, CH_2CH_3), 14.65 (4C, durene CH_3), 12.28, 11.68 (4C, 2,8,12,18-CH_3). Mol Wt. found by high resolution mass spectrometry: 692.4866; $^{12}C_{48}{}^1H_{60}{}^{14}N_4$ required 692.4818. *Anal.* calcd. for $C_{48}H_{60}N_4 \cdot CH_3OH$: C 81.22, H 8.84, N 7.73; found: C 81.50, H 8.90, N 7.72.

*7,17-Diethyl-2,8,12,18-tetramethyl-3,13-[2,3,5,6-tetramethylphenylene-1,4-bis(tetramethylene)]porphyrin (**34**b)*

The bisdipyrromethane **32***b* was decarboxylated as described for **32***a*. Because of the lower solubility of the intermediate **33***b*, the DMF solution was concentrated, diluted with THF instead of CH_2Cl_2, and cyclized under high dilution, as described earlier. The crude porphyrin was chromatographed initially on activity I silica gel as before but the partially purified porphyrin was rechromatographed on activity III neutral alumina. Toluene was used initially as the eluant, which was later changed to CH_2Cl_2. Yields varied between 11 and 16%; mp 272.0–273.0°C. Visible spectrum (CH_2Cl_2), λ_{max} (nm) (log ε): 400.7 (5.22), 502.0 (4.04), 538.0 (4.07), 571.5 (3.76), 626.0 (3.64); ^{1}H nmr (δ, $CDCl_3$): 9.83 (s, 2H, 10-H and 20-H), 9.61 (s, 2H, 5-H and 15-H), 4.06 (m, 4H, -CH_2CH_3), 3.82 (m, 2H, chain protons), 3.62 (m, 8H, two CH_3 and 2 chain protons), 3.32 (s, 6H, two CH_3), 1.88 (t, J = 7.5 Hz, 6H, -CH_2CH_3), 1.71 (s, 2H, chain protons), 1.43 (m, 4H, chain protons), 1.30 (m, 2H, chain protons), 0.29 (s, 6H, durene CH_3), 0.21 (s, 6H, durene CH_3), −1.51 (m, 2H, chain protons), −1.72 (m, 2H, chain protons), −3.54 (bs, 2H, N–H); ^{13}C nmr (δ, 10% TFA/$CDCl_3$): 146.54, 144.87, 143.00, 140.94, 140.31, 139.57, 139.42, 138.62 (16C, α- and β-pyrrolic carbons), 135.69, (2C, durene 1,4), 129.49, 129.17 (4C, durene 2,3,5,6), 99.93, 98.84 (4C, *meso* 5,10,15,20), 28.66, 28.00, 27.55, 25.20 (8C, chain carbons), 20.07 (2C, CH_2CH_3), 16.38 (2C, CH_2CH_3), 14.46 (4C, durene CH_3), 12.00, 11.59 (4C, 2,8,12,18-CH_3). Mol. Wt. found by high resolution mass spectrometry: 664.4495; $^{12}C_{46}{}^1H_{56}{}^{14}N_4$ requires 664.4509. *Anal.* calcd. for $C_{46}H_{56}N_4 \cdot H_2O$: C 80.99, H 8.56, N 8.20; found: C 81.06, H 8.20, N 8.20.

*7,17-Diethyl-2,8,12,18-tetramethyl-3,13[2,3,5,6-tetramethylphenylene-1-4-bis(heptamethylene)]porphyrin (**34**c)*

This was synthesized in a manner similar to that described for its analogue **34***a*. The second chromatographic purification of this material was performed on activity III neutral alumina. Some forerunning brown impurities were removed by using 25% hexane–toluene initially. The porphyrin product was then eluted cleanly using 20% CH_2Cl_2–toluene and was crystallized from CH_2Cl_2–CH_3OH. Yields varied between 9 and 13%, mp 314.5–315.5. Visible spectrum (CH_2Cl_2), λ_{max} (nm) (log ϵ): 397.0 (5.16), 495.5 (4.12), 528.5 (3.98), 565.0 (3.81), 618.5 (3.72); ^{1}H nmr (δ, $CDCl_3$): 10.04 (s, 2H, 10-H and 20-H), 10.02 (s, 2H, 5-H and 15-H), 4.41 (m, 2H, chain protons), 4.16 (m, 2H, chain protons), 3.97 (m, 4H, -CH_2CH_3), 3.60 (s, 6H, two CH_3), 3.57 (s, 6H, two CH_3), 2.31 (m, 2H, chain protons), 2.05 (m, 2H, chain protons), 1.84 (t, J = 7.5 Hz, 6H, -CH_2CH_3), 1.57 (m, 2H, chain protons), 1.38 (m, 2H, chain protons), 1.30–0.95 (m, 12H, chain protons), −0.01 to −0.16 (m, 4H, chain protons), −0.20 (s, 12H, durene CH_3), −3.71 (bs, 2H, N–H); ^{13}C nmr (δ, 10% TFA/$CDCl_3$): 145.45, 143.45, 142.68, 142.46, 141.65, 140.85, 139.71, 138.78 (16C, α- and β-pyrrolic carbons), 135.52 (2C, durene 1,4), 130.60 (4C, durene 2,3,5,6), 99.28 (4C, *meso* 5,10,15,20), 31.19, 29.85, 29.26, 28.44, 28.37, 27.76, 26.82 (14C, chain carbons), 20.15 (2C, CH_2CH_3), 16.43 (2C, CH_2CH_3), 15.20 (4C, durene CH_3), 12.19, 11.66 (4C, 2,8,12,18-CH_3). Mol Wt. found by high resolution mass spectrometry: 748.5446; $^{12}C_{52}{}^{1}H_{68}{}^{14}N_4$ requires 748.5444. *Anal.* calcd. for $C_{52}H_{68}N_4 \cdot 1/2H_2O$: C 82.38, H 9.17, N 7.39; found: C 82.58, H 9.34, N 7.30.

Acknowledgements

This work was supported by the U.S. National Institutes of Health (AM17989) and the Natural Sciences and Engineering Research Council of Canada. B.R.J. and D.D. thank Charles McDowell for his vision and support.

1. D. Brault and M. Rougee. Biochemistry, **13**, 4591 (1974).
2. B. R. James. *In* The porphyrins. Vol. V. *Edited by* D. Dolphin. Academic Press, New York. 1978. p. 205.
3. R. D. Jones, D. A. Summerville, and F. Basolo. Chem. Rev. **79**, 139 (1979).
4. A. L. Balch, Y.-W. Chan, R. J. Cheng, G. N. La Mar, L. Latos-Grazynski, and M. W. Renner. J. Am. Chem. Soc. **106**, 7779 (1984).
5. (*a*) J. P. Collman, R. R. Gagne, T. R. Halbert, J. C. Marchon, and C. A. Reed. J. Am. Chem. Soc. **95**, 7868 (1973); (*b*) J. P. Collman, R. R. Gagne, C. A. Reed, T. R. Halbert, G. Lang, and W. T. Robinson. J. Am. Chem. Soc. **97**, 1427 (1975).
6. (*a*) J. P. Collman, J. I. Brauman, T. J. Collins, G. L. Iverson, G. Lang, R. B. Pettman, J. L. Sessler, and M. A. Walters. J. Am. Chem. Soc. **105**, 3038 (1983); (*b*) J. P. Collman, J. I. Brauman, B. L. Iverson, J. L. Sessler, R. M. Morris, and Q. H. Gibson. J. Am. Chem. Soc. **105**, 3052 (1983).
7. (*a*) J. Almog, J. E. Baldwin, R. L. Dyler, and M. K. Peters. J. Am. Chem. Soc. **97**, 226 (1975); (*b*) J. Almog, J. E. Baldwin, M. J. Crossley, J. F. Debernadis, R. L. Dyer, J. R. Huff, and M. K. Peters. Tetrahedron, **37**, 3589 (1981); (*c*) T. Hashimoto, R. L. Dyer, M. J. Crossley, J. E. Baldwin, and F. Basolo. J. Am. Chem. Soc. **104**, 2101 (1982).
8. T. G. Traylor, D. Campbell, S. Tsuchiya, M. Mitchell, and D. V. Stynes. J. Am. Chem. Soc. **102**, 5939 (1980); (*b*) T. G. Traylor, M. J. Mitchell, S. Tsuchiya, D. H. Campbell, D. V. Stynes, and N. Kogan. J. Am. Chem. Soc. **103**, 5234 (1981).
9. (*a*) M. Momenteau, B. Loock, J. Mispelter, and E. Bisagni. Nouv. J. Chim. **3**, 77 (1979); (*b*) M. Momenteau, J. Mispelter, B. Loock, and E. Bisagni. J. Chem. Soc. Perkin. Trans. **1**, 189 (1983).
10. M. Momenteau, B. Loock, D. Laveletti, C. Tetreau, and J. Mispelter. J. Chem. Soc. Chem. Commun. 962 (1983).
11. A. R. Battersby, A. J. Bartholomew, and T. Nitta. J. Chem. Soc. Chem. Commun. 1291 (1983).
12. S. David, D. Dolphin, and B. R. James. *In* Frontiers of bioinorganic chemistry. *Edited by* A. V. Xavier. VCH Verlagsgesellschaft, Weinheim, Germany. 1985. p. 163.
13. B. Morgan and D. Dolphin. Structure Bonding (Berlin), **64**, 115 (1987).
14. (*a*) A. D. Adler, F. R. Longo, J. D. Finarelli, J. Goldmatcher, J. Assow, and L. Korsakoff. J. Org. Chem. **32**, 476 (1967); (*b*) A. D. Adler, F. R. Longo, and W. Shergalis. J. Am. Chem. Soc. **86**, 3146 (1964).
15. H. Dieckmann, C. K. Chang, and T. G. Traylor. J. Am. Chem. Soc. **93**, 4068 (1971).
16. T. P. Wijesekera, J. B. Paine III, and D. Dolphin. J. Org. Chem. **50**, 3832 (1985).
17. T. P. Wijesekera, J. B. Paine III, D. Dolphin, F. W. B. Einstein, and T. Jones. J. Am. Chem. Soc. **105**, 6747 (1983).
18. T. P. Wijesekera, J. B. Paine III, and D. Dolphin. J. Org. Chem. **53**, 1345 (1988).
19. S. David, D. Dolphin, B. R. James, J. B. Paine III, T. P. Wijesekera, F. W. B. Einstein, and T. Jones. Can. J. Chem. **64**, 208 (1986).
20. A. P. Krapcho, J. F. Weimaster, J. M. I. Elderidge, E. G. E. Jahngen, Jr., A. J. Lovey, and W. P. Stephens. J. Org. Chem. **43**, 138 (1978).
21. G. G. Kleinspehn. J. Am. Chem. Soc. **77**, 1546 (1955).
22. J. B. Paine III. *In* The porphyrins. Vol. 1. *Edited by* D. Dolphin. Academic Press, New York. 1978. p. 101.
23. J. B. Paine III, R. B. Woodward, and D. Dolphin. J. Org. Chem. **41**, 2826 (1976).
24. (*a*) S. David, B. R. James, and D. Dolphin. J. Inorg. Biochem. **28**, 125 (1986); (*b*) Can. J. Chem. **65**, 1098 (1987).
25. S. David. Ph.D. thesis, University of British Columbia (1985).

Can. J. Chem. Downloaded from www.nrcresearchpress.com by 112.217.228.212 on 09/07/12
For personal use only.

Catalytic decarbonylation of aldehydes using iron(II) porphyrin complexes, and the crystal structure of (5,10,15,20-tetraphenylporphinato)bis(tri-*n*-butylphosphine)iron(II)[1]

RAMESH M. BELANI, BRIAN R. JAMES, DAVID DOLPHIN, AND STEVEN J. RETTIG
Department of Chemistry, University of British Columbia, Vancouver, B.C., Canada V6T 1Y6

Received February 26, 1988

This paper is dedicated to Professor Charles A. McDowell, on the occasion of his seventieth birthday

RAMESH M. BELANI, BRIAN R. JAMES, DAVID DOLPHIN, and STEVEN J. RETTIG. Can. J. Chem. **66**, 2072 (1988).

The complex (5,10,15,20-tetraphenylporphinato)bis(tri-*n*-butylphosphine)iron(II), **1**, has been isolated in a triclinic crystal form, $a = 12.499(3)$, $b = 12.528(2)$, $c = 12.039(2)$ Å, $\alpha = 116.39(1)$, $\beta = 109.79(1)$, $\gamma = 98.13(1)°$, $Z = 1$, space group $P\bar{1}$. The structure was solved by conventional heavy atom methods and was refined by full-matrix least-squares procedures to $R = 0.060$ and $R_w = 0.070$ for 3551 reflections with $I \geq 3\sigma(I)$. The molecule, which has crystallographic 1-C_i symmetry, displays a relatively undistorted pseudo-octahedral coordination geometry with Fe—P = 2.346(1) and Fe—N = 1.998(3) and 1.993(3) Å. In CH_2Cl_2 solution, **1** reacts with CO and aldehydes to generate the carbonyl(phosphine) derivative, and decarbonylation of phenylacetaldehyde to toluene becomes catalytic under an Ar stream. The aldehyde decarbonylations involve radical pathways via carbonyl loss from $PhCH_2\dot{C}O$. The hydrogen abstraction/initiation reaction probably utilizes trace O_2 (and possibly trace (water); speculative mechanisms are discussed.

RAMESH M. BELANI, BRIAN R. JAMES, DAVID DOLPHIN et STEVEN J. RETTIG. Can. J. Chem. **66**, 2072 (1988).

On a isolé le complexe (tétraphényl-5,10,15,20 porphinato)bis(tris-*n*-butylphosphine)fer(II), **1**, sous la forme de cristaux tricliniques avec $a = 12,499(3)$, $b = 12,528(2)$ et $c = 12,039(2)$ Å, $\alpha = 116,39(1)$, $\beta = 109,79(1)$ et $\gamma = 98,13(1)°$, $Z = 1$ et groupe d'espace $P\bar{1}$. On a résolu la structure par les méthodes conventionnelles aux atomes lourds et on l'a affinée par la méthode des moindres carrés (matrice entière) jusqu'à des valeurs de $R = 0,060$ et $R_w = 0,070$ pour 3551 réflexions avec $I \geq 3\sigma(I)$. La molécule, qui possède une symétrie cristallographique 1-C_i, se présente sous une géométrie de coordination pseudo-octaédrique qui n'est pas déformée, avec Fe—P = 2,346(1) et Fe—N = 1,998(3) et 1,993(3) Å. En solution dans le CH_2Cl_2, le composé **1** réagit avec le CO et avec les aldéhydes pour donner le dérivé carbonyl (phosphine) et la décarbonylation du phénylacétaldéhyde en toluène devient catalytique sous un jet d'Ar. Les décarbonylations d'aldéhydes impliquent des voies radicalaires par le biais de la perte du carbonyle du $PhCH_2CO$. La réaction d'initiation par enlèvement d'hydrogène utilise probablement des traces de O_2 (et possiblement des traces d'eau); on spécule sur divers mécanismes possibles.

[Traduit par la revue]

Introduction

Carbonylation reactions provide key steps in a range of homogeneously catalyzed processes of industrial importance (1, 2). Decarbonylation (for example, of aldehydes: RCHO → RH + CO) might appear unattractive commercially, but is of potential, *if done catalytically*, in terms of (*a*) recycling of a branched aldehyde side-product formed in hydroformylation of olefins (ref. 2, Chapt. 4), and (*b*) in organic synthesis of fine chemicals, where conversion of a formyl substituent to hydrogen is required. Further, nature has learned how to effect catalytic decarbonylation at ambient conditions, for example, within (*a*) an uncharacterized metal-containing decarbonylase that generates from aldehydes less prevalent hydrocarbons containing odd numbers of carbon atoms (3), and (*b*) a nickel–zinc–iron–sulfur cluster containing carbon monoxide dehydrogenase that *reversibly* decarbonylates acetyl coenzyme A (4). It should be noted that reports on the enzymatic systems appeared subsequent to the rhodium and ruthenium catalysts discussed below.

Stoichiometric decarbonylation of aldehydes (and acid chlorides) by platinum metal complexes is well documented (5), but it is generally difficult to remove the coordinated carbonyl from the resulting complex either thermally (5) or photolytically (6). However, effective thermal catalysts (in refluxing toluene) for such decarbonylation were first provided by $Rh(P—P)_2^+$ complexes, because the $Rh(CO)(P—P)_2^+$ species generated lose CO quite readily (7). Then, early observations on stoichiometric decarbonylation of acetic acid (8) and dimethylformamide (9) by ruthenium(II) porphyrin complexes led us to develop an efficient catalytic system for decarbonylation of aromatic and aliphatic aldehydes at ambient conditions (10): the system, a purely thermal one, required the presence of tertiary phosphines, which were considered necessary to displace coordinated carbonyl via established, labile equilibria such as shown in eq. [1] (10).

[1] $Ru(porp)(CO)(PR_3) + PR_3 \rightleftharpoons Ru(porp)(PR_3)_2 + CO$

(R = Ph, ^{n}Bu)

The studies led to a "recipe" for a practical procedure for decarbonylation of aldehydes starting with solutions containing $Ru(porp)(PR_3)_2$ complexes, but the mechanism remained poorly defined, although radical pathways have been established (10). An obvious follow-up to this ruthenium work was extension to the first-row, cheaper iron(II) systems and at the time this work was initiated in 1982 (11), bis(tertiary phosphine)(porphyinato)iron(II) complexes had not been isolated in the solid state.

Of note, there have been recent developments in the use of tertiary phosphines as structural probes for heme environments (12), and indeed the first published work on isolation of $Fe(porp)(PR_3)_2$ and $Fe(porp)[P(OR)_3]_2$, which appeared in 1984, was motivated by this bioinorganic interest (13). We first made such complexes at the same time (11), and report here on the full characterization of $Fe(TTP)(P^nBu_3)_2$ including an X-ray structural analysis, and use of the complex for catalytic decarbonylation of aldehydes. The data have been reported at

[1] ABBREVIATIONS. P—P = the chelating ditertiaryphosphines $PPh_2(CH_2)_nPPh_2$ n = 1–4; porp = a porphyrin dianion; TPP = 5,10,15,20-tetraphenylporphyrin dianion; pip = piperidine.

Can. J. Chem. Downloaded from www.nrcresearchpress.com by 112.217.228.212 on 09/07/12
For personal use only.

Can. J. Chem. Downloaded from www.nrcresearchpress.com by 112.217.228.212 on 09/07/12
For personal use only.

meetings (14), and the structure appears to be the first reported for a hemephosphine complex.[2]

Experimental

All solvents were distilled, stored, and handled under argon, the purification methods being outlined in the literature (15). Liquid aldehydes were distilled under N_2 at reduced pressures, while solid aldehydes were recrystallized from appropriate solvents (15). The phosphines were from Strem Chemicals, the P^nBu_3 being fractionally distilled under vacuum and the purity checked by ^{31}P nmr ($\delta(C_6H_6)$ 31.8). C.P. grade CO, N_2, and Ar were obtained from Canada Liquid Air Ltd. All manipulations, including preparation of the complexes, were carried out under Ar using Schlenk techniques. General procedures used for recording optical, infrared, nmr, and mass spectra have been given elsewhere (16, 17) (^{31}P nmr shifts are relative to 85% H_3PO_4, downfield being positive). Gas chromatography (thermal conductivity) was performed on a Hewlett-Packard 5830A instrument using 6 ft. × 0.125 in. 6% OV101 and OV17 packed columns. Gas chromatography/mass spectrometry was carried out on a Carlo-Erba Fractovap 4160-Kratos MS80RFA instrument.

The compounds H_2TPP (18), Fe(TPP)Cl (19), $[Fe(TPP)]_2O$ (20), and $Fe(TPP)(pip)_2$ (21), were made according to the literature procedures.

Synthesis of $Fe(TPP)(PR_3)_2$ complexes; R = ^{n}Bu (1), Ph (2)

To Fe(TPP)Cl (140 mg, 0.2 mmol) in 30 mL CH_2Cl_2 under Ar was added P^nBu_3 (3 mL), and the solution refluxed for 20 min. The volume was then reduced to about 5 mL by bubbling Ar through the solution; addition of MeOH (10 mL) precipitated purple crystals of **1** that were filtered off, washed with methanol, and dried under Ar (95% yield). *Anal.* calcd. for $C_{68}H_{82}N_4P_2Fe$: C 76.14, H 7.65, N 5.22; found: C 75.9, H 7.7, N 5.1. λ_{max} nm (log ϵ), CH_2Cl_2: 358(4.69), 455(5.11), 562(4.20), 603(4.37), in good agreement with the literature (13). Nuclear magnetic resonance (C_6D_6, 20°C, *in vacuo*): δ_H −2.0 (br, CH_2P, 12H), −0.87(br, CH_2CH_2P, 12H), 0.5 (t, CH_2CH_3, 18H), 0.6 (m, CH_2CH_3, 12H), 7.5–7.6 (m, *m*-H, *p*-H, 12H), 8.32 (m, *o*-H, 8H), 8.74 (s, pyrrole-H, 8H). δ_P 5.65(s).

To Fe(TPP)Cl (140 mg, 0.2 mmol) in 20 mL CH_2Cl_2 under Ar were added PPh_3(210 mg, 0.8 mmol), and $Na_2S_2O_4$ (70 mg, 0.4 mmol) dissolved in 5 mL degassed water, and the mixture stirred at 30°C for 30 min. The organic layer was syringed out, evaporated to about 5 mL, and MeOH (10 mL) added. The resulting solid (**2**) was collected and dried under vacuum (60% yield). *Anal.* calcd. for $C_{80}H_{58}N_4P_2Fe\cdot CH_3OH$: C 79.42, H 5.06, N 4.57; found: C 79.4, H 5.7, N 3.8. λ_{max} nm, CH_2Cl_2, in the presence of added PPh_3: 590, 550, 450, and 345.

Procedure for catalytic aldehyde decarbonylation

The reactions were carried out in a side-armed flask, fitted with a reflux condenser connected to a dry ice/acetone trap. The system was continually flushed with Ar, that could be deoxygenated by passage through a BASF catalyst maintained at 45°C, and be dried by passage through P_2O_5, KOH, and Drierite columns. The aldehyde (10^{-1}–10^{-2} *M*) was added to the Fe(II) porphyrin complex dissolved at 10^{-3}–10^{-5} *M* in chosen solvents and temperatures, and the reaction monitored (uv/vis and gc) by withdrawing samples with a gas-tight syringe. Organic reactants and products collected also in the cold trap, the amounts depending on the reaction time and temperature. Quoted conversions and turn-overs include total concentration detected in the reaction vessel and cold-trap.

X-ray crystallographic analysis of $Fe(TPP)(P^nBu_3)_2$

A crystal bounded by the ten faces (followed by the distances in mm between parallel faces): {0 1 0}, 0.18, {1 0 0}, 0.30, {1 0 − 1}, 0.50, {0 1 −1}, 0.52, {0 0 1}, 0.51 was mounted in a general orientation. Unit-cell parameters were refined by least-squares on 2 sin θ/λ values for 25 reflections (2θ = 30–37°) measured on a diffractometer with Mo-$K\alpha$ radiation ($\lambda(K\alpha_1)$ = 0.70930, $\lambda(K\alpha_2)$ = 0.71359 Å). Crystal data at 22°C are:

$C_{68}H_{82}FeN_4P_2$ f.w. = 1073.2

Triclinic, a = 12.499(3), b = 12.528(2), c = 12.039(2) Å, α = 116.39(1), β = 109.79(1), γ = 98.13(1)°, V = 1492.3(6) Å^3, Z = 1, ρ_c = 1.194 Mg m^{-3}, F (000) = 574, μ(Mo-$K\alpha$) = 3.5 cm^{-1}. Absent reflections: none, space group $P\bar{1}$ (reduced cell, Donnay convention) from structure analysis.

Intensities were measured with graphite-monochromatized Mo-$K\alpha$ radiation on an Enraf-Nonius CAD4-F diffractometer. An ω–2θ scan at 0.9–10.0° min^{-1} over a range of (0.85 + 0.35 tan θ) degrees in ω (extended by 25% on both sides for background measurement) was employed. Data were measured to 2θ = 55°. The intensities of three check reflections, measured every 3600 s throughout the data collection, showed only small random variations. Of the 6835 independent reflections measured and processed,[3] 3551 (52%) had intensities greater than or equal to 3σ(I) above background where $\sigma^2(I) = S + 2B + (0.04(S - B))^2$ with S = scan count and B = normalized background count. No absorption correction was made in view of the low value of μ.

The E-statistics and the Patterson function were consistent with the centrosymmetric space group $P\bar{1}$. The coordinates of the P atoms were determined from the Patterson function, the iron atom being constrained by space group symmetry to lie at a crystallographic inversion centre; the coordinates of the remaining non-hydrogen atoms were determined from a subsequent difference map. An attempt to refine the structure in the non-centrosymmetric space group $P1$ resulted in a singular matrix. Non-hydrogen atoms were refined with anisotropic thermal parameters and hydrogen atoms were fixed in idealized positions (staggered methyls, C(sp^2)—H = 0.97, C(sp^3)—H = 0.98 Å, $U_H \propto U_{bonded\ atom}$). Scattering factors for all atoms and anomalous scattering corrections for Fe and P were taken from ref. 22. The weighting scheme $w = 1/\sigma^2(F)$, where $\sigma^2(F)$ is derived from the previously defined $\sigma^2(I)$, gave uniform average values of $w(|F_o| - |F_c|)^2$ over ranges of both $|F_o|$ and sin θ/λ and was employed in the final stages of full-matrix refinement of 340 variables. Reflections with $I < 3\sigma(I)$ were not included in the refinement. Convergence was reached at R = 0.060 and R_w = 0.070 for 3551 reflections with $I \geq 3\sigma(I)$. The function minimized was $\Sigma w(|F_o| - |F_c|)^2$, $R = \Sigma||F_o| - |F_c||/\Sigma|F_o|$ and $R_w = (\Sigma w(|F_o| - |F_c|)^2/\Sigma w|F_o|^2)^{1/2}$.

On the final cycle of refinement the mean and maximum parameter shifts corresponded to 0.03 and 0.20σ, respectively. The mean error in an observation of unit weight was 2.681. The final difference map showed no unusual features. The final positional and thermal parameters appear in Tables 1 and 5,[4] respectively. Measured and calculated structure factors have been placed in the Depository of Unpublished Data. Bond lengths and angles appear in Tables 2 and 3, respectively. Calculated hydrogen parameters (Table 4), torsion angles (Table 6), and intra-annular torsion angles (Table 7), are also included as supplementary material.

[2]Professor Simonneaux and his group at the Université de Rennes have recently isolated several $Fe(TPP)(PR_3)_2$ species and characterized structurally the bis(dimethylphenylphosphine) complex (private communication).

[3]The computer programs used include locally written programs for data processing and locally modified versions of the following: ORFLS, full-matrix least-squares, and ORFFE, function and errors, by W. R. Busing, K. O. Martin, and H. A. Levy; FORDAP, Patterson and Fourier syntheses, by A. Zalkin; ORTEP II, illustrations, by C.K. Johnson.

[4]The structure factor table, Table 5 (anisotropic thermal parameters), and other supplementary material mentioned in the text (Tables 4, 6, 7), may be purchased from the Depository of Unpublished Data, CISTI, National Research Council of Canada, Ottawa, Ont., Canada K1A 0S2.

Can. J. Chem. Downloaded from www.nrcresearchpress.com by 112.217.228.212 on 09/07/12
For personal use only.

TABLE 1. Final positional (fractional × 10^4, Fe and P × 10^5) and isotropic thermal parameters (U × 10^3 Å^2) with estimated standard deviations in parentheses

Atom	x	y	z	U_{eq}
Fe	50000	50000	50000	38
P(1)	35635(10)	58212(10)	55788(12)	54
N(1)	4847(3)	3950(3)	5831(3)	41
N(2)	3688(3)	3584(3)	3163(3)	45
C(1)	5537(3)	4268(4)	7170(4)	45
C(2)	5182(4)	3234(4)	7340(4)	55
C(3)	4291(4)	2277(4)	6108(4)	55
C(4)	4089(3)	2725(3)	5167(4)	44
C(5)	3261(3)	1975(4)	3756(4)	47
C(6)	3076(4)	2393(4)	2830(4)	52
C(7)	2213(4)	1649(4)	1396(4)	66
C(8)	2258(4)	2367(4)	858(4)	66
C(9)	3185(4)	3569(4)	1938(4)	51
C(10)	3525(3)	4583(4)	1781(4)	44
C(11)	2541(4)	634(4)	3190(4)	53
C(12)	1434(4)	307(4)	3139(6)	76
C(13)	759(5)	−961(6)	2556(7)	94
C(14)	1224(7)	−1874(5)	2040(6)	101
C(15)	2322(7)	−1554(5)	2119(8)	122
C(16)	2989(6)	−311(5)	2693(7)	98
C(17)	2824(4)	4446(4)	409(4)	52
C(18)	1836(4)	4830(5)	193(5)	66
C(19)	1180(4)	4727(6)	−1062(6)	84
C(20)	1499(5)	4208(6)	−2124(6)	84
C(21)	2478(7)	3845(6)	−1913(6)	101
C(22)	3146(5)	3970(6)	−651(5)	88
C(23)	3298(4)	7057(5)	5247(5)	66
C(24)	2374(5)	7639(5)	5595(6)	78
C(25)	2529(6)	8893(6)	5745(7)	99
C(26)	1633(8)	9497(7)	6127(8)	135
C(27)	3980(6)	6591(6)	7485(7)	94
C(28)	4717(9)	7864(9)	8391(7)	169
C(29)	5292(10)	8501(9)	10151(13)	201
C(30)	4406(13)	8249(15)	10383(15)	242
C(31)	2100(5)	4689(5)	4963(6)	84
C(32)	1217(5)	4145(6)	3548(6)	99
C(33)	31(6)	3134(7)	3104(8)	120
C(34)	−806(7)	2404(8)	1675(9)	159

TABLE 2. Bond lengths (Å) with estimated standard deviations in parentheses

Bond	Length (Å)	Bond	Length (Å)
Fe —P(1)	2.3457(11)	C(11)—C(12)	1.358(6)
Fe —N(1)	1.998(3)	C(11)—C(16)	1.364(6)
Fe —N(2)	1.993(3)	C(12)—C(13)	1.400(7)
P(1) —C(23)	1.809(5)	C(13)—C(14)	1.354(9)
P(1) —C(27)	1.885(6)	C(14)—C(15)	1.333(9)
P(1) —C(31)	1.823(5)	C(15)—C(16)	1.374(8)
N(1)—C(1)	1.376(5)	C(16)—C(18)	1.373(6)
N(1)—C(4)	1.372(5)	C(17)—C(22)	1.374(6)
N(2)—C(6)	1.384(5)	C(18)—C(19)	1.389(7)
N(2)—C(9)	1.383(5)	C(19)—C(20)	1.377(8)
C(1)—C(2)	1.431(5)	C(20)—C(21)	1.348(8)
C(1)—C(10)′[a]	1.397(5)	C(21)—C(22)	1.388(7)
C(2)—C(3)	1.343(5)	C(23)—C(24)	1.528(6)
C(3)—C(4)	1.440(5)	C(24)—C(25)	1.476(7)
C(4)—C(5)	1.400(5)	C(25)—C(26)	1.523(8)
C(5)—C(6)	1.395(6)	C(27)—C(28)	1.395(11)
C(5)—C(11)	1.497(5)	C(28)—C(29)	1.718(14)
C(6)—C(7)	1.428(6)	C(29)—C(30)	1.262(14)
C(7)—C(8)	1.326(6)	C(31)—C(32)	1.439(7)
C(8)—C(9)	1.433(6)	C(32)—C(33)	1.555(8)
C(9)—C(10)	1.395(5)	C(33)—C(34)	1.417(10)
C(10)—C(17)	1.500(5)		

[a]Here and elsewhere primed atoms have coordinates related to those in Table 1 by the symmetry operation (1 − x, 1 − y, 1 − z).

Results and discussion

Synthesis and characterization of the complexes

The Fe(TPP)(P^{n}Bu$_3$)$_2$ complex **1** is easily prepared by treating Fe(TPP)Cl with excess of the free phosphine, which presumably acts as the reducing agent; the nature of the redox process has not been elucidated but it may be akin to the well documented H-atom abstraction radical process involved in a corresponding reaction of Fe(TPP)Cl with piperidine to give Fe(TPP)(pip)$_2$ (21). Formation of the bis(triphenylphosphine) complex **2** requires addition of dithionite (or borohydride) as reductant. The synthesis of **1** parallels that discovered independently and reported earlier by Ohya *et al.* (13); this group has already discussed the "hyper" uv/visible spectra (i.e. the presence of a split Soret bond) generated by the bis(tertiary phosphine) and bis(tertiary phosphite) complexes. The uv/visible spectrum obeys Beer's Law and is independent of added P^{n}Bu$_3$, showing that dissociation of a phosphine to give a five-coordinate species is negligible; the same behaviour with this strongly basic phosphine has been noted earlier for the corresponding Ru(II) complex (16). The ^{1}H nmr spectrum of **1**, not studied previously (13), is very typical of that of a six-coordinate, diamagnetic porphyrin complex, and resembles closely that of the Ru(TPP)(P^{n}Bu$_3$)$_2$ complex, resonances of the butyl groups being shifted upfield because of the porphyrin ring current (16).

The crystal structure of Fe(TPP)(P^{n}Bu$_3$)$_2$ consists of well-separated molecules (Fig. 1) having crystallographic $\bar{1}$-C_i symmetry. As a result of this imposed symmetry, the FeN_4 unit is rigorously planar. The iron atom has a tetragonally distorted octahedral coordination geometry. Bond angles at the metal are essentially undistorted from the "ideal" values of 90 and 180°, the largest deviation being 0.42(9)°. The Fe—N distances are equal within the experimental error, the mean Fe—N distance of 1.996(4) Å agreeing well with the value of 2.000(1) Å for Fe(TPP)(PMe$_2$Ph)$_2$[2] and values of 1.98(3)–2.02(3) Å observed for other low-spin Fe(II) TPP complexes (23–27). The Fe—P bond length of 2.346(1) Å is significantly longer than the corresponding distance of 2.284 Å in Fe(TPP)(PMe$_2$Ph)$_2$, as well as those in other (non-porphyrin) octahedral, low-spin Fe(II) complexes with *trans* phosphine ligands, the longest, to our knowledge, being 2.312(8) Å in *trans*-Fe[PPh$_2$(CH$_2$)$_2$PPh$_2$]Cl$_2$ (28). The present Fe—P distance, however, is still substantially shorter than those reported for high-spin complexes which are typically 2.5–2.7 Å (29). The longer Fe—P bond in **1** compared to that in Fe(TPP)(PMe$_2$Ph)$_2$ is almost certainly steric in origin; within **1**, the hydrogens on carbons 27, 28, 31, and 32 are 2.50, 2.49, 2.71, and 2.44 Å respectively, from the porphyrin, less than the normal packing distance of 2.9 Å (30).

The porphyrin core is not rigorously planar, the maximum deviation from the mean plane being 0.045 Å. The pyrrole and phenyl rings are either planar within experimental error or are slightly, but significantly, non-planar (maximum deviation

TABLE 3. Bond angles (deg) with estimated standard deviations in parentheses

Bonds	Angle (deg)	Bonds	Angle (deg)
P(1)—Fe —N(1)	90.20(9)	C(5)—C(6)—C(7)	124.7(4)
P(1)—Fe —N(2)	90.42(9)	C(6)—C(7)—C(8)	107.9(4)
P(1)—Fe —P(1)′	180	C(7)—C(8)—C(9)	107.2(4)
P(1)—Fe —N(1)′	89.80(9)	N(2)—C(9)—C(8)	110.3(4)
P(1)—Fe —N(2)′	89.58(9)	N(2)—C(9)—C(10)	124.8(4)
N(1)—Fe —N(2)′	90.16(11)	C(8)—C(9)—C(10)	124.9(4)
N(1)—Fe —N(1)′	180	C(9)—C(10)—C(17)	118.1(3)
N(1)—Fe —N(2)′	89.84(11)	C(9)—C(10)—C(1)′	124.2(3)
N(2)—Fe —N(2)′	180	C(17)—C(10)—C(1)′	117.7(3)
Fe —P(1)—C(23)	116.48(15)	C(5)—C(11)—C(12)	122.3(4)
Fe —P(1)—C(27)	113.4(2)	C(5)—C(11)—C(16)	119.9(4)
Fe —P(1)—C(31)	117.4(2)	C(12)—C(11)—C(16)	117.8(4)
C(23)—P(1)—C(27)	102.5(2)	C(11)—C(12)—C(13)	121.2(5)
C(23)—P(1)—C(31)	108.2(2)	C(12)—C(13)—C(14)	119.2(6)
C(27)—P(1)—C(31)	96.0(3)	C(13)—C(14)—C(15)	119.8(5)
Fe —N(1)—C(1)	127.4(2)	C(14)—C(15)—C(16)	121.2(6)
Fe —N(1)—C(4)	127.4(2)	C(11)—C(16)—C(15)	120.8(5)
C(1)—N(1)—C(4)	105.0(3)	C(10)—C(17)—C(18)	119.8(4)
Fe —N(2)—C(6)	127.5(3)	C(10)—C(17)—C(22)	122.5(4)
Fe —N(2)—C(9)	128.0(3)	C(18)—C(17)—C(22)	117.7(4)
C(6)—N(2)—C(9)	104.5(3)	C(17)—C(18)—C(19)	121.0(5)
N(1)—C(1)—C(2)	110.4(3)	C(18)—C(19)—C(20)	120.1(5)
N(1)—C(1)—C(10)′	125.6(3)	C(19)—C(20)—C(21)	119.3(5)
C(2)—C(1)—C(10)′	124.0(4)	C(20)—C(21)—C(22)	120.5(5)
C(1)—C(2)—C(3)	107.4(4)	C(17)—C(22)—C(21)	121.3(5)
C(2)—C(3)—C(4)	106.5(4)	P(1)—C(23)—C(24)	119.6(3)
N(1)—C(4)—C(3)	110.7(3)	C(23)—C(24)—C(25)	114.2(5)
N(1)—C(4)—C(5)	125.6(3)	C(24)—C(25)—C(26)	114.7(6)
C(3)—C(4)—C(5)	123.7(3)	P(1)—C(27)—C(28)	119.2(5)
C(4)—C(5)—C(6)	124.1(3)	C(27)—C(28)—C(29)	119.2(9)
C(4)—C(5)—C(11)	118.4(4)	C(28)—C(29)—C(30)	106.7(10)
C(6)—C(5)—C(11)	117.5(4)	P(1)—C(31)—C(32)	117.9(4)
N(2)—C(6)—C(5)	125.3(4)	C(31)—C(32)—C(33)	113.7(6)
N(2)—C(6)—C(7)	110.1(4)	C(32)—C(33)—C(34)	117.5(7)

Can. J. Chem. Downloaded from www.nrcresearchpress.com by 112.217.228.212 on 09/07/12
For personal use only.

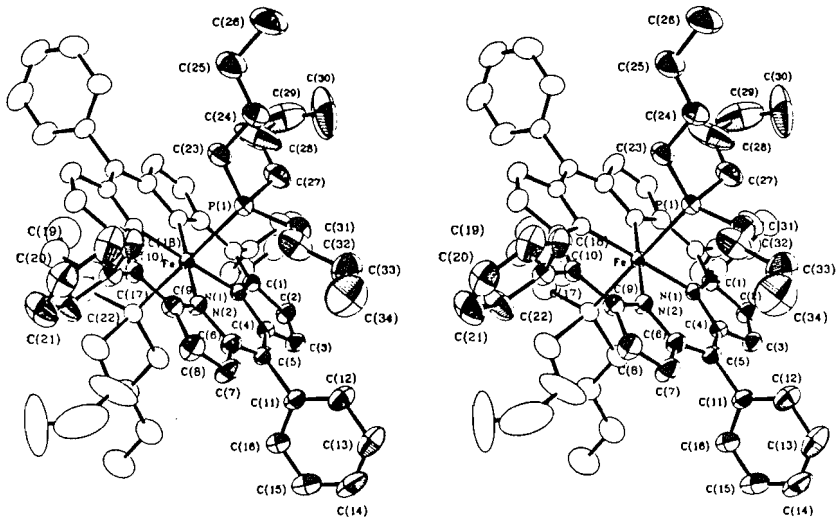

FIG. 1. Stereoscopic view of the (5,10,15,20-tetraphenylporphyinato)bis(tri-*n*-butylphosphine)iron(II) molecule; 33% probability thermal ellipsoids are shown and hydrogen atoms have been omitted for the sake of clarity.

Can. J. Chem. Downloaded from www.nrcresearchpress.com by 112.217.228.212 on 09/07/12
For personal use only.

from the mean plane = 0.03(7) Å). The dihedral angles between the normals to the porphyrin and phenyl mean planes are 91.7 and 92.9°. The mean bond lengths and angles in the porphyrin core are normal (31). Anomalous bond distances are noted within two of the *n*-butyl groups and may be ascribed to high thermal motion and/or minor unresolved disorder.

The $Fe(TPP)(PPh_3)_2$ complex **2** is probably not isolated in a pure state. Associated methanol is observed (the mass spectrum shows a 31 peak (CH_3O^+) as well as the 668 and 334 peaks of $Fe(TPP)^+$ and $Fe(TPP)^{2+}$), and although the C, H elemental analysis is satisfactory, that for N is not. In solution, **2** is very air-sensitive and also dissociates a phosphine ligand, at least at $\sim 10^{-5}$ *M*, because excess phosphine has to be added to generate the uv/visible spectrum typical of a six-coordinate bis(phosphine) species. The degrees of air-sensitivity, and ligand dissociation to give a five-coordinate species, are almost certainly related properties (32). The more basic and less sterically demanding P^nBu_3 ligand does not measurably dissociate from complex **1** at 10^{-5} *M*, which is more readily handled in solution than **2**, although is still air-sensitive (see below). The ^1H nmr spectrum of **2** is complicated by phosphine dissociation and exchange, and the tendency of **2** to oxidize. More careful, detailed studies are required on this system, although it is clear that the hydrogens of the coordinated PPh_3 are shifted upfield, as in $Ru(TPP)(PPh_3)_2$ (16). Attempts to purify **2** via recrystallization were unsuccessful.

Carbonylation/decarbonylation studies using CO

Solutions of $Fe(TPP)(P^nBu_3)_2$ react rapidly and reversibly with CO according to eq. [2].

$$[2]\quad \underset{\mathbf{1}}{Fe(TPP)(P^nBu_3)_2} + CO \overset{K}{\rightleftharpoons} \underset{\mathbf{3}}{Fe(TPP)(CO)(P^nBu_3)} + P^nBu_3$$

The Soret band of **1** (455 nm) is replaced by that of the (carbonyl) phosphine species **3** (438 nm). That the reaction follows the stoichiometry of equation [2] is readily demonstrated by a standard spectrophotometric titration technique (33, 34). The analysis of the data gives $K = 0.65$ at 23°C in toluene (11), which is comparable to that determined by Stynes *et al.* (34) for the corresponding protoporphyrin IX dimethylester system (K = 1.7, 25°C in toluene). The ir spectrum of **3** formed in situ in CH_2Cl_2 reveals ν_{CO} at 1993 cm^{-1}. The equilibrium constant for reaction [2] shows that **1** and **3** are readily interconvertible at easily attainable concentrations of added phosphine and CO, whose solubility in toluene, for example, is 7.6×10^{-3} *M* atm^{-1} at 25°C (35), thus making **1** an appropriate complex to test for catalytic decarbonylation. The K value for reaction [2] involving the Ru analogues of **1** and **3** is 0.054 at 26°C in toluene (36), showing that thermodynamically CO is more readily replaced by P^nBu_3 in the Ru system, although it should be noted that the Ru-catalyzed aldehyde decarbonylation reactions involve a mixed P^nBu_3/PPh_3 system (10). Complex **1** was indeed found to effect such catalysis, but the contribution of these K equilibria reactions within the overall mechanism (free radical in nature — see below) is not clear. Nevertheless, an equilibrium for a reaction comparable to [2], but with $Fe(TPP)(pip)_2$ as reactant, has $K = 15\,000$ (23°C, toluene) (33), showing much higher CO affinity, and the amine system was not an effective catalyst. The K value does serve as a qualitative guide for catalytic potential. The presence of the relatively strong *trans*-effect ligands CO and P^nBu_3 in **3** (compared to CO and pip) is consistent with a higher K value for the amine system, but differences in the labilities of the axial L ligands in the $Fe(TPP)L_2$ complexes (L = P^nBu_3, pip) may also be a factor (34).

Decarbonylation of aldehydes

Treatment of **1** at 10^{-4}–10^{-5} *M* in CH_2Cl_2 at room temperature with a variety of aromatic aldehydes (at $\sim 10^{-3}$ *M*): benzaldehyde and substituted ones (*p*-dimethylamino-, *p*-nitro-, 2,6-dichloro-, 3-methoxy-4-hydroxy-, 2,4,6-trimethoxy-, salicyaldehyde, piperonal), and phenylacetaldehyde, generated the (carbonyl)phosphine species **3** as detected by uv/vis spectroscopy; the reaction times were not reproducible for any one aldehyde, and varied from $t_{1/2}$ values of a few hours to several days. Heptanal-1 and 2-ethylbutanal similarly with **1** gave "irreproducible" formation of **3**. Vacuum pumping (or Ar flushing) the optical cells containing a solution of **3** and excess aldehyde regenerated **1** (eq. [2]), thus establishing the plausibility of catalytic decarbonylation of the aldehydes.

The most extensive studies were carried out using phenylacetaldehyde as substrate because the decarbonylation reaction always proceeded with this substrate and at a reasonable rate; further, the gc retention times for this aldehyde and toluene (the decarbonylation product) were well separated (typically in the 15 and 4 min range), respectively, with a temperature programmed OV101 separation (60°C/5 min and the 5°C/min to 180°C). Samples of catalytically active solutions taken during Ar flushing (see Experimental) revealed the 455 nm band of **1**, while discontinuation of the Ar flow allowed for growth of the 438 nm band of **3**. At room temperature using $PhCH_2CHO$ at $\sim 10^{-3}$ *M* and **1** at $\sim 10^{-5}$ *M* in CH_2Cl_2, essentially complete conversion to toluene occurred with turnovers in the range of 5–20 min^{-1}; at 40°C (refluxing CH_2Cl_2) turnovers a high as 100 min^{-1} were recorded. Of importance, a small amount of bibenzyl was sometimes detected by gc/ms. Flushing with a CO atmosphere (instead of Ar), or addition of $\geq$ 1.0 equivalent of P^nBu_3/Fe, inhibited the decarbonylation completely. All the necessary control experiments were done, and decarbonylation does require the presence of **1**. Addition of a radical inhibitor such as hydroquinone or 2,6-ditertiarybutyl-*p*-cresol at $\sim 10^{-4}$ *M* (which show no reactivity with **1**) prevented any decarbonylation, even stoichiometric, of the aldehyde.

Addition of air or oxygen to CH_2Cl_2 (or toluene) solutions containing $Fe(TPP)(P^nBu_3)_2$, either in the presence or absence of aldehydes, caused a rapid, irreversible colour change (red to greenish red); the Soret was shifted from 455 to 415 nm (log ϵ 4.95 based on [**1**]), while the visible maxima remained essentially unchanged in position but increased slightly in intensity. Such solutions containing the 415 nm band did not effect aldehyde decarbonylation; indeed, if sufficient O_2 gets into the active catalytic solutions to generate the "415 nm species" (e.g. during sampling), and only small amounts are necessary, the catalysis is suppressed. We have been unable to isolate any characterizable complex. One plausible oxidation product $[Fe(TPP)]_2O$ (20, 37) is ruled out because the Soret maximum of the μ-oxo species in CH_2Cl_2 is seen at 403 nm; a less likely product Fe(TPP)Cl exhibits the Soret maximum at 418 nm in CH_2Cl_2. The "oxidized" solution may well contain the five-coordinate phosphine oxide complex $Fe(TPP)(O{=}P^nBu_3)$; the corresponding triphenylphosphine oxide species is said to result from treatment of *in situ* $Fe(TPP)(PPh_3)_2$ with O_2, but no characterization details were presented (37). The 415 nm species could be readily reconverted to **1** by treatment with P^nBu_3. This could be a ligand substitution reaction, although a redox reaction comparable to that seen in the

synthesis of **1** from Fe(TPP)Cl cannot be ruled out; however, the visible spectral changes do not indicate changes in oxidation state of the iron. As noted above, excess phosphine inhibits decarbonylation and so cannot be used to protect against adventitious oxygen.

It should be emphasized that with substrates other than phenylacetaldehyde, catalytic decarbonylation occurred rarely and when catalysis was not observed the 415 nm band was always evident, even though every effort had been made to exclude trace O_2. It is possible that trace impurities in the aldehydes were problematic (either promoting reactivity for the phenylacetaldehyde substrate, or deactivating the other systems). Benzaldehyde was sometimes decarbonylated (the maximum turn-over at 20°C being 0.2 min^{-1}); salicylaldehyde and piperonal were never catalytically decarbonylated. Our earlier catalytic Ru systems were most efficient in MeCN or PhCN solution (10), but use of these solvents was not effective for the Fe(TPP)(P^nBu_3)$_2$/phenylacetaldehyde system; with neat aldehyde as solvent/substrate, temperatures of 200°C and reaction times of 1 h were necessary before decarbonylation products were detected.

Speculation on mechanisms

An attempt to rationalize the general findings can be made only in terms of radical mechanisms, and the evidence for such processes is strong (irreproducibility, inhibition experiments, and detection of bibenzyl with the phenylacetaldehyde substrate). Further, the "standard" decarbonylation mechanism (5, 7) involving oxidative-addition of aldehyde, CO migration (with subsequent elimination), and reductive elimination of hydrocarbon product, seems unlikely at a metalloporphyrin site (10), where one-electron, radical processes more generally are becoming increasingly well documented (38).

It is possible that trace dioxygen initiates a radical mechanism for the Fe-catalyzed decarbonylations, although there is no direct evidence for this; any attempts to add small amounts of O_2 led to formation of the "415 nm species" and inactivity. The irreproducibility in the data, especially within the stoichiometric reactions, certainly suggests that trace O_2 (air) is involved, and there is precedent for O_2 playing a role in assisting hydrogen abstraction from an aldehyde to give an acyl radical in the presence of, for example, a cobalt complex (39). Organic peroxides, whose formation can be catalyzed by metal ions in the presence of O_2 (40*a*), can also generate acyl radicals by reaction with aldehydes (41). Once the acyl radical is formed, catalytic decarbonylation may be accommodated by the processes shown in [3]:

[3] $R\dot{C}O \rightarrow R^{\cdot} + CO;\ R^{\cdot} + RCHO \rightarrow RH + R\dot{C}O$

The decarbonylation of acyl radicals is well known (40*b*), and the sometimes detected bibenzyl must come from the $PhCH_2\cdot$ radical.

That the catalysis is completely inhibited by addition of small, measured amounts of O_2 tends to suggest that initiation via Fe(III) as in eq. [4] (40*c*) is unlikely. Oxygenated species such as trace amounts of $Fe^{II}O_2$ ($Fe^{III}O_2^-$) could act as a chain initiator; H atom abstraction would then give coordinated

[4] $RCHO + Fe^{III} \rightarrow R\dot{C}O + Fe^{II} + H^+$

or free $HO_2^-\cdot$, and such a reaction has been suggested previously (42). The O_2-oxidation of Fe(II) porphyrin phosphine species involves bridged-peroxo and oxo intermediates (37), and H-abstraction by either of these seems plausible (37, 43). Trace protons (from water) can promote formation of superoxide (stabilized as $HO_2\cdot$) from reaction of O_2 with hexacoordinate metalloporphyrins via a one-electron outer-shere process (44, 45), and H-abstraction by $HO_2\cdot$ could also be envisaged. Our findings that isolated 5-coordinate Ru(porp)(PR_3) complexes in benzene do not react with rigorously purified benzaldehyde in the absence or presence of dry O_2, or with dry O_2 alone (32), suggest that the radical mechanism for aldehyde decarbonylation by the Ru system perhaps follows a different initiation pathway to that of the Fe system. Further, some unpublished work on the stoichiometric decarbonylation of phenylacetaldehyde by Ru(TPP)(P^nBu_3)$_2$ in CH_2Cl_2 had shown that the reaction rate increased generally with increasing O_2 at least up to 0.4 atm (36), but this O_2 had not been rigorously dried.

Further work is in progress in an attempt to unravel the complexities of these free-radical initiated catalytic decarbonylations. The studies, however, are difficult and frustrating because of the irreproducible data obtained. Trace impurities seem to be of key importance, and findings are leaning toward the conclusion that if the various ingredients for the recipes are "really highly purified", reactivity may cease. Nevertheless, effective catalytic systems have been discovered, and a search for their understanding continues to expand the coordination chemistry of five- and six-coordinate metalloporphyrins of the iron sub-group metals containing tertiary phosphine ligands. The relation, if any, of these free-radical type decarbonylations to the more recently discovered enzymatic systems (see Introduction) remains to be established.

Acknowledgements

We thank the Natural Sciences and Engineering Research Council of Canada and the National Institutes of Health (Grant No. Am 17989) for research grants, Professor J. Trotter for use of crystallographic facilities, and Johnson Matthey Ltd. for the loan of ruthenium.

1. A. MONTREUX and F. PETIT (*Editors*). *In* Industrial applications of homogenous catalysis. Reidel, Dordrecht. 1988. (*a*) p.l; (*b*) p. 19.
2. R. A. SHELDON. Chemicals from synthesis gas. Reidel, Dordrecht. 1983.
3. T. M. CHEESBROUGH and P. E. KOLATTUKUDY. Proc. Natl. Acad. Sci. U.S.A. **81**, 6613 (1984).
4. S. A. RAYBUCK, N. R. BASTIAN, L. D. ZYDOWSKY, K. KOBAYASHI, H. G. FLOSS, W. H. ORME-JOHNSON, and C. T. WALSH. J. Am. Chem. Soc. **109**, 3171 (1987).
5. J. TSUJI. *In* Organic synthesis via metal carbonyls. Vol. 2. *Edited by* I. Wender and P. Pino. Wiley, New York. 1977. p. 595.
6. G. L. GEOFFROY, D. A. DENTON, M. E. KEENEY, and R. R. BUCKS. Inorg. Chem. **15**, 2382 (1976).
7. D. H. DOUGHTY and L. H. PIGNOLET. *In* Homogeneous catalysis with metal phosphine complexes. *Edited by* L H. Pignolet. Plenum Press, New York. 1983. p. 343; B. R. JAMES and D. MAHAJAN. 7th Canadian symposium on catalysis. Preprints, Vol. 1. Alberta Research Council, Edmonton. 1980. p. 58.
8. B. C. CHOW and I. A. COHEN. Bioinorg. Chem. **1**, 57 (1971).
9. B. R. JAMES, A. W. ADDISON, M. CAIRNS, D. DOLPHIN, N. P. FARRELL, D. R. PAULSON, and S. WALKER. *In* Fundamental research in homogeneous catalysis. Vol. 3. *Edited by* M. Tsutsui. Plenum Press, New York. 1979. p. 751.
10. G. DOMAZETIS, B. TARPEY, D. DOLPHIN, and B. R. JAMES. J. Chem. Soc. Chem. Commun. 939 (1980); G. DOMAZETIS, B. R. JAMES, B. TARPEY, and D. DOLPHIN. ACS Symp. Ser. **152**, 243 (1981).

Can. J. Chem. Downloaded from www.nrcresearchpress.com by 112.217.228.212 on 09/07/12
For personal use only.

11. R. BELANI. M.Sc. Dissertation. The University of British Columbia. Vancouver. 1985.
12. G. SIMONNEAUX, A. BONDON, and P. SODANO. Inorg. Chem. **26**, 3636 (1987), and references therein.
13. T. OHYA, H. MOROHOSHI, and M. SATO. Inorg. Chem. **23**, 1303 (1984).
14. B. R. JAMES. Proc. NATO Conf. on Carbonylation Reactions Montebello, Quebec. 1985; B. R. JAMES. Proc. 4th Japan/China/USA Symposium on Organometallic Chemistry and Catalysis. Univ. of Tsukuba. Japan. 1986. p. 103.
15. D. D. PERRIN, W. L. F. ARMAREGO, and D. R. PERRIN (*Editors*). Purification of laboratory chemicals. 2nd ed. Pergamon Press, Sydney. 1982.
16. S. ARIEL, D. DOLPHIN, G. DOMAZETIS, B. R. JAMES, T. W. LEUNG, S. J. RETTIG, J. TROTTER, and G. M. WILLIAMS. Can. J. Chem. **62**, 755 (1984).
17. D. C. THACKRAY, S. ARIEL, T. W. LEUNG, K. MEMON, B. R. JAMES, and J. TROTTER. Can. J. Chem. **64**, 2440 (1986).
18. A. D. ADLER, F. R. LONGO, J. D. FINARELLI, J. GOLDMACHER, J. ASSOUR, and L. KORSAKOFF. J. Org. Chem. **32**, 476 (1967).
19. H. KOBAYASHI, T. HIGUCHI, Y. KAIZU, H. OSADA, and M. AUKI. Bull. Chem. Soc. Jpn. **48**, 3137 (1975).
20. E. B. FLEISHER and T. S. SRIVASTAVA. J. Am. Chem. Soc. **91**, 2403 (1969).
21. J. DEL GAUDIO and G. N. LAMAR. J. Am. Chem. Soc. **98**, 3014 (1976); L. M. EPSTEIN, D. K. STRAUB, and C. MARICONDI. Inorg. Chem. **6**, 1720 (1967).
22. International tables for X-ray crystallography. Vol. IV. Kynoch press, Birmingham. 1974. pp. 99–102 and 149.
23. L. J. RADANOVICH, A. BLOOM, and J. L. HOARD. J. Am. Chem. Soc. **94**, 2073 (1972).
24. W. R. SCHEIDT and M. E. FRISSE. J. Am. Chem. Soc. **97**, 17 (1975).
25. S. M. PENG and J. A. IBERS. J. Am. Chem. Soc. **98**, 8032 (1976).
26. G. B. JAMESON and J. A. IBERS. Inorg. Chem. **18**, 1200 (1979).
27. T. MASHIKO, C. A. REED, K. J. HALLER, M. E. KASTNER, and W. R. SCHEIDT. J. Am. Chem. Soc. **103**, 5758 (1981).
28. F. CECCONI, M. DI VAIRA, S. MIDOLLINI, A. ORLANDINI, and L. SACCONI. Inorg Chem. **20**, 3423 (1981).
29. F. CECCONI, M. DI VAIRA, and L. SACCONI. Cryst. Struct. Commun. **10**, 1523 (1981).
30. W. R. SCHEIDT and M. GOUTERMAN. *In* Iron porphyrins. Vol. 1. *Edited by* A. B. P. Lever and H. B. Gray. Addison Wesley, New York. 1983. p. 106.
31. W. R. SCHEIDT and C. A. REED. Chem. Rev. **81**, 543 (1981).
32. C. SISHTA, M. J. CAMENZIND, B. R. JAMES, and D. DOLPHIN. Inorg. Chem. **26**, 1181 (1987).
33. B. R. JAMES, K. J. REIMER, and C. T. WONG. J. Am. Chem. Soc. **99**, 4815 (1977), and references therein.
34. D. V. STYNES, D. FLETCHER, and X. CHEN. Inorg. Chem. **25**, 3483 (1986).
35. L. R. FIELD, E. WILHELM, and R. BATTINO. J. Chem. Thermodyn. **6**, 237 (1974).
36. B. TARPEY. M.Sc. Dissertation. The University of British Columbia, Vancouver. 1982.
37. D. H. CHIN, G. N. LAMAR, and A. L. BALCH. J. Am. Chem. Soc. **102**, 4344 (1980); **102**, 5945 (1980).
38. M. KE, S. J. RETTIG, B. R. JAMES, and D. DOLPHIN. J. Chem. Soc. Chem. Commun. 1110 (1987); M. D. FARNOS, B. A. WOODS, and B. B. WAYLAND. J. Am. Chem. Soc. **108**, 3659 (1986); R. S. PAONESSA, N. C. THOMAS, and J. HALPERN. J. Am. Chem. Soc. **107**, 4333 (1985).
39. W. F. BRILL and F. J. LISTER. J. Org. Chem. **26**, 565 (1961); A. MISONO, T. OSA, and Y. OHKATSU. Adv. Chem. Ser. **75**, 120 (1968).
40. R. A. SHELDON and J. K. KOCHI. Metal catalyzed oxidations of organic compounds. Academic Press, New York. 1981. (*a*) Chapt. 3; (*b*) Chapt. 12; (*c*) Chapt. 5.
41. W. H. URRY, D. J. TRECKER, and H. D. HARTZLER. J. Org. Chem. **29**, 1663 (1964).
42. C. E. CASTRO. *In* The porphyrins. Vol V. *Edited by* D. Dolphin. Academic Press, New York. 1978. Chapt. 1; D. V. STYNES, H. C. STYNES, J. A. IBERS, and B. R. JAMES. J. Am. Chem. Soc. **95**, 1142 (1973).
43. J. T. GROVES. J. Chem. Educ. **62**, 928 (1985); *In* cytochrome P-450. Structure, mechanism, and biochemistry. *Edited by* P. Ortiz de Montellano. Plenum Press, New York. 1985. Chapt. 1.
44. M. M. L. CHU, C. E. CASTRO, and G. M. HATHAWAY. Biochemistry. **17**, 481 (1978).
45. B. R. JAMES, S. R. MIKKELSEN, T. W. LEUNG, G. M. WILLIAMS, and R. WONG. Inorg. Chim. Acta, **85**, 209 (1984).

Can. J. Chem. Downloaded from www.nrcresearchpress.com by 112.217.228.212 on 09/07/12
For personal use only.

Synthesis, spectroscopic and magnetic properties of some pyrazine-bridged iron(II) sulfonate complexes

JOHN S. HAYNES, JOHN R. SAMS, AND ROBERT C. THOMPSON
Department of Chemistry, University of British Columbia, 2035 Main Mall, Vancouver, B.C., Canada V6T 1Y6

Received

This paper is dedicated to Professor Charles A. McDowell on the occasion of his seventieth birthday

HAYNES, J. S., SAMS, J. R., and THOMPSON, R. C. 1988. Can. J. Chem. **66**, 2079 (1988).

Six new pyrazine-bridged complexes of iron(II) have been prepared and studied using magnetic susceptibility, differential scanning calorimetry, and vibrational, electronic, and Mössbauer spectroscopic methods. $Fe(pyz)(CF_3SO_3)_2$ exhibits a susceptibility maximum at 4.4 K and analysis of the magnetic data according to a two-dimensional $S = 2$ system in the (isotropic) Heisenberg limit yields best-fit values of $J = -0.26 cm^{-1}$ and $g = 2.20$. Variable temperature Mössbauer spectra between 4.2 and 1.6 K are also reported for this compound and show the onset of magnetic hyperfine splitting below ~3.8 K. Analysis of magnetic data for $Fe(pyz)_2(CH_3SO_3)_2$ and $Fe(pyz)_2(CF_3SO_3)_2 \cdot CH_3OH$ according to the two-dimensional Heisenberg model also indicates the presence of weak antiferromagnetic exchange in these complexes ($J = -0.18$ and $-0.20 cm^{-1}$, respectively). No clear evidence for magnetic concentration was obtained from our studies on $Fe(pyz)_2(ClO_4)_2$, $Fe(pyz)(p\text{-}CH_3C_6H_4SO_3)_2$, and $Fe(pyz)(p\text{-}CH_3C_6H_4SO_3)_2.2CH_3OH$; any antiferromagnetic coupling in these complexes must be considerably weaker than in the other complexes studied.

HAYNES, J. S., SAMS, J. R., et THOMPSON, R. C. 1988. Can. J. Chem. **66**, 2079 (1988).

On a préparé six nouveaux complexes du fer (II) contenant un pont pyrazine et on les a étudié en faisant appel à la suceptibilité magnétique, à la calorimétrie de balayage différentiel et à des méthodes de spectroscopies vibrationnelle, électronique et de Mössbauer. Le $Fe(pyz)(CF_3SO_3)_2$ présente une susceptibilité maximale à 4,4 K et une analyse des données magnétiques à l'aide d'un système bidimensionnel $S = 2$, dans la limite isotrope d'Heisenberg, conduit à des valeurs de $J = -0{,}26 cm^{-1}$ et $g = 2{,}20$. Sur ce composé, on a aussi déterminé les spectres de Mössbauer à températures variables entre 4,2 et 1,6 K; il commence à présenter un couplage magnétique hyperfin en dessous d'environ 3,8 K. Une analyse des données magnétiques du $Fe(pyz)_2(CH_3SO_3)_2$ et du $Fe(pyz)_2(CF_3SO_3)_2 \cdot CH_3OH$ à l'aide du modèle bidimensionnel d'Heisenberg indique aussi la présence de faibles échanges antiferromagnétiques dans ces complexes ($J = -0{,}18$ et $-0{,}20 cm^{-1}$, respectivement). Nos études sur le $Fe(pyz)_2(ClO_4)$, le $Fe(pyz)(p\text{-}CH_3C_6H_4SO_3)_2$ et le $Fe(pyz)(p\text{-}CH_3C_6H_4SO_3)_2 \cdot 2CH_3OH$ n'ont pas permis de mettre en évidence la présence d'une concentration magnétique; dans ces complexes, les couplages antiferromagnétiques doivent être beaucoup plus faibles que ceux observés dans les autres complexes étudiés.

[Traduit par la revue]

Introduction

A recent report describing magnetic susceptibility and Mössbauer studies on $Fe(pyz)_2(NCS)_2$ and $Fe(pyz)(NCO)_2$ (1) demonstrated clearly that bridging pyrazine (1,4-diazine, pyz) ligands are capable of transmitting significant magnetic exchange effects between iron(II) centres. The thiocyanate compound has a two-dimensional layer structure with sheets consisting of a square array of iron atoms bridged by pyrazine and axially coordinated by —NCS groups; it exhibits a maximum in magnetic susceptibility at ~8 K, indicating a transition to a magnetically ordered state. The cyanate derivative contains bridging bidentate >NCO groups forming linear chains cross-linked by pyrazine ligands; it exhibits a broad susceptibility maximum at ~38 K.

Not all pyrazine-bridged complexes of iron show such strong magnetic concentration, however. Magnetic susceptibility studies on $Fe(pyz)_2X_2$ (X = Cl, Br, I) from 300 to 4.2 K and on $Fe(pyz)Cl_2$ from 300 to 1.9 K gave no conclusive evidence for exchange coupling in these complexes (2, 3). Mössbauer studies provide some evidence for incipient magnetic ordering in $Fe(pyz)_2Cl_2$ below 0.5 K, while no evidence of ordering was observed for $Fe(pyz)Cl_2$ down to 0.33 K (4, 5).

As part of a general search for and study of magnetic exchange effects in pyrazine-bridged iron compounds, we have investigated the complexes formed between pyrazine and some iron(II) sulfonates. Two types of complexes were obtained: mono(pyrazine) derivatives of the type $Fe(pyz)(RSO_3)_2$, where R is CF_3 and $p\text{-}CH_3C_6H_4$, and bis(pyrazine) complexes $Fe(pyz)_2(RSO_3)_2$, where R is CH_3 and CF_3 (the latter being obtained as a methanol solvate).

Since none of the complexes described here was obtained in a form suitable for structure determination by single crystal X-ray diffraction studies we have had to rely on indirect methods including vibrational, electronic and Mössbauer spectroscopy and differential scanning calorimetry. Comparisons with related compounds are also useful and we report here our investigation of two such complexes, $Fe(pyz)_2(ClO_4)_2$ and the pyridine complex, $Fe(py)_2(CF_3SO_3)_2$. A preliminary report of low temperature Mössbauer studies on $Fe(pyz)(CF_3SO_3)_2$ has appeared elsewhere (7).

Experimental section

Materials and syntheses

All chemicals used in this study were of at least reagent grade quality and obtained from commercial sources. Solvents were dried prior to use as follows: methanol was refluxed in the presence of magnesium methoxide; diethyl ether was refluxed over sodium benzophenone ketyl; pyridine was refluxed over barium oxide. After drying, solvents were distilled under a dry nitrogen atmosphere. The iron(II) complexes prepared are air- and moisture-sensitive; thus all manipulations were carried out either using standard vacuum-line techniques, or in a nitrogen atmosphere glove box.

The complexes were prepared either by a solution or a thermolytic route. The choice of temperature for preparative scale thermolysis was found to be quite critical and was determined by heating at gradually increasing temperature and monitoring changes in both the infrared spectrum and microanalytical data.

Can. J. Chem. Downloaded from www.nrcresearchpress.com by 112.217.228.212 on 09/07/12
For personal use only.

Can. J. Chem. Downloaded from www.nrcresearchpress.com by 112.217.228.212 on 09/07/12
For personal use only.

Bis(pyridine)iron(II) trifluoromethanesulfonate, $Fe(py)_2(CF_3SO_3)_2$

Heating of $Fe(pyz)_4(CF_3SO_3)_2$ (7) *in vacuo* at a temperature of approximately 360 K for 22 h resulted in loss of 2 mol of pyridine and production of $Fe(py)_2(CF_3SO_3)_2$. Further heating at this temperature caused no additional loss of pyridine. *Anal.* calcd. for $FeC_{12}H_{10}N_2F_6S_2O_6$: C 28.14, H 1.97, N 5.47; found: C 28.15, H 2.04, N 5.63.

Bis(pyrazine)iron(II) trifluoromethanesulfonate methanol solvate, $Fe(pyz)_2(CF_3SO_3)_2 \cdot CH_3OH$

A solution of pyrazine (0.55 g, 6.9 mmol) in methanol (5 mL) was added to iron(II) trifluoromethanesulfonate (8) (0.741 g, 2.09 mmol) dissolved in methanol (5 mL). A yellow solution resulted and after 24 h, precipitation of a yellow solid was facilitated by the addition of diethyl ether (30 mL). The product was removed by filtration and washed with diethyl ether (yield, 72%). *Anal.* calcd. for $FeC_{11}H_{12}N_4F_6S_2O_7$: C 24.19, H 2.21, N 10.26; found: C 24.12, H 2.34, N 10.27.

Bis(pyrazine)iron(II) methanesulfonate, $Fe(pyz)_2(CF_3SO_3)_2$

Pyrazine (1.28 g, 16.0 mmol) was dissolved in methanol (5 mL) and this solution was added to a solution of iron(II) methanesulfonate (8) (1.09 g, 4.43 mmol) in methanol (20 mL). A yellow precipitate formed immediately. The product was isolated in 83% yield after filtration and washing with methanol and diethyl ether. *Anal.* calcd. for $FeC_{10}H_{14}N_4S_2O_6$: C 29.56, H 3.48, N 13.79, O 23.63; found: C 29.47, H 3.66, N 13.50, O 23.95.

Bis(pyrazine)iron(II) perchlorate, $Fe(pyz)_2(ClO_4)_2$

The preparation of the dihydrate, $Fe(pyz)_2(ClO_4)_2 \cdot 2H_2O$, has been reported recently (9). The method involved the addition of a solution of hydrated iron(II) perchlorate to a solution of the ligand, both reagents being dissolved in the minimum amount of water. In the previous report, it was noted that drying the product over silica gel at reduced pressure failed to produce the anhydrous species. The same procedure was followed here and the dihydrate was isolated; this was subsequently dehydrated by applying more stringent conditions. The dihydrate was heated in an Aberhalden drying pistol at a temperature of approximately 390 K for a period of 46 h at reduced pressure, in the presence of P_4O_{10}. The anhydrous compound was isolated in 72% yield. *Anal.* calcd. for $FeC_8H_8N_4Cl_2O_8$: C 23.16, H 1.94, N 13.50, O 30.85; found: C 23.13, H 1.92, N 13.46, O 31.00.

Mono(pyrazine)iron(II) trifluoromethanesulfonate, $Fe(pyz)(CF_3SO_3)_2$

$Fe(pyz)_2(CF_3SO_3)_2 \cdot CH_3OH$, prepared as described above, was heated *in vacuo* for 15 h at 380 K in the presence of P_4O_{10} in an Aberhalden drying pistol. The infrared spectrum of the product shows significant changes from that of the starting material, and the analytical data are consistent with the formation of the unsolvated mono(pyrazine) complex. Heating for longer periods of time at the same temperature resulted in no further loss of pyrazine. *Anal.* calcd. for $FeC_6H_4N_2F_6S_2O_6$: C 16.60, H 0.93, N 6.45; found: C 16.85, H 0.98, N 6.38.

Mono(pyrazine)iron(II) p-toluenesulfonate bis(methanol) solvate, $Fe(pyz)(p\text{-}CH_3C_6H_4SO_3)_2 \cdot 2CH_3OH$

Iron (II) *p*-toluensulfonate (8) (0.87 g, 2.2 mmol) was dissolved in methanol (10 mL). Pyrazine (0.77 g, 9.6 mmol) dissolved in methanol/diethyl ether (12 mL, 1:5v/v) was then added to this solution. Small orange–yellow crystals formed after 0.5 h, and after 3 days the solid was removed by filtration and the product washed with a small amount of diethyl ether (yield 66%). *Anal.* calcd. for $FeC_{20}H_{26}N_2S_2O_8$: C 44.29, H 4.83, N 5.16; found: C 44.05, H 4.71, N 4.93.

Mono(pyrazine)iron(II)p-toluenesulfonate, $Fe(pyz)(p\text{-}CH_3C_6H_4SO_3)_2$

The unsolvated compound was prepared by heating the solvate, prepared as described above, at approximately 340 K *in vacuo* for 16 h. *Anal.* calcd. for $FeC_{18}H_{18}N_2S_2O_6$: C 45.20, H 3.79, N 5.85, O 20.07; found: C 44.98, H 3.77, N 5.77, O 19.86.

Physical measurements

Electronic and infrared spectra and differential scanning calorimetry data were obtained using equipment and procedures described previously (8). ^{57}Fe Mössbauer spectra were recorded at 78 and 293 K in transmission mode, with a constant acceleration spectrometer of conventional design. For $Fe(pyz)(CF_3SO_3)_2$ spectra were also obtained in the 1.6–4.2 K range. The Doppler velocity scale was calibrated with an iron foil absorber, and isomer shifts are quoted relative to the centroid of the iron spectrum.

Magnetic susceptibility measurements between 80 and 300 K employed the Gouy technique (8); a vibrating sample magnetometer (10) was used for measurements between 1.9 and 120 K. Magnetic susceptibilities were also measured at room temperature with a Faraday magnetic balance (11) at three different values of $H \cdot dH/dx$. No field dependence was observed. Molar magnetic susceptibilities were corrected for the diamagnetism of the metal ion and ligands. Corrections used were: Fe^{2+}, −13; $CF_3SO_3^-$, −46; $CH_3SO_3^-$, −35; $p\text{-}CH_3C_6H_4SO_3^-$, −89; CH_3OH, −34; pyridine, −49; pyrazine, −45 (in units of $10^{-6}cm^3mol^{-1}$).

Analyses for C, H, N, and O were performed by P. Borda of this department.

Results and discussion

Thermal studies

Thermolysis of tetrakis(pyridine) and bis(pyrazine) complexes often occurs by stepwise loss of neutral ligand, allowing convenient preparation of the corresponding bis(pyridine) and mono(pyrazine) derivatives. Previous studies of the thermal stabilities of tetrakis(pyridine) complexes of iron(II) sulfonates by differential scanning calorimetry (DSC) (7) suggested the possibility of a thermolytic route to the corresponding bis(pyridine) complexes. Long and co-workers (12, 13) have also used thermolysis as a preparative technique for obtaining bis(pyridine) derivatives.

We have succeeded in preparing $Fe(py)_2(CF_3SO_3)_2$ and $Fe(pyz)(CF_3SO_3)_2$ by thermolysis of $Fe(py)_4(CF_3SO_3)_2$ and $Fe(pyz)_2(CF_3SO_3)_2 \cdot CH_3OH$, respectively. In the former case the DSC curve showed an endothermic event at 465 K ($\Delta H = 95$ kJ mol^{-1}), with a weight loss corresponding to the removal of two pyridines (7). In the preparative thermolysis reported here, this same change was accomplished by heating at 360 K *in vacuo*. Similarly, for $Fe(pyz)_2(CF_3SO_3)_2 \cdot CH_3OH$ there is a thermal event at 415 K ($\Delta H = 104$ kJ mol^{-1}), the weight loss of 21% corresponding to the removal of the methanol of solvation and 1 mol of pyrazine; the same change was accomplished *in vacuo* at 380 K. The DSC results for $Fe(py)_2(CF_3SO_3)_2$ and $Fe(pyz)(CF_3SO_3)_2$ show thermal events at 557 K and 606 K respectively, due to the removal of the remaining neutral ligands to yield $Fe(CF_3SO_3)_2$. The thermal analysis of $Fe(pyz)_2(CH_3SO_3)_2$ shows two endothermic events at 503 and 583 K due to the successive loss of pyrazine ligands. Although it should be possible to obtain the mono(pyrazine) derivative of this sulfonate by preparative thermolysis, this has not yet been achieved.

The DSC curve for $Fe(pyz)(p\text{-}CH_3C_6H_4SO_3)_2 \cdot 2CH_3OH$ is more complex than that for the unsolvated species. Two thermal events at relatively low temperatures (329 and 367 K) are observed for the solvated species, probably associated with the consecutive loss of the two methanol molecules. The ΔH values, 13 and 33 kJ mol^{-1}, respectively, indicate that one methanol molecule is more strongly held than the other. After removal of solvent molecules from $Fe(pyz)(p\text{-}CH_3C_6H_4SO_3)_2 \cdot 2CH_3OH$, the thermogram is similar to that of $Fe(pyz)(p\text{-}CH_3C_6H_4SO_3)_2$, as expected. One broad endothermic peak occurs at approximately 545 K in both instances, probably associated with the removal of the pyrazine ligand.

Spectroscopic studies

Mössbauer spectra were recorded for all complexes at liquid nitrogen and room temperatures, and the results are given in

TABLE 1. ^{57}Fe Mössbauer parameters[a]

Compound	T (K)	δ (mm s^{-1})	ΔE_Q (mm s^{-1})	Γ_1 (mm s^{-1})	Γ_2 (mm s^{-1})
$Fe(py)_2(CF_3SO_3)_2$	293	1.19	1.65	0.31	0.28
	78	1.22	2.45	0.35	0.34
$Fe(pyz)(CF_3SO_3)_2$	293	1.19	2.79	0.52	0.44
	78	1.27	3.59	0.36	0.35
$Fe(pyz)_2(CF_3SO_3)_2 \cdot CH_3OH$	293	1.16	3.45	0.32	0.32
	78	1.25	3.71	0.40	0.38
$Fe(pyz)_2(CH_3SO_3)_2$	293	1.14	3.08	0.46	0.46
	78	1.23	3.20	0.43	0.43
$Fe(pyz)(p\text{-}CH_3C_6H_4SO_3)_2 \cdot 2CH_3OH$	293	1.18	3.21	0.47	0.39
	78	1.29	3.49	0.44	0.39
$Fe(pyz)(p\text{-}CH_3C_6H_4SO_3)_2$	293	1.22	2.54	0.43	0.40
	78	1.24	2.80	0.56	0.50
$Fe(pyz)_2(ClO_4)_2$	293	1.07	3.24	0.36	0.32
	78	1.16	3.74	0.35	0.33

[a]Estimated precision of parameters is ±0.01 mm s^{-1}.

Table 1. At 78 K and above, all the spectra consist of symmetric quadrupole-split doublets, with isomer shift (IS) and quadrupole splitting (QS) values typical of pseudooctahedral high-spin iron(II) complexes. The three bis(pyrazine) complexes have QS values in excess of 3 mm s^{-1} at both temperatures studied, values which are diagnostic of orbitally non-degenerate ($^5B_{2g}$) ground states. Thus, our results indicate ground states with the d_{xy} orbital lying lowest in energy, corresponding to a tetragonal compression of the octahedron and a positive value of V_{zz}, the principal component of the electric field gradient (EFG). The close similarity between these results and those for the tetrakis(pyridine)iron(II) sulfonates (7), where X-ray crystallography shows axially compressed octahedra of approximately D_{4h} symmetry, suggests a similar tetragonal compression of the FeN_4O_2 chromophores formed by bridging pyz ligands and axially coordinated anions in the bis(pyrazine) derivatives, with V_{zz} presumably directed along the pseudo-tetragonal O—Fe—O axis.

The room temperature IS values for the two bis(pyrazine)iron(II) sulfonate complexes are slightly higher than those of the corresponding tetrakis(pyridine) compounds (7). This suggests a somewhat greater degree of covalency in the pyridine derivatives, consistent with the relative base strengths of pyridine and pyrazine.

Similar Mössbauer spectra are observed for the bis(pyridine) and mono(pyrazine) complexes, although the QS values are somewhat smaller for $Fe(py)_2(CF_3SO_3)_2$ and $Fe(pyz)(p\text{-}CH_3C_6H_4SO_3)_2$ than for the other derivatives reported here. In all cases, however, the QS at 78 K is substantially greater than 2 mm s^{-1}, indicative of a ground state that is orbitally non-degenerate. We assume that in all these complexes V_{zz} is positive, as previously found for $Fe(pyz)Cl_2$ (2) and $Fe(pyz)(NCO)_2$ (1), and confirmed below for $Fe(pyz)(CF_3SO_3)_2$. Thus, the ground state can be described approximately as $^5B_{2g}$ in these complexes also.

The electronic spectra of the complexes are also consistent with high-spin distorted octahedral complexes of iron(II). The complexes exhibit, in the near infrared region, broad absorption bands (Table 2) which may be assigned to unresolved electronic transitions from the $^5B_{2g}$ ground state to the $^5A_{1g}$ and $^5B_{1g}$ levels derived from ^5E_g in octahedral symmetry. The energies of the band maxima of the three bis(pyrazine) derivatives lie in a range (10 800 – 11 600 cm^{-1}) comparable to that reported earlier for the tetrakis(pyridine)sulfonates (7), thus supporting an FeN_4O_2 chromophore for the former group of compounds with bridging pyrazine ligands and monodentate anion coordination.

For the bis(pyridine) complex and the three mono(pyrazine) complexes the position of the absorption maximum occurs at approximately the same frequency (~10 800 cm^{-1}), which is strong evidence to suggest the same chromophore in all instances. A likely structure for these would involve an FeN_2O_4 chromophore with a bidentate bridging pyrazine ligand (or two monodentate pyridine ligands) and bidentate sulfonate anions. The modes of anion coordination proposed here are supported by infrared studies.

Vibrational assignments for the complexes were made on the basis that the absorption bands originate from two constituent parts, namely, the neutral ligands and the anions. Partial infrared data with assignments (8, 14, 15) are given in Table 3. The anion bands tend to be intense and broad, particularly in the S—O (or Cl—O) stretching regions, and to some extent mask the neutral ligand vibrations. The anion bands are considered first.

The spectrum of $Fe(py)_2(CF_3SO_3)_2$ gives clear evidence for reduction in anion symmetry below C_{3v}, i.e., below that of the free ion. A clear indication of this reduction of anion symmetry is the splitting of the asymmetric SO_3 stretching mode ν_4. Importantly, the magnitude of this band splitting is different from that observed in $Fe(py)_4(CF_3SO_3)_2$ (7), suggesting different modes of anion coordination. In $Fe(py)_4(CF_3SO_3)_2$, where the anions are monodentate and *trans*-disposed, the ν_4 splitting is only 85 cm^{-1} (7). For $Fe(py)_2(CF_3SO_3)_2$, the splitting of this band is 111 cm^{-1}. The degree of splitting of the ν_4 band has been used to suggest bidentate bridging anion coordination in $(CH_3)_2Sn(FSO_3)_2$ (16), a situation subsequently confirmed by X-ray crystallography (17). It was noted that the ν_4 splitting was substantially larger in this tin complex than in complexes where the anion is coordinated in a unidentate fashion. The large splitting seen here for the bis(pyridine) derivative suggests a bidentate bridging mode of anion coordination, to give a linear

Can. J. Chem. Downloaded from www.nrcresearchpress.com by 112.217.228.212 on 09/07/12
For personal use only.

Can. J. Chem. Downloaded from www.nrcresearchpress.com by 112.217.228.212 on 09/07/12
For personal use only.

TABLE 2. Electronic spectra and magnetic moments

Compound	Absorption maximum[a] (10^3 cm^{-1})	Magnetic moment (BM) 4.2 K	80 K	300 K
$Fe(py)_2(CF_3SO_3)_2$	10.8	3.61	5.65	5.54
$Fe(pyz)(CF_3SO_3)_2$	10.9	2.94	5.20	5.42
$Fe(pyz)_2(CF_3SO_3)_2 \cdot CH_3OH$	10.8	3.34	5.18	5.31
$Fe(pyz)_2(CH_3SO_3)_2$	11.6 9.5 sh	3.38	4.92	5.08
$Fe(pyz)(p\text{-}CH_3C_6H_4SO_3)_2 \cdot 2CH_3OH$	10.8 8.9 sh	4.88	5.24	5.32
$Fe(pyz)(p\text{-}CH_3C_6H_4SO_3)_2$	10.8 8.9 sh	4.34	5.24	5.32
$Fe(pyz)_2(ClO_4)_2$	11.4	4.31	5.07	5.12

[a]Nujol mull, sh = shoulder.
[b]$\mu_{eff} = 2.828\ (\chi_m T)^{1/2}$ where χ_m is the molar magnetic susceptibility corrected for the diamagnetism of all atoms.

TABLE 3. Infrared spectra, selected vibrations

Compound	Infrared frequencies (cm^{-1})[a] and assignments: Anion vibrations[b] $\nu_4(E)$	$\nu_1(A_1)$	$\nu_4(A_1)$	$\nu_3(A_1),\nu_5(E)$	Neutral ligand vibrations[c]	
$Fe(py)_2(CF_3SO_3)_2$	1316 s 1205 s	1039 s	769 w	635 s 522 m	1610 m	430 m 424 sh
$Fe(pyz)(CF_3SO_3)_2$	1320 s 1205 s	1037 s	773 w	639 s 524 m	806 s	477 m
$Fe(pyz)_2(CF_3SO_3)_2 \cdot CH_3OH$	1331, 1325 s 1236 s	1033 s	756 w	639 s 529 w 520 m	836 m 827 m 815 w	480 m 472 m
$Fe(pyz)_2(CH_3SO_3)_2$	1264 s 1160 s	1038 s	783 s	565 s 558 sh 548 m 519 s	848 m 826 m	478 m 468 m
$Fe(pyz)(p\text{-}CH_3C_6H_4SO_3)_2 \cdot 2CH_3OH$	1248 s 1158 s	1037 s	686 s	573 s 557 m	827 m 808 s	476 m
$Fe(pyz)(p\text{-}CH_3C_6H_4SO_3)_2$	1257 s 1141 s	1045 s	682 s	584 m 555 s	821 m 812 s	473 m
$Fe(pyz)_2(ClO_4)_2$	1145 s	1026 s	918 s	637 m 626 s 617 s	825 sh 820 m	475 m 466 m

[a]s = strong, m = medium, w = weak, sh = shoulder.
[b]Sulfonate assignments (CSO_3 part, C_{3v} symmetry) from ref. 8; perchlorate assignment (C_{3v} symmetry) from ref. 19.
[c]Pyridine bands correspond to strong bands at 1580 and 405 cm^{-1} in the free ligand. Pyrazine bands correspond to a strong band at 804 cm^{-1} and a medium-intensity band at 417 cm^{-1} in the free ligand.

chain or two-dimensional sheet structure with trans pyridine ligands. The infrared data clearly eliminate the possibility that the product of the thermolysis of $Fe(py)_4(CF_3SO_3)_2$ is an equimolar mixture of this compound and $Fe(CF_3SO_3)_2$. In particular, infrared spectroscopy would detect the unsolvated sulfonate compound through the presence on an intense band at 1239 cm^{-1} (8), and this is not observed in the spectrum of $Fe(py)_2(CF_3SO_3)_2$.

The infrared spectra of the other triflate complexes are also informative. The spectrum of $Fe(pyz)(CF_3SO_3)_2$ is virtually identical (in regard to anion vibrations) to that of $Fe(py)_2(CF_3SO_3)_2$, consistent again with bidentate, likely bridging, triflate anions. In contrast, the spectrum of $Fe(pyz)_2(CF_3SO_3)_2 \cdot CH_3OH$ is almost identical to that of $Fe(py)_4(CF_3SO_3)_2$, where monodentate anion coordination is known to occur (7). In this bis(pyrazine) complex the six-fold coordination about iron is likely filled by two bridging pyz ligands and two monodentate anions, with the methanol present as solvent of crystallization.

Can. J. Chem. Downloaded from www.nrcresearchpress.com by 112.217.228.212 on 09/07/12
For personal use only.

The methanesulfonate anion spectra are virtually identical for $Fe(py)_4(CH_3SO_3)_2$ and $Fe(pyz)_2(CH_3SO_3)_2$ and we conclude the presence of monodentate anions in both, proven by X-ray studies (7) in the case of the former. The spectrum of $Fe(pyz)(p\text{-}CH_3C_6H_4SO_3)_2$ is, on the other hand, different from that of the pyridine complex $Fe(py)_4(p\text{-}CH_3C_6H_4SO_3)_2$. In particular, the splitting of ν_4 is greater (116 cm^{-1} vs. 90 cm^{-1} for the pyridine complex), supporting the assignment of a bidentate bridging mode of coordination in this complex. The spectrum of the bis(methanol) solvate of this complex differs from that of its ansolvated counterpart principally in regard to the ν_4 region. The splitting here is comparable to that of the pyridine analogue. This may be a consequence of the effects of H-bonding between methanol molecules and the anions; however, in this case we cannot rule out the possibility that the methanol molecules are, in fact, coordinated to iron with monodentate anions and bridging pyrazine molecules completing the coordination sphere.

Turning now to $Fe(pyz)_2(ClO_4)_2$, it is relevant to note that for the free perchlorate ion (point group T_d) there are four normal modes, of which only ν_3 and ν_4, the asymmetric stretching and bending modes, respectively, are infrared active. In ionic perchlorates these infrared active bands generally occur at approximately 1110 and 630 cm^{-1}, respectively (18), the former appearing as a very broad strong band which is occasionally split. Upon coordination through a single oxygen atom, the symmetry is reduced at least to C_{3v}; a splitting of the two triply degenerate normal modes results, the two symmetric modes become infrared active, and six bands may appear in the infrared spectrum. The infrared spectrum of $Fe(pyz)_2(ClO_4)_2$ shows splitting of both ν_3 and ν_4 (in T_d symmetry) and a strong absorption at 918 cm^{-1}, indicating a lowering of anion symmetry. If we assume C_{3v} symmetry for the anion in $Fe(pyz)_2(ClO_4)_2$, the assignments given in Table 3 are obtained. These assignments are very similar to those made for some $M(py)_4(ClO_4)_2$ complexes where unidentate anion coordination has been proposed (19), and indicate a similar coordination mode in $Fe(pyz)_2(ClO_4)_2$.

Selected neutral ligand vibrations are given in Table 3 for each complex. The pyridine bands listed for $Fe(py)_2(CF_3SO_3)_2$ are shifted to higher frequencies from those of the free ligand as expected for coordinated pyridine (7). Free pyrazine exhibits two bands of medium to strong intensity below 900 cm^{-1}, at 804 and 417 cm^{-1}. It was noted previously (2) that the 417 cm^{-1} band in particular shifts to higher frequencies (~470 cm^{-1}) upon coordination. In the complexes studied here both of these bands are shifted and, in addition, some band splitting is observed particularly in the case of the bis(pyrazine) derivatives, where both bands are split by 10 to 20 cm^{-1}. Such band splitting is not uncommon in pyrazine complexes and it has been suggested that it may arise from interactions between adjacent pyrazine rings or from different orientations of pyrazine rings giving rise to slightly different environments (2). It seems doubtful the splitting arises from significantly different structural environments for pyrazine rings as occurs in, for example, $Cu(pyz)_2(CH_3SO_3)_2$ (20). In this complex bridging pyrazine groups are of two types, one occupying equatorial positions and the other axial positions in the copper coordination sphere. This gives rise to band splittings of 33 and 54 cm^{-1} for the ~800 and ~470 cm^{-1} bands, respectively. In principle, it should be possible to prove the absence of unidentate pyrazine in these complexes since such ligands would give rise to bands at approximately 1230, 920, and 750 cm^{-1} (1, 2, 21, 22). Unfortunately, these regions are largely obscured by rather broad and intense anion absorptions.

In summary, the spectroscopic studies have shown that all the compounds under consideration here are pseudo-octahedral complexes of high-spin iron(II). The bis(pyrazine) complexes contain bridging pyrazine ligands and unidentate anions, with structures very probably similar to that of $Cu(pyz)_2(CH_3SO_3)_2$ (20) in which metal ions are bridged in a square array by neutral ligands and anions occupy trans-axial positions. The sulfonate anions in the bis(pyridine) and the three mono(pyrazine) complexes are coordinated in a bidentate fashion yielding chromophores of the type FeN_2O_4. Although it is possible the anions are coordinated in a chelating fashion, this is considered unlikely given the strain that accompanies four membered chelate rings. This point has been made previously in a review article on coordinated fluorosulfate and trifluoromethanesulfonate (23). It seems more likely that the anions are bridging to form either linear chains or sheet-like structures (**2** and **3** in ref. 1). For the mono(pyrazine) complexes the chains or sheets formed by the bridging anions will be cross-linked by pyrazine ligands. These chains or sheets will be effectively isolated in $Fe(py)_2(CF_3SO_3)_2$.

Magnetic measurements

Magnetic susceptibility and magnetic moment data as functions of temperature (4.2–300 K) are given in Table 4.[1] Magnetic moment data at three selected temperatures are given in Table 2. As we are interested in magnetic exchange effects, it will be useful in discussing these data to refer to the magnetic properties of the $Fe(py)_4(RSO_3)_2$ complexes (7). X-ray crystallography has shown that these compounds are monomeric, there is no evidence for magnetic concentration, and the temperature dependence of the magnetic moment arises solely from single-ion effects. Thus these complexes can serve as a benchmark from which magnetic exchange effects in the present sulfonate derivatives can be measured.

The magnetic properties of the bis(pyrazine) complexes $Fe(pyz)_2(CF_3SO_3)_2 \cdot CH_3OH$ and $Fe(pyz)_2(CH_3SO_3)_2$ are significantly different from those of the $Fe(py)_4(RSO_3)_2$ compounds. The differences are not significant at room temperature, where the magnetic moments for all these compounds are within the range 5.1–5.5 μ_B, typical of high-spin iron(II) derivatives. The bis(pyrazine) complexes, however, exhibit much stronger temperature dependencies in their moment values than do the tetrakis(pyridine) complexes, and at 4.2 K the magnetic moments for the two groups of compounds diverge by about 1.3 μ_B. A comparison of the temperature dependence of magnetic moment for $Fe(py)_4(CH_3SO_3)_2$ and $Fe(pyz)_2(CH_3SO_3)_2$ is shown in Fig. 1. A similar divergence exists for the tetrakis(pyridine) and bis(pyrazine) triflate derivatives. Unlike $Cu(pyz)_2(CH_3SO_3)_2$, which shows a maximum in its magnetic susceptibility vs. temperature plot at 6.9 K (20), the bis(pyrazine)iron(II) species do not exhibit susceptibility maxima down to 4.2 K. There is thus no conclusive evidence of this type for antiferromagnetic exchange interactions in these iron complexes.

It is often possible to analyze the temperature dependence of the magnetic moment as a function of distortion from O_h symmetry, spin–orbit coupling, and electron delocalization (24, 25). For the tetrakis(pyridine)iron(II) sulfonates this approach gave reasonable fits to the experimental data above

[1]Table 4 may be purchased from the Depository of Unpublished Data, CISTI, National Research Council of Canada, Ottawa, Ont., Canada K1A 0S2.

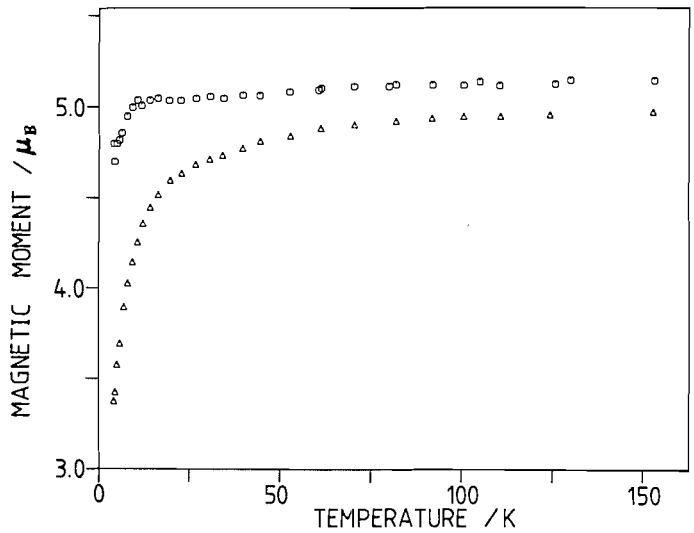

FIG. 1. Magnetic moment versus temperature for $Fe(py)_4(CH_3SO_3)_2$ (□) and $Fe(pyz)_2(CH_3SO_3)_2$ (△).

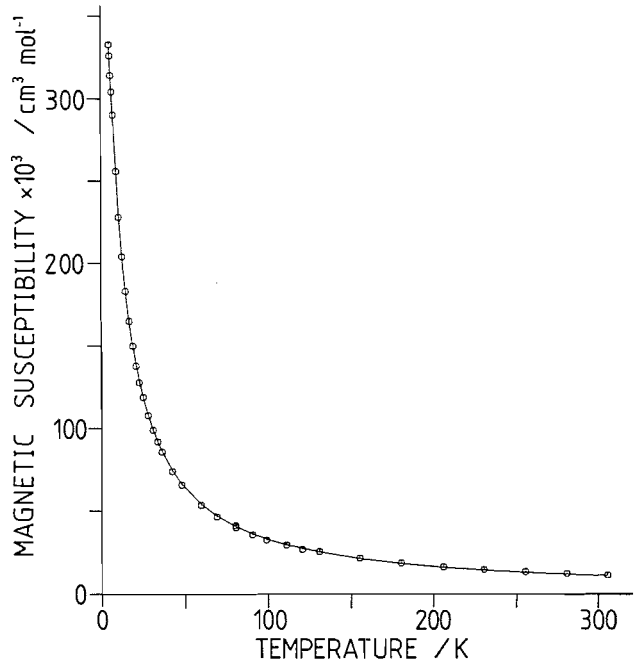

FIG. 2. Magnetic susceptibility versus temperature for $Fe(pyz)_2(CH_3SO_3)_2$. Two-dimensional model; solid line generated with $J = -0.18$ cm^{-1} and $g = 2.07$.

about 20 K, although there was disagreement at low temperatures between observed moments and those calculated from the simple crystal field model (7). For the bis(pyrazine)iron(II) sulfonates on the other hand, such a model is entirely unsatisfactory and quite incapable of reproducing the observed magnetic moment behaviour. The experimental values are always substantially below any values which the model generates. We therefore conclude that the strong temperature dependence of the magnetic moments for the bis(pyrazine) complexes arises either from a large zero-field splitting of the spin quintet ground state or from weak antiferromagnetism.

To see if zero-field splitting effects could account for the magnetic properties of these two complexes, we have analyzed the data using the magnetic susceptibility equation for zero-field splitting of the $S = 2$ ground multiplet (26). By least-squares fitting of the temperature dependence of the molar magnetic susceptibilities, we have obtained the zero-field splitting parameters D and isotropic g values given in Table 5. There is insufficient information in the powder susceptibility data to determine the sign of D; we have assumed $D > 0$, so that the $M_s = 0$ state lies lowest. To reproduce the magnetic susceptibility data for the bis(pyrazine) complexes it is necessary to employ D values that are approximately three times larger than those used for the analogous tetrakis(pyridine) complexes. (The standard deviations of the fits are about three times larger for the bis(pyrazine) complexes as well.) As both groups of compounds contain FeN_4O_2 chromophores and would be expected to have similar single-ion effects, it would seem very difficult to rationalize the extremely large D values suggested by this treatment for the bis(pyrazine) complexes, and we consider them unrealistic.

In view of the proposed two-dimensional structure of the bis(pyrazine) complexes, we have analyzed the magnetic susceptibility data using Lines' high-temperature series expansion for a two-dimensional square-planar $S = 2$ system in the (isotropic) Heisenberg limit (27). Excellent agreement between calculated and observed data was obtained with the parameter values given in Table 5. The agreement between experiment and theory for $Fe(pyz)_2(CH_3SO_3)_2$ is illustrated in Fig. 2. The small negative values of the exchange coupling constant J indicate that any exchange interactions present are of a weak antiferromagnetic nature. This is consistent with our previous results for $Fe(pyz)_2(NCS)_2$ and $Cu(pyz)_2(CH_3SO_3)_2$, where antiferromagnetic phase transitions were observed. The excellent fits obtained here using the two-dimensional exchange model provides strong support for the conclusion that weak exchange effects are present in these complexes, and that it is the bridging pyrazine ligands that provide the pathway for antiferromagnetic coupling of the Fe centres.

For $Fe(pyz)_2(ClO_4)_2$ a weaker temperature dependence of the magnetic moment is found, the value at 4.2 K being 4.31 μ_B, compared to about 3.36 μ_B for the bis(pyrazine) sulfonate derivatives. Although we have not analyzed the suspectibility data for $Fe(pyz)_2(ClO_4)_2$ in terms of Lines' model, it seems clear that any exchange effects in this complex are even weaker than in the sulfonates. Spectroscopic evidence suggests a structure for the perchlorate that is similar to that of the copper analogue (28), which shows a maximum in the magnetic susceptibility at 12.1 K (29), and we might have expected stronger magnetic exchange interactions in $Fe(pyz)_2(ClO_4)_2$.

Of the mono(pyrazine) and bis(pyridine) complexes studied here, $Fe(pyz)(CF_3SO_3)_2$ exhibits the most interesting magnetic properties. The room temperature magnetic moment is 5.4 μ_B, but decreases to 1.6 μ_B at 2 K, and there is a maximum in the magnetic susceptibility vs. temperature curve at approximately 4.4 K. This is a clear indication of antiferromagnetic exchange interactions; however, these interactions are considerably weaker in the triflate than in $Fe(pyz)(NCO)_2$, where the susceptibility maximum occurs at approximately 38 K (1).

The presence of a complex bridging network involving both the pyrazine ligands and triflate anions would seem to complicate the analysis of the susceptibility data for $Fe(pyz)(CF_3SO_3)_2$, as it is likely the exchange mechanisms through the two types of groups are different. At one extreme, if a single exchange mechanism is dominant, the magnetic susceptibility may be best represented by a one-dimensional linear chain model. On the other hand, if exchange proceeds nearly equally through both

Can. J. Chem. Downloaded from www.nrcresearchpress.com by 112.217.228.212 on 09/07/12
For personal use only.

TABLE 5 Parameters from fits of magnetic data

Compound	Zero-field splitting parameters			Two-dimensional exchange parameters		
	D (cm^{-1})	g	F^a	$-J$ (cm^{-1})	g	F
$Fe(pyz)_2(CH_3SO_3)_2$	13.5	2.03	0.0354	0.18	2.07	0.0143
$Fe(pyz)_2(CF_3SO_3)_2 \cdot CH_3OH$	14.5	2.11	0.0353	0.20	2.16	0.0122

[a]The fitting function F is as defined in ref. 1.

Can. J. Chem. Downloaded from www.nrcresearchpress.com by 112.217.228.212 on 09/07/12
For personal use only.

bridging ligands, a two-dimensional Heisenberg model is more appropriate. In the case of $Fe(pyz)(NCO)_2$, we found that on the low-temperature side of the susceptibility maximum the experimental data fell between the curves predicted by these two treatments, consistent with the anisotropic (Ising-like) two-dimensional characteristics of the complex (1).

For $Fe(pyz)(CF_3SO_3)_2$ we have analyzed the susceptibility data in terms of both a linear chain model and a two-dimensional model for $S = 2$ in the Heisenberg limit. Two approximation methods have been developed for an antiferromagnetic Heisenberg chain with $S = 2$. Weng (30) developed an interpolation scheme, and we have employed the coefficients given by Hiller *et al.* (31) to reproduce Weng's numerical results. The other approach is that of Wagner and Friedberg (32) who have scaled the exact results of Fisher (33) to the series expansion of Rushbrooke and Wood (34) to develope an equation for the temperature dependence of the susceptibility. Both these models produce similar curves and neither gives a satisfactory fit to the experimental data in the region of the maximum. Results obtained from the Weng model are shown in Fig. 3*a*.

On the other hand, agreement between experimental and calculated magnetic susceptibility data from Lines' square-planar Heisenberg model is excellent for $Fe(pyz)(CF_3SO_3)_2$ (Fig. 3*b*), with $J = -0.26\ cm^{-1}$ and $g = 2.20$. The success of the two-dimensional Heisenberg model in this case is interesting. If the structure consists of a linear chain in which the Fe centres are bridged by anions with the chains being cross-linked through pyrazine (which is clearly the case for $Fe(pyz)(NCO)_2$), then the present results suggest that pyrazine and triflate groups are essentially equal in their ability to propagate superexchange effects. On the other hand, if $Fe(pyz)(CF_3SO_3)_2$ adopts a sheet-like structure with bridging triflate anions in the equatorial plane and axial pyrazine groups bridging the sheets, our results may imply that exchange through the anions predominates, with the pyrazine ligands assisting to bring about long range three-dimensional ordering. In the absence of an X-ray structural determination, the susceptibility data are not able to distinguish between these possibilities.

The magnetic moment data for $Fe(py)_2(CF_3SO_3)_2$, $Fe(pyz)(p\text{-}CH_3C_6H_4SO_3)_2$, and $Fe(pyz)(p\text{-}CH_3C_6H_4SO_3)_2 \cdot 2CH_3OH$ all decrease with decreasing temperature, but none of these complexes shows a maximum in the magnetic susceptibility, so there is no conclusive evidence for magnetic interactions. It is clear that if such interactions are indeed present, they are considerably weaker in these derivatives than in $Fe(pyz)(CF_3SO_3)_2$.

Spectroscopic evidence indicates a close structural similarity between $Fe(pyz)(p\text{-}CH_3C_6H_4SO_3)_2$ and $Fe(pyz)(CF_3SO_3)_2$, i.e., bridging pyrazine and bridging anions. The magnetic properties of the two materials, however, are quite distinct, the *p*-tosylate derivative exhibiting a much weaker temperature dependence

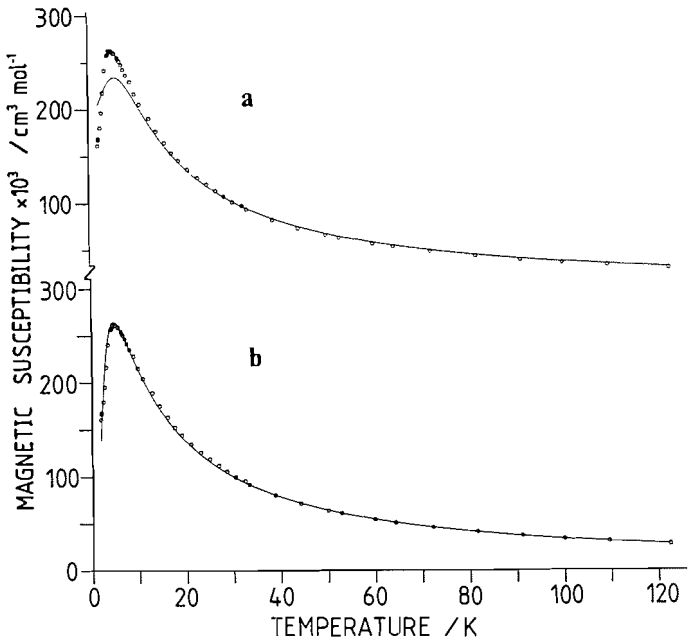

FIG. 3. Magnetic susceptibility versus temperature for $Fe(pyz)(CF_3SO_3)_2$. (*a*) Weng linear chain model; solid line generated with $J = -0.76\ cm^{-1}$, $g = 2.25$. (*b*) Two-dimensional model; solid line generated with $J = -0.26\ cm^{-1}$ and $g = 2.20$.

of the magnetic moment. As there is no X-ray structural evidence for the complexes it is difficult to rationalize these differences, but a possible explanation may lie in the more weakly basic nature of the triflate relative to the *p*-tosylate anion. This could result in a stronger iron–pyrazine interaction in the triflate derivative and an enhanced exchange effect via pyrazine.

The four iron(II) triflate derivatives containing pyridine or pyrazine that we have now prepared and studied provide an interesting comparison (Table 2 and ref. 7). For each compound the magnetic moment at 300 K lies in the narrow range 5.3–5.5 μ_B, whereas at 4.2 K a significant spread in moment values occurs. At 4.2 K the magnetic moment values are in the order: $Fe(py)_4(CF_3SO_3)_2 > Fe(py)_2(CF_3SO_3)_2 > Fe(pyz)_2(CF_3SO_3)_2 \cdot CH_3OH > Fe(pyz)(CF_3SO_3)_2$. This order indicates an increase in antiferromagnetic interactions from the tetrakis(pyridine) complex to the mono(pyrazine) complex, which appears to be in agreement with the proposed nature of the bridging system in each complex: the absence of a bridging network in $Fe(py)_4(CF_3SO_3)_2$, bridging triflate only in $Fe(py)_2(CF_3SO_3)_2$, bridging pyrazine in $Fe(pyz)_2(CF_3SO_3)_2 \cdot CH_3OH$, and both bridging pyrazine and bridging triflate in $Fe(pyz)(CF_3SO_3)_2$. No magnetic interactions are observed in the complex which lacks bridging ligands and

Can. J. Chem. Downloaded from www.nrcresearchpress.com by 112.217.228.212 on 09/07/12
For personal use only.

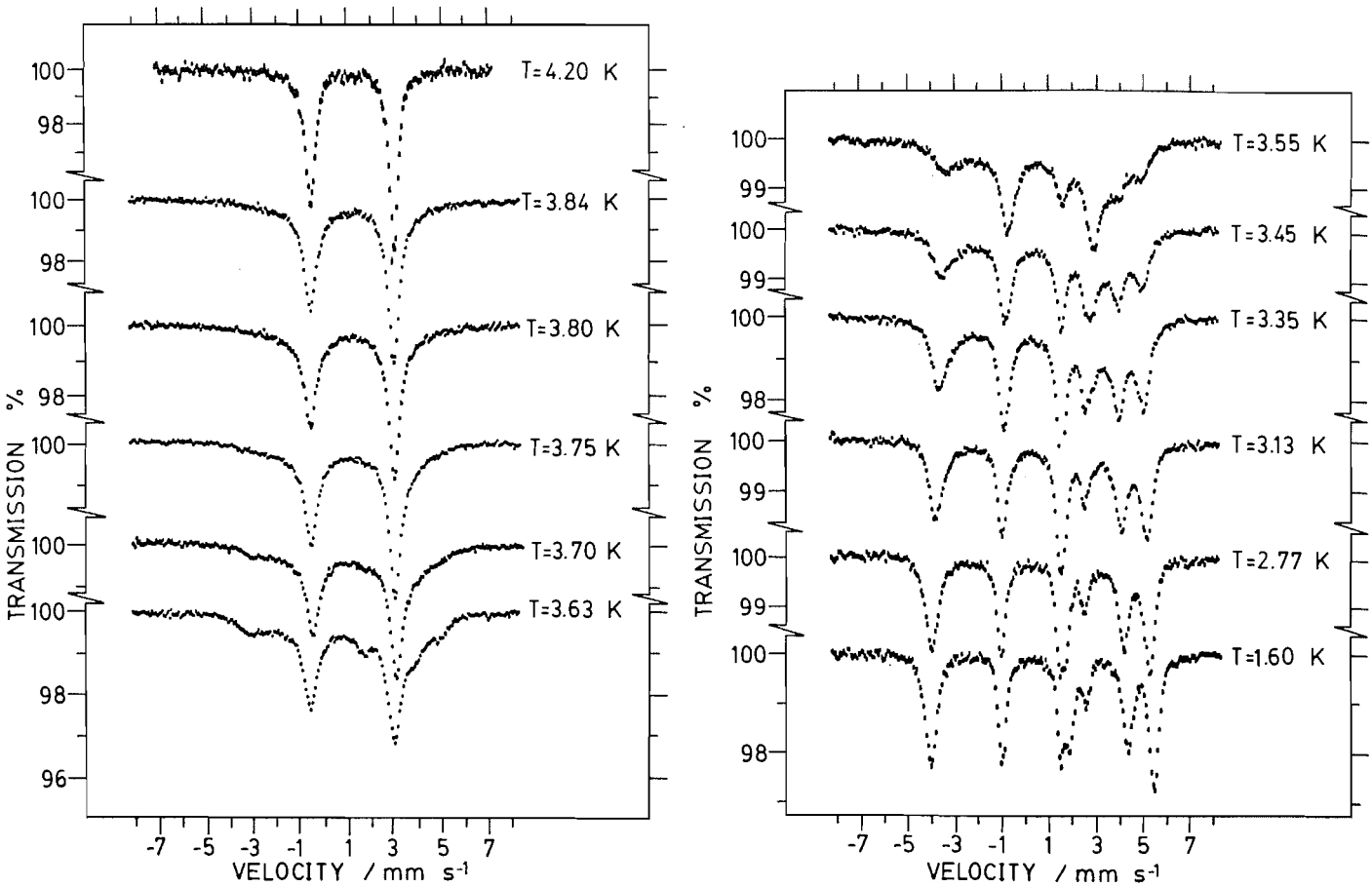

FIG. 4. Low-temperature Mössbauer spectra of $Fe(pyz)(CF_3SO_3)_2$.

the magnetic interaction increases with increasing number of bridging ligands. Clearly the combination of bridging triflate and bridging pyrazine groups provides the most facile magnetic exchange pathway in this series of complexes.

In view of the 4.4 K susceptibility maximum observed for $Fe(pyz)(CF_3SO_3)_2$, and the consequent possibility of observing magnetic ordering in the Mössbauer spectra below this temperature, additional spectra were measured for this complex between 4.2 and 1.6 K. These spectra are shown in Fig. 4.

The spectrum at 4.2 K shows considerable asymmetry, mainly in intensity, which may be attributable to a texture effect, to relaxation effects occurring within the Mössbauer frequency window ($\sim 10^7$ s^{-1}), or to some combination of these. As the lines are also substantially broadened, and as no significant asymmetry was observed at 78 K, we favour an explanation in terms of relaxation effects. Between 3.84 and 3.70 K further line broadening is seen, as well as the development of a magnetic hyperfine pattern. Below 3.70 K the spectra clearly show the combined effects of magnetic and quadrupolar interactions, but with some line broadening persisting down to 1.60 K.

The nature of these low-temperature spectra makes it impossible to estimate the Neel temperature precisely, nor can the spectra be simulated accurately by a static molecular field model (35). In principle, the line broadening seen between 4.2 and 1.6 K could be due either to soliton dynamics (36, 37) or to slow single-ion spin relaxation. We plan to carry out detailed analysis of these spectra employing methods discussed by de Jongh *et al.* (38), in an attempt to distinguish between these two possibilities.

Preliminary simulations of the spectrum obtained at 1.60 K using a static model (35) indicate that the line positions can be reproduced quite well, although there are discrepancies in intensities due presumably to dynamic effects. Although the parameter values obtained by this process must clearly be considered tentative, they are still of some interest. Specifically, they indicate that V_{zz} is positive, that the EFG is effectively axially symmetric, and that the internal hyperfine field at the iron nucleus is approximately 25 T. Of the polar angles θ and ϕ that specify the orientation of the hyperfine field with respect to the EFG principal axis system, the indications are that θ is approximately 77° and ϕ is indeterminate because of the axial symmetry.

These results are very different from those obtained for $Fe(pyz)(NCO)_2$ (1), where both angles were found to be approximately 90° (i.e., the hyperfine field H_{eff} is pinned along the y-axis of the EFG), and the asymmetry parameter was 0.47. In this complex, we have argued (1) that the most reasonable choice of EFG axes is to take the *y*-axis along the linear chain direction in **2** of ref. 1, the *x*-axis along the pyz—Fe—pyz direction, and the *z*-axis normal to the sheets of cross-linked linear chains. If a similar cross-linked linear chain structure obtains for $Fe(pyz)(CF_3SO_3)_2$, then the axial symmetry would require that the EFG *z*-axis now lies along the pyz—Fe—pyz direction. On the other hand, it is possible that $Fe(pyz)(NCO)_2$ and $Fe(pyz)(CF_3SO_3)_2$ are not isostructural, and that the latter adopts the cross-linked sheet structure **3** of ref. 1, where it would be entirely natural to take V_{zz} along the N—Fe—N direction. In either case the positive V_{zz} would require some-

what shorter Fe—N distances than Fe—O distances. In view of the X-ray crystallographic evidence for the tetrakis(pyridine)-iron(II) sulfonates, where the Fe—N bonds are at least 0.1 Å *longer* than the Fe—O bonds, such a structure would be unusual. However, a final resolution of these questions must await a satisfactory treatment of the dynamic effects.

Acknowledgements

We thank the Natural Sciences and Engineering Research Council of Canada for financial support. J.S.H. also thanks the U.B.C. Graduate Scholarship Committee for scholarship awards.

1. J. S. HAYNES, A. KOSTIKAS, J. R. SAMS, A. SIMOPOULOS, and R. C. THOMPSON. Inorg. Chem. **26**, 2630 (1987).
2. J. S. HAYNES, J. R. SAMS, and R. C. THOMPSON. Inorg. Chem. **25**, 3740 (1986).
3. K. RACHLEWEIZ, J. PIETRZYK, and K. DRABENT. Polyhedron, **4**, 1777 (1985).
4. W. M. REIFF, J. H. ZHANG, J. TAKACS, and L. TAKACS. Proc. Int. Conf. Appl. Mössbauer Eff., paper 2.04 (1985).
5. W. M. REIFF. Personal communication.
6. J. S. HAYNES, A. KOSTIKAS, J. R. SAMS, A. SIMOPOULOS, and R. C. THOMPSON. Hyp. Int. **28**, 815 (1986).
7. J. S. HAYNES, S. J. RETTIG, J. R. SAMS, R. C. THOMPSON, and J. TROTTER. Can J. Chem. **64**, 429 (1986).
8. J. S. HAYNES, J. R. SAMS, and R. C. THOMPSON. Can. J. Chem. **59**, 669 (1981).
9. M. D. CHILD, G. A. FOULDS, G. C. PERCY, and D. A. THORNTON. J. Mol. Struct. **75**, 191 (1981).
10. J. S. HAYNES, K. W. OLIVER, S. J. RETTIG, R. C. THOMPSON, and J. TROTTER. CAN. J. CHEM. **62**, 891 (1984).
11. F. G. HERRING, B. LANDA, R. C. THOMPSON, and C. F. SCHWERDTFEGER. J. Chem. Soc. A, 528 (1971).
12. B. F. LITTLE and G. J. LONG. Inorg. Chem. **17**, 3401 (1978).
13. G. J. LONG, D. L. WHITNEY, and J. E. KENNEDY. Inorg. Chem. **10**, 1406 (1971).
14. C. S. ALLEYNE and R. C. THOMPSON. Can. J. Chem. **52**, 18 (1974).
15. C. H. KLINE and J. TURKEVICH. J. Chem. Phys. **12**, 300 (1944).
16. P. A. YEATS, J. R. SAMS, and F. AUBKE. J. Chem. Soc. Chem. Commun. 791 (1969).
17. P. A. ALLEN, J. A. LERBSCHER, and J. TROTTER. J. Chem. Soc. A, 2507 (1971).
18. B. J. HATHAWAY and A. E. UNDERHILL. J. Chem. Soc. 3091 (1961).
19. (*a*) C. S. ALLEYNE, M.Sc. Thesis, University of British Columbia. 1973; (*b*) D. H. BROWN, R. H. NUTTALL, J. MCAVOY, and D. W. A. SHARP. J. Chem. Soc. A, 892 (1966).
20. J. S. HAYNES, S. J. RETTIG, J. R. SAMS, R. C. THOMPSON, and J. TROTTER. Can J. Chem. **65**, 420 (1987).
21. M. GOLDSTEIN, F. B. TAYLOR, and W. D. UNSWORTH. J. Chem. Soc. Dalton Trans. 418 (1972).
22. M. GOLDSTEIN and W. D. UNSWORTH. Spectrochim. Acta Part A, **27A**, 1055 (1971).
23. G. A. LAWRENCE. Chem. Rev. **86**, 17 (1986).
24. B. N. FIGGIS, J. LEWIS, F. E. MABBS, and G. A. WEBB. J. Chem. Soc. A, 442 (1967).
25. E. KONIG, A. S. CHAKRAVARTY, and K. MADEJA. Theor. Chim. Acta, **9**, 171 (1967).
26. C. L. KLEIN, C. J. O'CONNOR, R. J. MAJESTE, and L. M. TREFONAS. J. Chem. Soc. Dalton Trans. 2419 (1982).
27. M. E. LINES. J. Phys. Chem. Solids, **31**, 101 (1970).
28. J. DARRIET, M. S. HADDAD, E. N. DUESLER, and D. N. HENDRICKSON. Inorg. Chem. **18**, 2679 (1979).
29. M. S. HADDAD, D. N. HENDRICKSON, J. P. CANADY, R. S. DRAGO, and D. S. BIEKYSA. J. Am. Chem. Soc. **101**, 898 (1979).
30. C. H. WENG. Ph.D. Thesis, Carnegie-Mellon University. 1968.
31. W. HILLER, J. STRAHLE, A. DATZ, M. HANACK, W. E. HATFIELD, and P. GUTLICH. J. Am. Chem. Soc. **106**, 329 (1984).
32. G. R. WAGNER and S. A. FRIEDBERG. Phys. Lett. **9**, 11 (1964).
33. M. E. FISHER. Am. J. Phys. **32**, 343 (1964).
34. G. S. RUSHBROOKE and P. S. WOOD. Mol. Phys. **1**, 257 (1958).
35. W. KUNDIG. Nucl. Instrum. Methods, **48**, 219 (1967).
36. H. J. M. DE GROOT, L. J. DE JONGH, R. C. THIEL, and J. REEDIJK. Phys. Rev. B**30**, 4041 (1984).
37. H. H. A. SMIT, H. J. M. DE GROOT, R. C. THIEL, L. J. DE JONGH, C. E. JOHNSON, and M. F. THOMAS. Solid State Commun. **53**, 573 (1985).
38. L. J. DE JONGH, H. J. M. DE GROOT, M. ELMASSALAMI, H. H. A. SMIT, and R. C. THIEL. Proc. Int. Conf. Appl. Mössbauer Eff. paper INV-9. 1985.

Can. J. Chem. Downloaded from www.nrcresearchpress.com by 112.217.228.212 on 09/07/12
For personal use only.

The infrared spectrum of aminodifluoroborane, NH_2BF_2: Partial assignment of the fundamentals and analysis of the 2_0^1 band near 1608 cm^{-1}

H. M. JEMSON,[1] W. LEWIS-BEVAN,[2] AND M. C. L. GERRY[3]

Department of Chemistry, The University of British Columbia, 2036 Main Mall, Vancouver, B.C., Canada V6T 1Y6

Received January 24, 1988

This paper is dedicated to Professor Charles A. McDowell on the occasion of his 70th birthday

H. M. JEMSON, W. LEWIS-BEVAN, and M. C. L. GERRY. Can. J. Chem. **66**, 2088 (1988).

The infrared spectrum of gas phase aminodifluoroborane, NH_2BF_2, has been observed for the first time. A partial assignment to the fundamental vibrations has been made. The 2_0^1 band has been recorded at high resolution, and the rotational and centrifugal distortion constants of $NH_2{}^{11}BF_2$ have been obtained in both the ground and 2^1 levels. A small rotational perturbation in the 2^1 level has been attributed to a perpendicular Coriolis interaction. Using a newly written least-squares fitting program, spectroscopic constants of the unseen level have been evaluated, including its band origin and the Coriolis coupling coefficient. Possible identities of the unseen level are suggested.

H. M. JEMSON, W. LEWIS-BEVAN et M. C. L. GERRY. Can. J. Chem. **66**, 2088 (1988).

On a déterminé le spectre infrarouge de l'aminodifluoroborane, NH_2BF_2, en phase gazeuse pour la première fois. On a effectué une attribution partielle des vibrations fondamentales. On a enregistré la bande 2_0^1 à haute résolution et on a obtenu les constantes de distorsion de rotation ainsi que de centrifugation du $NH_2{}^{11}BF_2$ tant à l'état fondamental qu'au niveau 2^1. On a attribué une faible perturbation au niveau 2^1 à une interaction de Coriolis perpendiculaire. Utilisant un nouveau programme développé récemment pour ajuster les moindres carrés,on a évalué les constantes spectroscopiques du niveau qui n'est pas visible, y compris sa bande d'origine ainsi que son coefficient de couplage de Coriolis. On suggère des identités possibles pour le niveau qui n'est pas visible.

[Traduit par la revue]

Introduction

The aminoboranes, of general formula $R_2N—BR'_2$, can often be prepared by the pyrolysis of borane–amine complexes:

$$R_3NBR'_3 \longrightarrow R_2N—BR'_2 + RR'$$

For example, the parent compound, aminoborane, H_2NBH_2, the inorganic analog of ethylene, is prepared by pyrolysis of NH_3BH_3 (1). Similarly, gaseous aminodifluoroborane, NH_2BF_2, the inorganic analog of $CH_2 = CF_2$, may be prepared by heating ammonia boron trifluoride, NH_3BF_3. Early studies (2) of this reaction above 125°C suggested that it takes place according to:

$$4NH_3BH_3 \longrightarrow 3NH_4^+ BF_4^- + BN$$

However, it was shown later that no BN is present in the decomposition products, which do, however, contain several HNBF species (3). The mass spectrum of the volatile decomposition products of the pyrolysis of NH_3BF_3 at 185°C was monitored carefully by Rothgery *et al.* (4), and showed that primarily NH_2BF_2 is formed, along with some trifluoroborazine, $(HNBF)_3$. The vapour can also be condensed to form polymeric aminodifluoroborane (4, 5).

Lovas and Johnson (6) have studied the microwave spectrum of NH_2BF_2, which was produced in this case in a simple gas phase reaction of a mixture of NH_3 and BF_3, and later by the revaporization of the condensation products of this reaction by heating to 140°C. The measurement of the rotational constants of six isotopic species confirmed the ethylene-like planar structure of the molecule. The work also produced ground state centrifugal distortaion constants and a value for the dipole moment.

No infrared data are available in the literature for NH_2BF_2. The aim of this study was therefore to measure the infrared spectrum of this molecule in the gas phase, and to evaluate the wavenumbers of the fundamental vibrations. The rotational structure of the 2_0^1 band was also investigated at high resolution to improve the accuracy of the ground state constants, and to measure for the first time rotational parameters of the 2^1 level. A newly written Coriolis least-squares fitting program has been used to account for a small perturbation in the band.

Experimental

NH_2BF_2 was prepared by heating solid NH_3BF_3:

$$NH_3BF_3(s) \xrightarrow[125–140°C]{\Delta} NH_2BF_2(g) + HF(g)$$

The adduct had previously been prepared by passing a stream of NH_3 gas over a stirred solution of boron trifluoride etherate (Aldrich) diluted with twice its volume of diethyl ether. The white precipitate of NH_3BF_3 that was formed was filtered off, washed with diethyl ether, and dried under vacuum. Care was taken to keep the reaction flask flushed with nitrogen because NH_3BF_3 hydrolyses easily.

The spectrum of NH_2BF_2 was recorded with a Bomem DA3.002 interferometer equipped with a multiple reflection Wilks-type cell with flat KBr windows. The path length used was 8.25 m. Because the compound is unstable it was observed using a flow system. Solid NH_3BF_3 was loosely packed in a 20-cm Pyrex tube and heated to between 125 and 140°C; the reaction products were flowed through the cell. Initially only residual solvent, diethyl ether, was produced, but gradually the spectrum of NH_2BF_2 was detected, although some diethyl ether was still present, contaminating the spectrum. When the NH_3BF_3 was heated to higher temperatures the more stable trifluoroborazine, $(HNBF)_3$, started to appear; above 180°C the sample decomposed rapidly and the spectrum diasappeared. In any case very little vapour pressure could be maintained, probably because NH_2BF_2 was polymerizing in the cell, and the spectra obtained were not very intense.

The spectrum was recorded between 400 and 3700 cm^{-1}, using a globar light source. A KCl beamsplitter was used above 550 cm^{-1} and a

[1]Present address: Sci-Med New Zealand Limited, 60–66 France Street, South Newton, P.O. Box 68-232, Auckland, New Zealand.

[2]Present address: Department of Chemistry and Biochemistry, Southern Illinois University, Carbondale, IL 62901, U.S.A.

[3]Author to whom correspondence may be addressed.

Can. J. Chem. Downloaded from www.nrcresearchpress.com by 112.217.228.212 on 09/07/12
For personal use only.

Mylar beamsplitter below. The detectors were InSb above 1900 cm^{-1}, HgCdTe from 700 to 1800 cm^{-1}, both cooled with liquid nitrogen, and Ge:Cu below 700 cm^{-1}, cooled with liquid helium. Digital and optical filters were used to restrict the amplified band width so that only data in the range of interest were collected. Portions of the spectrum were recorded at 0.05 and 0.01 cm^{-1} resolution to identify the fundamentals.

The 2_0^1 band near 1608 cm^{-1} was recorded at 0.004 cm^{-1} resolution. For this band, after every 10 high-resolution scans, a low-resolution survey spectrum was obtained to ensure continued presence of NH_2BF_2. Ninety high-resolution scans were coadded for the final spectrum, which took about 5 h to record. The interferogram was transformed with no apodization (boxcar truncation); the resulting spectrum was ratioed against the spectrum of the empty cell and finally converted to absorbance units. The Bomen software peak-find routine, which differentiates the peaks, was used to determine line positions. The absolute calibration was checked against the absorption spectrum of H_2O (7). The accuracy of the line centers is estimated as follows: relative accuracy, ±0.0002 cm^{-1}, absolute accuracy, ±0.0005 cm^{-1}, for the stronger lines.

A deuterated sample, ND_2BF_2, was obtained by heating ND_3BF_3 that had been prepared as above using gaseous ND_3 (MSD isotopes, 99.2 at.% D). Low-resolution (0.05 cm^{-1}) spectra were recorded, as above.

Assignment and analysis

(a) Assignment of fundamentals

NH_2BF_2 is a planar, oblate, near-symmetric rotor (κ = 0.8326) having C_{2v} symmetry; the symmetry axis is the *a*-inertial axis. The 12 normal modes transform as $5A_1 + A_2 + 2B_1 + 4B_2$ (Mulliken's convention (8)). The fundamentals with A_1, B_2, and B_1 symmetry give rise to type A, type B, and type C bands, respectively; the A_2 mode, the torsion, is infrared inactive.

Unfortunately only a partial assignment of the normal modes could be made in this study. While some bands could be clearly identified, many were too weak to be observed or were overlapped. The chief criteria for assignment were the contours of the bands (9), in combination with the line spacings in their P and R branches. For a planar oblate rotor the spacings in a parallel (type C) band are ~$(A + B)$, while those in perpendicular (type A or B) bands are ~$(1/2)$ $(A + B)$ (assuming only small differences in rotational constants between vibrational states). Extra information was provided by comparison with the wavenumbers of the fundamentals of NH_2BH_2, (1)[4] and HBF_2 (10, 11), and from the wavenumbers obtained from an *ab initio* SCF calculation (12). The spectrum of the deuterated species was very weak, and provided only a little information.

The spectrum of NH_2BF_2 at low resolution, from 800 to 3800 cm^{-1}, is shown in Fig. 1. The pair of fundamentals at ~3500 cm^{-1} is assigned to the NH stretching vibrations by analogy with NH_2BH_2: the band at 3468 cm^{-1} has a type A contour and thus corresponds to ν_1, while the band at 3576 cm^{-1} has a type B contour and is thus ν_9. The band near 1608 cm^{-1} is also of type A; it is shown at 0.05 cm^{-1} resolution in Fig. 2. It is assigned to ν_2, largely the NH symmetric bend, again following NH_2BH_2.

In the range 1300–1460 cm^{-1} the spectrum is very complex and clearly contains several bands, though there is considerable likelihood of overlap with bands of residual diethyl ether. In an attempt to make an assigmnent it was investigated at 0.01 cm^{-1} resolution. A very weak type B band could be seen near 1339 cm^{-1}, and is tentatively assigned to ν_{10}, the BF_2 asymmetric stretch. Between 1360 and 1460 cm^{-1} the complexity is such that no clear assignment could be made, though there are what appear to be Q branches near 1396, 1419, 1445, and 1459 cm^{-1}. One or more could correspond to ν_3, the BN stretch. No properly resolved fine structure was observed.

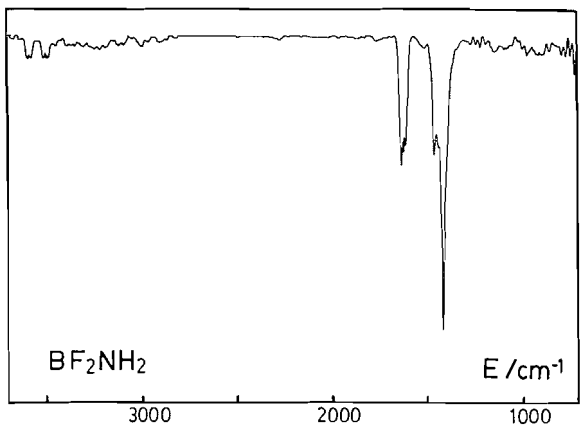

FIG. 1. Low resolution transmittance spectrum of NH_2BF_2 in the region 750–3700 cm^{-1}.

Two bands were observed for NH_2BF_2 between 400 and 700 cm^{-1}. The first, a type C band at 661 cm^{-1} (Fig. 3) is assigned to ν_7, the BF_2 out-of-plane bend, following the theoretical calculations. Very weak absorptions were also found nearby, with similar boron isotope shifts, for ND_2BF_2; these would seem to confirm the assignment, though it is interesting that corresponding wavenumbers of the deuterated species are slightly higher than those of the normal species. The band at 439 cm^{-1} (Fig. 4) is seemingly, from the apparent structure of its P branch, also a type C band, presumably the NH_2 out-of-plane bend. The spike at 464 cm^{-1} might then result from the ^{10}B species. It is curious, though, that if this is the case both type C bands would have the same boron isotopic dependence. Another possible assignment of this spike is to ν_5, the lowest frequency A_1 mode. It is interesting that vibrational satellites were observed in the microwave spectrum suggesting that the lowest frequency mode is near 450 cm^{-1} (6).

Three further bands were observed in searches for the spectrum of ND_2BF_2; they were centered near 2990, 1043, and 963 cm^{-1}. All showed PQR contours. Of these, only the band near 1043 cm^{-1} can be confidently assigned to this molecule. It has the correct spacing in its P and R branches for a perpendicular (type A) band. Its *B* isotopic shift is very small (~1 cm^{-1}); its assignment is unclear. There is a good chance that the other two bands were due to impurities. Their rotational structures are not so easily accounted for, and indeed the band near 2990 cm^{-1} shows no structure at all. Because only a very small amount of ND_3BF_3 was available, it was heated for much longer than the NH_3BF_3, thus increasing the probability of producing impurity gases.

A summary of the assignments is given in Table 1, along with those of any $NH_2{}^{10}BF_2$ band centres that could be identified. They are compared with the *ab initio* calculated wavenumbers, which are consistently higher than the measured values for both NH_2BF_2 and NH_2BH_2 (for which wavenumbers were also calculated (12)). Table 1 also contains a comparison of the

[4]W. D. Anderson, J. A. Barry, D. T. Cramb, M. C. L. Gerry, W. Lewis-Bevan, M. P. J. Lyne, A. J. Merer, J. Parikh, and D. M. Steunenberg, personal communication.

Can. J. Chem. Downloaded from www.nrcresearchpress.com by 112.217.228.212 on 09/07/12
For personal use only.

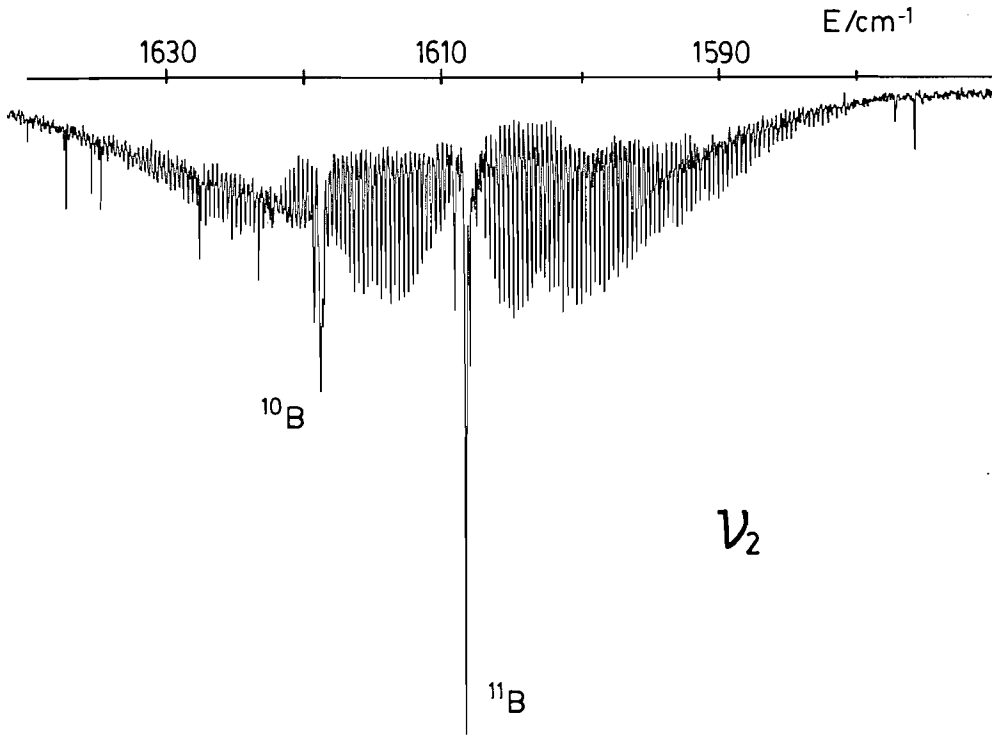

FIG. 2. The 2_0^1 band of NH_2BF_2, recorded as transmittance at 0.05 cm^{-1} resolution. The band origins due to $NH_2{}^{10}BF_2$ and $NH_2{}^{11}BF_2$ are indicated.

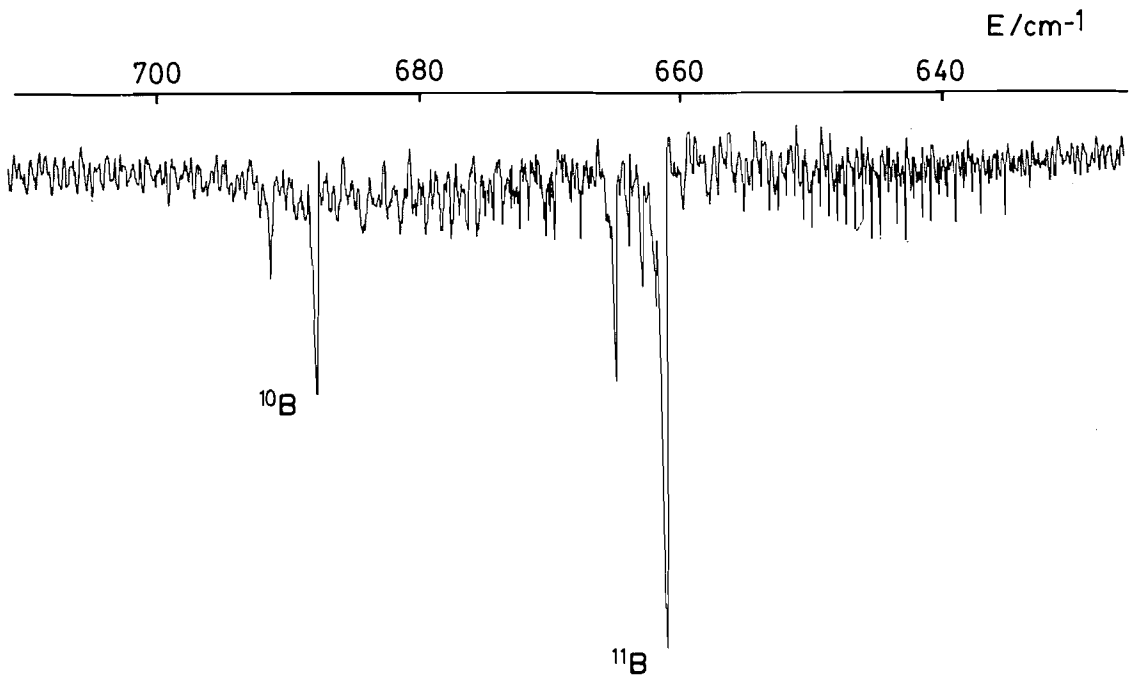

FIG. 3. The 7_0^1 band of NH_2BF_2, recorded at 0.05 cm^{-1} resolution. The band origins due to $NH_2{}^{10}BF_2$ and $NH_2{}^{11}BF_2$ are indicated.

assigned fundamentals of NH_2BF_2 with the corresponding values of NH_2BH_2 and HBF_2.

(b) Analysis of the 2_0^1 band

The 2_0^1 band near 1608 cm^{-1} (Fig. 2) is a type A band of an oblate near-symmetric rotor, following the rotational selection rules $\Delta J = 0, \pm 1$; $\Delta K_a = 0, \pm 2, \ldots$; and $\Delta K_c = \pm 1, \pm 3, \ldots$ It shows two intense central Q-branch features belonging to the overlapping Q-branch lines of $NH_2{}^{11}BF_2$ and $NH_2{}^{10}BF_2$. On either side of the band center lie clusters of R- and P-branch transitions; this clustering is common in planar oblate near-symmetric rotors when the rotational constants do not change much on vibrational excitiation, and $C \sim (\frac{1}{4})(A + B)$ (13). Each cluster has a different value of $(2J - K_c)$; they alternate between even and odd K_c. Within a given cluster the lower state quantum numbers of the transitions are $(J, K_c = J)$, $(J - 1, K_c = J - 2), \ldots$

Can. J. Chem. Downloaded from www.nrcresearchpress.com by 112.217.228.212 on 09/07/12
For personal use only.

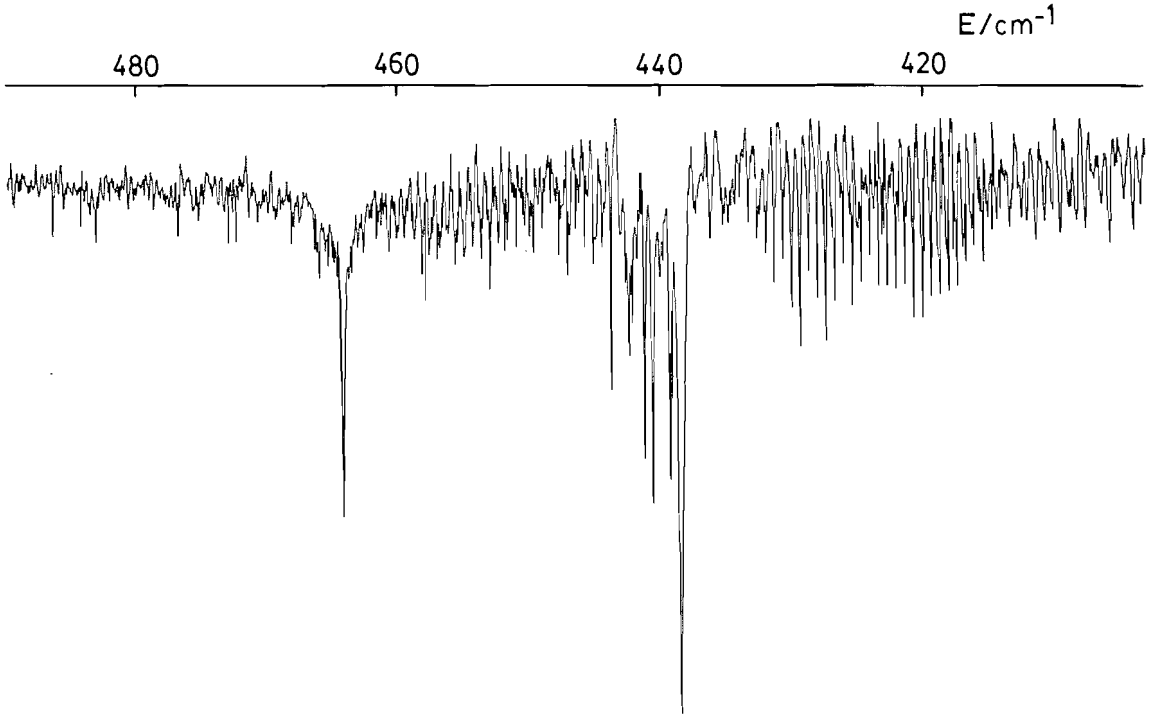

FIG. 4. The infrared transmittance spectrum of NH_2BF_2 in the region 400–490 cm^{-1}. The spike at 439 cm^{-1} is probably the origin of 8_0^1 of $NH_2{}^{11}BF_2$.

TABLE 1. Vibrational wavenumbers of NH_2BF_2 (in cm^{-1}), in comparisons with *ab initio* values[a] and values for NH_2BH_2[b] and HBF_2

Species	Mode	$NH_2{}^{11}BF_2$	$NH_2{}^{10}BF_2$	$ND_2{}^{11}BF_2$	$NH_2{}^{11}BH_2$[b]	$H^{11}BF_2$	Calculated[a]	Description
A_1	ν_1	3487			3451		3629	NH_2 symmetric str.
	ν_2	1608	1619		1617		1793	NH_2 symmetric bend
	ν_3	[c]			1337		1590	BN stretch
	ν_4					1167	940	BF_2 symmetric str.
	ν_5	[d]				544	488	BF_2 symmetric bend
A_2	ν_6	inactive					553	Torsion
B_1	ν_7	661	687	684			713	BF_2 out-of-plane
	ν_8	439	464		1005		562	NH_2 out-of-plane
B_2	ν_9	3576			3534		3736	NH_2 asym. str.
	ν_{10}	1339				1404	1663	BF_2 asym. str.
	ν_{11}				1122		1061	NH_2 asym. bend
	ν_{12}						417	BF_2 asym. bend

[a]Reference 12.
[b]Footnote 4.
[c]Several possible Q branches were observed, at 1396, 1419, 1445, and 1459 cm^{-1}.
[d]The spike observed at 464 cm^{-1} (Fig. 4) may be the origin of this band.

down to $((J + 1)/2, K_c = 1)$ or $(J/2, K_c = 0)$. The spectrum consequently becomes more dense away from the band center, both to high and low wavenumbers. A section of the P branch is shown in Fig. 5. In some cases asymmetry splitting was observed, and showed the 5:3 intensity ratio predicted from the spin statistics of two pairs of equivalent Fermions.

Initial assignments of the quantum numbers of the ^pP and ^rR branch transitions, which were the strongest lines of the spectrum, were made using ground state Δ_2F combination differences calculated from the microwave constants of Lovas and Johnson (6). Once correct assignments had been made in this way the remaining assignments were clear from the spectral patterns.

A global fit of 229 ground state combination differences and the 32 microwave measurements (6) of $NH_2{}^{11}BF_2$ was made to the ground state rotational and quartic centrifugal distortion constants, using Watson's *A*-reduced Hamiltonian in its I^r representation (14). The microwave data were given uncertainties 100 times smaller than those of the combination differences; the weights were proportional to $(\text{uncertainty})^{-2}$. The results are in Table 2, along with a comparison with the microwave constants. Clearly a significant improvement has been made in the precision of the constants; two of the distortion constants have been measured for the first time.

Finally, a least-squares fit was made using measured wavenumbers to the constants of $NH_2{}^{11}BF_2$ in the 2^1 state. In the fit the ground state constants were held fixed at the values calculated above. All measured ^pP, ^pQ, and ^rR branch transi-

Can. J. Chem. Downloaded from www.nrcresearchpress.com by 112.217.228.212 on 09/07/12
For personal use only.

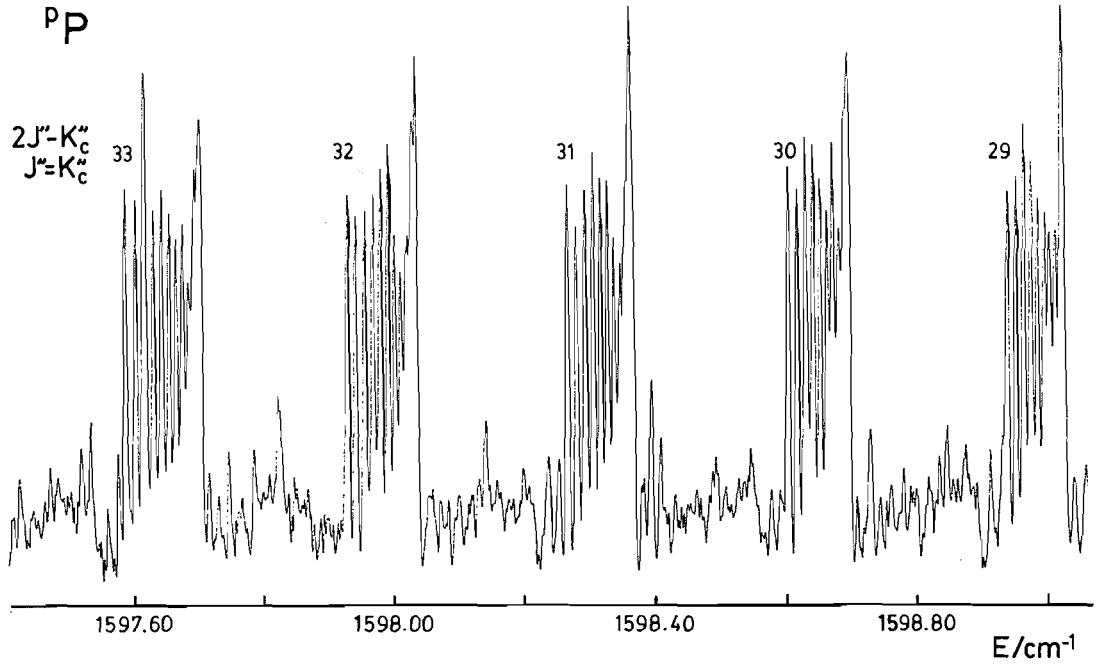

FIG. 5. A portion of the PP branch of the 2_0^1 band of gaseous NH_2BF_2, recorded as absorbance at 0.004 cm^{-1} resolution. The value of $2J - K_c$ for the *ground* state of each cluster of lines is indicated. This is also the value of J'' and K''_c for the line at the lowest wavenumber side of each cluster; in a given cluster J decreases by 1 and K_c by 2 for adjacent lines moving to higher wavenumbers.

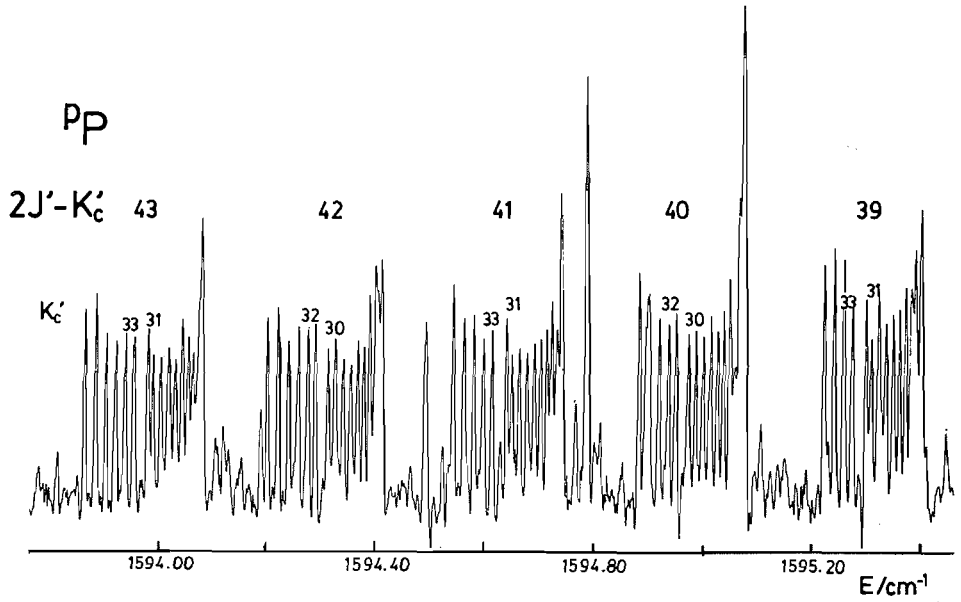

FIG. 6. A portion of the PP branch of the 2_0^1 band of NH_2BF_2, recorded as absorbance, showing a small Coriolis perturbation. The value of $2J - K_c$ for the 2^1 *level* is indicated for each cluster, as well as the value of K'_c for the lines on each side of the gap in the rotational structure.

tions were included, up to $J' = 53$ and $K'_c = 50$, with the exception of lines with $K'_c = 29$–33, for which a small perturbation was observed. Watson's *A*-reduced Hamiltonian in its I^r representation (14) was again used, and the results are also in Table 2. Once again accurate values have been obtained for the rotational and quartic distortion constants, all for the first time for this level, along with an accurate value for the band origin, T_0. Table 3 contains all the measured wavenumbers with their assignments and weights; the goodness of fit is also indicated.

(c) Perturbations in the 2^1 level

Some of the rotational structure of the 2_0^1 band is significantly perturbed by a Coriolis interaction. This is clearly shown in Fig. 6: a gap appears in both the PP- and RR-branch clusters at the same value of K'_c. Rotational levels in the region $K'_c = 29$–33 are shifted, with the largest shifts for $K'_c = 31$ and 32. These shifts, which are evaluated from the differences between the observed and calculated frequencies in the upper state, are indicated in Table 3; they are relatively small ($<\sim 0.01$ cm^{-1}) and are roughly proportional to $(J(J + 1)$–

Can. J. Chem. Downloaded from www.nrcresearchpress.com by 112.217.228.212 on 09/07/12
For personal use only.

TABLE 2. Spectroscopic constants (in cm^{-1}) of BF_2NH_2 in the ground and 2^1 states

Parameter	Ground state: This work[a]	Ground state: Microwave data[b]	2^1 state[c]
Rotational constants			
A	0.33421379(34)[d]	0.3342132(17)	0.3342446(13)
B	0.31990223(32)	0.3199009(17)	0.3196907(11)
C	0.16320694(31)	0.1632092(17)	0.16303482(12)
Quartic centrifugal distortion constants			
$10^6\Delta_J$	0.17560(23)	0.188(24)	0.17726(87)
$10^7\Delta_{JK}$	0.335(10)	—	0.420(52)
$10^6\Delta_K$	0.2067(14)	0.233(58)	0.1819(65)
$10^7\delta_J$	0.7669(16)	0.688(12)	0.7746(44)
$10^6\delta_K$	0.21307(41)	—	0.2204(18)
Band centre (T_0)			1608.70692(7)
Standard deviation of fit			0.00046

[a]Calculated from combination differences of the 2_0^1 band and microwave data of ref. 6.
[b]Values of ref. 6 converted to the A-reduction I^r representation (14), and to cm^{-1} using $c = 2.99792458 \times 10^8$ m s^{-1}.
[c]Calculated from observed cm^{-1}, omitting transitions with $K_c' = 29$–33, and with ground state constants fixed at the value of column 1.
[d]Numbers in parentheses are one standard deviation in units of the last significant figures.

$K_c'(K_c' \pm 1)$) for values of $K_c' = 29$–33. This implies a perpendicular Coriolis interaction in the symmetric rotor limit. Since NH_2BF_2 is an oblate rotor the interaction would be about the a- or b-inertial axis, and the interacting mode should thus be of species A_2 or B_1, respectively.

The directions of the shifts indicate that the interaction is probably $\Delta K_c' = -1$, with a vibrational level lying just below the 2^1 level. Since the levels involving $K_c' = 31$ and 32 have been pushed to higher and lower energies respectively, by similar amounts, one can deduce that the unseen vibrational state has K_c values of 30 and 31 lying between the $K_c' = 31$ and 32 levels of the 2^1 state. Figure 7 shows a plot of the rotational energies of the 2^1 level (solid lines) and those of the unseen level (dashed lines) vs. $J(J + 1)$. A rough estimate of ξ^α (with $\xi^x \equiv X\zeta^x$ etc.) using second order perturbation theory gave a value of $\xi^\alpha \sim 0.004$, and the origin of the unseen band at $\sim 1598.4\ cm^{-1}$.

With this information, least-squares Coriolis fits, using a newly written program, were undertaken to refine these constants. As before, the I^r representation was used, and fits were carried out assuming both x- and z-axis (b- and a-axis, respectively) Coriolis type interactions. (An attempted fit assuming a y-axis interaction failed.) The fits were made to the energy *levels* of the 2^1 state; these had been calculated by adding the measured infrared wavenumbers to the ground state energy levels calculated from the ground state fit. The levels were weighted according to the number of times they were measured in the infrared spectrum. All the constants obtained earlier for the 2^1 level were included in the fits, along with ξ^α, and T_0 and $(A + B)$ of the unseen level. The remaining constants of the unseen level were held at the ground state values. $(A + B)$ was floated because it determines the relative spacing of the K_c states.

The results of the Coriolis fits are summarized in Table 4, which includes the derived constants for both fits, along with the energies of the levels of the 2^1 state with $K_c' = 29$–33 (the levels where the perturbation is clearly evident) and the standard deviations of the fits. The constants of the unseen state are completely uncorrelated with those of the 2^1 state.

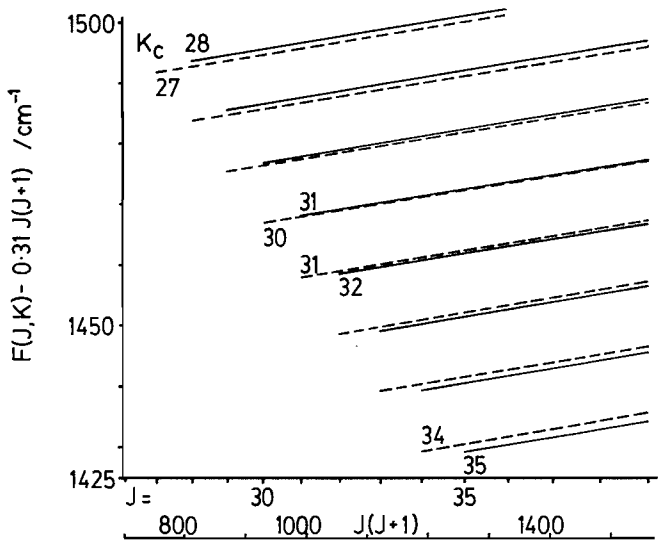

FIG. 7. A plot of energy levels (minus a factor of 0.31 $J(J + 1)$) vs. $J(J + 1)$ for the observed 2^1 vibrational state (solid lines) and the unseen state (dashed lines). $K_c' = 30$ and 31 of the unseen state are sandwiched between $K_c' = 31$ and 32 for the 2^1 state, allowing an unique solution of the position of the unseen vibration to be obtained.

From a comparison of Tables 2 and 4, it is clear that the perturbation is equally well accounted for by an a- or b-type Coriolis interaction. Even the value of ζ^α derived from the constants is essentially the same for both interactions (Table 4). Consequently, the identity of the perturbing level is rather obscure. It cannot be a fundamental, because the shifts are too small, there are no bands overlapping the 2_0^1 band, and it is highly unlikely that the torsion would lie at such a high energy. Also, since it cannot be an overtone level, which must be of species A_1, it must thus be a combination, of which there are several possibilities. On the basis of the calculated wavenumbers (11), one candidate is $\nu_7 + \nu_{11}$ (species A_2); another is $\nu_4 + \nu_7$ (species B_1). There are several others in which three

Can. J. Chem. Downloaded from www.nrcresearchpress.com by 112.217.228.212 on 09/07/12
For personal use only.

TABLE 3. Observed transitions[a] of the 2_0^1 band of $NH_2{}^{11}BF_2$

J'	K_a'	K_c'		J''	K_a''	K_c''	Observed Wavenumber (cm^{-1})	Deviation[b] (cm^{-1})	wt
7	6	1	-	7	6	2	1609.00782	0.00099	1.0
10	8	2	-	10	8	3	1609.29221	0.00031	1.0
12	10	2	-	12	10	3	1609.15825	0.00010	1.0
13	12	2	-	13	10	3	1609.97439	-0.00100	0.5
17	15	2	-	17	15	3	1608.83907	-0.00028	1.0
10	7	3	-	10	7	4	1609.77937	0.00034	0.5
13	10	3	-	13	10	4	1609.63509	-0.00001	0.5
16	14	3	-	16	12	4	1610.05901	0.00088	1.0
17	14	3	-	17	14	4	1609.30735	-0.00040	1.0
19	16	3	-	19	16	4	1609.12434	0.00040	1.0
23	20	3	-	23	20	4	1608.82850	0.00074	1.0
19	16	4	-	19	14	5	1610.20648	0.00070	1.0
15	10	5	-	15	10	6	1610.44393	-0.00059	0.5
19	14	5	-	19	14	6	1610.34238	0.00006	1.0
29	24	5	-	29	24	6	1609.34268	-0.00032	0.5
33	27	6	-	33	27	7	1609.60848	0.00050	0.0
17	10	7	-	17	10	8	1611.10701	-0.00004	0.5
28	22	7	-	28	20	8	1610.94147	-0.00058	0.5
24	16	8	-	24	16	9	1611.36588	-0.00069	1.0
29	22	8	-	29	20	9	1611.27648	0.00035	1.0
24	16	9	-	24	14	10	1611.70818	-0.00053	0.5
25	16	9	-	25	16	10	1611.69607	-0.00014	1.0
26	18	9	-	26	16	10	1611.68203	-0.00063	1.0
27	18	9	-	27	18	10	1611.66761	-0.00001	1.0
28	20	9	-	28	18	10	1611.65109	-0.00055	1.0
29	20	9	-	29	20	10	1611.63377	0.00042	1.0
24	14	10	-	24	14	11	1612.04373	-0.00089	0.5
25	16	10	-	25	14	11	1612.03355	-0.00043	1.0
26	16	10	-	26	16	11	1612.02231	-0.00012	1.0
27	18	10	-	27	16	11	1612.01002	0.00008	1.0
28	18	10	-	28	18	11	1611.99600	-0.00038	1.0
29	20	10	-	29	18	11	1611.98277	0.00100	0.5
25	14	11	-	25	14	12	1612.36714	-0.00048	1.0
26	16	11	-	26	14	12	1612.35685	-0.00059	1.0
27	16	11	-	27	16	12	1612.34540	-0.00107	0.5
29	18	11	-	29	18	12	1612.32214	0.00014	1.0
30	20	11	-	30	18	12	1612.30828	-0.00011	1.0
25	14	12	-	25	12	13	1612.69848	-0.00027	1.0
26	14	12	-	26	14	13	1612.68872	-0.00075	0.5
27	16	12	-	27	14	13	1612.67959	0.00005	1.0
28	16	12	-	28	16	13	1612.66904	0.00012	1.0
29	18	12	-	29	16	13	1612.65807	0.00050	1.0
33	22	12	-	33	20	13	1612.60350	-0.00052	1.0
34	22	12	-	34	22	13	1612.58842	0.00006	1.0
28	16	13	-	28	14	14	1613.00037	-0.00020	1.0
30	18	13	-	30	16	14	1612.97884	-0.00022	1.0
33	20	13	-	33	20	14	1612.94114	-0.00038	1.0
34	22	13	-	34	20	14	1612.92659	-0.00087	1.0
27	14	14	-	27	12	15	1613.33917	-0.00052	1.0
28	14	14	-	28	14	15	1613.33110	0.00063	1.0
29	16	14	-	29	14	15	1613.32132	0.00062	0.5
29	14	15	-	29	14	16	1613.65006	0.00019	1.0
30	16	15	-	30	14	16	1613.64000	-0.00006	1.0
31	16	15	-	31	16	16	1613.62992	0.00020	1.0
32	18	15	-	32	16	16	1613.61868	-0.00014	1.0
33	18	15	-	33	18	16	1613.60740	0.00007	1.0
34	20	15	-	34	18	16	1613.59538	0.00014	1.0
29	14	16	-	29	12	17	1613.97753	-0.00050	1.0
31	16	16	-	31	14	17	1613.95759	-0.00114	1.0
32	16	16	-	32	16	17	1613.94732	-0.00100	1.0
33	18	16	-	33	16	17	1613.93626	-0.00113	1.0
34	18	16	-	34	18	17	1613.92511	-0.00081	1.0
35	20	16	-	35	18	17	1613.91359	-0.00029	1.0
36	20	16	-	36	20	17	1613.90205	0.00080	0.0
37	22	18	-	37	20	17	1613.88882	0.00081	0.0
28	12	17	-	28	10	18	1614.31307	-0.00107	0.5
29	12	17	-	29	12	18	1614.30506	-0.00040	0.5
30	14	17	-	30	12	18	1614.29501	-0.00134	0.5
31	14	17	-	31	14	18	1614.28617	-0.00061	1.0
32	16	17	-	32	14	18	1614.27555	-0.00120	0.5
33	16	17	-	33	16	18	1614.26511	-0.00113	1.0
38	22	17	-	38	20	18	1614.20612	0.00028	0.0
27	10	18	-	27	8	19	1614.64863	-0.00029	1.0
30	12	18	-	30	12	19	1614.62281	-0.00064	1.0
31	14	18	-	31	12	19	1614.61336	-0.00077	1.0
32	14	18	-	32	14	19	1614.60329	-0.00109	0.5
33	16	18	-	33	14	19	1614.59413	-0.00005	1.0
30	12	19	-	30	10	20	1614.95057	0.00048	0.5
31	12	19	-	31	12	20	1614.94043	-0.00053	1.0
32	14	19	-	32	12	20	1614.93104	-0.00037	1.0
33	14	19	-	33	14	20	1614.92115	-0.00030	1.0
34	16	19	-	34	14	20	1614.91099	-0.00006	1.0
35	16	19	-	35	16	20	1614.90014	-0.00006	1.0
36	18	19	-	36	16	20	1614.88935	0.00045	1.0
37	18	19	-	37	18	20	1614.87803	0.00090	0.5
37	18	20	-	37	16	21	1615.20411	-0.00071	1.0
38	18	20	-	38	18	21	1615.19282	-0.00005	1.0
27	6	21	-	27	6	22	1615.62738	0.00045	0.5
32	12	21	-	32	10	22	1615.58494	0.00074	0.5
36	16	21	-	36	14	22	1615.54387	0.00070	0.5
37	16	21	-	37	16	22	1615.53276	0.00087	0.5
38	18	21	-	38	16	22	1615.51972	-0.00045	1.0
39	18	21	-	39	18	22	1615.50853	0.00051	1.0
8	8	0	-	9	8	1	1603.37680	-0.00028	0.5
9	9	0	-	10	9	1	1602.81860	0.00038	1.0
10	10	0	-	11	10	1	1602.26439	0.00066	1.0
18	18	0	-	19	18	1	1597.79291	-0.00085	0.5
6	6	1	-	7	6	2	1604.76733	-0.00040	0.5
15	14	1	-	16	14	2	1599.23696	0.00032	1.0
17	16	1	-	18	16	2	1598.14563	-0.00028	1.0
7	6	2	-	8	6	3	1604.32426	-0.00063	0.5
10	9	2	-	11	9	3	1602.43630	-0.00001	1.0
11	10	2	-	12	10	3	1601.82009	0.00037	1.0
13	11	2	-	14	11	3	1600.24008	0.00083	0.5
13	12	2	-	14	12	3	1600.60674	-0.00023	0.5
15	14	2	-	16	14	3	1599.41917	-0.00064	0.5
16	14	2	-	17	14	3	1598.41132	0.00041	1.0
22	20	2	-	23	20	3	1595.11046	0.00002	1.0
9	7	3	-	10	7	4	1603.31075	-0.00001	0.5
10	7	3	-	11	7	4	1602.60636	-0.00097	0.5
11	8	3	-	12	8	4	1601.92855	0.00082	0.5
12	10	3	-	13	10	4	1601.36807	-0.00072	1.0
13	10	3	-	14	10	4	1600.55278	0.00055	1.0
14	12	3	-	15	12	4	1600.09635	0.00008	1.0
15	12	3	-	16	12	4	1599.17593	0.00105	1.0
16	14	3	-	17	14	4	1598.84859	0.00012	0.5
17	14	3	-	18	14	4	1597.82844	-0.00076	0.5
19	16	3	-	20	16	4	1596.54227	-0.00076	0.5
20	18	3	-	21	18	4	1596.43440	-0.00089	0.5
23	20	3	-	24	20	4	1594.19505	0.00077	0.5
24	21	3	-	25	21	4	1593.64903	0.00039	0.5
15	12	4	-	16	12	5	1599.69579	0.00070	1.0
17	14	4	-	18	14	5	1598.39699	-0.00007	1.0
18	14	4	-	19	14	5	1597.54070	-0.00073	1.0
18	15	4	-	19	15	5	1597.75401	-0.00040	1.0
19	15	4	-	20	15	5	1596.84069	0.00057	0.5
19	16	4	-	20	16	5	1597.11720	0.00002	1.0
20	16	4	-	21	16	5	1596.14154	-0.00007	1.0
21	18	4	-	22	18	5	1595.86234	0.00051	1.0
21	17	4	-	22	17	5	1595.45063	-0.00016	0.5
24	20	4	-	25	20	5	1593.46526	-0.00065	1.0
23	18	5	-	24	18	6	1594.52741	0.00060	0.5
28	22	6	-	29	22	7	1591.51134	0.00101	0.5
29	22	7	-	30	22	8	1591.33413	0.00025	1.0
20	4	16	-	21	4	17	1600.32116	-0.00020	0.5
21	6	16	-	22	6	17	1599.66391	-0.00032	0.5
20	4	17	-	21	4	18	1600.64589	0.00005	0.5
21	4	17	-	22	4	18	1599.98857	-0.00007	0.5
22	6	17	-	23	6	18	1599.33106	-0.00032	0.5
24	8	17	-	25	8	18	1598.01624	-0.00042	1.0
25	8	17	-	26	8	18	1597.35896	-0.00025	1.0
21	4	18	-	22	4	19	1600.31255	-0.00038	0.5
22	4	18	-	23	4	19	1599.65527	-0.00032	0.5
23	6	18	-	24	6	19	1598.99859	0.00039	0.5
24	6	18	-	25	6	19	1598.34090	0.00014	1.0
25	8	18	-	26	8	19	1597.68309	-0.00016	1.0
27	10	18	-	28	10	19	1596.36765	-0.00045	1.0
28	10	18	-	29	10	19	1595.71034	-0.00010	0.5
29	12	18	-	30	12	19	1595.05288	0.00014	0.5
34	16	18	-	35	16	19	1591.76342	-0.00006	0.5
21	2	19	-	22	2	20	1600.63697	-0.00013	1.0
22	4	19	-	23	4	20	1599.98013	0.00044	1.0
23	4	19	-	24	4	20	1599.32229	0.00007	1.0
24	6	19	-	25	6	20	1598.66451	-0.00018	1.0
25	6	19	-	26	6	20	1598.00678	-0.00035	0.5
26	8	19	-	27	8	20	1597.34931	-0.00020	1.0
27	8	19	-	28	8	20	1596.69150	-0.00036	1.0
28	10	19	-	29	10	20	1596.03358	-0.00059	1.0
29	10	19	-	30	10	20	1595.37666	0.00022	1.0
30	12	19	-	31	12	20	1594.71874	0.00006	0.5
31	12	19	-	32	12	20	1594.06123	0.00034	0.5
33	14	19	-	34	14	20	1592.74489	-0.00030	0.5
22	2	20	-	23	2	21	1600.30358	-0.00010	0.5
23	4	20	-	24	4	21	1599.64588	-0.00024	1.0
24	4	20	-	25	4	21	1598.98841	-0.00010	1.0
25	6	20	-	26	6	21	1598.33097	0.00012	1.0
26	6	20	-	27	6	21	1597.67319	0.00002	1.0
27	8	20	-	28	8	21	1597.01523	-0.00021	1.0
28	8	20	-	29	8	21	1596.35741	-0.00028	1.0
29	10	20	-	30	10	21	1595.69982	-0.00009	1.0
30	10	20	-	31	10	21	1595.04199	-0.00012	1.0
31	12	20	-	32	12	21	1594.38406	-0.00022	1.0

Can. J. Chem. Downloaded from www.nrcresearchpress.com by 112.217.228.212 on 09/07/12
For personal use only.

TABLE 3 (*continued*)

J'	K_a'	K_c'		J''	K_a''	K_c''	Observed Wavenumber (cm^{-1})	Deviation[b] (cm^{-1})	wt
32	12	20	-	33	12	21	1593.72612	-0.00031	0.5
33	14	20	-	34	14	21	1593.06851	-0.00006	1.0
22	2	21	-	23	2	22	1600.62768	0.00009	1.0
23	2	21	-	24	2	22	1599.96993	0.00001	1.0
24	4	21	-	25	4	22	1599.31222	0.00001	1.0
25	4	21	-	26	4	22	1598.65418	-0.00029	1.0
26	6	21	-	27	6	22	1597.99660	-0.00009	1.0
27	6	21	-	28	6	22	1597.33914	0.00026	1.0
28	8	21	-	29	8	22	1596.68079	-0.00025	1.0
29	8	21	-	30	8	22	1596.02343	0.00024	1.0
30	10	21	-	31	10	22	1595.36520	-0.00012	1.0
31	10	21	-	32	10	22	1594.70788	0.00044	1.0
32	12	21	-	33	12	22	1594.05011	0.00057	1.0
33	12	21	-	34	12	22	1593.39194	0.00030	1.0
36	16	21	-	37	16	22	1591.41817	0.00026	1.0
23	2	22	-	24	2	23	1600.29370	0.00004	1.0
24	2	22	-	25	2	23	1599.63589	0.00005	1.0
25	4	22	-	26	4	23	1598.97815	0.00017	1.0
26	4	22	-	27	4	23	1598.32024	0.00014	1.0
27	6	22	-	28	6	23	1597.66236	0.00017	1.0
28	6	22	-	29	6	23	1597.00442	0.00016	1.0
29	8	22	-	30	8	23	1596.34651	0.00020	1.0
30	8	22	-	31	8	23	1595.68889	0.00053	0.5
31	10	22	-	32	10	23	1595.03080	0.00040	1.0
32	10	22	-	33	10	23	1594.37292	0.00049	1.0
33	12	22	-	34	12	23	1593.71465	0.00018	0.5
34	12	22	-	35	12	23	1593.05698	0.00047	1.0
23	0	23	-	24	0	24	1600.61747	0.00014	1.0
24	2	23	-	25	2	24	1599.95941	0.00002	1.0
25	2	23	-	26	2	24	1599.30149	0.00007	1.0
26	4	23	-	27	4	24	1598.64337	-0.00005	1.0
27	4	23	-	28	4	24	1597.98547	0.00007	1.0
28	6	23	-	29	6	24	1597.32762	0.00026	1.0
29	6	23	-	30	6	24	1596.66989	0.00058	0.5
30	8	23	-	31	8	24	1596.01199	0.00073	1.0
31	8	23	-	32	8	24	1595.35366	0.00046	1.0
32	10	23	-	33	10	24	1594.69557	0.00042	1.0
33	10	23	-	34	10	24	1594.03741	0.00031	1.0
34	12	23	-	35	12	24	1593.37961	0.00054	1.0
35	12	23	-	36	12	24	1592.72192	0.00087	1.0
36	14	23	-	37	14	24	1592.06313	0.00008	1.0
37	14	23	-	38	14	24	1591.40568	0.00061	1.0
24	0	24	-	25	0	25	1600.28279	-0.00010	1.0
25	2	24	-	26	2	25	1599.62471	-0.00009	1.0
26	2	24	-	27	2	25	1598.96689	0.00021	1.0
27	4	24	-	28	4	25	1598.30904	0.00051	1.0
28	4	24	-	29	4	25	1597.65102	0.00064	1.0
29	6	24	-	30	6	25	1596.99278	0.00057	1.0
30	6	24	-	31	6	25	1596.33462	0.00058	0.5
31	8	24	-	32	8	25	1595.67648	0.00060	1.0
32	8	24	-	33	8	25	1595.01800	0.00028	1.0
33	10	24	-	34	10	25	1594.36011	0.00054	1.0
34	10	24	-	35	10	25	1593.70169	0.00025	1.0
35	12	24	-	36	12	25	1593.04377	0.00043	1.0
37	14	24	-	38	14	25	1591.72751	0.00031	1.0
25	0	25	-	26	0	26	1599.94846	0.00034	1.0
26	2	25	-	27	2	26	1599.29035	0.00048	1.0
27	2	25	-	28	2	26	1598.63214	0.00054	1.0
28	4	25	-	29	4	26	1597.97396	0.00064	1.0
29	4	25	-	30	4	26	1597.31603	0.00100	0.5
30	6	25	-	31	6	26	1596.65707	0.00034	1.0
31	6	25	-	32	6	26	1595.99889	0.00044	1.0
32	8	25	-	33	8	26	1595.34013	-0.00004	1.0
33	8	25	-	34	8	26	1594.68236	0.00045	1.0
35	10	25	-	36	10	26	1593.36572	0.00026	1.0
38	14	25	-	39	14	26	1591.39136	0.00033	1.0
26	0	26	-	27	0	27	1599.61280	-0.00022	1.0
27	2	26	-	28	2	27	1598.95472	0.00010	1.0
28	2	26	-	29	2	27	1598.29652	0.00032	1.0
29	4	26	-	30	4	27	1597.63820	0.00043	1.0
30	4	26	-	31	4	27	1596.98024	0.00089	0.5
31	6	26	-	32	6	27	1596.32147	0.00054	1.0
32	6	26	-	33	6	27	1595.66280	0.00028	1.0
33	8	26	-	34	8	27	1595.00426	0.00012	1.0
34	8	26	-	35	8	27	1594.34637	0.00059	1.0
35	10	26	-	36	10	27	1593.68821	0.00076	0.5
36	10	26	-	37	10	27	1593.02982	0.00067	1.0
37	12	26	-	38	12	27	1592.37196	0.00106	1.0
27	0	27	-	28	0	28	1599.27775	0.00016	1.0
28	2	27	-	29	2	28	1598.61946	0.00043	1.0
29	2	27	-	30	2	28	1597.96110	0.00064	1.0
30	4	27	-	31	4	28	1597.30266	0.00076	1.0
31	4	27	-	32	4	28	1596.64439	0.00105	0.5
32	6	27	-	33	6	28	1595.98573	0.00093	1.0
33	6	27	-	34	6	28	1595.32685	0.00057	0.5
34	8	27	-	35	8	28	1594.66831	0.00053	1.0
35	8	27	-	36	8	28	1594.01010	0.00078	1.0
38	12	27	-	39	12	28	1592.03470	0.00051	1.0
41	14	27	-	42	14	28	1590.06036	0.00080	1.0
28	0	28	-	29	0	29	1598.94182	-0.00001	1.0
29	2	28	-	30	2	29	1598.28320	0.00008	1.0
31	4	28	-	32	4	29	1596.96650	0.00080	1.0
32	4	28	-	33	4	29	1596.30771	0.00070	1.0
33	6	28	-	34	6	29	1595.64918	0.00083	0.5
34	6	28	-	35	6	29	1594.99053	0.00082	0.5
35	8	28	-	36	8	29	1594.33175	0.00064	0.5
36	8	28	-	37	8	29	1593.67407	0.00153	0.0
37	10	28	-	38	10	29	1593.01547	0.00144	0.0
39	12	28	-	40	12	29	1591.69803	0.00086	1.0
29	0	29	-	30	0	30	1598.60610	0.00036	0.0
30	2	29	-	31	2	30	1597.94714	0.00027	0.0
31	2	29	-	32	2	30	1597.28862	0.00060	0.0
32	4	29	-	33	4	30	1596.63032	0.00114	0.0
33	4	29	-	34	4	30	1595.97144	0.00108	0.0
34	6	29	-	35	6	30	1595.31311	0.00154	0.0
35	6	29	-	36	6	30	1594.65436	0.00155	0.0
36	8	29	-	37	8	30	1593.99587	0.00177	0.0
37	8	29	-	38	8	30	1593.33685	0.00141	0.0
39	10	29	-	40	10	30	1592.02101	0.00272	0.0
38	10	29	-	39	10	30	1592.67918	0.00234	0.0
40	12	29	-	41	12	30	1591.36292	0.00310	0.0
41	12	29	-	42	12	30	1590.70416	0.00275	0.0
42	14	29	-	43	14	30	1590.04754	0.00445	0.0
43	14	29	-	44	14	30	1589.38697	0.00212	0.0
30	0	30	-	31	0	31	1598.26967	0.00035	0.0
31	2	30	-	32	2	31	1597.61113	0.00083	0.0
32	2	30	-	33	2	31	1596.95213	0.00083	0.0
33	4	30	-	34	4	31	1596.29381	0.00149	0.0
34	4	30	-	35	4	31	1595.63530	0.00192	0.0
35	6	30	-	36	6	31	1594.97648	0.00201	0.0
36	6	30	-	37	6	31	1594.31817	0.00257	0.0
37	8	30	-	38	8	31	1593.65939	0.00261	0.0
38	8	30	-	39	8	31	1593.00087	0.00285	0.0
39	10	30	-	40	10	31	1592.34239	0.00306	0.0
42	12	30	-	43	12	31	1590.36630	0.00262	0.0
31	0	31	-	32	0	32	1597.93477	0.00220	0.0
32	2	31	-	33	2	32	1597.27748	0.00408	0.0
33	2	31	-	34	2	32	1596.62023	0.00597	0.0
34	4	31	-	35	4	32	1595.96220	0.00705	0.0
35	4	31	-	36	4	32	1595.30359	0.00752	0.0
36	6	31	-	37	6	32	1594.64485	0.00781	0.0
37	6	31	-	38	6	32	1593.98507	0.00701	0.0
38	8	31	-	39	8	32	1593.32727	0.00813	0.0
39	8	31	-	40	8	32	1592.66925	0.00897	0.0
40	10	31	-	41	10	32	1592.01092	0.00943	0.0
41	10	31	-	42	10	32	1591.35230	0.00951	0.0
43	12	31	-	44	12	32	1590.03560	0.00997	0.0
44	14	31	-	45	14	32	1589.37687	0.00967	0.0
32	0	32	-	33	0	33	1597.59521	-0.00028	0.0
33	2	32	-	34	2	33	1596.93477	-0.00141	0.0
34	2	32	-	35	2	33	1596.27517	-0.00172	0.0
35	4	32	-	36	4	33	1595.61486	-0.00279	0.0
36	4	32	-	37	4	33	1594.95434	-0.00410	0.0
37	6	32	-	38	6	33	1594.29447	-0.00482	0.0
38	6	32	-	39	6	33	1593.63479	-0.00541	0.0
39	8	32	-	40	8	33	1592.97432	-0.00685	0.0
40	8	32	-	41	8	33	1592.31421	-0.00801	0.0
33	0	33	-	34	0	34	1597.25803	-0.00006	0.0
34	2	33	-	35	2	34	1596.59823	-0.00040	0.0
35	2	33	-	36	2	34	1595.93771	-0.00149	0.0
36	4	33	-	37	4	34	1595.27843	-0.00139	0.0
37	4	33	-	38	4	34	1594.61860	-0.00189	0.0
39	6	33	-	40	6	34	1593.29904	-0.00298	0.0
40	8	33	-	41	8	34	1592.63995	-0.00294	0.0
41	8	33	-	42	8	34	1591.98103	-0.00281	0.0
42	10	33	-	43	10	34	1591.32172	-0.00315	0.0
43	10	33	-	44	10	34	1590.66203	-0.00397	0.0
45	12	33	-	46	12	34	1589.34341	-0.00517	0.0
34	0	34	-	35	0	35	1596.92035	-0.00000	1.0
35	2	34	-	36	2	35	1596.26045	-0.00030	1.0
36	2	34	-	37	2	35	1595.60077	-0.00041	1.0
37	4	34	-	38	4	35	1594.94065	-0.00102	0.5
38	4	34	-	39	4	35	1594.28149	-0.00073	0.5
39	6	34	-	40	6	35	1593.62154	-0.00129	0.0
40	6	34	-	41	6	35	1592.96208	-0.00143	0.0
41	8	34	-	42	8	35	1592.30236	-0.00192	0.0
42	8	34	-	43	8	35	1591.64345	-0.00169	0.0
35	0	35	-	36	0	36	1596.58224	-0.00005	1.0
36	2	35	-	37	2	36	1595.92264	0.00010	1.0
37	2	35	-	38	2	36	1595.26254	-0.00030	1.0
38	4	35	-	39	4	36	1594.60217	-0.00103	0.5
39	4	35	-	40	4	36	1593.94321	-0.00041	0.5
40	6	35	-	41	6	36	1593.28315	-0.00096	0.5
41	6	35	-	42	6	36	1592.62325	-0.00144	0.0
42	8	35	-	43	8	36	1591.96371	-0.00165	0.0
43	8	35	-	44	8	36	1591.30443	-0.00169	0.0
44	10	35	-	45	10	36	1590.64502	-0.00196	0.0
45	10	35	-	46	10	36	1589.98550	-0.00245	0.0
36	0	36	-	37	0	37	1596.24373	-0.00018	1.0
37	2	36	-	38	2	37	1595.58368	-0.00033	1.0
38	2	36	-	39	2	37	1594.92357	-0.00060	1.0
39	4	36	-	40	4	37	1594.26383	-0.00057	1.0
40	4	36	-	41	4	37	1593.60372	-0.00098	1.0
41	6	36	-	42	6	37	1592.94403	-0.00105	0.0
42	6	36	-	43	6	37	1592.28443	-0.00112	0.0

Can. J. Chem. Downloaded from www.nrcresearchpress.com by 112.217.228.212 on 09/07/12
For personal use only.

TABLE 3 (*continued*)

J'	K_a'	K_c'	J''	K_a''	K_c''	Observed Wavenumber (cm^{-1})	Deviation[b] (cm^{-1})	wt
37	0	37	38	0	38	1595.90518	-0.00001	0.5
38	2	37	39	2	38	1595.24527	0.00012	1.0
39	2	37	40	2	38	1594.58460	-0.00058	1.0
40	4	37	41	4	38	1593.92471	-0.00057	1.0
41	4	37	42	4	38	1593.26466	-0.00080	1.0
42	6	37	43	6	38	1592.60441	-0.00131	0.0
43	6	37	44	6	38	1591.94494	-0.00115	0.0
44	8	37	45	8	38	1591.28549	-0.00106	0.0
46	10	37	47	10	38	1589.96755	-0.00027	0.0
47	10	37	48	10	38	1589.30794	-0.00070	0.0
38	0	38	39	0	39	1595.56594	-0.00021	1.0
40	2	38	41	2	39	1594.24524	-0.00063	1.0
41	4	38	42	4	39	1593.58534	-0.00050	1.0
42	4	38	43	4	39	1592.92482	-0.00108	1.0
43	6	38	44	6	39	1592.26494	-0.00111	0.5
44	6	38	45	6	39	1591.60534	-0.00097	1.0
46	8	38	47	8	39	1590.28738	0.00022	1.0
39	0	39	40	0	40	1595.22633	-0.00046	1.0
40	2	39	41	2	40	1594.56657	0.00010	1.0
41	2	39	42	2	40	1593.90602	-0.00021	1.0
42	4	39	43	4	40	1593.24561	-0.00046	1.0
43	4	39	44	4	40	1592.58526	-0.00075	1.0
44	6	39	45	6	40	1591.92523	-0.00083	0.5
48	10	39	49	10	40	1589.28700	-0.00040	1.0
40	0	40	41	0	41	1594.88696	-0.00014	1.0
41	2	40	42	2	41	1594.22612	-0.00052	1.0
42	2	40	43	2	41	1593.56605	-0.00022	1.0
43	4	40	44	4	41	1592.90532	-0.00067	1.0
48	8	40	49	8	41	1589.60612	-0.00015	1.0
41	0	41	42	0	42	1594.54711	0.00002	1.0
42	2	41	43	2	42	1593.88672	0.00023	1.0
43	2	41	44	2	42	1593.22594	-0.00005	1.0
44	4	41	45	4	42	1592.56600	0.00042	0.5
45	4	41	46	4	42	1591.90490	-0.00039	1.0
46	6	41	47	6	42	1591.24545	0.00034	1.0
47	6	41	48	6	42	1590.58455	-0.00050	1.0
49	8	41	50	8	42	1589.26533	-0.00002	1.0
42	0	42	43	0	43	1594.20696	0.00021	1.0
43	2	42	44	2	43	1593.54591	-0.00010	1.0
44	2	42	45	2	43	1592.88555	0.00017	1.0
45	4	42	46	4	43	1592.22505	0.00019	1.0
46	4	42	47	4	43	1591.56463	0.00018	1.0
48	6	42	49	6	43	1590.24423	0.00023	1.0
49	8	42	50	8	43	1589.58418	0.00019	1.0
43	0	43	44	0	44	1593.86618	0.00009	1.0
44	2	43	45	2	44	1593.20536	0.00014	1.0
45	2	43	46	2	44	1592.54467	0.00021	1.0
46	4	43	47	4	44	1591.88414	0.00033	1.0
47	4	43	48	4	44	1591.22373	0.00045	1.0
48	6	43	49	6	44	1590.56308	0.00019	1.0
44	0	44	45	0	45	1593.52488	-0.00022	1.0
45	2	44	46	2	45	1592.86409	-0.00001	0.5
46	2	44	47	2	45	1592.20353	0.00032	1.0
49	6	44	50	6	45	1590.22150	0.00020	1.0
50	6	44	51	6	45	1589.56130	0.00035	1.0
45	0	45	46	0	46	1593.18418	0.00039	1.0
46	2	45	47	2	46	1592.52304	0.00038	1.0
47	2	45	48	2	46	1591.86258	0.00094	1.0
46	0	46	47	0	47	1592.84288	0.00072	1.0
47	2	46	48	2	47	1592.18052	-0.00037	1.0
48	2	46	49	2	47	1591.51997	0.00022	1.0
50	4	46	51	4	47	1590.19727	-0.00062	1.0
51	6	46	52	6	47	1589.53639	-0.00079	1.0
47	0	47	48	0	48	1592.50067	0.00046	1.0
48	2	47	49	2	48	1591.83961	0.00080	1.0
49	2	47	50	2	48	1591.17770	0.00015	1.0
50	4	47	51	4	48	1590.51600	-0.00043	1.0
48	0	48	49	0	49	1592.15846	0.00053	1.0
49	2	48	50	2	49	1591.49657	0.00017	1.0
50	2	48	51	2	49	1590.83570	0.00068	1.0
51	4	48	52	4	49	1590.17299	-0.00079	1.0
52	4	48	53	4	49	1589.51310	0.00039	1.0
49	0	49	50	0	50	1591.81622	0.00089	1.0
50	2	49	51	2	50	1591.15367	-0.00001	1.0
51	2	49	52	2	50	1590.49192	-0.00025	1.0
51	2	50	52	2	51	1590.81168	0.00105	1.0
53	4	50	54	4	51	1589.48756	0.00001	1.0
4	2	2	4	4	1	1608.12571	-0.00020	1.0
6	4	2	6	6	1	1607.99352	0.00002	1.0
8	6	3	8	6	2	1607.99352	0.00000	1.0
9	7	3	9	7	2	1608.04104	0.00101	0.5
11	9	3	11	9	2	1608.15364	-0.00011	0.5
9	6	4	9	6	3	1607.58643	-0.00063	1.0
19	16	4	19	16	3	1608.19702	0.00079	1.0
17	12	5	17	14	4	1607.19364	-0.00106	0.5
20	16	5	20	16	4	1607.62849	0.00109	0.5
21	16	5	21	18	4	1606.97022	-0.00085	0.5
24	20	5	24	20	4	1608.02608	-0.00031	1.0
26	22	5	26	22	4	1608.21637	-0.00001	1.0
17	12	6	17	12	5	1606.93592	0.00001	1.0
18	13	6	18	13	5	1606.95420	0.00005	0.5
20	15	6	20	15	5	1607.01520	0.00079	1.0
22	16	6	22	18	5	1606.88061	0.00067	1.0
23	17	6	23	19	5	1606.85015	-0.00019	1.0
24	18	6	24	20	5	1606.80609	0.00022	1.0
25	20	6	25	20	5	1607.37633	-0.00055	1.0
30	24	6	30	26	5	1606.03947	0.00048	1.0
31	26	6	31	26	5	1608.06206	0.00008	1.0
22	16	7	22	16	6	1606.62273	-0.00050	1.0
24	18	7	24	18	6	1606.67447	-0.00046	1.0
29	23	7	29	23	6	1607.00520	0.00018	1.0
29	22	8	29	22	7	1606.36755	0.00030	1.0
13	12	1	12	12	0	1616.24413	0.00109	0.5
15	14	1	14	14	0	1617.35878	0.00098	1.0
4	2	2	3	2	1	1610.85825	-0.00024	1.0
6	4	2	5	4	1	1612.18069	-0.00015	0.5
8	6	2	7	6	1	1613.47266	0.00099	0.5
9	7	2	8	7	1	1614.09987	-0.00019	1.0
10	9	2	9	9	1	1614.43232	-0.00093	0.5
12	10	2	11	10	1	1615.90186	-0.00072	1.0
12	11	2	11	11	1	1615.60169	0.00037	1.0
5	2	3	4	2	2	1611.16229	0.00097	1.0
8	5	3	7	5	2	1613.16230	0.00063	0.5
9	6	3	8	6	2	1613.83575	0.00030	0.5
11	8	3	10	8	2	1615.17711	0.00079	1.0
12	9	3	11	9	2	1615.83590	0.00008	1.0
13	10	3	12	10	2	1616.48444	0.00066	0.5
13	11	3	12	11	2	1616.17545	-0.00037	1.0
14	11	3	13	11	2	1617.11752	-0.00049	1.0
15	12	3	14	12	2	1617.73720	0.00023	1.0
16	13	3	15	13	2	1618.33993	0.00026	1.0
4	0	4	3	0	3	1610.17261	-0.00055	1.0
12	8	4	11	8	3	1615.44955	-0.00019	0.5
20	16	4	19	16	3	1620.75309	-0.00018	1.0
26	22	4	25	22	3	1624.14082	-0.00061	0.5
5	0	5	4	0	4	1610.49770	-0.00019	0.5
14	9	5	13	9	4	1616.39025	0.00009	0.5
15	10	5	14	10	4	1617.05549	-0.00034	1.0
16	11	5	15	11	4	1617.72769	0.00064	0.5
17	12	5	16	12	4	1618.40447	0.00011	1.0
6	0	6	5	0	5	1610.82297	0.00066	0.5
18	13	6	17	13	5	1618.64664	0.00001	1.0
19	14	6	18	14	5	1619.29692	-0.00023	1.0
20	14	6	19	14	5	1619.99701	0.00003	1.0
23	18	6	22	18	5	1621.87636	-0.00096	1.0
21	14	7	20	14	6	1620.27901	0.00058	1.0
23	17	7	22	17	6	1621.57405	0.00059	1.0
15	8	8	14	8	7	1616.02968	0.00001	1.0
18	10	8	17	10	7	1617.98142	-0.00043	1.0
20	12	8	19	12	7	1619.28292	-0.00064	1.0
26	19	8	25	19	7	1623.19131	0.00004	1.0
19	10	9	18	10	8	1618.30216	0.00082	1.0
21	12	9	20	12	8	1619.60167	0.00057	1.0
16	6	10	15	6	9	1616.02203	-0.00003	0.5
17	8	10	16	8	9	1616.67183	-0.00030	0.5
18	8	10	17	8	9	1617.32189	-0.00008	1.0
19	10	10	18	10	9	1617.97132	-0.00028	1.0
21	12	10	20	12	9	1619.27004	-0.00027	1.0
22	12	10	21	12	9	1619.91930	-0.00013	1.0
24	14	10	23	14	9	1621.21735	0.00002	1.0
16	6	11	15	6	10	1615.69290	-0.00035	0.5
17	6	11	16	6	10	1616.34238	-0.00088	0.5
18	8	11	17	8	10	1616.99273	-0.00027	1.0
19	8	11	18	8	10	1617.64201	-0.00047	1.0
20	10	11	19	10	10	1618.29153	-0.00018	1.0
23	12	11	22	12	10	1620.23768	-0.00032	0.5
24	14	11	23	14	10	1620.88668	0.00033	0.5
25	14	11	24	14	10	1621.53412	-0.00038	1.0
26	16	11	25	16	10	1622.18225	-0.00024	1.0
27	16	11	26	16	10	1622.83056	0.00022	1.0
18	6	12	17	6	11	1616.66355	-0.00058	0.5
19	8	12	18	8	11	1617.31353	-0.00004	1.0
23	12	12	22	12	11	1619.90817	-0.00034	1.0
24	12	12	23	12	11	1620.55700	0.00043	1.0
25	14	12	24	14	11	1621.20441	0.00003	1.0
26	14	12	25	14	11	1621.85142	-0.00051	1.0
27	16	12	26	16	11	1622.49924	-0.00002	1.0
18	6	13	17	6	12	1616.33477	-0.00045	1.0
19	6	13	18	6	12	1616.98414	-0.00053	0.5
20	8	13	19	8	12	1617.63376	-0.00006	1.0
21	8	13	20	8	12	1618.28255	-0.00011	1.0
23	10	13	22	10	12	1619.57965	0.00021	0.5
24	12	13	23	12	12	1620.22703	-0.00034	1.0
25	12	13	24	12	12	1620.87484	-0.00016	1.0
26	14	13	25	14	12	1621.52232	-0.00002	1.0
27	14	13	26	14	12	1622.16960	0.00021	1.0
28	16	13	27	16	12	1622.81712	0.00097	0.5
29	16	13	28	16	12	1623.46269	0.00005	1.0
18	4	14	17	4	13	1616.00664	0.00046	0.5
19	6	14	18	6	13	1616.65488	-0.00081	0.5
20	6	14	19	6	13	1617.30472	-0.00015	1.0
21	8	14	20	8	13	1617.95386	0.00012	1.0
22	8	14	21	8	13	1618.60248	0.00019	1.0
23	10	14	22	10	13	1619.25056	0.00005	1.0
24	10	14	23	10	13	1619.89817	-0.00024	1.0
25	12	14	24	12	13	1620.54594	-0.00004	1.0

Can. J. Chem. Downloaded from www.nrcresearchpress.com by 112.217.228.212 on 09/07/12
For personal use only.

TABLE 3 (*continued*)

J'	K_a'	K_c'	J''	K_a''	K_c''	Observed Wavenumber (cm^{-1})	Deviation[b] (cm^{-1})	wt
26	12	14	- 25	12	13	1621.19241	-0.00081	1.0
27	14	14	- 26	14	13	1621.83936	-0.00078	1.0
29	16	14	- 28	16	13	1623.13227	-0.00074	1.0
18	4	15	- 17	4	14	1615.67739	0.00043	0.5
19	4	15	- 18	4	14	1616.32657	0.00003	0.5
20	6	15	- 19	6	14	1616.97512	-0.00068	0.5
21	6	15	- 20	6	14	1617.62431	-0.00042	1.0
22	8	15	- 21	8	14	1618.27344	0.00012	1.0
25	10	15	- 24	10	14	1620.21683	-0.00024	0.5
26	12	15	- 25	12	14	1620.86398	-0.00032	1.0
27	12	15	- 26	12	14	1621.51077	-0.00041	1.0
29	14	15	- 28	14	14	1622.80387	-0.00002	0.5
30	16	15	- 29	16	14	1623.45036	0.00064	1.0
31	16	15	- 30	16	14	1624.09525	0.00005	1.0
19	4	16	- 18	4	15	1615.99751	0.00030	0.5
21	6	16	- 20	6	15	1617.29525	-0.00031	1.0
22	6	16	- 21	6	15	1617.94403	-0.00020	1.0
23	8	16	- 22	8	15	1618.59238	-0.00017	1.0
24	8	16	- 23	8	15	1619.24066	0.00013	1.0
25	10	16	- 24	10	15	1619.88796	-0.00019	1.0
26	10	16	- 25	10	15	1620.53506	-0.00035	1.0
27	12	16	- 26	12	15	1621.18174	-0.00057	1.0
28	12	16	- 27	12	15	1621.82875	-0.00010	1.0
29	14	16	- 28	14	15	1622.47524	0.00023	1.0
30	14	16	- 29	14	15	1623.12092	0.00012	1.0
19	2	17	- 18	2	16	1615.66733	-0.00033	1.0
20	4	17	- 19	4	16	1616.31660	-0.00050	1.0
21	4	17	- 20	4	16	1616.96556	-0.00064	1.0
22	6	17	- 21	6	16	1617.61429	-0.00068	1.0
23	6	17	- 22	6	16	1618.26333	-0.00005	0.5
25	8	17	- 24	8	16	1619.55867	-0.00046	1.0
26	10	17	- 25	10	16	1620.20737	0.00091	0.5
27	10	17	- 26	10	16	1620.85337	-0.00005	1.0
28	12	17	- 27	12	16	1621.49984	-0.00016	1.0
29	12	17	- 28	12	16	1622.14581	-0.00039	1.0
30	14	17	- 29	14	16	1622.79214	0.00013	1.0
31	14	17	- 30	14	16	1623.43777	0.00033	1.0
32	16	17	- 31	16	16	1624.08261	0.00014	1.0
20	2	18	- 19	2	17	1615.98740	-0.00002	1.0
21	4	18	- 20	4	17	1616.63622	-0.00041	1.0
22	4	18	- 21	4	17	1617.28500	-0.00050	1.0
23	6	18	- 22	6	17	1617.93364	-0.00037	1.0
24	6	18	- 23	6	17	1618.58232	0.00015	1.0
25	8	18	- 24	8	17	1619.22995	-0.00001	1.0
26	8	18	- 25	8	17	1619.87749	0.00011	1.0
27	10	18	- 26	10	17	1620.52447	0.00004	1.0
28	10	18	- 27	10	17	1621.17110	0.00002	1.0
29	12	18	- 28	12	17	1621.81831	0.00096	0.5
30	12	18	- 29	12	17	1622.46269	-0.00054	1.0
31	14	18	- 30	14	17	1623.10861	-0.00009	1.0
20	2	19	- 19	2	18	1615.65778	0.00027	1.0
21	2	19	- 20	2	18	1616.30663	-0.00020	1.0
22	4	19	- 21	4	18	1616.95583	0.00002	1.0
23	4	19	- 22	4	18	1617.60419	-0.00025	1.0
24	6	19	- 23	6	18	1618.25277	0.00006	1.0
25	6	19	- 24	6	18	1618.90087	0.00026	1.0
27	8	19	- 26	8	18	1620.19561	0.00033	1.0
28	10	19	- 27	10	18	1620.84192	-0.00012	1.0
29	10	19	- 28	10	18	1621.48822	-0.00018	1.0
30	12	19	- 29	12	18	1622.13487	0.00051	1.0
31	12	19	- 30	12	18	1622.77944	-0.00048	0.5
33	14	19	- 32	14	18	1624.06998	0.00020	0.5
21	2	20	- 20	2	19	1615.97681	0.00002	1.0
22	2	20	- 21	2	19	1616.62590	0.00002	0.5
23	4	20	- 22	4	19	1617.27380	-0.00083	1.0
24	4	20	- 23	4	19	1617.92278	-0.00024	1.0
25	6	20	- 24	6	19	1618.57111	0.00007	1.0
27	8	20	- 26	8	19	1619.86601	0.00006	1.0
28	8	20	- 27	8	19	1620.51346	0.00064	1.0
29	10	20	- 28	10	19	1621.15973	0.00043	1.0
30	10	20	- 29	10	19	1621.80600	0.00063	1.0
31	12	20	- 30	12	19	1622.45124	0.00021	1.0
32	12	20	- 31	12	19	1623.09626	-0.00001	1.0
21	0	21	- 20	0	20	1615.64665	0.00017	1.0
22	2	21	- 21	2	20	1616.29548	-0.00023	1.0
23	2	21	- 22	2	20	1616.94426	-0.00032	1.0
24	4	21	- 23	4	20	1617.59302	-0.00007	1.0
25	4	21	- 24	4	20	1618.24114	-0.00010	1.0
26	6	21	- 25	6	20	1618.88905	0.00004	1.0
27	6	21	- 26	6	20	1619.53640	-0.00000	1.0
28	8	21	- 27	8	20	1620.18360	0.00020	1.0
29	8	21	- 28	8	20	1620.83064	0.00064	1.0
30	10	21	- 29	10	20	1621.47682	0.00063	1.0
31	10	21	- 30	10	20	1622.12226	0.00028	0.5
32	12	21	- 31	12	20	1622.76749	0.00016	1.0
34	14	21	- 33	14	20	1624.05633	-0.00043	0.5
22	0	22	- 21	0	21	1615.96546	0.00019	1.0
23	2	22	- 22	2	21	1616.61414	-0.00013	1.0
24	2	22	- 23	2	21	1617.26275	-0.00016	1.0
25	4	22	- 24	4	21	1617.91081	-0.00038	1.0
26	4	22	- 25	4	21	1618.55887	-0.00023	1.0
27	6	22	- 26	6	21	1619.20649	-0.00013	1.0
28	6	22	- 27	6	21	1619.85376	0.00000	1.0
29	8	22	- 28	8	21	1620.50078	0.00029	1.0
30	8	22	- 29	8	21	1621.14654	-0.00028	1.0
31	10	22	- 30	10	21	1621.79300	0.00027	1.0
32	10	22	- 31	10	21	1622.43862	0.00040	1.0
33	12	22	- 32	12	21	1623.08256	-0.00072	0.5
34	12	22	- 33	12	21	1623.72768	-0.00023	1.0
23	0	23	- 22	0	22	1616.28397	0.00028	1.0
24	2	23	- 23	2	22	1616.93225	-0.00022	1.0
25	2	23	- 24	2	22	1617.58039	-0.00050	1.0
26	4	23	- 25	4	22	1618.22885	-0.00009	1.0
27	4	23	- 26	4	22	1618.87667	0.00007	1.0
28	6	23	- 27	6	22	1619.52386	-0.00002	1.0
29	6	23	- 28	6	22	1620.17114	0.00039	1.0
30	8	23	- 29	8	22	1620.81809	0.00087	1.0
31	8	23	- 30	8	22	1621.46339	0.00011	1.0
32	10	23	- 31	10	22	1622.10897	0.00006	1.0
33	10	23	- 32	10	22	1622.75466	0.00055	1.0
35	12	23	- 34	12	22	1624.04352	0.00033	1.0
24	0	24	- 23	0	23	1616.60186	0.00010	1.0
25	2	24	- 24	2	23	1617.24997	-0.00035	1.0
26	2	24	- 25	2	23	1617.89828	-0.00023	1.0
27	4	24	- 26	4	23	1618.54628	-0.00004	1.0
28	4	24	- 27	4	23	1619.19324	-0.00050	1.0
29	6	24	- 28	6	23	1619.84079	0.00003	1.0
30	6	24	- 29	6	23	1620.48753	0.00015	1.0
31	8	24	- 30	8	23	1621.13453	0.00094	0.5
32	8	24	- 31	8	23	1621.77940	0.00003	1.0
34	10	24	- 33	10	23	1623.06977	0.00013	1.0
36	12	24	- 35	12	23	1624.35812	0.00000	1.0
25	0	25	- 24	0	24	1616.91961	0.00014	1.0
26	2	25	- 25	2	24	1617.56771	-0.00010	1.0
27	2	25	- 26	2	24	1618.21549	-0.00028	1.0
28	4	25	- 27	4	24	1618.86335	0.00001	1.0
29	4	25	- 28	4	24	1619.50968	-0.00084	0.5
30	6	25	- 29	6	24	1620.15710	-0.00019	1.0
31	6	25	- 30	6	24	1620.80407	0.00042	1.0
32	8	25	- 31	8	24	1621.44932	-0.00027	0.5
34	10	25	- 33	10	24	1622.74119	0.00101	0.5
35	10	25	- 34	10	24	1623.38528	0.00048	1.0
36	12	25	- 35	12	24	1624.02975	0.00078	1.0
26	0	26	- 25	0	25	1617.23638	-0.00044	1.0
27	2	26	- 26	2	25	1617.88481	-0.00012	1.0
28	2	26	- 27	2	25	1618.53285	0.00019	1.0
29	4	26	- 28	4	25	1619.17979	-0.00021	1.0
30	4	26	- 29	4	25	1619.82731	0.00038	1.0
31	6	26	- 30	6	25	1620.47371	0.00026	1.0
32	6	26	- 31	6	25	1621.11972	0.00016	1.0
33	8	26	- 32	8	25	1621.76567	0.00044	1.0
34	8	26	- 33	8	25	1622.41138	0.00091	1.0
35	10	26	- 34	10	25	1623.05575	0.00049	1.0
36	10	26	- 35	10	25	1623.70031	0.00071	1.0
37	12	26	- 36	12	25	1624.34284	-0.00063	0.5
27	0	27	- 26	0	26	1617.55367	-0.00014	1.0
28	2	27	- 27	2	26	1618.20148	-0.00022	1.0
30	4	27	- 29	4	26	1619.49643	0.00014	0.5
31	4	27	- 30	4	26	1620.14317	0.00019	1.0
32	6	27	- 31	6	26	1620.78997	0.00072	0.5
33	6	27	- 32	6	26	1621.43539	0.00029	1.0
28	0	28	- 27	0	27	1617.87020	-0.00025	1.0
29	2	28	- 28	2	27	1618.51823	0.00012	1.0
30	2	28	- 29	2	27	1619.16584	0.00047	1.0
32	4	28	- 31	4	27	1620.45934	0.00067	1.0
34	6	28	- 33	6	27	1621.75080	0.00053	0.5
35	8	28	- 34	8	27	1622.39629	0.00088	0.5
36	8	28	- 35	8	27	1623.04166	0.00156	0.0
37	10	28	- 36	10	27	1623.68653	0.00220	0.0
38	10	28	- 37	10	27	1624.32902	0.00093	0.0
29	0	29	- 28	0	28	1618.18741	0.00069	0.0
31	2	29	- 30	2	28	1619.48148	0.00030	0.0
32	4	29	- 31	4	28	1620.12855	0.00076	0.0
33	4	29	- 32	4	28	1620.77486	0.00087	0.0
34	6	29	- 33	6	28	1621.42094	0.00119	0.0
35	6	29	- 34	6	28	1622.06635	0.00127	0.0
39	10	29	- 38	10	28	1624.64466	0.00288	0.0
40	12	29	- 39	12	28	1625.28710	0.00233	0.0
30	0	30	- 29	0	29	1618.50320	0.00057	0.0
32	2	30	- 31	2	29	1619.79783	0.00121	0.0
33	4	30	- 32	4	29	1620.44419	0.00119	0.0
34	4	30	- 33	4	29	1621.09072	0.00177	0.0
35	6	30	- 34	6	29	1621.73652	0.00207	0.0
36	6	30	- 35	6	29	1622.38140	0.00188	0.0
37	8	30	- 36	8	29	1623.02678	0.00266	0.0
39	10	30	- 38	10	29	1624.31510	0.00317	0.0
31	0	31	- 30	0	30	1618.82146	0.00329	0.0
32	2	31	- 31	2	30	1619.46963	0.00448	0.0
33	2	31	- 32	2	30	1620.11729	0.00558	0.0
34	4	31	- 33	4	30	1620.76407	0.00623	0.0
35	4	31	- 34	4	30	1621.41066	0.00712	0.0
36	6	31	- 35	6	30	1622.05652	0.00773	0.0
39	8	31	- 38	8	30	1623.99080	0.00901	0.0
40	10	31	- 39	10	30	1624.63478	0.00961	0.0
41	10	31	- 40	10	30	1625.27769	0.00963	0.0

Can. J. Chem. Downloaded from www.nrcresearchpress.com by 112.217.228.212 on 09/07/12
For personal use only.

TABLE 3 (*concluded*)

J'	K_a'	K_c'	J''	K_a''	K_c''	Observed Wavenumber (cm^{-1})	Deviation[b] (cm^{-1})	wt
33	2	32	32	2	31	1619.77854	-0.00156	0.0
34	2	32	33	2	31	1620.42446	-0.00196	0.0
35	4	32	34	4	31	1621.06974	-0.00257	0.0
36	4	32	35	4	31	1621.71455	-0.00321	0.0
37	6	32	36	6	31	1622.35872	-0.00404	0.0
38	6	32	37	6	31	1623.00205	-0.00524	0.0
39	8	32	38	8	31	1623.64411	-0.00725	0.0
40	8	32	39	8	31	1624.28690	-0.00804	0.0
34	2	33	33	2	32	1620.09414	-0.00055	0.0
35	2	33	34	2	32	1620.74011	-0.00067	0.0
36	4	33	35	4	32	1621.38522	-0.00120	0.0
37	4	33	36	4	32	1622.02989	-0.00173	0.0
39	6	33	38	6	32	1623.31791	-0.00272	0.0
40	8	33	39	8	32	1623.96127	-0.00315	0.0
41	8	33	40	8	32	1624.60442	-0.00331	0.0
34	0	34	33	0	33	1619.76217	-0.00047	1.0
35	2	34	34	2	33	1620.40849	-0.00043	1.0
36	2	34	35	2	33	1621.05436	-0.00040	1.0
37	4	34	36	4	33	1621.69964	-0.00052	0.5
38	4	34	37	4	33	1622.34438	-0.00073	0.5
39	6	34	38	6	33	1622.98787	-0.00171	0.0
40	6	34	39	6	33	1623.63256	-0.00103	0.0
41	8	34	40	8	33	1624.27490	-0.00221	0.0
35	0	35	34	0	34	1620.07628	-0.00045	1.0
36	2	35	35	2	34	1620.72285	0.00007	1.0
37	2	35	36	2	34	1621.36792	-0.00046	0.5
38	4	35	37	4	34	1622.01324	-0.00030	1.0
39	4	35	38	4	34	1622.65785	-0.00038	0.0
40	6	35	39	6	34	1623.30081	-0.00163	0.0
41	6	35	40	6	34	1623.94488	-0.00130	0.0
42	8	35	41	8	34	1624.58814	-0.00129	0.0
43	8	35	42	8	34	1625.23067	-0.00151	0.0
36	0	36	35	0	35	1620.38998	-0.00048	1.0
37	2	36	36	2	35	1621.03618	-0.00009	1.0
38	2	36	37	2	35	1621.68216	0.00052	1.0
39	4	36	38	4	35	1622.32595	-0.00059	0.0
40	4	36	39	4	35	1622.96995	-0.00103	0.0
42	6	36	41	6	35	1624.25750	-0.00091	0.0
41	6	36	40	6	35	1623.61375	-0.00118	1.0
37	0	37	36	0	36	1620.70369	-0.00014	1.0
38	2	37	37	2	36	1621.34942	0.00002	1.0
39	2	37	38	2	36	1621.99414	-0.00038	1.0
40	4	37	39	4	36	1622.63857	-0.00061	1.0
41	4	37	40	4	36	1623.28271	-0.00065	1.0
38	0	38	37	0	37	1621.01647	-0.00035	1.0
39	2	38	38	2	37	1621.66193	-0.00023	1.0
41	4	38	40	4	37	1622.95183	0.00039	1.0
43	6	38	42	6	37	1624.23816	-0.00064	1.0
44	6	38	43	6	37	1624.88113	-0.00061	1.0
39	0	39	38	0	38	1621.32959	0.00014	1.0
40	2	39	39	2	38	1621.97483	0.00028	1.0
41	2	39	40	2	38	1622.61908	-0.00011	1.0
43	4	39	42	4	38	1623.90646	-0.00055	1.0
44	6	39	43	6	38	1624.54969	-0.00049	1.0
45	6	39	44	6	38	1625.19278	-0.00006	1.0
46	8	39	45	8	38	1625.83458	-0.00041	1.0
40	0	40	39	0	39	1621.64167	-0.00004	1.0
41	2	40	40	2	39	1622.28674	0.00016	1.0
42	2	40	41	2	39	1622.93064	-0.00032	1.0
44	4	40	43	4	39	1624.21834	0.00007	1.0
41	0	41	40	0	40	1621.95367	0.00006	1.0
43	2	41	42	2	40	1623.24251	0.00014	1.0
44	4	41	43	4	40	1623.88525	-0.00077	1.0
45	4	41	44	4	40	1624.52956	0.00039	1.0
46	6	41	45	6	40	1625.17194	0.00013	1.0
47	6	41	46	6	40	1625.81348	-0.00045	1.0
42	0	42	41	0	41	1622.26509	-0.00004	1.0
43	2	42	42	2	41	1622.90975	0.00024	1.0
45	4	42	44	4	41	1624.19667	-0.00013	1.0
46	4	42	45	4	41	1624.83937	-0.00032	1.0
43	0	43	42	0	42	1622.57611	-0.00018	1.0

[a]All measured transitions are included. Weights given are those used to obtain the 2^1 state constants given in Table 2.
[b]The deviation is the observed frequency minus that calculated using the constants obtained (Table 2) in the analysis omitting the Coriolis interaction.

modes are combined. If it is $\nu_7 + \nu_{11}$ or $\nu_4 + \nu_7$, this would set ν_{11} or ν_4 at $1598-661 = 937\,cm^{-1}$; no band was seen clearly here, however.

Discussion and conclusions

Good progress has been made in assigning for the first time the infrared spectrum of NH_2BF_2. It is somewhat of a pity that not all the normal modes could be accounted for. A major contributing factor to this difficulty was the rather low yield of desired product in the face of many competing reactions. This is entirely in keeping with the complex known chemistry of the system (4). Difficulties in removing all residual diethyl ether did not help either.

Of the bands that could be definitely assigned, the agreement

TABLE 4. Results of a Coriolis fit of the rotational levels of the 2^1 state

(*a*) Derived constants/cm^{-1}.

		a-type Interaction	b- type Interaction
2^1 level:	A	0.3342433(11)	0.3342443(12)
	B	0.31968975(98)	0.31968882(99)
	C	0.16303438(13)	0.16303437(13)
	$\Delta_J \times 10^6$	0.17650(64)	0.17649(64)
	$\Delta_{JK} \times 10^7$	0.362(46)	0.362(46)
	$\Delta_K \times 10^6$	0.1950(64)	0.1951(64)
	$\delta_J \times 10^7$	0.7719(32)	0.7719(32)
	$\delta_K \times 10^6$	0.2172(18)	0.2172(18)
	T_0	1608.70707(7)	1608.70707(7)
Unseen level:	(A + B)	0.653654(14)	0.653647(14)
	T_0	1598.5280(36)	1598.5301(36)
ξ^a		0.003191(19)	0.003019(18)
ζ^a		0.00955(6)	0.00944(6)
Std. dev. of fit		0.000360	0.000360

Can. J. Chem. Downloaded from www.nrcresearchpress.com by 112.217.228.212 on 09/07/12
For personal use only.

TABLE 4 (*concluded*)

(*b*) Goodness of the fit (levels with $K_c' = 29–33$)

Level	Energy	wt	obs.-calc./cm^{-1} a-type	obs.-calc./cm^{-1} b-type	Level	Energy	wt	obs.-calc./cm^{-1} a-type	obs.-calc./cm^{-1} b-type
29 0 29	1755.27878	0.66667	0.00041	0.00042	35 4 31	1863.02017	0.66667	0.00008	0.00010
30 2 29	1774.87919	0.33333	-0.00003	-0.00002	36 6 31	1886.52335	0.66667	-0.00004	-0.00002
31 2 29	1795.13006	0.66667	-0.00002	-0.00001	37 6 31	1910.67346	0.33333	-0.00128	-0.00125
32 4 29	1816.03091	0.66667	0.00029	0.00030	38 8 31	1935.47321	0.33333	-0.00055	-0.00053
33 4 29	1837.58064	0.66667	0.00014	0.00015	39 8 31	1960.92006	0.66667	-0.00001	0.00000
34 6 29	1859.77972	0.66667	0.00035	0.00036	40 10 31	1987.01352	0.66667	0.00023	0.00024
35 6 29	1882.62709	0.66667	0.00022	0.00022	41 10 31	2013.75304	0.66667	0.00004	0.00003
36 8 29	1906.12303	0.33333	0.00040	0.00040	43 12 31	2069.17023	0.33333	0.00003	-0.00001
37 8 29	1930.26613	0.33333	-0.00014	-0.00014	44 14 31	2097.84638	0.33333	-0.00043	-0.00049
38 10 29	1955.05801	0.33333	0.00062	0.00062	32 0 32	1786.08532	0.33333	0.00033	0.00032
39 10 29	1980.49649	0.66667	0.00090	0.00089	33 2 32	1807.64349	0.66667	-0.00026	-0.00028
40 12 29	2006.58112	0.66667	0.00065	0.00064	34 2 32	1829.85187	0.66667	0.00008	0.00004
41 12 29	2033.31209	0.33333	0.00050	0.00049	35 4 32	1852.70877	0.66667	0.00000	-0.00003
42 14 29	2060.69056	0.33333	0.00204	0.00202	36 4 32	1876.21418	0.66667	-0.00010	-0.00014
43 14 29	2088.71035	0.33333	-0.00047	-0.00050	37 6 32	1900.36806	0.66667	0.00012	0.00008
30 0 30	1765.22203	0.66667	0.00017	0.00018	38 6 32	1925.16970	0.66667	0.00035	0.00033
31 2 30	1785.47600	0.33333	0.00018	0.00019	39 8 32	1950.61800	0.66667	-0.00007	-0.00007
32 2 30	1806.37960	0.66667	0.00002	0.00004	40 8 32	1976.71414	0.66667	0.00049	0.00052
33 4 30	1827.93280	0.66667	0.00002	0.00003	33 0 33	1797.00624	0.33333	0.00027	0.00027
34 4 30	1850.13530	0.66667	0.00021	0.00022	34 2 33	1819.21802	0.66667	0.00013	0.00013
35 6 30	1872.98624	0.66667	0.00009	0.00011	35 2 33	1842.07873	0.66667	-0.00018	-0.00019
36 6 30	1896.48556	0.66667	-0.00002	-0.00001	36 4 33	1865.58861	0.66667	-0.00008	-0.00009
37 8 30	1920.63311	0.66667	0.00009	0.00010	37 4 33	1889.74658	0.66667	-0.00026	-0.00027
38 8 30	1945.42809	0.33333	0.00002	0.00002	39 6 33	1940.00617	0.66667	-0.00054	-0.00055
39 10 30	1970.87035	0.66667	0.00002	0.00002	40 8 33	1966.10732	0.66667	-0.00032	-0.00032
42 12 30	2051.07499	0.33333	-0.00124	-0.00127	41 8 33	1992.85546	0.66667	0.00012	0.00013
32 2 31	1796.40148	0.66667	-0.00012	-0.00015	42 10 33	2020.24989	0.33333	0.00051	0.00053
33 2 31	1817.95907	0.66667	0.00016	0.00015	43 10 33	2048.28955	0.33333	0.00022	0.00026
34 4 31	1840.16527	0.66667	0.00011	0.00012	45 12 33	2106.30538	0.33333	0.00023	0.00033

between the observed wavenumbers and those predicted from theory (Table 1) is rather poor (12). It is rather better for NH_2BH_2 (1),[4] but it seems that some new calculations would be in order.

The assignments and analysis of the 2_0^1 band are clear, however. This is one of the relatively rare examples of a perpendicular band of an oblate near-symmetric rotor from which spectroscopic constants have been obtained, others being OCF_2 (13) and CH_2CF_2 (15). The results of three analyses are presented; all give excellent constants. The rotational and distortion constants found when the perturbations are omitted (Tables 2 and 3) are very comparable to those found when they are included (Table 4); in the latter cases the Coriolis constant seems properly determined, although it is a pity we could not distinguish between *a*- or *b*-type interactions. The molecule is one of several (10) for which we have observed Coriolis effects in the rotational fine structure. It was to analyze these that our Coriolis fitting routine was written; results of the other analyses will appear in due course.

Acknowledgements

Financial support of the Natural Sciences and Engineering Research Council of Canada (to M.C.L.G.) in the form of Research Grants is gratefully acknowledged. H.M.J. acknowledges gratefully the award of a Commonwealth Scholarship.

1. M. C. L. GERRY, W. LEWIS-BEVAN, A. J. MERER, and N. P. C. WESTWOOD. J. Mol. Spectrosc. **110**, 153 (1985).
2. A. W. LAUBENGAYER and G. F. CONDIKE. J. Am. Chem. Soc. **70**, 2274 (1948).
3. I. G. RYSS and N. G. PARKHOMENKO. Russ. J. Inorg. Chem. (Engl. Transl.), **11**, 55 (1966).
4. E. F. ROTHGERY, H. A. MCGEE, JR., and S. PUSATCIOGLU. Inorg. Chem. **14**, 2236 (1975).
5. S. PUSATCIOGLU, H. M. MCGEE, JR., A. L. FRICKE, and J. C. HASSLER. J. Appl. Polym. Sci. **21**, 1561 (1967).
6. F. J. LOVAS and D. R. JOHNSON. J. Chem. Phys. **59**, 2347 (1973).
7. G. GUELACHVILI and K. N. RAO. Handbook of infrared standards. Academic Press, New York. 1986. pp. 424–427.
8. R. S. MULLIKEN. J. Chem. Phys. **23**, 1997 (1955).
9. G. HERZBERG. Infrared and Raman spectra of polyatomic molecules. Van Nostrand, New York. 1945. pp. 469–484.
10. M. PEREC and L. N. BECKA. J. Chem. Phys. **43**, 721 (1965).
11. A. G. ROBIETTE and M. C. L. GERRY. J. Mol. Spectrosc. **80**, 403 (1980).
12. T.-K. HA. J. Mol. Struct. (Theochem), **136**, 165 (1986).
13. W. LEWIS-BEVAN, A. J. MERER, M. C. L. GERRY, P. B. DAVIES, A. MORTON-JONES, and P. A. HAMILTON. J. Mol. Spectrosc. **113**, 458 (1985).
14. J. K. G. WATSON. *In* Vibrational spectra and structure, a series of advances. Vol. 6. *Edited by* J. R. Durig. Elsevier, Amsterdam. 1977. pp. 1–80.
15. W. J. LAFFERTY, J. P. SATTLER, T. L. WORCHESKY, and K. J. RITTER. J. Mol. Spectrosc. **87**, 416 (1981).

Can. J. Chem. Downloaded from www.nrcresearchpress.com by 112.217.228.212 on 09/07/12
For personal use only.

Synthesis and characterization of $(\eta^5\text{-}C_5Me_5)W(NO)I_2$, a monomeric, formally 16-electron complex

NEIL H. DRYDEN AND PETER LEGZDINS[1]
Department of Chemistry, The University of British Columbia, Vancouver, B.C., Canada V6T 1Y6
AND
FREDERICK W. B. EINSTEIN AND RICHARD H. JONES
Department of Chemistry, Simon Fraser University, Burnaby, B. C., Canada V5A 1S6

Received February 7, 1988

This paper is dedicated to Professor Charles A. McDowell on the occasion of his 70th birthday

NEIL H. DRYDEN, PETER LEGZDINS, FREDERICK W. B. EINSTEIN, and RICHARD H. JONES. Can. J. Chem. **66**, 2100 (1988).

The compound $(\eta^5\text{-}C_5Me_5)W(NO)I_2$ has been prepared by treating $(\eta^5\text{-}C_5Me_5)W(NO)(CO)_2$ with I_2. A single crystal X-ray crystallographic analysis establishes that the formally 16-electron complex possesses a monomeric, three-legged piano stool molecular structure in the solid state. Solution molecular weight measurements also indicate no significant degree of association of the compound.

NEIL H. DRYDEN, PETER LEGZDINS, FREDERICK W. B. EINSTEIN et RICHARD H. JONES. Can. J. Chem. **66**, 2100 (1988).

On a préparé le $(\eta^5\text{-}C_5Me_5)W(NO)I_2$ en faisant réagir du $(\eta^5\text{-}C_5Me_5)W(NO)(CO)_2$ avec du I_2. Faisant appel à une analyse par diffraction des rayons-X, on a établi que, à l'état solide, ce complexe comportant formellement 16 électrons possède une structure moléculaire monomère en forme de banc de piano à trois pieds. Des mesures de poids moléculaire effectuées sur des solutions indiquent que ce composé ne conduit pas à beaucoup d'association.

[Traduit par la revue]

Can. J. Chem. Downloaded from www.nrcresearchpress.com by 112.217.228.212 on 09/07/12
For personal use only.

Metal halide complexes serve as useful starting materials for the synthesis of many organometallic compounds (1). Indeed, the availability of the complexes

$$[(\eta^5\text{-}C_5R_5)M(NO)X_2]_n$$

R = Me, H

M = Mo, W

X = Cl, Br, I

n = 1 or 2

has enabled us to prepare various classes of Group 6 nitrosyl compounds (2–4). Although the dihalo species have been known for a long time, their molecular natures both in solution and in the solid state are still very uncertain. They have generally been formulated as halo-bridged dimers in the solid state (5) on the basis of satisfying an 18-electron, filled valence shell configuration for each metal centre. However, to the best of our knowledge, none of them has been structurally characterized. In this paper we wish to report the optimized synthesis of the title complex and to describe its solution and solid state physical characteristics, which clearly indicate that rather than being the dimer **A** it is the novel monomer **B**.

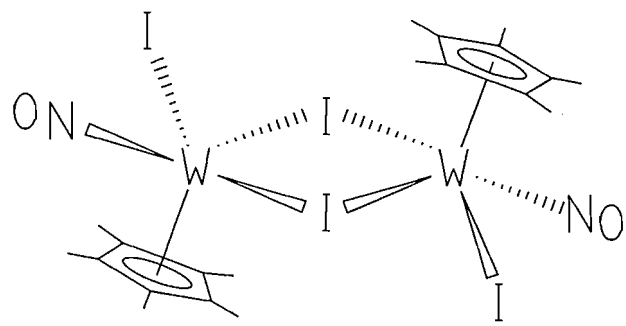

A

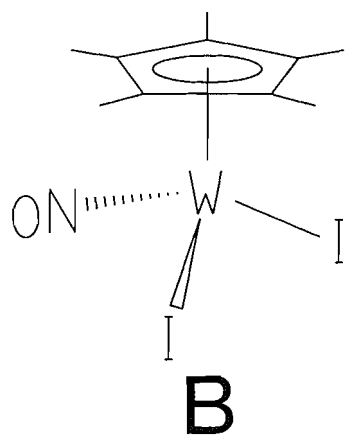

B

Experimental

All reactions and subsequent manipulations were performed under anaerobic and anhydrous conditions. General procedures employed in these laboratories have previously been described in detail (4). The solution molecular weight determination was effected by the Signer method (6) with azobenzene as the reference compound. A published procedure for the preparation of LiC_5Me_5 was used (7). All other chemicals were used as received from commercial suppliers.

Caution: Due to the evolution of CO gas during all of these syntheses, all reactions should be properly vented to a fumehood.

Preparation of $(\eta^5\text{-}C_5Me_5)W(NO)(CO)_2$

The complex was previously prepared (8) using NaC_5Me_5 as the permethylcyclopentadienyl source. In our opinion, a more efficient and convenient synthesis (especially for larger scale preparations) is the one described below.

A 1-L, 3-necked flask was charged with LiC_5Me_5 (17.5 g, 123 mmol) and was connected to a vacuum line. Then $W(CO)_6$ (44.0 g, 125 mmol) and THF (300 mL) were added. The initial pale yellow solution was refluxed gently with stirring for 4 days. The final

[1]Author to whom correspondence may be addressed.

Can. J. Chem. Downloaded from www.nrcresearchpress.com by 112.217.228.212 on 09/07/12
For personal use only.

red solution was cannulated into a 1-L sublimation flask. A yellow solution of Diazald (26.4 g, 123 mmol, Aldrich) in THF (150 mL) was added dropwise to the red solution via a pressure-equalized dropping funnel over a period of 30 min. Vigorous gas evolution occurred, and the reaction mixture was stirred for an additional 3 h after the Diazald addition was complete. Solvent was removed from the reaction mixture *in vacuo* to obtain an orange-tan solid. Initial sublimation of the solid material onto a water-cooled probe (10^{-3} Torr (1 Torr = 133.3 Pa), static vacuum, 60°C) for 3 h removed any unreacted W $(CO)_6$. Sublimation of the remaining solid onto a water-cooled probe (10^{-3} Torr, dynamic vacuum, 110–115°C) over 24 h yielded $(\eta^5\text{-}C_5Me_5)W(NO)(CO)_2$ as an orange crystalline solid (40.5 g, 81% yield based on LiC_5Me_5). The product was characterized by its distinctive nitrosyl and carbonyl infrared absorptions (CH_2Cl_2: ν(CO), 1992, 1912 cm^{-1}; ν(NO), 1633 cm^{-1}) and used without further purification.

Preparation of $(\eta^5\text{-}C_5Me_5)W(NO)I_2$

The synthesis of this compound has previously been described (9, 10). The method presented here is a modification of these earlier procedures.

An orange solution of $(\eta^5\text{-}C_5Me_5)W(NO)(CO)_2$ (8.1 g, 20 mmol) in toluene (100 mL) was rapidly cannulated into a stirred, dark red-purple solution of I_2 (5.0 g, 20 mmol) in toluene (150 mL). The reaction mixture evolved copious quantities of gas and became green in colour. After vigorous gas evolution ceased, the reaction mixture was warmed to 30–35°C, and the pressure in the flask was reduced. The flask was periodically reevacuated over 3 h to remove the remaining slowly evolving CO. Then the volume of solvent was reduced *in vacuo* to approximately 30 mL, resulting in the formation of a bright green, microcrystalline precipitate. Hexanes (50 mL) were added, and the mixture was cooled overnight at −15°C. Isolation of the resulting bright green microcrystals from the pale green supernatant by filtration on a glass frit and washing with hexanes (3 × 10 mL) afforded analytically pure $(\eta^5\text{-}C_5Me_5)W(NO)I_2$ (9.9 g, 83% yield); ir (CH_2Cl_2) ν: 1630 (NO) cm^{-1}; ^1H nmr ($CDCl_3$) δ: 2.18 (s, C-CH_3); $^{13}C\{^1H\}$ nmr ($CDCl_3$) δ: 117.5 (*C*-CH_3), 12.8 (C-*C*H_3). *Mol. Wt.* (20°C, CH_2Cl_2) calcd. for $C_{10}H_{15}NOI_2W$: 603 g/mol; measured: 606 g/mol. *Anal.* calcd. for $C_{10}H_{15}NOI_2W$: C 19.92, H 2.51, N 2.32; found: C 19.94, H 2.52, N 2.27.

Crystals suitable for X-ray crystallographic analysis were obtained from a toluene solution at −15°C.

Crystal structure analysis

Crystal data:

$C_{10}H_{15}NOWI_2$ fw = 602.89

Monoclinic, $P2_1/m$ (confirmed by refinement), a = 7.148(2), b = 13.073(10), c = 8.563(3) Å, β = 111.63(2)°, V = 743.81 Å^3, Z = 2, D_c = 2.692 g cm^{-3}, μ(MoKα) = 12.02 mm^{-1}, (MoKα$_1$) = 0.7093 Å.

A suitable crystal (0.21 × 0.17 × 0.16 mm) was mounted in a thin-walled glass capillary and transferred to an Enraf–Nonius CAD4F diffractometer equipped with graphite monochromated MoKα radiation. The unit-cell parameters were obtained from the accurate setting angles of 24 reflections ($21 < 2\theta < 33^0$). Data were collected in the range $4 < 2\theta \leq 50^0$, $h,k, \pm l$, using the θ–2θ scan technique. The scan width was 1.0 + 0.35 tan θ^0, and the scan speed varied between 0.75 and 2.75° min^{-1}. Two standard reflections measured every hour showed a marked decline in intensity with time (24%), and these standards were used to scale the data. The data were corrected for Lorentz polarization effects and analytically for absorption (11) (with transmission factors varying between 0.152 and 0.248). A total of 1395 reflections were collected, of which 990 having $I \geq 3\sigma(I)$ were used in the crystal structure analysis.

Models in both $P2_1$ and $P2_1/m$ were considered. Ultimately, the best justified model was that in $P2_1/m$ with disorder allowing the molecule to achieve site symmetry m. The disorder involved one iodine atom and the nitrosyl group. To achieve convergence, restraints were applied to the W—N, N—O, and the C—C(methyl) lengths together with the along-bond component of the anisotropic motion of the atoms in the pentamethylcyclopentadienyl group (12, 13). The hydrogen atoms of the methyl groups were geometrically placed and allowed to "ride" on the carbon atoms to which they were bonded. The variables included in the final cycles of refinement were scale, positional, and anisotropic thermal parameters for the non-hydrogen atoms, except for isotropic variables for the disordered nitrogen and oxygen atoms, and one isotropic thermal parameter for all the hydrogen atoms. Although an even more sophisticated model that would split all atom sites according to the disorder could be developed, our estimate of the displacements involved would be less than 0.05 Å for the tungsten atom splitting (since it is presumably mainly dependent on the difference between the W—I and W—"NO" bond lengths).

TABLE 1. Atomic coordinates (fractional × 10^4) and U_{eq} or U_{iso} ($U \times 10^4$ Å^2) for non-hydrogen atoms

Atom	x/a	y/b	z/c	U_{eq}/U_{iso}
W(1)	948(1)	2500	2041(1)	527
I(1)	2333(3)	2500	−442(3)	904
I(2)	2942(5)	3860(4)	4252(5)	911
N(1)	2385(48)	3582(20)	3125(43)	934(98)
O(1)	2928(93)	4331(35)	3934(68)	1736(299)
C(1)	−1827(36)	2500	2765(26)	715
C(2)	−1977(25)	3355(14)	1805(31)	787
C(3)	−2260(20)	3012(15)	146(22)	632
C(11)	−1725(71)	2500	4562(32)	1614
C(12)	−2116(37)	4450(18)	2310(54)	1289
C(13)	−2689(38)	3719(30)	−1333(37)	1351

The final residuals were R = 0.047, and R_w = 0.064, and the goodness of fit was 1.034. Refinement was by full-matrix least-squares minimization of the function $\Sigma w(|F_o| - |F_c|)^2$, where w was calculated from the three-term Chebyshev series, $w = [304.5t_o(x) + 397.3t_1(x) + 128.8t_2(x)]^{-1}$, where $x = F_o - F(\max)$ (14). The refinement was considered complete when the ratio of all shifts to esd's was less than 0.1. The highest peak in the final difference map was 3.10(17) e Å^{-3} and was situated 0.95 Å from the tungsten atom. Complex neutral atom scattering factors were taken from International tables for crystallography (15). Calculations were carried out on a Microvax II computer with use of the NRC VAX crystal structure system (16) and the CRYSTALS suite of programs (17). Positional parameters are given in Table 1. Selected bond distances and angles are listed in Table 2. Anisotropic thermal parameters, hydrogen atom coordinates, and tables of calculated and observed structure factors have been deposited as supplementary material.[2] A view of the molecule is given in Fig. 1 (18).

Results and discussion

The preparation of the title compound can be effected by the sequential transformations summarized in eq. [1]–[3] below.

[1] $W(CO)_6 + Li(C_5Me_5) \xrightarrow[-3\ CO]{THF,\ reflux} Li[(\eta^5\text{-}C_5Me_5)W(CO)_3]$

[2] $Li[(\eta^5\text{-}C_5Me_5)W(CO)_3] \xrightarrow[Diazald]{THF} (\eta^5\text{-}C_5Me_5)W(NO)(CO)_2$

[3*a*] $(\eta^5\text{-}C_5Me_5)W(NO)(CO)_2 \xrightarrow[I_2,\ -CO]{Toluene} (\eta^5\text{-}C_5Me_5)W(NO)(CO)I_2$

[3*b*] $(\eta^5\text{-}C_5Me_5)W(NO)(CO)I_2 \xrightarrow[35°C,\ in\ vacuo\ -CO]{Toluene} (\eta^5\text{-}C_5Me_5)W(NO)I_2$

[2] A complete set of data can be obtained at a nominal charge, from the Depository of Unpublished Data, CISTI, National Research Council of Canada, Ottawa, Ontario, Canada K1A 0S2.

Can. J. Chem. Downloaded from www.nrcresearchpress.com by 112.217.228.212 on 09/07/12
For personal use only.

TABLE 2. Bond lengths and angles

(*a*). Bond lengths with esd's in parentheses

Bond	Length (Å)
W(1)—I(1)	2.655(2)
W(1)—I(2)	2.605(3)
W(1)—N(1)	1.79*
W(1)—C(1)	2.29(2)
W(1)—C(2)	2.31(2)
W(1)—C(3)	2.37(1)
N(1)—O(1)	1.18*
C(1)—C(2)	1.37(2)
C(1)—C(11)	1.51*
C(2)—C(3)	1.43(3)
C(2)—C(12)	1.51*
C(3)—C(3)	1.34(4)
C(3)—C(13)	1.51*

*Denotes that a restraint was applied to this bond.

(*b*). Bond angles with esd's in parentheses

Bonds	Angle (deg)
I(2)—W(1)—I(1)	108.5(1)
N(1)—W(1)—I(1)	95.9(12)
N(1)—W(1)—I(2)	96.1(12)
O(1)—N(1)—W(1)	163.9(46)
C(2)—C(1)—C(2)	109.6(22)
C(2)—C(1)—C(11)	125.1(11)
C(3)—C(2)—C(1)	106.9(16)
C(1)—C(2)—C(12)	127.0(26)
C(3)—C(2)—C(12)	125.6(27)
C(3)—C(3)—C(2)	108.3(11)
C(2)—C(3)—C(13)	123.6(24)
C(3)—C(3)—C(13)	127.9(19)

The I_2 addition (eq. [3]) proceeds via a relatively stable intermediate complex, i.e., $(\eta^5\text{-}C_5Me_5)W(NO)(CO)I_2$, thereby making it necessary to warm the toluene solution under reduced pressure to induce the complete decarbonylation of this intermediate compound.

The final $(\eta^5\text{-}C_5Me_5)W(NO)I_2$ product is a bright green, crystalline solid. It is interesting that at approximately 25°C it displays reversible thermochromism, changing from bright green to golden yellow. This colour change is evident in both the solid state and in solution. To the best of our knowledge, this phenomenon is unique to this member of the family of compounds having the empirical composition $(\eta^5\text{-}C_5R_5)M(NO)X_2$. However, since the ^1H nmr spectrum of $(\eta^5\text{-}C_5Me_5)W(NO)I_2$ in $CDCl_3$ is invariant from 0 to 40°C, no inference concerning the physical basis for the observed thermochromism may be drawn at present.

Previous attempts to grow crystals of the analogous cyclopentadienyl tungsten diiodide complex suitable for X-ray crystallographic analysis were unsuccessful.[3] This was attributed to the low solubility of the cyclopentadienyl compounds in organic solvents (5). The replacement of the cyclopentadienyl ligand with its permethylcyclopentadienyl analogue can lead to marked increases in solubility and crystallizability (20), and this is indeed the case in this instance. In fact, the increased solubility of $(\eta^5\text{-}C_5Me_5)W(NO)I_2$ allows its solution molecular weight to be determined, something not possible for its cyclopentadienyl analogue (5). We measured the molecular weight of the diiodo complex in dichloromethane to be 606 g/mol. This value quite clearly indicates that there is no significant amount of association of the molecular units even in a non-coordinating solvent such as dichloromethane (21). Fortunately, the permethylated species also forms single crystals suitable for X-ray crystallographic analysis.

[3]J. T. Martin. Personal communication.

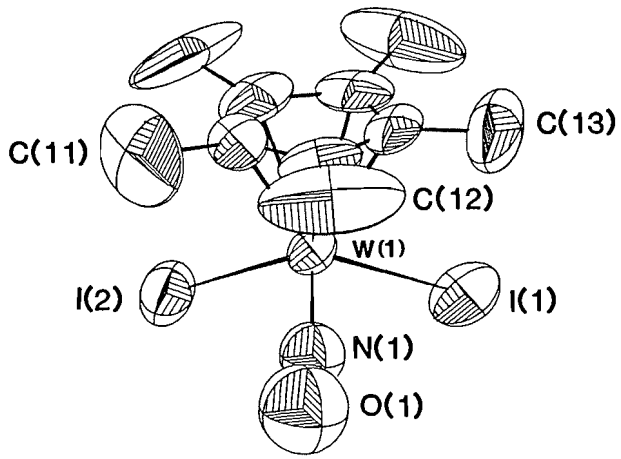

FIG. 1. SNOOPI plot of the molecular structure of $(\eta^5\text{-}C_5Me_5)W(NO)I_2$.

The crystal structure of $(\eta^5\text{-}C_5Me_5)W(NO)I_2$ consists of a closely packed array of monomeric molecular units, with normal van der Waals contacts between the units. Hence, the structure establishes unambiguously the monomeric nature of $(\eta^5\text{-}C_5Me_5)W(NO)I_2$ (Fig. 1). Discussion of the detailed intramolecular geometry of the monomer is unfortunately limited by the disorder of the nitrosyl group and one of the iodine atoms. Nevertheless, the unrestrained bond lengths in the $(\eta^5\text{-}C_5Me_5)W$ fragment are in good agreement with previously determined structures. Thus, the W—$(\eta^5\text{-}C_5Me_5)$–centroid distance of 2.006 Å is comparable to that found in $(\eta^5\text{-}C_5Me_5)W(NO)(CO)_2$ (2.008 Å)(8). The most noteworthy bond lengths are the W—I bonds (W—I(1) = 2.655(2) Å and W—I(2) = 2.605(3) Å (disordered)), which are significantly shorter than those seen in related 18-electron compounds, e.g., 2.803(1) Å in $(\eta^5\text{-}C_5H_5)W(NO)(\eta^3\text{-}C_3H_3)I$ (22), 2.864(av) Å in $(t\text{-}C_4H_9NC)_3W(CO)_2I_2$ (23), 2.845(2) Å in $W(CO)_4(PMe_3)I_2$ (24). A possible explanation for this may be the occurrence of some $W(d\pi)$–$I(p\pi)$ bonding in $(\eta^5\text{-}C_5Me_5)W(NO)I_2$. A similar inference can be drawn for $[WI(NEt_2)_2]_2$ where similar W—I bond lengths are observed (W—I = 2.682(av)) Å (25). Furthermore, similar multiple bonding has also been invoked in analogous electronically unsaturated, formally 16-electron molybdenum complexes. For instance, $Mo(d\pi)$–$N(p\pi)$ bonding has been suggested for the shortening of the Mo—N amido bonds in the pyrazolylborate complex $[\{Mo(NO)[HB(Me_2pz)_3]Cl\}_2(NC_4H_3N)]$ (26), and theoretical calculations have supported the existence of $Mo(d\pi)$–$S(p\pi)$ bonding in $(\eta^5\text{-}C_5He_5)Mo(NO)(SPh)_2$ to account for the observed shortening of the Mo—S bonds (27).

A formal 16-electron configuration for monomeric $(\eta^5\text{-}C_5Me_5)W(NO)I_2$, while novel for an organometallic halide, is not unreasonable. In our experience, the related 16-electron species

$(\eta^5\text{-}C_5H_5)M(NO)R_2$

M = Mo, W; R = CH_2SiMe_3

M = W ; R = SCH_2SiMe_3

are stable, isolable monometallic complexes (4, 27). Indeed, in the case of the thiolate complex, an 18-electron intermediate preferentially converts to the formally 16-electron product (19). It is possible, however, that the thiolate complex may also owe its thermal stability to the existence of some $W(d\pi)$–$S(p\pi)$ bonding (*vide supra*) (27).

The knowledge obtained from this study should prove useful in helping to understand the mechanisms by which the derivatives of $(\eta^5\text{-}C_5Me_5)W(NO)I_2$ are formed. In closing, it should be emphasized that the results presented in this paper do not imply anything about the degrees of association of the other $(\eta^5\text{-}C_5R_5)M(NO)X_2$ family members. Rather, they simply indicate that care should be taken when invoking the familiar 18-electron rule to deduce molecular structures without any other supporting evidence.

Acknowledgment

We are grateful to the Natural Sciences and Engineering Research Council of Canada for support of this work in the form of grants to F. W. B. E. and P. L. and a postgraduate scholarship to N. H. D.

1. J. P. COLLMAN, L. S. HEGEDUS, J. R. NORTON, and R. G. FINKE. Principles and applications of organotransition metal chemistry. 2nd ed. University Science Books, Mill Valley, CA. 1987. Chap. 3.
2. A. D. HUNTER, P. LEGZDINS, C. R. NURSE, F. W. B. EINSTEIN, and A. WILLIS. J. Am. Chem. Soc. **107**, 1791 (1985).
3. P. LEGZDINS, S. J. RETTIG, L. SANCHEZ, B. E. BURSTEN, and M. G. GATTER. J. Am. Chem. Soc. **107**, 1411 (1985).
4. P. LEGZDINS, J. T. MARTIN, and J. C. OXLEY. Organometallics, **4**, 1263 (1985).
5. R. B. KING. Inorg. Chem. **6**, 30 (1967).
6. E. P. CLARK. Ind. Eng. Chem. Anal. Ed. **13**, 820 (1941).
7. S. GAMBAROTTA, C. FLORIANI, A. CHIESI-VILLA, and C. GUASTINI. Inorg. Chem. **23**, 1739 (1984).
8. J. T. MALITO, R. SHAKIR, and J. L. ATWOOD. J. Chem. Soc. Dalton Trans. 1253 (1980).
9. C. R. NURSE. PhD. dissertation. University of British Columbia, 1983.
10. J. T. MARTIN. PhD. dissertation. University of British Columbia, 1987.
11. N. W. ALCOCK. *In* Crystallographic computing. *Edited by* F. R. Ahmed. Munksgaard, Copenhagen. 1969. p. 271.
12. J. WASER. Acta Crystallogr. **16**, 1091 (1963).
13. J. S. ROLLET. *In* Crystallographic computing. *Edited by* F. R. Ahmed. Munksgaard, Copenhagen. 1969. p. 169.
14. J. R. CARRUTHERS and D. J. WATKIN. Acta Crystallogr. Sect. A: Cryst. Phys. Diffr. Theor. Gen. Crystallogr. **35**, 698 (1979).
15. International tables for X-ray crystallography. Vol. IV. Kynoch Press, Birmingham, England. 1974. Tables 2.2B and 2.3.1.
16. A. C. LARSON, F. L. LEE, Y. LE PAGE, and E. J. GABE. The NRC VAX crystal structure system. Chemistry Division, National Research Council, Ottawa, Canada. 1984.
17. D. J. WATKIN, J. R. CARRUTHERS, and P. W. BETTERIDGE. CRYSTALS user guide. Chemical Crystallography Laboratory, University of Oxford, Oxford, England. 1985.
18. E. K. DAVIES. SNOOPI plot program. Chemical Crystallography Laboratory, University of Oxford, Oxford, England. 1984.
19. P. LEGZDINS and L. SANCHEZ. J. Am. Chem. Soc. **107**, 5525 (1985).
20. J. M. MANRIQUEZ, P. J. FAGAN, L. D. SCHERTZ, and T. J. MARKS. Inorg. Synth. **21**, 182 (1982).
21. U. VON MAYER, V. GUTMANN, and W. GERGER. Monatsh. Chem. **106**, 1235 (1975).
22. T. J. GREENHOUGH, P. LEGZDINS, D. T. MARTIN and J. TROTTER. Inorg. Chem. **18**, 3268 (1979).
23. E. B. DREYER, C. T. LAM, and S. J. LIPPARD. Inorg. Chem. **18**, 1904 (1979).
24. P. UMLAND and H. VAHRENKAMP. Chem. Ber. **115**, 3555 (1982).
25. M. H. CHISHOLM, F. A. COTTON, M. W. EXTINE, M. MILLAR, and B. R. STULTS. Inorg. Chem. **16**, 320 (1977).
26. N. AL OBADDI, T. A. HAMOR, C. J. JONES, J. A. MCCLEVERTY, and K. PAXTON. J. Chem. Soc. Dalton Trans. 2653 (1987).
27. M. T. ASHBY and J. H. ENEMARK. J. Am. Chem. Soc. **108**, 730 (1986).

Can. J. Chem. Downloaded from www.nrcresearchpress.com by 112.217.228.212 on 09/07/12
For personal use only.

The σ* molecular orbitals of perfluoroalkanes as studied by inner-shell electron energy loss and electron transmission spectroscopies

I. ISHII,[1] R. MCLAREN [2] AND A. P. HITCHCOCK
Department of Chemistry, McMaster University, Hamilton, Ont., Canada L8S 4M1
K. D. JORDAN AND Y. CHOI
Department of Chemistry, University of Pittsburgh, Pittsburgh, PA., 15260 U.S.A.
AND
M. B. ROBIN
AT&T BELL LABORATORIES, MURRAY HILL, NJ., 07974 U.S.A.

Received December 24, 1987

This paper is dedicated to Professor Charles A. McDowell on the occassion of his seventieth birthday

ISHII, I., MCLAREN, R., HITCHCOCK, A. P., JORDAN, K. D., CHOI, Y., and ROBIN, M. B. Can. J. Chem. **66**, 2104 (1988).

Absolute oscillator strength spectra in the C 1*s* (280–340 eV) and F 1*s* (680–740 eV) regions of the perfluoro-*n*-alkanes from C_2 to C_6 and perfluorocycloalkanes from C_3 to C_6 have been determined from inner-shell electron energy loss spectra recorded under electric-dipole scattering conditions. The spectral features are interpreted in terms of spatially localized transitions terminating at orbitals of predominantly σ*(C—F) and σ*(C—C) character. When compared to the spectra of the perfluoro-*n*-alkanes, both the C 1*s* and F 1*s* spectra of the perfluorocycloalkanes exhibit additional low-lying bands which are assigned to transitions terminating at σ*(C—C) orbitals which are shifted to low energy by the combination of the strain of cyclization and the inductive effect of the fluorination. The electron transmission spectra of selected perfluorocycloalkanes (which provide information on their anion states) show as well that the electron affinities of the cyclic systems are substantially lower than those of the corresponding perfluoro-*n*-alkanes, again as a result of a low-lying σ* orbital in the cyclic species. Quantum chemical calculations of the alkane and perfluoroalkane ground-state orbital structures support the experimental results. The localized character of the inner-shell excitations, indicated by the constancy of both term values and oscillator strengths with increasing chain length, contrasts with the more delocalized character of the states accessed in ultraviolet excitation or negative ion formation.

ISHII, I., MCLAREN, R., HITCHCOCK, A. P., JORDAN, K. D., CHOI, Y., et ROBIN, M. B. Can. J. Chem. **66**, 2104 (1988).

Utilisant les spectres de pertes d'énergie électronique des couches internes enregistrés dans des conditions de diffraction du dipôle électrique, on a déterminé les spectres de force absolute de l'oscillateur des régions C 1*s* (280 à 340 eV) et F 1*s* (680 à 740 eV) des perfluoro-*n*-alcanes (C_2 à C_6) et des perfluorocycloalcanes (C_3 à C_6). On interprète les caractéristiques spectrales en fonction de transitions qui sont localisées dans l'espace et qui se terminent avec les orbitales possédant des caractéres σ*(C—F) et σ*(C—C) prédominants. Lorsqu'on les compare aux spectres des perfluoro-*n*-alcanes, les spectres tant C 1*s* que F 1*s* des perfluorocycloalcanes présentent de faibles bandes additionnelles que l'on a attribuées à des transitions se terminant au niveau des orbitales σ*(C—C) qui sont déplacées vers les basses énergies par une combinaison de tensions de cycle et d'effet inductif des fluors. De plus, les spectres de transminnion électronique des ions négatifs de perfluorocycloalcanes choisis montrent que les affinitiés électroniques des systèmes cycliques sont beaucoup plus faibles que celles des perfluoro-*n*-alcanes correspondants; ces résultats sont encore une fois expliqués par la présence d'orbitales σ* basses dans les systèmes cycliques. Des calculs de chimie quantique effectués sur les structures des orbitales des états donsamentaux d'alcanes et de perfluorocycloalcanes sont en accord avec les résultats expérimentaux. Le caractère localisé des excitations de couches internes, tel qu'indiqué par la constance de chacun des termes des valeurs ainsi que des forces d'oscillation avec une augmentation de la longueur de la chaîne, est en opposition avec le caractère plus délocalisé des états atteints par les excitations ultraviolettes ou par la formation d'ions négatifs.
[Traduit par le revue]

1. Introduction

The fate of electronic transitions terminating at σ* MO's in the outer-shell (5–50 eV) and inner-shell (50–1000 eV) spectra of large organic molecules remains very much an open question. At first sight, the problem would seem to be that the transitions to σ* are rather high lying, and so are difficult to identify either because they fall among the clutter of transitions to Rydberg (R) orbitals or because they are autoionized in the ionization continua. However, the problem is more complex, for there is a very real possibility that a particular valence (V) σ* MO is mixed more or less with the R MO's of the same symmetry so that its valence identity becomes clouded; in extreme cases a σ* MO can dissolve in the Ryberg sea to such an extent as to lose its valence character completely (1, 2). Though valence transitions to σ* in the ionization continuum do appear as shape resonances (3, 4) and cannot be confused with transitions to R orbitals, assignment still can be ambiguous here as well, for other phenomena such as two-electron excitation, shake-up, and EXAFS interference also can contribute structure in this region (5). Finally, because the nature of the transitions to σ* MO's in the outer-shell and inner-shell spectra of the same molecule may be quite different, conclusions about σ* MO's reached in one type of study would not necessarily apply to the other.

In the present work, we have studied the inner-shell excitation energies and oscillator strength distributions of a series of perfluoro-*n*-alkanes (C_2—C_6) and perfluorocycloalkanes (C_3—C_6) as well as perfluoroneopentane. For certain of these compounds, we also have determined the negative-ion electron transmission spectra and performed *ab initio* ground state calculations. In our discussion of the spectral results, we address the following questions: (*1*) What are the energies and

[1]Present address: Department of Chemistry, George Washington University, Washington, DC., U.S.A. 20052.
[2]Present address: Department of Chemistry, University of Alberta, Edmonton, Alta., Canada T6G 2G2.

Can. J. Chem. Downloaded from www.nrcresearchpress.com by 112.217.228.212 on 09/07/12
For personal use only.

Can. J. Chem. Downloaded from www.nrcresearchpress.com by 112.217.228.212 on 09/07/12
For personal use only.

relative R/V characters of the σ* MO's accessed in the inner-shell and negative-ion spectroscopies of the perfluoroalkanes? (*2*) To what extent are σ* orbitals stabilized by perfluorination and/or ring strain? (*3*) Are the inner-shell and negative-ion excitations terminating at σ* in the perfluoroalkanes localized or delocalized?

Identification of transitions terminating at σ* is most readily approached through the study of inner-shell spectra, for in this case though the terminating MO manifold may be complex, at least the originating inner-shell MO manifold is simpler than the occupied valence MO manifold involved in outer-shell excitations. In addition, because of the smaller number of configurations of similar core-excitation energies, a one-electron orbital model is expected to be more applicable to inner-shell than to outer-shell excitation. Given the inner-shell ionization potential, usually from X-ray photoelectron spectroscopy, one knows that the corresponding R excitations will fall in a certain region below this limit (1). The energy difference between the ionization potential and the corresponding discrete excitation is called the term value. Term values for R states are usually between 0 and 5 eV. On the other hand, transitions to σ* orbitals can occur over a much wider spectral range; in this case, term values as large as 14 eV (F_2) and as small as −22 eV (C_2H_2) have been reported (4).

Recently it has been shown that the term value of a $1s \rightarrow \sigma^*$(A—B) transition can be estimated from empirical considerations of the atomic numbers of atoms A and B involved in forming the σ* MO and the A–B internuclear distance (3, 4). This correlation assumes that the σ* MO reached in an inner-shell excitation is strongly localized in the region of a localized core hole, even in systems of large size containing several equivalent and adjacent bonds. The localization of the $1s \rightarrow$ V(σ*) excitation could arise from a local character of the σ* orbital and/or spatial localization of the core hole.

In the case where inner-shell excitations to σ* and R orbitals are nearly degenerate, term value arguments are less compelling and the question arises as to the separate existence of near-degenerate R and V levels (1, 2). Although the answer to this is ambiguous in many cases, clear evidence for the coexistence of distinct V and R levels in the same spectrum has been presented for F_2O (6).

In addition to the term-value criteria, there are a number of effects that can assist in the determination of the relative R/V character of a particular spectroscopic feature. First, in the condensed phase, transitions to R levels are generally broadened significantly and shifted to higher energies so as to make the transitions effectively disappear (1, 7). In contrast, the transitions to V states persist virtually unchanged in a condensed phase. Second, there is a well-known upper limit to the oscillator strength of transitions to R states (1), whereas many transitions to V states have oscillator strengths which exceed the R limit. Third, the transition energies and oscillator strengths exhibit systematic variations through a homologous series of molecules which may help to distinguish transitions to R states from those to V states.

In a specific class of molecules, it has been found that σ* MO's can lie so low that their identification is not comprised by problems of congestion or orbital mixing. Thus, if a molecule has a bond between atoms A and B which has a strength of 60 kcal/mol or less, then the σ–σ* splitting will be abnormally small and the σ*(A—B) MO will be relatively low lying, as will inner-shell transitions such as A $1s \rightarrow \sigma^*$(A—B) and outer-shell transitions such as B $2p \rightarrow \sigma^*$(A—B). This lowering of the inner-shell and outer-shell energies for excitations to σ* has been called the weak-bond effect (2, 6).

In addition to the questions listed above, we also raise the question as to whether an *overall* molecular strain energy which weakens several bonds simultaneously also can result in a small σ–σ* split. If so, then such strained systems also will show unambiguous low-lying excitations to σ* with unusually large term values. In this regard, it is pertinent to note that C $1s \rightarrow \sigma^*$ transitions at lower-than-expected energies already have been observed in the spectra of cyclopropane and cyclobutane (8).

The opportunities for observing transitions to low-lying σ* MO's may be heightened yet again by perfluorinating the strained cyclic hydrocarbons. This could arise both from the introduction of strain energy due to F—F repulsions (9), and from the fact that fluorination of a molecule acts to lower both σ and σ* MO's due to the strong inductive effect of the F atom (6, 10). That the perfluoroalkanes may prove to be a rich hunting ground for low-lying transitions to σ* MO's was mentioned earlier following a comparison of the vacuum ultraviolet (VUV) spectra of alkanes and their perfluoro derivatives (1); related ideas can be found in discussions of the inner-shell spectra of the fluoromethane (1, 11–13) and chloromethane series (14).

In hydrocarbons consisting of several C—C bonds, the C $1s$ AO's on equivalent sites form a narrow band of width *ca.* 0.01 eV. It is generally believed that because of the narrow bandwidth, mobility of the $1s$ hole is so low that the originating orbital in the core-excited state can be localized at a single atomic site during the very short lifetime of the hole state (15–18). However, see the work of Schwartz *et al.* (19) for possible exceptions to this point of view. There clearly is a question at present as to the degree of localization of the core hole in the core excited states of molecules having the excited atoms in equivalent sites. Related aspects to this problem are the degree of delocalization of the σ* MO's populated in the core states, and the fact that the degree of delocalization of the optical orbital may differ depending upon the spectroscopy by which it is examined (20). That is, the potential experienced by the optical electron in a ($1s$, σ*) hole-localized excited state in the X-ray region of a given molecule is quite different from that appropriate to a delocalized (σ, σ*) state in the VUV excitation of that molecule. In these situations, the σ* MO's may be quite different both in spatial extent and term value.

The presence of low-lying, strain-induced σ* MO's in the perfluorocycloalkanes could be revealed not only in the inner-shell spectra but in their negative-ion spectra as well (21). Though the potential experienced by an electron in a σ* orbital is very different in the case of a negative-ion and inner-shell excitation in a neutral molecule, this avenue was felt to be worth exploring in spite of the possible differences. Inner-shell and negative-ion comparisons of this type have been found useful in studying the unoccupied orbitals of the fluorobenzenes (10) and fluoroethylenes (6).

In the present work, we have measured the negative-ion transmission spectra of the perfluoro-*n*-alkanes and the corresponding perfluorocycloalkanes. These results are compared with virtual-orbital calculations of the successive electron affinities of the linear and cyclic perfluoroalkanes. Negative-ion resonances in saturated molecules may involve not only σ* resonances, but Feshbach resonances as well, in which two electrons occupy a single R orbital. For purposes of assigning

Can. J. Chem. Downloaded from www.nrcresearchpress.com by 112.217.228.212 on 09/07/12
For personal use only.

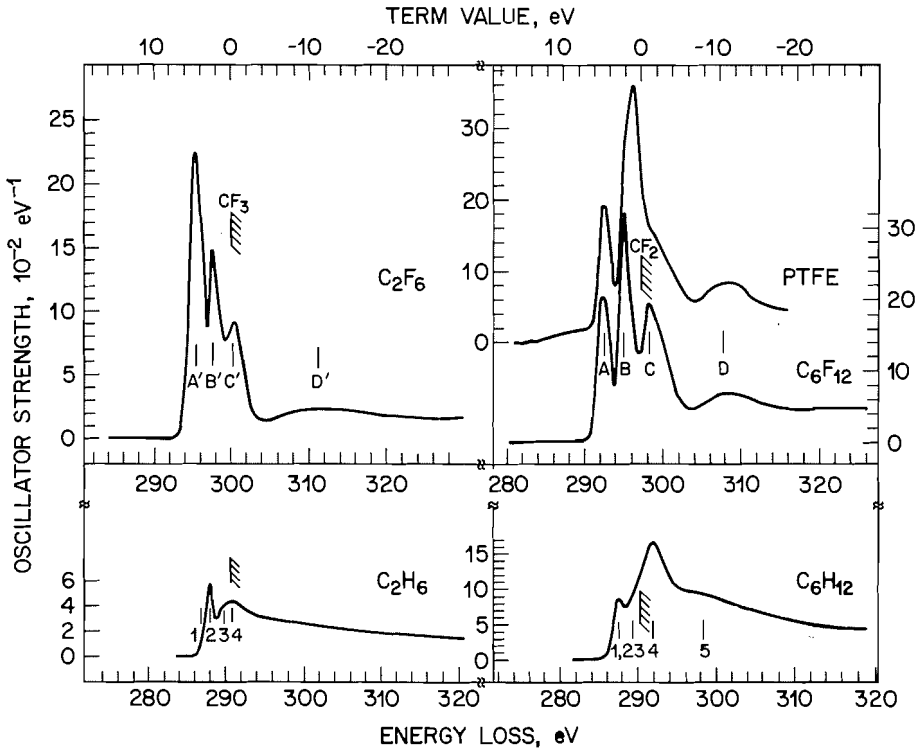

FIG. 1. Comparison of the oscillator strength spectra of C_2H_6 and C_6H_{12} with those of C_2F_6 and C_6F_{12}, as derived from energy-loss spectra recorded with 2.5 keV final electron energy, 2° scattering angle and 0.6 eV FWHM resolution. The spectra have been shifted so as to bring the C 1*s* ionization potentials into alignment. Also shown is the optical spectrum of PTFE, as recently reported by Ohta *et al.* (32), plotted on the same absolute energy scale as that of C_6F_{12}.

the negative-ion resonances, the strategy used here is to first assign the Feshbach resonances, using the well-known energy criteria for such excitations (1, 20, 22), and then assume that the remaining resonances involve occupation of the σ* MO's.

In this paper, we consider successively the C 1*s* spectra of the linear and branched perfluoroalkanes (sect. III) and compare these with the C 1*s* spectra of the cyclic perfluoroalkanes (sect. IV). Similar comparisons are drawn for the F 1*s* spectra of the same series of compounds (sect. V). The ordering of the virtual orbitals and their R/V characters as derived from these spectra are then compared with the conclusions deduced from the negative-ion spectra, as supported by *ab initio* calculations (sect. VI). These comparisons lead to a discussion of excitation localization/delocalization in these spectra (sect. VII).

II. Experimental

The C 1*s* and F 1*s* inner-shell spectra of the perfluoro-*n*-alkanes from C_2F_6 to C_6F_{14}, perfluoroneopentane, and the cyclic compounds from C_3F_6 to C_6F_{12} were recorded by electron energy loss spectroscopy using the McMaster inner-shell electron energy loss (ISEEL) spectrometer. Operating under conditions chosen to accentuate electric-dipole transitions (2.5 keV final electron energy and scattering angles less than 2°), a resolution of 0.6 eV FWHM was achieved. Further details of the spectrometer and operating procedures are presented elsewhere (3, 23). Each of the perfluoroalkanes was a commercial product except for perfluorocyclopropane, perfluorocyclopentane, and perfluoroneopentane which were gifts from Professor J. L. Adcock. Sample purity within the spectrometer cell was monitored mass spectrometrically and the energy loss spectra calibrated by the addition of appropriate gases of known transition energies. In all cases, the energy loss spectra reported here have had the underlying continuum intensity subtracted and have been converted to approximate absolute oscillator strength distributions (±20%) using corrections for kinematic effects and normalization to calculated atomic 1*s* photoionization oscillator strengths (24).

Negative-ion resonance energies were determined using an electron transmission spectrometer operating in the derivative mode. The technique is described in ref. 21. Negative-ion spectra were determined for selected members of both the linear and cyclic perfluoroalkanes, as well as for certain alkanes.

III. Inner-shell spectra of perfluoro-*n*-alkanes

The discrete transitions below the C 1*s* ionization potentials in the inner-shell spectra of the alkanes are of mixed R/V character (3, 8, 25). Since the general effect of fluorination is to accentuate the V character of the lower excitations, we must expect to see much stronger R/V mixing in the perfluoroalkanes or even low-lying transitions to relatively pure σ* MO's. In the latter case, the V levels may rest among the R levels or even precede them. Indeed, it is clear from earlier work (1, 12, 13, 26–30) that the C 1*s* spectrum of CF_4 involves comingling of transitions to both R MO's and to V σ*(C—F) levels. However, there is no *a priori* way of knowing how this will be reflected in the perfluoroalkane spectra.

Because the separation between the C 1*s*(CF_2) and C 1*s*(CF_3) ionization potentials is nearly 2 eV (31) in the perfluoro-*n*-alkanes, one has two partially overlapped inner-shell spectra and difficulties therefrom for perfluoro-*n*-alkanes larger than C_2F_6. In this case, it is best to first focus on a molecule containing only CF_3 groups (CF_3CF_3) and a molecule containing only CF_2 groups [$(CF_2)_6$], and then to apply this information toward interpreting the spectrum of $CF_3(CF_2)_xCF_3$, x = 1–4, which can be considered as a mixture of more or less weakly interacting CF_3 and CF_2 chromophores. The spectra of the molecular pair C_2H_6 and C_2F_6 and the pair C_6H_{12} and C_6F_{12} are

TABLE 1. Transition energies (E, eV), term values (TV, eV) and proposed assignments for features in the C 1*s* spectra of the perfluoro-*n*-alkanes

	C_2F_6		C_3F_8		*n*-C_4F_{10}		*n*-C_5F_{12}		*n*-C_6F_{14}		Assignment[b]	
Band[a]	E	TV	E	TV	E	TV	E	TV	E	TV	C 1*s*(CF_2)	C 1*s*(CF_3)
A			293.0	4.7	292.8	4.9	292.7	5.0	292.7	5.0	σ^*(C—F)$_\sigma$	
A'	295.4	4.5	295.3	4.4	295.4	4.3	295.2	4.5	295.3	4.4		σ^*(C—F)$_\pi$
B			295.3	2.4	295.4	2.3	295.2	2.5	295.3	2.4	σ^*(C—F)$_\sigma$	
B'	297.7	2.1	297.6	2.1	297.5	2.2	297.3	2.4	297.3	2.4		σ^*(C—F)$_\sigma$
IP			297.74	—	297.7[c]	—	297.7[c]	—	297.7[c]	—		
IP'	299.85	—	299.74	—	299.7[c]	—	299.7[c]	—	299.7[c]	—		
C			298.5	−0.8	298.9	−1.2	298.8	−1.1	298.6	−0.9	σ^*(C—C)	
C'	300.5	−0.7	300.8	−1.1	300.8	−1.1	302	−2.3	301	−1.3		σ^*(C—C)
D,D'	311	−11	311	−11	309	−11	308	−11	308	−11	Shape resonance or delayed onset	

[a]The unprimed bands originate at CF_2 groups whereas the primed bands originate at CF_3.
[b]Rydberg excitations to *3s*, *3p*, *4p*, etc. will fall at energies below the ionization potentials. However, they are either overlapped or mixed with the excitations to σ^* and do not appear as discrete features in these spectra.
[c]Ionization potentials assumed equal to those of C_3F_8 (31).

presented on common term value and oscillator strength scales (Fig. 1) to facilitate interpretation of the mixed chromophore systems. The spectrum of another possible CF_2 prototype, polytetrafluoroethylene (PTFE) $(CF_2)_x$ taken from the work of Ohta *et al.* (32) also appears in this figure.

III.1. The CF_3 spectrum

We consider CF_3CF_3 to be the prototypical CF_3 chromophore. This molecule has a spectrum in the C 1*s* region, Fig. 1 and Table 1, which not only is deeper by about 8 eV than that of CH_3CH_3, but also has a dramatically different oscillator strength distribution. Based on term values, analogy can be made between band *A'* of C_2F_6 (295.4 eV, 4.50 eV term value) and band 1 of C_2H_6 (286.9 eV, 3.69 eV term value) (25). In C_2H_6, this band has been assigned as terminating at a mixed $3s/\sigma^*$ MO with predominantly R character (1, 25). The increased term values of the transitions to $3s/\sigma^*$ upon fluorination of a wide variety of systems is well known (1, 2). What is more interesting here is that in C_2H_6 the C $1s \rightarrow 3s/\sigma^*$ transition is relatively weak and seems to be following the quasiatomic propensity rule forbidding $1s \rightarrow 3s$ transitions, whereas what appears to be the corresponding transition in C_2F_6 has more than 10 times the oscillator strength and is the most prominent band in the spectrum! Since the most intense Rydberg transitions in VUV spectroscopy have oscillator strengths of only 0.08 per degree of degeneracy (1) and R transitions in the inner-shell region will be much weaker still, both the 0.15 oscillator strength of the *A'* band of C_2F_6 and the increased term value indicate that the F atoms of C_2F_6 are strongly perturbing the $3s/\sigma^*$ orbital, acting to make it increasingly valence shell. In light of this, it follows that the 295.4 eV feature of C_2F_6 (band *A'*) can be considered as predominantly C $1s \rightarrow \sigma^*$(C—F). The spectral intensification and change of character from $3s/\sigma^*$-(C—H) to σ^*(C—F) on going from C_2H_6 to C_2F_6 has its parallels, for these changes also are observed on going from C_2H_4 to C_2F_4 (22, 24) and throughout the fluoromethane series (1, 12, 13, 26, 29).

Band *B'* of C_2F_6 with a term value of 2.09 eV has its counterpart in C_2H_6 (band 2), thought to be mixed $1s \rightarrow 3p$ and $1s \rightarrow \sigma^*$(C—H) (25, 33) with a term value of 2.70 eV. In this case, band *B'* has an oscillator strength which is threefold larger than that of band 2 in C_2H_6. Note that the observed increase of the *A'* term value, decrease of the *B'* term value and intensification of both transitions in C_2F_6 all follow naturally from a strong mixing of *3s* and *3p* orbitals among themselves along with further strong mixing with σ^* V orbitals. See sect. III.2 for further discussion of excitations to σ^*(C—F) in the CF_3 group.

The assignment of both *A'* and *B'* as transitions terminating at σ^*(C—F) is consistent with the bond length/term value correlation (4) which predicts a term value of 2.3 eV for the 1.326 Å C—F bond length in C_2F_6. This predicted value lies between the term values observed for features *A'* (4.5 eV) and *B'* (2.1 eV). Although the splitting of the σ^*(C—F) intensity into two peaks contradicts the bond-localized excitation assumption of the bond length correlation, this splitting (2.4 eV) is relatively small and the two observed lines straddle the predicted C $1s \rightarrow \sigma^*$(C—F) position. More dramatic examples of this type of deviation from the most simple implementation of the bond length correlation have been noted in the σ^*(C—C) resonances of benzene and the fluorobenzenes (10), as well as the σ^*(C—O) resonances of CO_2 (5).

Band *C'* of C_2F_6 (300.5 eV, 0.7 eV beyond the ionization potential) has its counterpart in C_2H_6 as band 4 (290.8 eV, 0.2 eV beyond the ionization potential). As in the CH_4/C_2H_6 comparison (3, 25), we see on comparing the CF_4 (26–30) and C_2F_6 (Fig. 1 and Table 1) inner-shell spectra, that the *C'* shape resonance of C_2F_6 does not appear in CF_4 and so must terminate at σ^*(C—C). The doubling of the C $1s \rightarrow \sigma^*$(C—C) oscillator strength upon perfluorinating C_2H_6 can be rationalized in terms of the potential barrier localization of the σ^*(C—C) orbital (34).

In C_2F_6, band *D'* can be assigned as either an unusually strong first EXAFS feature or alternatively, feature *D'* may represent the energy at which the C 1*s* photoelectron energy exceeds the height of the potential barrier associated with the large number of electronegative F atoms in this molecule (34). Within the framework of group-localized core excitations, the *D'* excitation energy is much too large to terminate at σ^*(C—C) or σ^*(C—F) (4). In the potential barrier interpretation, the spectral feature of interest is not the *D'* maximum, but rather the depressed C 1*s* continuum intensity between 302 and 310 eV which reaches a minimum value of 0.01 eV^{-1} at 305 eV compared to a value of 0.03 eV^{-1} at an equivalent photoelectron energy in C_2H_6 (Fig. 1). A strong suppression of the C 1*s*

Can. J. Chem. Downloaded from www.nrcresearchpress.com by 112.217.228.212 on 09/07/12
For personal use only.

TABLE 2. Oscillator strengths ($\times 10^{-2}$) for discrete and continuum regions in the C 1s spectra of the perfluoroalkanes and selected alkanes

Species	A^a	σ^{*b}	f(disc)^c	f/x^d	f''(cont)$/x^e$	f'(cont)^f	f'/x^g	f/f'
CF_4			36	36	5.7	25	25	1.4
C_2F_6			80	40	8.5	60	30	1.3
C_3F_8	12		107	36	8.2	82	27	1.3
C_4F_{10}	22		125	31	8.2	103	26	1.2
C_5F_{12}	27		135	27	7.6	118	24	1.1
C_6F_{14}	29		154	25	7.7	136	23	1.1
C_3F_6	7	7	84	26	7.7	68	23	1.2
C_4F_8	9	12	111	28	8.1	89	22	1.2
C_5F_{10}	14	15	139	28	7.4	119	24	1.3
C_6F_{12}	10[h]	30[h]	154	26	8.2	143	24	1.1
C_2H_6			14	7	11.7	61	31	0.23
C_6H_{12}			34	5.7	13.0	210	35	0.16
C_6H_{14}			36	6.1	10.7	179	30	0.20

[a]Oscillator strength for C 1s(CF_2) → σ^*(C—F), feature A, derived from curve fitting.
[b]Oscillator strength for C 1s(CF_2) → σ^*(C—C) derived from curve fitting.
[c]Oscillator strength summed from threshold to the C 1s ionization potential.
[d]Oscillator strength in the discrete region on a per-carbon-atom basis.
[e]f'' is the oscillator strength summed from 4 eV beyond the ionization potential to 12 eV beyond that point, on a per-carbon-atom basis.
[f]f' is the oscillator strength summed from the C 1s ionization potential to a point 25 eV beyond the IP.
[g]Oscillator strength in the continuum region (0–25 eV relative to the ionization potential) on a per-carbon-atom basis.
[h]This division of the total oscillator strength of the structured first band of C_6F_{12} (0.40) is derived from curve fitting.

Can. J. Chem. Downloaded from www.nrcresearchpress.com by 112.217.228.212 on 09/07/12
For personal use only.

near-continuum intensity of CF_4 relative to that in CH_4 was found in recent quantitative optical studies (29). If one follows the continuum intensity backward from high energy loss to the ionization potential, the slow rise in continuum begins to fall off approximately at the maximum of the apparent peak. If this is interpreted as the energy at which a potential barrier begins to depress the ionization cross section, then one arrives at an estimate of approximately 11 eV for the height of the centrifugal barrier in C_2F_8. It is interesting that this estimate is slightly greater than the estimate of 8 eV for the centrifugal barrier in C_2F_4 reached using slightly different arguments (24). That the potential barrier becomes larger as the number of electronegative F atoms surrounding the central C atom increases is intuitively acceptable. The depressed continuum intensity between 302 and 310 eV is found not only in C_2F_6 but also throughout all of the perfluoroalkanes. This is shown in Table 2, which compares on a per-C-atom basis the near-continuum intensity (from −4 to −12 eV term value) for all of the compounds studied in this work with those of the representative alkanes C_2H_6, C_6H_{12}, and C_6H_{14}.

Based on the above considerations, and with due allowance for the effects of fluorination on term values (1) and relative intensities (34), it is concluded that the A' and B' transitions of C_2F_6 are superficially related to those of C_2H_6 labelled 1 and 2 in Fig. 1, but whereas those of the latter are largely R in character, those of C_2F_6 are largely V. Shape resonances which closely resemble one another in energy and width are seen in C_2F_6 (band C') and C_2H_6 (band 4); both terminate at σ^*(C—C).

III.2. The CF_2 spectrum

We use perfluorocyclohexane $(CF_2)_6$ as a model of the CF_2 inner-shell spectrum and compare its spectrum with that of $(CH_2)_6$ in Fig. 1. As an alkane is lengthened, the term values for the excitations to $3s/\sigma^*$ and to $3p/\sigma^*$ orbitals converge upon one another at *ca.* 2.6 eV (1, 25). Accordingly, in C_6H_{12} (8), the transitions from C 1s to $3s/\sigma^*$ and $3p/\sigma^*$ no longer can be resolved, and instead form a single sharp feature (bands 1 and 2) with a term value of 2.60 eV. This coincidence is not expected in C_6F_{12}, for a large $3s/\sigma^*$–$3p/\sigma^*$ splitting (2–4 eV) often is observed in heavily fluorinated molecules. Indeed, the lowest two sharp bands (A and B) in the inner-shell spectrum of C_6F_{12} have term values of 4.8 and 2.11 eV, in the range characteristic of R transitions terminating at $3s$ and $3p$ orbitals, respectively. However, as with the bands of C_2F_6, these bands of C_6F_{12} when compared to those of C_6H_{12} are seen to have the greatly increased oscillator strengths more characteristic of valence transitions. The V bands in $(CF_2)_6$ are sufficiently broad that the C 1s → 4p transition (band 3 of the alkanes) does not appear. The dominance of C 1s → σ^*(C—F) and the relative weakness of C 1s → R transitions also is consistent with the potential barrier model for core excitation in perfluoro compounds (34). Features C (C 1s → σ^*(C—C)) and D appear in C_6F_{12} with term values close to those observed in C_2F_6. Feature C in C_6F_{12} has a high-energy shoulder and is broadened with respect to that in C_2F_6, consistent with contributions from several overlapping C 1s → σ^*(C—C) transitions in this region, as noted as well for the transitions to σ^*(C—C) in the longer alkanes.

If one considers the peak heights or oscillator strengths of bands A/A' and B/B' in C_6F_{12}/C_2F_6, one finds that, per carbon atom, the sum of the A' and B' oscillator strengths of C_2F_6 is roughly twice that of the A and B bands of C_6F_{12}, Table 2. This is somewhat larger than but similar to the relative numbers of C—F bonds in the CF_3 and CF_2 groups, for which C_2F_6 and C_6F_{12} are taken as prototypes. The oscillator strength per carbon atom of bands B and B' are approximately the same in the two species, whereas that for band A' in C_2F_6 is 2–3 times greater

Can. J. Chem. Downloaded from www.nrcresearchpress.com by 112.217.228.212 on 09/07/12
For personal use only.

than that for band A in C_6F_{12}. If one considers a local C_{2v} symmetry for the CF_2 group and local C_{3v} symmetry for the CF_3 group, the oscillator strengths then suggest that peaks B and B' correspond to C $1s$ excitations to the nondegenerate local σ^*(C—F) MO in both cases (a_1 in CF_3; a_1 or b_1 in CF_2). On the other hand, peaks A and A' then correspond to C $1s$ excitations to σ^*(C—F) levels of e symmetry in CF_3 groups but b_1 or a_1 symmetry in CF_2 groups. Thus in C $1s(CF_3)$ spectra, we label the A' band as $\sigma^*(C—F)_\pi$ and the B' band as $\sigma^*(C—F)_\sigma$. It should be noted that in this assignment scheme for CF_3, the A' and B' bands do not necessarily have the same symmetries as the $3s$ and $3p$ R orbitals, and so we are not dealing with the intensification of R transitions by mixing with V transitions, but rather with the overlapping of intense V transitions upon R transitions. It also should be noted that there is not necessarily a general one-to-one relationship between relative degeneracies and relative intensities. However, such a relationship is not unexpected when orbitals of similar character are involved.

Further support for a $\sigma^*(C—F)_\pi$ below $\sigma^*(C—F)_\sigma$ ordering of the CF_3 group orbitals in the C $1s$ excitation spectrum is found in the *ab initio* calculations for CF_3H and CF_2H_2 reported by Snyder and Basch (35). The C $1s$ spectra of CF_3H (14) and C_2F_6 are very similar except that the C_2F_6 spectral intensities are twice as large and there is additional intensity at the C $1s$ ionization potential associated with the C $1s \rightarrow \sigma^*$(C—C) promotion in C_2F_6. In the CF_3H ground state, a nondegenerate MO of σ^*(C—F) character ($8a_1$) is calculated to lie 1.8 eV above a degenerate pair of $\sigma^*(C–F)_\pi$ orbitals (*11, 12e*), in agreement with the $\sigma^*(C—F)_\pi$ below $\sigma^*(C—F)_\sigma$ ordering we assign for C_2F_6 on the basis of intensities.

Similarly, the discrete portion of the C $1s$ spectrum of CF_2H_2 resembles that of C_6F_{12}, although additional sharp structures associated with C $1s \rightarrow \sigma^*$(C—H) transitions are observed in CF_2H_2, the second σ^*(C—F) feature is much weaker, and the C $1s \rightarrow \sigma^*$(C—C) transition is absent. This provides further justification for our use of these compounds to model the C $1s(CF_3)$ and C $1s(CF_2)$ excitations in perfluoro-*n*-alkanes.

The ground-state virtual orbital eigenfunctions of CF_3H and CF_2H_2 calculated by Snyder and Basch (35) also can be used to estimate the relative intensities of C $1s(CF_3) \rightarrow \sigma^*$(C—F) and C $1s(CF_2) \rightarrow \sigma^*$(C–F) transitions and thus to provide further support for our spectral interpretation. In the absence of strong distortions by the core hole, the intensity of C $1s$ (F $1s$) excitations to a virtual orbital are expected to be proportional to the squares of the C $2p$ (F $2p$) atomic orbital coefficients on the core excited atom. This approach has been used recently to compare calculated and experimentally derived spatial distributions of the π^*(C—O) orbital in substituted carbonyls (36). According to the double-zeta GTO calculations (35), the ratio of the squared coefficients in the $\sigma^*_\pi/\sigma^*_\sigma$ orbitals of CF_3H is 1.5 (using the diffuse component) and 1.0 (using the compact component) (35), while the ratios of the squared C $2p$ coefficients in the first two virtual orbitals in CF_2H_2 are 0.8 (diffuse) and 1.2 (compact). Thus the ground state calculation suggests that the C $1s(CF_3) \rightarrow \sigma^*(C—F)_\pi$ transition should be more intense than the C $1s(CF_3) \rightarrow \sigma^*(C—F)_\sigma$ transition while the two C $1s(CF_2) \rightarrow \sigma^*$(C—F) excitations should be of similar magnitude. This is consistent with our interpretation of the virtual orbital ordering in C_2F_6 since the ratio of the areas of the first two peaks in the C $1s$ spectra is 2.7 in C_2F_6 and 0.7 in C_6F_{12}.

Further support for a $\sigma^*(C—F)_\pi$ below $\sigma^*(C—F)_\sigma$ ordering of the CF_3 group orbitals in the C $1s$ excitation spectrum is found in the *ab initio* calculation for C_2F_6 (see sect. VI). In this, we find the lowest virtual orbital to be C—F antibonding with overall e_u symmetry in the molecular point group; this corresponds to $\sigma^*(C–F)_\pi$. The virtual orbital corresponding to $\sigma^*(C–F)_\sigma$ is a_{2u} in the molecular point group, an orbital which is 2.92 eV higher in energy.

III.3. Condensed phase spectra

It is generally acknowledged (1, 7) that R states are very susceptible to perturbation by adjacent molecules in a condensed phase, whereas valence excitations are much less so. The R excitations of a solute molecule in a condensed phase of low electron mobility generally are shifted to higher energies and broadened so greatly as to make the transitions effectively disappear, whereas a valence transition to σ^* in the same molecule will suffer a much weaker perturbation, shifting slightly to lower energy. It is of great interest to use this difference to further illuminate the R/V characters of the inner-shell excitations in perfluoroalkanes. Possible problems which one might encounter using this approach are the effect due to a matrix/solvent of high electron mobility (rare gases, metal surfaces, matrices/solvents of near spherical symmetry, etc.) and the deperturbation which might be wrought by the matrix/solvent on a transition which in the gas phase is of mixed R/V character (37).

The electron yield spectrum of a thin film of PTFE recorded by Ohta *et al.* (32) using synchrotron radiation is plotted in Fig. 1 for comparison with that of C_6F_{12} in the vapor phase. A very similar spectrum of PTFE has been recorded by Fink *et al.* using inelastic electron scattering (38). There is a remarkably close correspondence between the bands of the $(CF_2)_x$ and $(CF_2)_6$ systems in spite of the fact that one of them is in the vapor phase and the other is a solid of low electron mobility. One argues from this that since the spectra of $(CF_2)_x$ and $(CF_2)_6$ are in one-to-one correspondence and since all of the observed bands of PTFE are necessarily valence, that all of the resolvable features of C_6F_{12} also are predominantly valence shell. It follows as well that since we are taking C_6F_{12} as prototypical of the CF_2 group excitation spectrum, all of the excitations attributed to the CF_2 group in whatever molecule are also strongly valence shell.

As with the PTFE/C_6F_{12} pair, comparison of the C $1s$ spectra of the analogous pair polyethylene (PE)/C_6H_{12} also shows a remarkably close correspondence of excitations (33). Further, these spectra bear close resemblance to those of the much smaller vapor phase *n*-alkanes (C_2H_6–C_6H_{14}). In the case of PE, polarization studies have been performed on the oriented material, leading to confirmation of the assignments of the two lowest energy features as valence excitations terminating at σ^*(C—H) and σ^*(C—C) MO's, respectively (32, 33). By analogy with the situation in PE, the B and C bands of oriented PTFE (292.7 and 296.0 eV), Fig. 1, should be polarized respectively perpendicular and parallel to the C—C direction.

III.4. The spectra of $CF_3(CF_2)_xCF_3$

It appears from the work quoted above that the inner-shell excitations in the CF_2 and CF_3 groups are very much localized. Working further in this approximation, one expects in zeroth order that the C $1s$ inner-shell spectrum of a perfluoro-*n*-alkane will be the sum of the spectra of its constituent CF_2 and CF_3 groups. Deviations from this may be due to inter-group interactions which spread the excitation over two or more CF_x groups. Thus, within the localization model, consideration of the C_2F_6 and C_6F_{12}/PTFE spectra leads to certain expectations

Can. J. Chem. Downloaded from www.nrcresearchpress.com by 112.217.228.212 on 09/07/12
For personal use only.

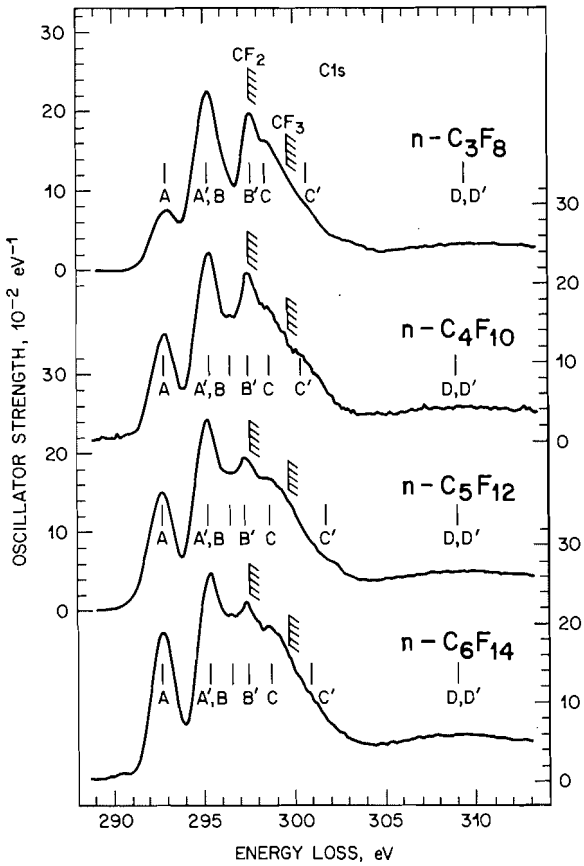

FIG. 2. Oscillator strength spectra of the perfluoro-*n*-alkanes in the C 1*s* region as derived from energy loss spectra (for details, see caption to Fig. 1). Inner-shell ionization potentials are shown by hatched areas. The unprimed transitions originate at CF_2 groups whereas the primed transitions originate at CF_3 groups.

in regard the spectra of perfluoro-*n*-alkanes: (*1*) On the term value scale, essentially the same spectral pattern is observed for CF_2 and CF_3 groups, although the relative intensities of the component transitions differ for the CF_2 and CF_3 chromophores. Thus the same transitions to σ*(C—F) and σ*(C—C) considered in sects. III.1 and III.2 will dominate the discrete structure of the perfluoro-*n*-alkane C 1*s* spectra, but with oscillator strengths proportional to the numbers of CF_2 and CF_3 groups in the molecule. (*2*) Spectra originating at CF_2 and CF_3 groups will be offset by the difference in the ionization potentials of these groups, typically 1.2–1.8 eV. Although the *A*/*B* and *A*′/*B*′ features are well separated in the spectrum of each chromophore, confusion may arise because their splitting in the perfluoro-*n*-alkanes will very nearly equal the splitting of the CF_2 and CF_3 ionization potentials. This leads to unavoidable coincidences of bands, e.g., the C $1s(CF_3) \rightarrow$ σ* *A*′ transitions will be accidentally degenerate (or nearly so) with C $1s(CF_2) \rightarrow$ σ* *B* transitions in all perfluoro-*n*-alkanes larger than C_2F_6. The characteristic relative intensities of bands *A* and *B* in the CF_2 and *A*′ and *B*′ in the CF_3 group spectra may assist in resolving this overlap.

Spectral analysis of the perfluoro-*n*-alkanes as a sum of CF_2 and CF_3 group excitations originating at C 1*s* is summarized in Table 1 and in Fig. 2; one sees a facile resolution of the spectra provided one accepts the unresolved coincidence of the *A*′ and *B* transitions in the C_3F_8–C_6F_{14} series. The (C 1*s*, σ*) term values of the lowest excitations increase very slowly with the size of the molecule, being 4.5 eV in C_2F_6 and reaching only 5.0 eV in C_6F_{14}. The term values for excitations originating at C $1s(CF_3)$ appear systematically smaller than those of the corresponding transitions originating at C $1s(CF_2)$. As expected from the localization model, the spectra of the perfluoro-*n*-alkanes can be interpreted as combinations of the spectra of the CF_2 and CF_3 groups. Only the transitions to σ* levels are seen. To some extent, this situation may result from the rather limited resolution (0.6 eV) of the present spectra, so that weak but discrete R features may be revealed with higher resolution studies. However, we expect them to be weaker and/or more congested than in CF_4 since the R structure in CF_4 is detected by our present apparatus.

The dramatic differences in the oscillator strength distributions for C 1*s* excitation in the perfluoro-*n*-alkanes as compared to the *n*-alkanes is emphasized by comparing the ratio of the sum of the discrete oscillator strengths to that obtained by integrating from the ionization potential to a point 25 eV beyond, Table 2. It is interesting to note that whereas the ratio of discrete to continuum oscillator strength values is 1.2 ± 0.1 for all of the perfluoro-*n*-alkanes (including CF_4), it is significantly lower for the *n*-alkanes (0.20 ± 0.05). It is clear as well that the oscillator strengths in the discrete regions of the C 1*s* spectra of the perfluoro-*n*-alkanes are many times larger than those in the corresponding *n*-alkanes, and much larger than expected solely from Rydberg excitations. This supports our interpretation of the discrete features in the perfluoro-*n*-alkanes as excitations to virtual orbitals of predominantly valence character. This also is consistent with the potential barrier model (34) since the intensities of transitions to inner-shell valence type orbitals are expected to be enhanced strongly in the core excitation spectrum of an atom surrounded by many highly electronegative atoms.

Our simplified view of the inner-shell spectra of the perfluoro-*n*-alkanes as sums of the CF_2 and CF_3 group excitations predicts that the intensity of a band such as *A* should scale linearly with the number of CF_2 groups in the molecule. In fact, if the C 1*s* spectra of C_2F_6 and C_6F_{12} are truly good models for the perfluoro-*n*-alkane spectra, then the oscillator strength of the *A* peak in a given $CF_3(CF_2)_xCF_3$ species should be predictable from the oscillator strength of the *A* peak in C_6F_{12}, scaled by $x/6$. As shown in Table 2, the oscillator strength of the first peak does increase systematically with x, but is almost twice as large as that predicted from C_6F_{12}. Our comparison of the C 1*s* oscillator strengths among these molecules must be treated with caution. The extrapolation of the background was made from a relatively short pre-edge region in some cases, and in all species the continuum intensity is very small relative to that of the discrete structure. Both factors contribute to the uncertainty in our determination of the C 1*s* continuum intensity at 25 eV beyond the ionization potential and thus to the estimated 20% uncertainty in the oscillator strength for peak A. If our results are confirmed by more precise measurements, it would appear that C_6F_{12} is not a perfect model for the C $1s(CF_2)$ excitations in the perfluoro-*n*-alkanes.

In our intensity analysis of band *A* in the perfluoro-*n*-alkanes, we have assumed that all of band *A* in C_6F_{12} corresponds to a transition to σ*(C—F). However, closer examination of this feature and comparison with the spectra of other perfluorocycloalkanes strongly suggest that there is a second transition to this band which terminates at σ*(C—C) and is common to all perfluorocycloalkanes (see sect. IV). In this regard, the spectrum of PTFE might be a better model for the perfluoro-*n*-alkanes than C_6F_{12}, especially if intensity information were available on it. Caution is therefore needed in applying an

Can. J. Chem. Downloaded from www.nrcresearchpress.com by 112.217.228.212 on 09/07/12
For personal use only.

independent-systems model to inner-shell spectra. Although this approach has worked well in the past (chloroethane (14) and methyl formate (39)), in the present case quantitative problems appear when comparing expectations with experiment. In view of the near degeneracy of the σ*(C—F) MO's within the CF_2 and CF_3 groups, mixing of these levels is not unexpected, and in part may be the reason behind the inconsistency between the observed and the predicted scaling of the *A*-band oscillator strengths with increasing numbers of CF_2 groups.

We similarly expect the peak at *ca.* 295 eV in the perfluoro-*n*-alkanes to grow in intensity with increasing chain length according to our assignment of it as overlapping *A'* and *B* transitions. However, the peak intensity of this feature is relatively constant at *ca.* 0.25 eV^{-1} in all species, contrary to the approximate doubling expected on going from C_3F_6 to C_6F_{12}. This suggests that the *A'* and *B* transitions possibly are not exactly aligned, but rather displaced so that the feature broadens rather than heightens as the chain length increases. This broadening is evident in Fig. 2, particularly on the high energy side.

III.5. Branched isomers

It is known from previous work (25) that there is little or no difference between the inner-shell spectra of the isomers *n*-pentane and neopentane, the reason being that at the present level of resolution there is no difference between the spectra of CH_2 and CH_3 groups. Because this is not true for CF_2 and CF_3 groups, it is anticipated that there will be significant differences between the C 1*s* spectrum of perfluoro-*n*-pentane and that of its isomer perfluoroneopentane since the latter contains no CF_2 groups. On the other hand, both contain CF_3 groups which should add their characteristic pattern to both spectra. There should be smaller differences in the F 1*s* spectra of these isomeric pentanes (see sect. V.2). The C 1*s* spectra of the two compounds appear in Figs. 2 and 3 and are summarized in Tables 1 and 3. Though C 1*s* ionization potentials are not known for $C(CF_3)_4$, the X-ray photoelectron spectra of other molecules (31) suggest ionization potentials of 293 eV for C 1*s*(C) and 300 eV for C 1*s*(CF_3). These reasonable values for the C 1*s* ionization potentials in turn result in quite reasonable term values for the observed transitions, Table 3.

The C 1*s* spectra of the C_5F_{12} isomers are similar in that they both show the *A'*, *B'*, *C'*, *D'* patterns of bands which correspond to transitions originating at the CF_3 groups. On the other hand, the four bands of perfluoro-*n*-pentane corresponding to transitions originating at the CF_2 groups (*A*, *B*, *C*, *D*) are replaced in perfluoroneopentane by only two relatively weak bands, *A* and *D*, which must originate at the central C atom of that molecule. The dominance of CF_3 group excitations in perfluoroneopentane leads to a remarkable similarity between its C 1*s* spectrum and that of C_2F_6 (Fig. 3), in spite of their very different symmetries. This similarity is reasonable if the C 1*s* holes are localized in the core excited states of each molecule, resulting in an effective C_{3v} symmetry at the core hole in each case.

Band *D* of $C(CF_3)_4$ originating at the central C atom has been assigned to a shape resonance or a delayed onset continuum feature, analogous to that discussed previously (see sect. III.1). The *A* band, while appearing relatively weak in the $C(CF_3)_4$ spectrum nonetheless has an oscillator strength of 0.095; though its term value of 2.6 eV is appropriate for a Rydberg upper state, the oscillator strength is too large for such an assignment. Thus the transition in question is assigned as C 1*s*(C) → σ*(C—F)$_\pi$.

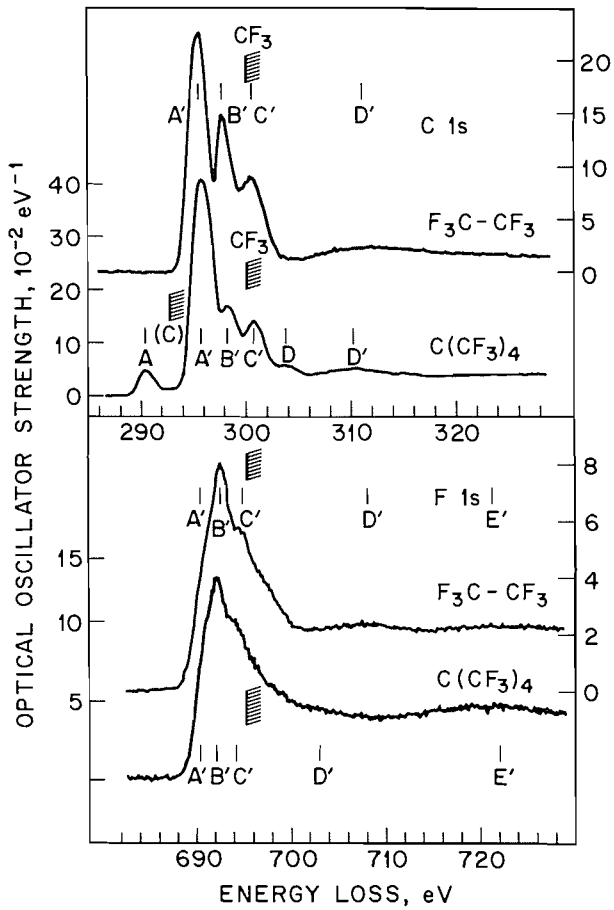

FIG. 3. Comparison of the oscillator strength spectra of C_2F_6 and $C(CF_3)_4$ in the C 1*s* (*upper panel*) and F 1*s* regions (*lower panel*). Primed and unprimed transitions originate with the CF_3 and C groups, respectively.

The term values of the C 1*s*(CF_3) → σ*(C—F)$_\pi$ and C 1*s*(CF_3) → σ*(C—F)$_\sigma$ transitions are 4.5 and 2.1 eV in C_2F_6 and 4.3 and 1.9 eV in $C(CF_3)_4$, respectively. The assignment of band *A* to C 1*s*(C) → σ*(C—F)$_\pi$ thus may seem strange based on the relatively low term value of 2.6 eV. However, it recently has been observed for a few well-defined cases (6) that transitions to highly localized molecular orbitals from the inner shells of atoms which are one atom removed from the localized bond show a decrease of 1–4 eV in their term value as compared to those in which the excitation involves a hole on an atom within the localized bond. A similar reduction of the term value also can be observed for valence excitations to the same σ* orbital. For example, inner-shell transitions to the local σ*(O—F) orbital of CF_3OF have term values of 11.1 and 11.0 eV in the O 1*s* and F 1*s*(OF) spectra, and are the dominant features of the spectra (6). Here the originating orbital has strong overlap with the terminating orbital and is highly localized. However, the C 1*s* → σ*(O—F) transition has a term value of only 7.0 eV and its oscillator strength is reduced by a factor of approximately 6 compared to the transition terminating at the same orbital in the O 1*s* and F 1*s*(OF) spectra. Similar discrepancies in term values and intensities also have been reported for inner-shell transitions to π* orbitals from local and distant sites in various carbonyls (36) and the fluoroethylenes (24).

The phenomenon of widely differing term values for transitions to a highly localized orbital when originating at atoms

TABLE 3. Transition energies (E, eV), term values (TV, eV), and proposed assignments for features in the C 1*s* and F 1*s* spectra of perfluoroneopentane

Band	E	TV (C)	TV (CF_3)	Assignment (C)	Assignment (CF_3)
C 1*s*					
A	290.4	2.6		$\sigma^*(C—F)_\sigma$	
A'	295.7[a]		4.3		$\sigma^*(C—F)_\pi$
B'	298.1		1.9		$\sigma^*(C—F)_\sigma$
IP(C)[b]	293				
IP'(CF_3)[b]	300				
C'	300.7		−0.7		$\sigma^*(C—C)$
D	303.8	−11		Shape resonance or delayed onset	
D'	310		−10		σ^*
F 1*s*					
A'	690		4.5	σ^*	
B'	692.0[c]		2.4	$\sigma^*(C—F)$	
C'	694.0		0.4	$\sigma^*(C—C)$	
IP(*F*)[b]	694.45		—		
D'	703		−9	Shape resonance or delayed onset	
E'	722		−27	EXAFS	

[a]Calibrated as 8.33 (5) eV above the C 1*s* → 1π* band of CO.
[b]Ionization potentials estimated by comparison with known values (31) of related compounds, i.e., $CF_3C{=}CSF_5$ (292.5); CF_3CH_3 (292.1); $CF_3C{\equiv}CCF_3$ (292.7); $CF_3C{\equiv}CH$ (292.2); CF_3CF_3 (299.8 eV).
[c]Calibrated as 157.8 (1) eV above the O 1*s* → 1π* band of CO.

which are distant rather than close to that orbital can be rationalized in terms of an energy penalty which must be paid when significant charge transfer is involved in the excitation.

IV. Low-lying σ* MO's in perfluorocycloalkanes

To this point, there is no evidence in the inner-shell spectra of the perfluoro-*n*-alkanes for a distinct transition to σ* which lies below the normal Rydberg region, although there is evidence for intense C 1*s* → σ* transitions overlapping the R transitions and most likely mixing with them. However, the C 1*s* excitations in several perfluorocycloalkanes, Fig. 4 and Table 4, are distinctly different from those of their linear counterparts in this regard, Fig. 2. Consider perfluorocyclopropane C_3F_6, as an example. The lowest-energy band in the C 1*s* spectrum of C_3F_6, Fig. 4 and Table 4, has a very large term value of 6.1 eV. Inasmuch as the lowest energy band of the corresponding linear system C_3F_8 has a term value of only 4.7 eV, Table 1, it is clear that the first band in the C 1*s* spectrum of C_3F_6 is unusually low lying due to the cyclization. We conclude that it is an additional transition to a σ* valence MO lying below those of C_3F_8 in the 293–300 eV region, with an enhanced term value due to molecular strain.

The C 1*s* → σ* transition is a prominent low-lying feature in the inner-shell spectrum of cyclopropane (8). According to X-α (8) and SCF-MO calculations (40), the lowest σ* MO in cyclopropane is a_2', an MO which is strictly C—C antibonding and has no C—H contribution whatsoever. Presumably, the additional band which is so low lying in C_3F_6 is a C 1*s* → a_2' σ*(C—C) transition. On the other hand, a virtual orbital calculation of C_3F_6 (sect. VII) shows that the a_2'(C—C) level is only second lowest, with a_2' σ*(C—F) being lower by *ca.* 1.2 eV.

The next band in the C 1*s* spectrum of C_3F_6 has a term value of 4.4 eV and so is assignable as C 1*s* → σ*(C—F), i.e., on the basis of its term value it corresponds to the *A* band for C 1*s* (CF_2) excitation. The *B*-band transition in C_3F_6 falls at 294.1 eV with a term value of 3.1 eV. This term value is unexpectedly high for a *B* band (Table 1), however, the upward shift of this spectral feature relative to its position in the perfluoro-*n*-alkanes may be a consequence of σ*(C—C) mixing with σ*(C—F).

The assignment of the lowest band of C_3F_6 to a transition to σ*(C—C) follows from the very high strain energy of 54 kcal/mol estimated for this molecule (9). In this regard, it is interesting then that Liebman *et al.* (9), have estimated the strain energy in perfluorocyclobutane, C_4F_8, as 14.5-18 kcal/mol, this being due in part to F—F repulsions. We argue that bond strain can be a significant factor in a four-membered ring such as C_4F_8, and as with C_3F_6, again may lead to a transition to a low-lying σ*(C—C) MO.

The *A* band in C_4F_8 at 293.1 eV (C 1*s* → σ*(C—F), 4.2 eV term value) is preceded by a prominent band which has a term value of 6.0 eV, Fig. 5. This term value is much larger than that expected for a transition to σ*(C—F) (Table 1), and thus the transition is assigned as terminating at a σ*(C—C) valence orbital which is shifted down due to molecular strain. The abnormal nature of the lowest excitation from C 1*s* in C_4F_8 (Table 4) is obvious when compared to the C 1*s* spectrum of C_4H_8 and the other cycloalkanes (8). Similarly, there is no complement of the low-lying σ* band of C_4F_8 to be found in C_4F_{10}. The narrow shape resonance at 302 eV in C_4F_8, Fig. 4, having a term value of −4.6 eV also is unique when compared with the spectra of the perfluoro-*n*-alkanes, and again suggests that there is something unusual going on in the σ* manifold of this compound.

Though the idea that molecular strain can lead to a low-lying transition to σ*(C—C) is an attractive one in view of the support

Can. J. Chem. Downloaded from www.nrcresearchpress.com by 112.217.228.212 on 09/07/12
For personal use only.

TABLE 4. Transition energies (E, eV), term values (TV, eV), and proposed assignments for features in the C 1*s* spectra of the cyclic perfluoroalkanes

	C_3F_6		C_4F_8		C_5F_{10}		C_6F_{12}		
Band	E	TV	E	TV	E	TV	E	TV	Assignment
σ*	291.1	6.1	291.2	6.0	291.7	5.5	292.2	5.0	σ*(C—C)
A	292.8	4.4	293.1	4.2	293.2	4.0	293.2	4.0	σ*(C—F)
B	294.1	3.1	295.0	2.3	295.1	2.1	295.1	2.1	σ*(C—F)
4	295.0	2.2	296.3	1.0	296.4	0.8	—	—	
IP	297.2[a]	—	297.2	—	297.2[a]	—	297.2[a]	—	
C	298	−0.8	297.4	−0.2	299	−2	298.3	−1.1	σ*(C—C)
6	—	—	301.9	−4.6			300.1	−2.9	σ*
D	309	−12	310	−13	309	−12	308.2	−11	EXAFS

[a]Taken as equal to that of C_4F_8 (31).

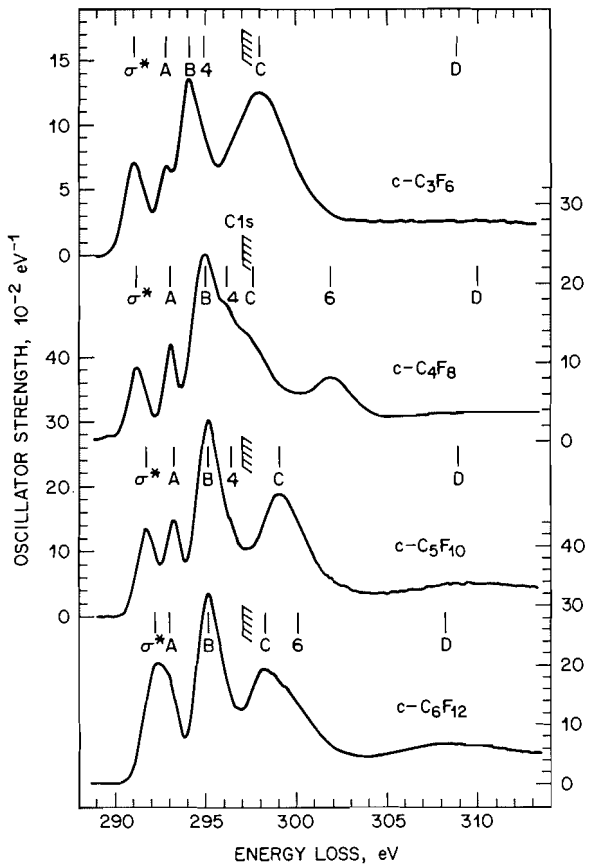

FIG. 4. Oscillator strength spectra of the perfluoro-*n*-alkanes in the C 1*s* region.

it receives from the C 1*s* spectra of C_3F_6, C_3H_6 (8) and C_4F_8, note too that the strain energy in C_4H_8 is 6 kcal/mol *higher* than in C_4F_8, yet there is no prominent, low-lying transition to σ*(C—C) in its inner-shell spectrum (8). Perhaps the low-lying position of the σ*(C—C) MO in C_4F_8 is due in part to its mixing with the low-lying σ*(C—F) levels. Note that an empirical analysis of the outer-shell spectrum of C_4H_8 (1) did lead to the suggestion of a valence excitation to σ* preceding the lowest R transition.

To this point, the role of strain in lowering σ* seems reasonable, with low-lying σ*(C—C) MO's appearing in the strained molecules C_3F_6 and C_4F_8, but not in the open chain relatives C_3F_8 and C_4F_{10}, nor apparently in C_6F_{12}. Though there is no data on molecular strain in C_5F_{10}, data on C_5H_{10} (41) shows it to be almost strain-free. Thus for C_5F_{10}, one might expect a C 1*s* spectrum much like that of C_6F_{12}. How surprising then to see, Fig. 6, that C_5F_{10} also shows a low-lying transition to σ*(C—C)!

The presence of an "extra" low-lying band in the spectra of the perfluorocycloalkanes is graphically illustrated in Figs. 5 and 6, where the C 1*s* spectra of the corresponding cyclic and linear perfluoroalkanes are compared on the basis of energy and intensity. One sees clearly from these comparisons that the lowest energy feature in the C_3, C_4, and C_5 linear compounds correspond to the second lowest in the cyclic compounds. The term values of the lowest bands in the cyclic systems, Table 4, are far too large for excitations to σ*(C—F) MO's, and so must terminate at σ*(C—C). A careful examination of the "C 1*s* → σ*(C—F)" transition of C_6F_{12} (Fig. 4) at 292.4 eV in fact shows that it too consists of two strongly overlapped transitions, the lower one of which is presumably a transition to σ*(C—C). With this feature in place, one sees a monotonic trend of the (C 1*s*, σ*(C—C)) term value from 6.1 to 4.8 eV as the ring strain decreases from C_3F_6 to C_6F_{12}.

It is at first sight anomalous that C_5F_{10} and C_6F_{12} would show low-lying excitations to σ*(C—C) due to strain (Fig. 6) when the C_5H_{10} and C_6H_{12} rings have strain energies of only 6.2 and 0.0 kcal/mol, respectively (41). However, it must be remembered that this argument neglects the F—F repulsions undoubtedly present in the perfluoro derivatives. The possibility that the σ*(C—C) level is low-lying in the perfluorocycloalkanes because the C 1*s* and σ* levels are delocalized around the rings leads to the expectation that, all other factors being equal, the (C 1*s*, σ*) term value will be largest in C_6F_{12} and smallest in C_2F_6, whereas the opposite is observed. The persistence of a low-lying σ*(C—C) level up to C_6F_{12} in the perfluorocycloalkanes may be due to mixing with low-lying σ*(C—F) levels (symmetry allowing) which amplifies the strain shift.

One can imagine that the $(CF_2)_x$ ring is formed by removing a CF_2 group from $(CF_2)_{x+1}$ and rejoining the terminal CF_2 groups. If this exercise is performed on perfluorocyclopropane, the result is tetrafluoroethylene, which we take for our purposes as a two-membered ring. In this two-membered ring, the MO conventionally taken as the "π" MO is the one that closes the ring; this MO is here relabelled σ′, while its antibonding counterpart (π*) is relabelled σ′*. Of course, the "two-membered ring" is extremely strained and so will have an unusually small σ′–σ′*

Can. J. Chem. Downloaded from www.nrcresearchpress.com by 112.217.228.212 on 09/07/12
For personal use only.

Can. J. Chem. Downloaded from www.nrcresearchpress.com by 112.217.228.212 on 09/07/12
For personal use only.

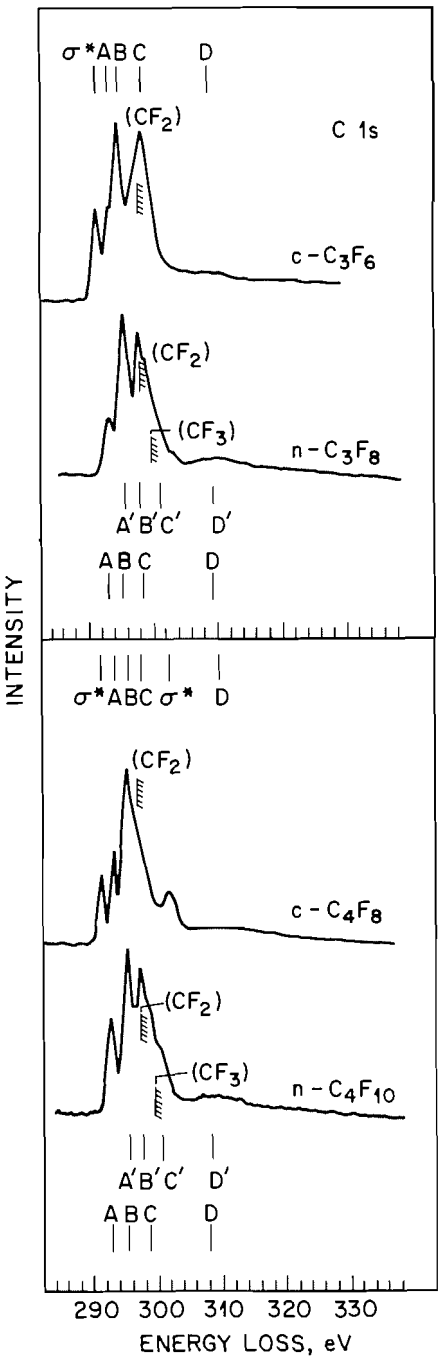

FIG. 5. Comparison of the C 1*s* spectra of the C_3 and C_4 perfluorocycloalkanes with those of corresponding perfluoro-*n*-alkanes.

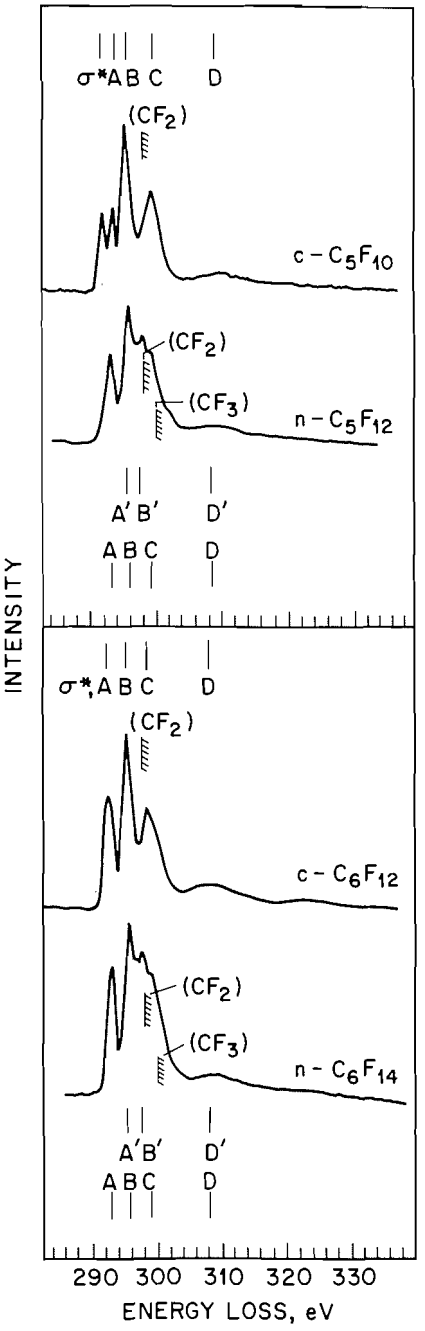

FIG. 6. Comparison of the C 1*s* spectra of the C_5 and C_6 perfluorocycloalkanes with those of the corresponding perfluoro-*n*-alkanes.

split. As anticipated from this, the C $1s \rightarrow \sigma'^*$ excitation of tetrafluoroethylene (conventionally written as C $1s \rightarrow \pi^*$) falls well below the lowest Rydberg excitation, having a term value of 6.47 eV (24). In this brief discussion, it is not our aim to propose a new nomenclature for olefins in which π/π^* and σ/σ^* are interchanged, but rather to show how the inner-shell spectra of unsaturates can be related to those of saturated compounds by virtue of the high strain in the former when considered as "cyclic" systems. If C_2F_4 is added to the list of strained perfluorocycloalkanes, then the term value trend for the C $1s \rightarrow \sigma^*$(C—C) transition stretches monotonically from 6.47 to 4.8 eV.

V. F 1*s* spectra of the perfluoroalkanes

Although not as well structured as those from C 1*s*, the F 1*s* spectra of the perfluoroalkanes also are of use when investigating low-lying transitions to σ^*. Note however, that ionization from F 1*s* in CF_4 is unusually broad (FWHM *ca.* 1.5 eV) due to dissociation of the F $1s^{-1}$ molecular ion (15). The strongly dissociative nature of F $1s^{-1}$ states is easily understood within the $Z + 1$ equivalent core model whereby the F 1*s* ionized atom is replaced by a Ne atom. This dissociation leads to very broad features in the F 1*s* inner-shell spectra of all of the perfluoroalkanes. In a previous study of the F 1*s* spectra of the

Can. J. Chem. Downloaded from www.nrcresearchpress.com by 112.217.228.212 on 09/07/12
For personal use only.

fluoromethanes, the first broad bands below the F 1*s* ionization potentials were assigned as terminating at antibonding V levels (42).

*V.1. The perfluoro-*n*-alkanes*

Our experience from earlier work on perfluorinated systems (10, 22, 24, 43) is that many of the transitions appearing in the C 1*s* spectra also appear in the F 1*s* spectra, though with poorer resolution and often with somewhat smaller term values. This is the case as well in the perfluoroalkanes. The F 1*s* spectra of the perfluoro-*n*-alkanes are plotted in Fig. 7, in comparison with those of the perfluorocycloalkanes. The spectral energies, term values and assignments are tabulated in Tables 3, 5, and 6. The poorly resolved character of the F 1*s* spectra is due not only to the large linewidths of the transitions to dissociative excited states (15), but also to the fact that the F 1*s*(CF_3) and F 1*s*(CF_2) ionization potentials are separated by only 1.5 eV (assuming that the measured ionization potentials of C_3F_8 (31) apply as well to the higher members of the perfluoro-*n*-alkanes series). Nonetheless, certain aspects of the F 1*s* spectra are clear:

(*1*) In the case of C_2F_6 (see Fig. 3), the F 1*s*(CF_3) $\rightarrow$ σ^*(C—F) *A'* band is expected to have a term value of *ca.* 4.3–5.0 eV, which fits for the barely perceptible shoulder at 690 eV having a 5.3 eV term value. In C_3F_8 the *A'* shoulder is more easily seen (689.9 eV) and is probably at 690–691 eV in the F 1*s* spectra of the other compounds in this series. Note too, there is an F 1*s*(CF_2) ionization in the C_3F_8–C_6F_{14} series which is *ca.* 1.5 eV lower than that from F 1*s*(CF_3), yet there are no signs whatever of the F 1*s*(CF_2) $\rightarrow$ σ^*(C—F) transitions! Since we are confident where these missing transitions should appear, we are led to conclude that the F 1*s*(CF_2) $\rightarrow$ σ^*(C–F) *A* band transitions are unusually weak. The 689.9 eV band of C_3F_8 is predominantly F 1*s*(CF_3) $\rightarrow$ σ^*(C—F). As in the C 1*s* spectra, there is nothing in the F 1*s* spectra of the perfluoro-*n*-alkanes to suggest a distinct σ^* MO lying below the R levels.

(*2*) Although the F 1*s* $\rightarrow$ σ^* *A* and *A'* transitions appear to be strongly electric-dipole forbidden, the F 1*s* $\rightarrow$ σ^* transitions *B* and *B'* should be strongly dipole allowed and thus the spectra should show two intense bands separate by *ca.* 1.5 eV, the difference of F 1*s* (CF_2) and F 1*s*(CF_3) ionization potentials. Indeed, the first two intense peaks in the F 1*s* spectra of C_3F_8 to C_6F_{14} are separated by *ca.* 1.5 eV.

(*3*) What appear to be high-energy shape resonances in the F 1*s* spectra of the perfluoro-*n*-alkanes from CF_4 to C_6F_{14} (features *D* and *D'*) have term values of *ca.* −14 eV, and seem to parallel those observed in the C 1*s* spectra with nearly the same term values (−11 eV). However, EXAFS or delayed continuum onset assignments also are possibilities here. The minima between *C* and *D* in the F 1*s* spectra are much less pronounced than the corresponding minima in the C 1*s* spectra. This is consistent with a potential barrier, delayed continuum onset interpretation of band *D*, since the F atoms are on the periphery of the molecule and thus should experience a smaller barrier.

(*4*) There are peaks in the F 1*s* spectra at 694–695 eV (*C'*) which are just at the F 1*s*(CF_3) ionization potential. It seems likely that these are F 1*s*(CF_2) $\rightarrow$ σ^*(C—C) shape resonances corresponding to band *C*, *C'* in the C 1*s* spectra.

(*5*) A very broad feature (*E*, *E'*) has a term value of *ca.* −28 eV in CF_4 to C_6F_{14}, and does not appear in any of the C 1*s* spectra. This is likely to be an EXAFS oscillation associated with backscattering from an F atom bonded to the same C atom as that to which the core-excited F atom is attached.

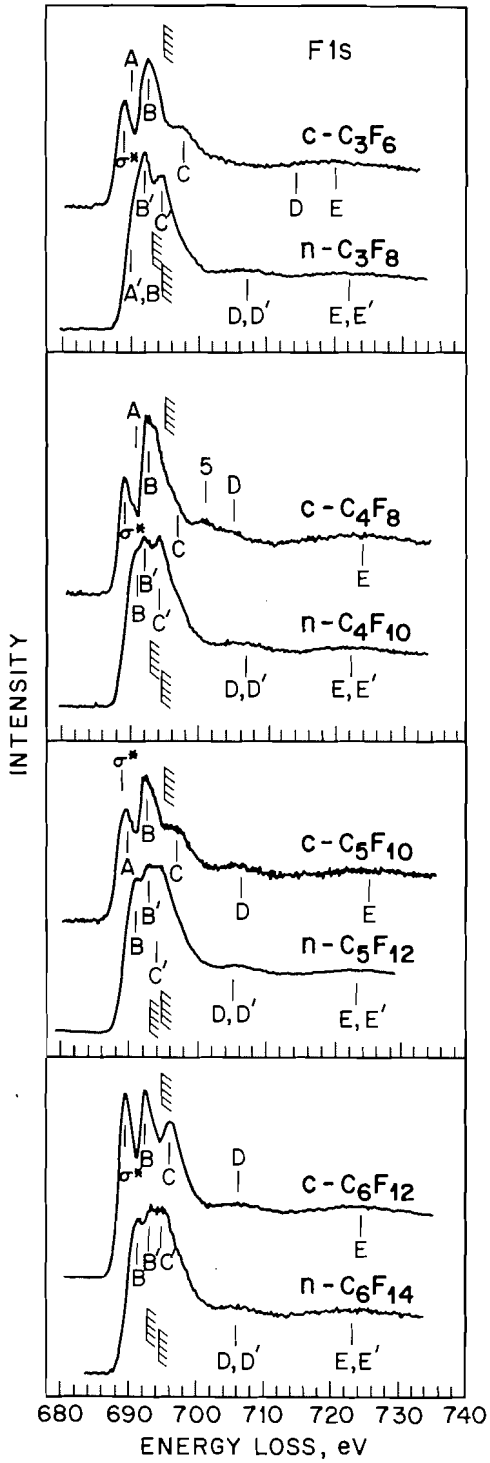

FIG. 7. Oscillator strength spectra of the perfluoro-*n*-alkanes and perfluorocycloalkanes in the F 1*s* region as derived from energy-loss spectra. Inner-shell ionization potentials are shown by hatched areas. The unprimed transitions originate at CF_2 groups whereas the primed transitions originate at CF_3 groups.

V.2. Branched perfluoroalkanes

Even more than with the C 1*s* spectra, the F 1*s* spectra of C_2F_6 and $C(CF_3)_4$ show a remarkable match, Fig. 3 and Tables 3 and 4. This close similarity arises not only because all of the F atoms in the two molecules are in CF_3 groups and thus are spectroscopically equivalent at our resolution, but also because of the apparent localization of the excitations to the CF_3 groups. This

TABLE 5 Transition energies (E, eV), term values (TV, eV), and proposed assignments for features in the F 1*s* spectra of the perfluoro-*n*-alkanes

	C_2F_6		C_3F_8		*n*-C_4F_{10}		*n*-C_5F_{12}		*n*-C_6F_{14}		Assignment	
Band[a]	E	TV	E	TV	E	TV	E	TV	E	TV	F 1*s*(CF_2)	F 1*s*(CF_3)
A'	690	5.3	689.9	4.7								$\sigma^*(C—F)_\pi$
B			689.9	3.1	691	2.1	691.0	2.1	691.3	1.8	$\sigma^*(C—F)$	
B'	692.7	2.6	692.0	2.6	692.2	2.4	692.7	1.9	693.3	1.3		$\sigma^*(C—F)_\sigma$
C'	694.7	0.6	694.4	0.2	694.3	0.3	694	0.6	694.9	−0.3		$\sigma^*(C—C)$
IP(CF_2)	—	—	693.07	—	693.1[b]	—	693.1[b]	—	693.1[b]	—		
IP'(CF_3)	695.33	—	694.61	—	694.6[b]	—	694.6[b]	—	694.6	—		
D,D'	708	−13	707	−13	706	−11	705	−10	706	−11	Shape resonance or delayed onset	
E,E'	721	−26	722	−28	722	−27	723	−28	723	−28	EXAFS	

[a]The unprimed bands originate at CF_2 groups whereas the primed bands originate at CF_3.
[b]Ionization potentials assumed to be equal to those of C_3F_8 (31).

TABLE 6. Transition energies (E, eV), term values (TV, eV), and proposed assignments for features in the F 1*s* spectra of the cyclic perfluoroalkanes

	C_3F_6		C_4F_8		C_5F_{10}		C_6F_{12}		
Band	E	TV	E	TV	E	TV	E	TV	Assignment
σ^*	689.2	5.9	689.5	5.6	689.4	5.7	—	—	$\sigma^*(C—C)$
A	690	5.1	690.8	4.3	690	5.1	689.8	5.3	$\sigma^*(C—F)$
B	692.8	2.3	693.2	1.9	692.4	2.7	692.7	2.4	$\sigma^*(C—F)$
IP	695.1[a]	—	695.1	—	695.1[a]	—	695.1[a]	—	
C	698.2	−3.1	697.0	−1.9	696.7	−1.6	696.3	−1.2	$\sigma^*(C—C)$
5			701	−6			—	—	
D	704	−9	705	−10	706	−11	706	−11	Shape resonance or delayed onset
E	720	−25	724	−29	725	−30	724	−29	EXAFS

[a]Taken as equal to that of C_4F_8 (31).

similarity includes not only spectral shape and peak positions but also intensities. The region below the F 1*s* ionization potential in $C(CF_3)_4$ has an integrated oscillator strength which is 1.7 times that of the corresponding region in C_2F_6, in reasonable agreement with the ratio of 2.0 between the number of F atoms in the two molecules. Indeed, on a per-F-atom basis, the oscillator strength in the discrete region of the F 1*s* spectra is remarkably constant, having a value of 0.53 (5) when averaged over all perfluoro species studied.

One dramatic difference between the F 1*s* spectra of C_2F_6 and $C(CF_3)_4$ is that band *D'* around 705 eV is not detected in $C(CF_3)_4$. This suggests that *D'*, a feature common to all of the perfluoroalkane F 1*s* spectra, may be a shape resonance or the first EXAFS oscillation associated with backscattering from an F atom on an adjacent C atom. These types of F—F distances do not exist in $C(CF_3)_4$. The presence of band *E'* with similar intensities in both C_2F_6 and $C(CF_3)_4$ is consistent with an EXAFS oscillation associated with backscattering from an F atom bonded to the same C atom as that to which the core-excited F atom is attached.

V.3. Perfluorocycloalkanes

The anomalous behavior of the C 1*s* spectra of the perfluorocycloalkanes (when compared with the linear species) persists in the F 1*s* spectra. Figure 7 compares the F 1*s* spectra of the cyclic and linear systems. One sees similar features in each case except for the addition of low-lying transitions to $\sigma^*(C—C)$ orbitals in the cyclic species. The (F 1*s*, σ^*) term values, Table 6, are esentially the same as those for the C $1s \rightarrow \sigma^*$ bands, Table 4. The observation of the low-lying excitations to $\sigma^*(C—C)$ in the F 1*s* spectra suggest that there is considerable interaction between the $\sigma^*(C—C)$ and $\sigma^*(C—F)$ orbitals on a single center. This implies that the MO induced to be so low-lying by strain and the inductive effect has both C—C and C—F antibonding character and is thus somewhat delocalized on its center.

VI. Negative-ion resonances

We now attempt to apply the lessons learned from the inner-shell excitation spectra of the alkanes and perfluoroalkanes in the 280–740 eV region to the interpretation of their negative-ion spectra in the 0–8 eV region. The thread connecting these two very different spectroscopies is a set of virtual orbitals assumed to be common to the transitions in each.

The electron affinities of selected perfluoroalkanes were determined by the electron transmission (ETS) technique (21), with results as shown in Fig. 8 for the linear species and in Table 7 for both linear and cyclic species. These data in some cases differ substantially from those of Christophorou *et al.* (44–46), who used the less direct technique of dissociative electron attachment (DEA) for determining the energetics of negative-ion formation. One major difference between ETS and DEA is that corresponding peaks generally appear at lower energy in

Can. J. Chem. Downloaded from www.nrcresearchpress.com by 112.217.228.212 on 09/07/12
For personal use only.

Can. J. Chem. Downloaded from www.nrcresearchpress.com by 112.217.228.212 on 09/07/12
For personal use only.

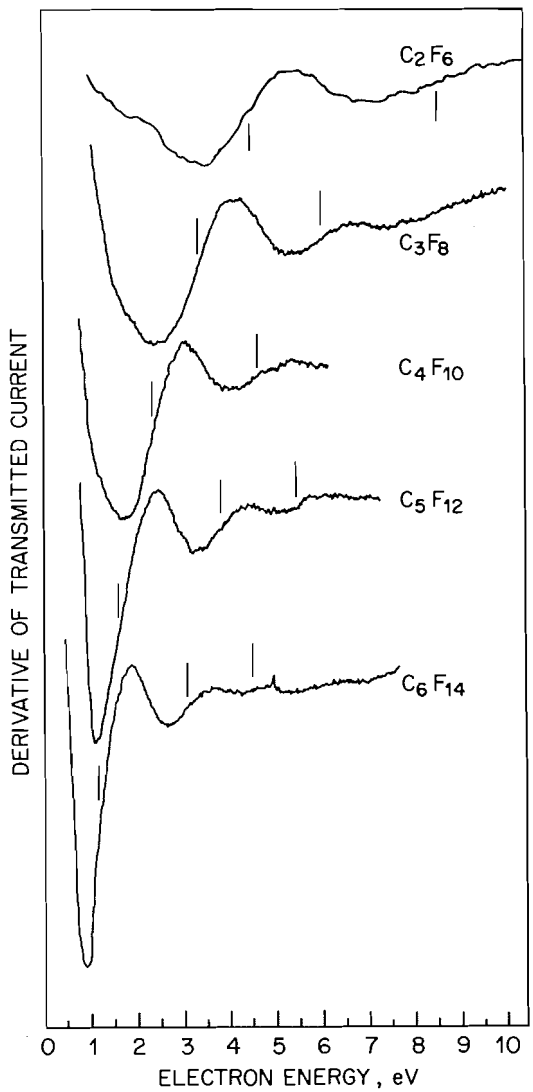

FIG. 8. Electron transmission spectra of the perfluorinated ethane, propane, *n*-butane, *n*-pentane, and *n*-hexane. Negative-ion resonance energies are indicated by the vertical bars.

DEA than in ETS because the attachment process is dissociative and so the survival probability of the anion decreases as the resonance energy increases from one end of the band to the other.

In each of the perfluoroalkanes investigated, two or more negative-ion resonances were observed. Since the target molecules are saturated, the negative ions must result either from electron capture into σ^* MO's or by formation of Feshbach resonances. In the latter, the incident electron excites a bound electron into an R orbital and is itself captured in an R orbital. Usually, but not always, the two electrons occupy the same R orbital. In the case where the R orbital in question is the $3s$ MO, it is known that the Feshbach resonance energy is very nearly 0.5 eV below the corresponding R excitation to $3s$ in the neutral molecule (1, 10, 22). That is to say, the $^1(\phi_i, 3s)$ R state has an electron affinity of +0.5 eV in forming the $^2(\phi_i, 3s^2)$ negative ion.

Referring to the uppermost valence ionization potentials in the perfluoro-*n*-alkanes as determined by photoelectron spectroscopy (1), one sees that the term values of the lowest transitions to $3s$ fall in the range 3.71–4.42 eV in the series CF_4 to C_6F_{14}. The corresponding transition energies to the $3s$ MO's are in the range 12.48–8.33 eV, thus placing the lowest possible Feshbach resonances for these compounds in the 12.0–7.8 eV range. For the *n*-alkanes CH_4 to C_6H_{14}, the corresponding limit below which negative-ion Feshbach resonances will not form is 9.2–7.2 eV. Any negative-ion states observed below these ranges necessarily must involve the occupation of σ^* MO's rather than R orbitals. If the qualitative conclusions of the inner-shell spectroscopic study carry over to the negative ions, then the σ^* resonances in the perfluoro-*n*-alkanes should lie considerably below those of the corresponding *n*-alkanes, and the σ^* negative ions should be particularly low lying in the highly strained perfluorocycloalkanes.

Negative-ion energies as determined by the electron transmission technique are summarized in Table 7. One sees that the negative-ion energies of the perfluoro-*n*-alkanes decrease as the size of the molecule increases. However, the incremental effect of each CF_2 group is diminished as the molecular chain is lengthened. All of the observed resonances are well below the region in which the lowest Feshbach resonances are expected, and so terminate at σ^*. Such behavior of the σ^* resonances is just that expected for delocalized σ^* valence MO's of large bandwidth, uncomplicated by the presence of R orbitals. Indeed, R MO's are irrelevant to the discussion of the binding of an electron to a neutral molecule because the electron does not experience a $-1/r$ potential. Unlike the electron transmission spectra of the perfluorinated alkanes, those of methane and *n*-hexane (47) provide no evidence of σ^* anion states below 6 eV. Thus the electron transmission spectra clearly show the strong stabilization of certain alkane σ^* MO's upon fluorination.

The lowest energy feature in the electron transmission spectrum of C_3F_6 occurs 1.27 eV above the ground state of the neutral molecule and is presumably due to the formation of the ground-state anion. Thus the lowest anion state of C_3F_6 is 2.17 eV more stable than that of acyclic C_3F_8. The electron transmission spectrum of C_3F_6 also shows structure due to anion states at 5.7 and 7.2 eV.

The electron transmission spectra of C_4F_8 and C_6F_{12} do not show structures due to anion formation below 3.7 eV. However, for each of these two compounds there is a feature just above the beam zero, the position of which varies with the retarding voltage. Experience shows that this often occurs when there is an anion state energetically slightly below the ground state of the neutral molecule. If the lowest anion states of these two molecules are indeed bound, this would imply that the ground-state anion of the cyclic C_4F_8 molecule is at least 2.37 eV more stable than that of the corresponding acyclic C_4F_{10}, and that the ground-state anion of the cyclic system C_6F_{12} is at least 1.20 eV more stable than that of acyclic C_6F_{14}. That the energy differences between the ground-state anions of the cyclic and acyclic compounds could be this large is clear from the above-mentioned results for the C_3 species. In light of the results discussed above for the inner-shell spectra, it is surprising that the drop in the electron affinity on going from C_4F_{10} to C_4F_8 is greater than that on going from C_3F_8 to C_3F_6. Perhaps this is due to the fact that the σ^* orbitals involved in the inner-shell spectra are localized while those in the electron transmission spectra are delocalized.

To aid in the assignments of the temporary-anion states, we have performed HF calculations on the ground states of the neutral molecules. In these calculations, the STO-3G basis set was employed and the geometries were fully optimized at the HF level. The virtual orbitals from these calculations are uniformly too high by about 9 eV as compared to the experimental electron

Can. J. Chem. Downloaded from www.nrcresearchpress.com by 112.217.228.212 on 09/07/12
For personal use only.

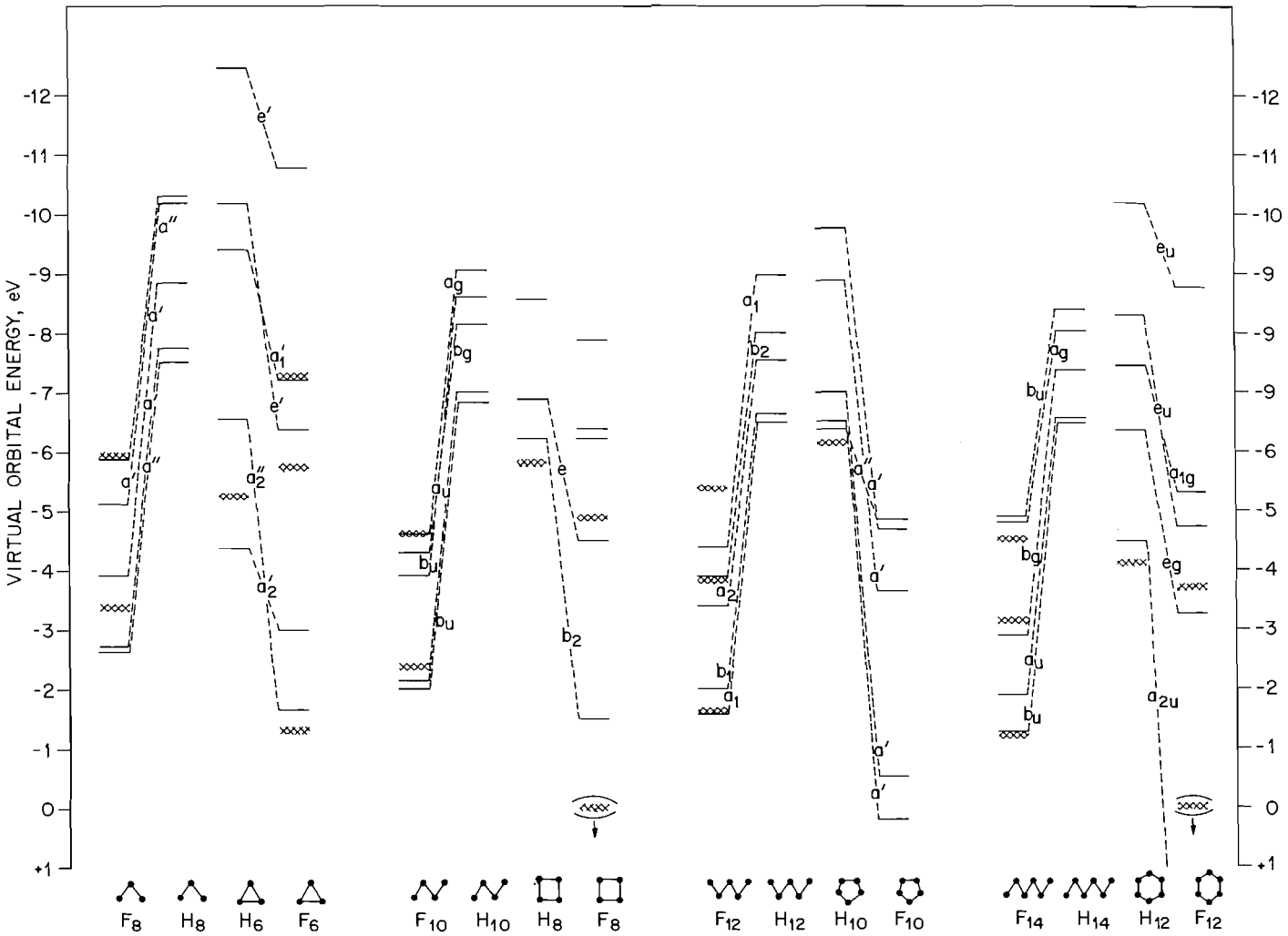

FIG. 9. Correlation of the computed virtual orbital energies of the linear and cyclic alkanes and perfluoroalkanes. All of the calculated energies have been shifted downward by 9 eV to improve agreement with experiment. The cross-hatched lines represent measured electron transmission resonance energies, with those in vertical parentheses being at energies greater than 0.0 eV, but otherwise of unknown magnitude.

affinities, and this quantity has been subtracted from the calculated eigenvalues. We note that this approach is quite crude, however more rigorous calculations would require introduction of continuum states for electron-molecule scattering, which is not yet practical for molecules of the complexity studied here.

One sees in Table 7 and Fig. 9 that the virtual MO approximation, naive though it is, does quite well in assigning the negative-ion features. In the perfluoro-*n*-alkanes series, the lowest resonance is observed to drop monotonically from 4.6 eV in C_2F_6 to 1.2 eV in C_6F_{14}, a trend which is semiquantitatively mirrored by the lowest predicted ngative-ion energies, which drop from 5.4 to 1.25 eV in the same series. The virtual MO calculations also predict that the lowest resonances in the perfluorocycloalkanes C_3F_6 and C_6F_{12} will be substantially below those of the corresponding perfluoro-*n*-alkanes, as observed. However, these calculations predict similar energies for the lowest anion states of C_4F_8 and C_4F_{10}, in contrast to the experimental evidence.

We also have performed calculations on selected hydrocarbons and the results are compared in Fig. 9 and Table 7 with the electron transmission results found in the literature (47, 48). In the *n*-alkane series C_2H_6 to C_6H_{14}, the lowest negative-ion resonance is predicted to drop by 2.39 eV, paralleling the drop of 2.49 eV observed for the corresponding perfluoro-*n*-alkanes. However, there is an almost uniform offset of 5 eV between the lowest anion energies in the two series of compounds, which would appear to be due to an inductive effect of the F atom.

As our electron transmission spectra of CH_4 and *n*-C_6H_{14} did not provide evidence for σ^* states below 6 eV, we presume that the transmission spectra of the intermediate *n*-alkanes also lack low-energy features due to anion formation. According to the calculations, Table 6, the lowest σ^* anion states in CH_4 through C_6H_{14} should fall between 6.5 and 7.0 eV above the neutral molecule ground states. Although this is indeed quite high in energy, it is interesting to observe that a peak due to anion formation shows clearly at 6.4 eV in the transmission spectrum of C_5H_{10} (this work). There are several factors which could cause the resonance in a cyclic system such as C_5H_{10} to be more visible than in the *n*-alkanes. First, the partial wave expansions of the lowest σ^* MO's of cyclic compounds are expected to contain greater contributions from high *l* values than are those of linear compounds. Second, at room temperature a significant

TABLE 7. Observed and calculated TNI energies (eV) in alkanes and their perfluoro derivatives

Molecule	Observed resonance energies	Calculated virtual orbital energies[a]
CF_4	$(-7.3)^b$	$-6.30(a_1)$; $-6.37\ (t_2)$
C_2F_6	-4.60; -8.86; $(-4.0)^b$	$-3.73(e_u)$; $-4.24(a_{2u})$; $-6.65(a_{2u})$
C_3F_8[c]	-3.34; -6.00; $(-2.55)^b$	$-2.61(a'')$; $-2.71(a')$; $-3.93(a')$
C_4F_{10}	-2.37; -4.63; $(-1.95)^b$	$-1.99(b_u)$; $-2.15(a_u)$; $-3.90(b_u)$
C_5F_{12}	-1.64; -3.82; -5.40; $(-1.55)^b$	$-1.57(a_1)$; $-1.97(b_1)$; $-3.37(a_2)$
C_6F_{14}	-1.20; -3.10; -4.50; $(-1.20)^b$	$-1.24(b_u)$; $-1.87(a_u)$; $-2.85(b_g)$
C_3F_6	-1.27; -5.74; -7.25	$-1.66(a'_2)$; $-3.02(a'_2)$; $-6.40(e')$
C_4F_8	>0; -4.91	$-1.47(b_2)$; $-4.48(e)$; $-6.21(a_1)$
C_5F_{10}	—	$0.21(a')$; $-0.50(a')$; $-3.66(a')$
C_6F_{12}	>0; -3.70	$4.44(a_{2u})$; $-3.22(e_g)$; $-4.71(a_{1g})$
CH_4	<-6	$-10.33(t_2)$; $-11.30(a_1)$
C_2H_6	—	$-8.84(e_u)$; $-9.70(a_{2u})$; $-11.05(a_{1g})$
C_3H_8[c]	—	$-7.55(a'')$; $-7.75(a')$; $-8.84(a')$
C_4H_{10}	—	$-6.84(b_u)$; $-7.01(a_u)$; $-8.17(b_g)$
C_5H_{12}	-6.1[d]	$-6.50(a_1)$; $-6.61(b_1)$; $-7.57(a_2)$
C_6H_{14}	<-6	$-6.45(b_u)$; $-6.49(a_u)$; $-7.40(b_g)$
C_3H_6	-5.29[e]	$-4.34(a'_2)$; $-6.57(a''_2)$
C_4H_8	-5.80	$-6.19(b_2)$; $-6.87(e)$; $-8.57(a_2)$
C_5H_{10}	-6.14	$-6.34(a'')$; $-6.50(a')$; $-6.97(a')$
C_6H_{12}	-4.11[e]	$-4.46(a_{2u})$; $-6.36(e_g)$; $-7.44(e_u)$

[a]Calculated values increased by 9.0 eV.
[b]Experimental values from Christophorou *et al.* (44–46).
[c]Calculated in C_s geometry.
[d]Experimental values for *n*-pentane are not available, however, a resonance energy of -6.14 eV is reported for neopentane (48).
[e]Experimental values from Howard and Staley (47).

fraction of the molecules in the vapor phase of an *n*-alkane will have geometries considerably removed from that of the lowest energy conformation. This will tend to broaden the electron-transmission peaks of alkanes, both due to the thermal motion and due to the fact that the empty σ* MO will tend to have more *s* wave character in the higher energy conformer. In general, resonance lifetimes are expected to decrease with symmetry lowering and with the accompanying increase in importance of low-*l* partial waves. If the resonance lifetimes become too short, the resonances are difficult to detect in the total scattering cross sections. The observation by Giordan and Moore (48) of a relatively sharp resonance in neopentane is compatible with the rules stated above.

A far more substantial difference between hydrocarbon and perfluorocarbon is seen in the cyclic compounds, where the lowest negative-ion resonance energy in the $(CF_2)_x$ series decreases monotonically with increasing x, whereas for the $(CH_2)_x$ compounds the trend is strongly upward for $x = 3$ to $x = 5$ and then downward at $x = 6$, as calculated.

Though the virtual orbital calculations would seem to give a satisfactory simulation of the observed negative-ion resonance energies in the perfluoroalkanes, a look at the wavefunctions raises some questions. The delocalized virtual orbital wavefunctions are inappropriate to a discussion of the localized inner-shell excitations (sect. VII), but may be better suited to a discussion of negative-ion states. Note however, Fig. 9, that on cyclizing C_3F_8 to C_3F_6, the virtual orbital which is predicted to be stabilized is the LUMO a'_2. This orbital is $\sigma^*(C—F)_\pi$ rather than σ*(C—C) as deduced from the inner-shell spectra. More sophisticated calculations on inner-shell excitation and negative-ion formation are needed to clarify some of the band assignments.

VII. Core hole and optical σ* orbitals; localization versus band formation

The two electron impact techniques used in this paper (inelastic electron scattering and electron transmission) were chosen because each should yield a clear picture of the role of σ* MO's in the virtual orbital manifolds of the perfluoroalkanes. However, we find that in the inner-shell spectra of unstrained systems, the excitations to σ* MO's have very nearly constant energies irrespective of the molecular size (Tables 1 and 5), whereas when studied by electron transmission, the σ* MO's have energies which decrease substantially with increasing molecular size (Table 7). Only in the strained molecules C_4F_8 and C_6F_{12} do the two techniques agree in placing a σ* MO at anomalously low energy. Yet a third technique, that of VUV spectroscopy (1), suggests that the σ* MO's in the perfluoro-*n*-alkanes descend with increased molecular size, in support of the trend displayed by the electron transmission spectra.

In order to rationalize the apparent contradiction between the trends in the inelastic electron impact and electron transmission data in regard to the behavior of σ* MO's in the perfluoroalkanes, one must recognize that the σ* MO's in the excited states of the two spectroscopies are very different. In the case of the σ* negative ions, the σ* MO is a global one, spanning the length of the molecule and having an orbital energy which decreases particle-in-a-box-like with increasing molecule size. In contrast, the energies for inner-shell excitations to the same σ* MO are very weakly dependent upon molecular size, suggesting to us that the 1*s* hole in the inner-shell excited states is localized which in turn localize the σ* MO. There is at the same time evidence in the inner-shell spectra for mixing of the σ*(C—C) and σ*(C—F) bond orbitals; we suggest that this only occurs

Can. J. Chem. Downloaded from www.nrcresearchpress.com by 112.217.228.212 on 09/07/12
For personal use only.

between such bond orbitals bonded to a common center, thus preserving the local character of the excitation.

It is relevant here to note the close similarity of the number of bands, their intensities and separations for the excitations to σ*(C—C) and σ*(C—F) in the perfluoroalkanes and in PTFE. The saturation of electronic band formation at relatively short chain lengths is consistent with the effective localization of the excitation during the lifetime of the core hole. Just such a conclusion was reached as well in regard the (1*s*, π*) localization in unsaturated hydrocarbons of increasing length (22). Paralleling the situation in the perfluoroalkanes, the spectra of the short-chain alkanes closely resemble those of PE, which again is understandable in terms of localized excitations to (1*s*, V) states (33). In addition, Hutson and Ramaker (49) conclude on the basis of comparisons of calculated and experimental Auger spectra that the (C 1*s*, σ*(C—C)) states in PE are appreciable localized. Although in these two cases we argue from saturation of band formation with chain length in favor of localized core hole excited states, it should be noted that the width of the occupied C 2*p* band of the alkanes is essentially constant above C_4H_{10} (50), yet the 2*p* orbitals are generally considered to be delocalized. Thus there are aspects to this problem yet to be understood.

VIII. Summary[3]

In summary, our interpretation of the inner-shell and negative-ion spectra of the perfluoroalkanes lead to the following qualitative picture of their σ* MO structures. In these species, the σ* levels are inherently lower and the inner-shell transitions to them more intense than in the corresponding alkanes; in the perfluoro-*n*-alkanes the lowest σ* MO has dominant (C—F) character. This valence character is confirmed by the lack of spectural perturbation observed on going into a condensed phase. On cyclizing the perfluoro-*n*-alkanes, a σ*(C—C) MO appears at yet lower energies. Its very large term value is related to molecular strain in the cyclic compounds. The uniquely low energy of the σ*(C—C) MO in the perfluorocycloalkanes is qualitatively confirmed by negative-ion spectroscopy and *ab initio* calculations, as is the relative stabilization of σ*(C—F) MO's in relation to σ*(C—H). However, the differences among inner-shell, negative-ion and VUV spectral shifts with chain length suggest that the core hole excited states are far more localized whereas the negative-ion states span the entire molecule.

IX. Acknowledgements

We are indebted to Professor J. L. Adcock for the generous gift of several perfluorinated hydrocarbons, to Professor J. Fink and to Professor T. Ohta and their students for access to their unpublished spectra of PTFE, and to K. Raghavachari for numerous discussions. Financial support in the form of research grants and a University Research Fellowship (APH) was provided by NSERC (Canada). A grant from the National Science Foundation to KDJ is gratefully acknowledged.

[3]NOTE ADDED IN PROOF: In this work and in earlier work as well (22), it was concluded on the basis of experiment that fluorination strongly increases the valence character of what are otherwise Rydberg upper levels. Just such an effect has recently been reported in theoretical calculations on the fluoroethylene series (51).

1. M. B. ROBIN. Higher excited states of polyatomic molecules. Vol. I. Academic Press, New York, 1974; Vol. II. Academic Press, New York. 1975; Vol. III. Academic Press, New York. 1985.
2. M. B. ROBIN. Can. J. Chem. **63**, 2032 (1985).
3. A. P. HITCHCOCK, S. BEAULIEU, T. STEEL, J. STÖHR, and F. SETTE. J. Chem. Phys. **80**, 3927 (1984).
4. F. SETTE, J. STÖHR, and A. P. HITCHCOCK. J. Chem. Phys. **81**, 4906 (1984).
5. M. N. PIANCASTELLI, D. W. LINDLE, T. A. FERRET, and D. A. SHIRLEY. J. Chem. Phys. **86**, 2765 (1987); A. P. HITCHCOCK and J. STÖHR. J. Chem. Phys. **87**, 3523 (1987).
6. I. ISHII, R. MCLAREN, A. P. HITCHCOCK, and M. B. ROBIN. J. Chem. Phys. **87**, 4344 (1987).
7. S. A. RICE and J. JORTNER. J. Chem. Phys. **44**, 4470 (1966).
8. A. P. HITCHCOCK, D. C. NEWBURY, I. ISHII, J. STÖHR, J. A. HORSLEY, R. D. REDWING, A. L. JOHNSON, and F. SETTE. J. Chem. Phys. **85**, 4849 (1986).
9. J. F. LIEBMAN, W. R. DOLBIER, JR., and A. GREENBERG. J. Phys. Chem. **90**, 394 (1986).
10. A. P. HITCHCOCK, P. FISCHER, A. GEDANKEN, and M. B. ROBIN. J. Phys. Chem. **91**, 531 (1987).
11. W. H. E. SCHWARZ, U. SEEGER, and R. SEEGER. Chem. Phys. To be published.
12. J. S. TSE, E. PELLACH, and G. M. BANCROFT. Can. J. Chem. **63**, 457 (1985).
13. W. H. E. SCHWARZ, L. MENSCHING, K. H. HALLMEIER, and R. SZARGAN. Chem. Phys. **82**, 57 (1983).
14. A. P. HITCHCOCK and C. E. BRION. J. Electron Spectrosc. Related Phenomena, **14**, 417 (1978).
15. O. GOSCINSKI, J. MÜLLER, E. POULAIN, and H. SIEGBAHN. Chem. Phys. Lett. **55**, 407 (1978).
16. L. C. SNYDER. J. Chem. Phys. **55**, 95 (1971); P. S. BAGUS and H. F. SCHAEFER. J. Chem. Phys. **56**, 224 (1972).
17. L. S. CEDERBAUM and W. DOMCKE. J. Chem. Phys. **66**, 5084 (1977).
18. J. NORDGREN, L. SELANDER, L. PETERSSON, C. NORDLING, K. SIEGBAHN, and H. AGREN. J. Chem. Phys. **76**, 3928 (1982).
19. W. H. E. SCHWARZ, T. CHANG, W. SEEGER, and K. H. HWANG. Chem. Phys. **117**, 73 (1987); W. H. E. SCHWARZ and T. CHANG. Unpublished results.
20. J. H. FOCK, H.-J. LAU, and E. E. KOCH. Chem. Phys. **83**, 377 (1984).
21. K. D. JORDAN and P. D. BURROW. Acc. Chem. Res. **11**, 341 (1978).
22. I. ISHII, R. MCLAREN, A. P. HITCHCOCK, and M. B. ROBIN. J. Electron Spectrosc. Related Phenomena. In press.
23. J. A. HORSLEY, J. STÖHR, A. P. HITCHCOCK, D. C. NEWBURY, A. L. JOHNSON, and F. SETTE. J. Chem. Phys. **83**, 6099 (1985).
24. R. MCLAREN, S. A. C. CLARK, I. ISHII, and A. P. HITCHCOCK. Phys. Rev. A**36**, 1683 (1987).
25. A. P. HITCHCOCK and I. ISHII. J. Electron Spectrosc. Related Phenomena, **42**, 11 (1987).
26. G. R. WIGHT and C. E. BRION. J. Electron Spectrosc. Related Phenomena, **4**, 327 (1974).
27. M. TRONC, G. C. KING, R. C. BRADFORD, and F. H. READ. J. Phys. B**9**, L555 (1976).
28. M. TRONC, G. C. KING, and F. H. READ. J. Phys. B**12**, 137 (1979).
29. Y. N. SIVKOV, V. N. AKIMOV, A. A. VINOGRADOV, and T. M. ZIMKINA. Opt. Spectrosc. USSR, **60**, 194 (1986).
30. F. C. BROWN, R. Z. BACHRACH, and A. BIANCONI. Chem. Phys. Lett. **54**, 425 (1978).
31. W. L. JOLLY, K. D. BOMBEN, and C. J. EYERMANN. At. Data Nucl. Data Tab. **31**, 433 (1978).
32. T. OHTA, K. SEKI, I. MORISADA, N. KOSUGI, T. USAMI, and S. HASHIMOTO. Abstracts, New opportunities in chemistry; applications of synchrotron radiation. Brookhaven, NY. Nov. 4–6, 1987.
33. J. STÖHR, D. A. OUTKA, K. BABERSCHKE, D. ARVANITIS, and J. A. HORSLEY. Phys. Rev. B, Rapid Commun. **36**, 2976 (1987).

Can. J. Chem. Downloaded from www.nrcresearchpress.com by 112.217.228.212 on 09/07/12
For personal use only.

34. J. L. DEHMER. J. Chem. Phys. **56**, 4496 (1972).
35. L. C. SNYDER and H. BASCH. Molecular wavefunctions and properties. Wiley, New York. 1972.
36. I. ISHII and A. P. HITCHCOCK. J. Chem. Phys. **87**, 830 (1987).
37. E. BOURSEY and J.-Y. RONCIN. Phys. Rev. Lett. **26**, 308 (1971).
38. J. FINK. Private communication.
39. I. ISHII and A. P. HITCHCOCK. J. Electron Spectrosc. **46**, 55 (1988).
40. H. BASCH, M. B. ROBIN, N. A. KUEBLER, C. BAKER, and D. W. TURNER. J. Chem. Phys. **51**, 52 (1969).
41. K. B. WIBERG. Angew. Chem. Int. Ed. **25**, 312 (1986).
42. R. E. LAVILLA. J. Chem. Phys. **58**, 3841 (1973).
43. A. P. HITCHCOCK and I. ISHII. To be published.
44. S. M. SPYROU, I. SAUERS, and L. G. CHRISTOPHOROU. J. Chem. Phys. **78**, 7200 (1983).
45. S. R. HUNTER and L. G. CHRISTOPHOROU. J. Chem. Phys. **80**, 6150 (1984).
46. S. M. SPYROU, S. R. HUNTER, and L. G. CHRISTOPHOROU. J. Chem. Phys. **83**, 641 (1985).
47. A. E. HOWARD and S. W. STALEY. Am. Chem. Soc. Symp. Ser. **263**, 183 (1984).
48. J. C. GIORDAN and J. H. MOORE. J. Am. Chem. Soc. **105**, 6541 (1983).
49. F. L. HUTSON and D. E. RAMAKER. Phys. Rev. B**35**, 9799 (1987).
50. E. E. KOCH. Top. Appl. Phys. **27**, 261 (1979).
51. R. S. PRASAD and R. SHARMA. Indian J. Phys. **61**B, 87 (1987).

Can. J. Chem. Downloaded from www.nrcresearchpress.com by 112.217.228.212 on 09/07/12
For personal use only.

Gas phase flash pyrolysis of 3-azido-1,2,4-triazole: generation and ultraviolet photoelectron spectrum of *N*-cyanomethanimine[1]

I. B'SHARY, C. GUIMON, M. GRIMAUD, AND G. PFISTER-GUILLOUZO

Université de Pau et des Pays de l'Adour, Laboratoire de physico-chimie moléculaire, Unité associée 474, Avenue de l'Université, 64000 Pau, France

AND

D. LIOTARD

Université de Pau et des Pays de l'Adour, Laboratoire de chimie structurale, Unité associée 474, Avenue de l'Université, 64000 Pau, France

Received January 27, 1988

I. B'SHARY, C. GUIMON, M. GRIMAUD, G. PFISTER-GUILLOUZO, and D. LIOTARD. Can. J. Chem. **66**, 2123 (1988).

A dimer of HCN, *N*-cyanomethanimine **6**, was prepared by flash pyrolysis (gas phase, 10^{-2} mbar) from 3-azido-1,2,4-triazole **1***a* and detected by ultraviolet photoelectron spectroscopy (HeI). Its ionization potentials were measured and the ionic states sequence proposed, with the aid of *ab initio* – CI (configuration interaction) calculations. The study of the MNDO potential hypersurface enabled us to propose a mechanism of the thermal reorganization of the precursor **1***a*. It is shown that the reaction path passes through the formation of the protomer **1***b* before thermal decomposition and the generation of the nitrene **2***b*.

I. B'SHARY, C. GUIMON, M. GRIMAUD, G. PFISTER-GUILLOUZO et D. LIOTARD. Can. J. Chem. **66**, 2123 (1988).

Un dimère de HCN, la *N*-cyanomethanimine **6**, a été préparé par flash thermolyse en phase gazeuse (10^{-2} mbar) à partir de l'azido-3 triazole-1,2,4 **1***a* et détecté par spectroscopie photoélectronique ultraviolette (HeI). Nous avons mesuré ses premiers potentiels d'ionisation et déterminé l'ordre de ses premiers états ioniques à l'aide de calculs *ab initio* avec interaction de configuration. L'analyse de l'hypersurface de potentiel MNDO nous a permis de proposer un mécanisme de la décomposition thermique du précurseur **1***a*. Ainsi nous avons pu montrer que le chemin de réaction passe par la formation du protomère **1***b* avant toute decomposition et avant la génération du nitrène **2***b*.

Introduction

In the chemistry of transient or highly reactive molecules, hydrocyanic acid dimers have created considerable interest both because of their probable presence in interstellar space (1) and as precursors in the prebiotic synthesis of amino acids (2–4).

Theoretical studies (5–9) have shown that only three forms have a sufficient stability to be detected in the gas phase. They are, in order of decreasing stability, iminoacetonitrile (HN=CH—C≡N), the linear hydrogen bonded complex (HC≡N···HC≡N), and *N*-cyanomethanimine (H_2C=N—C≡N). The first and third have been generated from various precursors by photolysis or thermolysis. Iminoacetonitrile, whose *N*-butyl derivative was prepared as early as 1970 (10), could be characterized by its infrared spectrum, by photolysis of azidoacetonitrile N_3CH_2CN at 308 nm in argon matrix (9), and by thermal degradation (1300 K) in a saturated atmosphere (2 Torr; 1 Torr = 133.3 Pa) (11) of dimethylcyanamide. The existence of *N*-cyanomethanimine, deduced from the analysis of the mass spectrum of the decomposition products of trimethylenetetrazole (12), was also generated by pyrolysis of dimethylcyanamide (13). This compound and its deuterated derivative (14, 15) have been the object of several detailed microwave spectrometry studies. In addition, a very recent photoelectron study (16) showed that the decomposition of trimethylenetetrazole yields *N*-cyanomethanimine and ethylene.

In the context of our work on the analysis of the electronic structure of transient molecules, using the combined techniques of photoelectron spectroscopy and quantum mechanical calculations, we have investigated the thermal decomposition of different azides (17, 18). These molecules lose a nitrogen molecule relatively easily (17–19) and form an unstable nitrene, which can undergo various rearrangements. We report the results obtained with 3-azido-1,2,4-triazole. Flash thermolysis of this compound leads to *N*-cyanomethanimine, which we have characterized from observed ionization potentials and for which we propose a mechanism of formation.

1. Thermal rearrangements of triazolonitrene

As we stated in the introduction, 3-azido-1,2,4-triazole loses a nitrogen molecule above a certain temperature and can undergo various rearrangements.

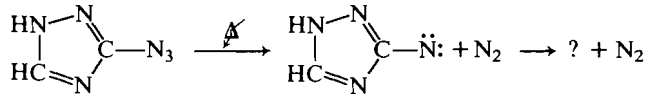

1*a* **2***a*

According to the results of Wentrup (20, 21) in the case of conjugated heterocyclic compounds and in addition to the nitrene rearrangement products in the triplet state leading to 3-amino-1,2,4-triazole, three main intramolecular mechanisms in the singlet state may occur (the hypothesis of spin conservation is generally admitted):

(a) Ring extension, already observed for 6-member rings (22, 23), would lead to a 6-member cyclic carbodiimide, which could open to yield linear compound **4**.

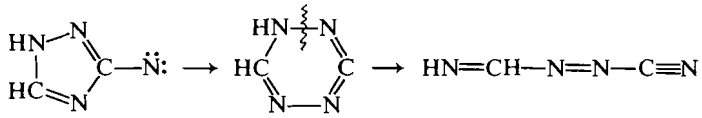

2*a* **3** **4**

In parallel, we determined the respective stability of the rearrangement products with MNDO calculations (Table 1).

[1]Part 35 of Applications of photoelectron spectroscopy to molecular properties. Part 34: S. Lacombe, J. L. Cabioche, B. Pellerin, J. M. Denis, and G. Pfister-Guillouzo. To be submitted.

Printed in Canada / Imprimé au Canada

Can. J. Chem. Downloaded from www.nrcresearchpress.com by 112.217.228.212 on 09/07/12
For personal use only.

TABLE 1. MNDO relative energies after optimization of all structural parameters

	1*a*	**1***b*	**2***a* + N_2	**2***b* + N_2	**3** + N_2	**4** + N_2	**5** + N_2	**6** + 2 N_2
Relative energy kJ mol^{-1})	0	29.9	117.3	164.4	155.4	−34.1	64.1	−160.3

Considering the low stability of **3** (the corresponding 7-member ring for which the carbodiimide group is less bent can be observed only at low temperature in an argon matrix), this possibility can be rejected in our experimental conditions (gas phase and high temperature).

(b) Ring opening has been postulated or demonstrated for other heterocyclic compounds such as 5-azido-1,2,4-triazole (24) and azido pyrazole (25, 26). In our case, this reaction would require the 1–3 migration of a hydrogen atom to form also **4**, which renders it improbable in spite of the relative stability of **4** (Table 1).

(c) Ring contraction occurs relatively easily in such 6-member heterocyclic compounds as the azido pyridines and azido pyrimidines (17, 20, 27–29). When the precursor heterocycle is a 5-member ring, this process generates a 4-member heterocycle (5) with an obviously reduced stability.

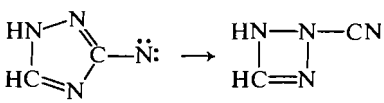

2*a* **5**

This instability, confirmed by MNDO calculations (30) (Table 1), thus renders this reaction highly improbable in our experimental conditions.

The last possibility, rarely suggested, is a sigmatropic rearrangement of the precursor by the 1–5 migration of a hydrogen even before the formation of the nitrene. This prototropic equilibrium **1***a* ⇄ **1***b* is possible if the associated activation barrier is of the same order as the energy required to form the nitrene **2***a*. In the opposite case, the 1–5 sigmatropic rearrangement of the nitrene is very improbable as a result of the thermodynamic instability of this species.

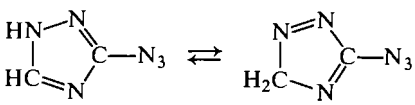

1*a* **1***b*

In addition to the decomposition of the azido group, the protomer **1***b* can lose the interacyclic N_2 fragment (12, 31) to yield *N*-cyanomethanimine **6**, a compound that is by far the most thermodynamically stable among the various possibilities proposed (Table 1).

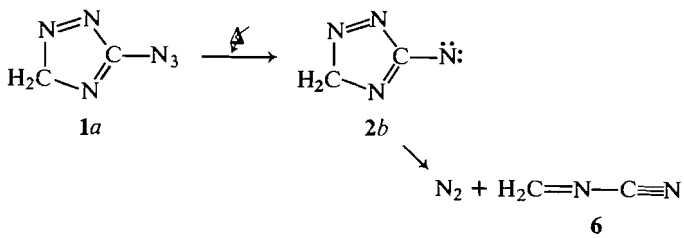

1*a* **2***b* **6**

2. Experimental results: photoelectron spectrum and structure of H_2CNCN

Figures 1 and 2 are the photoelectron spectra (HeI) of 3-azido-1,2,4-triazole before (380 K) and after pyrolysis (800 K). At this temperature (Fig. 2), there is first a very weak band around 9.4 eV, corresponding to the initial compound (Fig. 1), as well as bands (hatched) characteristic of hydrocyanic acid HCN and nitrogen (32, 33). Beginning at 1200 K, the spectra contain only the bands of these two molecules (Fig. 3).

If we refer to the photoelectron spectra of methanimine (34, 35) and its alkyl (36–38) and phenyl derivatives (39, 40), as well as acrylonitrile (41, 42), the remaining bands correspond to the expected spectrum of *N*-cyanomethanimine (Table 2). As is the case for simple imines, the first band, associated principally with the nonbonding orbital with σ symmetry of imino nitrogen (n_N) interacting with the $\pi'_{C=N}$ (π orbital in the σ plane of imine), is relatively broad and poorly resolved. The shift of the corresponding ionization potential (1 P) (11.25 eV) compared to that of the simple imine (10.52 eV) is explained by the considerable inductive effect of the C≡N group, which is not compensated by the interaction of the localized n_N and $\pi'_{C\equiv N}$ orbitals.

The shape of the second band is characteristic of the π system of imines, where we encounter a very pronounced vibrational structure. The main vibrational frequency of the ion (2000 cm^{-1}) is very close to that of acrylonitrile (42) (2080 cm^{-1}). In spite of the inductive effect of the cyano group, this second ionization potential (11.75 eV) is lower than that of methanimine. This results from a pronounced conjugation due to the strong interaction of $\pi_{C=N}$ and $\pi_{C\equiv N}$ orbitals. As a result of the substantial localization of the $\pi_{C=N}$ orbital on the nitrogen atom, this interaction is stronger than in the case of acrylonitrile, where we observe a stabilization of the corresponding orbital (11.1 eV) in comparison to ethylene (10.50 eV) (43).

The third band, which in light of its intensity could cover two ionizations, and the fourth band are associated with two bonding combinations, $\pi'_{C\equiv N} + n_N$, $\pi_{C\equiv N} + \pi_{C=N}$, and a σ type orbital delocalized on the skeleton of the molecule.[2]

This spectrum is confirmed by that obtained by subtraction between the spectrum of trimethylene tetrazole pyrolysis products and that of ethylene (16) (published during this study).

We wished to confirm this qualitative attribution and define the sequence of ionic states by calculating ionization potentials. In addition to the semi-empirical MNDO method used subsequently to follow reaction paths, two types of *ab initio* "beyond Koopmans" calculations were performed. The first (PSHONDO) considers only a portion of the polarization and specific

[2]It is possible that the band of HCN at 13.6 eV hides a band of H_2CNCN about 13.9 eV as suggested by HAM/3 calculations (made by D. T. Chong of Vancouver). The IP's calculated by this method are indeed very close to experimental IP's: 11.19, 12.00, 13.20, 13.92, and 14.61 eV.

Can. J. Chem. Downloaded from www.nrcresearchpress.com by 112.217.228.212 on 09/07/12
For personal use only.

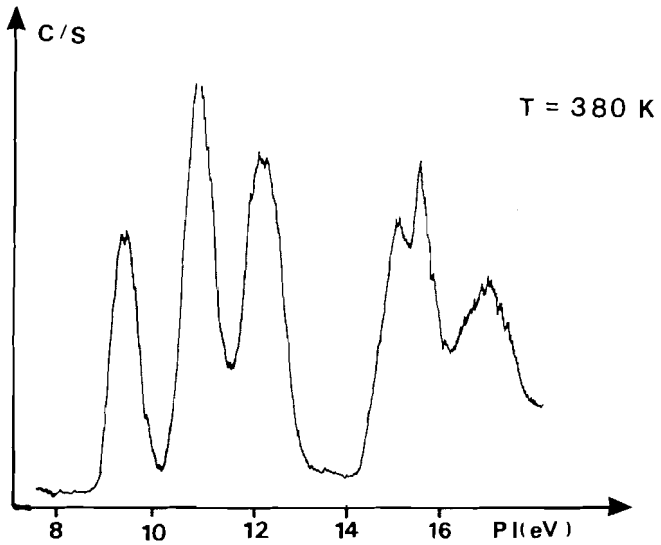

FIG. 1. Photoelectron spectrum (HeI) of 3-azido-1,2,4-triazole before pyrolysis.

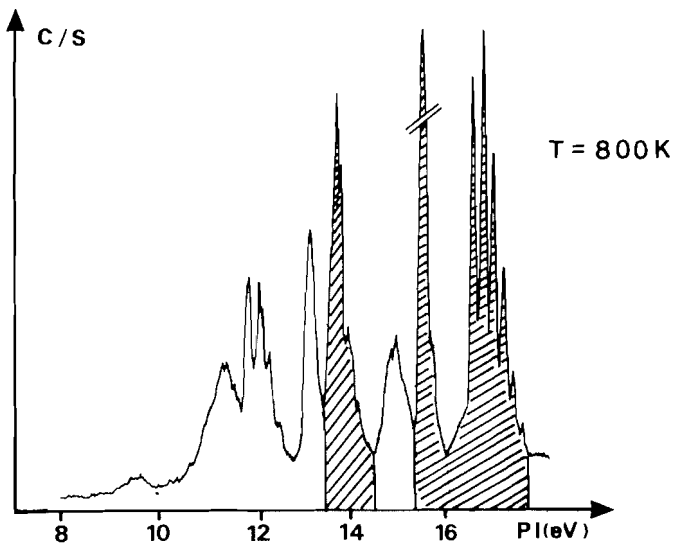

FIG. 2. Photoelectron spectrum (HeI) of 3-azido-1,2,4-triazole after pyrolysis (800 K).

correlation effects of the ions. The second (CIPSI) uses configuration interaction (CI) (see theoretical part). The results (Table 3) were obtained with optimized geometry (Fig. 4) using the MONSTERGAUSS program (see theoretical part).

It should first be noted that in contrast to the empirical MNDO method, the *ab initio* calculation furnishes an inversion of the first two ionization potentials at the level of the Koopmans approximation (IP $\sim -\epsilon_i$) (44). The sequence is reestablished by taking into account the specific correlation terms of the ions (reflected in the CI calculation by double excitations not invoking the ionic state considered) and above all the polarization terms (double excitations in which the determinant associated with this ionic state participates). The latter correction appears overestimated by the CI calculation at the level of the first ionization potential. This observation had already been mentioned in the theoretical study of other conjugated molecules (45). In contrast, the following four ionization potentials

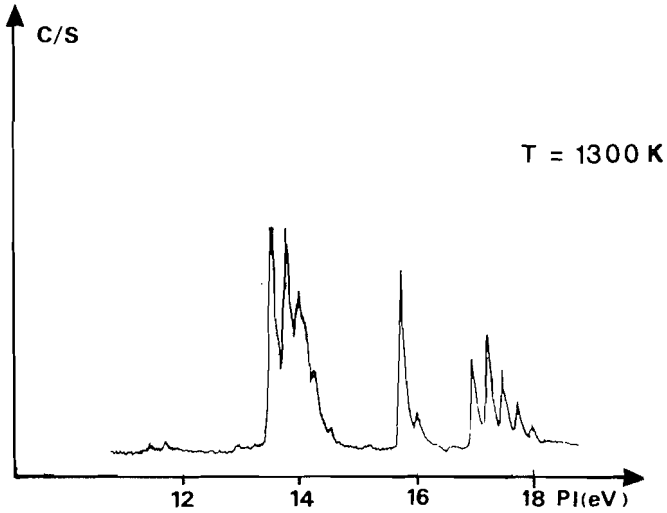

FIG. 3. Photoelectron spectrum (HeI) of 3-azido-1,2,4-triazole after pyrolysis (1300 K).

calculated with CIPSI are in good agreement with the experimental values, in contrast to the $-\epsilon_i$ values. In particular, the important polarization effect in the fourth ionic state should be noted, associated primarily with the σ orbitals of the skeleton, bringing the corresponding ionization potential to a value close to that associated with the third ionic state for which the main correction term is from specific correlation. Thus, in contrast to the proposal for acrylonitrile (42) (Table 2), the ionization potential characterizing the most stable π molecular orbital is much higher (1.8 eV) than that associated with the first bonding σ orbital, while the corresponding eigenvalues (ϵ_i) in the SCF calculations are of the same order (Table 3).

3. Reaction path

In parallel to these experimental data, we have carried out a theoretical analysis of the mechanism of *N*-cyanomethanimine formation from 3-azido-1,2,4-triazole. The reaction profile (MNDO) is shown in Fig. 5. We will analyze the different steps in this path, each corresponding to a saddle point, i.e., an activation energy barrier. We note that the first two steps (prototropic equilibrium and nitrene formation) require similar energies, supporting the hypothesis of a preliminary step involving a 1–5 prototropic migration.

3.1 1st step:3-azido-1,2,4-triazole(1H) 3-azido-1,2,4-triazole(5H) equilibrium

This step is a 1–5 migration of the hydrogen atom bound to a nitrogen. 1–5 Sigmatropic shifts are described in the literature in the cases of triazole (46, 47), pyrazole (48), and 1,2,4-diazaphosphole (49). They occur easily in solution, although we cannot speak of true unimolecular reactions. In the vapor phase and under low pressure the migration should be more difficult if we consider the barrier of 258 kJ mol^{-1} calculated in MNDO, a result confirmed by the temperature at which the change of 3-azido-1,2,4-triazole begins (700 K). The transition state TS_1 (Fig. 6) corresponds to what can be expected after applying Woodward–Hoffmann rules (50) for sigmatropic reactions (51, 52). The highest occupied orbitals of the ring and the corresponding radical are π type, and so in the transition state the migrating hydrogen atom is practically midway between the nitrogen and carbon atoms and above the plane (its ordinate with reference to the plane of the molecule is 1.08 Å).

Can. J. Chem. Downloaded from www.nrcresearchpress.com by 112.217.228.212 on 09/07/12
For personal use only.

TABLE 2. Experimental vertical ionization potentials of MO type of ethylene (43), cyanhydric acid (33), methanimine (34), acrylonitrile (42), and *N*-cyanomethanimine (this study)

$H_2C{=}CH_2$	$HC{\equiv}N$	$H_2C{=}NH$	$H_2C{=}CH{-}C{\equiv}N$	$H_2C{=}N{-}C{\equiv}N$
		10.52 (n_N)		11.25 ($n_N - \pi'_{C\equiv N}$)
10.5		12.43 ($\pi_{C=N}$)	11.1 ($\pi_{C=C} - \pi_{C\equiv N}$)	11.75 ($\pi_{C=N} - \pi_{C\equiv N}$)
	13.6 ($\pi'_{C\equiv N}$)		12.5 ($\pi'_{C\equiv N}$)	
	13.6 ($\pi_{C\equiv N}$)		13.0 ($\pi_{C\equiv N} + \pi_{C=C}$)	13.1, 14.9 ($\pi'_{C\equiv N} + n_N, \sigma, \pi_{C\equiv N} + \pi_{C=N}$)
	14.0 (σ_{CN})	15.13 (σ_{CN})	13.5 (σ_{CN})	

TABLE 3. Ionization potentials calculated in the Koopmans' approximation framework by MNDO and HONDO (4-31 G* basis set) in the first two columns, after a perturbational correction (see theoretical part) in the third column and after a configuration interaction (fourth column) compared to the experimental values (fifth column)

$-\epsilon_i$ (MNDO)	$-\epsilon_i$ (HONDO)	IP (HONDO)	IP (CIPSI)	IP (expt.)
11.56	12.03 ($n_N - \pi'_{C\equiv N}$)	11.73	10.60	11.25
11.83	11.98 ($\pi_{C=N} - \pi_{C\equiv N}$)	11.95	11.73	11.75
13.64	14.50 ($\pi'_{C\equiv N} + n_N$)	14.32	12.75	13.1
15.08	15.62 (σ)	14.39	12.77*	
14.98	15.81 ($\pi_{C\equiv N} + \pi_{C=N}$)	15.51	14.78	14.90

*That fourth state can be associated at a band hidden underneath the HCN band (about 13.6 eV, see footnote 2 in the text).

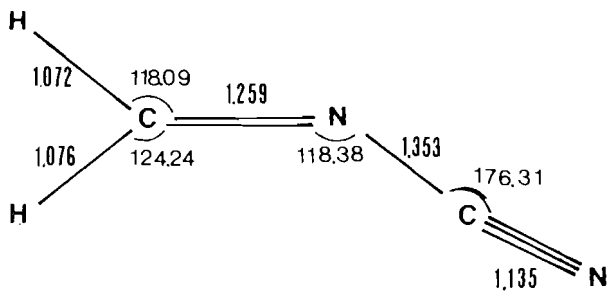

FIG. 4. *Ab initio* (Monstergauss program; 4-31 G* basis set) calculated structure of *N*-cyanomethanimine **6**.

3.2 2nd step: formation of 1,2,4-triazole(5H) nitrene

Whether the reaction by photolysis (53–55) or pyrolysis (56) of conjugated azides, the presence of an intermediate nitrene has often been proposed if not demonstrated. As a result of the energy proximity of the HOMO and LUMO frontier orbitals (degenerated in NH), the most stable state of these entities is a triplet (57, 58). Nevertheless, as we stated in the discussion of possible nitrene rearrangements, the thermal decomposition of azides preferentially yields a singlet nitrogen molecule (59) accompanied also by nitrene in the singlet state (20, 60). If we follow the changes in the frontier orbitals along the path **1***b* → **2***b* (Fig. 7), we observe a crossing between the HOMO and LUMO, leading to a relatively high activation barrier. In light of this crossing, it was necessary to search for the saddle point in the calculations by carrying out CI limited to the essential (frontier) orbitals.

Following this, it was found that the most stable singlet state of nitrene is not a closed shell state but rather open shell, i.e., presenting one electron on each orbital, schematically shown in Fig. 7. The same is true for the transition state TS_2, which is structurally close to nitrene (Fig. 6) according to the criterion of Hammond (61).

3.3. 3rd step:decomposition of 1,2,4-triazole(5H) nitrene

Nitrene **2***b* is metastable and easily loses nitrogen molecule to yield *N*-cyanomethanimine (Fig. 5). Contrary to the preceding step, there is no crossing between the occupied and virtual orbitals, explaining the low activation energy (57 kJ mol^{-1}). The corresponding transition state TS_3 is also close to the structure of nitrene, since it also presents a basic singlet state with two open shells. From its structure (Fig. 6) it appears that the departure of N_2 begins by a ring opening, which is consistent with general trends of cyclic nitrenes (see Sect. 1).

Passage of a singlet ground state with closed shells (more stable for the forms **1***a*, TS_1, **1***b*, and **6**) to a configuration with two open shells (more stable for TS_2, **2***b*, and TS_3) is shown in Fig. 8 by the dotted lines. In the crossing regions of the both S_0 and S_1 states, the slope of curve S_0 is much steeper than that of S_1, which shifts the maxima of the dotted curve (associated with TS_2 and TS_3) toward the intermediate minimum (**2***b*). This explains the structure of the two transition states TS_2 and TS_3, relatively close to that of nitrene **2***b*.

Conclusion

In this study, we have shown that the thermal decomposition (gas phase flash pyrolysis under low pressure) of 3-azido-1,2,4-triazole differs from the reaction paths usually proposed for this type of reaction of the heterocyclic series (extension, opening, or contraction of the ring). The formation of *N*-cyanomethanimine **6**, demonstrated by photoelectron spectroscopy, requires passage of the initial form via a tautomer (NH form → CH form). This tautomer then loses a nitrogen molecule to form a conjugated cyclic nitrene, which then splits into **6** + N_2. During this reaction, MNDO calculations have shown the

Can. J. Chem. Downloaded from www.nrcresearchpress.com by 112.217.228.212 on 09/07/12
For personal use only.

Can. J. Chem. Downloaded from www.nrcresearchpress.com by 112.217.228.212 on 09/07/12
For personal use only.

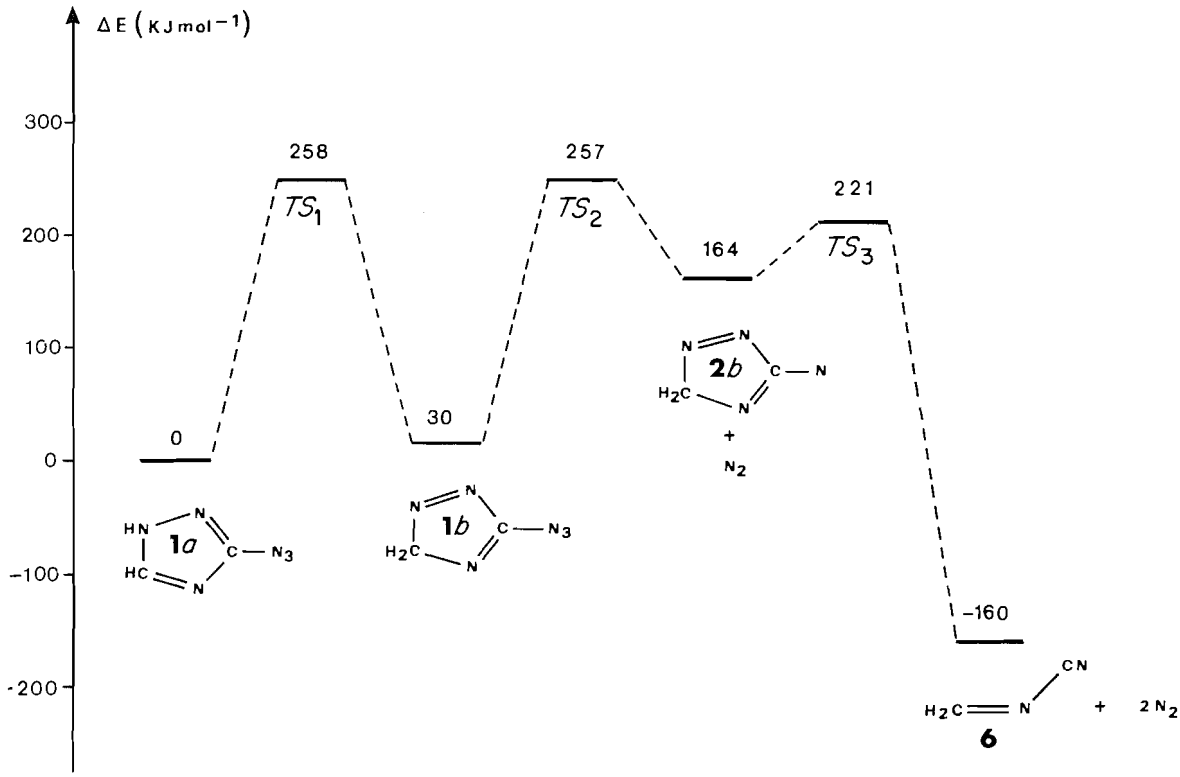

FIG. 5. MNDO energy profile of the thermal decomposition of 3-azido-1,2,4-triazole **1***a*.

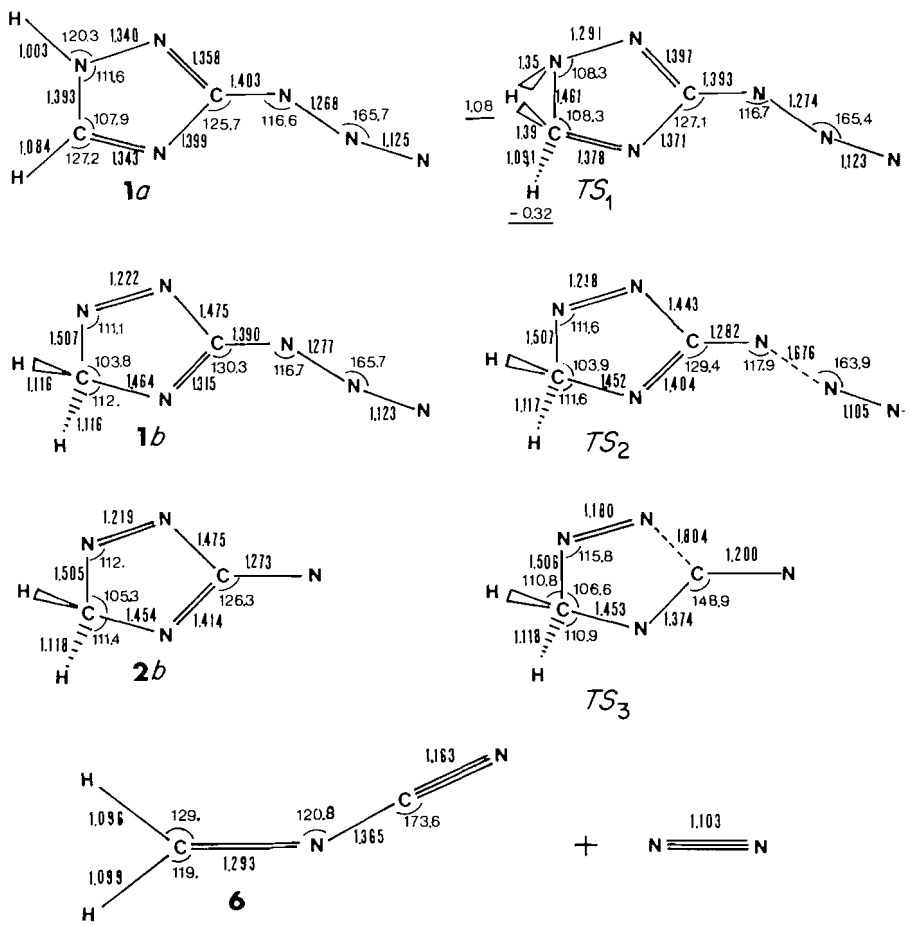

FIG. 6. MNDO calculated structure of the stable or metastable molecules (minima of the potential hypersurface) **1***a*, **1***b*, **2***b*, **6** and the transition states (saddle points) TS_1 TS_2, TS_3 shown in the reaction path of the Fig. 5.

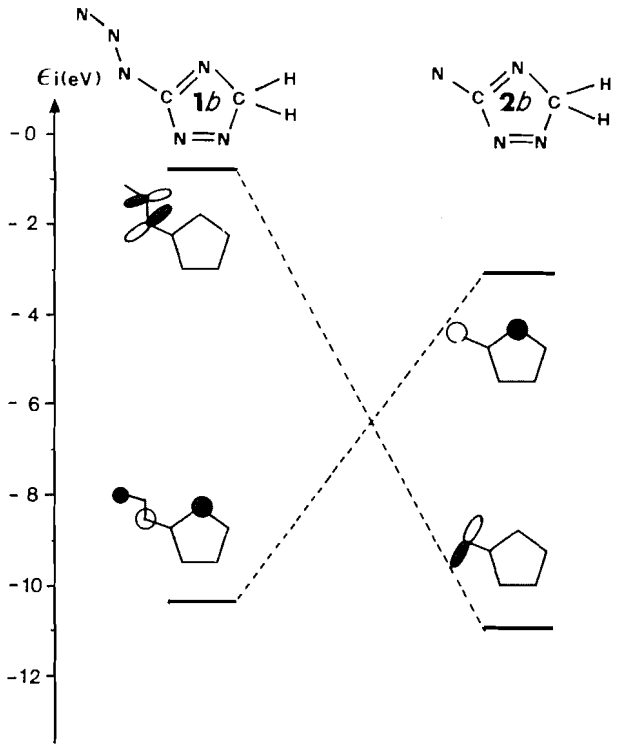

FIG. 7. HOMO–LUMO correlation for the decomposition of N_3 group.

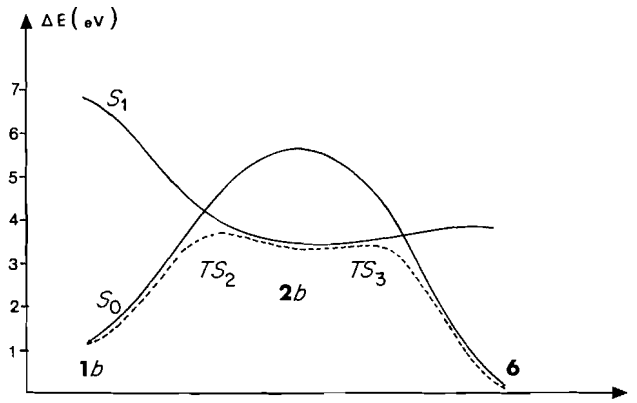

FIG. 8. Profile of the first two singlet states (S_0: closed shell singlet state; S_1: open shell singlet state); for the reaction $\mathbf{1}b \rightarrow \mathbf{6}$ (CI–MNDO calculations).

existence of crossing between the singlet states S_0 and S_1 due to the particular order of stability of nitrene (T_0, S_1, S_0).

The generation of *N*-cyanomethanimine in the ionization chamber of the photoelectron spectrometer also enabled us to determine the value of its first ionization potentials and to propose the sequence of the corresponding ionic states.

Experimental and computational details

As for most heterocyclic azides (62), 3-azido-1,2,4-triazole was obtained by the reaction of sodium azide with the diazonium chloride of 3-amino-1,2,4-triazole at 270 ± 2 K (mp 377 K, 80% yield).

The HeI photoelectron spectra were recorded on a PE spectrometer 0078 of Photoelectron Laboratories Ltd. with argon and xenon used as internal calibrants (12.126 and 13.443 eV for $^2P_{1/2}$ and $^2P_{3/2}$ of Xe; 15.755 and 15.93 eV for $^2P_{1/2}$ and $^2P_{3/2}$ of Ar). Flash pyrolysis was carried out with a variable-temperature probe (63) allowing us to heat the vapor above 1300 K in a ceramic tube during a few tenths of a second. The short pathway of about 5 cm between the end of the heating zone and the target chamber of the PE spectrometer allows recording of photoelectron spectra of transient compounds (ca. 0.1 s) or rearrangement derivatives.

The potential energy hypersurface of the $C_2N_6H_2$ system was calculated with the MNDO method (30), which gives for a reasonable price a quality of results close to *ab initio* double zeta results (64, 65). A saddle point search algorithm (66–68) was used in these calculations, enabling us to find the lowest saddle point on the pathway between two minima on the potential energy hypersurface.

The spectroscopic data were compared to the theoretical ionization potentials calculated with two different methods. We used the HONDO program (69) in which polarization and correlation effects are included after the SCF calculations by using a procedure based on a partial perturbative treatment (71, 72),[3] which calculates the energetic contributions of second-order corrective terms for the fundamental and ionic states. The basis set was of the 4-31 G type with *d* polarization orbitals on nitrogen. Several tests have shown the calculated IP were little influenced by polarization functions on carbon and hydrogen. We also performed a more rigorous calculation of the first ionization potentials by means of a program (73) using the CIPSI algorithm (74) (CI calculation on the ground states and the first ionic states).

A variational zeroth-order wave function was built in an iterative selection of the most important single and double excited determinants formed from the former reference subspace, the other ones being taken into account through a second-order Moller–Plesset perturbation. The configuration selection was based on the determinant coefficients in the correction of the zeroth-order function in the first order of the perturbation. In our case, the cutoff threshold was 0.02. So the reference subspace contained between 50 and 60 determinants. The number of determinants taken into account in the perturbative treatment was about 4×10^6.

The molecular geometries were fully optimized with respect to all structural parameters (bond lengths and angles) by the Broyden–Fletcher–Goldfard–Shanno gradient method (75) included in the MONSTERGAUSS program (70, 76) (same basis set as for HONDO calculations).

Acknowledgment

The authors wish to thank Dr D. P. Chong (University of British Columbia, Vancouver) for helpful suggestions and advice.

1. A. CARRINGTON and D. A. RAMSAY (*Editors*). Molecules in interstellar space. The Royal Society, London. 1982.
2. J. P. FERRIS, D. B. DONNER, and W. LOTZ. J. Am. Chem. Soc. **94**, 6968 (1972).
3. J. P. FERRIS, P. C. JOSHI, E. J. EDELSON, and J. C. LAWLESS. J. Mol. Evol. **11**, 293 (1978).
4. J. P. FERRIS and W. J. HAGAN, JR. Tetrahedron, **40**, 1093 (1984).
5. A. JOHANSON, P. KOLLMAN, and S. ROTHENBERG. Theor. Chim. Acta, **26**, 97 (1972).
6. W. YANG, R. MINAR, and C. N. MATTHEWS. J. Chem. Soc. Chem. Commun. 435 (1973).
7. J. B. MOFFAT. J. Chem. Soc. Chem. Commun. 888 (1975).
8. J. H. CLEMMONS, P. G. JASIEN, and C. E. DYKSTRA. Mol. Phys. **48**, 631 (1983).
9. P. LORENCAK, G. RAABE, J. J. RADZISZEWSKY, and C. WENTRUP. J. Chem. Soc. Chem. Commun. 916 (1986).
10. J. H. BOYER and H. DABEK. Chem. Commun. 1204 (1970).
11. Y. HAMADA, M. TSUBOI, T. NAKANAGA, H. TAKEO, and C. MATSUMURA. J. Mol. Spectrosc. **117**, 308 (1986).
12. C. WENTRUP. Tetrahedron, **27**, 1281 (1971).
13. B. BAK, O. J. NIELSEN, and J. SVANHOLT. Chem. Phys. Lett. **59**, 330 (1978).

[3]Also, J. P. Daudey, J. P. Malrieu, and G. Trinquier. Personal communication.

Can. J. Chem. Downloaded from www.nrcresearchpress.com by 112.217.228.212 on 09/07/12
For personal use only.

14. B. BAK and H. SVANHOLT. Chem. Phys. Lett. **66**, 387 (1979); **75**, 528 (1980); Acta Chem. Scand. Ser. A: **34**: 57 (1980).
15. M. WINNEWISSER and B. P. WINNEWISSER. J. Mol. Spectrosc. **105**, 193 (1984).
16. H. BOCK and R. DAMMEL. Angew Chem. Int. Ed. Engl. **26**, 504 (1987).
17. C. GUIMON, S. KHAYAR, G. PFISTER-GUILLOUZO, R. M. CLARAMUNT, and J. ELGUERO. Spectrosc. Lett. **15**, 435 (1982).
18. C. GUIMON and G. PFISTER-GUILLOUZO. Organometallics, **6**, 1387 (1987).
19. H. BOCK, R. DAMMEL, and S. AYGEN. J. Am. Chem. Soc. **105**, 7681 (1983).
20. C. WENTRUP. Top. Curr. Chem. **62**, 176 (1976), and ref. therein.
21. C. WENTRUP. React. Intermed. (Plenum), **1**, 263 (1980) and ref. therein.
22. W. D. CROW and C. WENTRUP. Tetrahedron Lett. 6149 (1968).
23. C. WENTRUP. Bull. Soc. Chim. Belg. **91**, 997 (1982).
24. P. A. S. SMITH, L. O. KRBECHER, and W. RESEMANN. J. Am. Chem. Soc. **86**, 2025 (1963).
25. P. A. S. SMITH, G. J. W. BREEN, M. K. HAJEK, and D. V. C. AWANG. J. Org. Chem. **35**, 2215 (1970).
26. P. A. S. SMITH and H. DOUNCHIS. J. Org. Chem. **38**, 2958 (1973).
27. W. D. CROW and C. WENTRUP. J. Chem. Soc. Chem. Commun. 1082 (1968); 1387 (1969).
28. C. WENTRUP and W. D. CROW. Tetrahedron, **27**, 361 (1971).
29. T. SASAKI, K. KANEMATSU, and M. MURATA. J. Org. Chem. **36**, 446 (1971).
30. M. J. S. DEWAR and W. THIEL. J. Am. Chem. Soc. **99**, 4899 (1977).
31. N. H. WERSTIUK, L. TAGUCHI, and J. WARKENTIN. Can. J. Chem. **55**, 3677 (1977).
32. C. BAKER and D. W. TURNER. Proc. R. Soc. London, A:**308**, 19 (1968).
33. K. KIMURA, S. KATSUMATA, Y. ACHIBA, T. YAMAZAKI, and S. IWATA. Handbook of HeI photoelectron spectra of fundamental organic molecules. Japan Scientific Societies Press, Tokyo. 1981.
34. J. B. PEEL and G. D. WILLETT. J. Chem. Soc. Faraday Trans, 2, **71**, 1799 (1975).
35. D. C. FROST, S. T. LEE, C. A. MCDOWELL, and N. P. C. WESTWOOD. J. Electron Spectrosc. Relat. Phenon. **12**, 95 (1977).
36. E. HASELBACH, J. A. HASHMALL, E. HEILBRONNER, and V. HORNUNG. Angew. Chem. Int. Ed. Engl. **8**, 878 (1969).
37. E. HASELBACH and E. HEILBRONNER. Helv. Chim. Acta, **53**, 684 (1970).
38. D. VOCELLE, A. DARGELOS, R. POTTIER, and C. SANDORFY. J. Chem. Phys. **66**, 2869 (1977).
39. T. BALLY, E. HASELBACH, S. LANIOVA, F. MARSCHNER, and M. ROSSI. Helv. Chim. Acta, **59**, 486 (1976).
40. D. C. FROST, N. P. C. WESTWOOD, N. H. WERSTIUK, L. C. TAGUCHI, and J. WARKENTIN. Can. J. Chem. **55**, 3677 (1977).
41. H. STAFAST and H. BOCK. Tetrahedron, **32**, 855 (1976).
42. G. BIERI, L. ASBRINK, and W. VON NIESSEN. J. Electron Spectrosc. Relat. Phenom. **27**, 129 (1982).
43. D. W. TURNER, C. BAKER, A. D. BAKER and C. R. BRUNDLE. Molecular photoelectron spectroscopy. Wiley Interscience, London. 1970.
44. T. KOOPMANS. Physica, 104 (1934).
45. C. LAFON. Doctoral thesis, Pau, France. 1987.
46. L. BIRKOFER, A. RITTER, and P. RICHTER. Chem. Ber. **96**, 2750 (1963).
47. L. BIRKOFER and P. WEGNER. Chem. Ber. **100**, 3485 (1967).
48. D. SEYFERTH and F. C. FLOOD. J. Organometal. Chem. **29**, C25 (1971).
49. W. ROSCH, U. HEES, and M. REGITZ. Chem. Ber. **120**, 1645 (1987).
50. R. HOFFMANN and R. B. WOODWARD. J. Am. Chem. Soc. **87**, 395 (1965).
51. R. B. WOODWARD and R. HOFFMANN. J. Am. Chem. Soc. **87**, 2511 (1965).
52. R. B. WOODWARD and R. HOFFMANN. Acc. Chem. Res. **1**, 17 (1968).
53. B. A. DEGRAFF, D. W. GILLESPIE, and R. J. SUNDBERG. J. Am. Chem. Soc. **96**, 7491 (1974).
54. V. A. SMIRNOV and S. B. BRIGHKIN. Chem. Phys. Lett. **87**, 548 (1982).
55. W. H. WADDELL and C. L. GO. J. Am. Chem. Soc. **104**, 5804 (1982).
56. A. REISER, H. M. WAGNER, R. MARLEY, and G. BOWES. Trans. Faraday Soc. **63**, 2403 (1967).
57. G. SMOLINSKY, E. WASSERMAN, and W. A. YAGER. J. Am. Chem. Soc. **84**, 3220 (1962).
58. W. LOWSKI. Nitrenes. Intersciences, New York. 1970.
59. G. HERZBERG. Molecular spectra and molecular structure: I. Spectra of diatomic molecules. 2nd ed. Van Nostrand, Princeton, NJ. 1950.
60. S. KHAYAR. Doctoral thesis, Pau, France. 1982.
61. H. S. HAMMOND. J. Am. Chem. Soc. **77**, 1288 (1955).
62. R. M. CLARAMUNT, J. ELGUERO, A. FRUCHIER, and M. J. NYE. Afinidad, **34**, 550 (1977).
63. H. J. LEMPKA. Helectros Developments, Beaconsfield, England. 1984.
64. H. L. MCKEE. J. Am. Chem. Soc. **107**, 1900 (1985).
65. S. SCHRODER and W. THIEL. J. Am. Chem. Soc. **107**, 4422 (1985).
66. D. LIOTARD. Doctoral thesis. Pau, France. 1979.
67. D. LIOTARD and J. P. PENOT. J. Chim. Phys. R11, 77 (1980).
68. D. LIOTARD and J. P. PENOT. *In* Numerical methods in the study of critical phenomena. *Edited by* J. Della-Rosa, J. Demongeot, and B. Locolle. Springer Verlag, Berlin. 1981. p. 213.
69. M. DUPUIS, J. RYS, and H. F. KING. J. Chem. Phys. **65**, 111 (1976).
70. W. C. DAVIDON and L. NAZARETH. Argonne Natl. Lab. Tech. Memos, 303, 306, Argonne, IL. 1981.
71. G. TRINQUIER. J. Am. Chem. Soc. **104**, 6969 (1982).
72. D. GONBEAU and G. PFISTER-GUILLOUZO. J. Electron Spectrosc. Relat. Phenom. **33**, 279 (1984).
73. M. PELISSIER. Doctoral thesis, Toulouse, France. 1980.
74. B. HURON, J. P. MALRIEU, and P. RANCUREL. J. Chem. Phys. **58**, 5745 (1973).
75. R. FLETCHER. Comput. J. **13**, 317 (1970).
76. M. PETERSON and R. POIRIER. Univ. of Toronto, Toronto, Ontario.

Can. J. Chem. Downloaded from www.nrcresearchpress.com by 112.217.228.212 on 09/07/12
For personal use only.

Tetracyclic triterpenes. X.[1] Solvent effect in reactions of tetrasubstituted triterpenoidal olefins with ozone. An allylic oxidation

ZDZISLAW PARYZEK[2] AND JACEK MARTYNOW
Faculty of Chemistry, A. Mickiewicz University, 60-780 Poznań, Poland

Received August 24, 1987[3]

ZDZISLAW PARYZEK and JACEK MARTYNOW. Can. J. Chem. **66**, 2130 (1988).

The highly hindered 8,9 double bond in lanostane derivatives was found susceptible to oxidation with ozone. The reaction depends on the polarity of the solvent. It is proposed that the structure of the initial complex formed between the olefin and ozone is influenced by the reaction medium. Reaction of 3β-acetoxy-5α-lanost-8-ene with ozone gives 8α,9α-epoxide in methylene chloride, while 3β-acetoxy-5α-lanost-8-en-7-one, an allylic oxidation product, is the main compound formed in ethyl acetate.

ZDZISLAW PARYZEK et JACEK MARTYNOW. Can. J. Chem. **66**, 2130 (1988).

On a trouvé que la double liaison très empêchée que l'on retrouve dans les positions 8,9 des dérivés du lanostane est très susceptible aux oxydations par l'ozone. La réaction est influencée par la polarité du solvant. On suggère que la structure du complexe qui se forme initialement entre l'oléfine et l'ozone est influencée par le milieu réactionnel. Dans le chlorure de méthylène, la réaction de l'acétoxy-3β 5α-lanostène-8 avec l'ozone conduit à l'époxyde 8α,9α; par ailleurs, dans l'acétate d'éthyle, le produit principal est l'acétoxy-3β 5α-lanostène-8 one-7, un produit provenant d'une oxydation allylique.

[Traduit par la revue]

Retropinacolic rearrangement of a triterpene 3-alcohol, for example 5α-lanostan-3β-ol (I), under the action of phosphorus pentachloride leads to the ring A contracted isopropylidene compound (II). Treatment of the olefin (II) with ozone provides a simple method of preparation of *A*-nor steroids (III). The sequence shown in eq. [1] has been described for pentacyclic (1)

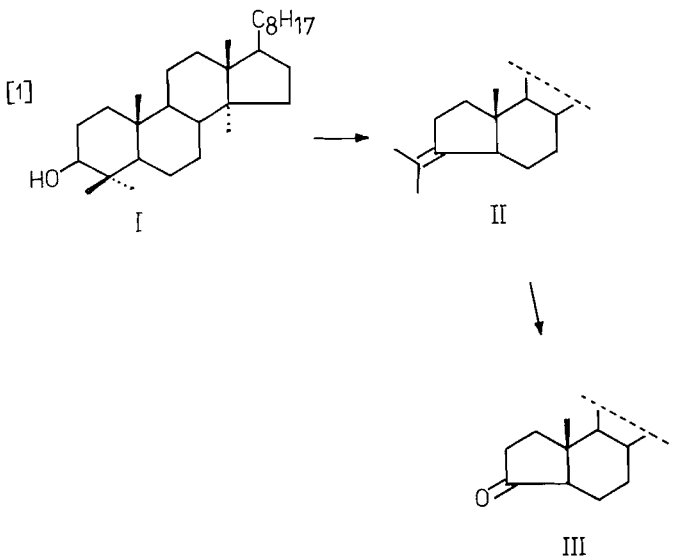

and tetracyclic (2) triterpenes, their derivatives possessing a degraded side chain (3), and for 4,4-dimethyl steroids (4). In the lanostane series, 14α-methyl-*A*-nor-steroids were prepared by this simple degradation route (5).

The literature search revealed, however, that ozonolysis of 3-izopropylidene-*A*-nor-steroids was only rarely performed on substrates possessing an additional olefinic double bond in the molecule. In these cases the reported yields of the degraded compounds were low (15–45%) (1*a*, 6).

In our approach to 14α-methyl-*A*-nor-5α-cholest-8-en-3-one (**9**), the isopropylidene compound **4**, which was prepared from dihydrolanosterol (**1**), was subjected to oxidative degradation with ozone. The reaction carried out in methylene chloride at −78°C gave the keto-diene **5**, which isomerized during work-up to the 5β-isomer **6** (2*b*). Thin-layer chromatographic monitoring of the reaction showed that the epoxy-ketone **7** was the primary product of the reaction. Dehydration of **7** to the diene **5** was catalyzed by an acid[4] formed from the solvent under ozonolysis conditions (7). This was evidenced by the isolation of the epoxy-ketone **7** (51% yield) and the enone **9** (5%) from the reaction of **4** carried out in the same solvent containing a small amount of pyridine (8). In the course of the ozonolysis of **4** in CH_2Cl_2 the reaction sample was analyzed after approximately 0.1 molar equivalent of ozone had reacted. It contained, besides the substrate, 7% of the diene **5** (uv test). This indicates that the reactivity of both the double bonds in **4** toward ozone is similar and the formation of the epoxide **7** was not a result of over-ozonation. Interestingly, the reactivity of the trisubstituted 24,25 double bond in 3β-acetoxy-5α-lanosta-8,24-diene exceeds significantly that of the tetrasubstituted olefinic linkage, thus making it possible to stop the ozonolysis at the stage of 24,25-ozonide, leading to the acid **11**.[5] In the light of these results it seemed of interest to study the reaction of ozone with other 8,9-olefins, both in the *A*-nor and in the "normal" lanostane series.

In the *A*-nor series, keto-olefin **9** gave the dienone **6** (48%) under acidic[4] conditions, while in methylene chloride–pyridine solution it was epoxidized to give **7**(34%). Similar epoxidation occurred when the olefin **12** (as a mixture of 3α- and 3β-epimers) was ozonized. The same reaction of 3β-acetoxy-5α-lanost-8-ene (**2**) and of 5α-lanost-8-en-3-one (**3**) gave the respective epoxides **13** (47%) and **14** (56%). Compound **2** gave 3β-acetoxy-5α-lanosta-7,9(11)-diene (65%) under acidic[4] conditions. In the course of all ozonations carried out in methylene chloride a remarkable destruction of the substrate was observed. This was probably a result of the attack of ozone on unactivated C—H bonds being more pronounced in the strained *A*-nor compounds.

[1]For Part IX, see ref. 9.

[2]Author to whom correspondence may be addressed.

[3]Revision received March 28, 1988.

[4]When oxygen–ozone mixture was passed through CH_2Cl_2 (50 mL) for 1 h an approximately 0.05 N acid solution was formed.

[5]Z. Paryzek and R. Wydra, unpublished results.

Printed in Canada / Imprimé au Canada

Can. J. Chem. Downloaded from www.nrcresearchpress.com by 112.217.228.212 on 09/07/12
For personal use only.

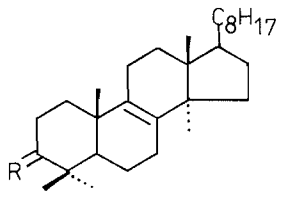

1 R = β-OH,H
2 R = β-OAc,H
3 R = O

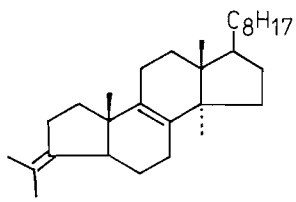

4

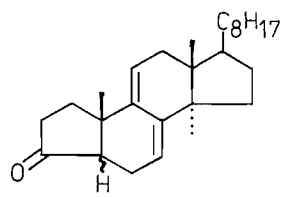

5 5α
6 5β

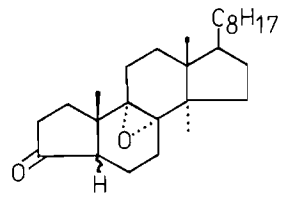

7 5α
8 5β

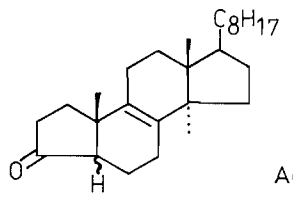

9 5α
10 5β

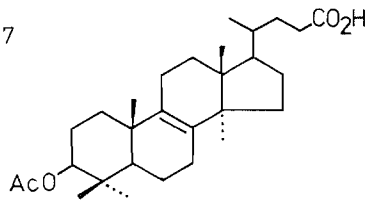

11

Diverse results were obtained when ozonations were carried out in nonpolar and unreactive solvent, *n*-hexane. The diene **4** was transformed to the enone **9** (78% yield) and only traces of the epoxide **7** could be detected in the reaction product. The two epimeric ozonides **15**, detected on tlc plates, were quite stable. One of them was isolated and characterized by its ^{1}H nmr and ir spectra. Ozonide **15** was stable toward reductive action of dimethyl sulfide and its decomposition was achieved by treatment with zinc in acetic acid or with potassium hydroxide in methanol–benzene solution. Olefin **2** was recovered unchanged after prolonged reaction with ozone in *n*-hexane.

The *trans* hydrindane-type ketone **9** isomerized easily in basic solution to the thermodynamically more stable 5β-ketone **10** (1*b*, 10). We found that epimerization at C(5) in *A*-nor-3-ketones was distinctly slower in the case of 8,9-olefins if compared with the 7,9(11)-dienes, which isomerized during the work-up and chromatography on silica gel. The characteristic spectral differences between 5α- and 5β-*A*-nor-3-ketones are summarized in Table 1. The 5β-configuration in **4** and **6** was confirmed by the positive Cotton effect associated with the $n \rightarrow \pi^*$ transition of the carbonyl group. High optical activity of the ketone **6** is determined by the asymmetry of the overlap between the 7,8 double bond and the carbonyl orbitals, which are in close proximity to each other in this γ,δ-unsaturated ketone.

The apparent solvent polarity dependance of the ozonations

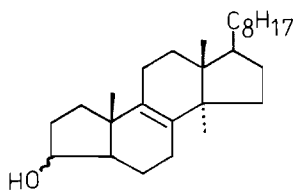

12

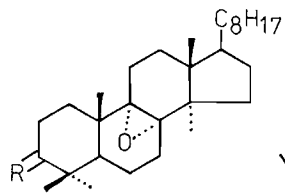

13 R = β-OAc,H
14 R = O

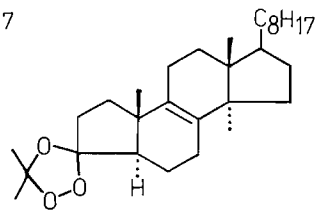

15

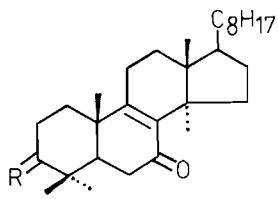

16 R = β-OAc,H
17 R = O
25 R = β-OH,H

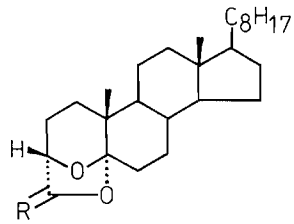

21 R = OH,H
22 R = O

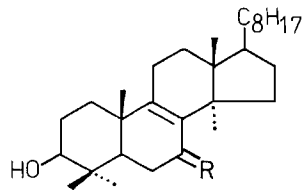

23 R = β-OH,H
24 R = α-OH,H

Can. J. Chem. Downloaded from www.nrcresearchpress.com by 112.217.228.212 on 09/07/12
For personal use only.

TABLE 1. Spectral data characteristic of 5α- and 5β-*A*-nor-3-ketones

Compound					
5β	5α	19-CH_3* (δ)	19-CH_3 (δ)	ν 3C=O (cm^{-1})	Δε (λ, nm)
6		29.3	1.33	1733	+6.41 (296)
8		25.2	1.30	1728	+2.60 (286)
					−0.08 (323)
10		25.4	1.22	1728	+3.14 (296)
	7	17.4	1.02	1731	−2.77 (297)
	9	19.4	0.90	1732	−2.63 (302)

*For the discussion of C-19 carbon shielding differences between 5α and 5β steroids see ref. 11.

studied here prompted the investigation of the reaction in more polar solvent. When olefin **2** dissolved in ethyl acetate reacted with ozone a mixture of two compounds formed. These were identified as the epoxide **13** (40%) and the enone **16** (46%). In similar conditions, compound **3** gave a mixture of the epoxide **14** (22%) and the enone **17** (57%). In another experiment epoxide **13** was excluded as a precursor of the enone **16**.

In spite of the large amount of work devoted to the elucidation of ozone reaction with alkenes and with olefins containing other functional groups, many aspects of the mechanism of ozonolysis (12) are still unclear. There are many reported cases where ozone is likely to be the epoxidation agent (12*b*). Formation of epoxides was observed in reactions of ozone with hindered triterpenoidal (13) and steroidal (14) olefins. These reactions do not conform with the concerted Criegee mechanism of ozonolysis (12*a*,*c*), which proceeds with the formation of 1,2,4-trioxolane as a final ozonide. In the case of crowded olefins, 1,2,3-trioxolanes as primary ozonides seem also to be excluded. Instead, open σ-complex, π-complex, and peroxy-epoxide are proposed as precursors from which epoxides may be formed (12*a*, 15).

[2]

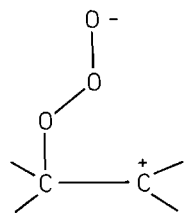

σ-complex

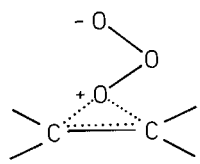

π-complex

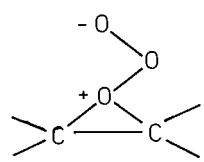

peroxy epoxide

Recently an intermediate primary ozonide, a diradical or zwitterion derived from the primary ozonide, and carbonyl oxide, which is the primary ozonide cleavage product, were evaluated as potential epoxidizing agents for the unreacted olefin (16). Experimental evidence was presented that epoxidation of olefins can be caused by carbonyl oxide (16*c*). However, considering activation energies (16*a*,*b*) and steric requirements for oxygen transfer, these intermediates have to be excluded as an effective source of oxygen in the epoxidation of crowded, triterpenoidal olefins.

Solvent effects in ozonolysis of alkenes were discussed in terms of the *cis–trans* ozonide ratio (12*c*, 15, 17) rather than the structure of the complex formed initially between ozone and an alkene. The effect of solvent on decomposition of the initial ozonide has also been reported (18). The observed influence of the solvent on reactions examined in this study suggests that the initial complex formed between ozone and the crowded triterpenoidal olefin may be stabilized by dipole–dipole interactions. On the basis of this assumption it is proposed that in methylene chloride (ε 8.93, μ5.17 × 10^{-30} $C \times m$) the structure of the ozone–olefin complex is of the π-complex type or rather the peroxy-epoxide **18**, stabilization of which is achieved by the elimination of oxygen molecule with formation of the α-epoxide **13**. In hexane (ε 1.88, μ 0.0), a complex of type **18** is not formed due to the lack of solvent stabilization. Thus no epoxide was isolated in reactions of **2** or **4** in *n*-hexane. In ethyl acetate (ε 6.02, μ 6.27 × 10^{-30} C·m), more effective solvent stabilization may result in formation of a complex with more pronounced charge separation, with structure similar to σ-complex **19**. Polar solvent stabilization would enhance the stability and increase the lifetime of **19**, thus increasing the opportunity for intramolecular oxygen transfer. This complex might rearrange to trioxolane **20**, which, due to steric congestion, eliminates an oxygen molecule with formation of the allylic alcohol, subsequently oxidized with excessive ozone to the enone **16** (Scheme 1).

Formation of the enone **16** might be explained assuming direct allylic oxidation and the intermediacy of hydrotrioxides. These have been postulated (19) in reactions proceeding with the 1,3-dipolar insertion of ozone into activated C—H bonds in ethers (20). However, these processes are of low regioselectivity.

The epoxide **13** was found stable toward ozone in ethyl acetate; therefore its isomerization to allylic alcohol as a possible pathway leading to the enone **16** could also be excluded.

Another possibility that might be considered is the oxidation of the olefin with the participation of singlet oxygen. In oxidations of olefins with ozone leading to epoxides, singlet oxygen is a by-product (21). Although $^1O_2$ is known to attack the unsaturated systems (22), this process may not be regarded as operating here for two reasons. First, singlet oxygen reactions are rather low yield processes, while the first oxidation step would require the effective transfer of $^1O_2$ to the unreacted olefin. Second, in the reaction of **3** with ozone the epoxide-to-enone ratio was approximately 1:2.5, thus excluding the epoxide as a source of singlet oxygen. Photooxygenation of 3β-acetoxy-5α-lanost-8-ene gave a low yield of several products among which 8-en-7-one and 7-hydroperoxy-8-ene were isolated in 16 and 6% yield (23).

Can. J. Chem. Downloaded from www.nrcresearchpress.com by 112.217.228.212 on 09/07/12
For personal use only.

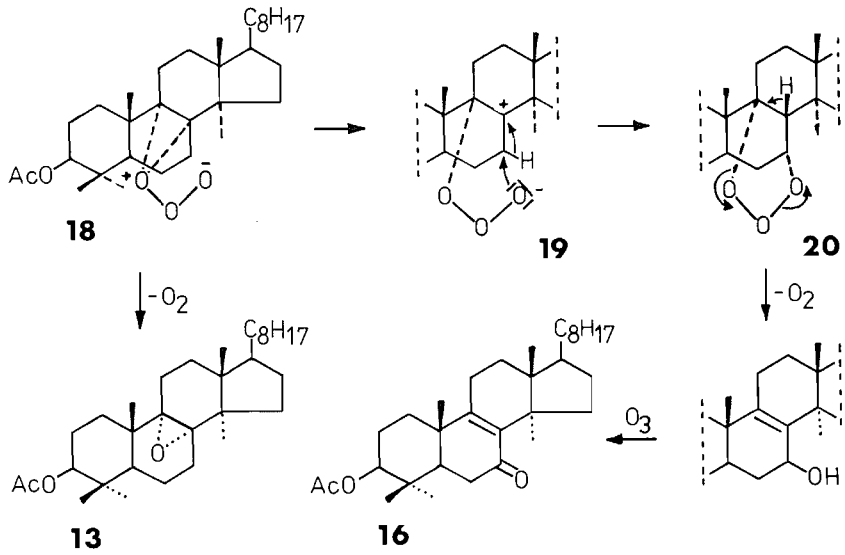

SCHEME 1

The oxidation of secondary alicyclic alcohols with ozone is known (24). Therefore, in view of the proposed intermediacy of allylic alcohol in ozonations under study, it was of interest to investigate the reaction of a model steroidal allylic alcohol with ozone in ethyl acetate at −78°C. Cholest-4-en-3β-ol was chosen as the model compound. However, the only product of this reaction (eq. [3]) had the structure **21**, which is in agreement with the Criegee mechanism of ozonolysis and is inconsistent with the abnormal ozonolysis pathway reported for allylic derivatives (25).

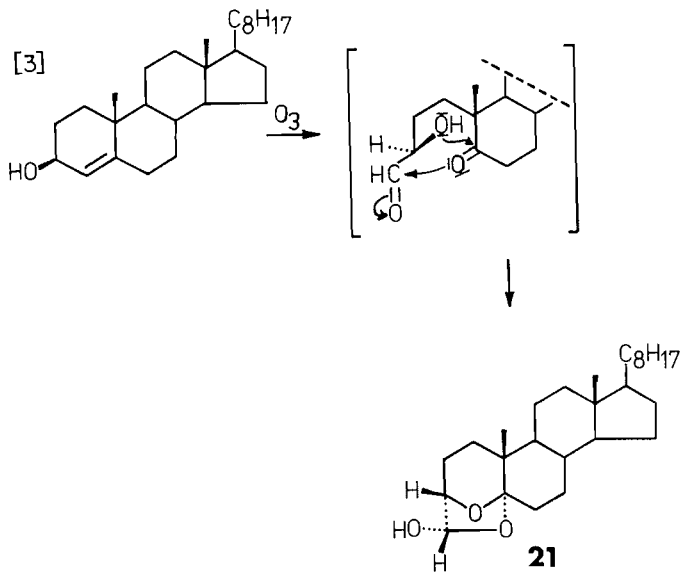

Identity of **21** obtained as a crystalline compound, was established by spectral data (Experimental) and by oxidation to the lactone **22**. Configuration *S* of C(4) in **21** was assigned on the basis of vicinal coupling (J = 8.8 Hz) between protons at C(4) and C(3) observed in the ^{1}H nmr spectrum. The structure of **21** was further supported by a ^{13}C nmr spectrum that revealed three deshielded signals recognized as arising from carbon atoms adjacent to one or two oxygen atoms. A singlet signal at 112.9 ppm and doublet signals at 81.4 and 96.4 ppm ascribed to C-5, C-3, and C-4, respectively, established the assigned structure definitively. Similar spontaneous (26) or acid catalyzed (27) intramolecular double acetalization has been reported.

The result of ozonolysis of cholest-4-en-3β-ol indicates that the allylic hydroxy group is not susceptible to oxidation with ozone, which preferably attacks the double bond. This evidence suggests that the most probable transformation of the postulated transient allylic alcohol (Scheme 1) is via the second oxidation step with formation of a complex similar to **19**, not necessarily involving formation of the 8,9-epoxy-7α-alcohol as an intermediate product.

The mechanistic proposal shown in Scheme 1 was supported by the following experiment. 3β-Acetoxy-5α-lanost-8-en-7-one was quantitatively reduced with lithium aluminum hydride to the mixture of 3β,7β- and 3β, 7α-diols **23** and **24** in the ratio 1.1:1. The assignment of the configuration of carbon 7 in **23** and **24** was based on the coupling pattern of the 7-H signal in the ^{1}H nmr spectra and on the characteristic up-field shift (4.5 ppm) of C-5 (28) in the ^{13}C nmr spectrum[6] of the pseudoaxial 7α alcohol **24**. The diol **24** was entirely transformed to the enone **25** upon treatment with ozone in ethyl acetate at −78°C.

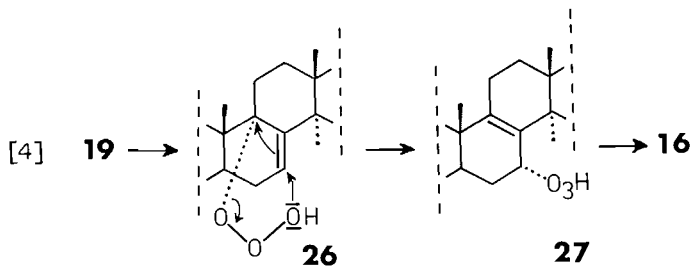

However, on the basis of the evidence presented, a reaction pathway involving the rearrangement of **19** (via the trioxide **20**, or alternatively via **26**) to the transient hydrotrioxide **27**, from which 8-en-7-one **16** may be formed directly (eq. [4]), cannot be excluded.

The reactions reported in this paper appear to be the first examples of solvent-dependent ozone oxidation of crowded olefins to the α-,β-unsaturated ketones.

[6]The full details of the ^{13}C nmr spectra of compounds described in this work will be discussed elsewhere.

Can. J. Chem. Downloaded from www.nrcresearchpress.com by 112.217.228.212 on 09/07/12
For personal use only.

Can. J. Chem. Downloaded from www.nrcresearchpress.com by 112.217.228.212 on 09/07/12
For personal use only.

Experimental

Melting points were determined on a Kofler hot-stage apparatus and are uncorrected. The ir spectra were determined with a Perkin Elmer 580 spectrophotometer for solutions in chloroform. The uv spectra were recorded with a Shimadzu 160 spectrophotometer for solutions in ethanol. The ^1H and ^{13}C nmr spectra were recorded with a JEOL FX 90Q spectrometer operating in the Fourier transform mode using solutions in deuteriochloroform. Mass spectra were recorded with a JEOL JMS-D 100 spectrometer using electron impact. The cd spectra were recorded with a Jobin–Yvon Dichrograph Mark III for solutions in dioxane.

Reactions of olefins with ozone. General procedure

The following solvents were used in ozonation reactions: procedure A: methylene chloride; procedure B: methylene chloride containing 1.5–3 molar equiv. of pyridine; procedure C: *n*-hexane; procedure D: ethyl acetate containing 1.5–3 molar equiv. of pyridine.

The olefin was dissolved in the solvent to get a 5–10% solution. Oxygen–ozone mixture was passed through this solution, cooled to −78°C and kept in the dark, until all the substrate disappeared (30–180 min, tlc test). Excessive ozone was removed with the stream of oxygen. An excess of dimethyl sulfide was added to the reaction mixture and it was left for 2 h at room temperature. Evaporation of the solvent under reduced pressure gave the crude product, which was purified by chromatography and crystallization.

Ozonation of ***4*** (procedure A)

The diene **4** (350 mg) gave an oily crude product (356 mg), which was chromatographed on silica gel to give pure 14α-methyl-*A*-nor-5β-cholesta-7,9(11)-dien-3-one (**6**) (170 mg, 52%), mp 85.5–86.5°C (methanol–water – diethyl ether) (lit. (*2b*) mp 85–87°C); ir ν_{max}: 1733 cm^{-1}; uv λ_{max} (ε): 237 nm (10 400) and 251 nm (h,7 700); cd Δε(λ): +4.11 (265), +5.22 (286), +6.41 (296), +5.96 (305), and +3.02 (316); ^1H nmr δ: 5.66 (1H, m), 5.39 (1H, m), 1.33, 0.90, 0.83, 0.79, and 0.56 (methyl signals); mass spectrum *m/z*: 382(M+,100%), 367, 349, 227, 157, and 43. *Anal.* calcd. for $C_{27}H_{42}O$: C 84.75, H 11.06; found: C 84.58, H 11.21.

Ozonation of ***9*** (procedure A)

The enone **9** (410 mg) gave a crude product, which was chromatographed on silica gel to give **6** (196 mg, 48%) identical in all respects with the compound described above.

Ozonation of ***2*** (procedure A)

Dihydrolanosteryl acetate **2** (400 mg) gave a crude product, which was chromatographed on alumina to give 3β-acetoxy-5α-lanosta-7,9(11)-diene, mp 167–168°C (methanol – methylene chloride) (lit. (*29a*) mp 164–166°C) and gave spectra in agreement with those of an authentic sample (*29b*).

Ozonation of ***4*** (procedure B)

Zinc (0.8 g) was added to the crude product obtained from the diene **4** (300 mg) and dissolved in a mixture of *n*-hexane (10 mL) and acetic acid (10 mL), and the mixture was stirred at room temperature for 1 h. After work-up the oily residue (305 mg) was chromatographed on silica gel. First compound **9** (15 mg, 5%) was eluted. This was an oil, which gave ir and ^1H nmr spectra identical with those obtained for the product of ozonation of **4** in hexane (*vide infra*). The further fractions contained epoxide **7**, as an oil (149 mg, 51%); ir ν_{max}: 1731, 1280, 1242, 1145, and 975 cm^{-1}; cd Δε(λ): −2.77(297), −2.71(290); ^1H nmr δ: 2.68 (1H, m, 5α-H), 2.21 (2H, m, 2α- and 2β-H), 1.02, 0.92, 0.90, 0.83, and 0.80 (methyl signals); mass spectrum *m/z*: 400 (M^+), 385, 382, 367 (100%), 259, 95, and 43. *Anal.* calcd. for $C_{27}H_{44}O_2$: C 80.94, H 11.07; found: C 80.62, H 10.94.

Ozonation of ***9***(procedure B)

The enone **9** (300 mg) gave a crude product (yellow oil), which after chromatography on silica gel afforded epoxy-ketone **7** (oil, 106 mg, 34%), identical (^1H nmr, ir) with **7** obtained in the previous experiment.

Ozonation of 3β-acetoxy-5α-lanost-8-ene (2) (procedure B)

The crude product obtained from **2** (400 mg) was purified on a short column of alumina and crystallized twice from methanol – diethyl ether mixture to give 3β-acetoxy-8α,9α-epoxy-5α-lanostane (**13**) (197 mg, 48%), which had mp 135–138°C (diethyl ether – methanol) (lit. (30) mp 140–142°C); this compound was identical in all respects with the original sample obtained from **2** upon epoxidation with *m*-chloroperbenzoic acid.

Ozonation of 5α-lanost-8-en-3-one (3) (procedure B)

The crude reaction product obtained from **3** (400 mg) was chromatographed on a column of silica gel to give 8α,9α-epoxy-5α-lanostan-3-one (**14**) (231 mg, 56%), which had mp 102–104°C (methanol); ir ν_{max}: 1702, 1235, 1119, and 970 cm^{-1}; ^1H nmr δ: 2.49 (2H,m), 1.25, 1.03, 1.01, 0.90, 0.82, and 0.79 (methyl signals); mass spectrum *m/z*: 442 (M^+), 427, 424, 409, 291 (100%), 152, and 43. *Exact Mass* calcd. for $C_{30}H_{50}O_2$: 442.3810; found: 442.3811.

Ozonation of ***4*** (procedure B)

The crude product obtained from **4** (400 mg) was dissolved in a solution of potassium hydroxide in methanol (5%) and left at room temperature for 18 h. The usual work-up and chromatography on a silica gel column gave **10** (30 mg, 8%), and 14α-methyl-8α,9α-epoxy-*A*-nor-5β-cholestan-3-one (**8**) (180 mg, 46%), which had mp 72–74°C (heptane); ir ν_{max}: 1728, 1155, 1118, and 970 cm^{-1}; cd Δε (λ): +2.60 (286 nm), +2.56 (292), and −0.08 (323); ^1H nmr δ: 2.33 (3H, m), 1.30, 0.90, 0.86, 0.83, and 0.79 (methyl signals); mass spectrum *m/z*: 400 (M^+), 385 (100%), 287, 180, and 44. *Anal.* calcd. for $C_{27}H_{44}O_2$: C 80.94, H 11.07; found: C 80.69, H 11.22.

Ozonation of ***12*** (procedure B)

Lithium aluminum hydride (100 mg) was added to the ketone **9** (100 mg) dissolved in tetrahydrofuran (5 mL) and the mixture was stirred under argon at room temperature for 25 min. The usual work-up gave an oil (78 mg), which was a mixture of epimeric alcohols **12** as evidenced by ^1H nmr signals at δ: 4.26 (1H, m, OH), 3.85, (0.2H, m), 3.72 (0.6H, m) and 3.60 (0.2H, m). This mixture was ozonized (procedure B) and the crude product was chromatographed on a silica gel column to give the oil (34 mg, 41%). This had ν_{max} 3360 cm, *m/z* 402 (M^+), and gave ^1H nmr signals at δ: 4.16 (1H, m, OH) and 3.90 (1H, bm, 3α- and 3β-H). Brief treatment of this material (18 mg) dissolved in chloroform with hydrogen bromide (0.2 mL, 40%) gave the product (an oil, 16 mg), which had spectral characteristics in accordance with the 7,9(11)-dien-3-ol structure: uv λ_{max} (ε): 243 (8 600); ^1H nmr δ: 5.45 (2H, m), 4.23 (1H, m, OH), 3.75 (1H, bm, 3α- and 3β-H); mass spectrum *m/z*: 384 (M^+), 366, 351, 197, 83 (100%), and 43.

Ozonation of ***4*** (procedure C)

Acetic acid (10 mL) and zinc (0.4 g) were added to the crude product obtained from the diene **4** (600 mg) and the mixture was stirred at room temperature for 1 h. The usual work-up gave an oily residue (596 mg), which was chromatographed on a silica gel column. First, starting material (51 mg) was eluted. The main fractions contained 14α-methyl-*A*-nor-5α-cholestan-3-one (**9**) as an oil (441 mg, 78%), which crystallized at −20°C as needles, mp 36–37°C (watered methanol); ir ν_{max}: 1732 cm^{-1}; cd Δε (λ): −2.51 (294) and −2.63 (302); ^1H nmr δ: 2.30–2.07 (7H, m), 0.90, 0.83, and 0.73 (methyl signals); mass spectrum *m/z*: 384 (M^+), 369 (100%), 215, 203, and 44. *Anal.* calcd. for $C_{27}H_{44}O_2$: C 84.31, H 11.53; found: C 84.21, H 11.63.

Isolation of the ozonide ***15*** (procedure C)

The crude product obtained from the diene **4** (1.0 g) was treated with dimethyl sulfide (2 mL) at room temperature for 16 h. The solvent was evaporated and the residue dissolved in *n*-hexane. After addition of methanol (5 mL) a white precipitate formed. This was filtered (347 mg) and the filtrate was evaporated to give an oily residue (600 mg), which was chromatographed on a silica gel column. The two compounds obtained, in order of their elution, were (1) ozonide **15** (oil, 101 mg), ir ν_{max}: 1250, 1220, 1180, 1115, and 980 cm^{-1}; ^1H nmr δ: 2.23–2.05 (5H, m), 1.49 (6H, s, 2 × CH_3), 0.95, 0.90, 0.87, 0.83, and 0.72; (2)

Can. J. Chem. Downloaded from www.nrcresearchpress.com by 112.217.228.212 on 09/07/12
For personal use only.

compound **9** (317 mg), identical with the sample obtained in the previous experiment.

Base catalyzed isomerization of the ketone 9

To the solution of ketone **9** (80 mg) in benzene (10 mL) a solution of potassium hydroxide in methanol (3 mL, 5%) was added and the mixture stirred at room temperature for 1 h. The benzene solution was washed with water, dried with sodium sulfate, and evaporated to yield 14α-methyl-*A*-nor-5β-cholestan-3-one (**10**) (72 mg), which had mp 81–82°C (watered methanol) (lit. (2*a*) mp 82–83.5°C); ir ν_{max}: 1728 cm^{-1}; cd $\Delta\epsilon$ (λ): +0.97 (267), +2.42 (287), +3.14 (296), +3.16 (306), and +1.75 (316); ^1H nmr δ: 1.22, 0.90, 0.83, 0.81, and 0.73 (methyl signals); mass spectrum *m/z*: 384 (M^+), 369 (100%), 203, 189, 105, and 44.

Ozonation of olefin 2 (procedure C)

Dihydrolanosteryl acetate (**2**) (100 mg) dissolved in hexane (50 mL) was ozonized at −78°C for 2.5 h. Thin-layer chromatography of the reaction mixture showed some polar material. The crude product was filtered through a short column of alumina (2 g). The pure fractions were combined, evaporated, and crystallized from methanol to give the substrate **2** (61 mg), which had mp 117–121°C (chloroform–methanol) and was identical with the original sample.

Ozonation of olefin 2 (procedure D)

The crude product obtained from **2** (400 mg) was chromatographed on a silica gel column. Two compounds obtained, in order of their elution, were 3β-acetoxy-8α,9α-epoxy-5α-lanostane (**13**) (166 mg, 40%), with mp 135–138°C (methanol) (lit. (30) mp 140–142°C) and spectra (ir, ^1H nmr, ms) in agreement with those of the original sample; and 3β-acetoxy-5α-lanost-8-en-7-one (**16**) (188 mg, 46%), with mp 149–150°C (*n*-heptane) and 145–146°C (diethyl ether – methanol) (lit. (31) mp 145–146°C) and spectra (^1H nmr, ir, uv, ms) in agreement with those of the original sample.

Ozonation of olefin 3 (procedure D)

The crude product obtained from **3** (420 mg) was chromatographed on a column of silica gel. Three compounds were obtained in order of their elution: the substrate **3** (36 mg, 8.5%); 8α,9α-epoxy-5α-lanostan-3-one (**14**) (94 mg, 22%), which had mp 102–104°C (methanol) and spectra (^1H nmr and ir) in accordance with those of the sample obtained in ozonation of **3** according to procedure B (above); and 5α-lanost-8-en-3,7-dione (**17**) (248 mg, 57%), which had mp 145–147°C (methanol) (lit. (32) mp 145–147°C); ir ν_{max}: 1704, 1652, and 1586 cm^{-1}; uv λ_{max} (ε): 253 nm (11 000) (lit. (32) λ_{max} (ε): 254 nm (12 600)); ^1H nmr δ: 2.52 (2H, m), 2.43 (2H, m), 1.12, 1.10, 0.94, 0.90, 0.83, and 0.68; mass spectrum *m/z*: 440 (M^+), 425 (100%), 327, 259, 149, and 44. *Anal.* calcd. for $C_{30}H_{48}O_2$: C 81.76, H 10.98; found C 81.58, H 11.12.

Ozonation of 13 (procedure D)

Treatment of **13** (35 mg) dissolved in ethyl acetate (20 mL) with ozone at −78°C for 1 h gave no reaction. Starting material was recovered and crystallized from methanol to give **13** (29 mg), which had mp 136–138°C and was identical (^1H nmr) with the authentic sample.

Ozonation of cholest-4-en-3β-ol

The crude product obtained from ozonolysis (procedure D) of cholest-4-en-3β-ol (320 mg) was dissolved in acetic acid (10 mL) and stirred with zinc powder (800 mg) at room temperature for 1 h. The reaction mixture was filtered and the filtrate was evaporated to dryness, purified by chromatography on an alumina column, and evaporated to give a white solid. This was crystallized from methanol – ethyl acetate mixture to give **21** (247 mg, 71%), which had mp 155–157°C. Recrystallization from acetonitrile gave white needles, mp 157–158°C; ir ν_{max}: 3570, 3425, 1137, 1095, 1072, 1049, 1029, 988, 937, and 868 cm^{-1}; ^1H nmr δ: 5.20 (1H, bd, J = 8.8 Hz, 4β-H), 4.20 (1H, d, J = 2 Hz, OH), 3.21 (1H, bd, J = 8.8 Hz, 3β-H), 1.02, 0.89, 0.82, and 0.64 (methyl signals); ^{13}C nmr δ: 112.9 (C-5), 96.4 (C-4), and 81.4 (C-3); mass spectrum *m/z*: 418 (M^+), 403, 372 (100%), 149, 95, and 44. *Anal.* calcd. for $C_{27}H_{46}O_3$: C 77.46, H 11.08; found: C 77.21, H 11.09.

Oxidation of bis-acetal 21 with Jones reagent

Compound **21** (25 mg) dissolved in acetone (15 mL) was oxidized with Jones reagent. After the substrate had reacted (tlc), methanol (0.5 mL) was added and the solvents evaporated. The residue was dissolved in benzene and this solution was filtered through an alumina (1 g) column. The product was compound **22** (22 mg, 88%). It had mp 130–131°C (acetonitrile); ir ν_{max}: 1783, 1278, 1250, 1195, 1060, 996, 987, 908, and 878 cm^{-1}; ^1H nmr δ: 4.44 (1H, m, $W_{\frac{1}{2}}$ = 4.8 Hz, 3β-H), 1.13, 0.93, 0.90, 0.86, 0.83, and 0.66 (methyl signals); mass spectrum *m/z*: 416 (M^+, 100%), 401, 372, 261, 149, and 44. *Anal.* calcd. for $C_{27}H_{44}O_3$: C 77.84, H 10.64; found: C 77.79, H 10.91.

Lithium aluminum hydride reduction of 3β-acetoxy-5α-lanost-8-en-7-one (16)

$LiAlH_4$ (600 mg) was added in portions to compound **16** (560 mg) dissolved in diethyl ether (80 mL) and the mixture was stirred at room temperature for 1 h. To this mixture, cooled to −78°C, was added a saturated aqueous solution of magnesium sulfate (20 mL). After warming up, the ether layer was separated and evaporated to give a white crystalline residue (474 mg), which was chromatographed on a column of silica gel. Two compounds were obtained: (1) 5α-lanost-8-en-3β,7β-diol (**23**) (202 mg, 39%), which had mp 167–168°C (acetonitrile); ir ν_{max}: 3610, 3440, 1240, 1027, 995, 980, 945, and 884 cm^{-1}; ^1H nmr δ: 4.35 (1H, m, $W_{\frac{1}{2}}$ = 23 Hz, 7α-H), 3.20 (1H, m, 3α-H), 1.07, 0.99, 0.90, 0.84, and 0.76 (methyl signals); ^{13}C nmr δ: 78.6 (C-3), 68.4 (C-7), and 49.5 (C-5); mass spectrum *m/z*: 444 (M^+), 426 (100%), and 411. *Anal.* calcd. for $C_{30}H_{52}O_2$: C 81.02, H 11.79; found: C 80.93, H 11.61; and (2) 5α-lanost-8-en-3β,7α-diol (**24**) (177 mg, 35%), which had mp 144–146°C (acetonitrile); ir ν_{max}: 3610, 3410, 1238, 1045, 1020, 1005, and 925 cm^{-1}; ^1H nmr δ: 4.20 (1H, m, $W_{\frac{1}{2}}$ = 10 Hz, 7β-H), 3.26 (1H, m, 3α-H), 1.03, 0.95, 0.90, 0.82, and 0.60 (methyl signals); ^{13}C nmr δ: 78.1 (C-3), 67.5 (C-7), and 45.0 (C-5); mass spectrum *m/z*: 444 (M^+), 426 (100%), and 411. *Anal.* calcd. for $C_{30}H_{52}O_2$: C 81.02, H 11.79: found: C 80.74, H 11.55.

Ozonation of 24 (procedure D)

The crude product obtained from **24** (100 mg) was a white solid (103 mg), which gave one spot on tlc. After crystallization from methanol 3β-hydroxy-5α-lanost-8-en-7-one (**25**) (63 mg) was obtained, which had mp 132–134°C (lit. (33) mp 135–136°C). This material was identical (ir, ^1H nmr, tlc) with an authentic sample.

Acknowledgements

We thank E Merck, Darmstadt, for a gift of "Lanosterin". Financial support of the work from the program RP II.13.2 is gratefully acknowledged.

1. (*a*) G. G. Allan, F. S. Spring, R. Stevenson, and W. S. Strachan. J. Chem. Soc. 3371 (1955); (*b*) G. V. Baddeley, T. G. Halsall, and E. R. H. Jones. J. Chem. Soc. 1715 (1960).
2. (*a*) L. Ruzicka, M. Montavon, and O. Jeger. Helv. Chim. Acta, **31**, 818 (1948); (*b*) C. Doree, J. F. McGhie, and F. Kurzer. J. Chem. Soc. 167 (1949); (*c*) W. Voser, D. E. White, H. Heuser, O. Jeger, and L. Ruzicka. Helv. Chim. Acta, **35**, 830 (1952); (*d*) P. Crabee, G. Ourisson, and T. Takahashi. Tetrahedron, **3**, 279 (1958); (*e*) D. H. R. Barton and D. Kumari. Annalen, **737**, 108 (1970).
3. (*a*) W. Voser, H. Heusser, O. Jeger, and L. Ruzicka. Helv. Chim. Acta, **36**, 299 (1953); (*b*) J. Fried and E. F. Sabo. J. Am. Chem. Soc. **84**, 4356 (1962); (*c*) G. R. Pettit and P. Hofer. J. Chem. Soc. 4439 (1963); (*d*) Helv. Chim. Acta, **46**, 2142 (1963).
4. J. F. Biellmann and G. Ourisson. Bull. Soc. Chim. Fr. 331 (1962); J. F. Biellmann, D. Kucan, and G. Ourisson. Bull. Soc. Chim. Fr. 337 (1962).

5. D. H. R. BARTON, D. A. J. IVES, and B. R. THOMAS. J. Chem. Soc. 903 (1954).
6. J. FRIED and D. W. ROSENTHAL. U.S. Patent 3,294,834 (1966); Chem. Abstr. **66**, 115889b (1967).
7. F. L. GREENWOOD, J. Org. Chem. **10**, 414 (1945).
8. G. SLOMP and J. L. JOHNSON. J. Am. Chem. Soc. **80**, 915 (1958).
9. R. WYDRA and Z. PARYZEK. Pol. J. Chem. **58**, 705 (1984).
10. W. KLYNE. J. Chem. Soc. 2916 (1952).
11. J. L. GOUGH, J. P. GUTHRIE, and J. B. STOTHERS. J. Chem. Soc. Chem. Commun. 879 (1972).
12. (*a*) R. CRIEGEE. Angew. Chem. Int. Ed. Engl. **14**, 745 (1975); (*b*) P. S. BAILEY. Ozonation in organic chemistry. Academic Press, New York. Vol. 1. 1978; Vol. 2 1982; (*c*) R. L. KUCZKOWSKI. Acc. Chem. Res. **16**, 42 (1983); (*d*) W. A. PRYOR, D. GIAMALVA, and D. F. CHURCH. J. Am. Chem. Soc. **107**, 2793 (1985); (*e*) D. CREMER and C. W. BOCK. J. Am. Chem. Soc. **108**, 3375 (1986).
13. O. JEGER. Prog. Chem. Org. Nat. Prod. **7**, 1 (1950); Y. TANAHASHI, Y. MORIYAMA, T. TAKAHASHI, F. PATIL, J.-F. BIELLMANN, and G. OURISSON. Bull. Soc. Chim. Fr. 1670 (1966); T. TSUYUKI, T. HOSHINO, H. ITO, and T. TAKAHASHI. Bull. Soc. Chim. Fr. 2895 (1968); E. SUOKAS and T. HASE. Acta Chem. Scand. Ser. B: **B31**, 231 (1977).
14. J. C. KNIGHT, D. J. WILKINSON, and C. DJERASSI. J. Am. Chem. Soc. **88**, 790 (1966); R. TAKASAKI. Chem. Pharm. Bull. **10**, 445 (1962).
15. R. W. MURRAY. Acc. Chem. Res. **1**, 313 (1968).
16. (*a*) P. S. NANGIA and S. W. BENSON. J. Am. Chem. Soc. **102**, 3105 (1980); (*b*) R. D. Bach and G. J. WOLBER. J. Am. Chem. Soc. **106**, 1410 (1984); (*c*) D. CREMER and C. W. BOCK. J. Am. Chem. Soc. **108**, 3375 (1986), and references cited therein.
17. N. L. BAULD, J. A. THOMPSON, C. E. HUDSON, and P. S. BAILEY. J. Am. Chem. Soc. **90**, 1822 (1968).
18. V. RAMACHANDRAN and R. W. MURRAY. J. Am. Chem. Soc. **100**, 2197 (1978).
19. H. J. SHINE and R. H. SNYDER. J. Am. Chem. Soc. **80**, 3064 (1958).
20. P. S. BAILEY and D. A. LERDAL. J. Am. Chem. Soc. **100**, 5820 (1978), and references cited therein.
21. R. W. MURRAY and M. L. KAPLAN. J. Am. Chem. Soc. **90**, 537 (1968); **90**, 4161 (1968); A. NICKON and W. L. MENDELSON. J. Am. Chem. Soc. **87**, 3921 (1965).
22. N. J. TURRO. *In* Modern molecular photochemistry. Benjamin/Cummings Publ. Co., Menlo Park, CA. 1978. Chap. 14; G. O. SCHENCK. ANGEW. CHEM. **64**, 12 (1952).
23. J. E. FOX, A. I. SCOTT, and D. W. YOUNG. J.Chem. Soc. Perkin Trans. **1**, 799 (1972).
24. W. L. WATERS, A. J. ROLLIN, C. M. BARDWELL, J. A. SCHNEIDER, and T. W. AANERUD. J. Org. Chem. **41**, 889 (1976).
25. K. AOKI, M. KATO, M. SUZUKI, Y. HAYAKAWA, H. NAKAMURA, and K. YAMADA. J. Chem. Soc. Chem. Commun. 618 (1973).
26. L. F. FIESER, T. GOTO, and B. K. BHATTACHARYYA. J. Am. Chem. Soc. **82**, 1700 (1960).
27. W. J. RODEWALD and Z. BONCZA-TOMASZEWSKI. Tetrahedron Lett. **3**, 169 (1979).
28. M. TSUDA, E. J. PARISH, and G. J. SCHROEPFER. J. Org. Chem. **44**, 1282 (1979).
29. (*a*) D. H. R. BARTON, J. F. MCGHIE, and P. L. BATTEN. J. Chem. Soc. (C), 1033 (1970); (*b*) Z. PARYZEK and R. WYDRA. Bull. Acad. Polon. Sci. Ser. Sci. Chim. **26**, 591 (1978).
30. I. G. GUEST and B. A. MARPLES. J. Chem. Soc. (C), 1468 (1971).
31. C. W. SHOPPEE and J. C. COLL. J. Chem. Soc. (C), 2158 (1969).
32. C. S. BARNES. Aust. J. Chem. **11**, 546 (1958).
33. W. S. GOLDER and T. R. WATSON. J. Chem. Soc. Perkin Trans. **1**, 422 (1980).

Can. J. Chem. Downloaded from www.nrcresearchpress.com by 112.217.228.212 on 09/07/12
For personal use only.

The thermodynamics of zinc sulphide transport in hydrogen chloride by modified entrainment

PETER J. GARDNER AND PETER PANG

Royal Holloway and Bedford New College, University of London, Egham Hill, Egham, Surrey, TW20 0EX, U.K.

Received December 1, 1987

PETER J. GARDNER and PETER PANG. CAN. J. CHEM. **66**, 2137 (1988).

The equilibrium ZnS(c,sphalerite) + 2HCl(g) = $ZnCl_2$(g) + H_2S(g) was studied by modified entrainment in the temperature range 1023 to 1263 K and the free energy equation, ΔG^0/J mol^{-1} = (95060 ± 2700) − (38.7 ± 2.4)T, was obtained. A free energy equation for the corresponding equilibrium, ZnS(c,sphalerite) + 2HCl(g) = $ZnCl_2$(l) + H_2S(g), was derived using ancillary thermodynamic data, ΔG^0/J mol^{-1} = (−28340 ± 2800) + (85.6 ± 2.4)T, (638–978 K).

PETER J. GARDNER et PETER PANG. CAN. J. CHEM. **66**, 2137 (1988).

Opérant dans l'intervalle de température allant de 1023 à 1263 K et faisant appel à une méthode modifiée d'entraînement, on a étudié l'équilibre ZnS(c, sphalérite) + 2HCl(g) = $ZnCl_2$(g) + H_2S(g) et on a déterminé que l'équation d'énergie libre est la suivante : ΔG^0/J mol^{-1} = (95060 ± 2700) − (38,7 ± 2,4)T. Utilisant des données thermodynamiques accessoires, on a déterminé que l'équation d'énergie libre de l'équilibre correspondant, ZnS(c,sphalérite) + 2HCl(g) = $ZnCl_2$(l) + H_2S(g) est la suivante : ΔG^0/J mol^{-1} = (−28340 ± 2800) + (85,6 ± 2,4)T, (638–978 K).

[Traduit par la revue]

Can. J. Chem. Downloaded from www.nrcresearchpress.com by 196.1.178.254 on 09/07/12
For personal use only.

Introduction

Molten zinc chloride is a selective catalyst for the hydrocracking of both coal and heavy crude oil residues to produce gasoline in good yield (1). A major problem encountered in the commercial exploitation of the process is the steady accumulation of ZnS in the melt, the sulphur arising from heteroatoms in the feedstock. Several regeneration procedures have been proposed (2) including passing hydrogen chloride through the melt so regenerating the chloride via eq. [1]

[1] $\quad ZnS(c) + 2HCl(g) = ZnCl_2(l) + H_2S(g)$

Reliable data for the temperature variation of K_1 and hence the likely efficiency of this regeneration route are scarce. Britske and Kapustinskii (3) have measured K_1 directly at 565 and at 635 K using a closed tube reactor. Jona and Mandel (4) have studied the kinetics of the corresponding vapour transport reaction, [2], over a wide range of HCl pressures at one temperature, 1268 K.

[2] $\quad ZnS(c) + 2HCl(g) = ZnCl_2(g) + H_2S(g)$

Equilibrium [2] has been examined between 1023 and 1263 K by modified entrainment to yield K_2 as a function of temperature. These results when combined with free energy data for the vaporization of zinc chloride (5) yield a definitive free energy equation for [1] within the liquid range of zinc chloride, 591 to 1005 K.

Experimental

The modified entrainment ring has been described in detail (6–8). Briefly, the zinc sulphide was contained in a spherical fused silica capsule suspended on one arm of a recording microbalance. The capsule was positioned in the central region of a vertically-mounted tube furnace and the carrier gas (argon) mixed with the transporting gas (hydrogen chloride) passed downwards over the capsule. The orifice of the capsule is a capillary (ca. 20 mm long × 1 mm internal diameter) which acts as a diffusive resistance to the transporting gas diffusing in and the reaction products diffusing out. Temperature (to ±2 K) was measured with a calibrated Pt – 13% Rh/Pt thermocouple mounted axially immediately below the capsule. Two separate capsules were used with diffusive resistances (l/r^2; l = length, r = internal radius) of 6.699 × 10^4 m^{-1} and 6.006 × 10^4 m^{-1}. The experimentally-determined quantity is the rate of mass loss of ZnS from the capsule at a known temperature, $\dot{\omega}(T)$. Four doping ratios of hydrogen chloride in argon (between 0.0602 and 0.0968) were used and are quoted as pressure fractions ($p_{HCl}/(p_{Ar} + p_{HCl})$) determined from a ratio of flow rates of Ar and HCl from calibrated mass flow controllers reading in cm^3(stp) min^{-1}. The total flow rate (Ar + HCl) was ca. 100 cm^3(stp) min^{-1} and 145 data points were recorded from 1023 K ($\dot{\omega} \approx 3.1 \times 10^{-11}$ kg s^{-1}) to 1263 K ($\dot{\omega} \approx 1.2 \times 10^{-10}$ kg s^{-1}). The ZnS transition (sphalerite → wurtzite) temperature is 1293 ± 10 K (9).

Materials

Argon was purified by passage through a commercial rare gas purifier (Model RGP-4, BOC Ltd.) which includes a titanium getter operating at 700°C to remove O_2 and N_2, copper oxide at 450°C to remove H_2, hydrocarbons, and CO, and molecular sieves to remove CO_2 and H_2O. Hydrogen chloride (electronic grade, 99.99%, Air Products Ltd.) was dried by passage through columns containing anhydrous magnesium perchlorate. Hydrogen was purified in a palladium diffuser (model H28/1, Johnson Matthey Ltd.).

Zinc sulphide (Aldrich Chemical Co., Gold Label, 99.99%, batch 0301 JK), a finely-divided pale yellow polycrystalline material, was characterized by X-ray diffraction (XRD), spectrographic and elemental analyses. Spectrographic analysis showed < 25 ppm of metallic impurities. Batches of stock ZnS were pretreated in flowing Ar or H_2 for at least 24 h, quenched rapidly, and subdivided in a dry box for XRD and elemental analysis. Hydrogen was selected for pretreatment as it is produced in small quantities from H_2S decomposition during entrainment, and it has been suggested (10) that its presence depresses the sphalerite → wurtzite conversion temperature (1293 ± 10 K). Sample sizes and irradiation times for XRD were such that the level of discrimination between the phases was about 5%. The results are collected in Table 1. This evidence confirmed that the material examined by modified entrainment was stoichiometric and was 95+% sphalerite (or β).

Results and discussion

Reaction stoichiometry

The H_2S produced in reaction [2] is significantly dissociated (K_5(1200 K) ≈ 500) in the experimental temperature range (1023–1263 K). The H_2 from the dissociation participates in reductive sublimation of ZnS. Further, $ZnCl_2$ undergoes slight dimerization below 1200 K (5, 11–13). The dissociative sublimation (eq. [4]) is known to be congruent (14) and the concentration of molecular ZnS in the vapour in our temperature range is negligible (15). Also, there is insignificant contribution from S_n(g) ($n > 2$ or $n = 1$) in the gas phase in this temperature range (16). Consequently, the eqs. [2]–[5] were considered as

Printed in Canada / Imprimé au Canada

Can. J. Chem. Downloaded from www.nrcresearchpress.com by 196.1.178.254 on 09/07/12
For personal use only.

the participating equilibria during entrainment

[2] $ZnS(c, \beta) + 2HCl(g) = ZnCl_2(g) + H_2S(g)$

[3] $2ZnCl_2(g) = Zn_2Cl_4(g)$

[4] $ZnS(c, \beta) = Zn(g) + \frac{1}{2}S_2(g)$

[5] $H_2(g) + \frac{1}{2}S_2(g) = H_2S(g)$

Notice that the reductive sublimation referred to above arises from the combination of [4] and [5] so is not included explicitly. The experimental temperature range overlaps with the liquid range of Zn(693–1186 K). However, the partial pressure of Zn in the modified entrainment experiments (see Table A3) is several orders of magnitude less than the corresponding saturation vapour pressure of zinc (17) and consequently it is correct to write zinc as Zn(g) in equilibrium [4].

Assumptions

The central assumption of the modified entrainment method (MEM) is that the diffusive resistance offered by the capillary above the sample is sufficiently high so that equilibrium partial pressures of all the gaseous species in [2] to [5] obtain within the capsule (6, 18). This condition is met provided the surface area of the condensed phase (ZnS here) is large compared with the cross-sectional area of the channel and that unfavourable surface kinetic effects do not intervene (18). Unfavourable surface kinetics may arise from (*i*) physical effects, e.g. a surface film of oxide may form on a liquid metal so hindering its vaporization or (*ii*) structural effects, e.g. the vaporization coefficient for *P*(red) is exceptionally small ($\approx 10^{-8}$) due to the structural reorganization in the solid → gas transition (8, 19). Liquids, most metals, and isotropically bonded solids have vaporization coefficients close to unity (20). Kinetic inhibition for reaction [2] at low partial pressures of HCl has been suggested (4) but this was in a closed tube reactor for which the diffusive resistance is five times smaller than in the MEM experiments. The equilibrium assumption is usually verified experimentally, as in this work, by conducting experiments with capsules having different channel dimensions and showing the results are self-consistent.

Equilibrium constants are written in terms of partial pressures and not fugacities. The standard state pressure is 101325 N m^{-2}. Non-ideality corrections are rarely available for the gaseous components of heterogeneous equilibria and such data that do exist suggest that at ca. 1000 K and 1 atm pressure, the correction will be small. For example, for $H_2O(g)$ at 1300 K and 10000 atm the non-ideality correction is ca. 10% (21).

The partial pressure (p_i^0) of any species depends on its flux (j_i) and diffusivity (D_i) in the channel and temperature (22).

$$[6] \quad \frac{p_i^0}{P} = \frac{j_i}{J} - \left[\frac{j_i}{J} - \frac{p_i^l}{P}\right]e^{-\xi_i}$$

$$[7] \quad \xi_i = \frac{JRTl}{D_iP}$$

In [6] and [7], J is the total flux, P is the total pressure (about 3 Torr above ambient pressure), p_i^l is the partial pressure of i at the open end of the channel, and D_i is a multicomponent diffusion coefficient of i into the mixture of the other species. The application of this equation and the estimation of the diffusion coefficients is outlined in the Appendix.

Ancillary data

In order to derive K_2 (or ΔG_2^0) and its temperature coefficient from the flux equations outlined in the Appendix it is necessary to know corresponding results for K_3, K_4, and K_5. Zinc chloride vaporization has been studied (5) by MEM and the results interpreted in terms of monomeric and dimeric species in the vapour. The free energy expression [8] was derived.

$$[8] \quad \Delta G_3^0/\text{J mol}^{-1} = -(162000 \pm 8000) + (202 \pm 11)T \qquad 638\text{–}978 \text{ K}$$

Although the temperature ranges of the zinc chloride work and these studies are not coincident, the zinc chloride dimer makes little contribution to the transport above 1000 K (see values of β in Table A1 and partial pressures in Table A3) so the non-coincidence is not a source of serious error. The dissociative sublimation of sphalerite (eq. [4]) has also been studied (23) by modified entrainment and eq. [9] obtained

$$[9] \quad \Delta G_4^0/\text{J mol}^{-1} = (374200 \pm 1100) - (190.4 \pm 1.0)T \qquad 1010\text{–}1270 \text{ K}$$

The free energies from this equation are within 2% of the free energies obtained from a recent independent study of [4] using a high temperature solid electrolyte cell (24). The thermodynamic parameters for the components in equilibrium [5] have been critically assessed by the compilers of the JANAF tables (25) and values of ΔG_5^0 were calculated at 100 K intervals from 900 to 1500 K using $\Delta G^0(T) = \Delta H_{298}^0 - T\Delta(\text{fef})$ where fef = $-(G_T^0 - H_{298}^0)/T$ and with the JANAF results for fef and ΔH_{298}^0. Regression of $\Delta G^0(T)$ with T gave

$$[10] \quad \Delta G_5^0/\text{J mol}^{-1} = -(90333 \pm 110) + (49.3 \pm 0.1)T \qquad 900\text{–}1500 \text{ K}$$

A recommended expression (26) for ΔG_5^0 over a much wider temperature range (298–1750 K) gave values for ΔG_5^0 within 0.3% of corresponding values from [10] in the experimental temperature range.

MEM results

The results from the MEM experiments with different channel sizes were first processed separately yielding two regression lines of the form $\Delta G_2^0 = a - bT$. Analysis of covariance showed there was no significant probability that the input data arose from different populations; this test confirms that equilibrium partial pressures obtain within the capsules. The results (145 data pairs, $\dot{\omega}(T)$) from the two different capsules and four different HCl doping levels (see Experimental) were then pooled and eq. [11] obtained by regression

$$[11] \quad \Delta G_2^0/\text{J mol}^{-1} = (95060 \pm 2700) - (38.7 \pm 2.4)T \qquad 1023\text{–}1263 \text{ K}$$

The uncertainty intervals in eqs. [8]–[11] are standard deviations of the regression coefficients. The equilibrium of central importance to this study is eq. [1]. The coefficients of eq. [11] were scaled to refer to 808 K (the mean temperature of the $ZnCl_2$ vaporization study, see below) using C_p results for HCl and H_2S from JANAF tables (25), for $ZnCl_2(g)$ from Givan and Loewenschuss (27) and for ZnS(β) from Pankratz and King (28)

TABLE 1. Zinc sulphide pretreatment regimes, XRD results and elemental analyses

Pretreatment	β(XRD)	α(XRD)	Zn:S ratio
973 K/24 h/H_2	Dominant	<5%	0.998±0.002
1073 K/24 h/H_2	Dominant	<5%	—
1173 K/24 h/H_2	Dominant	≈5%	0.999±0.002
1173 K/32 days/Ar + 1173 K/10 min/H_2	Dominant	5–10%	—

TABLE 2. Comparison of K_1 calculated from eq. [15] with literature results

Source	K (565 K)	K (635 K)
Bristske *et al.* (3)	0.072	0.021
This work	0.014±0.008	0.0072±0.0041

and Stuve (29). Thus,

$$[12] \quad \Delta G_2^0/\text{J mol}^{-1} = (98260 \pm 2700) - (42.0 \pm 2.4)T \quad \langle 808\ \text{K}\rangle$$

An independent study (5) of zinc chloride vaporization (eq. [13]) by modified entrainment in the range 638–978 K gave eq. [14].

$$[13] \quad ZnCl_2(l) = ZnCl_2(g)$$

$$[14] \quad \Delta G_{13}^0/\text{J mol}^{-1} = (126600 \pm 500) - (127.6 \pm 0.5)T \quad 638\text{–}978\ \text{K}$$

The mean temperature for the zinc chloride vaporization study was 808 K and combining eqs. [12] and [14] gives

$$[15] \quad \Delta G_1^0/\text{J mol}^{-1} = (-28340 \pm 2800) + (85.6 \pm 2.4)T \quad \langle 808\ \text{K}\rangle$$

which is valid over a temperature range of 638–978 K which is within the liquid range of $ZnCl_2$ (591–1005 K). Equilibrium constants calculated from eq. [15] are compared in Table 2 with the literature results of Britske and Kapustinskii (3). Although the proportional error in our K_1 is ca. 60%, the values are significantly different from those of Britske *et al.*

Third law and second law treatments

The free energy values for eq. [2] were analysed by the third law method. Free energy functions were taken from the literature (25, 27–29). Using values of $(H_{1143}^0 - H_{298}^0)$ from these same sources, the corresponding second law estimate of ΔH_{298}^0 was obtained from ΔH_2^0 (1143 K) = +95.1 ± 2.7 kJ mol^{-1} (from eq. [11]):

$$\Delta H_2^0(298\ \text{K}), \text{ second law} = 103.9 \pm 5.4\ \text{kJ mol}^{-1}$$

$$\Delta H_2^0(298\ \text{K}), \text{ third law} = 100.8 \pm 0.4\ \text{kJ mol}^{-1}$$

(uncertainty intervals in these and subsequent thermodynamic results are ± 2 (standard deviations of the mean)). The contribution to ΔH_2^0 from the $T\Delta$(fef) term in the third law analysis is ca. 50% and the coincidence between the second and third law results suggests the free energy functions for the components in eq. [2] are in good order.

Acknowledgements

The authors are indebted to Mr. K. Knight (British Petroleum plc) for X-ray diffraction studies, to Mr. S. Preston assistance with elemental analyses, to Drs. K. Holder, J. Counsell, and D. Clark (BP plc) for helpful discussion and to BP plc for financial support.

1. R. T. STRUCK and C. W. ZIELKE. Fuel, **60**, 795 (1981).
2. C. W. ZIELKE and W. A. ROSENHOOVER. U.S. Patent 4424111 (1984).
3. E. V. BRITSKE and A. F. KAPUSTINSKII. Zhur. fiz. Khim. **5**, 77 (1934).
4. F. JONA and G. MANDEL. J. Chem. Phys. **38**, 346 (1963); F. JONA. J. Phys. Chem. Solids. **23**, 1719 (1962).
5. P. J. GARDNER and P. PANG. Can. J. Chem. **66**, 566 (1988).
6. D. BATTAT, M. M. FAKTOR, I. GARRETT, and R. H. MOSS. J. Chem. Soc. Faraday I, **70**, 2267 (1974).
7. A. FINCH, P. J. GARDNER, E. TARBOX, and S. YARDLEY. J. Chem. Soc. Faraday I, **75**, 545 (1979).
8. B. DE LARGY, A. FINCH, P. J. GARDNER, and N. KELL. J. Chem. Soc. Faraday I, **79**, 383 (1983).
9. V. G. HILL. Can. Miner. **6**, 234 (1958).
10. S. D. SCOTT and H. L. BARNES. Geochim. Cosmochim. Acta, **36**, 1275 (1972).
11. F. J. KENESHEA and D. CUBICCIOTTI. J. Chem. Phys. **40**, 191 (1964).
12. O. G. POLYACHENOK, O. N. KOMSHILOVA, and G. A. TSIRMAN. Russ. J. Inorg. Chem. **14**, 912 (1969).
13. L. D. POLYACHENOK, K. NAZAROV, and O. G. POLYACHENOK. Russ. J. Phys. Chem. **50**, 1271 (1976).
14. G. DE MARIA, P. GOLDFINGER, L. MALASPINA, and V. PIACENTE. Trans. Faraday Soc. **61**, 2146 (1965).
15. P. GOLDFINGER and M. JEUNEHOMME. Trans. Faraday Soc. **59**, 2851 (1963).
16. M. GRADE and W. HIRSCHWALD. Z. Anorg. Allg. Chem. **460**, 106 (1980).
17. A. N. NESMEYANOV. Vapour pressure of the chemical elements. Elsevier. 1963.
18. M. M. FAKTOR, I. GARRETT, and M. H. LYONS. J. Cryst. Growth, **46**, 21 (1979).
19. G. M. ROSENBLATT. *In* Treatise on solid state chemistry. *Edited by* N. B. Hannay. Plenum Press, New York. 6A, 1976.
20. G. M. POUND. J. Phys. Chem. Ref. Data, **1**, 135 (1972).
21. K. SCHWERDTFEGER and E. T. TURKDOGAN. Techniques of metal research. Vol. IV. *Edited by* R. A. Rapp. Wiley. 1970. p. 321.
22. D. BATTAT, M. M. FAKTOR, I. GARRETT, and R. H. MOSS. J. Chem. Soc. Faraday I, **70**, 2302 (1974).
23. P. J. GARDNER and P. PANG. J. Chem. Soc. Faraday Transactions I. **84**, 1879 (1988).
24. S. C. SCHAEFER and N. A. GOKCEN. High Temp. Sci. **15**, 225 (1982).
25. D. R. STULL and H. PROPHET. JANAF Thermochemical Tables, NSRDS-NBS 37, Catalog No. C13.48:37, U.S. Govt. Printing Office, Washington, D.C., 1971 and supplements, J. Phys. Chem. Ref. Data, **3**, 311 (1974); **4**, 1 (1975); **7**, 793 (1978); **11**, 695 (1982).
26. O. KUBASCHEWSKI and C. B. ALCOCK. Metallurgical thermochemistry. Pergamon Press. 1979.
27. A. GIVAN and A. LOEWENSCHUSS. J. Chem. Phys. **68**, 2228 (1978).
28. L. B. PANKRATZ and E. G. KING. U.S. Bureau of Mines Reports of Investigation 6708 (1965).
29. J. M. STUVE. U.S. Bureau of Mines Report of Investigation 7940 (1974).
30. E. L. CUSSLER. Multicomponent diffusion. Elsevier. 1976.
31. D. BATTAT, M. M. FAKTOR, I. GARRETT, and R. H. MOSS. J. Chem. Soc. Faraday I, **70**, 2293 (1974).
32. P. J. GARDNER and P. PANG. Unpublished work.
33. T. R. MARRERO and E. A. MASON. J. Phys. Chem. Ref. Data, **1**, 3 (1972).
34. S. CHAPMAN and T. G. COWLING. The mathematical theory of non-uniform gases. Cambridge Univ. Press. 1960.
35. R. C. REID and T. K. SHERWOOD. The properties of gases and liquids. McGraw-Hill. 1966.
36. R. A. SVEHLA. NASA Tech. Rept. R-132, Lewis Research Centre, Cleveland, OH, U.S.A. 1962.
37. E. A. MASON and B. KRONSTADT. J. Chem. Ed. **44**, 740 (1967).

Appendix

The partial pressures of the gaseous species in eqs. [2]–[5] are calculated from eqs. [6] and [7]. As four interdependent equilibria are involved, three coupling parameters (β, δ, and θ) are defined,

$$[A1] \quad \beta = \frac{j(Zn_2Cl_4)}{j(ZnCl_2)}; \delta = \frac{j(Zn)}{j(S_2)}; \theta = \frac{j(H_2)}{j(H_2S)}$$

Can. J. Chem. Downloaded from www.nrcresearchpress.com by 196.1.178.254 on 09/07/12
For personal use only.

TABLE A1. Typical values of the coupling parameters (eq. [A1])

T/K	$10^5\beta$	θ	$10^4\delta$
1024	1.14	1.28	0.336
1159	0.278	2.60	11.5
1252	0.119	4.03	97.8

where j is the flux of the species in the channel. The net elemental fluxes are written in terms of the fluxes of the participating species, e.g.

[A2] $\text{Flux(Zn)} = j(ZnCl_2) + 2j(Zn_2Cl_4) + j(Zn)$

Combining the elemental flux equations with mass conservation equations permits the ratio of any individual flux to the total flux to be written in terms of a function (F_i) of the coupling parameters (22)

[A3] $$\frac{j_i}{J} = F_i(\beta, \theta, \delta)$$

There is mass conservation of both hydrogen and chlorine in this system in that there is zero net flux of each. For example, for hydrogen,

[A4] $j(HCl) + 2j(H_2S) + 2j(H_2) = 0$

For HCl in eq. [6],

[A5] $$\frac{p_i'}{P} = \epsilon$$

where ϵ is the pressure fraction of the transporting gas (HCl) in the carrier gas (Ar) plus HCl mixture — see Experimental. For all other species the ratio p_i'/P is zero as the carrier gas flushes these species away from the open end of the channel. The exponential term in [6] is expanded and truncated at O(2) — the error in this approximation is $\leq 5\%$ when the transport function, $\xi_i < 0.1$. Hence

[A6] $$\frac{p_i^0}{P} \approx \frac{j_i}{J}\xi_i$$

and

[A7] $$\frac{p^0(HCl)}{P} \approx \epsilon + \frac{j(HCl)}{J}\xi_{HCl}$$

assuming $\epsilon\xi_{HCl} \ll 1$.

The transport functions. (eq. [7]) are written in terms of the experimental parameter, $\dot{\omega}$(ZnS), and take the form

[A8] $$\xi_i = \frac{\dot{\omega}RTl}{AD_iMP}G(\beta, \theta, \delta)$$

where G is a universal function of the coupling parameters, M is the molecular mass of ZnS, and A is the cross-sectional area of the channel. Combining eqs. [A6] to [A8], the partial pressures are formed

[A9] $$p_i^0 = \frac{\dot{\omega}RTl}{AD_iM}F_iG \qquad (i \neq HCl)$$

[A10] $$p_{HCl}^0 = P\epsilon - \frac{\dot{\omega}RTl}{AD_{HCl}M}F_{HCl}G$$

Next, the equilibrium constants K_2 to K_5 are written in terms of the partial pressures and K_3 to K_5 are equated to analytical expressions taken from the literature (see Results and discussion — ancillary data). The resulting expressions for K_3 to K_5 are manipulated so as to solve for the three unknown coupling parameters (θ, δ, and β) which are then evaluated at each experimental temperature. These values are then back-substituted in the equation for K_2.

As more than two gaseous components are present in the channel at any time the effects of multicomponent diffusion (30) are taken into account. A second order treatment (31) of this effect permits the multicomponent diffusion coefficients (D_i) to be written in terms of the corresponding binary diffusion coefficient ($\mathcal{D}_{ij}$) when j is the majority component (in this work, Ar),

[A11] $$D_i = \frac{\mathcal{D}_{iAr}}{\gamma_i} = \frac{\mathcal{D}_{iAr}}{(1 + A_i\epsilon + B_i\xi_i)}$$

where A_i and B_i are functions of j_i, J, and $\mathcal{D}_{ij}$. Notice that γ_i in [A11] contains Σ_{j_i} which itself is a function of D_i. Hence a

TABLE A2. Typical values for the multicomponent diffusion correction coefficients (eq. [A11])

T/K	$\gamma[ZnCl_2]$	$\gamma[Zn_2Cl_4]$	γ[HCl]	$\gamma[H_2]$	γ[Zn]	$\gamma[S_2]$	$\gamma[H_2S]$
1024	0.9974	0.9969	0.9124	0.9989	0.9978	0.9981	0.9983
1159	0.9975	0.9965	0.9525	1.0010	0.9985	0.9993	0.9997
1252	0.9977	0.9959	0.9681	1.0028	0.9991	1.0002	1.0009

TABLE A3. Some equilibrium partial pressures (eqs. [A9] and [A10])

TK	$p^0(ZnCl_2)$ (N m^{-2})	$p^0(Zn_2Cl_4)$ (N m^{-2})	p^0(HCl) (N m^{-2})	$p^0(H_2)$ (N m^{-2})	p^0(Zn) (N m^{-2})	$p^0(S_2)$ (N m^{-2})	$p^0(H_2S)$ (N m^{-2})
1024	359.0	0.0066	5750.0	28.9	0.0022	106.0	101.0
1052	434.0	0.0058	5610.0	37.6	0.0064	138.0	111.0
1117	626.0	0.0043	5360.0	63.0	0.0598	230.0	133.0
1159	800.0	0.0035	5180.0	84.2	0.222	307.0	145.0
1222	1050.0	0.0025	4870.0	120.0	1.37	436.0	152.0
1252	1182.0	0.0022	4700.0	139.0	3.07	508.0	154.0

Can. J. Chem. Downloaded from www.nrcresearchpress.com by 196.1.178.254 on 09/07/12
For personal use only.

TABLE A4. Binary diffusion coefficients at 1 atm pressure between 1020 and 1450 K; parameters for eq. [A12]

i	$10^6\,\mathcal{D}^0_{i\mathrm{Ar}}/\mathrm{m}^2\,\mathrm{s}^{-1}$	$1+s$
$ZnCl_2$	8.624	1.760
Zn_2Cl_4	6.793	1.761
HCl	15.47	1.686
H_2	68.83	1.657
Zn	12.42[a]	1.793[a]
S_2	8.608	1.720
H_2S	14.80	1.682

[a]Experimental results (32).

reiterative procedure is employed, initializing all γ_i to unity and terminating when successive values of γ_i differ by less than 1 in 10^4. Some typical values of the coupling parameters, the multicomponent diffusion correction coefficients and partial pressures are collected in Table A1 to A3. All transport functions (ξ_i) were less than 0.007, so validating the exponential approximation ([A6] and [A7]).

Seven binary diffusion coefficients ($\mathcal{D}_{i\mathrm{Ar}}$) and their variation with temperature are required to complete the calculation (eq. [A11]). Experimental data are available for the Zn/Ar (32) and H_2/Ar (33) systems only. Kinetic theory for binary diffusion is well-established (34) and binary diffusion coefficients may be estimated (35) to a precision of ca. 7% if Lennard–Jones (L–J) potential parameters are available; such parameters exist (35) for Ar, H_2S, HCl, and H_2. Svehla's estimates (36) for L–J parameters were used for S_2. For $ZnCl_2$ and Zn_2Cl_4 a scaling procedure recommended by Mason and Kronstadt (37) was used. This requires a system of structural similarity (Ar/CO_2 was chosen) for which reliable experimental results are available (33). Estimates obtained in this manner have proved satisfactory in a study of zinc chloride vaporization by the MEM (5). Six estimated binary diffusivities each with a possible maximum error of $\approx 7\%$ are not the serious source of error as would initially appear. The coefficients usually occur in ratios and error cancellation is likely. The estimated values were regressed to equations of the form

$$[\mathrm{A12}]\quad \mathcal{D}_{i\mathrm{Ar}} = \mathcal{D}^0_{i\mathrm{Ar}} \left[\frac{T}{273.15}\right]^{1+s}$$

at 1 atm pressure over the temperature range 1020 to 1450 K; the constants for [A12] are collected in Table A4.

Can. J. Chem. Downloaded from www.nrcresearchpress.com by 196.1.178.254 on 09/07/12
For personal use only.

Étude expérimentale et modélisation théorique de la décomposition du radical éthyle

YVES SIMON, JEAN FRANÇOIS FOUCAUT ET GÉRARD SCACCHI[1]

Département de chimie physique des réactions, Unité associée n° 328 du Centre national de la recherche scientifique, Institut-national polytechnique de Lorraine – École nationale supérieure des industries chimiques, 1, rue Grandville, 54042 Nancy CEDEX, France

Reçu le 8 février 1988

YVES SIMON, JEAN FRANÇOIS FOUCAUT et GÉRARD SCACCHI. Can. J. Chem. **66**, 2142 (1988).

Une étude bibliographique sur la décomposition thermique du radical éthyle montre une assez grande dispersion des paramètres cinétiques pour les conditions limites haute et basse pression. C'est la raison pour laquelle nous avons repris une étude de ce processus élémentaire dans la pyrolyse de l'éthane, vers 800 K, en réacteur fermé et pour des pressions d'hydrocarbure pur comprises entre 1 et 300 Torr. Les résultats expérimentaux sont traités grâce à trois approches théoriques : la théorie RRKM et deux méthodes proposées par Troe. On obtient, chaque fois, un excellent ajustement des courbes théoriques aux points expérimentaux, ainsi que des expressions d'Arrhenius pour les constantes de vitesse à haute et basse pression. Une analyse critique détaillée de nos propres résultats et de ceux de la littérature montre qu'il n'existe pas encore une très bonne compatibilité entre les travaux les plus récents sur ce sujet. Néanmoins il est possible de donner deux expressions d'Arrhenius pour les constantes limite haute et basse pression qui représentent un bon compromis entre les résultats des divers auteurs :

$$k_\infty(s^{-1}) = 10^{13,2} \exp\left(-\frac{38\,000}{RT}\right)$$

$$k_0(cm^3 \cdot mol^{-1} \cdot s^{-1}) = 10^{18,3} \exp\left(-\frac{34\,900}{RT}\right)$$

YVES SIMON, JEAN FRANÇOIS FOUCAUT, and GÉRARD SCACCHI. Can. J. Chem. **66**, 2142 (1988).

A bibliographical study of the thermal decomposition of the ethyl radical shows that the kinetic parameters for the upper and lower limits of the pressure are rather scattered. This observation explains why we have carried out a new study of this elementary process in the pyrolysis of ethane, around 800 K, in a closed vessel and at pressures of the hydrocarbon varying from 1 to 300 Torr. The experimental results have been treated according to three theoretical approaches: the RRKM theory and two methods proposed by Troe. In each case, an excellent fit of the theoretical curves with the experimental data is obtained, as well as Arrhenius expressions for the reaction rate constants at high and low pressures. A detailed critical analysis of our results as well as those found in the literature shows that as yet there is no good agreement between recent studies on this subject. However, it is possible to present two Arrhenius expressions for the reaction rate constants at high and low pressures; these expressions represent a good compromise for the results obtained by various authors:

$$k_\infty(s^{-1}) = 10^{13,2} \exp\left(-\frac{38\,000}{RT}\right)$$

$$k_0(cm^3 \cdot mol^{-1} \cdot s^{-1}) = 10^{18,3} \exp\left(-\frac{34\,900}{RT}\right)$$

[Journal translation]

Introduction

La décomposition thermique du radical éthyle en éthylène et hydrogène atomique est une réaction élémentaire omniprésente dans les réactions en phase gazeuse d'hydrocarbures : pyrolyses, oxydations, chlorations, etc... Une bonne connaissance des paramètres thermochimiques et cinétiques de ce processus est donc nécessaire si l'on désire modéliser les réactions complexes précédentes. C'est la raison pour laquelle un certain nombre d'études expérimentales ont été consacrées, en particulier, à la variation de la constante de vitesse du processus avec la pression. Ce phénomène («fall-off»), observé d'abord dans la pyrolyse du butane (1), a été confirmé par des travaux sur la pyrolyse (2) et sur la décomposition photosensibilisée par le mercure (3) de l'éthane, ceci à des températures inférieures à 1000 K. Cette même réaction thermique a été étudiée plus récemment en tube à onde de choc entre 1200 et 1600 K (4) et vers 1000 K dans un réacteur «sans paroi» (5). Les différents auteurs de ces travaux proposent des expressions d'Arrhenius pour la constante de vitesse limite à haute pression (et parfois pour la constante bimoléculaire, à très basse pression) en utilisant des méthodes d'extrapolation ou de simulation théorique variées. On observe une assez grande dispersion des paramètres cinétiques et c'est la raison pour laquelle nous avons repris une étude expérimentale de la pyrolyse de l'éthane vers 800 K, en réacteur fermé.[2]

Pendant ce travail deux travaux importants, l'un sur le processus qui nous intéresse (7), l'autre sur le processus inverse (8, 9), ont été menés à bien. Une comparaison détaillée de ces nouveaux résultats et de ceux de notre étude sera présentée à la fin du présent article.

Conditions expérimentales

La pyrolyse de l'éthane a été étudiée en réacteur fermé, isotherme, à volume constant. L'éthane utilisé a été préparé par la Société l'Air Liquide. Il contient moins de 10 ppm d'éthylène et moins de 1 ppm d'oxygène. Par suite de la grande sensibilité de la réaction aux traces d'oxygène (10, 11), nous avons pris soin de dégazer soigneusement

1. Auteur à qui adresser toute correspondance.

2. Ce travail a été résumé dans le mémoire de Thèse de Doctorat de Troisième Cycle présenté par l'un d'entre nous (Y.S.) en mai 1986 à Nancy (6). Les principaux résultats ont fait l'objet d'une communication-poster au «IXth International Symposium on Gas Kinetics», Bordeaux (France), 20–25 juillet 1986.

Printed in Canada / Imprimé au Canada

Can. J. Chem. Downloaded from www.nrcresearchpress.com by 196.1.178.254 on 09/07/12
For personal use only.

Can. J. Chem. Downloaded from www.nrcresearchpress.com by 196.1.178.254 on 09/07/12
For personal use only.

le réactif avant chaque expérience par piégeage dans l'air liquide et pompage. Pour la même raison toute l'installation était équipée en robinets à soufflets métalliques, étanches à l'air. Il a été observé (12–15) que la décomposition thermique de l'éthane était sensible aux effets de parois, en particulier dans des réacteurs en silice. On pense (12, 14–16) que ce phénomène est dû aux terminaisons hétérogènes d'atomes d'hydrogène aux parois. Pour limiter l'importance de ce facteur nous avons choisi de pyrolyser l'éthane dans un réacteur en «Pyrex» où les effets de parois et les irreproductibilités sont moindres qu'avec la silice (15), de rapport surface/volume le plus faible possible. Un volume de un litre nous a paru un bon compromis entre un faible s/v (0,48 cm^{-1}) et une bonne homogénéité de température à l'intérieur du réacteur (moins facile à obtenir avec un réacteur plus gros). Les parois du réacteur ont été, de plus, traitées successivement à la soude puis à l'acide nitrique (17) pour diminuer encore ces effets perturbateurs.

L'utilisation du Pyrex à la place de la silice a limité la température maximale d'étude vers 540°C (813 K). La mesure du méthane, produit de transfert en faibles quantités, a imposé la température plancher vers 520°C (793 K). Le plus grand soin a été apporté au contrôle et à la mesure de la température. L'enregistrement continu de ce paramètre n'a jamais montré des variations de plus de 0,1 degré, ce qui correspond à une modification de l'avancement de 0,6% maximum.

Pour les raisons précédentes, nous avons donc mené à bien une étude de la pyrolyse de l'éthane entre 793 et 813 K (4 températures) et pour 13 pressions initiales d'éthane pur, comprises entre 1 et 300 Torr (1 Torr = 101 325/760 Pa). Les produits de la réaction, en particulier le méthane et l'éthylène, ont été suivis par chromatographie en phase gazeuse (colonne de 1,5 m de Carbo Sieve 100/120 mesh, à 135°C).

Principe de la mesure de la constante de vitesse et résultats expérimentaux

Il est généralement bien admis que la pyrolyse de l'éthane, vers 800 K, et à très faible avancement, relève d'un mécanisme radicalaire en chaînes (18) :

[1] $C_2H_6(+M) \rightarrow 2CH_3\cdot(+M)$

[x] $\cdot CH_3 + C_2H_6 \rightarrow CH_4 + \cdot C_2H_5$

[2] $C_2H_5\cdot(+M) \rightarrow C_2H_4 + H\cdot(+M)$

[3] $H\cdot + C_2H_6 \rightarrow H_2 + C_2H_5\cdot$

[4] $2C_2H_5\cdot \rightarrow n C_4H_{10}$ ou $C_2H_4 + C_2H_6$

On déduit de ce mécanisme les relations suivantes :

[5] vitesse d'amorçage = vitesse de terminaison :

$$k_1(C_2H_6)_0 = k_4(C_2H_5\cdot)^2$$

[6] vitesse initiale de production de C_2H_4 :

$$r^0_{C_2H_4} = k_2(C_2H_5\cdot)$$

[7] vitesse initiale de production de CH_4 : $r^0_{CH_4} = 2k_1(C_2H_6)_0$

Ces expressions amènent les commentaires suivants :

L'expression [5] suppose que l'unique processus de terminaison est [4]. Une étude détaillée (6) des rapports $(H\cdot)/(C_2H_5\cdot)$ et $(CH_3\cdot)/(C_2H_5\cdot)$, s'appuyant sur nos propres résultats et sur ceux de Pacey et Purnell (19), montre que les vitesses des processus de terminaison en $H\cdot + C_2H_5\cdot$, $2CH_3\cdot(+M)$ ou $H\cdot + CH_3\cdot(+M)$ sont toujours négligeables devant celle de [4]. En revanche, à très basse pression (1 Torr) il se peut que le processus

[8] $CH_3\cdot + C_2H_5\cdot \rightarrow C_3H_8$ ou $CH_4 + C_2H_4$

représente 3 ou 4% des terminaisons.

La relation [6] n'est correcte que si C_2H_4 provenant de [4] ou de [8] est négligeable devant C_2H_4 venant de [2], c'est-à-dire si les chaînes sont suffisamment longues. L'expérience (6) montre que la longueur de chaîne n'est jamais inférieure à 120 dans tout le domaine de pression et température exploré, ce qui justifie [6].

La relation [7] suppose que les radicaux $CH_3\cdot$ sont essentiellement produits par l'amorçage [1] et consommés par le transfert [x]. Là aussi une étude détaillée (6), utilisant nos propres résultats et des constantes de vitesse de la littérature, permet de montrer que les processus $H\cdot + C_2H_6 \rightarrow CH_4 + CH_3\cdot$ et $H\cdot + C_2H_5\cdot \rightarrow 2CH_3\cdot$ sont, dans tout le domaine expérimental couvert, négligeables devant l'amorçage [1]. Les processus : $CH_3\cdot + H\cdot(+M) \rightarrow CH_4(+M)$ et $2CH_3\cdot(+M) \rightarrow C_2H_6(+M)$ qui tendent à consommer des $CH_3\cdot$ sont également d'importance négligeable devant le transfert [x]. En revanche, comme il a été signalé plus haut, le processus [8] peut intervenir, très légèrement, à très basse pression pour concurrencer [x].

Des trois relations [5], [6] et [7] on tire :

[9] $$k_2 = (2k_4)^{1/2} r^0_{C_2H_4} (r^0_{CH_4})^{-1/2}$$

Cette expression est valable dans tout le domaine de pression et de température, à l'exception peut-être de la pression P_0 = 1 Torr. Il faudrait alors remplacer [9] par :

[10] $$k_2 = (2k_4)^{1/2} r^0_{C_2H_4} (r^0_{CH_4} - r_8)^{-1/2}$$

Si [8] représente environ 4% des terminaisons, donc 2% de $r^0_{CH_4}$, on voit que la correction sur k_2 est extrêmement faible, de l'ordre de grandeur des erreurs expérimentales sur les vitesses initiales.

En revanche il n'est pas possible de savoir quelle est l'importance et quelles sont les conséquences d'un processus de terminaison hétérogène du type :

[11] $H\cdot \rightarrow$ parois

signalé plus haut.

Vers 800 K et $P_0 \simeq 50$ Torr il a été montré (10, 15) que, dans un réacteur en Pyrex vide, [11] était complètement négligeable devant [4] mais ce travail n'a pas été fait pour P_0 = 1 Torr. Le fait que les courbes de formation de CH_4 et C_2H_4 pour P_0 = 1 Torr soient parfaitement régulières et que nous n'ayons pas observé d'irreproductibilité semble montrer que même à cette faible pression on peut négliger [11]. Dans son dernier article, Trenwith (7) pense, au contraire, que la variation qu'il observe du rapport dismutation/combinaison du processus [8] avec la pression ne peut s'expliquer que par la participation de [11]. Peut-être la nature des parois (silice) de son réacteur est-elle à l'origine du phénomène?

La figure 1 montre qu'à 813 K, les courbes de formation d'éthylène sont des fonctions linéaires du temps, à faible avancement (toujours inférieur à 1%). À plus fort avancement la courbure vers le bas deviendrait visible. Aux trois autres températures (793, 801 et 807 K) il en est de même. Seules les courbes correspondant aux deux pressions extrêmes sont montrées. Les pressions intermédiaires conduisent également à des droites. Les vitesses initiales $r^0_{C_2H_4}$ sont ainsi déterminées avec grande précision. Les courbes de formation de méthane (fig. 2) sont linéaires à très faible avancement mais on note, pour P_0 = 300 Torr, l'allure autoaccélérée au-delà de t = 2 min ($\simeq$0,2% d'avancement), due à la formation de méthane secondaire (20). Ce phénomène, visible uniquement à haute pression dans notre échelle de temps, ne perturbe pas la mesure des vitesses initiales $r^0_{CH_4}$.

En adoptant $k_4 \simeq 10^{13}$ $cm^3\cdot mol^{-1}\cdot s^{-1}$ (21–23), la relation [9] fournit les valeurs de k_2 (s^{-1}) du tableau 1.

Can. J. Chem. Downloaded from www.nrcresearchpress.com by 196.1.178.254 on 09/07/12
For personal use only.

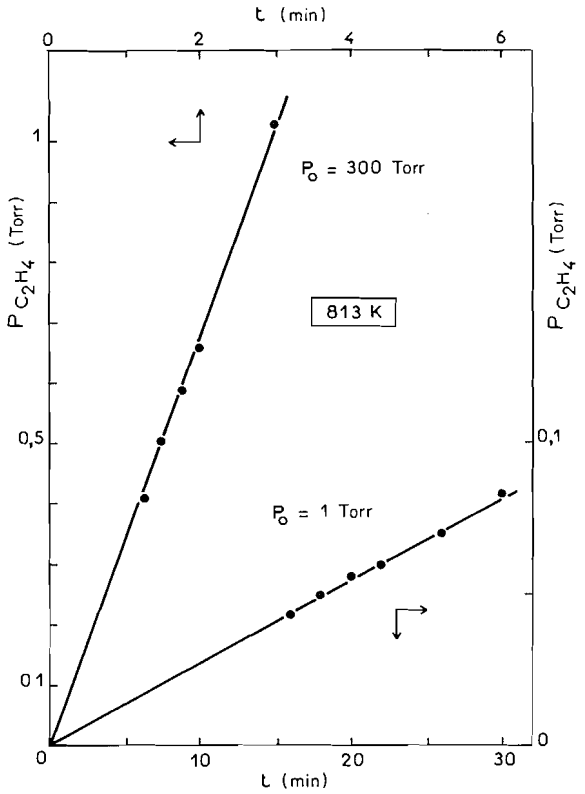

FIG. 1. Courbes de formation d'éthylène pour les deux pressions extrêmes d'éthane. Température de réaction : 813 K.

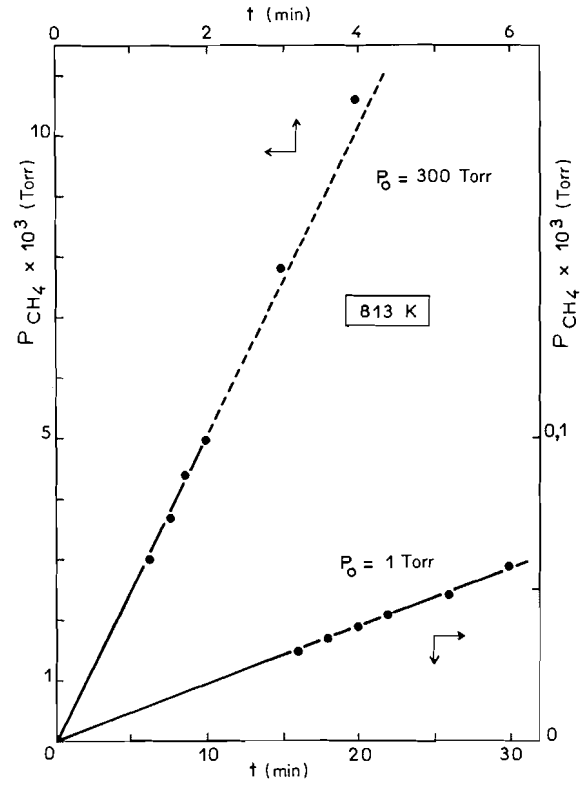

FIG. 2. Courbes de formation de méthane pour les deux pressions extrêmes d'éthane. Température de réaction : 813 K.

TABLEAU 1. Valeurs de k_2 (s^{-1}) aux différentes pressions et températures

	k_2 (s^{-1})			
P_0 (Torr)	793 K	801 K	807 K	813 K
300	272,3	351	418,5	554
200	233,2	306	365	472
100	178,6	230	274	337
70	152,8	201	234,5	289
50	129	167	203,3	244
30	101	130	152,5	182,2
25	90,4	117	138,5	166,8
20	82,5	107	125	146,5
15	68,4	—	102,2	122
10	55,3	67,7	82,5	98,7
5	33,3	—	—	—
3	22,8	28,4	33,4	39,6
1	—	—	13	16,3

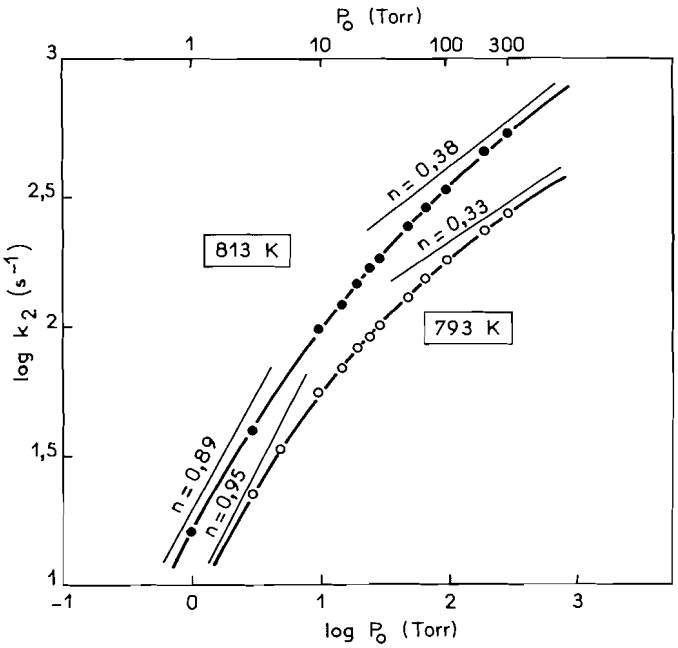

FIG. 3. Courbes de «fall-off» expérimentales aux deux températures extrêmes : 793 et 813 K.

La figure 3 montre les deux courbes de «fall-off», en coordonnées logarithmiques, pour les deux températures extrêmes 793 et 813 K. On voit qu'à 1 Torr l'ordre de k_2 est environ 0,90–0,95 : k_2 est très proche de la constante limite basse pression. En revanche, pour P_0 = 300 Torr, l'ordre est encore environ 0,35, donc assez éloigné de l'ordre théorique limite 0 à haute pression.

Exploitation des résultats expérimentaux

L'exploitation des résultats expérimentaux a été faite grâce à la théorie RRKM et à deux approches dues à Troe.

1. Théorie RRKM

Nous avons utilisé le programme mis au point par Gilbert (24).

Paramètres choisis pour le radical $C_2H_5\cdot$: fréquences (25, 26) en cm^{-1} : 2995 (5), 1432 (4), 1037 (2), 988 (2), 540 (1); rotation

TABLEAU 2. Méthode RRKM : valeurs de $k_{2,\infty}$, $k_{2,0}$ et des paramètres d'Arrhenius à pression infinie, aux différentes températures

T(K)	$k_{2,\infty}$ (s^{-1})	log $A_{2,\infty}$ (s^{-1})	$E_{2,\infty}$ (kcal·mol^{-1})	$k_{2,0}$ ($cm^3 \cdot mol^{-1} \cdot s^{-1}$)
793	516	14,00	40,97	$4,5 \times 10^8$
801	681	14,02	41,00	$5,55 \times 10^8$
807	824	14,02	41,02	$6,55 \times 10^8$
813	1030	14,04	41,04	$7,70 \times 10^8$

interne : $B = 14,1\ cm^{-1}$ ($I_{red} = 1,3$ uma Å^2); symétrie externe : $\sigma_{ext} = 1$; nombre d'isomères optiques : $n = 1$; symétrie interne : $\sigma_{int} = 6$.

Paramètres choisis pour le complexe activé : fréquences (25) en cm^{-1} : 3047 (4), 1466 (3), 1023 (2), 933 (3) plus *400* (2) cm^{-1}, fréquence ayant servi à obtenir le meilleur ajustement avec les points expérimentaux; symétrie externe : $\sigma^{\neq}_{ext} = 1$; nombre d'isomères optiques : $n^{\neq} = 1$.

Autres paramètres : énergie seuil à 0 K : $E^0 = 38,8$ kcal·mol^{-1}; diamètre «apparent» de collision : $\sigma = 2,9$ Å; rapport des moments d'inertie : $I^{\neq}/I = 1,14$–$1,20$ selon la température.

Le programme fournit, pour chaque température, les paramètres à pression infinie : $k_{2,\infty}$, $E_{2,\infty}$, et log $A_{2,\infty}$. L'ajustement entre les courbes théoriques et expérimentales se fait essentiellement, après que l'on s'est fixé E^0, grâce à la fréquence la plus basse du complexe activé (400 cm^{-1} ici), au rapport $I^{\neq}/I$ et au diamètre apparent de collision σ. En réalité c'est le facteur d'efficacité de désactivation λ, dans le produit $\lambda\sigma^2$, qui est le paramètre ajustable. Ainsi, si l'on admet pour $C_2H_5\cdot$ un diamètre de collision proche de celui de C_2H_6 : $\sigma_d = 4,45$ Å (valeur viscosimétrique (27)) l'adoption d'un diamètre apparent de 2,9 Å correspond à $\lambda \simeq 0,4$.

La figure 4 présente, pour les deux températures extrêmes, les courbes théoriques comparées aux points «expérimentaux» (ces points tiennent compte, dans cette représentation, de la valeur k_∞ donnée par le programme RRKM. Ils sont donc modifiés à chaque essai d'ajustement). L'accord est très bon, quelle que soit la température, la qualité de l'ajustement étant comparable pour les deux températures intermédiaires.

Le programme a permis le calcul de k_2 pour des pressions très basses : 0,01–0,1 Torr, en conservant les valeurs des paramètres ajustables précédents. La variation, linéaire, de k_2 dans ce domaine fournit la valeur de la constante bimoléculaire $k_{2,0}$.

Le tableau 2 regroupe les valeurs des paramètres à pression infinie données directement par le programme ainsi que les valeurs de la constante bimoléculaire $k_{2,0}$.

2. Première méthode de Troe (notée Troe 1)

Dans cette première méthode, Troe (28, 29) propose une expression modifiée de l'intégrale de Kassel :

$$[12]\quad I = \frac{k}{k_\infty} = \frac{1}{\Gamma(S_K)} \int_0^\infty \frac{x^{S_K - 1} \exp(-x)\, dx}{1 + \frac{k_\infty}{k_0 P_0} I_0(S_K, B_K) \left(\frac{x}{x + B_K}\right)^{S_K - 1}}$$

avec :

$$I_0(S_K, B_K) = \frac{1}{\Gamma(S_K)} \int_0^\infty (x + B_K)^{S_K - 1} \exp(-x)\, dx$$

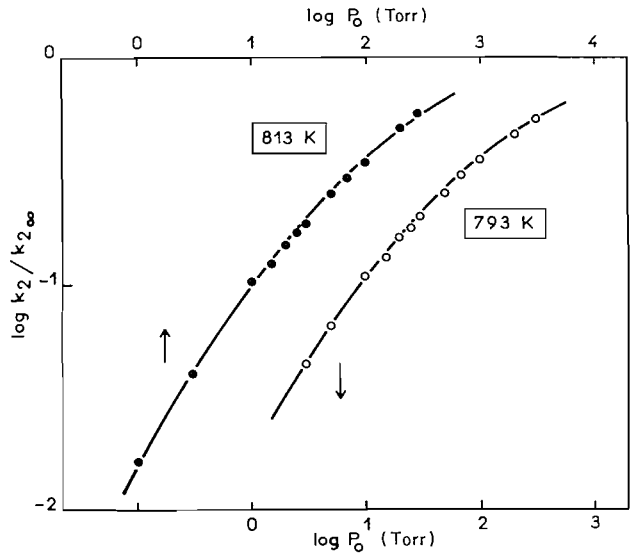

FIG. 4. Ajustement des courbes théoriques RRKM aux points expérimentaux, pour les deux températures extrêmes : 793 et 813 K.

où :

$$x = \frac{E - E^0}{k_B T}$$

E, énergie courante; E^0, énergie seuil à 0 K.

S_K et B_K sont les valeurs effectives des paramètres de Kassel S (paramètre ajustable dans la théorie RRK) et B ($= E^0/k_B T$ dans l'intégrale de Kassel). S_K et B_K sont calculables a priori à partir uniquement de E^0 et des fréquences de la molécule de réactif (28). On peut alors calculer l'intégrale I en fonction du paramètre $k_\infty/k_0 P_0$ où intervient la pression P_0 du réactif.

La méthode de détermination de k_∞ et k_0 à partir des résultats expérimentaux que nous avons mise au point est la suivante.

L'expression [12] se réécrit :

$$\log I = \log k - \log k_\infty$$

et

$$\log \frac{k_0 P_0}{k_\infty} = \log P_0 + \log \frac{k}{k_\infty} + \log \frac{k_0}{k}$$
$$= \log P_0 - \log k + \log k_0 + \log I$$

On peut alors tracer la courbe *théorique* : log I vs. log $(k_0 P_0/k_\infty)$ − log I en prenant $k_0 P_0/k_\infty$ comme paramètre soit encore log k − log k_∞ vs. log P_0 − log k + log k_0.

Les mesures expérimentales de k en fonction de P_0 peuvent être représentées par la courbe dite «*expérimentale*» : log k vs. log P_0 − log k.

Alors la courbe théorique se déduit de cette courbe expéri-

Can. J. Chem. Downloaded from www.nrcresearchpress.com by 196.1.178.254 on 09/07/12
For personal use only.

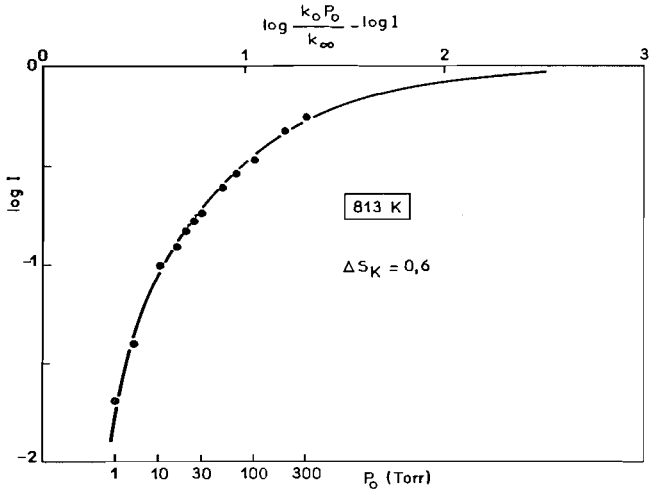

FIG. 5. Première méthode de Troe : ajustement de la courbe théorique transformée aux points «expérimentaux», permettant la détermination de $k_{2,\infty}$ et $k_{2,0}$ (cf. texte). Température : 813 K.

mentale par une translation selon l'axe des abscisses de $\log k_0$ et une translation selon l'axe des ordonnées de $-\log k_\infty$, ce qui permet l'évaluation de k_0 et k_∞.

Les valeurs de E^0 et des 14 fréquences de vibration de $C_2H_5\cdot$ sont les mêmes que pour le traitement RRKM et la rotation interne est ici remplacée par une vibration de fréquence 350 cm^{-1}. Les valeurs des paramètres efficaces sont alors, à 813 K : $S_K = 4{,}76$ et $B_K = 11{,}66$.

L'évaluation de k_0 et k_∞ se fait par optimisation au sens des moindres carrés, c'est-à-dire que l'on cherche le couple k_0, k_∞ qui donne la valeur minimale de la somme des carrés des distances entre les deux courbes expérimentales translatée et théorique, cette distance étant calculée pour chaque point expérimental.

Pour tenir compte de l'efficacité de désactivation (correspondant au facteur λ dans la théorie RRKM) Troe propose de modifier légèrement la valeur de S_K obtenue a priori par la formule qu'il préconise (28). Ainsi divers essais ont montré que le meilleur ajustement possible, à 813 K, de la courbe théorique aux points expérimentaux était obtenu pour $\Delta S_K = +0{,}6$. Ceci est illustré sur la figure 5. Le tableau 3 regroupe les valeurs de $k_{2,0}$ et $k_{2,\infty}$ obtenues par ajustement pour les quatre températures.

La courbe théorique de «fall-off» calculée, à 813 K, par la formule [12], à partir des valeurs $k_{2,\infty}$ et $k_{2,0}$ du tableau précédent est représentée, avec les points expérimentaux, sur la figure 6. Comme pour la théorie RRKM l'ajustement est de très bonne qualité. Il en est de même aux trois autres températures.

3. Deuxième méthode de Troe (notée Troe 2)

Troe et collaborateurs (29–33) ont proposé une représentation des courbes de «fall-off» en double échelle réduite, de la forme :

$$[13]\quad \log\frac{k}{k_\infty} = \log\frac{(k_0P_0/k_\infty)}{1+(k_0P_0/k_\infty)} + \frac{\log F_{cent}}{1+\left(\dfrac{\log(k_0P_0/k_\infty)}{0{,}75-1{,}27\log F_{cent}}\right)^2}$$

Le paramètre F_{cent} représente l'écart par rapport à la courbe de Lindemann–Hinshelwood (broadening factor) au centre de

TABLEAU 3. Première méthode de Troe : valeurs de $k_{2,\infty}$ et $k_{2,0}$ aux différentes températures

T (K)	$k_{2,\infty}$ (s^{-1})	$k_{2,0}$ ($cm^3\cdot mol^{-1}\cdot s^{-1}$)
793	385,5	$9{,}37 \times 10^8$
801	525,4	$1{,}16 \times 10^9$
807	646,4	$1{,}33 \times 10^9$
813	882,6	$1{,}55 \times 10^9$

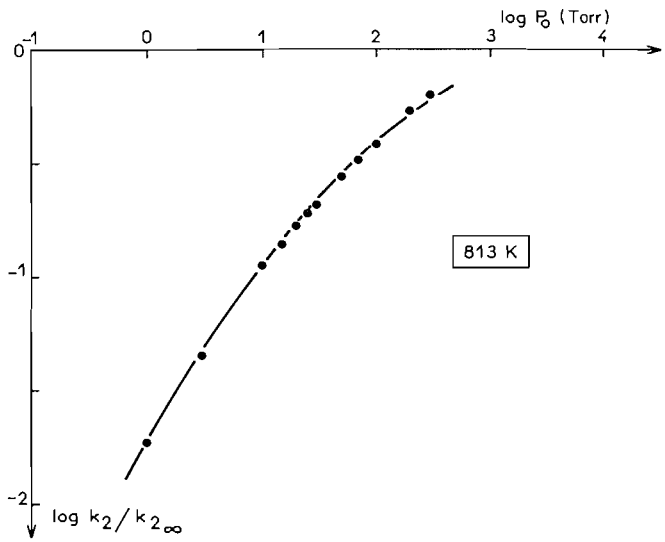

FIG. 6. Première méthode de Troe : courbe théorique, calculée à partir de $k_{2,\infty}$ et $k_{2,0}$ obtenus grâce à la figure 5, et points expérimentaux. Température : 813 K.

cette courbe (lorsque la variable réduite $y = k_0P_0/k_\infty$ vaut 1). F_{cent} se met sous la forme : $F_{cent} = F^{s.c.}{}_{cent} \times F^{w.c.}{}_{cent}$.

Le facteur $F^{s.c.}{}_{cent}$, correspondant à l'hypothèse des collisions fortes dans la désactivation de $C_2H_5\cdot$ activé, peut être estimé à partir des paramètres effectifs S_K et B_K évoqués dans la méthode précédente. Ceux-ci sont calculés (33) à partir de l'énergie seuil E^0 (= 38,8 $kcal\cdot mol^{-1}$) et des 14 fréquences de vibration du radical éthyle, la rotation interne étant prise en compte séparément (les 14 fréquences sont celles choisies dans la théorie RRKM).

À 813 K on obtient ainsi : $S_K = 4{,}76$ et $B_K = 12{,}29$ (formule un peu différente de celle utilisée dans la première méthode de Troe), d'où $F^{s.c.}{}_{cent} = 0{,}51$.

Le facteur $F^{w.c.}{}_{cent}$ est la correction à apporter lorsque les collisions sont faibles.

$F^{w.c.}{}_{cent} = \beta_c^{0,14}$ où β_c est l'efficacité de collision qui dépend de la température selon :

$$[14]\quad \frac{\beta_c}{1-\sqrt{\beta_c}} \simeq -\frac{\langle\Delta E\rangle}{F_E kT}$$

$\langle\Delta E\rangle$ est l'énergie moyenne échangée par collision. F_E, facteur statistique rendant compte de la dépendance de la densité d'états vibrationnels (harmoniques) $\rho_{vib.,h}$ vis-à-vis de l'énergie, est calculable (32) à partir de E^0 et des fréquences de vibration du radical éthyle.

Si l'on se donne $\langle\Delta E\rangle$ (cf. par exemple, réf. 31), la courbe $\log k/k_\infty$ vs. $\log k_0P_0/k_\infty$ peut ainsi être calculée a priori à partir de S_K, B_K et β_c. Si l'on désire comparer cette méthode aux deux précédentes, il est nécessaire de pouvoir passer de la

Can. J. Chem. Downloaded from www.nrcresearchpress.com by 196.1.178.254 on 09/07/12
For personal use only.

variable réduite $\log k_0P_0/k_\infty$ à la variable $\log P_0$, donc de connaître k_0 et k_∞. Troe propose l'expression factorisée de k_0 suivante :

[15] $$k_0 = \frac{\beta_c Z_{LJ} \rho_{vib,h}(E^0) k_B T}{Q_{vib}} \exp\left(-\frac{E^0}{k_B T}\right) F_E F_{anh} F_{rot} F_{rot.int.}$$

On indique ci-dessous la signification de ces différents termes, les grandeurs nécessaires à leur évaluation et leur valeur numérique à 813 K calculée à partir des formules de réf. 32. Z_{LJ} : fréquence de collision de Lennard–Jones; $\rho_{vib,h}(E^0)$: densité d'états vibrationnels (oscillateurs harmoniques) pour l'énergie seuil E^0; $Q_{vib.}$: fonction de partition vibrationnelle du réactif (oscillateurs harmoniques); F_E défini précédemment; F_{anh} : tient compte de l'anharmonicité des vibrations; $F_{rot.}$: rend compte du changement de moments d'inertie (rotations externes) entre réactif et complexe activé; $F_{rot.int.}$: représente la contribution des rotations internes du réactif.

Grandeurs nécessaires à l'évaluation des termes précédents : énergie seuil E^0 (38,8 kcal·mol^{-1}), nombre $S = 14$ et valeurs des fréquences vibrationnelles du réactif (celles de RRKM), diamètre de collision : $\sigma = 4{,}4$ Å (27); énergie d'interaction de Lennard–Jones : $\varepsilon_{A\text{-}M} = 1{,}79 \times 10^3$ J·mol^{-1} (27); nombre de rotations internes dans le réactif : $r = 1$; nombre d'oscillateurs qui disparaissent durant la réaction : $m = 3$; rapport des moments d'inertie I^*/I entre le complexe activé et le réactif : $I^*/I = 1{,}14$–$1{,}20$ selon la température. À 813 K on calcule ainsi : $Z_{LJ} = 3{,}96 \times 10^{11}$ cm^3·mol^{-1}·s^{-1}; $\rho_{vib.,h}(E^0) = 33{,}66$; $Q_{vib} = 4{,}80$; $F_E = 1{,}40$; $F_{anh} = 1{,}125$; $F_{rot} = 1{,}16$; $F_{rot.int.} = 1{,}79$.

Pour exploiter les résultats expérimentaux, plusieurs méthodes sont envisageables :

(*i*) On peut évaluer k_∞ par une méthode d'extrapolation comme celle de Oref et Rabinovitch (34), k_0 directement à partir des résultats expérimentaux à basse pression, en admettant que l'on se trouve dans le domaine bimoléculaire, et calculer F_{cent} par S_K, B_K et β_c (en se donnant une valeur, a priori, de $\langle \Delta E \rangle$; par exemple 10 kJ·mol^{-1} (31)). Dans cette méthode, adoptée par Trenwith (7), il n'y a pas de paramètre ajustable et la courbe théorique, calculée a priori, est comparée aux résultats expérimentaux.

(*ii*) Dans une étude du processus inverse $H\cdot + C_2H_4 \rightarrow C_2H_5\cdot$, Lightfoot et Pilling (9) envisagent une autre approche. Ils calculent F_{cent} a priori par S_K, B_K et en se donnant β_c et ils ajustent courbe théorique et points expérimentaux en prenant comme paramètres ajustables k_∞ et k_0. En revanche ils ne comparent pas, ensuite, la valeur de k_0 ainsi obtenue avec l'expression théorique [15] de Troe. On ne sait donc pas s'il y a ou non compatibilité.

(*iii*) Une autre méthode a été retenue. Nous calculons S_K et B_K a priori (33) et nous ajustons d'abord courbe expérimentale et points théoriques en prenant comme paramètres k_∞ et β_c et en déduisant k_0 de β_c par la formule [15]. Ce travail d'optimisation, aux quatre températures, permet de constater que β_c reste toujours voisin de 0,45 (entre 0,45 et 0,48). La valeur de β_c à 813 K (0,45) a alors été choisie pour calculer la valeur supposée indépendante de la température de $\langle \Delta E \rangle$ par la formule [14]. Cette valeur $\langle \Delta E \rangle = 13$ kJ·mol^{-1} permet de calculer β_c aux trois autres températures par [14] et k_0 par la formule [15]. L'ajustement, repris à 793, 801 et 807 K avec k_∞ comme unique paramètre, a conduit aux résultats du tableau 4.

La figure 7 montre l'excellente qualité de l'ajustement aux deux températures extrêmes. Il en est de même à 801 et 807 K.

TABLEAU 4. Deuxième méthode de Troe : valeurs de $k_{2,\infty}$, $k_{2,0}$, de l'efficacité de collision β_c et du paramètre F_{cent} («broadening factor») aux différentes températures

T(K)	β_c	F_{cent}	$k_{2,\infty}$(s^{-1})	$k_{2,0}$(cm^3·mol^{-1}·s^{-1})
793	0,459	0,463	530	$5{,}87 \times 10^8$
801	0,456	0,459	710	$7{,}43 \times 10^8$
807	0,453	0,457	860	$8{,}73 \times 10^8$
813	0,45	0,454	1100	$1{,}05 \times 10^9$

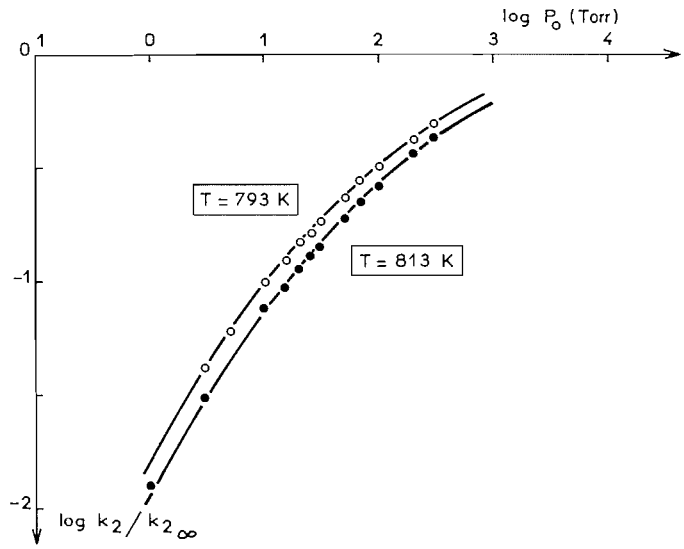

FIG. 7. Seconde méthode de Troe : ajustement des courbes théoriques aux points expérimentaux, pour les deux températures extrêmes : 793 et 813 K.

Discussion et comparaison avec les résultats de la littérature

Comme on vient de le voir, les trois méthodes précédentes permettent un très bon ajustement des courbes théoriques aux points expérimentaux. Parmi les différents travaux sur la décomposition du radical éthyle, seul le traitement RRKM, par Lin et Laidler (35), des résultats de Lin et Back (2) et de Loucks et Laidler (3), conduit à un ajustement de qualité comparable (pour des pressions supérieures à 30 Torr). Il a déjà été signalé (32, 36) que la détermination de k_∞ et k_0 à partir des courbes de «fall-off» est délicate et relativement peu précise, à moins de disposer de points expérimentaux dans un très grand domaine de pression, ce qui est rarement le cas. En particulier nous pensons, comme Clark et Quinn (36), que les méthodes d'extrapolation purement empiriques comme celle de Oref et Rabinovitch (34) ne conduisent pas à des valeurs précises de k_∞.

Néanmoins la comparaison des tableaux 2, 3 et 4 montre qu'en ce qui concerne $k_{2,\infty}$, la deuxième méthode de Troe fournit des valeurs qui ne diffèrent que de 5–6% de celles données par RRKM. Ce pourcentage est de 15–25% pour la première méthode de Troe. Dans le cas de $k_{2,0}$ la dispersion est plus importante : 30–35% pour Troe 2 par rapport à RRKM et un facteur 2 pour Troe 1. La cohérence entre les trois méthodes et en particulier entre RRKM et Troe 2 est donc très correcte.

Il est difficile de proposer des expressions d'Arrhenius précises, pour $k_{2,\infty}$ et $k_{2,0}$, lorsque les points expérimentaux ne couvrent qu'un domaine restreint de température (20°C). Un traitement d'Arrhenius sur les résultats des tableaux 2, 3 et 4 conduit aux paramètres figurant en bas du tableau 5, les valeurs

Can. J. Chem. Downloaded from www.nrcresearchpress.com by 196.1.178.254 on 09/07/12
For personal use only.

Can. J. Chem. Downloaded from www.nrcresearchpress.com by 196.1.178.254 on 09/07/12
For personal use only.

TABLEAU 5. Comparaison des expressions d'Arrhenius pour $k_{2,\infty}$ et $k_{2,0}$ proposées dans la littérature et dans le présent travail

Références	Méthodes d'exploitation	log $A_{2,\infty}$ (s^{-1})	$E_{2,\infty}$ (kcal·mol^{-1})	log $A_{2,0}$ ($cm^3 \cdot mol^{-1} \cdot s^{-1}$)	$E_{2,0}$ (kcal·mol^{-1})
2	Méthode de Powell (37) → k_∞ et k_0	13,43	38,0 ± 2	18,11	32,4 ± 2
3	Extrapolations par : Lindemann → k_∞ et k_0 et Oref et Rabinovitch (33) → k_∞ RRK	14,28	40,9	17,68	31,8
35	RRKM	14,35[a]	41,1[a]	18,39[a]	34,6[a]
4	Simulation informatique Seul paramètre ajustable : A_∞	12,75	38,0		
25	RRKM	14,85[b]	42,5[b]		
5	Simulation informatique Seul paramètre ajustable : k_∞	13,5 ± 0,7	41,8 ± 2,9		
7	Oref et Rabinovitch → k_∞	12,95 ± 0,20	38,0 ± 0,8		
	Résultats à basse pression → k_0				
Présent travail	RRKM	14,02 ± 0,02	41,0 ± 0,04	18,26	34,9
	Troe 1	16,80	51,5	17,93	32,5
	Troe 2	15,10	45,0	18,97	37,0

[a]Valeurs obtenues par un traitement d'Arrhenius (par nos soins) des résultats RRKM de l'article.
[b]Le traitement RRKM porte sur les résultats expérimentaux des réfs. 2 et 3 et sur ceux des auteurs lors de l'étude de l'activation chimique $H\cdot + C_2H_4 \rightarrow C_2H_5\cdot$. Le traitement d'Arrhenius a été fait par nos soins.

log $A_{2,\infty}$ et $E_{2,\infty}$ pour RRKM étant celles calculées directement par le programme (moyenne sur le tableau 2).

Le tableau 5 rassemble les paramètres proposés par les différents auteurs ainsi que les méthodes d'exploitation utilisées. Il faut noter que les expressions originales figurant dans les références 2, 3, 4, 25 et 35 ont été modifiées en prenant $k_4 = 10^{13}\,cm^3 \cdot mol^{-1} \cdot s^{-1}$ (au lieu de 2×10^{13}).

Comparaison des paramètres à pression infinie

Si l'on écarte les valeurs de $E_{2,\infty}$, manifestement trop élevées, données par les deux méthodes de Troe, on s'aperçoit que les autres se regroupent en deux domaines : l'un aux environs de 38 kcal·mol^{-1}, l'autre autour de 41 kcal·mol^{-1}. La valeur $\Delta H^0_f(C_2H_5\cdot) = 25{,}8$ kcal·mol^{-1} (300 K) couramment admise (38) conduisait à $\Delta H^0_{2(800\,K)} \simeq 40{,}0$ kcal·mol^{-1} soit $E_{2,\infty} - E_{-2,\infty} \simeq 38{,}4$ kcal·mol^{-1} donc $E_{2,\infty} \simeq 40{,}6$ kcal·mol^{-1}, compatible avec les valeurs expérimentales élevées. Mais il semble que des travaux (39–43), confirmés par l'étude récente de l'équilibre $H\cdot + C_2H_4 \rightleftarrows C_2H_5\cdot$ par Pilling et coll. (8), tendent à attribuer à $\Delta H^0_f(C_2H_5\cdot)$ une valeur plus élevée : $\simeq$28,4 kcal·mol^{-1} qui conduit à $E_{2,\infty} - E_{-2,\infty} \simeq 35{,}8$ kcal·mol^{-1} à 800 K. La valeur $E_{-2,\infty} = 2{,}16$ kcal·mol^{-1} proposée par Lightfoot et Pilling (9) vers 600 K donne alors : $E_{2,\infty} \simeq 38{,}0$ kcal·mol^{-1} en accord avec les faibles valeurs expérimentales, en particulier celle de Trenwith (7), ainsi qu'avec la valeur admise par Tsang (43) : 38,4 kcal·mol^{-1}, à 600 K.

En revanche, dans un article très récent, Grela et Colussi (44) estiment l'énergie d'activation $E_{2,\infty}$ à 0 K à 39,7 kcal·mol^{-1}, ce qui, compte-tenu des fréquences qu'ils adoptent pour le radical éthyle et le complexe activé (45), conduit à : $\Delta U_2^{0\neq} \simeq 40{,}2$ kcal·mol^{-1} à 800 K donc à une valeur élevée de $E_{2,\infty} \simeq 41{,}8$ kcal·mol^{-1} à 800 K. Il est à noter que ces auteurs admettent, dans leurs calculs, la nouvelle valeur de $\Delta H^0_f(C_2H_5\cdot) \simeq 28{,}2$ kcal·mol^{-1} et un jeu de fréquences qui leur permet de retrouver certaines caractéristiques de l'état de transition obtenues par les calculs «*ab initio*» de Schlegel (45) ainsi qu'un facteur de fréquence de $10^{13,5}\,s^{-1}$ à 600 K, très voisin de celui ($10^{13,4}\,s^{-1}$ à 600 K) retenu par Tsang (43). Malgré cela, il semble y avoir une incohérence interne dans ce travail puisque la nouvelle valeur de $\Delta H^0_f(C_2H_5\cdot)$ conduit, comme on l'a vu, à $E_{2,\infty} - E_{-2,\infty} \simeq 35{,}8$ kcal·mol^{-1} à 800 K, ce qui donnerait $E_{-2,\infty} \simeq 6$ kcal·mol^{-1}, valeur manifestement trop élevée.

Dans le tableau 6 on a rassemblé nos valeurs expérimentales de $k_{2,\infty}$ et $k_{2,0}$ à 813 K et celles, calculées, à 813 et 902 K, de ces mêmes grandeurs à partir des paramètres cinétiques du tableau 5. Figurent également les valeurs déduites des travaux de Pilling et coll. sur la thermochimie (8) et sur la cinétique de la réaction inverse (9). Enfin on y trouve les valeurs proposées à la seule température de 902 K par Pacey et Wimalasena (23) ainsi que celles calculées à partir des expressions de Tsang (43) et Grela et Colussi (44).

Compte-tenu de l'incertitude indiquée par Pilling, on voit qu'à 813 K, l'accord est excellent entre nos valeurs $k_{2,\infty}$ et la sienne. En particulier l'écart par rapport à notre valeur RRKM n'est que de 5%, ce qui est remarquable. Les résultats obtenus à partir de l'expression de Tsang sont également compatibles avec les précédents. Compte-tenu des incertitudes, la valeur proposée par Pacey est très voisine des précédentes à 902 K.

TABLEAU 6. Comparaison des valeurs numériques de $k_{2,\infty}$ et $k_{2,0}$ à 813 et 902 K, tirées des expressions du tableau 5 (à 813 K les valeurs du présent travail sont les valeurs «expérimentales»)

Références		$T = 813$ K		$T = 902$ K	
		$k_{2,\infty}$ (s^{-1})	$k_{2,0} \times 10^{-8}$ ($cm^3 \cdot mol^{-1} \cdot s^{-1}$)	$k_{2,\infty} \times 10^{-4}$ (s^{-1})	$k_{2,0} \times 10^{-9}$ ($cm^3 \cdot mol^{-1} \cdot s^{-1}$)
2		1636	25	1,7	18
3		1924	13	2,3	9,4
35		1998	12	2,4	10
4		342		0,35	
25		2650		3,6	
5		183		0,23	
7		542		0,55	
Présent travail	RRKM	1030	7,7	1,2	6,3
	Troe 1	883	15,5	2,1	11,3
	Troe 2	1100	10,5	1,6	10,1
8, 9		980 ± 120	$3,6 \pm 0,4$	$\simeq 1$	$\simeq 3,3$
23				$2,7 \pm 0,9$	5 ± 2
43		1200		1,3	
44		420		0,54	

Il n'en est pas de même pour les résultats de Trenwith, systématiquement trop bas, vraisemblablement à cause du faible facteur préexponentiel. Même remarque pour les valeurs récentes de Grela et Colussi, la raison étant cette fois la trop forte énergie d'activation.

Compte-tenu de ce qui précède on peut donc proposer une expression d'Arrhenius de la forme :

$$k_{2,\infty}(s^{-1}) = 10^{13,2} \exp\left(-\frac{38\,000}{RT}\right)$$

compatible avec les expressions fournies par Trenwith (7), Pilling (8, 9) et Tsang (43) et avec les valeurs expérimentales de Pacey (23) et les nôtres.

Comparaison des paramètres à basse pression

Comme le montre le tableau 5 il n'y a pas d'expression d'Arrhenius récente pour $k_{2,0}$ dans la littérature. On peut toutefois déduire des deux articles de Pilling et coll. (8, 9) l'expression : $k_{2,0} \simeq 10^{18,5} \exp(-37\,000/RT)\ cm^3 \cdot mol^{-1} \cdot s^{-1}$ vers 800 K. La valeur $E_{2,0} \simeq 37$ kcal·mol^{-1} correspond très exactement à celle obtenue, dans notre travail, par la méthode Troe 2. Rappelons que Pilling et coll. ont utilisé cette même méthode pour le traitement de leurs résultats sur la réaction inverse. Il y a donc là une excellente cohérence des deux travaux.

Néanmoins cette valeur est probablement trop forte. En effet, l'écart entre les valeurs $E_{2,\infty}$ et $E_{2,0}$ déduites de l'étude de Pilling est environ 1 kcal·mol^{-1}. Or il a été montré (32, 33) que $E_\infty - E_0 \simeq S_K RT$ soit ici environ 7,5 kcal·mol^{-1} (à 813 K). Même si l'incertitude sur S_K est 1, cette différence est encore de l'ordre de 5–6 kcal·mol^{-1}. Ce problème est encore aggravé par le fait que la valeur $E_{2,0} = 37$ kcal·mol^{-1} est déduite de travaux sur la réaction inverse utilisant l'hélium comme gaz inerte. Cette valeur correspondrait donc à la décomposition du radical éthyle dans le cas de collisions faibles. L'éthane étant un partenaire de choc plus efficace que l'hélium on devrait observer une valeur $E_{2,0} > 37$ kcal·mol^{-1}. On aurait alors une valeur $E_{2,0}$ voisine, ou même supérieure, à l'énergie critique E^0, ce qui n'est pas raisonnable (46).

Nous pensons que des valeurs $E_{2,0}$ de l'ordre de 34–35 kcal·mol^{-1} sont plus vraisemblables. Notons que notre valeur RRKM (34,9 kcal·mol^{-1}) est compatible avec la valeur correspondante $E_{2,\infty} = 41$ kcal·mol^{-1} et l'écart $E_{2,\infty} - E_{2,0}$ signalé plus haut. Il en est de même avec les expressions de Lin et Laidler (35) et également de Lin et Back (2), compte-tenu des incertitudes.

Comme le montre le tableau 6, il existe un facteur 2, à 813 K, entre notre valeur $k_{2,0}$ (RRKM) et la valeur obtenue à partir des travaux de Pilling. Ce facteur se retrouve à 902 K mais les deux résultats sont compatibles avec la valeur ponctuelle proposée par Pacey et coll. (23), ce qui est remarquable.

La cohérence des résultats entre le traitement RRKM effectué par Lin et Laidler (35) (sur les travaux de Lin et Back et Loucks et Laidler) et notre propre traitement RRKM nous amène à proposer, pour $k_{2,0}$, une expression du type :

$$k_{2,0}(cm^3 \cdot mol^{-1} \cdot s^{-1}) = 10^{18,3} \exp\left(-\frac{34\,900}{RT}\right)$$

qui conduit à une valeur à 902 K en très bon accord avec celle de Pacey.

Conclusion

L'analyse des résultats les plus récents sur la décomposition thermique du radical éthyle montre qu'il existe maintenant un assez bon accord entre les valeurs numériques de $k_{2,\infty}$ et $k_{2,0}$ obtenues, ponctuellement, à certaines températures. En revanche les expressions d'Arrhenius de ces deux constantes limites diffèrent encore sensiblement les unes des autres. Si l'on tient compte de la nouvelle valeur de $\Delta H^0_f(C_2H_5\cdot)$ et de la différence prévue théoriquement entre $E_{2,\infty}$ et $E_{2,0}$, il nous semble que les deux expressions :

$$k_{2,\infty}(s^{-1}) = 10^{13,2} \exp\left(-\frac{38\,000}{RT}\right)$$

$$k_{2,0}(cm^3 \cdot mol^{-1} \cdot s^{-1}) = 10^{18,3} \exp\left(-\frac{34\,900}{RT}\right)$$

représentent au mieux l'ensemble des résultats expérimentaux.

L'efficacité de désactivation λ ou β_c de la molécule d'éthane

Can. J. Chem. Downloaded from www.nrcresearchpress.com by 196.1.178.254 on 09/07/12
For personal use only.

semble être voisine de 0,4 vers 800 K (0,4 par RRKM et 0,45 par Troe 2), en parfait accord avec les travaux de Trenwith (7), ce qui correspond à $\langle \Delta E \rangle \simeq 13\ \text{kJ}\cdot\text{mol}^{-1}$. La valeur $\langle \Delta E \rangle \simeq 20\ \text{kJ}\cdot\text{mol}^{-1}$ (31), adoptée par Lightfoot et Pilling (9) paraît trop élevée et conduirait à une valeur $\beta_c \simeq 0{,}55$ vers 800 K, incompatible avec nos résultats et ceux de Trenwith.

1. J. H. Purnell et C. P. Quinn. Proc. R. Soc. London, A, **270**, 267 (1962).
2. M. C. Lin et M. H. Back. Can. J. Chem. **44**, 2357 (1966).
3. L. F. Loucks et K. J. Laidler. Can. J. Chem. **45**, 2795 (1967).
4. J. N. Bradley et M. Frend. J. Phys. Chem. **75**, 1492 (1971).
5. G. L. Pratt et D. Rogers. J. Chem. Soc. Faraday Trans. 1, **75**, 1089 (1979).
6. Y. Simon. Thèse de Troisième Cycle, Nancy (1986).
7. A. B. Trenwith. J. Chem. Soc. Faraday Trans. 2, **82**, 457 (1986).
8. M. Brouard, P. D. Lightfoot et M. J. Pilling. J. Phys. Chem. **90**, 445 (1986).
9. P. D. Lightfoot et M. J. Pilling. J. Phys. Chem. **91**, 3373 (1987).
10. G. Scacchi. Thèse de Doctorat d'État, Nancy (1969).
11. G. Scacchi, R. Martin et M. Niclause. C.R. Acad. Sci. Paris, Ser. C : **275**, 1347 (1972).
12. K. J. Laidler et B. W. Wojciechowski. Proc. R. Soc. London, A, **260**, 91 (1961).
13. C. P. Quinn. Proc. R. Soc. London, A, **275**, 190 (1963).
14. A. S. Gordon. Symposium. Kinetics of pyrolytic reactions. Ottawa (Canada). 9–11 sept. 1964.
15. J. Fusy, G. Scacchi, R. Martin, A. Combes et M. Niclause. C.R. Acad. Sci. Paris, **261**, 2223 (1965).
16. R. M. Marshall et C. P. Quinn. Trans. Faraday Soc. **61**, 2671 (1965).
17. A. Sepehrad, R. M. Marshall et H. Purnell. Int. J. Chem. Kinet. **11**, 411 (1979).
18. G. L. Pratt. Gas kinetics. Wiley, London. 1969.
19. P. D. Pacey et J. H. Purnell. J. Chem. Soc. Faraday Trans. 1, **68** (1972).
20. M. C. Lin et M. H. Back. Can. J. Chem. **44**, 2369 (1966).
21. D. A. Parkes et C. P. Quinn. J. Chem. Soc. Faraday Trans. 1, **72**, 1952 (1976).
22. D. M. Golden, K. Y. Choo, M. J. Perona et L. W. Piszkiewicz. Int. J. Chem. Kinet. **8**, 381 (1976).
23. P. D. Pacey et J. H. Wimalasena. J. Phys. Chem. **88**, 5657 (1984).
24. R. G. Gilbert. Programme QCPE n° 460, Chemistry Department, Indiana University, Bloomington, IN 47401, U.S.A.
25. J. V. Michael et G. N. Suess. J. Chem. Phys. **58**, 2807 (1973).
26. J. Pacansky et M. Dupuis. J. Chem. Phys. **68**, 4276 (1978).
27. R. C. Reid et T. K. Sherwood. The properties of gases and liquids. 2e ed. McGraw–Hill, New York. 1966.
28. J. Troe. Ber. Bunsen-ges. Phys. Chem. **78**, 478 (1974).
29. J. Troe. Ber. Bunsen-ges. Phys. Chem. **87**, 161 (1983).
30. R. G. Gilbert, K. Luther et J. Troe. Ber. Bunsen-ges. Phys. Chem. **87**, 169 (1983).
31. M. Quack et J. Troe. *Dans* Gas kinetics and energy transfer. Vol. 2. *Éditeurs* : P. G. Ashmore et R. J. Donovan. Chemical Society, London. 1977.
32. J. Troe. J. Phys. Chem. **83**, 114 (1979).
33. W. C. Gardiner, Jr. et J. Troe. *Dans* Combustion chemistry. *Éditeur* : W. C. Gardiner. Springer-Verlag, Berlin. 1984. Chap. 4.
34. I. Oref et B. S. Rabinovitch. J. Phys. Chem. **72**, 4488 (1968).
35. M. C. Lin et K. J. Laidler. Trans. Faraday Soc. **64**, 79 (1968).
36. J. A. Clark et C. P. Quinn. J. Chem. Soc. Faraday Trans. 1, **72**, 706 (1976).
37. R. E. Powell. J. Chem. Phys. **30**, 724 (1959).
38. D. F. McMillen et D. M. Golden. Annu. Rev. Phys. Chem. **33**, 493 (1982).
39. P. D. Pacey et J. H. Wimalasena. J. Phys. Chem. **84**, 2221 (1980).
40. W. Tsang. Int. J. Chem. Kinet. **10**, 821 (1980).
41. A. L. Castelhano, P. R. Marriot et D. Griller. J. Am. Chem. Soc. **103**, 4262 (1981).
42. J. R. Cao et M. H. Back. Int. J. Chem. Kinet. **16**, 961 (1984).
43. W. Tsang. J. Am. Chem. Soc. **107**, 2872 (1985).
44. M. A. Grela et A. J. Colussi. Int. J. Chem. Kinet. **19**, 869 (1987).
45. H. B. Schlegel. J. Phys. Chem. **86**, 4878 (1982).
46. M. J. Pilling et I. W. M. Smith (*Éditeurs*). Modern gas kinetics. Blackwell Scientific Publications, Oxford. 1987. p. 10.

Can. J. Chem. Downloaded from www.nrcresearchpress.com by 196.1.178.254 on 09/07/12
For personal use only.

The direct electrochemical synthesis of thiolato complexes of cobalt and nickel, and the crystal structure of bis(phenylthiolato)bis(1,10-phenanthroline)cobalt(III) perchlorate

RAJ K. CHADHA,[1] RAJESH KUMAR, JAIME ROMERO LOPEZ-GRADO,[2] AND DENNIS G. TUCK[3]

Department of Chemistry and Biochemistry, University of Windsor, Windsor, Ont., Canada N9B 3P4

Received November 9, 1987

RAJ K. CHADHA, RAJESH KUMAR, JAIME ROMERO LOPEZ-GRADO, and DENNIS G. TUCK. Can. J. Chem. **66**, 2151 (1988).

Cobalt(II) and nickel(II) thiolates, $M(SR)_2$, can be prepared in high yield by the electrochemical oxidation of a metal anode in an acetonitrile or acetone solution of RSH (R = C_6H_5, *o*-$CH_3C_6H_4$, 2-$C_{10}H_7$, 2,3,4,5-C_6F_4H; not all combinations). When 2,2-bipyridine or 1,10-phenanthroline (=L) is added to the electrolyte phase, the products are the adducts $M(SR)_2L_2$. In the case of $Co(SC_6H_5)_2(phen)_2$, aerial oxidation leads to the formation of the cobalt(III) cation $[Co(SC_6H_5)_2(phen)_2]^+$, isolated as the perchlorate salt. X-ray crystallographic analysis showed that this cation has a *cis*-$CoS_2(N_2)_2$ kernel.

RAJ K. CHADHA, RAJESH KUMAR, JAIME ROMERO LOPEZ-GRADO et DENNIS G. TUCK. Can. J. Chem. **66**, 2151 (1988).

Opérant avec des solutions de RSH (R = C_6H_5-, *o*-$CH_3C_6H_4$-, $C_{10}H_7$-2, F_4-2,3,4,5-C_6H-; pas toutes les combinaisons) dans l'acétonitrile ou l'acétone et faisant appel à une oxydation électrochimique d'une anode métallique, on peut préparer les thiolates de cobalt(II) ou de nickel(II), $M(SR)_2$, avec d'excellents rendements. Lorsqu'on ajoute de la bipyridine-2,2 ou de la phénanthroline-1,10 (=L) à la phase électrolytique, les produits qui se forment sont les adduits $M(SR)_2L_2$. Dans le cas du $Co(SC_6H_5)_2(phen)_2$, l'oxydation par l'air conduit à la formation du cation Co(III), $[Co(SC_6H_5)_2(phen)_2]^+$, qui est isolé sous la forme d'un perchlorate. Une analyse par diffraction des rayons-X a démontré que le noyau de ce cation est formé de $CoS_2(N_2)_2$-*cis*.

[Traduit par la revue]

Introduction

The thiolato derivatives of transition metal elements have been the subject of considerable recent interest, in large measure because a number of these compounds are believed to serve as models for active metal–sulphur sites in metalloproteins (1). In previous papers from this laboratory, we have shown that the technique of direct electrochemical synthesis can be used to prepare thiolato compounds of d^{10} metal ions in high yield by a simple one-step room temperature reaction (2–6). The present paper describes the successful application of this method to the synthesis of various $Co(SR)_2$ and $Ni(SR)_2$ compounds, and of a number of neutral adducts. In the course of working up one of the preparations, we obtained crystals of $[Co(SC_6H_5)_2(phen)_2]ClO_4$ (phen = 1,10-phenanthroline), and the crystal structure of this compound is also discussed.

Experimental section

Materials

Solvents were distilled from and stored over drying agents (acetonitrile – calcium hydride; acetone – anhydrous sodium sulphate). Thiols, and neutral ligands, were used as supplied (Aldrich). Cobalt was used as sheets 0.5 mm thick, and nickel as a wire (0.5 mm diameter), or better, as a rod (0.5 cm diameter). These metals were washed with dilute aqueous nitric acid and then distilled water, dried, and finally abraded with fine sandpaper.

Analysis and spectroscopy

Metal analysis was performed by atomic absorption spectrophotometry, using an IL 151/251 instrument. Microanalysis on selected compounds was performed by Guelph Chemical Laboratories Ltd. Infrared spectra were recorded on a Nicolet 5DX instrument. The magnetic susceptibility measurements were determined by the Gouy method using a Newport instrument with a VR3 power source.

Electrochemical procedures

The electrochemical syntheses utilized the methods described elsewhere (4,7). The cells were of the general type

$$Pt_{(-)}/CH_3CN(\text{or acetone}) + RSH\,(+\text{ ligand})\text{-}/M_{(+)}\,(M = Co, Ni)$$

using a 100-mL tall form beaker to contain the solution, with the anode suspended in the solution via a platinum wire. All experiments were carried out under an atmosphere of dry nitrogen, which also served to stir the reaction mixture as it bubbled gently through the solution. Details of solution composition, and the electrochemical conditions, are given in Table 1; isolation procedures are outlined below. Analytical results are reported in Table 2. Yields were generally in excess of 90%, based on the quantity of metal dissolved from the anode.

$M(SR)_2$ (M = Co, Ni; R = C_6H_5, 2,3,5,6-C_6F_4H, o-$CH_3C_6H_4$, 2-$C_{10}H_7$)

The brown–red products precipitated from the anode as the reaction proceeded, and were collected, washed with CH_3CN, or acetone (15 mL) and then *n*-pentane or diethyl ether (10 mL), and dried *in vacuo*. The products are all insoluble in aromatic solvents, acetonitrile, dimethylsulphoxide, and dimethylformamide, but are slightly soluble in pyridine; this latter solubility increases with temperature.

$M(SR)_2L_2$ (L = 2,2'-bipyridine, 1,10-phenanthroline)

As the electrolysis proceeded, the colour of the solution changed from pale brown to deep red–brown for cobalt, and to green for nickel. After the end of the electrolysis, the flow of nitrogen through the solution was continued for periods of 2–16 h during which time crystals deposited in the cell as the solvent slowly evaporated. These crystals were collected, washed with cold solvent and then diethyl ether, and dried *in vacuo*. The compounds are soluble in acetonitrile or dimethylsulphoxide, but insoluble in aromatics.

With chloroform, there is evidence of reaction, since colour changes were generally observed. In a brief study, $Ni(SC_6H_5)_2(phen)_2$ (0.61 g) was suspended in chloroform (60 mL) and the mixture stirred for 3 days at 20°C under nitrogen. The green solid gradually dissolved to give a yellow solution which slowly deposited a green–yellow solid which was collected, washed with $CHCl_3$ (10 mL) and dried *in vacuo*. Yield 0.51 g. Analysis Ni 9.8, Cl 11.3; c.f. $NiCl_2(phen)_2$: calcd. Ni 12.0, Cl 14.5; $NiCl(SC_6H_5)(phen)_2$: calcd. Ni 10.4, Cl 6.3. The filtrate from this reaction was taken to dryness, and the resultant red–yellow solid extracted with diethyl ether (100 mL). This extract contained $(C_6H_5)_2S_2$;

[1]Present address: Department of Chemistry, University of Manitoba, Winnipeg, Man., Canada R3T 2N2.

[2]Permanent address: Departamento de Quimica Inorganica, Facultad de Farmacia, Universidad de Santiago de Compostela, Spain.

[3]To whom correspondence should be addressed.

Can. J. Chem. Downloaded from www.nrcresearchpress.com by 112.217.228.212 on 09/07/12
For personal use only.

TABLE 1. Experimental conditions for the electrochemical synthesis of cobalt and nickel thiolato compounds

Thiol	Solvent[a]	Quantity RSH	Ligand[b]	Mass	Applied[c] voltage (V)	Time of electrolysis (h)	Metal dissolved (mg)	E_F (mol F^{-1})
M = Co								
C_6H_5SH	CH_3CN	1 mL			10	2	48	0.54
o-$CH_3C_6H_4SH$	CH_3CN	0.5 mL			10	2	39	0.44
2-$C_{10}H_7SH$	CH_3CN	0.25 g			15	2	47	0.53
C_6H_5SH	CH_3CN	1 mL	phen	0.30	20	3	51	0.39
o-$CH_3C_6H_4SH$	CH_3CN	1 mL	phen	0.35	15	2	36	0.41
2-$C_{10}H_7SH$	CH_3CN	0.3 g	phen	0.30	15	2	44	0.50
M = Ni								
C_6H_5SH	Acetone	1 mL			30	2	44	0.50
2,3,4,5-C_6F_4HSH	CH_3CN	0.5 mL			20	2	40	0.46
o-$CH_3C_6H_4SH$	Acetone	1 mL			15	2	27	0.31
2-$C_{10}H_7SH$	Acetone	0.3 g			20	1	21	0.47
C_6H_5SH	Acetone	0.75 mL	phen	0.30	25	2	39	0.44
2,3,4,5-C_6F_4HSH	CH_3CN	0.75 mL	phen	0.25	15	2	42	0.48
o-$CH_3C_6H_4SH$	Acetone	1 mL	phen	0.42	10	2.5	40	0.36
2-$C_{10}H_7SH$	Acetone	0.35 g	phen	0.30	20	1.5	37	0.56
C_6H_5SH	Acetone	1 mL	bpy	0.25	25	2	43	0.49
2,3,4,5-C_6F_4HSH	CH_3CN	0.85 mL	bpy	0.30	15	2.5	46	0.42
o-$CH_3C_6H_4SH$	Acetone	1 mL	bpy	0.30	10	2.5	33	0.30
2-$C_{10}H_7SH$	Acetone	0.35 g	bpy	0.25	20	1.5	33	0.50

[a]50 mL, containing ca. 40 mg Et_4NClO_4.
[b]phen = 1,10-phenanthroline; bpy = 2,2′-bipyridine.
[c]Voltage required to produce an initial current of 20 mA.

TABLE 2. Analytical and related results for cobalt and nickel thiolates

Thiol R=	Compound	Colour	Metal (%) Found	Metal (%) Calculated
C_6H_5	$Co(SR)_2$	Brown	20.9	21.3
	$Co(SR)_2(phen)_2$	Red–brown	8.7	9.3
o-$CH_3C_6H_4$	$Co(SR)_2$	Brown	18.6	19.3
	$Co(SR)_2(phen)_2$[a]	Red–brown	8.3	8.9
2-$C_{10}H_7$	$Co(SR)_2$	Brown	16.1	15.6
	$Co(SR)_2(phen)_2$	Red–brown	7.8	8.0
C_6H_5	$Ni(SR)_2$	Brown	22.1	21.2
	$Ni(SR)_2(phen)_2$[b]	Green	9.4	9.8
	$Ni(SR)_2(bpy)_2$	Green	10.5	10.0
2,3,4,5-C_6F_4H	$Ni(SR)_2$	Brown	14.1	13.9
	$Ni(SR)_2(phen)_2$[c]	Red–yellow	8.1	7.5
	$Ni(SR)_2(bpy)_2$	Yellow	8.3	8.0
o-$CH_3C_6H_4$	$Ni(SR)_2$	Brown	18.9	19.3
	$Ni(SR)_2(phen)_2$[d]	Yellow-gold	7.9	8.8
	$Ni(SR)_2(bpy)_2$	Red–brown	10.5	10.0
2-$C_{10}H_7$	$Ni(SR)_2$	Red-brown	16.6	15.6
	$Ni(SR)_2(phen)_2$[e]	Green	7.7	7.9
	$Ni(SR)_2(bpy)_2$	Green	8.6	8.5

[a] Found C 67.3, H 3.8, N 9.9; calcd. C 67.8, H 4.1, N 8.8.
[b] Found C 67.1, H 4.8, N 8.3; calcd. C 67.8, H 4.1, N 8.8.
[c] Found C 53.8, H 1.9, N 7.3; calcd. C 55.3, H 2.3, N 7.1.
[d] Found C 64.2, H 4.4, N 8.3; calcd. C 68.6, H 4.5, N 8.4.
[e] Found C 70.5, H 4.3, N 6.7; calcd. C 71.3, H 4.1, N 7.6.

mp 55°C (c.f. 58°C for a genuine sample), ^1H nmr spectrum identical with that of a genuine sample (7.07–7.63 m ppm from Me_4Si). The residue from this ether extraction (80 mg) had Ni 8.5%. This evidence does not allow us to identify the reaction unambiguously, but it appears to be similar to that observed with $CuSC_6H_5(phen)$, where $(C_6H_5)_2S_2$ and a copper(I) chloride derivative were identified (5).

[Co(SC$_6$H$_5$)$_2$(phen)$_2$]ClO$_4$(1)

In investigating the Co/C_6H_5SH/phen system, we observed a colour change from red–brown to green when the solution was exposed to air. In a subsequent experiment, oxygen was bubbled through a solution prepared in the way described above; green crystals deposited on slow evaporation of the cooled solution. These were collected,

Can. J. Chem. Downloaded from www.nrcresearchpress.com by 112.217.228.212 on 09/07/12
For personal use only.

Can. J. Chem. Downloaded from www.nrcresearchpress.com by 112.217.228.212 on 09/07/12
For personal use only.

TABLE 3. Crystallographic and related data for $[Co(SPh)_2(phen)_2]ClO_4$, $C_{36}H_{26}N_4S_2CoClO_4$

a (Å)	9.665(4)
b (Å)	13.044(5)
c (Å)	13.838(6)
α (°)	81.06(3)
β (°)	75.07(3)
γ (°)	71.79(3)
V (Å^3)	1596(1)
Crystal system	Triclinic
Space group	$P\bar{1}$
Mol. wt.	736.4
Z	2
ρ_c(g cm^{-3})	1.53
ρ_o(g cm^{-3})	1.51
Crystal dimensions (mm)	0.11 × 0.15 × 0.19
Radiation	Mo-K_α, 0.71069 Å
Monochromator	highly oriented graphite
Temperature (°C)	21
Absorption coefficient, μ (cm^{-1})	7.4
2 θ angle (°)	3–45
Scan type	Coupled θ (crystal)/2 θ (counter)
Scan width	$K\alpha_1 - 1°$ to $K\alpha_2 + 1°$
Scan speed (°min^{-1})	Variable, 1.50–3.91
Background time/scan time	0.5
Total reflections measured	4644
Unique data used	2687 [$I > 2\sigma(I)$]
No. of parameters (NP)	253
R	0.0995
R_w	0.101

washed with *n*-pentane (10 mL) and dried *in vacuo*. *Anal.* calcd. for $C_{36}N_{26}N_4S_2CoClO_4$: C 58.7, H 3.6, N 7.6, Co 8.0; found: C 59.3, H 3.4, N 7.6, Co 7.9.

The uv/visible spectrum of **1** had λ_{max} = 395 nm, $\epsilon = 2.2 \times 10^4$ mol^{-1} L cm^{-1}. A prominent feature of the infrared spectrum was a broad strong band at 1070 cm^{-1}, identified as ν_3 of ClO_4^-.

Crystallographic analysis

A suitable crystal of $[Co(SC_6H_5)_2(phen)_2]ClO_4$ (**1**), prepared by the method described above, was sealed in a capillary tube and mounted along the largest dimension in a Syntex $P2_1$ diffractometer. The cell dimensions (Table 3) were obtained from the least squares refinement of the setting angles of 15 high angle reflections ($15° > 2\theta > 30°$). The density was determined by flotation in carbon tetrachloride/benzene mixtures.

Relevant information on the X-ray crystallographic experiment is given in Table 3. The intensities of three mounted reflections did not change significantly during the data collection. Details of the collection and reduction of the experimental data, and the sources of the scattering factors and computer programmes used, have been described previously (8, 9).

The intensity statistics suggested a centric space group, and the space group $P\bar{1}$ was assumed, and subsequently confirmed by a successful refinement. The position of the cobalt atom was determined by a sharpened Patterson synthesis using SHELX, and the remaining atoms were revealed by subsequent difference maps. The cobalt, sulfur, nitrogen, chlorine, and oxygen atoms of **1** were refined anisotropically, and the remainder isotropically. Hydrogen atoms were included in the final refinements in ideal positions (C—H = 0.95 Å, CCH = 120°), with isotropic U-values set at 0.1 Å^2 greater than those of the corresponding carbon atoms. The function minimized in the least squares refinement was $(|F_o| - |F_c|)^2$, and a weighting scheme of the form $\omega = 1/[\sigma^2(F) + \rho f^2]$ was used, with a final ρ-value of 0.0001. No evidence of secondary extinction was found. The refinement converged at R = 0.0995, and R_w = 0.101. These high values are apparently related to the high thermal parameters of the oxygen atoms of the perchlorate anion and to an unresolved disorder problem in the anion; neither of these affect the details of the structure of the cation.

The final coordinates for the non-hydrogen atoms are given in Table 4 and important bond distances and angles in Table 5. Tables of fractional coordinates and thermal parameters for hydrogen atoms, of anisotropic thermal parameters, and of observed and calculated structure factors have been deposited, as has a packing diagram of the unit cell.[4]

Results and discussion

Preparative

As with other direct electrochemical syntheses developed in this laboratory, the anodic oxidation of cobalt or nickel in the presence of a thiol is a simple efficient one-step route to $Co(SR)_2$ and $Ni(SR)_2$ species. The present experiments involved the preparation of only small quantities of product in short experiments, but larger cells, or cells run in series, are easily operated for the synthesis of gram quantities of product. The characterization of these substances depended on elemental analysis, and on infrared spectroscopy which confirmed the presence of the appropriate SR and neutral donor ligands.

The average E_F value (defined as moles of metal dissolved per Faraday of charge) for the formation of $M(SR)_2$ (see Table 1) is 0.50 mol F^{-1} for Co, and 0.44 mol F^{-1} for Ni, although in the latter case the average is significantly affected by the result for *o*-$CH_3C_6H_4SH$, where the product adhered to the electrode thereby lowering the efficiency of the anode reaction. The overall average of ~0.50 mol F^{-1}, and the formation of H_2 at the cathode, is in keeping with the mechanism proposed previously (1):

$$\text{cathode: } 2RSH + 2e \rightarrow H_2 + 2RS^-$$

$$\text{anode: } 2RS^- + M \rightarrow M(SR)_2 + 2e$$

We may note here that this same E_F, and hence the same mechanism, applies to the formation of $M(SR)_2L_2$ adducts (L = bpy, phen), confirming that adduct formation follows the anodic oxidation process. A number of E_F values below 0.5 were observed, and in each case this was associated with the formation of materials adhering to the anode.

The insolubility of $M(SR)_2$ in common organic solvents other than pyridine for M = Co or Ni is similar to the behavior of other simple metal thiolates (2, 5, 10), and is most likely due to extensive secondary coordination, linking together $M(SR)_2$ units by S→M donation, which would be in keeping with the known ability of both Co^{II} and Ni^{II} to form four-coordinate $M(SR)_4^{2-}$ complexes (11, 12), and with the physical properties of these and other $M(SR)_2$ compounds.

All the cobalt(II) and nickel(II) $M(SR)_2$ compounds prepared form adducts with the bidentate donors bpy and phen. Surprisingly such compounds do not appear to have been reported previously. Given their solubility in organic solvents, and the known coordination chemistry of the two elements, these compounds can all be reasonably classified as monomeric species, with *cis*-$MS_2(N_2)_2$ coordination kernels. Magnetic studies on two such compounds, namely $Co(SC_6H_5)_2(phen)_2$ and $Ni(SC_6H_5)_2(phen)_2$, gave corrected values of μ_{eff} = 2.70 and 3.30 BM, respectively. For the nickel(II) compound, the magnetic moment is at the high end of the range of values reported for octahedral d^8 species (13), which is explicable in

[4]Complete set of data available upon request, at a nominal charge, from the Depository of Unpublished Data, CISTI, National Research Council of Canada, Ottawa, Ont., Canada K1S 0A2.

TABLE 4. Final fractional coordinates and isotropic thermal parameters for non-hydrogen atoms of $[Co(SC_6H_5)_2(phen)_2]ClO_4$, with standard deviations in parentheses

Atom	x	y	z	U_{eq}/U^a ($Å^2 \times 10^3$)
Co	0.5096(2)	0.2199(1)	0.1834(1)	24(1)
Cl	0.1080(5)	0.7342(3)	0.5715(4)	59(3)
S(1)	0.3759(4)	0.3440(3)	0.0789(3)	40(2)
S(2)	0.6313(4)	0.1372(3)	0.0383(3)	36(2)
N(1)	0.6433(11)	0.3106(8)	0.1651(8)	53(7)
N(2)	0.4064(13)	0.3014(9)	0.3026(7)	60(7)
N(3)	0.3792(12)	0.1244(9)	0.2099(8)	63(8)
N(4)	0.6215(12)	0.1073(9)	0.2694(8)	61(8)
O(1)	0.2624(11)	0.7252(10)	0.5634(9)	61(8)
O(2)	0.0202(17)	0.7970(20)	0.6447(22)	197(20)
O(3)	0.0831(15)	0.6347(12)	0.6013(14)	88(10)
O(4)	0.0730(23)	0.7616(25)	0.4831(19)	186(28)
C(11)	0.2825(15)	0.4633(11)	0.1447(10)	37(3)
C(12)	0.1480(17)	0.4708(12)	0.2130(11)	47(4)
C(13)	0.0800(19)	0.5581(13)	0.2696(13)	62(5)
C(14)	0.1444(19)	0.6428(15)	0.2515(14)	67(5)
C(15)	0.2767(18)	0.6371(13)	0.1819(12)	51(5)
C(16)	0.3454(17)	0.5477(12)	0.1260(11)	45(5)
C(21)	0.7165(14)	0.0009(10)	0.0744(9)	39(3)
C(22)	0.6431(16)	−0.0796(11)	0.0813(10)	32(4)
C(23)	0.7111(18)	−0.1871(13)	0.1057(12)	55(4)
C(24)	0.8525(19)	−0.2152(14)	0.1215(13)	62(5)
C(25)	0.9250(20)	−0.1401(14)	0.1165(13)	63(5)
C(26)	0.8608(15)	−0.0352(12)	0.0925(10)	41(4)
C(31)	0.2821(14)	0.2922(11)	0.3747(10)	32(3)
C(32)	0.2214(16)	0.3605(11)	0.4521(11)	41(4)
C(33)	0.2833(16)	0.4402(12)	0.4565(11)	46(4)
C(34)	0.4068(16)	0.4515(12)	0.3852(11)	42(4)
C(35)	0.4695(14)	0.3805(11)	0.3077(10)	31(3)
C(36)	0.5910(14)	0.3871(10)	0.2334(9)	26(3)
C(37)	0.6639(16)	0.4656(12)	0.2327(11)	43(4)
C(38)	0.7894(18)	0.4659(14)	0.1572(12)	60(5)
C(39)	0.8405(17)	0.3905(12)	0.0879(12)	49(4)
C(40)	0.7628(15)	0.3173(11)	0.0915(10)	37(4)
C(41)	0.4776(17)	0.5345(12)	0.3807(12)	51(4)
C(42)	0.5967(17)	0.5396(13)	0.3096(12)	55(4)
C(51)	0.2613(15)	0.1319(11)	0.1710(10)	32(3)
C(52)	0.1874(17)	0.0549(12)	0.1940(11)	50(4)
C(53)	0.2272(17)	−0.0326(13)	0.2569(12)	52(4)
C(54)	0.3485(17)	−0.0447(12)	0.3012(11)	48(4)
C(55)	0.4241(15)	0.0365(11)	0.2730(10)	38(4)
C(56)	0.5537(14)	0.0267(11)	0.3070(10)	32(3)
C(57)	0.6102(18)	−0.0620(13)	0.3725(12)	55(4)
C(58)	0.7385(18)	−0.0637(13)	0.4021(12)	57(5)
C(59)	0.8038(17)	0.0151(12)	0.3686(11)	51(4)
C(60)	0.7442(15)	0.0983(11)	0.3024(10)	37(3)
C(61)	0.4080(20)	−0.1356(15)	0.3692(13)	70(5)
C(62)	0.5268(18)	−0.1410(14)	0.4032(13)	61(5)

[a] U_{eq} for the non hydrogen atoms is calculated from the refined anisotropic thermal parameters ($U_{eq} = 1/3\ \Sigma_i\Sigma_j U_{ij} a_i^* a_j^* a_i \cdot a_j$).

terms of a strong distortion from O_h symmetry in the NiS_2N_4 kernel, plus a significant orbital contribution. The result for the cobalt complex shows that this is an example of the unusual low-spin d^7 state, arising from the presence of the high field 1,10-phenanthroline ligands and the low symmetry (13), which persists on oxidation as shown in the next section. The redox chemistry of such compounds might prove interesting, given the ease with which the cobalt(III) species **1** is formed by aerial oxidation.

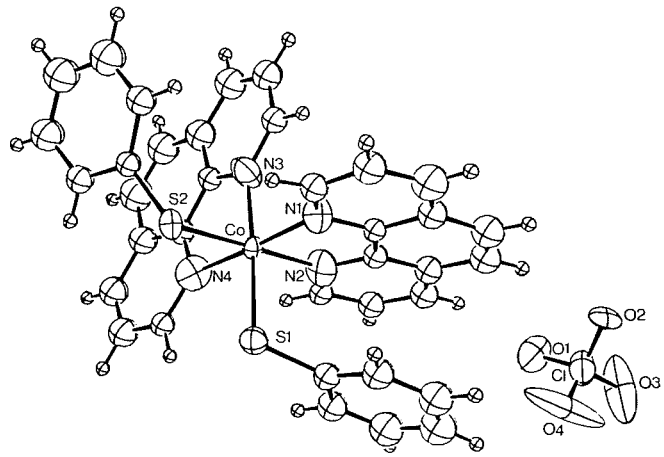

FIG. 1. Molecular structure of $[Co(SC_6H_5)_2(phen)_2]ClO_4$ showing the atomic numbering scheme. Ortep diagram, with 50% probability ellipsoids.

Structure of $[Co(SPh)_2(phen)_2]ClO_4$

The X-ray crystallographic results show unambiguously that **1** is indeed the 1:1 salt of a cobalt(III) complex, with the cation balanced by a perchlorato anion whose origin must be in the Et_4NClO_4 added to the electrolyte solution as part of our standard technique to enhance the initial conductivity (see Table 1). There is little doubt that the formation of this compound is the result of aerial oxidation, which is a common feature of the chemistry of cobalt(II). The structural features of the ClO_4^- anion in **1** are those of a slightly distorted tetrahedral anion, with r(Cl—O) = 1.35(3) Å (av) and O—Cl—O = 110(4)° (av), values which call for no special comment.

The cation (see Fig. 1), with its *cis*-CoS_2N_4 kernel of distorted octahedral geometry, is one of the few examples of a cobalt(III)–thiolato complexes, although several cobalt(II) compounds have been studied crystallographically (11, 12). Both mononuclear and polynuclear cobalt (III) structures with such ligands have been identified. The square-planar $[Co(S\text{-}2,4,6\text{-}i\text{-}Pr_3C_6H_2)_4]^-$ anion (**2**) has been investigated (14), as have polymeric $Co(SR)_3$ compounds (15, 16) and the square-planar $[Co(S_2\text{-}1,2\text{-}C_2H_4)_2]^-$ anion (17), and these provide a limited basis against which to compare the present results. The average Co—S bond distance in **1** is 2.297(4) Å, while in **2** the average is 2.207(3) Å, and this contraction is explicable in terms of the lower coordination number. The average Co—S distance in octahedral $Co^{III}S_6$ complexes has been given (18) as 2.27 Å, although there are no structures which are directly comparable with **1**. In the cation $[Co(ttcn)_2]^{3+}$ (ttcn = 1,4,7-trithiacyclononane, $C_6H_{12}S_3$), the average Co—S bond length in the CoS_6 octahedral kernel is 2.253(3) Å (19), and the analogous values in the cobalt(III)–thiosulphate complexes $[(en)_2Co(NO_2)(S_2O_3)]$ and $[(en)_2Co(S_2O_3)_2]^+$ are 2.281(3) and 2.263(3) Å, respectively (20), but such molecules are obviously different in ligand type from **1**, and the overall conclusion can only be that the present value is compatible with those in the literature as far as the comparisons can be made at present.

The Co^{III}—N bond distances in **1** give an average value of 1.97(1) Å. There are many reports of crystallographic studies of Co^{III}—N donors, but the most relevant and direct comparison is

Can. J. Chem. Downloaded from www.nrcresearchpress.com by 112.217.228.212 on 09/07/12
For personal use only.

TABLE 5. Bond distances (Å) and angles (°) for $[Co(SC_6H_5)_2(phen)_2]ClO_4$, with esd's in parentheses

Bond	Distance (Å)	Bonds	Angle (°)
Co—S(1)	2.305(4)	S(1)—Co—S(2)	83.1(1)
Co—S(2)	2.289(4)	S(1)—Co—N(1)	89.2(3)
Co—N(1)	1.96(1)	S(2)—Co—N(1)	94.1(3)
Co—N(2)	1.97(1)	S(1)—Co—N(2)	93.9(3)
Co—N(3)	1.97(1)	S(2)—Co—N(2)	175.7(3)
Co—N(4)	1.97(1)	N(1)—Co—N(2)	82.7(4)
Cl—O(1)	1.44(1)	S(1)—Co—N(3)	94.2(3)
Cl—O(2)	1.34(2)	S(2)—Co—N(3)	87.7(3)
Cl—O(3)	1.38(1)	N(1)—Co—N(3)	176.3(5)
Cl—O(4)	1.32(2)	N(2)—Co—N(3)	95.6(5)
S(1)—C(11)	1.79(1)	S(1)—Co—N(4)	176.7(3)
S(2)—C(21)	1.78(1)	S(2)—Co—N(4)	94.8(3)
N(1)—C(36)	1.37(2)	N(1)—Co—N(4)	93.4(4)
N(1)—C(40)	1.35(2)	N(2)—Co—N(4)	88.3(5)
N(2)—C(31)	1.37(2)	N(3)—Co—N(4)	83.2(5)
N(2)—C(35)	1.37(2)	O(1)—Cl—O(2)	111(1)
N(3)—C(51)	1.35(2)	O(1)—Cl—O(3)	110(1)
N(3)—C(55)	1.36(2)	O(2)—Cl—O(3)	105(1)
N(4)—C(56)	1.38(2)	O(1)—Cl—O(4)	111(1)
N(4)—C(60)	1.34(2)	O(2)—Cl—O(4)	116(2)
Ring C(11)—C(16)*		O(3)—Cl—O(4)	105(2)
mean C—C	1.38(2) Å	Co—S(1)—C(11)	106.8(5)
mean C—C—C	120(2)°	Co—S(2)—C(21)	106.7(4)
		Co—N(1)—C(36)	111.6(8)
Ring C(21)—C(26)		C(36)—N(1)—C(40)	117(1)
mean C—C	1.38(2) (Å)	Co—N(2)—C(31)	129.5(9)
mean C—C—C	120(2)°	Co—N(2)—C(35)	111.8(9)
Ring C(31)—C(42)		C(31)—N(2)—C(35)	119(1)
mean C—C	1.37(2) Å	Co—N(3)—C(51)	129.6(9)
mean C—C—C	120(2)°	Co—N(3)—C(55)	112.2(9)
Ring C(51)—C(62)			
mean C—C	1.37(2) Å	C(51)—N(3)—C(55)	118.1(11)
mean C—C—C	120(2)°	Co—N(4)—C(56)	112.4(8)
		Co—N(4)—C(60)	132(1)
		C(56)—N(4)—C(60)	115(1)
		S(1)—C(11)—C(12)	120(1)
		S(1)—C(11)—C(16)	119(1)
		S(2)—C(21)—C(22)	121(1)
		S(2)—C(21)—C(26)	122(1)

*The esd's on average values are calculated with the use of the "scatter formula": $\sigma = [\Sigma(d_i - \bar{d})^2/N - i)]^{1/2}$.

with the *cis*-$[Co(phen)_2CO_3]^+$ cation (21), in which Co—N = 1.929(7) (av) and the N—Co—N bite angle = 84.3(3) (av), values which are in reasonable agreement with those in Table 5. The structural features of benzenethiolate and 1,10-phenanthroline in **1** are essentially identical to those in other complexes containing these ligands (4).

Acknowledgements

This work was supported in part by Operating Grants (to D.G.T.) from the Natural Sciences and Engineering Research Council of Canada. Professor R. C. Rumfeldt is thanked for his comments on the magnetic results.

1. W. LOVENBERG (*Editor*). Iron–sulfur proteins. Vols. I and II. Academic Press, New York. 1973.
2. F. F. SAID and D. G. TUCK. Inorg. Chim. Acta, **59**, 1 (1982).
3. J. L. HENCHER, M. A. KHAN, F. F. SAID, and D. G. TUCK. Polyhedron, **4**, 1263 (1985).
4. J. L. HENCHER, M. A. KHAN, F. F. SAID, R. SIELER, and D. G. TUCK. Inorg. Chem. **21**, 2787 (1982).
5. R. K. CHADHA, R. KUMAR, and D. G. TUCK. Can. J. Chem. **65**, 1336 (1987).
6. M. A. KHAN, R. KUMAR, and D. G. TUCK. Polyhedron. **7**, 49 (1980).
7. C. OLDHAM and D. G. TUCK. J. Chem. Educ. **59**, 420 (1982).
8. M. A. KHAN, R. C. STEEVENSZ, D. G. TUCK, J. G. NOLTES, and P. W. R. CORFIELD. Inorg. Chem. **19**, 3407 (1980).
9. M. A. KHAN, C. PEPPE, and D. G. TUCK. Acta Crystallogr. C**39**, 1339 (1983).
10. S. J. BLACK, F. W. B. EINSTEIN, P. C. HAYES, R. KUMAR, and D. G. TUCK. Inorg. Chem. **25**, 4181 (1986).
11. I. G. DANCE. Polyhedron, **5**, 1037 (1986).
12. P. J. BLOWER and J. R. DILWORTH. Coord. Chem. Rev. **76**, 121 (1987).

Can. J. Chem. Downloaded from www.nrcresearchpress.com by 112.217.228.212 on 09/07/12
For personal use only.

13. B. N. FIGGIS. Introduction to ligand fields. Wiley, New York. pp. 289–290.
14. R. FIKAR, S. A. KOCH, and M. M. MILLAR. Inorg. Chem. **24**, 3311 (1985).
15. B. J. MCCORMICK and G. GORIN. Inorg. Chem. **2**, 928 (1963).
16. C. J. SWAN and D. L. TRIM. Chem. Ind. 1363 (1967).
17. J. R. DORFMAN, C. P. RAO, and R. H. HOLM. Inorg. Chem. **24**, 453 (1985).
18. R. D. SHANNON. *In* Structure and bonding in crystals. Vol. 2. *Edited by* M. O'Keeffe and A. Navrotsky. Academic Press, New York. 1981. Chap. 16.
19. H. J. KÜPPERS, A. NEVES, C. POMP, D. VENTUR, K. WIEGHARDT, B. NUBER, and J. WEISS. Inorg. Chem. **25**, 2400 (1986).
20. A. R. MURDOCK, T. TYREE, W. OTTERBEIN, L. KINNEY, M. CARRERAS, J. N. COOPER, and R. C. ELDER. Inorg. Chem. **24**, 3674 (1985).
21. E. C. NIEDERHOFFER, A. E. MARTELL, P. RUDOLF, and A. CLEARFIELD. Inorg. Chem. **21**, 3734 (1982).

Can. J. Chem. Downloaded from www.nrcresearchpress.com by 112.217.228.212 on 09/07/12
For personal use only.

Dérivés hydrosilylés des complexes (η-arène) tricarbonylchrome, de type (η C_6R_6)$(CO)_2$Cr(H)$SiHPh_2$; liaison à 2 électrons/3 centres, Cr—H—Si

ELISABETH MATARASSO-TCHIROUKHINE ET GÉRARD JAOUEN

École nationale supérieure de chimie de Paris, Unité Associée 403, 11, rue Pierre et Marie Curie, 75231 Paris CEDEX 05, France

Reçu le 26 octobre 1987

ELISABETH MATARASSO-TCHIROUKHINE et GÉRARD JAOUEN. Can. J. Chem. **66**, 2157 (1988).

L'action photochimique, à basse température, du diphénylsilane sur les complexes (η arène) tricarbonylchrome conduit à des dérivés hydrosilylés instables, de type (η C_6R_6)$(CO)_2$Cr(H)$SiHPh_2$, qui possèdent une liaison à 2 électrons/3 centres, Cr—H—Si. Le degré de cette liaison est supérieur à celui de la liaison Mn—H—Si dans les complexes isoélectroniques du manganèse, (η C_5R_5)L_2Mn(H)$SiHPh_2$, d'une part, et à celui de la liaison Cr—H—Si dans le complexe permethylé, (η C_6Me_6)$(CO)_2$Cr(H)$SiHPh_2$, d'autre part. La variation de $|^2J$(Cr—H—Si)| est discutée en fonction de la densité électronique sur le métal.

ELISABETH MATARASSO-TCHIROUKHINE and GÉRARD JAOUEN. Can. J. Chem. **66**, 2157 (1988).

Diphenylsilane reacts photochemically, at low temperature, on the η(tricarbonylchromium) arenes, to give unstables hydrosilylcomplexes, (η-C_6R_6)$(CO)_2$Cr(H)$SiHPh_2$ with a three-center two-electron bond, Cr—H—Si; according to ^{29}Si NMR data, the degree of this bond is higher than both the degree of the Mn—H—Si bond in isoelectronic manganese compounds, (η-C_5R_5)L_2Mn(H)$SiHPh_2$, and the degree of the three-center Cr—H—Si bond in the permethylated complex, (η-C_6Me_6)$(CO)_2$Cr(H)$SiHPh_2$, of chromium. The variation of $|^2J$(Si—Cr—H)| depending on the electron density of the metal is discussed.

Introduction

L'addition oxydante des silanes sur les métaux de transition se rattache à un problème qui a suscité beaucoup d'intérêt au cours des deux dernières décennies (1, 2); en effet, elle conduit à des complexes qui jouent un rôle d'intermédiaires important dans les hydrosilylations catalysées par ces métaux. Il a été suggéré que ces réactions procèdent en faisant intervenir une liaison à 2 électrons/3 centres (3–5) (cf. schéma 1).

Les complexes du manganèse de type (η $C_5R'_5$)L_2Mn(H)-$SiR^1R^2R^3$, décrits déjà en 1970–1971 (6, 7), ont été, depuis, l'objet d'études exhaustives (8, 9). En effet, la mise en évidence dans ces complexes d'une liaison à 2 électrons/3 centres Mn—H—Si, comparable à la liaison agostique C—H—M (10), permet de les considérer comme des états « gelés » des coordonnées de la réaction d'addition oxydante des silanes (11).

Afin d'étudier *l'influence sur le degré 2e/3c de la liaison M—H—Si* de la *nature du métal*, d'une part, et de la *densité électronique sur le métal*, d'autre part, nous avons étendu l'étude de l'addition oxydante du diphénylsilane aux complexes (η arène) tricarbonylchrome.[1]

Résultats et discussion

Les complexes (η arène) tricarbonylchrome **1**(*a–d*) réagissent sur le diphénylsilane, par irradiation UV à basse température et sous atmosphère inerte, pour conduire aux complexes **2**(*a–d*) (cf. schéma 2), caractérisés par spectroscopie RMN des ^{1}H, ^{29}Si et ^{13}C.

Les complexes **2**(*a–d*) présentent, d'une part, *une très grande instabilité à l'air* et, d'autre part, *une très grande instabilité thermique*. Sous atmosphère inerte, à température ambiante, **2***a* est décomposé en quelques jours, **2**(*c* et *d*) instantanément et ils le sont rapidement au-dessus de −20°C.

Les complexes **2**(*a,b*) ont été isolés cristallisés; seul **2***a* a pu être purifié par recristallisation (**2***b* subit une décomposition).

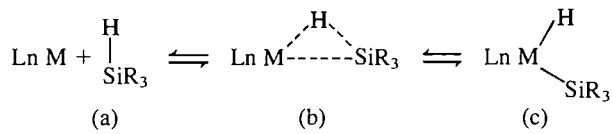

SCHÉMA 1

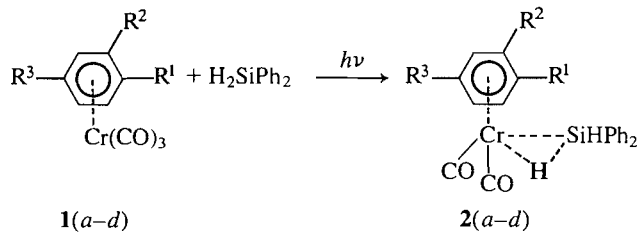

1(*a–d*) **2**(*a–d*)

1*a*, **2***a* $R^1 = R^2 = CH_3$; $R^3 = H$
1*b*, **2***b* $R^1 = CH_2N(CH_3)_2$; $R^2 = R^3 = H$
1*c*, **2***c* $R^1 = COOCH_3$; $R^2 = R^3 = H$
1*d*, **2***d* $R^1 = R^3 = COOCH_3$; $R^2 = H$

SCHÉMA 2

Les complexes **2**(*c,d*) très instables n'ont pu être cristallisés; les résultats obtenus, par specroscopie RMN des produits bruts, ont été confirmés par leur action sur PPh_3 qui conduit dans de bonnes conditions, par élimination réductrice du silane, aux complexes (η $R^1R^2C_6H_4$)$(CO)_2CrPPh_3$ (schéma 3).

Les complexes **2**(*a–d*) (cf. tableau 1) possèdent un proton lié au chrome (δ^1 H ~ −12 ppm) et un proton lié au silicium (δ^1 H ~ 6–7 ppm) dont le couplage $|^2J$(Si—Cr—H)| élevé, de l'ordre de 80 Hz, témoigne d'une liaison à 2 électrons/3 centres, Cr—H—Si. En effet, on sait (8) qu'une valeur élevée de $|^2J$(Si—M—H)|, comme $|^2J$(C—M—H)| pour la liaison agostique M—H—C (10), est caractéristique d'une liaison à 2 électrons/3 centres, M—H—Si, et sert de sonde pour la détermination du degré d'intéraction du silicium et de l'hydrogène: sa valeur absolue est en fonction croissante de cette

1. Pendant la dernière phase de ce travail est paru un article de U. Schubert *et al.* (12), concernant la structure et les propriétés du complexe (η Me_6C_6)$(CO)_2$Cr(H)$SiHPh_2$.

Printed in Canada / Imprimé au Canada

Can. J. Chem. Downloaded from www.nrcresearchpress.com by 196.1.178.254 on 09/07/12
For personal use only.

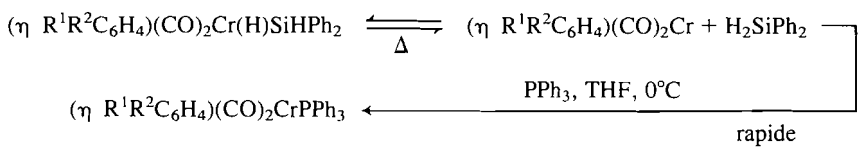

SCHÉMA 3

intéraction, c.a.d. du degré 2e/3c de la liaison à 2 électrons/3 centres M—H—Si.

Le degré 2e/3c de la liaison Cr—H—Si est supérieur à celui de la liaison Mn—H—Si dans les complexes du manganèse, de type (η $C_5R'_5$)(CO)LMn(H)(SiR_3) (8), pour lesquels ^2J(Mn—Si—H) ≤ 69 Hz; *^2J(Si—Cr—H) et ^1J(Si—H) sont fonction décroissantes de la densité électronique sur le métal* (cf. tableaux 1 et 2).[2]

L'accroissement de $|^1J$(Si—H)| a pour origine l'accroissement de l'électro-négativité du substituant au silicium (η C_6R_6)$(CO)_2$Cr (13).

L'accroissement de $|^2J$(Si—Cr—H)| peut avoir pour origine deux facteurs: (*a*) l'accroissement de l'électronégativité du substituant (η C_6R_6)$(CO)_2$Cr, au silicium, et (*b*) l'accroissement du degré de la liaison à 2 électrons/3 centres, Cr—H—Si.

Si l'on compare (cf. tableau 1) la variation, $\Delta|^2J|$ du couplage ^2J(Si—Cr—H) à la variation, $\Delta|^1J|$, du couplage ^1J(Si—H), il apparaît que :

1. *Lorsqu'on passe du dérivé perméthylé au complexe* **2**a $\Delta|^2J|$ *(~13%) est important par rapport à* $\Delta|^1J|$ *(~2%)*, ce qui permet de conclure à un *accroissement du degré de la liaison à 2 électrons/3 centres, Cr—H—Si.*

2. Lorsqu'on passe *du complexe* **2**a *au complexe* **2**d $\Delta|^2J|$ *(~2%) est faible par rapport à* $\Delta|^1J|$ *(~10%)* et peut avoir pour origine aussi bien la diminution de la densité électronique sur le métal que l'accroissement du degré de la liaison 2e/3c Cr—H—Si.

Toutefois, *l'instabilité thermique des complexes* **2**(*a–d*), également fonction décroissante de la densité électronique sur le métal, témoignerait en faveur de cette dernière hypothèse. En effet, on sait que l'instabilité thermique de ce type de complexes est liée à la tendance du silane à une élimination réductrice d'autant plus aisée que le degré d'intéraction Si—H est grand, nous avons montré par action de PPh_3 que l'élimination réductrice du silane dans le cas du complexe **2***c*, très lente à −40°C, devient aisée à 0°C, la vitesse de la réaction étant déterminée par la dissociation du complexe (14, 15) (cf. schéma 3).

La très faible variation de ^2J (dans les limites des erreurs expérimentales) observée (cf. tableau 1) en dépit d'une variation consistante de la densité électronique sur le métal, comme l'indique en spectroscopie IR la variation des fréquences $\nu(CO)_{Cr}$ (cf. tableau 2), suggère que la densité électronique sur le métal n'a qu'une influence très faible, sinon nulle, sur le caractère 2e/3c de la liaison Cr—H—Si pour les complexes **2**(*a–d*) de la série (η C_6R_6)$(CO)_2$Cr(H)$SiHPh_2$ étudiée.

Le dérivé perméthylé (η C_6Me_6)$(CO)_2$Cr(H)$SiHPh_2$ (12) se situe à part dans la série, avec un degré 2e/3c de la liaison Cr—H—Si, $|^2J$(Si—Cr—H)| = 70,8 Hz (12), relativement faible par rapport à ceux des autres complexes de la série $|^2J$(Si—Cr—H)| ~ 80 Hz, qui représenteraient des états gelés des coordonnées de l'addition oxydante du silane moins avancés, en d'autres termes, des états plus proche de (b) (cf. schéma 1).

Le déplacement chimique $\delta\,^{29}Si$ évolue vers les champs forts, lorsque la densité électronique sur le métal décroit. Un résultat analogue a été observé pour les complexes isoélectroniques du manganèse (η C_5R_5)(CO)LMn(H)$SiHPh_2$ (8).

L'addition oxydante du diphénylsilane aux complexes (η arène) tricarbonylchrome **1**(*c,d*), s'accompagne, dans les conditions expérimentales mises en jeu, d'une réaction secondaire non négligeable, qui conduit à des composés renfermant l'entité (SiH), mis en évidence dans le milieu réactionnel, en particulier, par la RMN du ^{29}Si.

Une première approche conduit à penser que ce sont des produits d'hydrosilylation, dont les complexes **2**(*c,d*) seraient les espèces précurseurs. Leur étude est en cours et fera l'objet d'une publication ultérieure.

Partie expérimentale

Toutes les manipulations concernant les produits sensibles à l'air ont été conduites en atmosphère inerte (argon) en utilisant la technique de Schlenk. Tous les solvants ont été distillés sur benzophénone Na avant usage. H_2SiPh_2 est préparé au laboratoire selon la réf. 16; il est distillé et conservé sous argon. $C_6H_5(COOCH_3)$, débarrassé de l'acide qu'il pouvait contenir, a été distillé sous argon sur hydrure de calcium et gardé sous argon. $C_6H_4(COOCH_3)_2$ et $Cr(CO)_6$, commerciaux, ont été dégazés sous pression réduite (environ 0,1 Torr; 1 Torr = 133,3 Pa) et gardés sous argon.

Complexes (η-arène) tricarbonyle chrome

Les complexes **1***a,b* ont été fournis par Monsieur G. Jaouen; les complexes **1***c,d* ont été préparé au laboratoire par action de $Cr(CO)_6$ sur l'arène correspondant avec une modification des techniques décrites (17, 18).[3]

$CH_3COOC_6H_5Cr(CO)_3$ ***1****c*: Une solution de $C_6H_5(COOCH_3)$ (6 mL) et de $Cr(CO)_6$ (2 g, 42) dans de l'oxyde de butyle (75 mL) à 10% de THF est portée à reflux à l'aide d'un bain d'huile à 130°C pendant 62 h. Le solvant est éliminé au rotavapor. Le solide résiduel est dissout dans du benzène et chromatographié sur colonne de silice, éluant hexane/benzène/éther (5:1:1); trois fractions sont isolées: I (têtes) (produits secondaires et $C_6H_5(COOCH_3)$ n'ayant pas réagit; II (**1***c*, produits secondaires et traces de $C_6H_5(COOCH_3)$; III (orangée), qui conduit au $C_6H_5(COOCH_3)Cr(CO)_3$ (**1***c*) par élimination du solvant au

2. Une conclusion identique a été émise (8) dans le cas des dérivés du manganèse, de type (η $C_5R'_5$)(CO)LMnHSiR_3, L = CO, PR_3, $P(OR)_3$, CNR. L'effet inverse observé dans le cas des composés (η C_5Me_5)$(CO)_2$Mn(H)$SiHPh_2$, ^2J = 65,4 Hz, et (η C_5H_4Me)$(CO)_2$-Mn(H)$SiHPh_2$, ^2J = 63,5 Hz, a été attribué à un effet stérique du noyau permethylé (8).

3. Les réactions sont délicates à conduire du fait de réactions secondaires et, à notre connaissance, non signalées dans la littérature, conduisant, en particulier à $C_6H_6Cr(CO)_3$, **1**′*c*, et $CH_3C_6H_5Cr(CO)_3$, **1**″*c*. Les vitesses de la complexation, ainsi que de la formation des complexes secondaires (qui atteint rapidement 100%), sont fonctions croissantes de la température de la réaction; il existe un rapport optimum *t*°C)/temps de la réaction.

Can. J. Chem. Downloaded from www.nrcresearchpress.com by 196.1.178.254 on 09/07/12
For personal use only.

TABLEAU 1. Données spectroscopiques RMN[a] des complexes arène $Cr(CO)_2(H)SiHPh_2$, **2**(*a–d*)

Arène	δ (Cr H)[b]	δ (Si–H)[b]	δ (^{13}CO)	δ ^{29}Si[c]	^1J(Si—H)/Hz	^2J(Si—Cr—H)/Hz
Me_6C_6 (12)	−11,5	+6,1		+21,2	197,0	70,8
ϕ-$Me_2C_6H_4$ (**2***a*)	−12,09[d]	+6,47[(d)]	+239,15	+17,6	201	80
$(CH_3)_2NCH_2C_6H_5$ (**2***b*)	−11,9	+6,7	+238,7	+17,08	203,5	79 ± 2
$(COOCH_3)C_6H_5$ (**2***c*)[e]	−12,15	+6,63	+236,6	+12,8	212 ± 1,5	81 ± 1
$(COOCH_3)_2C_6H_4$ (**2***d*)	−12,10		+235,75	+2,9	221,5 ± 2	82,5 ± 2

[a]En ppm, rapportées au TMS, $t = -40$°C; solvant : toluène-d_8, sauf indication contraire.
[b]Doublet.
[c]Quadruplet.
[d]^3J(H—Cr—Si—H) = 5,6 Hz.
[e]THF-d_8.

TABLEAU 2. Données spectroscopiques IR des composés arène $Cr(CO)_3$, **1**(*a–d*), et arène $Cr(CO)_2(H)SiHPh_2$, **2**(*a–d*)

	Arène $Cr(CO)_3$	Arène $Cr(CO)_2(H)SiHPh_2$	
Arène	$\nu(CO)_{Cr}/cm^{-1}$[a]	$\nu(CO)_{Cr}/cm^{-1}$	ν(Si–H)/cm^{-1}
Me_6C_6 (12)		1922 (vs), 1868(vs)	2016 (w)
ϕ-$Me_2C_6H_4$ (**2***a*)	1975 (s), 1910 (s)	1943 (s), 1885(s)[a]	2035 (w)
$(CH_3)_2NCH_2C_6H_5$ (**2***b*)	1980 (s), 1910 (s)	1945 (s), 1892[b] 1930, 1917, 1867, 1853[c]	2037 (w)
$(COOCH_3)C_6H_5$ (**2***c*)	1992 (s), 1931 (s)	1958 (s), 1907 (s)[b]	
$(COOCH_3)_2C_6H_4$ (**2***d*)	1994 (s), 1931 (s)	1965 (s), 1915 (s)[b]	

[a]Hexane.
[b]3-Me-pentane.
[c]Fluorolub, Nujol.

TABLEAU 3. Conditions expérimentales de la réaction photochimique d'hydrosilylation (cf. schéma 2)

Complexes **1**(*a–d*)	H_2SiPh_2	Solvant	*T* du liquide réfrigérant (°C)	Durée de l'irradiation (h)	*t* d'élimination du solvent (°C)	Complexes **2**(*a–d*)
1*a* 447 mg ≃ 1,85 mmol	1,4 mL ≃ 7,5 mmol	3-Me pentane, 50 mL Toluène, 10 mL	−15	3	0	**2***a* Cristaux jaunes purifiées par recristallisation[a]
1*b* 530 mg ≃ 1,96 mmol	1,5 mL ≃ 8 mmol	3-Me pentane, 50 mL Toluène, 10 mL	−26	4–5	−40 la fin à −28	**2***b* Cristaux jaunes non recristallisés (décomposition)
1*c* 220 mg ≃ 0,75 mmol	1 mL ≃ 5,4 mmol	Toluene, 30 mL	−36	4	−20	**2***c* Non isolé du mélange réactionnel brut rouge-brun
1*d* 318 mg ≃ 0,96 mmol	1 mL ≃ 5,4 mmol	Toluene, 35 mL	−35 à −30	2,5	−20	**2***d* Non isolé du mélange réactionnel brut

[a]*Anal.* calc. : C 65,12; H 5,54; Cr 13,06; Si 7,03%; tr. : C 66,33; H 5,50; Cr 12,11; Si 6,90%.

rotavapor; Rdt = 1,52 g soit 50%; RMN ^{1}H (toluène-d_8) δ ppm/TMS[4] : 3,32(s)(CH_3); 4,23(t), 4,52(t), 5,52(d). Dans les fractions de tête on a identifié par spectroscopie IR et RMN ^{1}H les complexes (*a*) $C_6H_6Cr(CO)_3$ **1**′*c* (majoritaire); IR (hexane) $\nu(CO)_{Cr}$ cm^{-1} : 1985; 1917; RMN ^{1}H (toluène-d_8) δ ppm/TMS : 4,28(s) aromatiques; et (*b*) $CH_3C_6H_5Cr(CO)_3$ **1**″*c*; IR (hexane) $\nu(CO)_{Cr}$ cm^{-1} : 1975, 1909; RMN ^{1}H (toluène-d_8) δ ppm/TMS : 1,54(s) (CH_3); 4,21–4,55 (aromatiques).

4. s : singulet; d : doublet; t triplet.

*$(CH_3COO)_2C_6H_4Cr(CO)_3$ **1**d :* Même procédé que pour **1***c*. **1***d* : RMN ^{1}H (benzène-d_6) δ ppm/TMS : 3,31(s) (CH_3); 5.49(s) aromatiques.

*Complexes (η arène) $Cr(CO)_2(H)SiHPh_2$, **2*** (a–d)

Le tableau 3 rassemble les conditions expérimentales de la réaction photochimique. De façon générale, on irradie par une lampe Hanovia-450W, refroidie par une gaine à ciculation d'eau en quartz et placée à 5–10 cm du mélange réactionnel, une solution du complexe arène tricarbonyle chrome et de diphényle silane en excès, contenue dans un réacteur en Pyrex à double paroi, qui permet de refroidir le mélange

Can. J. Chem. Downloaded from www.nrcresearchpress.com by 196.1.178.254 on 09/07/12
For personal use only.

réactionnel par la circulation d'un liquide approprié maintenu à basse température. Durant l'irradiation on fait passer un faible courant d'argon dans le mélange réactionnel agité. La réaction est suivie par spectroscopie infra-rouge, dans la région 2200–1700 cm^{-1} (cf. tableau 2). La réaction terminée, le traitement du mélange réactionnel varie légèrement suivant le complexe **2**(*a*–*d*) obtenu.

Dans le cas du composé **2***a*, qui est obtenu cristallisé dans le mélange réactionnel, le solvant est siphoné et le solide résiduel lavé plusieurs fois au 3-Me-pentane. Il est recristallisé à −40°C par addition de 3-Me-pentane, jusqu'à un léger trouble, à sa solution dans le minimum de toluène. Dans le cas du complexe **2***b* le mélange réactionnel est réduit à 1–2 mL en éliminant les solvants sous pression réduite, 20 mL de 3-Me-pentane sont ajoutés à la solution (formation d'un précipité flaconneux jaune) qui est maintenue à −40°C pendant 48 h. Un produit cristallisé, jaune-orangé, est ainsi obtenu; il est lavé plusieurs fois avec du 3-Me-pentane; les traces de solvant sont éliminées sous pression réduite à −40°C. Le produit brut ne se prête pas à la recristallisation selon la technique mise en jeu pour le composé **2***a* (décomposition). Dans le cas des complexes **2**(*c*,*d*), l'élimination du solvant à basse température conduit à un produit rouge-brun cristallisé pâteux.[5] Les tentatives de recristallisation ayant échoué (décomposition), les études spectroscopiques ont été réalisées sur les produits bruts.

Les spectres IR ont été enregistrés soit sur appareil Bomem-Michelson 100, soit sur appareil Bruker FT–IR 45.

Les spectres RMN ont été enregistrés sur appareil Bruker AM 250; les déplacements chimique de ^{29}Si ont été déterminés par rapport au diphénylsilane, pris comme référence interne, et reconvertis par rapport au TMS en prenant δ ^{29}Si diphenylsilane/TMS = −33,254 ppm, obtenu sur le même appareil avec le TMS comme référence interne.

5. Dans le cas du complexe **2***d*, en opérant comme dans le cas du complexe **2***b*, une seule et unique fois on a pu isoler des cristaux rouge vif se décomposant instantanément par élévation de *t* ou au contact de l'air. Il est vraisemblable que des traces d'impuretés accélèrent considérablement la décomposition.

Remerciements

Nous remercions Madame Hélène Le Pesant et Monsieur Yvon Besace pour leur assistance technique en spectroscopie IR–FT et RMN.

1. E. Lukevics, Z. V. Belyakova, M. G. Pomerantseva et M. G. J. Voronkov. J. Organomet. Chem. Libr. **5**, 1 (1975), et références citées.
2. J. L. Speier. Adv. Organomet. Chem. **17**, 407 (1979).
3. A. J. Chalk et J. F. Harrod. J. Am. Chem. Soc. **87**, 16 (1965).
4. J. F. Harrod, C. A. Smith et Khim Aye Than. J. Am. Chem. Soc. **94**, 8321 (1972).
5. C. Eaborn, D. J. Tune et D. R. M. Walton. J. Chem. Soc. Dalton Trans. 2255 (1973).
6. W. Jetz et W. A. G. Graham. Inorg. Chem. **10**, 4 (1971).
7. W. L. Hutcheon. Ph.D. thesis, University of Alberta, Edmonton. 1971.
8. U. Schubert, G. Schulz, J. Muller, K. Ackermann, B. Worle, et R. F. D. Stansfield. J. Organomet. Chem. **306**, 303 (1986), et références citées.
9. E. Colomer, R. J. P. Corriu, C. Marzin et A. Vioux. Inorg. Chem. **21**, 368 (1982), et références citées.
10. M. Brookhart et M. L. H. Green. J. Organomet. Chem. **250**, 395 (1983).
11. H. D. Kaesz. Adv. Chem. Ser. **167**, 215 (1978).
12. U. Schubert, J. Muller et H. G. Alt. Organometallics, **6**, 469 (1987).
13. Cf. H. Marsmann. NMR: Basic Princ. Prog. **17**, 120 (1981).
14. G. Kraft, C. Kalbas et U. Schubert. J. Organomet. Chem. **289**, 247 (1985).
15. A. J. Hart Davis et W. A. G. Graham. J. Am. Chem. Soc. **93**, 4388 (1971).
16. R. A. Benkeser, H. Landesman et D. J. Foster. J. Am. Chem. Soc. **74**, 648 (1952).
17. C. A. L. Mahaffy et P. L. Pauson. Inorg. Snyth. **19**, 154 (1979).
18. S. Top et G. Jaouen. J. Organomet. Chem. **182**, 154 (1979).

Can. J. Chem. Downloaded from www.nrcresearchpress.com by 196.1.178.254 on 09/07/12
For personal use only.

Symmetries of configurations of charges on a sphere

R. H. FRICKEL AND B. V. BRONK

Chemical Research Development and Engineering Center, Aberdeen Proving Ground, Maryland 21010-5423, U.S.A.

Received June 1, 1987[1]

R. H. FRICKEL and B. V. BRONK. Can. J. Chem. **66**, 2161 (1988).

New equilibrium figures are obtained for finite numbers of point charges confined to a sphere and interacting via a Coulomb potential. The symmetries of the configurations are classified for all cases up to a charge number of forty. Features of the geometry of the configurations are discussed and shown on equal area projections. The substantial number of configurations now available permit study of frequency of occurrence of various symmetries and persistence of certain geometries over a range of charge numbers, as well as detailed comparison of similarities and differences of the present global minimum energy figures with corresponding close packed structures.

R. H. FRICKEL et B. V. BRONK. Can. J. Chem. **66**, 2161 (1988).

On a obtenu de nouvelles valeurs pour les équilibres de charges ponctuelles à nombres finis, confinées a une sphère et qui interagissent par le biais d'un potentiel de Coulomb. Pour tous les cas jusqu'à quarante charges, on a pu établir une classification des symétries de configuration. On discute des caractéristiques de la géométrie des configurations et on les présente sur des aires de projection qui sont égales. Le très grand nombre de configurations qui sont maintenant disponibles permet d'étudier la fréquence d'apparition de diverses symétries et la persistance de certaines géométries pour des valeurs très différentes de nombres de charges ainsi que de faire une comparaison détaillée des similarités et des différences qui existent entre les valeurs actuelles de l'énergie globale minimale avec les structures correspondantes fermées.

[Traduit par la revue]

Can. J. Chem. Downloaded from www.nrcresearchpress.com by 196.1.178.254 on 09/07/12
For personal use only.

Introduction

The problem of arranging points on a sphere subject to extremal conditions is well-known to relate to many problems in physical chemistry. These include applications as basic as using minimal configurations to predict the polyhedral shapes of molecules as in the lone electron-pair model (1, 2). Further, many more contemporary problems such as arrangements of molecules on the surface of microdroplets, atoms in clusters (3), self-assembly of virus particles into macromolecular polyhedra, and examples of structural phase changes (4) are related to such configurations (see also refs. 5, 6, and 7).

In the present paper we examine the symmetries and changes of symmetry which occur when charged particles interact with each other via coulomb forces but are constrained to remain on the surface of a sphere. We reexamine the early examples studied by Foeppl (8) as well as more recent tabulations of the Coulomb case (9) and extend that case for n up to 40. We present several new equilibrium figures with lower Coulomb energy than that previously presented for the same charge number. We also present tabulations which allow one to see which symmetries recur most often and note the persistence of certain patterns for configurations. The present problem is a special case of the more general problem of finding the minimum energy configuration on a sphere for n particles interacting with energy

$$[1] \quad E = \tfrac{1}{2} \sum_{i=1}^{n} \sum_{\substack{j=1 \\ j \neq i}}^{n} \left| \bar{r}_i - \bar{r}_j \right|^{-m}$$

where $\bar{r}_i$ is the position of the i^{th} particle and m is arbitrary. Melnyk *et al.* (10) reviewed the relationship among equilibrium figures for various values of m for n between 3 and 16. The closest packing of hard spheres or inflexible circles ($m = \infty$) was recently extended for values of n up to 40 by Clare and Kepert (11).

[1]Revision received February 25, 1988.

Printed in Canada / Imprimé au Canada

2. Approach

In our calculations we fix the center of the sphere at the origin, set $r_i = 1$ and minimize the energy as defined in eq. [1] for $m = 1$, starting from arbitrarily specified initial charge positions on the sphere's surface. The charges are recursively moved, each by a small displacement proportional to the tangential force on it due to all the other charges, until the positions converge to an equilibrium configuration. We will subsequently use the abbreviation CCn to refer to the lowest-energy coulomb-equilibrium charge configurations (MCEC's) that we have computed (or recomputed) in this way.

Each configuration produced by this scheme was computed at least twice from independent initial configurations. Except in one instance for $n = 16$ and one for $n = 32$, discussed below, only one lowest-energy equilibrium configuration was found for each charge number.

We examined the symmetries using equal area projections, different edge lengths in each configuration being represented by different line types. As seen in Figs. 1–3, this representation allows configuration symmetries as well as similarities and differences between different configurations to be much more readily visualized than do more commonly encountered symmetry diagrams.

3. Discussion and results

The results of the present study and comparison with previous studies are presented in Tables 1 and 2. The total coulomb energy, point group, and the number of sets of equivalently situated charges suffice to identify the configuration. (Specific angular coordinates for most of the cases presented here are available in ref. 12.) Sources for previously reported MCEC's are listed in Table 1; data for other coulomb equilibrium configurations of interest are displayed at the end of the table. The point group classifications are summarized in Table 2.

3.1. Previous work

The symmetry and general structure of MCEC's presented by

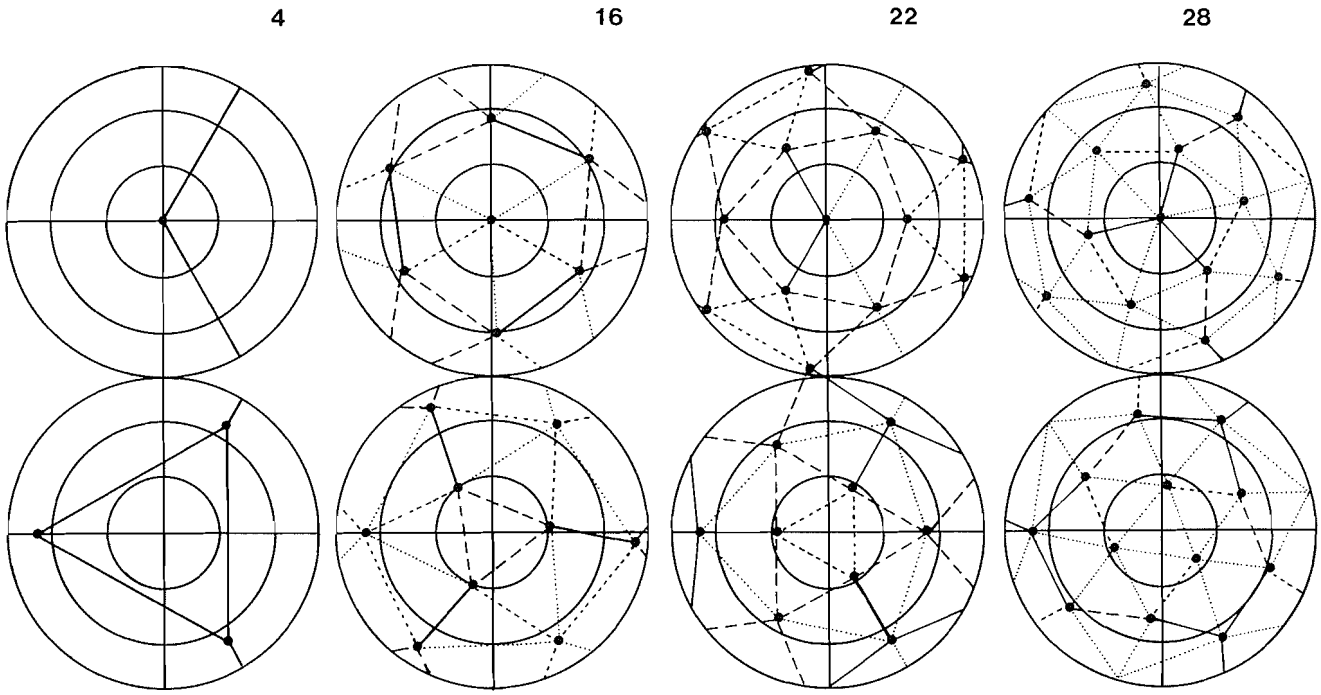

FIG. 1. Equal-area projections of the four tetrahedral configurations (CC4, CC16, CC22, and CC28). Both hemispheres are shown as seen from above. The four corners of the tetrahedron are shown in the same positions in all four configurations. For each configuration the edges of shortest length are shown as solid lines, the next shortest as long-dashed lines, and the next as short-dashed lines. Edges of greater length are shown as dotted lines. These edge-length keys also apply to the Figs. 2 and 3.

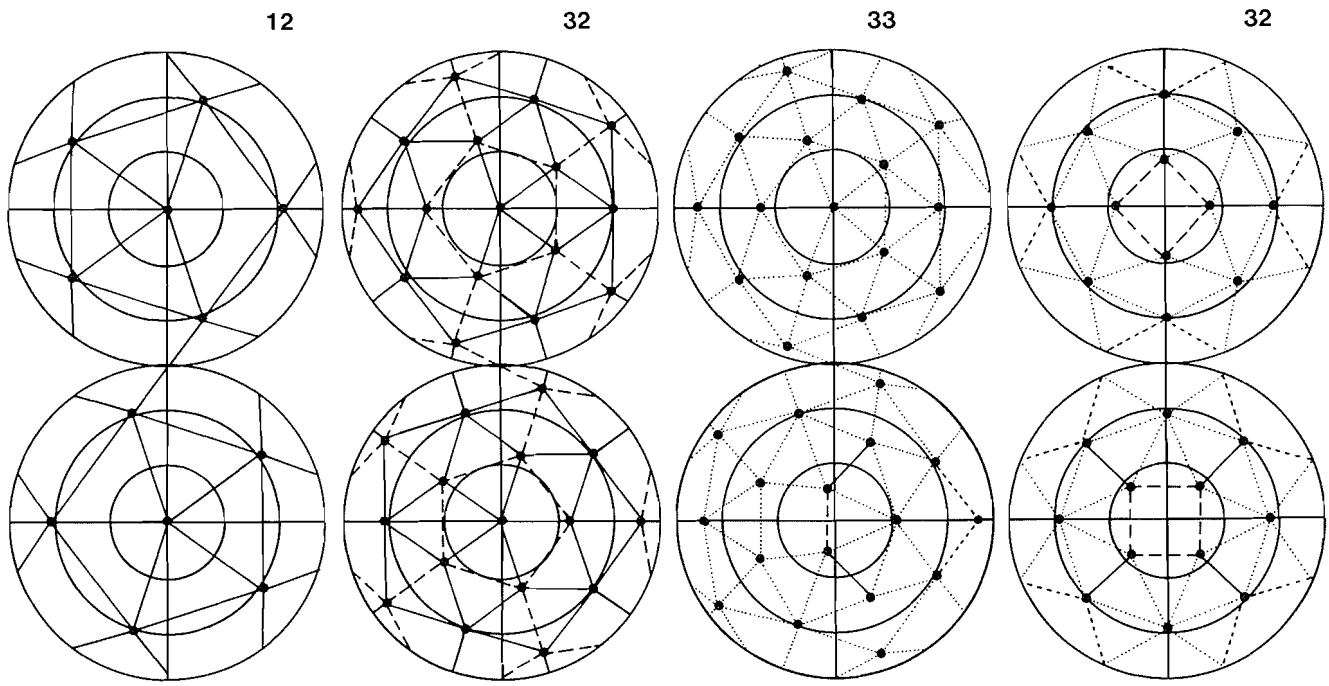

FIG. 2. CC12, CC32, and CC33. CC12 (the icosahedron) and CC32 (which has all the points of both the icosahedron and the dodecahedron) belong to the I_h group. CC33 has only a reflection plane (the horizontal axis in the diagram) but one can see that the upper hemisphere almost retains the structure and the C_5 symmetry of CC32. In the lower hemisphere the 33rd point appears to have been inserted near the pole, altering the structure. The anomalous D_{4d} 32-charge configuration is also shown.

Foeppl (8) for $n = 2$ through 8, 10, 12, and 14, by Cohn (13) for $n = 9$ and 11, and by Melnyk (10) for $n = 13$ and 15 were confirmed (or reconfirmed) by us. We also confirmed the coulomb energies as well as the structures presented by Munera (9) for $n = 4$ through 10, 12, 14, 17, and 18. The configurations presented by Munera for $n = 11$, 13, and 15 have higher coulomb energies than those computed by Melnyk. Munera's configurations for $n = 19$ and 20 have higher energies than those we computed. Our first computation (12) for $n = 16$ produced the D_{4d} double antiprism offered by both Melnyk and Munera.

Can. J. Chem. Downloaded from www.nrcresearchpress.com by 196.1.178.254 on 09/07/12
For personal use only.

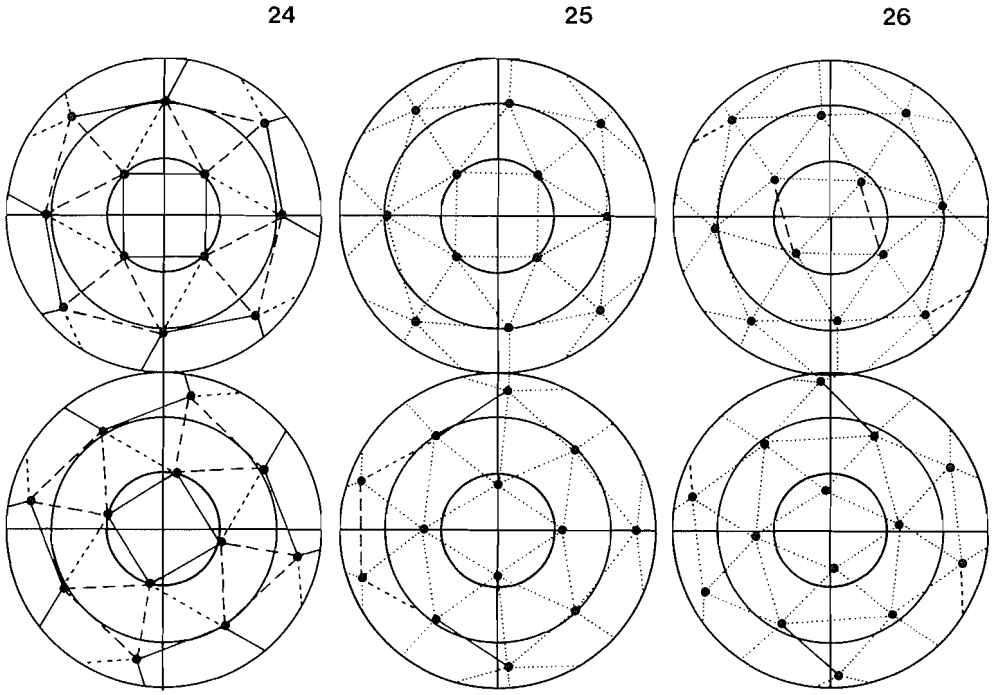

FIG. 3. Configurational continuity (CC24, CC25, and CC26). CC24 belongs to point group O. It has a square at each pole and four squares around the equator. CC25 is only C_s and CC26 only C_2. In the upper hemisphere the structure of CC24 is somewhat retained in CC25 and CC26. In the lower hemisphere the structure has been altered by the apparent insertion of the 25th and then the 26th charge.

TABLE 1. Equilibrium configuration energies

n	PG*	PS*	Energy	Ref.*	n	PG	PS	Energy	Ref.	n	PG	PS	Energy	Ref.
Lowest minimum energy configurations														
2	$D_{\infty}h$	1	0.500000	8,mc	15	D_3	3	80.670244	10,m	28	T	3	310.491542	
3	D_{3h}	1	1.732051	8,mc	16	T	2	92.911655		29	D_3	6	334.634439	
4	T_d	1	3.674235	8,mc	17	D_{5h}	3	106.050405	9,m	30	D_2	8	359.603946	
5	D_{3h}	2	6.474691	8,mc	18	D_{4d}	3	120.084467	9,m	31	C_{3v}	9	385.530838	
6	O_h	1	9.985281	8,mc	19	C_{2v}	7	135.089468		32	I_h	2	412.261275	mc
7	D_{5h}	2	14.452977	8,L	20	D_{3h}	4	150.881568	m	33	C_s	20	440.204057	
8	D_{4d}	1	19.675288	8,m	21	C_{2v}	9	167.641622		34	D_2	9	468.904853	
9	D_{3h}	2	25.759986	13,m	22	T_d	3	185.287536		35	C_2	18	498.569872	
10	D_{4d}	2	32.716949	8	23	D_3	5	203.930191		36	D_2	9	529.122408	
11	C_{2v}	5	40.596450	13	24	O	1	223.347074	m	37	C_2	19	560.627973	
12	I_h	1	49.165253	8,mc	25	C_s	15	243.812760		38	C_{2v}	13	593.048943	
13	C_{2v}	6	58.853231	10	26	C_2	13	265.133326		39	D_{3h}	6	626.389009	
14	D_{6d}	2	69.306363	8	27	D_{5h}	4	287.302615	m	40	D_2	10	660.725304	
Additional higher energy equilibrium configurations														
7	C_{3v}	3	14.458581		14	O_h	2	69.342378	L	30	I_h	1	361.314417	L
8	O_h	1	19.740774	L	16	D_{4d}	2	92.920354		32	D_{4d}	4	412.468397	
11	C_{5v}	3	40.615117		20	I_h	1	151.798621	L					

*PG is the point group; PS is the number of sets of equivalent points; Ref. number cites earlier reference; "m" indicates same symmetry and a similar looking polyhedron to a closest packed configuration cited by Mackay *et al.* (14) but present figure is congruent to close packed figure only in cases labeled with a "c". All figures labeled with both m and c satisfy the Leech (15) criteria for equilibrium. "L" indicates a figure which meets the Leech criteria but is of different symmetry from the closest packed solution.

Subsequent computation produced the new tetrahedrally symmetric configuration we present in Table 1, which has a lower energy (92.9117 vs. 92.9204) than the D_{4d} configuration.

Melynk proffered a bicapped square prism + 4 configuration for $n = 14$ as having lower energy for small m than Foeppl's bicapped pentagonal antiprism (the latter was also presented by Munera); however, the coulomb energy for Melnyk's configuration, which we computed to be minimal when the square prism is a cube and the structure is hence O_h, is higher (69.3424 vs. 69.3064) than that for Foeppl's D_{6d} structure.

3.2. *New configurations*

In addition to CC16, the tetrahedral $n = 16$ configuration, we have computed new equilibrium configurations for $n = 19$ through 40, for which we have not found any previous references (Table 1). The symmetry groups for these configura-

Can. J. Chem. Downloaded from www.nrcresearchpress.com by 196.1.178.254 on 09/07/12
For personal use only.

tions range from C_s and C_2 to T_d and I_h. No completely unsymmetrical minimum-energy configuration was found for $n \leq 40$.

CC21 is C_{2v}, but the angular position of the charges varies from C_{4v} symmetry by fractions of a degree. An effort was made to force the configuration into C_{4v} symmetry, but the charges always returned to the C_{2v} configuration.

CC16 and CC28 belong to point group T and CC22 to T_d. They are displayed in Fig. 1, along with CC4, the regular tetrahedron.

CC24 (Fig. 3) is a slightly distorted snub cube (see Sect. 3.3); it belongs to point group O. CC32 (point group I_h) is a rhombic triacontahedron distorted by bending each of its faces into two triangles so as to make it inscribable in a sphere. CC32 is shown in Fig. 2, along with CC12, the regular icosahedron, and CC33 (see Sect. 3.4). Our first computation for $n = 32$ produced a C_{4d} configuration having a higher coulomb energy than the spherical triacontahedron, but subsequent computations done from a variety of initial configurations always produced CC32.

Almost all the faces of the convex polygons defined by the charge configurations are triangles. CC8 (a square antiprism) and CC24 have some square faces. CC19 has a rectangular face at one of the poles. CC25 and CC33 are C_s and each has a quadrilateral face lying across the reflection plane. CC25 had five and CC33 has seven single charges scattered irregularly on the reflection-plane great circle.

3.3. *Relationship to the close-packing solutions*

A few of these newly computed minimum-coulomb-energy configurations have been previously presented as solutions (CPS's) for the close-packing problem, to wit, maximizing the minimum distance between charges (i.e., $m = \infty$). Indeed, structures in the same symmetry groups and having the same structural type as the corresponding MCEC's have been presented as CPS's for $n = 2$ through 6, 8, 9, 12, 15, 17, 18, 20, 24, 27, and 32 (10, 14). However, except for the structures demonstrated by Leech (15) to be in equilibrium independently of the nature of the interaction force (equatorial polygons with or without charges at the poles and certain figures related to the regular polyhedra), the CPS's are not congruent with the corresponding MCEC's. Melynk (10), for instance, points out that for $n = 8$ the CPS square antiprism is not congruent with the MCEC square antiprism; the former is equilateral, while in the latter the edges of the square faces are shorter than the edges connecting the square faces. Similarly the CPS for $n = 24$ is a snub cube (14, 16), which must be distorted to produce the MCEC CC24.[2] The CPS's are congruent with the corresponding MCEC's only for $n = 2$ through 6, 12, and 32 in agreement with Leech's criteria. (Tarnay and Gaspar (17) have produced a closer packing for $n = 32$ by distorting the spherical triacontahedron, and also new closer packings for $n = 17$ and 18.)

[2]The snub cube itself is a CPS and not a coulomb-equilibrium configuration. It does not satisfy Leech's criterion and is in equilibrium only for $m = \infty$. Construction of CC24 from the snub cube (which is equilateral) can be visualized as follows: The square faces are moved slightly closer to the center of the sphere; this lengthens their edges and shortens the edges connecting their corners. Each square face is then rotated slightly (through 1.0113°) within its plane, further altering the lengths of the connecting edges. The minimum edge length of the resulting MCEC (CC24) is 42.0653° compared with 43.6908 for the snub cube; its coulomb energy is 223.3471 vs. 223.4551 for the snub cube.

TABLE 2. Summary of point group classifications

PG	n	PG	n	PG	n
C_s	25,33	C_{2v}	11,13,19,21,38	D_{3h}	3,5,9,20,39
C_2	26,35,37	C_{3v}	31,7*	D_{5h}	7,17,27
D_2	30,34,36,40	C_{5v}	11*	$D_{\infty h}$	2
D_3	15,23,29	D_{4d}	8,10,18,16*,32*	O_h	6,8*,14*
T	16,28	D_{6d}	14	I_h	12,32,20*,30*
O	24	T_d	4,22		

*This symbol indicates an additional equilibrium configuration with higher energy.

3.4. *Other equilibrium configurations*

A number of configurations in equilibrium under coulomb forces but not lowest-energy configurations are listed at the end of Table 1. The CPS configuration for $n = 7$, a C_{3v} capped modified triangular antiprism, is not in electrostatic equilibrium. The C_{3v} structure listed in Table 1 is the corresponding coulomb-equilibrium configuration; the minimum interval between particles is 73.2823° vs. 77.8659° for the CPS (and 72° for the D_{5h} MCEC). The CPS for $n = 11$ is the regular icosahedron minus one particle — a C_{5v} capped pentagonal antiprism. This structure is modified to achieve electrostatic equilibrium by moving both pentagonal faces of the antiprism away from the polar charge; they are then no longer congruent. The $n = 14$ and $n = 16$ non-minimum configurations are discussed above. The 30-particle I_h configuration is the vertex-figure derivative of the icosahedron. The 32-particle configuration is a D_{4d} figure achieved once during our computations, subsequent trials producing the spherical triacontahedron. This configuration is shown in Fig. 2.

3.5. *Relationships between adjacent configurations*

Similarities between configurations with adjacent charge numbers can sometimes be observed even when the symmetries are very different. In Fig. 2, for example, CC33 is shown beside CC32. We recall that CC32 displays very high (icosahedral) symmetry, while CC33 has only a reflection plane. Nevertheless, the C_5 symmetry of CC32 is almost retained in the upper hemisphere of CC33. The 33rd charge of CC33 appears to have been inserted near the lower pole of CC32, obliterating the C_5 symmetry in the lower hemisphere. It should be noted that CC32 and CC33 were independently derived from arbitrary initial conditions.

Figure 3 shows CC24, CC25, and CC26. Although CC24 displays octahedral symmetry, while CC25 and CC26 have only a reflection plane and a C_2 axis, respectively, the upper hemispheres of these three figures correspond point for point and almost edge for edge; the quadrilateral at the pole of CC24 is retained in CC25 (though no longer a square), and also appears, now bent into two triangles, at the pole of CC26. In the lower hemisphere one can see in CC25 where the 25th charge appears to have been inserted near the left-hand edge of the configuration, destroying the C_4 symmetry of CC24 and breaking the polar square into two triangles. The lower hemispheres of CC25 and CC26 also correspond closely; one can see where the 26th charge appears to have been inserted near the right-hand edge of CC26. Again we note that CC24, CC25, and CC26 were computed independently.

3.6. *Energy vs. symmetry*

The energy of a charge of magnitude n uniformly distributed

Can. J. Chem. Downloaded from www.nrcresearchpress.com by 196.1.178.254 on 09/07/12
For personal use only.

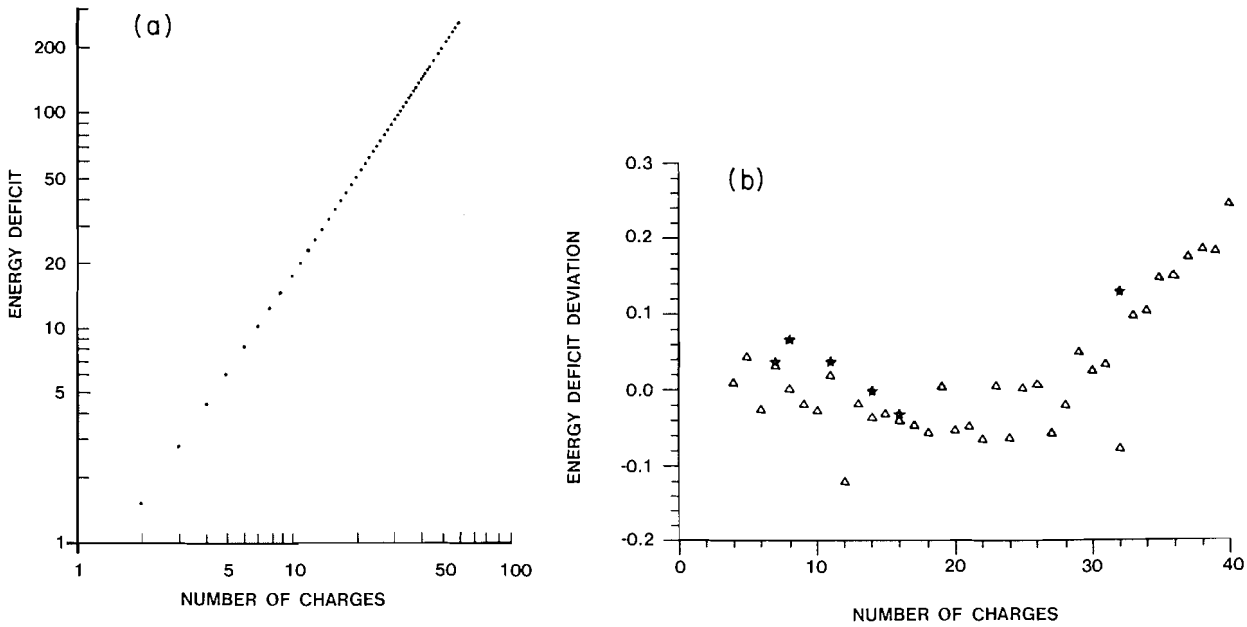

FIG. 4. (*a*) The energy deficit $n^2/2 - E(n)$ vs n. (*b*) The deviation of the calculated energy deficit from a least squares straight-line through the log-log plot in 4*a*. Higher-energy configurations have higher deviation values. The values for minimal-energy configurations are displayed as triangles. Those for the non-minimal-energy configurations are shown as stars. The values for the dodecahedron and the icosadodecahedron are out of the scale of the plot.

over the surface of a unit sphere is $n^2/2$. The excess of this quantity over the energy E_n of the minimum-energy configuration for n unit charges

[2] $E_0 = n^2/2 - E_n$

is shown in Fig. *4a* plotted against n. Figure *4b* shows the deficit of E_0 with respect to a least squares straight-line fit to the previous plot. Higher values of this excess correspond to higher values of E_n. Configurations of higher symmetry tend to have lower values than their neighbors, but this comparison cannot be made globally over the whole range of n. For the most part, a high degree of symmetry tends to be associated with low configuration energy (see Sect. 3.5), but this is not a general rule. The cube ($n = 8$) and the regular dodecahedron ($n = 20$) are neither MCEC's nor CPS's despite being regular polyhedra, nor is the O_h configuration for $n = 14$. The CC20 polyhedron has four sets of equivalent points and edges of seven different lengths, as compared with one each for the regular dodecahedron, but nevertheless CC20 has a lower configuration energy.

4. Conclusion

We have determined a number of new equilibrium configurations for a small number of charged particles confined to the surface of a sphere and interacting with a Coulomb force. These are zero temperature equilibrium configurations. We note that many of these configurations are closely related to solutions to the close-packing problem. A problem of interest to us is the behavior of objects interacting with realistic forces at finite temperatures on the surface of a spherical particle. An attractive initial step to the study of this problem would be to set up computer programs for calculating the molecular dynamics of the system. This computational system can be checked thermodynamically in the ideal gas case and can later be related to situations with more complex interactions and also to the symmetrical configurations studied here as the temperature is reduced sufficiently to induce phase changes.

1. I. S. DIMITRIEV. Symmetry in the world of molecules (Engl. Ed.). MIR, Moscow. 1979.
2. R. L. DE KOCK and H. B. GRAY. Chemical structure and bonding. Benjamin/Cummings. 1980. pp. 111–114.
3. D. L. KEPERT. Stereochemistry. Springer, Berlin. 1982.
4. A. A. BEREZIN. J. Math. Phys. **27**(6), 1533 (1986).
5. A. A. BEREZIN. Am. J. Phys. **54**(5), 403 (1986).
6. T. TARNAI. Ann. Univ. Sci. Budapest Sect. Math. **27**, 199 (1985).
7. M. G. CALKIN, D. KIANG, and D. A. TINDALL. Nature **319**, 454 (1986).
8. L. FOEPPL, J. REINE ANGEW. Math. **141**, 2511 (1912).
9. H. A. MUNERA. Nature **320**, 597 (1986).
10. T. W. MELNYK, O. KNOP, and W. R. SMITH. Can. J. Chem. **53**, 1745 (1977).
11. B. W. CLARE and D. L. KEPERT. Proc. R. Soc. London, A**405**, 329 (1986).
12. R. H. FRICKEL and B. V. BRONK. CRDEC-TR-87040. Configurations of charges on a sphere. April 1987.
13. H. COHN. Tables Aids Comput. **10**, 117 (1956).
14. A. L. MACKAY, J. L. FINNEY, and K. GOTOH. Acta Crystallogr. A**33**, 98 (1977).
15. J. LEECH. Math. Gaz. **XLI**, (1957).
16. R. M. ROBINSON. Math. Ann. **318**, 296 (1969).
17. T. TARNAI and Z. GASPAR. Math. Proc. Camb. Phil. Sc. **93**, 191 (1983).

Can. J. Chem. Downloaded from www.nrcresearchpress.com by 196.1.178.254 on 09/07/12
For personal use only.

A comparative study on the dynamics of epimeric 1-hydroxymethyl quinolizidines: II. The solvent and concentration dependence of the association properties

K. KULIŃSKA AND M. WIEWIÓROWSKI

Institute of Bioorganic Chemistry, Polish Academy of Sciences, Noskowskiego 12,61-704 Poznan, Poland

Received December 11, 1987

K. KULIŃSKA and M. WIEWIÓROWSKI. Can. J. Chem. **66**, 2166 (1988).

The homo and heteroassociation patterns of lupinine and epilupinine in different solvents and at various concentrations have been studied. In *n*-hexane, *n*-heptane, CCl_4, and $C_2H_4Cl_2$ solvents, lupinine monomers with an intramolecular OH...N hydrogen bond dominate over homoassociates with an OH...O′ intermolecular hydrogen bond even in concentrated solutions. Homoassociation of lupinine by intermolecular OH...N′ hydrogen bonding is observed only in saturated solutions. In chloroform solution any intermolecular homoassociation is effectively blocked because of significant affinity of chloroform molecules acting as a weak acid toward the free electron pairs of the oxygen atom from the hydroxyl group that would be otherwise engaged in intramolecular OH...N hydrogen bonding. Epilupinine in *n*-hexane, *n*-heptane, CCl_4, $C_2H_4Cl_2$, and chloroform solutions forms possible homoassociates both by OH...N′ and OH...O′ intermolecular hydrogen bonding. In dioxane-d_8, DMSO, and D_2O solvents both lupinine and epilupinine form heteroassociates with solvent molecules.

K. KULIŃSKA et M. WIEWIÓROWSKI. Can. J. Chem. **66**, 2166 (1988).

On a étudié les modèles d'homoassociation et d'hétéroassociation de la lupinine et de l'épilupinine dans différents solvants et à différentes concentrations. Dans le *n*-hexane, le *n*-heptane, le CCl_4 et le $C_2H_4Cl_2$ les monomères de la lupinine ayant des liaisons hydrogènes OH...N intramoléculaires dominent les composés homoassociés ayant des liaisons hydrogènes OH...O′ intermoléculaires même en solutions concentrées. On observe l'homoassociation de la lupinine par des liaisons hydrogènes intermoléculaires OH...N'uniquement dans des solutions saturées. En solution dans le chloroforme, toute homoassociation intermoléculaire est effectivement bloquée à cause de la très grande affinité des molécules de chloroforme agissant comme un acide faible en présence de la paire d'électrons libres de l'atome d'oxygène du groupe hydroxyle qui, par ailleurs, peut-être impliqué dans une liaison hydrogène intramoléculaire OH...N. L'epilupinine en solution dans le *n*-hexane, le *n*-heptane, le CCl_4, le $C_2H_4Cl_2$ et le chloroforme forme les deux types possibles de composés homoassociés par des liaisons hydrogènes intermoléculaires OH...N'et OH...O′. La lupinine et l'épilupinine dans le dioxanne-d_8, le DMSO, et le D_2O forment toutes deux des composés d'hétéroassociation avec les molécules de solvant.

[Traduit par la revue]

Introduction

The similarity of the conformations of biologically active molecules in water solution and as crystals is a crucial problem of structural study. Many proposed mechanisms of interaction on the molecular level are based on identical conformations in solution and in crystals. In effect, the preferred solution conformation of biomolecules seems to be generally similar to its crystal structure (1). Lupinine molecule (1-hydroxymethyl-quinolizidine) belongs to those rare biomolecules whose crystal structure deviates significantly from its structure in solution (2). Its epimer, epilupinine, differs from lupinine in the configuration of the exocyclic hydroxymethyl group, but this relatively small structural change has a great influence on the molecular and intermolecular dynamism of both epimers. Epilupinine retains in its crystal structure the preferred conformation from solution. Conformational dynamics in CCl_4, $CDCl_3$, and D_2O solutions, and in the liquid as compared with the solid state of both epimers, has been elucidated from spectroscopic ir and nmr data in the previous paper of this series (2). In this paper we attempt to determine the homo and heteroassociation patterns of lupinine and epilupinine in different solvents and at various concentrations to explain why the predominant tendency of lupinine to intramolecular self-association does not lead to crystals with a similar structure, but always to the homopoly-associated form, which is rarely present even in a concentrated solution and is very similar to that existing in crystalline epilupinine. The observations presented may be useful for a proper understanding of very important equilibrium processes between intra and intermolecular hydrogen bonds.

Experimental

Infrared spectra were measured on a Perkin–Elmer ir spectrometer, type 180. The ^1H nmr spectra were recorded on JEOL FX-90Q Fourier transform impulse equipment by a standard method. For details refer to our previous paper (2).

Results and discussion

Lupinine and epilupinine possess analogous proton-donor and -acceptor centres. There are two main possible modes of intermolecular hydrogen bonding formation: (*i*) between the hydroxyl group of one molecule and the nitrogen atom of another: OH...N′; (*ii*) between the hydroxyl group of one molecule and the oxygen atom of another: OH...O′. Moreover, intramolecular OH...N self-association is possible in lupinine in the *syn*/−60° conformation, as opposed to epilupinine where the equatorial position of the CH_2OH group renders this interaction impossible (2).

In effect, inter and intramolecular interactions of this type are fully or partially manifested in the ir spectra in the region of the stretching vibrations of the hydroxyl groups (Table 1 and Figs. 2–6). In dilute CCl_4 lupinine solutions two forms of monomers occur: 90% of the monomers, with the OH group engaged in intramolecular hydrogen bonds, are manifested in the ir spectra by ν(OH...N) at 3295 cm^{-1} (L_1 in Figs. 1 and 2) and about 10% of the monomers, with a free OH group, are manifested by the ν(OH) band (L_2 in Figs. 1 and 2) (2, 3). In dilute CCl_4 epilupinine solutions 100% of the monomers possess a free OH group (E in Figs. 1 and 2) and vibrate with the same frequency as the L_2 lupinine monomers at ν(OH) of 3640 cm^{-1} (2, 3).

Printed in Canada / Imprimé au Canada

Can. J. Chem. Downloaded from www.nrcresearchpress.com by 196.1.178.254 on 09/07/12
For personal use only.

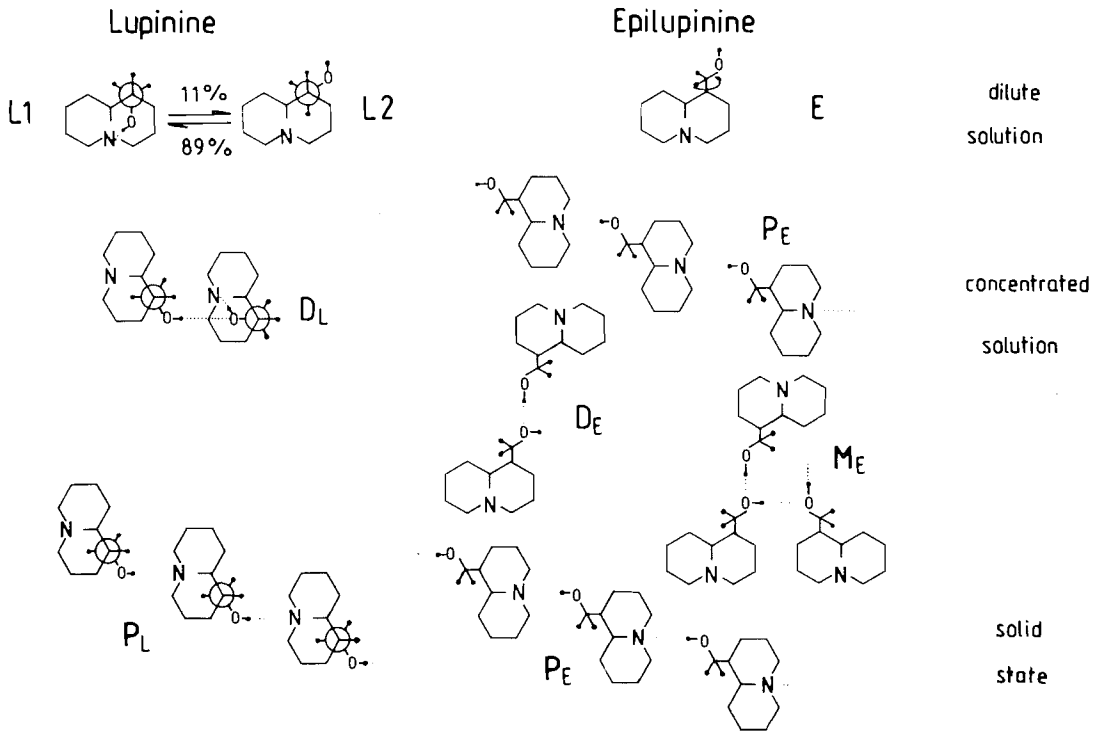

FIG. 1. The association pattern of lupinine and epilupinine in dilute and concentrated solutions and in the solid state.

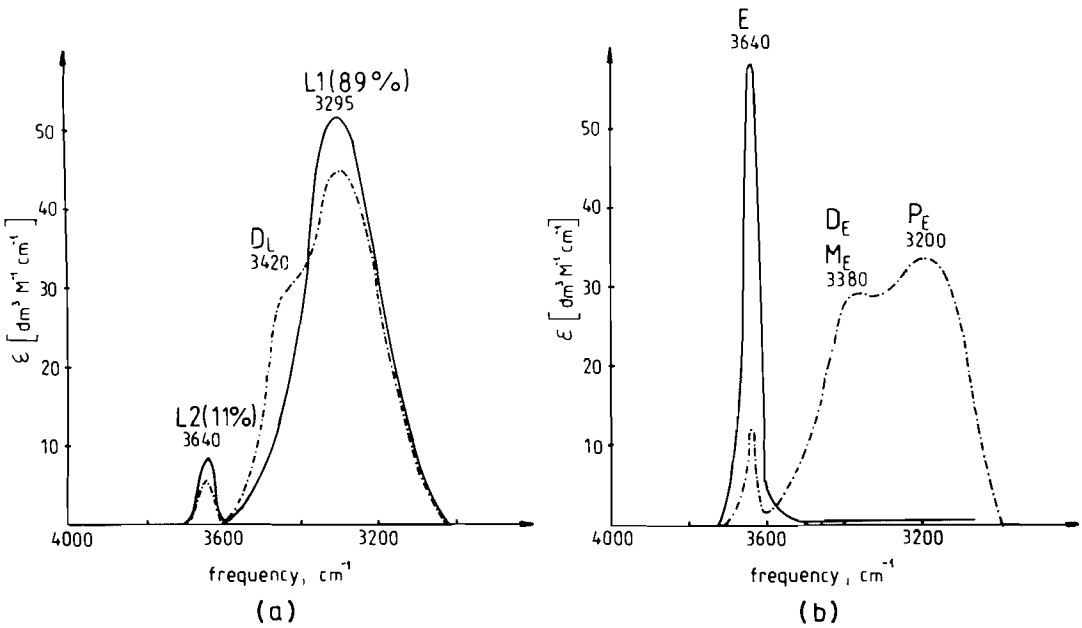

FIG. 2. Infrared spectra of lupinine (a) and epilupinine (b) in carbon tetrachloride (CCl_4) solutions of different concentrations: c = 0.03 M (————); c = 1.0 M (—·—·—·—).

Upon increased lupinine concentration only one new band, ν(OH...O'), appears at about 3420 cm^{-1} in the stretching vibration region of the ir spectra (Fig. 2, Table 1). This band has been assigned to homoassociates by an intermolecular OH...O' hydrogen bonding involving two lupinine molecules, one with an intramolecular hydrogen bonding L_1 and the other with a free OH group L_2 (D_L in Figs. 1 and 2). The assignment is deduced from a simultaneous intensity decrease of both monomer bands ν(OH) and ν(OH...N) and the growth of intensity of the homoassociate band ν(OH...O'), which is due to increasing lupinine concentration in solution. The integrative absorption rate of both monomer bands ν(OH) and ν(OH...N) as a function of concentration remains constant.[1] The position and intensity of the absorption band ν(OH...N) originating from the stretch-

[1]The integrative absorption rate was calculated from the concentration effect on the ir spectra of CCl_4 and $C_2H_4Cl_2$ lupinine solutions in the concentration ranges 0.003–1.5 M and 0.03–1.5 M, respectively (2).

Can. J. Chem. Downloaded from www.nrcresearchpress.com by 196.1.178.254 on 09/07/12
For personal use only.

TABLE 1. The stretching vibrations of the OH group (cm^{-1}) of lupinine and epilupinine in 0.7 M solutions of different solvents compared with the solid and liquid states (intensity of bands is denoted by w, weak; m, medium; s, strong; sh, shoulder)

	Lupinine					Epilupinine			
Solvent	OH[a]	OH...O'[b]	OH...N'[c]	OH...N'[b]	OH...O'$_{solv}$[d]	OH[a]	OH...O'[b]	OH...N'[b]	OH...O'$_{solv}$[d]
n-Hexane[e]	3640w	3430m	3325s	3220sh		3640m	3430m	3230s	—
n-Heptane									
CCl_4	3640w	3420m	3295s	—	—	3640m	3380m	3200s	—
$C_2H_4Cl_2$	3610w	3400m	3250s	—	—	3610m	3360m	3190s	—
$CDCl_3$	3630w	3400m	3220s	—	—	3630m	3320m	3170s	—
Dioxane-d_8	—	—	3270m	—	3490s	—	—	3190w	3490s
DMSO	—	—	—	—	3445s	—	—	—	3445s
D_2O	—	—	—	—	3400s	—	—	—	3400s
Solid state[f]	—	—	—	3170s	—	—	—	3160s	
Liquid state[f]	—	3420m	3310m	—	—	—	3410m	3200m	—

[a]Solvated monomers.
[b]Homoassociates.
[c]Intramolecular hydrogen bond.
[d]Heteroassociates with solvent molecules.
[e]Saturated solution, $c = 0.1$ M.
[f]For details see ref. 2.

ing vibration of the hydroxyl groups engaged in intramolecular hydrogen bonds depend on the concentration (concentration increase leads to a decrease of integrative absorption of the ν(OH...N) band —see Fig. 2), and solvent (the position of the ν(OH...N) band changes from 3325 cm^{-1} in *n*-hexane to 3220 cm^{-1} in chloroform—see Table 1). Due to the presence of two free electron pairs at the oxygen atom, lupinine monomer L_1 may act as a proton acceptor both for lupinine monomers L_2 forming dimers D_L (Figs. 1 and 2) and for proton-donor solvent molecules like 1,2-dichloroethane and chloroform. These interactions of the proton-donor group with free electron pairs at the oxygen atom partially reduce its negative charge, thus increasing the acidity and donor properties of the OH group. The intramolecular OH...N hydrogen bond becomes stronger, as indicated by the shifts of the ν(OH...N) bands to shorter wavenumbers (see Table 1). As one can see in Table 1, band ν(OH...N) shows the greatest shift to shorter wavenumbers in chloroform, being located at 3220 cm^{-1}. This indicates that in chloroform solutions the intramolecular OH...N hydrogen bond is the strongest. Acidic C—H hydrogen from chloroform molecules can stabilize the intramolecular OH...N hydrogen bond by acting as a proton donor with a free electron pair at the oxygen atom. In this way, intermolecular homoassociation is effectively blocked in chloroform solution and no homoassociate band is present in the ir spectra. Only at a saturated concentration, when crystallization processes start, homoassociates by intermolecular OH...N' hydrogen bonding similar to those in the crystal structure appear.

The intensity of the D_L dimer ν(OH...O')and in *n*-hexane, *n*-heptane, CCl_4, and $C_2H_4Cl_2$ solutions never exceeds that of monomers L_1 with an intramolecular ν(OH...N) hydrogen bond even in saturated solutions, where processes of crystallization start. The band of lupinine homoassociates by intermolecular OH...N' hydrogen bonding is observed only in the ir spectra of *n*-hexane and *n*-heptane saturated lupinine solutions at about 3220 cm^{-1}.

The intermolecular OH...N' hydrogen bond is stronger than the OH...N intramolecular one (ν(OH...N) − ν(OH...N') = 125 cm^{-1} in *n*-hexane lupinine solution), but it is not sufficiently strong to bind two lupinine molecules in solution into a stable dimer. The intramolecular OH...N hydrogen bond does not repress the diffusive movements of lupinine molecules in solution. Although the intramolecular hydrogen bond is weaker than the intermolecular OH...N' hydrogen bond it is kinetically more favourable. Probably this is the reason why homoassociates by intermolecular OH...N' hydrogen bonding are not observed in an unsaturated lupinine solution.

The homoassociation pattern of epilupinine is drastically different from that of lupinine. As the concentration of epilupinine increases, several new homoassociate bands appear in the stretching vibration region of the ir spectra. First of all a band appears at 3190 cm^{-1} in $C_2H_4Cl_2$ solution, at 3200 cm^{-1} in CCl_4 solution, and at 3230 cm^{-1} in *n*-hexane and *n*-heptane (see Table 1). This band is attributed to intermolecular OH...N' hydrogen bonding due to the formation of homoassociates, linear polymeric structures like those in the solid state (P_E in Fig. 1). At higher concentration another band of homoassociates appears at about 3500 cm^{-1}. The position of this band is concentration dependent and shifts towards shorter wavenumbers (3500 cm^{-1} → 3380 cm^{-1} in CCl_4, 3470 cm^{-1} → 3360 cm^{-1} in $C_2H_4Cl_2$; see Fig. 3) with increasing concentration. This band is attributed to the OH...O' intermolecular interaction. At lower concentrations linear dimers (D_E in Fig. 1) are probably formed, which at higher concentration transform into a linear multimer (M_E in Fig. 1) affecting the shift of the ν(OH...O') band as in other alcohols (4).

The pattern of epilupinine homoassociation presented above is similar for *n*-hexane, *n*-heptane, CCl_4, $C_2H_4Cl_2$, and even chloroform epilupinine solutions. Solvation of epilupinine molecules by chloroform proceeds similarly to the case of lupinine molecules, but does not hinder homoassociation because of the absence of intramolecular hydrogen bonding in epilupinine. The free OH groups of both epimers interact with the chlorine atom of solvent molecules to form very weak hydrogen bonds. The position of band ν(OH) = 3630 cm^{-1} is identical in lupinine and epilupinine chloroform solutions (see Fig. 4). The CH proton-donor group from chloroform (or CD from deuterochloroform) interacts with the free acceptor centres

Can. J. Chem. Downloaded from www.nrcresearchpress.com by 196.1.178.254 on 09/07/12
For personal use only.

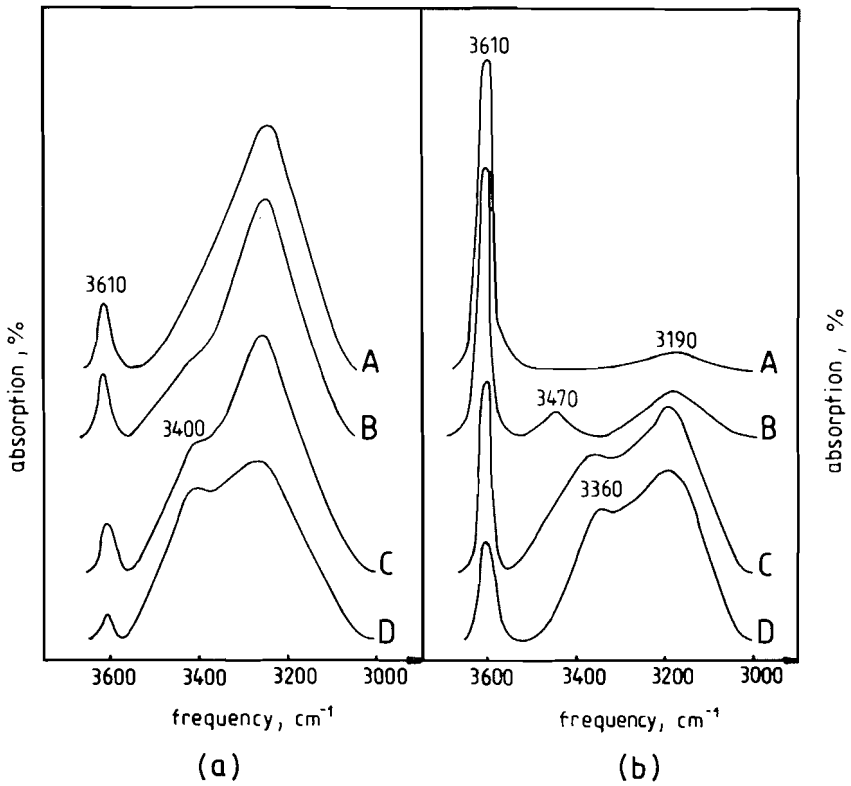

FIG. 3. Infrared spectra of lupinine (a) and epilupinine (b) in 1,2-dichloroethane ($C_2H_4Cl_2$) solutions of different concentrations: A, 0.03 M; B, 0.07 M; C, 0.7 M; D, 1.5 M.

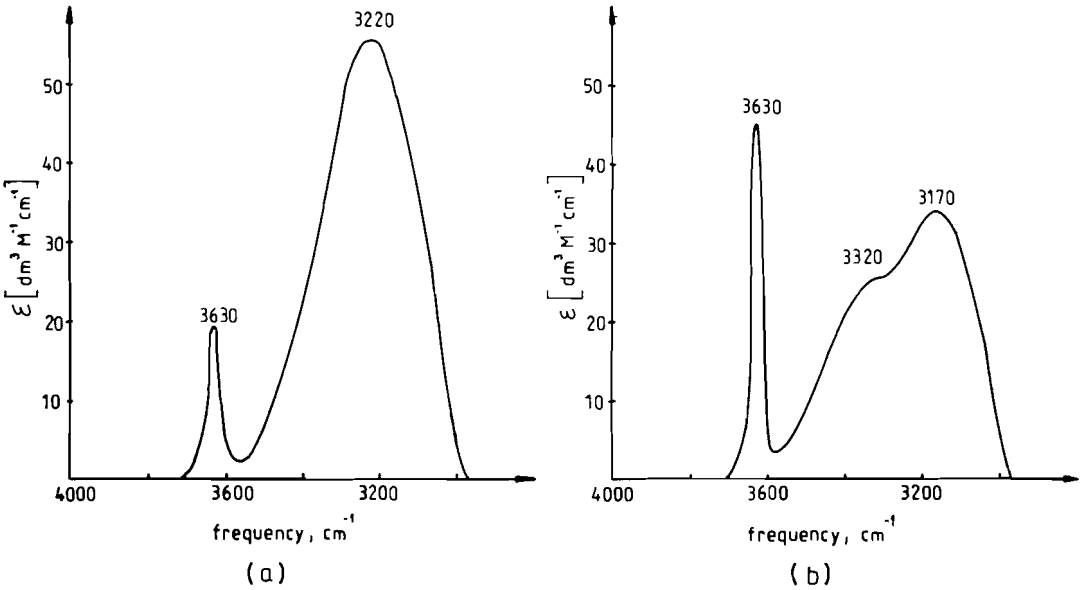

FIG. 4. Infrared spectra of lupinine (a) and epilupinine (b) in deuterochloroform ($CDCl_3$) solutions (c = 0.7 M).

of both epimers, i.e., the free electron pairs of oxygen atoms, but this interaction does not hinder epilupinine homoassociation.

In more polar solvents such as dioxane, DMSO, and D_2O, lupinine and epilupinine form heteroassociates with the molecules of the solvents (Table 1, Fig. 5). In dioxane, oxygen atoms with free electron pairs possess strong proton acceptor abilities and a majority of lupinine and epilupinine molecules form heteroassociates with the solvent molecules (ν(OH...O'$_{solv}$) = 3490 cm^{-1}). However, a significant percentage of lupinine molecules (about 40%) retain the monomeric form L_1 with an intramolecular hydrogen bond. In epilupinine dioxane solutions about 20% of epilupinine molecules form homoassociates by OH...N' hydrogen bonding (ν(OH...N') = 3190 cm^{-1}). In DMSO and D_2O both epimers form only heteroassociates with molecules of the solvents (ν(OH...O'$_{solv}$) = 3445 and 3400 cm^{-1} respectively).

The concentration effect observed in the ^{1}H nmr spectra confirms the association pattern of lupinine and epilupinine in

Can. J. Chem. Downloaded from www.nrcresearchpress.com by 196.1.178.254 on 09/07/12
For personal use only.

Can. J. Chem. Downloaded from www.nrcresearchpress.com by 196.1.178.254 on 09/07/12
For personal use only.

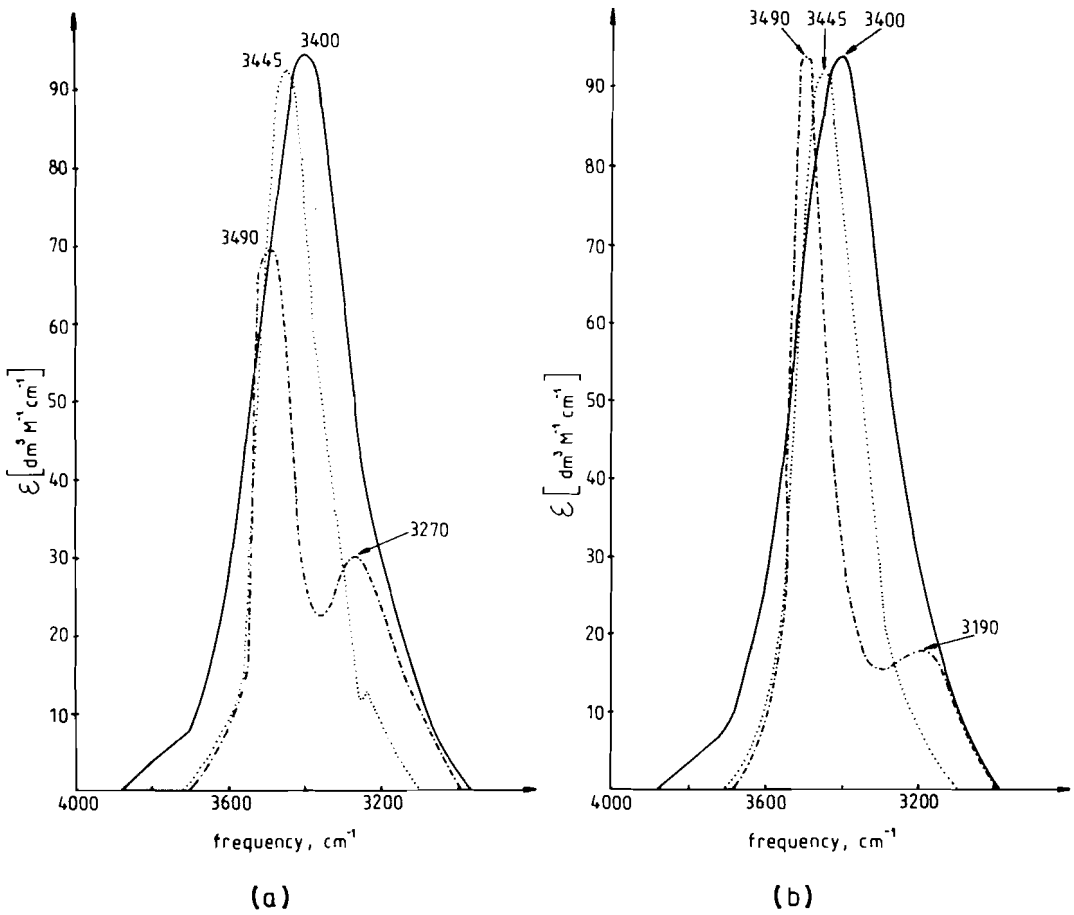

FIG. 5. Infrared spectra of lupinine (a) and epilupinine (b) in solutions of active solvents: dioxane-d_8 (—·—·—·—); dimethylsulfoxide-d_6 (DMSO) (--------); D_2O (————).

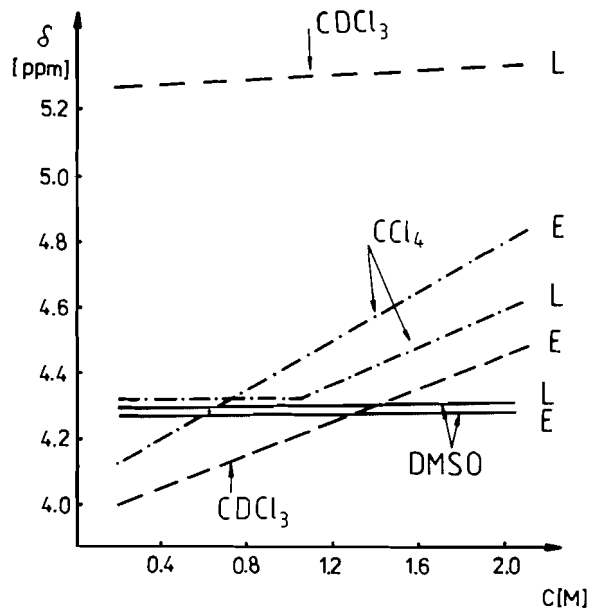

FIG. 6. Scheme of dependence of the chemical shift of the hydroxyl proton versus concentration in the ^1H nmr spectra of lupinine (L) and epilupinine (E) solutions: CCl_4 (—·—·—·—); $CDCl_3$ (————); DMSO (————).

CCl_4, $CDCl_3$, and DMSO solutions (Fig. 6). The chemical shift of the hydroxyl proton signal of lupinine or epilupinine reflects the different average magnetic environments of those protons, between which a quick chemical exchange takes place. Every turbulence of conformational and association equilibrium in solution results in a change of position of the hydroxyl proton signal. Positions of the hydroxyl proton signals in ^1H nmr spectra of lupinine and epilupinine CCl_4 solutions undergo shifts induced by changes in solution concentration. In the case of epilupinine the dependence is monotonic throughout the concentration range investigated (0.2–2.0 M), whereas the hydroxyl signal of lupinine is independent of concentration below 1 M. This is most probably due to a very low percentage of associates in these solutions. The signal of the hydroxyl proton in the ^1H nmr spectrum of lupinine solution in $CDCl_3$ is located in a field lower by approximately 1 ppm with respect to its position in CCl_4 and DMSO solutions. It is almost concentration independent in the whole range investigated. The insensitivity of δ (OH) of lupinine in chloroform solutions of different concentrations is evidence of the stability of the lupinine conformational and association equilibrium in this solution. A weaker screening of the hydroxyl proton of lupinine in $CDCl_3$ confirms that the intramolecular hydrogen bonds are stronger in chloroform than in other solvents. The signal of the hydroxyl proton of epilupinine in chloroform solutions is sensitive to

concentration changes just as in the case of epilupinine solutions in CCl_4. In the entire range of concentrations investigated the dependence is linear. In the ^1H nmr spectra of lupinine and epilupinine solutions in DMSO the chemical shift of the hydroxyl protons is concentration independent in the range of 0.2–2.0 M, which could mean that basic DMSO molecules solvate both epimeric amino alcohols in a very similar manner.

Summary

In spite of the fact that lupinine and epilupinine possess analogous proton-donor and -acceptor centres, the different configurational and conformational dynamics of those molecules are responsible for their different capabilities of homo and heteroassociation.

In nonpolar solvents lupinine closes its active groups, N and OH, by forming an intramolecular hydrogen bond. This type of intramolecular interaction probably also exists in isolated molecules of the argon matrix but is always in equilibrium with monomers weakly solvated by molecules of nonpolar solvents. Even in concentrated solutions these monomers dominate over dimeric lupinine molecules associated by an intermolecular OH...O′ hydrogen bonding. Polyassociation of lupinine with an intermolecular OH...N′ hydrogen bonding is blocked up to saturated solutions. The blocking of homoassociation processes in lupinine chloroform solution is caused by significant affinity of chloroform molecules acting as a weak acid toward the free electron pairs of the oxygen atom from the hydroxyl group engaged in intramolecular OH...N hydrogen bonding. This interaction causes an additional strengthening of the intramolecular OH...N hydrogen bond in lupinine.

In polar solvents such as dioxane, DMSO, and D_2O, the intramolecular hydrogen bond in lupinine is partly or totally broken, and OH groups of lupinine interact specifically with the proton-acceptor centres of solvent molecules forming heteroassociates. In dioxane, a significant number of lupinine molecules form an intramolecular OH...N hydrogen bonding, whereas none in H_2O solution and very few in DMSO do so.

On the other hand, in all nonpolar solvents, chloroform included, epilupinine forms both types of homoassociates by OH...N′ and OH...O′ intermolecular hydrogen bonding. In polar solvents epilupinine behaves similarly to lupinine and forms heteroassociates with the solvent molecules.

1. A. J. HAPFINGER. Intermolecular interactions, and biomolecular organization. Wiley–Interscience, New York. 1977. p. 376.
2. K. KULIŃSKA and M. WIEWIÓROWSKI. Can. J. Chem. **65**, 205 (1987).
3. H. S. AARON and C. P. FERGUSON. Tetrahedron, **30**, 803 (1974).
4. S. N. VINOGRADOV and R. H. LINNELL. Hydrogen bonding. Van Nostrand Reinhold, New York. 1971. p. 57.

Can. J. Chem. Downloaded from www.nrcresearchpress.com by 196.1.178.254 on 09/07/12
For personal use only.

Stepwise reduction of samarium cryptates in propylene carbonate: anions and water concentration effects on the redox behavior of the Sm(III)/Sm(II) couple

EDOUARD LAURENT LOUFOUILOU

Laboratoire de Chimie Physique, U.A. au CNRS n° 405, E.H.I.C.S., I rue Blaise Pascal, 67000 Strasbourg, France

AND

JEAN PAUL GISSELBRECHT

Laboratoire d'Electrochimie et de Chimie Physique du Corps Solide, U.A. au CNRS n° 405, Université Louis Pasteur, 4 rue Blaise Pascal, 67000 Strasbourg, France

Received January 4, 1988

EDOUARD LAURENT LOUFOUILOU and JEAN PAUL GISSELBRECHT. Can. J. Chem. **66**, 2172 (1988).

The polarographic reduction of samarium(III) cryptates with cryptands 222, 221, and 22 was investigated in propylene carbonate. The samarium(III) cryptates are reduced in two consecutive steps, the first step was reversible and corresponded to the reduction of the Sm(III) to the Sm(II) cryptate. The Sm(III)/Sm(II) redox potential of the cryptates depended on the anion used in the complex and, in the case of the cryptate with chloride anions, a stable mixed complex was observed in propylene carbonate. The Sm(III)/Sm(II) redox potentials of the cryptates were more cathodic than the redox potential of the uncomplexed Sm(III)/Sm(II) couple, which is typical of a lower stability of the reduced cryptate. Propylene carbonate does not stabilize low oxidation states of lanthanides by cryptation. This is at variance with behavior observed previously in other media like water and methanol. Variations of redox potentials as a function of increasing amounts of water were accounted for by solvent shielding of samarium(III) upon encapsulation in cryptands.

EDOUARD LAURENT LOUFOUILOU et JEAN PAUL GISSELBRECHT. Can. J. Chem. **66**, 2172 (1988).

La réduction polarographique de cryptates de samarium(III) en utilisant les cryptands 222, 221 et 22 a été étudiée dans le carbonate de propylene. Les cryptates de samarium(III) sont réduits en deux étapes consécutives dont la première était réversible et correspondait à la réduction du cryptate de samarium(III) en cryptate de samarium(II). Le potentiel rédox du couple Sm(III)/Sm(II) pour les cryptates étudiés dépendait énormément de la nature de l'anion du cryptate étudié et, dans le cas des cryptates dont l'anion était l'anion chlorure, un complexe mixte et stable a été mis en évidence dans le carbonate de propylène. Les potentiels rédox du couple Sm(III)/Sm(II) des cryptates étudiés était plus cathodique que le potentiel rédox du couple Sm(III)/Sm(II) non complexé, ce qui est caractéristique d'une plus faible stabilité du cryptate réduit par rapport à la forme oxydée. Dans le carbonate de propylène la complexation d'ions lanthanides par les cryptands ne permet pas de stabiliser leurs bas degrés d'oxydation comme cela a été observé antérieurement dans d'autres solvants tel l'eau et le méthanol. D'autre part, l'évolution des potentiels rédox des cryptates en fonction de la teneur en eau du carbonate de propylène, a montré clairement que ceux-ci évoluaient de manière plus conséquente pour le samarium(III) non complexé que pour les cryptates, confirmant l'effet d'écran du cryptand vis à vis de la solvatation.

Can. J. Chem. Downloaded from www.nrcresearchpress.com by 196.1.178.254 on 09/07/12
For personal use only.

Introduction

Up to now the encapsulation of lanthanide ions by macrocycles has been much less explored than that of alkaline, earth-alkaline, and transition metals ions (1). A recent review (2) on rare earth complexes with neutral macrocyclic ligands showed that the electrochemical studies on these species are still scarce in the literature.

The published electrochemical studies on such cryptates aimed mainly at stabilizing low oxidation states. It has been shown in water (3, 4) and methanol (5) that the complexation of lanthanides ions by cryptands stabilized low oxidation states, especially for Eu, Sm, Yb, whereas this stabilization was not observed in propylene carbonate (5). In propylene carbonate low oxidation states were stabilized with crown ethers (2, 5, 6).

The aim of the present work was to investigate the electrochemical properties of samarium(III) cryptates involving the cryptands 222, 221, and 22, to understand why these samarium(II) cryptates are not stabilized in propylene carbonate as indicated electrochemically by the observed cathodic shift of the redox potential of the Sm(III)/Sm(II) couple in the cryptate with respect of the uncomplexed couple, and to assess solvent shielding effects when samarium ions become complexed with macrocycles. While this research was in progress (7) Tabib *et al.* (8) reported that redox potentials of europium, samarium, and ytterbium cryptates with 222 and 221 in different solvents may be used as probe of solvent shielding effects in lanthanide cryptates (8).

Experimental

All electrochemical measurements were carried out in propylene carbonate (PC) (Merck) purified according to the method proposed by Gosse and Denat (9). Tetraethylammonium perchlorate (TEAP) (Fluka) was used as supporting electrolyte and was recrystallized in methanol before use (10).

Electrochemical measurements were performed with a multipurpose PRG4 device (SOLEA, Tacussel), on a dropping mercury electrode as working electrode (m = 0.085 mg/s; h = 40 cm). The reference electrode was a saturated calomel electrode (SCE) electrically connected to the electrolysis cell by a bridge filled with CP + 0.1 *M* TEAP.

The ligands 222, 221, 22 (Kryptofix, Merck) were used without further purification.

The samarium(III) trifluoromethanesulfonate was prepared according to the procedure described by Massaux and Duyckaerts (11) and dried under vacuum at 60°C for 24 h.

The complexes [222 Sm]Cl_3, [221 Sm]Cl_3, [22 Sm]Cl_3 were prepared as described by Seminara and Musumeci (12).

For the cryptates with trifluoromethanesulfonate (triflate) as anions an original synthetic route was used: 1 mmol of $Sm(CF_3SO_3)_3$ in 10 mL methanol was dried by trimethyl orthoformate — $CH(OCH_3)_3$ — (Jansen Chemica) according to Massaux and Musumeci (11). Acetonitrile (20 mL) was added and the methanol was removed by distillation. Then, a solution of 1.1 mmol of ligand in 10 mL acetoni-

Printed in Canada / Imprimé au Canada

Can. J. Chem. Downloaded from www.nrcresearchpress.com by 196.1.178.254 on 09/07/12
For personal use only.

trile was added to the samarium(III) solution in a dry box. The mixture was heated under reflux for half an hour at 40°C. White crystals precipitated. After filtration the solid was washed with hexane and dichloromethane and dried under vacuum at 40°C for 48 h. The complexes were slightly hygroscopic but they were easier to dry than the perchlorate salts.

To introduce chloride or water into the solutions we always added a precise volume of a stock solution containing tetraethylammonium chloride (TEACl) or water, of which concentration was exactly known.

Results

Reduction of samarium(III) triflate in CP

The polarographic reduction of samarium(III) occurs in two consecutive diffusional waves at − 1.14 V/SCE and −2.0 V/SCE corresponding, respectively, to the reduction of Sm(III) to Sm(II) and Sm(II) to Sm(0). This reduction behaviour was described previously (5, 11, 13, 14). The log plot (log $(I/I_d - I)$ versus E) was linear and the slopes were equal to 66 and 29 mV per log unit, respectively. The wave heights were proportional to the concentration over the range 2×10^{-4} M to 2.5×10^{-3} M, the slopes of the $I = f(C)$ plot being 0.23 and 0.45 μA/mM under our experimental conditions, respectively. Cyclic voltammetry performed between −0.5 to −2.0 V/SCE (Fig. 1) showed a reversible reduction of Sm(III) to Sm(II) and an irreversible reduction from Sm(II) to Sm(0). The samarium was reoxidized around −0.7 V/SCE. Cyclic voltammetry on the first reduction step between −0.9 and −1.4 V/SCE showed that this reduction occurs quasireversibly: $I_{p_c} = f(v^{1/2})$ linear and crossing the origin (I_{p_c} = reduction peak current), $E_{p_c} = f(\log v)$ non-linear and E_{p_c} shifted cathodically with increasing scan rate (Ep_c = reduction peak potential), the peak potentials difference $E_{p_c} - E_{p_a}$ increasing from −130 mV at 2 V/s to −380 mV at 100 V/s. At low scan rates (10 to 100 mv/s) (5) the difference $E_{p_c} - E_{p_a}$ was equal to −70 mV. From the evolution of the peak potential difference $E_{p_c} - E_{p_a}$, with scan rate, it was possible, according to Nicholson (15), to determine the charge transfer rate constant $k_s = (8.3 + 0.3) \times 10^{-2}$ cm s^{-1}.

Reduction of samarium in propylene carbonate with increasing water content

Increasing amounts of water added to a solution of $Sm(CF_3SO_3)_3$ shifted cathodically the Sm(III)/Sm(II) reduction potential but had no effect on the wave height. The redox potential moved up to −1.40 V/SCE (from −1.14 V/SCE) for a water concentration equal to 0.56 M (the value observed in water was −1.78 V/SCE (13, 14)). The limit of water solubility in propylene carbonate is approximately 4.5 M (16).

By cyclic voltammetry, like in polarography, the redox potential of the Sm(III)/Sm(II) couple became also more negative with increasing water concentration as shown on Fig. 1. Analysis of the voltammetric curves related to the first reduction (from −0.4 to −1.4 V/CE), proved that the system remained reversible, after addition of water. The ratio I_{p_a}/I_{p_c} remained constant and close to unity over the scan range 2 to 100 V/s, as water was added to the solution. Also the peak potentials difference $|E_{p_c} - E_{p_a}|$ increased, with scan rate, but the rate of the charge transfer slowed down against dry PC. Indeed, the calculated rate constant, according to Nicholson (15), became $k_s = (5.4 + 0.3) \times 10^{-2}$ cm s^{-1} for a water concentration in PC equal to 0.48 ML^{-1}.

Thus, the electrochemical behaviour of samarium(III) in the presence of water indicated that the redox potential of the

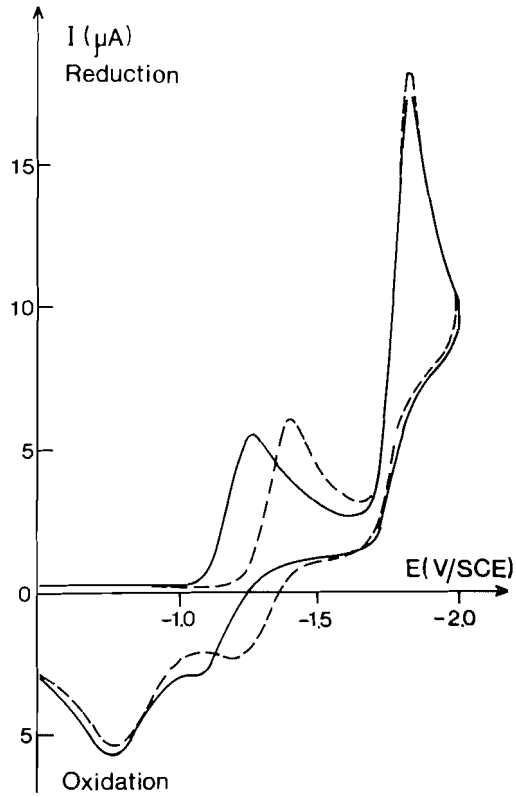

FIG. 1. Cyclic voltammogram of $Sm(CF_3SO_3)_3$ ($C = 2.52 \times 10^{-3}$ M) in PC + 0.1 M TEAP (v = 10 V/s). ——— Anhydrous CP; --------- PC + H_2O ($C_{H_2O}/C_{Sm} = 68$).

Sm(III)/Sm(II) couple depended very much on the water concentration in the propylene carbonate. As the redox potential of Sm(II)/Sm(0) remained unaffected by water concentration, it may be expected that only Sm(III) was strongly hydrated. This result was not surprising taking into account the very high hydration energy of about 800 kcal/mol for Sm(III) (17) whereas it is only 200 kcal/mol for calcium(II) which has about the same ionic radius. It explains why the reduction potential of Sm(III) was not water independent, like the reduction potential of Ca(II).

On the other hand, the high hydration energy of samarium(III) might explain why no significant encapsulation occurred by adding a cryptand to the samarium(III) solution. In fact, in interaction between samarium–cryptand indeed occurred. When cryptand was added to a samarium(III) solution, the Sm(III)/Sm(II) wave decreased and vanished as soon as the cryptand samarium ratio reached unity. Simultaneously, a new irreversible wave appeared at −1.85 V/SCE (5) who could be attributed to the reduction of an exclusive complex, the inclusive cryptate being reduced reversibly at a more anodic potential as demonstrated hereafter.

Reduction of samarium cryptates with [222], [221], [22] cryptands

Each of the different cryptates studied was dissolved in propylene carbonate. In the case of the [22 Sm]Cl_3 the solubility limit was about 5×10^{-3} M and for higher concentrations the solution became opalescent. Each cryptate was reduced in two distinct steps whose polarographic characteristics are summarized in Table 1.

The limiting current of each two reduction waves was

TABLE 1. Characteristics of the polarographic reduction of samarium cryptate in propylene carbonate

Cryptates	$E_{1/2}$ (III/II) (V/SCE)	$\log (I/I_d-I)$ (mV)	$E_{p_c} - E_{p_a}$ (mV)(10 V/s)	$E_{1/2}$ (II/0) (V/SCE)
[222 $SmCl_3$]	−1.46	69	− 88	<−2.6
[221 $SmCl_3$]	−1.62	61	−100	−2.6
[22 $SmCl_3$]	−1.74	95	−139	−2.36
[222 $Sm(CF_3SO_3)_3$]	−1.12	61	− 68	−2.40
[221 $Sm(CF_3SO_3)_3$]	−1.34	63	− 80	−2.30
[22 $Sm(CF_3SO_3)_3$]	−1.46	59	− 90	−2.35

proportional to the concentration on the range 0.2 to 3×10^{-3} M. We checked, using the chronoamperometric criterion developed in this aim (18) that the reduction limiting currents were diffusion controlled. Also, the slope of $\log (I/I_d - I) = f(E)$ indicated that the first reduction step was a reversible monoelectronic reduction step, except for [22 Sm]Cl_3. As the half-wave potential of the first reduction was independent on cryptate concentration, the reduction occurred without change in the metal/ligand stoichiometry. Thus the first step corresponded to the reduction of the complexed samarium(III) to the complexed samarium(II). The second reduction observed at more negative potentials corresponded to the reduction of the samarium(II) cryptate to free ligand and zerovalent samarium.

Another remarkable characteristic in these reductions was that the half wave potential of the first step depended upon the nature of the anion in the cryptate (Table 1): the $SmLCl_3$ cryptates were reduced at more cathodic potentials — about 0.3 V — than the corresponding $SmL(CF_3SO_3)_3$ cryptates. That behaviour will be discussed later on.

Cyclic voltammetry performed on the two reduction steps showed that the first step was a reversible one — presence of an anodic peak — whereas the second step was irreversible. The reduction parameters of the first reduction step were obtained from cyclic voltammetry performed on this first step only: $Ip_c = f(v^{1/2})$ was linear and crossing the origine, $Ep_c = f(\log v)$ was not linear (Ep_c shifting cathodically with increasing scan rate), the difference $|Ep_c - Ep_a|$ increased with scan rate, Ip_a/Ip_c was equal to unity. These parameters clearly indicated that the first reduction step of the studied Sm(III) cryptates was a quasi reversible monoelectronic reduction.

The reduction of [22 Sm]Cl_3 was also chemically reversible, as shown by the observed anodic peak in cyclic voltammetry (Fig. 2). However, the slope of the log plot and the peak potentials difference (Table 1) denoted a non Nernstian process. Cyclic voltammetry performed on the first reduction step showed that the evolution of the reduction parameters were similar to those described above, however the difference $|E_{p_c} - E_{p_a}|$ was higher, ranging from 100 mV at 50 mV/s to 160 mV at 20 V/s. These parameters indicated that the rate determining step was a slow charge transfer in this first reduction. Figure 2 shows also clearly the second reduction peak, as well as the reoxidation peak of the samarium(0) at −0.7 V/SCE.

Water concentration effects on the redox behaviour of samarium cryptate, in propylene carbonate

Adding increasing amounts of water to propylene carbonate had different effects on the first reduction potentials of the samarium(III) cryptates, depending on the anions used. For $SmLCl_3$ the redox potential shifted anodically as the water

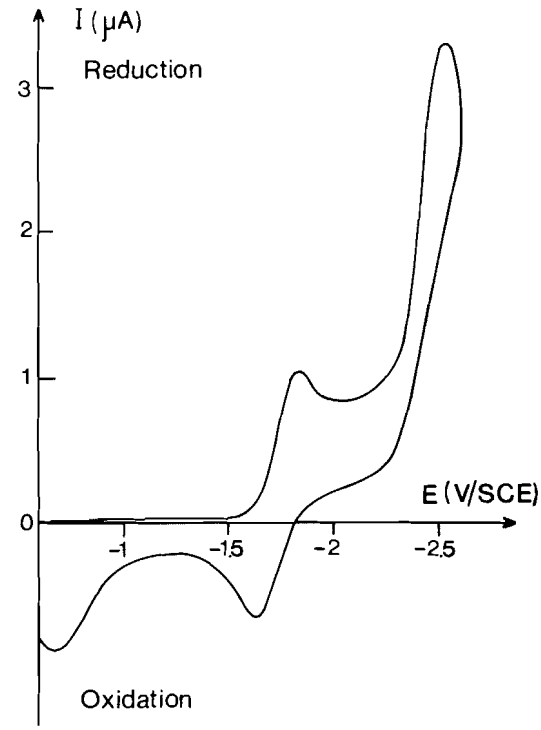

FIG. 2. Cyclic voltammogram of Sm 22 Cl_3 ($C = 5 \times 10^{-3}$ M) in PC + 0.1 M TEAP (v = 10 V/s).

content increased whereas a cathodic shift was observed with $SmL(CF_3SO_3)_3$. In other words, $SmLCl_3$ and $SmL(CF_3SO_3)_3$ cryptates exhibited closer reduction potentials after addition of water (Table 2).

It shall be noticed that addition of water shifted cathodically the Sm(III)/Sm(II) redox potential for derivatives having triflates as anions, when Samarium ions were complexed and when they were not complexed as well. However, the cathodic shift with water concentration was much smaller for the cryptates than for the uncomplexed samarium(III). On the other hand, the observed anodic shift in the derivatives with chloride anions was probably due to the dissociation of the chloride from the cryptate by water. This explanation will be discussed hereafter, but we have also checked that, in water and with a given cryptand involved, $SmLCl_3$ and $SmL(CF_3SO_3)_3$ cryptates have the same reduction potential, as expected for a total dissociation of these salts in water.

This behaviour led us to studying the changes in the redox potential of $SmL(CF_3SO_3)_3$ cryptates dissolved, in dry propylene carbonate, when increasing amounts of chloride were added to this solution.

Can. J. Chem. Downloaded from www.nrcresearchpress.com by 196.1.178.254 on 09/07/12
For personal use only.

TABLE 2. Redox potentials changes in PC as a function of water concentration for chlorinated and triflated cryptates[a]

	$E_{1/2}$ (V/SCE)			
Ligand	Sm Cl_3		$Sm(CF_3SO_3)_3$	
222	−1.46 (0 *M*)	−1.35 (0.69 *M*)	−1.19 (0.85 *M*)	−1.12 (0 *M*)
221	−1.62 (0 *M*)	−1.56 (0.66 *M*)	−1.44 (0.55 *M*)	−1.34 (0 *M*)

Values in parentheses are for water concentration.

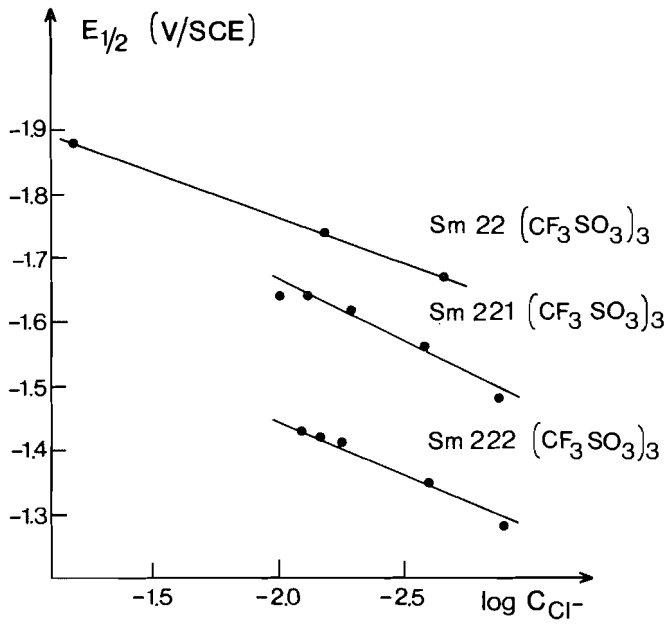

FIG. 3. Plot of half-wave potentials as a function of chloride concentration.

TABLE 3. Effect of the chloride concentration on the redox potential of the couple Sm(III)/Sm(II), in solutions of $Sm(CF_3SO_3)_3$ cryptates[b]

Ligand	$E_{1/2}$ (V/SCE)	Slope $\Delta E_{1/2}/\Delta \log (C_{Cl-})$	$p - q$
222	−1.12	180±10	3
221	−1.34	190±20	3
22	−1.46	110±10	2

[b]Solvent: PC + 0.1 *M* TEAP; *p* and *q* denote the number of chlorides coordinated with Sm(III) and Sm(II), respectively.

Changes in the redox potential of triflated Sm(III)/Sm(II) cryptates, in the presence of added chloride

Upon addition of tetraethylammonium chloride to the solution, the Sm(III)/Sm(II) redox potential in the different cryptates shifted cathodically with increasing chloride concentration. Also, the reduction potential measured in the presence of stoechoimetric amount of chloride added to the triflate solution (i.e. 3 Cl/1 Sm) was the same as the potential measured, in the same solvent, after dissolution of the corresponding $SmLCl_3$ cryptate. From the plots of the potential versus the logarithm of the chloride concentration (Fig. 3 and Table 3), the relation established by Stackelberg (19) led to calculate the stoechiometry change of coordinated chloride during the reduction of Sm(III) to Sm(II). Also, the stability constant of the mixed complex corresponding to the equilibrium $SmL + nCl^- \rightleftharpoons SmLCl_n$ was determined (Table 4).

TABLE 4.

Overall stability constants $\beta = \dfrac{(SmLCl_n)}{(SmL)\,(Cl^-)^n}$ of $SmLCl_n$ complexes

Ligand	Stoichiometry M^{3+}	: L :	nCl^-	log β
222	1	1	3	11.6
221	1	1	3	11.5
22	1	1	2	9.1

The values obtained for log β (Table 4) illustrated that the $SmLCl_n$ cryptates are very stable in solution, thus explaining why the redox behaviour of the $SmLCl_n$ cryptates, were so different from that of the corresponding $SmL(CF_3SO_3)_3$ cryptates.

Discussion

The present results obtained in propylene carbonate may be compared with previous studies in water (3, 4) and in methanol (5), where divalent lanthanides became stabilized by complexation by cryptand, as documented electrochemically for samarium(III) by the observed anodic shift of the redox potential of Sm(III)/Sm(II) in the cryptate with respect to the measured potential of the uncomplexed Sm(III)/Sm(II) couple. The present results clearly indicate that no stabilization of samarium(II) occurred by complexation with cryptand in propylene carbonate, with the exception of [222 Sm]$(CF_3SO_3)_3$, for which the 20 mV anodic shift of the redox potential indicated a very small stabilization of Sm(II) compared to Sm(III).

On the other hand, the addition of water to propylene carbonate shifted cathodically the redox potential of Sm(III)/Sm(II) in species with triflate anions. The effect was much greater for uncomplexed samarium(III) — from −1.12 to −1.40 V/SCE for 0.56 *M* of water, i.e. about +280 mV — than for the samarium cryptate: about 100 mV for 0.6 *M* of water. For example, for a 0.56 *M* water concentration the redox potential of Sm(III)/Sm(II) in $Sm(CF_3SO_3)_3$ became more cathodic ($E_{1/2}$ = −1.40 V/SCE) than the potential of Sm(III)/Sm(II) in [222 Sm]$(CF_3SO_3)_3$ ($E_{1/2}$ = −1.16 V/SCE). Therefore, in PC + 0.56 *M* H_2O, the uncomplexed Sm(III)/ Sm(II) potential was much less positive relative to 221 Sm(III)/221 Sm(II) than in anhydrous PC. It was expected that further addition of water will invert the sequence. This was actually observed in pure water and in methanol (3, 5). These results are consistent with the donor numbers of PC and water (20). It shall

Can. J. Chem. Downloaded from www.nrcresearchpress.com by 196.1.178.254 on 09/07/12
For personal use only.

Can. J. Chem. Downloaded from www.nrcresearchpress.com by 196.1.178.254 on 09/07/12
For personal use only.

also be noticed that, in anhydrous PC, it was possible to obtain stable complexes of Sm(III) with cryptand and chloride, which were dissociated in the presence of water. Such mixed complexes have previously been obtained in water with europium(III) and ytterbium(III) with fluoride and hydroxide in excess, but not with chloride (3). Our results are in agreement with the solvating properties of propylene carbonate according to Gutmann (20). The above results illustrate clearly the shielding effect of complexation by cryptand towards solvation. This shielding effect of the cryptand towards the cation-solvent interactions was assessed in one of our previous studies on cryptates in PC, where a levelling effect of complexation by cryptand was observed on the stokes radii of diffusing alkali ions in presence of 222 (21). That result was interpreted assuming that the 222 ligand replaced the first solvation shell around the complexed cation.

From the redox potentials obtained in the present paper and from the stability constants of lanthanide(III) cryptates determined by Loufouilou and co-workers (22), in PC, it was possible to calculate the stability constants of the corresponding samarium(II) cryptates, using Stackelberg's relationship (19) applied to the present reduction scheme:

$$ML_p^{n+} + (n\text{-}m)\ e \rightleftharpoons ML_q^{n+} + (p\text{-}q)\ L$$

(p and q correspond to the number of ligands attached to Sm^{n+} and Sm^{m+}, respectively).

The relationship has the form

$$\Delta E_{1/2} = [0.059/(n\text{-}m)] \times \log \beta_{red}/\beta_{ox} - (p\text{-}q) \times [0.059/(n\text{-}m)] \times \log L$$

(where β denotes the stability constant).

In the present case, the stoichiometry of the oxidized and of the reduced species is the same. Thus, $p\text{-}q = 0$ and the above relationship become

$$\Delta E_{1/2} = [0.059/(n\text{-}m)] \times \log \beta_{red}/\beta_{ox}$$

From Table 1 and from the stability constants of samarium(III) cryptates given in Table 5, we calculate the corresponding stability of samarium(II) cryptates (Table 5).

These results show, for the 22 ligand, that the highest stability is not attained as soon as the ionic radius of the metal cations fits the radius of the cavity, as observed for alkali and earth alkaline cryptates. This is probably due to the fact that the complexation in lanthanides is not only due to electrostatic interactions but also to covalent bonding.

If we compare the complexing properties of cyclic polyethers like 18-crown-6 (18-C-6) reported in Table 5 with the 22 cryptand which has the same ring size, it is well established that cryptates form more stable complexes than crown-ethers. However, there is no satisfactory explanation why cyclic polyethers stabilize Sm(II), whereas the 22 cryptand does not.

The complexing mechanisms between Sm(III) on the one hand and the ligand 22 and 18-C-6 on the other hand are likely to be different: the complexation of Sm(III) by 18-C-6 occurred easily in PC while the complexation of Sm(III) by the 22 cryptand had to be carried out in dry solvating media such as CH_3CN or ethanol–acetonitrile mixtures. A very crucial step in the complexation reaction of lanthanides is the desolvation of the cation to be complexed. As the desolvation of a cation is facilitated by a polar surrounding of the complexation site (27), the above results would indicate that the crown ether is more polar than the cryptand. Thus, the complexation with 18-C-6 is facilitated.

TABLE 5. Stability constants of Sm(III) and Sm(II) cryptates in PC[f]

Cation	Stability constant 222 (1.40 Å)[a]	221 (1.10 Å)[a]	22 (1.40 Å)[a]	18-C-6 (1.40 Å)[b]
Sm^{3+} (0.96 Å)[c]	17.3[e]	19.0[d]	16.5[e]	8.1[d]
Sm^{2+} (1.22 Å)[c]	17.6	15.6	11.2	8.9[d]

[a]See ref. 23.
[b]See ref. 24.
[c]See ref. 25.
[d]See ref. 26.
[e]See refs. 7 and 22.
[f]Values in parentheses are ionic radii of the cavities and the cations.

Acknowledgment

We thank Professor M. Gross for useful discussions and continuing interest in this work.

1. R. M. IZATT, J. S. BRADSHAW, S. A. NIELSEN, J. D. LAMB, and J. J. CHRISTENSEN. Chem. Rev. **85**, 271 (1985).
2. J. C. G. BUNZLI and D. WESSNER. Coord. Chem. Rev. **60**, 191 (1984).
3. O. A. GANSOW, A. R. KAUSAR, K. M. TRIPLETT, M. J. WEAVER, and E. L. YEE. J. Am. Chem. Soc. **99**, 7087 (1977).
4. E. L. YEE, O. A. GANSOW, and M. J. WEAVER. J. Am. Chem. Soc. **102**, 2278 (1980).
5. M. C. ALMASIO, F. ARNAUD-NEU, and M. J. SCHWING-WEILL. Helv. Chim. Acta, **66**, 1296 (1983).
6. J. MASSAUX and J. F. DESREUX. J. Am. Chem. Soc. **104**, 2967 (1982).
7. L. E. LOUFOUILOU. Thèse, Strasbourg. March, 1986.
8. J. TABIB, J. T. HUPP, and M. J. WEAVER. Inorg. Chem. **25**, 1916 (1986).
9. B. GOSSE and A. DENAT. J. Electroanal. Chem. **56**, 5129 (1974).
10. G. RITZLER, F. PETER, and M. GROSS. J. Electroanal. Chem. **146**, 285 (1983).
11. J. MASSAUX and G. DUYCKAERTS. Anal. Chim. Acta, **73**, 416 (1974).
12. A. SEMINARA and A. MUSUMECI. Inorg. Chim. Acta, **26**, 263 (1978).
13. G. PEYCHAL-HEILING and V. GUTMANN, Z. Anal. Chem. **248**, 6 (1969).
14. L. O. DE S. BULHOES and T. RABOCKAI. Electrochim. Acta, **27**, 1071 (1982).
15. R. S. NICHOLSON. Anal. Chem. **37**, 1351 (1965).
16. T. FUJINAGA and K. IZUTZU. Pure Appl. Chem. **27**, 275 (1971).
17. R. MORSS. J. Phys. Chem. **75**, 392 (1971).
18. M. GROSS and J. JORDAN. J. Electroanal. Chem. **75**, 163 (1977).
19. M. N. STACKELBERG. Polarographische Arbeits Methoden. Walter de Gruyter, Berlin. 1950.
20. V. GUTMANN. Electrochim. Acta, **21**, 661 (1976).
21. F. PETER, J. P. GISSELBRECHT, and M. GROSS. J. Electroanal. Chem. **86**, 115 (1978).
22. F. ARNAUD-NEU, E. L. LOUFOUILOU, and M. J. SCHWING-WEILL. J. Chem. Soc. Dalton Trans. 2629 (1986).
23. J. M. LEHN. Struct. Bonding, **16**, 1 (1973).
24. N. K. DALLEY. Synthetic multidentate macrocyclic compounds. *Edited by* R. M. Izatt and I. J. Christensen. Academic Press, New York. 1978.
25. R. D. SHANNON. Acta Crystallog. **B32**, 751 (1976).
26. M. C. ALMASIO. Thèse Docteur Ingénieur, Strasbourg. 1983.
27. J. M. GIRODEAU. Thèse Docteur Ingénieur, Strasbourg. 1977.

Fast atom bombardment (FAB) and chemical ionization (CI) mass spectrometry of γ-carboxyglutamic acid, 5-substituted-4,4-dicarboxyprolines, and their monodecarboxy derivatives glutamic acid and 5-substituted-4-carboxyprolines

R. CAPASSO,[1] P. PUCCI, AND G. RANDAZZO[2]

Dipartimento di Chimica Organica e Biologica, Università degli Studi di Napoli, Via Mezzocannone, 16, 80134 Napoli, Italy

AND

A. MALORNI

Istituto di Chimica di Molecole di Interesse Biologico del Consiglio Nazionale delle Ricerche e Servizio di Spettrometria di Massa, c/o II[a] Facoltà di Medicina e Chirurgia dell'Università degli Studi di Napoli, Via Pansini, 5, 80100 Napoli, Italy

Received January 7, 1987[3]

R. CAPASSO, P. PUCCI, G. RANDAZZO, and A. MALORNI. Can. J. Chem. **66**, 2177 (1988).

DL-γ-Carboxyglutamic acid (Gla) reacts easily and quantitatively with aldehydes to give the racemic diastereoisomers of 5-substituted-4,4-dicarboxyprolines. After heating at 100°C for 30 minutes these amino acids lose a carboxyl group from C-γ of Gla and C-4 of the proline ring to give glutamic acid and the racemic diastereoisomers of cyclic analogs of glutamic acid respectively. This paper reports a study of the above-mentioned compounds by using FAB mass spectrometry in comparison with CI analysis. FAB turned out to be an adequate ionization technique for dealing with such nonvolatile and thermolabile amino acids, and may thus allow the development of a rapid and sensitive method for detecting γ-carboxyglutamic acid in urine and in other biological matrices in pathological cases (i.e., renal stones and blood serum).

R. CAPASSO, P. PUCCI, G. RANDAZZO et A. MALORNI. Can. J. Chem. **66**, 2177 (1988).

L'acide γ-carboxyglutamique (Gla) réagit facilement et quantitativement avec les aldéhydes pour donner des diastéréoisomères racémiques des dicarboxy-4,4 prolines substitués en position 5. Par chauffage à 100°C pendant 30 minutes ces acides aminés perdent un groupe carboxyle à partir du carbone en position γ du Gla et du carbone en position 4 du cycle de la proline pour donner respectivement l'acide glutamique et les diastéréoisomères des analogues cycliques de l'acide glutamique. On rapporte une étude de ces composés en faisant appel à la spectrométrie de masse BFA conjointement avec l'analyse par IC. Le BFA se révèle être une technique adéquate d'ionisation pour acides aminés non volatils et thermolabiles. Il peut ainsi constituer une méthode sensible de détection de l'acide γ-carboxyglutamique dans l'urine et dans d'autres matrices biologiques dans des cas pathologiques (c.-à.-d. calculs rénaux, serum sanguin).

[Traduit par la revue]

Introduction

γ-Carboxyglutamic acid (Gla) has been found in proteins involved in blood clotting (1–4). Gla-containing proteins have also been identified in calcified tissues such as the organic matrix of bone (5), renal stones (6), and atherosclerotic plaque (7). Free Gla has been found in human urine (8) as a metabolic product of the catabolism of Gla-containing proteins (8, 9). In pharmacological therapy with warfarin (10) and in diseases such as osteoporosis (11), abnormal levels of Gla have been detected in the urine.

In this regard an analytical method to determine Gla in the urine, based on the quantitative and simple reaction of the amino acid with acetaldehyde, has been proposed (12).

Recently it has been shown, mainly by ^{1}H nmr (13), that DL-Gla generally reacts with aldehydes to give the racemic diastereoisomers of the 5-substituted-4,4-dicarboxyprolines. With the ultimate aim of finding a sensitive mass spectrometric method to detect Gla in the urine in pathological cases, the CI and FAB behaviour of the compounds mentioned has been investigated. The CI technique, which was successfully applied to the analysis of naturally occurring amino acids (14), failed in studying these derivatives on account of the high temperature required at the ms source to vaporize such nonvolatile and thermolabile tricarboxyamino acids. The FAB technique, on the contrary, proved to be very suitable in dealing with such polar compounds. Furthermore, the behaviour of these compounds after exposure at 100°C for 30 min in H_2O has been studied: they lose a carboxyl group from C-γ of Gla and from C-4 of proline derivatives, giving rise to glutamic acid and racemic diastereoisomers of the cyclic analogs of glutamic acid (13) respectively.

Experimental

FAB mass spectra were recorded on a Kratos MS 50 double focusing mass spectrometer, equipped with an M-scan source and an M-scan gun, using xenon as bombarding gas. Spectra were recorded at 8-kV acceleration potential, at 100 s/decade scan rate on Kodak paper Linagraph direct print. Samples were dissolved in 5% AcOH and loaded (0.1–10 μg) into a glycerol-coated probe tip. A significant improvement in the FAB spectra of some compounds was obtained by adding concentrated hydrochloric acid to the sample.

Linked scans at constant B/E (B/E linked scan) were performed by scanning the magnetic sector field-strength B and the electrostatic sector field-strength E simultaneously, holding the accelerating voltage constant. The B/E ratio is maintained at a constant value determined by the ratio of the two field-strengths, which transmit the selected precursor ion whose fragment-ion spectrum is required.

The CI mass spectra were obtained on a Kratos MS 80 mass spectrometer, using isobutane or ammonia as reagent gas, at a pressure of 0.8 Torr (1 Torr = 133.3 Pa) and at 350–400 eV. The sample (5–10

[1]Present address: Istituto di Chimica Agraria, Facoltà di Agraria, Università degli Studi di Napoli, Via Università, 100, 80055 Portici, Napoli, Italy.

[2]Present address: Istituto di Chimica Biologica, Facoltà di Medicina e Chirurgia, Università degli Studi di Cagliari, 09100 Cagliari, Italy.

[3]Revision received March 7, 1988

Printed in Canada / Imprimé au Canada

Can. J. Chem. Downloaded from www.nrcresearchpress.com by 196.1.178.254 on 09/07/12
For personal use only.

TABLE 1. FAB data for the amino acids **1–6** and some corresponding monodecarboxy derivatives **1***a*, **2***a*$_1$, **2***a*$_2$, **3***a*$_1$, **3***a*$_2$, **4***a*$_1$, and **4***a*$_2$ obtained by heating at 100°C for 30 min in H_2O and D_2O

Compound	MH^+	$MH^+ - CO_2$	Compound	MH^+	$(MD)H^+$
1	192 (100)	—	**1***a**	148 (100)	
2	—	—	**2***a*$_1$	160 (100)	
			2*a*$_2$		161 (100)
3	218 (100)	—	**3***a*$_1$	174 (100)	
			3*a*$_2$		175 (100)
4	280 (53)	236 (100)	**4***a*$_1$	236 (100)	
			4*a*$_2$		237 (100)
5	310 (86)	266 (100)			
6	325 (52)	281 (100)			

*This value is observed in the spectra of glutamic acid and the product obtained by heating γ-carboxyglutamic acid at 100°C for 30 min.

μg) was placed in a glass capillary tube, inserted into the probe of the mass spectrometer, and heated at 250–300°C.

Glu was purchased from Sigma and Gla from Bachem Biochemicals. The amino acid 4,4-dicarboxy-5-methylproline **3** (Fig. 1) was prepared by reaction of γ-carboxyglutamic acid with acetaldehyde as previously described (13), but the purification was performed as follows. The product (4.5 mg) was chromatographed on a DEAE-cellulose column, (1.5 × 10 cm) equilibrated and eluted with 0.3 M pyridine-acetate buffer pH 4.75. The fractions were analyzed by thin-layer chromatography (tlc) (Kieselgel Merck 0.25 mm 60 F_{254}, *n*-butanol – acetic acid – water 60:15:25, as eluent) and those giving a yellow spot with ninhydrin were pooled and lyophilized at least three times before the ms analyses. The amino acids 4,4-dicarboxyproline **2**, 4,4-dicarboxy-5-phenylproline **4**, -5-(*p*-OCH_3-phenyl)-proline **5**, and -5-(*p*-NO_2-phenyl)-proline **6** (Fig. 1) were prepared by reaction of carboxyglutamic acid with formaldehyde, benzaldehyde, *p*-methoxybenzaldehyde, and *p*-nitrobenzaldehyde respectively, as previously reported (13). The normal and C-4 deuterated amino acids were prepared by heating the parent amino acids **1–6** for 30 min at 100°C in H_2O or D_2O (99%). The solutions were cooled at room temperature, lyophilized, and the residue was directly analyzed by mass spectrometry.

The amino acids considered were identified by ^1H nmr analysis as already published (13).

Results and discussion

The FAB mass spectrum of γ-carboxyglutamic acid **1** (Fig. 1 and Table 1) shows a strong protonated molecular ion at *m/z* 192. The CI spectra (with isobutane and ammonia), of the same compound **1** and its monodecarboxy derivative, obtained by heating at 100°C for 30 min display the same characteristic fragmentation pattern as that of glutamic acid (14) (Table 2).

Furthermore, the FAB spectrum of glutamic acid **1***a* and the decarboxy derivative of Gla are identical (Table 1). These results strongly suggest that during CI experiments decarboxylation of Gla occurs in the mass spectrometer source, probably due to the high temperature (250°C) required to vaporize the nonvolatile and thermolabile Gla, according to the malonic acid nature of the carboxyl groups.

The data of positive FAB spectra of amino acids **3–5** are reported in Table 1. All the spectra, with the exception of product **2**, show two signals with different intensities, corresponding to MH^+ and $MH^+ - 44$ (Table 1). The latter refers to the monodecarboxy derivative formed by loss of CO_2 from C-4 of the proline ring as discussed below.

The 4,4-dicarboxyproline **2** (Fig. 1) does not afford signals,

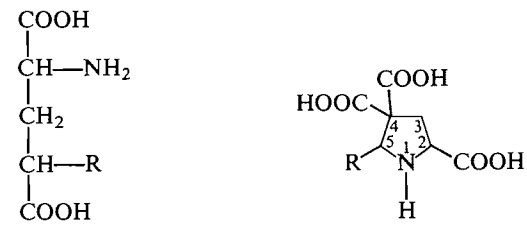

1 R = -COOH
1*a* R = -H

2 R = -H
3 R = -CH_3
4 R = -C_6H_5
5 R = -$C_6H_4OCH_3$
6 R = -$C_6H_4NO_2$

FIG. 1. Structure of Gla, Glu, 4,4-dicarboxyproline, and 5-substituted-4,4-dicarboxyprolines.

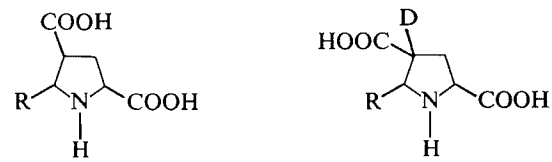

3*a*$_1$ R = -CH_3
4*a*$_1$ R = -C_6H_5
2*a*$_1$ R = -H

3*a*$_2$ R = -CH_3
4*a*$_2$ R = -C_6H_5
2*a*$_2$ R = -H

FIG. 2. Structure of 4-carboxyproline and 5-substituted-4-carboxyprolines with a hydrogen or deuterium atom on C-4.

while the 4,4-dicarboxy-5-methlyproline **3** does not show any CO_2 loss from the molecular ion. The reason for this behaviour remains unclear.

All the samples were heated at 100°C for 30 min in H_2O and D_2O and the resulting derivatives were analyzed by FAB mass spectrometry. The sample heated in D_2O showed a protonated molecular ion shifted up one mass unit in comparison to the derivatives obtained in H_2O. The statistical replacement of one of the carboxyl groups on C-4 by a deuterium atom provides 5-substituted-4-carboxy-4-D-prolines, as already demonstrated by ^1H nmr data (13). As examples, the data of the FAB spectra of 4-carboxyproline **2***a*$_1$, -4D-proline **2***a*$_2$, 4-carboxy-5-methylproline **3***a*$_1$, -4-D-5-methylproline **3***a*$_2$, 4-carboxy-5-phenylproline **4***a*$_1$, and -4-D-5-phenylproline **4***a*$_2$ (Fig. 2) are reported for

Can. J. Chem. Downloaded from www.nrcresearchpress.com by 196.1.178.254 on 09/07/12
For personal use only.

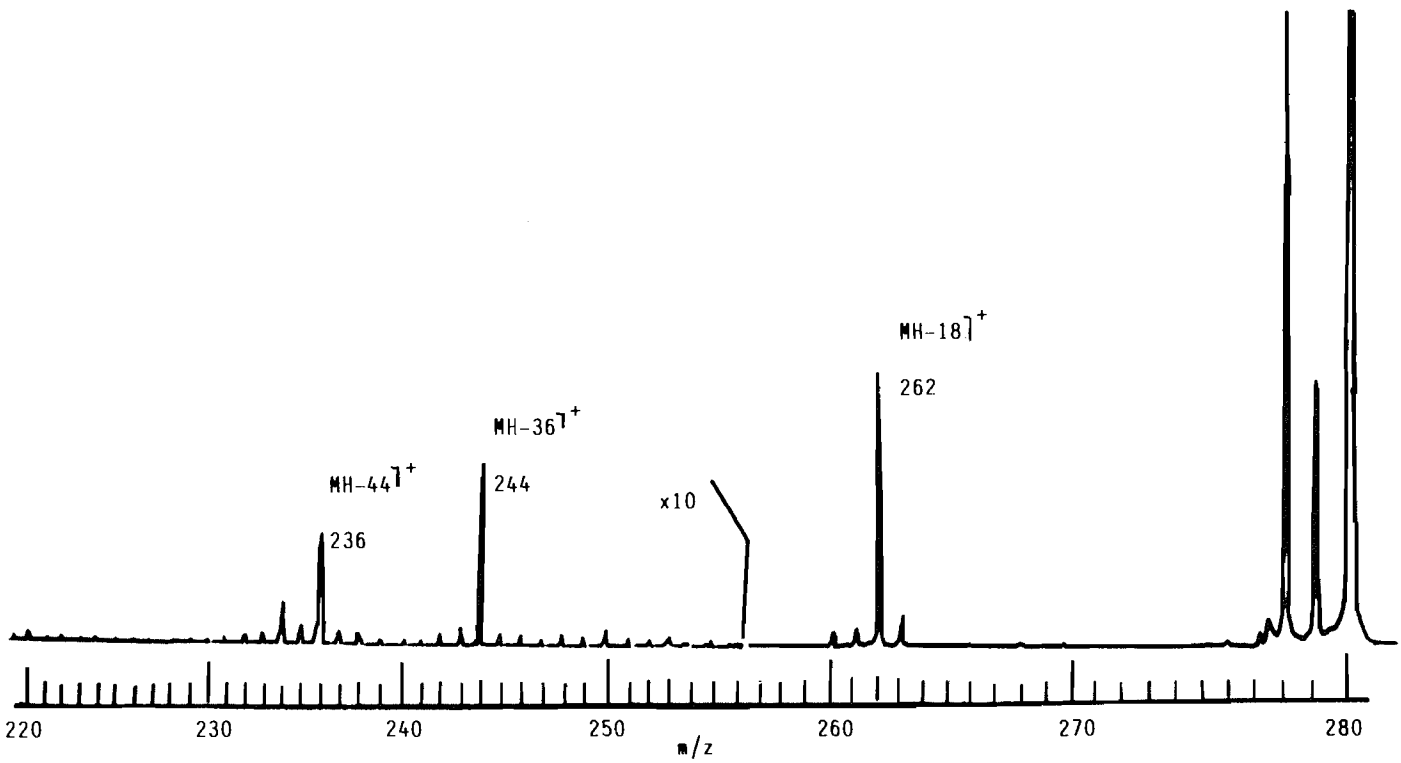

FIG. 3. Positive ion FAB B/E-linked scan spectrum of 4,4-dicarboxy-5-phenylproline **4**.

TABLE 2. CI data of the amino acids **1**, **3**, **6**, and corresponding monodecarboxy derivatives $\mathbf{1}a_1$, $\mathbf{3}a_1$, and $\mathbf{6}a_1$ obtained by heating at 100°C for 30 min in H_2O

Compound	$MH^+ - CO_2$	$MH^+ - CO_2$ —H_2O	$MH^+ - CO_2$ —$COOH_2$	$MH^+ - CO_2$ —$COOH_2$ —H_2O	Compound	MH^+	$MH^+ - H_2O$	MH^+ —$COOH_2$	$MH^+ - H_2O$ —$COOH_2$
1	148 (1)* (6)†	130 (100)* (68)†	102 (1)* (17)†	84 (30)* (100)†	$\mathbf{1}a$‡	148 (1)†	130 (55)†	102 (3)†	84 (100)†
2	—	—	—	—	$\mathbf{2}a_1$	160 (42)†	142 (100)†	—	—
4	236 (18)* (25)†	218 (17)* (12)†	190 (100)* (100)†	172 (70)* (60)†	$\mathbf{4}a_1$	236 (24)*	218 (14)*	190 (100)*	172 (75)*

*Relative intensity data with ammonia gas.
†Relative intensity data with isobutane gas.
‡This kind of fragmentation is identical to that of glutamic acid.

comparison in Table 1. The mass difference between the two MH^+ ions is clearly detectable.

Finally, B/E-linked scan experiments performed on 4,4-dicarboxy-5-phenylproline **4** demonstrate that the CO_2 loss originates from the protonated molecular ion, as shown by the presence of the peak at m/z 236 in the corresponding spectrum (Fig. 3). Moreover the FAB spectrum of **4** is reported as an example in Fig. 4. In this spectrum smaller peaks at m/z 262 and 244 appear in addition to m/z 280 and 236 and are attributed to the loss of H_2O, as indicated in the B/E-linked scan spectrum (Fig. 3). This kind of fragmentation (the loss of H_2O) is not observed in the FAB spectra of the other amino acids.

Compounds **2–6** were analyzed by CI technique in the same way as compound **1**. Samples **2**, **3**, **5**, and **6** did not give reproducible spectra, while the decarboxy derivative $\mathbf{2}a_1$ gave a clear and reproducible spectrum (Table 2). The spectrum of 4,4-dicarboxy-5-phenylproline **4** did not show the molecular ion at m/z 280 because of the thermolability of the carboxyl group on the C-4. The fragmentation pattern showed peaks at m/z 236 ($MH^+ - CO_2$), 218 ($MH^+ - CO_2$—H_2O), 190 ($MH^+ - CO_2$—$COOH_2$), and 172 (MH^+—H_2O). This spectrum is identical to that displayed by the compound $\mathbf{4}a_1$, obtained by heating sample **4** at 100°C for 30 min. All the data are summarized in Table 2.

These results confirm the failure of this method in analyzing such very polar, nonvolatile, and thermolabile compounds; the CI technique provides limited information only on a few samples, and therefore it does not seem the ideal technique for

Can. J. Chem. Downloaded from www.nrcresearchpress.com by 196.1.178.254 on 09/07/12
For personal use only.

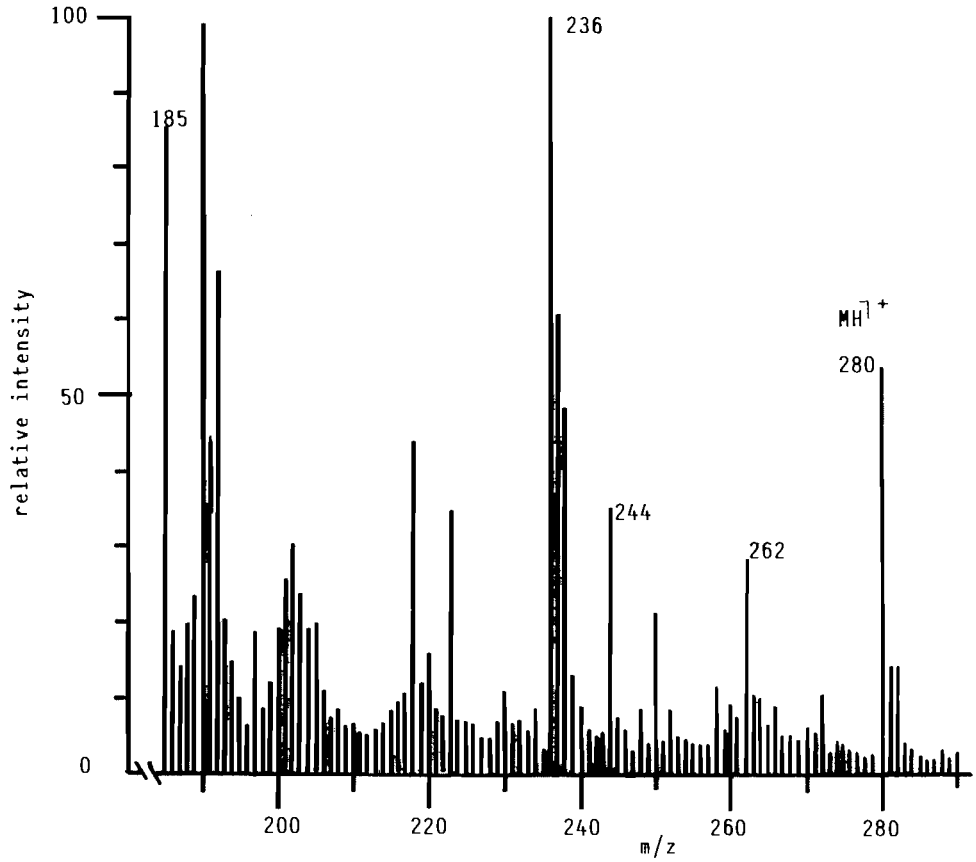

FIG. 4. Positive ion FAB spectrum of 4,4-dicarboxy-5-phenylproline **4**.

dealing with such compounds, as it has been in studies on naturally occurring amino acids (14).

The FAB ionization mode allows the mass spectrometric analysis of both the tricarboxyamino acids Gla and those formed by reacting Gla with aldehydes, and the decarboxy derivatives obtained by heating, permitting their detection at low levels. These findings suggest that FAB mass spectrometry could be used for quantitative analysis of the above-stated compounds, as already shown for other polar molecules (15–18), and we have therefore been encouraged in developing a FAB mass spectrometric method to detect Gla in biological matrices.

Acknowledgements

We are grateful to Mr. Antonio Cantilena of the Dipartimento di Chimica Organica e Biologica, Università di Napoli, for the CI mass spectra. The authors thank Professor G. Marino for helpful discussions. This work was supported by grants from the "Ministero della Pubblica Istruzione."

1. E. W. DAWIE and K. FUJIKAWA. Annu. Rev. Biochem. **44**, 799 (1975).
2. T. H. ZYTKOVICZ and G. L. NELSESTUM. Biochem. Biophys. Acta, **444**, 344 (1976).
3. D. BUCHER, E. NEBELIN, J. THOMSEN, and J. STENFLO. FEBS Lett. **68**, 293 (1976).
4. P. V. HAUSCHKA. Anal. Biochem. **80**, 212 (1977).
5. P. V. HAUSCHKA, J. B. LIAN, and P. M. GALLOP. Proc. Natl. Acad. Sci. U.S.A. **72**, 3925 (1975).
6. J. B. LIAN, E. L. PRIEN, JR., M. J. GLIENCHER, and P. M. GALLOP. J. Clin. Invest. **59**, 1151 (1977).
7. J. B. LIAN, W. STURMER, M. J. GLIENCHER, and P. M. GALLOP. Biochem. Biphys. Res. Commun. **73**, 349 (1975).
8. P. FERNLUND. Clin. Chim. Acta, **72**, 147 (1976).
9. D. V. SHAM, Y. K. TEWIS, A. E. HARPER, and J. W. SUTTIE. Biochem. Biophys. Acta, **539**, 209 (1978).
10. R. G. LEVY and J. B. LIAN. Clin. Pharmacol. Ther. **25**, 562 (1979).
11. R. G. LEVY, J. B. LIAN, C. GUNDBERG, and P. M. GALLOP. *In* Vitamin K metabolism and vitamin K-dependent proteins. *Edited by* J. W. Suttie. Univ. Park Press, Baltimore, MD. 1980. p. 375.
12. L. PECCI and D. CAVALLINI. Anal. Biochem. **118**, 70 (1981).
13. R. CAPASSO, G. RANDAZZO, and L. PECCI. Can. J. Chem. **61**, 2657 (1983).
14. G. W. A. MILNE, T. AXENROOD, and H. M. FALES. J. Am. Chem. Soc. **92**, 5170 (1970).
15. D. S. MILLINGTON, C. R. RAE, and D. A. MALTBY. Biomed. Mass Spectrom. **11**, 236 (1984).
16. G. MONETI, G. AGATI, M. G. GIOVANNINI, M. PAZZAGLI, R. SALERNO, G. MESSERI, and M. SERIO. Clin. Chem. (Winston-Salem, N.C.) 31 (1985).
17. M. BAMBAGIOTTI ALBERTI, S. PINSANTI, G. MONETI, G. AGATI, V. GIANNELLINI, S. A. CORAN, and F. F. VINCERI. J. Pharm. Biomed. Anal. **2**, 409 (1984).
18. S. J. GASKELL, B. G. BROWNSEY, P. W. BROOKS, and B. M. GREEN. Biomed. Mass Spectrom. **10**, 215 (1983).

Can. J. Chem. Downloaded from www.nrcresearchpress.com by 196.1.178.254 on 09/07/12
For personal use only.

Constant composition study of crystal growth of dicalcium phosphate dihydrate. The influence of polyphosphates, phosphonates, and phytate

ZAHID AMJAD

The BF Goodrich Company, Avon Lake Technical Center, Avon Lake, OH 44012, U.S.A.

Received September 29, 1987

ZAHID AMJAD. Can. J. Chem. **66**, 2181 (1988).

The influence of inhibitors of varying functional groups on the crystal growth of calcium phosphate dihydrate ($CaHPO_4 \cdot 2H_2O$, DCPD) on DCPD seed crystals at pH 6.00, 37°C, has been studied using the constant composition technique. The inhibitors studied include: (*a*) polyphosphate (sodium pyrophosphate, sodium hexametaphosphate, SHMP), (*b*) phosphonates (nitrilotris(methylene phosphonic acid), NTMP; 1-hydroxyethylidene-1,1-diphosphonic acid, HEDP; ethylenediaminetetra (methylene phosphonic acid), ETMP; hexamethylenediaminetetra(methylene phosphonic acid), HMDP); and (*c*) myoinositol hexaphosphoric acid (phytic acid). The effect of these inhibitors on the growth kinetics have been studied at several inhibitor concentrations. The retarding effect of these inhibitors is discussed in relation to calcium–inhibitor complex formation on the DCPD seed crystals and the structural features of the inhibitor molecules. The fit of the Langmuir adsorption to experimental data supports a mechanism of inhibition through molecular adsorption of the inhibitor ions on the surface of growing crystals. Based upon the kinetic data, the overall order of inhibitors effectiveness is

ETMP > HMDP > phytic acid > hexametaphosphate > HEDP > pyrophosphate

ZAHID AMJAD. Can. J. Chem. **66**, 2181 (1988).

Opérant à un pH de 6,0, à une température de 37°C et utilisant la technique de la composition constante, on a étudié l'influence des inhibiteurs portant divers groupements fonctionnels sur la croissance cristaux de phosphate de calcium dihydrate ($CaHPO_4 \cdot 2H_2O$, DCPD) sur des cristaux de DCPD ensemences. Les inhibiteurs examinés comportent; (*a*) des polyphosphates (pyrophosphate de sodium, hexamétaphosphate de sodium, HMPS), (*b*) des phosphonates (nitrilotris(acide méthylène phosphonique), NTMP; acide hydroxy-1 éthylidène diphosphonique-1,1, HEDP; éthylènediaminetétra(acide méthylène phosphonique), HMDP; et (*c*) l'acide hexaphosphorique du myoinositol (acide phytique). On a étudié l'effet de ces inhibiteurs sur la cinétique de la croissance à plusieurs concentrations d'inhibiteurs. On discute de l'effet retardant de ces inhibiteurs en relation avec la formation d'un complexe calcium–inhibiteur sur les cristaux de DCPD ensemencés et en relation avec les caractéristiques des structures des molécules d'inhibiteurs. L'ajustement de l'adsorption de Langmuir aux données expérimentales supporte un mécanisme d'inhibition impliquant l'adsorption moléculaire des ions inhibiteurs sur la surface des cristaux en croissance. En se basant sur les données cinétiques, l'ordre d'efficacité globale des inhibiteurs est le suivant :

ETMP > HMDP > acide phytique > hexamétaphosphate > HEDP > pyrophosphate

[Traduit par la revue]

Introduction

The importance of calcium phosphates as the main inorganic constituents of biological hard tissue (1–3) and urinary calculi (4,5) has stimulated the extensive research on the precipitation of these compounds. In addition, calcium phosphate compounds are involved in wastewater treatment processes, in agriculture as fertilizers, and in industrial water systems as hard deposits on heat exchanger surfaces. During the precipitation process at ambient temperature, the following calcium phosphate phases have been shown to be formed depending upon the level of supersaturation, pH, and ionic medium: dicalcium phosphate dihydrate ($CaHPO_4 \cdot 2H_2O$, DCPD), octacalcium phosphate ($Ca_8H_2(PO_4)_6 \cdot 5H_2O$, OCP), tricalcium phosphate ($Ca_3(PO_4)_2$, TCP), hydroxyapatite ($Ca_5(PO_4)_3OH$, HAP), and amorphous calcium phosphate, ACP (6–9). Results of previous studies have shown that the kinetically favored precursor phases such as ACP, DCPD, OCP, and TCP are formed prior to the formation of the thermodynamically stable HAP phase. Moreover, it has been suggested that such precursor phases can be stabilized by the presence of certain additives (10, 11).

The influence of naturally occurring substances such as pyrophosphate and polyphosphates on the precipitation of calcium phosphates at physiological conditions has also been the subject of numerous investigations (12–14). The results of these studies suggest that these substances, when present at low concentrations, greatly inhibit the precipitation of calcium phosphates from supersaturated solutions. Polyphosphates have been known much longer for their inhibitory role and they are commercially in use, preventing scale formation on heat exchanger surfaces in industrial water systems. Physical and chemical studies by Francis (13) and Varsanik (15) on the organophosphonates, a series of compounds similar to polyphosphates, led to their use as biological mineralization inhibitors and industrial scale control agents. The diphosphonates are characterized by —P—C—P— bonds in place of —P—O—P bonds of polyphosphates and have the advantage of being resistant to hydrolysis.

Phytic acid is another constituent of cells and cereals that may be involved in calcium metabolism (16). Excessive phytates in the diet may precipitate calcium in the intestine and cause calcium deficiency disease (17–19). Phytates may also adsorb to tooth surfaces and reduce cavities (20, 21). The inhibitory effect of phytate and HEDP on the crystal growth of HAP at low supersaturation has been studied recently using the constant composition technique (22). Results of this investigation indicate that phytate is about 25 times less effective than HEDP in reducing the rate of crystallization of HAP. A surface adsorption mechanism involving a simple Langmuir isotherm model was proposed to explain marked inhibitory action of these inhibitors.

Results of previous crystal growth studies (2, 22–25) on sparingly soluble salts in the presence of inhibitors have shown that the constant-composition technique is particularly useful in evaluating the effectiveness of inhibitors since their effect on the

Printed in Canada / Imprimé au Canada

Can. J. Chem. Downloaded from www.nrcresearchpress.com by 196.1.178.254 on 09/07/12
For personal use only.

TABLE 1. Structures of inhibitors

Inhibitor	Structure
Sodium pyrophosphate	$Na_4P_2O_7 \cdot 10H_2O$
Sodium hexametaphosphate	$(NaPO_3)_6$
Myo-inositol hexaphosphoric acid (phytic acid)	$C_6H_6(OPO_3H_2)_6$
Nitrilotri(methylene phosphoric acid) (NTMP)	$N(CH_2PO_3H_2)_3$
1-Hydroxyethilidine-1,1-diphosphonic acid (HEDP)	$CH_3C(OH)(PO_3H_2)_2$
Hexamethylenediaminetetra(methylene phosphonic acid) (HMDP)	$(CH_2PO_3H_2)_2N(CH_2)_6N(CH_2PO_3H_2)_2$
Ethylenediaminetetra(methylene phosphonic acid) (ETMP)	$CH—N(CH_2PO_3H_2)_2$ | $CH—N(CH_2PO_3H_2)_2$

crystal growth process can be accurately studied. The advantages of using the constant-composition technique, in which the concentration of the solution species is kept constant by the stoichiometric addition of reactants, to study the crystal growth of DCPD have been discussed previously (23).

In the present work, the constant-composition technique has been used to investigate the influence of a variety of inhibitors at constant supersaturation upon the kinetics of crystal growth of DCPD. The inhibitors tested include: (*a*) polyphosphate: sodium pyrophosphate, $Na_4P_2O_7$; sodium hexametaphosphate, $(NaPO_3)_6$; (*b*) phosphonates: nitrilotris(methylenephosphonic acid), NTMP; 1-hydroxyethylidine-1,1-diphosphonic acid; HEDP; hexamethylenediaminetetra (methylene phosphonic acid), HMDP; ethylenediaminetetra (methylenephosphonic acid), ETMP; and (*c*) phytic acid. The structures of these inhibitors are shown in Table 1.

Experimental

Reagent grade chemicals and grade A glassware were used. Potassium hydroxide solutions were prepared from Dilut-it reagents (J. T. Baker Co.) which were standardized by titration with potassium hydrogen phthalate using phenolphthalein as indicator. Phosphate solutions were prepared from potassium dihydrogen phosphate (J. T. Baker Co., Ultrex) and were standardized both by potentiometeric and by titration with standard potassium hydroxide solutions with thymolphthalein blue as indicator. Calcium chloride solutions were standardized by ion-exchange and atomic absorption spectroscopy. Sodium pyrophosphate and sodium hexametaphosphate solutions were prepared from reagent grade chemicals, and the phosphonates used in this study were prepared from samples that were kindly donated by Monsanto Chemical Co., St. Louis, MO. The DCPD seed crystals were prepared and characterized as previously described (23). After aging, DCPD crystals were filtered and dried to a constant weight in a desiccator over silica gel and used in subsequent experiments as seed materials.

Crystal growth experiments were made in a double-walled Pyrex cell at 37°C using the constant composition technique. The stable supersaturated solutions of calcium phosphate with a molar ratio of total calcium, T_{Ca}, to total phosphate, T_P = 1.00, were prepared by adjusting the pH of the premixed solution of calcium chloride and potassium dihydrogen phosphate to a value of 6.00 by slow addition of 0.1 *M* potassium hydroxide. Hydrogen ion measurements were made with a glass/Ag–AgCl electrode pair equilibrated at 37°C. The electrode pair was standardized before and after each experiment using NBS standard buffer solutions. The solutions were continuously stirred (325 rpm) while nitrogen gas, presaturated with water at 37°C, was bubbled through the solution to exclude carbon dioxide. Following the addition of DCPD seed crystals, the crystal growth reaction was monitored by the addition of titrant solutions from mechanically coupled automatic burettes mounted on a modified pH stat (pH meter model 632; dosimet model 655; impulsomat model 614, Brinkmann Instruments, Westbury, NY). The titrant solutions in the burettes consisted of calcium chloride, potasssium phosphate, potassium hydroxide, and inhibitor. The molar concentration ratio of the titrants corresponded to the stoichiometry of DCPD. Potassium chloride was added to the calcium phosphate supersaturated solutions in order to maintain the ionic strength to within ±1%. The constancy of solution composition was verified by analyzing the filtered samples which were withdrawn at various time intervals, for total calcium and total phosphate by a combined spectrophotometric method (26). The rates of crystallization were determined from the rates of addition of mixed titrants, and corrected for surface area changes (23).

TABLE 2. Crystallization of DCPD in the presence of inhibitors[a]

Exp.	Inhibitor	Concentration × 10^6 (*M*)	Rate × 10^6 (mol min)	$R_0/(R_0 - R_i)^b$
3	—	—	1.24	—
5	—	—	1.30	—
6	—	—	2.88[c]	—
8	P_2O_7	0.025	1.20	—
9	P_2O_7	0.200	0.835	3.06
11	P_2O_7	0.250	0.758	2.57
14	P_2O_7	0.300	0.651	2.11
13	P_2O_7	0.500	0.505	1.69
12	P_2O_7	1.00	0.251	1.25
10	P_2O_7	2.00	0.186	1.18
17	$(NaPO_3)_6$	0.025	0.749	2.52
21	$(NaPO_3)_6$	0.050	0.532	1.76
20	$(NaPO_3)_6$	0.100	0.266	1.27
22	Phytic acid	0.010	0.865	3.33
24	Phytic acid	0.025	0.526	1.65
23	Phytic acid	0.100	0.175	1.16
26	Phytic acid	0.200	<0.1	—
27	NTMP	0.0135	0.859	3.26
29	NTMP	0.0250	0.635	2.05
28	NTMP	0.050	0.355	1.40
30	HEDP	0.025	0.841	3.11
32	HEDP	0.050	0.588	1.92
33	HMDP	0.010	0.749	2.52
34	HMDP	0.025	0.445	1.56
36	ETMP	0.010	0.542	1.73
38	ETMP	0.025	0.206	1.20

[a]Initial conditions: $T_{Ca} = 4.18 \times 10^{-3}$ *M*, $T_P = 4.18 \times 10^{-3}$ *M*, pH = 6.00, 37°C, KCl = 0.023 *M*, DCPD = 14 mg, $-\Delta G$ (kJ mol^{-1}): DCPD, 0.99; OCP = 1.25; HAP = 4.18.

[b]$R_0(R_0 - R_i)^{-1}$: R_0 and R_i are the growth rates in the absence and presence of inhibitor, respectively.

[c]DCPD = 32 mg.

Results and discussion

Concentrations of ionic species in solutions were calculated from previously reported dissociation constants for phosphoric acid, phosphonic acids, phytic acid, and association constants of calcium-inhibitor complex formation (2, 22, 27–30). An iterative computational procedure for the ionic strength, involving mass balance and electroneutrality expressions, was used

Can. J. Chem. Downloaded from www.nrcresearchpress.com by 196.1.178.254 on 09/07/12
For personal use only.

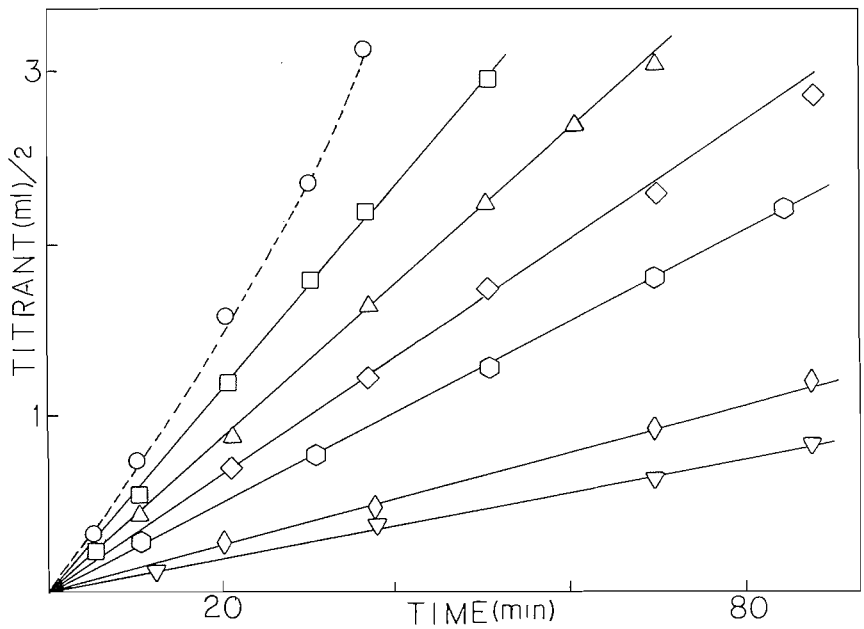

FIG. 1. Crystal growth of DCPD at constant supersaturation. Plots of volume of titrants added as a function of time in the presence of pyrophosphate (10^{-6} *M*). (□), ○; (△), 0.20; (◇), 0.30; (⬡), 0.50; (◇), 1.00; (▽), 2.00. Dotted line corresponds to experiment 3, uncorrected for surface area changes.

(22). The free energy term is computed from the equation:

[1] $\Delta G = -RT \ln (IP/K_s)^{1/n}$

in which n is the number of ions in a formula unit, IP is the activity product, and K_s, the thermodynamic solubility product for the precipitated calcium phosphate phase. The ΔG values obtained by using the above equation for various calcium phosphate phases indicate the thermodynamic instability of the experimental solutions compared to solutions in thermodynamic equilibrium with that particular phase.

The results of crystal growth experiments are summarized in Table 2. Typical plots of titrant volume needed to maintain the calcium and phosphate concentrations constant during DCPD seeded growth crystallization in experiment 5 are illustrated in Fig. 1. It can be seen in Fig. 1 that crystal growth began immediately upon the addition of seed crystals. Changes in surface area were calculated from these data, assuming the crystallites to be perfect spheres and the ordinate values, normalized to initial seed surface area (23), are also shown as corrected curves in Fig. 1. The slopes of the lines are used to calculate the growth rates expressed as mol of DCPD in Table 2. The excellent reproducibility is illustrated by the agreement between the results of experiments 3 and 5, respectively. In experiments 5 and 6 the weight of seed used to initiate the reaction was varied. It can be seen in Table 2 that the rate of crystallization is directly proportional to the amount of seed crystals added initially. This confirms that crystallization occurred only on seed crystals, without any secondary nucleation or spotaneous precipitation.

The effect of pyrophosphate on the crystal growth of DCPD from calcium phosphate supersaturated solutions was studied by a series of experiments summarized in Table 2. The analytical data of a typical crystal growth experiment in the presence of pyrophosphate (2.95×10^{-7} *M*, experiment 14) are summarized in Table 3. It can be seen that the stochiometry of the precipitating phase (Table 3) was constant with a calcium to phosphate molar ratio of 1.00 ± 0.02 for more than 70 min of reaction. The amount of newly grown DCPD phase was more than 170% of the original seed materials. Plots of moles of newly grown DCPD as a function of time for crystal growth experiments in the presence of pyrophosphate are shown in Fig. 1 and rate data summarized in Table 2. It can be seen that pyrophosphate at a concentration of 2.5×10^{-8} *M* (experiment 8) did not exhibit any significant inhibition on the crystal growth of DCPD. However, increasing the pyrophosphate concentration to 5.00×10^{-7} *M* (experiment 13) resulted in ~70% reduction in the rate of crystallization.

TABLE 3. Effect of pyrophosphate on crystal growth of DCPD[a]

Time (min)	[Ca] × 10^2 (*M*)	[P] × 10^2 (*M*)	Extent of crystallization (% original seed)
0	0.418	0.418	0
20	0.426	0.419	20
40	0.414	0.420	42
50	0.416	0.419	58
60	0.427	0.423	83
70	0.422	0.415	112
80	0.419	0.416	172

[a] T = 37°C, pH = 6.00, $[P_2O_7] = 3.00 \times 10^{-7}$ *M*, experiment 14.

The influence of the —P—O—P chain length in polyphosphate on crystal growth of DCPD is shown in Table 2. Under conditions used in the present work, sodium hexametaphosphate, at a concentration of 5.0×10^{-8} *M* (experiment 21) retarded crystal growth of DCPD to a greater degree than pyrophosphate ion at a concentration of 2.50×10^{-7} *M* (experiment 11). Results of crystal growth experiments in the presence of polyphosphates shown in Table 2 reveal that the inhibition by polyphosphate ion increases as the chain length increases. It should be noted that similar inhibitory effect of these polyphosphates has been recently reported (31) for HAP crystal growth from aqueous solution. In agreement with these results, it has been shown that polycarboxylic acids of high

Can. J. Chem. Downloaded from www.nrcresearchpress.com by 196.1.178.254 on 09/07/12
For personal use only.

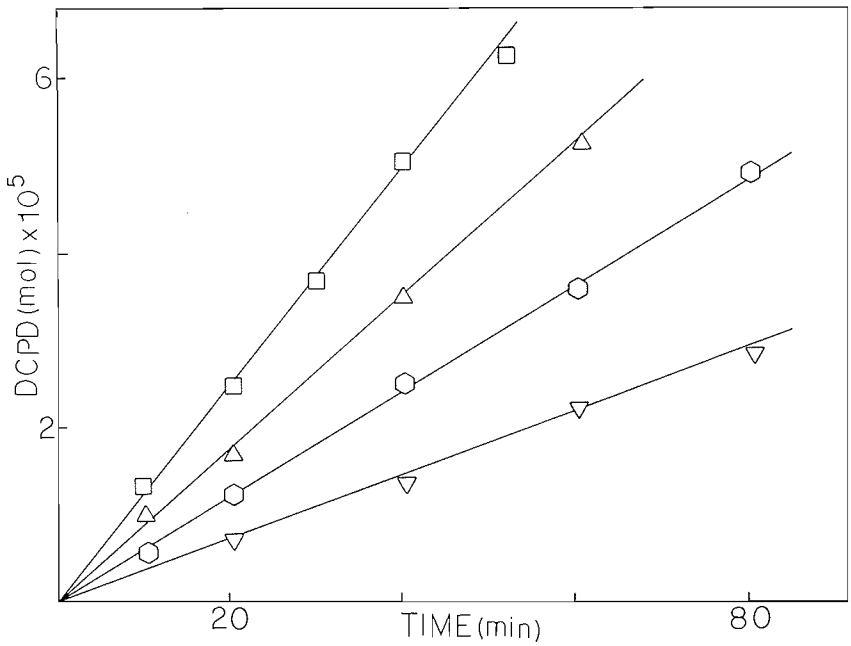

FIG. 2. Crytal growth of DCPD at constant supersaturation. Plots of moles of DCPD crystallized as a function of time in the presence of nitrilotris(methylene phosphonic acid) (10^{-7} *M*). (□), 0; (△), 0.135; (○), 0.250; (▽), 0.50.

TABLE 4. Effect of phosphonate (NTMP) on crystal growth of DCPD[a]

Time (min)	[Ca] × 10^2 (*M*)	[P] × 10^2 (*M*)	Extent of crystallization (% original seed)
0	0.418	0.418	0
20	0.415	0.424	13
40	0.425	0.420	34
50	0.412	0.416	52
60	0.416	0.424	80
70	0.426	0.421	126

[a] T = 37°C, pH = 6.00, [NTMP] = 2.50 × 10^{-8} *M*, experiment 29.

molecular weight are much more effective as $CaSO_4 \cdot 2H_2O$ crystal growth inhibitors than the simple uni-, di-, or tricarboxylic acids (32).

Another class of inhibitors that has proved to be effective in inhibiting calcification and mineral scale formation is the organic phosphonates. These inhibitors are characterized by the relatively inert P—C—P and P—C—N—C linkages which substitute for the hydrolyzable P—O—P bond of polyphosphate (Table 1). Crystal growth experiments made in the presence of phosphonates are summarized in Table 3 and mol DCPD grown as a function of time in the presence of NTMP are shown in Fig. 2. It can be seen that the presence of low concentrations of phosphonates markedly reduce the rate of DCPD crystallization. Analytical data of crystal growth experiment in the presence of NTMP (2.50 × 10^{-8} *M*, experiment 24) are summarized in Table 4. The observed T_{Ca}/T_P molar ratio of 1.00 ± 0.02 suggests that despite the marked inhibition, DCPD is the exclusively grown phase in the presence of NTMP.

The influence of other phosphonates such as HEDP, HMDP, and ETMP on the crystallization of DCPD was also studied by a series of experiments summarized in Table 2. Figure 3 shows the plots of mol of newly grown DCPD on DCPD seed crystals as a function of time in the presence of 2.5 × 10^{-8} *M* of each phosphonate present initially in the supersaturated solution. Based upon the rate data (Table 2) the order of effectiveness for phosphonates as crystal growth inhibitors is as follows:

ETMP > HMDP > NTMP > HEDP

The rate data for phytic acid as DCPD crystal growth inhibitor is summarized in Table 2. Plots of the mol of DCPD grown in the presence of phytic acid of varying concentrations are shown in Fig. 4. It can be seen (Table 2) that the presence of low concentrations of phytic acid markedly reduces the rate of DCPD crystallization. For example, rates of DCPD crystal growth obtained in the presence of 1.0 × 10^{-8} and 1.0 × 10^{-7} *M* phytic acid are 0.865 × 10^{-6} and 0.175 × 10^{-6} mol min, respectively, compared to 1.24 × 10^{-6} mol min obtained in the absence of phytic acid.

The results summarized in Table 2 indicate that the striking effect of the inhibitors, i.e. polyphosphates, phosphonates, phytate, etc. at low concentrations in reducing the rate of DCPD crystal growth cannot be attributed simply to the change in supersaturation due to calcium-inhibitor complex formation (the percent calcium complexed at the highest inhibitor concentration accounts for less than 5% of total calcium).

If we assume that the reduction in rate of DCPD crystal growth results from the adsorption of inhibitor at the DCPD crystal surface, then some form of adsorption model should be applicable. In many instances the Langmuir adsorption model, which was developed for the adsorption of ideal gases onto solid surfaces, has been used to describe empirically the reduction in crystal growth rates of sparingly soluble salts due to the adsorption of a wide variety of inhibitors. If the adsorbed inhibitor of concentration [C] covers a fraction α of the total available surface, then the rate of adsorption may be expressed as $k_a[C](1 - \alpha)$ and the rate of desorption as $k_d\alpha$, where k_a and k_d are the corresponding rate constants. At equilibrium it can be shown that:

$$[2] \quad R_0/(R_0 - R_i) = 1 + k_a/k_d[C]^{-1}$$

where R_0 and R_i are the growth rate constants in the absence and presence of inhibitors, respectively. Equation [2] shows that

Can. J. Chem. Downloaded from www.nrcresearchpress.com by 196.1.178.254 on 09/07/12
For personal use only.

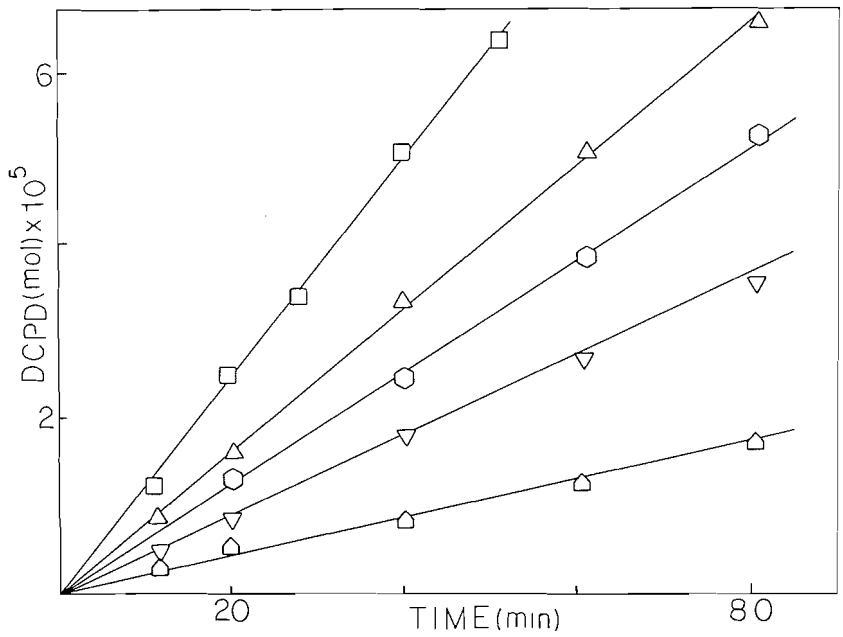

FIG. 3. Comparative effect of inhibitors on crystal growth of DCPD on DCPD seed crystals at constant supersaturation. Plots of moles of DCPD crystallized as a function of time in the presence of 2.50×10^{-8} M phosphonates. (□), 0; (▽), HEDP; (○), NTMP; (▽), HMDP; (△), ETMP.

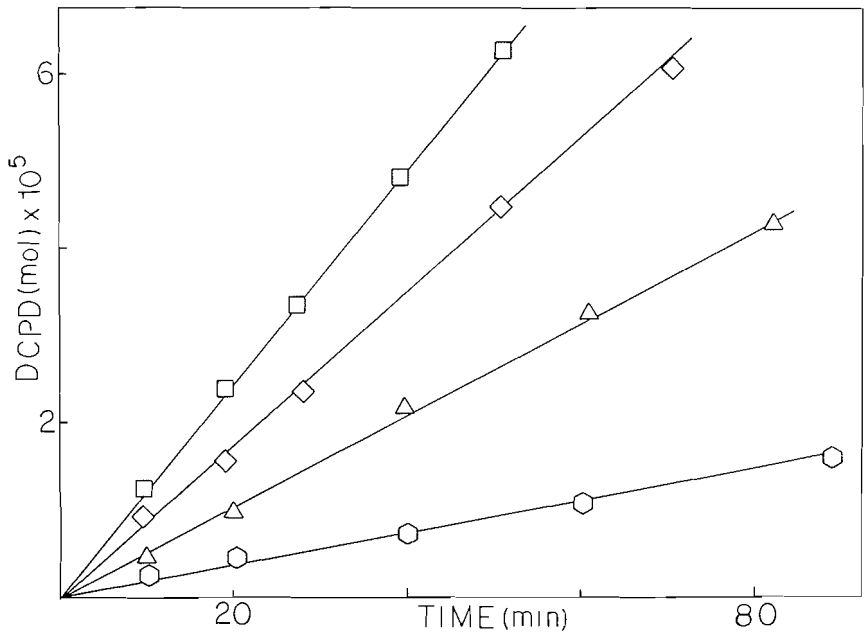

FIG. 4. Crystal growth of DCPD at constant supersaturation. Plots of moles of DCPD crystallization as a function of time in the presence of phytic acid (10^{-7} M). (□), 0; (◇), 0.10; (△), 0.25; (○), 1.00.

this model predicts a linear relationship between $R_0/(R_0 - R_i)$ and $[C]^{-1}$. The constant k_a/k_d, can be calculated from the slope of the resulting straight line. The ratio k_a/k_d, can be called "affinity constant", but it should be noted that it is not an equilibrium constant. If k_a is large or k_d is small, then the apparent affinity is of the adsorbing molecule to the substrate will be high.

Plots of $R_0(R_0 - R_i)^{-1}$ against $[C]^{-1}$ are shown in Fig. 5 for DCPD crystal growth in the presence of polyphosphates and phosphonates. The linear plots shown in Fig. 5 suggest that the inhibitor effect is due to the adsorption on the seed crystals. Application of the Langmuir model in this case is an oversimplification, because the prerequisites for the application of such a model are not valid. However, plots like that of Fig. 5 are useful for comparative purposes, since the slope of such plots is a measure for the affinity of a certain inhibitor for the particular solid substrate (22, 23). The values of "affinity constant" for polyphosphates, phosphonates, and phytic acid, as calculated from kinetic data shown in Table 2, are summarized in Table 5.

Based upon the kinetic data (Table 2), the order in terms of decreasing effectiveness for P—O—P bond containing inhibitors such as pyrophosphate, hexametaphosphate, and phytic

Can. J. Chem. Downloaded from www.nrcresearchpress.com by 196.1.178.254 on 09/07/12
For personal use only.

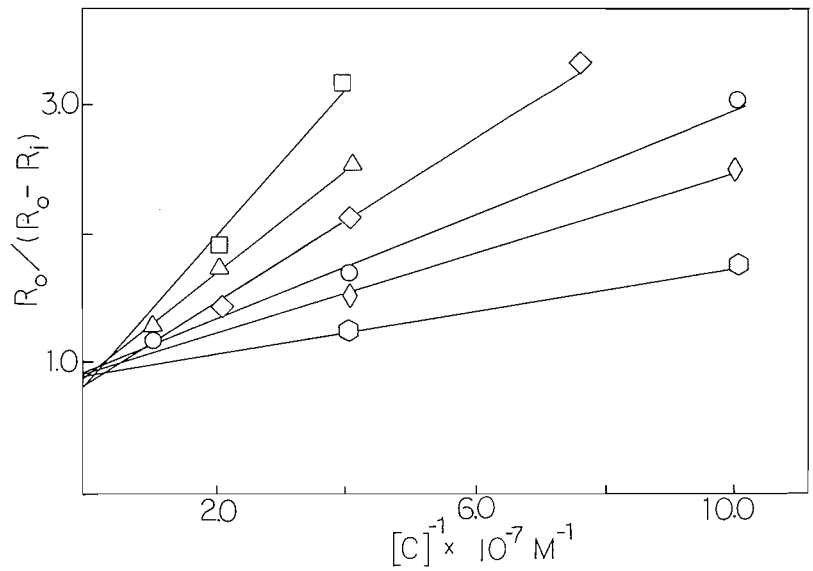

FIG. 5. Langmuir adsorption isotherms. Plots of $R_0/(R_0 - R_i)$ against $[C]^{-1}$ for polyphosphate and phosphonates. (□), HEDP; (△), SHMP; (○), NTMP; (◇), HMDP; (⬡), ETMP.

TABLE 5. Comparative data on calcium-inhibitor complex constants (K_{ML}) and affinity constant (K_a) for various inhibitors[a]

Inhibitor	log K_{ML}	Reference	$K_a \times 10^5$	Reference
Pyrophosphate	3.2	35	21.4	This work
Pyrophosphate	3.2	35	5.5[b]	14
Hexametaphosphate	7.6	35	210	This work
Phytic acid	3.2	35	410	This work
NTMP	6.9	36	312	This work
HEDP	7.1	36	170	This work
HMDP	5.4	36	560	This work
ETMP	9.3	36	1120	This work

[a]37°C.
[b]25°C.

acid is:

phytic acid > hexametaphosphate > pyrophosphate

It may be pointed out that in the case of HAP seeded growth (31) in the presence of polyphosphates, the order of effectiveness suggested was:

hexametaphosphate > phytic acid > pyrophosphate

The differences observed in the effectiveness of polyphosphates for HAP (31) and for DCPD as found in the present study, may be due to several factors including different rates of adsorption/desorption of polyphosphates on the two different types of calcium phosphate substrates namely, HAP and DCPD.

Varsanik (15) studied the spontaneous precipitation of calcium phosphates in the presence of phosphonates and concluded that the two most effective inhibitors were NTMP and HEDP, whereas ETMP and HMDP showed lower effectiveness as inhibitors for calcium orthophosphate. This is in contrast to the results obtained in the recent study (31) where only HAP exclusively grew on HAP seed crystals in the presence of phosphonates compared to the formation of calcium phosphate precursor phase(s) under spontaneous precipitation (15). Thus it is likely that phosphonates may have a different effect on the formation and subsequent transformation of the precursor phase (15) than on the formation of the thermodynamically stable HAP phase.

The effect of low levels of phosphonates on the crystal growth on calcium carbonate has also been investigated (33). Results of this study indicate that the effectiveness of the various phosphonates at a fixed weight concentration of 0.50 ppm, is in the order:

HEDP > HMDP > ETMP > NTMP

It is of interest to note that in the case of calcium oxalate monohydrate precipitation in the presence of phosphonates (34) the relative abilities of the phosphonates in retarding the precipitation was found to vary with varying experimental conditions. At 4.0×10^{-6} M phosphonate concentrations the order of effectiveness reported was:

HMDP > HEDP > ETMP and ETMP > HMDP > HEDP

for spontaneous and seeded growth, respectively. The observed results were interpreted in terms of both adsorption and complexation phenomena.

The differences in the ability of the various inhibitors, (viz., pyrophosphate, NTMP, HEDP, HMDP, ETMP, phytic acid, etc.) to retard or inhibit crystallization of DCPD could be rationalized in terms of their abilities to form a complex with the calcium ion. Table 5 summarizes the comparative data on the calcium-inhibitor complexation constant K_{ML} and the "affinity constant" for a variety of inhibitors. It can be seen that on the basis of "affinity constant" values, the order of effectiveness for the polyphosphate and phosphonates is:

ETMP > HMDP > NTMP > HEDP > pyrophosphate

whereas the values of the complexation constants follows the order:

ETMP > HEDP > NTMP > HMDP > pyrophosphate

A better assessment could only be gained by comparing the structural arrangement of phosphonate groups. The most effective of the inhibitors, ETMP, is structurally similar to the strong complexing agent EDTA (ethylenediamine tetraacetic acid) and would also be expected to be a strong complexing agent for calcium ion situated at DCPD crystal surface sites. The relative weakness of HMDP, containing four additional methylene groups compared to ETMP, as a potential inhibitor may be

Can. J. Chem. Downloaded from www.nrcresearchpress.com by 196.1.178.254 on 09/07/12
For personal use only.

attributed to the difficulty in grouping all the phosphonates groups around one calcium site. The higher "affinity" value (21.4×10^5) for DCPD obtained in the present study for pyrophosphate at 37°C may be compared with 5.5×10^5 obtained at 25°C (14).

Results summarized in Table 2 for the inhibitory effect of phytic acid indicate that low levels (2.0×10^{-7} *M*) of PA completely inhibits DCPD crystal growth for at least 20 h. The value of the "affinity constant" (Table 5) for phytic acid is 4.10×10^7 which can be compared with 1.7×10^7 obtained for HEDP. It is of interest to note that values of "affinity constant" of phytic acid and HEDP for HAP crystal growth (31) were 8.4×10^5 and 208×10^5, respectively. The change in order of inhibitor effectiveness of PA and HEDP for DCPD and HAP crystallization may be due to several factors including different rates of adsorption and desorption of these inhibitors on two different types of substrates, i.e. DCPD and HAP crystals.

Summary

In the present work it has been shown that the presence of inhibitors viz. polyphosphates, phosphonates, and phytic acid, at low concentration can significantly inhibit the crystal growth of DCPD on DCPD seed crystals from calcium phosphate supersaturated solution maintained at constant supersaturation. The marked inhibitory influence of the inhibitors may be explained by adsorption of inhibitor molecules at the active growth sites. Based upon the kinetic data effectiveness of the inhibitors follows the order:

polyphosphates: phytic acid > hexametaphosphate > pyrophosphate

phosphonates: ETMP > HMDP > NTMP > HEDP

1. W. E. Brown. Clin. Orthop. **44**, 205 (1966).
2. Z. Amjad. *In* Absorption on and surface chemistry of hydroxyapatite. *Edited by* D. N. Misra. Plenum Press, New York. 1984.
3. P. G. Koutsoukos, Z. Amjad, M. B. Tomson, and G. H. Nancollas. J. Am. Chem. Soc. **102**, 1533 (1980).
4. K. D. Lonsdale. Nature (London), **217**, 56 (1968).
5. K. D. Lonsdale, J. D. Sutor, and S. E. Wooley. Brit. J. Urol. **40**, 402 (1968).
6. M. D. Francis. Ann. N.Y. Acad. Sci. **131**, 694 (1965).
7. A. E. Sobel, M. Burger, and S. Nobel. Clin. Orthop. **17**, 103 (1960).
8. J. L. Meyer and E. D. Eanes. Calcif. Tiss. Res. **25**, 59 (1978).
9. D. G. A. Nelson, H. Salimi, and G. H. Nancollas. J. Colloid Interface Sci. **110**, 32 (1986).
10. A. L. Boskey and A. S. Posner. Mat. Res. Bull. **9**, 907 (1974).
11. E. D. Eanes and A. S. Posner. Calcif. Tiss. Res. **2**, 38 (1968).
12. H. Fleisch and W. F. Newman. Am. J. Physical. **200**, 1296 (1961).
13. M. D. Francis. Calcif. Tiss. Res. **3**, 151 (1969).
14. R. W. Marshal and G. H. Nancollas. J. Phys. Chem. **73**, 3838 (1969).
15. R. G. Varsanik. Mater. Perform. **14**, 16 (1975).
16. W. C. Thomas and M. T. Tilden. John Hopkins Med. J. **131**, 133 (1972).
17. H. M. Bruce and R. K. Callow. Biochem. J. **28**, 517 (1934).
18. J. T. Lowe and H. Steenbock. Biochem. J. **30**, 1991 (1936).
19. E. Mellanby. J. Physiol. 109, 488 (1949).
20. G. N. Jenkins, M. G. Foster, and R. L. Spiers. Brit. Dent. J. **106**, 362 (1959).
21. G. N. Jenkins, M. G. Foster, R. L. Spiers, and I. Kleinberg. Brit. Dent. J. **106**, 195 (1959).
22. P. G. Koutsoukos, Z. Amjad, and G. H. Nancollas. J. Colloid Interface Sci. **83**, 599 (1981).
23. Z. Amjad. J. Colloid Interface Sci. **117**, 98 (1987).
24. M. E. Sheehan and G. H. Nancollas. Invest. Urol. **17**, 446 (1980).
25. T. F. Kazmierczak, M. B. Tomson, and G. H. Nancollas. J. Phys. Chem. **86**, 103 (1982).
26. M. B. Tomson, J. P. Barone, and G. H. Nancollas. At. Absorpt. Newl. **16**, 117 (1977).
27. R. L. Carroll and R. R. Irani. Inorg. Chem. **6**, 1944 (1967).
28. H. Wada and Q. Fernando. Anal. Chem. **44**, 1640 (1970).
29. R. P. Carter, R. L. Carroll, and R. R. Irani. Inorg. Chem. **6**, 939 (1967).
30. R. J. Motekaitis, I. Murase, and A. E. Martell. J. Inorg. Nucl. Chem. **33**, 3353 (1971).
31. Z. Amjad. Langmuir. In press.
32. E. R. McCartney and A. E. Alexander. J. Colloid Sci. **13**, 383 (1958).
33. G. H. Nancollas and M. M. Reddy. *In* Aqueous environmental chemistry of metals. *Edited by* A. J. Rubin. Ann Arbor Science, Ann Arbor, MI. 1974.
34. E. N. Rizkalla and M. N. Moawad. J. Chem. Soc. Faraday Trans. **80**, 1617 (1984).
35. R. E. Gosselin and E. R. Coghlan. Biochem. Biophys. **45**, 301 (1953).
36. New product bulletin on Dequest^R 2060, Monsanto Industrial Chemicals Co., St. Louis, Mo.

Can. J. Chem. Downloaded from www.nrcresearchpress.com by 196.1.178.254 on 09/07/12
For personal use only.

Étude thermodynamique du mélange chlore – acide isocyanurique en milieu aqueux

BERNARD SOLASTIOUK ET XAVIER DEGLISE[1]

Laboratoire de photochimie appliquée (Unité associée n° 238 du Centre national de la recherche scientifique), Université de Nancy I, Boite postale 239, 54506 Vandoeuvre-les-Nancy CEDEX, France

Reçu le 8 février 1988

BERNARD SOLASTIOUK et XAVIER DEGLISE. Can. J. Chem. **66**, 2188 (1988).

Nous présentons un mode de calcul permettant d'obtenir les concentrations à l'équilibre en solution aqueuse, de l'acide cyanurique et de ses dérivés chlorés en fonction du pH, du rapport chlore/acide cyanurique et de la concentration en ions chlorures. Une étude de l'influence de chacun de ces paramètres sur les différents équilibres est présentée, dans des conditions proches de celles de l'utilisation de ces composés dans les eaux de piscines.

BERNARD SOLASTIOUK and XAVIER DEGLISE. Can. J. Chem. **66**, 2188 (1988).

A method of calculation of the equilibrium concentrations in aqueous solution of cyanuric acid and its chlorinated derivatives as a function of pH, molar ratio of chlorine/cyanuric acid, and chloride ion concentration is presented. The influence of each of these parameters is studied in conditions close to those used for these compounds in swimming pools.

Can. J. Chem. Downloaded from www.nrcresearchpress.com by 196.1.178.254 on 09/07/12
For personal use only.

Introduction

Les dérivés *N*-chlorés de la triazine-1,3,5 trione-2,4,6 ou acide cyanurique(Cy) sont des produits couramment utilisés comme sources de chlore dans les détergents et les eaux de piscines. En effet ces produits solides représentent une source de chlore plus facilement transportable et utilisable par exemple que l'eau de javel ou le chlore gazeux. Ils empêchent surtout la photolyse rapide du chlore car les molécules mono-, di-, et trichlorées de l'acide cyanurique ($CyCl$, $CyCl_2$, $CyCl_3$) tout en conservant un pouvoir chlorant efficace pour la désinfection des eaux sont d'une relative stabilité vis à vis du rayonnement solaire.

Les constantes d'équilibres entre ces composés ont été déterminées par O'Brien *et al.* (1, 2) et c'est à partir de ces valeurs que nous déterminons la composition d'une solution aqueuse de ces produits. Dans ces équilibres il n'est pas tenu compte des différentes formes tautomères que peuvent prendre ces molécules (voir figure 1).

1. Le chlore en solution aqueuse

Le chlore moléculaire dissous dans l'eau est soumis à différents équilibres et forme de façon rapide et réversible différentes espèces (acide hypochloreux, hypochlorites, et ions trichlorures) dont les proportions sont régies par les équilibres suivants :

$$Cl_2 + H_2O \rightleftarrows ClOH + H^+ + Cl^-$$

$$K_1 = \frac{[ClOH][Cl^-][H^+]}{[Cl_2]} = 3{,}94 \times 10^{-4}\ M^2 \text{ à } 298\ K$$

$$ClOH \leftrightarrows ClO^- + H^+$$

$$K_2 = \frac{[ClO^-][H^+]}{[ClOH]} = 2{,}88 \times 10^{-8}\ M \text{ à } 298\ K$$

$$Cl_2 + Cl^- \leftrightarrows Cl_3^-$$

$$K_3 = \frac{[Cl_3^-]}{[Cl_2][Cl^-]} = 0{,}18\ M^{-1} \text{ à } 298\ K$$

Bell et Gells (7) ont étudié la stabilité en solution aqueuse du cation Cl^+ et du cation solvaté $H_2O{\cdot}Cl^+$. Eigen et Kustin (8) quant à eux ont estimé celle de Cl_2OH^-. Ces espèces restant dans toutes conditions très minoritaires, sinon inexistantes, en solution aqueuse; nous n'en tenons donc pas compte.

Nous regroupons sous le terme générique de «chlore libre» indifféremment les quatre espèces Cl_2, $ClOH$, ClO^- et Cl_3^-, par opposition au chlore lié aux atomes d'azote.

Les ions chlorures sont pris en excès par rapport au chlore actif total en sorte que leurs concentrations puissent être considérées comme invariantes aux cours des différentes mises à l'équilibre considérées ($[Cl^-] \gg [Cl]_{total}$).

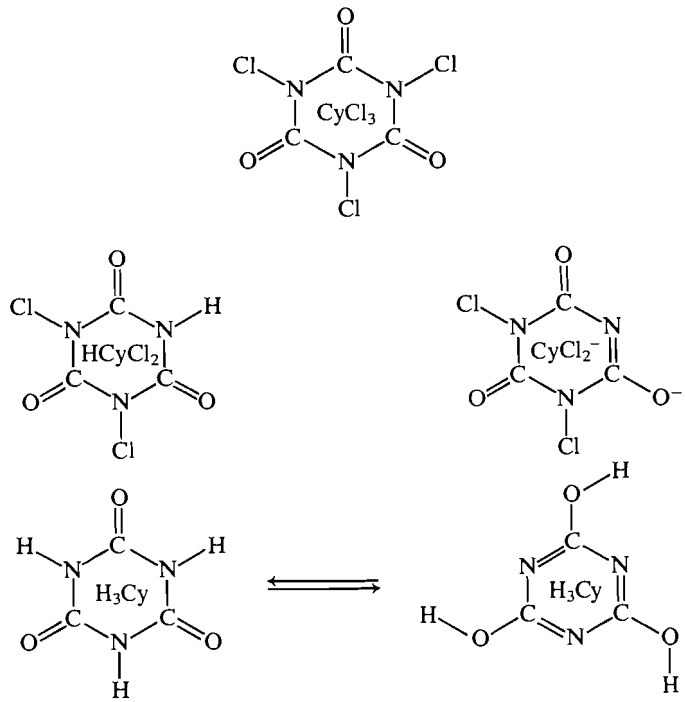

s Triazine trione — *s* Triazine triol

FIG. 1. Structures moléculaires des dérivés concernés. $CyCl_3$: acide trichlorocyanurique (*N*-trichloro-2,4,6 *s* triazine trione-1,3,5); $HCyCl_2$: acide dichlorocyanurique (*N*-dichloro-2,4 *s* triazine trione); $CyCl_2^-$: ion dichlorocyanurates; H_3Cy : acide cyanurique (*s* triazine-2,4,6 trione-1,3,5 et *s* triazine-2,4,6 triol-1,3,5).

2. Le mélange chlore – acide cyanurique en solution aqueuse

Lorsqu'on mélange chlore et acide cyanurique en solution aqueuse chaque azote du cycle triazinique est susceptible de fixer un atome de chlore (1–4).

1. Auteur à qui adresser toute correspondance.

Printed in Canada / Imprimé au Canada

Can. J. Chem. Downloaded from www.nrcresearchpress.com by 196.1.178.254 on 09/07/12
For personal use only.

Pour décrire ce système, les valeurs des constantes d'équilibre seront données pour les équilibres types suivants (où x est compris entre 0 et 2) :

$$Cl_{(3-x)}CyH_x + H_2O \rightleftarrows HOCl + Cl_{(2-x)}CyH_{(x+1)}$$

De plus les propriétés acido-basiques de ces dérivés imposent de tenir compte d'espèces supplémentaires plus ou moins ionisées.

Le schéma suivant (schéma 1) présente ces différents produits et les équilibres dans lesquels ils interviennent :

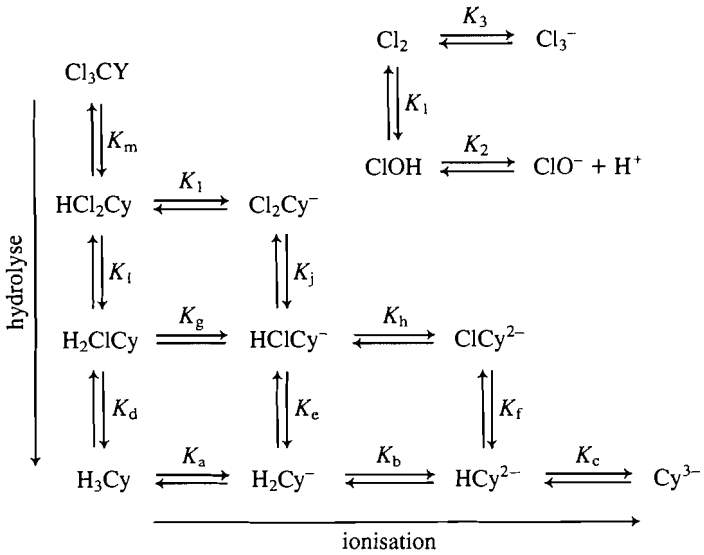

SCHÉMA 1

Les dix espèces comprenant un noyau cyanurique ($C_3N_3O_3$), et les quatre formes de chlore libre, sont susceptibles d'échanger protons et atomes de chlore.

3. Mode de calcul

Nous voulons étudier le devenir à l'équilibre d'une solution aqueuse d'un mélange d'acide cyanurique (H_3Cy) et de chlore en tenant compte :

- de la concentration initiale en acide cyanurique : $C_0 = [H_3Cy]_0$;
- de la concentration initiale en chlore considérée comme multiple de C_0 $[Cl_2]_0 = G \cdot C_0$;
- du pH : $h = [H^+] = 10^{-pH}$;
- de la concentration en chlorure : $Cl = [Cl^-]$;
- des valeurs des constantes d'équilibres;
- de la température supposée constante et égale à 25°C.

Nous utilisons les notations suivantes pour les différentes sommes des concentrations molaires

des dérivés du chlore libre (Chl) :

$$\Sigma_{Chl} = [ClOH] + [ClO^-] + [Cl_2] + [Cl_3^-]$$

des dérivés non-chlorés :

$$\Sigma_{(0)} = [H_3Cy] + [H_2Cy^-] + [HCy^{2-}] + [Cy^{3-}]$$

des dérivés monochlorés :

$$\Sigma_{(I)} = [H_2ClCy] + [HClCy^-] + [ClCy^{2-}]$$

des dérivés dichlorés :

$$\Sigma_{(II)} = [HCl_2Cy] + [Cl_2Cy^-]$$

et pour le dérivé trichloré :

$$\Sigma_{(III)} = [Cl_3Cy]$$

La concentration de chacune des 14 espèces présentes en solution est une inconnue. Pour résoudre ce système nous disposons de deux bilans (bilan en chlore et bilan en noyaux cyanuriques) et de 15 lois d'action de masse, il suffit d'en choisir arbitrairement 12 qui soient indépendantes.

Avec nos notations les bilans s'écrivent :

$$C_0 = \Sigma_{(0)} + \Sigma_{(I)} + \Sigma_{(II)} + \Sigma_{(III)}$$

(Bilan en noyaux cyanuriques)

$$G \cdot C_0 = \Sigma_{Chl} + \Sigma_{(I)} + 2\Sigma_{(II)} + 3\Sigma_{(III)}$$

(Bilan en chlore)

Et à partir de l'expression des constantes d'équilibre on peut exprimer les sommes en fonction de la concentration de l'espèce non ionisée de la série :

$$\Sigma_{(0)} = [H_3Cy]\{1 + K_a/h + K_aK_b/h^2 + K_aK_bK_c/h^3\} = [H_3Cy]\alpha$$

$$\Sigma_{(I)} = [H_2ClCy]\{1 + K_g/h + K_gK_h/h^2\} = [H_2ClCy]\beta$$

$$\Sigma_{(II)} = [HCl_2Cy]\{1 + K_1/h\} = [HCl_2Cy]\gamma$$

$$\Sigma_{(III)} = [Cl_3Cy]$$

La somme des concentrations des espèces de chlore libre peut s'exprimer à partir de celle de ClOH

$$\Sigma_{Chl} = [ClOH](1 + (Cl \cdot h/K_1) + (K_3 \cdot Cl^2 \cdot h/K_1) + (K_2/h)) = [ClOH]\delta$$

Les coefficients α, β, γ et δ sont évidemment facilement calculables et constants pour un pH et une concentration en chlorures donnés.

Les bilans s'écrivent alors :

bilan en noyaux cyanuriques :

$$C_0 = \alpha[H_3Cy] + \beta[H_2ClCy] + \gamma[HCl_2Cy] + [Cl_3Cy]$$

bilan en chlore :

$$G \cdot C_0 = \delta[ClOH] + \beta[H_2ClCy] + 2\gamma[HCl_2Cy] + 3[Cl_3Cy]$$

et sont exprimés en fonction de [ClOH] et $[H_3Cy]$:

$$C_0 = [H_3Cy]\left(\alpha + \beta\frac{[ClOH]}{K_d} + \gamma\frac{[ClOH]^2}{K_dK_i} + \frac{[ClOH]^3}{K_dK_iK_m}\right)$$

$$G \cdot C_0 = \delta[ClOH] + [H_3Cy]\left(\beta\frac{[ClOH]}{K_d} + 2\gamma\frac{[ClOH]^2}{K_dK_i} + 3\frac{[ClOH]^3}{K_dK_iK_m}\right)$$

En remplaçant dans la seconde équation la valeur de $[H_3Cy]$ par celle obtenue à partir de la première on trouve, après simplification et regroupement des différents termes, l'équation :

$$[1]\quad \left\{\frac{\delta}{K_dK_iK_m}\right\}[ClOH]^4 + \left\{\frac{\delta\gamma}{K_dK_i} + (3\text{-}G)\frac{C_0}{K_dK_iK_m}\right\}[ClOH]^3 + \left\{\frac{\delta\beta}{K_d} + (2\text{-}G)\frac{\gamma C_0}{K_dK_iK_m}\right\}[ClOH]^2 + \left\{\delta\alpha + (1\text{-}G)\frac{\beta C_0}{K_d}\right\}[ClOH]^2 - G\alpha C_0 = 0$$

équation du quatrième degré qui, résolue numériquement, nous

Can. J. Chem. Downloaded from www.nrcresearchpress.com by 196.1.178.254 on 09/07/12
For personal use only.

TABLEAU 1. Valeurs des constantes d'équilibre

Équilibres	K (298 K)	pK	N°	Réf.
$H_3Cy \rightleftarrows H_2Cy^- + H^+$	$1{,}32\times10^{-7}$	6,88	a	1
$H_2Cy^- \rightleftarrows HCy^{2-} + H^+$	$3{,}98\times10^{-12}$	11,40	b	1
$HCy^{2-} \rightleftarrows Cy^{3-} + H^+$	$3{,}16\times10^{-14}$	13,50	c	1
$H_2ClCy + H_2O \rightleftarrows H_3Cy + ClOH$	$8{,}51\times10^{-5}$	4,07	d	1
$HClCy^- + H_2O \rightleftarrows H_2Cy^- + ClOH$	$2{,}40\times10^{-6}$	5,62	e	1
$ClCy^{2-} + H_2O \rightleftarrows HCy^{2-} + ClOH$	$1{,}26\times10^{-7}$	6,90	f	1
$H_2ClCy \rightleftarrows HClCy^- + H^+$	$4{,}68\times10^{-6}$	5,33	g	1
$HClCy^- \rightleftarrows ClCy^{2-} + H^+$	$7{,}59\times10^{-11}$	10,12	h	1
$HCl_2Cy + H_2O \rightleftarrows H_2ClCy + ClOH$	$1{,}17\times10^{-3}$	2,93	i	1
$Cl_2Cy^- + H_2O \rightleftarrows HClCy^- + ClOH$	$3{,}09\times10^{-5}$	4,51	j	1
$HCl_2Cy \rightleftarrows Cl_2Cy^- + H^+$	$1{,}78\times10^{-4}$	6,90	l	1
$Cl_3Cy + H_2O \rightleftarrows HCl_2Cy + ClOH$	$1{,}58\times10^{-2}$	1,80	m	1
$Cl_2 + H_2O \rightleftarrows ClOH + Cl^- + H^+$	$3{,}94\times10^{-4}$	3,40	1	5
$ClOH \leftrightarrows ClO^- + H^+$	$2{,}88\times10^{-8}$	7,54	2	6
$Cl_2 + Cl^- \leftrightarrows Cl_3^-$	$1{,}80\times10^{-1}$	0,74	3	9

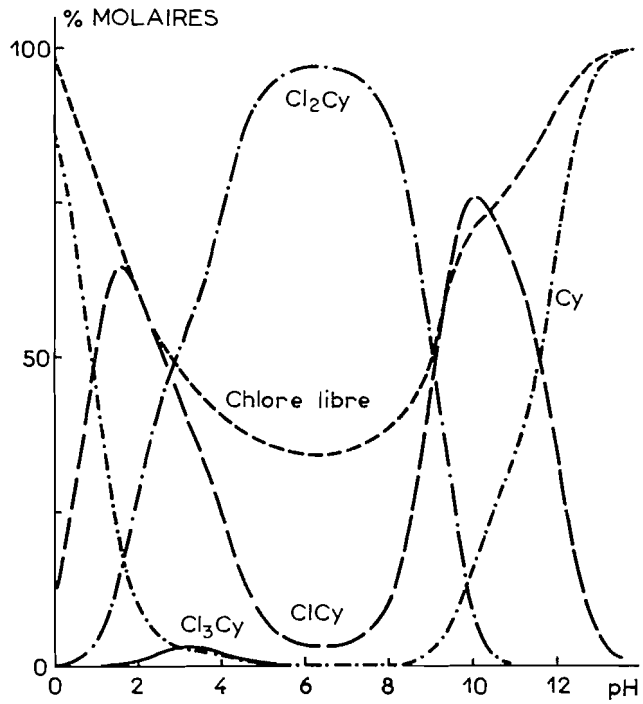

FIG. 2. Influence du pH sur la composition du mélange chlore – acide cyanurique en solution aqueuse. $[H_3Cy]_0 = 10^{-3}$ M; $[Cl_2]_0 = 3 \times 10^{-3}$ M équivalent à $[CyCl_3]_0 = 10^{-3}$ M (232 mg/L); $[Cl^-] = 10^{-1}$ M. (——) Cl_3Cy; (—·—·) Cl_2Cy somme des composés dichlorés; (— —) ClCy somme des composés monochlorés; (·····) Cy somme des composés non-chlorés; (----) chlore libre (Cl_2, ClOH, ClO^-, Cl_3^-).

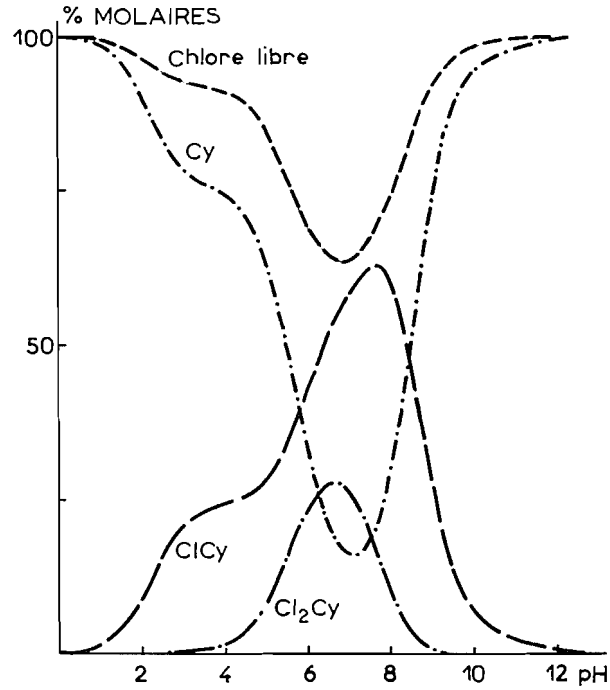

FIG. 3. Influence du pH sur la composition du mélange chlore – acide cyanurique en solution aqueuse. $[H_3Cy]_0 = 10^{-5}$ M; $[Cl_2]_0 = 3 \times 10^{-5}$ M équivalent à $[CyCl_3]_0 = 10^{-5}$ M (2,32 mg/L); $[Cl^-] = 10^{-1}$ M. (—·—) Cl_2Cy somme des composés dichlorés; (——) ClCy somme des composés monochlorés; (·····) Cy somme des composés non-chlorés; (----) chlore libre (Cl_2, ClOH, ClO^-, Cl_3^-).

donnera la valeur de [ClOH] pour les conditions fixées. La résolution de cette équation ne présente pas de difficulté particulière, en effet la racine recherchée $[ClOH]_{eq}$, prend une valeur forcément comprise entre 0 et la concentration en chlore initiale soit $G \times C_0$. Il est d'ailleurs facile de vérifier que pour $C = 0$ la fonction prend la valeur négative $-\alpha G \cdot C_0$ alors que pour $C = G \times C_0$ elle prend la valeur :

$$\frac{G^4(\delta-1)+G^3}{K_iK_dK_m}C_0^4 + \gamma\frac{G^3(\delta-1)+2G^2}{K_iK_d}C_0^3 + \beta\frac{G^2(\delta-1)+G}{K_i}C_0^3 + \alpha G(\delta-1)C_0$$

qui est positive, les coefficients δ étant toujours supérieurs ou égaux à 1. Un simple calcul informatique permet d'extraire rapidement cette racine.

Les concentrations des autres espèces se déduisent linéairement de la valeur de [ClOH]. Nous avons mis au point un logiciel bâti autour de ce calcul qui nous donne, pour une composition et un pH donnés, toutes les concentrations recherchées.

Les valeurs des différentes constantes d'équilibres que nous avons utilisées sont reportées dans le tableau 1.

4. Résultats

4.1 Influence du pH

Les figures 2 et 3 sont obtenues par le calcul précédent

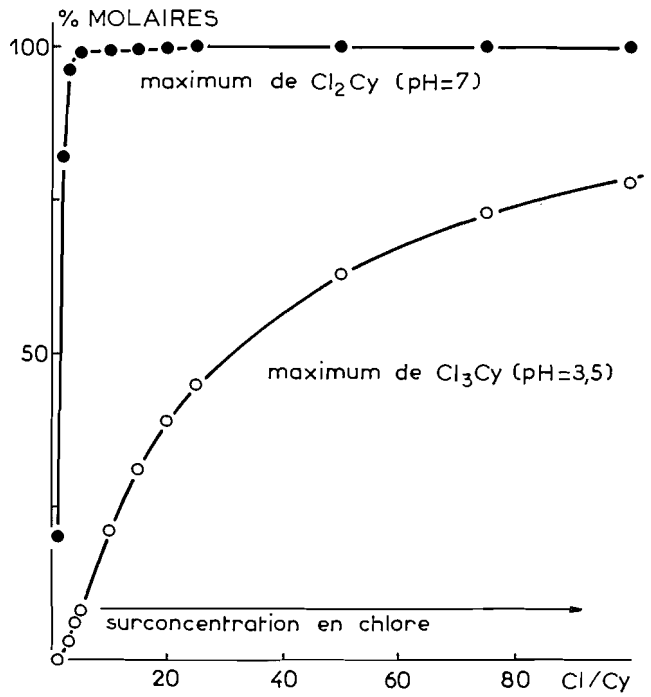

FIG. 4. Influence de la surconcentration en chlore; ● : proportion maximale de Cl_2Cy; ○ : proportion maximale de Cl_3Cy. $[H_3Cy]_0 = 10^{-3}$ M; $[Cl^-] = 10^{-1}$ M.

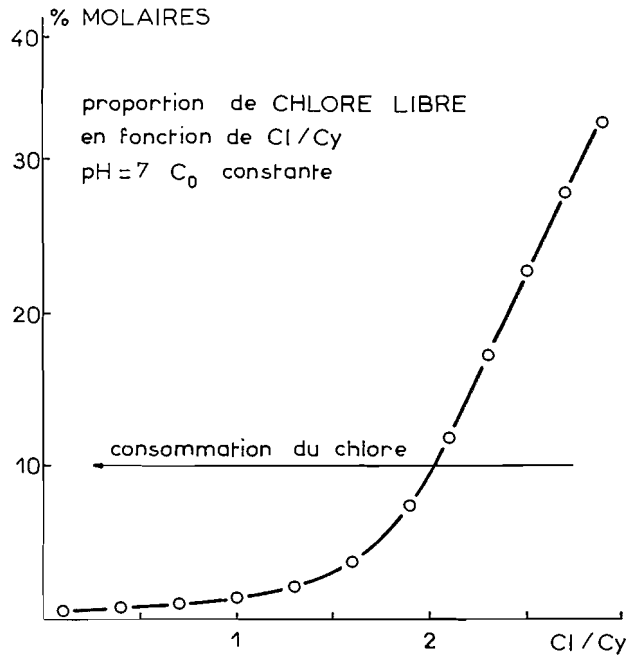

FIG. 5. Influence de la baisse du rapport Cl/Cy (dispariton du chlore) : proportion de chlore libre. $[H_3Cy]_0 = 10^{-3}$ M; $[Cl^-] = 10^{-1}$ M.

effectué dans tout le domaine de pH d'une solution aqueuse. Elles correspondent à deux dilutions différentes de Cl_3Cy, respectivement 10^{-3} M (232 mg/L) et 10^{-5} M (2,3 mg/L).

Les courbes qui y apparaissent représentent les pourcentages molaires pour chaque catégorie de composés, chlore libre ($\Sigma_{Chl}/(G \times C_0)$), mono, di, et trichloré ($\Sigma_{(i)}/C_0$) en fonction du pH.

La figure 2 montre une certaine symétrie, avec au centre (de pH 4–8) une large zone de prédominance du composé dichloré, cette plage correspond aussi au minimum de chlore libre en solution. Notons que les pH d'utilisation des dérivés chlorés de l'acide cyanurique se situent dans cette zone proche de la neutralité (eau de piscine par exemple) et à un minimum de chlore libre en solution correspond un minimum de la vitesse de disparition du chlore actif par photolyse.

De part et d'autre de cette plage apparaissent deux zones de prédominance du composé monochloré en milieu acide (pH 1–3) et milieu basique (pH 9–12) et pour des solutions très acides ou très basiques l'*hydrolyse* est totale.

Dans les conditions de calcul de cette figure, c'est à dire trois chlores pour un noyau cyanurique, la proportion maximale de trichlorocyanurique en solution ne dépasse pas 4 ou 5%. Par dissolution de Cl_3Cy on obtient donc dans des pH proches de la neutralité principalement Cl_2Cy, le tiers de chlore restant étant libéré sous forme d'acide hypochloreux.

Pour la figure 3 la symétrie précédente est conservée avec une baisse très sensible de la proportion des formes les plus chlorées, Cl_3Cy n'y apparait plus en quantité notable et Cl_2Cy n'est plus majoritaire à pH 7. Ceci est général, pour un même rapport Cl/Cy, plus la dilution est grande plus le chlore libre est abondant par rapport au chlore lié aux atomes d'azote des cycles cyanuriques.

4.2 Influence de la surconcentration en chlore

Il est évident à priori que plus le chlore sera en excès dans le milieu (plus le rapport Cl/Cy sera grand) plus la chloration relative de ces composés sera forte.

La figure 4 montre l'évolution des maxima en acide dichloro et trichlorocyanurique en fonction de ce rapport.

Il apparait que pour une faible surconcentration de chlore on obtient facilement au pH adéquat une proportion proche de 100% en Cl_2Cy alors qu'il est très difficile d'obtenir une grande proportion de Cl_3Cy.

La figure 5 montre la quantité de chlore libre par rapport au chlore actif total pour des valeurs du rapport chlore/acide cyanurique comprises entre 0 et 3. La baisse de Cl/Cy peut représenter la consommation du chlore dans une eau où l'on aurait dissous Cl_3Cy.

Cette figure montre que la dissolution du dérivé dichloré (rapport Cl/Cy = 2) amène moins de chlore libre, donc moins de chlore sensible à une photodégradation rapide en solution.

Pour mieux illustrer ce fait la figure 6 montre, à quantité de chlore actif total constant, l'influence directe du rapport Cl/Cy sur la proportion de chlore libre.

$$[\text{Cl actif}] = [\text{Cl lié à Cy}] + [\text{Cl libre}]$$

Nous avons pris dans cet exemple [Cl actif] = 1,5 mg/L, ce qui est de l'ordre de grandeur requis dans l'eau d'une piscine. (La quantité de chlore résiduel conseillé après surchloration et stabilisation d'une eau de piscine est de 1 à 1,5 ppm.)

4.3 Influence de la dilution (C_0)

Il existe un effet de dilution pour un même rapport Cl/Cy; la chloration est plus complète à concentration élevée en noyaux cyanurique.

La figure 7 représente la proportion maximale du dérivé dichloré en fonction du logarithme de $[H_3Cy]_0$ pour un rapport Cl/Cy constant et égal à 3.

4.4 Influence des ions chlorures

Hormis l'influence de la force ionique, les ions chlorures ont un effet sur la composition du mélange en milieu acide, plus la

Can. J. Chem. Downloaded from www.nrcresearchpress.com by 196.1.178.254 on 09/07/12
For personal use only.

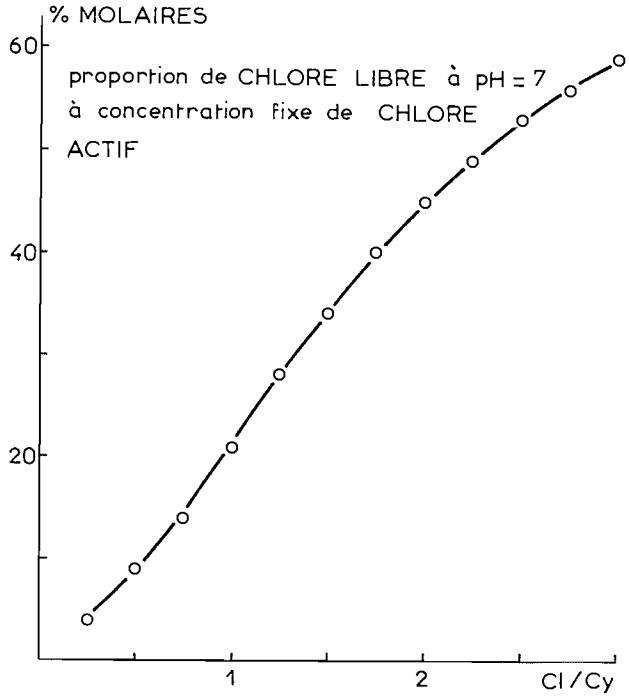

FIG. 6. Influence du rapport Cl/Cy sur la proportion de chlore libre à quantité de chlore actif constante : proportion de chlore libre. $[Cl_2]_0 = 1.5$ mg/L; $[Cl^-] = 10^{-1}$ M.

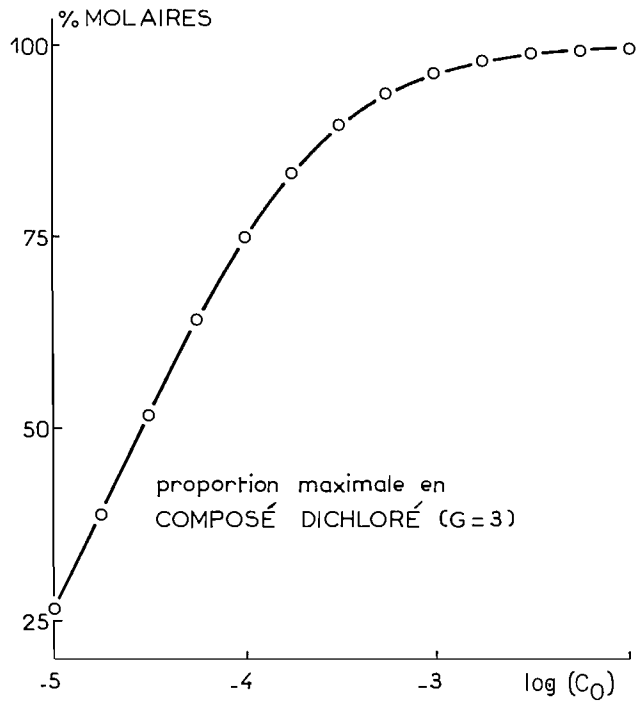

FIG. 7. Influence de la dilution globale : proportion maximale de dichlore versus $\log_{10}$ (C_0). Rapport Cl/Cy = constante = 3. $[H_3Cy]_0$ (C_0) variant de 10^{-5} à 10^{-2} M; $[Cl^-] = 10^{-1}$ M.

concentration en ions chlorures augmente plus la formation du dérivé trichloré est défavorisée.

Sur la figure 8 les concentrations en ions chlorures variant de 0,1 à 1 M; nous avons représenté le pourcentage maximum de $CyCl_3$ par rapport à la concentration initiale de noyaux cyanuriques en fonction de $[Cl^-]$, ceci en négligeant l'effet de

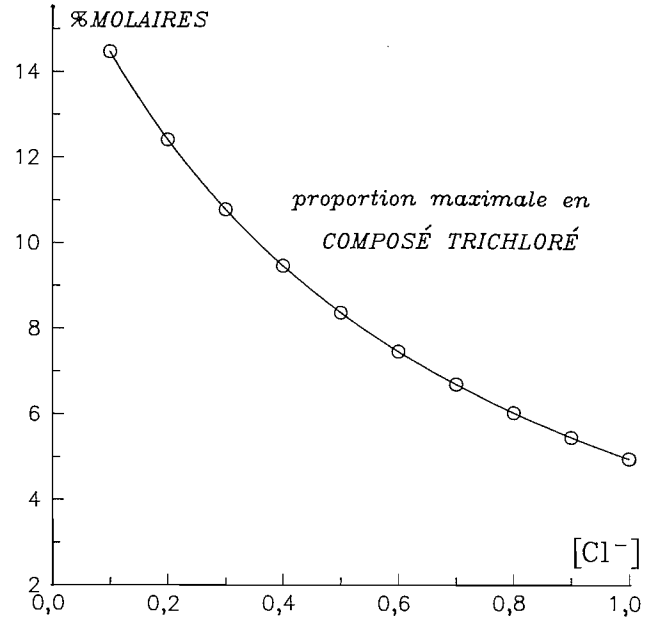

FIG. 8. Influence des ions chlorure : proportion maximale de trichlore versus $[Cl^-]$. Rapport Cl/Cy = 5. $[H_3Cy]_0 = 2 \times 10^{-3}$ M; $[Cl^-]$ variant de 0,1 à 1 M.

la force ionique du milieu sur les coefficients d'activités et les déplacements d'équilibres susceptibles d'en résulter.

Ces précautions étant prises, il apparait clairement qu'une forte concentration en ions chlorures favorise l'hydrolyse de $CyCl_3$.

En milieu basique les ions chlorures n'influencent pas directement la composition de la solution.

Conclusions

Le calcul utilisé ici permet de trouver facilement par la résolution de l'équation [1] les concentrations de toutes les espèces en solution aqueuse du système chlore/acide isocyanurique dans toutes les conditions de pH et de dilution voulues. Ceci est du au fait que nous tenons compte de toutes les espèces de chlore libre qu'il est possible de trouver en équilibre rapide et réversible sur toute la gamme de pH alors qu'habituellement la plupart des auteurs ne tiennent compte que des espèces ClOH et ClO^-. Le fait de prendre en compte la formation éventuelle de Cl_2 et Cl_3^- permet l'étude du milieu acide ce qui peut présenter un intérêt vis-à-vis de problèmes de synthèse (de Cl_3Cy en particulier).

Nous avons pu constater que l'acide trichlorocyanurique n'était majoritaire en solution qu'en présence d'un large excès de chlore, soit dans des conditions très différentes de celles des eaux de piscines; dans les conditions normales d'utilisation la dissolution des dérivés chlorocyanuriques conduit principalement à la formation d'acide dichloro et monochlorocyanurique.

Les résultats obtenus rejoignent les conclusions de O'Brien *et al.* (2) qui corrèlent la plus forte inhibition de la photodécomposition du chlore au minimum de chlore libre par rapport au chlore total entre pH 6 et 8, et celles de Pinsky et Hu (3) qui relie logiquement cette inhibition à la surconcentration en acide cyanurique.

Dans la mesure où le chlore lié aux noyaux isocyanurates reste actif en ce qui concerne son rôle désinfectant, il s'avère, pour gérer la composition d'une eau de piscine que à une teneur en chlore donnée, qu'il est préférable de maintenir un rapport

Can. J. Chem. Downloaded from www.nrcresearchpress.com by 196.1.178.254 on 09/07/12
For personal use only.

Cl/Cy le plus faible possible, ceci permettant d'obtenir un «reservoir» de chlore actif peu sensible à la plus grande partie du rayonnement solaire.

1. J. E. O'BRIEN. Thèse, Harvard University, Cambridge, MA. 1972.
2. J. E. O'BRIEN, J. C. MORRIS et J. N. BUTLER. Chem. Water Supply Treat. Distrib. Symp. (1973) (Pub. 1974). pp. 333–358.
3. M. L. PINSKY et HUA-CHING HU. Environ. Sci. Technol. **15**, 423 (1981).
4. J. CARREL MORRIS. Environ. Impact Water Chlorination, Proc. Conf. 1975. *Edited by* Robert L. Jolley. NTIS. 1976. pp. 21–35.
5. R. E. CONNICK et Y. T. CHIA. J. Am. Chem. Soc. **81**, 1280 (1959).
6. J. CARREL MORRIS. J. Phys. Chem. **70**(12), 3798 (1966).
7. R. P. BELL et E. GELLS. J. Chem. Soc. 2734 (1951).
8. M. EIGEN et K. KUSTIN. J. Am. Chem. Soc. **84**, 1355 (1962).
9. G. ZIMMERMANN et F. C. STRONG. J. Am. Chem. Soc. **79**, 2063 (1957).

Can. J. Chem. Downloaded from www.nrcresearchpress.com by 196.1.178.254 on 09/07/12
For personal use only.

Synthesis and X-ray crystal structure of the novel Mo—Cu complex, $(Ph_2PCH_2CH_2PPh_2)_2Cu^+[(HBpz''_3)Mo(CO)_3]_2Cu^-$ (where pz'' = 3,5-dimethylpyrazolyl, $N_2C_5H_7$)

STEVEN J. RETTIG, ALAN STORR, AND JAMES TROTTER

Department of Chemistry, University of British Columbia, 2036 Main Mall, Vancouver, B.C., Canada V6T 1Y6

Received March 3, 1988

RETTIG, S. J., STORR, A., and TROTTER, J. 1988. Can. J. Chem. **66**, 2194 (1988).

The novel complex, $(Ph_2PCH_2CH_2PPh_2)_2Cu^+[(HBpz''_3)Mo(CO)_3]_2Cu^-$ (where pz'' = 3,5-dimethylpyrazolyl), has been synthesized by reacting the $(HBpz''_3)Mo(CO)_3^-$ anionic ligand with CuI in the presence of a stoichiometric amount of $Ph_2PCH_2CH_2PPh_2$. Crystals of $(Ph_2PCH_2CH_2PPh_2)_2Cu^+[(HBpz''_3)Mo(CO)_3]_2Cu^- \cdot 3.5C_6H_6 \cdot CH_2Cl_2$ are triclinic, a = 13.421(1), b = 14.931(3), c = 28.523(5) Å, α = 90.41(2), β = 90.19(1), γ = 104.65(1)°, Z = 2, space group $P\bar{1}$. The structure was solved by heavy atom methods and was refined by full-matrix least-squares procedures to R = 0.047 and R_w = 0.049 for 8779 reflections with $I \geq 3\sigma(I)$. The crystal structure consists of $(Ph_2PCH_2CH_2PPh_2)_2Cu^+$ cations having irregular tetrahedral coordination geometry about the copper atom (Cu—P = 2.263(2)–2.304(2) Å and P—Cu—P = 88.30(7)– 134.62(8)°) and novel $[(HBpz''_3)Mo(CO)_3]_2Cu^-$ anions having exact C_i and approximate D_{3d} symmetry. The central Cu atom of the anion is bonded to two Mo atoms in a linear fashion and also interacts with six semi-bridging carbonyl ligands, three from each $(HBpz''_3)Mo(CO)_3^-$ ligand. Average bond lengths and angles for the anion are Mo–Cu = 2.565, Mo—C = 1.955, Mo—N = 2.256, Cu—C = 2.309, C—O = 1.174 Å, Mo—C—O = 171.7° and Cu—C—O = 114.7°.

RETTIG, S. J., STORR, A., et TROTTER, J. 1988. Can. J. Chem. **66**, 2194 (1988).

On a synthétisé le nouveau complexe, $(Ph_2PCH_2CH_2PPh_2)_2Cu^+[(HBpz''_3)Mo(CO)_3]_2Cu^-$ (où pz'' = diméthyl-3,5 pyrazolyl), en faisant réagir le ligand anionique $(HBpz''_3)Mo(CO)_3^-$ avec le CuI en présence de quantités stochiométriques de $Ph_2PCH_2CH_2PPh_2$. Les cristaux de $(Ph_2PCH_2CH_2PPh_2)_2Cu^+[(HBpz''_3)Mo(CO)_3]_2Cu^- \cdot 3.5C_6H_6 \cdot CH_2Cl_2$ sont tricliniques et appartiennent au groupe d'espace $P\bar{1}$ avec a = 13,421(1), b = 14,931(3), c = 28,523(5) Å, α = 90.41(2), β = 90,19(1), γ = 104.65(1)°, Z = 2. On a résolu la structure par la méthode des moindres carrés (matrice complète) jusqu'à des valeurs de R = 0.047 et de R_w = 0.049 pour 8779 réflexions avec $I \geq 3\sigma(I)$. La structure du cristal consiste en des cations $(Ph_2PCH_2CH_2PPh_2)_2Cu^+$ ayant une géométrie de coordination irrégulière autour de l'atome de cuivre (Cu—P = 2,263(2)–2,304(2) Å et P—Cu—P = 88,30(7)–134.62(8)°) et des nouveaux anions $[(HBpz''_3)Mo(CO)_3]_2Cu^-$ ayant exactement C_i et une symmétrie approximative D_{3d}. L'atome de cuivre central de l'anion est lié de façon linéaire à deux atomes de Mo et est en interaction avec six ligands carbonyles en position de demi-pont, chaque ligand $(HBpz''_3)Mo(CO)_3^-$ fournissant trois unités de ce demi-pont. Les longueurs moyennes de liaison et les angles moyens de l'anion sont Mo—Cu = 2,565, Mo—C = 1,955, Mo—N = 2,256, Cu—C = 2,309, C—O = 1,174 Å, Mo—C—O = 171,7° et Cu—C—O = 114,7°.

[Traduit par la revue]

Can. J. Chem. Downloaded from www.nrcresearchpress.com by 112.217.228.212 on 09/07/12
For personal use only.

Introduction

Earlier publications (1, 2) have described a number of complexes of the type (RE"pz"$_3$)Mo(CO)$_3$CuL (where R = Me when E = Ga and "pz" = $N_2C_3H_3$, L = PPh_3; where R = H when E = B and "pz" = $N_2C_3H_3$ for L = PPh_3 or tmed, or "pz" = $N_2C_5H_7$ for L = tmed). In these complexes a Mo—Cu bond is complimented by semi-bridging CO groups and the Cu centre is further ligated by a monodentate Ph_3P ligand or by the bidentate tmed molecule. The complexes where L = Ph_3P are unusual in their coordinative unsaturation about the copper centre, especially when compared to complexes of the type CpM(CO)$_3$Cu-$(Ph_3P)_2$ where M = Mo or W (3).

The Cp^- ligand has been likened to the trispyrazolylborate and -gallate ligands, RE"pz"$_3^-$, in that all three ligand systems are six-electron donors, facially tridentate chelating and uninegative. Consequently many "isoelectronic" series of complexes incorporating these ligands have been reported (4–7). The different compositions of the triphenylphospine complexes produced with the $CpMo(CO)_3^-$ and $(RE"pz"_3)Mo(CO)_3^-$ anions are thought to be manifestations of the different steric requirements of the two ligand types. The present study was an attempt to exploit this steric effect to produce a Cu diphos complex with a "dangling" diphenylphosphino functionality, viz, $(HBpz''_3)Mo(CO)_3CuPh_2PCH_2CH_2PPh_2$ (where pz'' = 3,5-dimethylpyrazolyl, $N_2C_5H_7$). The complex isolated did indeed display this stoichiometry but the novel molecular arrangement observed was unexpected and totally without precedent.

Experimental

Starting materials

Air-sensitive materials were handled in a nitrogen atmosphere. Tetrahydrofuran (THF), benzene, CH_2Cl_2, and hexane were dried by refluxing over Na/benzophenone, potassium, CaH_2, and $CaSO_4$, respectively, followed by distillation. A THF solution of the ligand $K^+[(HBpz''_3)Mo(CO)_3]^-$ was prepared as described previously (2).

Preparation of $(Ph_2PCH_2CH_2PPh_2)_2Cu^+[(HBpz''_3)Mo(CO)_3]_2Cu^-$

To a solution of $K^+[(HBpz''_3)Mo(CO)_3]^-$ (1.494 mmol) (2) in 200 mL THF was added a slurry of CuI (0.284 g, 1.494 nmol) and $Ph_2PCH_2CH_2PPh_2$ (0.594 g, 1.494 mmol) in CH_2Cl_2/THF. The mixture was stirred for ~16 h at room temperature and then the solvents were removed under vacuum. The residue was extracted with CH_2Cl_2 and filtered. Hexane and benzene were added to the clear filtrate and the mixed solvents allowed to evaporate slowly. Golden yellow crystals of the product were solvated with 3.5 C_6H_6 and one CH_2Cl_2 solvate molecules per ion pair. Yield ~60%. *Anal.* calcd. for $(Ph_2PCH_2CH_2PPh_2)_2Cu^+[(HBpz''_3)Mo(CO)_3]_2Cu^- \cdot 3.5C_6H_6 \cdot CH_2Cl_2$: C 59.07, H 5.15, N 7.52; found: C 58.60, H 5.08, N 7.64. ^{1}H nmr

Can. J. Chem. Downloaded from www.nrcresearchpress.com by 112.217.228.212 on 09/07/12
For personal use only.

(d^6-acetone, τ ($(CD_3)_2CO$) = 7.89 ppm): 7.58 s, 7.43 s (pz—Me); 4.32 s (CH_2Cl_2); 4.23 s (pz—H^4); 2.69 m, 2.56 m (P—Ph, C_6H_6). Infrared spectra: (KBr pellet) 1885, 1801, 1760 cm^{-1}; (CH_2Cl_2) 1885, 1785, 1750 cm^{-1}.

Spectra

The ir spectra were recorded on a Perkin-Elmer 598 spectrometer. The ^1H nmr spectrum was recorded on a Varian 300 MHz instrument using FT techniques.

X-ray crystallographic analysis of bis[1,2-bis(diphenylphosphino)ethane]copper(I) bis[(hydrotris(3,5-dimethylpyrazolyl)borato)tricarbonylmolybdenum]copper(2Mo—Cu) benzene dichloromethane solvate

A crystal bounded by the six faces (followed by the distances in mm between parallel faces): {0 0 1}, 0.22, {0 1 1}, 0.09, {1 0 1}, 0.65, was mounted in a general orientation. Unit-cell parameters were refined by least squares on 2 sin θ/λ values for 25 reflections (2θ = 35–38°) measured on a diffractometer with Mo–$K\alpha$ radiation ($\lambda(K\alpha_1)$ = 0.70930, $\lambda(K\alpha_2)$ = 0.71359 Å). Crystal data at 22°C are as follows:

$C_{88}H_{92}B_2Cu_2Mo_2N_{12}O_6P_4 \cdot 3.5C_6H_6 \cdot CH_2Cl_2$ f.w. = 2236.59 Triclinic, a = 13.421(1), b = 14.931(3), c = 28.523(5) Å, α = 90.41(2), β = 90.19(1), γ = 104.65(1)°, V = 5530(1) Å^3, Z = 2, ρ_c = 1.343 Mg m^{-3}, $F(000)$ = 2306, μ(Mo-$K\alpha$) = 18.7 cm^{-1}. Absent reflections: none, space group $P\bar{1}$ (C_i^1, No. 2, reduced cell) from structure analysis.

Intensities were measured with graphite-monochromated Mo-$K\alpha$ radiation on an Enraf-Nonius CAD4-F diffractometer. An ω scan at 2.0–20.1° min^{-1} over a range of (0.90 + 0.35 tan θ) degrees in ω (extended by 25% on both sides for background measurement) was employed. Data were measured to 2θ = 50°. The intensities of three check reflections, measured every 6000 s throughout the data collection, showed only small random variations (<4%). After data reduction, an absorption correction was applied using the Gaussian integration method. Transmission factors ranged from 0.820 to 0.939 for 96 integration points. Of the 19350 independent reflections measured, 8779 (45.4%) had intensities greater than or equal to $3\sigma(I)$ above background where $\sigma^2(I) = S + 2B + (0.04(S-B))^2$ with S = scan count and B = normalized background count. Pseudo-I-centering of the crystal lattice is partially responsible for the relatively small fraction of significant data, half of the total number being systematically weak.

The structure analysis was initiated in the centrosymmetric space group $P\bar{1}$ (which was confirmed by subsequent calculations). The structure was solved by heavy atom methods, the metal atom coordinates being determined from the Patterson function. The solution was complicated by the fact that there are two independent, centrosymmetric, $[(HBpz''_3)Mo(CO)_3]_2Cu^-$ anions located about the lattice points (0,0,0) and (1/2,1/2,1/2), and having the linear Mo—Cu—Mo moieties parallel. This results in considerable overlapping of the Patterson function peaks. The remaining non-hydrogen atoms of the cation and anion were positioned from a subsequent difference Fourier map. After further refinement the solvent molecules were located (three benzene molecules in general positions and one at a centre of symmetry and one molecule of dichloromethane). In the final stages of refinement the non-hydrogen atoms were refined with anisotropic thermal parameters and hydrogen atoms were fixed in idealized positions (B—H = 1.09, (C(sp^2)—H = 0.97, C(sp^3)—H = 0.98 Å, $U_H \alpha U_{\text{bonded atom}}$, methyl orientations based on observed hydrogen positions). Scattering factors for all atoms and anomalous scattering corrections for Mo, Cu, Cl, and P were taken from ref. 8. The weighting scheme $w = 1/\sigma^2(F)$, where $\sigma^2(F)$ is derived from the previously defined $\sigma^2(I)$, gave uniform average values of $w(|F_o|-|F_c|)^2$ over ranges of both $|F_o|$ and sin θ/λ and was employed in the final stages of full-matrix refinement of 1264 variables. Reflections with $I < 3\sigma(I)$ were not included in the refinement. Convergence was reached at R = 0.047 and R_w = 0.049 for 8779 reflections with $I \geq 3\sigma(I)$. The function minimized was $\Sigma w(|F_o|-|F_c|)^2$, $R = \Sigma(||F_o|-|F_c||/\Sigma|F_o|$ and $R_w = (\Sigma w(|F_o|-|F_c|)^2/\Sigma w|F_o|^2)^{1/2}$.

On the final cycle of refinement the mean and maximum parameter shifts corresponded to 0.04 and 0.83 σ, respectively. The mean error in an observation of unit weight was 1.763. The final difference map showed maximum fluctuations of −1.0 and 0.6 e Å^{-3} in the vicinity of the Mo atoms and was essentially featureless elsewhere. The final positional and thermal parameters appear in Tables 1 and 6[2], respectively. Measured and calculated structure factors have been placed in the Depository of Unpublished Data.[1] Selected bond lengths and bond angles appear in Tables 2 and 3, respectively. Intra-annular torsion angles, calculated hydrogen atom parameters, anisotropic thermal parameters, and complete lists of bond lengths, bond angles, and torsion angles (Tables 4–9) have also been deposited.[1]

Results and discussion

The ability of the tricarbonyl anions $(RE''pz''_3)Mo(CO)_3^-$ to form complexes with both transition metal and main group metal moieties in which heteronuclear metal–metal bonds are featured has been demonstrated in earlier publications (1, 2, 9). That the steric requirements of these anions are much greater than those of the comparable $CpMo(CO)_3^-$ anion is evidenced by the two different formulations for the Cu triphenylphosphine complexes, viz. $(RE''pz''_3)Mo(CO)_3CuPPh_3$ (1, 2) vs. $CpMo(CO)_3Cu(PPh_3)_2$ (3). Cognizant of this phenomenon, we have investigated the reaction of $(HBpz''_3)Mo(CO)_3^-$ with $CuI/Ph_2PCH_2CH_2PPh_2$ with the expectation that steric effects would prevent chelation of the diphos ligand at the Cu centre and a complex with a dangling "Ph_2P" moiety would result, viz. $(HBpz''_3)Mo(CO)_3$-$CuPh_2PCH_2CH_2PPh_2$. The golden yellow crystals isolated in moderate yield did in fact have the above stoichometry with additional benzene and dichloromethane solvate molecules. Surprisingly, however, the molecular arrangement was unique and totally unexpected, consisting of a $(Ph_2PCH_2CH_2PPh_2)_2Cu^+$ cation together with a trimetallic anion $[(HBpz''_3)Mo(CO)_3]_2$-Cu^-, the latter displaying a linear arrangement for the Mo_2Cu unit and six semi-bridging carbonyls around the Cu centre.

The solution ^1H nmr spectrum of the complex in d^6-acetone shows all the pyrazolyl rings to be in equivalent environments, as established in the solid state (see below). The ir spectra in both the solid state and in solution displayed three strong ν_{CO} bands, somewhat surprising considering the threefold symmetry of the complex which would be expected to give two ν_{CO} vibrations (a and e modes). Perhaps, as was noted earlier in the solid state spectrum of the complex $(MeGapz_3)Mo(CO)_3CuPPh_3$

[1]The structure factor table, Table 6 (anisotropic thermal parameters) and other material mentioned in the text may be purchased from the Depository of Unpublished Data, CISTI, National Research Council of Canada, Ottawa, Ont., Canada K1A 0S2.

TABLE 1. Final positional (fractional × 10^4; Mo, Cu, and P × 10^5) and isotropic thermal parameters ($U \times 10^3$ Å^2) with estimated standard deviations in parentheses

Atom	x	y	z	U_{eq}
Mo(1)	64246(4)	42069(4)	48086(2)	42
Mo(1′)	14175(4)	−8704(4)	1108(2)	46
Cu(1)	50000	50000	50000	63
Cu(1′)	0	0	0	66
Cu(2)	72117(6)	58545(6)	22817(3)	46
P(1)	85402(13)	59124(13)	28037(6)	47
P(2)	65067(14)	43877(13)	25170(6)	49
P(3)	78174(13)	65145(13)	15904(6)	45
P(4)	64040(13)	70148(13)	24182(6)	47
Cl(1)	3576(7)	3052(7)	1179(2)	385
Cl(2)	2160(7)	3850(7)	1237(3)	433
O(1)	6853(4)	5580(4)	5660(2)	74
O(2)	5750(4)	5403(4)	4037(2)	64
O(3)	4331(4)	2943(3)	5156(2)	70
O(1′)	234(4)	−1117(4)	−844(2)	88
O(2′)	−426(4)	−1327(4)	808(2)	76
O(3′)	2031(4)	1272(4)	249(2)	83
N(1)	6447(4)	3150(4)	4245(2)	47
N(2)	7347(4)	2891(4)	4149(2)	50
N(3)	7241(4)	3309(4)	5209(2)	49
N(4)	7945(4)	2935(4)	4978(2)	49
N(5)	8042(4)	4838(4)	4559(2)	44
N(6)	8675(4)	4275(4)	4452(2)	45
N(1′)	2489(4)	−975(4)	714(2)	52
N(2′)	3133(4)	−1552(4)	672(2)	47
N(3′)	2883(4)	−708(4)	−298(2)	49
N(4′)	3589(4)	−1210(4)	−172(2)	47
N(5′)	1390(4)	−2382(4)	29(2)	50
N(6′)	2291(4)	−2665(4)	54(2)	50
C(1)	6631(5)	5094(6)	5333(3)	57
C(2)	5921(5)	4963(5)	4348(2)	44
C(3)	5087(5)	3468(5)	5025(2)	50
C(4)	5725(5)	2649(5)	3954(2)	50
C(5)	6162(6)	2096(5)	3674(3)	62
C(6)	7178(6)	2260(5)	3807(3)	61
C(7)	7147(5)	2959(5)	5641(3)	59
C(8)	7778(6)	2350(5)	5681(3)	68
C(9)	8258(5)	2348(5)	5272(3)	58
C(10)	8588(5)	5707(5)	4517(2)	48
C(11)	9588(5)	5708(6)	4380(2)	57
C(12)	9626(5)	4813(6)	4350(2)	53
C(13)	4631(5)	2719(5)	3953(3)	70
C(14)	7987(7)	1834(7)	3609(3)	100
C(15)	6457(6)	3196(6)	6004(3)	82
C(16)	9012(7)	1817(6)	5122(3)	89
C(17)	8152(6)	6517(5)	4609(3)	67
C(18)	10532(5)	4420(6)	4243(3)	77
C(1′)	635(5)	−968(5)	−470(3)	58
C(2′)	238(5)	−1126(5)	533(3)	53
C(3′)	1722(5)	467(5)	189(3)	58
C(4′)	2561(5)	−675(5)	1154(3)	58
C(5′)	3257(6)	−1054(6)	1402(3)	65
C(6′)	3587(5)	−1590(5)	1092(3)	57
C(7′)	3322(5)	−148(5)	−638(3)	54
C(8′)	4302(5)	−260(5)	−731(3)	58
C(9′)	4440(5)	−924(5)	−438(3)	54
C(10′)	671(5)	−3137(5)	−91(2)	54
C(11′)	1074(6)	−3901(5)	−152(3)	61
C(12′)	2113(6)	−3563(6)	−56(3)	57
C(13′)	1962(7)	−38(7)	1343(3)	93
C(14′)	4347(6)	−2181(6)	1166(3)	86
C(15′)	2801(6)	516(5)	−869(3)	75
C(16′)	5369(5)	−1313(6)	−383(3)	79
C(17′)	−452(6)	−3125(6)	−136(3)	84
C(18′)	2922(6)	−4101(5)	−63(3)	81
B	8278(6)	3223(6)	4480(3)	52
B′	3299(6)	−1963(6)	195(3)	51
C(19)	7787(5)	5226(5)	3279(2)	49
C(20)	7197(5)	4294(5)	3076(2)	56
C(21)	7866(5)	7726(5)	1730(2)	54
C(22)	6816(5)	7786(5)	1912(2)	50
C(23)	9444(5)	5224(5)	2666(2)	49
C(24)	10190(6)	5121(6)	2997(3)	77
C(25)	10837(7)	4572(8)	2886(4)	101
C(26)	10806(8)	4154(7)	2465(4)	99
C(27)	10094(8)	4248(7)	2136(3)	101
C(28)	9424(6)	4813(6)	2245(3)	70
C(29)	9343(5)	6949(5)	3073(3)	54
C(30)	9065(6)	7361(6)	3460(3)	68
C(31)	9688(8)	8177(7)	3633(3)	81
C(32)	10590(8)	8589(6)	3421(4)	92
C(33)	10896(7)	8202(8)	3039(5)	107
C(34)	10277(7)	7388(7)	2846(3)	90
C(35)	5159(5)	4006(5)	2674(3)	52
C(36)	4444(7)	3329(7)	2444(3)	92
C(37)	3415(8)	3079(8)	2585(5)	118
C(38)	3117(8)	3525(9)	2949(5)	102
C(39)	3777(9)	4224(8)	3177(3)	97
C(40)	4800(6)	4473(6)	3036(3)	74
C(41)	6713(5)	3461(5)	2146(3)	61
C(42)	6932(7)	3614(6)	1682(3)	86
C(43)	7099(10)	2936(9)	1389(4)	120
C(44)	7035(10)	2081(10)	1559(5)	133
C(45)	6821(10)	1890(7)	2022(5)	136
C(46)	6656(8)	2584(7)	2320(3)	94
C(47)	9108(5)	6502(6)	1399(2)	51
C(48)	9953(6)	7169(6)	1542(3)	82
C(49)	10942(7)	7097(8)	1428(4)	107
C(50)	11076(7)	6375(10)	1187(4)	97
C(51)	10250(8)	5710(9)	1038(3)	108
C(52)	9255(6)	5773(7)	1139(3)	86
C(53)	7044(5)	6341(4)	1056(2)	42
C(54)	6078(6)	5710(5)	1054(2)	61
C(55)	5451(6)	5624(6)	663(3)	76
C(56)	5767(7)	6151(6)	278(3)	73
C(57)	6710(7)	6780(6)	279(3)	69
C(58)	7325(5)	6877(5)	662(2)	53
C(59)	4998(5)	6804(5)	2397(2)	52
C(60)	4428(6)	6011(6)	2195(3)	72
C(61)	3368(7)	5831(7)	2151(4)	100
C(62)	2891(7)	6480(9)	2319(4)	101
C(63)	3455(8)	7272(8)	2524(4)	108
C(64)	4506(6)	7451(6)	2572(3)	79
C(65)	6745(5)	7748(5)	2933(2)	51
C(66)	6359(6)	7432(6)	3363(3)	62
C(67)	6602(7)	7963(8)	3765(3)	81
C(68)	7243(8)	8824(9)	3745(3)	95
C(69)	7662(7)	9152(6)	3323(4)	92
C(70)	7410(6)	8640(6)	2919(3)	71
C(71)	4543(16)	658(11)	5112(6)	153
C(72)	5449(14)	915(8)	4926(5)	119
C(73)	5905(10)	264(15)	4813(5)	158
C(74)	985(16)	1782(13)	3952(6)	151
C(75)	1745(16)	2130(12)	4198(9)	158
C(76)	2046(11)	1666(18)	4556(9)	174
C(77)	1481(16)	868(13)	4679(6)	156

Can. J. Chem. Downloaded from www.nrcresearchpress.com by 112.217.228.212 on 09/07/12
For personal use only.

TABLE 1. (*concluded*)

Atom	*x*	*y*	*z*	$U_{eq.}$
C(78)	607(15)	486(9)	4403(8)	164
C(79)	386(11)	966(15)	4024(7)	147
C(80)	−459(14)	244(13)	1965(5)	156
C(81)	−806(16)	938(18)	1977(6)	204
C(82)	−600(16)	1545(14)	2306(9)	195
C(83)	−21(18)	1369(18)	2690(6)	219
C(84)	478(18)	791(21)	2635(9)	342
C(85)	60(13)	38(10)	2361(8)	165
C(86)	3996(46)	337(47)	2778(24)	305
C(87)	4660(34)	−80(21)	2884(16)	224
C(88)	4665(27)	−353(14)	3315(19)	188
C(89)	3985(38)	−181(21)	3639(10)	212
C(90)	3329(18)	307(26)	3464(19)	220
C(91)	3439(54)	601(45)	2973(36)	331
C(92)	2071(13)	2630(11)	1261(7)	245

TABLE 2. Selected bond lengths (Å) with estimated standard deviations in parentheses

Bond	Length (Å)	Bond	Length (Å)
Mo(1)—Cu(1)	2.5493(6)	Cu(2)—P(2)	2.263(2)
Mo(1)—N(1)	2.250(6)	Cu(2)—P(3)	2.270(2)
Mo(1)—N(3)	2.249(5)	Cu(2)—P(4)	2.296(2)
Mo(1)—N(5)	2.257(5)	P(1)—C(19)	1.847(6)
Mo(1)—C(1)	1.962(9)	P(1)—C(23)	1.819(7)
Mo(1)—C(2)	1.965(7)	P(1)—C(29)	1.811(8)
Mo(1)—C(3)	1.959(7)	P(2)—C(20)	1.866(7)
Mo(1′)—Cu(1′)	2.5808(5)	P(2)—C(35)	1.813(7)
Mo(1′)—N(1′)	2.269(5)	P(2)—C(41)	1.812(8)
Mo(1′)—N(3′)	2.249(5)	P(3)—C(21)	1.834(7)
Mo(1′)—N(5′)	2.261(6)	P(3)—C(47)	1.822(7)
Mo(1′)—C(1′)	1.944(8)	P(3)—C(53)	1.821(7)
Mo(1′)—C(2′)	1.953(7)	P(4)—C(22)	1.850(6)
Mo(1′)—C(3′)	1.946(9)	P(4)—C(59)	1.833(7)
Cu(1)—C(1)	2.354(7)	P(4)—C(65)	1.813(7)
Cu(1)—C(2)	2.244(6)	O(1)—C(1)	1.169(8)
Cu(1)—C(3)	2.322(7)	O(2)—C(2)	1.163(7)
Cu(1′)—C(1′)	2.283(8)	O(3)—C(3)	1.177(7)
Cu(1′)—C(2′)	2.354(6)	O(1′)—C(1′)	1.187(8)
Cu(1′)—C(3′)	2.299(7)	O(2′)—C(2′)	1.171(7)
Cu(2)—P(1)	2.304(2)	O(3′)—C(3′)	1.178(8)

(ν_{CO} = 1890, 1805, and 1780 cm^{-1}) (1), a splitting of the *e* mode is occurring due to packing or solvent effects.

The crystal structure of $(Ph_2PCH_2CH_2PPh_2)_2Cu^+[(HBpz''_3)Mo(CO)_3]_2Cu^- \cdot 3.5C_6H_6 \cdot CH_2Cl_2$ consists of $(Ph_2PCH_2CH_2PPh_2)_2Cu^+$ cations, $[(HBpz''_3)Mo(CO)_3]_2Cu^-$ anions, and solvated molecules of benzene and dichloromethane. The shortest distance between structural entities involving non-hydrogen atoms is the cation–anion contact O(2′)...C(48)($x-1$, $y-1$, $-z$) = 3.213(9) Å. There are four cation–anion C—H...O interactions of possible significance: C(40)—H(40)...O(2), C(57)—H(57)...O(3′)($1-x$, $1-y$, $-z$), C(58)—H(58)...O(2′)($1+x,1+y,z$), and C(67)—H(67)...O(3) ($1-x,1-y,-z$); H...O = 2.52, 2.52, 2.56, and 2.51 Å; C...O = 3.28(1), 3.34(1), 3.515(9), and 3.48(1) Å; C—H...O = 136, 143, 168, and 177°, respectively. The solvate molecules are fairly well resolved, but generally display a high degree of thermal motion. This factor combined with possible unresolved disorder leads to some anomalous geometrical features; a significant non-planarity of the C(80)—C(85) benzene ring has been noted in addition to other features apparent in Tables 7 and 8. All of the solvate molecules occupy spaces in the crystal lattice between anions.

The $(Ph_2PCH_2CH_2PPh_2)_2Cu^+$ cation (Fig. 1) has a highly irregular tetrahedral coordination geometry about the Cu(I) centre with P—Cu—P bond angles (88.30(7) to 134.62(8)°) similar to those reported for the Cu(I) species $[Cu(1,2\text{-}(Me_2As)_2C_6H_4)(pz_4B)]$ and $[Cu(1,2\text{-}(Me_2As)_2C_6H_4)_2]^+$ (10). As noted for the above complexes, steric factors are most likely responsible for the irregular geometry, which in the present example includes significant differences between the Cu(2)—P distances, two of which (Cu(2)—P(1) = 2.304(2) and Cu—P(4) = 2.296(2) Å) are significantly longer than the other two (Cu(2)—P(2) = 2.263(2) and Cu(2)—P(3) = 2.270(2) Å). The average Cu(2)—P distance of 2.283 Å is similar to the corresponding average value of 2.299 Å reported for $CpW(CO)_3Cu(PPh_3)_2$ (3).

The most interesting feature of the structure is the novel $[(HBpz''_3)Mo(CO)_3]_2Cu^-$ anion. The asymmetric unit contains two crystallographically independent centrosymmetric anions. One of these is shown in Fig. 2 while the second is essentially identical and is labelled in the same way, the atoms of the second anion being denoted by primed atom labels. The anions have exact C_i and approximate D_{3d} symmetry. The deviations from D_{3d} symmetry as well as the differences between the two independent half-ions are statistically, but not chemically, significant and are probably the result of packing effects. The central Cu atom is bonded to two Mo atoms in a linear fashion and also interacts with six semi-bridging carbonyl ligands to form a 1:3:3:1 bicapped octahedron. The Ω values ($\Omega = \exp[D(Cu—C)/D(Cu—O)]$) for $[(HBpz''_3)Mo(CO)_3]_2Cu^-$ range from 2.144 to 2.185 and average 2.16, consistent with a semi-bridging interaction (11). The 3:3:1 capped octahedral coordination geometry about the Mo atoms is similar to that reported for $(MeGapz_3)Mo(CO)_3CuPPh_3$ (1), which has three semi-bridging carbonyl groups, and for the complexes $(MeGapz_3)Mo(CO)_3SnPh_3$ (9), $(HBpz''_3)Mo(CO)_3SnMe_2Cl$ (2), and $(HBpz_3)Mo(CO)_3SnPh_3$ (2), which all have three terminal carbonyl ligands.

The $[(HBpz''_3)Mo(CO)_3]_2Cu^-$ anion is closely related to the $(MeGapz_3)Mo(CO)_3CuPPh_3$ molecule where the triphenylphosphine ligand has been replaced by a second $(RE"pz"_3)Mo(CO)_3^-$ ligand. The average Mo—Cu, Mo—C, Mo—N, Cu—C, and C—O bond lengths and Mo—C—O and Cu—C—O bond angles of 2.565, 1.955, 2.256, 2.309, and 1.174 Å, 171.7 and 114.7° are similar to the corresponding values of 2.513, 1.967, 2.257, 2.320, and 1.164 Å, 170.9 and 117.7° observed for $(MeGapz_3)Mo(CO)_3CuPPh_3$ (1). The M—Cu bond lengths in related molecules having a 3:4 piano stool geometry about the M atom (M = Mo or W) with two semi-bridging carbonyl ligands and one terminal carbonyl ligand are significantly longer: 2.592 Å in $CpMo(CO)_3Cu(tmed)$ (12), 2.639 Å in $(HBpz_3)Mo(CO)_3Cu(tmed)$ (2), and 2.721 and 2.771 Å in two crystalline modifications of $CpW(CO)_3Cu(PPh_3)_2$ (3).

Can. J. Chem. Downloaded from www.nrcresearchpress.com by 112.217.228.212 on 09/07/12
For personal use only.

Can. J. Chem. Downloaded from www.nrcresearchpress.com by 112.217.228.212 on 09/07/12
For personal use only.

TABLE 3. Selected bond angles (deg) with estimated standard deviations in parentheses

Bonds	Angle (deg)	Bonds	Angle (deg)
Cu(1)—Mo(1)—N(1)	128.5(1)	Mo(1′)—Cu(1′)—Mo(1′)*	180
Cu(1)—Mo(1)—N(3)	134.7(1)	Mo(1′)—Cu(1′)—C(1′)*	133.4(2)
Cu(1)—Mo(1)—N(5)	129.0(1)	Mo(1′)—Cu(1′)—C(2′)*	133.7(2)
Cu(1)—Mo(1)—C(1)	61.3(2)	Mo(1′)—Cu(1′)—C(3′)*	133.4(2)
Cu(1)—Mo(1)—C(2)	57.9(2)	C(1′)—Cu(1′)—C(2′)	77.8(3)
Cu(1)—Mo(1)—C(3)	60.3(2)	C(1′)—Cu(1′)—C(3′)	79.5(3)
N(1)—Mo(1)—N(3)	81.3(2)	C(1′)—Cu(1′)—Mo(1′)*	133.4(2)
N(1)—Mo(1)—N(5)	83.3(2)	C(1′)—Cu(1′)—C(1′)*	180
N(1)—Mo(1)—C(1)	170.2(2)	C(1′)—Cu(1′)—C(2′)*	102.2(3)
N(1)—Mo(1)—C(2)	89.7(2)	C(1′)—Cu(1′)—C(3′)*	100.5(3)
N(1)—Mo(1)—C(3)	90.4(2)	C(2′)—Cu(1′)—C(3′)	76.1(3)
N(3)—Mo(1)—N(5)	81.4(2)	C(2′)—Cu(1′)—Mo(1′)*	133.7(2)
N(3)—Mo(1)—C(1)	90.5(2)	C(2′)—Cu(1′)—C(1′)*	102.2(3)
N(3)—Mo(1)—C(2)	167.4(2)	C(2′)—Cu(1′)—C(2′)*	180
N(3)—Mo(1)—C(3)	90.8(2)	C(2′)—Cu(1′)—C(3′)*	103.9(3)
N(5)—Mo(1)—C(1)	90.3(2)	C(3′)—Cu(1′)—Mo(1′)*	133.4(2)
N(5)—Mo(1)—C(2)	88.8(2)	C(3′)—Cu(1′)—C(1′)*	100.5(3)
N(5)—Mo(1)—C(3)	170.6(2)	C(3′)—Cu(1′)—C(2′)*	103.9(3)
C(1)—Mo(1)—C(2)	97.5(3)	C(3′)—Cu(1′)—C(3′)*	180
C(1)—Mo(1)—C(3)	95.1(3)	P(1)—Cu(2)—P(2)	88.30(7)
C(2)—Mo(1)—C(3)	98.1(3)	P(1)—Cu(2)—P(3)	110.89(7)
Cu(1′)—Mo(1′)—N(1′)	133.5(2)	P(1)—Cu(2)—P(4)	111.95(7)
Cu(1′)—Mo(1′)—N(3′)	128.1(1)	P(2)—Cu(2)—P(3)	134.62(8)
Cu(1′)—Mo(1′)—N(5′)	131.6(1)	P(2)—Cu(2)—P(4)	121.21(7)
Cu(1′)—Mo(1′)—C(1′)	58.6(2)	P(3)—Cu(2)—P(4)	90.15(7)
Cu(1′)—Mo(1′)—C(2′)	60.7(2)	Cu(2)—P(1)—C(19)	98.3(2)
Cu(1′)—Mo(1′)—C(3′)	59.1(2)	Cu(2)—P(1)—C(23)	117.5(2)
N(1′)—Mo(1′)—N(3′)	81.4(2)	Cu(2)—P(1)—C(29)	126.0(2)
N(1′)—Mo(1′)—N(5′)	81.6(2)	C(19)—P(1)—C(23)	101.2(3)
N(1′)—Mo(1′)—C(1′)	167.8(3)	C(19)—P(1)—C(29)	106.9(3)
N(1′)—Mo(1′)—C(2′)	90.8(2)	C(23)—P(1)—C(29)	103.5(3)
N(1′)—Mo(1′)—C(3′)	91.1(3)	Cu(2)—P(2)—C(20)	103.8(2)
N(3′)—Mo(1′)—N(5′)	81.4(2)	Cu(2)—P(2)—C(35)	121.4(2)
N(3′)—Mo(1′)—C(1′)	90.3(2)	Cu(2)—P(2)—C(41)	117.1(3)
N(3′)—Mo(1′)—C(2′)	171.1(2)	C(20)—P(2)—C(35)	103.6(3)
N(3′)—Mo(1′)—C(3′)	89.7(2)	C(20)—P(2)—C(41)	105.1(3)
N(5′)—Mo(1′)—C(1′)	88.4(3)	C(35)—P(2)—C(41)	103.9(4)
N(5′)—Mo(1′)—C(2′)	93.3(2)	Cu(2)—P(3)—C(21)	99.4(2)
N(5′)—Mo(1′)—C(3′)	169.2(2)	Cu(2)—P(3)—C(47)	119.8(2)
C(1′)—Mo(1′)—C(2′)	96.7(3)	Cu(2)—P(3)—C(53)	122.5(2)
C(1′)—Mo(1′)—C(3′)	97.8(3)	C(21)—P(3)—C(47)	106.1(3)
C(2′)—Mo(1′)—C(3′)	94.8(3)	C(21)—P(3)—C(53)	101.1(3)
Mo(1)—Cu(1)—C(1)	47.0(2)	C(47)—P(3)—C(53)	104.8(3)
Mo(1)—Cu(1)—C(2)	47.9(2)	Cu(2)—P(4)—C(22)	102.4(2)
Mo(1)—Cu(1)—C(3)	47.1(2)	Cu(2)—P(4)—C(59)	121.8(3)
Mo(1)—Cu(1)—Mo(1)''	180	Cu(2)—P(4)—C(65)	119.6(2)
Mo(1)—Cu(1)—C(1)''	133.0(2)	C(22)—P(4)—C(59)	102.6(3)
Mo(1)—Cu(1)—C(2)''	132.1(2)	C(22)—P(4)—C(65)	105.5(3)
Mo(1)—Cu(1)—C(3)''	132.9(2)	C(59)—P(4)—C(65)	102.6(3)
C(1)—Cu(1)—C(2)	79.9(3)	Mo(1)—C(1)—Cu(1)	71.7(3)
C(1)—Cu(1)—C(3)	76.4(3)	Mo(1)—C(1)—O(1)	171.8(6)
C(1)—Cu(1)—Mo(1)''	133.0(2)	Cu(1)—C(1)—O(1)	116.2(5)
C(1)—Cu(1)—C(1)''	180	Mo(1)—C(2)—Cu(1)	74.2(2)
C(1)—Cu(1)—C(2)''	100.1(3)	Mo(1)—C(2)—O(2)	169.8(5)
C(1)—Cu(1)—C(3)''	103.6(3)	Cu(1)—C(2)—O(2)	115.7(5)
C(2)—Cu(1)—C(3)	80.9(2)	Mo(1)—C(3)—Cu(1)	72.5(2)
C(2)—Cu(1)—Mo(1)''	132.1(2)	Mo(1)—C(3)—O(3)	172.7(6)
C(2)—Cu(1)—C(1)''	100.1(3)	Cu(1)—C(3)—O(3)	114.7(5)
C(2)—Cu(1)—C(2)''	180	Mo(1′)—C(1′)—Cu(1′)	74.8(3)
C(2)—Cu(1)—C(3)''	99.1(2)	Mo(1′)—C(1′)—O(1′)	170.5(6)
C(3)—Cu(1)—Mo(1)''	132.9(2)	Cu(1′)—C(1′)—O(1′)	114.7(5)
C(3)—Cu(1)—C(1)''	103.6(3)	Mo(1′)—C(2′)—Cu(1′)	72.9(2)
C(3)—Cu(1)—C(2)''	99.1(2)	Mo(1′)—C(2′)—O(2′)	174.1(6)
C(3)—Cu(1)—C(3)''	180	Cu(1′)—C(2′)—O(2′)	113.0(5)
Mo(1′)—Cu(1′)—C(1′)	46.6(2)	Mo(1′)—C(3′)—Cu(1′)	74.4(3)
Mo(1′)—Cu(1′)—C(2′)	46.3(2)	Mo(1′)—C(3′)—O(3′)	171.5(6)
Mo(1′)—Cu(1′)—C(3′)	46.6(2)	Cu(1′)—C(3′)—O(3′)	114.1(5)

[a]'' and * denote the symmetry operations: $1-x$, $1-y$, $1-z$, and $-x,-y,-z$.

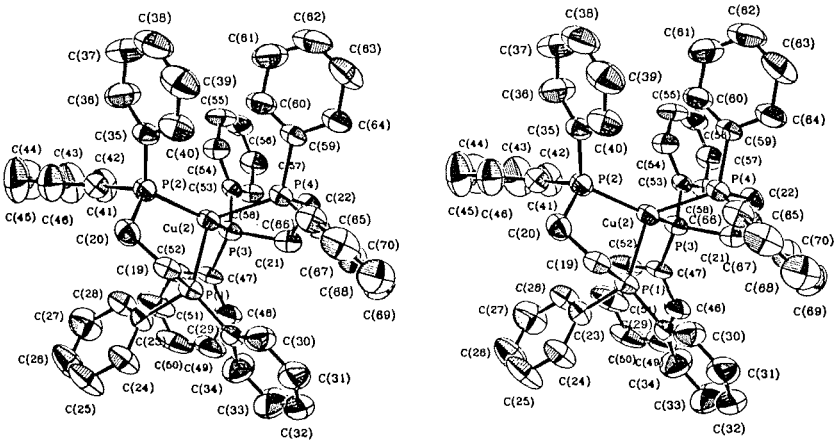

FIG. 1. Stereoscopic view of the $(Ph_2PCH_2CH_2PPh_2)_2Cu^+$ cation; 50% probability thermal ellipsoids are shown. Hydrogen atoms have been omitted for clarity.

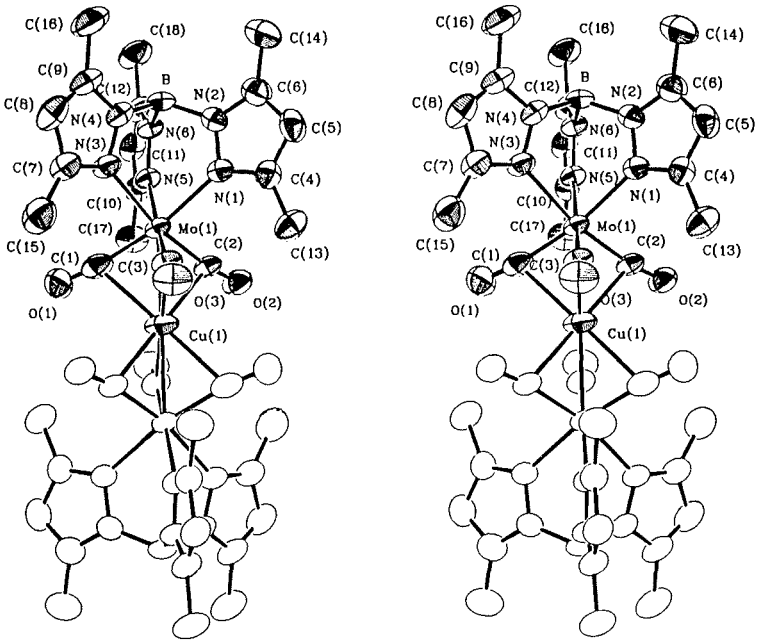

FIG. 2. Stereoscopic view of one of the two independent $[(HBpz''_3)Mo(CO)_3]_2Cu^-$ anions; 50% probability thermal ellipsoids are shown. Hydrogen atoms have been omitted for clarity.

Acknowledgments

We thank the Natural Sciences and Engineering Research Council of Canada for financial support and the University of British Columbia Computing Centre for assistance.

1. G. A. BANTA, B. M. LOUIE, E. C. ONYIRIUKA, S. J. RETTIG, and A. STORR. Can. J. Chem. **64**, 373 (1986).
2. Y.-Y. LIU, A. MAR, S. J. RETTIG, A. STORR, and J. TROTTER. Can. J. Chem. In press.
3. L. CARLTON, W. E. LINDSELL, K. J. MCCULLOUGH, and P. N. PRESTON. J. Chem. Soc. Dalton Trans. 1963 (1984).
4. S. TROFIMENKO. Prog. Inorg. Chem. **34**, 115 (1986).
5. K. R. BREAKELL, S. J. RETTIG, D. L. SINGBEIL, A. STORR, and J. TROTTER. Can. J. Chem. **56**, 2099 (1978).
6. K. R. BREAKELL, S. J. RETTIG, A. STORR, and J. TROTTER. Can. J. Chem. **57**, 139 (1979).
7. B. M. LOUIE, S. J. RETTIG, A. STORR, and J. TROTTER. Can. J. Chem. **62**, 633 (1984).
8. International tables for X-ray crystallography. Vol. IV. Kynoch press, Birmingham. 1974. pp. 99–102 and 149.
9. E. C. ONYIRIUKA, S. J. RETTIG, and A. STORR. Can. J. Chem. **64**, 321 (1986).
10. O. M. ABU SALAH, M. I. BRUCE, P. J. LOHMEYER, C. L. RASTON, B. W. SKELTON, and A. H. WHITE. J. Chem. Soc. Dalton Trans. 962 (1980).
11. C. P. HORWITZ and D. F. SHRIVER. Adv. Organomet. Chem. **23**, 219 (1984).
12. G. DOYLE, K. A. ERIKSEN and D. VAN ENGEN. Organometallics, **4**, 2201 (1985).

Can. J. Chem. Downloaded from www.nrcresearchpress.com by 112.217.228.212 on 09/07/12
For personal use only.

Transformation of resin sandaracopimaric acid into androstane analogs

FRANCISCO BERMEJO GONZALEZ, MARAVILLAS BORDELL MARTIN, AND ALFONSO FERNANDEZ MATEOS[1]
Departamento de Química Orgánica, Facultad de Químicas, Pza. de los Caídos 1–5, 37008 Salamanca, Spain

Received February 25, 1988

FRANCISCO BERMEJO GONZALEZ, MARAVILLAS BORDELL MARTIN, and ALFONSO FERNANDEZ MATEOS. Can. J. Chem. **66**, 2200 (1988).

Preparation of the α,β-unsaturated 15-ketosteroid **13** by acid-promoted cyclization of the pimarane diterpene β-hydroxyacid **5** is described.

FRANCISCO BERMEJO GONZALEZ, MARAVILLAS BORDELL MARTIN et ALFONSO FERNANDEZ MATEOS. Can. J. Chem. **66**, 2200 (1988).

La cyclisation, catalysée par les acides, du β-hydroxyacide **5**, possédant le squelette pimarane, conduit à la cétone stéroïdique α,β-insaturée **13**.

[Traduit par la revue]

Can. J. Chem. Downloaded from www.nrcresearchpress.com by 196.1.178.254 on 09/07/12
For personal use only.

Introduction

The transformation of resin acids and their derivatives into biologically active steroid intermediates has attracted the attention of several research groups over the past three decades (1).

Although much of the attention has been focused on the transformation of diterpene derivatives with a podocarpane (2) and abietane (3) type of skeleton, several recent contributions have led to the conversion of pimaradienic diterpenes into androstane derivatives by acid-catalyzed cyclization (4), intramolecular carbon–hydrogen insertion (5), and radical cyclization (6) processes.

Since the closure of acylium and carbonium ions from 4,5- and 5,6-unsaturated acids (7), aldehydes (8), and alcohols (9) are well-known reactions, we envisaged that the selective functionalization of the vinyl portion of sandaracopimaric acid derivatives would lead to substrates that could undergo acid-promoted cyclizations.

In the present work we describe the preparation of several of these substrates (**3**, **4**, **5**, **6**, **7**, and **10**) and the results obtained under acid-promoted cyclization conditions.

Results and discussion

(a) Preparation of the substrates

The methyl ketone **2** was prepared by a previously described procedure (10): oxymercuriation of methyl sandaracopimarate **1** followed by $NaBH_4$ reduction and further Jones oxidation led to **2** (62%, from **1**).

Treatment of **2** with vinyl magnesium bromide in refluxing THF led to a mixture of epimeric allylic alcohols **3** (74%) (Scheme 1), according to the evidence obtained from the ^1H nmr spectrum.

Reformatsky reaction of **2** with ethyl bromoacetate under standard conditions (11) led to a mixture of epimeric hydroxyesters **4**, with 76% isolated yield (flash chromatography).

Selective saponification of **4** with aqueous KOH in refluxing ethanol yielded a mixture of β-hydroxy acids **5** (83%), whose structure is based on ir and ^1H nmr evidence.

Treatment of **4** with $POCl_3$ in pyridine at 100°c afforded the diester **6** (64%). The presence of an α,β-unsaturated ester **6** (Fig. 1) is substantiated by the uv spectrum (CH_3OH); λ_{max}: 220 nm (log ε: 4.1). Furthermore, the ir and ^1H nmr spectra corroborated the structure corresponding to **6**. The δ value obtained for the methyl on the side chain (δ 2.02 ppm) confirms the *E* configuration of the double bond according to accurate nmr studies (12).

Selective saponification of **6** with 2 N methanolic KOH at room temperature yielded the α,β-unsaturated acid **7** (81%) whose structure was established from the uv, ir, and ^1H nmr spectra.

Preparation of the α,β-unsaturated aldehyde **10** (Fig. 1) from diester **6** was accomplished by a three-step sequence: (*i*) Reduction of **6** with $LiAlH_4$ in refluxing ether yielded diol **8** (93%). (*ii*) MnO_2 oxidation of the allylic alcohol **8** led to hydroxy aldehyde **9** (92%). The uv, ir, and ^1H nmr spectra confirm the proposed structure for the oxidation product. (*iii*) Treatment of **9** with acetic anhydride in pyridine led to the corresponding acetate **10** (82%) whose structure is apparent from the spectroscopic data.

(b) Cyclization attempts

The ring-forming reaction of a 5,6-unsaturated cation or an acylium ion in a pimarane diterpene derivative requires that the side chain have sufficient freedom of motion to attain the necessary transition state. The nucleophilic attack of the double bond on the electrophilic center must achieve the required trajectory to form the final bond (8, 13).

We found that the presence of a 2,3 double bond on the side chain led to failure in the ring-forming reaction, even when the existence of a *cis-trans* isomerization of the type shown in Scheme 2 could make the *E* configuration of the double bond (substrates **3**, **6**, **7**, and **10**) completely irrelevant.[2]

Treatment of allylic alcohol **3** with formic acid at room temperature led to the isolation of the rearranged formate **11** in quantitative yields. Increases in the reaction temperature did not change our first result.

Attempts to cyclize **6** with $ZnBr_2$, either in THF or in benzene at room temperature and under refluxing conditions, led to recovery of the starting material. The same result was obtained when the α,β-unsaturated acid **7** was treated with polyphosphoric acid in sulfolane under the cyclization conditions described by Nakatani and Kawashima (15).

Charge delocalization of the cationic cyclization intermediate

[1]Author to whom correspondence may be addressed.

[2]Presumably, the acid-catalyzed interconversion of the *trans* and *cis* derivatives **A** and **C** is faster than the cyclization because of the charge delocalization possible in the allylic cation **B**, which gives this intermediate a sufficiently long lifetime to permit *cis–trans* isomerization (14).

Printed in Canada / Imprimé au Canada

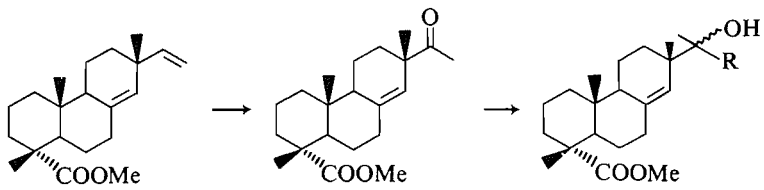

1 **2** **3** R = $CH{=}CH_2$; **4** R = CH_2COOEt; **5** R = CH_2COOH

SCHEME 1

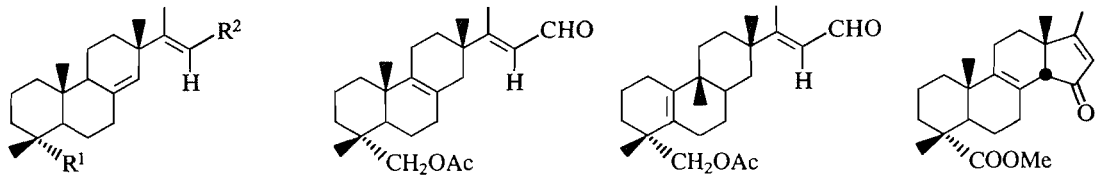

6 R^1 = COOMe R^2 = COOEt
7 R^1 = COOMe R^2 = COOH
8 R^1 = CH_2OH R^2 = CH_2OH
9 R^1 = CH_2OH R^2 = CHO
10 R^1 = CH_2OAc R^2 = CHO
11 R^1 = COOMe R^2 = CH_2OCOH

12*a* **12***b* **13**

FIG. 1

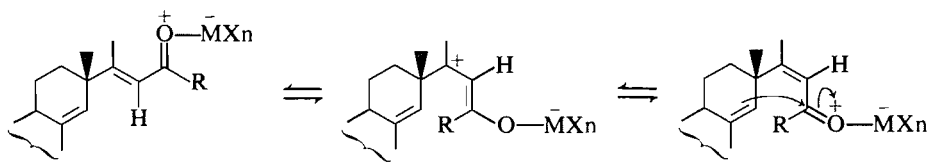

A **B** **C**

SCHEME 2

(Scheme 2) and the decreased cationic character due to the positive inductive effect of the ethoxy group might account for our discouraging results.

Treatment of the acetoxy aldehyde **10** with $SnCl_4$ (8) in either CH_3NO_2 or CH_2Cl_2 at room temperature led to recovery of starting material. An increase in the reaction temperature (refluxing CH_2Cl_2) yielded a rearranged aldehyde **12** whose structure is currently undetermined since the position of the internal double bond ($\Delta^{8,9}$ in **12***a*, or $\Delta^{5,10}$ in **12***b*) requires further spectroscopic evidence.

The above disappointing results prompted us to try the cyclization on a substrate with a completely saturated side chain. Presumably, the unsaturated character of the side chain in pimarane derivatives such as **6**, **7**, and **10** restricts the relative motion of the terminal carbonium ion (or equivalent) for undergoing efficient overlap with the π system of the internal double bond.

Treatment of the β-hydroxy acid **5** with *p*-toluenesulfonic acid in acetic anhydride at room temperature for 20 h gave **13** (76%), mp 128–130°C (hexane); $C_{23}H_{32}O_3$ (M^+ 356).

The location of an α,β-unsaturated ketone in **13** follows from uv spectroscopic evidence (CH_3OH): λ_{max}: 231 nm (log ε: 4.03); ir (ν_{max}: 1680, 1630 cm^{-1}). Inspection of the ^1H nmr spectrum reveals the presence of an olefinic proton (δ 5.70 (s,1H)) coupled to a methyl on the double bond (δ 2.00 (d, J = 1.5 Hz,3H)).

The optical rotatory dispersion (ord) curve of **13** showed a negative Cotton effect ($\Delta\varepsilon_{225}$: −48.13), which, according to Djerassi and co-workers (16), could correspond to an α,β-unsaturated 15-ketosteroid with a 14β-H configuration. However, according to the same authors the Cotton effect shown by this type of chromophore is highly dependent on the configuration of the adjacent rings. The 2D nOe (bidimensional nuclear Overhauser enhancement) technique was used for assigning the 14-H configuration. Thus, irradiation at δ 1.15 (13-Me) affected the signal at δ 2.39 (14-H), showing the spatial proximity of the 13-Me to the 14-H. This observation revealed that 13-Me and 14-H are oriented on the same plane.

We believe that the mechanism of formation of **13** involves the mixed anhydride, which collapses to an acylium

Can. J. Chem. Downloaded from www.nrcresearchpress.com by 196.1.178.254 on 09/07/12
For personal use only.

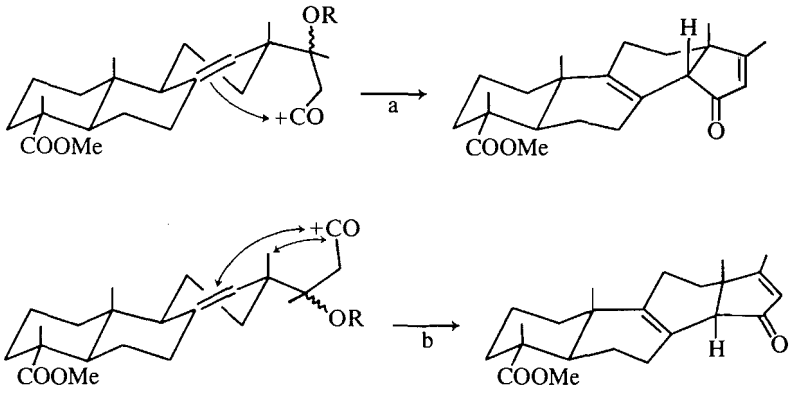

SCHEME 3

intermediate by acid catalysis. Ring closure takes place and dehydration occurs, giving **13** as the final product.

Nucleophilic attack at the α-face (pathway a, Scheme 3) should be favoured because attack at the β-side would have to overcome the strain due to the 1,3-diaxial interaction between the C-18 methyl and the acylium portion of the molecule (pathway b).

Experimental

Organic extracts were dried with commercially dried Na_2SO_4 and evaporated under reduced pressure below 40°C. Melting points were determined on a Kofler hot-stage apparatus. Optical rotations were determined on a digital Perkin Elmer 241 polarimeter in a 1-dm cell. The ^1H nmr spectra were recorded on a Hitachi Perkin Elmer R-24 60-MHz spectrometer and on a Bruker WP-200-SY spectrometer operating at 200 MHz. Nuclear Overhauser enhancements (nOe's) were obtained as described previously. The ir spectra were determined on a Beckman 33-IR spectrophotometer as indicated in each case. The uv absorptions were measured on a digital Varian 8-654 spectrophotometer. Optical rotatory dispersion curves were measured on a Jobin–Ybon Dichrograph III. Mass spectra were measured on a V.G. TS-250 apparatus. Microanalyses were performed using a Carlo Erba 1106 elemental analyser. All compounds discussed in this paper were obtained in a chromatographically homogeneous state.

Methyl 15-ethenyl-15-hydroxy-8(14)-isopimar-en-18-oate (3)

A solution of vinyl bromide (1 mL, 14.3 mmol) in dry THF (2 mL) was slowly added under nitrogen to a 100-mL flask containing Mg turnings (243 mg, 10 mmol) and freshly distilled THF (3 mL). Addition proceeded with a gentle reflux of the reaction mixture and, at the end of the addition, temperature was maintained at 60°C for 30 min. The reaction mixture was allowed to cool to 0°C and a solution of **2** (500 mg, 1.5 mmol) in freshly distilled THF (3 mL) was added. The reaction was stirred overnight. Following this an aqueous saturated NH_4Cl solution (5 mL) was added and the reaction mixture was extracted with ethyl acetate. The combined organic layers were washed with brine, dried (Na_2SO_4), filtered, and evaporated to afford crude material (500 mg). Partition of the crude by silica gel chromatography afforded **3** (400 mg, 74%), eluted with hexane-ether (8:2) as a colorless gum; $[\alpha]_D^{20}$ +24.3° (*c* 2.72, $CHCl_3$); ν_{max} (film): 3500, 1740, 940, 915 cm^{-1}; ^1H nmr (60 MHz, $CDCl_3$) δ : 0.80 (s, 3H), 1.00 (s, 3H), 1.20 (s, 6H), 3.60 (s, 3H); ABX system: 4.96 (dd, J_1 = 6 Hz, J_2 = 3 Hz, 1H), 5.18 (dd, J_1 = 13 Hz, J_2 = 3 Hz, 1H), 6.00 (dd, J_1 = Hz, J_2 = 6 Hz, 1H), 5.40 (s, 1H) ppm. *Anal.* calcd. for $C_{23}H_{36}O_3$: C 76.66 H 10.00; found: C 76.81, H 10.06.

Methyl 15-(ethoxycarbonyl)methyl-15-hydroxy-8(14)-en-18-isopimarate (4)

A solution of **2** (19 g, 5.7 mmol) in a benzene-ether (1:1) mixture (20 mL) and ethyl bromoacetate (1.7 mL, 15.3 mmol) was added dropwise, with stirring and under nitrogen, to a gently refluxing suspension of activated Zn powder (4.1 g, 63 mmol) in a benzene–ether (1:1) mixture (43 mL) with iodine. Stirring was continued for 5 h. The mixture was allowed to cool to room temperature and 10% H_2SO_4 (6 mL) was added. The Zn was decanted and the two layers separated. The aqueous layer was washed with ether, and the combined organic layers were washed with $NaHCO_3$ (5%) and brine, dried (Na_2SO_4), filtered, and evaporated to afford crude product (2.2 g). Chromatography of the crude on silica gel (30 g) afforded **4** (1.8 g, 70%), eluted with hexane–ether (90:10); ν_{max} (film): 3000, 1730, 1260 cm^{-1}; ^1H nmr ($CDCl_3$, 60 Mhz) δ :0.80 (s, 3H), 1.00 (s, 3H), 1.12 (s, 3H), 1.15 (s, 3H), 1.23 (t, J = 7 Hz, 3H), 3.56 (s, 3H), 4.18 (q, J = 7 Hz, 2H), 5.45 (s, 1H) ppm. *Anal.* calcd. for $C_{25}H_{40}O_5$: C 71.42, H 9.52; found: C 71.63, H 9.56.

Methyl 15-carboxymethyl-15-hydroxy-8(14)-en-18-isopimarate (5)

A stirred mixture of **4** (1.8 g, 4.3 mmol), KOH (0.5 g, 9.2 mmol), and H_2O (2 mL) was refluxed under nitrogen for 1 h. The reaction mixture was allowed to cool to room temperature and evaporated to dryness. The residue was dissolved in water, acidified with 4 N HCl, and extracted with ether. The extract was dried (Na_2SO_4), filtered, and evaporated to afford **5** (1.5 g, 90%); ν_{max} (film): 3250, 1715, 1695, 1240 cm^{-1}; ^1H nmr ($CDCl_3$, 60 MHz) δ : 0.80 (s, 3H), 1.00 (s, 3H), 1.20 (s, 3H), 1.25 (s, 3H), 3,60 (s, sH), and 5.40 (s, 1H) ppm.

Methyl 15-(ethoxycarbonyl)methylidenyl-8(14)-en-18-isopimarate (6)

Phosphorus oxychloride (0.2 mL, 2.14 mmol was added to a stirred solution of **4** (330 mg, 0.78 mmol) in dry pyridine (1 mL) at 0°C. The mixture was kept at room temperature for 1 h and then heated at 100°C for 1 h. The mixture was allowed to cool to room temperature and extracted with ether. The combined organic layers were washed with 2 N HCl, $NaHCO_3$ (5%) and brine, dried (Na_2SO_4), filtered, and evaporated to afford **6** (230 mg, 64%); $[\alpha]_D^{20}$ −10.5° (*c* 2.28, $CHCl_3$); ν_{max} (film): 1735, 1635, 860 cm^{-1}; ^1H nmr (60 MHz, CCl_4) δ : 0.85 (s, 3H), 1.12 (s, 3H), 1.15 (s, 3H), 1.23 (t, J = 7 Hz, 3H), 2.02 (s, 3H), 3.55 (s, 3H), 4.00 (q, J = 7 Hz, 2H), 5.20 (s, 1H), 5.50 (s, 1H) ppm. *Anal.* calcd. for $C_{25}H_{38}O_4$: C 74.63, H 9.45; found: C 74.69, H 9.50.

Methyl 15-carboxymethylidenyl-8(14)-en-18-isopimarate (7)

A 2 N methanolic solution (2 mL) was added to a stirred solution of **6** (92 mg, 0.25 mmol) in MeOH (2 mL) at room temperature. After 18 h, the MeOH was evaporated and the residue was dissolved in water. The aqueous solution was acidified and extracted with ether. The extract was washed with brine, dried (Na_2SO_4), filtered, and evaporated to afford **7** (77 mg, 80%); ν_{max} (film): 3500–3000 (br), 1730, 1690, 870 cm^{-1}; ^1H nmr (60 MHz, $CDCl_3$) δ : 0.85 (s, 3H), 1.15 (s, 3H), 1.20 (s, 3H), 2.10 (s, 3H), 3.65 (s, 3H), 5.25 (s, 1H), 5.75 (s, 1H) ppm. *Anal.* calcd. for $C_{23}H_{34}O_4$: C 73.80, H 9.09; found: C 73.87, H 9.05.

15-(2'-Hydroxy)ethylidenyl-8(14)-en-isopimar-18-ol (8)

Lithium aluminium hydride (76 mg, 2 mmol) was added to a solution of **6** (400 mg, 1 mmol) in dry ether (2 mL). The mixture was stirred at room temperature for 2 h. Then, H_2O (1 mL) and aqueous NaOH (15%) (0.1 mL) were successively added. The mixture was extracted with

Can. J. Chem. Downloaded from www.nrcresearchpress.com by 196.1.178.254 on 09/07/12
For personal use only.

Can. J. Chem. Downloaded from www.nrcresearchpress.com by 196.1.178.254 on 09/07/12
For personal use only.

ether. The combined organic layers were washed with brine, dried (Na_2SO_4), filtered, and evaporated to afford **8** (330 mg, 90%); ν_{max} (film): 3350, 1050 cm^{-1}; ^1H nmr (60 MHz, $CDCl_3$) δ : 0.80 (s, 3H), 0.85 (s, 3H), 1.10 (s, 3H), 1.60 (s, 3H), 3.20 (AB system, 2H), 4.15 (d, J = 7 Hz, 2H), 5.30 (s, 1H), 5.40 (m, 1H) ppm. *Anal.* calcd. for $C_{22}H_{36}O_2$: C 79.52, H 10.84; found: C 79.59, H 10.53.

15-(2'-Oxo)ethylidenyl-8(14)-en-isopimar-18-ol (9)

Activated MnO_2 (1 g, 11.50 mmol) was added to a solution of **8** (100 mg, 0.30 mmol) in acetone (5 mL). The mixture was stirred at room temperature under nitrogen for 7 h. The solid was then filtered and washed with acetone. Distillation of the solvent of the combined organic layers afforded crude **9** (91 mg). Partition of the crude material by chromatography on silica gel afforded **9** (61 mg, 60%), eluted with hexane–ether (40:60); $[\alpha]_D^{20}$ +59.8° (*c* 3.04, $CHCl_3$); ν_{max} (film): 3400, 2780, 1680, 880, 860 cm^{-1}; ^1H nmr (60 MHz, $CDCl_3$) δ : 0.75 (s, 3H), 0.85 (s, 3H), 1.15 (s, 3H), 2.12 (s, 3H), 3.18 (AB system, 2H), 5.25 (s, 1H), 5.85 (d, J = 8 Hz, 1H), 9.95 (d, J = 8 Hz, 1H) ppm. *Anal.* calcd. for $C_{22}H_{34}O_2$: C 80.00, H 10.30; found: C 80.08, H 10.38.

Acetate of 15-(2'-oxo)ethylidenyl-8(14)-en-isopimar-18-ol (10)

A solution of **9** (180 mg, 0.54 mmol) in Ac_2O (2 mL) and pyridine (1 mL) was allowed to stand overnight at room temperature. Ice was then added and the mixture was extracted with ether. The combined organic layers were washed with 2N HCl, aqueous $NaHCO_3$ (5%) and brine, dried (Na_2SO_4), filtered, and evaporated to afford the crude material (175 mg). Partition of the crude by chromatography over silica gel gave **10** (80 mg, 39%) eluted with hexane–ether (80:20); $[\alpha]_D^{20}$ −21.1° (*c* 1.03, $CHCl_3$); ν_{max} (film): 2750, 1745, 1670, 1630, 1245, 880, 860 cm^{-1}; ^1H nmr (60 MHz, $CDCl_3$) δ : 0.85 (s, 6H), 1.15 (s, 3H), 1.98 (s, 3H), 2.05 (s, 3H), 3.68 (AB system, 2H), 5.18 (s, 1H), 5.75 (d, J = 8 Hz, 1H), 9.82 (s, 1H), ppm. *Anal.* calcd. for $C_{24}H_{36}O_3$: C 77.42, H 9.68; found: C 77.49, H 9.73.

Methyl 15-(2'-formyloxy-ethylidenyl-8(14)-isopimaren-18-oate (11)

A solution of **3** (50 mg, 0.14 mmol) in formic acid (98%) (1 mL) was stirred for 30 min at room temperature. The reaction mixture was then poured over an aqueous saturated $NaHCO_3$ solution and extracted with chloroform. The combined organic layers were washed with brine, dried (Na_2SO_4), filtered, and evaporated to afford the crude material (60 mg). Filtration of the crude fraction through a silica gel column afforded **11** (53 mg, 98%) as a colorless gum; $[\alpha]_D^{20}$ −27.5° (*c* 2.32, $CHCl_3$); ν_{max} (film): 2680, 1740, 1665 cm^{-1}; ^1H nmr (60 MHz, CCl_4) δ : 0.85 (s, 3H), 1.08 (s, 3H), 1.18 (s, 3H), 1.65 (s, 3H), 3.57 (s, 3H), 4.52 (d, J = 7 Hz, 1H), 5.15 (m, 24), 7.85 (s, 1H), ppm. *Anal.* calcd. for $C_{24}H_{36}O_4$: C 74.22, H 9.28; found: C 74.43, H 9.45.

α,β-Unsaturated aldehyde (12)

Freshly distilled stannic choride (0.2 mL, 1.7 mmol) was slowly added to a stirred solution of **10** (80 mg, 0.21 mmol) at 0°C under nitrogen. After 18 h, 1 N HCl (10 mL) was added and the reaction mixture was extracted with CH_2Cl_2. The combined organic layers were washed with 2N HCl, aqueous $NaHCO_3$ (5%) and brine, dried (Na_2SO_4), filtered, and evaporated to afford the crude material (64 mg). Partition of the crude fraction by chromatography on silica gel gave **12** (44 mg, 56%) eluted with hexane–ether (90:10); $[\alpha]_D^{20}$ +76.9° (*c* 1.1, $CHCl_3$); ν_{max} (film): 2780, 1740, 1670, 1620, 1240 cm^{-1}; ^1H nmr (60 MHz, $CDCl_3$) δ : 0.75 (s, 3H), 0.90 (s, 3H), 1.00 (s, 3H), 1.96 (s, 3H), 2.05 (s, 3H), 3.65 (AB system, 2H), 5.45 (d, J = 8 Hz, 1H), 9.85 (s, 1H), ppm. *Anal.* calcd. for $C_{24}H_{36}O_3$: C 77.42, H 9.68; found: C 77.49, H 9.73.

4 β,-17-Dimethyl-4α-methoxycarbonyl-8,16-androstadien-14 β-15-one (13)

A mixture of **5** (1.2 g, 2.9 mmol), acetic anhydride (7 mL), and *p*-toluenesulfonic acid (722 mg, 3.8 mmol) was stirred under nitrogen for 24 h. Then brine (25 mL) was added and the mixture was stirred for 1 h. The two phases were separated and the aqueous layer was extracted with ether. The combined organic layers were washed with brine, dried (Na_2SO_4), filtered, and evaporated to afford the crude product (1 g). Partition of the crude by column chromatography on silica gel gave **13** (722 mg, 73%) eluted with hexane-ether (80:20); mp 128–130°C (hexane); $[\alpha]_D^{20}$ +238.2° (*c* 1.3, $CHCl_3$); λ_{max} (film): 1740, 1710, 1640, 1260 cm^{-1}; uv (CH_3OH) λ_{max}: 210 (ε 11 500), 231 (10 700); cd (CH_3OH) $\Delta\varepsilon_{205}$: +42.8, $\Delta\varepsilon_{225}$: −48.13, $\Delta\varepsilon_{320}$: +1.20; ^1H nmr ($CDCl_3$, 200 MHz) δ : 0.96 (s, 3H), 1.15(s, 3H), 1.19 (s, 3H), 2.01 (d, J = 1.2 Hz, 3H), 2.39 (s, 1H), 3.62 (s, 3H), 5.83 (d, J = 1.2 Hz, 1H) ppm; irradiation of the signal at δ 1.15 ppm gave a 10.96% nOe at δ 2.39 ppm; ^{13}C nmr ($CDCl_3$, 200 MHz) δ: 13.96, 16.38, 17.92, 19.07,20.69, 21.16, 27.10, 30,60, 32.80, 35.02, 36.17, 37.53, 46.04, 46.87, 47.29, 51.46, 60.49, 123.76, 130.37, 140.57, 178.32, 181.02, 204.85 ppm; ms (E.I)) *m/e* (%) :356 (M^+, 58), 296 (19), 282 (23), 281 (100), 110 (18), 105 (18), 91 (20), 55 (22), 41 (43). *Anal.* calcd. for $C_{23}H_{32}O_3$: C 77.53, H 8.99; found: C 77.46, H 8.90.

1. (*a*) E. Fujita, K. Fuji, Y. Nagao, M. Node, and M. Ochiai. Bull. Inst. Chem. Res. Kyoto Univ. **43** (1965)–**62** (1984); (*b*) J. De Pascual, F. Bermejo, A. F. Mateos, F. Conde, and M. E. Romero. An. Quim. Ser. C: **79**, 447 (1983), and references cited therein.
2. (*a*) D. M. S. Wheeler and P. R. Witt. J. Org. Chem. **37**, 4211 (1972); (*b*) R. C. Cambie, W. A. Denny, T. J. Fullerton, and R. C. Hayward. Aust. J. Chem. **27**, 1317 (1974); (*c*) B. R. Davis and W. B. Watkins. Tetrahedron, **23**, 2165 (1968).
3. (*a*) A. Tahara, M. Shimagaki, M. Itoh, Y. Harigaya, and M. Onda. Chem. Pharm. Bull. (Jpn.) **23**, 3189 (1975); (*b*) H. Steindl and E. Haslinger. J. Org. Chem. **50**, 3749 (1985); (*c*) J. W. Huffman and P. G. Arapakos. J. Org. Chem. **30**, 1604 (1965); (*d*) R. C. Cambie and R. A. Franich. Aust. J. Chem. **24**, 117 (1971); (*e*) A. Tahara, M. Shimagaki, M. Itoh, Y. Harigaya, and M. Onda. Chem. Lett. 651 (1974); (*f*) T. Wirthlin, H. Wehrli, and O. Jeger. Helv. Chim. Acta, **57**, 358 (1974); (*g*) R. L. Settine and A. A. Gawish. J. Org. Chem. **48**, 2309 (1983).
4. P. Cecchereli, M. Curini, M. Tingoli, and R. Pelliciari. J. Chem. Soc. Perkin Trans. 1, 1924 (1980).
5. E. Wenkert, L. L. Davis, L. Banavara, L. Mylari, M. F. Solomon, R. R. Da Silva, S. Shulman, and R. J. Warnet. J. Org. Chem. **47**, 3242 (1982).
6. B. Arreguy San Miguel, B. Maillard, and B. Delmond. Tetrahedron Lett. 2127 (1987).
7. (*a*) P. E. Eaton and R. H. Mueller. J. Am. Chem. Soc. **94,** 1014 (1972); (*b*) M. F. Semmelhack, J. S. Foos, and S. Katz, J. Am. Chem. Soc. **95**, 7325 (1973).
8. R. C. Cookson and S. A. Smith. J. Chem. Soc. Chem. Commun. 145 (1979), and references cited therein.
9. (*a*) J. A. Brewster and H. O. Bayer. J. Org. Chem. **29**, 116 (1964); (*b*) M. El Idrissi and M. Santelli. Tetrahedron Lett. 2583 (1987).
10. (*a*) W. Herz and L. Hall Allen. J. Org. Chem. **39**, 11 (1974); (*b*) J. W. ApSimon and H. Krehm. Can. J. Chem. **47**, 2859 (1969).
11. W. E. Bachmann, W. Cole, and A. L. Wilds. J. Am. Chem. Soc. **62**, 824 (1940).
12. S. Bory, H. Fetizon, and P. Laszlo. Bull. Soc. Chim. Fr. 2310 (1963).
13. J. E. Baldwin. J. Chem. Soc. Chem. Commun. 734 (1976).
14. (*a*) H. O. House and J. K. Larson. J. Org. Chem. **33**, 448 (1968); (*b*) F. G. Baddar, M. F. El Neweihy, and R. O. Loutfy. J. Chem. Soc. (C), 620 (1970).
15. Y. Nakatani and K. Kawashima. Synthesis, 147 (1978).
16. (*a*) A. R. Van Horn and C. Djerassi. J. Am. Chem. Soc. **89**, 651 (1967); (*b*) C. Djerassi. Optical rotatory dispersion. McGraw–Hill Book Co. Inc., New York, NY. 1967; (*c*) P. Crabbe. Optical rotatory dispersion and circular dichroism in organic chemistry. Holden Day Inc., San Francisco, CA. 1965. Chap. 5.

Lithum ion complexation effects on stereochemical dynamics of 14-crown-4 ethers in solution as studied by ^{13}C nuclear magnetic resonance

G. W. BUCHANAN, R. A. KIRBY, K. BOURQUE, AND C. MORAT[1]

Ottawa–Carleton Chemistry Institute, Department of Chemistry, Carleton University, Ottawa, Ont., Canada K1S 5B6

Received December 2, 1987

G. W. BUCHANAN, R. A. KIRBY, K. BOURQUE, and C. MORAT. Can. J. Chem. **66**, 2204 (1988).

The barrier to ring inversion for the *cis–syn–cis* isomer of dicyclohexano-14-crown-4 has been determined via ^{13}C nuclear magnetic resonance coalescence temperature measurements to be 42.3 ± 0.8 kJ/mol. For the LiNCS complex of this isomer, the inversion barrier increases by ca. 5 kJ/mol. For the Li^+ complex of the *cis–anti–cis* isomer, evidence for two dynamic conformational processes in solution is presented, with Li complexation inducing an increase in the barrier to degenerate cyclohexane ring inversion similar to that found in the *cis–syn–cis* isomer. ^{13}C T_1 measurements indicate a substantial decrease in the mobilities of both isomers in the presence of Li^+ ions in solution.

G. W. BUCHANAN, R. A. KIRBY, K. BOURQUE et C. MORAT. Can. J. Chem. **66**, 2204 (1988).

Faisant appel à des mesures de températures de coalescence des bandes de la résonance magnétique nucléaire du ^{13}C, on a déterminé que la barrière à l'inversion de cycle de l'ismère *cis–syn–cis* du dicyclohexano-14-éther-4 est de 42,3 ± 0,8 kJ/mol. La formation de complexes entre cet isomère et des ions lithium (LiNCS) augmente la barrière à l'inversion par environ 5 kJ/mol. Pour le complexe entre l'ion Li^+ et l'isomère *cis–anti–cis*, on présente des données suggérant que, en solution, deux processus conformationnels dynamiques sont impliqués; on observe que la complexation avec le lithium induit une augmentation de la barrière à la dégénérescence de l'inversion du noyau cyclohexane qui est semblable à celle observée avec l'isomère *cis–syn–cis*. Des mesures de T_1 dans les spectres rmn du ^{13}C indiquent que, lorsque chacun des isomères est mis en solution, leurs mobilités diminuent d'une façon importante lorsqu'ils sont placés en présence d'ions Li^+.

[Traduit par la revue]

Introduction

A recent communication from these laboratories (1) has dealt with the nature of conformational equilibria present in solution for the *cis–anti–cis* isomer, **1**, of dicyclohexano-14-crown-4. Using 100.6-MHz ^{13}C nmr at low temperature, the existence of two unequally populated conformations was demonstrated. These conformations appear to be present in a ratio of ca. 2:1 at 173 K and are interconvertible by inversion of just one of the two

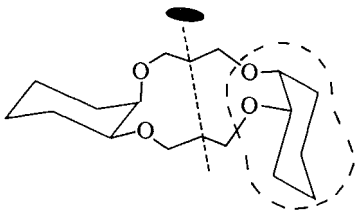

1A

$K \approx 2$

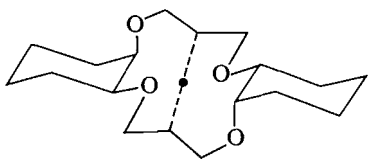

1B

cyclohexane rings present in the molecule, accompanied by a reorganization of the 14-membered ring geometry. This process is depicted above.

[1]Permanent address: LEDSS, Université scientifique, technique et médicale de Grenoble, B.P. 68, St-Martin d'Hères, France.

Presently we wish to report results regarding conformational equilibria for the previously unavailable *cis–syn–cis* isomer, **2** (below), as well as its LiNCS complex. Also, although it has not been possible to isolate a Li^+ complex of **1**, strong evidence for its existence in solution has been obtained from the T_1 measurements and low temperature spectra.

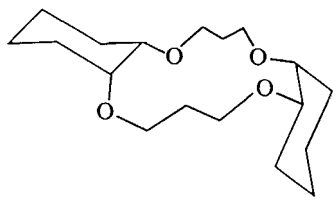

2

Results and Discussion

The structures and numbering schemes for **1** and **2** and the LiNCS complex of **2** are depicted in Fig. 1. The dispositions of the cyclohexane rings in each case are consistent with the recently obtained X-ray data (2).

Chemical shifts and coalescence data

These data are collected in Table 1. The chemical shift assignments at 293 K are made as a result of several considerations. Initially distinction between resonances for CH vs. CH_2 carbons bearing oxygen is made on the basis of the APT experiment (3). The resonance for C-4,15 is evident from its low relative intensity in nOe suppressed experiments, while distinction between C-8,11,19,22 and C-9,10,20,21 can be made on the basis of the known β-deshielding substituent effect of oxygen (4) on cyclohexyl ring carbon resonances.

The conformational equilibrium for free **1** in solution has been studied previously (1). The preferred conformation, **1*B***, (K ~ 2), at low temperatue appears to be the form with a centre of symmetry, which is also the structure found in the crystal (2).

Can. J. Chem. Downloaded from www.nrcresearchpress.com by 196.1.178.254 on 09/07/12
For personal use only.

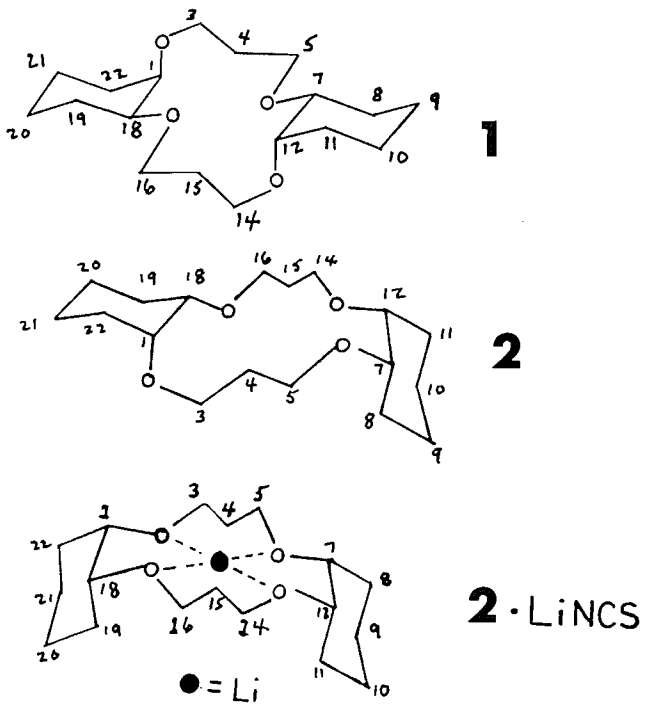

FIG. 1. Structures and numbering schemes.

All attempts to isolate LiNCS and $LiClO_4$ complexes of **1** have failed; however, there is strong evidence for its existence in solution. The 75.4-MHz spectra of a 1:1 mixture of **1** and LiNCS in CD_2Cl_2 as a function of temperature are presented in Fig. 2. At the low temperature limit of 165 K, eight resonances of approximately equal intensity are observed in the 64–80 ppm range for the oxygenated carbons. This suggests that there is only one conformation present in which no elements of symmetry are present. In the 18–30 ppm region for non-oxygenated carbon, one would expect to observe ten ^{13}C resonances in the low temperature limit for the case of a single asymmetric conformation. In fact, eight signals appear of which two are double intensity, specifically those at 16.87 and 21.98 ppm.

A detailed analysis of the temperature dependence of the spectra indicates that there exist two dynamic conformational processes, which have substantially different free energies of activation. To aid in the analysis of the spectra, the changes with temperature are depicted in a simplified way in Fig. 3. The five-line ^{13}C spectrum at room temperature is represented in the figure by the designation A, B, C, D and E. The A line represents the carbinyl carbons bearing oxygen i.e., C-1, 7, 12, and 18 appears at δ_C 77.17 and are depicted by B. The C-4, 15 carbons appear at δ_C 28.99 and are represented by C in the line spectra. Similarly the D line at 24.91 ppm depicts C-8, 11, 19, 22 while the most shielded resonance at δ_C 20.99 is represented by E and arises from the C-9, 10, 20, and 21 sites.

As the temperature is lowered gradually the lines A, B, D, and E each split into equal intensity components represented by A_1, A_2, B_1, B_2, D_1, D_2, E_1, and E_2 respectively. These four coalescence phenomena provide four independent measurements of the free energy of activation for this degenerate process. The coalescence temperatures and chemical shift differences are listed in Table 1. From these data the average value for $\Delta Gs5^{\ddagger}$ is calculated to be 47.2 ± 0.5 kJ/mol. We attribute this process to the degenerate double cyclohexane ring inversion since the observed shift differences at individual carbon sites are very similar to those found for cyclohexane ring inversion in related molecules (5). For example, the chemical shift difference for the carbinyl carbons at 230 K is 4.2 ppm (i.e., $A_1 - A_2$), which is consistent with expectations for carbons bearing axial and equatorial oxygenated substituents, the carbon bearing the axial function being the more shielded. The cyclohexyl carbons, which are γ to the oxygen atoms, also show large chemical shift differences at 230 K, i.e., $E_1 - E_2 = 5.06$ ppm. The more shielded resonance can be assigned to C-10, 21, which bear *gauche*-γ relationships to the axial oxygen atoms O-13 and O-2 respectively (1). For the methylene carbons bearing oxygen, the chemical shift difference at 230 K, i.e., $B_1 - B_2$, is 2.30 ppm. In the absence of an X-ray structure, it is difficult to make unambiguous assignments for these sites. If one employs uncomplexed **1** as a model, however, one could tentatively assign the more shielded resonance to C-5, 16, i.e., the carbons bonded to equatorial oxygen (1, 2). The smallest resolvable chemical shift difference, $D_1 - D_2 = 0.96$ ppm, at 230 K occurs for the cyclohexyl ring carbons β to oxygen. Due to the number of factors contributing to the ^{13}C shift at these carbons, no attempt will be made at this point to distinguish the C-8, 19 vs. the C-11, 22 pairs.

Comparison of the barrier to degenerate ring inversion in free **1** (1) with the LiNCS complex studied herein indicates an increase of ca. 4 kJ/mol in the barrier for the complex.

Temperature reduction below 230 K causes further spectral changes until a "limiting slow exchange" spectrum is obtained at 165 K. Figure 3 depicts the additional splitting of resonances that occurs in the $A_1, A_2, B_1, B_2, C, D_1$, and D_2 lines respectively. From the coalescence data in Table 1, $\Delta G^{\ddagger}$ for this second process can be calculated to be 39.6 ± 1.4 kJ/mol. The magnitude of this barrier is ca. 4 kJ/mol lower than that found for cyclohexane inversion in simple disubstituted cyclohexanes (5). Hence it is tempting to suggest that this second barrier represents the free energy of activation for 14-membered ring conformational change, which is taking place after the cyclohexanes are stereochemically "locked" on the nmr time scale. Support for this hypothesis comes from the lack of further splitting of the C-9, 10, 20, 21 lines below 230 K. Since these carbons are the most remote from the 14-membered ring, it is reasonable to expect that they would be least affected by stereochemical changes in that region of the molecule. Interestingly, the C-4, 15 site, whose resonance at δ_C 28.99 did not decoalesce as a result of ring inversion becoming slow on the nmr time scale, is split into two equal-intensity components with a chemical shift dif-

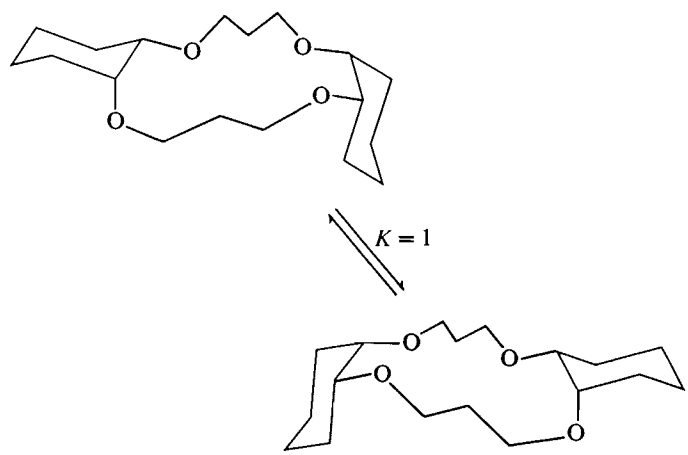

Can. J. Chem. Downloaded from www.nrcresearchpress.com by 196.1.178.254 on 09/07/12
For personal use only.

Can. J. Chem. Downloaded from www.nrcresearchpress.com by 196.1.178.254 on 09/07/12
For personal use only.

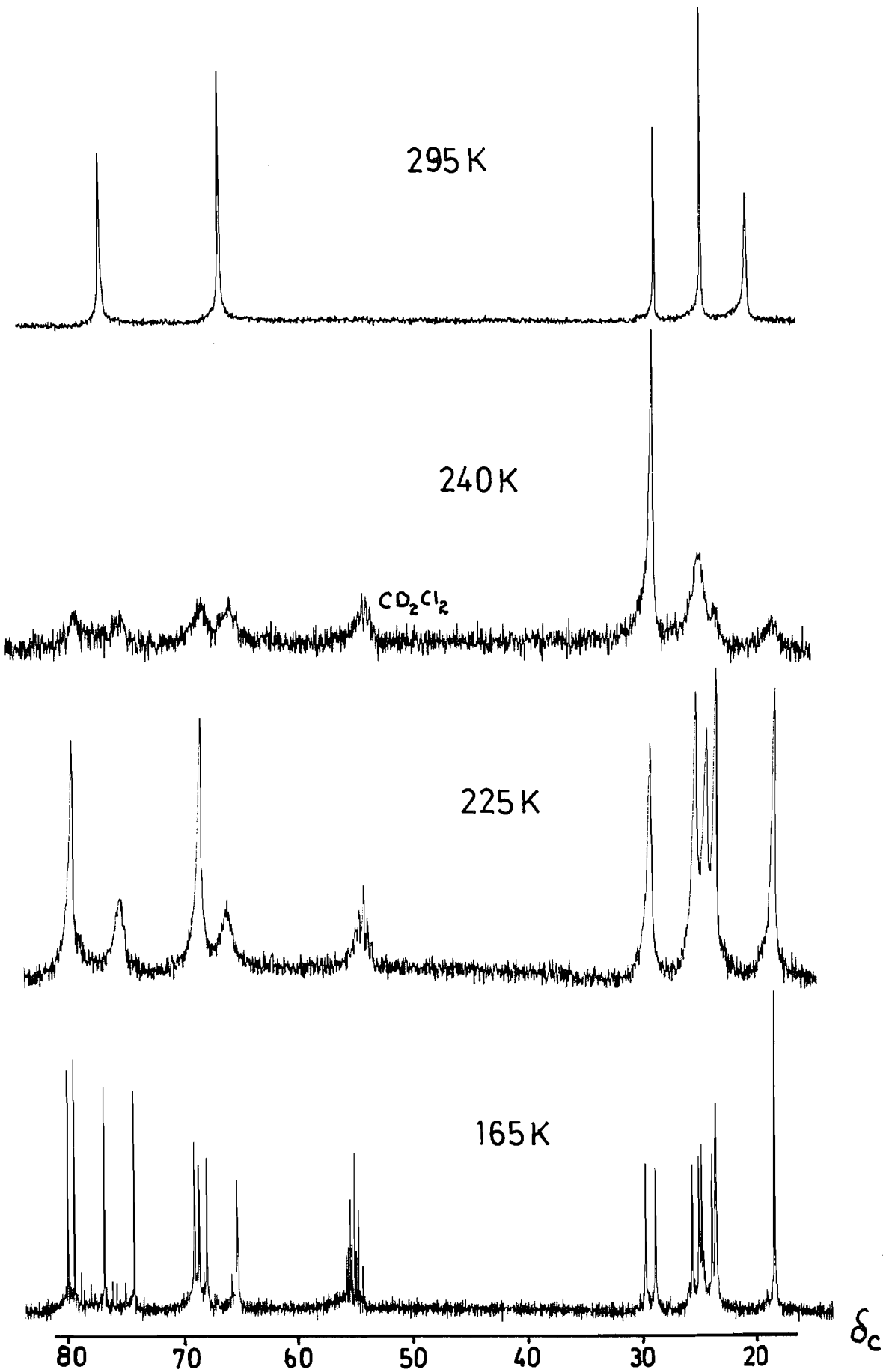

FIG. 2. The 75.5-MHz ^{13}C nmr spectra of **1** + 1 equivalent LiNCS as a function of temperature.

TABLE 1. ^{13}C chemical shifts ($\delta_C \pm 0.01$) and coalescence data

Compound	Carbon	δ_C(at 293 K)	$\Delta\nu$(Hz)[a]	T_c(K) ±1	$\Delta G^{\ddagger}$ (kJ mol^{-1})
1 + 1 equiv. LiNCS	1,7,12,18	77.17	314($A_1 - A_2$)[c]	250	47.2
	3,5,14,16	66.71	180($B_1 - B_2$)[c]	242	46.7
	4,15	28.99		Not observed	
	8,11,19,22	24.91	72($D_1 - D_2$)[c]	239	47.9
	9,10,20,21	20.99	380($E_1 - E_2$)[c]	250	46.8
					Average[b] = 47.2 ± 0.5 (Process no. 1)
	1,7,12,18		194($A_{21} - A_{22}$)[c]	215	41.1
	3,5,14,16		202($B_{21} - B_{22}$)[c]	215	40.9
	3,5,14,16		30($B_{11} - B_{12}$)[c]	183	37.6
	4,15		62($C_1 - C_2$)[c]	195	39.0
					Average[b] = 39.6 ± 1.4 no. (Process no. 2)
2	1,7,12,18	78.53	319	223	41.9
	3,5,14,16	64.85	189	218	43.6
	4,15	31.37		Not observed	
	8,11,19,22	28.41	305	223	41.9
	9,10,20,21	22.69	225	220	41.8
					Average[b] = 42.3 ± 0.8
2·LiNCS	1,7,12,18	77.53	201	238	45.8
	3,5,14,16	67.45	125	243	47.7
	4,15	29.74	32	223	46.2
	8,11,19,22	25.49	21	223	46.9
	9,10,20,21	21.58	256	253	48.3
					Average[b] = 47.0 ± 0.9

[a]At 75.5 MHz for **1** + 1 equiv. LiNCS; at 50.3 MHz for **2** and **2**·LiNCS.
[b]Uncertainties in $\Delta G^{\ddagger}$ are standard deviations.
[c]See Fig. 3.

Can. J. Chem. Downloaded from www.nrcresearchpress.com by 196.1.178.254 on 09/07/12
For personal use only.

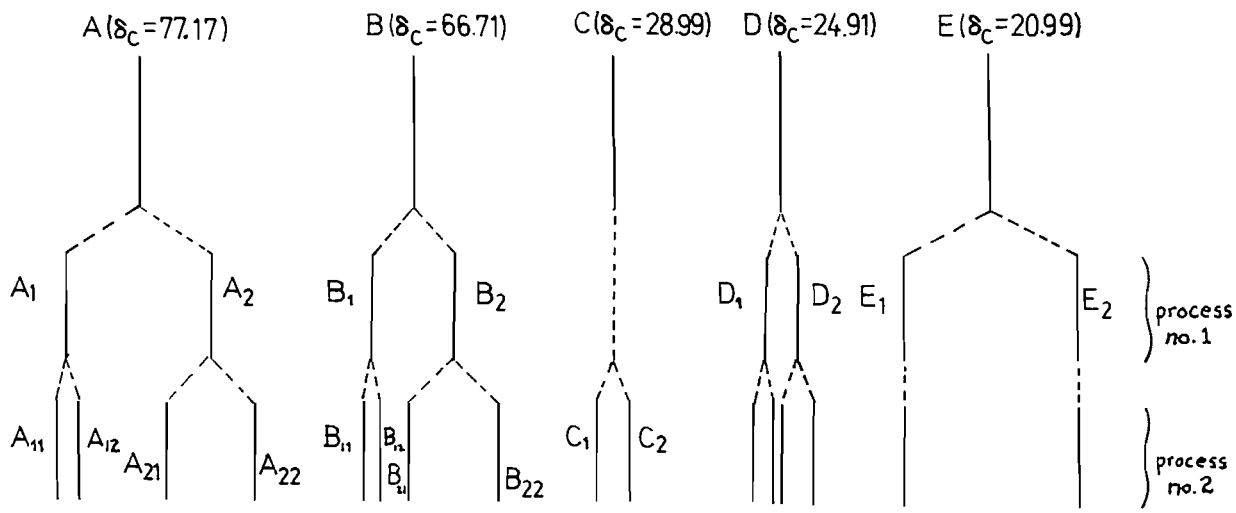

FIG. 3. Schematic analysis of the temperature dependent processes occurring in the ^{13}C nmr spectra of **1** + 1 equivalent LiNCS.

ference of ca. 1 ppm as a result of the 14-membered ring conformational process being retarded.

For **2**, reduction of the temperature produces ^{13}C nmr spectral changes consistent with a single degenerate conformational process becoming slow on the nmr time scale. The five-line spectrum at 293 K shows nine lines in the slow exchange limit, there being one position, C-4, 15, whose chemical shift differences are insufficient for resolution.

From the coalescence temperatures (T_C) and the limiting chemical shift differences ($\Delta\nu$) in Table 1, one can use the Eyring equation to calculate $\Delta G^{\ddagger}$, the free energy of activation for the process. For **2**, the average of the results for four sites is

42.3 ± 0.8 kJ/mol. This is nearly identical to values obtained for ring inversion in simple 1,2-disubstituted cyclohexanes (5). Hence we attribute the present results to degenerate ring inversion of both cyclohexane rings of **2**, accompanied by a reorganization of the 14-membered ring geometry as depicted below.

The simple degenerate conformational equilibrium for **2** is in contrast to the situation for its isomer **1** (1).

For the complex of **2** with LiNCS, the coalescence data are included in Table 1. In this case the five-line ^{13}C spectrum at 293 K becomes, in the low temperature limit, five pairs of equal-intensity doublets indicative of a single degenerate conformational process becoming slow on the nmr time scale. For each of the five exchanging pairs, the chemical shifts are sufficiently large to give five indepenent measures of the free energy of activation for the conformtional interconversion. The average value for $\Delta G^{\ddagger}$ is 47.0 ± 0.9 kJ/mol, i.e., ca 5 kJ/mol *higher* than for free **2**.

From X-ray data (2) the structure of **2**·LiNCS is as illustrated below. It is interesting to note that one of the cyclohexane rings has undergone an inversion in the complex, compared to the structure for free **2**. The four oxygens are found to be in a plane and bind to the lithium cation, which is situated 0.53 Å out of the plane of the ethereal oxygens.

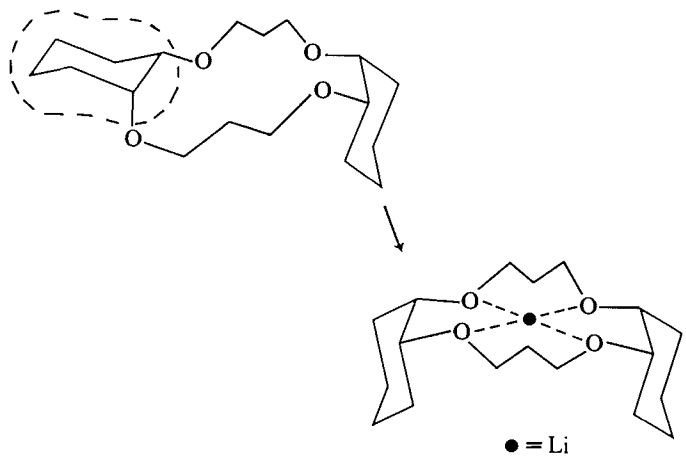

For ring inversion to occur, some disruption of this Li--O binding phenomenon must take place, and hence an increase in the free energy of activation for the degenerate double ring inversion process depicted below is intuitively reasonable.

Interestingly, the observed increase in the barrier in the present case is almost identical to the increase in the ring inversion barrier for the corresponding dicyclohexano-18-crown-6 systems upon complexation with the K^+ ion (6).

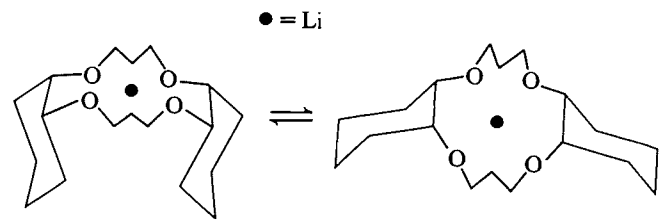

Spin-lattice relaxation times (T_1)

These data were determined by the inversion–recovery method (7) and are presented in Table 2. Measurement of nuclear Overhauser enhancements indicated that spin-lattice relaxation in these molecules is dominated by the dipole–dipole mechanism to the extent of over 90% for all carbon sites. For systems of molecular weight of less than 1000, it is reasonable to assume that the motional narrowing limit conditions apply, and hence the correlation time τ_C for the C–H vector is proportional to $1/T_1$.

TABLE 2. ^{13}C Spin-lattice relaxation times (T_1)

Compound	Site	T_1(s)
1	1,7,12,18	2.08±0.38
1 + 1 equiv. LiNCS		1.27±0.02
2		2.68±0.31
2·LiNCS		1.24±0.15
1	3,5,14,16	1.19–±0.09
1 + 1 equiv. LiNCS		0.75±0.02
2		1.60±0.08
2·LiNCS		0.75±0.04
1	4,15	1.33±0.05
1 + 1 equiv. LiNCS		0.77±0.02
2		1.27±0.08
2·LiNCS		0.88±0.06
1	8,11,19,22	1.39±0.12
1 + 1 equiv. LiNCS		0.82±0.01
2		1.45±0.06
2·LiNCS		0.88±0.02
1	9,10,20,21	1.22±0.04
1 + 1 equiv. LiNCS		0.75±0.02
2		1.39±0.05
2·LiNCS		0.73±0.10

Initially it is of interest to compare the T_1 data for uncomplexed **1** and **2**. Within the limits of uncertainty, results for the C-4, 15 and C-8, 11, 19, 22 sites are identical while those for the C-9, 10, 20, 21 sites are very nearly so. By contrast, the T_1's for the oxygenated carbons are substantially longer for **2** than for **1**. The greatest difference, ca. 34%, is found between the C-3, 5, 14, 16 sites, implying that the increase in mobility in **2** relative to **1** is most pronounced at this position. For the C-9, 10, 20, 21 carbon, the T_1 for **2** is ca. 29% longer than that of **1**. It is noteworthy that **2**, which appears to have a greater degree of segmental motion than **1** in the oxygenated portion of the molecule, is the isomer that more readily forms the LiNCS complex. Indeed X-ray data (2) indicate that one cyclohexane ring of **2** inverts its conformation upon complex formation.

In the LiNCS complex of **2** the T_1's at all sites are considerably reduced relative to the free crown ether. the most pronounced differences occur at the oxygenated carbons, however, a result that is consistent with the observed binding of the lithium by the four coplanar oxygen atoms in the complex (2).

Although we have not been able to isolate the complex of **1** with LiNCS, the T_1 data for **1** + 1 equivalent of LiNCS indicate very substantial specific interactions beteen these two species in solution. Indeed, the reductions in mobility of **1** upon addition of the LiNCS are comparable to those present in the LiNCS complex of **2** relative to free **2**.

Our present X-ray results (2) indicate that the effective 14-membered ring cavity diameter for **2** is 1.88 Å. This is too small to fit even the Li cation (effective diameter 1.18–1.52 Å (8) within the plane of the four oxygen atoms.

Experimental

(a) Spectra

The ^{13}C spectra were obtained at 50.3 MHz using a Varian XL-200 nmr spectrometer. Sample concentrations were 0.2 M in CD_2Cl_2 contained in 5 mm o.d. tubes. Routinely spectra were recorded with

Can. J. Chem. Downloaded from www.nrcresearchpress.com by 196.1.178.254 on 09/07/12
For personal use only.

complete ^1H noise decoupling. Normal conditions were as follows: sweep width = 10 kHz with 32K data points; pulse width = 7 μs (45°) and a repetition rate of 1.0 s. The number of accumulations for the low temperature spectra was typically 2000. Temperatures were calibrated using a copper–constantan thermocouple.

The ^{13}C spectra at 75.5 MHz were recorded on a Bruker MSL-300 instrument. For the low temperature experiments a sweep width of 7 kHz was employed using 8K data points. Resonances due to the solvent were eliminated via the DEPT (9) sequence using a 60° sorting pulse. The sequence was carried out assuming a J value of 140 Hz. An acquisition time of 0.6 s and a pulse delay of 2.0 s were employed. Typically, under these conditions, 400 accumulations provided adequate signal-to-noise ratios. The $\pi/2$ ^1H and ^{13}C pulses were 19 and 9.2 μs respectively.

^{13}C spin-lattice relaxation times were determined at 50.3 MHz via the inversion–recovery sequence (7) on 0.2 M solutions. Data were processed using the standard XL-200 software.

(b) Materials

Synthetic procedures for all materials employed herein have been described previously (2).

Acknowledgements

G.W.B. thanks the National Sciences and Engineering Research Council of Canada (NSERC) for continued support via operating grants. C.M. acknowledges financial aid from the NSERC France–Canada Scientific Exhange Program and the NRC Visiting Scientist Program. We thank Drs. J. A. Ripmeester and C. I. Ratcliffe for providing access to the MSL-300.

1. G. W. Buchanan and R. A. Kirby. Tetrahedron Lett. **28**, 1507 (1987).
2. G. W. Buchanan, R. A. Kirby, and J. P. Charland. J. Am. Chem. Soc. **110**, 2477 (1988).
3. S. L. Patt and J. N. Shoolery. J. Magn. Reson. **46**, 535 (1982).
4. H.-J. Schneider and V. Hoppen. Tetrahedron Lett. 579 (1974).
5. S. Wolfe and J. R. Campbell. Chem. Commun. 874 (1967).
6. G. W. Buchanan, K. Bourque, J. W. Bovenkamp. A. Rodrigue, and R. A. B. Bannard. Tetrahedron Lett. **25**, 3963 (1984).
7. R. L. Vold, J. S. Waugh, M. P. Klein, and D. E. Phelps. J. Chem. Phys. **48**, 3831 (1968).
8. R. D. Shannon. Acta Crystallogr. Sect A: Cryst. Phys. Diffr. Theor. Gen. Crystallogr. **32**, 751 (1976).
9. D. T. Pegg, D. M. Doddrell, W. M. Brooks, and M. R. Bendall. J. Magn. Reson. **44**, 32, (1981).

Can. J. Chem. Downloaded from www.nrcresearchpress.com by 196.1.178.254 on 09/07/12
For personal use only.

Ion chemistry of transition metals in hydrocarbon flames. I. Cations of Fe, Co, Ni, Cu, and Zn

QUANG TRAN, NICHOLAS S. KARELLAS, and JOHN M. GOODINGS
Department of Chemistry, York University, 4700 Keele Street, North York, Ont., Canada M3J 1P3

Received February 19, 1988

QUANG TRAN, NICHOLAS S. KARELLAS, and JOHN M. GOODINGS.. Can. J. Chem. **66**, 2210 (1988).

A fuel-rich, premixed, conical, methane–oxygen flame at 2200 K and atmospheric pressure is doped with approximately 1 ppm of the transition metals Fe, Co, Ni, Cu, and Zn. Metallic ions of these metals and their compounds formed by chemical ionization reactions with H_3O^+ are observed by sampling the flame through a nozzle into a quadrupole mass spectrometer. Concentration profiles of individual and total cations are measured as a function of distance along the flame axis, and also mass spectra at a fixed point in the burnt gas. For a given metal A, the mass spectra are dominated by the atomic ion A^+ with smaller amounts of the molecular ions AH^+, AOH^+, $A(OH)H^+$, $A(OH)_2H^+$, and ACO^+ and their hydrates. The spectra for Fe, Co, Ni, and Cu are very similar, but no ions are observed for Zn. The ion chemistry is dominated by proton transfer reactions from H_3O^+ to A and to the metallic compounds AO, AOH, and $A(OH)_2$ which exist in the flame. In addition, A^+ can be formed from the reaction of H_3O^+ with A by a charge transfer process. Also, some ions are formed by three-body association and free radical stripping reactions. The chemistry is discussed in detail to explain the relative magnitudes of the ion signals observed. In particular, when the atomic A^+ ion is dominant, its concentration can reach a superequilibrium level early in the burnt-gas region before it slowly decays downstream; the phenomenon is similar to the free radical overshoot which occurs in hydrogen flames.

QUANG TRAN, NICHOLAS S. KARELLAS et JOHN M. GOODINGS.. Can. J. Chem. **66**, 2210 (1988).

Opérant à 2200 K et à la pression atmosphérique, on a dopé une flame méthane–oxygène, conique, pré-mélangée et riche en carburant, avec environ 1 ppm des métaux de transition Fe, Co, Ni, Cu et Zn. En faisant un échantillonage de la flamme par le biais d'un spectromètre de masse quadripolaire, on a pu observer les ions métalliques de ces métaux ainsi que leurs composés qui se sont formés par des réactions d'ionisation avec le H_3O^+. On a mesuré les profils de concentration des cations individuels et totaux en fonction de la distance le long de l'axe de la flamme ainsi que les spectres de masse à un point fixe dans les gaz d'échappement. Pour un métal donné A, le spectre de masse est dominé par l'ion atomique A^+ accompagné de quantités plus faibles des ions moléculaires AH^+, AOH^+, $A(OH)H^+$, $A(OH)_2H^+$ et ACO^+ ainsi que leurs hydrates. Les spectres obtenus avec le Fe, le Co, le Ni et le Cu sont très semblables; on n'a toutefois pas observé d'ions avec le Zn. La chimie des ions est dominée par les réactions de transfert de protons de H_3O^+ vers A et vers les composés métalliques AO, AOH et $A(OH)_2$ qui existent dans la flamme. L'ion A^+ peut aussi se former par la réaction de H_3O^+ avec A par un processus de transfert de charge. En plus, quelques ions se forment par une association de trois composantes et par des réactions de dépossession de radicaux libres. On discute de cette chimie en détail afin d'expliquer les amplitudes relatives des signaux des ions. En particulier, lorsque l'ion atomique A^+ domine, sa concentration peut atteindre un niveau de super-équilibre très tôt dans les gaz d'échappement et sa concentration diminuer lentement alors qu'on évolue plus loin; le phénomène est semblable dépassement qui se produit avec les radicaux libres dans les flammes d'hydrogène.

[Traduit par la revue]

Can. J. Chem. Downloaded from www.nrcresearchpress.com by 112.217.228.212 on 09/07/12
For personal use only.

Introduction

We recently had occasion to consider the ion chemistry of alkali and alkaline earth metals in a premixed, fuel-rich, CH_4–C_2H_2–O_2 flame (1). This arose in the context of soot suppression by metallic additives involving an ionic mechanism (2, 3). We have now extended these studies to include chemical ionization (CI) processes for the first row of ten transition metals, Sc to Zn (atomic numbers 21–30). The last five including Fe, Co, Ni, Cu, and Zn are described here; the first five including Sc, Ti, V, Cr, and Mn present some different features, and are the subject of a second paper.

A premixed, fuel-rich, CH_4–O_2 flame doped with metallic additive is sampled into a mass spectrometer to ascertain what metallic cations are present and where in the flame they occur. The interest in the problem stems from the considerable variety of oxidation states known for these metals, and the bond formation and structural configurations which they may exhibit at high temperature.

Basically two mass-spectrometric flame studies involving cations of some of these transition metals have appeared in the past. In hydrogen flames, Hayhurst and Telford (4) observed ions for Cr, Mn, Fe, and Cu, and also other metals, in the course of measuring rate constants attributed to the charge transfer reaction

[1] $$H_3O^+ + A \rightarrow A^+ + H_2O + H$$

where A is the metal atom. In a CO/H_2 diffusion flame doped with benzene and containing $Fe(CO)_5$ as an impurity, Ham and McAllister (5) observed a considerable variety of iron molecular ions in addition to Fe^+. In this kind of flame having a relatively low temperature, molecular metallic ion signals are enhanced although their identification is complicated by the simultaneous observation of many C—H—O, non-metallic ions. The metallic ion chemistry is discussed in some detail.

A large and impressive body of research on organometallic ion chemistry involving transition metals in the gas phase has been published during the past few years. This work has been carried out near room temperature in many laboratories making use of ion cyclotron resonance (ICR), Fourier-transform mass spectrometry (FTMS), laser desorption/ionization (LDI), photodissociation and guided ion beams. The scope and versatility of FTMS, LDI, and photodissociation for metallic ion studies have been reviewed with excellent examples by Freiser (6). Only a small part of this work is applicable to the present flame studies since metal–carbon bond formation, except for carbonyl coordination, was not observed even when the flame is fuel-rich. Nevertheless, data obtained near room temperature for "inorganic" species are relevant involving metal–oxygen and metal–hydrogen bond formation in metallic oxides, hydroxides, hydrides, and their hydrates, both ionic and neutral. These thermodynamic data include proton affinities, bond dissociation energies, gas-phase basicities, ligand (e.g. hydrate)

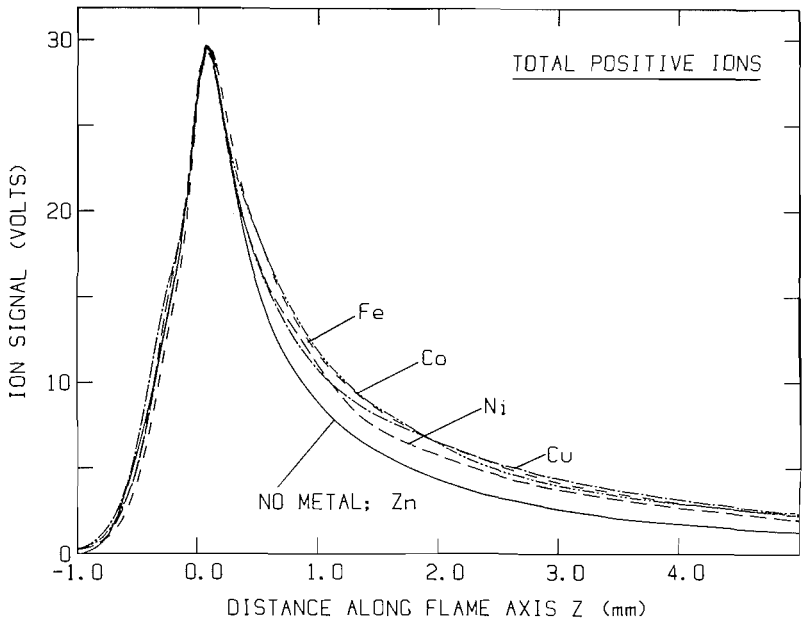

FIG. 1. Total ionization profiles along the flame axis with metal absent, and with the flame doped with equal molar concentrations (~1 ppm) of Fe, Co, Ni, Cu, and Zn. The luminous reaction zone is located upstream of $z = 0$.

binding energies, etc. They are assembled and referenced below.

Experimental

The flame employed for these studies was a premixed, laminar, CH_4–O_2 flame of fuel-rich composition (equivalence ratio $\phi = 2.15$) whose natural cation chemistry we have studied extensively in the past (7). It has a burnt-gas temperature of 2200 K and rise velocity of approxiamtely 1 m s^{-1}. Its small, conical, luminous, reaction zone (height 5 mm, base diameter 3 mm, thickness 0.3 mm) facilitates sampling along the flame axis into the mass spectrometer. The flame is stabilized at atmospheric pressure on a simple, tubular, quartz burner (2.3 mm i.d.) and surrounded by a flowing argon shield to minimize the entrainment of atmospheric air.

Transition metals (Fe, Co, Ni, Cu, and Zn) were introduced by spraying a 0.25 *M* aqueous solution of the metallic chloride into the premixed flame gas as an aerosol derived from a pneumatic atomizer (8). The atomizer was operated by part of the burner's oxygen supply. Alternatively, Fe was also introduced as $Fe(CO)_5$ vapour in a small flow of argon using a gas saturator technique. The use of flowing oxygen was not suitable since a brown deposit, presumably Fe_2O_3, was produced on the walls of the interconnecting tubing. The small argon flow, amounting to 2% of the total premixed gas, did not noticeably alter the flame characteristics. In fact, the whole range of ion signals observed with iron introduced as $FeCl_3$ aerosol or as $Fe(CO)_5$ vapour was remarkably similar. Moreover, the $Fe(CO)_5$ gas saturator technique provided a means of calibrating the tiny atomizer used with this flame. Spraying a 0.25 *M* solution introduced very nearly 1 ppm (8.7×10^{-7} mole fraction) of metal into the unburnt flame gas.

The burner was mounted on a motor-driven carriage and the flame axis was accurately aligned with the sampling orifice of the mass spectrometer. The calibrated burner drive provided spatial resolution of ±0.02 mm along the flame axis (designated *z*) for measurements of ion concentration profiles. The flame-ion mass spectrometer has been described previously in detail (7). The flame burned against a 60° conical, chromium, sampling nozzle of orifice diameter ca. 0.1 mm mounted in a water-cooled flange of the type described by Hayhurst and Telford (9). The sampled ions pass through two stages of differential pumping into a quadrupole mass filter. The mass-analyzed ions are detected with a parallel-plate Faraday collector connected to a vibrating reed electrometer having a grid-leak resistance of 10^{10} ohms.

The ion signals given in the figures have been corrected at low resolution for mass discrimination in the filter against ions of high *m/e* measured at high resolving power. The dynamic range of sensitivity of the apparatus is five orders of magnitude. A method has been described (7) involving a relatively sharp minimum in the pressure profile of the sampled gas for locating a reproducible origin ($z = 0$) in the flame (not referred to the burner). It corresponds to the downstream edge of the luminous reaction zone on the flame axis. In this way, a family of ion profiles at different mass numbers *m/e* can be accurately overlaid on the distance scale *z*. It is also an important consideration, when comparing mass spectra at a fixed point on the flame axis, to be able to return to the same point reproducibly.

Some ion signals are subject to distortion during sampling by the mass spectrometer. The flame gas is cooled in passing through the thermal boundary layer surrounding the sampling orifice, and again during the expansion to supersonic velocity which proceeds for a few orifice diameters just inside the sampling nozzle. This can affect the signal ratio of two ionic species participating in a fast ion–molecule reaction having a reaction time (relaxation time) comparable to, or less than, the sampling time (of order 1 μs). In these circumstances, the ratio will change in favour of the product ion in the exothermic direction of the reaction. These sampling effects for flames have been discussed in a series of papers by Hayhurst and co-workers of which refs. 10–12 are particularly relevant. A common case is the production of hydrate ions since a high water concentration in the burnt gas of the flame produces a high rate of hydration. Thus, Knewstubb and Sugden (13) concluded that the hydrate ions $H_3O^+.nH_2O$ ($n = 1$–4) are formed largely during sampling in contrast to H_3O^+ ($= H^+.H_2O$) which is a genuine flame ion. For metallic ions in cases where most of the hydrate is formed during sampling, the hydrate ion signal only amounts to a few percent of the parent ion signal (10). A larger ratio of hydrate/parent may indicate that the hydrate is a genuine flame ion. A notable example occurs for lithium where $Li^+.H_2O = Li(OH)H^+$ is relatively large, arising from protonation of the hydroxide which is a major metallic species in the flame (1, 10, 12). Similar cases will be encountered for the transition metal ions discussed below.

Results and discussion

Figure 1 shows total positive ion profiles measured as a function of distance along the flame axis in the absence of metal and with Fe, Co, Ni, Cu, and Zn present. The profiles are obtained with the d.c. voltages to the quadrupole mass filter

Can. J. Chem. Downloaded from www.nrcresearchpress.com by 112.217.228.212 on 09/07/12
For personal use only.

TABLE 1. Data for the first-row transition metals Fe–Zn

Metal A	Fe		Co		Ni		Cu		Zn	
				(*a*) Enthalpies of formation, $\Delta H_{f,0}^{0}$[a]						
A	413.96	(14,15)	423.082	(14,15)	427.659	(14,15)	337.15	(14,15)	130.181	(14,15)
AH	510±13	(16)	464±13	(16)			293[b]	(14)		
AO	276	(17)	310	(17)	314	(14)	306±42	(18)		
AO_2	<142±29	(19)	<142±29	(19)						
AOH	133±17	(20)								
$A(OH)_2$	−323±2	(18)								
A^+	1173.3	(14,15)	1181	(14,15)	1164.3	(14,15)	1082.6	(14,15)	1036.6	(14,15)
AH^+	1185±6	(15,21)	1206±6	(15,22)	1218±8	(15,22)	1210±13	(15,22)	1009	(15,23)
A_2O^+	<1075±29	(19)	<1079±19	(19)						
				(*b*) Bond dissociation energies, D_T^{0c}						
A—H	124±13	(24)	177±13	(24)	251±13	(24)	251±13	(24)	85.8±2.1	(24)
A—O	389±13	(20)	364±17	(25)	360	(14)	278±44	(18)		
A—OH	322±17	(20)					>406	(26)		
A^+—H	205±6	(21)	191±6	(22)	162±8	(22)	89±13	(22)	244	(14,23)
A^+—O	304±19	(20)	136±33	(27)	136±33	(27)	136±33	(27)	136±33	(27)
A^+—OH	318±19	(20)	297±13	(17)						
AO^+—H	450±20	(20)	456	(28)						
				(*c*) Proton affinities, PA_{298}^{0}[d]						
A	761±6	(15,21)	749±6	(15,22)	741±8	(15,22)	659±13	(15,22)	653	(15,23)
AO	916±21	(17,29)	916±21	(17,29)						
				(*d*) Ionization energies, IE_0^{0a}						
A	7.870	(15)	7.86	(15)	7.635	(15)	7.726	(15)	9.394	(15)
AH	7.00	(16,21)	7.69	(16,22)			9.50	(15,22)		
AO	8.71±0.10	(30)	9.0	(15)	9.5±0.3	(15)				
AO_2	9.5±0.5	(30)								
AOH	7.9±0.2	(20)								
Natural abundances of the isotopes (%)	^{54}Fe	5.82	^{59}Co	100.00	^{58}Ni	68.274	^{63}Cu	69.09	^{64}Zn	48.89
	^{56}Fe	91.66			^{60}Ni	26.095	^{65}Cu	30.91	^{66}Zn	27.81
	^{57}Fe	2.19			^{61}Ni	1.134			^{67}Zn	4.11
	^{58}Fe	0.33			^{62}Ni	3.593			^{68}Zn	18.57
					^{64}Ni	0.904			^{70}Zn	0.62
Oxidation numbers	2,3,6		2,3		2,3		1,2		2	

[a]Energy values for the gas phase are quoted in kJ mol^{-1} at 0 K unless otherwise noted.
[b]Referred to 298 K.
[c]The temperature T is sometimes unspecified but usually refers to an experimental temperature near 298 K. In general, the correction to 0 K will lie within the experimental error.
[d]Many of these values are given in the evaluated compilation of proton affinities by Lias *et al.* (29) and its supplements (in preprint form, not yet published).
[e]Quoted in eV. In a few cases, the temperature is unspecified.

switched off. The luminous flame reaction zone is located upstream of $z = 0$ (negative z). No change of the total ion signal is observed in the reaction zone, nor at the profile peak. The signal is enhanced downsteam throughout the burnt gas for Fe, Co, Ni, and Cu, but no enhancement is observed for Zn. These observations imply that the metals do not participate in any new chemi-ionization process, at least in the flame reaction zone. Certainly thermal ionization is an unlikely process since these metals, and their compounds which might exist in the flame, all have relatively high ionization energies (IE) > 7 eV. Known thermochemical data for the metals, their compounds, and associated cations are assembled in Table 1.

Downstream in the burnt gas with metal absent, the ion signal is overwhelminghly H_3O^+ and its first hydrate, $H_3O^+.H_2O$ (1, 7), most of which is formed on sampling (13). Thus, it is logical that the enhanced ion profiles observed downstream with metal present result from chemical ionization (CI) reactions of H_3O^+ with the metal or its compounds. Evidence that H_3O^+ serves as a reagent cation is given in Fig. 2 where it is shown that the H_3O^+ profile magnitude decreases when Fe, Co, Ni, or Cu are present in the flame; no change is observed for Zn, however. It is not necessary to invoke a new chemi-ionization source to explain the enhanced signal observed downstream in Fig. 1 with metal present. In the absence of metal, H_3O^+ disappears by the relatively fast, two-body, dissociative, electron–ion recombination reaction

$$[2] \quad H_3O^+ + e^- \rightarrow H + H + OH \text{ (or } H + H_2O)$$

With metal present, if H_3O^+ reacts to form metallic ions and an appreciable fraction of the product ions is the atomic ion A^+ of the metal, the A^+ ions disappear by relatively slow, three-body, atomic recombination

$$[3] \quad A^+ + e^- + M \rightarrow A + M$$

where M is a third body. For Fe, Co, Ni, and Cu, the atomic ion signals A^+ are much larger than any of those observed for molecular metallic ions. Atomic ion profiles are given in Fig. 3, whose signal magnitudes decrease in the order $Fe^+ > Co^+ > Ni^+ > Cu^+$; although the profile for the isotope of major natural abundance (see Table 1) was measured for each of Fe^+, Ni^+, and Cu^+, the signal magnitudes have been corrected to include the natural abundances of the other isotopes. For each profile,

Can. J. Chem. Downloaded from www.nrcresearchpress.com by 112.217.228.212 on 09/07/12
For personal use only.

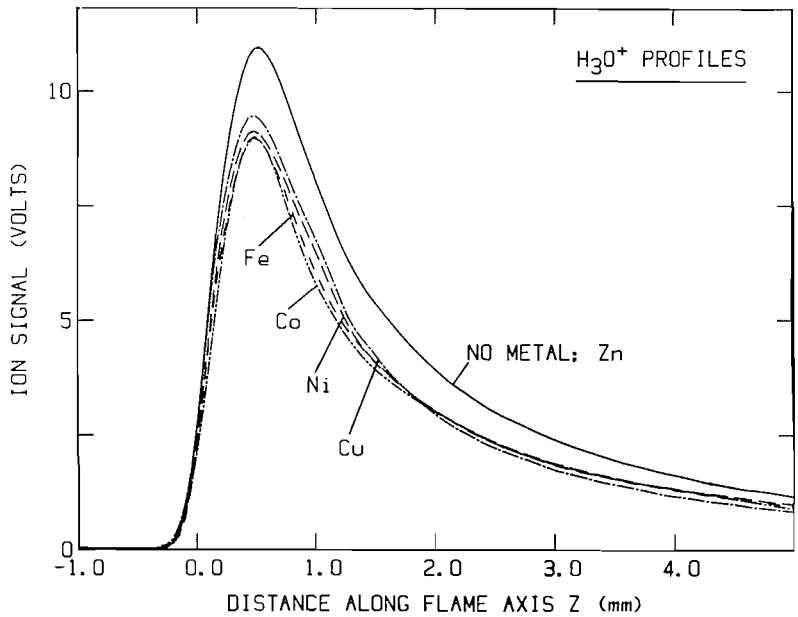

FIG. 2. Axial H_3O^+ profiles with metal absent, and with the flame doped with equal molar concentrations (~1 ppm) of Fe, Co, Ni, Cu, and Zn. The luminous reaction zone is located upstream of $z = 0$.

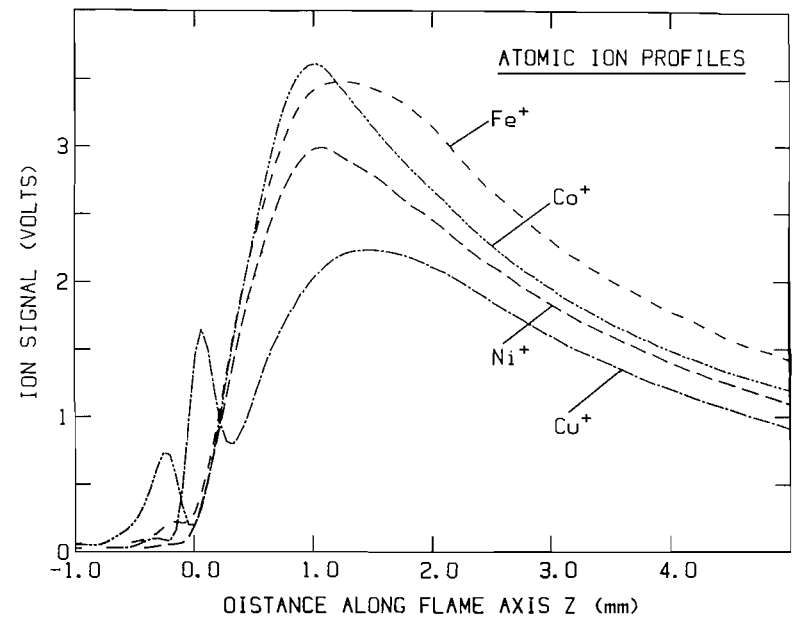

FIG. 3. Axial profiles of the dominant atomic ions A^+ observed when the flame is doped with equal molar concentrations (~1 ppm) of Fe, Co, Ni, and Cu. The luminous reaction zone is located upsteam of $z = 0$.

the small peak or peaks in and around the reaction zone near $z = 0$ stem from natural C—H—O ions at the same mass number as A^+. No signal was detected for Zn^+. Thus, the increased total ion signal observed downstream appears to result from a decreased overall loss rate rather than a new source term for ion formation.

In addition to A^+, a maximum of nine molecular ions including hydrates could be observed for Fe, Co, Ni, and Cu below 120 u. We were unable to observe any metallic ions with Zn. Profiles for the metallic ions of Co are given in Figs. 4 and 5. The profile peaks around the reaction zone near $z = 0$ stem from natural C—H—O ions at the same mass numbers as the metallic ions, but this is not the case downstream.

Cobalt offers the least ambiguity in the assignment of ions since ^{59}Co has a natural abundance of 100%. Similar sets of profiles were obtained for Fe, Ni, and Cu (not shown). Apart from profiles, mass spectra were measured at a fixed point in the flame. These are given in Fig. 6 for (*a*) Fe, (*b*) Co, (*c*) Ni, and (*d*) Cu measured at $z = 1.25$ mm downstream. From these spectra and the known isotopic abundances, the relative contributions of the various metallic ions for Fe, Ni, and Cu could be sorted out with reasonable certainty. The relative contributions for the four metals at $z = 1.25$ mm downstream are given in Table 2 as percentages of the total metallic ions present. Various structures are suggested for some of these ions in Table 2. In some cases at least, it is probable that only one isomeric structure is involved.

Can. J. Chem. Downloaded from www.nrcresearchpress.com by 112.217.228.212 on 09/07/12
For personal use only.

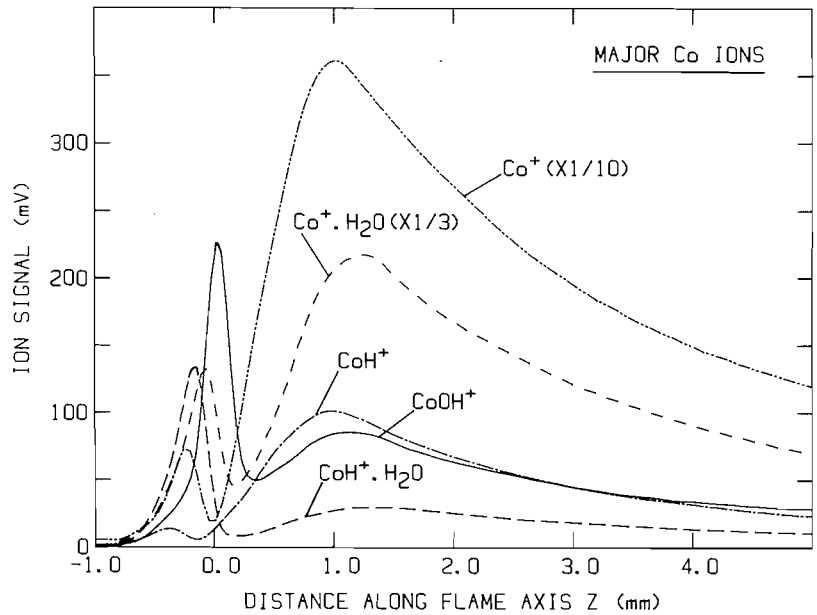

FIG. 4. Axial profiles of the large metallic ion signals obtained when the flame is doped with ~1 ppm of Co. The luminous reaction zone is located upstream of $z = 0$.

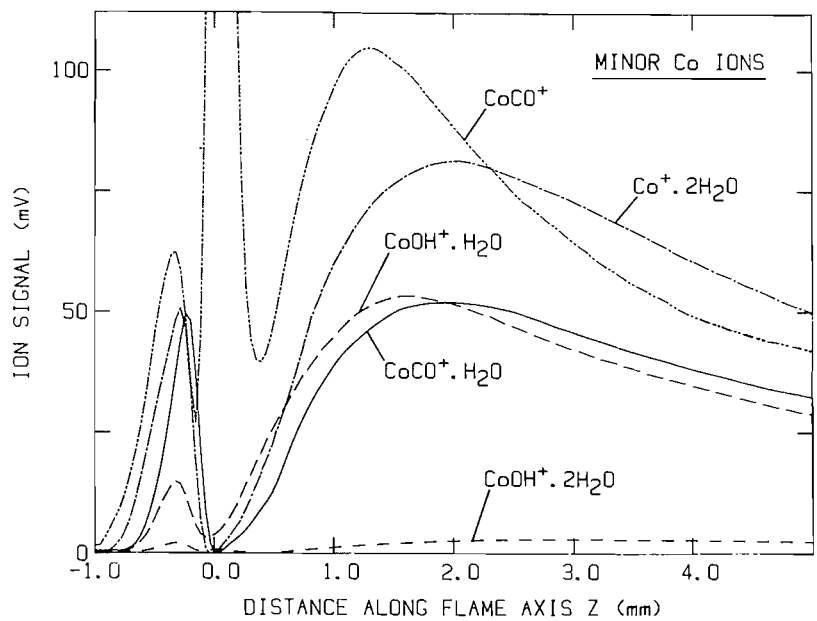

FIG. 5. Axial profiles of the small metallic ion signals obtained when the flame is doped with ~1 ppm of Co. The luminous reaction zone is located upstream of $z = 0$.

For example, the general designation AOH_2^+ refers to the same ionic structure whether formed by protonation of AOH represented by $A(OH)H^+$, or by hydration of A^+ represented by $A^+.H_2O$.

It should be emphasized that the ions shown in Fig. 6 and given in Table 2, apart from H_3O^+ and its hydrates, represent all of the ion signals observable at 1.25 mm downstream. That is, all of the signals logically correspond to metallic ions. This is in contrast to the observations of Ham and McAllister (5) using a diffusion flame doped with Fe at a considerably lower temperature where many C—H—O ions were observed in addition to metallic species. Also, their experimental conditions appear to enhance hydrate ions which may be formed largely during sampling. On the other hand, our premixed flame at higher temperature tends to enhance the atomic A^+ ion such that many of the molecular metallic ion signals are small.

Consideration is now given to the metallic neutral species which might be present in the the flame at 2200 K. Thermodynamic data are available (18, 31–33) for Fe and Co to calculate the approximate equilibrium distribution of total metal amongst the species A, AOH, AO, and $A(OH)_2$. The values are given as percentages of total metal in Table 3. However, the table may well be incomplete since gas-phase data for other possible neutrals are not known; e.g., $Fe(OH)_3$ as invoked by Ham and McAllister (5). Both Jensen and Jones (34) and Farber *et al.* (35) identified the presence of FeO, FeOH, and $Fe(OH)_2$ in addition to Fe in flames. Also for Fe (and Cr), the situation may be complicated by the presence of solid oxide particles detected

Can. J. Chem. Downloaded from www.nrcresearchpress.com by 112.217.228.212 on 09/07/12
For personal use only.

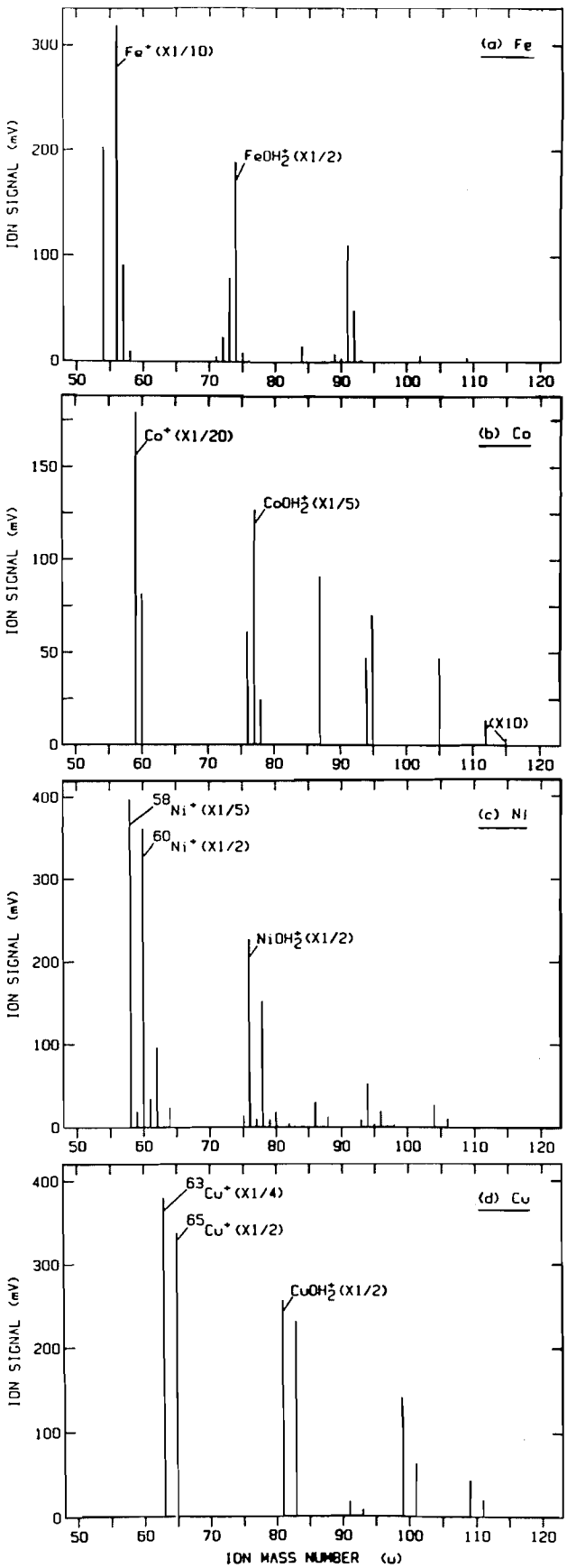

FIG. 6. Mass spectra observed at a fixed point on the flame axis at z = 1.25 mm downstream when the flame is doped with equal molar concentrations (~1 ppm) of (*a*) Fe, (*b*) Co, (*c*) Ni, and (*d*) Cu.

TABLE 2. Percentages of total metallic ions observed at z = 1.25 mm downstream

Ions of metal A	Concentration (%)			
	Fe	Co	Ni	Cu
A^+	83.2	77.2	77.2	68.0
$A^+.H_2O$ or $A(OH)H^+$	9.6	13.7	17.0	23.0
$A^+.2H_2O$ or $A(OH)H^+.H_2O$	1.4	1.5	2.0	6.3
AH^+	0.4	1.8	0.7	
$AH^+.H_2O$		0.5	0.2	
AOH^+	2.0	1.3	0.5	
$AOH^+.H_2O$ or $A(OH)_2H^+$	2.9	1.0	0.3	
ACO^+	0.4	2.0	1.1	0.8
$ACO^+.H_2O$	0.1	1.0	1.0	1.9
	100.0	100.0	100.0	100.0

TABLE 3. Percentages of metallic neutral species known to be present in the flame for equilibrium at 2200 K[a]

Neutral species	Concentration (%)	
	Fe	Co
A	24.08	91.31
AO	0.33	5.96
AOH	73.11	0.87
$A(OH)_2$	2.48	1.86
	100.00	100.00

[a]Jensen and Jones (33) attach large uncertainty factors ≥ 10 to the equilibrium constants from which these relative concentrations are calculated.

by Padley (36). For a premixed, fuel-rich, H_2—O_2—N_2 flame at 2025 K doped with Cu, Hayhurst and Telford (4) have done a statistical mechanical calculation using the data of Bulewicz and Sugden (37, 38) and Gaydon (39) which gives equilibrium concentrations for CuO, CuH, and CuOH of 3, 2, and 0.2%, respectively.

With this background, it remains to discuss the ion chemistry of these metals in hydrocarbon flames where H_3O^+ is the primary reagent cation. There are basically two reaction mechanisms of A with H_3O^+ to form A^+ involving charge transfer and proton transfer. The charge transfer reaction [1] might easily be dismissed on the grounds that it is endothermic for all five metals Fe–Zn; however, it is considered further in the discussion of signal magnitudes given below. With regard to the proton transfer mechanism, only recently has it been recognized that metallic atoms can have high proton affinities (see Table 1) such that

$$[4] \quad H_3O^+ + A \rightleftharpoons AH^+ + H_2O$$

is exothermic for Fe, Co, and Ni, and only somewhat endothermic for Cu and Zn. The observed AH^+ signals given in Table 2 for Fe, Co, and Ni are small, and an obvious route back to the atomic ion is provided by the radical reactions

$$[5a] \quad AH^+ + H \rightleftharpoons A^+ + H_2$$

$$[5b] \quad AH^+ + OH \rightleftharpoons A^+ + H_2O$$

which are exothermic for all five metals. In the equilibrium burnt gas of this fuel-rich flame, the mole fractions of H and OH amount to 3.63×10^{-3} and 3.05×10^{-4}, respectively.

Can. J. Chem. Downloaded from www.nrcresearchpress.com by 112.217.228.212 on 09/07/12
For personal use only.

Can. J. Chem. Downloaded from www.nrcresearchpress.com by 112.217.228.212 on 09/07/12
For personal use only.

Reaction [4] would seem to be an improbable CI source for Cu ions; certainly CuH^+ was not detected. Although its endothermicity is only slight, it is comparable to that for Zn for which no metallic ions of any kind could be detected. The existence of CuH in flames (37, 38) raises the possibility of the proton transfer reaction

[6] $H_3O^+ + CuH \rightarrow CuH_2^+ + H_2O$

followed by thermal decomposition of the product ion in one step

[7] $CuH_2^+ + M \rightarrow Cu^+ + H_2 + M$

or, more likely, in two steps involving dehydrogenation by radical attack

[8] $CuH_2^+ + H, OH \rightarrow CuH^+ + H_2, H_2O$

[9] $CuH^+ + H, OH \rightarrow Cu^+ + H_2, H_2O$

The energetics of the overall reaction [6] + [7]

[10] $H_3O^+ + CuH \rightarrow Cu^+ + H_2 + H_2O$

(or similarly for [6] + [8] + [9]) yield the relationship $\Delta H^0_{10} = PA^0(H_2O) - PA^0(CuH) + D^0(HCu^+—H) + D^0(Cu^+—H) - D^0(H—H)$; that is, $PA^0(H_2O) - PA^0(CuH) = 317 - D^0(HCu^+—H)$ kJ mol^{-1} at 298 K. This means that reaction [6] will be exothermic only if $D^0(HCu^+—H)$ exceeds 317 kJ mol^{-1}. Although possible, the $HCu^+—H$ bond is unlikely to be so strong, such that the proton affinity of CuH is probably less than 697 kJ mol^{-1}, the proton affinity of water. In corroboration, we were unable to detect any ion signal downstream in the flame at 67 u, the mass number of $^{65}CuH_2^+$.

In common with the alkali and alkaline earth metals (1), the oxides and hydroxides of Fe, Co, Ni, and Cu might be expected to have high PA's greater than that of H_2O. Certainly this is the case for FeO and CoO whose PA values of 916 ± 21 kJ mol^{-1} have been measured (17). These componds will chemically ionize in proton tranfer reactions with H_3O^+

[11] $H_3O^+ + AO \rightleftharpoons H_2O + AOH^+$

[12] $H_3O^+ + AOH \rightleftharpoons H_2O + A(OH)H^+$ or $A^+.H_2O$

[13] $H_3O^+ + A(OH)_2 \rightleftharpoons H_2O + A(OH)_2H^+$ or $AOH^+.H_2O$

The pairs of alternative formulae given in reactions [12] and [13] almost certainly refer to the same ionic structure. For all of these molecular ions, reaction paths back to the atomic ion A^+ occur by way of thermal dissociation or radical attack by H atoms

[14] $A(OH)_2H^+$ or $AOH^+.H_2O + M \rightleftharpoons AOH^+ + H_2O + M$

[15] $AOH^+ + H \rightarrow A^+ + H_2O$

[16] $A(OH)H^+$ or $A^+.H_2O + M \rightleftharpoons A^+ + H_2O + M$

Finally, higher hydrates of any of these ions may form in consecutive three-body reactions with H_2O; e.g.,

[17] $A^+.H_2O + H_2O + M \rightleftharpoons A^+.2H_2O + M$

where the calculated equilibrium mole fraction of H_2O in the burnt gas of this flame amounts to 0.251. As mentioned above, hydrates tend to be enhanced when the flame gas cools during sampling, and may not represent genuine flame ions (10–13). Typically, such hydrates give signals amounting to a few percent of the parent ion signals (1) depending on the quality of the sampling technique. When they are appreciably larger than this, it is an indication that the hydrate ions are truly present in the flame. An obvious example occurs in Table 2 for $AOH^+.H_2O = A(OH)_2H^+$ compared with AOH^+; evidently the dihydroxide really is involved in the proton transfer equilibria. In addition, it is not surprising that "hydration" also occurs with CO in this fuel-rich flame where the mole fraction of CO is large, amounting to 0.298

[18] $A^+ + CO + M \rightleftharpoons ACO^+ + M$

followed by further hydration with water to form $ACO^+.H_2O$. Whether metal–carbon bond formation is involved rather than AOC^+ formation is not clear from these experiments.

The relative signal magnitudes for the five metals require further discussion; namely, why the total ion signals observed with Fe, Co, Ni, and Cu are similar, but no ions are observed for Zn (see Fig. 1). Relevant data for a comparison of the charge transfer reaction [1]

[1] $H_3O^+ + A \rightleftharpoons A^+ + H_2O + H$

with the overall proton transfer mechanism [4] + [5a] or [4] + [5b]

[19a] $H_3O^+ + A + H \rightleftharpoons A^+ + H_2O + H_2$

[19b] $H_3O^+ + A + OH \rightleftharpoons A^+ + 2H_2O$

are given in Table 4. From the $PA^0_{298}(A)$ values in Table 1 and $PA^0_{298}(H_2O) = 697$ kJ mol^{-1} (29), the proton tranfer step [4] of reactions [19a] or [19b] to form AH^+ is exothermic for Fe, Co, and Ni, but slightly endothermic for Cu and Zn (see Table 4). Also from Table 4, the overall reactions [19a] or [19b] at 2200 K are exothermic and exoergic for all five metals. If the proton transfer mechanism and the endothermic reaction [4] are operative for Cu, why not for Zn as well for which no ions were observed? A possible solution to this dilemma comes from a further consideration of the charge transfer reaction [1]. The enthalpy of reaction is not a good criterion; from Table 4, ΔH^0_1 at 2200 K is considerably endothermic for all five metals. The proper criterion is ΔG^0_1 which is exoergic for Fe, Co, Ni, and Cu but slightly endoergic for Zn. The large entropy term in reaction [1] is not surprising since two reagent particles form three products. Thus, both reaction mechanisms for the production of Zn^+ are energetically unfavourable. However, for Cu where no CuH^+ was observed because reaction [4] is endothermic, presumably reaction [1] becomes the dominant path for the chemical ionization of copper.

This does not mean that reaction [19] is inoperative for the other metals since AH^+ was observed for Fe, Co, and Ni (see Table 2). In addition, for a metal like iron where FeOH is a major neutral species in the flame (see Table 3), production of Fe^+ can also proceed by reaction [12] to form $Fe(OH)H^+$ (or $Fe^+.H_2O$) followed by the dehydration reaction [16]. Reactions [11] + [15] provide yet another path to A^+ via the oxide AO which is appreciable in the case of Co (see Table 3). Presumably zinc exists in the flame entirely as Zn atoms such that these other production reactions for Zn molecular ions are not possible.

It is further necessary to explain why the ion signals for Fe, Co, Ni, and Cu have similar magnitudes fairly early in the burnt-gas region (see Figs. 1–3). The concentration data given in Table 4 show that this will not be the case far downstream when full thermodynamic equilibrium is attained. The equilibrium concentrations have been calculated at 2200 K on the assumption that the only ions present are A^+ and H_3O^+; quasi-neutrality requires that $[e^-] = [A^+] + [H_3O^+]$. Note that the total ionization levels represented by $[e^-]$ vary by a factor of 30. The equilibrium value for $[Zn^+]$ is much smaller than $[A^+]$ for

TABLE 4. Comparative data for the production of A^+ by charge transfer [1] and proton transfer [19a,b][a]

Parameter	Value				
	Fe	Co	Ni	Cu	Zn
$\Delta H^0_{4,298}$	−64	−52	−44	38	44
$\Delta H^0_{19a,2200}$	−277	−270	−293	−295	−140
$\Delta H^0_{19b,2200}$	−338	−331	−353	−356	−201
$\Delta G^0_{19a,2200}$	−311	−303	−406	−441	−175
$\Delta G^0_{19b,2200}$	−347	−338	−441	−477	−211
$\Delta H^0_{1,2200}$	178	185	163	160	315
$\Delta G^0_{1,2200}$	−122	−113	−216	−252	14
$[A^+]_{eq}$	2.94(7)	2.02(7)	5.94(8)	1.56(9)	2.32(4)
$[H_3O^+]_{eq}$	3.94(7)	4.29(7)	4.53(6)	1.74(6)	5.20(7)
$[e^-]_{eq}$	6.88(7)	6.31(7)	5.98(8)	1.56(9)	5.20(7)
$([A^+]/[H_3O^+])_{eq}$	0.747	0.469	131	898	4.45(−4)

[a]Energy values calculated from the JANAF Tables (18) are quoted in kJ mol^{-1} at 2200 K, and concentrations in particles mL^{-1}; e.g., 2.94(7) represents 2.94×10^7 mL^{-1}; eq denotes equilibrium at 2200 K.

Can. J. Chem. Downloaded from www.nrcresearchpress.com by 112.217.228.212 on 09/07/12
For personal use only.

the other metals, stemming ultimately from the high ionization energy of Zn (see Table 1). A large variation of $[A^+]/[H_3O^+]$ at equilibrium is evident, and yet the observed ratio is comparable for Fe, Co, Ni, and Cu (from Figs. 1–3).

Fairly early in the burnt gas, the explanation comes from chemical kinetic rather than thermodynamic considerations. The ion ratio is determined by the difference of the rates of production and loss of metallic ions. The rate of production, given by $k[H_3O^+][A]$, will be approximately constant if the rate constants k_1 and k_4 are similar for all four metals. (The same will be true if k_{12} and k_{11} are comparable when hydroxides and oxides are involved, respectively.) It is important to recognize that the increase in *total* ion signal shown in Fig. 1 with Fe, Co, Ni, and Cu present reflects the degree to which reaction [3] contributes to the overall rate of ion loss. Reaction [3] involves the slow, three-body recombination of e^- with A^+. For $k_3 = 10^{-27}$ mL^2 $molecule^{-2}$ s^{-1} (taken from ref. 33 which lists similar rate constants for alkali metal recombination) and $[e^-] < 10^{10}$ mL^{-1}, the relaxation time for reaction [3] amounts to $\tau_3 \simeq 1/k_3[e^-][M] > 30$ ms, corresponding to more than 30 mm of flame for a burnt-gas velocity of 1 m s^{-1}. Since $[A^+]$ (including a fraction of $[A^+.H_2O]$ formed during sampling) has similar values for Fe, Co, Ni, and Cu, and since their k_3 values should be roughly equal, it is reasonable that the profiles given in Figs. 1–3 are similar for the four metals. The overall chemical picture is interesting. In general, A^+ is produced by relatively fast, two-body processes, but is ultimately lost by a slow, three-body reaction. Thus, $[A^+]$ may achieve a superequilibrium level early in the burnt gas, but subsequently takes a long time downstream to fall to the equilibrium concentration given in Table 4. This situation for ions resembles the phenomenon of neutral radical overshoot which occurs for H, OH, and O in hydrogen flames (40).

Hayhurst and Telford (4) measured rate coefficients k for the rate of dissappearance of H_3O^+ in fuel-rich, H_2–O_2–N_2 flames doped with Fe and Cu as well as other metals. For example, in a flame of composition 4.0–1.0–4.0 at 2025 K, they measured k_{Fe} and k_{Cu} to be 1.2×10^{-9} and 4.1×10^{-10} mL $molecule^{-1}$ s^{-1}, respectively. They suggest that k_{Fe} and k_{Cu} represent a weighted mean for reaction [11] with AO and the reaction

[20] $H_3O^+ + A \rightleftharpoons AOH^+ + H_2$

which is exothermic for both metals. We do not favour reaction [20] because, in contrast to the transfer of a single particle (H^+, H, or e^-), a good deal of chemical rearrangement is involved; namely, the simultaneous breaking of two bonds and the formation of two others. More probably, k_{Fe} represents a weighted average (in approximate decreasing order; see Table 3) of reactions [12], [1], [4], [13], and [11], all of which are exothermic. For Cu, reactions [1], [11], and [12] would seem to be involved. Hayhurst and Telford (4) rejected reaction [1] for Fe and Cu because it is endothermic; they were unaware that it is exoergic for both metals because the thermodynamic data were not available at the time of their study. Similarly, the proton affinities of metallic atoms involved in reaction [4] were not known at that time.

It is of interest to compare our results for a premixed flame at 2200 K with those of Ham and McAllister (5) for a CO/H_2 diffusion flame at much lower temperature. In both flames, H_3O^+ is the primary CI source ion. In decreasing order of magnitude, they observed $Fe(OH)_2H^+$, $Fe(OH)_3H^+$, $Fe(OH)H^+.H_2O$, $Fe(OH)H^+$, and $Fe(OH)_2H^+.H_2O$, all of which involve proton transfer from H_3O^+. Of these, only $Fe(OH)_3H^+$ was not observed by us; presumably appreciable $Fe(OH)_3$ can only exist in a flame at lower temperature. In decreasing order, they next observed the curious ion $FeO(OH)_2^+$ (or $FeO_2^+.H_2O$) having an Fe oxidation state of 5 (not observed by us), followed by Fe^+. Finally, they observed $Fe(OH)_3^+$ and a small $Fe(OH)_2^+$ signal which we did not detect.

For these latter two ions of the type $Fe(OH)_n^+$, Ham and McAllister (5) hypothesize a CI source reaction analogous to reaction [1]

[21] $H_3O^+ + Fe(OH)_n \rightarrow Fe(OH)_n^+ + H_2O + H$

which is exothermic only if IE $[Fe(OH)_n] < 6.4$ eV. That is, reaction [21] is expected to be very endothermic for $Fe(OH)_2$ and $Fe(OH)_3$ (see, for example, $IE^0_O(FeOH)$ in Table 1). Since proton transfer to these compounds by H_3O^+ is probably exothermic, we would favour a two-step mechanism

[22] $H_3O^+ + Fe(OH)_n \rightarrow Fe(OH)_nH^+ + H_2O$

[23] $Fe(OH)_nH^+ + H, OH \rightarrow Fe(OH)_n^+ + H_2, H_2O$

[24] $H_3O^+ + Fe(OH)_n + H, OH \rightarrow Fe(OH)_n^+ + H_2O + H_2, H_2O$

The overall net reaction [24] is less endothermic than reaction [21] by 103 (for H) or 118 (for OH) kJ mol^{-1}. In summary, the results for Fe ions in these two flames are surprisingly different, both as to relative magnitude and type.

Conclusions

Equal concentrations (~1 ppm) for Fe, Co, Ni, Cu, and Zn are introduced into a fuel-rich, premixed, CH_4–O_2 flame at 2200 K and atmospheric pressure in which CO is a major component of the burnt gas (0.298 mole fraction). These metals exist in flames as atoms A and the metallic compounds AO, AOH, and $A(OH)_2$ in varying amounts. Most of these species appear to possess high proton affinities. The metallic ions observed include A^+ which is predominant, and the molecular ions AH^+, AOH^+, $A(OH)H^+$, $A(OH)_2H^+$, ACO^+ together with their hydrates. These ions are formed mainly by proton transfer reactions of H_3O^+ to the metallic neutral species including A, supplemented by three-body association and free radical stripping reactions. Also, A^+ can be formed by the reaction of H_3O^+ with A in a charge transfer process. In general, the hydrate ion signals are enhanced when the flame gas is cooled during sampling by the nozzle into the mass spectrometer. In some cases, however, the ion hydrates have the same structure as protonated metallic neutrals, and are genuine flame ions; examples include $A^+.H_2O = A(OH)H^+$ and $AOH^+.H_2O = A(OH)_2H^+$. The only flame ion observed to exhibit the possible formation of a metal–carbon bond is the carbonyl compound ACO^+ in contrast to studies of ion–molecule reactions near room temperature. The ion profiles for Fe, Co, Ni, and Cu are very similar as to relative magnitude and shape. No ions are observed for Zn, however. If the atomic A^+ ion is dominant, its concentration can reach a superequilibrium level early in the burnt-gas region before it slowly decays downstream; the phenomenon is similar to the free radical overshoot which occurs in hydrogen flames. Finally, the ion chemistry is surprisingly different from that observed by Ham and McAllister (5) for Fe in a diffusion flame at lower temperature.

Acknowledgement

Support of this work by the Natural Sciences and Engineering Research Council of Canada under Grant No. A-1604 is acknowledged.

1. J. M. Goodings and S. M. Graham. Int. J. Mass Spectrom. Ion Processes, **56**, 193 (1984).
2. S. M. Graham and J. M. Goodings. Int. J. Mass Spectrom. Ion Processes, **56**, 205 (1984).
3. J. M. Goodings, S. M. Graham, and N. S. Karellas. Int. J. Mass Spectrom. Ion Processes, **69**, 343 (1986).
4. A. N. Hayhurst and N. R. Telford. Trans. Faraday Soc. **66**, 2784 (1970).
5. N. S. Ham and T. McAllister. Aust. J. Chem. **36**, 1299 (1983).
6. B. S. Freiser. Talanta, **32**, 697 (1985).
7. J. M. Goodings, D. K. Bohme, and C.-W. Ng. Combust. Flame, **36**, 27 (1979).
8. J. M. Goodings, S. M. Graham, and W. J. Megaw. J. Aerosol Sci. **14**, 679 (1983).
9. A. N. Hayhurst and N. R. Telford. Combust. Flame, **28**, 67 (1977).
10. N. A. Burdett and A. N. Hayhurst. J. Chem. Soc. Faraday Trans. I, **78**, 2997 (1982).
11. A. N. Hayhurst and D. B. Kittelson. Combust. Flame, **28**, 137 (1977).
12. A. N. Hayhurst and N. R. Telford. Proc. R. Soc. London A, **322**, 483 (1971).
13. P. F. Knewstubb and T. M. Sugden. Proc. R. Soc. London A, **255**, 520 (1960).
14. D. D. Wagman, W. H. Evans, V. B. Parker, R. H. Schumm, I. Halow, S. M. Bailey, K. L. Churney, and R. L. Nuttall. The NBS tables of chemical thermodynamic properties. J. Phys. Chem. Ref. Data, **11**, Suppl. No. 2. 1982.
15. H. M. Rosenstock, K. Draxl, B. W. Steiner, and J. T. Herron. Energetics of gaseous ions. J. Phys. Chem. Ref. Data, **6**, Suppl. No. 1. 1977.
16. L. Sallans, K. R. Lane, R. R. Squires, and B. S. Freiser. J. Am. Chem. Soc. **107**, 4379 (1985).
17. C. J. Cassady and B. S. Freiser. J. Am. Chem. Soc. **106**, 6176 (1984).
18. M. W. Chase, Jr., C. A. Davies, J. R. Downey, Jr., D. J. Frurip, R. A. McDonald, and A. N. Syverud. JANAF Thermochemical Tables, 3rd ed. J. Phys. Chem. Ref. Data, **14**, Suppl. No. 1. 1985.
19. D. B. Jacobson and B. S. Freiser. J. Am. Chem. Soc. **108**, 27 (1986).
20. E. J. Murad. J. Chem. Phys. **73**, 1381 (1980).
21. J. L. Elkind and P. B. Armentrout. J. Phys. Chem. **90**, 5736 (1986).
22. J. L. Elkind and P. B. Armentrout. J. Phys. Chem. **90**, 6576 (1986).
23. P. L. Po, T. P. Radus, and R. F. Porter. J. Phys. Chem. **82**, 520 (1978).
24. R. R. Squires. J. Am. Chem. Soc. **107**, 4385 (1985).
25. R. F. Grimley, R. P. Burns, and M. G. Inghram. J. Chem. Phys. **45**, 4158 (1966).
26. D. A. Weil and C. L. Wilkins. J. Am. Chem. Soc. **107**, 7316 (1985).
27. M. M. Kappes and R. H. Staley. J. Phys. Chem. **85**, 942 (1981).
28. C. J. Cassady and B. S. Freiser. J. Am. Chem. Soc. **108**, 5690 (1986).
29. S. G. Lias, J. F. Liebman, and R. D. Levin. Evaluated gas phase basicities and proton affinities of molecules; heats of formation of protonated molecules. J. Phys. Chem. Ref. Data, **13**, 695 (1984).
30. R. D. Levin and S. G. Lias. Ionization and appearance potential measurements, 1971–1981. NSRDS-NBS 71, U.S. Government Printing Office, Washington, DC. 1982.
31. D. E. Jensen and G. A. Jones. J. Chem. Phys. **60**, 3421 (1974).
32. D. E. Jensen and G. A. Jones. J. Chem. Soc. Faraday Trans. I, **72**, 2618 (1976).
33. D. E. Jensen and G. A. Jones. Combust. Flame, **32**, 1 (1978).
34. D. E. Jensen and G. A. Jones. J. Chem. Soc. Faraday Trans. I, **69**, 1448 (1973).
35. M. Farber, S. P. Harris, and R. D. Srivastava. Combust. Flame, **22**, 191 (1974).
36. P. J. Padley. Ph.D. Thesis, University of Cambridge. 1959.
37. E. M. Bulewicz and T. M. Sugden. Trans. Faraday Soc. **52**, 1475 (1956).
38. E. M. Bulewicz and T. M. Sugden. Trans. Faraday Soc. **52**, 1481 (1956).
39. A. G. Gaydon. Dissociation energies and spectra of diatomic molecules. 3rd edition. Chapman and Hall, London. 1968.
40. E. M. Bulewicz, C. G. James, and T. M. Sugden. Proc. R. Soc. London A, **235**, 89 (1956).

Can. J. Chem. Downloaded from www.nrcresearchpress.com by 112.217.228.212 on 09/07/12
For personal use only.

Ion chemistry of transition metals in hydrocarbon flames. II. Cations of Sc, Ti, V, Cr, and Mn

JOHN M. GOODINGS, QUANG TRAN, AND NICHOLAS S. KARELLAS
Department of Chemistry, York University, 4700 Keele Street, North York, Ont., Canada M3J 1P3

Received February 19, 1988

JOHN M. GOODINGS, QUANG TRAN, and NICHOLAS S. KARELLAS. Can. J. Chem. **66**, 2219 (1988).

The same fuel-rich, premixed, conical, methane–oxygen flame at 2200 K and atmospheric pressure used for studies of Fe, Co, Ni, Cu, and Zn in Part I (1) is doped with the same concentration (~1 ppm) of Sc, Ti, V, Cr, and Mn to complete the first row of ten transition metals. Metallic ions of these metals and their compounds formed by chemical ionization reactions with H_3O^+ are observed by sampling the flame through a nozzle into a quadrupole mass spectrometer. Concentration profiles of individual and total cations are measured as a function of distance along the flame axis, and also mass spectra at a fixed point in the burnt gas. If A is the metal atom, the observed ions can be represented by four hydrate series including (*a*) $A^+.nH_2O$, (*b*) $AOH^+.nH_2O$, (*c*) $AO^+.nH_2O$, and (*d*) $AO_2H^+.nH_2O$ with $n = 0$–3 or 4, giving a maximum of four ligands around the metal atom. However, alternative isomeric structures are possible for each of the four basic series (e.g. $AO^+.2H_2O \sim A(OH)_2{}^+.H_2O \sim A(OH)_3H^+$). The ions observed with Cr and Mn, in common with those of Fe, Co, Ni, and Cu, strongly favour series (*a*). On the other hand, Sc is completely different; the ions of series (*c*) are dominant. All four series are observed with each of Ti and V. Series (*b*) dominates for Ti and series (*c*) for V; ions from series (*d*) were observed for the first time. The ion chemistry of these metals is discussed in detail with emphasis on the probable chemical ionization reactions responsible for metallic ion formation. The pre-eminent role of proton transfer processes is apparent.

JOHN M. GOODINGS, QUANG TRAN et NICHOLAS S. KARELLAS. Can. J. Chem. **66**, 2219 (1988).

Opérant dans les mêmes conditions que celles utilisées alors qu'on avait dopé une flamme méthane–oxygène, conique, pré-mélangée et riche en carburant, avec environ 1 ppm des métaux de transition Fe, Co, Ni, Cu et Zn (1), on a dopé cette flamme avec la même concentration (~1 ppm) des métaux Sc, Ti, V, Cr et Mn et on a ainsi complété l'examen de la première rangée des dix métaux de transition. Utilisant un échantillonnage de la flamme dans un spectromètre de masse quadripolaire, on a observé la formation des ions métalliques de ces métaux ainsi que celle de leurs composés formés par des réactions d'ionisation chimique avec le H_3O^+. On a mesuré les profiles de concentration des cations individuels et totaux en fonction de la distance le long de l'axe de la flamme ainsi qu'à un point fixe dans les gaz d'échappement. Si A est l'atome métallique, les ions observés peuvent être représentés par quatre séries d'hydrates comprenant; (*a*) $A^+.nH_2O$, (*b*) $AOH^+.nH_2O$, (*c*) $AO^+.nH_2O$ et (*d*) $AO_2H^+.nH_2O$ avec $n = 0$ à 3 ou 4 et conduisant à un maximum de quatre ligands autour des atomes métalliques. Toutefois, d'autres structures isomères peuvent exister pour chacune des quatre séries de base (par exemple, $AO^+.2H_2O \sim A(OH)_2{}^+.H_2O \sim A(OH)_3H^+$). Les ions observés avec le Cr et le Mn, de même qu'avec le Fe, le Co, le Ni et le Cu, favorisent fortement la série (*a*). Par ailleurs, le Sc est complètement différent; les ions de la série (*c*) dominent. Les quatre séries sont observées avec le Ti ainsi que le V. La série (*b*) domine avec le Ti et la série (*c*) avec le V; on a observé des ions de la série (*d*) pour la première fois. On discute en détail de la chimie ionique de ces métaux en mettant de l'emphase sur les réactions d'ionisation chimique qui sont probablement responsables de la formation d'ions métalliques. Le rôle prépondérant des processus de transfert de protons est apparent.

[Traduit par la revue]

Introduction

In the preceding paper designated Part I (1), we considered the ion chemistry of Fe, Co, Ni, Cu, and Zn in a fuel-rich, premixed, CH_4–O_2 flame at 2200 K and atmospheric pressure. This work follows on from our previous studies of chemical ionization reactions of alkali and alkaline earth metals in hydrocarbon flames in which the role of proton transfer reactions was emphasized (2). The present paper is a continuation of Part I for Sc, Ti, V, Cr, and Mn in order to complete the first row of ten transition metals.

We are not aware of any previous observations of flame ions for Sc, Ti, and V. Soundy and Williams (3) measured the reaction of H_3O^+ with Cr and Mn (and also Li, Cu, and Pb) in one flame at 2368 K but their electrostatic probe technique without mass analysis leaves the nature of the ions in doubt. Hayhurst and Telford (4) introduced Cr and Mn as well as a number of other metals into fuel-rich, H_2–O_2–N_2 flames containing natural flame ions, principally H_3O^+, arising from small amounts of hydrocarbon impurities. Using a mass spectrometer, they measured rate constants for the disappearance of H_3O^+ reacting with metallic atoms A, or with oxides AO, hydroxides AOH and $A(OH)_2$, or even hydrides AH if these compounds exist in flames for a particular metal. The ion–molecule reactions involved are discussed in detail below.

Part of the interest in these metals stems from the considerable number of common oxidation states which they exhibit in their chemistry at room temperature. It is, therefore, not surprising that a corresponding variety of different metallic ions are observed in flames. Broadly speaking, the ions of Cr and Mn show much in common with each other, and with those of Fe, Co, Ni, and Cu discussed in Part I in which the atomic ion A^+ is heavily favoured. In contrast, the ions observed for Sc with its single oxidation state of +3 are quite different. Finally, the ions of Ti and V are the most varied, show nearly all of the aspects observed for the other transition metals, and exhibit certain new features in addition.

Experimental

Exactly the same experimental procedures described in Part I were used in the present study. Equal concentrations (8.7×10^{-7} mole fraction; i.e., ~1 ppm) of the metals were introduced into the same conical, fuel-rich, premixed, CH_4–O_2 flame at 2200 K and atmospheric pressure by spraying a 0.25 *M* aqueous solution of the metallic chloride from an atomizer into the premixed gas feeding the burner. The single exception was Ti which was introduced as $TiCl_3$ vapour using a gas saturator technique. An equivalent concentration was assured by making the molar flow rate of $TiCl_3$ equivalent to that of $Fe(CO)_5$ vapour from the same saturator; the flow of Fe as $Fe(CO)_5$ was, in turn, made equivalent to that introduced by spraying a 0.25 *M*

Can. J. Chem. Downloaded from www.nrcresearchpress.com by 112.217.228.212 on 09/07/12
For personal use only.

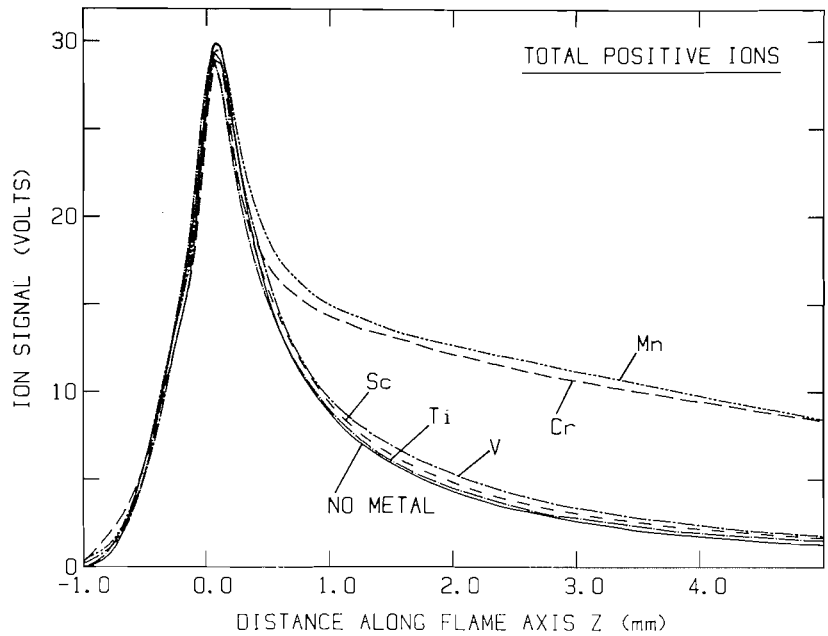

FIG. 1. Total ionization profiles along the flame axis with metal absent, and with the flame doped with equal molar concentrations (~1 ppm) of Sc, Ti, V, Cr, and Mn. The luminous reaction zone is located upstream of $z = 0$.

aqueous solution of $FeCl_3$ in the atomizer. Ion concentration profiles were measured along the flame axis z and also mass spectra at a fixed point $z = 1.25$ mm downstream of the flame reaction zone. This was done by sampling the flame along its axis through a chromium nozzle into a quadrupole mass spectrometer as described in Part I.

Results and discussion

Figure 1 shows total positive ion profiles measured as a function of distance along the flame axis in the absence of metal and with equal concentrations of Sc, Ti, V, Cr, and Mn present. The profiles were obtained with the d.c. voltages to the quadrupole mass filter rods switched off. Essentially no change of the total ion signal is observed at the profile peak nor in the flame reaction zone ($z < 0$, upstream). The signal is enhanced downstream in the burnt gas for all five metals, very slightly for Sc, Ti, and V, and very considerably for Cr and Mn. These observations imply that the metals do not participate in any new chemi-ionization process, at least in the flame reaction zone. Certainly thermal ionization is unlikely since all of these metals and their compounds which might exist in the flame have high ionization energies, IE > 6 eV. Known thermochemical data for the metals, their compounds, and associated cations are assembled in Table 1. These data come from the many studies of the gas-phase ion chemistry of transition metals carried out near room temperature using a variety of techniques: ion cyclotron resonance (ICR) and Fourier-transform mass spectrometry (FTMS), laser desorption/ionization (LDI), photodissociation, and guided ion beams. These various studies are referenced in Table 1.

The logical source of the metallic ions observed in the flame begins with the classic chemi-ionization reaction for hydrocarbons

$$[1] \qquad CH + O \rightarrow HCO^+ + e^-$$

In our flame where water is a major product in the burnt gas (equilibrium mole fraction 0.251), HCO^+ undergoes exothermic proton transfer to H_2O

$$[2] \qquad HCO^+ + H_2O \rightleftharpoons H_3O^+ + CO$$

In the absence of a metallic additive, H_3O^+ and its first hydrate, most of which is formed during sampling (see Part I), are by far the most abundant ionic species present downstream in the flame. With a metal present in the form of atoms or compounds, H_3O^+ serves as a chemical ionization (CI) source for the formation of metallic ions. The resulting depletion of H_3O^+ is shown for the five metals in Fig. 2. The depletion is small for Sc, Ti, and V, but large for Cr and Mn in correspondence with Fig. 1. Normally ions are lost in the burnt gas by the two-body, electron–ion recombination reaction

$$[3] \qquad H_3O^+ + e^- \rightarrow H + H + OH \text{ (or } H_2O + H)$$

It is evident in Fig. 1 that the loss rate for total ions is considerably reduced with Cr or Mn present. This is explained by the partial replacement of reaction [3] by the much slower three-body process involving atomic ion–electron recombination

$$[4] \qquad Cr^+, Mn^+ + e^- + M \rightarrow Cr, Mn + M$$

where M is a third body. Clearly, Cr^+ and Mn^+ must be the major metallic ions formed with these metals to affect the total ion loss rate so markedly. But even for Sc, Ti, and V, Fig. 1 is explicable in terms of a slightly decreased ion loss rate in the burnt gas; there is no evidence for any new chemi-ionization source reaction akin to reaction [1] involving metallic neutral species.

The results and discussion of the five metals will be presented in groups based on similarities of the ion chemistry. First, Cr and Mn are much the same, and have many features in common with Fe, Co, Ni, and Cu discussed in Part I. Secondly, the ion chemistry of Sc is markedly different. Thirdly, Ti and V show most of the features of all the other metals and present some new aspects in addition. To serve as a sort of index, percentages of the total metallic ions for each metal are given in Table 2, observed on the flame axis at a fixed point $z = 1.25$ mm downstream in the burnt gas. For Ti and Cr (and V to a small extent), the percentages have been corrected to allow for the contributions to a given ion of the various isotopes of the metal whose natural abundances are given in Table 1. For many of the

Can. J. Chem. Downloaded from www.nrcresearchpress.com by 112.217.228.212 on 09/07/12
For personal use only.

TABLE 1. Data for the first-row transition metals Sc–Mn

Parameter	Value									
	Sc		Ti		V		Cr		Mn	
(*a*) Enthalpies of formation, $\Delta H^0_{f,0}$[a]										
A	376.02	(5,6)	467.14	(5,6)	510.95	(5,6)	394.51	(5,6)	279.37	(5,6)
AH					573±13	(7)	444±13	(7)		
AO	−56.5	(5)	54±8	(8)	128±21	(8)	188±42	(8)	125	(5)
AO_2			−303±13	(8)	−231±42	(8)	−74±42	(8)		
AO_3							−293±42	(8)		
A^+	1008	(5,6)	1125	(5,6)	1161	(5,6)	1047.3	(5,6)	996.7	(5,6)
AH^+	993±10	(6,9)	1111±10	(6,10)	1180±6	(6,11)	1132±11	(6,10)	1014±14	(6,12)
(*b*) Bond dissociation energies, D^{0b}_T										
A—H	199±8	(13)	159±13	(13)	159±13	(13)	172±13	(13)	<134	(13)
A—O			660±8	(8)	630±21	(8)	453±42	(8)	402±13	(14)
OA—O			604±21	(8)	605±63	(8)	508±84	(8)		
O_2A—O							466±84	(8)		
A—OH									305±13	(14)
A^+—H	232±10	(9)	231±10	(10)	198±6	(11)	131±11	(10)	199±14	(12)
A^+—O			~854	(15)	565±67	(15)			105–167	(15)
(*c*) Proton affinities, PA^0_{298}[c]										
A	915±10	(6,9)	888±10	(6,10)	863±6	(6,11)	794±11	(6,10)	797±14	(6,12)
(*d*) Ionization energies, IE^{0d}_0										
A	6.55	(5,6)	6.82	(6)	6.74	(6)	6.766	(6)	7.434	(6)
AH					6.29	(7,11)	7.13	(7,10)		
AO			6.8±0.5	(17)	8±1	(17)	8.4±0.5	(6)		
AO_2			9.54±0.1	(17)	10±2	(17)	10.3±0.5	(6)		
AO_3							11.6±0.5	(6)		
(*e*) Natural abundances of the isotopes(%)	^{45}Sc	100.00	^{46}Ti	7.93	^{50}V	0.24	^{50}Cr	4.31	^{55}Mn	100.00
			^{47}Ti	7.28	^{51}V	99.76	^{52}Cr	83.76		
			^{48}Ti	73.94			^{53}Cr	9.55		
			^{49}Ti	5.51			^{54}Cr	2.38		
			^{50}Ti	5.34						
(*f*) Oxidation numbers	3		2,3,4		2,3,4,5		2,3,6		2,4,6,7	

[a]Energy values for the gas phase are quoted in kJ mol^{-1} at 0 K unless otherwise noted.
[b]The temperature T is sometimes unspecified but usually refers to an experimental temperature near 298 K. In general, the correction to 0 K will lie within the experimental error.
[c]Many of these values are given in the evaluated compilation of proton affinities by Lias *et al.* (16) and its supplements (in preprint form, not yet published).
[d]Quoted in eV. In a few cases, the temperature is unspecified.

ions, more than one chemically reasonable isomer is possible corresponding to the same empirical formula.

Chromium and manganese

Profiles along the flame axis of the major metallic ions observed for Mn are given in Fig. 3. The subsidiary peaks in the flame reaction zone upstream of $z = 0$ stem from natural C—H—O ions at the same mass numbers. The profiles of Mn are straightforward because the isotope ^{55}Mn has a natural abundance of 100%. Mass spectra of the metallic ions measured at a fixed point on the flame axis $z = 1.25$ mm downstream are given in Fig. 4 (*a*) for Cr and (*b*) for Mn; the various isotopes of Cr are apparent.

The next consideration involves the metallic neutral species present in the flame which are available for chemical ionization by H_3O^+. Spectroscopic studies of H_2—O_2—N_2 flames doped with manganese revealed the presence of appreciable MnO such that [MnO]/[Mn] = 0.3 for a near-stoichiometric flame at 2200 K (14); a very small amount of MnOH was also detected (14, 18). In our flame at 2000 K, the amounts of total manganese present as Mn, MnO, and MnOH on a molar percentage basis are approximately 83, 17, and <1%, respectively. A similar and very detailed study of chromium revealed the presence of solid Cr_2O_3 particles which, however, amounted to <10% of the total chromium added (19). Of the gaseous chromium present, hydroxides appeared to be negligible. Using data from the JANAF Tables (8) for our flame at 2200 K, the relative amounts of Cr, CrO, CrO_2, and CrO_3 on a molar percentage basis are 63, 31, 6, and ≪1%, respectively. Bulewicz and Padley (7) also present evidence for the presence of $HCrO_3$ with $[HCrO_3]/[Cr] \geq 0.2$, but little information is available other than its estimated atomization energy of 1940 ± 40 kJ mol^{-1}. In summary, appreciable fractions of both metals are present as strongly-bound, gaseous oxides in the burnt gas of the flame (see Table 1).

The ion chemistry for chromium and manganese has many aspects in common with that of Fe, Co, Ni, and Cu already discussed in Part I. Proton transfer from H_3O^+ to the metallic atoms is exothermic for the first eight transition metals, Sc–Ni (see Table 1, and Table 1 in Part I; proton affinity of water $PA^0_{298}(H_2O)$ = 697 kJ mol^{-1})

$$[5] \qquad H_3O^+ + A \rightleftharpoons AH^+ + H_2O$$

although a small, steady-state signal for the AH^+ intermediate

Can. J. Chem. Downloaded from www.nrcresearchpress.com by 112.217.228.212 on 09/07/12
For personal use only.

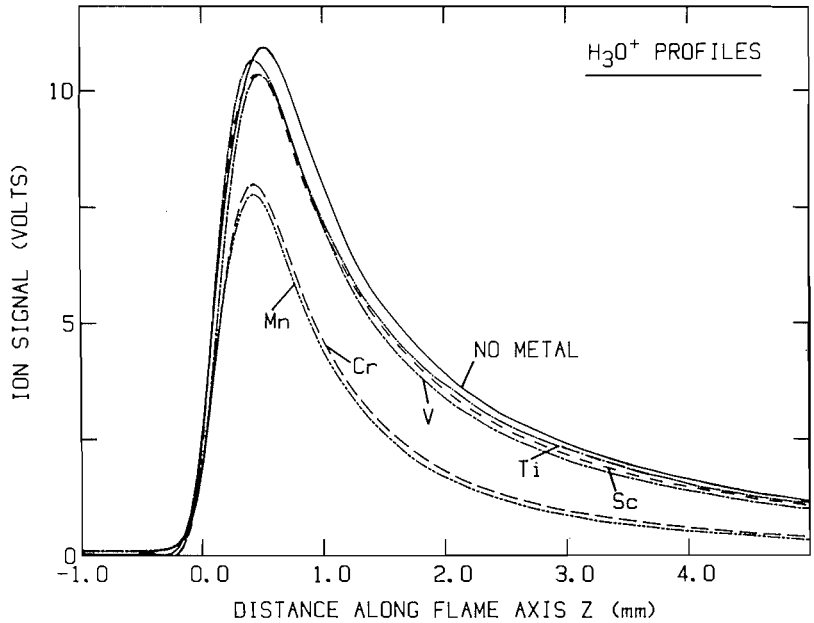

FIG. 2. Axial H_3O^+ profiles with metal absent, and with the flame doped with equal molar concentrations (~1 ppm) of Sc, Ti, V, Cr, and Mn. The luminous reaction zone is located upstream of $z = 0$.

TABLE 2. Percentages of total metallic ions observed at $z = 1.25$ mm downstream

Ions of metal A					Concentration (%)				
					Sc	Ti	V	Cr	Mn
AH^+									0.2
A^+							2.9	92.1	93.0
$A^+.H_2O$	or	$A(OH)H^+$			0.2	0.7	0.7	6.6	4.3
$A^+.2H_2O$	or	$A(OH)H^+.H_2O$				1.1		0.2	
$A^+.3H_2O$	or	$A(OH)H^+.2H_2O$				11.7			
$A^+.4H_2O$	or	$A(OH)H^+.3H_2O$			0.7	0.1			
AOH^+						34.9	4.0	0.4	1.3
$AOH^+.H_2O$	or	$A(OH)_2H^+$				26.0	3.5	0.5	1.2
$AOH^+.2H_2O$	or	$A(OH)_2H^+.H_2O$				14.7			
$AOH^+.3H_2O$	or	$A(OH)_2H^+.2H_2O$				4.4			
AO^+					3.1	0.9	51.6	0.1	
$AO^+.H_2O$	or	$A(OH)_2^+$			43.9	3.8	22.2	0.1	
$AO^+.2H_2O$	or	$A(OH)_2^+.H_2O$	or	$A(OH)_3H^+$	48.4	0.8	6.4		
$AO^+.3H_2O$	or	$A(OH)_2^+.2H_2O$	or	$A(OH)_3H^+.H_2O$	3.7	0.2	0.7		
AO_2H^+						0.6	2.7		
$AO_2H^+.H_2O$	or	$A(OH)_3^+$				0.1	5.0		
$AO_2H^+.2H_2O$	or	$A(OH)_3^+.H_2O$	or	$A(OH)_4H^+$			0.3		
					100.0	100.0	100.0	100.0	100.0

was detected only for Mn. Presumably the same exothermicity is valid for the monoxides as well

[6] $H_3O^+ + AO \rightleftharpoons AOH^+ + H_2O$

The preponderance of Cr^+ and Mn^+ in Table 2 implies the subsequent occurence of fast stripping reactions with radicals

[7a, b] $AH^+ + H, OH \rightleftharpoons A^+ + H_2, H_2O$

[8] $AOH^+ + H \rightleftharpoons A^+ + H_2O$

The latter reaction has been previously suggested by Schofield and Sugden (20) for the AOH^+ ions of the alkaline earth metals, particularly Mg (2). In Table 2 for Cr, there is the hint of an alternative channel for reaction [8] to produce the oxide ion, AO^+

[9a, b] $AOH^+ + H, OH \rightleftharpoons AO^+ + H_2, H_2O$

although the detected signal is small.

Any of these ions can undergo subsequent hydration in a three-body process, particularly as a consequence of cooling during sampling as discussed in Part I; for example

[10] $A^+ + H_2O + M \rightleftharpoons M + A^+.H_2O$ or $A(OH)H^+$

[11] $AO^+ + H_2O + M \rightleftharpoons M + AO^+.H_2O$ or $A(OH)_2^+$

Using our conical, sharp-edged, chromium sampling nozzles, a

Can. J. Chem. Downloaded from www.nrcresearchpress.com by 112.217.228.212 on 09/07/12
For personal use only.

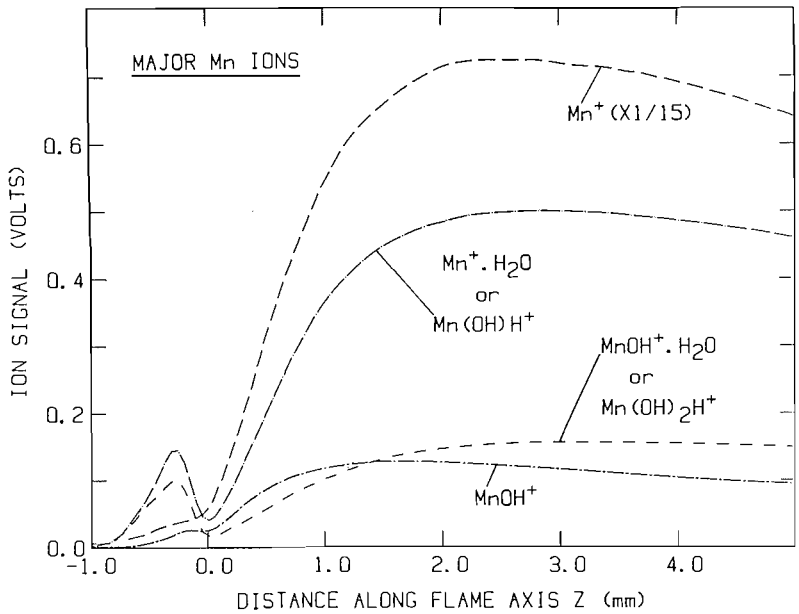

FIG. 3. Axial profiles of the major metallic ions observed when the flame is doped with ~1 ppm of Mn. The luminous reaction zone is located upstream of $z = 0$.

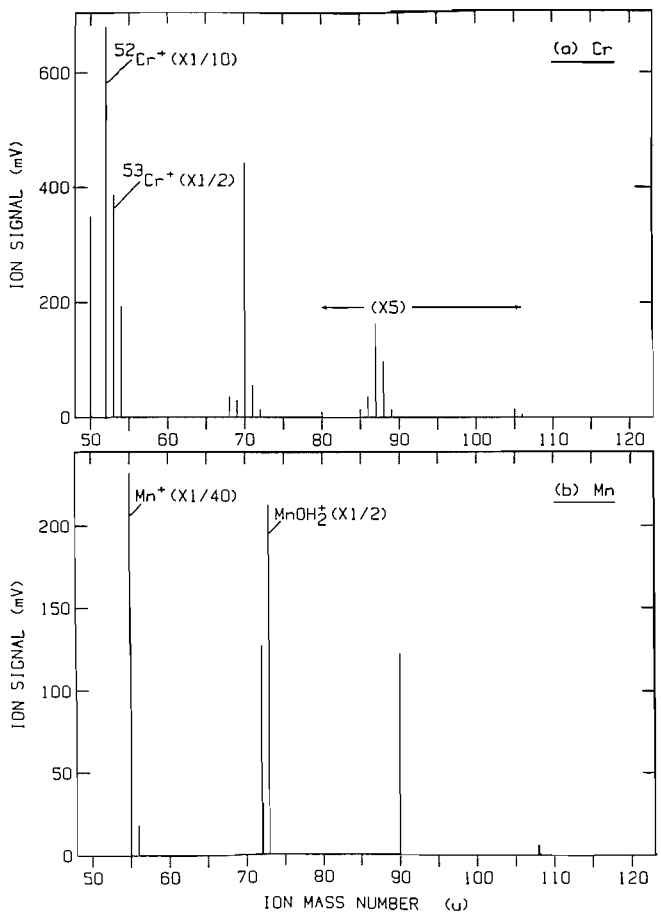

FIG. 4. Mass spectra observed at a fixed point on the flame axis at $z = 1.25$ mm downstream in the burnt gas when the flame is doped with equal molar concentrations (~1 ppm) of (*a*) Cr and (*b*) Mn.

typical hydrate ion signal is generally observed to be a few % of the parent ion signal. This ratio appears to have been exceeded in the present observations such that proton transfer to the monohydroxide cannot be ruled out

[12] $H_3O^+ + AOH \rightleftharpoons H_2O + A(OH)H^+$ or $A^+.H_2O$

and possibly to the dihydroxide as well

[13] $H_3O^+ + A(OH)_2 \rightleftharpoons H_2O + A(OH)_2H^+$ or $AOH^+.H_2O$

All of these ion–molecule reactions have been written above showing both the forward and reverse directions because the ion signals tail out a long way through the burnt gas as in Fig. 3 for the Mn profiles.

Hayhurst and Telford (4) also detected $[AOH^+]$ in amounts up to approxiately 5% of the $[A^+]$ ion signal for Cr and Mn. They invoke the chemical ionization reaction [6] and also

[14] $H_3O^+ + A \rightarrow AOH^+ + H_2$

followed by reaction [8], as well as

[15] $H_3O^+ + MnO \rightarrow Mn^+.H_2O + OH$

as an additional possibility for manganese. However, at the time of their study, it was not known that metallic atoms and oxides could possess high PA values. We believe that it is not necessary to invoke reactions as complicated as [14] and [15] from a point of view of chemical rearrangement in order to explain the ion signals observed.

It remains to discuss why the total ion signals detected with Cr and Mn present are so large compared with those of the other transition metals (see Fig. 1, and also the similar Fig. 1 in Part I for Fe, Co, Ni, and Cu). As explained in Part I, the overall mechanisms responsible for the production of A^+ involve proton transfer by [5] + [7] when A is the reagent

[16a, b] $H_3O^+ + A + H, OH \rightleftharpoons A^+ + H_2O + H_2, H_2O$

Can. J. Chem. Downloaded from www.nrcresearchpress.com by 112.217.228.212 on 09/07/12
For personal use only.

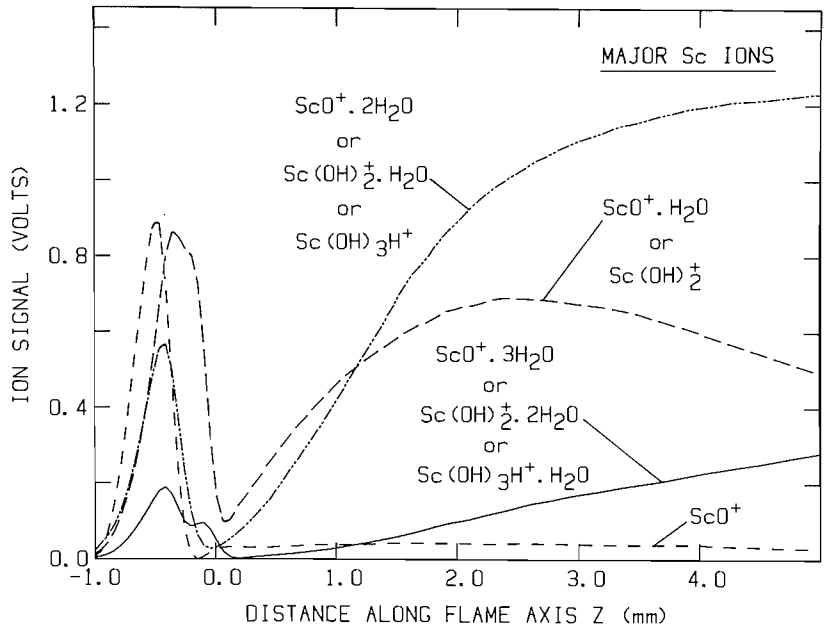

FIG. 5. Axial profiles of the major metallic ions observed when the flame is doped with ~1 ppm of Sc. The luminous reaction zone is located upstream of $z = 0$.

or by [6] + [8] with the oxide AO as reagent

[17] $H_3O^+ + AO + H \rightleftharpoons A^+ + 2H_2O$

or may involve charge transfer in a single step

[18] $H_3O^+ + A \rightleftharpoons A^+ + H_2O + H$

The detection of MnH^+ indicates that reaction [5] followed by [7a], [7b] (i.e., the overall reaction [16]) is operative, at least for manganese; presumably reaction [18] occurs as well. The reactions are all energetically favourable. Using data from the JANAF Tables (8) at 2200 K, the ΔG^0 values for reactions [16a], [16b], [17], and [18] are −408, −443, −411, and −218 kJ mol^{-1} for Cr, respectively. With Mn, the ΔG^0 values for reactions [16a], [16b] and [18] are −349, −384, and −159 kJ mol^{-1}, respectively; reaction [17] will certainly be exoergic but $\Delta G^0_{f,2200}(MnO)$ is not available. At full thermodynamic equilibrium under these flame conditions, $[Cr^+]/[H_3O^+] = 144$ and $[Mn^+]/[H_3O^+] = 5.82$; the calculated equilibrium concentrations of $[A^+]$, $[H_3O^+]$, and $[e^-] = [A^+] + [H_3O^+]$ are 6.22×10^8, 4.33×10^6, and 6.26×10^8 mL^{-1} for Cr, respectively, and 1.16×10^8, 1.99×10^7, and 1.36×10^8 mL^{-1} for Mn, respectively.

Chromium and manganese represent an extreme case of the behaviour already discussed in Part I for Fe, Co, Ni, and Cu. The enhancement of the total ion profiles in Fig. 1 with Cr and Mn present reflects the degree to which slow, three-body, atomic recombination of A^+ replaces the faster, two-body, dissociative recombination of H_3O^+ with e^- by reaction [3]. Since Cr^+ and Mn^+ are formed rapidly by reactions [16] and [18] with a corresponding loss of H_3O^+, reaction [4] soon dominates reaction [3]. That is, $[Cr^+]$ and $[Mn^+]$ reach superequilibrium levels early in the burnt gas, and take a long time to decrease to their equilibrium values much further downstream. A similar enhancement of the profiles in Fig. 1 for Sc, Ti, and V was not observed because the atomic A^+ ions, if present, are minor species (see Table 2). In general, molecular metallic ions will recombine with free electrons by fast, two-body, dissociative processes just like reaction [3] for H_3O^+. The fact that the total metallic ion signals for Sc, Ti, and V are not large (this is evident from Fig. 2 since the decrease in $[H_3O^+]$ is small) means that the formation reactions are not very exoergic, leading to small values of the equilibrium constants.

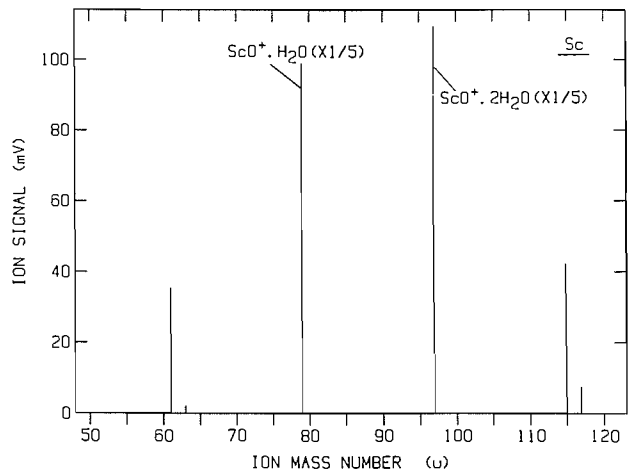

FIG. 6. Mass spectrum observed at a fixed point on the flame axis at z = 1.25 mm downstream in the burnt gas when the flame is doped with ~1 ppm of Sc.

Scandium

Axial concentration profiles for the major scandium ions are shown in Fig. 5. The upstream peaks in the reaction zone ($z < 0$) arise from natural C—H—O ions which are present when no metal is added to the flame. A mass spectrum measured at z = 1.25 mm downstream showing six metallic ions for ^{45}Sc which has a natural abundance of 100% is given in Fig. 6. These signals are represented in Table 2 as percentages of the total metallic ion signal observed.

We are not aware of any available information about scandium neutral species present in flames. Since no Sc^+ nor ScH^+ ions were observed, and since Sc has the highest PA of any first-row transition metal (see Table 1), it is unlikely that an

Can. J. Chem. Downloaded from www.nrcresearchpress.com by 112.217.228.212 on 09/07/12
For personal use only.

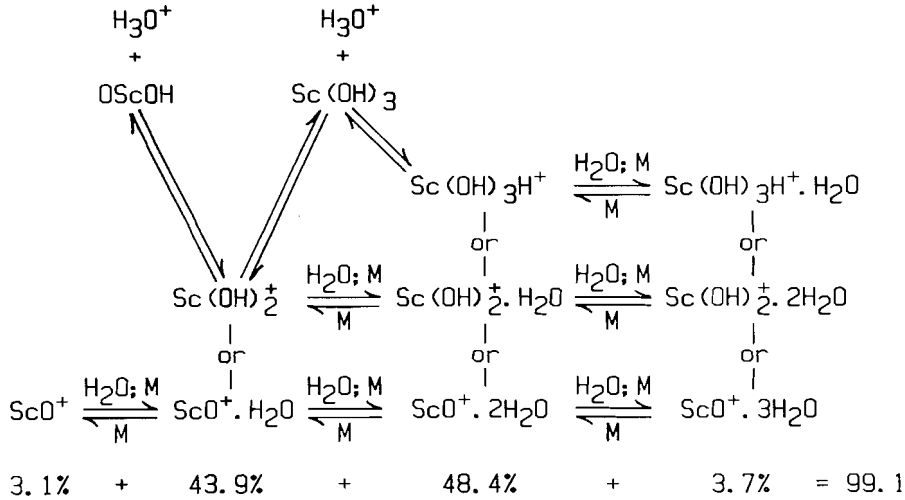

FIG. 7. Reaction flow diagram showing the dominant flame-ion chemistry for Sc. Three hydrate series involving isomeric ion structures are apparent.

appreciable quantity of the metal exists in the flame as Sc atoms. Near room temperature in solutions and solids, Sc exhibits only the single oxidation state of +3. Certainly this same oxidation number is favoured in the gas phase as flame temperature. The four major Sc ions in Figs. 5 and 6 or Table 2 can be interpreted as $ScO^+.nH_2O$ (n = 0–3), the series ending when Sc is surrounded by an electron octet, although the octet stability may have little significance for a transition metal. The octet occurs with four ligands around the metal atom, and the steric effect of a tetrahedral structure against further ligand addition is probably the more important consideration. Alternatively, the last three members of the series can be represented by $Sc(OH)_2^+.nH_2O$ (n = 0–2), or the last two by $Sc(OH)_3H^+.nH_2O$ (n = 0, 1) based on the protonated trihydroxide. In addition, two very small signals shown in Table 2 were observed for just two members of the series $Sc^+.nH_2O$ (n = 1, 4) or, alternatively, $Sc(OH)H^+.nH_2O$ (n = 0, 3) based on the protonated monohydroxide. In the last member, the Sc atom is surrounded by 10 electrons.

An insight into the chemistry leading to the formation of these ions comes from the profiles given in Fig. 5. The shapes of these profiles indicate that $Sc(OH)_2^+$ and perhaps $Sc(OH)_3H^+$ are formed first, which then dehydrate and hydrate, respectively, to form the other two members of the $ScO^+.nH_2O$ (n = 0, 3) series. Plausible Sc neutral species present in the flame which maintain the Sc(III) oxidation state are O=Sc—OH (the oxyhydroxide) and $Sc(OH)_3$. These could react with H_3O^+ to form the two major ions by the reactions

[19] $H_3O^+ + OScOH \rightleftharpoons Sc(OH)_2^+ + H_2O$

[20a] $H_3O^+ + Sc(OH)_3 \rightleftharpoons Sc(OH)_3H^+ + H_2O$ proton transfer

[20b] $\rightleftharpoons Sc(OH)_2^+ + 2H_2O$ charge transfer

Reaction [19] is preferred to form $Sc(OH)_2^+$ because reaction [20b] must be rather endothermic in the forward direction. This $ScO^+.nH_2O$ (n = 0–3) series of four ions accounts for 99% of the total Sc ions observed. A convenient summary of the ion chemistry is given in Fig. 7. Recall from Figs. 1 and 2 that the total metallic ion signal for Sc was small compared with those for Cr and Mn. If reactions [19] and [20a] are dominant and not very exoergic, their equilibrium constants may be close to unity giving low values for the $[Sc(OH)_2^+]/[H_3O^+]$ and $[Sc(OH)_3H^+]/[H_3O^+]$ ratios.

It is difficult to be definitive about formation processes for the minor ions $Sc^+.H_2O$ and $Sc^+.4H_2O$ recorded in Table 2. If a small amount of atomic Sc is present, the proton transfer reaction [5]

[5] $H_3O^+ + Sc \rightleftharpoons ScH^+ + H_2O$

invoked above for Cr and Mn, and also for Fe, Co, Ni, and Cu in Part I, is a logical starting point. The reactive radical cation ScH^+ might be expected to lose H by reaction [7] to form Sc^+, but the latter ion was not observed. Conceivably, it might react with water to form the first hydrate directly according to

[21] $ScH^+ + H_2O \rightleftharpoons H + Sc^+.H_2O$ (or $HScOH^+$)

The alternative structure given in parentheses indicates that reaction [21] is not necessarily a simple H/H_2O switching reaction. Written as the hydrate, $Sc^+.H_2O$ would constitute an unusual example of the Sc(I) oxidation state. The same ion could be produced by proton transfer to :ScOH if the monohydroxide were present in the flame. The structure of the observed ion depends on the protonation site; i.e., whether the O atom or the lone pair of electrons on Sc is the more basic. The former gives the hydrate $:Sc^+.H_2O$ involving Sc(I), while the latter amounts to hydride formation giving $H—Sc—OH^+$ which retains the common Sc(III) oxidation state.

Alternatively, $Sc^+.H_2O$ (or $HScOH^+$) could be produced from the large $Sc(OH)_2^+$ ion identified as primary in Fig. 5; e.g.

[22] $HOScOH^+ + H_2 \rightleftharpoons HScOH^+ + H_2O$

The reaction is attractive because of the high mole fraction (0.412) of H_2 in the burnt gas of this fuel-rich flame. The mechanism would seem to favour $HScOH^+$ rather than the hydrate structure. Once formed, the ion could undergo further hydration to form $Sc^+.4H_2O$ (or $HScOH^+.3H_2O$), the other tiny signal given in Table 2. The intermediate hydrates were not observed; the relative signal size merely depends on the values of the equilibrium constants for the various steps in the hydration sequence.

In summary, it is possible to interpret all of the Sc ions observed as members of various series of hydrates based on ScO^+, $HOScOH^+$, or $HScOH^+$, all of which maintain the Sc(III) oxidation state.

Can. J. Chem. Downloaded from www.nrcresearchpress.com by 112.217.228.212 on 09/07/12
For personal use only.

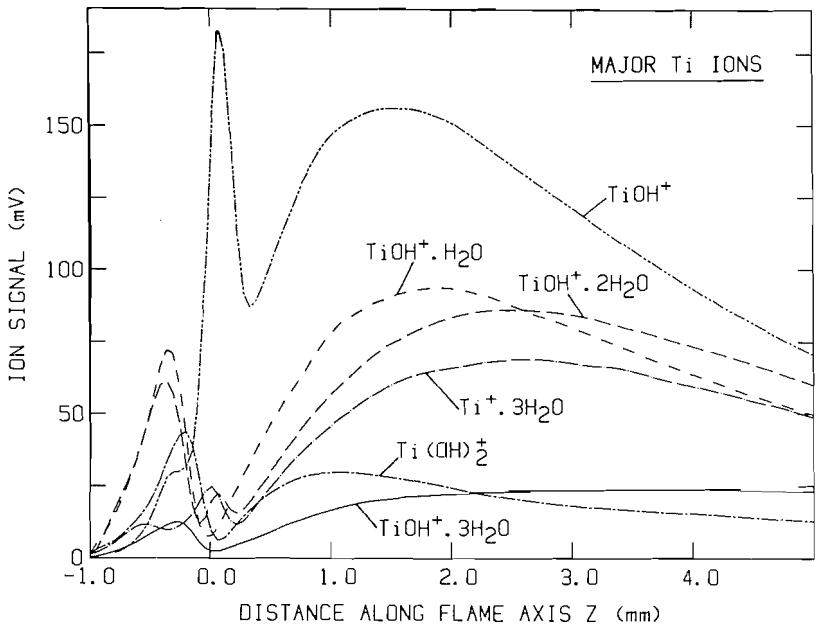

FIG. 8. Axial profiles of the major metallic ions observed when the flame is doped with ~1 ppm of Ti. The luminous reaction zone is located upstream of $z = 0$.

Titanium and vanadium

Axial profiles for the six major ions observed with titanium additive are given in Fig. 8, corrected to include contributions from the five stable Ti isotopes listed in Table 1. The various isotopes are evident in the mass spectrum of Ti ions measured at $z = 1.25$ mm downstream given in Fig. 9(*a*). A similar mass spectrum for V ions is shown in Fig. 9(*b*). These ion signals are presented in Table 2 as percentages of the total metallic ion signal observed for each metal.

Little is known about the chemistry of either of these metals in flames. Several common oxidation states are known for them near room temperature, and certainly they give rise to the greatest variety of flame ions of any of the first-row transition metals. On this basis, a considerable variety of neutral compounds of these metals in flames would not be surprising. A perusal of Table 2 indicates that much of the ion chemistry already discussed for Cr and Mn on the one hand, and for Sc on the other, will also be applicable to Ti and V; it will not be repeated here. The exception is the series of $AO_2H^+.nH_2O$ ions observed for the first time with Ti and V. However, it is of interest to consider why particular members of the various hydrate series give rise to uncommonly large signals.

For titanium, the $TiOH^+.nH_2O$ ($n = 0$–3) series, which includes the $Ti(OH)_2H^+.nH_2O$ ($n = 0$–2) as a sub-series, accounts for 80.0% of the Ti ions and emphasizes the Ti(II) oxidation state. The first member is explained by the protonation of TiO via reaction [6], and the second member by protonation of $Ti(OH)_2$ involving reaction [13]. The inference is that most of the Ti is present in the flame as TiO and/or $Ti(OH)_2$, both of which may have PA values > $PA(H_2O)$. The third member must be formed by hydration but its signal is exceptionally large for a hydrate. Since Ti has four valence electrons, this ion may have a special stability associated with the metal atom surrounded by an inert-gas octet of electrons. As with the Sc example discussed above, it is not clear whether protonation occurs on the lone pair of Ti to give $H:Ti(OH)_2^+.H_2O$ or on an O atom giving $:TiOH^+.2H_2O$. Further hydration produces the fourth and last member of the series in which the Ti atom is surrounded by 10 electrons.

For vanadium having five valence electrons, the same chemistry is in evidence but to a much smaller extent. Only the first two members of the $VOH^+.nH_2O$ ($n = 0$, 1) series were observed, both of which are radical cations, and the V(II) oxidation state is less prominent. The emphasis shifts to the $VO^+.nH_2O$ ($n = 0$–3) series involving the V(III) oxidation state. Similarities with the Sc ion chemistry are expected; the large ion signals are down-shifted to the next lower member of the series since V contains an extra electron pair compared with Sc. The major ion chemistry for V is essentially the same as that shown for Sc in Fig. 7. The third member of the series has a relatively large magnitude compared with the second, and completes an electron octet around the V atom. The fourth member terminates the series with 10 electrons surrounding V. The inference for vanadium neutral compounds present in the flame is that much of the V is present as $V(OH)_3$ and/or OVOH; presumably HVO_2 is a much less probable entity.

Similar reasoning indicates why this same series of ions is much less prominent for titanium involvng the Ti(III) oxidation state. The first four members are observed but amount to only 5.7% of the total Ti ions. All the members are, of course, radical cations; even if they were to be formed at appreciable rates, presumably the relatively high reactivity of such species mitigates against high steady-state concentrations. The second member of the series, $Ti(OH)_2^+$, is relatively prominent. Its profile given in Fig. 8 peaks early in the burnt gas, probably because of its subsequent reactivity further downstream. It might be formed by radical attack on the major $Ti(OH)_2H^+$ ion according to

$$[23a, b] \quad Ti(OH)_2H^+ + H, OH \rightleftharpoons Ti(OH)_2^+ + H_2, H_2O$$

which is similar to reaction [7] involving the dehydrogenation of the metallic hydride ions.

The $AO_2H^+.nH_2O$ ($n = 0$–2) series of ions, which includes the $A(OH)_3^+.nH_2O$ ($n = 0$, 1) sub-series, was observed for the first time with Ti and V. If the flame with Ti additive contains a small amount of TiO_2 involving the Ti(IV) oxidation state, it can protonate according to

Can. J. Chem. Downloaded from www.nrcresearchpress.com by 112.217.228.212 on 09/07/12
For personal use only.

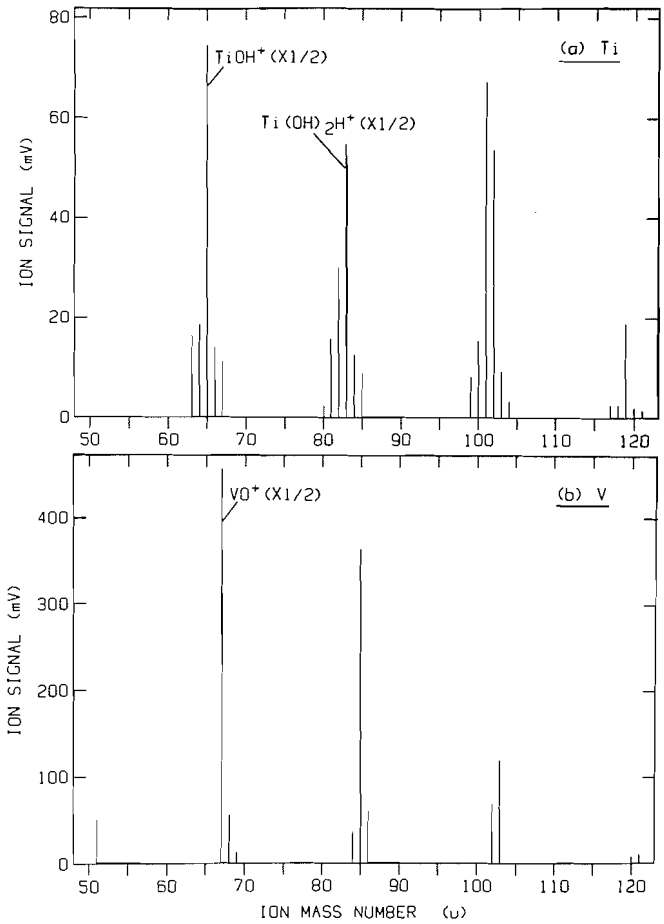

FIG. 9. Mass spectra observed at a fixed point on the flame axis at z = 1.25 mm downstream in the burnt gas when the flame is doped with equal molar concentrations (~1 ppm) of (*a*) Ti and (*b*) V.

[24] $H_3O^+ + TiO_2 \rightleftharpoons TiO_2H^+ + H_2O$

with subsequent hydration of the parent ion. The same production mechanism may also apply to V, although alternative reactions can be envisaged involving the major $VO^+.nH_2O$ ions as precursors. For example, to produce the one ion $VO_2H^+.H_2O$ (or $V(OH)_3^+$), possible reactions include

[25] $VO^+.H_2O$ or $V(OH)_2^+ + H_2O \rightleftharpoons H + VO_2H^+.H_2O$ or $V(OH)^+$

[26a, b] $V(OH)_2^+.H_2O$ or $V(OH)_3H^+ + H, OH \rightleftharpoons V(OH)_3^+ + H_2, H_2O$

with similar reactions for other members of the series. All the vanadium ions in this series are free radicals. In particular, the comparatively large signal obtained for the second member, assumed to be $V(OH)_3^+$ with 7 electrons around the metal atom, is remarkable. Whether the ion structure is pyramidal or planar trigonal and the character of the odd electron are not clear but the symmetry of the possible structures is noteworthy. Another strikingly similar example for Ti will be encountered below.

The last $A^+.nH_2O$ ion series includes the $A(OH)H^+.nH_2O$ ions as a sub-series. Only the first two members were observed for vanadium in Table 2 and probably arise by protonation of V atoms followed by H-atom abstraction and subsequent hydration in the manner already discussed for Cr and Mn via reactions [5], [7], and [10]. The uncommon V(I) oxidation state is involved in V^+ but V(III) can be invoked for its first hydrate if it is $HVOH^+$. The chemistry for Ti must be different because the first four hydrates were observed but not Ti^+ (see Table 2). One obvious explanation is protonation of TiOH by reaction [12] with subsequent hydration. The major $AOH^+.nH_2O$ ions could be involved as precursors in reactions such as

[27a, b] $TiOH^+.nH_2O + H_2, H_2O \rightleftharpoons H, OH + HTiOH^+.nH_2O$ or $Ti^+.(n+1)H_2O$

[28] $TiOH^+.nH_2O + H \rightleftharpoons Ti^+.nH_2O + H_2O$

All of the ions are odd-electron species. A remarkably large signal is obtained for one member of the series, assumed to be $Ti^+.3H_2O$ with 9 electrons around the metal atom in the unusual Ti(I) oxidation state. The considerations already noted for $V(OH)_3^+$ involving structure, character of the odd electron and molecular symmetry apply equally in the present case. That these two radical cations are particularly stable against chemical attack in the burnt gas of the flame is noteworthy. In general, if chemical reactivity is enhanced by irregularities in the electron density distribution around a molecule, surely such irregularities are reduced when the molecular symmetry is increased.

Summary and conclusions

The same fuel-rich, premixed, CH_4–O_2 flame at 2200 K and atmospheric pressure was doped with the same concentration (~1 ppm) of Sc, Ti, V, Cr, and Mn as was employed in Part I (1) for similar studies of Fe, Co, Ni, Cu, and Zn. Chemical ionization by H_3O^+ of these metal atoms A and a number of their compounds which may exist in flames including AOH, AO, OAOH (oxyhydroxide), $A(OH)_2$, $A(OH)_3$, and AO_2 produces series of metallic ions in the burnt-gas region which were observed by sampling the flame into a mass spectrometer. Apart from MnH^+, the observed ions can be described by four hydrate series, each of which contains one or two isomeric sub-series; namely, (*a*) $A^+.nH_2O$ (containing $A(OH)H^+.(n-1)H_2O$ as a sub-series), (*b*) $AOH^+.nH_2O$ (containing $A(OH)_2H^+.(n-1)H_2O$ as a sub-series), (*c*) $AO^+.nH_2O$ (containing $A(OH)_2^+.(n-1)H_2O$ as a sub-series, which contains $A(OH)_3H^+.(n-2)H_2O$ as a second sub-series), and (*d*) $AO_2H^+.nH_2O$ (containing $A(OH)_3^+.(n-1)H_2O$ as a sub-series, which contains $A(OH)_4H^+.(n-2)H_2O$ as a second sub-series). The value of n ranges from 0 to 4 for (*a*), 3 for (*b*) and (*c*), and 2 for (*d*). Thus, the observed series all terminate with four ligands around the central metal atom, and not five or six as is often the case for solutions and solids of transition metals near room temperature. This limited number of ligands may be caused by the high temperature, and also by the gas phase; in condensed phases, the ligands' electrons will be more delocalized by hydrogen bonding. All of the series of observed ions terminate with a maximum of 10 electrons around the metal atom with the single exception of $Ti^+.4H_2O$ which has 11. Not all metals exhibit all of the series. Some of the higher hydrates are undoubtedly enhanced by cooling during sampling into the mass spectrometer.

The ion chemistry of Cr and Mn has much in common with that of Fe, Co, Ni, and Cu discussed in Part I. It is dominated by series (*a*) involving proton transfer to A followed by dehydrogenation to form A^+ with subsequent hydration. The preponderance and slow electron–ion recombination of A^+ for Cr and Mn are responsible for the comparatively large metallic ion signal obtained for these two metals in the burnt gas. Series (*b*) involving proton transfer to AO and/or $A(OH)_2$ is much less prominent. In contrast, the ion chemistry of Sc is completely different; series (*c*) accounts for 99% of the observed ions. The major ions appear to involve proton transfer to OScOH and $Sc(OH)_3$. This

Can. J. Chem. Downloaded from www.nrcresearchpress.com by 112.217.228.212 on 09/07/12
For personal use only.

interpretation maintains Sc(III) as the single oxidation state exhibited by all of the ions and neutral species. It is even true for the minor ions of series (*a*) if $Sc^+.H_2O$ does, in fact, have the $HScOH^+$ structure formed by protonation of HScO.

For Ti and V, ions were observed from all four series. Ions from series (*d*) involving proton transfer to AO_2 were encountered for the first time. The major Ti ions in series (*b*) appear to arise by protonation of TiO and $Ti(OH)_2$; the Ti(II) oxidation state is favoured. For V, like the ion chemistry for Sc with two additional electrons, the major ions in series (*c*) appear to form by protonation of OVOH and $V(OH)_3$; the V(III) oxidation state is favoured. Series (*a*) and (*c*) for titanium emphasizing Ti(III), and series (*a*) and (*b*) for vanadium emphasizing V(I) and V(II) are less prominent. Two radical cations interpreted as $Ti^+ \cdot 3H_2O$ and $V(OH)_3^+$ yield unexpectedly large signals. Their stability against chemical attack in the burnt gas region of the flame is attributed to their high degree of symmetry, whether pyramidal or planar trigonal.

Acknowledgements

Support of this work by the Natural Sciences and Engineering Research Council of Canada under Grant No. A-1604 is acknowledged. We wish to thank Professors D. V. Stynes and A. B. P. Lever for a number of helpful discussions.

1. Q. Tran, N. S. Karellas, and J. M. Goodings. Can. J. Chem. **66**, 2210 (1988).
2. J. M. Goodings and S. M. Graham. Int. J. Mass Spectrom. Ion Processes, **56**, 193 (1984).
3. R. G. Soundy and H. Williams. 26th AGARD Propulsion and Energetics Panel, Pisa, Italy, AGARD Conference Proceedings No. 8. Vol. I. *Edited by* H. O. Wilsted. 1965.
4. A. N. Hayhurst and N. R. Telford. Trans. Faraday Soc. **66**, 2784 (1970).
5. D. D. Wagman, W. H. Evans, V. B. Parker, R. H. Schumm, I. Halow, S. M. Bailey, K. L. Churney, and R. J. Nuttall. The NBS tables of chemical thermodynamic properties. J. Phys. Chem. Ref. Data, **11**, Suppl. No. 2. 1982.
6. H. M. Rosenstock, K. Draxl, B. W. Steiner, and J. T. Herron. Energetics of gaseous ions. J. Phys. Chem. Ref. Data, **6**, Suppl. No. 1. 1977.
7. L. Sallans, K. R. Lane, R. R. Squires, and B. S. Freiser. J. Am. Chem. Soc. **107**, 4379 (1985).
8. M. W. Chase, Jr., C. A. Davies, J. R. Downey, Jr., D. J. Frurip, R. A. McDonald, and A. N. Syverud. JANAF Thermochemical Tables, 3rd ed. J. Phys. Chem. Ref. Data, **14**, Suppl. No. 1. 1985.
9. L. Sunderlin, N. Aristov, and P. B. Armentrout. J. Am. Chem. Soc. **109**, 78 (1987).
10. J. L. Elkind and P. B. Armentrout. J. Phys. Chem. **91**, 2037 (1987).
11. J. L. Elkind and P. B. Armentrout. J. Phys. Chem. **89**, 5626 (1987).
12. J. L. Elkind and P. B. Armentrout. J. Chem. Phys. **84**, 4862 (1986).
13. R. R. Squires. J. Am. Chem. Soc. **107**, 4385 (1985).
14. P. J. Padley and T. M. Sugden. Trans. Faraday Soc. **55**, 2054 (1959).
15. M. M. Kappes and R. H. Staley. J. Phys. Chem. **85**, 942 (1981).
16. S. G. Lias, J. F. Liebman, and R. D. Levin. Evaluated gas phase basicities and proton affinities of molecules; heats of formation of protonated molecules. J. Phys. Chem. Ref. Data, **13**, 695 (1984).
17. R. D. Levin and S. G. Lias. Ionization and appearance potential measurements, 1971–1981. NSRDS-NBS 71, U.S. Government Printing Office, Washington, D.C. 1982.
18. E. M. Bulewicz, L. F. Phillips, and T. M. Sugden. Trans. Faraday Soc. **57**, 921 (1960).
19. E. M. Bulewicz and P. J. Padley. Proc. R. Soc. London A, **323**, 377 (1971).
20. K. Schofield and T. M. Sugden. Tenth Symposium (International) on Combustion, The Combustion Institute, Pittsburgh, PA. 1969. p. 589.

Can. J. Chem. Downloaded from www.nrcresearchpress.com by 112.217.228.212 on 09/07/12
For personal use only.

Effect of residual linear orientation on the optical properties of cholesteric films

ANNA M. RITCEY,[1] GÉRARD CHARLET,[2] AND DEREK G. GRAY

Pulp and Paper Research Institute of Canada and Department of Chemistry, McGill University, 3420 University St., Montreal, P.Q., Canada H3A 2A7

Received November 9, 1987

ANNA M. RITCEY, GÉRARD CHARLET, and DEREK G. GRAY. Can. J. Chem. **66**, 2229 (1988).

The apparent circular dichroism arising from the selective reflection of circularly polarized light by cholesteric films of (hydroxypropyl)cellulose is extremely sensitive to residual linear orientation. The introduction of a uniaxially oriented film in the spectropolarimeter beam in front of a liquid crystalline sample may change both the intensity and the sign of the observed mesophase reflection band. The results can be understood by a simple consideration of the way in which the polarization state of light is altered as it traverses the birefringent film. These observations emphasize a potential problem in the use of circular reflectivity as a method to characterize the reflection properties of polymeric cholesteric liquid crystals. The presence of linear orientation in such samples can give rise to artifacts.

ANNA M. RITCEY, GÉRARD CHARLET et DEREK G. GRAY. Can. J. Chem. **66**, 2229 (1988).

Lorsque des films cholestériques d'(hydroxypropyl)cellulose réfléchissent sélectivement de la lumière polarisée d'une façon circulaire, on observe un dichroïsme circulaire apparent qui est très sensible à l'orientation linéaire des résidus. Lorsqu'on introduit un film orienté dans un seul axe dans le faisceau d'un spectropolarimètre, devant un échantillon de cristal liquide, il peut se produire un changement tant de l'intensité que du signe de la bande observée pour la réflexion de la mésophase. On peut comprendre facilement les résultats en faisant appel à une considération simple impliquant le façon dont l'état de polarisation de la lumière est altérée lorsqu'elle traverse le film biréfringent. Ces observations suggèrent que des problèmes peuvent surgir lors de l'utilisation de la réflectivité circulaire pour caractériser les propriétés de réflexion des cristaux liquides cholestériques de polymères. La présence d'orientations linéaires dans de tels échantillons peut donner lieu à des artéfacts.

[Traduit par la revue]

Can. J. Chem. Downloaded from www.nrcresearchpress.com by 112.217.228.212 on 09/07/12
For personal use only.

Introduction

Since the initial report (1) of the formation of a cholesteric liquid crystalline phase in concentrated aqueous solutions of (hydroxypropyl)cellulose (HPC), many other cellulose derivatives have been found to form similar ordered phases (2, 3). These liquid crystals possess unique optical properties arising from the selective reflection of light by the helicoidal arrangement of molecules found within them. This twisted supramolecular structure, illustrated schematically in Fig. 1, is characterized by its handedness and by the pitch, P, which is the distance through which a vector representing the average molecular orientation completes a 360° rotation. DeVries (4) formulated a theory for the optical properties of the cholesteric mesophase, predicting the reflection of circularly polarized light. For an incident beam parallel to the helicoidal axis, the wavelength of reflected light corresponds to the pitch. In addition to being selective with respect to wavelength, this reflection is also selective with respect to handedness: right-handed cholesteric liquid crystals reflect only right circularly polarized light and, similarly, left-handed cholesterics reflect only left circularly polarized light. At wavelengths within the reflection band, the intensity of light transmitted by a cholesteric mesophase will therefore be different for incident light of the two circular polarizations and the reflection properties can be monitored as apparent circular dichroism (CD) or "circular reflectivity".

The optical properties of dry HPC films cast from mesophase solution have recently been reported (5). When heated, these HPC films reflect circularly polarized light, indicating that the cholesteric order present in the lyotropic solution is retained on drying. This is the case for the films cast from a mesophase sample in the unperturbed cholesteric state. We would like to report here an additional optical effect, which is observed if the mesophase solution is sheared and then dried before the system can relax to the equilibrium cholesteric structure. Such samples sometimes show a reversal in sign of the CD peak. Normally this would indicate a reversal of the cholesteric structure from a right- to a left-handed helicoidal arrangement. This is physically improbable. The molecular orientation (6, 7) induced by shear and frozen-in during rapid drying may, however, drastically affect the circular reflectivity spectra of these films, and the presence of linear orientation in such samples can give rise to major artifacts.

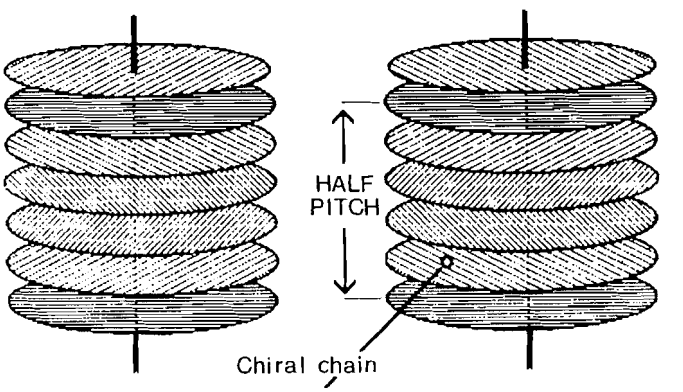

FIG. 1. Schematic representation of the molecular order found in cholesteric liquid crystals. The cholesteric phase can be pictured as consisting of a series of molecular layers perpendicular to the cholesteric axis. The molecules within each layer point in the same general direction and each layer is twisted relative to the next so as to generate a helicoidal supramolecular structure.

The problems associated with circular dichroism measurements of optically active chromophores in the presence of linear orientation have been treated in the literature (8–10). This paper illustrates that similar considerations are very significant in the

[1]Present address, Max-Planck Institute for Polymer Research, Postfach 3148, D-6500 Mainz, West Germany.

[2]Present address, Departement de chimie, Université Laval, Québec (Québec), Canada G1K 7P4.

characterization of the cholesteric reflection properties of polymeric liquid crystals. In these systems linear orientation is promoted by the ease with which molecular alignment is achieved under shear and the relatively high viscosities that restrict relaxation.

A theoretical analysis of the optical properties of samples that exhibit both linear and circular birefringence is complex since these two properties cannot be treated separately. The required Mueller matrix formalism is well described in the literature (9) and no attempt will be made to apply this approach in the present case. However, since the characterization of cholesteric liquid crystals by apparent circular dichroism is rapid and convenient, but subject to artifacts introduced by linear birefringence, a brief quantitative discussion is presented of results for a simplified model system consisting of a birefringent film and a cholesteric liquid crystal placed separately in the spectrometer beam. This provides a simple illustration of the observed artifacts.

Experimental

Sample preparation

Dry films were prepared from aqueous mesophase solutions of (hydroxypropyl)cellulose (Aldrich Chemical Co., nominal molecular weight 100 000) having a concentration of ~65% polymer by weight. The mesophase samples were pressed between two glass slides and allowed to relax to the equilibrium cholesteric structure, characterized by the appearance of a uniform reflection colour. The two slides were then separated by sliding lengthwise. The resulting thin HPC films dry rapidly at ambient conditions. Complete drying was achieved under vacuum.

Banded textures were observed with a Reichert polarizing microscope equipped with a rotating stage.

Reflectivity spectra

Circular reflectivity (CR) spectra were recorded with a Jasco J-500C spectropolarimeter. Temperature control was achieved by placing samples in a microscope hot stage (Mettler FP52) mounted in the spectrometer beam. All heating experiments were performed at a rate of 0.2°C/min.

Results and discussion

Optical properties

HPC films cast from mesophase solutions that have been sheared and then dried before relaxation to the equilibrium cholesteric structure is complete unexpectedly show a *positive* circular reflection band. At room temperature this reflection band is situated below 300 nm but, as is the case for cholesteric HPC films, moves to longer wavelengths on heating. Spectra recorded for this type of sample when heated at 150°C are shown in Fig. 2. This behaviour is very similar to that observed for the cholesteric films cast under equilibrium conditions, indicating that the peaks shown in Fig. 2 are cholesteric reflection bands. However, the reflection bands for sheared and equilibrium films are of opposite signs.

The lyotropic cholesteric liquid crystals formed by HPC (11), as well as the thermotropic mesophases formed by ester derivatives of HPC (12, 13), are right-handed and therefore preferentially reflect right circularly polarized light and give negative CR spectra. It is unlikely, however, that the positive reflection band observed here arises from the selective reflection of left circularly polarized light from a left-handed cholesteric arrangement. The method of sample preparation suggests that these films are uniaxially oriented and this is confirmed by the linear birefringence observed when the films are viewed between crossed polars. The polarization state of light will therefore be altered as it traverses such a sample and this change in polarization will in turn affect the recorded CR spectrum. In some cases, as shown below, the result can be a reversal in the sign of a CR spectrum.

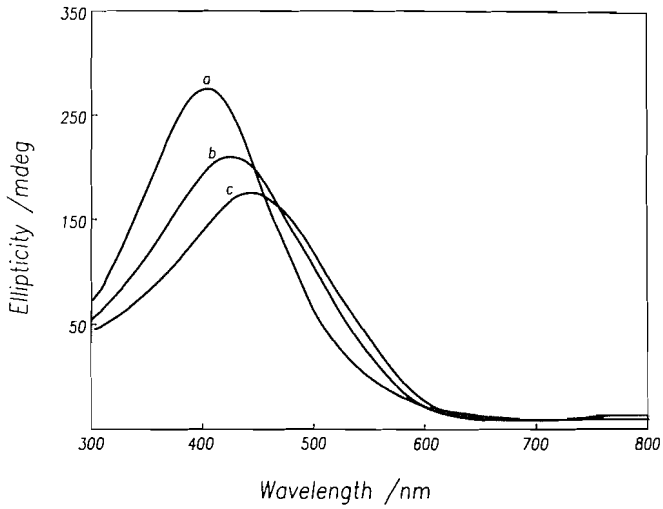

FIG. 2. Circular reflectivity spectrum of an HPC film cast from aqueous mesophase solution under shear recorded (a) 2, (b) 12, and (c) 40 minutes after heating from room temperature to 150°C.

The structure of the films cast under shear is quite complex in that the molecular orientation varies across the thickness of the sample. In addition to being linearly oriented, such a film must also possess the cholesteric component responsible for the observed reflection band. This cholesteric component can be eliminated by the preparation of very thin (<5 μm) samples, which dry almost immediately after shear. The composite nature of films that give positive reflection spectra can be modeled by placing one or more of these thin uniaxially oriented samples in the spectrometer beam along with a well-ordered lyotropic cholesteric mesophase.

The CR spectra obtained for such a combination of samples are shown in Fig. 3. The bottom curve (a) is the reflection band of the lyotropic liquid crystal alone. In this case the sample is an aqueous HPC mesophase and the reflection band is negative as expected. The presence of a birefringent HPC film, placed in the spectrometer beam in front of the mesophase sample, significantly reduces the intensity of the reflection band (curve b). The introduction of a second piece of the same film affects the spectrum differently, depending on the orientation of its shear direction relative to that of the first. Two oriented films placed so that the shear direction of one is perpendicular to that of the other have no effect on the mesophase spectrum, while the introduction of a second oriented film parallel to the first reverses the sign of the peak (curve c). If the samples are placed so that the spectrometer beam first passes through the mesophase sample and then the oriented film, the reflection spectrum is unchanged from that recorded for the mesophase alone.

These CR spectra can be understood through the following simple consideration of the polarization state of the light incident on the mesophase sample. The spectropolarimeter monitors the intensity of light transmitted by a sample as the incident radiation is modulated between left and right circularly polarized light. This cirularly polarized light can be decomposed into two perpendicular plane-polarized waves that are 90° out-of-phase. As these two perpendicular waves pass through a birefringent sample an additional phase difference, δ, develops between them. If the sheared sample has a birefringence such that $\delta = \pm 90°$ (i.e., the oriented sample is a quarter-wave plate),

Can. J. Chem. Downloaded from www.nrcresearchpress.com by 112.217.228.212 on 09/07/12
For personal use only.

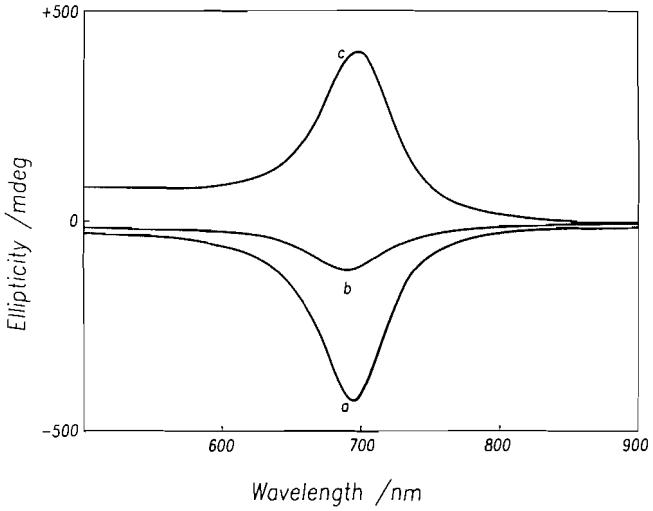

FIG. 3. Circular reflectivity spectrum of an aqueous HPC mesophase: (a) alone in the spectrometer beam; (b) with one HPC oriented film in beam; (c) with two oriented HPC films in the beam.

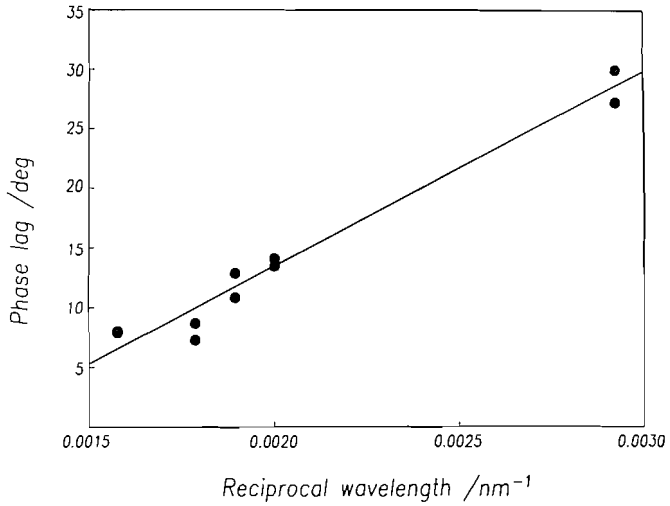

FIG. 4. Wavelength dependence of the phase lag introduced between two perpendicular waves on traversing an oriented HPC film. The phase lag was calculated from the observed decrease in the ellipticity of the reflection band of various HPC aqueous mesophases.

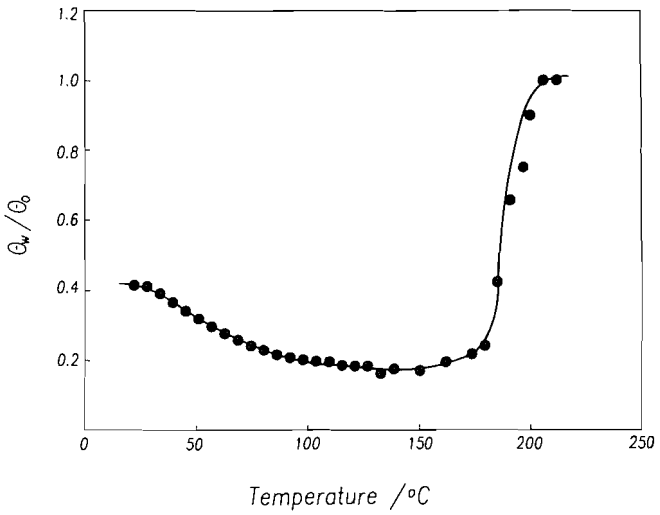

FIG. 5. Effect of waveplate temperature on the observed maximum of a CD spectrum of an HPC aqueous mesophase. θ_0 and θ_w are the ellipticity at the peak maximum in the absence and presence of the waveplate, respectively.

the resultant of the two waves after traversing the birefringent film will be plane polarized. The mesophase sample will then reflect the same intensity of light regardless of the handedness of the circularly polarized light being produced by the CD modulator, and the CR reflection band will therefore vanish. If, on the other hand, $\delta = \pm 180°$ (i.e., the oriented sample is a half-wave plate), the birefringent film will reverse the handedness of each of the circular polarizations produced by the CD modulator. In this case the recorded CR peak of the mesophase probe is reversed in sign.

In the intermediate cases the incident circularly polarized light is converted to elliptically polarized light as it passes through the birefringent film. It may be shown (see Appendix) that the observed maximum intensity of the reflection peak, θ_w, is related to that of the mesophase alone, θ_0, by

$$[1] \quad \theta_w/\theta_0 = 1 - \sin\delta$$

for $0° \leq \delta \geq 90°$. (Since the handedness of the radiation was not considered in the deviation, these limits for δ restrict eq. [1] to cases that do not involve a change in the sign of the observed peak.)

The phase shift δ is related to the birefringence, $n_1 - n_2$, of the oriented sample by

$$[2] \quad \delta = \frac{2\pi\,\Delta z}{\lambda}(n_1 - n_2)$$

where Δz is the film thickness, λ is the wavelength of the incident light, and n_1 and n_2 are the refractive indices parallel and perpendicular to the orientation direction.

For a given oriented film, δ can be determined as a function of wavelength by measuring θ_w/θ_0 for a number of lyotropic mesophase samples of various concentrations and therefore different wavelengths of maximum reflection. Values of δ determined in this way are plotted against reciprocal wavelength in Fig. 4. The film birefringence is calculated as 0.009 from the slope when the film thickness is taken as 5 μm. This value is of the same order of magnitude as the birefringence measured for several HPC cholesteric mesophases (14).

The molecular orientation responsible for the retardation plate behaviour of these HPC films persists to relatively high temperatures. The ratio of the observed maximum (θ_w) to the true intensity (θ_0) of a mesophase reflection band is plotted in Fig. 5 as a function of the temperature of the oriented HPC film. The true reflection band of the mesophase is observed only when the temperature of the oriented sample reaches 200°C. The light intensity transmitted by the sample between crossed polars also decreases sharply near this temperature, indicating a loss of birefringence.

Banded texture

When viewed between crossed polars, oriented films of HPC cast from a sheared mesophase exhibit the banded texture that has been reported for HPC films prepared in a similar manner (6, 7), for shear oriented films prepared from the thermotropic melt (15), and as an intermediate structure in the relaxation of HPC lyotropic mesophases after shear (16). The general behaviour of these bands when the sample is rotated agrees with previous observations (6, 17). However, the material and molecular

Can. J. Chem. Downloaded from www.nrcresearchpress.com by 112.217.228.212 on 09/07/12
For personal use only.

relaxation processes that cause the bands to form after a liquid crystalline polymer has been sheared remain obscure.

Like the birefringence of the oriented films, the banded texture persists to relatively high temperatures. The bands are difficult to discern in samples heated at 185°C since the field begins to darken as the birefringence vanishes. The bands and the birefringence, however, reappear when such samples are cooled.

Conclusions

Residual shear-induced orientation in cholesteric liquid crystals complicates the interpretation of the circular reflectivity spectra of such samples. However, the optical properties of partially oriented films indicate a potential use in the preparation of single component optical devices possessing the necessary properties for applications both as filters or circular polarizers and as waveplates (18).

Acknowledgements

We thank the Natural Sciences and Engineering Research Council of Canada for support.

1. R. S. Werbowyj and D. G. Gray. Mol. Cryst. Liq. Cryst. (Letters), **34**, 97 (1976).
2. R. D. Gilbert and P. A. Patton. Prog. Polym. Sci. **9**, 115 (1983).
3. D. G. Gray. J. Appl. Polym. Sci.: Appl. Polym. Symp. **37**, 179 (1983).
4. H. L. deVries. Acta. Crystallogr. **4**, 219 (1951).
5. G. Charlet and D. G. Gray. Macromolecules, **20**, 33 (1987).
6. M. Horio, S. Ishikawa, and K. Oda. J. Appl. Polym. Sci.: Appl. Polym. Symp. **41**, 269 (1985).
7. Y. Nishio, T. Yamane, and T. Takahashi. J. Polym. Sci.: Polym. Phys. Ed. **23**, 1053 (1985).
8. R. L. Disch and D. I. Sverdlik. Anal. Chem. **41**, 82 (1969).
9. H. P. Jensen, J. A. Schellman, and T. Troxell. Appl. Spectrosc. **32**, 192 (1978).
10. Y. Shindo and Y. Ohmi. J. Am. Chem. Soc. **107**, 91 (1985).
11. R. S. Werbowyj and D. G. Gray. Macromolcules, **17**, 1512 (1984).
12. G. V. Laivins and D. G. Gray. Polymer, **26**, 1435 (1985).
13. S. N. Bhadani and D. G. Gray. Mol. Cryst. Liq. Cryst. **99**, 29 (1983).
14. S. Suto, S. Kimura, and M. Karasawa. J. Appl. Polym. Sci. **33**, 3019 (1987).
15. Y. Nishio and T. Takahashi. J. Macromol. Sci. Phys. *b***23**, 483 (1985).
16. A. M. Donald, C. Viney, and A. P. Ritter. Liq. Cryst. **1**, 287 (1986).
17. P. Navard and A. E. Zachariades. J. Polym. Sci.: Polym. Phys. **25**, 1089 (1987).
18. S. D. Jacobs. *In* CRC Handbook of Laser Science and Technology. Vol. 4. Optical Materials: Part 2. *Edited by* M. J. Weber. CRC Press, Cleveland, OH. 1986. p. 409.
19. Jasco model J-500 spectropolarimeter instruction manual. Jasco International Company, Tokyo, Japan.

Appendix

Derivation of equation [1]

The Jasco J-500C spectropolarimeter monitors the intensity of light transmitted by a sample while an incident radiation of constant intensity, I_0, is modulated between left and right circularly polarized states. If the sample preferentially absorbs or reflects light of one of these polarizations, the intensity reaching the detector will depend on the polarization of the incident beam. If we choose as the sample a right-handed cholesteric mesophase, the time dependence of the intensity reaching the detector will be as illustrated in Fig. A1. Assuming that right circularly polarized light is reflected with a reflectivity R, and that all left circularly polarized light is transmitted, the intensity reaching the detector for incident right and left circularly polarized light is $I_R = I_0 - RI_0$ and $I_L = I_0$ respectively.

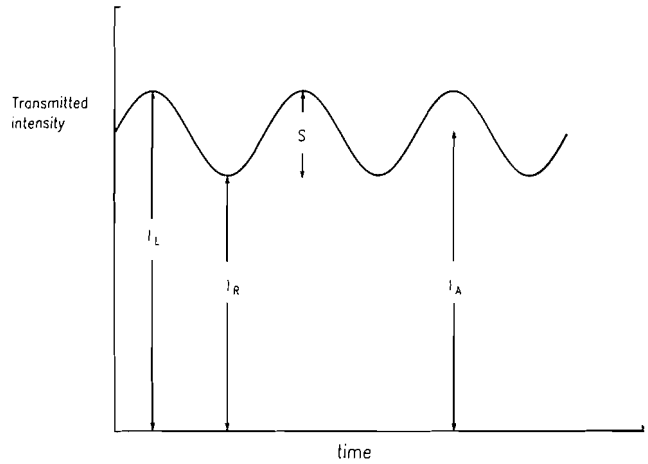

FIG. A1. Intensity of light reaching the detector of the spectropolarimeter as a function of time when a sample that preferentially reflects right circularly polarized light is placed in the beam. I_L and I_R are the transmitted intensities when the CD modulator is producing left and right circularly polarized light, respectively. S is the difference between these two intensities and I_A is their average.

The spectropolarimeter reports the spectrum as ellipticity, θ, as a function of wavelength. The recorded ellipticity is directly proportional to the parameters S and I_A:

$$[3] \quad \theta = C S/I_A$$

where C is a constant (19) and S and I_A are defined in Fig. A1.

The relationship between the observed ellipticity at the wavelength of maximum reflection and the reflectivity of the mesophase is then

$$[4] \quad \theta = \frac{-CR}{(1-R/2)}$$

Circularly polarized light can be decomposed into two linearly polarized components out-of-phase by 90°. The electric vector, $\boldsymbol{E}$, of right circularly polarized light propagating along the z-axis is given by

$$[5] \quad \boldsymbol{E} = E_0 \sin(\omega t)\,\boldsymbol{i} + E_0 \cos(\omega t)\,\boldsymbol{j}$$

where ω is angular frequency, t is time, and $\boldsymbol{i}$ and $\boldsymbol{j}$ are the unit vectors along the x- and y-axes, respectively. As these waves traverse the birefringent film where $n_i \neq n_j$, an additional phase lag, δ, develops between them, and now

$$[6] \quad \boldsymbol{E} = E_0 \sin(\omega t + \delta)\,\boldsymbol{i} + E_0 \cos(\omega t)\,\boldsymbol{j}$$

Therefore, at any point along the beam path

$$[7] \quad E_x = E_0 \sin(\omega t + \delta)$$

and

$$[8] \quad E_y = E_0 \cos(\omega t)$$

These equations can be combined to give

Can. J. Chem. Downloaded from www.nrcresearchpress.com by 112.217.228.212 on 09/07/12
For personal use only.

[9] $E_x^2 - 2E_xE_y \sin \delta + E_y^2 = E_0^2 \cos^2 \delta$

This is the equation of an ellipse with major axis tilted at 45° to the x- and y-axes. After rotation of the axes by 45° the general form of an ellipse is obtained:

[10] $$\frac{E_x^2}{E_0^2(1 + \sin \delta)} + \frac{E_y^2}{E_0^2(1 - \sin \delta)} = 1$$

for $-90° \leq \delta \leq 90°$.

The birefringent film therefore serves to change the light reaching the mesophase sample from alternating right and left *circularly* polarized light to alternating right and left *elliptically* polarized light. The selective reflection of elliptically polarized light from the cholesteric mesophase can be evaluated by considering this polarization as the sum of a circularly polarized component and a plane-polarized component. The intensities of these two components, I_{cir} and I_{pl} respectively, are given by

[11] $I_{cir} = 2E_0^2 (1 - \sin \delta)$

[12] $I_{pl} = 2E_0^2 (1 - \cos \delta)$

for $0° \leq \delta \leq 90°$. When the instrument is producing right circularly polarized light the sample will reflect R times the circularly polarized component and $\frac{1}{2}R$ times the plane-polarized component:

[13] $I_R = I_0 - RI_0(1 - \sin \delta) - \frac{1}{2}I_0R(1 - \cos \delta)$

When the instrument is producing left circularly polarized light the same proportion of the linearly polarized component is reflected, but all of the circularly polarized component is transmitted:

[14] $I_L = I_0 - \frac{1}{2}I_0R(1 - \cos \delta)$

The presence of the waveplate therefore serves to increase I_R and decrease I_L. For relatively low reflectivities it is reasonable to assume that I_A is unaffected by the waveplate, and that the major effect on the observed spectrum is through S. S in the presence of the waveplate, S_W, will be given by

[15] $S_w = I_0R(1 - \sin \delta)$

Therefore the ratio of the observed ellipticity in the presence of the waveplate, θ_w, to the observed ellipticity in the absence of the waveplate, θ_0, is

[16] $\theta_w/\theta_0 = (1 - \sin \delta)$

for $0° \leq \delta \leq 90°$.

This derivation treats only the simplified case when the linear birefringence and the circular reflectivity are physically separated. Consideration of the optical behaviour of birefringent cholesteric films, where a single polymer sample displays simultaneously these two optical properties, requires a more complex approach (9).

Can. J. Chem. Downloaded from www.nrcresearchpress.com by 112.217.228.212 on 09/07/12
For personal use only.

Ozonolysis of tetramethoxyethene[1]

KARL R. KOPECKY, JOSÉ MOLINA,[2] AND RODRIGO RICO[3]
Department of Chemistry, University of Alberta, Edmonton, Alta., Canada T6G 2G2

Received December 1, 1987

KARL R. KOPECKY, JOSÉ MOLINA, and RODRIGO RICO. Can. J. Chem. **66**, 2234 (1988).

Ozonolysis of tetramethoxyethene **1** produces 20–40% of dimethyl carbonate **3**, 35–60% of methyl trimethoxyacetate **7**, and 20–35% of the dioxetane **8** of **1**. Yields vary with initial concentration of **1**, temperature, and solvent. Singlet oxygen is produced, which reacts with **1** to form **8** and can be trapped with 2,5-dimethylfuran. No evidence for the formation of the molozonide of **1** was obtained. Up to 2.5 moles of **1** are consumed per mole of ozone. Ozonolysis of a mixture of **1** and 2,3-dimethyl-2-butene **12** gave the epoxide of **12** and three times the expected amount of the allylic hydroperoxide of **12**. A competing radical chain oxidation reaction is proposed to account for these products and the stoichiometry of the ozonolysis. The initial reaction in the ozonolysis of **1** is proposed to be an electron transfer reaction that is calculated to be exothermic by >35 kcal/mol. The resulting radical ions initiate the radical chain oxidation and combine to form the oxygenated epoxide **9** of **1**. Loss of singlet oxygen from **9** forms the epoxide **10**, which rearranges to **7**. At −95°C the zwitterion from **10** is trapped by CD_3OD to produce a mixture of **7** with one α OCD_3 group and pentamethoxyethanol with one β OCD_3 group from which a CH_3OD group is lost at ~ −10°C to form more deuterated ester.

KARL R. KOPECKY, JOSÉ MOLINA et RODRIGO RICO. Can. J. Chem. **66**, 2234 (1988).

L'ozonolyse du tétraméthoxyéthène (**1**) fournit de 20 à 40% de carbonate de diméthyle (**3**), de 35 à 60% de triméthoxyacétate de méthyle (**7**) et de 20 à 35% du dioxétane **8** du composé **1**. Les rendements varient avec la concentration initiale du composé **1**, avec la température et avec le solvant. Il se produit de l'oxygène singulet qui réagit avec le composé **1** pour donner du produit **8**; on peut le piéger avec du diméthyl-2,5 furanne. On n'a pas obtenu de résultats suggérant qu'il se forme du molozonide du composé **1**. Pour chaque molécule d'ozone, il y a 2,5 moles du composé **1** qui sont consommées. L'ozonolyse d'un mélange du composé **1** et du diméthyl-2,3 butène-2 (**12**) fournit l'époxyde **12** ainsi que de l'hydroperoxyde allylique de **12** qui se forme en quantités trois fois plus grandes que ce qu'on avait prévu. On suggère l'existence d'une réaction compétitive d'oxydation radicalaire en chaîne pour expliquer la formation de ces produits ainsi que la stoechiométrie de l'ozonolyse. On suggère que la réaction initiale, lors de l'ozonolyse du composé **1**, est une réaction de transfert électronique qui, d'après nos calculs, serait exothermique par >35 kcal/mol. Les ions radicaux qui en résultent initient la réaction d'oxydation radicalaire en chaîne et se combinent pour former l'époxyde oxygéné **9** du composé **1**. Par perte d'oxygène singulet, le composé **9** fournit l'époxyde **10** qui se transpose en composé **7**. À −95°C, le zwitterion provenant du composé **10** est piégé par le CD_3OD pour conduire à un mélange du composé **7** portant un groupement OCD_3 en α et de pentaméthoxyéthanol portant un groupement OCD_3 en β qui, par perte de CH_3OD à ~ −10°C, forme d'autre ester deutéré.

[Traduit par la revue]

Introduction

A general synthesis of tetraalkoxy-1,2,4,5-tetroxanes was required as part of a search for new luminescent molecules. There appear to be no examples of this class of compound but it would seem to be possible to prepare them by ozonolysis of tetraalkoxyethenes, which are readily available (1).

Studies were thus initiated with the simplest of these alkenes, tetramethoxyethene **1**. According to the commonly accepted mechanism of ozonolysis (2), treatment of **1** with ozone should result, via the molozonide **2**, in the formation of dimethyl carbonate **3** and tetramethoxy-1,2,4,5-tetroxane **5**, Scheme 1. In the participating solvent, methanol, dimethyl carbonate oxide **4** should be trapped to yield trimethoxymethyl hydroperoxide **6**.

In fact the ozonolysis of **1** was studied some time ago (3). Only 70% of the theoretical amount of ozone was consumed. The only products identified, by gas chromatography, were **3** and methyl trimethoxyacetate **7**. Both of these products were formed in the participating solvent, methanol, as well as in the inert solvents, chloroform and hexane. A 15% yield of peroxidic material, as determined by iodometric titration, was formed in methanol. These results indicate that peroxidic products are formed to only a minor extent.

Since compounds as sensitive as **5** and **6** might not survive the conditions of the gas chromatographic analysis used, the ozonolysis of **1** was reinvestigated using nmr spectroscopy at low temperature as a nondestructive method of analysis. The reaction proved to be more complex than anticipated. The dioxetane of **1** is a major product along with **3** and **7**, and there is evidence that a radical chain reaction contributes to product formation.

Results and discussion

Identification of dioxetane 8

Initially, ozonolyses were carried out at −78°C in nmr tubes and the reaction mixtures analyzed immediately by ^1H nmr spectroscopy at −70°C. Actually, the products were found to be stable for several hours at 20°C in inert solvents, but not in CD_3OD, if all traces of acid were removed from solvent and glassware. In addition to signals due to **3** and **7**, the nmr spectrum of the reaction mixture also exhibited a strong signal at δ 3.50 (CD_2Cl_2). This was originally thought to be due to the desired tetroxane **5**. However, the solution had only 49% of the

[1]Supported in part by a grant from the Natural Sciences and Engineering Research Council of Canada. Presented in part at the 189th National Meeting of the American Chemical Society, Miami Beach, FL, May 1985, Abstracts ORGN 0070, and at the 70th Canadian Chemical Conference, Quebec City, P.Q., June 1987, Abstracts ORG-32-D1.

[2]Recipient of a travel grant from the Consejeria de Education y Ciencia, Junta de Andalucia, 1986. Present address: Departamento de Quimica Organica, Universidad de Granada, 18071 Granada, Spain.

[3]Present address: Departamento de Quimica Organica, Universidad de Malaga, 29071 Malaga, Spain.

Can. J. Chem. Downloaded from www.nrcresearchpress.com by 112.217.228.212 on 09/07/12
For personal use only.

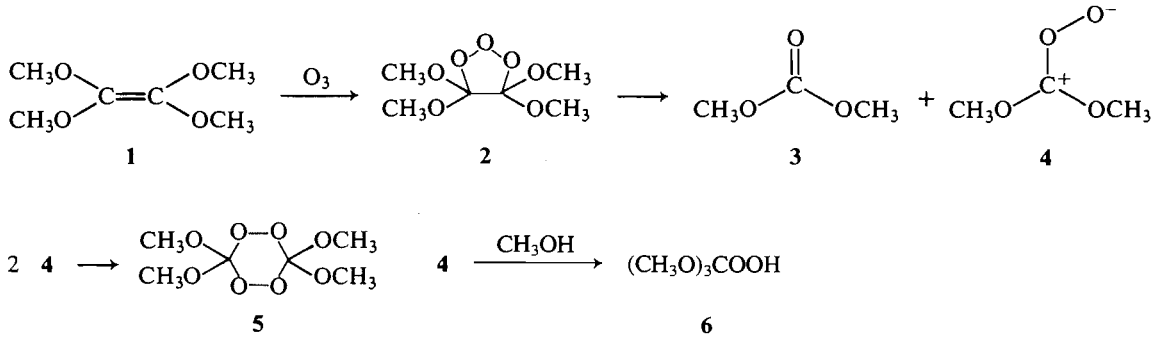

SCHEME 1

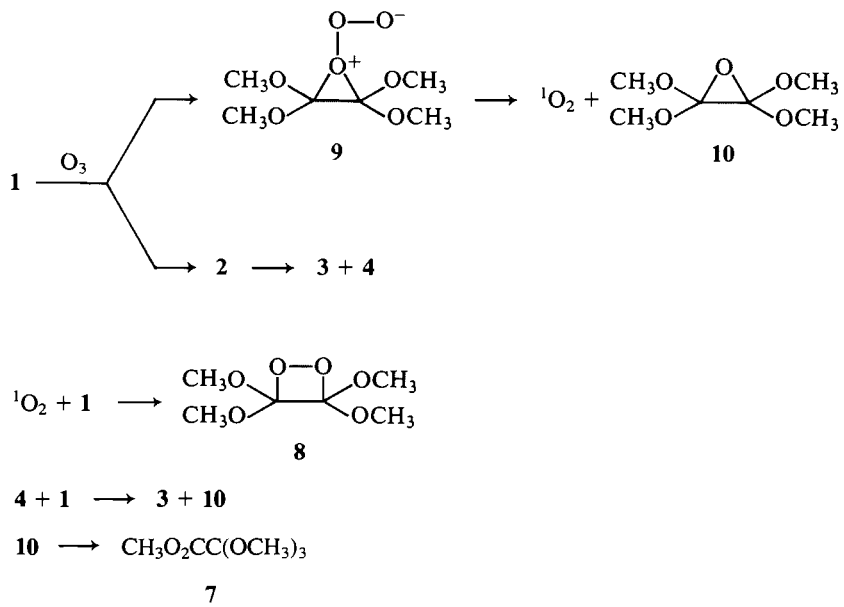

SCHEME 2

Can. J. Chem. Downloaded from www.nrcresearchpress.com by 112.217.228.212 on 09/07/12
For personal use only.

active oxygen content expected, as determined by iodometric titration. This suggested that the third product might be tetramethoxy-1,2-dioxetane **8**, and, in fact, the ^1H and ^{13}C nmr spectra of this product were identical with those of authentic **8** (4), which was prepared by oxidation of **1** with singlet oxygen. The dioxetane **8** is also formed upon ozonolysis of **1** in CD_3OD. The presence of a dioxetane was further confirmed by observation of bright luminescence upon addition of some of the reaction mixtures in CD_2Cl_2 or CD_3OD to hot toluene containing 9,10-dibromo- and 9,10-bis(phenylethynyl)anthracene. More evidence for the dioxetane structure was obtained by observation of the very rapid disappearance of the ^1H nmr signal attributed to **8** upon addition of a trace of $CuCl_2$ to an ozonolysis mixture in CD_3OD at $-60°C$. The intensity of the signal due to carbonate increased by a corresponding amount. Dioxetanes have been shown to be cleaved rapidly to carbonyl compounds by transition metal ions (5).

The yields of products formed in inert solvents vary with temperature, the initial concentration of **1**, and a little with solvent. They range from 20 to 40% **3**, 35 to 55% **7**, and 20 to 35% **8**, Table 1. Amounts of dioxetane formed are thus quite significant. There is no evidence that any other products are formed in the ozonolysis of **1** in inert solvents or, above $-50°C$, in CD_3OD. Higher temperatures and low initial concentrations of **1** result in increased yields of carbonate **3**. Highest yields of dioxetane occur at low temperature and higher initial concentrations of **1**. Under a given set of conditions product yields are quite reproducible. There is only a small change in product distribution when a stream of ozone in argon is used rather than a stream of ozone in oxygen.

Possible reaction pathways

Initial attempts to understand how the products are formed were based on reactions for which there was already precedent, Scheme 2. Formation of the ester **7** and dioxetane **8** could occur via the oxygenated epoxide **9**. Such species have been postulated on numerous occasions, mainly to rationalize epoxide formation in ozonolysis of very hindered alkenes (2), which **1** is not. Thus, **9** would fragment to the epoxide **10** and singlet oxygen (6). Rearrangement of **10** would result in ester **7** and the singlet oxygen would react with a second molecule of **1** to form **8**.

Evidence in favor of the formation of **8** by reaction between **1** and singlet oxygen was obtained by conducting the ozonolysis of **1** in the presence of 2,5-dimethylfuran **11**, an efficient singlet oxygen scavenger. No (<5%) dioxetane was formed when a 6:1 mixture of **11**:**1** was ozonized to 25% consumption of **1** although **3** and **7** were still formed in the normal ratio, eq. [1].

Can. J. Chem. Downloaded from www.nrcresearchpress.com by 112.217.228.212 on 09/07/12
For personal use only.

TABLE 1. Product distribution and stoichiometry in ozonolysis of **1**[a]

Solvent	Temperature, °C	Concentration, M	Per cent **1** consumed	Consumption $1/O_3$[b]	Relative ^1H nmr peak areas **3**	**7**	**8**
$CDCl_3$	−60	0.25	100	—	25	52	24
CD_2Cl_2	−95	0.30	100	—	28	44	28
		0.09	44	—	21	48	31
			45	—	21	46	30
			50	—	22	47	31
	−78	0.18	100	—	28	48	24
	−78	—[c]	100	—	45	90	0
	−60	—[c]	100	—	38	71	0
CD_3OD[d]	−50	0.25	100	—	20	56	24
	−35	0.25	100	—	20	61	20
	−20	0.25	100	—	23	60	17
CD_3COCD_3	−95	0.09	62	—	45	78	53
			58	—	44	74	46
			57	—	46	74	48
			54[e]	—	31	69	36
	−78	0.001	47	—	37	44	18
		0.01	59	—	32	42	27
		0.07	89	1.5	27	49	24
		0.14	49	1.9	28	49	23
		0.27	30	2.1	22	52	26
		0.54	54	2.2	19	56	26
		1.4[f]	47	2.5	24	40	36
		0.07[g]	83	1.3	30	46	22
		0.14[g]	54	1.4	25	41	34
		0.27[g]	37	1.6	24	43	33
	−64	0.1	58	—	28	43	28
	−45	0.1	68	—	34	40	26
	−23	0.1	56	—	37	37	26

[a]A stream of ozone in oxygen was used unless noted otherwise.
[b]Moles of **1** consumed per mole of ozone delivered.
[c]Inverse addition, 2.5 mg of **1** in 10 μL of CD_3COCD_3 added slowly to excess ozone in CD_2Cl_2.
[d]Below −50°C additional products are formed.
[e]The solution contained 10^{-2} M 2,6-di-*tert*-butylphenol.
[f]The solution was not homogeneous, so the actual concentration of **1** was less than this.
[g]Ozone in argon was used.

[1] **1** + 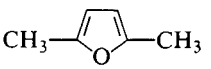 $\xrightarrow[-78°C]{O_3/CD_2Cl_2}$

11

3 + **7** + 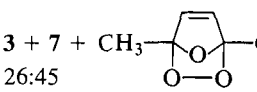

26:45

13

Essentially complete scavenging of singlet oxygen under these conditions would be expected since tetraethoxyethene and 2,3-dimethyl-2-butene **12** show similar reactivities toward this species, the rate constants for the reactions are 4.5×10^7 (acetone) (7) and 4.7×10^7 (methanol) (8), respectively, at room temperature, and **11** has been shown to be 11 times as reactive as **12** at −78°C (9). This was confirmed by carrying out competitive oxygenations of **1** and **12** sensitized by rose bengal at −78°C. These show that the latter alkene is more reactive toward singlet oxygen by a factor of 1.3 in CD_3COCD_3 and 1.6 in CD_3OD, in excellent agreement with the room temperature reactivities of **12** and tetraethoxyethene. Thus, **11** is 14–16 times as reactive as **1** toward singlet oxygen.

The formation of **3** and **7** in the normal ratio in ozonolysis of **1** in the presence of excess **11** shows that the reactions by which these two materials are formed are unaffected by the presence of **11**. The endoperoxide **13** of **11**, identified by its ^1H nmr spectrum (9), was present in about twice the expected amount, based on the relative yield of **8** formed in the absence of **11**. The reason for the larger than expected amount of **13** is unknown. Control experiments show that none is formed as a result of ozonolysis of **11** alone. It appears that **11** is much less reactive toward ozone than is **1**. At least 50% of the measured amount of ozone that was delivered was consumed by **1** based on the amount of **3** and **7** that were formed. Only weak signals were present in the ^1H nmr spectrum of the reaction mixture that could be attributed to ozonolysis products from **11**.

This evidence that **8** is formed by the reaction between **1** and singlet oxygen eliminates another conceivable route to **7** and **8**. The formation of **8** upon ozonolysis of **1** is reminiscent of earlier reports (10) that dioxetanes can be prepared by ozonolysis of alkenes under certain conditions. A peroxydioxetane intermediate was proposed to be the initial ozonolysis product that could transfer an oxygen atom to a suitable acceptor or rearrange to form the conventional molozonide. While these reports of

dioxetane formation were soon shown to be incorrect (11), the possibility that peroxydioxetanes could be intermediates in ozonolysis of alkenes has not been excluded in a general way. Applying this concept to the present work, the alkene **1** would serve as an oxygen atom acceptor from the peroxydioxetane **14**, eq. [2]. However, it is very unlikely that such a route to **7** and

[2] 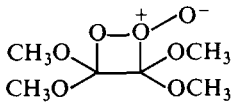 + 1 → 8 + 10 → 7

14

8 would be affected by the presence of **11**. Thus, while the formation of **14** would provide an economical route to **7** and **8** according to eq. [2], these products are not formed in this way.

Lack of evidence for carbonyl oxide 4

The formation of **7** and **8** can be rationalized on the basis of the intermediate formation of the oxygenated epoxide **9**, but an additional reaction is required to account for the formation of the carbonate **3**. An obvious route to **3** would involve an initial competing reaction to form the molozonide **2**, followed by its cleavage to **3** and the carbonyl oxide **4**, the reaction that was anticipated at the outset. If **3** were formed by this sequence, the lack of formation of **5**, the dimer of **4**, in inert solvents might be attributed to the transfer of an oxygen atom from **4** to **1**, a reaction of carbonyl oxides that has been proposed in other systems (12). This would result in an additional molecule of **3** and the epoxide **10**, which would then undergo rearrangement to **7**. However, this oxygen atom transfer would have to be especially efficient because no sign of any product in addition to **3**, **7**, and **8** could be detected even in experiments when the initial concentration of **1** was as low as 10^{-3} M and when **1** was added to excess ozone in CD_2Cl_2. In this inverse addition reaction **1** should never be present in any appreciable amount in solution, thus enhancing the possibility of dimerization of any **4** that might be formed. The amount of dioxetane **8** that was formed in the inverse addition experiments was always lower than in the other experiments and became insignificant when the addition of **1** was slow. The lack of formation of **8** under these conditions could be due to the rapid reaction between ozone and **1**, which greatly depletes the amount of **1** available to react with singlet oxygen, and a possible reaction between singlet oxygen and ozone.

Trapping a precursor of 7 in CD_3OD

Carbonyl oxides are efficiently scavenged by alcohols (2) but attempts to confirm the presence of **4** by conducting the ozonolysis reaction in solvent CD_3OD were unsuccessful.

Only **3**, **7**, and **8** are formed on ozonolysis of **1** in CD_3OD above −50°C and the relative intensities of the ^1H nmr signals of the CH_3O_2C and $C(OCH_3)_3$ groups of **7** are 1:3.0. This ratio decreases as the temperature at which the reaction is carried out is decreased from −50°C. At −95°C it is 1:2.1. Also three additional signals appear in the ^1H nmr spectra of the reaction mixtures when the reactions are conducted below −50°C and become more intense as the temperature of the reaction is lowered. One of these signals, 32 Hz downfield from that of the $C(OCH_3)_3$ group of **7** (−60°C), is due to CH_3OD. Its intensity corresponds to the missing intensity of the $C(OCH_3)_3$ group. The other signals are 17 and 41 Hz downfield from that of the $C(OCH_3)_3$ group and are of similar intensity. These signals remain upon warming the reaction mixture until about −10°C. At this temperature both signals disappear simultaneously.

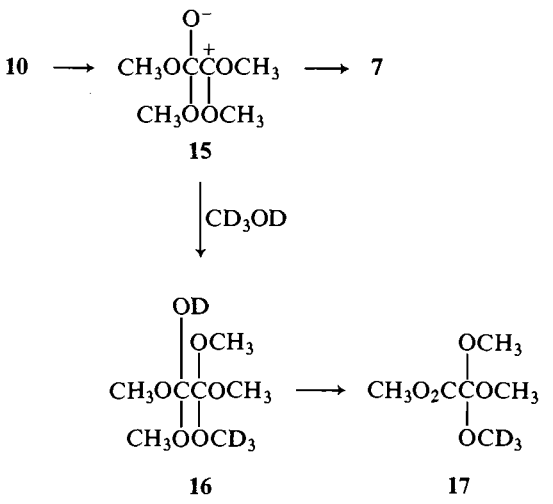

SCHEME 3

Those due to CH_3OD and **7** increase in intensity. The signals of **3** and **8** do not change in intensity. These observations show that a precursor to **7** is trapped by CD_3OD in a reaction that becomes competitive with rearrangement of the precursor to **7** below −50°C. A mixture of the relatively stable hemiorthoester **16** and the partially deuterated ester **17** result, Scheme 3. The amount of **16** formed increases as the temperature of the ozonolysis reaction decreases, but is not reproducible at any given temperature. At −95°C the yield of **16** varies from 7 to 14%. Since **16** is formed in neutral solution it is much longer lived than previously observed molecules of this class, which were not prepared in neutral solution (13).

The scheme depicts the zwitterion **15** as arising from **10**, but there is no evidence that any **10** is ever formed in ozonolysis of **1**, and the zwitterion may arise in another way. Attempts to detect **10** by ^1H nmr were unsuccessful. Samples of **1** were injected rapidly into ozone in CD_2Cl_2 at −90°C in the probe of the nmr spectrometer. The ^1H nmr spectra taken within 2 s contained signals of **7** that increased little in intensity with time. If any **10** is formed in the reaction it must have a half-life of less than 2 s at −90°C.

No evidence for the formation of any adduct **6** could be detected by ^1H nmr even when initial concentrations of **1** were 10^{-3} M. Thus, if any **4** were formed and it could not be trapped by CD_3OD because of a more rapid oxygen transfer reaction with **1**, the rate constant for the latter reaction would have to be $\sim 10^5$ that for the reaction between **4** and 24 M CD_3OD. While **4** might be less reactive than other carbonyl oxides toward CD_3OD, such a great lack of reactivity appears to be unprecedented. It is thus difficult to avoid the conclusion that no **4** is ever formed during ozonolysis of **1** and, further, that the molozonide **2** is not formed either.

Evidence for a radical chain reaction

Additional difficulties arise when attempting to account for the ozonolysis of **1** in terms of the reactions in Scheme 2. According to this scheme the ester **7** is formed in two ways. One mole of **7** would be formed for each mole of **8** produced, and another mole of **7** would result for each 2 moles of carbonate formed. Thus, the amount of **7** formed would be equal to the sum of the amounts of **3** and **8**. The results of the initial experiments, carried out at −95 to −65°C and ~0.1 M **1** in inert solvents, were tantalizingly close to this. However, at different temperatures and concentrations of **1** the product distribution deviates significantly from this expectation.

Can. J. Chem. Downloaded from www.nrcresearchpress.com by 112.217.228.212 on 09/07/12
For personal use only.

TABLE 2. Product distribution in ozonolysis of mixtures of **1** and **12**, 0.14 *M* each, at −95°C

Solvent	Per cent alkene consumed		Relative ^{1}H nmr peak areas						
	1	**2**	**3**	**7**	**8**	**18**	$(CH_3)_2CO$	**19**	**20**
CD_3COCD_3	70	46	32	72	17	44	26	15	—
CD_3OD	81	76	21	118[a]	14	73	77	>15	<77[b]
	33	33	6	25[a]	8	23	13	>5	<13[b]

[a]The sum of 4/3 the area of the signals of **17** and twice the area of the signal of a $(CH_3O)_2C$ group of **16**.

[b]The signals of **19** and **20** are superimposed. The area due to **20** is taken to be equal to the area due to acetone. The area due to **19** is taken to be the difference between those observed for **19** plus **20** and acetone. The areas given for **19** and **20** are minimum and maximum values, respectively, since some acetone is formed by a radical chain reaction that does not form **20**.

According to Scheme 2 each mole of ozone should consume 2 moles of **1**. The actual amount of **1** consumed varies with the initial concentration of **1** and ranges from 1.5 moles per mole of ozone at 0.1 M **1**, in agreement with the original work (3), to 2.5 in saturated solutions of **1** (~1 M) in CD_3COCD_3 at −78°C, Table 1, when a stream of ozone in oxygen is used. The consumption of **1** is lower with a stream of ozone in argon. These results point to a contribution from a radical chain oxidation reaction with both oxygen and ozone.

Further evidence for a radical chain contribution was obtained from ozonolysis of mixtures of **1** and **12**. The object of these experiments was to confirm the formation of singlet oxygen upon ozonolysis of **1** by observing the formation of 3-hydroperoxy-1-butene **18**, the product of reaction between **12** and singlet oxygen. Equimolar mixtures of **1** and **12** were treated with a limited amount of ozone in CD_3COCD_3 and CD_3OD at −95°C. The products of the reaction in CD_3OD are shown in eq. [3]. Based on the relative reactivities of **1** and **12** toward singlet oxygen, somewhat more **18** than **8** would be expected to be formed. Actually, more than twice as much of **18** as of **8** was formed in CD_3COCD_3 and between 3 and 5 times as much in CD_3OD, Table 2.

Another unexpected result from the ozonolysis of mixtures of **1** and **12** is the formation of significant amounts of 2,3-epoxy-2,3-dimethylbutane **19** in both solvents. In the reaction in CD_3COCD_3 this is evidenced by the presence of a sharp singlet 5 Hz upfield from the signal of the *gem*-dimethyl group of **18** in the ^{1}H nmr spectrum. Addition of some authentic **19** enhanced the intensity of this signal. The signals of the products formed from the carbonyl oxide of acetone (14) do not interfere with the signals of the other products. In CD_3OD the ^{1}H nmr signals of **19** and the acetone carbonyl oxide – CD_3OD adduct **20** coincide exactly and the amount of **19** formed was estimated from the difference in the areas of the signals due to acetone and to **19** and **20**. The areas of the signals due to acetone and **20** are exactly equal when **12** alone is ozonized in CD_3OD. Control experiments showed that neither **18** nor **19** was formed upon ozonolysis of **12** alone in either solvent.

The formation of the epoxide **19** together with excess allylic hydroperoxide **18** points to a contribution from a radical chain oxidation when **1** and **12** are ozonized together. Since **18** and **19** are not formed on ozonolysis of **12** alone, the presence of **1** is required to initiate the radical reaction. Thus, a radical chain reaction very likely contributes to product formation in ozonolysis of **1** alone. This would provide a route for the formation of carbonate **3**, Scheme 4, and account for the consumption of more than 2 moles of alkene per mole of ozone delivered to high initial concentrations of **1**. This radical reaction would also result in the formation of some ester **7**, which is always formed in higher yield than dioxetane **8** in ozonolysis of **1**. The nature of the initiator in Scheme 4 will be addressed later.

The free radical auto-oxidation of alkenes not having allylic hydrogen atoms results in epoxide formation and cleavage to carbonyl compounds (15). It has been shown that **3** and **7** do result from **1** (3). The auto-oxidation of neat **12** to low conversion at 50°C under 4 atmospheres of oxygen (1 atm = 101.3 kPa) results in the formation of allylic hydroperoxides, **19**, and acetone in a 8.6:3.1:2.1 ratio (16). The 3° allylic hydroperoxide **18** was found to predominate over the 1° isomer by a factor of 18 to 1. These oxidations of **1** and **12** were carried out under conditions much different from those used in the present ozonolysis studies. To assess the magnitude of the contribution of the radical chain oxidation to the ozonolysis

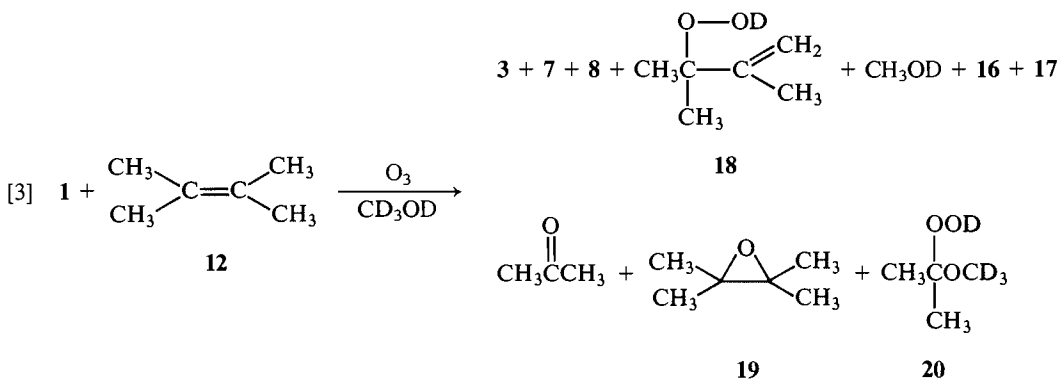

Can. J. Chem. Downloaded from www.nrcresearchpress.com by 112.217.228.212 on 09/07/12
For personal use only.

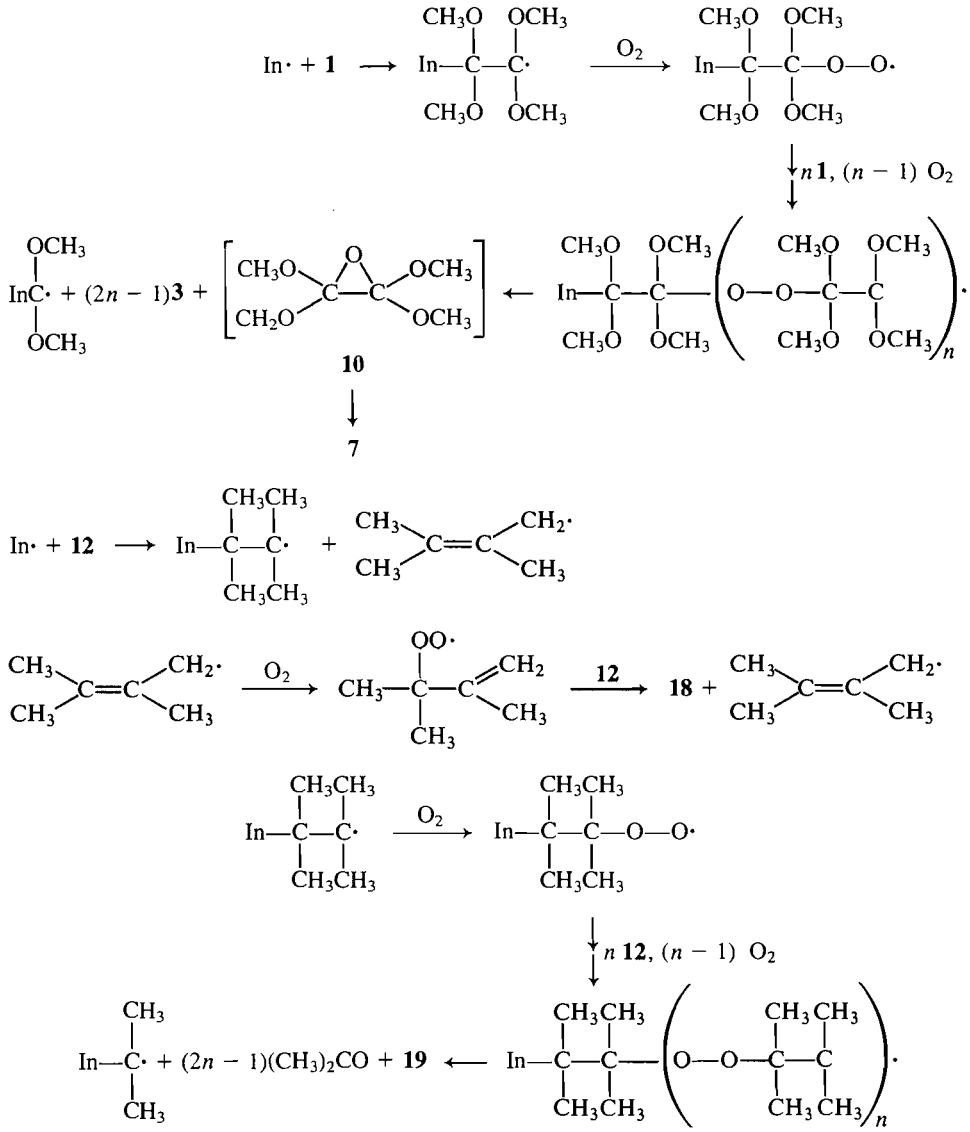

SCHEME 4

reactions the product distributions were determined for the auto-oxidation reactions alone by photolysis of solutions of **1** and **12** in CD_3COCD_3 containing azoisobutyronitrile at −78°C while oxygen was passed through, Table 3. Surprisingly, a small amount (~12% of the total of **3**, **7**, and **8**) of dioxetane **8** was formed from **1**. It was identified by the position of its ^{1}H nmr signal and by the observation of luminescence upon addition of the reaction mixture to hot toluene containing 9,10-dibromo- and 9,10-bis(phenylethynyl)anthracene. It is not clear how **8** is formed. Perhaps some singlet oxygen is generated during the photolysis. Several other unidentified products were formed but **3** and **7** and **8** made up about 80% of the total product. Some minor unidentified products were formed during auto-oxidation of **12** but **18**, **19**, and acetone predominated greatly. These were formed in a ratio of about 18:4:1. This ratio is not greatly different from that at higher temperature and oxygen pressure. When mixtures of **1** and **12** were oxidized this product ratio was 5.5:3.5:1. The change is probably due to the participation of **1** in the chain. The ratio **3**:**7**:**8** was about 4:3:1 when **1** was oxidized either alone or in the presence of **12**. The ratios cited here are the ratios of the areas of the ^{1}H nmr signals of the products.

It should be possible to estimate the yield of ester **7** formed in the ozonolysis of **1** by applying the results of the auto-oxidation experiments. If all the carbonate **3** were produced by the radical chain oxidation and all the dioxetane **8** were formed by the reaction between **1** and singlet oxygen, which, in turn, results from the oxygenated epoxide **9**, then the yield of **7** should be equal to the yield of **8** plus about 2/3 the yield of **3**. The agreement between the experimentally found and calculated quantities of **7** is only fair. There is almost always more **7** found than calculated. Perhaps not all the oxygen formed from **9**, or a precursor of **9**, see below, is singlet oxygen. On the other hand the formation of relatively large amounts of allylic hydroperoxide **18** in the ozonolysis of mixtures of **1** and **12** is well accounted for by the inclusion of a contribution from a radical chain oxidation reaction. The yield of **18** should be equal to about the yield of **8** (from singlet oxygen) plus about twice the yield of epoxide **19**. For the one experiment in which a mixture of **1** and **12** were ozonized in CD_3COCD_3 the agreement

Can. J. Chem. Downloaded from www.nrcresearchpress.com by 112.217.228.212 on 09/07/12
For personal use only.

TABLE 3. Product distribution from auto-oxidation of **1** and **12** at −78°C in CD_3COCD_3

Concentration, M		Per cent consumed		Relative ^1H nmr peak areas					
1	**12**	**1**	**12**	**3**	**7**	**8**	**18**[a]	**19**	$(CH_3)_2CO$
0.21	0	25	—	32	21	7			
0	0.21	—	7	—	—	—	226	60	12
0	0.21	—	10	—	—	—	168	30	9
0.21	0.21	10	6	160	110	30	112	72	20

[a]Taken as twice the area of the *gem*-dimethyl group. The signal of the allylic methyl group is obscured by that of the initiators.

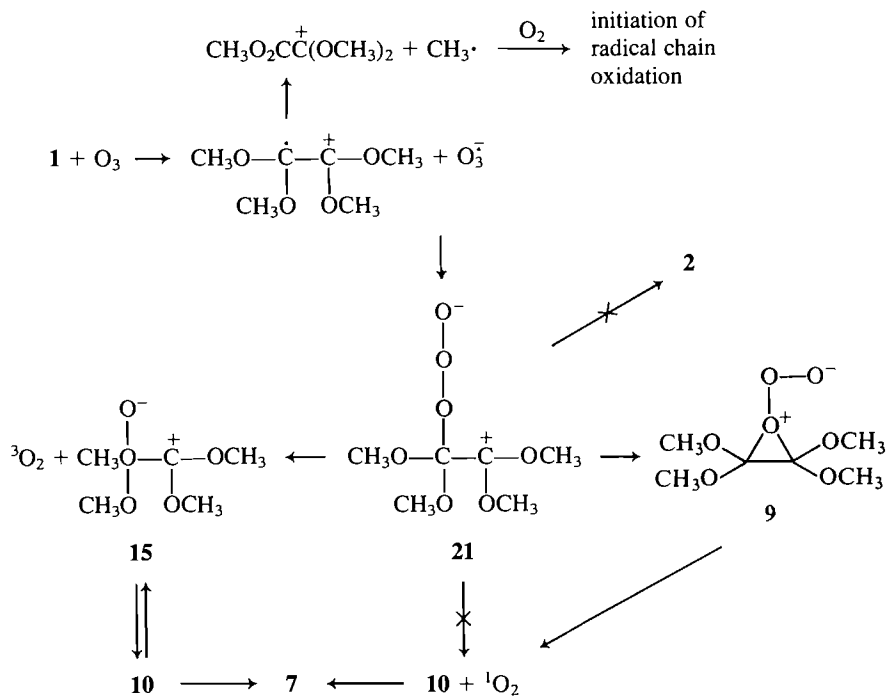

SCHEME 5

between the observed, 44, and calculated, 47, relative amounts of **18** formed is quite good.

A different attempt to verify a contribution from a radical chain oxidation in the ozonolysis of **1** was inconclusive. The product distribution was affected by the presence of the inhibitor 2,6-di-*tert*-butylphenol, but the effect was relatively small, less than might be expected for a long chain length reaction.

Initial electron transfer

All the products from the reaction between ozone and **1** can be accounted for without requiring the initial formation of any molozonide **2**. There appear to be no steric or energetic impediments to the formation of **2**: all the available evidence indicates that the reaction between ozone and **12** forms the molozonide; the methoxy group is considered to be less sterically demanding than the methyl group (17, 18); and the reaction to form **2** can be calculated, using group additivity values (18–20), to be exothermic by 71 kcal/mol. Thus, there must be another reaction that intervenes as the molecules of ozone and **1** approach each other. A likely candidate for this reaction, which can lead to a series of reactions to give all the observed products, is electron transfer to produce the ozone radical anion and the radical cation of **1**, Scheme 5. Formation of the radical ion pair provides a path for the initiation of the radical chain oxidation reaction. There is no evidence on the nature of the initiating species but a possible one might be methyl radical formed by fragmentation of the radical cation. Competing with this, or another, radical forming reaction would be collapse of the pair to give the zwitterion **21**. A rapid reaction of **21** should be cyclization to the molozonide **2**. This should be an irreversible reaction since the dioxetane **8**, which has much more ring strain, is stable in methanol to 10°C. Since there is no evidence that any **2** is ever formed, **21** must be produced in a conformation from which direct ring closure cannot occur and which allows another rapid reaction that forms singlet oxygen and ultimately the ester **7** to compete effectively. Several reactions could occur: cyclization to **9**, which would then undergo fragmentation to form singlet oxygen and the epoxide **10**; a concerted fragmentation and ring closure to form these products; and a fragmentation without ring closure to form

Can. J. Chem. Downloaded from www.nrcresearchpress.com by 112.217.228.212 on 09/07/12
For personal use only.

triplet oxygen and the zwitterion **15**. This last reaction could account for the excess of ester **7** formed, which was noted above.

The paths to singlet oxygen suggested here are preferred to the fragmentation of **21** to **15** and singlet oxygen on energetic grounds. The reaction of eq. [4] has been calculated to be endothermic by 11 kcal/mol, while the corresponding, spin forbidden, reaction to form triplet oxygen is exothermic by 11 kcal/mol (19). The energetics of the fragmentation of **21** to **15** and oxygen should be similar. The fragmentation of **9** with the neutral **10** as the leaving group should be exothermic enough to produce singlet oxygen.

[4] $HOOO^- \longrightarrow HO^- + {}^1O_2$

[5] $HOOO^- \longrightarrow HO^- + {}^3O_2$

The reactions of Scheme 5 are identical to those suggested some time ago (21) to explain luminescence during ozonolysis of 10,10′-dimethyl-9,9′-biacridylidene. A radical chain oxidation with oxygen was also discussed.

The electron transfer reaction would have to be quite exothermic to compete with molozonide formation. The enthalpy of the electron transfer reaction, eq. [6], depends on the ionization potential IP of **1**, the electron affinity EA of the

[6] $\Delta H^0_{et} = \mathrm{IP}(\mathbf{1}) - \mathrm{EA}(O_3) - \underset{\text{attraction}}{\text{Coulombic}} - \underset{\text{energy}}{\text{solvation}}$

$= \mathrm{IP}(\mathbf{1}) - 2.2\ \mathrm{eV} - 5.4\ \mathrm{eV} + 1\ \mathrm{eV}$

ozone, the coulombic attraction of the ion pair and the difference between the solvation energies of the neutral molecules and the ion pair. The values of the last two terms are taken to be equal to those used to calculate the energy of reaction between ozone and alkanes or alcohols (19) that leads initially to ion pairs. The IP of **1** is unknown but it should be considerably less than that of **12**, which is 8.45 eV (22). Replacement of a methyl group in propene or 2-methyl-2-butene or of an isobutyl group in 4-methyl-1-pentene by an alkoxy group results in a decrease of about 0.6 eV in the πIP (23). The effect of four such substitutions on **12** would probably not be additive, but it is unlikely that the πIP of **1** is greater than 7 eV. An IP of this magnitude would result in the ΔH^0 of the electron transfer reaction to be about −35 kcal/mol. This might be exothermic enough to compete with molozonide formation since electron transfer can occur at a greater separation of reactants than molozonide formation.

The radical chain reaction oxidation initiated by the electron transfer reaction here appears to be quite different from the cation radical catalyzed chain oxygenation of alkenes that has recently received intensive study (24). In particular, according to this type of reaction, dioxetane **8** would be formed as shown in Scheme 6. However, dimethylfuran would not be expected to interfere so effectively with dioxetane formation if **8** were formed in this way. Also, this reaction results in the formation of considerable acetone and pinacolone with **12** as the substrate. In the present study, ozonolysis of mixtures of **1** and **12** gives acetone as a minor product and no evidence for the presence of any pinacolone was found. Oxidation of **1** alone with oxygen at −78°C in CD_2Cl_2 catalyzed with a trace of $(4\text{-}BrC_6H_4)_3\dot{N}^+$ resulted mainly in carbonate. Only a little **7** and a trace of dioxetane **8** were formed. Significant amounts of several other,

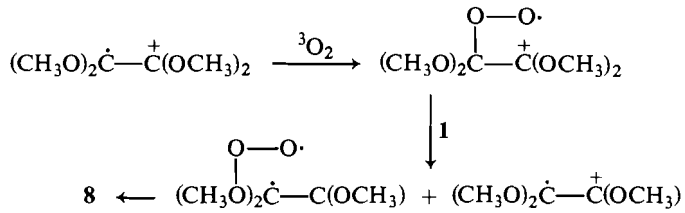

SCHEME 6

unidentified, compounds were formed, presumably products of an acid-catalyzed reaction of **1**.

A reaction between ozone and **1** to form the zwitterion **21** directly without initial electron transfer seems unlikely since the reaction between the alkenes **22**, **23**, and **24** and ozone, which could form zwitterions where the positive charge is similarly stabilized as in **21**, results in exclusive molozonide formation as judged from product distribution. Carbonate **3** and aldehyde or ketone carbonyl oxide products are formed in quantitative yield.[4] There is no evidence for formation of any epoxide or dioxetane from these materials.

$CH_2{=}C(OCH_3)_2$ **22** $CH_3CH{=}C(OCH_3)_2$ **23** $(CH_3)_2C{=}C(OCH_3)_2$ **24**

Electron transfer in other ozonolyses

Ozonolysis of the *Z*-dimethoxystilbene **25** produces about 20% of dioxetane and about 40% of an unidentified product, which may be an epoxide or a rearrangement product analogous to **7**, in addition to methyl benzoate. Also, 1.3 moles of **25** are consumed by 1 mole of ozone.[4] These results suggest that a process similar to that in ozonolysis of **1** is occurring. No dioxetane is formed on ozonolysis of the *E*-isomer **26**, one molecule of **26** is consumed by 1 mole of ozone and, in CD_3OD solvent, methyl benzoate and the CD_3OD adduct of the carbonyl oxide of methyl benzoate are the only products formed in equal amount.[4] Clearly this reaction proceeds via the molozonide.

Ozonolysis of other electron-rich alkenes may also proceed according to Scheme 5. The ozonolysis of 10,10′-dimethyl-9,9′-biacrildylidene (21) has already been noted. Recently, direct evidence of dioxetane formation in an acenaphthylene derivative oxygenated at the 1 and 2 positions has been obtained (25). Ozonolysis of the dimethoxynorbornene derivative **27** forms ~50% of **28** (26), a product analogous to **7**.

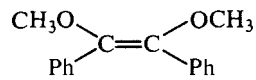

25

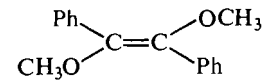

26

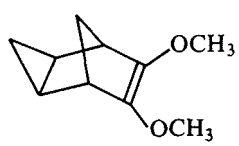

27

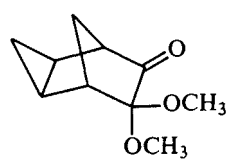

28

A variety of hindered alkenes containing two or three alkyl groups on the double bond give epoxides, sometimes in quite high yield, upon ozonolysis (27). The πIP of such materials

[4] J. Molina, unpublished results.

Can. J. Chem. Downloaded from www.nrcresearchpress.com by 112.217.228.212 on 09/07/12
For personal use only.

TABLE 4. The ^{1}H nmr chemical shifts for compounds at −50°C

Compound (protons)	δ CD_3OD	δ CD_3COCD_3
1	3.56	3.50
3	3.73	3.70
7 (CH_3O_2C)	3.80	3.78
7 ($(CH_3O)_3C$)	3.27	3.22
8	3.48	3.46
11 (CH_3)		2.19[a]
12	1.64	1.59
13 (CH_3)		1.78[a]
18 ($(CH_3)_2C$	1.29	1.24
18 (CH_3)	1.79	1.76
18 (CH_2)	4.90, 4.87	4.87, 4.85
19	1.31	1.22
20	1.31	

[a]In CD_2Cl_2.

should be 8.8–9.0 eV and electron transfer with ozone would be endothermic. In these reactions oxygenated epoxides corresponding to **9** were proposed to be formed directly and evidence for the formation of singlet oxygen was reported.

Experimental

Tetramethoxyethene 1

The procedure using dimethoxyethane as solvent (1) resulted in material that could be obtained in a high state of purity, >99%, by recrystallization from isopentane followed by distillation. The procedure using diglyme as solvent (28) resulted in material that contained 4–5% of impurities despite repeated attempts at purification. These impurities gave ^{1}H nmr signals in the region where the ozonolysis products of **1** absorbed.

Ozonolysis of 1

The ozonolysis reactions were carried out in nmr tubes. The product distributions were determined by ^{1}H nmr on a Bruker WH 200 spectrometer. Initially, the effluent stream from an ozonizer was divided and one portion of the stream passed through the solutions of **1**. The ^{1}H nmr chemical shifts of the compounds formed in the various reactions are shown in Table 4. Most reactions were carried out by taking up the ozone–oxygen mixture from the effluent stream of the ozonizer into a 50- to 200-mL gas syringe and then delivering the gas into the solution through a 1-mm Teflon tube that reached to the bottom of the nmr tube. The plunger fell of its own weight at a rate that delivered the required amount of gas over about a 5-min period. The ozone–oxygen mixture could be stored in the syringe for several hours at room temperature with no loss in ozone content. The nmr tubes were freed of acid by soaking in ammonia solution, draining, and drying at 120°C. Syringes used to deliver solvent were similarly treated except that they were dried with an air stream. Halogenated solvents were filtered slowly through a plug of powdered potassium carbonate. Even with these precautions by-products were formed in numerous runs that interfered with the ^{1}H nmr analysis. These were probably the result of acid-catalyzed reactions of **1** because they were formed quickly during the ozonolyses and did not build up in concentration as the ozonolyses progressed.

The amount of **1** consumed by ozone was measured as follows. Known volumes of the ozone–oxygen mixtures were delivered into excess 2,3-dimethyl-2-butene **12** in CD_3OD at −78°C. The reaction mixtures were analyzed by ^{1}H nmr, measuring the areas of the signals due to remaining **12**, acetone, and **20**. Solutions containing known amounts of **1** were then treated with the calibrated ozone–oxygen mixtures.

Ozone in argon mixtures were made by taking up ozone that had been adsorbed on silica gel with a stream of argon into a syringe. The ozone–argon mixture was passed back and forth between two syringes about 10 times to ensure uniform mixing.

Identification of tetramethoxy-1,2-dioxetane 8

A solution of 0.26 g **1** in 5 mL CD_2Cl_2 was ozonized at −90°C until all of **1** was consumed. The resulting solution was shaken with aqueous sodium hydroxide at 0°C until all **3** and **7** had been removed and only the signal of **8** was present in the ^{1}H nmr spectrum at δ 3.50. The ^{13}C nmr spectrum had signals at δ 51.37 and 118.64. Iodometric titration (29) showed 98% of the active oxygen content expected for **8**.

Authentic **8** was prepared by photooxygenation (4) of **1** in CD_3OD or in CD_2Cl_2. The ^{1}H and ^{13}C nmr signals of **8** prepared in this way in CD_2Cl_2 were identical to those of the sample prepared by ozonolysis; ^{1}H nmr (CD_2Cl_2): 3.50; ^{13}C nmr (CD_2Cl_2): 51.51, 118.66.

Competitive photooxygenation of 1 and 12

Mixtures of **1** and **12**, each 0.1 M, in CD_3COCD_3 or CD_3OD that contained some rose bengal adsorbed on silica gel were irradiated with a 200-W incandescent bulb while kept in a glass Dewar flask at −78°C. A slow stream of oxygen was bubbled through the mixtures. The resulting solutions were analyzed by ^{1}H nmr and the relative reactivities toward singlet oxygen calculated as described (30).

Auto-oxidation of 1 and 12

Solutions of **1** and **12** and mixtures of **1** and **12** in CD_3COCD_3 that contained 3.0×10^{-2} M azoisobutyronitrile, in nmr tubes kept in a Dry Ice – acetone bath, were removed and irradiated for 2-s intervals with light from a 200-W Hanovia mercury lamp. Intermittent irradiation followed by cooling was continued until several per cent of the alkenes were oxidized. The product distributions were determined by ^{1}H nmr. The signal for CH_3COCH_3 is 2 Hz downfield from the downfield peak of CHD_2COCD_3. Its area could be determined quite accurately.

Search for 18 and 19 in ozonolysis of 12

Solutions 1 M in **12** in CD_3OD and CD_3COCD_3 were ozonized at −78°C so that about 30% of **12** was consumed. The solutions were examined by ^{1}H nmr. In particular, no peaks due to the *gem*-dimethyl group of **18** could be detected in either solvent, no peak due to **19** could be detected in the CD_3COCD_3 solution, and the peaks due to acetone and **20** had exactly the same integral in CD_3OD.

Acknowledgement

The authors thank both referees for helpful comments.

1. J. W. SCHEEREN, R. J. F. M. STRAPS, and R. J. F. NIVARD. Recl. Trav. Chim. Pays-Bas, **92**, 11 (1973).
2. (*a*) R. CRIEGEE. Rec. Chem. Prog. **18**, 111 (1957); (*b*) P. S. BAILEY. Ozonation in organic chemistry. Vol. 1. Academic Press, New York. 1978.
3. R. W. HOFFMANN and J. SCHNEIDER. Chem. Ber. **100**, 3698 (1967).
4. (*a*) S. MAZUR and C. S. FOOTE. J. Am. Chem. Soc. **92**, 3225 (1970); (*b*) T. WILSON, D. E. GOLAN, M. S. HARRIS, and A. L. BAUMSTARK. J. Am. Chem. Soc. **98**, 1086 (1976).
5. (*a*) P. D. BARTLETT, A. L. BAUMSTARK, and M. E. LANDIS. J. Am. Chem. Soc. **96**, 5557 (1974); (*b*) P. D. BARTLETT and J. S. MCKENNIS. J. Am. Chem. Soc. **99**, 5334 (1977).
6. (*a*) P. S. BAILEY, J. W. WARD, R. E. HORNISH, and F. E. POTTS III. Adv. Chem. Ser. **122**, 1 (1972); (*b*) P. S. BAILEY, J. W. WARD, T. P. CARTER, JR., E. NIEH, C. M. FISHER, and Q. Y. KHASHAB. J. Am. Chem. Soc. **96**, 6136 (1974).
7. A. P. SCHAAP and A. ZAKLIKA. *In* Singlet oxygen. *Edited by* H. H. Wasserman and R. W. Murray. Academic Press, New York. 1979. Chap. 7.
8. K. GOLLNICK. Adv. Chem. Ser. **77**, 78 (1968).
9. P. D. BARTLETT and G. D. MENDENHALL. J. Am. Chem. Soc. **92**, 210 (1970).
10. (*a*) P. R. STORY, E. A. WHITED, and J. A. ALFORD. J. Am.

Can. J. Chem. Downloaded from www.nrcresearchpress.com by 112.217.228.212 on 09/07/12
For personal use only.

Chem. Soc. **94**, 2143 (1972); (*b*) N. C. YANG and R. V. CARR. Tetrahedron Lett. 5143 (1973).
11. (*a*) K. R. KOPECKY, P. A. LOCKWOOD, J. E. FILBY, and R. W. REID. Can. J. Chem. **51**, 468 (1973); (*b*) P. S. BAILEY, T. P. CARTER, JR., C. M. FISCHER, and J. A. THOMPSON. Can. J. Chem. **51**, 1278 (1973); (*c*) R. CRIEGEE and A. BANCIU. Can. Ztg. **98**, 261 (1974); (*d*) N. C. YANG and J. LIBMAN. J. Org. Chem. **39**, 1782 (1974).
12. T. A. HINRICHS, V. RAMACHANDRAN, and R. W. MURRAY. J. Am. Chem. Soc. **101**, 1282 (1979).
13. (*a*) B. CAPON and D. McL. A. GRIEVE. J. Chem. Soc. Perkin Trans. 2, 300 (1980); (*b*) M. AHMAD, R. G. BERGSTROM, M. J. CASHEN, Y. CHIANG, A. J. KRESGE, R. A. MCLELLAND, and M. F. POWELL. J. Am. Chem. Soc. **101**, 2669 (1979).
14. M. F. MCGARRITY and J. PRODOLLIET. J. Org. Chem. **49**, 4465 (1984).
15. F. R. MAYO. Acc. Chem. Res. **1**, 193 (1968).
16. D. E. VAN SICKLE, F. R. MAYO, R. M. ARLUK, and M. G. SYZ. J. Am. Chem. Soc. **89**, 967 (1967).
17. D. S. NOYCE and L. J. DOLBY. J. Org. Chem. **26**, 3619 (1961).
18. S. W. BENSON. Thermochemical kinetics. John Wiley and Sons, New York. 1976.
19. P. S. NANGIA and S. W. BENSON. J. Am. Chem. Soc. **102**, 3105 (1980).
20. J. HINE and A. W. KLUEPPEL. J. Am. Chem. Soc. **96**, 2924 (1974).
21. E. G. JANZEN, L. G. LOPP, and J. W. HAPP. Chem. Commun. 1140 (1970).
22. P. D. MOLLERE, K. N. HOUK, D. S. BOMSE, and T. H. MORTON. J. Am. Chem. Soc. **98**, 4732 (1976).
23. (*a*) D. A. KRAUSE, J. W. TAYLOR, and R. F. FENSKE. J. Am. Chem. Soc. **100**, 718 (1978); (*b*) P. MASCLET, D. GROSJEAN, G. MOUVIER, and G. DUBOIS. J. Electron Spectrosc. Relat. Phenom. **2**, 225 (1973); (*c*) H. FRIEGE and M. KLESSINGER. J. Chem. Res. (S), 208 (1977); (*d*) C. BATICH, E. HEILBRONNER, C. B. QUINN, and J. R. WISEMAN. Helv. Chim. Acta, **59**, 512 (1976).
24. S. F. NELSON. Acc. Chem. Res. **20**, 269 (1987).
25. T.-S. FANG and W.-P. MEI. Tetrahedron Lett. **28**, 329 (1987).
26. P. G. GASSMAN and X. CREARY. Tetrahedron Lett. 4407 (1972); 4411 (1972).
27. (*a*) S. MUNAVALLI and G. OURISSON. Bull. Soc. Chim. Fr. 729 (1964); (*b*) C. A. HENRICK and P. R. JEFFERIES. Aust. J. Chem. **17**, 915 (1964); (*c*) A. R. HOCHSTETLER. J. Org. Chem. **40**, 1536 (1975); (*d*) C. R. ENZELL and B. R. THOMAS. Tetrahedron Lett. 225 (1965); (*e*) C. R. ENZELL and B. R. THOMAS. Acta Chem. Scand. **19**, 1875 (1965); (*f*) C. R. ENZELL. Acta Chem. Scand. **15**, 1191 (1961); (*g*) C. R. ENZELL. Acta Chem. Scand. **16**, 1553 (1962).
28. D. BELLUS, H. FISCHER, H. GREUTER, and P. MARTIN. Helv. Chim. Acta, **61**, 1784 (1978).
29. H. B. KNIGHT and D. SWERN. *In* Organic synthesis. Coll. Vol. 4. *Edited by* N. Rabjohn. John Wiley and Sons, Inc., New York. 1963. p. 895.
30. R. HIGGINS, C. S. FOOTE, and H. CHENG. Adv. Chem. Ser. **77**, 102 (1968).

Can. J. Chem. Downloaded from www.nrcresearchpress.com by 112.217.228.212 on 09/07/12
For personal use only.

Molar volumes and refractivities of highly concentrated solutions of ammonium and potassium thiocyanates in water and dimethylsulphoxide

PETR PACÁK AND ZDENĚK KODEJŠ

Institute of Inorganic Chemistry, Czechoslovak Academy of Sciences, Majakovského 24, 160 00 Prague 6, Czechoslovakia

Received December 11, 1987

PETR PACÁK and ZDENĚK KODEJŠ. Can. J. Chem. **66**, 2244 (1988).

Densities and refractive indices of highly concentrated solutions of ammonium and potassium thiocyanates in water and dimethylsulphoxide have been measured at 333.2 K in the composition range from $x_s = 0.01$ up to saturated solutions. Molar volumes and apparent molar volumes have been calculated from density measurements and their concentration dependences are discussed. All the systems are volumetrically non-ideal and exhibit negative deviations from additivity. The molar refractivities were calculated from the refractive indices using the Lorentz–Lorenz equation. The refractivity values of individual ions were estimated in infinitely dilute solutions and were used for discussion of ion–solvent interactions.

PETR PACÁK et ZDENĚK KODEJŠ. Can. J. Chem. **66**, 2244 (1988).

Opérant à 333,2 K et à des composition en x_s allant de 0,01 à des solutions saturées, on a mesuré les densités et les indices de réfraction de solutions très concentrées de thiocyanates d'ammonium et de potassium, dans l'eau et le diméthylsulfoxyde. A partir des mesures de densité, on a calculé les volumes molaires ainsi que les volumes molaires apparents et on discute de leurs dépendances sur la concentration. D'un point de vue volumétrique, aucun système n'est idéal et chacun présente des déviations négatives par rapport à l'additivité. Utilisant l'équation de Lorentz–Lorenz, on a calculé les réfractivités molaires à partir des indices de réfraction. On a calculé les valeurs de réfractivité des ions individuels à dilution infinie et on les a utilisées pour discuter des interactions ion–solvant.

[Traduit par la revue]

Introduction

One of the reasons for studying the volumetric properties of electrolyte solutions is to formulate and to test models and equations useful both for experimental data fitting and for extrapolation of the volumetric properties into experimentally inaccessible concentration regions.

In our previous studies (1–4), water was used as a solvent and, of the ionic salts, mainly nitrates have been studied because of their high solubility. The relation between the deviation from ideal volumetric behaviour of binary salt + molecular solvent systems and parameters characterizing solute–solvent interactions were studied and an equation was derived for the dependence of the molar volume on composition of the solution from the concept of the apparent molar volume of water (3, 4). Experimental data on systems with dimethylsulphoxide (DMSO) as a solvent (5) were used to test the general validity of our model. Alternative approaches to the problem have been described by several authors (6–10).

The refractive index and molar refractivity yield valuable information on the electronic polarizability of individual ions in solutions. The molar refractivity corresponds to the actual volume of the ions (molecules) in one mole of the substance and thus it can be compared with the volumetric properties calculated from density measurements. The dependence of the refractivity on the salt concentration was investigated in the previous paper (11) for solutions of some univalent chlorides and nitrates in water and dimethylsulphoxide. The results can serve as a basis for discussions on the interactions of other ions with the two solvents.

In the present paper, the results of experimental study of volumetric and refractometric properties of highly concentrated solutions of thiocyanates in water and DMSO are presented to form a basis for consideration of ion–ion and ion–solvent interactions in dependence on the composition of electrolyte solutions. Dimethylsulphoxide was used as an alternative solvent for its capability to dissolve many inorganic salts. It is an aprotic solvent with a boiling point of 462 K. The solvation ability of DMSO and water can be compared on the basis of the concept of the donor number, D_N. The scale proposed by Gutmann (12) gives values of 18 and 30 for water and DMSO, respectively, indicating much stronger interaction of DMSO with electrolytes. The strength of ion–solvent interactions depends also on the solvent permanent dipole moment. The values for water and DMSO are 1.83 D and 3.96 D, respectively. Thiocyanates were chosen for their high solubility in both solvents.

Experimental

Reagent-grade NH_4SCN and KSCN ("pro analysi", Merck) were vacuum desiccated and stored over P_2O_5. Reagent-grade dimethylsulphoxide ("pro analysi", Merck) containing less than 0.03 mass% of water was used as received. Mixtures for measurements were prepared by weighing.

The density of the solutions was measured at 333.2 K using a DMA 40 digital vibration densimeter (Paar). The accuracy of the measured density values was estimated to be better than $\pm 4 \times 10^{-4}$ g cm^{-3} from analysis of the calibration method and the precision of temperature control.

The density of molten NH_4SCN was measured by the pycnometric method at 428 K, the pycnometer (approximately 25 cm^3) was calibrated at 298.2 K with water and the thermal expansion coefficient of glass was used for calculation of the volume of the pycnometer at 428 K. The uncertainty in the density value of molten NH_4SCN does not exceed $\pm 4 \times 10^{-3}$ g cm^{-3}.

The refractive index was determined with a Pulfrich refractometer (type PR-2, Zeis, Jena) at a wavelength of $\lambda = 587.6$ nm (helium D-line) with an accuracy of $\pm 5 \times 10^{-5}$ units. The molar refractivity values were calculated from the refractive index with an accuracy of ± 0.02 cm^3 mol^{-1}.

Results and discussion

Molar volumes

The measured values of the density, d, of the solutions of NH_4SCN and KSCN in H_2O and DMSO at different salt concentrations, x_s, at 333.2 K are reported in Table 1 together with the refractive index values, n.

Printed in Canada / Imprimé au Canada

Can. J. Chem. Downloaded from www.nrcresearchpress.com by 196.1.178.254 on 09/07/12
For personal use only.

TABLE 1. Experimental values of the density, d, and refractive index, n, together with the values of the molar volume, V_m, and molar refractivity, $[R]_{soln}$, of the solutions of NH_4SCN and KSCN in H_2O and DMSO at 333.2 K

x_s	d (g cm^{-3})	n	V_m (cm^3 mol^{-1})	$[R]_{soln}$ (cm^3 mol^{-1})
		$NH_4SCN + H_2O$		
0.01	0.9926	1.33643	18.73	3.89
0.02	1.0002	1.34527	19.17	4.08
0.03	1.0076	1.35377	19.61	4.26
0.04	1.0142	1.36184	20.05	4.45
0.05	1.0204	1.37018	20.50	4.64
0.10	1.0505	1.40535	22.68	5.56
0.20	1.0962	1.45619	27.04	7.35
0.30	1.1276	1.49398	31.44	9.15
0.40	1.1514	1.52258	35.83	10.94
		$KSCN + H_2O$		
0.01	1.0084	1.33610	18.65	3.87
0.02	1.0307	1.34450	19.01	4.03
0.03	1.0521	1.35255	19.38	4.20
0.04	1.0711	1.35994	19.75	4.36
0.05	1.0914	1.36786	20.13	4.53
0.10	1.1777	1.40030	22.02	5.34
0.15	1.2504	1.42720	23.90	6.14
0.20	1.3101	1.44914	25.84	6.93
0.25	1.3605	1.46723	27.79	7.71
0.30	1.4037	1.48273	29.75	8.49
		NH_4SCN + DMSO		
0.01	1.0667	1.46442	73.23	20.22
0.02	1.0690	1.46579	73.05	20.22
0.035	1.0704	1.46860	72.93	20.29
0.05	1.0739	1.47097	72.66	20.31
0.10	1.0846	1.47944	71.85	20.39
0.15	1.0939	1.48712	71.15	20.47
0.20	1.1023	1.49430	70.51	20.54
0.25	1.1101	1.50125	69.93	20.61
0.30	1.1181	1.50774	69.34	20.66
0.35	1.1262	1.51516	68.75	20.74
0.40	1.1340	1.52217	68.19	20.80
0.45	1.1425	1.52967	67.59	20.87
0.50	1.1506	1.53723	67.03	20.94
0.55	1.1586	1.54437	66.48	21.00
		KSCN + DMSO		
0.01	1.0692	1.46368	73.25	20.20
0.02	1.0754	1.46523	73.01	20.19
0.035	1.0848	1.46786	72.64	20.19
0.05	1.0935	1.47024	72.32	20.19
0.10	1.1242	1.47880	71.19	20.18
0.15	1.1555	1.48446	70.09	20.07
0.20	1.1874	1.49317	69.01	20.06
0.25	1.2166	1.49892	68.14	20.00
0.30	1.2469	1.50645	67.27	20.00
0.35	1.2769	1.51224	66.41	19.94

Molar volumes, V_m, i.e. volume of the solution containing 1 mol of the components (salt + solvent), were calculated from the density data by means of the equation

$$[1] \quad V_m = \frac{x_s M_s + (1 - x_s)M}{d}$$

where x_s is the salt mole fraction, M_s and M are the molecular weights of the salt and solvent, respectively, and d is the density of the solution.

Theoretically an electrolyte solution can be prepared by isothermal mixing of the solvent and liquid (molten) salt. In our case, i.e. at 333.2 K, the liquid salt would be in a hypothetical undercooled state. There is some uncertainty in the value of the molar volume of both salts at this temperature as it was obtained by extrapolation from the literature (13) and our experimental data. We found the density of the melt of NH_4SCN as d = 1.175 g cm^{-3} at 428 K; the uncertainty in this value is given mainly by the slow decomposition of the melt at the temperature of measurement.

For extrapolation of the density of KSCN from the experimental temperature range (473–537 K) to 333.2 K, the value of thermal coefficient for the density $b = 5 \times 10^{-4}$ g cm^{-3} K^{-1} was calculated from the literature data (13). The value of b for NH_4SCN melt cannot be determined experimentally as the melt decomposes above its melting point. The density of the solutions $NH_4SCN + H_2O$ and NH_4SCN + DMSO was measured in the temperature range from 298 to 333 K and the value of b were calculated for individual solutions. The value of b for NH_4SCN melt was estimated from the composition dependence of the thermal coefficients for the density, b, of the $NH_4SCN + H_2O$ solutions by extrapolation to the molten salt. The value of $b = 5 \times 10^{-4}$ g cm^{-3} K^{-1} was used for molten NH_4SCN and the values 58.9 and 62.5 cm^3 mol^{-1} for the molar volume of KSCN and NH_4SCN, respectively, were calculated by extrapolation to a temperature of 333.2 K. The uncertainty in the values of the molar volumes of the pure salts is estimated to be about ±0.4 cm^3 mol^{-1}. The value of the molar volume of pure KSCN is in a reasonable agreement with the value of 57.5 cm^3 mol^{-1} reported in the literature (14). The value has been obtained by the extrapolation of molar volume isotherm of $Ca(NO_3)_2.4H_2O$ + KSCN melt to the molten KSCN at 323 K.

The calculated values of the molar volumes are plotted against the salt mole fraction in Fig. 1. It is evident that all the systems are volumetrically non-ideal; the deviations from ideality, i.e. from purely additive behaviour, are negative and are more pronounced when DMSO is used as a solvent (Fig. 2). This conclusion is in agreement with earlier results (5) and the difference in the solvent permanent dipole moment can be invoked to explain this fact.

A relation between the type of anion and the magnitude of the deviations from ideality can be deduced from their numerical values at a fixed salt concentration, e.g. at x_s = 0.2. For NH_4NO_3, we found the deviations to be −0.1 and −1.0 cm^3 mol^{-1} at 333.2 K in H_2O and DMSO, respectively (4, 5), while for NH_4SCN the deviations are −0.12 and −0.9 cm^3 mol^{-1}, respectively. At this salt concentration, the effect of the SCN^- anion on the molar volume of the solution is similar to that of the NO_3^- anion.

An interesting insight into the problem of volumetric properties can be obtained from the concept of the apparent molar volume of the salt, Φ. This value is defined by the relation

$$[2] \quad V_m = x_s\Phi + (1 - x_s)V_1^0$$

where V_1^0 is the molar volume of the pure solvent. Even if the value of Φ is evaluated mainly at infinite dilution, where the partial molar volume and the apparent molar volume of the electrolyte are equal, it can also be used to discuss ion–solvent interactions in concentrated solutions.

The dependence of Φ on the composition of the solution for

Can. J. Chem. Downloaded from www.nrcresearchpress.com by 196.1.178.254 on 09/07/12
For personal use only.

Can. J. Chem. Downloaded from www.nrcresearchpress.com by 196.1.178.254 on 09/07/12
For personal use only.

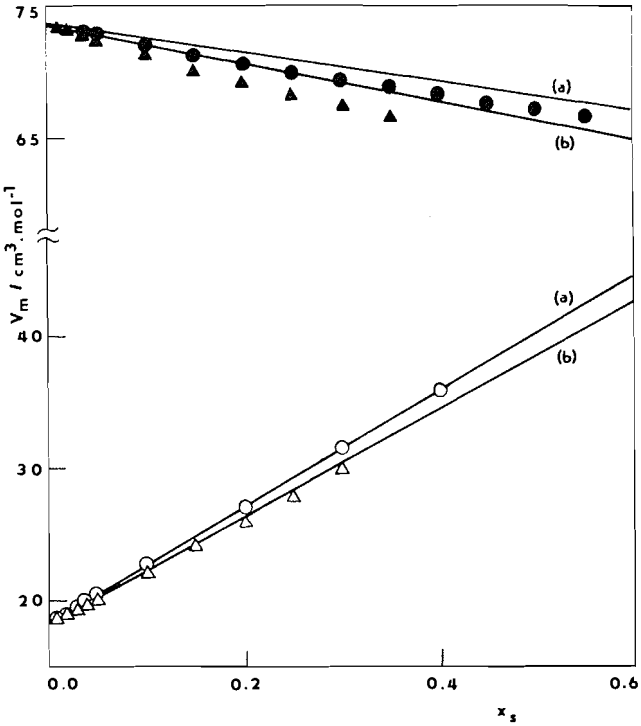

FIG. 1. Molar volumes of the solutions, V_m, as a function of the mole fraction of the salt, x_s, at 333.2 K. ○, $NH_4SCN + H_2O$; ●, NH_4SCN + DMSO; △, KSCN + H_2O; ▲, KSCN + DMSO. Full line — the ideal purely additive volumetric behaviour for NH_4SCN solutions, (*a*) and KSCN solutions, (*b*).

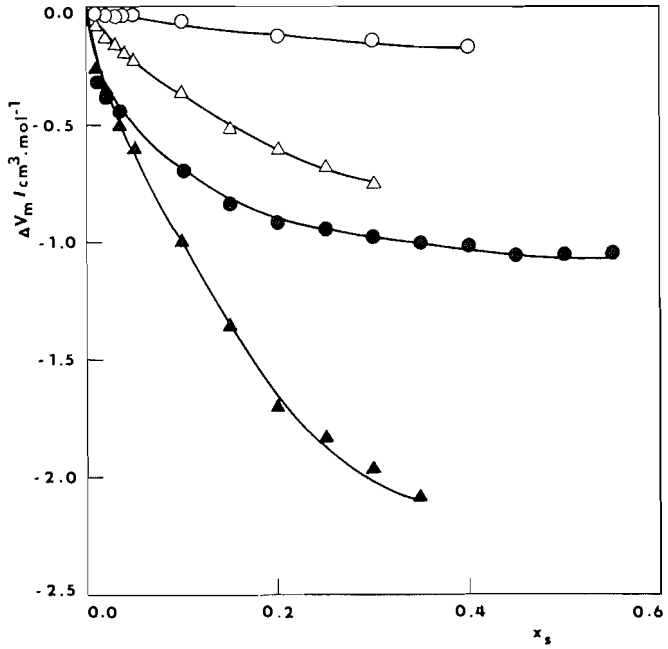

FIG. 2. Deviations of the molar volumes of the solutions, V_m, from the additive behaviour. ○, $NH_4SCN + H_2O$; ●, NH_4SCN + DMSO; △, KSCN + H_2O; ▲, KSCN + DMSO.

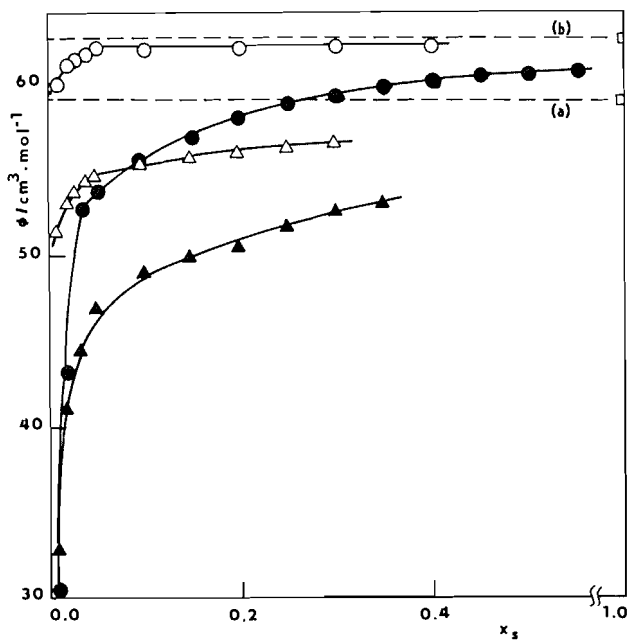

FIG. 3. Apparent molar volume of the salt, Φ, as a function of the mole fraction of the salt in the solution, x_s. Broken lines — the molar volume of the pure molten (undercooled) salt of 333.2 K: (*a*), KSCN; (*b*), NH_4SCN. ○, $NH_4SCN + H_2O$; ●, NH_4SCN + DMSO; △, KSCN + H_2O; ▲, KSCN + DMSO.

the studied systems is depicted in Fig. 3. The apparent molar volume concept is based on the value of the molar volume of the solvent, V_1^0, which is experimentally accessible, in contrast to the value of the molar volume of the molten salt, V_2^0, which is mostly a hypothetical value. In this concept, all the deviations from additivity between V_1^0 and V_2^0 are included in the value of the apparent molar volume of the salt. It may seem natural to discuss the deviations in terms of changes in the molar volume of the salt, but this approach is probably acceptable only in dilute solutions of electrolytes where the solvent molecules form a "continuum", but even then it is preferable to speak about the "mode of accommodation" of the ions in the solvent structure. Different modes of "ion accommodation" can be employed to explain, e.g. a difference between the values of Φ of a salt in H_2O and DMSO. Dimethylsulphoxide molecule is larger than water and thus there is also a larger intermolecular space in the structure of DMSO and only small expansion with respect to the original solvent structure is necessary to form "holes" for accommodation of ions. Utilization of the free volume in the solvent structure is reflected in lower value of Φ for both salts in DMSO than in water (Fig. 3). The effective molar volume of solvent molecules that are in contact with ions is lower than V_1^0. This is another, even if not so significant, contribution to the negative deviation from additivity between V_1^0 and V_2^0.

In salt-rich systems the above explanation of deviations from additivity is not applicable. In this range all solvent molecules are distinctly affected by ions and are accommodated in a quasi-lattice structure of ions. The difference between the effective molar volume of solvent molecules and V_1^0 is responsible for the deviations from additivity beween V_1^0 and V_2^0. A contribution of interionic space can explain the differences in the effective molar volume of solvent in different salt + solvent systems.

The shape of the experimental dependences in Fig. 3 is completely in agreement with the above assumptions. The difference between the straight line (ideal behaviour) and the experimental curves is smaller for aqueous than for

TABLE 2. Salt refractivities in infinitely dilute aqueous and DMSO solutions, $[R^0]$, in the crystalline state, $[R]_c$, and the refractivity change accompanying the transition of the salt from crystals to infinite dilution, $\Delta[R^0]_{c\text{-}x}$

Salt	$[R^0]_{H_2O}$	$[R]_c$[a]	$\Delta[R^0]_{c\text{-}H_2O}$	$[R^0]_{DMSO}$	$\Delta[R^0]_{c\text{-}DMSO}$
KSCN	20.10	18.57	1.53	18.90	0.23
NH_4SCN	22.20	21.00	1.20	21.38	0.38

[a]Values calculated from data in ref. 21.

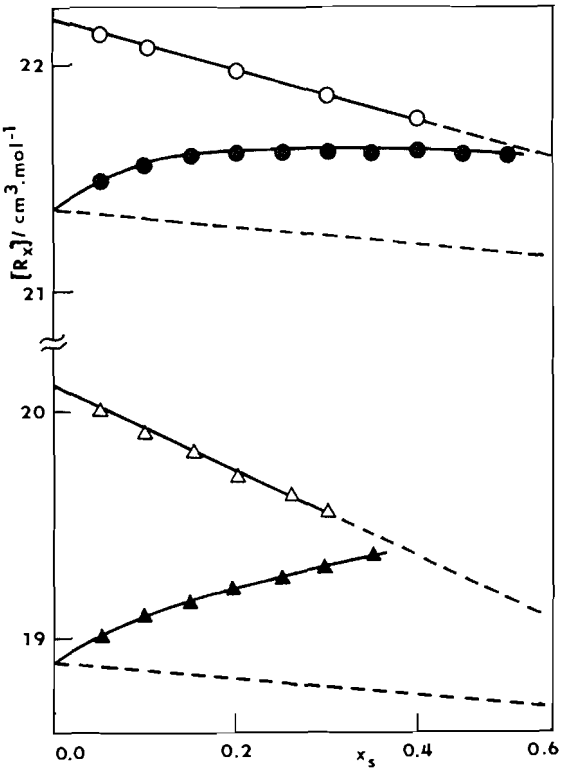

FIG. 4. Molar refractivity of the salt, $[R_x]$, as a function of the mole fraction in the solution, x_s. Broken lines represent the additive behaviour. ○, $NH_4SCN + H_2O$; ●, NH_4SCN + DMSO; △, KSCN + H_2O; ▲, KSCN + DMSO.

DMSO solutions, indicating higher deformability of the DMSO molecules.

There is another aspect of coordinate system used in Fig. 3. It can be used for the extrapolation of Φ to $x_s = 1$ and to estimate a value for the molar volume of the pure molten salt, V_2^0, at this temperature. The precision of this estimation is influenced by rather long extrapolation to the molten salt end and there is no simple model for mathematical form (shape) of the isotherm Φ vs. x_s. It means that the method can be used only as a rough test of the value obtained from the density data of molten salt.

Molar refractivity

Aqueous solutions

The molar refractivity of the solution, defined by the Lorentz–Lorenz equation

$$[3] \quad [R]_{soln} = \frac{n^2 - 1}{n^2 + 2} V_m$$

(V_m is the molar volume of the solution, n is the refractive index for a given wavelength) reflects the changes in the properties of the ions due to polarization or deformation of their electron shells under the influence of the electric field of the neighbouring ions. It is assumed that the refractivity of a system can be calculated in a strictly additive manner from the individual refractivities of the components. Every deviation from additivity is regarded as an indication of interactions between the components.

According to Fajans (15), the refractivity of anions is decreased by neighbouring cations. The stronger the electric field of a cation and, thus, the stronger the interactions between the cation and an anion, the more the refractivity of the anion is lowered. On the other hand, anions should increase the refractivity of cations. The joining of ions into molecules or crystals is then accompanied by a net decrease in the refractivity, $\Delta[R]$, when the effect of the cation on the anion outweighs the effect of the anion on the cation.

As the solution becomes more concentrated, the ions displace the solvent molecules and unite to form complex ions or ion pairs. These effects appear as a change in the refractivity of the ions. The refractivity values of the individual ions in the free gaseous state $[R]_g$, calculated by Pauling (16) and Fajans (17), can be used as a measure of their respective deformabilities. The change in the refractivity of a salt accompanying transition from the gaseous state to an infinitely dilute solution, $\Delta[R^0]$, is then expressed as

$$[4] \quad [R^0_{salt}] = [R_{cat}]_g + [R_{an}]_g + \Delta[R^0]$$

We subtracted the refractivity of the pure solvent (taken from ref. 18) from the refractivity of the solution, $[R]_{soln}$, containing 1 mole of the salt. This procedure is analogous to the calculation of the apparent molar volume of the salt. The molar refractivity values of the salt, $[R_x]$, thus obtained at various concentrations, were plotted as a function of the salt concentration (Fig. 4) and the refractivity of the salt in infinitely dilute solution, $[R^0]$, was obtained by extrapolation to the concentration, $x_s = 0$ (Table 2). The ionic refractions in infinitely dilute solutions were found to be additive both in aqueous (19) and in DMSO solutions (11). The refractivity values, $[R^0]_{H_2O}$, of NH_4^+ and K^+ cations in infinitely dilute aqueous solutions were estimated by Fajans (19) (Table 3), so that refractivity of the SCN^- anion can be estimated: $[R^0_{SCN^-}] = [R^0_{salt}] - [R^0_{cat}]$. The values of 17.84 and 17.89 calculated from KSCN and NH_4SCN, respectively, are in good agreement and the average value of $[R^0_{SCN^-}] = 17.86$ was adopted and is given in Table 3.

Cations and anions not only influence one another, but also affect the solvent molecules surrounding them in the solution. It was estimated earlier that the K^+ cation has no polarizing effect on water (19) and its refractivity value in the gaseous state is the same as in infinitely dilute solution, whereas the NH_4^+ cation

Can. J. Chem. Downloaded from www.nrcresearchpress.com by 196.1.178.254 on 09/07/12
For personal use only.

TABLE 3. Refractivity of ions in the free gaseous state, $[R]_g$, in infinitely dilute aqueous solutions, $[R^0]_{H_2O}$, and the refractivity accompanying transition from the gaseous state to infinite dilution, $\Delta[R^0]_{g\text{-}H_2O}$

Ion	$[R]_g$	$[R^0]_{H_2O}$	$\Delta[R^0]_{g\text{-}H_2O}$
K^+	2.26[a]	2.26[a]	0.0
NH_4^+	4.61[b]	4.31[a]	−0.3
SCN^-	17.86	17.86	0.0

[a]Values taken from ref. 19.
[b]Reference 11.

TABLE 4. Refractivity of ions in infinitely dilute DMSO solutions, $[R^0]_{DMSO}$, and the refractivity change accompanying the transition from the gaseous state to infinite dilution, $\Delta[R^0]_{g\text{-}DMSO}$

Ion	$[R^0]_{DMSO}$	$\Delta[R^0]_{g\text{-}DMSO}$
K^+	1.90	−0.36
NH_4^+	4.38[a]	−0.23
SCN^-	17.00	−0.86
NO_3^-	10.38[a]	−0.64
Cl^-	8.61[a]	−0.45

[a]Values taken from ref. 11.

lowers the refractivity of water by 0.3 (11). The effect of the SCN^- anion on water cannot be estimated using eq. [4] because the refractivity value of SCN^- anion in the free gaseous state is not known. We can, however, compare the refractivity change accompanying dissolution of the crystalline salts in water: $[R_{salt}]_{c\text{-}H_2O} = [R^0_{salt}]_{H_2O} - [R_{salt}]_c$ (Table 2). The value for NH_4SCN is by 0.33 lower than that for KSCN. Since the NH_4^+ cation lowers the refractivity of water by 0.33 (11), it seems that the SCN^- anion has no polarizing effect upon water and thus $[R^0_{SCN^-}]_{H_2O} = [R_{SCN^-}]_g$. This result is reasonable considering the high refractivity value of SCN^-.

With increasing salt concentration, water molecules are replaced by cations and anions which approach more closely to each other. Cations have a stronger polarizing effect on the SCN^- anions than on water as follows from comparison of the refractivity values of the salts in infinitely dilute aqueous solutions with those for crystals (Table 2). Thus, a decrease in the salt refractivity with increasing salt concentration was observed (Fig. 4). The refractivity changes linearly with changing concentration and extrapolation to the concentration of $x_s = 1$, i.e. the pure salt, yields a value which is the same as that given in Table 2 for the refractivity of the crystal. This behaviour is considered to be additive and no formation of complexes or ion pairs is expected.

DMSO solutions

The refractivities of the salts in infinitely dilute solutions are lower than those for aqueous solutions. The DMSO molecule is more polarizable than the water molecule (18) and is influenced more strongly by cations and anions. The concentration dependence of the salt refractivities is depicted in Fig. 4 and the values extrapolated to infinite dilution ($x_s = 0$), $[R^0_{salt}]_{DMSO}$, are listed in Table 2. The refractivities of the SCN^- anion and K^+ cation in infinitely dilute DMSO solution were evaluated from these values and the known value of $[R^0_{NH_4^+}]_{DMSO} = 4.38$ (11) ($[R^0_{SCN^-}] = [R^0_{salt}] - [R^0_{NH_4^+}]$, etc.) and are given in Table 4. The effect of the ions on the DMSO molecule, $\Delta[R^0]_{g\text{-}DMSO}$, can be estimated by comparing the $[R^0]_{DMSO}$ values of ions with their refractivities in the gaseous state, $[R]_g$ (see Table 4). The K^+ cation decreases the refractivity of DMSO by 0.36, the effect being stronger than that of the NH_4^+ cation. The SCN^- anion lowers the refractivity of DMSO by 0.86, which is more than for nitrate and chloride anions (11).

As the DMSO solutions become more concentrated, the salt refractivity increases and positive deviations from the additivity between $[R^0]$ and $[R]_c$ were observed. This behaviour is explained by the formation of complex solvates of the cations with the DMSO. The cations are surrounded by DMSO molecules, preventing approach by anions. Consequently, interactions between the ions are limited. The actual content of DMSO decreases with increasing salt concentration, so that the relative effect of the cation on DMSO also decreases. A positive term is thus introduced into the concentration dependence of the salt refractivity. The SCN^- anions have a similar effect as they also influence the DMSO molecule. The positive deviations from additivity are higher for K^+ than for NH_4^+ salt because of the stronger effect of the K^+ cation on DMSO which introduces a higher positive component into the refractivity change (Fig. 4). It is assumed that, if a higher concentration of the salt in the solution can be attained, the refractivity would decrease toward the refractivity value for the crystal.

Conclusions

Solutions of NH_4SCN and KSCN in water and dimethylsulphoxide are volumetrically non-ideal. Deviations from additivity are negative in both solvents.

The strength of the solute–solvent interactions that depends among others on the value of the solvent dipole moment and easier deformability of the DMSO molecules can be used to explain the more distinct deviations from volumetric ideality in solutions of both salts in DMSO than in water and the positive deviations from additivity in the concentration dependence of the salt refractivity.

The effect of K^+ cations on the DMSO molecule was found to be stronger than the effect of NH_4^+, both from refractometric and volumetric measurements. The effect of the SCN^- anion on DMSO is stronger than the effect of NO_3^- or Cl^-, but SCN^- has no effect on the water molecules. A similar conclusion was drawn on the basis of the solvent activity data in solutions of KSCN and KNO_3 in DMSO (20). The stronger interaction of the DMSO molecule with SCN^- than with NO_3^- is not unexpected for the stronger solvation of voluminous and polarizable anions in dipolar aprotic solvents.

1. Z. KODEJŠ, I. HORSAK, and I. SLÁMA. Rev. Roum. Chim. **24**, 293 (1979).
2. Z. KODEJŠ, J. NOVAK, and I. SLÁMA. Collect. Czech. Chem. Commun. **48**, 1810 (1983).
3. Z. KODEJŠ and I. SLÁMA. Chem. Zvesti, **34**, 335 (1980).
4. Z. KODEJŠ and G. A. SACCHETTO. J. Chem. Soc. Faraday Trans. I, **78**, 3529 (1982).
5. Z. KODEJŠ and G. A. SACCHETTO. Z. Phys. Chem. N.F. **134**, 187 (1983).
6. Z. KODEJŠ and P. PACÁK. Chem. Papers, **40**, 523 (1986).
7. M. ABRAHAM. J. Chim. Phys. **81**, 207 (1984).
8. I. HORSÁK and I. SLÁMA. J. Chem. Eng. Data, **31**, 434 (1986).

Can. J. Chem. Downloaded from www.nrcresearchpress.com by 196.1.178.254 on 09/07/12
For personal use only.

9. P. CLAES and J. GLIBERT. Ionic liquids. *Edited by* D. Inmann and D. Lovering. Plenum Press, New York. 1981. p. 291.
10. S. K. JAIN. J. Phys. Chem. **82**, 1272 (1978).
11. P. PACÁK. J. Phys. Chem. In press.
12. V. GUTMANN. The donor–acceptor approach to molecular interactions. Plenum Press, New York. 1978. Chapt. 2.
13. P. DULIEU and P. CLAES. Bull. Soc. Chim. Belg. **82**, 639 (1973).
14. N. ISLAM and K. ISMAL. J. Phys. Chem. **79**, 2180 (1975).
15. K. FAJANS. Trans. Faraday Soc. **23**, 357 (1927).
16. L. PAULING. Proc. R. Soc. London, A **114**, 198 (1927).
17. K. FAJANS and G. JOOS. Z. Physik, **23**, 1 (1924).
18. P. PACÁK. J. Solution Chem. **16**, 71 (1987).
19. K. FAJANS and R. LUHDEMANN. Z. Physik. Chem. **29**, 150 (1935).
20. Z. KODEJŠ, H. ŠPALKOVÁ, and G. A. SACCHETTO. J. Chem. Thermodyn. **20**, 363 (1988).
21. Handbook of chemistry and physics. Chemical Rubber Publ. Co. 1955.

Can. J. Chem. Downloaded from www.nrcresearchpress.com by 196.1.178.254 on 09/07/12
For personal use only.

Interpretation of *n*-donor specific solvent effect on electronic spectra of copper acetate and chloride complexes by intermolecular perturbation theory

MARIOLA SZPAKOWSKA

Zakład Chemii Fizycznej, Instytut Chemii i Technologii Nieorganicznej, Politechnika Gdańska, Ul. Majakowskiego 11/12, 80-952 Gdańsk, Poland

AND

OTTÓ B.NAGY[1]

Laboratoire de Chimie Organique Physique, Université Catholique de Louvain, Bâtiment Lavoisier, 1 Pl. Pasteur, 1348-Louvain-la-Neuve, Belgium

Received October 26, 1987

MARIOLA SZPAKOWSKA and OTTÓ B.NAGY. Can. J. Chem. **66**, 2250 (1988).

A simple second order intermolecular perturbation theory is proposed in the Fukui approximation to account for the electronic spectral behavior of electron acceptor solutes dissolved in pure *n*-donor solvents. This double perturbation theory considers explicitly both the solvating and complexing effects of the solvent. Using the electronic spectral data of mono- and binuclear copper acetate and chloride complexes obtained in pure pyridine derivatives it is shown that the predicted shifts brought about by increasing *n*-donor ability of solvent are fully corroborated by experiment. The sensitivity of mononuclear copper complexes to steric effects is also confirmed and it is shown that binuclear ones are not sensitive to this effect. New ionization potential values have also been determined using a simple interpolation–standardization procedure.

MARIOLA SZPAKOWSKA et OTTÓ B.NAGY. Can. J. Chem. **66**, 2250 (1988).

Une théorie simple de perturbation intermoléculaire d'ordre deux est proposée dans l'approximation de Fukui afin d'interpréter le comportement spectroscopique de solutés accepteurs d'électrons dissouts dans des solvants purs *n*-donneurs. Cette théorie de double perturbation considère explicitement les effets solvatants et complexants du solvant. En utilisant les données de la spectroscopie électronique de complexes d'acétate et de chlorure de cuivre mono- et binucléaires obtenues dans des dérivés purs de pyridine, il est démontré que les déplacements prédits, provoqués par le pourvoir *n*-donneur croissant du solvant, sont complètement corroborés par l'expérience. La sensibilité de complexes de cuivre mononucléaires aux effets stériques est aussi confirmée et il est démontré que les complexes binucléaires ne sont pas sensibles à ces effets. De nouvelles valeurs de potentiel d'ionisation ont été aussi déterminées en utilisant une simple procédure d'interpolation et de standardisation.

Can. J. Chem. Downloaded from www.nrcresearchpress.com by 112.217.228.212 on 09/07/12
For personal use only.

Introduction

In analyzing medium effects on physico-chemical properties of molecules it seems useful to distinguish between general (caused by polarity and polarizability) and specific (*n*-donor, π-donor, and hydrogen bond forming ability) solvent effects (1, 2). When the latter are present they usually dominate the overall medium effect (1–5). An immediate consequence of this situation is that aprotic solvents cannot be treated the same way but rather should be divided into several solvent classes (1, 2). The discovery of these classes (1, 2) lead to a better understanding of medium effects and allowed the interpretation of the seemingly anomalous behavior of *n*-donor solvents (1, 6).

A first successful explanation could be found in a particular solvation shell structure stemming from the presence of free electron pairs and the asymmetric charge distribution in solvent molecules (1). Another explanation was obtained from intermolecular perturbation theory (7). It has been shown that a simple intermolecular second order perturbation theory developed in the Fukui molecular orbitals (FMO) approximation (8, 9) can account successfully for the specific solvent effects observed for 2 + 4 cycloaddition reactions. The same theoretical method has also been used to study the behavior of *n*-donor solvents (7). It was predicted that in the case of π–π donor–acceptor molecular complexes the first electronic transition energy should increase with increasing *n*-donor ability of solvents (7), in full agreement with the previous explanation (1) and experimental observations (1, 2, 7).

An important limiting case is obtained when the electron acceptor molecule is dissolved in pure *n*-donor solvent. In this case the solvent is not only solvating but also complexing the acceptor solute, i.e. it takes over the role played by the electron donor complexing partner. In the present paper this specific complexing–solvating property of *n*-donor solvents will be studied using mono- and binuclear copper complexes (10, 11) as electron acceptor solutes, and substituted pyridine derivatives as *n*-donor solvents. Our choice was guided by the fact that these copper complexes proved to be very useful in realizing an extreme situation of microscopic partitioning according to the competitive preferential solvation (COPS) theory (3, 12), i.e. a full coordination of the competing solvent molecules. When copper acetate $[Cu(CH_3CO_2)_2H_2O]$ is dissolved in pure pyridine derivatives (L) a new complex is formed, $[Cu(CH_3CO_2)_2L_2]$, in which two molecules of the solvation shell are singled out by coordination (10). This mononuclear complex may also be in equilibrium with its binuclear form (10).

On the other hand, copper chloride may complex three or four pyridine molecules ($[Cu(Cl)_2L_n]$ with $n = 3, 4$).

Theoretical part

According to the previously proposed perturbation theory (7, 9) the *n*-donor solvent molecule (S) interacts with the lowest unoccupied orbital ($|l_A\rangle$, energy E_{lu}^{A}) of the electron acceptor solute (A) mainly through its highest occupied molecular orbital ($|h_S\rangle$, energy E_{ho}^{S}) (8). This solvating interaction leads to a new species AS, having the following Fukui energy levels:

$$[1] \quad E_{lu}^{AS} = E_{lu}^{A} + \frac{\langle l_A|H^S|h_S\rangle^2}{E_{lu}^{A} - E_{ho}^{S}}$$

[1]To whom all correspondence should be addressed.

Printed in Canada / Imprimé au Canada

Can. J. Chem. Downloaded from www.nrcresearchpress.com by 112.217.228.212 on 09/07/12
For personal use only.

and

$$[2] \quad E_{ho}^{AS} = E_{ho}^{S} + \frac{\langle h_S|H^S|l_A\rangle^2}{E_{ho}^{S} - E_{lu}^{A}}$$

as can be shown easily by standard perturbation theory (H^S represents the interaction Hamiltonian). In particular, second order calculation is needed here since the perturbation is intermolecular. The lowest unoccupied orbital of AS has the form

$$[3] \quad |l_{AS}\rangle = \left[1 + \left(\frac{\langle l_A|H^S|h_S\rangle}{E_{lu}^{A} - E_{ho}^{S}}\right)^2\right]^{-1/2}\left(|l_A\rangle + \frac{\langle l_A|H^S|h_S\rangle}{E_{lu}^{A} - E_{ho}^{S}}|h_S\rangle\right)$$

The solvent is also complexing the solute. This complexing interaction can be taken into account by admitting that the lowest unoccupied orbital of AS ($|l_{AS}\rangle$) in turn interacts with the highest occupied orbital of the complexing solvent molecule. Again, the Fukui energy levels of the resulting solvated-complexed solute (SAS) will be

$$[4] \quad E_{lu}^{SAS} = E_{lu}^{AS} + \frac{\langle l_{AS}|H^C|h_S\rangle^2}{E_{lu}^{AS} - E_{ho}^{S}}$$

$$[5] \quad E_{ho}^{SAS} = E_{ho}^{S} + \frac{\langle h_S|H^C|l_{AS}\rangle^2}{E_{ho}^{S} - E_{lu}^{AS}}$$

with the usual notations.

Let us note that in this simple perturbational calculation the Hamiltonian operators are not considered explicitly. Their matrix elements H_{ij}^C and H_{ij}^S are taken as parameters as in the simple Hückel approximation of molecular orbital theory. It should only be remembered that in general $H_{ij}^C > H_{ij}^S$ for obvious physico-chemical reasons. In more detailed calculations H^C is taken as the usual Hamiltonian of molecular systems containing electronic kinetic and potential energies as well as electronic and nuclear repulsion terms. H^S may be either constructed in the same way as H^C or one may use some alternative formulation based on current models of medium effects (point dipole approximation, reaction field effect, ...) (27).

The variation of energy levels brought about by the solute–solvent interaction is depicted in Fig. 1. The first electronic transition energy of species SAS will have the value: $\Delta E = E_{lu}^{SAS} - E_{ho}^{SAS}$. A more explicit expression can be obtained by substituting eqs. [1] and [3] into eqs. [4] and [5]. By adopting the zero differential overlap (ZDO) approximation (i.e., S—S interaction is neglected) and neglecting the small fourth order term which appears in the denominator of eqs. [4] and [5], we obtain, after some algebra, the following expression:

$$[6] \quad \Delta E = (E_{lu}^{A} - E_{ho}^{S}) + \frac{\langle l_A|H^S|h_S\rangle^2}{E_{lu}^{A} - E_{ho}^{S}} + 2\langle l_A|H^C|h_S\rangle^2\left[(E_{lu}^{A} - E_{ho}^{S}) + 2\frac{\langle l_A|H^S|h_S\rangle^2}{E_{lu}^{A} - E_{ho}^{S}}\right]^{-1}$$

It appears that this equation represents the limiting case of a more general expression obtained for the donor–acceptor complex – n-donor solvent interaction by similar double perturbation treatment (7). Equation [6] shows that the electronic transition energy depends on the energy gap separating the interacting orbitals in a rather complicated way. When the n-donor ability of the solvent increases, $E_{lu}^{A} - E_{ho}^{S}$ will decrease and the interaction matrix element increases. As a result, the last two terms in eq. [6] increase. However, the first term is the dominating one (24) as it can also be verified easily by numerical simulation. Therefore, it can be predicted that *with increasing* n*-donor ability of the solvent the electronic transition energy of the solute decreases.* This conclusion is just opposite to that obtained for the n-donor solvent effect on the electronic excitation energy of π–π complexes where a blue shift was predicted (7) and confirmed experimentally (1, 7).

In the case of a transition metal complex solute the complexing action of the solvent is strongly controlled by symmetry restrictions. As a matter of fact, the coordination of solvent molecules to the central metal ion takes place according to a well-defined geometry. Consequently, only those solute–solvent orbitals can interact which belong to the same irreducible representation of the actual symmetry point group. On the other hand, the solvating action of the solvent is not subject to such limitations because of the dynamic character of the solvation shell structure.

All the complexes considered here have a tetragonally distorted octahedral geometry and therefore they belong to the D_{4h} symmetry point group.

In both mono- and binuclear copper acetate complexes with n-donor solvents such as pyridine derivatives, the complexing solvent molecules occupy the axial positions along the z-axis (25). Molecular orbital calculations show (25, 26) that the highest occupied and the lowest unoccupied orbitals are mainly centered on the metal, receiving only slight contributions from the ligands. They have essentially the character of metal d orbitals and will be designated by $|h_M\rangle$ (energy E_{ho}^{M}) and $|l_M\rangle$ (energy E_{lu}^{M}), respectively (Fig. 1; note that for clarity, the metal is designated by F instead of M for chloride complexes). This result is in full agreement with the experimental observation that the electronic transitions considered here are essentially of d–d type. A potential field of D_{4h} symmetry splits the d orbital energy levels in such a way that the orbital d_{z^2} becomes the highest occupied (occupation number: 2), while the orbital d_{xy} becomes the lowest unoccupied (occupation number: 1) orbital of the complex (25). d_{z^2} and d_{xy} belong to the a_{1g} and b_{2g} irreducible representations of D_{4h}, respectively. Considering only σ-type metal–pyridine interactions (π-type interactions can influence neither $|l_M\rangle$ nor $|h_M\rangle$ for symmetry reasons), it can be seen that the pyridine lone pair electron orbital ($|h_S\rangle$, symmetry: a_{1g}, energy E_{ho}^{S}) can interact only with d_{z^2}, leading to the new highest occupied orbital $|h_{MS}\rangle$ (energy: E_{ho}^{MS}). Solvating action of pyridine affects both $|h_{MS}\rangle$ and $|l_{MS}\rangle$ ($\equiv |l_M\rangle$) (see above) and the final energy level positions are given in Fig. 1. Using the same procedure and applying the same approximations as for the derivation of eq. [6], the following expression is obtained for the metal d–d transition energy perturbed by the complexing–solvating ability of the n-donor solvent ($\Delta E_a = E_{lu}^{SMS} - E_{ho}^{SMS}$):

$$[7] \quad \Delta E_a = (E_{lu}^{M} - E_{ho}^{M}) + \frac{\langle l_M|H^S|h_S\rangle^2}{E_{lu}^{M} - E_{ho}^{S}} - \frac{\langle h_M|H^C|h_S\rangle^2}{E_{ho}^{M} - E_{ho}^{S}} - \langle h_M|H^S|h_S\rangle^2\left[(E_{ho}^{M} - E_{ho}^{S}) + 2\frac{\langle h_M|H^C|h_S\rangle^2}{E_{ho}^{M} - E_{ho}^{S}}\right]^{-1}$$

Again, if the n-donor ability of solvent increases, i.e. $E_{lu}^{M} - E_{ho}^{S}$ (and $E_{ho}^{M} - E_{ho}^{S}$) decreases, all terms, except the first one, increase. But, since the negative contribution (3rd and 4th terms) is greater than the positive one (2nd term), the overall

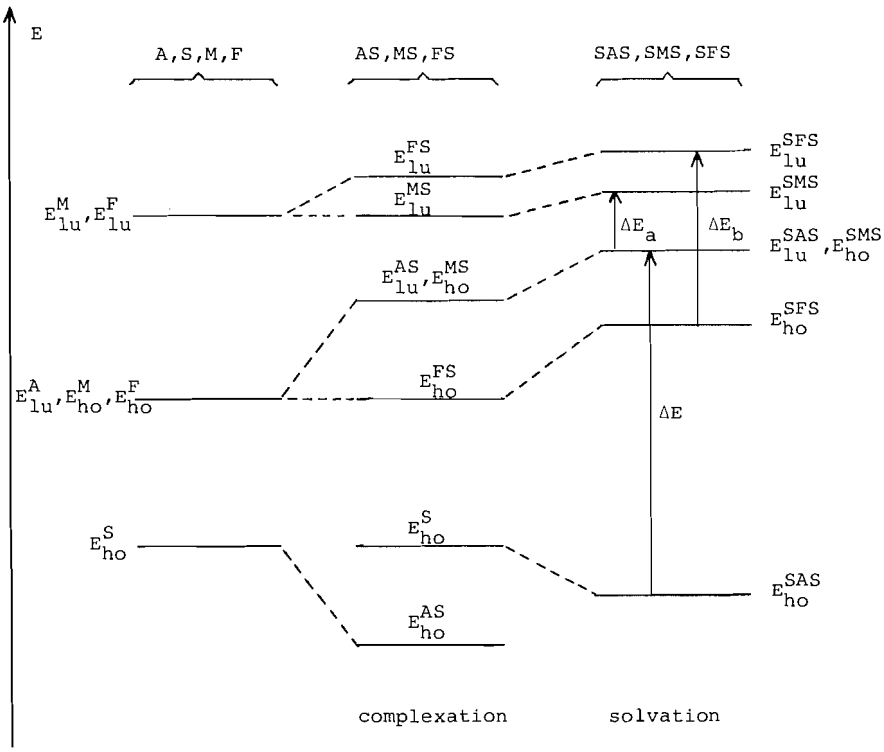

FIG. 1. Effect of complexing–solvating perturbation on the electronic levels of electron acceptor solutes.

transition energy will decrease and a *red shift* must be observed. It will be seen that this prediction is fully borne out by experiment.

In those copper chloride – pyridine complexes where four pyridine molecules are present, the latter occupy the equatorial xy plane of the distorted octahedron. Therefore the complexing solvent molecules interact mainly with the singly occupied d_{xy} metal orbital pushing it to higher energies, while the highest occupied orbital (d_{z^2}) remains unaffected for symmetry reasons. Here also solvation effect is not submitted to symmetry restrictions (Fig. 1). The same perturbational treatment as applied before to the acetate complexes results in the following expression for the metal d–d transition energy ($\Delta E_b = E^{SFS}_{lu} - E^{SFS}_{ho}$):

$$[8]\quad \Delta E_b = (E^F_{lu} - E^F_{ho}) - \frac{\langle h_F|H^S|h_S\rangle^2}{E^F_{ho} - E^S_{ho}} + \frac{\langle l_F|H^C|h_S\rangle^2}{E^F_{lu} - E^S_{ho}} + \langle l_F|H^S|h_S\rangle^2\left[(E^F_{lu} - E^S_{ho}) + 2\frac{\langle l_F|H^C|h_S\rangle^2}{E^F_{lu} - E^S_{ho}}\right]^{-1}$$

Here the positive contributions (3rd and 4th terms) will dominate and an increase of n-donor ability of solvent (i.e. $E^F_{lu} - E^S_{ho}$ decreases) provides a *blue shift* of the d–d metal transition. The opposite predictions of eqs. [7] and [8] show clearly that the same n-donor ability of solvent can influence differently the electronic spectrum of a given transition metal complex solute depending on the geometry and electronic structure of the latter.

Results and discussion

The electronic transition energies obtained for the mono- and binuclear forms of copper acetate complexes in pure n-donor solvents are collected in Table 1. Since the ionization potential (I_S) of the solvent represents in fact the energy of its highest occupied molecular orbital (i.e. $I_S = -E^S_{ho}$, Koopman's theorem), it was taken as an experimental parameter to express the n-donor power of the solvent molecules. The paucity of I_S values in the literature prompted us to work out a simple approach to determine the lacking data either by interpolation or by standardization. The basic principle is the existence of possible linear relationship between basicity (pK_a) and ionization potential.

As a starting point a standard series was chosen using only I_S values which have been well established both theoretically and experimentally (13). Using the ionization potentials of pyridine derivatives 3, 4, 7, and 8 from Table 1, of 3-methyl- (pK_a = 5.68; I_S = 9.68 eV), 4-methyl- (pK_a = 6.02; I_S = 9.63 eV), 2,5-dimethyl- (pK_a = 6.40; I_S = 9.57 eV), 2,3-dimethyl- (pK_a = 6.57; I_S = 9.57 eV), and 2,4,6-trimethyl- (pK_a = 7.59; I_S = 9.42 eV) pyridines (13), and of 4-cyano- (pK_a = 1.90; I_S = 10.25 eV) and 3-fluoro- (pK_a = 2.97; I_S = 10.09 eV) pyridines (14), the following linear relationship could be established between pK_a and I_S values (all acidity constants are from ref. 15):

$$[9]\quad pK_a = 71.12(\pm 1.13) - 6.76(\pm 0.12)I_S \qquad (r = 0.9987;\ \sigma = 0.093)$$

This equation was taken as standard and it was used to determine unknown ionization potentials by direct interpolation. On the other hand, it was noted that other ionization potential values (14) also lay on a line parallel to that given by eq. [9]. The average distance between the two parallel lines is 0.2 eV. This observation suggests that if the ionization potentials situated on this parallel line are corrected by increasing their values by +0.2 eV, useful estimates can be obtained for unknown I_S values. The results arrived at by this standardization procedure are collected in Table 2 (see also Table 1).

As it was shown above, eq. [7] predicts that when the n-donor ability of the solvating-complexing solvent molecules increases

Can. J. Chem. Downloaded from www.nrcresearchpress.com by 112.217.228.212 on 09/07/12
For personal use only.

TABLE 1. Electronic transition energies of mononuclear $[Cu(CH_3CO_2)_2L_2]$ and binuclear $[Cu_2(CH_3CO_2)_4L_2]$ copper acetate complexes in pure ligand (L) solutions ($T = 298 \pm 0.1$ K)

Ligand	pK_a[a]	I_S (eV)	Mononuclear form $\bar{\nu}_{max}$ (kK)	Mononuclear form ϵ_{max}	Binuclear form $\bar{\nu}_{max}$ (kK)	Binuclear form ϵ_{max}
1. 2-Chloropyridine[e]	0.72	10.45[c]	—	—	14.285	430
2. 3-Chloropyridine[f]	2.84	10.0[c]	15.384	84	14.084	475
3. Pyridine[f]	5.17	9.76[b]	15.197	82	13.850	470
4. 2-Methylpyridine[f]	5.97	9.65[b]	16.666	73	13.831	450
5. 2-Ethylpyridine[g]	5.97	9.64[d]	—	—	13.888	440
6. 4-Ethylpyridine[h]	6.02	9.63[d]	15.267	85	13.888	460
7. 2,6-Dimethylpyridine[g]	6.72	9.55[b]	16.129	68	13.717	450
8. 2,4-Dimethylpyridine[g]	6.63	9.52[b]	16.666	74	13.698	450
9. 3,4-Dimethylpyridine[f]	6.46	9.52[c]	15.151	78	13.793	450
10. Isoquinoline	5.40	9.19[c]	15.151	95	13.850	420

[a]Reference 15.
[b]Reference 13.
[c]Values from ref. 14 incremented by +0.2 eV (standardization procedure, see text).
[d]Interpolated value using eq. [9].
[e]Reference 11.
[f]Reference 10.
[g]Reference 16.
[h]Copper propionate complexes, ref. 17.

TABLE 2. New ionization potentials for pyridine derivatives obtained by interpolation (eq. [9])

Pyridine derivatives	pK_a[a]	I_S (eV)
1. 3,5-Dimethylpyridine	6.15	9.62
2. 3-Ethylpyridine	5.70	9.68
3. 2-Cyanopyridine	−0.26	10.57
4. 3-Cyanopyridine	1.45	10.31
5. 2-Fluoropyridine	−0.44	10.57[b]
6. 2-Bromopyridine	0.90	10.40
7. 3-Bromopyridine	2.84	10.11
8. 2-Iodopyridine	1.82	10.26
9. 3-Iodopyridine	3.25	10.05
10. 2-Hydroxypyridine	0.75	10.42
11. 3-Hydroxypyridine	4.72	9.83
12. 4-Hydroxypyridine	3.12	10.07
13. 2-Methoxypyridine	3.28	10.04
14. 3-Methoxypyridine	4.88	9.81
15. 4-Methoxypyridine	6.62	9.52[b]

[a]Reference 15.
[b]Values taken from ref. 14 and incremented by +0.2 eV (see text).

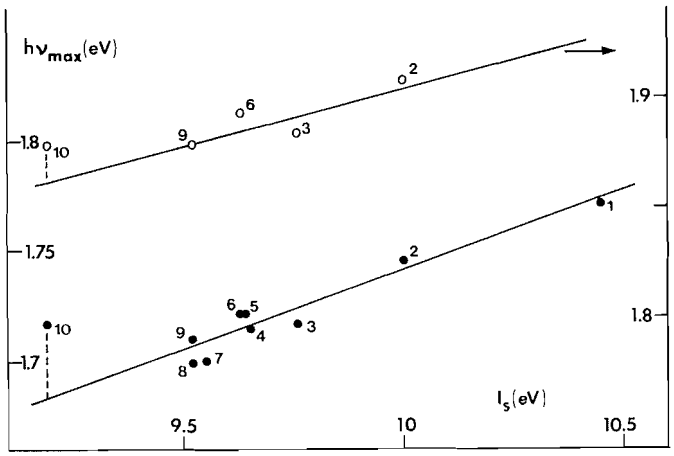

FIG. 2. Influence of n-donor power of solvent on the first electronic transition energy of mononuclear (○) and binuclear (●) copper acetate complexes (Table 1).

the first excitation energy of the solute should decrease. Figure 2 shows that this is indeed the case. The linear relations governing this correlation for both mono- and binuclear copper acetate complexes are given by eqs. [10] and [11] respectively:

$$[10] \quad h\nu_{max}\,(\text{eV}) = 1.384(\pm 0.218) + 0.052(\pm 0.022)I_S \qquad (r = 0.8543;\ \sigma = 0.008)$$

$$[11] \quad h\nu_{max}\,(\text{eV}) = 1.012(\pm 0.077) + 0.073(\pm 0.007)I_S \qquad (r = 0.9615;\ \sigma = 0.006)$$

It should be remembered, however, that these relationships are linear only in first approximation.

It can be seen that the slopes of eqs. [10] and [11] are very similar, showing that both mono- and binuclear complexes are sensitive to n-donor properties of solvent in a rather similar extent. It is important to note that the actual values of the slopes are much smaller than unity. It is well known that unit slopes are characterizing weak molecular interactions (22, 23). On the other hand, it has been suggested that the smaller the value of the slope, the stronger is the interaction between the donor–acceptor partners (24). As a matter of fact, full coordination of the donor to the acceptor represents the case where the interaction is very strong, i.e. considerably stronger than in loose molecular complexes. Therefore, according to the above suggestion (24), a slope much smaller than unity is expected in the present case when the first electronic transition energy is plotted vs. the ionization potential of the n-donor molecules. It can be seen that this is fully borne out by experiment (Fig. 2 and eqs. [10] and [11]).

Let us note that the points representing the complexes with isoquinoline do not fall on the straight lines obtained for pyridine derivatives. This is a natural consequence of the fact that in perturbation theory only the members of a given homologous series can be compared.

Can. J. Chem. Downloaded from www.nrcresearchpress.com by 112.217.228.212 on 09/07/12
For personal use only.

TABLE 3. Electronic transition energies of mononuclear $[Cu(Cl)_2L_n]$ copper chloride complexes in pure ligand (L) solutions ($T = 298 \pm 0.1$ K)

Ligand	pK_a[a]	I_S (eV)[a]	$\bar{\nu}_{max}$ (kK)	ϵ_{max}
1. Pyridine	5.17	9.76	12.886 (12.903[b])	141
2. 4-Ethylpyridine	6.02	9.63	13.037 (13.157[c])	140
3. 2,4-Dimethylpyridine	6.63	9.52	14.492 (14.814[d])	128
4. Isoquinoline	5.40	9.19	13.106 (13.157[e])	167

[a]See notes of Table 1.
[b]Reference 18.
[c]Reference 19.
[d]Reference 20.
[e]Reference 21.

On the other hand, it is well known (10, 16) that mononuclear species are very sensitive to steric effects. This is why points representing pyridine derivatives able to provoke strong steric effect (numbers 4, 7, and 8 in Table 1) fall completely off the line obtained for mononuclear complexes (not shown on Fig. 2). Interestingly enough, the same points follow closely eq. [11], showing that binulcear copper complexes are not sensitive to steric effects. As a matter of fact, the particular geometrical structure of these complexes neutralizes in a large extent the influence of steric crowding. It should be noted that all the interpolated and standardized ionization potentials behave in a coherent way with known I_S values, i.e. they obey the same perturbational relationship (eq. [7]). This allows to consider the new I_S values given in Tables 1 and 2 as a good first approximation to the unknown ionization potentials. It also supports the validity of the present standardization–interpolation procedure.

Some copper chloride complexes have been also reinvestigated and the new experimental results are given in Table 3 (the older, less accurate data are also included in parentheses for comparison).

It can be seen that increasing *n*-donor ability of solvent molecules brings about a blue shift as predicted by eq. [8], with isoquinoline falling again out of the homogeneous series of pyridine derivatives as it has been observed already for copper acetate complexes. Unfortunately, the data in Table 3 cannot be compared directly on account of the existing structural differences. While the complexes with pyridine and 2,4-dimethylpyridine contain four pyridine molecules, the complex with 4-ethylpyridine has only three (19, 20). Thus, only the cases of pyridine and 2,4-dimethylpyridine really corroborate the theoretical predictions. Further investigations are therefore necessary to establish definitively whether copper chloride complexes obey eq. [8] or show different behavior.

The above analysis shows that simple second order intermolecular perturbation theory developed here in the Fukui approximation can account successfully for the spectroscopic behavior of solutes which enter into solvating-complexing interactions with *n*-donor solvent molecules. The presently proposed theory is based on a double perturbation taking into account explicitly the two roles played by the solvent: complexation and solvation. The predicted spectral shifts brought about by increasing *n*-donor ability of solvent are fully borne out by experiment. This should also be compared to the blue shift predicted by this same theory for donor–acceptor molecular complex solutes in complete agreement with experimental observations (7).

Experimental

Solid copper acetate and chloride complexes with pyridine derivatives were obtained as described previously (10, 18, 21). The pyridine derivatives were dried by standing over KOH and distilled from molecular sieves (4 Å) *in vacuo*.

Electronic spectra (340–800 nm) were recorded on a Beckmann U.V. 5270 spectrophotometer in thermostatted stoppered cells at 298 ± 0.1 K. The experimental error of the band maxima is about ±0.5 nm.

All the measured electric conductivities of the various solutions were less than $10^{-7}\,\Omega^{-1}\,cm^{-1}$ at copper concentrations of $10^{-3}\,M$.

Copper analysis were realized by the standard EDTA titration procedure.

All manipulations were carried out in a dry box in the presence of P_2O_5.

Acknowledgements

This work was realized within the Belgian–Polish Cultural Exchange Program and was supported by the Polish Academy of Sciences (Grant no CPBP-01.12 and Grant of the Committee of Chemical Sciences).

1. O. B.NAGY, J. B.NAGY, and A. BRUYLANTS. J. Chem. Soc. Perkin II, 968 (1972).
2. S. DUPIRE, J. M. MULINDABYUMA, J. B.NAGY, and O. B.NAGY. Tetrahedron, **31**, 135 (1975).
3. O. B.NAGY, M. WAMUANDA, and J. B.NAGY. J. Phys. Chem. **83**, 1961 (1979).
4. J. B.NAGY, O. B.NAGY, and A. BRUYLANTS. Bull. Soc. Chim. Belg. **82**, 539 (1973).
5. O. B.NAGY, V. REULIAUX, N. BERTRAND, A. VANDERMENSBRUGGHE, J. LESEUL, and J. B.NAGY. Bull. Soc. Chim. Belg. **94**, 1055 (1985).
6. P. H. EMSLIE and R. FOSTER. Rec. Trav. Chim. **84**, 255 (1965).
7. O. B.NAGY and M. SZPAKOWSKA. *In* Physical organic chemistry 1986; Studies in organic chemistry. Elsevier Science Publishers, Amsterdam. 1987. Vol. 31. p. 593.
8. K. FUKUI, T. YONEZAWA, and C. NAGATA. Bull. Chem. Soc. Jpn. **27**, 423 (1954).
9. O. B.NAGY. Can. J. Chem. **63**, 1382 (1985).
10. M. SZPAKOWSKA, I. URUSKA, and J. ZIELKIEWICZ. J. Chem. Soc. Dalton Trans. 1849 (1985).
11. M. SZPAKOWSKA and I. URUSKA. Spectrochim. Acta, **43**A, 763 (1987).
12. O. B.NAGY, M. WAMUANDA, and J. B.NAGY. J. Chem. Soc. Faraday Trans. I, **74**, 2210 (1978).
13. T. NAKAJIMA and A. PULLMAN. J. Chim. Phys. **55**, 793 (1958).
14. D. H. AUE and M. T. BOWERS. Gas phase ion chemistry. Academic Press, New York. 1979. p. 30.
15. A. KATRITZKY. Physical methods in heterocyclic chemistry. Vol. I. Academic Press, New York. 1972.

Can. J. Chem. Downloaded from www.nrcresearchpress.com by 112.217.228.212 on 09/07/12
For personal use only.

16. M. SZPAKOWSKA and I. URUSKA. To be published.
17. Ł. RADECKA. M.Sc. Thesis, Gdańsk. 1987.
18. W. LIBUŚ, S. K. HOFFMANN, M. KLUCZKOWSKI, and H. TWARDOWSKA. Inorg. Chem. **19**, 1625 (1980).
19. M. SZPAKOWSKA, S. K. HOFFMANN, and I. URUSKA. Pol. J. Chem. **55**, 2463 (1981).
20. M. SZPAKOWSKA and I. URUSKA. Coord. Chem. In press.
21. I. URUSKA and M. SZPAKOWSKA. J. Chem. Soc. Faraday Trans. I, **72**, 2545 (1976).
22. G. BRIEGLEB. Elektronen–Donator–Acceptor–Komplexe. Springer Verlag, Berlin. 1961.
23. O. B.NAGY, S. DUPIRE, and J. B.NAGY. Tetrahedron, **31**, 2453 (1975).
24. R. S. MULLIKEN and W. B. PERSON. Molecular complexes, a lecture and reprint volume. Wiley-Interscience, New York. 1969.
25. R. LINN BELFORD, M. CALVIN, and G. BELFORD. J. Chem. Phys. **26**, 1165 (1957).
26. A. E. HANSEN and C. J. BALLHAUSEN. Trans. Faraday Soc. **61**, 631 (1965).
27. P. SCHUSTER, W. JAKUBETZ, and W. MARIUS. Topics in Current Chemistry, Springer Verlag, Berlin. 1975. Vol. 60. p. 1.

Can. J. Chem. Downloaded from www.nrcresearchpress.com by 112.217.228.212 on 09/07/12
For personal use only.

Alkylation of *tert*-butyl lithiohydrazones of aldehydes and ketones

SHAO-FANG WANG[1] AND JOHN WARKENTIN[2]
Department of Chemistry, McMaster University, Hamilton, Ont., Canada L8S 4M1

Received December 9, 1987

SHAO-FANG WANG and JOHN WARKENTIN. Can. J. Chem. **66**, 2256 (1988).

Treatment of the *tert*-butylhydrazones of formaldehyde, acetaldehyde, and acetone with butyllithium afforded the corresponding *tert*-butyl lithiohydrazones, which were alkylated with alkyl, allyl, and benzyl halides. Fourteen new *tert*-butylazo compounds were prepared in yields ranging from 38 to 86%.

SHAO-FANG WANG et JOHN WARKENTIN. Can. J. Chem. **66**, 2256 (1988).

La réaction des *tert*-butylhydrazones du formaldéhyde, de l'acétaldéhyde et de l'acétone avec le butyl-lithium conduit aux *tert*-butylhydrazones lithiées correspondantes qui peuvent être alkylées par les halogénures d'alkyle, d'allyle et de benzyle. On a préparé 14 nouveaux composés *tert*-butylazo, avec des rendements variant de 38 à 86%.

[Traduit par la revue]

Introduction

The alkylation of hydrazone salts of aldehydes and ketones (1–5) occurs primarily at carbon rather than at nitrogen, if the substituent at N is a large one, such as *tert*-butyl (reaction [1]).

[1] $R^1CH{=}N{=}NC(CH_3)_3^- Li^+ + R^2X \rightarrow R^1R^2CHN{=}NC(CH_3)_3 + LiX$

That selectivity has been used for a variety of useful synthetic purposes (1–5) including the overall conversion of aldehydes into ketones (reactions [1], [2]). The latter conversion is achieved by taking advantage of the fact that the azo/hydrazone equilibrium lies very much to the hydrazone side.

[2] $R^1R^2CHN{=}NC(CH_3)_3 \xrightarrow{F_3CCO_2H} R^1R^2C{=}NNHC(CH_3)_3 \xrightarrow{H^+,\ H_2O} R^1R^2CO$

We were interested in the azo compounds themselves, as substrates for intramolecular radical cyclizations to form heterocycles (6), and we therefore sought to apply the method of reaction [1] to their synthesis. We report the syntheses of 14 new azo compounds, including six prepared from formaldehyde *tert*-butylhydrazone, which had been used only once before to prepare two ketones by sequential anion formation, alkylation, isomerization, anion formation, and alkylation (3).

Methods, results, and discussion

Tetrahydrofuran (THF) was used as solvent throughout. One equivalent of tetramethylethylenediamine (TMEDA) enhanced the yields from reactions with formaldehyde *tert*-butylhydrazone and in reactions of hydrazone salts with 1-chloro-3-iodopropane.

The order of mixing of the reactants was not important in many cases but, for alkylation with 1-bromo-3-iodopropene, the preferred method involved addition of a solution of the preformed lithiohydrazone to a solution of the alkylating agent. Significantly lower yields were obtained for that case if the alkylating agent was added gradually to a solution of the lithiohydrazone. Reaction conditions and yields for the preparation of some *tert*-butylazo compounds, according to reaction [3], are given in Table 1.

[3] $R^1R^2C{=}NNHC(CH_3) \xrightarrow[2.\ R^3X]{1.\ BuLi,\ THF} R^1R^2R^3CN{=}NC(CH_3)_3 + LiX$

1 **2** **3**

1,3-Dibromopropane and 1,3-diiodopropane did not afford the expected azo compounds from reactions with the lithio derivative of **1***a*. Major products from 1,3-diiodopropane were the bis substitution product **4** (~20%) and the allyl derivative

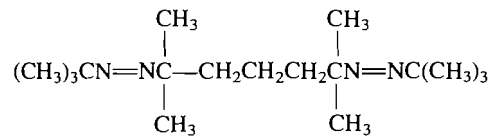

4

3*i* (~15%). The latter was the major product isolated from treatment of 1,3-dibromopropane with the lithium salt of **1***a*. We were unable to find reaction conditions to circumvent the double substitution and (or) elimination reactions that afford those products, and the only azo compounds of type $X(CH_2)_3CR^1R^2N{=}NC(CH_3)_3$ that we were able to prepare in good yield were **3***k* and **3***l* (X = Cl) from the dihalide 1-chloro-3-iodopropane.

The azo compounds (**3**) of Table 1, all of which are new,[3] were purified by vacuum distillation or by chromatography as described in the experimental section. They are identified from their ^1H nmr and high resolution mass spectra (Table 2).

Experimental

The tetrahydrofuran solvent was freshly distilled from sodium and benzophenone. Tetramethylethylenediamine and butyllithium (2.5 or 10.1 M, in hexanes) were used as received from Aldrich. Halides **2** were used as received from Aldrich except for **2***b* and **2***d*, which were prepared.

tert-*Butylhydrazone of acetone*, *1*a

A suspension of *tert*-butylhydrazine hydrochloride (30 g, 0.24 mol) and sodium carbonate (13 g, 0.12 mol) in a solvent made from 40 mL of acetone, 2 mL of water, and 60 mL of benzene was heated for 3 h at the reflux temperature. It was cooled to room temperature and dried over $MgSO_4$. The solid was removed by filtration and washed twice with benzene. The combined filtrate was distilled and the fraction boiling at

[1]Visiting Scholar, Xian Modern Chemistry Research Institute, 1986–1988.

[2]Author to whom correspondence may be addressed.

[3]Compounds **3***a*, **3***b*, **3***c*, **3***e*, **3***k*, and **3***m* were reported, without spectroscopic data or experimental detail, in a preliminary communication (3).

Can. J. Chem. Downloaded from www.nrcresearchpress.com by 112.217.228.212 on 09/07/12
For personal use only.

TABLE 1. *tert*-Butyl azo compounds

Reactants		Temperature	Time	Product[a]
$R^1R^2C{=}NNHC(CH_3)_3$	R^3X	(°C)	(h)	(% yield)
1*a*, $R^1 = R^2 = CH_3$	**2***a*, R^3 = *o*-BrBz,[b] X = Br	65	28	**3***a* (42)
1*a*	**2***b*, R^3 = *o*-IBz,[b] X = Br	65	35	**3***b* (38)
1*b*, $R^1 = CH_3$, $R^2 = H$	**2***a*	15	14	**3***c* (77)
1*c*, $R^1 = R^2 = H$[c]	**2***a*	0–10	3	**3***d* (86)
1*a*	**2***c*, R^3 = Bz, X = Br	65	20	**3***e* (67)
1*c*[c]	**2***c*	5	2	**3***f* (67)
1*a*	**2***d*, $R^3 = BrCH{=}CHCH_2$[d]; X = I	10–15	1	**3***g*[d] (69)
1*c*[c]	**2***d*	−10–0	1	**3***h* (70)
1*a*	**2***e*, $R^3 = CH_2{=}CHCH_2$, X = Cl	60	70	**3***i* (65)
1*c*[c]	**2***e*	35	1.5	**3***j* (43)
1*a*	**2***f*, $R^3 = ClCH_2CH_2CH_2$, X = I	20	7	**3***k* (67)[e]
1*c*[c]	**2***f*	4–6	2	**3***l* (62)
1*a*	**2***g*, $R^3 = CH_3CH_2CH_2$, X = I	20	14	**3***m* (62)
1*c*[c]	**2***g*	8–12	2	**3***n* (40)

[a]All products were oils at room temperature. Yields are average values from two to four runs.
[b]Abbreviations: *o*-BrBz = *ortho*-bromobenzyl; *o*-IBz = *ortho*-iodobenzyl; Bz = benzyl.
[c]One equivalent of TMEDA present.
[d]The starting material (R^3X) was a mixture of *cis*/*trans* isomers, as was the corresponding product.
[e]Yields from runs with one equivalent of TMEDA. Lower yields were obtained without TMEDA.

128–134°C was collected. The yield of **1***a* was 18.1 g (44%); ^{1}H nmr ($CDCl_3$) δ: 1.16 (s, 9H), 1.68 (s, 3H), 1.90 (s, 3H).

tert-*Butylhydrazone of acetaldehyde,* ***1****b*

A suspension of *tert*-butylhydrazine hydrochloride (30 g, 0.24 mol) and sodium carbonate (13.5 g, 0.13 mol) in a solution prepared from acetaldehyde (11.8 g, 0.27 mol), water (5 mL), and ether (50 mL) was stirred at 0°C for 2.5 h. Enough water was then added to bring all the suspended solid into solution. The organic layer was separated and the aqueous layer was extracted (2 × 25 mL) with ether. The combined organic layers were dried and the solvent was removed with a rotatory evaporator to leave 23.1 g (84%) of **1***b*. Distillation at 32–36°C (14 Torr; 1 Torr = 133.3 Pa) gave pure **1***b* as a mixture of *E* and *Z* isomers, *E*/*Z* ratio ≃ 1.4, assignments (7) and ratio by ^{1}H nmr spectroscopy of the mixture; ^{1}H nmr ($CDCl_3$) *E* isomer, δ: 1.11 (s, 9H), 1.84 (d, *J* = 5.5 Hz, 3H), 5.08 (s, br), 7.16 (q, *J* = 5.5 Hz, 1H); *Z* isomer, δ: 1.10 (s, 9H), 1.68 (d, *J* = 6.0 Hz, 3H), 5.08 (s, br), 6.64 (q, *J* = 6.0 Hz, 1H).

Hydrazone **1***b* was not distillable at atmospheric pressure. A sample of **1***b* solidified on heating to 100°C.

tert-*Butylhydrazone of formaldehyde,* ***1****c*

A solution of *tert*-butylhydrazine hydrochloride (6.04 g, 0.048 mol) and sodium carbonate (2.64 g, 0.025 mol) in water (30 mL) and methanol (20 mL) was cooled to −22(±2)°C with a Dry Ice – acetone bath. Formaldehyde (6 mL of 37% aqueous solution, 0.074 mol) was dropped in and the resulting solution was aged at −22(±2)°C for 30 min before it was extracted with ether. The ether extract was washed with water and dried over $MgSO_4$.

The ether solvent was evaporated with a rotatory evaporator, with the flask containing **1***c* in ice water. The residue was distilled, bulb-to-bulb, at room temperature in a closed system at ca. 0.06 Torr, to afford 2.2 g (40%) of **1***c*; ^{1}H nmr ($CDCl_3$), δ: 1.00 (s, 9H), 4.95 (s, br, 1H), 6.08 (d, *J* = 13.5 Hz, 1H), 6.62 (d, *J* = 13.5 Hz, 1H). Compound **1***c* could be stored for several days at the temperature of Dry Ice.

o-*Iodobenzyl bromide,* **2**b

Bromination of *o*-iodotoluene with *N*-bromosuccinimide (8) afforded **2***b*; ^{1}H nmr (90 MHz, $CDCl_3$), δ: 4.58 (s, 2H), 6.8–8.2 (m, 4H).

1-Bromo-3-iodopropene, **2**d

To 1,3-dibromopropene (3.7 g, 18.5 mmol, isomer ratio 1.6, *trans*:*cis*), prepared by the procedure of Hatch (5), was added a solution of sodium iodide (3.7 g, 29 mmol) in acetone (25 mL). The reaction mixture was stirred overnight at room temperature before evaporation of most of the acetone, addition of water, and extraction with ether. The ether extract was dried over $MgSO_4$ and the solvent was evaporated. Kugelrohr distillation (50°C, 0.06 Torr) afforded 2.7 g of the *trans*/*cis* isomers of **2***d*; ^{1}H nmr ($CDCl_3$), δ: 3.8–4.0 (m, 2H), 6.2–6.5 (m, 2H). Isomer ratio by integration of the ^{1}H nmr spectrum ca. 1.6.

Alkylation of lithiohydrazones

The following procedure is typical of those in which the *tert*-butylhydrazone of formaldehyde or 1-chloro-3-iodopropane was one reactant.

A 3-necked, 50-mL flask fitted with a magnetic stirrer, a pressure-equalizing addition funnel, a condenser topped with an inlet for N_2, and a septum was charged with THF (6 mL). The flask was cooled to between −20 and −25°C with a bath of acetone to which Dry Ice had been added. Formaldehyde *tert*-butylhydrazone (1.23 g, 12.3 mmol) was added to the THF, followed by butyllithium (5 mL of 2.5 M solution, 12.5 mmol) and TMEDA (1.4 mL, 9.3 mmol). The reaction mixture was left under N_2 at −20 to −25°C for 15 min before the temperature was allowed to rise to −5°C. *ortho*-Bromobenzylbromide (2.71 g, 10.8 mmol) was then added during 5 min. When addition was complete, the reaction mixture was kept for 3 h at a temperature between 0 and 10°C. Work-up involved acidification of the slurry with dilute aqueous HCl, extraction with ether, washing of the ether extract successively with dilute potassium carbonate solution and with water, and, finally, drying of the ether layer with $MgSO_4$. Evaporation of the ether left **3***d* (2.5 g, 86%) containing a minor impurity that was removed by column chromatography on silica gel, using ether (1.5%) in petroleum ether (bp 40–60°C). Spectra of pure **3***d*, an oil, are in Table 2.

The following procedure is typical of those used to prepare azo compounds from the *tert*-butylhydrazone of acetone, with the exception of **3***k*.

In a three-necked flask, equipped as described above, was placed **1***a* (2.5 g, 19.5 mmol) in 15 mL of THF. The flask was cooled with ice water before BuLi (2.15 g, 21.5 mmol, 10.1 M solution in hexane) was added by syringe through the septum. After the resulting solution had aged for 15 min, benzyl bromide (**2***c*, 2.36 g, 19.5 mmol) in THF (10 mL) was added and the resulting solution was kept at 60°C for 20 h. The work-up, analogous to that described above, afforded 4.77 g (67%) of slightly impure **3***e*. It was distilled to afford pure **3***e*, bp 63–64°C, 0.5 Torr, as an oil.

The following procedure is typical of those used to prepare allylic compounds such as **3***g*.

Can. J. Chem. Downloaded from www.nrcresearchpress.com by 112.217.228.212 on 09/07/12
For personal use only.

TABLE 2. Proton nmr and mass spectra of **3**

Compound	^{1}H nmr (90 MHz, δ, $CDCl_3$)	ms (m/z)[a]
3*a*	1.12 (s, 6H), 1.15 (s, 9H), 3.27 (s, 2H), 6.9–7.6 (m, 4H)	297.0966 297.0970[b]
3*b*	1.14 (s, 6H), 1.16 (s, 9H), 3.28 (s, 2H), 6.8–7.9 (m, 4H)	345.0828 345.0834[c]
3*c*	1.10 (s, 9H), 1.27 (d, J = 6.0 Hz, 3H), 3.20 (m, 2H), 3.87 (sextet, J = 6.0 Hz, 1H), 6.9–7.6 (m, 4H)	282.0732 282.0730[b]
3*d*	1.14 (s, 9H), 3.24 (t, J = 6.3 Hz, 2H), 4.07 (t, J = 6.3 Hz, 2H), 7.0–7.6 (m, 4H)	268.0575 268.0562[b]
3*e*	1.07 (s, 6H), 1.13 (s, 9H), 2.98 (s, 2H), 7.23 (s, br, 5H)	218.1783 218.1779[b]
3*f*	1.14 (s, 9H), 3.07 (t, J = 6.3 Hz, 2H), 4.07 (t, J = 6.3 Hz, 2H), 7.28 (s, 5H)	190.1469 190.1461[b]
3*g*	1.12 (s, 15H), 2.30 (d, J = 6.0 Hz) and 2.50 (d, J = 6.0 Hz) sum 2H, 5.9–6.3 (m, 2H)	247.0810 247.0807[d]
3*h*	1.20 (s, 9H), 2.4–2.8 (m, 2H), 3.83 (t, J = 6.8 Hz) and 3.85 (t, J = 6.8 Hz) sum 2H, 6.0–6.3 (m, 2H)	218.0419 218.0427[b]
3*i*	1.10 (s, 6H), 1.16 (s, 9H), 2.38 (d, J = 6.9 Hz, 2H), 4.9–6.0 (m, 3H)	169.1705 169.1702[d]
3*j*	1.18 (s, 9H), 2.50 (q, J = 6.3 Hz, 2H), 3.85 (t, J = 6.3 Hz, 2H), 5.0–6.0 (m, 3H)	141.1391 141.1393[d]
3*k*	1.09 (s, 6H), 1.13 (s, 9H), 1.7–1.9 (m, 4H), 3.48 (t, J = 6.6 Hz, 2H)	205.1472 205.1475[d]
3*l*	1.18 (s, 9H), 1.7–2.0 (m, 4H), 3.57 (t, J = 6.0 Hz, 2H), 3.80 (t, J = 6.0 Hz, 2H)	176.1080 176.1082[b]
3*m*	0.88 (t, J = 6.3 Hz, 3H), 1.07 (s, 6H), 1.14 (s, 9H), 1.3–1.7 (m, 4H)	
3*n*	0.94 (t, J = 6.3 Hz, 3H), 1.17 (s, 9H), 1.4–1.9 (m, 4H), 3.80 (t, J = 6.0 Hz, 2H)	142.1470 142.1462[d]

[a]High resolution. The numbers are given in the order calcd. followed by found.
[b]EI.
[c]CI(NH_3).
[d]CI(CH_4).

In a three-necked flask, described above, were placed **1***a* (0.71 g, 5.5 mmol) and THF (6 mL). The solution was cooled to ice temperature before BuLi (5.5 mmol, 2.2 mL of 2.5 M solution) was injected from a syringe. After 10 min, the resulting solution of lithium salt was withdrawn from the flask into the syringe. A solution of 1-bromo-3-iodopropenes (**2***d*, 1.08 g, 4.4 mmol) in THF (6 mL) was introduced into the flask and the contents of the syringe were then added over a 17-min interval. The solution so formed was kept at 10–15°C for 1 h. Work-up, as described above, afforded **3***g* (0.78 g, 69%) containing traces of impurities that were removed by column chromatography on silica gel using ether (2%) in petroleum ether (bp 40–60°C). The *trans*/*cis* isomer ratio, estimated from the ^{1}H nmr spectrum, was 1.8.

The three procedures described above serve as models for the 14 syntheses reported. Additional information can be found in Table 1.

Bis substitution product **4** *(2,2,5,5,9,9,12,12-octamethyl-3,4,10,11-tetraazatrideca-3,10-diene)*

To the three-necked flask, described above, was added **1***a* (0.70 g, 5.5 mmol) in 7 mL of THF. The solution was cooled with ice and BuLi (5.5 mmol, 2.2 mL of 2.5 M solution) was added during 10 min. After 15 min more at 0°C, 1,3-diiodopropane (1.7 g, 5.7 mmol) in THF (5 mL) was dropped in over 10 min. The temperature was allowed to rise to ambient and the mixture was worked up after stirring overnight. Work-up afforded a residue containing mostly 1,3-diiodopropane and **4**, which were separated by tlc on silica gel plates using ether (3%) in petroleum ether (bp 40–60°C) as the developing solvent; ^{1}H nmr ($CDCl_3$), δ of **4**: 0.98 (s, 12H), 1.10 (s, 18H), 1.38–1.80 (m, 6H).

Mixing the reactants in the inverse order afforded **3***i* and unreacted 1,3-diiodopropane, but not **4**. Analogous reactions with 1,3-dibromopropane instead of 1,3-diiodopropane gave **3***i* and unreacted 1,3-dibromopropane from both the normal addition mode and the inverse addition mode.

Acknowledgements

This work was financed from a grant provided by the Natural Sciences and Engineering Research Council of Canada. The assistance of Dr. R. Smith and of Mr. F. A. Ramelan with the acquisition of the mass spectra is also gratefully acknowledged.

1. R. M. ADLINGTON, J. E. BALDWIN, J. C. BOTTARO, and M. W. D. PERRY. J. Chem. Soc. Chem. Commun. 1040 (1983).
2. J. E. BALDWIN, J. C. BOTTARO, J. N. KOLHE, and R. M. ADLINGTON. J. Chem. Soc. Chem. Commun. 22 (1984).
3. J. E. BALDWIN, R. M. ADLINGTON, J. C. BOTTARO, J. N. KOLHE, M. W. D. PERRY, and A. U. JAIN. Tetrahedron, **40**, 4223 (1986).
4. J. E. BALDWIN, R. M. ADLINGTON, J. C. BOTTARO, J. N. KOLHE, I. M. NEWINGTON, and M. W. D. PERRY. Tetrahedron, **40**, 4235 (1986).
5. J. E. BALDWIN, R. M. ADLINGTON, and I. M. NEWINGTON. J. Chem. Soc. Chem. Commun. 176 (1986).
6. A. L. J. BECKWITH, S.-F. WANG, and J. WARKENTIN. J. Am. Chem. Soc. **109**, 5289 (1987).
7. G. J. KARABATSOS, J. D. GRAHAM, and F. M. VANE. J. Am. Chem. Soc. **84**, 753 (1962).
8. R. G. R. BACON and W. S. LINDSAY. J. Chem. Soc. 1375 (1958).

Can. J. Chem. Downloaded from www.nrcresearchpress.com by 112.217.228.212 on 09/07/12
For personal use only.

Voltammetric stabilization of electrofaceted (100)-type platinum electrodes in acidic solutions

SARA ALFONSINA DORA ALDABE DE BILMES, MARÍA CRISTINA GIORDANO, AND ALEJANDRO JORGE ARVIA

Instituto de Investigaciones Fisicoquímicas Teóricas y Aplicadas (INIFTA), Facultad de Ciencias Exactas, Universidad Nacional de La Plata, Sucursal 4, Casilla de Correo 16, (1900) La Plata, Argentina

Received June 23, 1987[1]

SARA ALFONSINA DORA ALDABE DE BILMES, MARÍA CRISTINA GIORDANO, and ALEJANDRO JORGE ARVIA. Can. J. Chem. **66**, 2259 (1988).

The voltammetric stabilization of electrofaceted (100)-type Pt electrodes prepared from polycrystalline Pt by fast repetitive triangular potential cycling are followed by conventional voltammetry in the H-electroadsorption/electrodesorption potential range in either 1 *M* H_2SO_4 (0 to 35°C) or 0.5 *M* $HClO_4$ (−2 to 35°C). The influence of CO adsorption on the stabilized voltammetric profile is also considered. Depending on the potential cycling used in conventional voltammetry, two well-defined stabilized profiles at 0.1 V/s in the H-electroadsorption/electrodesorption range can be obtained, namely, that corresponding to the H-adsorption stabilized electrofaceted (100)-type Pt, and that related to the O-adsorption stabilized electrofaceted (100)-type Pt.

The changes in the conventional voltammetric profiles can be interpreted in terms of surface modifications basically associated with either adsorption or electroadsorption processes. The influence of the anion (electrolyte composition) prevailing in solution is accounted for in terms of a competitive adsorption between anions and H-adatoms. The influence of temperature in the range covered by this work is smaller than that of the structure of the solution at the electrode/solution interface.

SARA ALFONSINA DORA ALDABE DE BILMES, MARÍA CRISTINA GIORDANO et ALEJANDRO JORGE ARVIA. Can. J. Chem. **66**, 2259 (1988).

Opérant soit dans du H_2SO_4 1 *M* (0 à 35°C) ou dans du $HClO_4$ 0,5 *M* (−2 à 35°C) et faisant appel à la voltamétrie conventionnelle dans l'écart de potentiel d'électroadsorption/électrodésorption du H, on a examiné la stabilisation voltamétrique d'électrodes de Pt du type (100) qui ont été facettées d'une façon électrochimique et qui ont été préparées à partir de Pt polycristallin par un cyclage rapide et répétitif d'un potentiel triangulaire. On a aussi considéré l'influence de l'adsorption de CO sur le profil voltamétrique stabilisé. Suivant le potentiel de cyclage utilisé lors de la voltamétrie conventionnelle, on a obtenu deux profils stabilisés bien définis, à 0,1 V/s, dans l'écart de potentiel d'électroadsorption/électrodésorption du H; il s'agit, d'une part, de celui qui correspond au Pt de type (100) facetté d'une façon électrochimique et stabilisé par adsorption de H et, d'autre part, à celui du Pt de type (100) facetté d'une façon électrochimique et stabilisé par adsorption de 0.

On peut interpréter les changements dans les profils voltamétriques conventionnels en fonction de modifications de surface qui sont essentiellement associées avec des processus soit d'adsorption ou d'électroadsorption. On explique l'influence de l'anion (composition de l'électrolyte) prédominant en solution en fonction d'une adsorption compétitive entre des anions et des atomes de H. L'influence de la température dans la zone couverte par notre travail est beaucoup plus faible que celle de la structure de la solution à l'interface électrode/solution.

[Traduit par la revue]

Introduction

It has been recently found that the voltammetric characteristics of polycrystalline Pt can be modified by applying fast potential cycling in acid electrolytes (1–3). Results obtained at present show that those electrodes exhibiting (100)-type preferred orientations behave in a very reproducible way and exhibit a very clear faceting (3–5). Nevertheless, the stabilized voltammetric response of these electrodes can be achieved only after they have been potential cycled under certain conditions within the potential range of bulk water stability. In this potential range the H-electroadsorption/electrodesorption in the 0 to ca. 0.45 V range, and the O-electroadsorption/electrodesorption in the 0.7 to 1.4 V range take place. The voltammetric features of both processes depend on the electrolyte composition (4–13), electrode treatment (14–16), and particularly, on the surface crystallographic orientation and defects (11–19).

The present work is devoted to study the stabilization of (100)-type preferred oriented Pt electrodes resulting after the electrochemical faceting treatment (1–3). The different stabilization stages are followed by conventional voltammetry and they depend on the potential cycling programme, electrolyte composition, temperature and adsorption/electroadsorption of foreign species. The voltammetric changes observed with electrofaceted (100)-type Pt are, in principle, comparable to those resulting from Pt(100) single crystal electrodes (12, 17–20). In both types of electrodes the voltammetric changes resulting from the potential cycling before the stable voltammogram is obtained can be associated with electrode surface modifications which are influenced by the proper potential cycling and the electrolyte solution composition adjacent to the electrode.

Experimental

The experimental work can be divided into two parts, namely, the preparation of the electrofaceted Pt electrodes and the voltammetric stabilization by means of repetitive triangular potential cycles at 0.1 V/s.

The electrofaceted (100)-type Pt electrodes were prepared from polycrystalline Pt wires (0.20 cm^2 apparent area) by applying a repetitive triangular potential cycling (RTPS) between 0.08 and 1.42 V, at 1.9×10^4 V/s, for 8 h in 1 *M* H_2SO_4 at 25°C. The experimental setup which was extensively used in previous works (1, 2) consisted of an about 10 mL capacity cell with the virgin pc Pt wire electrode (0.5 mm diameter, Johnson Matthey Chemicals Co., spectroscopically pure) symmetrically surrounded by a spiral shaped platinized platinum wire of about 5 cm^2 geometric area. The potential

[1]Revision received March 23, 1988.

Printed in Canada / Imprimé au Canada

Can. J. Chem. Downloaded from www.nrcresearchpress.com by 112.217.228.212 on 09/07/12
For personal use only.

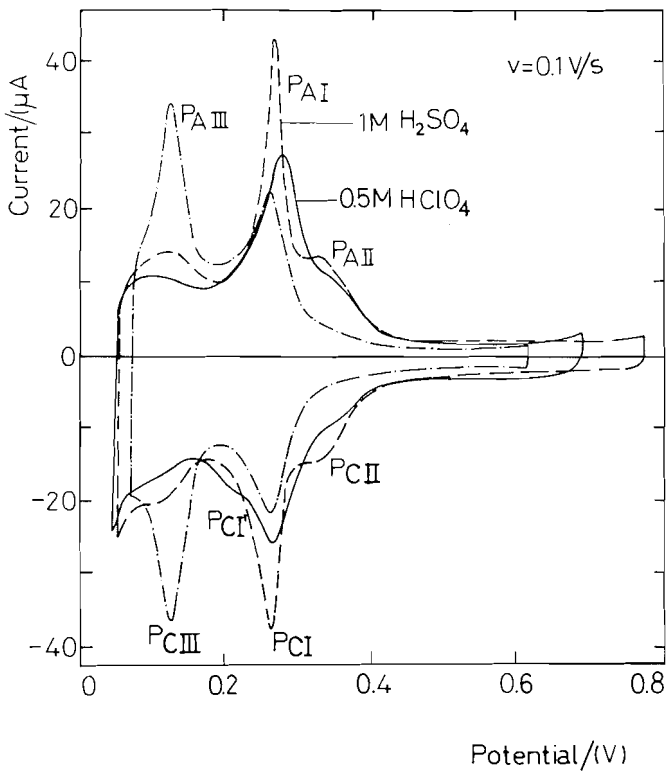

FIG. 1. Stable voltammograms obtained with polycrystalline Pt and HASE electrodes in acidic solutions at 0.1 V/s and 25°C: (···) polycrystalline Pt in 1 *M* H_2SO_4; (---) (100)-type Pt in 1 *M* H_2SO_4; (—) (100)-type Pt in 0.5 *M* $HClO_4$; $E_{s,c}$ = 0.07 and 0.05 V; $E_{s,a}$ = 0.61, 0.77, and 0.68 V.

of the working electrode was measured against a reversible hydrogen electrode in the same solution placed in a separate compartment provided with a Luggin tip passing through the counterelectrode spiral. The electrode arrangement assured the best current distribution compatible with the simplest cell design. A M-5 LYP potentiostat coupled to a LYP square wave generator was used. The characteristics of the potentiostat were as follows: output potential, ±30 V; output current, ±1 A; resolution, ±1 mV; slew rate, 2 V/μs; accuracy, 0.2%; linearity, 0.25%; ohmic drop compensation, up to 100 kΩ; and rise time, 5 μs. The SEM micrographs of the electrode surface were in agreement with those already published for this type of faceted Pt surfaces (4, 5).

The voltammetric stabilized studies of the electrofaceted electrodes were performed at a sweep rate of 0.1 V/s. These runs were made in a conventional three compartment Pyrex glass cell of about 50 mL with a jacket for thermostatic liquid circulation. Solutions, 1 *M* H_2SO_4 and 0.5 *M* $HClO_4$, were prepared from 98% Merck p.a. H_2SO_4 and 70% Merck Suprapure $HClO_4$, respectively. The triply distilled water satisfied the purity requirements usually accepted for electrocatalysis (21). Experiments were performed between −2 to 35°C with the temperature controlled to ±0.1°C. The voltammogram of the electrofaceted (100)-type Pt electrodes in 1 *M* H_2SO_4 in the 0.06–0.7 V range (Fig. 1) reproduces exactly the one previously reported in the literature (1–4) and is also very similar to the voltammogram of a Pt(100) single crystal electrode under the same conditions (12, 17–20). The roughness factor of electrofaceted (100)-type Pt electrodes was 1.1 as determined by comparing the experimental H-adatom voltammetric charge density to that of the H-adatom monolayer calculated for a Pt(100) single crystal surface (15).

Results

1. Conventional voltammetry. Data for $E_{s,a} < 0.8$ *V at 25°C*

Figure 1 shows stable voltammograms run at 0.1 V/s after repetitive cycling between the cathodic switching potential,

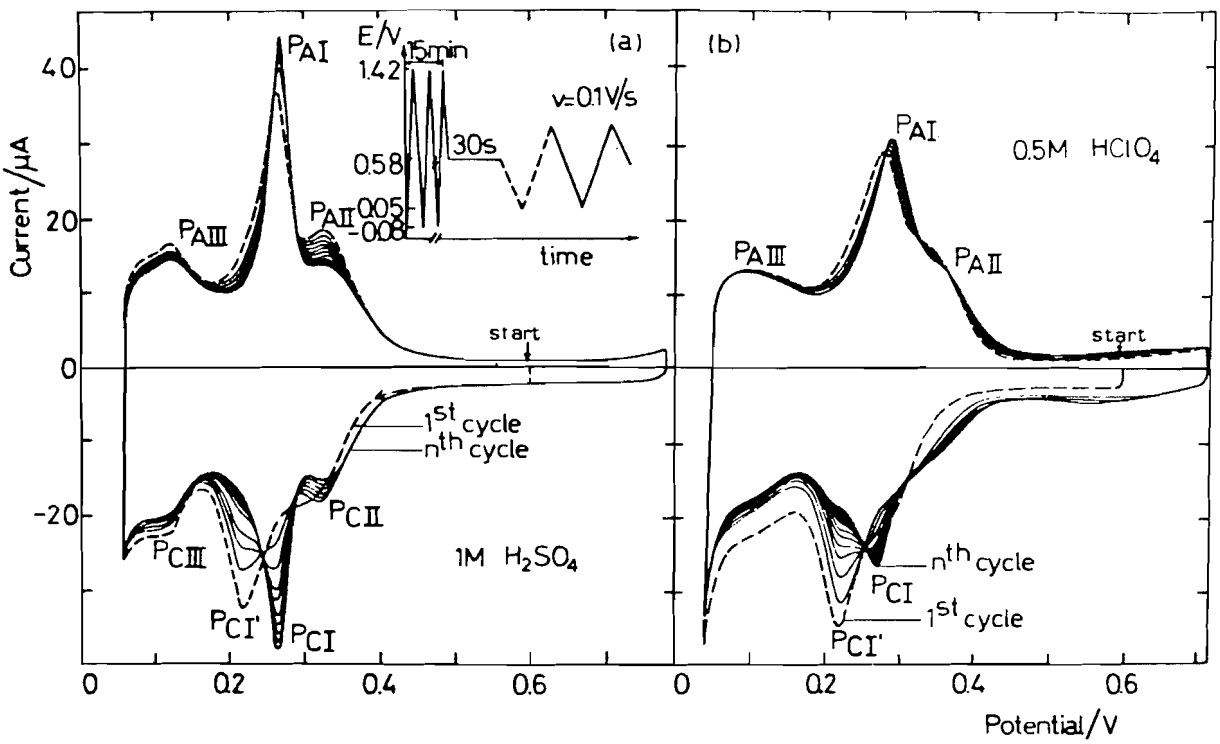

FIG. 2. Voltammetric evolution of H-adatom electroadsorption/electrodesorption peaks from a (100)-type Pt electrode to a HASE after RTPS. T = 25°C, 0.1 V/s. (*a*) 1 *M* H_2SO_4; (*b*) 0.5 *M* $HClO_4$.

Can. J. Chem. Downloaded from www.nrcresearchpress.com by 112.217.228.212 on 09/07/12
For personal use only.

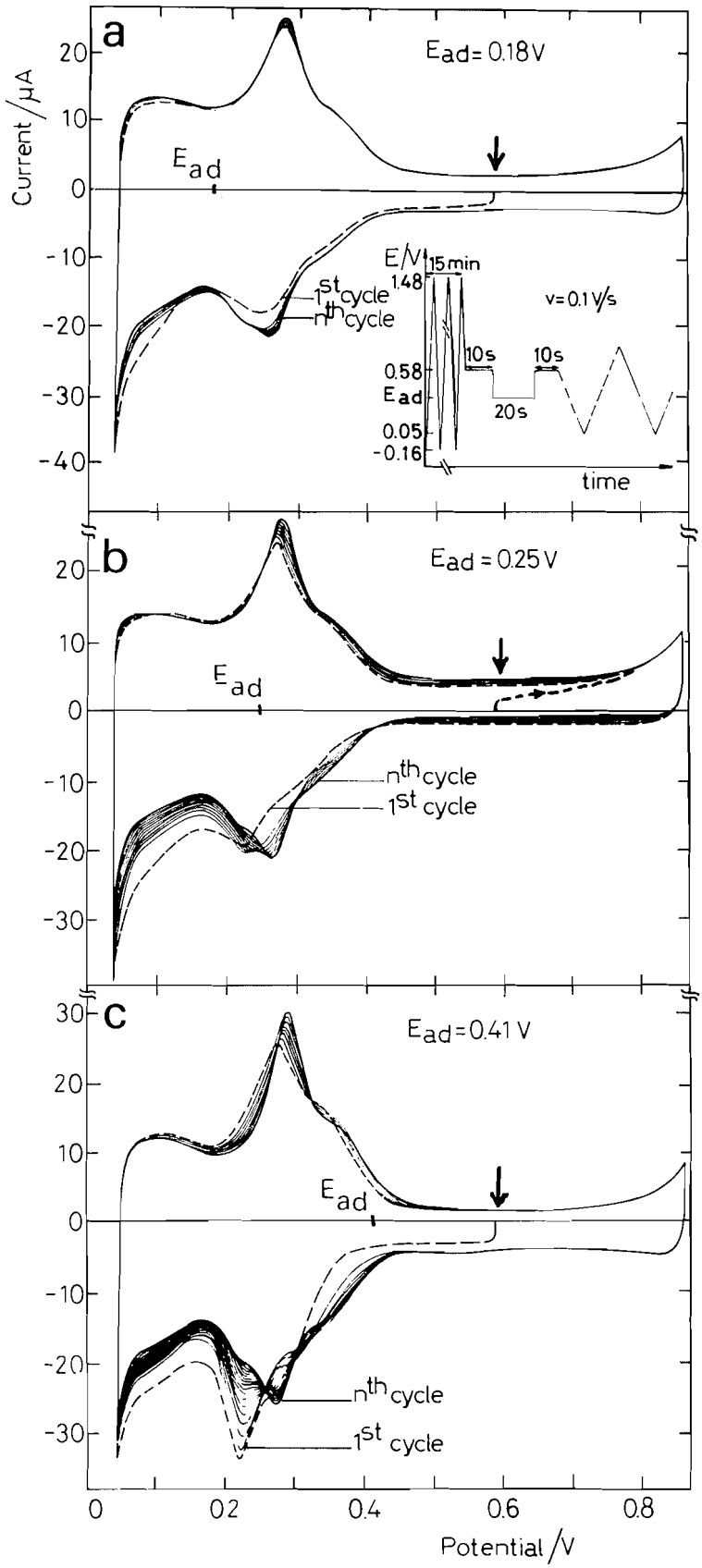

FIG. 3. Voltammetric evolution of H-adatom electroadsorption/electrodesorption peaks to a HASE after H-adsorption at different E_{ad} in 0.1 *M* $HClO_4$ at 25°C. (*a*) E_{ad} = 0.18 V, (*b*) E_{ad} = 0.25 V, (*c*) E_{ad} = 0.41 V; *n*th cycle = 20th cycle.

Can. J. Chem. Downloaded from www.nrcresearchpress.com by 112.217.228.212 on 09/07/12
For personal use only.

$E_{s,c}$ = 0.05 V, and the anodic switching potential, $E_{s,a}$ = 0.78 V in either 1 *M* H_2SO_4 or 0.5 *M* $HClO_4$ at 25°C with a polycrystalline Pt and an electrofaceted (100)-type Pt electrode. The latter type of electrode is denoted as HASE (hydrogen adsorption stabilized electrode).

The voltammetric response of a HASE shows a main pair of conjugated current peaks at ca. 0.26 V (PAI/PCI) and two satellite pairs of conjugated current peaks at each side, namely (PAII/PCII) at 0.35 V and (PAIII/PCIII) at 0.12 V. The pair of peaks PAI/PCI becomes sharper in 1 *M* H_2SO_4 than in 0.5 *M* $HClO_4$ probably due to the difference in the adsorbabilities of HSO_4^- and ClO_4^- ions (22). In 0.5 *M* $HClO_4$ a shoulder (PCI′) at 0.2 V is also recorded during the negative potential going scan.

The voltammetric response of HASE closely resembles that previously reported by several authors for a Pt(100) single crystal electrode under comparable sweep rate conditions (12, 17–20), except for small differences in the pair of peaks PAII/PCII. The contribution of peaks PAIII/PCIII can be attributed to residual Pt(111) faces remaining on the electrofaceted (100)-type Pt electrode after the preparation of the oriented surface from a polycrystalline Pt.

The evolution of the H-adatom electroadsorption profile under cycling, starting from that of a freshly prepared electrofaceted electrode is depicted in Fig. 2*a*,*b* for both 1 *M* H_2SO_4 and 0.5 *M* $HClO_4$ at 25°C. The first voltammogram (Fig. 2*a*) swept cathodically from 0.58 V in 1 *M* H_2SO_4 shows an asymmetric pair of peaks PCI′/PAI at 0.21 and 0.26 V, respectively, as major current contributions. The height of PAII is greater in the first cycle than that of HASE. The H-electroadsorption current peak PCI′ gradually moves to PCI after 9 min RTPS to achieve the voltammogram of the HASE in 1 *M* H_2SO_4. The interconversion of PCI′ to PCI is better defined in 1 *M* H_2SO_4 than in 0.5 *M* $HClO_4$ (Fig. 2*b*). For the latter, the corresponding HASE voltammogram after a prolonged RTPS still shows a remaining contribution of PCI′.

Isopotential values ($E_{i,c}$) at 0.24 V in 1 *M* H_2SO_4 and at 0.25 V in 0.5 *M* $HClO_4$ are observed during the accomplishment of the stable H-electroadsorption voltammogram for HASE. These isopotentials suggest an intra/interconversion of at least two states of H-adatoms promoted during cycling. Hence, the pair of conjugated peaks PCI/PAI can be ascribed to the stable H-adatom adsorption configuration for HASE. The HASE configuration emerges from the first voltammogram only when the potential step, E_{ad} preceding the RTPS is more negative than $E_{i,c}$ as seen from the comparison of Figs. 3*a*, *b*, and *c* for $E_{ad} < E_{i,c}$, $E_{ad} \simeq E_{i,c}$, and $E_{ad} > E_{i,c}$, respectively. Likewise, a voltammogram similar to that of the HASE in 0.5 *M* $HClO_4$ can be accomplished after the electrooxidation of adsorbed CO on freshly prepared electrofaceted Pt (Fig. 4*a*). In this case, CO adsorption was performed from a CO saturated solution at E_{ad} = 0.58 V (23) using a microflow cell (24), and then the solution was replaced by 0.5 *M* $HClO_4$. The voltammogram run immediately after the electrooxidation of adsorbed CO (Fig. 4*b*) becomes similar to that depicted in Fig. 3 in the H-adatom potential range for a HASE (25). These results demonstrate that the initial energy distribution in the freshly prepared electrofaceted (100)-type Pt surface is gradually changed through adsorbate–substrate interactions. The stronger the interaction the shorter the time to reach a stable surface configuration.

2. Data for $E_{s,a} > 0.8$ *V at 25°C*

The voltammogram in the H-electroadsorption/electrodesorption region substantially changes when the RTPS applied to the HASE in 1 *M* H_2SO_4 or in 0.5 *M* $HClO_4$ extends over the oxygen electroadsorption potential region (Fig. 5*a*,*b*). Similar changes are also observed just by extending $E_{s,a}$ towards increasingly positive potentials. In any case, after several RTPS in the 0.03–1.37 V range another stabilized voltammogram is obtained. The resulting electrode is denoted as OASE (oxygen adsorption stabilized electrode). The first potential excursion up to 1.4 V exhibits a rather poor definition of the O-electroadsorption current peaks (Fig. 5). Nevertheless, the electrooxidation current at ca. 1.2 V decreases progressively during the RTPS in both acids, whereas the O-electroadsorption at ca. 0.8 V increases. Finally, two oxidation current peaks are recorded in the O-electroadsorption range when the OASE voltammogram is achieved. The voltammetric changes observed in the O-electroadsorption/electrodesorption potential range are accompanied by simultaneous modifications in the H-electroadsorption/electrodesorption potential range. Thus, peaks PAI/PCI become wider than those already described for the HASE; the heights of peaks PAIII/PCIII increase considerably and, peak PCII is no longer observed.

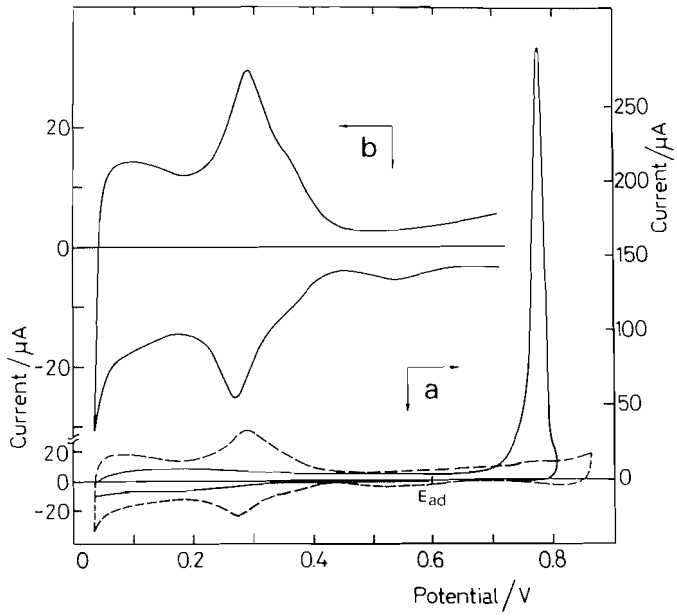

FIG. 4. Voltammogram run with a (100)-type Pt electrode after CO adsorption and electrooxidation: 0.1 V/s, *T* = 25°C, 0.5 *M* $HClO_4$. (*a*) (—) CO electrooxidation (microflow cell) (24), (---) 2nd cycle; (*b*) 3rd cycle expanded scale (equivalent to a HASE).

The voltammetric changes above described which are followed in 0.5 *M* $HClO_4$ better than in 1 *M* H_2SO_4, indicate that the O-electroadsorption/O-electrodesorption produces a partial rearrangement of the HASE surface structure.

Comparable results can be drawn from runs made by stepwise increasing $E_{s,a}$ from 0.70 to 1.4 V. As $E_{s,a}$ moves within the 0.7 to 0.9 V range the changes observed in the H-electroadsorption/electrodesorption process in 0.5 *M* $HClO_4$ are comparatively greater than in 1 *M* H_2SO_4. This difference can be assigned to the delay of O-electroadsorption due to HSO_4^- ion adsorption (9, 13, 15).

3. The influence of temperature in the conventional voltammograms

The variation of temperature from 0 to 35°C in 1 *M* H_2SO_4 and from −2 to 35°C in 0.5 *M* $HClO_4$ (Figs. 6 and 7) produces

Can. J. Chem. Downloaded from www.nrcresearchpress.com by 112.217.228.212 on 09/07/12
For personal use only.

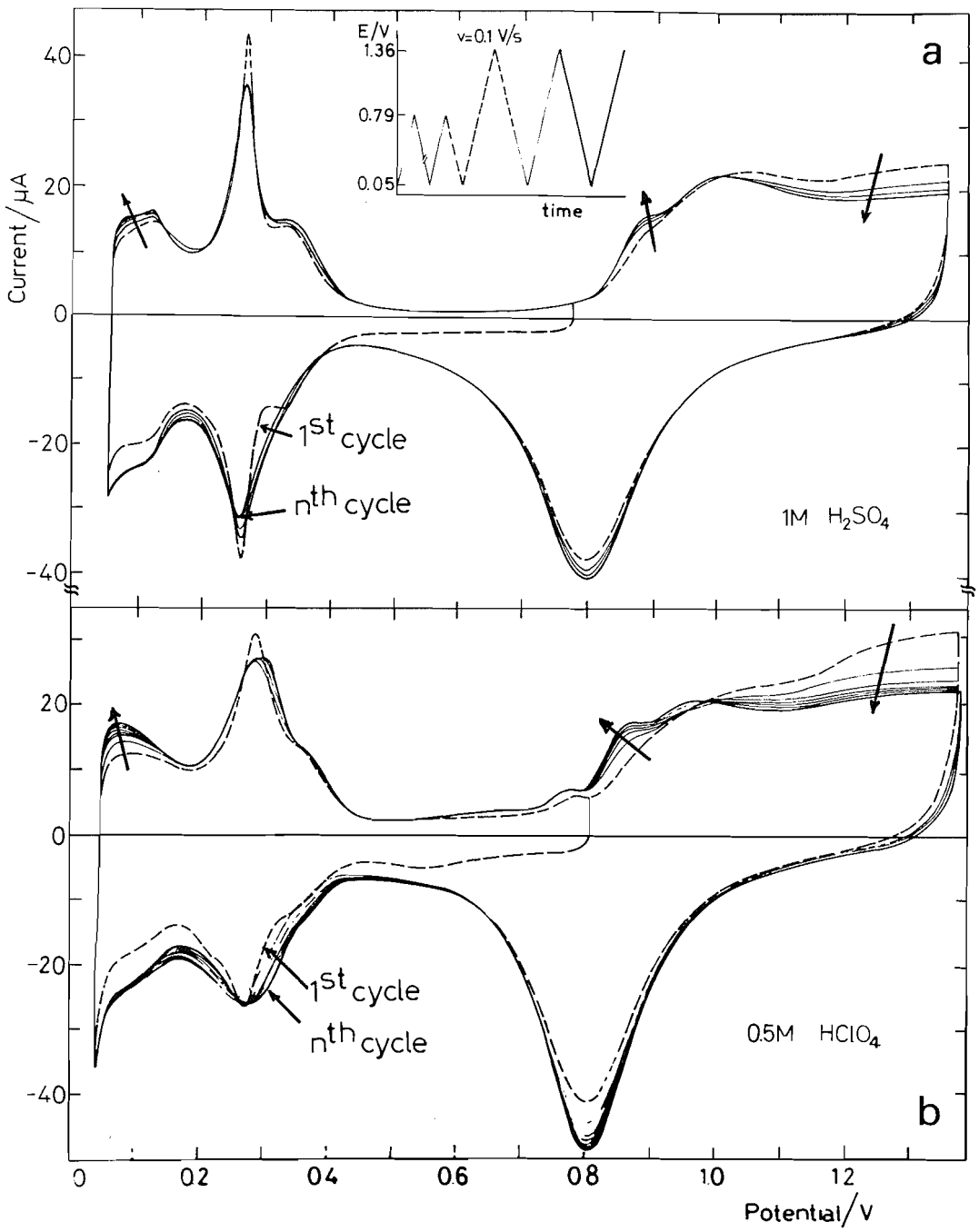

FIG. 5. Stabilized voltammogram from a HASE after RTPS between 0.05 and 1.4 V at 0.1 V/s; T = 25°C. (*a*) 1 *M* H_2SO_4, *n*th cycle = 5th cycle. (*b*) 0.5 *M* $HClO_4$, *n*th cycle = 10th cycle.

voltammetric changes qualitatively similar to those already described at 25°C. The higher the temperature, the lower the number of RTPS at 0.1 V/s required to get the voltammetric response of HASE, although the influence of temperature in 1 *M* H_2SO_4 is considerably greater than in 0.5 *M* $HClO_4$, that is, the time required for the voltammetric stabilization in each acid is different, although for both acids the potential difference between PCI′ and PCI decreases as the temperature increases.

The effect of O-electroadsorption/electrodesorption in the development of the OASE voltammogram is little influenced by temperature in both electrolytes. Although as it can be seen in Fig. 7 for 0.5 *M* $HClO_4$, the increase in temperature produces a considerable decrease of the O-electroadsorption threshold potential. This effect cannot be observed in 1 *M* H_2SO_4 at least in the potential range covered in Fig. 6.

Discussion

The initial voltammetric response of an electrofaceted (100)-type Pt electrode is very sensitive to the electrolyte composition, potential cycling conditions and temperature. Two different stabilized voltammetric profiles are obtained depending whether the value of $E_{s,a}$ is lower or greater than the threshold potential for the O-electroadsorption process. The two types of stabilized voltammetric profiles are denoted as HASE and OASE depend-

Can. J. Chem. Downloaded from www.nrcresearchpress.com by 112.217.228.212 on 09/07/12
For personal use only.

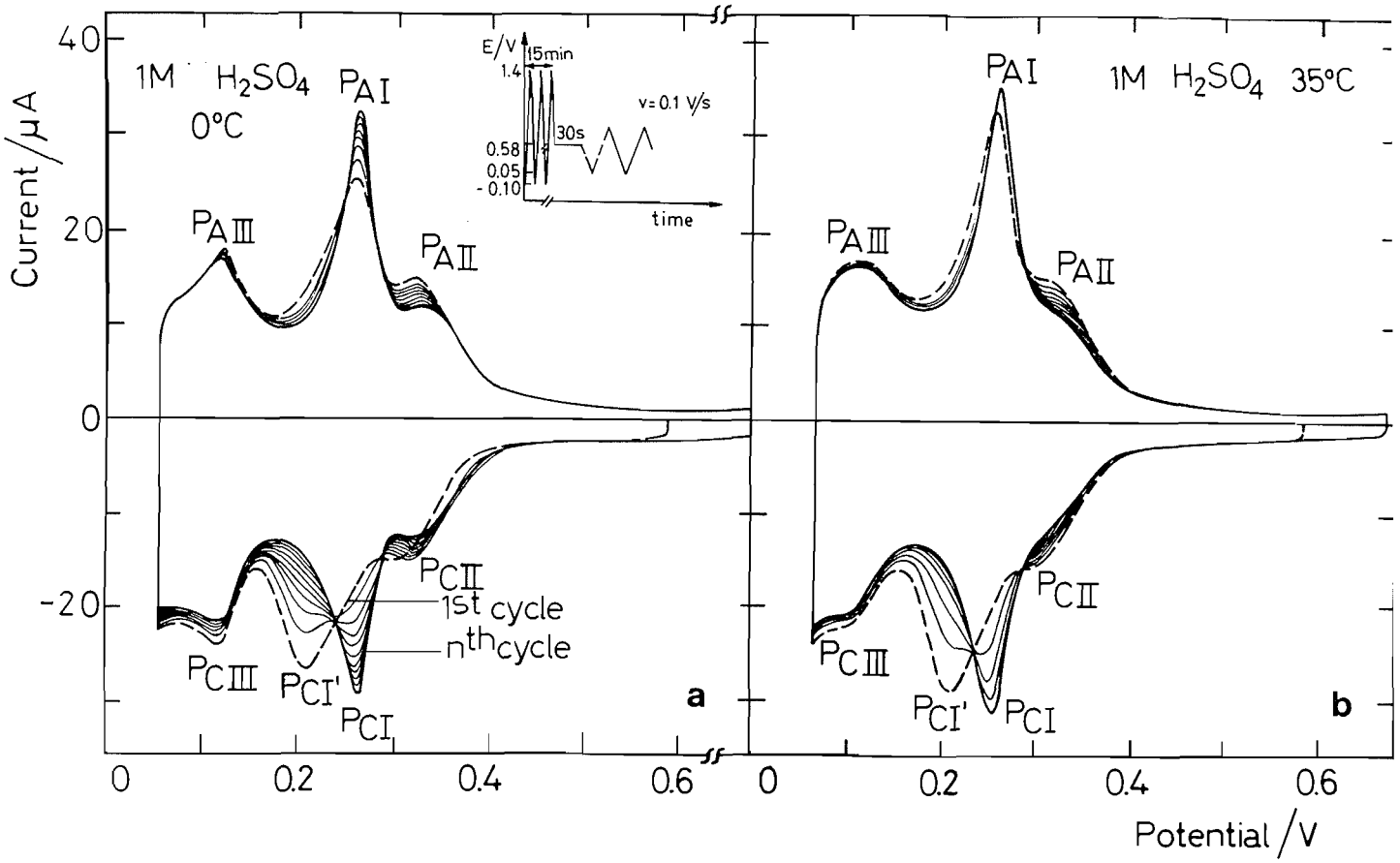

FIG. 6. Influence of temperature on the voltammetric evolution of H-adatom electroadsorption/electrodesorption peaks from (100)-type Pt to a HASE after RTPS in 1 *M* H_2SO_4 at 0.1 V/s. (*a*) 0°C; (*b*) 35°C.

ing whether stabilization is performed by H-electroadsorption/electrodesorption or O-electroadsorption/electrodesorption processes.

The changes observed on an electrofaceted (100)-type Pt electrode by H-electroadsorption/electrodesorption could be associated with an order-forming surface modification. This conclusion is supported by the fact that the definition of the pair of peaks PAI/PCI, which is considered as a fingerprint for a Pt(100) plane, is certainly improved in a HASE.

On the other hand, the pair of peaks PAI/PCI becomes broader and more poorly defined with an OASE. This fact indicates that the irreversible O-electroadsorption/electrodesorption process actually distorts in some way the surface order found with a HASE. For the latter, the substrate–adsorbate interaction energy must be of outmost importance in defining the type of surface modification suffered by the initial electrofaceted Pt electrode, such as the displacement of some metal atoms from their original positions in the polycrystalline surface during the adsorption/electroadsorption halfcycle. For low adsorption energies, the metal atom displacement is probably less than the average atom-to-atom distance at the metal surface. The metal atoms can be restored to their rest position in the lattice during the desorption/electrodesorption halfcycle which for most atoms is different from the original one (3, 26). Furthermore, for a small substrate–adsorbate interaction energy (<20 kJ/mol) such as that of H atoms or H_2O species on Pt (27), the adsorbate interferes the metal surface atom rearrangement by promoting a less dence crystallographic packing of metal atoms at the surface. This can be the case of HASE where the voltammetric characteristics of the (100) crystallographic plane is enhanced. The changes in the voltammogram occurring during the RTPS before attaining the HASE response are mainly observed in the H-electroadsorption region.

The electroadsorption of OH from water is the primary stage for the O-electroadsorption reaction. The adsorbed OH species may participate in various different reactions, such as the platinum electrodissolution and surface oxide electroformation, including place exchange reactions (9, 13, 15). For either a partial or a complete O-electroadsorption coverage the substrate–adsorbate interaction energy becomes greater than that corresponding to H-electroadsorption/electrodesorption, hence larger surface modifications should be expected. The initial electrofaceting would tend to be smeared out since during O-electrodesorption the partially "bare" Pt surface lasts a sufficiently long time ($>10^{-3}$ s) to rearrange in different ways. This leads to a poorly defined voltammetric response. In the long term a structure approaching polycrystalline Pt free from residual strains (16, 26) would be expected.

The H-atom electroadsorption/electrodesorption on both HASE and OASE electrofaceted (100)-type Pt is characterized by three pairs of conjugated peaks PAI/PCI; PAII/PCII, and PAIII/PCIII. Recent results (28) have shown that each process has a different time constant. Peaks PAI/PCI and PAII/PCII correspond closely to the H-adsorption peaks observed on a

Can. J. Chem. Downloaded from www.nrcresearchpress.com by 112.217.228.212 on 09/07/12
For personal use only.

Can. J. Chem. Downloaded from www.nrcresearchpress.com by 112.217.228.212 on 09/07/12
For personal use only.

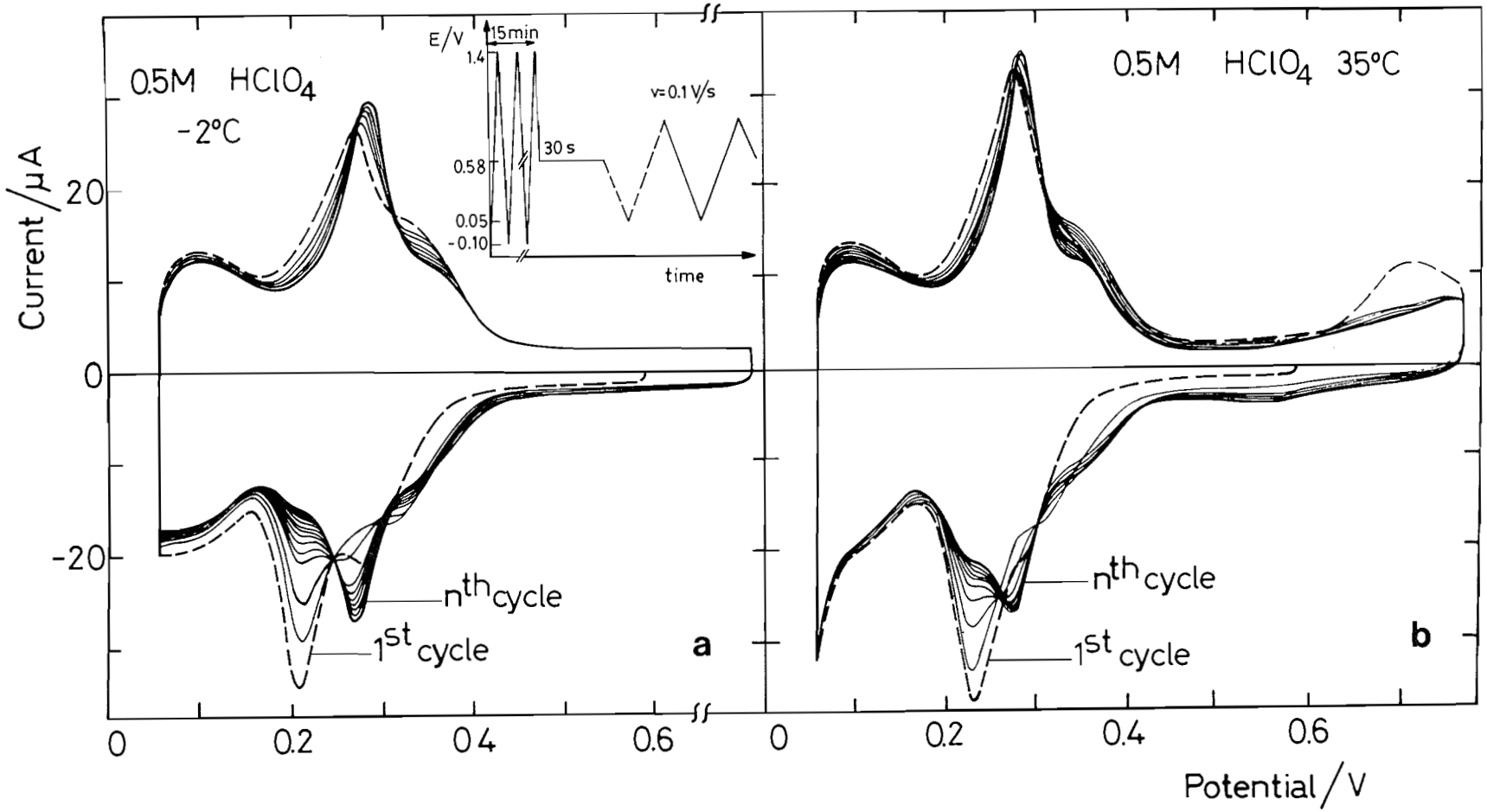

FIG. 7. Influence of temperature on the voltammetric evolution of H-adatom electroadsorption/electrodesorption peaks from (100)-type Pt to a HASE after RTPS in 0.5 *M* $HClO_4$ at 0.1 V/s. (*a*) −2°C; (*b*) 35°C.

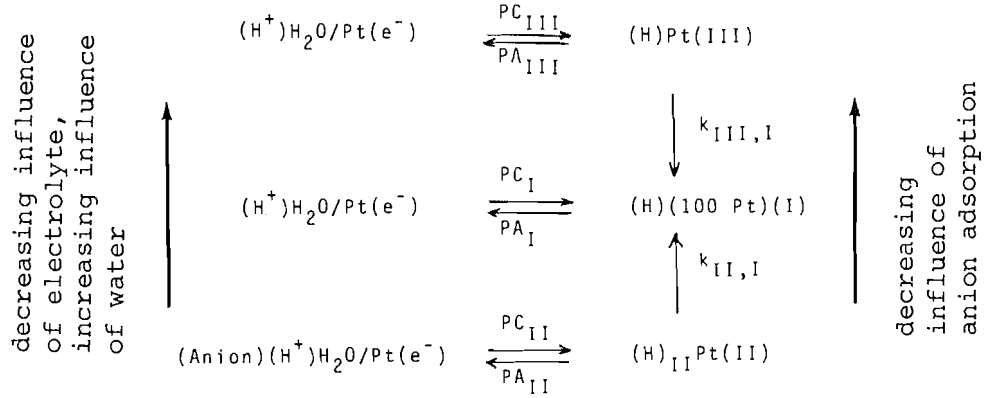

FIG. 8. Reaction scheme related to the different H-electroadsorption/electrodesorption voltammetric peaks. $k_{II,I}$ and $k_{III,I}$ denote the rate constants of adatom surface reactions.

Pt(100) single crystal electrode in 1 *M* H_2SO_4 (12). The electrolyte composition has little influence on the conjugated electrochemical reaction related to the pair of peaks PAIII/PCIII located at the negative potential side of the potential of zero charge of Pt in the acid electrolyte. This suggests that a relatively rapid electron–proton transfer should take place without requiring some previous slow rearrangements of the water–electrolyte structure. This agrees, in principle, with the structure of water in contact with Pt as recently discussed (29). Conversely, the largest influence of anions on the reaction should be expected in the potential range of peaks PAII/PCII as quite likely they are located at the positive potential side of the potential of zero charge of any crystallographic plane of a Pt single crystal (30). The influence of anion adsorption on the H-electroadsorption process related to PCII and PCI is accounted for in terms of a competitive adsorption between anions and H-adatoms as a sweep rate of 0.1 V/s is not sufficiently fast to suppress anion adsorption. This competitive adsorption can explain the change in the voltammogram from PCI′ to PCI on potential cycling (Figs. 2 and 3). The influence of anion adsorption should become increasingly important as the anion–metal interaction energy increases. All these effects are qualitatively summarized in the diagram for the H-adatom electroadsorption/electrodesorption depicted in Fig. 8, consisting of three electron transfer steps in parallel.

The number of cycles required to turn the voltammogram of a freshly prepared electrofaceted (100)-type Pt electrode into that of a HASE, or the latter into the voltammogram of OASE decreases on increasing the temperature. The resulting stable voltammograms exhibit a voltammetric response which depends on the electrolyte composition. The influence of the solution composition becomes more remarkable in the region where the strongest H-metal adsorption interaction is expected. The temperature affects the whole H-electroadsorption/electrodesorption profile, and in particular influences the pair of peaks PAIII/PCIII and PAI/PCI. The electrolyte composition and temperature are variables both acting simultaneously on the electrochemical system making it difficult to deal with each effect independently.

Conclusions

The voltammetric response at 0.1 V/s in 1 *M* H_2SO_4 and in 0.5 *M* $HClO_4$ of a freshly electrofaceted (100)-type Pt electrode cycled in the H-electroadsorption potential range approaches a first stable level which corresponds to an electrode surface denoted as HASE. The voltammogram of the latter is similar to that reported in the literature for Pt(100) single crystal electrode at 0.1 V/s in the same electrolyte. The rate of the voltammetric change to achieve the HASE response depends on both the electrolyte composition and the temperature. The HASE voltammetric response is also obtained from either H-adatom electroadsorption/electrodesorption or CO adsorption followed by adsorbate electrooxidation on the freshly electrofaceted electrode surface.

Surface rearrangements produced on the electrofaceted (100)-type Pt electrodes after O-electroadsorption–electrodesorption in both 1 *M* H_2SO_4 and 0.5 *M* $HClO_4$ turn the voltammogram of HASE into a second stable level denoted as OASE.

Acknowledgments

This work was financially supported by the Consejo Nacional de Investigaciones Científicas y Técnicas of Argentina, the Comisión de Investigaciones Científicas de la Provincia de Buenos Aires and the Regional Program for the Scientific and Technological Development of the Organization of the American States.

1. R. M. CERVIÑO, W. E. TRIACA, and A. J. ARVIA. J. Electrochem. Soc. **132**, 266 (1985); J. Electroanal. Chem. **182**, 51 (1985).
2. J. C. CANULLO, W. E. TRIACA, and A. J. ARVIA. J. Electroanal. Chem. **175**, 337 (1984).
3. W. E. TRIACA, T. KESSLER, J. C. CANULLO, and A. J. ARVIA. J. Electrochem. Soc. **134**, 1165 (1987).
4. R. M. CERVIÑO, A. J. ARVIA, and W. VIELSTICH. Surf. Sci. **154**, 623 (1985).
5. A. J. ARVIA, J. C. CANULLO, E. CUSTIDIANO, C. L. PERDRIEL, and W. E. TRIACA. Electrochim. Acta, **31**, 1359 (1986).
6. H. ANGERSTEIN-KOZLOWSKA, B. E. CONWAY, and W. B. A. SHARP. J. Electroanal. Chem. **43**, 9 (1973).
7. J. C. HUANG, W. E. O'GRADY, and E. YEAGER. J. Electrochem. Soc. **124**, 1732 (1977).
8. P. N. ROSS. J. Electroanal. Chem. **76**, 139 (1977).
9. H. ANGERSTEIN-KOZLOWSKA and B. E. CONWAY. J. Electroanal. Chem. **95**, 1 (1979).
10. B. H. LOO and T. E. FURTAK. Electrochim. Acta, **25**, 505 (1980).
11. J. CLAVILIER. J. Electroanal. Chem. **107**, 211 (1980).
12. C. L. SCORTICHINI and C. N. REILLEY. J. Electroanal. Chem. **139**, 233 (1982); **139**, 247 (1982); **139**, 265 (1982).
13. H. ANGERSTEIN-KOZLOWSKA, B. E. CONWAY, B. BERNET, and J. MOZOTA. J. Electroanal. Chem. **100**, 417 (1979).

Can. J. Chem. Downloaded from www.nrcresearchpress.com by 112.217.228.212 on 09/07/12
For personal use only.

14. V. S. BAGOTSKY, YU. B. VASSILIEV, and I. I. PYSHNOGRAEVA. Electrochim. Acta, **16**, 2141 (1971).
15. T. BIEGLER and R. WOODS. J. Electroanal. Chem. **20**, 73 (1969); R. WOODS. *In* Advances in electroanalytical chemistry. Vol. 9. *Edited by* A. J. Bard. Marcel Dekker Inc., New York. 1977. Chap. 1.
16. A. C. CHIALVO, W. E. TRIACA, and A. J. ARVIA. J. Electroanal. Chem. **146**, 93 (1983).
17. A. T. HUBBARD, R. M. ISHIKAWA, and J. KATEKARU. J. Electroanal. Chem. **86**, 271 (1978).
18. K. YAMAMOTO, D. M. KOLB, R. KOTZ, and G. LEHMPFUHL. J. Electroanal. Chem. **96**, 233 (1979).
19. P. N. ROSS. Surf. Sci. **102**, 463 (1981).
20. J. CLAVILIER, D. ARMAND, and B. L. WU. J. Electroanal. Chem. **135**, 159 (1982).
21. B. E. CONWAY, H. ANGERSTEIN-KOZLOWSKA, W. B. A. SHARP, and E. CRIDDLE. Anal. Chem. **45**, 1331 (1973).
22. I. I. LABKOVSKAYA, V. I. LUK'YANYCHEVA, and V. S. BAGOTSKII. Elektrokhimiya, **5**, 580 (1969); J. C. HUANG, W. E. O'GRADY, and E. YEAGER. J. Electrochem. Soc. **124**, 1732 (1977).
23. S. A. BILMES, N. R. DE TACCONI, and A. J. ARVIA. J. Electroanal. Chem. **164**, 129 (1984).
24. E. P. M. LEIVA and M. C. GIORDANO. J. Electrochem. Soc. **130**, 1305 (1983).
25. E. P. M. LEIVA, E. SANTOS, M. C. GIORDANO, R. M. CERVIÑO, and A. J. ARVIA. J. Electrochem. Soc. **133**, 1660 (1986).
26. A. C. CHIALVO, W. E. TRIACA, and A. J. ARVIA. Anal. Asoc. Quím. Arg. **73**, 23 (1985).
27. P. ROSS and F. WAGNER. *In* Advances in electrochemistry and electrochemical engineering. Vol. 13. Wiley and Sons, New York. 1984.
28. S. A. BILMES, M. C. GIORDANO, and A. J. ARVIA. J. Electroanal. Chem. **227**, 183 (1987).
29. A. BEWICK, K. KUNIMATSU, J. ROBINSON, and J. W. RUSSELL. J. Electroanal. Chem. **119**, 175 (1981); A. BEWICK and J. W. RUSSELL. J. Electroanal. Chem. **132**, 329 (1982).
30. J. C. LLOPIS and F. COLOM. *In* Encyclopedia of electrochemistry of the elements. Vol. IV. *Edited by* A. J. Bard. Marcel Dekker Inc., New York. 1976. p. 169.

Can. J. Chem. Downloaded from www.nrcresearchpress.com by 112.217.228.212 on 09/07/12
For personal use only.

Bridged-ring steroids. V. The total synthesis of 1,4-methano steroids by a modified Torgov sequence[1]

PETER YATES, STEPHEN P. DOUGLAS, SUSHIL K. DATTA, AND JEFFREY F. SAWYER
Lash Miller Chemical Laboratories, University of Toronto, Toronto, Ont., Canada M5S 1A1

Received February 23, 1988

PETER YATES, STEPHEN P. DOUGLAS, SUSHIL K. DATTA, and JEFFREY F. SAWYER. Can. J. Chem. **66**, 2268 (1988).

The Diels–Alder adduct, **17**, of cyclopentadiene and 2-methoxy-5-methyl-1,4-benzoquinone was reduced with sodium borohydride to the ketol **18**, whose acetate **19** was further reduced with zinc amalgam to the monoketone **20**. Reaction of **20** with vinyllithium gave the allylic alcohol **21**, which underwent very ready dehydration with rearrangement to give the tricyclic enol ether **27**, which was hydrolyzed to ketone **28***a*. Hydrogenation of **19** gave the dihydro product **30**, which was reduced with zinc amalgam to the ketone **31**. Treatment of the latter with vinyllithium gave the allylic alcohol **32**. This was more stable than its analogue **21**, but underwent hydrolysis and dehydration to the dienone **33**. Treatment of **32** with 2-methyl-1,3-cyclopentanedione (**5**) in the presence of Triton B gave the tricyclic intermediate **35**, its hydrolysis product **36**, and the hydroxy derivative of the latter, **37**. In the absence of base, **32** and **5** gave largely product **36**. Hydrogenation of **36** gave the dihydro product **38**, which on treatment with methanolic potassium hydroxide gave (±)-(1β,4β,5β,8α,9β,10β,13β,14β)-14-hydroxy-1,4-methanoandrostane-7,17-dione (**39**). Dehydration of **39** with *p*-toluenesulfonic acid gave first (±)-(1β,4β,5β,9β,10β,13β)-1,4-methanoandrost-8(14)-ene-7,17-dione (**40**), which was converted in turn to (±)-(1β,4β,5β,8α,9β,10β,13β,14β)-1,4-methanoandrost-15-ene-7,17-dione (**41**). Similar dehydration of **36** gave (±)-(1β,4β,5β,10β,13β,14β)-1,4-methanoandrosta-8,15-diene-7,17-dione (**45**).

PETER YATES, STEPHEN P. DOUGLAS, SUSHIL K. DATTA et JEFFREY F. SAWYER. Can. J. Chem. **66**, 2268 (1988).

Sous l'action du borohydrure de sodium, l'adduit **17** provenant de la condensation de Diels–Alder du cyclopentadiène sur la méthoxy-2 méthyl-5 benzoquinone-1,4 conduit au cétol **18**; son acétate **19**, par réduction à l'aide de l'amalgame de zinc, conduit à la monocétone **20**. La réaction du composé **20** avec le vinyllithium fournit l'alcool allylique **21** qui se déshydratate facilement, avec une transposition concomitante, pour conduire à l'éther énolique tricyclique **27** qui donne naissance, par hydrolyse, à la cétone **28***a*. L'hydrogénation du composé **19** fournit le composé dihydrogéné **30** qui, par réduction par l'amalgame de zinc, conduit à la cétone **31**. Par réaction avec le vinyllithium, cette dernière donne naissance à l'alcool allylique **32**. Celui-ci est plus stable que son analogue **21**; toutefois, son hydrolyse et sa déshydratation conduisent à la diénone **33**. Le composé **32**, par réaction avec la méthyl-2 cyclopentanedione-1,3 (**5**) en présence de Triton B, fournit l'intermédiaire tricyclique **35** ainsi que son produit d'hydrolyse **36** et le dérivé hydroxylé **37** de ce dernier. En l'absence de base, la réaction des composés **32** et **5** conduit principalement au produit **36**. L'hydrogénation du produit **36** fournit le dérivé dihydrogéne **38** qui, par traitement avec de l'hydroxyde de potassium en milieu méthanolique, conduit à la (±)-(1β,4β,5β,8α,9β,10β,13β,14β)-hydroxy-1,4 méthano-1,4 androstanedione-7,17 (**39**). La déshydratation du composé **39** par de l'acide *p*-toluènesulfonique conduit en premier lieu à la (±)-(1β,4β,5β,9β,10β,13β)-méthano-1,4 androstène-8(14) dione-7,17 (**40**) qui est ensuite transformée en (±)-(1β,4β,5β,8α,9β,10β,13β,14β)-méthano-1,4 androstène-15 dione-7,17 (**41**). Soumis à une déshydratation semblable, le composé **36** fournit de la (±)-(1β,4β,5β,10β,13β,14β)-méthano-1,4 androstadiène-8,15 dione-7,17 (**45**).

[Traduit par la revue]

Introduction

In our previous work on the synthesis of bridged-ring steroids (2–4) the routes have involved partial synthesis from other steroids. For example, 2,5-carbon-bridged steroids of type **1** have been obtained by introduction of the bridge into a steroid precursor via an ene reaction (3). We now report on the total synthesis of 1,4-carbon-bridged steroids of type **2** via a modified Torgov reaction sequence.

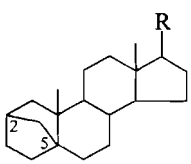

1

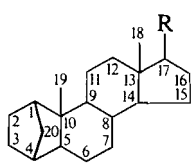

2

The conventional Torgov sequence (5, 6) provides a short and efficient route for the synthesis of steroids with an aromatic ring A. Thus treatment of 6-methoxy-1-tetralone (**3**) with vinylmagnesium bromide followed by condensation of the resulting allylic alcohol **4** with 2-methyl-1,3-cyclopentanedione (**5**) in the presence of benzyltrimethylammonium hydroxide (Triton B) gave the dione **6** (Scheme 1), which underwent acid-catalyzed cyclization to the steroid **7**; this was reduced to (±)-estrone methyl ether (**8**) (6). Kuo, Taub, and Wendler (7) showed subsequently that a basic catalyst was not required for the reaction of **4** with **5** to give **6** and that this conversion could best be effected via the isothiuronium salt **9**.[2] Wiechert (8) and Valenta (9) and their co-workers modified the Torgov sequence to make it applicable to the synthesis of non-aromatic ring A steroids; thus dione **10** was converted to the steroid **13** via the allylic halide **11** and trione **12**.

There appeared to us to be two critical features of the original Torgov sequence (5–7): (*i*) ready formation of a cationic intermediate of type **14** that leads to C-12—C-13 bond[3] formation and (*ii*) ready formation of a cationic intermediate of type **15** that results in C-8—C-14 bond formation in the acid-catalyzed cyclization of **6**. In both cases cation formation would be expected to be facilitated by the *p*-anisyl ring. In Valenta's modified sequence (9), the closure of ring C was effected by base-catalyzed aldol condensation involving the anion formed from the trienone system in **12**. It was clear that neither of these

[1]For Part IV see ref. 1*a*; for a preliminary communication concerning part of this work see ref. 1*b*.

[2]The use of such salts is limited, however, because of their insolubility in organic solvents.

[3]Steroid numbering is used throughout this account (cf. **2**).

Can. J. Chem. Downloaded from www.nrcresearchpress.com by 196.1.178.254 on 09/07/12
For personal use only.

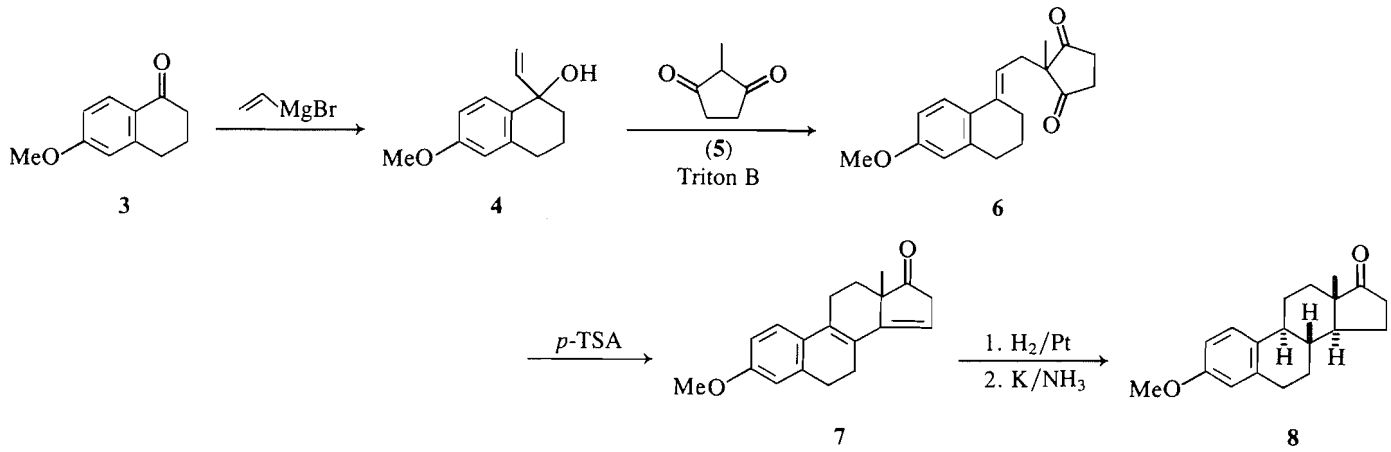

3 4 6 7 8

SCHEME 1

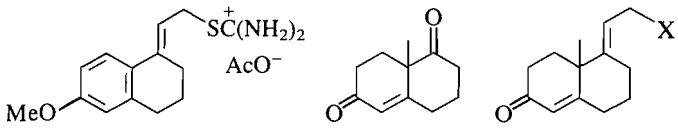

9 10 11

X = Cl or Br

enabling features could be called into play in the synthesis of a bridged ring A system of type **2**.[4] We therefore devised a further modification of the Torgov synthesis, involving the cation **16** as an intermediate. It was anticipated that this would be readily formed from the allylic alcohol **21** analogous to **4** and that subsequent closure of ring C could be effected by either acid- or base-catalyzed processes.

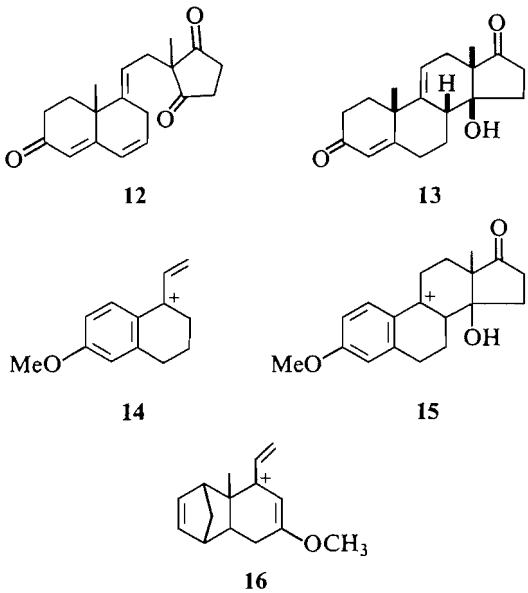

12 13 14 15 16

Results and discussion

Synthesis and rearrangement of the allylic alcohol 21

We synthesized **21** by the route shown in Scheme 2. Compound **17**, the Diels–Alder adduct of 2-methoxy-5-methyl-1,4-benzoquinone (10) and cyclopentadiene (11), was reduced chemospecifically to the alcohol **18** with sodium borohydride in methanol buffered with ammonium chloride, conditions that had previously been used by Cavill and Quinn (12) for the chemoselective reduction of **22** to **23**. The presence of only 13 signals in its ^{13}C nmr spectrum showed that the alcohol **18** was formed as a single diastereomer. The *endo* nature of the hydroxyl substituent was established by the ^{1}H nmr signal arising from the proton at C-6, a broad doublet (J = 10 Hz) at δ4.80. The dihedral angle measured from a model of **18** between the *exo* C-5—H bond and the *exo* C-6—H bond is approximately 0°, indicating that there would be a large coupling between protons with these orientations. Since there is a coupling constant of 10 Hz between the C-5 and C-6 protons the hydroxyl group must have the *endo* configuration. The stereochemistry of **18** was confirmed by its cyclization to an iodo ether (13).

Cavill and Quinn (12) acetylated **23** to form **24** and then removed the acetyloxy group with calcium and liquid ammonia to give **25**. We acetylated **18** to give **19**, which was then treated with calcium and liquid ammonia. However, in the present case the reaction was found to be very capricious, with the yield of **20** varying from 0 to 40%; the low yields appear to result from over-reduction. Attempted reduction of **19** with aluminum amalgam (14), chromous chloride or acetate (15), or zinc in acetic acid (16) was fruitless. Aluminum amalgam gave results similar to those with calcium and liquid ammonia, chromous salts did not effect reduction, and zinc in acetic acid led to hydrolysis of the enol ether function. The chromous salts were prepared by treatment of chromic chloride with an acidic slurry of zinc amalgam. This led us to compare the reduction potentials of Zn(0), Cr(II), and Ca(0). These are in the order Ca > Zn > Cr^{2+} (17), which suggested that zinc amalgam might have a reactivity intermediate between the reactivities of the other two reductants.

We were gratified to find that reaction of **19** with zinc amalgam in mildly acidic aqueous acetone consistently furnished **20** in >95% yield. This reagent could also be used to reduce the alcohol **18** to **20**, but in reduced yield (70%).

The ir, ^{1}H nmr, and ^{13}C nmr spectra of compounds **17**–**20** are compared in Tables 1 and 2 and their relationship may be seen to be in accord with the structural assignments.

Our next goal was the conversion of **20** to the allylic alcohol **21**, by reaction with a suitable vinyl anion equivalent. The original Torgov procedure utilized vinylmagnesium bromide (6). This reagent was found to be completely unreactive with **20**, although it reacted with the enol methyl ether of 1,3-cyclohexanedione. Valenta and co-workers found, in the case of

[4]Although the Wiechert modification (8) might be applicable, the yields reported for this method are very low.

Can. J. Chem. Downloaded from www.nrcresearchpress.com by 196.1.178.254 on 09/07/12
For personal use only.

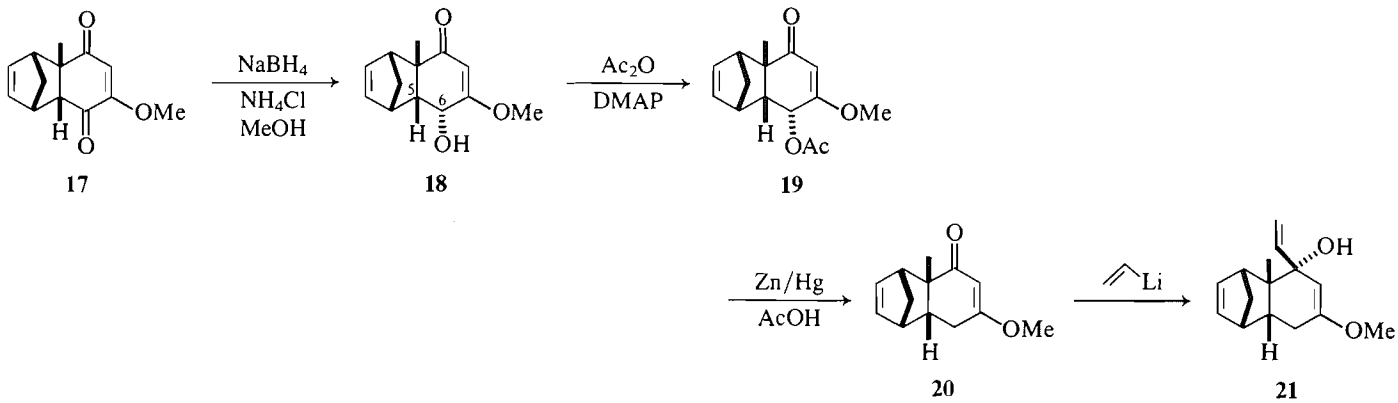

17 18 19 20 21

SCHEME 2

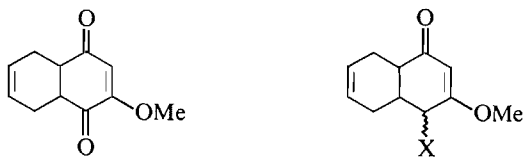

22 23 X = OH 24 X = OAc 25 X = H

dione **10**, that vinylmagnesium bromide was also unreactive and they devised a modification using lithium acetylide followed by catalytic hydrogenation (9). However, this reagent proved to be completely unreactive with **20**, although the reaction with the enol methyl ether of 1,3-cyclohexanedione proceeded smoothly. We next investigated the use of vinyllithium and, after extensive experimentation, found conditions (see Experimental) under which **20** was quantitatively converted to **21**.

The gross structure of **21** was apparent from its spectra. In its ^{1}H nmr spectrum, the C-methyl and O-methyl signals at δ1.19 and 3.42, respectively, were shifted upfield relative to those of compounds **17**–**20**. The low-field region of the spectrum showed the retention of the norbornene ethylenic proton signals (δ6.03 (m, 2H)) together with signals characteristic of a vinyl group. The product appears to be very largely a single diastereomer. The stereochemistry at C-9 is considered to be that shown in **21**, with attack from the less-hindered *exo* face (cf. the *exo* attack in the reduction of **17** to **18** with sodium borohydride).

The allylic alcohol **21** proved to be very unstable and did not survive even mild heating. A solution of the alcohol in deuterochloroform was left to stand at room temperature; the solution had separated into two phases (aqueous and organic) after 1 day. A new methoxyl signal appeared in the ^{1}H nmr spectrum of the organic product in addition to new vinylic proton signals. Also, a new C-methyl signal appeared at δ1.95, downfield from that of the starting material, indicative of the situation of the methyl group on a double bond or adjacent to a carbonyl group. After several days the methoxyl signal was absent and the spectrum remained constant. A structure, **27**, for the initially formed product consistent with the spectroscopic data and a route leading to its formation are shown in Scheme 3.

It is postulated that **21** is protonated by traces of adventitious acid and that loss of water occurs with cleavage of the bicyclo[2.2.1]heptene system. Reaction of the resulting allylic cation **26** with the enol methyl ether system and loss of a proton would furnish the enol ether **27**.

The ir spectrum (5.80 μm) and the ^{1}H nmr[5] and ^{13}C nmr spectra (Table 3) of the final rearrangement product are in accord with the assignment to it of structure **28***a*. Salient peaks in its mass spectrum are also in consonance with this assignment (Scheme 4). Its formation would result from hydrolysis of the enol ether **27**.

Hydrogenation of **28***a* over 5% palladium on carbon in ethyl acetate gave tetrahydro-**28***a*, in accord with the presence in **28***a* of three ethylenic double bonds, one of which is tetrasubstituted. The product, which is assigned structure **29**, featured only signals for C(sp^3) protons in its ^{1}H nmr spectrum: these included signals attributable to a vinylic methyl group (δ1.79) and the methyl group of a C-ethyl moiety (δ0.95 (t, J = 8 Hz)). A strong band at 5.83 μm was present in its ir spectrum. Its ^{13}C nmr spectrum showed two olefinic carbon signals (both singlets in the SFORD spectrum) instead of the six in the spectrum of **28***a*, and two C-methyl carbon signals corresponding to the methyl proton signals observed in the ^{1}H nmr spectrum.

The formation from **21** of an alternative rearrangement product, **28***b*, can also be envisaged. This could arise from the allylic cation **26**, postulated as an intermediate in the formation of **28***a* (Scheme 5). However, structure **28***a* is favored over **28***b* because of the similarity of the splitting patterns of the signals of the two cyclopentene ethylenic protons in the ^{1}H nmr spectrum of the product.

Our perception that the facile rearrangement of **21** involved the intermediacy of the allylic cation **26** led us to synthesize and investigate the utilization of the allylic alcohol **32**, a dihydro derivative of **21** that would not be expected to undergo such facile opening of the bicyclo[2.2.1]heptane system.

Synthesis of the allylic alcohol 32 and its conversion to 1,4-methano steroids

Acetate **19** was hydrogenated over 10% palladium on carbon to give **30**, which was treated with zinc amalgam to produce **31** (Scheme 6). The ir spectrum of **30** showed strong absorption bands at 5.73 and 6.18 μm, which are assigned to the ester and enone carbonyl-stretching frequencies, respectively. The ^{1}H nmr spectrum of **30** displayed the signal of the proton under the acetoxyl group as a multiplet at δ5.91. The enol ether vinyl proton gave rise to a doublet (J = 2 Hz) at δ5.35 and the signal of the methoxyl protons was little changed from its position in **19** at δ3.70. The signal for the acetyl methyl protons appeared at δ2.15 and the C-methyl protons gave rise to a singlet at δ1.22.

[5] Spin-decoupling experiments at 200 MHz confirmed many of the assignments (13).

Can. J. Chem. Downloaded from www.nrcresearchpress.com by 196.1.178.254 on 09/07/12
For personal use only.

TABLE 1. The ir and ^{1}H nmr spectra of compounds **17**–**20**[a]

Parameter	Compound 17	18	19	20
λ_{max}, μm ($CHCl_3$)[b]				
O—H	—	3.03	—	—
O—C=O	—	—	5.74	—
C=O (6)	5.89	—	—	—
C=O (9)	6.03	6.14	6.13	6.20
C=C	5.19			
$^H\delta$ ($CDCl_3$)[c]				
H-1,4	3.0–3.2	2.8–2.9	2.8–3.0*	2.9
	3.3–3.6	3.2–3.4		
2,3	5.97	5.88	6.0	6.0
	6.18	6.09		
5	2.88	2.70	2.8–3.0*	2.1–2.6*
	(d, *J* 3)	(dd, *J* 10, 3)		
6	—	4.80	5.92	1.4–1.7**
		(br d, *J* 10)	(dd, *J* 10, 2)	2.1–2.6*
8	5.85 (s)	5.16	5.26	5.22
		(d, *J* 2)	(d, *J* 2)	(br s)
CH_2 (bridge)	1.5–1.7	1.5–1.65	1.4–1.6	1.4–1.7**
$CH_3C(10)$	1.48 (s)	1.49 (s)	1.46 (s)	1.40 (s)
CH_3O	3.73 (s)	3.75 (s)	3.69 (s)	3.62 (s)
CH_3CO_2	—	—	2.21 (s)	—
OH	—	2.85	—	—

[a]Steroid numbering for ring system (see text).
[b]Bands are strong unless otherwise indicated.
[c]Signals are multiplets unless otherwise indicated, and their relative areas are in accord with the assignments; overlapping signals within a given spectrum are indicated with asterisks; *J* values are in Hz.

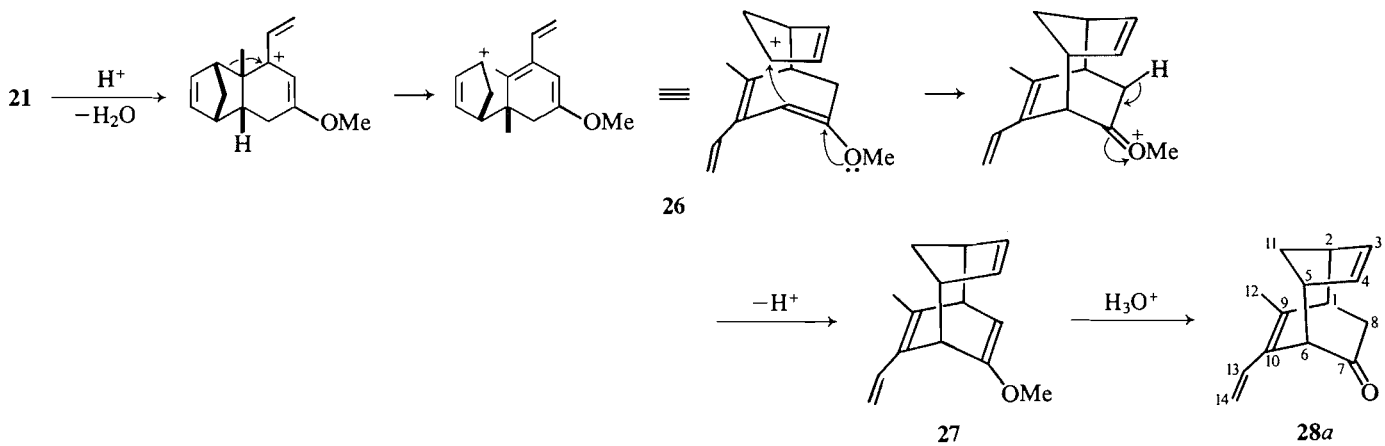

SCHEME 3

The conversion of **30** to **31** was made apparent by the absence of the acetyl methyl signal in the ^{1}H nmr spectrum of the latter. The enol ether vinyl proton signal appeared as a broad singlet at δ5.41, the methoxyl protons gave rise to a singlet at δ3.71, and the signal for the C-methyl protons appeared as a singlet at δ1.21. The ir spectrum of **31** displayed a strong band at 6.17 μm.

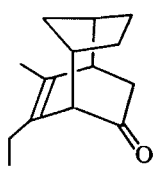

29

Reaction of **31** with vinyllithium under the same conditions as those used with **20** gave allylic alcohol **32** in excellent yield. The ^{1}H nmr spectrum of **32** established the completeness of the reaction by the absence of the signal of the methoxyl group at δ3.71 and its replacement with a methoxyl signal at δ3.50. Other assignable signals included a doublet of doublets (J_{AX} ~ 16 Hz, J_{MX} ~ 10 Hz) at δ5.70 arising from the X proton of the vinyl AMX system, a doublet of doublets (J_{AM} ~ 2 Hz) at δ5.01 from the A proton, a doublet of doublets at δ4.80 from the M proton, a doublet (J = 2 Hz) at δ4.54 arising from the

Can. J. Chem. Downloaded from www.nrcresearchpress.com by 196.1.178.254 on 09/07/12
For personal use only.

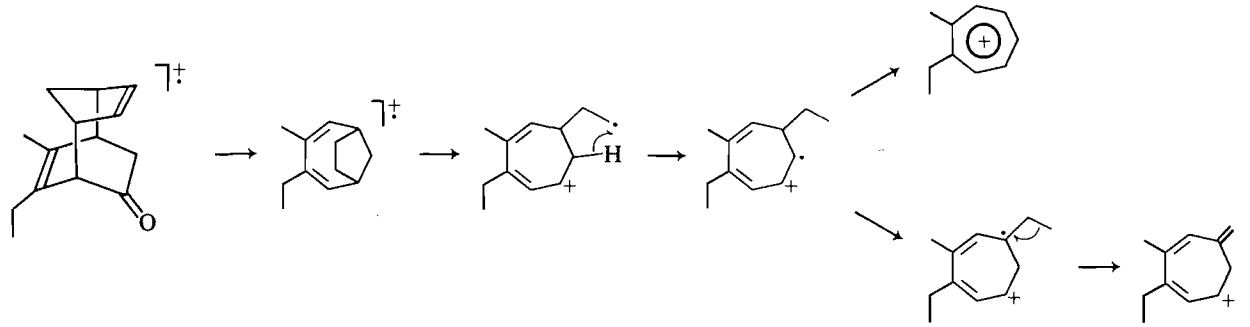

SCHEME 4

TABLE 2. The ^{13}C nmr spectra of compounds **17–20**[a]

Carbon	$^{C}\delta$ ($CDCl_3$)[b] 17	18	19	20
C-1	53.3	48.9	46.9	49.2
2	133.8	134.7	133.8	133.1
3	138.5	136.9	137.3	139.9
4	49.4	45.6	45.8	41.8
5	56.1	55.3	54.5	52.9
6	202.0	65.2	66.2	29.5
7	162.4	172.9	169.8	175.3
8	113.9	102.7	104.3	101.7
9	194.1	202.8	201.5	203.7
10	53.3	51.7	51.6	51.1
CH_2 (bridge)	46.3	46.3	46.3	45.7
$CH_3C(10)$	26.4	25.3	25.6	27.5
CH_3O	57.0	56.0	55.8	55.3
CH_3CO_2	—	—	20.3	—
CH_3CO_2	—	—	169.6	—

[a]See footnote *a* in Table 1.
[b]Signal multiplicities in SFORD spectra are in accord with the assignments.

TABLE 3. The ^1H and ^{13}C nmr spectra of compound **28***a*[a]

	$^{H}\delta$ ($CDCl_3$)[b]		$^{C}\delta$ ($CDCl_3$)[c,d]
H-1	2.70	C-1,2	39.5, 44.9*
2	2.60	3,4	129.4, 131.1**
3	5.57	4	131.1**
4	5.29	5	48.3*
5	3.20	6	51.6
6	3.54 (d, *J* 2.2)	7	212.9
8	2.13	8	38.1***
11*endo*	2.00	9	138.7
11*exo*	2.50	10	128.4
12	1.95 (s)	11	40.2***
13	6.56 (dd, *J* 17.5, 11.2)	12	18.8
14*c*	4.91 (d, *J* 11.2)	13	132.2**
14*t*	5.10 (d, *J* 17.5)	14	111.5

[a]For numbering, see structure **28***a* in text.
[b]See footnote *b* in Table 1.
[c]See footnote *b* in Table 2.
[d]Asterisks indicate assignments that are interchangeable.

enol ether vinyl proton, and a singlet at δ0.95 from the C-methyl group. Medium absorption at 5.99 μm in the ir spectrum of **32** is assigned to the double bond stretching vibrations.

We were happy to find that allylic alcohol **32** was not only more stable than **21** but that it reacted as desired with dione **5** (*vide infra*). However, **32** was readily converted to dienone **33**

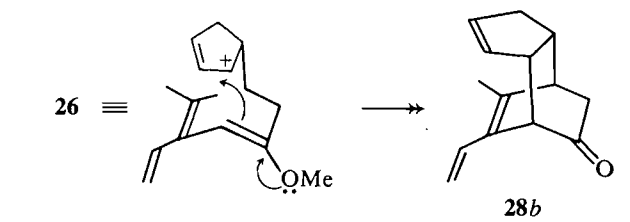

SCHEME 5

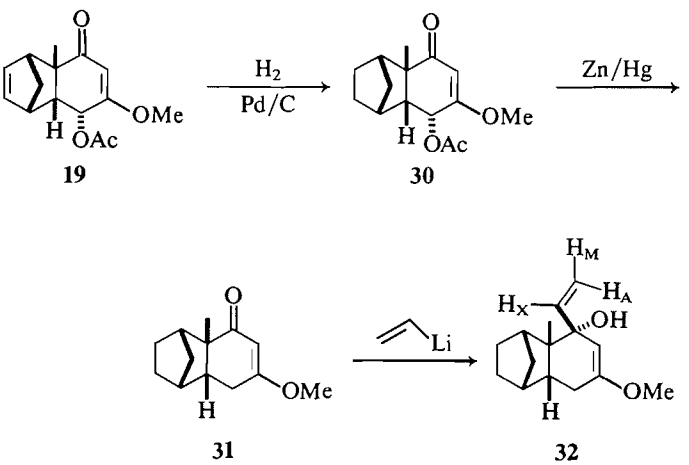

SCHEME 6

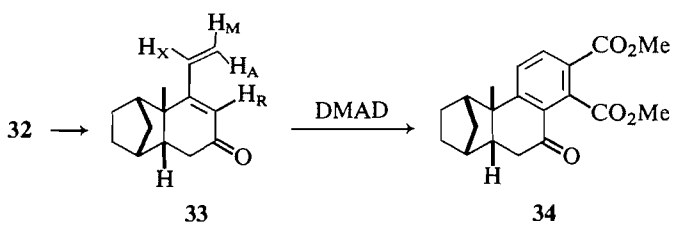

SCHEME 7

upon attempted purification (Scheme 7). The ^1H nmr spectrum of **33** displayed a complex olefinic region from which could be extracted the signal for H_X at δ6.35 (J_{AX} ~ 16 Hz, J_{MX} ~ 10 Hz), H_A at δ5.68 (J_{AM} = 2 Hz), H_M at δ5.34, and H_R at δ6.19. A C-methyl singlet at δ1.12 was the only other assignable peak. Its ir spectrum displayed a carbonyl-stretching band at 6.04 μm with a shoulder at 6.17 μm. The ultraviolet spectrum of **33** indicated that the unsaturated system was in the *s-cis* conformation, based on the magnitude of the extinction coefficient (18) of the maximum at 244 nm (ε = 5800); the n → π* absorption band appeared at 332 nm (ε = 120).

Heating a mixture of **33** with dimethyl acetylenedicarboxyl-

Can. J. Chem. Downloaded from www.nrcresearchpress.com by 196.1.178.254 on 09/07/12
For personal use only.

Can. J. Chem. Downloaded from www.nrcresearchpress.com by 196.1.178.254 on 09/07/12
For personal use only.

ate (DMAD) in benzene at 100°C for 15 h gave the aromatic product **34** in low yield together with several other compounds that were not isolated (Scheme 7). Compound **34** must arise by oxidation of the initially formed cycloadduct of the 1,3-diene **33**.

In view of the poor yield obtained in this Diels–Alder reaction of **33** we elected not to investigate an approach to steroid synthesis (19) that utilizes this method. We did explore the possibility of a Michael addition reaction of dione **5** to the dienone **33** as the key reaction to form an ABD steroid skeleton, a type of reaction for which precedent exists (20). However, attempts to catalyze the reaction with bases (21) and with potassium fluoride (22) were uniformly unsuccessful, as was the titanium(IV) chloride-mediated reaction (23) with the trimethylsilyl enol ether of **5**.

We therefore returned to the Torgov-type reaction and treated alcohol **32** with a slight excess of dione **5** in boiling toluene in the presence of a trace of Triton B, and obtained **35** and its hydrolysis product **36** in poor yield, together with a third product (**37**, *vide infra*) (Scheme 8). When the reaction was carried out in *tert*-butyl alcohol and xylenes in the absence of Triton B the main product isolated was **36**, which was obtained in 73% overall yield from **31**.

The ^{1}H nmr spectrum of **35** featured a one-proton, broad singlet at δ5.55 assigned to the C-8 proton. The C-11 proton gave rise to a triplet (J = 8 Hz) at δ4.82. The signal for the methoxyl protons appeared at δ3.73 and the signals for the two C-methyl groups at δ1.16 and 1.14. The four cyclopentanedione methylene protons are accidentally equivalent at δ2.67. The ir spectrum of **35** displayed a strong carbonyl-stretching band at 5.80 μm and a medium dienol ether band at 6.08 μm.

The ^{1}H nmr spectrum of the trione **36** displayed a signal for the vinyl proton as a broad singlet at δ5.85, a singlet for the cyclopentanedione protons at δ2.77, and a six-proton C-methyl singlet at δ1.16. Its ir spectrum showed strong stretching bands for the enone and the cyclopentanedione carbonyl groups at 6.02 and 5.80 μm, respectively.

The third product from the reaction carried out in the presence of Triton B is considered to have structure **37**. Exact mass measurement showed that it differed in composition from compound **36** by the presence of an additional oxygen atom. This fact and comparison of its ir and ^{1}H nmr spectra (see Experimental) and its ^{13}C nmr spectrum with those of **36** (Table 4) led to the conclusion that it was a hydroxy derivative of **36**. The presence of the hydroxyl group was confirmed by its conversion to an acetate. A heteronuclear correlation (HETCOR) nmr experiment (24) was performed[6] to determine the position of the hydroxyl group. The direct correlation chart established the direct ^{1}H–^{13}C connectivity ($^1J_{CH}$) of the proton signal at δ4.0, arising from attachment to the carbon atom bearing the hydroxyl group, and the carbon signal at δ70.0. The indirect correlation chart established the indirect ^{1}H–^{13}C connectivity ($^2J_{CH}$ or $^3J_{CH}$) of the carbonyl carbon signal at δ200.4 and the proton signal at δ4.0. Thus the hydroxyl group is located on C-6, next to the carbonyl carbon C-7.

The origin of **37** is problematic. It cannot arise from "carry through" of the hydroxyl group in **18**, since intermediates in the sequence were purified. Thus it must arise via oxidation during the reaction of **31**, but the nature of the oxidation process is uncertain. In the absence of Triton B no **37** was formed. Since the hydrolysis product **36**, which is needed for the next step, is the major product under the latter conditions, these are clearly to be preferred.

[6]We thank Mr. N. Plavac and Professor W. F. Reynolds for their assistance in this experiment.

TABLE 4. The ^{13}C nmr spectra of compounds **36** and **37**[a]

	$^c\delta$ ($CDCl_3$)[b,c]	
Carbon	**36**	**37**
C-1,4	45.7, 46.6*	40.6, 41.5
2,3	20.0, 27.5	24.9, 26.7
5	44.3*	52.1
6	36.1**	71.0
7	198.1	200.4
8	128.7	127.2
9	168.3	169.7
10	43.8	48.2
11	21.0	22.8
12	32.9**	32.2
13	56.3	56.2
14,17	215.5, 215.5	215.4, 215.6
15,16	34.9	35.0
18	26.5	32.0
19	35.4	36.5
20	35.4**	36.5

[a]See footnote *a* in Table 1.
[b]See footnote *b* in Table 2.
[c]See footnote *d* in Table 3.

Hydrogenation of **36** gave a dihydro compound that is assigned structure **38** on the basis of spectroscopic data and the fact that a molecular model indicates that the less-hindered side of the cyclohexene ring is the β face. The ^{1}H nmr spectrum of **38** featured the cyclopentanedione proton signal at δ2.77 and the signals of the two C-methyl groups at δ1.14 ppm and 1.05. Its ir spectrum displayed bands for the carbonyl groups at 5.79 μm (cyclopentanedione) and 5.84 μm (cyclohexanone).

A methanolic solution of compound **38** was stirred at 70°C overnight in the presence of a catalytic amount of potassium hydroxide. Upon work-up, compound **39** (Scheme 9), the first 1,4-methano bridged steroid to be synthesized, was obtained as a white crystalline solid. The prominent features of the ^{1}H nmr spectrum of **39** were the singlets for the two methyl groups at δ1.00 and 1.09. Its ir spectrum showed a hydroxyl stretching band at 3.00 μm, and carbonyl-stretching bands at 5.76 μm (cyclopentanone) and 5.90 μm (cyclohexanone). The spectra of **39** and related compounds are compared in Tables 5 and 6 (*vide infra*).

Examination of molecular models suggested that of the four possible transition states for carbon–carbon bond formation in the aldol reaction leading from **38** to the steroid, the one giving the diastereomer depicted as **39** is freest of steric interactions (13). Since this diastereomer also appears to be thermodynamically favored, we tentatively assigned the relative configura-

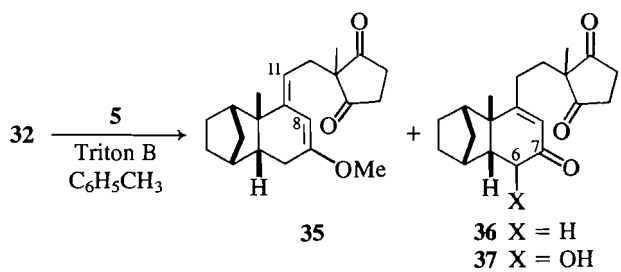

35 **36** X = H **37** X = OH

SCHEME 8

TABLE 5. The ir, uv, and ^{1}H nmr spectra of compounds **39–41** and **45**[a]

Parameter	39	40	41	42
λ_{max}, μm ($CHCl_3$)[b]				
OH	3.00 (w)	—	—	—
C=O (7)	5.76	5.74	—	5.84
C=O (17)	5.90	5.94	5.94 (vs)	6.04
C=C	—	6.20	6.24 (w)	6.14 (w), 6.24 (w)
λ_{max}, nm (ε) (EtOH)				
	—	265 (6710)	225 (7290)	235 (br)[c] (9550)
$^H\delta$ ($CDCl_3$)[d]				
H-14				3.93 (m)
15			8.13 (dd, *J* 5.8, 2.7)	7.46 (dd, *J* 5.6, 2.7)
16			6.12 (dd, *J* 5.8, 1.7)	6.02 (dd, *J* 5.6, 1.7)
18	1.00 (s)	1.12 (s)	1.05 (s)	1.04 (s)
19	1.09 (s)	1.25 (s)	1.10 (s)	1.14 (s)

[a]See footnote *a* in Table 1.
[b]See footnote *b* in Table 1.
[c]See text and footnote 7.
[d]See footnote *c* in Table 1.

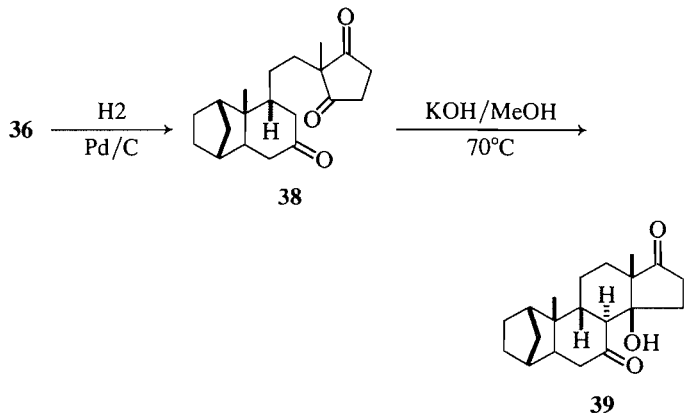

SCHEME 9

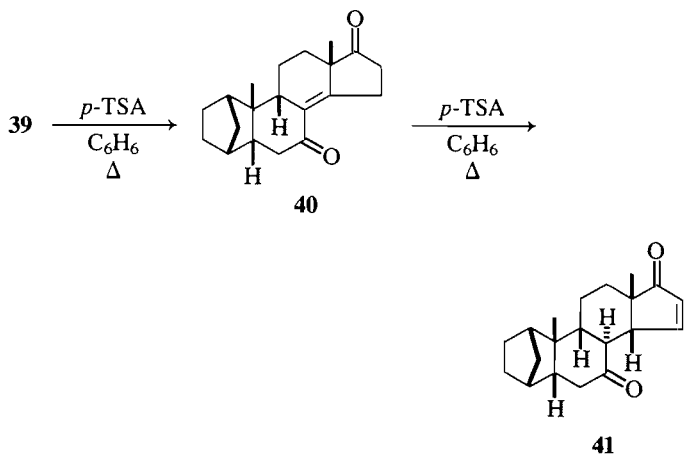

SCHEME 10

tion shown in **39** to the single diastereomer obtained from the aldol reaction. The gross structure of the steroid was confirmed and its relative configuration established as in **39** by a single crystal X-ray diffraction analysis (25).

Treatment of **39** with *p*-toluenesulfonic acid (*p*-TSA) in boiling benzene for 24 h gave as the major product the simple dehydration product **40** and a small amount of a second, isomeric product. The latter became the major product when the concentration of *p*-toluenesulfonic acid and the reaction time were increased; it is assigned structure **41** (Scheme 10). Their uv spectra (Table 5) show that both have α,β-unsaturated ketone chromophores. The position of the maxima are in accord with the structural assignments, and their intensities also correspond to those expected for an *s-cis*-2-enone and a 2-cyclopentenone derivative without double bond substituents (18). The ir spectrum of **40** shows carbonyl-stretching bands that are attributable to the cyclopentanone (5.74 μm) and 2-enone (5.94 μm)

TABLE 6. The ^{13}C nmr spectra of compounds **39–41** and **45**[a]

	$^C\delta$ ($CDCl_3$)[b,c]			
Carbon	39	40	41	45
C-1,4,5	42.3, 43.8 46.8	44.2, 45.5 46.5	43.05, 44.0 46.95	44.35, 44.6 46.55
2,3	21.7, 24.8	21.5, 22.5	21.8, 22.1	21.2, 25.8
6	26.2	23.8	26.0	26.5
7	216.5	202.5	213.1	196.0
8	47.0	131.0	47.05	129.0
9	53.7	47.25	50.5	163.5
10	39.1	40.4	40.5	44.0
11	30.1*	26.4*	29.2	31.5
12	31.0*	28.5*	39.2*	35.4*
13	55.0	50.8	46.9	46.8
14	80.15	154.0	54.1	48.35
15	34.6	35.2	130.5	130.0
16	39.3**	39.2**	167.0	165.0
17	218.6	219.0	215.0	213.2
18	19.9	23.5	24.1	25.5
19	31.3	30.5	31.6	27.2
20	41.8**	41.5**	40.0*	36.7*

[a]See footnote *a* in Table 1.
[b]See footnote *b* in Table 2.
[c]See footnote *d* in Table 3.

Can. J. Chem. Downloaded from www.nrcresearchpress.com by 196.1.178.254 on 09/07/12
For personal use only.

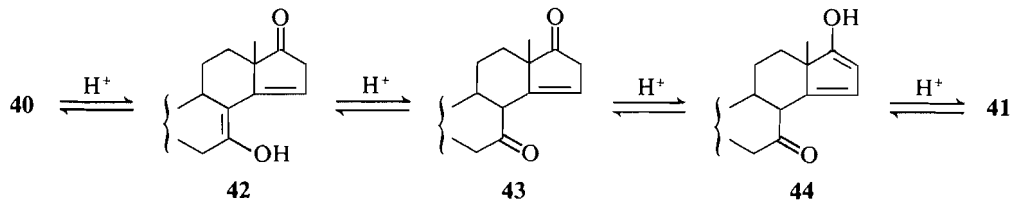

SCHEME 11

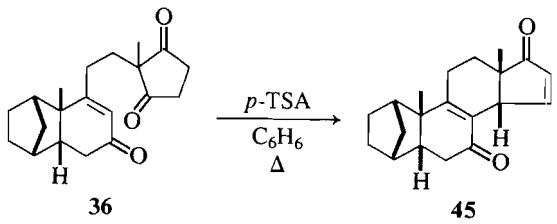

SCHEME 12

systems. The single, carbonyl-stretching band in the spectrum of **41**, which is very strong, can be attributed to overlap of bands arising from the cyclohexanone and 2-cyclopentenone systems. Both compounds show ethylenic stretching bands, with that of **40** being unusually strong as expected for an *s-cis*-2-enone (26). Prominent features in the ^{1}H nmr spectra of **40** and **41** are given in Table 5. The former shows the presence of the two angular methyl groups and the absence of vinyl protons. The latter again shows the presence of the two angular methyl groups and also two vinyl protons with signals at δ6.11 and 8.13, assigned to the C-16 and C-15 protons, respectively. The unusually low-field position of the latter is attributable to anisotropic deshielding by the carbonyl group at C-7. The vicinal coupling constant ($J_{15,16}$) of the vinyl protons is 5.8 Hz, while the values for $J_{14,15}$ and $J_{14,16}$ are 2.7 and 1.7 Hz, respectively (cf. the corresponding values for 2-cyclopentenone (5.5, 2.7, and 1.5 Hz)). The ^{13}C nmr spectra of **40** and **41** are compared with the spectrum of **39** in Table 6, and corroborate the structural assignments (*vide infra*).

The conversion of **39** to **40** clearly involves conventional acid-catalyzed dehydration of an aldol via the α-enol of the β-hydroxy ketone system. The subsequent conversion of the $\Delta^{8(14)}$ 7-keto compound **40** to the Δ^{15} 17-keto compound can readily be interpreted as involving acid-catalyzed isomerization of the enol **42** of **40** to the 3-ene-1,6-dione **43** followed by isomerization of this via the enol **44** to **41** (Scheme 11). It is of interest that the 2-cyclopentenone **41** with a disubstituted ethylenic double bond is favored over the 2-enone **40** with a tetrasubstituted ethylenic double bond.

It may be noted that there is no facile acid-catalyzed route for the isomerization of **40** to the corresponding $\Delta^{8(9)}$ 7-keto steroid.

Finally, we investigated the acid-catalyzed cyclization of the enetrione **36**, the immediate precursor of the trione **38**. Treatment with *p*-toluenesulfonic acid in boiling benzene gave a product that is assigned structure **45** (Scheme 12). Its uv spectrum showed a single maximum at 235 nm, which is considered to result from overlap of maxima arising from the two 2-en-1-one systems. As expected for such overlap, the band is exceptionally wide with the width at half-height ($W_{1/2}$) equal to 50 nm (for compound **40**, $W_{1/2}$ = 30 nm).[7] In its ir spectrum **45** shows 2-cyclopentenone and 2-cyclohexenone carbonyl-stretching bands at 5.84 and 6.04 μm, respectively, together with two weak ethylenic double bond stretching bands at 6.14 and 6.24 μm. Its ^{1}H nmr spectrum shows prominent signals analogous to those observed in the spectrum of **41**. These are again assigned to the two angular methyl groups and the unsubstituted 2-cyclopentenone system. In the present case the interpretation of the coupling pattern of the vinyl protons (Table 6) was corroborated by a decoupling experiment. Irradiation at the frequency of a one-proton multiplet at δ3.93, which is assigned to the C-14 proton, led to the collapse of each of the vinyl proton signals to a doublet with J = 5.6 Hz, confirming that the fine splitting of each vinyl proton signal in the original spectrum arises from coupling with the C-14 proton. The relative stereochemistry of **45** has not been established unambiguously since it cannot be excluded that the relative configurations at C-13 and C-14 are different from those in **39**.

Compound **45** is considered to arise via enolization of **36** to **46** and acid-catalyzed cyclization of this to the aldol **47** (Scheme 13); dehydration would then lead to the dienedione **48**, which could lead as in Scheme 11 to the 3-cyclopentenone **49**. Two acid-catalyzed enolizations of this would lead to the bis 3-enone system of **45**. In this case the $\Delta^{8,15}$ 7,17-diketo steroid is preferred to the $\Delta^{8,9}$ 7,17-diketo steroid **48**. This can be attributed at least in part to the greater degree of conjugation in **45**. It may be noted that here there is no facile route for the acid-catalyzed conversion of the $\Delta^{8(9)}$ 7-keto system of **45** to the corresponding $\Delta^{8(14)}$ 7-keto system.

The bridged steroids **39–41** and **45** we have described all have an "unnatural" *syn* relationship between the C-19 methyl group (at C-10) and the C-9 hydrogen atom. This, combined with the *cis* A/B ring fusion and the ring A bridge, results in an unusually compact stereostructure (cf. **50** ≡ **39**). It seems probable that our general method can be adapted in its later stages for the synthesis of other types of stereoisomer. Thus, for example, reduction of **36** with reducing metals rather than by hydrogenation could lead to products with an *anti* relationship between the C-19 methyl group and the C-9 hydrogen atom.

Experimental

Melting points were determined with a Thomas Hoover capillary melting point apparatus and are uncorrected.

Infrared (ir) spectra were obtained from solutions in chloroform, unless otherwise specified. Band positions in microns (μm) are reported relative to the 6.24-μm band of polystyrene; unless denoted as medium (m) or weak (w), their intensities are strong. Ultraviolet (uv) spectra were recorded in 95% ethanol. Proton magnetic resonance (^{1}H nmr) spectra of solutions in deuterochloroform (unless otherwise specified) were acquired at 60 MHz and at 200 MHz. Signal positions are reported on the delta (δ) scale in parts per million (ppm) downfield from tetramethylsilane as internal standard; coupling constants, J, are reported in hertz (Hz). Carbon-13 magnetic resonance (^{13}C nmr) spectra were acquired from deuterochloroform solutions, unless otherwise specified, on a Varian CFT-20, XL-200, or XL-400 spectrometer. The chemical shifts, obtained in the proton noise-decoupled mode, are reported on the delta scale in ppm and are referenced to the signal

[7]The value for the extinction coefficient is lower than might be expected for the overlap of the two chromophores; this is attributable to deviation from coplanarity of the 2-cyclohexen-1-one system.

Can. J. Chem. Downloaded from www.nrcresearchpress.com by 196.1.178.254 on 09/07/12
For personal use only.

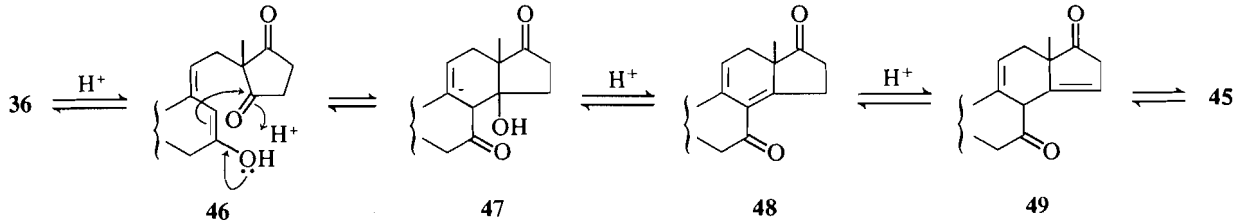

SCHEME 13

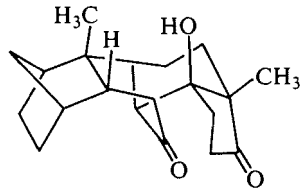

50

for the middle line of $CDCl_3$ at 77.9 ppm. Signal multiplicities were determined from the single-frequency off-resonance decoupled (SFORD) spectra (CFT-20) or from APT or DEPT experiments (XL-200 and XL-400).[8]

Low resolution mass spectra were recorded at 70 eV with a Bell and Howell CEC 21-490 single focussing mass spectrometer. Peak positions are reported in mass-to-charge units (m/z) followed by the relative abundances in parentheses. Exact mass measurements were determined from high resolution mass spectra obtained on a AEI MS-3074 double focussing mass spectrometer with a DS-50 data system.

The apparatus for reactions performed under anhydrous conditions was either oven-dried for at least 24 h at 110°C or flame-dried and then cooled in a desiccator prior to assembly. Argon (99.99%, supplied by Canox) was used as an inert atmosphere.

Analytical thin-layer chromatography was carried out on aluminum-backed plates that had been pre-coated with 0.20 mm of silica gel 60 containing a fluorescent indicator (Merck). Preparative thin-layer chromatography was performed on 20 × 20 cm plates coated with 2 mm of silica gel 60 containing a fluorescent indicator (Merck). Compound visualization was effected by ultraviolet light. On the preparative scale, bands were scraped off the plate and stirred with methanol for at least 0.5 h, and the extracts were filtered and concentrated. The compounds were isolated from the residue by solution in dichloromethane followed by filtration and concentration. Silica gel (grade 923, 100–200 mesh, Grace Davison) was used for column chromatography. Flash chromatography was carried out on 40–60 μm silica gel (Merck grade 60, 230–400 mesh, 60 Å mean pore diameter).

2-Methoxy-5-methyl-1,4-benzoquinone

The title compound was synthesized by the method of Woodward *et al.* (10); mp 175–177°C (lit. (10) mp 174–175.5°C); ir λ_{max}: 5.98, 6.08, 6.26 μm; ^{1}H nmr δ: 2.07 (d, J = 2 Hz, 3H), 3.83 (s, 3H), 5.91 (s, 1H), 6.53 (q, J = 2 Hz, 1H).

Diels–Alder reaction of cyclopentadiene with 2-methoxy-5-methyl-1,4-benzoquinone. Formation of ***17***

A solution of cyclopentadiene (100 mL, 1.21 mmol) and 2-methoxy-5-methyl-1,4-benzoquinone (35.0 g, 0.23 mmol) in hexanes (1000 mL) and ethyl acetate (500 mL) was boiled under reflux for 24 h. Additional cyclopentadiene (20 mL) was added and the mixture was heated for another 24 h. The mixture was concentrated and dicyclopentadiene was removed by high vacuum pumping at 40°C. The crude solid product was recrystallized from ethyl acetate/hexanes to give **17** in 87% yield; mp 118–120°C (lit. (11) mp 119–120°C).

When the reaction was carried out in boiling chloroform for 24 h and the reaction mixture was worked up in similar fashion, **17**, mp 119–120°C, was obtained in 93% yield.

[8]Spectroscopic data for many of the products are given in the Discussion or the tables.

Reduction of ***17*** *with sodium borohydride. Formation of ketol* ***18***

Sodium borohydride (1.10 g, 26.8 mmol) was added in small portions to a chilled (ice bath), stirred solution of diketone **17** (15.00 g, 68.7 mmol) and ammonium chloride (1.51 g, 28.2 mmol) in methanol (250 mL). The cooling bath was removed after the completion of addition and the mixture was stirred for an additional 30 min. Water (1500 mL) was added and multiple extractions with dichloromethane yielded, after concentration, ketol **18** as a white solid (14.86 g, 98%), which was recrystallized from acetone; mp 121–123°C. *Anal.* calcd. for $C_{13}H_{16}O_3$: C 70.89, H 7.32; found: C 70.77, H 7.32.

Acetylation of ***18****. Formation of acetate* ***19***

A mixture of alcohol **18** (6.50 g, 29.5 mmol) and freshly distilled acetic anhydride (3.82 mL, 40.5 mmol) in pyridine (25 mL) was treated with a crystal of 4-(dimethylamino)pyridine and stirred for 24 h. High vacuum pumping removed all unconsumed reagent and solvent to leave a solid, which was recrystallized from acetone/hexanes to give **19** (6.50 g, 90%) as colorless rods, mp 74–76°C. *Anal.* calcd. for $C_{15}H_{18}O_4$: C 68.68, H 6.92; found: C 68.36, H 6.88.

Reduction of ***19*** *with zinc amalgam. Formation of enone* ***20***

To a rapidly stirred solution of mercuric chloride (1.60 g, 5.89 mmol) in water (40 mL) was added concentrated hydrochloric acid (2 mL) and then zinc dust (20.9 g) in small portions (0.25 g). The cloudy mixture resulting after each addition was allowed to clarify and the resulting solid was crushed with a glass rod to prevent aggregation. After half the zinc was added the quantity of each addition could be doubled and the solid amalgam was checked periodically for the formation of large particles. The suspension was stirred for 15 min; the aqueous layer was decanted and the fluffy amalgam was washed several times with water. Water (50 mL) and hydrochloric acid (1.75 mL, 21.0 mmol) were added to the amalgam and the mixture was chilled in an ice bath. A solution of acetate **19** (1.40 g, 5.35 mmol) in acetone (50 mL) was added, the cooling bath was removed, and the reaction mixture was stirred for 20 min. The liquid phase was decanted, the amalgam was washed with acetone, and the combined liquid phases were concentrated. The product was isolated from the resulting concentrate by extraction with dichloromethane. The dichloromethane was evaporated giving **20** (1.01 g, 93%) as an oil, which crystallized from hexanes; mp 64.5–65.5°C. *Anal.* calcd. for $C_{13}H_{16}O_2$: C 76.44, H 7.90; found: C 76.06, H 7.90.

Addition of vinyllithium to ***20****. Formation of* ***21***

To a magnetically stirred solution of vinyl bromide (1 mL, ~14 mmol) in ether (30 mL) at −78°C in a Dry Ice/acetone bath was added dropwise 2.0 M *tert*-butyllithium (10.0 mL, 20 mmol). The mixture was stirred for 40 min and a solution of ketone **20** (0.403 g, 1.97 mmol) in ether (25 mL) was added slowly. The Dry Ice/acetone bath was replaced with a Dry Ice/carbon tetrachloride bath and the reaction mixture was stirred for 1 h at −23°C. The temperature of the mixture was lowered again to −78°C with a Dry Ice/acetone bath, and acetic acid (1.2 mL, 21 mmol) was added slowly. The cooling bath was removed after 30 min and the mixture was allowed to warm up. At ~0°C saturated aqueous sodium bicarbonate (20 mL) was added and the layers were separated. The aqueous phase was extracted with ether (2 × 5 mL) and the combined organic phases were concentrated after the addition of benzene (100 mL) to give the allyl alcohol **21** as an oil; ^{1}H nmr δ: 1.0–2.8 (m, 8H), 1.19 (s, 3H), 3.42 (s, 3H), 4.37 (s, 1H), 4.85 (dd, J = 14, 2 Hz, 1H), 5.06 (dd, J = 10, 2 Hz, 1H), 5.86 (dd, J = 14, 10 Hz, 1H), 6.03 (m, 2H).

Can. J. Chem. Downloaded from www.nrcresearchpress.com by 196.1.178.254 on 09/07/12
For personal use only.

Can. J. Chem. Downloaded from www.nrcresearchpress.com by 196.1.178.254 on 09/07/12
For personal use only.

*Rearrangement of **21**. Formation of **27** and **28**a*

A solution of allylic alcohol **21** in deuterochloroform on standing for 1 day gave an initial product, **27**, as an oil, showing new C-methyl, methoxyl, and vinyl proton signals in its ^{1}H nmr spectrum. On standing for several days this gave the final product, ***28a***, in quantitative yield as a viscous oil; this was also obtained on treatment of **21** with wet silical gel in methanol; ms *m/z*: 200 (31), 135 (100). *Exact Mass* calcd. for $C_{14}H_{16}O$: 200.1201; found: 200.1205.

*Hydrogenation of **28**a. Formation of **29***

A solution of triene ***28a*** (0.036 g, 0.18 mmol) in ethyl acetate (10 mL) was hydrogenated over 5% palladium on carbon (0.008 g) at atmospheric pressure until uptake of hydrogen ceased. The mixture was filtered through Celite and concentrated to give **29** (tetrahydro-***28a***) as an oil; ms *m/z*: 204 (M; 22), 162 (98), 133 (100).

*Hydrogenation of acetate **19**. Formation of **30***

A stirred mixture of acetate **19** (4.46 g, 17.0 mmol) and 10% palladium on carbon (0.22 g) in ethyl acetate (200 mL) was hydrogenated at atmospheric pressure until no more hydrogen was taken up. The solution was filtered through Celite and concentrated to give **30** (4.40 g, 98%) as a solid, which was recrystallized from acetone/hexanes; mp 76–78°C. *Anal.* calcd. for $C_{15}H_{20}O_4$: C 68.16, H 7.63; found: C 68.31, H 7.63.

*Reduction of **30** with zinc amalgam. Formation of enone **31***

The amalgam was prepared as described above by adding zinc dust (44.0) to mercuric chloride (3.55 g, 13.1 mmol) in water (150 mL) containing concentrated hydrochloric acid (4.4 mL). To the freshly prepared amalgam was added water (60.0 mL) and concentrated hydrochloric acid (2.23 mL, 26.8 mmol). The stirred mixture was chilled (ice bath) and a solution of the acetate **30** (2.98 g, 11.3 mmol) in acetone (40 mL) was added. The cooling bath was removed and the reaction mixture was stirred vigorously for 30 min. The reaction mixture was filtered and the amalgam was washed with acetone (25 mL). The combined liquid phases were concentrated and enone **31** was recovered (2.00 g, 86%) as an oil from the resulting solution by multiple extraction with dichloromethane followed by concentration. *Exact Mass* calcd. for $C_{13}H_{18}O_2$: 206.1307; found: 206.1303.

*Addition of vinyllithium to **31**. Formation of **32***

To a stirred solution of vinyl bromide (2.1 mL, 30 mmol) in ether (20 mL) under argon cooled in a Dry Ice/acetone bath was added dropwise 1.7 M *tert*-butyllithium (5.88 mL, 10 mmol). After 70 min a solution of ketone **31** (0.538 g, 2.56 mmol) in ether (40 mL) was added slowly. The Dry Ice/acetone bath was removed and replaced with a Dry Ice/carbon tetrachloride bath and the mixture was stirred for 1 h. The Dry Ice/acetone bath was restored and after 5 min acetic acid (2.06 mL, 46 mmol) was added. The cooling bath was removed after the reaction mixture had been stirred for 0.5 h and, when the temperature of the solution was between −20 and 0°C, saturated aqueous sodium bicarbonate (10 mL) was added. The aqueous layer was extracted with ether and the combined organic phases were dried (Na_2SO_4). Removal of the solvent gave **32** as an oil (0.40 g), which was used without further purification.

*Hydrolysis of **32**. Formation of **33***

Attempted purification of the above product **32** by chromatography on silica gel with elution with ethyl acetate/hexanes led to the formation of dienone **33** as an oil. *Exact Mass* calcd. for $C_{14}H_{18}O$: 202.1353; found: 202.1339.

*Diels–Alder reaction of **33** and dimethyl acetylenedicarboxylate. Formation of **39***

A mixture of dienone **33** (0.176 g, 0.87 mmol) and dimethyl acetylenedicarboxylate (0.214 mL, 1.74 mmol) in benzene (10 mL) was sealed in a glass-lined stainless steel reaction vessel with a Teflon-lined bronze screw-cap and heated for 15 h at 95°C. Solvent and unconsumed dienophile were removed under high vacuum to give a mixture of compounds, which were separated on a preparative tlc plate with elution with 30% ethyl acetate in hexanes. The fraction with R_f 0.3–0.4 was collected to give **34** (0.03 g, 10%) as an oil; ir λ_{max}: 5.77, 5.89 μm; ^{1}H nmr δ: 1.0–2.8 (m, 11H), 1.37 (s, 3H), 3.85 (s, 3H), 3.95 (s, 3H), 7.39 (d, *J* = 8 Hz, 1H), 8.10 (d, *J* = 8 Hz, 1H). *Exact Mass* calcd. for $C_{20}H_{22}O_5$: 342.1461; found: 342.1450.

*Torgov reaction of **32** and 2-methyl-1,3-cyclopentanedione (**5**). Formation of **35**, **36**, and **37***

(i) In the presence of Triton B

To a mixture of crude allylic alcohol **32** (0.23 g, 1.0 mmol) and dione **5** (0.171 g, 1.5 mmol) in toluene (30 mL) was added 40% methanolic Triton B (55 μL; 0.1 mmol). The mixture was boiled gently under reflux for 15 h, cooled, and then washed with aqueous 5% potassium hydroxide (5 mL) and water (5 mL). After concentration the residual reaction product was chromatographed (silica gel, 30% ethyl acetate in hexanes) to give first dienol ether **35** as an oil (0.060 g, 18%) with R_f 0.48.

Trione **36** was next eluted as an oil (0.082 g, 26%) with R_f 0.16. *Exact Mass* calcd. for $C_{20}H_{26}O_3$: 314.1882; found: 314.1841.

The third component, **37**, of the reaction mixture was the most polar fraction; it was recovered as an oil (0.042 g, 14%); ir λ_{max}: 2.89 (w), 5.81, 5.98 μm; ^{1}H nmr δ: 1.1–2.6 (m, 13H), 1.14 (s, 3H), 1.18 (s, 3H), 2.78 (s, 4H), 3.22 (m, 1H, OH), 4.04 (d, *J* = 7 Hz, 1H), 5.81 (br s, 1H). *Exact Mass* calcd. for $C_{20}H_{26}O_4$: 330.1831; found: 330.1824.

(ii) In the absence of Triton B

To a mixture of crude allylic alcohol **32** (0.508 g, 2.17 mmol) and dione **5** (0.359 g, 3.2 mmol) were added dry *tert*-butyl alcohol (4 mL) and dry xylene (4 mL) and the mixture was boiled under reflux for 40 h under argon. The reaction mixture was cooled, diluted with ether, and washed with aqueous 5% potassium hydroxide. The organic solution was dried (Na_2SO_4) and the solvent was evaporated to afford a thick, pale yellow oil (0.620 g, 91%). Purification by preparative thin-layer chromatography with elution with hexane/ethyl acetate (7:3 v/v) gave **36** (R_f 0.16; 0.500 g, 73%).

*Acetylation of **37**. Formation of **37**-acetate*

A mixture of alcohol **37** (0.20 g, 0.605 mmol) and acetic anhydride (5 mL) in pyridine (10 mL) was treated with a crystal of 4-(dimethylamino)pyridine and was stirred for 15 h. Unconsumed acetic anhydride and pyridine were removed under high vacuum and the resulting oil was dissolved in dichloromethane. The solution was washed with dilute hydrochloric acid and concentrated to give ***37-acetate*** as an oil; ir λ_{max}: 5.77 μm; ^{1}H nmr δ: 1.2–2.7 (m, 13H), 1.19 (s, 6H), 2.10 (s, 3H), 2.79 (s, 4H), 5.11 (d, *J* = 7 Hz, 1H), 5.81 (br s, 1H).

*Hydrogenation of **36**. Formation of **38***

A mixture of enone **36** (0.314 g, 1.00 mmol) and 10% palladium on carbon (0.02 g) in ethanol (100 mL) was hydrogenated at atmospheric pressure until the calculated amount of hydrogen had been taken up (16 h). The catalyst was removed by filtration through Celite and the solution was concentrated to give **38** in quantitative yield as an oil; ms *m/z*: 316 (M; 23), 204 (100).

*Base treatment of **38**. Formation of (1β,4β,5β,8α,9β,10β,13β,14β)-14-hydroxy-1,4-methanoandrostane-7,17-dione[9] (**39**)*

To a solution of **38** (0.316 g, 1.00 mmol) in methanol (150 mL) was added potassium hydroxide (0.060 g, 1.1 mmol) and the mixture was heated to 75°C for 15 h under argon. The solvent was evaporated and water was added to the residue. The mixture was extracted with benzene. The combined extracts were washed with aqueous potassium bicarbonate, dried, and concentrated to give **39** as a white solid (0.316 g, 100%), mp 209–211°C, which was crystallized from methanol; mp 210–212°C. *Anal.* calcd. for $C_{20}H_{28}O_3$: C 75.91, H 8.92; found: C 75.65, H 9.02.

[9]Formally, compounds **39–41** and **45** should be named as cyclopentaphenanthrene derivatives. We consider it preferable, however, to expand the meaning of "androstane" to include variations in configuration at all of its chiral centers and to use this expanded version as a basis for naming steroids of the type synthesized in the present work.

Can. J. Chem. Downloaded from www.nrcresearchpress.com by 196.1.178.254 on 09/07/12
For personal use only.

Dehydration of ***39***

*(i) Formation of (±)-(1β,4β,5β,9β,10β,13β)-1,4-methanoandrost-8(14)-ene-7,17-dione (**40**)*

A solution of **39** (0.143 g, 0.45 mmol) and anhydrous *p*-toluenesulfonic acid (0.0774 g, 0.45 mmol) in dry benzene (15 mL) was boiled at reflux under argon for 24 h. The reaction mixture was cooled to room temperature and poured into water (10 mL). The layers were separated and the aqueous phase was extracted with ether (3 × 10 mL). The combined organic layers were washed with water (3 × 10 mL), saturated aqueous sodium bicarbonate (10 mL), and saturated aqueous sodium chloride (10 mL). The solution was dried (Na_2SO_4) and concentrated to give a thick semisolid residue (0.130 g), which on trituration with ether gave **40** as a white solid (0.060 g), mp 153–154°C. Preparative thin-layer chromatography on silica of the solid from the ethereal extract with hexanes/ethyl acetate (7:3 v/v) as eluent provided additional product (0.21 g; total yield 60%), mp 153–154°C. Recrystallization from aqueous methanol afforded **40** as white crystals, mp 155–156°C. *Anal.* calcd. for $C_{20}H_{26}O_2$: C 80.49, H 8.78; found: C 80.25, H 9.08.

A small amount of a second product could be detected in the ^1H nmr spectrum of the crude product. This was subsequently identified as **41** (*vide infra*).

*(ii) Formation of **40** and (±)-(1β,4β,5β,8α,9β,10β,13β,14β)-1,4-methanoandrost-15-ene-7,17-dione (**41**)*

A solution of **39** (0.100 g, 0.316 mmol) and anyhydrous *p*-toluenesulfonic acid (0.172 g, 1.00 mmol) in dry benzene (15 mL) was boiled under reflux for 48 h under argon. Work-up as in (*i*) gave a pale yellow semisolid residue (0.090 g). Purification by preparative thin-layer chromatography on silica with elution with hexanes/ethyl acetate (7:3 v/v) gave **41** (R_f 0.31), which was crystallized from aqueous methanol to give white needles (0.045 g, 48%), mp 170–171°C. *Anal.* calcd. for $C_{20}H_{26}O_2$: C80.49, H 8.78; found: C 80.49, H 8.80.

Compound **40** (0.035 g, 37%) crystallized out from the mother liquor on standing at room temperature as white crystals, mp 154–155°C. The ir and nmr spectra of this product were identical with those of the product that was obtained by procedure (*i*).

*Acid treatment of **36**. Formation of (±)-(1β,4β,5β,10β,13β,14β)-1,4-methanoandrosta-8,15-diene-7,17-dione (**45**)*

A solution of **36** (0.50 g, 1.59 mmol) and anhydrous *p*-toluenesulfonic acid (0.11 g) in dry benzene (50 mL) was boiled under reflux for 24 h under argon. After cooling to room temperature, the solution was poured into water (25 mL). The aqueous phase was extracted with ether (3 × 20 mL). The combined organic layers were washed with water (3 × 15 mL), saturated aqueous sodium bicarbonate (20 mL), and saturated aqueous sodium chloride (15 mL). The solution was dried (Na_2SO_4) and evaporated to give a light brown oil (0.43 g). Preparative thin-layer chromatography on silica with hexanes/ethyl acetate (7:3 v/v) as eluent gave crystalline **45** (R_f 0.28; 0.25 g, 53%), mp 147–149°C. Recrystallization from methanol gave **45** as white crystals, mp 149–150°C. *Anal.* calcd. for $C_{20}H_{24}O_2$: C 81.04, H 8.16; found: C 80.69, H 8.29.

Acknowledgment

We thank the Natural Sciences and Engineering Research Council of Canada for support of this work.

1. (*a*) F. M. Winnik and P. Yates. Magn. Reson. Chem. **23**, 822 (1985); (*b*) S. P. Douglas, J. F. Sawyer, and P. Yates. Tetrahedron Lett. **26**, 5955 (1985).
2. P. Yates and F. M. Walliser. Can. J. Chem. **54**, 3508 (1976).
3. P. Yates and F. M. Winnik. Can. J. Chem. **59**, 1641 (1981).
4. P. Yates and F. M. Winnik. Can. J. Chem. **63**, 2501 (1985).
5. S. N. Ananchenko, V. Ye. Limanov, V. N. Leonov, V. N. Rzheznikov, and I. V. Torgov. Tetrahedron, **18**, 1335 (1963); S. N. Ananchenko and I. V. Torgov. Tetrahedron Lett. 1553 (1963).
6. I. N. Nazarov, S. N. Ananchenko, and I. V. Torgov. Izv. Akad. Nauk SSR, Otd. Khim. 103 (1959); Chem. Abstr. **59**, 16088i (1959); I. N. Nazarov, I. V. Torgov, and G. N. Verkholetova. Dokl. Akad. Nauk SSR, **112**, 1067 (1957); Chem. Abstr. **51**, 14647d (1957).
7. C. H. Kuo, D. Taub, and N. L. Wendler. J. Org. Chem. **33**, 3126 (1968); Angew. Chem. Int. Ed. Engl. **4**, 1083 (1965).
8. J. Ruppert, U. Eder, and R. Wiechert. Chem. Ber. **106**, 3636 (1973).
9. A. R. Daniewski, P. S. White, and Z. Valenta. Can. J. Chem. **57**, 1397 (1979).
10. R. B. Woodward, F. Sondheimer, D. Taub, K. Heusler, and W. M. McLamore. J. Am. Chem. Soc. **74**, 4223 (1952); J. N. Ashley. J. Chem. Soc. 1471 (1937); S. Heitz and R. Heitz. C. R. Seances Acad. Sci. Ser. C: **261**, 3158 (1965).
11. G. Mehta, D. S. Reddy, and A. V. Reddu. Tetrahedron Lett. **25**, 2275 (1984).
12. G. W. K. Cavill and R. J. Quinn. Aust. J. Chem. **26**, 595 (1973).
13. S. P. Douglas. Ph.D. thesis. University of Toronto (1986).
14. A. M. M. Hossain, D. N. Kirk, and G. Mitra. Steroids, **27**, 603 (1976).
15. H. O. House and R. G. Carlson. J. Org. Chem. **29**, 74 (1964); S. Danishefsky, P. Schuda, and K. Kato. J. Org. Chem. **41**, 1081 (1976).
16. L. F. Fieser. J. Am. Chem. Soc. **75**, 4377 (1953); R. B. Woodward, F. E. Bader, H. Bickel, A. J. Frey, and R. W. Kierstead. Tetrahedron, **2**, 1 (1958).
17. D. A. Skoog and D. M. West. Fundamentals of analytical chemistry. 3rd ed. Holt, Rinehart and Winston, New York, NY. 1976. p. 782.
18. A. I. Scott. Interpretation of the ultra-violet spectra of natural products. Pergamon Press, Oxford. 1964. Chap. 2.
19. J. Das, R. A. Dickinson, M. Kakushima, G. M. Kingston, G. R. Reid, Y. Sato, and Z. Valenta. Can. J. Chem. **62**, 1103 (1984).
20. T. B. Windholz, J. H. Fried, H. Schwam, and A. A. Patchett. J. Am. Chem. Soc. **85**, 1707 (1963).
21. G. Nomine, G. Amiard, and V. Toreli. Bull. Soc. Chim. Fr. 3664 (1968); J. A. Adamcik and E. J. Miklasiewicz. J. Org. Chem. **28**, 336 (1963); F. Kido, K. Tsutsumi, R. Maruta, and A. Yoshikoshi. J. Am. Chem. Soc. **101**, 6420 (1979).
22. F. Kido, Y. Noda, T. Maruyama, C. Kabuto, and A. Yoshikoshi. J. Org. Chem. **46**, 4264 (1981).
23. K. Narasaka, K. Soai, and T. Mukaiyama. Chem. lett. 1223 (1974); K. Narasaka, K. Soai, Y. Aikawa, and T. Mukaiyama. Bull. Chem. Soc. Jpn. **49**, 779 (1976).
24. A. Bax and G. A. Morris. J. Magn. Reson. **42**, 501 (1981); K. Hallenga and G. Van Binst. Bull. Magn. Reson. **2**, 343 (1980).
25. S. P. Douglas, J. F. Sawyer, and P. Yates. Acta Crystallogr. Sect. C: Cryst. Struct. Commun. **43**, 1372 (1987).
26. A. D. Cross. Introduction to practical infrared spectroscopy. 2nd ed. Butterworths, London. 1964. p. 64.

The structures and stabilities of singlet and triplet dithiatriazines: a computational study

R. E. HOFFMEYER, W.-T. CHAN, J. D. GODDARD, AND R. T. OAKLEY

Guelph–Waterloo Centre for Graduate Work in Chemistry, Department of Chemistry and Biochemistry, University of Guelph, Guelph, Ont., Canada N1G 2W1

Received February 25, 1988

R. E. HOFFMEYER, W.-T. CHAN, J. D. GODDARD, and R. T. OAKLEY. Can. J. Chem. **66**, 2279 (1988).

Ab initio molecular orbital and Møller–Plesset perturbation theory calculations have been carried out on two model dithiatriazines RCN_3S_2 (R = H, NH_2). With geometry optimization and the inclusion of electron correlation both of these dithiatriazines are predicted to be ground state singlets. Both molecules have low-lying triplet excited states, with energy gaps of 6.6 (R = H) and 13.0 (R = NH_2) kcal mol^{-1}. The singlet dithiatriazines distort from high (C_{2v}) to low (C_s) symmetry, and these changes are important in determining the relative energies of the singlet and triplet molecules. The structural distortions experienced by these molecules are related to Hartree–Fock and Jahn–Teller instabilities in other thiazene heterocycles.

R. E. HOFFMEYER, W.-T. CHAN, J. D. GODDARD et R. T. OAKLEY. Can. J. Chem. **66**, 2279 (1988).

On a effectué des calculs d'orbitales moléculaires *ab initio* et d'autres calculs suivent la théorie des perturbations de Møller–Plesset sur deux dithiatriazines modèles, RCN_3S_2 (R = H, NH_2). Si on introduit une optimisation de la géométrie et qu'on inclut une corrélation électronique, les calculs prédisent que, dans leur état fondamental, chacune de ces dithiatriazines existera sous forme de singulet. Pour chacune de ces molécules, les états triplets excités sont à des niveaux relativement bas; les différences d'énergies sont respectivement de 6,6 (R = H) et de 13,0 (R = NH_2) kcal mol^{-1}. Les dithiatriazines à l'état singulet adoptent des symétries déformées allant d'élevée (C_{2v}) à basse (C_s); ces changements sont importants lorsqu'on détermine les énergies relatives des molécules dans les états singulet et triplet. On a établi une corrélation entre les distorsions de structure que subissent ces molécules et les instabilités de Hartree–Fock et de Jahn–Teller observées dans d'autres thiazènes.

[Traduit par la revue]

Introduction

Since the inception of the Hückel $4n + 2$ rule (1) chemists have been intrigued by molecular systems that violate it. Traditionally the concepts of aromaticity and anti-aromaticity (2) have been associated with organic chemistry, but the ideas are no less relevant to inorganic frameworks. Studies of the chemistry of heterocyclic thiazenes have, in particular, provided considerable conceptual and experimental information as to the relative stabilities, both kinetic and thermodynamic, of $4n$ and $4n + 2$ π-systems constructed from inorganic units. The empirical analyses of binary sulphur–nitrogen (SN) rings by Banister in the early 1970's (3) stressed the importance of the Hückel rule as a guideline for molecular stability, and correctly predicted the existence of the planar 10π-electron $S_3N_3^-$ anion. The degree of aromatic character in this, and other binary SN rings, with both $4n + 2$ and $4n$ π-electron counts, has recently been probed by Gimarc, Jurić, and Trinajstić (4), who extended the concept of Dewar resonance energies (5) to these "electron-rich" π-systems.

While adherence to the $4n + 2$ rule is the norm in SN chemistry, there are both old and new examples of exceptions. The cage-like structure of S_4N_4 (6) itself has long been used to demonstrate, in a somewhat *a posteriori* way, one possible fate of a high symmetry anti-aromatic (12π) system, i.e. to distort to lower symmetry (7). Heterocycles of the general formula EN_3S_2 have also attracted attention. Generically, these dithiatriazine rings (E = R_2P, SO_2^-, RC) can all be considered as derivatives of the anti-aromatic 8π-electron $S_3N_3^+$ cation. *Ab initio* molecular orbital (MO) studies have confirmed a triplet ground state for this latter species (in D_{3h} symmetry), by virtue of the "high spin" occupancy of the degenerate e'' orbitals (see Fig. 1) (8). This degeneracy is lifted by the replacement of one (charged) sulphur atom with an isoelectronic fragment E; the two e'' orbitals transform, in C_{2v} symmetry, as b_1 and a_2 representations. With an electropositive perturbation the b_1 MO energy is raised relative to the a_2, which is nodal at the heteroatom site. With large perturbations, as expected for E = R_2P **1** (9) and SO_2^- **2** (10), the b_1–a_2 splitting is sufficient to favour a "low spin" singlet ground state. In the solid state these compounds are monomeric, albeit with structures quite distorted from ideal C_{2v} symmetry; their intense low energy absorption bands (*ca.* 550 nm) have been assigned to a b_1–a_2 excitation.

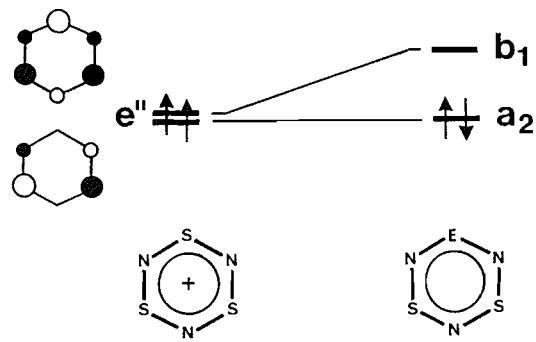

FIG. 1. Splitting of the degenerate e'' orbitals of $S_3N_3^+$ by the incorporation of a less electronegative atom E, and its effect on ground state multiplicity.

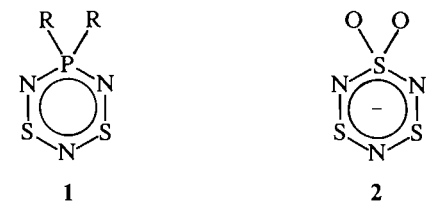

1 **2**

In the case of an S^+/CR replacement, the orbital electronegativity difference is less acute, and the energetic separation between the high (triplet) and low (singlet) spin states cannot be anticipated readily from purely one-electron arguments. MNDO calculations on a variety of model RCN_3S_2 derivatives **3** (R = H, NH_2, F, Ph) favour the triplet by 12–15 kcal mol^{-1} (11).

Can. J. Chem. Downloaded from www.nrcresearchpress.com by 196.1.178.254 on 09/07/12
For personal use only.

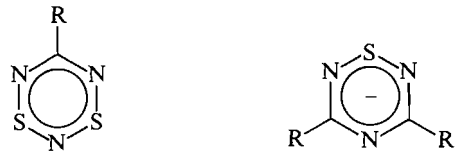

3 4

Interestingly, analogous calculations on the isoelectronic thiatriazine anion $H_2C_2N_3S^-$, **4** (R = H) predict the singlet to be considerably more stable than the triplet (by 28 kcal mol^{-1}) (12). Hartree–Fock–Slater (HFS) results on **3** have been far from definitive (13); convergence to a singlet ground state could only be achieved for R = NH_2, and no data on the corresponding triplet was provided.

Efforts to prepare discrete RCN_3S_2 species have had mixed success. The reduction of $RCN_3S_2Cl_2$ (R = CF_3 (14) and NMe_2 (13*b*)) has afforded red solid materials with the anticipated (for **3**) elemental and/or mass spectral analysis, but no structural or molecular weight data were reported. The reduction of $PhCN_3S_2Cl_2$, **5**, also leads to a compound with the correct empirical composition (eq. [1]) (11). In this case, however, the structure of the product has been established crystallographically as the cofacial dimer **6**, in which two $PhCN_3S_2$ are fused through two long S---S contacts (mean length 2.527 Å).

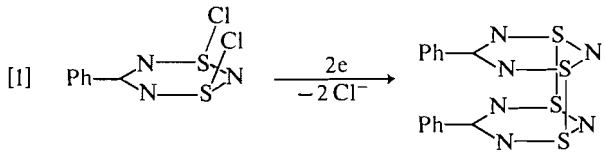

[1]

5 6

As part of ongoing studies of heterocyclic thiazenes, in particular the electronic and molecular structures of $4n$ π-systems, we have been anxious to remove some of the uncertainties surrounding the electronic structures of monomeric dithiatriazines, **3**. In the present paper we provide the results of a series of *ab initio* MO and electron correlation calculations, the latter using Møller–Plesset (MP) perturbation theory, on two model compounds **3** (R = H and NH_2). Our purpose has been to study the relative stabilities of the singlet and triplet states of these models, and also to ascertain what kind of internal structural changes might alter the energetic balance between the two multiplicities.

Computational methods

Ab initio calculations were carried out with the MONSTERGAUSS (15) version of GAUSSIAN80 adapted to the UNIX operating system of a SUN 3/160 workstation and with GAUSSIAN82 (16) running on a VAX 11/785. Geometries for the lowest closed shell singlet and triplet states were optimized at the SCF level (UHF for the triplets) employing gradient methods. The STO-3G* basis set (17) was used in the geometry optimizations as it has been found to give reasonable geometries for such molecules as $S_3N_3^-$ (18) and for cyclic phosphazenes (19). Stationary point geometries were checked as to their nature (minima, transition structures) by analytic evaluation of the harmonic vibrational frequencies. The effects of basis set extension were examined by use of the 3-21G* basis (20) at the STO-3G* geometries. The effects of electron correlation which are expected to be crucial in determining the relative stabilities of any pair of singlet and triplet species were included by Møller–Plesset perturbation theory through third order (MP2, MP3) (21, 22). Tests of stability of the STO-3G*

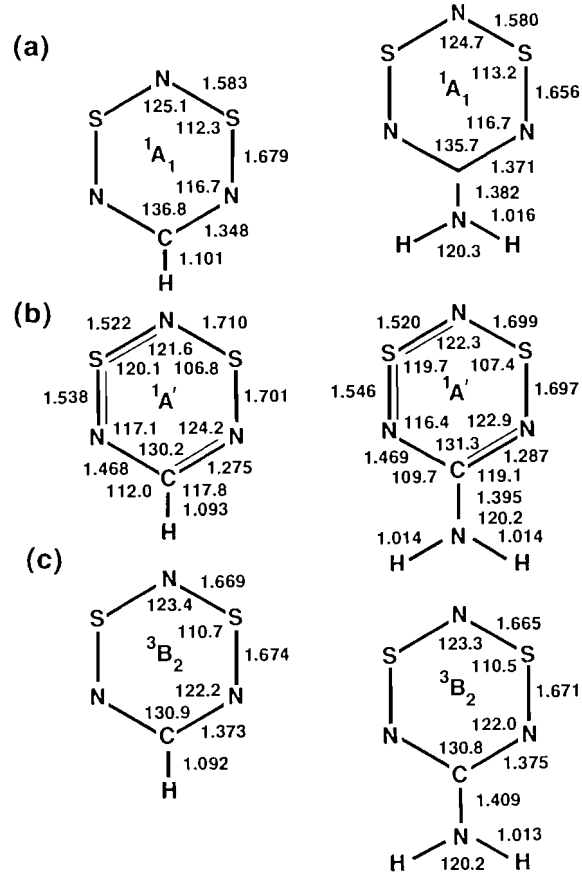

FIG. 2. STO-3G* SCF optimized geometries of HCN_3S_2 and $H_2NCN_3S_2$: (*a*) C_{2v} $^1A_1$, (*b*) C_s $^1A'$, (*c*) C_{2v} $^3B_2$.

wavefunctions for the singlet state H-substituted dithiatriazine, **3** (R = H) at the STO-3G* optimized equilibrium geometries (C_{2v} and C_s) were performed using the codes of Seeger and Pople (23) available as a part of GAUSSIAN82.

Results

Geometries and vibrational frequencies

The STO-3G* SCF optimized geometries for **3** (R = H and NH_2) are presented in Fig. 2. In $S_3N_3^-$, assuming D_{3h} symmetry, the STO-3G* basis predicts an SN distance of 1.616 Å (18), in very reasonable agreement with experimental values (range 1.584–1.626 Å) (24). Thus, although the optimized geometries for **3** (R = H and NH_2) originate from relatively small basis sets, they can be inferred to be reasonably accurate relative to the (unknown) experimental geometries of monomeric dithiatriazines.

The harmonic vibrational frequencies for the dithiatriazines are reported in Tables 1 and 2. These frequencies are not so much predictions of experimental results as they are conclusive demonstrations that at the STO-3G* SCF level both of the singlet dithiatriazines are unstable to geometrical distortions (note the imaginary b_2 frequencies) from C_{2v} to C_s nuclear frameworks. In the case of singlet $H_2NCN_3S_2$ (C_{2v}), a second imaginary frequency (b_1) is associated with pyramidalization of the tricoordinate nitrogen of the NH_2 group. Such a distortion is plausible but is not of energetic consequence. Further geometry optimization was thus performed with a planarity constraint.

Clearly the most interesting geometrical results are the rather

Can. J. Chem. Downloaded from www.nrcresearchpress.com by 196.1.178.254 on 09/07/12
For personal use only.

Can. J. Chem. Downloaded from www.nrcresearchpress.com by 196.1.178.254 on 09/07/12
For personal use only.

TABLE 1. STO-3G* SCF harmonic vibrational frequencies (cm^{-1}) for HCN_3S_2

ν	S_0 (C_{2v})		S_0 (C_s)		T_1 (C_{2v})	
1	a_1	3603	a'	3653	a_1	3665
2	b_2	1617	a'	1962	b_2	1573
3	a_1	1386	a'	1578	b_2	1361
4	b_2	1356	a'	1445	a_1	1347
5	b_1	1106	a'	1325	b_2	1092
6	a_1	976	a''	1033	b_1	901
7	a_1	892	a'	1008	a_1	880
8	b_2	861	a'	908	b_2	797
9	a_1	812	a'	818	a_1	755
10	a_1	518	a'	762	a_1	689
11	b_2	501	a'	540	b_2	460
12	b_1	410	a''	517	a_1	458
13	b_1	287	a'	454	b_1	450
14	a_2	75	a''	332	a_2	154
15	b_2	2019i	a''	117	b_1	59

TABLE 2. STO-3G* SCF harmonic vibrational frequencies (cm^{-1}) for $H_2NCN_3S_2$

ν	S_0 (C_{2v})		ν	S_0 (C_{2v})	
1	b_2	4288	12	b_1	690
2	a_1	4051	13	a_2	626
3	a_1	1838	14	b_2	525
4	a_1	1586	15	a_1	484
5	b_2	1434	16	b_2	399
6	a_1	1241	17	b_1	370
7	b_2	1235	18	b_1	125
8	a_1	926	19	a_2	18
9	b_2	906	20	b_2	1472i
10	a_1	858	21	b_1	359i
11	a_1	708			

large changes in ring bond lengths which accompany the distortions of both the H- and NH_2-substituted singlet structures. The C_s geometries are highly suggestive of two SN double bonds, two SN single bonds, one conjugated CN single, and one CN double bond around the ring, i.e. reminiscent of the valence bond formulation **7** (eq. [2]). In the C_{2v} structures the

[2] 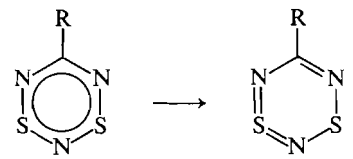

3 7

CN distances must be equal by symmetry and, at 1.348 or 1.371 Å are nicely intermediate between the distances in the C_s form (H, 1.468, 1.275, mean 1.372 Å; NH_2, 1.469, 1.287, mean 1.378 Å). The short SN distances of 1.52 to 1.54 Å and the long distances of 1.70 to 1.71 Å in the C_s minima average to ca. 1.67 while the SN distances in the C_{2v} transition structures are 1.58 Å to the unique nitrogen and 1.656 or 1.679 Å on the sides.

The triplet electronic state C_{2v} minima have geometries which are somewhat "looser" (longer SN and CN ring bond lengths) than the singlet C_{2v} structures. The bond distances in the H- and NH_2-substituted triplet models are remarkably similar.

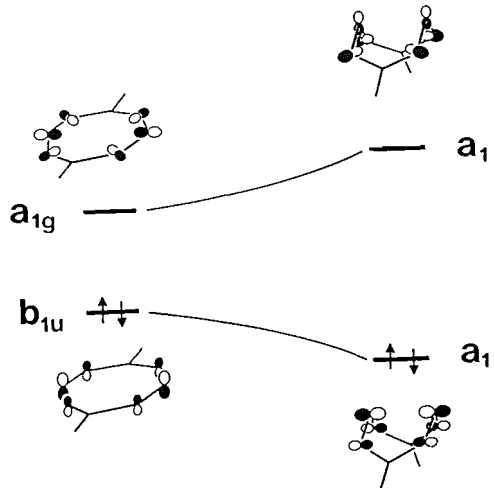

FIG. 3. The a_{1g}–b_{1u} orbital mixing that drives the second order Jahn–Teller distortion of dithiatetrazocines from D_{2h} to C_{2v} symmetry.

The singlet–triplet energy gap in dithiatriazines

Table 3 summarizes the total energies and energies relative to the C_s singlet minima for both dithiatriazine models at four levels of computation, STO-3G* SCF, 3-21G* SCF, 3-21G* MP2, and 3-21G* MP3. The geometries correspond to those specified in Figs. 2 and 3, i.e. STO-3G* SCF optimized structures.

Basis set limitations and truncation of the perturbation series at third order notwithstanding, the localized (C_s) singlet is more stable than the delocalized (C_{2v}) version. The relative energies vary with the level of calculation, the C_s form being favoured by 13 to 18 kcal mol^{-1} for R = H and by 7 to 11 kcal mol^{-1} for R = NH_2. The best predictions are 14.3 (R = H) and 11.3 (R = NH_2) kcal mol^{-1} for the exothermicities of the distortions from C_{2v} to C_s symmetry. These differences were slightly reduced, e.g. from 14.3 to 11.4 kcal mol^{-1} for R = H, when the STO-3G* harmonic frequencies were used to calculate the zero point energies of the C_{2v} and C_s forms.

Of considerable interest is the ground state multiplicity of simple monomeric dithiatriazines. With the inclusion of electron correlation by MP2 and MP3 calculations, which is essential in comparing states with different numbers of unpaired electrons, both dithiatriazine models are predicted to be singlet stable. The singlet/triplet separation is 6.6 kcal mol^{-1} for R = H (4.0 kcal mol^{-1} if zero point energies are used), and increases to 13.0 kcal mol^{-1} for R = NH_2; the difference can be attributed to the π-donor properties of the NH_2 group, which lead to conjugative destabilization of the b_1 MO (Fig. 1) and hence double occupancy of the a_2 MO.

Discussion

The term "electron-rich", which pervades many discussions of the electronic structures of heterocycles comprised of catenated —S=N— units, emphasizes the importance of π-electron count on overall molecular stability; increased occupation of anti-bonding π^*-levels reduces overlap populations. At the same time π-electron repulsion is increased, but since the extent of these interactions is not easily extracted from the total electronic energy, explicit discussion of their involvement tends to be avoided. There is another, also often overlooked, aspect of the electronic structures of SN heterocycles that contributes to their fragility, and that is the extent of electron repulsion between the in-plane non-bonding orbitals, the "lone pairs" on sulphur and nitrogen. The destabilizing influence of such lone

TABLE 3. Total energies (Hartree au) and relative energies (kcal mol^{-1}) for HCN_3S_2 and $H_2NCN_3S_2$ at various levels of calculation; all calculations are at STO-3G* SCF level optimized geometries

	STO-3G* SCF	3-21G* SCF	3-21G* MP2	3-21G* MP3
		Total energies		
HCN_3S_2				
$^1A_1$	−985.55023	−991.81851	−992.49503	−992.49189
$^1A'$	−985.57913	−991.83846	−992.52270	−992.51470
$^3B_2$	−985.63948	−991.88435	−992.48079	−992.50417
$H_2NCN_3S_2$				
$^1A_1$	−1039.89020	−1046.57532	−1047.35744	−1047.35372
$^1A'$	−1039.90723	−1046.58624	−1047.37180	−1047.37180
$^3B_2$	−1039.95831	−1046.61895	−1047.33041	−1047.35102
		Relative energies		
HCN_3S_2				
$^1A_1$	+18.1	+12.5	+17.4	+14.3
$^1A'$	0	0	0	0
$^3B_2$	−37.9	−28.8	+26.3	+6.6
$H_2NCN_3S_2$				
$^1A_1$	+10.7	+6.9	+9.0	+11.3
$^1A'$	0	0	0	0
$^3B_2$	−32.1	−20.5	+26.0	+13.0

pair interactions in molecules constructed from the later first and second row elements (e.g. nitrogen halides) has long been recognized (25). The large endothermic heats of formation of SN compounds, e.g. 110 kcal mol^{-1} for S_4N_4 (26), are direct manifestations of this effect. It is prudent, therefore, to remember that thiazine heterocycles are σ-electron-rich as well as π-electron-rich; the associated electronic instabilities in both systems can influence molecular structure.

Frequently, however, it is more appealing to ascribe major structural changes to π-effects. The structural dichotomy observed for 1,5-dithiatetrazocines provides a useful example. These compounds can be planar, e.g. **8**, or puckered, e.g. **9**,

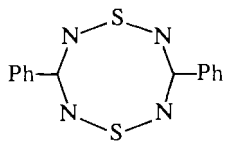

8

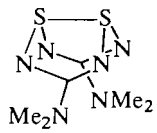

9

depending on the nature of the exocyclic ligand (27). The distortion is conveniently rationalized as being driven by a second order Jahn–Teller (SOJT) instability (28) in the π system. Accordingly ring puckering is precipitated by the destabilizing influence of π-donor ligands at the 1,5-positions (29), and consequent mixing of the high lying π-HOMO with a low-lying virtual σ-orbital (Fig. 3) (30).

In the case of the dithiatriazine system HCN_3S_2, the observed slippage from C_{2v} into C_s symmetry (eq. [2]) maintains the σ/π distinction. The interpretative problem that arises is to decide whether the symmetry lowering is driven by instabilities in the σ-system, the π-system, or a combination of both. These issues have been highlighted by several recent papers by Bénard, Laidlaw, and Paldus (31) in which they have probed the symmetry breaking (32) of the Hartree–Fock (HF) wavefunctions of several binary rings (e.g. $S_3N_3^-$, $S_4N_4^{2+}$, S_2N_2) when all the SN bonds are stretched to a length about 20% greater than their equilibrium values. They concluded that the mixing of occupied and unoccupied σ-orbitals was at least as important as the more easily anticipated π*/π* process.

As in the dithiatetrazocine system noted above, the π-instability rationalization in **3** is conceptually appealing. The conventional SOJT description for the C_{2v} to C_s distortion involves a mixing of the frontier π*-orbitals, specifically the a_2 HOMO and b_1 LUMO to yield two a'' orbitals (Fig. 1). This view is supported by analysis of the changes in these two orbitals as the distortion proceeds (Fig. 4). Of particular note is (*i*) the large change in the orbital eigenvalues as the two orbitals mix, i.e. $\Delta < \Delta'$, and (*ii*) the change in the eigenvector coefficients, in particular those of the lower orbital, whose bonding and antibonding properties reflect, broadly speaking, the bond localization apparent in the valence bond representation **7**.

In order to relate our results to those of Bénard, Laidlaw, and Paldus (31), we tested the STO-3G* HF wavefunctions of HCN_3S_2 at both the C_{2v} and C_s calculated equilibrium geometries for instabilities by following the methods of Seeger and Pople (23). In both geometries the wavefunctions were singlet stable. Such a result is in complete agreement with the earlier work on $S_3N_3^-$, $S_4N_4^{2+}$, and S_2N_2 (31), where the wavefunctions were always stable at the optimized *equilibrium* geometries, and showed broken symmetry solutions only when the SN bond lengths were increased.

In the light of these results the HF stability of the C_{2v} wavefunction of HCN_3S_2 was further examined by uniformly increasing all bond lengths by 20% and retesting the wavefunction. The wavefunction was still stable. In assessing the significance of this result it is important to recall from the earlier work that symmetry breaking was only observed from a high symmetry point group, i.e. D_{3h}, D_{4h}, or D_{2h}, down to C_{2v} (31). Instabilities involving a C_{2v} to C_s symmetry loss could not be induced, even at large SN separations. In the dithiatriazines studies here we have "chemically" broken the symmetry relative to $S_3N_3^+$ by introducing the CR group in place of S^+. Viewed in this way it is not surprising that a HF instability in HCN_3S_2 leading to a C_s wavefunction appears difficult to obtain.

Can. J. Chem. Downloaded from www.nrcresearchpress.com by 196.1.178.254 on 09/07/12
For personal use only.

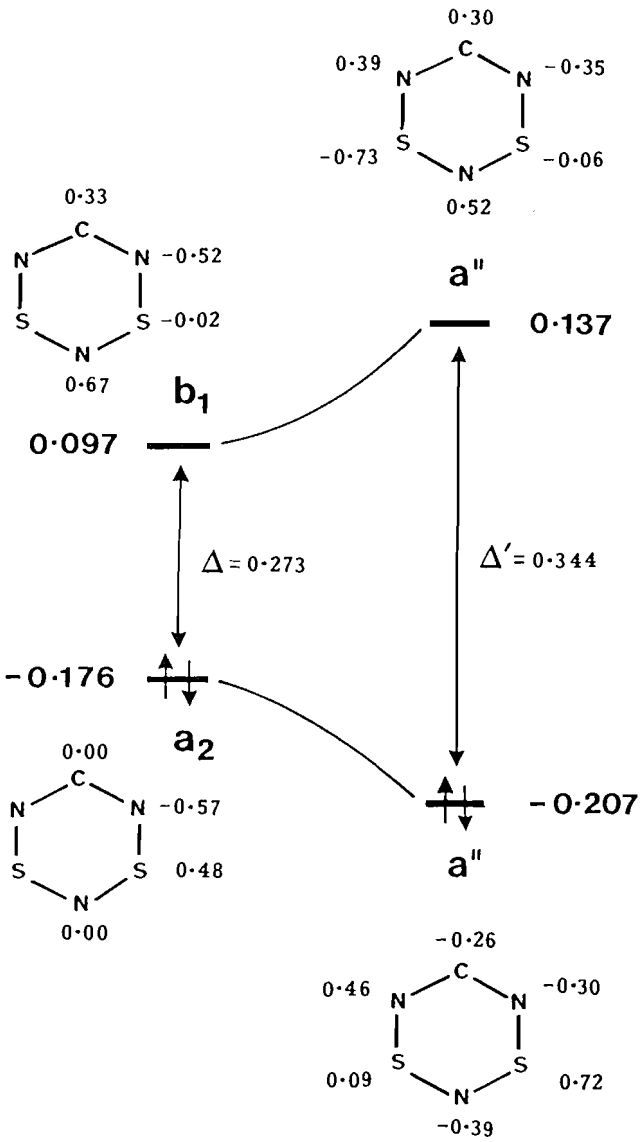

FIG. 4. Orbital energy (in Hartree au) and distribution changes in the a_2 HOMO and b_1 LUMO of HCN_3S_2 accompanying a distortion from C_{2v} to C_s symmetry. The eigenvector coefficients shown are the largest $p\pi$ components (STO-3G*).

Conclusion

Singlet C_{2v} dithiatriazines have been demonstrated to be unstable with respect to a distortion of the nuclear framework to C_s symmetry. There has been speculation that in any system a HF symmetry breaking instability in the electronic wavefunction may drive a nuclear framework distortion (33). Indeed a formal relationship between the relaxation component of the negative force constant in the SOJT distortion mechanism and the HF stability matrix has been derived (34). However, it would appear from both the results of this work and the distinctions drawn earlier (31) between HF instabilities and Jahn–Teller effects that a nuclear distortion conventionally rationalized by the SOJT model need not require a HF instability, nor does a HF instability imply a SOJT distortion.

There is, to date, no evidence for monomeric dithiatriazines **3**. The structural characterization of the dimer **6** shows that, at least for this derivative, the formation of two weak interannular S---S bonds is energetically preferred to a valence bond "slump" (10), i.e. slippage of delocalized rings **3** into the low symmetry form **7**. Such a conclusion would perhaps not be too surprising to an organic chemist; the dimerization of **3** (R = Ph) represents the fate of many strongly anti-aromatic species, i.e. to self-associate.

Acknowledgements

It is a pleasure to acknowledge several valuable discussions with Professor W. G. Laidlaw of the University of Calgary. Financial support by the Natural Sciences and Engineering Research Council of Canada (NSERC) through operating grants to J.D.G. and R.T.O. is also acknowledged.

1. E. HÜCKEL. Z. Physik, **79**, 204 (1931).
2. P. J. GARRATT. Aromaticity. Wiley Interscience, NY. 1986.
3. A. J. BANISTER. (*a*) Nature, **237**, 204 (1972); (*b*) **239**, 69 (1972).
4. B. M. GIMARC, A. JURIĆ, and N. TRINAJSTIĆ. Inorg. Chim. Acta, **102**, 105 (1985).
5. (*a*) M. J. S. DEWAR. The molecular orbital theory of conjugated systems. McGraw-Hill, New York. 1969; (*b*) R. C. HADDON. J. Am. Chem. Soc. **101**, 1722 (1979).
6. (*a*) B. SHARMA and J. DONOHUE. Acta Crystallogr. **16**, 891 (1961); (*b*) M. L. DELUCIA and P. COPPENS. Inorg. Chem. **17**, 2336 (1978).
7. R. GLEITER. J. Chem. Soc. 3174 (1970).
8. W. M. LAU, N. P. C. WESTWOOD, and M. H. PALMER. J. Am. Chem. Soc. **108**, 3229 (1986).
9. N. BURFORD, T. CHIVERS, A. W. CORDES, W. G. LAIDLAW, M. C. NOBLE, R. T. OAKLEY, and P. N. SWEPSTON. J. Am. Chem. Soc. **104**, 1282 (1982).
10. T. CHIVERS, A. W. CORDES, R. T. OAKLEY, and W. T. PENNINGTON. Inorg. Chem. **22**, 2429 (1983).
11. R. T. BOERÉ, C. L. FRENCH, R. T. OAKLEY, A. W. CORDES, J. A. J. PRIVETT, S. L. CRAIG, and J. B. GRAHAM. J. Am. Chem. Soc. **107**, 7710 (1985).
12. R. T. BOERÉ, A. W. CORDES, P. J. HAYES, R. T. OAKLEY, R. W. REED, and W. T. PENNINGTON. Inorg. Chem. **25**, 2445 (1986).
13. (*a*) O. TREU JR. and M. TRSIC. J. Mol. Struct. Theochem. **133**, 1 (1985); (*b*) T. CHIVERS, F. EDELMANN, J. F. RICHARDSON, N. R. M. SMITH, O. TREU JR., and M. TRSIC. Inorg. Chem. **25**, 2119 (1986).
14. H.-U. HÖFS, G. HARTMANN, R. MEWS, and G. M. SHELDRICK. Z. Naturforsch. **39b**, 1389 (1985).
15. M. R. PETERSON and R. A. POIRIER. MONSTERGAUSS. Department of Chemistry, University of Toronto, Toronto. 1986.
16. J. S. BINKLEY, M. FRISCH, K. RAGHAVACHARI, D. DEFREES, H. B. SCHLEGEL, R. WHITESIDE, E. FLUDER, R. SEEGER, and J. A. POPLE. GAUSSIAN82. Department of Chemistry, Carnegie–Mellon University, Pittsburgh, PA. 1983.
17. J. B. COLLINS, P. v. R. SCHLEYER, J. S. BINKLEY, and J. A. POPLE. J. Chem. Phys. **64**, 5142 (1976).
18. J. D. GODDARD. Unpublished results.
19. R. C. HADDON. Chem. Phys. Lett. **120**, 372 (1985).
20. W. J. PIETRO, M. M. FRANCL, W. J. HEHRE, D. J. DEFREES, J. A. POPLE, and J. S. BINKLEY. J. Am. Chem. Soc. **104**, 5039 (1982).
21. C. MØLLER and M. S. PLESSET. Phys. Rev. **46**, 618 (1934).
22. J. A. POPLE, R. SEEGER, and R. KRISHNAN. Int. J. Quantum Chem. Symp. **11**, 149 (1977).
23. R. SEEGER and J. A. POPLE. J. Chem. Phys. **65**, 265 (1976).
24. J. BOJES, T. CHIVERS, W. G. LAIDLAW, and M. TRSIC. J. Am. Chem. Soc. **101**, 17 (1979).
25. C. A. COULSON. Valence. 2nd ed. Oxford University Press. 1961.

Can. J. Chem. Downloaded from www.nrcresearchpress.com by 196.1.178.254 on 09/07/12
For personal use only.

26. C. K. BARKER, A. W. CORDES, and J. L. MARGRAVE. J. Phys. Chem. **69**, 334 (1965).
27. I. ERNEST, W. HOLICK, G. RIHS, D. SCHOMBURG, G. SHOHAM, D. WENKERT, and R. B. WOODWARD. J. Am. Chem. Soc. **103**, 1540 (1981).
28. (*a*) J. K. BURDETT. Molecular shapes. Wiley–Interscience, New York. 1980; (*b*) R. G. PEARSON. Proc. Natl. Acad. Sci. U.S.A., **72**, 2104 (1975); (*c*) L. S. BARTELL. J. Chem. Ed. **45**, 754 (1968); (*d*) R. F. W. BADER. Can. J. Chem. **40**, 1164 (1962).
29. (*a*) N. BURFORD, T. CHIVERS, P. W. CODDING, and R. T. OAKLEY. Inorg. Chem. **21**, 982 (1982); (*b*) R. T. OAKLEY. Can. J. Chem. **62**, 2763 (1984); (*c*) J.-P. BOUTIQUE, J. RIGA, J. J. VERBIST, J. DELHALLE, J. G. FRIPIAT, R. C. HADDON, and M. L. KAPLAN. J. Am. Chem. Soc. **106**, 312 (1984); (*d*) S. MILLEFIORI, A. MILLEFIORI, and G. GRANOZZI. Inorg. Chim. Acta, **90**, L55 (1984); (*e*) R. GLEITER, R. BARTETZKO, and D. CREMER. J. Am. Chem. Soc. **106**, 3437 (1984).
30. R. T. OAKLEY. Prog. Inorg. Chem. **36**, 299 (1988).
31. (*a*) M. BÉNARD, W. G. LAIDLAW, and J. PALDUS. Can. J. Chem. **63**, 1797 (1985); (*b*) M. BÉNARD and W. G. LAIDLAW. Theoret. Chim. Acta, **70**, 17 (1986); (*c*) M. BÉNARD, W. G. LAIDLAW, and J. PALDUS. Chem. Phys. **103**, 43 (1986); (*d*) W. G. LAIDLAW and M. BÉNARD. J. Comput. Chem. **8**, 727 (1987).
32. D. J. THOULESS. The quantum mechanics of many body systems. Academic Press, New York. 1961.
33. (*a*) J. ČÍŽEK and J. PALDUS. J. Chem. Phys. **47**, 3976 (1967); (*b*) J. PALDUS and J. ČÍŽEK. Can. J. Chem. **63**, 1803 (1985).
34. K. DEGUCHI, K. NISHIKAWA, and S. AONO. J. Chem. Phys. **75**, 4165 (1981).

Can. J. Chem. Downloaded from www.nrcresearchpress.com by 196.1.178.254 on 09/07/12
For personal use only.

The synthesis and unimolecular decomposition of four novel Δ^1-1,2,4-triazolines[1]

ADRIAN L. SCHWAN[2] AND JOHN WARKENTIN[3]

Department of Chemistry, McMaster University, Hamilton, Ont., Canada L8S 4M1

Received December 4, 1987

ADRIAN L. SCHWAN and JOHN WARKENTIN. Can. J. Chem. **66**, 2285 (1988).

Treatment of 4-*tert*-butyl-3,3-dimethyl-5-methylene-Δ^1-1,2,4-triazoline (**3**) with benzonitrile oxide (**9**), diphenylnitrile imine (**10**), phenyl azide, and *p*-nitrophenyl azide led, in each case, to 1,3-dipolar cycloaddition. The products, Δ^1-1,2,4-triazolines that are spiro-fused to another 5-membered ring, could be isolated in pure form in three of the four cases. All four are thermally unstable and decompose by loss of N_2 from the Δ^1-1,2,4-triazoline moiety to form an azomethine ylide. Subsequent reactions of those ylides are described.

ADRIAN L. SCHWAN et JOHN WARKENTIN. Can. J. Chem. **66**, 2285 (1988).

La réaction de la *tert*-butyl-4 diméthyl-3,3 méthylène-5 Δ^1-triazoline-1,2,4 (**3**) avec l'oxyde du benzonitrile (**9**), l'imine du diphénylnitrile (**10**), l'azoture de phényle ou de *p*-nitrophényle conduit, dans chaque cas, à une cycloaddition dipolaire-1,3. Les produits, des Δ^1-triazolines-1,2,4 qui sont spiro-condensées à un autre cycle à cinq chaînons, ont pu être isolés à l'état pur dans trois cas sur quatre. Les quatre sont instables d'un point de vue thermique et ils se décomposent par perte de N_2, de la part de la portion Δ^1-triazoline-1,2,4, pour conduire à un ylure d'azométhine. On décrit des réactions subséquentes de ces ylures.

[Traduit par la revue]

Can. J. Chem. Downloaded from www.nrcresearchpress.com by 196.1.178.254 on 09/07/12
For personal use only.

Although there are now a variety of methods available for the generation of azomethine ylides (**2**) (1–3), a very attractive route, the extrusion of N_2 from Δ^1-1,2,4-triazolines (**1**) as proposed by Kellogg (4) (reaction [1]), has still not been developed.

Our efforts toward the synthesis of Δ^1-1,2,4-triazoline (**1**) precursors of azomethine ylides have led to the synthesis of triazoline **3** (5, 6), the first Δ^1-1,2,4-triazoline without heteroatom substituents, and to aziridines **4**, **5**, and **6**, obtained by treating **3** (an enamine as well as a triazoline) with the appropriate electrophilic substrates. Presumably those aziridines arise from azomethine ylides derived from very thermolabile triazolines such as **7** (7) (reaction [2]). Thus, although triazolines of type **1** have been prepared as transient intermediates (e.g., **7**), none have been isolated.

[1] 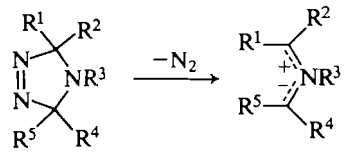

1 **2**

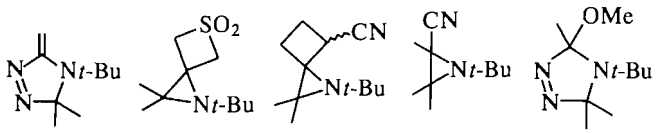

3 **4** **5** **6** **8**

[2] 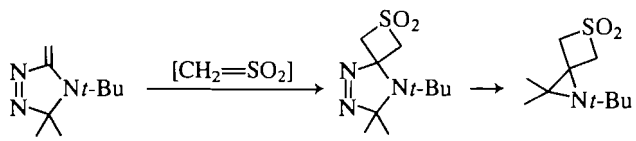

3 **7** **4**

We have, however, obtained evidence that triazolines with a heteroatom attached to one of the two sp^3 ring carbons (e.g., **8**) may have more inherent stability than those with all carbon substituents (7). Thus, methoxytriazoline **8** was observed by ^{13}C and ^1H nmr spectroscopy when **3** was dissolved in acidified methanol. The persistence of **8** in that medium indicated a resistance to N_2 extrusion substantially greater than those associated with triazolines such as **7**.

Although **8** was thermally stable in methanol solution, attempts to isolate **8** were unsuccessful. We reasoned that analogues of **8**, in which the heteroatom substituent was itself part of a ring, might be isolable. To test that hypothesis we treated **3** with 1,3-dipoles bearing a heteroatom at one of their termini.

Results and discussion

The first two 1,3-dipoles chosen for reaction with **3** were benzonitrile oxide, Ph—C≡$\overset{+}{N}$—O^- (**9**) and diphenylnitrile imine, PhC≡$\overset{+}{N}$—$\overset{-}{N}$Ph (**10**). They were selected not only because they provided a heteroatom at the desired position but also because both are known to react with enamines at ambient or lower temperatures (8). Indeed such a cycloaddition between **3** and both **9** and **10** was achieved. Treatment of **3** with benzoyl chloride oxime (**11**) (9) and triethylamine at −30°C for 10 min afforded **12** in 75% yield (reaction [3]). Benzoyl chloride phenylhydrazone (**14**) (10) together with triethylamine and **3** provided **15** in 84% yield after 40 h at room temperature (reaction [4]).

Structures **12** and **15** were assigned as the triazolines resulting from 1,3-dipolar cycloaddition of **11** and **14** to **3** on the basis of spectroscopic data. In the ^1H nmr spectra both **12** and **15** showed two magnetically nonequivalent methyl groups and the methylene protons appeared as an AB quartet, demonstrating their nonequivalence.[4] The ^{13}C nmr spectra provided evidence that the cycloaddition proceeded with the expected regiochemistry (8) and that the azo function was still present in the products. The triazoline ring carbons resonated at 128.63 and 104.68 ppm for **12** and at 119.58 and 102.68 ppm for **15**. These values are in keeping with expectations based on the number of

[1]Presented in part at the Fifth Annual Graduate Student Symposium, State University of New York at Buffalo, Buffalo, New York, May 1987.

[2]Holder of an NSERC of Canada Post-graduate Scholarship, 1983–1987. Present address: Department of Chemistry, State University of New York at Albany, Albany, NY 12222, U.S.A.

[3]Author to whom correspondence may be addressed.

[4]The methylene protons of **12** resonated as a singlet in $CDCl_3$ but the AB q pattern was evident in C_6H_6.

TABLE 1. The nmr chemical shifts of aromatic heterocycles

Heterocycle	Chemical shift (ppm)[a]			
	^{1}H	^{13}C		
	4-H	3-C	4-C	5-C
Isoxazole	6.41[b]	149.1[c]	103.7	157.9
3-Phenyl-5-methyl isoxazole	6.20[d,e]	169.6[f]	100.3	160.3
13	6.37	162.36	98.1	181.2
1H-pyrazole	6.31[g]	134.6[h,i]	105.8	134.6
3-Phenyl-*1H*-pyrazole	6.60[g]	150.2[h,i]	103.7	134.4
1-Phenyl-*1H*-pyrazole	6.46[g]	140.7[j]	107.3	126.2
16	6.57	149.98	102.5	154.16
1-Phenyl-1,2,3-triazole (**29***a*)[k]	7.81	—	134.0	121.7
1-Phenyl-5-(isopropylaminomethyl)-1,2,3-triazole[l]	7.66	—	133.3	136.3
21	7.64	—	132.04	138.58

[a]In $CDCl_3$ unless otherwise noted.
[b]Reference 12.
[c]Reference 13.
[d]In CCl_4.
[e]Reference 14.
[f]Reference 15.
[g]Reference 16.
[h]In CD_2Cl_2.
[i]Reference 17.
[j]Reference 18.
[k]Reference 19.
[l]Reference 20.

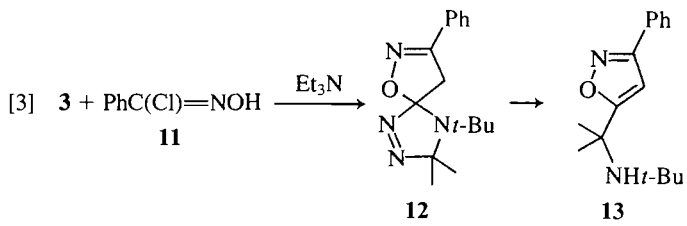

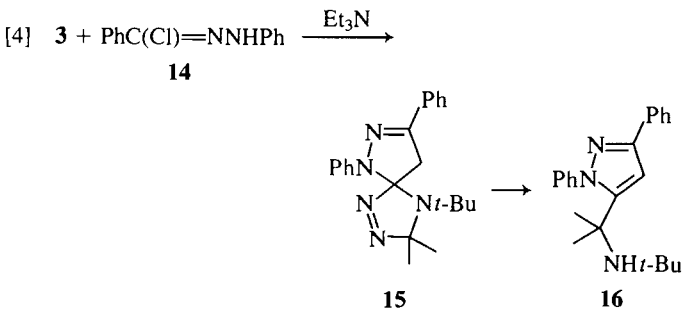

adjacent heteroatoms (cf. the values for **4**, **5**, and **6** (7)). Moreover, the presence of a strong band in the 1590–1600 cm^{-1} region of the Raman spectra of **12** and **15** is indicative of a *cis* azo function (11).

The mass spectral data for **12** and **15**, although less informative, are in keeping with the assignments. Molecular ions from neither **12** nor **15** were observable under electron impact (ei) conditions. Weak signals at $m/z = (M - N_2)^+$ and strong signals corresponding to $m/z = (M - N_2 - CH_3)^+$ fragments were observed. Under chemical ionization (ci) conditions, the expected $(M + 1)^+$ ions were observed. All spectroscopic data can be found in the Experimental.

Triazolines **12** and **15** are the first isolable Δ^1-1,2,4-triazolines with sp^3 ring carbons. With those in hand, we proceeded to investigate their thermolysis chemistry, with the hope that they would be useful precursors of azomethine ylides.

Thermolysis of **12** and **15** in benzene afforded isoxazole **13** (89%) and pyrazole **16** (94%) respectively, in high yield (reactions [3], [4]). Unfortunately those were also the products when the thermolyses were done in methyl acrylate or in dimethyl acetylenedicarboxylate (DMAD), two efficient dipolarophiles (8). Heterocycles **13** and **16** were identified on the basis of the spectroscopic data, which correspond well with those of similar known aromatic heterocycles (Table 1) (12–20). A significant feature of the nmr data is that the two methyl groups that are not part of the *t*-Bu substituent are magnetically equivalent, providing strong evidence that the 1,2,4-triazoline ring of **12** and **15** is not present in **13** and **16**.

The infrared spectra showed NH stretching bands at 3355 (**13**) and 3378 cm^{-1} (**16**). The mass spectra of **13** and **16** showed a weak signal at $m/z = M^+$ under ei conditions. A signal at $m/z = (M - CH_3)^+$ was significant in both instances. Under ci conditions the expected $m/z = (M + 1)^+$ peaks were observed. Finally, the background in the spectra of **12** and **15** contained the characteristic spectra of **13** and **16**, respectively. This is presumably due to some thermolysis of **12** and **15** in the heated inlet system of the mass spectrometer.

The mechanism of the transformation of **12** to **13**, and similarly of **15** to **16**, can be rationalized as outlined in Scheme 1. As we have observed with more thermolabile triazolines (6, 7), loss of N_2 to yield an azomethine ylide **17** is probably the first step. Ylide **17** would be expected to close quickly to aziridine **18** due to the large nonbonding interactions of the five ylide substituents. Electrocyclic ring closures of ylides are common and sterically congested ylides such as **17** are known to form 3-membered rings with rate constants large enough to prevent cycloaddition to a dipolarophile (7, 21–23). Thus the failure of methyl acrylate or DMAD to trap **17** (or its analog from **15**) is not surprising.

Ring opening of **18** (Scheme 1) may occur by an intramolecular dipolar mechanism leading to **19**. Finally, proton transfer from the ring to the negatively charged nitrogen forms the aromatic heterocycle **13**.

Other mechanisms may be possible but two features must be part of any proposal. The carbon bearing two methyl groups in **12** must end up attached to the ring in **13** and the bond that held

Can. J. Chem. Downloaded from www.nrcresearchpress.com by 196.1.178.254 on 09/07/12
For personal use only.

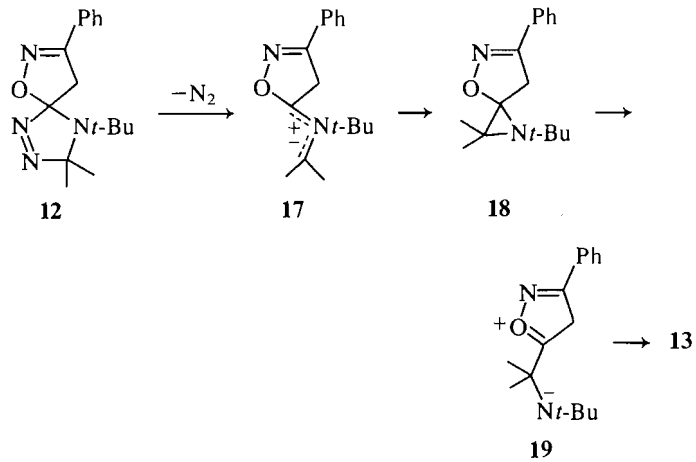

SCHEME 1

the N(*t*-Bu) group to the spiro atom of **12** must be broken. Precedent for the C—N cleavage can be found in the commonplace conversion of 5-aminoisoxazolines to deaminated isoxazoles (24). The transformation of 5-aminopyrazolines to deaminated pyrazoles, known to proceed readily (25), serves as a model for the analogous steps from **15** to **16**.

To estimate activation parameters for thermal decomposition of **12** and **15**, degassed solutions of the triazolines in benzene were sealed into nmr tubes, which were immersed in a constant temperature bath. Periodic integration of the ^{1}H nmr spectra gave first-order rate constants. The activation parameters, from data for the range 40–80°C, were $\Delta H^{\ddagger}$(**12**) = 26, $\Delta H^{\ddagger}$(**15**) = 26 kcal mol^{-1}, $\Delta S^{\ddagger}$(**12**) = −2, and $\Delta S^{\ddagger}$(**15**) = 0 eu. Although the nmr method for measuring reaction rate constants is rough, the values of $\Delta S^{\ddagger}$ obtained are in good agreement with values from the literature (26) for concerted unimolecular extrusions of N_2. The kinetic parameters are therefore supportive of the proposed mechanism (Scheme 1), with the first step irreversible and rate limiting. All the rate constants are compiled in Table 2.

Two other 1,3-dipoles were treated with **3**. Phenyl azide would not react with **3** at room temperature in a variety of solvents. Heating to 80°C was sufficient but heating reduced the chances of isolating spirotriazoline **20**, and only compounds believed to be derived from **20** were isolated (reaction [5]).

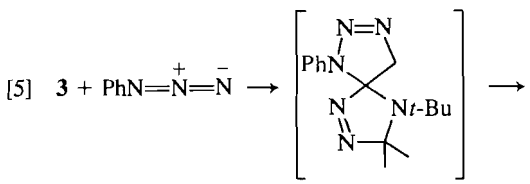

20

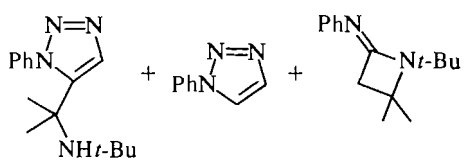

Triazoline **3** is also an enamine and therefore the 1,3-dipolar cycloaddition with azides is predicted to be controlled by the energy gap between the HOMO of the dipolarophile and the LUMO of the dipole. Since a *para*-nitro group is known to lower the LUMO of phenyl azide and to render it more reactive

TABLE 2. Decomposition rates of **12** and **15** (benzene)

T(°C)	k/s^{-1} for **12**[a]	k/s^{-1} for **15**[a]
40	3.8×10^{-6}	2.1×10^{-6}
50.5[b]	1.5×10^{-5}	8.2×10^{-6}
60	4.7×10^{-5}	2.4×10^{-5}
69	1.47×10^{-4}	7.9×10^{-5}
80	4.4×10^{-4}	2.8×10^{-4}
80[c]	4.6×10^{-4}	2.7×10^{-4}
$\Delta H^{\ddagger}$	26 kcal mol^{-1}	26 kcal mol^{-1}
$\Delta S^{\ddagger}$	−2 eu	0 eu

[a]Initial concentrations = 0.069 M in benzene unless otherwise indicated.
[b]51°C for **15**.
[c][**12**]$_i$ = 0.104 M; [**15**]$_i$ = 0.100 M.

toward π-excessive double bonds (8), *p*-nitrophenyl azide was treated with **3**. An isolable triazoline (**22**) was obtained as a solid (reaction [6]).

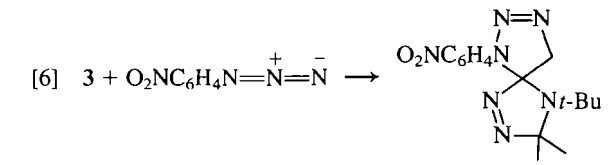

22

The spectroscopic properties of **22** were similar to those of **12** and **15**. In the ^{1}H nmr spectrum the *gem*-dimethyl group furnished two singlets while the methylene protons appeared as an AB quartet. The ^{13}C nmr spectrum was supportive of the assignment, with triazoline ring carbon signals (at δ114.12 and 104.11) comparable to those of **12** and **15**.

The ei mass spectrum of **22** provided a peak at m/z = $(M - N_4)^+$ while the ci (CH_4) spectrum gave the expected peak at $m/z = (M + 1)^+$. The Raman spectrum of **22** showed a band at 1596 cm^{-1} along with intense nitro group signals.

Cycloadduct **22** is a unique spiro species containing both a Δ^2-1,2,3-triazoline and a Δ^1-1,2,4-triazoline ring. Whereas the background regarding the thermolysis chemistry of Δ^1-1,2,4-triazolines is limited to that from this laboratory (5–7, 27), very much is known about N_2 loss from Δ^2-1,2,3-triazolines (28, 29). Those triazolines are known to decompose via a zwitterion, rather than an ylide, to give aziridines via ring closure and (or) imino species by means of an alkyl group shift (Scheme 2).

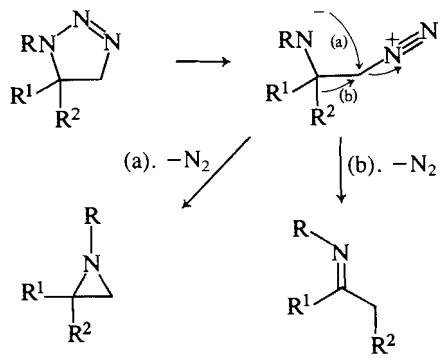

SCHEME 2

Can. J. Chem. Downloaded from www.nrcresearchpress.com by 196.1.178.254 on 09/07/12
For personal use only.

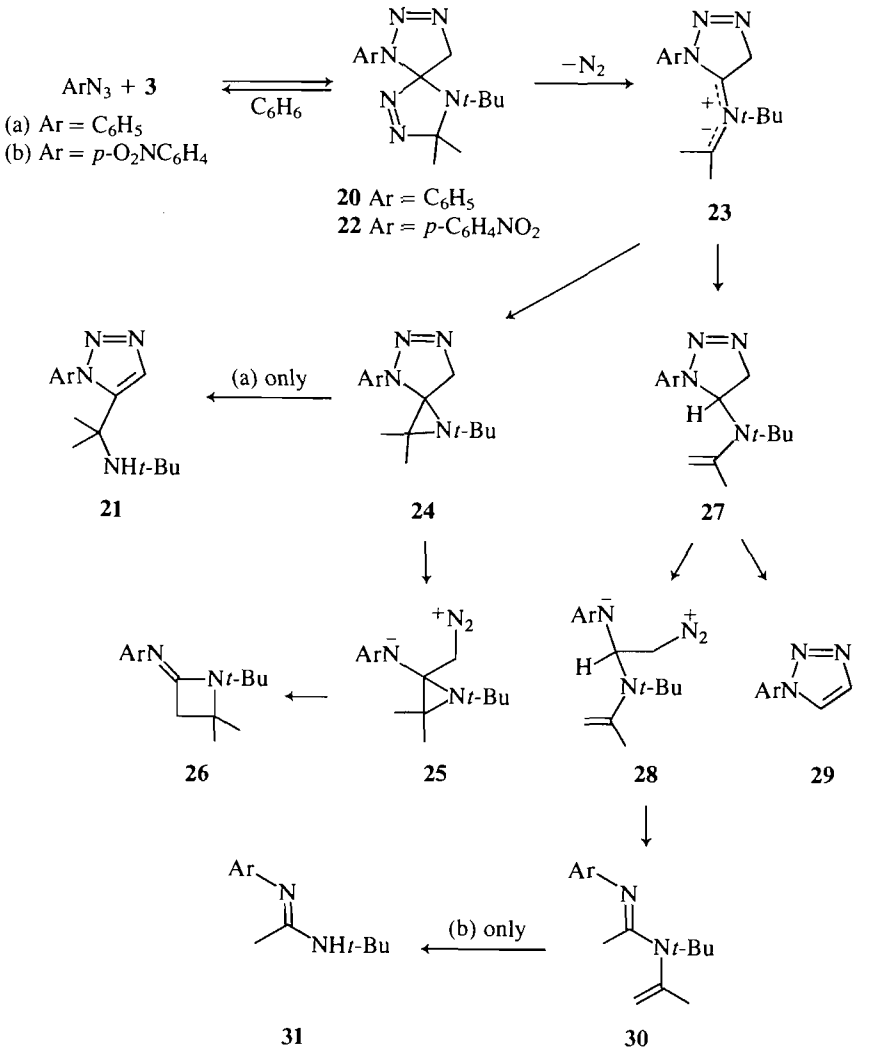

SCHEME 3

One would expect the Δ^1-1,2,4-triazoline ring of **25** to be the more labile of the two rings due to the conjugatively stabilized azomethine ylide that results from loss of molecular nitrogen. Breakdown of the 1,2,3-triazoline portion to yield the nonstabilized zwitterion, as depicted in Scheme 2, could follow extrusion of N_2 from the 1,2,4-triazoline ring. That sequence was assumed. It is known that aziridines rarely result from the breakdown of 5-amino-1,2,3-triazolines[5] (28), most of which decompose to 1,2,3-triazoles via loss of amine. When the 1-position of the 5-amino triazolines bears an electron-withdrawing group, loss of N_2 leading to an amidine (Scheme 2, $R^1 = NR_2^3$), becomes significant and may compete with deamination to the triazole (28). Finally, spiro Δ^2-1,2,3-triazolines tend to give ring-expanded imino compounds.

With these trends in mind, the thermal decomposition products of the assumed intermediate **20** and of **22** could be identified and rationalized readily (Scheme 3). Unfortunately the decomposition of **22** did not proceed with clean loss of one or two molecules of N_2. Cycloadduct **25** also reverts to **3** and *p*-nitrophenyl azide. There is precedent for this cycloreversion reaction and the equilibrium favours azide at higher temperatures (32). This complication prevented the straightforward acquisition of a unimolecular decomposition rate constant for **22**.

The decomposition of **22** was usually carried out without its isolation, and thermolysis of **20** was necessarily performed in this manner since it could not be isolated in pure form.

Refluxing a solution of phenyl azide and **3** in benzene followed by chromatographic separation provided products **21**, **26***a*, and **29***a*, in the yields indicated in Table 3. Analogous treatment of *p*-nitrophenyl azide with **3** in benzene afforded compounds **26***b*, **27***b*, **29***b*, **30***b*, **31***b*, and *p*-nitroaniline. Of these **29***b* was not isolated. Its presence in the crude mixture (in ca. 1% yield) was inferred from an ^{1}H nmr spectrum at 500 MHz.

Triazole **21** was identified by comparison of its spectra to those of similar heteroaromatic compounds including those of 1-phenyl-5-(isopropylaminomethyl)-1,2,3-triazole (20) (Table 1). Triazoles **29** are known species and the spectral data and physical properties for **29** were totally consistent with those reported previously (19, 32, 33).

Amidines **26** were identified by way of comparison of their spectroscopic data with those of amidine **33** (20). The C=N stretching frequency in the infrared spectra of **26***a* and **26***b* appeared at 1674 and 1652 cm^{-1}, respectively. The ^{1}H nmr

[5]For two exceptions to this general rule, the reader is referred to refs. 30 and 31.

Can. J. Chem. Downloaded from www.nrcresearchpress.com by 196.1.178.254 on 09/07/12
For personal use only.

TABLE 3. Yields of products from decomposition of **20**

Solvent	% Yield of product			
	21	**26***a*	**29***a*	**30***a*
C_6H_6	7	16	32	—
C_6H_6[a]	3	14	14	5
CH_3CN	40	Trace	—	—

[a]Initial thermolysis in benzene followed by extended heating in toluene.

TABLE 4. The ^{1}H nmr data of 5-amino-1,2,3-triazolines

Triazoline	^{1}H chemical shifts (δ)			Coupling constants (Hz)		
	H-4 *cis*	H-4 *trans*	H-5	*J cis*	*J trans*	*J gem*
34[a,b]	4.00	4.49	5.32	9.0	3.0	17.0
27*a*[c]	4.08	4.58	5.47	10.5	3.2	17.4
27*b*[c]	4.19	4.72	5.50	10.0	2.9	17.7

[a]Reference 35.
[b]60 MHz.
[c]500 MHz.

spectra showed singlets for the methylene groups of **26***a* and **26***b* and for their geminate methyl substituents. The ^{13}C nmr spectra showed signals at 156.66 ppm (**26***a*) and 157.49 ppm (**26***b*) for the amidine carbons. Both values are in the range expected for amidines (20, 35). Although the geometry about the C=N bond cannot be determined from the spectroscopic data, amidines **20** were assigned the *E* geometry on the basis of the fact that amidines with the *Z* configuration are rare and are known to isomerize readily to the *E* form (35, 36).

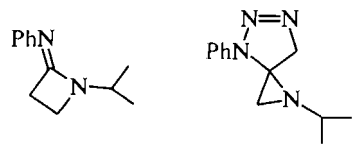

33 **32** **34**

Amidines **30***b* and **31***b* showed spectroscopic characteristics quite similar to those of **26**. The ^{1}H nmr spectrum of **30***b* permitted assignment of the signals from the two sp^2-bound methyl groups. The acetamidine methyl signal at 1.88 ppm is very sharp while the isopropylidene methyl peak at 1.97 ppm is broader due to allylic coupling. The nmr data and the mass spectrum of **31***b* indicated that it did not have the N-isopropenyl moiety of **30***b* but an NH moiety instead, as evidenced by the presence of an N—H stretching band at 3422 cm^{-1} in the ir spectrum.

Finally Δ^2-1,2,3-triazoline **27***b* was identified by way of its ^{1}H nmr spectrum. The ABX pattern of the ring protons of 5-dialkylamino-Δ^2-1,2,3-triazolines is a readily recognizable feature (Table 4) (37). The other spectral data of **27***b* were totally consistent with the assignment.

An ^{1}H nmr spectrum of the crude reaction mixture from phenyl azide and **3** also showed the distinctive ABX pattern and this is ascribed to the presence of **27***a* in the crude mixture. Only small amounts of **29***a* could be detected in this crude mixture and, because **29***a* was obtained in higher yield as the ultimate product, it follows that **27***a* is deaminated to **29***a* during chromatography.

Scheme 3 offers a series of pathways that rationalize the formation of the observed products. Cycloaddition between **3** and azide yields **20** or **22**, which should break down with rate constants similar to those for the decay of **12** or **15**. Such cycloreversions would generate azomethine ylides **23**. Two reactions of **23** then lead to the series of products obtained. A [1,4]-hydrogen shift leads to Δ^2-1,2,3-triazolines **27**. This sigmatropic rearrangement is a known reaction of azomethine ylides (6, 27, 38, 39). 1,2,3-Triazoline **27***a* deaminates to **29***a* upon chromatography. Analogue **27***b* survives chromatography but does decompose to *p*-nitroaniline and other products with prolonged manipulation. Presumably the nitro group of **27***b* renders the sp^3 nitrogen of the triazoline ring less nucleophilic, thereby reducing the rate of deamination.

Triazolines **27** also break down thermally by a mechanism different from that of deamination to **29**. Zwitterion **28***b*, from heterocyclic cleavage of the triazoline ring, is postulated. A hydride shift and loss of N_2 affords amidine **30***b* from **27***b*. Amidine **31***b* is the product of enamine hydrolysis of **30***b*. When the thermolysis mixture from **20** was heated for long periods of time, **30***a* was detected and lower yields of **29***a* were obtained even after chromatography. Identification of **30***a* followed from the similarity of its spectra to those of **30***b*. Extended refluxing of the mixture from **22** led to greater yields of *p*-nitroaniline and **30***b* at the expense of **27***b*. Presumably **27***b* is decomposed gradually to **30***b*, which is hydrolyzed slowly to **31***b*. The latter is apparently hydrolyzed more rapidly, to *p*-nitroaniline.

The other unimolecular reaction of ylides **23** is the ring closure to **24**. Crandall *et al.* (20) have proposed spiroaziridine **32** as an intermediate in the reaction of phenyl azide and *N*-isopropylmethyleneaziridine (20). Species **32** decomposed rapidly to 1-phenyl-5-(isopropylaminomethyl)-1,2,3-triazole and amidine **33**. The proposed decomposition pathway of **33** is analogous to that displayed in Scheme 3 for the breakdown of **24**. Only **24***a* gives the deaminated triazole (**21**). When **24***a* is generated in CH_3CN, **21** becomes the major product, most likely because the dipolar intermediate involved in the process is stabilized in that solvent. Presumably the mechanism suggested for the formation of heterocycles **13** and **16** is also suitable for rationalizing the presence of **21**.

Amidines **26** are formed by cleavage of the 1,2,3-triazoline (**24**) to **25**, which undergoes an alkyl shift and loss of molecular nitrogen to afford the ring-expanded species (**26**). In view of the known greater thermal stability of 1-phenyl-1,2,3-triazolines over their 1-*p*-nitrophenyl counterparts, it is not surprising that **24***a* forms **21** as well as **26***a*, whereas **24***b* does not lead to the analogue of **21**.

When a pure sample of **22** was decomposed in methyl acrylate, an efficient trap for azomethine ylides (1), no new products arising from **23***b* were detected.

On the whole, all of the products obtained from **3** and aryl azides can be rationalized with ample precedent. The pathways of Scheme 3 are fairly secure because **27***a* can be detected and **27***b* can be isolated. As well, the likelihood that **32** is an intermediate in the reaction of phenyl azide with *N*-isopropyl methyleneaziridine (20) lends credence to the proposal that **24** lies on the pathway to **21** and **26**. Although the mechanism of Scheme 3 is sufficient, the possibility that there is another concurrent decomposition pathway cannot be ruled out. Scheme

Can. J. Chem. Downloaded from www.nrcresearchpress.com by 196.1.178.254 on 09/07/12
For personal use only.

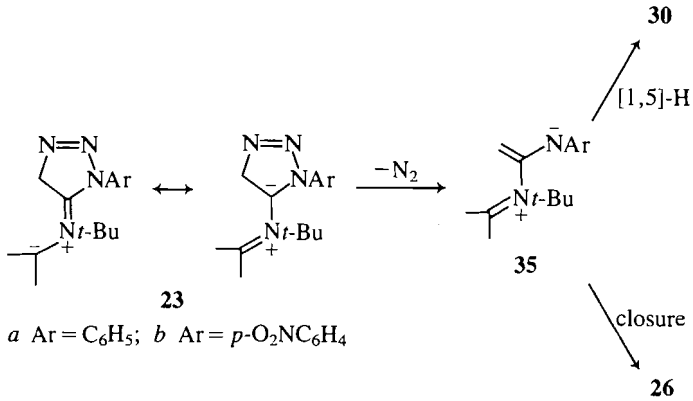

SCHEME 4

4, for example, depicts an alternative pathway from **23** to **26** and to **30**. In that mechanism, ylide **23** loses N_2 from the 1,2,3-triazoline ring to form zwitterionic species **35**, which then closes to **26** or transfers a proton intramolecularly from a methyl group, affording **30**. This latter step can also be perceived as a [1,5]-hydrogen transfer, assisted, at least in part, by the polarity of **35**. Species **35***b* would be more stable than **35***a* due to the conjugative effects of the *p*-nitro group. The pathway of Scheme 4, if it competes at all, may therefore be more important for the decay of **23***b* than of **23***a*. Unfortunately there is no model system with which the reactivity of **23**, with respect to loss of N_2, can be assessed. Deprotonations of Δ^2-1,2,3-triazolines that have been carried out have occurred from C-4 (40). Two examples are supportive of the proposal depicted in Scheme 4. Deprotonation from the 4-position of pyrazolines **36** enhances the rate of nitrogen loss by a factor of 10^{12} for X = CO_2Me (41) and by a factor of 10^{29} for X = CN (8, 42).

A closer analogy is the mechanism suggested by Padwa *et al.* to account for the decomposition of heterocycle **37** (43). Deprotonation from the 5-position of **37** yielded enolate **38** via anionic cycloreversion of the type that follows deprotonation from the 2-position of THF with formation of ethylene and acetaldehyde enolate (44).

Based on the examples above, some credibility can be given to the alternative mechanism for the formation of **26** and **30** as

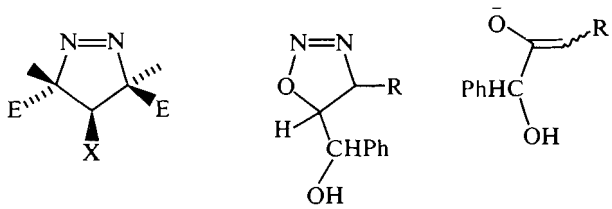

36 **37** **38**

depicted in Scheme 4, even if there is not a full negative charge at the 4-position of the 1,2,3-triazoline ring of **23**.

The fact that triazolines **12** and **15** can be isolated is truly surprising in light of the thermal instability of triazolines such as **7**. Intuitively, one would expect the additional heteroatom substituent at the spiro carbon atom to have a destabilizing effect. Analysis of all the examples from this and previous papers (6, 7, 26) allows one to conclude that the ring size of the spiro ring, if present, has little effect on the stability of the triazoline.

The observed stability of triazolines **12**, **15**, and **22** could be attributed to the relative energies of the ground state triazolines or of the corresponding ylides. Considering the ylide energy levels, ylides **17** and **23** are unlikely to be destabilized relative to those resulting from triazolines represented by **7**, based on the calculated substituent effects on carbonyl ylides (45). Addition of the amino substituent to a terminus of an unsubstituted carbonyl ylide provides 5 kcal mol^{-1} of stabilization (45). The corresponding stabilization of azomethine ylides is probably somewhat lower since they are considered to be more π-excessive than carbonyl ylides (1, 8) and therefore have less to gain from a donor substituent.

By process of elimination it seems necessary to postulate a ground state effect for the observed stability of **12**, **15**, and **22**, although the origin of such an effect is obscure.

Experimental

Melting points were determined on a Thomas Hoover capillary melting point apparatus and are uncorrected. Proton nuclear magnetic resonance (^{1}H nmr) spectra were recorded on a Varian EM 390 or a Bruker AM-500 instrument using TMS as the internal standard. Carbon-13 nuclear magnetic resonance (^{13}C nmr) spectra were obtained with either a Bruker WM-250 (62.90 MHz), WP-80/90 (22.62 MHz), or AM-500 (125.26 MHz) machine. Samples for nmr analysis were dissolved in $CDCl_3$ in all instances. Infrared spectra (ir) were obtained with a Perkin–Elmer model 283 instrument and are calibrated against the 1601.4 cm^{-1} band of polystyrene. Ultraviolet spectra (uv) were taken with a Hewlett–Packard model 8451A diode array spectrometer. Mass spectra (ms) were recorded on either a VG 70-70F or a VG ZAB-E spectrometer.

For Raman spectra, a Coherent model Innova 90 argon laser giving up to 3.5 W at 5145 Å was used for excitation. The spectrometer was a Spex Industries model 14018 double monochromator equipped with 1800 grooves/mm holographic gratings. Slit widths were set at 100 or 200 μm. The power setting was 50 or 100 mW. The scan rate was set at 1 or 2 cm^{-1} s^{-1}. Raman shifts quoted are believed to be accurate to ±2 cm^{-1}.

Centrifugal chromatography was carried out on a Chromatotron 7924T instrument equipped with silica-coated glass plates (coating 2 mm thick, 12 cm in radius, Merck Kieselgel 60 PF_{254}, using distilled solvents. Plastic-backed, Merck Kieselgel 60 PF_{254} 0.2 mm silica plates or plastic-backed polygram ALOX, N/UV_{254}, 0.2 mm neutral alumina plates were used for analytical thin-layer chromatography (tlc).

All reaction solvents were distilled from P_2O_5 before use.

The synthesis of **3** has been published (6).

Reaction of 3 with benzonitrile oxide

A flask containing 4 mL of dry CH_2Cl_2 and benzoyl chloride oxime (9) (162 mg, 1.14 mmol) was stirred at −30°C (alcohol – Dry Ice). A solution of **3** (162 mg, 0.97 mmol) and Et_3N (150 mg, 1.49 mmol) in 4 mL CH_2Cl_2 was added all at once. After 15 min, 4 volumes of ether were added and the solution was filtered. The filtrate was concentrated (aspirator) and applied to a basic Al_2O_3(II) column. Elution was with 40% ether in light petroleum. The fraction eluting with R_f 0.28 (40% ether) contained **12** (193 mg, 0.75 mmol) 77%. Recrystallization from light petroleum provided white crystals, mp 120–122°C (dec.). Spectral data for **12**: uv ($CHCl_3$), λ_{max} (log ε): 264 nm (3.88), 317 nm (2.95); ir (film), cm^{-1}: 1596 (vw), 1580 (vw), 1450, 1420, 1399, 1366, 1310, 1258, 1208; Raman, cm^{-1}: 1600, 1592 (N=N), 1564; ^{1}H nmr (90 MHz) δ: 1.36 (s, 9H), 1.58 (s, 3H), 1.67 (s, 3H), 3.59 (s, 2H, (ab q, J = 18 Hz in C_6H_6)), 7.38–7.58 (m, 3H), 7.67–7.82 (m, 2H); ^{13}C nmr (62.90 MHz), δ: 26.85, 27.88 (Me's), 31.99 (*t*-Bu), 42.63 (CH_2), 53.08 (CMe_3) 104.68 (ring C), 128.63 (spiro C), 126.61, 128.95, 129.99, 130.47 (Ph C's), 157.59 (C=N); ms (ei), *m/z* (%): 258(5), 257(4), 244(18), 243(89), 187(58), 186(62), 159(31), 103(30), 77(27), 58(100), 57(47); ms (ci, CH_3), *m/z* (%): 287(19), 259(22), 243(48), 203(29), 201(30), 186(31), 159(56), 118(70), 114(100), 104(86), 99(50), 84(36); ms (ei, high resolution), *m/z* calcd. for $C_{16}H_{22}N_2O$ [$M^+ - N_2$]: 258.1732; found: 258.1748; calcd. for $C_{15}H_{19}N_2O$ [$M^+ - N_2 - CH_3$]: 243.1497; found: 243.1503.

Reaction of 3 with diphenylnitrilimine

A flask containing **3** (236 mg, 1.41 mmol), benzoyl chloride phenyl-

Can. J. Chem. Downloaded from www.nrcresearchpress.com by 196.1.178.254 on 09/07/12
For personal use only.

Can. J. Chem. Downloaded from www.nrcresearchpress.com by 196.1.178.254 on 09/07/12
For personal use only.

hydrazone (10) (326 mg, 1.41 mmol), Et_3N (300 mg, 2.87 mmol), and 5 mL of dry CH_2Cl_2 was stirred at room temperature for 44 h. At this time, 4 volumes of ether were added and the solution was filtered. After concentration of the filtrate, the residue was applied to a basic Al_2O_3(II) column. Development with 10% ether in light petroleum afforded **15** (425 mg, 1.18 mmol) 84%, as a solid, mp 110°C (dec.), R_f 0.10 (10% ether). Spectral data for **15**: uv (hexanes), λ_{max} (log ε): 240 nm (4.14), 298 nm (3.93), 326 nm (4.18), 352 nm (4.10); ir (film), cm^{-1}: 1599, 1581(w), 1563(w), 1493, 1445(w), 1384, 1378, 1365, 1313, 1273, 1232, 1218; Raman, cm^{-1}: 1595 (N=N), 1562; ^1H nmr (90 MHz), δ: 1.28 (s, 9H), 1.49 (s, 3H), 1.70 (s, 3H), 3.42 (AB q, 2H, J = 18.3 Hz), 6.83–7.86 (m, 10H); ^{13}C nmr (125.76 MHz), δ: 26.85, 27.16 (Me's), 31.99 (*t*-Bu), 43.30 (CH_2), 52.72 (CMe_3), 102.68 (ring C), 119.58 (spiro C), 117.80, 121.80, 125.61, 128.47, 128.75, 128.93, 132.88, 143.15 (Ph C's), 146.51 (C=N); ms (ei), *m/z* (%): 333(1), 318(26), 262(32), 261(31), 143(26), 117(21), 77(100), 58(45); ms (ci, NH_3), *m/z* (%): 362(85), 334(100), 261(92), 74(46); ms (ei, high resolution), *m/z* calcd. for $C_{21}H_{24}N_3$ [$M^+ - N_2 - CH_3$]: 318.1970; found: 318.1974.

*Conversion of **12** to **13***

Triazoline **12** (104 mg, 0.36 mmol) was heated in 5 mL of benzene at 80°C for 3 h. After cooling and concentration, centrifugal chromatography of the residue (10% ethyl acetate in light petroleum) afforded **13** (83 mg, 0.32 mmol) 89%, obtained as a solid, mp 56–58°C (light petroleum), R_f 0.65 (25% EtOAc in petroleum, Al_2O_3). Spectral data for **13**: uv (MeOH), λ_{max} (log ε): 240 nm (4.04); ir (film), cm^{-1}: 3352 (br), 3121, 1597, 1576, 1508, 1467, 1438, 1405, 1391, 1379, 1362, 1214 (br); ^1H nmr (90 MHz), δ: 1.08 (s, 9H), 1.60 (s, 6H), 1.85 (s, br, 1H), 6.37 (s, 1H), 7.43–7.55 (m, 3H), 7.79–7.92 (m, 2H); ^{13}C nmr (125.76 MHz), δ: 30.64 (di-Me), 31.77 (*t*-Bu), 52.05, 52.76 (quat. C's), 98.10 (C-4), 126.63, 129.04, 129.57, 130.02 (Ph C's), 162.36 (C-3), 181.20 (C-5); ms (ei), *m/z* (%): 258(1), 243(79), 187(36), 186(38), 77(13), 58(100); ms (ci, CH_4), *m/z* (%): 259(8), 243(43), 186(26), 114(100), 74(9); ms (ei, high resolution), *m/z* calcd. for $C_{15}H_{19}N_2O$ [$M^+ - CH_3$]: 243.1497; found: 243.1503.

*Conversion of **15** to **16***

Triazoline **15** (95 mg, 0.25 mmol) was heated in benzene at 80°C for 3 h. After cooling and concentration, centrifugal chromatography (10% EtOAc in petroleum) afforded **16** (82 mg, 0.25 mmol) 94%, as a solid, mp 104–105°C (petroleum), R_f 0.63 (25% EtOAc in petroleum, Al_2O_3). Spectral data for **16**: uv (hexane), λ_{max} (log ε): 258 nm (4.24); ir (film), cm^{-1}: 3378 (br), 3063, 1599, 1538(w), 1498, 1460, 1421(w), 1389, 1377, 1363, 1213 (br); ^1H nmr (90 MHz), δ: 0.99 (s, 9H), 1.47 (s, 6H), 1.92 (s, br, 1H), 6.57 (s, 1H), 7.20–7.76 (m, 8H), 7.81–7.98 (m, 2H); ^{13}C nmr (125.76 MHz), δ: 31.71 (*t*-Bu), 32.28 (di-Me), 51.70, 52.80 (quat. C's), 102.50 (C-4), 125.57, 127.51, 128.49 (br), 128.54, 128.65, 133.28, 142.33 (Ph C's), 149.98 (C-3), 154.16 (C-5); ms (ei), *m/z* (%): 333(2), 318(61), 262 (80), 261(100), 77(18), 58(26); ms (ei, high resolution), *m/z* calcd. for $C_{22}H_{27}N_3$: 333.2205; found: 333.2210.

*Decomposition kinetics of triazolines **12** and **15***

Medium-walled nmr tubes were charged with the substrate and with sufficient benzene to give solutions with the concentrations indicated in Table 2. The solutions were degassed by means of three "freeze–pump–thaw" cycles before the tubes were sealed and immersed in constant temperature baths controlled to ±0.1°C.

Progress of the decomposition was monitored by ^1H nmr spectroscopy. Integration of the *tert*-butyl and *gem*-dimethyl signals of all components provided the normalizing integrals. Decompositions were followed to at least 85% conversion. Good fits of the data to the first-order rate law were obtained. The activation parameters listed in Table 2 were calculated from the Eyring equation.

*Synthesis of triazoline **22***

A flask was charged with **3** (171 mg, 1.03 mmol), *p*-nitrophenyl azide (46) (168 mg, 1.01 mmol), and 5 mL of dry CH_3CN. The contents were stirred at room temperature for 5 days. At this time the contents were concentrated (aspirator) and applied to a basic Al_2O_3(II) column. Elution was with 33% ether in light petroleum. The fraction with R_f 0.20 (33% ether) was collected and concentration afforded **22** (220 mg, 0.66 mmol) 65% as a yellow solid, mp 80°C (dec.) (light petroleum). Spectral data for **22**: uv ($CHCl_3$), λ_{max} (log ε): 280 nm (3.75), 332 nm (4.19); ir (film), cm^{-1}: 1604, 1524, 1502, 1400(w), 1382(w), 1370, 1341, 1328, 1300(w), 1290, 1272, 1172; Raman, cm^{-1}: 1596 (C—N=N—C), 1589, 1329, 1290, 1113; ^1H nmr (90 MHz), δ: 1.12 (s, 9H), 1.64 (s, 3H), 1.88 (s, 3H), 4.63 (AB q, 2H, J = 18.6 Hz), 7.40 (d, 2H, J = 9.3 Hz), 8.30 (d, 2H, J = 9.3 Hz); ^{13}C nmr (125.76 MHz), δ: 26.82, 27.05 (Me's), 31.60 (*t*-Bu), 53.04 (CMe_3), 73.03 (CH_2), 104.11 (sp^3 ring C), 114.12 (spiro C), 116.62, 125.13, 143.64, 144.48 (Ph C's); ms (ei), *m/z* (%): 275(16), 218(24), 163(50), 138(42), 117(21), 98(38), 82(73), 58(44), 57(100); ms (ci, NH_3), *m/z* (%): 332(8), 276(48), 246(47), 168(100), 140(38), 113(75), 111(40), 109(81); ms (ei, high resolution), *m/z* calcd. for $C_{15}H_{21}N_3O_2$ [$M^+ - N_4$]: 275.1634; found: 275.1633.

*Reaction of **3** and phenyl azide in benzene*

Triazoline **3** (384 mg, 2.30 mmol) and phenyl azide (47) (375 mg, 3.15 mmol) were heated together in 30 mL of benzene at 80°C for 43 h. After cooling, the benzene was removed (aspirator) followed by the excess phenyl azide (vacuum line). The residue was applied to a neutral Al_2O_3(II) column. Development with 2% ether in petroleum afforded **26** (85 mg, 0.37 mmol) 16% as a white solid, mp 52–54°C (light petroleum), R_f 0.28 (2% ether). Increasing the solvent polarity to 20% ether gave **21** and **29*a*** as a mixture (R_f 0.10, 20% ether). Centrifugal chromatography of this mixture (5% EtOAc in petroleum) gave pure **29*a*** (107 mg, 0.74 mmol) 32%, obtained as a solid, mp 52–53.5°C (light petroleum) (lit. (33) mp 55–56°C). Product **21** could not be recovered. The yield of **21** (7%) was estimated from the ^1H nmr spectrum of the crude reaction mixture. Spectral data for **26*a***: uv (MeOH), λ_{max} (log ε): 246 nm (4.01); ir (film), cm^{-1}: 1674 (vs), 1594, 1489, 1368, 1271, 1251, 1230, 1131; ^1H nmr (90 MHz), δ: 1.41 (s, 9H), 1.42 (s, 6H), 2.52 (s, 2H), 6.78–7.28 (m, 5H); ^{13}C nmr (125.76 MHz), δ: 28.27 (di-Me), 28.39 (*t*-Bu), 44.14 (CH_2), 55.30 (CMe_3), 61.01 (sp^3 ring C), 121.65, 122.71, 128.79, 150.66 (Ph C's), 156.42 (C=N); ms (ei), *m/z* (%): 230(38), 173(18), 139(28), 118(100), 98(25), 82(60), 57(77); ms (ei, high resolution), *m/z* calcd. for $C_{15}H_{22}N_2$: 230.1783; found: 230.1780. Partial ^1H nmr data for **27*a***, from ^1H nmr spectrum of crude reaction mixture (500 MHz), δ: 1.24 (s, 9H), 1.53 (s, 3H), 4.08 (dd, 1H, J = 10.5 and 17.4 Hz), 4.54 (s, br, 1H), 4.58 (dd, 1H, J = 3.2 and 17.4 Hz), 4.83 (s, br, 1H), 5.47 (dd, 1H, J = 3.2 and 10.5 Hz).

*Extended heating of **3** and phenyl azide*

Triazoline **3** (354 mg, 2.12 mmol) and phenyl azide (140 mg, 3.48 mmol) were heated in 30 mL of benzene at 80°C for 30 h. After removal of the benzene and the phenyl azide as described above, toluene (20 mL) was added. This solution was refluxed for 22 h before cooling and removal of the toluene by vacuum distillation. The residue was applied to a neutral Al_2O_3(II) column. Elution was with 1% ether in petroleum and afforded **30*a*** (24 mg, 0.10 mmol) 5%, R_f 0.48 (1% ether), followed by **26*a*** (68 mg, 0.30 mmol) 14%. Increasing the solvent polarity provided **21** and **29*a*** as a mixture. Centrifugal chromatography of this mixture provided **29*a*** (43 mg, 0.30 mmol) 14%. The yield of **21** was estimated to be 3%. Spectral data for **30*a***: uv (hexanes), λ_{max} (log ε): 236 nm (4.23); ir (film), cm^{-1}: 3061, 1610 (vs), 1592, 1482, 1370, 1345, 1267, 1223; ^1H nmr (90 MHz), δ: 1.53 (s, 9H), 1.79 (s, 3H), 1.93 (s, br, 3H), 4.91 (s, br, 1H), 5.20 (s, br, 1H), 6.61–7.17 (m, 5H).

*Reaction of **3** and phenyl azide in CH_3CN*

Triazoline **3** (176 mg, 1.05 mmol) and phenyl azide (317 mg, 2.66 mmol) were heated in 5 mL of CH_3CN at 65°C for 3 days. After cooling the CH_3CN was removed (aspirator), followed by the phenyl azide (vacuum line). Centrifugal chromatography (10% EtOAc in petroleum) of the residue provided pure **21** (109 mg, 0.42 mmol) 40%, obtained as a solid, mp 55–56°C (light petroleum), R_f 0.17 (Al_2O_3, 10% EtOAc). Product **26*a*** was detected by analytical gc in <1%

Can. J. Chem. Downloaded from www.nrcresearchpress.com by 196.1.178.254 on 09/07/12
For personal use only.

yield. Spectral data for **21**: uv (MeOH) λ_{max} (log ε): 262 nm (3.43); ir (film), cm^{-1}: 3340(br), 3158, 1600, 1537(w), 1581, 1471(w), 1452, 1413(w), 1390, 1380, 1363, 1311, 1230, 1220, 1201, 1180, 1169, 1164, 1127; ^1H nmr (90 MHz), δ: 1.02 (s, 9H), 1.50 (s, 6H), 7.57–7.63 (m, 5H), 7.64 (s, 1H); ^{13}C nmr (125.76 MHz), δ: 32.01 (di-Me), 32.15 (*t*-Bu), 51.91, 52.01 (sp^3 C's), 127.99, 128.71, 129.85, 147.21 (Ph C's), 132.04 (4-C), 138.58 (5-C); ms (ei), *m/z* (%): 258(2), 243(25), 186(21), 158(16), 114(24), 77(20), 58(100); ms (ei, high resolution), *m/z* calcd. for $C_{15}H_{22}N_4$: 258.1844; found: 258.1839.

Reaction of ***3*** *and* p*-nitrophenyl azide in benzene*

Triazoline **3** (260 mg, 1.56 mmol) and *p*-nitrophenyl azide (260 mg, 1.58 mmol) were heated together in 15 mL of benzene at 80°C for 20 h. After cooling, the benzene was removed (aspirator) and the residue was triturated with 3 × 30 mL of hot 30–60°C petroleum ether. The petroleum extracts were combined and put in a freezer at −20°C for 12 h. The liquid was decanted from the solid film that had fallen from solution. The liquid was concentrated and applied to a neutral Al_2O_3(II) column. Development with 2% ether in light petroleum provided *p*-nitrophenyl azide (R_f 0.39, 2% ether) followed by amidine **30***b* (82 mg, 0.30 mmol) 19%, as a yellow solid, mp 90–92°C (light petroleum), R_f 0.57 (10% ether). Gradual increase of the polarity to 10% ether afforded amidine **26***b* (128 mg, 0.47 mmol) 30%, mp 93–94°C (petroleum), R_f 0.32 (10% ether), followed by **31***b* (15 mg, 0.06 mmol) 4%, as a yellow solid, mp 137–138°C (from $CHCl_3$ in light petroleum), R_f 0.12 (10% ether).

The solid that fell from the cold petroleum ether solution was taken up in a small amount of solvent and applied to a neutral Al_2O_3(II) column. Development with 33% ether in light petroleum provided 1,2,3-triazoline **27***b* (99 mg, 0.33 mmol) 21%, mp 120–122°C, R_f 0.61 (33% ether), followed by *p*-nitroaniline (4 mg, 0.03 mmol) 2%, R_f 0.09 (33% ether). Spectral data for **26***b*: uv ($CHCl_3$), λ_{max} (log ε): 372 nm (4.52); ir (film), cm^{-1}: 1652(br), 1578(br), 1502, 1381, 1369, 1327, 1260, 1219, 1168, 1131, 1104, 1073; ^1H nmr (90 MHz), δ: 1.51 (s, 9H), 1.57 (s, 6H), 2.66 (s, 2H), 6.91 (d, 2H, J = 9.3 Hz), 8.13 (d, 2H, J = 9.3 Hz); ^{13}C nmr (22.62 MHz), δ: 27.94 (di-Me), 28.21 (*t*-Bu), 44.39 (CH_2), 55.97 (CMe_3), 62.18 (sp^3 ring C), 122.48, 125.10, 141.96, 157.62 (Ph C's), 157.49 (C=N); ms(ei), *m/z* (%): 275(32), 218(26), 204(17), 163(41), 139(49), 98(30), 82(67), 58(38), 57(100); ms (ei, high resolution), *m/z* calcd. for $C_{15}H_{21}N_3O_2$: 275.1634; found: 275.1633. Spectral data for **27***b*: uv (hexanes), λ_{max} (log ε): 220 nm (3.66), 3.38 nm (3.79), ir (film), cm^{-1}: 3042, 1578(br), 1502, 1383, 1370, 1329, 1208; ^1H nmr (500 MHz), δ: 1.31 (s, 9H), 1.53 (s, 3H), 4.19 (dd, 1H, J = 10.0 and 17.7 Hz), 4.53 (s, br, 1H), 4.72 (dd, 1H, J = 2.9 and 17.7 Hz), 4.85 (s, br, 1H), 5.50 (dd, 1H, J = 2.9 and 10.0 Hz), 7.56 (d, 2H, J = 9.2 Hz), 8.23 (d, 2H, J = 9.2 Hz); ^{13}C nmr (125.76 MHz), δ: 25.12 (Me), 29.78 (*t*-Bu), 55.17 (CMe_3), 66.90 (CH), 71.71 (CH_2), 116.82 (=CH_2), 114.87, 125.57, 140.75, 146.02 (Ph C's), 145.96 (vinyl C); ms, (ei), *m/z* (%): 275(7), 204(11), 177(33), 121(87), 82(60), 57(100), 41(72). Spectral data for **30***b*: uv (hexanes), λ_{max} (log ε): 222 nm (4.11), 330 nm (4.23); ir (film), cm^{-1}: 3100, 1617(br), 1582(br), 1499, 1372, 1360, 1325, 1285, 1239, 1191, 1165, 1105; ^1H nmr (90 MHz), δ: 1.56 (s, 9H), 1.88 (s, 3H), 1.97 (s, br, 3H), 4.92 (s, br, 1H), 5.23 (s, br, 1H), 7.16 (d, 2H, J = 9.3 Hz), 8.29 (d, 2H, J = 9.3 Hz); ^{13}C nmr (22.62 MHz), δ: 18.30 (N=C-*Me*), 25.12 (C=C-*Me*), 28.72 (*t*-Bu), 57.61 (CMe_3), 118.02 (=CH_2), 121.62, 125.25, 141.64, 158.65 (Ph C's), 145.86 (vinyl C), 153.75 (C=N); ms (ei), *m/z* (%): 275(11), 219(38), 218(100), 163(92), 117(52), 82(92), 57(67); ms (ei, high resolution), *m/z* calcd. for $C_{15}H_{21}N_3O_2$: 275.1634; found: 275.1636. Spectral data for **31***b*: uv ($CHCl_3$), λ_{max} (log ε): 350 nm (3.90); ir (film), cm^{-1}: 3422(br), 1644, 1584, 1526, 1487, 1323, 1261, 1202, 1611, 1102; ^1H nmr (90 MHz), δ: 1.46 (s, 9H), 1.79 (s, 3H), 4.38 (s, br, 1H), 6.78 (d, 2H, J = 9.0 Hz), 8.16 (d, 2H, J = 9.0 Hz); ^{13}C nmr (22.62 MHz), δ: 18.81 (Me), 28.74 (*t*-Bu), 51.84 (CMe_3), 122,21, 125.09, 142.03, 159.08 (Ph C's), 153.21 (C=N); ms (ei), *m/z* (%): 235(44), 179(24), 178(100), 163(38), 138(100), 108(38), 76(36), 57(57); ms (ei, high resolution), *m/z* calcd. for $C_{12}H_{17}N_3O_2$: 235.1320; found: 235.1324. ^1H nmr data for **29***b* obtained from crude reaction mixture (34) (500 MHz), δ: 7.92 (s, 1H), 8.00 (d, 2H, J = 9.1 Hz), 8.13 (s, 1H), 8.43 (d, 2H, J = 9.1 Hz).

Extended heating of ***3*** *and* p*-nitrophenyl azide*

Triazoline **3** (219 mg, 1.31 mmol) and *p*-nitrophenyl azide (220 mg, 1.34 mmol) were heated in benzene at 80°C for 24 h. After cooling, concentration, and trituration of the mixture into 3 × 30 mL of hot 30–60°C petroleum, the petroleum was concentrated (aspirator) and the residue was taken up in 10 mL of toluene. This solution was heated for 12 h at 110°C. After cooling and removal of the toluene by vacuum distillation, the residue was triturated with 3 × 30 mL of hot petroleum ether. The combined petroleum ether extracts were put in a freezer for 12 h.

Chromatography of the components remaining in solution was done as described above and afforded **30***b* (94 mg, 0.34 mmol) 26%, **26***b* (115 mg, 0.42 mmol) 32%, and **31***b* (15 mg, 0.07 mmol) 5%.

Chromatography of the solid that fell from the cold petroleum solution afforded *p*-nitroaniline (27 mg, 0.20 mmol) 15%.

Partial decomposition of ***22*** *in benzene*

Triazoline **22** (20 mg in 3 mL of benzene) was heated at 80°C for 2 h. After cooling, tlc indicated the presence of **26***b*, **27***b*, **30***b*, **31***b*, and *p*-nitroaniline as well as starting material **22**, *p*-nitrophenyl azide, and triazoline **3**.

1. J. W. Lown. *In* 1,3-Dipolar cycloaddition chemistry. Vol. 1. *Edited by* A. Padwa. Wiley–Interscience, New York, NY. 1984. p. 653.
2. E. Vedejs and F. G. West. Chem. Rev. **86**, 941 (1986).
3. A. Padwa, W. Dent, M. Tomas, Y.-Y. Chen, and U. Chiacchio. *In* Lectures in heterocyclic chemistry. Vol. 8. *Edited by* R. N. Castle and V. Snieckus. Heterocorporation, Tampa, FL. 1985. p. 21.
4. R. M. Kellogg. Tetrahedron, **32**, 2165 (1976).
5. A. L. Schwan and J. Warkentin. J. Chem. Soc. Chem. Commun. 1721 (1986).
6. A. L. Schwan and J. Warkentin. Can. J. Chem. **65**, 1200 (1987).
7. A. L. Schwan and J. Warkentin. Can. J. Chem. **66**, 155 (1988).
8. R. Huisgen. *In* 1,3-Dipolar cycloaddition chemistry. Vol. 1. *Edited by* A. Padwa. Wiley–Interscience, New York, NY. 1984. p. 1.
9. K. C. Liu, B. R. Shelton, and R. K. Howe. J. Org. Chem. **45**, 3916 (1980).
10. D. L. Rector, S. D. Folz, R. D. Conklin, L. H. Nowakowski, and G. Kaugars. J. Med. Chem. **24**, 532 (1981).
11. N. B. Colthup, L. H. Daly, and S. E. Wiberley. Introduction to infrared and Raman spectroscopy. Academic Press, New York, NY. 1975. p. 331.
12. R. Huisgen and M. Christl. Angew. Chem. Int. Ed. Engl. **5**, 456 (1967).
13. J. Gainer, G. A. Haworth, W. Hoyle, and S. M. Roberts. Org. Magn. Reson. **8**, 226 (1976).
14. S. D. Sokolov, I. M. Yudintseva, and P. V. Petrovskii. J. Org. Chem. (USSR), **6**, 2594 (1970).
15. D. H. Reid and R. G. Webster. J. Chem. Soc. Perkin Trans. 1, 2115 (1975).
16. J. Elguero, R. Jacquier, and H. C. N. Tien Duc. Bull. Soc. Chim. Fr. 3727 (1966).
17. J. Elguero, C. Marzin, and J. D. Roberts. J. Org. Chem. **39**, 357 (1974).
18. M. Begtrup. Acta Chem. Scand. **27**, 3101 (1973).
19. J. K. Crandall, N. W. Conover, and J. B. Komin. J. Org. Chem. **40**, 2042 (1975).
20. J. K. Crandall, L. C. Crawley, and J. B. Komin. J. Org. Chem. **40**, 2045 (1975).
21. J. A. Deyrup and W. A. Szabo. J. Org. Chem. **40**, 2048 (1975).

22. C. W. MARTIN, H. S. GILL, and J. A. LANDGREBE. J. Org. Chem. **48**, 1898 (1983).
23. J. BUTER, S. WASSENAAR, and R. M. KELLOGG. J. Org. Chem. **37**, 4045 (1972).
24. (*a*) K. BAST, M. CHRISTL, R. HUISGEN, W. MACK, and R. SUSTMANN. Chem. Ber. **106**, 3258 (1978); (*b*) P. CARAMELLA, P. FRATTINI, and P. GRUNANGER. Tetrahedron Lett. 3817 (1971); (*c*) S. MORROCCHI, A. RICCA, and L. VELO. Chem. Ind. (Milan), **49**, 168 (1967).
25. (*a*) R. HUISGEN, R. SUSTMANN, and G. WALLBILLICH. Chem. Ber. **100**, 1786 (1967); (*b*) R. FUSCO, G. BIANCHETTI, and D. POCAR. Gazz. Chim. Ital. **91**, 1233 (1961); (*c*) M. E. KUEHNE, S. J. WEAVER, and P. FRANZ. J. Org. Chem. **29**, 1582 (1964).
26. H. MEIER and K.-P. ZELLER. Angew. Chem. Int. Ed. Engl. **16**, 835 (1977).
27. A. L. SCHWANN and J. WARKENTIN. Can. J. Chem. **66**, 385 (1988).
28. P. K. KADABA, S. STANOVNIK, and M. TISLER. Adv. Heterocycl. Chem. **37**, 219 (1984).
29. P. SCHEINER. *In* Selective organic transformations. Vol. 1. *Edited by* B. S. Thayagarajan. Wiley–Interscience, New York, NY. 1970. p. 327.
30. L. CITERIO, M. L. SACCARELLO, and R. STRADI. Synthesis, 305 (1979).
31. Y. NOMURA, Y. TAKEUCHI, S. TOMODA, and M. M. ITO. Bull. Chem. Soc. Jpn. **54**, 2779 (1981).
32. (*a*) L. M. ROSSI and P. TRIMARCO. Synthesis, 465 (1978); (*b*) J. Heterocycl. Chem. **17**, 1545 (1980); (*c*) D. POCAR, M. C. RIPAMONTI, R. STRADI, and P. TRIMARCO. J. Heterocycl. Chem. **14**, 1545 (1977); (*d*) F. TEXIER and J. BOURGOIS. J. Heterocycl. Chem. **12**, 505 (1975); (*e*) J. BOURGOIS, F. TONNARD, and F. TEXIER. Bull. Soc. Chim. Fr. 2025 (1976).
33. H. EL KHADEM, H. A. K. MANSOUR, and H. M. MESHREKI. J. Chem. Soc. C, 1329 (1968).
34. J. ELGUERO, R. JACQUIER, and G. TARRAGO. Bull. Soc. Chim. Fr. 1346 (1970).
35. J. OSZCZAPOWICZ, E. RACZYNSKA, and J. OSEK. Magn. Reson. Chem. **24**, 9 (1986).
36. (*a*) A. F. HEGARTY and A. CHANDLER. Tetrahedron Lett. 885 (1980); (*b*) J. Chem. Soc. Chem. Commun. 130 (1980).
37. R. STRADI, D. POCAR, and G. BIACHETTI. Org. Magn Reson. **4**, 247 (1972).
38. R. SMITH and T. LIVINGSTONE. Tetrahedron **41**, 3559 (1985).
39. (*a*) A. A. LEONE and P. S. MARIANO. Rev. Chem. Intermed. **4**, 81 (1981); (*b*) A. G. SCHULTZ. Acc. Chem. Res. **16**, 210 (1983).
40. R. HUISGEN, G. SZEIMIES, and L. MOBIUS. Chem. Ber. **99**, 475 (1966).
41. P. EBERHARD and R. HUISGEN. J. Am. Chem. Soc. **94**, 1345 (1972).
42. R. HUISGEN. J. Org. Chem. **41**, 403 (1976).
43. A. PADWA, P. CIMILUCA, and D. EASTMAN. J. Org. Chem. **38**, 805 (1973).
44. R. B. BATES, L. M. KROPOSKI, and D. E. POTTER. J. Org. Chem. **37**, 560 (1972).
45. K. N. HOUK, N. G. RONDAN, C. SANTIAGO, C. J. GALLO, R. W. GANDOUR, and G. W. GRIFFIN. J. Am. Chem. Soc. **102**, 1504 (1980).
46. (*a*) H. H. HODGSON and W. H. H. NORRIS. J. Chem. Soc. 786 (1949); (*b*) P. A. S. SMITH and J. H. BOYER. Org. Synth. **31**, 14 (1951).
47. R. O. LINDSAY and C. F. H. ALLEN. Org. Synth. Coll. Vol. III, 710 (1955).

Can. J. Chem. Downloaded from www.nrcresearchpress.com by 196.1.178.254 on 09/07/12
For personal use only.

Vanadium(V) oxyanions. The dependence of vanadate alkyl ester formation on the pK_a of the parent alcohols

ALAN S. TRACEY, BRUNO GALEFFI, AND SOROUSH MAHJOUR
Department of Chemistry, Simon Fraser University, Burnaby, B.C., Canada V5A 1S6

Received January 22, 1988

ALAN S. TRACEY, BRUNO GALEFFI and SOROUSH MAHJOUR. Can. J. Chem. **66**, 2294 (1988).

The interaction of vanadate ($VO_4H_2^{1-}$) with a variety of alkyl alcohols (ROH) covering about seven pK_a units of acidity have been studied in aqueous solution by ^{51}V nuclear magnetic resonance spectroscopy. A linear free energy relationship between the equilibrium constant for the formation of the vanadate monoester ($HOVO_3R^{1-}$) and the acidity of the alcohol was established at 23°C. The correlation was found to be log $1/K = -(0.09 \pm 0.02)pK_a^{ROH} + 2.1 \pm 0.3$ where $K = [HOVO_3R^{1-}]/[VO_4H_2^{1-}][ROH]$. This correlation was shown not to extend to ligands with π-bonding capability such as phenols or phosphates, where the products are highly favoured relative to the alkyl esters. An interesting correlation between pK_a values of the product esters and the pK_a of the parent alcohols was also observed. It was found that below a pK_a^{ROH} of about 15 the pK_a values of the esters were essentially constant. However, above this value of 15 the pK_a of the ester was found to increase rapidly with an increase in pK_a of the alcohol. This result may indicate that the electron accepting ability of the metal is exhausted with the higher pK_a alcohols, and the extra electron density is transferred to the oxygens, thus causing an increase in pK_a of the ester.

ALAN S. TRACEY, BRUNO GALEFFI et SOROUSH MAHJOUR. Can. J. Chem. **66**, 2294 (1988).

Operant en solution aqueuse et utilisant la spectroscopie rmn du ^{51}V, on a étudié l'interaction du vanadate ($VO_4H_2^{1-}$) avec un grand nombre d'alcools aliphatiques (ROH) couvrant sept unités de pK_a. À 23°C, on a pu établir une relation linéaire d'énergie libre entre la constante d'équilibre pour la formation du monoester de vanadate ($HOVO_3R^{1-}$) et l'acidité des alcools. On a trouvé que la corrélation prend la forme de log $1/K = -(0{,}09 \pm 0{,}02)pK_a^{ROH} + 2{,}1 \pm 0{,}3$, dans laquelle $K = [HOVO_3R^{1-}]/[VO_4H_2^{1-}][ROH]$. On a démontré que cette corrélation ne s'étend pas aux ligands présentant une capacité de liaison par des électrons π, comme les phénols ou les phosphates; dans ces cas, les produits sont très favorisés par rapport aux esters d'alkyles. On a aussi observé une corrélation intéressante entre les valeurs des pK_a des esters qui se forment comme produits et les pK_a des alcools qui leur donnent naissance. On a trouvé qu'en-dessous d'une valeur de 15 pour le pK_a^{ROH}, les valeurs des pK_a des esters augmentent rapidement avec une augmentation du pK_a des alcools. Ce résultat semble indiquer que la facilité du métal à accepter des électrons est épuisée avec les alcools de pK_a élevé et que la densité électronique additionnelle est transférée aux oxygènes; ceci provoque une augmentation du pK_a de l'ester.

[Traduit par la revue]

Can. J. Chem. Downloaded from www.nrcresearchpress.com by 196.1.178.254 on 09/07/12
For personal use only.

Introduction

The aqueous chemistry of the higher oxidation states of vanadium is attracting increasing attention in chemistry and biochemistry. There is considerable evidence that vanadium is an essential element for animals (1, 2). Vanadium is found in the enzyme systems of some nitrogen-fixing bacteria (3, 4) and is apparently utilized in the halogenation processes of a variety of seaweeds (4). Vanadium(V) (vanadate) and vanadium(IV) (vanadyl) oxyanions can have a large effect on the function of a variety of enzymes either as an activator or inhibitor of the enzyme function (1, 5). The ability of vanadate to affect enzyme function seems to arise, at least in part, from the ability of vanadate to act as a phosphate analogue.

The condensation of phosphate with hydroxylic compounds to form a phosphate derivative is, to a significant extent, dependent on the acidity of the hydroxyl group. Thus, the formation constant for phosphate esters of alkyl alcohols is comparatively favourable, comparable in fact to the formation constant for alkyl vanadates as for instance in the case of formation of phosphate and vanadate esters of ethanol (6). The formation of phosphate esters of phenols is, by comparison, highly unfavourable when compared with those for ethyl phosphate and phenyl vanadate (7). An investigation of this phenomenon has shown that there is a direct relationship between the acidity constant, K_a, of the parent hydroxylic compound and the formation or hydrolysis constant for the phosphate ester (8).

The equilibrium constant for hydrolysis of the phosphate ester dianion is related to the pK_a of the parent hydroxyl group by eq. [1],

$$[1] \quad \log K = -1.35pK_a^{ROH} + 7.50$$

where K is the hydrolysis constant defined by eq. [2] and pK_a^{ROH} is the pK_a of the hydroxyl group of interest (8). In eq. [2]

$$[2] \quad HOPO_3^{2-} + H^+ + RO^- \underset{K}{\rightleftharpoons} ROPO_3^{2-}$$

$$K = [HOPO_3^{2-}][H^+][RO^-]/[ROPO_3^{2-}]$$

the formation of water is not explicitly considered. In view of the linear free energy relationship between product formation and the pK_a of the hydroxyl group expressed by eq. [1] for phosphate, it was decided to investigate the vanadate system in more detail, particularly in view of the fact that the available information suggested that the vanadate system showed much more complex behaviour.

^{51}V nuclear magnetic resonance (NMR) spectroscopy allows direct measurement of the equilibria since separate signals from the vanadium products and precursors, in general, are observed in the NMR spectra. Simple correlations, determined as a function of ligand or vanadate concentration, or of pH provide the requisite information.

Experimental

Materials

Reagent grade chemicals were used without further purification. Proton NMR spectra indicated that all the alkyl alcohols used in this

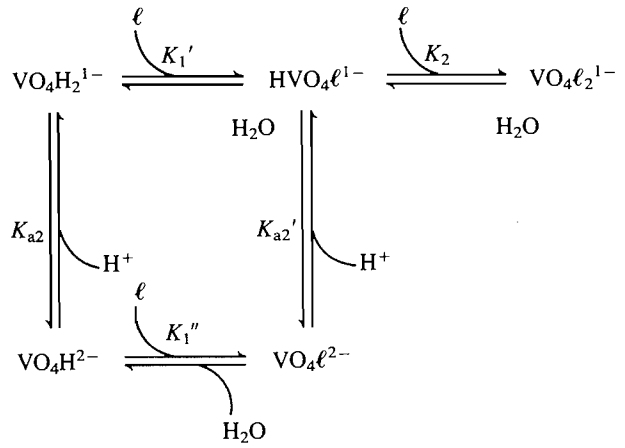

SCHEME 1

study were greater than 97% pure. Preparation of stock solutions and final solutions followed procedures previously described (6, 9).

Spectroscopy

All ^{51}V NMR spectra were obtained at ambient temperature from a Bruker WM-400 NMR spectrometer operating at the vanadium frequency of 105.2 MHz. Spectral widths of 40 kHz, 50° pulse widths and 0.05 s acquisition times were used for all spectra. Relative signal intensities were obtained using the integration routine supplied by the instrument manufacturer. No effort to obtain more accurate integrals through use of line-fitting or other methods was made. Chemical shifts are reported relative to that of $VOCl_3$ at 0.0 ppm.

Methods

The methods employed for determination of equilibrium constants for formation of the vanadate esters have been described in detail elsewhere as have the procedures employed for the determination of the pK_a values for those compounds with ionizable protons (6). No significant changes have been made to those methods in this study.

Results and discussion

The vanadate ion spontaneously and reversibly condenses with a variety of molecules containing hydroxyl groups to provide esterified vanadate derivatives (6, 7, 9, 10). This condensation has been shown to be reasonably favourable both for the ions VO_4H^{2-} and $VO_4H_2^-$ with the individual condensations apparently occurring in the manner indicated in Scheme 1 where l refers to the ligand.

In Scheme 1 the esterification reactions tend to be slow on the NMR time scale and as a consequence separate NMR signals can generally be observed for vanadate and its mono- and diesters. Proton exchange, on the other hand, is fast and because of the rapid proton exchange it is not possible to measure K_1' and K_1'' independently of each other in an NMR experiment but, rather, only an observed equilibrium, K_1, which is dependent on K_{a2} and K_{a2}', can be measured, K_1 is defined by eq. [3], and water formation is not explicitly considered. In eq. [3], T_i refers to tetrahedral vanadate, $VO_4H_2^-$ plus VO_4H^{2-}, and Tl to the product esters.

$$[3] \quad T_i + l \overset{K_1}{\rightleftharpoons} Tl \quad [T_i][l]K_1 = [Tl]$$

Expressing K_1 in terms of K_1', K_{a2} and K_{a2}' of Scheme 1 yields eq. [4].

$$[4] \quad K_1 = \frac{K_1'(1 + K_{a2}'/[H^+])}{1 + K_{a2}/[H^+]}$$

It is evident that if K_1 is determined for a variety of pH values near K_{a2} and K_{a2}', then all the constants of eq. [4] can be determined and as well K_1'' of Scheme 1. In practice, it is easier to measure K_{a2} and K_{a2}' directly since these values can be determined by the effect of pH on the chemical shifts of the ^{51}V NMR signals corresponding to T_i and Tl. A change in protonation state of vanadate or its monoester has a substantial effect on the shielding of the vanadium nucleus. At a pH well below the pK_{a2} of vanadate, the vanadate species in solution is $VO_4H_2^{1-}$, which is characterized by a chemical shift δ_l at a pH well above pK_{a2}, the species in solution is VO_4H^{2-} with the chemical shift δ_h. At intermediate pH values the observed shift, δ, is related to the pH and pK_a by eq. [5],

$$[5] \quad pH = pK_a + \log \frac{\delta - \delta_l}{\delta_h - \delta}$$

It is useful to note that when the logarithmic term is plotted against pH the slope of the straight line should be 1. This provides a convenient test of the applicability of eq. [5] to the system being studied. Equation [5] is also applicable to the vanadate monoester but not the diester $VO_4l_2^{1-}$, since the diester has no proton to lose. In this case the ^{51}V chemical shift should be pH-independent. This has been demonstrated for the vanadate/ethanol system (6) and has been observed here. Table 1 gives the chemical shifts and pK_a values for vanadate and its esters for a variety of alcohol solutions.

Knowledge of the K_{a2} and K_{a2}' values for vanadate and its esters then provides K_1' simply by determining K_1 of eq. [2] at any pH and applying eq. [4]. Of course K_1 must be determined within a pH range much lower than the pK_a for the alcohol or pK_{a3} of vanadate and well above pK_{a1} for vanadate or its ester. If this is not done, Scheme 1 must be expanded appropriately. Fortunately the pK_{a1} values are low, about 3.0 for vanadate (11, 12), while pK_{a3} of vanadate and the pK_a of the alcohols except for hexafluoroisopropanol are quite high (pK_a for CF_3-$CHOHCF_3$ = 9.3, pK_a (VO_4H^{2-}) ~ 13 (12)). From the various equilibrium constants measured at a pH near 7 and the known K_a values the respective K_1' and K_1'' were calculated and collected into Table 2.

From the entires of Table 2 it can be seen that the K_a values for the alcohols of this study range over about 7 orders of magnitude from pK_a = 9.3 for $(CF_3)_2CHOH$ to ~16.8 for *t*-butanol. Despite this large change in pK_a values, the formation constants of the various esters ranges only from about $0.20\,M^{-1}$ for the higher pK_a values to $0.06\,M^{-1}$ for the lower values. The decrease in formation constants, although small, follows the decrease in pK_a of the alcohols. This result does show that ester formation is not particularly sensitive to the pK_a of the alcohol. It can, however, be shown that, with the exception of the methyl and *t*-butyl vanadate esters, there is a linear free energy relationship between the pK_a of the alcohol and the hydrolysis (or formation) constant of the ester as can be seen by plotting $\log(1/K_1')$ versus the pK_a of the parent alcohol. When this was done a straight line of slope -0.09 ± 0.02 and intercept $+2.1 \pm 0.3$ as shown in Fig. 1 was obtained. The very small slope of this correlation illustrates the insensitivity of ester formation to the electron withdrawing ability of the ligand, RO^-.

This line has a slope of -1.09 ± 0.02 when cast into the form of eq. [1], for which a slope of -1.0 indicates that ester formation is independent of the pK_a of the parent alcohol. It is

Can. J. Chem. Downloaded from www.nrcresearchpress.com by 196.1.178.254 on 09/07/12
For personal use only.

TABLE 1. Vanadate and vanadate ester pK_a values and ^{51}V chemical shifts determined for various aqueous alcohol solutions[a,b]

Alcohol	$VO_4H_2^{1-}$ δ_l	δ_h	pK_{a2}	$ROVO_3H^{1-}$ δ_l	δ_h	pK'_{a2}	pK''_{a2}	$(RO)_2VO_2^{1-}$ δ	[ROH] M	Reference
Methanol	−560.8	−535.2	9.22±0.02	−551.0	−528.2	9.42±0.02	8.4	−543.3	7.4	15
Ethanol	−561.0	−534.0	8.3 ±0.1	−555.0	−532.0	8.9 ±0.1	8.8	−552.4	1.25	6
Isopropanol	−560.5	−535.7	8.83±0.03	−561.8	−539.0	9.61±0.04	9.0	−564.6	5.1	10
2-Butanol	−560.5	−535.5	8.69±0.02	−562.2	−538.6	9.67±0.02	9.2	−564.8	0.94	This work
t-Butanol	−561.0	−535.7	8.72±0.01	−574.6	−553.2	9.98±0.03	9.5		1.35	10
2-Cyanoethanol	−560.8	−537.5	8.67±0.03	−561.0	−537.0	8.65±0.05	8.2	−564.6	2.68	This work
2,2,2-Trifluoroethanol	−560.5	−535.8	8.81±0.02	−562.9	−532.4	8.79±0.02	8.2	−566.5	6.86	This work
Propargyl alcohol	−561.1	−536.3	8.54±0.04	−557.8	−531.8	8.56±0.05	8.2	−556.1	1.63	This work
1,1,1,3,3,3-Hexafluoro-2-propanol	−561.2	−536.0	8.27±0.03	−568.0	−531.8	8.05±0.03	8.0		3.16	This work
Ethylene glycol	−560.4	−535.9	8.8 ±0.1	−556.1	−533.4	8.9 ±0.1	8.3	−551.9	5.64	16

[a] pK_a values were determined by varying the pH under conditions of 20 mM HEPES buffer and the indicated concentrations of alcohol.
[b] Abbreviations are: δ_l, limiting ^{51}V chemical shift at low pH; δ_h, limiting shift at high pH; δ, ^{51}V chemical shift for the vanadate diester; ROH, the alcohol being considered.

TABLE 2. Formation constants for vanadate ester anions derived from a variety of alcohols

Alcohol	pK_a	K'_1 (M^{-1})	K''_1 (M^{-1})	K_2 (M^{-1})	Alcohol	pK_a	K'_1 (M^{-1})	K''_1 (M^{-1})	K_2 (M^{-1})
CH_3OH	15.07	0.09	0.06	0.02	CH_3CH_2OH	15.83	0.21	0.05	0.04
$CH_3CHOHCH_2CH_3$[c]	16.7	0.20	0.02	0.10	$NCCH_2CH_2OH$	14.03	0.15	0.16	0.10
CF_3CH_2OH	12.32	0.07	0.07	0.02	$HCCH_2OH$	13.57	0.13	0.13	0.03
$(CF_3)_2CHOH$	9.3	0.06	0.10		CH_2OHCH_2OH[d]	15.11	0.17	0.14	0.05
$(CH_3)_3COH$	16.84	0.09	0.005		$(CH_3)_2CHOH$	16.57	0.25	0.014	0.09

[a] Equilibrium constants are those defined by Scheme 1 and were determined as discussed in the text. Estimated errors for all equilibrium constants are about 10% of the reported values except for the K_2 values where the errors are about ±0.01 M^{-1} for all measurements.
[b] Alcohol pK_a values were taken from tabulations in ref. 17.
[c] The pK_a for this alcohol was estimated from values for related compounds tabulated in ref. 17.
[d] The statistical factor of two is removed from reported formation constants (ref. 16) to give the formation constants K'_1 and K''_1.

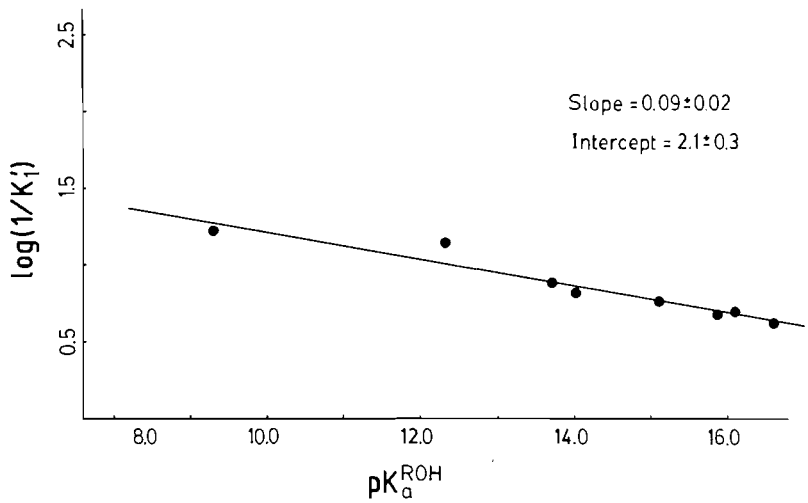

FIG. 1. The linear free energy relationship between the vanadate ester hydrolysis constants and the acidity constants of the product alcohols is shown. The experimental points are taken from the data of Table 2.

evident then, that phosphate alkyl ester formation is considerably more sensitive than vanadate alkyl ester formation to the pK_a of the alcohol. In fact the formation of vanadate alkyl esters shows a sensitivity to neighbouring substituents which is comparable to that attributable to electron withdrawal or donation as is evident for the formation of *t*-butyl vanadate, $K'_1 = 0.095 \pm 0.005 M^{-1}$ (10), 1-vanado-3-hydroxybutane, $K'_1 = 0.25 \pm 0.01 M^{-1}$ (10), 1-hydroxy-3-vanadobutane, $K'_1 = 0.29$

Can. J. Chem. Downloaded from www.nrcresearchpress.com by 196.1.178.254 on 09/07/12
For personal use only.

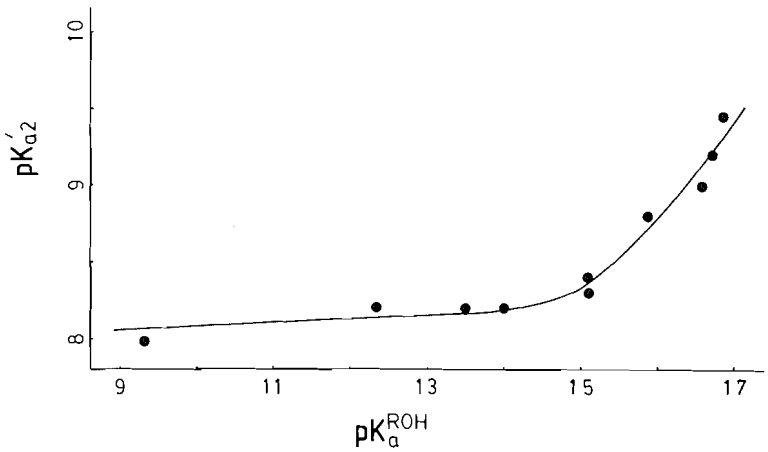

FIG. 2. The free energy relationship between the acidity constant of the vanadate esters, $HOVO_3R$, and those of the parent alcohols, ROH. The experimental points are taken from Table 1. (Note that the pK'_{a2} of this figure corresponds to the pK''_{a2} of Table 1.)

$\pm 0.02 M^{-1}$ (10) and 2-vanadopropionate, $K'_1 = 0.54 \pm 0.05 M^{-1}$ (13).

Interestingly enough, when an attempt was made to expand the considerations of pK_a to include hydroxylic compounds other than the alkyl alcohol systems of Table 2, no simple relationship between the pK_a of the parent hydroxyl and product formation was found. For instance, phosphate ($PO_4H_2^-$) with a pK_a of 6.70 readily forms a phosphovanadate anhydride, from $VO_4H_2^-$, with a formation constant of $64 \pm 3 M^{-1}$ (9). This value is much larger than the formation constants for vanadate esters from alkyl alcohols (Table 2) and clearly shows the presence of strong product stabilizing interactions which oppose the destabilizing interactions of electron withdrawal. Such stabilizing interactions apparently are much less significant for the case of formation of pyrophosphate from phosphate since pyrophosphate is a high energy phosphate product.

Somewhat similar behaviour is observed in the case of phenol. Phenylvanadate is formed with a formation constant of $1.0 M^{-1}$ (7), a value about 15 times larger than that expected for alkyl vanadates formed from alkyl alcohols of a similar pK_a^{ROH}, but about 4 orders of magnitude larger than phenyl phosphate formation (7). Behaviour such as this may indicate that the enhanced stabilization arises from vanadium *d*-orbital interactions with the π-system of the ligand. A variety of substituted phenols is currently being studied in an attempt to obtain more information concerning the factors influencing vanadate condensation reactions.

An additional point to be made from the information of Table 2 is that as the pK_a of the parent alcohol increases, the formation (K''_1) of $ROVO_3^{2-}$ from VO_4H^{2-} becomes increasingly favoured relative to the formation (K'_1) of $ROVO_3H^-$ from $VO_4H_2^-$. For example, for the very high pK_a alcohols such as *t*-butanol and *s*-butanol the proportion $K'_1 : K''_1$ is about 20:1 whereas with the low pK_a alcohols this proportion is about 1:1.

The effect that the aqueous solutions of the different alcohols have on the pK_{a2} of vanadate is rather small but significant. In general, the alcohol tends to increase the pK_a thus favouring the least ionized form of vanadate. Similar considerations also apply to the vanadate ester. If the effects of alcohol on the pK_a of $VO_4H_2^{1-}$ and on the pK_a of the ester $ROVO_3H^{1-}$ are similar, then the pK_a of the ester in dilute solution can be estimated by applying a correction factor obtained by comparing the pK_a of $VO_4H_2^{1-}$ in water ($pK_{a2} = 8.2$) to that observed for the aqueous alcoholic solutions in which the pK_a was measured (Table 1). The ester pK_a values estimated by this procedure are tabulated in Table 1 under pK''_{a2}. Corrections obtained by this type of procedure have been shown to be valid from studies of the effect of solvent on acid/base equilibria where it was concluded that solvent does not affect the relative strengths of acids as long as they are the same charge and same chemical type (14).

An interesting point of this study is revealed when the pK''_{a2} values of the alkyl esters and their parent alcohols are compared as shown in Fig. 2. From this graph it is seen that for alcohols with a pK_a below about 15, the pK''_{a2} values of the product esters are essentially constant; however, at a pK_a^{ROH} of about 15, the pK''_{a2} of the esters rise rapidly with increase in pK_a of the parent alcohols. The reason for this is not clear, but the behaviour indicates that the vanadium centre becomes saturated with electrons and any further electrons inductively introduced to the coordination centre are redistributed to the oxygens of the vanadate thus increasing pK''_{a2}. Below the critical pK_a^{ROH} the electron density may be localized to the vanadium centre. This behaviour is reminiscent of that observed for a homologous series of bidentate ligands where it was found that the coordination geometry and protonation state of the product vanadium(V) derivative depended in a rather subtle manner on the oxidation state of the ligand (13).

Acknowledgement

Thanks are gratefully extended to the Natural Sciences and Engineering Research Council of Canada for its support of this work.

1. N. D. CHASTEEN. Struct. Bonding Berlin, **53**, 105 (1983).
2. E. ERDMANN, K. WARDEN, W. KRAWIETZ, W. SCHMITZ, and H. SCHOLZ. Biochem. Pharmacol. **33**, 945 (1984).
3. B. J. HALES, E. E. CASE, J. E. MORNINGSTAR, M. F. DZEDA, and L. A. MAUTERER. Biochemistry, **25**, 7251 (1986).
4. R. WEVER, E. DE BOER, H. PLAT, and B. E. KRENN. FEBS Lett. **216**, 1 (1987).
5. T. RAMASARMA and F. L. CRANE. Curr. Top. Cell. Regul. **20**, 247 (1981).
6. M. J. GRESSER and A. S. TRACEY. J. Am. Chem. Soc. **107**, 4215 (1985).

Can. J. Chem. Downloaded from www.nrcresearchpress.com by 196.1.178.254 on 09/07/12
For personal use only.

7. A. S. TRACEY and M. J. GRESSER. Proc. Natl. Acad. Sci. USA, **83**, 609 (1986).
8. N. BOURNE and A. WILLIAMS. J. Org. Chem. **49**, 1200 (1984).
9. M. J. GRESSER, A. S. TRACEY and K. M. PARKINSON. J. Am. Chem. Soc. **108**, 6229 (1986).
10. A. S. TRACEY and M. J. GRESSER. Can. J. Chem. In press.
11. L. PETTERSSON, B. HEDMAN, A.-M. HENNER, and I. ANDERSSON. Acta Chem. Scand. **1739**, 499 (1985).
12. M. T. POPE and B. W. DALE. Chem. Soc. London, Q. Rev. **22**, 527 (1968).
13. A. S. TRACEY, M. J. GRESSER, and K. M. PARKINSON. Inorg. Chem. **27**, 629 (1986).
14. C. H. ROCHESTER. The chemistry of the hydroxyl group. Pt. 1. *Edited by* S. Patai. Interscience Publishers. 1971. p. 380.
15. A. S. TRACEY and M. J. GRESSER. Inorg. Chem. **27**, 157 (1988).
16. M. J. GRESSER and A. S. TRACEY. J. Am. Chem. Soc. **108**, 1935 (1986).
17. S. TAKAHASHI, L. A. COHEN, H. K. MILLER, and E. G. PEAKE. J. Org. Chem. **36**, 1205 (1971).

Can. J. Chem. Downloaded from www.nrcresearchpress.com by 196.1.178.254 on 09/07/12
For personal use only.

Fungal biotransformation of 1,3-oxathiolanes

HERBERT L. HOLLAND AND BENITO MUNOZ
Department of Chemistry, Brock University, St. Catharines, Ont., Canada L2S 3A1

Received January 14, 1988

HERBERT L. HOLLAND and BENITO MUNOZ. Can. J. Chem. **66**, 2299 (1988).

A series of 2,2-disubstituted 1,3-oxathiolanes has been incubated with fungi known to be capable of efficient asymmetric oxidation of sulfides to sulfoxides. In three cases (2-phenyl-1,3-oxathiolane, 2-methyl-2-phenyl-1,3-oxathiolane, and 2-*tert*-butyl-2-phenyl-1,3-oxathiolane), sulfoxidation occurred to give a single diastereomer of sulfoxide, whose relative stereochemistry has been assigned by ^{1}H nuclear magnetic resonance analysis. The sulfoxides were obtained as racemates or had low enantiomeric enrichment. In some cases ketones, assumed to be formed by spontaneous hydrolysis of oxathiolane sulfoxides, were obtained, together with their reduction products, secondary alcohols.

HERBERT L. HOLLAND et BENITO MUNOZ. Can. J. Chem. **66**, 2299 (1988).

On a soumis une série d'oxathiolanes-1,3 disubstitués en position-2,2 à une incubation avec des champignons qui sont connus pour leur capacité de provoquer une oxydation asymétrique des sulfures en sulfoxydes. Dans trois cas (phényl-2, méthyl-2 phényl-2 et *tert*-butyl-2 phényl-2 oxathiolanes-1,3), la réaction de sulfoxydation se produit pour conduire à un seul sulfoxyde diastéréomère dont la stéréochimie relative a été déterminée par une analyse du spectre en résonance magnétique nucléaire du ^{1}H. Les sulfoxydes ont été obtenus sous la forme de racémates ou de mélanges pour lesquels l'enrichissement énantiomérique est faible. Dans quelques cas, on a obtenu des cétones, qui se sont vraisemblablement formées par une hydrolyse spontanée des sulfoxydes d'oxathiolanes, ainsi que les alcools secondaires qui proviennent de leur réduction.

[Traduit par la revue]

Can. J. Chem. Downloaded from www.nrcresearchpress.com by 112.217.228.212 on 09/07/12
For personal use only.

The use of actively growing or resting cultures of fungi to convert organic sulfides of type R^1—S—R^2 to the corresponding sulfoxides, with introduction of chirality at the sulfur atom, represents, in many cases, the most efficient method for the preparation of such chiral molecules (1–3). Not only can this enzymatic reaction occur with selective oxidation of the enantiotopic electron pairs of sulfur (1–3), but, with appropriate substrates such as the 1,3-dithianes (**1**), enzymic sulfoxidation can also result in enantioenrichment at C-2 by selection between the two enantiotopic sulfur atoms (4, 5).

We have studied a range of substituted 1,3-oxathiolanes (**2**) as substrates for sulfoxidation by four fungi known to be capable of efficient asymmetric sulfoxidation of sulfides, namely *Mortierella isabellina* (2, 6) *Helminthosporium* species (6), *Aspergillus niger* (1), and *Rhizopus arrhizus* (5). These substrates, readily prepared from the corresponding ketones by treatment with 2-mercapto ethanol, offer the possibility of induction of chirality at C-2 concomitant with selective oxidation at the single sulfur atom. Neither 1,3-oxathiolanes nor the corresponding dithiolanes, dithio ethylene ketals, have been previously studied as substrates for fungal biotransformation.

Of the range of oxathiolane substrates studied, only three (**2***a*–**2***c*) were converted to sulfoxides (**3***a*–**3***c*, respectively) by *M. isabellina*, in a low yield (see Table 1). Of the other fungi studied, only *R. arrhizus* gave a sulfoxide product, **3***c*. In some cases (**2***a*–**2***d* and **2***g* with *M. isabellina*, and **2***c* and **2***d* with *R. arrhizus*), products were obtained that were identified as the corresponding ketones **5** and (or) the secondary alcohols **6**. Since these fungi are known to be capable of reducing a carbonyl group (7, 8), the latter products were presumably produced by the enzymic reduction of the corresponding ketones (**5**). In two cases (**5***a* → **6***a* and **5***c* → **6***d*) this was confirmed by the use of the ketones as substrates for *M. isabellina*; the alcohols produced in this way had the same enantiomeric enrichments and predominant absolute stereochemistries as those isolated from the use of oxathiolane substrates, strongly suggesting the intermediacy of ketones in the production of alcohols from oxathiolanes.

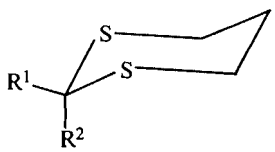

1

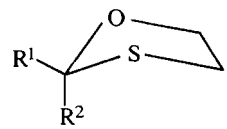

2

a; R^1 = Ph, R^2 = H
b; R^1 = Ph, R^2 = CH_3
c; R^1 = Ph, R^2 = *t*-C_4H_9
d; R^1 = R^2 = Ph
e; R^1 = CH_3, R^2 = C_2H_5
f; R^1 = CH_3, R^2 = *n*-C_3H_7
g; R^1 = CH_3, R^2 = *t*-C_4H_9
h; R^1 = CH_3, R^2 = cyclo-C_6H_{11}

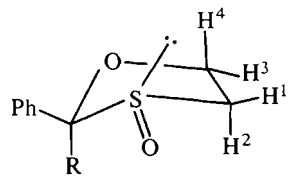

3

a; R = H
b; R = CH_3
c; R = *t*-C_4H_9

$PhCH(CH_3)SCH_2CH_2OH$

4

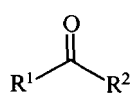

5

a; R^1 = Ph, R^2 = CH_3
b; R^1 = Ph, R^2 = *t*-C_4H_9
c; R^1 = CH_3, R^2 = *t*-C_4H_9

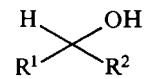

6

a; R^1 = Ph, R^2 = CH_3
b; R^1 = Ph, R^2 = *t*-C_4H_9
c; R^1 = R^2 = Ph
d; R^1 = CH_3, R^2 = *t*-C_4H_9
e; R^1 = Ph, R^2 = H

The ketones **5** could be produced as the hydrolysis products of either the oxathiolane **2** or the corresponding sulfoxide, **3**. We favour the intermediacy of the latter for the following reasons: control experiments with inactivated enzymes (auto-

TABLE 1. Biotransformation of oxathiolanes **2** by fungi

Substrate	Conditions*	Products (% yield) *M. isabellina*	*R. arrhizus*	*H. species*	*A. niger*
2*a*		**3***a*(8), **6***e*(4)	—	—	—
2*b*		**3***b*(5), **5***a*(2), **6***a*(2)	None	None	None
2*b*	pH 7.1	**5***a*(3)	—	—	—
2*b*	Autoclaved fungus	**2***b*(88)	—	—	—
2*c*		**3***c*(3), **5***b*(1) **6***b*(3)	**3***c*(3), **5***b*(1), **6***b*(3)	None	None
2*d*		**6***c*(20)	**6***c*(5)	None	None
2*d*	Autoclaved fungus	**2***d*(82)	—	—	—
2*e*		None	None	None	None
2*f*		None	None	None	None
2*g*		**5***c*(1), **6***d*(2)	None	None	None
2*g*	Autoclaved fungus	**2***g*(70)	—	—	—
2*h*		None	None	None	None

*Normal (see Experimental) unless otherwise stated.

claved fungus) suggest that the oxathiolanes are stable to non-enzymic hydrolysis under the conditions of the incubation. Thus **2***b*, **2***d*, and **2***g* were recovered unchanged, and unaccompanied by ketone, from incubation with inactivated *M. isabellina* (Table 1). Furthermore, oxathiolane sulfoxides, as discussed below and noted by others,[1] are hydrolytically labile. These observations suggest that, in cases where ketone and (or) alcohol products were observed in the absence of isolated sulfoxide (e.g., from **2***d* and **2***g*), the latter may have been formed but subsequently hydrolysed in the aqueous incubation medium.

The oxathiolane sulfoxides **3***a*–**3***c* were all characterized by spectral means. All were racemic ($[\alpha]_D$ 0°) with the exception of **3***c* produced by *M. isabellina*, which had an enantiomeric excess determined by ^{1}H nmr in the presence of chiral shift reagent to be less than 10%. In no case, however, was any evidence found either chromatographically or spectroscopically for the presence of more than one diastereomer of sulfoxide. The compounds were all hydrolytically labile, rapidly producing the corresponding ketone together with unidentified lower molecular weight species on standing on the bench or in wet organic solvents. The stability is in the order **3***c* ≫ **3***b* > **3***a*: the former compound can be stored for weeks under a dry argon atmosphere at −20°C, the latter surviving no more than a few days even under these conditions, and only a few hours in chloroform solution. In view of the rapid decomposition of **3***a* under analytical conditions (e.g., during acquisition of nmr and optical rotation data), the incubation of **2***a* was performed only with *M. isabellina*.

The relative stereochemistry of the oxathiolane sulfoxides was determined by ^{1}H nmr analysis of the spectrum of **3***b*, and then correlation of this spectrum with those of **3***a* and **3***c* (see Table 2). The ^{1}H nmr spectrum of **3***b* showed, in addition to signals attributed to the phenyl and methyl groups, a clearly defined set of four multiplet signals assigned to H-1–H-4 of **3***b* as follows: of the S-methylene proton signals centred at δ 2.8 and 3.0 ppm, the lower field set were assigned to H-2, *cis* to the sulfoxide oxygen, with the signals of H-1 assigned at 2.8 ppm. The downfield shift of signals from hydrogens *cis* to sulfoxide oxygen has previously been used for the assignment of relative stereochemistry of substituted dithiane sulfoxides derived from **1** (4, 5).

TABLE 2. The ^{1}H nmr data for **2***a*–**2***c*

Protons	δ, ppm **2***a*	**2***b*	**2***c*
H-1	2.8	2.8	2.5
H-2	3.0	3.0	2.9
H-3	4.5	4.4	4.2
H-4	4.7	4.7	4.8
	Coupling constants, Hz		
$J_{1,2}$	13.5	14.7	13.6
$J_{1,3}$	7.1	6.4	7.3
$J_{1,4}$	6.8	6.6	6.4
$J_{3,4}$	9.6	10.5	8.9
$J_{2,4}$	7.0	7.5	6.9
$J_{2,3}$	5.4	5.3	5.2

The other two sets of methylene signals in the spectrum of **3***b* belonged to the O-methylene protons, and appeared as multiplets centred at δ 4.4 and 4.7 ppm. They were assigned to H-3 and H-4 respectively, on the grounds of the expected downfield shift in the presence of a 1,3 phenyl substituent, and on the basis of 2-D COSY and selective proton decoupling experiments that gave the following coupling constants, consistent with the resonance assignments: $J_{1,2(gem)}$ = 14.7 Hz, $J_{1,4}$ = 6.6 Hz, $J_{1,3}$ = 6.4 Hz, $J_{2,4}$ = 7.5 Hz, $J_{2,3}$ = 5.3 Hz, and $J_{3,4(gem)}$ = 10.5 Hz.

Irradiation at δ 1.7 ppm (C-CH_3) caused a nuclear Overhauser enhancement (nOe) of the signals assigned to H-2 (45%) and H-3 (10%), but no effect on the signals of H-1 or H-4, confirming the *cis* placement of methyl and H-2, and therefore indirectly the *cis* arrangement of methyl and sulfoxide oxygen shown in structure **3***b*.

The methylene proton signals of **3***b* could be closely simulated by Intercal or NMRcal programs, and were almost identical with those observed for **3***a* and **3***c*, with minor chemical

[1]O. de Lucci. Personal communication.

Can. J. Chem. Downloaded from www.nrcresearchpress.com by 112.217.228.212 on 09/07/12
For personal use only.

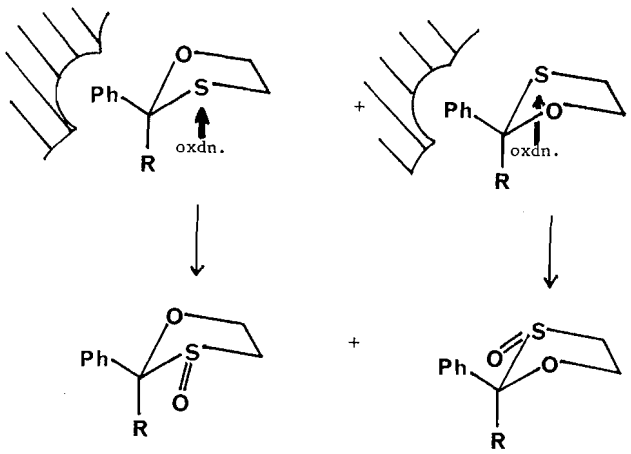

FIG. 1. Binding and sulfoxidation of 2-phenyl-1,3-oxathiolanes.

shift and J differences (see Table 2). No nOe enhancements were observed between the C-2 substituent and methylene hydrogens of **3***c*, and the experiment was not carried out on **3***a* because of instability problems, but the close correspondence between the methylene splitting patterns of **3***a*–**3***c* confirm that all three compounds have the same relative configuration.

Diastereomeric sulfoxides derived from chemical oxidation of **2***b* under modified Sharpless conditions have recently been reported, but without assignment of any relative or absolute stereochemistry (9). In our hands, routine chemical methods of sulfoxidation of **2***b* (*m*-chloroperoxybenzoic acid in methylene chloride or two-phase buffered systems, sodium metaperiodate, or hydrogen peroxide) all resulted in the isolation of acetophenone as the only reaction product.

The chemical oxidation of **2***b* referred to above (9) produces a close to racemic mixture of diastereomers (diastereomeric ratio 78:22, ee 3% by nmr) (9). Although the enzymic oxidations described herein produce only a single diastereomer, with one exception (see above), **3***a*–**3***c* were also obtained as racemates. This is surprising in view of the apparent specific aryl binding capability of the sulfoxidizing enzyme(s) of *M. isabellina* (3), but can be explained by the hypothesis outlined in Fig. 1, in which random but phenyl-dependent binding is followed by diastereospecific oxidation from the side opposite to the aromatic substituent. *Mortierella isabellina* is capable of sulfoxidation of benzyl thioethers in 10–40% yield (10), but nothing is known about the stereochemistry of the reaction.

To investigate the possibility that racemization of **3** may occur by reversible ring opening, the open-chain oxathiolane analogue **4** was used as substrate for *M. isabellina*. The only biotransformation product, the corresponding sulfoxide, was produced in 12% yield and was stable under normal conditions, but close to racemic ($[\alpha]_D^{20}$ −0.85°), suggesting an intrinsic lack of stereoselectivity in the sulfoxidation of benzyl thioethers. In the absence of a sample of oxathiolane sulfoxide of moderate to high optical purity, however, the possibility of racemization by ring opening cannot be eliminated from consideration, nor can other possible routes for racemization. Selective further metabolism of one sulfoxide enantiomer, as reported for some 1,3-dithiane sulfoxides (4, 5), may be occurring, but the hydrolytic lability of the oxathiolane sulfoxides precludes their use as substrates for biotransformation, so no data are available on this possibility.

It is therefore apparent that, although the fungal sulfoxidation of 2-phenyl-1,3-oxathiolanes produces racemic or nearly racemic material, the method does, unlike the only successful chemical method of oxidation (9), produce a single diastereomer of product in a consistent manner.

Experimental

Apparatus, materials, and methods

Melting points were determined on a Gallenkamp apparatus and are uncorrected. Infrared spectra were recorded with an Analect FX-6260 FTIR interfaced with a MAP-66 data system. The ^{1}H nmr spectra were obtained at 200 MHz and ^{13}C nmr at 50.3 MHz using a Bruker AC-200 FT instrument, $CDCl_3$ as solvent, and TMS as internal standard. Fast atom bombardment (FAB) mass spectra were obtained with a Kratos MS30 instrument with a saddle field gun (Ion Tech), operating at 7 keV using a glycerol sample matrix and argon beam. Electron impact (EI) mass spectra were recorded on a Kratos/AEI MS30 at 70 eV. Optical rotation measurements were obtained with a Rudolph Autopol III using a 10-cm cell and ethanol as solvent.

Computer simulated ^{1}H nmr spectra were generated using an Iteration of Calculated NMR Spectrum using Least Squares Criteria (ITRCAL) or a Nuclear Magnetic Resonance Spectrum Calculation (NMRCAL) program.

Flash column chromatography was performed using Merck silica gel 9385 (230–400 mesh), and thin-layer chromatography on Merck silica gel 60F 254.

Enantiomeric excesses were determined by ^{1}H nmr in CCl_4 solution in the presence of tris[3-(trifluoromethylhydroxymethylene)-(+)-camphorato], europium III derivative, at a relative concentration of 0.8–1.2 M, as previously described by us (7).

Mortierella isabellina NRRL 1757, *Aspergillus niger* ATCC 9142, and *Rhizopus arrhizus* ATCC 11145 were grown at 28°C and maintained at 4°C on malt agar slopes. *Helminthosporium* species NRRL 4671 was grown at 28°C and maintained at 4°C on V-8 juice agar slopes (ATCC medium 343).

Preparation of substrates

1,3-Oxathiolanes **2**a–**2**h

These were prepared from the corresponding ketone or aldehyde in 83–92% yield using the method of Djerassi and Gorman (11). All compounds gave satisfactory spectral and analytical data. The procedure is outlined below for the case of **2***b*.

A solution of acetophenone (17 g), 2-mercaptoethanol (10 g), and *p*-toluenesulfonic acid monohydrate (1 g) in anhydrous benzene (100 mL) was refluxed in a flask fitted with a Dean–Stark trap until no more water appeared in the separator (3 h). The solution was then cooled, washed ($NaHCO_3$, H_2O), and dried (Na_2SO_4). Evaporation yielded 2-methyl-2-phenyl-1,3-oxathiolane (**2***b*), (21.5 g); oil; ir, no CO stretch; ^{1}H nmr, δ: 1.9 (3H, s, CH_3), 2.4–3.1 (2H, m, —CH_2—S—), 3.8–4.5 (2H, m, —CH_2—O—), and 7.0–7.5 (5H, m, phenyl H) ppm; EI ms *m/z* (%): 180(10), 165(2), 120(3), 78(100). *Anal.* calcd. for $C_{10}H_{12}OS$: C 66.63, H 6.71, S 17.78%; found: C 66.42, H 6.61, S 17.92%. Other physical properties were identical with those reported (12).

1-Phenylethyl 2′-hydroxyethyl sulfide (4)

2-Mercaptoethanol (5 g) was added slowly to a stirred suspension of sodium hydride (2.5 g) in anhydrous benzene (25 mL), and the resulting mixture refluxed gently during subsequent addition of 1-chloro-1-phenylethane (9 g). The reaction mixture was refluxed for a further 24 h, then poured onto water (50 mL), and extracted with ether. The combined ethereal extract was dried (Na_2SO_4) and evaporated to give **4** (5.2 g). Purification by flash column chromatography using ethyl acetate:hexane (4:1) as solvent gave pure **4** (2.8 g), whose physical properties were identical with those reported (12); ir ν_{max}: 3300 (OH), but absence of 2650 (SH) cm^{-1}; ^{1}H nmr, δ: 1.5 (3H, d, —CH_3), 2.0 (1H, br s, —OH), 2.5 (2H, t, —CH_2—S—), 3.5 (2H, t, —CH_2—O—), 3.9 (1H, q, CH), and 7.1 (5H, br s, phenyl H) ppm.

Growth of microorganisms

Mortierella isabellina

The growth medium used in the cultivation of *M. isabellina* con-

Can. J. Chem. Downloaded from www.nrcresearchpress.com by 112.217.228.212 on 09/07/12
For personal use only.

Can. J. Chem. Downloaded from www.nrcresearchpress.com by 112.217.228.212 on 09/07/12
For personal use only.

sisted of a mixture of glucose (40 g), soy grits (5 g), yeast extract (5 g), sodium chloride (5 g), and dibasic potassium phosphate (5 g) per litre of distilled water. The growth medium (150 mL) was transferred to 1-L flasks, and the flasks were stoppered with sponge plugs and sterilized at 15 psi (1 psi = 6.9 kPa) and 121°C for 15 min, following which they were allowed to cool to room temperature. The fungus was transferred from slopes into the growth medium under sterile conditions, and the flasks placed on a rotary shaker (180 rpm) for 3 days at 26°C.

After 3 days, the mycelial growth was isolated by filtration, and washed with distilled water. The resulting fungal growth was divided into equal parts and resuspended in distilled water (150 mL/flask). The substrate was dissolved in 95% ethanol in the ratio of 1.0 g of substrate to 10 mL of solvent, and to each flask was added 1 mL of substrate solution. Incubations were carried out for 72 h, and the medium and fungal growth then separated by filtration.

The medium was continuously extracted over a 72-h period with dichloromethane, dried over anhydrous sodium sulfate, and evaporated. The medium residue was chromatographed either by using a benzene–ether stepwise gradient or by using mixtures of hexane and ethyl acetate as eluants. The fractions were analyzed by tlc and appropriate fractions pooled and subjected to ^{1}H nmr, ^{13}C nmr, ir, optical rotation, and mass spectrometric analysis.

The filtered fungus was blended twice in a Waring Blender with dichloromethane (200 mL) and the filtrate dried and evaporated.

Aspergillus niger

Aspergillus niger was grown in a Czapek Dox broth medium (35 g/L). The growth medium (150 mL) was transferred to 1-L flasks. Standard sterilization, filtration, incubation, extraction, and analysis procedures as outlined above were then followed.

Helminthosporium *species*

A procedure similar to that described above was followed for this fungus, using a growth medium consisting of V-8 juice (200 mL) and calcium carbonate (3 g) per litre of distilled water, adjusted to a pH of 7.2.

Rhizopus arrhizus

The procedure was similar to those previously described with two alterations: firstly, the growth medium consisted of a mixture of glucose (40 g), peptone (20 g), and corn steep liquor (5 mL) per litre of distilled water. Secondly, prior to incubation with the substrate, the fungus was blended in a Waring Blender for approximately two 1-s periods.

Incubation of substrates

The results are summarized in Table 1.

*2-Phenyl-1,3-oxathiolane (2*a)

Incubation of **2***a* (1 g) with *M. isabellina* gave extracts from the medium (0.09 g) and fungus (0.12 g). The latter extract contained only **2***a*. Chromatography of the medium extract yielded benzyl alcohol (**6***e*) (0.04 g), followed by the sulfoxide, **3***a* (0.08 g), as an unstable oil; $[\alpha]_D^{20}$ +0.008 ± 0.05°; ir ν_{max}: 1050 (S=O) cm^{-1}; ^{1}H nmr, δ: 2.5–2.9 (2H, m, —CH_2—S(O)—), 4.4–4.8 (2H, m, —CH_2—O—), 5.4 (1H, s, —CH), and 7.4 (5H, br s, phenyl H) ppm. Details of assignments and coupling constants are in Table 2; ^{13}C nmr, δ: 52.7 (—CH_2—S(O)—), 69.8 (—CH_2—O—), 111.65 (C(O)S), 125.9 and 128.9 (aromatic *o*- and *m*-C's), 129.4 (aromatic *p*-C), and 133.3 (aromatic C-1) ppm; EI ms *m/z* (%): 182 (16, M^+), 154(27), 126(12), 105(100), 77(65).

*2-Methyl-2-phenyl-1,3-oxathiolane (2*b)

(*i*) Incubation of 1 g of **2***b* with *M. isabellina* gave medium and fungal extracts of 0.26 g and 0.2 g respectively. The latter contained only **2***b*; chromatography of the former extract gave, in order of elution, **2***b* (0.01 g), acetophenone (**5***a*) (0.02 g), 1-phenylethanol (**6***a*) (0.02 g) ($[\alpha]_D^{20}$ −21.1°, ee 51%), and the sulfoxide **3***b* (0.05 g), mp 77–79°C; $[\alpha]_D^{20}$ +0.08 ± 0.1°; ir ν_{max}: 1040 (S=O) cm^{-1}; ^{1}H nmr δ: 1.7 (3H, s, CH_3), 2.7–3.0 (2H, m, —CH_2—S(O)—), 4.3–4.8 (2H, m, —CH_2—O—), and 7.3 (5H, br s, phenyl H's) ppm. Details of assignments and coupling constants are in Table 2; ^{13}C nmr, δ 22.2 (CH_3), 51.1 (—CH_2—S(O)—), 68.1 (—CH_2—O—), 106.7 (C(O)S), 125.2 and 128.9 (aromatic *o*- and *m*-C's), 128.5 (aromatic *p*-C), and 139.0 (aromatic C-1) ppm; FAB ms *m/z* (%): 197 (13, M + 1), 196 (19, M^+), 126(6), 121(34), 105(21), 97(14), 77(71).

(*ii*) Incubations of **2***b* with *R. arrhizus*, *H.* species, or *A. niger* resulted only in the recovery of **2***b* from either medium or fungal extracts.

(*iii*) Incubation of **2***b* with *M. isabellina* in 0.1 M phosphate buffer, pH 7.1, under conditions otherwise identical with those described above, afforded a medium extract (0.2 g) from which only acetophenone (0.03 g) was recovered. The fungal extract contained **2***b* as the only exogenous material.

(*iv*) Incubation of **2***b* (1 g) with autoclaved cells of *M. isabellina* gave extracts from the fungus (0.86 g) and medium (0.26 g) from which a total of 0.88 g of **2***b* was recovered as the only exogenous material.

*2-*tert*-Butyl-2-phenyl-1,3-oxathiolane (2*c)

(*i*) Incubation of **2***c* (1 g) with *M. isabellina* gave a medium extract (0.22 g) that upon chromatography gave recovered **2***c* (0.015 g), 2,2-dimethylpropiophenone (**5***b*) (0.01 g), 2,2-dimethyl-1-phenyl-1-propanol (**6***b*) (0.03 g), and the sulfoxide **3***c* (0.03 g), mp 64–66°C; $[\alpha]_D^{20}$ −13.3 ± 0.1°, ee 4%; ir ν_{max}: 1050 (S=O) cm^{-1}; ^{1}H nmr, δ: 1.12 (9H, s, CH_3), 2.4–2.9 (2H, m, —CH_2—S(O)—), 4.2–4.8 (2H, m, —CH_2—O—), 7.4 (5H, br s, phenyl H) ppm; ^{13}C nmr δ: 27.0 (CH_3), 39.4 ($C(CH_3)_3$), 50.7 (—CH_2S(O)—), 67.7 (—CH_2—O—), 112.9 (C(O)S), 126.9 and 128.4 (*o*- and *m*-aromatic C's), 128.2 (*p*-aromatic C), and 136.1 (C-1 aromatic C) ppm; FAB ms *m/z* (%): 238 (50, M^+), 195(6), 163(93), 146(24), 119(31), 105(67), 77(100).

(*ii*) Incubation of **2***c* (1 g) with *R. arrhizus* gave a medium extract (0.22 g) that afforded **5***b* (0.01 g), **6***b* (0.03 g), and **3***c* (0.03 g), mp 63–67°C, identical with the sample described above except that $[\alpha]_D^{20}$ = 0.5 ± 0.1°.

(*iii*) Incubation of **2***c* with *H.* species or *A. niger* resulted in the recovery of **2***c* as the only exogenous material.

*2,2-Diphenyl-1,3-oxathiolane (2*d)

(*i*) Incubation of 1 g of **2***d* with *M. isabellina* or *R. arrhizus* gave medium extracts that contained diphenyl methanol **6***c* as the only exogenous materials in yields of 20% and 5%, respectively. Incubation of **2***d* with the other fungi used in this study resulted only in the recovery of unchanged substrate.

(*ii*) Incubation of **2***d* with autoclaved *M. isabellina* gave medium and fungal extracts from which a total of 82% of **2***d* was recovered as the only exogenous material.

*2-*tert*-Butyl-2-methyl-1,3-oxathiolane (2*g)

(*i*) Incubation of **2***g* (1 g) with *M. isabellina* gave a medium extract (0.25 g) that upon chromatography afforded **2***g* (0.015 g), *tert*-butyl methyl ketone (**5***c*) (0.01 g), and 2,2-dimethyl-3-butanol (**6***d*) (0.02 g); $[\alpha]_D^{20}$ +0.5 ± 0.1°. Only unchanged substrate was recovered following incubation of **2***g* with *R. arrhizus*, *H.* species, or *A. niger*.

(*ii*) Incubation of **2***g* (0.5 g) with autoclaved *M. isabellina* gave a total recovery of 70% of unchanged substrate from medium and fungal extracts.

*2-Ethyl-2-methyl-1,3-oxathiolane (2*e), *2-methyl-2-*n*-propyl-1,3-oxathiolane (2*f), *and 2-cyclohexyl-2-methyl-1,3-oxathiolane (2*h)

The above substrates were recovered unchanged in yields of 50–80% following incubation with any of the fungi used in this study.

*Acetophenone (5*a)

Incubation of **5***a* with *M. isabellina* to yield *S*-(−)-1-phenylethanol in a yield of 87% and ee of 54% has previously been described (7).

*tert-Butyl methyl ketone (5*c)

Incubation of **5***c* (2 g) with *M. isabellina* gave extracts from the fungus (0.26 g) and medium (1.52 g). The latter extract afforded 2,2-dimethyl-3-butanol (1.45 g, 72%), with $[\alpha]_D^{20}$ +0.6 ± 0.1°.

Acknowledgements

Financial support was provided by the Natural Sciences and Engineering Research Council of Canada as an operating grant

to H.L.H. and by the Ontario Ministry of Education as a graduate scholarship to B.M. We are grateful to F. M. Brown for maintenance of the culture collection, and to T. R. B. Jones and D. Vukmanic for assistance in acquisition of spectral data.

1. B. J. Auret, D. R. Boyd, H. B. Henbest, and S. Ross. J. Chem. Soc. C, 2371 (1968).
2. H. L. Holland, H. Pöpperl, R. W. Ninniss, and P. C. Chenchaiah. Can. J. Chem. **63**, 1118 (1985).
3. H. L. Holland. Chem. Rev. **88**, 473 (1988).
4. B. J. Auret, D. R. Boyd, F. Breen, R. M. E. Greene, and P. M. Robinson. J. Chem. Soc. Perkin Trans. 1, 930 (1981).
5. B. J. Auret, D. R. Boyd, E. S. Cassidy, R. Hamilton, F. Turley, and A. F. Drake. J. Chem. Soc. Perkin Trans. 1, 1547 (1985).
6. E. Abushanab, D. Reed, F. Suzuki, and C. J. Sih. Tetrahedron Lett. 3415 (1978).
7. H. L. Holland, E. J. Bergen, P. C. Chenchaiah, S. H. Khan, B. Munoz, R. W. Ninniss, and D. Richards. Can. J. Chem. **65**, 502 (1987).
8. H. L. Holland, F. M. Brown, B. Munoz, and R. W. Ninniss. J. Chem. Soc. Perkin. Trans. 2. In press.
9. O. Bortolini, F. Di Furia, G. Licini, G. Modena, and M. Rossi. Tetrahedron Lett. **27**, 6257 (1986).
10. H. L. Holland and I. M. Carter. Can. J. Chem. **60**, 2420 (1982).
11. C. Djerassi and M. Gorman. J. Am. Chem. Soc. **75**, 3704 (1953).
12. E. L. Eliel, L. A. Pilato, and V. G. Badding. J. Am. Chem. Soc. **84**, 2377 (1962).

Can. J. Chem. Downloaded from www.nrcresearchpress.com by 112.217.228.212 on 09/07/12
For personal use only.

EPR study of the long-range effect of a β-carbon chiral center on the magnetic equivalence of β-methylene protons[1]

PETER SMITH[2] AND WILLIAM HARLEY DONOVAN

Paul M. Gross Chemical Laboratory, Department of Chemistry, Duke University, Durham, NC 27706, U.S.A.

Received February 25, 1988

PETER SMITH and WILLIAM HARLEY DONOVAN. Can. J. Chem. **66**, 2304 (1988).

Using aqueous $TiCl_3$-based continuous-flow, radical-generating methods at 25°C we have carried out a comprehensive EPR study of hydroxyl- and aminyl-radical addition to eight alkene substrates that yielded radicals of general formula XCH_2—$\dot{C}Y$—C*HR^1R^2, where C* is a chiral center, to investigate the magnetic inequivalence of β-CH_2 protons arising from a nonadjacent β-C chiral center. We attribute the observed nonequivalence to the long-range influence of the chiral center in these radicals, and note that our results are consistent with the reasonable expectation that the presence of bulky groups in the radicals is likely to favor particular conformations, leading to more easily observed inequivalence of the β-CH_2 proton splittings.

PETER SMITH et WILLIAM HARLEY DONOVAN. Can. J. Chem. **66**, 2304 (1988).

Opérant à 25°C et utilisant des méthodes de production de radicaux basées sur des écoulements continus de solutions aqueuses de $TiCl_3$, on a réalisé une étude rpe détaillée d'additions des radicaux hydroxyle et aminyle sur huit alcènes conduisant à des radicaux de formule générale XCH_2—CY—C*HR^1R^2 dans lesquels C* est un centre chiral; ces expériences ont été réalisées afin d'évaluer si les protons CH_2 en β, qui sont soumis à l'influence d'un centre chiral qui n'est pas adjacent, sont équivalents. On a observé qu'ils ne sont pas équivalents et on attribue ce résultat à l'influence à longue distance du centre chiral présent dans ces radicaux; de plus, on note que nos résultats sont en accord avec les attentes qu'on peut raisonnablement avoir si on admet que la présence de groupements volumineux dans les radicaux devrait favoriser des conformations particulières et ainsi conduire à une inéquivalence plus facilement observable des couplages des protons CH_2 en β.

[Traduit par la revue]

Introduction

Recently (1), we presented the results of an EPR study of three XCH_2—$\dot{C}H$—$CH(OH)CH_2X$ radicals, with -X = -CN, -COOH, and -OH, formed from symmetrical 1,2-disubstituted alkenes in aqueous solution at ca. 25°C with use of the $TiCl_3$–H_2O_2, continuous-flow, radical-generating method (2). Two of these radicals showed magnetic inequivalence of their β-CH_2 protons due to the presence of a nonadjacent β-chiral carbon, an EPR phenomenon that has received little attention (3–7) and, in the case of acyclic C-centered radicals, no systematic study (5–7). Similar long-range effects of molecular asymmetry are numerous in the NMR literature (8–12), and the adjacent chiral effect, namely, magnetic inequivalence of β-CH_2 protons adjacent to a γ-C chiral center or of γ-CH_2 protons adjacent to a β-C chiral center, is common in EPR spectroscopy (13–23).

Previously (1), we stressed the importance to spectral interpretation of recognizing the possibility of there being inequivalent β-CH_2 protons in radicals with a nonadjacent chiral center. The present investigation successfully extends our previous study of the nonadjacent chiral effect; specifically, to determine how often inequivalence of β-CH_2 protons can occur in radicals of general structure XCH_2—$\dot{C}Y$—CHR^1R^2, derived from mono-, di-, and tri-substituted alkenes employing the $TiCl_3$–H_2O_2 and –NH_2OH reaction systems. With this larger body of data now available, we are able to substantially reinforce and extend the major conclusions of the earlier, more limited study (1).

Experimental

The experimental arrangements and procedures were essentially as before (15). However, the spectrum-simulation program was that of Oehler and Janzen (24). The field-modulation amplitude was normally 0.50×10^{-1} to 2.00×10^{-1} G and all reported results refer to that range. The substrates examined were 2-acetoxy-3-butenenitrile, **1** (97%), 3-butene-2-ol, **2** (99%), *cis*-2-butene-1,4-diol, **3** (91%), *cis*-1,4-diacetoxy-2-butene, **4** (92%), 1,4-dicyano-2-butene, **5** (97%), *trans*-β-hydromuconic acid, **6** (98%), and 3-butene-1,2,3-tricarboxylic acid **7** (97%), all from Aldrich, except **4** (American Tokyo Kasei) and **7** (Lancaster Synthesis), and used as received; and (*E*)-propene-1,2,3-tricarboxylic acid, **8**, which we synthesized via a standard procedure (25).

When employing the $TiCl_3$–H_2O_2 method, the reducing stream was 0.004 M in $TiCl_3$, the oxidizing stream 0.1 M in H_2O_2, and both streams 0.1 M in H_2SO_4 and 0.02–0.10 M in substrate; also, the total flow rate (4–6 mL s^{-1}) was equally distributed between the two streams. When using the $TiCl_3$–NH_2OH system, the reaction conditions were as for the $TiCl_3$–H_2O_2 work except that we replaced the H_2O_2 in the oxidizing stream by 0.5 M $NH_2OH \cdot HCl$ (96%, Eastman) and made the total flow rate 2 mL s^{-1}. All results presented refer to 25.0 ± 1.0°C, unless otherwise noted. In any case where line broadening was evident or suspected at 25°C, we also ran spectra at 15 and 40 ±1.0°C. In an effort (20, 26) to reduce the linewidths of spectra obtained with both radical-generating systems using **7** and **8**, we made both streams 1.0 M in H_2SO_4, with no perceptible improvement in resolution.

Results and discussion

Table 1 summarizes the EPR spectroscopic data for all radicals characterized in the present study and includes results obtained previously in our laboratory (1, 15). All radicals listed that were generated in the present work resulted from individual studies of **1**, **4**, **7**, and **8** in the $TiCl_3$–H_2O_2 system, and of **1**–**8** in the $TiCl_3$–NH_2OH system, and there was no evidence for the formation of species other than those shown. To illustrate the quality of the spectra obtained in this study, Fig. 1 presents the higher-field half of the spectrum from **15** and a matching computer-generated plot.

In general, our results were consistent with expectation on three counts (31, 32). First, when reacting **1** and **8**, for example, we were able to add the hydroxyl radical to both carbons in their

[1]Supported by the National Science Foundation and the North Carolina Board of Science and Technology.

[2]Author to whom correspondence may be addressed.

Printed in Canada / Imprimé au Canada

Can. J. Chem. Downloaded from www.nrcresearchpress.com by 196.1.178.254 on 09/07/12
For personal use only.

Can. J. Chem. Downloaded from www.nrcresearchpress.com by 196.1.178.254 on 09/07/12
For personal use only.

TABLE 1. EPR spectroscopic data

Radical	Splitting constants[a](G) α-CH	β-CH	β-CH_2	γ-CH	γ-N	Δ(β-CH_2)[b]	ΔH_{pp}[c]	g-Value[d]	Reference[e]
$HOCH_2$—$\dot{C}H$—$CH(CN)OC(O)CH_3$, **9**	21.98(4)	13.18(4)	24.46(3),25.64(3)	—	—	1.18	0.7	2.00234	*f*
$\cdot CH_2$—$CH(OH)CH(CN)OC(O)CH_3$, **10**	22.18(3)	23.55(5)	—	0.81(2)	—	—	0.6	2.00244	*f*
H_2NCH_2—$\dot{C}H$—$CH(CN)OC(O)CH_3$, **11**	22.20(3)	15.37(3)	24.47(4)	—	4,56(3)	$<0.3_5$	0.7	2.00246	—
$HOCH_2$—$\dot{C}H$—$CH(OH)CH_3$, **12**	21.28(1)	17.41(1)	21.80(2)	0.95(2)[g]	—	<0.1	0.2_5	2.00238	*i*
H_2NCH_2—$\dot{C}H$—$CH(OH)CH_3$, **13**	21.53(5)	20.42(2)	22.22(5)	0.83(2)[g]	5.69(2)	$<0.2_5$	0.5	2.00245	—
$HOCH_2$—$\dot{C}H$—$CH(OH)CH_2OH$, **14**	21.40(2)	17.66(1)	22.30(2),22.68(2)	0.34(1)[h]	—	0.38	0.2	2.00239	1
$HOCH_2$—$\dot{C}H$—$CH(NH_2)CH_2OH$, **15**	21.69(2)	15.24(2)	24.48(4),25.42(2)	0.43(2)[j]	5.30(3)	0.94	0.3	2.00247	—
$CH_3C(O)OCH_2$—$\dot{C}H$—$CH(OH)CH_2OC(O)CH_3$, **16**	21.75(3)	18.82(3)	19.29(2)	0.58(2)[h]	—	<0.2	0.3_5	2.00237	—
$CH_3C(O)OCH_2$—$\dot{C}H$—$CH(NH_2)CH_2OC(O)CH_3$, **17**	21.98(3)	16.08(3)	20.90(3)	0.45(2),0.73(2)	4.88(2)	<0.2	0.4	2.00245	—
$NCCH_2$—$\dot{C}H$—$CH(OH)CH_2CN$, **18**	22.28(2)	20.61(1)	24.28(2),22.61(2)	0.64(1)[h]	—	1.67	0.3_5	2.00250	1
$NCCH_2$—$\dot{C}H$—$CH(NH_2)CH_2CN$, **19**	22.52(4)	14.07(2)	25.39(4)	0.79(1)[j]	5.26(4)	<0.2	0.4	2.00257	—
$HOOCCH_2$—$\dot{C}H$—$CH(OH)CH_2COOH$, **20**	21.90(2)	18.67(2)	22.86(2)	—	—	<0.2	0.4	2.00252	1
$HOOCCH_2$—$\dot{C}H$—$CH(NH_2)CH_2COOH$, **21**	22.18(4)	14.97(2)	22.18(4),24.11(4)	0.69(1)[h]	5.97(2)	1.93	0.5_5	2.00260	—
$HOCH_2$—$\dot{C}(COOH)$—$CH(COOH)CH_2COOH$, **22**	—	4.84(5)	22.17(3),23.43(4)	—	—	1.26	1.0	2.00309	*k*
H_2NCH_2—$\dot{C}(COOH)$—$CH(COOH)CH_2COOH$, **23**	—	5.41(2)	14.64(4),16.44(4)	—	5.41(2)	1.80	1.2	2.00314	—
$HOOCCH_2$—$\dot{C}(COOH)$—$CH(OH)COOH$, **24**	—	10.01(3)	13.35(2),14.53(2)	—	—	1.18	0.4	2.00325	*l*
$\cdot CH(COOH)$—$C(OH)(COOH)CH_2COOH$, **25**	20.74(3)	—	—	—	—	—	0.6	2.00319	*m*
$HOOCCH_2$—$\dot{C}(COOH)$—$CH(NH_2)COOH$, **26**	—	5.72(1)	12.26(2),17.91(2)	—	4.22(1)	5.65	0.4_5	2.00327	—

[a]Unless otherwise indicated, all protons of a given designation are magnetically equivalent. Each number in parentheses is the standard deviation of the mean, σ_{n-1}, times 10^2. The maximum error limits of the *a* values are ca. $\pm 2\sigma_{n-1}$ based on the error limits of the field standard (27).

[b]The difference between the β-CH_2 proton splittings.

[c]Of lines not broadened by restricted-rotation effects.

[d]σ_{n-1} is ±0.00001 and the maximum error limit ±0.00006, based on the error limits for the standard (27, 28). All values listed are unexceptional (29).

[e]Except as otherwise noted, present work (pH, ca. 1.5).

[f]**[9]**/**[10]** ≅ 4.

[g]γ-CH_3 protons.

[h]γ-CH_2 protons, not magnetically equivalent; the *a* value listed is for one such proton, that for the other is $\leq \Delta H_{pp}/2$.

[i]Corrected data based on previously recorded spectra (15).

[j]γ-CH_2 protons.

[k]Our spectra and listed results agree with the literature, bearing in mind that these earlier data (5) may refer to temperatures other than 25.0 ± 1.0°C.

[l]As in footnote *k*, but see also ref. 30.

[m]As in footnote *k* except that the earlier data are in refs. 5 and 30.

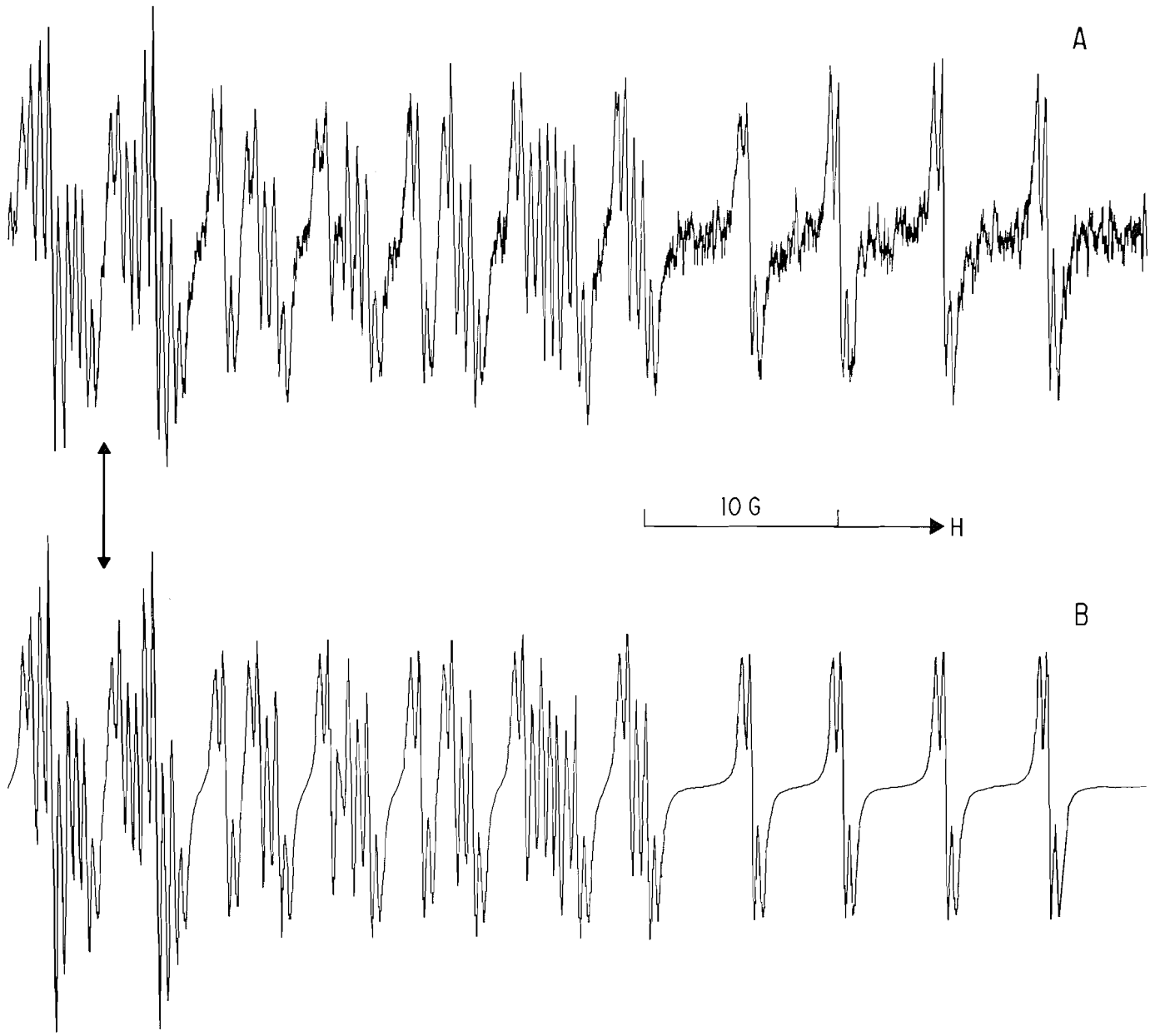

FIG 1. (A) The upper-field half of the EPR spectrum observed for the $TiCl_3$-NH_2OH/**3** reaction; t_p, 40.0 ± 1.0°C; [$TiCl_3$], 0.004 M in the reducing stream; [NH_2OH], 0.5 M in the oxidizing stream; [H_2SO_4], 0.1 M, and [**3**], 0.02 M, in both streams; total flow rate 4 mL s^{-1} equally divided between the two streams; modulation amplitude, 0.20 G; fieldscan rate, 1.33 G min^{-1}; time constant, 3.0 s; receiver gain, 6.3×10^4; microwave power, 20 mW. (B) Simulation of the spectrum of **15**; ΔH_{pp}, 0.30 G; the fraction Lorentzian, 0.90; the *a* values for α-CH, β-CH, β-CH_2, β-CH_2', γ-CH, and γ-N, respectively, 21.60(2), 15.34(2), 24.28(2), 25.23(2), 0.44(1), and 5.34(1) G. The arrow indicates the center of the experimental and simulated spectra.

Can. J. Chem. Downloaded from www.nrcresearchpress.com by 196.1.178.254 on 09/07/12
For personal use only.

double bonds, while, with the aminyl radical, there was evidence only for addition to the less hindered carbon (31, 32). Secondly, in the spectrum from a particular aminyl-radical adduct, the ΔH_{pp} values of the lines not broadened by restricted rotation were equal to or larger than those from the corresponding hydroxyl-radical adduct (31). Finally, relative to the $TiCl_3$–H_2O_2 system, the $TiCl_3$–NH_2OH system was less effective in yielding an observable signal from hydrogen-atom abstraction radicals (31, 32).

Considering those hydroxyl-radical adducts not already reported in the literature, namely, **9**, **10**, and **16**, we assigned the splittings for **9** and **10** by comparison with those of similar radicals (1, 15, 31, 33–36). Also, the splittings for **16** are analogous to those for **9**. However, while the assignment of the α-CH proton splitting in **16** was straightforward, there were two conceivable assignments for the β-CH and -CH_2 protons, which were very close in size, namely, (A) the β-CH_2 protons were nonequivalent, with splittings 18.8 and 19.3 G, requiring the $\alpha_{\beta\text{-H}}$(CH) value to be 19.5 G, and (B) the β-CH_2 protons were equivalent, 19.3 G, making $\alpha_{\beta\text{-H}}$(CH) equal to 18.8 G. The latter alternative seems more probable as $\alpha_{\beta\text{-H}}(CH_2) > \alpha_{\beta\text{-H}}(CH)$ for all radicals of structure similar to that of **9** in this study.

The assignments of the *a*-values for the aminyl-radical adduct **11** were analogous to those in **9** except that the β-CH_2 protons were equivalent (within the linewidth) and there was an expected (31) γ-nitrogen splitting. In the case of the other

Can. J. Chem. Downloaded from www.nrcresearchpress.com by 196.1.178.254 on 09/07/12
For personal use only.

aminyl-radical adducts in Table 1, the assignments of the splittings for **13**, **15**, **17**, **19**, and **21** were essentially as for **11**, and likewise for **23** and **26**, bearing in mind their lack of an α-CH proton.

In general, we would expect the β-CH_2 protons in the radicals with a nonadjacent chiral carbon center, namely, **9**, **11–24**, and **26**, to be nonequivalent. However, for **11–13**, **16**, **17**, **19**, and **20** the nonequivalence was too small to be observable. Likewise, the γ-CH_2 protons in the radicals bearing an adjacent chiral carbon center, namely, **14–23**, should also be nonequivalent. Indeed, in **14**, **16**, **18**, and **21**, our observations fitted this expectation as only one γ-CH_2 proton splitting was resolvable, the other being within the linewidth. In **17**, the γ-CH_2 proton splittings were nonequivalent and measurable. However, for **15** and **19**, the difference between the $a_{\gamma\text{-H}}$ (CH_2)-values was undetectable, so that we observed small (1:2:1)-triplets. For **20**, **22**, and **23**, no γ-CH_2 proton splittings were discernible.

The results in Table 1 show that $a_{\alpha\text{-H}}$(CH) for each aminyl-radical adduct of type $H_2NCH(X)—\dot{C}HY$ is slightly larger than that for the corresponding hydroxyl-radical adduct, a relationship that is true in all analogous cases in the literature of which we are aware (31, 32, 37–39). That the aminyl-radical adducts do display a greater α-CH proton splitting than the corresponding hydroxyl-radical adducts is in line with the relative sizes of the Fischer Δ-functions for $-CH_2OH$ and $-CH_2NH_2$ and the reasonable assumption that the effect stems primarily from changes in the unpaired π-electron spin density at the α-C in these species (31). This observation supports our earlier assignments (1), as it is reasonable to expect the α-CH proton splittings to vary over a much smaller range than those of the β-CH and $-CH_2$ protons for a series of radical adducts as presented here.

The spectra of **13–17**, **22**, **24**, and **26** displayed selective line broadening (40) to some degree. We can attribute this phenomenon to hindered interconversion between equilibrium conformations, a view supported by our finding that in each case the degree of the broadening decreased with increase in temperature. However, the effect manifested itself spectroscopically in three qualitatively different ways.

Radicals **13**, **24**, and **26** showed selective broadening of their $M_\beta = 0$ lines, a phenomenon treated in detail elsewhere (13, 14). The spectra of **24** and **26** both showed broadening of the inner relative to the outer lines in each (1:1:1:1)-quartet, consistent with out-of-phase modulation of the β-CH_2 protons during interconversion between conformations. The spectrum from **13** was similar except that the inequivalence of the β-CH_2 protons was unobservable due to the line broadening. Presumably, in all three cases, the small magnetic inequivalence of the β-CH_2 protons renders the $M_\beta = 0$ line more susceptible to exchange broadening than would be the case were there no asymmetry in these radicals.

Radicals **14–17** showed a small degree of line broadening seemingly unrelated to the β-CH_2 protons. Rather, we find this feature to be consistent with restricted rotation about the $C_\beta—C_\gamma$ bond, resulting in a modulation of the hyperfine splittings of the β-CH and the detectable γ-CH_2 protons. For the radicals in which the nuclear-spin orientation of these protons is the same, either αα or ββ, no field shift of the corresponding lines results from $C_\beta—C_\gamma$ bond rotation (41). Hence, half of the lines in the spectrum of **14** and **16** remained sharp and the rest displayed minor broadening. A similar effect also appeared to be present in **15** and **17**, although it was even less noticeable and, consequently, a definitive analysis was not possible.

For **22**, the line broadening was as described recently (5), where the outer rather than the inner lines of the (1:1:1:1)-quartet from the β-CH_2 protons were broadened, consistent with in-phase modulation of the β-CH_2 protons during interconversion between conformations (42).

Previous comprehensive EPR investigations of the adjacent chiral effect in nitro-anion and nitroxyl radicals of the forms $R^1R^2R^3CCH_2—NO_2^{\cdot-}$ (13) and $R^1R^2R^3CCH_2—N(t\text{-Bu})O\cdot$ (14), respectively, and of the nonadjacent chiral effect in 1,3-dioxolan-4-yl radicals of the type $\dot{C}H_2—CH—OCR^1R^2O$ (3), suggest that the magnitude of the Δ(β-CH_2) values, see Table 1, corresponds directly to the steric constraints imposed by the R groups attached to the chiral carbon. Our results for $XCH_2—\dot{C}Y—CHR^1R^2$ radicals are in general agreement with this size-inequivalence relationship, and illustrate the magnitude of methylene-proton inequivalence that we can expect in typical radicals of this sort. The Δ(β-CH_2) values in the radicals derived from the monosubstituted alkenes tended to be so small as to be seldom detectable, while those of the radicals produced by the disubstituted alkenes were usually, but not always, resolvable, and the trisubstituted alkenes gave rise to radicals with large Δ(β-CH_2) values. However, within this general trend, there are instances where it is impossible to predict what the size of Δ(β-CH_2) will be, see Table 1. Hence it follows that one must apply the general rule relating substituent size and number to the magnetic inequivalence with caution. That this is so is in line with the recognized complex nature of factors that influence nonequivalence (11).

Our results combined with relevant examples in the literature (5–8) show that the nonadjacent chiral effect is capable of rendering methylene protons detectably inequivalent in high-resolution EPR spectra of a variety of acyclic carbon-centered radicals. This effect appears to be somewhat more pronounced in cyclic carbon-centered radicals (3, 4). As far as we are aware, all reported cases of the nonadjacent chiral effect in EPR spectroscopy involve a separation of the methylene protons and the chiral center by only two single C—C bonds. Based on the attenuation of Δ(β-CH_2) values observed when comparing radicals with γ-C chiral center adjacent to a β-methylene group (13–23) to those we present here, we may reasonably speculate that methylene-proton inequivalence is not likely to be detectable in an acyclic radical with a chiral carbon three or more single C—C bonds removed from the methylene protons. This result contrasts with NMR findings where, for example, in an acyclic molecule, chemical shift nonequivalence of CH_3 protons can arise from asymmetry as far as six single C—C bonds away (9).

1. P. Smith and W. H. Donovan. J. Magn. Reson. **77**, 155 (1988).
2. W. T. Dixon and R. O. C. Norman. J. Chem. Soc. 3119 (1963).
3. K. H. Lee, K.-L. Chin, and S. Brumby. J. Chem. Soc. Perkin Trans. **2**, 161 (1985).
4. K. H. Lee and S. Brumby. J. Chem. Soc. Perkin Trans. **2**, 1071 (1983).
5. B. C. Gilbert, N. R. McLay, and D. J. Parry. J. Chem. Soc. Perkin Trans. **2**, 329 (1987).
6. H. Taniguchi. J. Phys. Chem. **88**, 6245 (1984).
7. F. Moriya, K. Makino, N. Suzuki, S. Rokushika, and H. Hatano. J. Phys. Chem. **84**, 3614 (1980).
8. G. M. Whitesides, D. Holtz, and J. D. Roberts, J. Am. Chem. Soc. **86**, 2628 (1964).
9. M. Schwarz, R. B. Bradley, H. M. McIntyre, and E. D. Becker. Org. Magn. Reson. **65**, 625 (1974).
10. E. D. Becker. *In* High resolution NMR: theory and chemical applications. Academic Press, New York. 1980. Chap. 7.

11. W. B. JENNINGS. Chem. Rev. **75**, 307 (1975).
12. J. C. RANDALL, J. J. MCLESKEY, III, P. SMITH, and M. E. HOBBS. J. Am. Chem. Soc. **86**, 3229 (1964).
13. B. C. GILBERT, and M. TRENWITH. J. Chem. Soc. Perkin Trans. **2**, 1834 (1973).
14. B. C. GILBERT, J. P. LARKIN, and R. O. C. NORMAN. J. Chem. Soc. Perkin Trans. **2**, 1272 (1972).
15. P. SMITH, K. R. MAPLES, C. C. DEVLIN, and G. MCCROHAN. J. Magn. Reson. **67**, 539 (1986).
16. R. C. SEALY, L. HARMAN, P. R. WEST, and R. P. MASON. J. Am. Chem. Soc. **107**, 3401 (1985).
17. B. C. GILBERT, and R. O. C. NORMAN. Can. J. Chem. **60**, 1379 (1982).
18. K. MAKINO, F. MORIYA, and H. HATANO. J. Chromatogr. **332**, 71 (1985).
19. C. C. FELIX and R. C. SEALY. J. Am. Chem. Soc. **103**, 2831 (1981).
20. W. T. DIXON, J. FOXALL, and G. H. WILLIAMS. J. Chem. Soc. Faraday Trans. 2, **70**, 1614 (1974).
21. F. L. RUPEREZ, J. C. CONESA, and J. SORIA. J. Chem. Soc. Perkin Trans. **2**, 1517 (1982).
22. M. KAMACHI, Y. KUWAE, and S. NOZAKURA. Polym. J. **13**, 919 (1981).
23. B. C. GILBERT and D. J. PARRY. J. Chem. Soc. Perkin Trans. **2**, 1345 (1986).
24. U. M. OEHLER and E. G. JANZEN. Can. J. Chem. **60**, 1542 (1982).
25. A. H. BLATT. Org. Synth. Coll. Vol. 2, 12 (1969).
26. Y. KIRINO and R. W. FESSENDEN. J. Phys. Chem. **79**, 834 (1975).
27. R. J. FABER and G. K. FRAENKEL. J. Chem. Phys. **47**, 2462 (1967).
28. J. Q. ADAMS, S. W. NICKSIC, and J. R. THOMAS. J. Chem. Phys. **45**, 654 (1966).
29. A. J. DOBBS. *In* Electron spin reson. Spec. Period. Rep., Chem. Soc. London **2**, 281 (1974).
30. B. B. ADELEKE and J. A. FANIRAN. Can. J. Chem. **57**, 1500 (1979).
31. P. SMITH, R. A. KABA, and P. B. WOOD. J. Phys. Chem. **78**, 117 (1974).
32. B. RÅNBY. Appl. Polym. Symp. **26**, 327 (1975).
33. W. T. DIXON, R. O. C. NORMAN, and A. L. BULEY. J. Chem. Soc. 3625 (1964).
34. P. SMITH, R. A. KABA, T. C. SMITH, J. T. PEARSON, and P. B. WOOD. J. Magn. Reson. **18**, 254 (1975).
35. P. SMITH and P. B. WOOD. Can. J. Chem. **45**, 649 (1967).
36. P. SMITH and K. K. KARUKSTIS. J. Magn. Reson. **46**, 469 (1982).
37. C. CORVAJA, H. FISCHER, and G. GIACOMETTI. Z. Phys. Chem. Neue Folge, **45**, 1 (1965).
38. W. E. GRIFFITHS, G. F. LONGSTER, J. MYATT, and P. F. TODD. J. Chem. Soc. (B), 530 (1967).
39. P. SMITH and K. K. KARUKSTIS. J. Magn. Reson. **46**, 200 (1982).
40. P. J. KRUSIC, P. MEAKIN, and J. P. JESSON. J. Phys. Chem. **75**, 3438 (1971).
41. J. E. WERTZ and J. R. BOLTON. *In* Electron spin resonance: elementary theory and practical applications. McGraw–Hill, New York. 1972. Chap. 9.
42. J. K. KOCHI. Adv. Free Radical Chem. **5**, 189 (1975).

Can. J. Chem. Downloaded from www.nrcresearchpress.com by 196.1.178.254 on 09/07/12
For personal use only.

Protium–deuterium exchange of styrenes in dilute acid at elevated temperatures

NICK HENRY WERSTIUK AND GEORGE TIMMINS
Department of Chemistry, McMaster University, Hamilton, Ont., Canada L8S 4M1

Received February 25, 1988

NICK HENRY WERSTIUK and GEORGE TIMMINS. Can. J. Chem. **66**, 2309 (1988).

A modified high temperature – dilute acid method is used to synthesize phenylethene-2,2-d_2 ("styrene-2,2-d_2") (**1***b*), 2-phenylpropene-1,1,3,3,3-d_5 ("α-trideuteriomethylstyrene-2,2-d_5") (**2***b*), and *E*-1-phenylpropene-2-*d* ("*trans*-β-methylstyrene-2-*d*") (**3***b*) from phenylethene ("styrene") (**1***a*), 2-phenylpropene ("α-methylstyrene") (**2***a*), and *E*-1-phenylpropene ("*trans*-β-methylstyrene") (**3***a*), respectively. The deuteriated substitution product *E*-1,3-diphenyl-1-butene-2,4,4,4-d_4 (**4***b*) is also obtained from **1***a*. Labelled substitution products 1,3,3-tri-trideuteriomethyl-1-phenylindane-2,2-d_{11} (**5***b*), 4-trideuteriomethyl-2,4-diphenyl-1-pentene-1,1,3,3,5,5,5-d_{10} (**6***b*), and *E*-4-trideuteriomethyl-2,4-diphenyl-2-pentene-1,1,1,3,5,5,5-d_{10} (**7***b*) are obtained from 2-phenylpropene.

NICK HENRY WERSTIUK et GEORGE TIMMINS. Can. J. Chem. **66**, 2309 (1988).

On a utilisé une méthode modifiée impliquant une température élevée et de l'acide dilué pour synthétiser le phényléthène-d_2-2,2 (« styrène-d_2-2,2 ») (**1***b*), le phényl-2 propène-d_5-1,1,3,3,3 (« α-trideutérométhylstyrène-d_5-2,2 ») (**2***b*) et le phényl-1 propène-*d*-2-(*E*) (« β-méthylstyrène-d2-*d*-*trans* ») (**3***b*) à partir respectivement du phényléthène (« styrène ») (**1***a*), du phényl-2 propène (« α-méthylstyrène ») (**2***a*) et du phényl-1 propène-(*E*) (« β-méthylstyrène-*trans* ») (**3***a*). On a aussi obtenu le diphényl-1,3 butène-1-d_4-2,2,4,4-(*E*) (**4***b*) à partir du composé **1***a*. Utilisant le phényl-2 propène, on a aussi préparé les produits marqués suivants : tri-trideutérométhyl-1,3,3 phényl-1 indane-d_{11}-2,2 (**5***b*), trideutérométhyl-4 diphényl-2,4 pentène-1-d_{10}-1,1,3,3,5,5,5 (**6***b*) et trideutérométhyl-4 diphényl-2,4 pentène-2-d_{10}-1,1,1,3,5,5,5-(*E*) (**7***b*).

[Traduit par la revue]

Can. J. Chem. Downloaded from www.nrcresearchpress.com by 196.1.178.254 on 09/07/12
For personal use only.

Introduction

In continuing to detail the scope and limitations of the high temperature – dilute acid (HTDA) method for hydrogen-isotope labelling of alkenes and aromatic compounds (1–10), we have studied the H–D exchange of phenylethene (**1***a*), 2-phenylpropene (**2***a*), and *E*-1-phenylpropene (**3***a*). To reduce the extent of substitution (polymerization) of these substrates, a modified HTDA method (7, 9) was used. An inert cosolvent was added to "dilute" the water-insoluble substrate and the reaction mixture was shaken to facilitate phase transfer. The results of our studies on **1***a*, **2***a*, and **3***a*, which are summarized in Table 1, establish that the HTDA mehod provides a simple, inexpensive route to phenylethene-2,2-d_2 (**2***b*), 2-phenylpropene-1,1,3,3,3-d_5 (**2***b*), *E*-1-phenylpropene-2-*d* (**3***b*), as well as *E*-1,3-diphenyl-1-butene-2,4,4,4-d_4 (**4***b*), 1,3,3-tri-trideuteriomethyl-1-phenylindane-2,2-d_{11} (**5***b*), 4-trideuteriomethyl-2,4-diphenyl-1-pentene-1,1,3,3,5,5,5-d_{10} (**6***b*), and *E*-4-trideuteriomethyl-2,4-diphenyl-2-pentene-1,1,1,3,4,4,4-d_{10} (**7***b*).

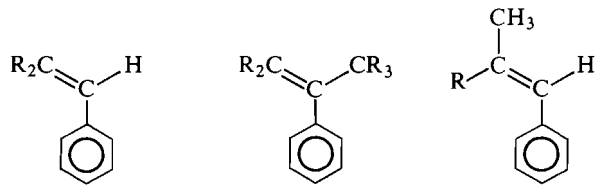

1
a, R = H
b, R = D

2
a, R = H
b, R = D

3
a, R = H
b, R = D

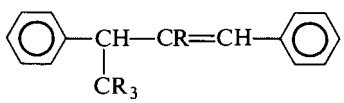

4
a, R = H
b, R = D

Results and discussion

H–D exchange of phenylethene (1a)

When **1***a* was heated in 0.26 M HCl/H_2O at 170°C with decalin as a cosolvent, 54.3% of **1***a* remained and 39.3% of **4***a* was obtained along with 6.4% of five other minor components that were not identified. Substituted butene **4***a* was identified as the major substitution product by its ^{1}H nmr and mass spectrum. When the reaction was carried out in deuteriated medium (entry 2, Table 1), ^{1}Hmr, ^{2}Hmr, and mass spectrometry indicated that **1***a* at C-2 was equilibrated with the deuterium pool. Mass spectrometry established that **4***b* contained 3.35 D atoms in excess of natural abundance and consisted of 8.91% d_2, 18.1% d_3, 59.8% d_4, 2.7% d_5, and 0.4% d_6 species. Signals at δ 6.4 and δ 1.5 in the ^{2}Hmr spectrum of deuteriated **4***b* corresponded to C2-D and the CD_3 group, respectively. There was a weak signal at δ 2.6, but no detectable peaks in the aromatic region. At a lower temperature (entries 3 and 4), more starting material remained, and, after 7.5 h at 145°C, 1.54 D atoms are incorporated into **1***a*. Additional studies were carried out in nondeuteriated medium. When the cosolvent decalin was used as an internal standard for the gc analysis, it was established that 25% of **1***a* and 50% of **4***a* were present relative to the amount of **1***a* present initially. It is conceivable that higher molecular weight products are formed that do not pass through the gc column and that **1***a* polymerizes in the gc injector block. When the reaction was carried out with pentane as the cosolvent, to facilitate recovery of the deuteriated compound, **1***b* was isolated in 21% yield. Although the yield is quite low, the method does provide a simple inexpensive route to **1***b* and **4***b*. It is noteworthy that H–D exchange of **1***a* competes with polymerization. This is probably due to the fact that the concentration of the styrene in the aqueous phase is kept low.

H–D exchange of 2-phenylpropene (2a)

When **2***a* was reacted in 0.26 M HCl/H_2O (entry 5), in addition to a short-retention-time product, which was **2***a* according to its ^{1}Hmr and mass spectrum, three higher molecular weight products were present. The components were separated by preparative gc and 250-MHz ^{1}Hmr spectra were

TABLE 1. H–D exchange of phenylethene and phenylpropenes

Entry	Substrate	Conditions[a]	Products[b] (rel % yields)	D atoms incorporated[c]
1	**1***a*	H, dec 170°C, 12 h	**1***a*(54.3), **4***a*(39.3) other (6.4)	
2	**1***a*	D, dec, 170°C, 12 h	**1***b*(38.6), **4***b*(53.2), other (8.2)	**1***b*(1.95), **4***b*(3.35)
3	**1***a*	D, dec, 145°C, 7.5 h	**1***b*(74.5), **4***b*(20.8), other (4.7)	**1***b*(1.54) **4***b*[d]
4	**1***a*	D, dec, 165°C, 12 h	**1***b*(62.2), **4***b*(36.2), other (1.6)	**1***b*(1.94) **4***b*[d]
5	**2***a*	H, cyc, 170°C, 12 h	**2***a*(31.2), **5***a*(3.7), **6***a*(31.7), **7***a*(32.6), other (0.8)	
6	**2***a*	D, cyc, 170°C, 12 h	**2***b*(32.2), **5***b*(8.9), **6***b*(28.4), **7***b*(28.7), other (1.8)	**2***b*(4.91)
7	**2***a*	D, dec, 205°C, 15 h	**2***b*(30.9), **5***b*(25.0), **6***b*(15.7), **7***b*(26.8)	**2***b*(5.10)
8	**3***a*	H, cyc, 170°C, 12 h	Other (7.9), **3***a*(89.5), dimers (1.4), other (1.2)	
9	**3***a*	D, cyc, 170°C, 12 h	Other (7.6, **3***b*(89.2), dimers (1.3), other (2.3)	**3***b*(0.88)
10	**3***a*	D, dec, 205°C, 15 h	Other (16), **3***b*(56.7), dimers (24.2), other (3.1)	**3***b*(−2.37)
11	**3***a*	D, cyc, 212°C, 69 h	Other (3.1), **3***b*(23.1), dimers (73.2), other (0.6)	**3***b*(7.16)

[a]H indicates 0.26 M HCl/H_2O, D indicates 0.26 M DCl/D_2O, dec indicates decalin and cyc indicates cyclohexane as the cosolvent. The reactions were agitated using a rocking motion of the pressure vessel. The temperatures were controlled to ±3°C.

[b]The products are listed in order of increasing gc retention time. Dimers refers to substitution products, which were not identified.

[c]Determined mass spectrometrically at low ionizing voltage (12–15 eV).

[d]Deuterium content was not determined.

obtained. The higher molecular weight component obtained in lowest yield exhibited signals at δ 1.03 (s, 3H), δ 1.35 (s, 3H), δ 1.69 (s, 3H), δ 2.19 (d, 1H), δ 2.42 (d, 1H), and δ 7.1–7.3 (m, 9H) in keeping with the spectrum expected for **5***a*. The other two products were assigned structures **6***a* (signals at δ 1.23 (s, 6H), δ 2.48 (s, 2H), δ 4.79 (d, 1H), δ 5.14 (d, 1H), and δ 7.2–7.3 (m, 10H)) and **7***a* (signals at δ 1.53 (s, 6H), δ 1.58 (s, 3H), δ 6.14 (s, 1H), and δ 7.2–7.4 (m, 10H)) on the basis of their ^{1}Hmr, ^{2}Hmr, and mass spectra. While **5***a* is formed by cyclization of the 4-methyl-2,4-diphenyl-2-pentyl cation (Scheme 1), **6***a* and **7***a* result from loss of protons from C-1 and C-3, respectively.

Treatment of **2***a* in 0.26 M DCl/D_2O/cyclohexane at 170°C for 12 h (entry 6) followed by distillation of the cyclohexane yielded a product consisting of **2***b* (32.2%), **5***b* (8.9%), **6***b* (28.4%), and **7***b* (28.7%) from which **2***b* (0.48 g, 27%) was isolated by distillation at reduced pressure. Mass spectral analysis indicated that **2***b* incorporated 4.91 D atoms and consisted of 11.6% d_4, 85.7% d_5, and 2.7% d_6 species. The ^{2}Hmr spectrum of **2***b* exhibited intense signals at δ 2.1 (CD_3), δ 5.05, and δ 5.35 (vinyl C-Ds); a weak signal (<5%) in the aromatic region established that only a small amount of deuterium was incorporated in the ring while the side chain was equilibrated with the deuterium pool. As established by ^{2}Hmr, even at 205°C (entry 7), there was little exchange (<5%) of the aromatic ring. The labelled substitution products **5***b*, **6***b*, and **7***b* were separated by preparative gc and their 250-MHz ^{1}Hmr spectra showed only weak signals (<5% relative to the arene protons), due the aliphatic and vinylic protons, thereby indicating essentially complete deuteriation of the aliphatic portions of these molecules. Thus, the reactions of **1***a* and **2***a* in deuteriated medium provide unique routes to **4***b*, **6***b*, and **7***b*.

H–D exchange of E*-1-phenylpropene (***3***a)*

When **3***a* was reacted under the same conditions as **2***a* (entries 5 and 8), very little substitution occurred, in contrast to the reaction of **2***a*. That the major component was **3***a* was established by ^{1}Hmr. Analytical gc analysis established that 8% of *Z*-1-phenylpropene was present. Mass spectral analysis of **3***b* isolated in 73% yield by preparative gc from a reaction in deuteriated medium (entry 9) established that **3***a* incorporated 0.88 D atoms and that it consisted of 22.4% d_0, 67.4% d_1, 9.6% d_2, and 0.5% d_3 species. Its ^{2}Hmr spectrum exhibited a strong signal at δ 6.2 with a shoulder and two weak signals (<5%) in the aromatic region, indicating that the deuterium was located predominantly at C-2. At 205°C (entry 10), 2.37 D atoms (0.4% d_0, 21.7% d_1, 37.3% d_2, 26.2% d_3, 10.4% d_4, 3.3% d_5, and 0.8% d_6) are incorporated into **3***a*. It was established by ^{2}Hmr

Can. J. Chem. Downloaded from www.nrcresearchpress.com by 196.1.178.254 on 09/07/12
For personal use only.

Can. J. Chem. Downloaded from www.nrcresearchpress.com by 196.1.178.254 on 09/07/12
For personal use only.

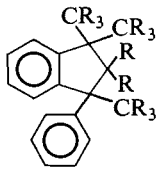

5
a, R = H
b, R = D

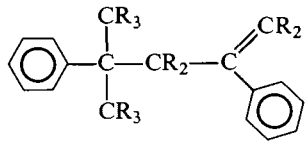

6
a, R = H
b, R = D

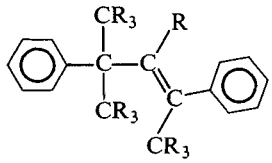

7
a, R = H
b, R = D

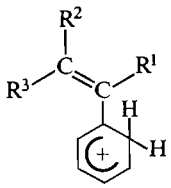

8
a, $R^1 = R^3 = H$; $R^2 = CH_3$
b, $R^1 = CH_3$; $R^2 = R^3 = H$

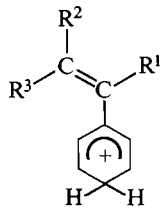

9
a, $R^1 = R^3 = H$; $R^2 = CH_3$
b, $R^1 = CH_3$; $R^2 = R^3 = H$

spectroscopy (Fig. 1) that deuterium is located at C-2 (0.93 D), C-1 (0.20 D), in the benzene ring (1.06 D), and in the methyl group. Although additional nmr studies were not carried out, the relative intensities (2:1) of the peaks in the aromatic region indicate that exchange occurs predominantly at the *ortho* and *para* positions; this is expected on the basis of the activating effect of the 1-propenyl substituent. It is interesting to note that the phenyl group of **3***a* undergoes exchange significantly faster than the phenyl group of **2***a* (*vide supra*). This observation establishes that vinyl cyclohexadienyl cations **8***a* and **9***a* are more stable than isomers **8***b* and **9***b*, a point that cannot be established easily by any other study because the double bond is substantially more reactive towards electrophiles than the benzene ring. Under more forcing conditions (entry 11), **3***a* incorporated 7.16 D atoms of deuterium (0.3% d_3, 1.2% d_4, 6.3% d_5, 18.5% d_6, 32.7% d_7, 31.1% d_8, 8.8% d_9, and 1.0% d_{10} species). Analysis by ^{1}Hmr and ^{2}Hmr spectroscopy established that the vinylic positions were equilibrated with the deuterium pool and that there were approximately three and two

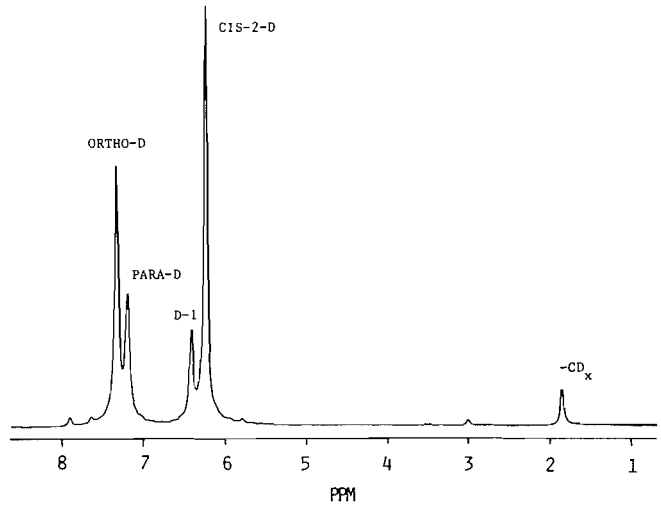

FIG. 1. The ^{2}Hmr spectrum (38.4 MHz, CCl_4) of *E*-1-phenylpropene-$d_{2.37}$.

deuterium atoms located in the ring and the methyl group, respectively. Although additional nmr studies were not carried out, based on the relative intensities of the signals in the aromatic region, we expect that the deuterium in the ring is located at the *ortho* and *para* positions. Gas chromatographic analysis established that there was substantial conversion (73%) to other products, which were not identified.

Computation studies on cations **9**a *and* **9**b

AM1 calculations (11) were carried out to probe the structures of cations **9***a* and **9***b*. According to AM1 the heats of formation of **9***a* and **9***b* are 867.4 and 901.5 kJ/mol, respectively. That AM1 predicts **9***a* to be lower in energy than **9***b* by 34.1 kJ/mol is in keeping with the fact that **3***a* undergoes H–D exchange of the aromatic ring faster than **2***a*. The difference in stability is due to two factors: steric interactions twist the double bond of **9***b* away from coplanarity with the cyclohexadienyl π-system. According to AM1, the twist angle is 29.5°C in this case. In the case of **9***a*, the double bond is almost complanar with the cyclohexadienyl π-system; the twist angle is 11.5°C. Furthermore, the methyl group at C-2 of **9***a* provides additional stabilization not available in the case of **9***b*.

Conclusions

This study established that a modified high temperature – dilute acid method provides a simple, inexpensive route to deuterium labelled phenylethene ("styrene"), 2-phenylpropene ("α-methylstyrene"), and *E*-1-phenylpropene ("*trans*-β-methylstyrene") as well as several substitution products. It should be a

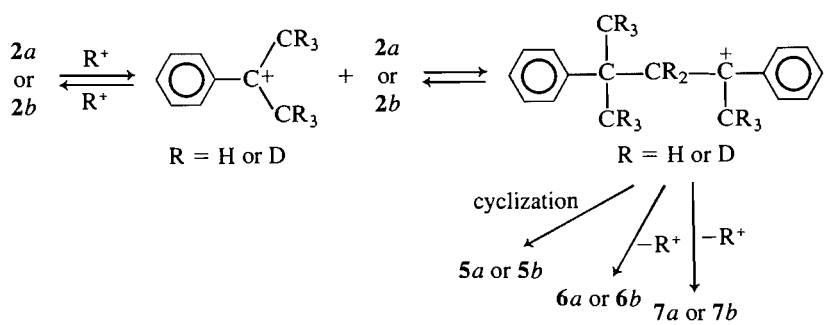

SCHEME 1

simple matter to tritiate these substrates by substituting tritiated water of the appropriate activity for the D_2O and to label other substituted derivatives with this methodology.

Experimental

Analyses were carried out on a Tracor model 560 chromatograph equipped with a Varian Aerograph model 485 electronic integrator using a 6 ft × 4 mm i.d. 3% OV-1 on 100/120 mesh Supelcoport column. Preparative collections were performed on a Varian A-700 gas chromatograph equipped with a 5 ft × 1/4 in. 15% SE-30 on 80/100 Chromosorb W column. The yields were not corrected for collection losses. Products were characterized by ^{1}Hmr and ^{2}Hmr spectroscopy (Varian EM-390 and Bruker WM-250 spectrometers). Deuterium analyses were carried out on a VG Micromass 7070F mass spectrometer at low ionizing voltage (12–15 eV).

*H–D exchange of phenylethene (**1**a)*

In a typical reaction, **1***a* (0.20 g), 0.27 M HCl/H_2O or 0.27 M DCl/D_2O (5 mL), and decalin (1 mL) were sealed under vacuum in a medium-walled Pyrex tube after the solution was degassed via three freeze–pump–thaw cycles. Tubes were heated in a 600-mL Parr pressure vessel containing water to equalize the pressure. Mixing was accomplished by a rocking motion of the vessel. The tubes were cooled, opened, the decalin layers were withdrawn, analyzed by analytical gc, and the products were isolated by preparative gc. The results are given in Table 1.

In a large scale preparation, six tubes each containing **1***a* (0.25 g), pentane (1.5 mL), and 0.27 M DCl/D_2O (5 mL) were prepared in the usual manner and heated with agitation at 137 ± 3°C for 24 h in a Parr pressure vessel. The tubes were opened, the pentane layers were withdrawn, and the combined aqueous layers were saturated with NaCl and extracted with pentane (3 × 10 mL). The extracts were dried, filtered, and the pentane was removed on a rotatory evaporator. Several crystals of hydroquinone were added to the residue and **1***b* (0.31 g, 21%) was flash distilled under vacuum through a short-path apparatus; ms: 5.8% d_6, 27.7% d_2, 66.9% d_2, 1.2% d_3, and 9.3% d_4 species; 1.64 D atoms per molecule.

*H–D exchange of 2-phenylpropene (**2**a)*

In a typical reaction **2***a* (0.20 g), 0.27 M DCl/D_2O or 0.27 M HCl/H_2O (5 mL), and decalin or cyclohexane (1 mL) were reacted and the products isolated as described for the case of **1***a*.

For a larger scale reaction, three tubes each containing **2***a* (0.60 g), cyclohexane (3 mL), and 0.27 M DCl/D_2O (10 mL) were heated at 175 ± 3°C for 12 h with agitation. The organic layers were withdrawn and washed with aqueous $NaHCO_3$ saturated with NaCl. The $NaHCO_3$ solution was extracted with cyclohexane (2 × 5 mL) and the combined cyclohexane layers were dried over Na_2SO_4. Most of the cyclohexane was taken off on the rotatory evaporator. The residue was kept under rotatory pump vacuum for several minutes, several crystals of hydroquinone were added, and **2***b* (0.43 g, 27%) was isolated by rapid distillation at approximately 4 Torr (1 Torr = 133.3 Pa) using a short path distillation apparatus; ms: 11.6% d_4, 85.7% d_5, and 2.7% d_0 species; 4.91 D atoms per molecule.

H–D exchange of E*-1-phenylpropene (**3**a)*

In a typical reaction **3***a* (0.20 g), 0.27 M DCl/D_2O or 0.27 M HCl/H_2O (5 mL), and decalin or cyclohexane (1 mL) were reacted and the products isolated as described for **1***a*.

For a larger scale reaction, three tubes each containing **3***a* (0.50 g), cyclohexane (3 mL), and 0.27 M DCl/D_2O (10 mL) were heated for 12 h at 175 ± 3°C with agitation. The organic layers were withdrawn and washed with aqueous $NaHCO_3$ saturated with NaCl. The $NaHCO_3$ solution was extracted with cyclohexane (2 × 5 mL) and the combined cyclohexane layers were dried over Na_2SO_4. Most of the cyclohexane was taken off on the rotatory evaporator. The residue was kept under rotatory pump vacuum for several minutes, several crystals of hydroquinone were added, and **3***b* (0.99 g, 65.2%) was isolated by rapid distillation at 1 Torr using a short path distillation apparatus; ms: **3***b*, 16.4% d_0, 71.7% d_1, and 0.7% d_2 species; 0.96 D atoms per molecule.

Acknowledgements

We thank the Natural Sciences and Engineering Research Council of Canada for financial support. We are indebted to Mr. B. Sayer for obtaining the ^{2}Hmr spectra.

1. N. H. Werstiuk and T. Kadai. Can. J. Chem. **51**, 1485 (1973).
2. N. H. Werstiuk and T. Kadai. Can. J. Chem. **52**, 2169 (1974).
3. N. H. Werstiuk and T. Kadai. U.S. patent 3,989,705 (1976).
4. N. H. Werstiuk and T. Kadai. Canadian Patent 1 048 556 (1979).
5. N. H. Werstiuk and G. Timmins. Can. J. Chem. **59**, 1022 (1981).
6. N. H. Werstiuk and G. Timmins. Can. J. Chem. **59**, 3218 (1981).
7. N. H. Werstiuk and G. Timmins. Can. J. Chem. **63**, 530 (1985).
8. N. H. Werstiuk and G. Timmins. Can. J. Chem. **64**, 1072 (1986).
9. N. H. Werstiuk and G. Timmins. Can. J. Chem. **64**, 1569 (1988).
10. N. H. Werstiuk. Hydrogen isotope exchange of organic compounds in dilute acid at elevated temperatures. *In* Isotopes in physical and biomedical sciences. Vol. 1. Labelled compounds (Part A). *Edited by* J. R. Jones and E. Buncel. Elsevier, Amsterdam. 1987. pp. 122–155.
11. AMPAC; Austin method 1 package (QCPE 506). Dewar research group and J. P. Stewart. QCPC Bull. 6, 2 (1986).

Can. J. Chem. Downloaded from www.nrcresearchpress.com by 196.1.178.254 on 09/07/12
For personal use only.

Electronic structure of zinc phthalocyanine

N. EL KHATIB, B. BOUDJEMA, AND M. MAITROT
Universite Claude Bernard Lyon 1, 43 bd du 11 novembre 1918, F-69622 Villeurbanne Cedex, France

AND

H. CHERMETTE AND L. PORTE
Institut de Physique Nucleaire (et IN2P3), Universite Claude Bernard Lyon 1, 43 bd du 11 novembre 1918, F-69622 Villeurbanne Cedex, France

Received December 10, 1987

N. EL KHATIB, B. BOUDJEMA, M. MAITROT, H. CHERMETTE, and L. PORTE. Can. J. Chem. **66**, 2313 (1988).

The electronic structure of zinc phthalocyanine is investigated through MSXα computations and XPS experiments. Reasonable argeement is found between the qualitative structure of the molecular orbital diagram and the XPS spectrum. The visible spectrum is also discussed and the calculation is compared to previous semi-empirical computations. On the other hand, it is shown that a similar calculation on the zinc tetraazaporphyrin — selected as a model molecule — cannot be used to interpret the electronic properties of the phthalocyanine.

N. EL KHATIB, B. BOUDJEMA, M. MAITROT, H. CHERMETTE, et L. PORTE. Can. J. Chem. **66**, 2313 (1988).

La structure électronique de la phtalocyanine de zinc a été étudiée au moyen de la méthode MSXα et par spectrométrie XPS. Un bon accord est trouvé entre la structure qualitative du spectre et le diagramme d'orbitales moléculaires. Le spectre visible est aussi discuté et le calcul est comparé aux calculs semi-empiriques connus. D'autre part, il est montré qu'un calcul similaire sur la tétraazaporphyrine de zinc, qui pourrait être considérée comme une molècule modèle de celle étudiée, ne peut pas être utilisée pour interpéter les propriétés électroniques de la phtalocyanine.

Can. J. Chem. Downloaded from www.nrcresearchpress.com by 84.22.46.98 on 09/08/12
For personal use only.

1. Introduction

Zinc phthalocyanine (ZnPc) is a well-known compound first prepared in the thirties (1). If its use as a paint pigment is quite old, it has been more recently studied for its electrical properties. In fact, its thermal stability (up to 500°C, no chemical degradation is observed) and its ability to sublime are remarkable. High purity can be obtained by successive sublimations, so it would be possible to use ZnPc as a molecular electronic components: although its conductivity is rather low ($\sigma = 10^{-9}$, 10^{-10} (ohm cm)$^{-1}$) for a thin evaporated layer at room temperature, it is not much lower than the conductivity of usual disordered mineral electronic components like SiH. Moreover, doping agents are available with a very high efficiency(2). Firstly, some dopants like oxygen and iodine were introduced into the ZnPc layers by gas or vapour diffusion (3). However, larger molecules, more stable in the phthalocyanine, can be used as p or n dopant: for instance by using the coevaporation method (3*b*) it was predicted that at low dopant concentration, pn junctions could probably be made, and perhaps some other electronic components such as field effect transistors or diodes. On the other hand, the contact properties of ZnPc have been thoroughly studied: diode effects were tested with Al or Ni electrodes, the photovoltaic effect was also studied in Schottky diodes, but up to now, a low efficiency has been obtained.

Moreover, numerous properties of metallophthalocyanines (1*b*) are well known for metallophthalocyanine structures from X-ray diffraction measurements, the macrocycle being planar to within 0.03 nm, so that the symmetry of the molecule is approximately D_{4h}. The spectroscopic properties like MCD spectra, electronic absorption spectra or photoemission spectra, can be used as tests of theoretical models (4). Some other properties, such as redox potentials or ESR measurements, important to characterize the electronic structure of ZnPc (5, 6), are also available. Thus, in spite of the large dimensions of the molecule (diameter equal to 1.5 nm), a fully theoretical calculation of the electronic structure of this compound should be interesting both for experimentalists (for instance, to assign electronic spectra) and for theoreticians to investigate what degree of confidence can be obtained in such "first principles" calculations at the one-electron level.

2. Experimental

Preparation

Linstead and co-workers in the 1930's (1) have given several methods to synthesize the metâllophthalocyanines. ZnPc is obtained by reacting 1,2-dicyanobenzene with the finely dispersed metal at 250–300°C. Many sublimations are used in a nitrogen atmosphere to purify the phthalocyanine.

The impurities still present in the powder consist mostly of hydrogen phthalocyanine (ca. 0.1%) which is eliminated in the evaporation step by using a cache to hide the plate, since the sublimation temperature of H_2Pc is slightly lower than that of ZnPc.

The film polycrystallinity is rather small and depends mainly on the temperature of the target. At low temperature (we used −70°C) the film is totally amorphous, and this is much better for electronic applications since interfaces between the crystallites are avoided. To obtain thin layers of ZnPc (100 to 1000 nm), the powder is evaporated onto a glass plate (10^{-7} Torr) (electrical or optical studies) in a strict absence of oxygen or onto a conducting plate (XPS measurements); the evaporation rate is kept low and constant (0.1–0.5 nm s^{-1}) during all the evaporation process.

Photoemission spectrum

The sample of about 300 nm thickness has been evaporated on a copper support. The X-ray photoelectron (XPS) spectrum was taken in a "Hewlett-Packard 5950 A" electron spectrometer, using the monochromatized AlKα X-ray (1487 eV) with a resolution equal to 0.85 eV.

Spectra were recorded at room temperature and the base pressure in the analysis chamber was in the 10^{-9} Torr range. Neither radiation damage nor outgassing was observed and measurements recorded on different samples were reproducible. No charging effects or peak deformation were observed and the spectra were recorded without flood gun compensation. Binding energies (BE) were measured taking the AU 4*f* 7/2 core line as reference (BE = 84.0 eV).

Printed in Canada / Imprimé au Canada

TABLE 1. Coordinates, α values and radii for the unique atoms

	out	Zn	N1	N2	C1	C2	C3	C4	H1	H2
x	0.000	0.000	6.166	2.646	5.195	6.469	9.022	9.547	10.290	11.374
y	0.000	0.000	0.000	2.646	2.185	4.598	5.229	7.890	3.961	8.252
z	0.000	0.000	0.000	0.000	0.000	0.000	0.000	0.000	0.000	0.000
r	14.782	2.640	1.475	1.475	1.512	1.512	1.512	1.512	0.819	0.819
α	0.762	0.707	0.752	0.752	0.758	0.758	0.758	0.758	0.777	0.777

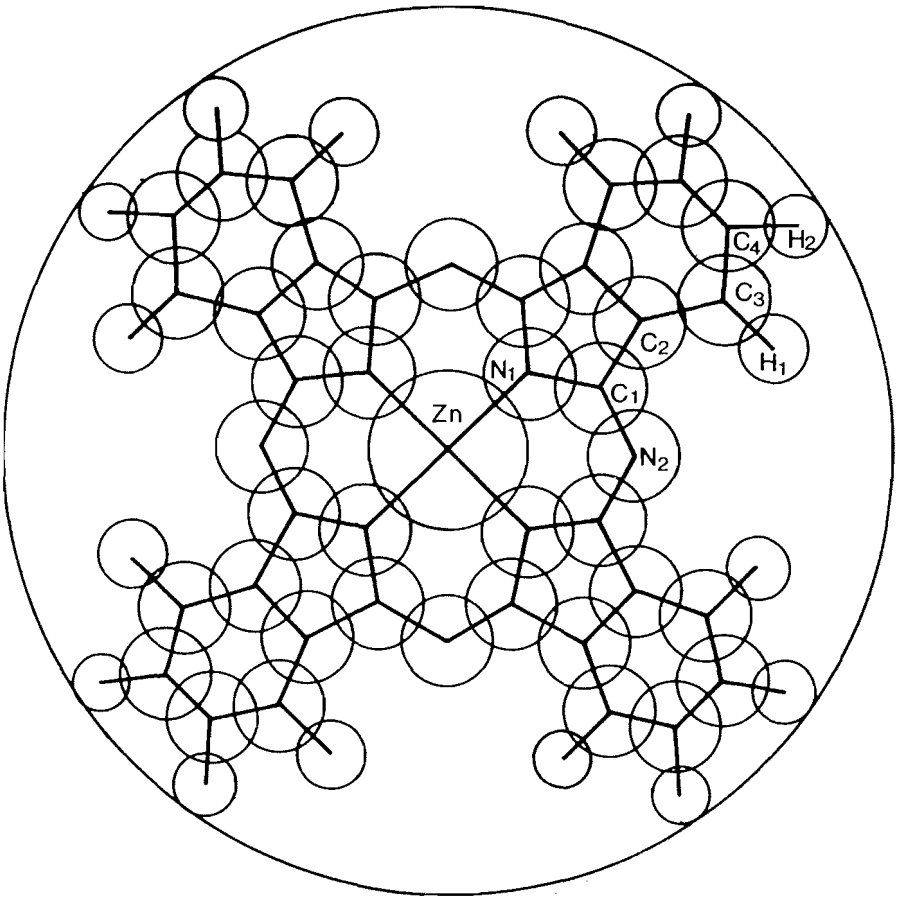

FIG. 1. Zinc phthalocyanine in the muffin-tin approximation.

3. Theoretical calculations

Calculations have been performed with the MS-Xα method with standard parameters. Although the muffin-tin approximation may be rather severe for such a molecule with a planar structure, quite good results have been obtained in the past for calculations on TCNQ and other planar molecules (7), so that we were confident to obtain at least semiquantitative results. The crudeness of the muffin-tin approximation is related here to the large volume of the intersphere region in which the potential is approximated as constant.

Computational details

D_{4h} symmetry was retained for a geometry deduced from the data of Scheidt and Dow (8). Slightly overlapping spheres were used, with radii obtained partly by Norman's criterion (9) along with the requirement to keep the same radii for similar atoms (10). The selected overlapping ratios were taken equal to 1.15 and 1.25 for C—N bonds, to 1.10 for Zn—N bonds, between 1.10 and 1.15 for C—C bonds, and equal to 1.30 for C—H bonds. Parameters were taken from Schwarz's compilation (11) and the basis set was limited to f waves ($l = 3$) for Zn, to p waves ($l = 1$) for N, C, and H atoms, and g waves ($l = 4$) for the outersphere. The coordinates, the α values, and the radii of unique atoms are displayed in Table 1.

4. Results and discussion

Ground state

The phthalocyanine is a neutral 294 electron system that consists of one Zn, 8 N, 32 C, and 16 H. Figure 1 depicts the inequivalent atoms in the molecule. On the other hand, the 294 electrons can be divided into two sets: the first one consists of 98 core electrons, namely $1s$, $2s$, $2p$, $3s$, and $3p$ for Zn, and $1s$ for nitrogen and carbon atoms. The second group gathers the valence electrons which are classically $1s$ for hydrogen, $4s$ and

Can. J. Chem. Downloaded from www.nrcresearchpress.com by 84.22.46.98 on 09/08/12
For personal use only.

TABLE 2. Eigenvalues of ZnPc (eV)

a_{1g}	a_{1u}	a_{2g}	a_{2u}	b_{1g}	b_{1u}	b_{2g}	b_{2u}	e_g	e_u
(12.7)	(9.8)	19.15	(10.72)	17.71	(10.61)	20.67	(11.62)	(10.27)	18.02
18.47	14.22	24.27	(11.30)	19.20	(12.55)	22.19	15.03	(11.18)	19.18
22.27	16.31	26.59	15.65	23.82	15.76	22.64	19.99	(13.61)	22.10
22.51		27.97	17.05	24.68	17.62	23.73		15.21	22.38
24.44		30.42	17.73	26.66	19.87	24.33		15.77	23.64
24.57		34.74	21.42	27.55		25.62		17.59	23.80
26.30				28.81		27.82		18.36	24.35
27.55				30.59		29.22		20.97	24.54
29.31				39.27		32.43		27.05	26.32
32.63						33.64			26.84
34.30						34.29			28.05
36.24						37.23			29.05
39.60									30.49
									32.52
									34.12
									34.12
									34.30
									36.78

$3d$ for zinc, $2s$ and $2p$ for nitrogen, and $2s$ and $2p$ for carbon, for a total of 196 electrons.

In the Xα ground state there are 50 doubly occupied orbitals and 24 quadruply occupied orbitals. Table 2 lists all these molecular orbitals (MO) with their eigenvalues; the atomic character of the most important valence orbitals is also indicated in the energy diagram (Fig. 2). In Table 3 are mentioned the core energy levels. One can notice the characteristics of two frontier MO's:

The LUMO: (Lowest Unoccupied Molecular Orbital) belongs to the e_g irreducible representation which mainly exhibits carbon character with small nitrogen contributions.

The HOMO: (Highest Occupied Molecular Orbital) belongs to the a_{1u} irreducible representation; it exhibits only carbon character since nitrogen character is symmetry forbidden in the a_{1u} irreducible representation.

It appears that the Zn(d) band is spanned mainly in four irreducible representations, namely $6a_{1g}$, $4b_{1g}$, $6b_{2g}$, and $1e_g$ with an atomic d character varying from 56% (b_{2g}) to 99% (e_g). Then the d bandwidth equals 0.8 eV and the d band is only slightly mixed with the other orbitals of the valence band VB. However, a slight, but significant, mixing involves levels as far as 3 eV from the center of the d band. This is clearly apparent in Fig. 2.

Comparison between Xα and EHT calculations

To our knowledge, only one Extended Huckel (EHT) calculation (12) and one PPP calculation (13) have so far been performed on the ZnPc molecule. In Fig. 3 are given the energy diagram from Xα (present work) and EHT calculations (the diagram is limited to the upper MO's).

Let us recall that the Xα eigenvalues (and more generally local spin-density eigenvalues) do not have the same significance as the EHT energies, as already pointed out by Case and Karplus (14). The EHT energies do not take explicitly the electronic repulsion into account, while the Xα eigenvalues contain a spurious self-energy interaction which can be extracted through a straightforward calculation (one shot iteration) as depicted in ref. 15. This self-interaction is strongly related to the localization of MO's exhibiting a similar delocalization over the molecule. This term is responsible for the apparently non satisfied Fermi statistics of the ground state of some molecules like Cu porphyrin (14) and possibly lithium phthalocyanine (16).

However, a qualitative comparison can be made between the two kinds of calculations, and it shows the following points:

(*1*) The calculated Xα levels are deeper than the corresponding Huckel ones. This effect is mainly due to the muffin-tin approximation in our calculation: to be more precise, the effect is due to the large size of the outersphere (required to be tangent to the outermost atomic spheres) leading to a large intersphere zone for which the potential is assumed constant. This effect is discussed in detail in a recent work (17).

(*2*) The LUMO levels are found to belong to the same irreducible representation (e_g) in both calculations but the HOMO is (a_{1u}) in Xα and (b_{1g}) in EHT. The authors of the EHT calculation pointed out, however, that their calculation leads to an erroneous result for the nature of the HOMO which should be of (a_{1u}) symmetry to agree with experimental properties such as the optical spectrum. Our result is then in accord with what the authors were expecting, i.e. the experimental conclusions.

(*3*) The two methods give almost the same gap value (0.6 eV). However, the gap in Xα calculations should be calculated through a Slater transition state calculation, in order to remove the self-interaction energy and take the electronic relaxation into account. But since both the HOMO and LUMO exhibit a similar π or π* character, their self-interactions are rather similar and the electronic relaxation has to be small (no charge transfer involved). Consequently the theoretical gap should not reach a value far from 0.6 ± 0.1 eV.

(*4*) The pattern of the first unnoccupied levels is rather similar if one excludes the $13a_{1g}$ level we found which has no equivalent in the EHT calculation. This MO exhibits a strong (for a virtual level) Zn ($4s$) atomic character (50%). Its exact position among the virtual levels may be subject to discussion because of the muffin-tin approximation involved in the calculation. In silver chloride calculations, the Ag ($5s$) level was found (with a smaller atomic $4s$ character) about 2 eV lower than required by the experimental spectrum (18).

Can. J. Chem. Downloaded from www.nrcresearchpress.com by 84.22.46.98 on 09/08/12
For personal use only.

Can. J. Chem. Downloaded from www.nrcresearchpress.com by 84.22.46.98 on 09/08/12
For personal use only.

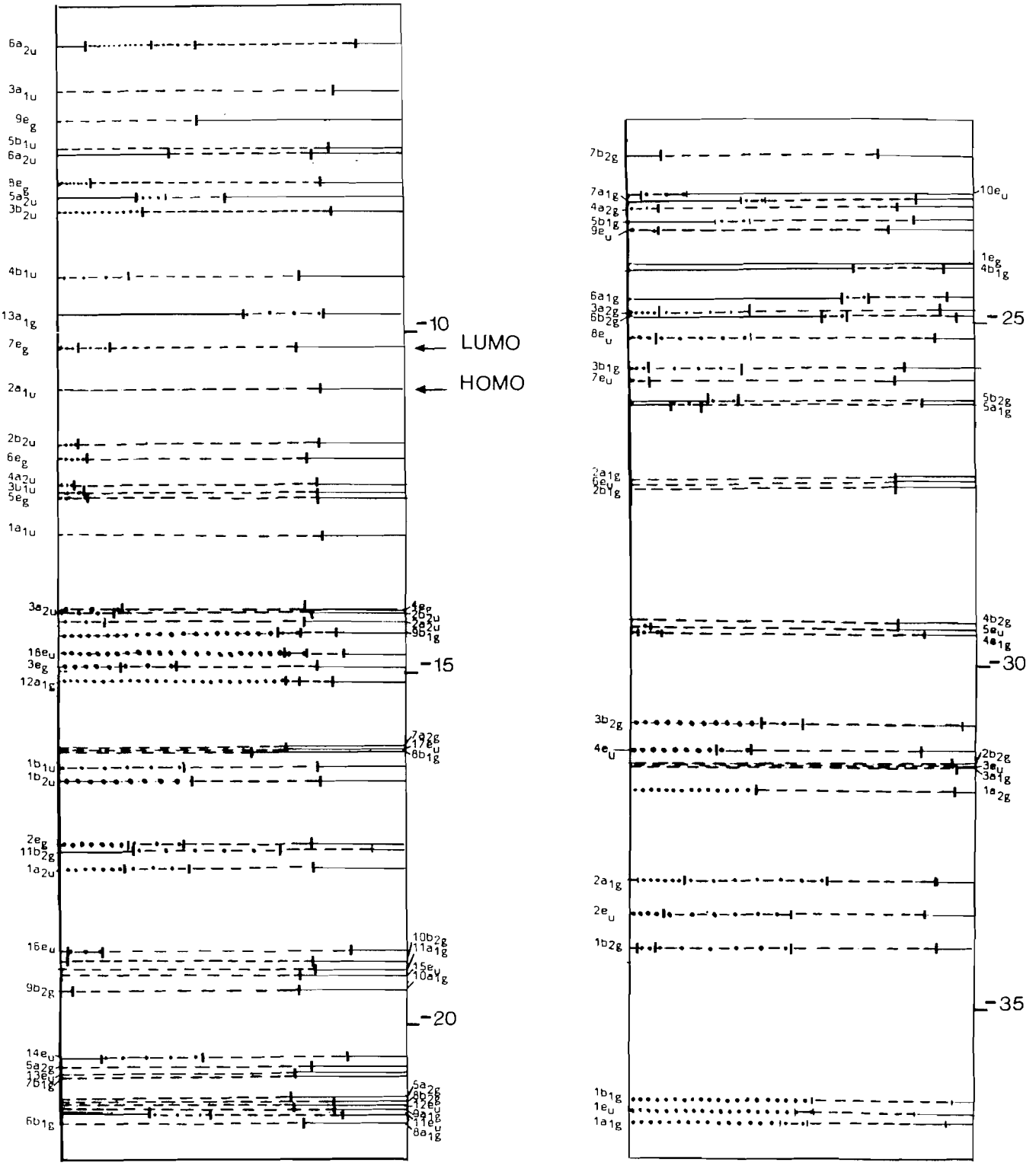

FIG. 2. Xα energetic diagram of ZnPc. ---, Zn contribution; . . . . . , N1 contribution; -·-·-·, N2 contribution; – – –: all carbon contribution.

(5) The order of the occupied levels is very different, between the two calculations and no one-to-one correspondence can be made since the authors did not give the full list of them (and the VB width).

Comparison between ZnPc and a similar smaller molecule zinc tetraazaporphyrin (ZnTAP)

This kind of molecule has also been the subject of several experimental determinations and theoretical calculations (19), however, to our knowledge no calculation has been performed on the zinc complex. One should emphasize that the geometry used for our calculation is that of ZnPc from which the benzo groups have been removed and after having saturated the dangling bonds by hydrogen atoms. This is not the experimental geometry which should, however, not be very different. Consequently, the same parameter set has been retained for the

TABLE 3. Theoretical core energy levels (eV)

Zn:	1*s*	2*s*	2*p*	3*s*	3*p*	
	9414.0	1148.0	1015.0	138.5	96.32	
1*s*:	N1	N2	C1	C2	C3	C4
	391.1	392.1	285.6	282.6	281.1	279.5

calculation, the outersphere radius excepted, since it is taken tangent to the most external atomic spheres in both cases.

The experimental spectrum of this kind of molecule is known to be quite different from the ZnPc spectrum (19): however, this calculation should be compared to both experimental and theoretical ZnPc spectram.

We did not find a ZnTAP photoemission spectrum in the literature but some qualitative features should be derived from the other transition elements TAP spectra described by Koch (19).

The experimental valence band width amounts to 24.0 eV, which is smaller than the calculated one. This is due to the geometry retained for the calculation, which is neither optimized in the calculation, (since the calculation aimed to mimic the phthalocyanine molecule) nor the experimental one.

If one compares now the ZnTAP to the ZnPc molecules, a smaller valence band width is expected because of a smaller π cloud over the molecule. the HOMO–LUMO gap is also expected to be found rather different since it involves orbitals belonging (in part) to peripheral atoms. On the other hand, the frame could be expected to be not significantly different from the previous one. In fact we found the two frontier MO's (HOMO, LUMO) belonging to the irreducible representations $5a_{2g}$ (10.08 eV, carbon character) and $5a_{2u}$ (9.875 eV, nitrogen character) respectively. This leads to a forbidden gap equal to 0.22 eV, much smaller than the gap of ZnPc. On the other hand, the valence band width is larger than the VB of ZnPc, since it is equal to 39.74 eV instead of 25.76 eV.

In order to compare the two VB of ZnPc and ZnTAP we begin with the two spectra Fig. 4 (*a*) and (*b*) where the total densities of state of ZnPc and ZnTAP are respectively given. These densities of states are obtained by convolution of the discrete levels by gaussian of 0.6 eV HWHM. The intensity of each level is given by its occupation number, while in partial or local densities of states, this intensity is weighted by the partial charges (*s*, *p*, *d*) of the selected atoms (Table 4). Finally the theoretical spectra are sums of partial densities of states weighted by atomic cross sections. As just mentioned, the valence band is narrower in ZnPc than in ZnTAP. On the (*a*) spectrum the characteristics of some peaks (purely 2*s* or *d* peaks) are given, the other peaks corresponding to mixed orbitals. The lack of C3(2*s*) and C4(2*s*) peaks in ZnTAP spectrum can be observed, and so the two peaks N1(2*s*) and N2(2*s*) are pulled nearer the Zn(3*d*) peak when the two atoms C3 and C4 are removed (i.e. going from ZnPc to ZnTAP). Moreover, a wide shift of the whole spectrum towards the lower energies is observed when going from ZnPc to ZnTAP. This is related to the size of the outersphere (i.e. the volume of the intersphere region), as previously stated. The order of magnitude of this shift can be deduced from the two spectra (*c*) and (*d*). On (*c*), the ZnPc molecule is given after setting to 0 the cross section of C3, C4, H1, and H2 atoms. On (*d*) a spectrum of ZnPc is given with a null cross section for H atoms, so that theoretically, the same molecules should be obtained. Although

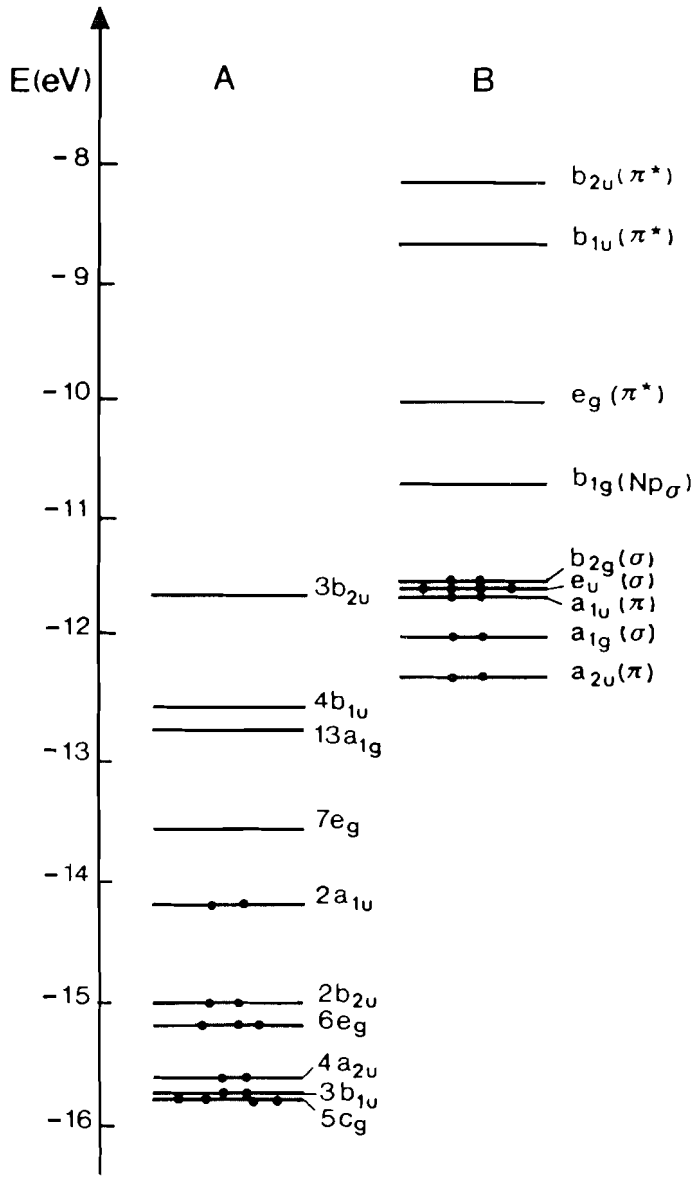

FIG. 3. Comparison between Xα and EHT calculations of the electronic structure of ZnPc.

the two spectra compared exhibit a similar shape, it can be deduced that the N1(2*s*) and N2(2*s*) peak shift amounts to 13 eV while the Zn(3*d*) peak shift is only about 4 eV.

Two spectra (not displayed here) can be calculated for ZnPc and ZnTAP with the usual atomic cross sections taken from Scofield's table (2). These two spectra do not differ significantly from the (*c*) and (*d*) spectra because the cross sections of the other orbitals N(2*p*), C(2*p*), and H(1*s*) are very weak in comparison to 3*d* (3*d*) cross section.

Extending this comparison to the C1(2*s*) and C1(2*p*) spectra, it clearly appears that these electrons are delocalized over all the MO's in both ZnPc and ZnTAP. However, the C2(2*s*) electrons localized at one place on the (*g*) spectrum (ZnPc) become localized at two places in the (*h*) spectrum (ZnTAP): this is not true for C2(2*p*) electrons which are delocalized over the whole spectrum in both cases. Therefore, the "truncation" of the ZnPc not only affects the qualitative distribution of these electrons, it also leads to a quantitative difference in the relative positions of the different peaks.

Can. J. Chem. Downloaded from www.nrcresearchpress.com by 84.22.46.98 on 09/08/12
For personal use only.

Can. J. Chem. Downloaded from www.nrcresearchpress.com by 84.22.46.98 on 09/08/12
For personal use only.

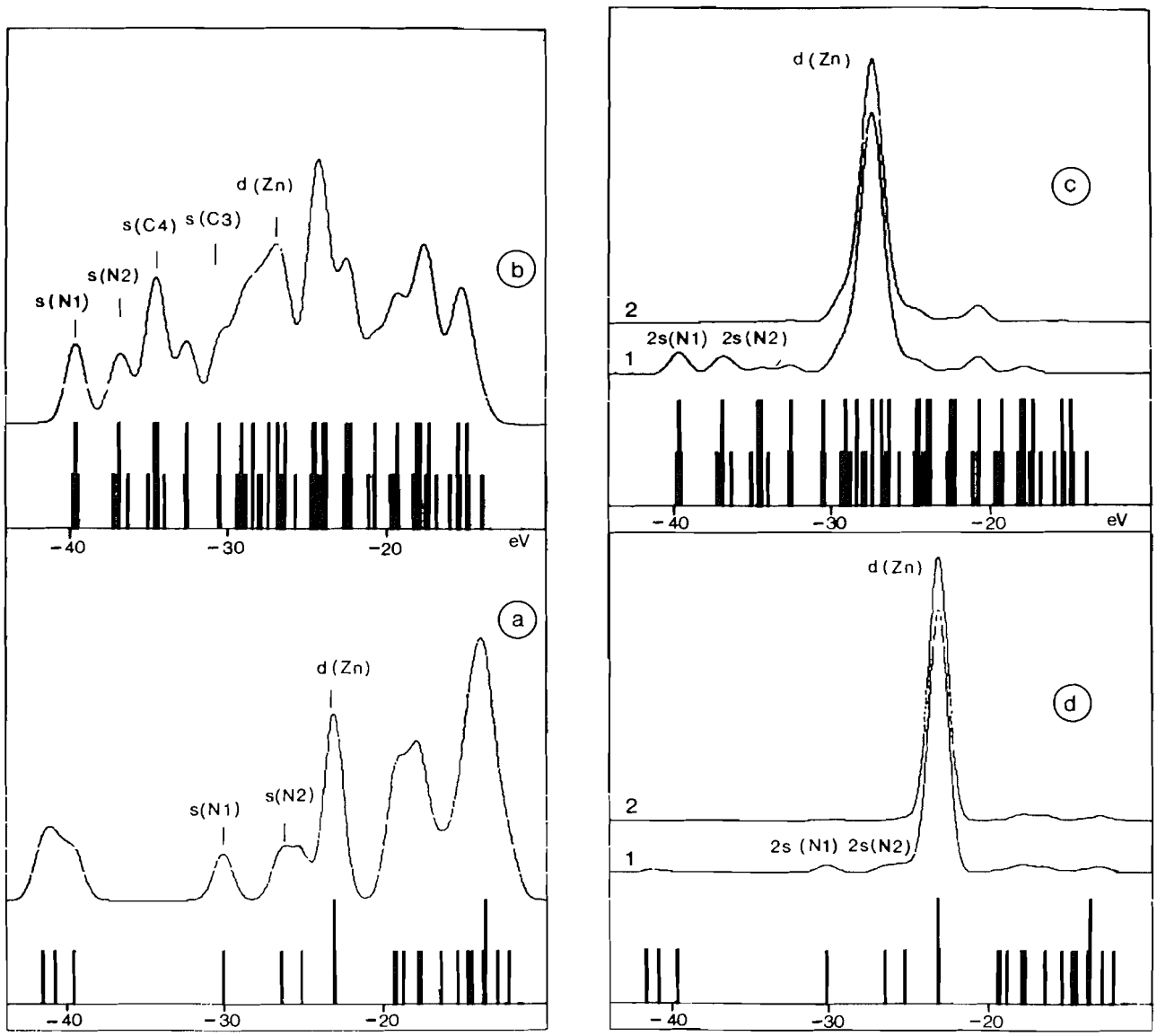

FIG. 4. (*a*) density of states of ZnPc with $\sigma = 1$; (*b*)density of states of ZnTAP with $\sigma = 1$; (*c*) *1*, skeleton of ZnPc (σ C3 = σ C4 = σ H1 = σ H2 = 0), *2*, contribution of Zn in ZnPc; (*d*) *1*, skeleton of ZnTAP (σ H1 = 0), *2*, contribution of Zn in ZnTAP; (*e*) theoretical spectrum of ZnPc: *1*, contribution of C1; *2*, contribution of C1(2*s*); *3*, contribution of C1(2*p*). (*f*) theoretical spectrum of ZnTAP: *1*, contribution of C1(2*s*) which is identical to the (C1) spectrum; *2*, contribution of C1(2*p*). (*g*) theoretical spectrum of ZnPc; *1*, contribution of (C2); *2*, contribution of C2(2*s*); *3*, contribution of C2(2*p*); (*h*) theoretical spectrum of ZnTAP: *1*, contribution of C2(2*s*); *2*, contribution of C2(2*p*).

5. Valence band photoemission spectra of ZnPc

Figure 5(*a*) reproduces the XPS spectrum of ZnPc in the valence band region; one notices the peak with the highest intensity lying at 11.0 eV BE, which is the Zn 3*d* peak. This peak shows that the energy of the (*d*) orbitals is concentrated in a narrow band.

Figure 5(*b*) gives a theoretical XPS spectrum obtained after having weighted the partial DOS (Fig. 5(*c*) by atomic cross sections, and a convolution with gaussians of 0.6 eV FWHM. The last two spectra show that the role of the cross section is dominant so that we cannot make direct comparisons between experiment and the DOS. On the other hand, the use of Scofield's values (20) allow a good agreement between the theoretical spectrum and the experimental one.

However, the theoretical photoemission spectrum should involve the transition state energies of all the MO's rather than the ground state eigenvalues, in order to take into account the electronic relaxation during the ionisation process and to remove the self-interaction, as already stated. This is hardly possible for reasons of computational cost, but we know that for orbitals exhibiting the same atomic character, the relaxation is similar (21). Accordingly, we can gather the VB MO's in three groups: the π orbitals, the (C,N)2*s orbitals and the Zn(3d)* orbitals. Therefore, we computed a transition state for one MO of each group in order to determine semi-quantitatively the shift to apply to each group. We found "relaxations" (i.e. self-

TABLE 4. Electronic sphere charges

out	int	Zn	N1	N2	C1	C2	C3	C4	H1	H2
0.029	31.47	30.30	6.45	6.40	5.30	5.42	5.38	5.51	0.49	0.47

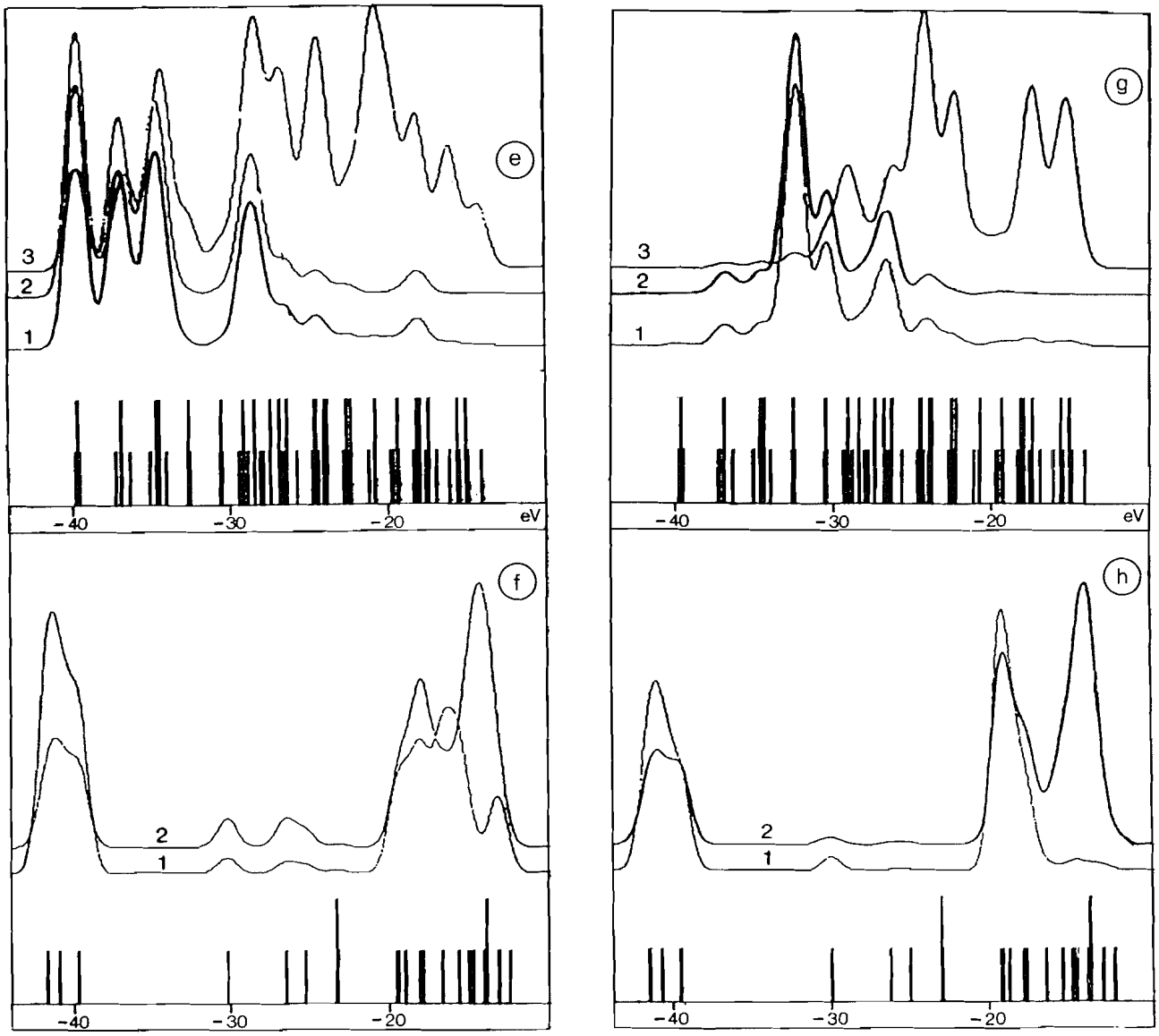

FIG. 4. (*Concluded*)

interaction energies + relaxation energies) as large as 5.8 eV for Zn(3*d*) MO's (calculated on the $1e_g$) and 1.7 eV for π^* MO's (HOMO). An intermediated value probably equal to 4 to 5 eV should be obtained for the 2*s* peaks since these orbitals are localized on one kind of symmetry-equivalent atoms. We did not compute it since a correct calculation should be performed in C_1 symmetry to let the ionization hole localize over one of the (4 or more- symmetry-equivalent atoms of the molecule in D_{4h} symmetry. These values compare well to the relaxation shift found by Tossell (22) for ZnS or Zn halides. On the other hand, the relaxation found for π orbitals is much larger than the 0.5 eV relaxation found by Ellis *et al.* in a DV-SCC calculation of SiTAP (23).

Therefore, the theoretical spectrum given in Fig. 5(*b*) may be discussed and compared to experiment if one keeps in mind that the Zn peak has to be shifted (by 4 eV) towards larger binding energies, as well as the left part of the spectrum (2s peaks, by ca. 3 eV) relatively to the π peaks.

The theoretical and experimental spectra given in Fig. 5(*a*) and (*b*) are rather similar if one performs a shift of 13 eV towards the lower energies in the theoretical spectrum with respect to the experimental one, and if one takes this shift to align the peaks of Zn(3*d*) we can observe the correspondence between the two peaks which are found at 24.0 eV and 20.5 eV BE in the experimental spectrum and the orbitals N1(2*s*) and N2(2*s*) peaks, respectively; an analogous correspondence can be established for the peaks which are found at 17.75 eV and 13.95 eV Be corresponding to the orbitals C4(2*s*) and C(2*s*), respectively.

The comparison between the experimental and theoretical values once this shift is performed, is summarized in Table 5. These values show that the differences between theoretical and experimental peak energies amounts to values as small as 0.5 eV, which are rather small, since a part of them can be attributed to the difference in the relaxation energies of the different oribtals through the ionization process.

In the experimental spectrum, the first peak lies at 3.7 eV below the Fermi level: it corresponds to the first peak of the DOS

Can. J. Chem. Downloaded from www.nrcresearchpress.com by 84.22.46.98 on 09/08/12
For personal use only.

Can. J. Chem. Downloaded from www.nrcresearchpress.com by 84.22.46.98 on 09/08/12
For personal use only.

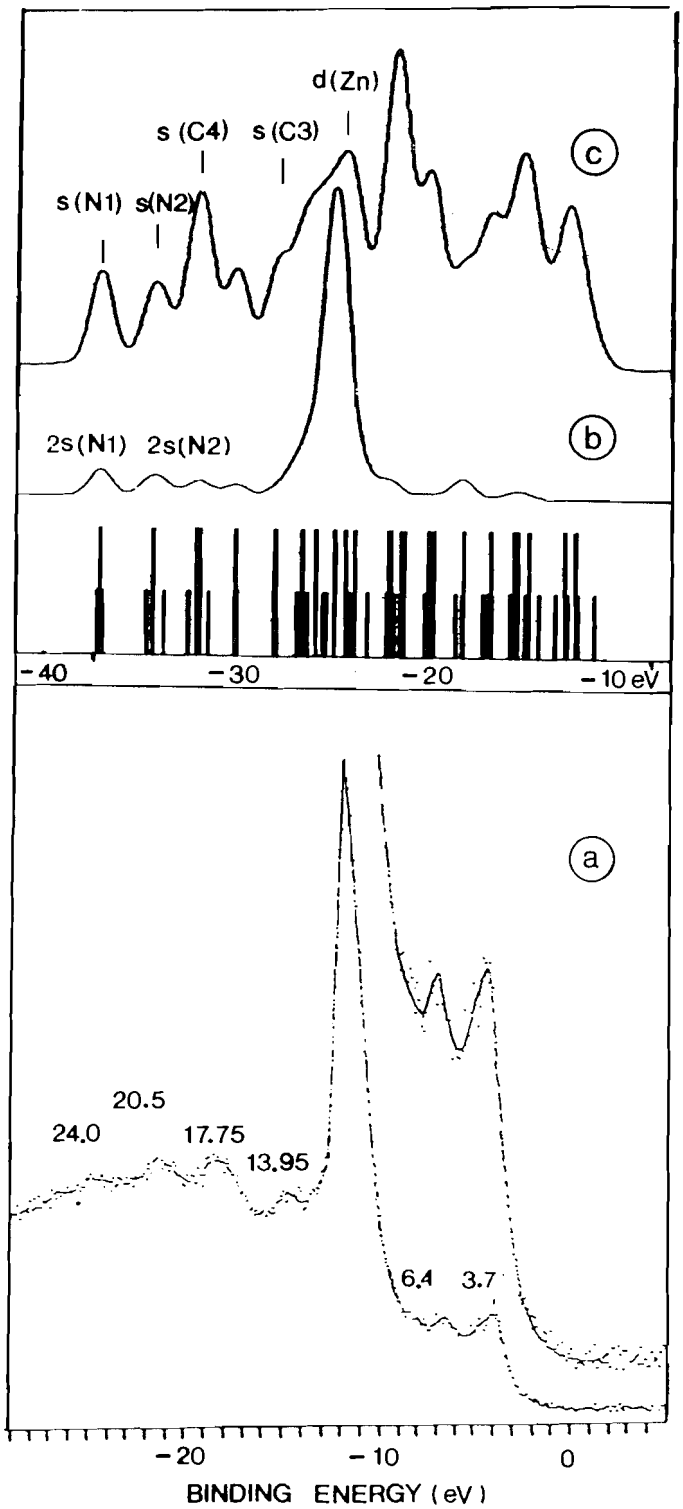

FIG. 5. (*a*) Experimental XPS spectrum of ZnPc, (*b*) theoretical XPS spectrum of ZnPc, (*c*) DOS of ZnPc.

and it arises essentially from the photoionization of the π electrons which are delocalized over the carbons.

Finally, let us recall that the shift of 13.9 eV is related to the too large value for the outersphere radius, or more precisely, to the large size of the intersphere volume in the muffin-tin representation of the potential. As already stated, this effect of increased binding energies of large (planar) molecules has been studied in detail in a forthcoming paper (17).

TABLE 5. Comparison between theoretical and experimental XPS values (C or N 2*s* band)

	XPS values			
Source	N1(2*s*)	N2(2*s*)	C3(2*s*)	C4(2*s*)
Experimental	24.0	20.5	13.95	17.75
Theoretical	23.25	20.4	14.24	18.24

6. Absorption spectrum

Figure 6 gives the experimental spectrum of a thin layer obtained in the laboratory by evaporation under vacuum. We have compared in this figure this absorption spectrum to that obtained in the vapor phase by Eastwood *et al.* (24), in solution by Lever (25), and more recently by Nyokong *et al.* (4*a*).

The absorption spectrum of a metal-phthalocyanine usually composes of two intense bands in the 300–400 nm zone (the Soret band) and the 600–700 nm zone (the Q band) (26). The absorption coefficient in these bands is very large. Thin film (300 nm) spectra have been recorded in the 0.2–2 μm range and exhibit no absorption in the 800 nm–2 μm range, therefore the first electronic transition does not lie in the infrared region and should be found in the visible spectrum.

Edward and Gouterman (21) have studied the absorption spectrum of the ZnPc and other phthalocyanines in the vapour phase between 800 nm and 300 nm. Generally, the metal effect is relatively weak in the 300 to 800 nm zone, since the specific band of the metal is found in the infrared range. In the uv a wide band exists at 180–160 nm. On the other hand, these authors have also compared the spectra in the vapor phase and in the solution state. These spectra differe slightly. However, more important changes occur when one goes from solution to solid state: one observes a widening of the Q band with the appearance of the Davidov splitting (27) which is clearly apparent in the thin film spectrum (Fig. 6). We notice the widening of the peak when one goes from the solution state to the solid state. On the other hand, the peaks are not of the same intensity ratio. The Q band is thus modified: the peak at 880 nm in the vapor phase is found at 707 nm in the solid phase spectrum, the peak at 600 nm which represents a shoulder is more intense than the band at 707 nm, and is shifted to 617 nm. This last peak also exhibits a shoulder. On the other hand, the Soret band lies at lower energies and is more intense than the Q peak, slightly wider, and has a shoulder at 380 nm.

In the literature some interpretations of the absorption spectra by molecular orbital theories can be found. The EHT method used by Gouterman *et al.* allowed to interpret the Q band as a $\pi \rightarrow \pi^*$ transition of $a_{1u} \rightarrow e_g$ type, the Soret band being also a $\pi \rightarrow \pi^*$ transition of $a_{2u} \rightarrow e_g$ symmetry. This would also be in agreement with PPP calculations.

The most detailed analysis of the absorption spectrum of ZnPc is given in Nyokong's paper (4*a*) in which the assignment is obtained through a correlated analysis of the absorption and the MCD spectra.

The energy diagram of ZnPc given in the previous paragraph shows for the forbidden gap ($2a_{1u}$–$7e_g$) an energy at 0.6 eV, which is at variance with the experimental electrochemical gap of about 1.7 eV (25–31). This discrepancy cannot be attributed only to the solvation of the molecule used for the experiment, and which is not taken into account in the calculation. On the other hand, solid state effects like the stacking of the ZnPc rings cannot be invoked since the vapor uv spectrum is rather similar

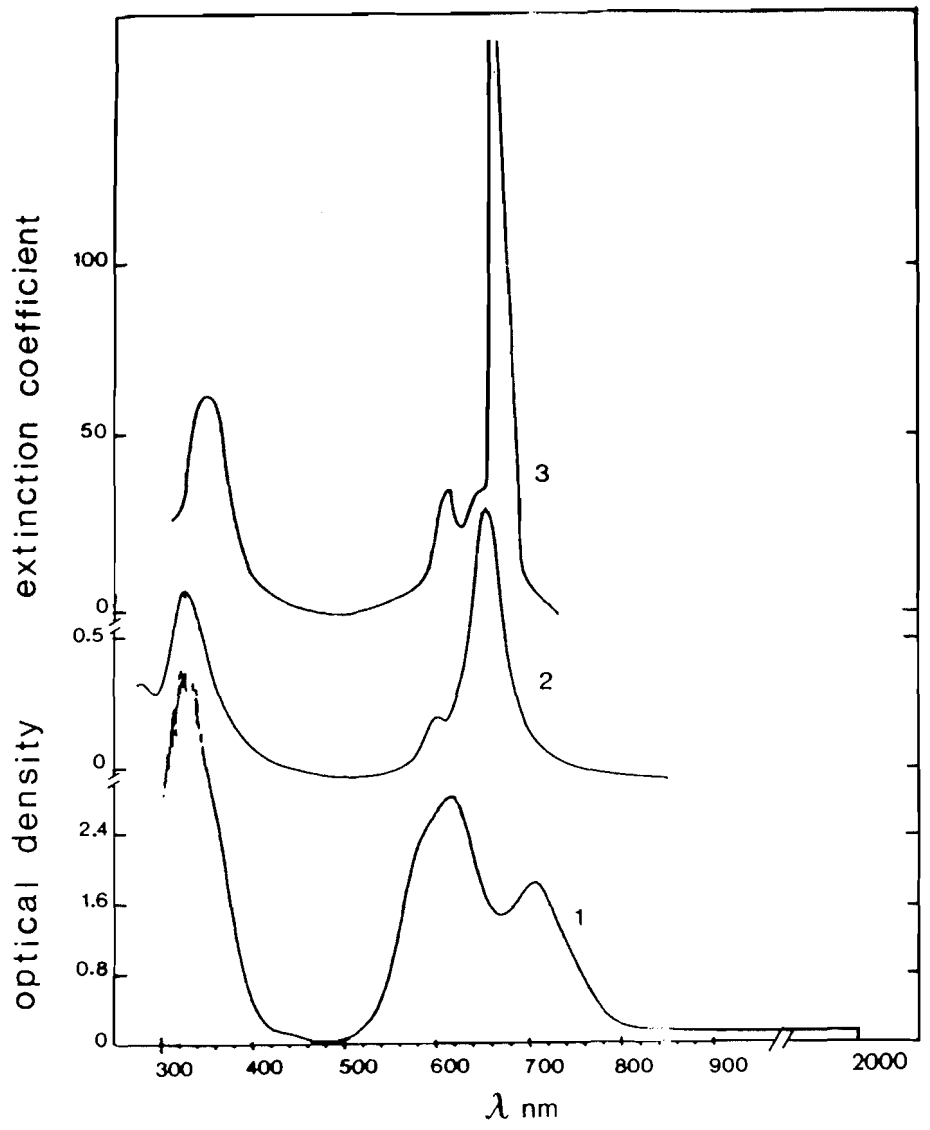

FIG. 6. Absorption spectra of ZnPc: (*1*) thin layer phase; (*2*) vapor phase (24); (*3*) in solution (25).

TABLE 6. Allowed transitions in the Xα calculation

	Label	Transition	Raw value* E (eV)	corrected value by 1.2 eV shift E (eV)	corrected value by 1.2 eV shift E (cm^{-1})	Experimental (ref. 4*a*)
	Q	$2a_{1u} \rightarrow 7e_g$	0.61	1.81	14600.	14906.
	N	$1a_{1u} \rightarrow 7e_g$	2.70	3.90	31400.	29778.
$a_{1u} \rightarrow e_g$						
	L	$2a_{1u} \rightarrow 8e_g$	3.04	4.24	34200.	35437.
		$1a_{1u} \rightarrow 8e_g$	5.13	6.33	51000.	
	B	$4a_{2u} \rightarrow 7e_g$	2.04	3.24	26150.	27513.
	C	$3a_{2u} \rightarrow 7e_g$	3.44	4.64	37400.	40655.
		$2a_{2u} \rightarrow 7e_g$	4.12	5.32	42900.	
$a_{2u} \rightarrow e_g$						
		$4a_{2u} \rightarrow 8e_g$	4.47	5.67	45700.	
		$3a_{2u} \rightarrow 8e_g$	5.87	7.07	57000.	
		$2a_{2u} \rightarrow 8e_g$	6.55	7.75	62500.	
$a_{2u} \rightarrow a_{1g}$		$4a_{2u} \rightarrow 13a_{1g}$	2.89	4.09	33000.	
		$3a_{2u} \rightarrow 13a_{1g}$	3.29	4.49	36200.	

*Difference of ground state eigenvalues.

Can. J. Chem. Downloaded from www.nrcresearchpress.com by 84.22.46.98 on 09/08/12
For personal use only.

Can. J. Chem. Downloaded from www.nrcresearchpress.com by 84.22.46.98 on 09/08/12
For personal use only.

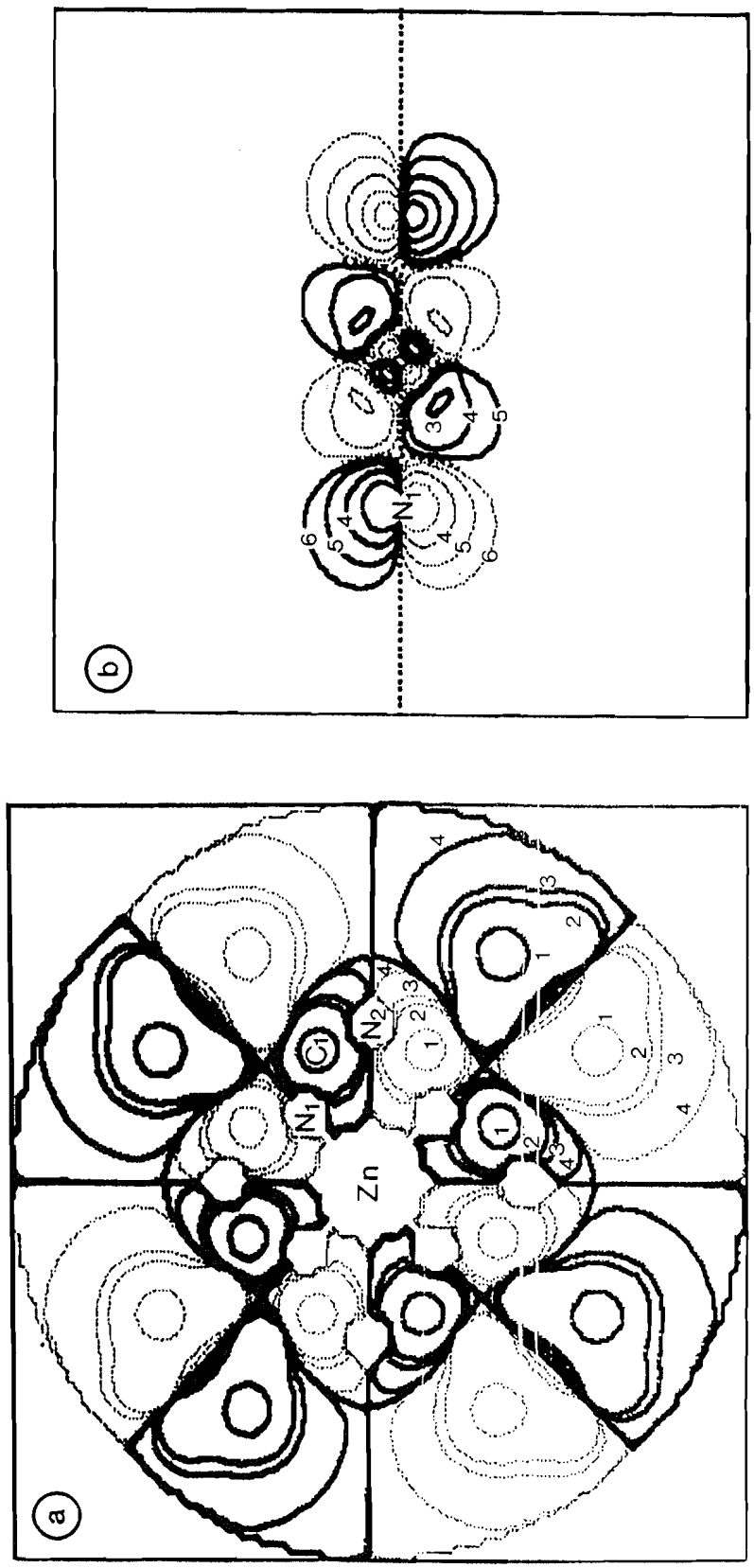

FIG. 7. Contour maps of selected MO's. *a*, HOMO ($2a_{1u}$); *b*, *c*, LUMO ($7e_g$); *d*, $13a_{1g}$; *a*, plane // to *x*O*y*; *b*, y*O*z plane; *c*, *d*: *xy*/O*z* plane. The contours values are (in electron$^{1/2}$ bohr$^{-3/2}$) (*1*) 5×10^{-2}; (*2*) 3×10^{-3}; (*3*) 7×10^{-5}; (*4*) 3×10^{-6}; (*5*) 0.

Can. J. Chem. Downloaded from www.nrcresearchpress.com by 84.22.46.98 on 09/08/12
For personal use only.

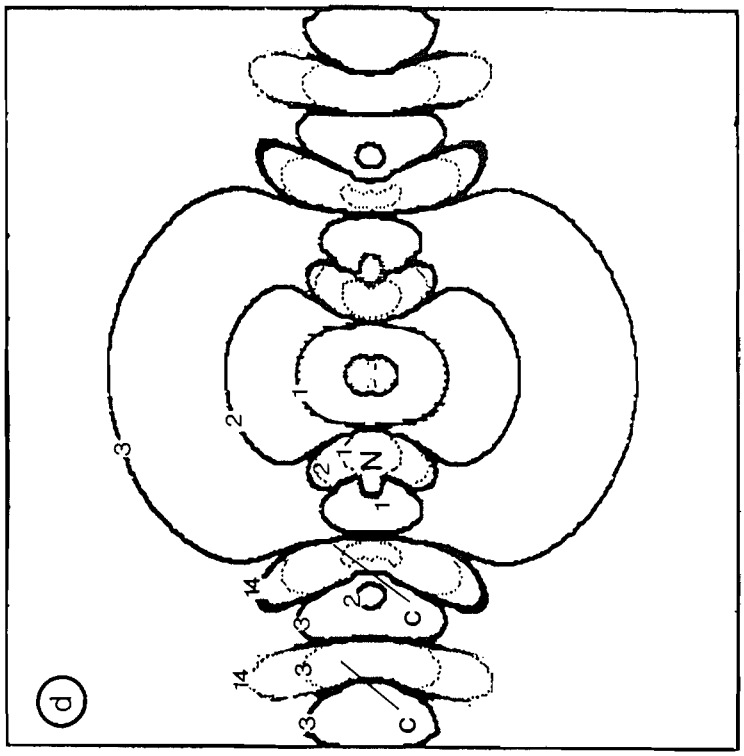

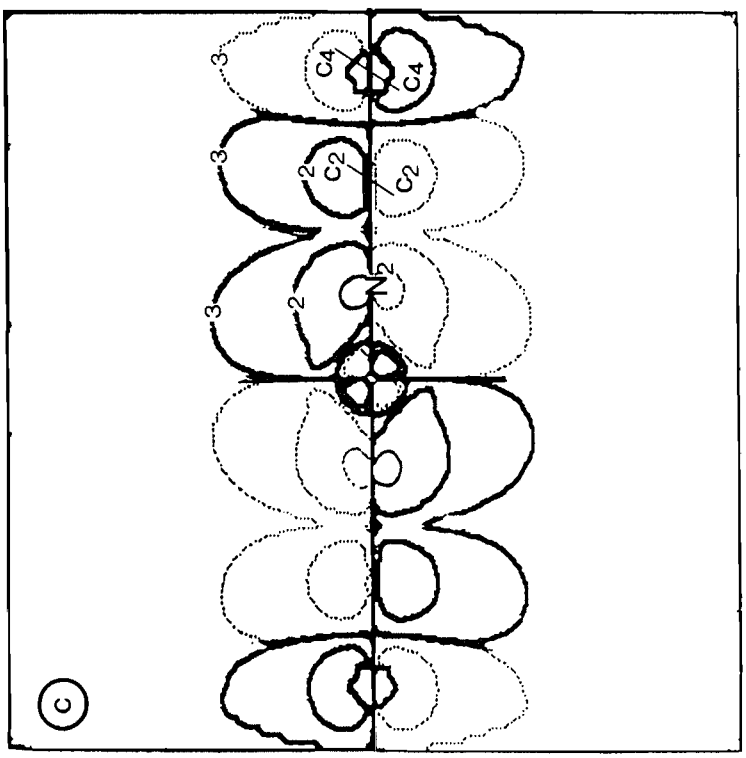

FIG. 7. (*Concluded*)

to the solid state one. The electronic gap and the electronic transitions are definitely underestimated, but if one adds 1.2 eV to the virtual level eigenvalues one obtains the optically allowed transition energies which are listed in Table 6. With this shift the HOMO–LUMO $2a_{1u}$–$7e_g$ transition corresponds well to the Q band which lies at 1.8 eV, i.e., 690 nm while the Soret $4a_{2u}$–$7e_g$ transition lies near 390 nm. Indeed, the correlation with Nyokong's assignment (4*a*) becomes surprisingly good since the four QBNL bands are found to agree within 5% (Table 6).

In order to get a better view of the MO's in the optical transitions some contour maps have been plotted in Fig. 7 for frontier orbitals $2a_{1u}$, $7e_g$, and the $13a_{1g}$ MO's. Their π or π^* character is clearly apparent in the views which are taken either in the *y*O*z* or the *xy*/O*z* planes. One also clearly sees the strong Zn(4*s*) character in the $13a_{1g}$ MO. The overlap between these π and π^* MO's is quite large, leading to high absorption coefficients. One should also expect in the far uv region, intense transitions involving the $13a_{1g}$ MO which exhibits a Zn(4*s*) character as already indicated.

Finally one can conclude that the energy level diagram allows the correct interpretation of the electronic absorption spectrum, as well as the XPS spectrum. This lead us to expect that it may be used with success to calculate the doping of this material by donor or acceptor molecules of similar shape. This work is now in progress.

1. (*a*) R. P. Linstead. J. Chem. Soc. 1016 (1934); (*b*) R. P. Linstead, and J. M. Robertson. J. Chem. Soc. 1195 (1936); 1636 (1936).
2. J. Simon and J. J. Andre. Molecular semiconductors, Springer Verlag. 1984.
3. (*a*) M. Martin, J. J. Andre, and J. Simon. J. Appl. Phys. **54**: 2792 (1983); (*b*) M. Maitrot, G. Guillaud, B. Boudjema, J. J. Andre, and J. Simon. J. Appl. Phys. **60**, 2396 (1986).
4. (*a*) T. Nyokong, Z. Gasyna, and M. Stillman. Inorg. Chem. **26**, 1087 (1987); (*b*) M. J. Stillman and A. J. Thomson. J. Chem. Soc. Faraday Trans. 2, **70**, 805 (1974); (*c*) M. J. Stillman and A. J. Thomson. J. Chem. Soc. Faraday Trans. 2, **70**, 790 (1974).
5. T. Nyokong, Z. Gasyna, and M. Stillman. Inorg. Chem. **26**, 548 (1987).
6. J. Simon, J. J. Andre, and M. Maitrot. Solid and liquid crystalline molecular semiconductors. *In* Proceedings of the 4th International School on Condensed Matter Physics Molecular Electronics, 253.
7. I. P. Batra, B. I. Bennett, and F. Herman. Phys. Rev. **11**, 4927 (1975).
8. W. R. Scheidt and W. Dow. J. Am. Chem. Soc. **99**, 1101 (1977).
9. J. G. Norman, Jr. J. Chem. Phys. **61**, 4630 (1974).
10. F. M. Michel-Calendini and H. Chermette. J. Phys. C, **14**, 1179 (1981).
11. K. Schwarz. Phys. Rev. **85**, 2466 (1972); Theor. Chim. Acta, **34**, 225 (1974).
12. A. M. Schaffer and M. Gouterman. Theoret. Chim. Acta, **25**, 62 (1972).
13. A. J. McHugh, M. Gouterman, and M. Weiss. Theoret. Chim. Acta, **24**, 346 (1972).
14. D. A. Case and M. Karplus. J. Am. Chem. Soc. **99**, 6182 (1977).
15. S. H. Lamson and R. P. Messmer. Phy. Rev. B**36**, 986 (1980).
16. M. Benkaddour, H. Chermette, N. El-Khatib, and M. Maitrot. To be published.
17. N. El-Khatib, H. Chermette, and M. Maitrot. Int. J. Quantum Chem. To be published.
18. C. Pedrini, H. Chermette, A. B. Goldberg, D. S. Macure, and B. Moine. Phys. Stat. Sol. (b) **120**, 753 (1983).
19. E. E. Koch, M. Iwan, K. Hermann, and P. S. Bague. Chem. Phys. **59**, 249 (1981).
20. J. H. Scofield. J. Electron. Spectrosc. Relat. Phenom. **8**, 129 (1976).
21. L. Edwards and M. Gouterman. J. Mol. Spectrosc. **33**, 292 (1970).
22. T. A. Tossell. Inorg. Chem. **16**, No. 11, 2944 (1977).
23. D. E. Ellis and Z. Berkovitch-Yellin. J. Chem. Phys. **74**, 2427 (1981).
24. D. Estwood, L. Edwards, M. Gouterman, and J. Steinfeld. J. Mol. Spectrosc. **20**, 281 (1966).
25. A. B. P. Lever. Adv. Inorg. Radiochem. **7**, 27 (1965).
26. P. C. Minor, M. Gouterman, and A. B. P. Lever. Inorg. Chem. **24**, 1895 (1985).
27. L. B. Sillinsh. Organic molecular crystals. Springer Verlag, 1980.
28. A. Volberg and J. Manassen. J. Am. Chem. Soc. **92**, 2982 (1970).
29. A. Giraudeau, F. R. Fan, and A. J. Bard. J. Am Chem. Soc. **102**, 5137 (1980).
30. J. Manasse and A. Bar-Irlan. J. Catal. **17**, 86 (1970).
31. A. B. P. Lever and J. P. Wilshire. Can. J. Chem. **54**, 2514 (1976).

Can. J. Chem. Downloaded from www.nrcresearchpress.com by 84.22.46.98 on 09/08/12
For personal use only.

The kinetics of gas phase reactions studied in a "homogeneous reactor"

JOHN M. ROSCOE
Department of Chemistry, Acadia University, Wolfville, N.S., Canada B0P 1X0

Received January 28, 1988

JOHN M. ROSCOE. Can. J. Chem. **66**, 2325 (1988).

The use of a "well-stirred" or "homogeneous" reactor in kinetic studies of gas phase reactions has been examined to assess the sensitivity of the method to the criteria upon which its use is based. The effects of heterogeneous and homogeneous secondary reactions are considered and the validity of the assumption of homogeneity has been examined experimentally for conditions similar to those which have been used elsewhere. The atom sink presented by the excess reagent under pseudo first order conditions results in failure of the homogeneity assumption. However, it is found that homogeneity is not required for successful use of the method provided the analytical measurements have good spatial resolution and the reaction volume is well-defined. The method is illustrated by using it to study some reactions of $O(^3P)$.

JOHN M. ROSCOE. Can. J. Chem. **66**, 2325 (1988).

On a examiné l'utilisation d'un réacteur "bien agité" ou "homogène" dans les études cinétiques des réactions en phase gazeuse, dans le but d'établir la sensibilité de la méthode face à ses critères d'utilisation. On a considéré les effets des réactions secondaires hétérogènes et homogènes et on a examiné expérimentalement la validité de l'hypothèse d'homogénéité dans des conditions semblables à celles déjà utilisées. Le puits d'atomes présenté par l'excès de réactifs dans des conditions de pseudo ordre 1 est dû à l'insuffisance de l'hypothèse d'homogénéité. On a trouvé que l'homogénéité n'est pas nécessaire pour une utilisation fructueuse de la méthode en admettant que les mesures analytiques ont une bonne résolution spatiale et que le volume réactionnel est bien défini. On applique la méthode à l'étude de quelques réactions du $O(^3p)$.

[Traduit par la revue]

Can. J. Chem. Downloaded from www.nrcresearchpress.com by 196.1.178.254 on 09/07/12
For personal use only.

Introduction

The principles of kinetic measurements in a "well-stirred" or "homogeneous" reactor, first developed by Denbigh (1, 2), have had sporadic application to the study of gas phase reactions of atoms and radicals (3–15). While considerable success has been attained at the relatively low pressures of the VLPP method of Benson and co-workers (10, 11), the validity of the homogeneity assumption at the higher pressures used in other work (3–9, 12–15) is unclear and has not been examined directly. The criteria for efficient mixing have received some attention (4, 9, 12), but the effect on the use of homogeneous reactors of the homogeneous atom sink represented by the excess reactant has been largely neglected in this higher pressure region. On the other hand, there are several theoretical and experimental evaluations of the relative importance of diffusive and convective mass transport in conventional flow systems operated at pressures of a few Torr (1 Torr = 133.3 Pa) and containing both homogeneous and localized heterogeneous atom sinks (16–20).

Homogeneous reactors operated at pressures above about 0.1 Torr represent a potentially simple and convenient way to study the kinetics of atom and free radical reactions. Although much of the work in the literature which uses this method has employed relatively expensive instrumentation (4–9), it has also been used successfully with much less costly apparatus (12–14). We were surprised, then, when our initial efforts to apply the homogeneous reactor method gave results which were in very poor agreement with data reported in the literature. Our results suggested that the criterion of homogeneity was not satisfied in our apparatus even though the physical criteria for homogeneity (9) were met and the homogeneous reactor equation relating concentrations of reactants to the rate constant for the reaction was evidently obeyed. This led us to investigate the implications at these pressures of a homogeneous atom sink for the principles upon which the method is based. The validity and necessity of the assumption of homogeneity were examined directly over a range of conditions encompassing most of those used in previous work (4–9, 12–15) and the reliability of the method was examined by using it to study the kinetics of some reactions of $O(^3P)$ for which good agreement exists among recent results in the literature.

Theory

Neglecting radial concentration gradients, the steady-state balance of atoms (A) entering and leaving a cross-section of a cylindrical gas kinetics flow reactor is

$$[1] \quad D\frac{\partial^2[A]}{\partial x^2} - v\frac{\partial[A]}{\partial x} - \sum_i k_i [A]^{n_i}[S]^{m_i} = 0$$

where D is the diffusion coefficient for A, v is the velocity of gas flow through the reactor, S is the substrate with which A reacts, x is the axial distance in the direction of flow, and k_i, n_i, and m_i are the rate constant and appropriate reaction orders for the ith reaction removing A. For simplicity, consider the removal of atoms by a single reaction which is first order in both S and A and which occurs under conditions which are pseudo first order in A (excess S). Equation [1] then becomes

$$D\frac{\partial^2[A]}{\partial x^2} - v\frac{\partial[A]}{\partial x} - k_1[A] = 0$$

where $k_1 = k[S]$ is the pseudo first order rate coefficient. Solution of this equation for [A] at any point x along the axis of the flow tube gives

$$[2] \quad [A]_x = [A]_0 e^{Rx}$$

where $[A]_0$ and $[A]_x$ are the atom concentrations at the inlet of the flow reactor and at some point x downstream from the inlet and R is given by

$$R = \frac{v}{2D} - \left[\left(\frac{v}{2D}\right)^2 + \frac{k_1}{D}\right]^{1/2}$$

It may be easily shown that, under the conditions encountered in conventional flow experiments (large v and small D), the second derivative term in eq. [1] becomes negligible and $R = -k_1/v$ as required.

Can. J. Chem. Downloaded from www.nrcresearchpress.com by 196.1.178.254 on 09/07/12
For personal use only.

Two methods of using homogeneous reactors have appeared in the literature. In the first method (4–7, 12–15), the inlet and exit atom concentrations are measured and are related to the rate constant for the reaction by

$$[3] \quad [A]_0 - [A]_L = k[S][A]_L V/\dot{V}$$

where $[A]_0$ and $[A]_L$ are the inlet and exit atom concentrations respectively, $\dot{V}$ is the volumetric flow rate through the reactor and V is the reactor volume. The assumption is made that diffusional mixing is so fast that the exit atom concentration equals the bulk (homogeneous) atom concentration.

The second method (9) measures an average atom concentration within the reactor and again uses eq. [3] on the assumption that diffusional mixing is so fast that the measured atom concentration equals the exit atom concentration. Since it is uncertain how much of the reactor was sampled in these experiments, the relationship of the measured atom concentration to the volumetric average atom concentration within the reactor is also uncertain.

Because it is desired to test the assumptions outlined above, two additional equations will be developed. If the reactor is sufficiently short, axial homogeneity can, in principle, be achieved to an arbitrarily good degree of approximation. Under such conditions eq. [3] can be differentiated, for a cylindrical reactor with constant [S] and of radius r, to give

$$-\mathrm{d}[A] = \frac{k[S]\pi r^2}{\dot{V}}\,\mathrm{d}([A]x)$$

where x is the axial distance from the reactor inlet. Substituting eq. [2] for [A] on the right hand side avoids the necessity of assuming axial homogeneity and leads to

$$\int_{[A]}^{[A]_0} \mathrm{d}[A] = \frac{k[S][A]_0\pi r^2}{\dot{V}} \int_0^x (1 + Rx)\mathrm{e}^{Rx}\mathrm{d}x$$

Integration gives on rearrangement

$$[4] \quad \left[\frac{[A]_0}{[A]} - 1\right] = \frac{k[S]V}{\dot{V}}$$

which is equivalent to the homogeneous reactor eq. [3] but does not rely in its derivation upon rapid diffusional mixing. It does, however, assume good spatial resolution in measuring [A] so that the volume defined by the limits of integration is the same as that to which $[A]_0 - [A]$ applies.

When the spatial average concentration is measured, the following approach applies. The volumetric average concentration of A up to a point at a distance L from the reactor inlet is given by

$$\langle[A]\rangle = \frac{1}{L}\int_0^L [A]_0\mathrm{e}^{Rx}\mathrm{d}x$$

This gives

$$\frac{\langle[A]\rangle}{[A]_0} = \frac{\mathrm{e}^{RL} - 1}{RL}$$

If we define $\langle x\rangle$ as the axial distance at which $[A] = \langle[A]\rangle$, use of eq. [2] gives

$$[5] \quad \langle x\rangle = \frac{1}{R}\ln\left\{\frac{(\mathrm{e}^{RL} - 1)}{RL}\right\}$$

Equation [4] may now be used with the realization that use of $\langle[A]\rangle$ requires integration between 0 and $\langle x\rangle$ so that V is replaced by $\langle V\rangle = \pi r^2\langle x\rangle$. The result is

$$[6] \quad \frac{[A]_0}{\langle[A]\rangle} - 1 = \frac{k[S]V}{\dot{V}}\frac{\langle x\rangle}{L}$$

The homogeneous reactor assumption, using the geometric volume, will give an apparent rate constant which is too small and which varies with $\langle x\rangle$ unless the pressure is sufficiently small that $\langle x\rangle = L$.

Experimental

Two reaction vessels of similar design were used in this work. The basic design is shown in Fig. 1. The reactor used to examine homogeneity differed from that used for the rest of the work in having a reactant inlet approximately in the center of the reactor, as shown in Fig. 1(*a*), and in having only the observation port used for viewing along the axis of the reactor. This reactor was not enclosed in a furnace so that measurements could be made at any point along its axis with a movable photomultiplier tube. The reactors used for most of the kinetic measurements had observation ports viewing the reactor at right angles to the direction of flow. In one reactor, these were located between the inlet and exit tubes as shown in Fig. 1(*a*). In the other reactor, shown in Fig. 1(*b*), the observation ports were located just outside the reaction volume at the inlet and exit. These reactors were also enclosed in a furnace to provide temperature control.

Most of the experiments were made at pressures ranging from 0.8 to 1.7 Torr and at room temperature. The flowrates of the carrier gases, N_2 and He, were measured with calibrated capillary flowmeters. Flowrates of the other components were determined by measuring the increase in pressure when the gas whose flowrate was required was allowed to enter a bulb of known volume for a measured length of time.

Atomic oxygen was produced by adding NO to $N(^4S)$ atoms formed in a microwave discharge through N_2 or a mixture of a few percent of N_2 in He. The purification procedures used for these gases are standard and have been described elsewhere (17, 18). This method of producing $O(^3P)$ has the advantage of minimizing interference by ground state or electronically excited molecular oxygen. The concentration of $O(^3P)$ was controlled by adjusting the composition of the gas passing through the discharge or by varying the ratio of gas flowrates through the discharge and through a bypass around the discharge while maintaining a constant total flowrate. This made it possible to achieve ratios of reactant concentration to $O(^3P)$ concentration of as much as several thousand. This was necessary in some cases to avoid interference by secondary reactions and to ensure both pseudo first order disappearance of $O(^3P)$ and constant stoichiometry.

The concentration of $O(^3P)$ was monitored by measuring the chemiluminescence produced by the reaction between $O(^3P)$ and a small amount of NO (less than about 10% of $[O(^3P)]$). The titration of $N(^4S)$ with NO was used to calibrate the chemiluminescence signal in terms of $[O(^3P)]$. When two photomultipliers were used to measure this chemiluminescence at two positions the signals produced by them in the absence of a second reactant were made equal by adjusting the high voltage applied to each detector. In all cases, the dark currents produced by these detectors were within 30% of each other and were no greater than 10% of the smallest signal recorded in the kinetic measurements. In most measurements the dark current was less than 1% of the signal produced by the NO_2 chemiluminescence. In all the kinetic measurements the ratio of substrate concentration to $O(^3P)$ concentration was at least 200 and in most cases was several thousand. This should have ensured pseudo first order loss of $O(^3P)$ and, except in the reaction of $O(^3P)$ with NO, a stoichiometric coefficient of unity.

Results and discussion

The reaction of $O(^3P)$ with CH_3OH was selected as the test reaction because its rate constant is known with reasonable accuracy (22–25) and is of a convenient magnitude at room temperature for use in evaluating the performance of the available apparatus. Two other reactions were subsequently

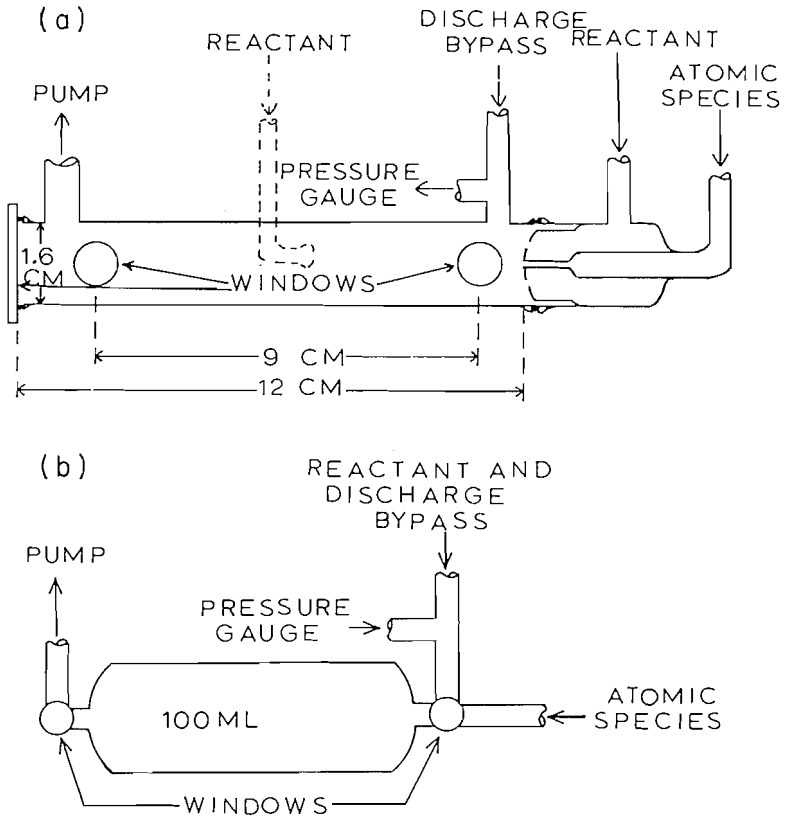

FIG. 1 (*a*). Basic reactor design for investigation of homogeneity; (*b*). Design of the reactor used in the kinetic measurements.

examined in the same system to provide additional information about its reliability and the useful range of operating conditions.

Experimental test of homogeneity:

Radial homogeneity was examined in the reactor shown in Fig. 1(*a*) by adding a small amount of NO to the $O(^3P)$ stream before it entered the reactor. The intensity of the resulting NO_2 chemiluminescence was observed at several points across the diameter of the window mounted on the end of the reactor. Uniform intensity was found both in the presence and absence of methanol indicating that efficient radial mixing had occurred by the time the gas stream had reached the downstream end of the reactor. No variation in this behaviour was found for residence times in the range 30 to 400 milliseconds.

Axial homogeneity was examined by generating NO_2 chemiluminescence as above but using a movable photomultiplier tube to observe the intensity at various positions along the axis of the reactor. In the absence of methanol, the intensity of the NO_2 chemiluminescence was uniform along the full length of the reactor indicating good axial homogeneity. However, when methanol was added through the central inlet the intensity of the NO_2 chemiluminescence remained constant from the atom inlet to within about a centimeter of the central inlet. It then decreased steadily from the central inlet to the reactor outlet. This behaviour is illustrated in Fig. 2. The criterion for efficient mixing in the absence of an atom sink is (9) $t_D/t_R \simeq r^2\dot{V}/2DV << 1$ where r is a characteristic distance over which diffusion occurs in maintaining homogeneity, t_R is the residence time in the reactor, t_D is the time required for diffusion over a distance r, and the other symbols are as defined earlier. The value of r for a cylindrical reactor has been taken as the radius in other work (9) and this practice is followed here as well to provide a consistent means of comparison with the conditions used by others. For the least favourable conditions (largest $\dot{V}$) in our experiments $r^2\dot{V}/2DV = 0.016$ which is smaller than the value attained in much of the work in the literature. The data of Fig. 2 show that the homogeneity criterion clearly fails in the presence of a homogeneous atom sink although homogeneity was observed experimentally in the absence of the sink.

It is clear from the foregoing that kinetic data calculated from eq. [6] using average concentrations or from eq. [4] on the assumption that [A] is constant throughout the reactor and equal to the exit concentration will be incorrect. One may, however, test the applicability of eq. [4] using atom concentrations measured at various points along the reactor as outlined above. Equation [4] predicts that a plot of $(I_0/I - 1)\dot{V}$ against $[CH_3OH]$ should be linear, passing through the origin. Figure 3 indicates that such plots are linear and that, within the scatter of the experimental points, they pass through the origin. Equation [4] also predicts that the slopes of the lines of Fig. 3, divided by the rate constant for the reaction, should give the reactor volume up to the observation point. These experiments were made at substantially larger concentrations of $O(^3P)$ than those described later in this work with the result that the accessible values of $[CH_3OH]/[O(^3P)]$ were less than required for a stoichiometric coefficient of unity (22–25). The stoichiometric coefficient has been measured for $[CH_3OH]/[O(^3P)]$ ratios comparable to those used here (22) and the product of this stoichiometric coefficient and the absolute rate constant was used in obtaining the results presented in Table 1. The data of Table 1 indicate that in all cases the volume calculated from eq. [4] is much greater than the corresponding geometric volume. Although the volumes calculated from eq. [4] vary linearly with distance from the reactant inlet, as required for a cylindrical

Can. J. Chem. Downloaded from www.nrcresearchpress.com by 196.1.178.254 on 09/07/12
For personal use only.

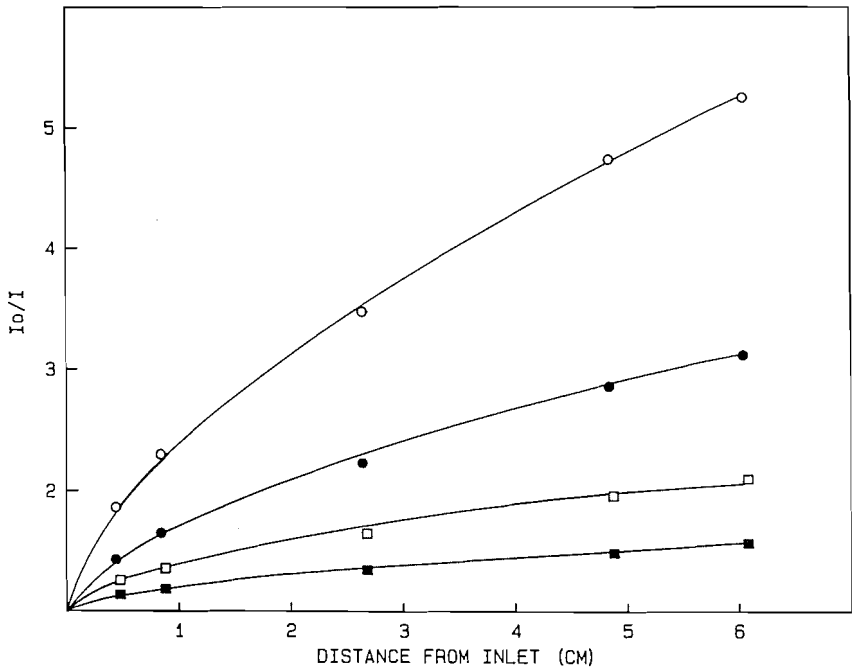

FIG. 2. Variation in $O(^3P)$ signal with distance from the central reactant inlet along the axis of the reaction vessel. ○, $[CH_3OH] = 4.0 \times 10^{-6}$ mol L^{-1}; ●, $[CH_3OH] = 2.0 \times 10^{-6}$ mol L^{-1}; □, $[CH_3OH] = 1.0 \times 10^{-6}$ mol L^{-1}; ■, $[CH_3OH] = 5.0 \times 10^{-7}$ mol L^{-1}. Pressure = 0.46 Torr ± 2%, volumetric flowrate = 190 cm^3 s^{-1} ± 10% $[O(^3P)] = 7.0 \times 10^{-8}$ mol L^{-1}.

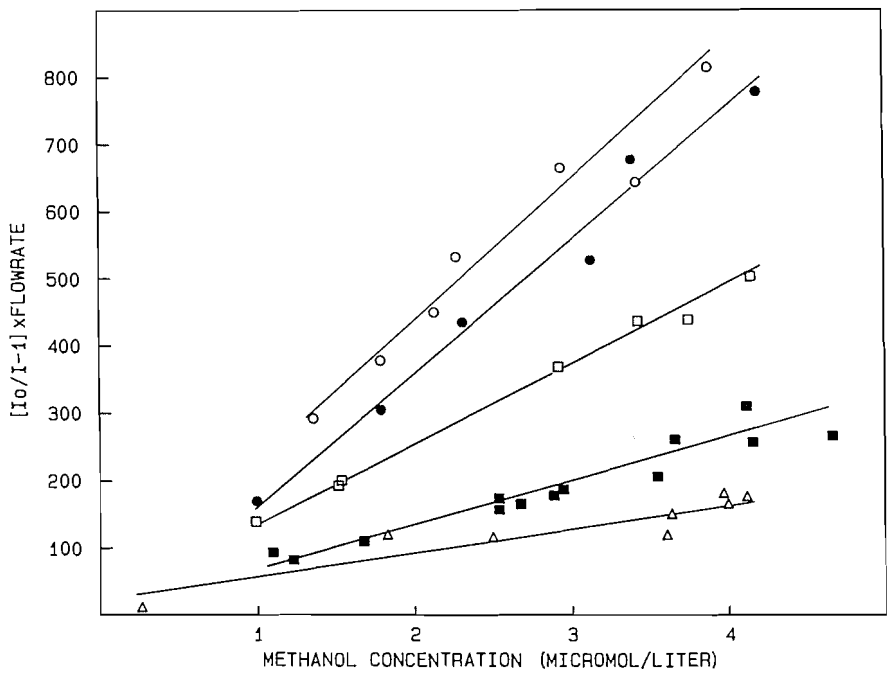

FIG. 3. Analysis of the data of Fig. 2 in terms of eq. [4] at different distances L from the reactant inlet. ○, L = 6.04 cm; ●, L = 4.84 cm; □, L = 2.64 cm; ■, L = 0.84 cm; △, L = 0.44 cm.

reactor, the intercept is not at the origin and the slope (3.12 cm^2) is significantly greater than the value of πr^2 (2.01 cm^2) appropriate to the cylindrical reactor used in these experiments.

A possible source of the difficulty with this application of eq. [4] could stem from the ability of a substrate such as CH_3OH to quench the emission from excited NO_2 (see, for example, ref. 26). This would make the effective sensitivity of the $O(^3P)$ measurement less in the presence of CH_3OH than in its absence and would make the ratio I_0/I larger than it would be in the absence of quenching. Moreover, this effect would become more severe as the concentration of CH_3OH increased. For Stern–Volmer quenching, it may be shown that, for a constant total flowrate through the reactor,

$$[7] \quad \left[\frac{I_0}{I} - 1\right]\frac{\Sigma \dot{V}}{[CH_3OH]} = a[CH_3OH] + b$$

where a depends on both the rate constant and the Stern–Volmer

Can. J. Chem. Downloaded from www.nrcresearchpress.com by 196.1.178.254 on 09/07/12
For personal use only.

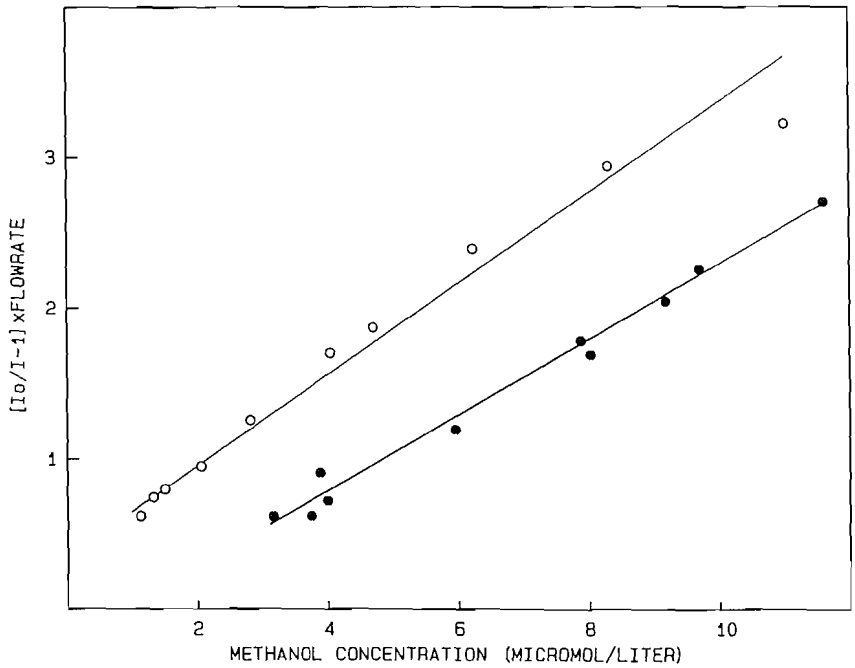

FIG. 4. Representative results of experiments designed to correct for quenching of the NO_2 chemiluminescence by methanol at 298 ± 1 K. ○, Pressure = 1.11 Torr ± 2%, $[O(^3P)] = 9.24 \times 10^{-8}$ mol L^{-1}; ●, pressure = 1.02 Torr ± 2%, $[O(^3P)] = 9.20 \times 10^{-10}$ mol L^{-1}.

TABLE 1. Evaluation of the use of eq. [4] with the reactor described in Fig. 1(*a*) and the reaction $O + CH_3OH \rightarrow OH + CH_2OH$[a]

Distance from reactor inlet (cm)	*kV* {eq. [4]} ($cm^3 L s^{-1} mol^{-1}$)	"Experimental" volume (cm^3)	Geometric volume (cm^3)
0.44	4.31×10^7	4.4	0.88
0.84	6.49×10^7	6.4	1.69
2.64	1.24×10^8	12.7	5.31
4.84	1.87×10^8	19.2	9.73
6.04	2.13×10^8	21.9	12.1

[a]Temperature = 299 K, pressure = 0.46 Torr ± 2%, total volumetric flowrate = 190 $cm^3 s^{-1}$ ± 10%. Experimental volumes were calculated from the values in the second column using the following expression for the rate constant of the reaction (23) combined with the stoichiometric coefficient, 1.9 ± 0.2 (22), measured with comparable values of $[CH_3OH]/[O(^3P)]$: $k = 9.79 \times 10^9 \exp(-2267/T)$ L mol^{-1} s^{-1}.

quenching constant while *b* depends only on the rate constant. This would produce upward curvature in plots such as those of Fig. 3 when a sufficiently wide range of concentrations of substrate is used. Such behaviour was, in fact, observed in experiments in which the CH_3OH concentration covered an order of magnitude or more and plots of the left hand side of eq. [7] against $[CH_3OH]$ were linear as expected. This leads to the conclusion that at least a significant part of the difficulty in applying the homogeneous reactor equations was a result of quenching of the NO_2 chemiluminescence by methanol.

Quenching does not affect the accuracy of rate constants measured under conditions of pseudo first order atom loss in a conventional flow tube reactor because the atom signals which are used in the calculation are all obtained with an effectively constant substrate concentration. This ensures that the sensitivity of the atom signal is reduced by the same fraction over the entire length of the reactor. The two-window versions of the reactor indicated in Fig. 1 take advantage of this by comparing the atom signals at the two windows in the presence of identical concentrations of CH_3OH, the excess reactant. The ratio I_0/I is then unaffected by quenching and it should now be possible to use eq. [4]. In these experiments, the signals from the photomultipliers viewing the two observation ports were made equal in the absence of methanol by adjusting the high voltage applied to them. These signals remained equal over a wide range of NO concentrations and varied linearly with [NO] verifying that loss of $O(^3P)$ in the reactor was either negligible or constant in the absence of CH_3OH. In these and subsequent experiments with CH_3OH the ratio $[CH_3OH]/[O(^3P)]$ was in the range 200 to 10^4 to avoid the stoichiometric complications of the earlier experiments. The effects of this ratio on the stoichiometric coefficient have been fully discussed elsewhere (22–25).

Experiments were first made in the two-window version of the reactor indicated in Fig. 1(*a*). This provides data under experimental conditions which differ from those above only in providing a means of compensating for quenching. While it is clear that the concentrations in the reactor are not homogeneous, it is equally certain that diffusional mixing is significant under the flow conditions used in these experiments and the time resolution at the two windows at which $O(^3P)$ concentrations were measured is likely to be poor. These experiments should indicate the effect of this poor resolution. The reaction of $O(^3P)$ with CH_3OH was again used as the test reaction. Representative results of these experiments are shown in Fig. 4 and these indicate that good linearity was obtained over a range of values of $[CH_3OH]$ which gave distinct curvature in the experiments using a single window at the end of the reactor. The effect of quenching seems, then, to have been eliminated. The slopes of the lines in Fig. 4 should give the volume of the portion of the reactor between the windows if good time resolution has been achieved. The experiments gave an average volume of 51 cm^3 ± 4% which is much larger than the geometric volume of 20 cm^3 between the windows. The effect of diffusional mixing, while not sufficient to produce homogeneity along the axis of the reactor, is clearly substantial and prevents adequate time

Can. J. Chem. Downloaded from www.nrcresearchpress.com by 196.1.178.254 on 09/07/12
For personal use only.

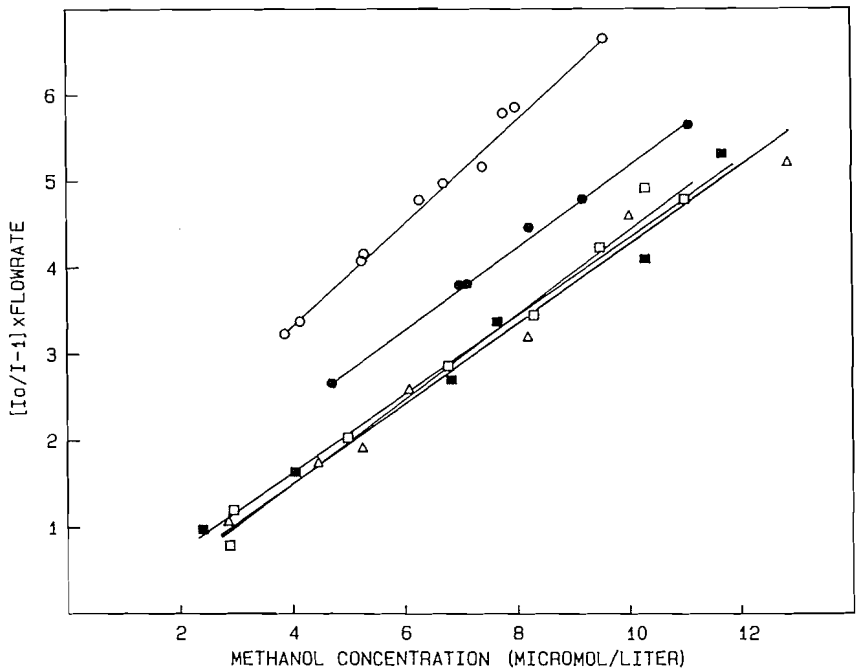

FIG. 5. "Calibration" of the effective reaction volume of the reactor of Fig. 1(*b*) using the reaction of $O(^3P)$ with methanol. Temperature = 299 ± 2 K. ○, pressure = 1.51 Torr ± 2%, residence time = 0.170 s ± 3%; ●, pressure = 1.34 Torr ± 2%, residence time = 0.185 s ± 3%; □, pressure = 1.47 Torr ± 2%, residence time = 0.175 s ± 3%; ■, pressure = 1.42 Torr ± 2%, residence time = 0.195 s ± 3%; △, pressure = 1.33 Torr ± 1%, residence time = 0.200 s ± 3%.

resolution for accurate kinetic measurements based on concentration measurements within the reactor.

Kinetic measurements

It is clear from the foregoing that conditions adequate for accurate application of eq. [4] require a two-window reactor to eliminate the effect of quenching and a design which provides good temporal resolution at the inlet and exit of the reactor. The reactor illustrated in Fig. 1(*b*) was constructed with these requirements in mind. Figure 5 and Table 2 show the data obtained on the test reaction of $O(^3P)$ with CH_3OH. As noted earlier, the ratio $[CH_3OH]/[O(^3P)]$ was kept in the range 200 to 10^4 to avoid the need for stoichiometric corrections. The pseudo first order rate constants calculated from eq.[4] may represent the sum of a homogeneous pseudo first order rate constant and a heterogeneous first order rate constant representing the efficiency of oxygen atom loss at the wall. This is represented as

$$k_{obs}\, V = kV[CH_3OH] + k_0$$

The values of k_0 represent a correction to be applied to the experimental pseudo first order rate constants and are included in Table 2. They were always small and were frequently zero within the accuracy of the measurements. As Fig. 5 indicates, linearity of these plots was good. The slopes of these lines, divided by the value of k, gives the effective volume of the reactor. The value of k used for this purpose was calculated from the Arrhenius expression reported in ref. 23. The average reactor volume obtained with these measurements was 107 cm^3 ± 11% which compares favourably with the geometric volume, including an estimate of the volume at the window locations, of 100 cm^3 ± 5%. No dependence of the calculated volume on the ratio $[CH_3OH]/[O(^3P)]$ was discernable.

In experiments such as these there is always the possibility of fortuitous agreement between experiment and theory as a result of selection of a specific value of a rate constant from among those available in the literature. To examine the validity of our use of the kinetic data of ref. 23 as a basis for the "calibration" of the reactor, two other reactions were studied. These were selected for (*a*) reliability of the reported rate constants and (*b*) coverage of a sufficient range of reaction rates to delineate the range of application of the 100 cm^3 reactor.

The reaction

$$[8] \quad O(^3P) + NO + M \rightarrow NO_2 + M$$

has been studied extensively (27) with specific evaluation of the rate constant for M = He in two cases with good agreement (28, 29). Since the above reaction is followed by the comparatively rapid reaction

$$[9] \quad O(^3P) + NO_2 \rightarrow NO + O_2$$

the experimental rate constants are related to the absolute rate constant for reaction [8] by

$$[10] \quad k_{obs} = 2\, k_8\, [NO]P/RT + k_0$$

The results calculated for a reactor volume of 107 cm^3 are indicated in Table 3 and Fig. 6 and give a rate constant of 2.48×10^{10} $L^2\ mol^{-2}\ s^{-1}$ ± 13% at 298 K. This agrees well with the values of refs. 28 (2.1×10^{10}) and 29 (2.24×10^{10}) and provides encouraging support of the calibration procedure for the reactor. Linearity of the plot of k_{obs} against $[NO]P/RT$ is good. Although there appears to be some gentle upward curvature at high NO concentrations, one cannot be certain of this within the scatter of the measurements. The intercepts are again small. Although it is tempting to interpret these intercepts as heterogeneous loss terms, they may also include an accumulation of other effects such as approximately constant absolute errors in pressure or in the concentration of NO. The origin of the negative values of these intercepts is therefore not clear and they are probably best regarded simply as empirical correction terms.

Can. J. Chem. Downloaded from www.nrcresearchpress.com by 196.1.178.254 on 09/07/12
For personal use only.

TABLE 2. Summary of the results of the reactor "calibration" experiments using the reaction $O + CH_3OH \rightarrow OH + CH_2OH$ at room temperature

Pressure (Torr)	Inlet flowrates ($cm^3\ s^{-1}$) N_2	He	CH_3OH	Total	$[O]_0/[O]$	$k_{obs}\,V$ ($cm^3 s^{-1}$)
1.49	5	573	29	607	6.32	3230
1.53	5	557	39	601	7.93	4160
1.53	5	557	56	618	9.37	5170
1.52	5	561	60	626	10.25	5790
1.51	5	564	31	600	6.62	3370
1.51	5	565	76	646	11.30	6660
1.51	5	565	39	609	7.70	4080
1.51	5	565	51	621	9.02	4980
1.51	5	564	48	617	8.76	4790
1.51	5	565	62	632	10.27	5860
	$V = 126\ cm^3 \pm 3\%$, $k_0 = 890\ cm^3\ s^{-1} \pm 16\%$					
1.33	5	514	37	556	5.79	2670
1.33	5	515	56	576	7.60	3800
1.34	5	511	75	591	9.11	4800
1.36	5	503	91	599	10.44	5660
1.33	5	514	68	587	8.60	4460
1.33	5	515	57	577	7.60	3810
	$V = 100\ cm^3 \pm 3\%$, $k_0 = 490\ cm^3\ s^{-1} \pm 20\%$					
1.45	15	546	21	582	2.27	740
1.47	15	538	21	574	3.00	1150
1.47	15	539	36	590	4.37	1990
1.49	14	532	49	595	5.73	2810
1.49	14	532	61	607	6.60	3400
1.49	14	531	72	617	7.78	4190
1.49	14	531	86	631	8.52	4750
1.49	14	528	78	620	8.87	4880
	$V = 110\ cm^3 \pm 5\%$, $k_0 = -490\ cm^3\ s^{-1} \pm 40\%$					
1.40	10	490	16	516	2.79	920
1.41	10	486	27	523	4.04	1590
1.42	10	483	47	540	5.91	2650
1.42	10	483	54	547	7.08	3330
1.43	10	480	74	564	8.19	4060
1.42	10	483	87	580	10.09	5280
	$V = 100\ cm^3 \pm 6\%$, $k_0 = -200\ cm^3\ s^{-1} \pm 125\%$					
1.34	11	458	100	569	10.10	5180
1.33	11	462	75	548	9.32	4560
1.33	11	462	60	533	6.92	3150
1.32	11	465	43	519	5.91	2550
1.33	11	462	36	509	4.68	1870
1.32	11	465	31	507	4.36	1700
1.32	11	464	20	495	3.08	1030
	$V = 97\ cm^3 \pm 6\%$, $k_0 = -200 \pm 108\%$					

TABLE 3. Summary of kinetic data obtained at 298 K for the reaction $O + NO + M \rightarrow NO_2 + M$

Pressure (Torr)	Inlet flowrates ($cm^3\ s^{-1}$) N_2	He	NO	Total	$[O]_0/[O]$	k_{obs} (s^{-1})
0.793	17.8	880	9.24	907	1.050	0.420
0.793	17.8	881	20.1	919	1.179	1.53
0.824	17.1	848	38.7	904	1.449	3.79
0.839	16.8	833	72.6	922	1.997	8.59
0.824	17.1	848	48.3	913	1.593	5.06
0.824	17.1	848	38.9	904	1.389	3.28
0.801	17.6	872	27.9	918	1.264	2.26
0.793	17.8	881	11.6	910	1.094	0.799
0.785	18.0	890	3.99	912	1.035	0.302
0.785	18.0	890	7.45	915	1.068	0.580
	$k = 2.60 \times 10^{10}\ L^2\ mol^{-2}\ s^{-1} \pm 5\%$; $k_0 = -0.5\ s^{-1} \pm 40\%$					
0.912	47.3	954	4.83	1006	1.005	0.045
0.953	45.2	912	26.3	984	1.260	2.39
0.936	46.1	929	12.6	988	1.091	0.842
0.903	47.7	963	6.34	1017	1.019	0.182
0.920	47.7	963	20.2	1004	1.068	0.642
0.953	45.2	913	26.1	984	1.231	2.12
0.945	45.6	920	31.1	997	1.326	3.04
0.970	44.4	897	49.0	990	1.724	6.70
0.970	44.4	897	65.7	1007	2.065	10.02
0.961	44.8	905	56.6	1006	1.769	7.22
	$k = 2.89 \times 10^{10}\ L^2\ mol^{-2}\ s^{-1} \pm 6\%$; $k_0 = -1.1\ s^{-1} \pm 27\%$					
1.004	144	891	13.1	1048	1.075	0.730
1.012	143	883	5.14	1031	1.009	0.085
1.012	143	884	6.29	1033	1.027	0.261
1.012	143	883	12.9	1039	1.085	0.825
1.030	140	868	16.8	1025	1.144	1.38
1.021	141	875	22.2	1039	1.216	2.09
1.021	141	876	24.9	1042	1.250	2.44
1.030	140	868	29.0	1037	1.290	2.81
1.030	140	868	30.9	1039	1.363	3.53
1.038	139	861	45.4	1046	1.562	5.50
	$k = 2.28 \times 10^{10}\ L^2\ mol^{-2}\ s^{-1} \pm 4\%$; $k_0 = -0.8 \pm 14\%$					
0.978	29.3	991	11.0	1031	1.118	1.13
0.995	28.8	974	16.1	1019	1.152	1.45
0.995	28.7	973	16.9	1019	1.204	1.94
0.995	28.8	974	23.7	1026	1.246	2.36
1.004	28.5	965	27.4	1021	1.315	3.01
1.004	28.5	965	36.1	1030	1.371	3.57
0.995	28.8	974	40.2	1043	1.448	4.37
1.004	28.5	965	47.0	1040	1.529	5.14
1.012	28.3	958	47.9	1034	1.603	5.83
1.021	28.0	949	56.6	1034	1.724	7.00
0.995	28.8	974	39.4	1042	1.444	4.33
	$k = 2.16 \times 10^{10}\ L^2\ mol^{-2}\ s^{-1} \pm 4\%$; $k_0 = -0.4\ s^{-1} \pm 49\%$					

It seemed useful to examine the reliability of the homogeneous reactor method with a reaction having a more complex mechanism than the reaction of $O(^3P)$ with NO and in which secondary reactions of $O(^3P)$ are known to have an important effect on the kinetics of the reaction if a sufficient excess of the second reactant is not maintained. The reaction of $O(^3P)$ with acetone satisfies these criteria. The rate constant for this reaction has been measured as a function of temperature by two quite different methods (30, 31). The Arrhenius parameters obtained in the two studies are in excellent agreement and lead to numerical values of the rate constants at 298 K which agree within some 20%. The results of one set of experiments (30) cover conditions in which $O(^3P)$ was in large excess of the acetone and the rate constant was based on the measured decrease in acetone concentration with time. The other experiments (31) were made in the presence of a large (as much as 1000-fold) excess of acetone and the rate constant was based on the measured decrease in $O(^3P)$ concentration with time. Both studies indicated that when one or other of the reactants was not in sufficient excess substantial stoichiometric corrections were required to obtain a value for the absolute rate constant of the reaction. These potential mechanistic complications have been discussed elsewhere (30, 31) and the experiments reported here were made with $[(CH_3)_2CO]/[O(^3P)]$ ratios which had been found in other work (31) to be large enough to avoid stoichiometric corrections. The results obtained with the homo-

Can. J. Chem. Downloaded from www.nrcresearchpress.com by 196.1.178.254 on 09/07/12
For personal use only.

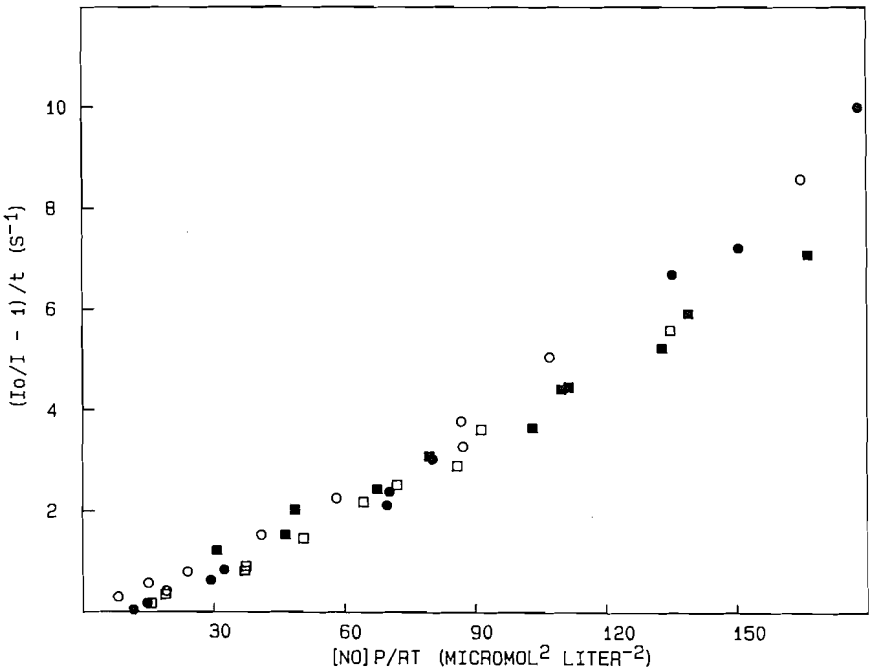

FIG. 6. Concentration dependence of the pseudo first order rate constants for the reaction of $O(^3P)$ with NO at 298 K. ○, Pressure = 0.816 Torr ± 3%, residence time = 0.120 s ± 1%; ●, pressure = 0.936 Torr ± 4%, residence time = 0.105 s ± 2%; □, pressure = 1.02 Torr ± 2%, residence time = 0.105 s ± 1%; ■, pressure = 1.00 Torr ± 2%, residence time = 0.105 s ± 1%.

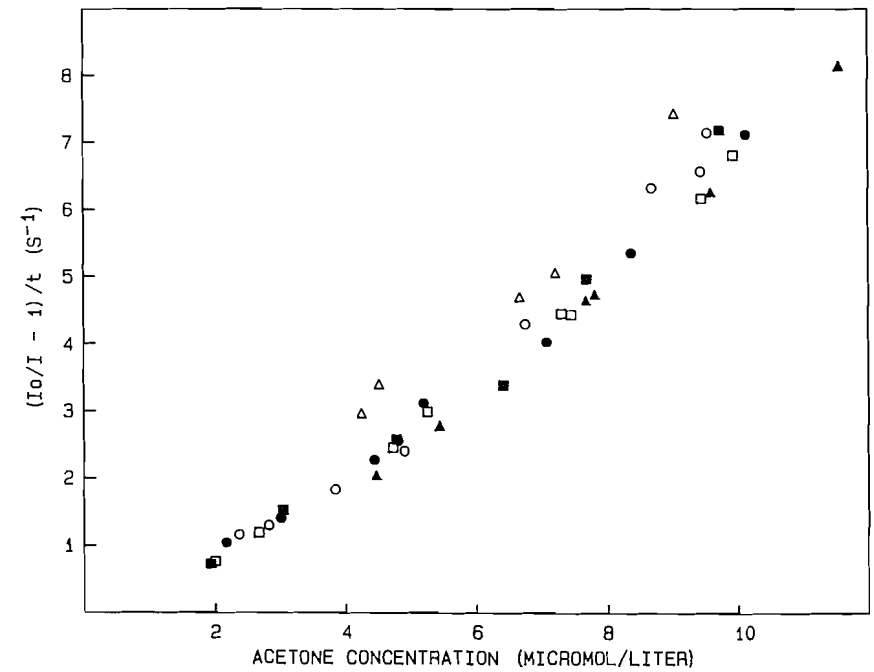

FIG. 7. Concentration dependence of the pseudo first order rate constants for the reaction of $O(^3P)$ with acetone at 296 ± 1 K. ○, Pressure = 0.985 Torr ± 1%, residence time = 0.105 s ± 8%; ●, pressure = 0.950 Torr ± 1%, residence time = 0.105 s ± 9%; □, pressure = 0.868 Torr ± 3%, residence time = 0.105 s ± 7%; ■, pressure = 0.804 Torr ± 1%, residence time = 0.105 s ± 9%; △, pressure = 0.845 Torr ± 3%, residence time = 0.105 s ± 5%; ▲, pressure = 0.844 Torr ± 1%, residence time = 0.100 s ± 8%.

geneous reactor, based on a reaction volume of 107 cm^3, are presented in Table 4 and Fig. 7. Agreement with the results of refs. 30 (4.04×10^5 L mol^{-1} s^{-1}) and 31 (5.33×10^5 L mol^{-1} s^{-1}) is not as good as with the other reactions examined. The slopes of plots of the data according to the equation

$$[11] \quad k_{obs} = k[(CH_3)_2CO] + k_0$$

lead to a rate constant of 8.13×10^5 L mol^{-1} s^{-1} ± 6% which is nearly double the reference values cited above. Linearity of the plots is again good and, although there is some indication of upward curvature at large acetone concentrations, one cannot be certain of this within the scatter of the data. The values of k_0 are again negative and are of the same order of magnitude as they were in the experiments with NO. If the data are fitted to a quadratic, as suggested by eq. [7], rather than a straight line, the correlation coefficient is virtually the same as for the linear fit.

Can. J. Chem. Downloaded from www.nrcresearchpress.com by 196.1.178.254 on 09/07/12
For personal use only.

TABLE 4. Summary of kinetic data obtained at 298 K for the reaction
$O + (CH_3)_2CO \rightarrow OH + CH_2C{:}OCH_3$

Pressure (Torr)	Inlet flowrates ($cm^3\ s^{-1}$) N_2	He	$(CH_3)_2CO$	Total	$[O]_0/[O]$	k_{obs} (s^{-1})
0.979	7.4	907	42.9	957	1.130	1.16
0.991	7.3	896	50.3	954	1.147	1.31
0.979	7.4	907	71.5	986	1.198	1.83
0.991	7.3	897	91.1	995	1.259	2.41
0.979	7.4	907	134	1048	1.439	4.30
0.991	7.3	897	175	1079	1.628	6.33
0.991	7.3	896	193	1096	1.643	6.58
0.991	7.3	906	201	1114	1.687	7.15
$k = 8.48 \times 10^5$ L mol^{-1} s^{-1} ± 5%; $k_0 = -1.2$ s^{-1} ± 25%						
0.956	7.6	889	219	1116	1.683	7.13
0.956	7.6	890	174	1072	1.535	5.36
0.956	7.6	890	143	1041	1.415	4.03
0.956	7.6	890	100	998	1.335	3.12
0.956	7.6	889	84.3	981	1.249	2.28
0.956	7.6	890	55.6	953	1.158	1.41
0.956	7.6	889	39.3	936	1.118	1.04
0.944	7.6	901	94.4	1003	1.273	2.56
$k = 7.57 \times 10^5$ L mol^{-1} s^{-1} ± 5%; $k_0 = -0.9$ s^{-1} ± 22%						
0.862	8.4	883	38.4	930	1.080	0.696
0.839	8.6	907	55.8	971	1.124	1.13
0.862	8.4	883	98.8	990	1.258	2.39
0.862	8.4	883	112	1003	1.313	2.93
0.862	8.4	882	167	1057	1.442	4.37
0.874	8.3	872	157	1039	1.452	4.39
0.897	8.0	848	205	1061	1.616	6.11
0.897	8.0	849	219	1076	1.672	6.75
$k = 7.48 \times 10^5$ L mol^{-1} s^{-1}; $k_0 = -0.9$ s^{-1} ± 22%						
0.804	9.0	847	245	1101	1.692	7.12
0.804	9.0	848	182	1039	1.506	4.91
0.816	8.9	837	142	988	1.360	3.32
0.804	9.0	847	104	960	1.280	2.51
0.804	9.0	847	62.9	919	1.170	1.46
0.792	9.1	861	39.5	910	1.078	0.659
$k = 8.01 \times 10^5$ L mol^{-1} s^{-1} ± 9%; $k_0 = -1.1$ s^{-1} ± 36%						
0.815	8.8	883	92.9	985	1.315	2.90
0.822	8.7	879	97.8	985	1.363	3.34
0.851	8.4	849	142	999	1.496	4.64
0.874	8.2	826	147	981	1.545	5.00
0.839	8.6	860	212	1081	1.729	7.37
$k = 8.65 \times 10^5$ L mol^{-1} s^{-1} ± 12%; $k_0 = -0.8$ s^{-1} ± 88%						
0.832	8.6	867	181	1057	1.472	4.67
0.847	8.5	852	224	1084	1.612	6.20
0.855	8.4	844	280	1132	1.764	8.08
0.832	8.6	866	177	1052	1.465	4.58
0.832	8.6	866	118	993	1.292	2.71
0.839	8.5	859	92.7	960	1.221	1.98
$k = 8.58 \times 10^5$ L mol^{-1} s^{-1} ± 2%; $k_0 = -1.9$ s^{-1} ± 5%						

However, the value of the rate constant is now 5.3×10^5 L mol^{-1} s^{-1}. While this is much closer to the reference values, the distribution of the residual errors is not significantly different from the linear fit and the standard deviation in the rate constant is much worse, largely as a result of fitting the additional coefficient. The y-intercept is somewhat smaller but is still negative and of the same order of magnitude as before. This indicates the sensitivity of the results to the method selected for analyzing the data. Use of eq. [4] in this case leads to a rate constant which is evidently almost a factor of two too large. Use of eq. [7], on the assumption that correction for quenching is incomplete, leads to a rate constant which is in better agreement with those in the literature. However, a statistical analysis by itself would provide no indication whether the linear fit or the quadratic fit is a better description of the data. It is clear that the method can only provide reliable results if extraneous effects such as quenching are absent and there is no ambiguity concerning the method of analyzing the data.

Conclusions

The experiments described here indicate that the type of reactor used can provide accurate kinetic information. However, the reactors are not accurately described as homogeneous at the pressures at which they are most commonly used and should be described by some alternative term such as "fixed residence time" or "plug flow". The reactor designs used in conjunction with mass spectrometers (4–7) seem to have incorporated sampling into the mass spectrometer with good spatial resolution at the inlet and exit from the reactor. The use of eq. [4] was therefore appropriate. The reactor designs used in conjunction with esr spectrometers (8, 9) cannot be treated as easily. Particularly in the experiments of ref. (9), the volume to which the measured atom concentrations apply is uncertain. In fact, some difficulty was noted in that work with respect to the rate constants obtained for several of the reactions that were examined. It may be that at least some of this difficulty can be traced to a lack of homogeneity within the reactor. The nature of their experiments made it impossible to directly examine homogeneity. Finally, the reactor design used in the most recent application of such reactors (12–14) and which also used a chemiluminescent method to measure the atom concentration was quite similar to that of Fig. 1(*b*) although it was of substantially greater volume. While the atom concentrations were measured at the entrance and exit of the reactor, evidently with good spatial resolution, the other reactants were added through a separate inlet. This may have led to some interference due to quenching but the extent to which this was a problem is not clear. Successful use of such reactors for measurement of rate constants clearly requires careful attention to provision of good spatial resolution and avoidance of extraneous effects such as quenching.

Acknowledgments

Financial support for this work was provided by the Natural Sciences and Engineering Research Council of Canada. The author is indebted to Mr. Timothy D. Locke and Mr. Dennis Curran for their assistance in some of the initial experiments with "homogeneous" reactors.

1. K. G. DENBIGH. Trans. Faraday Soc. **40**, 352 (1944).
2. K. G. DENBIGH and F. M. PAGE. Discuss. Faraday Soc. **17**, 145 (1954).
3. J. P. LONGWELL and M. A. WEISS. Ind. Eng. Chem. **47**, 1634 (1955).
4. G. B. KISTIAKOWSKY and G. G. VOLPI. J. Chem Phys. **27**, 1141 (1957).
5. E. L. WONG and A. E. POTTER. J. Chem. Phys. **39**, 2211 (1963).
6. E. L. WONG and A. E. POTTER. J. Chem. Phys. **43**, 3371 (1965).
7. E. L. WONG and A. E. POTTER. Can. J. Chem. **45**, 367 (1967).
8. M. F. R. MULCAHY, J. R. STEVEN, and J. C. WARD. J. Phys. Chem. **71**, 2124 (1967).
9. A. A. WESTENBERG, N. DEHAAS, and J. M. ROSCOE. J. Phys. Chem. **74**, 3431 (1970).

Can. J. Chem. Downloaded from www.nrcresearchpress.com by 196.1.178.254 on 09/07/12
For personal use only.

10. S. W. BENSON and G. N. SPOKES. J. Am. Chem. Soc. **89**, 2525 (1967).
11. D. M. GOLDEN, G. N. SPOKES, and S. W. BENSON. Angew. Chem. Internt. Edit. **12**, 534 (1973).
12. I. M. CAMPBELL and B. J. HANDY. J. Chem. Soc. Faraday Trans. I, **71**, 2097 (1975).
13. I. M. CAMPBELL and B. J. HANDY. J. Chem. Soc. Faraday Trans. I, **74**, 316 (1978).
14. I. M. CAMPBELL, J. S. ROGERSON,and B. J. HANDY. J. Chem. Soc. Faraday Trans. I, **74**, 2672 (1978).
15. D. L. BAULCH, I. M. CAMPBELL, and R. HAINSWORTH, J. Chem. Soc. Faraday Trans. I, **80**, 2525 (1984).
16. H. WISE and C. M. ABLOW. J. Chem. Phys. **29**, 634 (1958).
17. H. WISE and C. M. ABLOW. J. Chem. Phys. **35**, 10 (1961).
18. J. E. MORGAN and H. I. SCHIFF. J. Chem. Phys. **38**, 2631 (1963).
19. J. E. MORGAN and H. I. SCHIFF. Can. J. Chem. **42**, 2300 (1964).
20. P. B. RUDNICK and S. TOBY. Can. J. Chem. **46**, 3899 (1968).
21. J. M. ROSCOE and S. G. ROSCOE. Can. J. Chem. **51**, 3671 (1973).
22. C. M. OWENS and J. M. ROSCOE. Can. J. Chem. **54**, 984 (1976).
23. R. L. FAILES, D. L. SINGLETON, G. PARASKEVOPOULOS, and R. S. IRWIN. Int. J. Chem. Kinet. **14**, 371 (1982).
24. H. H. GROTHEER and TH. JUST. Chem. Phys. Lett. **78**, 71 (1981).
25. D. G. KEIL, T. TANZAWA, E. G. SKOLNIK, R. B. KLEMM, and J. V. MICHAEL. J. Chem. Phys. **75**, 2693 (1981).
26. L. F. KEYSER, S. Z. LEVINE, and F. KAUFMAN. J. Chem. Phys. **54**, 355 (1971).
27. D. L. BAULCH, R. A. COX, R. F. HAMPSON, JR., J. A. KERR, and J. TROE. J. Phys. Chem. Ref. Data, **9**, 295 (1980).
28. H. HIPPLER, C. SCHIPPERT, and J. TROE. Int. J. Chem. Kinet. Symp. **1**, 27 (1975).
29. J. V. MICHAEL, W. A. PAYNE, and D. A. WHYTOCK. J. Chem. Phys. **65**, 4830 (1976).
30. J. H. LEE and R. B. TIMMONS. Int. J. Chem. Kinet. **9**, 133 (1977).
31. J. M. ROSCOE. Can. J. Chem. **64**, 1458 (1986).

Can. J. Chem. Downloaded from www.nrcresearchpress.com by 196.1.178.254 on 09/07/12
For personal use only.

Catalytic polarographic waves of cobalt(II) in the presence of sodium sulfide (SH^- form) in borax – ammonium chloride

DOLORES MARIN AND CARMEN TEIJEIRO

Departamento de Química Física, Química Analítica e Ingeniería Química, Universidad de Alcalá de Henares, Alcalá de Henares (Madrid), Spain

Received January 14, 1988

DOLORES MARIN and CARMEN TEIJEIRO. Can. J. Chem. **66**, 2335 (1988).

The presence of SH^- ions in a medium containing ammonia (borax–NH_4Cl) and cobalt(II) gives rise to a catalytic cobalt(II) prewave and a catalytic hydrogen wave, both of which manifest more positive potentials than the cobalt(II) reduction wave. The effects of time, sulfide and cobalt concentrations, mercury column height, and gelatine and neutral salts addition are discussed. In addition, the characteristics of the current–time and electrocapillary curves are shown. The results obtained suggest a mechanism whereby a cobalt(II) prewave is produced by a cobalt(II) complex with SH^- in the 1:2 relationship. Hydrogen catalytic evolution is attributed to the reduction of a protonated complex.

DOLORES MARIN et CARMEN TEIJEIRO. Can. J. Chem. **66**, 2335 (1988).

La présence d'ions SH dans un milieu contenant de l'ammoniaque (borax–NH_4Cl) et du cobalt(II) donne lieu à une pre-vague catalytique du cobalt et à une vague due à l'hydrogène catalytique qui toutes deux ont des potentiels plus positifs que le vague de réduction du cobalt(II). On discute des effets du temps, des concentrations en sulfide et en cobalt, de la hauteur de la colonne de mercure, et de la gélatine et des sels neutres. De plus, on montre les courbes caractéristiques du courant en fonction du temps et les courbes d'électrocapillarité. Les résultats obtenus suggèrent un mécanisme par lequel un complexe de cobalt(II) avec SH dans la proportion 1:2, produit une pre-vague de cobalt(II). On attribue le dégagement catalytique de l'hydrogène la réduction du complexe protoné.

[Traduit par la revue]

Introduction

In the presence of certain complexing substances, cobalt and nickel ions give rise to catalytic currents (1–3). Complexing substances have specific active groups and generally, the —SH group is considered the most characteristic for catalytic processes in the presence of cobalt. One of the principal reasons limiting our understanding of the phenomenon is the fact that the structure of these substances, which give rise to catalysis, is usually organic and extremely complicated (4, 5). Calusaru and Kuta (6) state: "The most favorable case would be represented by the simplest molecule, the one with the smallest number of functional groups. It can be noted that even as the catalytic process is considered to be appreciably tied to the sulfide groups in the molecule, they alone are not enough for the activity to be expressed, and it can be manifested with the presence of other groups like amino or carboxilic groups".

This paper studies catalytic waves of cobalt(II) and a simple inorganic ligand, free SH^- ion.

Experimental technique

Polarograms and i–t curves were obtained with an Amel 473 Polarographic Analyzer using a polarographic cell equipped with three electrodes, one of which, a saturated calomel electrode (SCE), was used as the reference electrode. At a mercury reservoir height of 45 cm, the dropping mercury electrode (DME) used in these experiments had the following characteristics: $m = 2.08$ mg s^{-1} and $t = 3.86$ s at -700 mV (vs. SCE) in 0.06 M borax – 0.70 M NH_4Cl. The pH values were measured with a Model 62 Radiometer pH-meter.

The hexamminocobalt trichloride employed was Fluka purum grade and all other chemicals were Merck reagent grade. The mercury used in the DME was first purified chemically and subsequently distilled twice.

The stock sulfide solution was freshly prepared every week from $Na_2S.xH_2O$ ($x = 7$–9) in doubly-distilled water with enough ammonium hydroxide for pH > 12 and de-aerated before each set of experiments. The $Na_2S.xH_2O$ concentration was tested with iodometry. The sulfide solution is lifted to its SH^- form at alkaline pH.

Since an ammonium medium is necessary for prewave appearance, a borax–NH_4Cl (0.06–0.70 M) buffer was used (pH = 8.4).

As stated in the Introduction, this paper aims to study the cobalt(II)–SH^- system; however, cobalt(II) sulfides are very insoluble. On the other hand, catalytic waves need an ammoniacal medium to appear but cobalt(II) aquo-ammoniacal complexes are very unstable. As a result, only very diluted sulfide concentrations can be used with cobalt(II) in ammoniacal medium.

Cobalt(III) is reduced in two steps. The first step is cobalt(III) reduction to cobalt(II) at -0.20 V and the other is cobalt(II) reduction to cobalt(0) at -1.15 V. Cobalt(II) is reduced in a step that, at equal cobalt(III) and cobalt (II) concentrations, it is identical to the second cobalt(III) step (Fig. 1(*I*)).

The first cobalt(III) wave is unaltered and the other behaves the same as the cobalt(II) wave in presence of SH^- (Fig. 1(*II*)).

From the above we conclude that cobalt(III) can be substituted for cobalt(II) to study the cobalt(II)–SH^- system, since cobalt(III) electrogenerates cobalt(II) at -0.20 V. Since aquo-ammoniacal cobalt(III) complexes are very stable, the sulfide concentrations that can be used with cobalt(III) are much higher that the ones that can be used with cobalt(II).

Given the foregoing and even though we use cobalt(III) in the solutions, we speak of cobalt(II) reduction wave — second cobalt(III) step — and cobalt(II) catalytic wave.

The intensity of the catalytic waves diminishes over time, thus every polarogram was made at the same time: 2 min from mixing the solutions.

Results

Cobalt(III) in the presence of sulfide in a borax–NH_4Cl medium presents two waves at more positive potentials than those of cobalt(II) reduction (Fig. 1). The first is a catalytic prewave of cobalt(II) and the second a hydrogen catalytic wave, as we will demonstrate in this paper.

As can be seen in Fig. 2, catalytic wave intensity diminishes with time. The decrease is more noticeable in the first catalytic wave than in the second. For both waves, the decreases deepen as the cobalt(III) concentration increases.

The effect of the sulfide concentration on the catalytic waves has been studied between 3×10^{-6} and 1.5×10^{-4} M at a constant cobalt(III) concentration, 5×10^{-4} M (Fig. 3). The

Printed in Canada / Imprimé au Canada

Can. J. Chem. Downloaded from www.nrcresearchpress.com by 196.1.178.254 on 09/07/12
For personal use only.

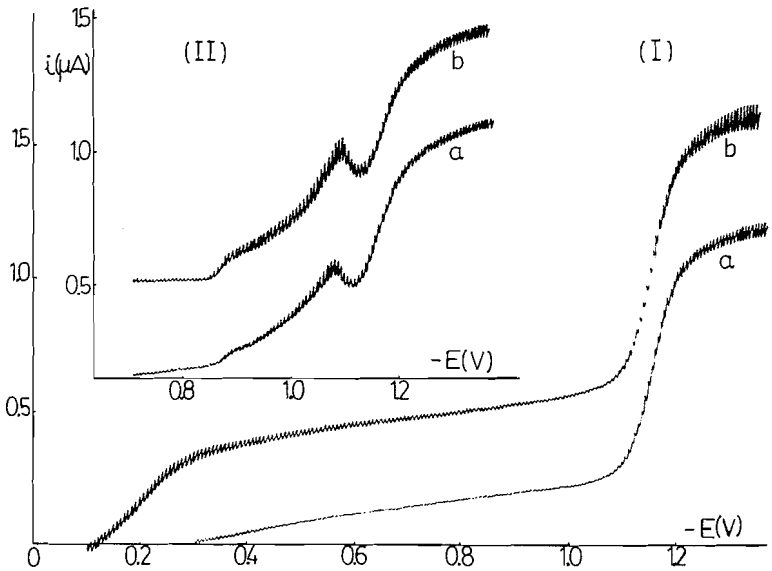

FIG. 1. (*I*) Polarograms in 0.06 *M* borax – 0.70 *M* NH_4Cl; (*a*) 10^{-4} *M* Co(II), (*b*) 10^{-4} *M* Co(III). (*II*) The same as (*I*) with the addition of 4×10^{-5} *M* SH^- in both cases.

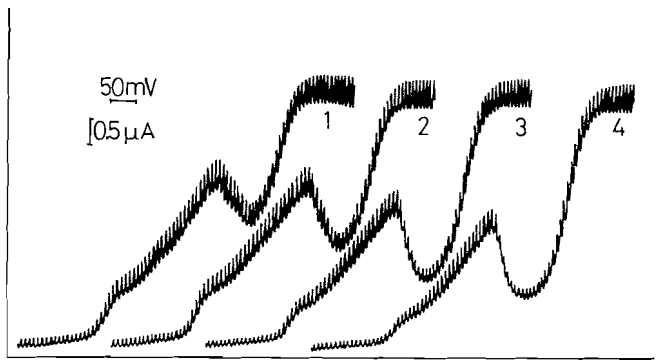

FIG. 2. Polarograms in 0.06 *M* borax – 0.70 *M* NH_4Cl; 5×10^{-4} *M* Co(III); 3.62×10^{-5} *M* SH^-. Time: (*1*) 2; (*2*) 8; (*3*) 20; (*4*) 32 min from mixing the solutions. Start potential −700 mV (SCE).

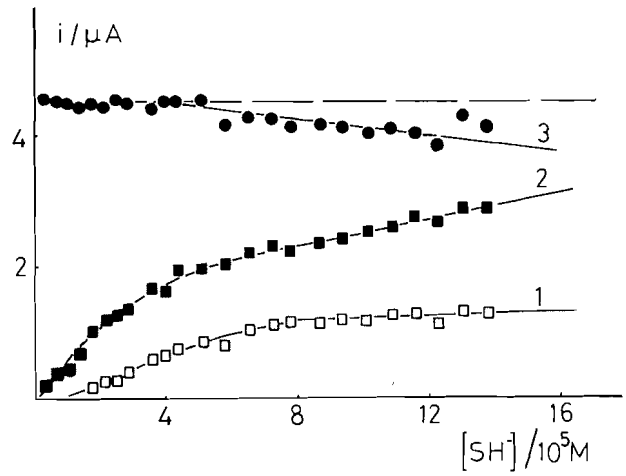

FIG. 3. SH^- concentration effect: 0.06 *M* borax – 0.70 *M* NH_4Cl; 5×10^{-4} *M* Co(III). (*1*) First catalytic wave; (*2*) second catalytic wave; (*3*) Co(II) reduction wave.

first catalytic wave was studied with a sulfide concentration higher than 2.5×10^{-5} *M* since the wave is not observable at lower concentrations. The intensity of this wave increases with sulfide concentration tending toward a limiting value which is approximately 30% of the value of the cobalt(II) reduction current. The second catalytic wave, which also presents a maximum, increases continually with sulfide concentration. At sulfide concentrations greater than 5×10^{-5} *M* the solution is darkened by cobalt(II) sulfides and as a result, cobalt(II) reduction current decreases. In spite of the turbidity, it was necessary to increase the sulfide concentration in order to find the limit of these waves.

The half-wave potential for the first catalytic wave is constant with the sulfide concentration. However, the peak potential of the second wave changes toward more negative potentials reaching a limit of −1100 mV.

At constant sulfide concentration, the intensity of the two catalytic waves varies linearly with cobalt(III) concentration (Fig. 4).

In order to establish the character of the catalytic waves, the *i–t* curves, the effect of the mercury column height, the electrocapillary curves, and the effect of neutral salt additions have been studied.

The dependence of the second catalytic wave height on

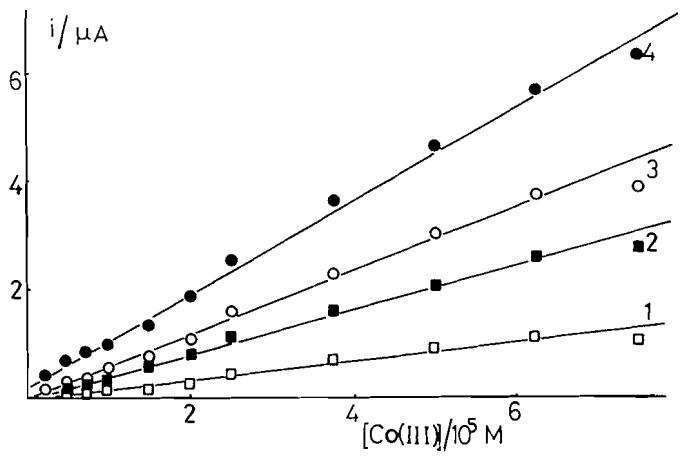

FIG. 4. Cobalt(III) concentration effect: 0.06 *M* borax – 0.70 *M* NH_4Cl; 3.62×10^{-5} *M* SH^-. (*1*) First catalytic wave; (*2*) second catalytic wave; (*3*) total intensity of first and second catalytic waves; (*4*) Co(II) reduction wave.

Can. J. Chem. Downloaded from www.nrcresearchpress.com by 196.1.178.254 on 09/07/12
For personal use only.

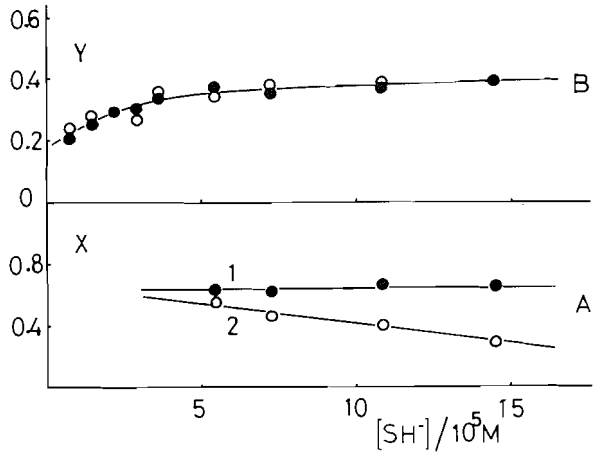

FIG. 5. Exponent variation of the equations (*A*) $i = f(H^x)$, (*B*) $i = f(t^y)$ on SH^- concentration: 5×10^{-4} *M* Co(III) in 0.06 *M* borax – 0.70 *M* NH_4Cl. (*1*) First catalytic wave; (*2*) second catalytic wave.

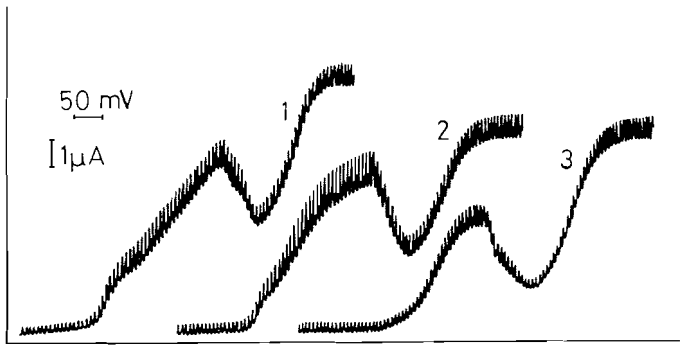

FIG. 6. Polarograms of 5×10^{-4} *M* Co(III) and 5.4×10^{-5} *M* SH^- in 0.06 *M* borax – 0.70 *M* NH_4Cl containing different gelatine concentrations: (*1*) 0; (*2*) 0.005; (*3*) 0.010%. Start potential −700 mV.

mercury column height, *H*, changes with the sulfide concentration. In Fig. 5*A* the exponent *x*, from the $i = f(H^x)$ equation, is plotted vs. the sulfide concentration at a constant cobalt(III) concentration. The *x* exponent remains constant for the first catalytic wave at a value of 0.65, and for the second it ranges from 0.5 to 0.2.

Logarithmic analysis of the *i*–*t* curves obtained at the limiting current potential of the first catalytic wave and the peak potential of the second wave gives the exponent for the $i = f(t^y)$ equation. This exponent increases with sulfide concentration and tends to a limiting value of 0.4 in both waves (Fig. 5*B*).

The electrocapillary curves obtained in the absence and in the presence of sulfide and cobalt(III) do not show adsorption phenomena.

The effect of neutral salts on the catalytic waves has been studied by adding several amounts of different chlorides to a 5×10^{-4} *M* cobalt(III) and 3.62×10^{-5} *M* sodium sulfide in 0.06 *M* borax – 0.70 *M* NH_4Cl solution. An increase in the ionic strength due to the addition of a salt is accompanied by a decrease in the catalytic currents. The decreasing effect is $(C_4H_9)_4N^+ > K^+ \simeq Na^+ \simeq Li^+$, that is, the effect grows with cation size and, consequently, when the absolute value of the ψ potential is smaller. The half-wave potential of the first catalytic wave and the peak potential of the second do not change with neutral salt addition.

Figure 6 shows the effect of gelatine on the catalytic waves. The first catalytic wave decreases with gelatine addition until it disappears. Gelatine on the second catalytic wave only rounds the maximum.

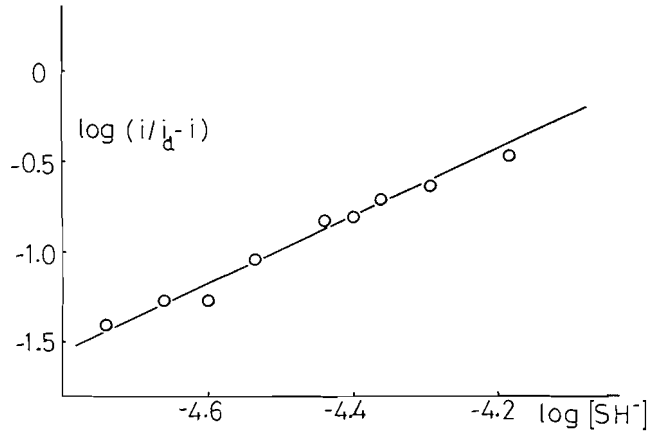

FIG. 7. Log $i/(i_d - i)$ vs. log $[SH^-]$ plot for the first catalytic wave, where *i* and i_d are respectively the average limiting currents of the prewave and the Co(II) reduction wave; 5×10^{-4} *M* Co(III) in 0.06 *M* borax – 0.70 *M* NH_4Cl.

Discussion

The catalytic character of the waves under study is clear since their intensities are higher than the intensity expected from the low sulfide concentration in the solution.

It was thought that both waves were cobalt(II) prewaves. However, the second wave presents a maximum which does not disappear with gelatine addition and reaches a higher intensity than do cobalt(II) reduction wave intensity. Electrolysis at the peak potential of this wave results in the appearance of bubbles on the DME. So, the first wave is a cobalt(II) prewave and the second a catalytic hydrogen wave.

The cobalt catalytic prewave is produced by a cobalt(II) complex with SH^-, discharged before the reduction cobalt(II) wave. The composition of the complex is not known, but it is obvious, as was remarked above, that ammonia is necessary to form the complex which produce the prewave. Therefore, we can express the catalytic complex as $[Co(II)(SH^-)_z(NH_3)_w]^{2-z}$, although it may include some other ligand. The variation in the prewave intensity (tending to a limit value) with sulfide concentration is characteristic of catalytic processes. In the electrodic process the ligand is regenerated and so the prewave current is larger than the diffusion current expected from the cobalt-sulfide complex. The SH^-:cobalt(II) relationship in the complex can be calculated using an approximate method for catalytic current (7). If the electrodic process takes place on the surface of the electrode, the catalytic current and the ligand concentration are related by the following equation $\log i/(i_d - i) = \text{constant} + z \log [SH^-]$ where *i* is the average cobalt(II) limiting catalytic current of the prewave, i_d the average cobalt(II) reduction limiting current, $[SH^-]$ the sulfide concentration, and *z* the complex stoichiometric coefficient. Figure 7 shows that this equation is valid, and the resulting slope is close to two (1.83). The catalytic complex is then formed between SH^- and cobalt(II) in the relationship of 2:1.

The catalytic hydrogen wave appears at a potential of −1100 mV, which means that hydrogen overvoltage has diminished substantially. Under some conditions an ill-defined new wave is observed together with the hydrogen wave. When this wave is not observed, it may be that it has been overlapped by the hydrogen wave. This kind of overlapping is found frequently in

Can. J. Chem. Downloaded from www.nrcresearchpress.com by 196.1.178.254 on 09/07/12
For personal use only.

the literature (1, 7). The catalytic hydrogen wave may be attributed to the reduction of a protonated complex of cobalt(II or 0) and sulfide. We think that the second prewave is due to a complex of cobalt(II) and sulfide which catalyses hydrogen evolution before electroreduction. Taking into account values of x and y, which range from 0.5 to 0.2 and 0.2 to 0.4, respectively, the character of this wave changes with sulfide concentration from a diffusion control to a mixed diffusion–kinetic control.

There are no adsorption phenomena in any of these waves since, (*a*) the electrocapillary curves did not change with sulfide addition, (*b*) the half-wave potential and the peak potential did not change with ionic strength, and (*c*) gelatine did not change the intensity of the hydrogen catalytic wave; the prewave intensity decreased with gelatine and, therefore, we attribute a surface character to this wave.

Acknowledgement

C. F. Warren of the UAH ICE for her editorial assistance.

1. P. MADER, I. M. KOLTHOFF, and V. VESELA. Electrochim. Acta, **27**, 1393 (1982).
2. J. GALVEZ, D. MARIN, T. FUENTE, and M. SARABIA. Electrochim. Acta, **27**: 1253 (1982); **29**, 253 (1984).
3. M. A. GOMEZ-NIETO, M. D. LUQUE DE CASTRO, and M. VALCARCEL. Electrochim. Acta, **29**, 611 (1984).
4. F. G. BANICA and A. CALUSARU. J. Electroanal. Chem. **158**, 47 (1983).
5. B. L. JOHANSSON and S. WENDSJOE. J. Electroanal. Chem. **176**, 165 (1984).
6. A. CALUSARU and J. KUTA. Collection Czech. Commun. **31**, 814 (1966).
7. J. M. LOPEZ FONSECA, P. SANZ PEDRERO, and C. GONZALEZ POSA. J. Chim. Phys. **77**, 825 (1980).

Can. J. Chem. Downloaded from www.nrcresearchpress.com by 196.1.178.254 on 09/07/12
For personal use only.

Conversion of some azaheterocyclic-acetic esters and -acetonitriles into fused heterocycles

DAVID M. MCKINNON, PERRY SPEVACK, AND GRAHAM TIPPLES
Chemistry Department, University of Manitoba, Winnipeg, Man., Canada R3T 2N2

Received August 6, 1987[1]

DAVID M. MCKINNON, PERRY SPEVACK, and GRAHAM TIPPLES. Can. J. Chem. **66**, 2339 (1988).

Various heterocyclic acetic esters and nitriles of the pyridine, thiazole, and imidazole series react with 3-methylthio-4-phenyl-1,2-dithiolium perchlorate to form fused pyridinethiones or dithiolylidene esters. These esters or nitriles also react with trichloromethanesulfenyl chloride to form fused isothiazoles.

DAVID M. MCKINNON, PERRY SPEVACK et GRAHAM TIPPLES. Can. J. Chem. **66**, 2339 (1988).

Divers esters et nitriles acétiques hétérocycliques de la pyridine, du thiazole et de l'imidazole réagissent avec le perchlorate du méthylthio-3 phényl-4 dithiolium-1,2, pour former des pyridinethiones condensés ou des esters dithiolylidène. Ces esters ou ces nitriles réagissent également avec le chlorure de trichlorométhanesulphényle pour former des isothiazoles condensés.

[Traduit par la revue]

Introduction

The possession by azaheterocyclic acetic acid derivatives of both a reactive methylene group and a reactive nitrogen atom allows many fruitful syntheses of fused heterocyclic systems with bridgehead nitrogen atoms, by cyclocondensation with numerous substrates. Two useful additions to this repertoire have been investigated: the reaction with 3-methylthio-4-phenyl-1,2-dithiolium perchlorate (**1**) and with trichloromethanesulfenyl chloride (**2**).

In an earlier paper (1), the reaction of methyl pyridine-2-acetate (**3***a*) with 1,2-dithiolium salts was reported. While most reacted to form 1,2-dithiolylidenepyridine-2-acetate derivatives, the salt **1** reacted by an alternative mechanism to form a quinolizinethione derivative. This suggested that related azaheterocyclic acetic esters might react analogously to form a number of nitrogen fused pyridinethione analogues (Scheme 1). Likewise, it appeared likely that these compounds could react with trichloromethanesulfenyl chloride, which, providing a suitable carbon–sulfur unit, would form other sulfur-containing fused five-membered rings. In its reaction with certain amino-pyridine and -pyrimidines such chemistry is observed (2, 3), and it is suggested that the reaction of some thiazoleacetamides with the related chlorothioformyl chloride forms thiazolothiazoles (4).

Results and discussion

The starting esters or nitriles were either available commercially, or synthesized by literature methods or by modifications. The benzimidazole **4***a* was made by reaction of methyl cyanoacetate with 2-methylaminoaniline, and the benzothiazole and benzimidazole (**5***a*, **4***b* respectively) were made by reaction of ethyl malonate with 2-mercaptoaniline or 2-methylaminoaniline respectively. The benzothiazole **5***a* had been reported (5) to decompose on distillation but no difficulties were encountered on distillation at 1.5 Torr (1 Torr = 133.3 Pa). In these reactions small amounts of di(benzothiazol-2-yl)methane **6***a* and di(1-methylbenzimidazol-2-yl)methane **6***b* respectively were also obtained.

Reactions of these esters or nitriles with the dithiolium salt **1** were carried out in acetonitrile/dioxane mixtures. In the case of the benzimidazoles **4***a*, *b*, better results were obtained in the presence of triethylamine.

The reaction of pyridine-2-acetonitrile (**3***b*) with **1** gave two products. The major product had properties consistent with the cyanoquinolizinethione **7***a* formed by initial reaction of **3***b* at

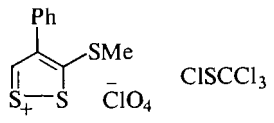

1

2

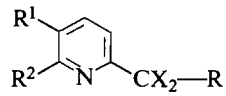

3

a R = CO_2Me; $R^1 = R^2 = X = H$
b R = CN; $R^1 = R^2 = X = H$
c R = CO_2Et; $R^1, R^2 = (—CH=CH—)_2$, X = H
d R = CO_2Me; $R^1 = R^2 = H$; X = Cl

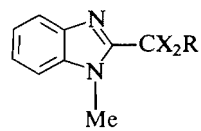

4

a R = CN; X = H
b R = CO_2Et; X = H
c R = CO_2Et; X = Cl

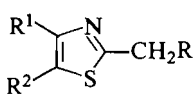

5

a R = CO_2Et; $R^1, R^2 = (—CH=CH—)_2$
b R = CO_2Me; $R^1 = R^2 = CH_3$
c R = CO_2Me; $R^1 = H$; $R^2 = CH_3$

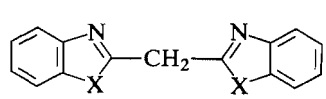

6

a X = NCH_3
b X = S

[1]Revision received April 26, 1988.

Can. J. Chem. Downloaded from www.nrcresearchpress.com by 196.1.178.254 on 09/07/12
For personal use only.

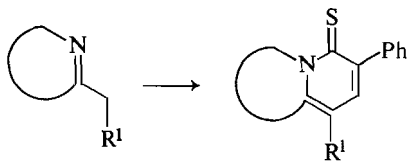

$R^1 = CO_2R, CN$

SCHEME 1

the unsubstituted 5-position of the dithiole ring, followed by ring opening and recyclization. This compound exhibits a strong absorption at 1129 cm^{-1}, tentatively assigned to the thiocarbonyl group. A related quinolizinethione absorbs in this region (1110 cm^{-1}) (6) and 3-phenylquinolizine-4-thione, prepared earlier (1), absorbs at 1084 cm^{-1}. The compound **7***a* exhibited a λ_{max} at 423 nm, while that of 3-phenylquinolizine-4-thione was at 440 nm. The other product is tentatively assigned the structure **8**, or a tautomer. It exhibits an ion in the mass spectrum at $M^+ = 296$ and a broad band in the nmr at $\delta = 8.6$ ppm, consistent with this structure. A plausible scheme for its formation would involve attack of the nitrile at the 3-position of the dithiolium salt, forming 2-(1,2-dithiolylidene)-2-pyridylacetonitrile by elimination of methanethiol, which further reduces the 1,2-dithiole ring to form **8**.

The reaction of **1** with the thiazoleacetic ester **5***b* gave two products. One of these was the desired fused system **9***b*. The other product was a material that had a consistent mp, nmr, and mass spectrum even after many recrystallizations, but on the basis of its nmr spectrum, especially from the appearance of two singlets at δ 2.93 and 3.80 ppm, appears to be a mixture of two compounds. The nmr spectrum indicates that these are two geometrical isomers **10***b* and **11***b* of a 1,2-dithiolylidenethiazoleacetic ester. In the isomer **10***b*, which has a phenyl group close to the ester function, the latter experiences shielding effects by the aromatic ring and absorbs at relatively high field. In the isomer **11***b*, no such shielding is possible and the methyl group absorbs in a normal range. The relative intensities of the peaks indicate that the predominant isomer is that with the more shielded methyl group. When the ester **5***c* was treated with the dithiolium salt, related compounds were obtained, the pyrido[2,1-*b*]thiazole ester **9***c*, and what appear to be the geometrical isomers **10***c*, **11***c* of a 1,2-dithiolylidenethiazoleacetic ester, with once more the shielded isomer **10***c* formed in greater amount. However, these compounds were accompanied by a dark violet material that also appears to be a mixture of two components. Mass spectral and analytical data were consistent with a formula of $C_{26}H_{21}NS_5O_2$, thus this material is formed by a reaction of the ester **5***c* with two molecules of dithiole. The structures **12**, **13** are tentatively assigned to these on the following basis. In the spectra of **10***c*, **11***c* above, two nmr signals at $\delta = 6.45$ and 6.75 ppm are assigned to their respective thiazole protons, as the compounds **10***b*, **11***b* lack signals in this range. In the violet material above, no signals in this range are evident; thus it appears that the hitherto free position of the thiazole ring is involved in a further reaction. Also the mass spectrum showed a large ion at $M^+ = 290$, which is consistent with a cleavage at the bond adjacent to the 2-carbon of thiazole ring in **12** or **13**. Significantly, no violet material could be isolated from the reaction of the ester **5***b*, which lacks a free thiazole position.

The reaction of the ester **5***a* with **1** gave the pyridobenzothiazole **9***a* as a major product. No products corresponding to **10***a* or **11***a* could be isolated. Likewise the benzimidazoles **4***a*,*b* gave the pyridobenzimidazoles **9***d*, *e* respectively as major products. No material corresponding to dithiolylidenebenzimidazole esters was isolated, yet curiously the reaction of the 2-quinolineacetic ester **3***c* under standard conditions gave only a dithiolylidenequinolineacetic ester. As the nmr of this indicates that it is a single compound, and the methylene protons of the ethyl group are evident as a quartet centered at δ = 3.40 ppm, it thus appears that this is the isomer **14**, i.e., that in

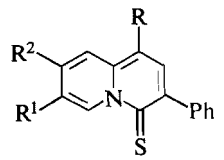

7

a R = CN; $R^1 = R^2 = H$
b R = CO_2Et; $R^1, R^2 = (—CH=CH—)_2$

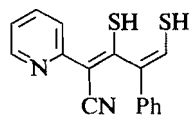

8

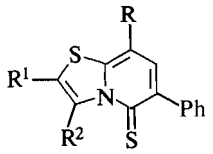

9

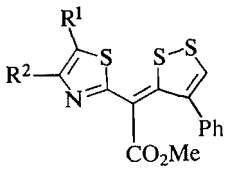

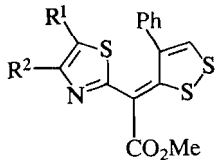

10 **11**

a R = CO_2Et; $R^1, R^2 = (—CH=CH—)_2$
b R = CO_2Me; $R^1 = R^2 = Me$; X = S
c R = CO_2Me; $R^1 = H$; $R^2 = Me$; X = S
d R = CN; $R^1, R^2 = (—CH=CH—)_2$; X = NMe
e R = CO_2Et; $R^1, R^2 = (—CH=CH—)_2$, X = NMe

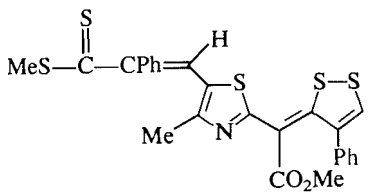

12

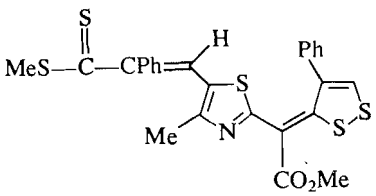

13

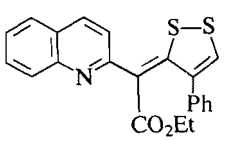

14

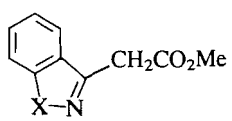

15

a X = S
b X = O

Can. J. Chem. Downloaded from www.nrcresearchpress.com by 196.1.178.254 on 09/07/12
For personal use only.

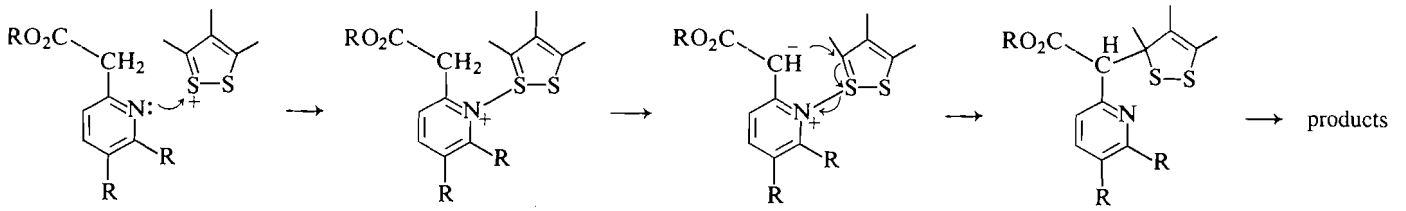

SCHEME 2

which the ester function is shielded by the phenyl group. When the ester **3***c* reacted with **1** in the presence of triethylamine, the ester **14** was still formed as the major product but it was accompanied by the benzoquinolizinethione **7***b*.

Surprisingly the benzisothiazole and benzisoxazoleacetic esters **15***a*,*b* failed to react.

While the above reactions show that there are two modes of reaction of the azaheterocyclic esters and the dithiolium salt, and product formation may be rationalized in terms of which position of the dithiolium salt is preferentially attacked, the reason for the substantial differences in the products from the different substrates is not clear. The difference in products between methyl pyridine-2-acetate and ethyl quinoline-2-acetate is especially striking.

Steric factors do not provide a suitable explanation, as there appears to be little difference in steric accessibility of the reactive groups in **3***a* or **3***c*.

Also, the results do not correlate in terms of attack of anions derived from **3***a*, **3***c* on the 3- or 5-position of **1**, using hard–soft acid–base theory, using data from pK_a's of 2-picoline and 2-methylquinoline (7), and calculated electron densities of the 2-mercapto-1,2-dithiolium ion (8) taken as models. However, if the reactions involve prior attack of the heterocyclic nitrogen at a ring sulfur (Scheme 2), with subsequent reaction as shown, there is a correlation of results with basicities of 2-picoline and 2-methylquinoline (9). Relative nucleophilicities of pyridine and quinoline nitrogen atoms are more extreme (10) and it is reasonable that thiophilicities will show large differences. Thus the former would initially attack S-1 of the salt, the latter, S-2. The results of the reaction of **3***c* in the presence of triethylamine may be interpreted as attack of a more strongly nucleophilic resonant anion from **3***c* attacking at the ring sulfur (S-1) bearing the greater positive charge.

Reactions of the esters or nitriles with trichloromethanesulfenyl chloride were carried out in acetonitrile.

With the ester **3***a*, using an equivalent quantity of halide **2**, a complex mixture was obtained, from which were isolated in low yield what appear to be the pyrido[1,2-*b*]isothiazoles **16***a*,*b*,*c*, and the ester **4***b*. Chlorination of pyridine side chains by **2** is reported (11). For the formation of **16***a*,*b*,*c*, it is likely that a dichloro compound **16***d* is the initial product, which by reaction with water or more ester forms **6***a* or *c* respectively. Further halogenation on sulfur, and hydrolysis, would form **16***b*. While it is possible that these compounds have the isomeric fused pyridothiazole system, **17**, we favour isothiazole formulation on the basis of ^{13}C studies of a benzothiazole ester product below. Also in β-aminocrotonic esters, whose tautomeric form has structural relationship to the pyridine esters, reaction with trichloromethanesulfenyl chloride produces isothiazoles (12, 13). With two equivalents of sulfenyl halide the compound **16***c* was obtained in a higher yield, along with another compound to which the dithietane structure **18** is tentatively assigned, arising by dimerization of a thioketene **19**. This was also obtained from the reaction of **3***a* with thiophosgene.

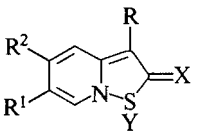

16

a Y = :; X = O; R = CO_2Me, $R^1 = R^2 = H$
b Y = X = O; R = CO_2Me, $R^1 = R^2 = H$
c Y = O; X = C(CO_2Me)2-Py, R = CO_2Me; $R^1 = R^2 = H$
d Y = :; X = Cl; R = CO_2Me; $R^1 = R^2 = H$
e Y = O; X = C(CN)2-py, R = CN; $R^1 = R^2 = H$
f Y = :; X = O; R = CO_2Et; R^1, R^2 = (—CH=CH—)$_2$
g Y = :; X = C(CO_2Et)2-quinolinyl; R^1, R^2 = (—CH=CH—)$_2$

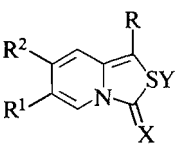

17

Although the compound **17***c* has potential for exhibiting hypervalency of the sulfur atom, and thereby becoming symmetrical like structure **20**, for example, similarly to related compounds (14, 15), the nmr spectrum of **17***c* exhibited two methyl peaks, consistent with an unsymmetrical structure. This lack of symmetry may be due to steric interference, preventing planarity and hence utilization of sulfur *d* orbitals, or it may be an electronic effect, as the electron-withdrawing ester functions reduce electron density on the rather weak S—N bonds.

Reaction of pyridine-2-acetonitrile **3***b* with trichloromethanesulfenyl chloride gave similar products (**18***b*, **16***e*). While the nitrile group in **16***d* should exhibit much less steric interference, its colour was not consistent with a hypervalent sulfur formulation. It was too insoluble for nmr studies. The reaction of the benzothiazole-2-acetate **5***a* with **2** gave as the main product a pale yellow compound, whose properties were consistent with the ketone **21***a*. This is probably formed by a 1:1 reaction of **5***a* with **2** to form a dichloro compound, which during work-up forms the ketone by hydrolysis. This structure, rather than the isomeric thiazolothiazole **22**, is favoured on the basis of its ^{13}C nmr spectrum, which exhibited two peaks at

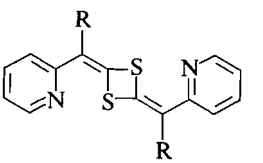

18

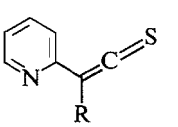

19

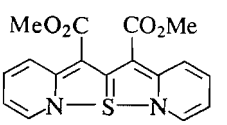

20

Can. J. Chem. Downloaded from www.nrcresearchpress.com by 196.1.178.254 on 09/07/12
For personal use only.

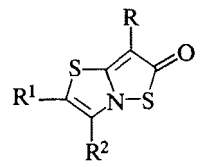

21

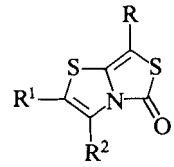

22

a R = CO_2Et; R^1, R^2 = (—CH=CH—)$_2$
b R = CO_2Me; R^1 = H; R^2 = Me

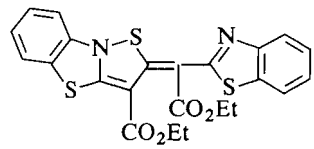

23

δ = 161.6 and 165.7 ppm, consistent with two rather similarly situated carbonyl groups. Data for thiazolinone structures such as **22** indicate that these absorb around δ = 172 ppm (16). The only other major component in this reaction was a reddish solid that failed to give a sharp mp. Mass spectra and nmr data suggest that it is a mixture of the two geometrical isomers of a 2:1 reaction product **23**.

The thiazole ester **5***c* reacted with **2** similarly. The only product isolated was the thiazoloisothiazolone **21***b*. However, ethyl 1-methylbenzimidazole-2-acetate **4***b* failed to give new heterocyclic rings. Instead the dichloro ester **4***c* was obtained as the sole isolable product, arising by halogenation of the side chain.

Ethyl quinoline-2-acetate (**3***c*) reacted to give the fused isothiazoles **16***f* and **16***g* in rather poor yield.

Experimental

The ^{1}H nmr spectra were obtained in deuteriochloroform solution using tetramethylsilane as an internal standard, on Varian model EM360 or AM300 spectrometers. The ^{13}C spectra were obtained on a Bruker WH90 spectrometer and mass spectra were obtained on a VG 7070E spectrometer. Thick-layer chromatography was performed on Merck-type 60PF_{254} silica gel. Infrared (ir) spectra were performed as mulls in liquid paraffin using a Perkin–Elmer model 881 spectrometer.

Starting esters, trichloromethanesulfenyl chloride, and thiophosgene were purified by distillation prior to use. Where necessary, solutions were dried over anhydrous magnesium sulfate.

Reactions of heterocyclic acetic esters or acetonitriles with 3-methylthio-4-phenyl-1,2-dithiolium perchlorate

General procedure

Equimolar quantities of the reagents in the approximately tenfold weight of a 50:50 acetonitrile:dioxane mixture were heated under reflux for 2 h. In the case of imidazole reagents an equivalent quantity of triethylamine was also added. Products were isolated by dilution with water, neutralization with sodium bicarbonate, and chloroform extraction. Evaporation gave oils that were separated by chromatography using varying amounts of chloroform in benzene. The fastest running bands, dark red and orange, were decomposition products of the dithiolium salt and were not examined. Products of type **7** or **9** were usually evident as yellow bands, and those of type **10**, **14** were as reddish bands.

Reaction of 2-pyridine acetonitrile

Chromatography indicated a complex mixture, but with yellow and red bands formed in the greatest amounts. Work-up of the yellow band gave **7**. It recrystallized from nitromethane as yellow needles, mp 170–172°C (41%). The ir spectrum: 2230 (C≡N), 1129 (C=S) cm^{-1}. The uv spectrum in ethyl acetate, λ_{max}: 433, 318, 287, 263. The ^{1}H nmr spectrum of **7***a*, δ: 7.34–7.56 (6H, complex m, the aromatic and one pyridine ring protons), 7.81 (1H, s, H2), 7.89 (1H, dd, tentatively H7), 8.23 (1H, d, H8), 10.81 (1H, d, H5) ppm. The ^{13}C nmr spectrum, δ: 175.85 (C=S), 114.52 (C≡N) ppm. The mass spectrum, M^+ 262; M calcd.: 262. Ions at 261 ($M^+ - 1$), 218 (M^+ – (C=S)), and 149 (M^+ – CNC—CH=C—Ph) were also evident. *Anal.* calcd. for $C_{16}H_{10}N_2S$: C 73.28, H 3.82, N 10.68, S 12.21; found: C 73.31, H 3.62, N 10.80, S 12.08.

Work-up of the red band gave **8** as a solid that crystallized from nitromethane as red needles, mp 204°C (19%). The nmr spectrum of **8** indicated only a series of bands, δ 7.15–8.48 ppm, and a broad band at δ 8.6 ppm. The latter disappeared on shaking with D_2O. The mass spectrum, M^+ 296; M calcd.: 296. *Anal.* calcd. for $C_{16}H_{12}NS_2$: C 64.86, H 4.05, N 9.46, S 21.62; found: C 64.77, H 4.11, N 9.63, S 21.53.

Reaction of methyl 4,5-dimethylthiazole-2-acetate

Chromatography of the reaction mixture gave two main bands isolated as yellow and red semicrystalline solids.

The yellow material crystallized from ethanol giving **9***b* as yellow needles, mp 126–128°C (48%). The nmr spectrum of **9***b*, δ: 2.40, 2.97 (two, 3H, s, the thiazole methyls), 3.93 (4H, s, the O-methyl), 7.20–7.67 (5H, bands, the aromatic protons), 7.71 (1H, s, the heterocyclic proton) ppm. The mass spectrum, M^+ 329; M calcd.: 329. *Anal.* calcd. for $C_{17}H_{15}NS_2O_2$: C 62.01, H 4.56, N 4.26, S 19.45; found: C 61.77, H 4.28, N 4.04, S 19.23.

The red material crystallized from acetonitrile giving **10***b*, **11***b* as small red prisms, mp 152–154°C (18%). The nmr spectrum indicated that this was an approximately 55:45 mixture of the two components, **10***b*, **11***b* respectively, tentatively assigned; for isomer **10***b*, δ: 2.07, 2.43 (two 3H, s, the thiazole methyls), 2.93 (3H, s, the shielded O-methyl), 7.43 (5H, s, the aromatic protons), 7.70 (1H, s, the dithiole proton) ppm. For isomer **11***b*, δ: 1.90, 2.37 (two 3H, s, the thiazole methyls), 3.80 (3H, s, the O-methyl), 7.08 (5H, br s, the aromatic protons), 7.75 (1H, s, the dithiole proton) ppm. The mass spectrum, M^+ 361; M calcd.: 361. *Anal.* calcd. for $C_{17}H_{15}NS_3O_2$: C 56.51, H 4.16, N 3.88, S 27.59; found: C 56.77, H 4.03, N 4.01, S 27.32.

Reaction of methyl 4-methylthiazole-2-acetate

Chromatography of the reaction mixture gave three main reaction products, visible as yellow, violet, and red bands in order of elution.

The yellow material crystallized from ethanol giving **9***c* as yellow needles, mp 148°C (30%). The ir spectrum, 1690 (C=O), 1140 (C=S) cm^{-1}. The nmr spectrum of **9***c*, δ: 3.17 (3H, s, the thiazole methyl), 3.93 (3H, s, the O-methyl), 6.93 (1H, s, the thiazole proton), 7.28–7.65 (5H, br, the aromatic protons), 7.87 (1H, s, the pyridyl proton) ppm. The mass spectrum, M^+ 315; M calcd.: 315. *Anal.* calcd. for $C_{16}H_{13}NO_2S_2$: C 60.95, H 4.13, N 4.44, S 20.32; found: C 61.11, H 4.21, N 4.50, S 20.04.

The violet material crystallized from nitromethane giving **12** and **13** as fine dark red needles with a green reflex, mp 175°C (17%). The nmr spectrum indicated that these were present in approximately 70:30 amounts, respectively. These are tentatively assigned; for **12**, δ: 2.65, 2.70 (two 3H, s, the thiazole and S-methyls), 2.86 (3H, s, the O-methyl), 7.78 (1H, s, the dithiole proton), 8.50 (1H, s, the side-chain proton) ppm. For **13**, δ: 2.16, 2.64 (two 3H, s, the thiazole and S-methyl protons), 3.69 (3H, s, the O-methyl), 7.67 (1H, s, the dithiole proton), 8.14 (1H, s, the side-chain proton) ppm. All other protons in both isomers gave complex bands between δ 6.90 and 7.55 ppm. The mass spectrum, M^+ 539; M calcd.: 539. *Anal.* calcd. for $C_{26}H_{21}NO_2S_5$: C 43.25, H 3.90, N 2.60, S 29.68; found: C 43.55, H 4.01, N 2.63, S 29.52.

The red material crystallized from acetonitrile giving **10***c*, **11***c* as reddish brown prisms, mp 130°C (32%). The nmr spectrum indicated that it was a mixture of the two components in approximately 60:40 amounts, respectively. These are tentatively assigned; for **10***c*, δ: 2.57 (3H, s, the thiazole methyl), 2.91 (3H, s, the O-methyl), 6.75 (1H, s, the thiazole proton), 7.70 (1H, s, the dithiole proton) ppm. For isomer **11***c*, δ: 2.01 (3H, s, the thiazole methyl), 3.79 (3H, s, the

Can. J. Chem. Downloaded from www.nrcresearchpress.com by 196.1.178.254 on 09/07/12
For personal use only.

Can. J. Chem. Downloaded from www.nrcresearchpress.com by 196.1.178.254 on 09/07/12
For personal use only.

O-methyl), 6.45 (1H, s, the thiazole proton), 7.03 (1H, s, the dithiole proton) ppm. For both isomers other protons were evident as bands, δ 6.95–7.45 ppm. The mass spectrum, M^+ 347; M calcd.: 347. *Anal.* calcd. for $C_{10}H_{13}NO_2S_3$: C 55.33, H 3.75, N 4.03, S 27.67; found: C 55.07, H 3.81, N 4.17, S 27.92.

Reaction of ethyl benzothiazole-2-acetate

Chromatography gave two main products, evident as yellow and red bands in order of elution. The yellow material crystallized from a toluene:ethanol 1:1 mixture giving **9***a* as golden yellow needles, mp 181–182°C (68%). The ir spectrum: 1686 (C=O) and 1131 (C=S) cm^{-1}. The nmr spectrum of **9***a*, δ: 1.20, 4.19 (3H, t, and 2H, q, resp., the ethyl protons), 7.32–7.75 (9H, bands, the aromatic protons), 7.91 (1H, s, the pyridyl proton) ppm. The mass spectrum, M^+ 365; M calcd.: 365. *Anal.* calcd. for $C_{20}H_{15}NO_2S_2$: C 65.75, H 4.11, N 3.84, S 17.53; found: C 66.01, H 4.32, N 3.72, S 17.44.

The red band could not be purified satisfactorily, but its nmr spectrum displayed two ethyl groups at δ 0.90 and 3.32 ppm (3H, t, and 2H, q, resp.), and δ 1.25 and 4.22 ppm (3H, t, and 2H, q, resp.), consistent with the isomers **10***a*, **11***a*.

Reaction of 1-methylbenzimidazole-2-acetonitrile

Evaporation of the solvent and dilution with water gave an oily solid, which was collected and crystallized from nitromethane giving **9***d* as yellow needles, mp 240°C (76%). The ir spectrum: 2208 (C≡N), 1117 (C=S) cm^{-1}. This was too insoluble in chloroform for a satisfactory nmr spectrum. The mass spectrum, M^+ 315; M calcd.: 315. *Anal.* calcd. for $C_{19}H_{13}N_3S$: C 72.38, H 4.13, N 13.30, S 10.16; found: C 72.28, H 4.07, N 13.22, S 9.95.

Reaction of ethyl 1-methylbenzimidazole-2-acetate

Chromatography of the reaction mixture indicated only one yellow band as a main product. Isolation gave a yellow solid that crystallized from nitromethane giving **9***e* as lemon yellow needles, mp 183°C (62%). The nmr spectrum of **9***e*, δ: 1.42, 4.40 (3H, t, and 2H, q, resp., the ethyl protons), 3.89 (3H, s, the N-methyl), 7.95 (1H, s, the pyridyl proton) ppm. *Anal.* calcd. for $C_{21}H_{18}NO_2S$: C 69.61, H 4.97, N 7.73, S 8.34; found: C 69.54, H 5.07, N 7.72, S 8.96.

Reaction of ethyl quinoline-2-acetate

Chromatography of the crude reaction product gave a strongly absorbed red band as a major reaction product. Work-up gave **14** as a red oil (82%). The nmr spectrum of **14**, δ: 1.06 and 3.40 (3H, t, and 2H, q, resp., the ethyl protons), 7.36–8.55 (12H, bands, the aromatic and heterocyclic protons) ppm. The mass spectrum, M^+ 391; M calcd.: 391. *Anal.* calcd. for $C_{22}H_{17}NS_2O_2$: C 67.52, H 4.35, N 3.58, S 16.98; found: C 67.55, H 4.41, N 3.68, S 17.10.

When the reaction was carried out using one equivalent of triethylamine as a catalyst, the ester was accompanied by another deep red material, which was separated by repeated chromatography. A red oil was obtained, which crystallized under ethanol. It was recrystallized from acetonitrile as dark red prisms, mp 171–172°C (13%). The nmr spectrum of **7***b*, δ: 1.41, 4.42 (3H, t, and 2H, q, the ethyl protons), 7.35–7.91 (9H, bands, the aromatic protons), 7.90 and 8.91 (2H, d, the pyridine ring protons) ppm. The mass spectrum, M^+ 359; M calcd.: 359. *Anal.* calcd. for $C_{22}H_{17}NSO_2$: C 73.54, H 4.74, N 3.90, S 8.91; found: C 73.01, H 4.83, N 3.77, S 8.82.

Attempted reactions of methyl 1,2-benzisoxazole-2-acetate and methyl 1,2-benzisothiazole-2-acetate

No apparent reaction products could be isolated under a variety of reaction conditions.

Reactions of heterocyclic esters or nitriles with trichloromethanesulfenyl chloride

General procedure

Equimolar quantities of reagents (≈10 mmol); were heated under reflux in acetonitrile (20 mL) for 2 h. Solutions were worked up by dilution with water, neutralization with sodium bicarbonate, and chloroform extraction. The dried chloroform extracts were treated with charcoal and evaporated. In some cases the products crystallized on evaporation. In others chromatography was necessary.

Reactions with methyl pyridine-2-acetate

A complex mixture was obtained. Examination by chromatography of the major bands gave, in order of elution, a yellow solid, a colorless oil, a yellow oil, a pale yellow solid, and an orange solid.

The yellow solid crystallized from ethanol giving **16***b* as amber needles, mp 126–127°C (8%). The nmr spectrum of **16***b*, δ: 3.87 (3H, s, the methyl protons), 8.22–8.90 (4H, m, the pyridine ring protons) ppm. The mass spectrum M^+ 225; M calcd.: 225. *Anal.* calcd. for $C_9H_7NSO_4$: C 48.00, H 3.11, N 6.22, S 14.22; found: C 48.26, H 3.09, N 6.21, S 14.07.

The colorless oil **3***d* failed to crystallize. It was purified by rechromatography (3%). The nmr spectrum of **3***d*, δ: 3.91 (3H, s, the methyl protons), 7.34–8.80 (4H, bands, the pyridine protons) ppm. The mass spectrum showed M^+ ions at 219, 221, 223; M calcd.: 219, 221, 223. This material was not analyzed.

The yellow oil crystallized under methanol and was recrystallized from methanol, giving **16***a* as yellow needles, mp 81–82°C (6%). The nmr spectrum of **16***a*, δ: 3.86 (3H, s, the methyl protons), 6.51 (1H, t), 7.10 (1H, t), 7.89 (1H, d), 8.08 (1H, d, the pyridine ring protons) ppm. The mass spectrum, M^+ 209; M calcd.: 209. *Anal.* calcd. for $C_9H_7NSO_3$: C 51.67, H 3.35, N 6.70, S 15.31; found: C 51.82, H 3.64, N 6.29, S 15.07.

The pale yellow solid recrystallized from nitromethane, giving **18***a* as pale yellow needles, mp 214–218°C (5%). The nmr spectrum, of **18***a*, δ: 3.96 (two 3H, s, the ester methyls), 8.61–7.02 (8H, bands, the pyridine protons) ppm. The mass spectrum, M^+ 386; M calcd.: 386. *Anal.* calcd. for $C_{18}H_{14}N_2S_2O_4$: C 55.96, H 3.63, N 7.25, S 16.58; found: C 56.13, H 3.88, N 7.03, S 16.49.

The orange material recrystallized from toluene, giving **16***c* as orange prisms, mp 217–218°C (8%). The nmr spectrum of **16***c*, δ: 3.76, 3.89 (two 3H, s, the ester methyls), 5.91–8.82 (8H, bands, the pyridine protons) ppm. The mass spectrum, M^+ 342; M calcd.: 342. *Anal.* calcd. for $C_{17}H_{14}N_2SO_4$: C 59.63, H 4.13, N 8.18, S 9.36; found: C 59.71, H 4.22, N 8.16, S 9.51.

When this reaction was performed with a 2:1 ratio of ester to sulfenyl halide, work-up gave a dark red solid. Recrystallization from toluene after a charcoal treatment gave the ester **16***c* as orange prisms (18%).

Reactions of pyridine-2-acetonitrile

Reagents here were heated for 10 min. Work-up gave a brown solid that was chromatographed using chloroform as an eluent. A yellow and an orange band, in order of elution, were evident.

The yellow band gave **18***b* as a yellow solid that crystallized from dioxane as a yellow powder, mp 350°C, darkening above 330°C (31%). The ir spectrum: 2214 (C≡N) cm^{-1}. It was too insoluble for a satisfactory nmr spectrum. The mass spectrum, M^+ 320; M calcd.: 320. *Anal.* calcd. for $C_{16}H_8N_4S_2$: C 60.00, H 2.50, N 17.50, S 20.00; found: C 60.33, H 2.65, N 17.21, S 19.85.

The orange band gave an orange powder that crystallized from dioxane, giving **16***e* as an orange microcrystalline powder, mp 288–294°C (42%). It was too insoluble for a satisfactory nmr spectrum. The mass spectrum, M^+ 276; M calcd.: 276. *Anal.* calcd. for $C_{15}H_8N_4S$: C 65.22, H 2.90, N 20.29, S 11.59; found: C 65.26, H 2.97, N 20.14, S 11.73.

Reaction of ethyl benzothiazole-2-acetate

Work-up gave a red oil, which was separated by chromatography into a pale yellow band and a more strongly adsorbed red band.

The pale yellow band gave a yellow solid that crystallized from micromethane, giving **21***a* as pale yellow needles, mp 139–140°C (41%). The ^1H nmr spectrum of **21***a*, δ: 1.36, 4.34 (3H, t, and 2H, q, resp., the ethyl protons), 7.20–8.32 (4H, m, the aromatic protons) ppm. The ^{13}C spectrum, δ: 161.32 and 165.52 ppm, the two carbonyl carbons. The mass spectrum, M^+ 279; M calcd.: 279. *Anal.* calcd. for $C_{12}H_9NS_2O_3$: C 51.61, H 3.23, N 5.02, S 22.94; found: C 51.90, H 3.15, N 5.11, S 23.08.

The red band on work-up gave an orange powder that recrystallized from nitromethane, giving **23** as red prisms, mp 168–172°C (9%). The nmr spectrum of **23**, δ: 0.95 and 4.01 (3H, t, and 2H, q, resp.,

the ethyl group), 7.01–7.78 (8H, bands, the aromatic protons) ppm. The mass spectrum, M^+ 482; M calcd.: 482. *Anal.* calcd. for $C_{23}H_{18}N_2S_3O_4$: C 57.26, H 3.73, N 5.81, S 19.92; found: C 57.51, H 3.82, N 5.66, S 20.20.

When the reaction was allowed to reflux for 24 h the ester **23** was the major product (22%).

Reaction of methyl 4-methylthiazole-2-acetate

The crude dark red oil gave a faster running yellow band and a slower red band on chromatography. The yellow band on elution and evaporation gave a yellow oil that crystallized under ethanol. It was crystallized from acetonitrile, giving **22***b* as yellow needles, mp 214°C (19%). The nmr spectrum of **22***b*, δ: 2.53 (3H, s, the thiazole methyl), 4.07 (3H, s, the ester methyl), 6.90 (1H, s, the thiazole proton) ppm. The mass spectrum, M^+ 229; M calcd.: 229. *Anal.* calcd. for $C_8H_7NS_2O_3$: C 41.92, H 3.05, N 6.11, S 27.95; found: C 42.06, H 3.11, N 5.95, S 27.64.

Further chromatography of the red band indicated that it was very complex and it was not further examined.

Reaction of ethyl 1-methylbenzimidazole-2-acetate

A work-up gave a thick yellow oil, which gave only one major band on chromatography. It was further purified by rechromatography, giving **4***c* as a pale yellow oil (31%). The nmr spectrum of **4***c*, δ: 1.13 (3H, t, the ester methyl), 3.72 (3H, s, the N-methyl), 4.27 (2H, q, the ester methylene), 6.95–7.75 (4H, bands, the aromatic protons) ppm. The mass spectrum, M^+ ions at 286, 288, 290; M calcd.: 286, 288, 290. *Anal.* calcd. for $C_{12}H_{12}Cl_2N_2O_2$: C 50.17, H 4.18, Cl 24.74, N 9.76; found: C 50.33, H 4.21, Cl 24.43, N 9.73.

Reaction of ethyl quinoline-2-acetate

Reaction gave a dark red oil, which separated on chromatography into a yellow and a more strongly adsorbed red band. These were isolated and purified by rechromatography.

The yellow band gave a dark yellow crystalline solid that crystallized from acetonitrile, giving **16***f* as dark yellow needles, mp 138–140°C (3%). The nmr spectrum of **16***f*, δ: 1.45, 4.41 (3H, t, and 2H, q, resp., the ethyl group), 7.07–8.13 (6H, bands, the heterocyclic and aromatic protons) ppm. The mass spectrum, M^+ 273; M calcd.: 273. *Anal.* calcd. for $C_{14}H_{11}NO_3S$: C 61.40, H 4.03, N 5.13, S 11.72; found: C 61.66, H 4.07, N 4.98, S 11.64.

The red band gave a red solid that recrystallized from nitromethane, giving **16***g* as fine red prisms, mp 285–290°C (dec.) (2%). It was too insoluble for a satisfactory nmr spectrum. The mass spectrum, M^+ 470; M calcd.: 470. *Anal.* calcd. for $C_{27}H_{22}N_2O_4S$: C 68.94, H 4.68, N 5.96, S 6.81; found: C 68.67, H 4.43, N 6.02, S. 6.76.

Reaction of methyl pyridine-2-acetate with thiophosgene

The ester **3***a* (3.2 g, 0.02 mol) and thiophosgene (2.3 g, 0.02 mol) in acetonitrile (20 mL) were refluxed for 1 h. The mixture was cooled, diluted with saturated sodium bicarbonate solution, and extracted with chloroform. Evaporation gave a dark yellow oil that gave two main bands on chromatography. Separation gave the dithietane **18***a* (11%) and pyridoisothiazole **16***c* (12%) identical to those obtained above.

Preparation of ethyl benzothiazole-2-acetate (5a)

2-Aminobenzenethiol (12.5 g, 0.1 mol) and ethyl malonate (16 g, 0.1 mol) in toluene (100 mL) were refluxed for 24 h. The evaporated solution was cooled for 1 day, crystalline material removed, and the liquid distilled *in vacuo*. The fraction, bp 145°C at 1.5 Torr (1 Torr = 133.3 Pa), was collected, giving **5***a* as a pale yellow oil (55%). The crystalline precipitate was recrystallized from ethanol, giving **6***b* as fine pale yellow plates, mp 82°C (5%). The nmr spectrum of **6***b*, δ: 5.03 (2H, s, the methylene protons), 7.45–8.20 (8H, bands, the aromatic protons) ppm. The mass spectrum, M^+ 282; M calcd.: 282. *Anal.* calcd. for $C_{15}H_{10}N_2S_2$: C 63.83, H 3.55, N 9.93, S 22.70; found: C 63.77, H 3.46, N 10.09, S 22.84.

Preparation of 1-methylbenzimidazole-2-acetonitrile (4a)

2-Methylaminoaniline (2.44 g, 0.02 mol) and methyl cyanoacetate (3 g, 0.03 mol) were refluxed gently for 3 h and cooled for 16 h. The crystalline product was collected and recrystallized from ethanol as colorless needles, mp 132–134°C (lit. (17) mp 132–134°C) (62%).

Preparation of ethyl 1-methylimidazole-2-acetate (4b)

2-Methylaminoaniline (2.44 g, 0.02 mol) and ethyl malonate (1.6 g, 0.01 mol) were heated gently under reflux for 24 h. The boiling point, initially 150°C, had decreased to 100°C. The mixture was cooled, allowed to stand for 1 day, and filtered to remove the crystalline precipitate of **6***a*. The liquid was distilled *in vacuo* and the fraction, bp 170–180°C at 1.5 Torr, was collected. This crystallized on standing and was recrystallized from ethanol as colorless needles, mp 66–67°C (lit. (18) mp 66–67°C) (63%).

The solid **6***a* recrystallized from nitromethane as colorless needles, mp 196°C (11%). The nmr spectrum of **6***a*, δ: 3.90 (6H, s, the N-methyl protons), 4.71 (2H, s, the methylene protons), 7.11–7.73 (8H, bands, the aromatic protons) ppm. The mass spectrum, M^+ 276; M calcd.: 276. *Anal.* calcd. for $C_{17}H_{16}N_4$: C 73.91, H 5.80, N 20.29; found: C 73.88, H 5.67, N 20.02.

Acknowledgments

We wish to thank the Natural Sciences and Engineering Research Council of Canada for financial support of this work. We also wish to thank Mr. W. Buchannon for the preparation of mass spectra, and Mr. K. Marat for nmr spectra.

1. D. M. McKinnon, K. Duncan, A. M. McKinnon, and P. A. Spevack. Can. J. Chem. **63**, 882 (1985).
2. K. T. Potts and J. Kane. J. Org. Chem. **38**, 3087 (1973).
3. K. T. Potts and J. Kane. J. Org. Chem. **40**, 2600 (1975).
4. H. Schaefer and K. Gewald. J. Prakt. Chem. **316**, 684 (1974).
5. P. Baudet and C. Otten. Helv. Chim. Acta, **53**, 1683 (1970).
6. H. N. Al-Jalbo and F. W. Al-Azawi. J. Heterocycl. Chem. **10**, 139 (1973).
7. G. Seconi, E. Eaborn, and A. Fischer. J. Organomet. Chem. **117**, 129 (1979).
8. D. Gonbeau, C. Guiman, and G. Pfister-Guillouzo. Tetrahedron, **29**, 3599 (1973).
9. E. F. V. Scriven. Pyridines and their benzo derivatives. ii. Reactivity at ring atoms. *In* Comprehensive heterocyclic chemistry. Vol. 2. *Edited by* A. J. Boulton and A. McKillop. Pergamon Press, Oxford. 1984.
10. J. A. Zoltewicz and L. W. Deady. J. Am. Chem. Soc. **94**, 2765 (1972).
11. V. Traynelis and J. N. Rieck. J. Org. Chem. **38**, 4334 (1973).
12. J. A. Waite and K. H. R. Wooldridge. Tetrahedron Lett. 3273 (1972).
13. A. Tanaka and T. Usui. Chem. Pharm. Bull. Jpn. **26**, 3576 (1978).
14. K. T. Potts and J. Kane. J. Org. Chem. **39**, 3783 (1974).
15. R. L. N. Harris. Aust. J. Chem. **25**, 993 (1972).
16. I. W. J. Still, N. Plavac, D. M. McKinnon, and M. S. Chauhan. Can. J. Chem. **54**, 1660 (1970).
17. W. Ozegowski and D. Krebs. J. Prakt. Chem. **29**, 18 (1965).
18. D. Chapman, J. K. Elwood, D. N. Heseltine, H. M. Hess, and D. N. Kurz. J. Org. Chem. **42**, 2474 (1977).

Can. J. Chem. Downloaded from www.nrcresearchpress.com by 196.1.178.254 on 09/07/12
For personal use only.

Orientation specific Diels–Alder addition of isoprene to an activated 4,4-dimethylcyclohexenone. An improved route to himachalenes

HSING-JANG LIU, ERIC N. C. BROWNE,[1] AND SEW YEU CHEW
Department of Chemistry, University of Alberta, Edmonton, Alta., Canada T6G 2G2

Received February 29, 1988

HSING-JANG LIU, ERIC N. C. BROWNE, and SEW YEU CHEW. Can. J. Chem. **66**, 2345 (1988).

Diels–Alder addition of isoprene to enone-ester **3** proceeds exclusively to the *para*-addition product **6**. The specificity of this route constitutes a significant improvement in the previously reported total synthesis of himachalenes via **6**. The mechanistic significance of the observed specificity of addition is discussed.

HSING-JANG LIU, ERIC N. C. BROWNE et SEW YEU CHEW. Can. J. Chem. **66**, 2345 (1988).

L'addition de Diels–Alder de l'isoprène sur l'ester énonique **3** conduit exclusivement au produit d'addition en *para* **6**. La spécificité de cette voie d'accès constitue une amélioration significative des synthèses totales connues des himachalènes par l'intermédiaire du composé **6**. On discute de l'importance du mécanisme de cette addition spécifique observée.

[Traduit par la revue]

Can. J. Chem. Downloaded from www.nrcresearchpress.com by 112.217.228.212 on 09/07/12
For personal use only.

Introduction

We previously reported on the Diels–Alder reactions of dienone-ester **1** and dienone **2** with various dienes (1–3). In particular, we described, and provided a mechanistic rationale for, the unusual regioselectivity observed in additions of isoprene (2–5) to these dienophiles. We used an isoprene adduct of **1** in the total synthesis of himachalenes (4). We now report on additions of isoprene to the enone-ester **3** that contrast with the regiochemical outcome of additions to **1** and **2** but very clearly complement the mechanistic rationale we presented for regiochemical effects in this dienophile system. The new results constitute a formal improvement of the total synthesis of himachalenes.

Results and discussion

The enone-ester **3** was prepared in three steps (78% overall yield) from 4,4-dimethyl-2-cyclohexen-1-one **4** (6). Catalytic hydrogenation of **4** (H_2, Pd/C, EtOAc) gave 4,4-dimethylcyclohexanone, which was carbomethoxylated with dimethyl carbonate (NaH, 1,2-dimethoxyethane (DME), reflux). Dehydrogenation of the product, saturated keto-ester **5**, in one pot, by phenylselenenylation (PhSeCl, pyridine, CH_2Cl_2) and oxidative elimination (aqueous H_2O_2) gave the target dienophile **3**.

The Diels–Alder reaction of **3** with isoprene was examined using three Lewis acid catalysts and a variety of conditions, which are summarized in Table 1. Exclusive generation of the "*para*"-addition product **6**[2] was observed in all cases regardless of catalyst or temperature. This is in striking contrast to the high selectivity of **2** for the "*anti-para*"-addition product **9** (2, 3) and the catalyst dependent selectivity of **1** in which the formation of the *anti-para*-addition product **8** cannot be completely excluded (3, 4). The effect of catalyst selection on the relative order of reaction rates for **3** ($FeCl_3 > SnCl_4 > BF_3 \cdot Et_2O$) and of reaction yields ($SnCl_4$ best, $BF_3 \cdot Et_2O$ poorest) corresponds to

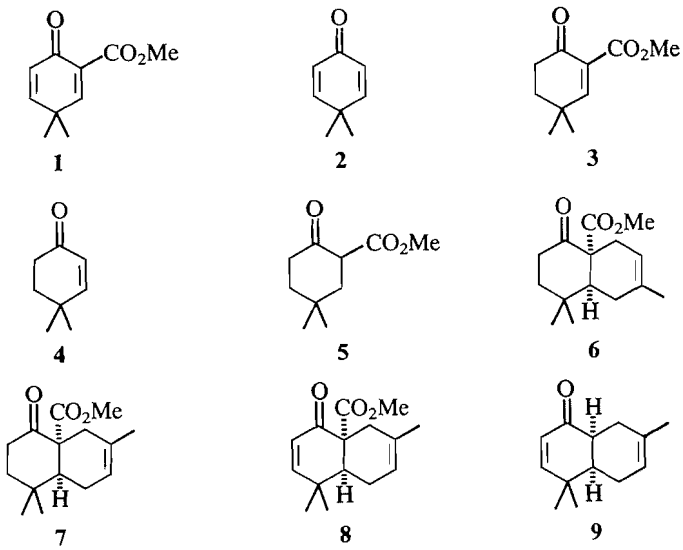

that observed for dienophile **1**, although in general the rates are slower and yields poorer for **3**. With increased proportion of catalyst the yields are seen to improve for $BF_3 \cdot Et_2O$ and $SnCl_4$ catalysis, and reaction rates increased for all three cases.

The regiochemical result of these additions implies that the preference for transition states **A**, having secondary orbital interaction with the ketone carbonyl observed in additions to **1** (3), is not present in additions to **3**. The difference in behavior of **1** and **3** under these reaction conditions would arise from a relative reduction in secondary orbital effect stabilization of the **A**-type transition states due to chemical reduction of the C5—C6 double bond and loss of its contribution to the cross-conjugated π-orbital system. Potential steric interaction between the quasi-axial proton of the C5 methylene of **3** and the diene would also contribute to the observed effect. Likely, these two effects combine to completely eliminate any addition by **A**-type transition states. In the **B**-type transition states, the usual directing effects are unmodified and the *para*-addition product via **6B** is formed exclusively. The retained specificity of orientation in the product, even under low temperature conditions (Entries 6–8) where the product of the most stable transition state would be more favoured, confirms this conclusion.

The observed high selectivity for adducts arising from secondary orbital overlap with the ethyl ester group in the case of the related dienophile **10** (8) follows similarly from combined

[1]Present address: Ayerst Laboratories, 1025 Laurentian Blvd., St. Laurent, P.Q., Canada H4R 1J6.

[2]The structure of adduct **6** derived from Diels–Alder addition to **1** has been conclusively demonstrated (4, 5). The adduct derived from **3** is identical in its ^{1}Hmr, ir, and ^{13}Cmr spectra. The regioisomer **7** has been prepared from the enone-ester **8** and shows spectral characteristics (7) distinctly different from those of **6**; ^{1}Hmr for **7**, δ:5.40 (br s, 1H, =CH—), 3.72 (s, 3H, $-OCH_3$), 1.65 (br s, 3H, $=\overset{|}{C}CH_3$), 1.00 (s, 3H, $-CH_3$), and 0.90 (s, 3H, $-CH_3$).

TABLE 1. Lewis acid catalyzed Diels–Alder addition of isoprene to enone-ester **3**

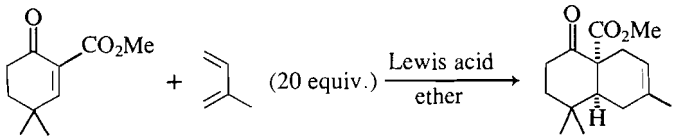

3 **6**

Entry	Lewis acid	(equiv.)	Temperature (°C)	Time (h)	Yield (%)
1	$BF_3 \cdot Et_2O$	(0.5)	20	140	< 5[a,b]
2	$BF_3 \cdot Et_2O$	(1.0)	20	29	33
3	$SnCl_4$	(0.5)	20	44	58
4	$SnCl_4$	(1.0)	20	18	87
5	$FeCl_3$	(0.5)	20	2	52
6	$FeCl_3$	(0.5)	0	18	67[a,c]
7	$FeCl_3$	(1.0)	0	9	59
8	$FeCl_3$	(0.5)	−20	48	49[a,d]

[a]Based on the consumed starting material. The starting material was recovered as indicated:
[b]In 63%.
[c]In 14%.
[d]In 49%.

changes in steric and secondary orbital effects and likewise gives exclusively the *para*-addition product with isoprene. The enone-aldehydes **11** (9) and **12** (10) can be predicted to show a similar reversal of regioselectivity. Indeed **12** has already been shown (11) to give Diels–Alder addition products specifically via secondary orbital overlap of the ketone carbonyl. In contrast, in the addition to unactivated enones **4** and **13** the only possible secondary orbital effect stabilized transition states overlap the ketone carbonyl and consequently the product

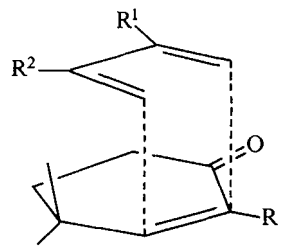

A

6A R = CO_2Me, R^1 = H, R^2 = CH_3
7A R = CO_2Me, R^1 = CH_3, R^2 = H

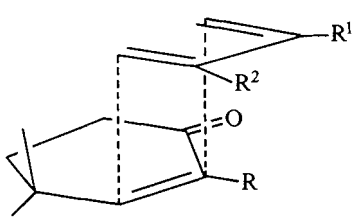

B

6B R = CO_2Me, R^1 = H, R^2 = CH_3
7B R = CO_2Me, R^1 = CH_3, R^2 = H

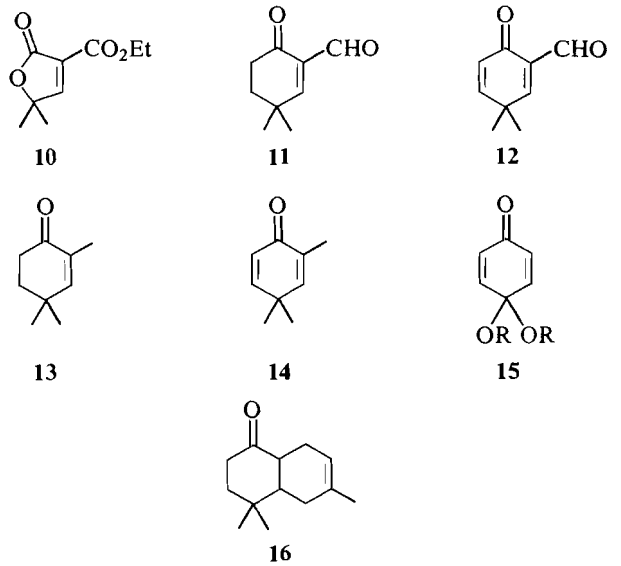

10 **11** **12**

13 **14** **15**

16

mixtures contain *para* and *anti-para* adducts of isoprene in equal or nearly equal amounts (12, 13).[3]

The preparation of **6**, the key intermediate in the synthesis of himachalenes in 68% yield (four step) from **4** is a significant improvement over the previous approach (4), which accomplished the conversion of **4** to **6** in 37% yield (five steps). This improved approach, formally giving the key intermediate **16** in 58% yield (five steps) from **4**, remains superior in both its regiospecificity and in overall yield to a recently reported direct approach to this intermediate (12), which gives a 38% yield of the correct regioisomer (as a *cis*/*trans* mixture) contaminated with an equal amount of the difficultly separable incorrect regioisomer.

Conclusion

Further to our previous illustration of the role of catalyst selection in the regiochemistry of Diels–Alder additions, the effect of a remote structural feature such as the cross-conjugated double bond in this dienophile system has been shown to play a significant role in the regiochemical and stereochemical outcome of the Diels–Alder reaction. That such an effect may occur through slight modifications of steric and electronic environments of the substrate serves to draw increased attention to the importance of secondary orbital effects in cycloadditions.

Experimental

General

Melting points were determined on a Kofler hot stage apparatus and are uncorrected. Elemental analyses were performed by the microanalytical laboratory of this department. The ir spectra were recorded on a Nicolet 7199 FT-IR spectrophotometer and were obtained in neat film. The ^{1}Hmr and ^{13}Cmr spectra were recorded on a Bruker AM 300 spectrometer and were obtained on solutions in deuteriochloroform using tetramethylsilane as internal reference. Mass spectra (ms) were recorded using an A.E.I. model MS 50 mass spectrometer. Unless stated otherwise, anhydrous magnesium sulfate was used for drying organic solutions.

4,4-Dimethylcyclohexanone

A solution of 13.026 g (0.105 mol) of enone **4** (6) in ethyl acetate

[3]The specificity of the dehydro derivatives of **4** and **13**, **2** and **14** respectively, for *anti-para* addition and generation of equal mixtures of *para* and *anti-para* adducts of ketals **15** (R = Me or Et or R,R = $-CH_2CH_2-$), has already been demonstrated (2, 14, 15).

Can. J. Chem. Downloaded from www.nrcresearchpress.com by 112.217.228.212 on 09/07/12
For personal use only.

Can. J. Chem. Downloaded from www.nrcresearchpress.com by 112.217.228.212 on 09/07/12
For personal use only.

(200 mL) was hydrogenated using palladium on activated carbon (260 mg) as catalyst at 15 psi (1 psi = 6.9 kPa) for 3 h. Filtration (with a layer of Celite) and concentration of the reaction mixture gave the product (12.772 g, 96% yield) as a white solid; mp 44–45°C (lit. (16) mp 38–40°C); ir: 1706 (C = O) cm^{-1}; ^{1}Hmr δ:1.10 (s, 6H, 2 × CH_3), 1.67 (t, 4H, J = 7 Hz, 2 × -CH_2-), and 2.35 (t, 4H, J = 7 Hz, 2 × -CH_2CO-). *Exact Mass* calcd. for $C_8H_{14}O$: 126.1045; found (ms): 126.1046.

4,4-Dimethyl-2-carbomethoxycyclohexanone (5)

Sodium hydride (80% dispersion in oil, 3.108 g, 0.103 mol, washed with petroleum ether and DME (freshly distilled over sodium/benzophenone)) was suspended in DME (40 mL) under an atmosphere of argon, and dimethyl carbonate (21.998 g, 0.244 mol) was added. The suspension was heated at reflux while stirring with a mechanical stirrer. A solution of 5.967 g (0.047 mol) of 4,4-dimethylcyclohexanone in DME (15 mL) was added dropwise. Heating was continued for 3 h and then the mixture was cooled to 0°C. An aqueous 10% acetic acid solution (100 mL) was added dropwise with stirring and the mixture was extracted with ether (3 × 50 mL). The extracts were washed with water, saturated aqueous sodium bicarbonate, water and saturated aqueous sodium chloride, dried, filtered, and concentrated. Flash chromatography of the residue on silica gal, eluting with 3–14% ether in petroleum ether, gave keto ester **5** (7.778 g, 85% yield) as a light yellow liquid. This compound existed mostly (~94% by ^{1}Hmr integration) in the corresponding enol form. The following ir and ^{1}Hmr data were attributed to the enol form: ir: 1659 (ester) and 1620 (enol) cm^{-1}; ^{1}Hmr δ:0.95 (s, 6H, -CH_3), 1.44 (t, 2H, J = 6 Hz, —CH_2—CH_2—C(OH)=), 2.03 (t, 2H, J = 1 Hz, —CH_2—C=), 2.29 (tt, 2H, J = 6, J' = 1 Hz, —CH_2—C(OH)=), 3.75 (s, 3H, -OCH_3), and 12.15 (s, 1H, =C—OH). The following ir and ^{1}Hmr data were attributed to the keto form: ir: 1750 (ester) and 1720 (ketone) cm^{-1}; ^{1}Hmr δ:1.07 (s, 3H —CH_3), 1.19 (s, 3H, —CH_3), and 3.75 (s, 3H, —OCH_3). *Exact Mass* calcd. for $C_{10}H_{16}O_3$: 184.1100; found (ms): 184.1101.

4,4-Dimethyl-2-carbomethoxy-2-cyclohexen-1-one (3)

At 0°C, pyridine (2.82 g, 0.036 mol) was added to a solution of phenylselenenyl chloride (6.89 g, 0.036 mol) in dichloromethane (200 mL) under an argon atmosphere. After stirring for 10 min, keto-ester **5** (5.529 g, 0.03 mol) in 30 mL of dichloromethane was added. After 4 h, the reaction mixture was washed with 1 M aqueous hydrochloric acid (2 × 100 mL). The organic solution was placed in a flask and cooled to 0°C. A 30% aqueous hydrogen peroxide solution (6 mL) was added. After stirring for 10 min, an additional 6 mL of 30% aqueous hydrogen peroxide was added. After 1.5 h, water was added and the layers separated. The organic layer was washed with saturated aqueous sodium bicarbonate, dried, filtered, and concentrated. The residue was distilled in a Kugelrohr apparatus at reduced pressure (aspirator) and enone-ester **3** (5.246 g, 96% yield) was obtained as a yellow oil; ir: 1747 (ester), 1719 (conjugated ester and ketone), and 1698 (conjugated ketone) cm^{-1}; ^{1}Hmr δ:1.24 (s, 6H, 2 × -CH_3), 1.90 (m, 2H, -CH_2-), 2.54 (m, 2H, -CH_2—C-), 3.80 (s, 3H, -OCH_3), and 7.36 (t, 1H, J = 1 Hz, =CH—). *Exact Mass* calcd. for $C_{10}H_{14}O_3$: 182.0943; found (ms) 182.0943.

8a-Carbomethoxy-4,4,6-trimethyl-3,4,4a,5,8,8a-hexahydro-1(2H)-naphthalenone (6)

At 0°C, anhydrous tin(IV) chloride (0.18 mL, 1.5 mmol) was added to a solution of enone-ester **3** (0.273 g, 1.5 mmol) and isoprene (3 mL, 30 mmol) in ether (11 mL; freshly distilled over sodium and benzophenone). The reaction mixture was stirred at room temperature under an atmosphere of argon for 18 h. Saturated aqueous sodium bicarbonate (6 mL) was added and the resulting mixture was extracted with ether. The extracts were washed with water, dried, filtered, and concentrated. Flash chromatography of the residue on silica gel, eluting with 10–20% ether in Skelly B, gave keto-ester **6** (0.329 g, 87% yield) as a colourless oil; ir: 1744, 1730 (ester), and 1709 (ketone) cm^{-1}; ^{1}Hmr δ:5.38 (m, 1H, -CH=), 3.72 (s, 3H, -OCH_3), 1.64 (d, 3H, =C—CH_3), 1.11 (s,3H, -CH_3), and 1.01 (s, 3H, -CH_3); ^{13}Cmr δ: 209.3 (C1), 173.7 (-COO-), 132.0 (C6), 117.6 (C7), 59.6 (C8a), 52.5 (-OCH_3), 44.8 (C4a), 38.5, 35.6, 33.4 (C2, C3, C4), 30.7 (-CH_3), 29.6, 28.6 (C5, C8), 23.8, and 23.5 (2 × -CH_3). *Exact Mass* calcd. for $C_{15}H_{22}O_3$: 250.1569; found (ms): 250.1571. *Anal.* calcd. for $C_{15}H_{22}O_3$: C 71.97, H 8.86; found: C 72.09, H 8.77.

Using the same procedure, Diels–Alder reactions of enone-ester **3** and isoprene were carried out with different Lewis acid catalysts. The results are summarized in Table 1.

Acknowledgements

We are grateful to the Natural Sciences and Engineering Research Council of Canada and the University of Alberta for financial support.

1. H. J. Liu and E. N. C. Browne. Tetrahedron Lett. 2919 (1977).
2. H. J. Liu and E. N. C. Browne. Can. J. Chem. **57**, 377 (1979).
3. H. J. Liu and E. N. C. Browne. Can. J. Chem. **65**, 1262 (1987).
4. H. J. Liu and E. N. C. Browne. Can. J. Chem. **59**, 601 (1981).
5. E. N. C. Browne. Ph.D. thesis, The University of Alberta. 1980.
6. R. L. N. Harris, F. Komitsky, and C. Djerassi. J. Am. Chem. Soc. **89**, 4765 (1967).
7. L. A. K. Nelson. Ph.D. thesis, The University of Alberta. 1986.
8. H. J. Liu, E. N. C. Browne, and P. R. Pednekar. Can. J. Chem. **60**, 921 (1982).
9. W. L. Meyer, M. J. Brannon, C. G. Burgos, T. E. Goodwin, and R. W. Howard. J. Org. Chem. **50**, 438 (1985).
10. H. V. Secor, M. Bourlas, and J. F. Debardeleben. Experientia, **27**, 18 (1971).
11. D. Liotta, C. Barnum, R. Puleo, G. Zima, C. Bayer, and H. S. Kezar. J. Org. Chem. **46**, 2920 (1981).
12. F. Fringuelli, F. Pizzo, A. Taticchi, and E. Wenkert. Synth. Commun. **16**, 245 (1986).
13. E. C. Angell, F. Fringuelli, L. Minuti, F. Pizzo, A. Taticchi, and E. Wenkert. J. Org. Chem. **51**, 5177 (1986).
14. F. Fringuelli, L. Minuti, F. Pizzo, A. Taticchi, T. D. J. Halls and E. Wenkert. J. Org. Chem. **48**, 1810 (1983).
15. M. C. Carreno, F. Farina, A. Galan, and J. L. G. Ruano. J. Chem. Res. (S), 370 (1981); J. Chem. Res. (M), 4310 (1981).
16. Dictionary of organic compounds. 5th ed. Vol. 2. Chapman and Hall, New York, NY. 1982. p. 2110.

Electron microprobe studies of chemical reactions in ancient painted murals: The Beni Hasan Tombs, Egypt[1]

K. M. WILSON-YANG AND GEORGE BURNS
Lash Miller Chemical Laboratories, University of Toronto, Toronto, Ont., Canada M5S 1A1

Received August 31, 1987[2]

K. M. WILSON-YANG and GEORGE BURNS. Can. J. Chem. **66**, 2348 (1988).

The Egyptian tombs at Beni Hasan (ca. 2100 B.C.) have developed an ubiquitous, progressive grey surface layer which disfigures their painted surfaces. Recently, we published a series of X-ray photoelectron spectra of samples from these tombs and proposed a mechanism for surface layer formation. It involves CO_2-saturated condensed water which gradually erodes the mural substrate. However, no direct evidence for this erosion was available. To test the proposed mechanism, light microscopy was used to study cross-sections of the murals. Areas of repeated solution and precipitation, in the form of dendritic structures were discovered in the subsurface regions, especially in yellow pigmented samples. In red pigmented samples, this degradation is not seen to the same extent. A series of electron microprobe analyses of the surface and subsurface regions of small painted fragments also were performed. Porous, heterogenous subsurface regions with pockets of phosphates have been found, predominantly in the yellow samples. These findings support the mechanism proposed earlier. Pore size measurements, estimated by photographic measurements, indicate that subsurface alteration took place before the bulk of the surface deposit layer had formed and that the existing surface deposit protects, as well as obscures, the painted walls. The surface layer development described here has some aspects common to other natural systems, i.e. the interaction of CO_2 in water with carbonate-bearing rocks and deposits. However, at Beni Hasan there is effectively no source of groundwater and the painted surfaces are sheltered from direct exposure to the environment. Therefore the Beni Hasan deterioration has unique mechanistic features.

K. M. WILSON-YANG et GEORGE BURNS. Can. J. Chem. **66**, 2348 (1988).

Les tombes égyptiennes à Beni Hasan (environ 2100 B.C.) ont développées une couche superficielle grise qui défigure progressivement les surfaces peintes. Récemment, on a publié une série de spectres photo-électroniques des rayons-X effectués sur des échantillons provenant de ces tombes et on a proposé un mécanisme pour expliquer la formation de ces couches superficielles. Il implique de l'eau saturée par du CO_2 qui provoque une érosion graduelle des murales. Toutefois, on ne possédait aucune donnée directe concernant cette érosion. Afin de vérifier le mécanisme proposé, on a utilisé la microscopie lumineuse pour étudier des sections droites des murales. Sous la surface, on a découvert des surfaces ayant subi des solutions et précipitations répétées, sous la forme de structures dendritiques et particulièrement dans les échantillons pigmentés avec du jaune. Dans les régions pigmentées en rouge, on n'a pas observé un tel degré de dégradation. On a aussi effectué une série d'analyses par micro-sondes électroniques à la surface et dans les régions sous la surface de petits fragments peints. Dans les échantillons pigmentés en jaune, on a observé sous la surface des régions poreuses et hétérogènes qui forment des poches de phosphates. Ces résultats sont en accord avec le mécanisme proposé antérieurement. Des mesures faites à l'aide de photographies ont permis de déterminer la grosseur des pores; elles indiquent que les modifications qui se sont produites sous la surface sont antérieures au dépôt de la couche que l'on retrouve en surface et que les dépôts qui se sont faits sur la surface existante protège, et en même temps obscurcissent, les peintures murales. Le développement de la couche superficielle qui est décrit ici ressemble à d'autres systèmes naturels comme l'interaction du CO_2 de l'eau avec les roches et les dépôts contenant du carbonate. Toutefois, à Beni Hasan il n'y a effectivement pas de source d'eau dans le sol et les surfaces peintes sont protégées d'une exposition directe à l'environnement. La détérioration observée à Beni Hasan possède donc des caractéristiques mécanistiques unique.

[Traduit par la revue]

Introduction

The Beni Hasan tombs are man-made structures, cut in the cliffs overlooking the east bank of the Nile River. Their environment is essentially desert, although irrigation and agriculture are practised in the plain below them. The walls of these tombs are obscured by an opaque deposit (1) consisting of calcite ($CaCO_3$) and sand components (2, 3). Earlier studies (4) indicate that this deposit is recent, accelerating and progressive. Such deterioration is often evidence of environmental disturbances. This paper is concerned with the development of this surface degradation.

Several mechanisms for the formation of the disfiguring layer at Beni Hasan have been proposed (1–3). A recent X-ray photoelectron spectroscopic (XPS) study (5) indicated that none of these mechanisms is complete: neither the recent formation of the surface layer nor the consequences to the subsurface regions had been previously recognized or predicted. It was possible to propose a mechanism which predicted subsurface deterioration. However, this mechanism was based on information from XPS analyses which provides information only at the nanometer level on the painted surfaces.

To assess this new mechanism it was necessary to look beyond the nanometer level into the regions of the bulk surface deposit and into the subsurface structure of the painted walls. In studies below, electron microprobe analyses and light microscopy have been used to establish the elemental compositions and structural characteristics, respectively, of small, authentic fragments of the painted walls. These procedures provide cross-sectional information from the first few micrometers of the surface deposit into the rock substrate to a depth of several hundred micrometers.

[1]Based on the Progress Report, submitted to the Egyptian Antiquities Organization, Cairo, January 1987.

[2]Revision received March 31, 1988.

Can. J. Chem. Downloaded from www.nrcresearchpress.com by 112.217.228.212 on 09/07/12
For personal use only.

TABLE 1. Sample descriptions, origins, sampling heights above tomb floor and surface layer thickness

Sample designation	Origin	Sampling height (m)	Surface layer thickness (μm)
15-I[a]Y	Tomb 15, yellow	1.8	50–60[b]
15-IR[c]	Tomb 15, red	2.3	20–25
17-IY	Tomb 17, yellow	2.3	60–65[b]
33-IR[c]	Tomb 33, red	1.5	20–70
33-IRY(a)	Tomb 33,[d] red, ca. 600 A.D./ yellow, ca. 2150 B.C.	1.5	30–50
33-IRY(b)	Tomb 33, red, ca. 2150 B.C.	1.5	30–50
33-IRY(c)	Tomb 33, red, ca. 600 A.D.	1.5	30–50
2-M[e]RC[c]	Tomb 2, red, cleaned	1.8	20–35
3-MY[c]	Tomb 3, yellow	1.2	—
3-MR[c]	Tomb 3, red	1.2	15–20
3-MRC	Tomb 3, red,[f] cleaned	1.2	25–45[b]
2-MR	Tomb 2, red	0.9	15–20
2-MY	Tomb 2, yellow	2.1	50–75[b]
23-MY(a)[c]	Tomb 23, yellow	2.3	30–75[b]
23-MY(b)	Tomb 23, yellow	2.3	50–70[b]

[a]First intermediate period: I.
[b]Surface layer and apparent pigment.
[c]XPS sample, see ref. 5.
[d]The sample was taken near the edge of a Coptic cross which had been incised into a wall of Tomb 33 and then outlined in red. The surfaces of Tomb 33 are uniformly blackened and are assumed to have suffered smoke damage.
[e]Middle Kingdom: M.
[f]Sample presentation allows the analysis of the subpigment and rock regions only.

Experimental

Sampling

Samples were selected on the basis of the appearance of the surface layer and the historical importance of the tomb of origin. Since surface degradation processes and underlying transport phenomena were to be investigated, only red and yellow pigmented samples were assembled. This reduced the number of variables involved in the interpretation of results. The samples were removed from the wall surfaces with a stainless steel scalpel, handled with disposable plastic gloves. Care was taken not to remove any archaeological information and/or unique painted features. Samples were stored in pre-cleaned, plastic, screw-topped vials (PROVIAL and NALGENE) packed with glass wool and sealed with strips of PARAFILM (American Can).

Table 1 provides descriptions of the samples. The sample number is built up from four pieces of information: the number of the tomb of origin (as assigned in the Egyptological literature (6)), the period in which the tomb was constructed (6, 7) and the sample's apparent colour. Thus, sample 15-IY is from Tomb 15, which was constructed in the First Intermediate Period "I", and the sample's colour is yellow, "Y". Middle Kingdom tombs are designated "M" and red samples are denoted with "R". The designation "C" indicates that the sample had been cleaned, on site, by conservators. Cleaning of mural surfaces has taken place intermittently for the last 20 years and has involved the use of HCl. Subsamples with identical sample numbers after all designations were made, are further noted by (a), (b), or (c).

Photography

Specimens were photographed under reflected light using a Wild-Leitz 160959 Microscope and also by plane-polarized light using a Leitz petrographic microscope with and without crossed-nicols. Both black and white film (Kodak PANATOMIC X) and colour slide film (Kodak EKTACHROME W) were employed. Measurements of layer thicknesses, particle-size estimates and pore-size estimates were made using graticules photographed on the same film as were the samples.

Electron microprobe analyses

Samples were grain-mounted in discs of epoxy resin (METSET SW, Metaserv). Cross-sections were exposed by cutting perpendicular to the painted surface with a diamond saw (Buehler ISOMET). The cross-sections were polished with alumina powders and diamond polishing preparations and then coated with a layer of carbon approximately 10 μm thick to minimize charging effects during analysis.

All analyses were performed on an ETEC electron microprobe controlled by a PDP-11 computer at the University of Toronto. Samples were fitted into a moveable stage and were observed directly by an off-angle refracting optics microscope (8) fitted on the sample chamber. Spectra were collected using a focussed beam 1 μm in diameter at an energy of 20 keV for a fixed time of 100 s. The analyzed spot size was approximately 2 μm in diameter due to electron beam spreading in the sample, as estimated from the cathodoluminscence of a willamite standard. The coordinates of the focussed beam were known at all times. No element with $Z < 11$ can be detected by electron microprobe.

Results

Photography

The cross-sectional photographs show that in general, the Beni Hasan samples have four layer structures: a surface deposit layer or encrustation, a pigmented layer, a subpigment region, and a rock substrate. This is unusual in that only two or three layer structures should have been observed.

On the whole, the surface deposit layer appears as a heterogeneous coating ranging in thickness from 15 to 70 μm. Individual grains, ranging in diameter from 5 to 20 μm can be seen (Fig. 1). This suggests that sediments are of wind-borne origin which are typically ≤50 μm (9) in size. The estimated pore width in the surface deposit layer ranges from ≤5 to 10 μm in all samples. Ranges of surface deposit layer thicknesses are given in Table 1 for each sample.

Pigmented layers are seen below the surface encrustation in all red samples (Fig. 1). These pigment layers have an average thickness of 30 ± 10 μm. In the yellow samples, the distinc-

Can. J. Chem. Downloaded from www.nrcresearchpress.com by 112.217.228.212 on 09/07/12
For personal use only.

Can. J. Chem. Downloaded from www.nrcresearchpress.com by 112.217.228.212 on 09/07/12
For personal use only.

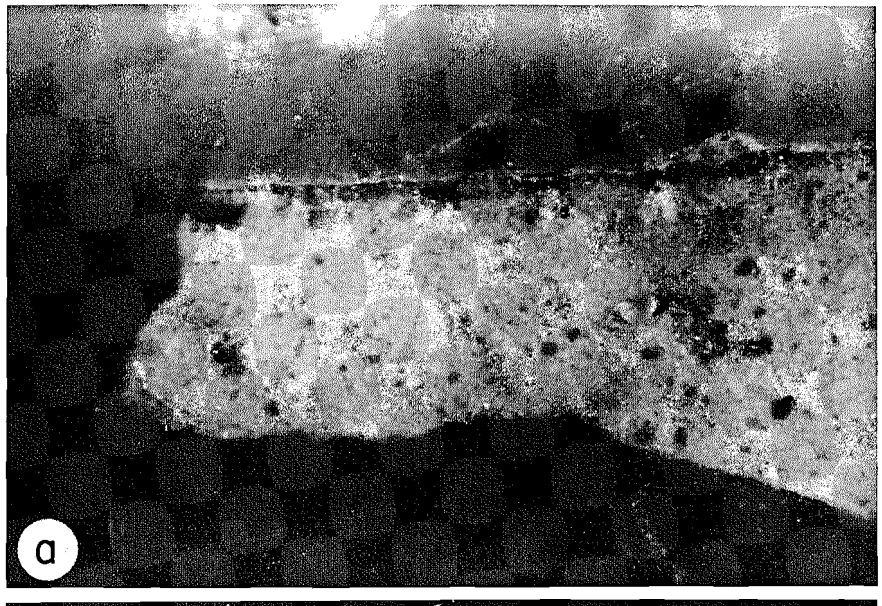

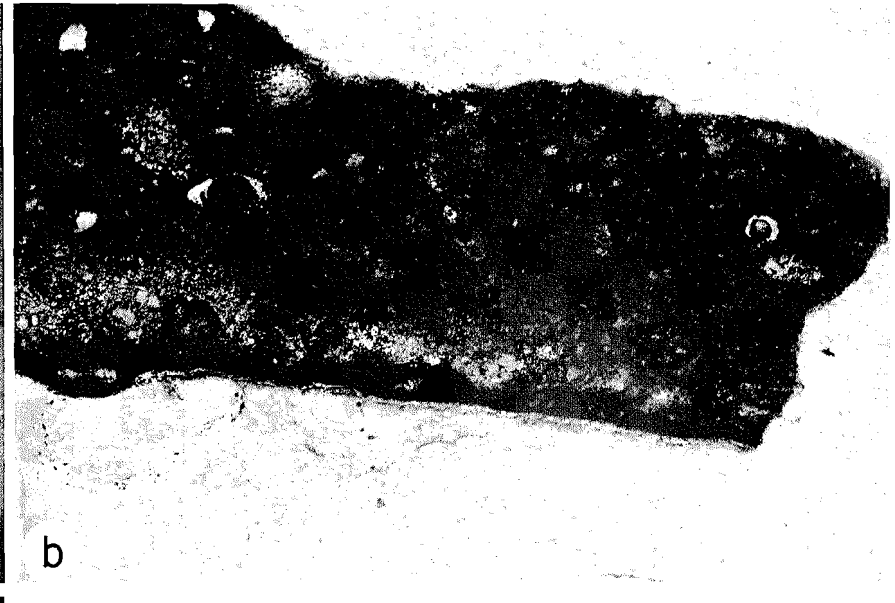

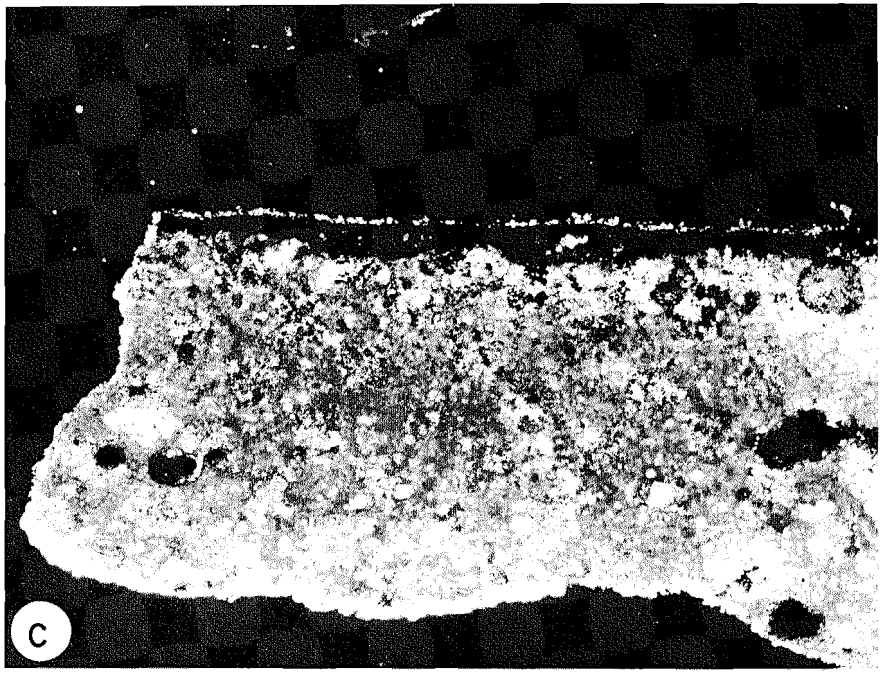

FIG. 1. Sample 2-MRC in cross-section: this sample has a red pigment layer which is visible under a granular surface deposit. The sample was removed from a portion of a painting in Tomb 2 which had been cleaned approximately 20 years ago. The sample cross-section is 700 μm in width at its widest point. (*a*) Photograph taken under reflected light; magnification 50× on 35 mm negative; three layers are visible: surface deposit, pigment, and substrate rock. (*b*) Photograph taken under plane-polarized light; magnification is 63× on a 35 mm negative. (*c*) Photograph taken under crossed-nicols; magnification is 63× on a 35 mm negative.

Can. J. Chem. Downloaded from www.nrcresearchpress.com by 112.217.228.212 on 09/07/12
For personal use only.

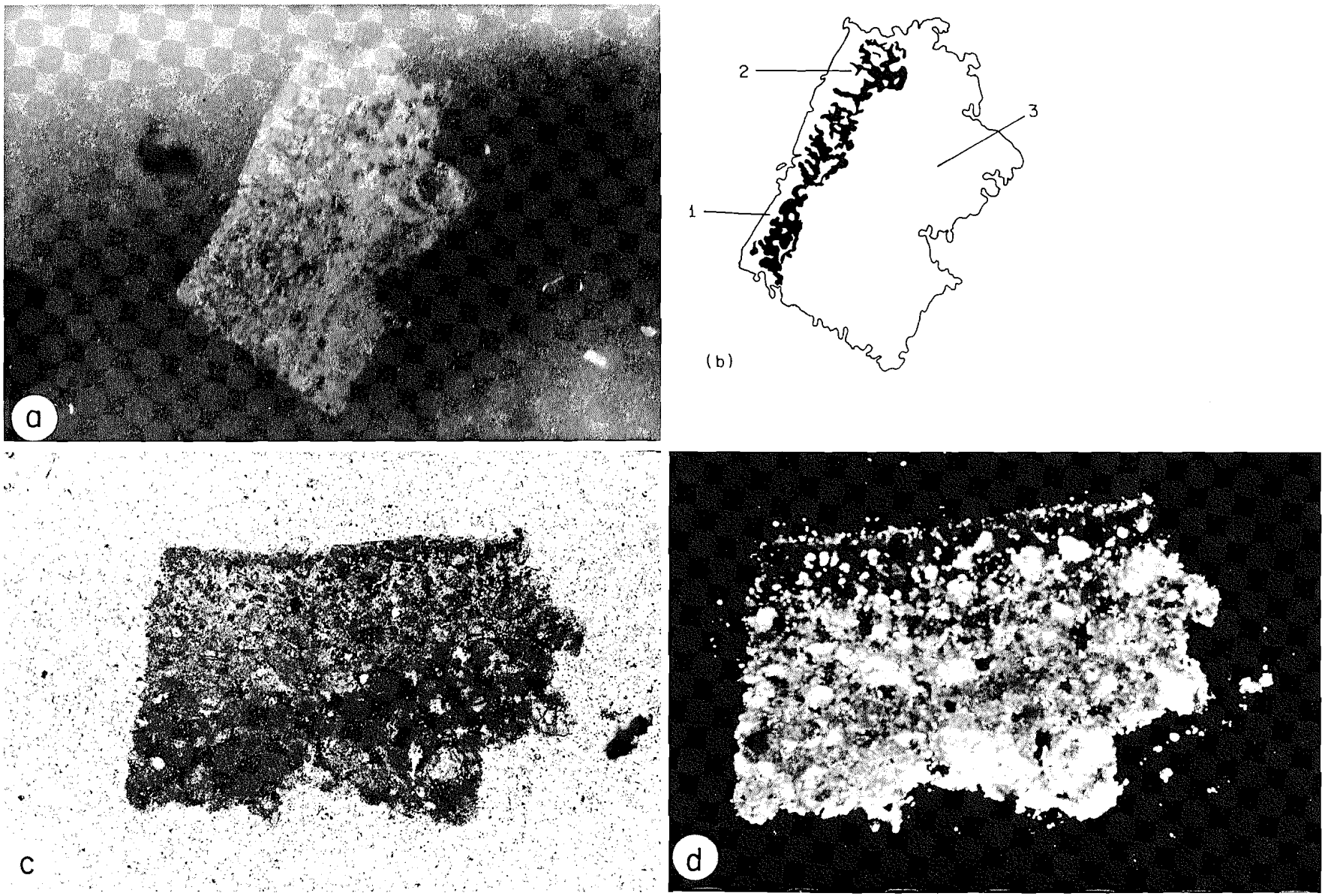

FIG. 2. Sample 23-MY(a) in cross-section: this sample is a yellow pigmented fragment from Tomb 23. A clearly defined pigment layer is not seen, instead a visually inhomogeneous, dendritic, subsurface region appears under magnification. (*a*) Photograph taken under reflected light; magnification 50× on a 35 mm negative; the sample cross-section is 620 μm in width at its widest point. (*b*) Schematic of (*a*) showing surface: *1*; dendritic layer: *2*; and substrate rock: *3*. (*c*) Photograph is taken under plane-polarized light; magnification is 63× on a 35 mm negative. The dendritic region is dark. (*d*) Photograph is taken under crossed-nicols; magnification is 63× on 35 mm negative. The dendritic layer remains dark thus indicating a region of porosity or microcrystalline material.

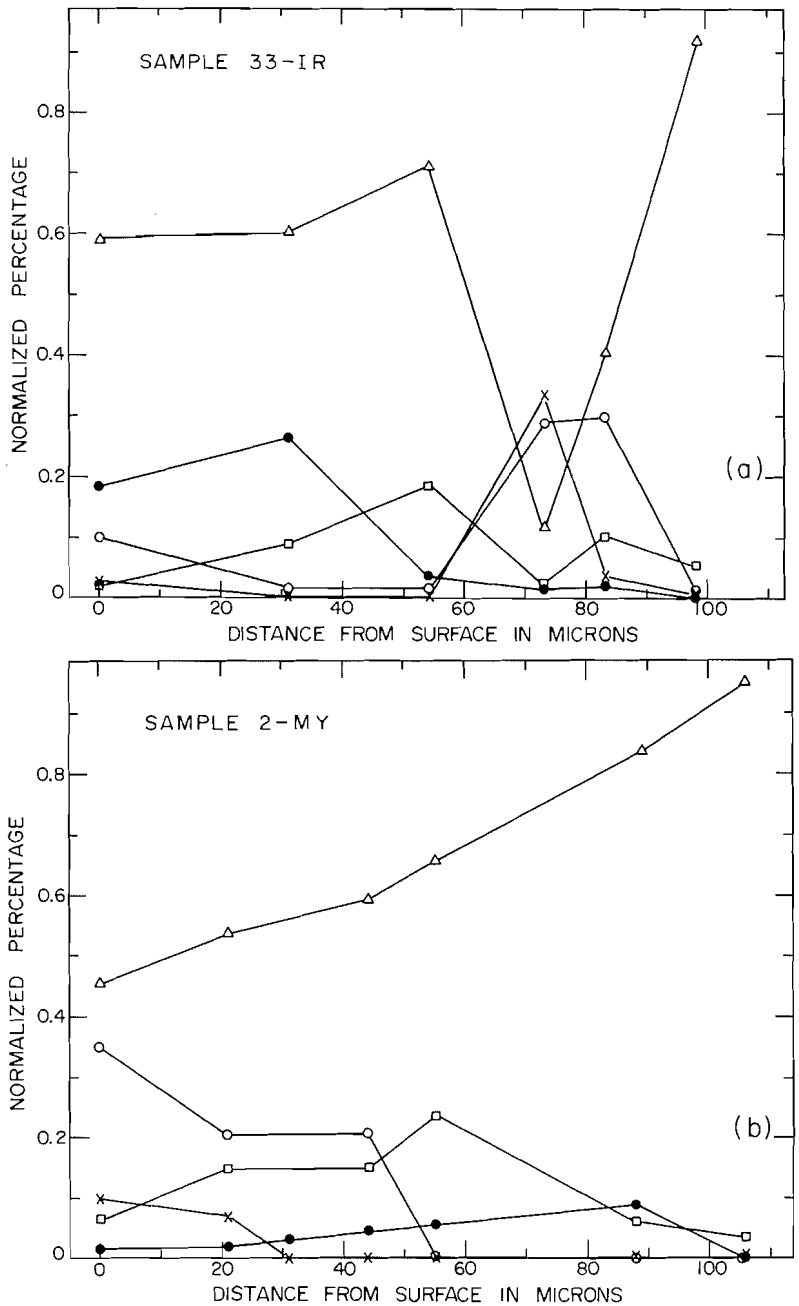

FIG. 3. Cross-sectional scans of Beni Hasan fragments. The abscissa is measured in microns from the beginning of the surface deposit. The ordinate is normalized elemental weight percent. The elements are identified as follows:

△, Ca; ○, Si; □, P; ×, Fe; ●, S.

Errors are estimated as 1 s.d. based on the sample-average s.d. (Table 3). (*a*) Sample 33-IR. The pigment layer is identified by the Fe peak between 70 and 80 μm. Ca and S both drop in this region. (*b*) Sample 2-MY. No Fe maximum is seen. Phosphorus attains a plateau above rock levels between 20 and 60 μm.

tion between the surface layer, the pigment layer and the subpigment region is not as well defined.

In five of the red-pigmented samples, 2-MRC, 2-MR, 3-MRC, 3-MR, and 15-IR, and in two of the six yellow-coloured samples, 15-IY and 3-MY, the surface deposit is found directly upon the pigment layer which in turn appears to be placed directly on the rock substrate. The rock substrate has a pore width of ≤5 μm. In sample 33-IR, a dark subpigment layer 35 to 70 μm thick with an estimated pore width of 40 μm is visible under crossed-nicols and, in sample 33-IRY(b), a white opaque layer 50 to 100 μm in thickness is seen below the pigment by reflected light. Three of the yellow samples, 2-MY, 23-MY(a), and 23-MY(b) display a region with irregularly branched or dendritic features with a pore or dendrite width range of 20–90 μm extending 55 to 230 μm under the surface encrustation. By reflected light, this dendritic region is opaque white and grey; it is dark when observed under plane-polarized light as well as through crossed-nicols (Fig. 2). The dark regions seen under crossed-nicols can indicate (*a*) a total lack of material, (*b*) a region of high porosity, (*c*) the presence of microcrystalline or amorphous material, i.e., with particle size <5 μm. Because of the white appearance of these regions under reflected

Can. J. Chem. Downloaded from www.nrcresearchpress.com by 112.217.228.212 on 09/07/12
For personal use only.

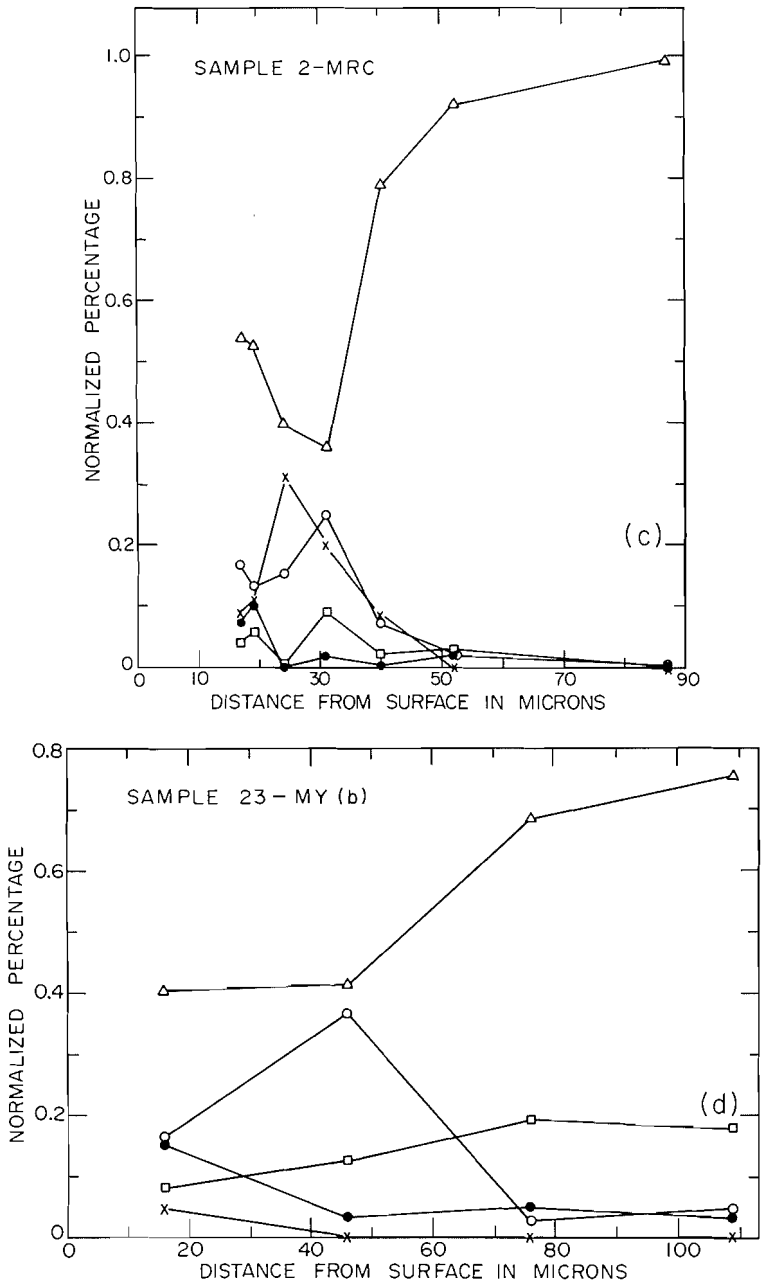

FIG. 3. (*c*) Sample 2-MRC. This scan shows similar features to 33-IR. The Fe peak is situated between 20 and 30 μm. (*d*) Sample 23-MY(b). Si peaks between 40 and 50 μm. There is a high phosphorus plateau extending past 100 μm from the surface. This indicates movement of soluble phosphates downward under the action of solvent with movement of soluble substrate material upward. Ca at 100 μm is lower than that in Fig. 3 (*a*)–(*c*).

light, either one of the latter two explanations is probable. The remaining yellow sample, 17-IY, has granular, dendritic subpigment region, but it did not appear dark under crossed-nicols. The significance of these dendritic regions is discussed in detail below.

Electron microprobe

Peak areas from the electron microprobe spectra were reduced to elemental weight-percentages by a ZAF procedure (10, 11) which uses calibration data from standard minerals.[3] If samples and standards are well-matched both in composition and homogeneity, accurate elemental analysis of the sample can be obtained. However, because the samples studied were both multilayered and heterogeneous, standards cannot match the samples well. None the less, it is possible to establish the error associated with the method of analysis using the ZAF procedure and standard minerals of known composition containing the same elements as the unknowns but in different matrices. The inherent error due to this method of quantification is 10% for major elements and 50 to 100% for elements near the detection limit. The detection limit is estimated as 0.5% by weight which translates as 0.01 normalized percent.

Samples were analyzed to establish (*i*) the average elemental compositions of each identifiable layer in each sample, referred

[3]The standard minerals were apatite: $Ca_5F(PO_4)_3$, pyrite: FeS, diopside: $CaMgSi_2O_6$ and scapolite: a silicate mineral without a well-defined composition which includes sodium, calcium, chlorine, sulphur and CO_3^{2-}.

Can. J. Chem. Downloaded from www.nrcresearchpress.com by 112.217.228.212 on 09/07/12
For personal use only.

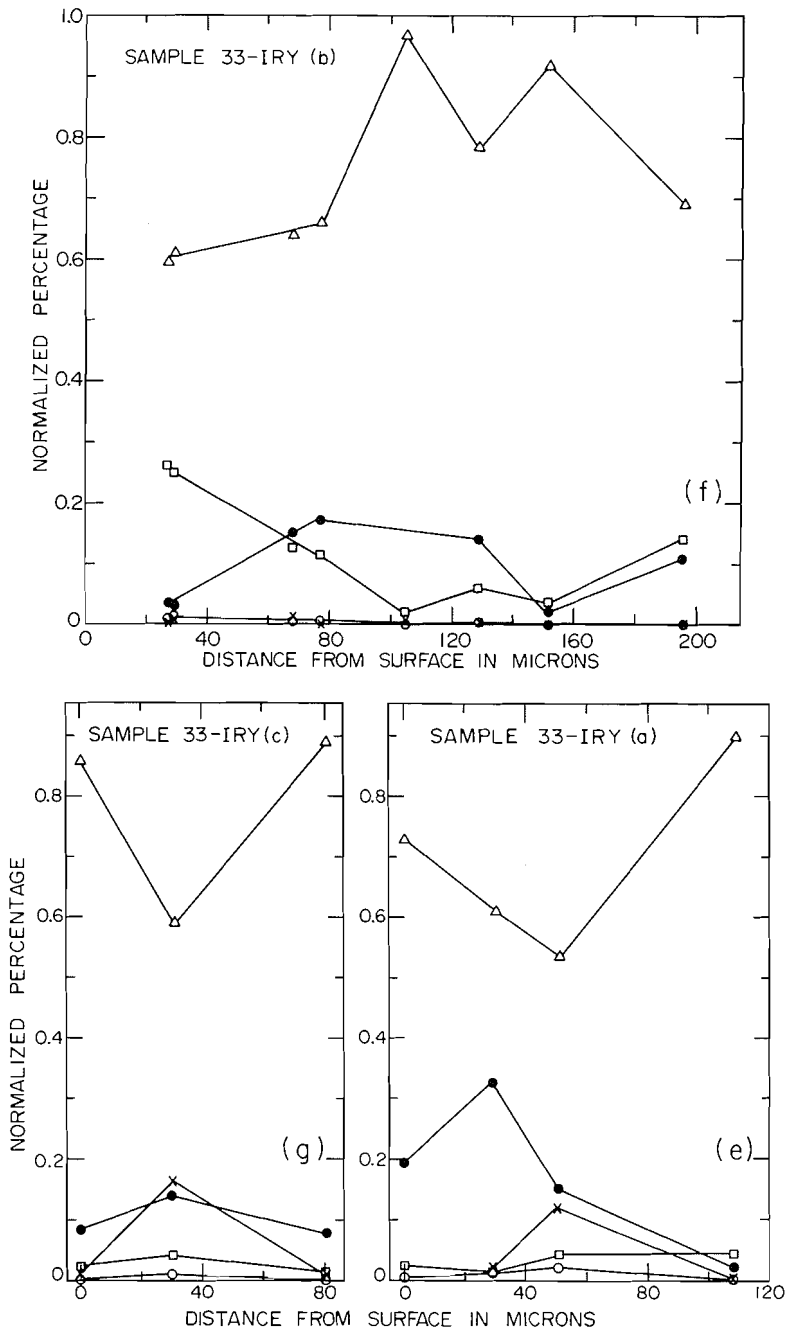

FIG. 3. (*e*) Sample 33-IRY(a) shows a Fe maximum from a Coptic (600 A.D.) red pigment. (*f*) Sample 33-IRY(b) appeared red. It has a high phosphorus content between 30 and 80 μm but has no indication of a red pigment. (*g*) Sample 33-IRY(c) has an Fe maximum from a Coptic (600 A.D.) red pigment.

herein as sample-averages and (*ii*) the average elemental composition of all four layers throughout the site as a whole, referred to as site-averages. Individual analyses performed at known distances were assembled to obtain elemental composition as a function of depth in the sample (Fig. 3).

The elemental weight percentages were normalized by dividing them by the total percentage of analyzed elements in each analysis. The analysis totals are indicators of the density of matter, excluding elements which have $Z < 11$, in the analysis region. The analysis totals are affected by surface roughness and by inherent porosity. Analysis totals have been correlated to porosity (12) and to degree of vitrification (13) in ceramic ware. Elemental weight-percentages have been normalized by dividing them by the analysis totals to obtain elemental normalized percentages. This normalization procedure removes variations between samples as well as fluctuations in instrument conditions during analysis. It does not remove the effects of inhomogeneous elemental spatial distributions. The elemental normalized percentages form the body of the data used for comparisons among samples and among layer structures.

Site-averages

The sample-average values for each element were used to calculate averages for each element for the whole site. These site-averages, their pooled standard deviations (14), and 95% confidence limits for Ca, P, S, Si, Fe, Al, Cl, Na, Mg, and K

Can. J. Chem. Downloaded from www.nrcresearchpress.com by 112.217.228.212 on 09/07/12
For personal use only.

TABLE 2. Electron microprobe analysis: site-averages, total analysed elements; elemental normalized percents; weight percent compounds

Layer; total elements[a]	Element	Site-averages norm. percents ± 95% C.I.	Weight percent compounds ±95% C.I.	Compound
Surface	Ca	0.59±0.06	27±3[b]	$CaCO_3$[c]
$\bar{x} = 35 \pm 5$[a]	Si	0.08±0.04	6±3	SiO_2
$n = 28$[d]	P	0.07±0.03	12±5	$Ca_3(PO_4)_2$
$k = 7$[e]	S	0.14±0.03	21±4	$CaSO_4 \cdot 2H_2O$
	Fe	0.03±0.02	1.4±0.9	Fe_2O_3
	Al	0.03±0.02	2±1	Al_2O_3
	Cl	0.04±0.05	1±2	Cl
	Na	0.01±0.01	0.3±0.3	Na
	Mg	0.01±0.01	0.3±0.3	Mg
	K	0.01±0.01	0.3±0.3	K
Pigment	Ca	0.4 ±0.2	13±6	$CaCO_3$
$\bar{x} = 44 \pm 5$	Si	0.06±0.08	6±8	SiO_2
$n = 14$	P	0.03±0.03	8±8	$Ca_3(PO_4)_2$
$k = 4$	S	0.12±0.09	30±20	$CaSO_4 \cdot 2H_2O$
	Fe	0.3 ±0.2	20±10	Fe_2O_3
	Al	0.05±0.05	4±4	Al_2O_3
	Cl	0.02±0.01	0.9±0.4	Cl
	Na	0.01±0.01	0.4±0.4	Na
	Mg	0.01±0.01	0.4±0.4	Mg
	K	0.01±0.02	0.4±0.8	K
Subpigment	Ca	0.68±0.05	26±2	$CaCO_3$
$\bar{x} = 36 \pm 4$	Si	0.03±0.04	2±3	SiO_2
$n = 42$	P	0.11±0.03	20±5	$Ca_3(PO_4)_2$
$k = 11$	S	0.14±0.04	26±8	$CaSO_4 \cdot 2H_2O$
	Fe	0.01±0.02	0.4±0.8	Fe_2O_3
	Al	0.01±0.01	0.7±0.7	Al_2O_3
	Cl	0.01±0.01	0.4±0.4	Cl
	Na	0.01±0.01	0.4±0.4	Na
	Mg	0.01±0.01	0.4±0.4	Mg
	K	0.00±0.00	0±0	K
Rock	Ca	0.89±0.06	60±4	$CaCO_3$
$\bar{x} = 32 \pm 3$	Si	0.01±0.01	0.6±0.6	SiO_2
$n = 29$	P	0.06±0.03	9±4	$Ca_3(PO_4)_2$
$k = 10$	S	0.03±0.03	5±5	$CaSO_4 \cdot 2H_2O$
	Fe	0.00±0.00	0±0	Fe_2O_3
	Al	0.00±0.00	0±0	Al_2O_3
	Cl	0.01±0.01	0.3±0.3	Cl
	Na	0.00±0.00	0±0	Na
	Mg	0.00±0.00	0±0	Mg
	K	0.00±0.00	0±0	K

[a]Total analysed elements in percent ± 95% C.I. for elements with $Z > 11$.

[b]Error is reported as a 95% confidence limit based on the compound standard deviation:

$$((s)^2_{\text{norm. percent}} + (s)^2_{\text{total}})^{1/2}$$

the normalized percentages were reconverted to elemental percentages before use in the calculation of compound percentage composition.

[c]The percentage $CaCO_3$ was calculated by first calculating the percentage $Ca_3(PO_4)_2$ and then $CaSO_4 \cdot 2H_2O$ and assigning the remainder of Ca to $CaCO_3$.

[d]Total number of analyses is denoted "n".

[e]Total number of samples is denoted "k".

are given in Table 2. Only red sample data were used to calculate site-averages for the pigment layer. The percentage composition as compounds are also given in Table 2 as a general guide only. The nature of the compounds is suggested by evidence from previous XPS analyses (5).

As a preliminary check, a one-way analysis of variance (14) was performed on the site-average values. A one-way analysis of variance is a statistical method for the simultaneous comparison of more than one mean to establish the existence of significant differences. In the current application, a one-way analysis of variance tests if the expected variance of the elemental site-average between layers is greater than the expected variance within layers. Here, the large variances contributed by individual sample-averages to the site-averages removed any significant differences between layers at the 95% level except in the cases of Fe and Ca. A pairwise t-test (14) at the 95%

Can. J. Chem. Downloaded from www.nrcresearchpress.com by 112.217.228.212 on 09/07/12
For personal use only.

TABLE 3. Electron microprobe analyses: sample-averages, $\bar{x}$; elemental normalized percent

Sample		Ca	S	P	Fe	Si	Al	Total
				I, surface				
2-MRC	$\bar{x}$	0.6	0.07 L[a]	0.04	0.07 H[b]	0.17 H	0.07 H	34
$n = 5$[c]	s.d.[d]	0.1	0.06	0.02	0.03	0.05	0.01	5
2-MY	$\bar{x}$	0.50 L	0.02 L	0.13 H	0.07 H	0.2 H	0.04	34
$n = 5$	s.d.	0.06	0.01	0.07	0.04	0.1	0.04	8
3-MR	$\bar{x}$	0.57	0.12	0.18 H	0.01	0.03 L	0.01	34
$n = 3$	s.d.	0.07	0.03	0.05	0.01	0.03	0.01	2
15-IR	x	0.64	0.05 L	0.22 H	0.01	0.01 L	0.01	41.43 H
$n = 1$								
17-IY	x	0.97 H	0.00 L	0.01 L	0.00 L	0.00 L	0.00 L	36.68
$n = 1$								
23-MY(a)	$\bar{x}$	0.64	0.2 H	0.02 L	0.01	0.05	0.02	33
$n = 5$	s.d.	0.07	0.1	0.01	0.01	0.02	0.01	5
23-MY(b)	$\bar{x}$	0.65	0.2 H	0.01 L	0.01	0.03	0.01	31
$n = 3$	s.d.	0.04	0.2	0.01	0.01	0.01	0.01	6
33-IR	$\bar{x}$	0.61	0.2 H	0.06	0.01	0.04	0.01	41 H
$n = 5$	s.d.	0.08	0.1	0.05	0.01	0.04	0.02	8
33-IRY(a)		0.73 H	0.20 H	0.02 L	0.01	0.00 L	0.01	36.39
$n = 1$								
33-IRY(b)	$\bar{x}$	0.63	0.21 H	0.06	0.01	0.03	0.01	36
$n = 3$		0.02	0.09	0.04	0.01	0.01	0.01	6
33-IRY(c)		0.86 H	0.08	0.02 L	0.01	0.00 L	0.01	39.27
$n = 1$								
				II, pigment				
2-MRC	$\bar{x}$	0.4	0.10	0.03	0.3	0.11	0.04	32 L
$n = 5$	s.d.	0.2	0.09	0.02	0.2	0.05	0.03	3
33-IR	$\bar{x}$	0.3	0.10	0.06	0.3	0.1	0.10 H	47
$n = 4$	s.d.	0.2	0.10	0.05	0.1	0.1	0.08	4
33-IRY(a)	$\bar{x}$	0.3	0.17	0.02	0.4	0.02	0.03	50 H
$n = 2$	s.d.	0.1	0.01	0.01	0.2	0.01	0.00	9
33-IRY(c)	$\bar{x}$	0.6	0.12	0.04	0.17	0.01	0.03	45
$n = 3$	s.d.	0.2	0.07	0.00	0.08	0.00	0.01	3
15-IY	x	0.38	0.05	0.08	0.10	0.22 H	0.08	31.03
$n = 1$								
				III, subpigment				
2-MRC	$\bar{x}$	0.9 H	0.01 L	0.01 L	0.02	0.03	0.01	21 L
$n = 4$	s.d.	0.9	0.01	0.01	0.04	0.03	0.01	6
2-MY	$\bar{x}$	0.64	0.03 L	0.27 H	0.00	0.01	0.00	30
$n = 3$	s.d.	0.03	0.01	0.02	0.00	0.01	0.01	20
$n = 3$	$\bar{x}$	0.8 H	0.1	0.05 L	0.00	0.01	0.00	30 L
	s.d.	0.1	0.1	0.05	0.01	0.01	0.00	10
$n = 3$	$\bar{x}$	0.66	0.04 L	0.24 H	0.00	0.00	0.00	43
	s.d.	0.00	0.01	0.01	0.00	0.00	0.00	2
3-MR	x	0.77 H	0.03 L	0.10	0.01	0.06	0.01	28.63 L
$n = 1$								
3-MY	$\bar{x}$	0.82 H	0.04 L	0.08	0.00	0.02	0.00	39.9
$n = 3$	s.d.	0.08	0.04	0.07	0.00	0.03	0.00	0.2
15-IY	$\bar{x}$	0.57 L	0.38 H	0.03 L	0.00	0.00	0.00	45
$n = 3$	s.d.	0.00	0.01	0.01	0.00	0.00	0.00	5
$n = 2$	$\bar{x}$	0.58 L	0.32H	0.07 L	0.00	0.01	0.00	50 H
	s.d.	0.01	0.00	0.00	0.00	0.00	0.00	3
$n = 3$	$\bar{x}$	0.56 L	0.39H	0.03 L	0.00	0.00	0.00	47
	s.d.	0.01	0.03	0.02	0.00	0.00	0.00	3

Can. J. Chem. Downloaded from www.nrcresearchpress.com by 112.217.228.212 on 09/07/12
For personal use only.

TABLE 3. (*Concluded*)

Sample		Ca	S	P	Fe	Si	Al	Total
17-IY	$\bar{x}$	0.61 L	0.06 L	0.13	0.02	0.08 H	0.03 H	35
$n = 6$	s.d.	0.06	0.03	0.06	0.01	0.03	0.03	6
23-MY(a)	$\bar{x}$	0.70	0.1	0.13	0.00	0.00	0.00	14 L
$n = 3$	s.d.	0.09	0.2	0.06	0.00	0.00	0.00	1
23-MY(b)	$\bar{x}$	0.6 L	0.07 L	0.13	0.00	0.2 H	0.01	22 L
$n = 2$	s.d.	0.2	0.05	0.08	0.00	0.3 H	0.01	3
33-IR	$\bar{x}$	0.7	0.05 L	0.13	0.05 H	0.03	0.02 H	36
$n = 4$	s.d.	0.2	0.00	0.08	0.08	0.04	0.03 H	4
33-IRY(a) $n = 1$		0.61 L	0.33 H	0.01 L	0.01	0.00	0.01	39.23
33-IRY(b) $n = 1$		0.58 L	0.04 L	0.24 H	0.01	0.01	0.01	55.06 H
				IV, rock				
2-MRC	$\bar{x}$	0.96 H	0.01	0.02 L	0.00	0.01	0.00	26 L
$n = 2$	s.d.	0.05	0.02	0.02	0.00	0.01	0.00	4
2-MY	$\bar{x}$	0.91	0.02	0.05	0.01 H	0.01	0.00	33
$n = 7$	s.d.	0.05	0.03	0.03	0.00	0.01	0.00	2
2-MR	$\bar{x}$	0.93	0.01	0.04	0.00	0.01	0.00	28 L
$n = 2$	s.d.	0.03	0.00	0.00	0.00	0.02	0.00	2
3-MRC	$\bar{x}$	0.8 L	0.05	0.08	0.00	0.02 H	0.00	37 H
$n = 2$	s.d.	0.2	0.05	0.07	0.00	0.01	0.00	1
3-MY $n = 1$	x	0.98 H	0.00	0.00 L	0.00	0.01	0.00	36.81 H
23-MY(a)	$\bar{x}$	0.8	0.04	0.08	0.00	0.01	0.00	25 L
$n = 6$	s.d.	0.1	0.06	0.07	0.00	0.01	0.00	9
23-MY(b) $n = 1$	x	0.76 L	0.03	0.18 H	0.00	0.00	0.00	21.45 L
33-IR	$\bar{x}$	0.90	0.01	0.06	0.00	0.00	0.00	38 H
$n = 2$	s.d.	0.02	0.01	0.01	0.00	0.00	0.00	6
33-IRY(b)	$\bar{x}$	0.9	0.04	0.07	0.00	0.01	0.00	37 H
$n = 5$		0.1	0.04	0.05	0.00	0.01	0.00	2
33-IRY(c) $n = 1$		0.99 H	0.00	0.00 L	0.00	0.00	0.00	41.10 H

[a]L signifies that the sample-average lies outside the lower confidence limit.
[b]H signifies that the sample-average lies outside the higher confidence limit.
[c]No. of analyses is denoted "n".
[d]Standard deviation is denoted "s.d.".

level was used to identify the layers which were the source of these differences in Fe and Ca contents. It was found that the rock is significantly higher in Ca than all other layers: this finding provides additional proof, over and above that provided in the photographs, that rock was indeed sampled in these thin (<1 mm thick) specimens. The red pigment layer is significantly higher in Fe than all other layers. Furthermore, in these samples, the surface layer has a higher Fe content than the rock and the pigment layer has a lower Ca content than the subpigment regions.

Sample-averages

To examine the replicate analyses, and any single analysis, of each sample, a reference distribution function estimated by the elemental site-average (Table 2) and its pooled standard deviation (14) is constructed for each element. The 95% confidence band of the elemental site-average (Table 2) is used to identify values which lie outside the estimated reference distribution at this level of probability. The sample-averages are presented in Table 3 and the samples which lie outside the confidence bands on both the high and low sides are identified. As one expects, the more heterogeneous is the layer, the more samples are found outside the confidence limits.

The surface and subpigment regions have the greatest number of results which lie outside their respective confidence limits (Table 3). The red pigment layer was found to be the most homogeneous. The rock, although exhibiting some data outside the 95% confidence limits, is not as heterogeneous, overall, as the surface and subpigment layers.

The sulphur site-average for the subpigment regions is dominated by one high sample-average, that of 15-IY. Nine of the remaining twelve samples are below the site-average sulphur content. When this obvious disparity is removed from the site-average, the site-average sulphur content drops to 0.06 ± 0.05

Can. J. Chem. Downloaded from www.nrcresearchpress.com by 112.217.228.212 on 09/07/12
For personal use only.

Can. J. Chem. Downloaded from www.nrcresearchpress.com by 112.217.228.212 on 09/07/12
For personal use only.

(95% C.I.) normalized percent or about 10% $CaSO_4 \cdot 2H_2O$ in the subpigment regions. A one-way analysis of variance again does not indicate significant differences between layers.

Sample 2-MY is noteworthy because of the existence of pockets of phosphorus and sulphur enrichment in its subpigment dendrites which have sample-averages outside the 95% confidence limits of the respective elements. The estimated size of these pockets is 20 μm. In addition, the opaque white subpigment layer seen in 33-IRY(b) (see previous section) was found to be phosphate-rich.

Analysis totals

A one-way analysis of variance of the site-averages for the elemental-analysis totals (Table 2) indicates that a significant difference in these averages does not exist between the four layers.

One can compare the sample-average values of the elemental-analysis totals (Table 3) with the elemental-analysis totals reference distribution at a 95% confidence level. It is found that samples 33-IR and 15-IR have high surface layer average totals. The pigmented layer of 2-MRC has the lowest total of all the red pigmented regions and 33-IRY(a) has the highest. The subpigment totals of 2-MRC, 3-MR, 23-MY(a), 23-MY(b), and the sulphate-rich dendrite of 2-MY are below the site-average and the high sulphate subpigment region of 15-IY is well above it. The samples 23-MY(a) and 23-MY(b) have low rock totals as do 2-MRC and 2-MR whereas the samples 33-IRY, 33-IR, 3-MRC, and 3-MY have high totals.

Cross-sectional scans

Cross-sectional scans were performed on all samples which had well-defined, parallel layers: 2-MRC, 2-MY, 23-MY(b), 33-IRY(a), (b), and (c), and 33-IR. Scans were assembled in steps starting at zero distance defined at the outside edge of the surface layer and preceding at known distances across the sample. One analysis per step was performed. These scans are presented in Fig. 3. Data are entered as normalized percentages. Only Ca, P, Si, S, and Fe are shown. The error associated with these normalized percentages is estimated as one standard deviation where the best available estimate of the standard deviation is the respective sample-average standard deviation. The error in distance is ±1 μm.

Trends that appear in the sample-averages presented above (Table 3) are also found in the cross-sectional scans. It can be seen from the cross-sectional scans that: (*i*) with the exception of 33-IRY(b), only the red-pigmented samples have Fe maxima, the depth of which depends on the thickness of the surface deposited layer, (*ii*) no sulphur maxima are seen in the subpigment regions, and (*iii*) the subpigment regions contain noticeable contributions from P and Si in the samples with dendritic or altered regions as seen in the photographs, these being 23-MY(b), 2-MY, 33-IRY(b), and to a lesser extent, 33-IR. These alterations are not seen in samples 2-MRC, 33-IRY(c), and 33-IRY(a).

Discussion

The surface deposits at Beni Hasan are, on average, 30 μm thick. They contain, in order of decreasing abundance based on the site-average (see previous section) Ca, S, P, Si, Fe, Al, Cl, and traces of Na, Mg, and K (Table 2). Egyptian desert sand consists primarily of silicates and aluminosilicates. However, it has been found that, in some cases, it may contain up to 35% soluble material, mostly gypsum, NaCl, and KCl in the particle-size fraction ≤74 μm (15). It is recognized that the proportion of soluble material can be site-specific. The Si component of the surface deposits as well as some soluble material likely arise from wind-blown sand. Bats are known to inhabit these calcitic tombs and their deposits are seen on the walls, hence soluble phosphates (16) and calcium phosphates are expected in the local tomb dust as is some $CaCO_3$. Iron occurs in the surface layer, originating in part from iron silicates in the sand; its surface deposit site-average abundance is greater than that of the rock. Correlations between surface deposited layer thicknesses or composition with sampling height (Table 1) have not been found in this sample population.

Aside from the above general description, one cannot say that there is a fixed composition of the surface deposit layer, as studied by the electron microprobe, in all tombs. Every sample has at least one sample-average which lies outside its respective reference distribution at the 95% level. Based on the information given in Table 3, there are six samples which have three or more elemental sample averages lying outside the 95% bands. A high Ca, low Si and P surface is found in samples 33-IRY(a), (c), and 17-IY; samples 2-MRC and 2-MY have a surface type which is high in Si and Fe but low in S. Sample 2-MY is also significantly low in Ca; the cleaned sample, 2-MRC, has a Ca content that lies just inside the lower bound. Sample 15-IR exhibits, in a single analysis, a surface which is high in P and low in S and Si. By considering the surface deposits of the remaining samples to have an intermediate composition, three and possibly four surface compositions are seen by the electron microprobe. The surface deposit layer types seen by the electron microprobe are representative of the surface layer growth and deterioration process integrated over time.

Earlier XPS results (5) indicated the presence of three distinct surface types detected the point of growth of the surface deposit i.e. at the nanometer level: a high Si – low Ca surface, a low Si – high Ca surface, and surfaces which were intermediate in the abundances of these elements. The observation of these surface types by XPS has lead to the suggestion (5) that there are two ways to initiate surface layer growth, one involving deposition of silica-containing dust and sand and a resulting increase in surface area and the increased possibility of capillary condensation of CO_2-enriched water vapour, and a second involving direct deposition of dew-point condensation. Subsurface attack and movement of soluble components of the substrate, including $CaCO_3$, was proposed as a consequence of the action of solvent water (5). The electron microprobe surface deposit layers represent the end products in these cumulative processes and their compositions may indicate the dominant mode of surface layer growth at localized spots.

We now have evidence, both from photographs and from bulk analyses, that subsurface depletion or alteration of the soluble components of rock and subpigment regions has occurred indeed under the inward movement of solvent (Fig. 2). The dendritic regions seen in the yellow pigmented fragments and the samples from the severely disfigured Tomb 33, on top of the calcite-rich rock, are direct evidence of alteration in particle size due to repeated solution from above and subsequent reprecipitation. The attack of acid rain on urban marbles has been found to produce a similar type of alteration in subsurface particle size (17, 18). Porosity (see Table 3 and previous section) is seen in the subpigment layers of these samples and also in the rock regions of three of the yellow samples. Pockets of phosphates in the altered regions are observed also. The exis-

Can. J. Chem. Downloaded from www.nrcresearchpress.com by 112.217.228.212 on 09/07/12
For personal use only.

tence of phosphate pockets is significant since the movement and subsequent immobilization of soluble phosphate deposits can be considered a marker for inward movement of solvent water.

A cohesive pigment layer is not seen in the yellow samples. The pigment yellow ochre is expected at this site. The yellow pigment orpiment, As_2S_3, is not seen in wall paintings until the 18th dynasty (ca. 1560 B.C.) (19). Yellow ochre is hydrated Fe_2O_3 admixed with silica, clay, and sometimes gypsum (20) (see also Table 3, pigment layer, sample 15-IY). However, the iron abundance of yellow iron pigments can be close to the detection limit of the microprobe and still be sufficient to yield colouration in the pigment layer visible to the human eye. Furthermore, it is known that the yellow, hydrated iron oxides are more soluble in acids and water than are the anhydrous iron oxides (21, 22) on which the red pigment at this site is based (19, 23). The differences seen in the red and yellow pigmented samples suggest that solvent water does not penetrate through the red pigment layers but does penetrate the more soluble and porous yellow pigment layer.

The effects of stronger acids may be evident in sample 2-MRC. This sample was cleaned approximately 20 years ago with HCl. However, Cl was not detected in the surface deposit or the rock layer of sample 2-MRC and was just detected in pigment and subpigment regions. However, sample 2-MRC has been found to have significantly low pigment layer, subpigment layer and rock totals at the 95% level based on the analysis-totals reference distribution (see previous section) even though these layers appear unaltered in photographs (Fig. 1). Material depletion from these layers may be a possible result of the application of strong acid. Further detailed analyses are on-going to investigate the effects of acid-cleaning.

No sulphate plaster layer exists in this tomb system. The significantly high sulphate sample-averages of 15-IY arise from the analyses of an inclusion approximately 450 μm in diameter below the surface and *not* from a continuous layer. The use of $CaCO_3$-based whitewash for preparing the rock wall for the execution of mural paintings is a possible alternative to the use of gypsum. Its employment has been cited and the presence of gypsum impurities in the whitewash noted (20). It is also possible that the rock walls were painted directly without a final wall preparation or polishing. The mechanistic consequence of the lack of a sulphate-rich plaster is that the surface layer is not dominated by sulphate even though subsurface attack and removal of soluble components, including sulphate, has occurred.

In natural limestone caves, water in the form of groundwater is almost always present. Calcite, in these situations, precipitates when CO_2 is degassed from the solvent water when the solvent water moves from high P_{CO_2} to low P_{CO_2} regions or to regions of higher temperature (24, 25). This is the case in the painted caves at Lascaux where groundwater enriched in CO_2 from biological soil processes (25, 26) has formed surface deposits. These deposits range in appearance from "cauliflower-like" concentrations to thin translucent films (26). In Beni Hasan there is no evidence for subsurface water flow or water flow over entire walls although a very few fissures, stained with iron-oxides, do appear in some Beni Hasan tombs. Stalactites and stalagmites are not seen by us anywhere in these tombs. The most probable source of water is condensation, both the dew-point and the capillary type (27, 28). Hence, we have a deposit which has formed in the presence of *atmospheric* CO_2 and in the absence of continuous excess solvent water.

Other deposits in which rain or dew provide solvent action have been described. Many open-air North American petroglyph and rock art sites have layers of silcrete and calcrete[4] deposited under the action of rain and groundwater (29, 30). These layers often form both substrate and surface deposit on these carved or painted rock faces (31, 32). The thin (<1 mm thick) dark coloured deposit known as rock or desert varnish is also formed on exposed outcrops from the dissolution of rock and dust rich in Fe and Mn silicates (33, 34) by dew and rain. Desert varnish can contain up to 30% Mn and Fe oxides (33). In the formation of coastal deposits known as aeolinites (35) on coastal outcrops and dunes, windborne materials such as SiO_2, Fe_2O_3, and $CaSO_4 \cdot 2H_2O$ are cemented in place by $CaCO_3$. At Beni Hasan, the deteriorating surfaces are in relatively enclosed spaces, the surface deposit layer compositions show the effects of material originating from the immediate tomb surroundings and subsurface attack as well as windborne sand. The recent formation (during the past 150 years) of the surface deposit indicates an environmental change which most likely involves the availability of solvent. It is unlikely that these tombs have been exposed to regular dew-fall such as occurs in the open desert (15) over the first four millennia of the tombs' existence. Therefore, although it has some features in common with other deposits, the Beni Hasan phenomenon has aspects which are unique and which have general significance in the understanding of the degradation processes of ancient painted surfaces.

The system CO_2–H_2O–$CaCO_3$ provides, to a first approximation, a description of the physical chemistry in the limestone-walled tombs of Beni Hasan. The solubility of $CaCO_3$ may be calculated (25, 35), for illustrative purposes, by considering the equilibria for carbonate dissolution in neutral water in the presence of CO_2. Continuous contact with an atmospheric source of CO_2, as is the case at Beni Hasan, is also assumed.

$$2CO_2(g) + H_2O \rightleftharpoons CO_2(aq) + H_2CO_3 \quad K_H K_0$$
$$H_2CO_3 \rightleftharpoons H^+ + HCO_3^- \quad K_1$$
$$HCO_3^- \rightleftharpoons CO_3^{2-} + H^+ \quad K_2$$
$$CaCO_3 \rightleftharpoons Ca^{2+} + CO_3^- \quad K_{sp}$$
$$H_2O \rightleftharpoons OH^- + H^+ \quad K_w$$

Amounts of dissolved Ca^{2+} calculated on the basis of concentration have been found. Experimental solubility data (36) for the Henry's law constant, K_H, and a value of 600 for the equilibrium constant for the hydration of CO_2, K_0, (37) were used. The amounts found are 53 ppm Ca^{2+} at 20°C at a P_{CO_2} of 3.0×10^{-4} atm and at a partial pressure of CO_2 comparable to that in human breath, 5.5×10^{-2} atm (38), 6400 ppm at 20°C. Thus, although the high levels of CO_2 typically seen in ground waters in cave environments (5×10^{-3} to 2×10^{-2} atm (25)) are not available at Beni Hasan, the influence of human activity may compensate. More exhaustive calculations of calcite solubilities based on activities, and including contributions from ion pairs and molecular species, have been cited in the literature (25) for temperatures and pressures expected in cave environments.

The kinetics of the dissolution and precipitation of $CaCO_3$ have been investigated (25, 39–44). At Beni Hasan, we are most interested in these processes in porous media (42, 43) and in thin films (41, 44).

The dissolution mechanism of calcite within the rock matrix has been investigated both experimentally and by solving transport equations in pores at varying flow velocities (42, 43).

[4]Silcrete typically has an SiO_2 content of 87–98% (29); calcrete typically has a $CaCO_3$ content of 80% (30).

Can. J. Chem. Downloaded from www.nrcresearchpress.com by 112.217.228.212 on 09/07/12
For personal use only.

Within the assumption that chemical reactions in the system are instantaneous (42), the rate of dissolution was found to depend on transport processes, i.e., the ability of the solute to diffuse away or be carried, from the dissolving pore-walls. When the rates of chemical surface reactions are also considered (43), it has been shown that for high flow rates (or short residence times of solvent water) surface reaction kinetics and chemical reaction kinetics become rate determining. In stagnant or low-flow regimes, the rate of dissolution again becomes dependent upon transport processes. In both the model which ignores surface reactions and the model which includes them, the incoming solution will become saturated within a distance comparable to the radius of a pore in a low-flow situation (42, 43). The extent of structural alteration in porous limestone is then just the distance that CO_2-saturated water will travel through the pore-network before becoming saturated with $CaCO_3$. The attainment of saturation may take a few minutes or several hours depending on the thickness or depth of the water film in the porous surface and below. In films approximately 500 μm thick, diffusion of CO_2 in the solvent is the rate-determining step (41, 44). In very thin films, such as are expected at Beni Hasan, i.e. $\leq$30 μm, the rate-determining step (44) for the dissolution of calcite is the slow (45) hydration of CO_2.

At Beni Hasan, the surface-layer pore width, estimated from photographic measurements, is approximately 5 μm and the rock pore width is $\leq$5 μm. The current depth limit of alteration in a single exposure to unsaturated solvent can be estimated at 5 μm in the surface layer. The width of the dendrites in the depleted region, however, is $\geq$20 μm. This is roughly four times as large as the surface pore size. Individual samples, notably 33-IR, show larger differences between surface layer pore sizes and subsurface dendrite widths. This difference in pore and dendrite width is evidence that there has been repeated dissolution caused by solvent entering from the surface in the initial stages of surface layer growth. The existing surface deposit, which at present disfigures the painted surfaces, is concurrently acting as a barrier to further substrate attack. The kinetics of the multistep degradation process on-going at this site is currently being modelled by us.

Acknowledgements

The authors wish to thank the Egyptian Antiquities Organization and its Permanent Committee for Archaeology for their permission, given in 1980, to take samples from the tombs at Beni Hasan. Special thanks are extended to Dr. Ali el Khouli, Mr. Mottawi Balboosh, and Mr. Gamal M. Amin for their advice and assistance. Drs. M. Gorton and C. Cermignani and Mr. George Taylor, Department of Geology, University of Toronto, provided advice on the electron microprobe analyses. Dr. J. M. Allen, also of the Department of Geology, made available a petrographic microscope for photography. Dr. D. Spanel, Virginia Museum, Richmond, VA., provided valuable discussions on the Egyptological aspects of these investigations. Dr. Jean Vouvé, Dr. M. del Monte, Dr. el Goresy, and Mr. Ian Wainwright provided reprints of their articles.

This work was supported by the University of Toronto, the Natural Sciences and Engineering Research Council of Canada, and the UNESCO/CIDA Assistance Programme.

1. A. Stoppeleare. Annales du Service des Antiquitiés de l'Egypte, **40**, 941 (1940).
2. H. J. Plenderlith, P. Mora, G. Torraca, and G. De Guichen. Conservation problems in Egypt. UNESCO Consultant Report, Contract No. 33.591. 1970.
3. G. Torraca. Deterioration processes of mural paintings. Application of science in the examination of works of art. *Edited by* Wm. Young. Museum of Fine Art, Boston. 1970. p. 170.
4. K. M. Wilson-Yang and G. Burns. J. Am. Research Center in Egypt, **19**, 119 (1982).
5. K. M. Wilson-Yang and G. Burns. Can. J. Chem. **65**, 1058 (1987).
6. P. E. Newberry. Beni Hasan. Vol. 1. Egyptian Exploration Fund, London, 1893–4.
7. W. S. Smith. The art and architecture of ancient Egypt. 2nd ed. *Revised by* W. K. Simpson. Pelican Books Ltd., Harmondsworth, Middlesex. 1981. p. 199.
8. J. C. Rucklidge. Instrumentation. Microbeam techniques short course handbook. Vol. 1. Mineralogical Assoc. of Canada, Edmonton. 1976. p. 3.
9. Z. Kukal. Geology of recent sediments. *Translated by* H. Zarubova. Academic Press, New York, NY. 1971. p. 121.
10. P. J. Statham. Ph.D. Thesis. University of Cambridge. 1975.
11. L. S. Birks. Electron probe microanalysis. Wiley Interscience, New York, NY. 1971. Chap. 7.
12. S. P. De Atley and J. S. Olin. Comparison of data obtained by neutron activation and electron microprobe analyses of ceramics. Archaeological ceramics. *Edited by* J. S. Olin and A. D. Franklin. Smithsonian Institute Press, Washington, D.C. 1982. p. 79.
13. I. C. Freestone, M. S. Tite, and M. Bimson. Archaeometry, **24**, 99 (1982).
14. G. E. P. Box, W. G. Hunter, and J. S. Hunter. Statistics for Experimenters. Wiley, New York, NY. 1978. Chap. 6.
15. F. Rizk, A. El-Arabaty, and A. El-Sarky. IEEE, PAS-**94**, 1770 (1975).
16. D. R. Stoddart and T. P. Scoffin. Phosphate rock on coral reef. Chemical sediments and geomorphology. *Edited by* A. S. Goudie and K. Pye. Academic Press, Toronto. 1983. p. 383.
17. M. Del Monte and O. Vittori. Endeavour, **9**, 117 (1985).
18. J. I. Feddema and T. C. Meiring. Atm. Environ. **21**, 143 (1987).
19. A. el Goresy, H. Jakseh, M. A. Razek, and K. L. Weiner. Ancient pigments in wall paintings of Egyptian tombs and temples: an archaeometric project. MPIH-1986-v.12 Max-Planck Institute für Kernphysik, Heidelberg.
20. A. Lucas and J. R. Harris. Ancient Egyptian materials and industries. 4th ed. J. R. Harris and Edward Arnold, London. 1962.
21. M. Pourbaix *et al.* Atlas d'equilibres electrochemiques. Gauthier-Villars, Paris. 1963. p. 311.
22. W. C. McCrone, and J. G. Delly. The particle atlas. Vol. II. 2nd. ed. Ann Arbor Publ., Ann Arbor. 1973. p. 445.
23. R. J. Gettens and G. L. Stout. Painting materials. Dover, New York, NY. 1966. p. 134.
24. J. N. Jennings. Karst geomorphology. Basil Blackwell, New York, NY. 1985.
25. R. G. Picknett, L. N. Bray, and R. D. Stenner. The chemistry of cave waters. The science of speleology. *Edited by* T. D. Ford and C. H. D. Cullingford. Academic Press, New York, NY. 1976. Chap. 7.
26. J. Vouve, J. Brunet, P. Vidal, and J. Marsal. Stud. Conserv. **28**, 97 (1983).
27. A. D. Zimon. The adhesion of dust and powders. 2nd ed. Consultants Bureau, New York, NY. 1982. p. 109.
28. S. J. Gregg and K. S. V. Sing. Adsorption, surface area and porosity. Academic Press, London. 1967. Chap. 3.
29. M. A. Summerfield. Silcrete. Chemical sediments and geomorphology. *Edited by* A. S. Goudie and K. Pye. Academic Press, Toronto. 1983. p. 59.
30. A. S. Goudie. Calcrete. Chemical sediments and geomorphology. *Edited by* A. S. Goudie and K. Pye. Academic Press, Toronto. 1983. p. 93.
31. J. M. Taylor. J. Can. Conserv. Inst. **3**, 20 (1978).
32. R. Myers, J. M. Taylor, and I. N. M. Wainwright. Bull. Am. Inst. Conserv. **14**, 28 (1974).
33. W. B. Whalley. Desert varnish. Chemical sediments and geo-

morphology. *Edited by* A. S. Goudie and K. Pye. Academic Press, Toronto. 1983. p. 197.
34. R. A. M. GARDNER. Aeolinites. Chemical sediments and geomorphology. *Edited by* A. S. Goudie and K. Pye. Academic Press, Toronto. 1983. p. 265.
35. R. M. GARRELS and C. L. CHRIST. Solutions, minerals and equilibria. Harper and Row, New York. 1965. Chap. 3.
36. G. W. C. KAYE and T. H. LABY. Tables of physical and chemical constants. 14th ed. Longman, London. 1973. p. 184.
37. F. A. COTTON and G. WILKINSON. Advanced inorganic chemistry. 3rd ed. Interscience. 1972. p. 296.
38. D. N. BARON. Chemical pathology. 3rd ed. English Universities Press, London. 1973. p. 32.
39. L. N. PLUMMER, T. M. L. WIGLEY, and D. L. PARKHURST. Am. J. Sci. **2**, 179 (1978).
40. E. L. SJOBERG and D. T. RICKARD. Chem. Geol. **42**, 119 (1984).
41. W. DREYBRODT. Chem. Geol. **29**, 89 (1985).
42. P. K. WEYL. J. Geol. **66**, 163 (1958).
43. J. BAUMANN, D. BUHMANN, W. DREYBRODT, and H. D. SCHULZ. Chem. Geol. **53**, 219 (1985).
44. D. BUHMANN and W. DREYBRODT. Chem. Geol. **48**, 189 (1985).
45. M. D. KERN. J. Chem. Ed. **37**, 14 (1960).

Can. J. Chem. Downloaded from www.nrcresearchpress.com by 112.217.228.212 on 09/07/12
For personal use only.

Formation constants of trivalent lanthanide metal ions and hydrazone β-diketones in 75% dioxane – water solvent

BASHEIR A. EL-SHETARY, SHAKER L. STEFAN,[1] MOHAMED S. ABDEL-MOEZ, AND MAHMOUD M. MASHALY
Chemistry Department, Faculty of Education, Ain-Shams University, Roxy, Cairo, Egypt

Received May 6, 1987[2]

BASHEIR A. EL-SHETARY, SHAKER L. STEFAN, MOHAMED S. ABDEL-MOEZ, and MAHMOUD M. MASHALY. Can. J. Chem. **66**, 2362 (1988).

A new series of hydrazone β-diketone organic ligands were prepared: 3-(2-acetylphenylhydrazone)pentane-2,4-dione (2-APHA), 2-(2-acetylphenylhydrazone)-1-phenyl-1,3-butane dione (2-APHB), 2-(2-acetylphenylhydrazone)-1,3-diphenyl-1,3-propane dione (2-APHDB), 3-(2-acetylphenylhydrazone) 1,1,1-trifluoropentane-2,4-dione (2-APHTA) and 2-(2-acetylphenylhydrazone)-5,5-dimethyl-1,3-cyclohexane dione (2-APHDm). The step formation constants of their 1:1 and 1:2 rare-earth complexes were determined at 30°C by pH titration in 75% (v/v) dioxane–water solvent. The ionization constant of ligands were also measured. A curious odd–even stability differential was apparent in the (2-APHDm) ligand with the heavier rare earths Gd–Lu. The differential was apparent in both log K_1 and log β values and may be sufficient to cause reversal of the usual ion-exchange elution sequence.

BASHEIR A. EL-SHETARY, SHAKER L. STEFAN, MOHAMED S. ABDEL-MOEZ et MAHMOUD M. MASHALY. Can. J. Chem. **66**, 2362 (1988).

On a préparé une nouvelle série de ligands organiques dérivés d'hydrazones de β-dicétones : (acétyl-2 phénylhydrazone)-3 pentanedione-2,4 (2-APHA), (acétyl-2 phénylhydrazone)-2 phényl-1 butanedione-1,3 (2-APHB), (acétyl-2 phénylhydrazone)-2 diphényl-1,3 propanedione-1,3 (2-APHDB), (acétyl-2 phénylhydrazone)-3 trifluoro-1,1,1 pentanedione-2,4 (2-APHTA) et (acétyl-2 phénylhydrazone)-2 diméthyl-5,5 cyclohexanedione-1,3 (2-APHDm). Opérant à 30°C, dans un mélange dioxanne/eau à 75% (v/v), on a déterminé les constantes de formation par étape de leurs complexes 1:1 et 1:2 avec des terres rares. On a aussi mesuré la constante d'ionisation des ligands. On a déterminé qu'il existe une curieuse de stabilité différentielle dans les complexes pair et impair du ligand 2-APHDm avec les terres rares plus lourdes de la série Gd à Lu. On peut remarquer les différences tant dans les valeurs du log K_1 que du log β et ces différences sont telles qu'elles peuvent être suffisantes pour renverser la séquence habituelle d'élution lors de l'échange d'ions.

[Traduit par la revue]

β-Diketones are well-known chelating agents, capable of forming stable complexes with metal ions. Lanthanide β-diketones have also been found to have wide application (2), including chromatographic separation of the lanthanide series (3). Azo compounds are also used as complexing agents (4), and the combination of azo compounds and β-diketones are good ligands (5). The chelation between similar ligands and lanthanide metal has been studied (6, 7).

The coupling product of the diazonium salt of 2-aminoacetophenone with different β-diketones such as acetylacetone, benzoylacetone, dibenzoyl methane, trifluoroacetylacetone, and 5,5-dimethylcyclohexane-1,3-dione (dimedone) produces a series of 3-(2-acetylphenylhydrazone)diketone ligands. The present study determined the acid dissociation constants of these ligands and the formation constants of their trivalent lanthanide complexes. The structure and basicity effects of the ligands on the stability of the formed complexes are discussed and some correlations attempted. These complexing agents may be useful in the separation of the lanthanides.

Experimental

(i) Materials and methods

Stock solutions of lanthanide nitrates were prepared from their metal oxides (BDH 99.9%) as mentioned previously (7). The acidity of the metal ion solutions was adjusted to between pH 4.0 and 4.5. The exact concentration was determined by titration with EDTA using xylenol orange as indicator (7). Dioxane was freshly purified by refluxing with $LiAlH_4$ and sodium metal for 8 h and then distilled. Oxygen-free nitrogen gas was passed through the solutions during the titrations.

Titrations of 5×10^{-3} *M* free ligands, as well as mixtures of the free ligands and 1×10^{-3} *M* lanthanide ions, were carried out against standard KOH in 75% dioxane – water (v/v) to avoid precipitation. Dilute solutions (10^{-3} *M*) were used to reduce the possibility of formation of polynuclear species. All titrations were done in duplicate; the curves agreed within 0.03 pH units in all cases. The formation of lanthanide–nitrate complexes was assumed negligible.

The ligands used in this study did not undergo hydrolysis under the above experimental conditions. This was indicated by rapid attainment of equilibrium during titration and by the absence of any significant drift in the pH even after a half hour (8). pH titrations were carried out using a WTW digital pH meter 520 fitted with combination electrode at 30°C and <0.025 ionic strength in 75% (v/v) dioxane – water solvent.

The dissociation constants pK_H were calculated as mentioned before (9). As 75% dioxane – water (v/v) was used as a solvent, a correction value of 0.28 pH unit was added as recommended by Irving and Mahnot (10). The adopted method by Irving and Rossotti (11) was employed to determine the parameters $\bar{n}$ and pL. Linear plots of $\bar{n}/(1 - \bar{n})$ and $\log [(\bar{n} - 1)/(2 - \bar{n})]$ vs. pL were drawn to obtain the best values of stepwise formation constants. Also correlation coefficients were calculated and found to be equal to or better than 98%.

(ii) Preparation of ligands

The organic ligands used in this investigation were prepared by coupling the diazonium salt of 2-aminoacetophenone with different diketones in sodium acetate medium (12). The crude materials were crystallized twice from acetic acid to obtain pure products.

The purity of the ligands was checked by infrared, thin layer chromatography, and elemental analysis.

3-(2-Acetylphenylhydrazone)pentane-2,4-dione (2-APHA), I

This compound was obtained as yellow crystals from acetic acid, mp 159.0–159.5°C; ir (KBr) ν: 3080–3020 (NH) (mb), 1663 (C=O) (s), 1570 (C=N) (s) cm^{-1}. *Anal.* calcd. for $C_{13}H_{14}N_2O_3$: C 63.41, H 5.69, N 11.38; found: C 63.60, H 5.80, N 10.67.

[1]Author to whom correspondence should be addressed.
[2]Revision received March 4, 1988.

Printed in Canada / Imprimé au Canada

Can. J. Chem. Downloaded from www.nrcresearchpress.com by 196.1.178.254 on 09/07/12
For personal use only.

*2-(2-Acetylphenylhydrazone)-1-phenyl-1,3-butane dione (2-APHB), **II***

This compound was obtained as yellow crystals from acetic acid, mp 114.0–114.5°C; ir (KBr) ν: 3260–3100 (NH) (mb), 1642 (C=O) (s), 1570 (C=N) (s) cm^{-1}. *Anal.* calcd. for $C_{18}H_{16}N_2O_3$: C 70.12, H 5.19, N 9.09; found: C 69.96, H 5.42, N 8.89.

*2-(2-Acetylphenylhydrazone)-1,3-phenyl-1,3-propane dione (2-APHDB), **III***

This compound was obtained as yellow crystals from acetic acid, mp 78.0–78.5°C; ir (KBr) ν: 3180–3100 (NH) (mb), 1625 (C=O) (s), 1567 (C=N) (s) cm^{-1}. *Anal.* calcd. for $C_{23}H_{18}N_2O_3$: C 74.59, H 8.46, N 5.56; found: C 74.80, H 5.17, N 7.8.

*3-(2-Acetylphenylhydrazone)-1,1,1-trifluoropentane-2,4-dione (2-APHTA), **IV***

This compound was obtained as yellow crystals from acetic acid, mp 103.0–103.5°; ir (KBr) ν: 3160–3050 (NH) (mb), 1660 (C=O) (s), 1572 (C=N) (m) cm^{-1}. *Anal.* calcd. for $C_{13}H_{11}N_2O_3F_3$: C 52.00, H 3.66, N 9.33; found: C 52.10, H 3.69, N 9.64.

*2-(2-Acetylphenylhydrazone)-5,5-dimethyl-1,3-cyclohexane dione (2-APHDm), **V***

This compound was obtained as deep yellow crystals from acetic acid, mp 141.0–141.5°C; ir (KBr) ν: 3400–3300 (NH) (wb), 1675 (C=O) (s), 1570 (C=N) (s) cm^{-1}. *Anal.* calcd. for $C_{16}H_{18}N_2O_3$: C 67.13, H 6.29, N 9.79; found: C 67.60, H 6.13, N 9.92.

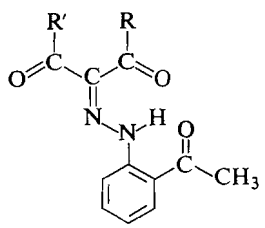

(I–IV)

3-(2-Acetylphenylhydrazone)-pentane-2,4-dione

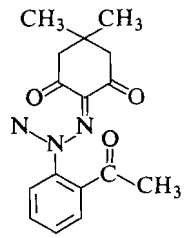

(V)

2-(2-Acetylphenylhydrazone)-5,5-dimethyl-1,3-cyclohexane dione (2-APHDm)

I	2-APHA	CH_3—	CH_3—
II	2-APHB	CH_3—	C_6H_5—
III	2-APHDB	C_6H_5—	C_6H_5—
IV	2-APHTA	CH_3—	CH_3—

Results and discussion

(i) Dissociation constants

The titration curves of free ligand in 75% dioxane – water (v/v) reveals that the ligands behave as weak monoprotic acids. The pK_H values of the different ligands were observed to be affected by the terminal groups of the β-diketone in the ligands.

2-APHA ligand has the highest value of dissociation constant (pK = 14.43). This may be attributed to the increase in electron density on the hydrazone moiety caused by the electron repelling property of the methyl group, which retards removal of the ligand proton and increases its basicity. For 2-APHB ligand the presence of one electron-withdrawing phenyl group in the β-diketone branch decreases its basicity (pK = 13.99). The effect of phenyl group substitution on the basicity of ligand becomes more obvious in the 2-APHDB ligand since the value of the dissociation constant is 12.54. The effect of the electron-withdrawing group on the basicity of ligands is clear in comparing the pK_H values of 2-APHA (pK_H = 14.43) and 2-APHTA (pK_H = 12.5). The decreased value of the latter is attributed to the presence of fluorine atoms. The order of

TABLE 1. Formation constants of 1:1 and 1:2 trivalent lanthanide metal ions – hydrazone-β-diketone ligands in 75% (v/v) dioxane – water mixture at 30 + 0.5°C*

	2-APHTA, pK = 12.50 ± 0.02			2-APHDB, pK = 12.54 ± 0.03			2-APHDm, pK = 13.13 ± 0.02			2-APHB, pK = 13.99 ± 0.03			2-APHA, pK = 14.43 ± 0.04		
Metal ion	log K_1	ΔG_1	log β	log K_1	ΔG_1	log β	log K_1	ΔG_1	log β	log K_1	ΔG_1	log β	log K_1	ΔG_1	log β
La^{3+}	7.82	44.73	14.07	9.45	54.05	16.67	8.37	47.88	15.15	9.33	53.37	17.00	10.20	58.34	18.83
Ce^{3+}	8.12	46.45	14.94	9.82	56.17	17.51	9.89	50.85	16.28	9.68	55.37	18.07	10.27	58.74	19.87
Pr^{3+}	8.33	47.65	15.25	10.14	58.01	17.97	9.35	53.48	17.15	10.07	57.60	18.72	10.50	60.06	19.58
Nd^{3+}	8.47	48.45	15.51	10.43	59.66	18.71	9.87	56.46	17.88	10.37	59.32	19.12	10.75	61.49	20.09
Sm^{3+}	8.80	50.34	16.12	10.90	62.35	19.60	10.73	61.38	19.50	10.56	60.40	19.76	10.85	62.06	20.53
Eu^{3+}	8.88	50.80	16.22	11.05	63.21	19.85	11.01	62.98	19.81	10.91	62.41	19.74	10.83	61.95	20.46
Gd^{3+}	8.95	51.20	16.25	11.00	62.92	19.75	11.32	64.76	20.20	11.03	63.10	19.89	11.05	63.21	20.48
Tb^{3+}	8.75	50.05	16.20	10.92	62.46	19.62	10.58	60.52	19.67	10.50	60.06	19.66	10.97	62.75	20.75
Dy^{3+}	8.85	50.63	16.41	10.94	62.58	19.47	9.93	56.80	18.53	10.90	62.35	20.53	11.10	63.50	21.08
Ho^{3+}	8.83	50.51	16.43	10.63	60.81	18.47	9.74	55.71	18.23	10.58	60.52	19.83	10.98	62.81	20.84
Er^{3+}	8.96	51.25	16.54	11.35	64.92	20.49	10.45	59.77	19.50	10.80	61.78	20.30	11.58	66.24	21.88
Yb^{3+}	9.43	53.94	17.53	11.32	64.76	20.17	10.85	62.06	20.07	10.96	62.69	20.73	11.63	66.52	21.96
Lu^{3+}	9.30	53.20	17.30	11.02	63.04	19.35	10.85	60.52	19.70	11.00	62.92	20.60	11.32	64.76	21.40

* ΔG_1 in kJ/mol; the values log K_1 – log K_2 ranged between 1.07 and 1.25. The uncertainty in the stability constants ranged between ±0.01 and ±0.03, and the correlation coefficient (r) ranged between 0.95 and 0.99.

Can. J. Chem. Downloaded from www.nrcresearchpress.com by 196.1.178.254 on 09/07/12
For personal use only.

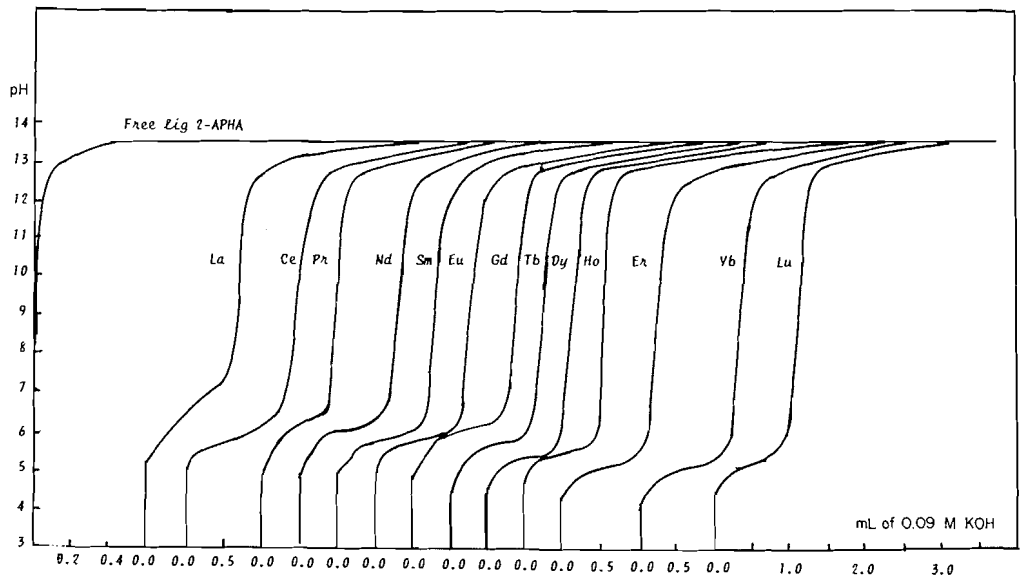

FIG. 1. Potentiometric titration curves for 5×10^{-3} *M*, 3-(2-acetylphenylhydrazone)pentane-2,4-dione in the absence and presence of 1×10^{-3} *M* lanthanide ion, $T = 30°C$, 75% (v/v) dioxane – water, $V^0 = 40$ mL.

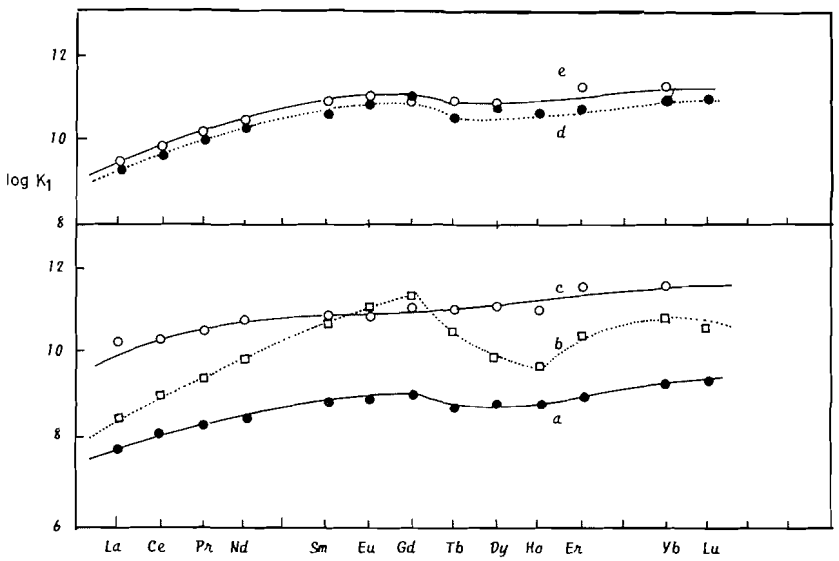

FIG. 2. log K_1 as a function of atomic number for lanthanide(III) complexes at 30°C in 75% (v/v) dioxane – water mixture. (*a*) Ln(III)–2-APHTA, (*b*) Ln(III)–2-APHDm, (*c*) Ln(III)–2-APHA, (*d*) Ln(III)–2-APHB, and (*e*) Ln(III)–2-APHDB.

dissociation constants of the studied ligands decreases in the same manner as that of the β-diketone themselves (1). The decreased basicity of the 2-APHDm ligand ($pK_H = 13.13$) relative to the 2-APHA ligand ($pK_H = 14.43$) may be due to both the cyclic structure and the distant location of the methyl groups from the hydrazone moiety. Considering substitution effects, the investigated ligands can be arranged according to increased basicity in the following order: 2-APHTA < 2-APHDB < 2-APHDm < 2-APHB < 2-APHA.

(ii) Formation constants

Titration curves of the 2-APHA ligand (Fig. 1) are greatly altered in the presence of Ln^{3+} ion (Lu = La, Ce, Pr, Nd, ..., Lu) as a result of complex formation.

The lanthanide ions (1×10^{-3} *M*) and organic ligand mixtures in a ratio of 1:5 were titrated with KOH at 30 ± 0.5°C and <0.025 *M* ionic strength in 75% dioxane – water (v/v) solvent. A sharp inflection was observed at $m = 2$, where m = mole of base per mole of ligand, indicating that the highest complex formation ratio is 1:2 metal-to-ligand. The lighter and heavier lanthanides all form ML and ML_2 complexes. Therefore, stepwise formation constants (log K_1 and log K_2) can be evaluated (Table 1). A plot of the formation constants (log K_1) for these complexes vs. atomic number of lanthanide elements shows a regular increase from lanthanum (La) to europium (Eu) with a break after gadolinium (Fig. 2). The increase in formation constant values of the light lanthanide complexes La^{3+} to Gd^{3+}) may be attributed mainly to electro-

Can. J. Chem. Downloaded from www.nrcresearchpress.com by 196.1.178.254 on 09/07/12
For personal use only.

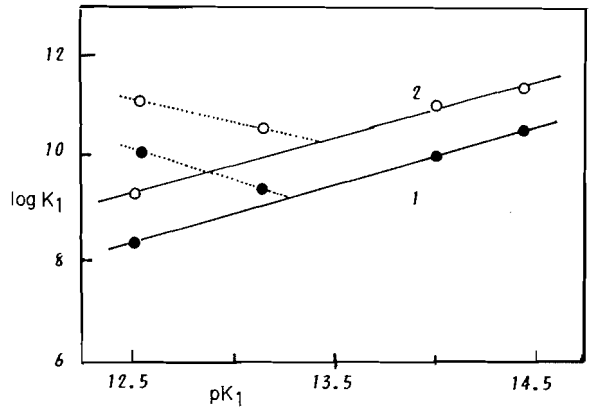

FIG. 3. Comparison of stabilities of 1:1 Ln–chelate reagent complexes. (*1*) Pr^{3+} complexes. (*2*) Lu^{3+} complexes.

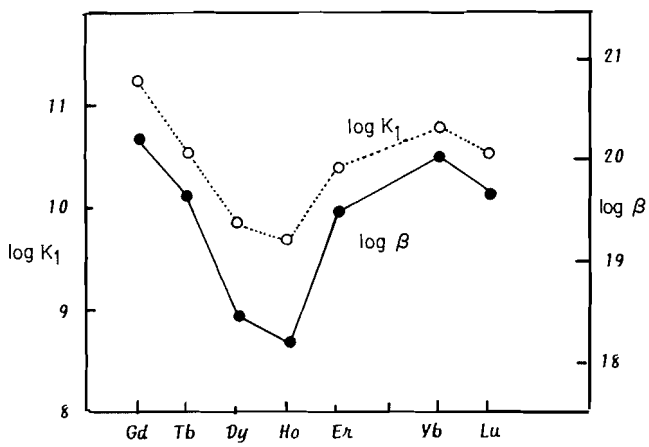

FIG. 4. Apparent odd–even effect in chelate stabilities noted with the heavier rare-earth–2-APHDm species.

static attraction. The behaviour observed in these ligands agrees very well with that of other chelating agents (13–15). On the other hand, the formation constants (log K_1) of the heavier lanthanide complexes (Tb^{3+} to Lu^{3+}) show a very slight increase (Fig. 2). The latter increase is 0.27, 0.35, 0.02, and 0.09 units for 2-APHTA, 2-APHDB, and 2-APHB, respectively. However, differences between consecutive log K_1 values for lanthanide complexes from La to Gd (light lanthanides) was 0.12, 0.16, and 0.23, and 0.24 units for the same order of ligands. The smaller increase in the formation constants for the heavier lanthanide complexes cannot be explained by electrostatic bond interactions. In terms of electrostatic considerations, the gadolinium break may be attributed to the discontinuity of the crystal radius at gadolinium (16). The deviation of the ligand stability constants from linearity is not peculiar, but seems to be common for most rare earth complexes with several chelating agents, such as 2,4-pentanedione (17), 1-phenyl-1,3-butane dione (18) and *N*-hydroxyethylenediamine triacetic acid (14). This agreement in behaviour of the studied ligands with those cited in literature (17–20) may be due to the similarity of the coordination sites of the ligands.

The plots of stability constants of the 2-APHDm lanthanide chelates vs. the atomic number of the lanthanides in Fig. 2 suggests the presence of ionic interaction through the light lanthanide elements. However, the stability values of the heavier lanthanide complexes decrease to Ho^{3+} and then increase to Lu^{3+}. Figure 3 shows the relationship between the acid dissociation constant pK_H and the formation constant log K_1 of the Ln chelates (Pr^{3+} and Lu^{3+} are given as examples). The stabilities of the complexes of the flexible ligands exhibit a dependance on the acid dissociation constant while the stabilities of the complexes of the rigid 2-APHDm ligand do not follow the trend. The stability constant values of the Ln(III) complexes (Table 1) for the different ligands have been found to be related to their basicities and structures. The general trend observed is that by increasing the basicity of the organic ligands, the formation constants of the lanthanide complexes are increased in the order: 2-APHDm > 2-APHA > 2-APHB > 2-APHDB > 2-APHTA.

Formation constants of the Ln–(2-APHDm) complexes have been found to deviate from the general trend. This deviation may be due to the rigid structure of the 2-APHDm ligand with respect to the other ligands. The effect of ligand structure is obvious in the stability values of the Ln complexes (Table 1). Values for the flexible branches 2,4-pentanedione, 1-phenyl-1,3-butane dione, and 1,3-diphenyl-1,3-propane dione decreased gradually. This may be due to the bulky methyl and phenyl groups present. The results obtained agree with those cited in the literature (21, 22).

A literature (14, 17, 23) survey showed that the lanthanides can form 1:1, 1:2, and 1:3 complexes with β-diketones, but in this study only 1:1 and 1:2 types were obtained. This may be due to steric effects of the ligands which hinder interaction of the ligands around the metal ions.

The 2-(2-acetylphenylhydrazone)-5,5-dimethyl-1,3-cyclohexanedione–lanthanide complexes (Fig. 4) show a curious odd–even effect from Gd^{3+} and Lu^{3+} for both log K_1 and log β. The difference in both log K_1 and log β between the pairs of lanthanide series is outside the experimental error (Fig. 4, Table 1). We conclude that the 2-APHDm ligand might be valuable for the separation of rare earth mixtures by ion exchange techniques.

1. D. D. PERRIN. Stability constants of metal ions complexes. Part B. Organic ligand, IUPAC Chemical Data Series No. 22. Pergamon Press, Oxford. 1979.
2. N. AHMED, N. S. BHACCA, J. SERBIN, and J. W. WANDER. J. Am. Chem. Soc. **93**, 2564 (1971).
3. E. W. BERG and J. J. CHIANG ACOSTA. Anal. Chem. Acta, **40**, 101 (1968).
4. J. R. KIRBY and R. M. MILBURN. Anal. Chem. Acta, **26**, 458 (1962).
5. A. G. EVANS, J. C. EVANS, B. A. EL-SHETARY, C. C. ROWLANDS, and R. H. MORGAN. J. Coord. Chem. **9**, 19 (1979).
6. A. M. ZAHRA, B. A. EL-SHETARY, and A. ISMAIL. J. Chinese Chem. Soc. **28**, 47 (1981).
7. G. R. CHOPPIN and J. A. CHOPPORIAN. J. Inorg. Nucl. Chem. **22**, 97 (1961).
8. M. S. MAYADEO, S. S. PUROHIT, and S. H. HUSSAIN. J. Indian Chem. Soc. **59**, 952 (1982).
9. A. ALBERT and E. SERJEANT. Ionization constants of acids and bases. 1st ed. Methun & Co. Ltd., London. 1962. p. 162.
10. H. M. H. IRVING and U. S. MAHNOT. J. Inorg. Nucl. Chem. **30**, 1215 (1968).
11. H. M. IRVING and H. S. ROSSTTI. J. Chem. Soc. 3397 (1953); 2904 (1954).
12. R. ADAMS. Organic reaction. Vol. 10. Chapman Hall, London. 1959. Chapt. 1, pp. 1–120.

Can. J. Chem. Downloaded from www.nrcresearchpress.com by 196.1.178.254 on 09/07/12
For personal use only.

13. E. N. RIZKALLA, A. T. RAMADAN, and M. H. SEADA. Polyhedron, **2**, 1155 (1983).
14. F. H. SPEDDING, J. E. POWELL, and J. W. WRIGHT. J. Am. Chem. Soc. **78**, 34 (1956).
15. T. F. GRITNON, H. P. GOEDKEN, and G. R. CHOPPIN. J. Inorg. Nucl. Chem. **39**, 2021 (1977).
16. S. K. GRAY, S. MUKHERJEE, B. S. GARG, and R. P. SINGH. J. Indian Chem. Soc. **59**, 1038 (1982).
17. I. GRENTHE and W. C. FERNELIUS. J. Am. Chem. Soc. **82**, 6258 (1960).
18. N. K. DAVIDENKO and A. A. ZHOLDAKOV. J. Inorg. Chem. USSR, **12**, 633 (1967).
19. A. DADGAR and G. R. CHOPPIN. J. Coord. Chem. **1**, 179 (1971).
20. R. STAMPFLI and G. R. CHOPPIN. J. Coord. Chem. **1**, 173 (1971).
21. N. K. DUTT and P. BANDYAPADHYAY. J. Inorg. Nucl. Chem. **26**, 729 (1964).
22. S. P. SINHA. Complexes of the rare earths. Pergamon Press, London. 1966.
23. A. S. BERLIAND, A. E. BVPKE, and L. E. MARTINEKO. J. Inorg. Chem. USSR, **13**, 2106 (1969).

Can. J. Chem. Downloaded from www.nrcresearchpress.com by 196.1.178.254 on 09/07/12
For personal use only.

Preparations, X-ray crystal structures, and spectral studies of seleninyl bis(trifluoromethanesulfonate) and seleninyl bis(acetate)

RAMESH KAPOOR, POONAM WADHAWAN, and PRATIBHA KAPOOR
Chemistry Department, Panjab University, Chandigarh-160014, India

AND

JEFFERY F. SAWYER
Lash Miller Chemical Laboratories, University of Toronto, Toronto, Ont., Canada M5S 1A1

Received November 17, 1987[1]

RAMESH KAPOOR, POONAM WADHAWAN, PRATIBHA KAPOOR, and JEFFERY F. SAWYER. Can. J. Chem. **66**, 2367 (1988).

The compounds seleninyl bis(trifluoromethanesulphonate) (**1**) and seleninyl bis(acetate) (**2**) have been prepared and characterized by elemental analysis, ir and Raman spectroscopy, and X-ray crystallography. Crystals of **1** are monoclinic, space group $P2_1/n$ with $a = 12.735(1)$ Å, $b = 5.163(4)$ Å, $c = 16.133(2)$ Å, $\beta = 96.426(8)°$, $U = 1054$ Å^3, $D_x = 2.48$ g cm^{-3} for $Z = 4$, $R = 0.038$ for 1745 observed reflections with $I > 2.5\sigma(I)$. Those of **2** are orthorhombic, space group $Pcab$ with $a = 6.845(3)$ Å, $b = 8.992(2)$ Å, $c = 23.560(9)$ Å, $U = 1450$ Å^3, $D_x = 1.95$ g cm^{-3} for $Z = 8$, $R = 0.074$ for 1073 observed reflections with $I > 3.0\sigma(I)$. The primary geometry of the Se atom in $SeO(O_3SCF_3)_2$ is AX_3E with a Se═O distance of 1.571(3) Å and Se—O bond lengths to the CF_3SO_3 ligands of 1.902(3) and 1.922(3) Å. Completing the overall coordination geometry of the Se atom are 2 intramolecular and 4 intermolecular Se...O contacts which are less than van der Waals limits. The overall coordination geometry is somewhat irregular since the two triflate anions are significantly differently arranged with respect to the SeO_3E tetrahedron. The crystal packing consists of layers of interacting molecules. In **2** there is some disorder. However, the major arrangement of the molecule has Se═O and Se—O(1), Se—O(3) distances to the acetate ligands of lengths 1.575(9), 1.847(7), and 1.831(8) Å respectively. The overall geometry of the Se atom in this compound is completed by two intramolecular secondary Se...O contacts involving the second O atoms of both acetates and two intermolecular contacts involving the seleninyl oxygen atom and atom O(2) of an acetate group in two different symmetry related molecules. Overall, the crystal packing consists of essentially centrosymmetric dimeric units linked together through Se═O—Se bridges. A 1:2 adduct of **1** with pyridine has also been prepared and characterised.

RAMESH KAPOOR, POONAM WADHAWAN, PRATIBHA KAPOOR et JEFFERY F. SAWYER. Can. J. Chem. **66**, 2367 (1988).

On a préparé les composés séléninyl bis(trifluorométhanesulfonate) (**1**) et séléninyl bis(acétate) (**2**) et on les a caractérisés par des analyses élémentaires, des spectres ir et Raman et par diffraction des rayons-X. Les cristaux du composé **1** sont monocliniques, groupe d'espace $P2_1/n$, avec $a = 12,735(1)$, $b = 5,163(4)$ et $c = 16,133(2)$ Å, $\beta = 96,426(8)$, $V = 1054$ Å^3, $D_x = 2,48$ g cm^{-3}, $Z = 4$ et $R = 0,038$ pour 1745 réflexions observées avec $I > 2,5\sigma(I)$. Ceux du composé **2** sont orthorhombiques, groupe d'espace $Pcab$, avec $a = 6,845(3)$, $b = 8,992(2)$ et $c = 23,560(9)$ Å, $U = 1450$ Å^3, $D_x = 1,95$ g cm^{-3}, $Z = 8$ et $R = 0,074$ pour 1073 réflexions observées avec $I \geq 3,0\sigma(I)$. La géométrie primaire de l'atome de Se dans $SeO(O_3SCF_3)_2$ est AX_3E avec une distance Se═O de 1,571(3) Å et des longueurs de liaison Se—O dans les ligands CF_3SO_3 de 1,902(3) et 1,922(3) Å. Pour compléter la géométrie globale de coordination de l'atome de Se, il existe deux contacts intramoléculaires et quatre contacts intermoléculaires Se...O qui sont à l'intérieur des limites de van der Waals. La géométrie globale de coordination est assez irrégulière puisque deux anions triflates sont arrangés d'une façon assez différente par rapport au tétraèdre du SeO_3E. L'empilement cristallin comporte des couches de molécules qui interagissent. Dans le composé **2**, il y a un peu de désordre. Toutefois, l'arrangement principal de la molécule comprend des distances Se═O, Se—O(1) et Se—O(3) avec les ligands acétates qui sont respectivement de 1,575(9), 1,847(7) et 1,831(8) Å. La géomètrie globale de l'atome de Se de ce composé cet complétée par deux contacts intramoléculairer secondaires Se...O impliquant les deuxièmes atomes de O de chacun des acétates et deux contacts intermoléculaires impliquant l'oxygène d'atome du séléninyle et l'atome O(2) d'un groupement acétate qui sont situés dans deux molécules qui sont différentes du point de vue de la symétrie. Dans l'ensemble, l'empilement cristallin comprend essentiellement des unites dimères centrosymétriques qui sont liées entre elles par le bias de ponts Se═O—Se. On a aussi préparé un adduit 1:2 du composé **1** avec la pyridine et on l'a caractérisé.

[Traduit par la revue]

Introduction

Earlier studies on seleninyl compounds included the synthesis of $SeO(SO_3F)_2$ (1), $SeO(C_2O_4)$ and $SeO(OOCCH_3)_2$ (2). Ionic dissociation into $SeOSO_3F^+$ and SO_3F^- was proposed to account for the high electrical conductivity of $SeO(SO_3F)_2$ (1). On the basis of infrared measurements alone a trigonal pyramidal SeO_3 group with a planar covalently bonded oxalate and planar covalently bonded acetate groups to Se has been proposed for $SeO(C_2O_4)$ and $SeO(OOCCH_3)_2$. In this paper we report the syntheses of $SeO(SO_3CF_3)_2$ and $SeO(OOCCH_3)_2$, their X-ray crystal structures and other spectral measurements. The complex of **1** with pyridine, $SeO(SO_3CF_3)_2.2C_5H_5N$, has also been isolated.

[1]Revision received April 15, 1988.

Experimental methods

Seleninyl chloride (Alfa) and trifluoromethanesulfonic acid anhydride (Aldrich) were used without further purification. All the reagents involved were highly hygroscopic and required handling in a nitrogen atmosphere dry box. Selenium was determined in its elemental form by reduction of the compounds with hydrazine hydrochloride and SO_2 solution in water. Sulphur was determined as $BaSO_4$. C, H, and N were determined microanalytically.

Preparations

Seleninyl bis(trifluoromethanesulfonate), $SeO(SO_3CF_3)_2$

Reaction was carried out in a two-bulb glass vessel incorporating a Rotoflow valve and a teflon covered stirring bar. In a typical experiment, 1.52 g (9.2 mmol) of $SeOCl_2$ was distilled into one arm of the double ampule vessel followed by 3.1 mL (5.2 g, 18.4 mmol) of trifluoromethanesulfonic acid anhydride with the help of a calibrated

Printed in Canada / Imprimé au Canada

Can. J. Chem. Downloaded from www.nrcresearchpress.com by 112.217.228.212 on 09/07/12
For personal use only.

TABLE 1. Crystal data, details of intensity measurements, and structure refinements[a]

Compound	$SeO(O_3SCF_3)_2$	$SeO(O_2C_2H_3)_2$
System	Monoclinic	Orthorhombic
a (Å)	12.735(1)	6.845(3)
b (Å)	5.163(4)	8.992(2)
c (Å)	16.133(2)	23.560(9)
β (deg)	96.426(8)	
U (Å^3)	1054	1450
fw	393.1	213.0
Z/D_x (g cm^{-3})	4/2.48	8/1.95
Space group	$P2_1/n$	*Pcab*
μ(Mo Kα)(cm^{-1})	40.2	50.9
Reflections in cell determination	$25 - (10.4 < \theta < 15.5)$	$25 - (10.6 < \theta < 15.1)$
Scan widths (deg)	$0.65 + 0.35 \tan\theta$	$0.75 + 0.35 \tan\theta$
Maximum scan time (s)	80	75
Standard reflections (number/interval in s)	3/6500[b]	3/7200
Maximum 2θ (deg)/Octants	$55/h,k,\pm l$	$55/h,k,\pm l$
Total number data collected	2881 (inc. stds.)	3927 (inc. stds.)
Unique data	2209[c]	2557
Structure solution	Patterson(Se), least-squares, Fourier	
Absorption corrections	Needle	Block
Faces: distance from origin (cm)	(0,1̄,0): 0.0180 {1,0,1}: 0.0042 (2,1,1): 0.0040	{1,0,0}: 0.0125 {0,1,0}: 0.0125 {0,0,1}: 0.0125
Grid used in calculations	8 × 14 × 8	10 × 8 × 8
Transmission range	0.698–0.765	0.316–0.390
Number observed data	$1745[I \geq 2.5\sigma(I)]$	$1073[I \geq 3\sigma(I)]$
Final $R_1(R_2)$	0.038(0.046)	0.074(0.083)
Maximum Δ/σ final cycle	0.39 (for g)	0.11
Weights, value p	0.04[d]	0.00384[e]
Extinction Corr., value of g	$2.0(4) \times 10^{-7}$	—
Esdouw, S	1.34	—
Maximum peak final ΔF map (e Å^{-3})	0.72 (0.9 Å from Se)	1.25 (1.0 Å from Se)
Programs	Enraf-Nonius SDP package on PDP 11/23 computer; Shelx on Gould 9705 computer.	
Scattering factors	From International Tables for X-Ray Crystallography	

[a]Enraf-Nonius CAD4 diffractometer; Mo Kα (graphite monochromater); λ = 0.71069 Å; T = 298 K; θ–2θ mode.

[b]No significant losses in intensities observed.

[c]105 [123] standard reflections and a further 484 [883] reflections which were systematically absent or had $F_{obs} = 0.0$ rejected. 83 [364] symmetry equivalent data then averaged ($R_{merge}(F) = 0.023$ [0.053] — no change after absorption correction) to give indicated number of unique data. Values in square brackets are for $SeOAc_2$.

[d]Weights given by $4F^2/[\sigma^2(I) + (pF^2)^2]^{-1}$.

[e]Weights given by $[\sigma^2(F) + pF^2]^{-1}$.

glass syringe in the dry-box. The contents were stirred in a warm water bath at ca. 60°C, while keeping the other arm of the ampule in an ice–water bath. After a few hours, a colourless liquid distilled over to the other side and a yellow crystalline (needle-shaped) product separated out. After about 8–10 h, the mother liquor was distilled into the other arm by cooling it in a dry ice – acetone bath. The arm containing the yellow crystalline product was then flame sealed.

The product was analysed to be $SeO(SO_3CF_3)_2$. *Anal.* calcd. for $SeC_2F_6S_2O_7$: C 6.11, Se 20.09. S 16.29; found: C 6.02, Se 20.2, S 16.1. The mother liquor distilled at 31–32°C and was identified as CF_3SO_2Cl by its Raman spectrum (3). The following bands were observed (cm^{-1}): 1454(m), 1269(vs), 1236(w), 1123(m), 782(vs), 702(s), 640(w), 592(w), 564(m), and 546(m). The band at 702 cm^{-1} is assigned to a S—Cl stretch.

The adduct of $SeO(SO_3CF_3)_2$ with pyridine was prepared by adding an excess amount of pyridine to the suspension of the compound in light petroleum ether at 0°C. The pale-white product was filtered under vacuum and dried *in vacuo*. *Anal.* calcd. for $SeC_{12}H_{10}N_2F_6S_2O_7$: C 26.13, N 5.08, S 11.62, Se 14.33; found: C 26.02, N 5.20, S 11.3, Se 14.0.

Seleninyl bis(acetate)

This was prepared by the literature method (2). In a typical experiment seleninyl chloride (2.45 g, 0.0148 mol) was stirred with anhydrous sodium acetate (2.44 g, 0.0298 mol) in dry diethylether (30 mL) for about 8 to 10 h and the precipitated silver chloride was filtered off. The solution was reduced to one-third of its volume by pumping off the solvent. The solution gave colourless needle-shaped crystals on cooling to about 3–4°C. The crystals were removed by vacuum filtration and dried. *Anal.* calcd. for $SeC_4H_6O_5$: C 22.54, H 2.82, Se 37.08; found: C 22.36, H 2.67, Se 38.0.

The infrared spectrum of $SeO(SO_3CF_3)_2$ was recorded as a neat sample on silver chloride plates and that of $SeO(OOCCH_3)_2$ as a KBr pellet by the use of a Perkin-Elmer model 283 spectrophotometer. Raman spectra were recorded with a Spex Industries Model 1400 spectrometer equipped with a double monochromator, an RCA C31034 phototube detector, an electrometer amplifier and a recorder. The exciting radiation was the green 5145 Å line of a Spectra-Physics Model 140 Ar^+ laser. Both solid and liquid samples were sealed in 1/4 in. o.d. Pyrex tubes. A ^{19}F nmr spectrum was recorded on a Bruker WM 250 spectrometer operating at 235.35 MHz.

X-ray crystallography

Crystals of **1** and **2** as thin colorless needles or blocks were selected and sealed in 0.2–0.3 mm Lindemann capillaries in a dry box under a N_2 atmosphere. Further work on an Enraf-Nonius CAD4 diffractometer gave the crystal data summarized in Table 1, which also contains a summary of the intensity measurements and structure refinements undertaken. Lorentz and polarization corrections were applied to all data collected. Absorption corrections were made at a

Can. J. Chem. Downloaded from www.nrcresearchpress.com by 112.217.228.212 on 09/07/12
For personal use only.

later stage of the refinements by the use of the progam ABSORB of the Enraf-Nonius SDP package (4). Least-squares refinement minimizing $\Sigma w\Delta F^2$ and including extinction corrections for **1** then converged to the indicated residuals. The final atomic positional and equivalent isotropic thermal parameters are given in Table 2, bond lengths, bond angles, and information about the secondary bonding in Table 3. Tables of anisotropic thermal parameters and final structure factor amplitudes for both compounds have been deposited.[2]

Results and discussion

Seleninyl bis(trifluoromethanesulfonate)

Reaction of seleninyl chloride with trifluoromethanesulphonic acid anhydride yields seleninyl bis(trifluoromethanesulphonate) in quantitative yield according to:

$$SeOCl_2 + 2(CF_3)_2S_2O_5 = SeO(SO_3CF_3)_2 + 2CF_3SO_2Cl$$

This compound is highly sensitive to moisture, fumes in moist air, and is reduced to elemental selenium. It has a pungent smell, is soluble in most of the common organic solvents such as CCl_4, CH_3CN, CH_3NO_2, $C_6H_5NO_2$, and DMF, and decomposes in DMSO to give elemental Se. Its millimolar solution in acetonitrile is non-conducting, thereby suggesting the covalent nature of $SeO(SO_3CF_3)_2$. The ^{19}F nmr spectrum shows a single peak at −73.6 ppm from external $CFCl_3$. This resonance occurs in a region characteristic for trifluoromethanesulphonates (5).

The ir and Raman spectra of $SeO(SO_3CF_3)_2$ are given in Table 4. Earlier vibrational studies on trifluoromethanesulphonates have provided information on ionic SO_3CF_3 groups (6), covalently bonded monodentate OSO_2CF_3 groups (7) and bidentate bridging SO_3CF_3 groups (8). Problems exist for accurate assignments for the SO_3CF_3 group owing to the possibility of S—O and C—F vibrations of identical symmetry being observed in the same spectral region (9, 10). Some band assignments in Table 4 have been made assuming that the C_{3v} symmetry for an isolated CSO_3 moiety (or a tridentate trifluoromethanesulphonate group) which would be responsible for six fundamentals, three E [$\nu_{as}(SO_3)$, $\delta_{as}(SO_3)$, and $\delta_s(SO_3)$] and three A [$\nu_s(SO_3)$, ν(S—C), and $\delta_s(SO_3)$] modes of ir-active vibrations is lowered to C_s as may be the case for a monodentate type of coordination. In the latter case the three E modes are split to give six bands and a total of nine ir-active bands. In the vibrational spectrum of $SeO(SO_3CF_3)_2$ both ν_4 and ν_5 modes are split indicating that the CSO_3 symmetry is reduced below C_{3v} and is consistent with a SO_3CF_3 coordination in which one oxygen is more strongly bonded to the selenium than the other two as is evident from the X-ray diffraction data below. Similarly, the selenium–oxygen vibration of the seleninyl bond at 1024 cm^{-1} is higher than that for $SeOCl_2$ (955 cm^{-1}) (11), $SeOF_2$ (1012 cm^{-1}) (12), and SeO_2F_2 (1014 cm^{-1}) (13) but significantly lower than that observed for $SeO(SO_3F)_2$ (1055 cm^{-1}) (1).

The Lewis acid character of $SeOCl_2$ is well known (14). Similar behaviour of $SeO(SO_3CF_3)_2$ has not been demonstrated and it was also possible that two or more monodentate ligands could displace the trifluoromethanesulfonate ligand(s) from this compound. In order to distinguish between these two possibilities, we have investigated the reaction of $SeO(SO_3CF_3)_2$ with pyridine which results in the formation of a 1:2 addition complex, $SeO(SO_3CF_3)_2.2C_5H_5N$. Comparison of the infrared spectrum of this adduct with that of the original compound suggests that bands due to S—O and Se=O stretching modes are observed at frequencies very close to those observed in the parent compound. Bands due to C—C, C—N, ring-breathing frequencies, and the three in-plane C—H deformations are observed at considerably higher frequencies than in pure pyridine. This is consistent with coordination to selenium through the nitrogen of pyridine (15).

Seleninyl bis(acetate)

This compound is soluble in all common organic solvents, very hygroscopic, and on exposure to moist air undergoes decomposition. It has a pungent smell, typical of selenium compounds. The ir spectrum of **2** is reported in Table 4. Several ir studies of the acetate ion have been reported and band assign-

[2]These tables are available, at a nominal charge, from the Depository of Unpublished Data, CISTI, National Research Council of Canada, Ottawa, Ont., Canada K1A 0S2.

TABLE 2. Table of positional parameters and their estimated standard deviations

(*a*) $SeO(O_3SCF_3)_2$

Atom	*x*	*y*	*z*	B (Å^2)[a]
Se	0.64753(4)	0.3315(1)	0.60969(3)	2.501(8)
S1	0.59552(9)	0.2485(2)	0.41946(7)	2.41(2)
S2	0.86712(9)	0.2423(2)	0.69191(7)	2.42(2)
F11	0.7893(3)	0.406(1)	0.4321(2)	7.8(1)
F12	0.7178(4)	0.350(1)	0.3076(2)	8.9(1)
F13	0.7664(3)	0.028(1)	0.3826(3)	10.2(1)
F21	0.9267(3)	0.5735(8)	0.5853(2)	5.96(9)
F22	0.9983(3)	0.2008(9)	0.5803(2)	7.3(1)
F23	1.0467(3)	0.459(1)	0.6809(2)	7.8(1)
O1	0.6774(3)	0.6141(7)	0.5848(2)	3.52(7)
O11	0.6232(3)	0.1423(7)	0.5081(2)	2.88(7)
O12	0.5368(3)	0.0592(7)	0.3711(2)	3.55(7)
O13	0.5600(3)	0.5097(7)	0.4208(2)	3.71(8)
O21	0.7824(2)	0.1596(7)	0.6210(2)	2.87(6)
O22	0.9137(3)	0.0206(7)	0.7328(2)	3.74(8)
O23	0.8288(3)	0.4479(7)	0.7381(2)	3.14(7)
C1	0.7248(5)	0.258(2)	0.3835(4)	5.3(2)
C2	0.9661(4)	0.378(1)	0.6301(3)	4.2(1)

[a]Anisotropically refined atoms are given in the form of the isotropic equivalent thermal parameter defined as: $(4/3) \times [a^2 \times \beta(1,1) + b^2 \times \beta(2,2) + c^2 \times \beta(3,3) + ab(\cos\gamma), \times \beta(1,2) + ac(\cos\beta) \times \beta(1,3) + bc(\cos\alpha) \times \beta(2,3)]$.

(*b*) $SeO(OOCCH_3)_2$

Atom	*x*	*y*	*z*	B/B_{eq}(Å^2)[a]
Se	0.4834(1)	0.3690(1)	0.09307(4)	2.76(3)
O	0.5854(14)	0.2182(10)	0.0764(4)	4.1(2)
O1	0.6920(11)	0.4878(8)	0.1135(3)	2.9(2)
O2	0.7035(14)	0.5115(11)	0.0191(3)	4.7(2)
C1	0.7696(15)	0.5464(13)	0.0656(4)	2.8(2)
C2	0.9399(22)	0.6505(17)	0.0750(8)	5.1(5)
O3	0.4463(12)	0.3323(9)	0.1688(4)	3.4(2)
O4a	0.2894(14)	0.5488(10)	0.1729(3)	4.3(2)
C3a	0.3379(17)	0.4367(14)	0.1962(4)	3.2(3)
C4a	0.3093(26)	0.3972(18)	0.2607(7)	6.6(6)
O4b[b]	0.402(10)	0.139(6)	0.102(2)	4.8(12)[c]
C3b[b]	0.458(17)	0.167(14)	0.165(5)	7.0(24)[c]
C4b[b]	0.439(9)	0.117(6)	0.221(3)	2.5(9)[c]
O1b[b]	0.642(5)	0.137(4)	0.092(1)	2.8(5)[c]
O1c[b]	0.279(15)	0.294(11)	0.062(5)	3.3(19)[c]

[a]Anisotropically refined atoms are given in the form of the equivalent isotropic thermal parameter, $B_{eq} = (1/3)$ trace **B**.

[b]Population parameters: O4b, C3b, and C4b = 0.175; O1b = 0.250 and O1c = 0.075.

[c]Refined isotropically.

Can. J. Chem. Downloaded from www.nrcresearchpress.com by 112.217.228.212 on 09/07/12
For personal use only.

TABLE 3. Selected bond lengths (Å), contact distances (Å), and related bond angles (deg) with estimated standard deviations in parentheses

(*a*) $SeO(O_3SCF_3)_2$

Bond	Length	Bond	Length	Bond	Length
Se—O(1)	1.571(3)	Se—O(13)	3.256(3)	Se—O(22)^{III}	2.908(3)
—O(11)	1.902(3)	—O(13)^{I}	2.756(3)	—O(23)	2.984(3)
—O(12)^{II}	3.134(3)	—O(21)	1.922(3)	—O(23)^{IV}	3.141(3)

	Length			Length	
Bond	$n = 1$	$n = 2$	Bond	$n = 1$	$n = 2$
S(n)—O(n1)	1.535(3)	1.541(3)	C(n)—F(n1)	1.317(7)	1.310(6)
—O(n2)	1.410(3)	1.418(3)	—F(n2)	1.307(7)	1.311(7)
—O(n3)	1.423(3)	1.415(3)	—F(n3)	1.296(8)	1.308(6)
—C(n)	1.806(5)	1.828(5)			

(*ii*) Bond angles at Se, X—Se—Y (deg)[a]

X/Y	O(11)	O(12)^{II}	O(13)	O(13)^{I}	O(21)	O(22)^{III}	O(23)	O(23)^{IV}
O(1)	106.1	145.9	64.3	86.2	102.3	90.5	78.4	141.3
O(11)		72.7	48.2	86.4	84.5	152.9	137.7	110.0
O(12)^{II}			95.3	59.8	111.4	81.5	126.2	61.7
O(13)				61.8	115.3	128.7	138.5	154.4
O(13)^{I}					169.0	73.2	135.7	109.4
O(21)						113.3	54.1	68.2
O(22)^{III}							65.7	62.6
O(23)			$\sigma \approx 0.07$–$0.15°$					65.5

[a]Symmetry operations: ^{I}, $1-x, 1-y, 1-z$; ^{II}, $1-x, -y, 1-z$; ^{III}, $3/2-x, 1/2+y, 3/2-z$; and ^{IV}, $3/2-x, -1/2+y, 3/2-z$.

(*iii*) Other bond angles (deg)

	Angle			Angle	
Bonds	$n = 1$	$n = 2$	Bonds	$n = 1$	$n = 2$
O(n1)—S(n)—O(n2)	108.6(2)	110.1(2)	O(n2)—S(n)—O(n3)	121.0(2)	120.8(2)
—O(n3)	111.3(2)	110.1(2)	—O(n4)	106.6(3)	106.5(2)
—O(n4)	100.8(2)	99.8(2)	O(n3)—S(n)—O(n4)	106.5(3)	107.4(2)
S(n)—C(n)—F(n1)	110.7(4)	110.6(4)	F(n1)—C(n)—F(n2)	108.4(6)	108.9(4)
—F(n2)	109.9(4)	110.5(4)	—F(n3)	108.0(6)	108.8(5)
—F(n3)	111.6(5)	108.8(3)	F(n2)—C(n)—F(n3)	108.2(6)	109.2(5)
Se—O(n1)—S(n)	128.1(2)	119.1(2)			

(*b*) $SeO(OOCCH_3)_2$[a]

(*i*) Bond lengths (Å)

Bond	Length	Bond	Length	Bond	Length
Se—O	1.575(9)	Se...O(4a)	2.814(7)	O(1)—C(1)	1.355(12)
—O(1)	1.847(7)	...O(2)^{I}	3.126(8)	O(2)—C(1)	1.227(12)
...O(2)	2.637(9)	...Se^{II}	4.036(1)	C(1)—C(2)	1.511(17)
—O(3)	1.831(8)	...O^{II}	2.862(10)	O(3)—C(3a)	1.360(14)
				O(4a)—C(3a)	1.194(14)
				C(3a)—C(4a)	1.573(18)

Can. J. Chem. Downloaded from www.nrcresearchpress.com by 112.217.228.212 on 09/07/12
For personal use only.

TABLE 3 (*concluded*)

(*ii*) Angles around Se, X—Se—Y (deg)

X/Y	O(1)	O(2)	O(3)	O(4a)	$O(2)^{I}$	O^{II}
O	102.7	90.0	98.6	150.5	105.4	98.7
O(1)		56.6	87.5	81.8	109.7	158.5
O(2)			144.2	115.6	60.5	125.9
O(3)				52.2	145.9	87.3
O(4a)					100.0	78.5
$O(2)^{I}$		$\sigma \approx 0.3$–4				65.7

(*iii*) Other bond angles (deg.)

Bonds	Angle	Bonds	Angle
Se—O(1)—C(1)	108.1(6)	Se—O(3)—C(3a)	114.4(7)
Se—O(2)—C(1)	75.2(6)	Se—O(4a)—IC(3a)	72.0(6)
O(1)—C(1)—O(2)	120.0(10)	O(3)—C(3a)—O(4a)	121.1(10)
O(1)—C(1)—C(2)	115.0(10)	O(3)—C(3a)—C(4a)	111.8(11)
O(2)—C(1)—C(2)	125.0(11)	O(4a)—C(3a)—C(4a)	126.8(11)
Se—O...Se^{III}	128.6(5)	Se—O(2)...Se^{I}	119.5(3)

[a]Symmetry operations: ^{I}, $1-x, 1-y, -z$; ^{II}, $-1/2+x, 1/2-y, z$; ^{III}, $1/2+x, 1/2-y, z$.

TABLE 4. Spectral data for compounds $SeO(SO_3CF_3)_2$ (**1**) and $SeO(O_2CCH_3)_2$ (**2**)[a]

Band assignments for XSO_3 moiety	IR frequencies of (**1**) (cm^{-1})	Raman frequencies of (**1**) (cm^{-1})	IR frequencies of (**2**)[b] (cm^{-1})	Band assignments for acetate group
SO_3 as stretch[c]	1385 s	1240 m	1702vs	C—O as. str.
	1200 vs		1424 w	CH_3 defn.
			1365 m	CH_3 sym. defn.
SO_3 sym. stretch	1020 vs	1024 vs	1200 vs	C—O sym. str.
+			1038 w	CH_3 rock
νSe═O			995 w	
C—S stretch	756 m	767 m	955 vs	Se═O str.
SO_3 as. defn.[c]	620 s		880 s	C—C str.
	605 s		680 s	COO sym. defn.
SO_3 sym. defn.	570 m	580 w	595 w	COO out of plane
S—X defn.[c] + CF_3	1180 s	1223 m	525 w	
	1145 sh	1190 m	400 w	
	920 m	423 vs	360 w	Unassigned
	510 s	405 vs	330 w	
	495 w	350 m		
	475 sh	316 m		
		206 m		
		185 m		

[a]vs very strong; s strong, m medium, w weak and sh shoulder.
[b]Raman spectrum could not be recorded due to visible destruction of the sample in the lasar beam.
[c]*E* modes for isolated $CF_3SO_3^-$ ion of C_{3v} symmetry — split in a unidentate or bidentate covalently bonded group of local symmetry C_s.

ments have been made (16, 17). In **2** two intramolecular Se...O contacts involving the second oxygen atoms of the acetate groups are observed so that the coordination of the acetate group to selenium may be classed as unsymmetrically bidentate (18). The difference $\Delta\nu$ ($\nu_1(COO^-)-\nu_s(COO^-)$) is suggested to be somewhat indicative of the mode of coordination of the acetate group in different complexes with the separation in the free ion values (ca. 1560 and 1416 cm^{-1}) increasing in unidentate complexes and when the acetate bridges two metal centres due to the increasing difference in the carbon–oxygen bond orders (18, 19). In the present compound the slight differences in the acetate coordination modes observed in the crystal structure (see below) are not apparent in the spectra and the large $\Delta\nu$ separation of 500 cm^{-1} is consistent with an unidentate mode in which the interaction of the second oxygen atoms of the acetates with the selenium is quite weak.

Another notable feature in the spectrum is the observation of a Se═O stretching band at 955 cm^{-1} in seleninyl bis(acetate). This band is observed at a much lower value than that in seleninyl bis(trifluoromethanesulfonate) (1024 cm^{-1}) although

Can. J. Chem. Downloaded from www.nrcresearchpress.com by 112.217.228.212 on 09/07/12
For personal use only.

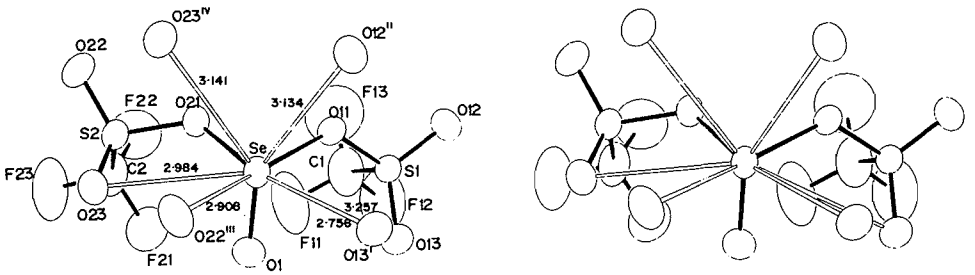

FIG. 1. Stereoscopic view of $SeO(O_3SCF_3)_2$ showing the complete coordination geometry of the Se atom. Secondary bonds are indicated by the unfilled bonds.

the selenium–oxygen distances (1.575 Å in $SeO(OOCCH_3)_2$ and 1.571 Å in $SeO(O_3SCF_3)_2$) are the same and do not suggest that there should be any shift towards higher wave numbers in the acetate. Such a correlation between Se—O bond distance and its stretching frequency is very difficult to draw without X-ray structures. The lowering in selenium–oxygen stretching frequency in $SeO(OOCCH_3)_2$ may be attributed to intermolecular interactions btween the oxygen of the Se=O group and the Se atom of another molecule.

Discussion of crystal structures

(1) Seleninyl bis(trifluoromethanesulfonate)

The primary geometry of the selenium atom in $SeO(O_3SCF_3)_2$ is AX_3E with a Se=O distance of 1.571(3) Å and Se—O bond lengths to the trifluoromethanesulfonate ligands of 1.902(3) and 1.922(3) Å. Completing the overall coordination geometry of this Se atom are two intramolecular and four further intermolecular Se...O contacts which are less than the sum of the neutral atom van der Waals radii for Se and O (3.35 Å). This overall Se coordination geometry is not easily described since the two triflate anions are significantly differently rotated about the Se—O(11) and Se—O(21) bonds so that the molecule has no overall molecular symmetry. This can be seen in the difference between the two torsion angles τ(Se—O(21)—S(2)—O(23)) = −1.4(3) and τ(Se—O(11)—S(1)—O(13)) = −16.5(3)° and the enlargement of the angle Se—O(11)—S(1) = 128.1(2)° over Se—O(21)—S(2) = 119.1(2)°. Similarly this results in the two atoms O(13) and O(23) forming the intramolecular contacts being 0.913(3) and −0.761(3) Å, respectively below and above the O(1)—O(11)—O(21) basal plane (Se is −0.860 Å above the plane). The long Se...O(13) intramolecular contact (3.257(3) Å) is however, compensated for by the fairly short intermolecular Se...$O(13)^I$ contact (2.758(3) Å). This latter contact and the intermolecular contact Se...$O(22)^{III}$ are approximately *trans* to the Se—O(11) and Se—O(21) bonds (O(11)—Se...$O(22)^{III}$ = 152.9(5)°; O(21)—Se...$O(13)^I$ = 169.0(1)°) and with the two remaining intermolecular contacts to $O(12)^{II}$ and $O(23)^{IV}$ clearly avoid and help define the position of the expected lone pair on Se (Fig. 1).

Secondary bonding is invariably present in seleninyl compounds and their related ions and adducts (14, 20) but it is rare to observe as large a number of contacts as that found for the present compound. By the use of a formalism proposed (21) for the description of the overall primary and secondary geometries of Sb(III) and related compounds the geometry in the present compound might be approximately denoted as $AX_3(Y')Y'_2Y_3E$ with O(23), O(13), and O(12) as the face capping [Y] contacts, $O(23)^{III}$ and $O(22)^{IV}$ the edge bridges [Y'] and the intramolecular contact to O(13) is considered to bridge the O(1)...O(11) edge of the polyhedron. The arrangement of the present intermolecular contacts is similar to the overall geometry of one of the Se atoms in the compound $(Se_4S_2N_4)(AsF_6)_2$ (see Fig. 3 in ref. 22) and has been observed in other compounds, e.g. the environment of the Sb(III) atom in $CsSbClF_3$ (21).

The strengths of these and other secondary bonding interactions can usually be approximately calculated using the bond valence curves of Brown and others (23). For Se(IV)—O interactions the curve has the form $S = S_0 (R/R_0)^{-N}$ with $S = 1.0$, $R = 1.796$ Å, and $N = 4.0$, and its application results in a bond valence sum Σs for all the selenium–oxygen distances indicated in Fig. 1 of 4.03, compared to the expected value of 4.0. The six longer intra- and intermolecular contacts account for 19% of this sum.

The primary and secondary bond lengths in $SeO(O_3SCF_3)_2$ are compared to values for other seleninyl compounds in Table 5. It is notable that the present Se=O distance has the same value as that in the $SeOCl_2$·dioxane solvate (14) although the O atom in the latter compound is also involved in Se...O secondary bonding (2.902(11) Å). Both of these values are somewhat shorter than other values in the table and nominally Se=O distances in compounds such as H_2SeO_3 (Se=O = 1.643 Å) (24). Similarly, the Se—O single bonds to the triflate anions are significantly different due to the different arrangement of the anions as noted above. Both distances are enlarged over distances observed in selenates or selenites (⟨Se—O⟩ = 1.641 and 1.704 Å respectively) (20*b*). The long weak Se—O(11), O(21) and short, strong Se—O(1) bonds explain the contracted small O(11)—Se—O(21) bond angle of 84.5(1)° and enlarged O=Se—O bond angles (102.3(2), 106.1(2)°). The significant 3.8° difference in the latter angles is consistent with the Se—O(11), O(21) bond lengths since the smaller angle involves the longer Se—O(21) bond, although the intermolecular contacts will also affect these angles slightly.

As a consequence of the intermolecular contacts, the crystal packing (Fig. 2) consists of layers of interacting molecules in the $(\bar{1},0,1)$ plane held together by F...F contacts between the CF_3 groups on the upper and lower surfaces of each layer.

In the trifluoromethanesulfonate groups the C—F and S—C bond lengths are normal (25). In ionic examples the lengths of the S—O bonds, however, are a function of hydrogen bonding and other contacts (26) but are typically ≤1.46 Å in length. Similarly, in two organometallic examples where the ligand is directly bonded to the metal the S—O distances of 1.456(6) Å (aquodimethyl(trifluoromethanesulfonato)gold(III)) (27) and 1.441(8) Å (trifluoromethanesulfonato)-(3-(diethylamino)-propionyl)(diethylamine)palladium(II)) (28) are still significantly shorter than the present S(1)—O(11) and S(2)—O(21) distances (1.535(3) and 1.541(3) Å). Moreover, these

Can. J. Chem. Downloaded from www.nrcresearchpress.com by 112.217.228.212 on 09/07/12
For personal use only.

TABLE 5. Bond lengths and secondary contacts in some seleninyl compounds

Compound	Se=O (Å)	Se—X (Å)	Se...Y (Å)
$SeOF_2$[a]	1.62(3)	1.68(2), 1.72(3)	2.68(3)[O], 2.83(3)[O], 3.03(3)[F]
$SeOCl_2$[b]	1.612(5)	2.204(5)[x2]	Electron diffraction
$SeOBr_2$[c]	1.61(1)	2.351(2)–2.366(2)	3 contacts present — no other details
$SeO(O_3SCF_3)_2$[d]	1.571(3)	1.902(3), 1.922(3)	2.984, 3.257 (intra) 2.756, 3.134, 2.908, 3.142[O] (inter)
$SeO(O_2CCH_3)_2$[d]	1.575(9)	1.847(7), 1.831(8)	2.637(9), 2.814(7) [O] (intra) 2.862, 3.126 [O] (inter)
SeO_3(monomeric)[e]	1.69(1)		Electron diffraction
$SeOCl_2$.dioxan[f]	1.571(11)	2.235(5), 2.202(7)	2.902(11), 2.614(13), 2.724(15) [O]

[a]Reference 20*a*.
[b]Reference 14.
[c]Reference 20*c*.
[d]This work.
[e]See ref. 30.
[f]Reference 14.

Can. J. Chem. Downloaded from www.nrcresearchpress.com by 112.217.228.212 on 09/07/12
For personal use only.

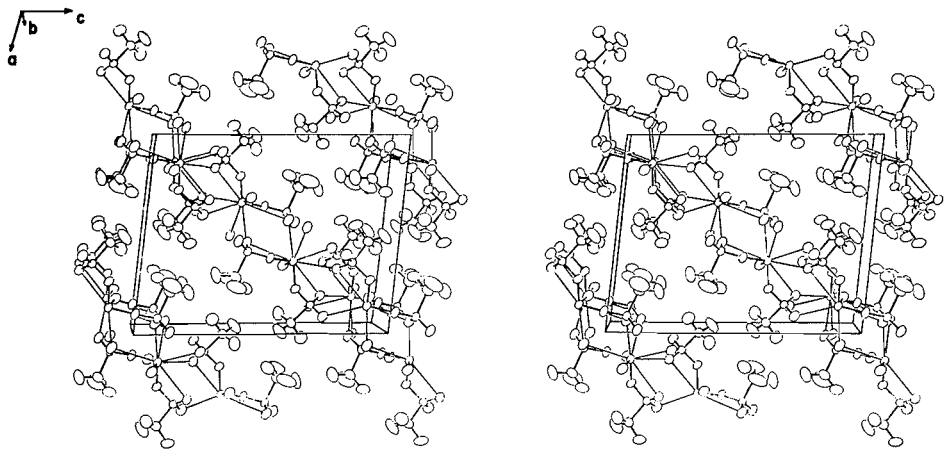

FIG. 2. Stereoscopic view down *b* of the crystal packing of $SeO(O_3SCF_3)_2$.

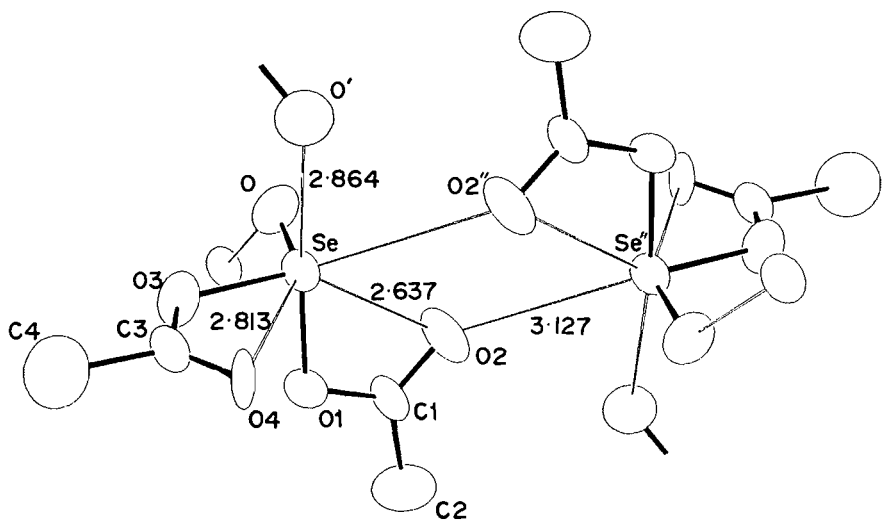

FIG. 3. View of the dimeric unit and the further interactions involving the seleninyl group in the structure of $SeO(OOCCH_3)_2$. Secondary bonds are indicated by the thin bonds.

distances and the short S(1)—O(12), O(13), and S(2)—O(22), O(23) distances as well as the OSO and CSO bond angles are more compatible with the dimensions of trifluoromethane sulfonic acid (S—OH = 1.531(4), S—O = 1.412, 1.424(3) Å) (29).

(2) Seleninyl bis(acetate)

There is some disorder in this compound involving a few residual peaks representing up to ca. 25% of an oxygen atom (Table 2). The peaks denoted O(4b), C(3a), and C(4a), along

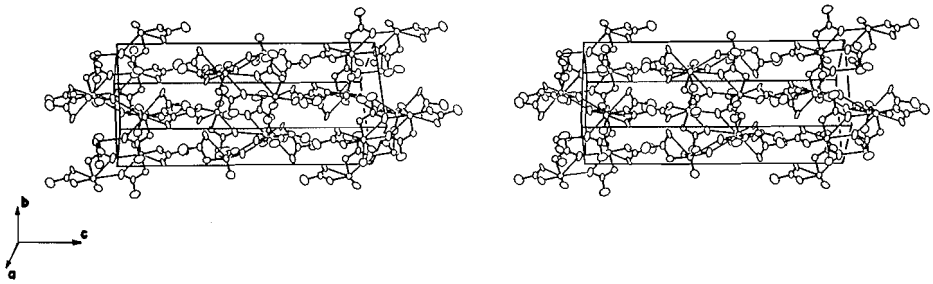

FIG. 4. Stereoscopic view approximately down *a* of the crystal packing of $SeO(OAc)_2$. Secondary bonds are indicated by the unfilled bonds.

Can. J. Chem. Downloaded from www.nrcresearchpress.com by 112.217.228.212 on 09/07/12
For personal use only.

with O(4a) appear to define an alternative arrangement of one acetate; those denoted O(1b) and O(1c) result in alternative bridging arrangements involving the seleninyl group or even possibly the presence of $SeOCl(OOCCH_3)$ in the lattice. The following discussion is, however, limited to the geometry and packing of the major component atoms. As with $SeO(O_3SCF_3)_2$ above, the primary geometry of the Se atom in $SeO(OOCCH_3)_2$ consists of a Se=O bond of length 1.575(9) Å and Se—O bonds to the acetate ligands of lengths 1.847(7) and 1.831(8) Å. Both of the latter distances are significantly shorter than the Se—O distances to the triflate ligands. Completing the overall geometry of the Se atom are two intramolecular contacts involving the acetate oxygen atoms O(2) and O(4a) of lengths 2.637(9) and 2.814(7) Å and two intermolecular contacts involving the seleninyl oxygen atom (2.862(10) Å) and O(2) (3.126(8) Å) of symmetry related molecules. Overall the packing consists of centrosymmetric dimeric units linked by the interactions involving O(2) which are further enchained by the bridging Se=O...Se interactions (Figs. 3 and 4).

The environment of the Se atom might be designated as $AX_3Y_3Y'E$ representing a monocapped octahedral arrangement of ligands and lone pair which is further distorted by the second intermolecular contact involving O(2). As with $SeO(O_3SCF_3)_2$, a bond valence calculation gives a Σs of 4.16 for all the selenium–oxygen interactions in $SeO(OOCCH_3)_2$ with the longer secondary interactions accounting for 15% of this sum.

Consistent with the stronger Se—O(Ac) bonding in the present compound it is notable that the O(1)—Se—O(3) angle between the acetate ligands is ca. 3° larger (87.5(4)°) and the O=Se—O(1),O(3) angles are ca. 3° smaller (102.7, 98.6(4)°) than corresponding values in $SeO(O_3SCF_3)_2$ above (84.5(1), 106.1, and 102.3(2)°). In the acetate groups it is notable that the interactions involving O(2) results in a smaller Se—O(1)—C(1) angle (108.1(6) cf.Se—O(3)—C(3)=114.4(7)°) and an apparent lengthening of the C(1)—O(2)=1.227(12) Å bond (cf. C(3a)—O(4a)=1.194(14) Å).

Acknowledgement

We thank the Natural Sciences and Engineering Research Council of Canada for a grant for the diffractomer and one of us (P.W.) thanks U.G.C. (India) for a research fellowship.

1. H. A. CARLIN and F. AUBKE. Inorg. Nucl. Chem. Lett. **5**, 999 (1969).
2. R. PAETZOLD. Z. Chem. **6**, 72 (1966).
3. R. N. HASZELDINE and J. M. KIDD. J. Chem. Soc. 2901 (1955).
4. Enraf-Nonius Structure Determination Package. B. A. Frenz and Associates, College St., TX.
5. C. H. DUNGON, and J. R. VAN WAZER. Compilation of reported ^{19}F chemical shifts 1951–67, Wiley-Interscience, New York 1970.
6. F. A. SCHRODER, B. GANSWEIN, and G. BRAVER. Z. Anorg. Allg. Chem. **391**, 295 (1972).
7. M. WECHSBERG, P. A. BULLINER, F. O. SLADKY, R. MEWS, and N. BARTLETT. Inorg. Chem. **11**, 3063 (1972).
8. P. A. YEATS, J. R. SAMS, and F. AUBKE. Inorg. Chem. **11**, 2634 (1972).
9. M. G. MILES, G. DOYLE, R. P. COONEY, and R. S. TOBIAS. Spectrochim. Acta, Part A, **25**, 1515 (1969).
10. H. BURGER, K. BUROZYK, and A. BLASCHETTE. Monatsh. Chem. **101**, 102 (1970).
11. H. GERDING. Rec. Trav. Chim. **60**, 728 (1941).
12. J. A. ROLFE and L. A. WOODWARD. Trans. Faraday Soc. **51**, 778 (1955).
13. T. BIRCHALL and R. J. GILLESPIE. Spectrochim. Acta, **22**, 681 (1966).
14. N. W. ALCOCK and J. F. SAWYER. J. Chem. Soc. Dalton Trans. 115 (1980).
15. N. N. GREENWOOD and K. WADE. J. Chem. Soc. 1130 (1960).
16. K. ITOH and H. J. BERNSTEIN. Can. J. Chem. **34**, 170 (1956).
17. K. NAKAMEINE. Chem. Soc. Jpn. **79**, 1411 (1958); **79**, 1420 (1958).
18. N. W. ALCOCK, V. M. TRACY, and T. C. WADDINGTON. J. Chem. Soc. Dalton Trans. 2243 (1976).
19. K. NAKAMOTO. Infrared spectra of inorganic and coordination compounds. 2nd ed. Wiley-Interscience, New York. 1970. p. 232.
20. (*a*) J. C. DEWAN and A. J. EDWARDS. J. Chem. Soc. Dalton Trans. 2433 (1976); (*b*) A. W. CORDES. *In* Selenium. *Edited by* R. A. Zingaro and W. C. Cooper. Van Nostrand Reinhold, NY. 1974; (*c*) B. KREBS, M. HUCKE, and A. SCHAFFER. Z. Krist. **159**, 84 (1982).
21. J. F. SAWYER and R. J. GILLESPIE. Prog. Inorg. Chem. **34**, 65 (1986).
22. R. J. GILLESPIE, J. P. KENT, and J. F. SAWYER. Inorg. Chem. **20**, 4053 (1981).
23. I. D. BROWN and K. K. WU. Acta Crystallogr. **B32**, 1957 (1976).
24. F. K. LARSEN, M. S. LEHMANN and I. SOTOFTE. Acta Chem. Scand. **25**, 1233 (1971).
25. R. G. DELAPLANE, J.-O. LUNDGREN, and I. OLOVSSON. Acta Crystallogr. **B31**, 2202 (1975).
26. J.-O. LUNDGREN. Acta Crystallogr. **B34**, 2428, (1978); **B34**, 2432 (1978).
27. S. KOMIYA, J. C. HUFFMAN, and J. K. KOCHI. Inorg. Chem. **16**, 2138 (1977).
28. O. P. ANDERSON and S. B. PACKARD. Inorg. Chem. **18**. 1129 (1979).
29. R. G. DELAPLANE, J.-O. LUNDGREN, and I. OLOVSSON. Acta Crystallogr. **B31**, 2208 (1975).
30. A. K. BRISDON and J. S. OGDEN. J. Mol. Struct. **157**, 141 (1987).

Prototropic reactions for 1-, 2-, and 4-fluorenamides in the ground and excited singlet states

RAMASAMY MANOHARAN AND SNEH K. DOGRA[1]
Department of Chemistry, I.I.T. Kanpur, Kanpur-208 016, India

Received November 26, 1987

RAMASAMY MANOHARAN and SNEH K. DOGRA. Can. J. Chem. **66**, 2375 (1988).

Absorption and fluorescence spectra of 1-, 2- and 4-fluorenamides (1-FAm, 2-FAm, 4-FAm) were studied in different solvents and at various acid concentrations. This study indicates that the long wavelength absorption band is long-axis polarised in 2-FAm whereas in 1-FAm and 4-FAm, it is composed of long- and short-axis polarised transitions. The —$CONH_2$ group in 1-FAm and 4-FAm is coplanar with the fluorene moiety, whereas the same group in 2-FAm is non-coplanar with the fluorene ring in non-polar solvents, both in S_0 and S_1 states, but attains coplanarity in the polar and hydrogen bonding solvents in the S_1 state. Hammett's acidity scale is not valid for the protonation reaction of amides and a medium effect is observed on the absorption spectra of the monocations in strong sulphuric acid. The prototropic equilibrium for the protonation of ring carbon atom is not established in the S_1 state, due to the slower rate of protonation reaction. Proton-induced fluorescence quenching of the monocations is followed before the monocations are being protonated.

RAMASAMY MANOHARAN et SNEH K. DOGRA. Can. J. Chem. **66**, 2375 (1988).

Utilisant différents solvents et des concentrations différentes d'acide, on a étudié les spectres de fluorescence des fluorénamides-1, -2 et -4 (FAm-1, FAm-2, FAm-4). Ces études indiquent que la grande longueur d'onde d'absorption est polarisée selon le grand axe dans le composé FAm-2 tandis que dans les composés FAm-1 et FAm-2 cette longueur d'onde est composée de transitions polarisées selon les deux axes. Le groupe —$CONH_2$ du compé FAm-1 et l'unité fluorène sont coplanaires, tandis que dans le composé FAm-2, cette coplanéarité n'existe pas dans les solvants non-polaires dans les états S_0 et S_1, mais on l'observe dans l'état S_1 dans les solvants polaires et dans les solvants contenant des liaisons hydrogènes. L'échelle d'acidité de Hammett n'est pas valable pour la réaction de protonation des amides et on observe un effet du milieu sur les spectres d'absorption des monocations dans l'acide sulfurique fort. On n'a pas pu déterminer l'équilibre prototropique de la protonation de l'atome de carbone du cycle dans l'état S_1, à cause de la vitesse plus lente de la réaction de protonation. On observe l'arrêt de fluorescence du monocation, induit par le proton, avant la protonation des monocations.

[Traduit par la revue]

Introduction

Many organic molecules possess more than one site of protonation or deprotonation and determining which of these is the main reaction is not always simple. Amides are one group of such molecules where the site of protonation can be either the carbonyl oxygen or the nitrogen atom of the amino group. Stewart (1) has recently reviewed this subject. Liler (2) favoured the site to be the amino-nitrogen atom. This was based on the fact that (*i*) the hydroxide-catalysed reaction is faster than the hydronium-catalysed one (3–5) and (*ii*) the pK_a values for the prototropic reactions (~−2) are not consistent with the pK_a values (~−7) of similar reactions of other carbonyl groups in carboxylic acids and esters (6, 7). Liler (2) also proposed that while in aqueous sulphuric acid the protonation occurs at the amino-nitrogen group, in concentrated or anhydrous sulphuric acid, it occurs at the carbonyl oxygen atom, indicating the presence of tautomerism.

However the vast majority of workers in this field have concluded that the site of protonation is the carbonyl oxygen atom and a large amount of evidence now exists in favour of oxygen protonation (8–16). Their studies also include (*i*) Hammett's acidity scale cannot be used to calculate the pK_a value for this prototropic reaction (8–11); thus a new scale, H_A, was developed to calculate the pK_a value in the real thermodynamic sense (10); (*ii*) the absorption spectra of the monocations of the amides depend on the environment and a regular red shift in the absorption spectrum is observed with an increase in acidity (11*c*, *d*).

Unfortunately, theoretical studies have not been able to solve this controversy. Although they favour oxygen protonation in the gas phase, they predict that increasing "pyramidization" of the —NH_2 group, which might occur in solution, increases the nitrogen basicity and decreases the oxygen basicity (17).

Our aim in the present study of 1-fluorenamide (1-FAm), 2-fluorenamide (2-FAm), and 4-fluorenamide (4-FAm) is to study the effect of solvents and acid concentration on the absorption and fluorescence spectra of these amides. At the same time, we have tried to assign the nature of the transition of the longest wavelength band and to calculate the pK_a values for the various prototropic reactions in the ground and excited singlet states.

Materials and methods

Acid chlorides of 1-fluorenecarboxylic acid (1-FA), 2-fluorenecarboxylic acid (2-FA), and 4-fluorenecarboxylic acid (4-FA) were prepared by the thionyl chloride method (18). After purification, these carbonyl chlorides were reacted with cold aqueous ammonia to give their corresponding amides. All the amides were recrystallised from ethanol and purity was checked by noting the melting points, elemental analysis, ir spectra, nmr spectra, and obtaining similar fluorescence spectra excited with different wavelengths. The data as listed in Table 1 agree reasonably well with the data of compounds containing similar functional groups. Analytical grade sulphuric acid, sodium hydroxide, *o*-phosphoric acid, and trifluoroacetic acid (TFA), all of BDH, were used as such. Analytical grade cyclohexane (SDS), dioxane (BDH), acetonitrile (E. Merck), and methanol (E. Merck) were further purified according to the procedure described in the literature (19). Triply distilled water was used for aqueous solutions. The modified Hammett's acidity scale (H_0) (20), as well as the H_A scale (10) for H_2SO_4–H_2O mixtures below pH 1 and Yagil's basicity scale (21) for NaOH–H_2O mixtures, above pH 13, were used.

Absorption spectra were recorded on a Shimadzu UV 190 spectro-

[1]To whom all correspondence should be addressed.

Printed in Canada / Imprimé au Canada

Can. J. Chem. Downloaded from www.nrcresearchpress.com by 112.217.228.212 on 09/07/12
For personal use only.

TABLE 1. Characteristics of 1-, 2-, and 4-fluorenamides

Compound	Melting point (°C)	Elemental analyses (%) C	H	N	Infrared (cm^{-1})	NMR(^1H)
1-FAm	247	79.8 (80.4)	5.4 (5.3)	6.1 (6.7)	3325 3150 1660 1620	7.3–8.3[a] (m) 4.2 (s) 4.5 (bs)
2-FAm	228	81.0 (80.4)	5.2 (5.3)	6.4 (6.7)	3360 3160 1650 1610	7.3–8.3[b] (m) 4.1 (s) 5.3 (bs)
4-FAm	137	79.2 (80.4)	5.6 (5.3)	6.2 (6.7)	3360 3170 1635 1600	7.2–8.3[c] (m) 6.1 (bs) 3.9 (s)

[a]DMSO:TMS.
[b]DMSO/CD_3Cl:TMS.
[c]$CDCl_3$:TMS.

photometer, equipped with a U 135 recorder. Fluorescence measurements were made on a scanning spectrofluorimeter, fabricated in our laboratory, details of which are reported elsewhere (22). Both the excitation and emission monochromator were calibrated with a low pressure mercury lamp from time to time. The band width used for excitation is 8 nm. The quantum yields in different solvents were calculated for solutions with absorbance less than 0.1. The fluorescence spectra were corrected according to the procedure of Parker (23), and quinine sulphate in 0.1 N H_2SO_4 was used as a fluorescence standard (24). The excitation wavelength used for 1-FAm is 313 nm. 2-FAm and 4-FAm were excited at 300 nm. The fluorescence spectrum at 77 K was recorded in an aqueous medium with varying concentrations of acid. This system does not form a perfect glass and a lot of scattering was observed. The fluorescence spectrum of the different species at 77 K was obtained by scanning the solutions with and without fluorophore. The experiments in these solutions were designed to observe if the different prototropic species, which were non-fluorescent at 298 K, are fluorescent at 77 K. The concentrations of the solutions used were 2×10^{-5} M, containing no more than 1% (v/v) ethanol. For absorptiometric and fluorimetric titrations, the solutions were prepared just before taking measurements. The fluorescence intensity at any analytical wavelength was measured by exciting the solutions at their isosbestic points. The pH of the solutions in the range of 1–13 was measured on a Toshniwal pH meter model CL 44A.

Results

Effect of solvents

The absorption and fluorescence spectra of 1-FAm, 2-FAm, and 4-FAm were recorded in different solvents (shown in Fig. 1) and at various acid concentrations (shown in Fig. 2). The relevant data are compiled in Table 2. The data of Table 2 clearly show that the long wavelength absorption maximum of 1-FAm is more diffuse and largely red-shifted as compared to the maxima of 4-FAm, 2-FAm, and fluorene (25). In the case of 4-FAm, the absorption spectrum is broad and featureless. The absorption spectra of 2-FAm and 4-FAm resemble those of the respective carboxylic acids (26) but in case of 1-FAm, the spectrum is blue-shifted in comparison to 1-FA (1-fluorenecarboxylic acid) (27). In all cases, absorption spectra are unaffected by the nature of the solvent environment.

The fluorescence spectrum of 2-FAm is structured in cyclohexane but this structure is lost as the solvent polarity or proton donor/acceptor property of the solvent increases. The fluorescence spectral profile of 2-FAm resembles that of 2-FA (2-fluorene carboxylic acid) (26). On the other hand, the fluorescence spectra of 1-FAm and 4-FAm are broad and red-shifted, both with respect to fluorene (25) and to 2-FAm. Similar to 2-FAm, the fluorescence spectra of 1-FAm and 4-FAm are progressively red-shifted upon increasing the polarity and hydrogen bonding ability of the solvents. It can be noted from the data on Table 2 that the fluorescence band maxima of any one amide in any one solvent is blue shifted with respect to the corresponding acids, the blue shift being especially large for 1-FAm in water. The fluorescence quantum yield increases with increasing proton donor capacity of the solvents.

Effect of acid concentration

The absorption spectra of all the species remain unchanged in the range of H_- 16 to pH 0, except that a large red-shift is observed in the case of 4-FAm, after pH 14. Below pH 0, a red-shift is observed in all the amides. Clear isosbestic points are observed till $H_0 - 4$ followed by a continuous red-shift upto $H_0 - 7$ (Fig. 4). Similar behaviour is observed in other primary amides. The former behaviour is due to the formation of a monocation, whereas the latter behaviour is due to a medium effect (11*d*). A blue shift is observed after $H_0 - 7$, because of the dication species formed by protonating the ring carbon atom. Similar to the absorption spectra, the fluorescence spectra of the monocations are red shifted as compared to the neutral species, except that the monocation of 1-FAm is non-fluorescent in aqueous medium but fluorescent in cyclohexane + 2% TFA (v/v). Below $H_0 - 2$, the fluorescence intensities of monocations start decreasing without the appearance of any other new band. This has been assigned to the proton-induced fluorescence quenching of monocations as observed in naphthamides (28, 29). The blue-shifted fluorescence band below $H_0 - 4$ for 2-FAm is assigned to the dication, formed by the protonation of cabonyl oxygen atom and the ring carbon atom, but similar species of 1-FAm and 4-FAm are non-fluorescent at 298 K (*vide infra*). The fluorescence spectra of the neutral amides and monocations at H_0 0 and -6 (where the monocations are non-fluorescent at 298 K) and the dications at $H_0 - 10$ were recorded at 77 K. Unlike room temperature studies, all the species, are fluorescent and a normal blue shift is observed

Can. J. Chem. Downloaded from www.nrcresearchpress.com by 112.217.228.212 on 09/07/12
For personal use only.

Can. J. Chem. Downloaded from www.nrcresearchpress.com by 112.217.228.212 on 09/07/12
For personal use only.

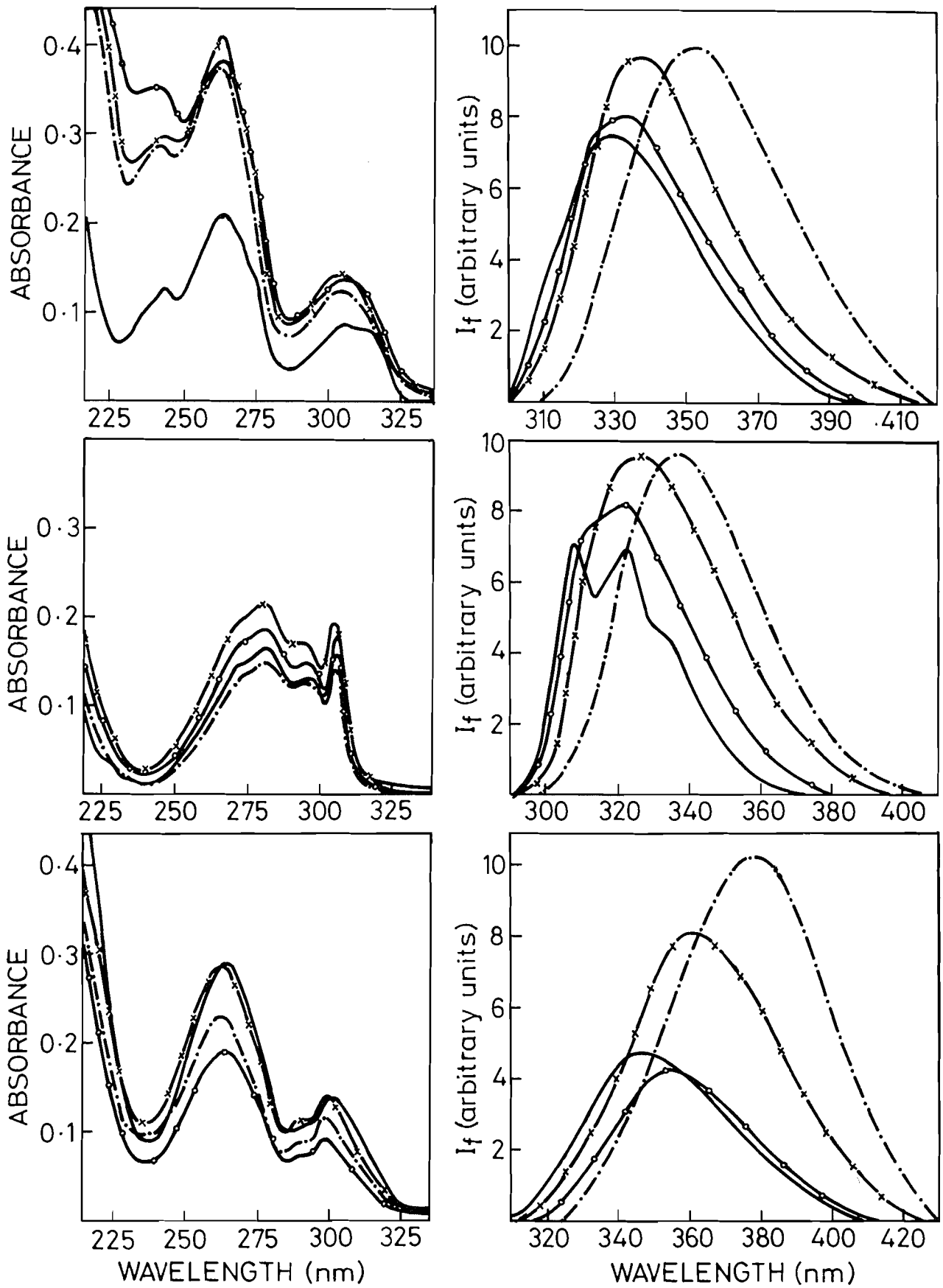

FIG. 1. Absorption (left panel) and fluorescence (right panel) spectra of 1-FAm, 2-FAm, and 4-FAm in different solvents at 298 K (—, cyclohexane; –○–○–, dioxane; –×–×–, acetonitrile, –·–·–, methanol).

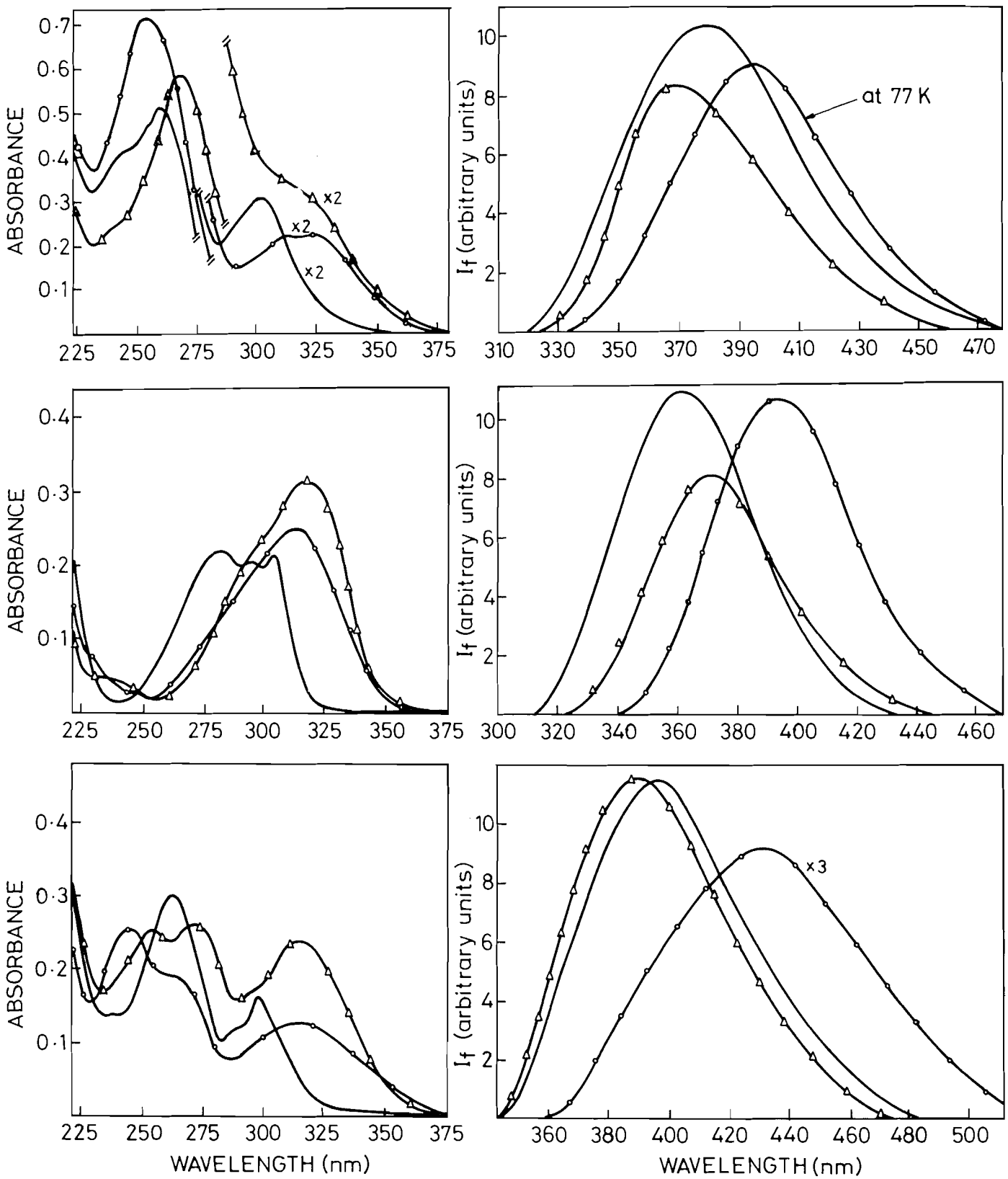

FIG. 2. Absorption (left panel) and fluorescence (right panel) spectra of different prototropic species of 1-FAm, 2-FAm, and 4-FAm (—, neutral; –○–○–, monocation; –△–△–, dication).

Can. J. Chem. Downloaded from www.nrcresearchpress.com by 112.217.228.212 on 09/07/12
For personal use only.

TABLE 2. Absorption and fluorescence spectral data of 1-FAm, 2-FAm, and 4-FAm in various solvents and at different proton concentrations[e]

Solvent/pH	1-Fluorenamide		2-Fluorenamide		4-Fluorenamide	
	λ_a (log ϵ)	λ_f (ϕ_f)	λ_a (log ϵ)	λ_f (ϕ_f)	λ_a (log ϵ)	λ_f (ϕ_f)
1	2	3	4	5	6	7
Cyclohexane	314 305 273.5 268.5 262 257.5 240.5 234	328 (0.011)	306 297.5 293.5 283 270 234.5	307 322 (0.007) 335	300 290 275 265 255	347 (0.006)
Dioxane	313 (3.62) 304 (3.75) 273.5 (3.91) — 262 (4.12) — 239 (4.08) 235 (4.08)	323 334 (0.01)	306.5 (4.32) 295 (4.24) 281.5 (4.37) 271 (4.36) 233.5 (4.26)	311 323 (0.005)	298 288.5 275 263.5 254	352 (0.004)
Acetonitrile	312.5 (3.64) 302.5 (3.73) — 262 (4.08) 239 (4.00) 235 (3.80)	338 (0.023)	305 (4.20) 294 (4.16) 280.5 (4.25) 270.5 (4.19) 233 (3.75)	325 (0.008)	297 288 275 262.5 253	360 (0.009)
Methanol	314 (3.68) 304 (3.78) — 261 (4.21) 250 (4.09) 239 (3.90)	352 (0.11)	304 (4.41) 293 (4.39) 281 (4.45) 269.5 (4.37) 233 (3.65)	338 (0.156)	296 287.5 275 262 —	380 (0.1)
Neutral (pH 6)	315 (3.64) 302.5 (3.76) 261 (4.30) 242.5 (4.21) — —	382 (0.33) 334[a]	303.5 (4.36) 293.5 (4.35) 281.5 (4.39) 269 (4.33) — —	360 323[a]	296 287.5 261	395 (0.23) 352[a]
Monocation (H_0 − 4)	322 (3.64) 314 (3.63) 254 (4.47)	408[e] 395[b] 400[c]	313 (4.46) 287.5 (4.24) 277 (3.95)	396 363[b] 365[c]	316 303 290 262.5 245	433 390[b] 395[c]
Dication (H_0 − 10)	320 (4.08) 282.5 (4.47) 268 (4.61) 237.5 (4.21)	— 368[a]	316 (4.57) 291.5 (4.4) 242 (3.66) 225 (3.95)	372 360[a]	313 — 297 271.5 — 253.5	— 390[a]
Anion[d]	—	—	—	—	325 314 285 262.5	—

[a] 77 K.
[b] H_0 0, 77 K.
[c] H_0 − 4, 77 K.
[d] 1-FAm and 2-FAm get precipitated after pH 14.
[e] In cyclohexane + 2% TFA medium.

Can. J. Chem. Downloaded from www.nrcresearchpress.com by 112.217.228.212 on 09/07/12
For personal use only.

TABLE 3. Acidity constants of fluorenamides in the ground and first excited singlet states[a]

Equilibrium	pK_a	pK_a^*	Förster cycle method (pK_a^*)		
			a	*f*	Average
1-FAmH$_2^{2+}$ ⇌ 1-FAmH$^+$ + H$^+$	−8.5				
1-FAmH$^+$ ⇌ 1-FAm + H$^+$	−1.87	2.1	−0.4	7.8	3.7
1-FAm ⇌ 1-FAm$^-$ + H$^+$	>16	13.8	—	—	—
2-FAmH$_2^{2+}$ ⇌ 2-FAmH$^+$ + H$^+$	−8.3	−7.8			
2-FAmH$^+$ ⇌ 2-FAm + H$^+$	−1.95	2.0	1.6	3.3	1.8
2-FAm ⇌ 2-FAm$^-$ + H$^+$	>16	13.6	—	—	—
4-FAmH$_2^{2+}$ ⇌ 4-FAmH$^+$ + H$^+$	−8.1	—			
4-FAmH$^+$ ⇌ 4-FAm + H$^+$	−2.2	1.8	1.8	5.6	3.0
4-FAm ⇌ 4-FAm$^-$ + H$^+$	>16	15.3	—	—	—

[a]pK_a^* (Förster) of 1-FAm and 4-FAm were calculated by using low temperature (77 K) fluorescence data.

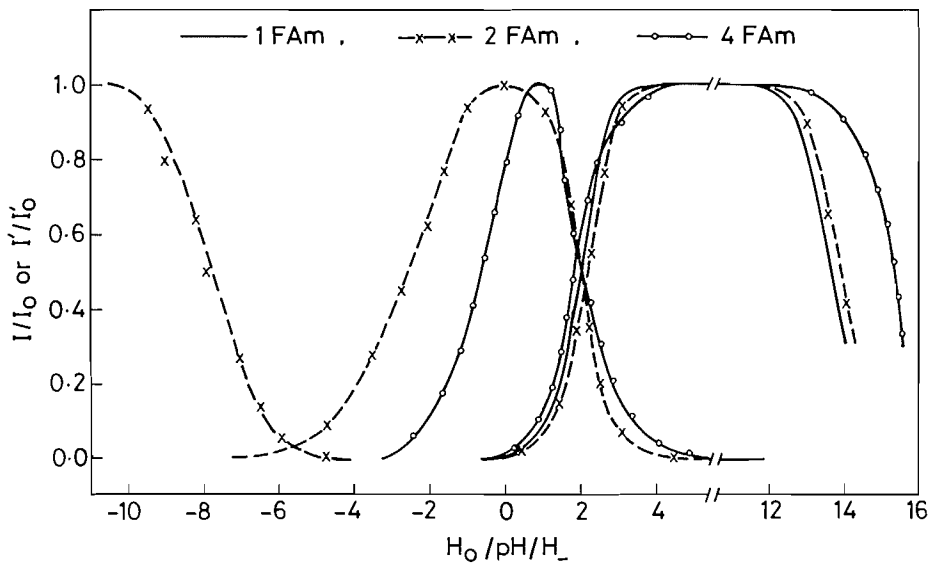

FIG. 3. Plot of I/I_0 vs. H_0/pH/H_-.

in the fluorescence spectra of each species as compared to those recorded at 298 K. Further at 77 K, the monocations are fluorescent at the acid concentration where they are non-fluorescent at 298 K. Under these conditions, the fluorescence spectra of the dications are blue shifted as compared to monocations. Similar behavior has also been observed for 2-FAm at 298 K. The fluorescence intensity of each amide also starts decreasing below pH 12, without the appearance of other new band.

The pK_a values for monocation–neutral and dication–monocation equilibria have been determined spectrophotometrically and are listed in Table 3, whereas the pK_a value for neutral–monoanion equilibrium cannot be determined as the formation of anion is not complete even in the highly basic medium used. The pK_a's in the excited state have been determined with the help of fluorimetric titrations (Fig. 3). The values are also listed in Table 3. The Förster-cycle method has been used wherever applicable to calculate the pK_a^* values listed in Table 3.

Discussion

Effect of solvents

It is well known that the moderately intense 300 nm and strong 265 nm absorption bands of fluorene are long-axis polarised, whereas the weak 287 nm band is short-axis polarised (30, 31). In 1-FAm and 4-FAm, the —$CONH_2$ group is along the shorter axis, whereas in 2-FAm, it is along the axis which predominantly affects the long-axis polarised transition. If the —$CONH_2$ group in any amide is coplanar with the fluorene moiety, the absorption transition of fluorene, polarised along that particular direction will be perturbed more than the other. The similarity of the spectral profile of 2-FAm and fluorene indicates that the conjugation between the π cloud of —$CONH_2$ group and fluorene moiety is minimal (Fig. 1). In other words, the —$CONH_2$ group is non-coplanar with the fluorene moiety in the S_0 state. The small red-shift of 3 to 4 nm observed in the long wavelength band of the fluorene molecule is due to the inductive effect of the —$CONH_2$ group. Whereas the large red-shift observed in the absorption spectrum of fluorene in 1-FAm and 4-FAm indicates that the —$CONH_2$ group is coplanar with the fluorene moiety. This is based on the following observations: (*i*) Unlike the fluorene spectrum, the long-wavelength bands of these compounds are broad and featureless. (*ii*) The long-wavelength absorption band is a mixture of the 300 nm band, which is not affected at all by the presence of the amide group and the weak 287 nm band, which is perturbed by the

Can. J. Chem. Downloaded from www.nrcresearchpress.com by 112.217.228.212 on 09/07/12
For personal use only.

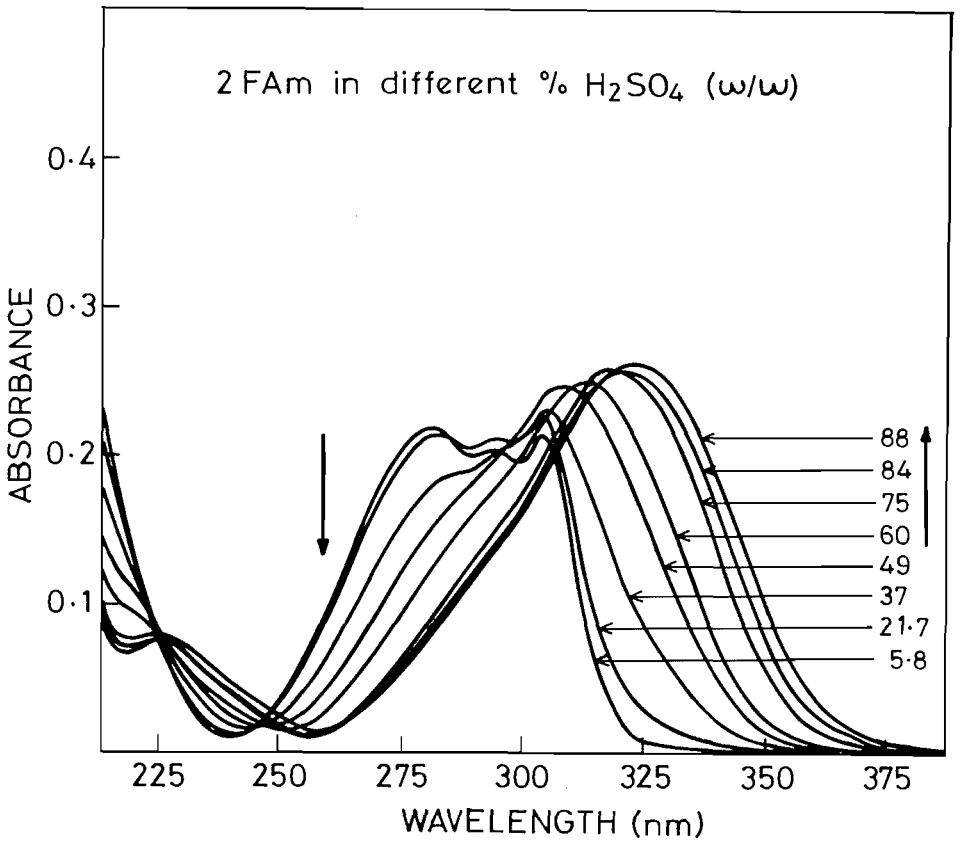

FIG. 4. Absorption spectra of 2-FAm in different wt.% H_2SO_4 acid.

amide group. (*iii*) The molecular extinction coefficient data (25) of fluorene indicate that the first vibrational peak of the long wavelength band is more intense than the others toward the short-wavelength side, and than the 287 nm band. 4-FAm follows the same trend, therefore the 287 nm band is not stabilised enough to replace the 300 nm band.[2] However, the molecular extinction coefficient data of 1-FAm suggest that its short-axis polarised band (287 nm) is more stabilised than the long-axis polarised band (300 nm) and that it is of lower energy. This is explained by the fact that the molecular extinction coefficient of the first long-wavelength peak is less than that of the second peak in the 287 nm band. This may be due to more coplanarity of —$CONH_2$ group with the fluorene moiety and it may be due to the hydrogen bonding between the hydrogen atom at the 9-position and the amide group in 1-FAm. Similar behaviour is observed in 2-phenylbenzimidazole (33), where the phenyl group is coplanar with the benzimidazole moiety. On the other hand, the phenyl groups are non-coplanar in biphenyl (34). The higher pK_a value for the dissociation of 1-FA compared to the values for 2-FA, 3-FA, and 4-FA is due to hydrogen bonding from the hydrogen at the 9-position (35). The planarity of the phenyl and naphthalene rings in 1-fluoro-2-phenylnaphthalene in the S_0 and S_1 states have been explained on the basis of hydrogen bonding between the fluorine atom and the hydrogen atom of the C—H bond of the phenyl ring (34). The blue shift observed in the absorption spectra of 1-FAm and 4-FAm with respect to their respective carboxylic acids (26) is due to the presence of the amino group rather than to the presence of the hydroxy group. The amino group is a

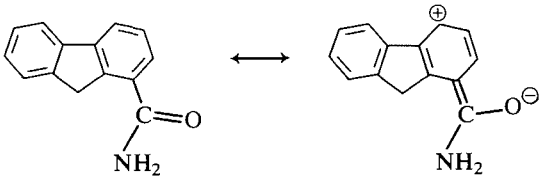

I II

better charge donor than the hydroxy group and thus will increase the charge density at the carboxyl group. Due to the increased charge density at the carbonyl group, the canonical structure **II** is not very important in the resonance interaction as is observed in 1-FA. This consequently reduces the π electronic interaction between the two chromophores.

The fluorescence spectrum of 2-FAm in a non-polar solvent is different from that of 1-FAm or 4-FAm. The former shows a vibrational spacing $\sim 1420\,cm^{-1}$, whereas the latter are broad. The absorption and fluorescence spectra of fluorene are very complex and it has been shown that many vibrational modes are active in the long-wavelength electronic transition (30, 31) which is long-axis polarised. The absorption spectrum of 2-FAm illustrates this kind of behaviour and the vibrational frequencies observed in the absorption spectrum are close to 800, 500, and $1420\,cm^{-1}$. On the other hand, the fluorescence spectrum of 2-FAm shows only one vibrational mode with a frequency near $1400\,cm^{-1}$. This vibrational mode is one of the frequencies observed in the absorption spectrum indicating that fluorescence is taking place from the electronic state governing the absorption. This is also clear from the near-equivalence of the 0–0 transition observed in the absorption and fluorescence spectrum of 2-FAm.

The Stokes shifts ($\bar{\nu}_{max}$(abs) − $\bar{\nu}_{max}$(flu)) for 1-FAm, 2-FAm,

[2]This is based on the absorbance data as the molecular extinction coefficients could not be determined.

Can. J. Chem. Downloaded from www.nrcresearchpress.com by 112.217.228.212 on 09/07/12
For personal use only.

Can. J. Chem. Downloaded from www.nrcresearchpress.com by 112.217.228.212 on 09/07/12
For personal use only.

TABLE 4. Stokes shift (cm^{-1}) observed for 1-FAm, 2-FAm, and 4-FAm in different solvents and at various proton concentrations

Solvent	Stokes shift		
	1-FAm	2-FAm	4-FAm
Cyclohexane	1360	110	4515
Dioxane	2010	420	5160
Acetonitrile	2365	2020	5890
Methanol	3540	3310	7470
Water	5570	5120	8470
Monocation	—	6696	—
Dication	—	4764	—

and 4-FAm have been calculated in various solvents and recorded in Table 4. The long-wavelength maximum in the absorption spectrum matches the short-wavelength maximum in the fluorescence spectrum in non-polar solvents for 2-FAm. Very small Stokes shifts observed in non-polar solvents indicate that the geometry of the molecule (2-FAm) in the excited state is not different from that in the ground state and thus 2-FAm in non-polar solvents can be assigned to class-2 type molecules as suggested by Berlman (36). Molecular models demonstrate that the steric hindrance experienced by the amide group of 2-FAm from the adjacent hydrogen atoms is quite a bit less than that experienced by the amide group at the 1-position of 1-FAm. Substitution of the amide group at position 2 of fluorene should therefore be expected to impart more substantial changes in the absorption and fluorescence spectra of fluorene than substitution at position 1. Contrary to this, the absorption and fluorescence spectra of 2-FAm are structured compared to those of 1-FAm and 4-FAm, indicating that the amide group in 2-FAm is not coplanar with the fluorene ring in the ground and excited states. This is supported by the Stokes shift observed in cyclohexane for 2-FAm. This behaviour is similar to that observed for 2-FA (27), but quite different from that of many other carboxylic acids, where the —COOH group is not coplanar in the S_0 state but attains coplanarity with the parent aromatic molecule on excitation (37–39).

The vibrational structure is lost in more polar and hydrogen-bond forming solvents, indicating strong interaction between solute and solvent. Correspondingly large Stokes shifts are observed in more polar and better hydrogen-bonding solvents. The Stokes shifts observed in polar and hydrogen-bonding solvents (e.g. methanol and water) are so large for 2-FAm that this cannot be explained by simple solute–solvent interaction, especially where the amide group is not coplanar in a non-polar solvent. It seems that in polar and proton donor or proton acceptor solvents, the resonance form **II** becomes more favour-

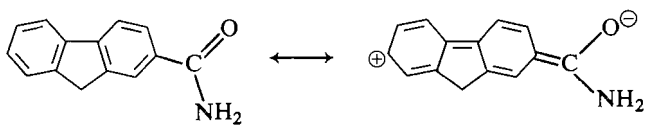

I **II**

able in the excited state. This is due to a change in the electron density induced by the long-axis polarised transition dipole moment and is confirmed by the large Stokes shift observed in methanol and water as solvents. As might be expected, significant hydrogen bonding interaction with the solvent is better transmitted to the ring via coplanar configuration. The Stokes shift observed in the above environments for 1-FAm and 4-FAm are greater than those observed for 2-FAm, indicating that charge migration from the fluorene ring to the amide group of 1-FAm and 4-FAm is greater than that in 2-FAm in the first excited singlet state.

The increase in the fluorescence quantum yields of the amides in polar and hydroxylic solvents can be explained along the same lines as has been done by Lim and Yu (40) provided the $^1\pi\pi^*$ is the lowest singlet state and the energy gap between the $^1\pi\pi^*$ and the next singlet $^1n\pi^*$ is not too large, i.e., solvent dependent fluorescence from $^1\pi\pi^*$ singlet can be based on the assumption that efficient radiationless transition to the triplet states can occur through the vibronic interaction of the lowest excited singlet state with the $n\pi^*$ singlet state and the extent of this interaction depends upon the energy gap between these two states. In polar and hydroxyl solvents, the energy gap between $^1\pi\pi^*$ and $^1n\pi^*$ singlets will increase. This will decrease the vibronic interaction between these two states and thereby reduce the rate of intersystem crossing to triplet states. In other words, an increase in fluorescence intensity will be noticed in hydroxylic solvents. It has been shown that $^1\pi\pi^*$ is the lowest singlet state in benzoic acid and benzamide (41). It can also be speculated that $^1\pi\pi^*$ will be lowest energy singlet in the compounds studied here and based on our results it can be concluded that the energy gap between the $^1\pi\pi^*$ and $^1n\pi^*$ singlets is not very large.

Effect of acid concentration

Ground state

Monocations of primary amides can be obtained either by protonating the carbonyl oxygen or by protonating the nitrogen atom of the amino group, though more evidence exists for the former. It is very difficult from our study to locate the site of protonation, yet based on our study of the prototropic reactions of 2-benzimidazolone (42) (**1**) and 3-indazolinone (**2**) (43) we

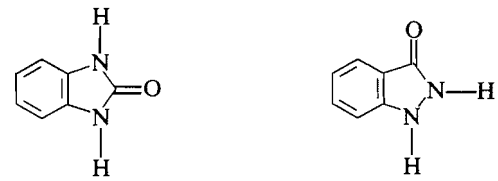

1 **2**

conclude that the protonation in amides occurs on the carbonyl oxygen. In the case of molecule **1**, the first protonation in aqueous (where this structure is more stable) solutions should have occurred at pH ~ 4 and monocations should have been formed by protonating the >N—H group adjacent to benzene ring. On the other hand, the pK_a value observed for this reaction is −2.1. This pK_a is in the right region for carboxamide, which proves that the protonation has occurred at the carbonyl oxygen, rather than that at >NH group. Further protonation of the monocation of molecule **1** leads to a reorganization of bonds resulting in the benzimidazole structure as inferred from the absorption spectrum of the monocation. If the protonation had occurred at the >NH group, structural reorganization to the benzimidazole moiety would have also required the migration of proton from $>NH_2^+$ to the carbonyl oxygen atom, which is less favourable than simple charge migration in case

TABLE 5. Ground state pK_a of monocation–neutral equilibria of amides, using different data (see text)

Compound	Scale	Case a[b]	Case b[b]	Difference in hydration number (39) (see text)
1-FAm	H_0	Slope 0.46 pK_a −2.75	Slope 0.63 pK_a −2.15	$(n - r) = 2.25$ pK_a −1.87
	H_A	Slope 0.68 pK_a −2.25	Slope 0.99 pK_a −1.85	
2-FAm	H_0	Slope 0.29 pK_a −4.1	Slope 0.78 pK_a −2.25	$(n - r) = 2.58$ pK_a −1.95
		Slope 0.68 pK_a −2.55	Slope 1.0 pK_a −1.97	
4-FAm	H_0	Slope 0.62 pK_a −3.3	Slope 0.68 pK_a −2.45	$(n - r) = 2.16$ pK_a −2.2
	H_A	Slope 0.88 pK_a −2.6	Slope 1.0 pK_a −2.0	

[a]For equilibrium inside the range 5.8–84% H_2SO_4 (w/w).
[b]For equilibrium inside the range 5.8–60% H_2SO_4 (w/w).

of protonation at the carbonyl group. Similar results also exist for molecule **2**, as well as for *N*-methyl-2-benzimidazolone and *N*,*N*′-dimethyl-2-benzimidazolone (44, 45).

Two conclusions evident from the earlier studies on the prototropic reactions of the amides are (*i*) Hammett's acidity scale is not valid (10) and (*ii*) a continuous red-shift is observed with an increase in acid concentration (11*d*). As said earlier, the clear isosbestic points are observed up to $H_0 - 4$ to -5 but the red-shift in absorption spectra of the amides are observed up to $H_0 - 7$. If the red-shift in the absorption spectrum up to $H_0 - 7$ is because of the protonation of amides and the Hammett's acidity scale is valid, one should get a slope equal to -1 from the plot of H_0 vs. $\log [BH^+]/[B]$, where $[BH^+]$ and [B] are the concentration of the acid and its conjugate base, respectively. pK_a values have been calculated using H_0 and H_A scales and the relevant data are compiled in Table 5. It is clear from Table 5 that the H_0 acidity scale is not at all valid even for data up to $H_0 - 4$, whereas the H_A scale is followed when the data points are used up to $H_A - 4$. This clearly indicates that Hammett's acidity scale is not valid for these primary amides and that a medium effect is observed for the monocations. This is consistent with the literature, as said earlier.

Lovell and Schulman (46) have proposed that the failure of Hammett's acidity scale for the prototropic reactions of amides is because of the different hydration requirements of the prototropic reactions of the carboxamides relative to the hydration requirements of the dissociations of the primary amines, used as indicators to establish the H_0 scale. The following equation has been derived

$$H_0 - \log \frac{[B]}{[BH^+]} = pK_a - (n - r) \log a_w$$

where $(n - r)$ is the difference in the hydration number as described above and a_w is the activity of water. The slopes and intercepts from the plot of left hand side vs. $\log a_w$ are listed in Table 5. The a_w values were taken from a curve constructed from the data of Giauque *et al.* (47). The pK_a values obtained for each amide agree nicely with those calculated using the H_A scale. Slopes also indicate that two fewer water molecules are involved in the dissociation reactions of the protonated amides than in the dissociation reactions of ammonium ions used in the establishment of H_0 scale.

Acid hydrolysis of the amide group is possible. If the hydrolysis of the amide group had occurred, it would have yielded the monocations of the respective acids, formed by protonating the carbonyl group. This possibility is rejected on the ground that monocations of the respective acids are highly fluorescent and the fluorescence band maxima are at a longer wavelength (26, 27) than those of the neutral species. This indicates that even though acid hydrolysis of amides is possible, it is too slow to affect our results. The pK_a values for dication–monocation equilibrium are consistent with the value obtained for the prototropic reaction of fluorene (48). The pK_a for 4-FAm is the lowest and that for 2-FAm is the highest. In fluorene the electrophilic substitution takes place first at position 2 and then at positions 7 and 4 (25). In the case of 2-FAm, the second protonation will be at position 7 and the presence of an electron-withdrawing group at position 2 will decrease the charge density at position 7. On the other hand, in the case of 1-FAm and 4-FAm, the charge densities will be lowered at positions 2 and 3, respectively, i.e. *ortho* to each other. Thereby position 2 will be susceptible to attack by a proton in the case of 4-FAm, followed by 1-FAm and 2-FAm. Our results are also consistent with this argument.

First excited singlet state

Fluorimetric titrations clearly show that the amide group becomes more basic in the S_1 state. The pK_a^* for dication–monocation equilibrium has been calculated for 2-FAm, as the dications of the other amides are non-fluorescent at 298. The results obtained agree with similar protropic reactions of aromatic hydrocarbons (49–51) in the sense that the rate of protonation for aromatic hydrocarbon is so small that the prototropic equilibrium is not established during the lifetimes of the conjugate acid–base pair. The decrease in the fluorescence intensity of the neutral amide at pH > 12, could be due to either the base hydrolysis of the amides, hydroxyl-induced fluorescence quenching or formation of the monoanion, obtained either by deprotonation of the methylene group at posi-

Can. J. Chem. Downloaded from www.nrcresearchpress.com by 112.217.228.212 on 09/07/12
For personal use only.

tion 9 or the $—NH_2$ group. The first possibility is rejected on the ground that the base hydrolysis of amides will lead to the formation of carboxylate anions and the anions of the respective carboxylic acids are fluorescent under these conditions (26, 27). Unfortunately, the monoanion obtained by the deprotonation of methylene group of fluorene and by the deprotonation of aromatic amines (52–54) (with few exceptions (55, 56)) are non-fluorescent. Further, pK_a^* obtained from the fluorimetric titrations for both the above equilibria nearly fall in the same region. This study indicates that it is not easy to find out whether the decrease in fluorescence intensity is due to hydroxyl-induced fluorescence quenching or to the formation of monoanions.

Lastly, fluorescence quenching of the monocations by protons is consistent with the results of Watkins (28) and Hussain and Wyatt (29). The quenching rate constants k_q cannot be calculated because of the unavailability of the lifetimes of the monocations. Strickler and Berg's (32) equation cannot be used because the appropriate absorption envelopes of the monocations are mixtures of two transitions, especially for 1-FAm and 4-FAm.

The fluorescence band maxima observed at 77 K are consistent with the earlier results that the blue-shift, observed as compared to the results at 298 K, is due to a reduced solvent interaction at low temperature. These results also indicate that the absence of fluorescence of the monocation of 1-FAm and the dications of 1-FAm and 4-FAm at 298 K is due to collisional quenching.

The formation of dication produces a blue shift, both in absorption and fluorescence relative to the monocation species. The pK_a values, calculated for the dication–monocation equilibrium, indicate that the protonation occurs at a ring carbon atom. As said earlier, the electrophilic attack on fluorene takes place first at position 2, then at positions 7 and 4 (25). In the case of 2-FAm, the protonation will occur at position 7. This will inhibit charge transfer, i.e., structure **II** will be unfavourable and hence the polarity of the dication will decrease. This will lead to a decrease in solvent interaction, thus increasing the gap between the two states. Similar arguments can be given for the other two amides. Similar results are also observed for the second protonation of fluorene carboxylic acids (26, 27).

Conclusions

The following conclusions can be drawn from this study. (*i*) The longest wavelength band in 2-FAm is long-axis polarised, whereas those of 1-FAm and 4-FAm are a mixture of long- and short-axis polarised transitions. (*ii*) The amide group in 1-FAm and 4-FAm is coplanar with the fluorene moiety, both in S_0 and S_1 states, whereas the same group in 2-FAm is not coplanar with fluorene, in both the S_0 and S_1 states in non-polar solvents, but attains coplanarity in polar and hydrogen bonding solvents in the S_1 state. (*iii*) Hammett's acidity scale is not valid for the prototropic reactions of the amides and a medium effect is observed in the absorption spectra of the monocations of the amides in concentrated sulphuric acid. (*iv*) The amide group becomes a stronger base in the S_1 state. (*v*) Proton-induced fluorescence quenching is observed for the monocations. (*vi*) The rate of protonation of the ring carbon atom is slow as compared to the rate of emissive decay.

Acknowledgement

The authors thank the Department of Science and Technology, New Delhi, for financial support of the project "Proton transfer reactions in the excited states".

1. R. STEWART. The proton: applications to organic chemistry. Vol. 46. Academic Press, New York. 1985. p. 185.
2. M. LILER. (*a*) Adv. Phys. Org. Chem. **11**, 267 (1975); (*b*) J. Chem. Soc. Perkin Trans. 2, 334 (1971); (*c*) J. Chem. Soc. Perkin Trans. 2, 71 (1974).
3. A. BERGER, A. LOEWENSTEIN, and S. MEIBOOM. J. Am. Chem. Soc. **81**, 62 (1959).
4. I. M. KLOTZ and B. FRANK. J. Am. Chem. Soc. **87**, 2721 (1965).
5. F. A. BOVEY and G. V. D. TIERS. J. Polym. Sci. **A18**, 849 (1963).
6. W. L. PAUL and S. G. SCHULMAN. Anal. Chem. **45**, 415 (1973).
7. S. G. SCHULMAN, P. J. KOVI, and J. F. YOUNG. J. Pharm. Sci. **62**, 1197 (1973).
8. A. R. KATRITZKY, A. J. WARING, and K. YATES. Tetrahedron, **19**, 465 (1963).
9. J. T. EDWARDS and I. C. WANG. Can. J. Chem. **40**, 966 (1962).
10. K. YATES, J. B. STEVENS, and A. R. KATRITZKY. Can. J. Chem. **42**, 1957 (1964).
11. (*a*) K. YATES and J. B. STEVENS. Can. J. Chem. **43**, 529 (1965); (*b*) R. A. COX and K. YATES. J. Am. Chem. Soc. **100**, 3861 (1978); (*c*) R. A. COX and K. YATES. Can. J. Chem. **59**, 1560 (1981); (*d*) R. A. COX and K. YATES. Can. J. Chem. **59**, 1568 (1981).
12. R. B. HOMER and C. D. JOHNSON. Chemistry of amides. *Edited by* J. Zabicky. Interscience, London. 1970. Chap. 3.
13. C. R. SMITH and K. YATES. Can. J. Chem. **50**, 771 (1972).
14. (*a*) C. L. PERRIN. J. Am. Chem. Soc. **96**, 5628 (1974); (*b*) C. L. PERRIN and E. R. JOHNSON. J. Am. Chem. Soc. **103**, 4697 (1981); (*c*) C. L. PERRIN, E. R. JOHNSON, C. P. LOLLO, and P. A. KOBRIN. J. Am. Chem. Soc. **103**, 4691 (1981); (*d*) C. L. PERRIN, C. P. POLLO, and E. R. JOHNSON. J. Am. Chem. Soc. **106**, 2749 (1984).
15. (*a*) R. J. GILLESPIE and T. BIRCHALL. Can. J. Chem. **41**, 148 (1963); (*b*) T. BIRCHALL and R. J. GILLESPIE. Can. J. Chem. **49**, 2642 (1963).
16. A. R. FERSHT. J. Am. Chem. Soc. **93**, 3504 (1971).
17. J. CATALAN and M. YANEJ. Tetrahedron, **36**, 665 (1980).
18. B. S. FURNISS, A. J. HANNAFORD, V. ROGERS, P. W. G. SMITH, and A. TATCHELL. *In* Vogels text book of practical organic chemistry. 4th ed. ELBS London. 1980. p. 792.
19. J. A. RIDDICK and W. B. BUNGER. *In* Organic solvents. Wiley Interscience, New York. 1970. pp. 632, 695, 801.
20. M. J. JORGENSON and D. R. HARTTER. J. Am. Chem. Soc. **85**, 878 (1963).
21. G. YAGIL. J. Phys. Chem. **71**, 1034 (1967).
22. M. SWAMINATHAN and S. K. DOGRA. Indian J. Chem. **22A**, 853 (1983).
23. C. A. PARKER. *In* Photoluminescence of solutions with applications to photochemistry and analytical chemistry. Elsevier, Amsterdam. 1968. pp. 265–268.
24. S. R. MEECH and D. PHILLIPS. J. Photochem. **23**, 193 (1983).
25. H. H. JAFFE and M. ORCHIN. *In* Theory and application of ultraviolet spectroscopy. Wiley, New York. 1962. p. 356.
26. R. MANOHARAN and S. K. DOGRA. J. Photochem. Photobiol.: A. Chem. **43**, 119 (1988).
27. R. MANOHARAN and S. K. DOGRA. Spectrochim. Acta, **43A**, 91 (1987).
28. A. WATKINS. Z. Phys. Chem. (N.F.), **78**, 103 (1972).
29. S. K. HUSSAIN and P. A. H. WYATT. J. Chem. Soc. Faraday I, **68**, 130 (1972).
30. A. BREE and R. ZWARICH. J. Chem. Phys. **57**, 903 (1969).
31. J. W. HOFSTRAAT, G. PH. HOORNWEG, C. GOOIER, and N. H. VELTHORST. Anal. Chim. Acta, **169**, 125 (1985).
32. S. J. STRICKLER and R. A. BERG. J. Chem. Phys. **37**, 814 (1962).
33. A. K. MISHRA and S. K. DOGRA. Spectrochim. Acta, **39A**, 609 (1983).
34. T. C. WERNER. *In* Modern fluorescence spectroscopy. *Edited by* E. L. Wehry. Plenum Press, New York. 1976. p. 286.

Can. J. Chem. Downloaded from www.nrcresearchpress.com by 112.217.228.212 on 09/07/12
For personal use only.

35. P. H. GRANTHAM, E. K. WEISBURGER, and J. H. WEISBURGER. J. Org. Chem. **26**, 1008 (1961).
36. I. B. BERLMAN. J. Phys. Chem. **74**, 3085 (1970).
37. J. J. AARON, A. TINE, M. E. WOJCIECHOWSKA, and C. PARKANYI. J. Lumin. **33**, 33 (1985).
38. T. C. WERNER and D. M. HERCULES. J. Phys. Chem. **73**, 2005 (1969); **74**, 1030 (1970).
39. P. J. KOVI and S. G. SCHULMAN. Anal. Chim. Acta, **63**, 39 (1973).
40. E. C. LIM and J. M. U. YU. J. Chem. Phys. **45**, 4742 (1966).
41. C. J. SELISKAR, O. S. KHALIL, and S. P. MCGLYNN. *In* Excited states. *Edited by* E. C. Lim. Academic Press. 1974. p. 231.
42. A. K. MISHRA and S. K. DOGRA. J. Photochem. **31**, 333 (1985).
43. M. KRISHNAMURTHY and S. K. DOGRA. Chem. Phys. **103**, 325 (1986).
44. L. S. EFFROS and A. V. EILSOV. J. Gen. Chem. U.S.S.R. **27**, 755 (1957).
45. S. SRIVASTAVA and S. K. DOGRA. Indian J. Chem. In press.
46. M. W. LOVELL and S. G. SCHULMAN. Anal. Chim. Acta, **127**, 203 (1981).
47. W. F. GIAUQUE, E. M. HORNUNG, J. F. KUNZLER, and T. R. RUBIN. J. Am. Chem. Soc. **82**, 62 (1960).
48. R. MANOHARAN and S. K. DOGRA. J. Photochem. Photobiol.: A. Chem. **43**, 81 (1988).
49. R. L. FLURRY JR. and P. G. LYKOS. J. Am. Chem. Soc. **85**, 1033 (1963).
50. R. L. FLURRY JR. J. Am. Chem. Soc. **88**, 5393 (1966).
51. H. SHIZUKA and S. TOBITA. J. Am. Chem. Soc. **104**, 6919 (1982).
52. A. K. MISHRA and S. K. DOGRA. J. Photochem. **23**, 163 (1983); J. Chem. Soc. Perkin Trans. 2, 943 (1984).
53. M. SWAMINATHAN and S. K. DOGRA. Can. J. Chem. **61**, 1064 (1983).
54. M. SWAMINATHAN and S. K. DOGRA. J. Am. Chem. Soc. **105**, 6223 (1983).
55. A. K. MISHRA, M. SWAMINATHAN, and S. K. DOGRA. J. Photochem. **28**, 87 (1985).
56. TH. FORSTER. Z. Elektrochem. **54**, 531 (1950).

Can. J. Chem. Downloaded from www.nrcresearchpress.com by 112.217.228.212 on 09/07/12
For personal use only.

Polynuclear silver complexes of 2,5-dimethyl-2,5-diisocyanohexane (TMB). Influence of the anions

MICHÈLE DARTIGUENAVE,[1] YVES DARTIGUENAVE,[1] ALAIN MARI, AND ANDRÉ GUITARD
Laboratoire de Chimie de Coordination du CNRS, 205, route de Narbonne, 31400 Toulouse-Cedex, France

AND

MARC J. OLIVIER AND ANDRÉ L. BEAUCHAMP[1]
Département de Chimie, Université de Montréal, C.P. 6128, Succursale A, Montréal (Qué.), Canada H3C 3J7

Received January 12, 1988

MICHÈLE DARTIGUENAVE, YVES DARTIGUENAVE, ALAIN MARI, ANDRÉ GUITARD, MARC. J. OLIVIER, and ANDRÉ L. BEAUCHAMP. Can. J. Chem. **66**, 2386 (1988).

Two series of complexes have been prepared by reaction of 2,5-dimethyl-2,5-diisocyanohexane (TMB) with AgX (X = NO_3^-, BF_4^-, PF_6^-, ClO_4^-). Complexes of the first series, Ag(TMB)X, have been obtained with X = NO_3^-, BF_4^-, PF_6^-. The structures have been determined by X-ray diffraction for X = NO_3^- and BF_4^-. The crystals contain infinite chains of silver atoms alternating with bridging TMB ligands. When X = NO_3^-, the Ag atom is best described as (2 + 2)-coordinated, with two of the coordination sites filled by NO_3^- acting as a bidentate ligand. When X = BF_4^-, the Ag—TMB chain is of a different type and Ag can be considered two-coordinated and weakly interacting with a monodentate BF_4^- ion. The second series includes $Ag_2(TMB)_3X_2$ complexes whose structure consists of pairs of chains cross-linked by extra TMB ligands leading to a ladder-like pattern. A weak unidentate interaction involving ClO_4^- or PF_6^- is also apparent. The infrared data are in agreement with the X-ray results, since the highest $\nu(C{\equiv}N)$ value is obtained for $Ag(TMB)BF_4$, where Ag—CN distance is the shortest. The conformation of TMB is always *trans* about the central CH_2—CH_2 bond. The methyl groups render one of the staggered orientations of the —$C(CH_3)_2(NC)$ groups unfavorable, leaving two conformations for coordinated TMB, both of which are observed in the Ag complexes.

MICHÈLE DARTIGUENAVE, YVES DARTIGUENAVE, ALAIN MARI, ANDRÉ GUITARD, MARC. J. OLIVIER et ANDRÉ L. BEAUCHAMP. Can. J. Chem. **66**, 2386 (1988).

Deux séries de complexes ont été préparés par réaction du diméthyl-2,5 diisocyano-2,5 hexane (TMB) avec AgX (X = NO_3^-, BF_4^-, PF_6^-, ClO_4^-). Des complexes de la première série, de formule Ag(TMB)X, ont été obtenus avec X = NO_3^-, BF_4^- et PF_6^-. La structure a été déterminée par diffraction des rayons X pour X = NO_3^- et BF_4^-. Les cristaux contiennent des chaînes infinies d'atomes Ag alternant avec des ligands TMB pontants. Pour X = NO_3^-, l'atome Ag possède une coordination (2 + 2), deux des sites de coordination étant occupés par NO_3^- jouant le rôle de ligand bidentate. Lorsque X = BF_4^-, la chaîne Ag—TMB est d'un type différent, alors que Ag peut être considéré comme étant bicoordiné et participant à une faible interaction avec un ion BF_4^- monodentate. La deuxième série comprend des complexes $Ag_2(TMB)_3X_2$ dont la structure consiste en paire de chaînes Ag—TMB reliées entre elles par d'autres ligands TMB, qui donnent naissance à un motif en échelle. Il y a une faible interaction monodentate des ions ClO_4^- ou PF_6^- avec Ag. Les données infrarouges sont en bon accord avec les résultats cristallographiques, puisque la valeur la plus élevée de $\nu(C{\equiv}N)$ est obtenue pour $Ag(TMB)BF_4$, où la liaison Ag—CN est la plus courte. La conformation du TMB est toujours *trans* autour du lien CH_2—CH_2 central. Les groupes méthyles défavorisent l'une des orientations décalées des groupes —$C(CH_3)_2(NC)$, ce qui laisse pour le TMB coordiné deux conformations, qui sont toutes deux observées dans les complexes de l'argent.

Introduction

Although isonitriles are commonly used ligands, the potential of aliphatic diisonitriles has not been much explored as yet. End-on coordination at the terminal carbons and linear geometry at nitrogen impart to these molecules structural characteristics that have been used for developing unusual architectures in metal complexes of low nuclearity. For instance, a series of Rh(I) complexes containing Rh—Rh bonds have been shown by Gray, Mann, and their co-workers (1–3) to possess valuable photoredox properties. A mixed Rh—Mn compound has also been obtained (4). With Ni(II) and Pd(II), dinuclear species without direct metal–metal bonding show the interesting characteristic of being able to encapsulate halide ions (5). Aromatic diisonitriles, on the other hand, have been found to give rise to two-dimensional polymeric compounds which attracted attention for their potential use in heterogeneous catalysis (6).

Our research has been recently directed at assembling Ag atoms into complexes of low nuclearity. Diisonitriles were considered as potential ligands to bring together silver atoms, which do not usually form Ag—Ag bonds, but can be positioned side-by-side by trifluoroacetate (7), adenine (8), and other ligands (9). In a previous paper (10), we reported on the 2:3 $AgClO_4$ complex with 2,5-dimethyl-2,5-diisocyanohexane (TMB = "tetramethylbridge" (2)). This material was shown to be polymeric with the diisonitrile in an extended conformation and one ClO_4^- oxygen occupying a coordination site about silver. By using counter-anions whose Lewis basicity is either higher (NO_3^-) or lower (BF_4^-, PF_6^-), these compounds could show different coordinating characteristics. They are described in the present paper.

Experimental section

TMB (2,5-dimethyl-2,5-diisocyanohexane) was prepared as previously reported (10, 11). $AgNO_3$, $AgBF_4$, $AgPF_6$ (Fluka) were used as received. All the silver complexes were protected from light.

The infrared spectra were recorded on Perkin Elmer 577 or 983 spectrophotometers, as Nujol mulls between KBr disks or as KBr pellets.

Electrical conductivity of powdered samples was measured on compressed pellets with a Wayne and Kerr Model B 605 Automatic Com-

[1]To whom correspondence may be addressed.

Printed in Canada / Imprimé au Canada

Can. J. Chem. Downloaded from www.nrcresearchpress.com by 112.217.228.212 on 09/07/12
For personal use only.

TABLE 1. Crystal data

Parameter	Value		
	$Ag(TMB)NO_3$, **3**	$Ag(TMB)BF_4$, **4**	$Ag_2(TMB)_3(PF_6)_2 \cdot 2CH_3CN$, **2**
Formula	$C_{10}H_{16}AgN_3O_3$	$C_{10}H_{16}AgBF_4N_2$	$C_{34}H_{54}Ag_2F_{12}N_8P_2$
Fw	334.13	358.92	1080.5
Crystal system	Orthorhombic	Monoclinic	Triclinic
Space group	*Pbca*	*C*2/*c*	$P\bar{1}$
a, Å	8.590(7)	27.307(4)	8.896(5)
b, Å	15.125(2)	8.032(2)	9.099(7)
c, Å	21.075(3)	15.707(5)	16.462(6)
α, deg	90	90	97.61(4)
β, deg	90	122.53(2)	92.14(4)
γ, deg	90	90	116.71(5)
V, Å^3	2738.1	2904.5	1172.8
Z	8	8	1
D_c, g cm^{-3}	1.621	1.641	1.529
μ, cm^{-1}	14.6	14.0	9.7
T	295 K	295 K	170 K
Crystal dimensions, mm (indices)	0.16 (001–00$\bar{1}$)	0.09 (100–$\bar{1}$00)	0.12 (100–$\bar{1}$00)
	0.16 (010–0$\bar{1}$0)	0.18 (210–2$\bar{1}$0)	0.14 (010–0$\bar{1}$0)
	0.38 (100–$\bar{1}$00)	0.037 ($\bar{1}$02–10$\bar{2}$)	0.17 (001–00$\bar{1}$)
Octants	*hkl*	*hkl*, *hk*$\bar{l}$	*hkl*, *hk*$\bar{l}$, *h*$\bar{k}$*l*, *h*$\bar{k}$$\bar{l}$
$2\theta_{max}$	45.0	45.0	50.0
No. measured reflection	1788	1897	4112
Rejection criterion, $I/\sigma(I)$	<3.0	<3.0	<3.0
No. observed reflection	1177	1310	3596
Standards, number and average fluctuation	3, ±2.1%	3, ±1.7%	3, ±1.8%
R^a	0.028	0.034	0.039
$R_w{}^a$	0.035	0.045	0.049
Goodness-of-fit ratio	1.27	1.76	2.11
No. variables	218	227	359
Residual electron density, e Å^{-3}	±0.15	±0.4	±0.4
		± |0.4–0.6| near BF_4^-	± |0.4–0.90| near Ag

$^a R = \Sigma||F_o| - |F_c||/\Sigma|F_o|$, $R_w = [\Sigma w(|F_o| - |F_c|)^2/\Sigma w|F_o|^2]^{1/2}$.

ponent Bridge. The resistance of the pressed pellet was measured directly in the "conductivity press" while applying a force of 700 kg on 2 mm diameter pistons moving in a glass capillary.

Ag(TMB)(NO$_3$), 3

TMB (2 mmol, 0.32 g) dissolved in acetonitrile (40 mL) was added to a stirred solution of $AgNO_3$ (0.34 g; 2 mmol) in methanol (20 mL). After 30 min, the solution was concentrated to 30 mL. A layer of ether (30 mL) was poured very delicately. White crystals appeared as the solvents diffused. They were filtered, washed with cold ether, and dried *in vacuo*. Yield: 80%. *Anal.* calcd. for $C_{10}H_{16}AgN_3O_3$: C 35.95, H 4.83, N 12.58; found: C 35.62, H 5.03, N 12.29.

Ag$_2$(TMB)$_3$(PF$_6$)$_2$·2CH$_3$CN, 2; Ag(TMB)(PF$_6$), 5

TMB (5 mmol, 0.82 g) dissolved in 50 mL of methanol was slowly added to 5 mmol (1.26 g) of $AgPF_6$ dissolved in 50 mL of methanol. Immediate precipitation of a white powder occurred, which was filtered, washed with ether, and dried *in vacuo*. Recrystallization overnight at −30°C in acetonitrile gave white crystals, which were filtered cold and washed with cold ether. They turned into a powder by drying *in vacuo* (ir, $\nu(C{\equiv}N) = 2235\ cm^{-1}$). *Anal.* calcd. for $C_{10}H_{16}AgF_6N_2P$, **5**: C 28.80, H 3.87, N 6.72; found: C 29.00, H 3.83, N 6.75. Recrystallization of **5** in acetonitrile gave, after 15 days at −25°C, white crystals of **2**, which were isolated following the same procedure, but not dried *in vacuo* (ir, $\nu(C{\equiv}N) = 2195\ cm^{-1}$). *Anal.* calcd. for $C_{34}H_{54}Ag_2F_{12}N_8P_2$, **2**: C 37.79, H 5.04, N 10.37; found: C 36.71, H 4.75, N 10.10.

Ag(TMB)(BF$_4$), 4

Same procedure as above using 11.8 mmol (2.30 g) of $AgBF_4$ in 25 mL methanol and 11.8 mmol (1.87 g) of TMB in 25 mL methanol/dichloromethane (40/10). Yield: 90%. *Anal.* calcd. for $C_{10}H_{16}AgBF_4N_2$: C 33.46, H 4.49, N 7.80; found: C 33.33, H 4.41, N 7.99. Recrystallization in methanol at 0°C yielded the crystals used for X-ray work (ir, $\nu(C{\equiv}N) = 2225\ cm^{-1}$). When recrystallized from a methanol/ether mixture, the microcrystalline precipitate consisted mainly of the above 1:1 complex ($\nu(C{\equiv}N) = 2225\ cm^{-1}$), together with a small amount of a compound whose $\nu(C{\equiv}N)$ vibration (2195 cm^{-1}) would be consistent with $Ag_2(TMB)_3(BF_4)_2$. However, this 2:3 complex, presumably similar to the PF_6^- compound, was not isolated in a pure form.

Crystallographic measurements and structure determination

An Enraf-Nonius CAD-4 diffractometer was used to obtain the cell dimensions, space group, and intensity data for compounds **2**, **3**, and **4**. A series of 20–25 randomly distributed reflections created by the automatic search procedure were centered in the counter. The reduced triclinic cell through these reflections was calculated by the autoindexing routine and checked by means of long-exposure oscillation photographs, which showed the expected layer line spacing about each of the crystallographic axes. Inspection of the Niggli matrix indicated that no higher symmetry was present for the PF_6^- compound, leaving *P*1 and $P\bar{1}$ as possible space groups. For the NO_3^- compound, Laue mirrors on the three oscillation photographs confirmed the orthorhom-

Can. J. Chem. Downloaded from www.nrcresearchpress.com by 112.217.228.212 on 09/07/12
For personal use only.

Can. J. Chem. Downloaded from www.nrcresearchpress.com by 112.217.228.212 on 09/07/12
For personal use only.

TABLE 2. Refined fractional coordinates ($\times 10^4$, Ag $\times 10^5$, H $\times 10^3$) and equivalent isotropic temperature factors ($\times 10^3$)[a]

(*a*) $Ag(TMB)NO_3$

Atom	*X*	*Y*	*Z*	U_{eq}
Ag	9714(6)	16730(3)	22312(2)	62
O(1)	−536(5)	1986(3)	1231(2)	86
O(2)	−1226(5)	757(3)	1645(2)	84
O(3)	−2154(6)	1151(3)	737(2)	101
N(1)	−1314(5)	1293(3)	1195(2)	64
N(1A)	3336(5)	203(3)	1656(2)	47
N(2A)	−125(5)	−2195(3)	1526(2)	45
C(1A)	2621(6)	779(3)	1843(2)	55
C(2A)	4124(6)	−579(3)	1413(2)	44
C(3A)	2897(6)	−1312(3)	1379(2)	46
C(4A)	1451(6)	−1076(3)	1002(2)	47
C(5A)	260(6)	−1818(3)	902(2)	47
C(6A)	−414(6)	−2547(4)	1982(2)	52
C(7A)	4787(7)	−352(4)	765(3)	60
C(8A)	5409(6)	−803(4)	1882(3)	60
C(9A)	−1235(7)	−1443(4)	619(3)	65
C(10A)	896(8)	−2587(4)	512(3)	67
H(11A)	117(6)	−236(3)	12(2)	86(18)
H(12A)	11(6)	−305(3)	47(2)	66(15)
H(13A)	193(6)	−284(4)	68(2)	86(17)
H(31A)	331(5)	−181(3)	120(2)	63(15)
H(32A)	265(5)	−147(3)	182(2)	53(14)
H(41A)	92(5)	−61(3)	125(2)	47(13)
H(42A)	169(5)	−79(3)	63(2)	50(14)
H(71A)	389(6)	−12(3)	50(2)	61(15)
H(72A)	523(6)	−96(4)	58(2)	84(17)
H(73A)	553(5)	12(3)	79(2)	55(15)
H(81A)	596(5)	−132(4)	175(2)	73(16)
H(82A)	621(5)	−37(3)	190(2)	63(15)
H(83A)	499(6)	−87(3)	230(2)	85(17)
H(91A)	−94(6)	−122(3)	20(2)	71(16)
H(92A)	−164(6)	−95(3)	90(2)	89(18)
H(93A)	−211(6)	−194(3)	65(2)	83(17)

(*b*) $Ag(TMB)BF_4$

Atom	*X*	*Y*	*Z*	U_{eq}
Ag	14265(2)	27624(6)	49268(4)	66
F(1)	1724(4)	2246(13)	3315(6)	259
F(2)	940(6)	2972(13)	1999(11)	333
F(3)	992(5)	1185(22)	3025(7)	356
F(4)	1221(6)	552(16)	2098(9)	305
N(1B)	2269(2)	−349(7)	5954(4)	53
N(1C)	581(2)	5902(6)	4256(3)	48
C(1B)	1988(3)	773(9)	5627(5)	61
C(2B)	2621(2)	−1877(7)	6309(4)	47
C(3B)	2754(4)	−2379(13)	5532(6)	88
C(7B)	3206(4)	−1464(13)	7274(8)	84
C(8B)	2301(4)	−3132(13)	6543(9)	87
C(1C)	882(3)	4805(9)	4520(5)	60
C(2C)	181(2)	7355(7)	3891(4)	44
C(3C)	−179(3)	7289(9)	2737(4)	45
C(7C)	557(4)	8895(10)	4335(7)	66
C(8C)	−212(3)	7122(12)	4304(6)	63
B	1232(6)	1781(12)	2604(8)	87
H(31B)	296(3)	−145(12)	541(6)	129(36)
H(32B)	297(3)	−337(9)	575(5)	69(20)
H(71B)	345(3)	−243(9)	762(6)	81(22)
H(72B)	314(3)	−94(11)	775(6)	97(30)
H(73B)	340(3)	−72(10)	709(6)	83(29)
H(81B)	223(3)	−274(9)	700(6)	78(27)
H(82B)	193(3)	−341(9)	593(5)	77(23)
H(83B)	253(3)	−413(10)	684(6)	92(25)
H(31C)	−41(3)	628(9)	252(5)	64(20)
H(32C)	−42(3)	822(8)	251(5)	67(21)
H(71C)	86(3)	888(9)	422(5)	71(24)
H(72C)	33(3)	985(9)	405(5)	82(24)
H(73C)	73(3)	895(9)	506(5)	75(24)
H(81C)	0(3)	725(8)	503(6)	78(21)
H(82C)	−50(3)	797(9)	402(5)	79(23)
H(83C)	−40(3)	605(10)	412(5)	86(26)

TABLE 2. (*Concluded*)

(*c*) $Ag_2(TMB)_3(PF_6)_2 \cdot 2CH_3CN$

Atom	*X*	*Y*	*Z*	U_{eq}
Ag	45768(4)	4462(4)	24008(2)	25
P	1250(2)	2247(2)	2922(1)	33
F(1)	193(5)	3085(5)	2597(2)	67
F(2)	2021(4)	2291(4)	2066(2)	54
F(3)	2202(6)	1270(7)	3229(2)	96
F(4)	524(6)	2228(6)	3786(2)	82
F(5)	−246(6)	453(5)	2535(3)	93
F(6)	2704(6)	3991(6)	3274(3)	110
N(1)	6000(14)	4157(15)	616(5)	146
N(1D)	5426(5)	8479(5)	3752(2)	27
N(2D)	7411(5)	4435(5)	2952(2)	29
N(1E)	2271(5)	−772(5)	614(2)	30
C(1)[b]	4589(10)	5742(9)	1415(4)	75
C(2)[b]	5417(11)	4823(11)	983(5)	82
C(1D)	5007(6)	9031(6)	3238(3)	34
C(2D)	6091(5)	7976(6)	4442(3)	27
C(3D)	6707(6)	6717(5)	4096(3)	29
C(4D)	7999(6)	7291(6)	3488(3)	34
C(5D)	8780(6)	6087(6)	3249(3)	35
C(6D)	6388(6)	3088(6)	2736(3)	33
C(7D)	7533(6)	9590(6)	4920(3)	33
C(8D)	4669(6)	7179(6)	4975(3)	32
C(9D)	9895(8)	6644(8)	2561(5)	59
C(10D)	9777(7)	5963(7)	3982(4)	52
C(1E)	3001(5)	−419(5)	1255(3)	27
C(2E)	1469(6)	−1084(6)	−226(3)	32
C(3E)	697(7)	129(7)	−271(3)	42
C(7E)	2867(7)	−629(8)	−795(3)	48
C(8E)	233(7)	−2941(7)	−420(3)	49
H(11D)	1066(7)	712(7)	421(4)	56(17)
H(12D)	1031(9)	539(9)	386(5)	89(23)
H(13D)	909(7)	557(7)	433(4)	55(17)
H(31D)	712(7)	645(6)	456(3)	45(15)
H(32D)	586(6)	586(6)	387(3)	33(13)
H(41D)	750(6)	751(6)	297(3)	41(14)
H(42D)	889(7)	833(6)	372(3)	45(15)
H(71D)	839(7)	1032(7)	457(4)	65(19)
H(72D)	804(8)	923(8)	532(4)	74(20)
H(73D)	717(7)	1026(6)	517(3)	47(15)
H(81D)	393(7)	623(6)	467(3)	50(16)
H(82D)	504(7)	681(7)	546(4)	57(17)
H(83D)	428(7)	785(7)	517(4)	51(16)
H(91D)	1090(7)	789(7)	274(4)	56(17)
H(92D)	1033(7)	597(6)	243(3)	45(15)
H(93D)	930(8)	672(7)	216(4)	66(19)
H(31E)	12(7)	−4(7)	−87(4)	54(16)
H(32E)	157(6)	118(6)	−11(3)	36(13)
H(71E)	370(6)	40(6)	−64(3)	32(13)
H(72E)	241(7)	−69(7)	−130(4)	58(17)
H(73E)	337(7)	−148(7)	−84(3)	48(15)
H(81E)	−54(9)	−333(8)	−98(4)	79(21)
H(82E)	79(6)	−353(5)	−41(3)	27(12)
H(83E)	−58(7)	−334(6)	2(4)	52(16)

[a]Isotropic *U* for hydrogen atoms.
[b]Acetonitrile molecule.

TABLE 3. Infrared and structural data for the TMB—Ag complexes

Complex		$\nu(C\equiv N)$ (cm^{-1})	Coordination	Ag—C (Å)	C—Ag—C (deg)
TMB		2120			
$Ag_2(TMB)_3(ClO_4)_2$	**1**	2170	(3 + 1)	2.139(12)	118.7(4)
$Ag_2(TMB)_3(PF_6)_2 \cdot 2CH_3CN$	**2**	2195	(3 + 1)	2.153(5)	119.7(2)
$Ag(TMB)(NO_3)$	**3**	2180	(2 + 2)	2.107(5)	144.9(2)
$Ag(TMB)(BF_4)$	**4**	2225	2	2.073(8)	167.8(3)
$Ag(TMB)(PF_6)$	**5**	2235	(2?)	—	—

bic system suggested by the 90° angles of the reduced cell. The systematic absences ($0kl$, $k \neq 2n$, $h0l$, $l \neq 2n$; $hk0$, $h \neq 2n$) revealed by the full data set identified *Pbca* as the only possible space group. The Niggli matrix and the presence of a Laue mirror for oscillation about the 8.03 Å axis pointed to a *C*-centered monoclinic cell for the BF_4^- complex. The axes were redefined accordingly. Space groups *Cc* and *C2/c* were consistent with the systematic absences ($h0l$, $l \neq 2n$; $hk0$, $h + k \neq 2n$) noted in the data set.

The intensity data were collected following the method described earlier (10), using graphite-monochromatized MoKα radiation (λ = 0.71069 Å). The data were corrected for polarization and the Lorentz effect. They were not corrected for absorption owing to the low absorption coefficients.

The three structures were solved by the heavy-atom method and refined on $|F_o|$ by full-matrix least-squares procedures. For the BF_4^- and PF_6^- compounds, where two space groups were possible, resolution was first attempted in the centric space groups. This choice was confirmed by successful refinement. In each case, the Ag atom was located from a Patterson synthesis, and the remaining non-hydrogen atoms were found from a difference Fourier (ΔF) map phased on Ag. These atoms were refined isotropically, then anisotropically. All hydrogen atoms were visible in the subsequent ΔF map. They were introduced into the model and isotropically refined, simultaneously with the non-hydrogen atoms, which were anisotropically refined. The final ΔF map showed no significant electron density.

The conditions used for data collection and the results of the refinement are summarized in Table 1. The scattering curves were taken from Cromer and Waber (12), except for hydrogen (13). The anomalous dispersion contributions f' and f'' were included for Ag and P (14).

The refined positional parameters are listed in Table 2. The anisotropic temperature factors and the structure factor amplitudes are provided in the supplementary material.[2]

Results and discussion

All complexes are white solids, soluble in polar solvents such as methanol and acetonitrile. Two series of compounds are formed: $Ag(TMB)X$ ($X = NO_3^-$, BF_4^-, PF_6^-), *type 1*, and $Ag_2(TMB)_3X_2$ ($X = ClO_4^-$, BF_4^-, PF_6^-), *type 2*. With ClO_4^-, only a *type 1* complex has been obtained, and with NO_3^-, only a *type 2* complex. Both types were found to exist with PF_6^- and BF_4^-.

The infrared data are reported in Table 3 together with the Ag—C distances observed for the different complexes by X-ray diffraction (*vide infra*).

Coordination of the anion to silver is detected by infrared only for NO_3^-, which acts as a bidentate ligand ($\nu(NO_3^-)$ = 1470, 1275, 1030 cm^{-1}). These values are very similar to those reported for $Ni(dien)(NO_3)_2$: 1480, 1300, 1021 cm^{-1} (15, 16). Coordination of ClO_4^- is not apparent since only a broad ν_3 band is present at 1075 cm^{-1}. Similarly, only broad bands are observed for BF_4^- (ν_3 = 1075 cm^{-1}) and PF_6^- (ν_3 = 840 cm^{-1}).

Of particular interest is the $\nu(C\equiv N)$ vibration of the isonitrile ligand. Previous studies on the bonding in M—CNR groups have shown a direct correlation between $\nu(C\equiv N)$ and the strength of the M—CNR bond. Moreover, the decrease of the $\nu(C\equiv N)$ frequency was found to parallel the increase of the isonitrile/metal molar ratio and the charge on the metal (17–21). The experimental values in Table 3 are consistent with these trends. Higher values are observed for the *group 1* complexes **4** and **5** (TMB/Ag = 1) compared with the *group 2* species **1** and **2** (TMB/Ag = 1.5). Also, for *group 1* complexes, the greatest $\nu(C\equiv N)$ value is observed for complex **4**, that is, the one with the greatest Ag—C distance. Complex **3** behaves differently, which can be related to the higher Lewis basicity of NO_3^- compared to ClO_4^- or PF_6^-.

Electrical conductivity in the solid state was checked for **2** and **4**. As expected, both are insulators.

Crystal structure of $Ag_2(TMB)_3(PF_6)_2 \cdot 2CH_3CN$

Despite the presence of acetonitrile in $Ag_2(TMB)_3(PF_6)_2 \cdot 2CH_3CN$, this compound is structurally so close to $Ag_2(TMB)_3(ClO_4)_2$ (10) that they are virtually isomorphous. Comparison of Fig. 1 with the stereoview for the perchlorate analog (Fig. 2 in ref. 10) strikingly shows that the Ag—TMB frameworks are nearly superimposable. Both symmetry-independent TMB ligands exist as the extended conformer, with a *trans* conformation about the central C(3)—C(4) bond (see Fig. 2 for numbering scheme). This conformation invariably generates polymeric chains rather than dinuclear units. The —Ag—CN NC—Ag—CN NC—Ag— chains oriented along the ***b*** axis occur by pairs in the crystals. Junction is achieved by TMB molecules cross-linking corresponding Ag atoms in the two parallel chains, thereby defining a ladder-like pattern, in which the main chains of TMB ligands (type D) and silver atoms define the side arms, whereas the cross-linking ligands (type E) are the rungs.

Silver forms three coplanar Ag—C bonds of 2.135(5), 2.140(5), and 2.186(5) Å, respectively (Table 4). Departure from the ideal 120° values for the C—Ag—C angles (119.6, 110.5, 129.0, σ = 0.2°) is significant, but relatively small. Beside these three strong bonds, there is a long Ag—F(3) contact of 2.873(6) Å with the PF_6^- anion, which is found roughly at the same place as the ClO_4^- ion in the perchlorate analog (10). This Ag—F contact is weak compared with those of the bidentate PF_6^- ion (Ag—F = 2.668(14) Å) in the *t*-$Bu_3C_6H_2NC$ complex (22). In spite of the good affinity of Ag(I) for nitriles, the CH_3CN molecule is not coordinated to the metal, but simply fills space in the unit cell, interacting with its surroundings by normal van der Waals contacts. The intensity data for this compound were collected at 170 K. At this temperature, the PF_6^- ion and CH_3CN molecule have higher

[2]Lists of anisotropic temperature factors, weighted least-squares planes, distances and angles involving hydrogen, and structure factor amplitudes for the three structures may be purchased from the Depository of Unpublished Data, CISTI, Natural Research Council of Canada, Ottawa, Ont., Canada K1A 0S2.

Can. J. Chem. Downloaded from www.nrcresearchpress.com by 112.217.228.212 on 09/07/12
For personal use only.

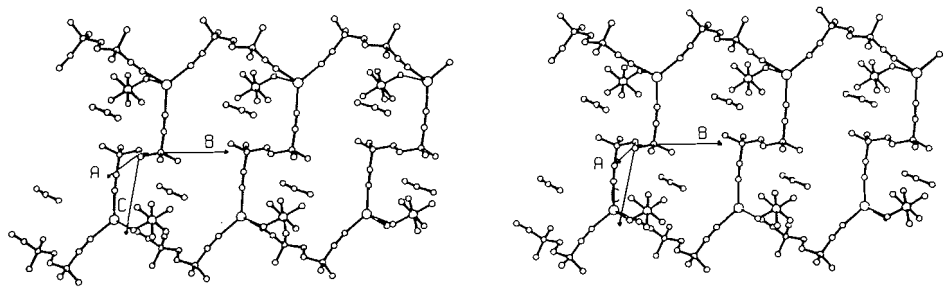

FIG. 1. Stereo view of molecular packing for $Ag_2(TMB)_3(PF_6)_2 \cdot 2CH_3CN$ down the a^* direction. Hydrogens are omitted for simplicity. The atoms are shown as spheres of arbitrary sizes, the larger ones corresponding to Ag. The anions, with thin bonds representing the contacts with Ag, are easily recognized.

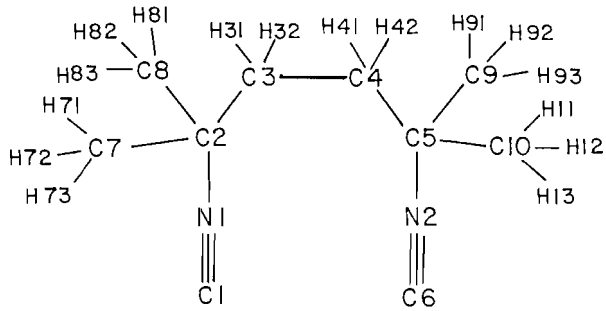

FIG. 2. Numbering scheme in the TMB ligand. Letters (A to G) are used to identify individual ligands in the various compounds.

thermal motion than the rest of the structure (Table 2), but they show no evidence for disorder, except for the methyl hydrogens of CH_3CN which were not located. At room temperature, however, the crystals remain stable only in sealed vials. In open air, they lose their crystallinity within a few minutes by evaporation of the lattice acetonitrile molecule.

Crystal structures of Ag(TMB)X, X = BF_4^- and NO_3^-

In contrast with the PF_6^- and ClO_4^- complexes, the BF_4^- and NO_3^- compounds contain one diisonitrile per metal. Again, the extended conformer of TMB alternating with Ag atoms generates infinite chains in both cases. However, these two compounds show different chain arrangement and metal–anion interaction.

The zigzag chains observed in the BF_4^- complex are shown in Fig. 3. These chains are built up from two symmetry-independent types of TMB ligands showing different relative orientations of their terminal $-CMe_2(NC)$ units. In type B ligands, the two roughly antiparallel $-N{\equiv}C$ groups bridge two silver atoms in the straight portion of the chain. Ligands of type C with their $-N{\equiv}C$ groups oriented ~60° apart define the bent portions. These interlocked chains generate layers parallel to the ***b*** axis and the cell ***ac*** diagonal. Layer thickness corresponds to the length of the extended TMB conformer, as the ligands C(2)—C(5) vectors are perpendicular to the layer surface. Cohesion between the layers is achieved by normal van der Waals forces.

In this BF_4^- compound, silver forms only two strong Ag—C bonds with a C—Ag—C angle of 167.8(3)°. Departure from the ideal 180° value is large, but not uncommon in silver chemistry. The Ag—C bonds (2.073(8) Å) are shorter than in the PF_6^- and ClO_4^- complexes, reflecting the reduction in coordination number from 3 to 2 (15). A long Ag—F(3) contact of 2.850(11) Å is also found. Thermal motion is very high for the BF_4^- anion in this crystal, whose intensities were collected at room temperature (see Fig. 5, supplementary material).

The nitrate compound contains a single type of diisonitrile (labelled A). Whereas the Ag—BF_4^- interaction is very weak, the better coordinating NO_3^- anion is found to interact to a much greater extent and in a bidentate manner via O(1) and O(2) (Fig. 4). The Ag—O distances (2.519(5) and 2.647(4) Å), although not the shortest known, are on the low side of the range for this type of interaction (23). The Ag—O contacts found here are definitely stronger than those observed in the ClO_4^- compound (Ag—O = 2.733(13) Å) (10). Greater donor ability of NO_3^- is also evidenced from the Ag—C bond lengths (2.123(5) and 2.091(5) Å) being greater than in the BF_4^- compound, and in the greater deviation of the C—Ag—C angle (144.9(2)°) from 180°. Thus, the Ag atom is best described here as (2 + 2)-coordinated, but the overall geometry around the metal does not fit a common polyhedron.

The NO_3^- ion is planar within 1σ (0.005 Å), but the metal lies at a large distance (0.23 Å) from this plane. This is probably due to intermolecular contacts involving the free O(3) atom. Coordination of O(1) and O(2) leaves the N—O bonds unchanged (1.245(6) and 1.250(6) Å) compared with the uncoordinated NO_3^- ion, but the distance to the free oxygen O(3) is shorter (1.224(7) Å). The O(1)—N(1)—O(2) angle (117.9(5)°) is also slightly reduced compared with those involving O(3) (120.8(5) and 121.3(5)°). Although these changes are significant only at the ~3σ level, they follow the trends noted for bidentate nitrate coordination (24).

The packing pattern (Fig. 4) shows layers of thickness ***c***/2, parallel to the ***ab*** plane. Cohesion between the layers is achieved by van der Waals contacts involving hydrogen atoms of TMB and the O(3) atom of the nitrate group. Within the layers, zigzag chains running roughly along the ***b*** direction are interlocked to fill space efficiently.

The structure of the ligand in the various complexes is compared in Table 5. The —C—N≡C portions of TMB should be linear and the lone pair should lie along this direction. There is a small, but significant, bend at nitrogen (C—N≡C = 173.6–179.1°) and a greater departure from linearity at the donor atom (Ag—C≡N = 169.3–176.8°, Table 4). These angles are likely to be very sensitive to crystal packing. The remaining distances and angles in TMB are normal (Table 5).

Conformation of the TMB ligand

The conformation of TMB in the complexes can be discussed from the torsion angles listed in Table 6. For all seven unequivalent ligands in four silver compounds, the diisonitrile adopts the *trans* conformation about the central C(3)—C(4) bond: deviation from 180° is less than 12°. Rotation about C(3)—C(4) toward a *trans–gauche* conformation is opposed by mutual repulsion between the substituents in the $-CMe_2(NC)$ terminal groups. On the other hand, each $-CMe_2(NC)$ group

Can. J. Chem. Downloaded from www.nrcresearchpress.com by 112.217.228.212 on 09/07/12
For personal use only.

TABLE 4. Selected interatomic distances (Å) and bond angles (deg)

(*a*) $Ag(TMB)NO_3$

Bond	Distance	Bond	Distance
Ag—C(1A)	2.123(5)	Ag—O(1)	2.519(5)
Ag—C(6A)[a]	2.091(5)	Ag—O(2)	2.647(4)
N(10)—O(1)	1.245(6)	N(10)—O(3)	1.224(7)
N(10)—O(2)	1.250(6)		

Bonds	Angle	Bonds	Angle
C(1A)—Ag—C(6A)[a]	144.9(2)	C(6A)[a]—Ag—O(1)	116.1(2)
C(1A)—Ag—O(1)	98.1(2)	C(6A)[a]—Ag—O(2)	120.1(2)
C(1A)—Ag—O(2)	87.9(2)	O(1)—Ag—O(2)	48.8(1)
Ag—C(1A)—N(1A)	169.3(4)	Ag—C(6A)[a]—N(2A)[a]	173.7(5)
O(1)—N(10)—O(2)	117.9(5)	N(10)—O(1)—Ag	99.7(3)
O(1)—N(10)—O(3)	120.8(5)	N(10)—O(2)—Ag	93.3(3)
O(2)—N(10)—O(3)	121.3(5)		

(*b*) $Ag(TMB)BF_4$

Bond	Distance	Bond	Distance
Ag—C(1B)	2.074(8)	B—F(1)	1.256(17)
Ag—C(1C)	2.071(8)	B—F(2)	1.280(17)
Ag—F(3)	2.850(11)	B—F(3)	1.250(21)
		B—F(4)	1.258(17)

Bonds	Angle	Bonds	Angle
C(1B)—Ag—C(1C)	167.8(3)	F(1)—B—F(2)	112.3(13)
C(1B)—Ag—F(3)	89.2(4)	F(1)—B—F(3)	105.0(13)
C(1C)—Ag—F(3)	101.7(4)	F(1)—B—F(4)	116.5(13)
N(1B)—C(1B)—Ag	175.9(7)	F(2)—B—F(3)	112.6(14)
N(1C)—C(1C)—Ag	176.8(7)	F(2)—B—F(4)	108.9(13)
Ag—F(3)—B	110.1(10)	F(3)—B—F(4)	101.1(13)

(*c*) $Ag_2(TMB)_3(PF_6)_2 \cdot 2CH_3CN$

Bond	Distance	Bond	Distance
Ag—C(6D)	2.186(5)	P—F(1)	1.571(5)
Ag—C(1E)	2.135(5)	P—F(2)	1.588(4)
Ag—C(1D)[c]	2.140(5)	P—F(3)	1.590(6)
Ag—F(3)	2.873(6)	P—F(4)	1.583(4)
C(1)—C(2)	1.477(13)[b]	P—F(5)	1.597(5)
C(2)—N(1)	1.100(16)[b]	P—F(6)	1.543(5)

Bonds	Angle	Bonds	Angle
C(6D)—Ag—C(1E)	119.6(2)	F(1)—P—F(5)	89.7(3)
C(6D)—Ag—C(1D)[c]	110.5(2)	F(1)—P—F(6)	89.7(3)
C(6D)—Ag—F(3)	86.7(2)	F(2)—P—F(3)	91.0(3)
C(1E)—Ag—C(1D)[c]	129.0(2)	F(2)—P—F(4)	178.7(2)
C(1E)—Ag—F(3)	92.1(2)	F(2)—P—F(5)	87.9(2)
C(1D)[a]—Ag—F(3)	100.0(2)	F(2)—P—F(6)	90.7(3)
C(1)—C(2)—N(1)	175.5(11)	F(3)—P—F(4)	88.4(3)
Ag—C(1D)—N(1D)	170.2(4)	F(3)—P—F(5)	86.1(3)
Ag—C(6D)—N(2D)	174.5(4)	F(3)—P—F(6)	94.4(3)
Ag—C(1E)—N(1E)	173.9(4)	F(4)—P—F(5)	93.2(3)
F(1)—P—F(2)	89.3(2)	F(4)—P—F(6)	88.1(3)
F(1)—P—F(3)	175.8(3)	F(5)—P—F(6)	178.6(3)
F(1)—P—F(4)	91.4(2)		

[a] $-x, \frac{1}{2} + y, \frac{1}{2} - z$.
[b] CH_3CN molecule.
[c] $x, y - 1, z$.

Can. J. Chem. Downloaded from www.nrcresearchpress.com by 112.217.228.212 on 09/07/12
For personal use only.

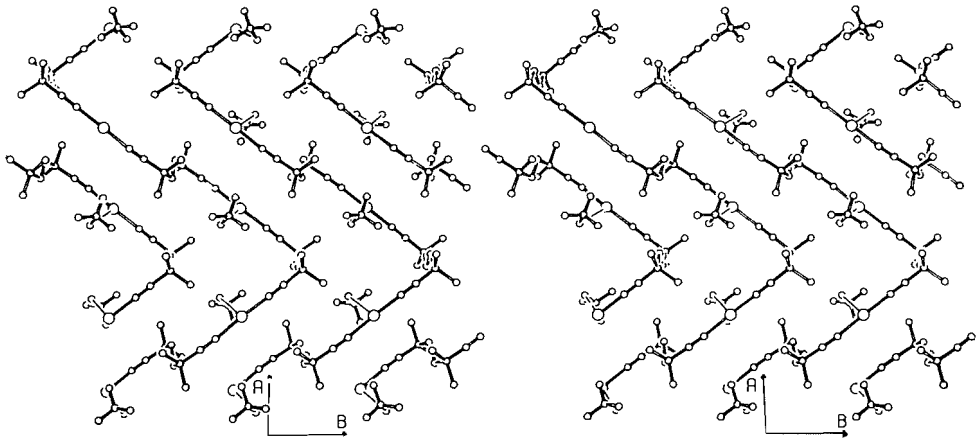

FIG. 3. Stereo view of molecular packing for $Ag(TMB)BF_4$ down the *c* axis. Conditions as in Fig. 1.

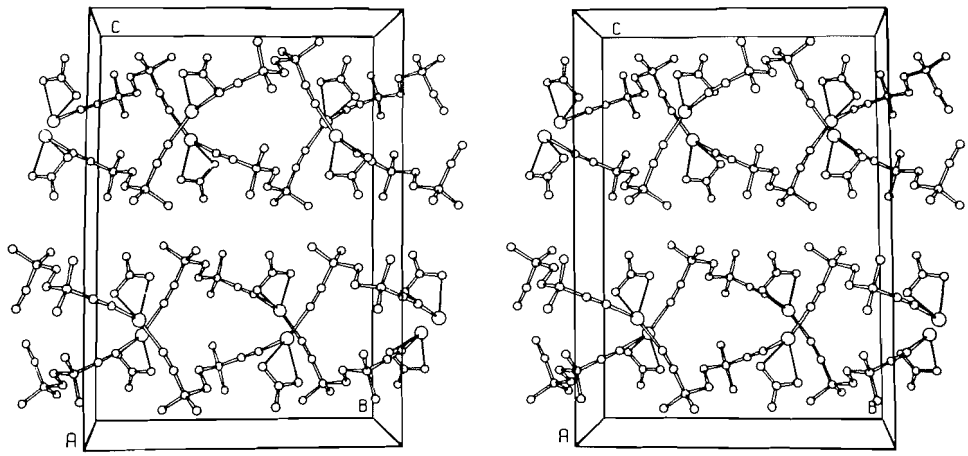

FIG. 4. Stereo view of the unit cell of $Ag(TMB)NO_3$ down the *a* axis. Conditions as in Fig. 1.

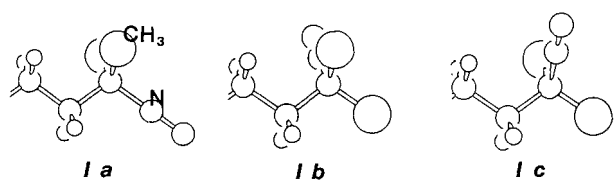

SCHEME 1

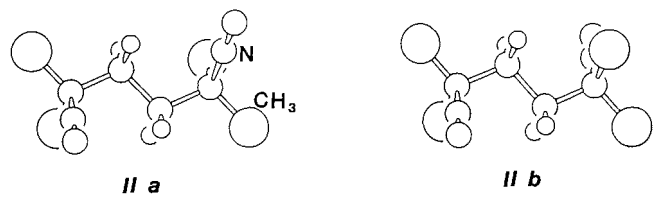

SCHEME 2

can adopt three possible staggered conformations (Scheme 1) with respect to the adjacent methylene group. However, Table 6 shows that only **I***b* and **I***c* are observed. A N(1)—C(2)—C(3)—C(4) angle of 180° (conformation **I***a*) would force both methyl groups close to the β methylene hydrogens. This is energetically unfavorable compared with **I***b* and **I***c*, where a methyl group is replaced by a less bulky isonitrile group in these β interactions. Combining the *trans* conformation about C(3)—C(4) with these two possible orientations for each of the $—CMe_2(NC)$ groups, four possible combinations (**II***a*, **II***b*, and their mirror images, see Scheme 2) are found for the relative orientations of the isonitrile groups in TMB. In conformer **II***b*, the —N≡C groups are oriented in opposite directions. This conformer is found for ligands B, E, and G (Table 6). For conformer **II***a*, the isonitrile groups are pointing 60° apart. This conformation occurs for ligands A, C, D, and F. Thus, these two conformations are found with roughly the same probability among the Ag compounds studied here. This reflects their probable similarity in energy.

These torsion angles (Table 6) can be compared with those found for $Rh_2(TMB)_4(PF_6)_2$, which are typical of systems where TMB is bridging two metal atoms in dinuclear species (2–4, 25). In the Rh complex, TMB conformation can be regarded as derived from **II***a*, by applying strain in the chain to bring the —N≡C groups closer together. This constraint changes only to a small extent the N(1)—C(2)—C(3)—C(4) and N(2)—C(5)—C(4)—C(3) angles, which are controlled by the steric effect of the methyl groups. Most of the distortion is absorbed by the central C(3)—C(4) region, where the system has moved from the *trans* conformation toward a less favorable *trans–gauche* orientation (C(2)—C(3)—C(4)—C(5) ~ 145°). In order to overcome this expense in energy, there must be a net im-

Can. J. Chem. Downloaded from www.nrcresearchpress.com by 112.217.228.212 on 09/07/12
For personal use only.

TABLE 5. Geometry of the 2,5-dimethyl-2,5-diisocyanohexane ligand

(*i*) Bond lengths

Bond	Length					
	A	B[b]	C[b]	D	E[b]	Mean[a]
C(1)—N(1)	1.136(7)	1.114(9)	1.121(9)	1.168(6)	1.145(6)	1.137
N(1)—C(2)	1.456(6)	1.471(8)	1.487(8)	1.477(6)	1.464(6)	1.468
C(2)—C(3)	1.531(7)	1.504(12)	1.529(8)	1.534(7)	1.547(8)	1.534
C(2)—C(7)	1.519(7)	1.535(13)	1.517(11)	1.532(7)	1.524(8)	1.523
C(2)—C(8)	1.520(7)	1.503(14)	1.535(12)	1.524(7)	1.525(8)	
C(3)—C(4)	1.517(7)	1.504(13)	1.514(11)	1.510(7)	1.505(9)	1.510
C(4)—C(5)	1.533(7)			1.558(7)		
C(5)—C(9)	1.525(8)			1.519(9)		
C(5)—C(10)	1.525(8)			1.517(9)		
C(5)—N(2)	1.471(6)			1.448(6)		
N(2)—C(6)	1.126(7)			1.147(6)		

(*ii*) Bond angles

Bonds	Angle					
	A	B	C	D	E	Mean[a]
C(1)—N(1)—C(2)	174.9(5)	175.8(7)	179.1(7)	173.6(5)	174.6(5)	175.5
N(1)—C(2)—C(3)	106.5(4)	108.1(6)	107.5(5)	109.2(4)	108.2(4)	108.0
N(1)—C(2)—C(7)	107.9(4)	108.4(6)	106.7(6)	105.6(4)	107.3(4)	107.2
N(1)—C(2)—C(8)	106.9(4)	107.8(7)	106.1(6)	108.4(4)	106.6(4)	
C(3)—C(2)—C(7)	112.3(4)	106.4(7)	114.7(6)	112.2(4)	107.2(4)	111.6
C(3)—C(2)—C(8)	111.6(4)	116.4(7)	110.3(6)	110.1(4)	116.2(5)	
C(7)—C(2)—C(8)	111.3(4)	109.7(7)	111.1(6)	111.2(4)	111.0(5)	110.9
C(2)—C(3)—C(4)	114.7(4)	117.1(8)	114.2(6)	115.5(4)	114.2(5)	115.1
C(3)—C(4)—C(5)	116.5(4)			113.8(4)		
C(4)—C(5)—N(2)	108.1(4)			108.3(4)		
C(4)—C(5)—C(9)	110.1(4)			110.2(5)		
C(4)—C(5)—C(10)	113.2(4)			112.1(5)		
N(2)—C(5)—C(9)	107.7(4)			108.4(4)		
N(2)—C(5)—C(10)	105.5(4)			107.5(4)		
C(9)—C(5)—C(10)	112.0(4)			110.3(5)		
C(5)—N(2)—C(6)	174.6(5)			175.8(5)		

[a]Means calculated assuming equivalence of the two halves of the molecule and of the four methyl groups (see Fig. 2).
[b]The two halves of the ligand are related by crystallographic symmetry.

TABLE 6. Torsion angles in the 2,5-dimethyl-2,5-diisocyanohexane ligand

Bonds	Torsion angle							
	NO_3^-	BF_4^-		PF_6^-		ClO_4^- (10)[b]		$[Rh_2(TMB)_4](PF_6)_2$ (2)
	A	B	C	D	E	F	G	
N(1)—C(2)—C(3)—C(4)	54.4(5)	−55.7(10)	−57.4(8)	55.3(5)	−63.6(6)	55.8(12)	57.4(13)	64.1(13)
C(2)—C(3)—C(4)—C(5)	174.4(4)	179.8(8)	−175.6(6)	171.7(4)	180.0[a]	168.6(10)	180.0[a]	−147.0(11)
C(3)—C(4)—C(5)—N(2)	52.8(5)	55.8(10)	−57.4(8)	54.6(5)	63.7(6)	52.8(13)	−57.4(13)	64.1(13)

[a]Middle of the C(3)—C(4) bond on a crystallographic inversion centre.
[b]Ladder-like structure, ligands F are in the side arms, ligands G are cross-linking.

provement in overall isonitrile–metal binding energy in the dinuclear system, compared with the formation of the same number of bonds with two remote metal atoms. In the rhodium complexes, Rh—Rh bonding obviously overcomes this expense in energy. In the case of silver, the absence of Ag—Ag bonding leaves no energetically favorable alternative to the polymerized system. Therefore, TMB does not act as a dinucleating ligand for silver and it is unlikely to have marked potential to induce metal assembling in systems containing no otherwise preassembled metal atoms.

Acknowledgments

We are grateful to the Centre National de la Recherche Scientifique (France) and the Natural Sciences and Engineer-

Can. J. Chem. Downloaded from www.nrcresearchpress.com by 112.217.228.212 on 09/07/12
For personal use only.

ing Research Council (Canada) for financial support. This work was made possible by travel grants in the framework of the Programme d'Échanges Universitaires Franco-Québécois (A.G.). We thank Dr. R. Vicente for measuring the electrical conductivity, and L. Grenier who participated in the crystallographic work for the BF_4^- compound.

1. K. R. MANN and H. B. GRAY. Inorganic compounds with unusual properties—II. Am. Chem. Soc., Washington, DC. Adv. Chem. Ser. No. 173, 225 (1979).
2. S. J. MILDER, R. A. GOLDBECK, D. S. KLIGER, and H. B. GRAY. J. Am. Chem. Soc. **102**, 6761 (1980); K. R. MANN, J. A. THICH, R. A. BELL, C. L. COYLE, and H. B. GRAY. Inorg. Chem. **19**, 2462 (1980); W. L. GLADFELTER, M. W. LYNCH, W. P. SCHAEFER, D. N. HENDRICKSON, and H. B. GRAY. Inorg. Chem. **20**, 2390 (1981).
3. K. R. MANN, M. H. DIPIERRO, and T. P. GILL. J. Am. Chem. Soc. **102**, 3965 (1980); K. R. MANN. Cryst. Struct. Commun. **10**, 451 (1981).
4. D. A. BOHLING, T. P. GILL, and K. R. MANN. Inorg. Chem. **20**, 194 (1981).
5. C. M. CHE, F. H. HERBSTEIN, W. P. SCHAEFER, R. E. MARSH, and H. B. GRAY. Inorg. Chem. **23**, 2572 (1984); W. L. GLADFELTER and H. B. GRAY. J. Am. Chem. Soc. **102**, 5909 (1980).
6. A. EFRATY, I. FEINSTEIN, F. FROLOW, and L. WACKERLE. J. Am. Chem. Soc. **102**, 6341 (1980); A. EFRATY, I. FEINSTEIN, L. WACKERLE, and F. FROLOW. Angew. Chem. Int. Ed. Engl. **19**, 633 (1980); A. EFRATY, I. FEINSTEIN, F. FROLOW, and A. GOLDMAN. J. Chem. Soc. Chem. Commun. 864 (1980).
7. R. G. GRIFFIN, J. D. ELLETT, JR., M. MEHRING, J. G. BULLITT, and J. S. WAUGH. J. Chem. Phys. **57**, 2147 (1972).
8. C. GAGNON, J. HUBERT, R. RIVEST, and A. L. BEAUCHAMP. Inorg. Chem. **16**, 2469 (1977).
9. P. JENNISCHE and R. HESSE. Acta Chem. Scand. **25**, 423 (1971).
10. A. GUITARD, A. MARI, A. L. BEAUCHAMP, Y. DARTIGUENAVE, and M. DARTIGUENAVE. Inorg. Chem. **22**, 1603 (1983).
11. W. P. WEBER, G. W. GOKEL, and I. K. UGI. Angew. Chem. Int. Ed. Engl. **11**, 530 (1972).
12. D. T. CROMER and J. T. WABER. Acta Crystallogr. **18**, 104 (1965).
13. R. F. STEWART, E. R. DAVIDSON, and W. T. SIMPSON. J. Chem. Phys. **42**, 3175 (1965).
14. D. T. CROMER. Acta Crystallogr. **18**, 17 (1965).
15. C. C. ADDISON and D. SUTTON. Prog. Inorg. Chem. **8**, 195 (1967).
16. N. F. CURTIS and Y. M. CURTIS. Inorg. Chem. **4**, 804 (1965).
17. K. NAKAMOTO. Infrared and Raman spectra of inorganic and coordination compounds. 3rd ed., Wiley Interscience, NY. 1978.
18. Y. YAMAMOTO. Coord. Chem. Rev. **32**, 193 (1980).
19. P. M. TREICHEL. Adv. Organomet. Chem. **11**, 21 (1973).
20. D. T. PLUMMER and R. J. ANGELICI. Inorg. Chem. **22**, 4063 (1983).
21. Y. YAMAMOTO and H. YAMAZAKI. Inorg. Chem. **25**, 3327 (1986).
22. Y. YAMAMOTO, K. AOKI, and H. YAMAZAKI. Inorg. Chim. Acta, **68**, 75 (1982).
23. R. A. STEIN and C. KNOBLER. Inorg. Chem. **16**, 242 (1977); J. H. MEINERS, J. C. CLARDY, and J. G. VERKADE. Inorg. Chem. **14**, 632 (1975); T. J. KISTENMACHER, M. ROSSI, and L. G. MARZILLI. Inorg. Chem. **18**, 240 (1979); P. F. RODESILER and E. L. AMMA. Inorg. Chem. **11**, 388 (1972).
24. C. C. ADDISON, N. LOGAN, S. C. WALLWORK, and C. D. GARNER. Q. Rev. **25**, 289 (1971).
25. J. S. NAJDZIONEK and B. D. SANTARSIERO. Acta Crystallogr. **C39**, 577 (1983).

Can. J. Chem. Downloaded from www.nrcresearchpress.com by 112.217.228.212 on 09/07/12
For personal use only.

The first ^1H and ^{14}N ENDOR spectra of an oxygen-centered radical adduct of DMPO-type nitrones[1]

D. Larry Haire, Uwe M. Oehler, H. Duane Goldman,[2] Robert L. Dudley,[2] and Edward G. Janzen[3]

Department of Chemistry and Biochemistry, Guelph–Waterloo Centre for Graduate Work in Chemistry, University of Guelph, Guelph, Ont., Canada N1G 2W1

Received January 20, 1988

D. Larry Haire, Uwe M. Oehler, H. Duane Goldman, Robert L.Dudley, and Edward G. Janzen. Can. J. Chem. **66**, 2395 (1988).

We report the first ^1H and ^{14}N electron nuclear double resonance (ENDOR) spectra of oxygen-centered radical adducts (i.e., derived from the addition of *tert*-butoxyl radicals) of 5,5-dimethyl-1-pyrroline-*N*-oxide (DMPO) as well as the related cyclic nitrones: 4-phenyl-5,5-dimethyl-1-pyrroline-*N*-oxide (4-Ph-DMPO) and 3,3,5,5-tetramethyl-1-pyrroline-*N*-oxide (M_4PO). Features of the electron paramagnetic resonance (EPR) and ENDOR spectra of these cyclic (pyrrolidine) aminoxyl (nitroxide) species along with some deuterated analogues in liquid toluene solutions are highlighted. For instance, we found several long-range γ-H hyperfine splittings (HFS's) detectable by ENDOR that provide unique spectral signatures for these radical adducts. Conformational assignments of the pyrrolidine aminoxyl structures based upon the EPR and ENDOR findings are also discussed. Signs of the various hyperfine splittings (i.e., a^N, a_β^H, a_γ^H) investigated by cross-relaxation intensity sequence patterns (CRISP) in the ENDOR spectra are also presented.

D. Larry Haire, Uwe M. Oehler, H. Duane Goldman, Robert L.Dudley et Edward G. Janzen. Can. J. Chem. **66**, 2395 (1988).

On rapporte pour la première fois les spectres de résonnance double nucléaire électronique (RDNE) du ^1H et du ^{14}N d'un adduit radicalaire ayant un oxygène central c.-à-d. qui dérive de l'additon de radicaux *tert*- butoxyles), du diméthyl-5,5 pyrroline-1 *N*-oxyde (DMPO) aussi bien que ceux des nitrones cycliques apparentés : phenyl-4 diméthyl-5,5 pyrroline-1 *N*-oxyde (Ph-4 DMPO) et tétraméthyl-3,3,5,5 pyrroline-1 *N*-oxyde (M_4PO). On met en évidence les caractéristiques des spectres de RDNE et de résonnance paramagnétique électronique (RPE) de ces espèces cycliques (pyrrolidine) aminoxyle (nitroxide) ainsi que ceux de quelques analogues deutériés dans des solutions de toluène liquide. Nous avons trouvé, par exemple, plusieurs dédoublements hyperfins (DHF) à longue distance γ-H décelables par RDNE qui constituent des caractéristiques spectrales uniques de ces adduits radicalaires. On discute également des attributions conformationnelles des structures aminoxyle pyrrolidine à partir des spectres de RDNE et de RPE. On présente également les traces des divers dédoublements hyperfins (c.-à-d. a^N, a_β^H, a_γ^H) étudiés par relaxation croisée faisant appel au modèle d'intensité sequentielle (CRISP).

[Traduit par la revue]

Introduction

Cyclic nitrones were introduced in the mid 1970's (1–4) for the detection and identification of transient free radicals by EPR spin trapping (5) (eq. [1], below).[4] Since that time there has been a steady interest in these compounds as probes for free radicals in a variety of chemical and biochemical systems. Recently, the focus of attention has been on the trapping of oxygen-centered radicals such as hydroxyl, alkoxyls, and peroxyls (e.g., superoxide anion) (10–13).[5] For instance, these spin trapping studies have suggested that oxygen-centered radicals may be important intermediates in radiolysis (14) and sonolysis (15) reactions, ozone-related chemistry (16, 17), xanthine/xanthine oxidase systems (18), carcinogenesis (19), antitumour drug redox interactions (20–22), cigarette smoke (23), drug/skin phototoxicity (24, 25), neutrophil action (26*a*–*c*), peroxidation reactions (27–31), as well as myocardial ischemia/reperfusion injury (32*a*–*c*).

[1] 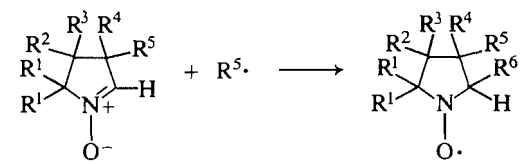

DMPO-type spin trap | Transient radical (R^6) | Radical spin adduct (aminoxyl)

DMPO (**1**)	$R^1 = CH_3$,	$R^2 = H$	$R^3 = R^4 = R^5 = H$
4-Ph-DMPO (**2**)	$R^1 = CH_3$,	$R^2 = C_6H_5$,	$R^3 = R^4 = R^5 = H$
4-Ph-DMPO-d_7 (**3**)	$R^1 = CH_3$,	$R^2 = C_6H_5$,	$R^3 = D$, $R^4 = R^5 = H$
M_4PO (**4**)	$R^1 = R^4 = R^5 = CH_3$,	$R^2 = R^3 = H$	

Solution ENDOR spectroscopy has proven to be a valuable tool for gleaning detailed structural and environmental information about aminoxyl (nitroxide) spin probes, spin labels, as well as radical spin adducts (33–67). There are a number of important advantages of studying aminoxyls by ENDOR (Electron Nuclear Double Resonance). These include the ability

[1]Some of the initial work was presented at the 28th Rocky Mountain Conference on Analytical Chemistry (9th International EPR Symposium), Denver, CO, U.S.A., August 3–8, 1986.

[2]Work done at the University of Georgia, Athens, GA 30061, U.S.A.

[3]Author to whom correspondence may be addressed.

[4]For a recent general review of EPR spin trapping see also ref. 6. For two recent reviews of EPR spin trapping in biochemical systems see refs. 7 and 8. For a compilation of EPR hyperfine splittings of spin adducts see ref. 9.

[5]It is noteworthy that the kinetics for spin trapping certain oxygen-centered radicals with cyclic nitrones is fast, e.g., 2.0×10^9 M^{-1} s^{-1} for hydroxyl with DMPO (ref. 10). Alkoxyl radicals are also efficiently trapped (e.g., $\sim 10^8$ M^{-1} s^{-1} for *tert*-butoxyl with DMPO): ref. 11. Resonance-stabilized oxygen-centered species such as superoxide and hydroperoxyl radicals are trapped considerably more slowly than alkoxyls (e.g., $\sim 10^1$ and $\sim 10^4$ M^{-1} s^{-1} respectively with DMPO), yet the relative persistence of these cyclic nitrone adducts enables spin trapping to be feasible (12). The sulfur analogues of alkoxyl radicals (thiyls) are also trapped at fast rate constants ($\sim 10^8$ M^{-1} s^{-1}) (13).

Can. J. Chem. Downloaded from www.nrcresearchpress.com by 196.1.178.254 on 09/07/12
For personal use only.

Can. J. Chem. Downloaded from www.nrcresearchpress.com by 196.1.178.254 on 09/07/12
For personal use only.

to detect long-range hyperfine splittings (HFS's) as well as the possibility of determining the signs of HFS's by CRISP (Cross Relaxation Intensity Sequence Pattern) (44) or Triple (51) modifications of the ENDOR experiment. Very recently aminoxyl ENDOR has also been applied to investigate heterogeneous systems such as micelles (33) and inverse micelles (39), as well as biological systems (e.g., imaging of plant stems with aminoxyl probes) (35).

In favourable cases the spin trapping of radicals by nitrones (e.g., phenyl-*N*-*tert*-butyl nitrones (PBN)) (34, 37, 44, 52, 59), or by C-nitroso compounds (e.g., 2-methyl-2-nitrosopropane (MNP)) (41, 46) leads to aminoxyl concentrations ($\sim 10^{-4}$–10^{-5} M) that are sufficient for analysis by ENDOR spectroscopy. To date, no ENDOR spectroscopic studies of radical adducts of "DMPO-type" nitrones, or any other 5-membered ring nitrogen heterocycle (e.g., pyrrolidine aminoxyls) with a β-hydrogen, has appeared in the literature. In this account we describe the first successful ENDOR experiments on these types of sytems. Specifically, ^{1}H and ^{14}N ENDOR spectra of *tert*-butoxyl radicals adducts of DMPO-type nitrones are reported.

Experimental

The *tert*-butoxyl radical adducts were produced by the thermolysis (25°C) of 50 mM di-*tert*-butylperoxalate (2, 3) in toluene solutions containing 50 mM nitrone.[6] Alternatively, these alkoxyl radical adducts were produced by the photolysis (low pressure 75-W Xenon lamp, Oriel model 6137) of 2-mL solutions of di-*tert*-butylperoxide (Lucidol–Penwalt) containing 50 mM nitrone in 13 × 100-mm borosilicate glass test tubes, followed by evaporation of this solvent and redissolution in toluene. Samples were deoxygenated by four freeze–pump–thaw cycles and sealed on a vacuum line prior to EPR and ENDOR analysis.

The EPR and ENDOR spectra were recorded with a Bruker ER-200D EPR spectrometer (ST 4102 and EN 801 X-band cavities, respectively) coupled to an ER-140 (Aspect 2000) computer system. The ENDOR spectra were obtained with an E-N A-300 amplifier with 12.5-kHz radiofrequency modulation. The EPR field was centered around 3400 gauss. Thus, the ENDOR doublets for ^{1}H and ^{14}N are centered about 14.47 and 1.046 MHz, respectively. The sample temperature was controlled with a Bruker ER 4111 VT unit. The *g* values were determined with Fremy's salt (sodium peroxylamine disulfonate, available from Sigma) in saturated sodium bicarbonate (a^N = 13.091 gauss, g = 2.00550) (70) in a capillary tube attached to the walls of the 4-mm o.d. quartz EPR and ENDOR cells.

All ENDOR spectra were generated from the $M_I = 0$ branch of the EPR line unless otherwise noted. The relevant settings during ordinary EPR and EPR for ENDOR were the following: modulation amplitude = 0.125 gauss, sweep time = 50 s, and time constant = 50 ms. Note, the microwave power was 20.4 mW for the former and 129.0 mW for the latter. Also, the spectrometer gain was generally 10 times higher during ENDOR. The settings for the full ENDOR spectrum (23 MHz) and the expanded view (4 MHz) were as follows: radiofrequency power = 102.0 mW and 65.0 mW, radiofrequency modulation depth = 100 kHz and 20 kHz, ENDOR start frequency = 4 and 12.5 MHz, ENDOR spectrum width = 23 and 4 MHz, ENDOR sweep time = 23 and 10 s.

The cyclic nitrones, 5,5-dimethyl-1-pyrroline-*N*-oxide (DMPO) (71, 72) and 3,3,5,5-tetramethyl-1-pyrroline-*N*-oxide (M_4PO) (72) were prepared by literature methods but are available commercially (e.g., Aldrich or Sigma). The phenylated nitrone, 4-phenyl-5,5-dimethyl-1-pyrroline-*N*-oxide (4-Ph-DMPO) was prepared by the procedure of Bapat and Black (73). The analogous deuterated nitrone required synthesis of *trans*-3-deuterio-cinnamaldehyde (available from a directed aldol reaction between benzaldehyde-1-*d* (available from MSD Isotopes) and acetaldehyde) (74). Addition of 2-nitropropane-d_6 (available from the reaction of acetone-d_6 (available from MSD Isotopes) and sodium nitrite) (75) to *trans*-3-deuterio-cinnamaldehyde gave 4-methyl-4-nitro-3-phenylpentanal-d_7. This nitroaldehyde was converted to the cyclic nitrone, 4-phenyl-5,5-dimethyl (d_6)-4-deuterio-1-pyrroline-*N*-oxide (4-Ph-DMPO-d_7), as described previously (73).

[6]Please note that di-*tert*-butylperoxybutylate is *shock-sensitive* (68). Professor L. R. C. Barclay (Mount Allison University) has suggested that di-*tert*-butylhyponitrite, $(CH_3)_3CON{=}NOC(CH_3)_3$, may be a better thermal source of *tert*-butoxyl radicals (69). The *trans*-sodium hyponitrite precursor may be obtained from G. D. Mendenhall at the Department of Chemistry and Chemical Engineering, Michigan Technical University, Houghton, MI 49931, U.S.A.

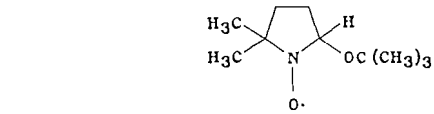

DMPO–OC(CH$_3$)$_3$

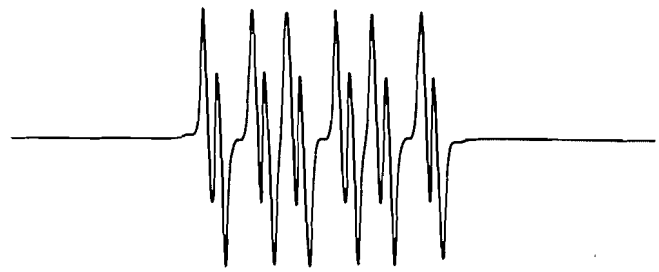

FIG. 1. EPR spectrum of the *tert*-butoxyl radical adduct of DMPO in toluene at room temperature.

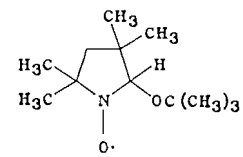

M$_4$PO–OC(CH$_3$)$_3$

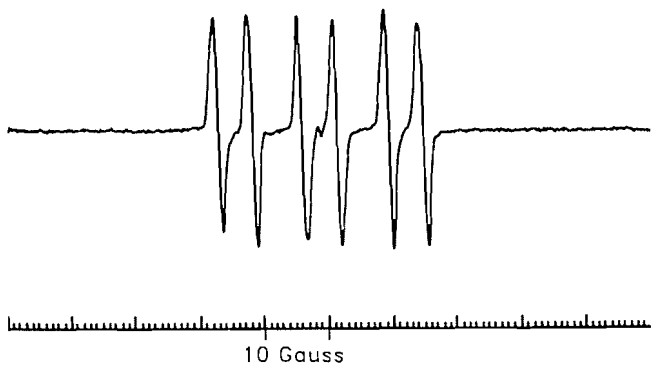

FIG. 2. EPR spectrum of the *tert*-butoxyl radical adduct of M_4PO in toluene at room temperature.

Results and discussion

Magnitudes and signs of the hyperfine splittings (HFS's) of the *tert*-butoxyl radical adducts of the DMPO-type nitrones are collected in Table 1. The HFS's are indicated by Greek subscripts to designate by the number of intervening bonds between the nucleus in question and the aminoxyl radical center (i.e., N-a_α-b_β-c_γ-d_δ-e_ϵ- etc.). EPR and ENDOR spectra of these radical adducts are provided in Figs. 1–3 and Figs. 4–6, respectively.

TABLE 1. Magnitudes and signs of the hyperfine splittings (HFS's) of the *tert*-butoxyl radical adducts of the DMPO-type nitrones determined by EPR and ENDOR spectroscopy[a]

Nitrone	Experiment type	HFS[b,c,d]					
		a^N	a_β^H	a_γ^{H5}	$a_\gamma^{H3,4}$	a_γ^{H2}	a_γ^{H1}
DMPO	EPR	13.12	7.59	1.94	N.R.	N.R.	N.R.
	ENDOR	+36.96	+21.41	−5.48	−2.02	−0.87	−0.34
		(13.15)	(7.62)	(1.95)	(0.72)	(0.31)	(0.12)
		g value = 2.00601					
					a_γ^{H3}	a_γ^{H2}	a_γ^{H1}
M_4PO	EPR	13.23	5.38	—	N.R.	N.R.	N.R.
	ENDOR	+37.39	+15.03	—	−1.26	−0.67	−0.31
		(13.29)	(5.35)	—	(0.45)	(0.24)	(0.11)
		g value = 2.00605					
					a_γ^{H4}	a_γ^{H2}	a_γ^{H1}
4-Ph-DMPO	EPR	13.11	6.41	1.99	N.R.	N.R.	N.R.
	ENDOR[e]	+36.78	+17.37	−5.37	−1.96	−0.85	−0.34
		(13.09)	(6.18)	(1.91)	(0.70)	(0.30)	(0.12)
		g value = 2.00607					
					a_γ^{H4}	a_γ^{H2}	a_γ^{H1}
4-Ph-DMPO-d_7	EPR	13.12	6.41	1.99	0.70	—	N.R.
	ENDOR[e]	+36.84	+17.48	−5.37	−1.97	—	−0.34
		(13.11)	(6.22)	(1.91)	(0.70)	—	(0.12)
		g value = 2.00607					

[a]All hyperfine splittings (HFS's) were determined in toluene solutions. ^1H and ^{14}N ENDOR values were obtained at 200 and 230 K, respectively. The EPR values are listed in gauss and the ENDOR values are given in MHz with the gauss values in brackets (conversion of MHz to gauss: division by 2.81).

[b]The numbering for the γ-HFS's follows that for the pyrrolidine ring shown in eq. [1].

[c]Signs of the HFS's were determined by examination of the relative intensities of the ENDOR lines (i.e., cross-relaxation intensity sequence patterns (CRISP) (37, 42, 44) as different branches of the EPR aminoxyl triplet ($M_I = +1$ vs. $M_I = 0$ vs. $M_I = -1$) were saturated). The signs of the γ-hydrogen hyperfine splittings (HFS's) are tentative because successful CRISP experiments required temperatures at or above 230 K where ENDOR resolution is not optimum. Sign information from TRIPLE resonance experiments proved to be inconclusive.

[d]N.R. indicates small long-range hyperfine splittings (HFS's), which contribute to the EPR linewidth but are not resolvable.

[e]The *tert*-butoxyl radical adducts of 4-Ph-DMPO and 4-Ph-DMPO-d_7 are diastereomeric. The EPR hyperfine splittings (HFS's) are: $a^N = 13.42$, $a_\beta^H = 14.99$ gauss for the *cis* isomer. ENDOR spectra of this isomer were not obtained. For the HFS's of the *trans* isomer, see the table.

Can. J. Chem. Downloaded from www.nrcresearchpress.com by 196.1.178.254 on 09/07/12
For personal use only.

EPR spectra of the DMPO-type radical adducts

In contrast to carbon-centered radical adducts of DMPO (e.g., methyl, phenyl, etc.) (1), the EPR spectra of oxygen-centered radical adducts (e.g., *tert*-butoxyl, Fig. 1) in organic solvents usually exhibit a small extra doublet splitting (~2 gauss) in additon to the β-hydrogen doublet and nitrogen triplet hyperfine splittings (HFS's). Since this extra splitting is absent in comparable oxygen-centered adducts of M_4PO (76) (e.g., *tert*-butoxyl, Fig. 2) it is expected that this γ-hydrogen splitting originates from one of the hydrogen nuclei attached to the 3-position of the pyrrolidine ring (which may form a favourable geometric "W-type" arrangement with the aminoxyl p_π orbital) (77). It is noteworthy that of the oxyl family of DMPO spin adducts the hydroxyl adduct is anomalous in that it does not exhibit the characteristic small doublet splitting in organic (or aqueous) solvents (9).

The *tert*-butoxyl radical adduct of 4-phenyl-DMPO (Fig. 3) is a diastereomeric mixture of radical adducts due to the asymmetric centers (*) at the 2- and 4-positions of the pyrrolidine ring (**5**). One of these isomers exhibits an EPR hyperfine splitting pattern that is quite similar to that observed for the *tert*-butoxyl adduct of DMPO (i.e., $a^N = 13.12$, $a_\beta^H = 7.59$, $a_\gamma = 1.94$ vs. $a^N = 13.11$, $a_\beta^H = 6.41$, $a_\gamma = 1.99$ gauss, respectively, Table 1). Since the *trans*-2-*tert*-butoxyl-4-phenyl species should more closely resemble the analogous DMPO adduct (less perturbation of the pyrrolidine aminoxyl ring structure) the EPR pattern is assigned to this isomer. The other component (i.e., $a^N = 13.42$, $a_\beta^H = 14.99$ gauss) is attributed to the corresponding *cis* isomer.

When 4-Ph-DMPO is substituted with 4-Ph-DMPO-d_7 the resulting DMPO-like *tert*-butoxyl radical adduct exhibits one more γ-hydrogen hyperfine splitting (i.e., a 0.70-gauss doublet appears) due to the sharper EPR lines afforded by the deuterated nitrone (cf. Fig. 3B vs. Fig. 3A).

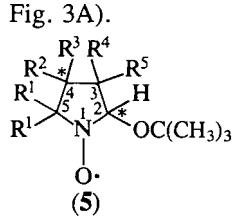

(**5**)

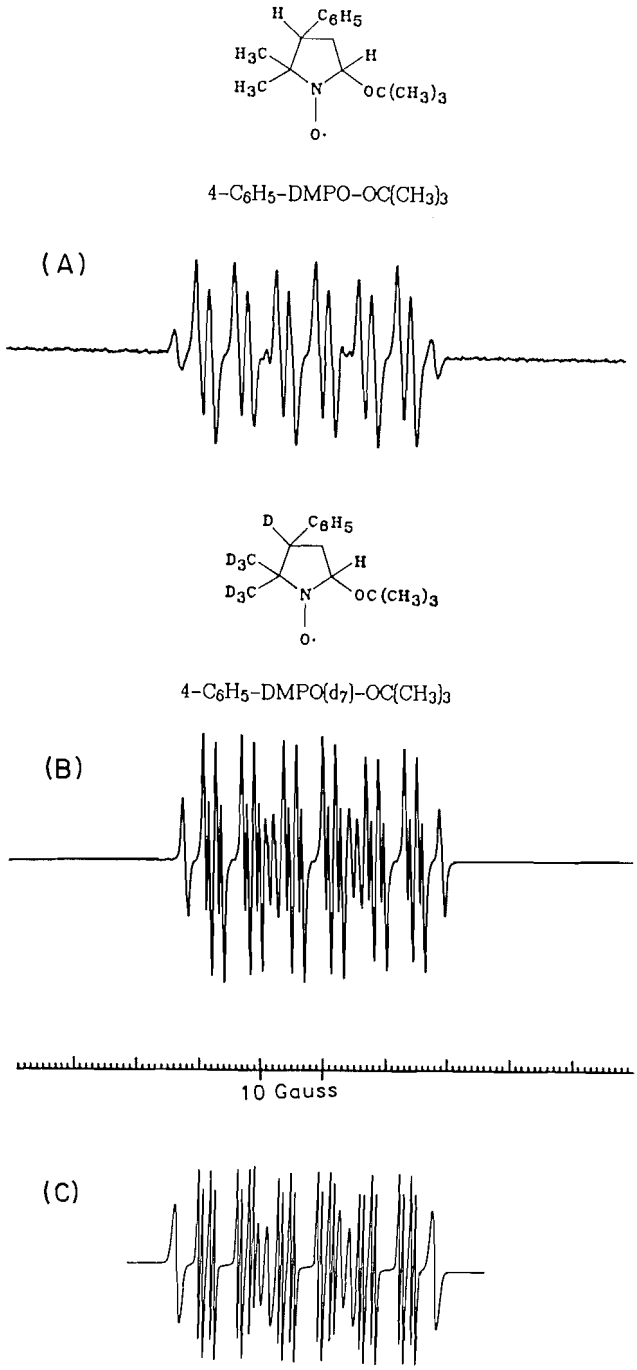

FIG. 3. (A) EPR spectrum of the *tert*-butoxyl radical adduct of 4-Ph-DMPO in toluene at room temperature. (B) EPR spectrum of the *tert*-butoxyl radical adduct of 4-Ph-DMPO-d_7 in toluene at room temperature. (C) Computer simulation of the EPR spectrum of the *tert*-butoxyl radical adduct of 4-Ph-DMPO-d_7.

ENDOR spectra of the DMPO-type radical adducts

ENDOR spectra of a variety of 5-membered ring (i.e., pyrrolidine) aminoxyls have appeared in the literature. For instance, pyrrolidine spin labels and spin probes (33, 40, 45, 53, 54, 64) as well as the heteroatom substituted 3-aza (53), 3-oxa (53, 57), 3-aza-*N*-oxide (imidazole-type) (48), 3-aza and 2-oxa 4,5-aryl fused (36, 49) analogues have been successfully analyzed by ENDOR spectroscopy. It is noteworthy that all of the above studies have involved 2,2,5,5-tetra-α-substituted aminoxyls, which are indefinitely stable compounds. In contrast, the ENDOR spectra we present here deal with 2,5,5-tri-α-substituted pyrrolidine aminoxyls (**5**) (R^1 = CH_3 or CD_3, and R^5 = $OC(CH_3)_3$), which are known to be considerably less persistent (e.g., second-order decay rate constant for DMPO–$OC(CH_3)_3$ ~ 10^3 M^{-1} s^{-1}) (11).

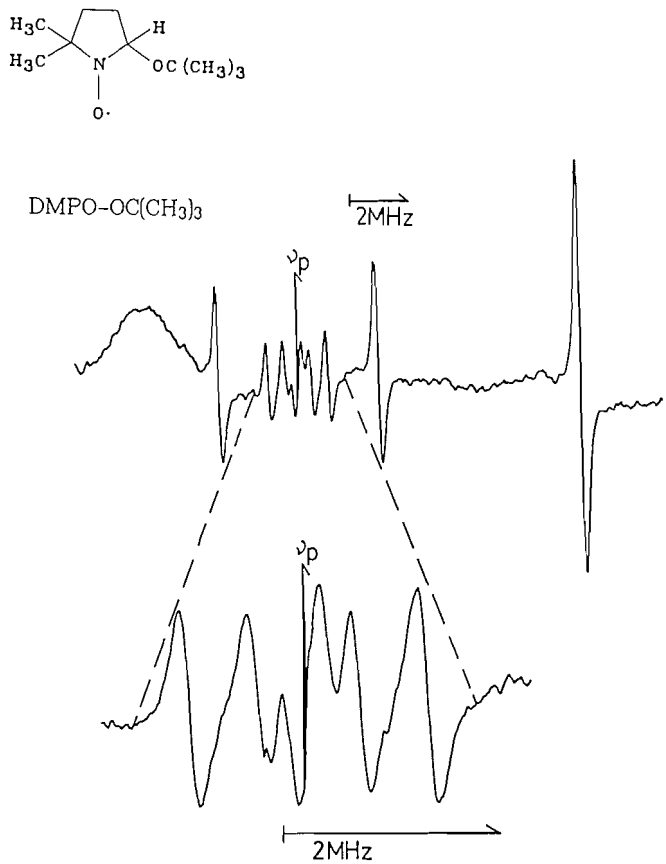

FIG. 4. ENDOR spectrum of the *tert*-butoxyl radical adduct of DMPO in toluene at 200 K. Note: The left side of the β-H ENDOR doublet is not shown due to instrumental noise in this low-frequency region (49).

ENDOR spectra of radical adducts of DMPO-type nitrones seem to be more difficult to obtain than from the related spin labels and spin probes alluded to earlier. Notwithstanding the problems of low spin adduct concentrations due to EPR spin trapping kinetics considerations (i.e., spin adduct formation and decay rate constants), the substitution around the pyrrolidine ring seems to affect the ease of obtaining ENDOR spectra. Of the *tert*-butoxyl radical spin adducts studied, M_4PO–$OC(CH_3)_3$ gave the strongest ENDOR response. The 4-substituted derivatives 4-Ph-DMPO–$OC(CH_3)_3$ and 4-Ph-DMPO-d_7–$OC(CH_3)_3$ provided slightly weaker spectra, with spectra from DMPO–$OC(CH_3)_3$ substantially (>5×) weaker than those from M_4PO–$OC(CH_3)_3$. To compensate for these intrinsically weaker ENDOR responses (e.g., as with DMPO–$OC(CH_3)_3$ these ENDOR spectra were accumulated accordingly longer. Thus, ring rigidity induced by pyrrolidine ring substitution may play a role in determining the ENDOR response, perhaps due to alteration of the electronic or nuclear relaxation behavior of the cyclic radicals.

DMPO–$OC(CH_3)_3$

There are at least seven types of magnetically distinct hydrogen nuclei in the *tert*-butoxyl radical adduct of DMPO (**6**). These include the β-H, the four H's at the 3- and 4-positions, the

Can. J. Chem. Downloaded from www.nrcresearchpress.com by 196.1.178.254 on 09/07/12
For personal use only.

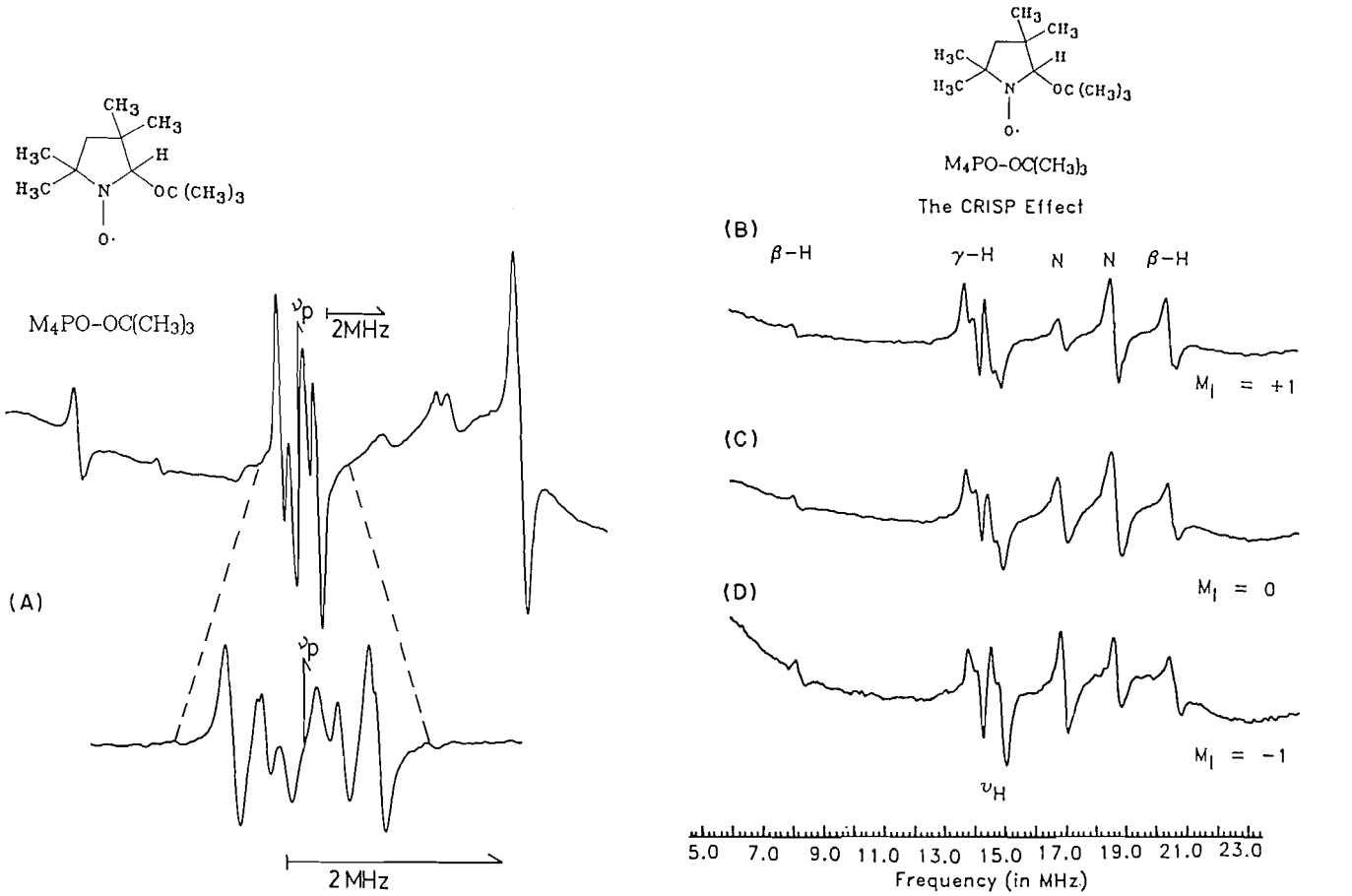

FIG. 5. (A) ENDOR spectrum of the *tert*-butoxyl radical adduct of M_4PO in toluene at 200 K. (B), (C), and (D) refer to the ENDOR spectra of the *tert*-butoxyl radical adduct of M_4PO in toluene at 230 K while saturating the $M_I = +1$, 0, and -1 branches of the EPR aminoxyl triplet.

Can. J. Chem. Downloaded from www.nrcresearchpress.com by 196.1.178.254 on 09/07/12
For personal use only.

γ-H's of the methyl groups at the 5-position, and the ϵ-H's of the *tert*-butoxyl group at the 2-position. The numbering for the various γ-H HFS's will be indicated according to that shown in eq. [1]. In Fig. 4 the ^1H ENDOR spectrum in toluene at 200 K reveals five of them. Since the *tert*- butoxyl H's are too distant (ϵ with respect to the aminoxyl nitrogen) to be observable even by ENDOR spectroscopy, only one type of hydrogen nucleus remains unaccounted for. Thus, this hyperfine splitting is either below the ENDOR resolution limit or its magnitude accidentally coincides with that of another hydrogen HFS.

Assignment of the β-H is straightforward due to its very large magnitude (Table 1, Fig. 4). One of the H's at the 3-position generates $a^H_{\gamma 5}$ (for assignment arguments, see the EPR spectra of DMPO–$OC(CH_3)_3$ vs. M_4PO–$OC(CH_3)_3$). Additionally, one of the H's at the 4-position is assigned to a^{H2}_{γ} (see Table 1) due to the remarkable spectral similarities with *trans*-4-phenyl-DMPO–$OC(CH_3)_3$ (see later).

The observed isotropic EPR linewidth of only ~1.1 gauss (Fig. 1) should contain contributions from a 1:6:15:20:15:6:1 septet due to the six H's on the methyl groups at the 5-position. Thus, the HFS from these H's may correspond to a^{H1}_{γ} because six times this value (i.e., 6 × 0.12 gauss) yields a reasonable linewidth contribution. Six times any other γ-H value (i.e., 6 × 1.95 vs. 6 × 0.72 vs. 6 × 0.31 gauss) produces a contribution to the linewidth that by itself may be too large for the linewidth actually observed.

By elimination, $a^H_{\gamma 3,4}$ is assigned to one of the remaining hydrogen nuclei at the 3- and 4-positions. For the HFS assignments for DMPO–$OC(CH_3)_3$ (**6**), see Table 1.

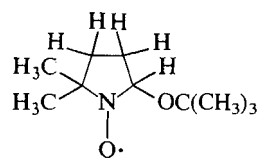

DMPO–$OC(CH_3)_3$
(**6**)

M_4PO–$OC(CH_3)_3$

Assignment of the hydrogen HFS due to the methyls at the 5-position (a^{H1}_{γ}) is based on arguments analogous to those developed for DMPO–$OC(CH_3)_3$. The δ-H's of the methyls at the 3-position are expected to be too small to detect. The remaining HFS's (i.e., a^{H2}_{γ} and a^{H3}_{γ}) for M_4PO–$OC(CH_3)_3$ therefore may be due to H's at the 4-position (**7**), Table 1).

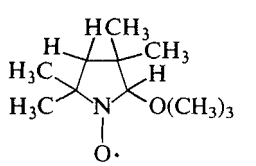

M_4PO–$OC(CH_3)_3$
(**7**)

Can. J. Chem. Downloaded from www.nrcresearchpress.com by 196.1.178.254 on 09/07/12
For personal use only.

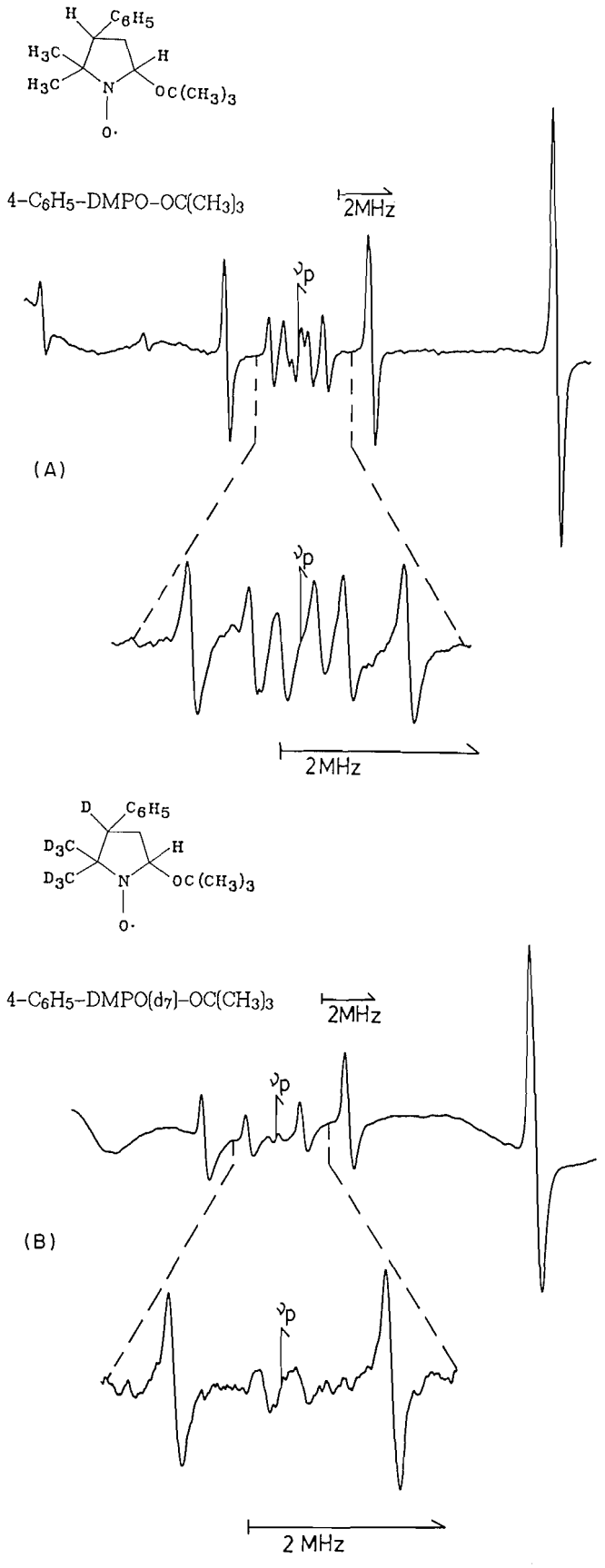

FIG. 6. (A) ENDOR spectrum of the *tert*-butoxyl radical adduct of 4-Ph-DMPO in toluene at 200 K. (B) ENDOR spectrum of the *tert*-butoxyl radical adduct of 4-Ph-DMPO-d_7 in toluene at 200 K. Note: The left side of the β-H ENDOR doublet is not shown due to instrumental noise in this low-frequency region (49).

4-Ph-DMPO–$OC(CH_3)_3$ and 4-Ph-DMPO-d_7–$OC(CH_3)_3$

The hyperfine splitting for the γ-H at the 4-position can be definitively assigned because this HFS ($a_\gamma^{H_3}$) disappears upon deuteration (see Fig. 6A vs. 6B). The 1.99-gauss splitting is assigned (by analogy to DMPO–$OC(CH_3)_3$) to one of the H's at position 3 (i.e., $a_\gamma^{H_5}$). Long-range phenyl HFS's are not expected to contribute ENDOR signals because these nuclei are ϵ- or further away from the aminoxyl radical centre. Because deuteration of the methyl groups at the 5-position is only around 93% (according to mass spectroscopy) some residual ENDOR response may be detected ($a_\gamma^{H_1}$). The remaining HFS (i.e., $a_\gamma^{H_4}$) for *trans*-4-phenyl-DMPO–$OC(CH_3)_3$ (**8**) therefore may arise from the second hydrogen nucleus at the 3-position, see Table 1.

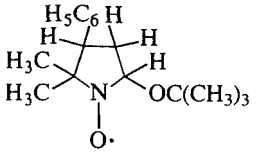

trans-4-Ph-DMPO–$OC(CH_3)_3$
(**8**)

Sign determination in the DMPO-type radical adducts

Signs of the HFS's were estimated by comparing the relative intensities of the ^1H and ^{14}N ENDOR peaks during saturation of different wings of the aminoxyl triplet (37, 42, 44) and are listed in Table 1. We have suggested the term CRISP (cross relaxation intensity sequence patterns) be used to describe this process (37, 44).

The *tert*-butoxyl radical adduct of M_4PO at 230 K in toluene solution was chosen to demonstrate the CRISP effect (Figs. 5B–5D). As the $M_I = +1$ branch of the EPR line is saturated the intensity ratio of high frequency to low frequency ^{14}N ENDOR lines decreases (Fig. 5B). Conversely, as the $M_I = -1$ wing is saturated this ratio increases (Fig. 5D). Because optimum temperatures for ^1H ENDOR are lower (i.e., ~200 K) than those for ^{14}N ENDOR (and CRISP) (i.e., ~230 K), sign determination (especially for the γ-H's) is tentative. Additional support for the negative γ-H HFS's for these DMPO-type spin adducts comes from the fact that other *N*,*N*-dialkylaminoxyls (e.g., spin adducts of α-phenyl *N*-*tert*-butyl nitrone (PBN)) (37, 44) also exhibit negative γ-H HFS's, as would be expected if a spin polarization mechanism of spin transfer from the aminoxyl nitrogen were operative. We have observed distinctly positive γ-H HFS's in certain *N*-acyl, *N*-alkylaminoxyls (nitroxones); however, the bonding characteristics in these species seem to be rather special compared to *N*,*N*-dialkylaminoxyls (78).

Summary

The first ^1H and ^{14}N ENDOR spectra of oxygen-centered radical adducts of DMPO-type nitrones (namely, the *tert*-butoxyl adducts) are shown to be useful because they can uncover extra diagnostic HFS's hidden in the EPR linewidth and also because the relative signs of the HFS's may be deduced by CRISP (37, 44) techniques. In addition to the hyperfine splittings from the β-H and ^{14}N nuclei, a number of γ-H splittings from the 3- and 4-positions as well as the methyls at the 5-position of the pyrrolidine aminoxyl are readily observable by ENDOR spectroscopy. Applications of these or other EPR resolution enhancement techniques (79–81)[7] to detect

[7]For "90° out-of-phase" resolution enhancement EPR see ref. 79. For "post-experiment" resolution enhancement by Fourier transform and related techniques see refs. 80 and 81.

characteristic long-range HFS's (either from the spin trap moiety or from the radical addend itself) appear to be viable new methodologies to assist in the confirmation of EPR spin adduct assignments. Additionally, we have found that deuteration of the cyclic nitrone nucleus (e.g., as in 4-Ph-DMPO-d_7) also leads to reduced linewidths and hence higher spectral resolution.

Acknowledgements

The authors would like to thank the Natural Sciences and Engineering Research Council of Canada (NSERC) for the purchase of the ENDOR spectrometer and for continuing support of this research.

Can. J. Chem. Downloaded from www.nrcresearchpress.com by 196.1.178.254 on 09/07/12
For personal use only.

1. E. G. JANZEN and J. I.-P. LIU. J. Magn, Reson. **9**, 510 (1973).
2. E. G. JANZEN, C. A. EVANS, and J. I.-P. LIU. J. Magn. Reson. **9**, 513 (1973).
3. E. G. JANZEN and C. A. EVANS. J. Am. Chem. Soc. **95**, 8205 (1973).
4. J. R. HARBOUR, V. CHOW, and J. R. BOLTON. Can. J. Chem. **52**, 3549 (1974).
5. E. G. JANZEN. Acc. Chem. Res. **4**, 31 (1971).
6. M. J. PERKINS. *In* Advances in physical organic chemistry. Vol. 17. *Edited by* Y. Gold and D. Bethell. Academic Press, New York. 1980. pp. 1–64.
7. P. J. THORNALLEY. *In* Life chemistry reports. Vol. 4. Harwood Academic, U.K. 1986. pp. 57–112.
8. R. P. MASON. *In* Spin labeling in pharmacology. *Edited by* J. L. Holtzman. Academic Press, New York. 1984. pp. 87–129.
9. G. R. BUETTNER. Free Radical Biol. Med. **3**, 259 (1987).
10. P. R. MARRIOTT, M. J. PERKINS, and D. GRILLER. Can. J. Chem. **58**, 803 (1980).
11. D. L. HAIRE and E. G. JANZEN. Can. J. Chem. **60**, 1514 (1982).
12. E. FINKELSTEIN, G. M. ROSEN, and E. J. RAUCKMAN. J. Am. Chem. Soc. **102**, 4994 (1980).
13. M. J. DAVIES, L. G. FORNI, and S. L. SHUTER. Chem.–Biol. Interact. **61**, 177 (1987).
14. A. SAMUNI, A. J. CARMICHAEL, A. RUSSO, J. B. MITCHELL, and P. RIESZ. Proc. Natl. Acad. Sci. U.S.A. **83**, 7393 (1986).
15. K. MAKINO, M. M. MOSSOBA, and P. RIESZ. J. Am. Chem. Soc. **104**, 3537 (1982).
16. A. R. FORRESTER and V. PURUSHOTHAM. J. Chem. Soc. Faraday Trans. 1, **83**, 211 (1987).
17. W. A. PRYOR, C. K. GOVINDAN, and D. F. CHURCH. J. Am. Chem. Soc. **104**, 7563 (1982).
18. C. MOTTLEY, H. D. CONNOR, and R. P. MASON. Biochem. Biophys. Res. Commun. **141**, 622 (1986), and references cited therein.
19. B. G. TAFFE, N. TAKAHASHI, T. W. KENSLER, and R. P. MASON. J. Biol. Chem. **262**, 12143 (1986).
20. B. D. HILTON, R. MISRA, and J. L. ZWEIER. Biochemistry, **25**, 5533 (1986).
21. J. H. DOROSHOW and K. J. A. DAVIES. J. Biol. Chem. **261**, 3068 (1986).
22. C. A. PRITSOS, P. P. CONSTANTINIDES, T. R. TRITTON, D. C. HEIMBROOK, and A. C. SARTORELLI. Anal. Biochem. **150**, 294 (1985).
23. A. HALPERN and J. KNIEPER. Z. Naturforsch. B: Anorg. Chem. Org. Chem. **40B**, 850 (1985).
24. W. H. KOCH and M. R. CHEDEKEL. Photochem. Photobiol. **44**, 703 (1986).
25. K. RESZKA, R. D. HALL, and C. F. CHIGNELL. Photochem. Photobiol. **40**, 707 (1984).
26. (*a*) M. S. COHEN, B. E. BRITIGAN, D. J. HASSETT, and G. M. ROSEN. Free Radical Biol. Med. **5**, 81(1988); (*b*) F. W. KLEINHANS and S. T. BAREFOOT. J. Biol. Chem. **262**, 12452 (1987); (*c*) E. G. JANZEN, L. T. JANRISITS, and D. L. BARBER. Free Radical Res. Commun. **4**, 115 (1987).
27. M. J. DAVIES and T. F. SLATER. Biochem. J. **245**, 167 (1987).
28. K. MAKINO, H. IMAICHI, S. MORINISHI, T. TAKEUCHI, and Y. FUJITA. Biochem. Biophys. Res. Commun. **141**, 381 (1986).
29. M. J. DAVIES and T. F. SLATER. Biochem. J. **240**, 789 (1986).
30. B. KALYANARAMAN, C. MOTTLEY, and R. P. MASON. J. Biol. Chem. **258**, 3855 (1983).
31. P. J. THORNALLEY, R. J. TROTTA, and A. STERN. Biochem. Biophys. Acta, **759**, 16 (1983).
32. (*a*) J. H. KRAMER, C. M. ARROYO, B. F. DICKENS, and W. B. WEGLICKI. Free Radical Biol. Med. **3**, 153 (1987); (*b*) J. L. ZWEIER, J. M. LUBER, JR., N. RUJIKARN, and P. S. RAO. 19th Annual Southeastern Magnetic Resonance Conference, Research Triangle Park, N.C., U.S.A. October 7–9, 1987; (*c*) P. B. GARLICK, M. J. DAVIES, D. J. HEARSE, and T. F. SLATER. Circ. Res. **61**, 757 (1987).
33. Y. KOTAKE and E. G. JANZEN. Can. J. Chem. **66**, 1895 (1988).
34. D. L. HAIRE, Y. KOTAKE, and E. G. JANZEN. Can. J. Chem. **66**, 1901 (1988).
35. E. G. JANZEN, Y. KOTAKE, and U. M. OEHLER. J. Chem. Soc. Faraday Trans. 1. In press.
36. M. BRUSTOLON, A. L. MANEIRO, U. SEGRE, and L. GRECI. J. Chem. Soc. Faraday Trans. 1, **83**, 69 (1987).
37. E. G. JANZEN, U. M. OEHLER, D. L. HAIRE, and Y. KOTAKE. J. Am. Chem. Soc. **108**, 6858 (1986).
38. E. G. JANZEN and Y. KOTAKE. J. Magn. Reson. **69**, 567 (1986).
39. E. G. JANZEN, Y. KOTAKE, G. A. COULTER, and U. M. OEHLER. Chem. Phys. Lett. **126**, 205 (1986).
40. Y. KOTAKE, Y. TOMITA, and K. KUWATA. J. Phys. Chem. **89**, 207 (1985).
41. J. C. EVANS, S. K. JACKSON, C. C. ROWLANDS, and M. D. BARRATT. Biochim. Biophys. Acta, **835**, 421 (1985).
42. J. YAMAUCHI and Y. DEGUCHI. Chem. Lett. 111 (1985).
43. M. BRUSTOLON, A. L. MANEIRO, and U. SEGRE. Mol. Phys. **55**, 713 (1985).
44. E. G. JANZEN and U. M. OEHLER. Chem. Lett. 1233 (1984).
45. Y. KOTAKE and K. KUWATA. Chem. Lett. 83 (1984).
46. J. C. EVANS, S. K. JACKSON, C. C. ROWLANDS, and M. D. BARRATT. Biochim. Biophys. Acta, **792**, 239 (1984).
47. M. BRUSTOLON, A. L. MANEIRO, and C. CORVAJA. Mol. Phys. **51**, 1269 (1984).
48. R. Z. SAGDEEV, A. Z. GOGOLEV, I. A. GRIGORIEV, G. I. SHCHUKIN, L. B. VOLODARSKY, W. MOHL, and K. MÖBIUS. Chem. Phys. Lett. **105**, 223 (1984).
49. E. G. JANZEN and U. M. OEHLER. Tetrahedron Lett. 669 (1983).
50. J. YAMAUCHI and Y. DEGUCHI. Chem. Lett. 257 (1983).
51. Y. DEGUCHI, K. OKADA, J. YAMAUCHI, and K. FUJII. Chem. Lett. 1611 (1983).
52. Y. KOTAKE and K. KUWATA. Can. J. Chem. **60**, 1610 (1982).
53. B. KIRSTE, A. KRÜGER, and H. KURRECK. J. Am. Chem. Soc. **104**, 3850 (1982).
54. M. P. EASTMAN, D. E. PATTERSON, R. A. BARTSCH, Y. LIU, and P. G. ELLER. J. Phys. Chem. **86**, 2052 (1982).
55. F. OHZEKI, L. D. KISPERT, C. ARROYO, and M. STEFFAN. J. Phys. Chem. **86**, 4011 (1982).
56. W. PLATO, W. LUBITZ, and K. MÖBIUS. J. Phys. Chem. **85**, 1202 (1981).
57. S. S. EATON, H. VAN WILLIGEN, M. J. HEINIG, and G. R. EATON. J. Magn. Reson. **38**, 325 (1980).
58. H. THOMANN, B. H. ROBINSON, L. R. DALTON, A. H. BETH, R. C. PERKINS, and J. H. PARK. Chem. Phys. Lett. **73**, 131 (1980).
59. Y. KOTAKE, M. OKAZAKI, and K. KUWATA. J. Am. Chem. Soc. **99**, 5198 (1977).
60. N. M. ATHERTON and M. BRUSTOLON. Mol. Phys. **32**, 23 (1976).
61. H. VAN WILLIGEN, M. PLATO, K. MÖBIUS, K.-P. DINSE, H. KURRECK, and J. REUCH. Mol. Phys. **30**, 1359 (1975).
62. K. ISHIZU, H. NAGAI, K. MUKAI, M. KOHNO, A. NAKAJIMA, and Y. DEGUCHI. Tetrahedron Lett. 1537 (1974).
63. K. ISHIZU, H. NAGAI, K. MUKAI, M. KOHNO, and T. YAMAMOTO. Chem. Lett. 1261 (1973).
64. K. P. DINSE, K. MÖBIUS, M. PLATO, R. BIEHL, and H. HAUSTEIN. Chem. Phys. Lett. **14**, 196 (1972).

65. R. D. ALLENDOERFER and J. H. ENGELMANN. Mol. Phys. **20**, 569 (1971).
66. D. S. LENIART, J. C. VEDRINE, and J. S. HYDE. Chem. Phys. Lett. **6**, 637 (1970).
67. J. S. HYDE. *In* Magnetic resonance in biological systems. *Edited by* A. Ehrenberg, B. G. Mälmstrom, and T. Vanngard. Pergammon, Oxford. 1967. pp. 63–84.
68. P. A. BARTLETT, E. P. BENZING, and R. E. PINCOCK. J. Am. Chem. Soc. **82**, 1762 (1960).
69. G. D. MENDENHALL. Tetrahedron Lett. **24**, 451 (1983).
70. J. Q. Adams and J. R. THOMAS. J. Chem. Phys. **39**, 1904 (1963).
71. D. L. HAIRE, J. W. HILBORN, and E. G. JANZEN. J. Org. Chem. **51**, 4298 (1986).
72. R. BONNETT, R. F. C. BROWN, V. M. CLARK, I. O. SUTHERLAND, and A. TODD. J. Chem. Soc. 2094 (1959).
73. J. B. BAPAT and D. S. C. BLACK. Aust. J. Chem. **21**, 2483 (1968).
74. G. WITTIG and A. HESSE. Org. Synth. **50**, 66 (1970).
75. N. KORNBLUM, H. O. LARSON, R. K. BLACKWOOD, D. M. MOOBERRY, E. P. OLIVITO, and G. E. GRAHAM, J. Am. Chem. Soc. **78**, 1497 (1957).
76. E. G. JANZEN, R. V. SHETTY, and S. M. KUNANEC. Can. J. Chem. **59**, 756 (1981).
77. F. W. KING. Chem. Rev. **76**, 157 (1976).
78. U. M. OEHLER. PhD dissertation, University of Guelph (1986).
79. M. M. MOSSOBA, K. MAKINO, P. RIESZ, and R. C. PERKINS, JR. J. Phys. Chem. **88**, 4717 (1984).
80. P. TROUSSON and Y. LION. J. Phys. Chem. **89**, 1954 (1985).
81. K. ROTH and B. KIRSTE. J. Magn. Reson. **63**, 360 (1985).

Can. J. Chem. Downloaded from www.nrcresearchpress.com by 196.1.178.254 on 09/07/12
For personal use only.

Ion–dipole complexes in the unimolecular reactions of isolated organic ions. Fragmentation of protonated and cationated formate and acetate esters

ADAM W. MCMAHON AND ALEX. G. HARRISON
Department of Chemistry, University of Toronto, Toronto, Ont., Canada M5S 1A1

Received March 14, 1988

ADAM W. MCMAHON and ALEX. G. HARRISON. Can. J. Chem. **66**, 2403 (1988).

The unimolecular fragmentation reactions occurring on the metastable ion time scale have been determined for protonated alkyl formates and acetates and for the adducts of CD_3^+ and $C_2H_5^+$ with these esters. The protonated esters, $R^1CO_2RH^+$, fragment to form $R^+ + R^1CO_2H$ or, by internal hydrogen transfer, $R^1CO_2H_2^+ + (R - H)$ with the relative yields depending on the identity of R^1 and R. Using deuterium labelling it has been shown that the added proton interchanges with hydrogens of the R group prior to fragmentation. The methyl-d_3-cationated esters, $R^1CO_2R.CD_3^+$, mostly fragment to give $R^1CO_2CD_3$, H^+ by elimination of (R − H), although R^+ formation is observed in a few cases. The ethyl-cationated esters fragment primarily to give $R^1CO_2C_2H_5.H^+$ by elimination of (R − H); specifically no elimination of C_2H_4 is observed. All of the results can be rationalized in terms of a step-wise mechanism of fragmentation involving initial formation of an ion–dipole complex of the alkyl ion R^+ with a carbonyl compound. This complex may either fragment to form R^+ or may proceed by way of an ion–dipole complex of a protonated carbonyl and an olefin to the protonated species plus (R−H). The results indicate that primary alkyl ions are not formed but rather that rearrangement to the more stable secondary or tertiary structure occurs. There is some evidence that *s*-butyl cations are not formed, but that these too rearrange to the *t*-butyl structure.

ADAM W. MCMAHON et ALEX. G. HARRISON. Can. J. Chem. **66**, 2403 (1988).

On a déterminé les réactions de fragmentation unimoléculaire se produisant à l'échelle de temps des ions métastables des formiates et des acétates d'alkyle protonés et des adduits du CD_3^+ et du $C_2H_5^+$ avec ces esters. Les esters protonés $R^1CO_2RH^+$ se fragmentent pour donner du $R^+ + R^1CO_2H$, ou par transfert d'hydrogène interne, du $R^1CO_2H_2^+ + (R - H)$ dont les rendements relatifs dépendent des groupes R^1 et R. L'utilisation du marquage au deutérium a permis de mettre en évidence un échange entre le proton ajouté et les hydrogènes du groupe R avant la fragmentation. Les esters cationiques méthyl-d_3, $R^2CO_2R.CD_3^+$, se fragmentent principalement surtout pour donner du $R^1CO_2CD_3.H^+$ par élimination de (R − H) en dépit du fait que dans certains cas on observe la formation du groupe R^+. Les esters éthyliques cationiques se fragmentent principalement pour donner le composé $R^1CO_2C_2H_5.H^+$ par élimination de (R − H) et on n'a pas observé d'élimination spécifique de C_2H_4. On peut rationnaliser tous ces résultats en terme d'un mécanisme de fragmentation par étapes impliquant la formation initiale d'un complexe ion-dipôle de l'ion alkyle R^+ avec le composé carbonylé. Ce complexe peut soit se fragmenter pour donner R^+ soit se transformer via un complexe ion–dipôle d'un carbonyle protoné et d'une oléfine en l'espèce protoné plus (R−H). Les résultats indiquent que les ions alkyle primaire ne se forment pas mais qu'ils se transposent de préférence en ions secondaire ou tertiaire plus stable. On a la preuve que les cations *s*-butyles ne se forment pas mais qu'ils se transposent en cations *t*-butyle.

[Traduit par la revue]

Can. J. Chem. Downloaded from www.nrcresearchpress.com by 112.217.228.212 on 09/07/12
For personal use only.

Introduction

The reactions of isolated gaseous ions can be investigated conveniently using mass spectrometers (for a recent review, see ref. 1). Particularly useful information may be acquired from the study of the fragmentation reactions occurring on the metastable ion time frame where the excess energies in the transition state are similar to those involved in solution reactions (ref. 2, for reviews emphasizing the usefulness of metastable ion investigations, see ref. 3). For such reactions the relative rates are determined primarily by relative critical reaction energies and the results frequently can be understood in terms of potential energy profiles (3). Thus, the study of the unimolecular fragmentation reactions of metastable ions probes the fragmentation pathways of lowest critical reaction energy. The present study reports such a study of protonated, methyl-cationated and ethyl-cationated ethyl through butyl formates and acetates. The proton-transfer chemical ionization mass spectra of esters have received extensive study (4–11) and the major fragmentation pathways of higher energy protonated species have been delineated. However, the threshold fragmentation reactions which explore the potential energy profiles for fragmentation have not been examined. In addition, the fragmentation reactions of the methyl-cationated and ethyl-cationated species have not been studied systematically. Extensive studies have shown that species comprising an incipient cation and a neutral, held together by ion–dipole attractive forces frequently play a role in the chemistry of isolated ions (12–26). Much of the earlier evidence for these ion–dipole complexes derived from the behaviour of closed-shell "onium" ions generated by dissociative ionization of alcohols, ethers, and amines (12–16). More recently, such complexes have been shown to be involved in the fragmentation of closed-shell species produced by bimolecular ion/molecule reactions (18–26). The present results provide further examples of the role of ion–dipole complexes in the fragmentation of closed-shell species.

Experimental

The unimolecular fragmentation reactions of the protonated, deuteronated, and ethyl-cationated esters, which occur on the metastable ion time frame, were investigated by the MIKES technique (2) using a VG Analytical ZAB-2FQ mass spectrometer (27). Kinetic energy releases were evaluated from the peak widths at half-height after correction for the main beam width. The MIKES spectra of the methyl-cationated species were complicated by artifact peaks and by fragmentation of the MH^+ ion of the next higher homologous ester which was present as a low level impurity. To eliminate the latter complication the methyl-d_3-cationated esters were studied. To eliminate the first complication the appropriate ion was transmitted to the rf-only quadrupole cell of the instrument where unimolecular fragmentation occurred (in the absence of collision gas) with the products being analyzed by the final stage quadrupole mass analyzer; the extra stage of mass/energy selection eliminated the artifact peaks. The collision-induced dissociation mass spectra of the protonated esters were

TABLE 1. Metastable ion fragmentation of protonated formate esters, $HCOOR.H^+$ by MIKES technique

	$HCO_2H_2^+ + (R—H)$		$R^+ + HCO_2H$		$C_nH_{2n}D^+$
R	Yield	ΔH^0react[a]	Yield	ΔH^0react[a]	$C_nH_{2n+1}^+$
C_2H_5	100	99	0	188	—
n-C_3H_7	0	97	100	171(104)[b]	2.3
i-C_3H_7	1	115	99	122	2.5
n-C_4H_9	0	92	100	159(84)[b]	4.5
i-C_4H_9	0	97	100	263(29)[c]	0.9
s-C_4H_9	0	107	100	106	7.1
t-C_4H_9	0	118	100	60	1.2

[a]In kJ mol^{-1}.
[b]Value in parentheses, ΔH^0 for formation of secondary ion.
[c]Value in parentheses, ΔH^0 for formation of t-butyl$^+$.

TABLE 2. Metastable ion fragmentation of protonated acetate esters, $CH_3COOR.H^+$ by MIKES technique

	$CH_3CO_2H_2^+ + (R—H)$		$R^+ + CH_3CO_2H$		$CH_3CO_2HD^+$ / $CH_3CO_2H_2^+$
R	Yield	ΔH^0react	Yield	ΔH^0react	
C_2H_5	100	108	0	236	
n-C_3H_7	100	100	0	213(146)[b]	3.2
i-C_3H_7	97	119	3	165	1.1
n-C_4H_9	99	107	1	207(132)[b]	1.6
i-C_4H_9	15	93	85	208(74)[c]	1.0
s-C_4H_9	100	111	0	149	0.5
t-C_4H_9	7	118	93	99	1.5

[a]In kJ mol^{-1}.
[b]Value in parentheses: ΔH^0 for formation of secondary ion.
[c]Value in parentheses: ΔH^0 for formation of t-$C_4H_9^+$.

determined over the collision energy range 5 to 100 eV by mass selecting the appropriate MH^+ ion by the double-focussing (BE) mass spectrometer, decelerating the ions to the appropriate energy and injecting them into the rf-only quadrupole cell with N_2 used as collision gas. The products of dissociation were analyzed with the final quadrupole mass analyzer.

For metastable ion studies the protonated esters were prepared by CH_4 chemical ionization in a combined EI/CI source operating in the CI mode. Substitution of CD_4 for the CH_4 reagent gas yielded the deuteronated ester. For the CID studies the protonated ester was prepared by isobutane chemical ionization to minimize unimolecular fragmentation. The methyl-d_3-cationated species were prepared by using CD_3Br as reagent gas while the ethyl-cationated species were prepared by using C_2H_5Br as reagent gas. The exact reaction(s) forming the cationated esters is (are) not known, however, in both systems the dialkyl bromonium ion R_2Br^+ (R = CD_3 or C_2H_5) was a major species and alkyl ion transfer by this species to the ester undoubtedly is occurring. The ion source was operated at ~200°C with 50 eV ionizing electron energy and 8 kV ion accelerating potential.

The esters either were commercially available or were prepared by standard methods.

Results and discussion

Fragmentation of protonated esters

Table 1 records the relative fragment ion intensities observed as a result of fragmentation of protonated formate esters as metastable ions while Table 2 records the similar data obtained for the fragmentation of protonated acetate esters. For metastable ions two fragmentation reactions are observed, elimination of a carboxylic acid forming an alkyl ion (reaction [1]) and elimination of an olefin forming the protonated acid (reaction [2]). Also included in the tables for each ester are the enthalpies of reactions [1] and [2] calculated from the thermochemical

$$[1]\quad R^1\text{-}C(OH^+)\text{-}OR \rightarrow R^1COOH + R^+$$

$$[2]\quad \rightarrow R^1CO_2H_2^+ + (R—H)$$

data listed in the Appendix. On the metastable ion time scale protonated ethyl formate fragments by reaction [2] while the protonated propyl and butyl formates fragment by reaction [1]. The protonated acetates fragment primarily by reaction [2] with the exception of protonated i-butyl and t-butyl acetates which fragment primarily by reaction [1]. These results are in accord with the proton-transfer chemical ionization mass spectra reported earlier (11) in that for each ester the dominant fragment ion observed in the CI mass spectrum is the same as that observed in the metastable ion mass spectrum.

The results obtained for the metastable ion fragmentation of the deuteronated esters are particularly relevant to a discussion of the mechanism of fragmentation of protonated esters. The MD^+ ion of ethyl formate forms HCO_2HD^+ exclusively in metastable ion fragmentation reactions. The MH^+ ions of the remaining formates fragment to form the appropriate alkyl ions; for the MD^+ ions this products was observed both as C_nH_{2n+1} and as $C_nH_{2n}D^+$, the observed $C_nH_{2n}D^+/C_nH_{2n+1}$ ratios

Can. J. Chem. Downloaded from www.nrcresearchpress.com by 112.217.228.212 on 09/07/12
For personal use only.

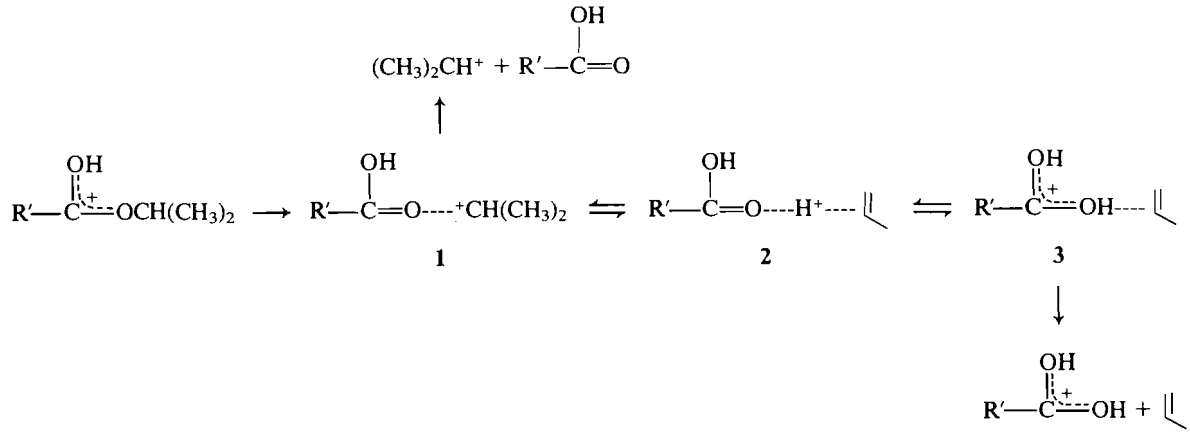

SCHEME 1

being given in Table 1. The protonated acetates fragment to give protonated acetic acid; for the deuteronated acetates both $CH_3CO_2HD^+$ and $CH_3COH_2^+$ were observed, the $CH_3CO_2HD^+/CH_3CO_2H_2^+$ ratios being given in Table 2. Note that only $CH_3CO_2HD^+$ is observed in the ethyl acetate system. In addition to these results the butyl ions produced from the *i*-butyl and *t*-butyl esters showed substantial deuterium incorporation: $C_4H_8D^+/C_4H_9^+ = 0.7$ (*i*-butyl) and 2.6 (*t*-butyl). Initial protonation/deuteronation of the esters presumably occurs at the carbonyl oxygen (the most basic site (28)) and the present results clearly show that, except for the ethyl esters, this added hydrogen/deuterium undergoes substantial interchange with the hydrogens of the alkyl group. Such interchange reactions have been observed previously for protonated ethanol (25) and protonated methyl isopropyl ether (29) and have been rationalized (25) in terms of partial equilibration between the ion–dipole complexes proposed as intermediates in the fragmentation of protonated molecules. This mechanism, applied to the case of protonated esters and using a protonated isopropyl ester as an example, is shown in Scheme 1. If partial equilibration between the intermediate complexes **1** and **3** occurs, hydrogen interchange between oxygen and the alkyl group will be observed. In line with earlier arguments (25), such equilibration should be observed as long as **1** is lower in energy than the final products $R^1CO_2H_2^+ + (R—H)$. The complex **1** should be stabilized, relative to $R^+ + R'CO_2H$, by ion–dipole interactions which may amount to as much as 40–60 kJ mol^{-1} (12), so that, as long as $\Delta H_1 - \Delta H_2 \leq 40$–60 kJ mol^{-1}, **1** will be lower in energy than $R^1CO_2H_2^+ + (R—H)$ and hydrogen interchange should occur. Perusal of the thermochemical data of Tables 1 and 2 shows that the protonated ethyl esters do not meet this requirement and, indeed, hydrogen interchange is not observed. Based on this criterion, hydrogen interchange is predicted for the remaining protonated acetates *provided* we assume relatively facile rearrangement of the incipient primary alkyl cations in **1** to the more stable secondary or tertiary structure. This point will be returned to below. Similarly, hydrogen interchange is predicted for the protonated propyl and butyl formate esters with the possible exception of *t*-butyl formate. In this case one would expect that the complex **3** is higher in energy than the products $t\text{-}C_4H_9^+ + HCO_2H$; consequently any complexes **1** which have energy to reach **3** will have more than enough energy to fragment. Nevertheless, hydrogen interchange is observed, although to a smaller extent than for the *n*-butyl and *s*-butyl esters. Clearly, the hydrogen interchange data provide strong evidence for the participation of ion–dipole complexes in the fragmentation of protonated closed-shell species.

It should be noted that the reaction enthalpies for [1] and [2] are the same, within experimental uncertainty, for the protonated propyl formates, yet $C_3H_7^+$ is the only product observed in metastable ion fragmentation reactions. This may indicate that there is a barrier in addition to the reaction endothermicity for formation of $R^1CO_2H_2^+$. Alternatively the results may be interpreted in tems of similar energy barriers, but with the reaction forming the alkyl ion being favoured entropically because it is a simple bond fission reaction with a loose transition state, while the reaction forming $R^1CO_2H_2^+$ involves H^+ transfer and has a tight transition state. Support for the latter hypothesis comes from low variable-energy collision-induced dissociation (ERMS) (30–32) studies. It is well established (33–37) that, in such low energy collisional experiments, the energy deposited in the ion as internal energy increases with increasing collisional energy; thus, by varying the collision energy, the energy dependence of the competing reactions can be examined over an extended range such that not only relative critical energies, but also relative frequency factors play a role in determining the relative rates. In the present study, it was observed that, for those systems where alkyl ion formation (reaction [1]) dominated the metastable ion mass spectrum, the same ion dominated the breakdown graph (fractional fragment ion intensities as a function of collision energy). Typical results are shown in Fig. 1 for the protonated *i*-propyl formate system. In these systems formation of $R^1CO_2H_2^+$ cannot compete with formation of R^+ at higher internal energies because of the lower frequency factor for the former reaction. By contrast, for those systems where rearrangement to form $R^1CO_2H_2^+$ is the energetically favoured reaction and this ion dominates the metastable ion spectrum, formation of the alkyl ion R^+ increases markedly in importance with increasing collision energy. Typical results are shown in Fig. 2 for the protonated *s*-butyl acetate system; similar results were obtained for the protonated propyl acetates and protonated *n*-butyl acetate. In these cases formation of R^+, although there is a higher critical reaction energy, there is also a more favourable frequency factor (loose transition state) and the reaction competes effectively with the formation of $R^1CO_2H_2^+$ at higher internal energies as the latter reaction has a lower frequency factor (tight transition state).

The results reported in Tables 1 and 2 have been rationalized above, in part, by assuming that the incipient primary alkyl ions undergo facile rearrangement to the more stable secondary or tertiary structure. There is substantial evidence that small

Can. J. Chem. Downloaded from www.nrcresearchpress.com by 112.217.228.212 on 09/07/12
For personal use only.

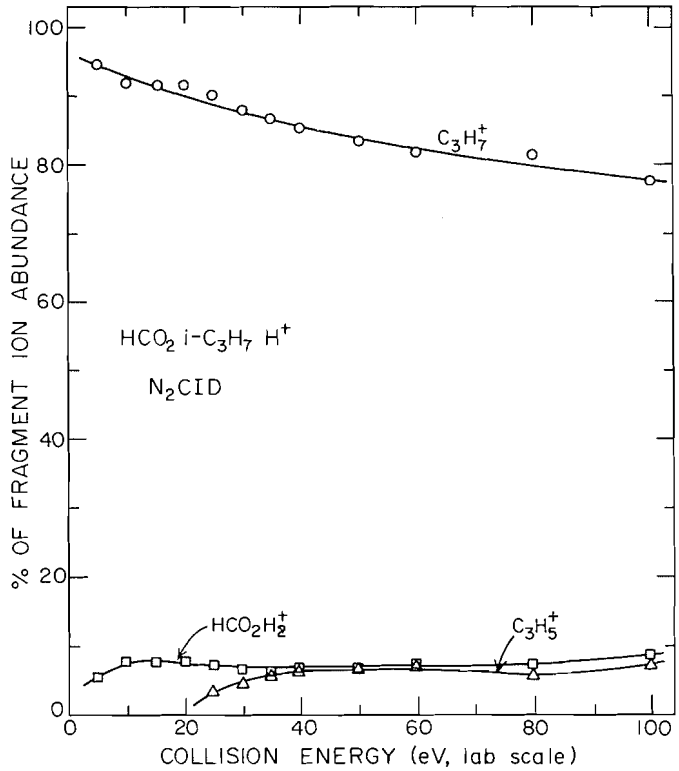

FIG. 1. Breakdown graph for protonated *i*-propyl formate.

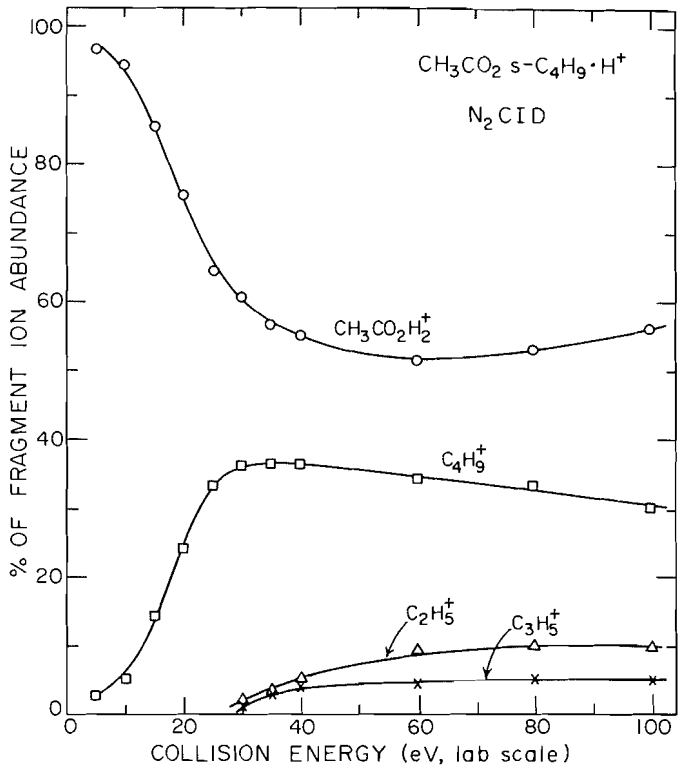

FIG. 2. Breakdown graph for protonated *s*-butyl acetate.

hydrocarbon ions undergo facile isomerizations prior to unimolecular dissociation in the gas phase (38) and under solvolytic conditions in condensed phases (39); indeed, it appears that free primary alkyl ions are not stable species (40). Further information relevant to the question of the rearrangement of the incipient alkyl ions comes from measurements of the kinetic energy releases associated with the fragmentation reaction [1] occurring on the metastable ion time scale. The results of such measurements are presented in Table 3. The results for the *t*-butyl and *i*-butyl esters are particularly informative. The kinetic energy release associated with reaction [1] is 2.0 meV for protonated *t*-butyl formate and 3.1 meV for protonated *t*-butyl acetate. These low kinetic energy releases are consistent with a reaction which is continuously endothermic along the reaction coordinate. By contrast, the corresponding protonated *i*-butyl esters show much larger kinetic releases (14.3 and 15.7 meV, respectively). These larger kinetic energy releases are inconsistent with a continuously endothermic reaction leading to formation of the *i*-butyl cation, but are consistent with an exothermic rearrangement of the incipient *i*-butyl cation to the *t*-butyl structure. There is ample evidence (18, 41) that dissociation of gaseous ions which are preceded or accompanied by an exothermic isomerization of the incipient cation are associated with an increased kinetic energy release. The isomerization from the *i*-butyl to the *t*-butyl structure presumably occurs by a hydride ion migration (42) in the *i*-butyl$^+$–R^1CO_2H complex. This complex should be 40–56 kJ mol^{-1} more stable than the separated *i*-$C_4H_9^+$ + R^1CO_2H products. However, since ΔH_f^0(*i*-$C_4H_9^+$) − ΔH_f^0(*t*-$C_4H_9^+$) = 134 kJ mol^{-1} (Appendix) it is clear that this complex is higher in energy than the final products, leading to an exothermic fragmentation reaction and an increased kinetic energy release. On the other hand, protonated *i*-propyl formate and protonated *n*-propyl formate show essentially identical kinetic energy releases in metastable ion fragmentation reactions to form $C_3H_7^+$, although it is probable that *i*-$C_3H_7^+$ is formed in both cases. However, ΔH_f^0 (*n*-$C_3H_7^+$) − ΔH_f^0 (*i*-$C_3H_7^+$) = 67 kJ mol^{-1} and it is likely that the stabilization energy in the *n*-$C_3H_7^+$–HCO_2H complex is of this order of magnitude so that the complex is not significantly higher in energy than the final products, *i*-$C_3H_7^+$ + HCO_2H, in this case; consequently no significant increase in kinetic energy release would be expected. Schwarz and Stahl (18) have observed that fragmentation of $C_3H_7OH_2^+$ to $C_3H_7^+$ + H_2O gave the same low kinetic energy release for both isomers but that fragmentation of $C_3H_7CO^+$ to $C_3H_7^+$ + CO gave a considerably higher kinetic energy release for the *n*-C_3H_7 isomer because of the decreased ion–dipole stabilization associated with interaction with CO compared to interaction with H_2O. Our system should be comparable to the $C_3H_7^+$–H_2O system.

TABLE 3. Kinetic energy release ($T_{1/2}$) in fragmentation $R^1CO_2R.H^+ \rightarrow R^1CO_2H + R^+$

$R^1CO_2R.H^+$	$T_{1/2}$(meV ± 0.3)
HCO_2.*i*-C_3H_7	3.2
HCO_2.*n*-C_3H_7	4.0
HCO_2.*t*-C_4H_9	2.0
HCO_2.*i*-C_4H_9	14.3
HCO_2.*s*-C_4H_9	15.2
HCO_2.*n*-C_4H_9	14.4
CH_3CO_2.*t*-C_4H_9	3.1
CH_3CO_2.*i*-C_4H_9	15.7

Can. J. Chem. Downloaded from www.nrcresearchpress.com by 112.217.228.212 on 09/07/12
For personal use only.

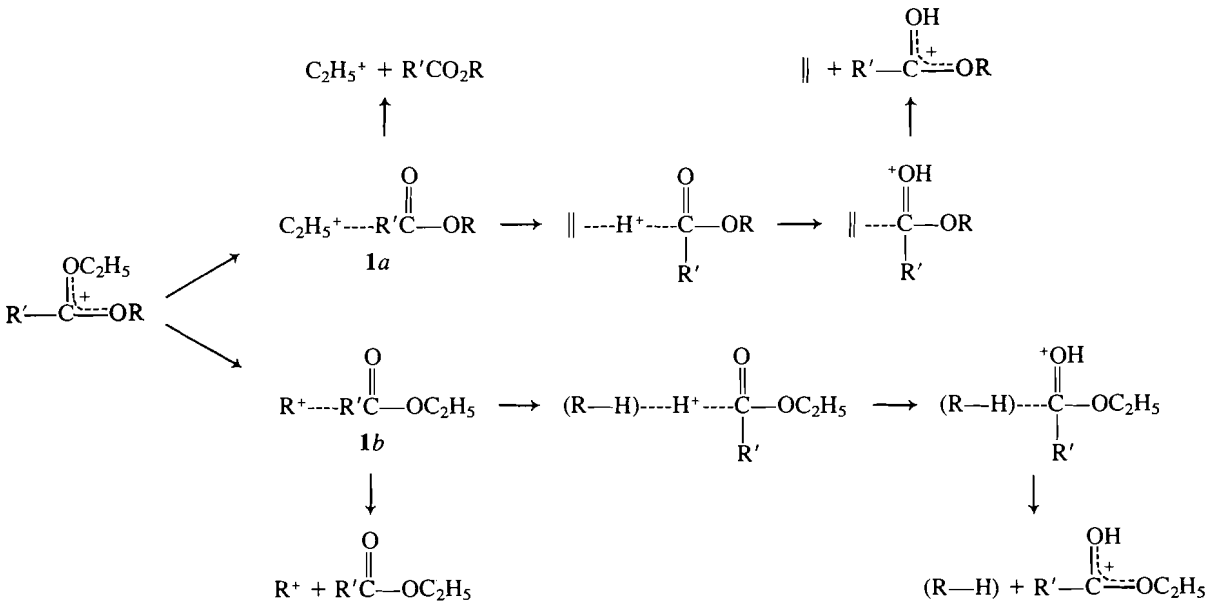

SCHEME 2

The most intriguing result in Table 3 is the relatively large kinetic energy release associated with reaction [1] for protonated *s*-butyl formate. Such a large kinetic energy release is not expected if simple bond fission to form *s*-$C_4H_9^+$ + HCO_2H occurs. It appears probable, therefore, that fragmentation of this protonated ester is accompanied by exothermic rearrangement to the *t*-butyl cation structure. Such a rearrangement has been proposed (43) to occur through the *i*-butyl$^+$ structure. It is interesting to note that the *s*-butyl$^+$ ion rearranges to the tertiary structure in the solution phase at −60°C (39). It is probable that fragmentation of the protonated *n*-butyl ester also involves rearrangement of the alkyl group to the *t*-butyl structure.

Fragmentation of methyl-cationated esters

Unimolecular fragmentation of the CD_3^+ adducts on the metastable ion time scale gave, with two exceptions, the protonated ester $R^1CO_2CD_3.H^+$ (reaction [3])

[3] $R^1CO_2RCD_3^+ \rightarrow R^1CO_2CD_3.H^+ + (R—H)$

The two exceptions were the *i*-butyl formate system where $C_4H_9^+$ was the only fragment ion observed and the *t*-butyl formate system where 73% $HCO_2CD_3.H^+$ and 27% $C_4H_9^+$ were observed; these latter data are uncertain because of the extremely low intensity of the adduction.

Calculation of the heats of formation of products reveals that reaction [3] is the thermochemically favoured reaction except for the adducts with *i*-butyl formate and *t*-butyl formate where formation of *t*-$C_4H_9^+$ becomes the thermochemically favoured reaction. (This, of course, assumes rearrangements from the *i*-butyl to the *t*-butyl structure). In effect, the proton affinities of the methyl esters are sufficiently high to direct the reaction to formation of this product in most cases. As examples, the proton affinity of methyl formate (797 kJ mol^{-1} (Appendix) is higher than that of 2-butene (761 kJ mol^{-1} (43)) (the conjugate base of *s*-butyl$^+$) but lower than that of *i*-butene (824 kJ mol^{-1} (43)) (the conjugate base of *t*-butyl$^+$). On the other hand, the proton affinity of methyl acetate (829 kJ mol^{-1} (Appendix)) is greater than that of *i*-butene.

Fragmentation of ethyl-cationated esters

Unimolecular fragmentation reactions of the $C_2H_5^+$ adducts with the propyl and butyl formates and acetates were examined, with the exception of the adduct with *t*-butyl formate where no significant adduct ion signal was observed. Earlier work (44) has shown that the $C_2D_5^+$ adduct of ethyl acetate fragments by loss of C_2D_4 and C_2H_4. Four fragmentation reactions, [4] to [7], are possible for fragmentation of these adducts.

[4] $R^1CO_2R{\cdot}C_2H_5^+ \rightarrow R^1CO_2R{\cdot}H^+ + C_2H_4$

[5] $\rightarrow R^1CO_2C_2H_5{\cdot}H^+ + (R—H)$

[6] $\rightarrow C_2H_5^+ + R^1CO_2R$

[7] $\rightarrow R^+ + R^1CO_2C_2H_5$

Thermochemical calculations show that the reactions enthalpies of [4] and [5] are the same within experimental uncertainty (±17 kJ mol^{-1}); in several cases reaction [5] appears to be thermochemically favoured. Despite this, no evidence was found for loss of C_2H_4 in the metastable ion fragmentation reactions. The dominant fragmentation reaction, with one exception, was elimination of (R—H), reaction [5]. The one exception was the adduct with *i*-butyl formate which formed both $HCO_2C_2H_5{\cdot}H^+$ (39%) and $C_4H_9^+$ (61%) in metastable ion fragmentation reactions; for this case the thermochemical data show that reactions [5] and [7] have very similar reaction enthalpies.

At first sight the domination of reaction [5] over reaction [4] is surprising given that the reaction enthalpies are very similar. However, the results are readily rationalized if olefin elimination occurs by a step-wise mechanism involving ion–dipole complexes (Scheme 2) rather than by a concerted mechanism. The ion–dipole complex, **1***a*, which leads to elimination of C_2H_4 will be of higher energy than the ion–dipole complex **1***b*, and higher in energy than the products $R^1CO_2C_2H_5.H^+$ + (R—H). This is illustrated by the following representative data

Can. J. Chem. Downloaded from www.nrcresearchpress.com by 112.217.228.212 on 09/07/12
For personal use only.

		ΔH_f^0 (products) (kJ mol^{-1})
$HCO_2.i\text{-}C_4H_9.C_2H_5^+$	$\rightarrow HCO_2.i\text{-}C_4H_9.H^+ + C_2H_4$	343
	$\rightarrow HCO_2C_2H_5.H^+ + i\text{-}C_4H_9$	331
	$\rightarrow C_2H_5^+ + HCO_2.i\text{-}C_4H_9$	489
	$\rightarrow C_4H_9^+ + HCO_2C_2H_5$	460 (i-butyl$^+$)
		326 (t-butyl$^+$)
$CH_3CO_2.s\text{-}C_4H_9.C_2H_5^+$	$\rightarrow CH_3CO_2.s\text{-}C_4H_9.H^+ + C_2H_4$	238
	$\rightarrow CH_3CO_2C_2H_5.H^+ + 2\text{-}C_4H_8$	238
	$\rightarrow C_2H_5^+ + CH_3CO_2.s\text{-}C_4H_9$	414
	$\rightarrow s\text{-}C_4H_9^+ + CH_3CO_2C_2H_5$	322

The complexes **1***a* and **1***b* should have similar stabilization energies (40–60 kJ mol^{-1}) relative to the separated alkyl ion plus ester products and that leading to ethylene elimination will be considerably higher in energy because of the high enthalpy of formation of $C_2H_5^+$. This is particularly true if we assume facile rearrangement of incipient primary propyl and butyl ions to the more stable secondary and tertiary structures. Clearly these results also provide strong evidence for the role of ion–dipole complexes on the fragmentation of even-electron species. It should be noted that an explanation similar to the above has been presented to rationalize the elimination of C_3H_6 rather than C_2H_4 from protonated ethyl isopropyl amine activated by chemical means or by multi-photon absorption (19, 20).

Acknowledgements

The authors are indebted to the Natural Sciences and Engineering Research Council of Canada for continued financial support. A.G.H. gratefully acknowledges the award of a Killam Research Fellowship (1985–1987) by the Canada Council.

1. J. L. Holmes. Org. Mass Spectrom. **20**, 169 (1985).
2. R. G. Cooks, J. H. Beynon, R. M. Caprioli, and G. R. Lester. Metastable ions. Elsevier, Amsterdam 1973.
3. R. D. Bowen, D. H. Williams, and H. Schwarz. Agnew. Chem. Int. Ed. Engl. **18**, 451 (1979); R. D. Bowen and D. H. Williams. *In* Rearrangements in ground and excited states. *Edited by* P. de Mayo. Vol. 1. Academic Press, New York. 1980. Chap. 2.
4. M. S. B. Munson and F. H. Field. J. Am. Chem. Soc. **88**, 4337 (1966).
5. B. L. Jelus, J. Michnowicz, and B. Munson. J. Org. Chem. **39**, 2130 (1974).
6. C. V. Peschek and S. E. Buttrill. J. Am. Chem. Soc. **96**, 6027 (1974).
7. C. W. Tsang and A. G. Harrison. J. Chem. Soc. Perkin Trans. 2, 1718 (1975).
8. A. G. Harrison and C. W. Tsang. Can. J. Chem. **54**, 2029 (1976).
9. F. M. Benoit and A. G. Harrison. Org. Mass Spectrom. **13**, 128 (1978).
10. A. C. Hopkinson, G. I. Mackay, and D. K. Bohme. Can. J. Chem. **57**, 2996 (1979).
11. J. A. Herman and A. G. Harrison. Can. J. Chem. **59**, 2133 (1981).
12. R. D. Bowen and D. H. Williams. Int. J. Mass Spectrom. Ion Phys. **29**, 47 (1979).
13. R. D. Bowen. J. Chem. Soc. Perkin Trans. 2, 409 (1980).
14. T. H. Morton. J. Am. Chem. Soc. **102**, 1596 (1980).
15. R. D. Bowen and D. H. Williams. J. Am. Chem. Soc. **102**, 2752 (1980).
16. R. D. Bowen. J. Chem. Soc. Perkin Trans. 2, 1219 (1980).
17. T. H. Morton. Tetrahedron, **38**, 3195 (1982).
18. H. Schwarz and D. Stahl. Int. J. Mass Spectrom. Ion Phys. **36**, 285 (1980).
19. C. R. Moylan and J. I. Brauman. J. Am. Chem. Soc. **107**, 761 (1985).
20. P. Ausloos and S. G. Lias. J. Am. Chem. Soc. **108**, 1972 (1986).
21. U. Filges and H.-F. Grutzmacher. Org. Mass Spectrom. **21**, 673 (1986).
22. E. J. Reiner, R. A. Poirier, M. R. Peterson, I. G. Csizmadia, and A. G. Harrison. Can. J. Chem. **64**, 1652 (1986).
23. W. Tumas, R. F. Foster, M. J. Pellerite, and J. I. Brauman, J. Am. Chem. Soc. **109**, 961 (1987).
24. M. Weiss, R. A. Crombie, and A. G. Harrison. Org. Mass Spectrom. **22**, 216 (1987).
25. A. G. Harrison. Org. Mass Spectrom. **22**, 216 (1987).
26. R. D. Bowen, A. G. Harrison, and E. J. Reiner. J. Chem. Soc. Perkin Trans. 2. 1009 (1988).
27. A. G. Harrison, R. S. Mercer, E. J. Reiner, A. B. Young, R. K. Boyd, R. E. March, and C. J. Porter. Int. J. Mass Spectrom. Ion Processes, **74**, 13 (1986).
28. F. M. Benoit and A. G. Harrison. J. Am. Chem. Soc. **99**, 3980 (1977).
29. J. K. Terlouw, T. Weiske, H. Schwarz, and J. L. Holmes. Org. Mass Spectrom. **21**, 665 (1986).
30. S. A. McLuckey, G. L. Glish, and R. G. Cooks. Int. J. Mass Spectrom. Ion Phys. **39**, 219 (1981).
31. D. D. Fetterolf and R. A. Yost. Int. J. Mass Spectrom. Ion Phys. **44**, 37 (1982).
32. S. A. McLuckey and R. G. Cooks. *In* Tandem mass spectrometry. *Edited by* F. W. McLafferty. Wiley, New York. 1983.
33. D. J. Douglas. J. Phys. Chem. **86**, 185 (1982).
34. P. H. Dawson. Int. J. Mass Spectrom. Ion Phys. **50**, 287 (1983).
35. P. H. Dawson and W. F. Sun. Int. J. Mass Spectrom. Ion Phys. **44**, 51 (1982).
36. S. Nacson and A. G. Harrison. Int. J. Mass Spectrom. Ion Processes, **63**, 325 (1985).
37. J. J. Zwinselman, S. Nacson, and A. G. Harrison. Int. J. Mass Spectrom. Ion Processes, **67**, 93 (1985).
38. (*a*) B. J. Stapleton, R. D. Bowen, and D. H. Williams. Tetrahedron **34**, 259 (1978); (*b*) R. D. Bowen, B. J. Stapleton, and D. H. Williams. Org. Mass Spectrom. **31**, 2431 (1978).
39. G. A. Olah and J. A. Olah. *In* Carbonium ions. Vol. II. *Edited by* G. A. Olah and P. v. R. Schleyer. Wiley-Interscience, New York. 1974. Chap. 17.
40. P. K. Bischof and M. J. S. Dewar. J. Am. Chem. Soc. **97**, 2378 (1978).
41. (*a*) T. J. Mead and D. H. Williams. J. Chem. Soc. Perkin Trans. 2, 876 (1972); (*b*) R. D. Bowen and D. H. Williams. J. Am. Chem. Soc. **99**, 6822 (1977); (*c*) D. H. Williams, B. J. Stapleton, and R. D. Bowen. Tetrahedron Lett. 2919 (1978); (*d*) R. D. Bowen, B. J. Stapleton, and D. H. Williams. J. Chem. Soc. Chem. Commun. 24 (1978); (*e*) R. D. Bowen and D. H. Williams. Int. J. Mass Spectrom. Ion Phys. **29**, 47 (1979); (*f*) R. D. Bowen, D. H. Williams, H. Scwarz, and C. Wesdemiotis. J. Chem. Soc. Chem. Commun. 261 (1979); (*g*) R. D. Bowen, D. H. Williams, H. Schwarz, and C. Wesdemiotis. J.

Can. J. Chem. Downloaded from www.nrcresearchpress.com by 112.217.228.212 on 09/07/12
For personal use only.

TABLE 4. Thermochemistry (kJ mol^{-1}) of carboxylic compounds at 298 K

R^1—COOR	$\Delta H_f^0(R^1COOR)$	$PA(R^1COOR)$	$\Delta H_f^0(R^1COOR.H^+)$
HCOOH	−379	756	396
$HCOOCH_3$	−350	797	384
$HCOOC_2H_5$	−371	811	349
HCOO.*n*-C_3H_7	−397	814	320
HCOO.*i*-C_3H_7	−414	815	302
HCOO.*n*-C_4H_9	−418	810	303
HCOO.*i*-C_4H_9	−427	813	291
HCOO.*s*-C_4H_9	−435	815	281
HCOO.*t*-C_4H_9	−456	815	260
CH_3COOH	−432	795	304
CH_3COOCH_3	−410	829	292
$CH_3COOC_2H_5$	−443	840	248
CH_3COO.*n*-C_3H_7	−464	842	225
CH_3COO.*i*-C_3H_7	−481	844	206
CH_3COO.*n*-C_4H_9	−485	844	202
CH_3COO.*i*-C_4H_9	−494	844	193
CH_3COO.*s*-C_4H_9	−502	844	185
CH_3COO.*t*-C_4H_9	−519	844	168

Am. Chem. Soc. **101**, 4681 (1979); (*h*) C. WESDEMIOTIS, R. WOLFSCHUTZ, and H. SCHWARZ. Tetrahedron, **36**, 275 (1980).
42. D. H. WILLIAMS. Acc. Chem. Res. **10**, 280 (1977).
43. A. G. HARRISON. Chemical ionization mass spectrometry. CRC Press, Boca Raton. 1983.
44. A. G. HARRISON. Can. J. Chem. **64**, 1051 (1986).
45. P. KEBARLE. Ann. Rev. Phys. Chem. **28**, 445 (1977).
46. D. H. AUE and M. T. BOWERS. *In* Gas phase ion chemistry. Vol. 2. *Edited by* M. T. Bowers. Academic Press, New York. 1979.
47. J. D. COX and G. PILCHER. Thermochemistry of organic and organometallic compounds. Academic Press, New York. 1970.
48. H. M. ROSENSTOCK, K. DRAXL, B. W. STEINER, and J. T. HERRON. J. Phys. Chem. Ref. Data, **6**, Suppl. 1 (1977).
49. S. W. BENSON. Thermochemical kinetics. Wiley-Interscience, New York, NY. 1976.
50. F. P. LOSSING and A. MACCOLL. Can. J. Chem. **54**, 990 (1976).

Appendix

The thermochemical data relevant to the enthalpies of formation of protonated carboxylic acids and esters are summarized in Table 4. The proton affinities are taken from Kebarle (45) or are estimated and are adjusted to $PA(NH_3)$ = 857.7 kJ mol^{-1} as recommended by Aue and Bowers (46). The neutral enthalpies of formation are literature values (47, 48) or are estimated by group equivalent methods (49). Other relevant enthalpies of formation (kJ mol^{-1}) are $C_2H_5^+$, 916; *n*-$C_3H_7^+$, 870; *i*-$C_3H_7^+$, 803; *n*-$C_4H_9^+$, 841; *i*-$C_4H_9^+$, 833; *s*-$C_4H_9^+$, 766; *t*-$C_4H_9^+$, 699, all taken from ref. 50. Neutral enthalpies of formation, from refs. 47 and 48, are (in kJ mol^{-1}): C_2H_4, 52; C_3H_6, 21; 1-C_4H_8, −1; 2-C_4H_8, −8; −8; *i*-C_4H_8, −18. All data are for the temperature of 298 K.

Can. J. Chem. Downloaded from www.nrcresearchpress.com by 112.217.228.212 on 09/07/12
For personal use only.

Determination of the dissociation constant of D_2O_2 in D_2O by a conventional method and via muonium kinetics

JEAN-CLAUDE BRODOVITCH, PAUL W. PERCIVAL, AND DEREK POTERYKO
Department of Chemistry and TRIUMF, Simon Fraser University, Burnaby, B.C., Canada V5A 1S6

Received March 3, 1988

JEAN-CLAUDE BRODOVITCH, PAUL W. PERCIVAL, and DEREK POTERYKO. Can. J. Chem. **66**, 2410 (1988).

The dissociation constant of deuterium peroxide has been determined from measurements of the pH of mixtures of D_2O_2/NaOD in D_2O. At 25°C, $pK_a = 12.35$ (5), confirming the value previously deduced from a kinetic study of the reactions of muonium with H_2O_2 and D_2O_2. The enthalpy and entropy of dissociation of D_2O_2 are estimated to be 34.7 (8.8) kJ mol^{-1} and -120 (30) J K^{-1}, respectively.

JEAN-CLAUDE BRODOVITCH, PAUL W. PERCIVAL et DEREK POTERYKP. Can. J. Chem. **66**, 2410 (1988).

La constante de dissociation du péroxyde de deutérium déduite ailleurs à partir d'une étude de la cinétique des reactions des péroxydes d'hydrogène et de deutérium avec le muonium, a été confirmée en mesurant directement le pH d'une série de mélanges D_2O_2/NaOD en milieu D_2O. On a estimé l'enthalpie et l'entropie de dissociation de D_2O_2 à 34.7 (8.8) kJ mol^{-1} et -120 (30) J K^{-1} respectivement. A 25°C, on a obtenu $pK_a = 12.35$ (5).

Can. J. Chem. Downloaded from www.nrcresearchpress.com by 196.1.178.254 on 09/07/12
For personal use only.

We have recently completed an extensive study of the kinetics of the reactions Mu + H_2O_2 and Mu + D_2O_2 in aqueous solution. Muonium (Mu) is the exotic atomic system μ^+e^-, and behaves as a light radioactive isotope of H (see ref. 1 for a general introduction and references to the literature of Mu chemistry and the μSR technique). Muonium decay rates were measured for various conditions of peroxide concentration (0 to 3 m*M*), acidity of the medium (pH 3 to pH 12.4 for H_2O_2, pD 3 to pD 13.7 for D_2O_2) and temperature (0 to 50°C). A preliminary account and most of the data are to be found in a conference report (2). Full experimental details and interpretation of the results in terms of mechanism and isotope effects will be reported in a full publication elsewhere. This short note is intended to highlight a "spin-off" of the kinetics study, namely, the determination of the ionisation constant of D_2O_2, and to report an independent determination by more conventional means.

The H_2O_2 data are consistent with the following reaction scheme:

[1] $\mathrm{Mu} + \mathrm{H_2O_2} \xrightarrow{k_1} \text{products}$

[2] $\mathrm{Mu} + \mathrm{HO_2^-} \xrightarrow{k_2} \text{products}$

[3] $\mathrm{Mu} + \mathrm{OH^-} \xrightarrow{k_3} \text{products}$

[4] $\mathrm{H_2O_2} \overset{K_a}{\rightleftharpoons} \mathrm{HO_2^-} + \mathrm{H^+}$

[5] $\mathrm{H_2O} \overset{K_w}{\rightleftharpoons} \mathrm{OH^-} + \mathrm{H^+}$

For such a scheme, the first order decay rate for the disappearance of Mu is given by (1):

$$[6]\quad \lambda_{obs} = \frac{k_1[H^+] + k_2K_a}{[H^+] + K_a} \cdot [H_2O_2]_t + \frac{k_3K_w}{[H^+]} + \lambda_0$$

where $[H_2O_2]_t = [H_2O_2] + [HO_2^-]$ is the nominal peroxide concentration, and λ_0 is the decay rate measured for pure water. A similar reaction scheme and an analogous expression to [6] was assumed for the Mu + D_2O_2 system. The purpose of the kinetics study was to determine k_1 and k_2 and their equivalents in the D_2O_2 scheme. They may be obtained by fitting [6] to the experimental data, using k_1, k_2, and k_3 as adjustable parameters. In the case of the H_2O_2 system we used literature values of K_a (3). However, we were unable to find any reported values for the corresponding dissociation constant of D_2O_2. Therefore, we used the kinetic data to determine K_a by performing a fit to expression [6] with K_a as an extra adjustable parameter.

By processing the D_2O_2 data in this manner we have determined K_a to be $6.8(6) \times 10^{-13}$ *M* ($pK_a = 12.2(2)$) at 25°C. (For H_2O_2 $pK_a = 11.66$ at this temperature (4).) However, to obtain meaningful fits some constraints had to be imposed on K_a during the calculations. Specifically, the variation of pK_a with temperature was required to be equal for H_2O_2 and D_2O_2, in similar fashion to the temperature dependence of pK_w for H_2O and D_2O. In terms of the activation parameters for the dissociation of D_2O_2, this is equivalent to imposing the same ΔH^0 value as that of H_2O_2 while leaving ΔS^0 a free parameter. The pK_a value found for D_2O_2 is larger than that of H_2O_2, which seems reasonable given the relative dissociation constants of H_2O and D_2O: $pK_w(H_2O) = 14.0$ compared to $pK_w(D_2O) = 14.9$ at 25°C (5).

The determination of K_a by such a procedure suffers from some serious drawbacks. First, the results are imprecise due to the insensitivity of the fit to K_a; second, the value of K_a obtained is very much dependent on the model chosen to explain the kinetic data; third, the results are biased by the restriction imposed on the fit; fourth, the technique of μSR is not yet widely known, so a constant such as a pK_a derived in this manner warrants independent confirmation. Aside from these considerations, the parameters of principal interest to us are the rate constants associated with the various reaction channels, and their determination will be more reliable if we can reduce the number of degrees of freedom of the fit by employing definite values of K_a.

With this in mind, we decided to make an independent measurement of the pK_a of D_2O_2. We followed the procedure of Evans and Uri (6) in their determination of the pK_a of H_2O_2. It involves the measurement of the pH (more precisely here the pD $= -\log_{10}[D^+]$) of known mixtures of NaOD and D_2O_2 as a function of the ionic strength of the medium, which is adjusted with $NaClO_4$. The pK_a can be calculated from the pD value extrapolated to zero ionic strength.

A solution (~3 *M*) of D_2O_2 was prepared by reacting an excess of D_3PO_4 (obtained from D_2O + P_2O_5) with Na_2O_2, followed by vacuum distillation of the D_2O_2 evolved into a cold

TABLE 1. Results of pH analysis of D_2O_2 solutions*

t/°C	pH_0	pK_a	c
20.0	11.04(5)	12.44(6)	0.038(86)
35.0	10.75(2)	12.15(4)	0.035(38)

*Conditions: $[NaOD]_0$ = 0.051(2) M, $[D_2O_2]_0$ = 0.5592(11) M, I = 0.05 to 1.0 M.

trap (7). This solution was standardized by titration against $KMnO_4$ solution.

A CO_2-free solution of ~0.3 M NaOD was obtained by addition of D_2O to Na(Hg) amalgam prepared by the technique described by Vogel (8). It was standardized by titration against HCl solution.

To prepare a ~5 M solution of sodium perchlorate, commercially available $NaClO_4$ was recrystallized in H_2O, thoroughly dried in a vacuum oven, then the required amount dissolved in D_2O. This solution was determined by acid–base titration of the H^+ released after passing an aliquot through a REXYN-101 cation exchange column.

Wherever necessary, the solvent was D_2O (>99 atom% D) obtained from MSD ISOTOPES.

The test solution was contained in a jacketed flask attached to a circulating bath to control the temperature (±0.02°C). pH measurements were made with a digital pH-meter (Cole-Parmer model 5985-80) equipped with a saturated NaCl glass electrode. The pH-meter was calibrated with two buffer solutions (pH 7 and pH 10 from BDH). The effect of temperature on the electrode response was taken into account by using the built-in temperature compensator of the pH meter. No attempt was made to correct the reading for Na^+ activity.

Care was taken to exclude atmospheric CO_2 during sample manipulations by continuous bubbling with purified wet N_2.

We first checked our set-up and technique by repeating Evans and Uri's experiment with H_2O_2. The pH can be expressed by the Henderson buffer equation (6):

$$[7]\quad pH = pH_0 - 0.5I^{1/2} + cI$$

with

$$[8]\quad pH_0 = pK_a + \log_{10}\frac{[NaOH]_0}{[H_2O_2]_0 - [NaOH]_0}$$

where I is the ionic strength and c a small empirical constant. The conditions $[H_2O_2]_0$ = 0.55 M and $[NaOH]_0$ = 0.05 M are chosen such that the log term in eq. [8] is equal to −1(6). The pH was measured at four ionic strengths (I = 0.05 to 1.0 M) and two temperatures. The results were then fitted to eq. [7] in which pH_0 and c are the free parameters. The pK_a value is readily calculated from eq. [8].

For H_2O_2, we obtained pK_a values of 11.80(11) at 20°C and 11.44(7) at 30°C; at these temperatures the literature values range from 11.75 to 11.85 and 11.48 to 11.58, respectively (4).

The experiment was then repeated with D_2O_2 under essentially identical conditions and following the same procedure. The pH extrapolated to zero ionic strength was converted to pD_0 using (9):

$$[9]\quad pD = pH + 0.40$$

and the pK_a value was calculated from [8]. The results are summarized in Table 1. From these two data points, we derive the following values of the thermodynamic parameters for the ionisation of D_2O_2: ΔH^0 = 34.7(8.8) kJ mol^{-1}, ΔS^0 = −120(30) J K^{-1}, and ΔG^0 = 69.8(3) kJ mol^{-1} at 20°C; the corresponding quantities for H_2O_2 are 34.3 kJ mol^{-1}, −107.4 J K^{-1}, and 69.04 kJ mol^{-1}, respectively (6). At 25°C, pK_a = 12.35(5), in agreement with the value (12.2(2)) deduced from our kinetic measurements. The restriction imposed in our fitting procedure appears to be justified; the values of ΔH^0 are very similar (i.e. same slope of plot of pK_a vs. $1/T$) for both peroxides as is the case for H_2O and D_2O (55.76 kJ mol^{-1} vs. 58.4 kJ mol^{-1}, respectively (5). Further discussion on the values of these thermodynamic parameters is not warranted in view of the large uncertainties of the present determination.

In conclusion, we have obtained values for the pK_a of D_2O_2 directly from pH measurements and indirectly from kinetics data. The determinations agree within experimental errors, which we interpret as evidence to support our reaction scheme. This is the first example of the use of μSR data in the determination of an ionisation constant, but we do not advocate it as a general method.

Acknowledgments

This work was funded by the Natural Sciences and Engineering Research Council of Canada and, through TRIUMF, by the National Research Council of Canada. Derek Poteryko received an NSERC Undergraduate Research Award in 1986 and was supported in part from a Challenge '87 award in 1987.

1. E. RODUNER. Prog. Reaction Kinet. **14**, 1 (1986).
2. P. W. PERCIVAL, J.-C. BRODOVITCH, and K. E. NEWMAN. NBS special publication No. 716. NBS, Washington. 1986. p. 547.
3. N. A. LANGE. Handbook of chemistry. 10th ed. McGraw-Hill, New York. 1961.
4. D. D. DOUGLAS. Ionisation constants of inorganic acids and bases. 2nd ed. Pergamon Press, New York. 1982.
5. CRC handbook of chemistry and physics. 61st ed. CRC Press Inc. 1981. p. D-168.
6. M. G. EVANS and N. URI. Trans. Faraday Soc. **45**, 244 (1949).
7. C. MARTINS and G. SHORRE. Ann. Chem. **570**, 140 (1950).
8. A. I. VOGEL. Quantitative inorganic analysis. 3rd ed. Longmans, London. 1962.
9. R. G. BATES. Determination of pH. 2nd ed. Wiley, New York. 1973.

Can. J. Chem. Downloaded from www.nrcresearchpress.com by 196.1.178.254 on 09/07/12
For personal use only.

Enhanced nucleophile selectivity in the photoaddition to styrene. Comparison with the thermal addition

STEVEN W. ANDERSON[1] AND KEITH YATES[2]

Lash Miller Chemical Laboratories, University of Toronto, Toronto, Ont., Canada M5S 1A1

Received January 29, 1988

This paper is dedicated to Professor John T. Edward on the occasion of his 65th birthday

STEVEN W. ANDERSON and KEITH YATES. Can. J. Chem. **66**, 2412 (1988).

The reactivity–selectivity properties of the *sec*-phenethyl carbenium ion and its analogues have been examined in binary-aqueous solutions of alcohols (ROH; R = Me, Et, CF_3CH_2, *n*-Bu, *t*-Bu, *n*-Pr, *i*-Pr), acetic acid, and in solutions containing external nucleophiles such as thiophenol, ethanethiol, acetate, and benzenesulfinate. Selectivity ($S = k(\text{Nuc})/k(H_2O)$) is observed to be a function of the nucleophile, the ring substituent, thermal or photochemical conditions, irradiation time, and medium acidity. In the case of styrene, the photochemically generated (usually 254 nm, 1 h) species exhibits greater selectivity (up to two orders of magnitude) than its thermal counterpart, generated (usually 80°C, 2–4 d) in identical media, particularly in aqueous-rich solvent compositions. A rationale for these differences, supported by fluorescence quenching experiments, and the other effects upon selectivity will be discussed.

STEVEN W. ANDERSON et KEITH YATES. Can. J. Chem. **66**, 2412 (1988).

On a étudié les propriétés de réactivité–sélectivité de l'ion *sec*-phénéthyl carbenium et de ses analogues dans des solutions aqueuses binaires d'alcool (ROH; où R = Me, Et, CF_3CH_2, *n*-Bu, *t*-Bu, *n*-Pr, *i*-Pr), et acide acétique et dans des solutions contenant des nucléophiles externes tels le thiophénol, l'éthanethiol, l'acétate et le benzènesulfinate. On a observé que la sélectivité ($S = k(\text{Nuc})/k(H_2O)$) dépend du nucléophile, du substituent sur le cycle, des conditions thermiques et photochimiques, du temps d'irradiation et de l'acidité du milieu. Dans le cas du styrène, les espèces générées photochimiquement (généralement 254 nm, 1 h) montrent une plus grande sélectivité (jusqu'à deux ordres de grandeur) que celles générées thermiquement (généralement 80°C, 2–4 d) dans un milieu identique; particulièrement dans des solvants binaires riches en eau. On discute de la rationalisation de ces différences, que supporte des expériences d'extinction de fluorescence, et des autres effets sur la sélectivité.

[Traduit par la revue]

Previous studies in our laboratories (1, 2) have shown that the photohydrations of ring-substituted styrenes are generally subject to acid catalysis, the reaction proceeding via a polarized S_1 state (eq. [1] (R = H, OMe, F, 3,4(C_4H_4)).

[1] 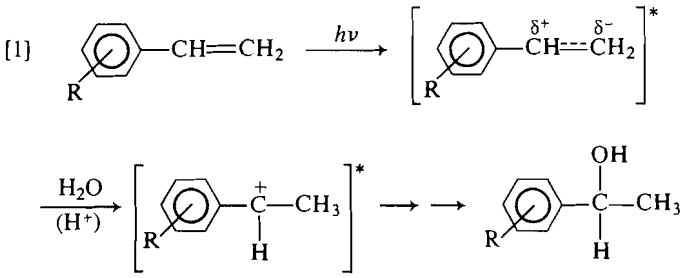

The nitrostyrenes, however, exhibit anomalous behavior leading to *anti*-Markownikov addition products, which were shown to arise from a reverse-polarized T_1 state. It is conceivable that the *sec*-phenethyl carbenium ion generated by acid catalysis, photochemically or thermally, could be intercepted by a nucleophile other than water. Such attack could occur on carbenium ions that, intrinsically, would be expected to exhibit different reactivity, e.g., those in an electronically excited state, a vibrationally "hot" ground (electronic) state, or an electronic (and vibrational) ground state. To test this hypothesis we have investigated the acid-catalyzed photoaddition of various nucleophiles to styrene. Several compositions of binary-aqueous alcohols and aqueous solutions containing charged and neutral species of greater or less nucleophilicity than water were employed. A comparison with the acid-catalyzed thermal reaction has also been carried out. Factors influencing the observed selectivity, such as acid concentration, ring substitution (Chart 1), nucleophilicity, steric bulk, solvating ability of the nucleophile, solvent composition, and irradiation time, have also been explored.

Although the literature is replete with studies of thermal- and photo-addition reactions of nucleophiles (frequently with a sensitizer or catalyst present) to alkenes and alkynes, very few papers have examined reactivity–selectivity relationships and, in these instances, only indirectly. It is therefore appropriate that we briefly summarize these now, since they will have an important bearing on our later discussion.

Nozaki and co-workers observed (3) that both direct and acetophenone sensitized irradiation of 1-phenyl-cyclohexene or -cycloheptene (eq. [2]) with solvent of 0.003 mole fraction

[2] 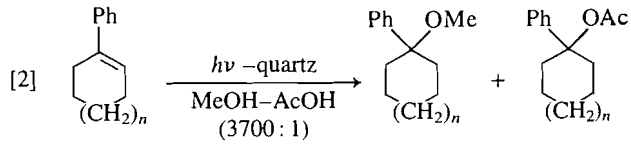

$n = 1$	direct yield, %	26 (23)	19 (14)
$n = 2$	(sensitized yield) %	27 (25)	19 (18)

acetic acid in methanol gave more than one-third yield of the acetate in comparison to the ether. Selectivities ($S = k(\text{MeOH})/k(\text{AcOH})$) for both conditions are essentially invariant and independent of the ring size. The average is approximately 0.005, reflecting a strong preference for reaction with acetic acid. Nozaki has reasoned that the intermediate (the *trans* alkene) is sufficiently long-lived to capture the more favorable partner (carboxylic acid) and form a benzyl carbocation and

[1]Present address: Department of Chemistry, University of Wisconsin–Whitewater, Whitewater, WI 53190, U.S.A.

[2]Author to whom correspondence may be addressed.

Can. J. Chem. Downloaded from www.nrcresearchpress.com by 112.217.228.212 on 09/07/12
For personal use only.

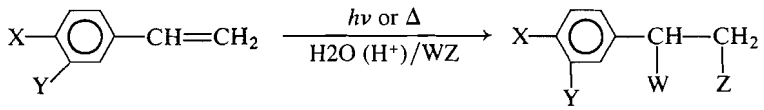

Compound	X	Y	W	Z
1	H	H	OH	H
2	H	H	OMe	H
3	H	H	OEt	H
4	H	H	*n*-PrO	H
5	H	H	*i*-PrO	H
6	H	H	*n*-BuO	H
7	H	H	*t*-BuO	H
8	H	H	CF_3CH_2O	H
9	H	H	AcO	H

Compound	X	Y	W	Z
10	H	H	PhS	H
11	H	H	EtS	H
12	H	H	$PhSO_2$	H
13	MeO	H	OH	H
14	MeO	H	OMe	H
15	H	NO_2	H	OH
16	H	NO_2	H	OMe
17	H	NO_2	CH_2OH	H
18	H	NO_2	H	CH_2OH

CHART 1

carboxylate anion pair, which ultimately recombine to give the ester.

The photolysis of 2-phenylnorborn-2-ene in aqueous methanol containing 0.72 mole fraction of methanol was found by Kropp (4) to give predominantly the methyl ether adduct (eq. [3]). A selectivity value ($S = k(\text{MeOH})/k(H_2O)$) of 0.62

[3] 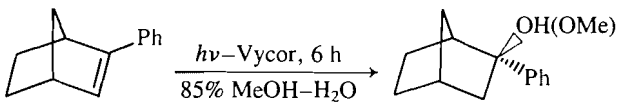

32%(51%)

can be calculated based upon these results. This reaction apparently involves a singlet excited state. Use of *tert*-butanol gave only the reduction product. Similarly, irradiation of (+)-carene in aqueous solvent of 0.19 mole fraction *tert*-butanol with benzene as sensitizer gave only isomerization and alcohol products (5). Presumably the latter results are largely a consequence of the steric bulk of *tert*-butanol.

Results

Acid-catalyzed photo and thermal addition of binary-aqueous organic solvents to styrene

Selectivity values for the competitive reaction between a nucleophile and water with the intermediate were calculated (6) by eq. [4] (where R = 1-phenethyl-, 1-(4-methoxyphenyl)ethyl-, and 1-(3-nitrophenyl)ethyl-),

[4] $S = k(\text{Nuc})/k(H_2O) = ([\text{RNuc}][H_2O]/[\text{ROH}][\text{Nuc}])$

the product ratio being determined by glc analysis.

Selectivity values for the photochemical and thermal reactions are listed along with product ratios for 28 solvent compositions in Table 1. It is readily seen that the S values remain relatively constant up until 10% of the organic cosolvent and then increase proportionally with water content, this increase being most pronounced in aqueous ethanol. It is also apparent that the photochemically generated carbenium ion exhibits greater selectivity than its thermal counterpart generated in identical media at 80°C. At 50.1°C, for 10–1% aqueous methanol (footnote *c*, Table 1), the observed selectivity for the thermal reaction was much lower. In sharp contrast, regardless of the solvent composition, the S values in aqueous acetic acid remained essentially constant, independent of the solvent composition or conditions. We also found that there was no correlation of mass balance (i.e., the percentage of recovered styrene and solvent adducts) with solvent composition or conditions. Ideally, we would have preferred to compare solvent nucleophilicities with the obtained S values. The greatest changes in selectivity, however, occur for solvent compositions less than 10% (by volume) of the organic component, for which solvent nucleophilicity data are not currently available. N_{OTs} values decrease only by 7% in going from 10% cosolvent (acetone, ethanol, methanol) to pure water (Table 2 and ref. 7). To accommodate this gap we have calculated weighted nucleophilicities, which take into account the nucleophilicities of the pure components and their proportion (mole fraction) in various solvent compositions. In eq. [5] we define C_i as the weighted

[5] $C_i = x_i n_i$

nucleophilicity of the ith component where x and n are the corresponding mole fraction and antilog of the nucleophilicity (N_{OTs}) of the pure solvent. It follows that, for a binary mixture, $S_n = C_A + C_B$, where S_n is defined as the sum-weighted nucleophilicity of a mixture of A and B. If the intermediate (or substrate) reacts with the solvent components according to their effective (or relative) concentration and nucleophilicity (taken together), then S should be a 1:1 function of C_A/S_n and a plot of S vs. C_A/S_n should pass through the origin, where as C_A/S_n approaches zero (or $-\infty$ for a logarithmic plot), S does also. Four important assumptions inherent in this analysis are (1) the intermediate (or substrate) reacts with solvent components according to their effective (or relative) concentrations and nucleophilicities, (2) ground-state nucleophilicities are applicable to excited-state reactions, (3) catalytic acid equally perturbs the effective nucleophilicities of both solvent components, and (4) side reactions of the products are negligible. Logarithmic plots of C_{MeOH}/S_n vs. S are depicted in Figs. 1 and 2 for the thermal and photochemical reactions, respectively. The correlation between C_{MeOH}/S_n is quite reasonable for the photochemical reactions in aqueous ethanol, methanol, and TFE ($r > 0.970$), yet the thermal reactions (and the photochemical reaction in acetic acid) give a very poor correlation ($r < 0.770$).

Structural, nucleophilic, and solvation effects upon selectivity

In an attempt to ascertain whether S values are controlled predominantly by one factor of the nucleophile (e.g., steric bulk, nucleophilicity, or solvation effects) we have examined the photoaddition reaction, at constant acidity and irradiation time, in six binary-aqueous compositions of seven alcohols. The results are listed in Table 3. In general, S values decrease in the order MeOH, EtOH > *n*-PrOH > *i*-PrOH > *n*-BuOH, *t*-BuOH > TFE. Of particular interest is the observation that the

Can. J. Chem. Downloaded from www.nrcresearchpress.com by 112.217.228.212 on 09/07/12
For personal use only.

TABLE 1. Photo and thermal addition of binary-aqueous organic solvents to 6.5×10^{-4} M styrene

Conditions					
254 nm, 5% H_2SO_4,[a] 1 h			80.8°C, 5% H_2SO_4,[a] 4–6 d		
% ROH[a]	Ether/alcohol	S^b	% ROH	Ether/alcohol	S^b
R = Me			R = Me[c]		
80	44	25	80	35	19
50	4.7	11	50	57	130
40	5.6	19	40	13	45
20	2.4	22	20	0.82	7.4
10	0.93	19	10	0.89	18
1	0.88	194	1	0.068	16
0.1	1.1	2400	0.1	0.0011	2.3
0.01	0.25	5700	0.01	0.00050	210
0.002	[d]				
R = Et			R = Et		
80	18	15	80	45	36
50	0.23	0.74	50	15	48
40	1.5	7.2	40	3.9	19
20	2.0	25	20	2.0	26
10	1.2	36	10	0.31	9.0
1	0.66	210	1	0.038	12
0.1	0.84	2700	0.1	0.028	94
0.01	0.39	13000	0.01	0.034	1100
R = Ac			R = Ac		
80	2.4	1.9	80	5.7	4.6
60	1.1	2.3	60	1.8	3.8
40	0.35	1.7	40	1.1	5.1
20	0.084	1.1	20	0.51	6.4
10	0.037	1.1	10	0.062	1.8
1	0.010	3.2	1	[d]	—
R = CF_3CH_2					
20	0.043	0.69			
10	0.11	4.0			
1	0.010	4.0			
0.1	0.0097	40			
0.01	0.0014	710			

[a]Percentage by volume at 21°C; 5% MeCN also present.

[b]Ratio of specific rate constants for reaction of intermediate ionic species with the organic solvent and water, respectively (see text); all runs done, at least, in duplicate.

[c]At 50.1°C, the following values were obtained, % MeOH, S: 10, 6.6; 1, 22; 0.1, 48; 0.01, alcohol adduct (**1**) only.

[d]Only alcohol adduct (**1**) detected.

photochemical reaction has a distinct preference for the organic component, independent of N_{OTs} values (Table 2).

Selectivity as a function of acid concentration

The photoaddition of 1 and 10% aqueous methanol to styrene as a function of added sulfuric acid (0–25% by volume) concentration was studied. Except for the acid concentration, the conditions for these reactions were identical to those listed in Table 1. No systematic behavior was evidenced at either concentration of methanol. In 1% methanol, the S values ranged from a minimum of 33 (at 15% H_2SO_4) to a maximum of 423 (at 3% H_2SO_4) with significant fluctuations at the other points. In 10% methanol, the S values spanned from a maximum of 21 (at 5% H_2SO_4) to a minimum of 2 (at 3% H_2SO_4). Similar fluctuations were observed here. However, the range of S values was much smaller. There is no direct correspondence between medium acidity and selectivity nor between the selectivity trends in the two methanol compositions. This lends support to our third assumption (*vide supra*), that catalytic acid equally perturbs the effective nucleophilicities of both solvent components.

Irradiation time/product stability

The photoaddition of 10% aqueous methanol to styrene in the presence of 5% sulfuric acid (same conditions as outlined in Table 1, except for the irradiation time) was found to increase in selectivity with irradiation time from a minimum of 7 at 10 and 20 min, to 16 at 40 min, and a maximum of 21 at 60 min. Irradiation for a longer period (80 min) gave a corresponding drop in the selectivity to 11. We also studied the variation in

Can. J. Chem. Downloaded from www.nrcresearchpress.com by 112.217.228.212 on 09/07/12
For personal use only.

TABLE 2. Solvent parameters

Solvent	N_{OTs}[a]	α[b]	β[c]	pK_a[d]	Y[e]
i-PrOH	0.2	0.76	0.95	17.1	−2.73
EtOH	0.00	0.83	0.77	15.9	−2.03
MeOH	−0.04	0.93	0.62	15.5	−1.09
H_2O	−0.44	1.17	0.18	15.7	3.49
AcOH	−2.35	1.12		4.75	−1.68
TFE	−2.67[f]	1.51	0.00	12.4[g]	1.05
t-BuOH		0.68	1.01	19.2	−3.26

[a]Ground-state nucleophilicity values, obtained from ref. 7.
[b]Measures the ability of a solvent to donate a proton in a solvent–solute hydrogen bond; values from ref. 36.
[c]Measures the ability of a solvent to accept a proton in a solute–solvent hydrogen bond; values from ref. 36.
[d]Values taken from ref. 19, except where otherwise indicated.
[e]Grunwald–Winstein solvent ionizing power; values drawn from ref. 37.
[f]Value taken from ref. 38.
[g]Value obtained from ref. 39.

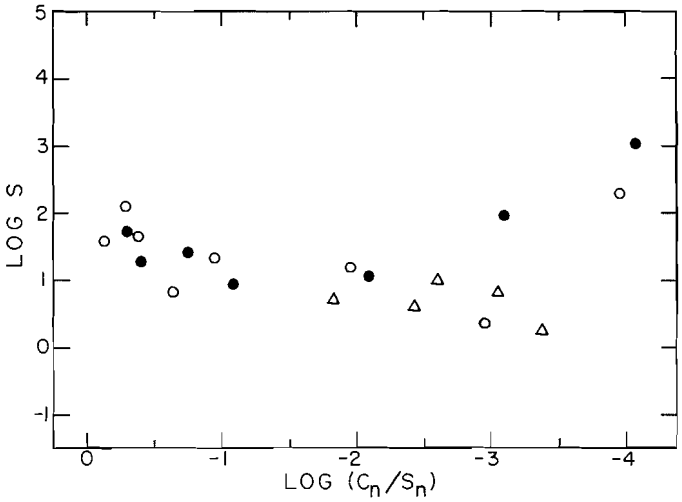

FIG. 1. Logarithmic plot of selectivity vs. weighted nucleophilicity for thermal additions to styrene at 80.8°C. (Closed circles are for EtOH–H_2O, open circles for MeOH–H_2O, and triangles for AcOH–H_2O).

selectivity with irradiation time for four different compositions of aqueous methanol (Table 4) at the concentrations where fluctuations in selectivity are significant. The most pronounced selectivity changes (ca. two orders of magnitude) are manifested only at 60 min; at shorter irradiation times the changes in selectivity (ca. one order of magnitude) are attenuated. When the data are extrapolated back to zero time, where secondary photochemistry is presumably excluded, the selectivity trend is still in the same direction. That is, the selectivity still increases proportionally with the water content of the mixed solvent.

We have also studied the decomposition of authentic samples of the ether (**2**) and alcohol (**1**) products under the same conditions used for the photo and thermal addition reactions to styrene (Table 5). Use of both "uncorrected" and "corrected" selectivity values indicates that the alcohol reacts slightly faster (1–1.5 times) than the ether in both the photo and thermal reactions.

Reactions with neutral and anionic external nucleophiles

Extensive secondary photochemistry was observed when thiols were employed as nucleophiles. The photolysis of styrene

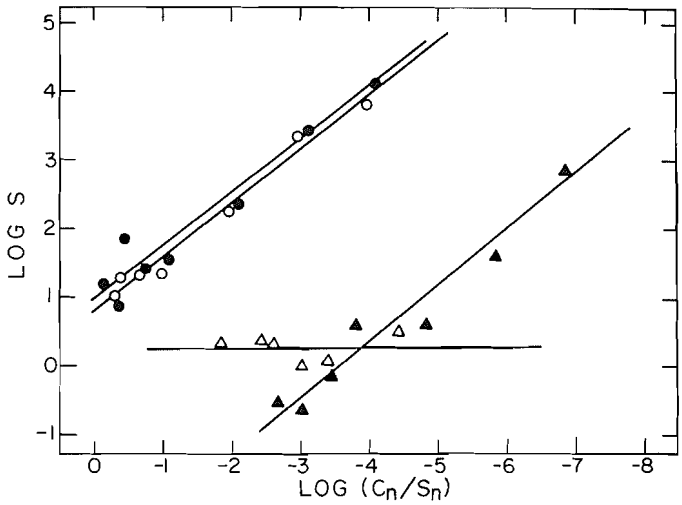

FIG. 2. Logarithmic plot of selectivity vs. weighted nucleophilicity for photoadditions to styrene. (Closed circles are for EtOH–H_2O, open circles for MeOH–H_2O, closed triangles for AcOH–H_2O, and open triangles for TFE–H_2O.)

with thiophenol or ethanethiol under a variety of conditions afforded between 0.5 and 11% of the expected thioethers (**10** and **11**), trace amounts of the alcohol (**1**), and variable amounts of unreacted styrene. The bulk of the reaction mixtures consisted of several unidentified products and intractable polymer. Lower limits for selectivity values were calculated and gave 380 with thiophenol and 1.4×10^5 for ethanethiol.

The photoaddition of aqueous solutions of the benzenesulfinate anion to styrene (same conditions as given in Table 1 except without acid catalyst) gave the expected adduct (**12**), with calculated S values of ca. 33,000 for a 2.4-fold molar excess and ca. 2900 for a 28-fold molar excess. The amount of unreacted styrene varied from zero up to ca. 80% and no major by-products were detected. It was found that the thermal addition (80°C, 7 d, 0.1% H_2SO_4, 2.4-fold molar excess of $PhSO_2^-$) gave an S value of 1420. Sodium acetate, present in a 37-fold molar excess, gave a lower selectivity value of 281.

Ring substitution

The effects upon the selectivity of introducing either a *p*-methoxy or *m*-nitro substituent to the styrene ring are summarized in Table 6. The thermally generated carbenium ion from *p*-methoxystyrene (at 40°C) exhibits greater selectivity than that from styrene in the same compositions of aqueous methanol. In contrast, the photochemically generated species is less selective than for styrene. However, similar dichotomy in selectivity between the photo and thermal reactions is observed, as with styrene (except for the crossover at 0.01% MeOH). In other words, the photochemical reaction still exhibits greater selectivity than its thermal counterpart.

The photochemically generated species from *m*-nitrostyrene is decidedly less selective than either styrene or *p*-methoxystyrene. In fact, no methyl ether was detected at methanol compositions of 0.1 and 0.01% by volume. In line with the photohydrations *m*- and *p*-nitrostyrene (1, 2), the *anti*-Markownikov addition products (**15** and **16**) were observed. No products resulting from Markownikov addition were detected.

Fluorescence quenching

Six compositions of aqueous methanol containing styrene, prepared in a manner identical to the solutions used for the

Can. J. Chem. Downloaded from www.nrcresearchpress.com by 112.217.228.212 on 09/07/12
For personal use only.

Can. J. Chem. Downloaded from www.nrcresearchpress.com by 112.217.228.212 on 09/07/12
For personal use only.

TABLE 3. Structural and nucleophilic effects upon selectivity in the photoaddition of binary-aqueous alcohols to styrene[a]

% ROH[b]	Ether/alcohol	S[c]	% ROH[b]	Ether/alcohol	S[c]
40, MeOH	5.6	19	1, EtOH	0.70	226
EtOH	1.5	7	MeOH	0.80	178
n-PrOH	0.82	5	*t*-BuOH[e]	0.073	38
TFE[d]	0.04	0.2	*n*-PrOH	0.026	12
			n-BuOH	0.020	10
20, MeOH	2.4	22	TFE	0.01	4
EtOH	1.2	16			
n-PrOH	0.30	5	0.1, EtOH	0.84	2720
TFE	0.04	0.7	MeOH	1.0	2260
			TFE	0.0097	40
10 EtOH	1.2	36	*n*-BuOH	0.0072	37
MeOH	1.0	21			
n-PrOH	0.26	10	0.01, EtOH	0.39	12700
t-BuOH[e]	0.18	8	MeOH	0.28	6400
i-PrOH[f]	0.11	4	TFE	0.018	710
TFE	0.11	4	*n*-BuOH	0.0034	180

[a]Irradiation at 254 nm for 1 h; details in experimental section.
[b]Percentage by volume of the alcohol in water at 21°C; 5% MeCN and 5% H_2SO_4 also present.
[c]See footnote *b* in Table 1.
[d]2,2,2-Trifluorethanol.
[e]Without acid catalyst.
[f]The percentages were not response calibrated; products confirmed by ^1H nmr analysis.

TABLE 4. Selectivity as a function of irradiation time in the photoaddition of aqueous methanol to 6.5×10^{-4} M styrene[a]

	S[b]							
% MeOH	t(min): 60	40	20	10	5	0[c]	r[d]	F[e]
10	19	16	6.9	8.0	3.4	3.2 ± 1.5	0.963	38
1.0	194	3.3	9.2	4.2	—	5.5 ± 3.7	0.980	12
0.1	2420	7.5	8.6	—	4.8	7.0 ± 2.8	0.974	9
0.01	5660	461	189	161	—	212 ± 134	0.989	22

[a]Conditions identical to those described in Table 1 except for the irradiation times.
[b]As defined in Table 1.
[c]Extrapolated to zero time using polynomial regression analysis of the data; a two-term polynomial gave the best fit in all cases except for 10% MeOH, where a linear relationship was found to be satisfactory.
[d]Single or multiple correlation coefficient.
[e]*F*-statistic.

TABLE 5. Product decomposition data in aqueous methanol

Conditions							
254 nm, 5% H_2SO_4,[a] 1 h				80.8°C, 5% H_2SO_4,[a] 4–6 d			
% MeOH[a]	Ether/alcohol	S[b]	S'[d]	Substrate[c]	Ether/alcohol	S[b]	S'[d]
80	0.72	0.4	0.56	$PhCH(OCH_3)CH_3$	7.8	4	0.51
10	0.89	18	20	$PhCH(OCH_3)CH_3$	0.88	18	18
1					0.05	12	220
80	0.11	0.06	0.70	$PhCH(OH)CH_3$	12	6	0.57
10	0.67	13	21	$PhCH(OH)CH_3$	0.97	19	21
1				$PhCH(OH)CH_3$	0.08	14	310

[a,b]As defined in Table 1.
[c]Concentration is 6.5×10^{-4} *M*.
[d]"Corrected" selectivity values where the initial purities of the ether (99%) and alcohol (98%) substrates are taken into account.

TABLE 6. Effect of ring substitution upon selectivity

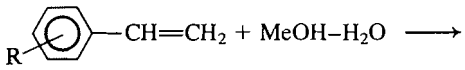

	Conditions				
	254 nm,[a] 5% H_2SO_4[b]			40.6°C, H_2SO_4,[b] 24 h	
R	% MeOH[b]	Ether/alcohol	S[c]	Ether/alcohol	S[c]
p-OMe[d]	51	6.2	14	—	[f]
	10	2.3	40	2.2	46
	1	0.73	163	0.25	55
	0.1	0.12	262	0.03	60
	0.01	0.018	410	—	[g]
m-NO_2[e]	10	0.17	3.4		
	1	0.014	3.2		
	0.1	—	[h]		
	0.01	—	[h]		

[a]Irradiation time was 1 h for R = *p*-MeO and 10 h for *m*-NO_2.
[b]Percentage by volume at 21°C; 5% MeCN also present.
[c]See footnote *b* in Table 1.
[d]Concentration of 2.9×10^{-4} M in 5% MeCN.
[e]Concentration of 3.4×10^{-3} M in 17% MeCN. It was necessary to conduct these runs in the absence of acid catalyst as the addition products otherwise decompose during the prolonged irradiation time.
[f]No alcohol adduct (**13**) detected.
[g]No methyl ether adduct (**14**) detected.
[h]No methyl ether adduct (**16**) detected.

photolyses, were measured for possible fluorescence quenching. These and data for other binary-aqueous organic solvents are listed in Table 7. In proceeding from 80 to 0.01% methanol a 41% drop in the fluorescence quantum yield occurred. Fluorescence quenching was also observed in aqueous ethanol (a 19% reduction from 80 to 0.01%), the isomeric propanols, and in 2,2,2-trifluorethanol (TFE). In aqueous acetic acid, the trend was reversed with Φ_{fl} increasing from 0.012 to 0.14 from 80 to 0.01% of the organic component. Only two emission bands, centered at 294 and 305 nm, could be detected for styrene. No others could be found at longer wavelengths with maximum instrument sensitivity.

Discussion

Selectivity trends in thermal and photochemical solvent addition

We can propose two different explanations for the observed trends. Symon's theory of water reactivity (8) can accommodate our results if we consider that addition of a basic cosolvent (e.g., MeOH, MeCN) to water will free lone pairs on the water molecules, thereby increasing their bulk nucleophilicity (eq. [6]). Therefore, as we increase the concentration of the

$$(H_2O)_{bulk} \rightleftharpoons (OH)_{free} + (\text{lone pairs})_{free} \quad (4\text{–}8\%)$$
$$\text{Base} + (OH)_{free} \rightleftharpoons \text{Base----(HO)} \qquad [6]$$

basic cosolvent, water molecules can compete more effectively in trapping the intermediate and the observed selectivity will be lower. Alternatively, as the water concentration of the mixed solvent is increased, the medium polarity will simultaneously increase, thereby stabilizing the developing carbenium ion. Of the solvents investigated, water has the largest Y value (Table 2) and its high polarity will best stabilize the developing carbenium ion by dipole–dipole interactions. Either of these explanations could account for the observed trends. The anomalous behavior in aqueous acetic acid (nearly constant selectivity) is primarily due to competitive photosolvolysis of the addition products (demonstrated by control experiments) or the result of the lower availability of "free" acetic acid by virtue of its known self-association in monomer–dimer equilibria (9–11), which favors the dimer. The latter argument does not appear to be supported, however, by the fluorescence quenching data (Table 7) where the greatest total quenching is observed in 80% acetic acid and varies by a factor of 12 from 0.01%. It is difficult to see why the correlation between the weighted nucleophilicity (C_{MeOH}/S_n) and S (Figs. 1 and 2) is very good for the photochemical reactions, yet poor for the thermal reactions in light of the fact that the weighted nucleophilicity is derived from thermal kinetic data. These results suggest that some other factors than nucleophilicity are operative. Even if the nucleophilicity values could be modified for the photochemical reactions, all of the results could still not be explained. As we shall discuss shortly, secondary photochemistry of the addition products also occurs in the other solvent systems, but is much slower. Nonetheless, the fact that selectivity trends are in the same direction in aqueous methanol for four different irradiation times (Table 4), even when extrapolated back to zero time, sugests that *we can make qualitative predictions, despite this secondary photochemistry*. We could not resort to irradiation of styrene at longer wavelengths because its molar absorptivity approaches zero at 300 nm. The methyl ether (**2**) and alcohol (**1**) adducts possess molar absorptivities of ca. 300 at this wavelength. At 254 nm, however, styrene is the principal absorber (ϵ_{max} (243 nm) = 13,360) while the alcohol and ether products have lower (<4900) molar absorptivities. Since selectivity changes were most pronounced at 60 min, all irradiations were conducted for this duration. Trends might have otherwise been indistinguishable in the less nucleophilic TFE–H_2O mixtures. It remains for us to delineate why the photochemical reaction should exhibit much higher selectivity than its thermal counterpart.

Fluorescence quenching

Our results (Table 7) indicate that there is preferential solvation of styrene by the organic component in the binary-aqueous solvent. We believe that this is due to a pre-association step involving hydrogen bonding, which is retained or enhanced in the excited state. The latter effect is possibly due to the increase in π-bond basicity in the excited state for styrenes, ca. 8–10 pK_a units (1). An alternative explanation considered, involving a HOMO–LUMO interaction between styrene and the nucleophile in the excited state, is unlikely to be correct since Whitten and co-workers (12) could not spectrally detect exciplexes in the photoaddition of nucleophiles to electron-deficient alkenes, substrates ideally suited for such an interaction. Furthermore, scanning of our solutions of aqueous methanol with styrene at longer wavelengths and maximum instrument sensitivity did not reveal an emission band (usually broad), characteristic of an exciplex. Fluorescence quenching due to hydrogen bonding has previously been observed with 9-trimethylsilylanthracene in methanol (13) and 1-aminopyrene in pyridine/hexane (14).

Structural, nucleophilic, and solvation effects upon selectivity

The local concentration of organic solvent molecules about

Can. J. Chem. Downloaded from www.nrcresearchpress.com by 112.217.228.212 on 09/07/12
For personal use only.

TABLE 7. Absolute fluorescence quantum yields for styrene in binary-aqueous organic solvents[a]

ROH, vol.%	Φ_{fl}[b,c,d]						
	MeOH	EtOH	*n*-PrOH	*i*-PrOH	*n*-BuOH	TFE	AcOH
80	0.22	0.19				0.16	0.012
40	0.18	0.20	0.27				
20							
10	0.11	0.19		0.18		0.14	0.10
1	0.13	0.16		0.16			
0.1	0.13	0.16	0.15		0.15	0.14	
0.01	0.13	0.16		0.16		0.14	0.14
0.00	0.12						

[a]Containing 5% H_2SO_4 and 5% MeCN; styrene concentration = 6.5×10^{-4} *M*.
[b]Relative to Rhodamine-B at 298 K; error in the values presented in no greater than ±5%.
[c]Condirston and Laposa (40) obtained values of 0.24 and 0.25 in 3-methylpentane and cyclohexane, respectively (at 298 K), relative to biphenyl.
[d]Excitation wavelength at 249 nm.

Can. J. Chem. Downloaded from www.nrcresearchpress.com by 112.217.228.212 on 09/07/12
For personal use only.

styrene, just alluded to, might also be due in part to other factors. A lower than expected nucleophilicity for water in acetonitrile has been explained (15) in terms of solvent clusters held together by weak hydrogen bonds that diminish the nucleophilic character of water, in accord with Symon's theory (8). A similar rationale has been proposed by Jencks and co-workers (16) for aqueous TFE mixtures. From thermochemical measurements (by mass spectroscopy) of mixed water–methanol cationic clusters ($(H_2O)_n(MeOH)_mH^+$), Meot-Ner (17) has found that the H^+ (charged) center will be preferentially solvated by methanol molecules. In other words, the most stable isomers will have the methanol molecules situated near the charged center. It is not unreasonable to presume that this line of argument could be extended to conclude that styrene molecules would prefer to reside within such a cluster, if the hydrophobic nature of styrene is considered. On the basis of solubility alone, styrene would be expected to be better solvated by the organic solvent component. Moreover, we would anticipate that the selectivity should increase with better solvating organic solvents (e.g., propanol vs. methanol). The only consistent trend in this particular study (Table 3) is that the *sec*-phenethyl carbenium ion reacts preferentially with the organic solvent component. The approximate order of selectivity we observed does not correlate with ground-state solvent nucleophilicity values, the solvatochromatic parameters α and β, pK_a, or *Y* values (Table 2). Kobayashi *et al.* observed (15) a similar disparity between the ground-state and "apparent" excited-state nucleophilicity order (MeOH > EtOH > *i*-PrOH > H_2O > *t*-BuOH) in the decay of vinyl cations generated via flash photolysis. Our results imply that selectivity is governed by an interplay of steric bulk, solvating ability, and solvent composition, with all other variables remaining equal. It is quite remarkable that a preference is shown even for weakly nucleophilic TFE in the presence of water. Clearly, its solvating power as well as superior hydrogen-bonding ability must be factors in this behavior.

Medium acidity

The discordant results obtained in 1 and 10% aqueous methanol are not easily interpreted. One likely possibility is that the thermal addition is competitive at higher acid concentrations (>15% H_2SO_4). Even though precautions were taken (cooling during mixing of components and use of a cold finger during irradiation) this still seems to be a viable explanation. Wan has noted (1, 18) that the ground-state hydration of styrene becomes significant at $H_0 < -1.4$ (ca. 15% H_2SO_4). In addition to this, acid-catalyzed photosolvolysis and (or) suppression of solvent autoionization (particularly in 1% MeOH–H_2O) could be occurring.

Irradiation time/product stability

At first it was speculated the results (a parabolic increase and decrease in selectivity with irradiation time) might be due to selective photosolvolysis of the alcohol adduct. Initially, this seemed unlikely since the leaving groups (methanol and water) differ by only 2 pK_a units (Table 2) and are of approximately the same pK_a ($\Delta pK_a = 0.3$) when methanol is in dilute solution (19, 20). At other compositions of aqueous methanol, it was found that *S* does not always increase from 20 to 40 min (Table 4), yet the most significant changes are at 60 min and later. The most reasonable explanation for this trend is that there is another, completely different reaction of the primary photoaddition (photosolvolysis) product(s), which has a much lower quantum yield, or which requires one of the initially formed products to react with it. Our decomposition study, however, does reveal that the alcohol (**1**) reacts 1–1.5 times faster than the ether (**2**) during a comparable time period (60 min) in various compositions of aqueous methanol. This rate variation, in itself, does not make a significant enough contribution to explain the time dependent irradiation behavior.

Reactions with external nucleophiles

The results with thiophenol and ethanethiol (<11% of the thioether adduct) imply that competitive photochemistry of the thiol and (or) adduct is occurring. One inherent problem is that styrene and thiophenol have comparable molar absorptivities (21). A competitive radical pathway initiated by homolytic dissociation of the thiols is consistent with earlier photochemical studies by Sivertz and co-workers (22, 23). This may explain why the observed selectivity is greater with ethanethiol, which does not absorb light as strongly.

The benzenesulfinate anion was the most potent nucleophile (24) we examined. The molar absorptivity of $PhSO_2^-$ was found to be very low (ϵ_{max} (269 nm) = 1004 in water) thus mitigating against competitive absorption with styrene. Our observed fluctuation in selectivities with nucleophile concentrations, for both the acetate and benzenesulfinate ions, suggests an interplay between substrate/nucleophile solubility at higher

Can. J. Chem. Downloaded from www.nrcresearchpress.com by 112.217.228.212 on 09/07/12
For personal use only.

nucleophile concentrations. At lower nucleophile concentrations, the barrier to desolvation of acetate to allow it to approach the developing carbenium ion must be of higher energy than that required for the benzenesulfinate ion, which parallels an argument set forth by Richard and Jencks for carboxylate anions (25). Polymerization of styrene is not likely to compete at such low concentrations; i.e., 10^{-4} M. It would be hazardous to speculate upon the selectivity difference in the photo and thermal addition of $PhSO_2^-$ to styrene, due to the difference in medium acidity.

Ring substitution

On the basis of simple resonance effects, it was anticipated that *p*-methoxystyrene might exhibit greater selectivity than styrene in both the thermal and photochemical addition reactions. On the other hand, we expected *m*-nitrostyrene to give lower selectivity and *anti*-Markownikov addition products for the photoaddition. Addition at the carbinol carbon, in light of partial diradicaloid character (1), could also conceivably compete. The increased selectivity of *p*-methoxystyrene over styrene in the thermal addition of aqueous methanol (Table 6) is clearly consistent with resonance stabilization of the developing carbenium ion by the *p*-methoxy substituent. Results from the photoaddition were initially puzzling; they are in direct contradiction to the reactivity–selectivity principle (RSP; 6, 26). Excitation of styrenes (analogous to normal alkenes) presumably leads to an S_1 state where a weakening of the π-bond results in a preferred nonplanar conformation of the *p*-orbitals (1, 27, 28). This partial disruption of the extended π-system might explain the attenuation in resonance stabilization. Alternatively, introduction of a ring substituent may also contribute to a shorter lifetime by providing an energy sink for the excited-state species, i.e., additional vibrational degrees of freedom afforded by a "free rotor" effect. Previous measurements in our laboratories (1, 2, 18) gave fluorescence lifetimes of 7.5 and 1 ns for styrene and *p*-methoxystyrene, respectively, in acetonitrile–water at pH 7. It was found that these lifetimes decreased with increasing medium acidity. Hence, the lower selectivity of *p*-methoxystyrene as compared to styrene is quite reasonably explained either by attenuated resonance effects and (or) a shorter intermediate lifetime. The *sec*-phenethyl carbenium ion has also been generated in a photosolvolytic reaction. McKenna and co-workers observed (29) that both the thermal- and photo-solvolysis of (−)-1-(4-methoxyphenyl)-ethyltrimethylammonium iodide in aqueous methanol (containing 0.31 mole fraction methanol) gave a strong preference for formation of the methyl ether rather than the alcohol (eq. [7]).

[7] 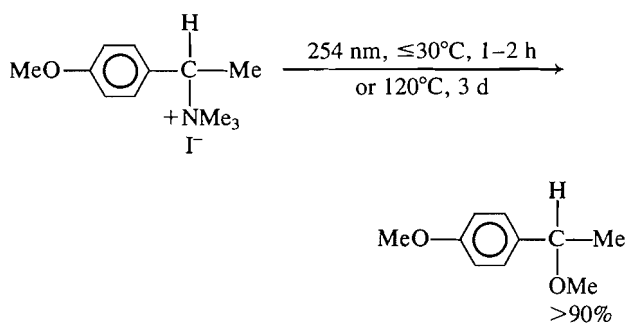

From the yield of the ether product, it was calculated that the capture ratio (k(MeOH)/H_2O)) is at least 20. The similarity of capture by methanol under both conditions indicates the photochemically generated carbenium ion is most likely thermally equilibrated prior to coordination with the solvent molecule(s). The large selectivity (e.g., S values of 1.5–2.8 were found for the benzyl analogues in the same solvent) was ascribed to stabilization of the ion pair by the *p*-methoxy group. It is not entirely clear why our photochemical results, but not the thermal, agree with McKenna's (29) solvolytic data. Ion pairs in the solvolysis reaction might be one significant point of departure. The thermal S values are also close to the previously described results of Richard and Jencks (25). The fact that our observations differ from those of McKenna demonstrates that there is no appreciable thermal equilibration of the photochemically generated carbenium ion from *p*-methoxystyrene prior to coordination with the solvent molecule(s).

m-Nitrostyrene, which reacts via a T_1 state, has a considerably longer lifetime of ca. 460 ns (18). The very low selectivity that we have observed with the *meta* derivative appears to be the result of largely one effect. It could be due to the reverse-polarized or diradicaloid character of the intermediate, which would render it less susceptible to nucleophilic attack. This is consistent with the previous observation (1, 2) that photohydration of the nitrostyrenes was not subject to acid catalysis. As we anticipated, no products that would arise from attack at the carbinol carbon (**17** and **18**) were detected.

Conclusions

Our study has demonstrated that selectivity in the acid-catalyzed addition of nucleophiles to styrene is a function of several variables. While the selectivities we have measured are not absolute by any means, the results do indicate a marked difference between the photochemically and thermally generated carbenium ions. Our data further argue against proton transfer to styrene (or *p*-methoxystyrene) leading to an intermediate that funnels from the excited-state energy surface to the corresponding ground-state surface. Indeed, the results suggest that the photochemical reaction involves either a hot cation, an excited state, or a blend of these possibilities. Some of our observations have also raised further questions as to the validity of the RSP (30). Fluorescence quenching measurements in aqueous methanol mixtures have supported our hypothesis that the difference in selectivity between the photochemical and thermal reaction is due to retention or enhancement of hydrogen bonding of the organic solvent to styrene in the excited state. This also might be attributed to a "local" concentration effect as a result of the rapid intermediate generation in the photochemical reaction. The longer time period for the thermal reaction allows for greater solvent reorganization.

Experimental

Instrumentation

Infrared (ir) absorption spectra were recorded using a Nicolet 5DX FT-IR grating spectrophotometer, in a potassium bromide matrix or neat. The ^1H nmr spectra were measured using a Varian T-60 spectrometer at 60 MHz with deuterochloroform as solvent and tetramethylsilane as an internal standard. Capillary melting points (mp) were determined on a Gallenkamp apparatus. Both melting points and boiling points (bp) are uncorrected. Ultraviolet (uv) absorption spectra were measured using a Varian 2300 uv–vis spectrometer with 1-cm cells. Analytical glc analyses were performed on either a Varian 3400 gas chromatograph (using a 15 m × 0.25 mm fused silica (0.25 μm) capillary column packed with OV-101) or on a Varian Aerograph 2700 gas chromatograph (using a 6 ft × 2 mm column packed with either 3% OV-101 on 80/100 mesh Chromosorb G or 3% OV-17 on 80/100 mesh Chromosorb W) with a Varian 4270 integrator (error estimated at ±5%). *m*-Dimethoxybenzene was employed in nearly all cases

Can. J. Chem. Downloaded from www.nrcresearchpress.com by 112.217.228.212 on 09/07/12
For personal use only.

as an internal standard for response calibration to the detectors. Fluorescence spectra were recorded on Perkin Elmer MPF-44B or MPF-66 fluorescence spectrophotometers at 20°C using argon degassed solutions. Unless otherwise specified, all preparative irradiations were conducted with 525-mL solutions using a Rayonet RPR-100 reactor equipped with 254-nm lamps. Solutions were outgassed with argon for at least 20 min prior to irradiation. A 0.6-L Vycor quartz tube was employed with a cold finger connected to tap water. During irradiations, the outlet water temperature was found to be ca. 5°C. Stirring of the reaction mixture was effected with a magnetic bar. Thermal runs were carried out in either tightly stoppered volumetric flasks or in sealed ampoules placed in a constant temperature bath maintained within ±0.2°C.

Materials

Benzene and acetonitrile were Caledon ACS reagent grade and used as received. All of the alcohol solvents, except for 2,2,2-trifluoroethanol (TFE, Aldrich Gold Label) and *tert*-butanol (Fisher), were Caledon ACS reagent grade. The alcohols and acetic acid (Baker glacial, ACS reagent grade) were used as received without further purification. All of these solvents were used together with distilled water to prepare binary solutions on a volume/volume basis at 21°C. The appropriate volume of sulfuric acid (BDH or Fisher) was then added. Styrene (Fisher), *p*-methoxystyrene (K & K), and *m*-nitrostyrene (Fairfield) were distilled from hydroquinone under reduced pressure prior to use. Substrates **1** and **15** were purchased from Aldrich Chemical Company. Other substrates, except for those described specifically below, were prepared following literature procedures. Compound **10** was prepared by the reaction of thiophenol and **1** according to the method of Scretas and Scretas (31). Substrate **11** was synthesized from the reaction of ethanethiol (Aldrich) and **1** by the procedure of Guindon *et al.* (32). 1-Phenethyl bromide and 1-(4-methoxyphenyl)ethyl bromide were prepared from the corresponding alcohols by treatment with constant boiling hydrobromic acid as described by McKenna and co-workers (29). Substrates **2**, **4**, **6**, **7**, **8**, and **14** were synthesized from the appropriate alkyl bromide and the corresponding alcohol by the method of McKenna (29). Compound **13** was prepared by sodium borohydride reduction of *p*-methoxyacetophenone (Aldrich) in ethanol. Substrate **3** was synthesized according to the method of Dauben *et al.* (33) by reaction of ethyl iodide with **1**. Compound **9** was prepared by a Fischer esterification of acetic acid and **1**. The above synthesized compounds were purified and identified by their melting or boiling points and spectroscopic data, which were, in all cases, in good agreement with the literature values.

1-Phenethylbenzenesulfinate (12)

In a manner analogous to the preparation of 1-adamantyl methyl sulfide (34), *sec*-phenethyl bromide (2.00 g) and sodium benzenesulfinate (3.55 g, Aldrich) were reacted in refluxing acetonitrile for 24 h. The reaction mixture was concentrated (rotary evaporator) and gave, upon standing overnight at room temperature, yellow platelets. Recrystallization from benzene gave a pale yellow solid and repeated washing with ether and pentane afforded 0.7 g (26% yield) of a fine white powder, mp 112–114°C; ir (KBr) ν_{max}: 1299 and 1286 (asym. SO_2), 1142 and 1139 (sym. SO_2); uv λ_{max} (H_2O): 269 nm (ϵ 1044), 228 nm (ϵ 2419); ^{1}H nmr ($CDCl_3$) δ: 1.82 (d, CH_3, 3H, J = 7 Hz), 4.27 (q, CH, 1H, J = 7 Hz), 7.28 (m, 2 Ph, 10H).

3-Nitrophenethyl methyl ether (15)

Following the procedure of Merz (35), a solution of **15** (1.99 g, Aldrich) and tetra-*n*-butylammonium iodide (0.072 g) in dry benzene (20 mL) and 50% aqueous NaOH (7.5 mL) was equilibrated by vigorous stirring for 30 min. Dimethylsulfate (4.4 mL) was then added dropwise, with cooling during a 15-min period at a rate such that the temperature did not exceed 45°C. The whole was next brought to reflux and stirred for 6 d whereupon glc analysis (OV-101 column) showed complete disappearance of starting material. This was followed by quenching with concentrated NH_4OH (40 mL), extraction with ether (3 × 30 mL), and drying of the combined extracts over $MgSO_4$. Removal of solvent followed by distillation of the crude product under reduced pressure afforded 1.3 g (60% yield) of a pale, clear yellow liquid, bp 112–114°C (0.65 Torr; 1 Torr = 133.3 Pa); ir (neat) ν_{max}: 1529, 1525 (asym. N=O), 1349 (sym. N=O), 1115 (C—O—C); ^{1}H nmr ($CDCl_3$) δ: 2.92 (t, CH_2OH, 2H, J = 6 Hz), 3.32 (s, CH_3O, 3H), 3.64 (t, $PhCH_2$, 2H, J = 6 Hz), 7.23–8.18 (m, Ph, 4H).

Irradiations

The following experiment was representative of the procedure employed. A solution of styrene (34 mg in 25 mL of MeCN and 500 mL of 1% aqueous ethanol containing 5% H_2SO_4) was outgassed with argon for 20 min and then irradiated for 1 h at 254 nm in a Vycor tube equipped with a cold finger. The solution was then saturated with NaCl and extracted with CH_2Cl_2 (3 × 100 mL). The combined organic extracts were neutralized with saturated aqueous $NaHCO_3$ solution. Subsequent drying over $MgSO_4$, solvent removal (rotary evaporator), and response-calibrated glc analysis (OV-17 column) of the crude product revealed the presence of 0.5% styrene, 41.1% of **3**, and 58.9% of **1**. These components comprised approximately 62% of the total reaction mixture, the remainder consisting of several unidentified higher boiling by-products.

Thermal runs

In a typical experiment, a solution of *p*-methoxystyrene (10 mg in 5 mL of MeCN and 95 mL of 0.1% aqueous methanol containing 5% H_2SO_4) in a 250-mL volumetric flask was placed in a constant temperature bath thermostatted at 40.6°C for 28.5 h. The solution was then saturated with NaCl, extracted with CH_2Cl_2 (3 × 30 mL), the combined extracts neutralized with saturated aqueous $NaHCO_3$, and then dried over $MgSO_4$. Removal of solvent (rotary evaporator) followed by response-calibrated glc analysis (OV-101 column) revealed the presence of peaks corresponding to starting material (1.6%), **13** (95.4%), and **14** (3.0%). These components made up approximately 29% of the total reaction mixture, the remainder again consisting of numerous by-products possessing longer retention times.

Fluorescence quenching

Solutions for fluorescence quenching studies were prepared by injecting 10 μL of a stock solution of styrene (4.00×10^{-4} M in CH_3CN) into the appropriate mixed solvent (3 mL), which had been degassed for 1 min, in a quartz cuvette. The resulting styrene concentration was 1.33×10^{-6} *M*. Corrected fluorescence spectra of these solutions were then recorded under identical conditions employing Rhodamine-B as a standard.

Acknowledgements

The continued financial support of the Natural Sciences and Engineering Research Council of Canada is appreciated. We also express our gratitude for helpful discussions with T. W. Bentley, M. K. Boyd, W. J. Leigh, and J. G. E. McEwen.

1. P. Wan, S. C. Culshaw, and K. Yates. J. Am. Chem. Soc. **104**, 2509 (1982).
2. P. Wan and K. Yates. J. Org. Chem. **48**, 869 (1983).
3. S. Fujita, Y. Hayashi, T. Nomi, and H. Nozaki. Tetrahedron, **27**, 1602 (1971).
4. P. J. Kropp. J. Am. Chem. Soc. **95**, 4611 (1973).
5. P. J. Kropp and H. J. Krauss. J. Am. Chem. Soc. **89**, 5199 (1967).
6. A. Pross. Adv. Phys. Org. Chem. **14**, 69 (1977).
7. T. W. Bentley and G. E. Carter. J. Org. Chem. **48**, 579 (1983).
8. M. C. R. Symons. J. Chem. Soc. Chem. Commun. 418 (1978).
9. N. A. Pohl, M. E. Hobbs, and P. M. Gross. J. Chem. Phys. **9**, 408 (1941).
10. A. A. Maryott, M. E. Hobbs, and P. M. Gross. J. Am. Chem. Soc. **71**, 1671 (1949).
11. J. T. Harris, Jr. and M. E. Hobbs. J. Am. Chem. Soc. **76**, 1419 (1954).
12. J. W. Happ, M. T. McCall, and D. G. Whitten. J. Am. Chem. Soc. **93**, 5496 (1971).

13. J.-P. DESVERGNE, H. BOUAS-LAURENT, A. CASTELLAN, E. YUREK, and A. DEHAUT DESIGY. J. Chem. Soc. Chem. Commun. 82 (1986).
14. N. IKEDA, H. MIYASAKA, T. OKADA, and N. MATAGA. J. Am. Chem. Soc. **105**, 5206 (1983).
15. S. KOBAYASHI, T. KITAMURA, H. TANIGUCHI, and W. SCHNABEL. Chem. Lett. 1117 (1983).
16. J. P. RICHARD, M. E. ROTHENBURG, and W. P. JENCKS. J. Am. Chem. Soc. **106**, 1361 (1984).
17. M. MEOT-NER. J. Am. Chem. Soc. **108**, 6189 (1986).
18. P. WAN. Ph.D. thesis, University of Toronto. 1983.
19. G. M. LOUDON. Organic chemistry. Addison–Wesley, Don Mills, Ont. 1984. p. 693.
20. E. M. ARNETT. Prog. Phys. Org. Chem. **1**, 223 (1963).
21. R. M. SILVERSTEIN, G. C. BASSLER, and T. C. MORRILL. Spectrometric identification of organic compounds. John Wiley and Sons, New York. 1981.
22. R. H. PALLEN and C. SIVERTZ. Can. J. Chem. **35**, 723 (1957).
23. R. BACK, G. TRICK, C. MCDONALD, and C. SIVERTZ. Can. J. Chem. **32**, 1078 (1954).
24. C. D. RITCHIE. J. Am. Chem. Soc. **97**, 1170 (1975).
25. J. P. RICHARD and W. P. JENCKS. J. Am. Chem. Soc. **106**, 1373 (1984).
26. R. D. LEVINE. Isr. J. Chem. **26**, 320 (1985); A. PROSS. Isr. J. Chem. **26**, 390 (1985), and other contributions in this "Reactivity and Selectivity" symposium issue.
27. P. J. KROPP. Org. Photochem. **4**, 1 (1979).
28. P. WAN and K. YATES. Rev. Chem. Intermed. **5**, 157 (1984).
29. V. LILLIS, J. MCKENNA, J. M. MCKENNA, M. J. SMITH, P. S. TAYLOR, and I. H. WILLIAMS. J. Chem. Soc. Perkin Trans. 2, 83 (1980), and references cited therein.
30. E. M. ARNETT and K. E. MOLTER. Acc. Chem. Res. **18**, 339 (1985), and references cited therein.
31. M. SCRETAS and C. G. SCRETAS. J. Org. Chem. **42**, 1462 (1977); M. MICHA-SCRETAS. J. Org. Chem. **44**, 713 (1979).
32. Y. GUINDON, R. FRENNETE, R. FORTIN, and J. ROKACH. J. Org. Chem. **48**, 1357 (1983).
33. W. G. DAUBEN, J. H. SMITH, and J. SALTIEL. J. Org. Chem. **34**, 261 (1969).
34. D. N. KEVILL and S. W. ANDERSON. J. Am. Chem. Soc. **108**, 1579 (1986).
35. A. MERZ. Angew. Chem. Int. Ed. Engl. **12**, 846 (1973).
36. M. J. KAMLET, J.-L. M. ABBOUD, M. H. ABRAHAM, and R. W. TAFT. J. Org. Chem. **48**, 2877 (1983).
37. C. REICHARDT. Solvent effects in organic chemistry. Verlag Chemie, Weinheim, Germany. 1979. p. 233.
38. B. ALLARD, A. CASADEVALL, E. CASADEVALL, and C. LARGEAU. Nouv. J. Chim. **3**, 335 (1979).
39. W. P. JENCKS and J. REGENSTEIN. *In* Handbook of biochemistry. *Edited by* H. A. Sober. The Chemical Rubber Co., Cleveland, OH. 1968. p. J-150.
40. D. A. CONDIRSTON and J. D. LAPOSA. Chem. Phys. Lett. **63**(29), 313 (1979).

Can. J. Chem. Downloaded from www.nrcresearchpress.com by 112.217.228.212 on 09/07/12
For personal use only.

Solvation properties in iso-acidic media involving phosphoric acid

C. Louis, A. Bebba, and J. Bessière

Laboratoire de Chimie et Electrochimie Analytique, Faculté des Sciences, Université de Nancy 1, B.P. 239, 54506 Vandoeuvre Les Nancy CEDEX, France

Received October 23, 1987[1]

C. Louis, A. Bebba, and J. Bessière. Can. J. Chem. **66**, 2422 (1988).

Concentrated solutions of mineral acids (phosphoric, hydrochloric, perchloric, sulfuric) are characterized, for an equal value of their water activity, by an equal R_0(H) acidity level (iso-acidic solutions). By mixing them, we prepare what we call iso-acidic mixtures which keep the same acidity level as the constitutive solutions whatever the proportions; their redox and solvating properties depend both on the nature and on the ratio of the constitutive solutions. Reactivity variations for ionic species: Cl^-, Br^-, I^-, diethyldithiophosphate (LET^-), $Si(W_3O_{10})_4^{4-}$, $Si(W_3O_{10})_4^{5-}$, Cu^{2+}, Cu^+, Pb^{2+}, Sn^{2+}, Cd^{2+}, Zn^{2+}, Ag^+, Fe^{3+}, Fe^{2+}, UO_2^{2+}, U^{4+} in the iso-acidic mixtures are characterized by their f solvation-transfer activity coefficients. Relations between f coefficient values and complexation properties are established and it is shown that phosphoric acid has comparatively weak solvating properties toward most species. The possibility for anticipating reaction changes with the iso-acidic mixture composition by using the f coefficients is demonstrated in the case of cadmium ionic flotation with diethyldithiophosphate and silver extraction with dithizone in carbon tetrachloride.

C. Louis, A. Bebba et J. Bessière. Can. J. Chem. **66**, 2422 (1988).

On a caractérisé des solutions concentrées d'acides minéraux (phosphorique, chlorhydrique, perchlorique, sulfurique), ayant la même activité dans l'eau et le même niveau d'acidité R_0(H) (solutions iso-acides). En les mélangeant, on a préparé ce que l'on peut appeler des mélanges iso-acides qui gardent le même niveau d'acidité que les solutions qui les constituent quelles que soient les proportions. Leurs propriétés de solvatation et redox dépendent à la fois de la nature et du rapport des solutions de départ. On a caractérisé les variations de réactivité des espèces ioniques Cl^-, Br^-, I^-, diethyldithiophosphate (LET^-), $Si(W_3O_{10})_4^{4-}$, $Si(W_3O_{10})_4^{5-}$, Cu^{2+}, Cu^+, Pb^{2+}, Sn^{2+}, Cd^{2+}, Zn^{2+}, Ag^+, Fe^{3+}, Fe^{2+}, UO_2^{2+}, U^{4+}, des mélanges iso-acides en se basant sur leur coefficient d'activité de transfert de solvatation f. On a établi des relations entre les valeurs du coefficient f et les propriétés de complexation et on montre que de tous les acides, c'est l'acide phosphorique qui solvate moins bien la plupart des espèces. Utilisant la flottation de l'ion cadmium par le diethyldithiophosphate d'éthyle et l'extraction à l'argent avec la dithizone dans le tétrachlorure de carbone, on démontre qu'il est possible de se servir du coefficient f, pour prévoir le comportement des réactions en fonction de la composition du mélange iso-acide.

[Traduit par la revue]

Introduction

It has been shown recently that concentrated solutions of mineral acids (phosphoric, hydrochloric, perchloric, sulfuric) having the same water activity, are characterized by an equal value of the R_0(H) acidity function (1). By mixing these solutions, we prepare what we call iso-acidic mixtures which have the same acidity level as the constitutive solutions, whatever the proportions (2). Nevertheless, their solvation and redox properties are assumed to be different, depending both on the nature and the proportions of the constitutive solutions.

The concept of iso-acidity is important to anticipate changes of equilibria with the composition of concentrated acid mixture. We intend to apply it in particular to the analysis of the acidic dissolution processes of minerals (apatites, mineral fluorides ...) which generally lead to complex acid mixtures. As we did in the case of concentrated phosphoric acid solutions (3), we characterize the variation of ionic species reactivity in iso-acidic solutions involving phosphoric acid with their solvation-transfer activity coefficients (f) and analyze these data to find out if ionic species having weak chemical interactions with the solvent anions keep the same reactivity when the composition of the iso-acidic mixture is changed.

We consider binary iso-acidic mixtures involving phosphoric acid on the one hand and hydrochloric acid, sulfuric acid, or perchloric acid on the other. Hydrochloric and sulfuric acids have been selected for their complexing properties and perchloric acid for its lack of complexing properties.

Changes in the precipitation reaction of cadmium with diethyldithiophosphate (LET^-) and the extraction reaction of silver with dithizone (acidic extractant H_2Dz) are then analyzed taking into account variations of the solvation characteristics of the involved species.

Variations of solute solvation: theoretical aspects

Variations of solute solvation are characterized by means of the solvation-transfer activity coefficients (f). They are calculated from normal potential values of the corresponding redox systems according to the relations [1]–[4].

M^{n+}/M system

[1] $$\log f_{M^{n+}} = n(E_0^a - E_0^w)/0.058$$

$M^{n+}/M^{(n-m)+}$ system

[2] $$\log f_{M^{n+}}/f_{M^{(n-m)+}} = m(E_0^a - E_0^w)/0.058$$

$MO_p^{n+}/MO_q^{[n+2(p-q)-m]+}$ system

[3] $$\log f_{MO_p^{n+}}/f_{MO_q^{[n+2(p-q)-m]+}} = m(E_0^a - E_0^w)/0.058 + 2(p-q)R_0(H) + (p-q)\log a_{H_2O}$$

AX_n/A system

[4] $$\log f_{X^-} = (E_0^w - E_0^a)/0.058$$

E_0^w represents the normal potential of the considered redox system in water, E_0^a its value in an iso-acidic medium characterized by its acidity level, R_0(H) (4–7), and its water activity, a_{H_2O} (8). Both are referred to the ferricinium/ferrocene (Fc^+/Fc) comparison system (9, 10).

The f coefficients have been alternatively determined from

[1]Revision received May 11, 1988.

Printed in Canada / Imprimé au Canada

Can. J. Chem. Downloaded from www.nrcresearchpress.com by 112.217.228.212 on 09/07/12
For personal use only.

TABLE 1. E_0 mV vs. Fc^+/Fc ($R_0(H) = -1.9$ (5.5 M H_3PO_4 + 3.25 M H_2SO_4))

5.5 M H_3PO_4 + 3.25 M H_2SO_4 (vol%)	E_0					
	0%	25%	50%	75%	100%	H_2O
$E_{0\,AgCl/Ag}$	−80	−97	−102	−120	−120	−178
$E_{0\,AgBr/Ag}$	−247	−253	−253	−260	−260	−329
$E_{0\,AgI/Ag}$	−442	−453	−459	−459	−459	−552
$E_{0\,AgLET/Ag}$	−58	−58	−64	−65	−65	−203
$E_{0\,Si(W_3O_{10})_4^{4-}/Si(W_3O_{10})_4^{5-}}$	−276	—	—	—	−266	−522
$E_{0\,Cu^{2+}/Cu}$	−2	−25	−40	−45	−45	−60
$E_{0\,Pb^{2+}/Pb}$	−415	—*	—*	—*	—*	−520
$E_{0\,Sn^{2+}/Sn}$	−454	−448	−448	−446	−443	−530
$E_{0\,Cd^{2+}/Cd}$	−593	−620	−632	−640	−658	−800
$E_{0\,Zn^{2+}/Zn}$	−1004	−1018	−1040	−1052	−1060	−1160
$E_{0\,Ag^{+}/Ag}$	498	469	458	446	446	400
$E_{0\,Fe^{3+}/Fe^{2+}}$	144	173	213	254	312	370
$E_{0\,UO2^{2+}/U^{4+}}$	226	223	243	270	312	−66

*Precipitation in mixtures containing H_2SO_4.

solubility product values according to the relation [5]

MX compound

$$[5] \quad pK_s^a - pK_s^w = \log f_{M^+} + \log f_{X^-}$$

where K_s^a represents the solubility product of the MX compound in the iso-acidic medium and K_s^w its value in water.

In the case of cadmium ionic flotation with diethyldithiophosphate as a collector, there is a direct relationship [6] between the precipitation of cadmium with the LET^- collector and the cadmium ionic flotation yield (R) (6, 11).

$$[6] \quad K_s = (1 - R)(\Phi - 2R)^2 C_0^3$$

where K_s is the solubility product and C_0 the initial concentration of cadmium. R represents the ratio of collected Cd^{2+} to initial Cd^{2+} and Φ the ratio of initial concentration of the collector to initial concentration of cadmium.

The precipitation reaction of Cd^{2+} with LET^-

$$[7] \quad Cd(LET)_2 \downarrow \leftrightarrow Cd^{2+} + 2LET^-$$

is characterized in water and in an acidic mixture, respectively, by the constants:

$$[8] \quad K_s^w = [Cd^{2+}][LET^-]^2$$

$$[9] \quad K_s^a = [Cd^{2+}]_a[LET^-]_a^2$$

which are related according to

$$[10] \quad pK_s^a = pK_s^w + \log f_{Cd^{2+}} + 2 \log f_{LET^-}$$

with $pK_s^w = 9.9$.

Extraction constants are related to the activity coefficients of the extracted species. If the extraction of a metallic cation (Ag^+) with an acidic extractant (dithizone H_2Dz) in an organic solvent (CCl_4) is considered (12), the extraction equilibrium

$$[11] \quad Ag^+ + H_2Dz^* \leftrightarrow AgHDz^* + H^+$$

*X = X species in the organic phase

is generally characterized by the constant

$$[12] \quad K = a_{H^+} a_{AgHDz} / a_{H_2Dz} a_{Ag^+}$$

If the concentrations of both the extracted species and the extractant are low and with an aqueous phase at pH = 0, the extraction constant is

$$[13] \quad K = K_{app}^w = [AgHDz]/[Ag^+][H_2Dz]$$

with $\log K_{app}^w = 7.0$ at pH = 0.

with an acidic aqueous phase (acidity level $R_0(H)$),

$$[14] \quad K_{app}^a = [AgHDz]/[Ag^+]_a[H_2Dz] = f_{Ag^+}[AgHDz]/a_{Ag^+}[H_2Dz] = Kf_{Ag^+}/a_{H^+}$$

$$[15] \quad \log K_{app}^a = \log K + \log f_{Ag^+} + R_0(H)$$

This relationship is valid in any acidic mixture provided the extraction equilibrium remains unchanged and the nature of the organic phase does not change when the composition of the acidic aqueous phase is modified.

Experimental

The normal potentials of some redox systems were determined directly by classical electrochemical methods: dc polarography and zero current potentiometry.

Direct current polarography was used in the case of Cd^{2+}/Cd, Pb^{2+}/Pb, Zn^{2+}/Zn, Cu^{2+}/Cu, Sn^{2+}/Sn, Fe^{3+}/Fe^{2+}, $Si(W_3O_{10})_4^{4-}/Si(W_3O_{10})_4^{5-}$ (6, 13, 14). Normal potentials and half-wave potentials of rapid systems are equal as long as the diffusion coefficients of cations in solution and in the amalgam are the same. In concentrated media, diffusion coefficient variations are determined and the correction is calculated, the correction is significant in iso-acidic media with an $R_0(H)$ acidity level lower than −5.9.

Normal potentials were determined by potentiometry at the silver electrode (Nernst law verification) in the case of the redox systems: $AgCl\downarrow/Ag\downarrow$, $AgBr\downarrow/Ag\downarrow$, $AgI\downarrow/Ag\downarrow$, $AgLET\downarrow/Ag\downarrow$. The potentials were all measured at 20°C by reference to the following electrode: aqueous SCE in a separate compartment containing 0.1 M H_3PO_4.

Normal potentials of uranium were calculated from the equilibrium constants of the reaction

$$[16] \quad U(VI) + 2Fe(II) \leftrightarrow U(IV) + 2Fe(III)$$

in acidic media with an $R_0(H)$ acidity level higher than −2.0.

Can. J. Chem. Downloaded from www.nrcresearchpress.com by 112.217.228.212 on 09/07/12
For personal use only.

TABLE 2. E_0 mV vs. Fc^+/Fc ($R_0(H) = -1.9$ (5.5 *M* H_3PO_4 + 3.4 *M* $HClO_4$))

5.5 *M* H_3PO_4 + 3.4 *M* $HClO_4$ (vol%)	E_0					
	0%	25%	50%	75%	100%	H_2O
$E_{0\,AgCl/Ag}$	−80	−85	−85	−91	−96	−178
$E_{0\,AgBr/Ag}$	−247	−247	−253	−253	−260	−329
$E_{0\,AgI/Ag}$	−442	−447	−453	−460	−465	−552
$E_{0\,AgLET/Ag}$	−58	−58	−60	−62	−58	−203
$E_{0\,Si(W_3O_{10})_4^{4-}/Si(W_3O_{10})_4^{5-}}$	−276	—	—	—	−266	−522
$E_{0\,Cu^{2+}/Cu}$	−2	−2	−2	+1	+4	−60
$E_{0\,Pb^{2+}/Pb}$	−415	−418	−421	−427	−433	−520
$E_{0\,Sn^{2+}/Sn}$	−454	−452	−448	−448	−446	−530
$E_{0\,Cd^{2+}/Cd}$	−598	−605	−617	−634	−646	−800
$E_{0\,Zn^{2+}/Zn}$	−1004	−1010	−1024	−1030	−1035	−1160
$E_{0\,Ag^{+}/Ag}$	498	498	492	487	481	400
$E_{0\,Fe^{3+}/Fe^{2+}}$	144	167	196	230	242	370
$E_{0\,UO2^{2+}/U^{4+}}$	226	227	228	230	241	−66

TABLE 3. E_0 mV vs. Fc^+/Fc
($R_0(H) = -1.9$ (5.5 *M* H_3PO_4 + 3.85 *M* HCl))

5.5 *M* H_3PO_4 + 3.85 *M* HCl (vol%)	E_0					
	0%	25%	50%	75%	100%	H_2O
$E_{0\,Pb^{2+}/Pb}$	−415	−488	−553	−562	−582	−520
$E_{0\,Cu^{2+}/Cu^{+}}$	—	249	271	289	283	−247
$E_{0\,Cu^{+}/Cu}$	—	−246	−330	−358	−378	120
$E_{0\,Cu^{2+}/Cu}$	—	+2	−29	−34	−47	−60
$E_{0\,Cd^{2+}/Cd}$	−598	−685	−759	−766	−781	−800
$E_{0\,Ag^{+}/Ag}$	498	132	85	40	12	400
$E_{0\,Fe^{3+}/Fe^{2+}}$	144	232	266	317	352	370

These equilibrium constants were determined from vis-spectrophotometric measurements on U(IV) species at 660 nm (15, 16).

Determinations involving ionic flotation were carried out in the following way: the acidic solution containing the cadmium and the collector (Φ ratio) is introduced in the Hallimond flotation cell (6). Air under controlled pressure is passed through. The foam which contains the cadmium-collector species is collected at the top and diluted in dimethylsulfoxide. The Cd^{2+} concentration is determined polarographically.

The extraction of AgHDz in CCl_4 is realized in the following conditions: shaking, 15 min; phase separation, 2 h; Ag species concentrations are calculated from [AgHDz]; spectrophotometric measurements at 463 nm (6).

The normal potentials (referred to the ferricinium/ferrocene system) are given in Tables 1, 2, 3, 7, 8. The solvation transfer activity coefficients ($\log f$) are given in Tables 4, 5, 6, 9, 10.

Discussion

1. Ion solvation

Solvation of Cl^-, Br^-, I^-, LET^- anions which are monovalent and have no basic properties except for the last one, does not change significantly when the composition of the iso-acidic mixture is modified (Tables 4, 5, 6, 9, 10). Consequently, reducing properties of metals which oxidize in the form of an insoluble halogenide and oxidizing properties of Cl_2, Br_2, I_2 species in gas or solid state or in solution in an immiscible solvent, do not change when the composition of the iso-acidic mixture is modified. In addition, the variation of the halogenide solubility product depends only on the variation of the cation solvation.

The normal potential of the redox system $Si(W_3O_{10})_4^{4-}/Si(W_3O_{10})_4^{5-}$ remains constant although large anions with several charges are involved. So far, we cannot generalize such a result. Some cations do not have the same reactivity in the various iso-acidic mixtures. Some others hold the same solvation characteristics (Tables 4, 5, 6, 9, 10). Solvation variations are summarized in Table 11.

Perchloric acid is said to have little complexing properties. It is then this medium which, for an equal water activity value, should have presented the weakest affinity toward metallic cations. Nevertheless, phosphoric solutions are generally the less solvating toward most cations.

Complexation phenomena can explain the variations observed in the $\log f$ values.

The effect of Cl^- on Ag^+, Pb^{2+}, Cd^{2+}, Cu^+ cations is apparent in the phosphoric–hydrochloric iso-acidic mixtures as soon as HCl is added to H_3PO_4. Ag^+, Pb^{2+}, Cu^+ are probably in the form of the soluble complexes $AgCl_2^-$, $PbCl_3^-$, $CuCl_2^-$. It has been shown (17) that $CdCl^{(n-2)2+}$ complexes exist in the phosphoric mixtures. Their stability is approximately the same as the one they have in water. Cd^{2+} and Zn^{2+} cations are less solvated in phosphoric acid than in perchloric acid. This can be explained by the formation of $CdClO_4^+$ and $ZnClO_4^+$ complexes. In water, $ZnClO_4^+$ pK_c value is 1.3. Since ClO_4^- has no basic properties, the interaction between zinc and perchlorate anion is possible in concentrated solutions as well. Zinc and cadmium have close chemical properties so that their similar behaviour appears logical.

SO_4^{2-} anions have basic properties ($pK_a = 1.9$), then their reactivity decreases as the acidity increases, nevertheless the higher the H_2SO_4 concentration in the iso-acidic medium, $R_0(H) = -1.9$, the stronger the Ag^+, Zn^{2+}, and Cd^{2+} solvation. Such a behaviour is analogous to the one of organic cations (Hammett indicator cations) which have no interaction with the solvent anions. In both cases, cations are more solvated

Can. J. Chem. Downloaded from www.nrcresearchpress.com by 112.217.228.212 on 09/07/12
For personal use only.

TABLE 4. $\log f$ (R_0(H) = −1.9 (5.5 M H_3PO_4 + 3.25 M H_2SO_4))

5.5 M H_3PO_4 + 3.25 M H_2SO_4 (vol%)	log f				
	0%	25%	50%	75%	100%
log f_{Cl^-}	−1.7	−1.4	−1.3	−1.0	−1.0
log f_{Br^-}	−1.4	−1.3	−1.3	−1.2	−1.2
log f_{I^-}	−1.9	−1.7	−1.6	−1.6	−1.6
log f_{LET^-}	−2.5	−2.5	−2.4	−2.4	−2.4
log $f_{Si(W_3O_{10})_4^{4-}}/f_{Si(W_3O_{10})_4^{5-}}$	+14.2	—	—	—	+14.8
log $f_{Cu^{2+}}$	+2.0	+1.2	+0.7	+0.5	+0.5
log $f_{Pb^{2+}}$	+3.6	—*	—*	—*	—*
log $f_{Sn^{2+}}$	+2.6	+2.8	+2.8	+2.9	+3.0
log $f_{Cd^{2+}}$	+7.0	+6.2	+5.8	+5.5	+4.9
log $f_{Zn^{2+}}$	+5.4	+4.9	+4.2	+3.7	+3.4
log f_{Ag^+}	+1.7	+1.2	+1.0	+0.8	+0.8
log $f_{Fe^{3+}}/f_{Fe^{2+}}$	−3.9	−3.4	−2.7	−2.0	−1.0
log $f_{UO_2^{2+}}/f_{U^{4+}}$	+2.3	+2.5	+3.0	+3.7	+5.2

*Precipitation in mixtures containing H_2SO_4.

TABLE 5. $\log f$ (R_0(H) = −1.9 (5.5 M H_3PO_4 + 3.4 M $HClO_4$))

5.5 M H_3PO_4 + 3.4 M $HClO_4$ (vol%)	log f				
	0%	25%	50%	75%	100%
log f_{Cl^-}	−1.7	−1.6	−1.6	−1.5	−1.4
log f_{Br^-}	−1.4	−1.4	−1.3	−1.3	−1.2
log f_{I^-}	−1.9	−1.8	−1.7	−1.6	−1.5
log f_{LET^-}	−2.5	−2.5	−2.6	−2.6	−2.5
log $f_{Si(W_3O_{10})_4^{4-}}/f_{Si(W_3O_{10})_4^{5-}}$	+14.2	—	—	—	+14.8
log $f_{Cu^{2+}}$	+2.0	+2.0	+2.0	+2.1	+2.2
log $f_{Pb^{2+}}$	+3.6	+3.5	+3.4	+3.2	+3.0
log $f_{Sn^{2+}}$	+2.6	+2.7	+2.8	+2.8	+2.9
log $f_{Cd^{2+}}$	+7.0	+6.7	+6.3	+5.7	+5.3
log $f_{Zn^{2+}}$	+5.4	+5.2	+4.7	+4.3	+4.3
log f_{Ag^+}	+1.7	+1.7	+1.6	+1.5	+1.4
log $f_{Fe^{3+}}/f_{Fe^{2+}}$	−3.9	−3.5	−3.0	−2.4	−2.2
log $f_{UO_2^{2+}}/f_{U^{4+}}$	+2.3	+2.2	+2.2	+2.4	+2.7

in the more ionized acid. In particular, solvation variations of Ag^+ and 4-nitro-2-aniline cations are very close in the mixture 5.5 M H_3PO_4 − 3.25 M H_2SO_4 (6). This analysis is also valid in the R_0(H) = −5.9 iso-acidic mixtures.

Cu^{2+} and Sn^{2+} cations are less solvated in the perchloric medium than in the phosphoric medium. These cations are characterized in 2.0 M phosphoric medium by negative log f values (15, 18) indicating a specific interaction with phosphoric acid at a low concentration. One can understand that the other iso-acidic media can be less solvating toward these cations as it is for Cu^{2+} in perchloric acid and for Sn^{2+} in sulfuric and perchloric acids.

The correlation which exists between complexation and solvation variations explains that log f cannot be calculated according to recently developed models (19–22) which assume no specific interaction between the particles, taking uniquely into account electrostatic interactions (short and mean distances) and not complexation.

2. Reaction evolution analysis

The LET^- anion is equally solvated in the various iso-acidic mixtures (Tables 4, 5), then according to relation [10], the less solvating the iso-acidic mixture toward Cd^{2+}, the easier the $Cd(LET)_2$ separation. The pK_s^{exp} values calculated from flotation experiments according to relation [6] and pK_s^{calc} values calculated according to relation [10] are fairly consistent (Table 12). Cd^{2+} ionic flotation yield is the higher in the phosphoric medium.

TABLE 6. $\log f$ (R_0(H) = −1.9 (5.5 M H_3PO_4 + 3.85 M HCl))

5.5 M H_3PO_4 + 3.85 M HCl (vol%)	log f				
	0%	25%	50%	75%	100%
log $f_{Cu^{2+}}$	+2.0	+2.1	+1.0	+0.9	+0.4
log $f_{Cu^{2+}}/f_{Cu^+}$	—	+8.5	+8.9	+9.0	+9.1
log f_{Cu^+}	—	−6.3	−7.7	−8.2	−8.6
log $f_{Pb^{2+}}$	+3.6	+1.1	−1.1	−1.4	−2.1
log $f_{Cd^{2+}}$	+7.0	+3.3	+1.4	+1.2	+0.6
log f_{Ag^+}	+1.7	−4.6	−5.4	−6.2	−6.7
log $f_{Fe^{3+}}/f_{Fe^{2+}}$	−3.9	−2.4	−1.8	−0.9	−0.3

Analysis of the partition coefficient P = [AgHDz]/[Ag^+] as a function of log [H_2Dz] indicates a linear variation (slope =

Can. J. Chem. Downloaded from www.nrcresearchpress.com by 112.217.228.212 on 09/07/12
For personal use only.

Can. J. Chem. Downloaded from www.nrcresearchpress.com by 112.217.228.212 on 09/07/12
For personal use only.

TABLE 7. E_0 mV vs. Fc^+/Fc ($R_0(H) = -5.9$ (11.5 M H_3PO_4 + 7.6 M H_2SO_4))

11.5 M H_3PO_4 + 7.6 M H_2SO_4 (vol%)	E_0					
	0%	25%	50%	75%	100%	H_2O
$E_{0\,AgCl/Ag}$	30	20	7	4	9	−178
$E_{0\,AgBr/Ag}$	−126	−149	−161	−171	−178	−329
$E_{0\,AgI/Ag}$	−354	−366	−383	−390	−401	−552
$E_{0\,Cu^{2+}/Cu}$	+183	+183	+180	+180	+177	−60
$E_{0\,Pb^{2+}/Pb}$	−244	—*	—*	—*	—*	−520
$E_{0\,Sn^{2+}/Sn}$	−220	−208	−200	−200	−176	−530
$E_{0\,Cd^{2+}/Cd}$	−420	−428	−432	−434	−443	−800
$E_{0\,Zn^{2+}/Zn}$	−812	−818	−823	−826	−826	−1160
$E_{0\,Ag^{+}/Ag}$	678	661	649	637	632	+400
$E_{0\,Fe^{3+}/Fe^{2+}}$	294	323	364	474	515	+370

*Precipitation in mixtures containing H_2SO_4.

TABLE 8. E_0 mV vs. Fc^+/Fc ($R_0(H) = -5.9$ (11.5 M H_3PO_4 + 7.15 M $HClO_4$))

11.5 M H_3PO_4 + 7.15 M $HClO_4$ (vol%)	E_0					
	0%	25%	50%	75%	100%	H_2O
$E_{0\,AgCl/Ag}$	30	25	13	7	2	−178
$E_{0\,AgBr/Ag}$	−126	−126	−131	−137	−143	−329
$E_{0\,AgI/Ag}$	−354	−354	−360	−360	−366	−552
$E_{0\,Cu^{2+}/Cu}$	183	218	224	224	230	−60
$E_{0\,Pb^{2+}/Pb}$	−244	−244	−244	−247	−247	−520
$E_{0\,Sn^{2+}/Sn}$	−220	−216	−212	−200	−180	−530
$E_{0\,Cd^{2+}/Cd}$	−420	−420	−426	−432	−432	−800
$E_{0\,Zn^{2+}/Zn}$	−812	−812	−812	−820	−826	−1160
$E_{0\,Ag^{+}/Ag}$	678	678	666	655	643	400
$E_{0\,Fe^{3+}/Fe^{2+}}$	294	341	375	404	457	370

TABLE 9. $\log f$ ($R_0(H) = -5.9$ (11.5 M H_3PO_4 + 7.6 M H_2SO_4))

11.5 M H_3PO_4 + 7.6 M H_2SO_4 (vol%)	$\log f$				
	0%	25%	50%	75%	100%
$\log f_{Cl^-}$	−3.6	−3.4	−3.2	−3.0	−2.9
$\log f_{Br^-}$	−3.5	−3.1	−2.9	−2.7	−2.6
$\log f_{I^-}$	−3.4	−3.2	−2.9	−2.8	−2.6
$\log f_{Cu^{2+}}$	+8.4	+8.4	+8.3	+8.3	+8.2
$\log f_{Pb^{2+}}$	+9.5	—*	—*	—*	—*
$\log f_{Sn^{2+}}$	+10.7	+11.1	+11.4	+11.4	+11.5
$\log f_{Cd^{2+}}$	+13.1	+12.8	+12.7	+12.6	+12.3
$\log f_{Zn^{2+}}$	+12.0	+11.8	+11.6	+11.5	+11.5
$\log f_{Ag^{+}}$	+4.8	+4.5	+4.3	+4.1	+4.0
$\log f_{Fe^{3+}}/f_{Fe^{2+}}$	−1.3	−0.8	−0.1	+1.8	+2.5

*Precipitation in mixtures containing H_2SO_4.

TABLE 10. $\log f$ ($R_0(H) = -5.9$ (11.5 M H_3PO_4 + 7.15 M $HClO_4$))

11.5 M H_3PO_4 + 7.15 M $HClO_4$ (vol%)	$\log f$				
	0%	25%	50%	75%	100%
$\log f_{Cl^-}$	−3.6	−3.5	−3.3	−3.2	−3.1
$\log f_{Br^-}$	−3.5	−3.5	−3.4	−3.3	−3.2
$\log f_{I^-}$	−3.4	−3.4	−3.3	−3.3	−3.2
$\log f_{Cu^{2+}}$	+8.4	+9.6	+9.8	+9.8	+10.0
$\log f_{Pb^{2+}}$	+9.5	+9.5	+9.5	+9.4	+9.4
$\log f_{Sn^{2+}}$	+10.7	+10.8	+11.0	+11.4	+12.1
$\log f_{Cd^{2+}}$	+13.1	+13.1	+12.9	+12.7	+12.7
$\log f_{Zn^{2+}}$	+12.0	+12.0	+12.0	+11.7	+11.5
$\log f_{Ag^{+}}$	+4.8	+4.8	+4.6	+4.4	+4.2
$\log f_{Fe^{3+}}/f_{Fe^{2+}}$	−1.3	−0.5	−0.1	+0.6	+1.5

+1) when the aqueous phase is 5.5 M H_3PO_4, 3.25 M H_2SO_4 or 3.4 M $HClO_4$ iso-acidic solutions ($R_0(H) = -1.9$). Conditions are then fulfilled for the calculation of the partition constants according to relation [15]. It is shown on Table 13 that K_{app}^{calc} partition constants calculated according to relation [15] and K_{app}^{exp} determined from extraction experiments are in good agreement. Ag^+ cation is less extracted in the acidic solutions than in water because lesser solvation Ag^+ in these solutions does not compensate for the acidity increase. When the iso-acidic solutions are compared, the extraction efficiency depends uniquely on Ag^+ solvation variations, then Ag^+ extraction in more efficient in the case of phosphoric medium.

TABLE 11. Solvation variation of metallic cations in iso-acidic media ($\Delta \log f = \log f_{H3PO4} - \log f_{H2SO4}$ or $- \log f_{HClO4}$ or $- \log f_{HCl}$) at $R_0(H) = -1.9$ and $R_0(H) = -5.9$

	$\Delta \log f$					
	H_3PO_4–H_2SO_4		H_3PO_4–$HClO_4$		H_3PO_4–HCl	
Cation	$R_0(H) = -1.9$	$R_0(H) = -5.9$	$R_0(H) = -1.9$	$R_0(H) = -5.9$	$R_0(H) = -1.9$	$R_0(H) = -5.9$
Cu^{2+}	+1.5	+0.2	−0.2	−1.6	+1.6	—
Cu^{+}	—	—	—	—	>+2.3	—
Pb^{2+}	—	—	+0.6	+0.1	+5.7	—
Sn^{2+}	−0.4	−0.8	−0.3	−1.4	—	—
Cd^{2+}	+2.1	+0.8	+1.7	+0.4	+6.4	—
Zn^{2+}	+2.0	+0.5	+1.1	+0.5	—	—
Ag^{+}	+0.9	+0.8	+0.3	+0.6	+8.4	—

TABLE 12. $Cd(LET)_2$ solubility product (experimental and calculated pK_s values) in 5.5 *M* H_3PO_4, 3.25 *M* H_2SO_4, and 3.4 *M* $HClO_4$ iso-acidic solutions ($R_0(H) = -1.9$)

	Value		
Parameter	5.5 *M* H_3PO_4	3.25 *M* H_2SO_4	3.4 *M* $HClO_4$
pK_s^{exp}*	11.7	9.8	10.1
$\log f_{Cd^{2+}}$	7.0	4.9	5.3
$\log f_{LET^-}$	−2.5	−2.4	−2.5
pK_s^{calc}†	11.9	10.0	10.2

*Calculated according to relation [6].
†Calculated according to relation [10].

TABLE 13. Ag^+ partition with dithizone in CCl_4 as the organic phase and 5.5 *M* H_3PO_4, 3.25 *M* H_2SO_4, or 3.4 *M* $HClO_4$ iso-acidic solutions ($R_0(H) = -1.9$) as the aqueous phase (experimental and calculated K_{app} values)

	Value		
Parameter	5.5 *M* H_3PO_4	3.25 *M* H_2SO_4	3.4 *M* $HClO_4$
$\log K_{app}^{exp}$*	6.7	5.6	6.2
$\log f_{Ag^+}$	1.7	0.8	1.4
$\log K_{app}^{calc}$†	6.8	5.9	6.5

*Experimental results.
†Calculated according to relation [15].

1. C. LOUIS and J. BESSIERE. Can. J. Chem. **63**, 908 (1985).
2. C. LOUIS, A. BEBBA, and J. BESSIERE. Can. J. Chem. **65**, 1353 (1987).
3. C. LOUIS and J. BESSIERE. Can. J. Chem. **64**, 608 (1986).
4. C. LOUIS and J. BESSIERE. Anal. Lett. **13**, 937 (1980).
5. D. BAUER and M. BOUCHET. C.R. Acad. Sc. Sér. C. Paris. **275**, 21 (1972).
6. A. BEBBA. Thèse de l'Université de Nancy 1. 1987.
7. D. BABALE. Thèse de Doctorat de 3° cycle. Yaounde. 1981.
8. F. COUSSEMANT, M. HELLIN, and B. TORCK. Les fonctions d'acidité et leur utilisation et catalyse acido-basique. Gordon and Breach, Paris, London, New York. 1969. pp. 46, 47.
9. H. M. KOEPP, H. WENDT, and H. STREHLOW. Z. Elektrochem. **64**, 483 (1960).
10. H. STREHLOW. Electrode potentials in non aqueous solvents. *In* The chemistry of non-aqueous solvents. Vol. 1. *Edited by* J. J. Lagowski. Academic Press, New York. 1966. Chap. 4, p. 129.
11. J. BESSIERE, M. BRUANT, E. A. JDID, and P. BLAZY. Int. J. Min. Process. **16**, 63 (1986).
12. A. BENAYADA. Thèse de Doctorat d'Etat, Nancy. 1986.
13. B. KEITA and L. NADJO. J. Electroanal. Chem. Interfac. **191**, 441 (1985).
14. B. KEITA and L. NADJO. J. Electroanal. Chem. Interfac. **199**, 229 (1986).
15. C. LOUIS and J. BESSIERE. Talanta, **34**, 763 (1987).
16. C. LOUIS and J. BESSIERE. Talanta, **34**, 771 (1987).
17. J. GONZALEZ-CHAVEZ. Unpublished results.
18. C. LOUIS and J. BESSIERE. J. Chem. Eng. Data, **31**, 472 (1986).
19. A. B. ZDANOVSKII. Trudy Solyanoi Laboratorii Akad. Nauk. SSSR, **6**, 1 (1936).
20. V. M. VDOVENKO and M. A. RYAZANOV. Radiokhimiya, **8**, 5 (1966).
21. J. LY. Thèse de Doctorat d'Etat, Paris. 1984.
22. R. GELY. Thèse de Doctorat d'Etat, Paris. 1986.

Can. J. Chem. Downloaded from www.nrcresearchpress.com by 112.217.228.212 on 09/07/12
For personal use only.

Density measurements in the succinonitrile–water system

LEE HONG NG AND DONALD ROBERT SADOWAY

Department of Materials Science and Engineering, Massachusetts Institute of Technology, Cambridge, MA 02139, U.S.A.

Received March 31, 1988

LEE HONG NG and DONALD ROBERT SADOWAY. Can. J. Chem. **66**, 2428 (1988).

The variation of density with temperature and composition in the succinonitrile–water system was measured by the direct Archimedean method. At fixed composition, density was found to vary linearly with temperature. At constant temperature, density was found to vary linearly with composition. Along the phase boundary there is a density reversal: at temperatures above 45°C the water-rich phase is denser; below 45°C the succinonitrile-rich phase is denser.

LEE HONG NG et DONALD ROBERT SADOWAY. Can. J. Chem. **66**, 2428 (1988).

Utilisant la méthode directe d'Archimède, on a mesuré la variation de la densité du système eau–succinonitrile en fonction de la température et de la composition du mélange. On a trouvé que pour une composition déterminée, la densité varie linéairement avec la température, tandis qu'à température constante la densité varie linéairement avec la composition. Il y a une inversion de la densité le long de la frontière des phases : la phase riche en eau est plus dense à une température supérieure à 45°C. En dessous de cette température c'est la phase riche en succinonitrile qui est plus dense.

[Traduit par la revue]

1. Introduction

Miscibility gaps are present in many technologically important systems. In order to attain microstructural goals in these systems it is imperative that phase separation phenomena be strictly controlled during materials processing operations. This requires a knowledge of the kinetics of phase transformation.

Classical studies of phase separation were restricted to solids where it is effectively impossible to observe microstructural evolution as it occurs. However, conclusions based on the final morphologies can be misleading (1–6). It is clear that the transformation must be studied in real time.

The novelty of the present work is that for the first time a liquid system was made the subject of a phase transformation study. The succinonitrile–water system was chosen because it is liquid at ambient temperature and transparent to visible light. The latter allows the use of noninvasive optical techniques for real time measurement of microstructure. However, this requires a knowledge of the variation of the index of refraction. Such data have not been reported for the succinonitrile–water system. As the index of refraction is related to density, the purpose of the present study was to measure the dependence of density on temperature and composition in this system.

2. Experimental

Density was measured by the direct Archimedean technique in which one monitors the weight change of a calibrated bob upon immersion in the solution under study (7). The apparatus is shown in Fig. 1. The upper limb is 66 cm long and houses the fused quartz spring; the lower limb is 16 cm long and holds the sample which is heated by circulating water. Water temperature is regulated by a constant temperature circulator.[1] The spring is centered by the ball and socket joint at the top of the upper limb and is raised and lowered by the pulley mechanism. During the experiment the sample is kept under an atmosphere of argon.

The density bob is made of borosilicate glass and weighs about 3 g. The bob is connected to the spring by means of a stainless steel wire, 0.5 mm in diameter. The fused quartz spring[2] has a sensitivity of 0.05 g cm^{-1} and extremely good linearity. Spring displacement was measured by cathetometer[3] which read to the nearest 0.1 mm and can measure a maximum length of 40 cm. In order to minimize calibration errors, an effective "cell constant" which relates spring displacement to the density of the sample was determined by measuring the temperature dependence of the density of water and comparing these results with those in the literature (8).

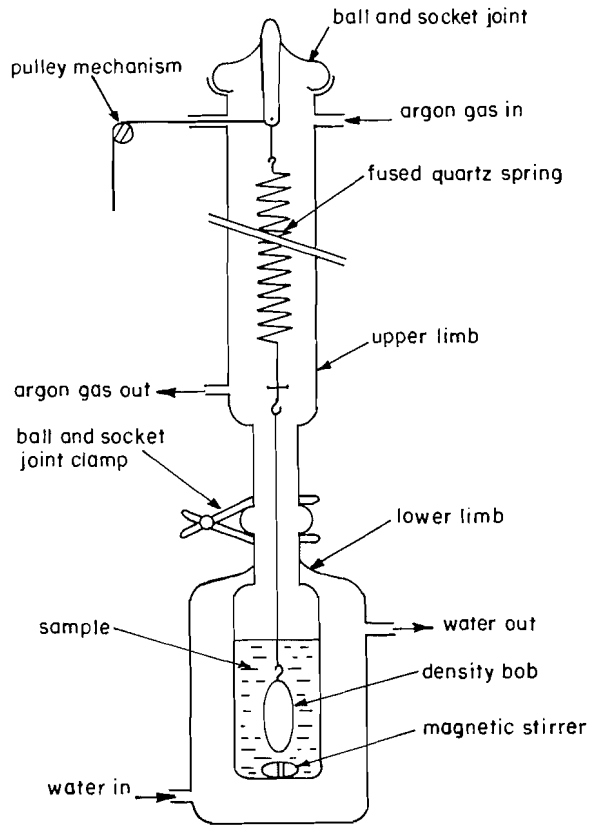

FIG. 1. Apparatus for the measurement of density.

Reagent grade succinonitrile[4] was vacuum distilled several times until a clear residue remained. The melting point of the distillate was measured by cryoscopy and taken to be a further indication of purity. Binary solutions of succinonitrile-water were prepared by adding high purity water to succinonitrile and heating the mixture to obtain a

[1]Model 800, Allied Fisher Scientific, Pittsburgh PA.

[2]Ruska Instrument Corporation, Houston TX.

[3]Model 5100, Eberbach Corporation, Ann Arbor MI.

[4]Eastman Kodak, Rochester NY.

Printed in Canada / Imprimé au Canada

Can. J. Chem. Downloaded from www.nrcresearchpress.com by 112.217.228.212 on 09/07/12
For personal use only.

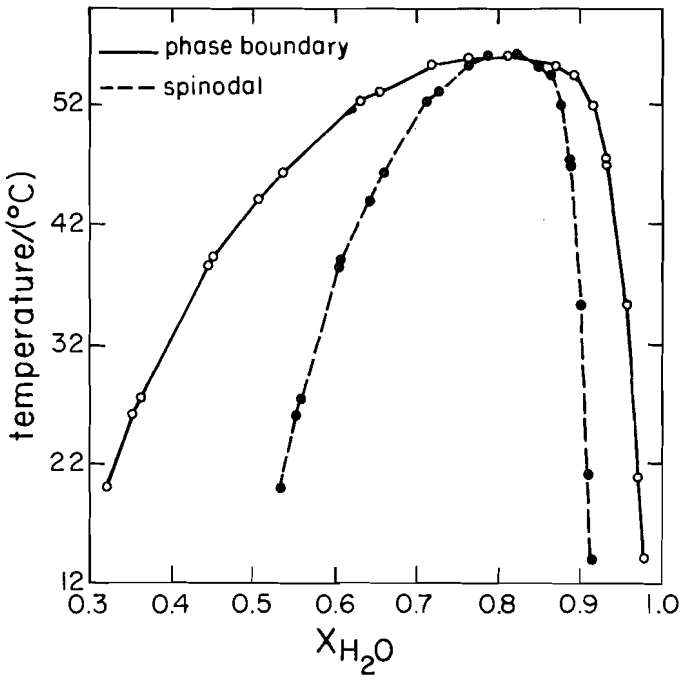

FIG. 2. Phase diagram of the succinonitrile–water system. Spinodal calculated by the "root three" rule.

homogeneous solution which was then transferred to the apparatus. The composition of the sample was then checked once again by comparing the temperature of the phase boundary as reported in the phase diagram (9) to the homogenization temperature as determined by heating the sample and visually inspecting for the presence of any second phase particles. The phase diagram is reproduced for the convenience of the reader in Fig. 2 which also gives the spinodal as calculated by the "root three" rule (10).

In a typical experiment the temperature of the sample, which weighed about 30 g, was varied from approximately 2 K above the solubility limit to a maximum temperature of 80°C. Once the temperature of the sample was set, it was mixed for 10 min by magnetic stirrer. Next, the bob was lowered into the solution, and the extension of the spring was measured by cathetometer. The bob was raised and lowered into the sample again, and another reading was taken. This was repeated at least four times before the temperature was changed. Care was taken to ensure that the immersion depth of the bob was constant in all measurements. The results were checked for reproducibility by performing the experiment on at least two different samples at every composition. The range of composition in this study was 0.3 to 0.97 mole fraction of water. In addition, the density of pure succinonitrile was measured between 60 and 80°C.

3. Results and discussion

At each composition the density measurements were fitted to the following linear function of temperature:

$$[1] \quad \rho/(\text{g cm}^{-3}) = a - bT$$

where T is in Kelvins. Equation [1] is valid only in the single-phase region outside the miscibility gap. The results are shown in Table 1. The fit was extremely good for all compositions, including that of pure succinonitrile. In consideration of the experimental errors associated with this technique, the accuracy of all the density measurements is assessed to be 0.2%.

There are no reports of the density of binary solutions of succinonitrile–water. However, Timmermans and Hennaut-Roland have measured the density of pure succinonitrile (11), and their results differ by less than 0.2% from the present work.

TABLE 1. Temperature dependence of density in the succinonitrile–water system. $\rho/(\text{g cm}^{-3}) = a - bT$, where T is in Kelvins

X_{H_2O}	$a/(\text{g cm}^{-3})$	$b/(\text{g cm}^{-3}\,\text{K}^{-1})$
1.000	1.1421	0.000479
0.970	1.1842	0.000599
0.950	1.2021	0.000653
0.900	1.2302	0.000739
0.827	1.2506	0.000803
0.700	1.2629	0.000847
0.600	1.2672	0.000861
0.500	1.2712	0.000873
0.400	1.2678	0.000861
0.300	1.2618	0.000842
0.000	1.2550	0.000823

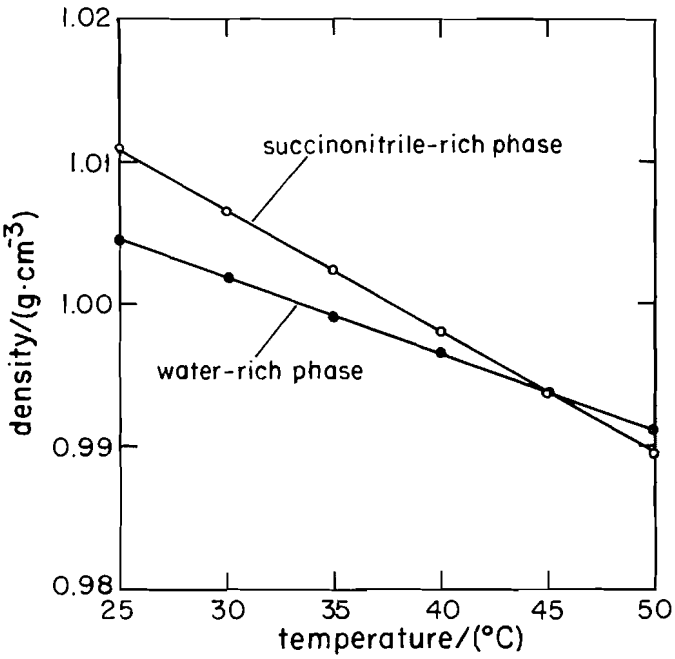

FIG. 3. Variation of density with temperature at compositions along the phase boundary.

The molar volume was calculated from the density data through the use of the equations in Table 1. The molar volume at a given composition is defined as the molar mass of the solution divided by its density. In a binary system the molar mass refers to the mass of one mole of solution and is calculated by adding the molar masses of the pure components weighted by their mole fractions. The molar volume isotherm was found to be a linear function of composition at any given temperature. At temperatures below the consolute the solutions separate into two phases, and the molar volume is undefined in this two-phase region. However, molar volume isotherms of the water-rich solutions and succinonitrile-rich solutions were piecewise linear and appear to lie on the same line when projected across the miscibility gap.

Equation [2] represents the variation in molar volume with composition at a constant temperature of 60°C.

Can. J. Chem. Downloaded from www.nrcresearchpress.com by 112.217.228.212 on 09/07/12
For personal use only.

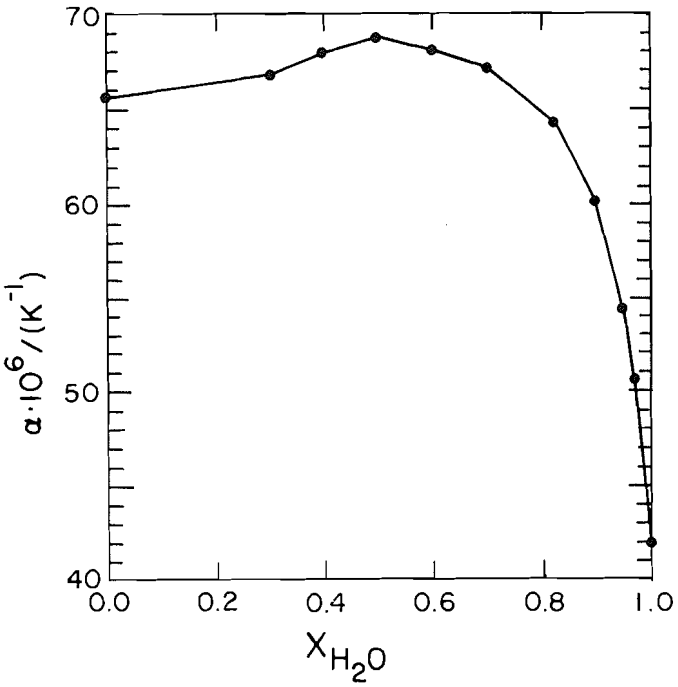

FIG. 4. Variation of thermal expansivity, α, with composition at a temperature of 60°C.

$$[2] \quad V_m/(cm^3) = 81.70 - 63.42X_{H_2O}$$

Equation [2] was constructed by computing the values of molar volume at 60°C from the least squares fits of density versus temperature at different compositions as measured in this study. For the molar volume of pure succinonitrile eq. [2] gives a value of 81.70 cm^3 which differs by less than 0.1% from the value calculated directly from the measured density of succinonitrile at this temperature.

Figure 3 shows the variation in density with temperature along the phase boundary. At each composition the density was calculated from the least-squares fit of density versus temperature evaluated at the corresponding phase boundary. There are two lines, one for the water-rich phase and one for the succinonitrile-rich phase.

This system exhibits density reversal. During the course of experiments the liquid phases were observed to exchange position at temperatures near 45°C. This is consistent with Fig. 3 which shows that at temperatures above 45°C the water-rich phase is denser and below 45°C the succinonitrile-rich phase is denser.

Figure 4 shows the isothermal variation of the thermal expansivity, α, with composition at 60°C. This temperature was chosen because it is above the consolute and thus provides access to the full compositional range. Furthermore, while the absolute magnitude of α changes with temperature, the relative magnitude of α across an isotherm is comparatively insensitive to temperature, i.e., the shape of the isotherm does not change much with temperature.

Figure 4 shows that α is effectively invariant with composition spanning the interval between pure succinonitrile and the consolute composition, 82.7 mol% water. At higher water contents the value of α drops sharply to that of pure water, which is only about half that of succinonitrile. Thus, as the temperature of a two-phase mixture within the miscibility gap is made to decrease, there is a more pronounced variation in density of the succinonitrile-rich phase. The result is that at temperatures below 45°C the succinonitrile-rich phase becomes denser in spite of the fact that at higher temperatures the water-rich phase is denser.

Acknowledgements

The authors wish to acknowledge the financial support of the National Aeronautics and Space Administration through the Materials Processing Center at the Massachusetts Institute of Technology, grant number NSG-7645.

1. J. W. CAHN and R. J. CHARLES. Phys. Chem. Glasses, **6**, 181 (1965).
2. W. HALLER. J. Chem. Phys. **42**, 686 (1965).
3. R. W. HOPPER and D. R. UHLMANN. Discuss. Faraday Soc. **56**, 166 (1970).
4. G. R. SRINIVASAN, J. TWEER, P. B. MACEDO, A. SARKER, and W. HALLER. J. Non-cryst. Solids, **6**, 221 (1971).
5. T. P. SEWARD III, D. R. UHLMANN, and D. TURNBULL. J. Am. Ceram. Soc. **51**, 634 (1968).
6. W. HALLER and P. B. MACEDO. Phys. Chem. Glasses, **9**, 153 (1968).
7. N. R. CARMICHAEL and S. N. FLENGAS. J. Electrochem. Soc. **126**, 2098 (1979).
8. GMELINS handbuch der anorganischen chemie, system-nummer 3, lieferung 5, Verlag Chemie, Weinheim. 1963. p. 1323.
9. J. E. SMITH, JR., D. O. FRAZIER, and W. F. KAUKLER. Scripta Met. **18**, 677 (1984).
10. H. E. COOK and J. E. HILLIARD. Met. Trans. AIME, **233**, 142 (1965).
11. M. J. TIMMERMANS and M. HENNAUT-ROLAND. J. Chim. Phys. **34**, 693 (1937).

Can. J. Chem. Downloaded from www.nrcresearchpress.com by 112.217.228.212 on 09/07/12
For personal use only.

Iodination and deuteration of catechin derivatives[1]

E. KIEHLMANN, N. LEHTO, AND D. CHERNIWCHAN
Department of Chemistry, Simon Fraser University, Burnaby, B.C., Canada V5A 1S6

Received March 1, 1988

E. KIEHLMANN, N. LEHTO, and D. CHERNIWCHAN. Can. J. Chem. **66**, 2431 (1988).

The preparation and ^1H and ^{13}C nuclear magnetic resonance spectra of ten monoiodocatechin derivatives are described. The iodination of catechin with *N*-iodosuccinimide (NIS) takes place regiospecifically at C-6 in acetone but preferentially at C-8 in dimethylformamide; both products can be derivatized at oxygen in alkaline medium but lose iodine in the presence of acid. 3′,4′,5,7-Tetra-*O*-methylcatechin reacts with NIS regiospecifically at C-8 while catechin pentaacetate resists iodination. The debromination of 6-bromo- and 6,8-dibromocatechin with sodium sulfite in CD_3CN/D_2O is accompanied by H/D-exchange at C-6 and C-8. The synthesis of catechin pentaacetate from partially deuterated catechin and its conversion to tetra-*O*-methylcatechin proceed without H/D-exchange and permit distinction between the H-6 and H-8 chemical shifts.

E. KIEHLMANN, N. LEHTO et D. CHERNIWCHAN. Can. J. Chem. **66**, 2431 (1988).

On décrit la préparation et les spectres de résonance magnétique nucléaire du ^1H et du ^{13}C de dix dérivés de la monoiodocatéchine. L'iodation de la catéchine avec la *N*-iodosuccinimide (NIS), dans l'acétone, est régiospécifique au niveau du carbone en position 6 mais se fait préférentiellement au niveau du carbone en position 8 dans le diméthylformamide. En milieu alcalin, on peut transformer les deux produits en dérivés oxygénés, mais en milieu acide, l'iode est éliminé. La tétra-*O*-méthyl-3′,4′,5,7 catéchine réagit de façon régiospécifique avec la NIS au niveau du carbone en position 8 tandis que le pentaacétate de catéchine résiste à l'iodation. La débromation des dérivés bromo-6 et dibromo-6,8 catéchines par le sulfite de sodium dans un mélange de CD_3CN/D_2O s'accompagne d'un échange de H/D au niveau des carbones en positions 6 et 8. La synthèse du pentaacétate de catéchine à partir de la catéchine partiellement deutérée et sa transformation en tétra-*O*-méthylcatéchine se font sans échange de H/D et permettent de discriminer les déplacements chimiques des protons H-6 et H-8.
[Traduit par la revue]

Introduction

In continuation of our studies of halogen as protecting group in flavanoid synthesis (1), we have investigated the iodination of catechin derivatives, the protodeiodination of iodocatechins, the deuteration of catechin, and the debromination of bromocatechins with sodium sulfite in deuterated solvents. A better understanding of the halogenation (2, 3), dehalogenation (4, 5), and deuteration mechanisms (6) is essential for the regiospecific introduction and removal of protecting groups prior to interflavanoid coupling at the unprotected nucleophilic centre (C-6 or C-8) of flavans. It was hoped that the large size and low electrophilicity of iodine might improve the regioselectivity of the halogenation step and facilitate subsequent dehalogenation. A recently published paper (7) on the coupling of mollisacacidin with 6-iodocatechin prompts us now to report our results.

Results and discussion

More than 80 years ago, Kostanecki and Lampe (8) prepared the first two iodocatechin derivatives, 8-iodotetra-*O*-methylcatechin (**3***f*) and its 3-acetate (**5***f*), by direct iodination of tetra-*O*-methylcatechin (**3***a*) with molecular iodine in ethanol and subsequent acetylation (eq. [1]). Repeating this procedure or using *N*-iodosuccinimide (NIS) in dimethylformamide (DMF) as more convenient iodinating agent, we obtained the same compounds in high yields, although **3***f* started to decompose (loss of iodine) at a lower temperature than quoted in the original paper. In sharp contrast to the analogous bromination of **3***a*, the use of two molar equivalents of iodine or NIS does not result in diiodination, indicating unfavourable steric interactions between a large halogen substituent at C-6 and two bulky *ortho*-methoxy groups. The structure assignments of **3***f* and its acetate **5***f*, especially the position of attachment of iodine to ring A (C-8 rather than C-6), are based on a comparison of their proton and carbon chemical shifts (Tables 1 and 2) with those of the 6-iodo isomers (**3***e* and **5***e*, *vide infra*) and the corresponding bromocatechins (1, 9), and on the nuclear Overhauser enhancement (nOe) of two methoxy signals when the aromatic ring A proton of **5***f* is saturated. Most of our ^1H nmr and mass spectrometry data for **5***f* (see Experimental) agree with those reported by Roux and co-workers (7) who obtained the compound in less than 1% yield from catechin by successive iodination, methylation, chromatographic purification of the intermediate tetramethyl ester, and acetylation. Methylation of the aliphatic hydroxy group (at C-3) of **3***f* with methyl iodide in DMF gives 8-iodo-3,3′,4′,5,7-penta-*O*-methylcatechin (**4***f*) in high yield.

The corresponding 6-iodo isomers are accessible by regioselective iodination of catechin and subsequent derivatization of the OH groups (eq. [2]). The medium for the reaction of catechin with NIS controls the regiochemistry: dimethylformamide leads primarily to 8-substitution (**2***f*/**2***e* ratio 4:1) while acetone yields almost exclusively 6-iodocatechin; 6,8-diiodocatechin is formed when two molar equivalents of NIS are used. Contrary to recently published data (7), we identified 8-iodocatechin (rather than the 6-iodo compound) as major reaction product in mixtures of the two solvents. The two regioisomers are readily distinguished by the characteristically different chemical shifts of their residual ring A aromatic protons (see Table 1), and by the nOe difference spectra of their tetramethyl ether acetates: saturation of H-8 of **5***e* enhances only one methoxy signal while saturation of H-6 of **5***f* enhances two. Additional verification of our structure assignments is provided by the excellent correlation of the nmr chemical shifts for all ten monoiodocatechin derivatives (Tables 1 and 2) with those for the corresponding bromo compounds (1, 9).

The discrepancies between our results and those of Roux and co-workers warrant detailed comment. In part 14 of their series on the synthesis of condensed tannins (7), Roux and co-workers

[1]Presented in part at the 42nd ACS Northwest Regional Meeting, 18 June 1987, Western Washington University, Bellingham, Washington, U.S.A.

Can. J. Chem. Downloaded from www.nrcresearchpress.com by 112.217.228.212 on 09/07/12
For personal use only.

[1]

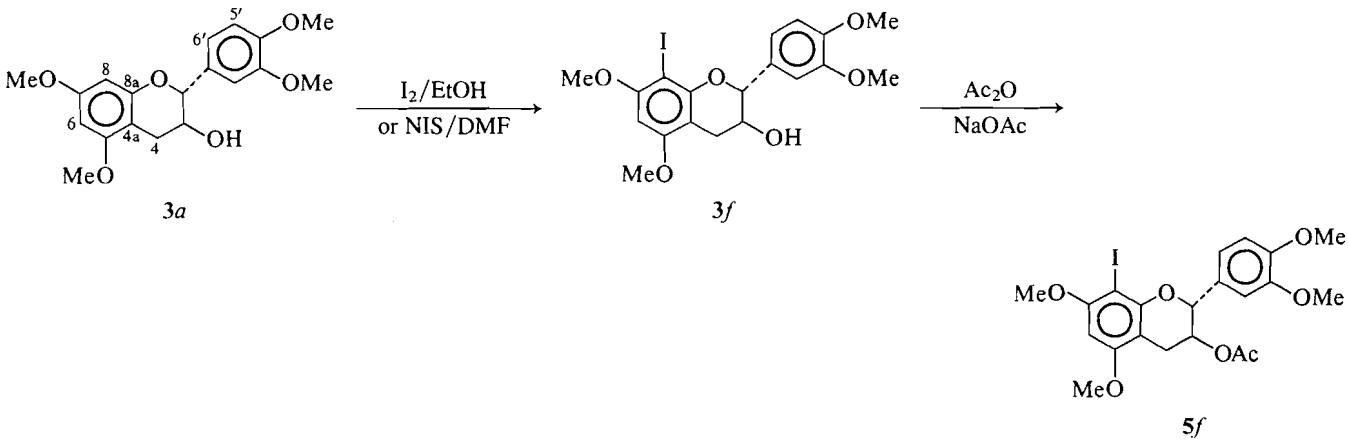

3*a* 3*f* 5*f*

TABLE 1. Proton chemical shifts[a] and coupling constants

	6-Iodocatechin derivatives					8-Iodocatechin derivatives				
Compound:	**2***e*[b]	**3***e*	**4***e*	**5***e*	**6***e*	**2***f*[b]	**3***f*	**4***f*	**5***f*	**6***f*
3,5,7,3′,4′-Substituents:	-$(OH)_5$	-$(OMe)_4$ 3-OH	-$(OMe)_5$	-$(OMe)_4$ 3-OAc	-$(OAc)_5$	-$(OH)_5$	-$(OMe)_4$ 3-OH	-$(OMe)_5$	-$(OMe)_4$ 3-OAc	-$(OAc)_5$
Proton										
H-6	—	—	—	—	—	6.251	6.137	6.122	6.131[c]	6.687
H-8	6.119	6.327	6.333	6.366	6.748	—	—	—	—	—
H-2′	6.855	6.960	6.886	6.853[c]	7.151	6.895	7.013	6.974	6.909	7.159
H-5′	6.79	6.913	6.865	6.829[c]	7.193	6.76	6.878	6.848	6.858	7.198
H-6′	6.71	7.005	6.933	6.887[c]	7.234	6.76	6.961	6.927	6.809	7.241
ArOR-5		3.807	3.771	3.740			3.837	3.825	3.803	
ArOR-7		3.814	3.807	3.834	2.28–		3.888	3.881	3.897	2.27–
ArOR-3′/4′		3.904	3.865/ 3.876	3.848/ 3.865	2.36		3.837/ 3.878	3.859/ 3.869	3.831/ 3.849	2.28
H-2	4.604	4.685	4.895	5.088	5.166	4.776	4.892	5.120	5.333[c]	5.329
H-3	4.019	4.064	3.672	5.347	5.238	4.034	4.054	3.703	5.434	5.260
RO-3			3.237	1.961	1.997			3.314	2.030	2.036
H-4a	2.932	3.245	3.052	2.973	2.87	2.782	2.946	2.808	2.728	2.827
H-4b	2.588	2.771	2.773	2.842	2.67	2.569	2.647	2.685	2.728	2.700
Coupling constant (Hz)										
J_{23}	7.5	8.5	7.1	6.3	5.7	6.7	7.3	6.3	4.8	5.5
J_{34a}	5.5	5.6	5.0	5.1			5.4	5.0		4.9
J_{34b}	8.0	9.4	7.7	6.5		7.5	8.0	6.2		5.8
J_{44}	16.1	16.1	16.3	16.6		16.2	16.5	16.6		17.0
$J_{2'6'}$	1.7	1.9	1.8	1.8	1.8		1.7	1.9	1.5	2.1
$J_{5'6'}$	8.1	8.2	8.3	8.3	8.4		8.3	8.3	8.4	8.4

[a]In ppm downfield from TMS in $CDCl_3$ (except **2***e* and **2***f*).
[b]In acetone-d_6.
[c]Chemical shifts deviate significantly from those reported in the literature (7).

have stated (on p. 2522):

> ... some progress towards regiospecific synthesis of [4,8]-isomers was possible through quantitative reaction of (+)-catechin with 1 mol. equiv. of NIS to give predominantly 6-iodo-(+)-catechin as intermediate. The point of substitution was established by the chemical shift of the residual 8-proton (8-H, δ 6.24) (cf. ref. 10), and also by reaction of an excess of the crude product of iodination with (+)-mollisacacidin in an acid medium (0.1 M HCl, 25°C) which led almost exclusively to a 1:1 ratio of [4,8]-3,4-*trans*- and [4,8]-3,4-*cis*-(−)-fisetinidol-(+)-catechins in a 44% combined yield. The sequence of 8-substitution and de-iodination at C-6 (during work-up) is supported by formation of only trace amounts of [4,6]-isomers and recovery of some 50% unsubstituted (+)-catechin.

Unfortunately, the literature reference (10) cited in support of their incorrect peak assignment does not contain ^{1}Hmr data on substituted catechins in their free phenolic form. Although a nearly quantitative reaction of catechin with NIS (1:1 molar ratio) is possible, as verified by recording the ^{1}Hmr spectrum of the crude product mixture shortly after sample preparation, both 6- and 8-iodocatechin are labile compounds that we were unable

Can. J. Chem. Downloaded from www.nrcresearchpress.com by 112.217.228.212 on 09/07/12
For personal use only.

Can. J. Chem. Downloaded from www.nrcresearchpress.com by 112.217.228.212 on 09/07/12
For personal use only.

[2]

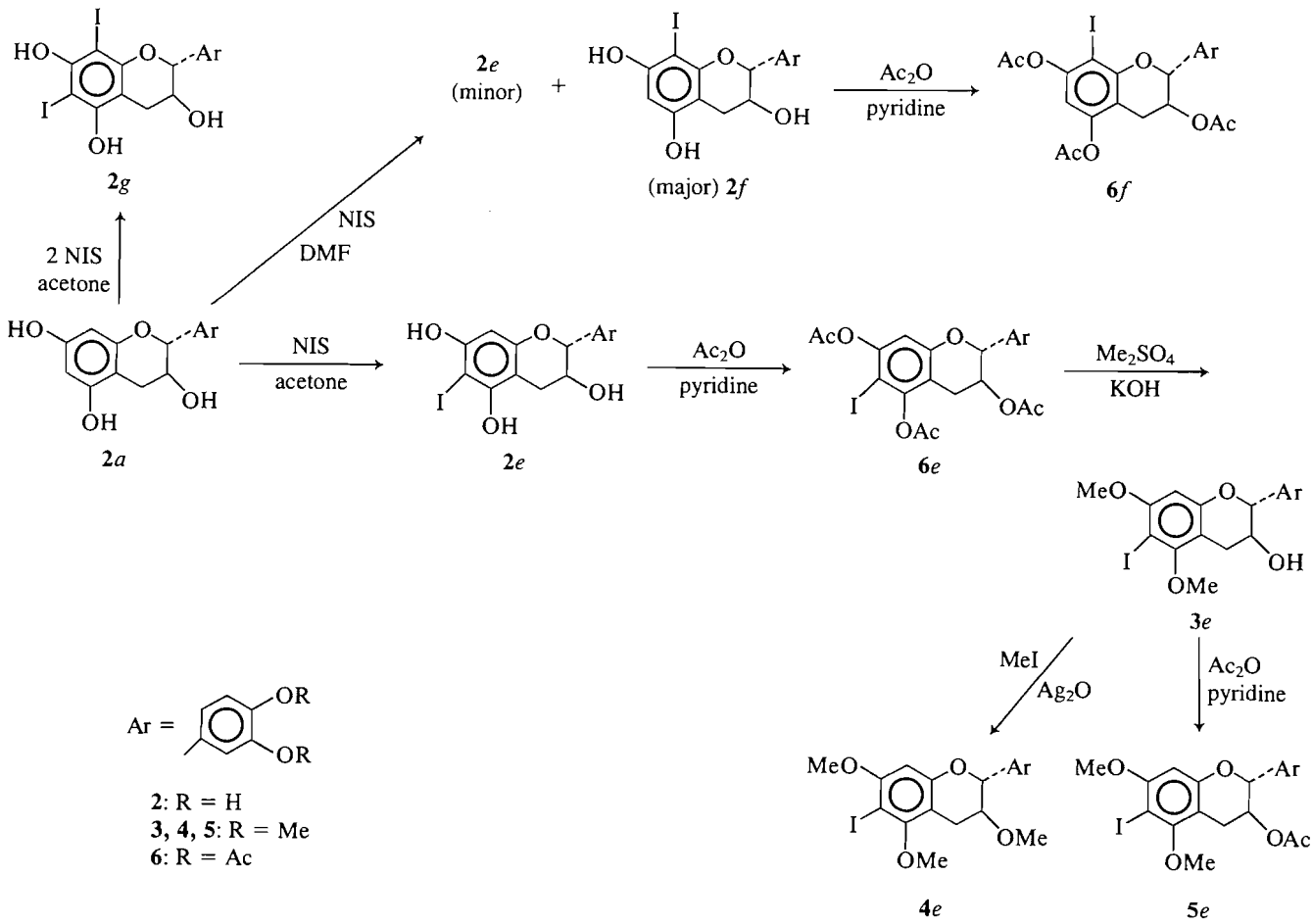

to isolate in pure form. Mixtures with the iodination by-product succinimide may be stored for several days in a desiccator with little decomposition but undergo slow deiodination (red colouration) on standing in acetone, more rapidly in the presence of acid (the most likely reason for the poor product yields obtained in the reaction of catechin with molecular iodine). A sample of **2***e* in acetone-d_6 was quantitatively converted to catechin 20 min after the addition of 2 μL concentrated HCl.

Since protodeiodination competes efficiently with (slow) interflavanoid coupling, the exclusive formation of the two diastereomeric [4,8]-fisetinidolcatechins observed by Roux must be attributed to the reaction of mollisacacidin with nonhalogenated catechin (preferential attack at C-8) rather than with 6-iodocatechin. The recovery of a large quantity of unsubstituted (+)-catechin, which cannot be explained by sequential substitution and deiodination at C-6, is indeed consistent with this interpretation. Clearly, Roux and co-workers also obtained 8- rather than 6-iodocatechin as major product of the initial halogenation step, as evidenced by the reported chemical shift of 6.24 ppm (our values: 6.25 ppm for **2***f*, 6.12 ppm for **2***e*). Therefore, the authors' claim of progress toward regiospecific synthesis of 4,8-coupled diflavanoids appears premature. We consider it a risky proposition to establish the point of substitution (by iodine) by reference to two subsequently formed interflavanoid coupling products (11) whose structures have never been unambiguously proved. The previously proposed criteria for the distinction between 6- and 8-substituted catechins are strictly limited to a few pairs of regioisomeric monoflavanoid methyl ethers (10). They do not apply to the corresponding free phenols (1), nor can they be indiscriminately extrapolated to diflavanoid derivatives without additional experimental structure proof.

The iodocatechin pentaacetates (**6***e* and **6***f*) are accessible only by acetylation of the respective free phenols (**2***e* and **2***f*) since catechin pentaacetate (**6***a*) is inert toward iodinating agents. However, it can be brominated to yield a 3:2 mixture of 6- and 8-bromocatechin pentaacetate (**6***c* and **6***d*) in quantitative yield (eq. [3]); no dibromination is observed even when more than two molar equivalents of *N*-bromosuccinimide are used.

[3]

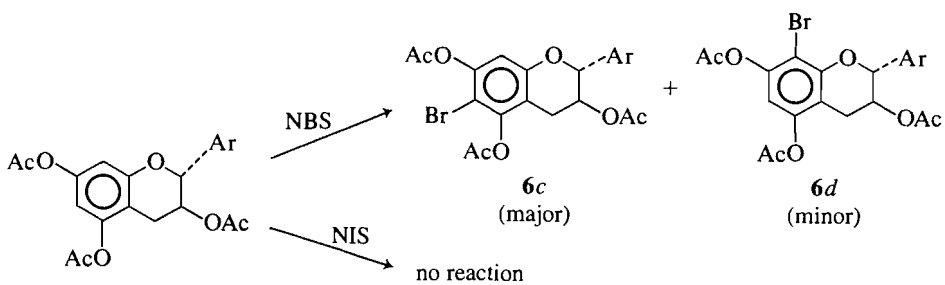

Can. J. Chem. Downloaded from www.nrcresearchpress.com by 112.217.228.212 on 09/07/12
For personal use only.

TABLE 2. Carbon chemical shifts: rings A and C[a,b]

Compound	3,3′,4′,5,7-Substituents	C-2	C-3	C-4	C-5	C-7	C-8a	C-4a	C-6	C-8	RO-3	RO-5	RO-7
6-Iodocatechin derivatives													
2e[c]	-(OH)$_5$	82.6	68.0	29.1	156.0	156.6	157.3	101.5	66.6	96.0			
3e	-(OMe)$_4$,3-OH	82.1	67.8	28.6	159.3	158.3	156.5	107.7	73.4	96.3		60.1	56.4
4e	-(OMe)$_5$	80.1	76.5	25.3	159.4	158.3	156.5	107.4	73.1	96.4	57.4	60.2	56.4
3e	-(OMe)$_4$,3-OAc	78.6	68.7	24.4	159.3	158.4	156.0	106.6	73.3	96.3	20.8/170.0	60.1	56.4
6e	-(OAc)$_5$	77.9	68.0	24.6	151.0	151.1	154.9	112.4	78.5	109.4	20.7/170.1	20.7/167.4	21.0/168.2
8-Iodocatechin derivatives													
2f[c]	-(OH)$_5$	83.1	68.1	27.9	157.6	156.7	155.2	101.7	96.0	63.7			
3f	-(OMe)$_4$,3-OH	81.8	67.9	26.9	159.2	158.4	153.7	102.6	88.8	65.9		55.6	56.5
4f	-(OMe)$_5$	79.4	76.5	23.8	159.1	158.4	153.7	102.7	88.9	66.2	57.1	55.5	56.6
5f	-(OMe)$_4$,3-OAc	78.1	68.6	22.8	159.0	158.3	153.0	101.8	88.7	65.9	21.0/170.4	55.4	56.4
6f	-(OAc)$_5$	78.5	68.1	23.6	149.9	150.9	153.7	110.6	109.9	78.7	20.8/170.2	20.5/168.0	21.0/168.3
6,8-Dihalocatechins													
2g[c]	-(OH)$_5$, 6,8-diI	83.3	67.7	28.8	156.4	155.0	155.4	102.5	66.3	64.7			
2h[c]	-(OH)$_5$, 6-Br,8-I	82.7	67.3	28.0	153.7	152.2	153.1	102.7	90.7	65.2			

[a]In ppm downfield from TMS in $CDCl_3$ (except **2e**, **2f**, **2g**, and **2h**).
[b]Ring B chemical shifts as reported in ref. 9.
[c]In acetone-d_6.

(X = H, Br or I) (Y = H or Br)

FIG. 1

In view of the aforementioned regiospecific 8-halogenation of catechin methyl ethers, the predominance of the 6-isomer (**6***c*) in the product mixture is at first surprising. However, an analysis of the most likely transition state geometries provides an explanation. Flavanyl ethers prefer to react at C-8 because this is the least crowded position in the crablike planar conformation A (Fig. 1), which permits maximum resonance stabilization of the initially formed cationic adduct and prevents electrophilic attack at C-6 for steric reasons. The alternate "paddle-wheel" conformation B should be less reactive, due to steric interference of the bulky methyl groups with the attacking electrophile, and is assumed to be the species leading to dibromination (Fig. 1, Y = Br). A large iodine atom at C-8 forces the 7-methyl carbon to rotate out of the ring plane; this relief of steric strain is accompanied by a loss of conjugative interaction between the oxygen lone pairs and the aromatic π-electrons that reduces the nucleophilicity of ring A sufficiently to prevent a second electrophilic substitution at C-6. In the preferred conformations of aryl acetates, on the other hand, the acetyl groups are oriented at 45–90°C angles relative to the ring plane (Fig. 1C), as shown by X-ray diffraction studies (12),[2] CNDO calculations (13), and dipole moment measurements (14). The oxygen lone pairs interact strongly with the electron-withdrawing carbonyl group instead of enhancing the reactivity of the *ortho* and *para* carbons (15). As a consequence, the weak electrophile iodine does not react at all, and bromination at C-6 is slightly favoured over C-8. van der Waals repulsion between AcO-7 and the first bromine leads to a reorientation of the bulky acetyl group toward the second nucleophilic centre, making the latter sterically inaccessible and thereby preventing dibromination.

This interpretation agrees with the results of our recent studies of stereoelectronic substituent effects on the carbon-13 chemical shifts of bromocatechin derivatives (9) and is confirmed by the ^{13}Cmr spectra of the corresponding iodo compounds (Table 2). The individual resonance lines were assigned as described for the bromo compounds. Except for the expected strong shielding of the ipso carbon (by 30.3 ± 1.1 ppm), the effect of iodination at C-6 or C-8 on the electron densities at the remaining ring A carbons is similar to that of bromination. This can be seen best by calculating the substituent chemical shifts (SCS) for transhalogenation (Table 3). The (hypothetical) replacement of bromine by iodine deshields the *ortho* (by 2.1–3.2 ppm) and *para* carbons (by 1.4–1.7 ppm) and shields (by 0.3–0.8 ppm) the *meta* carbons. The relatively large downfield shifts (by 3.1–3.2 ppm) measured for C-5 of **6***e* and C-7 of **6***f* are indicative of significant conformational changes of the

[2]A search of the CRYSTOR data base (CAN/SND, National Research Council of Canada, Ottawa) revealed 86 additional aryl acetate crystal structures (1935–1986) with a mean value of 75 ± 13° for the C—C—O—CO torsion angle.

TABLE 3. Transhalogenation[a] carbon-13 shift increments[b] for ring A (ppm)

Compound	5,7-Substituents	Halogenation position	C-4a	C-6	C-8	C-5	C-7	C-8a
2*e*[c]	-OH	6-I	−0.5	−24.4	−0.4	+2.8	+2.7	+1.7
3*e*, **4***e*, **5***e*[d]	-OMe	6-I	−0.3	−25.0	−0.5	+2.9	+2.3	+1.7
6*e*	-OAc	6-I	−0.4	−24.5	−0.3	+3.2	+3.1	+1.5
2*f*[c]	-OH	8-I	−0.5	−0.6	−25.6	+1.4	+2.6	+2.3
3*f*, **4***f*, **5***f*[d]	-OMe	8-I	−0.4	−0.5	−25.4	+1.6	+2.4	+2.1
6*f*	-OAc	8-I	−0.8	−0.3	−23.9	+1.6	+3.1	+2.4

[a] δ(C-I) − δ(C-Br) (see ref. 9).
[b] Positive (negative) values designate downfield (upfield) shifts.
[c] Solvent $CDCl_3$, except for **2***e* and **2***f* (acetone-d_6).
[d] Average of 3 values.

acetoxy group (rotation toward C-4 and C-6, respectively) resulting from steric interference with the adjacent iodine atom. The (hypothetical) isomerization of 6- to 8-iodo compounds is accompanied by the expected upfield shift of the C-8 signals (by 30.2–32.3 ppm), correspondingly large downfield shifts for C-6 of **2** (by 29.4 ppm) and **6** (31.4 ppm), and negligible changes in the absorption positions for C-5 and C-7, but unusually large upfield (by 4.7–5.1 ppm) and small downfield shifts (by 15.4–15.8 ppm) for C-4a and C-6, respectively, of the three methyl ethers (**3**, **4**, and **5**). When iodine is moved from C-6 to C-8, the relief of van der Waals strain at C-5 permits the 5-methoxy carbon to rotate into the ring plane, and the resulting interaction of the oxygen lone pairs with the aromatic π-electrons leads to shielding of the *ortho* carbons. Thus, as in the case of the bromo analogues, steric inhibition of resonance (which is insignificant in the free phenols and their acetates) explains the deshielding of the *meta* carbons and the exceptionally low shielding of the ipso carbon when iodine is introduced at C-6 of catechin methyl ethers (16). The same effect is observed for the 5-methoxy carbon of **3***e*, **4***e*, and **5***e*, which resonates at considerably lower field (60.1 ppm) than expected because the presence of two bulky *ortho* substituents (CH_2-4 and I-6) forces it to rotate out of coplanarity with the ring (17).

The absorption positions of the 5-methoxy protons, on the other hand, undergo little change on iodination (by −0.04 to +0.03 ppm) while the 7-methoxy proton signals shift significantly downfield when iodine is introduced at C-6 (by 0.06–0.07 ppm) or at C-8 (by 0.13–0.14 ppm). These trends parallel those observed previously (1) for bromocatechins and, in conjunction with nOe difference spectra, permit assignment of the methoxy peaks. The protons attached to the skeletal carbons of iodocatechins were generally found to resonate within ±0.03 ppm of the corresponding bromo compounds,[3] and 6-halogenation has again a larger deshielding effect on H-8 (by 0.19–0.20 ppm) than 8-halogenation on C-6 (by 0.03–0.04 ppm). The consistency of the ^{1}Hmr and ^{13}Cmr chemical shift values of the ten iodocatechin derivatives listed in Tables 1 and 2 and their more thoroughly studied bromo analogues (1) firmly establishes the point of halogen substitution in each molecule.

The unexpected regioselectivity of the reaction of catechin with NIS in different solvents suggested sequential iodination at C-6 (in acetone), bromination at C-8, and deiodination at C-6 as possible synthetic route to 8-bromocatechin. However, 6,8-dibromocatechin was formed as the major product of bromination of 6-iodocatechin with *N*-bromosuccinimide, together with minor quantities of iodobromo- and monohalocatechins. This result shows that iodine is weakly bonded to carbon, especially in dihalogenated molecules, and readily replaced by stronger electrophiles such as protons or bromonium ions. Only by recording a ^{13}Cmr spectrum within half an hour of sample preparation could we establish the presence of 8-iodo-6-bromocatechin (**2***h*), in addition to some unreacted starting material, in the crude reaction mixture obtained from 6-bromocatechin and NIS.

Our search for selective dehalogenation agents also led to a further investigation of the mechanism of debromination of bromocatechins by sodium sulfite (2). We reasoned that the replacement of Br-6 of 6-bromocatechin (**2***c*) by deuterium, monitored by ^{1}Hmr, should be accompanied by a shift of the H-8 resonance from 6.06 to 5.82 ppm (in CD_3CN) if dehalogenation is faster than hydrogen/deuterium exchange via keto/enol tautomerization. This would verify by chemical means the H-8 assignment in the ^{1}Hmr spectrum of catechin, which was previously determined by the enhancement of the aromatic ring A proton signals on gated decoupling of OH-5 and OH-7, respectively, in the presence of cadmium nitrate (1). In the event, the very slow replacement by deuterium of H-6 and H-8 of catechin in CD_3CN/D_2O (pH ~ 6) was speeded up by sodium sulfite (pH ~ 7.5), but during the debromination of **2***c* the ^{1}Hmr signals for *both* protons (δ 5.92 and 5.82 ppm) appeared simultaneously (equal intensities) before gradually fading away. When the amount of sulfite is insufficient for complete monodebromination of 6,8-dibromocatechin (**2***b*), i.e., less than two molar equivalents, dehalogenation stops as the pH drops below 7 (due to the formation of $NaHSO_4$), and the composition of the product mixture shows that the ease of bromine removal decreases in the order 8-Br of **2***b* > Br of **2***c* ≫ 6-Br of **2***b*; no 8-bromocatechin is formed but the initially produced 6-bromocatechin (**2***c*) is partially converted to catechin before the starting material has been completely 8-debrominated. Fortunately, the extent of catechin formation can be minimized by running the reaction at low temperature (2). Thus, H/D-exchange is accelerated by base, and complete H-6/H-8 scrambling accompanies rapid debromination. Similar results have been obtained for other polyhydric phenols: Furlong and Nudelman (6) investigated the rates of base-catalyzed deuteration of resorcinol and phloroglucinol at C-2, C-4, and C-6 (H-5 of resorcinol is not exchanged) in D_2O/MeOD; Äryä and Widén (19) attributed the slow disappearance of the C-5 signal

[3] In ref. 1 (Table 2), the chemical shifts for H-5′ and H-6′ of **5***d* in $CDCl_3$ were inadvertently exchanged; the correct assignments are δ 6.805 (H-5′) and 6.858 ppm (H-6′).

Can. J. Chem. Downloaded from www.nrcresearchpress.com by 112.217.228.212 on 09/07/12
For personal use only.

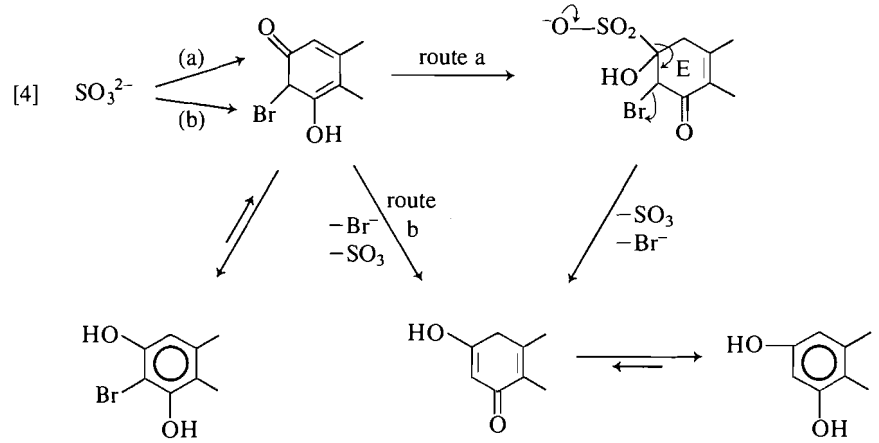

in the ^{13}Cmr spectrum of 2,4,6-trihydroxy-3-methylbutyrophenone in acetone-d_6/D_2O to H/D-exchange; Davis and Harrington (4) described the debromination of 2,4,6-tribromoresorcinol with sulfite in basic solution; and we have confirmed the replacement of H-2 (but not H-5) by deuterium when sodium carbonate is added to a solution of 4,6-dibromoresorcinol in acetone-d_6/D_2O.

In all cases, including a recent kinetic study of the epimerization of catechin (20), ketone structures have been invoked as intermediates. We conclude from these results that the reactive species is an α-bromoketone ("ketobromide", cf. refs. 4 and 21) that, for its formation in significant concentration, requires the presence of two *meta*-oriented OH groups on the aromatic ring. (In contrast to 4,6-dibromoresorcinol, 4,6-dibromo-3-methoxyphenol does not react with sodium sulfite.) Nucleophilic attack by sulfite at the carbonyl carbon yields an α-hydroxysulfonate that undergoes oxidation at sulfur and halide elimination at the α-carbon (eq. [4], route a). Alternatively, the product may be formed in a single step by nucleophilic displacement at halogen (route b). Analogous mechanisms have been proposed for the dehalogenation of 4-bromo-3-arylsydnones (22) and of α-haloketones (23) with sodium dithionite. In view of the isolation and characterization of several sulfite addition products to resorcinols and phloroglucinols in the past (24, 25, 33), we favour route a: Rapid intramolecular proton transfer from C-8 to C-6 (and vice versa) via the hydroxysulfonate function at C-7 (eq. [4], structure E) may be responsible for the observed scrambling of the aromatic ring A protons.

The reactivity differences exhibited by C-6 and C-8 of catechin toward halogen electrophiles and the slow H/D-exchange observed in neutral and acidic medium suggested the possibility of regioselective deuteration by recrystallization of catechin hydrate from heavy water. Integration of the ^{1}Hmr spectrum of a catechin sample kept for 2 h in D_2O solution at 90°C revealed the presence of 20% 8-deutero- (H-6 singlet at 6.01 ppm), 10% 6-deutero- (H-8 singlet at 5.86 ppm), 50% 6,8-dideuterocatechin, and 20% unreacted (protonated) starting material, i.e., preferred substitution at C-8. None of the B-ring aromatic protons had been replaced by deuterium, and exchange of the OH protons was incomplete. H-6 and H-8, whose chemical shifts have been previously identified by nOe difference spectroscopy (see before), could now be distinguished by their different peak areas. The invariance of the H-6 and H-8 peak area ratio (4:3) on conversion of the partially deuterated catechin to its tetramethyl ether **3***a* (H-6 at 6.12, H-8 at 6.03 ppm, solvent acetone-d_6) via the pentaacetate (**6***a*) intermediate (H-6 at 6.55, H-8 at 6.65 ppm, solvent CD_3CN) confirms that in the acetate, contrary to free catechin and its tetramethyl ether, H-6 resonates upfield from H-8 (1, 26). More importantly, it demonstrates that neither the acetylation with acetic anhydride and pyridine nor the reaction of **6***a* with dimethyl sulfate and 50% aqueous potassium hydroxide in methanol is accompanied by H/D-exchange at C-6 or C-8. It appears that the ester transmethylation in strongly alkaline medium involves nucleophilic aromatic substitution rather than sequential ester hydrolysis and etherification by phenoxide attack at the methyl carbon (27). Further studies of this mechanism are currently in progress.

In summary, the regioselectivity of electrophilic aromatic substitution in ring A of catechin depends strongly on the medium: both 6- and 8-iodocatechin (also 6,8-diiodocatechin) are accessible by direct iodination with *N*-iodosuccinimide but undergo protodeiodination in neutral or weakly acidic solution. The large size and low electrophilicity of iodine prevent iodination of tetra-*O*-methyl-8-iodocatechin at C-6 and of catechin pentaacetate. Catechin slowly exchanges H-6 and H-8 in heavy water (pH 6) but not during acetylation and methylation in alkaline medium.

Experimental

The ^{1}Hmr spectra of 0.02–0.04 M substrate solutions in acetone-d_6 (free phenols) or chloroform-*d* were recorded on a Bruker 400-MH FT spectrometer (unless specified otherwise) at a probe temperature of 30°C, ^{13}Cmr spectra of 0.3–0.7 M solutions at 21°C. Chemical shifts are reported in ppm downfield from TMS. Samples for nOe difference spectra were degassed immediately prior to the experiment. Melting points (uncorrected) were determined on a Fisher–Johns apparatus, elemental analyses with a Carlo Erba elemental analyzer model 1106. Anhydrous catechin (**2***a*) was obtained by drying commercial catechin hydrate (Sigma) under vacuum (12 h at 110°C) and converted to 6-bromocatechin (**2***c*) and 6,8-dibromocatechin (**2***b*) as previously described (2). Standard literature procedures were followed to derivatize the halogenated catechins:

(a) Acetylation (**2** → **6**, **3** → **5**, ref. 28): The free phenol or its tetramethyl ether (70–100 mg) is dissolved in a mixture of 0.5 mL acetic anhydride and 0.3 mL pyridine, allowed to stand at 25°C for 24 h, pipetted into 5 mL ice water, and refrigerated for 12 h. The product is isolated and purified by filtration, recrystallization from ethanol, and vacuum drying (P_2O_5).

(b) Acetate transmethylation (**6** → **3**, ref. 29): Three millilitres of 50% aqueous potassium hydroxide are added dropwise to a solution of the pentaacetate (1 mmol) in 3 mL methanol and 1 mL dimethyl sulfate. After brief boiling, the mixture is poured into ice water, and the product

Can. J. Chem. Downloaded from www.nrcresearchpress.com by 112.217.228.212 on 09/07/12
For personal use only.

Can. J. Chem. Downloaded from www.nrcresearchpress.com by 112.217.228.212 on 09/07/12
For personal use only.

is filtered, washed free of alkali, and vacuum dried. Preparative tlc (benzene/acetone 4:1) and recrystallization from ethanol gives the pure tetramethyl ether.

(c) Exhaustive methylation (**3** → **4**, ref. 30): To a magnetically stirred solution of the tetramethyl ether (0.2 mmol) in dry dimethylformamide (1.0 mL) are added silver oxide (150 mg) and methyl iodide (0.44 mL, added in 5 portions over a period of 4 days). After 5 days, the mixture is poured into water (50 mL) and extracted with chloroform (5 × 25 mL). The pentamethyl ether is obtained by solvent evaporation and vacuum drying (P_2O_5).

*8-Iodo-3′,4′,5,7-tetra-*O*-methylcatechin (**3**f)*

N-Iodosuccinimide (225 mg, 1.00 mmol) in 3 mL dimethylformamide (DMF) was added dropwise to a stirred solution of 3′,4′,5,7-tetra-*O*-methylcatechin (**3***a*) (348 mg, 1.00 mol) in 4 mL DMF (70 min). Filtration of the beige precipitate formed on pouring the reaction mixture into ice water (50 mL) and recrystallization (95% ethanol) gave **3***f* (63% yield), mp 173–175°C (lit. (8) mp 192–193°C (dec.); sinters and turns brown at 160°C). The nmr spectral parameters (Tables 1 and 2) are identical to those of the products formed (*i*) from **3***a* and 2 mol. equivs. NIS (quant. yield), and (*ii*) from **3***a* and molecular iodine (with trace of iodic acid) in ethanol (according to ref. 8); no 6,8-diiodo-3′,4′,5,7-tetra-*O*-methylcatechin was detected in either experiment. *Anal.* calcd. for $C_{15}H_{21}IO_6$: C 48.32, H 4.48; found: C 48.61, H 4.54%.

*8-Iodo-3-*O*-acetyl-3′,4′,5,7-tetra-*O*-methylcatechin (**5**f)*

Acetylation of **3***f* (procedure a) gives **5***f* (92% yield), mp 193–195°C (lit. (8) mp 189°C); ^{1}Hmr (nOe difference): saturation at 6.13 ppm (H-6) enhances signals at 3.80 (MeO-5) and 3.90 ppm (MeO-7). *Anal.* calcd. for $C_{21}H_{23}IO_7$: C 49.04, H 4.51; found: C 48.65, H 4.24%.

*8-Iodo-3,3′,4′,5,7-penta-*O*-methylcatechin (**4**f)*

From **3***f* by exhaustive methylation (procedure c) in 91% yield, mp 159–160°C (dec.). *Anal.* calcd. for $C_{20}H_{23}IO_6$: C 49.40, H 4.77; found: C 49.45, H 4.74%.

*Iodination of catechin (**2**a)*

(i) In acetone

Dropwise addition (10 min) of NIS (225 mg, 1.00 mmol) in 6 mL reagent acetone to a solution of catechin (290 mg, 1.00 mmol) in 10 mL acetone at 25°C, continued stirring (1 h), and solvent evaporation gave a fluffy beige solid that was shown by ^{1}Hmr to consist of 6-iodocatechin (**2***e*, >95%, H-8 at 6.12 ppm), 8-iodocatechin (**2***f*, <5%, H-6 at 6.25 ppm), succinimide (CH_2 at 2.67 ppm), and a trace of catechin. After 2 weeks of storage at 4°C, an ^{1}Hmr sample in acetone-d_6 had turned red-brown and contained approximately 5 mol% catechin. The addition of acid accelerated deiodination (acid/time/catechin percentage): 2 μL CF_3COOH/18 h/40%, 2 μL conc. HCl/15 min/90%, 14 μL 0.1 N HCl/24 h/25%.

(ii) In dimethylformamide

A solution of NIS (225 mg, 1.00 mmol) in 3 mL dry DMF was added dropwise (7 min) to a stirred solution of dry catechin (290 mg, 1.00 mmol) in 4 mL DMF. After 1 h of continued stirring at 25°C, the mixture was poured into 80 mL carbon tetrachloride and the layers were allowed to separate (12 h). Drainage of the CCl_4 layer and suspension of the remaining red oil in dichloromethane gave a beige solid that, after vacuum drying (P_2O_5), weighed 168 mg and contained (by ^{1}Hmr) 75% 8-iodocatechin (**2***f*), 15% 6-iodocatechin (**2***e*), 10% catechin (**2***a*), and traces of DMF and succinimide. Chromatographic separation of the iodocatechins from catechin was attempted but unsuccessful. When the *N*-iodosuccinimide was dissolved in acetone (rather than DMF), the acetone evaporated under nitrogen before work-up with CCl_4 and CH_2Cl_2, and the crude product immediately acetylated (procedure a), the molar ratio of the three pentaacetates **6***f*, **6***e*, and **6***a* (94% overall yield) was found to be 6:1:2 by integration of the ^{1}Hmr spectrum.

*6,8-Diiodocatechin (**2**g)*

The iodination of catechin (124 mg, 0.43 mmol) with 2 molar equivs. NIS in acetone (see above, procedure *i*), solvent evaporation under nitrogen, and vacuum drying (KOH) gave 316 mg of a brown solid containing **2***g* and catechin in the approximate molar ratio 13:1. The product underwent slow deiodination in acetone solution (^{1}Hmr sample), which was accelerated by the addition of CF_3COOH (**2***g*/**2***a* ratio 1:1 after 91 h); ^{1}Hmr of **2***g* (red solution in acetone-d_6) δ: 6.86 (H-2′), 6.74–6.77 (H-5′ and H-6′), 4.88 (d, *J* 6.5 Hz, H-2), 4.10 (m, H-3), and 2.88 (dd, *J* 5.3 and 16.2 Hz, H-4a) ppm.

*6-Bromo-8-iodocatechin (**2**h)*

The iodination of 6-bromocatechin (**2***c*, 0.5 mmol, ref. 2) with NIS (0.5 mmol) in acetone (see above, procedure *i*) gave 294 mg of a reddish-brown product containing **2***h* and **2***c* in the appropriate molar ratio 7:2 (by ^{1}Hmr).

*6-Iodocatechin pentaacetate (**6**e)*

Acetylation (procedure a) of the crude product of iodination of catechin (0.50 mmol) in acetone (>95% **2***e*) gave **6***e* (90% yield), mp 90–92°C (from 50% ethanol). *Anal.* calcd. for $C_{25}H_{23}IO_{11}$: C 47.94, H 3.70; found: C 47.79, H 3.75%.

*3′,4′,5,7-Tetra- and 3,3′,4′,5,7-penta-*O*-methyl-6-iodocatechin (**3**e and **4**e)*

Transmethylation (procedure b) of **6***e* (0.45 mmol) gave 93 mg (44% yield) of a yellow powder, which was subjected to preparative tlc (benzene/acetone 4:1): **3***e* (R_f 0.44, 74 mg), mp 129.5–130.5°C (from 95% EtOH), and **4***e* (R_f 0.64, 13 mg). *Anal.* calcd. for $C_{19}H_{21}IO_6$ (**3***e*): C 48.32, H 4.48; found: C 48.35, H 4.45%; calcd. for $C_{20}H_{23}IO_6$ (**4***e*): C 49.40, H 4.77; found: C 49.44, H 4.42%.

*6-Iodo-3-*O*-acetyl-3′,4′,5,7-tetra-*O*-methylcatechin (**5**e)*

Acetylation (procedure a) of **3***e* (0.14 mmol) gave **5***e* (83% yield), mp 64–71°C (after preparative tlc, benzene/acetone 9:1); ^{1}Hmr (nOe difference): saturation at 6.37 ppm (H-8) enhances the signal at 3.88 ppm (MeO-7). *Anal.* calcd. for $C_{21}H_{23}IO_7$: C 49.04, H 4.51; found: C 49.14, H 4.65%. Previously reported analytical data (7) are incorrect and apply to **2***e* ($C_{15}H_{13}IO_6$).

*8-Iodocatechin pentaacetate (**6**f)*

Acetylation (procedure a) of the crude product of iodination of catechin in DMF (see above, procedure *ii*) gave a beige solid, which was separated by preparative tlc (toluene/ethyl acetate 7:3) into two fractions: R_f 0.55 (**6***e*) and R_f 0.48 (**6***f* and **6***a*). Pure **6***f* was obtained from the latter by recrystallization from ethanol and aqueous methanol, mp 114–116°C. *Anal.* calcd. for $C_{25}H_{23}IO_{11}$: C 47.94, H 3.70; found: C 47.91, H 4.08%.

*Bromination of catechin pentaacetate (**6**a)*

A solution of catechin pentaacetate (500 mg, 1.00 mmol) and *N*-bromosuccinimide (356 mg, 2.00 mmol) in 7 mL DMF was magnetically stirred for 16 h, then poured into 40 mL water and filtered. The white precipitate was washed with water and vacuum dried (P_2O_5) to give 515 mg (89% yield) of a mixture (H-8/H-6 ^{1}Hmr peak area ratio 3:2) of 6-bromo- and 8-bromocatechin pentaacetate (**6***c* and **6***d*; see refs. 1 and 9 for nmr data) from which small samples of the pure components were obtained by fractional crystallization from ether (**6***c* is less soluble), and by repeated preparative tlc (poor separation) using toluene and ethyl acetate (7:3). No 6,8-dibromocatechin pentaacetate was detected by tlc or nmr. Repetition of the experiment with one molar equivalent NBS gave the same mixture in 80% yield, and ^{1}Hmr monitoring showed that the ratio of **6***c*/**6***d* does not change as a function of time.

*Debromination of 6-bromocatechin (**2**c) and 6,8-dibromocatechin (**2**b) in CD_3CN/D_2O*

The ^{1}Hmr spectra of catechin (**2***a*), 6-bromocatechin, and 6,8-dibromocatechin were recorded on an XL-100 spectrometer (CW mode) before and at various time intervals after the addition of sodium sulfite. Because of the limited miscibility of acetonitrile-d_3 and heavy water at the required substrate concentration levels, a rigorous kinetic study was not feasible. However, the observed variations in the relative

Can. J. Chem. Downloaded from www.nrcresearchpress.com by 112.217.228.212 on 09/07/12
For personal use only.

peak areas of the H-2 (ring C, δ 4.5–4.6 ppm), H-6/8 (ring A, δ 5.8–6.1 ppm), and H-2′/5′/6′ (ring B, δ 6.7–6.8 ppm) signals, designated below by the capital letters C, A, and B, gave a good indication of the reaction progress. Catechin (75 mg, 0.26 mmol) was dissolved in a mixture of 0.5 mL CD_3CN and 0.5 mL D_2O. After 16 h at 25°C the A:B:C ratio was essentially the same (2:3:1) as at time zero (no exchange). Forty minutes after the addition of 0.1 mL 2.2 M Na_2SO_3 in D_2O and vigorous shaking (several minutes) of the resultant two-phase system, the top layer was withdrawn by pipette and analyzed by ^{1}Hmr: the A/C ratio had decreased to one third of its original value, and 4 h later the H-6/8 signals had completely vanished.

Starting from a solution of 0.22 mmol 6-bromocatechin (**2***c*) in 0.4 mL CD_3CN and 0.2 mL D_2O (A/C ratio 1:1), the reaction with 0.1 mL 5 M Na_2SO_3 (excess) led initially (when the H-2 peak areas indicated debromination of one third of the starting material) to the appearance of both the H-6 and the H-8 doublet of catechin at the expense of H-8 of **2***c*, and after additional shaking (debromination half-complete) to their disappearance due to H/D-exchange. In the second series of experiments, a solution of **2***c* (92 mg, 0.25 mmol) in 0.6 mL CD_3CN and 0.2 mL D_2O was vigorously shaken with 0.1 mL 1.6 M Na_2SO_3, and the top layer analyzed by ^{1}Hmr (time: 6 min). Additional spectra of the top layer were recorded after recombination of the layers and continued shaking (times: 25, 44, and 61 min). A second portion of 0.1 mL 1.6 M Na_2SO_3 was added before the final analysis (time: 81 min). As the amount of sulfite was insufficient for complete debromination (0.25 mmol **2***c* requires 0.50 mmol Na_2SO_3), only one third of the organic substrate was initially converted to catechin: H-2 (**2***c*)/H-2 (**2***a*) peak area ratios 5:1 (6 min), 3:1 (25 min), 2:1 (44 min), and 2:1 (61 min). Relative to H-2, the area of the H-8 peak of **2***c* decreased from 0.75 to 0.50 over the same period, while the H-6/8 (**2***a*):H-8 (**2***c*) ratio increased substantially from 1:3 (6 min) to 1:1 (61 min), and finally to 2:1 after 81 min (rapid debromination). Twenty minutes after addition of the second sulfite portion, the reaction mixture contained equal amounts of **2***a* and **2***c* (equal H-2 areas), but the total aromatic ring A proton area was only half as large as would be expected in the absence of H/D-exchange.

Treatment of a solution of 6,8-dibromocatechin (**2***b*, 112 mg, 0.25 mmol) in 0.6 mL CD_3CN and 0.2 mL D_2O with sodium sulfite and monitoring by ^{1}Hmr (as described above for **2***c*, second series) gave the following results (mmol Na_2SO_3, time, product composition): 0.19 mmol, 6 min, 75% **2***b*/25% **2***c*; 0.38 mmol, 24 min, 50% **2***b*/50% **2***c*; 0.38 mmol, 84 min, 30% **2***b*/45% **2***c*/25% **2***a*; 0.57 mmol, 136 min, 25% **2***b*/40% **2***c*/35% **2***a*.

Debromination and deuteration of 4,6-dibromoresorcinol

To a stirred solution of 5.36 g (20.0 mmol) 4,6-dibromoresorcinol (31) in 20 mL methanol and 40 mL water were added 40 mL 1 M Na_2SO_3 during the first 15 min and 10 mL 1 N NaOH after 6.5 h. After 21 h the reaction mixture was acidified to pH 3 with 10% HCl, the methanol evaporated, and the aqueous solution extracted with ether (6 × 60 mL). The white powder (2.34 g, 62% yield) obtained after drying ($MgSO_4$), solvent evaporation, and recrystallization from benzene was washed with ice water (5 × 5 mL) and vacuum dried to give pure 4-bromoresorcinol, mp 97–100°C (lit. (32) mp 100–102°C); ^{1}Hmr (acetone-d_6) δ: 8.64 (OH), 7.24 (d, *J* 8.6 Hz, H-5), 6.52 (d, *J* 2.7 Hz, H-2), and 6.31 (dd, H-6) ppm; ^{13}Cmr (acetone-d_6) δ: 157.8 (C-1), 154.8 (C-3), 133.5 (C-5), 108.9 (C-6), 104.0 (C-2), and 99.4 (C-4) ppm. When 4,6-dibromoresorcinol was treated with 2 molar equivs. Na_2SO_3 and 2 molar equivs. NaOH under similar conditions, the product mixture was found (by ^{1}Hmr) to contain 52 mol% 4-bromoresorcinol, 24% resorcinol, and 12% unreacted starting material. A solution of 50 mg 4,6-dibromoresorcinol in 0.5 mL acetone-d_6 and 0.3 mL D_2O showed no evidence of ring deuteration (equal ^{1}Hmr peak areas for H-2 and H-5) over a period of 7 weeks. On addition of 5 mg K_2CO_3, H/D-exchange at C-2 started within 15 min and was 90% complete after 54 h (50% after 24 h) as measured by the decrease in the H-2 peak area relative to H-5.

Attempted debromination of 4,6-dibromo-3-methoxyphenol

A solution of 4,6-dibromo-3-methoxyphenol (282 mg, 1.00 mmol), prepared by bromination of 3-methoxyphenol as described in the literature (18), in 40 mL 50% aqueous methanol was treated with 2 mL 1 M Na_2SO_3 and 2 mL 1 N NaOH and stirred for 9 h at 25°C (pH 10–11). Acidification (10% HCl), flash evaporation of the methanol, extraction with ether (4 × 20 mL), drying ($MgSO_4$), and ether evaporation gave an oily residue (235 mg) that solidified on standing and was shown to be identical to the starting material; ^{1}Hmr (acetone-d_6) δ: 7.59 (H-5), 6.74 (H-2), and 3.82 (OMe) ppm; ^{13}Cmr (acetone-d_6) δ: 157.2 (C-3), 155.3 (C-1), 136.0 (C-5), 101.9 (C-2), 101.7 (C-4), 100.9 (C-6), and 56.8 (OMe) ppm. Refluxing the reagent mixture for 24 h, or doubling the amounts of Na_2SO_3 and NaOH, or omitting the NaOH addition (pH 7.5–8) had little effect: in all cases, 82–85% of the starting material was recovered.

Preparation of partially deuterated catechin and its derivatives

Catechin hydrate (1.54 g, 4.25 mmol) was dissolved in 12 mL hot D_2O. After 2 h at 90°C, the solution was cooled to 20°C and the white crystals were filtered and vacuum dried (110°C/5 h, P_2O_5) to give 1.17 g partially deuterated catechin. The product composition was determined by integration of the ^{1}Hmr spectrum (acetone-d_6 with trace of cadmium nitrate): the measured peak area ratio of 22:6.5:9:66 for H-2 (δ 4.54 ppm):H-8 (δ 5.86 ppm):H-6 (δ 6.01 ppm):H-2′/5′/6′ (δ 6.73–6.89 ppm) corresponds to approximately 10% 6-deutero-, 20% 8-deutero-, 50% dideuterocatechin, and 20% unreacted starting material. The integral of the OH signals (OH-5 at 8.28, OH-7 at 8.09, OH-3′/4′ at 7.99 and 7.93 ppm) indicated incomplete deuterium exchange (42%). Acetylation (procedure a) of this product gave partially deuterated catechin pentaacetate (81% yield) with the relative intensities of the downfield (H-8: 6.65 ppm in $CDCl_3$ and CD_3CN, 6.67 ppm in acetone-d_6) and upfield (H-6: 6.59 ppm in $CDCl_3$, 6.56 ppm in CD_3CN, 6.60 ppm in acetone-d_6) ^{1}Hmr signals for the aromatic ring A protons in the ratio 3:4. In all three solvents the singlets caused by the two monodeuterated compounds were found to overlap the upfield components of the H-6 and H-8 doublets of nondeuterated catechin. Transmethylation (procedure b) of this pentaacetate mixture (67% deuterated at C-6 and C-8) gave a mixture of 3′,4′,5,7-tetra- and 3,3′,4′,5,7-penta-*O*-methylcatechin (molar ratio 11:1) in 91% overall yield, which was 68% deuterated in ring A (H-6/8:H-2 peak area ratio 20:31), and contained more 8- than 6-deuterated product (intensity ratio of 25:19 for the H-6 and H-8 ^{1}Hmr signals at δ 6.12 and 6.03 ppm, respectively, in acetone-d_6).

Acknowledgements

We wish to thank T. Starr, R. Lauener, and C. Schafmeister for technical assistance, and the Natural Sciences and Engineering Research Council of Canada for financial support.

1. E. Kiehlmann and A. S. Tracey. Can. J. Chem. **64**, 1998 (1986).
2. E. Kiehlmann, P. J. van der Merwe, and H. K. L. Hundt. Org. Prep. Proced. Int. **15**, 341 (1983).
3. V. Calo and L. Lopez. J. Chem. Soc. Perkin Trans. 2, 1189 (1974).
4. T. L. Davis and V. F. Harrington. J. Am. Chem. Soc. **56**, 129 (1934).
5. J. M. Brittain, P. B. D. de la Mare, and P. A. Newman. J. Chem. Soc. Perkin Trans. 2, 32 (1981).
6. J. J. P. Furlong and N. S. Nudelman. Acta Sud Am. Quim. **3**, 129 (1983).
7. D. A. Young, A. Cronjé, A. L. Botes, D. Ferreira, and D. G. Roux. J. Chem. Soc. Perkin Trans. 1, 2521 (1985).
8. St. v. Kostanecki and V. Lampe. Chem. Ber. **40**, 4910 (1907).
9. E. Kiehlmann and A. S. Tracey. Magn. Reson. Chem. **26**, 204 (1988).
10. H. K. L. Hundt and D. G. Roux. J. Chem. Soc. Perkin Trans. 1, 1227 (1981).
11. J. J. Botha, D. Ferreira, and D. G. Roux. J. Chem. Soc. Perkin Trans. 1, 1235 (1981); p. 1213 incorrectly cited in ref. 7.
12. F. R. Fronczek, G. Gannuch, W. Mattice, R. W. Heming-

WAY, G. CHIARI, F. L. TOBIASON, K. HOUGLUM, and A. SHANAFELT. J. Chem. Soc. Perkin Trans. 2, 1383 (1985).
13. R. J. ABRAHAM, G. H. BARNETT, G. E. HAWKES, and K. M. SMITH. Tetrahedron, **32**, 2949 (1976).
14. B. A. ARBUZOV, A. P. TIMOSHEVA, S. G. VULFSON, and A. N. VERESHCHAGIN. Izv. Akad. Nauk SSSR, Ser. Khim. 1336 (1977); Engl. transl. p. 1234.
15. (*a*) C. G. SWAIN and E. C. LUPTON, JR. J. Am. Chem. Soc. **90**, 4328 (1968); (*b*) C. G. SWAIN, S. H. UNGER, N. R. ROSENQUIST, and M. S. SWAIN. J. Am. Chem. Soc. **105**, 492 (1983).
16. K. S. DHAMI and J. B. STOTHERS. Can. J. Chem. **44**, 2855 (1966).
17. J. N. ROITMAN and L. F. JAMES. Phytochemistry, **24**, 835 (1985).
18. M. KOHN. J. Am. Chem. Soc. **74**, 1601 (1952).
19. P. ÄRYÄ and C.-J. WIDÉN. Planta Med. **34**, 144 (1978).
20. P. KIATGRAJAI, J. D. WELLONS, L. GOLLOB, and J. D. WHITE. J. Org. Chem. **47**, 2910 (1982).
21. R. H. DE ROSSI and A. V. VEGLIA. Tetrahedron Lett. **27**, 5963 (1986).
22. K. TURNBULL and M. SALJOUGHIAN. Synth. Commun. **16**, 461 (1986).
23. S.-K. CHUNG and Q.-Y. HU. Synth. Commun. **12**, 261 (1982).
24. G. M. KHEIFETS. Zh. Org. Khim. **15**, 1763 (1979); Engl. transl. p. 1583.
25. (*a*) H. TH. BUCHERER and E. HOFFMANN. J. Prakt. Chem. [2], **229**, 113 (1929); (*b*) W. M. LAUER and C. M. LANGKAMMERER. J. Am. Chem. Soc. **56**, 1628 (1934); (*c*) J. PODSTATA, D. SNOBL, and Z. J. ALLAN. Collect. Czech. Chem. Commun. **31**, 3563 (1966).
26. L. Y. FOO and L. J. PORTER. J. Chem. Soc. Perkin Trans. 1, 1535 (1983).
27. R. SANCHE-OBREGON, G. HURTADO, H. BARRIOS, B. ORTIZ, and F. YUSTE. Org. Prep. Proced. Int. **18**, 145 (1986).
28. K. FREUDENBERG and L. PURRMANN. Liebigs Ann. Chem. **437**, 274 (1924).
29. K. FREUDENBERG. Liebigs Ann. Chem. **433**, 230 (1923).
30. T. PURDIE and J. C. IRVINE. J. Chem. Soc. **83**, 1021 (1903).
31. J. ZEHENTER. Monatsh. Chem. **8**, 293 (1887).
32. R. B. SANDIN and R. A. MCKEE. Org. Synth. Coll. Vol. II, 100 (1943).
33. R. J. HIGHET and I. V. EKHATO. J. Org. Chem. **53**, 2843 (1988).

Can. J. Chem. Downloaded from www.nrcresearchpress.com by 112.217.228.212 on 09/07/12
For personal use only.

The solvent deuterium isotope effect on the hydroxide-ion-catalyzed conversion of acetaldehyde to its enolate ion

J. R. KEEFFE[1] AND A. J. KRESGE

Department of Chemistry, University of Toronto, Toronto, Ont., Canada M5S 1A1

Received March 2, 1988

J. R. KEEFFE and A. J. KRESGE. Can. J. Chem. **66**, 2440 (1988).

Rates of proton transfer from acetaldehyde to the hydroxide ion were measured by iodine scavenging in H_2O and in D_2O solution at 25°C; the results give the solvent isotope effect $k_{HO^-}/k_{DO^-} = 0.73 \pm 0.02$. This value is somewhat more consistent with an estimate, made using fractionation factor theory, for hydron transfer directly from the substrate to the hydroxide ion than with another estimate, made similarly, for hydron transfer through an intervening water molecule.

J. R. KEEFFE et A. J. KRESGE. Can. J. Chem. **66**, 2440 (1988).

On a mesuré les vitesses de transfert du proton de l'acétaldéhyde à l'ion hydroxyde en utilisant l'iode comme piège dans l'eau et dans une solution de D_2O à 25°C. On obtient dans ces conditions un effet isotopique du solvant de $k_{HO^-}/k_{DO^-} = 0{,}73 \pm 0{,}02$. Cette valeur se rapproche davantage de l'évaluation faite, selon la théorie du facteur de fractionnement, pour le transfert direct de l'hydron du substrat vers l'ion hydroxyde, que d'une autre évaluation faite de la même façon, pour le transfert de l'hydron via la participation d'une molécule d'eau.

[Traduit par la revue]

Can. J. Chem. Downloaded from www.nrcresearchpress.com by 196.1.178.254 on 09/07/12
For personal use only.

There is much current interest in simple enols (for reviews, see ref. 1) and, in our recent examination of some of the chemistry of the simplest enol of all, vinyl alcohol, we determined the solvent deuterium isotope effect on the hydronium-ion-catalyzed formation of this substance from acetaldehyde, eq. [1] (2). We now wish to report the results of a companion

[1] 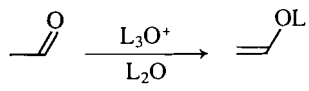

study, which provides the solvent isotope effect on the reaction of acetaldehyde with hydroxide ion to give the enolate ion, eq. [2].

[2] 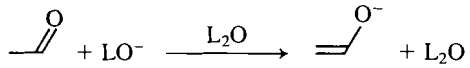

Experimental

Rates of reaction of acetaldehyde with hydroxide ion were measured as before (2) by using iodine to scavenge the enolate ion product as it formed. Initial stoichiometric aldehyde and iodine concentrations in the reaction mixtures were ca. 2×10^{-4} M and 1×10^{-3} M respectively. Reactions were followed to completion; the data obeyed the first-order rate law well, and observed first-order rate constants were calculated by least-squares fitting to an exponential function (3). Hydroxide ion concentrations were determined by acidimetric titration of spent reaction solutions.

Results

Acetaldehyde in aqueous solution is in rapidly established equilibrium with appreciable amounts of its hydrate, eq. [3],

[3] 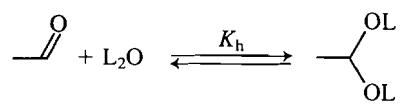

and, at the hydroxide ion concentrations used here, the hydrate is ionized to a significant extent, eq. [4].

[4] 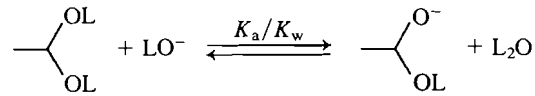

[1]Permanent address: Department of Chemistry, San Francisco State University, 1600 Holloway Avenue, San Francisco, CA 94132, U.S.A.

TABLE 1. Rate data for reaction of acetaldehyde with hydroxide ion in H_2O and D_2O at 25°C[a]

$[LO^-]/10^{-2}$ M	$k_{obs}/10^{-2}$ s^{-1}	k_{LO^-}/M^{-1} s^{-1}
H_2O		
9.38	4.33	1.07
8.88	4.15	1.07
D_2O[b]		
8.14	4.75	1.45
8.93	5.19	1.46

[a]Ionic strength = 0.1 M.
[b]Deuterium content of reaction mixtures was 98 at.%.

All of these species are consumed in the reaction studied here, but only the aldehyde is the reactive form. Corrections to observed rate constants allowing for this may be made according to eq. [5] where K_h is the hydration equilibrium constant,

$$[5] \quad k_{corr} = k_{obs}\{1 + K_h(1 + K_a[LO^-]/K_w)\}$$

K_a is the acidity constant of the hydrate, and K_w is the autoprotolysis constant of water.

For H_2O solution, $K_h = 1.06$ (4) and $K_a = 2.53 \times 10^{-14}$ M (5), both at 25°C. An isotope effect $K_{H_2O}/K_{D_2O} = 0.89$ is available for K_h at 15°C (4); it is unlikely that this would change very much over the short temperature interval 15–25°C, and use of the same value for 25°C leads to $(K_h)_{D_2O} = 1.19$. The isotope effect on K_w at 25°C has been measured: $K_{H_2O}/K_{D_2O} = 7.3$ (6). No isotope effect on K_a is available, but a reasonable value for an acid as weak as acetaldehyde hydrate would be $K_{H_2O}/K_{D_2O} = 6$ (7); the correction to k_{obs}, at any rate, is not a sensitive function of this constant.

Use of these values with the experimental data listed in Table 1 gives $k_{HO^-} = 1.07$ M^{-1} s^{-1}, in good agreement with $k_{HO^-} = 1.17$ M^{-1} s^{-1} measured before (2), and $k_{DO^-} = 1.46$ M^{-1} s^{-1}. The latter value refers to D_2O containing 2 at.% protium, and linear extrapolation to 100% D_2O leads to the isotope effect $k_{HO^-}/k_{DO^-} = 0.73$ with an estimated uncertainty of ±0.02. This result is consistent with $k_{HO^-}/k_{DO^-} = 0.68$ reported for acetone (8).

Can. J. Chem. Downloaded from www.nrcresearchpress.com by 196.1.178.254 on 09/07/12
For personal use only.

Discussion

Hydroxide-ion-consuming reactions, such as that investigated here, generally show inverse solvent deuterium isotope effects, $k_{HO^-}/k_{DO^-} < 1$. It is believed that this is because the hydroxide ion is strongly solvated in aqueous solution through hydrogen bond formation to three water molecules, as shown in **1** (9). Hydrogen bonding is known to lower the vibrational frequencies of bonds to the hydrogens involved, and these solvating water molecules consequently have weaker bonds, with less isotopically sensitive zero-point energy, than do ordinary water molecules in the bulk solvent (10). Destruction of the hydroxide ion, e.g., by hydron transfer from a substrate (eq. [6]), converts these solvating molecules into ordinary

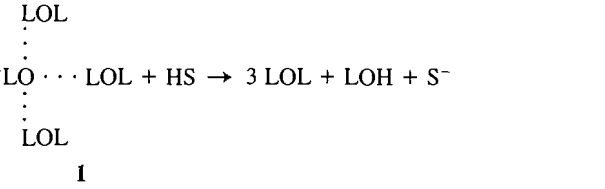

[6]

1

water, and that raises their isotopically sensitive zero-point energy and gives an inverse solvent isotope effect.

This picture of hydroxide ion solvent isotope effects can be used to make a quantitative prediction for the presently examined reaction. It is convenient to do this using fractionation factor theory, which expresses a kinetic isotope effect as the product of fractionation factors for all exchangeable hydrogens in the initial state, ϕ_i, divided by a like product for the transition state, $\phi_j^{\ddagger}$, eq. [7] (11). Application of this formalism to the

$$[7] \quad k_H/k_D = \pi_i\phi_i/\pi_j\phi_j^{\ddagger}$$

present system, eq. [8], leads to eq. [9], in which Φ_s is

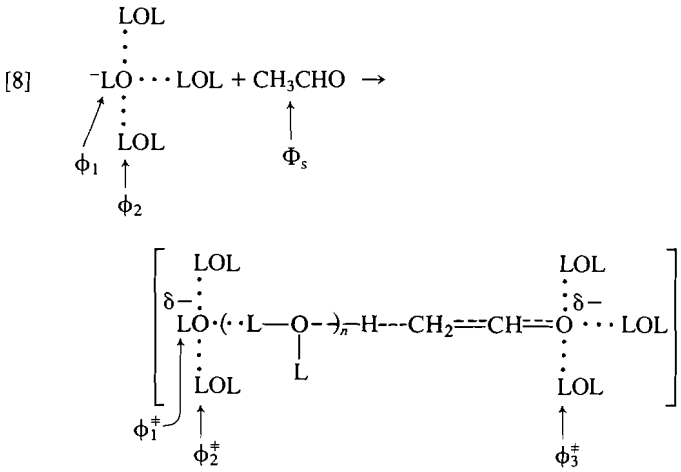

[8]

the fractionation factor of the water molecules solvating the acetaldehyde substrate.[2]

$$[9] \quad k_{HO^-}/k_{DO^-} = \phi_1(\phi_2)^3\Phi_s/\phi_1^{\ddagger}(\phi_2^{\ddagger})^{2+n}(\phi_3^{\ddagger})^3$$

If hydron transfer from acetaldehyde to the hydroxide ion takes place indirectly through one of the water molecules originally solvating the hydroxide ion, n in eqs. [8] and [9] will be equal to 1. If, on the other hand, hydron transfer is direct, then one of the solvating molecules must be lost before the transition state is reached, and $n = 0$. It has recently been shown that hydron transfer from a carbon acid to amines and alkoxide ions is direct, but it is not known whether this applies to hydron transfers involving the hydroxide and hydronium ions as well (12). Estimates will therefore be made for $n = 0$ and $n = 1$.

The more remote hydrogens of the water molecules solvating the hydroxide ion are believed to have fractionation factors similar to those of bulk water, $\phi = 1.00$; the other two kinds of hydrogen have been assigned the values $\phi_1 = 1.15$ and $\phi_2 = 0.72$ (9). In the transition state these latter hydrogens are on the way to becoming bulk water molecules and their fractionation factors, $\phi_1^{\ddagger}$ and $\phi_2^{\ddagger}$, should therefore lie between the corresponding initial state values and that for bulk water, i.e., unity. It would seem reasonable to assume that these fractionation factors will differ from unity in proportion to the amount of negative charge remaining on the oxygen atom they are solvating, and that this charge may be estimated as $1 - \beta$ where β is the Brønsted exponent for the system; it follows then that $\phi_1^{\ddagger} = (\phi_1)^{1-\beta}$ and $\phi_2^{\ddagger} = (\phi_2)^{1-\beta}$. A Brønsted exponent has not been measured for the ionization of acetaldehyde, but $\beta = 0.53$ is available for hydron transfer from isobutyraldehyde to a series of aryloxide ions (13), and use of the rounded value $\beta = 0.50$ leads to $\phi_1^{\ddagger} = 1.07$ and $\phi_2^{\ddagger} = 0.85$.

Fractionation factors for the hydrogens of water molecules solvating the oxygen atoms of enolate ions have not been determined, but a reasonable estimate might be $\phi_{E^-} = 0.75$; this is slightly greater than $\phi_1 = 0.72$ mentioned above for the more basic hydroxide ion and is consistent with $\phi = 0.75$ measured for the methoxide ion in methanol solution (14). A transition state value may be derived from this estimate, as before, by using the relationship $\phi_3^{\ddagger} = \phi_{E^-}^{x}$ where x is an index denoting the amount of negative charge developed on the enolate oxygen atom at the transition state. Because of transition state imbalance (15), x is not simply equal to β; rather, it has been estimated at $x = 0.38$ (2), and use of the rounded value $x = 0.40$ gives $\phi_3^{\ddagger} = 0.89$.

The substrate fractionation factor Φ_s has also not been determined directly, but an estimate may be made from the solvent isotope effect on the hydration of simple aldehydes and ketones (cf. eq. [3]). This isotope effect may be expressed as $K_{H_2O}/K_{D_2O} = \Phi_s/\phi_h^2$, and, on the assumption that $\Phi_s = 1.00$, $\phi_h = 1.08$ has been calculated for the hydroxyl hydrogens of the hydrates (16). It is not clear, however, that the fractionation factor of such hydrogens should be different from unity, which is the value usually found for uncharged hydroxyl groups. On the other hand, Φ_s could be significantly less than unity because carbonyl oxygen atoms of simple aldehydes or ketones bear an appreciable negative charge, and water molecules solvating such oxygens will be hydrogen bonded to them and will consequently have lowered fractionation factors. Taking $\phi_h = 1.00$ then leads to $\Phi_s = 0.86$; this estimate is consistent with the approximate value $\Phi_s = 0.83$ recently determined for isobutyrophenone.[3]

Use of these values in eq. [9] gives $k_{HO^-}/k_{DO^-} = 0.68$ for direct hydron transfer ($n = 0$) and $k_{HO^-}/k_{D_2O^-} = 0.80$ for transfer through a bridging water molecule. The experimentally determined value, $k_{HO^-}/k_{DO^-} = 0.73 \pm 0.02$ lies between these two estimates, but somewhat closer to that for direct transfer. This suggests that direct transfer is the more likely reaction mechanism, and it is interesting in this connection that analysis of our previously determined solvent isotope effect on the hydronium-ion-catalyzed enolization of acetaldehyde supported direct transfer for that reaction as well (2).

[2]In accord with ref. 11*b*, we use Φ to denote the aggregate isotopic fractionation produced by m sites with identical individual fractionation factors ϕ, i.e., $\Phi = \phi^m$.

[3]J. R. Keeffe, unpublished work.

Acknowledgements

We are grateful to the Natural Sciences and Engineering Research Council of Canada and the Donors of the Petroleum Research Fund, administered by the American Chemical Society, for financial support of this work.

1. H. HART. Chem. Rev. **79**, 515 (1979); J. TOULLEC. Adv. Phys. Org. Chem. **18**, 1 (1982); A. J. KRESGE. CHEMTECH, **16**, 250 (1986); Bull. Soc. Chim. France. In press.
2. Y. CHIANG, M. HOJATTI, J. R. KEEFFE, A. J. KRESGE, N. P. SCHEPP, and J. WIRZ. J. Am. Chem. Soc. **109**, 4000 (1987).
3. C. G. SWAIN, M. S. SWAIN, and L. F. BERG. J. Chem. Inf. Comput. Sci. **20**, 47 (1980).
4. J. L. KURZ. J. Am. Chem. Soc. **89**, 3524 (1967).
5. R. P. BELL and D. P. ONWOOD. Trans. Faraday Soc. **58**, 1557 (1962).
6. A. K. COVINGTON, R. A. ROBINSON, and R. G. BATES. J. Phys. Chem. **70**, 3820 (1966); V. GOLD and B. M. LOWE. J. Chem. Soc. A, 936 (1967).
7. P. M. LAUGHTON and R. E. ROBERTSON. *In* Solute–solvent interactions. Vol. 1. *Edited by* J. F. Coetzee and C. D. Ritchie. Marcel Dekker, New York. 1969. Chap. 7.
8. Y. POCKER. Chem. Ind. 1383 (1959).
9. V. GOLD and S. GRIST. J. Chem. Soc. Perkin Trans. 2, 89 (1972); Y. CHIANG, A. J. KRESGE, and R. A. MORE O'FERRALL. J. Chem. Soc. Perkin Trans. 2, 1832 (1980); R. A. MORE O'FERRALL and A. J. KRESGE. J. Chem. Soc. Perkin Trans. 2, 1840 (1980); A. J. KRESGE, R. A. MORE O'FERRALL, and M. F. POWELL. *In* Isotopes in organic chemistry. Vol. 7. *Edited by* E. Buncel and C. C. Lee. Elsevier, New York. 1987. Chap. 4.
10. M. M. KREEVOY and T. M. LIANG. J. Am. Chem. Soc. **102**, 3315 (1980).
11. (*a*) A. J. KRESGE. Pure Appl. Chem. **8**, 243 (1964); R. L. SCHOWEN. Prog. Phys. Org. Chem. **9**, 275 (1972); (*b*) W. J. ALBERY. *In* Proton transfer reactions. *Edited by* E. F. Caldin and V. Gold. Chapman and Hall, London. 1975. p. 263.
12. R. A. BEDNAR and W. P. JENCKS. J. Am. Chem. Soc. **107**, 7126 (1985).
13. J. HINE, J. G. HOUSTON, J. H. JENSEN, and J. MULDERS. J. Am. Chem. Soc. **87**, 5050 (1965).
14. V. GOLD and S. GRIST. Chem. Commun. 1216 (1968); J. Chem. Soc. (B), 1665 (1971); R. A. MORE O'FERRALL. Chem. Commun. 114 (1969).
15. C. F. BERNASCONI. Pure Appl. Chem. **54**, 2335 (1982); Tetrahedron, **41**, 3219 (1985).
16. R. BONE and R. WOLFENDEN. J. Am. Chem. Soc. **107**, 4772 (1985).

Can. J. Chem. Downloaded from www.nrcresearchpress.com by 196.1.178.254 on 09/07/12
For personal use only.

Halogen and pseudohalogen substitution of some adamantanoid chalcogenate clusters $[(\mu\text{-EPh})_6(MEPh)_4]^{2-}$ using methylmercury and triphenyltin derivatives. A multinuclear nuclear magnetic resonance study[1]

PHILIP A. W. DEAN[2] AND JAGADESE J. VITTAL
Department of Chemistry, University of Western Ontario, London, Ont., Canada N6A 5B7

Received March 15, 1988

PHILIP A. W. DEAN and JAGADESE J. VITTAL. Can. J. Chem. **66**, 2443 (1988).

Multinuclear nmr (^1H, ^{77}Se, $^{111/113}Cd$, ^{119}Sn, ^{199}Hg, as appropriate) has been used to study $Y^- - EPh^-$ exchange in Me_2CO or MeCN between $R_nM'Y$ (R_nM' = Ph_3Sn or MeHg; Y = Cl, Br, I, NCO, or NCS) and the adamantane-like anions $[(\mu\text{-EPh})_6(MEPh)_4]^{2-}$ (E = S, M = Zn, Cd, or Co; E = Se, M = Zn or Cd), as their tetraalkylammonium salts. Quantitative terminal substitution of the clusters occurs in most cases, giving $[(\mu\text{-EPh})_6(MEPh)_{4-x}(MY)_x]^{2-}$ (x = 1–4). However, reaction is incomplete for M = Cd, E = S or Se, $R_nM'Y$ = Ph_3SnNCO or Ph_3SnNCS and for M = Zn or Co, E = S, $R_nM'Y$ = MeHgI. Differences in the extents of reaction for Ph_3SnY and MeHgY are consistent with the position of equilibrium in MeHgY:Ph_3SnEPh mixtures.

Group interchange provides a convenient alternative synthesis of the known halogen-substituted clusters $[(\mu\text{-EPh})_6(MY)_4]^{2-}$ (M = Zn or Cd, Y = Cl, Br, or I; M = Co, Y = Cl), and the first syntheses of $[(\mu\text{-SPh})_6(CoY)_4]^{2-}$ (Y = Br or I) and various pseudohalogen-substituted adamantanoid anions. The nuclei used for full direct nmr characterization of the new clusters in solution were: ^{77}Se and ^{113}Cd for $[(\mu\text{-SePh})_6(CdSePh)_{4-x}(CdY)_x]^{2-}$ (x = 1–4; Y = NCO or NCS); ^{77}Se for $[(\mu\text{-SePh})_6(ZnSePh)_{4-x}(ZnY)_x]^{2-}$ (x = 1–4, Y = NCO or NCS); ^{113}Cd for $[(\mu\text{-SPh})_6(CdSPh)_{4-x}(CdY)_x]^{2-}$ (x = 1–4; Y = NCO or NCS); ^1H for $[(\mu\text{-SPh})_6(CoY)_4]^{2-}$ (Y = Br, I, NCO, or NCS). The first solution ^1H nmr spectrum of $[(\mu\text{-SPh})_6(CoCl)_4]^{2-}$ is also reported.

PHILIP A. W. DEAN et JAGADESE J. VITTAL. Can. J. Chem. **66**, 2443 (1988).

Faisant appel à la rmn multinucléaire (^1H, ^{77}Se, $^{111/113}Cd$, ^{119}Sn, ^{199}Hg selon le cas) on a étudié l'échange $Y^- - EPh^-$, dans le Me_2CO ou le MeCN, entre le $R_nM'Y$ (R_nM = Ph_3Sn ou MeHg; Y = Cl, Br, I, NCO ou NCS) et les anions du type adamantane $[(\mu\text{-EPh})_6(MEPh)_4]^{2-}$ (E = S, M = Zn, Cd ou Co; E = Se, M = Zn ou Cd) sous forme de sels de tétraalkylammonium. Dans la plupart des cas il se produit une substitution terminale quantative des aggrégats qui conduit à la formation de $[(\mu\text{-EPh})_6(MEPh)_{4-x}(MY)_x]^{2-}$ (x = 1–4). La réaction est cependant incomplète dans lorsque M = Cd, E = S ou Se, $R_nM'Y$ = Ph_3SnNCO ou Ph_3SnNCS et pour M = Zn ou Co, E = S et $R_nM'Y$ = MeHgI. Les différences constatées dans les réactions sont en accord avec la position d'équilibre dans les mélanges de MeHgY:SnEPh.

L'échange mutuel entre les groupes fournit une méthode de synthèse alternative des aggrégats connus ayant un halogène comme substituant $[(\mu\text{-EPh})_6(MY)_4]^{2-}$ (M = Zn ou Cd, Y = Cl, Br ou I; M = Co, Y = Cl) et la première synthèse du $[(\mu\text{-SPh})_6(CoY)_4]^{2-}$ (Y = Br ou I) et de divers anions de type adamantane ayant des substituants pseudohalogénés. On a utilisé les noyaux suivants pour caractériser les nouveaux composés en solution par rmn : le ^{77}Se et le ^{113}Cd pour $[(\mu\text{-SePh})_6(CdSePh)_{4-x}(CdY)_x]^{2-}$ (x = 1–4, Y = NCO ou NCS); le ^{77}Se pour $[(\mu\text{-SePh})_6(ZnSePh)_{4-x}(ZnY)_x]^{2-}$ (x = 1–4, Y = NCO ou NCS); le ^{113}Cd pour $[(\mu\text{-SPh})_6(CdSPh)_{4-x}(CdY)_x]^{2-}$ (x = 1–4, Y = NCO ou NCS); le ^1H pour $[(\mu\text{-SPh})_6(CoY)_4]^{2-}$ (Y = Br, I, NCO ou NCS). On rapporte également la première solution du spectre de rmn du $[(\mu\text{-SPh})_6(CoCl)_4]^{2-}$.

[Traduit par la revue]

Introduction

Adamantane-like anions, $[(\mu\text{-SPh})_6(MSPh)_4]^{2-}$, with a [4M-6S] core of (idealized) T_d symmetry, are known for various divalent metal ions including Mn(II), Fe(II), Co(II), Zn(II), and Cd(II) (1). For M = Zn and Cd, the related selenolate complexes, $[(\mu\text{-SePh})_6(MSePh)_4]^{2-}$, have also been reported (2). The $[(\mu\text{-EPh})_6(MEPh)_4]^{2-}$ clusters should have an interesting ligand substitution chemistry, but to date there has been very little work in this area.[3] In previous papers from these laboratories we have described substitution of the Zn_4 and Cd_4 clusters with halogens (2*b*, 5) and R'E' (2*a*, 2*b*).

Halogen substitution of $[(\mu\text{-EPh})_6(MEPh)_4]^{2-}$ (M = Zn or Cd; E = S or Se) according to eq. [1], allows complete terminal

[1] $[(\mu\text{-EPh})_6(MEPh)_4]^{2-} + 2X_2 \rightarrow [(\mu\text{-EPh})_6(MX)_4]^{2-} + 2Ph_2E_2$

[1a], X = Cl; [1b], X = Br; [1c], X = I

substitution (2*b*, 5). For incorporation of chlorine, $PhICl_2$ (6) acts as a useful alternative to the halogen itself (2*b*, 5), as shown in eq. [2]. So far as we are aware, these are the only studies

[2] $[(\mu\text{-EPh})_6(MEPh)_4]^{2-} + 2PhICl_2 \rightarrow [(\mu\text{-EPh})_6(MCl)_4]^{2-} + 2Ph_2E_2 + 2PhI$

in which halogen-substituted clusters have been made from the parent $[(\mu\text{-EPh})_6(MEPh)_4]^{2-}$ anions. At the outset of our work, the only other tetrahalo-anions that had been reported were $[(\mu\text{-SPh})_6(FeX)_4]^{2-}$ (X = Cl or Br), assembled from $FeCl_2$, Cl^- and SPh^-, or from $Fe(SPh)_4^{2-}$ and FeX_2, rather than by substitution of pre-formed $[(\mu\text{-SPh})_6(FeSPh)_4]^{2-}$ (7). Up to that time, attempts to build up tetrahalo-anions of Zn(II) (8) and Co(II) (9) in a similar manner had been unsuccessful, leading only to doubly terminally substituted products. Since the completion of our study, the synthesis of $(Bu_4N)_2[(\mu\text{-SPh})_6(CoCl)_4]$ from $(Bu_4N)[CoCl_3(PPh_3)]$ and $PhSSiMe_3$ has been reported, with characterization of the new tetranuclear anion by X-ray analysis (10).

Reaction [1c] is convenient to carry out, but there are drawbacks to [1a], [1b], and [2]. Quantitative addition of Cl_2 [1a] or Br_2 [1b] is difficult, and for [2] $PhICl_2$ must be freshly

[1]Presented in part at the 70th Canadian Chemical Conference, Quebec City, Quebec, June 1987.

[2]Author to whom correspondence should be addressed.

[3]Several groups have investigated *metal* substitution of such adamantanoid clusters (2*a*, 3, 4).

Can. J. Chem. Downloaded from www.nrcresearchpress.com by 112.217.228.212 on 09/07/12
For personal use only.

made for each synthesis. Further, the syntheses of reactions [1] and [2] cannot be extended straightforwardly to other substituents such as the common pseudohalogens, nor are they suitable for clusters of readily-oxidizable metals. Alternative methods of substitution clearly deserve exploration.

In this paper we have used multinuclear nmr to make a systematic investigation of substitution of the representative anions $[(\mu\text{-EPh})_6(\text{MEPh})_4]^{2-}$ (M = Zn or Cd, E = S or Se; M = Co, E = S) via interchange of groups with $R_nM'Y$ (R_nM' = MeHg or Ph_3Sn), as in eq. [3].

$$[3]\quad [(\mu\text{-EPh})_6(\text{MEPh})_4]^{2-} + 4R_nM'Y \rightarrow [(\mu\text{-EPh})_6(\text{MY})_4]^{2-} + 4R_nM'EPh$$

The organo-mercury and -tin compounds possess several features making them promising reagents for the interchange reaction of interest: (*i*) the "soft" organometallic centres bind the chalcogenate group strongly with a 1:1 stoichiometry;[4] (*ii*) a wide range of stable $R_nM'Y$ is readily available so that Y groups other than halides can be tried; (*iii*) the fate of R_nM' can be followed using ^{199}Hg or ^{119}Sn nmr;[5] and (*iv*) in future synthetic studies, the solubility of the organometallic reagents and products in non-polar solvents should allow easy separation from the ionic clusters. In addition, since [3] involves ligand exchange rather than oxidation by halogens (eqs. [1] and [2]), it reduces the possibility of problems due to metal oxidation.

Experimental

Materials

Literature syntheses without significant variation were used for $(Me_4N)_2[(\mu\text{-EPh})_6(\text{MEPh})_4]$ (E = S, M = Zn (3), Cd (13), or Co (9); E = Se, M = Zn (*5b*) or natural or ^{113}Cd-enriched Cd (*2a*)) and $(Et_4N)_2[(\mu\text{-SePh})_6(\text{ZnSePh})_4]$ (*2b*, *5b*). The synthesis of $(Pr_4N)_2[Cd_4(SPh)_{10}]$ paralleled that of the Me_4N^+ salt. MeHgNCS was prepared from MeHgI and AgSCN (14). The analogous synthesis using AgN_3 gave $MeHgN_3$, which was recrystallized from $CHCl_3$. Reported methods gave Ph_3SnY (Y = N_3 (15), NCO (16), or I (17)). Following ref. 17, Ph_3SnBr was prepared by the stoichiometric reaction of Sn_2Ph_6 with Br_2 in $CHCl_3$; it was recrystallized from dry propanol. The method of ref. 11, but with NaOMe (produced *in situ*) in place of Et_3N, yielded $Ph_3SnSePh$, which was recrystallized from $CHCl_3$. Two synthetic methods were used to produce Ph_3SnNCS: (*i*) reaction of Ph_3SnI and AgSCN in refluxing Et_2O, with subsequent solvent removal and recrystallization from toluene; or (*ii*) reaction of Ph_3SnCl with KSCN in refluxing MeOH, followed by precipitation with water, drying, and recrystallization from toluene (18). The compounds Ph_3SnSPh and MeHgEPh (E = S or Se) were obtained as the by-products of appropriate completely reacted mixtures of $R_nM'Y$ and $[(\mu\text{-EPh})_6(\text{MEPh})_4]^{2-}$ (M = Zn or Cd) (see below): following solvent removal from a completely reacted $[(\mu\text{-EPh})_6(\text{MEPh})_4]^{2-}$–$R_nM'Y$ mixture, $R_nM'EPh$ was extracted into C_6H_6. The crude products obtained by evaporation of C_6H_6 were recrystallized from $CHCl_3$. Ph_3SnCl (Aldrich) was recrystallized from dry propanol. MeHgY (Y = Cl, Br, or I) (all from Alfa) were used as received. All solvents were dried over 3A molecular sieves before use. Before preparation of solutions containing any of the chalcogenate clusters, solvents were also thoroughly de-oxygenated in a flow of Ar.

The purities of the organometallic reagents were checked using nmr: ^{119}Sn nmr[5] (together with ^{77}Se nmr[5] for $Ph_3SnSePh$) was used for the triphenyltin compounds and ^{1}H and/or ^{199}Hg nmr[5] for the organomercury compounds. Our nmr data are consistent with literature values, where available (19–21). We could find no published ^{119}Sn nmr data for several of the triphenyltin compounds. Metal nmr data for these, as solutions in inert solvents, are given in Table 1. Similarly, no ^{199}Hg nmr data seem to have been reported for $MeHgN_3$; we find $\delta_{Hg} = -904$ (relative to external $HgMe_2$), $^2J(^{199}Hg—^1H) = 191 \pm 3$ Hz at 293 K for a $CHCl_3$ solution containing 0.05 mol/L of solvent. The compound MeHgNCO has been only partially characterized in the literature (23). The synthesis and further characterization of this compound are described below.

Synthesis

MeHgNCO. An earlier brief report (23) of this substance described its synthesis from MeHgCl and ClNCO and characterization by osmometry and vibrational spectroscopy. From a ^{119}Hg nmr[5] study, we find the compound to be formed quantitatively when a 1:1 mixture of MeHgI and AgNCO is stirred for 12–18 h at room temperature in acetone. The crude product is obtained by removal of the solvent from the filtrate. On recrystallization from $CHCl_3$, pure MeHgNCO is isolated as white flakes. Isolated yield: 51%. Pmr (0.05 mol/L of $CDCl_3$): $\delta_H = 1.04$ ppm, $^2J(^{199}Hg—^1H) = 199 \pm 1$ Hz. In the ^{199}Hg nmr spectrum of this sample at 294 K, $\delta_{Hg} = -852$ ppm. *Exact mass* calcd. for $C_2H_3{}^{202}HgNCO$: 258.9921; found (ms at 70 eV): 258.9925.

Solid MeHgNCO deteriorates over a period of days on standing at room temperature, becoming gradually insoluble in $CHCl_3$. Because of this instability, as well as the high volatility of the compound (23), after our initial synthesis MeHgCO was not normally isolated. Instead, it was prepared *in situ* in acetone, as outlined above, with removal of AgI by filtration before use.

Nuclear magnetic resonance spectra

All samples were prepared on the basis of (mass of solute/volume of solvent). For solutions of the chalcogenate clusters, solvents were de-oxygenated in a flow of Ar.

Nuclear magnetic resonance spectra were measured using a Varian XL-200 or -300 spectrometer system. Conventional methods were used to obtain ^{1}H and ^{13}C nmr spectra, using samples in 5 mm od nmr tubes. For ^{199}Hg, ^{77}Se, $^{111/113}$Cd, and ^{119}Sn nmr spectroscopy[5] samples were prepared in 10 mm od nmr tubes. In these cases measurements of temperature, instrumental operating conditions and external referencing were generally similar to those used in earlier reports from this laboratory (*2a*, *2b*, *5b*, 13, 24). However, during the current work we made an inversion-recovery measurement of T_1 for ^{77}Se in $(Me_4N)_2[(\mu\text{-SePh})_6(\text{ZnI})_4]$ (*2b*) as a solution in deoxygenated acetone (0.05 mol/L of Me_2CO). At 57.20 MHz and 297 K, $T_1 = 0.75 \pm 0.02$ s, a much shorter T_1 than presumed[6] in our earlier work on PhSe-bridged clusters (*2b*, *5b*, *24a*). The conditions used here to collect ^{77}Se nmr spectra assume T_1 values of *ca.* 1–2 s, e.g. tip angles of *ca.* 60° with an acquisition (and repetition) time of 1 s, so that ^{77}Se data collection is more efficient than earlier.

Results and discussion

Anion exchange between methylmercury and triphenyltin compounds

Of interest in connection with the reaction shown in eq. [3] is a study of equilibrium [4] for various combinations of EPh and Y. To our knowledge, there are no literature data for this

$$[4]\quad MeHgY + Ph_3SnEPh \underset{}{\overset{K_4}{\rightleftharpoons}} MeHgEPh + Ph_3SnY$$

[4]We note, however, that organotin chalcogenates have sometimes been used as a source of the chalcogenate ion in synthesis (e.g. ref. 11), just as Me_3SiSPh is used as a *source* of SPh^- in the synthesis of $[(\mu\text{-SPh})_6(CoCl)_4]^{2-}$.

[5]The nuclei ^{199}Hg, ^{119}Sn, ^{111}Cd, ^{113}Cd, and ^{77}Se all have spin $I = 1/2$. Their % natural abundances and receptivities relative to ^{13}C are, respectively, 16.84 and 5.57, 8.58 and 25.6, 12.75 and 6.97, 12.26 and 7.67, and 7.58 and 3.01 (12).

[6]T_1 values of ^{77}Se are typically long for small molecules. For larger molecules that tumble more slowly, shorter relaxation times can occur (e.g. ref. 25).

Can. J. Chem. Downloaded from www.nrcresearchpress.com by 112.217.228.212 on 09/07/12
For personal use only.

TABLE 1. Tin-119 nmr data for some compounds Ph_3SnY at 294 ± 2 K[a]

Y	Solvent	δ_{Sn}[b]	$\Delta\nu_{1/2}$ (approx) (Hz)	Other
Br	CH_2Cl_2	−47.2	8	
SePh	CH_2Cl_2	−81.4	19	$^1J(^{119}Sn—^{77}Se) = 1167 \pm 5$ Hz $\delta_{Se} = -27.1$[c]
N_3	$CHCl_3$	−88.1	90	
NCO	$CHCl_3$	−118.0	75	
NCS	$CHCl_3$	−134.8	50	$^1J(^{119}Sn—^{14}N) = 88 \pm 3$ Hz[d]

[a]Measured at 74.61 MHz (38.16 MHz for ^{77}Se) for solutions with concentrations 0.05 mol per L of solvent.

[b]Relative to external pure $SnMe_4$; estimated error in measurement ±0.1 ppm.

[c]Relative to external pure Me_2Se; estimated error in measurement ±0.1 ppm; $\Delta\nu_{1/2} \approx 6$ Hz.

[d]For comparison, $^1J(^{119}Sn—^{14}N) = 136$ Hz for $(c\text{-}C_6H_{11})_3SnNCS$ in toluene (22*a*). Also $^1J(^{119}Sn—^{15}N) = 307.0$ Hz for Bu_3SnNCS (22*b*); from this, the calculated value of $^1J(^{119}Sn—^{14}N)$ in Bu_3SnNCS = 218.9 Hz.

particular equilibrium. However, Kravtsov *et al.* (26), have studied the position of equilibrium for $OAc^- - ArS^-$ exchange in mixtures of phenylmercury and triphenyltin derivatives. They found that the preference for ArS^- over OAc^- in $PhHg^+ > Ph_3Sn^+$, concluding that the organomercury centre is the softer acceptor. Also, Grant and Wardell (27) have shown that complete anion exchange occurs in mixtures of $Me_3SnSePh$ and PhHgCl.

Overall, Me_2CO was used most widely in the studies of reaction [3] described below. Accordingly, Me_2CO was also the solvent chosen to study [4].[7] As probes of the position of equilibrium[8] both ^{119}Sn and ^{199}Hg nmr were used.

In mixtures of MeHgY and MeHgEPh, there is rapid exchange of the MeHg group between sites (see, for example, ref. 28). Thus with a prior knowledge of δ_{Hg} for MeHgY and MeHgEPh separately,[9] the position of the exchange-averaged ^{119}Hg nmr signal can be used to indicate the position of [4]. This method will be least accurate when K_4 is very large or very small. Under these conditions the value found for K_4 will be most sensitive to the (comparatively small) variation of δ_{Hg}(MeHgEPh/Y) with concentration and with small changes in ambient probe temperature.

Our ^{119}Sn nmr studies show that on this nmr timescale there is no exchange of the Ph_3Sn group between sites in mixtures of Ph_3SnEPh (E = S or Se) and Ph_3SnY (Y = Cl, Br, I, N_3, NCO, or NCS) in acetone, with or without added methylmercury compound. Here the relative intensities of the separate ^{119}Sn signals[10,11] can be used to quantitate equilibrium [4], complementing the results of ^{199}Hg nmr. The intensity ratios, and hence the calculated values of K_4, are once more expected to be least accurate for extreme values of K_4.

TABLE 2. Equilibrium constants for [4] at 295 ± 2 K in Me_2CO[a]

	log K_4[b]	
Y	E = S	E = Se
Cl	2.2±0.2	2.5±0.2
Br	0.3±0.1	−1.0±0.2
I	−1.5±0.3	−1.3±0.2
NCO	>2.7[c]	>2.7[c]
NCS[d]	>2.7[c]	>2.7[c]
N_3	>2.7[c]	>2.7[c]

[a]Total concentrations of methylmercury and triphenyltin compounds are 0.05–0.2 mol/L of solvent.

[b]Estimated errors are quoted.

[c]K_4 was too large to be measured accurately.

[d]The thiocyanate group is S-bound in MeHgSCN and N-bound in Ph_3SnNCS (see text).

The values found for K_4 are given in Table 2. When E = S or Se and Y = NCO, NCS,[12] or N_3, the value of K_4 is too large to be measured accurately ($K_4 > 500$). For Y = halide, the values found using the two different metal nmr probes are in reasonable agreement; the average value is given. The data in Table 2 show that equilibrium [4] favours Ph_3SnEPh strongly for E = S, Y = I and for E = Se, Y = I or Br. Conversely, MeHgEPh is favoured strongly for E = S or Se and Y = Cl, NCO, N_3, or NCS, and slightly for E = S, Y = Br. In general then, MeHgY should be the more potent reagent for substitution of chalcogenate clusters when Y = Cl, NCO, NCS, or N_3, while Ph_3SnI should be more potent when Y = I. For Y = Br an

[7]Qualitatively similar results were found using MeCN as solvent.

[8]The equilibria are rapidly established compared with the rate at which the nmr spectra can be obtained.

[9]At 293 K, for Me_2CO solutions containing 0.05 mol/L of solvent, δ_{Hg} = −847, −958, −1147, −979, −918, −787, −615, and −682 for Y in MeHgY = Cl, Br, I, N_3, NCO, SCN, SPh, and SePh, respectively.

[10]At 295 K, for Me_2CO solutions containing 0.05 mol/L of solvent, δ_{Sn} = −103.7, −103.7, −121.6, −161.0, −185.8, −234.3 ($^1J(^{119}Sn—^{14}N)$ = 120 ± 10 Hz), −65.9 and −81.0 ($^1J(^{119}Sn—^{77}Se) = 1150 \pm 5$ Hz, $\delta_{Se} = -31.6$) for Y in Ph_3SnY = Cl, Br, I, N_3, NCO, NCS, SPh, and SePh, respectively.

[11]The large changes in δ_{Sn} for Ph_3SnY (Y = N_3, NCO, or NCS) and in $^1J(^{119}Sn—^{14}N)$ for Ph_3SnNCS that occur on change of solvent from $CHCl_3$ to Me_2CO (compare Table 1 and footnote 10) indicate coordinate of Me_2CO. The acceptor properties of these neutral pseudohalides are well established from other work, e.g. ref. 18*b* and references therein. Also it appears that Ph_3SnCl and Ph_3SnBr are ionized to $Ph_3Sn(OCMe_2)_x^+$ in Me_2CO: in this solvent the two compounds have identical ^{13}C as well as ^{119}Sn nmr spectra.

[12]It should be noted that S-bonded thiocyanate occurs in MeHgSCN (14, 28), and N-bonded thiocyanate in Ph_3SnNCS (29).

Can. J. Chem. Downloaded from www.nrcresearchpress.com by 112.217.228.212 on 09/07/12
For personal use only.

Can. J. Chem. Downloaded from www.nrcresearchpress.com by 112.217.228.212 on 09/07/12
For personal use only.

experimental determination of the better reagent would be safest.

Reaction of $[(\mu\text{-}EPh)_6(MEPh)_4]^{2-}$ and $R_nM'Y$

Relative extent of reaction must obviously be an important factor in the choice of a reagent, Ph_3SnY or MeHgY, for a particular reaction [3]. However, practical considerations also influence the choice. From the point of view of handling, the Ph_3SnY reagents are preferable: they are less volatile and therefore less hazardous. Also solid Ph_3SnNCO is thermally stable whereas solid MeHgNCO is not (see Experimental Section). A disadvantage of the MeHg(II) reagents is that MeHgY:$[M_4(EPh)_{10}]^{2-}$ mixtures give broader nmr signals in spectra measured at ambient probe temperature than do Ph_3SnY:$[M_4(EPh)_{10}]^{2-}$ mixtures (see below). This is not a problem in low temperature spectra however, and here the organomercury reagents have the advantage of generally greater solubility in Me_2CO.

Just as described above for MeHgY:Ph_3SnEPh mixtures, ^{119}Sn or ^{199}Hg nmr spectra of mixtures of $[(\mu\text{-}EPh)_6(MEPh)_4]^{2-}$ and $R_nM'Y$ in Me_2CO at ambient probe temperature can be used to obtain the $R_nM'EPh/R_nM'Y$ ratio and so obtain an initial indication of the extent of reaction. The *cleanness* of reaction must be found by other means. The two organometallic azides certainly undergo reaction with $[M_4(EPh)_{10}]^{2-}$, as judged by $^{119}Sn/^{119}Hg$ nmr, but we could not identify the non-organometallic products, though they are certainly not those expected from [3]. Accordingly, the azides are not considered further in the following discussion.

*(i) $[(\mu\text{-}SePh)_6(CdSePh)_4]^{2-}$ (**1**)*

On the basis of $^{119}Sn/^{199}Hg$ nmr, there is complete reaction of **1** with MeHgY (Y = Cl, Br, I, NCO, or NCS) and with Ph_3SnY (Y = Cl, Br, or I) up to $R_nM'Y/\mathbf{1} = 4$.[13] Reaction of **1** with Ph_3SnNCO and Ph_3SnNCS is incomplete. Detailed ^{77}Se and ^{113}Cd nmr studies of those reactions that appear complete by $^{119}Sn/^{199}Hg$ nmr confirm the completeness and show that all these reactions occur cleanly in accordance with eq. [3].

We have previously reported that ^{77}Se nmr spectra of **1** in Me_2CO or MeCN at ambient probe temperature show a single broad exchange-averaged signal (*2a*, *5b*), while for MeCN solutions at 234 K well-separated resonances, assignable to bridging and terminal PhSe groups ($PhSe_t$ and $PhSe_{br}$), are found at 18 and −62 ppm, respectively (*5b*). As part of the current work we have obtained more definitive low temperature ^{77}Se nmr spectra of **1**. At 213 K, a sample of **1** in Me_2CO (concentration 0.01 mol/L of solvent) showed sharp resonances with $\delta_{Se} = 26.4$ and −64.3 ppm, and relative intensities approximately 2 and 3. These signals can be assigned to $PhSe_t$ and $PhSe_{br}$ groups, respectively (*5b*). Satellites from one-bond coupling to $^{111/113}Cd$ can be picked out readily. In a sample with partial ^{113}Cd enrichment, $^1J(^{113}Cd—^{77}Se_t) = 144 \pm 3$ Hz, while $^1J(^{113}Cd—^{77}Se_{br}) = 165 \pm 3$ Hz. From the $^{111/113}Cd$ nmr[5] spectra of this sample, $^2J(^{113}Cd—Se—^{111}Cd) = 66 \pm 3$ Hz.

Addition of 4 mol equiv. of $R_nM'Y$ (R_nM' = Ph_3Sn or MeHg; Y = Cl, Br, or I) to **1**, leads to the tetrahalo anions $[(\mu\text{-}SePh)_6(CdY)_4]^{2-}$, which we have described earlier (*5*). Low temperature ^{77}Se and ^{113}Cd nmr spectra are in general agreement with those already reported (*5*) for these species. It is somewhat surprising that sharper spectra were obtained in the present work, using samples prepared *in situ*, than could be obtained previously using analytically pure samples (*5*). Hence it was possible to measure some couplings here that were previously obscured by the linewidth. At 237 K[14] in Me_2CO or MeCN $^1J(^{111/113}Cd—^{77}Se_{br})$ (from ^{77}Se nmr) and $^2J(^{113}Cd—^{111}Cd)$ (from ^{113}Cd nmr) are 58 ± 3 and *ca.* 33 Hz, and 80 ± 2 and *ca.* 38 Hz, for the tetrachloro and tetrabromo complexes, respectively. Only the two couplings for the tetraiodo complex (120 ± 10 and 52 ± 2 Hz, which we confirmed here) and an approximate value of $^1J(^{113/111}Cd—^{77}Se)$ for the tetrabromo complex were obtained previously (*5b*). Since $^1J(^{111/113}Cd—^{77}Se)$ and $^2J(^{113}Cd—^{111}Cd)$ share a common coupling pathway, they are expected to change in concert, as found here for the series of **1** and its tetrahalo-substituted derivatives.

When MeHgY (Y = NCO or SCN) is added stepwise to **1** in Me_2CO, ^{77}Se and ^{113}Cd nmr spectra of samples at 213 K[14] provide clear evidence for stepwise substitution of the pseudohalide into **1** to give $[(\mu\text{-}SePh)_6(CdSePh)_{4-x}(CdY)_x]^{2-}$ as components of equilibrium mixtures.[15] A typical ^{77}Se nmr spectrum, that of a mixture with MeHgNCO/**1** = 2, is shown in Fig. 1*a*. The first new cluster formed in the MeHgY:**1** mixtures is characterized by one new ^{77}Se nmr signal (relative intensity 1) in the $PhSe_t$ region and two new signals (each of relative intensity 1) in the $PhSe_{br}$ region. This spectrum reaches its maximum intensity with the concentration of addition of 1 mol equiv. of MeHgY. Following previous work (*2b*), the spectrum can be assigned to the anion with $x = 1$. The concentration of $[(\mu\text{-}SePh)_6(CdSePh)_2(CdY)_2]^{2-}$ reach a maximum at MeHgY/**1** = 2. This species has a ^{77}Se nmr spectrum consisting of a $PhSe_t$ signal (relative intensity 2) and three $PhSe_{br}$ signals (two of relative intensity 1, one of relative intensity 4), as expected (*2b*) for species of time-averaged C_2 symmetry. The anion $[(\mu\text{-}SePh)_6(CdSePh)(CdY)_3]^{2-}$, which has maximum concentration at MeHgY/**1** = 3, gives one ^{77}Se resonance (relative intensity 1) in the $PhSe_t$ region and two (both of relative intensity 3) in the $PhSe_{br}$ region, consistent (*2b*) with time-averaged C_3 symmetry. At MeHgY/**1** = 4, the major species is $[(\mu\text{-}SePh)_6(CdY)_4]^{2-}$. This anion is not the sole species present, however. Significant amounts of the species with $x = 3$ still exist at this ratio. The products corresponding to $x > 4$, which must also exist in the equilibrium mixture, remain unidentified. A similar redistribution equilibrium has been noted earlier for $[(\mu\text{-}SePh)_6(ZnCl)_4]^{2-}$ (*2b*).

The occurrence of a total of nine ^{77}Se nmr signals in the $PhSe_{br}$ region of the series $[(SePh)_6(CdSePh)_{4-x}(CdY)_x]^{2-}$ (Y = NCO or NCS), as exemplified in Fig. 1*a*, shows that the ^{77}Se resonances of $PhSe_{br}$ are sensitive to both geminal and more distant substitution, and assignments can be made on this basis (*2b*). The ^{77}Se nmr spectra of the two pseudohalide-substituted series so assigned are given in Table 3. The data for the two series of spectra are sufficiently similar to allow the conclusion that NCS^-, like NCO^-, is N-bonded in the Cd_4 anions. N-bound NCS^- also occurs in discrete[16] mononuclear cadmium complexes (e.g. ref. 31).

The low temperature[14] ^{113}Cd nmr spectra of mixtures of **1** and MeHgY (Y = NCO or SCN) give results consistent with

[13]Complete reaction occurs to higher $R_nM'Y/[M_4(EPh)_{10}]^{2-}$ ratios, but we have been unable as yet to characterize the products beyond the 4/1 ratio.

[14]At ambient probe temperature very broad lines are found.

[15]The distribution of the species $[(\mu\text{-}EPh)_6(MEPh)_{4-x}(MY)_x]^{2-}$ is close to statistical.

[16]Most Cd^{2+}–thiocyanate species are polymeric (e.g. ref. 30).

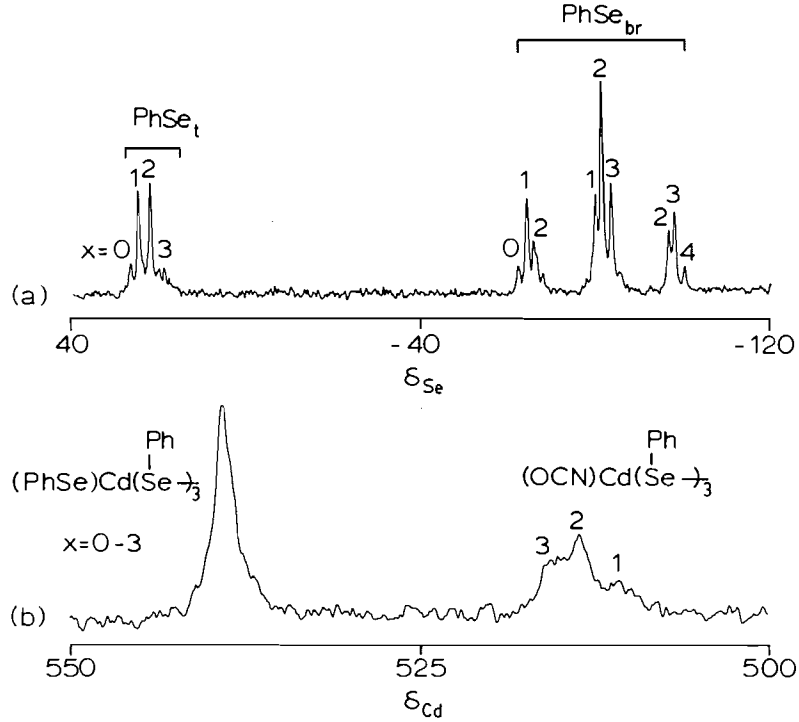

FIG. 1. Nuclear magnetic resonance spectra at 213 K of the supernatant liquid from a mixture of $(Me_4N)_2[(\mu\text{-SePh})_6(CdSePh)_4]$ (**1**):MeHgNCO = 1:2 in acetone, showing the formation of $[(\mu\text{-SePh})_6(CdSePh)_{4-x}(CdNCO)_x]^{2-}$. (*a*) ^{77}Se nmr spectrum at 38.15 MHz. (*b*) ^{113}Cd nmr spectrum at 44.37 MHz. The mixture was prepared using 0.05 mol of **1**/L of Me_2CO.

those from ^{77}Se nmr, though the ^{113}Cd nmr spectra with their larger linewidths were less well resolved. The ^{113}Cd nmr spectra of the series $[(\mu\text{-SePh})_6(CdSePh)_{4-x}(CdY)_x]^{2-}$ (Y = NCO or NCS; x = 0–4) give rise to signals in two regions, as illustrated in Fig. 1*b* for a mixture with MeHgNCO/**1** = 2. The two regions in the spectra must correspond to the two different first coordination spheres, $PhSeCd(\mu\text{-SePh})_3$ and $YCd(\mu\text{-SePh})_3$, that occur in these series (5, 32). The higher frequency region contains the signal of **1** itself and so can be assigned to the $PhSeCd(\mu\text{-SePh})_3$ grouping. Thus the more shielded region is due to $YCd(\mu\text{-SePh})_3$. The thiocyanate series shows further fine structure in both these regions and from the order of appearance of the signals and their relative intensities, the ^{113}Cd spectra of the five individual complexes can be assigned. For the species with x = 1, 2, and 3, the relative intensities in the $PhSeCd(\mu\text{-SePh})_3$ and $SCNCd(\mu\text{-SePh})_3$ regions are 3 and 1, 2 and 2, and 1 and 3, respectively. The anion $[(\mu\text{-SePh})_6(CdNCS)_4]^{2-}$ gives a signal in the $SCNCd(\mu\text{-SePh})_3$ region only. Similar spectra occur for the cyanato complexes (Fig. 1*b*) though these give resolved signals only in the $OCNCd(\mu\text{-SePh})_3$ region. Details of the ^{113}Cd nmr spectra of these new Cd_4 complexes are given in Table 4. The data confirm that N-bonding of the pseudohalide occurs in both series. Attachment of an S-bound thiocyanate to ^{113}Cd is expected (33) to produce *deshielding* relative to attachment of an N-bound cyanate. This is the reverse of what we observe.

Unlike the reactions of **1** with MeHgNCO and MeHgNCS, reactions with Ph_3SnNCO and Ph_3SnNCS do not proceed to completion. After addition of two equivalents of Ph_3SnNCO to **1** (0.01 mol/L of Me_2CO), ^{77}Se nmr at 213 K shows that the major species at equilibrium is still **1**; a smaller amount of $[(\mu\text{-SePh})_6(CdSePh)_3(CdNCO)]^{2-}$ is also evident, as is the co-produced $Ph_3SnSePh$. An identical experiment using Ph_3SnNCS shows that the major Cd_4 species present in this case is $[(\mu\text{-SePh})_6(CdSePh)_3(CdNCS)]^{2-}$. Even here though, less than 50% of the Ph_3SnNCS is converted to $Ph_3SnSePh$ at equilibrium. The different behaviours of methylmercury and triphenyltin pseudohalides towards **1** are consistent with results of MeHgSePh:Ph_3SnY (Y = NCO or NCS) mixtures.

*(ii) $[(\mu\text{-SePh})_6(ZnSePh)_4]^{2-}$ (**2**)*

From $^{119}Sn/^{199}Hg$ nmr there appears to be complete reaction of **2** with $R_nM'Y$ (R_nM' = Ph_3Sn or MeHg; Y = Cl, Br, I, NCO, or NCS) up to $R_nM'Y/2 = 4$.[13] Using ^{77}Se nmr, it can be shown that the reactions occur cleanly. In Me_2CO solution at ambient probe temperature, the anion **2** itself gives two well-separated ^{77}Se resonances at 46 and −7 ppm, that can be assigned to $PhSe_t$ and $PhSe_{br}$, respectively (2*b*). From ^{77}Se nmr spectra obtained at 298 K on stepwise addition of Cl_2 or $PhICl_2$, Br_2, or I_2 to **2**, we have earlier characterized the series $[(SePh)_6(ZnSePh)_{4-x}(ZnY)_x]^{2-}$ (Y = Cl, Br or I; x = 1–4) (2*b*). Under the same conditions, essentially identical spectra, with additional resonances from $Ph_3SnSePh$, are obtained here on stepwise addition of the corresponding Ph_3SnY. These results show that reaction [3] occurs cleanly as well as completely with the organotin halides. Using methylmercury halides very similar results are obtained except that the ^{77}Se nmr spectra, of species containing $PhSe_t$ in particular, are significantly broader. Sharp clean spectra can be obtained at reduced temperature, but it is clear that a new, as yet unidentified, exchange process occurs in the presence of methylmercury salts. The same phenomenon was observed whenever MeHgY was used.

Incremental addition of Ph_3SnY (Y = NCO or NCS) to **2** in Me_2CO at 298 K, causes ^{77}Se nmr spectral changes indicative of the formation of the new anions $[(\mu\text{-SePh})_6$-

Can. J. Chem. Downloaded from www.nrcresearchpress.com by 112.217.228.212 on 09/07/12
For personal use only.

TABLE 3. Selenium-77 nmr data for $[(\mu\text{-SePh})_6(MSePh)_{4-x}(MY)_x]^{2-}$ as equilibrium mixtures in acetone[a]

M	T (K)	x	δ_{Se} (terminal PhSe)[b] Y = NCO	δ_{Se} (terminal PhSe)[b] Y = NCS	Bridging PhSe: Geminal terminal groups	Bridging PhSe: Non-geminal terminal groups	δ_{Se}[b] Y = NCO	δ_{Se}[b] Y = NCS
Cd[c]	213	0[d]	28.4[e]	28.5[e]	PhSe, PhSe	PhSe, PhSe	−63.6[e]	−63.6[e]
		1[f]	24.6[g]	23.3[h]	PhSe, PhSe	PhSe, Y	−64.3[i]	−64.8[j]
					PhSe, Y	PhSe, PhSe	−80.1[k]	−82.5[l]
		2[f]	21.8	19.6[m]	PhSe, PhSe	Y, Y	−65.8	−66.7
					PhSe, Y	PhSe, Y	−81.5	−84.8
					Y, Y	PhSe, PhSe	−96.8	−101.4
		3[f]	18.8	15.5	PhSe, Y	Y, Y	−83.6[n]	−87.8
					Y, Y	PhSe, Y	−98.1	−103.9
					Y, Y	Y, Y	−100.5[f]	−106.2[o]
Zn	298	0[d,p]	45.7	46.1	PhSe, PhSe	PhSe, PhSe	−7.2	−6.5
		1[d,p]	42.9	42.5	PhSe, PhSe	PhSe, Y	−9.0	−10.0
					PhSe, Y	PhSe, PhSe	−21.7	−26.4
		2[d,p]	39.9	38.8	PhSe, PhSe	Y, Y	−11.1	−13.4
					PhSe, Y	PhSe, Y	−24.3	−30.3
					Y, Y	PhSe, PhSe	−34.7	−43.5
		3[o,p]	36.7	35.1	PhSe, Y	Y, Y	−27.2	−34.8
					Y, Y	PhSe, Y	−37.5	−47.9
		4[o,p]			Y, Y	Y, Y	−40.6	−52.4
	253	0[f,q]	41.3		PhSe, PhSe	PhSe, PhSe	−15.2	
		1[f,q]	38.6		PhSe, PhSe	PhSe, Y	−16.3	
					PhSe, Y	PhSe, PhSe	−29.1	
		2[f,q]	35.7		PhSe, PhSe	Y, Y	−17.8	
					PhSe, Y	PhSe, Y	−31.0	
					Y, Y	PhSe, Y	−41.5	
		3[f,q]	32.6		PhSe, Y	Y, Y	−33.4	
					Y, Y	PhSe, Y	−43.5	
		4[f,q]			Y, Y	Y, Y	−46.2	

[a]In equilibrium mixtures produced from $(R_4N)_2[(\mu\text{-SePh})_6(MSePh)_4]$ and $R_nM'Y$, with 0.05 mol of cluster per L of Me_2CO at room temperature. Some mixtures were saturated.

[b]Relative to external pure Me_2Se at 298 K.

[c]In $(Me_4N)_2[(Cd_4(SePh)_{10}]$–MeHgY mixtures.

[d]In a solution where $[M_4(SePh)_{10}]^{2-}$:$R_nM'Y$ = 1:1.

[e]In a solution of $(Me_4N)_2[Cd_4(SePh)_{10}]$ (0.01 mol per L of Me_2CO, enriched with ^{113}Cd to *ca.* 40 atom%) at 213 K, δ_{Se} and $^1J(^{113}Cd—^{77}Se)$ = 26.4 and 144 ± 3 Hz, and −64.3 and 165 ± 3 Hz, for terminal and bridging PhSe, respectively.

[f]In a solution where $[M_4(SePh)_{10}]^{2-}$:$R_nM'Y$ = 1:2.

[g]$^1J(^{111/113}Cd—^{77}Se) \approx 144$ Hz.

[h]$^1J(^{111/113}Cd—^{77}Se) \approx 164 \pm 10$ Hz.

[i]$^1J(^{111/113}Cd—^{77}Se) \approx 152 \pm 6$ Hz.

[j]$^1J(^{111/113}Cd—^{77}Se) \approx 151$ Hz.

[k]$^1J(^{111/113}Cd—^{77}Se) \approx 180$ Hz.

[l]$^1J(^{111/113}Cd—^{77}Se) \approx 178$ Hz.

[m]$^1J(^{111/113}Cd—^{77}Se) \approx 154$ Hz.

[n]$^1J(^{111/113}Cd—^{77}Se) \approx 162$ Hz.

[o]In a solution where $[M_4(SePh)_{10}]^{2-}$:$R_nM'Y$ = 1:3.

[p]In $(Me_4N)_2[Zn_4(SePh)_{10}]$–$Ph_3SnY$ mixtures; these mixtures also contain $Ph_3SnSePh$ (δ_{Se} = −30.3 to −30.8; $^1J(^{119}Sn—^{77}Se)$ = 1150 ± 5 Hz, at 298 K).

[q]In a $(Et_4N)_2[Zn_4(SePh)_{10}]$–MeHgNCO mixture; this solution also contains MeHgSePh (δ_{Se} = 156, $\Delta\nu_{1/2} \approx 45$ Hz, at 253 K).

$(ZnSePh)_{4-x}(ZnY)_x]^{2-}$ (Y = NCO or NCS) in equilibrium mixtures.[15] The ^{77}Se nmr spectral patterns of the individual clusters and the equilibrium mixtures are qualitatively similar to those of the series $[(\mu\text{-SePh})_6(CdSePh)_{4-x}(CdY)_x]^{2-}$ (Y = NCO or NCS) (see above) and $[(\mu\text{-SePh})_6(ZnSePh)_{4-x}(ZnY)_x]^{2-}$ (Y = Cl, Br, or I) (2*b*), and can be assigned in the same manner. At $Ph_3SnY/\mathbf{1}$ = 4, the major species is $[(\mu\text{-SePh})_6(ZnY)_4]^{2-}$, but the anion is in equilibrium with detectable amounts of the species with x = 3 and products corresponding to x > 4, which remain unidentified. The Cd_4 analogues and $[(\mu\text{-SePh})_4(ZnCl)_4]^{2-}$ redistribute similarly, as discussed above. Assigned ^{77}Se nmr spectra of the two pseudohalide-substituted series are given in Table 3. The similarity between the ^{77}Se nmr spectra of the two series shows that in these tetranuclear Zn_4 anions NCS^-, like NCO^-, is N-bonded. This is the case in mononuclear zinc complexes also (e.g. refs. 31*a*, 34).

Table 3 also contains data for a representative series of clusters formed using the methylmercury method. The spectra of MeHgNCO:**2** mixtures are broad at ambient probe temperature, but sharp at reduced temperature. Apart from expected

Can. J. Chem. Downloaded from www.nrcresearchpress.com by 112.217.228.212 on 09/07/12
For personal use only.

Can. J. Chem. Downloaded from www.nrcresearchpress.com by 112.217.228.212 on 09/07/12
For personal use only.

TABLE 4. Cadmium-113 nmr data for $[(\mu\text{-EPh})_6(\text{CdEPh})_x(\text{CdY})_{4-x}]^{2-}$ (E = S or Se; Y = NCO or NCS) at 213 K in acetone[a]

E	Y	x	δ_{Cd}[b] $(\mu\text{-EPh})_3\text{Cd(EPh)}$ kernel[c]	δ_{Cd}[b] $(\mu\text{-EPh})_3\text{CdY}$ kernel[c]
Se	—	0[d]	540.6[e]	—
	NCS	1[f]	539.1	489.4
		2[g]	538.0	494.4
		3[h]	537.2	497.3
		4[i]	—	497.6[j]
	NCO	1[d]	~539	510.6
		2[d]	~539	513.5
		3[h]	~539	515.8
		4[i]	—	516.9[k]
S	—	0[l]	592.9[m]	—
	NCS	1[f]	591.7[n]	528.8
		2[f]	589.2[n]	531.7
		3[h]	586.9	532.1
		4	—	530.4[o]
	NCO[p]	1[f]	591.8[q]	~546[r]
		2[g]	590.5	~548[r]
		3[g]	~589	~548[r]
		4[i]	—	548.5[s]

[a]In equilibrium mixtures produced from $(Me_4N)_2[(\mu\text{-EPh})_6(\text{CdEPh})_4]$ and MeHgY, with 0.05 mol of cluster per L of Me_2CO at room temperature, and using natural Cd, except where noted otherwise. Some mixtures were saturated.
[b]Relative to external 0.1 *M* $Cd(ClO_4)_2$ (aq) at 295 K.
[c]See text.
[d]In a solution of $(Me_4N)_2[Cd_4(SePh)_{10}]$ (0.01 mol/L of Me_2CO, enriched with ^{113}Cd to *ca.* 40 atom%).
[e]$^2J(^{113}Cd—Se—^{111}Cd)$ = 66 ± 3 Hz, confirmed in ^{111}Cd nmr spectrum.
[f]In a mixture where $[Cd_4(EPh)_{10}]^{2-}$:MeHgY = 1:1.
[g]In a mixture where $[Cd_4(EPh)_{10}]^{2-}$:MeHgY = 1:2.
[h]In a mixture where $[Cd_4(EPh)_{10}]^{2-}$:MeHgY = 1:3.
[i]In a mixture where $[Cd_4(EPh)_{10}]^{2-}$:MeHgY = 1:4.
[j]At 297 K, $\delta_{Cd} \approx 494$, $\Delta\nu_{1/2} \approx 425$ Hz in the 1:4 mixture.
[k]At 297 K, $\delta_{Cd} \approx 503$, $\Delta\nu_{1/2} \approx 275$ Hz in the 1:4 mixture.
[l]In a solution of $(Pr_4N)_2[Cd_4(SPh)_{10}]$ (0.05 mol/L of Me_2CO).
[m]$^2J(^{113}Cd—^{111}Cd) \approx 45$ Hz.
[n]$^2J(^{113}Cd—^{111/113}Cd) \approx 40$ Hz.
[o]At 297 K, $\delta_{Cd} \approx 527$, $\Delta\nu_{1/2} \approx 450$ Hz in the 1:4 mixture.
[p]Using $(Pr_4N)_2[Cd_4(SPh)_{10}]$.
[q]$^2J(^{113}Cd—^{111/113}Cd) \approx 56$ Hz.
[r]Poorly resolved.
[s]At 297 K, $\delta_{Cd} \approx 536$, $\Delta\nu_{1/2} \approx 370$ Hz.

(2*b*) temperature shifts, and the absence of the signals of $Ph_3SnSePh$, the ^{77}Se spectra of the complexes formed from MeHgNCO are identical to those formed from Ph_3SnNCO.

(iii) $[(\mu\text{-SPh})_6(CdSPh)_4]^{2-}$ (3)

When 4 mol equiv. of $R_nM'Y$ (R_nM' = Ph_3Sn or MeHg; Y = Cl, Br, or I) are added to **3** in Me_2CO or MeCN, ^{113}Cd nmr shows that the tetrahaloanions $[(\mu\text{-SPh})_6(CdY)_4]^{2-}$ are formed cleanly. Cadmium-113 nmr data have already been reported on these species (5), **3** (3, 12, 35), and the partially-substituted species $[(\mu\text{-SPh})_6(CdSPh)_{4-x}(CdY)_x]^{2-}$ (Y = Cl, Br, or I; x = 1–3) (5).

On incremental addition of up to 4[13] mol equiv. of MeHgNCO or MeHgNCS to **3** in Me_2CO, the changes occurring in the ^{113}Cd nmr spectra of the mixtures at 213 K[14] can be interpreted in terms of the formation $[(\mu\text{-SPh})_6(CdSPh)_{4-x}(CdY)_x]^{2-}$ (Y = NCO or NCS; x = 1–4). The spectra are generally similar to those of the corresponding $PhSe^-$ complexes discussed above, and can be assigned in the same way. The ^{113}Cd nmr spectra are summarized in Table 4. For the thiolate clusters, the linewidths are generally smaller than for the $PhSe^-$ analogues, and in several cases partially resolved cadmium satellites are evident. Whereas only $^2J(^{113}Cd—^{111}Cd)$ coupling is expected over the pathway PhS—Cd—S(Ph)—Cd—SPh in these tetranuclear complexes (12, 35), both ^{113}Cd–^{111}Cd and ^{113}Cd–^{113}Cd coupling can occur in the fragment PhS—Cd—S(Ph)—Cd—Y. The partially-resolved couplings observed (Table 4) will be a superimposition of these. As expected, the values of ^2J are similar to those of **3** (e.g. 47 ± 2 Hz at 295 K in Me_2CO (13)). From the data for $[(\mu\text{-SPh})_6(CdSPh)_{4-x}(CdY)_x]^{2-}$ (Y = NCO or NCS) in Table 4, it is again clear that in the thiocyanate complexes N-bonding of the ligand occurs.

Comparison of the ^{113}Cd nmr spectra of **3**:Ph_3SnY (Y = NCO or NCS) mixtures with those of the analogous **3**:MeHgY mixtures shows that reaction of the triphenyltin pseudohalides occurs cleanly but is incomplete. With 4 mol equiv. of $Ph_3Sn(IV)$ reagent added to **3** (0.05 mol/L of Me_2CO) only *ca.* 33% of the cadmium ions have been substituted at equilibrium. This is in agreement with the results of ^{119}Sn nmr. As noted above, the corresponding reactions with **1** are also incomplete.

The different behaviours of the triphenyltin and methylmercury pseudohalides towards **3** are consistent with the position of equilibrium [4] when E = S and Y = NCO or NCS.

(iv) $[(\mu\text{-SPh})_6(ZnSPh)_4]^{2-}$ (4)

Substitution of this cluster cannot be followed directly by nmr methods. The properties of the quadrupolar ^{67}Zn nucleus[17] make this an unattractive probe (see, for example, ref. 36), and the ^{13}C and ^1H nmr spectra of the PhS_{br} groups are insensitive to changes in the terminal substituents of the cluster (see, for example, ref. 5*b*). In this case, then, the cleanness of reaction cannot be assessed by nmr. The extent of reaction can be followed by ^{119}Sn or ^{199}Hg nmr, as above. From ^{119}Sn nmr of mixtures with $0 < Ph_3SnY/4 \leq 4$,[13] reaction [3] appears complete for Y = Cl, Br, I, NCO, and NCS. Similarly, from ^{199}Hg nmr, complete reaction seems to occur up to MeHgY/**4** for Y = Cl, Br, NCO, and SCN. In contrast, MeHgI does not react completely with **4**. The supernatant fraction of a mixture of **4** (0.05 mol/L of Me_2CO) with 4 mol equiv. of MeHgI at 295 K gives an exchange-averaged ^{199}Hg nmr signal at $\delta_{Hg} = -660$. This chemical shift shows that *ca.* 10% of the MeHgI remains unreacted at equilibrium. Thus Ph_3SnI is a better reagent for iodide-substitution of **4** than MeHgI. This is as expected from the position of equilibrium [4] when E = S and Y = I (see Table 2 and discussion above).

(v) $[(\mu\text{-SPh})_6(CoSPh)_4]^{2-}$ (5)

Earlier workers (3) have shown that at or below 346 K this paramagnetic complex gives six separate isotropically-shifted ^1H nmr signals, consistent with slow exchange between PhS_t and PhS_{br} groups. Assignments were made using deuterium labelling. In agreement with the earlier work, our spectra of **5** (0.02 mol/L of MeCN) at 294 K show six well-resolved signals (see Fig. 2*a* and Table 5).

Stepwise addition of Ph_3SnY (Y = Cl, Br, I, NCO, or NCS) to **5** (0.02 mol/L of MeCN) causes both the generation of new signals in each of the six regions of the ^1H nmr spectrum of **5**

[17] ^{67}Zn: 4.11% natural abundance; spin, I = 5/2; quadrupole moment 0.16 Q/m^2; receptivity relative to ^{13}C 0.670 (12).

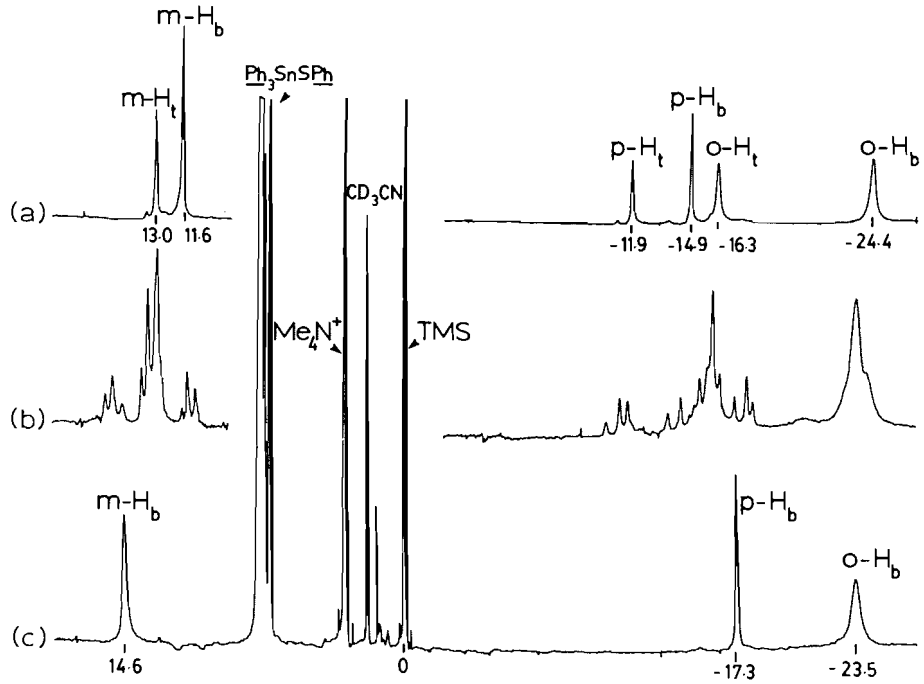

FIG. 2. Proton nmr spectra at 200.06 MHz and 294 K of $(Me_4N)_2[(\mu\text{-SPh})_6(CoSPh)_4]$ (**5**):Ph_3SnI mixtures in CD_3CN showing formation of $[(\mu\text{-SPh})_6(CoSPh)_{4-x}(CoI)_x]^{2-}$. (*a*) **5** alone. (*b*) Ph_3SnI:**5** = 2:1. (*c*) Ph_3SnI:**5** = 4:1. The mixtures were prepared using 0.02 mol of **5**/L of CD_3CN.

TABLE 5. Proton nmr spectra of some complexes $[(\mu\text{-SPh})_6(CoY)_4]^{2-}$ in MeCN at 294 ± 2 K[a]

Y	δ_H[b] ($\Delta\nu_{1/2}$ (approx)[c])		
	o-H[d]	*m*-H[d]	*p*-H[d]
SPh[e]	−24.4 (60)	11.60 (21)	−14.93 (21)
	−16.3 (45)[f]	12.98 (24)[f]	−11.87 (24)[f]
Cl	−23.9 (85)	14.60 (15)	−17.25 (15)
Br	−24.0 (100)	14.86 (17)	−17.50 (16)
I	−23.5 (105)	14.64 (45)	−17.31 (23)
NCO	−24.2 (110)	13.78 (18)	−16.76 (19)
NCS	−22.2 (85)	15.08 (17)	−16.73 (17)

[a]In an equilibrium mixture with $(Me_4N)_2[(\mu\text{-SPh})_6(CoSPh)_4]$:$Ph_3SnY$ = 1:4, prepared starting from a solution containing 0.02 mol of $[Co_4(SPh)_{10}]^{2-}$ per L of MeCN; see text.
[b]Relative to internal TMS.
[c]In Hz.
[d]Assignments are based on those of ref. 3.
[e]Data for $[(\mu\text{-SPh})_6(CoSPh)_4]^{2-}$ have been reported previously (3).
[f]Terminal SPh groups.

and a stepwise diminution in the Ph_t/Ph_{br} intensity ratio. A representative series of ^1H nmr spectra, from the system **5**–Ph_3SnI, are shown in Fig. 2. Overall, the results for the systems **5**–Ph_3SnY are quite consistent with the production of equilibrium mixtures of $[(\mu\text{-SPh})_6(CoSPh)_{4-x}(CoY)_x]^{2-}$. We have not attempted assignment of the spectra of all the individual members of the several series. Many lines are expected[18] and there is significant signal overlap (e.g. Fig. 2*b*).

However, assignment of the relatively simple spectra of all the fully terminally substituted complexes $[(\mu\text{-SPh})_6(CoY)_4]^{2-}$ was straightforward. Details of these spectra are given in Table 5. The complex $[(\mu\text{-SPh})_6(CoI)_4]^{2-}$ is the sole species present in Ph_3SnI:**5** mixtures at Sn/Co = 4 (see Fig. 2*c*). At this same ratio, a small amount of $[(\mu\text{-SPh})_6(CoSPh)(CoY)_3]^{2-}$ is present in the equilibrium mixtures when the other Ph_3SnY are used. Probably $[(\mu\text{-SPh})_6(CoY)_4]^{2-}$ exists in equilibrium with its redistribution products in these cases, since ^{119}Sn nmr shows no detectable amount of unreacted Ph_3SnY.

This is the first characterization of the tetra-substituted complexes with Y = Br, I,[19] NCO and NCS.[20] As noted in the Introduction, $[(\mu\text{-SPh})_6(CoCl)_4]^{2-}$ has been characterized in the solid state very recently (10). In the same work, an attempt to characterize this complex in solution using ^1H nmr was unsuccessful. We find that the ^1H nmr spectrum of $[(\mu\text{-SPh})_6(CoCl)_4]^{2-}$ is not unusually broad (see Table 5) and can offer no explanation for the earlier lack of success.

When MeHgY is used to substitute **5**, the ^1H nmr spectral changes observed are generally similar to those obtained using Ph_3SnY. However, noticeable broadening of the spectra is induced by the methylmercury compounds, and the ^1H nmr spectrum of MeHgSPh is also broad in these mixtures. Again these results suggest an intermolecular exchange process in the presence of MeHg(II). The broadness of the ^1H nmr lines in **5**:MeHgY mixtures makes it difficult to quantify the extent of reaction by pmr. However, judged by ^{199}Hg nmr, reaction is complete for Y = Cl, Br, NCO, or SCN up to MeHgY/**5** = 4.

[18]For $1 \leq x \leq 3$, every new member of the series should give rise to a new signal in each of the *o*-H_t, *m*-H_t, and *p*-H_t regions. For x = 1, 2, 3, and 4, there should be two, three, two, and one new signal(s), respectively, in each of the *o*-H_{br}, *m*-H_{br}, and *p*-H_{br} regions (c.f. discussion of the ^{77}Se nmr spectra of $[(\mu\text{-SePh})_6(MSePh)_{4-x}(MY)_x]^{2-}$ (M = Cd or Zn) above).

[19]We find that this complex can also be synthesized cleanly by treatment of **5** with 2 mol equiv. of I_2 in MeCN, as described earlier (5) for the Cd_4 and Zn_4 analogues.

[20]The bonding mode of NCS^- in $[(\mu\text{-SPh})_6(CoY)_4]^{2-}$ (Y = NCS) cannot be determined unambiguously from the ^1H nmr spectrum of the cluster. N-bonding seems most probable, since this bonding mode is well-established for Co(II) (e.g. ref. 34).

Can. J. Chem. Downloaded from www.nrcresearchpress.com by 112.217.228.212 on 09/07/12
For personal use only.

In contrast, reaction of **5** with MeHgI is incomplete. For example, when 4 mol equiv. of MeHgI are added to **5** (0.01 mol/L of MeCN), approximately 40% of the MeHgI reacts. As noted above, incomplete reaction with MeHgI is also observed for **4**.

Acknowledgments

We thank the Natural Sciences and Engineering Research Council of Canada for financial support of this work. We are grateful to Mrs. V. M. Richardson and Ms. S. Wilson, both of this Department, for expert technical assistance in obtaining some of the nmr spectra, and to Dr. Ivor Wharf of Dawson College, Montreal, P.Q., for helpful discussions about triphenyltin pseudohalides.

1. I. G. DANCE. Polyhedron, **5**, 1037 (1986) and references therein.
2. (*a*) P. A. W. DEAN and J. J. VITTAL. Inorg. Chem. **25**, 514 (1986); (*b*) P. A. W. DEAN and J. J. VITTAL. Inorg. Chem. **26**, 278 (1987); (*c*) P. A. W. DEAN, J. J. VITTAL, and N. C. PAYNE. Unpublished results.
3. K. S. HAGEN, D. W. STEPHAN, and R. H. HOLM. Inorg. Chem. **21**, 3928 (1982).
4. I. G. DANCE. Austral. J. Chem. **38**, 1745 (1985).
5. (*a*) P. A. W. DEAN and J. J. VITTAL. Inorg. Chem. **24**, 3722 (1985); (*b*) P. A. W. DEAN, J. J. VITTAL, and N. C. PAYNE. Inorg. Chem. **26**, 1683 (1987).
6. H. J. LUCAS and E. R. KENNEDY. Org. Synth. **22**, 69 (1942).
7. D. COUCOUVANIS, M. KANATZIDIS, E. SIMHON, and N. C. BAENZIGER. J. Am. Chem. Soc. **104**, 1874 (1982).
8. I. G. DANCE. Inorg. Chem. **20**, 2155 (1981).
9. (*a*) I. G. DANCE. J. Am. Chem. Soc. **101**, 6264 (1979); (*b*) I. G. DANCE and J. C. CALABRESE. J. Chem. Soc. Chem. Commun. 762 (1975).
10. D. FENSKE, J. MEYER, and K. MERZWEILER. Z. Naturforsch. **42**(B), 1207 (1987).
11. E. MACMULLIN and M. E. PEACH. J. Organomet. Chem. **52**, 355 (1973).
12. R. K. HARRIS. Nuclear magnetic resonance spectroscopy. Pitman, London. 1983. p. 230.
13. P. A. W. DEAN and J. J. VITTAL. J. Am. Chem. Soc. **106**, 6936 (1984).
14. J. RELF and R. P. COONEY. J. Organomet. Chem. **39**, 75 (1972).
15. J. S. THAYER and R. WEST. Inorg. Chem. **3**, 406 (1964).
16. A. S. MUFTI and R. C. POLLER. J. Chem. Soc. 5055 (1965).
17. J. BOESEKEN and J. J. RUTGERS. Rec. Trav. Chim. **42**, 1017 (1923).
18. (*a*) A. M. DOMINGOS and G. M. SHELDRICK. J. Organomet. Chem. **67**, 257 (1974); (*b*) I. WHARF, L. PIEHLER, B. M. SAILOFSKY, M. ONYSZCHUK, and M. G. SIMARD. Can. J. Chem. **65**, 639 (1987).
19. P. G. HARRISON. *In* Dictionary of organometallic compounds. Vol. 2. *Edited by* J. Buckingham. Chapman and Hall, London. 1984. p. 2152 et seq, and references therein.
20. J. L. WARDELL. *In* Dictionary of organometallic compounds. Vol. 1. *Edited by* J. Buckingham. Chapman and Hall, London. 1984. p. 1016 et seq, and references therein.
21. A. J. CANTY and A. J. CARTY. J. Inorg. Biochem. **19**, 133 (1983).
22. (*a*) K. C. MOLLOY, K. QUILL, S. J. BLUNDEN, and R. HILL. J. Chem. Soc. Dalton. 875 (1986); (*b*) G. J. JENKS. Austral. Dept. Supply, Defense Standards Lab., Techn. Note No. 87 (1966). *Quoted in* S. J. Blunden, P. A. Cusack and D. G. Gillies. J. Magn. Reson. **60**, 114 (1984).
23. H. LEIMEISTER and K. DEHNICKE. J. Organomet. Chem. **31**, C3 (1971).
24. (*a*) P. A. W. DEAN and J. J. VITTAL. Inorg. Chem. **26**, 4245 (1987); (*b*) P. A. W. DEAN and R. S. SRIVASTAVA. Inorg. Chim. Acta, **105**, 1 (1985).
25. J. D. ODOM, W. H. DAWSON, and P. D. ELLIS. J. Am. Chem. Soc. **101**, 5815 (1979).
26. D. N. KRAVTSOV, A. S. PEREGUDOV, and E. M. ROKHLINA. J. Organomet. Chem. **128**, C27 (1977).
27. D. W. GRANT and J. L. WARDELL. J. Organomet. Chem. **276**, 161 (1984).
28. R. D. BACH and A. T. WEIBEL. J. Am. Chem. Soc. **98**, 6241 (1976).
29. A. M. DOMINGOS and G. M. SHELDRICK. J. Organomet. Chem. **67**, 257 (1974).
30. M. CANNAS, G. CARTA, A. CRISTINI, and G. MARIONGIU. J. Chem. Soc. Dalton Trans. 300 (1976).
31. (*a*) J. A. KARGOL, R. W. CRECELY, and J. L. BURMEISTER. Inorg. Chem. **18**, 2532 (1979); (*b*) A. I. SHVELASHVILI, M. A. PORAI-KOSHITS, A. I. KVITASHVILI, B. M. SHCHEDRIN, and L. P. SARISHVILI. Zh. Strukt. Khim. **15**, 315 (1974) (Chem. Abstr. **81**, 69762q (1974)).
32. L. M. SEITZ and T. L. BROWN. J. Am. Chem. Soc. **88**, 2174 (1966).
33. M. F. SUMMERS. Coord. Chem. Rev. **86**, 43 (1988).
34. A. H. NORBURY. Adv. Inorg. Nucl. Chem. **17**, 298 (1975) and references therein.
35. I. G. DANCE and J. K. SAUNDERS. Inorg. Chim. Acta, **96**, L71 (1985).
36. G. K. CARSON and P. A. W. DEAN. Inorg. Chim. Acta, **66**, 157 (1982).

Can. J. Chem. Downloaded from www.nrcresearchpress.com by 112.217.228.212 on 09/07/12
For personal use only.

The effects of aggregation, counterion binding, and added NaCl on diffusion of aqueous methylene blue

DEREK G. LEAIST
Department of Chemistry, University of Western Ontario, London, Ont., Canada N6A 5B7

Received April 5, 1988

DEREK G. LEAIST. Can. J. Chem. **66**, 2452 (1988).

A simplified version of the Harned conductimetric technique is used to measure binary diffusion of the self-associating dye methylene blue chloride in water at 25°C. As the dye concentration is increased from 0.0006 to 0.02 mol dm^{-3}, aggregation of the dye monomers and binding of the chloride counterions cause the dye's binary diffusion coefficient to drop from 0.83×10^{-9} to 0.63×10^{-9} $m^2 s^{-1}$. Ternary diffusion coefficients for aqueous methylene blue chloride + NaCl solutions are also reported. These results show that small amounts of added NaCl (0.005 or 0.01 mol dm^{-3}) sharply reduce the diffusivity of the dye component, and that each mole of diffusing dye cotransports 0.2–0.7 mol NaCl. Diffusion of trace amounts of the dye in the presence of a large excess of an inert supporting electrolyte is discussed briefly.

DEREK G. LEAIST. Can. J. Chem. **66**, 2452 (1988).

On a utilisé une version simplifiée de la technique de conductimétrie de Harned pour mesurer la diffusion binaire du colorant auto-associé, le chlorure du bleu de méthylène dans l'eau à 25°C. Lorsque la concentration du colorant passe progressivement de 0,0006 à 0,02 mol dm^{-3}, l'aggrégation des monomères du colorant et la fixation des ions contraires du chlorure provoquent une chute du coefficient de diffusion binaire du colorant de $0,83 \times 10^{-9}$ à $0,63 \times 10^{-9}$ $m^2 s^{-1}$. On rapporte également les coefficients de diffusion ternaire des solutions aqueuses de chlorure de bleu de méthylène + NaCl. Ces résultats indiquent que l'addition de petites quantités de NaCl (0,005 ou 0,01 mol dm^{-3}) réduisent sensiblement la diffusibilité du colorant, et que la diffusion de chaque mole de colorant entraine celle de 0,2 à 0,7 mole de NaCl. On discute brièvement de la diffusion du colorant à l'état de traces en présence d'un grand excès d'un electrolyte agissant comme support inerte.

[Traduit par la revue]

1. Introduction

Methylene blue (1–13), like many other dyes (14, 15) and biochemicals (16), self-associates in aqueous solutions. The flat methylene blue cations stack like plates to form dimers, trimers, and larger aggregates. In this paper diffusion coefficients are reported for methylene blue chloride in water and in aqueous sodium chloride solutions. The work was undertaken to study the effects of aggregation, added salt, and counterion binding on the diffusion behavior of an ionic dye.

When methylene blue chloride diffuses in pure water, an electric field is generated to speed up the methylene blue aggregates and to slow down the smaller, relatively mobile chloride counterions, thereby preventing charge separation. If a supporting electrolyte such as NaCl is added, the electric field will produce a coupled flow of Na^+ ions at the expense of speeding up the methylene blue cations. As a result, the dye will diffuse more slowly (17, 18) and it will cotransport sodium ions. These features have practical implications for dyeing operations that use baths containing supporting electrolytes.

The aggregation of methylene blue has been the subject of numerous previous investigations. Sedimentation (1–3) and solvent extraction (5–9) techniques, for example, have been used with success to determine the stepwise association constants. Absorption spectroscopy (1, 4, 10, 11), osmometry (4), polarography (12), and electrical conductivity (13) measurements have also been used to study the speciation of the aqueous dye.

2. Experimental

Methylene blue chloride, 3,7-bis[dimethylamino]phenazothionium chloride (Sigma Chemical Co.), was recrystallized from ethanol (1) and dried in a vacuum oven at 80°C. Potentiometric titration against silver nitrate indicated a purity of 98%. Sodium chloride (BDH reagent grade) was dried at 110°C and used without further treatment. Solutions were made up with distilled deionized water in calibrated volumetric flasks.

The intense optical absorbance of the dye and its tendency to adsorb onto glass surfaces would complicate interferometric or diaphragm-cell diffusion measurements. Accordingly, diffusion coefficients were determined by using a simplified Harned conductimetric procedure (19–21). The initial concentration gradients were prepared by injecting electrolyte into the lower ends of columns of solution. The rate of diffusion was followed by measuring changes in electrical conductivity with pairs of small platinum electrodes positioned near the top and bottom of the columns. Plots of the logarithm of the difference between the upper and lower conductivity against time for binary diffusion of the dye (no added NaCl) were linear. This indicated that the dye sample was adequately pure for our experiments (19).

In the ternary diffusion experiments on methylene blue chloride + NaCl solutions, separate experiments were run with initial gradients in the methylene blue chloride component or the NaCl component. Moments analysis (22) of the conductivity versus time data was used to evaluate the ternary diffusion coefficients. The diffusion cells used in the present work had cylindrical diffusion channels (4.57 cm height, 1.27 cm diameter) that were milled from high-density polyethylene or polypropylene and fitted with 0.1 cm diameter electrodes.

3. Results

Methylene blue chloride (1) + water

Diffusion of the methylene blue chloride component transports chloride ions together with dye monomers, dimers, trimers, etc. Conveniently, electroneutrality and local equilibrium of the association reactions ensure that only one solute flow is independent (23, 24). Consequently, diffusion of the dye obeys the simple binary transport equation

$$[1] \quad -J_1 = D_{11}\nabla C_1$$

Here, C_1 stands for the concentration of the methylene blue chloride component in moles of total dye monomer (free plus aggregated monomers) per unit volume and J_1 is the flux density of the dye component in moles of total dye monomer per unit area per unit time.

Values of D_{11}, the binary diffusion coefficient of the dye, were determined at 25.00 ± 0.01°C and mean cell concentrations of dye from 0.00057 to 0.0197 mol dm^{-3}. The measured

Can. J. Chem. Downloaded from www.nrcresearchpress.com by 112.217.228.212 on 09/07/12
For personal use only.

TABLE 1. Measured binary diffusion coefficients for aqueous methylene blue chloride at 25°C

$10^3 C_1$/(mol dm^{-3})	$10^9 D_{11}$/(m^2 s^{-1})
0.574	0.831
0.821	0.838
1.63	0.825
2.87	0.796
4.09	0.774
6.56	0.727
9.02	0.706
14.0	0.675
16.4	0.646
19.7	0.629

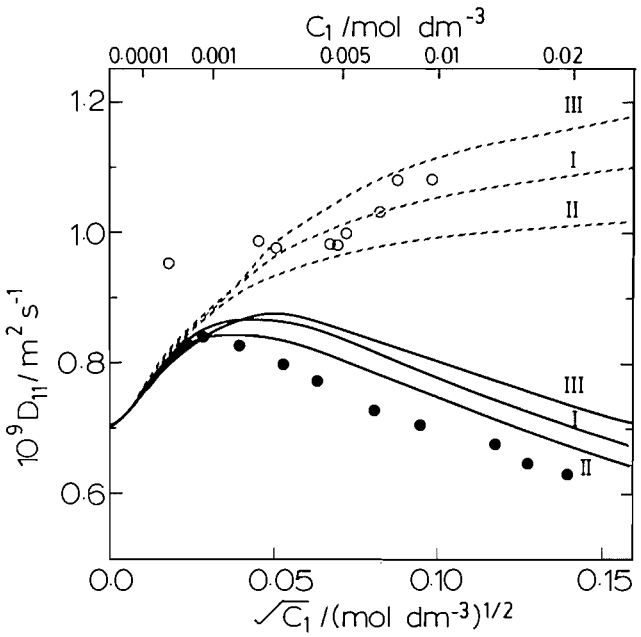

FIG. 1. Measured and predicted binary diffusion coefficients for aqueous dyes at 25°C. Methylene blue chloride: ●, measured D_{11} values; solid curves, predicted D_{11} values with chloride binding constant K_L = 45 dm^3 mol^{-1} and non-attenuated (I), attenuated (II), and isodesmic (III) association constants; dashed curves, predicted D_{11} with counterion binding omitted (K_L = 0). Methyl orange: ○, measured D_{11} values.

values of D_{11} drop from 0.83 × 10^{-9} to 0.63 × 10^{-9} m^2 s^{-1} with increasing concentration. The results of the experiments are summarized in Table 1.

Conductimetric diffusion data were reported recently for aqueous solutions of the sodium salt of methyl orange (25), a self-associating anionic azo dye. In contrast to the methylene blue diffusivities, the D_{11} values for methyl orange increase with concentration. The diffusion data for the two dyes are compared in Fig. 1.

The dye monomers become more extensively associated as the concentration rises. A qualitative analysis of the effect of aggregation on the diffusion behavior can be formulated by treating the dye as an n-univalent electrolyte, where n designates the mean aggregation number, the average number of dye monomers per aggregate. Methylene blue chloride, for example, may be assumed to dissolve as follows: MBCl = $(1/n)(MB)_n^{n+}$(aq) + Cl$^-$(aq). For this type of electrolyte, the mobility, U, and the thermodynamic driving force per mole of MBCl are given by (26)

$$[2] \quad U \cong \frac{1}{RT}\frac{nD_pD_{Cl}}{nD_p + D_{Cl}}$$

$$[3] \quad -\nabla\mu_1 \cong \frac{RT}{C_1}\left(1 + \frac{1}{n}\right)\nabla C_1$$

where D_p is the diffusion coefficient of the polyion that contains n dye monomers, D_{Cl} is the diffusion coefficient of the chloride counterions, and μ_1 is the chemical potential of the dye component. The factor $1 + (1/n)$ appearing in eq. [3] equals the number of moles of free solute particles per mole of dissolved dye. According to Stokes law, D_p should vary with n approximately as $n^{-1/3}$ (27). Therefore, as n increases with concentration, the mobility of the dye component should also increase and approach the mobility of the counterions.

Equations [2] and [3] lead to the following approximate expression for the binary diffusion coefficient (26)

$$[4] \quad D_{11} = C_1 U\frac{\partial\mu_1}{\partial C_1} \cong \frac{(n+1)D_pD_{Cl}}{nD_p + D_{Cl}}$$

which is identical to the expression for the limiting diffusion coefficient of an n-univalent electrolyte. It predicts that D_{11} should increase with n since, for large values of n, the predicted values of D_{11} for methylene blue chloride approach the diffusivity of the chloride counterions, about 2.0 × 10^{-9} m^2 s^{-1} at 25°C (28). The fact that the measured values of D_{11} actually decrease with concentration suggests that the simple model of free counterions diffusing with dye aggregates may require modification in the case of methylene blue. This point will be discussed later.

Methylene blue chloride (1) + NaCl (2) + water

Ternary diffusion in aqueous methylene blue chloride solutions with added NaCl is described by the coupled transport equations

$$[5] \quad -J_1 = D_{11}\nabla C_1 + D_{12}\nabla C_2$$

$$[6] \quad -J_2 = D_{21}\nabla C_1 + D_{22}\nabla C_2$$

where J_1 and J_2 are the molar flux densities of the methylene blue (1) and NaCl (2) components, and C_1 and C_2 are the respective concentrations of the components. Cross-diffusion coefficient D_{21} measures the flux of NaCl produced by the gradient in the concentration of the dye, and vice versa for D_{12}.

The ternary diffusion coefficients were determined in triplicate at the mean cell concentrations 0.002, 0.005, or 0.010 mol dm^{-3} methylene blue chloride and 0.005 or 0.01 mol dm^{-3} NaCl. The measured values of D_{ik} were reproducible within ±0.03 × 10^{-9} m^2 s^{-1}. The results of the ternary experiments are listed in Table 1.

As shown in Fig. 2, added NaCl sharply reduces the dye's diffusivity (D_{11}). The positive values of D_{21} confirm that the gradient in the concentration of the dye produces a significant co-current coupled flow of NaCl. It is evident from the values of the ratio D_{11}/D_{21} that each mole of diffusing dye cotransports 0.2 to 0.7 mol NaCl. The coupled flow of dye produced by the gradient in the concentration of NaCl is relatively small in the solutions that were studied. These and other features of the ternary diffusion behavior can be interpreted by treating the solutes as a simple mixture of $P_{1/n}$Cl + NaCl electrolytes. Extending eq. [4] to solutions with added NaCl gives (21, 30)

Can. J. Chem. Downloaded from www.nrcresearchpress.com by 112.217.228.212 on 09/07/12
For personal use only.

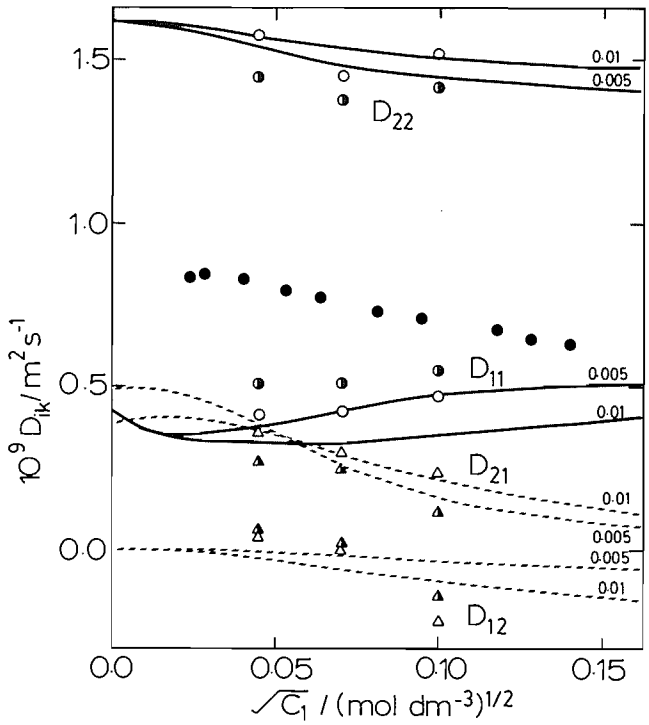

FIG. 2. Measured and predicted ternary diffusion coefficients for aqueous methylene blue chloride (1) + NaCl (2) solutions at 25°C. Measured values: △, ○, in 0.010 mol dm^{-3} NaCl; ▲, ◑, in 0.005 mol dm^{-3} NaCl; ●, binary diffusion coefficient D_{11} for NaCl-free methylene blue chloride solutions. Predicted values calculated with K_L = 45 dm^{-3} mol^{-1} and non-attenuated association constants (set I): solid curves, D_{11} and D_{22}; dashed curves, D_{12} and D_{21}.

[7] $D_{11} \cong D_p + t_p(D_{Cl} - D_p)$

[8] $D_{12} \cong t_p(D_{Cl} - D_{Na})/n^2$

[9] $D_{21} \cong t_{Na}(D_{Cl} - D_p)n^2$

[10] $D_{22} \cong D_{Na} + t_{Na}(D_{Cl} - D_{Na})$

Here t_i stands for the transference number of ion i

[11] $$t_i = c_i z_i^2 D_i \Big/ \sum_{k=1}^{3} c_k z_k^2 D_k$$

and c_i and z_i are the ionic concentrations and charges: $c_p = C_1/n$, $z_p = n$, $c_{Na} = C_2$, $z_{Na} = 1$, $c_{Cl} = C_1 + C_2$, $z_{Cl} = -1$. As the ratio of NaCl to methylene blue chloride increases, the transference number t_p of the methylene blue polyion drops to zero, and the predicted ternary diffusivity of the methylene blue chloride component, D_{11}, drops to D_p. As the NaCl:dye ratio increases, t_{Na} and hence D_{21} also increase.

4. Discussion

Aggregation

A more realistic treatment of diffusion in the methylene blue solutions with allowance for the polydispersity of the dye aggregates will now be attempted. Stepwise association of the dye cations will be described by using the series of reactions

$$MB^+ + (MB)_{i-1}^{(i-1)+} = (MB)_i^{i+}$$

with the association constants

[12] $K_i = c_i/c_1 c_{i-1}$

for the formation of an aggregate of i methylene blue monomers from an aggregate of $i - 1$ monomers. The concentration of the aggregate of i monomers is denoted by c_i.

Given the total dye concentration and values for the association constants (1, 6), the concentration of the free dye monomers, c_1, can be obtained by solving the mass balance equation

[13] $$C_1 = \sum_{i=1}^{\infty} i c_i = c_1 + 2K_2 c_1^2 + 3K_2 K_3 c_1^3 + \ldots$$

The concentrations of the methylene blue polymers can then be evaluated from $c_2 = K_2 c_1^2$, $c_3 = K_3 c_1 c_2$, etc. For the special case of isodesmic association (1, 6, 24), the various stepwise association constants are identical, $K_2 = K_3 = K_4 = \ldots = K$, and $C_1 = c_1/(1 - Kc_1)^2$.

Added NaCl

The diffusion coefficients for the solute components are most easily estimated (31) by first evaluating the Onsager L_{ik} transport coefficients defined by the flow equations

[14] $$-J_i = \sum_{k=1}^{2} L_{im} \nabla \mu_m$$

and then using the identity

[15] $$D_{ik} = \sum_{m=1}^{2} L_{im} \partial \mu_m / \partial C_k$$

Small electrophoretic interactions between the diffusing ions may be neglected for dilute solutions to give (26, 31)

[16] $L_{11} = (c_{Na} D_{Na} + c_{Cl} D_{Cl})A/B$

[17] $L_{12} = L_{21} = -c_{Na} D_{Na} A/B$

[18] $L_{22} = c_{Na} D_{Na}(c_{Cl} D_{Cl} + A)/B$

where A and B are abbreviations for

[19] $$A = \sum_{i=1}^{\infty} i^2 c_i D_i$$

[20] $B = RT(c_{Cl} D_{Cl} + c_{Na} D_{Na} + A)$

The values of $\partial \mu_m/\partial C_k$ required to estimate values of D_{ik} can be obtained by differention of eq. [13] together with the expressions

[21] $\mu_1 = \mu_1^0 + RT \ln [c_1(C_1 + C_2)]$

[22] $\mu_2 = \mu_2^0 + RT \ln [C_2(C_1 + C_2)]$

for the chemical potentials of the solute components.

In Fig. 1 the binary values of D_{11} for methylene blue chloride (no added NaCl) predicted by eqs. [12] and [22] are compared with the measured values. The association constants used in the calculations were taken from the solvent extraction study of Mukerjee and Ghosh (6). Three of their sets of recommended K_i values were used: I, "non-attenuated" association, K_2 = 2090 dm^3 mol^{-1} for the dimerization constant and $K_i (i > 2)$ = 2000 $(i - 1)/(i - 2)$ dm^3 mol^{-1} for the subsequent association constants; II, "attenuated" association, K_2 = 2160 dm^3 mol^{-1} and the slowly decreasing values $K_i (i > 2)$ = 8700/$(i - 1)$ dm^3 mol^{-1}; isodesmic association, $K_i (i > 1)$ = 2500 dm^3 mol^{-1}. The predicted values of D_{11} (dashed curves) and the measured values show poor agreement. The former increase with concentration whereas the latter decrease. The data in Fig. 1 are plotted against the square root of the dye concentration to help visualize the behavior at very low concentrations.

Can. J. Chem. Downloaded from www.nrcresearchpress.com by 112.217.228.212 on 09/07/12
For personal use only.

Can. J. Chem. Downloaded from www.nrcresearchpress.com by 112.217.228.212 on 09/07/12
For personal use only.

The value of the chloride ion diffusivity used in the calculations, 2.03×10^{-9} m^2 s^{-1}, was estimated from the limiting molar ionic conductance (28) $\Lambda_m^0(Cl^-) = 0.00763$. Although a precise value for the limiting conductance of the methylene blue cation is not known, extrapolation of Robinson's data for methylene blue chloride (13) gives the approximate value 0.0016 ($\pm$0.0002) for $\Lambda_m^0(MB^+)$, and hence $D_1 = 0.43 \times 10^{-9}$ m^2 s^{-1} for the methylene blue monomer. In order to estimate the diffusion coefficient of the dimer, we assumed that the dimer's volume is twice the volume of the monomer. Shape effects were taken into account by assuming that the monomer and dimer were oblate ellipsoids with minor axis:major axis ratios 1:4 and 2:4, respectively. Application of the well-known expression for the friction factor of an ellipsoid (32, 34) gave 0.38×10^{-9} m^2 s^{-1} for the diffusivity of the dimer, D_2. The trimer was assumed to have an axial ratio of 3:4, and so on for the higher polymers. This estimation procedure gave 0.34, 0.31, 0.29, 0.27, 0.25, 0.24, and 0.23 m^2 s^{-1} for $10^9 D_3$ through $10^9 D_9$.

It is conceivable that the large discrepancy between the measured and predicted values of D_{11} shown in Fig. 1 results from the neglect of activity coefficients which allow for departures from ideal solution behavior. However, these terms were thought to be relatively unimportant for the dilute solutions under consideration. As a check, the predicted values of D_{11} were recalculated by including ionic activity coefficients, y_i, estimated from the semi-empirical relation (35) $\ln y_i = -1.17 z_i^2 I^{1/2} (I + I^{1/2})^{-1}$. Significant improvement in the agreement between the measured and predicted values of D_{11} was not obtained. Terms for electrophoresis and changes in the solution viscosity can also be neglected in view of the low concentrations that were used.

Counterion binding

Up to this point in the analysis the simplifying assumption has been made that the chloride counterions do not bind to the stacks of the aggregated methylene blue cations. However, Braswell's sedimentation studies (3) have shown that the aqueous methylene blue chloride component is essentially unionized in solutions containing a large excess of NaCl. In a study of the protonation equilibria of methylene blue, Ghosh (8) was able to estimate the value 2.6 dm^3 mol^{-1} for the association constant for the reaction in which chloride ions pair with methylene blue dimers, $Cl^- + (MB)_2^{2+} = (MB)_2Cl^+$. The tendency of chloride ions to bind to the higher methylene blue polymers, which have larger positive charges, might be stronger.

These pieces of evidence suggest that the neglect of counterion binding might be a poor approximation. To include the chloride ions in the aggregation reactions, suppose that each $(MB)_i^{i+}$ species has i sites for chloride binding. The methylene blue dimers, for example, may then diffuse as the chloride-free $(MB)_2^{2+}$ species or as the $(MB)_2Cl^+$ and $(MB)_2Cl_2$ species. As a first approximation valid for small extents of binding, the various binding sites may be considered identical, regardless of whether the neighbouring sites are occupied. If this assumption holds, the fraction of the total sites that are filled, θ, followed the Langmuir isotherm (32)

$$[23] \quad \theta = K_L c_{Cl}/(1 + K_L c_{Cl})$$

where K_L is the binding equilibrium constant and c_{Cl} is the concentration of free chloride ions. Braswell's sedimentation data for dilute methylene blue chloride in 0.1 mol dm^{-3} NaCl solution indicate that approximately 82% of the chloride ions were bound to the dye cations (3). Substitution of $\theta = 0.82$ and $c_{Cl} = 0.1$ mol dm^{-3} into eq. [23] gives 45 dm^3 mol^{-1} for K_L.

TABLE 2. Measured ternary diffusion coefficients for aqueous solutions of methylene blue chloride (1) + sodium chloride (2) at 25°C

C_1*	C_2*	$10^9 D_{11}$†	$10^9 D_{12}$†	$10^9 D_{21}$†	$10^9 D_{22}$†
0.002	0.005	0.51	0.06	0.36	1.45
0.005	0.005	0.51	0.02	0.25	1.38
0.010	0.005	0.55	−0.14	0.12	1.42
0.002	0.010	0.41	0.04	0.27	1.56
0.005	0.010	0.42	−0.01	0.30	1.45
0.010	0.010	0.47	−0.17	0.24	1.52

*In mol dm^{-3}.
†In m^3 s^{-1}.

For each aggregate of i methylene blue monomers, $\theta^j(1 - \theta)^{i-j}$ gives the probability that a particular set of j sites will be occupied by chloride ions ($j \leq i$) and the remaining $i - j$ sites will be unoccupied. Since there are $i!/j!(i - j)!$ ways to distribute j chloride ions among the i sites, the concentration of the species consisting of i dye monomers and j chloride ions, c_{ij}, is given by

$$[24] \quad c_{ij} = [i!/j!(i - j)!]\theta^j(1 - \theta)^{i-j} c_i$$

where, as before, c_i is the total concentration of species containing i dye monomers, $c_i = \sum_{j=0}^{i} c_{ij}$. Counterion binding reduces the concentration of the free methylene blue cations, MB^+, from c_1 to c_{10}

$$[25] \quad c_{10} = (1 - \theta)c_1$$

Similarly, the concentration of the free chloride ions drops from $C_1 + C_2$ to the value given by

$$[26] \quad c_{Cl} = (1 - \theta)C_1 + C_2$$

To estimate the effects of counterion binding on the diffusion behavior of methylene blue solutions, the expressions for the L_{ik} transport coefficients were elaborated to include the $(MB)_iCl_j^{(i-j)+}$ species, as shown in the Appendix. Each $(MB)_iCl_j^{(i-j)+}$ species was assumed to have the same diffusivity as the $(MB)_i^{i+}$ species. The values of $\partial\mu_m/\partial C_k$ were obtained by differentiation of the modified expressions

$$[27] \quad \mu_1 = \mu_1^0 + RT \ln [(1 - \theta)C_1((1 - \theta)C_1 + C_2)]$$

$$[28] \quad \mu_2 = \mu_2^0 + RT \ln [C_2((1 - \theta)C_1 + C_2)]$$

In Fig. 1 the recalculated binary diffusion coefficients for methylene blue chloride (solid curves) are compared with the measured values. When the terms for counterion binding are included, the predicted values of D_{11} increase initially then decrease as the concentration is raised. This brings the predicted and measured values of D_{11} into good qualitative agreement. The counterion binding reduces the number of free solute particles per mole of dye, which in turn reduces the driving force and slows the rate of diffusion. For the solutions that were studied, the calculated fraction of bound chloride ions ranged from 0.024 for the most dilute solution to 0.35 for the most concentrated solution.

The remaining small discrepancies between the measured and predicted values of D_{11} shown in Fig. 1 may well be due to the approximations that were made in the model, such as the

assumption of identical ion binding sites and ideal solution behavior. Another likely source of error in the predictions are errors in the estimated values of the diffusivities of the dye aggregates.

In view of the uncertainties in the predicted values of D_{11}, it is not possible to decide here which of Mukerjee and Ghosh's sets of recommended association constants gives the most accurate description of the dye's aggregation. Nevertheless, it may be noted that sets I and II, which they regarded as more reliable than the isodesmic set III, lead to better agreement with the experimental results.

In Fig. 2 the measured D_{ik} values for the solutions with added NaCl are compared with the predicted ternary coefficients. (To emphasize the reduction in the dye's diffusivity caused by the added NaCl, the measured values of D_{11} for the NaCl-free solutions are also plotted (filled circles).) Although qualitative agreement is obtained, it is not as good as the agreement obtained for binary diffusion. The sodium ion diffusivity 1.33×10^{-9} m^2 s^{-1} (28) together with the diffusivities of the chloride ions and the methylene blue species quoted previously were used in the calculations.

Intradiffusion

Hillson and McKay (12) have used a polarographic technique to measure intradiffusion coefficients (36–39) for several dyes in aqueous solutions containing a large excess of KCl and other supporting electrolytes. They found that methylene blue's intradiffusion coefficient, designated here by D^*_{MB}, dropped by 40(±10)% as the total dye concentration was increased from 10^{-5} to 0.003 mol dm^{-3}. Absolute values of D^*_{MB} were not reported.

To test whether the polarographic result is consistent with the model of dye diffusion developed in the present report, values of D^*_{MB} were estimated by weighting the diffusivities of each dye-containing species in proportion to the fraction of the total dye it transports (36–39).

$$[29] \quad D^*_{MB} = \sum_{i=1}^{\infty} \sum_{j=0}^{i} ic_{ij}D_i/C_1 = \sum_{i=1}^{\infty} ic_iD_i/C_1$$

As shown in Fig. 3, the predicted values of D^*_{MB} drop from about 0.42×10^{-9} to 0.31×10^{-9} m^2 s^{-1} in the concentration range from 10^{-5} to 0.003 mol dm^{-3}. This 30% drop agrees reasonably well with the polarographic result.

Also shown in Fig. 3 are intradiffusion coefficients for the chloride counterions calculated according to the expression

$$[30] \quad D^*_{Cl} = \sum_{i=1}^{\infty} \sum_{j=0}^{i} jc_{ij}D_i/C_1$$

As the dye concentration increases, a higher proportion of the chloride ions is attached to the slowly-diffusing dye aggregates which causes a drop in the values of D^*_{Cl}. In order to measure D^*_{Cl} it would be necessary to use solutions containing small amounts of methylene blue chloride and an excess of an inert supporting electrolyte, such as $NaClO_4$.

5. Conclusions

Despite the myriad of different solute species, the simple binary diffusion equation can be used to describe diffusion of methylene blue chloride in water. The concentration dependence of the dye's binary diffusion coefficient can be understood in terms of aggregation of the dye ions and counterion binding. Aggregation and counterion binding tend to respectively increase and decrease the rate of diffusion. As a result, the binary diffusion coefficient of the dye is not sensitive to concentration. On the other hand, small amounts of added NaCl lead to a sharp reduction in the diffusivity of the dye in the ternary solutions.

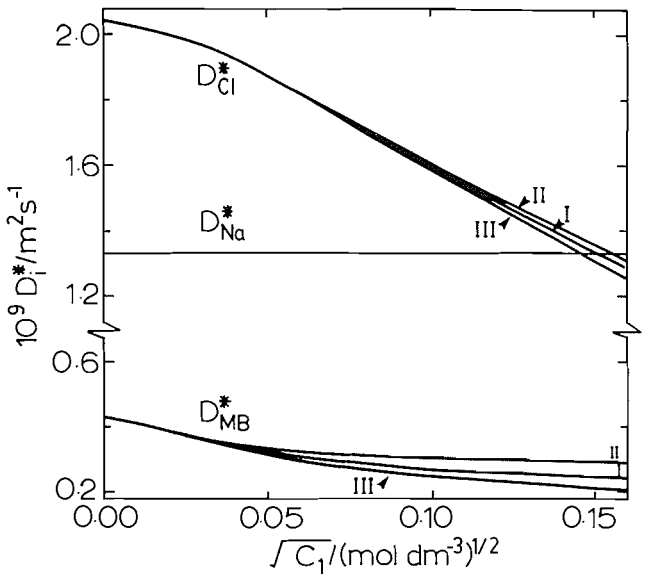

FIG. 3. Calculated tracer diffusion coefficients for aqueous methylene blue and chloride ions at 25°C. Non-attenuated association constants (set I) and $K_L = 45$ dm^3 mol^{-1} were used.

6. Acknowledgements

The author thanks P. Caskanette for help with the diffusion measurements. This work was supported by the Natural Sciences and Engineering Research Council of Canada.

1. E. H. BRASWELL. J. Phys. Chem. **88**, 3653 (1984).
2. E. H. BRASWELL and J. LARY. J. Phys. Chem. **85**, 1573 (1981).
3. E. H. BRASWELL. J. Phys. Chem. **76**, 4026 (1972).
4. E. H. BRASWELL. J. Phys. Chem. **72**, 2477 (1968).
5. P. MUKERJEE and A. K. GHOSH. J. Am. Chem. Soc. **92**, 6403 (1970).
6. A. K. GHOSH and P. MUKERJEE. J. Am. Chem. Soc. **92**, 6408 (1970).
7. A. K. GHOSH and P. MUKERJEE. J. Am. Chem. Soc. **92**, 6413 (1970).
8. A. K. GHOSH. J. Am. Chem. Soc. **92**, 6415 (1970).
9. P. MUKERJEE and A. K. GHOSH. J. Am. Chem. Soc. **92**, 6419 (1970).
10. K. BERGMAN and C. T. O'KONSKI. J. Phys. Chem. **67**, 2169 (1963).
11. E. RABINOVITCH and L. F. EPSTEIN. J. Am. Chem. Soc. **63**, 69 (1941).
12. P. J. HILLSON and R. B. MCKAY. Trans. Faraday Soc. **61**, 374 (1965).
13. C. ROBINSON. Trans. Faraday Soc. **31**, 245 (1935).
14. K. L. KENDRICK and W. R. GILKERSON. J. Solution Chem. **16**, 257 (1987).
15. R. L. REEVES, M. S. MAGGIO, and S. A. HARKAWAY. J. Phys. Chem. **83**, 2359 (1979).
16. H. HØILAND, A. SKAUGE, and I. STOKKELAND. J. Phys. Chem. **88**, 6350 (1984).
17. E. VALKÓ. Trans. Faraday Soc. **31**, 230 (1935).
18. G. S. HARTLEY and C. ROBINSON. Proc. R. Soc. **134A**, 20 (1931).
19. H. S. HARNED and R. L. NUTTALL. J. Am. Chem. Soc. **69**, 736 (1947).
20. D. G. LEAIST and P. A. LYONS. Aust. J. Chem. **33**, 1869 (1980).
21. D. G. LEAIST and P. A. LYONS. J. Phys. Chem. **86**, 564 (1982).

Can. J. Chem. Downloaded from www.nrcresearchpress.com by 112.217.228.212 on 09/07/12
For personal use only.

22. D. G. LEAIST. Can. J. Chem. **63**, 2933 (1985).
23. W. H. STOCKMAYER. J. Chem. Phys. **33**, 1291 (1960).
24. E. L. CUSSLER. Diffusion. Cambridge University Press, Cambridge. 1984. p. 165.
25. D. G. LEAIST. J. Colloid Interface Sci. In press.
26. D. G. LEAIST. J. Colloid Interface Sci. **111**, 230 (1986).
27. C. ROBINSON and H. E. GARRETT. Trans. Faraday Soc. **35**, 771 (1939).
28. R. A. ROBINSON and R. H. STOKES. Electrolyte solutions. 2nd ed. Academic Press, New York. 1959.
29. D. G. LEAIST. J. Phys. Chem. **90**, 6600 (1986).
30. D. G. LEAIST. J. Colloid Interface Sci. **111**, 240 (1986).
31. D. G. LEAIST. J. Chem. Soc. Faraday Trans. 1, **78**, 3069 (1982).
32. C. TANFORD. The physical chemistry of macromolecules. Wiley, New York. 1961. p. 327.
33. F. PERRIN. J. Phys. Radium. **7**, 1 (1936).
34. R. O. HERZOG, R. ILLIG, and H. KUDAR. Z. Phys. Chem. A**167**, 329 (1934).
35. E. A. GUGGENHEIM and J. C. TURGEON. Trans. Faraday Soc. **51**, 747 (1955).
36. H. SCHONERT. Z. Phys. Chem. N.F. **119**, 53 (1980).
37. P. C. CARMAN. J. Phys. Chem. **71**, 2565 (1967).
38. P. J. DUNLOP. J. Phys. Chem. **69**, 1693 (1965).
39. H. J. V. TYRRELL and K. R. HARRIS. Diffusion in liquids. Butterworths, London. 1984. Chap. 5.

Appendix

Multicomponent transport coefficients for diffusion of incompletely dissociated mixed electrolytes can be estimated by using the identity (31)

$$[A1] \quad \mathbf{L} = (\boldsymbol{\nu}^t(\hat{\boldsymbol{\nu}}\hat{\mathbf{l}}\hat{\boldsymbol{\nu}}^t)^{-1}\boldsymbol{\nu})^{-1}$$

where $\hat{\mathbf{l}}$ is the matrix of Onsager $\hat{l}_{ik}$ transport coefficients for the solute species, $\hat{\boldsymbol{\nu}}$ is the matrix of stoichiometric coefficients $\hat{\nu}_{ik}$ which give the number of moles of constituent ion i per mole of species k, and $\boldsymbol{\nu}$ is the matrix of stoichiometric coefficients ν_{im} which give the number of moles of constituent ion i per mole of electrolyte component m. $\boldsymbol{\nu}^t$ and $\hat{\boldsymbol{\nu}}^t$ denote the transpose of $\boldsymbol{\nu}$ and $\hat{\boldsymbol{\nu}}$. For dilute solutions, it is a good approximation to write $\hat{l}_{ii} = c_i D_i/RT$ and to assume the off-diagonal elements $\hat{l}_{ik}(i \neq k)$ are zero (31).

For the solutions of methylene blue chloride (component 1) + NaCl (component 2), the constituent ions were numbered as follows: 1 = MB^+, 2 = Na^+, 3 = Cl^-. For calculation purposes, the solute species were numbered as follows: 1 = MB^+, 2 = Na^+, 3 = Cl^-, 4 = $(MB)_2^{2+}$, 5 = $(MB)_2Cl^+$, 6 = $(MB)_2Cl_2$, 7 = $(MB)_3^{3+}$, 8 = $(MB)_3Cl^{2+}$, etc., and hence

$$[A2] \quad \boldsymbol{\nu} = \begin{pmatrix} 1 & 0 \\ 0 & 1 \\ 1 & 1 \end{pmatrix}$$

$$[A3] \quad \hat{\boldsymbol{\nu}} = \begin{pmatrix} 1 & 0 & 0 & 2 & 2 & 2 & 3 & 3 & \dots \\ 0 & 1 & 0 & 0 & 0 & 0 & 0 & 0 & \dots \\ 0 & 0 & 1 & 0 & 1 & 2 & 0 & 1 & \dots \end{pmatrix}$$

In practice, the speciation was truncated at $(MB)^{50+}$. The concentrations of the higher aggregates were negligible.

Can. J. Chem. Downloaded from www.nrcresearchpress.com by 112.217.228.212 on 09/07/12
For personal use only.

Methylmercury(II) complexes with tryptophan and its *N*-acetyl derivative

MARIE-CLAUDE CORBEIL AND ANDRÉ L. BEAUCHAMP[1]

Département de chimie, Université de Montréal, C.P. 6128, Succ. A, Montréal (Québec), Canada H3C 3J7

Received January 13, 1988

MARIE-CLAUDE CORBEIL and ANDRÉ L. BEAUCHAMP. Can. J. Chem. **66**, 2458 (1988).

CH_3HgOH reacts with tryptophan in aqueous ethanol to form a 2:1 neutral complex in which CH_3Hg groups are bound to the terminal amino group and to the deprotonated indole nitrogen. When this complex is dissolved in water, ^1H and ^{13}C nuclear magnetic resonance show that the indole CH_3Hg group hydrolyzes, leading to an amino-bound 1:1 species. Under the same conditions, *N*-acetyltryptophan forms a neutral 1:1 compound where the metal is bound to a carboxylate oxygen, and a neutral 2:1 complex in which an extra CH_3Hg group is fixed to the deprotonated indole ring. It is shown by ^1H and ^{13}C nuclear magnetic resonance that the 1:1 species is stable in DMSO-d_6, but that the 2:1 compound is readily hydrolyzed to the 1:1 compound by traces of water. The solid-state infrared and Raman spectra are discussed. In the crystal structure of the 2:1 tryptophan complex, the ligand adopts a conformation favoring a short intramolecular π interaction between Hg and the indole ring. No such π interaction is found in the crystal structure of the 1:1 carboxylate-bonded complex with acetyltryptophan.

MARIE-CLAUDE CORBEIL et ANDRÉ L. BEAUCHAMP. Can. J. Chem. **66**, 2458 (1988).

CH_3HgOH réagit avec le tryptophane dans l'éthanol aqueux pour former un complexe 2:1 neutre, dans lequel les groupes CH_3Hg sont liés à la fonction amino terminale et à l'azote déprotoné de l'indole. Quand ce complexe est dissous dans l'eau, les spectres de résonance magnétique nucléaire ^1H et ^{13}C indiquent que le groupe CH_3Hg lié à l'indole s'hydrolyse pour conduire à un composé 1:1 neutre, où la coordination se fait seulement à la fonction amine. Dans les mêmes conditions, le *N*-acétyltryptophane forme un composé 1:1 neutre où le métal est lié à un oxygène carboxylate, ainsi qu'un composé 2:1 neutre dans lequel le groupe CH_3Hg supplémentaire est fixé au cycle indole déprotoné. On montre par résonance magnétique nucléaire ^1H et ^{13}C que l'espèce 1:1 est stable dans DMSO-d_6, alors que le composé 2:1 s'hydrolyse en espèce 1:1 en présence de traces d'eau. Les spectres infrarouges et Raman des composés solides sont discutés. Dans la structure cristalline du complexe 2:1 du tryptophane, le ligand adopte une conformation qui favorise une interaction π intramoléculaire courte entre le mercure et le cycle indolique. Il n'y a pas d'interaction semblable dans la structure cristalline du complexe 1:1 de l'acétyltryptophane.

Can. J. Chem. Downloaded from www.nrcresearchpress.com by 196.1.178.254 on 09/07/12
For personal use only.

Introduction

The reactions of the methylmercury cation with S-containing amino acids have been thoroughly studied (1–5), because the major step in mercury poisoning involves soft sulfhydryl groups in proteins acting as primary targets for the soft mercury species (6). Much less effort has been devoted to sulfur-free amino acids, although the side chains of such residues in proteins may play an important part, for instance, by forming secondary bonds to stabilize the Hg-sulfhydryl complex and shield it from the surroundings, or by providing migration pathways in a detoxification process.

Our recent work with glycine, alanine, and glycylglycine (7, 8) confirmed earlier studies (9, 10) by showing that the methylmercury group remains bonded to the $-NH_2$ end of simple amino acids over a wide pH range. However, no evidence could be obtained from Raman spectroscopy for the presence of mercury-carboxylate species in water solution, even in the case of the $[(CH_3Hg)_2(\text{glycylglycinate})]^+$ ion, which was shown to contain a carboxyl-bonded methylmercury group in the solid state (8).

In a previous paper dealing with serine (11), the methylmercury ion was found not to form a primary bond with the weakly coordinating $-CH_2OH$ side chain. However, X-ray work revealed the presence of an intramolecular Hg...O contact in the NH_2-bonded complex, and this secondary interaction is strong enough to make the same conformation the most abundant one in aqueous solution.

In the present paper, we are reporting on the reactions with the tryptophan residue, whose side chain attracted our attention for two main reasons: (*i*) it contains an aromatic group, and interactions of aromatic units with the coordinated methylmercury group have been previously reported (9, 10, 12, 13); (*ii*) an endocyclic N-H group is also present, and it was of interest to determine the relative affinities of mercury for this potential coordination site and for oxygens. To account for both carboxylate and amide oxygens, we looked at *N*-acetyltryptophan as well.[2]

Experimental

Reagents

DL-Tryptophan (J. T. Baker) and *N*-acetyl-DL-tryptophan (Aldrich) were used without further purification. The source of CH_3Hg^+ ions was the hydroxide CH_3HgOH (1 M aqueous solution from Alfa Inorganics).

Nuclear magnetic resonance spectroscopy

The ^1H and ^{13}C nmr spectra were recorded on a Bruker WH-400 (^1H, 400.13 MHz; ^{13}C, 100.62 MHz) spectrometer at the Laboratoire Régional de RMN Haut Champ, located at the Université de Montréal.

The concentrations of the solutions were in the range 0.01–0.03 M, except for $(CH_3Hg)_2$(DL-Trp), for which the maximum concentration obtained was 0.005 M. The samples were prepared by dissolving the solids in 0.5 or 2.0 mL of either D_2O (Cambridge Isotope Laboratories or Aldrich) or Me_2SO-d_6 (Aldrich). For D_2O solutions, DSS (^1H, δ = 0.00 ppm from TMS) and 1,4-dioxan (^{13}C. δ = 63.4 ppm from TMS) were used as external references. For Me_2SO-d_6 solutions, the residual solvent signal was used as internal reference (^1H, δ = 2.50 ppm from TMS; ^{13}C, δ = 39.6 ppm from TMS).

Raman spectroscopy

The Raman spectra, excited by the 514.5-nm line from a Spectra Physics model 165 argon ion laser, were recorded on a Spex model 1400 microcomputer-controlled spectrometer. The samples were contained in capillary tubes that were mounted on a motor shaft and rotated at high speed in the laser beam. The laser power at the sample was ~200 mW for free tryptophan, and was kept very low for all

[1] Author to whom correspondence may be addressed.

[2] Abbreviations used for tryptophan: DL-H_2Trp (neutral), DL-$HTrp^-$ (monoanion), DL-Trp^{2-} (dianion); for *N*-acetyltryptophan, *N*-Ace-DL-H_2Trp (neutral), *N*-Ace-DL-$HTrp^-$ (monoanion), *N*-Ace-DL-Trp^{2-} (dianion). DL is often dropped from these abbreviations for simplicity.

Can. J. Chem. Downloaded from www.nrcresearchpress.com by 196.1.178.254 on 09/07/12
For personal use only.

other compounds (25–50 mW). For the highly light-sensitive acetyltryptophan complexes, the spectra were recorded using the back scattering Raman technique. All spectra were typically recorded with a 5 cm^{-1} spectral slit width, and a 2 s integration time at each 2 cm^{-1} frequency increment.

Infrared spectroscopy

The infrared spectra were recorded as KBr pellets on a Nicolet 7199 FTIR spectrometer equipped with a HeNe class II laser. The spectral resolution was 1 cm^{-1} and a typical spectrum required 200 scans.

Preparations

In the following procedures, the filtered crystalline solids were dried *in vacuo* at room temperature.

$(CH_3Hg)_2$(DL-Trp)

DL-Tryptophan (1 mmol, 204 mg) was suspended in a mixture of distilled water (15 mL) and 1 M CH_3HgOH (2 mL), and heated until complete dissolution. Ethanol (25 mL) was then added to the solution. After a few days at room temperature in a vented hood, the volume had reduced to ~30 mL and platelets had deposited. Yield: 120 mg (19%). *Anal.* calcd. for $C_{13}H_{16}Hg_2N_2O_2$: C 24.65, H 2.55, Hg 63.33, N 4.42; found: C 24.67, H 2.63, Hg 64.12, N 4.61.

(CH_3Hg)(N-Ace-DL-HTrp)

Acetyl-DL-tryptophan (1 mmol, 246 mg) was dissolved in absolute ethanol (50 mL) and 1 M CH_3HgOH (1 mL). Platelets formed after a few days, in the same conditions as above. Yield: 239 mg (52%). *Anal.* calcd. for $C_{14}H_{16}HgN_2O_3$: C 36.48, H 3.50, Hg 43.52, N 6.08; found: C 36.40, H 3.66, Hg 43.53, N 5.91.

$(CH_3Hg)_2$(N-Ace-DL-Trp)

One millimole of acetyl-DL-tryptophan was dissolved in propanol (25 mL) and 1 M CH_3HgOH (2 mL). Crystals precipitated within a few days. Yield: 304 mg (45%). *Anal.* calcd. for $C_{15}H_{18}Hg_2N_2O_3$: C 26.67, H 2.69, Hg 59.39, N 4.15; found: C 27.06, H 2.76, Hg 60.06, N 4.01.

Crystal structure of (CH_3Hg)(N-Ace-DL-HTrp)

$C_{14}H_{16}HgN_2O_3$ fw = 460.88

Monoclinic, $P2_1/c$, a = 8.330(2), b = 19.324(3), c = 9.380(3) Å, β = 96.76(2)°, V = 1499.4 $Å^3$, Z = 4, D_c = 2.041 g cm^{-3}, $\lambda(MoK\bar{\alpha})$ = 0.71069 Å (graphite monochromator), $\mu(MoK\alpha)$ = 102.6 cm^{-1}, T = 293 K.

A specimen of dimensions (mm) 0.18 (between the 100 and $\bar{1}00$ faces) × 0.19 (010 and $0\bar{1}0$) × 0.66 (001 and $00\bar{1}$) was used for X-ray work. Cell parameter determination and data collection were carried out with an Enraf–Nonius CAD4 diffractometer, as described elsewhere (14). Axial photographs were recorded about the three axes as a check for cell dimensions and Laue symmetry. Seven standard reflections monitored during the experiment showed random fluctuation within ±2.5%. A total of 2036 hkl and $hk\bar{l}$ reflections were measured, within a sphere limited by 2θ = 45°. Space group $P2_1/c$ was uniquely defined from the systematic absences ($0k0$, $k \neq 2n$; $h0l$, $l \neq 2n$). After rejection of the systematic absences, the data set consisted of 1955 independent reflections, of which 1528 were used to solve the structure ($I > 3.0\sigma(I)$). The data were corrected for the Lorentz effect, polarization, and absorption (Gaussian integration, grid 8 × 8 × 8, transmission ranges: 0.15–0.21).

The structure was solved by the heavy-atom method and refined on $|F_o|$. The mercury atom was located from a Patterson map and the non-hydrogen atoms were found from a difference Fourier (ΔF) map phased on Hg. The structure was refined isotropically by full-matrix least squares. Refinement was completed by block-diagonal least squares. All hydrogen atoms (except those of the two methyl groups, which were neglected) were fixed at ideal positions (C—H = 0.95 Å, N—H = 0.87 Å, B_{iso} = 4 $Å^2$). Their parameters were not refined, but their coordinates were recalculated after each least-square cycle. Anisotropic refinement of all non-hydrogen atoms converged to $R = \Sigma||F_o| - |F_c||/\Sigma|F_o| = 0.040$ and $R_w = [\Sigma w(|F_o| - |F_c|)^2/\Sigma w|F_o|^2]^{1/2} = 0.046$, and a goodness-of-fit ratio of 2.11. The highest residuals on the final ΔF map (±|1.2 − 1.4| e $Å^{-3}$) were around the Hg atom and the general background was below ±0.9 e $Å^{-3}$.

Crystal structural of $(CH_3Hg)_2$(DL-Trp)

$C_{13}H_{16}Hg_2N_2O_2$ fw = 633.47

Triclinic, $P\bar{1}$, a = 5.508(4), b = 9.497(5), c = 14.064(8) Å, α = 77.70(4), β = 87.62(6), γ = 80.83(5)°, V = 709.6 $Å^3$, Z = 2, D_c = 2.965 g cm^{-3}, $\lambda(MoK\bar{\alpha})$ = 0.71069 Å (graphite monochromator), $\mu(MoK\alpha)$ = 216.1 cm^{-1}, T = 143 K.

This compound gave crystals of poor quality. Several crystals were tried and the data from an untwinned specimen of dimensions (mm) 0.04 (010–$0\bar{1}0$) × 0.08 (001–$00\bar{1}$) × 0.68 (100–$\bar{1}00$) were retained. Cell parameters and data collection were done as above. The reduced triclinic cell obtained was checked with oscillation photographs, and the Niggli parameters indicated no symmetry higher than triclinic. The seven standards showed random fluctuation within ±5%. A set of 2500 hkl, $hk\bar{l}$, $h\bar{k}l$, and $h\bar{k}\bar{l}$ reflections ($2\theta \leq 50°$) was collected. A total of 1949 reflections was retained ($I > 3\sigma(I)$) for structure determination. The data were corrected for the Lorentz effect, polarization, and absorption (Gaussian integration, grid 8 × 8 × 8, transmission range: 0.19–0.46).

The structure was solved by the heavy-atom method and anisotropically refined. The final residuals were R = 0.073, R_w = 0.094, goodness-of-fit ratio = 3.39. The poor quality of the crystals is reflected in the rather high residuals. Other crystals from the same or different batches yielded data of comparable quality. Although the esd's on distances and angles are slightly higher than for the other compound, it is clear that the connectivity and the chemically significant features of this structure are reliably defined. The general background in the final ΔF map was ±1.0 e $Å^{-3}$, with a few peaks above background near the Hg atoms.

The scattering curves were from standard sources (15). The f' and f'' contributions of Hg to anomalous dispersion were included in the structure factor calculation (15). The refined coordinates and equivalent isotropic temperature factors are listed in Table 1.[3]

Results and discussion

In the absence of soft thiolate groups, amino acids usually bind the CH_3Hg^+ ion via the $-NH_2$ end. Our X-ray work (see below) shows that tryptophan follows this trend. However, the simple 1:1 complex could not be isolated. The solid precipitating from alcohol-rich water–ethanol mixtures contained an extra CH_3Hg^+ group bound to the deprotonated nitrogen of the indole ring. Even when lower metal:ligand ratios were used to favor the 1:1 (CH_3Hg)(HTrp) compound, the material isolated consisted of the 2:1 $(CH_3Hg)_2$(Trp) complex, sometimes containing unreacted tryptophan. Thus, despite the high pK_a (16.8) (16) of the indole N-H proton, substitution takes place under mild conditions and at low methylmercury concentration in this water-poor medium. Other cases are known of CH_3Hg^+ ions replacing very weakly acidic N-H protons under similar conditions (17).

[1] $2(CH_3Hg)(HTrp) \rightarrow (CH_3Hg)_2(Trp) + H_2Trp$

That a 1:1 complex was not obtained seems to originate mainly in its solubility being greater than those of either the

[3]Supplementary material. For the structures: temperature factors, structure factor amplitudes, hydrogen coordinates, ligand geometry, least-squares planes, and intermolecular distances and angles. For the free ligands and their complexes: lists of infrared and Raman frequencies. Copies may be purchased from the Depository of Unpublished Data, CISTI, National Research Council of Canada, Ottawa, Ont., Canada K1A 0S2. Hydrogen atom coordinates and ligand geometry have been deposited with the Cambridge Crystallographic Data Centre and can be obtained on request from The Director, Cambridge Crystallographic Data Centre, University Chemical Laboratory, Lensfield Road, Cambridge CB2 1EW, U.K.

Can. J. Chem. Downloaded from www.nrcresearchpress.com by 196.1.178.254 on 09/07/12
For personal use only.

TABLE 1. Coordinates ($\times 10^3$, Hg $\times$ 10^5) and equivalent temperature factors ($\times 10^3$) of the non-hydrogen atoms

$(CH_3Hg)_2$(DL-Trp)

Atom	x	y	z	U_{eq}
Hg(1)	−14342(20)	−10843(12)	76521(8)	30
Hg(2)	19251(18)	49371(10)	75581(7)	21
O(1)	−112(3)	415(2)	896(1)	19
O(2)	−82(3)	281(2)	1050(1)	26
N(1)	106(4)	27(2)	779(2)	21
N(2)	363(4)	457(2)	894(2)	20
C(1)	586(5)	253(3)	712(2)	32
C(2)	619(6)	248(4)	618(3)	47
C(3)	465(7)	177(4)	567(3)	51
C(4)	288(6)	109(3)	614(2)	37
C(5)	260(5)	101(3)	714(2)	23
C(6)	400(4)	168(3)	762(2)	21
C(7)	331(5)	139(3)	866(2)	20
C(8)	143(5)	53(3)	868(2)	18
C(9)	417(4)	188(2)	950(2)	15
C(10)	296(4)	336(3)	967(2)	18
C(11)	13(4)	346(3)	972(2)	17
C(12)	−392(5)	−239(3)	751(2)	30
C(13)	52(6)	549(4)	618(3)	44

(CH_3Hg)(*N*-Ace-DL-HTrp)

Atom	x	y	z	U_{eq}
Hg(1)	94235(6)	−6468(3)	85826(6)	68
O(1)	744(1)	1(1)	860(1)	71
O(2)	732(1)	−10(1)	626(1)	69
O(3)	698(1)	168(1)	593(1)	90
N(1)	6(1)	122(1)	716(1)	77
N(2)	497(1)	92(1)	579(1)	59
C(1)	331(2)	161(1)	980(1)	76
C(2)	270(2)	221(1)	1043(2)	99
C(3)	117(3)	248(1)	988(2)	114
C(4)	21(2)	215(1)	882(1)	80
C(5)	80(2)	161(1)	826(1)	66
C(6)	227(1)	130(1)	867(1)	56
C(7)	249(1)	73(1)	776(1)	55
C(8)	104(2)	71(1)	685(1)	66
C(9)	391(2)	27(1)	775(1)	66
C(10)	542(1)	65(1)	721(1)	54
C(11)	685(1)	15(1)	732(1)	57
C(12)	581(1)	142(1)	527(1)	65
C(13)	513(2)	166(1)	373(1)	80
C(14)	1144(2)	−127(1)	858(2)	92

2:1 complex or free tryptophan, so that the disproportionation reaction [1] is shifted to the right. However, on the basis of the nmr spectra, a 1:1 species results when the 2:1 complex is dissolved in water.

Both ^1H and ^{13}C nmr spectra have been reported for aqueous solutions of tryptophan (18), but the pH used is not known. The solutions were probably acidic, since the authors indicated in the experimental section that "the samples were pD adjusted with DCl". It may be assumed that tryptophan is present as the monocation in these samples. In contrast, our ^1H data listed in Table 2 correspond to D_2O solution whose pD was not adjusted, and the amino acid is present almost exclusively in the zwitterionic neutral form. This explains the small chemical shift differences between our results and those obtained in acidic solutions. Solubility at that pD was too low to obtain the ^{13}C spectrum.

The ^1H and ^{13}C data for the 2:1 complex dissolved in D_2O are given in Tables 2 and 3. Complexation to the NH_2 end is evidenced from the downfield shift (0.76 ppm) of the methine proton, also noted for the serine (11) complex. On the other hand, the ^1H indole signals do not differ significantly from those of free tryptophan. Since greater differences are expected for a mercurated indole unit (see below), it must be concluded that the CH_3Hg^+ group has been displaced by a proton to generate the amino-coordinated 1:1 complex. Thus, in water, formation of the 1:1 complex by hydrolysis (reaction [2]) becomes favorable. Nevertheless, all attempts to isolate the 1:1 species from aqueous solution yielded only a mixture containing free tryptophan, the 2:1 complex, and perhaps a small amount of a 1:1 complex.

[2] $(CH_3Hg)_2Trp + H_2O \rightarrow (CH_3Hg)HTrp + CH_3HgOH$

When the amino end of tryptophan is blocked by an acetyl group, the ligand exists as a normal carboxylic acid. The X-ray work discussed below shows that in the neutral 1:1 complex, the CH_3Hg^+ group has substituted the carboxylic proton and formed a Hg—O bond. By reacting two equivalents of CH_3HgOH per ligand, a 2:1 compound was isolated, which was shown, by infrared and Raman spectroscopy (see below), to be carboxylate and indole coordinated. As these compounds are insoluble in water, the nmr data (Tables 2 and 3) were obtained in DMSO-d_6, where solubility is still low, but acceptable.

Complexation via a carboxylic oxygen in the 1:1 complex is retained in DMSO. The low-field ^1H signal at 12.6 ppm for the carboxylic proton disappears in the complex, whereas the amide proton at 8.15 ppm is shifted to high field by 0.16 ppm. The methine and methylene protons remain virtually unmoved, whereas very small shifts are found for the corresponding ^{13}C signals. The methine and carboxylate ^{13}C resonances, however, have moved downfield by 2 ppm upon complexation. The CH_3Hg^+ signal is found at 0.73 ppm with a coupling constant of 226 Hz with ^{199}Hg, which is consistent with Hg—O coordination (9).

Coordination of the extra CH_3Hg^+ group to the indole ring of acetyltryptophan is detected by the disappearance of the indole N-H signal of the 1:1 complex and free ligand at 10.8 ppm, and by shifts on the ^1H signals for the protons near the complexation site (0.18 ppm on H4). Solubility was too low to obtain the ^{13}C spectrum. Just like the 2:1 tryptophan complex, the indole-bonded CH_3Hg^+ group is readily displaced by hydrolysis: small residual peaks for the 1:1 compound are detected in the baseline as a result of a reaction with the traces of water in DMSO-d_6, unless special care is taken to thoroughly dry the solvent.

Structure of [$(CH_3Hg)_2$(DL-Trp)]

The structure of the 2:1 complex with DL-tryptophan is shown in Fig. 1 with the atom numbering scheme. Selected interatomic distances and bond angles are listed in Table 4.

In addition to coordinating to the amino group as commonly observed with amino acids (1, 7, 10, 11), the CH_3Hg^+ ion is found to bind to the deprotonated N(1) site of the indole ring. The Hg—N and Hg—C distances are normal. Departure from linearity is significant, but small, at the amino-bonded Hg atom (C(13)—Hg(2)—N(2) = 173(1)°). For the other methylmercury group, the coordination is almost perfectly linear (179(1)°), but it does not take place exactly along the ideal direction of the indole nitrogen lone pair, as evidenced from the

TABLE 2. The ^1H nmr data for tryptophan, *N*-acetyltryptophan, and their methylmercury complexes

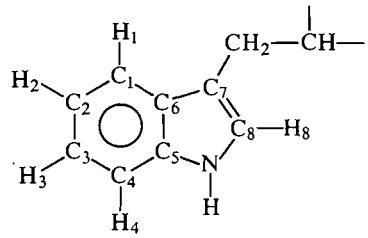

Proton	H_2Trp^a	$(CH_3Hg)(HTrp)^a$	*N*-Ace-H_2Trp^b	(CH_3Hg)(*N*-Ace-HTrp)^b	$(CH_3Hg)_2$(*N*-Ace-Trp)^b
H1	7.72	7.69	7.52	7.52	7.54
H2	7.18	7.19	6.98	6.96	6.84
H3	7.27	7.28	7.06	7.05	6.91
H4	7.52	7.53	7.33	7.32	7.50
H8	7.30	7.28	7.13	7.13	7.19
CH	4.04	4.80	4.45	4.47	4.45
CH_2	3.47	3.44	3.15	3.20	3.20
	3.29	3.22	2.98	2.98	2.98
N-H (indole)	—	—	10.84	10.79	—
N-H (amide)	—	—	8.15	7.99	7.95
COO-H	—	—	12.59	—	—
CH_3 (amide)	—	—	1.80	1.77	1.77
CH_3 (Hg)	—	0.01	—	0.73	0.76
$[^2J(^{199}Hg-^1H)]^c$	—	216	—	226	—[d]

[a] In D_2O.
[b] In DMSO-d_6.
[c] Coupling constant in Hz.
[d] Satellites not detected due to low solubility.

TABLE 3. The ^{13}C nmr data for tryptophan, *N*-acetyltryptophan, and their methylmercury complexes

Carbon	$(CH_3Hg)(HTrp)^a$	*N*-Ace-H_2Trp^b	(CH_3Hg)(*N*-Ace-HTrp)^b
C1	119.5	120.8	120.7
C2	120.4	118.1	118.1
C3	123.4	118.1	118.1
C4	113.2	111.3	111.3
C5	137.2	136.0	136.0
C6	128.0	127.2	127.3
C7	108.6	109.9	110.6
C8	126.2	123.4	123.2
COOH	179.6	173.3	175.3
CO-NH	—	169.1	168.7
CH	54.3	53.0	55.3
CH_2	26.7	27.2	28.0
CH_3 (amide)	—	22.4	22.6
CH_3Hg	−4.3	—	−0.6

[a] In D_2O.
[b] In DMSO-d_6.

difference of 14° between the two Hg(1)—N(1)—C angles. The distances and angles in the ligand (supplementary material) show no unusual features.

The amino-bonded Hg atom makes an intramolecular contact of 2.60(2) Å with the carboxylate oxygen O(1) atom. In this respect, the present complex compares well with those of other amino acids (1, 7, 10, 11). However, the present compound is peculiar in that the methylmercury group sits above the indole ring; more precisely, the methyl group is just above the middle of the six-membered ring, whereas the ring C(1) and C(6) atoms are at ~3.05 Å from Hg(2), and close to the plane through Hg(2) and perpendicular to the N(2)—Hg(2)—C(13) direction (Table 4). It is very likely that some Hg-ring π interaction is taking place, of the type proposed for the complexes of tyrosine (10) and other aromatic ligands (13), in which the methylmercury group is similarly positioned with respect to the phenyl ring.

This π interaction is responsible for the particular conformation adopted by the amino acid in the complex. For free DL-tryptophan in the solid state (19), the amino group is *trans* relative to the indole ring (N(2)—C(10)—C(9)—C(7) torsion angle = 169°), whereas the carboxylate group is *gauche*

Can. J. Chem. Downloaded from www.nrcresearchpress.com by 196.1.178.254 on 09/07/12
For personal use only.

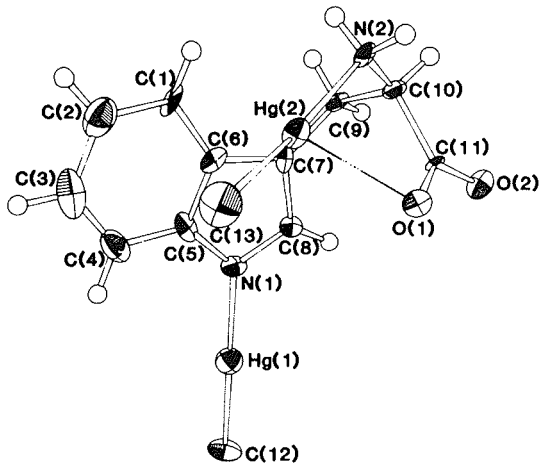

FIG. 1. Structure and numbering scheme for $(CH_3Hg)_2$(DL-Trp). The Hg(2)...O(1) contact is shown as a thin bond. Ellipsoids correspond to 50% probability.

TABLE 4. Selected interatomic distances (Å) and bond angles (deg)

Bond	Distance	Bonds	Angle
$(CH_3Hg)_2$(DL-Trp)			
Hg(1)—N(1)	2.07(2)	C(12)—Hg(1)—N(1)	179(1)
Hg(1)—C(12)	2.03(3)	Hg(1)—N(1)—C(8)	119(2)
Hg(2)—N(2)	2.13(3)	Hg(1)—N(1)—C(5)	133(2)
Hg(2)—C(13)	2.05(3)	C(13)—Hg(2)—N(2)	173(1)
Hg(2)—C(1)	3.03(3)	Hg(2)—N(2)—C(10)	116(2)
Hg(2)—C(6)	3.11(3)	N(2)—Hg(2)—C(1)	86.3(8)
Hg(2)—C(7)	3.37(3)	N(2)—Hg(2)—C(6)	84.8(8)
		N(2)—Hg(2)—C(7)	65.6(7)
(CH_3Hg)(*N*-Ace-HTrp)			
Hg(1)—O(1)	2.085(9)	C(14)—Hg(1)—O(1)	178.1(5)
Hg(1)—C(14)	2.07(1)	Hg(1)—O(1)—C(11)	109.9(7)

(C(11)—C(10)—C(9)—C(7) = −68°). In the $(CH_3Hg)_2$(DL-Trp) molecule, these torsion angles have become −70(3)° and 53(3)°, respectively, which corresponds to the carboxylate and amino groups both being *gauche* to the indole ring. Thus complexation induces a 120° rotation about the C(9)—C(10) bond, which makes it possible for a carboxylate oxygen and the aromatic ring to make simultaneous contacts with mercury: these interactions can take place simultaneously only if the amino, carboxylate, and indole units are in the same region of space, as in the observed conformation.

Cohesion in the unit cell is achieved mainly by intermolecular Hg...O contacts and N—H...O hydrogen bonds.

Structure of [(CH_3Hg)(N-Ace-HTrp)]

The complex is represented in Fig. 2. Interatomic distances and bond angles are listed in Table 4.

In this 1:1 compound where the tryptophan NH_2 end has been blocked by an acetyl group, the CH_3Hg^+ ion is bound to a carboxylate oxygen, and the indole unit retains its N-H proton.

The Hg(1)—O(1) distance (2.085(9) Å) is similar to the one observed for the 2:1 glycylglycine complex (8). Mercury shows the usual linear coordination (C(14)—Hg(1)—O(1) = 178.1(5)°). Considering the esd's, the interatomic distances and bond angles in the acetyltryptophan ligand do not differ

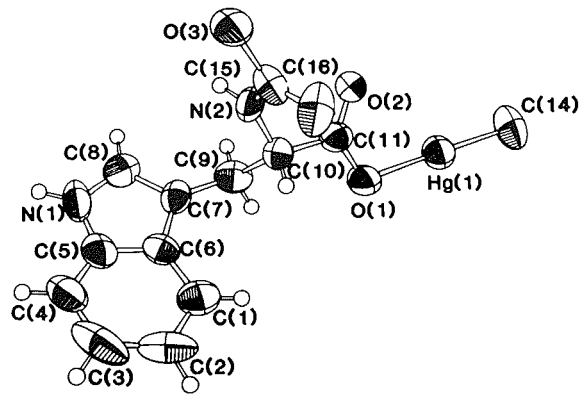

FIG. 2. Structure and numbering scheme for (CH_3Hg)(*N*-Ace-HTrp). Ellipsoids correspond to 50% probability.

significantly from those of its free form (20). However, the torsion angles around the C(10)—C(11) and C(10)—N(2) bonds are changed by ~20°.

Beside normal van der Waals contacts between organic groups, the lattice contains only hydrogen bonds (Fig. 3). Surprisingly, mercury is not involved in intra- or intermolecular Hg---O contacts, as commonly observed for other methylmercury – amino acid structures (1, 2, 7, 10, 11). The mercury cannot participate in a π interaction with the indole ring, as found in the crystal structure of $(CH_3Hg)_2$(DL-Trp), without inducing drastic perturbation in bond angles. The same situation was observed in the crystal structure of the [L-(2-amino-4-phenylbutanoato)]methylmercury(II) complex (10), where mercury is also five bonds away from the aromatic ring. However, in (CH_3Hg)(*N*-Ace-DL-HTrp), the oxygen-bonded mercury is located above the aromatic ring of a neighboring molecule.

Vibrational spectroscopy

H_2Trp and $(CH_3Hg)_2$(Trp)

The infrared and Raman frequencies are provided in Table 5 (supplementary material). Our assignments are based on those proposed by other groups (21–24) and on our previous work on methylmercury complexes with simple amino acids (7, 11).

The infrared spectrum of the $(CH_3Hg)_2$(DL-Trp) complex shows characteristic bands of the methylmercury group: ν(2915 cm^{-1}), δ(1198 cm^{-1}), and ρ(805 cm^{-1}). The ν and δ modes are also Raman active and give intense lines at 2918 and 1198 cm^{-1}, respectively. The vibrations involving the metal (ν Hg—C and ν Hg—N) are weak in infrared, but give rise to the most intense Raman lines. The ν Hg—C mode occurs at 560 cm^{-1}, while ν Hg—N is located at 484 cm^{-1}. These two bands are broader than those observed on the spectra of 1:1 complexes of alanine, glycine, and serine. This indicates that the frequencies of the two distinct CH_3Hg groups are close, but not exactly coincident, as noted by Alex and Savoie (25).

The infrared spectrum of free tryptophan shows a broad absorption, centered around 3000 cm^{-1} and assigned to ν NH_3^+. It is flanked by a sharp peak at 3406 cm^{-1} due to the indole NH stretching mode. This mode is Raman active and gives a strong line at 3350 cm^{-1}. Substitution of this NH proton by methylmercury removes this band from the infrared and Raman spectra. The broad ν NH_3^+ absorption is replaced by bands at 3110 and 3000 cm^{-1} corresponding to ν NH_2 vibrations of the -$NH_2(HgCH_3)$ group. The δ NH_3^+ bands (1665 and 1554 cm^{-1}) are replaced by a single δ NH_2 band at 1598 cm^{-1},

Can. J. Chem. Downloaded from www.nrcresearchpress.com by 196.1.178.254 on 09/07/12
For personal use only.

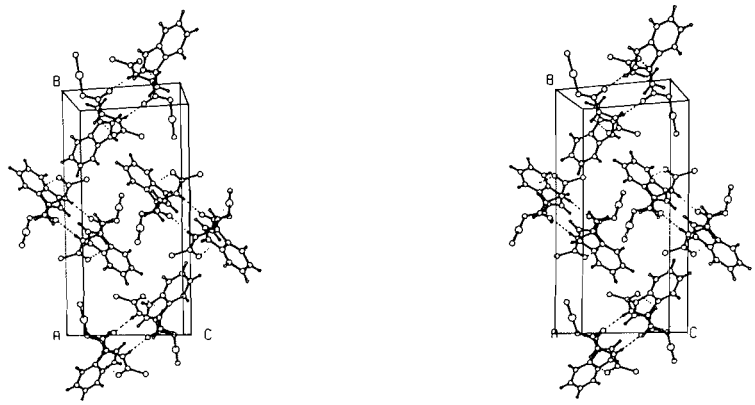

FIG. 3. Stereoview of the unit cell of (CH_3Hg)(*N*-Ace-HTrp). Atoms can be identified by reference to Fig. 2. Dashed lines correspond to hydrogen bonds.

Can. J. Chem. Downloaded from www.nrcresearchpress.com by 196.1.178.254 on 09/07/12
For personal use only.

but some intensity remains at $\sim 1530\ cm^{-1}$ because of coincidence with an indole ring vibration. The NH_3^+ group also has two rocking modes normally located between 1260 and $1100\ cm^{-1}$. The first one occurs at $1251\ cm^{-1}$ and disappears by complexation. The second mode probably produces one of the components in the $1166/1135\ cm^{-1}$ pair, the other originating from in-plane bending of the indole N-H group. Although both of these absorptions should be removed in the complex, this spectral region for the complex still shows bands, which are probably due to ω and (or) $\tau\ NH_2$ vibrations. The $\rho\ NH_2$ mode is believed to contribute to the band at $825\ cm^{-1}$, because of its characteristic broad shape. The indole NH group also produces an out-of-plane (γ) deformation mode. According to Lautié and co-workers (22), it occurs as a broad and intense band at $487\ cm^{-1}$ for indole. The infrared spectrum of tryptophan shows two such bands at 529 and $504\ cm^{-1}$. Upon complexation, they are replaced by a narrow peak at $532\ cm^{-1}$. One of these bands can be assigned to γ NH.

As noted for other methylmercury – amino acid complexes, the carboxylate vibrations are not greatly affected by complexation.

N-Ace-DL-H_2Trp and its methylmercury complexes

The spectra of acetyltryptophan and its methylmercury complexes are analyzed by comparison with the above discussion. The ν NH (amide and indole) and ν COOH modes were assigned by Battaglia *et al.* (26). The spectra of the methylamide have also been discussed by Matsuura *et al.* (27). The frequencies and tentative assignments are listed in Table 6 (supplementary material).

Carboxylate protonation and replacement of the NH_3^+ group of tryptophan by an acetyl group introduce changes in the high frequency region. There is a second sharp peak at $3340\ cm^{-1}$ for the amide ν NH band. The carboxylic ν OH mode produces a band at $2980\ cm^{-1}$, considerably narrower than the NH_3^+ absorption, which also occurred in this region for tryptophan.

The ν_a COOH mode appears as a strong doublet at $1722/1711\ cm^{-1}$, whereas the ν_s counterpart is located at $1236\ cm^{-1}$ (26). The very strong band at $1633\ cm^{-1}$ is broad and includes two indole ring vibrations, plus the amide I mode. The amide II and III bands are located at 1551 and probably $1249\ cm^{-1}$, respectively. The amide IV and V bands normally occur below $800\ cm^{-1}$. They are found at 663 and $711\ cm^{-1}$, respectively, for glycylglycine (8), but their frequencies are lower (602 and $684\ cm^{-1}$) for acetylglycine (28). The $682\ cm^{-1}$ band could be assigned to the amide V mode, this band being absent from the spectrum of tryptophan. However, the amide IV mode could not be identified.

The first methylmercury group reacts by substitution of the carboxylic proton, which removes the ν OH band from the spectrum. The ν_a and ν_s COO bands now occur at 1608 and $1381\ cm^{-1}$, respectively. The frequency difference between these two bands is thus reduced, as expected for carboxylate coordination to the metal (29). The observed frequencies are in good agreement with those reported by Battaglia *et al.* for acetyltryptophan chelates of copper (26).

Again, the presence of methylmercury is confirmed by its characteristic infrared (2923, 1191, and $806\ cm^{-1}$) and Raman bands (2934 and $1190\ cm^{-1}$). The Raman spectrum shows a strong ν Hg—C band at $554\ cm^{-1}$. The ν Hg—O band is located at $539\ cm^{-1}$ and coincides with the ρ COO mode, which usually produces a weak Raman line. The ν Hg—O band for the 2:1 glycylglycine complex was observed at $536\ cm^{-1}$ (8).

The spectral features described above for the 1:1 compound are also present for the 2:1 complex. In addition, spectral changes reflecting the deprotonation of the indole NH group are observed. The ν NH band disappears. The γ NH band, located at $565\ cm^{-1}$ in the infrared spectra of acetyltryptophan and its 1:1 complex, is removed from the spectrum of the 2:1 complex. The δ NH mode could not be reliably assigned.

The Raman spectrum of the 2:1 complex shows two sets of ν Hg—C and ν Hg—X (X = O and N) lines. The oxygen-bonded CH_3Hg group produces the ν Hg—C and ν Hg—O bands at 558 and $542\ cm^{-1}$, respectively. The CH_3Hg group bonded to the indole nitrogen atom gives rise to ν Hg—C and ν Hg—N bands located at 553 and $488\ cm^{-1}$, respectively. The frequency of the ν Hg—N band is almost the same as observed for the 2:1 tryptophan complex ($484\ cm^{-1}$).

Conclusion

The methylmercury complex with tryptophan incorporates two structural characteristics generally found for sulfhydryl-free amino acids, namely mercury coordination to the NH_2 end and an intramolecular secondary Hg...O bond with a carboxylate oxygen. The most interesting feature of the complex, however, is the side chain conformation that positions an indole ring C—C bond just above the methylmercury group. The Hg-ring π contact is probably strong enough to make this conformation the most favorable in solution, judging from the relatively deshielded positions of the ^1H and ^{13}C methylmercury nmr signals. Substitution of the indole N-H proton is found to

take place under mild conditions for both tryptophan and its *N*-acetylated derivative. In the latter case, blocking the NH_2 end by an acetyl group displaces the primary binding to a carboxylate oxygen. However, when methylmercury binds at this end, no low-energy conformation can bring the aromatic ring near mercury to produce π interactions.

Acknowledgments

We wish to thank the Natural Sciences and Engineering Research Council of Canada and the Fonds FCAR (Ministère de l'Éducation du Québec) for financial support. We are also grateful to M. J. Olivier who collected the X-ray data, and to S. Alex, M. Pigeon, and M. Savoie, who provided the Raman spectra.

1. Y. S. Wong, P. C. Chieh, and A. J. Carty. Can. J. Chem. **51**, 2597 (1973); Y. S. Wong, N. J. Taylor, P. C. Chieh, and A. J. Carty. J. Chem. Soc. Chem. Commun. 625 (1974); Y. S. Wong, A. J. Carty, and P. C. Chieh. J. Chem. Soc. Dalton Trans. 1157 (1977); Y. S. Wong, A. J. Carty, and P. C. Chieh. J. Chem. Soc. Dalton Trans. 1801 (1977).
2. Y. S. Wong, P. C. Chieh, and A. J. Carty. J. Chem. Soc. Chem. Commun. 741 (1973); N. J. Taylor, Y. S. Wong, P. C. Chieh, and A. J. Carty. J. Chem. Soc. Dalton Trans. 438 (1975).
3. M. T. Fairhurst and D. L. Rabenstein. Inorg. Chem. **14**, 1413 (1975); D. L. Rabenstein and M. T. Fairhurst. J. Am. Chem. Soc. **97**, 2086 (1975); R. S. Reid and D. L. Rabenstein. Can. J. Chem. **59**, 1505 (1981); D. L. Rabenstein and R. S. Reid. Inorg. Chem. **23**, 1246 (1984).
4. S. Alex and R. Savoie. J. Raman Spectrosc. **18**, 17 (1987).
5. P. G. Simpson, T. E. Hopkins, and R. Haque. J. Phys. Chem. **77**, 2282 (1973); Y. Hojo, Y. Sugiura, and H. Tanaka. J. Inorg. Nucl. Chem. **38**, 641 (1976); A. P. Arnold and A. J. Canty. Can. J. Chem. **61**, 1428 (1983).
6. A. Rothstein. *In* Mercury, mercurials and mercaptans. *Edited by* M. W. Miller and T. W. Clarkson. C. C. Thomas Publ., Springfield, IL. 1971.
7. M.-C. Corbeil, A. L. Beauchamp, S. Alex, and R. Savoie. Can. J. Chem. **64**, 1876 (1986).
8. S. Alex, R. Savoie, M.-C. Corbeil, and A. L. Beauchamp. Can. J. Chem. **64**, 148 (1986).
9. D. L. Rabenstein, R. Ozubko, S. Libich, C. A. Evans, M. T. Fairhurst, and C. Suvanprakorn. J. Coord. Chem. **3**, 263 (1974).
10. N. W. Alcock, P. A. Lampe, and P. Moore. J. Chem. Soc. Dalton Trans. 1324 (1978).
11. M.-C. Corbeil and A. L. Beauchamp. Can. J. Chem. **66**, 1379 (1988).
12. M. V. Hershberger and A. H. Maki. Biopolymers, **19**, 1329 (1980); P. Svejda, A. H. Maki, and R. R. Anderson. J. Am. Chem. Soc. **100**, 7138 (1978); R. R. Anderson and A. H. Maki. J. Am. Chem. Soc. **102**, 163 (1980).
13. A. J. Canty, N. Chaichit, and B. M. Gatehouse. Acta Crystallogr. Sect. B: Struct. Crystallogr. Cryst. Chem. **36**, 786 (1980); E. F. Kiefer, W. L. Waters, and D. A. Carlson. J. Am. Chem. Soc. **90**, 5127 (1968); R. D. Bach, A. T. Weibel, W. Schmonsees, and M. D. Glick. J. Chem. Soc. Chem. Commun. 981 (1974).
14. F. Bélanger-Gariépy and A. L. Beauchamp. J. Am. Chem. Soc. **102**, 3461 (1980).
15. D. T. Cromer and J. B. Mann. Acta Crystallogr. Sect. A: Cryst. Phys. Diffr. Theor. Gen. Crystallogr. **24**, 321 (1968); R. F. Stewart, E. R. Davidson, and W. T. Simpson. J. Chem. Phys. **42**, 3175 (1965); D. T. Cromer. Acta Crystallogr. **18**, 17 (1965).
16. G. Yagil. Tetrahedron, **23**, 2855 (1967).
17. J. P. Charland, M. T. Phan Viet, M. St-Jacques, and A. L. Beauchamp. J. Am. Chem. Soc. **107**, 8202 (1985); J. P. Charland, M. Simard, and A. L. Beauchamp. Inorg. Chim. Acta, **80**, L57 (1983); R. J. Kline, L. F. Systsma, and D. R. Shackle. Inorg. Nucl. Chem. Lett. **7**, 311 (1971).
18. S. Biagini, A. Lai, M. Monduzzi, and G. Saba. J. Chem. Soc. Faraday Trans. 2, **79**, 491 (1983).
19. O. Bakke and A. Mostad. Acta Chem. Scand. Ser. B: **B34**, 559 (1980).
20. T. Yamane, T. Andou, and T. Ashida. Acta Crystallogr. Sect. B: Struct. Crystallogr. Cryst. Chem. **33**, 1650 (1977).
21. A. Y. Hirakawa, Y. Nishimura, T. Matsumoto, M. Nakanishi, and M. Tsuboi. J. Raman Spectrosc. **7**, 282 (1978).
22. A. Lautié, M. F. Lautié, A. Gruger, and S. A. Fakhri. Spectrochim. Acta, Part A: **36A**, 85 (1980).
23. R. P. Rava and T. G. Spiro. J. Phys. Chem. **89**, 1856 (1985); J. Am. Chem. Soc. **106**, 4062 (1984).
24. S. A. Asher, M. Ludwig, and C. R. Johnson. J. Am. Chem. Soc. **108**, 3186 (1986).
25. S. Alex and R. Savoie. Can. J. Chem. **65**, 491 (1987).
26. L. P. Battaglia, A. Bonamartini Corradi, G. Marcotrigiano, L. Menabue, and G. C. Pellacani. J. Am. Chem. Soc. **102**, 2663 (1980).
27. H. Matsuura, K. Hasegawa, and T. Miyazawa. Spectrochim. Acta, Part A: **42A**, 1181 (1986).
28. M. V. Callahan and L. May. J. Mol. Struct. **2**, 154 (1968).
29. K. Nakamoto. Infrared and Raman spectra of inorganic and coordination compounds. John Wiley & Sons, New York. 1978. p. 306.

Can. J. Chem. Downloaded from www.nrcresearchpress.com by 196.1.178.254 on 09/07/12
For personal use only.

A 6-31G* chemistry of isoelectronic tetrahedral XL_4^{ϵ} and YL_4^{ϵ} (X = Li to F; Y = Na to Cl; L = H, F, Cl) species. Part 2. Energies, bond lengths, and critical radii[1]

S. C. Choi, Russell J. Boyd, and Osvald Knop
Department of Chemistry, Dalhousie University, Halifax, N.S., Canada B3H 4J3

Received January 20, 1988

S. C. Choi, Russell J. Boyd, and Osvald Knop. Can. J. Chem. **66**, 2465 (1988).

The 6-31G* *ab initio* treatment of isoelectronic tetrahedral species now covers the complete XL_4^{ϵ} and YL_4^{ϵ} series (X = Li to F; Y = Na to Cl; L = H, F, Cl). The optimized equilibrium molecular parameters comprise the total electronic energy E, bond lengths, critical radii r_c, MO energy levels, net charges, and electron densities at the bond critical points; only the first four are discussed in this part. The stability in terms of E, of the tetrahedral species relative to some competing systems, is examined. The energy requirements associated with the transfer of electronic charge from L to the central atom are reflected in the variation of the critical radii with the oxidation state m of X and Y, with important differences between the first- and the second-row elements. In an appendix it is shown that the $E_{\sim\text{HF limit}}$ energies of isoelectronic He-core (Li^+ ff.), Ne-core (Na^+ ff.), and Ar-core (K^+ ff.) series of ions can be represented analytically by quadratic polynomials in m to an accuracy of ~0.0023% of the $E_{\sim\text{HF limit}}$ range or better, and that these approximations for the three series are *qualitatively* of the type $E = -a(Z - b)^2$.

S. C. Choi, Russell J. Boyd et Osvald Knop. Can. J. Chem. **66**, 2465 (1988).

Le traitement *ab initio* au niveau 6-31G* des espèces tétraédriques isoélectroniques s'étend maintenant aux séries XL_4^{ϵ} et YL_4^{ϵ} (X = Li à F; Y = Na à Cl; L = H, F, Cl). Les paramètres optimisés de l'équilibre moléculaire comprennent : l'énergie électronique totale E, les longueurs de liaison, les rayons critiques r_c, les niveaux d'énergie OM, les charges nettes et les densités électroniques au niveau des points critiques de liaison. La discussion, dans cette étude, ne porte que sur les quatre premiers paramètres. On étudie la stabilité des espèces tétraédriques, en fonction de l'énergie électronique totale E, par rapport à quelques systèmes concurrents. Les énergies nécessaires au transfert de la charge électronique de l'atome L à l'atome central se réflètent dans la variation du rayon critique en fonction de l'état d'oxydation m de X et de Y, avec une différence importante entre les éléments de la première et de la deuxième période. On montre dans un appendice que les énergies $E_{\sim\text{HF limite}}$ des systèmes isolélectroniques suivants : He-squelette (Li^+ ff.), Ne-squelette (Na^+ ff.) et Ar-squelette (K^+ ff.) des ions peuvent être représentées analytiquement par des polynômes quadratiques de degré m avec une précision de l'ordre de ~0,0023% de $E_{\sim\text{HF limite}}$ ou mieux, et que ces approximations dans le cas de ces trois séries sont *qualitativement* de type $E = -a(Z - b)^2$.
[Traduit par la revue]

In Part 1 (1)[2] we dealt with the results of *ab initio* calculations at the 6-31G* level of isoelectronic tetrahedral YF_4^{ϵ} (Y = Na, Mg, S, Cl) and $YF_{4-n}Cl_n^{\epsilon}$ (Y = Al, Si, P; n = 0–4) species. This investigation has now been extended to the entire set XH_4^{ϵ}, $XF_{4-n}Cl_n^{\epsilon}$, $XF_{4-n}H_n^{\epsilon}$, YH_4^{ϵ}, and $YF_{4-n}Cl_n^{\epsilon}$, where X is an element of the first row (Li to F), Y an element of the second row (Na to Cl), and n = 0–4. In the following we compare the results on the homoligand species XL_4^{ϵ} and YL_4^{ϵ} (L = H, F, Cl); results on the mixed species will be communicated in subsequent papers. The notation, abbreviations, and the method of calculation are the same as in Part 1, to which the reader is also referred for a discussion of the validity of the 6-31G* treatment.[3]

Table 1 supplements the electronic energies (au) listed in Table 4 of Part 1 by the $E_{6\text{-}31G^*}$ and $E_{\sim\text{HF limit}}$ values for X = Li to Ne and for a few other ions. The differences for the 6-31G* and ~HF-limit pairs of values are on the average ten times smaller than for Y^{m+}, i.e., the 6-31G* basis set yields much better energies for X^{m+} than for Y^{m+}, as would be expected. Observations on analytic representations of the $E(X^{m+})$ and $E(Y^{m+})$ values are discussed in the appendix.

Table 1. Electronic energies (au) of selected ions

Ion	$E_{6\text{-}31G^*}$	$E_{\sim\text{HF limit}}$[a]	Difference
H^0	−0.49823	−0.5	0.00177
H^-	−0.42244	−0.48793	0.06549
He^0	−2.85516	−2.86168	0.00652
Li^+	−7.23554	−7.23641	0.00087
Be^{2+}	−13.60980	−13.61130	0.00150
B^{3+}	−21.98386	−21.98623	0.00237
C^{4+}	−32.35768	−32.36119	0.00351
N^{5+}	−44.73119	−44.73616	0.00497
O^{6+}	−59.10444	−59.11114	0.00670
F^+ (^3P)	−98.79206	−98.83170	0.03964
F^{7+}	−75.47742	−75.48612	0.00870
Ne^{4+} (^3P)	−120.46984	−120.54356	0.07372
Ne^{8+}	−93.85006	−93.86111	0.01105
Cl^+ (^3P)	−459.01502	−459.04841	0.03339
Ar^0	−526.77374	−526.81709	0.04335
Ar^{4+} (^3P)	−521.66642	−521.70978	0.04336

*These values are from ref. 3 except for $E(H^-)$, which is from ref. 4.

[1]Reference 1 is considered as Part 1 of this series.

[2]Errata for ref. 1: Page 1109, line 2 of French abstract: SF_4^{2+}, *not* SF^{2+}; l. 3, *m*, *not* m. Page 1110, Table 1, footnote *d*: thermal. Table 2: AlF_3Cl^-, FXF = 110.35°; SiF_2Cl_2, FXCl = 109.21°; $SiFCl_3$, ClXCl = 110.64°; PF_3Cl^+, FXF = 107.06°; $PF_2Cl_2^+$, FXCl = 109.12°; $PFCl_3^+$, ClXCl = 111.88°. Page 1114, rh column, l. 3 of 3rd para.: ~ 12τ, *not* = 12τ; l. 5, $\tau \sim -\delta$, *not* $\tau = -\delta$. Page 1120, lh column, l. 5 of 2nd para.: of, *not* for.

[3]The only departure from the optimization procedure employed earlier involves FF_4^{3+}, for which attempts to obtain SCF convergence with GAUSSIAN 80 failed. Convergence was achieved with GAUSSIAN 86 (2), but as this program has not yet been interfaced with the AIMPAC set of programs (cf. ref. 1), the molecular parameters of FF_4^{3+} related to the bond critical point (r_c(F), $\rho(r_c)$, ϵ(F), electron-density contours) are not available at present.

Can. J. Chem. Downloaded from www.nrcresearchpress.com by 196.1.178.254 on 09/07/12
For personal use only.

TABLE 2. The energies E (au), bond lengths (Å), critical radii r_c (Å), net charges ϵ (e), and electron densities at the bond critical points $\rho(r_c)$ (au) for XL_4^{ϵ} and YL_4^{ϵ} species of T_d equilibrium geometry[a]

Species	$E_{6\text{-}31G^*}$	(X,Y)—L	r_c(X,Y)	ϵ(X,Y)	ϵ(L)	$\rho(r_c)$
LiH_4^{3-}	−9.13094	2.5065	0.9486	−1.117	−0.471	0.00466
LiF_4^{3-}	−404.82174	2.1347	0.7982	0.145	−0.786	0.01545
$LiCl_4^{3-}$	−1845.41052	3.0523	0.9874	0.628	−0.907	0.00365
BeH_4^{2-}	−16.64299	1.5837	0.6237	−0.138	−0.466	0.04380
BeF_4^{2-}	−412.49979	1.5757	0.5536	0.675	−0.669	0.07012
$BeCl_4^{2-}$	−1852.81959	2.1068	0.6254	0.843	−0.711	0.04276
BH_4^{-}	−26.96510	1.2431	0.5165	−0.030	−0.242	0.14220
BF_4^{-}	−422.72513	1.3935	0.4583	0.957	−0.489	0.15723
BCl_4^{-}	−1862.84690	1.8726	0.5376	0.262	−0.316	0.12035
CH_4	−40.19517	1.0837	0.6814	−0.660	0.165	0.27717
CF_4	−435.64522	1.3018	0.4171	1.313	−0.328	0.30449
CCl_4	−1875.74483	1.7665	0.7918	−0.364	0.091	0.20645
NH_4^{+}	−56.53077	1.0135	0.7925	−0.951	0.488	0.32923
NF_4^{+}	−451.51941	1.2797	0.5786	1.487	−0.122	0.44562
NCl_4^{+}	−1891.84342	1.7491	0.9433	−0.731	0.433	0.19858
OH_4^{2+}	−76.19498	1.0335	0.8782	−0.804	0.701	0.24396
OF_4^{2+}	−470.78956	1.3908	0.7437	0.714	0.321	0.31931
OCl_4^{2+}	−1911.52229	1.8465	1.0124	−0.811	0.703	0.12350
FH_4^{3+}	−99.57452	1.3778	1.1847	−0.541	0.885	0.05028
FF_4^{3+}	−494.15800	1.8047		−0.220	0.805	
FCl_4^{3+}	−1935.23094	2.2064	1.1510	−0.553	0.888	0.03949
NaH_4^{3-}	−163.57075	2.7585	1.2620	−1.170	−0.458	0.00578
$NaCl_4^{3-}$	−1999.82839	3.3063	1.2980	0.681	−0.920	0.00419
MgH_4^{2-}	−201.67145	1.9634	0.9545	−0.372	−0.407	0.02714
$MgCl_4^{2-}$	−2037.84445	2.4299	0.9382	0.849	−0.712	0.02757
AlH_4^{-}	−244.21330	1.6513	0.8060	0.248	−0.312	0.06367
SiH_4	−291.22513	1.4753	0.7156	0.545	−0.136	0.11759
PH_4^{+}	−342.76158	1.3795	0.6711	0.523	0.119	0.18538
SH_4^{2+}	−398.89852	1.3534	0.9829	0.415	0.396	0.21319
SCl_4^{2+}	−2234.43763	1.9402	1.0037	0.386	0.403	0.19098
ClH_4^{3+}	−459.76672	1.4979	1.1852	0.168	0.708	0.11420
$ClCl_4^{3+}$	−2295.37996	2.4269	1.3366	−0.102	0.776	0.04724

[a]For previously presented results on YF_4^{ϵ} (Y = Na to Cl) and YCl_4^{ϵ} (Y = Al, Si, P) see Tables 2 and 3 of ref. 1.

Results and discussion

The values of the molecular parameters for the tetrahedral XL_4^{ϵ} and YL_4^{ϵ} species not reported in Part 1 are listed in Table 2. For a chemist to draw full benefit from these and additional results, their analysis must be reasonably complete and therefore of necessity somewhat lengthy. In order not to lose sight of the main conclusions and to keep our account manageable for the reader, the analysis presented in this paper is confined to the energies, bond lengths, and critical radii, all at the 6-31G* level unless stated otherwise. A sequel will deal with net charges, electron densities at the bond critical points, and electron-density distributions.

The discussion that follows is an extension of that in Part 1, in a similar format. However, some of the conclusions in Part 1 concerning trends in the molecular parameters have to be modified to take account of the much more complete present set of results. The curves in the figures are visual fits unless stated otherwise.

Stability relative to competing species

The sum $E(BeF_3^{-}, D_{3h}) + E(F^{-})$ was discovered to be lower than $E(BeF_4^{2-}, T_d)$. This would point to instability of the T_d ion relative to the two simpler species. However, crystalline salts of BeF_4^{2-} are well known,[4] whereas crystals containing discrete BeF_3^{-} units do not appear to have been reported. Comparisons of $E(T_d$ species) with E(competing system) values are therefore of limited usefulness for predicting the stability of as yet unobserved T_d species under ordinary conditions, except where the difference of the two values is large. In that case a large positive difference, E(competing system) − $E(T_d$ species), would indicate that the tetrahedral species is stable relative to the given alternative; a *large negative* difference would point to instability. Where the difference is negative but small, the tetrahedral species, if ionic, stands a good chance of being stabilized in a crystal by Coulombic energy, and the same would apply to small positive differences, for the sign of the difference is of uncertain significance when the difference is numerically small, especially where fluorine is involved (cf. ref. 1).

Although the stability, in terms of E, of the XL_4^{ϵ} and YL_4^{ϵ}

[4]Discrete BeF_4 tetrahedra occur, for example, in the orthorhombic A_2BeF_4 of the K_2SO_4 (A = Na, K, Rb, Cs, NH_4, Tl) and Al_2BeO_4 (A = Cs, $Li_{1/2}Na_{1/2}$) types, the hexagonal Na_2BeF_4 ($LiKSO_4$ type), the trigonal Li_2BeF_4 (Be_2SiO_4 type), and the orthorhombic $ABeF_4$ (A = Ba, Pb; $BaSO_4$ type).

Can. J. Chem. Downloaded from www.nrcresearchpress.com by 196.1.178.254 on 09/07/12
For personal use only.

TABLE 3. Stability, in terms of $E_{6\text{-}31G^*}$(au), of the tetrahedral species XL_4^{ϵ} and YL_4^{ϵ}(A) relative to competing systems (B)

A	B	E(B) − E(A)	A	B	E(B) − E(A)
LiH_4^{3-}	$LiH + 3H^-$	−0.11725	NaH_4^{3-}	$NaH + 3H^-$	−0.06902
LiF_4^{3-}	$LiF + 3F^-$	−0.16393	NaF_4^{3-}	$NaF + 3F^-$	−0.12843
$LiCl_4^{3-}$	$LiCl + 3Cl^-$	−0.17667	$NaCl_4^{3-}$	$NaCl + 3Cl^-$	−0.14923
BeH_4^{2-}	$BeH_2 + 2H^-$	0.03218	MgH_4^{2-}	$MgH_2 + 2H^-$	0.11100
BeF_4^{2-}	$BeF_2 + 2F^-$	0.12106	MgF_4^{2-}	$MgF_2 + 2F^-$	0.17421
	$BeF_3^- + F^-$	−0.07284	$MgCl_4^{2-}$	$MgCl_2 + 2Cl^-$	0.06530
$BeCl_4^{2-}$	$BeCl_2 + 2Cl^-$	0.00505	AlH_4^-	$AlH_3 + H^-$	0.17460
BH_4^-	$BH_3 + H^-$	0.15265	AlF_4^-	$AlF_3 + F^-$	0.23909
BF_4^-	$BF_3 + F^-$	0.17917	$AlCl_4^-$	$AlCl_3 + Cl^-$	0.12843
BCl_4^-	$BCl_3 + Cl^-$	0.06656	PH_4^+	$PH_3 + H^+$	0.31362
NH_4^+	$NH_3 + H^+$	0.34641	PF_4^+	$PF_3 + F^+$	0.31145
NF_4^+	$NF_3 + F^+$	0.18729	PCl_4^+	$PCl_3 + Cl^+$	0.17706
NCl_4^+	$NCl_3 + Cl^+$	0.09289	SH_4^{2+}	$SH_2 + 2H^+$	0.23120
OH_4^{2+}	$H_2O + 2H^+$	0.18423	SF_4^{2+}	$SF_2 + 2F^+$	0.12820
OF_4^{2+}	$OF_2 + 2F^+$	−0.24808	SCl_4^{2+}	$SCl_2 + 2Cl^+$	−0.09443
	$OF_3^{3+} + F^-$	1.33492	ClH_4^{3+}	$HCl + 3H^+$	−0.29326
OCl_4^{2+}	$OCl_2 + 2Cl^+$	−0.17589	ClF_4^{3+}	$FCl + 3F^+$	−0.61028
FH_4^{3+}	$HF + 3H^+$	−0.42839	$ClCl_4^{3+}$	$Cl_2 + 3Cl^+$	−0.57792
FF_4^{3+}	$F_2 + 3F^+$	−0.89594			
FCl_4^{3+}	$FCl + 3Cl^+$	−0.63364			

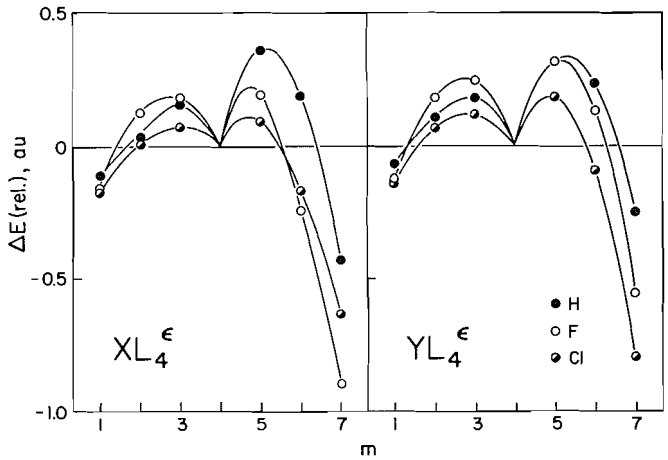

FIG. 1. Stability of the tetrahedral XL_4^{ϵ} and YL_4^{ϵ} species relative to the competing systems $XL_{4-|\epsilon|}^{0} + |\epsilon|L^{\epsilon/|\epsilon|}$ or $YL_{4-|\epsilon|}^{0} + |\epsilon|L^{\epsilon/|\epsilon|}$ (cf. Table 3). ΔE(rel.) = $E(XL_{4-|\epsilon|}^{0}) + |\epsilon|E(L^{\epsilon/|\epsilon|}) - E(XL_4^{\epsilon})$ and similarly for the Y species.

species relative to competing systems was not the subject of this work and has not been investigated systematically, a few dissociative schemes are listed in Table 3. The 6-31G* energies and geometric parameters of the pertinent product species will be found in Table 4. In the particular case of competing systems that involve the lower-coordinated neutral species, $XL_{4-|\epsilon|} + |\epsilon|L^{\epsilon/|\epsilon|}$ and $YL_{4-|\epsilon|} + |\epsilon|L^{\epsilon/|\epsilon|}$, it is found (Fig. 1) that gross instability occurs only with FL_4^{3+} and ClL_4^{3+}. The species OH_4^{2+}, SH_4^{2+}, and SF_4^{2+} might therefore be capable of being stabilized in the presence of suitable counter anions in crystals; for SCl_4^{2+} and OCl_4^{2+} the probability of this happening would seem much smaller (Table 3).

In fact, an account of an investigation of the stability of OH_4^{2+} relative to $H_3O^+ + H^+$ appeared while the present work was in progress (10). From a 6-31G* treatment (as well as from MP2/6-31G**, MP3/6-31G**, and MP4SDTQ/6-31G** refinements) the authors concluded that, although the thermodynamic stability (in terms of E) of the isolated OH_4^{2+} ion is unfavourable, the *kinetic* stability should be substantial. They suggest, from the results of their ^{17}O nmr experiments in $HF:SbF_5$, that OH_4^{2+} under such conditions might be stabilized by solvation. Since Coulombic energy in crystals containing divalent ions would provide at least as much stabilization, the possibility of existence of crystalline OH_4^{2+} salts cannot be dismissed.

Bond lengths

None of the calculated bond lengths is shorter than 1 Å, in agreement with observation. A comparison of the calculated and observed bond lengths can be made with reference to Table 5 and to Tables 1 and 2 of Part 1. Where experimental values are available, they are seen to agree with the calculated values to about 0.02 Å for the neutral and the singly charged species except AlH_4^-; in making these comparisons for the hydrogenic cations one must consider the lengthening effect of hydrogen bonding in crystals. For the higher-charged anionic species the extent of agreement is difficult to estimate, as such species have only been observed in crystals, where the bond length is invariably shorter (in the hydrogenic species especially so). This is the expected consequence of Coulombic compression as well as of the fact that species like LiH_4^{3-} or LiF_4^{3-} in crystals cannot be properly regarded as autonomous ionic units. No examples have been found of the doubly charged cationic species.

The trends reported in Part 1 for the variation with m of the internuclear distances Y—L in YF_4^{ϵ} (Y = Na to Cl) and YCl_4^{ϵ} (Y = Al, Si, P) are present in all six series (Fig. 2). In the XL_4^{ϵ} series the turn upward in the X—L vs. m curve occurs roughly at m = 5, whereas in the YL_4^{ϵ} series the corresponding change occurs at m = 6. The minima of the curves are quite flat and the shapes at large m give the impression of asymptotic

Can. J. Chem. Downloaded from www.nrcresearchpress.com by 196.1.178.254 on 09/07/12
For personal use only.

Can. J. Chem. Downloaded from www.nrcresearchpress.com by 196.1.178.254 on 09/07/12
For personal use only.

TABLE 4. Total electronic energies $E_{6\text{-}31G^*}$ and optimized equilibrium molecular geometries of species involved in the discussion of relative stabilities of the tetrahedral XL_4^{ϵ} and YL_4^{ϵ} species

Species	Symmetry	$E_{6\text{-}31G^*}$, au	Bond length, Å		Bond angle, deg		References
			calcd.	obsd.	calcd.	obsd.	
LiH	$C_{\infty v}$	−7.98087	1.6358	1.5957			5, 6
LiF	$C_{\infty v}$	−106.93423	1.5554	1.5639			5, 6
LiCl	$C_{\infty v}$	−467.00919	2.0722	2.0207			5, 6
BeH_2	$D_{\infty h}$	−15.76593	1.3342		180		5
BeF_2	$D_{\infty h}$	−213.67777	1.3712		180		5
BeF_3^-	D_{3h}	−313.22215	1.4606		120		This work
$BeCl_2$	$D_{\infty h}$	−933.76264	1.8046		180		This work
BH_3	D_{3h}	−26.39001	1.1883		120		5
BF_3	D_{3h}	−323.19548	1.3011	1.31	120		5, 7
BCl_3	D_{3h}	−1403.25434	1.7454	1.74	120		This work, 7
NH_3	C_{3v}	−56.18436	1.0025	1.015	107.21	106.6	5, 7
NF_3	C_{3v}	−352.54006	1.3279	1.371	102.69	102.2	5, 7
NCl_3	C_{3v}	−1432.73551	1.7224	1.75	110.22	106.8	This work, 7
OH_2	C_{2v}	−76.01075	0.9473	0.957	105.50	104.5	5, 8
OF_2	C_{2v}	−273.45352	1.3484	1.409	103.26	103.3	5, 7
OF_3^{3+}	D_{3h}	−370.10416	1.3032		120		This work
OCl_2	C_{2v}	−993.66814	1.6714	1.700	122.98	110.9	This work, 7
FH	$C_{\infty v}$	−100.00291	0.9110	0.9168			5, 6
F_2	$D_{\infty h}$	−198.67776	1.3449	1.4119			5, 6
FCl	$C_{\infty v}$	−558.81952	1.6126	1.6283			6
NaH	$C_{\infty v}$	−162.37245	1.9144	1.8873			5, 6
NaF	$C_{\infty v}$	−261.30170	1.8849	1.9259			6
NaCl	$C_{\infty v}$	−621.39962	2.3971	2.3608			6
MgH_2	$D_{\infty h}$	−200.71557	1.7177		180		5
MgF_2	$D_{\infty h}$	−398.60243	1.7231		180		This work
$MgCl_2$	$D_{\infty h}$	−1118.72715	2.1919		180		This work
AlH_3	D_{3h}	−243.61626	1.5841		120		5
AlF_3	D_{3h}	−540.45034	1.6205	1.63	120		This work, 7
$AlCl_3$	D_{3h}	−1620.57609	2.0774	2.06	120		This work, 7
PH_3	C_{3v}	−342.44796	1.4031	1.42	95.41	93.8	5, 7
PF_3	C_{3v}	−639.12923	1.5641	1.570	97.26	97.8	This work, 7
PCl_3	C_{3v}	−1719.21349	2.0480	2.04	100.78	100.3	This work, 7
SH_2	C_{2v}	−398.66732	1.3264	1.3356	94.37	92.1	5, 9
SF_2	C_{2v}	−596.31220	1.5864	1.59	98.01	98	This work, 7
SCl_2	C_{2v}	−1316.43524	2.0196	2.00	102.81	100	This work, 7
ClH	$C_{\infty v}$	−460.05998	1.2665	1.2746			5, 6
Cl_2	$D_{\infty h}$	−918.91282	1.9900	1.9879			5, 6

convergence (X,Y)—L → ∞ (or at any rate a large increase in the bond length) as $m \rightarrow 8$.

Assuming, as in Part 1, that the variation of (X,Y)—L with m can be represented as a sum of a bond-shortening (attractive) and a bond-lengthening (repulsive) term, and further that the internuclear distance tends to infinity as $m \rightarrow 8$, the (X,Y)—L distances were fitted to a function $a(m - b)^c + d(8 - m)^e$. The initial estimates of a, b, and c were obtained by fitting the (X,Y)—L values for $m = 1$–3 to a simple power function, and d and e were estimated from a power fit to the differences between (X,Y)—L and the $a(m - b)^c$ values calculated from the initial estimates of a, b, and c. All five parameters were then optimized by iterative least squares (Table 6). The goodness of fit σ ranges from ~0.4% of the observed Y—L range for YF_4^{ϵ} to ~2.4% for YCl_4^{ϵ} and appears adequate for our purposes.

Examination of the m_{eq} values at which $a(m - b)^c = d(8 - m)^e$ reveals that the repulsive interaction sets in later in the three Y series than in the three X series, but $m_{eq} > 7$ in all six series. The positions of m_{min} obtained from the analytic approximations confirm what is observed visually, viz. in the three X series the minimum occurs near $m = 5$, whereas in the three Y series it occurs near $m = 6$, although for YCl_4^{ϵ} the minimum is closer to Y = P than to Y = S.

Critical radii

Going from $m = 1$ to $m = 7$ the oxidation state and the nuclear charge Z of the central atom of XL_4^{ϵ} and YL_4^{ϵ} increase. As a result there is a progressive transfer of electronic charge from L to the central atom, i.e., $L^- \rightarrow L^0 \rightarrow L^+$ as $m \rightarrow 8$. These factors would be expected to decrease the effective size of X and Y as well as of L (as measured by r_c), thus progressively shortening the (X,Y)—L bond, reducing the positive charge on X and Y by $m - \epsilon(X,Y)$ and the negative charge on the ligand atom by $-1 - \epsilon(L)$.

These consequences are in fact observed, but not necessarily over the entire m range (Table 2, Fig. 3). The $r_c(X)$ and $r_c(L)$ vs. m curves for the X series fall from $m = 1$ to a minimum at $m = 3$ (at $m = 4$ for L = F), and the $r_c(Y)$ and $r_c(L)$ vs. m curves for the Y series fall from $m = 1$ to a minimum at $m = 5$ (at $m = 6$ for L = F). Beyond these minima the $r_c(X,Y)$ values increase with increasing m and the $r_c(L)$ values decrease, indicating that eventually enough electronic charge is transferred from L to the

TABLE 5. Literature values of experimentally determined bond lengths (Å) in tetrahedral XL_4^{ϵ} and YL_4^{ϵ} species[a]

Species	Bond length	Method[b]	Reference
LiH_4^{3-}	⟨1.94(8)⟩	$LiAlH_4$	11
	1.90–2.01	$ALiH_3$ (A = Eu, Sr, Ba)[c]	12
LiF_4^{3-}	⟨1.868(16)⟩	Li_2BeF_4	13
	⟨1.87(6)⟩	$CsLiF_2$	14
	1.88	$Li[LiNi]F_4$	15
	⟨1.883⟩	$Na_3Li(BeF_4)_2$	16
$LiCl_4^{3-}$	2.391(1)	$Li[LiMn]Cl_4$	17
BeF_4^{2-}	⟨1.532(3)⟩	$(NH_4)_2BeF_4$ (also nd)	18–20
	1.551(5) (corr.)	$(NH_4)_2BeF_4$	21
	⟨1.552⟩	$Na_3Li(BeF_4)_2$	16
	⟨1.554(6)⟩	Li_2BeF_4	13
	1.57(1)	Li_6BeZrF_{12}	22
BH_4^-	⟨1.255(20)⟩	$NaBH_4$, KBH_4, $RbBH_4$, nmr	23
BF_4^-	1.40 (corr.)	$Ca(BF_4)_2$	24
	⟨1.406(4)⟩ (corr.)	NH_4BF_4	25
CH_4	1.0940	vibr. spectr.	8
	1.094	*ab initio*[d]	26
	1.101	*ab initio*[e]	27
CF_4	1.320(5)	ed	28, 29
CCl_4	1.766(3)	ed	30
	1.773 (corr.)	CCl_4(II), 195 K	31
	1.763(6)	ed	28, 29
NH_4^+	⟨1.03(2)⟩	NH_4X (X = Cl, Br), nd	32
	1.030	*ab initio*[d]	26
	1.216	*ab initio*[e]	33
NF_4^+	1.301(6)	NF_4BF_4	[g]
	⟨1.31⟩	ir (est.)	35
	1.32	*ab initio* (level not stated)	36
NaH_4^{3-}	⟨2.50(1)⟩	$NaAlH_4$[f]	37
AlH_4^-	1.532(7)	$NaAlH_4$	37
	1.55(2)	$LiAlH_4$	11
	1.66	Raman (est.)	38
$AlCl_4^-$	⟨2.147(11)⟩ (corr.)	$(S_4N_4)[AlCl_4]_2$	39
	⟨2.146(9)⟩ (corr.)	$[N(SCl_2)]AlCl_4$	40
SiH_4	1.480	$SiHD_3$, ir	41
	1.475	*ab initio*[e]	27
PH_4^+	1.414(8) (corr.)	PH_4I, nd	42
	1.42(2)	PH_4I, PH_4Br, nmr	43
	1.680	*ab initio*[e]	33
PCl_4^+	⟨1.92(2)⟩	$(PCl_4)TeCl_5$	44
	⟨1.928(6)⟩	$(PCl_4)_2(SnCl_6)(PCl_6)$, $(PCl_4)SnCl_5$, $(PCl_4)Sn_2Cl_{10}$	34

[a]Compare also Table 1 of ref. 1.

[b]ed, electron diffraction; ir, infrared spectroscopy; nd, neutron diffraction; X-ray diffraction where no other indication.

[c]LiH_6^{2-} in cubic perovskites.

[d]An extended Gaussian basis set of *s* and *p* functions on the central atom and *s* functions on the H atoms.

[e]Single-centre expansion method with a basis set of 26 Slater-type orbitals.

[f]Na in 8-coordination, "(NaH_8^{7-})".

[g]K. O. Christe. Personal communication to O.K. (24/9/86).

central atom to start increasing the effective size of the latter whilst r_c(L) decreases further. The tendency of the central atom to acquire electronic charge from L increases steadily with m, but $L^- \rightarrow L^0$ and $L^0 \rightarrow L^+$ represent two stages of the charge transfer process from L with different energy requirements: for free atoms the second stage involves an approximately tenfold expenditure of energy over the first. It is therefore not surprising to find that the resulting compromise between the charge acquisition by X and Y and the charge surrender by L is reflected in the r_c vs. m or ϵ(L) curves, even though the course of the variation of r_c with m, ϵ(L), or ϵ(X,Y) cannot be predicted in detail.

Between $m = 1$ and the minimum the r_c(X) and r_c(Y) vs. m curves for L = H and Cl practically coincide and the curves for L = F parallel the respective curves for the hydrides and chlorides. This is also largely true of the r_c(H) and r_c(Cl) vs. m curves in the XL_4^{ϵ} and YL_4^{ϵ} series; the shapes of the corresponding curves for L = F are somewhat different. The increase in r_c(X,Y) for m values to the right of the minima is considerable: by $m = 7$ the r_c(X,Y) values in both the L = H

Can. J. Chem. Downloaded from www.nrcresearchpress.com by 196.1.178.254 on 09/07/12
For personal use only.

TABLE 6. Representation of the equilibrium internuclear distances in XL_4^{ϵ} and YL_4^{ϵ} by the composite power function $a(m - b)^c + d(8 - m)^e$

Parameter[a]	XH_4^{ϵ}	XF_4^{ϵ}	XCl_4^{ϵ}	YH_4^{ϵ}	YF_4^{ϵ}	YCl_4^{ϵ}
a	1.8469	1.6678	2.0941	2.2956	2.0071	2.6804
b	0.4878	0.5151	0.5909	0.3962	0.6001	0.5362
c	−0.4489	−0.2916	−0.3289	−0.3558	−0.2082	−0.2602
d	0.5823	0.8432	1.0760	0.3248	0.1165	0.7776
e	−1.8068	−1.2349	−0.7839	−1.7223	−2.3443	−1.7412
σ, Å	0.0242	0.0174	0.0263	0.0123	0.0044	0.0327
σ, % of range	1.62	2.04	2.02	0.87	0.44	2.39
m_{eq}	7.154	7.101	7.063	7.518	7.647	7.345
m_{min}	5.499	4.760	4.757	5.955	6.345	5.371

[a] m_{eq}, the value of m at which $a(m - b)^c = d(8 - m)^e$; m_{min}, the value of m at which the equilibrium distance is a minimum. The above optimized parameter values are believed to correspond to the absolute σ minima, but the possibility that they correspond to local minima close to the global minimum cannot be completely ruled out.

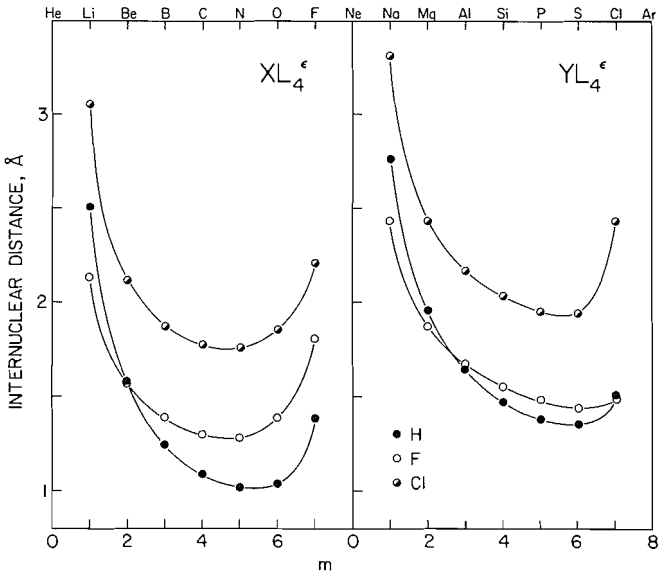

FIG. 2. Variation of the X—L and Y—L bond lengths in XL_4^{ϵ} and YL_4^{ϵ} (L = H, F, Cl) with the oxidation state m of X and Y.

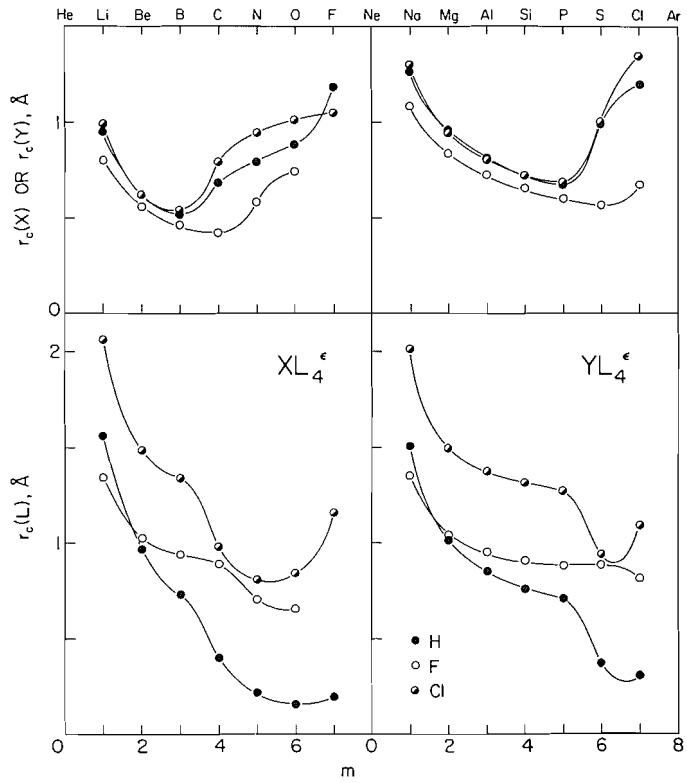

FIG. 3. Variation of the critical radii $r_c(L)$, $r_c(X)$, and $r_c(Y)$ in XL_4^{ϵ} and YL_4^{ϵ} with m.

and Cl series have reached or exceeded the corresponding values for $m = 1$. For L = F the trend is the same, although here the $r_c(X,Y)$ values do not regain, at high m, the values for $m = 1$.

The minima in the $r_c(X,Y)$ vs. m curves correspond to points of inflection in the $r_c(L)$ vs. m curves, and the minimum in the $r_c(H)$ vs. m curve for XH_4^{ϵ} corresponds to a point of inflection in the $r_c(X)$ curve for those hydrides. Such a correspondence might also exist in the curves for the other series, but the cutoff at $m = 7$ does not permit this to be verified. The rise, toward the end of the range, in the $r_c(H)$ and $r_c(Cl)$ values for XH_4^{ϵ}, XCl_4^{ϵ}, and YCl_4^{ϵ} must be considered together with the simultaneous increase in the bond length.

The electronic charge transfer from L to X and Y is more difficult for F than for H and Cl, especially in the YF_4^{ϵ} series; hence the $r_c(X,Y)$ vs. m curves for the fluorides reach their minima at higher values of m than is the case for H and Cl. The progress of the transfer is illustrated more dramatically by plotting the difference $r_c(L) - r_c(X,Y)$ against m or, more informatively, against $\epsilon(L)$ (Fig. 4). In the plot for the Y series in particular the uniformity of the features of these curves is clearly evident. Up to $\epsilon(L) \sim 0$ the r_c difference varies only slightly, i.e., $r_c(Y)$ and $r_c(L)$ for a given m decrease by the same amount (this is not quite true for Li). At $\epsilon(L) \sim 0$, however, further charge transfer from L produces a substantial drop in the value of the difference. This sudden drop, for $m = 6$ in the YH_4^{ϵ} and YCl_4^{ϵ} series and $m = 7$ in the YF_4^{ϵ} series, is caused by a simultaneous decrease in $r_c(L)$ and an increase in $r_c(Y)$, whereas for $m = 7$ the $r_c(Cl = L)$ value increases even though the value of the r_c difference drops.

In the X series (Fig. 4) the $r_c(L) - r_c(X)$ difference varies with $\epsilon(L)$ more gradually; for XH_4^{ϵ} from X = B to F the variation is almost linear. The turn downward occurs at $m = 4$ for L = F and at $m = 3$ for L = Cl, and for both at $\epsilon(L) \sim -0.2$. For X = H the turn at $m = 3$ and $\epsilon(H) \sim -0.2$ is less well

Can. J. Chem. Downloaded from www.nrcresearchpress.com by 196.1.178.254 on 09/07/12
For personal use only.

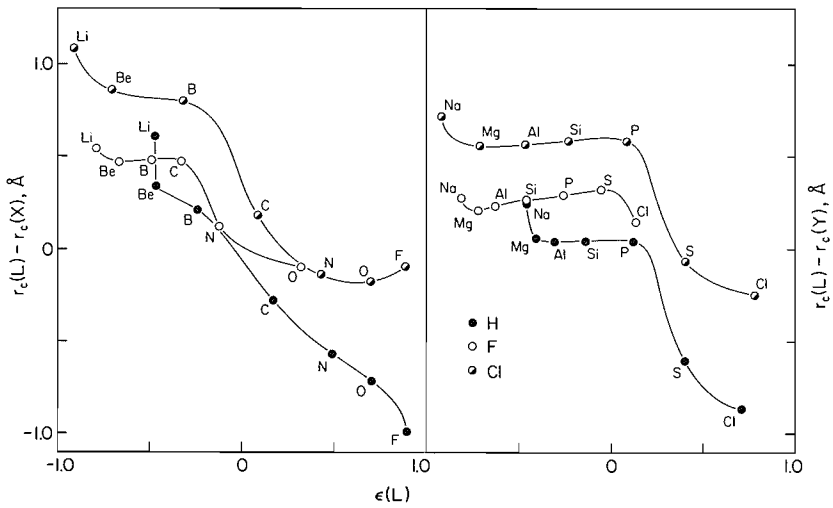

FIG. 4. Variation of the difference $r_c(L) - r_c(X,Y)$ of the critical radii with the net charge $\epsilon(L)$ on the ligand in XL_4^{ϵ}(*left*) and YL_4^{ϵ}(*right*).

Can. J. Chem. Downloaded from www.nrcresearchpress.com by 196.1.178.254 on 09/07/12
For personal use only.

defined. The earlier onset of the charge transfer from L in the X series may be attributed to the lower shielding of the nuclear charge on X.

The relative variation of $r_c(X,Y)$ and $r_c(L)$ is displayed even more clearly when these quantities are plotted against each other (Fig. 5). Implicit in this plot, unlike in Fig. 4, is the length of the (X,Y)—L bond. The $r_c(L)$ vs. $r_c(X,Y)$ curves therefore display an additional feature, viz. the onset of a repulsive interaction responsible for the bond lengthening that is observed toward the end of the m range in all six $(X,Y)L_4^{\epsilon}$ series (Fig. 2). This is best seen in the curves for XCl_4^{ϵ} and XH_4^{ϵ}, each of which contains unmistakably two turning points. The first, at a lower m, is consistent with the turning point of the curve in Fig. 4; the second, at a higher m, corresponds approximately to the minimum of the bond length. Although allowance must be made for the uncertainties of the visual fits of the points in Fig. 5, the *qualitative* similarity of the six curves cannot be denied. Further support for the existence of the repulsive interaction at high m will be presented in Part 3.

Position of the bond critical point

The relative position of the critical point in the Y—L bonds, $r_c(L)/(Y—L)$, in YL_4^{ϵ} varies little with m up to $m = 5$, after which the point moves suddenly toward the ligand nucleus (Fig. 6A). This shift is quite abrupt for L = H and Cl but less pronounced for L = F. The variation observed for XL_4^{ϵ} is similar except that the drop in $r_c(L)/(X—L)$ occurs already after $m = 3$. These trends are consolidated when the relative position of the critical point is plotted against $\epsilon(L)$ (Fig. 6B), in which case the plot resembles closely that of Fig. 4.

The internal consistency of the parameters involved is confirmed in Fig. 7, where the curves representing the visual fits carry more conviction.

Difference between X and Y elements

The variation of $r_c(X)$ with m is significantly different from that of $r_c(Y)$. The $r_c(Y)$ vs. m curves resemble those for $r_c(X)$ vs. m but are stretched along the m axis in such a way that the m_{min} values increase roughly by two units (Fig. 3). The maximum difference between the corresponding $r_c(X)$ and $r_c(Y)$ curves thus falls in the $m = 3$–5 region and reflects the difference in the bonding properties of the elements of the first and the elements of the second row. Figure 8 brings out this

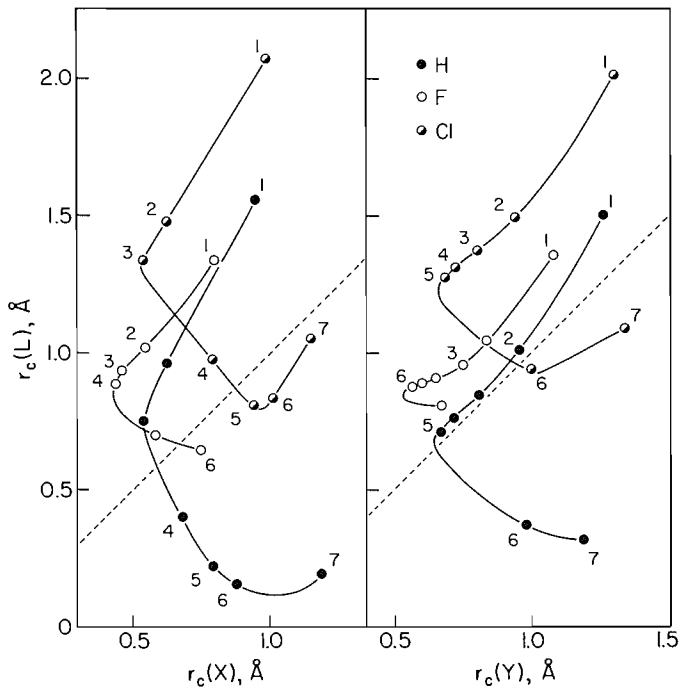

FIG. 5. Variation of the critical radii $r_c(L)$ in XL_4^{ϵ} and YL_4^{ϵ} with $r_c(X,Y)$.

difference more dramatically. In the $r_c(L)^X$ vs. $r_c(L)^Y$ plot the points for $m = 1$–2 and L = H, $m = 1$–4 and L = F, and $m = 1$–3 and L = Cl all lie, perhaps not surprisingly, close to the $r_c(L)^X = r_c(L)^Y$ line. For higher m values, however, there is a significant divergence due to $r_c(L)^X < r_c(L)^Y$; for the chloride series the points are situated on a loop, which for $m = 7$ returns to the 45° line. This behaviour seems to suggest association with a factor that intensifies with increasing m to a maximum and falls off again as $m \rightarrow 8$. The differences $\epsilon(L)^X - \epsilon(L)^Y$ and $[\epsilon(X) - \epsilon(L)^X] - [\epsilon(Y) - \epsilon(L)^Y]$ (i.e., the difference of bond "polarity") both have, qualitatively, this property, although lack of close *numerical* agreement indicates that these quantities alone do not account for the difference between $r_c(L)^X$ and $r_c(L)^Y$ for a given m. The F atoms would thus carry about the

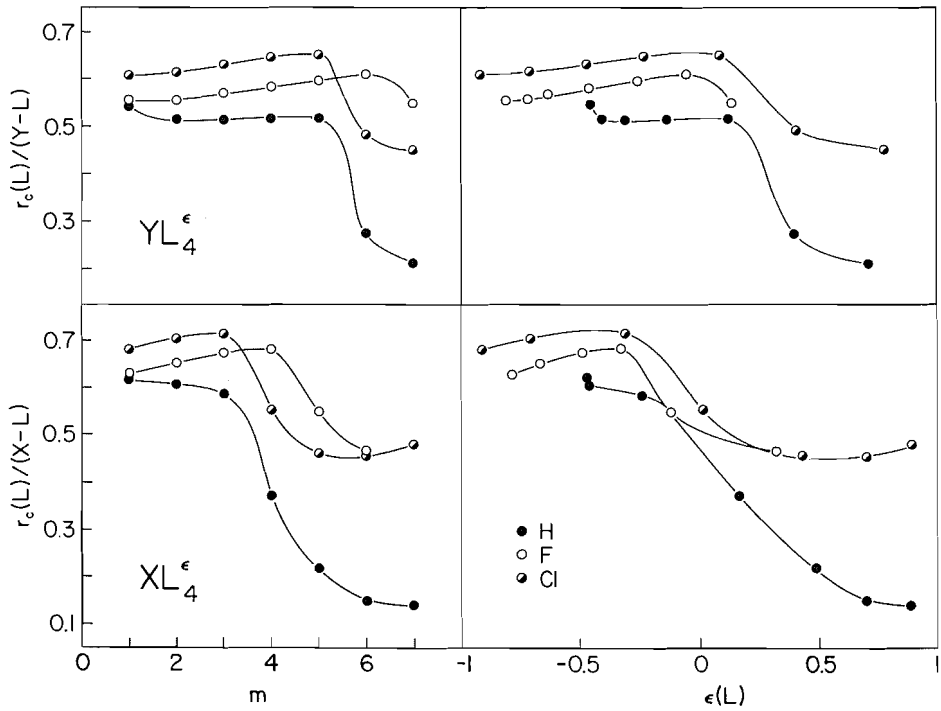

FIG. 6. Variation, with m (A, *left*) and ϵ(L) (B, *right*), of the relative position of the critical point in the X—L and Y—L bonds of XL_4^ϵ and YL_4^ϵ.

same net charge in CF_4 and SiF_4, but the Cl and H atoms in CL_4 would have significantly more electronic charge than in SiL_4, and the difference in the bond polarity between CL_4 and SiL_4 would be much larger for Cl and H than for F.

A somewhat analogous, and even more uniform, behaviour is observed in the plot of $r_c(X)_m$ vs. $r_c(Y)_m$ (Fig. 8). Here, however, $r_c(X)_m$ becomes larger than $r_c(Y)_m$ for $m > 4$. In the fluorides $r_c(Y)_m$ differs from $r_c(X)_m$ by a constant amount of ~0.3 Å up to $m = 4$, after which $r_c(Y)$ decreases only slightly with increasing m but $r_c(X)$ shows a rapid increase. Similar behaviour is observed in the chlorides and hydrides already after $m = 3$.

Critical vs. empirical radii

The $r_c(X^{m+})$ values for X = Li to B in the fluorides are, on the average, 0.054 Å smaller than those for L = H and Cl, and the $r_c(Y^{m+})$ values for Y = Na to P and L = F are 0.070 Å smaller than those for the corresponding hydrides and chlorides. For these m ranges the critical radii of X^{m+} and Y^{m+} in the fluorides correlate very well ($r^2 = 1.00$) with Shannon's effective covalent $r^{iv}(X^{m+})$ and $r^{iv}(Y^{m+})$ radii: $r^{iv}(X^{m+}) = -0.376 + 1.392 r_c(X^{m+})^F$ and $r^{iv}(Y^{m+}) = -0.698 + 1.691 r_c(Y^{m+})^F$. For YCl_4^ϵ and YH_4^ϵ the linear correlation is somewhat less good, while for XH_4^ϵ and XCl_4^ϵ the correlation is nonlinear. Since Shannon's set of effective radii was devised for use with oxides and fluorides (cf. ref. 1), the poorer agreement for L = Cl and H is not unexpected, but the difference between the $r_c(X^{m+},Y^{m+})$ values for L = F and those for L = Cl and H demonstrates the limitations of any quasi-universal additive set of effective radii.

If the sets of $r_c(X^{m+})$ and $r_c(Y^{m+})$ values correlate with Shannon's empirically derived additive set of effective radii only within a limited range of m values, Fig. 3 shows that there is little prospect of arriving at a self-consistent set of effective radii for the ligand atoms L. The critical radius $r_c(L)$ varies with m so widely that it would be meaningless to single out particular $r_c(L)$ values as representative except where L can be regarded

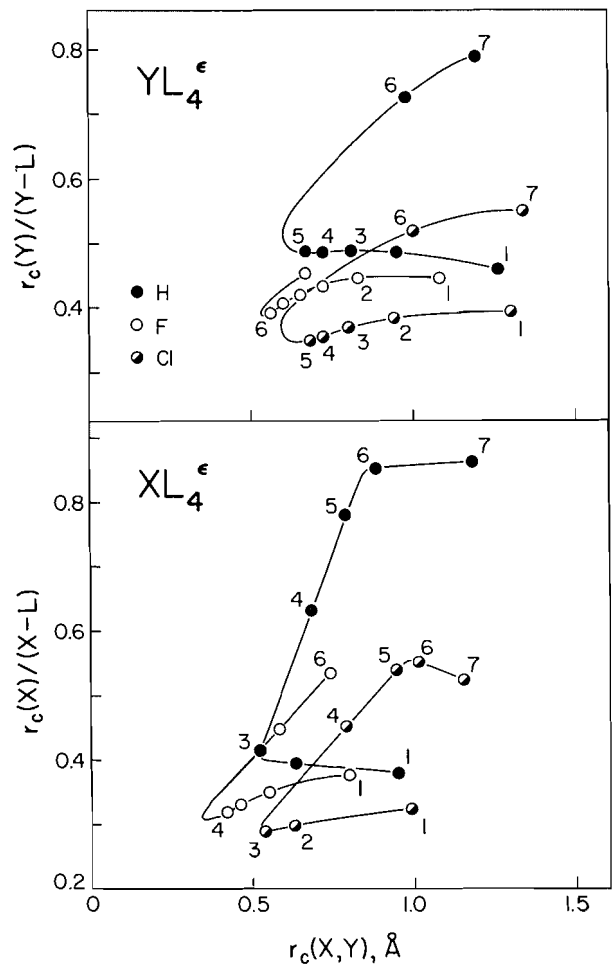

FIG. 7. Variation of the relative position of the bond critical point $r_c(X,Y)/[(X,Y)—L]$ in XL_4^ϵ and YL_4^ϵ with the critical radius $r_c(X,Y)$.

Can. J. Chem. Downloaded from www.nrcresearchpress.com by 196.1.178.254 on 09/07/12
For personal use only.

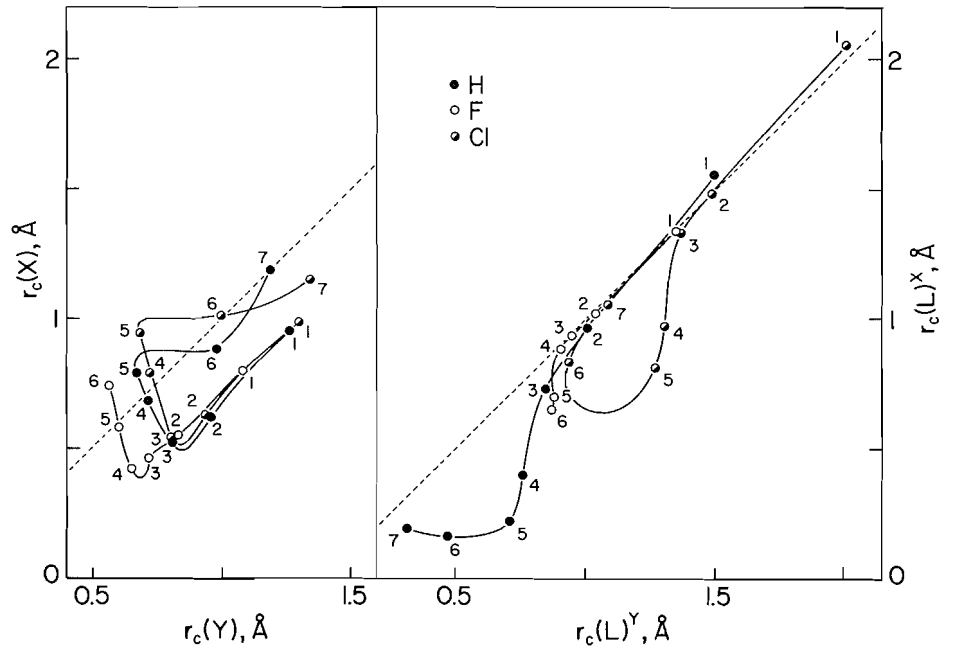

FIG. 8. Variation of $r_c(X)$ with $r_c(Y)$, and of $r_c(L)$ in XL_4^ϵ with $r_c(L)$ in YL_4^ϵ. The numbers represent m. The transfer of charge from L to the central atom is much more significant in the X than in the Y series after $m = 3$.

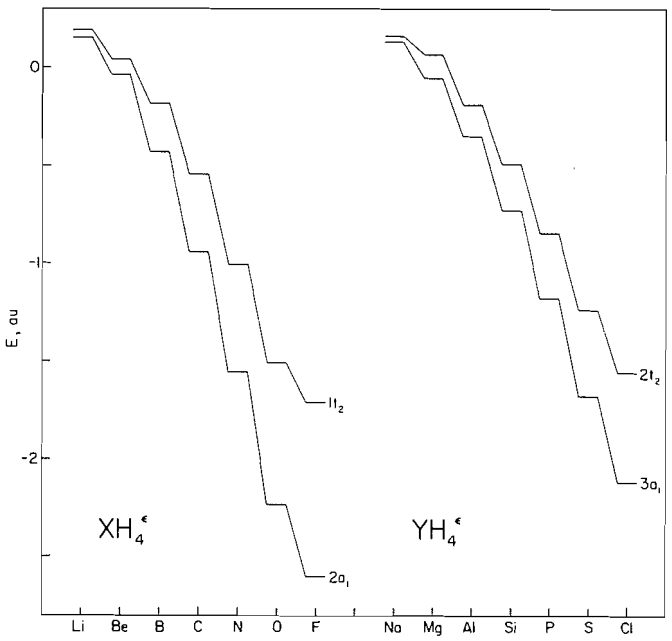

FIG. 9. MO energy levels in XH_4^ϵ and YH_4^ϵ (cf. Table 7 for numerical values).

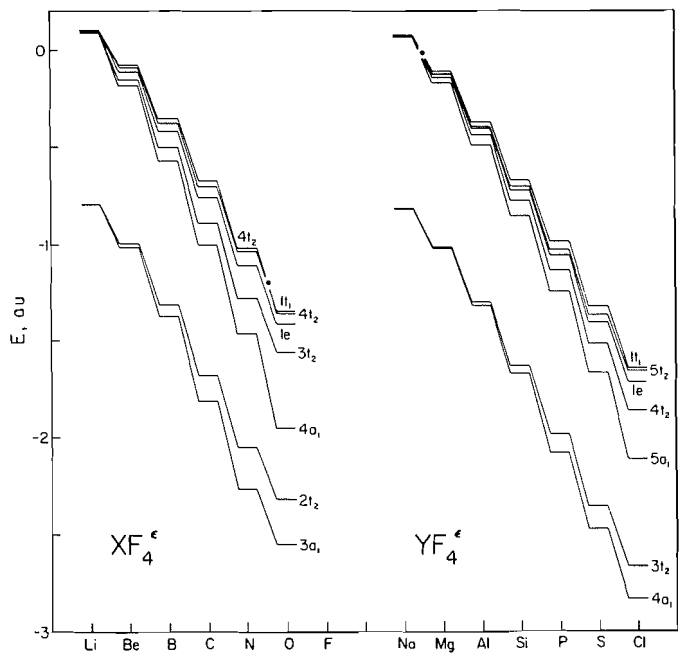

FIG. 10. MO energy levels in XF_4^ϵ and YF_4^ϵ (cf. Table 8 for numerical values). Crossover of two MO levels is indicated by a black dot.

as largely ionic, i.e., for $m = 1$–2. In that case the ratio $r_c(Cl)/r_c(F)$ is ca. 1.48(4), which approaches the values 1.40 and 1.36 for Shannon's covalent and ionic L radii, respectively, in six-coordination.

MO energy levels

In an attempt to discover the reasons for the minima in the bond length vs. m curves we have examined the individual MO energy levels (Figs. 9–11; Tables 7–9).[5] However, if such reasons are implicit in the MO levels, they are not self-evident in the gross features of Figs. 9–11. The steady decrease in energy with increasing m is the consequence of the increasing nuclear charge. For all three L the top occupied level in the YL_4^ϵ series is below that in the XL_4^ϵ series, but as m increases this order is preserved for L = F but reversed for L = H and Cl. Similarly, the lowest a_1 level is higher in the YL_4^ϵ than in the XL_4^ϵ series for L = H and Cl but not for L = F, where $4a_1$ is considerably below $3a_1$ of XF_4^ϵ.

For $m = 1$ the top five bonding levels of the fluorides and

[5]Copies of these tables can be purchased from the Depository of Unpublished Data, CISTI, National Research Council of Canada, Ottawa, Ont., Canada K1A 0S2.

Can. J. Chem. Downloaded from www.nrcresearchpress.com by 196.1.178.254 on 09/07/12
For personal use only.

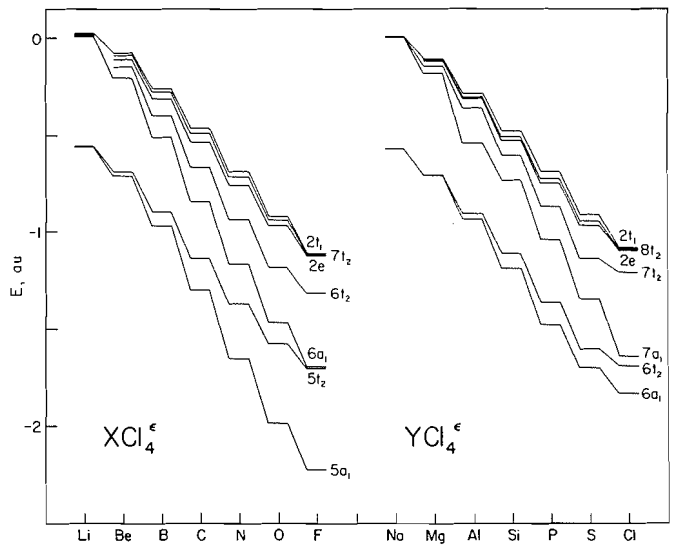

FIG. 11. MO energy levels in XCl_4^ϵ and YCl_4^ϵ (cf. Table 9 for numerical values).

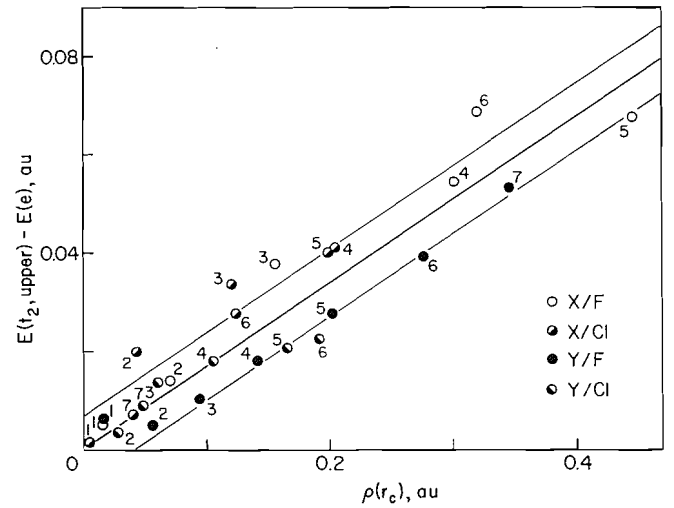

FIG. 12. Correlation of the MO energy difference $E(t_2, \text{upper}) - E(e)$ with the electron density $\rho(r_c)$ at the bond critical point in XF_4^ϵ, XCl_4^ϵ, YF_4^ϵ, and YCl_4^ϵ.

chlorides are very closely spaced. With increasing m their splitting increases but eventually decreases again, with the result that in the fluorides the upper t_2 and t_1 levels are again closely spaced, and in the chlorides the upper t_2, t_1, and e levels tend to coalesce. There is also a crossover of the $4t_2$ and $1t_1$ levels in the XF_4^ϵ series between N and O, and of the $5t_2$ and $1t_1$ in the YF_4^ϵ series between Na and Mg. In the hydrides the splitting of a_1 and t_2 increases steadily with m. The MO diagrams suggest that, in the $m \rightarrow 0$ limit, the bonding-orbital levels would coalesce to a single, 15-fold degenerate level, and for $m \rightarrow 8$ possibly to a 6-fold degenerate level in the fluoride species and an 8-fold degenerate level in the chlorides.

Further, more detailed, analysis would be required to determine how these progressive changes in the energy levels affect the equilibrium bond lengths of the tetrahedral species.

As a preliminary observation we note that the magnitude of the upper $t_2 - e$ splitting appears to correlate (roughly linearly, $r^2 = 0.88$, $\sigma = 0.00715$ au) with the electron density at the bond critical point, $\rho(r_c)$ (Fig. 12).

Conclusions

A complete set of equilibrium molecular geometries optimized at the 6-31G* level is now available for the isoelectronic T_d species XL_4^ϵ and YL_4^ϵ (X = Li to F; Y = Na to Cl; L = H, F, Cl). Analysis of the total electronic energies E, bond lengths, critical radii r_c, and MO energy levels brings to light the following main trends in the six series:

1. In each series the bond length decreases with the increasing formal oxidation state m of the central atom to a local minimum at $m \geq 4$ (Fig. 2). This variation can be approximated quite closely by the sum of a bond-contracting and a repulsive term: (X,Y)—L = $a(m - b)^c + d(8 - m)^e$, where $c, e < 0$.

2. The gross variation of r_c(X,Y) and r_c(L) with m resembles that of (X,Y)—L but the detail is more complex (Fig. 3). The r_c vs. m minimum in a particular series does not occur at the same m for r_c(X,Y) as for r_c(L), i.e., an increase in (X,Y)—L = r_c(X,Y) + r_c(L) with m may be produced by an increased r_c(X,Y) and a *decreased* r_c(L). The r_c values reflect the manner in which the electronic charge is progressively transferred from the ligand to the central atom as m increases.

3. The position r_c(L)/[(X,Y)—L] of the critical point in the bond remains at first relatively constant with m but then shifts suddenly toward L. This shift occurs in the vicinity of the zero net charge, ϵ(L) = 0, on the ligand in the YL_4^ϵ and at ϵ(L) ~ −0.3 in the XL_4^ϵ series (Fig. 6).

4. There are significant differences in the r_c vs. m variation between the first- and the second-row series after $m = 3$ (Fig. 8).

The net charges ϵ(X,Y) and ϵ(L), the electron densities at the bond critical points $\rho(r_c)$, and the geometry of the electron-density contours in XL_4^ϵ and YL_4^ϵ will be discussed in Part 3, in which we also intend to present more complete conclusions from this investigation.

Acknowledgments

This work was supported by grants from the Natural Sciences and Engineering Research Council of Canada to R.J.B. and O.K. We are pleased to acknowledge the assistance provided by Randy Barkhouse, Aidan Evans, and the staff of the Dalhousie University Computing and Information Services.

1. S. C. CHOI, R. J. BOYD, and O. KNOP. Can. J. Chem. **65**, 1109 (1987).
2. M. J. FRISCH, J. S. BINKLEY, H. B. SCHLEGEL, K. RAGHAVACHARI, C F. MELIUS, R. L. MARTIN, J. J. P. STEWART, F. W. BOBROWICZ, C. M. ROHLFING, L. R. KAHN, D. J. DEFREES, R. SEEGER, R. A. WHITESIDE, D. J. FOX, E. M. FLEUDER, and J. A. POPLE. GAUSSIAN 86. Carnegie–Mellon Quantum Chemistry Publishing Unit, Pittsburgh, PA. 1984.
3. E. CLEMENTI and C. ROETTI. At. Data Nucl. Data Tables, **14**, 177 (1974).
4. A. GUPTA and R. J. BOYD. J. Chem. Phys. **68**, 1951 (1978).
5. R. A. WHITESIDE, M. J. FRISCH, and J. A. POPLE. The Carnegie–Mellon quantum chemistry archive. 3rd ed. Department of Chemistry, Carnegie–Mellon University, Pittsburgh, PA. 1983.
6. K. P. HUBER and G. HERZBERG. Molecular spectra and molecular structure. Vol. 4. Van Nostrand, New York. 1979.
7. A. F. WELLS. Structural inorganic chemistry. 5th ed. Clarendon Press, Oxford. 1984.

Can. J. Chem. Downloaded from www.nrcresearchpress.com by 196.1.178.254 on 09/07/12
For personal use only.

Can. J. Chem. Downloaded from www.nrcresearchpress.com by 196.1.178.254 on 09/07/12
For personal use only.

8. G. HERZBERG. Molecular spectra and molecular structure. Vol. 3. Van Nostrand, New York. 1966.
9. R. L. COOK, F. C. DE LUCIA, and P. HELMINGER. J. Mol. Struct. **28**, 237 (1975).
10. G. A. OLAH, G. K. SURYA PRAKASH, M. BARZAGHI, L. LAMMERTSMA, P. VON R. SCHLEYER, and J. A. POPLE. J. Am. Chem. Soc. **108**, 1032 (1986).
11. N. SKLAR and B. POST. Inorg. Chem. **6**, 669 (1967).
12. A. J. MAELAND and A. F. ANDRESEN. J. Chem. Phys. **48**, 4660 (1968).
13. J. H. BURNS and E. K. GORDON. Acta Crystallogr. **20**, 135 (1966).
14. J. H. BURNS and W. R. BUSING. Inorg. Chem. **4**, 1510 (1965).
15. W. RÜDORFF, J. KÄNDLER, and D. BABEL. Z. Anorg. Allg. Chem. **317**, 261 (1962).
16. P. J. VICAT, D. TRANQUI, S. ALÉONARD, and P. RICHARD. Acta Crystallogr. Sect. B: Struct. Crystallogr. Cryst. Chem. **30**, 2678 (1974).
17. C. J. J. VAN LOON and J. DE JONG. Acta Crystallogr. Sect. B: Struct. Crystallogr. Cryst. Chem. **31**, 2549 (1975).
18. S. V. MISYUL, A. I. KRUGLIK, K. S. ALEKSANDROV, YU. Z. NOZIK, L. E. FYKIN, and S. P. SOLOV'EV. Kristallografiya, **24**, 932 (1979).
19. S. V. MUSYUL, A. I. KRUGLIK, and M. A. SIMONOV. Kristallografiya, **25**, 473 (1980).
20. A. ONODERA and Y. SHIOZAKI. Ferroelectrics, **31**, 27 (1981).
21. A. GARG and R. C. SRIVASTAVA. Acta Crystallogr. Sect. B: Struct. Crystallogr. Cryst. Chem. **35**, 1429 (1979).
22. D. R. SEARS and J. H. BURNS. J. Chem. Phys. **41**, 3478 (1964).
23. P. T. FORD and R. E. RICHARDS. Disc. Faraday Soc. **19**, 230 (1955).
24. T. H. JORDAN, B. DICKENS, L. W. SCHROEDER, and W. E. BROWN. Acta Crystallogr. Sect. B: Struct. Crystallogr. Cryst. Chem. **31**, 669 (1975).
25. A. P. CARON and J. L. RAGLE. Acta Crystallogr. Sect. B: Struct. Crystallogr. Cryst. Chem. **27**, 1102 (1971).
26. M. KRAUSS. J. Chem. Phys. **38**, 564 (1963).
27. R. MOCCIA. J. Chem. Phys. **40**, 2164 (1964).
28. L. O. BROCKWAY. Acta Crystallogr. **7**, 682 (1954).
29. L. S. BARTELL, L. O. BROCKWAY, and R. H. SCHWENDEMAN. J. Chem. Phys. **23**, 1854 (1955).
30. Y. MORINO, Y. NAKAMURA, and T. IIJIMA. J. Chem. Phys. **32**, 643 (1960).
31. S. COHEN, R. POWERS, and R. RÜDMAN. Acta Crystallogr. Sect. B: Struct. Crystallogr. Cryst. Chem. **35**, 1670 (1979).
32. H. A. LEVY and S. W. PETERSON. J. Am. Chem. Soc. **75**, 1536 (1953).
33. R. MOCCIA. J. Chem. Phys. **40**, 2176 (1964).
34. J. SHAMIR, S. LUSKI, A. BINO, S. COHEN, and D. GIBSON. Inorg. Chem. **24**, 2301 (1985).
35. K. O. CHRISTE. Spectrochim. Acta, Part A: **42**A, 939 (1986).
36. N. J. S. PETERS. Ph.D. dissertation, Princeton University. 1982. (Quoted in ref. 35.)
37. J. W. LAUHER, D. DOUGHERTY, and P. J. HERLEY. Acta Crystallogr. Sect. B: Struct. Crystallogr. Cryst. Chem. **35**, 1454 (1979).
38. L. A. WOODWARD and H. L. ROBERTS. Trans. Faraday Soc. **52**, 1458 (1956).
39. R. J. GILLESPIE, J. P. KENT, J. F. SAWYER, D. R. SLIM, and J. D. TYRER. Inorg. Chem. **20**, 3799 (1981).
40. O. GLEMSER, E. KINDLER, B. KREBS, R. MEWS, F.-M. SCHNEPEL, and J. WEGENER. Z. Naturforsch. B. Anorg. Chem. Org. Chem. **35**B, 657 (1980).
41. D. R. J. BOYD. J. Chem. Phys. **23**, 922 (1955).
42. A. SEQUEIRA and W. C. HAMILTON. J. Chem. Phys. **47**, 1818 (1967).
43. L. PRATT and R. E. RICHARDS. Trans. Faraday. Soc. **50**, 670 (1954).
44. P. H. COLLINS and M. WEBSTER. Acta Crystallogr. B, **28**, 1260 (1972).

Appendix

Analytic representation of $E(X^{m+})$ *and* $E(Y^{m+})$

While examining the energies of formation $E_f(XL_4^{\epsilon})$ and $E_f(YL_4^{\epsilon})$ we made the following observations, which we think worth reporting.

1. The total electronic energies $E(X^{m+})_{\sim\text{HF limit}}$ and $E(Y^{m+})_{\sim\text{HF limit}}$ $(m = 0\text{–}8)$ can be represented to a high accuracy by simple quadratic functions of m, and so can the $E_{\sim\text{HF limit}}$ of the third-row isoelectronic ions from Ar^0 to Ni^{10+}:

He-core ions, $E_{\sim\text{HF limit}} = -2.861616 - 3.374838m - 1.0000129m^2$, $\sigma = 0.00005$ au $\sim 5 \times 10^{-5}$% of range;

Ne-core ions, $E_{\sim\text{HF limit}} = -128.537413 - 31.141118m - 2.0048218m^2$, $\sigma = 0.00773$ au ~ 0.0023% of range;

Ar-core ions, $E_{\sim\text{HF limit}} = -526.786812 - 69.787000m - 2.4540177m^2$, $\sigma = 0.02019$ au ~ 0.0023% of range.

The listed $E_{\sim\text{HF limit}}$ values for the Ne- and Ar-core ions (3) are somewhat less accurate than those for X^{m+}. It is therefore possible that an improved accuracy of these two sets might result in quadratic expressions of even lower σ values. The accuracy of these simple representations is so high as to suggest that a simple polynomial is the proper functional representation of $E_{\sim\text{HF limit}}$ for such isoelectronic series. Similar representations, of lower accuracy, are obtained for the $E_{6\text{-}31G^*}$ sets.

2. The quadratic representations can be rewritten as $E_{\sim\text{HF limit}} = -a(Z - b)^2 - R$, where Z is the atomic number:

He-core ions, $a = 1.0000129$ au, $b = 0.312603 \sim 5/16$, $R = 0.01417$ au ~ 0.016% of range;

Ne-core ions, $a = 2.0048218$ au, $b = 2.233445$, $R = 7.607809$ au ~ 0.22% of range;

Ar-core ions, $a = 2.4540177$ au, $b = 3.781072$, $R = 30.638634$ au ~ 3.2% of range.

The form of this function suggests that the b term may be regarded as a shielding parameter, and the relative smallness of the R term suggests that the $E_{\sim\text{HF limit}}$ values could be approximated by a two-constant function to an accuracy probably no worse than 1%. Regressing $E_{\sim\text{HF limit}}$ on $-a(Z - b)^2$ and taking a(He-core ions) = 1 and a(Ne-core ions) = 2 gave these results:

He-core ions, $a = 1$ au, $b = 0.311539$, $\sigma = 0.00512$ au ~ 0.006% of range;

Ne-core ions, $a = 2$ au, $b = 2.068103$, $\sigma = 1.58170$ au ~ 0.46% of range;

Ar-core ions, $a = 2.4462$ au, $b = 3.4352$, $\sigma = 5.00$ au ~ 0.53% of range.

The accuracy of these two-constant regressions is considerably poorer than for the unconstrained quadratic fits. However, it is sufficiently good to suggest that the "effective" charge, which for the He-core ions involves a shielding parameter appropriate to the s electrons, in the case of the Ne- and Ar-core ions can similarly, to a first approximation, be expressed as $Z - b$, where b represents an overall shielding parameter due to *all* the *s and p* electrons.

Étude structurale de l'amino-5 dibenzyl-4,4 one-3 2*H*-thiadiazine-1,2,6 dioxyde-1,1

PIERRE BROUANT ET JACQUES BARBE[1]

Groupe d'études et de recherche en chimie thérapeutique organique et physique, Faculté de pharmacie, 27 boul. Jean-Moulin, 13385 Marseille CEDEX 5, France

ET

PILAR GOYA ET CARMEN OCHOA

Instituto de Quimica Medica, CSIC, Juan de la Cierva 3, Madrid 6, Espagne

Reçu le 9 décembre 1987

PIERRE BROUANT, JACQUES BARBE, PILAR GOYA et CARMEN OCHOA. Can. J. Chem. **66**, 2477 (1988).

La structure à l'état solide de l'amino-5 dibenzyl-4,4 one-3 2*H*-thiadiazine-1,2,6 dioxyde-1,1 a été déterminée par diffraction des rayons X. La structure montre que la molécule correspond au tautomère amino et qu'il y a disposition en feuillets des cycles aromatiques et hétérocycliques. Le noyau hétérocyclique non conjugué présente ici une structure plane alors qu'il est généralement plié chez les substances homologues. Les résultats obtenus en solution par spectroscopie en résonance magnétique nucléaire ^1H et par mesure du moment dipolaire sont compatibles avec cette géométrie.

PIERRE BROUANT, JACQUES BARBE, PILAR GOYA, and CARMEN OCHOA. Can. J. Chem. **66**, 2477 (1988).

5-Amino-4,4-dibenzyl-3-one-2*H*-1,2,6-thiadiazine-1,1-dioxide was structurally characterized in the solid state by X-ray diffraction. The structure shows that the title compound exists in the solid in a sheet-packed form and as the amino tautomer. The unconjugated heterocyclic ring, which in the structures of related compounds is usually folded, is planar in the present structure. ^1H nuclear magnetic resonance and dipole moment data indicate that the title compound has the same structure in the solid state and in solution.

Can. J. Chem. Downloaded from www.nrcresearchpress.com by 196.1.178.254 on 09/07/12
For personal use only.

Introduction

La configuration des hétérocycles thiadiaziniques-1,2,6 a été largement étudiée par radiocristallographie. Leur caractère non aromatique s'accorde avec les structures pliées qui sont décrites dans la littérature (1–8). Pour ce qui concerne plus particulièrement les dérivés de la 2*H*-thiadiazine-1,2,6 dioxyde-1,1, plusieurs activités biologiques différentes ont été mentionnées. Ainsi, on a décrit chez ces substances des propriétés bactéricide (9), antifongique (10–12) et antiparasitaire (12, 13). Cependant, si leur analogie apparente avec les bases pyrimidiniques planes se confirmait sur le plan topographique, ceci permettrait d'orienter les recherches vers l'élaboration et l'élucidation de nouvelles activités biologiques. C'est pourquoi, on a entrepris l'étude structurale de la molécule schématisée sur la figure 1 : l'amino-5 dibenzyl-4,4 one-3 2*H*-thiadiazine-1,2,6 dioxyde-1,1.

Partie expérimentale

1. Radiocristallographie

Les données cristallographiques sont rapportées dans le tableau 1. Le composé, préparé selon le mode opératoire décrit dans la référence 14, a été recristallisé dans le chloroforme. La densité a été mesurée par flottaison dans le mélange toluène – tétrachlorure de carbone. La détermination de la maille et l'enregistrement des intensités diffractées ont été effectués sur un diffractomètre automatique 4 cercles CAD-4 Enraf Nonius à monochromateur de graphite : $\lambda(\text{Mo K}\bar{\alpha}) = 0{,}7107$ Å. Les dimensions de la maille ont été obtenues par moindres carrés à partir des positions angulaires de 25 réflexions. Le groupe spatial a été déterminé par analyse des extinctions systématiques sur clichés de diffraction effectués en chambre en précession avec la radiation Cu Kα.

On a utilisé la technique de balayage θ–2θ. On a réalisé des contrôles d'orientation toutes les 300 mesures et des contrôles d'intensité toutes les 10 000 secondes. La déviation angulaire maximum tolérée a été de 0,12 et les variations d'intensité ont été inférieures à 1%.

Les intensités mesurées n'ont pas été corrigées pour l'absorption. La structure a été déterminée par méthode directe (15) avant d'être précisée par une succession de synthèses de Fourier-différences et de cycles d'affinements par moindres carrés.

Les atomes d'hydrogène, construits géométriquement à l'exception des trois hydrogènes portés par les atomes d'azote qui ont pu être localisés sur les cartes de Fourier-différences, ont été inclus et affinés dans les derniers cycles d'affinement qui ont eu lieu en matrice entière. Tous les atomes ont été affinés avec des coefficients d'agitation thermique anisotropes à l'exception des atomes d'hydrogène affectés d'un facteur d'agitation thermique isotrope. La fonction à minimiser est $\Sigma w(|F_o| - |F_c|)^2$. Le facteur d'accord R et le facteur d'accord pondéré Rw sont donnés par $R = \Sigma||F_o| - |F_c||/\Sigma F_o$ et $Rw = \Sigma\sqrt{w}||F_o| - |F_c||/\Sigma\sqrt{w}F_o$. Dans ces expressions $w = 1{,}6084/\sigma^2(F_o)$. Les facteurs de diffusion atomique proviennent de la référence 16. Tous les calculs ont été effectués sur ordinateur DEC PDP 11/44 sous logiciel SDP (17).

L'enregistrement des intensités diffractées et les calculs ont été réalisés dans le Service de Cristallochimie de l'Université d'Aix-Marseille III.

Le tableau 2 donne les coordonnées atomiques et les tableaux 3, 4 et 5 donnent les distances interatomiques, les angles de valence et de torsion les plus significatifs.[2]

La configuration cristalline est rapportée sur la figure 2.

2. Dipôlemétrie

Le moment dipolaire de l'espèce en solution dans le dioxanne a été mesuré à 10°C, 20°C, 25°C, 30°C, 35°C, 40°C, 45°C et 50°C. Les valeurs de la constante diélectrique et de l'indice de réfraction des solutions ont été extrapolés à dilution infinie selon la méthode de Guggenheim (18) et Smith (19). La pente à la concentration molaire $C = 0$, de la courbe donnant $(\varepsilon_{12} - n_{12}^2) - (\varepsilon_1 - n_1^2)fC$, permet alors le calcul du moment selon la relation :

$$\mu^2 = \frac{9kT}{4\pi N} \cdot \frac{3}{(\varepsilon_1 + 2)(n_1^2 + 2)} \cdot \frac{(\varepsilon_{12} - n_{12}^2)(\varepsilon_1 - n_1^2)}{C}$$

1. Auteur à qui la correspondance doit être adressée.

2. Les tableaux des facteurs thermiques anisotropes, des coordonnées des atomes d'hydrogène et des facteurs de structure calculés et observés sont disponibles. On peut les acheter en s'adressant au Dépôt de données non publiées, ICIST, Conseil national de recherches du Canada, Ottawa (Ontario), Canada K1A 0S2.

Printed in Canada / Imprimé au Canada

Can. J. Chem. Downloaded from www.nrcresearchpress.com by 196.1.178.254 on 09/07/12
For personal use only.

TABLEAU 1. Données cristallographiques

Formule :	$C_{17}H_{17}N_3O_3S$
Dimensions du cristal, mm :	0,4 × 0,4 × 0,1
Densité mesurée, D_m, g cm^{-3} :	1,30(2)
Densité calculée, D_c, g cm^{-3} :	1,322
Masse moléculaire relative, M_r :	343,41
Système cristallin :	Monoclinique
Groupe d'espace :	$P2_1/n$
Dimensions de la maille, a, Å :	10,514(3)
b, Å :	7,498(2)
c, Å :	22,233(5)
β, deg :	100,27(4)
Volume de la maille, Å^3 :	1724,8(8)
Nombre de molécules par maille, Z :	4
μ (Mo Kα), mm^{-1} :	2,08
$F(000)$:	720
Limites angulaires en θ :	0 et 30
Octants mesurés :	hkl et $\bar{h}kl$
Nombre total de mesures :	4724
Nombre de mesures avec $I > 3\sigma(I)$ utilisées pour la résolution et les affinements :	1572
Facteur d'accord sur toutes les intensités mesurées, R_{sym} :	0,041
Limite de rejet des pics de densité électronique en Fourier-différence, $(\Delta e)_{max}$ en e·Å^{-3} :	0,26
Facteur d'accord, R :	0,042
Facteur d'accord pondéré, R_w :	0,033
Variation sur erreur maximum, $(\lvert\Delta/\sigma\rvert)_{max}$:	0,027

où K est la constante de Boltzmann, N le nombre d'Avogadro, T la température absolue, ε et n les permittivités et les indices de réfraction du solvant (indice 1) et des solutions (indice 12). Les résultats sont schématisés sur la figure 3.

Les moments dipolaires ont, par ailleurs, été calculés tant par addition vectorielle d'incréments moléculaires et (ou) de liaison que par CNDO/2 (20). Les valeurs suivantes des moments dipolaires furent employées lors des calculs : aniline, 1,53 D; diméthylsulfone, 4,52 D; pyridine, 2,20 D; pyrrole, 1,81 D; toluène, 0,40 D; aziridine, 1,74 D (21); C=O, 2,35 D (22). Tous les calculs ont été effectués sur l'ordinateur MicroVax II du Service Commun d'Infographie de la Faculté de Pharmacie de Marseille.

Les résultats, dans les diverses hypothèses conformationnelles d'énergies précisées dans le tableau 6 et construites selon une géométrie idéale, à l'exception des angles O(11)S(1)O(12) : 115°, C(41)C(4)C(42) : 112°, C(4)C(41)C(411) et C(4)C(42)C(421) : 114°, sont présentés dans le tableau 7.

3. Résonance magnétique nucléaire ^1H

Le spectre du produit en solution dans l'acétone-d_6 a été enregistré à 20°C sur un spectrophotomètre Bruker AM 200.

Discussion

De l'étude par diffraction des rayons X, il ressort que l'hétérocycle est pratiquement plan. En effet, les atomes S(1) et C(4) sont respectivement à 0,085(1) Å et 0,010(4) Å du plan moyen formé par les atomes N(2), C(3), C(6) et N(6) ($\chi^2 = 86$). D'autre part, ces mêmes atomes sont respectivement à 0,040(1) Å et 0,022(4) Å du plan moyen formé par les six atomes du noyau hétérocyclique ($\chi^2 = 2260$). Enfin, S(1) est à 0,089(1) Å d'un plan moyen formé par les atomes N(2), C(3), C(4), C(5) et N(6) ($\chi^2 = 87$). Certes, d'un strict point de vue cristallographique, il ne s'agit pas là de plans véritables; néanmoins, on est ici loin des formes réellement pliées des composés homologues. En effet, les dérivés thiadiaziniques

TABLEAU 2. Coordonnées atomiques et déviations standard

Atome	x	y	z	B_{eq} (Å^2)*
S(1)	0,2777(1)	0,0455(1)	0,3631(1)	2,91
O(11)	0,3382(3)	0,1727(4)	0,3295(1)	4,47
O(12)	0,1697(3)	0,1094(4)	0,3871(1)	5,02
O(31)	0,5152(3)	−0,2106(4)	0,4810(1)	4,26
N(2)	0,3891(4)	−0,0158(4)	0,4221(1)	3,16
N(6)	0,2426(3)	−0,1270(4)	0,3228(1)	2,73
N(51)	0,2344(4)	−0,4189(5)	0,3026(2)	3,07
C(3)	0,4338(4)	−0,1830(5)	0,4355(2)	2,89
C(4)	0,3813(4)	−0,3383(5)	0,3946(2)	2,72
C(5)	0,2824(4)	−0,2869(5)	0,3384(2)	2,41
C(41)	0,3175(5)	−0,4671(6)	0,4356(2)	3,47
C(411)	0,2051(5)	−0,3849(6)	0,4589(2)	3,81
C(412)	0,2234(7)	−0,2943(7)	0,5142(3)	5,90
C(413)	0,1164(12)	−0,2179(10)	0,5342(4)	8,55
C(414)	−0,0046(10)	−0,2305(11)	0,4990(5)	8,97
C(415)	−0,0227(7)	−0,3197(10)	0,4455(4)	7,47
C(416)	0,0814(6)	−0,3944(8)	0,4255(3)	5,42
C(42)	0,4995(5)	−0,4267(6)	0,3728(2)	3,59
C(421)	0,5571(4)	−0,3117(6)	0,3289(2)	3,77
C(422)	0,5231(5)	−0,3346(8)	0,2662(2)	4,70
C(423)	0,5710(6)	−0,2235(9)	0,2259(3)	5,83
C(424)	0,6541(7)	−0,0899(11)	0,2465(4)	8,26
C(425)	0,6912(7)	−0,0682(11)	0,3083(4)	9,38
C(426)	0,6436(6)	−0,1776(9)	0,3493(3)	6,36

*Les atomes affinés de façon anisotrope sont donnés sous la forme d'équivalents isotropes définis ci-dessous :

$$B_{eq} = 4/3[a^2B(1,1) + b^2B(2,2) + c^2B(3,3) + ab(\cos\gamma)B(1,2) + ac(\cos\beta)B(1,3) + bc(\cos\alpha)B(2,3)]$$

TABLEAU 3. Longueurs de liaisons en Å et leurs déviations standard

Atomes	Longueur (Å)	Atomes	Longueur (Å)
S(1)—O(11)	1,429 (3)	C(411)—C(412)	1,388 (6)
S(1)—O(12)	1,421 (3)	C(411)—C(416)	1,380 (7)
S(1)—N(2)	1,659 (3)	C(412)—C(413)	1,404 (10)
S(1)—N(6)	1,580 (3)	C(413)—C(414)	1,373 (11)
O(31)—C(3)	1,220 (4)	C(414)—C(415)	1,348 (10)
N(2)—C(3)	1,353 (5)	C(415)—C(416)	1,373 (8)
N(6)—C(5)	1,297 (4)	C(42)—C(421)	1,507 (6)
N(51)—C(5)	1,312 (5)	C(421)—C(422)	1,387 (6)
C(3)—C(4)	1,519 (5)	C(421)—C(426)	1,377 (7)
C(4)—C(5)	1,526 (5)	C(422)—C(423)	1,382 (7)
C(4)—C(41)	1,560 (6)	C(423)—C(424)	1,354 (8)
C(4)—C(42)	1,561 (6)	C(424)—C(425)	1,369 (9)
C(41)—C(411)	1,503 (7)	C(425)—C(426)	1,385 (9)

possédant une ou deux doubles liaisons dans le cycle se présentent tous avec une configuration de type «enveloppe» dans laquelle l'atome de soufre, avec une élévation variant de 0,171 Å à 0,753 Å, est largement hors du plan N(2), C(3), C(4), C(5) et N(6) (1–5). De même, les espèces qui n'ont pas de double liaison intracyclique présentent une configuration de type «bateau», au demeurant plus ou moins applatie selon les substituants portés par les atomes d'azote en positions 2 et 6, dans lesquelles les atomes S et C(4) sont, en moyenne, à 0,46 Å et 0,35 Å du plan N(2), C(3), C(5) et N(6) (6–8). D'autre part, on doit noter que le plan moyen formé par les six atomes du noyau hétérocyclique est un pseudo-plan de symétrie pour toute la molécule. En effet, les substituants benzyles sont disposés

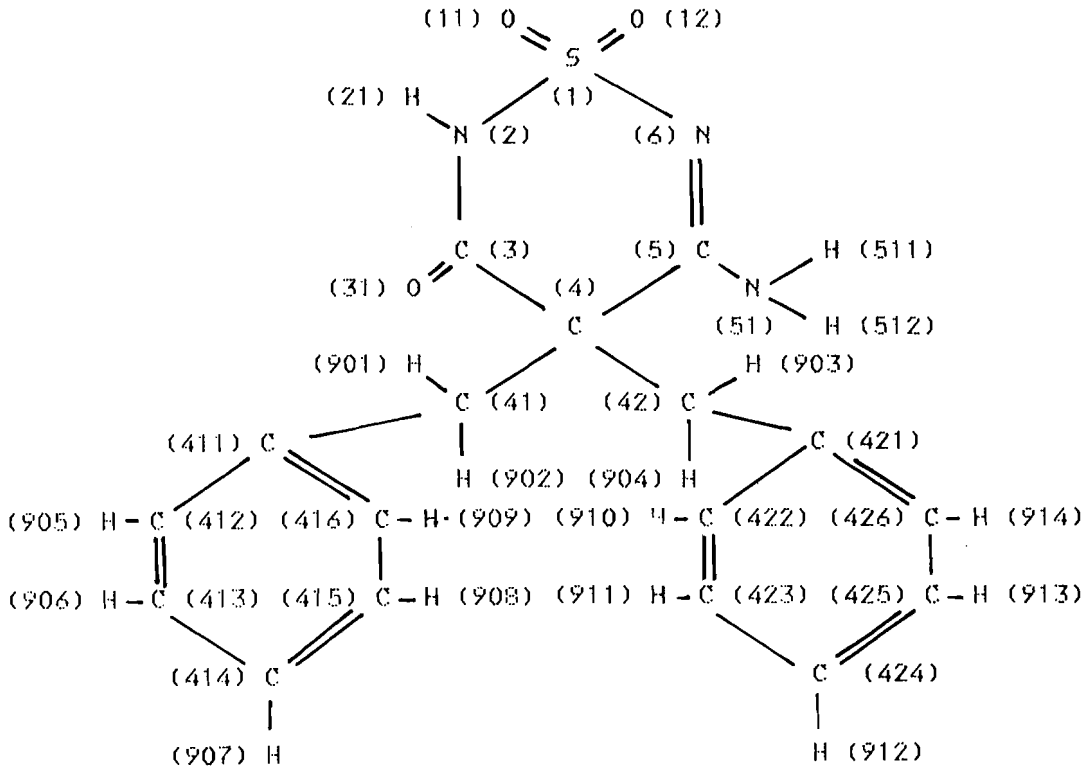

FIG. 1. Formule générale et numérotation.

TABLEAU 4. Angles de liaisons en degré et leurs déviations standard

Atomes	Angle (deg)	Atomes	Angle (deg)
O(12)—S(1)—O(11)	115,5(2)	C(3)—C(4)—C(41)	105,8(3)
O(12)—S(1)—N(2)	107,2(2)	C(3)—C(4)—C(42)	106,7(3)
O(31)—C(3)—N(2)	120,3(4)	C(4)—C(5)—N(51)	116,0(3)
O(31)—C(3)—C(4)	119,5(4)	C(5)—N(6)—S(1)	125,0(3)
N(2)—S(1)—O(11)	106,3(2)	C(5)—C(4)—C(41)	109,5(4)
N(2)—C(3)—C(4)	120,2(4)	C(5)—C(4)—C(42)	108,4(3)
N(6)—S(1)—O(11)	109,3(2)	C(411)—C(41)—C(4)	113,2(4)
N(6)—S(1)—O(12)	111,6(2)	C(412)—C(411)—C(41)	120,9(5)
N(6)—S(1)—N(2)	106,4(2)	C(413)—C(412)—C(411)	119,3(7)
N(6)—C(5)—N(51)	117,7(4)	C(414)—C(413)—C(412)	120,3(8)
N(6)—C(5)—C(4)	126,3(3)	C(414)—C(415)—C(416)	119,6(8)
C(3)—N(2)—S(1)	126,8(3)	C(415)—C(414)—C(413)	120,5(9)
C(3)—C(4)—C(5)	114,8(3)	C(415)—C(416)—C(411)	122,3(7)
C(3)—C(4)—C(41)	105,8(3)	C(416)—C(411)—C(41)	121,1(5)
C(3)—C(4)—C(42)	106,7(3)	C(416)—C(411)—C(412)	118,0(6)
C(4)—C(5)—N(51)	116,0(3)	C(42)—C(4)—C(41)	111,6(4)
C(5)—N(6)—S(1)	125,0(3)	C(421)—C(42)—C(4)	113,1(4)
C(5)—C(4)—C(41)	109,5(4)	C(422)—C(421)—C(42)	121,5(5)
C(5)—C(4)—C(42)	108,4(3)	C(422)—C(421)—C(426)	117,3(5)

symétriquement de part et d'autre de l'hétérocycle pour former ainsi un triple feuillet avec des angles dièdres de valeur moyenne 56°.

Il convient de souligner que cette configuration symétrique s'accorde avec le spectre rmn ^1H sur lequel on remarque, d'une part, l'équivalence des protons aromatiques (7,23 ppm; 10H) impliquant une conformation identique pour les groupements phényles et, d'autre part, le couplage AB avec une constante J_{gem} = 13,8 Hz pour les protons des deux groupements méthylènes (3,65 ppm, 2H; 3,47 ppm, 2H). Ainsi, les deux protons d'un même groupement méthylène ne sont pas équivalents, ce qui s'explique par un environnement différent, l'un étant soumis au champ de la fonction amine primaire, l'autre à celui de la fonction carbonyle. Ceci ne se conçoit qu'en admettant une conformation moléculaire en phase dissoute qui soit analogue à la configuration observée à l'état solide.

Néanmoins, le tableau 6 donnant l'énergie calculée par CNDO/2 de différentes conformation-limites possibles fait apparaître d'autres minimums que celui correspondant à la configuration décrite dans l'état solide. On a donc calculé par

Can. J. Chem. Downloaded from www.nrcresearchpress.com by 196.1.178.254 on 09/07/12
For personal use only.

TABLEAU 5. Angles de torsions en degré et leurs déviations standard

Atomes	Angle (deg)
O(11)—S(1)—N(2)—C(3)	−121.0(3)
O(12)—S(1)—N(2)—C(3)	114,9(3)
N(6)—S(1)—N(2)—C(3)	−4,5(2)
S(1)—N(2)—C(3)—O(31)	−179,0(3)
S(1)—N(2)—C(3)—C(4)	−0,1(2)
N(2)—C(3)—C(4)—C(5)	2,4(2)
N(2)—C(3)—C(4)—C(41)	−118,5(3)
N(2)—C(3)—C(4)—C(42)	122,6(3)
C(3)—C(4)—C(5)—N(6)	1,2(2)
C(3)—C(4)—C(5)—N(51)	−179,3(4)
C(4)—C(5)—N(6)—S(1)	−7,1(2)
C(5)—N(6)—S(1)—N(2)	8,0(3)
C(3)—C(4)—C(41)—C(411)	62,8(3)
C(5)—C(4)—C(42)—C(421)	54,6(3)

incrémentation vectorielle et CNDO/2 les moments dipolaires de ces structures. On doit noter que, parmi les constructions marquées **1***a*, **1***b* et **2***f* qui, le tableau 7 le montre, sont les seules à présenter des moments calculés dont la valeur soit proche de celle mesurée, les géométries **1***b* et **2***f*, impliquant une disymétrie moléculaire, sont incompatibles avec les résultats de rmn qui ont été rappelés. En revanche, il existe une géométrie globulaire autour d'un noyau hétérocyclique plan, **1***a*, qui n'est autre que celle décrite précédemment par radiocristallographie.

Il faut, cependant, souligner que cette comparaison entre les

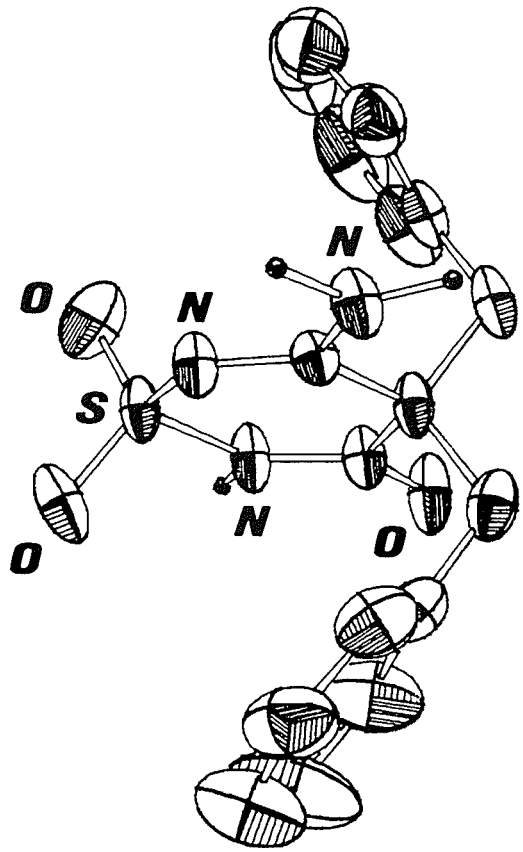

FIG. 2. Vue de la molécule.

TABLEAU 6. Energie totale (en unités atomiques) des différentes conformations-limites schématisées

	Géométrie du cycle*	Orientation du groupement dibenzyle 1	2	3	4
a	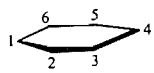	−234,8237	−234,8171	−234,8164	−234,8046
b	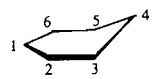	−234,8203	−234,8077	−234,8062	−234,7948
c	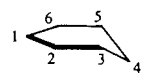	−234,8202	−234,8133	−234,8123	−234,8003
d	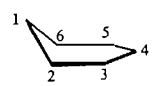	−234,8141	−234,8077	−234,8062	−234,7948
e	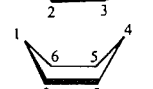	−234,8141	−234,8065	−234,8068	−234,7950
f	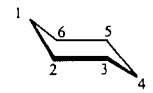	−234,8063	−234,8001	−234,7983	−234,7849

*On a retenu un angle d'élévation de 20° qui est ainsi la moyenne des angles d'élévation décrits dans les études radiocristallographiques antérieures. Cet angle représente, selon le cas figuré, le supplément de l'angle dièdre entre les plans C(3)C(4)C(5) et N(2)C(3)C(5)N(6) ou le supplément de l'angle dièdre entre les plans S(1)N(2)N(6) et N(2)C(3)C(5)N(6).

Can. J. Chem. Downloaded from www.nrcresearchpress.com by 196.1.178.254 on 09/07/12
For personal use only.

TABLEAU 7. Moments dipolaires, en debyes, calculés par incrémentation vectorielle (et par CNDO/2) pour les diverses conformations schématisées

Géométrie du cycle*	Fonctionnalisation	Orientation du groupement dibenzyle 1	2	3	4
a	Amine	5,48† (6,99)	4,87 (7,14)	4,87 (7,14)	4,26 (7,40)
	Imine	2,94	2,45	2,45	2,03
b	Amine‡	5,50 (6,90)	4,93 (6,97)	4,92 (7,18)	4,35 (7,35)
c	Imine‡	(7,04) 3,10	(7,27) 2,70	(7,10) 2,61	(7,44) 2,26
d	Amine	5,75 (7,19)	5,20 (7,33)	5,20 (7,36)	4,67 (7,61)
	Imine	4,11	3,81	3,81	3,58
e	Amine	5,64 (6,88)	5,07 (6,93)	5,17 (7,15)	4,60 (7,30)
	Imine	3,45	3,01	3,17	2,81
f	Amine	5,88 (7,47)	5,43 (7,69)	5,32 (7,56)	4,89 (7,86)
	Imine	4,87	4,72	4,52	4,44

*Voir note au bas du tableau 6.
†Configuration radiocristallographique.
‡Les moments calculés par incrémentation vectorielle sont identiques pour *b* et *c*, en raison de la symétrie moléculaire.

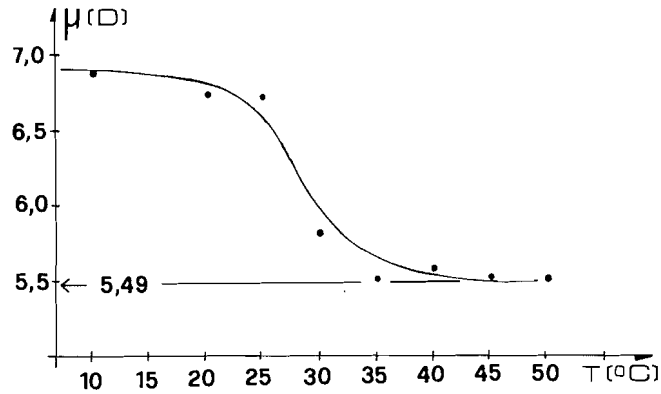

FIG. 3. Etude de μ $f(T)$ dans le dioxanne et extrapolation de la valeur du moment dipolaire expérimental de l'espèce isolée.

TABLEAU 8. Indices de liaison

Atomes	Indice
S(1)—N(2)	0,201
N(2)—C(3)	0,426
C(3)—O(31)	0,849
C(3)—C(4)	0,207
C(4)—C(5)	0,224
C(5)—N(51)	0,519
C(5)—N(6)	0,739
N(6)—S(1)	0,227

moments mesurés et calculés qui sert à la description structurale de la molécule, ne peut être valablement faite qu'après une étude en température. En effet, les associations soluté–solvant rendent, lorsqu'elles existent, la mesure du moment dipolaire dépendante de la température. Pour éviter alors, de considérer indûment le moment électrique d'une association comme celui du seul soluté, il est nécessaire de mesurer le moment dipolaire de l'espèce en solution à des températures croissantes et ce jusqu'à valeur constante (fig. 3). On peut ainsi extrapoler la valeur expérimentale du moment dipolaire de la molécule étudiée. De plus, à ce propos, on doit, ici, souligner la surévaluation des moments dipolaires calculés par CNDO/2, ce qui a d'ailleurs déjà été observé (4) chez des substances structuralement apparentées.

En revanche, le calcul par CNDO/2 des indices de liaison rassemblés dans le tableau 8 révèle une conjugaison partielle sur les fragments NH_2—C=N et NH—C=O. Il n'y aurait donc pas de conjugaison s'étendant sur l'ensemble de l'hétérocycle comme, d'ailleurs, les valeurs des longueurs de liaison obtenues par radiocristallographie (tableau 3) le laissaient effectivement penser mais contrairement à ce que la planéité du noyau aurait pu laisser croire.

Enfin, toutes les méthodes utilisées, que ce soit la résolution de la structure cristalline—où, en particulier, les deux hydrogènes du groupement amino ont pu être localisés sur les cartes de Fourier-différences—ou encore la comparaison du moment dipolaire expérimental avec les moments calculés pour les différentes fonctions (tableau 7), s'accordent avec l'existence du seul tautomère amine.

Can. J. Chem. Downloaded from www.nrcresearchpress.com by 196.1.178.254 on 09/07/12
For personal use only.

Conclusion

Étudiée dans divers états et sous diverses conditions expérimentales, l'amino-5 dibenzyle-4,4 one-3 2*H*-thiadiazine-1,2,6 dioxyde-1,1 montre une structure moléculaire constante, de forme générale globulaire avec un noyau hétérocyclique plan, non conjugué et fonctionnalisé en tant qu'amine. Cette géométrie diffère ainsi notablement des formes pliées antérieurement décrites pour des substances homologues.

1. C. Esteban-Calderon, M. Martinez-Ripoll et S. Garcia-Blanco. Acta Crystallogr. Sect. B: Struct. Sci. **B38**, 1124 (1982).
2. C. Esteban-Calderon, M. Martinez-Ripoll et S. Garcia-Blanco. Acta Crystallogr. Sect. B: Struct. Sci. **B38**, 1128 (1982).
3. C. Esteban-Calderon, M. Martinez-Ripoll et S. Garcia-Blanco. Acta Crystallogr. Sect. B: Struct. Sci. **B38**, 1340 (1982).
4. J. Elguero, C. Ochoa, M. Stud, C. Esteban-Calderon, M. Martinez-Ripoll, J. P. Fayet et M. C. Vertut. J. Org. Chem. **47**, 536 (1982).
5. H. A. Albrecht, J. F. Blount, F. M. Konzelmann et J. T. Plati. J. Org. Chem. **44**, 4191 (1979).
6. P. Goya, R. Nieves, C. Ochoa, C. Rodellas, M. Martinez-Ripoll et S. Garcia-Blanco. Can. J. Chem. **65**, 298 (1987).
7. P. Brouant, M. Pierrot, A. Baldy, C. Ochoa, P. Goya, J. C. Soyfer et J. Barbe. Acta Crystallogr. Sect. C: Cryst. Struct. Commun. **C42**, 892 (1986).
8. M. D. Cabezuelo, C. Foces-Foces, F. H. Cano et S. Garcia-Blanco. Acta Crystallogr. Sect. B: Struct. Crystallogr. Cryst. Chem. **34**, 3069 (1978).
9. M. Hori, K. Satq et T. Wada. Jpn. Kokai Tokkyo Koho, 78-121 774. 1978.
10. R. D. Acker, E. Ammermann et E. H. Pommer. Ger. Offen. DE 3 230 332. 1984.
11. R. D. Acker, E. Ammermann et E. H. Pommer. Ger. Offen. DE 3 230 923. 1984.
12. V. J. Aran, A. G. Bielsa, P. Goya, C. Ochoa, J. A. Paez, M. Stud, M. Contreras, J. A. Escario, M. I. Jimenez, E. A. Duran et C. Pueyo de la Cuesta. Farmaco, Ed. Sci. **41**, 862 (1986).
13. G. Garcia-Munoz, R. Madronero, C. Ochoa, M. Stud et W. Pfleiderer. J. Heterocycl. Chem. **13**, 793 (1976).
14. P. Goya, C. Molina, C. Ochoa et M. Stud. Heterocycles, **16**, 5 (1981).
15. P. Main, S. J. Fiske, S. E. Hull, L. Lessinger, G. Germain, J. P. Declercq et M. M. Woolfson. MULTAN 80. A system of computer programs for the automatic solution of crystal structures from X-ray diffraction data. Univ. York (Angleterre) et Louvain (Belgique). 1980.
16. International tables for X-ray crystallography. Tome IV. Kynoch Press, Birmingham. 1974; distribué par D. Reidel, Dordrecht.
17. B. A. Frenz. Computing in crystallography. *Edité par* H. Schenk, R. Olthof-Hazekamp, H. Van Koningsveld et G. C. Bassi. Delft Univ. Press, Pays-Bas. 1978. pp. 44–71.
18. E. A. Guggenheim. Trans. Faraday Soc. **45**, 714 (1949).
19. J. W. Smith. Trans. Faraday Soc. **46**, 394 (1950).
20. P. A. Dobosh. CNINDO. Q.C.P.E. 141 (1968).
21. A. L. McClellan. Tables of experimental dipole moments. Vol. 2. Rahara Enterprises, El Cerrito, 1974.
22. O. Exner. Dipole moments in organic chemistry. G. Thieme Pub., Stuttgart. 1975.

Can. J. Chem. Downloaded from www.nrcresearchpress.com by 196.1.178.254 on 09/07/12
For personal use only.

Air-stable binuclear alkoxytungsten complexes as catalyst precursors for olefin metathesis

JACQUES SAVARD AND HOWARD ALPER[1]

The Ottawa–Carleton Chemistry Institute, Department of Chemistry, University of Ottawa, Ottawa, Ont., Canada K1N 9B4

Received February 10, 1988

JACQUES SAVARD and HOWARD ALPER. Can. J. Chem. **66**, 2483 (1988).

The use of the air-stable complexes tetrachlorobis(μ-methoxy)bis(methanolo)dimethoxyditungsten (**1**) and tetrachlorobis(μ-ethoxy) tetraethoxyditungsten (**2**) as catalyst precursors for the metathesis of 1-octene is described. Using mild conditions, the latter was converted to 7-tetradecene (**4**) in fair yields when diethylaluminum chloride (**3**) was used as a cocatalyst. Product stereoselectivity was 4/1 in favor of the *trans* isomer. The reaction was also shown to be efficient for the production of 2-nonenes.

JACQUES SAVARD et HOWARD ALPER. Can. J. Chem. **66**, 2483 (1988).

Les tetrachlorobis(μ-methoxy)bis(methanolo)dimethoxyditungsten (**1**) et tetrachlorobis(μ-ethoxy)tetraethoxyditungsten (**2**), des complexes stables à l'air, ont été utilisés comme précurseurs de systèmes catalytiques pour la métathèse de l'octène-1. Ce dernier a ainsi été converti en tetradecène-7 (**4**), sous des conditions douces et avec de bons rendements, en utilisant le chlorure de diéthylaluminium (**3**) comme cocatalyseur. La stéréosélectivité des liaisons doubles est de 4 à 1 en faveur de l'isomère *trans*. La réaction s'est aussi avérée utile pour la préparation des nonènes-2.

Introduction

Olefin metathesis has been extensively investigated in recent years. Although many metal complexes have been examined with respect to metathesis activity, those of molybdenum and tungsten, including tungsten hexachloride and molybdenum pentachloride, have drawn the most attention (1).

The synthesis and chemistry of binuclear complexes containing metal–metal multiple bonds is another subject of considerable interest (2). Those complexes possessing metal–metal double bonds can, in principle, undergo metathesis reactions with olefins (like metal–metal triple bonds with alkynes). Such an approach may generate metal carbene complexes, which are known to readily undergo metathesis with alkenes (1). There are no publications, to our knowledge, of olefin metathesis using metal–metal double bond complexes as catalysts. We now describe the utilization of such a complex, and a related single bonded complex, as catalysts for the metathesis reaction.

A feature common to many known catalysts as well as to complexes containing metal–metal multiple bonds is the high reactivity to both oxygen and moisture. An exception is the double bonded tungsten–tungsten alkoxide dimers **1** which are quite air-stable, as are the W—W single bond species **2** (Fig. 1) (3). Complexes of type **1**, which can be prepared directly from tungsten tetrachloride, readily undergo alcohol exchange reactions, thus providing an entry into several higher homologues (3).

The use of **1** and **2** as catalysts for the metathesis of 1-octene is the subject of this paper. 1-Octene was chosen as the model compound because, if successful, tetradecene would be formed as one of the products: long chain systems, suitably functionalized, are of value in the areas of biophysics, polymers, and pharmaceuticals (e.g. liposomes, vesicles (4), prepolymers, synthons).

Results of discussions

No reaction occurred on exposure of 1-octene to **1** (R = methyl), in benzene at reflux for 24 h. A cocatalyst is therefore required. While tetralkyltin compounds (R_4Sn, R = CH_3, C_2H_5, C_4H_9) and triethylaluminum were inactive, both diethylaluminum chloride **3** and ethylaluminum dichloride induced metathesis of 1-octene by **1**. However, ethylaluminum dichloride was unsuitable for use due to its ability to catalyse Friedel–Crafts reaction of benzene. Consequently, diethylaluminum chloride **3** was the most useful of the cocatalysts which were screened for the metathesis process.

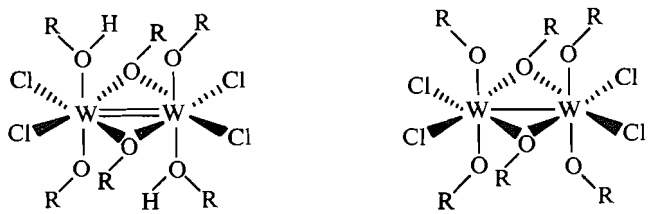

FIG. 1. Structures of **1** and **2**.

The proportion of cocatalyst to catalyst required to induce the formation of an active species is 4/1, in contrast to most cases where it is 1/1 (ref. 1, for analogous systems, see ref. 5). This difference may be a consequence of the presence of two alcohol molecules bound to the binuclear complex as ligands.

Conversion rate

Reacting **1** (R = methyl) in benzene with Et_2AlCl (**3**), followed by the addition of 1-octene, gave a dark brown suspension. The latter induced the conversion of the starting material to metathesis products (24 h at 80°C). Figure 2 shows the effect of temperature and time on conversion. It is also noteworthy that equilibrium is apparently reached within 6 to 7 h even at low temperature (20°C). No significant improvement could be obtained with longer reaction times. 1-Heptene and 1-hexene exhibited similar behavior to 1-octene.

Identical results were obtained when the red complex **2** (R = ethyl) was used instead of **1** (R = methyl) as the catalyst (Table 1), the conversion being 80% although the equilibrium was not reached for 24 h. However, an improvement of the conversion rate was observed when the reaction was run for 120 h at 50°C (56% to 71%). The yield of 7-tetradecene (**4**) did not significantly improve (34% to 42%). After 24 h, one could see lower molecular weight by-products becoming much more important.

Running reactions in boiling benzene while decreasing the

[1]To whom correspondence may be addressed.

Can. J. Chem. Downloaded from www.nrcresearchpress.com by 196.1.178.254 on 09/07/12
For personal use only.

Can. J. Chem. Downloaded from www.nrcresearchpress.com by 196.1.178.254 on 09/07/12
For personal use only.

TABLE 1. Metathesis of 1-Octene in benzene with Et_2AlCl (**3**) as cocatalyst[a]

Entry #	Cat. mol %	Cat.	C14 %	C13 %	C12 %	C11 %	C10 %	C9 %	Conversion %	Induction condition min (°C)
1[b]	0.6	**1**	—	—	—	—	—	—	0	10 (RT)
2[e]	0.6	**1**	1	2	1	—	—	4	8	10 (RT)
3	0.6	**1**	4	3	—	—	—	7	14	10 (RT)
4	0.6	**1**	8	8	2	—	1	14	34	10 (RT)
5	2	**1**	5	9	4	1	2	19	40	5 (30)
6[c]	2	**1**	6	2	—	—	—	7	15	10 (30)
7[e]	2	**1**	8	4	1	—	2	13	28	10 (30)
8	2	**1**	9	16	10	1	6	25	67	10 (30)
9	2	**1**	12	22	24	9	3	10	80	10 (RT)
10	2	**1**	10	12	3	1	2	22	50	10 (0)
11	2	**1**	12	14	6	2	4	25	63	17 (30)
12	2	**1**	4	8	5	2	8	22	49	10 (80)
13[f]	2	**1**	10	13	6	2	14	22	67	10 (RT)
14[f]	2	**1**	17	13	—	—	3	25	58	10 (RT)
15[f]	4	**1**	7	14	10	2	9	23	65	10 (RT)
16[f]	5	**1**	10	18	9	3	3	25	68	10 (RT)
17[e]	0.8	**2**	32	9	1	—	—	12	55	3 (RT)
18	0.8	**2**	4	19	31	11	3	10	77	4 (RT)
19[c]	0.8	**2**	23	—	—	—	—	—	23	4 (RT)
20[d]	0.8	**2**	18	1	—	—	—	2	21	4 (RT)
21[a]	0.8	**2**	34	12	2	—	—	21	56	10 (RT)
22[d]	0.8	**2**	17	—	—	—	—	1	18	4 (RT)
23[g]	0.8	**2**	19	1	—	—	—	2	22	4 (RT)
24[e]	0.8	**2**	40	15	3	1	—	9	68	4 (RT)

[a]Reactions done in boiling benzene except when mentioned. Other conditions are described in the table. Conversion is defined here as the summation of the yields of all metathesis products. The selectivity is defined as the ratio of the amount of compound to the % conversion. Compounds lighter than 1-octene were not monitored. For **1**: R = Me; **2**: R = Et.

[b]Reactions run without cocatalyst.

[c]Reactions run at 20°C.

[d]Reactions run at 35°C.

[e]Reactions run at 50°C.

[f]Reactions run under nitrogen for the complete reaction time.

[g]Reactions run in pentane.

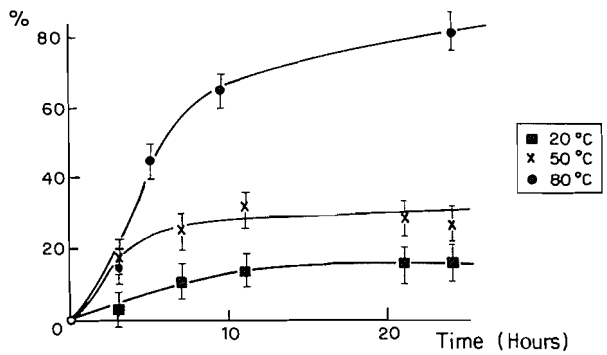

FIG. 2. Conversion rates induced by **1** in benzene as a function of time and temperature.

ratio of catalyst to olefin to 0.6% induced a major drop in the conversion rates (Table 1). Doubling the amount of catalyst provided no further improvement of the conversion rate. However, when the reaction was run at 50°C with 5 mol% the conversion rate increased from 28 to 68%. At this temperature a decrease of the catalyst concentration showed the same deleterious effect on the conversion as was observed in boiling benzene.

Chemoselectivity

A mixture of several octene isomers could undergo cometathesis with 1-octene and produce a complex mixture of lower molecular weight metathesis by-products. The normal metathesis products for 1-octene are 7-tetradecene (**4**) and ethylene. But if 2-octene is also present in the mixture, 6-tridecenes, 2-nonenes, 1-heptene, and propylene could also form. Other isomers of 1-octene could undergo similar pathways to produce a large number of different low molecular weight cometathesis by-products (from C3 to C13). Because very few systems are known to be selective for terminal olefins in long chain metathesis reactions (1), the effect of each parameter on the yields was examined for these lower molecular weight by-products (C9 to C13). It is interesting to note that internal alkenes hardly reacted with the catalyst to undergo metathesis. The use of both *cis*- and *trans*-2-nonene gave only 2% conversion to 7-tetradecene (**4**) using the more severe conditions. So the reaction of internal alkenes formed in the mixture may be regarded as coming from the interaction of the complex formed by a terminal double bond and the catalyst.

The isomerization process for terminal to internal olefins may be induced mainly by the cocatalyst since no isomerization occurs in the absence of any cocatalyst. It was reasoned that an

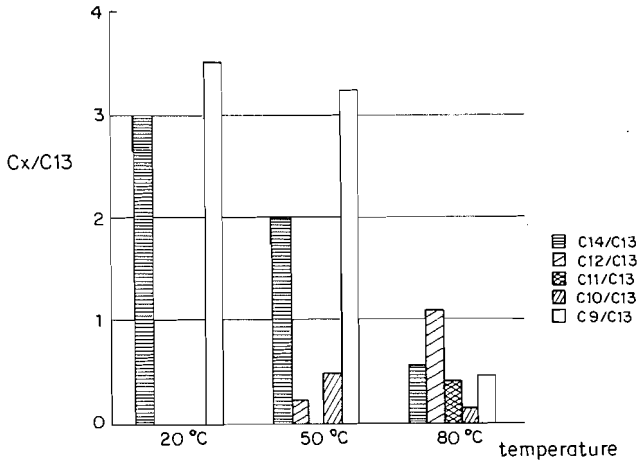

FIG. 3. Distribution of products with temperature after 24 h (from entries #6, 7, 9).

exact ratio of cocatalyst had to be used and that the generation of the active species had to be complete prior to the introduction of the substrate.

For both catalytic systems (**1** and **2**), product selectivity was dependent on the temperature as shown by the results in Fig. 3. Despite the increase in conversion rates at higher temperatures the expected reaction product (C14) is formed in low yields compared with lower molecular weight analogues (C12–C13). With **1** (R = methyl) room temperature reactions proved to be more useful as they provided higher selectivity and easily separable mixtures of 1-octene, 2-nonenes, and 7-tetradecene (**4**) (Fig. 3). For the reactions induced by **2**, 20°C was obviously the temperature of choice since after 24 h, the mixture showed almost exclusively 7-tetradecene **4** along with residual 1-octene.

It is also noteworthy that almost all reactions (including room temperature ones) gave around 25% of 2-nonenes. This corresponds to the coupling of the longer carbon chain of one olefin with the shorter chain of a second isomerized alkene (2-octene). The coupling of two long moieties which should lead to the formation of 6-tridecenes was always lower in yields than the former. This observation is similar to the well described, favored interchanges of methylenes in the degenerative metathesis of terminal olefins (6), such a phenomenon is probably also occurring in the selective production of 2-nonenes and 7-tetradecenes (**4**) under the less severe conditions (see Fig. 3) using the system described herein.

The reaction is sensitive to concentration effects. Using a more dilute solution (3×) of benzene to generate the catalytic system improved the selectivity at the expense of the conversion (2%) while a more concentrated solution (neat) was shown to be impracticable because the poor solubility of the catalyst in octene (0.5 mL) prevented good interaction between **1** and the cocatalyst. The solvent had no influence on either the selectivity or the conversion, as long as it was a non-polar one (benzene, pentane). Any traces of polar solvents (trichloroethylene, acetonitrile) or additives (propyl acetate) totally inhibit reaction.

An induction period was needed to allow the formation of the catalytic species. In this manner, the cocatalyst is transformed to the active species strong interaction with the substrate is thus prevented. Extensive olefin isomerization occurred using **1** (R = methyl) with a short induction period (0 and 5 min). A minimum of 10 min was required to observe a slight increase in the selectivity of the reaction. Similarly, a higher temperature (80°C), while generating the catalyst, increased the amount of isomerization by-products. It also reduced the total conversion of 1-octene and the actual yield of tetradecene. With **2**, the selectivity was best using an induction period of three minutes.

Stereoselectivity

Each reaction product was present as a mixture of *cis* and *trans* isomers, the relative composition of which was not determined except for 7-tetradecene (**4**). The stereochemistry of the double bond in the latter case was approximately 4/1 in favor of the *trans* isomer in all cases. This ratio appeared to be constant from the beginning of the reaction. Isomers of 2-nonenes were formed in equal amounts.

Conclusion

In conclusion complex **2** and, to some extent, **1**, are useful catalyst precursors for the metathesis of 1-octene to tetradecene and ethylene. These processes occur under mild conditions, although the conversion to tetradecene is not high.

Experimental section

1-Octene, purchased from Aldrich Chemical Co., was distilled and stored over molecular sieves. The other alkenes (Wiley Organics) and solutions of Et_2AlCl (**3**) (Aldrich Chemical Co.) were used as received. Tungsten chloride was synthesized according to procedures described elsewhere (7). Benzene was dried, distilled (over benzophenone ketyl), and degassed (nitrogen) prior to use. The analysis of product mixtures was performed on a Varian 3300 Gas Chromatograph equipped with a 4-m DB-1 capillary column (butylbenzene as internal standard).

Synthesis of catalysts

(a) Tetrachlorobis(μ-methoxy)bis(methanolo)dimethoxyditungsten (1)

Although the catalyst can be synthesized from the direct reaction of cooled methanol and WCl_4 a two-step procedure involving alcohol exchange was used because **1** was more readily isolated in high yield and purity (3, 8). Ethanol was reacted in the cold with WCl_4 and the dark green solid obtained by filtration under nitrogen was recrystallized from chloroform/ethanol (37%). The pure ethoxy complex was then refluxed in degassed methanol from which the light green compound **1** precipitated (57%). It was dried under vacuum for several hours and then stored under nitrogen.

(b) Tetrachlorobis(μ-ethoxy)tetraethoxyditungsten (2)

The precursor of **1** can be easily oxidized to the red complex **2** by simply bubbling O_2 through a room temperature solution of **1** (R = ethyl) in ethanol at room temperature. This complex was also prepared by the use of a mild oxidizing agent (3).

General procedure

The catalytic system was generated under a nitrogen stream at room temperature by adding four equivalents of Et_2AlCl (1.8 *M* solution in toluene) to a benzene suspension (3–4 mL) of either **1** or **2** (0.1 mmol). The mixture was then stirred at the desired temperatures for 10 min (except otherwise noted). The degassed alkene (≈0.5 g containing the internal standard and 0.5 mL of solvent) was then introduced with a syringe and the flask was placed in an oil bath preheated to the reaction temperature (or at room temperature). The nitrogen flow was turned off after several minutes to avoid loss of materials. Acetone (10 mL) was added, the solution was filtered, dried ($MgSO_4$), and the filtrate was analyzed by gas chromatography.

Acknowledgements

We are grateful to the Natural Sciences and Engineering Research Council and British Petroleum for support of this work. We also thank Dr. J. M. Fréchet for the use of his capillary gas chromatograph.

Can. J. Chem. Downloaded from www.nrcresearchpress.com by 196.1.178.254 on 09/07/12
For personal use only.

1. (*a*) K. J. IVIN. Olefin metathesis. Academic Press, Toronto. 1983; (*b*) V. DRAGUTAN, A. T. BALABAN, and M. DIMONIE. Olefin metathesis and ring-opening polymerization of cycloolefins. J. Wiley & Sons, New York. 1985.
2. F. A. COTTON and R. A. WALTON. Multiple bonds between metal atoms. J. Wiley & Sons, New York. 1982.
3. F. A. COTTON, L. R. FALVELLO, M. F. FREDRICH, and R. A. WALTON. J. Am. Chem. Soc. **105**, 3088 (1983).
4. J. H. FENDLER. Membranes mimetic chemistry. Wiley-Interscence, New York. 1984.
5. F. QUIGNARD, M. LECONTE, and J.-M. BASSET. J. Mol. Catal. **36**, 13 (1986); H. T. DODD and K. J. RUTT. J. Mol. Catal. **15**, 103 (1982).
6. J. MCGINNIS, T. J. KATZ, and S. HURWITZ. J. Am. Chem. Soc. **98**, 605 (1976).
7. M. A. SCHAEFER KING and R. E. MCKALLEY. Inorg. Chem. **12**, 1972 (1973).
8. W. J. REAGAN and C. H. BRUBAKER. Inorg. Chem. **9**, 827 (1970).

Can. J. Chem. Downloaded from www.nrcresearchpress.com by 196.1.178.254 on 09/07/12
For personal use only.

Open chain nitrogen compounds. Part XIII.[1] 1-Aryl-3-arylthiomethyl-3-methyltriazenes and 3-(arylazo)-1,3-thiazolidines

KEITH VAUGHAN[2] AND HARTFORD W. MANNING
Department of Chemistry, Saint Mary's University, Halifax, N.S., Canada B3H 3C3

AND

MARCUS P. MERRIN AND DONALD L. HOOPER
Department of Chemistry, Dalhousie University, Halifax, N.S., Canada B3H 4J3

Received February 9, 1988

KEITH VAUGHAN, HARTFORD W. MANNING, MARCUS P. MERRIN, and DONALD L. HOOPER. Can. J. Chem. **66**, 2487 (1988).

Reaction of 3-acetoxymethyl-1-aryl-3-methyltriazenes with sodium thiophenolate or thiocresolate in anhydrous dimethylformamide affords a new series of 3-arylthiomethyltriazenes (**2**), Ar-S-CH_2-NMe-N=N-Ar′. These triazenes are remarkably labile in aqueous buffer and may be good pro-drugs for the active metabolite of the antitumour dimethyltriazenes. The reaction of arenediazonium fluoroborates with 1,3-thiazolidine in aqueous acetone affords a new series of *N*-arylazo-1,3-thiazolidines (**4**); the arylazothiazolidines represent a new class of triazene in which the N3 nitrogen is incorporated into a heterocyclic unit, in this case a 1,3-thiazolidine. Nuclear magnetic resonance spectra of the arylazothiazolidines show evidence for rotational isomerism of the exocyclic N2—N3 bond in the triazene moiety.

KEITH VAUGHAN, HARTFORD W. MANNING, MARCUS P. MERRIN et DONALD L. HOOPER. Can. J. Chem. **66**, 2487 (1988).

La réaction des acétoxyméthyl-3 aryl-1 méthyl-3 triazènes avec le thiophénolate ou le thiocrésolate de sodium, dans le diméthylformamide anhydre, fournit une nouvelle série d'arylthiométhyl-3 triazènes (**2**), Ar-S-CH_2-NMe-N=N-Ar′. Dans des tampons aqueux, ces triazènes sont remarquablement labiles et, pour cette raison, ils peuvent être de bons précurseurs de drogues pour le métabolite actif des diméthyltriazènes antitumoraux. La réaction des fluoroborates d'arènediazonium avec la thiazolidine-1,3, dans de l'acétone aqueuse, fournit une nouvelle série de *N*-arylazothiazolidines-1,3 (**4**); les arylazothiazolidines correspondent à une nouvelle classe de triazène dans laquelle l'azote N3 est incorporé dans un hétérocycle; dans ce cas, il s'agit d'une thiazolidine-1,3. Les spectres en résonance magnétique nucléaire des arylazothiazolidines suggèrent l'existence d'une isomérie de rotation autour de la liaison exocyclique N2—N3 de la portion triazène.

[Traduit par la revue]

1-Aryl-3,3-dimethyltriazenes (**1***a*) are an important class of antitumour agents (1), which have been shown to undergo metabolic activation to the short-lived 3-hydroxymethyltriazene (**1***b*) (2). Because of the inherent instability of hydroxymethyltriazenes under physiological conditions (they lose formaldehyde rapidly in aqueous buffer), it has been suggested (3) that a stable derivative of the hydroxymethyltriazene might be a suitable pro-drug for the active metabolite of the dimethyltriazene, the monomethyltriazene (Ar-N=N-NHMe) formed by loss of formaldehyde from **1***b*. To this end several derivatives of **1***b* have been reported and do indeed have antitumour activity in animal models. Examples of such derivatives are the chemically reactive 3-acetoxymethyltriazenes (**1***c*; "acetates") and the relatively inert 3-methoxymethyltriazenes (**1***d*) (4).

Previous attempts to synthesize 3,3-dialkyltriazenes with an α-situated sulfur functionality in one of the alkyl groups have met with mixed success. Hemens and Vaughan (5) have found that the acetoxymethyltriazenes (**1***c*) reacted smoothly with methanol to give the methoxymethyltriazenes (**1***d*) but not at all with a pure thiol; the lack of reactivity of the thiol was accounted for by the poor ionizing ability of the thiol as solvent. More recently, Iley *et al.* (6) discovered that the hydroxymethyltriazene (**1***b*) can be converted directly to the methyl ether (**1***d*) by reaction in methanol with an acid catalyst; surprisingly, the acid treatment leaves the triazene unit unaffected and furthermore can be applied to catalyze the reaction of **1***b* with an alkane thiol to give the first reported example of an alkanethiomethyltriazene (**1***e*).

In this paper, we report a different approach to the synthesis of α-sulfur containing alkyltriazenes; the method is specific for *S*-aryl, rather than *S*-alkyl thioethers. In our method, the hydroxymethyltriazene (**1***b*) is first converted to the acetate (**1***c*), which is then reacted with the sodium thiophenolate in anhydrous dimethylformamide:

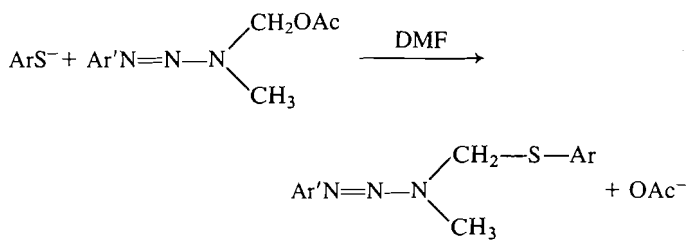

2

This reaction affords good yields of the 3-arylthiomethyltriazenes (**2**).

Identification of the new 3-arylthiomethyltriazenes is based on ir and nmr spectroscopic analysis, molecular weight determination by mass spectrometry, and elemental analysis of representative compounds (Table 1). The ir spectra show the expected absorption bands of the aryl substituent (X) and the absence of absorption from OH or acetate-carbonyl groups. The ^{1}H nmr spectra of **2** show the overlapping patterns of two aromatic nuclei in addition to N-Me resonance at δ 3.22–3.27, Ar-S-CH_2 resonance at δ 5.16–5.24, and the anticipated resonance from protons (when present) in the X and Y substituents.

We were initially perplexed at the relatively low-field

[1]For Part XII, see ref. 9.

[2]Author to whom all correspondence should be addressed.

Can. J. Chem. Downloaded from www.nrcresearchpress.com by 196.1.178.254 on 09/07/12
For personal use only.

TABLE 1. Yields and ^{1}H nmr data for the 1-aryl-3-arylthiomethyl-3-methyltriazenes (**2**)

Compound no.	X	Y	Yield[a] (%)	Melting point (°C)	δ (ppm) in $CDCl_3$ Arom.	CH_2	N-Me	X	Y	M^+ Found	Calcd.
2*a*	*p*-CH_3O_2C	H	84	111–114	7.16–8.02	5.21	3.23	3.88 (O-Me)	—	315.1033	315.1041
2*b*	*p*-EtO_2C	H	7	83–84	7.13–7.94	5.22	3.23	1.37 (t, *J* 7 Hz) 4.33 (q, *J* 7 Hz) (O-C_2H_5)	—	329.1200	329.1193
2*c*	*p*-O_2N	H	33	110–111	7.16–8.10	5.22	3.26	—	—	302.0839	302.0837
2*d*	*p*-NC	H	43	92–98	7.15–7.54	5.22	3.25	—	—		
2*e*	*p*-CH_3CO	H	6	100–103	7.18–7.88	5.24	3.24	2.58 (s, Ac)	—		
2*f*	*p*-CH_3O_2C	CH_3	17	108–110	7.08–7.95	5.19	3.25	3.91 (O-Me)	2.29	329.1202	329.1193
2*g*	*p*-EtO_2C	CH_3	23	79–81	7.04–7.93	5.16	3.22	1.37 (t, *J* 7 Hz) 4.33 (t, *J* 7 Hz) (O-C_2H_5)	2.26		
2*h*	*p*-O_2N	CH_3	15	108–110	7.06–8.13	5.18	3.27	—	2.27	316.1002	316.0990
2*i*	*p*-NC	CH_3	32	89–94	← see footnote *b* →						
2*j*	*o*-CF_3	H	34	Oil	6.93–7.60	5.22	3.24	—	—	325.0864	325.0857

[a]Not optimized.
[b]The ^{13}C nmr spectrum: ($CDCl_3$) 21.1 (CH_3-aryl), 33.9 (CH_3-N), 63.0 (CH_2), 108.5 (CN), 119.5, 121.4, 128.5, 129.9, 132.7, 134.1, 138.3, 153.3 (arom.).

resonance of the S-CH_2 protons in **2**, which occurs at almost exactly the same chemical shift as the methylene protons of the hydroxymethyltriazene (**1***b*) (7); an upfield shift might have been anticipated when replacing -OH by -SPh. However, in comparison with the nmr data of the 3-alkanethiomethyltriazenes (**1***e*) (6) the shift looks reasonable, since the CH_2 resonance in the *S*-alkyl compounds occurs at ca. δ 4.95. Additive chemical shift parameters for methylene protons (8) predict a downfield shift of 0.29 ppm for CH_2SAr compared to CH_2SR, consistent with our observations of compounds of type **2**.

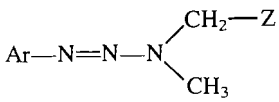

1*a* Z = H
b Z = OH
c Z = OAc
d Z = OMe
e Z = SR
f Z = N_3

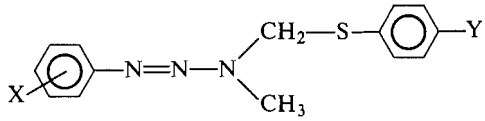

2*a* X = *p*-CH_3O_2C-, Y = H
b X = *p*-$C_2H_5O_2C$-, Y = H
c X = *p*-O_2N-, Y = H
d X = *p*-NC-, Y = H
e X = *p*-CH_3CO, Y = H
f X = *p*-CH_3O_2C-, Y = CH_3
g X = *p*-$C_2H_5O_2C$-, Y = CH_3
h X = *p*-O_2N-, Y = CH_3
i X = *p*-NC-, Y = CH_3
j X = *o*-CF_3, Y = H

The new 3-arylthiomethyltriazenes are, with one exception (**2***i*), crystalline solids. An important consideration for the possible pro-drug use of these new triazenes is their stability in buffer solution and their consequent facility to release a cytotoxic species in the cell. Other α-substituted triazenes show quite marked differences in stability in aqueous buffer, the facility for hydrolysis being influenced by the leaving group capacity of Z. Thus the methyl ethers (**1***d*), where Z is a poor leaving group, show no tendency to hydrolyse in buffer and are consequently not cytotoxic in vitro (3). In contrast, the acetates (**1***c*) possess a good leaving group (acetate ion), they hydrolyse rapidly in aqueous buffer, and are cytotoxic to tumour cells in vitro (3). It is intriguing to note that the 3-alkanethiomethyltriazenes (**1***e*) are stable in aqueous buffer, showing no apparent hydrolysis over a 24-h period.[3] Apparently the *O*-alkyl and *S*-alkyl groups, of **1***d* and **1***e* respectively, are similarly inert as leaving groups, within the 24-h time period studied.

In contrast, the 3-arylthiomethyltriazenes described here are remarkably labile in aqueous buffer (pH 7.2, 0.05 M phosphate), with half-lives, measured by following uv spectral decay, in the range 4–16 min. The comparison of stability of the *S*-alkyl and *S*-aryl compounds is quite striking and must reflect the enhanced leaving group ability of ArS^- over RS^-. The facility of hydrolysis of compounds of type **2** suggests that they may indeed be potential pro-drugs for the cytotoxic monomethyltriazene and the results of in vivo antitumour tests with representative compounds of this series are presented in Table 2. Compounds **2***a* and **2***f* were tested against the ADJ/PC6 solid tumour (3) and do indeed show activity comparable with other α-substituted alkyltriazenes (3). However, although comparable percent inhibition of tumour growth was achieved, much higher doses of the triazenes **2***a* and **2***f* were required to achieve the same percent inhibition as with compounds of type **1***c* (see Table 2). Thus the therapeutic index of compounds of type **2** is not as high as that of other triazenes tested by us.

The preparation of these 3-arylthiomethyltriazenes represents a further illustration of the usefulness of the acetoxymethyltriazenes (**1***c*) as synthetic intermediates for α-substituted triazenes. In previous studies we have shown that the acetates react with methanol to give the methyl ethers (**1***d*) (4) and with azide ion in aqueous acetone to afford the 3-azidomethyltriazenes (**1***f*) (10). Whereas reaction of the acetate with the pure thiol

[3]J. Iley, personal communication.

Can. J. Chem. Downloaded from www.nrcresearchpress.com by 196.1.178.254 on 09/07/12
For personal use only.

TABLE 2. Antitumour activity of 1-aryl-3-arylthiomethyl-3-methyltriazenes (**2**) against the ADJ/PC6 tumour

Compound no.	ID_{90} (mg/kg)	LD_{50} (mg/kg)	TI[a]	Optimal dose (mg/kg)	% Inhibition of tumour growth
2*a*	325	>800	2.46	800	97.5
2*f*	50	>400	>8	400	96.7
1*c*[b]	16.5	140	8.5	25	98.2

[a]TI = therapeutic index.
[b]Compound **1***c*, Ar = *p*-AcC_6H_4; ref. 3.

(RSH) failed to produce any alkanethiomethyltriazene (**1***e*) (5), we have now shown that conversion of the acetate to the thioether can be achieved by reaction with the stronger nucleophile, $Ar\text{-}S^-$. The requirement for the strong nucleophile and the polar aprotic solvent suggests that the conversion **1***c* → **2** may be an S_N2 process, but further work needs to be carried out with these nucleophiles to establish the mechanism clearly.

A heterocyclic analogue of the 3-hydroxymethyltriazene (**1***b*) is the arylazooxazolidine (**3**), in which the α-situated oxygen

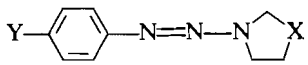

3 X = O
4*a* X = S, Y = CN
b X = S, Y = NO_2
c X = S, Y = CO_2Me
d X = S, Y = Cl

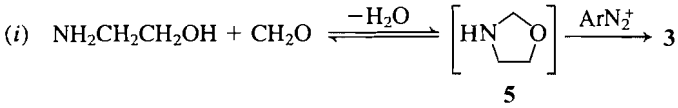

5

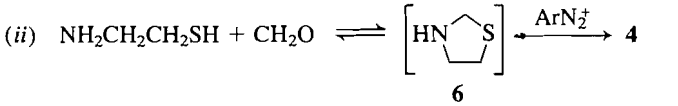

6

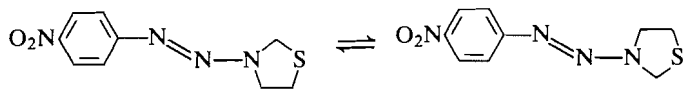

4*b*′ **4***b*″

is incorporated into the five-membered heterocyclic ring. In a previous report (11), we described the synthesis of the 3-arylazo-1,3-oxazolidines (**3**) by diazonium coupling with 1,3-oxazolidine (**5**). The oxazolidine was generated *in situ* from 2-ethanolamine and formaldehyde and coupled directly with the diazonium salt (eq. (*i*)). *In situ* generation of **5** was used because of the tendency of oxazolidines without an *N* substituent to polymerize (12). In the work described here, we sought to extend this approach to the sulfur analogues, the 3-arylazo-1,3-thiazolidines (**4**), which are the heterocyclic analogues of the 3-alkanethiomethyltriazenes (**1***e*).

Unlike oxazolidine (**5**), the 1,3-thiazolidine (**6**) is not readily polymerized and is commercially available (Aldrich 14969-1). However, the commercial product is more expensive by a factor of three, compared to its precursor, 2-aminoethanethiol. We therefore attempted the synthesis of compounds of type **2** by diazonium coupling with 1,3-thiazolidine (**6**) generated *in situ* in an aqueous medium from 2-amino ethanethiol and formaldehyde (eq. (*ii*)), as described in Method "A" in the experimental. This reaction did indeed afford the 3-arylazo-1,3-thiazolidines in low yield, but the products were not pure and did not respond well to conventional purification procedures. A low yield of a pure sample of the 3-(*p*-nitrophenylazo)-1,3-thiazolidine (**4***b*) was obtained by Method A, which also gave a moderate yield of the *p*-bromo analogue. However, recrystallization of the latter product failed to produce a sample with a sharp melting point. Thus, although the *in situ* thiazolidine method does give the expected products, the method does not show much promise for general synthetic application.

An alternative method in which the diazonium salt was coupled in aqueous solution with commercial thiazolidine was less successful. The initial products of these reactions were bright yellow solids but they proved to be unstable and were found to decompose to intractable tars within hours of preparation. The identity of the initially formed yellow solids has not been established.

A successful method (Method B) for the preparation of the 3-arylazo-1,3-thiazolidines (**4**) was developed using the diazonium salt as the fluoroborate, which was reacted with 1,3-thiazolidine in aqueous acetone. The solid products of these reactions required repeated crystallization and (or) column chromatography to achieve analytical purity, but the final products are apparently stable. Yields and physical data are given in Table 3; the yields of arylazothiazolidines are of the same order as those of the arylazooxazolidines previously reported (11). Analytical data for representative compounds are given in Table 4 and spectroscopic data in Tables 5 and 6.

The infrared spectra of the arylazo-1,3-thiazolidines show predictably no functional group distinguishing features other than those expected to arise from the Y substituent in the aryl moiety. However the nmr spectra are very diagnostic. The ^1H nmr spectra (Table 5) show aromatic AA′BB′ patterns and a 2 proton singlet at ca. 4.8 ppm arising from the methylene protons at C2. The other methylene protons attached to C4 and C5 give rise to triplets at ca. 4.1 ppm and ca. 3.1 ppm respectively; the assignments are based on the assumption that the chemical shift of the $N\text{-}CH_2$ protons at C4 will be shifted to lower field than those at C5, and on a comparison of the ^1H nmr spectrum with that of thiazolidine itself (H-2, 4.09; H-4, 3.11, and H-5, 2.79 ppm). All the thiazolidine ring protons in **4** are shifted downfield compared to the analogous protons in thiazolidine itself.

A significant feature of the ^1H nmr spectrum of the *p*-nitro derivative (**4***b*) is the extensive broadening of the signals of the C2 and C4 methylene protons, both of which are attached to nitrogen. The most logical explanation of this phenomenon is

Can. J. Chem. Downloaded from www.nrcresearchpress.com by 196.1.178.254 on 09/07/12
For personal use only.

TABLE 3. Yields and physical data for the 3-arylazo-1,3-thiazolidines (**4**)

Compound no.	Y	Method	Yield (%)	Melting point (°C)	Solvent
4*a*	CN	B	37	93.5–94.5	Hexane/toluene
4*b*	NO_2	A	6	128–129	[a]
		B	29[b]		
4*c*	CO_2Me	B	30	116–117	Hexane/toluene
4*d*	Cl	B	38	49–50	Pentane

[a]Resisted recrystallization; purified by repeated column chromatography.
[b]Crude yield; product did not respond to attempts at recrystallization.

TABLE 4. Elemental analysis of 3-arylazo-1,3-thiazolidines

Compound no.	Y	Formula	Calculated					Found				
			C	H	N	S	Cl	C	H	N	S	Cl
4*a*	CN	$C_{10}H_{10}N_4S$	55.05	4.59	25.69	14.68	—	55.11	4.63	25.60	14.42	—
4*c*	CO_2Me	$C_{11}H_{13}N_3O_2S$	52.59	5.18	16.73	12.75	—	52.70	5.17	16.70	12.67	—
4*d*	Cl	$C_9H_{10}N_3ClS$	47.47	4.40	18.46	14.07	15.60	47.36	4.41	18.36	14.03	15.73

TABLE 5. ^1H nuclear magnetic resonance spectroscopic data for the 3-arylazothiazolidines

Compound no.	Y	δ($CDCl_3$)				
		Aromatic (AA'BB')	$N-CH_2-S$	$N-CH_2$	$S-CH_2$	Y
4*a*	CN[a]	7.4–7.6(m)	4.82(s)	4.13(t)	3.10(t)	—
4*b*	NO_2[b]	8.15	4.81(s,	4.10(t,	3.09(t,	—
		8.13	br)	br)	J = 5.9 Hz)	
		7.46				
		7.44				
4*c*	CO_2Me[b]	8.04	4.87(s)	4.14(t,	3.11(t,	3.90(s)
		8.01		J = 6.3 Hz)	J = 6.3 Hz)	
		7.48				
		7.46				
4*d*	Cl[a]	7.30[c]	4.78(s)	4.02(t)	2.95(t)	—

[a]60 MHz spectra, Varian EM360 spectrometer.
[b]Nicolet 360 MHz spectra.
[c]These protons are fortuitously magnetically equivalent and in this case there is no AA'BB'.

the restricted rotation around the N2—N3 bond in the triazene unit, i.e., **4***b*′ ⇌ **4***b*″; hindered rotation of this sort is well known for other 1-aryl-3,3-dialkyltriazenes (13). Further evidence for this hindered rotation is seen in the ^{13}C nmr spectra of the *p*-nitrophenylazo-1,3-thiazolidine (**4***b*) and the *p*-chloro analogue (**4***d*) (Table 6). In the spectrum of the *p*-chloro derivative, the signals of the carbon atoms at C2 and C4 are broadened, but not that from the carbon atom at C5, which is well removed from the site of rotational isomerism. In the case of the *p*-nitro compound (**4***b*), the spectrum was recorded at low temperature, which resolved the signals of the C4 and C5 carbon atoms into two signals from each. However, the signal from the C2 carbon of **4***b* was still broadened and unresolved at −30°C.

The lack of resolution of the C2 signals of **4***b* at −30°C may need further explanation. The resolution of such signals depends on two factors: (*a*) the rate of interconversion of the two forms; (*b*) the chemical shift difference between the two signals. Presumably in the case of compound **4***b* the signals of C2 in the two forms are much closer in chemical shift than those of C4 or C5. Thus the signals of C4 and C5 are resolved at −30°C whereas those of C2 are not.

In conclusion, the new compounds reported here represent an important addition to the spectrum of derivatives of 3,3-dialkyltriazenes with α-substituents in one of the alkyl groups. The sulfur containing triazenes described here (**2** and **4**) and those reported by Iley *et al.* (6) (**1***e*) are of potential interest pharmacologically because of their close structural relationship to the 3-hydroxymethyltriazene (**1***b*), a metabolite of the antitumour 3,3-dimethyltriazene (7). Further studies are being undertaken to determine the pharmacological properties of these new triazenes.

Experimental

*1-Aryl-3-arylthiomethyl-3-methyltriazenes (2*a–j*)*

General procedure

Thiophenol (or *p*-thiocresol) was treated with 1 equivalent of sodium hydride in anhydrous dimethylformamide to give a resulting solution of the sodium thiophenolate with concentration 2 M. The appropriate

Can. J. Chem. Downloaded from www.nrcresearchpress.com by 196.1.178.254 on 09/07/12
For personal use only.

TABLE 6. ^{13}C nuclear magnetic resonance spectroscopic data for selected 3-arylazothiazolidines

Compound no.	Y	Temperature (°C)	δ($CDCl_3$) Aromatic	N-CH_2-S	N-CH_2	S-CH_2
4*b*	NO_2	−30	154.92 144.60 124.77 120.67	54.21(br)	48.53 47.85	29.29 28.10
4*d*	Cl	+20	148.61 131.88 128.96 122.11	51.63(br)	50.53(br)	29.01

acetoxymethyltriazene (**1***c*) (0.004 mol) was dissolved in anhydrous dimethylformamide (6.0 mL) and treated with a twofold excess of the sodium thiophenolate solution (4.0 mL). After stirring at room temperature for 2 h, the red reaction mixture was poured into water (25 mL), extracted with ether (3 × 20 mL), and the washed (water, aqueous $NaHCO_3$, water again) ether extracts were dried ($CaCl_2$) and evaporated. The residue was purified by column chromatography on silica gel with 1:1:1 hexane/ethyl acetate/carbon tetrachloride as eluant, followed by recrystallization from hexane/chloroform mixture, to afford the 1-aryl-3-arylthiomethyl-3-methyltriazenes (**2***a–j*). Yields and physical data are given in Table 1.

3-Arylazo-1,3-thiazolidines (4)

General procedure

Method A: The aniline (0.01 mol) was diazotized in 2 M hydrochloric acid (50 mL) with sodium nitrite (0.011 mol). The resulting diazonium salt solution was added dropwise to a cold (0°C) solution containing 2-aminoethanethiol (0.02 mol), formaldehyde (7.8 g of 40% aqueous solution), and sodium carbonate (5.24 g) in water (40 mL), acidified to pH 3 with 2 M hydrochloric acid. The resulting yellow solution was neutralized to pH 7.5 with sodium bicarbonate. A bright yellow precipitate forms (when Y = CN or NO_2) and is removed by filtration to afford the crude 3-arylazo-1,3-thiazolidine. These crude products did not respond well to recrystallization.

However, the *p*-nitrophenyl analogue (**4***b*) was purified by column chromatography and then recrystallized from hexane/methylene chloride to give a low yield (6%) of the pure *N*-arylazothiazolidine.

Method B: The arenediazonium fluoroborate (0.011 mol) was dissolved in acetone (15.0 mL). A solution of thiazolidine (0.011 mol) in water (10 mL) was added slowly to the diazonium salt solution at 0°C. A coloured (usually yellow to orange) precipitate formed immediately and was removed by filtration after stirring the mixture for a further 0.5 h. The product was purified by recrystallization or by column chromatography as follows:

*3-(*p*-Cyanophenylazo)-1,3-thiazolidine (4*a*)*. The crude product was an orange solid, which was treated with a boiling mixture of hexane/toluene (1:1). The insoluble dark greasy oil was discarded, but the mother liquor afforded a crystalline product on cooling. Further recrystallization from hexane/toluene afforded the pure arylazothiazolidine as reported in Table 3.

*3-(*p*-Methoxycarbonylphenylazo)-1,3-thiazolidine (4*c*)*. The crude product was a yellow-orange solid, which was purified by successive column chromatography, with alumina as the solid support and toluene as the eluant in the first column and 1:1 hexane/toluene as the eluant in the second. Further purification by two recrystallizations from hexane/toluene gave analyticallu pure material.

*3-(*p*-Chlorophenylazo)-1,3-thiazolidine (4*d*)*. The crude product was a red oily precipitate which was extracted into dichloromethane. The residue from the dried (Na_2SO_4) dichloromethane extracts was purified by column chromatography using alumina and 1:1 hexane/toluene in the first column and pure hexane as eluant in the second column. The product was purified further by recrystallization from *n*-pentane.

Acknowledgements

The financial support of the Natural Sciences and Engineering Research Council of Canada is gratefully acknowledged. The authors are grateful to the Atlantic Regional Magnetic Resonance Centre, Dalhousie University, for nmr spectra and to the Department of Chemistry at the University of Alberta for high resolution mass spectra. Antitumour testing was carried out by the Institute for Cancer Research, Royal Marsden Hospital, Sutton, U.K.

1. T. A. CONNORS, P. M. GODDARD, K. MERAI, W. C. J. ROSS, and D. E. V. WILMAN. Biochem. Pharmacol. **25**, 241 (1976).
2. G. F. KOLAR, K. MAURER, and M. WILDSCHUTTE. Cancer Lett. **10**, 287 (1980).
3. L. M. CAMERON, R. J. LAFRANCE, C. M. HEMENS, K. VAUGHAN, R. RAJARAMAN, D. C. CHUBB, and P. M. GODDARD. Anti-Cancer Drug. Des. **1**, 27 (1985).
4. C. M. HEMENS, H. W. MANNING, K. VAUGHAN, R. J. LAFRANCE, and Y. TANG. Can. J. Chem. **62**, 741 (1984).
5. C. M. HEMENS and K. VAUGHAN. J. Chem. Soc. Perkin Trans. 2, 11 (1986).
6. J. ILEY, E. ROSA, and L. FERNANDES. J. Chem. Res. (S), 264 (1987).
7. K. VAUGHAN, Y. TANG, G. LLANOS, J. K. HORTON, R. J. SIMMONDS, J. A. HICKMAN, and M. F. G. STEVENS. J. Med. Chem. **27**, 357 (1984).
8. H. M. BELL, L. K. BERRY, and E. A. MADIGAN. Org. Magn. Reson. **22**, 693 (1984).
9. R. J. LAFRANCE, H. W. MANNING, and K. VAUGHAN. Can. J. Chem. **65**, 292 (1987).
10. K. VAUGHAN, K. N. G. NICHOLAS, R. D. SINGER, M. ROY, and N. W. GIBSON. Anti-Cancer Drug Des. **2**, 279 (1987).
11. R. J. LAFRANCE, H. W. MANNING, and K. VAUGHAN. J. Org. Chem. **50**, 2229 (1985).
12. M. RIEHL and P. A. LAURENT. Bull. Soc. Chim. Fr. 1223 (1969).
13. M. H. A. KHTAR, R. S. MCDANIEL, M. FESER, and A. C. OEHLSCHLAGER. Tetrahedron, **24**, 3899 (1968).

Can. J. Chem. Downloaded from www.nrcresearchpress.com by 196.1.178.254 on 09/07/12
For personal use only.

^{15}N and ^{13}C nuclear magnetic resonance of deoxydinucleotide monophosphates. I. Protonation of deoxycytidylyl-(3′,5′)-guanosine in dimethylsulfoxide

GIOVANNA BARBARELLA,[1] MASSIMO LUIGI CAPOBIANCO, ANTONIO CARCURO, FRANCESCO PAOLO COLONNA, AND ANNA GARBESI

Istituto dei Composti del Carbonio Contenenti Eteroatomi e loro Applicazioni, Consiglio Nazionale delle Ricerche, Via della Chimica 8, 40064 Ozzano Emilia, Bologna, Italy

AND

VITALIANO TUGNOLI

Dipartimento di Biochimica, Sezione di Chimica e Propedeutica Biochimica, Facolta' di Medicina e Chirurgia, Universita', Via Selmi 2, 40126 Bologna, Italy

Received March 25, 1988

GIOVANNA BARBARELLA, MASSIMO LUIGI CAPOBIANCO, ANTONIO CARCURO, FRANCESCO PAOLO COLONNA, ANNA GARBESI, and VITALIANO TUGNOLI. Can. J. Chem. **66**, 2492 (1988).

The ^{15}N and ^{13}C chemical shifts of the sodium salt of deoxycytidylyl-(3′,5′)-guanosine have been measured in dimethylsulfoxide in the presence of variable amounts of CF_3COOH. N3(cyt) is protonated first, followed by N7(gua) and the phosphate anion. These results vary from those reported for the binding of the methylmercuric cation to d(CpG).

GIOVANNA BARBARELLA, MASSIMO LUIGI CAPOBIANCO, ANTONIO CARCURO, FRANCESCO PAOLO COLONNA, ANNA GARBESI et VITALIANO TUGNOLI. Can. J. Chem. **66**, 2492 (1988).

Opérant dans le diméthylsulfoxyde, en présence de quantités variables de CF_3COOH, on a mesuré les déplacements chimiques du ^{15}N et du ^{13}C du sel de sodium de la désoxycytidylyl-(3′,5′)-guanosine. Le N3(cyt) est le premier à se protoner, suivi du N7(gua) et de l'anion phosphate. Les résultats diffèrent de ceux publiés pour la liaison du cation méthylmercurique au d(CpG).

[Traduit par la revue]

Extensive work on nucleosides and mononucleotides has shown that ^{15}N nmr is the more direct and powerful method for establishing the sites of proton and metal-ion binding to DNA bases (1). ^{15}N chemical shifts of "pyridine-like" nitrogens of purine bases are considerably affected by the mean molecular excitation energy contribution to the paramagnetic shielding (2, 3). Since this term is dominated by the low energy $n \rightarrow \pi^*$ transitions, it increases and an upfield shift occurs (2, 3) when the lone pair of a pyridine-like nitrogen becomes involved in bonding, or even in weaker associations with electrophiles. Upfield shifts up to 100 ppm are found for proton or platinum binding to nitrogen (1, 4), while smaller but significant chemical shift changes are observed for nitrogen association to other "soft" metals such as Hg^{2+} (5). Unfortunately, owing to the high concentrations required to observe ^{15}N nmr signals at natural abundance (6), ^{15}N nmr data on DNA constituents beyond the mononucleotide level are very few.

A number of ^{13}C nmr studies on association of nucleobases with metals playing a biological role have shown that carbon chemical shifts as well as carbon–proton coupling constants are also very sensitive probes of binding sites (7). However, ^{13}C nmr data on oligonucleotides are also limited in number. A recent paper (8) on the interactions of d(CpG) with the methylmercuric cation shows that quite significant chemical shift changes are observed in the carbons flanking the binding site, N7(gua).

As a part of a program aimed to characterize the acid–base equilibria of deoxydinucleotides and their interactions with electrophiles in different solvents, we have investigated the protonation of these compounds in dimethylsulfoxide by means of ^{15}N and ^{13}C nmr. DMSO was chosen as the solvent to begin with, since work on nucleosides and mononucleotides has shown that a qualitative estimate of the relative basicities of protonation sites can be made in this solvent, owing to the lack of base–solvent proton exchange (1, 7). As well, the data in DMSO can be useful as a guideline for understanding the acid–base equilibria in water. Indeed, data obtained by potentiometry and calorimetry show that, although DMSO solutions are very different systems from aqueous ones, the pK values of several nitrogen bases in this solvent (including purines and related compounds) are only slightly smaller than in water (9).

We give here the initial results for the protonation of deoxycytidylyl-(3′,5′)-guanosine sodium salt (Fig. 1) in dimethylsulfoxide.

Results and discussion

The conformational features of d(CpG) have been investigated by proton nmr (10). A study of the X-ray structure of d(CpG) sodium salt has just been published (11). According to studies based on proton (10) and ^{13}C (8) nmr, d(CpG) gives significant stacking interactions in water. No data are available regarding d(CpG) in DMSO. Base stacking is not likely to occur in DMSO (12) where, however, hydrogen-bonded base pairs can be formed (13). Earlier studies based on ^{1}H (13) and ^{15}N (14) nmr in DMSO indicate that guanosine and cytidine associate to give Watson–Crick base pairs in DMSO. When hydrogen bonds are formed between guanosine and cytidine, the protons involved in bonding are shifted downfield, and a linear relationship between the magnitude of the downfield shifts and the concentration of the nucleoside is observed (13). We have found[2] that NH(gua), NH_2(gua), and NH_2(cyt) protons of d(CpG) show the same behavior when the concentration of d(CpG) in DMSO increases, a result that is consistent with the formation of intermolecular base pairs between the cytidylyl and guanosine residues of d(CpG) in this solvent.

To test the sensitivity of ^{13}C nmr to the variations of stacking and hydrogen-bonding interactions following a temperature

[1]Author to whom correspondence may be addressed.

[2]G. Barbarella. To be published.

Printed in Canada / Imprimé au Canada

Can. J. Chem. Downloaded from www.nrcresearchpress.com by 196.1.178.254 on 09/07/12
For personal use only.

TABLE 1. ^{13}C chemical shifts[a] of 0.02 M solutions of d(CpG) in D_2O and DMSO-d_6 at 25 and 80°C

3′-dCMP					5′-dGMP				
D_2O			DMSO-d_6		D_2O			DMSO-d_6	
25°C	80°C		25°C	80°C	25°C	80°C		25°C	80°C
157.0	[b]	C2	155.1	0.0	154.6	[b]	C2	153.6	0.0
166.2	[b]	C4	165.6	0.0	152.3	[b]	C4	150.9	0.0
97.0	−0.2	C5	94.1	0.0	117.0	[b]	C5	116.9	0.0
142.0	+0.5	C6	140.8	0.0	159.4	[b]	C6	156.8	0.0
86.7	+0.2	C1′	84.7	+0.1	138.3	[b]	C8	135.5	0.0
38.7	+0.1	C2′	[c]		84.0	+0.2	C1′	82.8	+0.2
76.1	−0.2	C3′	74.2	0.0	39.3	+0.1	C2′	[c]	
86.6	+0.1	C4′	86.1	+0.1	71.5	+0.2	C3′	71.2	+0.1
62.0	+0.1	C5′	61.6	+0.1	86.3	+0.1	C4′	86.0	0.0
					65.8	+0.1	C5′	64.6	+0.1

[a]In ppm.
[b]Not observed.
[c]Overlap DMSO-d_6.

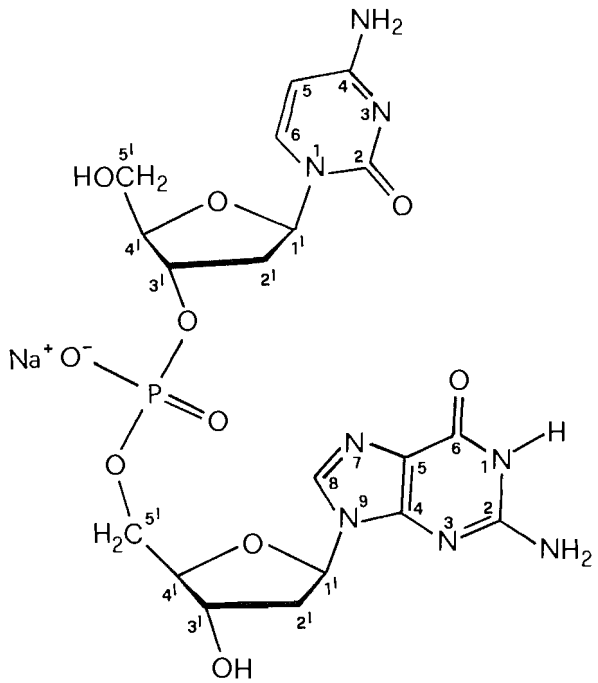

FIG. 1. Structure and numbering system of deoxycytidylyl-(3′,5′)-guanosine.

increase, we measured the ^{13}C chemical shifts of 0.02 M solutions of d(CpG) in water and DMSO at 22–25°C (probe T) and 80°C. The results are given in Table 1. It is apparent that only very small chemical shift changes are found in both solvents. The ^{13}C nmr is not very sensitive, at least in dilute solutions, to the conformational adjustments arising from variations in the interactions that occur in DMSO and water on temperature increase. In DMSO solution chemical shift changes within the experimental error (±0.1 ppm) are found. In aqueous solution the variations are slightly larger, though never exceeding 0.5 ppm, and are indicative of a higher degree of order in water compared to DMSO. Most of the carbons are *deshielded* at 80°C compared to probe temperature. Due to ring currents from the electrons of the bases, stacking generally leads to upfield shifts of near atoms (16*a*). Thus, the downfield shifts observed in the aqueous solution at 80°C are consistent with a decrease in the stacking interactions at high temperature.

The ^{15}N chemical shifts of a 0.35 M solution of d(CpG) in dimethylsulfoxide at varying amounts of added CF_3COOH are given in Table 2. Signal assignment is straightforward, as the chemical shifts of the neutral solution are nearly the same as those of cytidine and guanosine in DMSO (1*a*), also reported in Table 2 for comparison. The fact that N3 and NH_2 of the cytidylyl residue are *shielded* by 4.5 ppm and *deshielded* by 0.6 ppm, respectively, compared to the corresponding nitrogens of free cytidine, supports the hypothesis that Watson–Crick base-pairs are formed in dimethylsulfoxide (14).

Figure 2 is a plot of ^{15}N chemical shifts of d(CpG) vs. the molar equivalents of added acid. The chemical shift variations observed are proportional to the concentration of the protonated form, since for each acid addition the chemical shifts are weighted averages between the δ values for the neutral and the protonated species.

Several basic sites are present in d(CpG). There is a lot of evidence to show that in water as well as DMSO the most basic site of free cytidine and deoxycytidine is N3, whereas the most basic center of free guanosine and deoxyguanosine is N7 (16*b*). The pK_{BH^+} values assigned for ionization of the corresponding protonated bases (BH^+, first protonation step), are 4–4.5 for N3 and 2–2.5 for N7 (17), i.e., the N3 nitrogen of cytidine is more basic than the N7 nitrogen of guanosine by more than 2 pK units.

Figure 2 shows that, in line with the pK values for the free nucleosides, addition of up to 1.2 molar equivalents of CF_3COOH to d(CpG) perturbs essentially the cytidylyl residue. A progressive *shielding* of N3 (about −10 ppm for each 0.2 molar equiv. of added acid) is found, indicating that protonation at this site takes place. Chemical shift increments of N3 of nearly the same magnitude are found for free cytidine in DMSO.

Table 2 and Fig. 2 show that, parallel to the upfield shift observed for N3, a smaller but quite important *deshielding* of the amino group of the cytidylyl residue (about +2 ppm for each 0.2 molar equiv. of added acid) occurs, almost the same as that observed for cytidine in the same conditions.

Can. J. Chem. Downloaded from www.nrcresearchpress.com by 196.1.178.254 on 09/07/12
For personal use only.

TABLE 2. ^{15}N chemical shifts[a] of d(CpG),[b] cytidine,[b] and guanosine[b] in DMSO-d_6 as a function of added trifluoroacetic acid

	d(CpG)							
	3′-dCMP			5′-dGMP				
Molar equiv. of CF_3COOH	N1	N3	NH_2	N1	N3	N7	N9	NH_2
0.0	153.8	205.5	94.1	146.7	165.4	246.6	172.1	73.8
0.2	154.1	193.3	97.0	146.7	165.4	246.3	172.1	73.8
0.4	154.5	180.2	99.9	146.9	165.7	246.2	172.3	73.9
0.6	154.7	167.0	102.4	146.8	165.6	245.7	172.3	73.7
0.8	154.8	[c]	105.3	146.8	165.5	244.9	172.3	73.7
1.2	154.9	148.6	105.6	146.7	165.3	241.4	172.5	73.7
1.4	154.9	146.3	105.8	146.8	165.1	237.4	172.8	74.0
1.6	154.9	145.3	105.9	146.9	165.1	233.6	173.1	74.3
1.8	154.9	144.6	105.9	146.9	164.8	229.0	173.4	74.3
2.0	154.9	144.2	105.9	147.0	164.6	224.2	173.8	75.0
2.4	154.8	143.8	105.9	147.0	164.3	[c]	174.4	75.6
2.6	154.9	143.6	105.9	147.2	164.2	212.1	174.8	75.8
3.6	154.9	143.3	105.8	147.0	165.3	182.7	[c]	77.8
4.6	155.0	143.3	105.9	147.0	165.2	181.7	[c]	77.5
	Cytidine			Guanosine[d]				
	N1	N3	NH_2	N1	N3	N7	N9	NH_2
0.0	[c]	210.4	93.5	148.0	166.5	247.4	170.7	74.0
0.36				148.8	166.1	225.5	173.0	76.0
0.5	153.7	173.7	100.8					
1.0	[c]	148.0	105.5					
1.86				150.0	165.0	181.1	176.6	79.2

[a]In ppm, with respect to NH_3.
[b]0.35 M in DMSO-d_6.
[c]Not observed.
[d]Reference 1*a*.

As already known, in free cytidine there is delocalization of the lone pair belonging to the amino nitrogen over the ring system, leading to a partial double bond character of the C4—NH_2 bond (cf. resonance structure **B** of Fig. 3), and resulting in a shift of the amino nitrogen to lower fields (18). Comparison of the chemical shift for the amino nitrogen of cytidine with that of guanosine, in which there is no lone-pair delocalization, shows that the first resonates 20 ppm further downfield than the latter. Table 2 shows that in d(CpG) the same chemical shift difference between NH_2(cyt) and NH_2(gua) is found.

According to an X-ray study (19), delocalization of the lone pair of the amino nitrogen occurs also in protonated cytidine. Moreover, the contribution of the resonance structure **D** to the protonated form of cytidine is more important than that of **B** to the neutral form. If the same is true for d(CpG) in DMSO, the progressive deshielding of NH_2(cyt) upon protonation at N3(cyt) can be explained by the fact that contribution of **D** to the protonated cytidylyl residue is more important than that of **B** to the corresponding neutral form.

It is worth noting that a contribution of form **B** to the cytidylyl residue in neutral d(CpG) in DMSO implies a large distribution of negative charge at N3 and O2 and that this favours the formation of Watson–Crick base pairs (14).[2] On the other hand, protonation at N(3) should have an effect on the hydrogen-bonding capabilities of d(CpG) and lead to variations in the chemical shifts of NH(gua) and NH_2(gua) nitrogens. Unfortunately, guanosine nitrogens are much less sensitive to changes in hydrogen-bonding interactions (14) than those of cytidine. Consequently, the shielding variations in NH(gua) and NH_2(gua) for protonation of the cytidylyl residue at N3 are too small to give any useful information on this point.

Further addition of CF_3COOH to d(CpG) begins to affect the guanine residue of d(CpG). While only minor variations are found in NH_2(gua) on addition of acid, N7 is progressively *shielded* by several ppm. However, contrary to that observed in N3(cyt), the upfield shift of N7(gua) following addition of acid (roughly 4 ppm each 0.2 molar equivalents of added acid) is much smaller than that observed for guanosine under the same conditions (nearly 10 ppm for each 0.2 molar equiv. of added acid). Clearly, after addition of 2.6 molar equiv. of CF_3COOH, N7 is far from being fully protonated. Table 2 shows that the chemical shift of N7(gua) reaches the same value as that of protonated guanosine only after a large excess of added acid.

Table 3 gives the ^{13}C chemical shifts of a 0.19 M solution of d(CpG) in DMSO-d_6 at varying amounts of added CF_3COOH, together with those of the free nucleosides for comparison. Table 4 reports the variations of the significant carbon–proton coupling constants of d(CpG) upon addition of acid. That N(3) protonates first is clearly shown by the variation in the one-bond couplings of the cytidylyl moiety ($^1J_{C5H5}$ and $^1J_{C6H6}$), while the one-bond ($^1J_{C8H8}$) and the long-range ($^3J_{C5H8}$) coupling of the guanosine residue are unaffected. After addition of an excess of acid, $^1J_{C8H8}$ *increases* by 3.5 Hz and $^3J_{C5H8}$ *decreases*

Can. J. Chem. Downloaded from www.nrcresearchpress.com by 196.1.178.254 on 09/07/12
For personal use only.

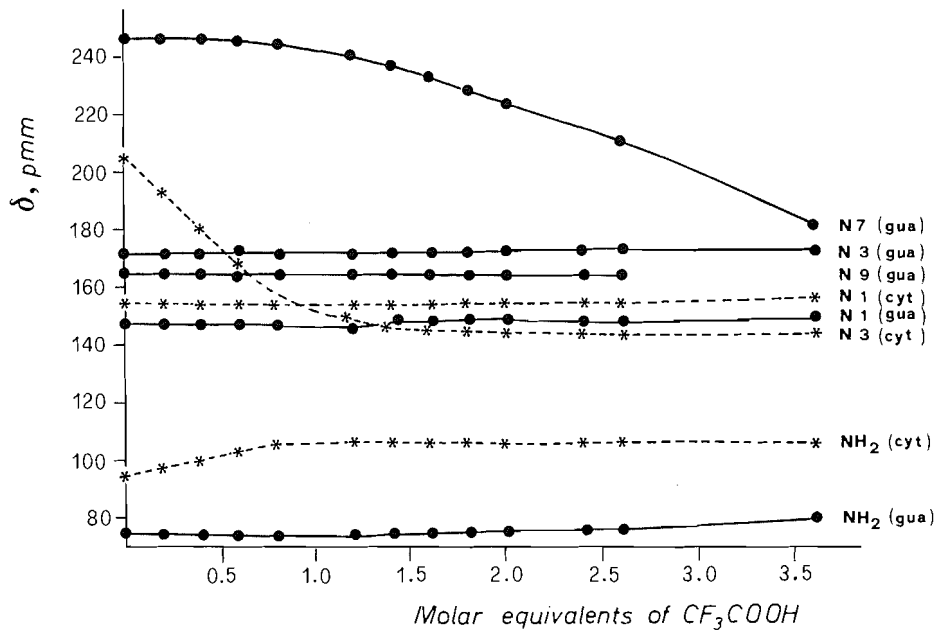

FIG. 2. ^{15}N chemical shifts of deoxycytidylyl-(3′,5′)-guanosine reported as a function of the molar equivalents of added CF_3COOH.

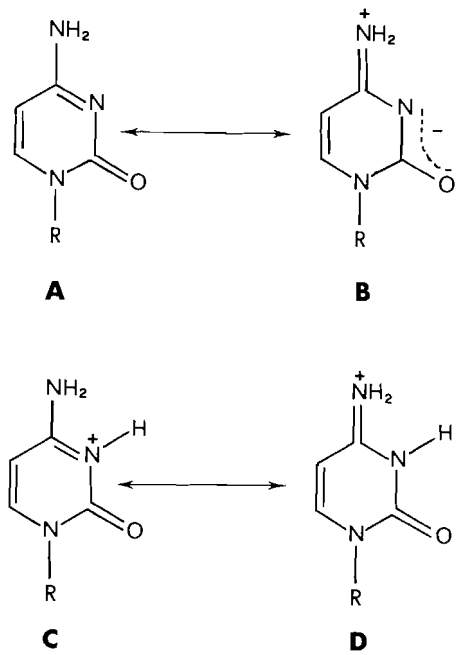

FIG. 3. Resonance forms of cytidine and N3 protonated cytidine.

by 4.9 Hz, as would be expected for protonation at N7 of purine bases (20).

As expected according to Grant's pioneering work on the protonation of purines (21), ^{13}C chemical shift variations on addition of acid are one order of magnitude smaller than those found for ^{15}N.

Examination of Table 3 shows that the trend of $\delta(^{13}C)$ upon addition of acid is similar to that found in $\delta(^{15}N)$.

It is seen that on addition of the first equivalent of CF_3COOH nearly the same variations as those observed for cytidine are found in the carbons flanking N3(cyt). In contrast, further addition of acid up to more than 3 molar equivalents does not affect the carbon atoms of the guanine moiety to the extent to which they are affected in guanosine upon protonation at N(7). Protonation of guanosine shields C5 by nearly 7 ppm, whereas C8, the other carbon next to the protonation site, is unchanged, probably due to cancelling effects. After addition of more than 3 molar equiv. of acid to d(CpG), C5(gua) is shifted upfield by only 3.6 ppm and the chemical shifts found in protonation of guanosine are reached only after addition of a large excess of acid.

Both ^{15}N and ^{13}C nmr results suggest that protonation at N7(gua) is competitive with protonation at another basic site, which is not a nitrogen atom, i.e., the phosphate group. Indeed, since it is reasonable to assume that the pK value for the first ionization step of $(HO)_3PO$ is close to that of a phosphate diester, its value, 2.2–2.5 (22), appears to be in the same range as that of N7(gua). Unfortunately, the chemical shift variations upon protonation found in the carbons near the phosphate center, namely C3′(cyt) and G5′(gua), are not very significant, not only because they are small, but also because it is impossible to distinguish between the contributions arising from protonation of the phosphate group and small perturbations in the distribution of conformers of the deoxyribose ring or minor adjustments of the sugar phosphate backbone. For the same reasons it would be difficult to get more direct evidence of protonation of the phosphate group by ^{31}P nmr. Determination of the pK_{BH^+} values of N3(cyt), N7(gua), and the phosphate group by other techniques such as uv spectroscopy (23), which would take into account the variations of ionic strength or the presence of competitive ions such as Na^+, is required.

The results of protonation of d(CpG) in dimethylsulfoxide vary from those of metallation of the same compound by the methylmercuric cation in water (8), which, for less than one molar equivalent of CH_3Hg^+ added, occurs at N7(gua).

It is generally considered that in cytosine and guanine protonation and metal ion coordination sites are the same (1*c*, 18). In agreement with this, mercuriation occurs at N3 in cytidine and cytidine-3′-monophosphate (5*a*, *c*, 24) and at N7 in guanosine and guanosine-5′-monophosphate (5*a*, *c*), in water and DMSO as the solvents.

Can. J. Chem. Downloaded from www.nrcresearchpress.com by 196.1.178.254 on 09/07/12
For personal use only.

Can. J. Chem. Downloaded from www.nrcresearchpress.com by 196.1.178.254 on 09/07/12
For personal use only.

TABLE 3. ^{13}C chemical shifts[a] of d(CpG), cytidine, and guanosine in DMSO-d_6[b] as a function of added trifluoroacetic acid

Molar equiv. of CF_3COOH	3′-dCMP								
	C2	C4	C5	C6	C1′	C2′	C3′	C4′	C5′
0.0	155.4	165.6	94.4	140.9	84.9	38.7	74.6	85.9	61.5
0.25	135.5	164.1	94.4	141.6	85.1	38.6	74.7	85.8	61.3
0.5	151.9	162.8	94.4	142.2	85.3	38.6	74.9	85.8	61.1
0.75	150.3	161.7	94.4	142.9	85.5	[c]	75.0	85.7	61.1
1.0	149.0	160.8	94.3	143.4	85.6	[c]	75.2	85.6	61.0
1.25	148.1	160.2	94.2	143.7	85.8	[c]	75.5	85.7	60.9
2.5	147.4	159.8	94.2	144.1	85.8	[c]	76.1	85.6	60.8
3.65	147.3	159.8	94.3	144.2	85.9	[c]	76.3	85.7	60.9
6.25	147.3	159.8	94.3	144.3	86.0	[c]	76.5	86.1	61.0
	5′-dGMP								
	C2	C4	C5	C6	C8	C1′	C2′	C3′	C4′	C5′
0.0	153.8	151.1	116.5	157.3	135.4	82.7	39.1	71.1	86.0	64.8
0.25	153.8	151.0	116.4	157.2	135.4	82.7	39.6	71.1	86.2	65.0
0.5	153.8	151.0	116.4	157.1	135.4	82.7	39.7	71.0	86.3	65.1
0.75	153.8	151.0	116.5	157.1	135.4	82.8	[c]	71.0	86.5	65.3
1.0	153.8	151.0	116.4	157.0	135.4	82.8	[c]	71.0	86.6	65.5
1.25	153.9	150.9	116.1	156.8	135.3	82.9	[c]	70.8	86.6	65.7
2.5	154.3	150.5	114.4	156.1	135.4	83.5	[c]	70.6	86.6	66.1
3.65	154.7	150.2	112.8	155.4	135.4	84.1	[c]	70.5	86.6	66.2
6.25	155.0	150.0	107.9	155.3		84.9	[c]	70.5	86.7	66.2
	Cytidine				Guanosine				
	C2	C4	C5	C6	C2	C4	C5	C6	C8	
0.0	155.4	165.5	93.8	141.4	153.6	151.3	116.5	156.9	135.8	
0.33	153.1	163.5	94.1	142.5						
0.5	151.6	162.4	94.1	143.0	154.7	150.5	112.7	155.5	135.6	
1.0	148.4	160.4	94.1	144.1	155.2	150.2	111.0	154.9	135.5	
2.0					155.8	150.0	109.5	154.4	135.6	

[a]In ppm, with respect to TMS as internal reference.
[b]0.2 M in DMSO-d_6.
[c]Not observed (overlap DMSO-d_6).

TABLE 4. Significant carbon–proton coupling constants[a] of d(CpG),[b] cytidine,[b] and guanosine[b] upon addition of CF_3COOH

Molar equiv. of CF_3COOH	d(CpG)			
	3′-dCMP		5′-dGMP	
	$^1J_{C5H5}$	$^1J_{C6H6}$	$^1J_{C8H8}$	$^3J_{C5H8}$
0.0	173.3	180.7	215.0	11.0
0.5	177.0	185.6	215.0	11.0
1.0	181.8	185.6	215.0	11.0
6.25	182.0	185.6	218.5	6.1
	Cytidine		Guanosine	
	$^1J_{C5H5}$	$^1J_{C6H6}$	$^1J_{C8H8}$	$^3J_{C5H8}$
0.0	173.3	180.7	214.5	11.3
0.33	175.8	183.1		
0.5	178.2	183.1	216.0	9.4
1.0	180.7	185.6	220.0	8.5

[a]In Hz.
[b]0.2 M in DMSO-d_6.

Since the reversal of the relative basicities of N3(cyt) and N7(gua) in water in respect to DMSO is unlikely (9, 17), it would have been expected that addition of less than one equivalent of CH_3Hg^+ would have brought about preferential binding at N3(cyt).

However, although in both processes the relative basicities of the potential binding sites play a crucial role, protonation and metallation are quite different reactions in terms of steric requirements and activation energies. Thus, the question arises whether the different results found for proton and CH_3Hg^+ addition to d(CpG) are due to steric reasons (the binding of CH_3Hg^+ at N3 being hindered by the presence of the flanking amino and keto groups) or are in some way related to the mini-helix structure of d(CpG) in water (10), or both. The question is not only in itself of obvious chemical interest but is especially relevant to the problem of the mutagenic action of several metals (25) or the activity of anticancer drugs such as cisplatin (26).

Experimental

The dinucleoside monophosphate, d(CpG), was prepared according to a published procedure (15). The sodium salt was obtained from the corresponding ammonium derivative by treatment with Dowex 50W8 (Na^+ form).

Natural abundance ^{15}N nmr spectra were obtained at 30.408 MHz with a Bruker CXP-300 spectrometer. A 10-mm dedicated probe was employed and the spectra run with inverse-gated decoupling to suppress the unfavorable $\{^{15}N-^{1}H\}$ nuclear Overhauser enhancement. Typical conditions were sweep width, 10 kHz; pulse width, 40°; repetition time, 7 s; data points, 16K. The free induction decays were zero-filled to 32K before transformation. The chemical shifts were measured with respect to an external 1 M solution of HNO_3 and converted to the NH_3 scale using the conversion factor $\delta_{NH_3}(HNO_3)$ = 376 ppm (2).

The ^{13}C spectra were run at 75.458 with the same instrument. The assignments were based on ref. 8. C1′(cyt), C4′(cyt), and C4′(gua) resonate at nearly the same frequency. The two signals showing a $^{13}C-^{31}P$ coupling were assigned to C4′(cyt) and C4′(gua); however, these could be interchanged. For the solutions in DMSO the chemical shifts were measured with respect to TMS as internal reference. For the solution in water the chemical shifts were measured with respect to internal dioxane and converted to the TMS scale using the conversion factor δ_{TMS} = 67.4 ppm.

1. (*a*) V. Markowski, G. R. Sullivan, and J. D. Roberts. J. Am. Chem. Soc. **99**, 714 (1977); (*b*) N. C. Gonnella, H. Nakanishi, J. B. Holtwick, D. S. Horowitz, K. Kanamori, N. J. Leonard, and J. D. Roberts. J. Am. Chem. Soc. **105**, 2050 (1983); (*c*) K. Kanamori and J. D. Roberts. Acc. Chem. Res. **16**, 35 (1983); (*d*) G. Remaud, J. Kjellberg, H. Bazin, N. G. Johansson, and J. Chattopahyaya. Tetrahedron, **42**, 5073 (1986); (*e*) G. Reamud, X-x. Zhou, C. J. Welch, and J. Chattopadhyaya. Tetrahedron, **42**, 4057 (1986); (*f*) G. Remaud, J. Kjellberg, N. G. Johansson, and J. Chattopadhyaya. Tetrahedron, **43**, 365 (1987).
2. G. C. Levy and R. L. Lichter. Nitrogen-15 nuclear magnetic resonance spectroscopy. J. Wiley & Sons, New York. 1979. Chap. 3.
3. J. B. Lambert and F. G. Riddel. The multinuclear approach to NMR spectroscopy. D. Reidel Publishing Company, Dordrecht, Boston. 1982. Chap. 2.
4. (*a*) M. Nee and J. D. Roberts. Biochemistry, **21**, 4920 (1982); (*b*) G. Barbarella, A. Bertoluzza, A. Morelli, M. R. Tosi, and V. Tugnoli. Gazz. Chim. Ital. In press.
5. (*a*) G. W. Buchanan and J. B. Stothers. Can. J. Chem. **60**, 787 (1982); (*b*) G. W. Buchanan and M. J. Bell. Can. J. Chem. **61**, 2445 (1983); (*c*) Magn. Reson. Chem. **24**, 493 (1986).
6. (*a*) G. E. Hawkes, E. W. Randall, and C. H. Bradley. Nature, **257**, 767 (1975); (*b*) J. Mason. Chem. Rev. **81**, 205 (1981); (*c*) W. von Philipsborn and R. Muller. Angew. Chem. Int. Ed. Engl. **25**, 383 (1986).
7. (*a*) K. Shinozuka, K. Wilkowski, B. H. Heyl, and L. G. Marzilli. Inorg. Chim. Acta, **100**, 141 (1985); (*b*) A. Bertoluzza, C. Fagnano, M. R. Tosi, V. Tugnoli, M. Morelli, and G. Barbarella. Anticancer Res. **6**, 1385 (1986).
8. G. W. Buchanan and M. J. Bell. Can. J. Chem. **64**, 2093 (1986).
9. R. L. Benoit, D. Boulet, L. Seguin, and M. Frechette. Can. J. Chem. **63**, 1228 (1985).
10. D. M. Cheng and R. H. Sarma. J. Am. Chem. Soc. **99**, 7333 (1977).
11. M. Coll, X. Solans, M. Font-Altaba, and J. A. Subirana. J. Biomol. Struct. Dyn. **4**, 797 (1987).
12. L. Katz and S. Penman. J. Mol. Biol. **15**, 220 (1966).
13. R. A. Newmark and C. R. Cantor. J. Am. Chem. Soc. **90**, 5010 (1968).
14. (*a*) C. Dyllick-Brenziger, G. R. Sullivan, P. P. Pang, and J. D. Roberts. Proc. Natl. Acad. Sci. U.S.A. **77**, 5580 (1980); (*b*) G. Barbarella, A. Bertoluzza, and V. Tugnoli. Magn. Reson. Chem. **25**, 864 (1987).
15. J. E. Marugg, M. Tromp, P. Jhurani, C. F. Hoyng, G. A. van der Marel, and J. H. van Boom. Tetrahedron, **40**, 73 (1984).
16. W. Saenger. Principles of nucleic acid structure. Springer-Verlag, New York. 1984. (*a*) Chap. 6; (*b*) Chap. 5; (*c*) Chap. (8).
17. R. M. Izatt, J. J. Christensen, and J. H. Rytting. Chem. Rev. **71**, 439 (1971).
18. P. Buchner, W. Maurer, and H. Ruterjans. J. Magn. Reson. **29**, 45 (1978).
19. R. Taylor and O. Kennard. J. Mol. Struct. **78**, 1 (1982).
20. M. Schumacher and H. Gunther. J. Am. Chem. Soc. **104**, 4167 (1982).
21. R. J. Pugmire and D. M. Grant. (*a*) J. Am. Chem. Soc. **90**, 4232 (1968); (*b*) J. Am. Chem. Soc. **93**, 1980 (1971).
22. The Merck Index. Merck & Co., Inc., Tenth Edition, 1983, p. 1059.
23. R. L. Benoit and M. Frechette. Can. J. Chem. **63**, 3053 (1985).
24. S. Mansy and R. S. Tobias. J. Am. Chem. Soc. **96**, 6874 (1974).
25. L. G. Marzilli, B. deCastro, J. P. Caradonna, R. C. Stewart, and C. P. Van Vuuren. J. Am. Chem. Soc. **102**, 916 (1980).
26. S. E. Sherman and S. J. Lippard. Chem. Rev. **87**, 1153 (1987).

Can. J. Chem. Downloaded from www.nrcresearchpress.com by 196.1.178.254 on 09/07/12
For personal use only.

Molecular structure of opiate alkaloids. Part I. Crystal structure of two 16-alkyl analogues of thebaine and oripavine

ANDRÉ G. MICHEL[1] AND M. PROULX
Laboratoire de chimie structurale, Université de Sherbrooke, Sherbrooke (Qué.), Canada J1K 2R1

G. EVRARD AND B. NORBERG
Facultés Universitaires Notre-Dame de la Paix, rue de Bruxelles, 61, B5000 Namur, Belgium

AND

E. MILCHERT
Politechnika Szczecinska, Szczecin, Poland, 0422141, PS PL

Received September 18, 1987[2]

Can. J. Chem. Downloaded from www.nrcresearchpress.com by 196.1.178.254 on 09/07/12
For personal use only.

ANDRÉ G. MICHEL, M. PROULX, G. EVRARD, E. MILCHERT, and B. NORBERG. Can. J. Chem. **66**, 2498 (1988).

The crystal structures of two 16-alkyl thebaine and oripavine analogues are described, in an attempt to put forward the particular requirements of these compounds to interact with the opiate receptor. Conformational congruencies accounting for the very high potency of these compounds are also emphasized.

In light of the crystal structures, the influence of the 16-alkyl substitution is discussed, as well as the differentiation in the agonist activity observed between diastereomers at C(19) characterizing these classes of opioids.

Significant distortions in the condensed ring system and the existence of an intramolecular hydrogen bonding are the main geometrical observations. They are invoked to account for particular modulations in the analgesic activity.

ANDRÉ G. MICHEL, M. PROULX, G. EVRARD, E. MILCHERT et B. NORBERG. Can. J. Chem. **66**, 2498 (1988).

Les structures cristallines de deux analogues 16-alkylés de la thébaine et de l'oripavine sont décrites, afin de mettre en évidence les propriétés conformationnelles caractérisant leurs intéractions spécifiques avec le récepteur opiacé.

L'influence du substituant 16-alkyl sur la conformation est discutée, ainsi que la différentiation dans l'activité agoniste observée pour les diastéréoisomères 19-*R* et 19-*S*, particularité propre à ces deux familles de composés.

Des déformations significatives dans le noyau polycyclique et la présence d'une liaison hydrogène intramoléculaire constituent les principaux éléments d'ordre structurel invoqués pour tenir compte des modulations particulières de l'activité analgésique de ces composés.

Introduction

In the past decade, crystal structure analysis of opiate alkaloids has proven to be extremely useful to probe the opiate receptor topography: more than 45 crystal structures have been reported. Nevertheless, very few of these are semi-rigid narcotic alkaloids of the oripavin and thebain families; their particular interest derives from the presence of a C(6)—C(14) etheno bridge, bearing various C(7) substituents.

In early attempts to establish structure–activity relationships of opiate multi-ring compounds, three interaction sites were postulated at the receptor level; an anionic center interaction with the nitrogen atom, and hydrophobic site, in relation with the aromatic ring A and finally a "hole" where C(15) and C(16) had to fit (1). This model had to be updated to explain the tremendous increase in the analgetic activity for 6,14-*endo*-ethenotetrahydrothebaine where not only is activity as much as 2200 times higher than that of morphine (2), but also the *R* diastereoisomers are much more potent than the *S* diastereoisomers.

In this study we have addressed two structure–activity questions; the influence of the alkyl substitution at the C(16) position and the differentiation in agonist activity between diastereomers at C(19) (2). Compounds **1** and **2** were chosen accordingly; they belong to the oripavin and thebain family respectively and differ by the C(16) substitution.

The effect of this alkyl substitution relates to the size of the particular "C(15)—C(16) hole" as mentioned in the opiate receptor model proposed by Beckett and Casy (1): all the 16-alkyl-6,14-*endo*-ethenotetrahydrothebaines are less active as analgetics than the unsubstituted compounds (2). In particular, a group larger than methyl (compound **2**) eliminates almost completely the analgesic activity. We were also interested in the effect of substitution on the distortion of the multi-ring system as an alternative hypothesis to take into account the loss of activity.

Concerning C(7) substitution and its stereospecificity, conformational studies of a series of oripavine suggested the formation of an intramolecular hydrogen bonding (4). These results were consistent with the crystallographic data available (7). In our study, a similar intra-hydrogen bonding also exists in compounds **1** and **2** this would be useful to explain the stereospecificity at C(7) and determine the size and the orientation of corresponding subsite to be taken into account in the opiate receptor modelisation.

Experimental

The preparations and pharmacological properties of the title compounds have been reported earlier (2).

Crystals of **1** were obtained by slow evaporation from a solution in methanol, kept at 5°C. Colourless transparent plates were prepared to be suitable for X-ray analysis. Crystals of **2** were obtained from an aqueous isopropanolic solution in a 1:1 ratio. Prismatic, colourless transparent crystals grew slowly at 5°C.

The cell constants and space groups were obtained with film

[1]To whom correspondence should be addressed.

[2]Revision received April 25, 1988.

Printed in Canada / Imprimé au Canada

TABLE 1. Crystallographic data

Parameter	Compound **1**	Compound **2**
Molecular formula	$C_{24}H_{31}NO_4$	$C_{26}H_{35}NO_4 \cdot \frac{1}{2}H_2O$
Molecular weight	397.50	434.56
Unit cell	Monoclinic	Orthorhombic
a (Å)	10.498 (1)	8.948 (1)
b (Å)	10.758 (1)	38.944 (4)
c (Å)	9.094 (1)	6.740 (5)
β (deg)	95.37 (1)	—
V (Å^3)	1022.54	2348.69
Z	2	4
d_{obs} (g cm^{-3})	1.30	1.23
d_c (g cm^{-3})	1.290	1.227
Space group	$P2_1$	$P2_12_12$
Radiation, K$\bar{\alpha}$ (Å)	1.54178	1.54178
T (°C)	20	20
Crystal size (mm)	0.22 × 0.19 × 0.06	0.06 × 0.10 × 0.35

TABLE 2. Experimental conditions for data collection and refinement

Parameter	Compound **1**	Compound **2**
$F(0,0,0)$	428.0	940.0
μ (cm^{-1})	6.4	5.62
Scan range (deg)	0.7 + 0.3 tan θ	0.7 + 0.3 tan θ
2θ range (deg)	4–144	4–144
h,k,l ranges	$-12 \leq h \leq 12$	$0 \leq h \leq 11$
	$0 \leq k \leq 13$	$0 \leq k \leq 48$
	$0 \leq l \leq 11$	$0 \leq l \leq 8$
Maximum fluctuation of standard reflection (%)	≤1	≤1
Number of reflections measured	2115	2692
Number of reflections observed	1464	1628
Threshold: $I \geq k\sigma(I)$, k =	2.5	2
$R = \Sigma\lvert\Delta F\rvert/\Sigma\lvert F_o\rvert$	0.031	0.041
$R_w = [\Sigma w\Delta F^2/\Sigma w(F_o)^2]^{1/2}$	0.022	0.037
S (goodness of fit)	4.476	0.899
$(\text{Displacement}/\sigma)_{max}$	0.642	0.908
$(\text{Displacement}/\sigma)_{average}$	0.2	0.855
Extreme fluctuations of residual electron density (e Å^{-3})	−0.150; 0.130	−0.093; 0.093

techniques and were confirmed using the diffractometer data. A total of 18 (compound **1**) and 25 (compound **2**) reflections were used to refine the cell dimensions. Independent reflections were collected on a Nonius CAD-4 automatic diffractometer. Experimental conditions related to the data acquisitions are given in Table 1.

Absorption corrections were not applied because of the small sizes of the crystals and the small values of linear absorption coefficients for CuKα. Lorentz and polarization corrections were applied.

The positions of the non-hydrogen atoms of both molecules were obtained from the E-map computed subsequently to the direct methods application (MULTAN programs) (5). The structure refinement of compound **1** was performed by isotropic and anisotropic refinements by full-matrix least squares applied to F's using the NRCVAX program (12). Counting statistics weights were used, H atoms located on difference Fourier maps and isotropically refined in subsequent calculations. The "y" coordinate of atom O(1) has been fixed during the refinements, $P2_1$ being a polar space group. The structure refinement of compound **2** has been achieved by isotropic and anisotropic refinements by full-matrix least squares; using the XTAL83 program (6) lowered the R value to 0.070. A Fourier difference synthesis revealed the coordinates of the H atoms, which were given the isotropic thermal parameters of their adjacent atoms. Counting statistics weights

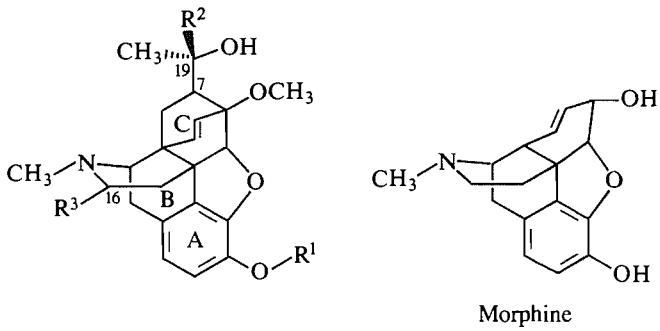

Morphine

1: R^1 = H, R^2 = methyl, R^3 = methyl, RX6414M*
6,14-*endo*-etheno-7α-(1-hydroxy-1-propyl)-16α-methyl 6,7,8,14-tetrahydrothebaine

2: R^1 = methyl, R^2 = methyl, R^3 = ethyl, RX7720M*
6,14-*endo*-etheno-7α-(1-hydroxy-1-propyl)-16α-ethyl 6,7,8,14-tetrahydrooripavine

3: R^1 = methyl, R^2 = cyclohexyl, R^3 = methyl, RX6420M*

4: R^1 = methyl, R^2 = cyclohexyl, R^3 = ethyl, RX6439M*

5: R^1 = methyl, R^2 = propyl, R^3 = H, propylthevinol

6: R^1 = H, R^2 = benzyl, R^3 = H

*Reckitt and Colman identifications

were used. Although not refined, the H atoms parameters were included in the subsequent calculations. High values for (displacement/σ) may be attributed to the relatively important mosaïcity of the crystals and resulting low quality of the measurements. The O(5) atom lies in a position very close to the 2-fold axis. Its factor of occupancy has been assigned to 0.5. For both compounds, the final refinement undertaken under the conditions listed in Table 2 yielded the atomic coordinates of the non-hydrogen atoms as given in Table 3. The positional parameters of the H atoms together with their isotropic temperature factors, as well as the lists of structure factors and anisotropic thermal parameters have been deposited as supplementary material.[3]

Results

The atomic numbering used for compounds **1** and **2** is indicated in Fig. 1, which shows the crystal structure of **2**. The atoms C(25) and C(26) are not present in **1**.

The numbering of the carbon atoms in the crystal structure corresponds to the commonly accepted conventions for the morphine class of molecules. The T shape of the rigid morphine-like part is displayed by both compounds. The bond distances for the two compounds are listed in Table 4 and bond angles in Table 5.

The molecular structures are similar to those of 19-propylthevinol hydrobromide described earlier (7). The piperidyl system is in the chair conformation with the *N*-methyl equatorial, in spite of the presence of the 16-β-alkyl substituent. In both compounds the O(4) hydroxyl oxygen forms an intramolecular hydrogen bond with the ether oxygen O(3), as observed in early X-ray studies (7) as well as predicted by conformational analysis (4).

[3]Tables of observed and calculated structure factor amplitudes, of anisotropic temperature factors for non-hydrogen atoms, of fractional coordinates and temperature factors for hydrogen atoms, and of torsional angles may be purchased from the Depository of Unpublished Data, CISTI, National Research Council of Canada, Ottawa, Ont., Canada K1A 0S2.

Can. J. Chem. Downloaded from www.nrcresearchpress.com by 196.1.178.254 on 09/07/12
For personal use only.

TABLE 3. Fractional coordinates and B_{eq} for non hydrogen atoms of compounds **1** and **2**

(*a*) Compound **1**

Atom	*x/a*	*y/b*	*z/c*	B_{eq}[a]
C01	0.9625(4)	0.0610(5)	0.6383(4)	2.96
C02	1.0464(4)	0.1109(5)	0.7504(4)	3.07
C03	1.1682(4)	0.1533(5)	0.7263(4)	2.83
C04	1.2010(3)	0.1462(5)	0.5822(4)	2.59
C05	1.3166(4)	0.1165(5)	0.3825(4)	2.71
C06	1.3816(4)	−0.0111(5)	0.3658(4)	2.97
C07	1.3707(4)	−0.0313(5)	0.1920(4)	2.72
C08	1.2274(4)	−0.0510(5)	0.1371(4)	2.72
C09	0.9971(4)	−0.0307(5)	0.2258(4)	2.78
C10	0.9239(4)	−0.0156(5)	0.3683(5)	3.11
C11	0.9956(4)	0.0579(5)	0.4919(4)	2.68
C12	1.1119(4)	0.1089(5)	0.4698(4)	2.51
C13	1.1734(4)	0.1037(5)	0.3277(4)	2.38
C14	1.1433(3)	−0.0278(5)	0.2648(4)	2.35
C15	1.1305(4)	0.2045(5)	0.2133(5)	2.93
C16	0.9907(4)	0.1929(5)	0.1467(5)	3.21
C17	1.1892(4)	−0.1209(5)	0.3832(4)	3.00
C18	1.3097(4)	−0.1120(5)	0.4355(5)	3.05
C19	1.5423(4)	0.3649(5)	0.8646(5)	3.44
C20	1.5538(6)	0.3685(8)	1.0329(6)	4.89
C21	1.5685(5)	0.2355(6)	0.8073(7)	4.46
C22	0.8375(5)	0.0412(6)	0.0324(6)	3.83
C23	0.8936(6)	0.2585(6)	0.2365(7)	4.31
C24	1.5530(6)	−0.0291(7)	0.5687(6)	5.26
N1	0.9636(3)	0.0622(4)	0.1092(3)	2.69
O1	1.32201(23)	0.1608	0.5373(3)	2.90
O2	1.24826(34)	0.1915(4)	0.8455(3)	3.92
O3	1.51611(25)	−0.0017(4)	0.4156(3)	4.14
O4	1.40914(28)	0.3930(4)	0.8200(4)	4.13

(*b*) Compound **2**

Atom	*x/a*	*y/b*	*z/c*	B_{eq}
C01	0.1722(5)	0.8177(1)	0.4093(8)	3.40
C02	0.0739(5)	0.8293(1)	0.2649(9)	3.97
C03	0.1185(5)	0.8492(1)	0.1017(8)	3.28
C04	0.2727(5)	0.8559(1)	0.0878(8)	2.77
C05	0.4983(5)	0.8831(1)	0.0315(7)	2.55
C06	0.5321(5)	0.9177(1)	0.1333(8)	3.22
C07	0.7048(5)	0.9146(1)	0.1841(8)	3.27
C08	0.7250(5)	0.8886(1)	0.3580(8)	3.21
C09	0.5934(5)	0.8360(1)	0.5170(8)	2.73
C10	0.4366(5)	0.8188(1)	0.5578(7)	3.10
C11	0.3257(5)	0.8241(1)	0.3897(8)	2.70
C12	0.3704(5)	0.8408(1)	0.2194(7)	2.33
C13	0.5269(5)	0.8535(1)	0.1794(7)	2.33
C14	0.5787(5)	0.8679(1)	0.3837(7)	2.51
C15	0.6333(5)	0.8265(1)	0.0954(7)	2.41
C16	0.6765(5)	0.7976(1)	0.2395(8)	2.58
C17	0.4654(5)	0.8944(1)	0.4510(8)	3.00
C18	0.4434(5)	0.9197(1)	0.3229(8)	3.35
C19	0.7867(6)	0.9490(1)	0.2224(10)	5.73
C20	0.7120(7)	0.9717(1)	0.3786(12)	7.90
C21	0.9517(6)	0.9418(1)	0.2782(11)	6.31
C22	0.7703(6)	0.7890(1)	0.5762(8)	4.16
C23	0.5688(5)	0.7666(1)	0.2368(8)	3.33
C24	0.3703(6)	0.9546(1)	−0.0658(10)	4.90
C25	0.0420(6)	0.8779(2)	−0.1989(9)	6.85
C26	0.5924(7)	0.7438(1)	0.0549(10)	5.97
N1	0.7075(4)	0.8128(1)	0.4343(6)	2.68
O1	0.3409(3)	0.8794(1)	−0.0358(5)	2.96
O2	0.0082(4)	0.8616(1)	−0.0193(6)	4.95
O3	0.5155(4)	0.9460(1)	0.0011(6)	4.22
O4	0.7968(4)	0.9669(1)	0.0347(8)	7.63
O5	1.9663(14)	1.0160(3)	1.7798(14)	10.73

[a] $B_{eq} = \frac{8\pi^2}{3}\sum_i\sum_j U_{ij}a_i^*a_j^*a_ia_j$.

To evaluate the distortions on the molecule structures induced by the 16-β-alkyl substituent, we have superimposed both compound **1** and compound **2** on compound **5**, propylthevinol, the unsubstituted thebaine derivative (7). Its activity is about 100 times more potent than morphine in tail pressure test in rats (10). The best molecular fittings have been made by exact superposition of the phenyl rings (ring A) constraining the six pairs of equivalent atoms to match perfectly. Resulting pictures are shown in Fig. 2. The "fit" option of the SYBYL molecular modelling system has been used (8).

In compound **1**, the crystal packing is assured by one intermolecular hydrogen bond between the O(2) hydroxyl oxygen and the O(4) 19-hydroxyl oxygen of another molecule, and by Van der Waals contacts. In compound **2**, the packing in the crystal is mainly achieved by hydrogen bonds between the O(5) atom of water and the hydroxyl O(4) atom, the corresponding values are given in Table 6. The H_2O molecule (O(5) atom) bridges two symmetry-related molecules, as can be seen in Fig. 3.

Although very different one from each other, the packings of compounds **1** and **2** do not induce significant modifications at the molecular level. Even the intramolecular hydrogen bond is conserved, although the O(4) hydroxyl atom of compound **2** is shared between an intra- and an intermolecular H-bond: donor to O(3) (intra) and acceptor from O(5) of the water (inter). Intervening protons have been represented in Fig. 3.

Discussion

Essential molecular characteristics for thebaine and oripavine narcotics appear from the present study and can be related to their specific agonist properties.

The presence of the 16-methyl (compound **1**) and 16-ethyl (compound **2**) as R^3 substituents has been shown to have minor effects on the N-lone pair orientation and cannot be invoked to justify the loss of activity (9). The argument of the steric hindrance as postulated in former models (1) remains the most plausible. Nevertheless, the examination of Figs. 2*a* and *b* shows that the distortion on the orientation of the C(7)—C(19) bond is in the order of 30° compared to the unsubstituted propylthevinol compound **5** (7). This observation might be reconsidered when the contribution of the R^2 to the pharmacophore would be precised. Particularly its relative position and orientation with respect to the tyramine part of the molecule would be of interest in the description of the opiate receptor.

This statement is corroborated by the presence of intramolecular hydrogen bonding O(3)...O(4) corresponding to O-methoxy and hydroxyl groups, respectively. This observation confirms NMR, IR, and quantum calculations predictions, reported earlier (3). The protons involved were located on Fourier-difference maps for both compounds. The geometrical characteristics are given in Table 6. Also observed for com-

Can. J. Chem. Downloaded from www.nrcresearchpress.com by 196.1.178.254 on 09/07/12
For personal use only.

Can. J. Chem. Downloaded from www.nrcresearchpress.com by 196.1.178.254 on 09/07/12
For personal use only.

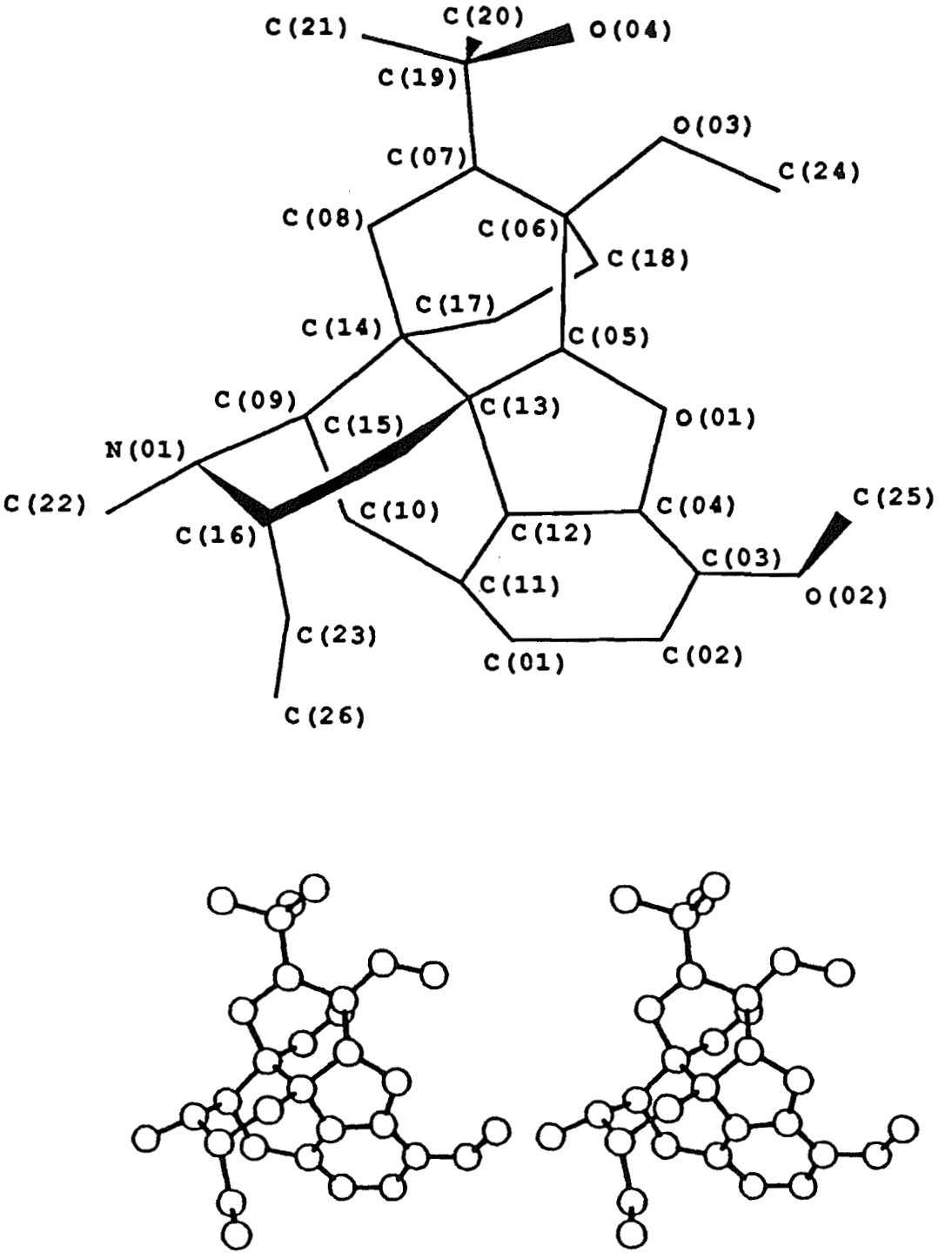

FIG. 1. Atoms numbering for **1** and **2**: represented by using the crystal structure of **2**: C(25) and C(26) are not present in **1**. The numbering corresponds to the chemical conventions.

pound **5**, this intramolecular constraint differentiates the *R* and *S* isomers at C(19), in consequence of the hindered rotation around the C(7)—C(19) bond. As a result, the torsional angles C(6)—C(7)—C(19)—O(4) are very similar: −60.3° for compound **1**, −70.0° for compound **2** and −66.2° for compound **5** (7). Molecular similarities are evident from Fig. 2: excellent molecular fits were obtained between compound **1** and compound **5** (Fig. 2*a*) as well as between compounds **2** and **5** (Fig. 2*b*) and between **1** and **2** (Fig. 2*c*). Similarities are also reflected by equivalent distances between atoms involved in the interaction with the opiate receptor. N(1)—O(3): 6.8 Å for compound **1**, 6.6 Å for compound **2**, to be compared with 6.7 Å in compound **5** (7). This finding may also explain the observed differentiation in the narcotic activity between the diastereoisomers at C(19). According to the Becket and Casy (1) receptor model, the C(7) substituents interact with a lipophilic receptor site. The presence of the hydrogen bond allows the *R* isomers to orient the C(7) substituent in the proper region of space and, hence, increase the agonist potency.

Computer modelling techniques demonstrated the similari-

Can. J. Chem. Downloaded from www.nrcresearchpress.com by 196.1.178.254 on 09/07/12
For personal use only.

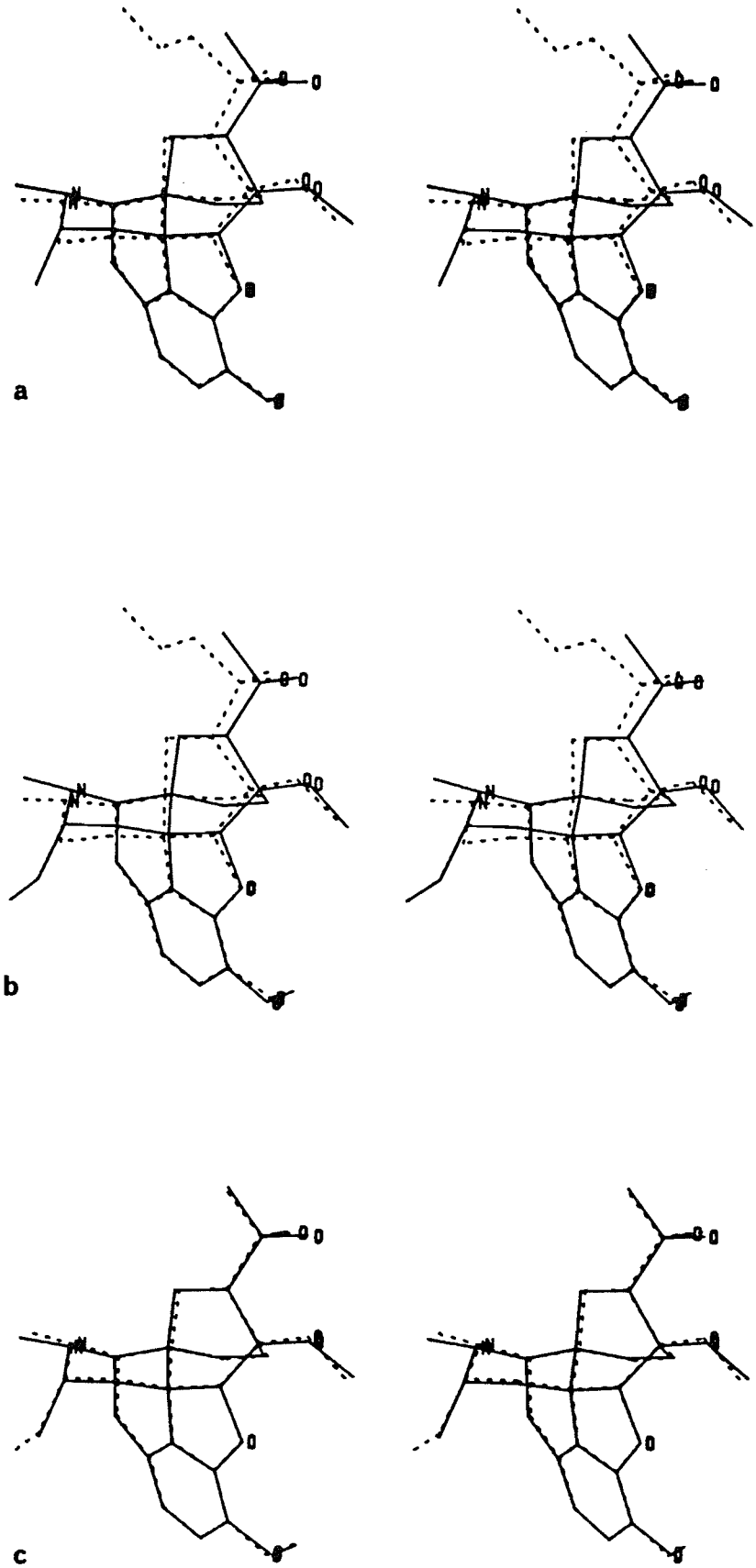

FIG. 2. Stereoviews of pairs of molecules superimposed by their phenyl rings. (*a*) Full lines: compound **1** dashed lines: compound **5**; (*b*) Full lines: compound **2**, dashed lines: compound **5**; (*c*) Full lines: compound **1**, dashed lines: compound **2**.

TABLE 4. Intramolecular bond distances for compounds **1** and **2** with estimated standard deviation in parentheses

Distance	1	2	Distance	1	2
C(02)—C(01)	1.391(6)	1.388(7)	C(10)—C(11)	1.515(6)	1.520(7)
C(11)—C(01)	1.407(5)	1.403(6)	C(12)—C(11)	1.370(6)	1.377(7)
C(03)—C(02)	1.395(6)	1.404(8)	C(13)—C(12)	1.499(5)	1.509(6)
C(04)—C(03)	1.388(5)	1.407(6)	C(14)—C(13)	1.547(7)	1.588(7)
O(02)—C(03)	1.371(5)	1.368(6)	C(15)—C(13)	1.541(6)	1.526(6)
C(12)—C(04)	1.379(5)	1.378(7)	C(17)—C(14)	1.516(6)	1.517(6)
O(01)—C(04)	1.379(4)	1.379(6)			
			C(16)—C(15)	1.504(6)	1.537(6)
C(06)—C(05)	1.547(7)	1.541(6)			
C(13)—C(05)	1.545(5)	1.546(6)	N(01)—C(16)	1.469(7)	1.467(6)
O(01)—C(05)	1.483(4)	1.487(5)	C(23)—C(16)	1.536(7)	1.545(6)
C(07)—C(06)	1.588(5)	1.587(7)	C(18)—C(17)	1.312(6)	1.325(7)
C(18)—C(06)	1.497(7)	1.506(7)			
O(03)—C(06)	1.445(5)	1.427(6)	C(20)—C(19)	1.525(7)	1.529(9)
			C(21)—C(19)	1.520(8)	1.549(8)
C(08)—C(07)	1.555(6)	1.561(7)	O(04)—C(19)	1.450(5)	1.447(8)
C(19)—C(07)	1.560(7)	1.548(7)			
			N(01)—C(22)	1.455(5)	1.447(7)
C(14)—C(08)	1.544(6)	1.548(6)			
			O(03)—C(24)	1.440(6)	1.415(7)
C(10)—C(09)	1.576(6)	1.579(6)			
C(14)—C(09)	1.543(5)	1.537(6)	C(26)—C(23)		1.528(8)
N(01)—C(09)	1.476(6)	1.472(6)			
			C(25)—O(02)		1.400(7)

Can. J. Chem. Downloaded from www.nrcresearchpress.com by 196.1.178.254 on 09/07/12
For personal use only.

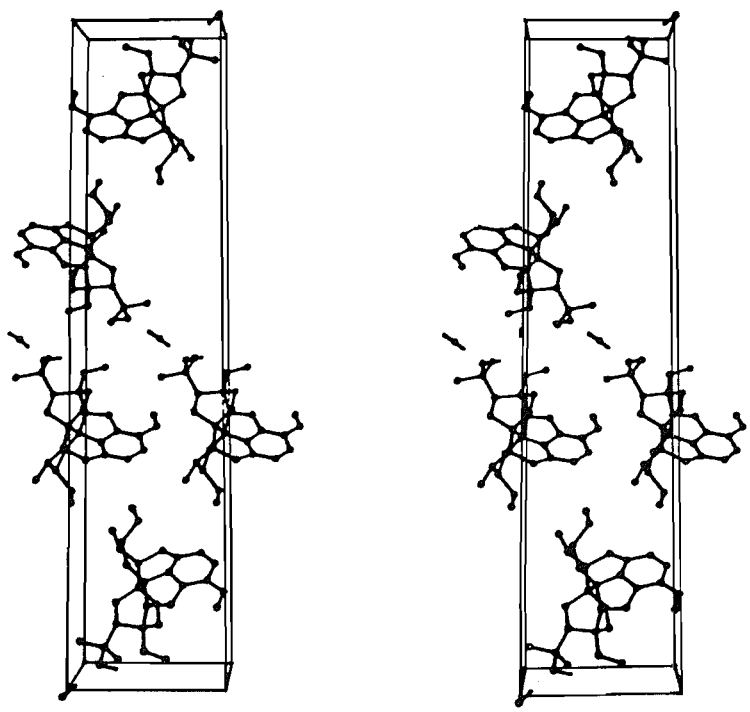

FIG. 3. Stereoviews of the molecules as packed into the unit cells for compound **2**. The *x* axis lies across the page, the *y* axis down page, and the 2-fold *z* axis points to the observer.

Can. J. Chem. Downloaded from www.nrcresearchpress.com by 196.1.178.254 on 09/07/12
For personal use only.

TABLE 5. Intramolecular valence angles for compounds **1** and **2** with estimated standard deviations in parentheses

Angle	1	2	Angle	1	2
C(02)—C(01)—C(11)	120.5(4)	119.7(5)	C(05)—C(13)—C(12)	101.7(3)	101.9(3)
			C(05)—C(13)—C(14)	111.1(4)	110.5(3)
C(01)—C(02)—C(03)	122.5(4)	123.3(4)	C(05)—C(13)—C(15)	111.7(4)	112.2(4)
			C(12)—C(13)—C(14)	105.3(3)	103.7(4)
C(02)—C(03)—C(04)	116.3(4)	115.7(4)	C(12)—C(13)—C(15)	115.7(4)	114.8(3)
C(02)—C(03)—O(02)	118.5(3)	117.1(4)	C(14)—C(13)—C(15)	111.0(3)	112.9(4)
C(04)—C(03)—O(02)	125.1(4)	127.1(4)			
C(03)—C(04)—C(12)	120.3(3)	120.0(4)	C(08)—C(14)—C(09)	116.8(3)	114.4(4)
C(03)—C(04)—O(01)	126.1(3)	126.6(4)	C(08)—C(14)—C(13)	109.3(4)	109.9(4)
C(12)—C(04)—O(01)	113.2(3)	113.1(4)	C(08)—C(14)—C(17)	105.2(4)	104.1(3)
			C(09)—C(14)—C(13)	105.5(4)	104.6(3)
C(06)—C(05)—C(13)	108.3(4)	109.4(4)	C(09)—C(14)—C(17)	113.2(4)	115.6(4)
C(06)—C(05)—O(01)	113.6(3)	114.0(3)	C(13)—C(14)—C(17)	107.5(3)	108.1(4)
C(13)—C(05)—O(01)	116.5(3)	106.2(3)			
			C(13)—C(15)—C(16)	114.6(4)	115.2(4)
C(05)—C(06)—C(07)	103.2(3)	102.8(3)			
C(05)—C(06)—C(18)	110.9(3)	108.7(4)	C(15)—C(16)—C(23)	114.1(4)	114.1(4)
C(05)—C(06)—O(03)	109.5(4)	112.2(4)	C(15)—C(16)—N(01)	109.0(4)	108.5(3)
C(07)—C(06)—C(18)	109.2(4)	109.5(4)	C(23)—C(16)—N(01)	116.1(4)	116.4(4)
C(07)—C(06)—O(03)	107.4(3)	107.1(3)			
C(18)—C(06)—O(03)	115.8(4)	115.7(4)	C(14)—C(17)—C(18)	116.2(4)	114.3(4)
C(06)—C(07)—C(08)	108.4(3)	108.9(4)	C(06)—C(18)—C(17)	114.0(4)	115.8(4)
C(06)—C(07)—C(19)	115.9(4)	115.6(4)			
C(08)—C(07)—C(19)	112.0(4)	112.5(4)	C(07)—C(19)—C(20)	108.6(4)	114.1(4)
			C(07)—C(19)—C(21)	114.3(4)	109.5(4)
C(07)—C(08)—C(14)	109.9(3)	108.9(4)	C(07)—C(19)—O(04)	109.7(4)	107.4(5)
			C(20)—C(19)—C(21)	111.6(5)	110.7(5)
C(10)—C(09)—C(14)	111.1(3)	111.5(4)	C(20)—C(19)—O(04)	105.0(4)	110.6(4)
C(10)—C(09)—N(01)	114.8(4)	115.0(3)	C(21)—C(19)—O(04)	107.2(4)	103.9(4)
C(14)—C(09)—N(01)	108.5(3)	109.5(4)			
			C(16)—C(23)—C(26)		112.2(4)
C(09)—C(10)—C(11)	114.6(3)	113.1(4)			
			C(09)—N(01)—C(16)	117.0(3)	117.1(4)
C(01)—C(11)—C(10)	124.3(4)	123.0(4)	C(09)—N(01)—C(22)	112.6(4)	114.4(4)
C(01)—C(11)—C(12)	115.6(4)	116.5(4)	C(16)—N(01)—C(22)	114.1(4)	113.9(3)
C(10)—C(11)—C(12)	119.2(3)	119.7(4)			
			C(04)—O(01)—C(05)	106.8(3)	107.5(3)
C(04)—C(12)—C(11)	124.0(3)	123.6(4)			
C(04)—C(12)—C(13)	109.4(3)	109.5(4)	C(03)—O(02)—C(25)		121.3(4)
C(11)—C(12)—C(13)	124.9(4)	124.9(4)			
			C(06)—O(03)—C(24)	117.1(4)	118.5(4)

TABLE 6. Hydrogen-bond distances (Å) and angles (deg) between donor and acceptor atoms

Compound	O—H ---O	O—H ---O (deg)	O---O (Å)	O—H (Å)	H---O (Å)
1	O(02)—H---O(04) $x, y, z \quad 1-x, \frac{1}{2}+y, 1-z$	152	2.759(5)	0.80	2.01
1[a]	O(04)—H---O(03)	157	2.614(5)	0.86	1.94
2	O(05)—H---O(04) $x, y, z \quad -x, -y, z$	155	2.985(1)	1.17	1.95
2[a]	O(04)—H---O(03)	132	2.654(5)	0.95	1.95

[a]Indicates an intramolecular bond.

ties between a cyclic enkephalin analogue and a rigid narcotic alkaloid (11), the structure of which was constructed on the basis of crystal data of compound **5**. Compounds **3** and **4** are now under investigation to accumulate structural informations. When these studies are completed, we will have reliable molecular structures for thebaine and oripavine narcotic alkaloids to describe the molecular basis of the opiate activity.

Acknowledgements

We thank Professor B. Belleau (McGill University, Mon-

tréal) for his support of this work and for fruitful discussions. Samples of both compounds were gifts from Reckitt & Colman to B. Belleau. Compound **1** is RX6414M, batch number PM786/1, and compound **2** is RX7720M, batch number PAF97/2. We gratefully acknowledge Drs. Lewis and Meyers (R & C, London) for their assistance. We are indebted to the Natural Sciences and Engineering Research Council of Canada (operating grant A-0329 to A.G.M.) for financial assistance.

1. A. H. BECKETT and A. F. CASY. J. Pharm. Pharmacol. **6**, 986 (1954).
2. J. W. LEWIS, K. W. BENTLEY, and A. COWAN. Ann: Rev. Pharmacol. **11**, 241 (1971).
3. J. W. LEWIS, P. A. MAYOR, and D. I. HADDLESEY. J. Med. Chem. **16**, 12 (1973).
4. G. H. LOEW and D. S. BERKOWITZ. J. Med. Chem. **22**, 603 (1979).
5. P. MAIN, S. J. FISKE, S. E. HULL, L. LESSINGER, G. GERMAIN, J. P. DECLERCQ, and M. M. WOOLFSON. Multan 80, a system of computer programs for the automatic resolution of crystal structures from X-ray diffraction data. University of York, England, and Louvain-La-Neuve, Belgium. 1980.
6. J. M. STEWART, S. R. HALL, R. A. ALDEN, R. OLTHOF-HAZEKAMP, and R. M. DOHERTY. The XTAL system of crystallographic programs: user's manual. Computer Science Technical Report Series no TR-1364. University of Maryland, Maryland 20742 (1983).
7. J. H. VAN DEN HENDE and N. R. NELSON. J. Am. Chem. Soc. **89**, 2091 (1967).
8. SYBYL: Molecular modeling software supplied by TRIPOS Associates Inc. St-Louis, Missouri 63117.
9. B. BELLEAU, T. CONWAY, F. R. AHMED, and A. D. HARDY. J. Med. Chem. **17**, 907 (1974).
10. K. W. BENTLEY, D. G. HARDY, and B. MEEK. J. Am. Chem. Soc. **89**, 3273 (1967).
11. J. DIMAIO, C. I. BAYLY, G. VILLENEUVE, and A. G. MICHEL. J. Med. Chem. **29**, 1658 (1986).
12. E. J. GABE, F. L. LEE, and Y. LE PAGE. The NRCVAX crystal structure system, in crystallographic computing 3: data collection, structure determination, proteins, and databases. Clarendon Press, Oxford. 1985. pp. 167–174.

Can. J. Chem. Downloaded from www.nrcresearchpress.com by 196.1.178.254 on 09/07/12
For personal use only.

Arylation of cyclic ethers by gaseous phenylium ions. Formation and behavior of phenoxenium ions in the gas phase

SIMONETTA FORNARINI[1]

Dipartimento di Studi di Chimica e Tecnologia delle Sostanze Biologicamente Attive, Università di Roma "La Sapienza", 00185 Roma, Italy

AND

MAURIZIO SPERANZA

Dipartimento di Agrobiologia ed Agrochimica, Università della Tuscia, 01100 Viterbo, Italy

Received March 28, 1988

SIMONETTA FORNARINI and MAURIZIO SPERANZA. Can. J. Chem. **66**, 2506 (1988).

Free, unsolvated phenylium ions formed by the spontaneous decay of 1,4-ditritiobenzene have been allowed to react with gaseous cyclic ethers (oxirane, propene oxide, and oxetane) and acetaldehyde in the pressure range 30–250 Torr and in the presence of a thermal radical scavenger (O_2, 4 Torr). The effects of a gaseous base (NMe_3, 20 Torr) and of an energy moderator (He, 630–720 Torr) were also investigated. Phenylium ion confirms its considerable site selectivity, demonstrated by the distinct preference for the *n*-type center of the substrate, although appreciable insertion into the carbocyclic structure of propene oxide and oxetane is observed as well. The stability features of the ionic intermediates from addition of phenylium ion to selected substrates have been evaluated as well as their fragmentation and isomerization mechanisms. The behavior of gaseous phenylium ion toward cyclic ethers, in particular its ability to formally abstract an oxygen atom from the ether to give the phenoxenium ion, a reaction first observed in the present study, is discussed and compared with previous mechanistic investigations carried out in the gas phase and in solution.

SIMONETTA FORNARINI et MAURIZIO SPERANZA. Can. J. Chem. **66**, 2506 (1988).

Opérant à des pressions allant de 30 à 250 Torr et en présence d'un piège à radicaux thermiques (O_2, 4 Torr), on a laissé réagir les ions phényliums libres et non-solvatés qui se forment par la décomposition spontanée du ditritio-1,4 benzène avec des éthers cycliques à l'état gazeux (oxiranne, oxyde de propène et oxétanne) ainsi qu'avec de l'acétaldéhyde. On a aussi évalué les effets de la présence d'une base gazeuse (NMe_3, 20 Torr) ainsi que d'un modérateur d'énergie (He, 630–720 Torr). L'ion phénylium confirme sa haute sélectivité qui est démontrée par sa préférence marquée pour le centre de type *n* du substrat même si on observe aussi une quantité appréciable d'insertion dans la structure carbocyclique de l'oxyde de propène et de l'oxétanne. On a évalué les caractéristiques de stabilité ainsi que les mécanismes de fragmentation et d'isomérisation des intermédiaires ioniques obtenus par l'addition de l'ion phénylium sur des substrats choisis. On discute du comportement de l'ion phénylium gazeux vis-à-vis des éthers cycliques, en particulier de sa facilité d'arracher formellement un atome d'oxygène de l'éther pour donner l'ion phénoxénium, une réaction qui a été observée pour la première fois dans cette étude; on compare ce comportement avec celui observé dans des études mécanistiques rapportées antérieurement et effectuées soit en phase gazeuse soit en solution.

[Traduit par la revue]

Can. J. Chem. Downloaded from www.nrcresearchpress.com by 196.1.178.254 on 09/07/12
For personal use only.

Introduction

Unsaturated carbenium ions are reactive intermediates in which the electron-deficient carbon is an integral part of a π-unsaturation. In the singlet configuration, the formally positive carbon atom has a nominally vacant orbital, which is orthogonal to a strongly polarized π system (1). As a consequence, the positive carbon center tends to acquire the character of a substituted singlet carbene (2), thus conferring on the unsaturated species a marked tendency for insertion into σ-bonds and π-bonds and addition to *n*-type electrons (3).

Experimental confirmation of this ability is provided by the pronounced reactivity of gaseous vinyl and aryl cations toward essentially all kinds of organic substrates. Of special interest is the mode of insertion of these ions into π- and σ-bonds of hydrocarbons (4), which is thought to proceed via two distinct consecutive steps (2). The first step is the electrophilic insertion of the vacant orbital of the ion into the hydrocarbon bond to yield a two-electron three-center bond. The second step is the nucleophilic coupling of the antibonding orbital of the hydrocarbon with the π system of the unsaturated ion to form a second σ-bond (2). This mode of attack accounts for the formation of indane from gas-phase insertion of singlet phenylium ion **1** into the C—C bonds of cyclopropane via the spiro

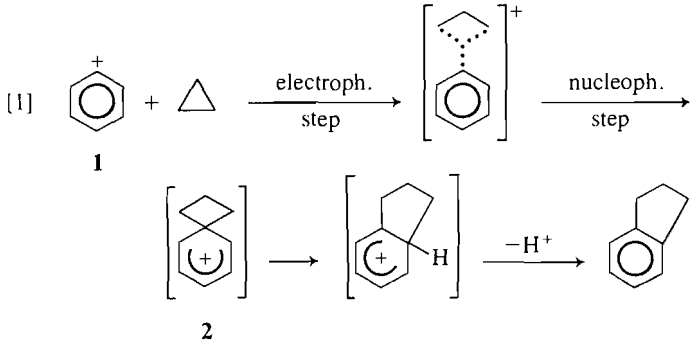

intermediate **2**, reaction [1] (5). In the same way, isomeric dihydronaphthalenes are produced in fair yields from gas-phase addition of **1** to the terminal carbons of 1,3-butadiene (6).

Simple addition to the *n*-type center is observed in the attack of **1** on molecules such as alkyl halides, alcohols, and ethers to yield the corresponding onium intermediates (7). In all circumstances an internal nucleophilic step, such as the one shown in reaction [1] involving alkyl group migration from the heteroatom to the π system of the onium intermediates, is hardly observed. Rather, the onium ions undergo unimolecular fragmentation with loss of an alkene in competition with a bimolecular displacement by an external nucleophile, whose

[1]Author to whom correspondence may be addressed.

Printed in Canada / Imprimé au Canada

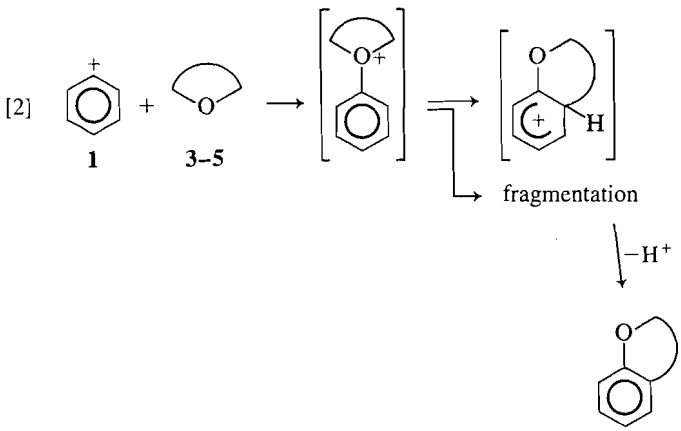

relative extent depends primarily upon the experimental conditions adopted (7).

To ascertain whether this is a general behavior of *n*-type molecules toward **1** or whether other mechanisms, similar to the one shown in reaction [1], are operative, the investigation is now extended to strained cyclic ethers, such as oxirane **3**, propene oxide **4**, and oxetane **5**. In this way, while we broaden our knowledge of the site selectivity of **1** in the gas phase, we expect to gain information about the relative stability of the oxonium intermediates from the gas-phase O-phenylation of **3–5** as well as on their propensity to relieve the strain energy via O-to-ring alkyl group migration, reaction [2]. The different strain energy and structural features of the selected cyclic ethers **3–5** might be expected to lead to remarkable differences in both extent and mechanism of fragmentation of the corresponding phenylated oxonium intermediates, and to influence the possibility of intramolecular isomerization to a ring alkylated structure.

Experimental

Materials

1,4-Ditritiobenzene, used as a precursor of the tritiated phenylium ion **1**, was synthesized and purified as previously described (8). He, NMe_3, and O_2 were obtained from Matheson Gas Products, Inc.; their stated purity exceeded 99.9 mol%.

Aldrich Chemical Co. and Fluka AG provided all the products used as glc standards or as components in the gas-phase experiments. Other aromatic compounds, not available commercially, such as α- and β-methyldihydrobenzofuran (9), phenyl vinyl ether (10), and all isomeric phenyl propenyl ethers (10, 11) were prepared according to established synthetic procedures. 2-Methylbenzodioxane was prepared by the reaction of *o*-dihydroxybenzene with 1,2-dibromopropane in aqueous KOH. The identity of the synthesized products was checked by conventional ir and nmr spectroscopy.

Decay experiments

The decay samples were prepared by introducing sealed glass capillaries containing ca. 1 mCi of tritiated benzene (specific activity: 80 mCi $mmol^{-1}$) into 300-mL Pyrex ampoules. The ampoules were connected to a vacuum line and thoroughly degassed. The organic substrate was then introduced, together with minor amounts (ca. 4 Torr; 1 Torr = 133.3 Pa) of oxygen, which was used as a scavenger of the radical species that could be formed by the passage of the energetic β-particle from the nuclear decay of tritiated benzene through the gaseous mixture. In some cases, either He (630–720 Torr) or NMe_3 (20 Torr) was added to the mixture. The ampoules were finally sealed and the capillary tube containing benzene broken with a glass hammer.

The decay mixtures were stored for about a year in the dark, at room temperature. The vessels were then opened under airtight conditions and their content analyzed by radio glc, using a C. Erba Fractovap 4200 gas chromatograph equipped with a high-sensitivity hot-wire detector (HWD), coupled in series with a Berthold proportional counter tube, kept at 180°C. The identity of the tritiated products was established by coincidence of the radiochemical peaks with the HWD signals from authentic reference compounds on both the following columns: (*i*) 2 m 5% SP 1200/5% Bentone-34 on 80–100 mesh Supelcoport, operated at 120°C; (*ii*) 5 m 15% 550 Silicone Oil on 60–80 mesh Chromosorb W-AW, operated at 130°C.

Over 40 reference compounds were tested, including those described in the previous section, arenes (e.g., styrene), aldehydes (e.g., phenylacetaldehyde), ketones (e.g., ethylphenylketone), cyclic (e.g., phenyloxirane) and acyclic ethers (e.g., cinnamyl methyl ether), alcohols (e.g., cinnamyl alcohol), phenols (e.g., *o*-allyl phenol), esters (e.g., phenyl acetate), and a variety of benzocyclic compounds (e.g., 1,3-dihydroisobenzofuran, 3,4-dihydro-1*H*-2-benzopyran, 3,4-dihydro-2*H*-1-benzopyran).

As the tritium-labelled products are formed in extremely small amounts (picogram level), their routine analysis can be performed only by radioanalytical methods. In some cases a further check on the identity of a product was sought by a derivatization procedure. An inactive carrier corresponding to the product of interest was added to the mixture of the decay experiment. A chemical reaction was then carried out (typically an electrophilic substitution on our aromatic compounds) and it was carefully noted whether the derived product possessed the expected fraction of radioactivity from its precursor.

Fourier-transform mass spectrometric (FT–MS) experiments

Phenylium-ion attack on oxirane and acetaldehyde was investigated by the FT–MS technique. All the mass spectrometric experiments were performed on a Nicolet FT–MS 1000 ICR spectrometer equipped with a 2.54-cm cubic trapping cell situated between the poles of a superconducting magnet operated at 2.0 T.

Sample pressures (uncorrected) were measured with a Granville–Phillips 280 Bayard–Alpert ion gauge. The FT–MS resolution was typically 1000 fwhh (full width half height) at mass 100. Inlet system and trapping cell were kept at room temperature. Ions were trapped in the cell by a differential trapping voltage of about 1.0 V. Typical operating conditions were as follows: nominal electron beam energy, 20 eV; electron beam pulse, 3 ms; emission current, 400 nA; total pressure, 10^{-7}–10^{-6} Torr. The reaction sequences involved attack of either phenylium ions (from EI (electron impact) on chlorobenzene) or phenoxenium ions (from EI on nitrobenzene) on the selected substrates and were investigated by multiple resonance experiments on the appropriate ionic species with variable reaction times up to 200 ms.

Results

Tables 1–3 show the relative and absolute yields of tritiated products recovered from the gas-phase attack of the 1,4-ditritiobenzene decay ions on oxirane, propene oxide, and oxetane, respectively. To extend the investigation of structural factors on the tritiated product distribution, decay runs were also carried out using an isomer of oxirane, namely acetaldehyde **6**, whose results are reported in Table 4. In all systems, reaction conditions were chosen to span a factor of over 7 in the substrate partial pressure (30–250 Torr). In some cases, He gas (630–720 Torr) was used as moderator of the energetic species. A powerful base, such as NMe_3 (20 Torr) was also introduced in the decay experiments carried out at the highest partial pressure of the substrate.

At variance with the results of related decay experiments carried out using alkyl halides, alcohols, and acyclic ethers (7), analysis of Tables 1–4 reveals comparatively limited absolute yields of tritiated products from the decay runs, never exceeding 30%. Radio glc analysis showed that low-boiling fragmentation products account for only a small fraction of the missing activity (<2%). We therefore proceeded in the quantitative measurement of the total activity of the crude reaction mixture as well as of the inner surface of the reaction vessel by liquid scintillation

Can. J. Chem. Downloaded from www.nrcresearchpress.com by 196.1.178.254 on 09/07/12
For personal use only.

TABLE 1. Tritiated product distribution from gas-phase attack of phenylium ions on oxirane

System composition (Torr)[a]			Relative yields of products (%)[b]					
	He	NMe_3					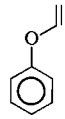	Total absolute yields (%)[c]
30	—	—	21	2	61	15	n.d.[d]	21
30	720	—	28	2	35	36	n.d.	22
220	—	—	37	n.d.	33	30	n.d.	19
220	—	20	15	4	3	n.d.	78	12

[a]All gaseous systems contain O_2 (4 Torr) and tritiated benzene (ca. 1 mCi).
[b]Expressed as a percentage of the total activity of the recovered aromatic products; uncertainty level of data, ca. 10%.
[c]Expressed as the percent ratio of the total activity of the end aromatic products to the activity originally contained in the nuclear-decay formed T-phenylium ion reactant.
[d]Below detection limit: ca. 1%.

TABLE 2. Tritiated product distribution from gas-phase attack of phenylium ions on propene oxide

System composition (Torr)[a]			Relative yields of products (%)[b]								
	He	NMe_3	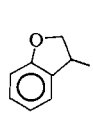	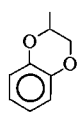	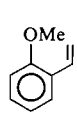	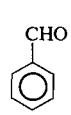	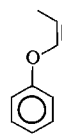	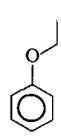	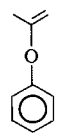	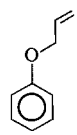	Total absolute yields (%)[c]
30	—	—	29	26	6	15	6	9	n.d.[d]	9	14
30	650	—	26	26	6	18	n.d.	12	n.d.	12	12
250	—	—	21	22	13	17	2	12	2	11	13
250	—	20	6	n.d.	n.d.	n.d.	34	22	10	n.d.	18

[a]See footnote *a*, Table 1.
[b]See footnote *b*, Table 1. In the runs with NMe_3, ca. 28% relative yields of unknown radioactive aromatic products are formed as well.
[c]See footnote *c*, Table 1.
[d]See footnote *d*, Table 1.

TABLE 3. Tritiated product distribution from gas-phase attack of phenylium ions on oxetane

System composition (Torr)[a]			Relative yields of products (%)[b]						
	He	NMe_3	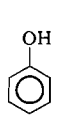	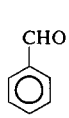	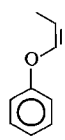	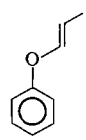	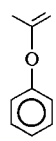	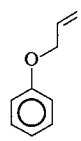	Total absolute yields (%)[c]
30	—		67	12	7	n.d.[d]	15	n.d.	11
30	640	—	50	15	14	9	7	3	16
250	—	—	81	6	6	6	n.d.	n.d.	15
250	—	20	30	n.d.	30	24	11	4	17

[a]See footnote *a*, Table 1.
[b]See footnote *b*, Table 1. In the runs with He and with NMe_3, low amounts (1–2%, relative yields) of unknown radioactive aromatic products are formed as well.
[c]See footnote *c*, Table 1.
[d]See footnote *d*, Table 1.

Can. J. Chem. Downloaded from www.nrcresearchpress.com by 196.1.178.254 on 09/07/12
For personal use only.

TABLE 4. Tritiated product distribution from gas-phase attack of phenylium ions on acetaldehyde

System composition (Torr)[a]			Relative yields of products (%)[b]		
			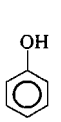	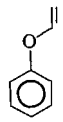	
CH_3CHO	He	NMe_3			Total absolute yields (%)[c]
30	—	—	100	n.d.[d]	20
30	630	—	100	n.d.	14
250	—	—	100	n.d.	27
250	—	20	39	61	23

[a]See footnote *a*, Table 1.
[b]See footnote *b*, Table 1.
[c]See footnote *c*, Table 1.
[d]See footnote *d*, Table 1.

counting. We observed that it largely exceeds the combined activity of the individual products identified by radio glc, thus indicating that most of the missing activity resides in high-boiling labeled products, i.e., polymers.

In conclusion, the activity balance is mostly accounted for by polymerization products, accompanied by minor yields of fragmentation products and monotritiated benzene, whose activity cannot be discriminated from that contained in the undecayed 1,4-ditritiobenzene, arising from possible hydride-ion transfer from **3**–**6** to phenylium ion **1**. The identity of a few radioactive products is left undefined, since it could not be safely assessed by comparison with authentic standard compounds. However, according to their retention volumes on the selected glc columns, these unknown products are most likely aromatic oligomers of the substrate and (or) their unimolecular fragmentation derivatives.

Analysis of Tables 1–4 reveals the formation of five different families of aromatic products from all decay experiments, namely benzofuran derivatives, benzodioxane derivatives, phenol, benzaldehyde, and acyclic alkenyl phenyl ethers. Their occurrence and relative yields depend on many factors, including the nature of the substrate, the presence of the base NMe_3, and the total pressure of the system. Thus, while benzofuran and benzodioxane derivatives are major products from the oxirane and propene oxide decay runs carried out in the absence of base, they are absent among the products from the oxetane and acetaldehyde decay experiments. Here, phenol is the predominant product at any system pressure in the absence of NMe_3. In the presence of base, the relative yields of the acyclic alkenyl phenyl ethers are increased significantly (by a factor greater than 2). This effect is consistent with the role of inhibitor of a cationic polymerization sequence.

In the oxirane set of experiments (Table 1), the increase of the ether pressure leads to an increase of the relative yield of dihydrobenzofuran (from 21 to 37%) and to a decrease of the relative yield of benzodioxane (from 61 to 33%). Formation of phenol is favored as well (from 15 to 30%). In contrast, phenol is absent from the products recovered in the propene oxide runs (Table 2). Here, the relative yields of 3-methyldihydrobenzofuran (21–28%) and 2-methylbenzodioxane (22–26%) are rather unaffected by large variations of the partial pressure of the ether.

In the absence of NMe_3, formation of cyclic and acyclic ethers in the propene oxide and oxetane decay experiments is accompanied by variable amounts of benzaldehyde, i.e., a tritiated product apparently derived from formal insertion of phenylium ion into the C—H and (or) C—C bonds of the ethers (Tables 2 and 3). Formation of benzaldehyde appears prevented in the phenylium-ion attack on oxirane and acetaldehyde (Tables 1 and 4). Finally, it should be pointed out that the same set of acyclic alkenyl phenyl ethers is generated from the decay experiments with isomeric substrates. Thus, while oxirane and acetaldehyde give rise only to phenyl vinyl ether, propene oxide and oxetane yield isomeric phenylpropenyl ethers and allyl phenyl ether, in proportions that are very similar in the presence of NMe_3 and significantly different in the absence of base.

To obtain independent information on the mechanism of formation of the decay products, phenylium ion was produced by 20-eV electron impact on chlorobenzene, and its reaction pattern towards oxirane and acetaldehyde was examined by Fourier-transform mass spectrometry (FT–MS). The adduct between phenylium ion and the substrate was not observed under the mass spectrometric conditions (source pressure: 10^{-7}–10^{-6} Torr), nor was it expected, but significant abundances of ionic species at masses 43, 91, and 93 (3:3:1) were produced from phenylium ion. These ions seem to be rather stable intermediates under FT–MS conditions since their relative abundances do not change much by increasing their residence time in the FT–MS cell up to 200 ms. The ionic fragment at $m/z = 43$ is presumably acetyl cation or some isomeric species arising from formal hydride-ion transfer from the substrate to phenylium ion.

The peak at $m/z = 91$ is probably the benzyl cation or some other isomeric species, whose formation indicates the possibility of formal attack of phenylium ion on the σ-bonds of the substrate. Unexpectedly, minor amounts of a fragment with $m/z = 93$ invariably accompany the above-mentioned species. This ionic intermediate does not display any Bronsted-acid properties toward the substrate, thus excluding its possible identification as protonated toluene.[2]

As a consequence, we are inclined to attribute to the $m/z = 93$ fragment the structure of the phenoxenium ion PhO^+, arising from attack of phenylium ion on the *n*-type center of the substrate and subsequent fragmentation of the ensuing excited phenyloxonium intermediate with loss of a C_2H_4 moiety.

To increase our knowledge of the reactivity properties of a gaseous phenoxenium ion, the known procedure (12) for preparing it in high yields by electron impact on nitrobenzene was exploited in our FT–MS cell, and its reactivity toward oxirane and acetaldehyde was examined by multiple resonance experiments. Phenoxenium ions from 20-eV electron bombard-

[2]In spite of the slightly higher proton affinity of toluene (P.A. = 189.9 kcal mol^{-1}) with respect to that of oxirane (P.A. = 187.9 kcal mol^{-1}) and acetaldehyde (P.A. = 186.6 kcal mol^{-1}), the enormous excess of neutral substrate vs. neutral toluene in the FT–MS cell would lead to the slow disappearance of a conceivable protonated toluene peak ($m/z = 93$) and increase of the $m/z = 45$ ion abundance at long reaction times, i.e., under conditions approaching thermodynamic equilibrium. The essential unreactivity of the $m/z = 93$ toward oxirane and acetaldehyde observed even at rather long reaction times (200 ms) excluded any significant contribution of the protonated toluene structure to the $m/z = 93$ peak. Consistent with these conclusions is the absence of any labelled toluene in all decay experiments involving the same substrates.

Can. J. Chem. Downloaded from www.nrcresearchpress.com by 196.1.178.254 on 09/07/12
For personal use only.

Can. J. Chem. Downloaded from www.nrcresearchpress.com by 196.1.178.254 on 09/07/12
For personal use only.

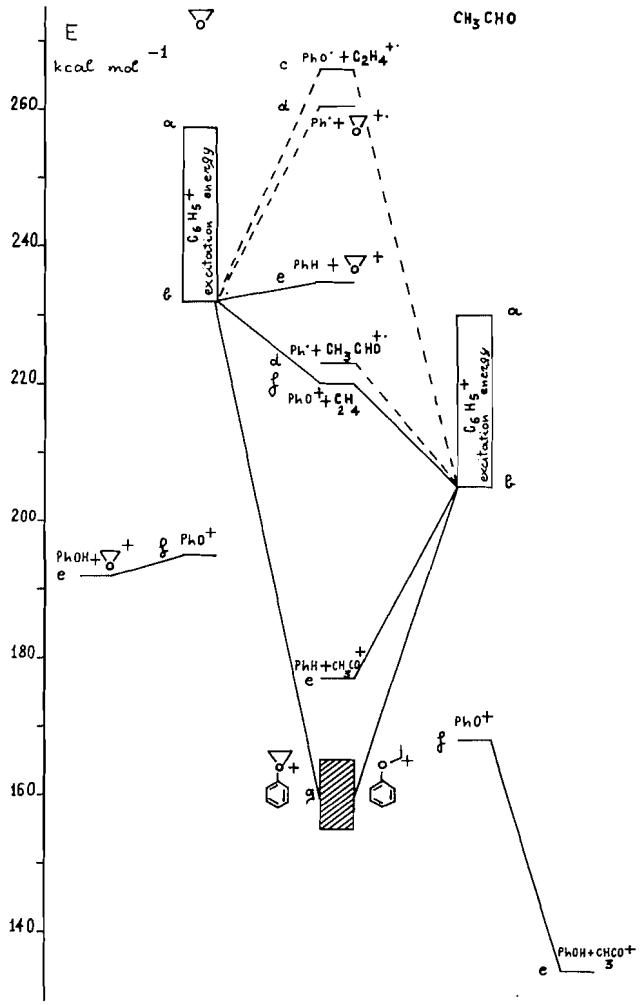

FIG. 1. Energetics of several relevant ion–molecule reactions involved in the gas-phase attack of phenylium ion on oxirane and acetaldehyde. (a) According to *ab initio* calculations (21), the ΔH_f^0 of a phenylium ion with the geometry of benzene is ca. 32 kcal mol^{-1} higher than that of a phenylium ion in a vibrational ground-state. Thus, the maximum formation enthalpy available to a phenylium ion formed by nuclear decay **1** is computed to be ca. 277 kcal mol^{-1}, which is in satisfactory agreement with the experimental value (ΔH_f^0 = 266–270 kcal mol^{-1}; ref. 22) derived from the ionization potential of the phenyl radical. (b) The ΔH_f^0 of a phenylium ion in a vibrational ground state has been calculated to be 244.8 kcal mol^{-1} (13). (c)–(f) Formation enthalpy data taken from ref. 14; (d) Ionization potential data taken from ref. 15; (e) Formation enthalpy data taken from refs. 14*b* and 16; (g) the ΔH_f^0's of **7** and **13** were estimated as several kilocalories per mol higher than that of dimethylphenyloxonium ion, ref. 7*d*.

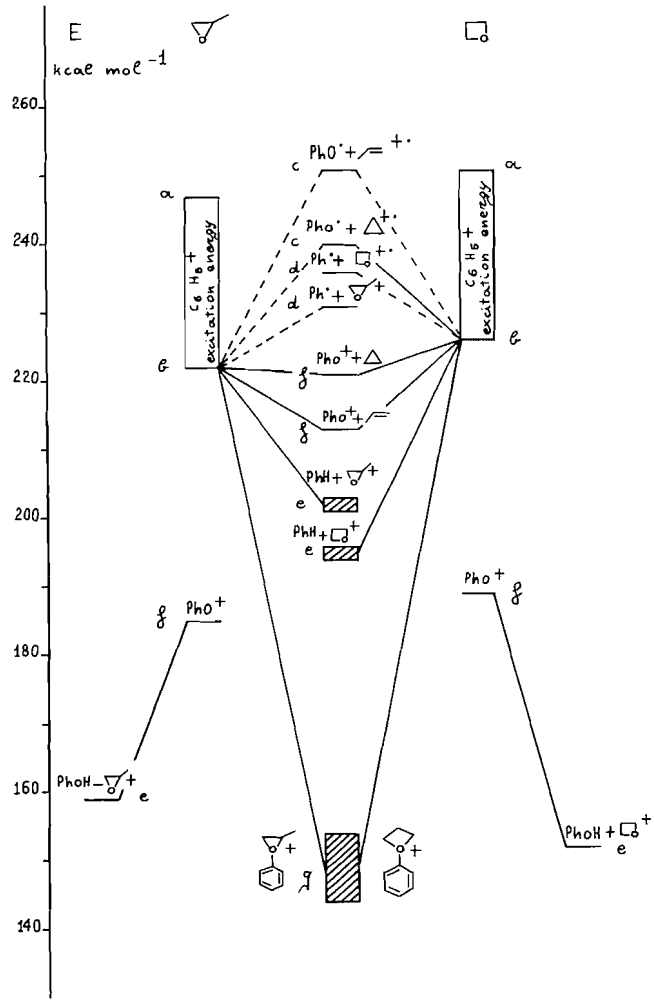

FIG. 2. Energetics of several relevant ion–molecule reactions involved in the gas-phase attack of phenylium ion on propene oxide and oxetane. (a)–(f) See (a)–(f) of Fig. 1; (g) The ΔH_f^0's of **14** and of the O-phenyloxetanium intermediate were estimated as several kilocalories per mol lower than that of dimethylphenyloxonium ion, ref. 7*d*.

ment on nitrobenzene display essentially the nature of a hydride-ion acceptor from acetaldehyde yielding efficiently the acetyl cation m/z = 43. The same reaction does not occur appreciably when oxirane is used as the neutral substrate.

Discussion

The attack of the phenylium ion

The nature and the properties of free phenylium ion **1** produced by nuclear decay in tritiated benzene and used in the present study as the electrophilic reactant have been previously described in detail (7).

Several reaction channels are open to phenylium ion **1** formed by nuclear decay, in its attack on the selected substrates, as illustrated in Figs. 1 and 2. The figures give approximate reaction enthalpies for the relevant gas-phase processes. For the sake of clarity, other plausible reaction pathways are not reported in the figures, either because they are highly endothermic or because they are not observed under FT–MS and nuclear-decay conditions. For instance, charge exchange (paths (d) of Figs. 1, 2) as well as O^- transfer between **1** and the substrate (paths (c) of Figs. 1, 2) to yield the molecular ion of the substrate or a $C_2H_4^+/C_3H_6^+$ fragment, respectively, are rather endothermic processes and, therefore, very inefficient reactions, as confirmed by the absence of m/z = 44 and m/z = 28 peaks among the daughter species of phenylium ion in the FT–MS runs with oxirane and acetaldehyde.

A significant exothermicity characterizes all the remaining processes of Figs. 1 and 2, namely (*i*) the addition of **1** to the *n*-type center of the substrate to yield the corresponding primary phenyloxonium intermediates (paths (g)); (*ii*) the subsequent fragmentation of these intermediates to give a phenoxenium ion and a neutral alkene moiety (paths (f)), allowed by the substantial excess energy of the phenyloxonium precursors from the preceding highly exothermic process; (*iii*) the hydride-ion transfer from the substrate to **1** to yield benzene and the

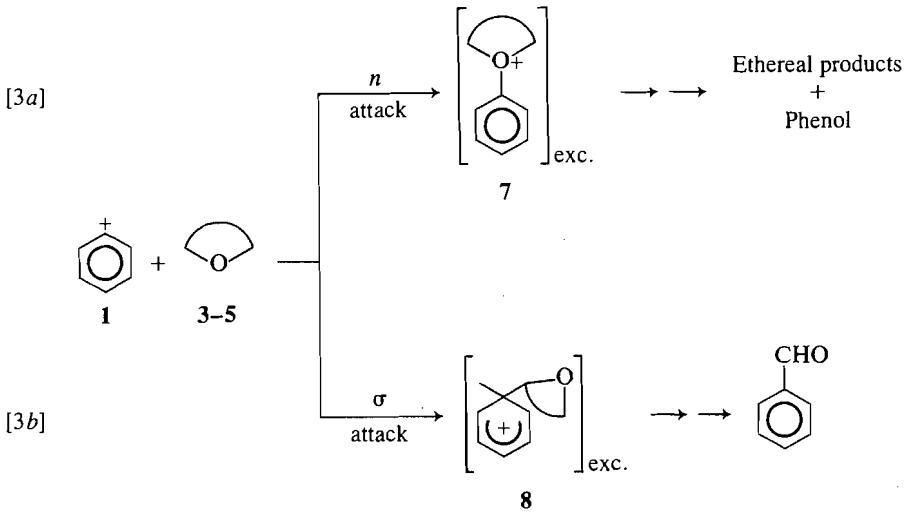

[substrate-H]$^+$ fragment (paths (e)). The latter two paths have been directly observed by FT–MS experiments. All the above exothermic processes, therefore, may be considered as potential ionic sources of radioactive products in the decay experiments, although the hydride-ion transfers (e) are "blind" (i.e., not leading to identifiable labeled products, other than the tritiated benzene precursor) reaction channels, which could partly account for the activity loss (over 70%) observed in all decay systems.

The results reported in Tables 1–4 confirm the remarkable affinity of **1** toward the *n*-center of the substrate, as inferred from the relatively high yields of cyclic and acyclic phenyl ethers and phenol (overall relative yield, 82–100%).

It is therefore suggested, in analogy with the conclusion reached in previous studies (7), that the phenylation process occurring in the decay systems involves competitive attack of **1** on the *n*- and σ-type centers of the substrate, to give the corresponding onium intermediate **7** in predominant yields, reaction [3], and minor, if any, amounts of arenium ions (e.g., **8** in reaction [3*b*]), respectively, with the latter responsible for the formation of benzaldehyde. It should be noted, in this connection, that measurable amounts of benzaldehyde are observed only among the labeled products from propene oxide and oxetane, namely from those isomeric cyclic ethers with the highest ratio of σ- vs. *n*-type centers.

In addition, the distinct site selectivity of **1** is extended to the different σ-bonds of propene oxide and oxetane as well. In fact, no measurable amounts of 1,3-dihydroisobenzofuran, 1,3-dihydro-1-methylisobenzofuran, and 3,4-dihydro-1*H*-2-benzopyran were recovered among the labeled decay products from these systems, thus confirming previous experimental evidence pointing to **1** as attacking exclusively the σ_{C-H} bonds of a saturated hydrocarbon chain, while ignoring the σ_{C-C} bonds (4*e*).

Isomerization and fragmentation of phenyloxonium intermediates 7

The fate of the phenyloxonium intermediates **7**, excited by the exothermicity of their formation processes [3*a*], appears to be highly sensitive to the nature of the parent oxygenated substrate and of the reaction environment. In the oxirane systems without added NMe_3 (Table 1), predominant formation of benzodioxane, dihydrobenzofuran, and phenol is observed, whose relative yields are dependent upon the total pressure of the system. Thus, while the relative yield of benzodioxane increases at low pressure (30 Torr), formation of both dihydrobenzofuran and phenol appears more favored at high ether pressure (220 Torr). Taking into account the FT–MS results for the same system, recovery of benzodioxane in significant yields, increasing at low pressure, i.e., under conditions favoring high-energy fragmentation processes, is attributed to the formation of a phenoxenium intermediate **9** from unimolecular fragmentation of the corresponding excited *O*-phenyloxiranium intermediate **7**, reaction [4*a*].

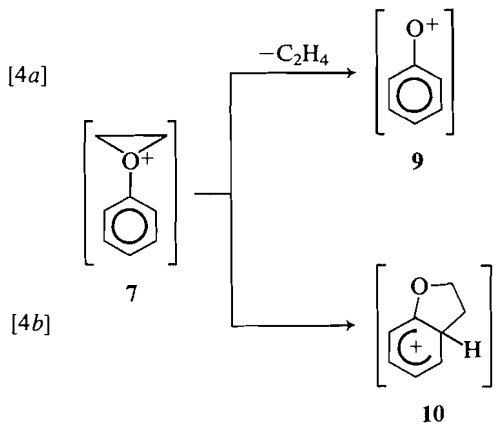

As for the isoelectronic phenylcarbenes and nitrenes, free phenoxenium ion **9** may exist in the singlet (**9s**) or a triplet (**9t**) state, but neither experimental nor theoretical data are available to date with regard to their relative stability and interconversion rate.

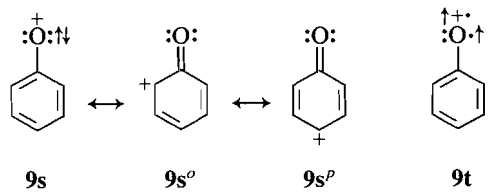

In the singlet state configuration, phenoxenium **9** can be represented by resonance structures, with the oxocyclohexadienylium canonical structures **9s**^{o} and **9s**^{p} reasonably contributing more than the **9s** one. As a consequence, singlet phenoxenium ion should act as a typical carbocationic electrophile adding to the high-electron density center of a nucleophilic substrate, with formation of *ortho* and *para* substituted phenols. On the contrary, triplet phenoxenium ion **9t** should formally

Can. J. Chem. Downloaded from www.nrcresearchpress.com by 196.1.178.254 on 09/07/12
For personal use only.

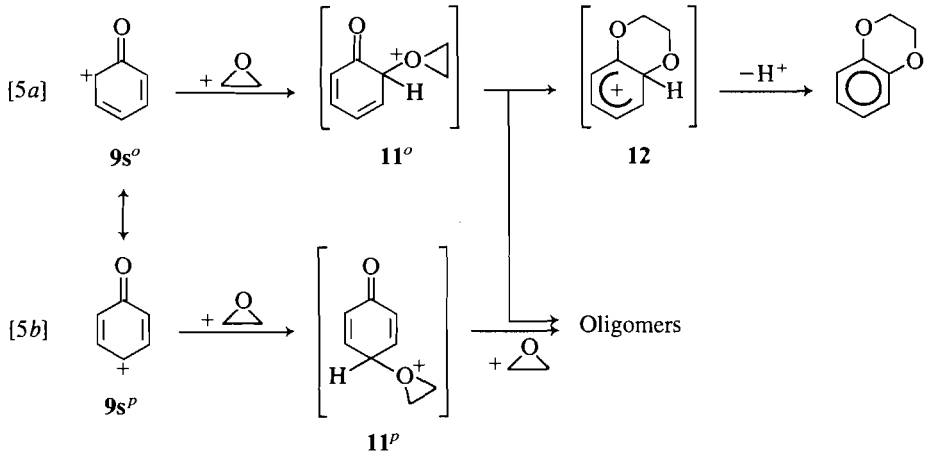

maintain most of the positive charge at the O center. Therefore it is expected that **9t** would attack predominantly the C and H centers of a substrate, yielding essentially phenyl ethers and phenol, respectively, as neutral end products.

On these grounds, formation of benzodioxane in the oxirane decay systems is attributed to the addition of a singlet phenoxenium intermediate to the *n*-type center of a second oxirane molecule to yield the oxocyclohexadienyl oxonium intermediates $\mathbf{11}^o$ and $\mathbf{11}^p$ (or their hydroxyphenyl oxonium tautomers), reactions [5*a*,*b*]. The subsequent fate of these intermediate species depends essentially on their structure. Thus, while both isomers $\mathbf{11}^o$ and $\mathbf{11}^p$ (or their tautomers) would proceed in undergoing further nucleophilic addition of oxirane at the side-chain carbon centers to give oligomeric structures, a competitive isomerization pathway [5*a*] is opened exclusively to the *ortho* isomer $\mathbf{11}^o$ (or its tautomer), involving internal nucleophilic attack of the ketonic (or phenolic) oxygen on one of the side-chain carbons and yielding directly a protonated benzodioxane structure, e.g., **12**.[3] In this perspective, sequence [4*a*] → [5*a*] in the oxirane decay systems is favored at the lowest ether partial pressure (30 Torr), because collisional quenching of excited **7**, competing with the fragmentation step [4*a*], is minimized, and because the extent of the secondary oligomerization process [5*b*] is proportionally reduced in favor of the parallel isomerization channel [5*a*].

A lower-energy process, competing with the high-energy fragmentation path [4*a*], is the isomerization of excited **7** to a protonated dihydrobenzofuran structure **10**, reaction [4*b*]. Intermediacy of open-chain transients in reaction [4*b*] appears unlikely on the following grounds. Extensive collisional activation analysis excludes that open-chain isomers of **7** may undergo significant cyclization even at relatively long ion lifetimes (17). This conclusion agrees with the absence of detectable yields of benzocyclic products from the acetaldehyde decay systems (Table 4), wherein only the open-chain 1-phenoxyethyl cations **13** are generated by attack of **1** on the O of the substrate. Hence, it is concluded, in analogy with the two-step mechanism of insertion of unsaturated carbenium ions into σ- and π-bonds (2), that the isomerization step [4*b*] is promoted by the intramolecular nucleophilic interaction of the π system of the phenyl group with the electrophilic C—O Walsh orbitals of the oxirane moiety

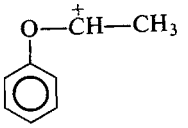

13

A reaction network similar to [4] → [5] appears operative in the propene oxide decay systems as well (Table 2). In fact, both 2-methylbenzodioxane and 3-methyldihydrobenzofuran represent the most abundant labeled products, in the absence of added NMe_3, whose yields slightly increase by lowering the ether partial pressure from 250 to 30 Torr. This observation is only consistent with a comparable efficiency of the two competing processes analogous to [4*a*,*b*]. In these cases, in fact, an O-phenylated propene oxide intermediate (**14**) is involved, which isomerizes exclusively to the protonated 3-methyldihydrobenzofuran structure (**15**), reaction [6*a*], the alternative isomerization pathway leading to 2-methyldihydrobenzofuran being essentially prevented. Following the previous conclusion concerning isomerization of **7**, this observation is consistent with an isomerization transition state wherein a partial positive charge is developed at the side-chain carbon center before significant interaction with the phenyl ring π orbital is established. It follows that the presence of an electron-releasing methyl substituent at the carbon center renders its migrating rate substantially higher than that of an unsubstituted carbon center. Therefore, it can be expected that the isomerization pathway [6*a*], involving the O-phenylated propene oxide intermediate **14**, is inherently faster than that involving **7**, to the point of becoming comparable to the rate of the competing fragmentation channel, analogous to [4*a*].

No benzocyclic products are recovered from the oxetane decay systems (Table 3). Here, in the absence of NMe_3, most of the activity resides in the aromatic ring of phenol. No simple rationale for the formation of phenol is presently available.[4]

[3] In the absence of NMe_3, neutralization of protonated intermediates such as **12** may occur by several mechanisms, including proton transfer to the substrate itself, to the walls of the reaction vessel, or to traces of nucleophiles invariably present or radiolytically formed in the gaseous decay system.

[4] A possible explanation of these results involves actual formation of O-phenylated oxetane, excited enough to dissociate to phenoxenium and a C_3H_6 moiety, much like the analogous intermediates **7** and **14**, reaction [4*a*]. Here, however, a phenoxenium ion **9t** with the triplet configuration would be preferentially formed, which reacts by hydride-ion abstraction from oxetane yielding preferentially phenol. However, the results obtained in the oxirane systems (Tables 1 and 2) indicate a distinct increase in the formation of products from phenoxenium intermediates with decreasing pressure. This behavior is not paralleled

Can. J. Chem. Downloaded from www.nrcresearchpress.com by 196.1.178.254 on 09/07/12
For personal use only.

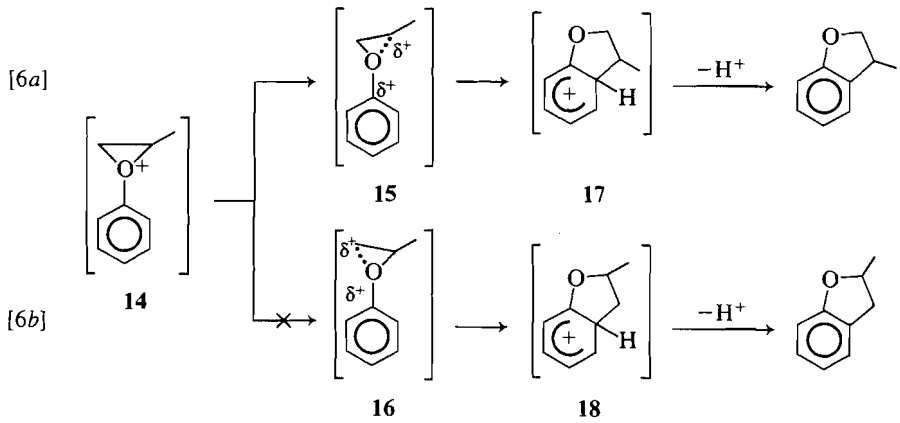

The peculiar behavior of oxetane with respect to the oxiranes **3** and **4** following attack of **1** is further shown by the absence of formation of any benzocyclic products. In fact, no observable amounts of 3,4-dihydro-2*H*-1-benzopyran or isomeric methyldihydrobenzofurans were recovered among the tritiated products from oxetane, in spite of specific search (Table 3). It is therefore concluded that O-phenylated oxetane, at variance with the more strained **7** and **14** analogues, has no tendency to fragment to **9** or to isomerize to protonated benzocyclic structures, but it is sufficiently long lived to undergo nucleophilic attack by an external oxetane molecule at a side-chain carbon center, initiating an oligomerization process.

The effect of the NMe_3 base

Addition of 8–9 mol% of a powerful base, such as NMe_3 (P.A. = 225.1 kcal mol^{-1}) (14*b*), to the gaseous mixtures leads to a pronounced increase of the absolute yield of alkenylphenyl ethers (over 3 times) and a profound modification of their isomeric composition (Tables 1–4). In fact, comparative analysis of Tables 2 and 3 reveals a substantially different distribution of alkenylphenyl ethers from propene oxide and oxetane in the absence of NMe_3, whereas, in the presence of base, a similar composition is observed, i.e., *cis*-propenylphenyl ether (43–51%) > *trans*-propenylphenyl ether (33–35%) > isopropenylphenyl ether (15–16%) > allylphenyl ether (0–6%). A rationalization of these results can be attempted by starting from the observation that addition of NMe_3 causes a 3-fold increase of the absolute yield of alkenylphenyl ethers from propene oxide, which is counterbalanced by a greater than 5-fold decrease of the overall yield of benzocyclic products (Table 2). In the oxetane systems, instead, the pronounced 6-fold increase of the absolute yield of alkenylphenyl ethers is accompanied by only a halving of the absolute yield of phenol. It follows that the main path responsible for the formation of alkenylphenyl ethers in the propene oxide/NMe_3 systems involves an NMe_3-induced β-elimination in the phenyloxonium intermediate **14**, although a contribution from deprotonation of its open-chain isomers cannot be excluded.[5] An analogous process is responsible for the formation of phenylvinyl ether in the oxirane/NMe_3 and acetaldehyde/NMe_3 systems (Tables 1, 4).

In the oxetane/NMe_3 systems, on the other hand, a number of ionic species may be involved in the base-induced formation of isomeric alkenylphenyl ethers, including the long-lived O-phenylated oxetane and its open-chain isomers, as well as the progeny of their oligomerization intermediates. Hence, it is suggested that the similar distribution of alkenylphenyl ether observed in the propene oxide/NMe_3 and oxetane/NMe_3 systems does not arise from the interaction of the base with a common intermediate or family of intermediates, but rather can be regarded as an accidental coincidence.

However, restricting the analysis to the relative yields of alkenylphenyl ether from the propene oxide/NMe_3 systems (Table 2), a hint into the regioselectivity of NMe_3 toward the phenyloxonium intermediate **14** can be obtained from the olefin distribution. The observed trend suggests that interaction of the base occurs preferentially with the most acidic hydrogens. In fact the positively charged oxirane ring hydrogens are highly favored over the methyl ones. Among the ring hydrogens the interaction of NMe_3 is mostly directed to the methylene hydrogens rather than to the methine one, due to the presence of the electron-releasing methyl group.

Conclusions

The present investigation confirms the view that the phenylium ion **1** may act essentially as a Lewis acid attacking both σ- and *n*-type bonds. As expected, it displays a large preference for the *n*-type centers as compared to the σ-type ones, as demonstrated by the product distribution of Tables 1–4. In the meantime, the reaction pattern following the attack of **1** at the *n*-center of the selected strained cyclic ethers is significantly different and appears to be related to the stability of the ensuing phenyloxonium intermediates. Thus, while the primary intermediate from O-phenylation of oxetane appears so stable as to undergo further oligomerization processes, intermediates **7** and **14** from O-phenylation of oxirane and propene oxide are rather unstable and readily isomerize to the corresponding benzocyclic isomers **10** and **17**, respectively.

Intramolecular nucleophilic interaction of the π-phenyl orbitals with the electrophilic C—O Walsh orbitals of the oxirane moiety promotes an isomerization process that is analogous to the nucleophilic step involved in the insertion of unsaturated carbenium ions into σ- and π-bonds of hydrocarbons. A high-energy unimolecular fragmentation process, competing with the isomerization pathway, leads to the forma-

by the yield of phenol from oxetane, thus casting doubts on a common reaction pathway.

A unified view may be obtained if, at low ether pressure, **9t** has partly converted to the conceivably more stable singlet configuration (**9s**). In this case, however, benzocyclic products containing two oxygen atoms are expected to be formed, contrary to experimental data.

[5]Deprotonation of open-chain isomers of **14** is probably the predominant source of alkenylphenyl ethers in the absence of added NMe_3.

Can. J. Chem. Downloaded from www.nrcresearchpress.com by 196.1.178.254 on 09/07/12
For personal use only.

tion of singlet phenoxenium ion from both **7** and **14** excited intermediates, both under FT–MS and nuclear decay conditions.

By analogy with the results of related solvolytic studies (18), singlet phenoxenium ion is able to attack its parent ether with the formation of a C—O bond, as demonstrated by the recovery of benzodioxane derivatives among the labeled product from these systems.

Thus, the present results have not only extended our knowledge of the reactivity of phenylium ion **1** toward *n*-type organic molecules, but have also opened up a way to investigating the intimate nature and the kinetic behavior of phenoxenium ions in the dense gas state and to compare them with those observed in solution.

In view of the considerable interest in the chemistry of phenoxenium ions, particularly in connection with phenol oxidation in general (19) and biosynthetic-type oxidative coupling reactions in particular (20), development of alternative procedures to generate and investigate singlet and triplet phenoxenium ions, such as those reported in the present study, deserves further attention.

Acknowledgements

The authors express their gratitude to Dr. Roberto Gabrielli of the FT–MS Service of the Area della Ricerca C.N.R. di Roma for his generous help in carrying out the FT–MS experiments.

The financial support of the Ministero della Pubblica Istruzione and Strategic Project "Molecular Dynamics and Catalysis" of the Consiglio Nazionale delle Ricerche is gratefully acknowledged.

1. P. J. Stang, Z. Rappoport, M. Hanack, and L. R. Subramanian. Vinyl cations. Academic Press, New York. 1979.
2. H. Kollmar and H. O. Smith. Angew. Chem. Int. Ed. Engl. **11**, 635 (1972).
3. (*a*) G. Modena and U. Tonellato. Adv. Phys. Org. Chem. **9**, 185 (1971); (*b*) A. E. Lodder, H. M. Buck, and L. J. Oosterhoff. Recl. Trav. Chim. Pays-Bas, **89**, 1229 (1970); (*c*) H. Hogeveen and C. F. Roobeek. Tetrahedron Lett. 3343 (1971); (*d*) H. U. Wagner and R. Gompper. Tetrahedron Lett. 4061 (1971); 4065 (1971).
4. (*a*) S. Fornarini, R. Gabrielli, and M. Speranza. Int. J. Mass Spectrom. Ion Proc. **72**, 137 (1986); (*b*) S. Fornarini and M. Speranza. J. Phys. Chem. **91**, 2154 (1987); (*c*) J. Am. Chem. Soc. **107**, 5358 (1985); (*d*) J. Chem. Soc. Chem. Commun. 1692 (1985); (*e*) G. Angelini, C. Sparapani, and M. Speranza. Tetrahedron, **40**, 4865 (1984).
5. M. Colosimo, M. Speranza, F. Cacace, and G. Ciranni. Tetrahedron, **40**, 4873 (1984).
6. S. Fornarini and M. Speranza. Gazz. Chim. Ital. **116**, 341 (1986).
7. (*a*) G. Angelini, S. Fornarini, and M. Speranza. J. Am. Chem. Soc. **104**, 4773 (1982); (*b*) M. Speranza, Y. Keheyan, and G. Angelini. J. Am. Chem. Soc. **105**, 6377 (1984); (*c*) Y. Keheyan and M. Speranza. Helv. Chim. Acta, **68**, 2381 (1985); (*d*) S. Fornarini and M. Speranza. J. Chem. Soc. Perkin Trans. 1, 171 (1984).
8. M. Speranza, F. Cacace, A. P. Wolf, and R. Erhenkaufer. J. Labelled Compd. Radiopharm. **19**, 905 (1982).
9. (*a*) B. J. Fairless, G. Ragsdale, and C. Kerby. J. Chem. Educ. **51**, 61 (1974); (*b*) W. D. Crow and H. McNab. Aust. J. Chem. **32**, 123 (1979).
10. V. L. Tweedie and B. G. Barron. J. Org. Chem. **25**, 20 (1960).
11. (*a*) C. C. Price and W. H. Snyder. J. Am. Chem. Soc. **83**, 1773 (1961); (*b*) E. Taskinen and P. Linkas. Acta Chem. Scand. Ser. B: **28**, 114 (1974); (*c*) P. Golborn and F. Scheinman. J. Chem. Soc. Perkin Trans. 1, 2870 (1973).
12. (*a*) M. Panczel and T. Baer. Int. J. Mass Spectrom. Ion Proc. **58**, 43 (1984); (*b*) M. Moini and J. R. Eyler. Int. J. Mass Spectrom. Ion Proc. **76**, 47 (1987); (*c*) C. J. Porter, J. H. Beynon, and T. Ast. Org. Mass Spectrom. **16**, 102 (1981); (*d*) J. H. Beynon, M. Bertrand, and R. G. Cooks. J. Am. Chem. Soc. **95**, 1739 (1973).
13. W. A. Castenmiller and H. M. Buck. Recl. Trav. Chim. Pays-Bas, **96**, 207 (1977); M. Tasaka, M. Ogata, and H. Ichikawa. J. Am. Chem. Soc. **103**, 1885 (1981).
14. (*a*) F. P. Lossing and J. L. Holmes. J. Am. Chem. Soc. **106**, 6917 (1984); (*b*) S. G. Lias, J. F. Liebman, and R. D. Levin. J. Phys. Chem. Ref. Data, **13**, 695 (1984).
15. V. I. Vedeneyev, L. V. Gurvich, V. N. Kondrat'yev, V. A. Medvedev, and Ye. L. Frankevich. *In* Bond energies, ionization potentials and electron affinities. E. Arnold Publ., London. 1966.
16. (*a*) R. H. Nobes, W. J. Bouma, and L. Radom. J. Am. Chem. Soc. **105**, 309 (1983); (*b*) R. D. Bach and J. M. Domagala. Tetrahedron Lett. **45**, 4025 (1976); (*c*) G. Bouchoux *et al.* Nouv. J. Chim. **9**, 453 (1985).
17. K. Levsen, H. Heimbach, C. C. Van de Sande, and J. Monstrey. Tetrahedron, **33**, 1785 (1977).
18. (*a*) R. A. Abramovich, G. Alvernhe, R. Bartnik, N. L. Dassanayake, M. N. Inbasekaran, and S. Kato. J. Am. Chem. Soc. **103**, 4558 (1981); (*b*) Y. Endo, K. Shudo, and T. Okamoto. J. Am. Chem. Soc. **104**, 6393 (1982); (*c*) H. Iijima, Y. Endo, K. Shudo, and T. Okamoto. Tetrahedron, **40**, 4981 (1984).
19. (*a*) P. D. McDonald and G. A. Hamilton. *In* Oxidation in organic chemistry, Part B. *Edited by* W. S. Trahanovsky. Academic Press, New York. 1973; (*b*) M. L. J. Mihailovic and Z. Cekovic. *In* The chemistry of the hydroxyl group, Part I. *Edited by* S. Patai. Wiley–Interscience, New York. 1971.
20. (*a*) D. H. R. Barton. Chem. Ber. **3**, 330 (1967); (*b*) W. I. Taylor and A. R. Battersby. *In* Oxidative coupling of phenols. M. Dekker, New York. 1967.
21. P. v. R. Schleyer, A. J. Kos, and K. Raghavachari. J. Chem. Soc. Chem. Commun. 1296 (1983).
22. H. M. Rosenstock, J. T. Larkins, and J. A. Walker. Int. J. Mass Spectrom. Ion Phys. **11**, 309 (1973).

Can. J. Chem. Downloaded from www.nrcresearchpress.com by 196.1.178.254 on 09/07/12
For personal use only.

Complexes of 15-crown-5 and cyclohexano-15-crown-5 with lithium, sodium, and potassium phenoxide having macrocycle:salt ratios of 1:1 and 1:2. The crystal structures of two polymorphs of 15-crown-5·2LiOPh

MICHAEL P. MURCHIE, JOHN W. BOVENKAMP,[1] AND ANDRÉ RODRIGUE
Defence Research Establishment Ottawa, Ottawa, Ont., Canada K1A 0Z4

AND

KIMBERLEY A. WATSON AND SUZANNE FORTIER[1]
Department of Chemistry, Queen's University, Kingston, Ont., Canada K7L 3N6

Received January 25, 1988

MICHAEL P. MURCHIE, JOHN W. BOVENKAMP, ANDRÉ RODRIGUE, KIMBERLEY A. WATSON, and SUZANNE FORTIER. Can. J. Chem. **66**, 2515 (1988).

The syntheses, in ethereal solvents, of the complexes of 15-crown-5 and cyclohexano-15-crown-5 with lithium, sodium, and potassium phenoxide are described. The two macrocycles form complexes with lithium and sodium phenoxide with host:guest ratios of 1:2. Potassium phenoxide, however, was complexed by the two macrocycles to give products with macrocycle:salt ratios of 1:1. Crystals of 15-crown-5·2LiOPh were obtained for X-ray diffraction structure determinations. In fact, the crystal structures of two co-crystallizing polymorphs of this complex (**1***a* and **1***b*) have been determined. Polymorph **1***a* crystallizes in space group $P\bar{1}$ with $a = 11.386(4)$, $b = 11.901(4)$, $c = 10.654(4)$ Å, $\alpha = 106.53(3)$, $\beta = 112.60(3)$, $\gamma = 106.52(3)°$, and $Z = 2$. Polymorph **1***b* crystallizes in space group $P2_1/n$ with $a = 15.355(4)$, $b = 11.642(2)$, $c = 13.595(6)$ Å, $\beta = 104.56(3)°$, and $Z = 4$. Both structures were solved by direct methods, and refined by full-matrix least-squares calculations to residuals, R, of 0.053 and 0.055 for polymorphs **1***a* and **1***b*, respectively. The structures of the two polymorphs differ only in the orientation of the phenoxides. The structures show a dimer, $(15\text{-crown-5}\cdot 2\text{LiOPh})_2$, which consists of an aggregate of four lithium phenoxide molecules complexed by two 15-crown-5 macrocycles. The two lithiums of each monomeric unit of this dimer have different crystallographic and chemical environments. One lithium is coordinated to all five oxygens of the macrocycle and to one of the phenoxide oxygens while the other lithium is coordinated to only one oxygen of the macrocycle and to three phenoxide oxygens.

MICHAEL P. MURCHIE, JOHN W. BOVENKAMP, ANDRÉ RODRIGUE, KIMBERLEY A. WATSON et SUZANNE FORTIER. Can. J. Chem. **66**, 2515 (1988).

On décrit les synthèses, dans des solvants éthérés, des complexes de la 15-couronne-5 et de la cyclohexano-15-couronne-5 avec les phénolates de lithium, de sodium et de potassium. Les deux macrocycles forment des complexes avec les phénolates de lithium et de sodium avec des rapports 1:2. Toutefois, le phénolate de potassium est complexé par les deux macrocycles et il donne des produits possédant des rapports de macrocycle à sel de 1:1. On a pu obtenir des cristaux du complexe 15-couronne-5·2LiOPh d'une qualité appropriée pour la diffraction des rayons-X. En fait, on a déterminé les structures cristallines de deux polymorphes de ce complexe (**1***a* et **1***b*) qui co-cristallisent. Le polymorphe **1***a* cristallise dans le groupe d'espace $P\bar{1}$, avec $a = 11{,}386(4)$, $b = 11{,}901(4)$ et $c = 10{,}654(4)$ Å, $\alpha = 106{,}53(3)$, $\beta = 112{,}60(3)$ et $\gamma = 106{,}52(3)°$ et $Z = 2$. Le polymorphe **1***b* cristallise dans le groupe d'espace $P2_1/n$, avec $a = 15{,}355(4)$, $b = 11{,}642(2)$ et $c = 13{,}595(6)$ Å, $\beta = 104{,}56(3)°$ et $Z = 4$. On a résolu les deux structures par des méthodes directes et on les a affinées par la méthode des moindres carrés (matrice entière) jusqu'à des valeurs résiduelles de R de 0,053 et de 0,055 respectivement pour les polymorphes **1***a* et **1***b*. Les structures des deux polymorphes ne diffèrent que par l'orientation des groupements phénolates. Les structures présentent un dimère, $(15\text{-couronne-5}\cdot 2\text{LiOPh})_2$, qui consiste en un agrégat de quatre molécules de phénolate de lithium qui sont complexées par deux macrocycles 15-couronne-5. Les deux lithiums de chacune des unités monomères de ce dimère possèdent des environnements cristallographique et chimique différents. Un des lithiums est coordonné à chacun des cinq oxygènes du macrocycle et à un oxygène de phénolate alors que l'autre lithium est coordonné à un seul oxygène du macrocycle et à trois oxygènes de phénolate.

[Traduit par la revue]

Introduction

In 1967, Pedersen (1) showed that crown ethers form stable complexes with alkali metal salts. Since then, crown ether complexes have been extensively studied. Several reviews (2–9) have been written on this topic. A large number of alkali metal salt complexes with 15-crown-5 (10–13), benzo-15-crown-5 (14–16), and cyclohexano-15-crown-5 (1) have been prepared and isolated in the solid state. The structures of several complexes of benzo-15-crown-5 and 15-crown-5 with alkali metal salts have been determined by X-ray crystallography; e.g. benzo-15-crown-5·X (X = Li(Pic)·$2H_2O$ (17), Na(Pic) (18), (1/2)(K(Pic)) (19), and Cs(Pic) (20); Pic = 2,4,6-trinitrophenolate) and 15-crown-5·Y (Y = NaSCN·(1/2)H_2O (10) and Na(ethylacetoacetate) (11)).

Complexes of 15-crown-5, benzo-15-crown-5, and cyclohexano-15-crown-5 with alkali metal salts have been shown to have macrocycle:salt stoichiometries of only 1:1 (for lithium and sodium salts) and 2:1 (for potassium salts); e.g. butylbenzo-15-crown-5·LiNCS (1), 15-crown-5·Na(ethylacetoacetate) (11) and $(\text{benzo-15-crown-5})_2\cdot$K(Pic) (19). The complexation of a cation by a macrocycle and the stoichiometry of the resulting macrocycle salt complex are dependent upon a number of factors; including (*i*) compatibility of cavity size and cation diameter, (*ii*) anion effects, and (*iii*) solvent effects (2–9). Recently, Rodrigue *et al.* (21) demonstrated the importance of solvent effects in the formation of 18-crown-6 macrocycle salt complexes. Using ethereal solvents such as 1,2-dimethoxyethane, tetrahydrofuran, and diethyl ether, complexes were isolated which exhibited novel macrocycle:salt ratios of 1:2 and 1:3; e.g. dicyclohexano-18-crown-6(isomer B)·2KOPh,

[1]Authors to whom correspondence may be addressed.

Can. J. Chem. Downloaded from www.nrcresearchpress.com by 196.1.178.254 on 09/07/12
For personal use only.

TABLE 1. The complexes, their host:guest ratios, the solvents used, and the yields obtained for the complexes

Complex number	Macrocycle[a] (mmol)	Salt[a] (mmol)	Macrocycle:salt[b] ratio	Solvent used[c] (mL)	% Yield of complex
1	15C5(5.43)	LiOPh(11.30)	1:2	Hexane(70) + Et_2O(90)	94
2	15C5(9.99)	NaOPh(20.83)	1:2	THF(50) + Et_2O(85)	70
3	15C5(10.19)	KOPh(10.18)	1:1	THF(50) + Et_2O(43)	80
4	C-15C5(2.10)	LiOPh(4.25)	1:2	Et_2O(30)	89
5	C-15C5(2.52)	NaOPh(5.11)	1:2	THF(2) + Et_2O(35)	78
6	C-15C5(5.50)	KOPh(2.73)	1:1	Et_2O(45)	57

[a]15C5 and C-15C5 represent 15-crown-5 and cyclohexano-15-crown-5, respectively.
[b]With the exception of **6**, the macrocycle:salt ratio remains unchanged when an excess or deficit of phenoxide salt is used (see Experimental).
[c]The solvent or solvent mixture in which the complex was formed. Et_2O and THF are used to designate diethyl ether and tetrahydrofuran. See Experimental for isolation and purification procedures.

Can. J. Chem. Downloaded from www.nrcresearchpress.com by 196.1.178.254 on 09/07/12
For personal use only.

dicyclohexano-18-crown-6(isomer A)·2NaOPh and 18-crown-6·3NaOPh. In each case, only 1:1 complexes would have been expected. X-ray crystal structures (22) have been obtained for dicyclohexano-18-crown-6(isomer B)·2KOPh and dicyclohexano-18-crown-6(isomer A)·2NaOPh.

The above results led to the present study in which the complexes of lithium, sodium, and potassium phenoxide with 15-crown-5 and cyclohexano-15-crown-5 have been isolated from the ethereal solvents tetrahydrofuran and diethyl ether. The preparation and characterization of six complexes that exhibit novel 1:2 (macrocycle:salt) ratios with lithium and sodium salts, and 1:1 ratios with potassium salts are described. These six complexes are as follows:

1 15-crown-5·2LiOPh

2 15-crown-5·2NaOPh

3 15-crown-5·KOPh

4 cyclohexano-15-crown-5·2LiOPh

5 cyclohexano-15-crown-5·2NaOPh

6 cyclohexano-15-crown-5·KOPh

The X-ray crystal structure of the complex formed between 15-crown-5 and lithium phenoxide (**1**) is reported and discussed.

Experimental

Anhydrous diethyl ether was dried over sodium wire. Hexane was dried over molecular sieves (Type 3A). Reagent grade tetrahydrofuran and 1,2-dimethoxyethane were distilled from lithium aluminum hydride and stored over molecular sieves. Lithium, sodium, and potassium phenoxides were prepared as described in refs. 21 and 23. Commercially obtained 15-crown-5 was stored over molecular sieves. Cyclohexano-15-crown-5 (*cis* isomer) was prepared and purified according to the procedure described in ref. 24.

Great care was taken throughout this work to protect the samples from atmospheric moisture. All complexation reactions, the preparation of samples for elemental analysis and the preparation of infrared, ultraviolet, and nmr spectroscopic samples were carried out in a Dri-Lab (Vacuum Atmospheres Corp.) under an argon atmosphere.

*Standard synthetic method used for complexes **1–5***

In this procedure, 1 equiv. of the macrocycle was added to a solution containing 2 equiv. of the salt in the cases of LiOPh and NaOPh, and 1 equiv. of the salt in the case of KOPh.

In a typical reaction, LiOPh (11.30 mmol) was dissolved in a mixture of diethyl ether (90 mL) and hexane (40 mL). The 15-crown-5 (5.43 mmol), dissolved in hexane (30 mL), was added to the LiOPh solution. A white precipitate was formed immediately upon addition of the 15-crown-5. The reaction mixture was stirred for 1.5 h at room temperature. The precipitate was isolated by suction filtration and then dried under high vacuum (<0.001 Torr) in a drying pistol at 56°C for 16 h. The white solid was identified by proton NMR spectroscopy and elemental analysis as 15-crown-5·2LiOPh, and the yield obtained was 5.12 mmol, which corresponds to a 94% yield based on 15-crown-5 (see Table 1).

In Table 1 are listed the amounts of reactants, the solvent (or solvent mixture) used and its volume, and the % yield for each of the complexes. Table 2 gives the melting point and elemental analysis obtained for each complex. The complexes were further characterized by ^1H nmr, infrared, and ultraviolet spectroscopy. Complex **1** was also characterized by single crystal X-ray diffraction techniques.

*Other methods used for complexes **1–5**. Reactions using an (a) excess or (b) deficit of phenoxide salt*

(a) Excess of phenoxide. A procedure similar to that described above was used (see below for details) except that 1 equiv. of the macrocycle was added to a solution containing at least 3 equiv. of the phenoxide salt in the cases of LiOPh and NaOPh, and 2 equiv. of the salt in the case of KOPh. In all cases, the macrocycle:salt ratios of the complexes formed were the same as those of the complexes formed by the standard method previously described and listed in Table 1.

In a typical reaction, LiOPh (3.98 mmol) was dissolved in a mixture of anhydrous solvents (diethyl ether (20 mL) and hexane (10 mL)). A solution of 15-crown-5 (1.00 mmol) dissolved in hexane (10 mL) was added to the LiOPh solution. A large quantity of white precipitate was formed immediately upon addition of the 15-crown-5. The reaction mixture was stirred for 2 h at room temperature. The white solid was isolated by suction filtration and then dried under vacuum (0.001 Torr) at 56°C for 16 h. The white solid was identified as 15-crown-5·2LiOPh, and the yield obtained was 0.98 mmol which corresponds to a 98% yield based on 15-crown-5.

(b) Deficit of phenoxide. Again, the procedure used was similar to that described for the standard synthetic method except that 1 equiv. of the macrocycle was added to a solution containing 1 equiv. of the salt in the cases of LiOPh and NaOPh, and half of an equivalent of the salt in the case of KOPh. The macrocycle:salt ratio of the complexes formed were the same as those of the complexes formed by the standard synthetic method, and listed in Table 1.

In a typical reaction, NaOPh (1.80 mmol) was dissolved in a mixture of tetrahydrofuran (1 mL) and diethyl ether (10 mL). A solution of cyclohexano-15-crown-5 (1.89 mmol) dissolved in diethyl ether (5 mL) was added to the NaOPh solution. After stirring at room temperature for 15 min, a white precipitate formed. The mixture was stirred at room temperature for a further 2 h. The solid was isolated by suction filtration and then dried under vacuum at 56°C for 17 h. The white solid was identified as cyclohexano-15-crown-5·2NaOPh, and the yield obtained was 0.74 mmol which corresponds to an 83% yield based on NaOPh.

*Synthesis of complex **6***

Diethyl ether (10 mL) was added to solid potassium phenoxide (2.73 mmol) forming a colorless solution over a white solid (potassium

TABLE 2. Melting points and elemental analyses of the complexes

Complex number	Melting point (°C)	Calculated					Found				
		C	H	Li	Na	K	C	H	Li	Na	K
1	196.0–197.0	62.84	7.19	3.30			63.02	7.26	3.58		
2	151.0–152.0	58.40	6.68		10.16		58.12	6.66		9.80	
3	169.0–170.5	54.52	7.15			11.09	54.30	7.36			11.30
4	185.0–185.6	65.81	7.65	2.92			66.10	7.90	2.95		
5	136.0–137.0	61.65	7.16		9.08		61.35	7.43		8.80	
6[a]	83–87	59.09	7.69			9.62	55.39	7.78			9.91

[a]A satisfactory elemental analysis could not be obtained for complex **6**. Several attempts were made but, although the integrated proton magnetic resonance spectra were in agreement with the 1:1 ratio shown in Table 1, the complex was too unstable to give either a sharp melting point or a satisfactory elemental analysis. The elemental analysis shown was the best result obtained.

TABLE 3. Crystal data[a]

Parameter	Crystal data	
	1*a*	**1***b*
Molecular formula	$Li_2O_7C_{22}H_{30}$	$Li_2O_7C_{22}H_{30}$
Molecular weight	420.36	420.36
Space group; Z	$P\bar{1}$:2	$P2_1/n$;4
a, Å	11.386(4)	15.355(4)
b, Å	11.901(4)	11.642(2)
c, Å	10.654(4)	13.595(6)
α, deg	106.53(3)	90
β, deg	112.60(3)	104.56(3)
γ, deg	106.52(3)	90
V, Å^3	1144.3	2352.1
Number of reflections used for the determination of unit cell parameters; 2θ range, deg	25; 16–27	25; 18–27
Density (calcd.), g cm^{-3}	1.220	1.187
Number of measured reflections	2129	2183
Number of observed reflections, $I \geq 3\sigma(I)$	1670	1179
2θ range scanned, deg	1–40	1–40
μ (MoKα), cm^{-1}	0.824	0.802
Crystal dimensions, mm	0.75 × 0.25 × 0.40	0.56 × 0.13 × 0.20
Isotropic secondary extinction correction, g	1.12×10^{-6}	1.22×10^{-7}
Final R; R_w	0.053; 0.083	0.055; 0.069
Largest shift/error in final least-squares cycle, Δ/σ	0.00	0.09
Maximum and minimum residual electron density in final difference Fourier map, e Å^{-3}	0.209; −0.271	0.191; −0.199
Standard deviation of an observation of unit weight	3.477	2.489

[a]Estimated standard deviations are shown in parentheses.

phenoxide is essentially insoluble in diethyl ether). Cyclohexano-15-crown-5 (5.50 mmol), dissolved in diethyl ether (35 mL), was added to the potassium phenoxide – diethyl ether mixture. After stirring for less than 5 min, a light brown – cloudy solution over a very small quantity of light-colored precipitate was observed. A powdery grey–brown precipitate at the bottom of a translucent yellow–brown solution was obtained after 24 h. The solution was concentrated to approximately 50% of its original volume, and the solid was isolated by suction filtration. The powder turned a purple colour while under vacuum (0.001 Torr) at 56°C for 20 h. The powder had the proton NMR spectrum expected for cyclohexano-15-crown-5·KOPh, and the yield obtained was 1.54 mmol which corresponds to a 57% yield based on KOPh. This compound is discussed further in the Results and discussion section.

X-ray crystal structures of polymorphs **1***a and* **1***b of 15-crown-5·2LiOPh*

Suitable crystals of 15-crown-5·2LiOPh were obtained from a solution of the complex (0.128 g) in a mixture of diethyl ether/dimethoxyethane (3 mL/5 mL). The solution was slowly evaporated to dryness in an argon atmosphere. Crystals of both polymorphs, **1***a* and **1***b*, were obtained from this sample. The discovery of the two polymorphs was by serendipity and was due to the fact that more than one crystal was selected for analysis. The proportion of the two polymorphs in the mixture is not known. The mixture of the crystalline polymorphs had a melting point of 196.5–197.0°C.

Pertinent data about the crystals used and the measurement of diffraction intensities are summarized in Table 3. The crystals used in the diffraction experiments were mounted inside glass capillaries in a moisture-free environment. The intensity data were collected on an Enraf-Nonius CAD-4 diffractometer using graphite monochromated MoKα (λ = 0.71073 Å) radiation. In each case, intensities were collected by the ω/2θ scanning procedure and three reflections were measured after every 7200 s of exposure time to check on the stability of the crystal. No evidence of crystal decay was detected in either case. The data were corrected for Lorentz and polarization effects; absorption corrections were not considered necessary. The structure of **1***b* was solved routinely by direct methods using the program

Can. J. Chem. Downloaded from www.nrcresearchpress.com by 196.1.178.254 on 09/07/12
For personal use only.

Can. J. Chem. Downloaded from www.nrcresearchpress.com by 196.1.178.254 on 09/07/12
For personal use only.

TABLE 4. Final fractional coordinates and equivalent isotropic temperature factors for **1***a* with estimated standard deviations in parentheses

Atom	*x*	*y*	*z*	B_{eq} (Å^2)[a]
O1	0.9636(3)	0.0269(3)	0.2168(3)	3.82
O4	0.7241(3)	−0.0178(3)	−0.0231(3)	4.13
O7	0.5537(3)	−0.2779(3)	−0.1925(3)	5.1
O10	0.6965(3)	−0.4033(3)	−0.0896(3)	5.2
O13	0.9528(3)	−0.1960(3)	0.0535(3)	4.40
O16	0.7157(3)	0.8430(3)	0.1920(3)	3.38
O23	1.0168(3)	−0.1132(3)	0.4657(3)	3.65
C2	0.9357(5)	0.1346(4)	0.2025(3)	4.1
C3	0.7786(5)	0.0881(4)	0.1185(5)	4.2
C5	0.5761(5)	−0.0647(5)	−0.1201(6)	5.2
C6	0.5245(5)	−0.1920(4)	−0.2574(5)	5.4
C8	0.5117(6)	−0.4033(5)	−0.3020(6)	6.1
C9	0.5559(6)	−0.4783(5)	−0.2136(6)	6.3
C11	0.7988(5)	−0.4143(5)	−0.1277(5)	5.4
C12	0.9426(5)	−0.3244(4)	0.0120(5)	5.1
C14	1.0863(4)	−0.0991(4)	0.1898(5)	3.9
C15	1.0889(4)	0.0303(5)	0.2156(5)	4.3
C17	0.6071(4)	0.8219(4)	0.2127(4)	3.0
C18	0.4675(4)	0.7409(4)	0.0943(4)	3.6
C19	0.3537(4)	0.7224(4)	0.1188(5)	4.6
C20	0.3741(4)	0.7807(4)	0.2637(5)	4.9
C21	0.5117(5)	0.8586(4)	0.3835(5)	4.6
C22	0.6257(4)	0.8792(5)	0.3576(5)	4.2
C24	1.0049(4)	−0.2317(4)	0.4246(4)	3.2
C25	1.1236(4)	−0.2571(4)	0.4582(5)	4.0
C26	1.1113(5)	−0.3835(5)	0.4081(6)	5.6
C27	0.9804(6)	−0.4909(5)	0.3281(6)	6.3
C28	0.8608(6)	−0.4664(5)	0.2968(6)	5.9
C29	0.8716(5)	−0.3419(5)	0.3424(5)	4.6
Li1	0.9055(7)	0.9591(7)	0.3610(7)	3.6
Li2	0.7485(8)	0.8080(8)	0.0288(8)	4.6

[a] $B_{eq} = (4/3)\Sigma_i\Sigma_j\beta_{ij}(\boldsymbol{a}_i.\boldsymbol{a}_j)$.

TABLE 5. Final fractional coordinates and equivalent isotropic temperature factors for **1***b* with estimated standard deviations in parentheses

Atom	*x*	*y*	*z*	B_{eq} (Å^2)[a]
O1	0.5419(3)	0.0605(5)	0.7188(4)	5.51
O4	0.4887(3)	−0.0788(5)	0.8525(4)	6.1
O7	0.3218(4)	−0.0198(6)	0.8684(4)	8.3
O10	0.2892(4)	0.1900(5)	0.7915(4)	8.1
O13	0.4559(3)	0.2400(5)	0.7787(4)	6.1
O16	1.0172(3)	−0.3866(4)	1.0263(3)	4.9
O23	0.8549(3)	−0.5155(5)	1.1259(3)	4.7
C2	0.6012(5)	−0.0293(7)	0.7688(6)	5.8
C3	0.5420(6)	−0.1256(7)	0.7907(6)	6.2
C5	0.4323(6)	−0.1619(8)	0.8801(7)	7.3
C6	0.3727(6)	−0.1032(9)	0.9353(7)	7.9
C8	0.2727(6)	0.065(1)	0.9149(6)	10.6
C9	0.2297(6)	0.139(1)	0.8408(7)	11.8
C11	0.3246(6)	0.3018(8)	0.8251(7)	8.1
C12	0.3917(6)	0.3287(7)	0.7669(7)	8.0
C14	0.5166(6)	0.2592(8)	0.7136(7)	7.4
C15	0.5825(5)	0.1721(8)	0.7336(7)	6.7
C17	1.0460(5)	−0.2834(6)	1.0548(5)	4.2
C18	0.9893(5)	−0.1950(7)	1.0703(6)	5.2
C19	1.0218(6)	−0.0863(7)	1.1014(6)	6.5
C20	1.1105(6)	−0.0620(8)	1.1186(6)	6.9
C21	1.1666(5)	−0.1453(8)	1.1013(6)	6.7
C22	1.1381(5)	−0.2565(7)	1.0707(6)	5.1
C24	0.7793(4)	−0.5020(6)	1.0569(5)	3.9
C25	0.7725(5)	−0.4282(7)	0.9730(5)	4.9
C26	0.6938(6)	−0.4138(7)	0.8987(7)	6.6
C27	0.6154(5)	−0.4692(8)	0.9062(7)	7.3
C28	0.6195(5)	−0.5425(7)	0.9866(6)	6.4
C29	0.6986(5)	−0.5614(7)	1.0599(5)	4.9
Li1	0.0388(8)	0.512(1)	0.9266(9)	4.9
Li2	0.3904(9)	0.068(1)	0.758(1)	5.4

[a] $B_{eq} = (4/3)\Sigma_i\Sigma_j\beta_{ij}(\boldsymbol{a}_i.\boldsymbol{a}_j)$.

MULTAN 80 (25). For **1***a*, a reasonable fragment could be found in the top MULTAN solution but it was not possible to extend it through standard Fourier techniques. As this suggested proper orientation but incorrect position of the fragment in the unit cell, the space group was relaxed to $P1$, and the partial structure was used for Karle recycling. After one cycle, all of the atoms were identified in the *E*-map and the correct position in $P\bar{1}$ was determined. The positions of all the hydrogen atoms for **1***a* were found in the difference Fourier map. For **1***b*, 28 of the total of 30 hydrogen atoms were located in the difference Fourier maps, the remaining two were calculated. The structures were refined by full-matrix least-squares using all reflections with $I \geq 3\sigma(I)$. Anisotropic temperature factors were used for the non-hydrogen atoms. The hydrogen atoms were assigned isotropic temperature factors equal in magnitude to the equivalent isotropic temperature factors of their parent atoms. They were included in the calculations but they were not refined. The function minimized was $\Sigma w||F_o| - |F_c||^2$, where $w = 1/\sigma^2(|F_o|)$. A correction for isotropic secondary extinction effect was included in each refinement. The scattering factors were taken from Cromer and Waber (26). The fractional coordinates and equivalent isotropic temperature factors of the non-hydrogen atoms are presented in Tables 4 and 5. All calculations were done on a PDP 11/23 computer using the Enraf-Nonius SDP program package (27).

Nuclear magnetic resonance spectra

Integrated proton magnetic resonance spectra of the complexes were obtained using a Varian XL-200 (at 200.058 MHz using a 5 mm computer switchable probe) spectrometer. Chemical shifts were referenced relative to internal TMS. Typically, 20–50 mg samples of the complexes were dissolved in CD_3OD (0.5 mL). The spectra were in agreement with the structure of the complexes shown in this paper.

Ultraviolet spectra of complexes 1–6 and the alkali metal phenoxides

The ultraviolet spectra were obtained using a Varian Cary 2300 spectrophotometer. The complexes and salts were dissolved in anhydrous 1,2-dimethoxyethane to concentrations of ca. 2×10^{-3} *M*. Samples of the resulting solutions were loaded into ultraviolet cells (0.1 cm). The reference cell contained anhydrous 1,2-dimethoxyethane.

Infrared spectra and elemental analyses of the complexes

Infrared spectra were obtained on a Perkin Elmer (model 283) infrared spectrophotometer using Nujol mulls of the complexes and ZnSe optically flat windows. The spectra obtained were in agreement with the structure of the complexes shown in this paper.

Elemental analyses for complexes **1–6** (see Table 2) were carried out by Guelph Chemical Laboratories Ltd., Guelph, Ontario.

Results and discussion[2]

Synthesis of complexes 1–6 and the novel macrocycle:salt ratios

Pure samples of complexes **1–5** were prepared in good yield by the addition of 15-crown-5 or cyclohexano-15-crown-5 to solutions of lithium, sodium, or potassium phenoxide in ethereal solvents. With the exception of complex **6**, the macrocycle:salt ratio in each complex was invariant regardless of the proportions of the reactants used in the synthesis.

[2]A complete set of supplementary material may be purchased from the Depository of Unpublished Data, CISTI, National Research Council of Canada, Ottawa, Ont., Canada K1A 0S2.

Can. J. Chem. Downloaded from www.nrcresearchpress.com by 196.1.178.254 on 09/07/12
For personal use only.

Complex **6** was isolated only from the reaction of cyclohexano-15-crown-5 and potassium phenoxide in a proportion of 2:1, respectively. Reactions of cyclohexano-15-crown-5 and potassium phenoxide at stoichiometries less than 2:1 led to tars. All attempts to isolate pure products from these tars were unsuccessful. Table 1 gives the amounts of reactants and solvents and the yields of the complexes obtained. Infrared spectra obtained on Nujol mulls of the complexes showed the absence of uncomplexed macrocycle and phenoxide. The macrocycle:salt ratios in complexes **1–6** were determined by dissolving the complexes in CD_3OD, obtaining the ^1H nmr spectra, and comparing the integrated areas of the aromatic protons with the 15-crown-5 resonances in the case of complexes **1–3**, and the aromatic protons with the macrocyclic ring and cyclohexano resonances in the case of complexes **4–6**. Complexes **1–5** gave good melting point ranges (Table 2). The macrocycle:salt ratios of complexes **1–5** were confirmed by elemental analysis (Table 2). Complex **6** could not be isolated in a pure state although several attempts were made. Integrated proton magnetic resonance spectra of **6** showed a 1:1 ratio, however, the complex was too unstable to give either a sharp melting point or a satisfactory elemental analysis. The elemental analysis result shown in Table 2 for **6** was the best result obtained.

Many alkali metal salts form aggregates in ethereal solvents such as tetrahydrofuran, diethyl ether, and dimethoxyethane. The degree of association of ion pairs is dependent on the solvent, and the size, charge density, and the hardness of both the cation and anion (28, 29). In Jackman and Lange's review (28), solvents are separated into four classes with respect to the occurrence of free ions, ion pairs, and aggregates of ion pairs. Weakly polar solvents like tetrahydrofuran and diethyl ether were termed class B solvents. In this class of solvents, lithium, sodium, and potassium phenoxide are expected to form hexamers, tetramers, and (or) dimers similar to those observed in the X-ray crystal structures of several alkali metal enolates; e.g. the hexameric species $[Li^+(pin^-)]_6$ and $[K^+(pin^-)\cdot THF]_6$ (30) (where pin^- = the enolate of pinacolone); the tetrameric species $[Na^+(pin^-)\cdot pinacolone]_4$ (30) and $[Li^+(methyl\text{-}3,3\text{-}dimethylbutanoate^-)\cdot THF]_4$ (31); and the dimeric species $[Li^+(tert\text{-}butylpropionate^-)\cdot TMEDA]_2$ and $[Li^+(tert\text{-}butyl\text{-}2\text{-}methylpropionate^-)\cdot TMEDA]_2$ (31) (where TMEDA = *N,N,N',N'*-tetramethylethylenediamine). In more polar solvents (class C and D) the phenoxide salts are expected to exist as more highly solvated monomers.

It has been shown that 15-crown-5, or its derivatives, generally react with alkali metal salts containing Li^+, Na^+, and K^+ to form complexes with macrocycle:salt ratios of 1:1 (Li^+ and Na^+) and 2:1 (K^+) (1, 6, 7, 9, 16). These ratios are often attributed to how well the cation fits into the cavity of the macrocycle. The cation diameters of Li^+ (1.52 Å) and Na^+ (2.04 Å) are compatible with the diameter of the 15-crown-5 cavity (1.72–1.84 Å) (9) and consequently, 1:1 complexes are formed; e.g. butylbenzo-15-crown-5·LiSCN (1) and 15-crown-5·NaSCN·(1/2)H_2O (10). On the other hand, the K^+ cation (diameter = 2.76 Å) (9) is too large to fit into the cavity of 15-crown-5, thus allowing 2:1 macrocycle:salt sandwich complexes to be formed; e.g. $(benzo\text{-}15\text{-}crown\text{-}5)_2\cdot KX$ (X = I^-, Pic, and Dnb·2HDnb; where Pic = picrate and Dnb = dinitrobenzoate) (16).

The present work clearly shows that, in weakly polar solvents, complexes of 15-crown-5 and cyclohexano-15-crown-5 with lithium and sodium phenoxide (i.e. complexes **1**, **2**, **4**, and **5**) are obtained with macrocycle:salt ratios of 1:2. The 1:2 ratio is attributed to the tendency of the alkali metal phenoxides to form aggregates in ethereal solutions. The complexing abilities of 15-crown-5 and cyclohexano-15-crown-5 are not sufficient to break up the alkali metal phenoxide aggregates into contact ion pairs.

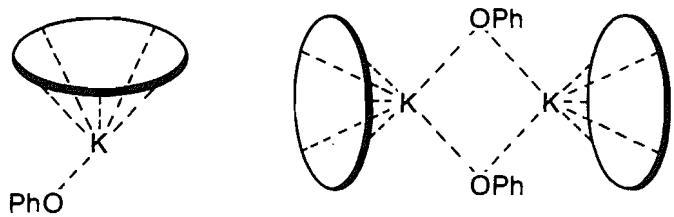

I II

FIG. 1. Possible orientations for the complexes with potassium phenoxide. The ovals represent the macrocycles.

The complexes with potassium phenoxide (i.e. **3** and **6**), which were expected to have the 2:1 macrocycle:salt ratio of a sandwich complex, had a 1:1 stoichiometry. Such a stoichiometry indicates that the structures of these complexes may consist of a contact ion pair complexed to the macrocycle (**I**) or a dimeric structure containing a potassium phenoxide aggregate (**II**) (see Fig. 1). We feel that the latter structure is the correct one and are attempting to prove this by obtaining suitable crystals of **3** for an X-ray diffraction structure determination (see section on ultraviolet spectra for further discussion).

*Crystal structures of 15-crown-5·2LiOPh (**1**a and **1**b)*

The 15-crown-5·2LiOPh complex crystallized to give two polymorphs (**1***a* and **1***b*). The ORTEP diagrams of **1***a* and **1***b* are shown in Figs. 2 and 3, respectively. Polymorphs **1***a* and **1***b* exhibit structures which differ only in the orientation of the phenoxides. The structures may simply be described as an aggregate of four lithium phenoxide units complexed by two crown ethers. Lithium–oxygen bond distances and angles appear in Table 6; average and range of bond distances and angles of the macrocycles and of the phenoxides are given in Table 7; and macrocyclic ring torsion angles are presented in Table 8.

The structures of **1***a* and **1***b* are very similar. The differences between them (Tables 6, 7, and 8) are very minor and therefore, discussion of the crystal structures will be limited to the former. In **1***a*, there is a center of a symmetry situated midway between O(16) and O(16′). There are two different chemical environments for the lithium atoms. Li(1) is coordinated to only one of the pentaether oxygens (i.e. O(1)) at a distance of 2.155(4) Å and to three phenoxide oxygens (i.e. O(16), O(16′), and O(23)) at an average distance of 1.90(3) Å. Figure 2 and the values in Table 6 indicate that the geometry around Li(1) is roughly tetrahedral. Li(2) lies 0.63(1) Å (0.65(1) Å in **1***b*) out of the mean plane defined by the five oxygens of the crown. It is coordinated to all five of the pentaether oxygens at distances ranging from 2.210(4)–2.531(5) Å with an average value of 2.3(1) Å. In addition, Li(2) is coordinated to one phenoxide oxygen, O(23), located at a distance of 1.866(4) Å. It is worth noting that the distance between the Li^+ ions and the phenoxide oxygens are all significantly shorter than those between the Li^+ ions and the crown oxygens. Thus, stronger interactions exist between the Li^+ cations and the phenoxide oxygens of the aggregate than the Li^+ ions and the crown oxygens.

The average lithium – pentaether oxygen distance for Li(2) in

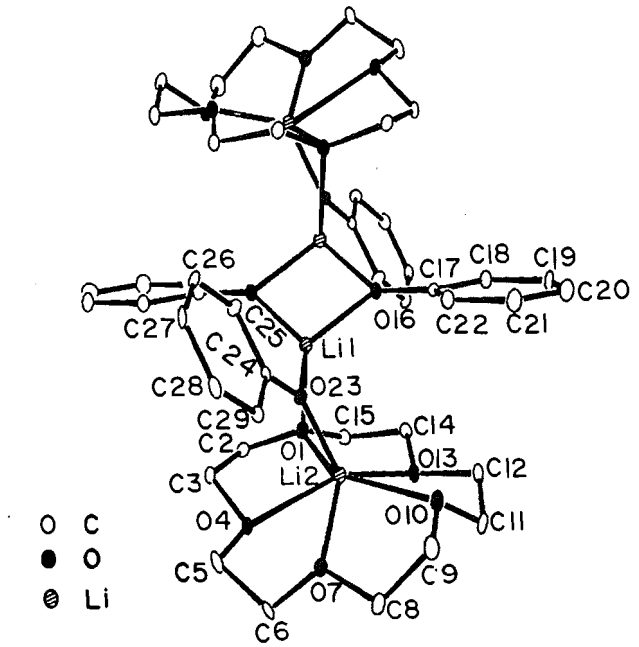

FIG. 2. ORTEP diagram and atom numbering scheme for 15-crown-5·2LiOPh (**1***a*).

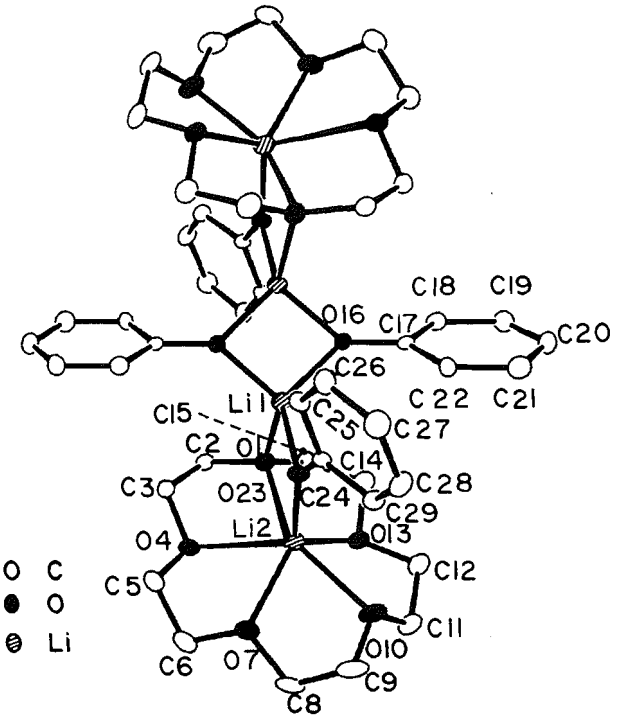

FIG. 3. ORTEP diagram and atom numbering scheme for 15-crown-5·2LiOPh (**1***b*).

15-crown-5·2LiOPh is longer than other lithium – crown ether oxygen distances found in the literature. For example, the average lithium – crown ether oxygen distance is 2.10 Å for 18,18′-spirobi-(19-crown-6)·2LiI·4H_2O (32), 2.10 Å for 18-crown-6·$LiClO_4$·2H_2O (33), 2.03 Å for 18-crown-6·2LiSCN·2H_2O (33), 2.07 Å for benzo-13-crown-4·LiNCS (34), and 2.04 Å for dibenzo-14-crown-4·LiNCS (35). This shows that for 15-crown-5·2LiOPh the $Li(2)^+$ – phenoxide oxygen interactions are stronger than the $Li(2)^+$ – pentaether oxygen interactions. This results in the $Li(2)^+$ ion being pulled out of the crown ether pocket with a subsequent lengthening of the Li(2) – pentaether oxygen distances. The lithium – phenoxide oxygen distances in 15-crown-5·2LiOPh are consistent with the lithium – enolate oxygen distances of 1.90–1.95 Å in lithium-*tert*-butylpropionate·TMEDA and lithium-*tert*-butyl-2-methylpropionate·TMEDA (31), and 1.849 Å in lithium-2,6-di-*tert*-butylphenoxide (36).

The 15-crown-5·2LiOPh dimer (Fig. 2) contains an Li_2O_2 four-membered ring comprised of Li(1), O(16), Li(1′), and O(16′). In this four-membered ring, the Li(1)—Li(1′) distance of 2.55(1) Å in **1***a* (2.58(1) Å in **1***b*) is shorter than the lithium–lithium bond distance of 2.67 Å in Li_2 (37, 38). Other complexes that exhibit short lithium–lithium distances are known. For example, lithium–lithium distances of 2.34 Å in [(*N*-(2-lithiocyclohexenyl)-*N*,*N*′,*N*′-trimethyl-1,3-propanediamine]$_2$ (39, 40), 2.37 Å in $(\eta^5\text{-}C_5H_4)_2Fe(N_3C_9H_{23})Li_2]_2$ (40, 41), 2.40 Å in cyclohexyl lithium (40, 42), and 2.57 Å in tetrameric methyllithium (40, 43) have been reported.

The structure of the phenoxide aggregate in the 15-crown-5·2LiOPh complex has many similarities to that described for dicyclohexano-18-crown-6(isomer A)·2NaOPh (22). In dicyclohexano-18-crown-6(isomer A)·2NaOPh, four sodium phenoxides form an aggregate, and the four sodium ions are complexed by two dicyclohexano-18-crown-6(isomer A) macrocycles. In addition, dicyclohexano-18-crown-6(isomer A)·2NaOPh contains two unique sodium ions, one of which is coordinated to one crown oxygen and three phenoxide oxygens; the other of which is coordinated to all six of the crown oxygens and only one phenoxide oxygen.

The bond lengths and angles of the 15-crown-5 ring (Table 7) are similar to those observed in other complexes such as 15-crown-5·NaSCN·(1/2)H_2O (10), 15-crown-5·$SnCl_4$·2H_2O (44), and 15-crown-5·$CuBr_2$·2H_2O (45). The C—C bond lengths in **1***a* show the characteristic shortening with an average value of 1.500(5) Å (1.46(3) Å in **1***b*). An unusually short carbon–carbon distance of 1.376(9) Å was observed for the C(8)—C(9) bond in **1***b*, however, the reason for such a short carbon–carbon bond distance is not apparent. The C—O bond lengths have an average value of 1.43(1) Å, and the O—C—C and C—O—C angles have averaged values of 108(1)° and 113(2)°, respectively. In undistorted cyclic polyethers the torsion angles about the C—C bonds are synclinal and those about C—O bonds are antiperiplanar. As can be seen from Table 8, these values are found in the present structures of **1***a* and **1***b* with the exception of the torsion angle around the C(9)—O(10) bond. This conformation of the 15-crown-5 ring is also present in the structures of 15-crown-5·Na(ethylacetoacetate) (11), 15-crown-5·NaSCN·(1/2)H_2O (10), and 15-crown-5·$SnCl_4$·2H_2O (44) (see Table 8).

Ultraviolet spectra of the complexes

The λ_{max} values from the ultraviolet spectra of the phenoxide anion in the complexes **1–6** and the alkali metal phenoxides in 1,2-dimethoxyethane are given in Table 9. The λ_{max} values for lithium, sodium, and potassium phenoxides themselves, which are expected to exist as dimers and (or) higher aggregates of ion pairs in this solvent, are similar to those reported previously by Zaugg and Schaeffer (46) and Rodrigue *et al.* (21). The λ_{max} values for the phenoxide in **1**, **2**, **4**, and **5**, all of which have 1:2 macrocycle:salt ratios, are essentially identical with those found for lithium and sodium phenoxide themselves. This indicates that the Li^+ and Na^+ ions are not being complexed strongly and

Can. J. Chem. Downloaded from www.nrcresearchpress.com by 196.1.178.254 on 09/07/12
For personal use only.

TABLE 6. Oxygen – alkali metal bond lengths and angles for **1***a* and **1***b* with estimated standard deviations in parentheses[a]

	Length (Å)			Angle (deg)	
Bond	**1***a*	**1***b*	Bonds	**1***a*	**1***b*
Li(1)—O(1)	2.155(4)	2.133(9)	O(1)—Li(1)—O(16)	117.2(2)	109.2(4)
Li(1)—O(16)	1.906(4)	1.890(8)	O(1)—Li(1)—O(16′)	103.0(2)	108.3(4)
Li(1)—O(16′)	1.855(4)	1.886(8)	O(1)—Li(1)—O(23)	90.1(2)	90.1(3)
Li(1)—O(23)	1.936(4)	1.939(8)	O(16)—Li(1)—O(16′)	94.5(2)	93.7(4)
Li(2)—O(1)	2.531(5)	2.512(9)	O(16)—Li(1)—O(23)	119.0(2)	124.4(4)
Li(2)—O(4)	2.353(5)	2.426(9)	O(16′)—Li(1)—O(23)	133.4(2)	129.7(5)
Li(2)—O(7)	2.210(4)	2.293(9)	O(1)—Li(2)—O(4)	67.1(1)	66.7(3)
Li(2)—O(10)	2.255(5)	2.237(9)	O(1)—Li(2)—O(7)	138.8(2)	134.5(4)
Li(2)—O(13)	2.257(5)	2.226(9)	O(1)—Li(2)—O(10)	139.4(2)	142.5(4)
Li(2)—O(23)	1.866(4)	1.836(9)	O(1)—Li(2)—O(13)	67.2(1)	69.4(3)
			O(1)—Li(2)—O(23)	81.0(2)	81.5(3)
			O(4)—Li(2)—O(7)	72.6(1)	69.9(3)
			O(4)—Li(2)—O(10)	140.6(2)	134.9(4)
			O(4)—Li(2)—O(13)	110.9(2)	111.5(4)
			O(4)—Li(2)—O(23)	98.0(2)	106.3(4)
			O(7)—Li(2)—O(10)	72.9(2)	71.8(3)
			O(7)—Li(2)—O(13)	122.7(2)	125.6(4)
			O(7)—Li(2)—O(23)	113.2(2)	114.9(4)
			O(10)—Li(2)—O(13)	73.7(2)	73.5(3)
			O(10)—Li(2)—O(23)	112.6(2)	111.0(4)
			O(13)—Li(2)—O(23)	122.2(2)	116.1(4)

[a]The primed atoms are related to the unprimed atoms by the following symmetry operation: $-x$, $-y$, $-z$.

TABLE 7. Average and range in the bond lengths (Å) and angles (deg) for the macrocyclic rings and phenoxides of **1***a* and **1***b* with estimated standard deviations in parentheses

	Value			Value	
Parameter	**1***a*	**1***b*	Parameter	**1***a*	**1***b*
Macrocyclic ring					
Average C—C	1.500	1.457	Average C—O	1.422	1.430
Range of C—C	1.485–1.515(4)	1.376–1.518(8)	Range of C—O	1.403–1.443(3)	1.408–1.457(6)
Average C—O—C	113.5	113.0	Average C—C—O	107.6	108.5
Range of C—O—C	112.3–114.5(2)	110.0–115.9(5)	Range of C—C—O	105.4–111.0(2)	106.7–113.2(5)
Phenoxides					
O(16)—C(17)	1.305(3)	1.311(5)	O(23)—C(24)	1.312(3)	1.307(5)
O(16)—C(17)—C(18)	122.0(2)	122.7(5)	O(23)—C(24)—C(25)	122.2(2)	121.6(4)
O(16)—C(17)—C(22)	121.6(2)	120.1(5)	O(23)—C(24)—C(29)	121.2(2)	122.9(4)
Average C—C	1.389	1.388	Average C—C—C	120.0	120.0
Range of C—C	1.365–1.405(4)	1.356–1.428(7)	Range of C—C—C	116.4–122.5(2)	115.5–123.1(5)

that the LiOPh and NaOPh salt molecules are associated more strongly with each other than with the macrocycles. In the case of 15-crown-5·2LiOPh, the X-ray crystal structure shows that the LiOPh molecules are associated more strongly with each other than with the macrocycles (*vide supra*). As found for 15-crown-5·2LiOPh (**1**), the ultraviolet data suggest that the 15-crown-5 macrocycles in **2**, **4**, and **5** form complexes with aggregates of lithium and sodium phenoxide. Therefore complexes **2**, **4**, and **5** may have structures similar to that of **1**. Work is underway to obtain crystal structures of these complexes.

A similar situation was observed for the 1:2 and 1:3 host:guest complexes of sodium and potassium phenoxide with 18-crown-6 and its derivatives (21). The λ_{max} value of dicyclohexano-18-crown-6(isomer A)·2NaOPh in dimethoxyethane was identical to the value obtained for NaOPh itself (21), indicating that the macrocycle very likely was complexed to an aggregate of NaOPh. The crystal structure of dicyclohexano-18-crown-6(isomer A)·2NaOPh (22) confirmed this and showed two macrocycles complexed to an aggregate of four NaOPh molecules.

The λ_{max} values for the 1:1 macrocycle:salt complexes **3** and **6** are also essentially identical to that obtained for potassium phenoxide itself. This indicates that, similar to the situation for LiOPh and NaOPh, the K^+ ions are not being complexed strongly and that the KOPh units are associated more strongly

Can. J. Chem. Downloaded from www.nrcresearchpress.com by 196.1.178.254 on 09/07/12
For personal use only.

TABLE 8. Macrocyclic ring torsion angles for complexes containing 15-crown-5[a]

Bonds	15-Crown-5 complexes[a]				
	1*a*[b]	**1***b*[b]	L·NaEAA[c]	L·NaSCN·(1/2)H_2O	L·$SnCl_4$·$2H_2O$[c]
O(1)—C(2)—C(3)—O(4)	−58.9(6)	−57.4(4)	−61	−61	−63.2
C(2)—C(3)—O(4)—C(5)	−177.9(5)	−174.9(3)	−176	174	170.7
C(3)—O(4)—C(5)—C(6)	−174.6(6)	−170.5(3)	−173	−171	−167.5
O(4)—C(5)—C(6)—O(7)	59.8(7)	61.3(4)	64	66	70.7
C(5)—C(6)—O(7)—C(8)	−167.7(6)	−180.0(4)	−178	−166	−162.6
C(6)—O(7)—C(8)—C(9)	176.8(7)	178.5(4)	152	−179	178.0
O(7)—C(8)—C(9)—O(10)	−50 (1)	−49.1(5)	−17	−58	−57.5
C(8)—C(9)—O(10)—C(11)	−97.5(9)	−86.0(5)	−127	−84	−89.5
C(9)—O(10)—C(11)—C(12)	174.2(6)	177.0(4)	174	174	176.2
O(10)—C(11)—C(12)—O(13)	−57.7(7)	−60.3(4)	−68	−65	−70.9
C(11)—C(12)—O(13)—C(14)	174.3(6)	179.1(3)	170	160	161.2
C(12)—O(13)—C(14)—C(15)	176.3(6)	176.3(3)	−177	176	−175.6
O(13)—C(14)—C(15)—O(1)	56.8(7)	53.3(4)	59	59	57.9
C(14)—C(15)—O(1)—C(2)	−160.7(6)	−165.2(3)	−158	−163	−170.2
C(15)—O(1)—C(2)—C(3)	154.0(5)	147.7(3)	162	163	168.3

[a]L = 15-crown-5; EAA = ethylacetoacetate.
[b]This work.
[c]Torsional angles for the pentaether in 15-crown-5·NaEAA, 15-crown-5·NaSCN·(1/2)H_2O and 15-crown-5·$SnCl_4$·$2H_2O$ were obtained from refs. 11, 10, and 44, respectively.

TABLE 9. λ_{max} from the ultraviolet spectra of the phenoxide anion in the complexes **1–6** and the phenoxide salts dissolved in dimethoxyethane

Complex number	Complex	λ_{max} (nm)
1	15-crown-5·2LiOPh	290
2	15-crown-5·2NaOPh	300
3	15-crown-5·KOPh	312
4	C-15-crown-5·2LiOPh	290
5	C-15-crown-5·2NaOPh	300
6	C-15-crown-6·KOPh	310
	LiOPh	293
	NaOPh	301
	KOPh	311

with each other than with the macrocycles. In contrast, the λ_{max} for the 1:1 KOPh complexes with 18-crown-6, its derivatives and cryptand [2.2.2] (21) were significantly greater than the value for the KOPh itself. This indicates that, very likely, the macrocycles were complexed to single ion pairs rather than associated ion pairs. Therefore, this suggests that aggregates of KOPh are to be expected in the 1:1 complexes with 15-crown-5 and cyclohexano-15-crown-5. One possible structure for complexes **3** and **6** is a KOPh dimer sandwiched between two macrocycles (see **II** in Fig. 1).

The dimeric structure depicted for **II** (Fig. 1) has been observed in the crystal structure of (18-crown-6·$RbNCS)_2$ (47), (18-crown-6·$CsNCS)_2$ (48), and [benzo-15-crown-5·Ba(3,5-dinitrobenzoate)$_2]_2$ (49).

Acknowledgements

The Natural Sciences and Engineering Research Council of Canada (NSERCC) is thanked for Visiting Scientist Fellowships for M.P.M. and A.R. Financial assistance in equipment grants for S.F. and scholarships for K.A.W. is also gratefully acknowledged. We are grateful to Dr. G. W. Buchanan for providing us with the cyclohexano-15-crown-5.

1. C. J. PEDERSEN. J. Am. Chem. Soc. **89**, 7017 (1967).
2. F. VÖGTLE and E. WEBER. *In* The chemistry of functional groups (Supplement E: the chemistry of ethers, crown ethers, hydroxyl groups and their sulphur analogues. Part 1). *Edited by* S. Patai. John Wiley and Sons, New York. 1980. Chap. 2.
3. E. WEBER and F. VÖGTLE. *In* Topics in current chemistry (Host guest complex chemistry I). Vol. 98. *Edited by* F. Vögtle. Springer-Verlag, Berlin. 1981. pp. 1–43.
4. F. DE JONG and D. N. REINHOUDT. *In* Advances in physical organic chemistry. Vol. 17. *Edited by* V. Gold and D. Bethell. Academic Press, New York. 1980. pp. 279–433.
5. G. A. MELSON (*Editor*). Coordination chemistry of macrocyclic compounds. Plenum Press, New York. 1979.
6. N. S. POONIA. *In* Progress in macrocyclic chemistry. Vol. 1. *Edited by* R. M. Izatt and J. J. Christensen. John Wiley and Sons, New York. 1979. pp. 115–155.
7. N. S. POONIA. J. Sci. Ind. Res. **37**, 202 (1978).
8. R. M. IZATT and J. J. CHRISTENSEN (*Editors*). Synthetic multidentate macrocyclic compounds. Academic Press, New York. 1978.
9. R. M. IZATT, J. S. BRADSHAW, S. A. NIELSEN, J. D. LAMB, J. J. CHRISTENSEN, and D. SEN. Chem. Rev. **85**, 271 (1985).
10. P. GROTH. Acta Chem. Scand. A**35**, 721 (1981).
11. C. CAMBILLAU, G. BRAM, J. CORSET, and C. RICHE. Can. J. Chem. **60**, 2554 (1982).
12. A. I. GORBUNOV, A. P. STOROZHENKO, L. V. IVAKINA, B. M. BULYCHEV, and A. I. GUSEV. Dokl. Akad. Nauk SSSR, **285**, 129 (1985).
13. N. P. RATH and E. M. HOLT. J. Chem. Soc. Chem. Commun. 665 (1985).
14. N. S. POONIA and M. R. TRUTER. J. Chem. Soc. Dalton Trans. 2062 (1973).
15. N. S. POONIA. J. Am. Chem. Soc. **96**, 1012 (1974).
16. N. S. POONIA, P. BAGDI, and K. S. SIDHU. J. Incl. Phenom. **4**, 43 (1986), and references therein.
17. V. W. BHAGWAT, H. MANOHAR, and N. S. POONIA. Inorg. Nucl. Chem. Lett. **16**, 373 (1980).

Can. J. Chem. Downloaded from www.nrcresearchpress.com by 196.1.178.254 on 09/07/12
For personal use only.

18. D. L. WARD, A. I. POPOV, and N. S. POONIA. Acta Crystallogr. C**40**, 238 (1984).
19. V. W. BHAGWAT, H. MANOHAR, and N. S. POONIA. Inorg. Nucl. Chem. Lett. **17**, 207 (1981).
20. K. VENKATASUBRAMANIAN, K. JOSHI, N. S. POONIA, W. R. MONTFORT, S. R. ERNST, and M. L. HACKERT. J. Incl. Phenom. **3**, 453 (1985).
21. A. RODRIGUE, J. W. BOVENKAMP, B. V. LACROIX, R. A. B. BANNARD, and G. W. BUCHANAN. Can. J. Chem. **64**, 808 (1986).
22. M. E. FRASER, S. FORTIER, A. RODRIGUE, and J. W. BOVENKAMP. Can. J. Chem. **64**, 816 (1986).
23. L. M. JACKMAN and C. W. DEBROSSE. J. Am. Chem. Soc. **105**, 4177 (1983).
24. G. W. BUCHANAN, K. BOURQUE, G. K. DIEDRICH, and M. Z. KHAN. Magn. Reson. Chem. **25**, 65 (1987).
25. P. MAIN, S. J. FISKE, S. E. HULL, L. LESSINGER, G. GERMAIN, J.-P. DECLERCQ, and M. M. WOOLFSON. MULTAN 80. A system of computer programs for the automatic solution of crystal structures from X-ray diffraction data. Universities of York, England, and Louvain, Belgium. 1980.
26. D. T. CROMER and J. T. WABER. International tables for X-ray crystallography. Vol. IV. Kynoch Press, Birmingham. 1979.
27. Enraf-Nonius. Structure determination package. *Revised by* B. A. Frenz. Enraf-Nonius, Delft. 1979.
28. L. M. JACKMAN and B. C. LANGE. Tetrahedron, **33**, 2737 (1977).
29. O. A. REUTOV and A. L. KURTS. Russ. Chem. Rev. **46**, 1040 (1977).
30. P. G. WILLIARD and G. B. CARPENTER. J. Am. Chem. Soc. **108**, 462 (1986).
31. D. SEEBACH, R. AMSTUTZ, T. LAUBE, W. B. SCHWEIZER, and J. D. DUNITZ. J. Am. Chem. Soc. **107**, 5403 (1985).
32. M. CZUGLER and E. WEBER. J. Chem. Soc. Chem. Commun. 472 (1981).
33. P. GROTH. Acta Chem. Scand. A**36**, 109 (1982).
34. G. SHOHAM, W. N. LIPSCOMB, and U. OLSHER. J. Am. Chem. Soc. **105**, 1247 (1983).
35. G. SHOHAM, W. N. LIPSCOMB, and U. OLSHER. J. Chem. Soc. Chem. Commun. 208 (1983).
36. B. CETINKAYA, I. GUMRUKCU, M. F. LAPPERT, J. L. ATWOOD, and R. SHAKIR. J. Am. Chem. Soc. **102**, 2086 (1980).
37. J. L. WARDELL. *In* Comprehensive organometallic chemistry. Vol. I. *Edited by* G. Wilkinson, F. G. A. Stone, and E. W. Abel. Pergamon Press, Oxford. 1982. p. 67.
38. J. E. HUHEEY. Inorganic chemistry. Harper and Row Publishers, New York. 1972. p. 695.
39. R. L. POLT, G. STORK, G. B. CARPENTER, and P. G. WILLIARD. J. Am. Chem. Soc. **106**, 4276 (1984).
40. W. N. SETZER and P. VON RAGUE SCHLEYER. *In* Advances in organometallic chemistry. Vol. 24. *Edited by* F. G. A. Stone and R. West. Academic Press, New York. 1985.
41. M. WALCZAK, K. WALCZAK, R. MINK, M. D. RAUSCH, and G. STUCKY. J. Am. Chem. Soc. **100**, 6382 (1978).
42. R. ZERGER, W. RHINE, and G. STUCKY. J. Am. Chem. Soc. **96**, 6048 (1974).
43. E. WEISS and G. HENCKEN. J. Organomet. Chem. **21**, 262 (1970).
44. E. HOUGH, D. G. NICHOLSON, and A. K. VASUDEVAN. J. Chem. Soc. Dalton Trans. 2335 (1986).
45. P. E. ARTE, J. FENEAU-DUPONT, J. P. DECLERCQ, G. GERMAIN, and M. VAN MEERSSCHE. Acta Crystallogr. B**35**, 1215 (1979).
46. H. E. ZAUGG and A. D. SCHAEFFER. J. Am. Chem. Soc. **87**, 1857 (1965).
47. M. DOBLER and R. P. PHIZACKERLEY. Acta Crystallogr. B**30**, 2746 (1974).
48. M. DOBLER and R. P. PHIZACKERLEY. Acta Crystallogr. B**30**, 2748 (1974).
49. D. L. WARD, A. I. POPOV, and N. S. POONIA. Acta Crystallogr. C**40**, 1183 (1984).

Can. J. Chem. Downloaded from www.nrcresearchpress.com by 196.1.178.254 on 09/07/12
For personal use only.

Kinetics of hydride transfer between nitrogen heteroaromatic cations

JOHN W. BUNTING AND MARK A. LUSCHER
Department of Chemistry, University of Toronto, Toronto, Ont., Canada M5S 1A1

Received March 14, 1988

JOHN W. BUNTING and MARK A. LUSCHER. Can. J. Chem. **66**, 2524 (1988).

The kinetics of the reduction of the 3-cyano-1-methylquinolinium, 4-cyano-2-methylisoquinolinium, and 2-methyl-5-nitroisoquinolinium cations by 9,10-dihydro-10-methylacridine, and also the reduction of these same three cations as well as the 10-methylacridinium cation by 5,6-dihydro-5-methylphenanthridine, have been investigated in 20% acetonitrile – 80% water, ionic strength 1.0, 25°C. The reactions of the 2-methyl-5-nitroisoquinolinium cation with both reductants, and also of the 4-cyano-2-methylisoquinolinium cation with 9,10-dihydro-10-methylacridine, display kinetic saturation effects in the pseudo-first-order rate constants as a function of heterocyclic cation concentration. These effects are consistent with the formation of 1:1 association complexes between hydride donor and acceptor prior to the rate-determining step of the reduction. The second-order rate constants for these reactions, and also those for analogous heterocyclic cation reductions by 1,4-dihydronicotinamides, show systematic variations as a function of the hydride donor and acceptor species.

JOHN W. BUNTING et MARK A. LUSCHER. Can. J. Chem. **66**, 2524 (1988).

Opérant à 25°C, à une force ionique de 1,0, dans une solution d'acétonitrile dans l'eau 20:80, on a étudié la cinétique de la réduction des cations cyano-3 méthyl-1 quinolinium, cyano-4 méthyl-2 isoquinolinium et méthyl-2 nitro-5 isoquinolinium par la dihydro-9,10 méthyl-10 acridine ainsi que la réduction de ces trois même cations ainsi que celle du cation méthyl-10 acridinium par la dihydro-5,6 méthyl-5 phénanthridine. Les réactions du cation méthyl-2 nitro-5 isoquinolinium avec chacun des réactifs ainsi que celle du cation cyano-4 méthyl-2 isoquinolinium avec la dihydro-9,10 méthyl-10 acridine présentent des effets de saturation cinétique des constantes de vitesse du pseudo premier ordre en fonction de la concentration de cation hétérocyclique. Ces effets sont en accord avec la formation de complexes d'association 1:1 entre le donneur et l'accepteur d'hydrure avant l'étape qui détermine la vitesse de la réduction. Les constantes de vitesse du deuxième ordre de ces réactions, ainsi que celles des réductions analogues de cations hétérocycliques par les dihydro-1,4 nicotinamides, présentent des variations systématiques en fonction des espèces qui donne ou qui accepte l'hydrure.

[Traduit par la revue]

The rates of reduction of nitrogen heteroaromatic cations (Q^+) by the dihydro derivatives of various nitrogen heteroaromatic species (i.e., derivatives of dihydropyridines (RH in eq. [1])) have been extensively investigated as part of the general exploration of non-enzymic hydride transfers that are relevant to the redox reactions of the nicotinamide coenzymes (1–32).

[1] $Q^+ + RH \rightarrow QH + R^+$

Many of these investigations have utilized 1,4-dihydronicotinamides for the reduction of a variety of pyridinium (1–9), quinolinium (10–14), isoquinolinium (15, 16), and acridinium (11, 13, 17–28) cations, since such reducing agents are most closely related to the biological NADH and NADPH species. However, a variety of 1,4-dihydroquinolines (11, 13, 24, 25, 29), 9,10-dihydroacridines (11, 13, 24, 25, 30, 31), and 5,6-dihydrophenanthridines (11, 13, 30, 32) have also been used as hydride donors in the continuing investigations of "model nicotinamide–coenzyme reactions". These reactions have also attracted interest as vehicles for the evaluation of some fundamental principles of physical organic chemistry (11, 13, 31, 32).

Some form of association complex between the hydride donor and acceptor species would be expected to precede the hydride transfer process between these relatively large organic species. In actual fact, such complexation has rarely been observed in reactions of the general class described by eq. [1] (14–16, 19), although evidence for the formation of association complexes is readily obtainable in the reactions of 1,4-dihydronicotinamides and their derivatives with flavins (33–36), quinones (37–42), and related species (43, 44). Such complexation between the two reactants becomes obvious in the form of a "kinetic saturation" for the dependence of pseudo-first-order rate constants upon the concentration of the excess reactant, or by the spectral observation of transient charge-transfer complexes. While lack of evidence for complexation between Q^+ and RH of eq. [1] might be simply ascribable to very small association constants for complex formation, the cases in which kinetic saturation has been reported imply that this phenomenon should be more widely encountered, especially in predominantly aqueous solutions.

The most extensive examples of complexation between hydride donor and acceptor species have been reported for the reduction of isoquinolinium (15, 16) and quinolinium (14) cations by 1,4-dihydronicotinamides in aqueous solutions containing 20% acetonitrile cosolvent. Pronounced kinetic saturation effects are found in the pseudo-first-order rate constants for these reactions, and these effects are consistent with the presence of 1:1 complexes between the two reactant species. As usual, the interpretation of complexation is complicated by the well-known kinetic conundrum, in which the formation of productive and (or) nonproductive complexes produces kinetically equivalent reaction mechanisms.

Weak complexation between these organic species is consistent with either weak π–π^* electronic interactions of the charge-transfer type or hydrophobic interactions between the reactant species. Either of these weak interactions would be expected to be significantly stronger for larger, and less polar, hydride donor species than for 1,4-dihydronicotinamides. That such complexation has not been reported when 1,4-dihydroquinolines, 9,10-dihydroacridines, or 5,6-dihydrophenanthridines have been used as the hydride donors, may be simply attributable to the fact that these reactions have usually been investigated in relatively nonpolar solvent systems, in which the minimization of aqueous interactions with large organic molecules is less of a factor in favour of complexation between organic species.

In the current work, we report an extension of our earlier

Can. J. Chem. Downloaded from www.nrcresearchpress.com by 196.1.178.254 on 09/07/12
For personal use only.

Can. J. Chem. Downloaded from www.nrcresearchpress.com by 196.1.178.254 on 09/07/12
For personal use only.

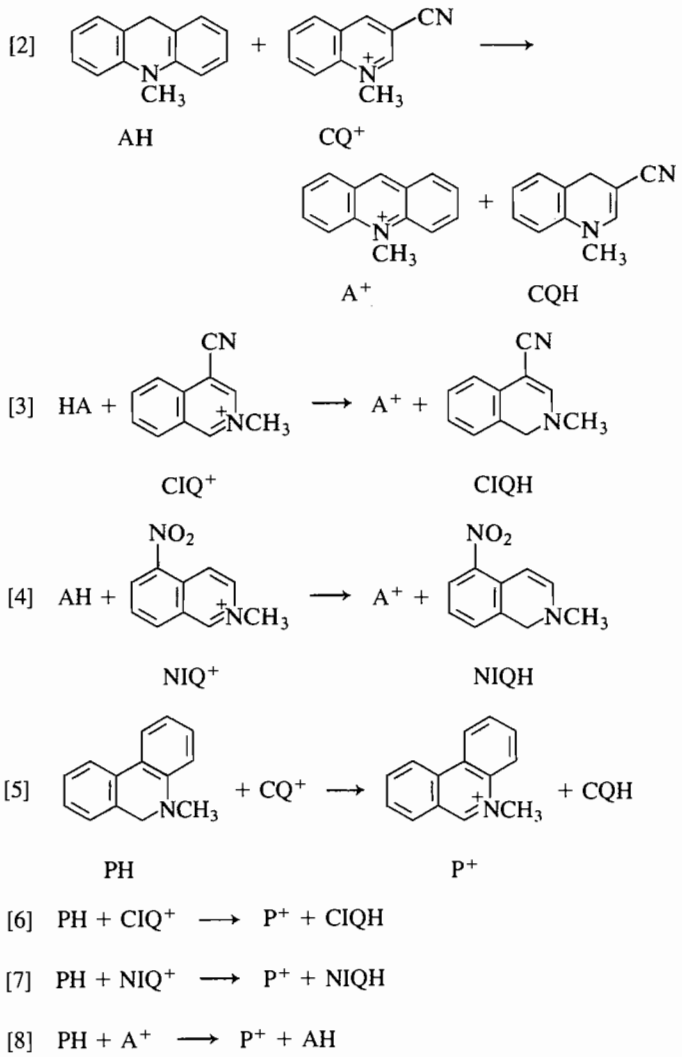

studies (in 20% acetonitrile in water) of the kinetics of the 1,4-dihydronicotinamide reduction of isoquinolinium (15, 16), quinolinium (14), and acridinium (24) cations to the reduction of some examples of these cations by 9,10-dihydro-10-methylacridine and 5,6-dihydro-5-methylphenanthridine in this same solvent (eqs. [2]–[8]). We have found that the expectations mentioned above, regarding the importance of complexation using these large hydride donors in a predominantly aqueous solvent, are justified. Furthermore, the current data allow a comparison of relative reactivities of hydride donor and acceptor species in our own solvent system, and in the less polar 80% 2-propanol – 20% water solvent, which has been extensively used by Kreevoy and co-workers (11–13, 30–32) in studies that parallel our own work in this area.

Experimental

10-Methylacridinium chloride dihydrate (45) and 4-cyano-2-methylisoquinolinium bromide (46) were available from earlier studies in this laboratory. These materials, as well as all other heterocyclic salts described below, were recrystallized and characterized by ^{1}H nmr spectroscopy prior to use.

5-Methylphenanthridinium iodide was prepared by stirring phenanthridine (2 g) in iodomethane (15 mL) in a pressure bottle for 3 days at room temperature. Since this iodide salt is air sensitive, it was converted to the corresponding chloride monohydrate by stirring with freshly prepared silver chloride in methanol, followed by recrystallization from aqueous acetone; mp 211–213°C (lit. (47) mp 215°C).

10-Methylacridinium iodide was prepared by stirring acridine (3.95 g) in acetone (3 mL) with iodomethane (3.4 mL) in a pressure bottle at room temperature for 3 weeks. The red powder was used for synthetic purposes without further purification.

3-Cyano-1-methylquinolinium iodide was prepared by stirring 3-cyanoquinoline (3 g) with iodomethane (20 mL) for 2 days. After the addition of diethyl ether (50 mL), the crude product was recrystallized several times from ethanol to give brown crystals of mp 243–244°C (dec.) (lit. (48) mp 207°C (?)).

2-Methyl-5-nitroisoquinolinium iodide was prepared by stirring 5-nitroisoquinoline (2 g) with iodomethane (20 mL) for 3 days. The crude product was treated with diethyl ether, and recrystallized from a methanol–2-propanol mixture; mp 165°C (dec.).

9,10-Dihydro-10-methylacridine

10-Methylacridinium iodide (2.17 g) was dissolved in 2:1 methanol–water (100 mL) and cooled to 10°C. An aqueous solution (10 mL) of sodium borohydride (310 mg) was added dropwise with stirring. The yellow solution turned black, then dark green, followed by light green, and finally deposited a creamy white precipitate. Water was added (100 mL), and the mixture was then extracted with dichloromethane. After evaporation of the solvent the crude product was recrystallized several times from aqueous methanol; mp 101–102°C (lit. (49) 102–103°C).

5,6-Dihydro-5-methylphenanthridine

5-Methylphenanthridinium iodide (2 g) was dissolved in 2:1 methanol–water (80 mL) and cooled to 10°C. An aqueous solution (7.9 mL) of sodium borohydride (185 mg) was added dropwise, to give a pale green solution. Water (200 mL) was added, and the mixture was stored in the dark under nitrogen for 30 min to allow the product to crystallize. After suction filtration, the crystals were dissolved in methanol (15 mL) under nitrogen. Water was added dropwise until the solution became slightly cloudy, whereupon a single crystal from the crude product was added to seed crystallization. When crystallization appeared complete, more water (150 mL) was added dropwise over a period of 1–2 h. The crystalline product was filtered off, and recrystallized again by the same procedure to give fine white crystals of mp 44–46°C (lit. (50) mp 48°C). This material was stored in the vacuum desiccator in the dark, and recrystallized biweekly to maintain purity.

Kinetic studies

Stock solutions of dihydropyridine derivatives (RH) in spectroscopic grade acetonitrile were freshly prepared each day, while neutral aqueous solutions of salts of the heterocyclic cations (Q^+) were replaced weekly, with refrigeration while not in active use. All kinetic and spectral studies were done at 25°C using a Cary 210 spectrophotometer in 20% acetonitrile – 80% water, at ionic strength 1.0 (potassium chloride), and buffered at pH 7.0 with 5 mM phosphate unless indicated otherwise. Reactions of the 4-cyano-2-methylisoquinolinium cation were studied at pH 5.0 (5 mM acetate) to avoid competing pseudobase formation by this cation (pK_{R^+} 7.80 (46)). This pH 5.0 buffer was also used for reactions of the 3-cyano-1-methylquinolinium cation to avoid a very slow decomposition of the 1,4-dihydroquinoline reaction product that was observed at higher pH.

The time dependence of the absorbance was recorded at appropriate wavelengths as discussed in the Results. These data were digitized by a microprocessor controlled by a Commodore 4048 computer into 75 data points usually covering at least 95% of the overall reaction. For pseudo-first-order kinetic studies, the rate constants were calculated from the appropriate logarithmic relationship by linear least-squares analysis. In a few cases when a poor correlation was obtained, or competing reactions were obvious (e.g., eq. [7] as discussed in the Results), the rate constant was calculated by fitting the absorbance (A_t) at time t to the relationship, $A_t = A_f + (A_0 - A_f) \exp(-k_{obs} \cdot t)$, via the Marquardt algorithm treating the initial absorbance (A_0), the final absorbance (A_f), and k_{obs} as parameters to be evaluated. This same algorithm was also used for parameter evaluation from the k_{obs} vs. $[Q^+]$ kinetic saturation curves (eq. [9]).

Can. J. Chem. Downloaded from www.nrcresearchpress.com by 196.1.178.254 on 09/07/12
For personal use only.

Results

Spectral observations

We have used spectrophotometric techniques to measure the rates of reduction of the 3-cyano-1-methylquinolinium cation (CQ^+), the 4-cyano-2-methylisoquinolinium cation (CIQ^+), and the 2-methyl-5-nitroisoquinolinium cation (NIQ^+) by 9,10-dihydro-10-methylacridine (AH) (eqs. [2]–[4]), and the reduction of these three cations and also the 10-methylacridinium cation (A^+) by 5,6-dihydro-5-methylphenanthridine (PH) (eqs. [5]–[8]) in 20% acetonitrile in water, buffered at an appropriate pH as described in the experimental section, at ionic strength 1.0 and 25°C. In initial experiments, the time dependences of the electronic absorption spectra of equimolar mixtures of the reactants were obtained for each of the reactions in eqs. [2]–[8]. In all cases, as indicated below, the spectral observations were consistent with the reaction products of eqs. [2]–[8].

The reduction of the 3-cyano-1-methylquinolinium cation by either AH (eq. [2]) or PH (eq. [5]) has been shown to occur exclusively at C-4 rather than at C-2 of this quinolinium cation (11, 13). Our spectral observations confirm this result. For the reaction of eq. [2], the appearance of the 10-methylacridinium cation reaction product is clear from its characteristic spectrum consisting of an intense sharp maximum at 357 nm and a less intense series of three peaks at 397, 416, and 439 nm. Superimposed upon this acridinium cation spectrum is a shoulder in the vicinity of 333 nm, which is derived from the absorption maximum of 3-cyano-1,4-dihydro-1-methylquinoline (CQH) (51). The product spectrum from the reaction of eq. [5] displayed a very broad absorption maximum in the vicinity of 330 nm and a shoulder at about 355 nm. The difference spectrum between this product mixture and an equimolar concentration of the 5-methylphenanthridinium cation displayed the characteristic spectrum of the 1,4-dihydroquinoline derivative. For each of these reactions, the time-dependent spectra show clean isosbestic points, which indicate that there is no significant formation of intermediate species in these reactions.

The product spectra from the reduction of the 4-cyano-2-methylisoquinolinium cation by either AH (eq. [3]) or PH (eq. [6]) were characterized by the spectra of the 10-methylacridinium and 5-methylphenanthridinium cations, respectively, superimposed upon the spectrum of 4-cyano-1,2-dihydro-2-methylisoquinoline (CIQH), which has also been shown to be the product of the reduction of this isoquinolinium cation by 1-benzyl-1,4-dihydronicotinamide (16). Clean isosbestic points indicate the absence of significant concentrations of intermediates in either of these reactions.

The spectra of the reaction mixtures containing the 2-methyl-5-nitroisoquinolinium cation (eqs. [4] and [7]) are complicated by the relative instability of the 1,2-dihydro-2-methyl-5-nitroisoquinoline (NIQH) reaction product (λ_{max} = 440 nm) over the lengthy periods required to observe these extremely slow reactions. In the reduction of this isoquinolinium cation by PH (eq. [7]) (both 0.06 mM), a broad absorbance centered near 440 nm, as expected for the NIQH reaction product, appears during the first few hours of the reaction. However, the lack of clean isosbestic points, and the subsequent decrease in the absorbance from the 440 nm maximum, suggest the decomposition of this product in competition with its formation in the reduction reaction. Similar observations have been reported (15) for the reduction of this cation by 1,4-dihydronicotinamides, and are attributable to the aerobic oxidation of the 1,2-dihydro product to 2-methyl-5-nitro-1-isoquinolinone, which does not absorb at $\lambda > 400$ nm.

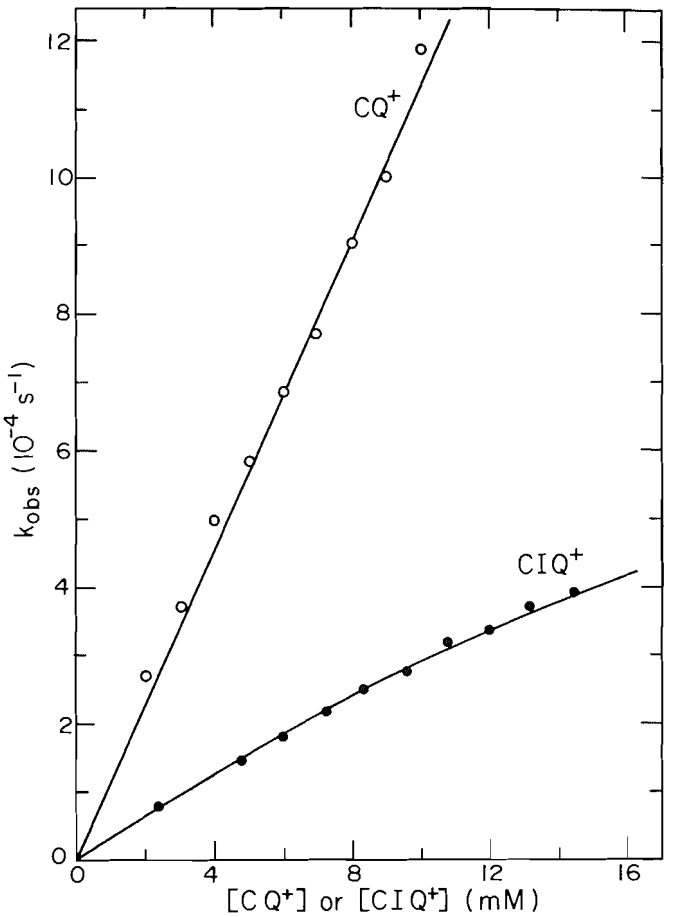

FIG. 1. Pseudo-first-order rate constant as a function of cation concentration for the reduction of CQ^+ and CIQ^+ by AH (eqs. [2] and [3]).

The reaction of equimolar concentrations of the 2-methyl-5-nitroisoquinolinium cation and AH is about 100 times slower than the reaction described above for the reduction of this cation by PH. Consequently, in this case decomposition of the immediate NIQH product is much faster than its formation, so that spectral observation shows only the clean formation of the characteristic 10-methylacridinium cation spectrum at $\lambda > 400$ nm. The reaction shows clean isosbestic points, indicating that there is no significant buildup of the NIQH reduction product as an "intermediate" prior to its aerial oxidation. Superimposed upon the 10-methylacridinium cation spectrum in the reaction product is an additional absorption of $\lambda_{max} \approx 340$ nm, which we attribute to 2-methyl-5-nitro-1-isoquinolinone.

The reaction of 5,6-dihydro-5-methylphenanthridine and the 10-methylacridinium cation (eq. [8]) is known to give 9,10-dihydro-10-methylacridine and the 5-methylphenanthridinium cation. The spectrum of our product mixture is consistent with this result. This product spectrum is identical to that of an equimolar mixture of the predicted reaction products, displaying an intense absorption maximum at 285 nm characteristic of AH, and absorption in the vicinity of 355 nm characteristic of the 5-methylphenanthridinium cation.

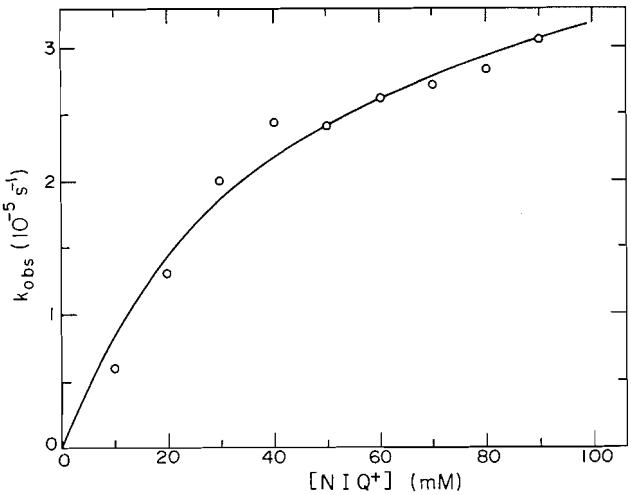

FIG. 2. Pseudo-first-order rate constant as a function of cation concentration for the reduction of NIQ^+ by AH (eq. [4]).

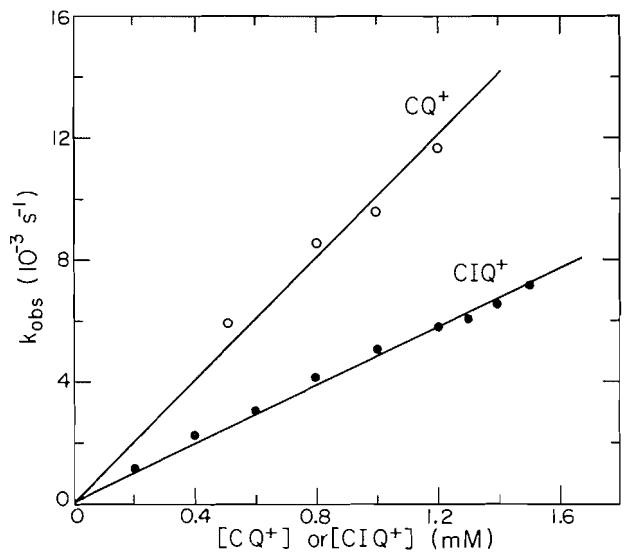

FIG. 3. Pseudo-first-order rate constant as a function of cation concentration for the reduction of CQ^+ and CIQ^+ by PH (eqs. [5] and [6]).

Kinetic studies

(i) Reactions of 9,10-dihydro-10-methylacridine (eqs. [2]–[4])

The rates of the reactions in each of eqs. [2]–[4] were followed by monitoring the appearance of the 10-methylacridinium cation at 416 nm (eqs. [2] and [3]) or 435 nm (eq. [4]) using an initial concentration of 0.06 mM for AH, and large excesses of the heteroaromatic cations. Pseudo-first-order rate constants (k_{obs}) were evaluated at a number of cation concentrations, and are displayed in Figs. 1 and 2. For the reduction of the 3-cyano-1-methylquinolinium cation (eq. [2]), k_{obs} is linear in cation concentration over the limited concentration range that is accessible. However, for each of the isoquinolinium cations in eqs. [3] and [4], k_{obs} is less than linearly dependent upon cation concentration. While the curvature in Fig. 1 is only slight for the 4-cyano-2-methylisoquinolinium cation, the curved dependence for the 2-methyl-5-nitroisoquinolinium cation in Fig. 2 is quite dramatic, with k_{obs} tending to a limit at high concentrations of isoquinolinium cation.

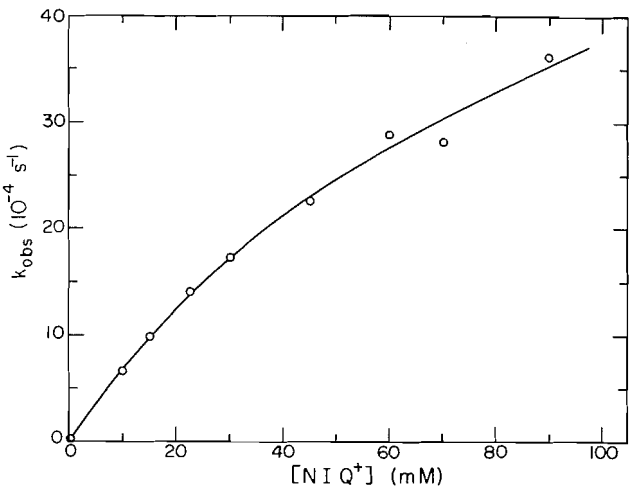

FIG. 4. Pseudo-first-order rate constant as a function of cation concentration for the reduction of NIQ^+ by PH (eq. [7]).

(ii) Reactions of 5,6-dihydro-5-methylphenanthridine (eqs. [5]–[8])

The reactions of eqs. [5] and [6] are characterized by extensive overlap between the spectra of reactant and product species at all wavelengths. Consequently, only limited concentration ranges of the heterocyclic cations were accessible for pseudo-first-order kinetic studies (at 365 nm for eq. [5], and 370 nm for eq. [6]). Within these regions, k_{obs} was strictly linear for the reduction of each of the cations in eqs. [5] and [6] (Fig. 3).

The formation of 1,2-dihydro-2-methyl-5-nitroisoquinoline in eq. [7] can be conveniently monitored in the vicinity of 440 nm; however, as described above, this species undergoes subsequent decomposition prior to completion of the reduction. Consequently, the absorbance due to this species as a function of time passes through a maximum. Fortunately, the decomposition reaction occurs sufficiently slowly, relative to the reduction, that accurate pseudo-first-order rate constants were accessible by analyzing the absorbance vs. time data over the first 70% of the reaction, during which complications from decomposition are insignificant. Values of k_{obs} for this reaction show a clear saturation effect (Fig. 4). From the time dependence of the disappearance of NIQH at long reaction times, we have estimated an apparent first-order rate constant of about 10^{-4} s^{-1} for the decomposition of the dihydroisoquinoline product under the current reaction conditions (20% CH_3CN – 80% H_2O, pH 7.0 phosphate buffer (5 mM), ionic strength 1.0, 25°C).

It is not possible to investigate the reaction of eq. [8] under pseudo-first-order conditions, because of the long wavelength absorbance by the 10-methylacridinium cation and the limited solubility of the 5,6-dihydro-5-methylphenanthridine in the predominantly aqueous solvent. Consequently, we have followed the disappearance of the acridinium cation at 416 nm, at similar concentrations of the two reactant species. Second-order kinetic plots ($1/[A^+]$ vs. time) are linear for approximately the first 50–60% of the reaction. However, during the second 50% of the reaction, curvature of the type shown in Fig. 5 becomes obvious. Such curvature, which implies an increase in apparent

Can. J. Chem. Downloaded from www.nrcresearchpress.com by 196.1.178.254 on 09/07/12
For personal use only.

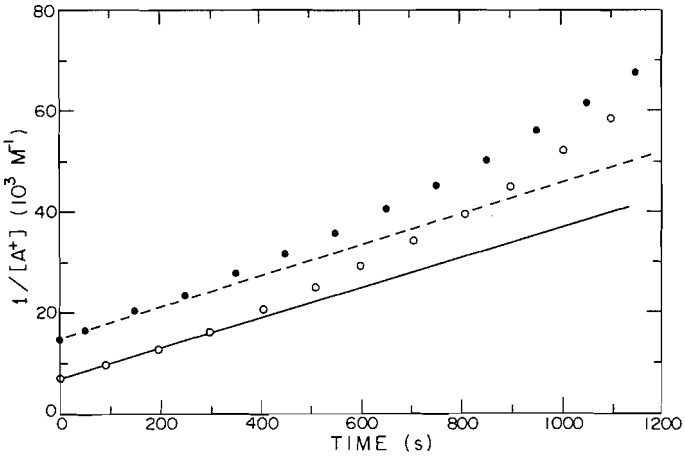

FIG. 5. Second-order kinetic plots for the reduction of A^+ by PH (eq. [8]). Initial reaction concentrations: ●, $[A^+]$ = [PH] = 0.167 mM; ○, $[A^+]$ = [PH] = 0.30 mM. Both lines represent second-order rate constants of $30\ M^{-1}\ s^{-1}$.

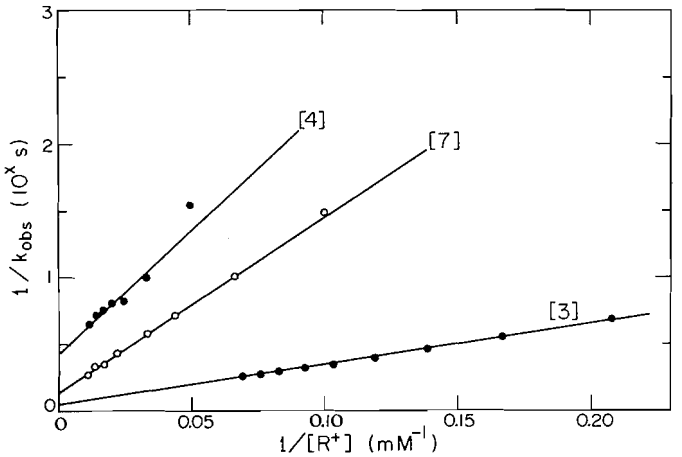

FIG. 6. Double reciprocal plots of pseudo-first-order rate constants for the reactions of eq. [3] ($x = 4$), eq. [4] ($x = 4.7$), and eq. [7] ($x = 5$) as indicated on the figure. Data from Figs. 1, 2, and 4.

second-order rate constant as the reaction progresses, is unchanged even after extensive repurification of both reactants, and is independent of the presence of significant added concentrations of either reaction product (up to at least 0.17 mM AH and 9 mM P^+). We have no ready explanation for this curvature at the present time. Second-order rate constants evaluated from the linear region of these kinetic plots during the first 50% of the reaction were found to be independent of either reactant or product concentration. It is this second-order rate constant that is reported for this reaction in Table 2.

Discussion

Kinetic saturation effects of the type shown in Figs. 1, 2, and 4 have previously been reported for the reduction of quinolinium (14) and isoquinolinium (15, 16) cations by 1,4-dihydronicotinamides. This phenomenon was shown to be consistent with the formation of a 1:1 association complex between hydride donor and acceptor, with complex formation being rapid relative to the hydride transfer process. Such a kinetic scheme predicts that $1/k_{obs}$ should be linearly dependent upon $1/[Q^+]$ where k_{obs} is the pseudo-first-order rate constant in the presence of a large excess of heterocyclic cation (Q^+). Double reciprocal plots of the nonlinear dependences in Figs. 1, 2, and 4 are shown in Fig. 6. These plots are clearly linear, and so indicate that these kinetic saturation effects are consistent with the formation of a 1:1 complex between the hydride donor and acceptor species.

We feel that an alternative possibility, that the kinetic saturation effects may arise from self-aggregation of ion pairs of the acceptor organic salt, can be ruled out on two different grounds. Firstly, the measured association constants for three different donors with NIQ^+ vary by more than fivefold (Y_{int}/slope of Table 1). These parameters should be independent of the hydride donor if they reflect self-aggregation of NIQ^+Cl^- ion pairs. Secondly, kinetic saturation effects in these reactions are only commonly observed in predominantly aqueous reaction media, and are rarely (if ever) reported for more hydrophobic solvents. This result is as expected for the association of neutral hydride donors with heteroaromatic cations since such complexes should be favoured by more polar solvents, whereas the reverse would be expected to be true for ion pairs.

The slope and ordinate intercept (Y_{int}) parameters that characterize the plots in Fig. 6 were evaluated from regression analyses of the kinetic saturation curves in Figs. 1, 2, and 4, according to the relationship in eq. [9]. These parameters are collected in Table 1, which also includes literature data for the reaction of 1-benzyl-1,4-dihydronicotinamide with the 2-methyl-5-nitroisoquinolinium cation, the 2-methylisoquinolinium cation, and the 1-methylquinolinium cation under the same reaction conditions.

$$[9] \quad k_{obs} = ([Q^+]/\text{slope})/(1 + Y_{int}[Q^+]/\text{slope})$$

The interpretation of these empirical parameters depends upon which of several kinetically equivalent reaction schemes is chosen (see below). However, independent of reaction scheme, the ratio Y_{int}/slope represents the overall association constant for 1:1 complex formation, and 1/slope has units of a second-order rate constant. These second-order rate constants are equivalent to the initial slopes of the curves in Figs. 1, 2, and 4 at low concentrations of heterocyclic cation, and are collected in Table 2, along with second-order rate constants evaluated from the slopes of the linear relationships in Figs. 1 and 3.

Clear trends are evident across each row and down each column in Table 2. These trends are quantified more clearly in Table 3, where the data are expressed as relative rate constants referenced to 5,6-dihydro-5-methylphenanthridine as a common reductant, or alternatively to the 3-cyano-1-methylquinolinium cation as a common oxidant. In both comparisons of relative rate constants, the value for the 1-benzyl-1,4-dihydronicotinamide reduction of the 2-methyl-5-nitroisoquinolinium cation appears to be somewhat anomalous and has not been included in the calculation of the following relative reactivities. This case will be considered further below. The relative reactivities of NH:PH:AH towards heteroaromatic cations are close to 10:1:0.01, while the relative reactivities of A^+:CQ^+:ClQ^+:NIQ^+ are approximately 3:1:0.3:0.008 for the oxidation of dihydro nitrogen heterocycles. These ratios should have useful predictive value in future studies in this area.

The association constants in Table 1 for HA with ClQ^+ and NIQ^+ and also PH with NIQ^+ are somewhat smaller than that for NH with NIQ^+, but are clearly much larger than those for NH with the parent *N*-methyl quinolinium and isoquinolinium cations. Extensive analysis (15, 16) of the association complexes

Can. J. Chem. Downloaded from www.nrcresearchpress.com by 196.1.178.254 on 09/07/12
For personal use only.

TABLE 1. Parameters describing kinetic saturation of pseudo-first-order rate constants according to eq. [9]

Reaction[a]	$1/Y_{int}$ (s^{-1})	1/slope ($M^{-1}\,s^{-1}$)	Y_{int}/slope (M^{-1})
AH + NIQ^+	$4.5\ (\pm0.4)\times10^{-5}$	$1.0\ (\pm0.1)\times10^{-3}$	23 (±4)
PH + NIQ^+	$7.2\ (\pm0.8)\times10^{-3}$	$7.4\ (\pm0.2)\times10^{-2}$	10 (±2)
NH + NIQ^+	2.1×10^{-3}	0.12	56[b]
AH + CIQ^+	$2.4\ (\pm0.3)\times10^{-3}$	$3.3\ (\pm0.1)\times10^{-2}$	14 (±2)
NH + IQ^+	3.9×10^{-4}	8.0×10^{-4}	2.1[c]
NH + Q^+	9.5×10^{-3}	5.0×10^{-3}	0.5[d]

[a]NH = 1-benzyl-1,4-dihydronicotinamide; IQ^+ = 2-methylisoquinolinium cation; Q^+ = 1-methylquinolinium cation (this table only); other reactants are defined by eqs. [2]–[8]. All data in 20% acetonitrile – 80% water; ionic strength 1.0; 25°C.
[b]Data from ref. 15.
[c]Data from ref. 16.
[d]Data from ref. 14.

TABLE 2. Second-order rate constants for reactions of eq. [1][a]

Reductant (RH)	Oxidant (Q^+)			
	A^+	CQ^+	CIQ^+	NIQ^+
NH	400[b]	121[c]	29[d]	0.12[e]
PH	30 (±4)	10 (±1)	4.6 (±0.2)	$7.4\ (\pm0.2)\times10^{-2}$
AH		0.103 (±0.003)	$3.3\ (\pm0.1)\times10^{-2}$	$1.0\ (\pm0.1)\times10^{-3}$

[a]Units: $M^{-1}\,s^{-1}$; reactants are defined by eqs. [2]–[8]; NH = 1-benzyl-1,4-dihydronicotinamide.
[b]Data from ref. 27.
[c]Data from ref. 14.
[d]Data from ref. 16.
[e]Data from ref. 15.

between 1,4-dihydronicotinamides and isoquinolinium cations has shown that the relatively large association constant observed between NH and NIQ^+ can only be simply interpreted as being due to the formation of a nonproductive complex between these two species. It has been established (16) that this complexation involves a specific interaction between the 5-NO_2 substituent of NIQ^+ and the 3-$CONH_2$ unit of NH. Since the AH and PH species lack such a carboxamide substituent, it seems unlikely that the association complexes between either of these species and NIQ^+ are structurally analogous to the NH–NIQ^+ complex. This view is supported by the similar association constants that are found for AH with NIQ^+ and CIQ^+.

These considerations are the basis for our suggestion above that the data in Table 3 for the NH reduction of NIQ^+ are not directly comparable with the other relative rate data in this table. The two simplest reaction schemes that generate kinetic saturation effects of the type observed in this work are shown in Scheme 1 (productive complex) and Scheme 2 (nonproductive complex). These two schemes represent the simplest cases from several, more general, kinetically equivalent schemes involving productive and nonproductive complexes. Detailed algebraic analyses of five schemes of this type have been previously presented (15).

$$Q^+ + RH \underset{}{\overset{K}{\rightleftharpoons}} C \xrightarrow{k_c} QH + R^+$$

$$\frac{-d[RH]}{dt} = \frac{k_c K[Q^+][RH]}{1 + K[Q^+]} = k_{obs}[RH] \qquad (\text{for } [Q^+] \gg [RH])$$

SCHEME 1

$$Q^+ + RH \overset{K_{NP}}{\rightleftharpoons} C_{NP}$$

$$Q^+ + RH \xrightarrow{k_2} QH + R^+$$

$$\frac{-d[RH]}{dt} = \frac{k_2[Q^+][RH]}{1 + K_{NP}[Q^+]} = k_{obs}[RH] \qquad (\text{for } [Q^+] \gg [RH])$$

SCHEME 2

Scheme 2, which was previously used (15) for the NH + NIQ^+ reaction, predicts that 1/slope for the double reciprocal plot should be the true second-order rate constant for a bimolecular reaction. On the other hand, Scheme 1 requires that 1/slope = $k_c \cdot K$ is an apparent rate constant containing contributions from both the association constant for productive complex formation and also a first-order rate constant for hydride transfer within such a complex. Thus if the saturation effects observed in the AH and PH reductions arise predominantly from productive complex formation as in Scheme 1, then the apparent second-order rate constants in Table 2 have different definitions for these species than for the NH + NIQ^+ reaction. Significantly, the NH reductions of A^+, CQ^+, and CIQ^+, which do not show observable saturation effects, seem to fit the general patterns discerned for the AH and PH reductions in Table 3, and this again points to the strong complexation observed between NH and NIQ^+ being of a quite different nature than that found for the other species.

If one accepts the productive complexation of Scheme 1 as a reasonable interpretation of the reactions in the current study, then one must also interpret the second-order rate constants

Can. J. Chem. Downloaded from www.nrcresearchpress.com by 196.1.178.254 on 09/07/12
For personal use only.

TABLE 3. Relative reactivities for reactions according to eq. [1][a]

Reductant (RH)	Oxidant (Q^+)			
	A^+	CQ^+	CIQ^+	NIQ^+
NH	13	12	6.3	1.6
PH	1	1	1	1
AH		0.010	0.0072	0.0135
NH	3.3	1	0.24	0.00099
PH	3.0	1	0.46	0.0074
AH		1	0.32	0.0097
NH[b]	17 (0.5)[c]			
PH[b]	1 (0.4)[c]	1 (0.13)[c]		
AH[b]	0.0036	0.0062 (0.08)[c]		

[a]Calculated from data in Table 2 (in 20% acetonitrile – 80% water, ionic strength 1.0, 25°C), unless indicated otherwise.

[b]Calculated from data in ref. 11 for 80% 2-propanol – 20% water.

[c]Ratio of second-order rate constant in 80% 2-propanol – 20% water (ref. 11) to that in 20% acetonitrile – 80% water (current work).

evaluated from the linear relationships of Figs. 1 and 3 in terms of $k_c \cdot K$ as defined by Scheme 1, with K being too small to produce significant nonlinearity in the accessible concentration ranges. It is certainly reasonable that such large organic species should be significantly associated in predominantly aqueous solutions, since there are numerous precedents for the association of neutral aromatic molecules with heteroaromatic cations, to form complexes that have been attributed to hydrophobic, charge-transfer, or $\pi-\pi^*$ donor–acceptor interactions. To a first approximation one might expect that the k_c and K parameters of Scheme 1 would both vary in a similar way upon changing the reactant species, since both hydride transfer and charge-transfer or $\pi-\pi^*$ interactions involve the redistribution of electron density from the formal hydride donor to the hydride acceptor species. In fact a weak charge-transfer complex has been shown (19) to be formed immediately upon mixing 1-benzyl-1,4-dihydronicotinamide and the 10-methylacridinium cation, with the rate of disappearance of this complex being identical to the rate of hydride transfer between these two species. A fuller exploration of the association of neutral aromatic species with the various heteroaromatic cations of this study is reported in the accompanying paper (52).

The earlier examples of complexation between 1,4-dihydronicotinamides and isoquinolinium (15, 16), quinolinium (14), or acridinium (19) cations have now been extended to include 9,10-dihydroacridines and 5,6-dihydrophenanthridines as hydride donors towards these heteroaromatic cations. Experimental limitations precluded the investigation of some of the current reactions at high enough concentrations to demonstrate the kinetic consequences of complexation between hydride donor and acceptor. Nevertheless, it is now clear that such association complexes must be seriously considered in all quantitative studies of hydride transfer according to eq. [1].

Table 3 includes data from Kreevoy and co-workers for those reactions which are common to their studies in 80% 2-propanol – 20% water and our own studies in 20% acetonitrile – 80% water. It is clear that the same qualitative relative reactivities are found in the two solvent systems, although the selectivities seem to be somewhat enhanced in the less polar medium. All reactions are slower in the less polar solvent than in our predominantly aqueous medium, with an indication that the solvent effect is somewhat dependent upon the cation involved. Thus, in 80% 2-propanol, acridinium cations are reduced at 40–50% of the rate in 20% acetonitrile, while the 3-cyano-1-methylquinolinium cation is reduced at only about 10% of the rate in the more aqueous medium. In the light of the general conclusions of the current study, the detailed interpretation of such comparisons will require quantitative information of the solvent dependences of both k_c and K of Scheme 1 as a function of hydride donor and acceptor.

Acknowledgement

We appreciate the continued support of this work by the Natural Sciences and Engineering Research Council of Canada.

1. G. CILENTO. Arch. Biochem. Biophys. **88**, 352 (1960).
2. M. J. SPIEGEL and G. R. DRYSDALE. J. Biol. Chem. **235**, 2498 (1960).
3. J. LUDOWIEG and A. LEVY. Biochemistry, **3**, 373 (1964).
4. J. B. JONES and K. E. TAYLOR. Can. J. Chem. **54**, 2974 (1976).
5. P. VAN EIKEREN and D. L. GRIER. J. Am. Chem. Soc. **99**, 8057 (1977).
6. C. BERNOFSKY and W. J. GALLAGHER. Biochim. Biophys. Acta, **659**, 1 (1981).
7. W. VAN GERRESHELM, C. KRUK, and J. W. VERHOEVEN. Tetrahedron Lett. **23**, 565 (1982).
8. J. W. BUNTING and J. C. BREWER. Can. J. Chem. **63**, 1245 (1985).
9. J. W. BUNTING and J. L. BOLTON. Tetrahedron, **42**, 1007 (1986).
10. N. BABA, K. NISHIYAMA, J. ODA, and Y. INOUYE. Agric. Biol. Chem. **40**, 1259 (1976).
11. R. M. G. ROBERTS, D. OSTOVIC, and M. M. KREEVOY. Faraday Disc. Chem. Soc. **74**, 257 (1982).
12. R. M. G. ROBERTS, D. OSTOVIC, and M. M. KREEVOY. J. Org. Chem. **48**, 2053 (1983).
13. D. OSTOVIC, I. H. LEE, R. M. G. ROBERTS, and M. M. KREEVOY. J. Org. Chem. **50**, 4206 (1985); M. M. KREEVOY, D. OSTOVIC, I. H. LEE, D. A. BINDER, and G. W. KING. J. Am. Chem. Soc. **110**, 524 (1988).
14. J. W. BUNTING and N. P. FITZGERALD. Can. J. Chem. **63**, 655 (1985).
15. J. W. BUNTING and S. SINDHUATMADJA. J. Org. Chem. **46**, 4211 (1981).
16. J. W. BUNTING, V. S. F. CHEW, and G. CHU. J. Org. Chem. **47**, 2303 (1982).
17. D. J. CREIGHTON, J. HADJU, G. MOOSER, and D. S. SIGMAN. J. Am. Chem. Soc. **95**, 6855 (1973).
18. J. HADJU and D. S. SIGMAN. J. Am. Chem. Soc. **97**, 3524 (1975).
19. J. HADJU and D. S. SIGMAN. J. Am. Chem. Soc. **98**, 6060 (1976).
20. J. HADJU and D. S. SIGMAN. Biochemistry, **16**, 2841 (1977).
21. S. SHINKAI, T. IDE, H. HAMADA, O. MANABE, and T. KUNITAKE. J. Chem. Soc. Chem. Commun. 848 (1977).
22. S. SHINKAI, T. IDE, and O. MANABE. Bull. Chem. Soc. Jpn. **51**, 3655 (1978).
23. A. OHNO, T. SHIO, H. YAMAMOTO, and S. OKA. J. Am. Chem. Soc. **103**, 2045 (1981).
24. M. F. POWELL and T. C. BRUICE. J. Am. Chem. Soc. **104**, 5834 (1982); J. Am. Chem. Soc. **105**, 7139 (1983).
25. T. T. ROMOFF, N. S. SAMPSON, and P. VAN EIKEREN. J. Org. Chem. **52**, 4454 (1987).
26. A. VAN LAAR, H. J. VAN RAMESDONK, and J. W. VERHOEVEN. Recl. Trav. Chim. Pays-Bas, **102**, 157 (1983).
27. J. W. BUNTING, V. S. F. CHEW, G. CHU, N. P. FITZGERALD, A. GUNASEKARA, and H. T. P. OH. Bioorg. Chem. **12**, 141 (1984).
28. J. W. VERHOEVEN, W. VAN GERRESHEIM, F. M. MARTENS, and S. M. VAN DER KERK. Tetrahedron, **42**, 975 (1986).
29. S. SHINKAI, T. TSUNO, and O. MANABE. Chem. Lett. 1203 (1981).

Can. J. Chem. Downloaded from www.nrcresearchpress.com by 196.1.178.254 on 09/07/12
For personal use only.

30. D. OSTOVIC, R. M. G. ROBERTS, and M. M. KREEVOY. J. Am. Chem. Soc. **105**, 7629 (1983).
31. M. M. KREEVOY and I. H. LEE. J. Am. Chem. Soc. **106**, 2550 (1984).
32. M. M. KREEVOY, D. OSTOVIC, D. G. TRUHLAR, and B. C. GARRETT. J. Phys. Chem. **90**, 3766 (1986).
33. T. C. BRUICE, L. MAIN, S. SMITH, and P. Y. BRUICE. J. Am. Chem. Soc. **93**, 7327 (1971).
34. D. J. T. PORTER, G. BLANKENHORN, and L. I. INGRAHAM. Biochem. Biophys. Res. Commun. **52**, 447 (1973).
35. G. BLANKENHORN. Eur. J. Biochem. **50**, 351 (1975); **67**, 67 (1976).
36. D. J. PORTER and H. J. BRIGHT. J. Biol. Chem. **255**, 7362 (1980).
37. S. FUKUZUMI and T. TANAKA. Chem. Lett. 1513 (1982).
38. S. FUKUZUMI, N. NISHIZAWA, and T. TANAKA. Chem. Lett. 1755 (1983).
39. S. FUKUZUMI, N. NISHIZAWA, and T. TANAKA. J. Org. Chem. **49**, 3571 (1984).
40. A. K. COLTER, G. SAITO, and F. J. SHAROM. Can. J. Chem. **55**, 2741 (1976).
41. G. SAITO and A. K. COLTER. Tetrahedron Lett. 3325 (1977).
42. C. C. LAI and A. K. COLTER. J. Chem. Soc. Chem. Commun. 1115 (1980).
43. A. OHNO and N. KITO. Chem. Lett. 369 (1972).
44. D. C. DITTMER, A. LOMBARDO, F. H. BATZOLD, and C. S. GREENE. J. Org. Chem. **41**, 2976 (1976).
45. J. W. BUNTING and G. M. KAUFFMAN. Can. J. Chem. **62**, 729 (1984).
46. J. W. BUNTING, V. S. F. CHEW, and S. SINDHUATMADJA. Can. J. Chem. **59**, 3195 (1981).
47. D. MAGRATH and J. N. PHILLIPS. J. Chem. Soc. 1940 (1949).
48. Y. KIKUGAWA, M. KURAMOTO, I. SAITO, and S. YAMADA. Chem. Pharm. Bull. **21**, 1914 (1973).
49. R. A. REED. J. Chem. Soc. 679 (1944).
50. P. KARRER, H. J. V. KRISHNA, and R. SCHWYZER. Helv. Chim. Acta, **30**, 294 (1950).
51. M. FERLES and O. KOCIAN. Collect. Czech. Chem. Commun. **44**, 2238 (1979).
52. J. W. BUNTING and M. A. LUSCHER. Can. J. Chem. **66**, 2532 (1988).

Can. J. Chem. Downloaded from www.nrcresearchpress.com by 196.1.178.254 on 09/07/12
For personal use only.

Charge transfer complexation of *N,N*-dimethyl-*p*-toluidine with nitrogen heteroaromatic cations as a model for association complexes in hydride transfer reactions

JOHN W. BUNTING AND MARK A. LUSCHER
Department of Chemistry, University of Toronto, Toronto, Ont., Canada M5S 1A1

Received March 14, 1988

JOHN W. BUNTING and MARK A. LUSCHER. Can. J. Chem. **66**, 2532 (1988).

Charge-transfer complexation of *N,N*-dimethyl-*p*-toluidine (DMT) with each of the following *N*-methyl cations has been investigated in acetonitrile solution at 25°C: acridinium; phenanthridinium; 3-X-quinolinium and 4-X-isoquinolinium (X = H, Br, $CONH_2$, CN); 5-nitroisoquinolinium; 3-X-pyridinium (X = $CONH_2$, CN) (also the *N*-benzyl pyridinium cations); *N,N'*-dimethyl-4,4'-dipyridylium dication. Charge-transfer absorption maxima are reported, and extinction coefficients (ε_{max}) at these maxima and association constants (K) for 1:1 complex formation have been evaluated from the dependence of absorbance upon [DMT]. In general, the longest wavelength absorption maximum increases with increasing association constant. There is a strictly linear relationship between ε_{max} and $1/K$. These observations are considered in the context of theories of charge-transfer spectra. Such charge-transfer species are considered as models for the association complexes that are believed to exist upon the reaction pathway for hydride transfer between heteroaromatic cations. Although some significant qualitative relationships are apparent, variations in susceptibility of heteroaromatic cations to charge-transfer complexation are much smaller than variations in the reactivity of these cations towards hydride donor species.

JOHN W. BUNTING et MARK A. LUSCHER. Can. J. Chem. **66**, 2532 (1988).

Opérant dans une solution d'acétonitrile, à 25°C, on a examiné la complexation par transfert de charge de la *N,N*-diméthyl *p*-toluidine (DMT) avec chacun des cations *N*-méthylés suivants : acridinium, phénanthridinium, X-3 quinolinium et X-4 isoquinolinium (X = H, Br, $CONH_2$, CN), nitro-5 isoquinolinium, X-3 pyridinium ainsi que les cations *N*-benzyl pyridinium (X = $CONH_2$, CN) et le dication *N,N'*-diméthyl dipyridinium-4,4'. On rapporte les maxima d'absorption des transferts de charge; en se basant sur la relation qui existe entre l'absorbance et la [DMT], on a évalué les coefficients d'extinction (ε_{max}) à ces maxima ainsi que les constantes d'association (K) pour la formation des complexes 1:1. Il existe une relation strictement linéaire entre le ε_{max} et $1/K$. On considère ces observations dans le contexte des théories des spectres de transfert de charge. On considère que de telles espèces de transfert de charge sont de bons modèles pour les complexes d'association qui existeraient lors du cheminement réactionnel des hydrures au cours de leur transfert entre des cations hétéroaromatiques. Même s'il semble exister des relations qualitatives importantes, les variations dans la susceptibilité des cations hétéroaromatiques à la complexation de transfert de charge sont beaucoup plus faibles que les variations observées dans la réactivité de ces cations vis-à-vis des espèces donneurs d'hydrure.

[Traduit par la revue]

The transfer of a hydride ion to a nitrogen heteroaromatic cation from a dihydro derivative of another heteroaromatic cation (eq. [1]) has been extensively investigated in recent years. Such studies, which are summarized in the accompanying paper (1), are of interest because of their relevance to the reactions of the biologically important hydride sources NADH and NADPH in a wide range of enzymic redox reactions.

[1] $A^+ + DH \rightarrow AH + D^+$

In general, one would expect (2–4) that the reaction of eq. [1] would be preceded by the formation of an association complex between A^+ and DH, and a minimal description of such reactions would be that shown in Scheme 1.

$$A^+ + DH \rightleftharpoons [A^+ \cdot DH]$$
$$[A^+ \cdot DH] \rightleftharpoons [AH \cdot D^+]$$
$$[AH \cdot D^+] \rightleftharpoons AH + D^+$$

SCHEME 1

From the observation of saturation kinetics for pseudo-first-order rate constants for reactions of the type shown in eq. [1], evidence is beginning to accumulate (1, 5–8) for the presence of 1:1 association complexes between the reactants in such reactions. Many such association complexes appear to be quite weak, and it is clear that, at least for predominantly aqueous solutions, limited solubilities of the reactants will often not permit studies at sufficiently high reactant concentrations to allow the observation of complexation and the evaluation of association constants. We have therefore sought an indirect method of estimating the likely extent of complexation of a variety of heteroaromatic cation hydride acceptors (A^+) with a common hydride donor (DH).

To a first approximation, one may characterize the $[A^+ \cdot DH]$ association complex as a charge-transfer complex between the DH electron donor and the A^+ acceptor (4). In fact, the formation of a charge-transfer complex between 1-benzyl-1,4-dihydronicotinamide (**1**) and the 10-methylacridinium cation (**2**) has been spectroscopically observed (5). This complex has λ_{max} in the vicinity of 550 nm in methanolic solution, which is quite similar to that reported (9) (λ_{max} = 555 nm) for the complex formed between *N,N*-dimethylaniline and this same cation. It is also intriguing that both of these charge-transfer spectra are quite similar to the spectrum reported (10–12) for the *N*-methylacridanyl radical (**3**) (λ_{max} = 520 nm), since one interpretation of the electronic structure of the $[A^+ \cdot DH]$ charge-transfer complex is in terms of a resonance contribution from the species $[A^{\cdot} \cdot DH^{\cdot +}]$. These considerations suggest that the complexation of aniline derivatives with heteroaromatic cations may be a reasonable simulation of the complexation of 1,4-dihydronicotinamides with such cations. There are a number of reports in the literature of the spectral observation of complexes between aniline derivatives (9, 13–16), or other π-excessive electron donors (17–26), and heteroaromatic cations. However, we have been unable to find any report of a systematic quantitative study of this phenomenon.

We now present an investigation of the charge-transfer complexation of *N,N*-dimethyl-*p*-toluidine (**4**) with many of the heterocyclic cations that have been used as hydride acceptors

Can. J. Chem. Downloaded from www.nrcresearchpress.com by 196.1.178.254 on 09/07/12
For personal use only.

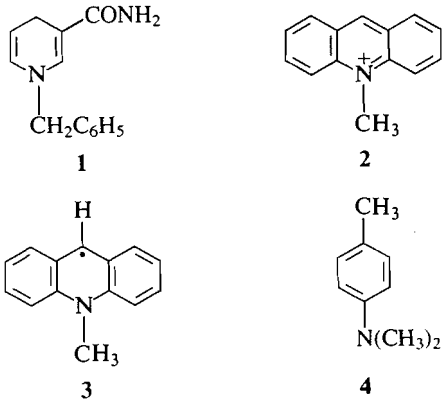

in recent investigations of reactions of the type described in eq. [1]. We present data upon the spectral characterization of such complexes, and also equilibrium constants for their formation, as a function of cation structure and substitution, for a variety of pyridinium (**5** and **6**), quinolinium (**7**), isoquinolinium (**8**), acridinium (**2**), and phenanthridinium (**9**) cations. The choice of *N*,*N*-dimethyl-*p*-toluidine as donor species was made so as to minimize interference from coupling reactions of the type described by Ballard *et al.* (15). In this initial study, acetonitrile was chosen as a solvent, rather than an aqueous or alcoholic medium, to minimize complications that may arise from nucleophilic addition to these cations. Such hydroxide or alkoxide adducts would also be potential donors in charge-transfer complexation with these heteroaromatic cations.

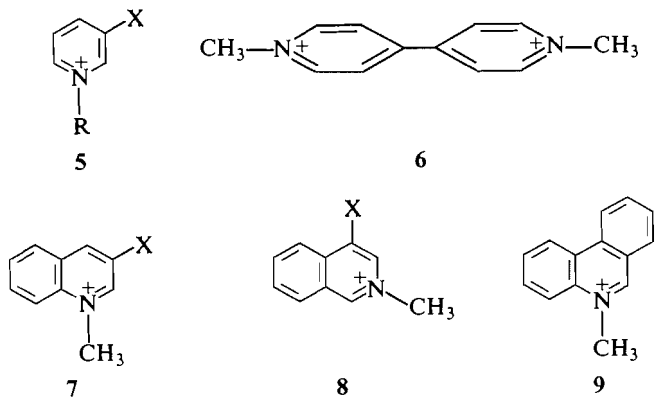

Experimental

Materials

Most of the *N*-methyl heteroaromatic cations were available as their chloride or bromide salts from recent or concurrent (1) studies in our laboratory. In all cases, these were recrystallized several times, and their identities were confirmed by ^{1}Hmr spectroscopy. The dibromide salt of the *N*,*N*′-dimethyl-4,4′-dipyridylium dication (**6**) was prepared by stirring 4,4′-dipyridyl with excess methyl bromide in a pressure bottle for several days at room temperature. The yellow solid was recrystallized several times from a 1:1 mixture of methanol and ethanol and characterized by ^{1}Hmr spectroscopy.

N,*N*-Dimethyl-*p*-toluidine (Aldrich Chemical Co.) was distilled several times under vacuum to give a very pale yellow liquid. Stock samples of this compound were redistilled weekly to ensure purity. All acetonitrile solutions were made from the hplc grade solvent supplied by Aldrich Chemical Co.

Spectroscopic studies

The charge-transfer absorbance spectrum was measured for each cation in a solution (3 mL) containing acetonitrile (2 mL) and *N*,*N*-dimethyl-*p*-toluidine (1 mL) and the chloride or bromide salt of the heterocyclic cation (usually 2 mM). Absorbance maxima (λ_{max}) were evaluated from these curves, but extinction coefficients were calculated from the subsequent spectrophotometric determination of the association constants. Studies of several cations, which were available as both the chloride and bromide salts, gave identical results for these two counterions.

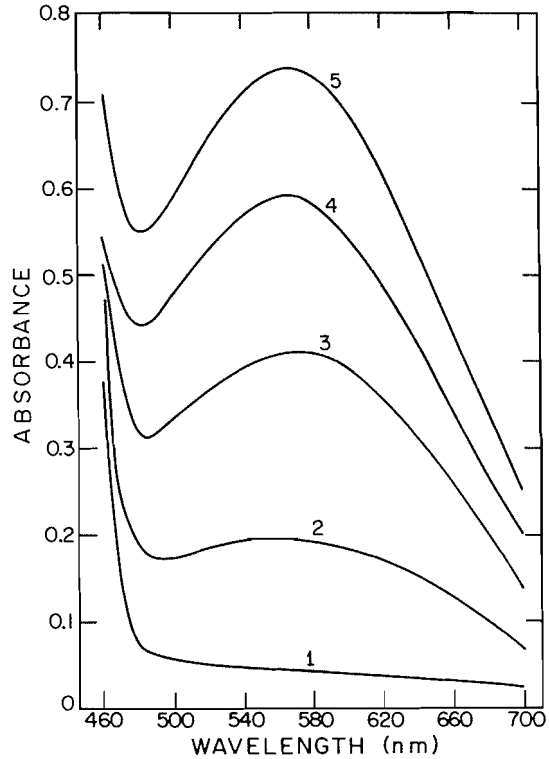

FIG. 1. The absorption spectrum (1-cm path) of 10-methylacridinium chloride (5 mM) in acetonitrile solution in the presence of the following concentrations (M) of *N*,*N*-dimethyl-*p*-toluidine: 1, 0; 2, 0.077; 3, 0.189; 4, 0.309; 5, 0.540.

All equilibrium constants were evaluated spectrophotometrically (Cary 210 spectrophotometer) in acetonitrile solution at 25°C. Absorbances were read at a wavelength in the vicinity of λ_{max} immediately upon preparation of solutions that were made by mixing appropriate volumes of a stock solution of the heterocyclic salt in acetonitrile, *N*,*N*-dimethyl-*p*-toluidine, and acetonitrile to give a final total volume of 3 mL. Each of these components was individually stored in a vial thermostatted at 25°C. Absorbances were measured at a constant concentration of the heterocyclic salt (usually 2 mM), and at about ten different concentrations of *N*,*N*-dimethyl-*p*-toluidine, covering at least a tenfold range in the concentration of this aniline. Equilibrium constants (K) and extinction coefficients (ε_{max}) of the complexes were evaluated as described below.

Results

Figure 1 shows the electronic absorption spectrum as a function of the concentration of *N*,*N*-dimethyl-*p*-toluidine (DMT) immediately upon mixing DMT with 10-methylacridinium chloride in acetonitrile solution. These spectra are somewhat unstable, and undergo small changes over a period of time; nevertheless the formation of a species of $\lambda_{max} \approx 572$ nm, having an absorbance that is dependent upon [DMT], is quite clear. The formation of this species absorbing at 572 nm appears to occur "instantaneously" upon mixing these solutions, with slight decreases in absorbance in this region usually accompanying the subsequent slow process mentioned above. All absorbance measurements used in the calculation of equilibrium

Can. J. Chem. Downloaded from www.nrcresearchpress.com by 196.1.178.254 on 09/07/12
For personal use only.

TABLE 1. Charge-transfer absorption maxima and equilibrium constants for complexation of *N*,*N*-dimethyl-*p*-toluidine with *N*-methyl heteroaromatic cations[a]

N-methyl cation	λ_{max} (nm)	ε_{max} ($M^{-1}cm^{-1}$)	$K(M^{-1})^b$	$K(M^{-1})^c$	$K(M^{-1})^d$	$K_c(M^{-1})^i$
Acridinium	572	625	0.54 (±0.03)	0.54	0.54	1.03
Phenanthridinium	425	900	0.29 (±0.01)	0.29	0.27	0.82
Quinolinium	427	2850	0.070(±0.007)	<0.10	0.11	0.60
3-$CONH_2$	440	1370	0.18 (±0.02)	0.18	0.23	0.71
3-Br	482	1080	0.269(±0.007)	0.269	0.30	0.80
3-CN	525	450	0.94 (±0.07)	0.97	0.72	1.47
Isoquinolinium	400	3930	0.048(±0.006)	<0.067	0.077	0.58
4-$CONH_2$	420	[e]	0.15 (±0.01)	0.16	0.21	0.68
4-Br	445	1050	0.227(±0.005)	0.233	0.234	0.76
4-CN	514	540	0.72 (±0.04)	0.69	0.54	1.25
5-NO_2	[f]	[f]	0.20 (±0.02)	0.26	0.29	0.73
4,4′-Dipyridylium dication	500	1180	0.22 (±0.02)	0.22	0.14	0.75
3-$CONH_2$-pyridinium[g]	<400[h]	[h]	0.070(±0.007)	<0.1	0.30	0.60
3-CN-pyridinium[g]	<400[h]	[h]	0.133(±0.005)	0.125	0.12	0.66
3-$CONH_2$-pyridinium	<400[h]	[h]	<0.05			
3-CN-pyridinium	<400[h]	[h]	<0.05			

[a]In acetonitrile solution at 25°C.
[b]Calculated by Wilkinson's iterative method using weighted data points.
[c]By direct fitting to eq. [2] using the Marquardt algorithm iterative method.
[d]From least-squares analysis of Benesi–Hildebrand plots.
[e]Stock solution was a saturated solution of uncertain concentration. *K* is not influenced by this concentration; however, accurate ε_{max} are not obtainable.
[f]No discrete maximum observable (see text).
[g]*N*-Benzyl cation.
[h]Absorption maximum is obscured by absorption from the high [DMT] required.
[i]Calculated from eq. [8] as described in text.

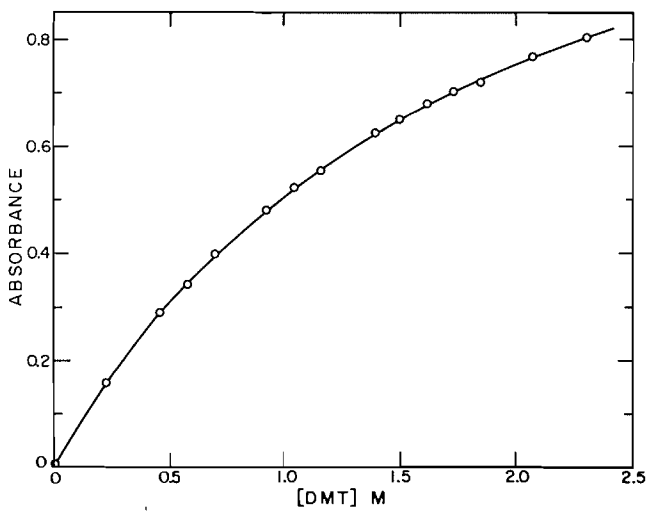

FIG. 2. Variation of the absorbance (1-cm path) of acetonitrile solutions of 10-methylacridinium chloride (2 mM) at 550 nm as a function of the concentration of *N*,*N*-dimethyl-*p*-toluidine (DMT).

constants were obtained within 30 s of mixing temperature-equilibrated solutions of the reactants. Studies of the time dependence of the absorbance at fixed wavelength indicated that extrapolations to "zero time" produced less than 1% change in these absorbances.

The variation of absorbance as a function of [DMT] is shown in Fig. 2 for mixtures of DMT with a fixed concentration of the 10-methylacridinium cation. This concentration dependence of the absorbance (A) is consistent with eq. [2], which is derived for 1:1 complexation between donor and acceptor, with the donor (D) being present in large excess (>10-fold) over the acceptor cation (total concentration $[A^+]_T$ of complexed and free cation), and the complex being the only species with a significant extinction coefficient (ε_c) at the wavelength under study. Fitting eq. [2] to the experimental data in Fig. 2 allows the evaluation of the association constant (K) and ε.

$$[2] \qquad A = \frac{\varepsilon K[D][A^+]_T}{1 + K[D]}$$

Similar spectral observations were made for solutions containing mixtures of DMT and a variety of other nitrogen heteroaromatic cations. The absorption maximum of the association complex is sensitive to the structure of the cationic acceptor (Table 1). Most cations show significant curvature in absorbance vs. [DMT] (e.g., Figs. 2 and 3) and equilibrium constants for 1:1 complex formation could be evaluated according to eq. [2]. For the *N*-methyl pyridinium cations, association with DMT appears to be so weak that absorbance vs. [DMT] is linear (Fig. 4), and consequently only lower limits for the association constants are accessible in these cases.

All absorption maxima (λ_{max}), extinction coefficients (ε_{max} at λ_{max}), and association constants (K) measured for DMT in the current study are collected in Table 1. In several cases, the charge-transfer absorption maximum is at sufficiently short wavelength that it is not readily accessible because of the absorbance by DMT at these wavelengths. A brown charge-transfer complex is formed immediately upon addition of DMT to solutions of the 2-methyl-5-nitroisoquinolinium cation;

Can. J. Chem. Downloaded from www.nrcresearchpress.com by 196.1.178.254 on 09/07/12
For personal use only.

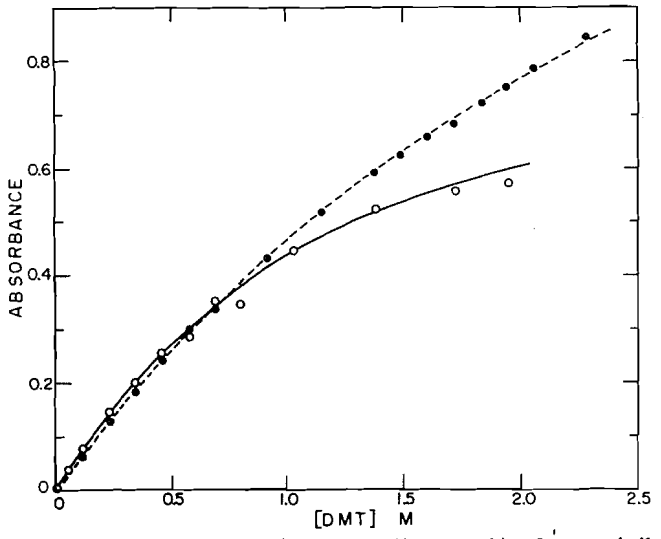

FIG. 3. Variation of the absorbance (1-cm path) of acetonitrile solutions of 3-cyano-1-methylquinolinium chloride (2 mM) (○) at 525 nm and 3-bromo-1-methylquinolinium chloride (2 mM) (●) at 482 nm as a function of the concentration of *N*,*N*-dimethyl-*p*-toluidine (DMT).

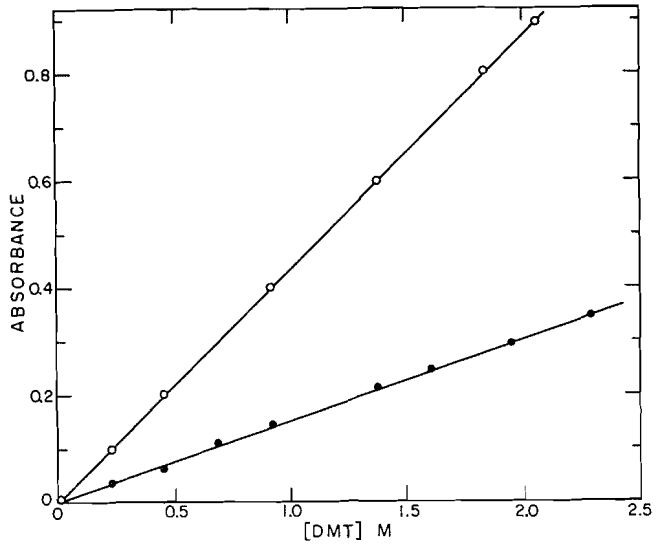

FIG. 4. Variation of the absorbance (1-cm path) of acetonitrile solutions of 3-cyano-1-methylpyridinium chloride (2 mM) (○) at 440 nm and 3-carbamoyl-1-methylpyridinium chloride (2 mM) (●) at 430 nm as a function of the concentration of *N*,*N*-dimethyl-*p*-toluidine (DMT).

however, the spectrum of this charge-transfer species appears to be very broad and featureless, with a tail extending to >700 nm, and a definitive absorbance maximum is not observed. Observation of λ_{max} for the charge-transfer species in this case is also complicated by the absorption spectrum of this cation, which shows a weak shoulder in the vicinity of 425 nm ($\varepsilon \approx 100\ M^{-1}\ cm^{-1}$) and a broad tail extending out to >550 nm at the concentrations used in the current study.

Methods for the evaluation of equilibrium constants for charge-transfer complex formation in studies of the current type have been reviewed on several occasions (27, 28). In Table 1 we present three values for each equilibrium constant. These values were obtained using three different methods of data analysis: (*i*) the classical Benesi–Hildebrand technique (29) using a plot of $1/A$ vs. $1/[D]$ in which K is given by the Y-intercept:slope ratio; (*ii*) evaluation of the parameters K and ε_{max} by directly fitting A as a function of [D] to eq. [2] using an iterative technique (30) based upon the Marquardt algorithm; and (*iii*) by using the weighted nonlinear regression iterative method developed by Wilkinson (31) for fitting steady-state rate data in enzyme kinetic studies to the Michaelis equation, which has the same analytical form as eq. [2]. In general there is good agreement for values of K evaluated by each of these techniques, with almost exact agreement from methods (*ii*) and (*iii*), although the latter of these methods is preferable since consecutive iterations converge upon a final set of parameters much more quickly when small equilibrium constants (<0.1) are involved. The upper limits for K that are given for several complexes in column 5 of Table 1 are the values obtained after arbitrarily stopping the iterative technique after 50 cycles of the Marquardt algorithm, which was begun using the Benesi–Hildebrand parameters as the initial estimates. Convergence in the Wilkinson method using these same data was complete after only four iterative cycles. We have used the parameters evaluated by Wilkinson's method (column 4 of Table 1) in all comparisons in the discussion that follows. While all Benesi–Hildebrand plots are quite linear for the current data sets ($r > 0.999$ in most cases), this method appears to significantly overestimate K for the weakest complexes ($K < 0.1$).

Discussion

All of the nitrogen heteroaromatic cations listed in Table 1 form charge-transfer complexes in the presence of *N*,*N*-dimethyl-*p*-toluidine in acetonitrile solution. In most cases plots of absorbance vs. [DMT] show saturation with increasing [DMT]. The [DMT] varies as high as 1 mL in a total solution volume of 3 mL (i.e., 2.31 M) suggesting that significant solvent effects may influence the absorbance vs. [DMT] curves of Figs. 2 and 3. However, the plots in Fig. 4 are clearly linear. These data cover the highest concentration ranges of DMT in any of these studies, and represent cases where complexation is expected to be weakest. The linearity of the plots in Fig. 4 can be taken as an indication that solvent effects are not an important influence in these studies, and this conclusion is also supported by the fact that curvature in the other plots is very dependent upon cation structure. We therefore confidently attribute the saturation effects in Figs. 2 and 3 to complexation that is consistent with 1:1 interaction between DMT and the heterocyclic cation. In all cases eq. [2], which is derived upon this assumption, gives a close fit to the experimental data.

From a perusal of the data in Table 1, it can be concluded that the charge-transfer absorption maxima (λ_{max}), the extinction coefficients (ε_{max}) at these maxima, and the equilibrium association constants (K) for charge-transfer complex formation all vary systematically with the structure and the substitution of the heterocyclic cation. In general, as discussed in more detail below, strong complexation (large K) is associated with the longest wavelength absorption maxima, but the weakest absorbance intensities at these maxima.

Quinolinium and isoquinolinium cations

We first consider substituent effects within the series of C-3 substituted (H, $CONH_2$, Br, CN) quinolinium cations (**7**), and also the corresponding series of C-4 substituted isoquinolinium cations (**8**). Within each of these two series of cations, K increases in the order $H < CONH_2 < Br < CN$, and λ_{max} also increases in this same order. The intensities (ε_{max}) of the

Can. J. Chem. Downloaded from www.nrcresearchpress.com by 196.1.178.254 on 09/07/12
For personal use only.

charge-transfer absorbance maxima in these series seem to decrease in this same order; i.e., ε_{max} decreases with increasing λ_{max}. In all cases, K is slightly larger, and the charge-transfer maximum (λ_{max}) is somewhat longer, for the quinolinium cation than for the correspondingly substituted isoquinolinium cation.

Within each of these two series of cations, the substituent effects upon K and λ_{max} follow closely the substituent Hammett σ_m values defined for the ionization of *meta*-substituted benzoic acids in aqueous solutions. The dependence of log K upon σ_m appears to be essentially linear, with a Hammett ρ value of 1.8 ($\pm$0.1) for the quinolinium cations (r = 0.993) and ρ = 1.90 ($\pm$0.05) for the isoquinolinium cations (r = 0.999). These ρ values are considerably smaller than are found (ρ = 5.9 (32)) for the pK_a values (which also correlate with σ_m) for deprotonation of the 3-X-quinolinium and 4-X-isoquinolinium cations. However, the sign and magnitude of these ρ values for log K clearly indicate significant transfer of fractional negative charge (electron density) to these cationic acceptors upon charge-transfer complexation with this donor.

Benzylogous heteroaromatic cations

Variations in λ_{max} for charge-transfer spectra in the order acridinium > phenanthridinium $\approx$ quinolinium > isoquinolinium > pyridinium for cationic acceptors with a constant donor have been reported several times in the literature (9, 15, 17, 19), and are again found in the current study (Table 1). Although individual λ_{max} are quite donor and solvent dependent, this order does not change and, as discussed by other workers, can be correlated with the energies of the LUMO's (9, 24) or the electron affinities (25) of these cationic acceptors. The relatively strong complex observed for the *N,N'*-dimethyl-4,4'-dipyridylium dication (also known as the methyl viologen or paraquat dication) is consistent with its ready susceptibility to one-electron reduction to the radical cation (33, 34). This observation stresses the importance of the relationship between the ability of a heteroaromatic cation to accept a single electron (35), and its susceptibility to charge-transfer complexation with an appropriate donor species such as DMT.

Literature data on equilibrium constants for charge-transfer complexation by these cationic acceptors are quite sparse. We have been unable to locate any report of equilibrium constants for complexation of the *N*-methyl acridinium, phenanthridinium, quinolinium, isoquinolinium, and pyridinium cations with a common donor. Kampar and Neiland (22) have reported K in the order quinolinium > isoquinolinium > pyridinium for complexation of the anions of several 2-(substituted phenyl)-1,2-indandiones with these *N*-methyl cations in ethanolic solution. These complexes are much stronger (K in the range 24–172 M^{-1}) than those investigated in the current study, although the relative values of K for the quinolinium and isoquinolinium cations are similar to those reported in Table 1. The only other K that we have located for these cationic acceptors are the data of Shinitzky (36) for association between acridine, quinoline, and isoquinoline and their corresponding cations. Although the acridinium cation does form the strongest of these complexes, these data cannot be simply related to the current study since they do not refer to a common donor species interacting with these various cations.

In Fig. 5, the relationship between log K for charge-transfer complexation with DMT and the pK_{R^+} value (37) for hydroxide ion addition to these heterocyclic cations is explored, with the thermodynamically more stable hydroxide adducts (C-2 or C-4 as the case may be) being considered for the quinolinium cations (38). For this purpose we have considered the cations of Table 1 in two distinct groups. The *N*-methyl acridinium, phenanthridinium, 3-bromoquinolinium, 4-bromoisoquinolinium, quinolinium, and isoquinolinium cations appear to describe a reasonably linear relationship between log K and pK_{R^+}:

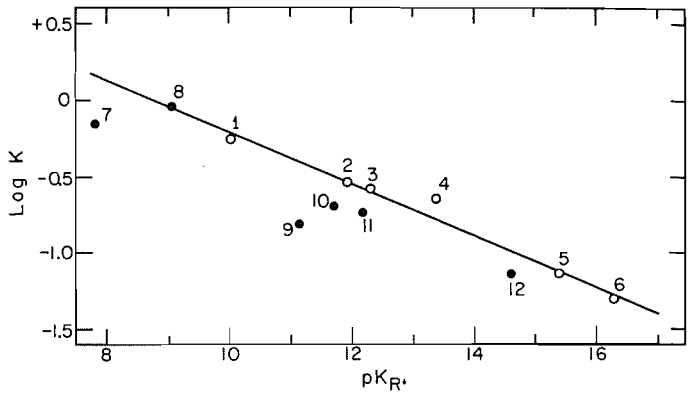

FIG. 5. Dependence of log K (from Table 1) upon pK_{R^+} for the following *N*-methyl cations: 1, acridinium; 2, phenanthridinium; 3, 3-bromoquinolinium; 4, 4-bromoisoquinolinium; 5, quinolinium; 6, isoquinolinium; 7, 4-cyanoisoquinolinium; 8, 3-cyanoquinolinium; 9, 4-carbamoylisoquinolinium; 10, 5-nitroisoquinolinium; 11, 3-carbamoylquinolinium; 12, 1-benzyl-3-carbamoylpyridinium. Correlation line is calculated for cations 1–6 only (see text).

[3] $$\log K = -0.17\ (\pm 0.02)\ pK_{R^+} + 1.5\ (\pm 0.2) \qquad (r = 0.982)$$

The remaining cations bear cyano, carboxamido, or nitro substituents, which are known (38, 39) to stabilize the hydroxide adducts via resonance effects that are not expected to be applicable to charge-transfer complexes. Consistent with this expectation, each of these cations is less efficient (although the 3-cyano-1-methylquinolinium cation is apparently an exception) as a charge-transfer acceptor than predicted by the correlation line (eq. [3]) for other cations in which such resonance effects are not present. That such cyano and carboxamido cations would deviate from eq. [3] is actually predictable from the correlations of log K with σ_m that are noted above, since pK_{R^+} is known (38, 39) to correlate with σ_p^- for 4-substituted isoquinolinium cations and 3-substituted quinolinium cations. The weak dependence of log K upon pK_{R^+} that is expressed by eq. [3] is presumably a reflection of the fact that hydroxide ion addition results in complete charge neutralization upon these cations, whereas charge-transfer complexation results in only a fractional transfer of electron density.

A general tendency for K to increase with λ_{max} while ε_{max} decreases with increasing λ_{max} seems to be apparent for the data in Table 1. A detailed analysis of these trends indicates that there is no simple general relationship between λ_{max} and either K or ε_{max}. However, a general relationship between ε_{max} and K, covering all examples in Table 1 for which both of these parameters are available, is apparent in Fig. 6. Least-squares analysis indicates that this relationship is linear (r = 0.998), and corresponds to eq. [4]:

[4] $$\varepsilon_{max} = 175\ (\pm 4)(1/K) + 330\ (\pm 30)$$

From quantum mechanical considerations, Mulliken's theoretical treatment of charge-transfer complexation (42, 46), and

Can. J. Chem. Downloaded from www.nrcresearchpress.com by 196.1.178.254 on 09/07/12
For personal use only.

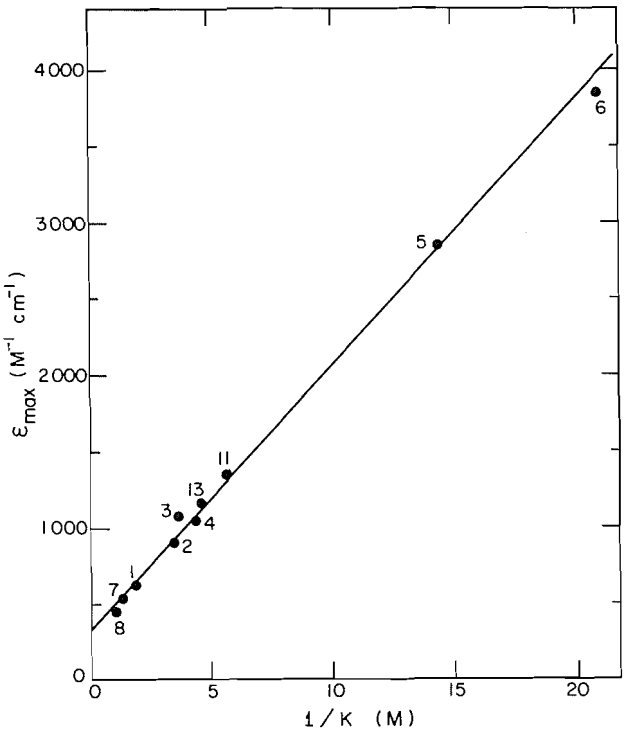

FIG. 6. Dependence of ε_{max} upon $1/K$ for *N*-methyl cations. Data points are as indicated in legend to Fig. 5; 13, *N*,*N*′-dimethyl-4,4′-dipyridylium dication.

its extension by Murakami (43), leads to a prediction that the intensity of the charge-transfer absorption band should increase with increasing complex strength within a series of structurally related complexes. However, the usual experimental result is actually the reverse of this prediction; i.e., ε_{max} is usually observed to decrease as the association constant increases. McGlynn (40) has commented upon this situation in detail, and we note this commonly observed trend is also reproduced by the data from our current study, and is expressed by eq. [4] above. The only earlier attempt at such a quantitative relationship seems to be the report of Tamres *et al.* (41) who found that ε_{max} is linearly dependent upon $1/\sqrt[3]{K}$ for the association of a series of five methylbenzenes with molecular iodine. The current relationship of eq. [4] appears to be the first reported for a common donor with a series of different acceptors, and also is the most extensive quantitative relationship of this type of which we are aware.

Since Mulliken's ideas form the basis of most modern theoretical considerations of charge-transfer complexation (44, 45), a rationalization of this divergence between theory and experimental result is essential. Two such rationalizations have been reported (46, 47), and these make use of two essentially independent hypotheses. The current data, and in particular eq. [4], will now be considered briefly in the context of each of these hypotheses.

Orgel and Mulliken (46) introduced the concept of contact charge-transfer absorption during random encounters between donor and acceptor molecules. Such contact species are assumed to contribute to the observed intensity of the charge-transfer band, but are such weak complexes that the association constants for their formation approach zero. In a system in which measurable association complexes exist in equilibrium with the donor, acceptor, and contact species, Orgel and Mulliken showed (46) that the experimentally determined extinction coefficient (ε_{max} in Table 1) is given by

$$[5] \quad \varepsilon_{max} = \varepsilon_c(1 + \rho/K)$$

where ε_c is the true extinction coefficient of a stable 1:1 charge-transfer complex formed with association constant K, and ρ is a function of the average number of possible contact sites for a donor molecule around an acceptor molecule under conditions of loose thermal contact. This model predicts that the evaluation of data according to eq. [2] gives the correct association constant for stable complexes, even though the apparent extinction coefficient is exalted by the presence of contact charge-transfer absorption. Combination of eqs. [4] and [5] gives

$$[6] \quad \varepsilon_c(1 + \rho/K) = 175/K + 330$$

An obvious solution to eq. [6] is $\varepsilon_c = 330$ and $\rho = 0.53$, which would require that the extinction coefficient of the charge-transfer species be independent of K.

An alternative hypothesis is due to Carter, Murrell, and Rosch (47), who emphasize the role played by solvation, and ignore any contribution from contact charge-transfer species. These workers assume an equilibrium of the form:

$$[7] \quad A{\cdot}S_n + D{\cdot}S_m \rightleftharpoons AD{\cdot}S_p + qS$$

where $q = (n + m - p)$ is the difference in the number of solvent molecules in the first solvation shells of the solvated complex ($AD{\cdot}S_p$) and the solvated donor and acceptor species, i.e., the number of solvent molecules "liberated" upon formation of one molecule of the complex. According to this model, the experimentally evaluated constants K and ε_{max} (according to eq. [2]) are given by

$$[8] \quad K = K_c - q(m + 1)/S_0$$

$$[9] \quad \varepsilon_{max} = \varepsilon_c K_c/K$$

where K_c is the equilibrium constant for eq. [7], ε_c is the extinction coefficient for the solvated charge-transfer complex, and S_0 is the molar concentration of the pure solvent. Equations [8] and [9] imply that analysis of experimental data according to eq. [2] underestimates the association constant, and overestimates the extinction coefficient for the complex. Combination of eqs. [8] and [9] leads to

$$[10] \quad \varepsilon_{max} = \varepsilon_c + \varepsilon_c q(m + 1)/(K_c S_0)$$

which in the light of eq. [4] requires $\varepsilon_c = 330$ and $q(m + 1) = 10$ ($S_0 = 19.2$ for acetonitrile). This value for $q(m + 1)$ is similar to values for this function obtained in other analyses of this type (47).

This solvation model, like the contact species model discussed above, gives an extinction coefficient that is independent of the acceptor species in the current study. The analysis according to eq. [8] requires that the true association constants defined by eq. [7] are given by $K_c = K + 0.53$. Values of K_c calculated in this way are included in the final column of Table 1. It is important to note that the same relative order is obtained for the susceptibilities of the various heteroaromatic cations to charge-transfer complex formation, irrespective of the model assumed in the evaluation of the association constants.

Complexation in hydride transfer reactions

The presence of association complexes (as described by Scheme 1) in hydride transfer reactions between heteroaromatic cations is supported by the observation (1, 5–8) of kinetic

Can. J. Chem. Downloaded from www.nrcresearchpress.com by 196.1.178.254 on 09/07/12
For personal use only.

Can. J. Chem. Downloaded from www.nrcresearchpress.com by 196.1.178.254 on 09/07/12
For personal use only.

saturation effects in some of these reactions, and also by the spectroscopic observations (5) of a charge-transfer complex (λ_{max} = 550 nm) in the reaction between the *N*-methylacridinium cation and 1-benzyl-1,4-dihydronicotinamide. However, it is not easy to demonstrate that such species are productive complexes upon the reaction coordinate. In fact, we have argued (6) that the strong complexation observed (K = 10–1800 M^{-1}) in the reduction of 5-nitroisoquinolinium cations by 1,4-dihydronicotinamides is only readily interpretable in terms of nonproductive species that lie off the reaction coordinate for hydride transfer. This conclusion is supported by the data in Table 1, which indicate that the 2-methyl-5-nitroisoquinolinium cation does not form unusually stable charge-transfer complexes relative to related heterocyclic cations. However, in the accompanying paper (1), we present data for other hydride transfers that can be sensibly interpreted in terms of productive 1:1 complexation between the hydride donor and acceptor species.

For a reaction according to eq. [1], which actually proceeds via a weak productive 1:1 complex between A^+ and DH, the apparent second-order rate constant (k_2) is equal to the product $k_c \cdot K$, where k_c is the first-order rate constant for hydride transfer within a complex formed with association constant K. It is well established that for the reduction of individual series of substituted quinolinium (8) and isoquinolinium cations (7) by 1-benzyl-1,4-dihydronicotinamide, the experimentally determined log k_2 is linearly correlated with pK_{R^+} for hydroxide ion addition to these cations. For a hydridic transition state (6, 48), one also would expect that, to a first approximation, log k_c would also be related to pK_{R^+}, and relationships such as eq. [3] now also predict a similar dependence upon pK_{R^+} for log K. The relatively small slope of this correlation line suggests that the deviations observable for some cations in Fig. 5 would only appear as a small experimental scatter in a log k_2 vs. pK_{R^+} correlation.

Acridinium cations are well established as being intrinsically more reactive in their reduction by hydride donors than are related phenanthridinium, quinolinium, isoquinolinium, or pyridinium cations. Such enhanced reactivity is apparent if one compares (49) the relative rates of reduction and of hydroxide ion addition to such cations. This enhanced reactivity for acridinium cations also emerges in terms of a lower intrinsic barrier towards reduction when the rate data are treated (4) in terms of the Marcus theory. One possible interpretation of such enhanced reactivity would be in terms of a much greater susceptibility of acridinium cations towards formation of productive complexes with the hydride donor species. The complex between the 10-methylacridinium cation and DMT is one of the more stable species in Table 1; however, the differences in the relative susceptibilities to complex formation by the various cations in this table are not large. While it may be that DMT is not a good model for 1,4-dihydronicotinamide and related hydride donor species, we feel that at the present time the equilibrium constants in Table 1 should be accepted as representative relative association constants for the various heteroaromatic cations, and alternative reasons shoud be sought for their observed differences in reactivity with hydride donors.

Acridinium cations show enhanced reactivity relative to other heteroaromatic cations even in degenerate hydride transfer processes (2). The relative rates of such degenerate hydride transfers vary over a range of 66-fold under constant experimental conditions, with the relative rates of such degenerate reactions following the order (9,10-dihydroacridine + acridinium) > (5,6-dihydrophenanthridine + phenanthridinium) > (1,4-dihydroquinoline + quinolinium) > (1,4-dihydropyridine + pyridinium). Again, in terms of Scheme 1, one would predict that variations in overall rate might be attributable to variations in the strength of complex formation between donor and acceptor pairs. Of course, in such degenerate reactions, one now also has the complication that both the donor and the acceptor species vary from one reaction to the next, and the association constant for complex formation depends both upon the donor and the acceptor species. If the relative abilities of the donors to form complexes vary in the same order as their cationic acceptors (Table 1), then, in the context of Scheme 1, the relative rates of such degenerate reactions are predicted to be in the order that is experimentally observed. In this regard, it is intriguing that the largest association constants that we have attributed (1) to productive complex formation are for 10-methyl-9,10-dihydroacridine and 5-methyl-5,6-dihydrophenanthridine as the hydride donor species. As indicated above, these donor species are also the most reactive in degenerate hydride transfers.

While the current study is not conclusive, it does further implicate the association complexes of Scheme 1 as important intermediates to be considered in hydride transfer reactions between heteroaromatic cations. The extension of this work to the quantitative evaluation of the charge-transfer complexation of other donors, which more closely resemble the structures of typical hydride donor species, should provide further insights into the role of association complexes in determining the rates of hydride transfer between heteroaromatic cations.

Acknowledgements

We appreciate the continued support of this work by the Natural Sciences and Engineering Research Council of Canada. Some preliminary investigations in this area were initiated in our laboratory by Mr. H. T. P. Oh.

1. J. W. Bunting and M. L. Luscher. Can. J. Chem. **66**, 2524 (1988).
2. R. M. G. Roberts, D. Ostovic, and M. M. Kreevoy. Faraday Disc. Chem. Soc. **74**, 257 (1982).
3. T. T. Romoff, N. S. Sampson, and P. Van Eikeren. J. Org. Chem. **52**, 4454 (1987).
4. M. M. Kreevoy, D. Ostovic, I. H. Lee, D. A. Binder, and G. W. King. J. Am. Chem. Soc. **110**, 524 (1988).
5. J. Hadju and D. S. Sigman. J. Am. Chem. Soc. **98**, 6060 (1976).
6. J. W. Bunting and S. Sindhuatmadja. J. Org. Chem. **46**, 4211 (1981).
7. J. W. Bunting, V. S. F. Chew, and G. Chu. J. Org. Chem. **47**, 2303 (1982).
8. J. W. Bunting and N. P. Fitzgerald. Can. J. Chem. **63**, 655 (1985).
9. S. F. Mason. *In* Physical methods in heterocyclic chemistry. Vol. II. *Edited by* A. R. Katritzky. Academic Press, New York. 1963. pp. 76–84.
10. K. S. Peters, E. Pang, and J. Rudzki. J. Am. Chem. Soc. **104**, 5535 (1982).
11. L. E. Manring and K. S. Peters. J. Am. Chem. Soc. **105**, 5708 (1983).
12. L. E. Manring and K. S. Peters. J. Am. Chem. Soc. **107**, 6452 (1985).
13. V. A. Trofimov, O. N. Chupakhin, and Z. V. Pushkareva. Dokl. Akad. Nauk SSSR, **191**, 1302 (1970); Dokl. Chem. (Engl. Transl.) **191**, 304 (1970).
14. G. E. Ivanov. Khim. Geterotsikl. Soedin. 663 (1973); Chem. Heterocycl. Compd. (Engl. Transl.) 611 (1973).

15. R. E. BALLARD, J. JONES, and E. SUTHERLAND. Tetrahedron Lett. **23**, 3677 (1982).
16. A. S. N. MURTHY and A. P. BHARDWAJ. Spectrochim. Acta, Part A: **39A**, 415 (1983).
17. S. F. MASON. J. Chem. Soc. 2437 (1960).
18. E. LE GOFF and R. B. LACOUNT. J. Am. Chem. Soc. **85**, 1354 (1963).
19. J. NASIELSKI and E. VANDER DONCKT. Theor. Chim. Acta, **2**, 22 (1964).
20. T. G. BEAUMONT and K. M. C. DAVIS. J. Chem. Soc. (B), 1010 (1968).
21. T. G. BEAUMONT and K. M. C. DAVIS. Nature, **225**, 632 (1970).
22. V. E. KAMPAR and O. YA. NEILAND. Zh. Org. Khim. **8**, 225 (1972); J. Org. Chem. USSR (Engl. Transl.), **8**, 225 (1972).
23. V. E. KAMPAR and O. YA. NEILAND. Zh. Org. Khim. **9**, 335 (1973); J. Org. Chem. USSR (Engl. Transl.), **9**, 360 (1973).
24. C. PARKANYI and G. J. LEU. Z. Naturforsch. B: Anorg. Chem. Org. Chem. **30B**, 984 (1975).
25. V. E. KAMPAR and O. YA. NEILAND. Zhur. Obshch. Khim. **47**, 442 (1977); J. Gen. Chem. USSR (Engl. Transl.), **47**, 406 (1977).
26. L. SOCCORSI, M. L. TOSATO, M. C. RAMUSINO, and M. CIGNITTI. J. Electroanal. Chem. **116**, 699 (1980).
27. R. FOSTER. Organic charge transfer complexes. Academic Press, London. 1969. Chap. 6.
28. R. FOSTER. *In* Molecular complexes. Vol. 2. *Edited by* R. Foster. Elek Science, London. 1974. Chap. 3.
29. H. A. BENESI and J. H. HILDEBRAND. J. Am. Chem. Soc. **71**, 2703 (1949).
30. D. W. MARQUARDT. J. Soc. Ind. Appl. Math. **11**, 431 (1963); P. R. BEVINGTON. Data reduction and error analysis for the physical sciences. McGraw–Hill Book Co., New York. 1969. p. 237.
31. G. N. WILKINSON. Biochem. J. **90**, 324 (1961).
32. J. CLARK and D. D. PERRIN. Q. Rev. Chem. Soc. **18**, 295 (1964).
33. C. L. BIRD and A. T. KUHN. Chem. Soc. Rev. **10**, 49 (1981).
34. M. HEYROVSKY. J. Chem. Soc. Chem. Commun. 1856 (1987).
35. O. N. CHUPAKHIN, V. N. CHARUSIN, J. M. SOSONKIN, E. G. KOVALEV, and I. YA. POSTOVSKII. Khim. Geterotsikl. Soedin. 690 (1977); Chem. Heterocycl. Compd. (Engl. Transl.) 562 (1977).
36. M. SHINITZKY. Isr. J. Chem. **6**, 491 (1968).
37. J. W. BUNTING. Adv. Heterocycl. Chem. **25**, 1 (1979).
38. J. W. BUNTING and N. P. FITZGERALD. Can. J. Chem. **62**, 1301 (1984).
39. J. W. BUNTING, V. S. F. CHEW, and S. SINDHUATMADJA. Can. J. Chem. **59**, 3195 (1981).
40. S. P. MCGLYNN. Chem. Rev. **58**, 1113 (1958).
41. M. TAMRES, D. R. VIRZI, and S. SEARLES. J. Am. Chem. Soc. **75**, 4358 (1953).
42. R. S. MULLIKEN. J. Am. Chem. Soc. **74**, 811 (1952).
43. H. MURAKAMI. Bull. Chem. Soc. Jpn. **27**, 268 (1954).
44. J. N. MURRELL. J. Am. Chem. Soc. **81**, 5037 (1959).
45. C. J. BENDER. Chem. Soc. Rev. **15**, 475 (1986).
46. L. E. ORGEL and R. S. MULLIKEN. J. Am. Chem. Soc. **79**, 4839 (1957).
47. S. CARTER, J. N. MURRELL, and E. J. ROSCH. J. Chem. Soc. 2048 (1965).
48. M. M. KREEVOY and I. H. LEE. J. Am. Chem. Soc. **106**, 2550 (1984).
49. J. W. BUNTING and J. L. BOLTON. Tetrahedron, **42**, 1007 (1986).

Can. J. Chem. Downloaded from www.nrcresearchpress.com by 196.1.178.254 on 09/07/12
For personal use only.

Studies on the kinetics of racemization of 2,4-disubstituted-5(4*H*)-oxazolones

MAREK SLEBIODA,[1] MARC A. ST-AMAND,[2] FRANCIS M. F. CHEN, AND N. LEO BENOITON[3]
Department of Biochemistry, University of Ottawa, Ottawa, Ont., Canada K1H 8M5

Received November 20, 1987[4]

MAREK SLEBIODA, MARC A. ST-AMAND, FRANCIS M. F. CHEN, and N. LEO BENOITON. Can. J. Chem. **66**, 2540 (1988).

The kinetics of racemization of 2,4-disubstituted-5(4*H*)-oxazolones obtained from *N*-acetyl, *N*-benzoyl, and *N*-benzyloxycarbonylglycyl-L-leucine, -valine, and -phenylalanine have been studied in several solvents alone and in the presence of tertiary amines. The influence of the nature of the substituents on the rate of the reaction has been evaluated, and the values of the activation parameters $\Delta H^{\neq}$ and $\Delta S^{\neq}$ for the base-catalyzed reactions have been determined. The racemization process is governed by electronic effects of the C(2)-substituents and steric effects of the C(4)-substituents of the oxazolones. The thermodynamic data suggest that the 2-substituted-4-benzyl-5(4*H*)-oxazolones racemize more readily than the 4-alkyl analogues (alkyl ≠ benzyl) because of the unique conformation assumed by the benzyl substituent. The rate of the base-catalyzed reaction depends on the extent of hindrance about the nitrogen atom of the tertiary amine as well as on its basicity. The data suggest that the relative rates of racemization of oxazolones are not a true reflection of the relative tendencies to racemize of the pertinent residues during couplings of the parent acids.

MAREK SLEBIODA, MARC A. ST-AMAND, FRANCIS M. F. CHEN et N. LEO BENOITON. Can. J. Chem. **66**, 2540 (1988).

Opérant dans divers solvants seuls ainsi qu'en présence d'amines tertiaires, on a étudié la cinétique de la racémisation de 4*H*-oxazolones-5 disubstituées en positions 2,4, qui ont été obtenues à partir des *N*-acétyl, *N*-benzoyl et *N*-benzyloxycarbonyl-glycyl-L-leucine, -valine et -phénylalanine. On a évalué l'influence de la nature des substituants sur la vitesse de la réaction et on a déterminé les valeurs des paramètres d'activation $\Delta H^{\neq}$ et $\Delta S^{\neq}$ pour les réactions catalysées par les bases. Le processus de racémisation est gouverné par les effets électroniques des substituants en C(2) et par les effets stériques des substituants en C(4) des oxazolones. Les données thermodynamiques suggèrent que les benzyl-4 (4*H*)-oxazolones-5 substituées en position 2 se racémisent plus facilement que leurs analogues alkylés en position 4 (alkyle ≠ benzyle); la cause de cette différence serait la conformation unique qu'adopte le substituant benzyle. La vitesse de la réaction catalysée par les bases dépend de l'empêchement stérique autour de l'atome d'azote de l'amine tertiaire ainsi que de sa basicité. Les données suggèrent que les vitesses relatives de racémisation des oxazolones ne reflètent pas nécessairement les tendances relatives à se racémiser des résidus correspondant au cours des couplages des acides parents.

[Traduit par la revue]

Introduction[5]

The main side-reaction which accompanies the activation and peptide-bond forming reactions which are used in peptide synthesis is racemization. The stereomutation results from the formation and tautomerism of the 2,4-dialkyl-5(4*H*)-oxazolone **2** (1–3). The degree of racemization and the factors contributing thereto during peptide synthesis have been extensively investigated (2, 3). However, few data on direct measurements of the rates of racemization of oxazolones can be found in the literature (4–6). This is undoubtedly due to the difficulties encountered in preparing pure oxazolones. Recognition that oxazolones survive washing a solution of the oxazolone with water has allowed us to obtain them in pure form using a soluble *N*,*N*′-dialkylcarbodiimide (7, 8). In the present article, we describe a study of the kinetics of the racemization which oxazolones undergo through an autocatalytic process (7, 9, 10), as well as the kinetics of their racemization in the presence of tertiary amines.

Results and discussion

Racemization was monitored by observing the change in optical rotation of a solution of the oxazolone. To demonstrate the validity of the approach, the stability of the oxazolones under the same conditions was examined by ^{1}H-nuclear magnetic resonance spectroscopy. Oxazolones exhibit a characteristic C(4)-proton signal which is different from that of the α-H in the precursor acid or any product generated by ring-opening, thus allowing the detection of 3–5% of impurity. Compounds **2***e*, **2***f* and **2***g* in deuteriochloroform, tetrahydrofuran-D_8 or dimethylformamide-D_7 showed no change for at least 6 h after the addition of 1% of triethylamine. In fact, there was no apparent change in the compounds kept for 18 h in tetrahydrofuran-D_8 in the presence of 0.5 equiv. of triethylamine. That oxazolones are relatively stable to hydrolysis is attested to by the fact that **2***c* could be isolated in near-quantitative yield 2 h after dissolution in tetrahydrofuran–water (1:1). We conclude that the change in optical activity of a solution of oxazolone in the presence of tertiary amines is due solely to the racemization process resulting from abstraction of the C(4)-proton (2).

In the cases studied, in aprotic solvents the racemization process involved parallel reactions [1] to [6]:

$$[1]\quad Ox_S \xrightarrow{k_1} Ox_R$$

$$[2]\quad Ox_R \xrightarrow{k_1} Ox_S$$

$$[3]\quad Ox_S + Ox_S \xrightarrow{k_2} Ox_R + Ox_S$$

$$[4]\quad Ox_R + Ox_R \xrightarrow{k_2} Ox_S + Ox_R$$

$$[5]\quad Ox_S + Ox_R \xrightarrow{k_2'} Ox_S + Ox_S$$

$$[6]\quad Ox_R + Ox_S \xrightarrow{k_2'} Ox_R + Ox_R$$

[1]On study leave. Permanent address: Department of Organic Chemistry, Technical University of Gdansk, 80-952 Gdansk, Poland.

[2]Holder of a Natural Sciences and Engineering Research Council Summer Studentship.

[3]To whom correspondence should be addressed.

[4]Revision received May 17, 1988.

[5]Abbreviations: Ac, acetyl; Bu, n-butyl; Bz, benzoyl; DIEA, diisopropylethylamine; Et, ethyl; NMM, *N*-methylmorpholine, $CH_3N(CH_2CH_2)_2O$; NMP, *N*-methylpiperidine, $C_5H_{10}NCH_3$; Z, benzyloxycarbonyl, $C_6H_5CH_2OCO$.

Can. J. Chem. Downloaded from www.nrcresearchpress.com by 196.1.178.254 on 09/07/12
For personal use only.

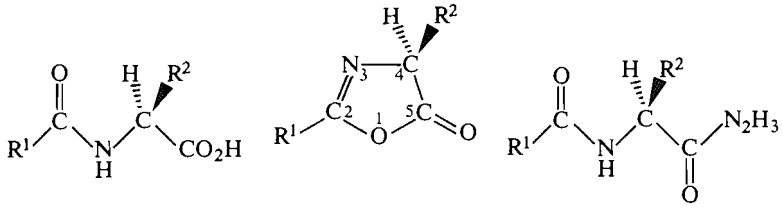

1 2 3

	1	R^1	R^2
a	Ac-Phe	CH_3	$C_6H_5CH_2$
b	Ac-Leu	CH_3	$(CH_3)_2CHCH_2$
c	Bz-Phe	C_6H_5	$C_6H_5CH_2$
d	Bz-Leu	C_6H_5	$(CH_3)_2CHCH_2$
e	Bz-Val	C_6H_5	$(CH_3)_2CH$
f	Z-Gly-Phe	$ZNHCH_2$	$C_6H_5CH_2$
g	Z-Gly-Leu	$ZNHCH_2$	$(CH_3)_2CHCH_2$
h	Z-Gly-Val	$ZNHCH_2$	$(CH_3)_2CH$
i	Z-Gly-Ala	$ZNHCH_2$	CH_3

Combining these reactions one can obtain the rate equation [7]:

$$[7]\quad \frac{d[Ox_S]}{dt} = k_1\{[Ox_R] - [Ox_S]\} + k_2\{[Ox_R]^2 - [Ox_S]^2\}$$

or

$$[8]\quad \frac{d[Ox_S]}{dt} = -\{k_1 + k_2[Ox_T]\}\{[Ox_S] - [Ox_R]\}$$

where $[Ox_T] = [Ox_S] + [Ox_R]$.

Since the observed optical rotation of the solution of oxazolone is equal to:

$$[9]\quad \alpha = \frac{\phi l}{10}\{[Ox_S] - [Ox_R]\} = \frac{\phi l}{10}\{2[Ox_S] - [Ox_T]\}$$

where l is the length of the polarimeter tube (dm) and ϕ is the molecular rotation which is equal to the specific rotation times the molecular weight divided by 100. One can note that:

$$[10]\quad \frac{d}{dt}\{[Ox_S] - [Ox_R]\} = \frac{d}{dt}\{2[Ox_S] - [Ox_T]\}$$
$$= 2\frac{d}{dt}[Ox_S]$$

Uniting [8], [9], and [10] gives

$$[11]\quad \frac{d\alpha}{dt} = -2\alpha\{k_1 + k_2[Ox_T]\}$$

This is a pseudo first-order reaction, in which

$$[12]\quad k_{obs} = 2\{k_1 + k_2[Ox_T]\}$$

and k_1 and k_2 may be found by plotting k_{obs} against $[Ox_T]$.

It is seen in Table 1 that the values of the rate constants for the racemization of a series of oxazolones in dichloromethane depend on the nature of the C(2) as well as the C(4)-substituents. There was an inverse relationship between the steric hindrance caused by the C(4)-substituent and the reaction rate, the rate diminishing over 70 times (at $[Ox_T] = 0.1$ mol dm^{-3}) in the order (R^2) benzyl > isobutyl >> isopropyl. In the extreme case of the isopropyl analogue, the first-order reaction rate was below the limit of detection. The relatively high rate constant of reaction of the 4-benzyl analogue in comparison to the 4-isobutyl analogue is probably due to the unique conformation

TABLE 1. Reaction rate constants for the autoracemization of oxazolones **2** in dichloromethane: $[Ox_T] = 0.05$–0.90 mol dm^{-3}, temperature = 23°C[a]

2	R^1	R^2	$k_1 \times 10^6$ (s^{-1})	$k_2 \times 10^5$ ($dm^{-3}mol^{-1}s^{-1}$)
a	CH_3	$C_6H_5CH_2$	0.05	0.37
f	$ZNHCH_2$	$C_6H_5CH_2$	1.15	2.05
c	C_6H_5	$C_6H_5CH_2$	1.70	5.35
d	C_6H_5	$(CH_3)_2CHCH_2$	0.85	2.20
e	C_6H_5	$(CH_3)_2CH$	0.05	0.34

[a]Relative mean error in k_1 and k_2 is $< \pm 4\%$.

assumed by the phenyl ring of the benzyl substituent (see below). The nature of R^1 affected the racemization rate to a similar extent, due to electronic rather than steric effects. The data substantiate the reports that oxazolones **2** undergo a chiral inversion process which is autocatalytic (7, 9, 10). Autoracemization, however, is unlikely to occur in the course of peptide synthesis, because of the relatively high concentration of bases present. Instead, the base-catalyzed reaction will predominate.

As seen in Table 2, the rate of racemization of oxazolone **2***f* in the presence of tertiary amines was markedly affected by the nature of the amine. There was no discernable correlation between the apparent rate constants and the accessibility of the nitrogen atom of the acyclic bases (DIEA < Bu_3N < Et_3N) in the two solvents, and also of the cyclic bases (<NMM/NMP) in dimethylformamide. The reasons for the differences in catalytic effects between NMM and NMP remain obscure.

The base-catalysed racemization of oxazolones **2** in tetrahydrofuran obeys simple pseudo first-order kinetics.

$$[13]\quad Ox_S + B \underset{k_4}{\overset{k_3}{\rightleftharpoons}} Ox^- + BH^+ \underset{k_3}{\overset{k_4}{\rightleftharpoons}} Ox_R + B$$

where B is the base, and Ox^- is the deprotonated oxazolone. Under steady-state conditions $d[Ox^-]/dt = 0$, the rate equation

$$[14]\quad -\frac{d[Ox_S]}{dt} = k_3[B][Ox_S] - k_4[Ox^-][BH^+]$$

becomes equal to

Can. J. Chem. Downloaded from www.nrcresearchpress.com by 196.1.178.254 on 09/07/12
For personal use only.

$$[15] \quad -\frac{d[Ox_S]}{dt} = k_3[B_T]\left\{[Ox_S] - \frac{[Ox_T]}{2}\right\}$$

where $[B_T] = [B] + [BH^+]$ is the total concentration of base. If $[Ox^-]$ is much less than $[Ox_T]$, the observed optical rotation of a solution of oxazolone can be expressed in terms of $[Ox_S]$ and $[Ox_T]$ (see eq. [9]) and eq. [15] can be written as

$$[16] \quad -\frac{d\alpha}{dt} = k_3[B_T]\alpha$$

which can be integrated to give

$$[17] \quad \ln\frac{\alpha_0}{\alpha} = k_3[B_T]t$$

On the basis of the dependence of the apparent rate constants, $k_{obs} = k_4[B_T]$ on the concentration of base, $[B_T]$, and the reaction temperature, the values of the catalytic rate constant, k_4, and the activation parameters of the reaction in the presence of several tertiary amines were obtained (Table 3). The values of the enthalpy of activation, $\Delta H^{\neq}$, of the reaction increased in the order $Et_3N < Bu_3N < NMM \simeq NMP \simeq DIEA$, which can be attributed not only to changes in the basicities of the amines but also to changes in the energetic expense required for the amine to approach the reaction centre, i.e., to steric interactions. On the other hand, despite the same values of $\Delta H^{\neq}$ for reactions in the presence of *N*-methylmorpholine and *N*-methylpiperidine, the catalytic rate constant of the NMP-catalysed reaction is unexpectedly high. This results from the relatively small entropy of activation of the latter reaction, which is probably due to solvation effects.

The influence of the nature of the substituents R^1 and R^2 on the reaction parameters for the base-catalysed racemization of oxazolones **2** in tetrahydrofuran was examined. It is seen in Table 4 that the effect was exerted mainly in changes in the values of enthalpy of activation. Thus, the enthalpy of activation of oxazolone **2***b* (oxazolone from Ac-Leu) was about 50% higher than that of **2***d* (oxazolone from Bz-Leu). However, racemization of the oxazolone from Z-Gly-Phe (**2***f*) was twice as rapid as that of the oxazolone from Z-Gly-Leu (**2***g*) due to the entropy effect. This could be caused by the folding of the side-chain phenyl ring over the oxazolone ring, a phenomenon observed for 4-oxazolidinones (12) and other heterocyclic compounds (13, 14). In fact, such a conformation has been suggested for 2-methyl-4-benzyl-5(4*H*)-oxazolone (**2***a*) on the basis of its ^{1}H-nmr spectrum (15) and is indicated when one compares the nmr spectra of the oxazolones **2***a–h* (16). Such a feature of the oxazolone molecule should diminish the steric interaction of the 4-benzyl substituent with the approaching tertiary amine, and the rotation around the C(4)—CH_2Ph bond should be frozen in the ground and transition states. On the other hand, the transition state of the 4-isobutyl analogue should be more restricted than its ground state because of the base–C(4)-substituent steric interactions. Indeed, the racemization of 2-$ZNHCH_2$-4-benzyl-5(4*H*)-oxazolone is favoured by 8 J mol^{-1} K^{-1} in entropy. Moreover, there would be almost no difference in rotation around the C(4)—CH_3 bond in the ground and transition states of the 4-methyl analogue, and the values of $\Delta S^{\neq}$ between the 4-benzyl and 4-methyl analogues differ only by 2 J mol^{-1} K^{-1}.

The influence of the C(2)-substituents on the rate of racemization is mainly of mesomeric and/or inductive nature (compare $\Delta H^{\neq}$ values in Table 4), and the reaction rate decreased in the order phenyl > $ZNHCH_2$ ≫ methyl. Nevertheless, small long-distance steric interactions between the C(2)- and C(4)-substituents are still possible, and the entropy of activation of the 2-$ZNHCH_2$ analogue is 5 J mol^{-1} K^{-1} lower than that of the 2-methyl analogue.

TABLE 2. Apparent rate constants of the base-catalyzed racemization of 2-($ZNHCH_2$)-4-benzyl-5(4*H*)-oxazolone (**2***f*): $[Ox_T] = 0.10$ mol dm^{-3}, $[B_T] = 4 \times 10^{-4}$ mol dm^{-3}

Base	pK_b in H_2O[a]	$k_{obs} \times 10^4$ (s^{-1}) in CH_2Cl_2	$k_{obs} \times 10^4$ (s^{-1}) in DMF
Et_3N	3.33	30.3	115
Bu_3N	4.07	7.2	65
NMP	3.92	3.4	190
DIEA	—	1.5	50
NMM	6.33	1.1	448

[a]Data from ref. 11. Relative mean error in k_{obs} is $< \pm 4\%$.

TABLE 3. Reaction parameters of the base-catalyzed racemization of 2-($ZNHCH_2$)-4-isobutyl-5(4*H*)-oxazolone (**2***g*) in tetrahydrofuran: $[Ox_T] = 0.08–0.11$ mol dm^{-3}, $[B_T] = (0.5–8.8) \times 10^{-3}$ mol dm^{-3}, temperature = 17.9–35.0°C[a]

Base	k_3 at 25°C (dm^3 mol^{-1} s^{-1})	$\Delta H^{\neq}$ (kJ mol^{-1})	$\Delta S^{\neq}$ (J mol^{-1} K^{-1})
Et_3N	1.16	26.3	−156
Bu_3N	0.17	32.0	−153
NMM	0.09	36.8	−142
NMP	1.22	37.2	−119
DIEA	0.05	38.5	−141

[a]Mean error: $\Delta H^{\neq}$, $< \pm 4$ kJ mol^{-1}; $\Delta S^{\neq}$, $< \pm 10$ J mol^{-1} K^{-1}.

In relation to the influence of the C(2)-substituent, it is of interest to note that although *N*-acetylamino acids undergo more racemization than the corresponding *N*-protected peptides when coupled with an amino group (3), the rate of racemization of the oxazolone from Ac-Leu (**2***b*) was almost 17 times less than that of the oxazolone from Z-Gly-Leu (**2***g*) (Table 4). Thus the relative rates of racemization of oxazolones are not a true reflection of the relative susceptibilities to racemization of residues during coupling. Other variables implicated in determining the stereomutation observed in a coupling are the rates of oxazolone formation, coupling, and aminolysis, as well as asymmetric induction.

Conclusions

2,4-Disubstituted-5(4*H*)-oxazolones **2** in solution undergo solvent-promoted and/or autocatalyzed racemization, both reactions being governed by electronic effects of the C(2)-substituents and steric effects of the C(4)-substituents. In the presence of tertiary amines, the base-catalyzed reaction takes place. The rate of this reaction depends on the steric interactions between the oxazolone and the amine molecules, and the basicity of the amine. Again, the influence of the C(2)-substituents of the oxazolone on the rate of reaction is mainly mesomeric and/or inductive in nature, whereas that of the C(4)-substituents is steric. The relatively rapid racemization of 2-substituted-4-benzyl-5(4*H*)-oxazolones compared to the 2-substituted-4-alkyl-5(4*H*)-oxazolones is due to the entropy

Can. J. Chem. Downloaded from www.nrcresearchpress.com by 196.1.178.254 on 09/07/12
For personal use only.

TABLE 4. Reaction parameters for the triethylamine-catalyzed racemization of oxazolones **2** in tetrahydrofuran: $[Ox_T] = 0.011–0.126$ mol dm^{-3}, $[Et_3N] = (0.3–4) \times 10^{-3}$ mol dm^{-3}, temperature = 17.9–35.1°C

2	R^1	R^2	k_3 at 25°C (dm^3 mol^{-1} s^{-1})	$\Delta H^{\neq}$ (kJ mol^{-1})	$\Delta S^{\neq}$ (J mol^{-1} K^{-1})
b	CH_3	$(CH_3)_2CHCH_2$	0.07[a]	34.6	−151
d	C_6H_5	$(CH_3)_2CHCH_2$	5.99	22.9	−153
g	$ZNHCH_2$	$(CH_3)_2CHCH_2$	1.16	26.3	−156
f	$ZNHCH_2$	$C_6H_5CH_2$	2.52	26.6	−148
j	$ZNHCH_2$	CH_3	0.95	28.6	−150
h	$ZNHCH_2$	$(CH_3)_2CH$	0.05	32.8	−160

[a]Lit. (4) $k_3 = 0.05$ dm^3 mol^{-1} s^{-1} under similar conditions. Mean error: $\Delta H^{\neq}$, $< \pm 2$ kJ mol^{-1}; $\Delta S^{\neq}$, $< \pm 5$ J mol^{-1} K^{-1}.

TABLE 5. Physical data of oxazolones **2** and hydrazides **3**

	Oxazolone **2**		Hydrazide **3**			
			From **2**		From ester	
Complex	mp (°C)	$[\alpha]_D^{23}$ (*c* CH_2Cl_2)	mp (°C)	$[\alpha]_D^{23}$	mp (°C)	$[\alpha]_D^{23}$ (*c* solv.)
a	oil	−173.4° (2.1)	173–175	+27.6°	180–181	+39.1° (1.8 H_2O)
c	93–95	−36.3° (2.0)	190–191	−29.6°	196–197	−45.6° (0.9 DMF)
d	51–52	−31.8° (2.5)	137–140	−20.6°	149–150[a]	−52.5° (1.2 $CHCl_3$)[a]
e	oil	−71.9° (2.4)	205–207	+30.0°	206–208	+42.3° (1.6 $CHCl_3$)
f	oil	−53.7° (2.0)	129–130	−5.2°	131–135	−6.6° (0.6 $CHCl_3$)

[a]Lit. (7) mp 147–148°C, $[\alpha]_D^{23}$ −56.6° (2.0 $CHCl_3$).

effect and it is probably caused by folding of the phenyl ring over the oxazolone ring.

Experimental

General

Amino acid derivatives and the carbodiimide were obtained from Sigma Chemical Co. (St. Louis, MO), tertiary amines were Aldrich products obtained from Terochem Labs (Edmonton, AL), solvents were HPLC-grade obtained from Fisher Scientific. Dimethylformamide was freshly distilled under reduced pressure before use. Optical rotations were measured with a Rudolph Research (Flanders, NJ) Autopol III automatic polarimeter using a 2-dm thermostated tube.

Kinetic determinations

Oxazolones were weighed in 10-mL volumetric flasks. Solvents and amine solutions at the appropriate temperatures were added and the solutions were immediately transferred to the polarimeter tube. The changes in optical rotation were recorded until an 80% decrease in the initial value had been reached. Experiments were carried out using the bivariable plan, i.e., the temperature and concentration of one of the reactants or the concentrations of the two reactants were varied at the same time according to the latin squares method. The ranges of values for the variables are given in the tables. Any results which are compared are from experiments carried out with the same batch of solvents.

*2,4-Disubstituted-5(4*H*)-oxazolones 2*

These were prepared by a slight modification of the published procedure (7). *N*-Ethyl-*N'*-(3-dimethylaminopropyl)-carbodiimide hydrochloride (1 mmol) was added to a solution of the *N*-substituted amino acid or dipeptide **1** (1 mmol) in 20 mL of dichloromethane at 0°C and the mixture was washed successively with cold 10% aqueous citric acid, water, 5% aqueous $NaHCO_3$ and water, the solution was dried ($MgSO_4$), and the solvent was removed with a rotary evaporator (bath temperature 35°C). The yields, mp's, and specific rotations of the products were in agreement with previous data (7). In some cases, the stereochemical purity of the oxazolones was verified by converting them into hydrazines **3** (7, 8, 17) by leaving the oxazolone (1 mmol) in 10 mL of methanol containing 85% hydrazine hydrate (1 mL) for 10 min. After removal of the solvent, the specific rotations of the products were compared with those of the same compounds prepared from the corresponding esters (7, 18) (Table 5).

Data handling and presentation

All the kinetic data are reported to within the last significant figure (at confidence level 0.05) and the confidence intervals are omitted in order to simplify the presentation of data. The values of the apparent rate constants were found for each pair of measurements (t_{i-1}, α_{i-1}), (t_i, α_i) according to:

$$[18] \quad k_{obs} = \frac{1}{t_i - t_{i-1}} \ln \frac{\alpha_{i-1}}{\alpha_i}$$

and the mean values are reported. The values of the enthalpy and entropy for the transition state reaction rate theory, and the catalytic rate constants were computed using the weighted least-squares technique (19) with a Sharp mini-computer, type PC-1401.

Acknowledgement

This research was financially supported by the Medical Research Council of Canada, of which N.L.B. is a Career Investigator.

1. M. GOODMAN and C. GLASER. *In* Peptides: chemistry and biochemistry. *Edited by* B. Weinstein and S. Lande. Marcel Dekker, New York. 1970. p. 267.
2. D. S. KEMP. *In* The peptides. Vol. 1. *Edited by* E. Gross and J. Meienhofer. Academic Press, New York. 1979. p. 315.
3. N. L. BENOITON. *In* The peptides. Vol. 5. *Edited by* E. Gross and J. Meienhofer. Academic Press, New York. 1983. p. 218.

Can. J. Chem. Downloaded from www.nrcresearchpress.com by 196.1.178.254 on 09/07/12
For personal use only.

4. I. Z. SIEMION and L. WILSCHOWITZ. Z. Naturforsch. **26**B, 762 (1971).
5. O. G. GRAHL-NIELSEN. J. Chem. Soc. Chem. Commun. 1588 (1971).
6. M. GOODMAN and W. J. MCGAHREN. Tetrahedron, **23**, 2031 (1967).
7. F. M. F. CHEN, K. KURODA, and N. L. BENOITON. Synthesis, 230 (1979).
8. N. L. BENOITON, K. KURODA, and F. M. F. CHEN. Int. J. Peptide Protein Res. **20**, 81 (1982).
9. K. KOWAK and I. Z. SIEMION. Roczniki Chem. **35**, 153 (1961).
10. I. Z. SIEMION and A. DZUGAJ. Roczniki Chem. **40**, 1699 (1969).
11. D. D. PERRIN. Dissociation constants of organic bases in aqueous solution. Butterworths, London. 1965.
12. T. POLONSKI. Tetrahedron, **39**, 3131 (1983); **39**, 3139 (1983).
13. K. D. KOPPLE and M. OHNISHI. J. Am. Chem. Soc. **91**, 962 (1969).
14. H. FUJIWARA, A. K. BOSE, M. S. MANHAS, and J. M. VAN DER VEEN. J. Chem. Soc. Perkin 2, 653 (1979).
15. I. Z. SIEMION and G. BARAN. Bull. Acad. Pol. Sci. **23**, 317 (1975).
16. F. M. F. CHEN and N. L. BENOITON. Int. J. Peptide Protein Res. **30**, 683 (1987).
17. M. GOODMAN and C. B. GLASER. J. Org. Chem. **35**, 1954 (1970).
18. B. W. WILLIAMS and J. T. YOUNG. J. Chem. Soc. 881 (1963).
19. D. MARGERISON. *In* Comprehensive chemical kinetics. Vol. 1. *Edited by* C. H. Bamford and C. F. H. Tipper. Elsevier, Amsterdam. 1969. p. 403.

Can. J. Chem. Downloaded from www.nrcresearchpress.com by 196.1.178.254 on 09/07/12
For personal use only.

The effect of substitution on the conformation in *para*-substituted ethylene glycol dibenzoate molecules

SUZANNE DEGUIRE AND FRANÇOIS BRISSE

Département de chimie, Université de Montréal, C.P. 6128, Succ. A, Montréal (Québec), Canada H3C 3J7

Received February 22, 1988

SUZANNE DEGUIRE and FRANÇOIS BRISSE. Can. J. Chem. **66**, 2545 (1988).

The series of ethylene glycol di-*para*-X-benzoates, where X = Me, OMe, CN, and NO_2, has been studied by infrared spectroscopy and solid state CP/MAS ^{13}C nuclear magnetic resonance. The crystal structures were established for X = Me and OMe. Bond distances, bond angles, and torsion angles were compared to those of related molecules (X = H, Ph, Cl). It was found that the conformation of the CO—O—CH_2—CH_2—O—CO sequence is either *trans-trans-trans* or *trans-gauche-trans*. (*trans* = *t*, *gauche* = *g*). The CH_2—CH_2 bond distance ranging from 1.471(2) to 1.499(3) Å is always very short. The O—CH_2—CH_2 bond angle is around 105° for the *ttt* conformation and 107° for the *tgt* conformation. It was confirmed that the infrared frequencies for the CH_2 bending, CH_2 wagging, C–C stretching, and CH_2 rocking modes are observed at 1470–1485, 1335–1340, 975–980, 845–855 cm^{-1} and at 1460, 1370–1375, 1040, 895–900 cm^{-1} for the *ttt* and *tgt* conformations respectively. The substitution effect on the nmr chemical shifts, both in solution and the solid state, can be rationalized in terms of induction and resonance contributions. On the basis of the ir and nmr spectra, it is proposed that for both the *p*-NO_2 and *p*-CN substituted molecules, for which no crystal structure has been established, the conformation of the methylenic sequence is *trans-trans-trans*.

SUZANNE DEGUIRE et FRANÇOIS BRISSE. Can. J. Chem. **66**, 2545 (1988).

Faisant appel à la spectroscopie infrarouge et à la résonance magnétique nucléaire CP/MAS du ^{13}C à l'état solide, on a étudié une série de di-*para*-X-benzoates de l'éthylène glycol dans laquelle X = Me, OMe, CN et NO_2. Pour les cas où X = Me et OMe, on a établi les structures cristallines. On a comparé les longueurs des liaisons, les angles des liaisons ainsi que les angles de torsion avec les valeurs correspondantes observées dans des molécules apparentées (X = H, Ph et Cl). On a trouvé que la conformation de la séquence CO—O—CH_2—CH_2—O—CO est soit *trans-trans-trans* soit *trans-gauche-trans* (*trans* = *t* et *gauche* = *g*). La longueur de la liaison CH_2—CH_2, qui varie de 1,471(2) à 1,499(3) Å, est toujours très courte. L'angle de la liaison O—CH_2—CH_2 est d'environ 105° pour la conformation *ttt* et de 107° pour la conformation *tgt*. Dans l'infrarouge, les vibrations des modes de déformation angulaire du CH_2, de vibration de balancement du CH_2, d'élongation C–C et de vibration de rotation du CH_2 sont observées 1470–1485, 1335–1340, 975–980 et 845–855 cm^{-1} et 1460, 1370–1375, 1040 et 895–900 cm^{-1} respectivement pour les conformations *ttt* et *tgt*. On peut rationaliser l'effet de substitution des déplacements chimiques en rmn, tant en solution qu'à l'état solide, en faisant appel à des contributions de l'induction ainsi que de la résonance. En se basant sur les spectres ir et rmn, on suggère que les molécules substituées tant par un *p*-NO_2 que par un *p*-CN, pour lesquelles les structures cristallines n'ont pas été établies, existent dans la conformation impliquant une séquence méthylénique *trans-trans-trans*.

[Traduit par la revue]

Introduction

Daubeny, Bunn, and Brown (1) were the first to determine the structure of the crystalline region of poly(ethylene terephthalate) or 2GT. The fiber repeat was found to be 0.15 Å shorter than expected for an all-*trans* conformation. The departure from planarity was mostly localized in the glycol group. Tomashpol'skii and Markova (2) and Arnott and Wonacott (3) reinvestigated the structure of 2GT. Their structures are in general agreement with that proposed earlier by Daubeny *et al.* However, there remains some puzzling discrepancies between the three structures. More accurate information about the geometry of the repeat unit had to be provided.

Pérez and Brisse (4, 5) tackled this problem by the model compound approach. They undertook a systematic study of ethylene glycol dibenzoates and *para*-substituted dibenzoates. The crystal structure of ethylene glycol dibenzoate, 2DBO (C_6H_5—CO—O—$(CH_2)_2$—O—CO—C_6H_5), showed some unusual geometrical features (4). The CH_2—CH_2 bond distance of 1.499(3) Å was significantly shorter than the expected $C(sp^3)$—$C(sp^3)$ distance of 1.535(3) Å (6). Simultaneously, the two C—C—O angles involving this CH_2—CH_2 bond were not as open as expected. Using these geometrical parameters, the distance between the centers of the aromatic rings of ethylene glycol dibenzoate was identical to the fiber repeat, *c*, reported by Daubeny *et al.* for poly(ethylene terephthalate).

The crystal structure of ethylene glycol di-*para*-chlorobenzoate, 2DBO-*p*-Cl (Cl—C_6H_4—CO—O—$(CH_2)_2$—O—CO—C_6H_4—Cl), was also determined (5). The same significant shortening of the ethylene part of the molecule was observed. The CH_2—CH_2 distance was only 1.493(2) Å. Unlike ethylene glycol dibenzoate, for which the O—CH_2—CH_2—O sequence was shown to be in the *trans* conformation, the same sequence was found to be in the *gauche* conformation in the case of 2DBO-*p*-Cl.

Since these two molecules, which differ only by the *para* substituent, have two different conformations, we undertook to study the *para*-substitution effect on the conformation. To do this, we chose substituents of different size, geometry, and electronegativity: methyl, methoxy, phenyl (7), nitro, and cyano groups.

Structural information about this series of model compounds was collected by means of X-ray structure determinations. Infrared spectroscopy was used to gain additional structural information on certain model compounds, for which no crystal suitable for X-ray structure determination could be obtained.

Solid-state CP/MAS ^{13}C nmr spectroscopy was also investigated. It has been shown previously that the γ-*gauche* effect and molecular packing interactions both affect the chemical shift to different degrees. By studying this series of model compounds we tried to quantify the factors influencing the chemical shift.

Can. J. Chem. Downloaded from www.nrcresearchpress.com by 196.1.178.254 on 09/07/12
For personal use only.

Can. J. Chem. Downloaded from www.nrcresearchpress.com by 196.1.178.254 on 09/07/12
For personal use only.

TABLE 1. Crystal data of interest

Parameter	2DBO-*p*-Me	2DBO-*p*-OMe
Molecular formula	$C_{18}H_{18}O_4$	$C_{18}H_{18}O_6$
Molecular weight	298.34	330.34
$F(000)$	632	348
Melting point (K)	390	388
Crystal system	Monoclinic	Triclinic
a (Å)	12.203(4)	5.807(2)
b (Å)	10.644(3)	10.943(1)
c (Å)	12.288(4)	13.622(2)
α (deg)	90.00	74.21(1)
β (deg)	75.80(3)	87.38(2)
γ (deg)	90.00	78.42(2)
V (Å^3)	1547.3	816.0
d_{obs} (g cm^{-3})	1.29	1.36
d_{calc} (g cm^{-3})	1.280	1.344
Z	4	2
Space group	$C2/c$	$P\bar{1}$
μ(CuKα) (cm^{-1})	6.97	8.04
T (°C)	20	20
Crystal size (mm)	0.16 × 0.22 × 0.32	0.14 × 0.23 × 0.50

Experimental

Ethylene glycol di-*para*-methylbenzoate, 2DBO-*p*-Me, ethylene glycol di-*para*-methoxybenzoate, 2DBO-*p*-OMe, ethylene glycol di-*para*-cyanobenzoate, 2DBO-*p*-CN, and ethylene glycol di-*para*-nitrobenzoate, 2DBO-*p*-NO_2, were prepared according to the method described by Heim and Poe (8), by reacting, in pyridine, solutions of ethylene glycol and of the *para*-methyl, *para*-methoxy, *para*-cyano, or *para*-nitro substituted benzoyl chlorides. Crystals of 2DBO-*p*-Me and 2DBO-*p*-OMe were obtained by slow evaporation from a chloroform solution.

X-ray diffraction

The orientation of the well-developed single crystals of 2DBO-*p*-Me and 2DBO-*p*-OMe and their unit-cell dimensions were obtained by a least-squares fit to the angular settings of 25 well-centered reflections on a Nonius CAD-4 diffractometer. Graphite monochromatized CuKα radiation was used ($\lambda CuK\bar{\alpha}$ = 1.54178 Å). Crystal data of interest are given in Table 1. The data collections were performed by the ω–2θ scan method. The orientation of the crystal was monitored every 100 reflections. The intensities of three reference reflections in both cases, measured every hour, showed a maximum random variation of 1.0% for 2DBO-*p*-Me and 1.6% for 2DBO-*p*-OMe over the duration of the data collection. The diffracted intensities were corrected for Lorentz and polarization effects. No absorption correction was applied since the absorption coefficients were small.[1]

The structures were solved by direct methods using MULTAN. All non-hydrogen atoms were revealed in the first computed E-map. The hydrogen atoms were located on subsequent difference Fourier syntheses. The weighted least-squares refinements of the atomic coordinates, minimizing $\Sigma w(|F_o| - |F_c|)^2$, were conducted with anisotropic temperature factors for C and O atoms and isotropically for H atoms. The details of the least-squares refinement of the two compounds are given in Table 2.

The scattering curves for C and O atoms were taken from ref. 13 and those for H atoms from ref. 14.

Infrared spectroscopy

The ir spectra were recorded from KBr pellets on a FTIR Nicolet 7199 equipped with a He–Ne class II laser with a resolution of 2 cm^{-1} and 200 scans per spectrum, while the background noise spectra were signal-averaged with 100 scans. The FTIR spectra of 2DBO and of the *p*-X-substituted derivatives where X = Me, OMe, Ph, Cl, CN, and NO_2 were thus recorded.

Nuclear magnetic resonance

The ^{13}C nmr solution spectra were measured on a Bruker 80 MHz spectrometer at a frequency of 20.11 MHz. Each compound (0.1 g) was dissolved in 2 mL of $CDCl_3$, and tetramethylsilane was used as reference. ^{13}C CP/MAS spectra were taken with a Varian CXP 300 MHz at a frequency of 75.31 MHz. An averaged contact time of 1.9 μs was used with a delay of around 5.0 s between sequences. An averaged number of 5138 contacts was used.[2]

Chemical shifts are given with respect to powdered hexamethylbenzene whose aromatic signal is at 132.1 ppm.

Results and discussion

Structural considerations

For 2DBO-*p*-Me, both the Cc or $C2/c$ space groups are compatible with the observed systematic absences. Since the refinement proceeded normally in $C2/c$, this choice was retained. Furthermore, the density indicated that there are only four molecules per unit cell and these lie about the twofold symmetry axes. In the case of 2DBO-*p*-OMe, the space group is $P\bar{1}$ and the density indicates two molecules in the unit cell. However, instead of having two centrosymmetrically related molecules, we find here that each molecule (A and B) has a crystallographic center of symmetry.

The final positional parameters and their standard deviations are presented in Table 3. The atomic numbering is shown in Fig. 1 and the molecular structures are presented as stereopairs in Fig. 2. The packing of the molecules is shown in Fig. 3. The bond distances and angles of 2DBO-*p*-Me and 2DBO-*p*-OMe are given in Table 4 where they are compared to the corresponding quantities for 2DBO-*p*-Ph, 2DBO-*p*-Cl, and 2DBO.

The benzoate groups

The C(sp^2)—C(sp^2) bond distances in the phenylene rings average 1.384 Å for 2DBO-*p*-Me, 2DBO-*p*-OMe, and 2DBO-*p*-Cl, 1.389 Å for 2DBO-*p*-Ph, and 1.379 and 1.384 Å for 2DBO. They are very close to the mean bond length of 1.379 Å computed from 78 C(sp^2)—C(sp^2) distances by Brisse and Sygusch (15). The average angle in each of the benzene rings is 120.0°.

There are some slight deviations from a perfect hexagonal symmetry. The angles affected by substitution, at C(1) and C(4), have been underlined in Table 4. They can be accounted for and confirm the rules established by Domenicano, Vaciago, and Coulson (16).

As usual the angles around the carbon atom C(7) of the ester groups are unequal. This disymmetry tends to open the C(1)—C(7)—O(1) angle while the C(1)—C(7)—O(2) angle is lowered. The mean value of the C(1)—C(7)—O(1) angle is 124.5°, the mean value of C(1)—C(7)—O(2) is 112.1°, while the angle O(1)—C(7)—O(2) has a mean value of 122.2°.

The methylenic sequence

As noted for 2DBO and 2DBO-*p*-Cl, the observed CH_2—CH_2 bond lengths are always significantly shorter than the expected C(sp^3)—C(sp^3) distance of 1.535(3) Å (6). The mean bond length is 1.490 Å. It varies from 1.471(3) to 1.499(3) Å. Bocelli

[1]The programs used here are modified versions of NRC-2, data reduction; NRC-3, absorption correction; NRC-10, bond distances and angles; and NRC-22, mean planes; FORDAP, Fourier and Patterson maps (A. Zalkin); MULTAN, multisolution program; NUCLS, least-squares refinement; and ORTEP, stereodrawing (9–12).

[2]^{13}C CP/MAS experimental details have been deposited together with H-atom coordinates, anisotropic thermal parameters, and structure factor tables of the X-ray determinations. Copies may be purchased from the Depository of Unpublished Data, CISTI, National Research Council of Canada, Ottawa, Ont., Canada K1A 0S2.

TABLE 2. Summary of data collection and refinement

Parameter	2DBO-*p*-Me	2DBO-*p*-OMe
Scan range (deg)	1.00 + 0.14 tan θ	1.00 + 0.14 tan θ
2θ max (deg)	140.0	140.0
hkl ranges	$0 \leq h \leq 14$	$0 \leq h \leq 7$
	$0 \leq k \leq 12$	$-13 \leq k \leq 13$
	$-14 \leq l \leq 14$	$-16 \leq l \leq 16$
Number of reflections, measured	1463	3095
Number of reflections, observed	1134	2217
When $I \geq k\sigma(I)$, k =	1.96	1.96
$R = \Sigma\|\Delta F\|/\Sigma\|F_o\|$	0.043	0.066
$Rw = [\Sigma w\Delta F^2/\Sigma wF_o^2]^{1/2}$	0.059	0.057
$S = [\Sigma w\Delta F^2/(m-n)]^{1/2}$	2.08	2.00
(Displacement/error) max	0.20	0.10
(Displacement/error) average	0.02	0.02
Extreme fluctuations of residual electron density (e Å^{-3})	−0.15, 0.18	−0.23, 0.22

TABLE 3. Fractional atomic coordinates and their esd's ($\times 10^4$ for C and O) and U_{eq} ($\times 10^4$) for 2DBO-*p*-Me and 2DBO-*p*-OMe (molecules A and B)

$$U_{eq} = \tfrac{1}{3}\sum_i\sum_j U_{ij}a_i^*a_j^*a_i\cdot a_j$$

Atom	*X*	*Y*	*Z*	U_{eq}
O(1)	4723(1)	1680(1)	4892(1)	761
O(2)	5458(1)	2115(1)	6343(1)	522
C(1)	5958(1)	3441(2)	4777(1)	452
C(2)	6796(2)	3998(2)	5196(2)	500
C(3)	7371(2)	5037(2)	4671(2)	541
C(4)	7119(2)	5549(2)	3727(2)	545
C(5)	6282(2)	4989(2)	3313(2)	597
C(6)	5701(2)	3944(2)	3829(2)	552
C(7)	5316(2)	2327(2)	5312(1)	500
C(8)	4882(2)	1034(2)	6931(2)	535
C(9)	7749(3)	6688(3)	3164(3)	776
O(11)	−4610(3)	−663(1)	1425(1)	718
O(12)	−1394(2)	−1319(1)	605(1)	639
O(13)	−5399(3)	−6445(1)	1697(1)	668
O(21)	225(3)	5717(1)	6338(1)	723
O(22)	3490(2)	6228(1)	5555(1)	646
O(23)	−290(3)	11416(1)	6747(1)	704
C(11)	−3764(3)	−2831(2)	1283(1)	475
C(12)	−2249(3)	−3759(2)	925(1)	561
C(13)	−2710(3)	−4983(2)	1056(1)	577
C(14)	−4732(3)	−5287(2)	1548(1)	504
C(15)	−6251(3)	−4374(2)	1932(1)	569
C(16)	−5763(3)	−3156(2)	1798(1)	548
C(17)	−3355(3)	−1502(2)	1129(1)	515
C(18)	−872(4)	−40(2)	411(2)	650
C(19)	−3960(4)	−7400(2)	1290(2)	699
C(21)	1145(3)	7778(2)	6244(1)	480
C(22)	2715(3)	8601(2)	5914(1)	543
C(23)	2304(3)	9820(2)	6069(1)	552
C(24)	293(3)	10231(2)	6561(1)	510
C(25)	−1301(3)	9413(2)	6907(2)	586
C(26)	−874(3)	8199(2)	6750(1)	551
C(27)	1518(3)	6476(2)	6073(1)	518
C(28)	3938(4)	4993(2)	5327(2)	671
C(29)	1238(4)	12301(2)	6380(2)	734

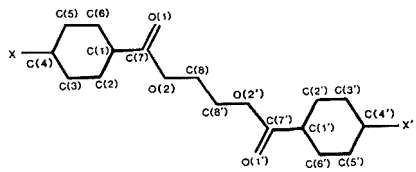

FIG. 1. Schematic representation of the molecules and atomic numbering.

and Grenier-Loustalot have observed a similar short distance for 2,3-butenediyl dibenzoate (17) and 1,2-propanediyl di(*p*-chlorobenzoate) (18). The C(8)—C(8′) distance measures 1.511(3) and 1.471(9) Å respectively in the above two compounds. All this justifies, after the fact, the short C—C distance that was adopted, without justification, by Daubeny *et al.* (1) in the structure of poly(ethylene terephthalate). Note also that the angle O(2)—C(8)—C(8′), involving the CH_2—CH_2 bond, has a mean value of 105.5° (it varies from 104.9(2) to 107.3(2)°). This angle is strikingly smaller than is usually accepted for molecules with no apparent strain. In 2,3-butanediyl dibenzoate this angle has a value of 103.6(2)°, and its values are 103.7(4) and 104.2(5)° in 1,2-propanediyl bis(*p*-chlorobenzoate). It seems that the value taken by this O—C—C angle depends upon the conformation (see below). We observe an angle of about 105° or less when the conformation is all-*trans*. When the conformation is *trans-gauche-trans*, the angle is slightly larger, about 107°.

Conformation

The conformational angles for the dibenzoates correspond to the calculated conformations, which are energetically stable. The torsional angles that characterize the methylenic sequence are defined by ϕ_1 = C(7)—O(2)—C(8)—C(8′), ϕ_2 = O(2)—C(8)—C(8′)—O(2′), and ϕ_1' = C(8)—C(8′)—O(2′)—C(7′). The values taken by these torsional angles are given in Table 5. We observe two types of conformation: *trans-trans-trans* and *trans-gauche-trans*. Bocelli and Grenier-Loustalot (17, 18) have observed a conformation relatively far from all-*trans* for the two compounds. The angle values of the methylenic sequence are −156.6, −179.0, and 146.4° for 2,3-butanediyl dibenzoate. In 1,2-propanediyl bis(*p*-chloro-

Can. J. Chem. Downloaded from www.nrcresearchpress.com by 196.1.178.254 on 09/07/12
For personal use only.

TABLE 4. Comparison of the bond distances and angles

Distances (Å) esd's:	2DBO-*p*-Me 0.002–0.003	2DBO-*p*-OMe 0.002–0.003 A	2DBO-*p*-OMe 0.002–0.003 B	2DBO-*p*-Ph 0.002–0.003	2DBO-*p*-Cl 0.002	2DBO 0.003	
C(1)—C(2)	1.386	1.384	1.384	1.386	1.392	1.387	1.391
C(2)—C(3)	1.382	1.381	1.379	1.389	1.380	1.374	1.382
C(3)—C(4)	1.383	1.379	1.377	1.389	1.378	1.375	1.381
C(4)—C(5)	1.383	1.392	1.394	1.395	1.382	1.377	1.386
C(5)—C(6)	1.386	1.380	1.375	1.386	1.379	1.379	1.376
C(6)—C(1)	1.386	1.386	1.394	1.389	1.392	1.381	1.387
C(1)—C(7)	1.483	1.478	1.478	1.487	1.482	1.478	1.476
C(7)—O(1)	1.203	1.201	1.203	1.202	1.204	1.209	1.202
C(7)—O(2)	1.339	1.336	1.337	1.336	1.344	1.339	1.339
O(2)—C(8)	1.446	1.443	1.439	1.444	1.452	1.442	1.441
C(8)—C(8′)	1.495	1.471	1.488	1.493	1.493	1.499	
Angles (deg) esd's	0.2	0.2 A	0.2 B	0.2	0.2	0.2	
C(1)—C(2)—C(3)	120.4	121.5	121.3	120.2	120.7	120.1	119.8
C(2)—C(3)—C(4)	121.0	119.4	119.5	121.2	118.9	120.3	120.3
C(3)—C(4)—C(5)	118.4	119.9	120.0	118.0	121.6	119.8	119.7
C(4)—C(5)—C(6)	121.2	120.0	120.0	121.0	119.1	120.5	120.5
C(5)—C(6)—C(1)	119.9	120.5	120.5	120.2	120.5	119.8	119.8
C(6)—C(1)—C(2)	119.1	118.7	118.7	119.3	122.8	119.8	119.9
C(1)—C(7)—O(1)	125.1	125.4	125.8	125.1	124.5	124.6	124.1
C(1)—C(7)—O(2)	112.0	112.0	111.7	111.5	112.5	113.1	112.8
O(1)—C(7)—O(2)	122.7	122.6	122.5	123.3	123.0	122.3	122.6
C(7)—O(2)—C(8)	116.6	115.7	115.1	116.0	115.8	115.9	115.5
O(2)—C(8)—C(8′)	106.6	105.1	104.6	104.9	107.3	104.7	105.2

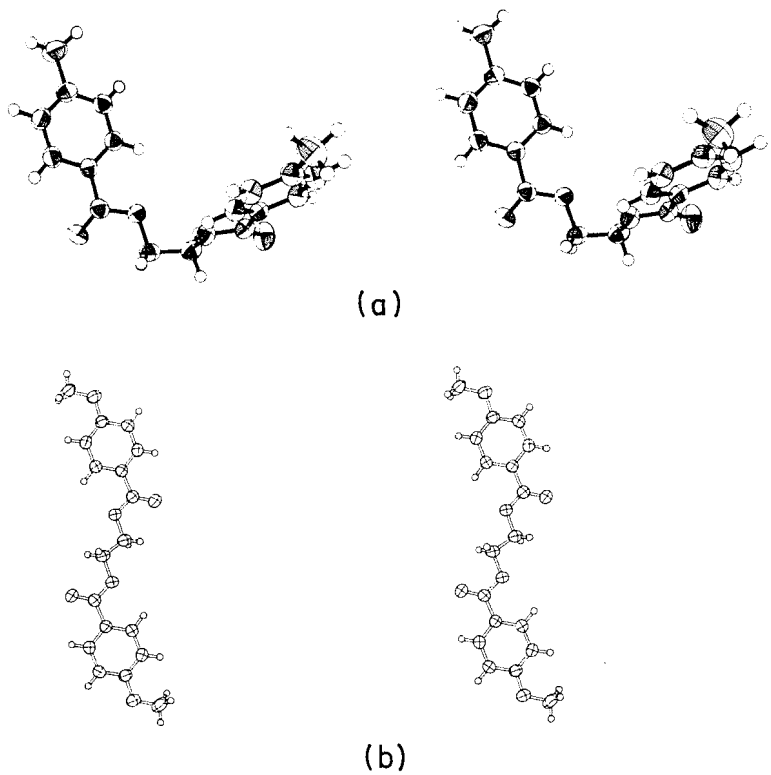

FIG. 2. Stereopairs of the two molecules. (a) Ethyleneglycol di-*para*-methylbenzoate. (b) Ethyleneglycol di-*para*-methoxybenzoate.

Can. J. Chem. Downloaded from www.nrcresearchpress.com by 196.1.178.254 on 09/07/12
For personal use only.

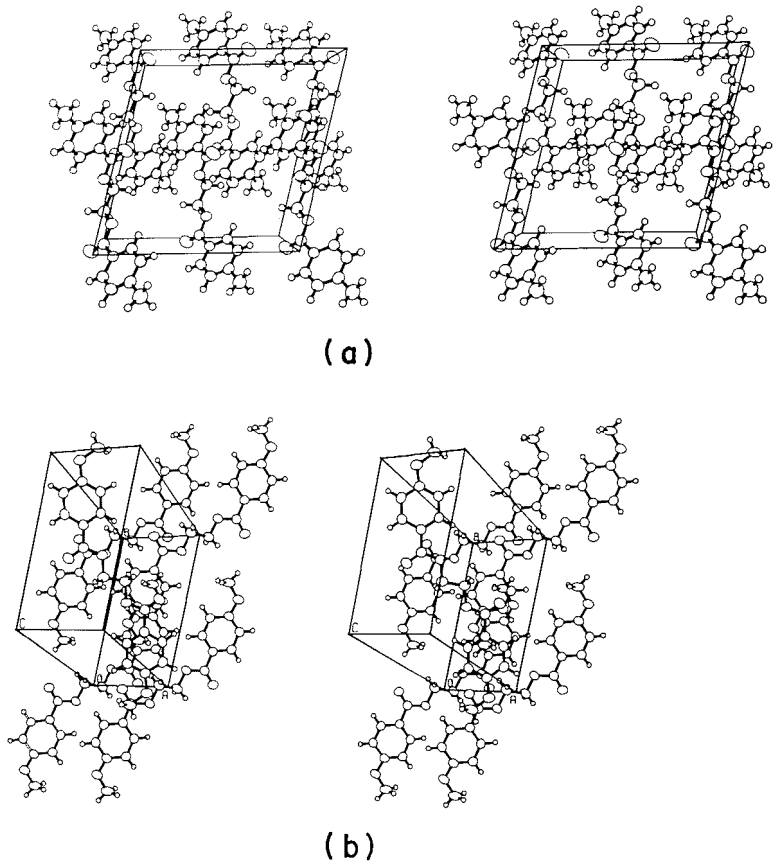

FIG. 3. Packing of the molecules. (a) Ethyleneglycol di-*para*-methylbenzoate. (b) Ethyleneglycol di-*para*-methoxybenzoate.

TABLE 5. Comparison between conformational analysis and crystallographic results

	Energy minima calculated by conformational analysis			Conformation of model compounds obtained by X-ray diffraction				
		Torsion angle		Torsion angle				
Minima	Energy (kcal/mol)	ϕ_1	ϕ_2	ϕ_1	ϕ_2	ϕ_1'	Molecule	Equivalent fiber repeat, p_c, Å
I	0.00	±100	±60					
II	0.52	180	180	−163.2(2)	180	163.3(2)	2DBO-*p*-OMe	10.74
				174.7(2)	180	−174.7(2)		10.75
				177.1(2)	180	−177.1(2)	2DBO-*p*-Ph	10.77
				175.6	−172.8	−176.0	2DBO	10.75
III	0.58	±177.5	±62.5	175.0	74.5	175.0	2DBO-*p*-Cl	9.27
				175.3(3)	67.6(2)	175.3(3)	2DBO-*p*-Me	10.27
IV	0.63	±80	±55					
V	1.12	±80	+175					

benzoate), the corresponding angle values are 152.1, −169.8, and −174.6°. It is the bulk of the methyl groups which is responsible for the deviation from the *trans* conformation. Poulin-Dandurand (19) calculated the conformational energy of an isolated molecule of ethylene glycol dibenzoate, 2DBO. The (ϕ_1, ϕ_2) pairs of torsion angles corresponding to the five lowest energy minima, all within 1 kcal/mol, are compared in Table 5 with the actual torsion angles of the dibenzoates.

Mean planes

The carboxylic groups are tilted by about 5° with respect to the corresponding phenyl plane. This is in good agreement with the systematic study of benzoate groups (7) in which it is found that the dihedral angle between the carboxylate group and the phenylene ring is in the interval of 0–10° with the most frequently observed value around 5°.

Relation to the parent polyester

The equivalent fiber repeat, p_c, is measured by the distance between the centers of the aromatic rings. In 2DBO, 2DBO-*p*-OMe, and 2DBO-*p*-Ph, p_c is very close to the observed fiber repeat, c = 10.75 Å, reported by Daubeny *et al.* (1) in

Can. J. Chem. Downloaded from www.nrcresearchpress.com by 196.1.178.254 on 09/07/12
For personal use only.

TABLE 6. Infrared absorption frequencies (cm^{-1}) characteristic of the methylene groups

	From refs. 20–22	2DBO	2DBO-*p*-Me	2DBO-*p*-OMe	2DBO-*p*-Ph	2DBO-*p*-Cl	2DBO-*p*-CN	2DBO-*p*-NO_2
trans-Conformation								
CH_2 bending	1470	1485		1470	1476		1481	1487
CH_2 wagging	1340	1339		1339	1335		1338	1336
C–C stretching for a *trans* glycol segment	975	984		976	986		979	979
CH_2 rocking	845	856			849		846	846
gauche-Conformation								
CH_2 bending	1450		1460			1458		
CH_2 wagging	1370		1370			1375		
C–C stretching for a *gauche* glycol segment	1040		1039			1039		
CH_2 rocking	898		897			894		

poly(ethylene terephthalate). In 2DBO-*p*-Me and 2DBO-*p*-Cl, p_c is 10.27 and 9.27 Å respectively, values much lower than the observed fiber repeat of 2GT.

For a planar chain, i.e., for the polyester in a fully extended conformation, the calculated fiber repeat is 10.9 Å. It is interesting to note that for the three model compounds with various combinations of bond distances, angles, and torsion angles, the equivalent fiber repeat is always shorter than that for an all-*trans* conformation and nearly matches the observed fiber repeat of poly(ethylene terephthalate).

Packing of the molecules

In all the molecules, none of the intermolecular contacts is less than 3.30 Å; therefore, the molecules are held in the crystal by van der Waals forces only.

In 2DBO, 2DBO-*p*-Ph, and 2DBO-*p*-OMe, the molecules are packed in a herringbone manner. In 2DBO-*p*-Me, the molecules are in an interlocking herringbone type of arrangement.

Infrared spectra

Since our interest was in the conformation of the methylenic sequence, the relevant absorption bands are those of the methylene groups. The FTIR bands observed for these vibrational modes for the dibenzoates are compared in Table 6.

The band assignment follows the work of Schneider *et al.* (20), Boitsov and Gotlib (21), and Ward and Wilding (22). They established a series of bands for the *trans* and the *gauche* conformations of a O—CH_2—CH_2—O segment. They assigned the absorption bands at 1470, 1340, 975, and 845 cm^{-1} to the *trans* conformation while the absorption bands at 1450, 1370, 1040, and 898 cm^{-1} were assigned to the *gauche* conformation. This assignment is confirmed in the case of the dibenzoates whose structures were determined in this work. We propose that in both 2DBO-*p*-CN and 2DBO-*p*-NO_2, for which compounds no crystal structure has been determined, the O—CH_2—CH_2—O sequence is in the *trans* conformation. All the absorption bands of 2DBO-*p*-CN and 2DBO-*p*-NO_2 fit very well with the assignment corresponding to a *trans* conformation. In the case of 2DBO-*p*-NO_2, the band at 1340 cm^{-1} is absent. It is probably hidden in the strong absorption of the symmetric stretching of the nitro group at 1336 cm^{-1}.

Another relevant absorption band is the ν(C=O) band of a benzoate group, normally observed at 1720 cm^{-1} (23). It is the resonance between the aromatic ring and the ester group which lowers the frequency with regard to that of a saturated ester whose band ν(C=O) is at 1735 cm^{-1} (24). The resonance between the aromatic ring and the ester group is influenced by the nature of the substituent on the six-membered ring. The effect of the substitution on the resonance between the phenylene ring and the ester group is qualitatively evaluated in Table 7 by taking into account the inductive effect and the resonance effect of the substituents (25). In the case of the methyl, phenyl, cyano, and nitro groups, there is no ambiguity in interpreting the observed shifts since both the inductive and resonance effects act in the same direction. In the case of 2DBO-*p*-Me and 2DBO-*p*-Ph, we observe an increase of the resonance between the aromatic ring and the ester group, and this is characterized by a ν(C=O) band observed at 1715 and 1708 cm^{-1} respectively. However, when the substituents are nitro or cyano groups, the ν(C=O) band is observed in both cases at 1724 cm^{-1}, as the resonance between the six-membered ring and the ester group is lowered. As for the methoxy and chloro groups, the two contributions have opposite effects. It is then difficult to evaluate their combined effect. We observe two ν(C=O) bands at 1715 and 1709 cm^{-1} for 2DBO-*p*-OMe, and one at 1714 cm^{-1} for 2DBO-*p*-Cl, thus indicating an increase of the resonance between the phenylene ring and the ester group. Therefore, the contribution of the resonance between the methoxy group and the aromatic ring is then larger than the contribution of the inductive effect.

TABLE 7. Contributions of the substituents on the resonance between the aromatic ring and the ester group

	Contributions*		Effect of the substituent on the resonance	
Substituent	Induction	Resonance	Predicted	Experimental
Me	+I	+R	Increase	Increase
OMe	−I	+R	?	Increase
Cl	−I	+R	?	Increase
Ph	—	+R	Increase	Increase
NO_2	−I	−R	Decrease	Decrease
CN	−I	−R	Decrease	Decrease

*−I: group takes on a negative charge by induction. +I: group takes on a positive charge by induction. −R: group takes on a negative charge by resonance. +R: group takes on a positive charge by resonance.

Can. J. Chem. Downloaded from www.nrcresearchpress.com by 196.1.178.254 on 09/07/12
For personal use only.

Can. J. Chem. Downloaded from www.nrcresearchpress.com by 196.1.178.254 on 09/07/12
For personal use only.

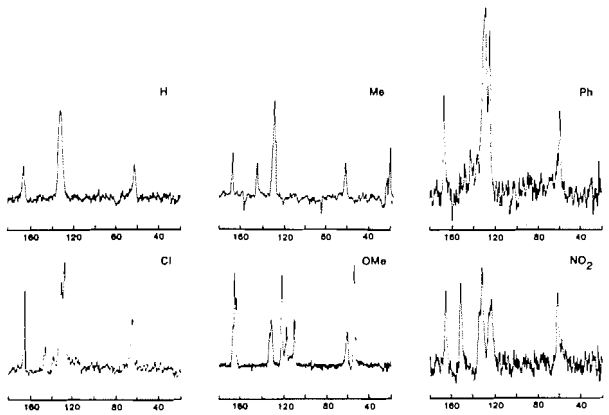

FIG. 4. ^{13}C nuclear magnetic resonance spectra of model compounds of polyethylene terephthalate.

^{13}C solid-state nuclear magnetic resonance

The ^{13}C solid-state nmr spectra of 2DBO, 2DBO-*p*-Me, 2DBO-*p*-OMe, 2DBO-*p*-Ph, 2DBO-*p*-Cl, and 2DBO-*p*-NO_2 are shown in Fig. 4. The chemical shifts in both the solid and liquid phases are given in Table 8.

In the cases of 2DBO-*p*-Me, 2DBO-*p*-Cl, and 2DBO-*p*-Ph, we observe only one peak for each pair of symmetrically related carbon atoms. This is because 2DBO-*p*-Me and 2DBO-*p*-Cl have a twofold axis of symmetry lying at the midpoint of the aliphatic chain while there is a center of symmetry in 2DBO-*p*-Ph.

Aliphatic region

These symmetry elements make the C(8), C(8′) and C(7), C(7′) atoms crystallographically equivalent in 2DBO-*p*-Me, -Cl, and -Ph. Thus, for these three compounds, only one peak is observed for C(8) and C(7). However, since there are two distinct centrosymmetrical molecules in the crystals of 2DBO-*p*-OMe, we observe two peaks for each of the C(8) and C(7) atoms. Finally, since there is no symmetry element in 2DBO there are also two peaks for each of the C(8) and C(7) atoms.

It has been shown that the γ-*gauche* effect and the molecular packing interactions both affect the chemical shift to different degrees. For the *para*-substituted dibenzoates, atoms C(8) and C(8′) are not affected by the γ-*gauche* effect since all the torsion angles (ω, ϕ_1) that could influence the chemical shift are *trans*. ω is the torsion angle C(7)—O(2)—C(8)—C(8′). However, the molecular packing interactions may still influence the chemical shift.

The averaged value of the chemical shift of C(8) in solution is 62.7 ppm and in the solid state it is 62.0 ppm. In both phases, the chemical shift does not vary significantly with the substitution. In solution, the extreme values are 62.4 and 63.2 ppm while in the solid phase they range from 60.2 to 62.5 ppm, except for 2DBO-*p*-Cl for which the chemical shift is 65.0 ppm. This value is out of the range observed here but it is quite similar to those obtained by Grenier-Loustalot and Bocelli for the ^{13}C solid-state nmr chemical shift of C(8) in butylene-1,4 dibenzoates substituted by chlorine in *ortho*, *meta*, and *para*, and in butylene-1,4 dibenzoate (28).

Aromatic ring

In solution, the chemical shift of the C(7) atom is influenced by the substitution of the aromatic ring, since the ester group is in resonance with the aromatic ring. Indeed, if the substituent is

TABLE 8. ^{13}C chemical shifts for the ethyleneglycol *para*-substituted dibenzoates in the solid phase and in solution

	2DBO		2DBO-*p*-Me		2DBO-*p*-OMe†		2DBO-*p*-Cl		2DBO-*p*-Ph		2DBO-*p*-NO_2	
Carbon	Solution	Solid	Solution	Solid	Solution	Solid	Solution	Solid	Solution	Solid	Solution	Solid
C1	131.1 (130.3)*	129.4	127.0 (127.4)	126.9	122.2 (122.6)	121.6	128.7 (128.4)	124.0	128.8 (129.6)	127.8	134.8 (136.1)	132.5–133.3
C2	129.6 (129.5)	129.4	129.6 (129.4)	128.7	131.6 (130.5)	131.1 *or* 132.8	131.0 (130.8)	128.0	130.1 (130.2)	127.8	130.7 (130.4)	130.5
C3	128.3 (128.3)	129.4	128.9 (129.0)	128.7	113.5 (113.9)	117.0	128.7 (128.7)	124.0	126.9 (127.4)	123.7	123.5 (123.5)	122.1
C4	133.0 (133.8)	129.4	143.7 (142.7)	143.4	163.4 (165.2)	163.3	139.7 (140.0)	143.9	145.8 (145.9)	140.3	150.6 (153.8)	150.5
C5	128.3 (128.3)	129.4	128.9 (129.0)	128.7	113.5 (113.9)	109.7	128.7 (128.7)	124.0	126.9 (127.4)	123.7	123.5 (123.5)	122.1
C6	129.6 (129.5)	129.4	129.6 (129.4)	128.7	131.6 (130.5)	131.1 *or* 132.8	131.0 (130.8)	128.0	130.1 (130.2)	127.8	130.7 (130.4)	130.5
C7	166.2	164.0	166.3	165.8	166.0	164.5	165.5	164.2	166.2	164.5	164.3	163.9
		163.4				166.0						
C8	62.6	61.9	62.4	62.3	62.4	61.0	62.8	65.0	62.7	60.2	63.2	61.1
		62.5				61.4						

*The values given in parentheses are for chemical shift calculated for the corresponding "methylbenzoate" (26, 27).
†In 2DBO-*p*-Me, *or* indicates that the assignment of C2/C6 could be interchanged.

strongly electron withdrawing, it will decrease the conjugation between the aromatic ring and the ester group, and thus C(7) will be shielded. In the case of the methyl, methoxy, chloro, and phenyl groups, their inductive and resonance effects increase the resonance between the aromatic ring and the ester group. For these substituents, the extreme values of the chemical shift of C(7) range from 165.5 to 166.3 ppm and their average is 166.0 ppm, a value quite similar to the chemical shift of C(7) in 2DBO (166.2 ppm). However, the nitro group is strongly electron withdrawing and it decreases the conjugation between the six-membered ring and the ester group. As expected, C(7) is shielded and its chemical shift is 164.3 ppm.

For the ^{13}C solid-state nmr, this effect is less remarkable. Indeed, the chemical shift of the C(7) atom ranges from 163.9 to 166.0 ppm and averages 164.7 ppm. In the solid state, the chemical shift of C(7) is also influenced by the γ-*gauche* effect related to the ϕ_1 torsion angle as well as by the molecular packing. In the case of the γ-*gauche* effect, this is negligible because, in all the compounds, the torsion angle of interest is always *trans*. The fluctuations of the chemical shift are then probably due to packing interactions.

As can be seen in Table 8, the observed chemical shifts of the aromatic ring carbons are quite similar to those calculated for the corresponding "methylbenzoate" in both solution and solid phase. In the case of 2DBO-*p*-OMe, the region of the aromatic carbons is more complicated in the solid-state spectra than in the solution spectra because the nuclei that are equivalent in solution (C(2), C(6) and C(3), C(5)) become nonequivalent in the solid. Indeed, the C(3) and C(5) atoms give rise to a doublet (see Table 8) separated by 7.3 ppm, while C(2) and C(6) are separated by 1.7 ppm although they are coincident in the liquid state. This is due to the nonsymmetric orientation of the methoxy group with respect to the aromatic ring. This has already been encountered in the study of *p*-alkoxybenzoic acids (29). Whereas free rotation about the methoxy bond may occur in solution, the molecule is locked in the solid state such that the C(3) and C(5) and the C(2) and C(6) atoms are no longer equivalent.

Conclusions

The study of these dibenzoates has served to establish that the CH_2—CH_2 bond length, whose average is 1.490 Å, is shorter than the expected C(sp^3)—C(sp^3) distance. The O—CH_2—CH_2 bond angles are not open as expected. It seems that this angle depends upon the value of the O—CH_2—CH_2—O torsion angle. We observe two types of conformation for the CO—O—CH_2—CH_2—O—CO sequence: all-*trans* and *trans-gauche-trans*. When the conformation is all-*trans* we observe an angle value of 105°, and when the conformation is *trans-gauche-trans* the angle value is 107°. No matter what the substituents are, the equivalent fiber repeat of those models in the all-*trans* conformation is always very close to that of the parent polyester.

The absorption bands in infrared spectroscopy confirm the conformation of the O—CH_2—CH_2—O sequence for the dibenzoates whose structures have been solved. For the two compounds for which no crystal structure has been determined, 2DBO-*p*-CN and 2DBO-*p*-NO_2, the observed absorptions allow us to propose, in both cases, a *trans* conformation.

For the molecules that have a twofold axis or a center of symmetry lying at the midpoint of the aliphatic chain, we observe in the nmr spectra only one peak for each pair of symmetrically related carbon atoms.

Acknowledgements

We wish to thank the Natural Sciences and Engineering Research Council of Canada for its financial support of this research. We also wish to acknowledge the help of Mr. M. J. Olivier for collecting the X-ray data.

1. R. DE P. DAUBENY, C. W. BUNN, and C. J. BROWN. Proc. R. Soc. London, A: **226**, 531 (1954).
2. Y. Y. TOMASHPOL'SKII and G. S. MARKOVA. Polym. Sci. USSR, **6**, 316 (1964).
3. S. ARNOTT and A. J. WONACOTT. Polymer, **7**, 157 (1966).
4. S. PÉREZ and F. BRISSE. Acta Crystallogr. Sect. B: Struct. Crystallogr. Cryst. Chem. **32**, 470 (1976).
5. S. PÉREZ and F. BRISSE. Can. J. Chem. **53**, 3551 (1975).
6. Molecular structures and dimensions. International Union of Crystallography, Cambridge. 1972.
7. S. DEGUIRE, J. GAGNÉ, F. BRISSE, and H. DUGAS. Can. J. Chem. **65**, 2291 (1987).
8. H. C. HEIM and C. P. POE. J. Org. Chem. **9**, 299 (1944).
9. F. R. AHMED, S. R. HALL, M. E. PIPPY, and C. P. HUBER. J. Appl. Crystallogr. **6**, 309 (1973).
10. P. MAIN, S. J. FISKE, S. E. HULL, L. LESSINGER, G. GERMAIN, J. P. DECLERCQ, and M. M. WOOLFSON. MULTAN80. A system of computer programs for the automatic solution of crystal structures from X-ray diffraction data. Universities of York, England, and Louvain, Belgium. 1980.
11. R. J. DOEDENS and J. A. IBERS. Inorg. Chem. **6**, 204 (1967).
12. C. K. JOHNSON. ORTEP. Report ORNL-3794. Oak Ridge National Laboratory, Tennessee. 1965.
13. D. T. CROMER and J. B. MANN. Acta Crystallogr. Sect. A: Cryst. Phys. Diffr. Theor. Gen. Crystallogr. **24**, 321 (1968).
14. R. F. STEWART, E. R. DAVIDSON, and W. T. SIMPSON. J. Chem. Phys. **42**, 3175 (1965).
15. F. BRISSE and J. SYGUSCH. Acta Crystallogr. Sect. B: Struct. Crystallogr. Cryst. Chem. **30**, 480 (1974).
16. A. DOMENICANO, A. VACIAGO, and C. A. COULSON. Acta Crystallogr. Sect. B: Struct. Crystallogr. Cryst. Chem. **31**, 221 (1975).
17. G. BOCELLI and M. F. GRENIER-LOUSTALOT. Acta Crystallogr. Sect. C: Cryst. Struct. Commun. **C39**, 633 (1983).
18. G. BOCELLI and M. F. GRENIER-LOUSTALOT. Acta Crystallogr. Sect. C: Cryst. Struct. Commun. **C40**, 1394 (1984).
19. S. POULIN-DANDURAND. M.Sc. thesis, Université du Québec à Montréal, 1978.
20. B. SCHNEIDER, P. SEDLACEK, J. STOKR, D. DOSKOCILOVA, and J. LOVY. Collect. Czech. Chem. Commun. **46**, 1913 (1981).
21. V. B. BOITSOV and Y. Y. GOTLIB. Opt. Spectrosc. **15**, 116 (1963).
22. I. M. WARD and M. A. WILDING. Polymer, **18**, 327 (1977).
23. M. AVRAM and G. D. MATEESCU. Spectroscopie infrarouge. Dunod, Paris. 1970. p. 523.
24. D. L. PAVIA, G. M. LAMPMAN, and G. S. KRIZ, JR. Introduction to spectroscopy. W. B. Saunders Company, Philadelphia, PA. 1979. p. 55.
25. N. L. ALLINGER, M. P. CAVA, D. D. DE JONGH, C. R. JOHNSON, N. A. LEBEL, and C. L. STEVENS. Organic Chemistry. Worth Publishers, Inc., New York, NY. 1976. p. 348.
26. R. J. ABRAHAM and P. LOFTUS. Proton and carbon-13 NMR spectroscopy. Heyden, London. 1980. p. 28.
27. E. BREITMAIER and G. BAUER. ^{13}C NMR spectroscopy, a working manual with exercises. Harwood Academic Publishers, Chur, Switzerland. 1984. pp. 61–62.
28. M. F. GRENIER-LOUSTALOT and G. BOCELLI. Eur. Polym. J. **20**, 957 (1984).
29. G. R. HAYS. J. Chem. Soc. Perkin Trans. 2, 1049 (1983).

Can. J. Chem. Downloaded from www.nrcresearchpress.com by 196.1.178.254 on 09/07/12
For personal use only.

Palladium phthalocyanine and its polymorphic forms

ARNOLD KEMPA AND JAN DOBROWOLSKI

Institute of Inorganic Chemistry and Technology, Technical University of Gdańsk, 80-952 Gdańsk, Majakowski Str. 11/12, Poland

Received July 6, 1987[1]

ARNOLD KEMPA and JAN DOBROWOLSKI. Can. J. Chem. **66**, 2553 (1988).

Pd(II) phthalocyanine (PdPc) was obtained by reaction of $PdCl_2$ with phthalimide and urea in the presence of ammonium molybdate in boiling nitrobenzene, resulting in a good yield equal to 68%. This method has not been used previously. The following polymorphic forms were obtained: metastable α- and γ-PdPc, not previous described in the literature, and stable β-PdPc. The IR spectra and X-ray powder diffraction spectra of these phases were measured and interpreted. The results were compared with the literature data on polymorphic forms of other phthalocyanines. At this time we do not know if any of the PdPc polymorphs are isomorphous with the various forms of nickel, copper, and platinum phthalocyanine.

ARNOLD KEMPA et JAN DOBROWOLSKI. Can. J. Chem. **66**, 2553 (1988).

Faisant appel à une méthode qui n'avait pas été utilisée jusqu'à maintenant, on a préparé le phtalocyanure de Pd(II) (PdPc) avec un rendement de 68% en faisant réagir du $PdCl_2$ avec de la phtalimide et de l'urée en présence de molybdate d'ammonium, dans du nitrobenzène bouillant. On a obtenu les formes polymorphes suivantes : les formes métastables α- et γ-PdPc qui ne sont pas décrites dans la littérature ainsi que le forme stable β-PdPc. On a déterminé les spectres ir et les spectres de diffraction des rayons-X des poudres de ces phases et on les a interprétés. On a comparé les résultats avec ceux retrouvés dans la littérature pour des formes polymorphes d'autres phtalocyanures. Sur la base de ces données, on ne peut pas affirmer que des formes polymorphes du PdPc sont isomorphes avec diverses formes de phtalocyanures de nickel, de cuivre ou de platine.

[Traduit par la revue]

Introduction[2]

Our investigations on synthesis and properties of PdPc complexes with iodine required preparation and examination of certain physical properties of various polymorphic forms of PdPc. No data on PdPc polymorphs are available from the literature. From the group of phthalocyanines of the d^8 ions of the VIII group metals, viz. Ni, Pd, and Pt, PdPc was the least examined. This is probably due to difficulties associated with its synthesis. In a reaction of $PdCl_2$ with phthalonitrile Cl-PdPc is formed (1–3). PdPc can be obtained from palladium black and phthalonitrile, but the product contains a mixture of H_2Pc and colloidal palladium which are very difficult to remove (4, 5). Other methods of preparation also yield PdPc mixed with H_2Pc (1, 6). We therefore decided to synthesize PdPc by reaction of $PdCl_2$ with phthalimide in the presence of urea and a catalyst. PdPc has not been prepared by this method up to now, while according to Moser and Thomas (7), under such conditions no H_2Pc is formed and the chlorination of phthalocyanines does not occur. Following synthesis and purification of PdPc, its polymorphic forms were synthesized. The terms α, β, γ were used, similar to the polymorphic forms of CuPc (7). X-ray powder diffraction spectra of α-, β-, and γ-PdPc were taken to reveal similarities with the known diffraction spectra of α-PtPc (8), β-NiPc (9), α-CuPc (8, 10–14), and β-CuPc (11, 12, 14), γ-CuPc (8, 13, 14), and α- and β-H_2Pc (15). Another technique used to differentiate between polymorphic forms of phthalocyanines is their IR spectra (16). Infrared spectra of α-, β-, and γ-PdPc were taken to find out if they are identical. For isomorphous forms of the same compound (PdPc) the IR spectra should be identical, while for non-isomorphous forms the IR spectra should be different.

Experimental

Materials

Analytical grade $PdCl_2$, urea, ammonium molybdate, isopropanol, NaOH, HCl, pyridine, methanol, xylene, and purum grade phthalimide made in Poland. Analytical grade nitrobenzene and acetone were obtained from Reactivul Bucuresti, and analytical grade H_2SO_4 was of Polish production.

Syntheses

PdPc was obtained using a method typical for synthesis of CuPc (7), adapted in a suitable way. $PdCl_2$, phthalimide, and urea (1:4:14 molar) were heated in boiling nitrobenzene for 4 h in the presence of ammonium molybdate (2% of mass of phthalimide) as a catalyst. A large amount of greasy impurities is formed during the reaction, probably because the formed PdPc catalyzes a number of side reactions (17). The resulting product was purified by washing in succession with isopropanol, 2–3% NaOH, and 2–3% HCl. PdPc was subsequently recrystallized four times from concentrated H_2SO_4. Usually during recrystallization the solution of phthalocyanine in concentrated H_2SO_4 is poured into distilled water (18). In this case the resulting particles are very fine, difficult to filter and to decant. As a result we used our method of precipitation. Since the use of pure water for precipitation results in an irreversible formation of very small crystallites, we used sulphuric acid of concentration decreasing gradually from 96 to nearly 0%. This proved to be a very convenient precipitation agent. A solution of H_2SO_4 was added slowly to a stirred solution of PdPc in concentrated H_2SO_4. PdPc precipitated this way consists of larger crystallities that are easy to filter and to decant. After complete recrystallization the PdPc obtained (γ-form) was further purified by Soxhlet extraction using in succession: py – water 1:9 by volume, methanol, and acetone. Yield, 68%. *Anal.* calcd. for PdPc: C 62.10, H 2.61, N 18.10, Pd 17.19; found: C 61.97, H 2.41, N 18.36, Pd 17.14.

α-PdPc, not previously known, was obtained by a method typical for synthesis of α-phthalocyanines (7). The solution of PdPc in concentrated H_2SO_4 was poured into a large amount of vigorously stirred distilled water. The product was filtered, the remaining acid washed out, and the phthalocyanine dried at 150°C.

β-PdPc was obtained by a method typical for synthesis of β-phthalocyanines (7), by heating PdPc for several hours in boiling xylene, subsequent filtration, and drying at 150°C.

[1]Revision received May 13, 1988.

[2]Abbreviations used in this article are as follows: PdPc, Pd(II) phthalocyanine; NiPc, Ni(II) phthalocyanine; CuPc, Cu(II) phthalocyanine; PtPc, Pt(II) phthalocyanine; H_2Pc, metal-free phthalocyanine; Cl-PdPc, Pd(II) monochlorophthalocyanine.

Printed in Canada / Imprimé au Canada

Can. J. Chem. Downloaded from www.nrcresearchpress.com by 196.1.178.254 on 09/07/12
For personal use only.

TABLE 1. Infrared spectra of the three polymorphic modifications of PdPc[a]

α-PdPc	γ-PdPc	β-PdPc	PdPc after sublimation at 550°C Kobayashi (19)	Cl-PdPc Keen (3)
1612 w[b]	1612 w	1612 w	1606 m	1614 ms
1589 w	1589 w	1589 w	1583 w	
1509 w	1509 w	1510 m	1503 s	1511 m
~ 1462 s (Nujol oil)			1480 sh	1481 w
				1464 w
1421 m	1421 m	1421 m	1418 s	1420 m
~ 1376 s (Nujol oil)				
1354 w	1354 mw	1354 w	1350 m	1354 w
1332 s	1332 s	1332 s	1330 s	1330 ms
1288 ms	1288 ms	1288 ms	1285 s	1289 m
				1257 w
1200 w	1200 w	1200 w		
			1188 w	
1170 s	1170 s	1170 s	1167 s	1170 m
			1125 sh	1124 s
			1120 vs	
1111 w	1111 w	1111 w	1107 s	
1072 m	1072 m	1072 w	1070 s	1076 wm
1028 w	1028 w			
				1011 w
1002 w	1002 w		1000 vw	
	948 w	951 w	949 m	955 w
	939 w		940 sh	
914 m	914 m	915 m	911 m	918 ms
		884 mw		
			880 w	876 w
	869 w			
	863 mw	862 w	860 w	
809 w	809 mw	809 mw	805 w	
		781 m	778 m	
769 m	769 s	769 mw	767 s	771 w
757 s	757 s	757 s	755 s	756 wm
		736 mw		
			730 sh	
723 s	722 s	726 s	723 vs	724 s

[a]Wavenumbers in cm^{-1}.
[b]v = very, s = strong, m = medium, w = weak, sh = shoulder.

We prepared γ-PdPc using a modification of Knudsen's method of synthesis of γ-CuPc (13). A solution of H_2SO_4 of concentration decreasing gradually from 96 to nearly 0% was added slowly to the solution of PdPc in concentrated H_2SO_4 in such a manner that the final concentration of H_2SO_4 was lower than 60%. The product was filtered, the remaining acid washed out, and the phthalocyanine dried at 130°C.

The IR spectra were recorded in Nujol suspension using NaCl plates and a Carl Zeiss Jena Specord 75 IR spectrophotometer. Polystyrene and indene served as standards.

X-ray spectra

Powder diffraction spectra were recorded using a DRON-2 X-ray diffractometer: CuK_α 35/20 radiation; slit arrangement 2, 2, 0.5. Range of pulse counter 4×10^3 pulses/s, gain 128, time constant 1 s, goniometer rate 2°/min. External standards β quartz, $Ca(H_2PO_4)_2 \cdot H_2O$. Angular range 5–50°.

Results and discussion

(*1*) It was found that the present method produced a 68% yield of PdPc (hence better than that in literature (5)), free of mixtures of Cl-PdPc and H_2Pc. The crude product, however, requires quite laborious purification. New α and γ phases of PdPc, not described in the literature, were synthesized; the stable β-PdPc was also obtained. The products are fine coloured crystalline powders with α reddish, β pale blue, and γ dark blue.

TABLE 2. X-ray powder diffraction spectra of α-, β-, and γ-PdPc

β-PdPc		α-PdPc		γ-PdPc	
d_{hkl}[a]	I/I_0	d_{hkl}	I/I_0	d_{hkl}	I/I_0
13.07	1.00			13.21	1.00
11.75	0.44	12.26	1.00	12.29	0.65
9.05	0.10			9.63	0.15
8.27	0.09			5.47	0.26
5.32	0.27			3.62	0.10
4.07	0.05	3.35	0.58	3.27	0.15
3.42	0.12	2.24	0.17	2.24	0.08
3.18	0.04	1.94	0.08	1.94	0.03
3.02	0.06				
2.24	0.06				

[a]In Å.

(*2*) Table 1 presents our IR absorption spectra; together with Kobayashi's results for high temperature (550°C) sublimed PdPc (19) and Keen's results for α Cl-PdPc (3). All peaks of the α form have been found in the spectrum of the γ polymorph which has several additional peaks. The phenomenon suggests a similarity in the crystalline structure of α- and γ-PdPc, which on the other hand differs from that of β-PdPc.

(*3*) Well developed X-ray powder diffraction spectra were obtained for β- and γ-PdPc. The spectrum of the α-phase, however, consists of only four low, insufficiently developed, broad peaks. Hence it is concluded that α-PdPc consists of crystallites smaller than 0.1 μm (8, 20–22). Using the Debye–Scherer equation (22), taking into account the broadening of peaks (including correction), the average size of crystallites of α-PdPc was calculated to be equal to 0.008 μm. Crystallites of β- and γ-PdPc must be much bigger, because spectra of these forms are well developed. Table 2 shows our diffraction spectra. The diffraction spectrum of β-PdPc is entirely different from the spectra of the remaining two polymorphs, which indicates that its crystalline structure is totally different from those of α and γ forms. All the peaks which occur in the spectrum of α-PdPc are also present in the spectrum of the γ form, which has several additional peaks. Hence, it can be supposed that the structure of α and γ polymorphs are similar, although small differences in structure are not excluded. By comparing literature data with our results, we find no similarity between the diffraction spectra of the PdPc phases and those of α-PtPc, α-, γ-CuPc, β-CuPc, and β-NiPc. Hence, we have no basis to correlate the isomorphism of the obtained α-, β-, and γ-polymorphic forms of PdPc with any of the above listed crystal phases.

Conclusions

It follows from our investigations that we obtained PdPc in one stable β-PdPc form and two metastable α and γ forms which are different from the β form on the basis of IR and X-ray diffraction. Further research is required to determine if the α and γ polymorphs are isomorphous or are somewhat different in structure, and to determine the structure of the stable β form.

Can. J. Chem. Downloaded from www.nrcresearchpress.com by 196.1.178.254 on 09/07/12
For personal use only.

Acknowledgements

The authors wish to thank Dr. A. Pielak for the X-ray powder diffraction spectra, and Dr. T. Suwińska for carrying out elemental analysis. This research was financed by grant MR-I-13 and CPBP-01.18.

1. P. A. BARRET, D. A. FRYE, and R. P. LINSTEAD. J. Chem. Soc. 1157 (1938).
2. I. M. KEEN. Plat. Met. Rev. **8**, 143 (1964).
3. I. M. KEEN and B. W. MALERBI. J. Inorg. Nucl. Chem. **27**, 1311 (1965).
4. G. E. FICKEN and R. P. LINSTEAD. J. Chem. Soc. 4846 (1952).
5. J. F. BOAS, P. E. FIELDING, and A. G. MACKAY. Aust. J. Chem. **27**, 7 (1974).
6. H. TOMODA, S. SAITO, and S. SHIRAISHI. Chem. Lett. 313 (1983).
7. F. MOSER and A. L. THOMAS. Phthalocyanine compounds. Reinhold Publishing Corp., New York, London. 1963.
8. B. HONIGMANN, H. U. LENNE, and R. SCHRÖDEL. Z. Kristall. **122**, 185 (1965).
9. J. ROBERTSON. J. Chem. Soc. 1195 (1936).
10. M. T. ROBINSON and G. E. KLEIN. J. Am. Chem. Soc. **74**, 6294 (1952).
11. M. SHIGEMITSU. Bull. Chem. Soc. Jpn. **32**, 607 (1959).
12. J. H. SHARP and M. ABKOWITZ. J. Phys. Chem. **77**, 477 (1973).
13. B. I. KNUDSEN. Acta Chem. Scand. **20**, 1344 (1966).
14. J. M. ASSOUR. J. Phys. Chem. **69**, 2295 (1965).
15. F. W. KARASEK and J. C. DECIUS. J. Am. Chem. Soc. **74**, 4716 (1952).
16. D. N. KENDALL. Anal. Chem. **25**, 382 (1953).
17. H. ECKERT. Ger. Offen. DE 3.121.478. 16 Dec., 1982.
18. H. LUBS (*Editor*). The chemistry of synthetic dyes and pigments. Hafner Publishing Corp., Darrien, CT. 1970.
19. T. KOBAYASHI, F. KUROKAWA, N. UYEDA, and E. SUITO. Spectrochim. Acta, **26A**, 1305 (1970).
20. B. HONIGMANN. J. Paint Tech. **38**, 77 (1966).
21. B. HONIGMANN. Ber. Bunsenges. Phys. Chem. **71**, 239 (1967).
22. J. SCHRÖDER. Prog. Org. Coat. **12**, 181 (1984).

Can. J. Chem. Downloaded from www.nrcresearchpress.com by 196.1.178.254 on 09/07/12
For personal use only.

The intermediates in the interaction of phenols with *N*-bromosuccinimide

YUAN L. CHOW,[1] DA-CHUAN ZHAO, AND CARL I. JOHANSSON
Department of Chemistry, Simon Fraser University, Burnaby, B.C., Canada V5A 1S6

Received March 17, 1988

YUAN L. CHOW, DA-CHUAN ZHAO, and CARL I. JOHANSSON. Can. J. Chem. **66**, 2556 (1988).

Phenols react with *N*-bromosuccinimide to generate 2-bromocyclohexadienone-type intermediates that enolize to 2-bromophenols thermally or photolytically with a wide range of rate constants depending on the parent phenol. A trace amount of acids not only accelerates the rates of the formation and decomposition of the 2-bromodienones, it also promotes the rearrangement of the 2-bromodienones to cross-conjugated 4-bromocyclohexadienones. The enolization of these last compounds affords 4-bromophenols. The occurrence of autocatalysis in dienone decompositions arising from more acidic bromophenols is also established. The reaction is assumed to occur by a bromophilic attack of phenols on the N—Br bond to form unstable hypobromites that rapidly rearrange to the 2-bromocyclohexadienone intermediates. The quantum yield of the photodecomposition of 2-bromo-(2*H*)-naphthalene-1-one in the vicinity of 365 nm was determined to be unity.

YUAN L. CHOW, DA-CHUAN ZHAO et CARL I. JOHANSSON. Can. J. Chem. **66**, 2556 (1988).

Les phénols réagissent avec le *N*-bromosuccinimide pour conduire à des intermédiaires du type bromo-2 cyclohexadiènones, qui s'énolisent en bromo-2 phénols d'une façon thermique ou photochimique et avec des constantes de vitesse très variables suivant la nature des phénols de base. L'addition de traces d'acides n'accélère pas uniquement les vitesses de formation ou de décomposition des bromo-2 diènones, elle provoque aussi la transposition des bromo-2 diènones en bromo-4 cyclohexadiènones avec une conjugaison croisée. L'énolisation de ces derniers composés conduit à des bromo-4 phénols. On a aussi démontré que des décompositions des diénones se produisent sous l'effet d'une autocatalyse qui est dûe aux bromophénols qui sont plus acides. On suppose que la réaction se produit par une attaque bromophile des phénols sur la liaison N—Br qui conduit à la formation d'hypobromites instables qui se transposent rapidement en intermédiaires bromo-2 cyclohexadiènones. On a établi que le rendement quantique de la photodécomposition de la bromo-2 (2*H*)-naphtalènone-1, autour de 365 nm, est égal à un.

[Traduit par la revue]

Can. J. Chem. Downloaded from www.nrcresearchpress.com by 196.1.178.254 on 09/07/12
For personal use only.

N-Bromosuccinimide (NBS) is a versatile brominating agent and has been used extensively in radical and ionic brominations (1–3).[2] We have observed that NBS reacts with phenols in aprotic solvent cleanly with second-order kinetics to form unstable intermediates that are shown to have dienone-type structures. The kinetics of formation and the behavior of these intermediates are described in this paper. Bromination of phenols with bromine has been studied extensively as a prototype electrophilic reaction (4–8). NBS has been used as an analytical reagent for phenols such as vanillin and thymol (9, 10), but its mechanistic aspects have scarcely received any attention. Semistable intermediates obtained from the reaction of NBS with estradiols have been suggested, such as the hypobromites **1** (11), although their nmr spectroscopic data are

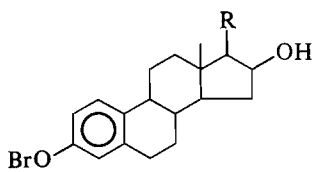

1

equally compatible with a hexadienone structure, i.e., structures analogous to those of **3** and **4** (*vide infra*) (4, 12, 13). Since the reaction of NBS with phenols is a simple and clean method of preparing monobromo derivatives of phenols, and some of their intermediates can be developed as secondary actinometers, we undertook mechanistic studies of this reaction.

Results

Upon admixing dilute solutions of 1-naphthol (1-NpOH) and NBS in methylene chloride at room temperature in the dark, the mixture immediately revealed a pale yellow colour and rapidly developed an absorption peak at 357 nm with two isobestic points at 269 and 323 nm (Fig. 1a). The absorption peak of the new product was confirmed further by a differential ultraviolet spectroscopic method in which the mixture was scanned against a reference containing solutions of the starting materials (1-NpOH and NBS in double concentrations) separately placed in a double-compartment cell (Fig. 1b). Under the dark, ambient conditions, the new product from 1-NpOH decomposed slowly, and completely in a few days, to give 2-bromo-1-naphthol **5** and a small amount of the 4-bromo isomer **6**. Other phenols also reacted with NBS under similar conditions to afford the corresponding intermediates, whose uv absorptions were determined (Table 1). Some of these spectral patterns are shown in Fig. 2. The decomposition of these intermediates gave the corresponding bromophenols, which were isolated (see Experimental). The mechanistic studies were carried out primarily using 1-NpOH as a model compound.

The nmr parameters of the intermediates derived from naphthols and NBS were obtained from solutions prepared from substrates without isolation and are shown in Table 2. While these data, as well as the uv absorption parameters (Table 1), were consistent with the intermediates possessing dienone-type structures (12, 13), they failed to exclude the possibility of hypobromite intermediates, since alkyl hypobromites are reported to show absorptions near 340 nm (14, 15). The ir spectrum of the intermediates formed *in situ* from 1-NpOH and NBS was obtained by subtracting the absorption due to residual NBS (Fig. 3). The absorption band at 1701 is in agreement with those reported for the extended dienone, 2-bromo-(2*H*)-naphthalene-1-one (**3**). The carbonyl stretching frequency was shifted to a higher wave number than usual owing to the 2-equatorial C—Br bond orientation in **3**. Extensive studies of these spectra failed to show conclusively the presence of corresponding hypobromite absorptions. The intermediates

[1]Author to whom correspondence may be addressed.

[2]There are many reports in the literature, some of which are cited in review articles in ref. 1.

Can. J. Chem. Downloaded from www.nrcresearchpress.com by 196.1.178.254 on 09/07/12
For personal use only.

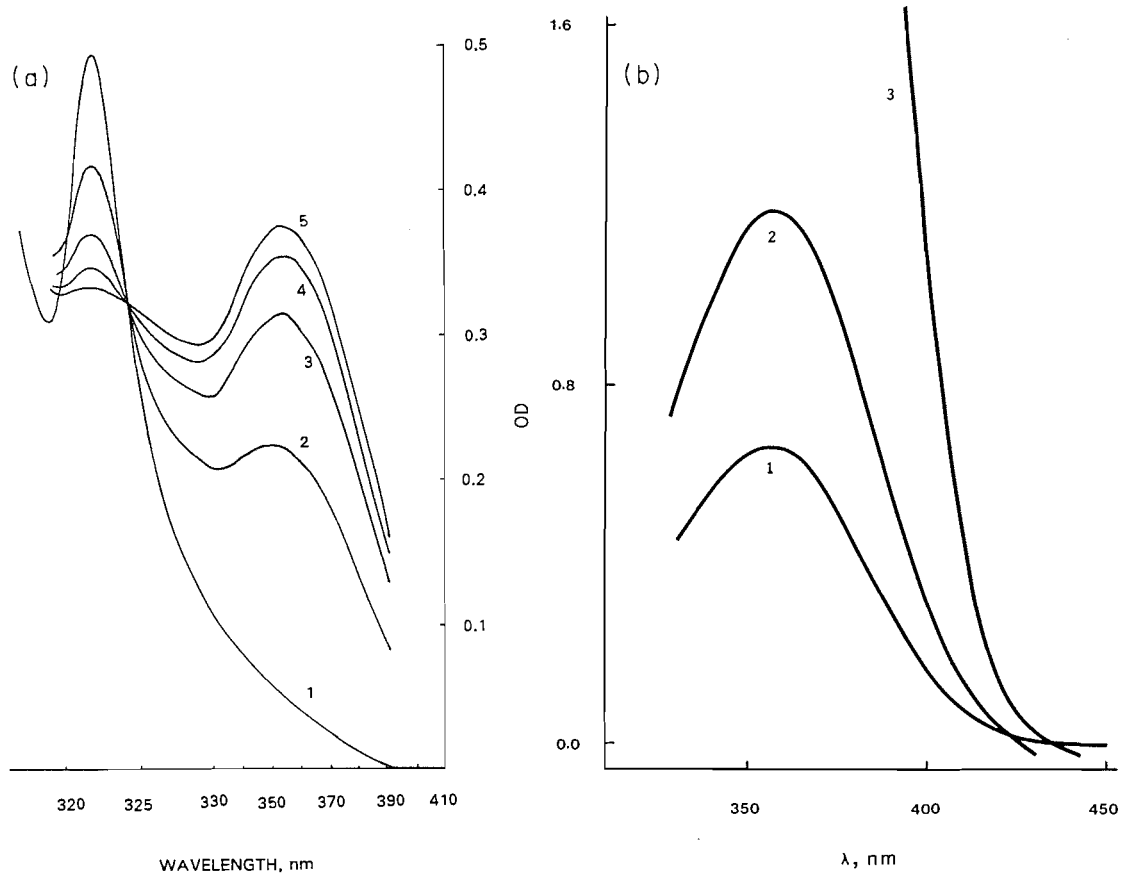

FIG. 1. Time-elapsed absorption spectra of the mixture of 1-NpOH (2.7×10^{-4} M) and NBS (2.0×10^{-2} M) in CH_2Cl_2 at 22 ± 2°C; (a) 10, 110, 210, 310, and 410 s after mixing. (b) Differential absorption spectra; the reference is a double-compartment cell, each compartment containing twice the concentration of the components in the solutions; curve 3, [1-NpOH] = 2.5×10^{-3} M, [NBS] = 2.0×10^{-3} M; curve 2, [1-NpOH] = 7.6×10^{-4} M, [NBS] = 1.6×10^{-3} M; curve 1, [1-NpOH] = 7.6×10^{-4} M, [NBS] = 3.2×10^{-4} M.

from other phenols were also assigned dienone structures by analogy with the 1-NpOH reaction as shown in Tables 1 and 2. As the intermediate solution decomposed to give a small amount of 4-bromo-1-naphthol **6**, 4-bromo-(4*H*)-naphthalene-1-one (**4**) could be present as a minor component. The failure to detect the ir absorptions corresponding to **4** suggested that **4** as well as **6** might be formed in a later stage by an autocatalytic process of phenolic products **5** and **6**, which are more acidic than 1-NpOH (*vide infra*). These dienone intermediates possessed reasonable thermal stability but were sensitive to light as well as acid catalysis. These properties precluded our effort to isolate the intermediates, but allowed us to study their photochemistry *in situ*.

The order of the reaction of 1-NpOH with NBS was determined under experimental conditions in which [1-NpOH] and [NBS] were in the vicinity of the $(2.7–5.4) \times 10^{-4}$ M range: doubling of the concentration of either reactant increased the absorbance at 365 nm by a factor of 2 ± 0.3 at 20 and 50 s after the mixing of reactant solutions. Since second-order reaction rate constants calculated from these traces were comparable and agreed within experimental error with those k_2 shown in Table 3 (*vide infra*), the reaction is first order in both reactants. The reaction order was further confirmed by experiments under pseudo-first-order conditions, i.e., an excess of 1-NpOH (3.74×10^{-3} M) in methylene chloride was allowed to react with increasing concentration of NBS ($2.5 \times 10^{-5} – 3.9 \times 10^{-4}$ M); the absorbance at 365 nm after the completion of the

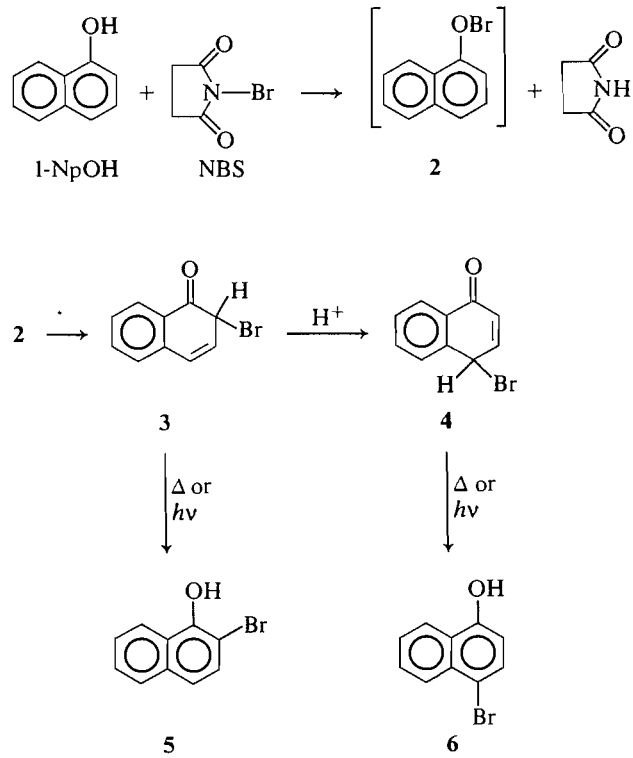

SCHEME 1

TABLE 1. Ultraviolet absorption peaks and stability of 2-bromodienones in CH_2Cl_2

Reactions	λ_{max}, nm	$10^{-3}\,\epsilon_{max}$	Remarks
1 1-NpOH → 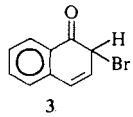 **3**	357	2.0	$\epsilon^{365\ nm} = 1.9 \times 10^3$ [a] $t_{1/2} = 15$ h
2 2-NpOH → 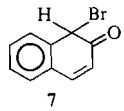 **7**	330	5.7	$\epsilon^{355\ nm} = 4.2 \times 10^3$ [a] $t_{1/2} = 14$ h
3 4-Cl-1-NpOH → 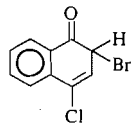 **8**	356	2.1	$\epsilon^{375\ nm} = 1.5 \times 10^3$ [a] $t_{1/2} = 16$ h
4 2-Br-4-Cl-1-NpOH → 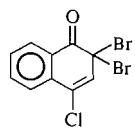 **9**	362	2.2	Stable
5 1-Anthrol → 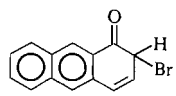	396 414 (sh)	2.4	$t_{1/2} = 800$ s
6 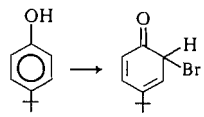	337	>0.039	$t_{1/2} = 5400$ s

[a]The ϵ values shown are obtained from the plot of OD against [NBS]. The ϵ_{max} values at λ_{max} were calculated with reference to these ϵ values. Other ϵ_{max} values were obtained from the highest absorbance of the kinetic traces at the λ_{max}.

TABLE 2. ^1H nuclear magnetic resonance parameters of naphthols and the corresponding dienones in $CDCl_3$[a]

Compound	H-1	H-2	H-3	H-4	H-5–H-8
1-NpOH	5.4(s)	6.85(dd) $J_{2,3} = 6.9$ $J_{2,4} = 1.6$	7.27(dd) $J_{3,4} = 8.3$	7.40(d)	7.45–8.14(m)
3	—	5.02(d) $J_{2,3} = 4.6$	6.38(dd) $J_{3,4} = 9.8$	6.70(d)	7.27–8.11(m)
2-NpOH	7.16(s)	5.0(s)	← 7.32–7.82 →		
7	5.43(s)	—	6.26(d) $J_{3,4} = 10.0$	← 7.16–8.0 →	
4-Cl-1-NpOH	5.3(s)	6.75(d) $J_{2,3} = 8.0$	7.40(d)	—	7.61–8.23
8	—	5.11(d) $J_{2,3} = 5.5$	6.56(d)	—	7.56–8.42
2-Br-4-Cl-1-NpOH	5.9(s)	—	7.61(s)	—	7.56–8.32
9	—	—	7.03(s)	—	7.53–8.29

[a]Chemical shifts are expressed in δ values calculated from $CHCl_3$ (7.27 ppm) as the internal standard.

Can. J. Chem. Downloaded from www.nrcresearchpress.com by 196.1.178.254 on 09/07/12
For personal use only.

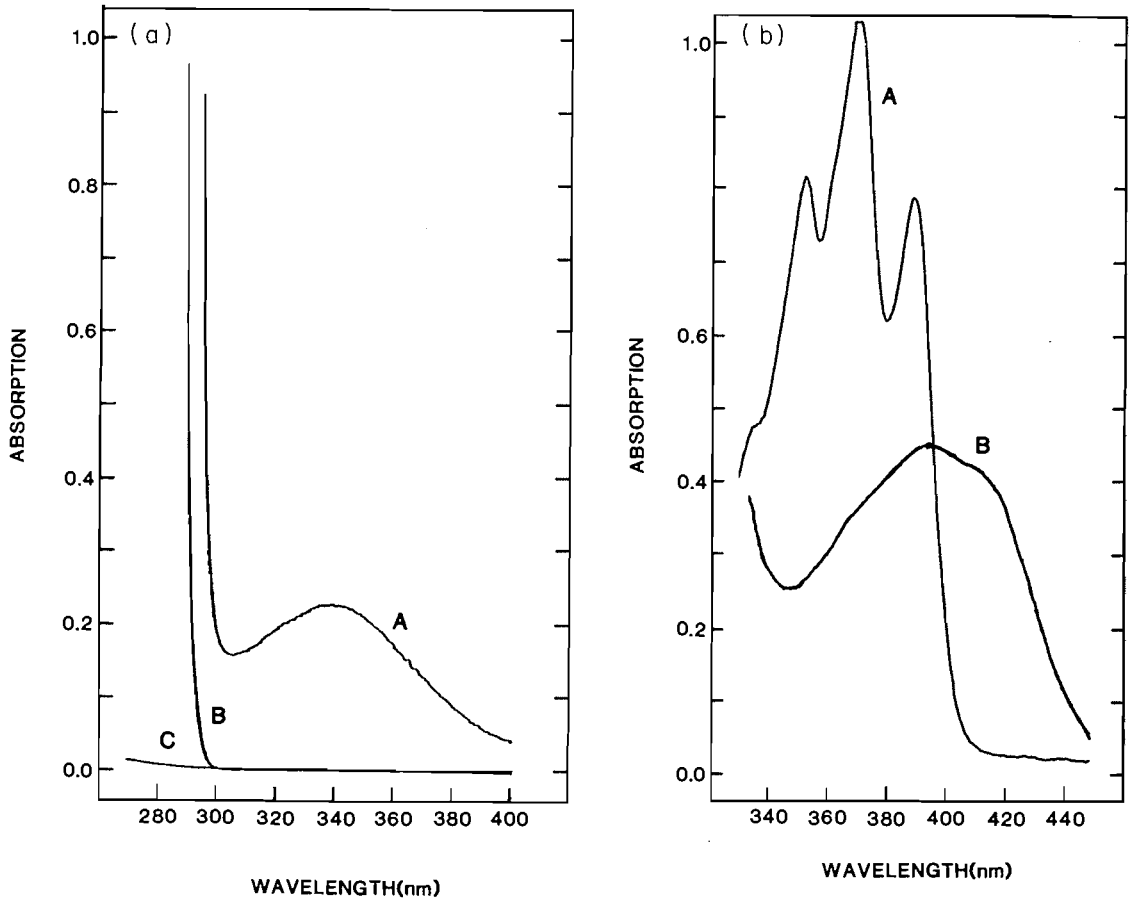

FIG. 2. Absorption spectra in CH_2Cl_2. (a) Curve A contains [NBS] = 4.63×10^{-4} M, [4-*tert*-butylphenol] = 1.34×10^{-2} M; curve B, [4-*tert*-butylphenol] = 1.34×10^{-2} M; curve C, [NBS] = 4.63×10^{-4} M. (b) Curve A contains [1-anthrol] = 5.0×10^{-5} M; curve B, [1-anthrol] = 5.0×10^{-5} M and [NBS] = 5.0×10^{-5} M.

reaction (~10 min) was plotted against NBS concentrations (Fig. 4) to give a straight line; the slope ($\epsilon = 1900$) represents the molar absorptivity of dienone **3** at 365 nm. Note that 365 nm was chosen since both reactants show nil absorption at this wavelength, which is not λ_{max} of the absorption peak.

In some of these experiments, a small amount of an olefin, either cyclohexene or 1,1-dichloroethene (10^{-4}–10^{-5} M), was added to scavenge bromine or bromine atom (16) in order to suppress radical pathways. However, it was found that if these reactions were conducted in the dark and completed in a matter of 10–30 min, the omission of olefins did not cause any observable difference in the kinetic curves and data. The concentrations of the reactants could be adjusted so that the kinetics of the dienone formation and (or) that of the decay could be followed readily. Usually, the reactions were carried out under pseudo-first-order reaction conditions using excess phenols, and the pseudo-first-order rate constants (k_{obs}) were obtained from kinetic traces such as shown in Fig. 5 and were converted to bimolecular rate constants (k_2 in Table 3). The rate constants of the formation of intermediate from other phenols and NBS were also determined and given in Table 3. Since the dienone intermediate derived from 1-anthrol decomposed relatively quickly, the kinetic measurement of the formation was carried out at higher substrate concentrations to avoid complications from the decomposition. The decomposition of the dienone intermediates derived from naphthols took more than 10 h. The decay curves monitored at a wavelength near the dienone λ_{max} did not afford a straight line according to second- or first-order kinetic analysis; the latter plots showed upward curvature, hinting at an autocatalytic process most likely arising from increased acidity of the brominated phenolic products. In Table 1 the times required for the absorptivity to decrease to its half-value are listed; these $t_{1/2}$ are not true half-life times because of kinetic complications.

The kinetics of the interaction of NBS with phenols as well as those of the decomposition of the intermediates were sensitive to impurities present in substrates and solvents; in particular, the presence of trace amounts of hydrochloric acid ($<10^{-5}$ M) could accelerate rates enormously (Table 3). The substrates and solvents must be carefully purified to ensure reproducible results as those given in this paper. The use of unpurified NBS and methylene chloride in the reaction with 2-NpOH gave rapid formation of the intermediate as well as the decay (Fig. 6). However, the decay curve of **7** as well as that of **3** in the presence of a trace amount of HCl gave good straight lines according to first-order analysis: The portion of acid catalysis arising from the phenolic products was apparently relatively unimportant under these conditions but the rate constants obtained did not represent the true unimolecular decomposition.

The reactions of other phenols with NBS under comparable conditions also showed a similar type of spectral changes and kinetic traces; two representative spectra are shown in Fig. 2.

Can. J. Chem. Downloaded from www.nrcresearchpress.com by 196.1.178.254 on 09/07/12
For personal use only.

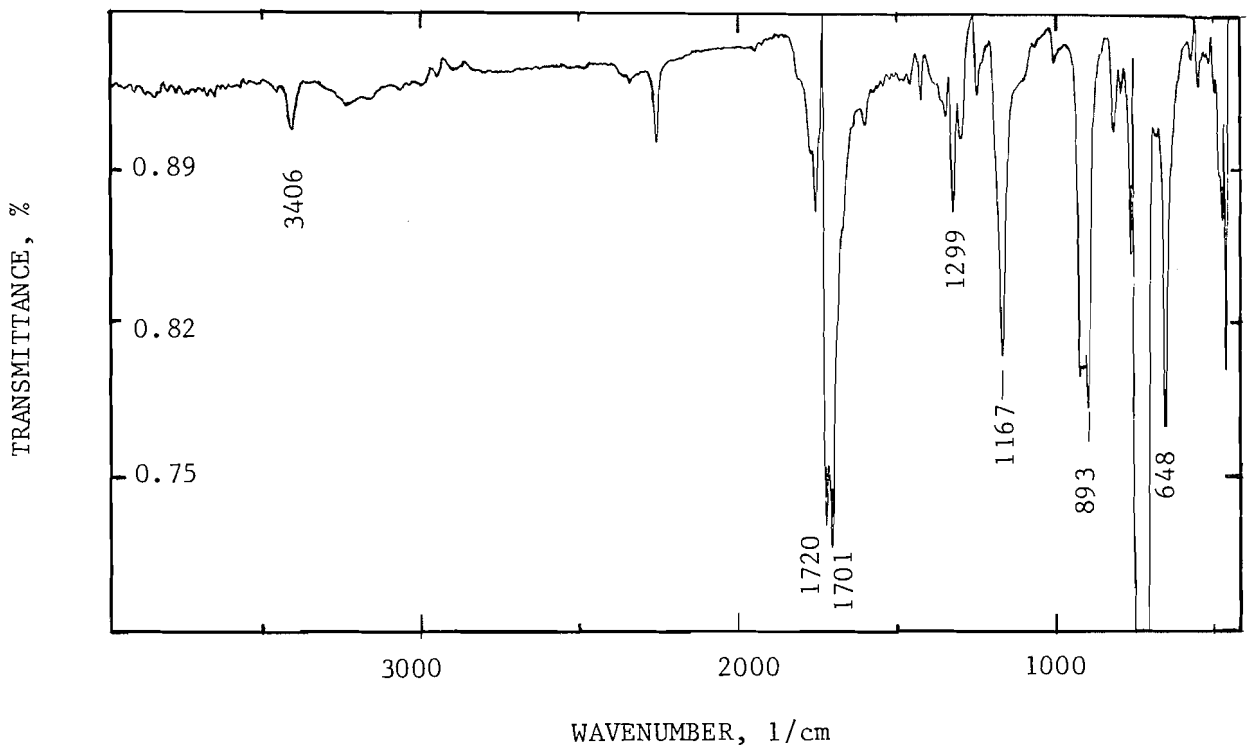

FIG. 3. The FT-IR spectrum, 35 s after mixing of CH_2Cl_2 solutions of 1-NpOH (4.4×10^{-2} M) and NBS (4.1×10^{-2} M); the absorption of NBS was subtracted.

TABLE 3. The rate constants of the formation of dienone intermediates in CH_2Cl_2 at 25 ± 1°C

[Phenols], M	[NBS], M	$10^4 k_{obs}$, s^{-1} [a]	$10k_2$, $M^{-1}s^{-1}$	λ (monitor), nm [b]
1-Naphthol				
7.97×10^{-3}	5.26×10^{-4}	30 ± 6	3.8 ± 0.8	360(5)
7.80×10^{-3}	5.09×10^{-4}	27 ± 4	3.5 ± 0.5	360(5)
8.06×10^{-3}	4.91×10^{-4}	98 ± 10	12 ± 10	360(2)[c]
1-AnOH				
6.1×10^{-3}	3.1×10^{-4}	1500	250	430(1)
3.5×10^{-4}	3.6×10^{-4}	—	200	430(1)[d]
2-Naphthol				
7.7×10^{-3}	4.25×10^{-4}	85 ± 11	11 ± 2	350(3)
9.73×10^{-4}	2.75×10^{-4}	—	1000	350(1)[d,e]
4-Chloro-1-naphthol				
6.93×10^{-3}	4.10×10^{-4}	7.3 ± 2.0	1.0 ± 0.3	365(2)
2-Bromo-4-chloro-1-naphthol				
6.92×10^{-3}	4.20×10^{-4}	2.5 ± 0.5	0.36 ± 0.07	370(2)
4-*tert*-Butylphenol				
9.10×10^{-3}	6.00×10^{-4}	14 ± 2	1.6 ± 0.2	340(2)

[a] The correlation coefficients are ≥0.999.
[b] The rate constants were obtained by the monitor of increases in the absorbance of the intermediates: the figures inside brackets are the number of runs.
[c] A trace amount of the HCl in CH_2Cl_2 (7×10^{-7} M) was added.
[d] The reactions were carried out under second-order reaction conditions.
[e] This reaction used unpurified NBS (see Fig. 6).

Can. J. Chem. Downloaded from www.nrcresearchpress.com by 196.1.178.254 on 09/07/12
For personal use only.

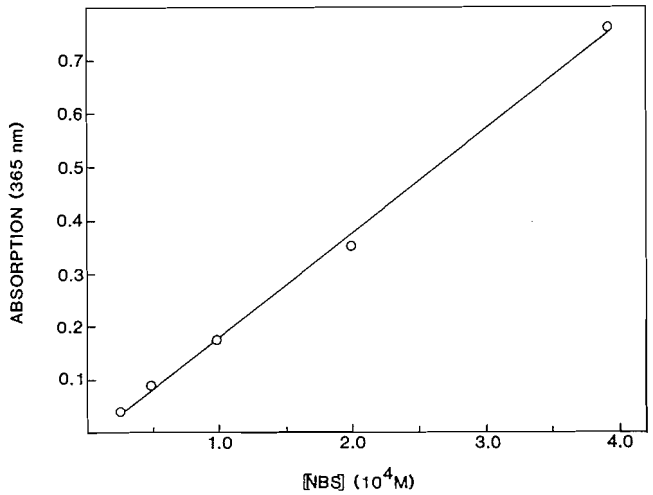

FIG. 4. The plot of the absorbance at 365 nm against the concentration of NBS in CH_2Cl_2 in the presence of [1-NpOH] = 3.74×10^{-3} M and [cyclohexene] = 1/5 [NBS]; the maximum absorbances were obtained after 5–10 min of mixing.

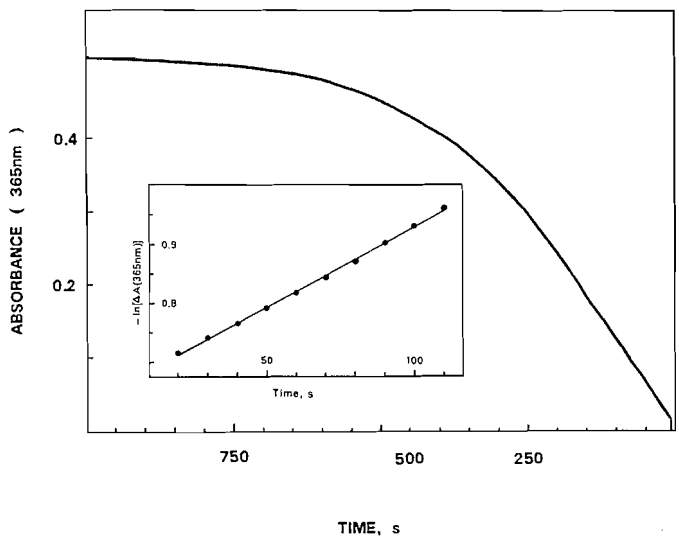

FIG. 5. The kinetic trace of the reaction of 1-NpOH (8.06×10^{-3} M) and NBS (2.80×10^{-4} M) in CH_2Cl_2 at 25 ± 1°C monitored at 360 nm.

For kinetic runs, a wavelength near the peak of the intermediate and where the starting materials showed no absorption was selected as the monitoring wavelength. The absorption maxima and extinction coefficients can be calculated from appropriate spectra in each case (Table 1). For 1-anthrol and *tert*-butylphenol, where the dienone intermediates underwent rapid decompositions, the ε-values were calculated from the highest optical density of kinetic runs (see Fig. 2), but these values must be smaller than the true values. The ε-values of the dienone intermediates derived from naphthols were determined more accurately using a plot similar to Fig. 2. Neither 4-nitro nor 4-cyano-phenol, on interaction with NBS, showed transient absorption under comparable conditions. Since no ring-brominated product was obtained after prolonged incubation in the dark (*vide infra*), it was concluded that the corresponding dienones were not formed from these phenols.

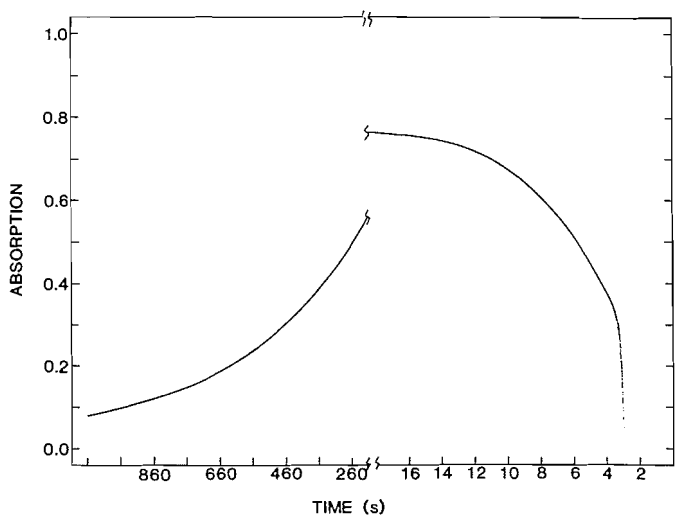

FIG. 6. Kinetic traces of the reaction of 2-NpOH with unpurified NBS in CH_2Cl_2 at 20 ± 1°C monitored at 335 nm; [NBS] = 2.75×10^{-4} M, [2-NpOH] = 9.73×10^{-4} M. The calculated rate constant of the formation is 100 M^{-1} s^{-1}, and that of the decomposition, 2.98×10^{-3} s^{-1}.

A methylene chloride solution of dienone **3** prepared *in situ* in quartz cuvettes was exposed to laboratory room light, unfiltered or filtered with a GWV filter (cutoff at <380 nm), and the absorbance at 365 nm was recorded at intervals. The plots of the absorbances, corrected for those due to thermal decomposition, against times of irradiation gave straight lines indicating a zero-order reaction up to 85% conversions. The quantum yield of the photoreaction of dienone **3** was measured using methylene chloride solutions prepared *in situ* and monochromatic light of 365 nm; benzophenone–benzhydrol actinometry was used as the secondary reference (19). The *observed* quantum yield of 0.66 was obtained for a solution of dienone **3** showing an absorbance change of 0.56–0.47: extrapolation to the total absorbance of incident light by the dienone gave the *actual* quantum yield of 0.9–1.0. For a methylene chloride solution of the dienone with the OD higher than unity, the observed quantum yield was 1.0 ± 0.1.

The product distribution in the photoreaction was studied in various solvents using a GWV filter to photoexcite the dienones alone at >380 nm. The dienone intermediate solutions were prepared *in situ* with an excess of 1-NpOH and the products were analysed by gc. The results are tabulated in Table 4. The percentage of 4-Br-1-NpOH **6** increased significantly as polarity of solvent increased, and also did so with unpurified NBS, obviously because of the presence of a trace amount of HBr. These solvent polarity effects are similar to that observed in bromination of phenols (17, 18). When the thermal decomposition of dienone was allowed to proceed for a longer time, the yield of **6** was also slightly increased. In certain photoreactions, 1-naphthyl methyl ether (1-$NpOCH_3$) was added to the intermediate solutions as a competing substrate. The amount of 4-bromo-1-methoxynaphthalene was negligibly small, indicating that dienone **3** is a poor brominating agent. NBS failed to react with 1-$NpOCH_3$ under prolonged incubation.

Some control and reference experiments were also carried out and results are shown in Table 5. They were competitive bromination of 1-NpOH and 1-$NpOCH_3$ in the absence and presence of K_2CO_3 and either in the dark or under illumination.

Can. J. Chem. Downloaded from www.nrcresearchpress.com by 196.1.178.254 on 09/07/12
For personal use only.

TABLE 4. The product distribution of photodecomposition of dienone intermediates

No.	10^2[1-NpOH], M	10^2[NBS], M	Solvent	% Products 2-Br-1-NpOH	% Products 4-Br-1-NpOH
1	1.4	0.49	Benzene	81	5.3
2	1.7	1.3	Benzene	85	2.6
3	2.6	1.4	Dioxane	75	6.0
4	2.5	1.2	Dioxane	82	5.0
5	5.9[a]	2.75	CCl_4	37	7
6	2.0	1.8	CH_2Cl_2	78	7
7	0.93[c]	0.60	CH_2Cl_2	67	5.8
8	1.8	1.4	CH_2Cl_2	85	9[b]
9	2.0[d]	2.0	CH_2Cl_2	65	12
10	0.5[f]	0.5	CH_2Cl_2	63	24
11	0.43	0.38	CH_3CN	50	17
12	0.62	0.57	CH_3CN	44	28[b]
13	2.4[f,g]	1.9	CH_3CN	29	46
14	2.4[e,f]	1.9	CH_3CN	29	44

[a]Heterogeneous reaction because of low solubility of NBS in CCl_4; the photolysate was washed with $NaHSO_3$ solution to destroy remaining NBS before gc analysis.
[b]For these two experiments the reaction was allowed to proceed for 1 h before photolysis; for other experiments the reaction was allowed for 10 min before photolysis.
[c]1-Methoxynaphthalene (8.65×10^{-3} M) was added and 4-bromo-1-methoxynaphthalene was detected in <1%.
[d]Decomposed in the dark as comparison.
[e]1-Methoxynaphthalene (4.35×10^{-3} M) was added and 4-bromo-1-methoxynaphthalene was detected in <1%.
[f]An unpurified NBS reagent was used.
[g]Dichloroethane (3.1×10^{-3} M) was added.

TABLE 5. Competitive bromination of 1-naphthol and 1-naphthyl methyl ether in CH_2Cl_2

10^2[1-NpOH], M	10^2[1-NpOCH$_3$], M	10^2[XBr], M[a]	Relative yields[a] 2-Br-1-NpOH	4-Br-1-NpOH	4-Br-1-NpOCH$_3$
1.2[b]	1.1	0.7	1.0	0.62	0.77
1.2[c]	1.1	0.7	1.0	0.57	0.87
1.3[d]	1.0	0.6	1.0	0.57	0.78
1.3[e]	1.0	0.6	1.0	0.62	0.50
0.9[a]	0.87	0.6	12	1.0	0.0

[a]The last experiment uses NBS; other experiments use Br_2.
[b]A bromine solution was added while the substrate solution was irradiated with 410 ± 6 nm light (200-W Xe/He lamp, Kratos intensive monochromator).
[c]This experiment was carried out in the dark for 30 min, at which time the solution became colourless.
[d]The solution containing $K_2CO_3/Br_2 \geq 5$ was exposed to room light.
[e]A bromine solution was added while the substrate solution was irradiated with a 450-W Hanovia lamp.

The results show that bromination by bromine on 1-NpOH occurred very rapidly, and more rapidly than that on 1-NpOCH$_3$ in the dark or under illumination, to give nearly the same product ratio. The trend of this reactivity is known (20). In contrast NBS reacted exclusively with 1-NpOH, showing no trace of reaction with 1-NpOCH$_3$.

Discussion

Using 1-NpOH as a model compound, we have demonstrated that NBS is a useful reagent to monobrominate 1-NpOH cleanly via the intermediacy of dienones **3** and **4** to give 2-bromo-1-naphthol **5** and 4-bromo-1-naphthol **6**. While the preparation can be simply executed, the mechanism is more complicated than had been expected. The overall reaction can be conveniently separated into two steps for discussion, namely: (*i*) the interaction of NBS with 1-NpOH to form the dienones, and (*ii*) the rearrangement of the dienones, induced either by thermolysis or photolysis, to give the brominated phenols. Though these dienones are reasonably stable in the dark, as shown in Table 1, they were not isolated owing to their sensitivity towards acid and light catalysis. Their rearrangements are essentially a carbon-to-oxygen prototropy accompanied by aromatization and should be irreversible reactions; i.e., **3** → **5** and **4** → **6**. As externally added 1-NpOCH$_3$ was not brominated (Table 4) in the photolysis (or thermolysis), there exists no other competing pathway. Photoexcitation of **3** and **4** obviously results in their prototropic reaction with the quantum yield of unity.

Can. J. Chem. Downloaded from www.nrcresearchpress.com by 196.1.178.254 on 09/07/12
For personal use only.

Can. J. Chem. Downloaded from www.nrcresearchpress.com by 196.1.178.254 on 09/07/12
For personal use only.

The presence of acid catalysis in the thermal rearrangement of dienone intermediates is confirmed by kinetic studies, which also indicate the presence of autocatalysis of the rearrangement arising from the production of more acidic bromophenols in the carefully controlled bromination reaction. It is known that brominated phenols are more acidic, by ca. one pK_a unit, than the parent phenols and that an acid could catalyse (17, 18) the rearrangement of an extended dienone such as **3** to a cross-conjugated dienone such as **4**. The results described above are consistent with the occurrence of the acid-catalysed process of the **3** → **4** rearrangement.

At the onset of the interaction of NBS with 1-NpOH, *only one intermediate, that of dienone 3, is formed as the initial product*, as indicated by (*i*) the occurrence of two isobestic points at 269 and 323 nm, and (*ii*) the lack of the ir bands of **4**. If dienone **4** were also formed concurrently, the isobestic points could not be obtained since **4** should absorb strongly in the 250–310 nm region (12, 13). Since the prototropy of **4** cannot give anything but **6**, and that of **3** but **5**, the yields of **6** in Table 4 must mean that **4** is formed at a certain point in the reaction: the high percentage yields of **6** in experiments no. 10, 13, and 14, where an unpurified NBS is used, clearly indicate that indeed a trace amount of acid impurities catalyses the rearrangement of **3** → **4**. Slightly higher percentage yields of **6** in experiments 8, 9, and 12 support the presence of autocatalysis to form **4** by more acidic bromonaphthols; prolonged thermal decompositions in these experiments allow the involvement of acid catalysis.

Bromination of phenols to give dienone intermediates has been recognized previously (5–8, 17, 18) and, with some 2- and 4-substituted phenols and naphthols, the corresponding dienones have been isolated and identified (5, 17). However, bromine as the reagent generally leads to uncontrollable bromination for two reasons: (*i*) a secondary bromination of dienones, and (*ii*) the generation of HBr, which catalyses the rapid rearrangement of dienones as well as their formation. Indeed we have found that 10^{-4} M HCl catalyses both reactions so rapidly that kinetic measurements become impossible. From this viewpoint, NBS is an excellent reagent to generate extended dienones such as **3** *in situ* and (or) to monobrominate at the *ortho* positions of phenols, provided that care is taken to eliminate trace amounts of acids.

We now turn to the question on hypobromite **2** as a short-lived precursor of dienones. The immediate question is the location of the attack of NBS on phenolic species; i.e., whether it is an attack at the O-centre or C-centre. NBS is formally regarded as a source of positive bromine, and its N—Br bond may be polarized but not dissociated to provide a bromonium ion in nonpolar media. Though we have failed to detect the O—Br stretching absorption by FT-IR spectroscopy, there is evidence to suggest that the primary product from NBS and 1-NpOH is hypobromite **2**, which rearranges rapidly to dienone **3**. The failure of NBS to brominate 1-$NpOCH_3$ in a competitive reaction between 1-NpOH and 1-$NpOCH_3$ (Table 5) suggests that the reaction might have occurred at the oxygen but not at the carbon at the 2-position. This is a reasonable conclusion in view of the fact that in contrast to the facile addition of bromine to a carbon–carbon double bond, NBS showed no such reactivity. It should be mentioned that the latter reaction at the C2 position may not lead to the dienone intermediate but should give the *ortho*-brominated product eventually if the bromination occurs at all. Indeed Br_2 does brominate 1-$NpOCH_3$, as shown in Table 5. In the bromination of phenol with NBS, bromine has been proposed as the actual reagent; i.e., NBS is the reservoir of a low concentration of Br_2 by HBr scavenging (18). This conclusion is obviously untenable, at least in aprotic nonpolar solution, for the same reason.

The rearrangement of hypobromite **2** to dienone **3** therefore must be very fast, and the observed rate constants (k_2 in Table 2) represent the slower rate-determining step of the formation of **2**. The latter conclusion has been supported by the comparable rate constants of the disappearance of 1-NpOH to that shown in Table 1; this kinetic trace is run with 1-NpOH as the limiting reagent and by following the decrease of the absorption of 1-NpOH at 322 nm. Although we do not have additional information to offer, **1** possesses nmr data as well as stability properties that are more consistent with a dienone structure. The formation of hypobromites from phenols and NBS in aprotic solvent can be regarded as an electrophilic attack of the polarized N—Br bond on the phenol or a nucleophilic attack of phenolic oxygen on the bromine atom of NBS. The latter mechanism is essentially a halophilic reaction (21). Whatever interpretation is used, the failure of *p*-nitro- and *p*-cyano-phenols to react with NBS clearly indicates that a low electron density at the O-center retards the reactivities.

The solutions of dienones derived from naphthols as shown in Table 1 can be used as secondary actinometric solutions for the region of 300–400 nm. These solutions are easily prepared and have a sufficient lifetime. The concentrations of dienones are readily determined by uv spectroscopy. The efficient and clean photorearrangement of these dienones (e.g., the quantum yield of unity for the case of 1-NpOH) makes them excellent compounds for actinometry.

Experimental

Chemicals and equipment

NBS (BDH, reagent grade) was recrystallized from hot water and dried over $CaCl_2$ under vacuum. Bromine (Anachemia, reagent grade) was used as supplied. Dichloromethane, dioxane, acetonitrile, carbon tetrachloride, and benzene were distilled after being dried with $CaCl_2$. Anhydrous K_2CO_3 (BDH, analytical grade) was ground to a powder and pumped in a vacuum line at 150°C for 24 h. Nitrogen (Union Carbide, 99.998%) was used as supplied. 1-NpOH, 4-chloro-1-naphthol (mp 117.5–118.5°C), and 2-NpOH (Anachemia) were recrystallized from toluene and sublimed. Other compounds were purified by distillation or recrystallization followed by sublimation. Gas chromatographic (gc) analysis used a Hewlett-Packard 5792A equipped with an OV-1 capillary column; nmr spectra were recorded with a Bruker SY100 spectrometer, and uv spectra with a Cary 210 spectrophotometer.

Kinetic measurements

A solution of phenol placed in a uv cell was set in the Cary 210 compartment at 25 ± 1°C under dark conditions. A solution of NBS thermostated at the same temperature was injected with a syringe equipped with plastic tubes. The scanning of OD against time or against wavelengths commenced immediately. To obtain reproducible results, (*i*) phenols must be sublimed; (*ii*) solvent must be freshly redistilled; (*iii*) an NBS solution should be prepared within a few hours and kept in the dark; and (*iv*) syringe and cells should be rinsed thoroughly with distilled solvent. Under the pseudo-first-order reaction conditions, the traces of the increases of new absorbance were analysed by plotting ln ($A_\infty - A$) vs. time, where A_∞ and A are the absorbance at the completion of and during the reaction. For the unstable dienone intermediate from 4-*tert*-butylphenol, only an initial portion of the curve was analysed using computer-assisted fitting to obtain the best A_∞ value (22).

Irradiation of the dienone solutions

Solutions of the required concentrations in 1-NpOH and NBS were prepared in a test tube or uv cuvette in the dark and purged with nitrogen for 10 min; by this time dienones were formed as shown by uv spectra. The solutions were irradiated with a 200-W Hanovia medium-pressure mercury lamp filtered through a GWV filter (cutoff < 380 nm). In 5 min the yellow solutions were bleached but irradiation was continued for another 5–10 min. The products were analysed by gc using anthracene as the internal standard (Table 3), and in some cases were isolated. 2-Bromo-1-naphthol (**5**) and 4-bromo-1-naphthol (**6**) were recrystallized from ethanol to afford crystals, mp 44–45°C (lit. (23) mp 44°C) for the former and mp 127–128°C (lit. (24) mp 129°C) for the latter. Other products were also purified similarly: 1-bromo-2-naphthol, mp 82–83°C (lit. (25) mp 84°C); 2-bromo-4-chloro-1-naphthol, mp 92.5–93.5°C (lit. (26) mp 96°C); 2-bromo-4-*tert*-butylphenol, mp 50–51°C (lit. (27) mp 52°C); and 2-bromo-1-anthrol, mp 98–99°C.

Quantum yield measurements

Irradiation was carried out with a 200-W Hg/Xe lamp and Kratos high intensity monochrometer. At 365 nm, the emission was determined to be $(2.3 \pm 0.1) \times 10^{-7}$ Einstein/min in a 1-cm quartz uv cell using benzophenone–benzhydrol actinometry ($\Phi = 0.74$ in benzene) (19). Two methylene chloride solutions 1.2×10^{-3} M in NBS and 1.9×10^{-3} M in 1-NpOH and each containing dichloroethene 1.28×10^{-3} M were mixed in a uv cell in the dark. The resulting solution showed an absorbance of 0.56, and was irradiated for 1.5 min to give a value of 0.47. The thermal reaction was run simultaneously as the control reaction: the subtraction of the absorbance due to the thermal reaction gave that due to photoreaction. This absorbance decrease gave an apparent quantum yield of 0.66. This figure was normalized to 99% absorption of light (OD = 2) to give the actual quantum yield of 0.95–1.0.

When similar solutions with OD of 1.95 and 1.89 were irradiated for 1.5 min, the OD decreased to 1.74 and 1.66, respectively. The quantum yields were calculated to be 0.96 and 1.05.

Spectroscopic determinations of dienone 3

NBS and naphthol concentrations of $\sim 5 \times 10^{-2}$ M in $CDCl_3$ were mixed in an nmr tube and nmr signals were obtained with single scan after 10 min (Table 3).

NBS solution (200 μL, 5.17×10^{-2} M) in CH_2Cl_2 was placed in an ir cell (0.2 mL) and sealed with a septum. 1-NpOH solution (50 μL, 2.22×10^{-1} M) was injected with a syringe and the solution was mixed. The ir cell was placed in the sample compartment of a Bruker IFS-85 FT-IR spectrophotometer that had been flushed with N_2 for 10 min. The ir spectra of the solution were recorded at intervals.

1. (*a*) D. Djerassi. Chem. Rev. **48**, 271 (1948); (*b*) L. Horner and E. H. Winkelman. Newer methods of preparative organic chemistry. Vol. III. *Edited by* W. Foerst. Academic Press, New York. 1964. p. 251.
2. C. K. Ingold. Structure and mechanism in organic chemistry. Cornell University Press, Ithaca, NY. 1969.
3. Y. L. Chow and Y. M. A. Naguib. Rev. Chem. Intermed. **5**, 325 (1984).
4. J. M. Brittain and P. B. D. de la Mare. *In* The chemistry of halides, pseudohalides and azides. Part I. Supplement D. *Edited by* S. Patai and Z. Rappoport. John Wiley, New York. 1983. p. 496.
5. P. D. B. de la Mare, O. M. H. El Dusouqui, J. G. Tillett, and M. Zeltner. J. Chem. Soc. 5306 (1964).
6. E. Baciocchi and G. Illuminati. J. Am. Chem. Soc. **89**, 4017 (1967).
7. M. Christen, W. Koch, W. Simon, and H. Zollinger. Helv. Chim. Acta, **45**, 2077 (1962); W. Koch and H. Zollinger. Helv. Chim. Acta, **48**, 554 (1965).
8. J. M. Brittain, P. B. D. de la Mare, and P. A. Newman. J. Chem. Soc. Perkin Trans. 2, 32 (1981).
9. P. F. Kruse, Jr., K. L. Grist, and T. A. McCoy. Anal. Chem. **26**, 1319 (1954).
10. M. Z. Barakat, A. S. Fayzalla, and S. T. El-Aassan. Analyst, **97**, 470 (1971).
11. D. S. Wilbur and H. A. O'Brien, Jr. J. Org. Chem. **47**, 359 (1982).
12. (*a*) A. J. Waring. Adv. Alicyclic Chem. **1**, 131 (1966); (*b*) W. G. Dauben, P. D. Hence, and W. K. Hayes. J. Am. Chem. Soc. **77**, 4609 (1955).
13. P. B. de la Mare and A. Singh. J. Chem. Soc. Perkin Trans. 2, 59 (1973).
14. M. Anbar and I. Dostrovsky. J. Chem. Soc. 1105 (1954).
15. R. A. Sneen and N. P. Matheney. J. Am. Chem. Soc. **86**, 5503 (1964).
16. Y. L. Chow and D. C. Zhao. J. Org. Chem. **52**, 1931 (1987).
17. V. Calò, L. Lopez, G. Pesce, F. Ciminale, and P. E. Todesco. J. Chem. Soc. Perkin Trans. 2, 1179 (1974).
18. V. Calò, L. Lopez, G. Pesce, and P. E. Todesco. J. Chem. Soc. Perkin Trans. 2, 1192 (1974).
19. G. S. Hammond and P. Leermakers. J. Phys. Chem. **66**, 1148 (1962).
20. S. Simakamasundari and R. Ganesan. Int. J. Chem. Kinet. **12**, 837 (1980).
21. (*a*) X. Y. Li, H. Q. Pan, and X. K. Jiang. Tetrahedron Lett. 4937 (1984); (*b*) X. Y. Li, X. K. Jiang, Y. F. Gong, and H. Q. Pan. Huaxue Xuebao, **43**, 260 (1985); (*c*) X. Y. Li, H. Q. Pan, X. K. Jiang, and Z. Y. Zhan. Angew. Chem. Int. Ed. Engl. **24**, 871 (1985).
22. M. J. J. Holt and A. C. Norris. J. Chem. Educ. **54**, 426 (1977).
23. F. Krollpfeiffer and A. Müller. Ber. Dtsch. Chem. Ges. **68**, 1169 (1935).
24. J. B. Shoesmith and H. Rubli. J. Chem. Soc. 3102 (1927).
25. F. Kroḧnke and H. Timmer. Ber. Dtsch. Chem. Ges. **69**, 614 (1936).
26. R. Willslatter and L. Schuler. Ber. Dtsch. Chem. Ges. **61**, 362 (1928).
27. B. Jones. J. Chem. Soc. 358 (1941).

Can. J. Chem. Downloaded from www.nrcresearchpress.com by 196.1.178.254 on 09/07/12
For personal use only.

The dependence of vanadate phenyl ester formation on the acidity of the parent phenols

BRUNO GALEFFI AND ALAN S. TRACEY[1]

Department of Chemistry, Simon Fraser University, Burnaby, B.C., Canada V5A 1S6

Received February 25, 1988

BRUNO GALEFFI and ALAN S. TRACEY. Can. J. Chem. **66**, 2565 (1988).

The condensation of vanadate ($VO_4H_2^{1-}$) with a variety of substituted phenols in aqueous acetone solution has been studied by ^{51}V nuclear magnetic resonance spectroscopy. The formation constants for the various product esters were determined, as were their respective pK_a values. Inductive and resonance contributions to vanadate ester formation were investigated using the dual substituent parameter approach. This procedure did not succeed particularly well, although trends were clearly observed. Correlations with Hammett constants were compared with those of the dual parameter approach. The observation of some linear free-energy relationships was interpreted to mean that the inductive and resonance parameters generally ascribed to the various phenols are not directly applicable to vanadate ester formation where *d* orbitals are probably involved. The results did indicate that resonance effects have a significantly greater influence on ester formation than do inductive effects.

BRUNO GALEFFI et ALAN S. TRACEY. Can. J. Chem. **66**, 2565 (1988).

Opérant en solution dans de l'acétone aqueuse et faisant appel à la résonance magnétique nucléaire du ^{51}V, on a étudié la condensation du vanadate ($VO_4H_2^{1-}$) avec divers phénols substitués. On a déterminé les constantes de formation des divers esters ainsi que les valeurs respectives de leurs pK_a. Utilisant l'approche du paramètre à double substituant, on a étudié les contributions relatives de l'induction et de la résonance sur la formation des esters du vanadate. Cette méthode n'est pas très appropriée, même si on peut clairement observer des tendances. On a comparé les corrélations avec les constantes de Hammett avec celles obtenues par l'approche du paramètre à double substituant. On a observé des relations linéaires d'énergie libre; on croit que ce résultat signifie que les paramètres d'induction et de résonance qui sont généralement attribués à divers phénols ne sont pas directement applicables à la formation des esters du vanadate qui implique probablement des orbitales *d*. Les résultats indiquent que les effets de résonance influencent beaucoup plus la formation de l'ester que les effets inductifs.

[Traduit par la revue]

Can. J. Chem. Downloaded from www.nrcresearchpress.com by 196.1.178.254 on 09/07/12
For personal use only.

Introduction

The aqueous chemistry of vanadium(V) oxyanions is highly complex with a variety of oligomeric products arising as a function both of concentration and of pH. Various studies have succeeded in unravelling many of the details of this system (1, 2). These studies are of increasing importance as it has become evident from recent work that vanadium has an important biological role both in nitrogen fixation (3, 4) and in halogenation reactions (4, 5). Earlier work had suggested that vanadium is an essential element but this has not been unequivocally established (6, 7). Vanadium oxyanions have a significant effect on the function of many enzymes, activating some and inhibiting others (6–8). Some of this biological activity derives from the ability of vanadate to act as a phosphate analogue.

In the presence of hydroxylic compounds, such as alcohols and acids, condensation with vanadate spontaneously occurs to form vanadate esters or anhydrides (9–11). An interesting facet of such condensations, in the case of alkyl alcohols, is that a decrease in pK_a of the parent alcohol to a small extent disfavours the formation of vanadate esters (12). This behaviour does not extend to include ligands such as phosphate ($PO_4H_2^{1-}$), vanadate ($VO_4H_2^{1-}$), and phenol. In fact, condensation with these ligands is favoured well over that with the alkyl alcohols.

The behaviour exhibited by vanadate ester formation with the alkyl alcohols is similar to that found for phosphate ester formation; however, in the case of phosphate, the correlation extends to include condensation with phenols and other oxygen donors, including phosphate itself (13). It seems evident that for vanadate, as opposed to phosphate, there are stabilizing interactions that arise from certain types of ligands, which override the destabilizing interactions of electron withdrawal that disfavour condensation. These interactions may have their source in the unoccupied *d* orbitals of the vanadate ion, which can accept electron density from the π system of the ligand, thus favouring product formation.

In an effort to evaluate the effects of electron release or withdrawal on the esterification process, the interaction of vanadate with a variety of substituted phenols has been studied. Somewhat similar studies have been carried out by other workers for the Fe(III)–phenolate system where a linear relationship between the pK_a of the phenol and the formation constant for the product was observed (14). In the present study, an analogous free-energy relationship for the condensation of vanadate with phenols has not been observed.

Experimental

Materials

The various phenols used in this study were purchased from a variety of chemical supply companies, and their purity checked by proton magnetic resonance spectroscopy. Those which were discoloured or impure by ^1H nmr spectroscopy were recrystallized or, in the case of 3-chlorophenol, distilled under vacuum. Vanadium(V) oxide 99.99% (Aldrich "Gold Label") and TRIS (Tris[hydroxymethyl]aminomethane) 99.9% (Aldrich "Gold Label") were used as supplied. Reagent quality acetone was used without further purification. Sodium vanadate stock solutions were prepared by combining vanadium(V) oxide with two molar equivalents of 1.0 M aqueous NaOH in sufficient water to provide a final vanadium atom concentration of a little over 0.1 M. The orange material was stirred overnight during which time all of the vanadium pentoxide dissolved and a colourless product was obtained. The solution was then diluted with sufficient water to give a 0.1 M vanadium atom concentration.

Solutions

Aqueous acetone solutions were prepared by dissolving the required weight of phenol in a 42% v/v acetone/H_2O solution of near the final volume. Sufficient TRIS base to give the desired final concentration of 20 mM was added, and the pH was adjusted to slightly below the desired value by adding a few drops of either aqueous HCl or aqueous NaOH. Sufficient sodium vanadate stock solution to provide the

[1]Author to whom correspondence may be addressed.

TABLE 1. Phenyl vanadate formation constants for a variety of substituted phenols in aqueous acetone solution

Phenol	pK_a[a]	K_1[b]	K_2[b]
2,4,6-Trichlorophenol	6.35	29±5	
4-Nitrophenol	7.50	3.3±0.2	
2,4-Dibromophenol	8.10	4.5±0.2	
3-Nitrophenol	8.71	3.0±0.2	
2-Chlorophenol	8.91	2.6±0.1	2.9±0.2
3-Chlorophenol	9.47	2.7±0.1	
4-Carboxyphenol	9.72	2.2±0.2	
4-Chlorophenol	9.76	2.0±0.1	2.4±0.2
3-Aminophenol	10.17	1.4±0.1	1.3±0.2
3-Carboxyphenol	10.20	1.6±0.3	
4-Fluorophenol	10.24	1.6±0.1	1.9±0.2
Phenol	10.34	1.8±0.1	1.1±0.1
4-Methylphenol	10.61	1.9±0.1	1.6±0.2
4-Aminophenol	10.65	2.4±0.2	1.2±0.2
2,6-Dimethylphenol	10.95	7.6±0.1	3.3±0.2
2,4-Diisopropylphenol	11.25	10±2	

[a]The pK_a values are for the various phenols in 42% v/v acetone/water and were corrected from the values for aqueous solution as discussed in the experimental section.

[b]These formation constants are defined in eq. [1], and were determined as described in the experimental section.

desired final concentration of vanadate was added, and the solution brought to the final volume by addition of 42% v/v acetone/H_2O. Final pH adjustment was made by addition of small amounts of NaOH. All samples were freshly prepared.

Nuclear magnetic resonance spectroscopy

All ^{51}V nmr spectra were obtained at 105 MHz from a Bruker WM-400 nmr spectrometer operating at ambient temperature in the broadband mode. Spectral widths of 20 kHz, 0.05-s acquisition times, and 45° pulse widths were used throughout. Spectra were zero-filled and a 35-Hz line broadening factor was applied before transforming the data to the frequency domain. All spectra were baseline corrected before signal intensities were determined using the instrument manufacturer's software. Chemical shifts are reported relative to an external reference of $VOCl_3$ at 0.0 ppm.

Proton nmr spectra were obtained at 100 MHz from a Bruker 100-SY nmr spectrometer.

pH and pK_a values

Measurements of pH in the acetone/water solvent solutions were made with a standard pH meter equipped with a combination electrode. The meter was standardized against aqueous buffer solutions prior to sample preparation and rechecked periodically. The pH of a mixed solvent system such as that employed here is not well defined; however, for the purposes of this study, it is important only that the *difference* between the hydrogen ion concentration and the measured pH not change significantly throughout the pH range employed, that is, pH 5.7–10.5.

The pK_a values of the phenols utilized in this study are also influenced by the solvent. Investigation of the *meta* and *para* nitrophenols by uv/visible spectroscopy showed that the pK_a value of the phenol in 42% aqueous acetone was 0.35 ± 0.1 unit higher than that for water. It has been shown that the relative pK_a values for phenols are essentially independent of the solvent (15), so the correction factor of 0.35 to the literature values (16–18) for the various phenols has been applied in the tabulation of Table 1.

Calculations

All the equilibrium constants were determined from at least five data points. Hydrogen ion concentration enters into the measured equilibrium constants via the pathway indicated in eq. [1]. The values of K_1 and K_2 are then pH-independent equilibrium constants as long as the phenol is not ionized. In eq. [1] water requirements are not explicitly considered.

$$\begin{array}{ccccc} H_2VO_4^- + ArOH & \overset{K_1}{\rightleftharpoons} & ArOVO_3H^- + ArOH & \overset{K_2}{\rightleftharpoons} & (ArO)_2VO_2^- \\ \Big\downarrow\uparrow K_{a2} & & \Big\downarrow\uparrow K'_{a2} & & \\ HVO_4^{2-} + H^+ & & ArOVO_3^{2-} + H^+ & & \end{array} \quad [1]$$

By working at sufficiently low pH, it was possible in most cases to avoid the ionization of the phenol itself. For the phenols having the lowest pK_a (4-nitrophenol and 2,4,6-trichlorophenol), the concentration of ionized phenol was easily determined by using the appropriate ionization constant, and the appropriate correction was made to K_1 and K_2.

The values of K_1 and K_2 can be calculated if pK_{a2} and pK'_{a2} are known. Deprotonation of both $H_2VO_4^-$ and $ArOVO_3H^-$ leads to substantial change in chemical shift of the ^{51}V nmr signal corresponding to the particular species. If δ_l and δ_h are the limiting chemical shifts at low and high pH for the monoanion and dianion, respectively, and δ_{obs} is the observed average chemical shift, then a simple calculation shows that the pK_a of the entity of interest is related to the chemical shifts and the pH by eq. [2].

$$[2] \quad pH = pK_a + \log \frac{\delta_{obs} - \delta_l}{\delta_h - \delta_{obs}}$$

A plot of the logarithm term versus pH then gives a straight line of unit slope and a y-intercept equal to the pK_a.

At a given pH, the total concentration of vanadate, of monoester, and of diester is provided by the respective signal intensities (at room temperature, ligand exchange is usually sufficiently slow to enable distinct resonances to be obtained for vanadate and its esters). The concentrations of $VO_4H_2^-$ and $ArOVO_3H^-$ can therefore be calculated at the considered pH using eqs. [3] and [4]. These values were used to obtain the equilibrium constants K_1 and K_2.

$$[3] \quad pH - pK_{a2} = \log \left(\frac{[\text{vanadate}]}{[VO_4H_2^-]} - 1 \right)$$

$$[4] \quad pH - pK'_{a2} = \log \left(\frac{[\text{monoester}]}{[ArOVO_3H^-]} - 1 \right)$$

Results and discussion

Vanadate reacts spontaneously with all of the phenols that were studied to form the corresponding phenyl vanadates. The condensation in all cases was a favourable one as is evident by comparing the formation constants, K_1, compiled in Table 1, for which K_1 is defined in eq. [1]. Of some note, as can be seen from this table, is the finding that the formation of phenyl

Can. J. Chem. Downloaded from www.nrcresearchpress.com by 196.1.178.254 on 09/07/12
For personal use only.

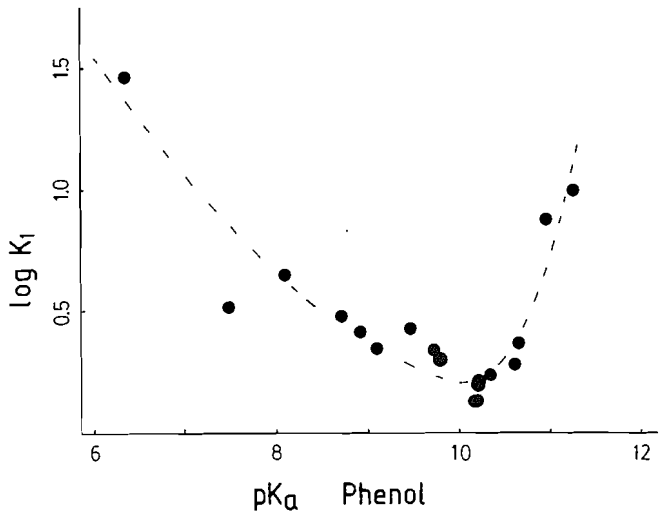

FIG. 1. The variation of the formation constant (K_1) for phenyl vanadate as a function of the pK_a of the parent phenol; K_1 = $[ArOVO_3H^-]/[VO_4H_2^-][ArOH]$.

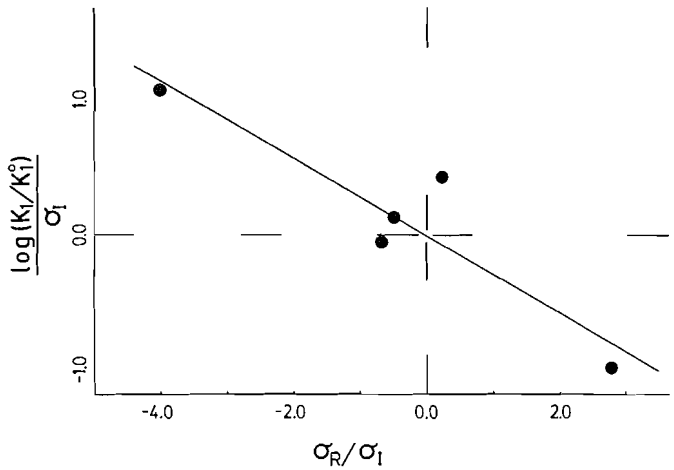

FIG. 2. The relationship between the inductive and resonance contributions to the formation of *para*-substituted phenyl vanadate esters is depicted.

vanadate from phenol and vanadate is among the least favoured reactions, while phenols of either higher or lower pK_a values more readily condense with vanadate to provide the ester. Figure 1 graphically depicts this behaviour and, since log K_1 is plotted in this figure, it is clear that there is no linear free-energy relationship between the formation constant of the product and the pK_a of the parent phenol. This result contrasts markedly with those of a similar study for which the interaction between phenols and iron(III) was studied (14). In this latter study, a very good linear free-energy relationship was observed, a behaviour also observed for the formation of alkyl vanadates (12).

The results of Table 1 suggest very strongly that there are at least two important substituent electronic contributions to vanadate ester formation. It is difficult to clearly identify these contributions. Attempts to correlate the observed ester formation constants with substituent inductive and resonance parameters via the Hammett constants did not succeed. The dual substituent parameter approach (19) was then utilized in an effort to separate the inductive and resonance contributions to the ester formation constants. The resonance and inductive electronic effects are related to the formation constants by eq. [5],

$$[5] \quad \log (K_1/K_1^0) = \rho_I\sigma_I + \rho_R\sigma_R$$

where σ_I and σ_R are the inductive and resonance factors determined from a variety of studies and ρ_I and ρ_R are the respective transmission factors for the system of interest. K_1 is the formation constant for the particular ester, and K_1^0 is that for the parent phenyl vanadate. Equation [5] can be rewritten as eq. [6], and the term on the left plotted versus σ_R/σ_I to give a line of intercept ρ_I and slope ρ_R.

$$[6] \quad \frac{\log (K_1/K_1^0)}{\sigma_I} = \rho_I + \frac{\rho_R\sigma_R}{\sigma_I}$$

From the values for σ_I and σ_R of ref. 19 and the measured equilibrium constants for the formation constants of the *para*-substituted products of Table 1, Fig. 2 was obtained.

It is evident from Fig. 2 that the *y*-intercept of the line must be near zero and also that the slope of the line is small, the least-squares values being 0.0 ± 0.2 and -0.3 ± 0.1, respectively. The small slope accounts for much of the apparent scatter in the plot of Fig. 2 but even so the correlation is rather poor. The fact that the intercept of this graph, which corresponds to ρ_I, is near zero means that vanadate ester formation is insensitive to inductive withdrawal or donation of electrons. A similar conclusion has previously been reached from a study of the formation of a number of alkyl vanadates (12). The slope of the line in this figure is quite small, -0.3, but its negative value indicates that resonance donation of electrons favours formation of vanadate esters, perhaps by allowing electron delocalization into the empty *d* orbitals of the vanadate moiety. Clearly this does not answer all questions since one must query why the formation of the 4-nitrophenyl, 2,6-dimethylphenyl, and 2,4-diisopropylphenyl vanadate esters is so highly favoured relative to what might be expected from the above considerations.

It does seem evident, however, that if electronic effects provide a dominating influence on ester formation, then those effects may be reflected in the pK'_{a2} values of the product vanadate esters as defined in eq. [1]. The pK_a values of vanadate and its esters were determined for the various reaction conditions of the different solutions by the procedure outlined in the experimental section and collected in Table 2. There is a significant variation in the values determined for the pK_a of $H_2VO_4^-$ from the solutions with different phenols. It has been shown (15) that relative strengths of acids of the same chemical type and same charge are essentially independent of solvent. On this basis, all pK_a values were corrected to the value for vanadate in 40% aqueous acetone and then plotted against the pK_a of the parent phenol (also determined for the aqueous acetone solvent). This plot is shown in Fig. 3 where two very good linear correlations are obtained. One correlation is between the pK_a of phenols substituted in the *meta* and *para* positions with slope = 0.19 and intercept = 7.52. The second correlation is with *ortho*-substituted phenols, and the slope and intercept are 0.28 and 7.01, respectively.

The observation of a good linear relationship between the pK_a values for the phenyl vanadates and the parent phenols (Fig. 3), and the lack of a similarly good correlation between vanadate ester formation constants and the polar and π-delocalization constants indicates that the dual substituent parameter approach employed here for investigation of the factors influencing vana-

Can. J. Chem. Downloaded from www.nrcresearchpress.com by 196.1.178.254 on 09/07/12
For personal use only.

TABLE 2. pK_{a2} values and chemical shifts for vanadate and its phenyl esters for various phenols in aqueous acetone solutions[a,b]

Phenol	$ArOVO_3H^-$			$VO_4H_2^-$		
	δ_l	δ_h	pK'_{a2}	δ_l	δ_h	pK_{a2}
2,4,6-Trichlorophenol	−562.6	—	—	−561.0	−535.5	9.46
4-Nitrophenol	−573.9	−550 ± 2	8.5	−561.2	−535.5	9.05
2,4-Dibromophenol	−566.3	−542	9.18	−560.0	−532.0	9.52
3-Nitrophenol	−570.0	−539	9.0	−561.0	−533.0	9.35
2-Chlorophenol	−565.0	−535	9.33	−560.2	−534.0	9.36
3-Chlorophenol	−567.8	−540	9.28	−560.2	−532.0	9.58
4-Carboxyphenol	−564.8	−535	9.06	−559.9	−534.0	9.22
4-Chlorophenol	−566.2	−536	9.37	−560.2	−533.6	9.47
3-Aminophenol	−564.1	−537.5	9.55	−560.2	−533.0	9.58
3-Carboxyphenol	−562.4	−535.5	9.03	−560.2	−534.5	9.11
4-Fluorophenol	−564.6	−535	9.52	−560.1	−532.0	9.60
Phenol	−564.9	−538	9.51	−559.8	−534.0	9.56
4-Methylphenol	−562.7	−538	9.61	−560.1	−534.1	9.51
4-Aminophenol	−555.9	−543	9.66	−560.0	−535.5	9.63
2,6-Dimethylphenol	−563.2	−545	10.16	−561.0	−535.0	9.70
2,4-Diisopropylphenol	−569.7	−561	10.28	−560.2	−534.0	9.70

[a]The pK_a values were determined for a 42% v/v acetone/water solution of the appropriate phenol using the procedure described in the experimental section.

[b]Estimated errors in δ_l, δ_h, pK_{a2}, and pK'_{a2} values are ±0.10, ±1.0, ±0.05, and ±0.10, respectively. δ_l is the chemical shift of $ROVO_3H^-$; δ_h, the chemical shift for $ROVO_3^{2-}$ where R = H or Ar.

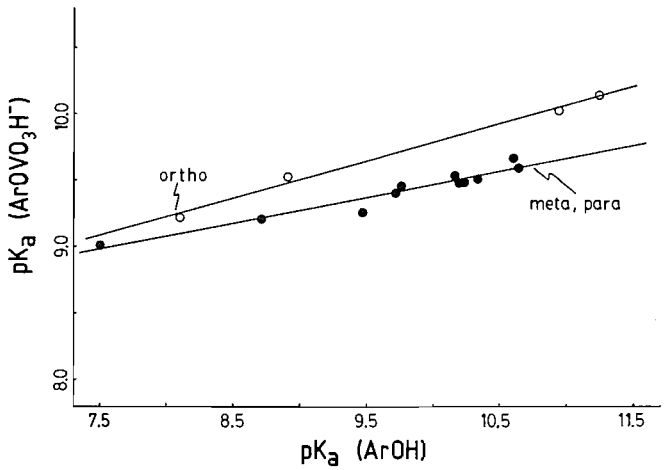

FIG. 3. The linear relationships between the pK_a of $ArOVO_3H^-$ and the parent phenols, ArOH, is revealed by this graph. The top plot is for *ortho*-substituted phenols, the bottom for a combination of *meta* and *para* substituents.

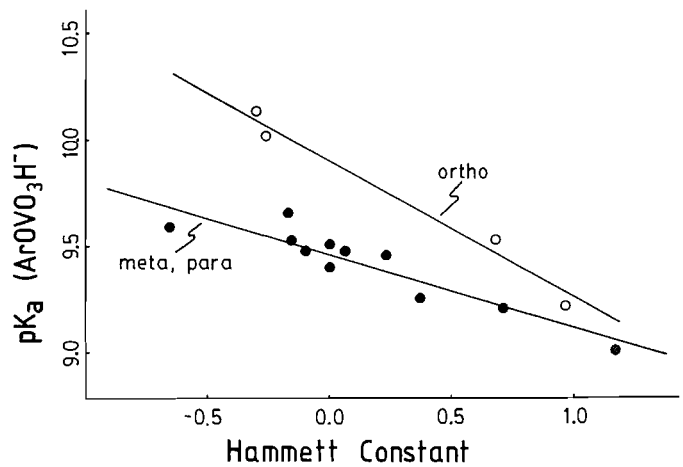

FIG. 4. Linear relationships between the pK_a values of a variety of substituted phenyl vanadates, $ArOVO_3H^-$, and the corresponding Hammett constants of the phenol precursors are depicted in this graph. The top plot is for *ortho*-substituted phenols, the bottom for *meta*- and *para*-substituted phenols.

date ester formation is not adequate. This view is reinforced if $(pK_a^{Tl} - pK_a^0)/\sigma_I$ is plotted against σ_R/σ_I, where pK_a^{Tl} is the pK_a of the individual vanadate esters and pK_a^0 is that for phenyl vanadate. This plot does not give a particularly good straight line, although a behaviour analogous to that of Fig. 2 is clearly observed. Interestingly enough, a plot of pK_a^{Tl} versus the Hammett constants for the various phenols does give a good straight line for the *meta*- and *para*-substituted phenols, and similarly a straight line for the *ortho*-substituted products as seen in Fig. 4. The Hammett constants represent some averaged value describing the electronic properties of the phenol. The linearity of pK_a^{Tl} versus the Hammett constants and the lack of a correspondingly good linearity in the dual substituent parameter approach means that, although the σ_I and σ_R values commonly employed (19) may not be adequate for a description of ester formation with vanadate where *d* orbitals are involved, a good separation of the electronic effects into inductive and resonance factors should be attainable.

An interesting facet of this investigation is the linear relationship between the pK_a values of the *meta*- and *para*-substituted phenyl vanadates ($ArOVO_3H^-$) and their respective vanadium chemical shifts. This relationship is depicted in Fig. 5. From the slope (5.03×10^{-2}) and intercept (37.9), the pK_a values for all the phenols studied here can be predicted to better than 0.1 pK_a unit, except for the *p*-aminophenyl vanadate ester, which is ~0.3 pK_a units from the line. It is not clear why parameters describing this latter compound deviate from the described line, or even if this linear relationship is a general one. It certainly does not apply to the *ortho*-substituted products.

Can. J. Chem. Downloaded from www.nrcresearchpress.com by 196.1.178.254 on 09/07/12
For personal use only.

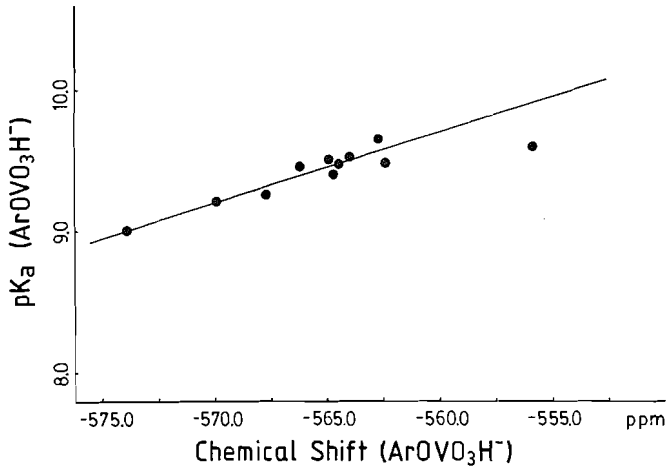

FIG. 5. The relationship between the chemical shifts of the vanadate ester monoanions ($ArOVO_3H^{1-}$) and their respective pK_a values is shown for *meta*- and *para*-substituted products.

The results of this study provide considerable insight into some of the factors governing vanadate ester formation and their acidity, but clearly much more work is necessary to obtain a good understanding of this system.

Acknowledgements

Thanks are gratefully extended to the Natural Sciences and Engineering Research Council of Canada for its financial support of this work in the form of operating grants to A.S.T.

1. E. HEATH and O. W. HOWARTH. J. Chem. Soc. Dalton Trans. 1105 (1981).
2. L. PETTERSSON, I. ANDERSSON, and B. HEDMAN. Chem. Scr. **25**, 309 (1985).
3. R. E. EADY, R. L. ROBSON, B. E. SMITH, D. J. LOWE, R. W. MILLER, and M. J. DILWORTH. Recl. Trav. Chim. Pays-Bas, **106**, 175 (1987).
4. R. WEVER, E. DE BOER, H. PLAT, and B. E. KRENN. FEBS Lett. **216**, 1 (1987).
5. R. WEVER, E. DE BOER, B. E. KRENN, and H. PLATT. Recl. Trav. Chim. Pays-Bas, **106**, 181 (1987).
6. N. D. CHASTEEN. Struct. Bonding (Berlin), **53**, 105 (1983).
7. T. RAMASARMA and F. L. CRANE. Curr. Top. Cell. Regul. **20**, 247 (1981).
8. M. J. GRESSER, A. S. TRACEY, and P. J. STANKIEWICZ. Adv. Protein Phosphatases, **4**, 35 (1987).
9. M. J. GRESSER and A. S. TRACEY. J. Am. Chem. Soc. **107**, 4215 (1985).
10. A. S. TRACEY and M. J. GRESSER. Proc. Natl. Acad. Sci. (USA), **83**, 609 (1986).
11. M. J. GRESSER, A. S. TRACEY, and K. M. PARKINSON. J. Am. Chem. Soc. **108**, 6229 (1986).
12. A. S. TRACEY, B. GALEFFI, and S. MAHJOUR. Can. J. Chem. **66**, 2294 (1988).
13. N. BOURNE and A. WILLIAMS. J. Org. Chem. **49**, 1200 (1984).
14. K. E. JABALPURWALA and R. M. MILBURN. J. Am. Chem. Soc. **88**, 3224 (1966).
15. C. H. ROCHESTER. *In* The chemistry of the hydroxyl group. *Edited by* S. Patai. Interscience, New York, NY. 1971. p. 380.
16. R. C. WEAST (*Editor*). Handbook of chemistry and physics. 66th ed. CRC Press, Cleveland, OH. 1985.
17. A. ALBERT and E. P. SERJEANT. The determination of ionization constants. 3rd ed. Chapman and Hall, New York. 1984.
18. P. J. PEARCE and R. J. J. SIMKINS. Can. J. Chem. **46**, 241 (1968).
19. S. EHRENSON, R. T. C. BROWNLEE, and R. W. TAFT. Prog. Phys. Org. Chem. **10**, 1 (1973).

Can. J. Chem. Downloaded from www.nrcresearchpress.com by 196.1.178.254 on 09/07/12
For personal use only.

The characterization of primary, secondary, and tertiary vanadate alkyl esters by ^{51}V nuclear magnetic resonance spectroscopy

ALAN S. TRACEY AND MICHAEL J. GRESSER
Department of Chemistry, Simon Fraser University, Burnaby, B.C., Canada V5A 1S6

Received March 29, 1988

ALAN S. TRACEY and MICHAEL J. GRESSER. Can. J. Chem. **66**, 2570 (1988).

A variety of alkyl vanadates has been studied by ^{51}V nuclear magnetic resonance spectroscopy. It was found that the equilibrium constant for condensation of vanadate with alcohols is insensitive to whether the hydroxyl group is primary, secondary, or tertiary. These products, however, have characteristic vanadium chemical shifts that allow assignment of nmr signals to the appropriate ester. It was also found that chemical shifts are additive in the sense that the chemical shifts of the esters $ROVO_3H^-$ are one half the chemical shift of the diesters $(RO)_2VO_2^-$ when those shifts are given relative to −559 ppm. This effect is independent of whether the signals are to high or low field of −559 ppm and the additivity extends to mixed ligand systems. This value of −559 ppm is close but not equal to the chemical shift of the vanadate monoanion, $H_2VO_4^{1-}$, which is at −561 ppm. These results are at variance with arguments concerning the effects of ligand bulkiness on chemical shifts of vanadium(V) complexes.

ALAN S. TRACEY et MICHAEL J. GRESSER. Can. J. Chem. **66**, 2570 (1988).

On a étudié un certain nombre de vanadates d'alkyles en faisant appel à la résonance magnétique nucléaire du ^{51}V. On a trouvé que la constante d'équilibre pour la condensation du vanadate avec les alcools n'est pas sensible au caractère primaire, secondaire ou tertiaire des groupements hydroxyles. Toutefois, ces produits possèdent des déplacements chimiques du vanadium qui sont caractéristiques et qui permettent d'attribuer les signaux rmn aux esters appropriés. On a trouvé que les déplacements chimiques sont additifs dans le sens que les déplacements chimiques des esters $ROVO_3H^-$ correspondent à la moitié des déplacements chimiques des diesters $(RO)_2VO_2^-$ lorsque ces déplacements sont donnés par rapport à −559 ppm. Cet effet ne dépend pas de la position de ces signaux par rapport à −559 ppm et cette additivité s'étend aux systèmes comportant des ligands mixtes. La valeur de −559 ppm s'approche du, mais elle n'est pas égale au, déplacement chimique du monoanion de vanadate, $H_2VO_4^{1-}$, qui est égal à −561 ppm. Ces résultats sont en opposition avec les arguments concernant les effets d'encombrement des ligands sur les déplacements chimiques des complexes de vanadium(V).

[Traduit par la revue]

Can. J. Chem. Downloaded from www.nrcresearchpress.com by 196.1.178.254 on 09/07/12
For personal use only.

Introduction

The aqueous chemistry of vanadium(V) oxyanions has, over recent years, become an area of considerable interest in chemistry and biochemistry, not only because vanadate has a significant effect on the function of many enzymes (1–4) but also because it is involved in nitrogen fixation (5, 6), in biological halogenation reactions (6–8), and may be useful in enzymic synthesis since vanadate esters can be accepted by some enzymes in lieu of the biological substrate, the analogous phosphate ester (9). There is also a potential use for vanadium in the treatment of the symptoms of diabetes and sickle-cell anemia (10–12).

Vanadate spontaneously and rapidly condenses with hydroxylic compounds to provide the corresponding vanadate ester derivatives (13–17). Previous work with aliphatic compounds has concentrated on primary alcohols. However, our studies of some systems have indicated that reaction with secondary alcohols to form the vanadate ester proceeds as readily as that for primary esters. These observations have been confirmed by this work and, as well, condensation of vanadate with the tertiary alcohol, *tert*-butanol, has been studied.

Studies of the condensation reactions of vanadate have utilized to a large extent ^{51}V nuclear magnetic resonance (nmr) spectroscopy (13–15, 18–20). Vanadium nmr offers the sensitivity to work conveniently at vanadate concentrations between 0.1 and about 4 mM, which, for many studies of condensation reactions, includes the optimum vanadate concentration range. It has become evident from nmr studies of vanadate complexes with alkyl alcohols (14, 16), vicinal diols (21), α-hydroxy acids (22, 23), and oxalate (18, 22) that the ^{51}V nmr signals from tetrahedral, octahedral, and pentacoordinate complexes containing these ligands tend to occur within rather restricted chemical shift regions of the ^{51}V nmr spectral range. Of these coordination geometries the vanadate products with tetrahedral coordination show a comparatively wide range of chemical shifts.

The chemical shifts of tetrahedral products are very sensitive to the state of protonation and the number of substituents. Beyond this, the nmr studies have indicated that the ^{51}V chemical shifts of vanadate esters of aliphatic alcohols have specific stereochemical dependencies that can be useful in structural assignments. In this work the results from previous studies have been utilized, together with those from some new systems, to obtain a cohesive picture of the effects of substitution and charge state on the ^{51}V nmr chemical shifts of alkyl vanadate esters.

Experimental

Materials

Vanadium pentoxide, 99.999% (Aldrich "Gold Label") and HEPES (N-2-hydroxyethylpiperazine-N'-2-ethanesulphonic acid, Sigma Chemical Co.) buffer were used as supplied. The purity of the various alcohols used in this study was checked by ^1H or ^{13}C nmr spectroscopy before use: all were used as supplied.

Methods

The procedures utilized in this study differed little from those of previous studies of other systems (14, 21). They have been recently described in detail in ref. 24 with the exception that no KCl was incorporated into the solutions. All ^{51}V nmr spectra were obtained at ambient temperature (21°C) using the broadband facility of a Bruker WM-400 nmr spectrometer. Signal intensities were determined using the instrument manufacturer's software. No attempt to obtain more accurate integrals was made.

The results of vanadium and alcohol concentration studies were analyzed according to Scheme 1 using the concentrations of the various

species given by the nmr spectra. The pK_a values for vanadate and the vanadate esters were determined by application of eq. [2] to the observed chemical shifts, which were determined relative to $VOCl_3$ at 0.0 ppm.

pH, as utilized in this study, refers specifically to the value provided by a standard pH meter equipped with a calomel electrode and calibrated with pH 4.00 and pH 10.00 buffer solutions. No effects resulting from the presence of alcohol in the aqueous solutions have been considered. As discussed in ref. 14, such effects are small except at high alcohol concentrations.

Results and discussion

The condensation of vanadate with alkyl alcohols to form the alkyl vanadate ester and water is a facile reaction which, at least for the case of ethanol, occurs in the millisecond time scale (14). The product can undergo a further condensation with a second alcohol to form the diester. Both vanadate and its monoester have the possibility of gaining or losing a proton since the second pK_a for these compounds has values within the range of pH utilized in this study. The dialkyl vanadate ester has no proton to lose since the first pK_a of vanadate is about 3.2 (25), and the first pK_a of its mono- and diesters should be similar to this. For the work described here, the pH was varied from about 6.5 to 10.5.

From the above discussion it is clear that the reactions of vanadate with alkyl alcohols are very simple. They are summarized in Scheme 1 where ROH refers to the alkyl alcohol

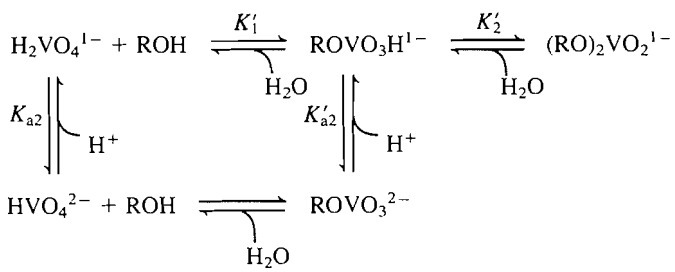

SCHEME 1

of interest. As a general rule, K_1' is not measured directly but rather K_1 as defined by eq. [1] is determined,

$$[1]\quad T_i + \ell \underset{H_2O}{\overset{K_1}{\rightleftharpoons}} T\ell \qquad [T_i][\ell]\,K_1 = [T\ell][H_2O]$$

where T_i refers to total tetrahedral vanadate ($H_2VO_4^{1-}$ + HVO_4^{2-}), $T\ell$ to its ester ($ROVO_3H^{1-}$ + $ROVO_3^{2-}$), and ℓ to the ligand. The chemical shift of tetrahedrally coordinated vanadate is quite sensitive to the protonation state, and consequently, by varying the pH, the changes in the observed chemical shift, δ_o, can be related to the shift of $ROVO_3H^{1-}$ (δ_l) and $ROVO_3^{2-}$ (δ_h) by eq. [2], and the pK_a values for vanadate

$$[2]\quad pH = pK_a + \log\left(\frac{\delta_o - \delta_l}{\delta_h - \delta_o}\right)$$

and its esters are therefore readily determined (14). The observed equilibrium constants, K_1, measured at any pH are related to the pH-independent K_1' of Scheme 1 and the K_{a2} values for vanadate and its esters by eq. [3].

$$[3]\quad K_1' = \frac{K_1(1 + K_{a2}/[H^+])}{(1 + K_{a2}'/[H^+])}$$

In practice, K_1 has generally been determined at a pH of 7.5 so that the correction to give K_1' is small since this pH is well below the pK_a of vanadate and its monoester.

As for K_1', the formation constant K_2' of Scheme 1 is, in general, not directly measured. K_2 as defined by eq. [4] is determined. This value is related to K_2'

$$[4]\quad T\ell + \ell \underset{}{\overset{K_2}{\rightleftharpoons}} T\ell_2 + H_2O \qquad [T\ell][\ell]K_2 = [T\ell_2][H_2O]$$

by eq. [5].

$$[5]\quad K_2' = K_2(1 + K_{a2}'/[H^+])$$

In this study the equilibrium constants for formation of vanadate esters from isopropanol, *sec*-butanol, *tert*-butanol, and 1,3-butane diol have been determined, and the pK_{a2} values for vanadate and the vanadate ester determined for each of the various solutions following procedures previously described for the formation of ethyl vanadate (14) as outlined below. The equilibrium constants K_1 and K_2 were readily obtained from the ^{51}V nmr spectra by first observing the appearance of the nmr signals corresponding to the vanadate ester and diester, respectively, then monitoring the changes in signal intensities as a function of alcohol concentration. The results of the concentration studies were then analyzed according to eqs. [1] and [4]. Variation of the hydrogen ion concentration at fixed ligand and total vanadate concentration allowed application of eq. [2] to provide the acidity constants and the limiting chemical shifts for low and high pH. These formation constants and the pK_a values are collected, together with values selected from other studies, in Table 1, which also tabulates the limiting chemical shifts, δ_l and δ_h of eq. [2], for each derivative. In Table 1, the formation constants are reported according to the formulation that the activity of liquid water is unity, so that the water concentration of eqs. [1] and [4] are not specifically considered. The pK_a values and formation constants for these and other vanadate esters have been discussed in detail elsewhere (26–28).

The formation constants listed in Table 1 are, however, of interest here. It is clear from this table that vanadate monoesters are formed, essentially, equally well, independent of whether the hydroxyl group being substituted is primary, secondary, or tertiary. It is particularly interesting to note that methyl vanadate has a formation constant almost identical to that for *tert*-butyl vanadate. The values for these two esters are approximately one half to one third those for most primary and secondary esters. The smaller formation constant for *tert*-butyl vanadate might be rationalized on steric grounds, but it is not clear why that for methanol is similar.

Except for methanol, vanadate ester formation is insensitive to whether the hydroxyl is secondary or primary. This is perhaps exemplified best in vanadate ester formation at the primary and secondary hydroxyls of 1,3-butane diol where, in fact, ester formation at the secondary position is slightly favoured over that at the primary position.

The insensitivity of ester formation to steric effects is evident also in the formation of vanadate diesters. Only with *tert*-butanol is there evidence of a steric effect on diester formation, since with this alcohol at concentrations up to 1.6 M no diester was observed. However, a low intensity signal ascribed to the di-*tert*-butyl vanadate was observed in a 50% acetone solution where higher concentrations of alcohol were obtainable.

It is evident from this work that in studies of systems containing a variety of hydroxyl groups, vanadate ester formation constants will not, in general, provide a reliable diagnostic

Can. J. Chem. Downloaded from www.nrcresearchpress.com by 196.1.178.254 on 09/07/12
For personal use only.

Can. J. Chem. Downloaded from www.nrcresearchpress.com by 196.1.178.254 on 09/07/12
For personal use only.

TABLE 1. ^{51}V nuclear magnetic resonance parameters and equilibrium constants describing vanadate and its mono- and diesters in a variety of aqueous alcoholic solutions[a]

Alkyl alcohol	Formation constants		$VO_4H_2^-$		VO_4H^{2-}		$ROVO_3H^-$	$ROVO_3^{2-}$	$(RO)_2VO_2^-$	
	$ROVO_3H^-$	$(RO)_2VO_2^-$	pK_{a2}	δ_l	δ_h	pK'_{a2}	δ_l	δ_h	$\delta_{T\ell_2}$	Reference
CH_3OH	0.094 ± 0.002	0.022 ± 0.002	9.22 ± 0.02	-560.8	-535.2	9.42 ± 0.02	-551.0	-528.2	-543.3	16
CH_3CH_2OH	0.21 ± 0.01	0.041 ± 0.004	8.3 ± 0.1	-561.0	-534.0	8.9 ± 0.1	-555.0	-532.0	-552.4	14
$(CH_3)_2CHOH$	0.24 ± 0.03	0.09 ± 0.01	8.83 ± 0.03	-560.5	-535.7	9.61 ± 0.02	-561.8	-539.0	-564.6	This work
$(CH_3)_3COH$	0.095 ± 0.005		8.72 ± 0.01	-560.9	-535.7	9.98 ± 0.03	-574.6	-553.2	-597.1^b	This work
$CH_3CH_2CHOHCH_3$	0.20 ± 0.01	0.10 ± 0.01	8.69 ± 0.01	-560.5	-535.3	9.67 ± 0.02	-562.2	-538.6	-564.8	This work
$CH_3CHOHCH_2CH_2OH$										
(Primary hydroxyl)	0.25 ± 0.01	0.074 ± 0.007	8.75 ± 0.05	-560.6	-535.4	9.09 ± 0.03	-556.0	-532.3	-552.9	This work
(Secondary hydroxyl)	0.29 ± 0.02	0.08 ± 0.01				9.37 ± 0.02	-564.0	-539.0	-569.5	
(Mixed hydroxyl)		0.11 ± 0.01							-560.9	
CH_2OHCH_2OH	0.34 ± 0.02	0.09 ± 0.01	8.8 ± 0.1	-560.4	-535.9	8.9 ± 0.1	-556.1	-533.4	-553.4	22
$CH_3C(CH_2OH)_3$	0.51 ± 0.10	0.18 ± 0.12	8.32 ± 0.02	-560.0	-536.3	8.65 ± 0.02	-556.1	-532.4	-553.0	27

[a]See experimental section for details.
[b]50% acetone solution.

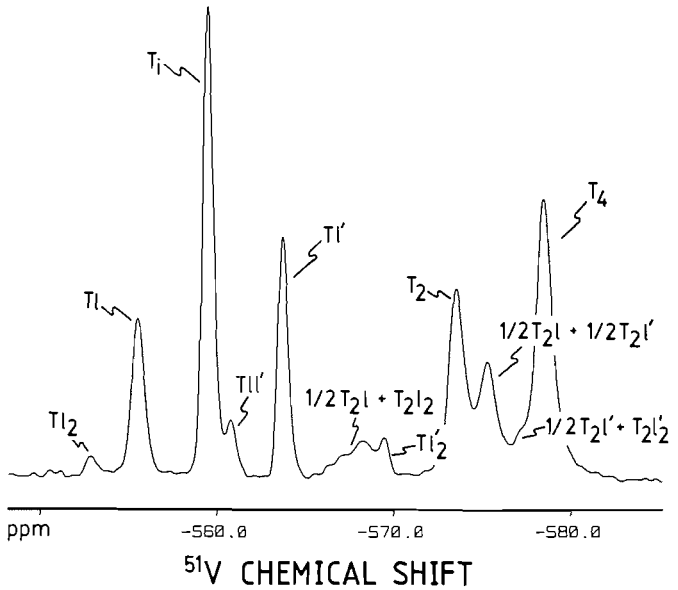

FIG. 1. ^{51}V nuclear magnetic resonance spectrum showing the products of the spontaneous condensation of vanadate with 1,3-butane diol in aqueous solution. In this figure the T represents the tetrahedrally coordinated vanadate; T_i, vanadate; T_2, divanadate; T_4, tetravanadate; ℓ, ligand complexed through the primary hydroxyl; ℓ', ligand complexed through secondary hydroxyl. The conditions of the experiment were 4.0 mM total vanadate, 1.11 M 1,3-butane diol, 20 mM HEPES buffer, and pH 7.5.

tool. It should be mentioned at this point that alkyl esters of divanadate are also formed. In general, a quantitative examination of their formation is difficult because the nmr signals are often not resolved from the signal of divanadate, T_2. A detailed study for the case of methanol has been reported (16). Signals in the nmr spectrum of 1,3-butane diol can be ascribed to the formation of divanadate esters, not only with the primary but also the secondary hydroxyls of the ligand, which are represented as ℓ and ℓ', respectively, in Fig. 1 where T is used to represent tetrahedral coordination about the vanadium nucleus. Other signals have been assigned to the esters of vanadate itself. A point to be made about the nmr spectrum of this system is that no signal ascribable to the product resulting from butane diol acting as a bidentate ligand is observed. This is in keeping with our observations with other 1,3-diol systems (27).

The assignment of ^{51}V nmr signals to vanadate products formed from 1,3-butane diol as depicted in Fig. 1 follows from the comparison of the chemical shifts reported in Table 1, from the study of methanol (16) and of 1-butanol, 2-butanol, and mixtures of the latter two. In this regard it should be mentioned that 1:1 mixtures of 1- and 2-butanol with vanadate provided ^{51}V nmr spectra virtually identical to spectra obtained from 1,3-butane diol. It is relevant to note that although the pK_{a2} for the vanadate monoanion, $H_2VO_4^{1-}$ (the predominant species at pH 7.5), is sensitive to the aqueous alcoholic solution in which it was measured, the ^{51}V nmr chemical shifts at low (δ_l) and high (δ_h) pH are remarkably constant near -561 ppm and -535 ppm, respectively. The pK_a values for the vanadate esters are also sensitive to solvent as well as to other effects such as the pK_a of the parent alcohol (28). However, as for vanadate itself, their chemical shifts are not sensitive to solvent, at least in the predominantly aqueous solutions employed here and for other studies. It is evident, however, from Table 1 that both the chemical shifts for $ROVO_3H^{1-}$ and $(RO)_2VO_2^{1-}$ vary considerably from one product to another. There does appear to

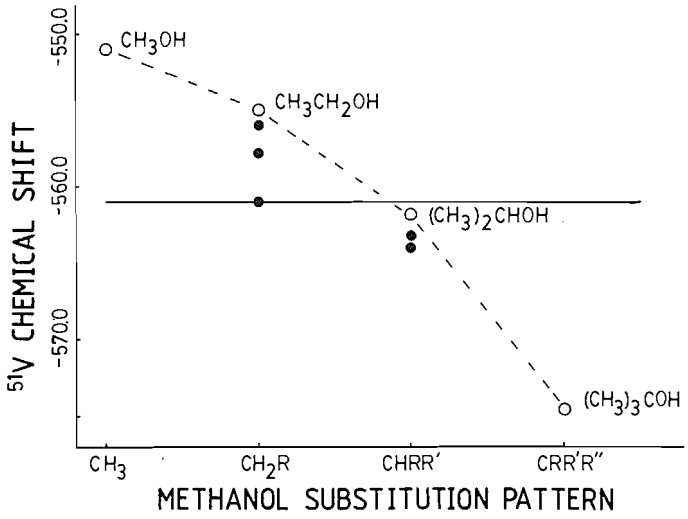

FIG. 2. A graphical representation of ^{51}V chemical shifts for $ROVO_3H^{1-}$ depicted as a function of the number of hydrogens of the methyl group of methanol replaced by alkyl substituents. The dashed line connects the chemical shifts for the products formed from the substituents CH_3OH, CH_3CH_2OH, $(CH_3)_2CHOH$, and $(CH_3)_3COH$. The solid line represents the chemical shift for $VO_4H_2^{1-}$ at −561 ppm. The open circles represent the specified alkyl alcohol, the solid circles, derivatives substituted at a methyl group. All chemical shifts are from Table 1.

be a systematic variation in these shifts, and this is exemplified in Fig. 2 where the chemical shift for $ROVO_3H^{1-}$ is compared to the number of methanol methyl hydrogens replaced by substituents and to the chemical shift of $H_2VO_4^{1-}$ (solid line at −561 ppm). It is seen from this figure that the chemical shifts of primary esters tend to be more positive than that of vanadate itself, while secondary esters are more negative. The only overlap of these ranges that we have observed to date is that of the fluorocarbon, 1,1,1-trifluoroethyl vanadate, which, with a δ_1 of −562.8 ppm, has a chemical shift to a slightly higher field than that of isopropyl vanadate (28). Certain other primary alkyl vanadates have chemical shifts very close to that of vanadate, such as 2-cyanoethyl vanadate (28). The chemical shifts from a variety of other compounds not explicitly considered here fall within the ranges depicted in Fig. 2.

In addition to the above finding, there also appears to be an additive property associated with ester and diester formation in that the ^{51}V chemical shifts of the diester monoanions for all the primary and secondary alcohols of Table 1 are close to twice as far away from −559.0 ppm as the chemical shifts of the corresponding monoester monoanions. This additivity of chemical shifts extends to mixed ligand species and can be used to calculate the chemical shift of the mixed diester formed from 1,3-butane diol T$\ell\ell'$ of Fig. 1. The value calculated is −561.0 ppm as compared to the observed value of −560.9.

It is interesting to speculate on the meaning of this unique chemical shift of −559 ppm. This shift, although close to that of the anion $H_2VO_4^-$ (−561 ppm) cannot be said to correspond to that value. It seems possible that it actually corresponds to the chemical shift of an $H_2VO_4^{1-}$ species that has some of the water of hydration removed or rearranged, similar to what would happen when an -OH is replaced by an -OR. This ion, which is not observable and indeed may not even exist under the conditions of these experiments, provides a reference frequency for the chemical shifts of the mono- and diesters. It is not possible to know if an analogous situation exists for the dianion HVO_4^{2-} since a diester cannot form with this ion. It is evident, though, from Table 1 that there is a systematic change in chemical shifts of the ester dianions, $ROVO_3^{2-}$, which parallels that of the monoanions, $ROVO_3H^{1-}$.

The dependence of chemical shift on the bulkiness of the alkyl group has been reported for vanadate esters in nonaqueous solution (29–31). An explanation (30) for this shift dependence, which invokes an increasing V—O bond length with increasing ligand bulkiness, and the associated effects on the paramagnetic term of the chemical shielding equation does not appear to provide an explanation for the results obtained here. The problem arises from considerations of the chemical shifts of the diesters relative to the monoesters. The incremental shifts, as we have seen above, are actually in opposite directions, dependent on whether the monoester, $ROVO_3H^-$, has a shift more positive or less positive than −559 ppm. Since incorporation of a second ligand necessarily increases total substituent bulkiness, it is clear that such an explanation is somewhat limited. An adequate description of chemical shielding should incorporate into it an explanation for a chemical shift of the special character of the −559 ppm observed here.

The characteristics of the chemical shift dependence of vanadate esters provide a useful diagnostic tool for analyzing ^{51}V nmr spectra. If the nmr spectra are obtained at a pH of 7.5 or less, where vanadate and its monoester are predominantly monoanions, then primary esters will, in general, resonate under, or to low field of, the vanadate signal, whereas signals from secondary or tertiary vanadates will generally occur to high field of the vanadate esters. Some consideration must also be given to rates of chemical exchange. Ethyl vanadate exchanges with vanadate in the millisecond timescale at 328°C. Other equilibration reactions could be faster than this so that, even at room temperature, signal coalescence might occur, particularly in cases where the chemical shifts of vanadate and its esters are close to each other. In this case some line broadening may be observable. Because of the additivity of the chemical shifts of mono- and diester vanadates, assignments of signal positions to either the monoester or the diester when one or the other signal is observed will be greatly facilitated. If the possibility for mixed diesters exists, then the chemical shift of the mixed species can be predicted from the chemical shifts of the two monoester precursors. Furthermore, as is evident from Fig. 1 and from a study of methanol/vanadate interactions (16), somewhat similar considerations apply to the chemical shifts of ester divanadates. In this case, it is the signal from the substituted vanadate moiety of the ester divanadate that is shifted by substitution, while the signal from the second vanadium nucleus shifts, at best, only a small amount. Esterification on the second vanadate to form the diester divanadate provides a symmetrical product with a resultant superposition of chemical shifts.

Acknowledgments

Thanks are gratefully extended to the Natural Sciences and Engineering Research Council of Canada for financial support in the form of operating grants to A.S.T. and M.J.G.

1. N. D. CHASTEEN. Struct. Bonding (Berlin), **53**, 105 (1983).
2. T. RAMASARMA and F. L. CRANE. Curr. Top. Cell. Regul. **20**, 247 (1981).
3. E. ERDMANN, K. WERDEN, W. KRAWIETZ, W. SCHMITZ, and H. SCHOLZ. Biochem. Pharmacol. **33**, 945 (1984).
4. F. BOSCH, A. M^A GOMEZ-FOIX, J. ARIÑO, and J. J. BUINOVART. Adv. Protein Phosphatases, **4**, 351 (1987).

Can. J. Chem. Downloaded from www.nrcresearchpress.com by 196.1.178.254 on 09/07/12
For personal use only.

5. H. VILTER. Phytochemistry, **23**, 1387 (1984).
6. R. WEVER, E. DE BOER, H. PLAT, and B. E. KRENN. FEBS Lett. **216**, 1 (1987).
7. R. R. EADY, R. L. ROBSON, B. E. SMITH, D. J. LOWE, R. W. MILLER, and M. J. DILWORTH. Recl. Trav. Chim. Pays-Bas, **106**, 175 (1987).
8. B. J. HALES, E. E. CASE, J. E. MORNINGSTAR, M. F. DZEDA, and L. A. MAUTERER. Biochemistry, **25**, 7251 (1986).
9. A. F. NOUR-ELDEEN, M. M. CRAIG, and M. J. GRESSER. J. Biol. Chem. **260**, 6836 (1986).
10. C. E. HEYLIGER, A. G. TAHILIANI, and J. H. MCNEILL. Science, **227**, 1474 (1985).
11. J. MEYEROVITCH, Z. FARFEL, J. SACK, and Y. SCHECHTER. J. Biol. Chem. **262**, 6658 (1987).
12. P. J. STANKIEWICZ, M. J. GRESSER, A. S. TRACEY, and L. F. HASS. Biochemistry, **26**, 1264 (1987).
13. D. REHDER and K. WIEGHARDT. Z. Naturforsch. B: Anorg. Chem. Org. Chem. **36B**, 1251 (1981).
14. M. J. GRESSER and A. S. TRACEY. J. Am. Chem. Soc. **107**, 4215 (1985).
15. M. J. GRESSER, A. S. TRACEY, and K. M. PARKINSON. J. Am. Chem. Soc. **108**, 6229 (1986).
16. A. S. TRACEY, M. J. GRESSER, and B. GALEFFI. Inorg. Chem. **27**, 157 (1988).
17. J. H. FERGUSON and K. KUSTIN. Inorg. Chem. **18**, 3349 (1979).
18. P. M. EHDE, I. ANDERSSON, and L. PETTERSSON. Acta Chem. Scand. Ser. A: **A40**, 489 (1986).
19. J. A. BONADIES and C. J. CARRANO. J. Am. Chem. Soc. **108**, 4088 (1986).
20. D. REHDER. Bull. Magn. Reson. **4**, 33 (1982).
21. M. J. GRESSER and A. S. TRACEY. J. Am. Chem. Soc. **108**, 1935 (1986).
22. A. S. TRACEY, M. J. GRESSER, and K. M. PARKINSON. Inorg. Chem. **26**, 629 (1987).
23. M. M. CALDEIRA, M. L. RAMOS, N. C. OLIVEIRA, and V. M. S. GIL. Can. J. Chem. **65**, 2434 (1987).
24. A. S. TRACY, M. J. GRESSER, and S. LIU. J. Am. Chem. Soc. In press.
25. M. T. POPE and B. W. DALE. Q. Rev. Chem. Soc. **22**, 527 (1968).
26. B. GALEFFI and A. S. TRACEY. Can. J. Chem. **66**, 2565 (1988).
27. A. S. TRACEY and M. J. GRESSER. Inorg. Chem. **27**, 1269 (1988).
28. A. S. TRACEY, B. GALEFFI, and S. MAHJOUR. Can. J. Chem. **66**, 2294 (1988).
29. D. REHDER. Z. Naturforsch. **326**, 771 (1977).
30. D. REHDER. J. Magn. Reson. **38**, 419 (1980).
31. D. REHDER. Chimie, **40**, 186 (1988).

Can. J. Chem. Downloaded from www.nrcresearchpress.com by 196.1.178.254 on 09/07/12
For personal use only.

Linear oligopeptides. 188.[1] Crystallographic characterization of the conformation of the 1-aminocyclopentane-1-carboxylic acid residue in simple derivatives

GIOVANNI VALLE, MARCO CRISMA, AND CLAUDIO TONIOLO[2]

Biopolymer Research Centre, C.N.R., Department of Organic Chemistry, University of Padova, 35131 Padova, Italy

Received November 6, 1987[3]

GIOVANNI VALLE, MARCO CRISMA, and CLAUDIO TONIOLO. Can. J. Chem. **66**, 2575 (1988).

The crystal structures of six derivatives of the $C^{\alpha,\alpha}$-dialkylated α-aminoacid residue 1-aminocyclopentane-1-carboxylic acid (Acc^5) have been determined. These are Z-Acc^5-OH, Z-Acc^5-OH acetone hemi-solvate, Fmoc-Acc^5-OH, mClAc-Acc^5-OH, *p*BrBz-Acc^5-OH, and the 5(4*H*)-oxazolone from *p*BrBz-Acc^5-OH. The values determined for the torsion angles about the N—C^α (ϕ) and C^α—CO (ψ) bonds correspond to folded, potentially $\alpha/3_{10}$-helical conformations for the Acc^5 residue of Z-Acc^5-OH, Z-Acc^5-OH acetone hemi-solvate, mClAc-Acc^5-OH, and *p*BrBz-Acc^5-OH. The structure of Fmoc-Acc^5-OH, however, is unusual in having a semi-extended conformation for the ϕ, ψ angles, accompanied by a *cis* arrangement of the amide group of the secondary urethane moiety. The dependence of the N—C^α—C′ bond angle on the ψ torsion angle and the asymmetry at the C^α atom are relevant features of the Acc^5 residues. The position of the cyclopentyl ring relative to the peptide chain and its puckering parameters for the six compounds are also discussed.

GIOVANNI VALLE, MARCO CRISMA et CLAUDIO TONIOLO. Can. J. Chem. **66**, 2575 (1988).

On a déterminé les structures cristallines de six dérivés $C^{\alpha,\alpha}$-dialkylés du résidu d'acide α-aminé, amino-1 cyclopentane-carboxylique-1 (Acc^5). Il s'agit du Z-Acc^5-OH, du Z-Acc^5-OH hémisolvaté par l'acétone, du Fmoc-Acc^5-OH, du mClAc-Acc^5-OH, du *p*BrBz-Acc^5-OH et de la (4*H*)-oxazolone-5 préparée à partir du *p*BrBz-Acc^5-OH. Les valeurs qui ont été obtenues pour les angles de torsion autour des liaisons N-C^α (ϕ) et C^α-CO (ψ) du résidu Acc^5 du Z-Acc^5-OH, du Z-Acc^5-OH hémisolvaté par l'acétone, du mClAc-Acc^5-OH et du *p*BrBz-Acc^5-OH correspondent à des conformations repliées qui sont possiblement $\alpha/3_{10}$-hélicoïdales. Toutefois, la structure du Fmoc-Acc^5-OH est inhabituelle; sur la base des angles ϕ et ψ elle possède une conformation semi-étendue qui est accompagnée par un arrangement *cis* du groupement amide de la portion secondaire de l'uréthane. Le fait que l'angle de la liaison N—C^α—C′ varie en fonction de l'angle de torsion ψ et de l'asymétrie du C^α et sont caractéristiques importantes des résidus Acc^5. On discute aussi de la position du cyclopentane par rapport à la chaîne peptidique ainsi que des paramètres de plissement des six composés.

[Traduit par la revue]

Introduction

The use of uncommon α-amino acid residues in the synthesis of peptides with restricted conformational flexibility has acquired increasing importance in the design of analogs of bioactive peptides (2). $C^{\alpha,\alpha}$-dialkylated α-amino acid residues have proven to be valuable in the construction of conformationally constrained peptide backbones (3–5).

While considerable attention has been paid to the crystal-state conformational preferences of $C^{\alpha,\alpha}$-dialkylated residues with linear substituents, like $C^{\alpha,\alpha}$-dimethylglycine or α-aminoisobutyric acid (Aib) (3–16), $C^{\alpha,\alpha}$-diethylglycine (Deg) (5, 10, 17), and $C^{\alpha,\alpha}$-di-*n*-propylglycine (Dpg) (5, 10, 18), relatively few studies have been reported on peptides containing 1-aminocycloalkane-1-carboxylic acids (Acc^n, where *n* is the number of carbon atoms in the cycloalkane ring). Recent X-ray diffraction investigations in our laboratory suggest that both 1-aminocyclohexane-1-carboxylic acid (Acc^6) (19–22) and 1-aminocyclopentane-1-carboxylic acid (Acc^5), earlier referred to as cycloleucine and abbreviated as Cle, Cyl, cycloLeu or *c*Leu (23) strongly prefer folded backbone conformations in the $3_{10}/\alpha$-helical region of the conformational space ($\phi \simeq \pm 60 \pm 20°$, $\psi \simeq \pm 30° \pm 20°$) (24).

As a part of a program aimed to a detailed investigation of the conformational properties of the Acc^5 residue (23), in this report we describe the X-ray diffraction structures of six Acc^5 derivatives, namely Z-Acc^5-OH (**1**) (Z, benzyloxycarbonyl), Z-Acc^5-OH acetone hemi-solvate (**2**), Fmoc-Acc^5-OH (**3**) (Fmoc, fluoren-9-ylmethyloxycarbonyl), mClAc-Acc^5-OH (**4**) (mClAc, monochloracetyl), *p*BrBz-Acc^5-OH (**5**) (*p*BrBz, *para*bromobenzoyl), and the 5(4*H*)-oxazolone from *p*BrBz-Acc^5-OH (**6**). In particular, the results permit a definition of the Acc^5 ϕ, ψ torsion angles (24) and the conformational features of the cyclopentyl side chain. X-ray diffraction structures of H-Acc^5-OH monohydrate (25), H-Acc^5-OH hydrobromide (26), and the 2,5-dioxopiperazine from Acc^5 and Ser (27) have already been published by other groups.

This study was expected to provide information on the structural effect produced by Acc^5 when inserted in analogs of bioactive peptides. To our knowledge, Acc^5-containing peptides synthesized so far range from analogs of the formyl-methionyl tripeptide chemoattractant (28–31) to the sweetening agent aspartame (32–34), from angiotensin II (35) to enkephalins (36, 37), from the antitumor and antiviral agents 2,5-dioxopiperazines (38) to angiotensin-converting enzyme (39), peptidyltransferase (40), and γ-glutamyl transpeptidase (41, 42) inhibitors, from penicillin (43) and somatostatin (44) to oxytocin (45, 46) and vasopressin (47).

Experimental

Materials

Z-Acc^5-OH (**1**) (48) and mClAc-Acc^5-OH (**4**) (48) were prepared by published procedures.

Fmoc-Acc^5-OH (**3**) was prepared as described by Paquet (49). Mp 187–188°C (from ethyl acetate). *Anal.* calcd. for $C_{21}H_{21}NO_4$ (351.4): C 71.8, H 6.0, N 4.0; found: C 71.6, H 6.1, N 3.9.

*p*BrBz-Acc^5-OH (**5**) was prepared as described by Toniolo *et al.* (8). Mp 236–237°C (from ethyl acetate). *Anal.* calcd. for $C_{13}H_{14}NO_3Br$ (312.2): C 50.0, H 4.5, N 4.5, Br 25.6; found: C 49.8, H 4.5, N 4.4, Br 25.4.

5(4*H*)-Oxazolone from *p*BrBz-Acc^5-OH (**6**) was prepared as des-

[1]For part 187: see ref. 1.

[2]Author to whom correspondence may be addressed.

[3]Revision received May 6, 1988.

Printed in Canada / Imprimé au Canada

Can. J. Chem. Downloaded from www.nrcresearchpress.com by 196.1.178.254 on 09/07/12
For personal use only.

cribed by Toniolo *et al.* (8). Mp 120–121°C (from toluene – petroleum ether). *Anal.* calcd. for $C_{13}H_{12}NO_2Br$ (294.2): C 53.1, H 4.1, N 4.8, Br 27.2; found: C 52.9, H 4.0, N 4.7, Br 27.0.

X-ray diffraction

Colorless crystals of Z-Acc^5-OH (**1**) were obtained from a diethyl ether solution by slow evaporation. Crystal data are as follows:

$C_{14}H_{17}NO_4$ fw = 263.3

Triclinic, a = 12.833(2), b = 8.580(2), c = 6.605(1) Å, V = 673.1 Å^3, α = 98.24(10), β = 103.58(10), γ = 103.22(10), ρ_o = 1.39(1), Z = 2, ρ_c = 1.396 g cm^{-3} (20°C; MoK$_\alpha$, λ = 0.7107 Å). Space group $P\bar{1}$.

Colorless crystals of Z-Acc^5-OH acetone hemi-solvate (**2**) were obtained from an acetone solution by slow evaporation. Crystal data are as follows:

$C_{14}H_{17}O_4.(1/2)(C_3H_6O)$ fw = 292.3

Orthorhombic, a = 31.282(3), b = 10.596(2), c = 9.621(2) Å, V = 3189.0 Å^3, ρ_o = 1.29(1), Z = 8, ρ_c = 1.30 g cm^{-3} (20°C; MoK$_\alpha$, λ = 0.7107 Å). Space group *Pbcn*.

Colorless crystals of Fmoc-Acc^5-OH (**3**) were obtained from an ethyl acetate solution by slow evaporation. Crystal data are as follows:

$C_{21}H_{21}NO_4$ fw = 351.4

Orthorhombic, a = 26.136(5), b = 13.854(4), c = 9.842(3) Å, V = 3563.7 Å^3, ρ_o = 1.30(1), Z = 8, ρ_c = 1.31 g cm^{-3} (20°C; MoK$_\alpha$, λ = 0.7107 Å). Space group *Pbca*.

Colorless crystals of mClAc-Acc^5-OH (**4**) were obtained from an acetone – petroleum ether mixture by slow evaporation. Crystal data are as follows:

$C_8H_{12}NO_3Cl$ fw = 205.6

Orthorhombic, a = 11.012(3), b = 9.541(3), c = 9.277(3) Å, V = 974.7 Å^3, ρ_o = 1.38(1), Z = 4, ρ_c = 1.39 g cm^{-3}, μ = 3.2 cm^{-1} (20°C; MoK$_\alpha$, λ = 0.7107 Å). Space group $P2_12_12_1$.

Colorless crystals (0.5, 0.5, 0.6 mm) of *p*BrBz-Acc^5-OH (**5**) were obtained from an ethyl acetate solution by slow evaporation. Crystal data are as follows:

$C_{13}H_{14}NO_3Br$ fw = 312.2

Orthorhombic, a = 21.313(5), b = 10.004(3), c = 12.158(3) Å, V = 2592.3 Å^3, ρ_o = 1.59(1), Z = 8, ρ_c = 1.60 g cm^{-3}, μ = 30.8 cm^{-1} (20°C; MoK$_\alpha$, λ = 0.7107 Å). Space group *Pccn*.

Colorless crystals (0.15, 0.15, 0.7 mm) of the 5(4*H*)-oxazolone from *p*BrBz-Acc^5-OH (**6**) were obtained from a toluene – petroleum ether mixture by slow evaporation. Crystal data are as follows:

$C_{13}H_{12}NO_2Br$ fw = 294.2

Triclinic, a = 12.635(3), b = 9.568(3), c = 5.490(2) Å, V = 615.5 Å^3, α = 100.1(3), β = 93.0(3), γ = 108.5(3), ρ_o = 1.57(1), Z = 2, ρ_c = 1.58 g cm^{-3}, μ = 32.4 cm^{-1} (20°C; MoK$_\alpha$, λ = 0.7107 Å). Space group $P\bar{1}$.

A total of 2368, 2811, 3139, 1718, 2288, and 2161 independent reflections for **1**, **2**, **3**, **4**, **5**, and **6**, respectively, were collected on a Philips PW 1100 four-circle diffractometer, using graphite-monochromatized MoK$_\alpha$ radiation at $4° < 2\theta < 50°$ with the θ–2θ scan mode. During data collection three standard reflections were measured every 180 min to check the stability of the crystal and the electronics. Intensities were corrected for Lorentz and polarization factors; no absorption corrections was applied.

The six structures were solved by direct methods using MULTAN 80 (50) and refined by block-diagonal least-squares (**1**, **2**, **3**, **5**, and **6**) or by full-matrix least-squares (**4**) with anisotropic thermal parameters for all non-hydrogen atoms with the exception of those of the acetone molecule of **2**. The hydrogen atoms of **1** and **2** were found on the difference Fourier map, but not refined; those of **3**, **4**, and **6** were found and refined isotropically. Part of the hydrogen atoms of **5** were found on the difference Fourier map while the others were calculated, and all were refined isotropically. All calculations were performed on the IBM 370/158 computer of the University of Padova, using SHELX 76 (51).

The final R values for the 745, 746, 1118, 1605, 1404, and 1432 observed reflections with $I \geq 3.0\sigma(I)$ of **1**, **2**, **3**, **4**, **5**, and **6**, respectively, were 0.077, 0.070, 0.064, 0.039, 0.052, and 0.052, respectively. For **1** and **2** the low percentages (31.5 and 26.5) of observed reflections might tentatively be attributed to the tiny crystals obtained in both cases and to the internal disorder existing particularly in the oxygen atom of the acetone molecule of **2**.

Tables of final atomic coordinates with esd's and thermal parameters, of bond lengths, bond angles, and torsion angles, and lists of observed and calculated structure factors are available from the Depository of Unpublished Data.[4]

Results and discussion

Perspective views of molecules **1** to **6** are shown in Figs. 1–6 with the atom numbering schemes. Average values of bond lengths and bond angles for the Acc^5 residue are listed in Fig. 7.

The Acc^5 residue

The Acc^5 residue of compounds **1**, **2**, **4**, and **5** is folded, the sets of ϕ, ψ_T torsion angles (24) falling in the region of the conformational energy map where both α- and 3_{10}-helices are found. The pertinent values are 60.9(13), 29.4(13)° for **1**, −58.2(11), −31.4(11)° for **2**; −62.6(4), −23.4(4)° for **4**; −61.9(8), −34.4(8)° for **5**. Conversely, the Acc^5 of **3** is semi-extended [−65.5(9), 160.9(6)°], as observed in Fmoc-Aib-OH, where the ϕ, ψ_T values are −78.6, 158.6° (52). In *t*-Boc-(Acc^5)$_2$-NHMe (*t*-Boc, *tert*-butyloxycarbonyl; NHMe, methylamino (23) the ϕ, ψ values for the two Acc^5 residues are −57.6, −38.1° and −60.2, −31.1° for the folded N- and C-terminal residues, respectively.

In general, bond lengths and bond angles of the Acc^5 residue agree well with those reported for the *trans* peptide unit (53, 54) and the Aib (54–57) and Acc^6 (21) residues. The average value for the N—C$^\alpha$—C′ (τ) bond angle is higher than the regular tetrahedral value, but the known dependence of this angle on the ψ torsion angle is found also in this study: in particular, the Acc^5 residue in the semi-extended conformation (compound **3**) shows a value closer to 109.5° than the Acc^5 residues in the helical conformation (compounds **1**, **2**, **4**, and **5**). The asymmetry at the C$^\alpha$ atom (bond angles involving the C$^{\beta L}$ as compared to those involving the C$^{\beta D}$ atom), already reported for the Aib and Acc^6 residues, stands out clearly also from the values of the Acc^5 residue listed in Fig. 7. As expected for a cyclopentyl ring (58), the endocyclic bond angles have values significantly lower than 109.5°.

As for the torsion angles relating the cyclopentyl ring to the peptide chain, N—C$^\alpha$—C$^{\beta L}$—C$^{\gamma L}$ and N—C$^\alpha$—C$^{\beta D}$—C$^{\gamma D}$, the sets of values observed (deposited) are half-way between the ideal *gauche* (g^+, g^-, or ±60°) and *skew* (s^+, s^-, or ±120°) conformations, with the single exception of the 5(4*H*)-oxazolone from *p*BrBz-Acc^5-OH (**6**), the values of which are reasonably close to the s^+, s^- conformation.

The endocyclic cyclopentane ring torsion angles of compounds **1** to **6** are listed in Table 1. As expected (58), the absolute values range from 0.3 (planar) to 41.0°. The values of ϕ, the phase angle of puckering (59), are 179.4(21), −42.5(21), 173.2(27), 171.6(7), 6.3(16), and 75.0(17)° for compounds **1**–**6**, respectively. In terms of the original cyclopentane model (60), values of ϕ = 0, 36, 72, 108, 144, 180° correspond to envelope conformations with C_s symmetry, while ϕ = 18, 54, 90, 126, 162° give half-chair (or twist) conformations with C_2 symmetry.

[4]These tables may be purchased from the Depository of Unpublished Data, CISTI, National Research Council of Canada, Ottawa, Ont., Canada K1A 0S2.

Can. J. Chem. Downloaded from www.nrcresearchpress.com by 196.1.178.254 on 09/07/12
For personal use only.

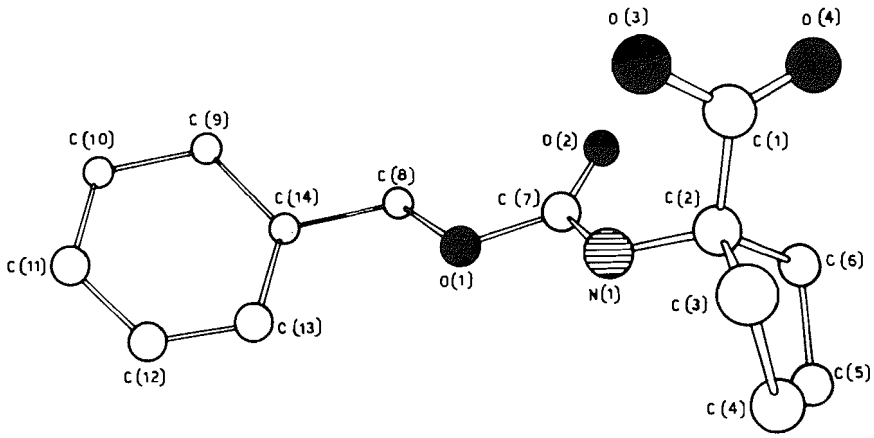

FIG. 1. Molecular structure of Z-Acc^5-OH (**1**) with numbering of the atoms.

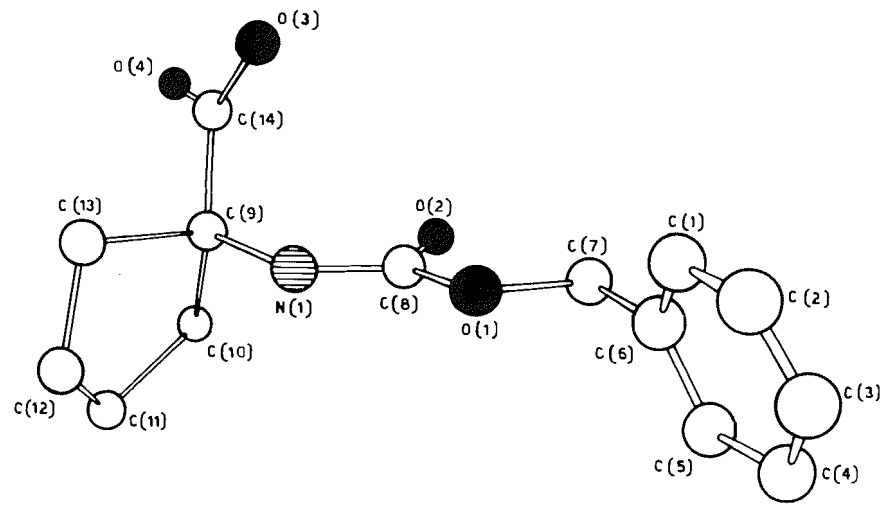

FIG. 2. Molecular structure of Z-Acc^5-OH acetone hemi-solvate (**2**) with numbering of the atoms.

N-terminal groups

The values of bond lengths and bond angles for the urethane group of the benzyloxycarbonyl compounds **1** and **2** (Figs. 1 and 2) are in agreement with literature data (61). In particular, the decrease of the bond angle at the carbonyl carbon, O(1)—C(7)—N(1) in **1** (110.4(9)°) and O(1)—C(8)—N(1) (109.2(8)°) in **2**, by about 5°, as compared with the corresponding bond angle C^{α}—C′—N in the peptide group (53, 54), must be ascribed to the reduced repulsion between the O(1) atom and the nearest substituent on the N-atom in urethane, compared with a corresponding repulsion involving the C^{α} atom of the peptide group. The θ_2 and θ_3 angles, giving the orientation of the phenyl ring relative to the urethane moiety (61), C(7)—O(1)—C(8)—C(14) and O(1)—C(8)—C(14)—C(13) in **1**, and C(8)—O(1)—C(7)—C(6) and O(1)—C(7)—C(6)—C(1) in **2**, have values of −162.5(9) and −45.9(14)° in **1**, and −173.2(9) and −76.6(14)° in **2**. Interestingly, in the observed distribution of θ_2 in crystalline Z-derivatives, the values are concentrated in three regions, close to 90, −90, and 180°, respectively; conversely, the distribution of θ_3 values is broad, extending over its entire range (61). The angle between normals to the average planes of the phenyl and urethane groups is 44.9° in **1** and 70.3° in **2**. The secondary urethane linkage is found in the usual *trans* conformation (61–63) in both **1** and **2**, the values of the ω_0 torsion angle (O(1)—C(7)—N(1)—C(2) in **1** and O(1)—C(8)—N(1)—C(9) in **2**) being −178.5(9)° in **1** and 179.3(7)° in **2**. This structural property, accompanied by the *trans* θ_1 torsion angle (179.1(9)° for N(1)—C(7)—O(1)—C(8) in **1**, while −178.3(9)° for N(1)—C(8)—O(1)—C(7) in **2**), allows us to classify the urethane moieties of **1** and **2** as the common type *b* (61–63).

Bond lengths and bond angles for the fluoren-9-ylmethyloxycarbonyl group of compound **3** (Fig. 3) compare well with those found in other Fmoc (52) and urethane (61, 62) derivatives. In particular, we note the following points: (*i*) The C(6)—C(7), C(12)—C(13), and C(1)—C(13) bond lengths of the fluorene system are 1.484(12), 1.535(13), and 1.511(13) Å, respectively. (*ii*) The tetrahedral bond angles about the C(13) atom are considerably spread (from 101.2(7) to 115.3(8)°) to help relieve the unfavorable interactions between the tricyclic moiety and the methyloxycarbonylaminoacyl chain. (*iii*) The C(13)—C(14) bond length (1.516(11) Å) is shorter than that quoted as standard for a paraffinic C—C single bond, 1.541 Å (64); by contrast, the C(14)—O(1) bond length (1.468(12) Å) is larger than that quoted as standard for an ether C—O single bond, 1.430 Å (64). The fluorene ring system, and the urethane and carboxylic acid groups are close to planarity. The angle between normals to the average planes of the two aromatic rings of the fluorene system is 3.8°. The angles between normals to the average plane of the urethane group and the average planes

Can. J. Chem. Downloaded from www.nrcresearchpress.com by 196.1.178.254 on 09/07/12
For personal use only.

Can. J. Chem. Downloaded from www.nrcresearchpress.com by 196.1.178.254 on 09/07/12
For personal use only.

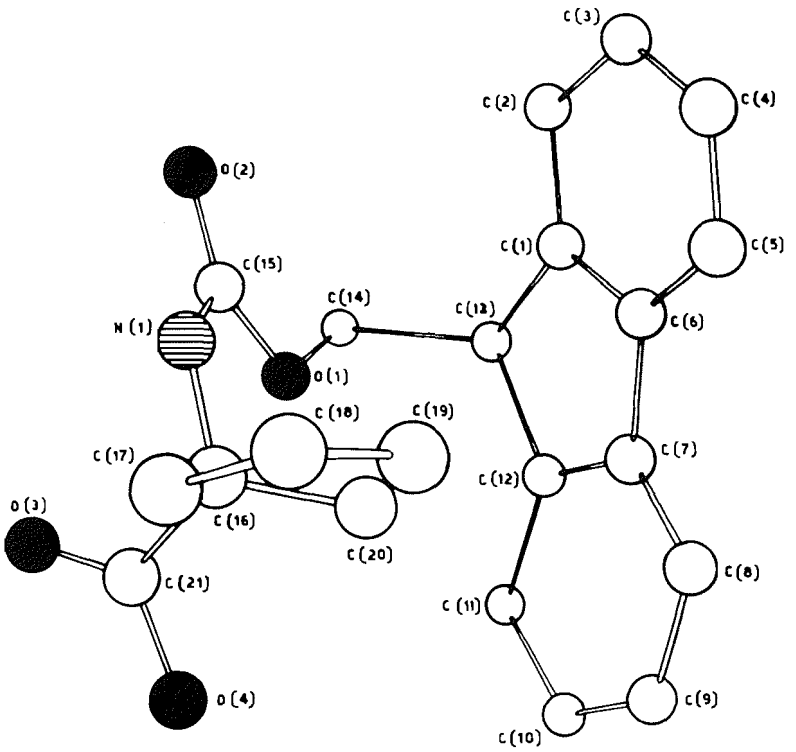

FIG. 3. Molecular structure of Fmoc-Acc^5-OH (**3**) with numbering of the atoms.

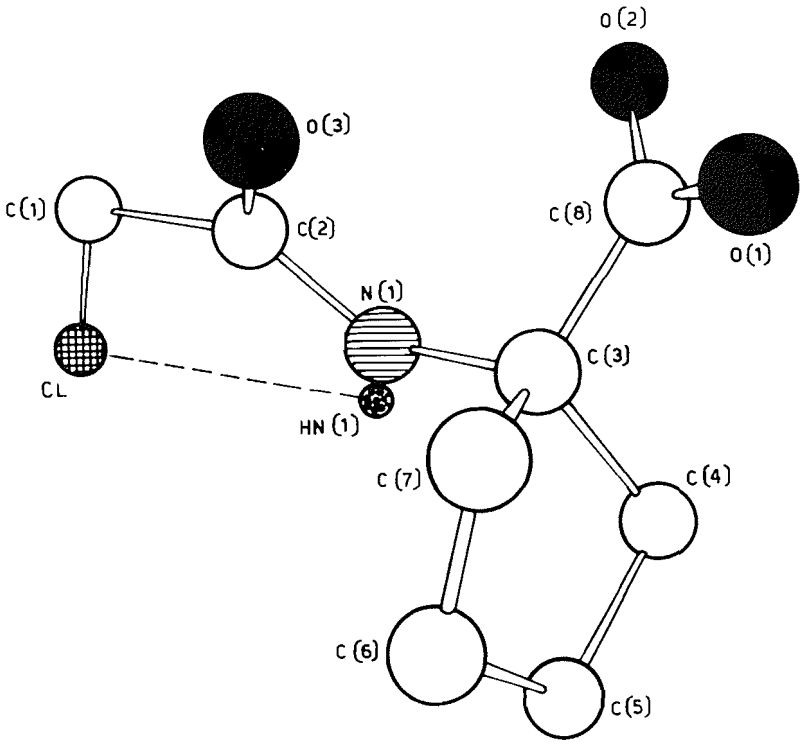

FIG. 4. Molecular structure of mClAc-Acc^5-OH (**4**) with numbering of the atoms. The intramolecular H-bond is shown as a dashed line.

of the central ring of the fluorene system and the carboxylic acid group are 116.9° and 104.6°, respectively. The secondary urethane moiety is in the relatively unusual type *a* (*trans*, *cis*) conformation (61–63), the two pertinent θ_1 and ω_0 torsion angles having values of −172.4(7) and −3.4(10)°, respectively. In Fmoc-Aib-OH (52), however, the urethane conformation is *trans*, *trans* (type *b*).

The dihedral angle δ between normals to the average planes of the amide and carboxylic acid groups of compound **4** (Fig. 4) is 107.8°. In *N*-acylamino acids this angle is known to have a preference for values near 20° or 90° (65). The alignment of the C(1)—Cl and the amide N(1)—H bonds is suggested by the value of the Cl—C(1)—C(2)—N(1) torsion angle (5.0(5)°). The presence of the intramolecularly H-bonded "C_5" conforma-

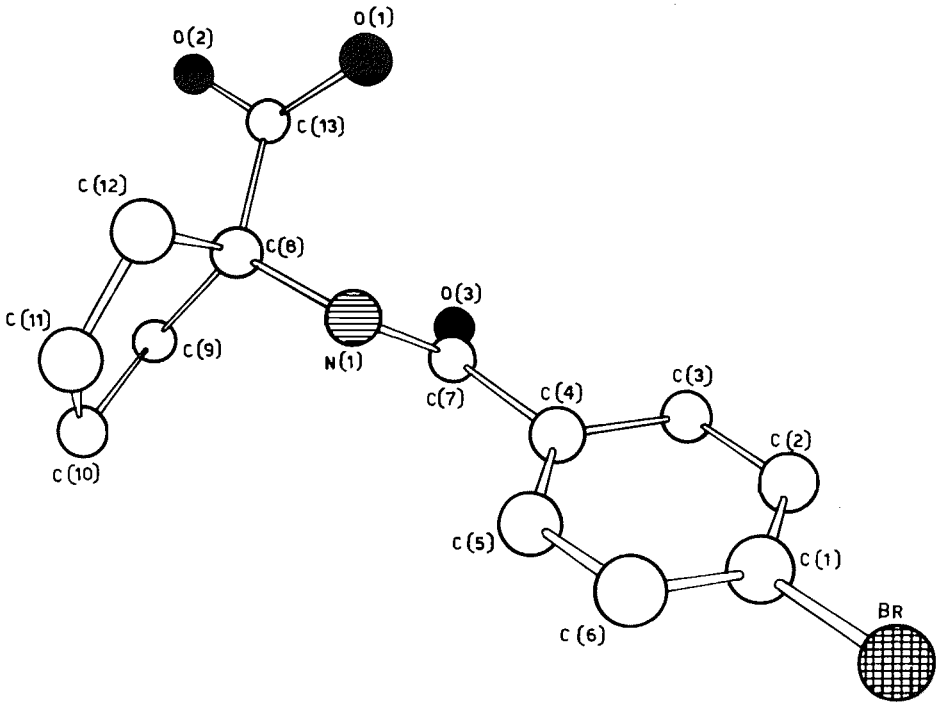

FIG. 5. Molecular structure of *p*BrBz-Acc^5-OH (**5**) with numbering of the atoms.

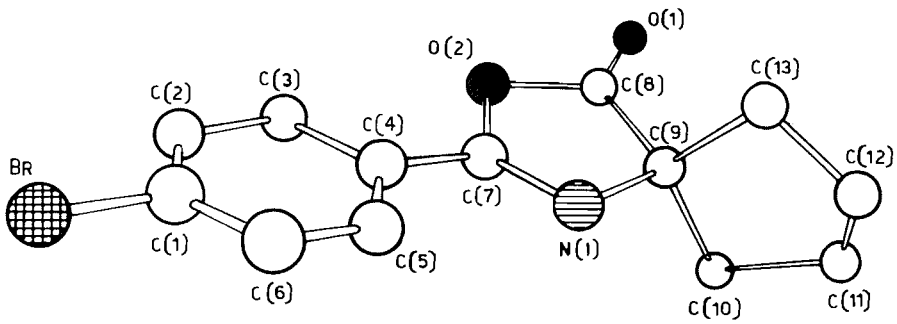

FIG. 6. Molecular structure of the 5(4*H*)-oxazolone from *p*BrBz-Acc^5-OH (**6**) with numbering of the atoms.

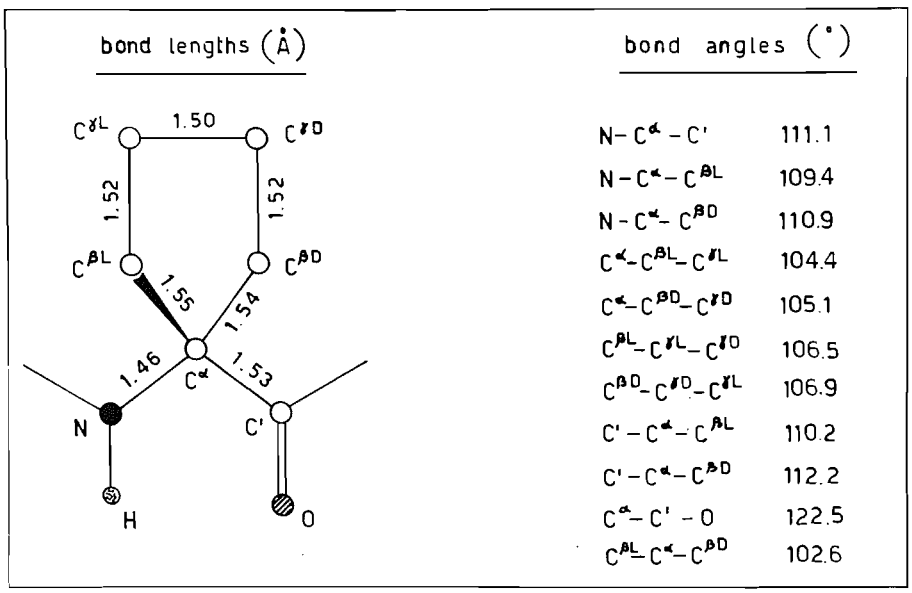

FIG. 7. Average geometry for an Acc^5 residue derived from an analysis of the crystal structures discussed in this work.

Can. J. Chem. Downloaded from www.nrcresearchpress.com by 196.1.178.254 on 09/07/12
For personal use only.

Can. J. Chem. Downloaded from www.nrcresearchpress.com by 196.1.178.254 on 09/07/12
For personal use only.

TABLE 1. Torsion angles (deg) in the cyclopentane rings of compounds **1** to **6**

Compound	Torsion angle									
	$C^{\beta D}$—C^{α}—$C^{\beta L}$—$C^{\gamma L*}$	C^{α}—$C^{\beta L*}$—$C^{\gamma L}$—$C^{\gamma D}$	$C^{\beta L}$—$C^{\gamma L}$—$C^{\gamma D}$—$C^{\beta D}$	$C^{\gamma L}$—$C^{\gamma D}$—$C^{\beta D}$—C^{α}	$C^{\gamma D}$—$C^{\beta D}$—C^{α}—$C^{\beta L}$
Z-Acc^5-OH (**1**)	37.1(10)	−22.8(12)	−0.3(13)	23.7(12)	−37.7(11)
Z-Acc^5-OH acetone hemi-solvate (**2**)	−17.1(11)	−4.8(13)	25.7(14)	−35.7(12)	32.7(11)
Fmoc-Acc^5-OH (**3**)	−31.6(10)	22.5(12)	−4.2(13)	−15.3(11)	28.6(9)
mClAc-Acc^5-OH (**4**)	36.7(4)	−19.3(4)	6.3(5)	29.6(4)	−41.0(3)
*p*BrBz-Acc^5-OH (**5**)	34.5(8)	−18.9(9)	−4.5(10)	26.1(9)	−37.1(7)
*p*BrBz-Acc^5-OH oxazolone (**6**)	−2.3(11)	25.2(12)	−39.1(12)	36.6(11)	−21.4(11)

*The C^{β} carbon atom in the Acc^5 residue that occupies the same position as C^{β} in an L-amino acid is designated as $C^{\beta L}$, and the other C^{β} atom is $C^{\beta D}$. Furthermore, the carbon atoms bonded to $C^{\beta L}$ and $C^{\beta D}$ are designated as $C^{\gamma L}$ and $C^{\gamma D}$, respectively.

tion (66) is corroborated by the following additional observations: (*i*) The secondary amide torsion angle, C(1)—C(2)—N(1)—C(3) is −178.1(3)°, the usual *trans* conformation (67). (*ii*) The intramolecular Cl···N(1) and Cl···HN(1) distances are 3.001(3) and 2.531(20) Å (22, 68–70).

Bond lengths and bond angles of the *p*BrBz moiety of compounds **5** (Fig. 5) and **6** (Fig. 6) agree well with those found in other *p*BrBz derivatives (8, 22, 71). The dihedral angle between normals to the average planes of the phenyl and amide groups in **5** is 36.3°, while the δ angle (65) is 77.8°. The phenyl and 5(4*H*)-oxazolone groups of **6** are nearly coplanar (the angle between normals to the average planes of these two groups being 8.2°), whereas the phenyl and cyclopentyl groups are nearly perpendicular to each other (the pertinent dihedral angle has a value of 78.8°). The secondary amide bond of **5** is *trans* (−175.4(6)°) (67), as found in *p*BrBz-Aib-OH (71).

C-terminal groups

In compounds **1**, **2**, **4**, and **5** the —COOH group adopts a conformation with respect to the C—N bond intermediate between the *anticlinal* and *antiperiplanar* conformations (72), the N—C^{α}—C′—O (carbonyl oxygen) torsion angles being −153.7(11), 156.3(9), 160.6(3), and 149.6(7)°, respectively. Conversely, this angle is −20.4(11) (intermediate between the *synperiplanar* and *synclinal* conformations) in **3**.

The N(1)—C(7) bond length, 1.271(12) Å, of the heterocyclic moiety of the 5(4*H*)-oxazolone from *p*BrBz-Acc^6-OH (**6**) is appropriate for a C—N double bond. This finding confirms the results obtained in the analysis of the amino acid and peptide 5(4*H*)-oxazolones the structures of which have been solved so far (22, 71, 73, 74), namely that this bond is not conjugated with the lactone moiety C(7), O(2), C(8), O(1), C(9). The O(2)—C(7) and O(2)—C(8) bond lengths are 1.384(11) and 1.392(11) Å, respectively, characteristic for an O—C(sp^2) bond (75). The exocyclic bond angles about the carbonyl C(8)—O(1) of the lactone moiety differ by 7.6°, with a larger value for the O(1)—C(8)—C(9) bond angle, 130.4(10)°. This latter value is probably the result of intramolecular interactions between O(1) and the two C(sp^3) substituents on the C(9). Again, this finding is in agreement with published data on other 5(4*H*)-oxazolones (22, 71, 73, 74). An additional result, common to all 5(4*H*)-oxazolones, is the widening of the N(1)—C(7)—C(4) exocyclic bond angle to >127°. The 5(4*H*)-oxazolone ring is nearly planar. The displacement of the atoms in the five-membered ring from its mean plane varies from −0.0074 to 0.069 Å (σ(m) = 0.0054 Å). The C(10) and C(13) atoms are displaced by nearly equal amounts on the opposite sides of the average plane of the 5(4*H*)-oxazolone ring (1.262 and −1.234 Å, respectively) (22, 71, 73, 74).

Crystal packing

The molecules of Z-Acc^5-OH (**1**) are held together across a crystallographic centre of symmetry by the formation of two intermolecular H-bonds of the N—H···O—C (acid) type, giving rise to a ten-membered cyclic dimer. The N(1)···O(3) $(1-x, 1-y, 1-z)$ distance is 3.085(12) Å, falling close to the most probable range for a length of a (peptide) N—H···O=C (peptide) H-bond, 2.9–3.0 Å (76, 77). There is an additional short distance involving heteroatoms in the crystals of **1**, namely O(2)···O(3) $(1-x, 1-y, -z)$ 2.644(10) Å (78, 79); however, the O(3)—*H*···O(2) separation is 2.726(20) Å. These findings are not in keeping with the principle that the maximum number of proton donors and acceptors will participate in the H-bonding scheme, recently put forward in a study of carboxylic acids and amides (80).

Can. J. Chem. Downloaded from www.nrcresearchpress.com by 196.1.178.254 on 09/07/12
For personal use only.

The packing mode of the molecules of Z-Acc^5-OH acetone hemi-solvate (**2**) is, however, completely different. We find an eight-membered cyclic dimer formed by two intermolecular H-bonds of the O—H···O=C (acid) type, the most commonly observed interlinking motif in carboxylic acids (81). The O(3)···O(4) ($-x$, $-y$, $1 - z$) separation is 2.652(10) Å (78, 79). In the crystal packing of this compound additional intermolecular H-bonds of the N—H···O=C (urethane) type are seen, ultimately producing chains of dimers along the z direction. The N(1)···O(2) (x, $-y$, $1/2 + z$) distance is 2.868(9) Å (76, 77). No interactions are seen between the acetone and the N-protected amino acid molecules.

The molecules of Fmoc-Acc^5-OH (**3**) are held together across a crystallographic centre of symmetry via two intermolecular H-bonds of the N—H···O=C (acid) type, forming a ten-membered cyclic dimer. The N(1)···O(3) ($1 - x$, $-y$, $2 - z$) separation is 3.035(8) Å (79, 80). Chains of dimers are produced along the y direction by the formation of O—H···O=C (urethane) intermolecular H-bonds. The O(2)···O(4) ($1 - x$, $1/2 + y$, $3/2 - z$) distance is 2.589(7) Å (78, 79).

In the crystals of mClAc-Acc^5-OH (**4**) rows of molecules are held together along the y direction through O—H···O=C (amide) intermolecular H-bonds. The O(2)···O(3) ($-x$, $1/2 + y$, $1/2 - z$) distance is 2.618(4) Å (78, 79). Chains of molecules are also observed along the z direction via N—H···O=C (acid) intermolecular H-bonds. The N(1)···O(1) ($1/2 - x$, $1 - y$, $-1/2 + z$) separation is 3.055(3) Å (76, 77). This is the most common packing motif of *N*-acyl amino acids (82). However, it is worth remembering that the N—H group is also participating in the intramolecular H-bond with the Cl atom (see above).

The packing mode of the *p*BrBz-Acc^5-OH (**5**) molecules involves cyclic dimer formation via two intermolecular H-bonds of the N—H···O=C (acid) type. The N(1)···O(1) ($-x$, $1 - y$, $-z$) distance is 3.118(7) Å (76, 77). Chain of dimers are eventually produced along the y-direction through O—H···O=C (amide) intermolecular H-bonds. The O(1)···O(3) ($-x$, $1/2 + y$, $-1/2 - z$) distance is 2.632(7) Å (78, 79).

Obviously, there are no intermolecular H-bonds connecting the molecules of the 5(4*H*)-oxazolone from *p*BrBz-Acc^5-OH (**6**) in the crystals, owing to the absence of potential H-bonding donors in this compound.

1. G. Valle, M. Crisma, and C. Toniolo. Acta Crystallogr. Sect. C. C**44**, 850 (1988).
2. A. F. Spatola. *In* Chemistry and biochemistry of amino acids, peptides and proteins. Vol. VII. *Edited by* B. Weinstein. Dekker, New York. 1983. pp. 267–357.
3. G. R. Marshall, H. E. Bosshard, N. C. E. Kendrick, J. Turk, T. M. Balasubramanian, S. M. H. Cobb, M. Moore, L. Leduc, and P. Needleman. *In* Peptides 1976. *Edited by* A. Loffet. Edit. de l'Univ. de Bruxelles, Bruxelles. 1976. pp. 361–368.
4. B. V. V. Prasad and P. Balaram. C.R.C. Crit. Rev. Biochem. **16**, 307 (1984).
5. E. Benedetti, B. di Blasio, V. Pavone, C. Pedone, A. Bavoso, C. Toniolo, G. M. Bonora, M. T. Leplawy, and P. M. Hardy. J. Biosci. **8**, 253 (1985).
6. E. Benedetti, A. Bavoso, B. di Blasio, V. Pavone, C. Pedone, M. Crisma, G. M. Bonora, and C. Toniolo. J. Am. Chem. Soc. **104**, 2437 (1982).
7. C. Toniolo, G. M. Bonora, A. Bavoso, E. Benedetti, B. di Blasio, V. Pavone, and C. Pedone. Biopolymers, **22**, 205 (1983).
8. C. Toniolo, G. M. Bonora, A. Bavoso, E. Benedetti, B. di Blasio, V. Pavone, and C. Pedone. Macromolecules, **19**, 472 (1986).
9. C. Toniolo, E. Benedetti, and C. Pedone. Gazz. Chim. Ital. **116**, 355 (1986).
10. C. Toniolo. British Polym. J. **18**, 221 (1986).
11. M. Kokkinidis, D. Tsernoglou, and H. Brückner. Biochem. Biophys. Res. Commun. **136**, 870 (1986).
12. R. Bosch, G. Jung, H. Schmitt, and W. Winter. Biopolymers, **24**, 961 (1985).
13. G. D. Smith, V. Z. Pletnev, W. L. Duax, T. M. Balasubramanian, H. E. Bosshard, E. W. Czerwinski, N. E. Kendrick, F. S. Mathews, and G. R. Marshall. J. Am. Chem. Soc. **103**, 1493 (1981).
14. N. Shamala, R. Nagaraj, and P. Balaram. J. Chem. Soc. Chem. Commun. 996 (1978).
15. R. Nagaraj and P. Balaram. Acc. Chem. Res. **14**, 356 (1981).
16. I. L. Karle, M. Sukumar, and P. Balaram. Proc. Natl. Acad. Sci. USA, **83**, 9284 (1986).
17. E. Benedetti, V. Barone, A. Bavoso, B. di Blasio, F. Lelj, V. Pavone, C. Pedone, G. M. Bonora, C. Toniolo, M. T. Leplawy, K. Kaczmarek, and A. Redlinski. Biopolymers. **27**, 357 (1988).
18. E. Benedetti, C. Toniolo, P. Hardy, V. Barone, A. Bavoso, B. di Blasio, P. Grimaldi, F. Lelj, V. Pavone, C. Pedone, G. M. Bonora, and I. Lingham. J. Am. Chem. Soc. **106**, 8146 (1984).
19. R. Bardi, A. M. Piazzesi, C. Toniolo, M. Sukumar, P. A. Raj, and P. Balaram. Int. J. Pept. Protein Res. **25**, 628 (1985).
20. P. K. C. Paul, M. Sukumar, R. Bardi, A. M. Piazzesi, G. Valle, C. Toniolo, and P. Balaram. J. Am. Chem. Soc. **108**, 6363 (1986).
21. V. Pavone, E. Benedetti, V. Barone, B. di Blasio, F. Lelj, C. Pedone, A. Santini, M. Crisma, G. M. Bonora, and C. Toniolo. Macromolecules. **21**, 2064 (1988).
22. G. Valle, M. Crisma, C. Toniolo, N. Sen, M. Sukumar, and P. Balaram. J. Chem. Soc. Perkin Trans. 2. 393 (1988).
23. R. Bardi, A. M. Piazzesi, C. Toniolo, M. Sukumar, and P. Balaram. Biopolymers, **25**, 1635 (1986).
24. IUPAC-IUB Commission on Biochemical Nomenclature. Biochemistry, **9**, 3471 (1970).
25. M. Mallikarjunan, K. K. Chacko, and R. Zand. J. Cryst. Mol. Struct. **2**, 53 (1972).
26. R. Chandrasekharan, M. Mallikarjunan, G. Chandrasekharan, and R. Zand. Curr. Sci. **37**, 91 (1968).
27. J. Symersky, K. Blaha, and V. Langer. Acta Crystallogr. Sect. C. **43**, 303 (1987).
28. R. J. Freer, A. R. Day, J. A. Radding, E. Schiffmann, S. Aswanikumar, H. J. Showell, and E. L. Becker. Biochemistry, **19**, 2404 (1980).
29. E. Schiffmann, S. Aswanikumar, K. Venkatasubramanian, B. A. Corcoran, C. B. Pert, J. Brown, E. Gross, A. R. Day, R. J. Freer, A. H. Showell, and E. L. Becker. FEBS Lett. **117**, 1 (1980).
30. M. Sukumar, P. A. Raj, P. Balaram, and E. L. Becker. Biochem. Biophys. Res. Commun. **128**, 339 (1985).
31. M. Iqbal, P. Balaram, H. J. Showell, R. J. Freer, and E. L. Becker. FEBS Lett. **165**, 171 (1984).
32. J. W. Tsang, B. Schmied, R. Nyfeler, and M. Goodman. J. Med. Chem. **27**, 1663 (1984).
33. M. Rodriguez, J. M. Bland, J. W. Tsang, and M. Goodman. J. Med. Chem. **28**, 1527 (1985).
34. M. Goodman. Biopolymers, **24**, 137 (1985).
35. W. K. Park, C. Choi, F. Rioux, and D. Regoli. Can. J. Biochem. **52**, 113 (1974).
36. R. Kishore and P. Balaram. Indian J. Chem. **23B**, 1137 (1984).
37. R. Kishore and P. Balaram. *In* The medicinal chemistry and molecular pharmacology of opioid peptides and the opiates. *Edited by* R. S. Rapaka, G. Barret, and R. L. Hawks. National Institute of Drug Abuse, U.S.A. Research Monograph 69. 1986. pp. 312–331.

38. E. KASAFIREK, J. VANZURA, I. KREJCI, J. KREPELKA, A. DLABAC, and M. VALCHAR. Patent Belg. BE 897, 843 (1984); Chem. Abstr. **100**, 192289*d* (1984).
39. W. H. ROARK, F. J. TINNEY, D. COHEN, A. D. ESSENBURG, and H. R. KAPLAN. J. Med. Chem. **28**, 1291 (1985).
40. S. CHLADEK and P. BHUTA. Biochim. Biophys. Acta, **696**, 212 (1982).
41. J. DANNER, M. H. COBB, W. HEAGY, H. M. LENHOFF, and G. R. MARSHALL. Biochem. J. **175**, 547 (1978).
42. S. D. MAGNAN, F. N. SHIROTA, and H. T. NAGASAWA. J. Med. Chem. **25**, 1018 (1982).
43. N. H. GRANT and H. E. ALBURN. J. Am. Chem. Soc. **86**, 3870 (1964).
44. D. VEBER, W. C. RANDALL, R. F. NUTT, R. M. FREIDINGER, S. F. BRADY, D. S. PERLOW, P. CURLEY, W. J. PALEVEDA, R. G. STRACHAN, F. W. HOLLY, and R. SAPERSTEIN. *In* Peptides 1982. *Edited by* K. Blaha and P. Malon. de Gruyter, Berlin. 1983. pp. 789–792.
45. V. J. HRUBY, T. W. ROCKWAY, V. VISWANATHA, and W. Y. CHAN. Int. J. Pept. Protein Res. **21**, 24 (1983).
46. V. J. HRUBY, H. J. MOSBERG, T. K. SAWYER, J. J. KNITTEL, T. W. ROCKWAY, J. ORMBERG, P. DARMAN, W. Y. CHAN, and M. E. HADLEY. Biopolymers, **22**, 517 (1983).
47. M. L. MOORE, W. F. HUFFMAN, W. M. BRYAN, J. SILVESTRI, H. L. CHANG, G. R. MARSHALL, F. STASSEN, J. STEFANKIEWICZ, L. SULAT, D. SCHMIDT, L. KINTER, J. MCDONALD, and D. ASHTON-SUE. *In* Peptides: structure and function. *Edited by* C. M. Deber, V. J. Hruby, and K. D. Kopple. Pierce Chem. Co., Rockford, IL. 1985. pp. 607–610.
48. P. TAILLEUR and L. BERLINGUET. Can. J. Chem. **39**, 1309 (1961).
49. A. PAQUET. Can. J. Chem. **60**, 976 (1982).
50. M. PAIN, S. J. FISKE, S. E. HULL, L. LESSINGER, G. GERMAIN, J. P. DECLERCQ, and M. M. WOOLFSON. MULTAN 80. A system of computer programs for the automatic solution of crystal structures from X-ray diffraction data. Univ. of York, England and Univ. of Louvain, Belgium. 1980.
51. G. M. SHELDRICK. SHELX 76. Program for crystal structure solution and refinement. Cambridge University, England. 1976.
52. G. VALLE, G. M. BONORA, and C. TONIOLO. Can. J. Chem. **62**, 2661 (1984).
53. E. BENEDETTI. *In* Chemistry and biochemistry of amino acids, peptides and proteins. Vol. VI. *Edited by* B. Weinstein. Dekker, New York. 1982. pp. 105–184.
54. T. ASHIDA, Y. TSUNOGAE, I. TANAKA, and T. YAMANE. Acta Crystallogr. Sect. B, **43**, 212 (1987).
55. G. VALLE, M. CRISMA, F. FORMAGGIO, C. TONIOLO, and G. JUNG. Liebigs Ann. Chem. 1055 (1987).
56. Y. PATERSON, S. M. RUMSEY, E. BENEDETTI, G. NEMETHY, and H. A. SCHERAGA. J. Am. Chem. Soc. **103**, 2947 (1981).
57. R. BOSCH, K.-P. VOGES, G. JUNG, and W. WINTER. Acta Crystallogr. Sect. C, **39**, 481 (1983).
58. J. B. HENDRICKSON. J. Am. Chem. Soc. **83**, 4537 (1961).
59. D. CREMER and J. A. POPLE. J. Am. Chem. Soc. **97**, 1354 (1975).
60. J. E. KILPATRICK, K. S. PITZER, and R. SPITZER. J. Am. Chem. Soc. **69**, 2483 (1947).
61. E. BENEDETTI, C. PEDONE, C. TONIOLO, M. DUDEK, S. NEMETHY, and H. A. SCHERAGA. Int. J. Pept. Protein Res. **21**, 163 (1983).
62. E. BENEDETTI, C. PEDONE, C. TONIOLO, G. NEMETHY, M. S. POTTLE, and H. A. SCHERAGA. Int. J. Pept. Protein Res. **16**, 156 (1980).
63. E. BENEDETTI, A. CIAJOLO, B. DI BLASIO, V. PAVONE, C. PEDONE, C. TONIOLO, and G. M. BONORA. Int. J. Pept. Protein Res. **14**, 130 (1979).
64. L. E. SUTTON (*Editor*). *In* Tables of interatomic distances and configuration in molecules and ions, Supplement. The Chemical Society, London. U.K. 1965.
65. C. S. CHEN and R. PARTHASARATHY. Int. J. Pept. Protein Res. **11**, 9 (1978).
66. C. TONIOLO. C.R.C. Crit. Rev. Biochem. **9**, 1 (1980).
67. P. CHAKRABARTI and J. D. DUNITZ. Helv. Chim. Acta, **65**, 1555 (1982).
68. R. BOSCH, H. BRÜCKNER, G. JUNG, and W. WINTER. Tetrahedron, **24**, 3579 (1982).
69. G. VALLE, G. M. BONORA, C. TONIOLO, P. M. HARDY, M. T. LEPLAWY, and A. REDLINSKI. J. Chem. Soc. Perkin Trans. 2, 885 (1986).
70. J. E. BALDWIN, R. M. ADLINGTON, B. J. RAWLINGS, and R. H. JONES. Tetrahedron Lett. 485 (1985).
71. G. VALLE, M. CRISMA, and C. TONIOLO. Z. Kristallogr. **175**, 73 (1986).
72. J. D. DUNITZ and P. STRICKLER. *In* Structural chemistry and molecular biology. *Edited by* A. Rich and N. Davidson. Freeman, San Francisco. 1968. pp. 595–602.
73. C. M. K. NAIR and M. VIJAYAN. Acta Crystallogr. Sect. B, **36**, 1498 (1980).
74. C. TONIOLO, G. M. BONORA, M. CRISMA, E. BENEDETTI, A. BAVOSO, B. DI BLASIO, V. PAVONE, and C. PEDONE. Int. J. Pept. Protein Res. **22**, 603 (1983).
75. L. NORSKOV-LAURITSEN, H. B. BÜRGI, P. HOFMANN, and H. R. SCHMIDT. Helv. Chim. Acta, **68**, 76 (1985).
76. C. RAMAKRISHNAN and N. PRASAD. Int. J. Protein Res. **3**, 209 (1971).
77. R. TAYLOR, O. KENNARD, and W. VERSICHEL. Acta Crystallogr. Sect. B, **40**, 280 (1984).
78. I. D. BROWN. Acta Crystallogr. Sect. A, **32**, 24 (1976).
79. J. MITRA and C. RAMAKRISHNAN. Int. J. Pept. Protein Res. **9**, 27 (1977).
80. M. ETTER. J. Am. Chem. Soc. **104**, 1095 (1982).
81. L. LEISEROWITZ. Acta Crystallogr. Sect. B, **32**, 775 (1976).
82. Z. BERKOVITCH-YELLIN, S. ARIEL, and L. LEISEROWITZ. J. Am. Chem. Soc. **105**, 765 (1983).

Can. J. Chem. Downloaded from www.nrcresearchpress.com by 196.1.178.254 on 09/07/12
For personal use only.

^{99}Tc-thiocyanate complexes: their extractions as ionic associations with Adogen 464

J. G. MARCH AND F. GRASES
Chemistry Department, Balearic Islands University, 07071-Palma de Malorca, Spain

Received June 23, 1987[1]

J. G. MARCH and F. GRASES. Can. J. Chem. **66**, 2583 (1988).

The extraction of the ionic species formed between two reduced Tc–SCN anionic complexes and trioctylmethyl ammonium cation has been studied spectrophotometrically in both oxygenated and deoxygenated media. The distribution ratio for each reduced complex has been determined as a function of tin(II) and Adogen 464 concentrations. The results indicate that, depending on the concentration of the Sn(II) reducing agent, a red Tc(IV) or a yellow Tc(III) complex can be formed.

J. G. MARCH et F. GRASES. Can. J. Chem. **66**, 2583 (1988).

Opérant tant dans des milieux tant oxygéné que désoxygéné et faisant appel à la spectrophotométrie, on a étudié l'extraction des espèces ioniques qui se forment entre deux complexes anioniques Tc–SCN réduits et le cation trioctylméthyl ammonium. On a déterminé le rapport de distribution de chacun des complexes réduits en fonction des concentrations de l'étain(II) et de l'Adogène 464. Les résultats indiquent que, suivant la concentration de l'étain(II) comme agent réducteur, il peut se former soit un complexe Tc(IV) rouge ou un complexe Tc(III) jaune.

[Traduit par la revue]

Introduction

The complex formation between reduced technetium and thiocyanate ion in aqueous media has been reported previously (1). The exact nature of that system has been examined by several workers (2–4). Depending on reaction conditions, either a red or yellow species are formed. Initially, the 500 nm band (red) was assigned to a Tc(V) complex, and the 400 nm band (yellow) to a Tc(IV) complex.

Subsequently, a thorough investigation (5) led to the proposal that the above two complexes formed a redox couple (eq. [1]).

[1] $[Tc(NCS)_6]^{2-} \leftrightharpoons [Tc(NCS)_6]^{-} + e^{-}$
yellow red

That study included the isolation of the two species. A red one, formulated as a Tc(V) compound $(Me_4N)[Tc(NCS)_6]$, and a yellow one, formulated as a Tc(IV) compound $(Me_4N)_2[Tc(NCS)_6]$.

More recently, the same system has been reinvestigated (6). Voltammetric studies in acetonitrile indicated that the two species were linked via electron transfer between $[Tc(NCS)_6]^{3-}$ (yellow technetium(III) complex) and $[Tc(NCS)_6]^{2-}$ (red technetium(IV) complex) (eq. [2]).

[2] $[Tc(NCS)_6]^{3-} \leftrightharpoons [Tc(NCS)_6]^{2-} + e^{-}$
yellow red

These conclusions agreed with the authors' potentiometric results which were obtained in aqueous media (9).

It should be noted that in most of the cases studied to date, the resulting technetium(V) complexes have either one or two oxo-groups remaining bonded to the metal (7). In fact, the oxo-technetium(V) thiocyanate complex, formulated as $[TcO(NCS)_5]^{2-}$, was prepared by ligand substitution on $[TcOCl_4]^{-}$ and characterized as tetraphenylarsonium salt (8).

Both thiocyanate species, the red and the yellow, were easily extractable from acid media in polar organic solvents (ether, butyl acetate, octanol). The extraction was assumed to take place through the formation of an ionic association between the complex (anion) and protonated molecules of the organic solvent (cation). The anion complex did not extract into non-polar organic solvents (e.g. chloroform, toluene, benzene).

According to the literature (5, 6, 9, 10), the molar ratio of Tc to NCS for both red and yellow species was 1:6. Therefore, the charge on the resulting thiocyanate complexes would appear to be directly related to the oxidation state of technetium in accordance with eq. [3].

[3] Tc oxidation state = 6 − negative charge on complex

The purpose of this work is to study the extraction of the Tc–NCS complexes into a non-polar organic solvent (toluene), using a liquid resin for anionic exchange (Adogen 464), through the formation of a ternary complex. Thus, the technetium oxidation state in the reduced complex can be determined by measuring the $Tc(NCS)_6$:resin molar ratio which corresponds to the charge on the complexes. In addition, this work proposes a new procedure for the extraction of technetium, which can be helpful in technetium purification processes.

Experimental

Chemicals and apparatus

^{99}Tc in solution form as ammonium pertechnetate (34.0 mg Tc/mL, 4.46 MBq/mL), was purchased from Amersham Searle Co., Arlington Heights, IL. A 10^{-3} *M* $^{99}TcO_4^-$ solution was prepared by dilution of the stock standard with water. A 0.1 *M* Sn(II) solution was prepared from reagent grade $SnCl_2 \cdot 2H_2O$ (Merck) in 6 *M* HCl; this solution was prepared daily and standardized by titration with KIO_3 (12). Stock solutions of reagent grade 4.2×10^{-3} *M* KSCN (Panreac) and 1.1×10^{-3} *M* trioctylmethyl ammonium chloride, commercially known as Adogen 464 (Serva), were prepared in water and in toluene, respectively. The Adogen 464 solution was deoxygenated before use.

A Perkin-Elmer 552 spectrophotometer equipped with 1-cm cell was used for taking absorbance measurements.

A Crison 517 potentiometer provided with a platinum indicator electrode and a calomel reference electrode was used for potential measurements.

The β-activity was determined by liquid scintillation counting (Beckman LS 1800) using a PPO/POPOP solution in xylene as fluor solution and a surfactant solution supplied by Aldabó & Juliá, Barcelona (Spain).

Method

A typical extraction procedure was as follows. In a separatory funnel, 1 mL of 10^{-3} *M* Tc(VII) solution, 5 mL of 4.2×10^{-2} *M* SCN^- solution, 4 mL of 6 *M* HCl solution, and enough water to ensure a final volume of 15 mL were placed. The mixture was deaerated by bubbling N_2 for 15 min. Then 15 μL of 0.1 *M* Sn(II) and 10 mL of $1:1 \times 10^{-3}$ *M* Adogen toluene solution were added. The system was shaken 45 min in a nitrogen atmosphere with a mechanical shaker. After phase separation, spectrophotometric measurements of the organic layer or

[1]Revision received May 27, 1988.

Printed in Canada / Imprimé au Canada

Can. J. Chem. Downloaded from www.nrcresearchpress.com by 196.1.178.254 on 09/07/12
For personal use only.

potentiometric measurements of the aqueous phase were carried out. The extractions were carried out at room temperature.

To obtain distribution ratio values the organic layer was oxygenated for 3 h, then absorbance measurements at 506 nm were made (as described below this transforms reduced Tc species to the red Tc(IV) thiocyanate complex). The technetium concentration in the organic phase was evaluated from the absorbance value by using a calibration graph obtained with an amount of Sn(II) that guaranteed reduction to the +4 oxidation state. The technetium concentration in the aqueous phase was obtained from the difference between the total concentration and the organic phase concentration.

Results and discussion

A systematic study showed that, in the presence of a large excess of ligand (Tc:SCN molar ratio 40 or higher), within the range 2.0 to 0.3 *M* hydrochloric acid concentration, and working in anaerobic conditions, the colour of the organic phase was either red or yellow, depending on the amount of reducing agent added. Thus, the solution was red if the amount of tin(II) added was less than or equal to the theoretical stoichiometric amount necessary to reduce Tc(VII) to Tc(IV). The solution was yellow when the amount of Sn(II) added was greater than or equal to the theoretical stoichiometric amount necessary to reduce Tc(VII) to Tc(III). Both Tc complexes were quantitatively extracted into toluene that contained an adequate excess of Adogen 464 (Tc:Adogen molar ratio 15 or higher for both red and yellow species). The quantitativeness of the extractions (99.99%) was determined by measuring the ^{99}Tc radioactivity remaining in the aqueous phase after extraction. On the other hand, it was shown that following the procedure described in the Experimental section, Tc(VII) was not reduced by the thiocyanate ligand at the above mentioned hydrochloric acid concentrations because, in the absence of tin(II), there was no visible reaction; moreover, the solution showed typical reactions corresponding to Tc(VII) (13–16). It was interesting to note that if the reaction was carried out in the absence of oxygen, no significant changes in the spectra took place during the extraction.

From these observations, the extraction equilibria can be represented by eq. [4]

$$[4]\quad Tc(NCS)_6^{n-} + nR_4N^+_{org} \rightleftharpoons [Tc(NCS)_6(R_4N)_n]_{org}$$

(R_4N^+ = Adogen 464). This is supported by the fact that only slight changes in the spectra of the aqueous species were observed, from which it is assumed that extraction is due to ion-pair formation. Consequently,

$$[5]\quad K = \frac{[Tc(NCS)_6(R_4N)_n]_{org}}{[Tc(NCS)_6^{n-}][R_4N^+]_{org}^n}$$

The distribution ratio is defined as follows

$$[6]\quad D = \frac{[Tc]_{org}}{[Tc]_{aq}} = \frac{[Tc(NCS)_6(R_4N)_n]_{org}}{[Tc(NCS)_6^{n-}]}$$

Combining [5] and [6], and taking the logarithm of both sides, yields

$$[7]\quad \log D = \log K + n \log [R_4N^+]_{org}$$

Therefore, the slope of a plot of log D versus log $[R_4N^+]_{org}$ gives the charge on the technetium thiocyanate complex.

The absorption spectrum of the extracted ion-pair when tin(II) was present in a molar excess of 1.5, as can be seen in Fig. 1(*a*), shows only one maximum at 506 nm (red). Figure 2(*a*) shows the variation of the absorbance at that wavelength as a function of the tin(II) concentration. The curve shows a pronounced maximum for a Sn(II):Tc(VII) molar ratio equal to 1.5, which corresponds to a Tc(IV) final oxidation state, assuming Sn(II) to Sn(IV) oxidation to be quantitative and technetium to be reduced to only one final oxidation state. The stoichiometry found for the extracted red ternary complex, as can be seen in Fig. 3(*a*), is 1:2 technetium-complex:resin. The value of the slope found by plotting log D against log $[R_4N^+]$

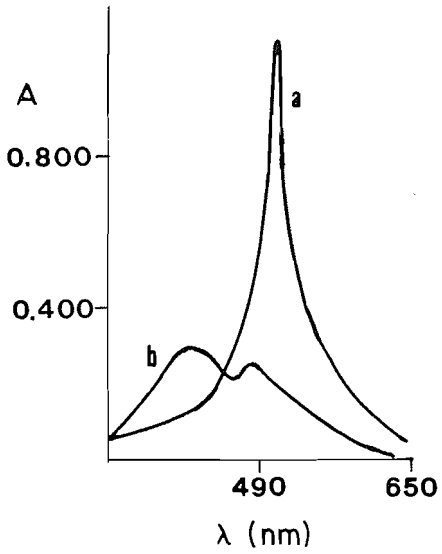

FIG. 1. Absorption spectra of Tc–NCS–Adogen ternary complex extracted in toluene corresponding to two different Sn(II):Tc(VII) molar ratios. [Tc(VII)] = 6.6×10^{-5} *M*, [SCN$^-$] = 1.4×10^{-2} *M*, [HCl] = 1.6 *M*, [Adogen]$_{org}$ = 1.1×10^{-3} *M*, V_{aq} = 15 mL, V_{org} = 10 mL, shaking time = 45 min. (*a*) [Sn(II)] = 1.0×10^{-4} *M*. (*b*) [Sn(II)] = 1.3×10^{-4} *M*.

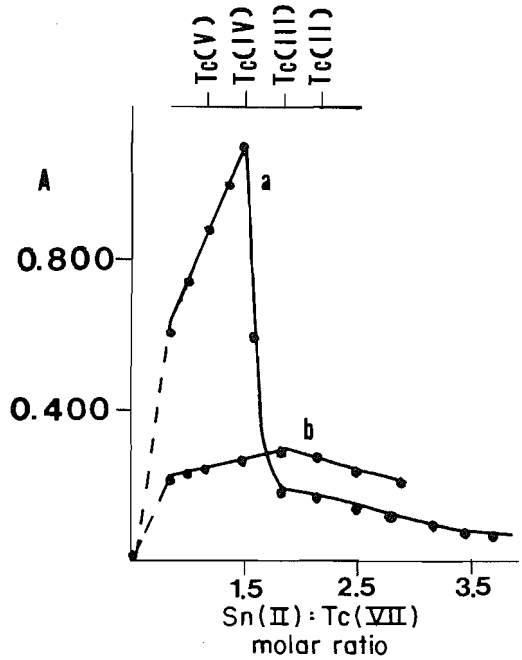

FIG. 2. Absorbance of the toluene phase at (*a*) λ = 506 nm, (*b*) λ = 414 nm, as a function of Sn(II):Tc(VII) molar ratio for [Tc(VII)] = 6.6×10^{-5} *M*, [SCN$^-$] = 1.4×10^{-2} *M*, [HCl] = 1.6 *M*, [Adogen]$_{org}$ = 1.1×10^{-3} *M*, V_{aq} = 15 mL, V_{org} = 10 mL, shaking time = 45 min. The figure includes an auxiliary axis denoting the final Tc oxidation state assuming complete oxidation of Sn(II) to Sn(IV).

Can. J. Chem. Downloaded from www.nrcresearchpress.com by 196.1.178.254 on 09/07/12
For personal use only.

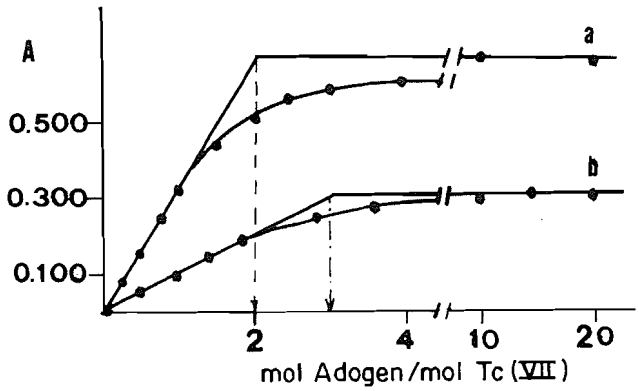

FIG. 3. Extraction of the two [Tc-SCN^-]–[Adogen] species as a function of Adogen/technetium molar ratio for two Sn(II):Tc(VII) molar ratios. [SCN^-] = 1.4×10^{-2} *M*, [HCl] = 1.6 *M*, V_{aq} = 15 mL, V_{org} = 10 mL, shaking time = 45 min. (*a*) [Sn(II)] = 6.0×10^{-5} *M*, [Tc(VII)] = 4.0×10^{-5} *M*, λ = 506 nm. (*b*) [Sn(II)] = 1.3×10^{-4} *M*, [Tc(VII)] = 6.6×10^{-5} *M*, λ = 414 nm.

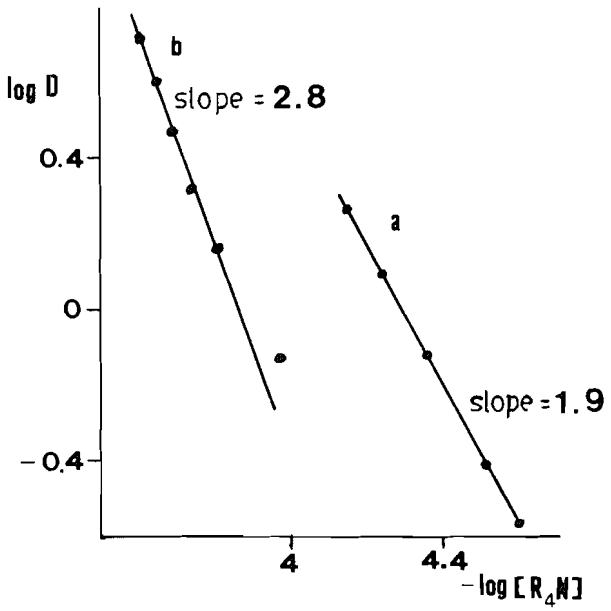

FIG. 4. Extraction ratio as a function of Adogen 464 (R_4N) concentration corresponding to two Sn(II):Tc(VII) molar ratios. Conditions: [SCN^-] = 1.4×10^{-2} *M*, [HCl] = 1.6 *M*, V_{aq} = 15 mL, V_{org} = 10 mL, shaking time = 45 min. (*a*) [Sn(II)] = 8.0×10^{-5} *M*, [Tc(VII)] = 5.3×10^{-5} *M*. (*b*) [Sn(II)] = 1.3×10^{-4} *M*, [Tc(VII)] = 6.6×10^{-5} *M*.

(see Fig. 4(*a*)), for that amount of reducing agent, was 1.9. These results indicate clearly that the oxidation state of technetium in the red ion-pair corresponds to Tc(IV).

The absorption spectrum obtained when tin(II) was present in a molar excess of 2, as can be seen in Fig. 1(*b*), shows maxima at 482 and 414 nm (yellow). A plot of A_{414} vs. Sn(II):Tc(VII) molar ratio (Fig. 2(*b*)) shows a maximum for a Sn(II):Tc(VII) molar ratio equal to 2. The stoichiometry found for the yellow ionic association was 1:3 technetium-complex:Adogen (Fig. 3(*b*)). The value of the slope of the curve log *D* vs. log [R_4N^+] (see Fig. 4(*b*)) was 2.8. Therefore the oxidation state of technetium in the yellow extracted ternary complex corresponds to Tc(III). As mentioned, in this case the absorption spectrum shows two maxima, suggesting two different species. In fact, an orange species was previously mentioned

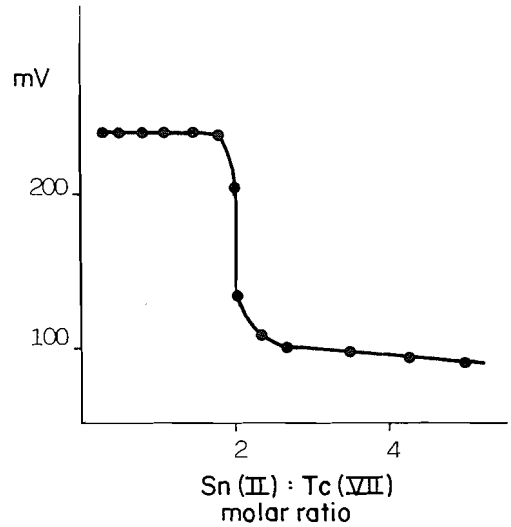

FIG. 5. Potential as a function of Sn(II):Tc(VII) molar ratio for [Tc(VII)] = 1.2×10^{-4} *M*, [SCN^-] = 2.6×10^{-2} *M*, [HCl] = 1.6 *M*, $[Adogen]_{org}$ = 2.0×10^{-3} *M*, V_{aq} = 15 mL, V_{org} = 10 mL, shaking time = 45 min.

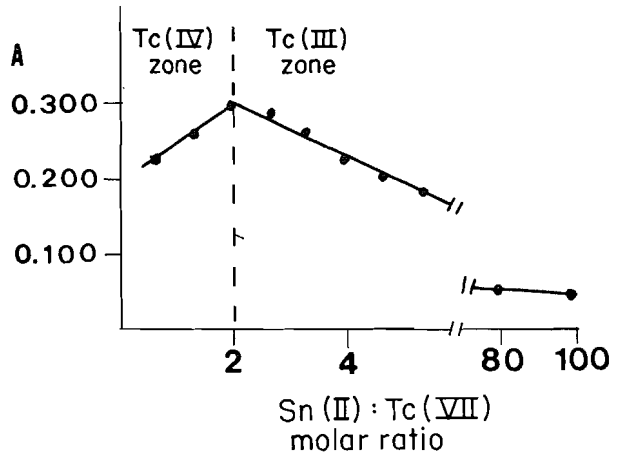

FIG. 6. Absorbance of the toluene phase at 414 nm as a function of Sn(II):Tc(VII) molar ratio. [Tc(VII)] = 6.6×10^{-5} *M*, [SCN^-] = 1.4×10^{-2} *M*, [HCl] = 1.6 *M*, $[Adogen]_{org}$ = 1.1×10^{-3} *M*, V_{aq} = 15 mL, V_{org} = 10 mL, shaking time = 45 min.

in the literature (6). A potentiometric study in aqueous media assigned to that compound a Tc(III) oxidation state (9).

In both water and toluene, exposure of the yellow complex to oxygen caused the absorption maxima at 414 and 482 nm to decrease as a function of time, and a corresponding increase in absorption at 506 nm. The red species was also obtained with the same yield under aerobic conditions, with a Sn(II):Tc(VII) molar ratio higher than 1.5. Under these conditions the yellow species is formed first but, during the extraction, the excess reducing agent is oxidized by oxygen, and the initial Tc(III) yellow complex is oxidized to the Tc(IV) red complex. This permitted establishment of a standard curve independent on Sn(II) concentration, and allowed determination of the distribution ratio spectrophotometrically.

The potentiometric data are summarized in Fig. 5, where the measured potential of the aqueous phase after extraction is plotted against the Sn(II):Tc(VII) molar ratio. As can be seen, the amount of tin(II) remaining in the aqueous phase increased abruptly when the Tc(III) oxidation state was reached. No

Can. J. Chem. Downloaded from www.nrcresearchpress.com by 196.1.178.254 on 09/07/12
For personal use only.

reduction of Tc(III) to lower oxidation states was detected under the conditions employed in this study.

In summary, we present here results indicating that the reduction of Tc(VII) by Sn(II) takes place stoichiometrically. A more interesting point is that, after Tc(III) was obtained with the Sn(II) stoichiometric amount, any excess (Fig. 6) produced a negative effect on the yield of the complex. The potentiometric study indicates no further Tc(III) reduction, thus indicating the possibility of Sn–thiocyanate interactions. This point should be considered in technetium-radiopharmacy research, where reductions are normally carried out in the presence of a high molar excess of reducing agent (11). We believe that a non-controlled excess of reductant (Sn(II)) can produce variability in tissue distribution of some ^{99m}Tc imaging agents in nuclear medicine (17). Thus it is necessary to keep in mind the Sn(II) concentration when optimizing chemical procedures for Tc-radiopharmaceutical preparations.

Acknowledgement

Financial support by CAICYT, grant 2060-83, is gratefully acknowledged.

1. C. E. CROUTHAMEL. Anal. Chem. **29**, 1756 (1957).
2. O. H. HOWARD and C. W. WEBER. Anal. Chem. **34**, 530 (1962).
3. F. JASIM, R. J. MAGEE, and C. J. WILSON. Talanta, **2**, 93 (1959).
4. A. K. LAVRUKINA and A. A. POZDNYAKOV. Analytical chemistry of technetium, promethium, astatine and francium. Ann Arbor-Humphrey Science Publishers, Ann Arbor, MI. 1970.
5. K. SCHWOCHAW, L. ASTHEIMER, and H. J. SCHENK. J. Inorg. Nucl. Chem. **35**, 2294 (1973).
6. H. S. TROP, A. DAVISON, A. G. JONES, M. A. DAVIS, D. J. SZALDA, and S. J. LIPPARD. Inorg. Chem. **19**, 1105 (1980).
7. A. DAVISON and A. G. JONES. Int. J. Appl. Radiat. Isot. **33**, 875 (1982).
8. A. DAVISON, A. G. JONES, L. MULLER, R. TATZ, and H. S. TROP. Inorg. Chem. **20**, 1160 (1981).
9. F. GRASES, G. FAR, and P. MARCH. Radiochim. Acta, **42**, 47 (1987).
10. V. V. MULLER. Acta Crystallogr. B**33**, 2197 (1977).
11. W. C. ECKELMAN and W. A. VOLKERT. Int. J. Appl. Radiat. Isot. **33**, 945 (1982).
12. A. I. VOGEL. A text-book of quantitative analysis. Longman, 3rd ed. London. 1961.
13. F. GRASES, J. G. MARCH, F. MATA, and A. PEÑAFIEL. Anal. Chim. Acta, **166**, 71 (1984).
14. F. GRASES, J. G. MARCH, and R. FORTEZA. J. Radioanal. Nucl. Chem. **102**, 121 (1986).
15. F. GRASES and J. G. MARCH. Analyst, **110**, 975 (1985).
16. F. GRASES, E. AMAT, and J. G. MARCH. Bull. Soc. Chim. Fr. **4**, 594 (1985).
17. I. IKEDA, O. INOUE, and K. KURATA. Int. J. Appl. Radiat. Isot. **27**, 681 (1976).

Can. J. Chem. Downloaded from www.nrcresearchpress.com by 196.1.178.254 on 09/07/12
For personal use only.

A gas phase study of the regioselective BH_4^- reduction of some 2-substituted maleic anhydrides

HANS VAN DER WEL AND NICO M. M. NIBBERING[1]
Laboratory of Organic Chemistry, University of Amsterdam, Nieuwe Achtergracht 129, 1018 WS Amsterdam, The Netherlands
AND
MARGARET M. KAYSER[1]
Division of Sciences, University of New Brunswick, P.O. Box 5050, Saint John, N.B., Canada E2L 4L5

Received August 31, 1987[2]

HANS VAN DER WEL, NICO M. M. NIBBERING, and MARGARET M. KAYSER. Can. J. Chem. **66**, 2587 (1988).

Gas phase ion/molecule reactions in a Fourier transform ion cyclotron resonance mass spectrometer have been carried out for reductions of isotopically labelled citraconic (methylmaleic), phenylmaleic, and ethoxymaleic anhydrides by BH_4^-. In citraconic anhydride the carbonyl group neighbouring the methyl substituent is reduced preferentially in agreement with the *ab initio* calculations, which show the higher LUMO coefficients at this site. Hydride ion transfer to the olefinic double bond occurs as well; however, in that case no preference for either of the carbon atoms is observed. In phenylmaleic anhydride strong indications are found for a theoretically unexpected hydride ion transfer to the phenyl ring. For ethoxymaleic anhydride experimental evidence is presented showing hydride ion transfer to the carbon atom carrying the ethoxy group, which is in agreement with the "best overlap" consideration predicting that this carbon atom bears the highest LUMO coefficient.

Most of the hydride transfers from BH_4^- to the molecules studied seem, therefore, to take place under orbital control rather than under control of long-range ion-induced dipole interactions between reactants.

HANS VAN DER WEL, NICO M. M. NIBBERING et MARGARET M. KAYSER. Can. J. Chem. **66**, 2587 (1988).

On a effectué des réactions ion/molécule en phase gazeuse dans un spectromètre de masse à résonance ionique par transformation de Fourier pour les réductions des anhydrides citraconique (méthylmaléique), phénylmaléique et éthoxymaléique par le BH_4^-. Dans le cas de l'anhydride citraconique, le groupement carbonyle adjacent du groupement méthyle subit une réduction préférentielle; ce résultat expérimental est en accord avec les calculs *ab initio* qui démontrent que le coefficient d'OM basse vacante se situe sur ce site. Il se produit aussi un transfert d'hydrure vers la double liaison oléfinique; toutefois, dans ce cas, on n'observe aucune préférence pour l'un ou l'autre des atomes de carbone. Dans le cas de l'anhydride phénylmaléique, on relève de fortes indications à l'effet qu'il se produirait un transfert d'hydrure vers le cycle aromatique; ce transfert est inattendu d'un point de vue théorique. Pour l'anhydride éthoxymaléique, on présente des données expérimentales démontrant qu'il se produit un transfert d'hydrure vers le carbone portant le groupement éthoxy; ce résultat est en accord avec les considérations de «meilleur recouvrement» qui prédisent que ce carbone porte le coefficient le plus élevé d'OM basse vacante.

Il semble donc que la plupart des transferts d'hydrure de BH_4^- vers les molécules étudiées ont lieu sous un contrôle orbitalaire plutôt que sous un contrôle d'interactions dipolaires à longue distance entre les réactifs, qui seraient induites par les ions.

[Traduit par la revue]

Introduction

Previously performed *ab initio* calculations for borohydride addition to formaldehyde to give a $CH_3OBH_3^-$ species have suggested a one-step process as the least energy demanding route (1). The calculated transition state is not a symmetrical four-center arrangement in which B—H bond-breaking and C—H and B—O bond-making occur simultaneously (structure **A**), but rather a nonsynchronous structure in which the BH_3^- group is transferred from the almost completely formed C—H bond to the oxygen atom (structure **B**). The energy of this transition state relative to the reactants was calculated to be 127 kJ/mol, thus suggesting that the noncatalyzed reaction is energetically unfavourable. The calculations carried out with a single molecule of water, hydrogen bonded to the formaldehyde oxygen atom (structure **C**), showed the activation energy to be only 38 kJ/mol. These results are in accord with the experimental findings (2, 3) and confirm the hypothesis that the simultaneous or prior association of the carbonyl oxygen with a counterion, proton, or protic solvent facilitates hydride transfer (4).

In view of the above it was predicted that in the gas phase a one-step formation of the $CH_3OBH_3^-$ species from BH_4^- and a "naked" formaldehyde, although calculated to be highly exothermic, should not occur, as the energy of the transition state of 127 kJ/mol is too high to be compensated by the stabilizing effect of the $BH_4^-...CH_2O$ complexation, calculated to be 31 kJ/mol (1). Similarly, a hydride transfer from BH_4^- to CH_2O to give free CH_3O^- and BH_3, which would be the first in a two-step formation of $CH_3OBH_3^-$, should not occur either since, according to the calculations, this highly endothermic step requires 149 kJ/mol (1). It was, therefore, not surprising that the ion cyclotron resonance study of the reaction between BH_4^- and CH_2O showed that no hydride transfer could be detected (5) even upon increasing the translational energy of BH_4^-. However, when one or more electron-withdrawing substituents are attached to the carbonyl function, the activation energy for hydride transfer should be lowered, thus facilitating the reaction.

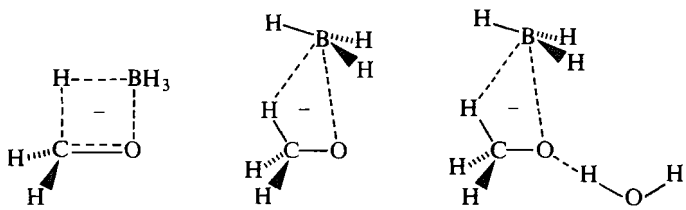

A **B** **C**

In solution chemistry the experimental evidence pointing in this direction was provided by Loupy *et al.*, who demonstrated

[1]Authors to whom correspondence may be addressed.
[2]Revision received June 10, 1988.

Printed in Canada / Imprimé au Canada

Can. J. Chem. Downloaded from www.nrcresearchpress.com by 196.1.178.254 on 09/07/12
For personal use only.

Can. J. Chem. Downloaded from www.nrcresearchpress.com by 196.1.178.254 on 09/07/12
For personal use only.

that a cation and (or) a protic solvent was not "essential" for the reduction of aromatic or conjugated ketones (6). The same trend appears to be true also in the gas phase. Although a recently reported list (7) of hydride affinities[3] shows that carbonyl compounds substituted with electron-withdrawing groups such as C_6H_5CHO, CF_3COCH_3, or CF_3CHO have a considerably lower hydride affinity than BH_3 (affinities ranging from 122 to 66 kJ/mol (7), we have found that hydride transfer from BH_4^- to hexafluoroacetone (reaction [1]) or to F_2CO (reaction [2]) *does occur*, with the relative abundance of the corresponding product ions approximately 90% and 5%, respectively.

[1] $BH_4^- + (CF_3)_2CO \rightarrow (CF_3)_2CHO^- + BH_3$
m/z 15 m/z 167

[2] $BH_4^- + CF_2O \rightarrow CF_2HO^- + BH_3$
m/z 15 m/z 67

Interestingly, preliminary experiments carried out on maleic and phthalic anhydrides showed that the gas phase hydride transfer from BH_4^- to these substrates did occur as well. This prompted us to examine further these reductions, particularly the question of regioselectivity of the hydride transfer. In solution, reductions of cyclic anhydrides by $NaBH_4$ yield lactones. These reductions are frequently highly selective, leading to preferential formation of one of the isomeric lactones in the case of unsymmetrical substituted anhydrides. Several factors influence the regioselectivity of these reactions (8). One of the effects appears to be the difference in the "intrinsic reactivity" (9) of the two carbonyl functions vis-a-vis a nucleophile. The difference in reactivity of the two carbonyl groups in cyclic anhydrides has been associated with the difference in the size of LUMO coefficients at the carbon atoms of the two carbonyl functions. At a short distance of approximately 2 Å the orbitals of the nucleophile and the substrate begin to merge. The best overlap between the nucleophile's HOMO and the carbonyl's LUMO leads to the more favourable lower energy transition state. Such a relationship between intrinsic reactivity and the regioselectivity of reductions of metal hydrides appears to hold for all succinic, maleic, and phthalic anhydrides studied (9–11). Yet, it is not possible to estimate the extent to which this effect is responsible for the control of regioselectivity, since in solution, counterions and (or) solvent also play an important role.

On the other hand, in the gas phase, solvent effects and counterions are absent; hence a gas phase study of the reduction of unsymmetrically substituted maleic anhydrides by BH_4^- should shed some light on the importance of intrinsic reactivity in the control of regioselectivity. For that purpose we carried out a Fourier transform ion cyclotron resonance (FT-ICR) mass spectrometric study (for recent reviews see ref. 12) of isotopically labelled maleic anhydrides, in combination with the *ab initio* calculations for a few model compounds.

Experimental

Ion cyclotron resonance spectra were measured with the FT-ICR instrument at the University of Amsterdam. The basic hardware (13*a*), software (13*b*), and general operation procedure (13*c*,*d*) of the instrument have been described previously. The partial pressures were kept around 4×10^{-5} Pa except for the anhydrides ($\sim 1 \times 10^{-5}$ Pa) and for the collision gas N_2O ($\sim 1 \times 10^{-4}$ Pa) during the collision induced dissociation (CID) experiments. These pressures were measured on an ionization gauge placed in a side arm of the main pumping line. The ionization gauge was calibrated against an MKS Baratron (type 170M, head type 94 AH-1) placed in the same side arm using N_2 as calibrant in the 10^{-1}–10^{-3} Pa pressure range.

Negative ions were trapped in the cubic FT-ICR cell (15.6 cm^3) at a magnetic field of 1.4 T by application of a small negative potential (~ -1.6 V) to the trapping plates.

General procedure

The BH_4^- ions were prepared by reaction of $O^{-\bullet}$ (generated from N_2O by electron impact with ~0.6 eV electrons) with B_2H_6.

In a typical experiment $^{11}BH_4^-$ ions were isolated in the cell by application of the so-called notch ejection technique (14) and the reactions with the anhyrides were studied as a function of the reaction time.

In some experiments, to confirm accurate mass measurements, the reactions of the $^{10}BH_4^-$ ions with the anhydrides were studied while the $^{11}BH_4^-$ isotopic ions were removed continuously from the cell.

Collision induced dissocation (CID) experiments (12)

CID experiments were performed with N_2O as collision gas. First the $(M + H)^-$ and $(M + BH_4)^-$ ions (M = anhydride) were isolated in the cell by application of the so-called notch-ejection technique (14) after 0.5–1 s reaction time, following isolation of the $^{11}BH_4^-$ ions in the cell. Then a short, but intense, radio-frequency pulse at the cyclotron frequency of the ions was used (0.02–0.03 ms duration, 10 V peak to peak) to excite the ions translationally. The fragment ions were detected 50–100 ms after the CID pulse (i.e., the "CID interaction time", during which time ion fragmentation occurred as a result of collisions with the target gas molecules).

Materials

B_2H_6 was prepared by reaction of KBH_4 with H_3PO_4 (15).

B_2D_6 (~85% D_6) was prepared by reaction of $NaBD_4$ with D_3PO_4 (made from D_2O and P_2O_5) (15).

Maleic and phthalic anhydrides were commercially available. The ^{13}C labelled substrates were prepared by few-step synthetic sequences (16).

Results and discussion

As mentioned in the introduction, preliminary experiments have shown that maleic and phthalic anhydrides **1** and **2** can be reduced by BH_4^- in the gas phase. These substrates react with BH_4^- essentially via two channels, as can be concluded from the product ions given in Table 1.

The major process is reduction of the anhydrides, while BH_4^- addition followed by elimination of either CO_2 or HBO or (HBO + H_2) plays a minor role. Although not only one of the carbonyl functions but also the double bond may be reduced, it is especially the CO_2 loss following BH_4^- addition that has given the impetus to study a possibly regioselective reduction in the case of unsymmetrically substituted maleic anhydrides. For the latter, citraconic (methylmaleic) anhydride **3**, phenylmaleic anhydride **4**, and ethoxymaleic anhydride **5** have been chosen, partly because these molecules could be labelled with ^{13}C rather easily at the carbonyl function indicated with an asterisk (16), partly because they are amenable to *ab initio* calculations.

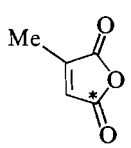

3

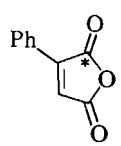

4

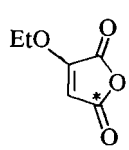

5

[3]The anhydride affinity of a neutral compound, HA(X), is defined as the enthalpy of dissociation of the corresponding anion HX^- to free hydride and the neutral compound X:

$$HX^- \xrightarrow{\Delta H} H^- + X$$

$$HA(X) = \Delta H = \Delta H_f(H^-) + \Delta H_f(X) - \Delta H_f(HX^-)$$

TABLE 1. Primary product ion distributions[a] for the reactions of BH_4^- with maleic and phthalic anhydrides **1** and **2**

Anhydride	$(M + H)^-$	$(M + BH_4 - CO_2)^-$	$(M + BH_4 - HBO)^-$	$(M + BH_4 - HBO/H_2)^-$
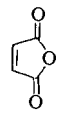 **1**	65	9	11	15
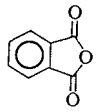 **2**	81	9	4	6

[a]The percentages were obtained after a reaction time of about 500 ms and correction for the secondary product ion formation (i.e., formation of the [primary product ion + BH_3]$^-$ ions) on the basis of double resonance experiments. Conversion into products was 50–80% and the error on the percentages is estimated to be around 15%.

Before presenting the results of the gas phase measurements and associated mechanistic interpretations, the relevant data from the *ab initio* calculations will be given.

Ab initio *calculations*

Citraconic anhydride

The *ab initio* calculations for citraconic anhydride show that the higher LUMO coefficient is located on the carbon of the carbonyl group neighbouring the substituent (9), see structure **6**. Hence, the citraconic anhydride – H^- supermolecule **7***a* is of lower energy than the isomeric complex **7***b* (10).

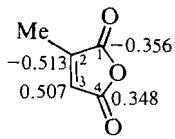

ϵ_{LUMO} = 0.16397 au

6

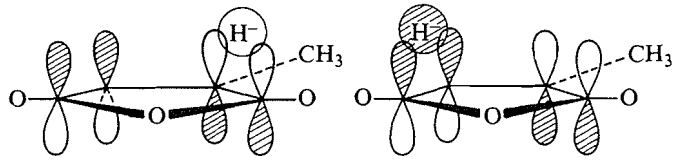

7*a* **7***b*

E = −7.5 kcal/mol E = 0 kcal/mol

Experimentally, the reductions of citraconic anhydride by a variety of metal hydrides in THF occur with a high regioselectivity at the carbonyl function next to the methyl substituent. The match between the forecast based on calculations and the experimental findings is only partially satisfactory. On the basis of "the best overlap" argument, the preferred hydride transfer should occur to the carbon atom with the LUMO coefficient of the highest absolute value; in citraconic anhydride it is C-2. The result of such a reaction would be the reduction of the double bond. For $NaBH_4$ reductions in solution, however, this is only a minor pathway, probably due to the interference of the Na^+ cation. The *ab initio* calculations for maleic anhydride – cation complexes show that the association of the cation with the oxygen atom of the carbonyl function modifies the LUMO coefficients, as shown in **8***a* and **8***b*.

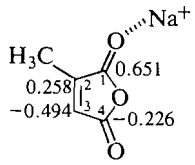

8*a*

ϵ_{LUMO} = − 0.10372 au

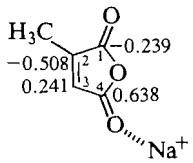

8*b*

ϵ_{LUMO} = −0.09943 au

Thus, the influence of the cation not only facilitates hydride transfer (LUMO lowered: compare **6** vs. **8***a* or **8***b*), but also favours the reaction at the C atom of the CO group next to the substituent (compare ϵ_{LUMO} **8***a* < ϵ_{LUMO} **8***b*; and C1 coefficient **8***a* > C4 coefficient **8***b*). In the gas phase, in the absence of cation or protic solvent, BH_4^- encounters naked anhydride molecules whose LUMO orbital coefficients are shown in structure **6**. In terms of the best overlap, we should expect considerable H^- transfer to the double bond. If, however, H^- is transferred to the carbon of the carbonyl function, C-1 should be preferred over C-4.

Phenylmaleic anhydride

The phenyl substituent on a double bond extends conjugation, hence lowering the energy of the LUMO and causing polarization similar to that observed for acrolein and cyanomaleic anhydride (Fig. 1(b)).

It should be noted here that the reaction of phenylmaleic anhydride with $NaBH_4$ in THF solution results principally in the reduction of the double bond. The yield of lactonic products with the *untouched* double bond is low, 30% (17).

Ethoxymaleic anhydride

Ab initio calculations were carried out for methoxymaleic anhydride, which is an excellent model for ethoxymaleic anhydride. Here, as in other maleic anhydrides, the LUMO coefficients are higher on the carbon atoms of the double bond (the highest being on the substituent-bearing C-2, see Fig. 1). Of the two carbonyl functions C-1 has a higher LUMO coefficient than C-4. Here it should be noted that ethoxymaleic anhydride is reduced by $NaBH_4$ in THF solution entirely at the carbonyl group adjacent to the substituent,[4] similarly to the methoxymaleic anhydride (10).

The regiospecificity of methoxymaleic anhydride reductions

[4]M. M. Kayser and L. Breau. Unpublished results.

Can. J. Chem. Downloaded from www.nrcresearchpress.com by 196.1.178.254 on 09/07/12
For personal use only.

Can. J. Chem. Downloaded from www.nrcresearchpress.com by 196.1.178.254 on 09/07/12
For personal use only.

TABLE 2. Primary product ion distributions[a,b] for the

Anhydride	$(M + H)^-$	$(M + BH_4 - CO_2)^-$	$(M + BH_4 - {}^*CO_2)^-$	$(M + BH_4 - C_2H_7BO)^-$
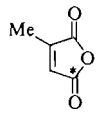 **3**	40	9	16	—
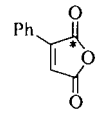 **4**	90	—	—	—
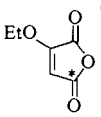 **5**	20	—	—	59

[a]See note *a*, Table 1.
[b]The percentages have been corrected for incomplete ^{13}C-labelling of the anhydrides (see experimental part).
[c]In small amounts m/z 98 ions are generated (~3% of the total product ion distribution), their exact origin being unknown.
[d]The origin of the $(M - C_2H_5)^-$ may be due to either a β-elimination reaction on the ethoxy group or an electron transfer reaction to the anhydride and loss of $C_2H_5^\cdot$ (the m/z 114 ions can easily be generated by electron impact on anhydride **5** with ~0.5 eV electrons and subsequent loss of $C_2H_5^\cdot$).

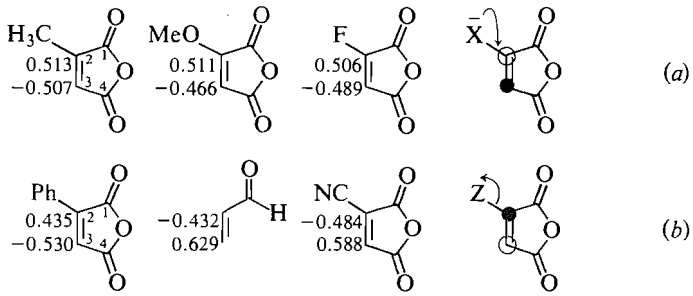

FIG. 1. (a) LUMO coefficients on the double bond for a series of maleic anhydrides bearing an electron-releasing substituent. (b) LUMO coefficients for a series of compounds with a conjugated double bond, including cyanomaleic anhydride. Here, the absolute values of the two LUMO coefficients are reversed compared to the (a) series.

in solution has been interpreted in terms of the important chelating effect by the reagent (19) or counterion (9) reinforced by various electronic effects (8).

Gas phase ion/molecule reactions

Citraconic anhydride

The primary product ions generated by reaction of BH_4^- with the ^{13}C-labelled citraconic anhydride **3** and also with the ^{13}C-labelled phenylmaleic and ethoxymaleic anhydrides **4** and **5**, which will be discussed below, have been summarized in Table 2.

As can be seen in this table, there is a minor $(M - H)^-$ formation, which is probably due to proton abstraction from the methyl group. Two other products, for which no mechanisms are given, result from the addition of BH_4^- and subsequent elimination of HBO and (HBO + H_2). The most relevant, however, to the problem of regioselectivity of BH_4^- attack on the anhydride is the observation that following BH_4^- addition $^{13}CO_2$ and CO_2 are lost in the ratio of 16:9. It is significant to note that in the corresponding product ions BH_4^- is retained, in contrast with the most abundant $(M + H)^-$ ion formation. This points, in our opinion, to a boron–oxygen bond formation, which is known to be very strong (>800 kJ/mol) (20). It seems therefore not unreasonable to suppose that the eliminations of $^{13}CO_2$ and CO_2 following BH_4^- addition are due to attack of BH_4^- upon the unlabelled and ^{13}C-labelled carbonyl groups, respectively, as visualized by reactions [3*a*] and [3*b*].

Although the structures of the final product ions of reactions [3*a*] and [3*b*] have not been proven experimentally, it has been demonstrated recently that vinylic anions can readily be generated as long-lived, stable species in the gas phase by CO_2 loss from carboxylate anions (21). It is gratifying to see that the preferential loss of $^{13}CO_2$ versus CO_2, i.e., a preferential attack of BH_4^- upon the carbonyl group neighbouring the substituent, is in line with the predictions made on the basis of the *ab initio* calculations (*vide supra*).[3]

Additional support for this interpretation is provided by collisionally induced dissociation (CID) experiments on the $(M + H)^-$ ions. Although the formation of these ions as such does not provide information on the site within the anhydride molecule to which the hydride ion has been transferred, the CID experiments show that the loss of $^{13}CO_2$ and CO_2 is in a 1:1 ratio (see Table 3), thus quite different from the 19:6 ratio following BH_4^- addition.

It seems likely, therefore, that in the long-lived $(M + H)^-$ ions, the double bond rather than one of the carbonyl groups has been reduced by BH_4^-, albeit without noticeable preference for H^- addition to one or the other carbon atom of the double bond (reactions [4*a*] and [4*b*]). This is further corroborated by the observation that the $(M + BH_4^-)$ ions, generated via reaction of

reactions of BH_4^- with the ^{13}C-labelled anhydrides **3**, **4**, and **5**

$(M + BH_4 - C_2H_4O/*CO_2)^-$	$(M + BH_4 - HBO)^-$	$(M + BH_4 - HBO/H_2)^-$	$(M - H)^-$	$(M - C_2H_5)^-$
—	19	14	2	—
—	7	3	—	—
6	—	—	—	12[d]

Can. J. Chem. Downloaded from www.nrcresearchpress.com by 196.1.178.254 on 09/07/12
For personal use only.

[3a] [3b]

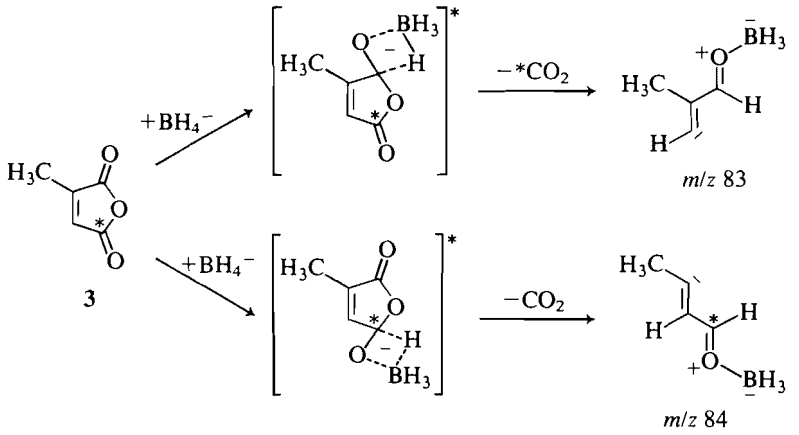

[4a] [4b]

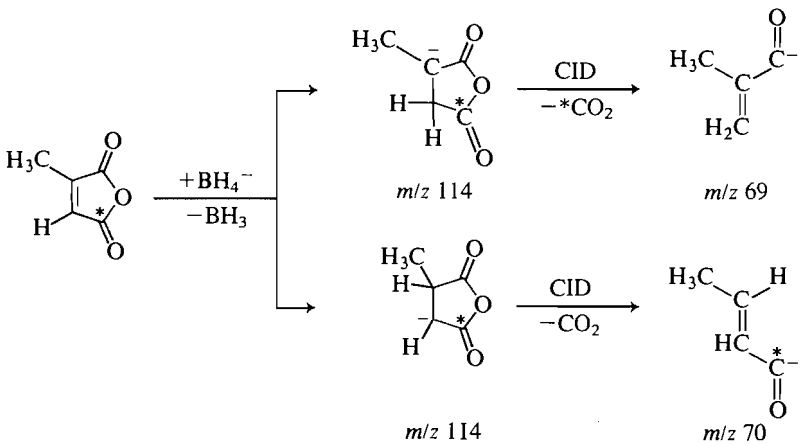

TABLE 3. Percentages of collisionally induced losses of $^{13}CO_2$, CO_2, and BH_3 from the $(M + H)^-$ and $(M + BH_4)^-$ ions of ^{13}C-labelled citraconic anhydride **3**

Ion	$^{13}CO_2$ loss (%)	CO_2 loss (%)	BH_3 loss (%)
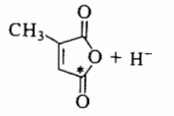 **3**	50	50	—
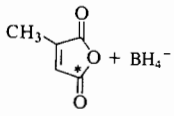 **3**	30	30	40

the $(M + H)^-$ ions with B_2H_6 according to eq. [5], eliminate upon CID $^{13}CO_2$ and CO_2 in a 1:1 ratio as well (see Table 3).

[5] $(M + H)^- + B_2H_6 \rightarrow (M + BH_4)^- + BH_3$

These eliminations can be visualized in the same way as suggested for the $(M + H)^-$ ions in reactions [4*a*] and [4*b*] with the modification that in the $(M + H)^-$ ions a BH_3 molecule is bonded to the oxygen atom of the carbonyl group that eventually is retained in the product ion.

In summary, the carbonyl group reduction of citraconic anhydride by BH_4^- seems to take place predominantly in a regioselectively controlled manner, but such selectivity is not observed for the BH_4^- reduction of the olefinic bond.

Phenylmaleic anhydride

Reaction of BH_4^- with phenylmaleic anhydride **4** yields a very abundant $(M + H)^-$ ion, but loss of carbon dioxide following BH_4^- addition as in the case of citraconic anhydride is not observed here (see the data in Table 2).

CID experiments on the $(M + H)^-$ ions of **4** show specific losses of $^{13}CO_2$ and $^{13}CO_2/CO$ occurring in a ratio of about 2:1. These observations seem to indicate that neither of the carbonyl groups has been reduced by BH_4^-. It is then logical to suppose that the hydride ion has been transferred to one of the carbon atoms of the olefinic bond, which should be C-3 according to the *ab initio* calculations (*vide supra*). However, such $(M + H)^-$ ions are expected to eliminate $^{12}CO_2$ and $^{12}CO_2/^{13}CO$ upon CID, as visualized by reaction [6], which is just opposite to the observations made.

Another possibility is that the hydride ion is transferred to C-2, which could explain the observed $^{13}CO_2$ and $^{13}CO_2/CO$ losses from the corresponding $(M + H)^-$ ion upon CID via routes similar to those given in reaction [6]. However, it is important to note that the $(M + H)^-$ ions of phenylmaleic anhydride react only slightly with B_2H_6 to give $(M + BH_4^-)$ ions, in contrast with the $(M + H)^-$ ions of citraconic anhydride, which do react to a large extent in this way (*vide supra*, reaction [5]). Such observation casts doubts on the importance of hydride ion transfer to either of the carbon atoms of the olefinic bond, as such transfer would enable the localization of the negative charge at the carbonyl oxygen atoms and thus promote the formation of an O—BH_3 bond during collision with B_2H_6.

[6] 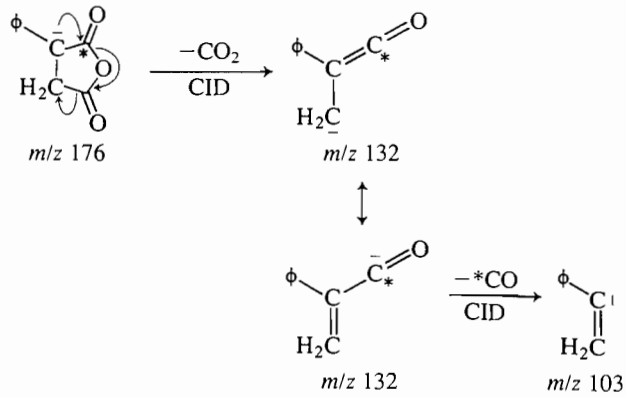

The last possibility for $(M + H)^-$ ion formation is that the hydride ion is transferred to the phenyl ring, which at first glance might seem peculiar but which permits delocalization of the negative charge over a large part of the ion, which contributes to stabilization of charged species in the gas phase. Assuming that the hydride ion is attached to the *para* position of the phenyl ring, reaction [7] can then account very well for the observed specific losses of $^{13}CO_2$ and $^{13}CO_2/CO$.

[7] 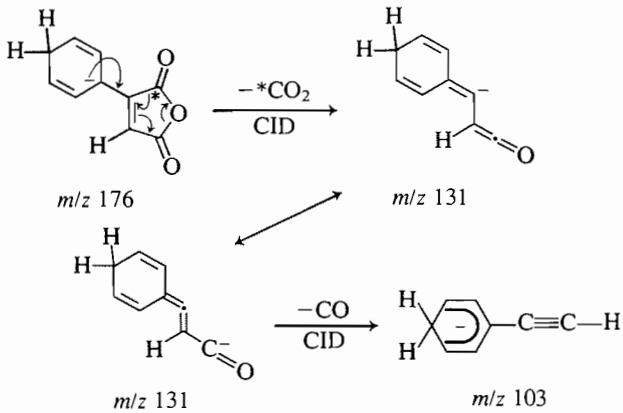

Support for such a route is provided by the observed exclusive losses of $^{12}CO_2$ and $^{12}CO_2/^{13}CO$ from the $(M - H)^-$ ions of citraconic anhydride **3** upon CID as summarized in reaction [8].

[8] 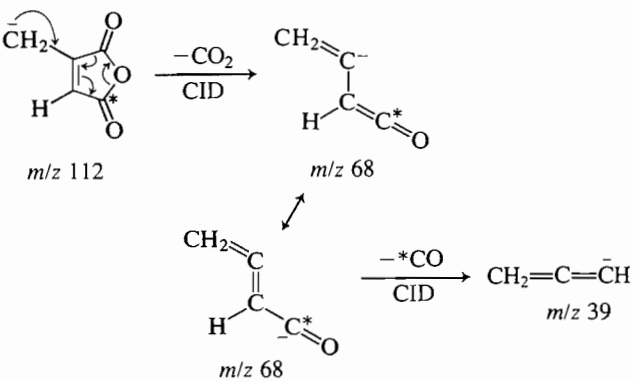

Finally, the reactions of methoxide and ethoxide ions with 2-phenylmaleic anhydride **4** should be mentioned. These ions both transfer a hydride ion (22) to generate $(M + H)^-$ ions, which upon CID show specific losses of $^{13}CO_2$ and $^{13}CO_2/CO$ and react via an addition–elimination channel where again specifically $^{13}CO_2$ and $^{13}CO_2/CO$ are lost from the corresponding collision complexes. Even the long-lived adduct between methoxide and 2-phenylmaleic anhydride **4**, generated by

Can. J. Chem. Downloaded from www.nrcresearchpress.com by 196.1.178.254 on 09/07/12
For personal use only.

Can. J. Chem. Downloaded from www.nrcresearchpress.com by 196.1.178.254 on 09/07/12
For personal use only.

reaction with methanol-solvated methoxide ion, shows specific losses of $^{13}CO_2$ and $^{13}CO_2/CO$ upon CID. The addition of a nucleophile to the phenyl ring, as suggested above for the hydride transfer reaction from BH_4^-, seems therefore to be rather general.

Ethoxymaleic anhydride

One of the major primary product ions that is formed upon reaction between BH_4^- and 2-ethoxymaleic anhydride **5** is the $(M + H)^-$ ion, as shown by the data in Table 2. CID experiments on this ion show losses of C_2H_5OH (~90%), C_2H_4/H_2 (~5%), and a neutral molecule of 44 daltons (~5%), which could be CO_2 and (or) C_2H_4O. The latter are both feasible in view of the fact that CID experiments on the corresponding $(M + H)^-$ ions of 2-methoxymaleic anhydride have shown both CO_2 and CH_2O loss together with CH_3OH and CH_4 loss in a ratio of 6:6:78:10, respectively.

The abundant loss of ethanol from the $(M + H)^-$ ion of **5** upon CID, which for the $(M + D)^-$ ions generated by reaction with BD_4^- becomes 65% C_2H_5OD loss and 35% C_2H_5OH loss, has been visualized by reaction [9] and is a strong argument for

[9]

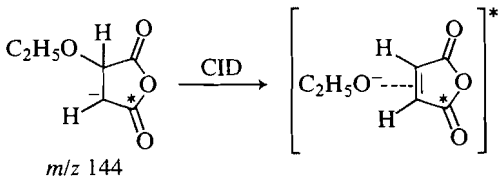

m/z 144

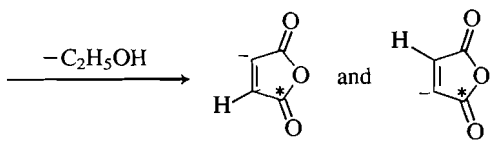

m/z 98

hydride ion transfer to C-2. This is in agreement with the results of *ab initio* calculations, which have indicated that C-2 has indeed the highest LUMO coefficient (*vide supra*).

The most abundant primary ion formed from reaction of BH_4^- with **5** (see Table 2) formally corresponds to elimination of $C_2H_5OBH_2$ from the collision complex, according to accurate mass measurements. In principle, this ion could also arise from the $(M + BH_4)^-$ collision complex by loss of C_2H_4O and BH_3, but this possibility is not likely because of the formation of $(M + BD_4 - C_2H_5D_2BO)^-$ ions in a much larger abundance than $(M + BD_4 - C_2H_4D_3BO)^-$ ions (~95:5%) when BD_4^- is used instead of BH_4^-. This indicates that mainly two deuterium atoms from BD_4^- are transferred to the anhydride. A possible route to explain the $(M + BH_4 - C_2H_5OBH_2)^-$ product formation might be that during the hydride transfer to C-2, BH_3 becomes bonded to the ether oxygen atom and that the energy released upon the boron–oxygen bond formation (bond strength > 800 kJ/mol; ref. 20) assists in the generation of an intermediate $C_2H_5OBH_3^-$/maleic anhydride complex. A subsequent hydride ion transfer in this complex would then result eventually in the formation of the most abundant primary $(M + BH_4 - C_2H_5OBH_2)^-$ ion (reaction [10]).

At any rate the elimination of $C_2H_5OBH_2$ from the collision complex points to hydride ion transfer to C-2, which is in line with the highest LUMO coefficient at that position.

Finally, a low abundant primary ion with *m/z* 69, which shifts to *m/z* 73 when BD_4^- is used, corresponds to expulsion of C_2H_4O and $^{13}CO_2$ from the BH_4^-/**5** collision complex

[10] $BH_4^- + \mathbf{5} \rightarrow$ *m/z* 15

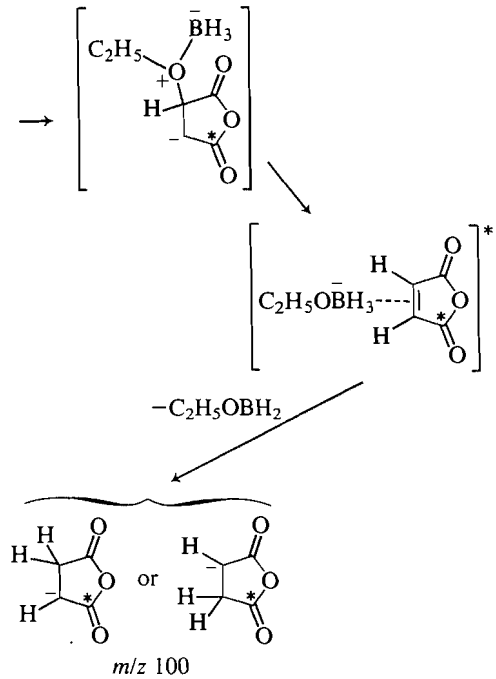

m/z 100

(see Table 2). The observation that boron is retained in the product ion and that $^{13}CO_2$, but not $^{12}CO_2$, is lost, points to boron–oxygen bond formation at the C-1 carbonyl group. Irrespective of the details of the expulsion of C_2H_4O and $^{13}CO_2$ from the BH_4^-/**5** collision complex, the attack upon the C-1 rather than the C-4 carbonyl group is again in agreement with the *ab initio* calculations, which have indicated that C-1 has a higher LUMO coefficient than C-4 (*vide supra*).

Conclusions

Most of the gas phase hydride-ion transfer reactions from BH_4^- to the unsymmetrically substituted maleic anhydrides studied appear to proceed under orbital control. That is, the hydride ion is transferred predominantly to those carbon atoms of the anhydride that on the basis of the *ab initio* calculations have the higher LUMO coefficients. In other words, the regioselectivity of these reactions appears to be under orbital rather than charge control. In view of that we may conclude that the lifetimes of the corresponding collision complexes are relatively long, which has been shown to be the case in many other gas phase reactions (18, 23).

Acknowledgements

H. v.d. W. and N.M.M.N. thank the Netherlands Organization of Pure Research (SON/ZWO) for financial support. Further financial assistance of this work was provided by a grant from NATO (M.M.K.).

1. O. Eisenstein, H. B. Schlegel, and M. M. Kayser. J. Org. Chem. **47**, 2886 (1982).
2. J. L. Pierre and H. Handel. Tetrahedron Lett. 2317 (1974).
3. H. Handel and J. L. Pierre. Tetrahedron, **31**, 997 (1975).
4. E. C. Ashby, J. R. Boone, and J. P. Oliver. J. Am. Chem. Soc. **95**, 5427 (1973).
5. M. M. Kayser and T. B. McMahon. Tetrahedron Lett. **25**, 3379 (1984).
6. A. Loupy, J. Seyden-Penne, and B. Tchoubar. Tetrahedron Lett. 1677 (1976).
7. R. R. Squires. Structure reactivity and thermochemistry of ions.

In Proc. NATO Adv. Study Inst. *Edited by* P. Ausloos and S. G. Lias. Reidel, Dordrecht, The Netherlands. 1987. p. 373.
8. M. M. KAYSER and G. WIPFF. Can. J. Chem. **60**, 1192 (1982).
9. M. M. KAYSER and O. EISENSTEIN. Can. J. Chem. **59**, 2457 (1981).
10. M. M. KAYSER, L. BREAU, S. ELIEV, P. MORAND, and H. S. IP. Can. J. Chem. **64**, 104 (1986).
11. C. SOUCY, D. FAVREAU, and M. M. KAYSER. J. Org. Chem. **52**, 129 (1987).
12. (*a*) D. A. LAUDE, JR., C. L. JOHLMAN, R. A. BROWN, D. A. WEIL, and C. L. WILKINS. Mass Spectrom. Rev. **5**, 107 (1986); (*b*) N. M. M. NIBBERING. Adv. Mass Spectrom. **10**, 417 (1985).
13. (*a*) J. H. J. DAWSON. Lect. Notes Chem. **31**, 331 (1982); (*b*) A. J. NOEST and C. W. F. KORT. Comput. Chem. **6**, 111 (1982); **6**, 115 (1982); **7**, 81 (1983); (*c*) J. C. KLEINGELD and N. M. M. NIBBERING. Org. Mass Spectrom. **17**, 136 (1982); (*d*) S. INGEMANN, N. M. M. NIBBERING, S. A. SULLIVAN, and C. H. DEPUY. J. Am. Chem. Soc. **104**, 6520 (1982).
14. J. C. KLEINGELD and N. M. M. NIBBERING. Tetrahedron, **24**, 4193 (1983).
15. O. EISENSTEIN, M. M. KAYSER, M. ROY, and T. B. MCMAHON. Can. J. Chem. **63**, 281 (1985).
16. L. BREAU and M. M. KAYSER. J. Labelled Compd. Radiopharm. **25**, 301 (1988).
17. M. M. KAYSER and P. MORAND. Can. J. Chem. **58**, 2484 (1980).
18. S. INGEMANN, N. M. M. NIBBERING, S. A. SULLIVAN, and C. H. DEPUY. J. Am. Chem. Soc. **104**, 6520 (1982).
19. D. W. KNIGHT and G. PATTENDEN. J. Chem. Soc. Perkin Trans. 1, 62 (1979).
20. R. C. WEAST (*Editor*). Handbook of chemistry and physics. 64th ed. CRC Press, Boca Raton, FL. 1983–1984. p. F-176.
21. S. W. FROELICHER, B. S. FREISER, and R. R. SQUIRES. J. Am. Chem. Soc. **108**, 2853 (1986).
22. S. INGEMANN, J. C. KLEINGELD, and N. M. M. NIBBERING. J. Chem. Soc. Chem. Commun. 1009 (1982).
23. C. H. DEPUY, J. J. GRABOWSKI, and V. M. BIERBAUM. Science, **218**, 955 (1982).

Can. J. Chem. Downloaded from www.nrcresearchpress.com by 196.1.178.254 on 09/07/12
For personal use only.

A reinvestigation of the interaction between triplet states of cyclohexenones and amines[1]

D. WEIR AND J. C. SCAIANO
Division of Chemistry, National Research Council of Canada, Ottawa, Ont., Canada K1A 0R6

AND

D. I. SCHUSTER
Department of Chemistry, New York University, New York, NY 10003, U.S.A.

Received January 22, 1988

D. WEIR, J. C. SCAIANO, and D. I. SCHUSTER. Can. J. Chem. **66**, 2595 (1988).

Laser flash photolysis studies lead to the conclusion that the short-lived triplet states of cyclohexenones are readily quenched by amines. For example, in the case of 2-cyclohexen-1-one (**I**) its triplet state (τ_T = 40 ns in acetonitrile) is quenched by triethylamine with a rate constant of (9.0 ± 0.8) × 10^7 M^{-1} s^{-1}. Cyclohexenone triplets are also quenched efficiently by DABCO and by triphenylamine leading to the formation of the corresponding amine radical cations. The new evidence reported rules out the involvement of long-lived detectable exciplexes.

D. WEIR, J. C. SCAIANO et D. I. SCHUSTER. Can. J. Chem. **66**, 2595 (1988).

Sur la base d'études de photolyse éclair au laser, on peut conclure que les états triplets de courtes vies des cyclohexènones sont facilement piégés par les amines. Par exemple, dans le cas de la cyclohexène-2 one-1 (**1**), sont état triplet (τ_T = 40 ns, dans l'acétonitrile) est piégé par la triéthylamine avec une constante de vitesse de (9,0 ± 0,8) × 10^7 M^{-1} s^{-1}. Les triplets des cyclohexènones sont aussi piégés d'une façon efficace par le DABCO ainsi que la triphénylamine; dans chacun des cas, il y a formation des radicaux cations des amines correspondantes. Les données obtenues éliminent la possibilité d'intervention d'exciplex à longues vies qui seraient détectables.

[Traduit par la revue]

Introduction

Triplet excited states of ketones are known to be quenched directly by amines, as demonstrated by nanosecond flash techniques as well as steady state studies (for a review, see ref. 1). Cohen and Peters and their co-workers have studied this process with benzophenone and related ketones, and have demonstrated convincingly that the quenching process involves electron transfer to give initially amine radical cations and ketone radical anions (2). Schuster and Brisimitzakis demonstrated that reactive 2,5-cyclohexadienone triplets are quenched by amines of appropriate ionization potential to give a set of products not observed in the absence of amines. In all cases, the amine interacts directly with ketone triplet (3).

Reactions of photoexcited α,β-unsaturated carbonyl compounds with amines are known to give 1:1 adducts, presumably via the enone triplet states (4). Dunn *et al.* have reported results of nanosecond flash studies on excitation of cyclohexanone **I** and analogues such as **II** (see Chart I) in the presence of 1,4-diazabicyclo[2.2.2]octane (DABCO) which demonstrate that long-lived DABCO radical cations (λ_{max} 450 nm) are formed from an intermediate which has the same lifetime (ca. 25 ns) as the transient species (λ_{max} 280 nm) generated on laser excitation of the enone in the absence of amines (5). This transient has been suggested by Bonneau (6) and by Schuster *et al.* (7) to be a highly twisted triplet excited state of these cyclohexenones. In the presence of even small amounts of DABCO, long-lived absorption is observed which interferes with analysis of the fast component of the decay curve at wavelengths in the range 270–300 nm; at the DABCO concentrations required for observation of the growth of the radical cation at 450 nm, the fast decay at 280 nm cannot be monitored (5, 8).

In contrast to the above findings, Pienta and McKimmey reported results of product analyses from excitation of **I** in the presence of triethylamine as a function of enone and amine concentrations which they interpreted in terms of a mechanism in which triplets of **I** do not interact directly with amines but rather react with ground state enone to give a dimeric species (excimer?) which is the species intercepted by triethylamine (9). Pienta later reported that on laser flash excitation of **I** in acetonitrile at 355 nm in the presence of triethylamine, the lifetime of the transient decay observed at 280 nm increases with increasing amine concentration (10). This was interpreted in terms of reversible formation of a long-lived enone–amine exciplex, which also absorbs at 280 nm, from the twisted π,π* state of the enone (the short-lived transient observed in the absence of amines). Equilibrium constants for formation of the triplet enone–amine exciplexes were calculated for **I** as well as for **II** and several other methylated analogs of **I** from the decays measured as a function of amine concentration (10). It was noted that components with microsecond rates become measureable at even the lowest concentrations of amines used in this study (36 m*M*); attempts to fit these slow decays to second order kinetics were unsuccessful. As in our later studies using DABCO (5, 8), the slow components increase with amine

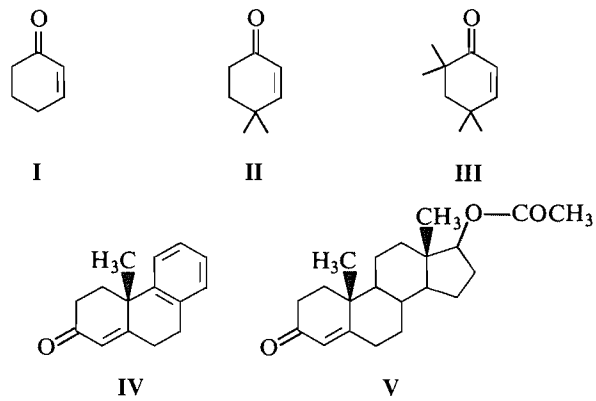

CHART 1

[1]NRCC No. 28932.

Printed in Canada / Imprimé au Canada

Can. J. Chem. Downloaded from www.nrcresearchpress.com by 196.1.178.254 on 09/07/12
For personal use only.

concentration at the expense of the fast decays and eventually the latter are obliterated. Mechanistically, these data were interpreted (in light of the product studies) to mean that the monomeric enone triplet interacts with amines to give a detectable exciplex which does *not* result in formation of products, in competition with formation of a dimeric enone triplet from which enone dimers as well as enone–amine adducts are derived (10).

Pienta's conclusions conflict with previous studies of interactions between amines and photoexcited ketones (1–5), as well as nanosecond flash data on **I**, **II**, and related compounds (5–8). Furthermore, we have observed that triethylamine, DABCO, and other amines quench the unimolecular photorearrangement of **II** and other cyclohexenones, as well as photocycloaddition to alkenes, with efficiencies (given by the Stern–Volmer slopes $k_q\tau_T$, where k_q is the bimolecular quenching rate constant and τ_T is the lifetime of the enone triplet) that depend inversely on the ionization potential of the amine (7, 8). Adducts of enone **II** and triethylamine were also formed under these conditions. In the case of **II** and DABCO, enone–amine adducts are not formed, but there is good agreement between the flash and steady-state quenching data (8). These results are readily rationalized by a mechanism involving electron transfer from the amines to the chemically reactive monomeric enone triplets.

As part of a detailed study of transient phenomena in cyclohexenone photochemistry, we have reexamined the interaction between triethylamine and other amines with the "280 nm transient" derived from **II** and other enones. This study was also prompted by examination of the decay curves from the earlier study (10) which were generously provided by Professor Pienta; we believe the conclusion from this study should be revised. Indeed, as detailed below, we now find that the fast decay rates measured at 280 nm on laser flash excitation of **II** and other enones at 337 nm are accelerated by low concentrations of triethylamine, and we find no evidence to support the prior claim for equilibration of these enone triplets with an enone–amine exciplex.

Experimental

Laser flash photolysis experiments were performed using the pulses from a Molectron UV-24 nitrogen laser (337.1 nm, ~8 ns, ≤10 mJ/pulse) for excitation. The monitoring system includes an arrangement of monochromator and photomultiplier, a Tektronix R7912 transient digitizer and a PDP11/23 computer which controls the acquisition, processing and display of the data. Other details on the system have been reported elsewhere (11). Samples of **I** and **II** were obtained from Aldrich and vacuum distilled before use. Triethylamine was refluxed over NaOH then fractionally distilled. DABCO (Aldrich) was recrystallized twice from ethanol before use.

The solvents acetonitrile, methanol, heptane, and cyclohexane were Aldrich Gold label and were used as received. The sources and purification of **III**, **IV**, and **V** were the same as in earlier work (7, 8).

Results

I. Quenching of enone triplets

A. Triethylamine

The quenching of the triplet of **I** with triethylamine (TEA) was carried out under conditions as identical as possible to those of Pienta (10). The solvent, concentration of **I** and concentration range of TEA additions were duplicated. Laser excitation wavelengths were slightly different (355 nm in Pienta's study, 337 nm in this study) but both wavelengths are encompassed in the same broad absorption band of **I**. Our measurements always include an emission correction. This correction is simply the subtraction of the signal recorded by the detector when the laser is incident on the sample with the analysing beam blocked. This correction takes into account a variety of emissive sources within the system, such as fluorescence, delayed fluorescence, scattered laser light, Raman emission, and monophotonic or multiphotonic emissions from optical components.

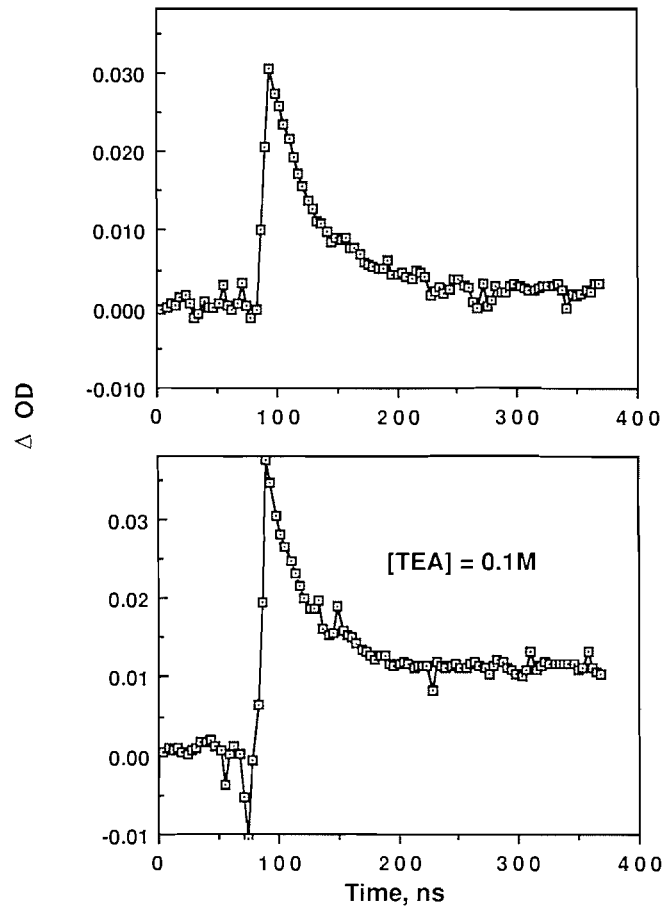

FIG. 1. Transient decay traces monitored at 280 nm following laser excitation of **I** in acetonitrile in the absence (top) and presence of 0.1 *M* triethylamine.

In the absence of quencher **I** gives a transient decay at 280 nm after 337 nm laser excitation, with lifetimes of 40, 28, and 27 ns in acetonitrile, cyclohexane, and methanol, respectively. These values agree well with those in the literature (7, 10), and specifically with the 36.7 ns lifetime in acetonitrile given by Pienta (10). The small difference between the two reported values is within the experimental error. It should be noted that both these values are significantly longer than a previous value of 24 ns estimated from the Stern–Volmer analysis of the kinetics for the growth of naphthalene triplet absorption at 413 nm upon quenching of triplet **I** (5).

We have also observed a long-lived residual signal of intensity 5–10% of the initial transient absorbance. This long-lived species is most likely a triplet-derived product (*vide infra*). The addition of triethylamine has two effects on the transient kinetic traces. The first is a definite shortening of the triplet lifetime. The second is an increase in the signal size (and thus concentration) of the long-lived species. Figure 1 shows two kinetic decay traces; the top trace with no TEA present and the bottom one with 0.1 *M* TEA. The quenching follows pseudo first order kinetics and can be represented by eq. [1].

Can. J. Chem. Downloaded from www.nrcresearchpress.com by 196.1.178.254 on 09/07/12
For personal use only.

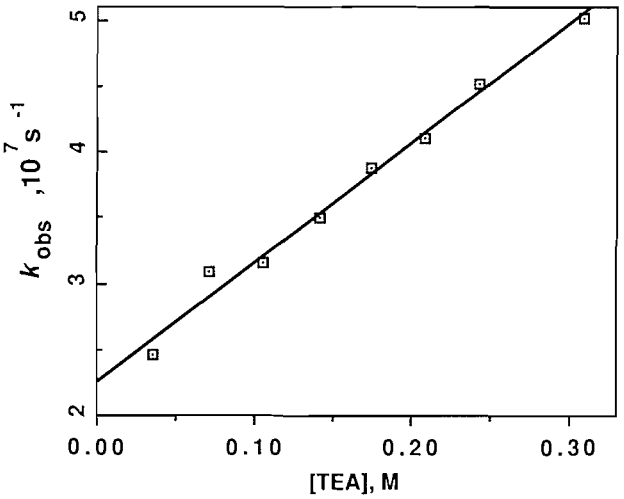

FIG. 2. Quenching of triplet **I** by triethylamine in acetonitrile, according to eq. [1].

TABLE 1. Triethylamine quenching of cyclohexenone triplets

Compound	Solvent	k_q (M^{-1} s^{-1})
I	Acetonitrile	$(9.0 \pm 0.8) \times 10^7$
	Cyclohexane	$(9.2 \pm 4.6) \times 10^7$
II	Methanol	$(1.1 \pm 0.4) \times 10^8$
	Acetonitrile	$(3.7 \pm 0.5) \times 10^7$
III	Cyclohexane	$(1.3 \pm 0.5) \times 10^8$
IV	Acetonitrile	$(2.0 \pm 0.6) \times 10^6$

[1] $k_{obs} = k_0 + k_q[TEA]$

The rate constants k_{obs}, k_0, and k_q correspond to the observed triplet decay, the decay in the absence of quencher (i.e. τ^{-1}) and the second order quenching constant, respectively. Equation [1] leads to a linear quenching plot (Fig. 2) from which we obtain $k_q = (9.0 \pm 0.8) \times 10^7\ M^{-1}\ s^{-1}$ (errors as $\pm 2\sigma$ throughout). A similar value was obtained in cyclohexane (see Table 1). The long-lived species does not decay in the time scale of these experiments and a straightforward offset of the data is sufficient to adequately analyze the kinetics.

Triethylamine quenching of some other enones was also examined. The triplet of **II** gave lifetimes of 40 ns and 28 ns in methanol and cyclohexane. The T–T absorption spectrum shows a maximum at 275–280 nm. **II** showed a much smaller residual absorbance than **I**, which increases upon addition of triethylamine. The triplet of **II** is quenched by TEA with $k_q = (1.1 \pm 0.4) \times 10^8\ M^{-1}\ s^{-1}$ in methanol. A slower quenching was observed in acetonitrile (Table 1).

One possibility that has not been previously tested is that the short-lived transients observed in these experiments are not due to the lowest triplet state of these enones but rather to short-lived triplet enols which are produced by a route such as that shown in Scheme 1 for cyclohexenone. To explore this possibility we examined compound **III** in which methyl groups block the 6-position, thus cutting off the possibility of photoenolization. When **III** is excited with a 337 nm laser pulse a species with $\lambda_{max} \sim 275$ nm with a lifetime of 34 ns in acetonitrile is observed. The presence of this transient shows that the species observed in the laser flash photolysis of **I**–**III** are all of the same

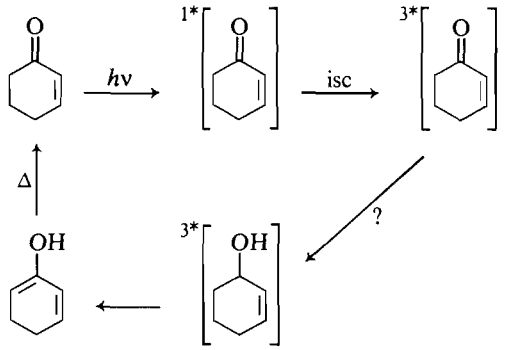

SCHEME 1

origin and must be assigned to the ketone triplet states and not the enols. The TEA quenching of **III** was also interesting in that, although it gave a quenching rate similar to **I** and **II**, it did not, even at the highest amine concentrations, give any significant residual absorbance.

B. Quenching with other amines

In a previous study the effect of adding 1,4-diazabicyclo-[2.2.2]octane (DABCO) to quench the triplet of **I** and **II** was examined and the resulting quenching rate constants in acetonitrile (derived from kinetics of appearance of DABCO radical cations) were $3.7 \times 10^8\ M^{-1}\ s^{-1}$ and $2.7 \times 10^8\ M^{-1}\ s^{-1}$, respectively (5). We have examined the direct quenching of triplet **IV** by DABCO, and obtained $k_q = (7.7 \pm 0.9) \times 10^7\ M^{-1}\ s^{-1}$ in acetonitrile. All DABCO quenching rates are significantly higher than the corresponding TEA values, which is reasonable given the lower oxidation potential of DABCO vs. TEA. Using the lifetime of **II** in ACN of 40 ns and the DABCO quenching rate of $2.7 \times 10^8\ M^{-1}\ s^{-1}$ one obtains $k_q\tau_T = 10.8\ M^{-1}$. This value is in very good agreement with a product study of DABCO quenching of the photocycloaddition of **II** to tetramethylethylene (TME) which gave a Stern–Volmer slope of $11.6\ M^{-1}$ (12). It should be noted that the triplet lifetime of **II** is not affected by TME (13), so these data can be compared.

The triplet of **V** was quenched with diphenylamine. The quenching could not be followed at 280 nm but the growth of the diphenylaminyl radical cation could be observed. The spectrum, with a maximum at 680 nm in the visible region is in good agreement with literature values (14–16). The quenching plot with a representative trace showing diphenylaminyl radical cation growth kinetics is shown in Fig. 3. The resulting quenching rate constant was $3.9 \times 10^9\ M^{-1}\ s^{-1}$.

II. Residual transient absorbance experiments

With the amine quenching of the triplets of these enones now well established, we also wished to identify the long-lived species which are observed in these experiments. The most important question is whether this species is a direct product of the triplet or whether it is created by a separate reaction pathway, possibly via the singlet manifold or by reactions of products built up during the laser experiment. To this end a Stern–Volmer analysis of the triethylamine quenching data of **I**, **II**, and **IV** was made according to eq. [2].

$$[2] \quad \frac{1}{\Delta OD_{obs}} = \chi + \frac{\chi k_0}{k_q[TEA]}$$

In this treatment ΔOD_{obs} is the concentration of the long-lived species as measured by its transient absorbance after the triplet signal has fully decayed, χ is an experimental parameter which includes a measure of the efficiency of the reaction, k_0 is the

Can. J. Chem. Downloaded from www.nrcresearchpress.com by 196.1.178.254 on 09/07/12
For personal use only.

Can. J. Chem. Downloaded from www.nrcresearchpress.com by 196.1.178.254 on 09/07/12
For personal use only.

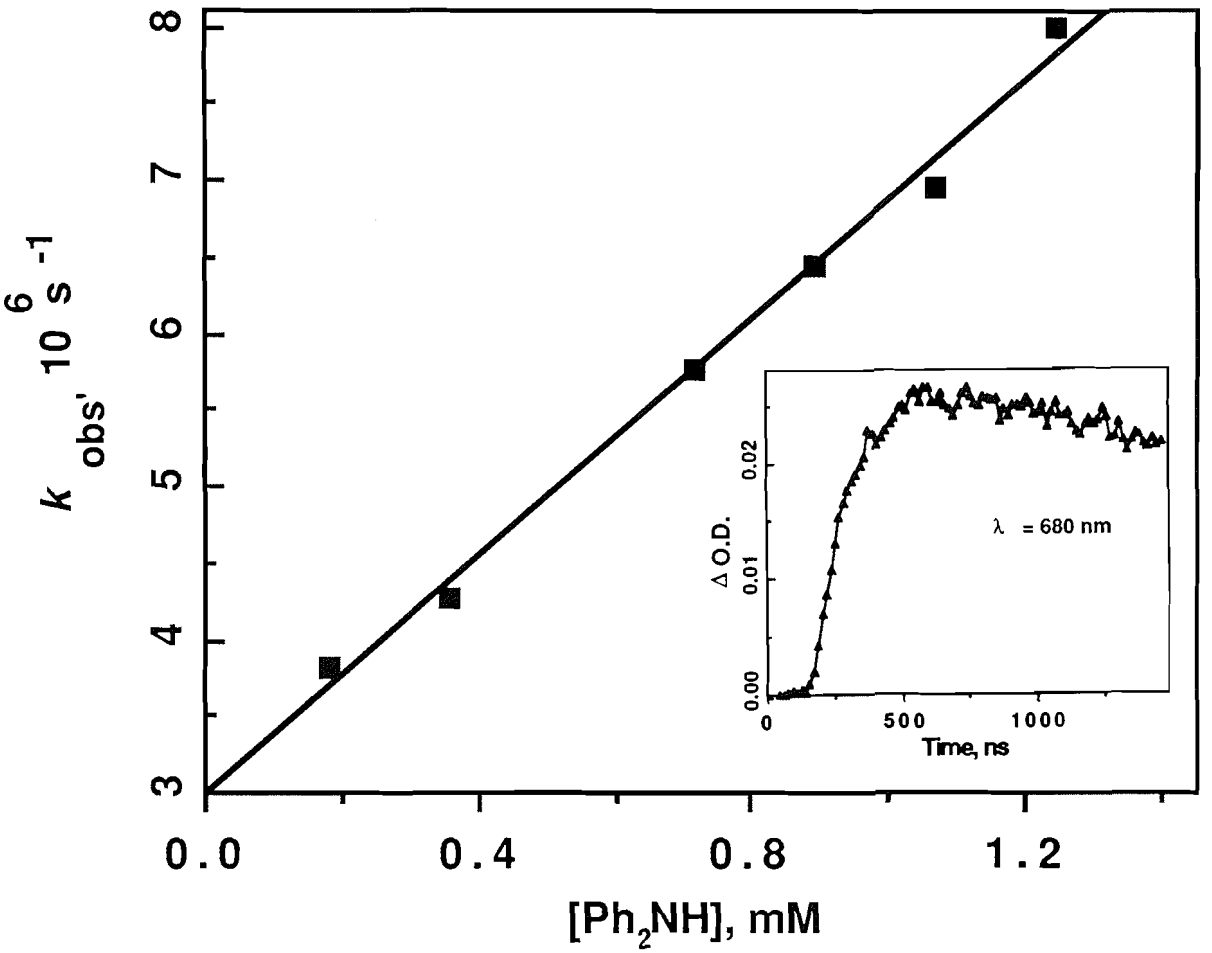

FIG. 3. Quenching of triplet **V** by diphenylamine in methanol, according to eq. [1]. *Insert*: Build-up of the diphenylamine radical cation obtained by reaction of triplet **V** with the amine present in 7.14×10^{-4} *M* concentration.

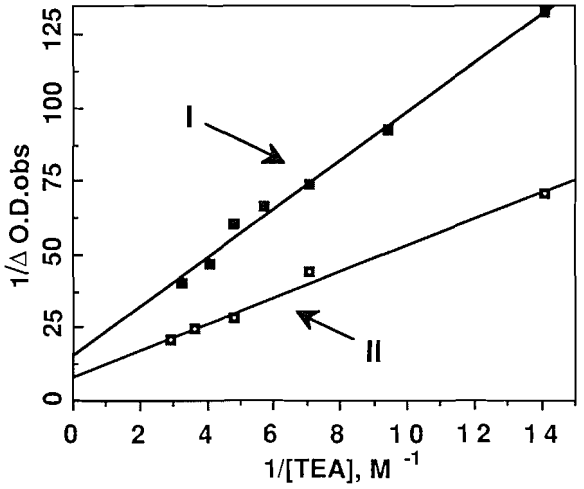

FIG. 4. Double reciprocal plots according to eq. [2] for the quenching of triplet **I** and **II** by triethylamine.

triplet decay rate in the absence of quencher, and k_q is the amine quenching rate constant. A plot of $(\Delta OD_{obs})^{-1}$ vs. $([TEA])^{-1}$ should be linear if the transient product is produced from only one state which is quenched by the amine. The intercept/slope ratio gives the Stern–Volmer constant, $k_q\tau_T$.

The plots for **I** and **II** according to eq. [2] are shown in Fig. 4. The values of $k_q\tau_T$ for the formation of the long-lived species in acetonitrile are 1.9, 1.8, and 0.13 M^{-1} for **I**, **II**, and **IV** (not shown), respectively. These values can be compared with independent values of k_q and τ_T also obtained in this study (*vide supra*) which give $k_q\tau_T$ values of 4.0 ± 0.6 for **I**, 1.2 ± 0.2 for **II** and 0.27 ± 0.05 M^{-1} for **IV**. Given the inherent error in trying to measure the residual OD in these experiments (especially at lower amine concentrations), as well as the large error in extrapolation to the intercept in plots of this type, the agreement within a factor of two is satisfactory and suggests that the long-lived species is a direct product of the triplet state. No Stern–Volmer plot could be produced for **III** since no residual ΔOD was observed upon amine addition.

Finally, the effect of solvent on the residual absorption of **V** was studied. The residual ΔOD was found to be present in both *n*-heptane or acetonitrile in the absence of amine. In protic solvents such as methanol or ethanol, however, little or no residual ΔOD was observed. If we assume that the extinction coefficients of these transient species are unlikely to change dramatically in going from acetonitrile to methanol, the likely explanation is that either the lifetime or the yield of this species is drastically reduced in protic solvents.

Discussion

Our results with compounds **I**–**III** clearly confirm that the short-lived transients observed at 270–280 nm upon laser

Can. J. Chem. Downloaded from www.nrcresearchpress.com by 196.1.178.254 on 09/07/12
For personal use only.

excitation of cyclic enones are due to the triplets of these molecules. The similarity of the lifetime and quenching rates of **III**, which cannot form an enol, to the results with **I** and **II** shows that enols do not play a role at the triplet manifold level. This seems to be true also for **IV** and **V** since they show similar behavior.

Pienta (10) has suggested that these triplets form detectable exciplexes, with lifetimes longer than the triplet, upon the addition of triethylamine. He reported no amine quenching of the triplets of **I** and **II**. Our study, which closely duplicates the conditions of those experiments, shows this conclusion to be incorrect. The triplet states of **I–IV** are quenched by triethylamine at rates comparable to amine quenching of other carbonyl triplets. We cannot fully explain the reasons for Pienta's observation of lifetime lengthening upon amine addition; however, we found that we can closely reproduce his observations if we exclude the emission correction from our measurements. However, Professor Pienta has indicated that a similar correction was also employed in his experiments (17).

The quenching by amines is likely to involve an electron transfer mechanism. This is supported by the observation of DABCO radical cation when DABCO is used to quench the triplets of **I**, **II**, and **IV** (5), as well as by the fact that the amine quenching rates follow the trend of amine oxidation potentials. While the quenching of the triplet of **V** by TEA could not be followed, quenching by diphenylamine was measurable. Again, the results showed simple bimolecular amine quenching. All these results are consistent with previous product studies which examined the effect of TEA and DABCO addition on the rearrangement of **II** (7, 12). The agreement of the $k_q\tau_T$ values of those studies and the independently obtained values of this study further confirm that amines quench the triplet of **II**. Thus, only simple amine quenching occurs in these systems and there is no evidence for the formation of long-lived ketone–amine exciplexes.

It should be noted that our results do not rule out the possible involvement of an exciplex. They simply establish that if involved, it is not directly detectable by this technique. Kelly *et al.* (18) recently reported that self-quenching plays a role in the decay of triplet 3-phenylcyclopent-2-enone which has a triplet lifetime of 2.9 μs at room temperature. In the case of ketones **I–III** their triplet lifetimes are much shorter and as a result self-quenching is unlikely to be of importance.

The residual ΔOD observed for ketones **I**, **II**, **IV**, and **V** is proposed to be due to the corresponding enols. For isophorone (reaction [3]) the enol has been implicated as the intermediate

[3] 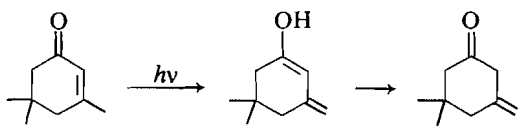

in the observed deconjugation reaction in heptane (19), while enol formation has also been suggested to play a role in the photochemistry of **VI** (20, 21), i.e.

[4] 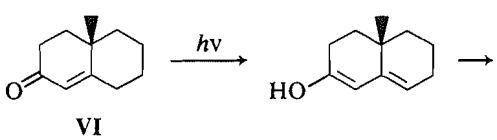

VI

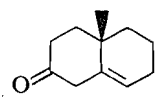

In the systems studied here the most efficient enol production would be via a hydrogen shift from the 6-position. In the case of **III** where the α-position is methyl substituted, no enol can be formed (22). This is consistent with the fact that no residual long-lived absorption was observed with **III** while it was with **I** and **II**. Upon the addition of amines this residual ΔOD increases. Since there is no evidence to suggest that different products are formed upon amine addition, and since the spectral and kinetic features are essentially the same whether TEA, DABCO, or diphenylamine is used as the quencher, it seems likely that the long-lived species observed in the amine quenching experiments is the same as that observed in the absence of amine. The effect of solvent on the residual ΔOD values also supports the assignment to the enol since in other systems some enols have reduced lifetimes in alcohols as opposed to alkanes or acetonitrile (10, 23).

Conclusion

Thus, our study demonstrates that there is nothing peculiar above the interaction of triplet states of cyclohexenones with amines, but rather that the dynamics of this interaction are similar to those observed with other carbonyl triplets (1–3). Mechanistic problems associated with Pienta's product analysis (9) remain to be resolved. Our results also illustrate the interpretative pitfalls that can arise in situations where complex decay kinetics are observed following flash excitation.

Acknowledgments

Thanks are due to Mr. S. E. Sugamori for technical assistance and to Professor N. J. Pienta for kindly providing some of the original traces obtained in his work. This work was supported in part by a grant (to D.I.S.) from the U.S. National Science Foundation (CHE-8320154).

1. R. S. Davidson. *In* Molecular association. Vol. 1. *Edited by* R. Foster. Academic Press, New York. 1975. p. 215.
2. J. B. Guttenplan and S. G. Cohen. J. Am. Chem. Soc. **94**, 4040 (1972); Tetrahedron Lett. 2163 (1972); A. H. Parola, A. W. Rosa, and S. G. Cohen. J. Am. Chem. Soc. **97**, 6202 (1975); S. Inbar, H. Linschitz, and S. G. Cohen. J. Am. Chem. Soc. **102**, 1419 (1980); K. S. Peters, S. C. Freilich, and C. G. Schaeffer. J. Am. Chem. Soc. **102**, 5701 (1980); C. G. Schaeffer and K. S. Peters. J. Am. Chem. Soc. **102**, 7566 (1980); J. D. Simon and K. S. Peters. J. Am. Chem. Soc. **103**, 6403 (1981).
3. D. I. Schuster and A. C. Brisimitzkas. Tetrahedron Lett. **23**, 4531 (1982); **23**, 4535 (1982).
4. R. C. Cookson, J. Hudec, and N. A. Mirza. Chem. Commun. 824 (1967).
5. D. A. Dunn, D. I. Schuster, and R. Bonneau. J. Am. Chem. Soc. **107**, 2802 (1985).
6. R. Bonneau. J. Am. Chem. Soc. **102**, 3816 (1980).
7. D. I. Schuster, R. Bonneau, D. A. Dunn, J. M. Rao, and J. Joussot-Dubien. J. Am. Chem. Soc. **106**, 2704 (1984).
8. D. A. Dunn. Ph.D. Dissertation. New York University, New York. 1985.
9. N. J. Pienta and J. E. McKimmey. J. Am. Chem. Soc. **104**, 5501 (1982).
10. N. J. Pienta. J. Am. Chem. Soc. **106**, 2704 (1984).
11. J. C. Scaiano. J. Am. Chem. Soc. **102**, 7747 (1980).
12. P. C. Tucker and D. I. Schuster. Unpublished results; P. C. Tucker. Ph.D. Dissertation. New York University, New York. 1988.
13. D. I. Schuster, P. B. Brown, L. J. Capponi, C. A. Rhodes,

J. C. SCAIANO, P. C. TUCKER, and D. WEIR. J. Am. Chem. Soc. **109**, 2533 (1987).
14. E. LEYVA, M. S. PLATZ, B. NIU, and J. WIRZ. J. Phys. Chem. **91**, 2293 (1987).
15. T. SHIDA and A. KIRA. J. Phys. Chem. **73**, 4315 (1969).
16. R. SCHEERER and M. GRATZEL. J. Am. Chem. Soc. **99**, 865 (1977).
17. N. J. PIENTA. Personal communication.
18. J. M. KELLY, T. B. H. MCMURRY, and D. N. WORK. J. Chem. Soc. Chem. Commun. 280 (1987).
19. J. D. SHILOFF and N. R. HUNTER. Can. J. Chem. **57**, 3301 (1979).
20. P. MARGARETHA and K. SCHAFFNER. Helv. Chim. Acta, **56**, 2884 (1973).
21. O. JEGER and K. SCHAFFNER. Pure Appl. Chem. **21**, 247 (1970).
22. P. G. SAMMES. Tetrahedron, **32**, 405 (1976).
23. G. PORTER and M. F. TCHIR. J. Chem. Soc. A, 3772 (1971).

Can. J. Chem. Downloaded from www.nrcresearchpress.com by 196.1.178.254 on 09/07/12
For personal use only.

A ^{13}C nuclear magnetic resonance study of selectivity in the binding of univalent counterions by heparin

PHOTIS DAIS
Department of Chemistry, University of Crete, 71110 Iraklion, Crete, Greece

AND

KEVIN R. HOLME AND ARTHUR S. PERLIN
Department of Chemistry, McGill University, Montreal, Quebec, Canada H3A 2A7

Received March 29, 1988

PHOTIS DAIS, KEVIN R. HOLME, and ARTHUR S. PERLIN. Can. J. Chem. **66**, 2601 (1988).

The binding selectivities of univalent counterions for heparin in the systems $Ca^{2+}/M^+/HEP$, where $M^+ = Li^+$, Na^+, K^+, Cs^+, TMA^+, have been studied by ^{13}C nuclear magnetic resonance spectroscopy. Chemical shift displacements of the various ^{13}C nuclei of heparin in these systems clearly indicate that the binding selectivity of the polymer for univalent counterions increases with an increase in the radius of the hydrated cation form, namely $Li^+ > Na^+ > K^+ > Cs^+ > TMA^+$. An explanation for this binding preference is offered on the basis of electrostatic and entropic terms, whereby the latter is reflected in changes in the hydration volumes of the univalent cations. Differences in the magnitude of these hydration volumes, in relation to the free energies of hydration, may account for a binding selectivity that favours the more highly hydrated ions.

PHOTIS DAIS, KEVIN R. HOLME et ARTHUR S. PERLIN. Can. J. Chem. **66**, 2601 (1988).

Faisant appel à la résonance magnétique nucléaire du ^{13}C et opérant dans les systèmes $Ca^{2+}/M^+/HEP$ dans lesquels $M^+ = Li^+$, Na^+, K^+, Cs^+ et TMA^+, on a évalué les sélectivités de liaison de contre-ions univalents pour l'héparine. Les déplacements chimiques des divers noyaux ^{13}C de l'héparine dans ces systèmes indiquent clairement que la sélectivité de liaison du polymère pour les contre-ions univalents augmente avec une augmentation du rayon de la forme hydratée du cation, soit $Li^+ > Na^+ > K^+ > Ca^+ > TMA^+$. On offre une explication pour cette préférence de liaison; elle est basée sur des termes électrostatiques et entropiques et ce dernier est le reflet de changements dans les volumes d'hydratation des cations univalents. Les différences dans l'amplitude de ces volumes d'hydratation, par rapport aux énergies libres d'hydratation, pourraient expliquer une sélectivité de liaison qui favorise les ions les plus hydratés.

[Traduit par la revue]

Introduction

^{13}C nuclear magnetic resonance spectroscopic studies on metal ion interactions with the biological polyelectrolyte heparin have been reported (1, 2) recently. The binding data for mixed counterion systems were correlated in a satisfactory manner with the two-variable theory of Manning (3, 4). A preliminary examination (2) of the binding selectivity of univalent counterions for heparin in the systems $Ca^{2+}/Na^+/HEP$ and $Ca^{2+}/K^+/HEP$ showed that Ca^{2+} binds to a greater extent in the presence of K^+ than of Na^+. This binding preference for Na^+ as compared with K^+, which is opposite to that observed in other experiments with heparin (5), invited clarification based on a systematic study using various alkali metal counterions.

In this report we present results obtained for the interaction of beef lung heparin with Ca^{2+} in the presence of a series of counterions covering a wide range of radii, namely, Li^+, Na^+, K^+, Cs^+, and also tetramethylammonium ion (TMA^+), all as chloride salts. The ^{13}C chemical shift displacements of the various carbons of heparin in these $Ca^{2+}/M^+/HEP$ systems show clearly that the binding selectivity of heparin for the univalent counterions increases as the radii of the cations in their hydrated forms increase.

Results and discussion

Table 1 summarizes the ^{13}C chemical shift displacements for all carbons of the main disaccharide unit (**1**) of heparin for the systems $Ca^{2+}/M^+/HEP$, where $M^+ = Li^+$, Na^+, K^+, Cs^+, TMA^+, at a total ionic strength of 0.4 M and constant ratio ($X = C_2/C_p = 1.0$) of Ca^{2+} ion (C_2) to heparin (C_p) concentration. In general, the chemical shift displacements for all carbons

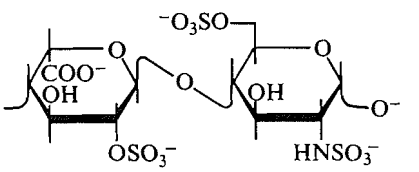

1

in these systems, reflecting the extent of binding of Ca^{2+} to heparin in the presence of the univalent counterion M^+, increase in the order $TMA^+ > Cs^+ > K^+ > Na^+ > Li^+$. This trend corresponds to a stronger binding of heparin by Ca^{2+} in the presence of ions Li^+ through TMA^+, and indicates that the binding selectivity of heparin for these univalent counterions follows in the order of an increase in the size of the hydrated ion. The same trend as shown in Table 1 was observed for all chemical shift displacements obtained by varying the X-ratio from 0.0 to 1.0 at constant total ionic strength.

Manning's theoretical (6) and experimental (7) studies on species selectivity suggest that site-binding mechanisms play no role in the association between univalent counterions and polyelectrolytes, and that counterion selectivity may be attributed to the local dielectric constant of the medium surrounding the polyelectrolyte. This dielectric constant is equivalent, perhaps, to a 1 M aqueous ionic solution (the local concentration of territorially bound univalent counterions is estimated (3, 6) to be of the order of 1 M for polyanions of typical charge densities). Using the Born approximation, Manning calculated the contribution of the molar free energy of transfer of a counterion from the bulk dilute solution of dielectric constant $D_{H_2O} = 78.3$ to the local polyanion environment with dielectric constants (8)

Printed in Canada / Imprimé au Canada

Can. J. Chem. Downloaded from www.nrcresearchpress.com by 196.1.178.254 on 09/07/12
For personal use only.

TABLE 1. Displacements in the chemical shifts[a] of the ^{13}C nuclei of univalent salts of beef lung heparin, induced by calcium ion[b,c]

Carbon atom	Univalent counterion				
	Li^+	Na^+	K^+	Cs^+	TMA^+
I-1	−16.3	−21.6	−21.6	−31.6	−31.7
I-2	−31.7	−35.4	−37.1	−59.6	−112.7
I-3	−43.3	−51.0	−48.6	−83.4	−145.0
I-4	−2.7	−1.6	−0.1	−25.6	−45.8
I-5	−1.2	+9.6	+9.1	−6.8	−28.2
I-6	+13.5	+30.7	+36.8	+53.3	+97.0
A-1	+23.6	+28.1	+35.8	+34.6	+38.5
A-2	−2.7	−2.6	−2.4	−6.1	−22.1
A-3	+3.9	+9.6	+8.4	+0.6	+16.2
A-4	+12.8	+11.1	+15.0	+25.7	+51.8
A-5	−5.7	−7.1	−7.4	−12.7	−13.8
A-6	+1.5	+3.0	+6.1	+10.3	+17.6

[a]Negative values denote upfield shift.
[b]In D_2O at 70°C.
[c]At $X = C_2/C_p = 1$ and total ionic strength 0.4 M. C_2 is $[Ca^{2+}]$ and C_p is $[M^+/HEP]$.

$D_{Cs^+} = 70.6$ and $D_{Na^+} = 66.7$, corresponding to their respective 1 M ionic solution. His results indicated that the polyelectrolyte is more selective for the larger Cs^+ counterion than the smaller Na^+ (in terms of their *non*-hydrated radii), because the positive free energy of transfer to an environment of lower dielectric constant was less for the larger ion. Alternatively, it is possible to express this selectivity in terms of the size of their hydrated forms, because hydrated Na^+ is larger than hydrated Cs^+. Although the use of crystal radii in the Born equation (6) seems justified for ions in solution, there are other pitfalls (9) in employing the Born-type model: (*a*) The radius of an ion, or even an uncharged species, changes on transfer from the gas to the liquid phase, where it is subject to compressional forces. (*b*) The radius of the dissolved species depends on its surface charge density. Hence any model of solvation that uses a continuous charging process to evaluate the electrostatic energy must include a variable parameter for the ion size. (*c*) The radius depends on the degree of dielectric saturation induced by the ion in the solvent. (*d*) Realistic functions must be used to represent the dielectric constants in the vicinity of the ions, rather than of the bulk solution. (*e*) By considering the dielectric continuum model, structural effects on the electrical interactions of ions and solvent molecules are omitted.

In view of the very small changes in the free energies of hydration accompanying the binding of monovalent counterions to heparin, as suggested earlier (6, 10), the aforementioned factors questioning the validity of the simple Born approximation may play a decisive role in determining the correct order of binding selectivity.

Although this assessment of size selectivity is supported by a number of experiments (5, 7, 10–14), the converse order of specificity has been observed in others (15–18), as well as the present ones, i.e., increased binding with an increase in the hydrated radius ($Li^+ > Na^+ > K^+$). These diverse findings raise the possibility that, apart from free energy changes accompanying the transfer of an ion from the bulk solution to the surface of the polyanion, entropy effects accounting for the relative space in which territorial binding occurs also play an important role in determining binding selectivity.

Some qualitative predictions can be made, on the basis of Manning's selectivity rule (6). In his treatment of binding selectivity, Manning derived the following thermodynamic equation:

$$[1] \quad \alpha = \frac{\theta_2/X_2}{\theta_1/X_1} = \frac{V_2}{V_1} e^{-(\delta\mu_2^0 - \delta\mu_1^0)/RT}$$

where θ_1 and θ_2 are the fractions of ions 1 and 2, respectively, bound to the polyanions, X_1 and X_2 are the ratios of the concentrations of free counterions 1 and 2, respectively, to the total concentration ($C_t = C_i + C_p$, $i = 1, 2$) of the solution, V_1 and V_2 are the volumes in which counterions 1 and 2 are considered bound, and $\delta\mu_1^0$ and $\delta\mu_2^0$ have the meaning of free energy of transfer from the bulk solution to the environment near the polyanion. Moreover (4, 6),

$$[2] \quad \delta\mu_i^0 = \mu_{ib}^0 - \mu_{if}^0, \quad i = 1, 2$$

where μ_{ib}^0 and μ_{if}^0 represent the free energy of hydration of ion i in the bound and free state, respectively. This means that $\delta\mu_i^0$ primarily measures the change in hydration free energy as a counterion passes from the free to the bound state.

In eq. [1], when $\alpha > 1$, then counterion 2 binds the polyanion more selectively than counterion 1. The value of α depends both on the relative magnitudes of V_1 and V_2, and of $\delta\mu_1^0$ and $\delta\mu_2^0$. There are several choices for the parameters $V_i e^{-\delta\mu_i^0/RT}$, some of which have been discussed in ref. 6:

(*i*) $V_1 e^{-\delta\mu_1^0/RT} = V_2 e^{-\delta\mu_2^0/RT}$ leads to $\alpha = 1$, which is contrary to the experimental observations on selectivity.

(*ii*) $V \neq V_2$ and $e^{-\delta\mu_1^0/RT} = {}^{-\delta\mu_2^0/RT}$ leads to $\alpha \gtrless 1$, depending on the relative magnitudes of V_1 and V_2. Although variations in the condensed volumes, depending on the nature of the counterion, have been suggested by many authors (14, 19, 20), equality in the ΔG values for the bound and free ions seems improbable because, then, the determining factor is not the electrostatic interaction, as the polyelectrolyte theories imply, but an entropic change accompanying a change in ion hydration.

(*iii*) $V_1 = V_2$ and $e^{-\delta\mu_1^0/RT} \neq e^{-\delta\mu_2^0/RT}$, according to the "monolayer condensation" model by Iwasa (21). In this case, selectivity is purely electrostatic in nature and depends solely on the relative magnitude of the free energy terms in eq. [1].

(*iv*) $V_1 \neq V_2$ and $e^{-\delta\mu_1^0/RT} \neq e^{-\delta\mu_2^0/RT}$; then, selectivity must depend on the relative magnitude of differences between volumes and free energies of hydration. If there are minute changes in the free energies $\delta\mu_2^0 - \delta\mu_1^0$ in the range of −0.2 to −0.5 kcal (at 25°C), as suggested in the literature (6, 10), and assuming that the less hydrated ion 2 binds to heparin in preference to ion 1, then

$$[3] \quad \alpha = \frac{V_2}{V_1} \times (e^{+0.2/RT} \text{ to } e^{+0.5/RT}) = \frac{V_2}{V_1} \times (1.4 \text{ to } 2.3)$$

If $V_1 > V_2$ (1.4 to 2.3), then α becomes less than unity and a reversal of binding selectivity is to be expected, favoring the more hydrated ion 1.

In the monolayer condensation model represented by case (*iii*), the condensation volumes for both ions 1 and 2 are taken to be equal. This choice of a constant condensation volume, which is a general hypothesis in the counterion condensation model (3, 4), has been criticized by many authors (11, 14, 19, 20), as already mentioned. If one has to assume territorial binding in which the counterions bound to the polyanion retain their primary hydration sheath, then the condensation volume, which may be approximated by the volume of the hydrated ion, must be different for each cation, and decrease from Li^+ through

Can. J. Chem. Downloaded from www.nrcresearchpress.com by 196.1.178.254 on 09/07/12
For personal use only.

TABLE 2. Intrinsic volumes (V_{in}, in Å^3), hydration numbers (h), and hydration volumes (V_h (M^+), in Å^3) of various counterions

Counterion	V_{in}[a]	h[b]	$V_h(M^+)$	h[c]	$V_h(M^+)$	h[d]	$V_h(M^+)$	h[e]	$V_h(M^+)$
Li^+	2.0	7	212	4.9	149	4.7	144	22	662
Na^+	6.4	5	156.4	3.1	102.5	3.6	114.4	13	396.4
K^+	15.3	2	75.3	2.1	78.3	2.0	75.3	7	225.3
Cs^+	25.5	1.5	70.5	1.0	55.5	1.4	67.5	6	205.5

[a]From refs. 24 and 25.
[b]Based on ionic mobility measurements (ref. 28).
[c]Based on nmr measurements (refs. 29 and 30).
[d]Based on entropy measurements (ref. 22, p. 57).
[e]Based on transference numbers (ref. 31).

Cs^+. According to eq. [3] and the aforementioned inequality $V_1 > V_2$ (1.4–2.3), this may account for the binding selectivity observed.

A possible way to evaluate these considerations in a quantitative, although simplified manner, is to calculate the hydration volumes, $V_h(M^+)$, of the various cations studied. In principle, hydration volumes can be calculated through empirical equations, using the parameters of the hydration number (h) determined experimentally, and the effective volume (V_h) taken up by one water molecule in the primary hydration sheath. The latter quantity is indefinite, but it can be approximated (22) by the volume occupied by a water molecule in liquid water at 25°C, which is 30 Å^3. According to Robinson and Stokes (22), the volume of the hydrated cation is

$$[4] \quad V_h(M^+) = 30h + V^+$$

where V^+ is the apparent molal volume of the cation in Å^3. V^+ can be either estimated from the apparent molal volume of the salt, V_{app}, in solution by means of the equation (22)

$$[5] \quad V^+ = V_{app} - 6.47Z_1 \cdot r_-^3$$

where Z_1 is the cation valency and r_- the crystal radius of the anion (in Å), or it can be equated with the intrinsic volume (V_{in}), which can be identified with the actual volume occupied by the unhydrated cation in solution (23). The latter volume will be used in eq. [4], since it has been determined experimentally from the concentration dependence of the compressibility of the solution (24, 25).

The selection of the hydration number is quite uncertain, as there is a broad range of values in the literature (26, 27) for the hydration number of each cation, depending on methods and assumptions used. Nevertheless, a general pattern of hydration numbers, decreasing steadily from Li^+ to Cs^+, has been observed experimentally (26, 27). For our calculations, we have used the results of methods that determine strongly bound water molecules in the primary hydration sheath, and also those solvent molecules more distant but still under the attractive influence of the cation.

Table 2 summarizes the intrinsic volumes, the hydration numbers from various sources, and the calculated hydration volumes of cations Li^+ through Cs^+. The hydration volumes decrease steadily from the former to the latter, following the decreasing order of the number of the water molecules bound to the cations. Although these data are only an approximation and lack the degree of accuracy necessary for physical relevance, they clearly indicate that the hydration volumes (eq. [1]) influence the binding selectivity according to their relative magnitude, as well as the magnitude of the free energy change accompanying the transfer of counterions from the free to the bound state.

Of all the cations studied, TMA^+ ion binds the least strongly to heparin. This is in accord with earlier findings (2, 13, 15, 32), in which tetraalkylammonium ions showed a much smaller affinity for polyelectrolytes than do metal ions. TMA^+ is considered to be unhydrated or sparingly so, as are other tetraalkylammonium salts (ref. 23, pp. 77–83; ref. 26, Chaps. 2, 3, 4), although its unhydrated form has a relatively large molecular volume (95.9 Å^3) (33). Presumably, the energetic factors in eq. [1] must be large enough to compensate for entropy changes in the binding process. Although the inclusion of entropic effects on binding selectivity in terms of hydration volumes appears to be valid, the absolute magnitude of these volumes requires an accurate determination of the hydration numbers of the ions in solution. Due to the wide disparity among literature values (23, 26, 27), the present results may serve more as a reflection of the trend in counterion binding selectivity than as a definitive statement.

Other factors to be considered in interpreting binding data are the nature of the functional groups of the polyanion, and the degree of uniformity in their distribution. Structural differences among polymers represent variations in the local environments of the functional groups and, hence, in their standard free energies, which may lead to differences in binding selectivity. This is clearly a possibility with heparin, because specimens of this polymer may differ widely in structure, depending on their origin and method of isolation. Although, usually, the major type of repeating sequence consists of (1→4) linked residues of α-L-iduronic acid 2-sulfate and 2-deoxy-2-sulfamino-α-D-glucose 6-sulfate (**1**), such constituents as β-D-glucuronic acid and 2-acetamido-2-deoxy-α-D-glucose are relatively more prominent in heparin from hog mucosa than from beef lung (34). The latter type has been used in our studies on counterion binding, by choice, because of its higher degree of structural homogeneity with respect to disaccharide unit **1**. As heparin of the hog mucosal type is much more readily available commercially, it is likely to have been used in some of the other studies on counterion binding. This may help to account for some disagreement on ion selectivity in the literature, such as between Na^+ and K^+, for which differences in binding affinities are relatively small. To facilitate quantitative studies on binding, a synthetic polyelectrolyte having carboxyl and sulfate groups distributed uniformly in a known pattern should serve as a useful model.

Experimental

Sodium heparin, isolated from beef lung, was supplied by Upjohn

Can. J. Chem. Downloaded from www.nrcresearchpress.com by 196.1.178.254 on 09/07/12
For personal use only.

Co. of Canada. Purified by dialysis against distilled water, the heparin gave an equivalent weight of 178, and a sulfate to carboxylate ratio of 2.4 (1). To prepare the required univalent salts of heparin, a 2.5% w/v solution of sodium heparin was passed through a column of Amberlite IR 120 (H^+) ion-exchange resin, and the acid eluate was divided into five equal portions. The eluate fractions were then immediately neutralized with 1.0 M solutions of LiOH, NaOH, KOH, CsOH, and tetramethylammonium (TMA) hydroxide, respectively, and freeze-dried to give the Li^+, Na^+, K^+, Cs^+, and TMA^+ salts of heparin.

For ^{13}C nmr spectroscopy, solutions were prepared by weighing appropriate amounts of the heparin salts, $CaCl_2$, and the respective chloride salt of the univalent counterion into the nmr tube, followed by 0.50 mL of deuterium oxide. The polymer concentration in all samples was 0.10 M (0.40 equiv./L) based on the equivalent weight of heparin, and the ionic strength (I) was 0.4 M. For each of the five univalent counterions, samples containing calcium ion concentrations of 0.00, 0.02, 0.05, 0.07, and 0.10 M were prepared. The ^{13}C nmr spectra were acquired at 70°C with a Varian XL300 spectrometer operating at 75.4 MHz, and the chemical shifts were referenced to internal DMSO at δ 39.6.

Acknowledgements

The authors express their gratitude to McGill University and the Natural Sciences and Engineering Research Council of Canada for generous support.

1. P. Dais, Q.-J. Peng, and A. S. Perlin. Carbohydr. Res. **168**, 163 (1987).
2. P. Dais, Q.-J. Peng, and A. S. Perlin. Can. J. Chem. **65**, 1739 (1987).
3. G. S. Manning. Q. Rev. Biophys. **2**, 179 (1978).
4. G. S. Manning. Acc. Chem. Res. **12**, 443 (1979).
5. J. Mattai and J. C. T. Kwak. Biochim. Biophys. Acta, **677**, 303 (1981).
6. G. S. Manning. J. Phys. Chem. **88**, 6654 (1984).
7. G. S. Manning. Biopolymers, **20**, 2337 (1981).
8. R. Rottel. *In* Water. Vol. 3. *Edited by* F. Franks. Plenum Press, New York. 1973.
9. B. Case. React. Mol. Electrodes, 45 (1971); B. Case and R. Parsons. Trans. Faraday Soc. **63**, 1224 (1967).
10. G. E. Boyd and D. P. Wilson. Macromolecules, **15**, 78 (1982).
11. J. Mattai and J. C. T. Kwak. Macromolecules, **19**, 1663 (1986).
12. T. J. Podlas and P. Ander. Macromolecules, **3**, 154 (1970).
13. C. Tondre and R. Zana. J. Phys. Chem. **75**, 3367 (1971).
14. J. Mattai and J. C. T. Kwak. J. Phys. Chem. **86**, 1026 (1982).
15. M. L. Bleam, C. F. Anderson, and M. T. Record, Jr. Proc. Natl. Acad. Sci. U.S.A. **77**, 3085 (1980).
16. N. Ise and T. Okubo. Macromolecules, **11**, 439 (1978).
17. V. P. Strauss and Y. P. Leung. J. Am. Chem. Soc. **87**, 1476 (1965).
18. M. Rinaudo and M. Milas. *In* Polyelectrolytes and their application. *Edited by* E. Sélègny. Reidel, Dordrecht, Holland. 1975. p. 31.
19. J. A. Marinsky, R. Baldwin, and M. M. Reddy. J. Phys. Chem. **89**, 5303 (1985).
20. M. Gueron and G. Weisbuch. Biopolymers, **19**, 353 (1980).
21. K. Iwasa. Biophys. Chem. **9**, 397 (1979).
22. R. A. Robinson and R. H. Stokes. Electrolyte solutions. Butterworth Scientific Publications, London. 1955. p. 249.
23. J. E. Desnoyers and C. Jolicoeur. Hydration effects and thermodynamic properties of ions. *In* Modern aspects of electrochemistry. No. 5. *Edited by* J. O'M. Bockris and B. E. Conway. Plenum Press, New York. 1969. Chap. 1. p. 26.
24. J. Padova. J. Chem. Phys. **40**, 691 (1964).
25. K. Tamura and T. Sasaki. Bull. Chem. Soc. Jpn. **36**, 875 (1963).
26. J. Burgess. Metal ions in solution. Ellis Harwood Ltd., Chichester. 1978. Chap. 5.
27. B. E. Conway and J. O'M. Bockris. Ionic solution. *In* Modern aspects of electrochemistry. No. 1. *Edited by* J. O'M. Bockris and B. E. Conway. Butterworth Scientific Publications, London. 1954. Chap. 2.
28. E. Glueckauf. Trans. Faraday Soc. **51**, 1235 (1955).
29. J. C. Hindman. J. Chem. Phys. **36**, 1000 (1962).
30. E. J. Sutter, D. M. Updegrove, and J. F. Harman. Chem. Phys. Lett. **36**, 49 (1985).
31. A. T. Rutgers and Y. Hendrikx. Trans. Faraday Soc. **58**, 2184 (1962).
32. C. F. Anderson, M. T. Record, Jr., and P. A. Hart. Biophys. Chem. **7**, 301 (1978).
33. J. T. Edward. J. Chem. Educ. **47**, 261 (1970).
34. A. S. Perlin, M. Mazurek, L. B. Jaques, and L. W. Kavanagh. Carbohydr. Res. **7**, 369 (1968); A. S. Perlin, B. Casu, G. R. Sanderson, and L. F. Johnson. Can. J. Chem. **48**, 2260 (1970).

Can. J. Chem. Downloaded from www.nrcresearchpress.com by 196.1.178.254 on 09/07/12
For personal use only.

Atrazine hydrolysis in aqueous suspensions of humic acid at 25.0°C[1]

DONALD S. GAMBLE[2] AND SHAHAMAT U. KHAN
Land Resource Research Centre, Agriculture Canada, Ottawa, Ont., Canada K1A 0C6

Received August 5, 1987[3]

DONALD S. GAMBLE and SHAHAMAT U. KHAN. Can. J. Chem. **66**, 2605 (1988).

The acidic properties of a Chernozemic humic acid were determined by equilibrium titration. The number of carboxyl groups is 2.828 (mmol/g) ± 0.5%. The results were used for an investigation of Brönsted acid catalysis of atrazine hydrolysis by a suspension of the humic acid. There is sufficient sorption so that the rates of change of atrazine and product hydroxyatrazine in solution differ both from each other and form the rate of atrazine conversion on the catalytic sites. An important objective of this work was the separate determination of the sorption equilibrium constants for atrazine and hydroxyatrazine, and the rate constant for atrazine conversion on the catalytic sites. All three constants are relevant to environmental research. The apparent rate constants for changes in solution are experimental artifacts however, not useful for such research. Calculated in terms of carboxyl sorption sites in the free acid form, the sorption equilibrium constants were 1.74×10^2, $\sigma = 0.03 \times 10^2$ and 8.5×10^2, $\sigma = 2.3 \times 10^2$, for atrazine and hydroxyatrazine, respectively. The rate constant for conversion on catalytic sites ranges from 1.8×10^{-1} day^{-1} ± 20% to 2.9×10^{-1} day^{-1} ± 20%, for atrazine coverage of sites from 9.0 (μmol/g) to 1.0 (μmol/g).

DONALD S. GAMBLE et SHAHAMAT U. KHAN. Can. J. Chem. **66**, 2605 (1988).

Faisant appel à une titrage à l'équilibre, on a déterminé les propriétés acides d'un acide humique Chernozémique. Le nombre de groupements carboxyliques est de 2,828 (mmol/g) ± 0,5%. On a utilisé ces résultats pour réaliser une étude de la catalyse acide de Brönsted sur l'hydrolyse de l'atrazine par une suspension de l'acide humique. La sorption est telle que, en solution, les taux de changement de l'atrazine et de son produit l'hydroxyatrazine diffèrent les uns des autres et qu'ils forment le taux de conversion de l'atrazine sur les sites catalytiques. Un objectif important de ce travail était de déterminer séparément les constantes d'équilibre de sorption de l'atrazine et de l'hydroxyatrazine ainsi que la constante de vitesse de conversion de l'atrazine sur les sites catalytiques. Les trois constantes sont importantes pour les recherches sur l'environnement. Toutefois, les constantes apparentes de vitesse pour les changements en solution sont des artéfacts qui ne sont pas utiles pour ces recherches. Si on les calcule en fonction des sites carboxyliques de sorption sous la forme d'acide libre, les constantes d'équilibre de sorption sont de $1{,}74 \times 10^2$, $\sigma = 0{,}03 \times 10^2$ et $8{,}5 \times 10^2$, $\sigma = 2{,}3 \times 10^2$ respectivement pour l'atrazine et pour l'hydroxyatrazine. La constante de vitesse pour la conversion des sites catalytiques varie de $1{,}8\ 10^{-1}$ jours^{-1} ± 20% à $2{,}9 \times 10^{-1}$ jours^{-1} ± 20% pour des couvertures des sites par l'atrazine allant de 9,0 (μmol/g) à 1,0 (μmol/g).

[Traduit par la revue]

Introduction

In general, chemical reactions and microbiological processes both contribute to the degradation of organic chemical pesticides in soils. For some pesticides, microbiological processes are dominant. In the case of atrazine, chemical reaction can be quite important. Because of their ion exchange properties, acid soils can have higher concentrations of acid catalysts inside of the soil particles than they do in the external soil solutions. If the ionic strength is sufficiently low, a nearly neutral soil solution pH might not indicate a lack of catalytic activity. The general importance of sorption processes and hydrolysis reactions is indicated by the fact that pesticide regulatory agencies in Canada, the United States and Europe require sorption and hydrolysis tests as part of the documentation for commercial pesticide registration.

Rao and Davidson have commented that multiple regression equations could not be developed from the available literature because the information for physical, chemical, and microbiological properties of soils was inadequate (1). Some information is available, however. Statistical correlations in the literature generally implicate humic materials as an important factor. A review of Stevenson for example (2), presents evidence for this accumulated since 1962 (3–13). A number of authors have consequently investigated the interactions of organic pesticides with humic materials (5, 7, 14–33). The acidic functional groups of humic materials are an important factor (32, 34–38), and Perdue has examined their effects from the point of view of Brönsted acid–base catalysis theory (39).

Atrazine sorption by soils has been reported to be not only pH dependent, but also reversible (40, 41). Previous work with atrazine in fulvic acid solutions has demonstrated interactions between atrazine and unionized carboxyl groups and hydrogen ions (42–45). The atrazine – fulvic acid solution phase work has indicated that unionized carboxyl groups are hydrogen bonding sites. In addition, the only two catalysts for atrazine hydrolysis identified were hydrogen ions and unionized carboxyl groups (44–47). Under field conditions, some atrazine could be sorbed from solution into water swollen particles, encountering an internal gel solution containing unionized carboxyl groups and free hydrogen ions. The stoichiometrically exact investigation of such a system will require a humic acid for which the acid properties have been standardized in a way comparable to that of the fulvic acid. Unlike some fulvic acids, however, no humic acid standardizations of this type have yet been reported.

Humic acid titration curves have been in the literature for many years (46–52). A new investigation is required however, for at least four reasons. (*1*) Every humic acid has its own numerical values for its acidic, solubility, and other polyelectrolyte properties. (*2*) A humic acid is a carboxylic type cation exchanger. Marinsky's work (53) has shown that a titration of such a system is affected by intraparticle diffusion and governed by the Donnan potential, as discussed by Helffrich (54). Simple solution phase calculations are therefore not applicable. (*3*) The pH dependent dissolution of the humic acid must be accounted for during the calculation and interpretation of titration data. (*4*) H^+ molarity measurements are

[1]Contribution No. 87-65 from Land Resource Research Centre.
[2]To whom correspondence should be addressed.
[3]Revision received May 31, 1988.

Can. J. Chem. Downloaded from www.nrcresearchpress.com by 196.1.178.254 on 09/07/12
For personal use only.

more useful for chemical calculations than conventional pH measurements are.

Heterogeneous catalysis experiments do not all have the same purposes. They therefore do not all have the same experimental design or the same calculation procedures. In particular, pesticide persistence and movement problems in soil create a need for the separate determination of sorption equilibrium constants and kinetic rate constants. For an atrazine–humic system, the mixture of chemically different catalytic sites and the possibility of catalyst poisoning by hydroxyatrazine product must be accounted for. It is also important that true rate constants be determined, and not just apparent rate constants which are experimental artifacts. Measurements which are confined to initial rate measurements and to the conventional determination of the algebraic products of a rate constant and a sorption equilibrium constant are not adequate for practical purposes.

A consideration of the above factors, the types of correlations referred to by Rao and Davidson (1), and the availability of an analytical chemical method for the simultaneous determination of atrazine and hydroxyatrazine in the solution phase led to two specific research objectives. (*1*) Acid–base standardization of the humic acid, with its pH dependent solubility accounted for. (*2*) Use of the standardized humic acid, for the separate determination of sorption equilibrium constants for atrazine and hydroxyatrazine and the conversion rate constant of atrazine on the catalytic sorption sites.

Theory[4]

I. Standardization of the humic acid

By definition, a humic acid is a humic fraction that is insoluble in the free acid form but soluble in the Na^+ salt form. Undissolved humic acid in an aqueous system can therefore be expected to behave as a carboxylic-type cation exchanger having pH dependent solubility. The important equilibria, such as cation exchange and solubility, are governed by the acidic functional groups. They especially include the carboxyl groups. The carboxyl groups are, however, distributed over the polymer molecules of polydisperse polyelectrolyte. At a given point in an acid–base titration curve, the most general case is that a particular polyelectrolyte molecule will have some of its carboxyl groups protonated and some of them unprotonated. When the mole fraction of its unprotonated carboxyl groups becomes sufficiently great, the polyelectrolyte molecule will go into solution. The numerical value of this mole fraction is not known, and the possibility of it being less than 1 must be allowed. The reason for this might include hydrogen bonding and high charge density. The most general possible postulate is that each of the two physical phases will have both unionized carboxyl groups and carboxylate anions. Whether or not unionized carboxyl groups can be detected and measured in the external solution and whether or not carboxylate anions can be detected and measured in the undissolved humic acid are analytical chemistry questions. The sorption of water creates an internal gel solution in the particles of undissolved humic acid, just as it does with other cation exchanges (42, 45, 54).

Equation [1] describes the acid dissociation equilibrium for the mixture of chemically nonidentical carboxyl groups in the internal gel phase.

$$[1] \quad HA \overset{\overline{K}_{GA}}{\rightleftharpoons} H^+ + A^-$$

$$\overline{K}_{GA} = \frac{M_{GH} M_{GA}}{M_{GAH}}$$

The subscripts designate the molarities of the carboxyl groups AH, free protons H^+, and carboxylate anions A^- in the gel solution. Because it is defined for a mixture of carboxyl groups, $\overline{K}_{GA}$ is known to be a weighted average equilibrium function (49, 55–60). In terms of the effects of humic acid on atrazine, this equilibrium is important for at least two reasons. One is that unionized carboxyl groups and free protons both act as catalysts for the hydrolysis of atrazine (39, 45, 58, 64). Since their catalytic effects are different, net hydrolysis rates should depend on the gel phase concentrations of both of them. The acid dissociation equilibrium function $\overline{K}_{GA}$ is therefore very relevant to the Brönsted acid catalysis of atrazine. Marinsky has demonstrated methods for estimating the gel phase K_A values of carboxylic cation exchangers (53). It is found, however, that pH dependent solubility prevents the proper use of Marinsky's method for humic acid. The detailed proof is available.[4] The acid–base standardization of the humic acid is therefore confined to a Gran's function method for the equivalence point, and a titration curve for total gel phase acid. Equation [2] gives the Gran's function in terms of the measured H^+ molarity.

$$[2] \quad Y = VM_H$$

V is sample solution volume in L. The total gel phase acid Q_{GH} is obtained from the simple material balance eqs. [3] and [4].

$$[3] \quad Q_{GH} = Q_H - (M_H - K_W/M_H)V$$

$$[4] \quad Q_H = Q_A - Q_B$$

where Q_A and Q_B are moles of initial acid and added base, respectively.

II. The heterogeneous catalysis system

Figure 1 shows the overall scheme for atrazine in a sample having undissolved humic acid and water. During the reaction, both atrazine and hydroxyatrazine have equilibrium distributions between sorption sites within the interior gel solutions of the humic acid particles, and the external solution. Assuming reversible labile equilibria, the sorption and desorption processes are expected to be quite fast relative to the chemical reaction that might have half lives of days or weeks.

The sorption sites are assumed to be unneutralized carboxyl groups —COOH, which act as catalytically active hydrogen bonding sites. The experimental evidence for this postulate has been provided by recent investigations of atrazine complexing by fulvic acid (42–44). The collection of chemically nonidentical carboxyl groups is expected to have a spectrum of weak acid K_a values (39, 46, 47, 51). According to Brönsted acid catalysis theory and the work of Perdue, this is expected to cause the reaction rate constant to vary with site coverage (39).

In a realistic experiment, the site coverage will be small so that site saturation will not occur. Atrazine and hydroxyatrazine might nonetheless compete for sorption sites. Since usually no two compounds will be equally strongly sorbed, it cannot be assumed that site coverage will remain constant during the course of an experiment. For the most general case, it is therefore seen from simple material balance arguments that

[4]The detailed development of the heterogeneous kinetics, accounting for variable site coverage below saturation, catalyst poisoning, and separate calculation of sorption equilibrium functions is available from the Depository of Unpublished Data. A complete set of data may be purchased from the Depository of Unpublished Data, CISTI, National Research Council of Canada, Ottawa, Ont., Canada K1A 0S2.

Can. J. Chem. Downloaded from www.nrcresearchpress.com by 196.1.178.254 on 09/07/12
For personal use only.

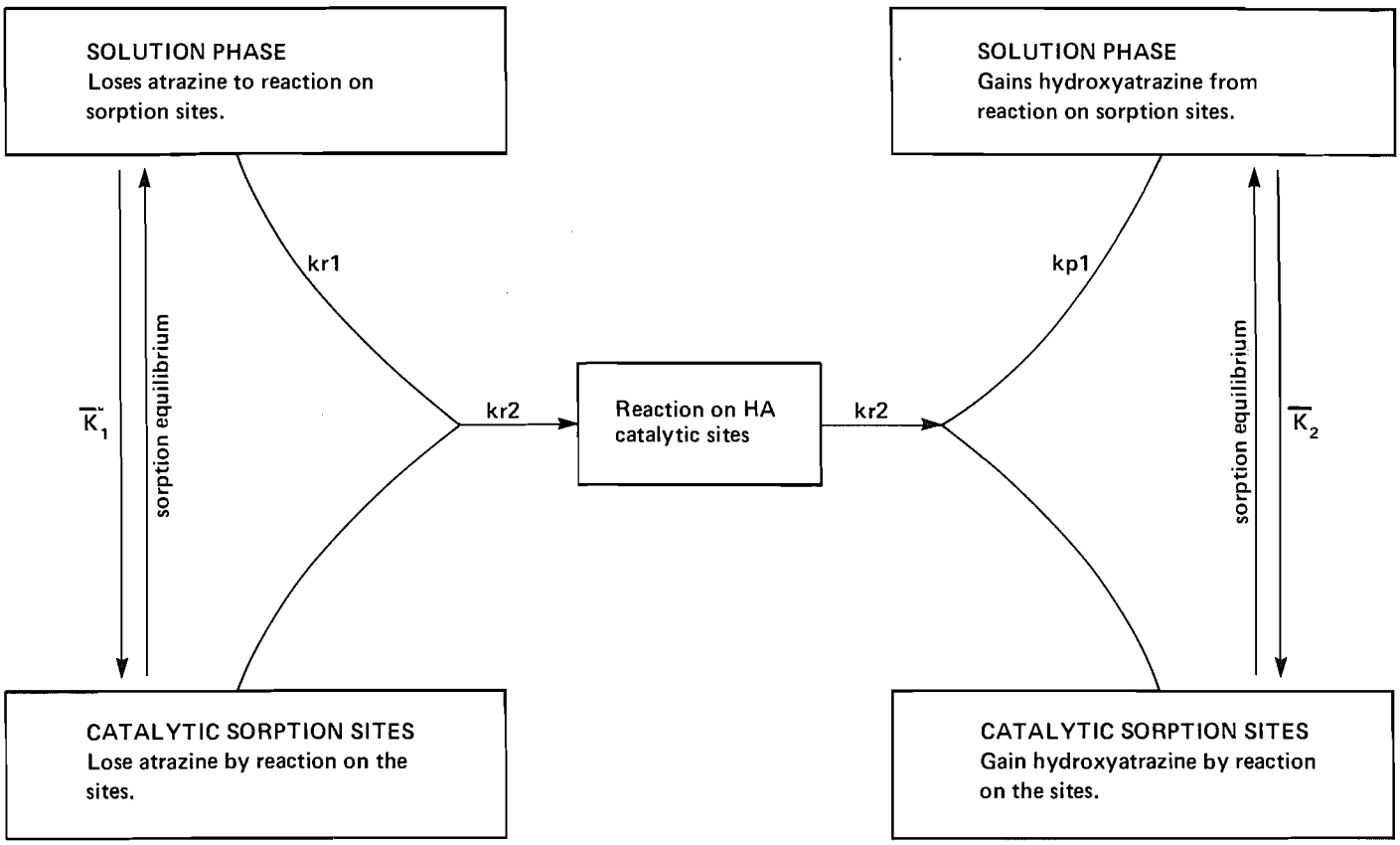

FIG. 1. Heterogeneous catalysis systems: a suspension of humic particles in an aqueous atrazine solution. The catalytic sorption sites are carboxyl groups in the H^+ form, in the ion exchange gel phase.

there are three processes for atrazine: (*i*) the conversion of atrazine to hydroxyatrazine on the catalytically active sorption sites; (*ii*) the net removal of atrazine from the sorption sites; (*iii*) the net removal of atrazine from the external solution. There are three corresponding processes for the accumulation of hydroxyatrazine. A direct consequence of these processes is that the rate at which atrazine disappears from solution and the rate at which hydroxyatrazine appears in solution cannot be assumed to be the same. From an environmental point of view, it is important to recognize that the apparent reaction rate constants and half lives measured directly in the solution could be quite different from the real reaction rate constants and half lives for the whole system. Misleading predictions could result if this is not clearly understood. The kinetic rate laws must therefore be formulated in a way that accounts for the phenomena described.

III. Sorption equilibria

Reversible labile equilibria are assumed to exist for the sorption of atrazine and of hydroxyatrazine from solution. The atrazine and hydroxyatrazine are also expected to compete for protonated carboxyl groups as sorption sites. Equation [5] defines the equilibrium function $\bar{K}_1$ for the sorption of atrazine. In the most general case, $\bar{K}_1$ will be a weighted average equilibrium function (47).

$$[5] \quad \mathrm{At} + \mathrm{HA} \overset{\bar{K}_1}{\rightleftharpoons} \mathrm{At.HA}$$

$$\bar{K}_1 = \frac{\theta_{At}}{M_{At}\theta_0}$$

M_{At} is the molarity of atrazine in the solution. θ_{At} is the moles of atrazine sorbed per g of humic acid. θ_0 is the moles of carboxyl groups unoccupied by sorbed molecules, per g of humic acid. In the same way, eq. [6] described the equilibrium sorption of hydroxyatrazine.

$$[6] \quad \mathrm{AtOH} + \mathrm{HA} \overset{\bar{K}_2}{\rightleftharpoons} \mathrm{AtOH.HA}$$

$$\bar{K}_2 = \frac{\theta_{AtOH}}{M_{AtOH}\theta_0}$$

where M_{AtOH} is the molarity of hydroxyatrazine in the solution and θ_{AtOH} is the moles of sorbed hydroxyatrazine per g of humic acid. The coverage of catalytic sorption sites might be important for two reasons. One is that the most strongly catalytic sites may be preferentially occupied. The other is that hydroxyatrazine sorption might cause catalyst poisoning. There is no available method however, for directly measuring the separate site coverages by atrazine and hydroxyatrazine. It is therefore important to estimate $\bar{K}_1$ and $\bar{K}_2$ by an indirect method. Because both compounds can be simultaneously monitored in the external solution throughout kinetics runs, this can be done. The calculation is based on eq. [7], which has been obtained from material balance relationships combined with eqs. [5] and [6].

$$[7] \quad Y_c = \bar{K}_1 M_{At} + \bar{K}_2 M_{AtOH}$$

$Y = (\theta_c/\theta_0)$ is the mole ratio of occupied to free carboxyl sorption sites. It is also an experimental quantity. The most general possible postulate for a system having a mixture of sorption sites is that $\bar{K}_1$ and $\bar{K}_2$ will depend on sorption site

Can. J. Chem. Downloaded from www.nrcresearchpress.com by 196.1.178.254 on 09/07/12
For personal use only.

Can. J. Chem. Downloaded from www.nrcresearchpress.com by 196.1.178.254 on 09/07/12
For personal use only.

coverage and hence on solution composition (47). Apparently constant values of the atrazine – fulvic acid binding equilibrium function have been observed experimentally however, by Haniff *et al.* (44). A possible reason for this result was that only a small fraction of the carboxyl binding sites was occupied by atrazine. For the same reason it is postulated that $\bar{K}_1$ and $\bar{K}_2$ will be experimentally indistinguishable from constants. This permits the use of the partial derivatives in eqs. [8] and [9].

$$[8] \quad \bar{K}_1 = \left(\frac{\partial Y_c}{\partial M_{At}}\right)_{M_{AtOH}}$$

$$[9] \quad \bar{K}_2 = \left(\frac{\partial Y_c}{\partial M_{AtOH}}\right)_{M_{At}}$$

Once $\bar{K}_1$ and $\bar{K}_2$ values are available, it is then possible to estimate θ_{At} and θ_{AtOH}, the site coverages by atrazine and hydroxyatrazine.

IV. Hydrolysis in solution

The two catalysts for atrazine hydrolysis that have been identified in humic materials are protons and unionized carboxyl groups (61). In the present case, the investigation of catalytically active sorption sites in the undissolved humic acid requires that proton catalysis in the solution phase be accounted for. This is easily done with the reported half-life relationship (61) in eq. [45].

$$[10] \quad t_{1/2} = \left[8.796\left(\frac{1.777 \times 10^{-2} \times 10^{-pH}}{2.45 \times 10^{-2} + 10^{-pH}} + M_{AH}\right)\right] \text{days}$$

The experiment was run at a pH of 4.0. With no carboxyl groups in solution, this gives a half life for atrazine in solution of 333.5 years. It would therefore not be possible to detect solution phase hydrolysis during the course of a 14 day experimental run. Catalysed hydrolysis will consequently only be determined for the undissolved humic acid phase.

V. Hydrolysis on catalytically active sorption sites

A. Atrazine disappearance

The total rate of change of atrazine coverage on the catalytic sorption sites is given by eq. [11].

$$[11] \quad -W_{HA}\left(\frac{d\theta_{At}}{dt}\right)_t = -W_{HA}\left(\frac{d\theta_{At}}{dt}\right)_r + V_s\frac{dM_{At}}{dt}$$

In the left hand term, W_{HA} is g of humic acid, and the subscript "t" indicates total change. The first term on the right is the rate of atrazine conversion on the catalytic sorption sites, as explained by eq. [12].

$$[12] \quad \left(\frac{d\theta_{At}}{dt}\right)_r = -k_{r2}\theta_{At}$$

When sorption equilibrium is accounted for with eq. [5], the differential rate law is obtained as eq. [13]. It has been simplified by the absence of solution phase hydrolysis.

$$[13] \quad \frac{dM_{At}}{dt} = -k_{r1}M_{At} - \left(\frac{W_{At}}{V_s}\right)\left(\frac{d\theta_{At}}{dt}\right)_t$$

Unlike the true rate constant k_{r2} to which it is related, the apparent rate constant k_{r1} is an experimental artifact dependent on the relative amounts of humic acid and solution. Equation [14] shows the relationship.

$$[14] \quad k_{r1} = \left(\frac{W_{HA}}{V_s}\right)\bar{K}_1 k_{r2}\theta_0$$

The integral rate law required for calculations is eq. [15].

$$[15] \quad \ln(M_{At}) + A_{At}\ln(\theta_{At}) = -k_{r1}t + B_{At}$$

The constants A_{At} and B_{At} are defined by eqs. [16] and [17].

$$[16] \quad A_{At} = \left(\frac{W_{HA}}{V_s}\right)\bar{K}_1\theta_0$$

$$[17] \quad B_{At} = \ln(M^0_{At}) + A_{At}\ln(\theta^0_{At})$$

The apparent rate constant k_{r1} may therefore be calculated from linear fits of $[\ln(M_{At}) + A_{At}\ln(\theta_{At})]$ vs. t.

B. Hydroxyatrazine appearance

A similar examination of hydroxyatrazine production yields the differential rate law, eq. [18].

$$[18] \quad \frac{dM_{AtOH}}{dt} = -\left(\frac{k_{p1}}{A_{AtOH}}\right)M_{AtOH} + B_{AtOH}\theta_c$$

M_{AtOH} is the hydroxyatrazine molarity in the external solution. Equations [19] to [21] define the three constants.

$$[19] \quad k_{p1} = -\left(\frac{W_{HA}}{V_s}\right)\bar{K}_2 k_{r2}\theta_0$$

$$[20] \quad A_{AtOH} = 1 + \left(\frac{W_{HA}}{V_s}\right)\bar{K}_2\theta_0$$

$$[21] \quad B_{AtOH} = \frac{(W_{HA}/V_s)k_{r2}}{A_{AtOH}}$$

k_{p1} is also an apparent rate constant related to the real rate constant k_{r2}. Equation [22] is the corresponding integral rate law, calculated over the time interval t_1 to t_2.

$$[22] \quad \ln(M_2/M_1) = -(k_{p1}/A_{AtOH})(t_2 - t_1) + B_{AtOH}\int_{t_1}^{t_2} X(t)dt$$

M_1 and M_2 are the integration limits for M_{AtOH}, and the function $X(t)$ is explained by eq. [23].

$$[23] \quad X(t) = (\theta_c/M_{AtOH})$$

The evaluation of the apparent rate constant is more difficult for hydroxyatrazine than it is for atrazine. The reasons are that eq. [22] must be rearranged, and numerical integration is required for the last term on the right.

C. Key parameters

Equations [14] and [19] for the experimental parameters k_{r1} and k_{p1} not only have exactly the same form, but also mostly the same constants. A consequence of this is that the ratio (k_{r1}/k_{p1}) gives the useful relationship in eq. [24].

$$[24] \quad \frac{k_{r1}}{k_{p1}} = \frac{\bar{K}_1}{\bar{K}_2}$$

The two ratios (k_{r1}/k_{p1}) and $(\bar{K}_1/\bar{K}_2)$ might be used either to test the quality of experimental data, or to determine whether the data are consistent with theory.

Because k_{r1} and k_{p1} depend on experimental design, they cannot be used directly for practical applications. It is therefore necessary to evaluate the rate constant k_{r2}. This is easily done with data for both atrazine and hydroxyatrazine, by using eqs. [25] and [26].

$$[25] \quad k_{r2} = (V_s/W_{HA})(k_{r1}/\bar{K}_1\theta_0)$$

$$[26] \quad k_{r2} = (V_s/W_{HA})(k_{p1}/\bar{K}_2\theta_0)$$

The rate constant k_{r2} probably depends on the acid strengths of the occupied carboxyl groups. It is, however, the only rate constant that should be used for the comparison of samples or experiments, or for the modelling of field phenomena. In addition, eqs. [25] and [26] could be used for testing data or theory. It is therefore important to have equilibrium and kinetics data for both atrazine and hydroxyatrazine.

Experimental

Reagents

The humic acid was obtained from the Ah horizon of an Alberta black Chernozem soil which had a pH of 6.5. Its preparation and analysis have been reported by Khan and Schnitzer (62–65) and by Schnitzer and co-workers (66). Atrazine and hydroxyatrazine were crystalline solids which were prepared and analysed as previously described (58). Orthophosphoric acid and sodium chloride were reagent grade. Water redistilled under N_2 was used for the preparation of all standard stock solutions, standards, and samples. Chromatography grade acetonitrile was used for HPLC work.

Standard stock solutions

HCl and NaOH solutions were 0.1 *N* analytical standard solutions. Other standard stock solutions were 1.5×10^{-4} *M* HCl, 1.0×10^{-4} *M* atrazine, 1.0×10^{-4} *M* hydroxyatrazine, and 1.5×10^{-4} *M* atrazine.

Analytical standards

The standardization of a pH meter was done with an orthophosphoric acid solution that was 1.0×10^{-3} *M*, containing 0.01 *M* NaCl. HPLC analyses employed mixed standards which ranged from 3.0×10^{-5} *M* atrazine and 0.0 *M* hydroxyatrazine, to 0.0 *M* atrazine and 3.0×10^{-5} *M* hydroxyatrazine.

Experimental samples

Each reaction sample consisted of about 25.0 mg of standardized Chernozem humic acid, suspended in 25.0 mL of reaction solution. The solutions contained 1.0×10^{-4} *M* HCl to prevent dissolution of the humic acid. Initial atrazine concentrations, before sorption or reaction, ranged from 0.5×10^{-5} *M* to 5.0×10^{-5} *M*.

Equipment

An Orion 801 digital pH meter was used with an Orion Ross type micro combination glass electrode, and a 5.00 mL microburett. Jacketed reaction vessels for titrations and kinetics samples were connected to a circulating constant temperature bath.

The HPLC consisted of two Altex Model 100 pumps and a Beckman Model 164 variable wavelength detector. The reverse phase column was an Altex Ultrasphere – ODFS with 5 μm particles size, 4.6 mm ID, and 25 cm length. A corresponding 2 cm guard column had the same diameter and packing.

Humic acid titrations

Each titration sample consisted of 0.05 g of humic acid in 20.0 mL of 0.1 *N* NaCl solution. Equilibrium titrations were conducted with 0.05 mL increments of standard base at 25.00°C. The samples were stirred so that suspensions were titrated. Volts vs. mL data points were recorded 10.0 min after the addition of standard base, when the dissolution and mass transfer processes had been replaced by the much slower electrode drift. An instrument calibration titration was run for each sample titration, for the preparation of H^+ molarity curves. The calibration runs used 100.00 mL aliquots of a standard stock solution containing 1.0×10^{-3} *M* H_3PO_4 and 0.01 *M* NaCl. The use of orthophosphoric acid titrations for H^+ molarity calibrations and the related calculations have been previously described (58, 59). Five replicate titrations were run. A single H^+ molarity vs. mL curve was produced by averaging the five replicate runs. This was done by applying least squares polynomial fits to decade ranges of H^+ molarity data.

The Gran's function $Y = VM_H$ was fitted to a quadratic equation, which was found to give the best least squares fit. Since the equivalence point V_{el} is found at $Y = 0$, the quadratic equation may be rearranged to give eq. [27].

$$[27] \quad V_{el} = \frac{C_0}{C_1 + C_2 V_{el}}$$

C_0, C_1, and C_2 are the quadratic constants. V_{el} was obtained by iterative calculations using eq. [27]. This was checked against graphical calculations. The results are presented in Fig. 2.

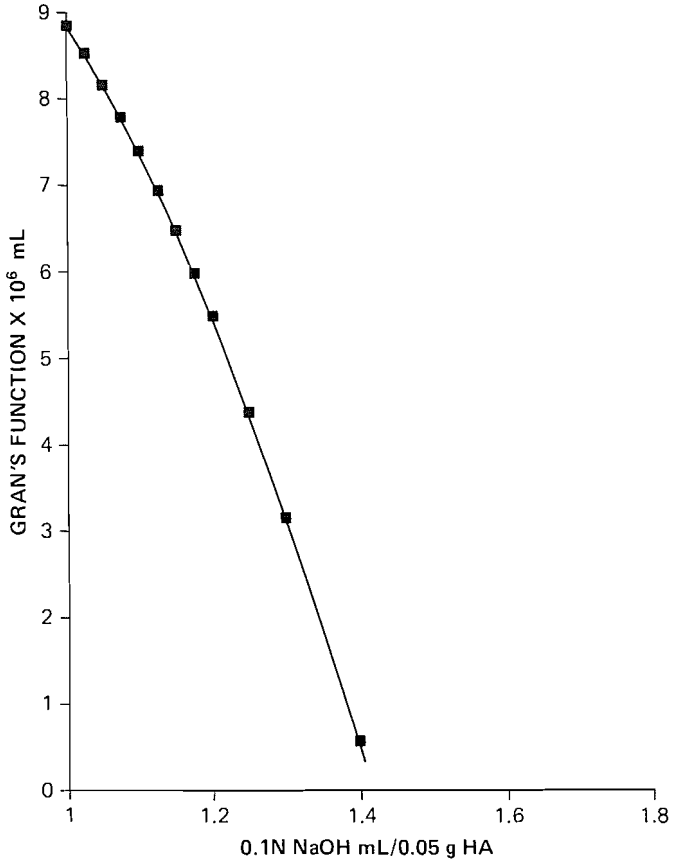

FIG. 2. The Gran's function, $Y = VM_H = -6.0006 \times 10^{-16} + 3.02446 \times 10^{-5} V - 2.13882 \times 10^{-5} V^2$. At $Y = 0$, $V = V_{el} = 1.414$ mL ± 0.5%.

A separate titration was carried out independently for an investigation of Na^+ uptake by undissolved humic acid. It was conducted in essentially the same way except that the external solution was monitored by 200 mm–300 mm UV scans for dissolved humate, and aliquots were drawn off at regular intervals for Na^+ analysis by atomic absorption spectroscopy.

Chemical kinetics runs

Each kinetics sample was kept in suspension by stirring, at a reaction temperature of 25.00°C. Air and light were excluded to prevent oxidation and photochemistry. Each sample was analysed daily at various recorded times for atrazine and hydroxyatrazine, during the course of a 12 day run. The analyses were done by HPLC with a mobile phase consisting of 50.0 vol% acetonitrile–H_2O containing 1.58×10^{-3} *M* HCl. The flow rate was 1.0 mL/min. Analysis aliquots were withdrawn from the reaction solutions through syringe tip filters. Every sample injection was bracketed by two standard injections, with atrazine and hydroxyatrazine peaks both being read from each injection. The atrazine and hydroxyatrazine peaks were read at 222.0 nm and 240.0 nm, respectively. The reaction solutions were examined by gas chromatography, to determine whether or not any products of dealkylation side reactions could be detected.

Can. J. Chem. Downloaded from www.nrcresearchpress.com by 196.1.178.254 on 09/07/12
For personal use only.

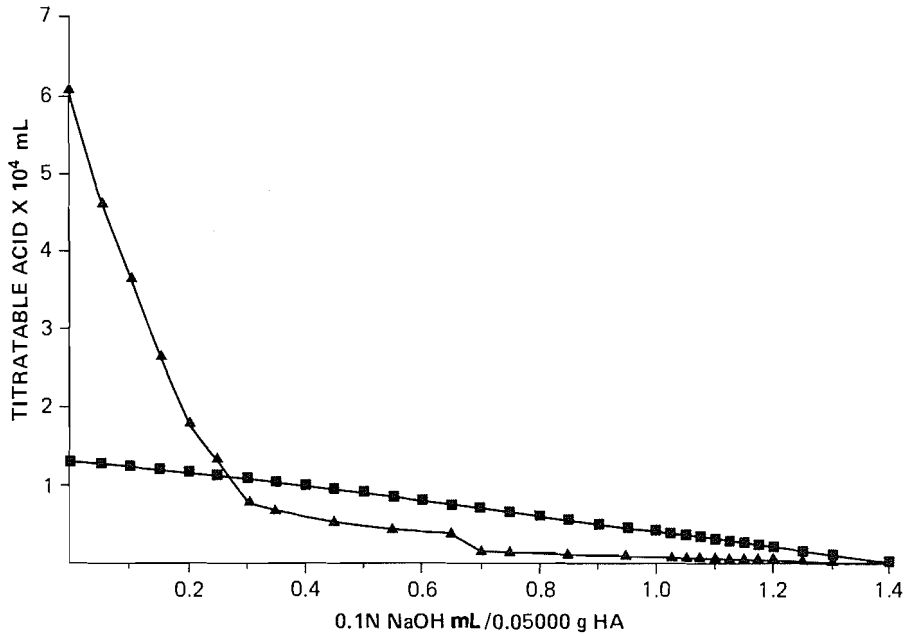

FIG. 3. The effects of titration on the quantities of acid remaining in the two physical phases of the sample. ▲, molarity of H^+ in the external solution; ■, (moles of acid/0.0500 g) in the gel phase. 25.0°C.

Results and discussion

I. Standardization of the humic acid

The Gran's function shown as the plot in Fig. 2 was quite conveniently used in the form $M_H V$ instead of the customary form $K10^{-kE_V}$, because the M_H data were available from the calibration. The data gave a very close least square fit to a quadratic equation. The titration equivalence point was calculated iteratively from the fitted constants, as indicated in Fig. 2. The simple graphical method gave the same equivalence point as did the Gran's plot in Fig. 2, to within the analytical error. A plot of M_H vs. mL of base gave a curve having the same general appearance of nearly the same extrapolation. The equivalence point value made it possible to calculate the amount of titratable acid remaining in the gel phase at each titration point. A titration scan curve for each of the two physical phases is consequently plotted in Fig. 3. These two curves represent a calibration of the acidic properties of the humic acid. The discontinuity in the gel phase at about 0.65 mL is probably a mathematical artifact caused by experimental scatter. About 0.6 mmol/g of carboxyl groups are more strongly acidic than the rest, which look rather similar to each other.

An important feature of Fig. 3 is that it shows the relationship between titratable acid found in the two phases. Atrazine, if present, would be affected differently by the protons in the external solution, and the combination of unionized carboxyl groups and free protons in the undissolved humic gel phase. Any attempts to make quantitative predictions of the atrazine sorption and hydrolysis must account separately for the amounts of acid species in both phases. At 0.28 mL of base, M_H is 1.0×10^{-4}. An examination of Fig. 4 and the titration curve shows that with an external solution pH of about 4, 85% of the original gel phase acid still remains. A pH of 5 is more common in soils. At 0.96 mL of base, the external solution has M_H equal to 1.0×10^{-5}. With the solution pH now approximately 5, solution phase hydrolysis of atrazine would be very slow (45). In the undissolved particles of humic acid, however, about 30 mol% of the original gel phase acid still remains to act as catalytically active sorption sites for atrazine. They are, however, the most weakly acidic fraction of the mixture of carboxyl groups. The most strongly acidic fraction of them were titrated by the first 0.3 mL of standard base. Not only can the fate of atrazine not be predicted by measuring the simple bulk mass of humic material present, it also cannot be predicted by measuring only the pH of the external solution. All of the information in Fig. 3 is required.

A polynomial least squares fit was produced for the gel phase curve in Fig. 3, so that it can be computerized for experimental design or for predictions. The polynomial constants are tabulated in Table 1. It should be noted that extra digits beyond the number of significant figures are recorded so that rounding off and truncation errors can be minimized. This calibration curve is only strictly valid for the experimental conditions actually used. Since it is the unneutralized acid functional groups that cause catalysis and control solubility and sorption, it is necessary to know what mol% of them remain unneutralized at any point in the acid–base titration curve. Figure 4, which was constructed for this reason, permits the mol% gel phase acid to be related to solution phase pH.

Humic acid solubility was monitored during titration with photometric absorbance measurements at 260 nm. The resulting A_{260} vs. mL curve is seen in Fig. 5. The solubility increased substantially between 0.3 and 1.0 (mL/0.05) g. This corresponds to the solution phase H^+ molarity range of 7.7×10^{-5} to 8.9×10^{-6}. Any changes in solubility that exist outside that range appear to be small. There would be an important practical advantage in monitoring the dissolution of carboxylate anions instead of monitoring the dissolution of chromophores, if an experimental method were available. The advantage would be that the amount of free protons in the humic gel phase could be estimated. Unfortunately, the dissolution of carboxylate anions could not be neglected and no successful method was found for measuring it in these experiments. Although it might be possible to use the approximation

$$M_A \approx N_B V_B$$

Can. J. Chem. Downloaded from www.nrcresearchpress.com by 196.1.178.254 on 09/07/12
For personal use only.

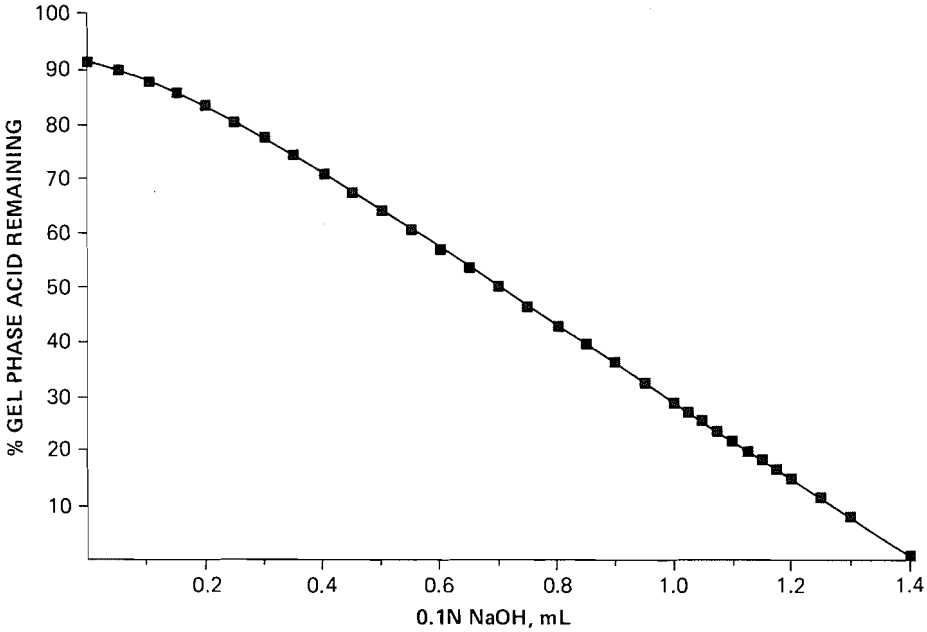

FIG. 4. Mol% of the titratable acid remaining in the gel phase during titration with standard base. Relative standard deviation, ±5%. 25.0°C.

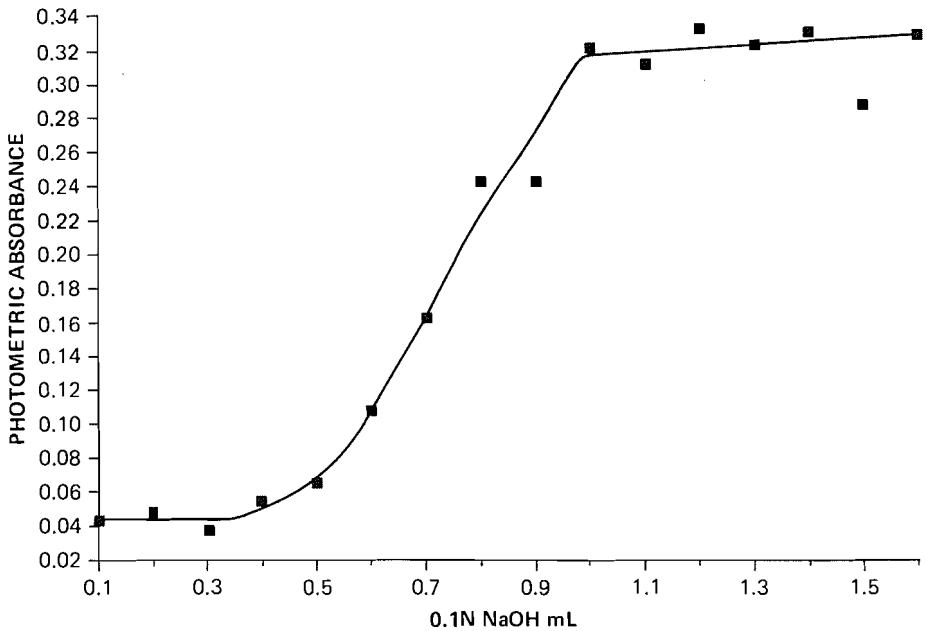

FIG. 5. Dissolution of the humic acid during titration, monitored by photometric absorbance at λ 260 nm.

it is not known how valid such an approximation would be, and it was not attempted. The errors in R found in Table 4 imply relatively large errors in values for the amount of free protons in the gel phase, near the equivalence point. Since the amounts of free gel phase protons should be small in this region of the titration curve, the errors may be less important than they seem. The best available option for atrazine – humic acid experiments is to correlate sorption and rate constant data with the total amounts of titratable gel phase acid.

Because it is important to have the calibration data in Tables 5 to 7 available for future calculations, they have been stored in numerical form[1]. The experimental errors found there are typical for glass electrode measurements (49, 58, 60).

Solution phase results obtained previously with a calibrated fulvic acid have demonstrated that a large reduction in experimental scatter may be achieved by correlating atrazine interaction parameters with numbers or concentrations of protons and protonated carboxyl groups (46, 56). A similar result is anticipated for two phase aqueous systems containing humic acid and atrazine.

II. Heterogeneous catalysis of the hydrolysis reaction

A. Sorption equilibria

Figure 6 shows a typical set of solution phase atrazine data. The top curve shows the loss of atrazine from solution. The bottom curve is the experimental plot of eq. [15] from which the apparent rate constant k_{r1} was calculated. The linearity of the plots indicates that atrazine attained sorption equilibrium quite

Can. J. Chem. Downloaded from www.nrcresearchpress.com by 196.1.178.254 on 09/07/12
For personal use only.

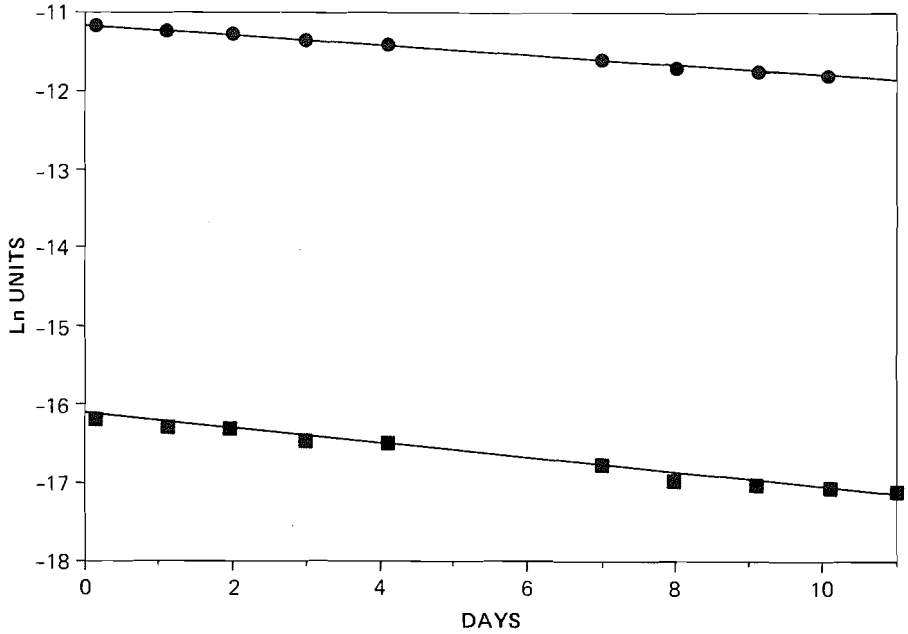

FIG. 6. Atrazine kinetics plots for the loss of atrazine from the external solution. Sample 4. ●, $\ln(M_{At})$; ■, $Y = [\ln(M_{At}) + A_{At}\ln(\theta_{At})]$. See eq. [57].

TABLE 1. Gel phase acid as a function of mL of 0.1 *N* NaOH added; 0.1 *M* initial NaCl, 25.0°C, $Q_{GH} = C_0 + C_1V_B + C_2V_B^2C_3V_B^3 + C_4V_B^4$ (mol/0.500 g), $\sigma = 2.23 \times 10^{-7}$

Coefficient	Calculated value
C_0	1.2933×10^{-4}
C_1	-3.9282×10^{-5}
C_2	-1.1754×10^{-5}
C_3	9.8163×10^{-5}
C_4	-2.9488×10^{-5}

quickly. In chemical kinetics terms, the atrazine established a steady state condition. A separate sorption experiment used for extrapolations to zero time has provided supporting evidence of this. The hypothetical sorption site coverages at zero time have been plotted against initial atrazine concentrations, in Fig. 7. Because no plateau was reached, the sorption was evidently well below saturation so that no sorption capacity was observed. While it is reasonable to assume that such a capacity exists, it must be somewhat greater than the atrazine complexing capacity of dissolved fulvic acid (43, 44). A possible reason for this is that the internal gel solution of the water swollen humic acid has a much higher concentration of carboxyl groups than dilute fulvic acid solutions. At least in principle, the mixture of chemically nonidentical carboxyl groups would be expected to give nonlinear sorption curves. The apparent linearity may simply reflect the fact that the total site coverage attained amounted to less than 6%. Each kinetics run covered such a small range of acidities that the change in catalytic activity could not be observed outside experimental error.

Hydroxyatrazine curves typically had the shape seen in Fig. 8. This contrasts sharply with the observed behaviour of atrazine in Fig. 6. Generally about 4 days were required for the establishment of sorption equilibrium. Sorption equilibrium calculations and steady state kinetics calculations were therefore confined to the region beyond 4 days. The measurements made during the first 4 days lacked the quality and quantity required for interpretive calculations. Only one kinetics sample had a fast equilibration of hydroxyatrazine sorption. Sample No. 1, which was prepared with about 25.0 mg of humic acid in 24.9 mL of 5.09×10^{-6} *M* atrazine solution, had a linear ln plot for hydroxyatrazine just about down to zero reaction time. The curve resembled that of Fig. 8 except that the initial fast rise was missing. The reason for this was that the atrazine sorption was sufficiently small so that the reaction rate was too small for large concentration gradients to develop.

$\bar{K}_1$ was calculated according to eqs. [7] and [8], by least squares fitting and interpolation. Y_c vs. M_{AtOH} and $M_{At}.M_{AtOH}$ curves were fitted by least squares for each of several experimental runs. Y_c vs. M_{At} data points were then obtained by interpolation, for selected values of M_{AtOH} as a parameter. $\bar{K}_1$ values were then obtained as the slopes of linear Y_c vs. M_{At} fits with constant values of M_{AtOH}. The calculated $\bar{K}_1$ values are listed in Table 2, together with the corresponding M_{AtOH} values. The relative standard deviation is only 1.8%, but there could also be a systematic error in $\bar{K}_1$. Because it is intended that the $\bar{K}_1$ value be available for subsequent calculations, an extra figure beyond the significant figures has been retained for the purpose of limiting errors from computer truncation. In principle, $\bar{K}_1$ should decrease with increasing coverage of protonated carboxyl groups. The values in Table 2 do not show such an effect outside the limits of error, however. The sorption equilibrium function for hydroxyatrazine, $\bar{K}_2$, was calculated in a similar way using eq. [9]. According to Table 3, the equilibrium function for hydroxyatrazine has a much larger standard deviation. It is also evident that hydroxyatrazine is somewhat more strongly sorbed, with an equilibrium function about five times as great as that of atrazine. If $\bar{K}_2$ has any of the expected dependence on site coverage, it is also obscured by experimental error.

Once the values of $\bar{K}_1$ and $\bar{K}_2$ were available in Tables 2 and 3, it became possible to estimate separately the sorption site coverages of atrazine and hydroxyatrazine during the course of an experiment. Because the total sorption could be calculated

Can. J. Chem. Downloaded from www.nrcresearchpress.com by 196.1.178.254 on 09/07/12
For personal use only.

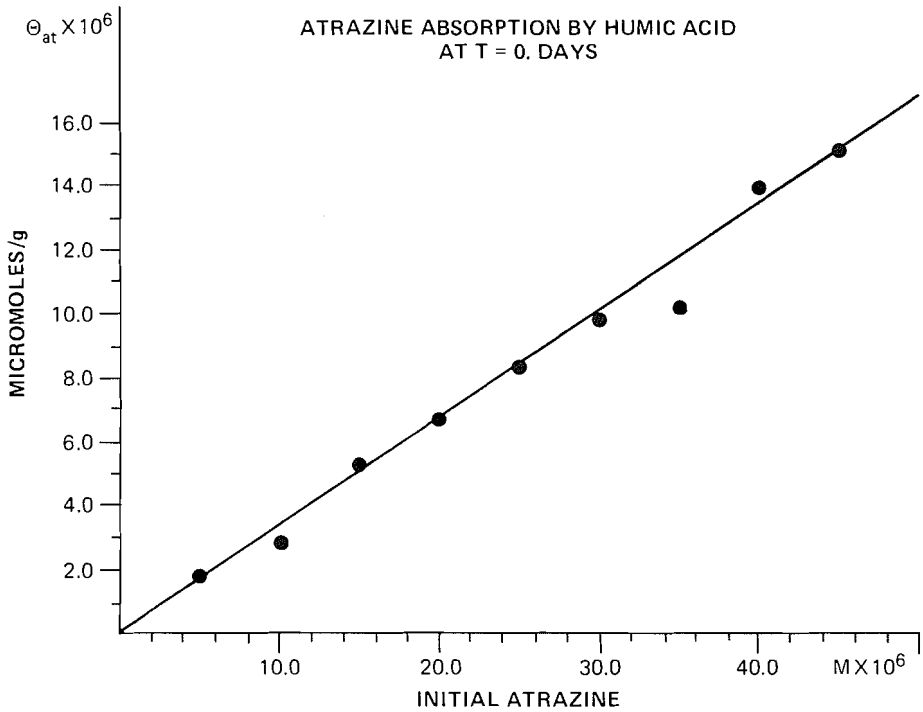

FIG. 7. Initial sorption of atrazine by humic acid at 25.0°C; prior to the hydrolysis reaction.

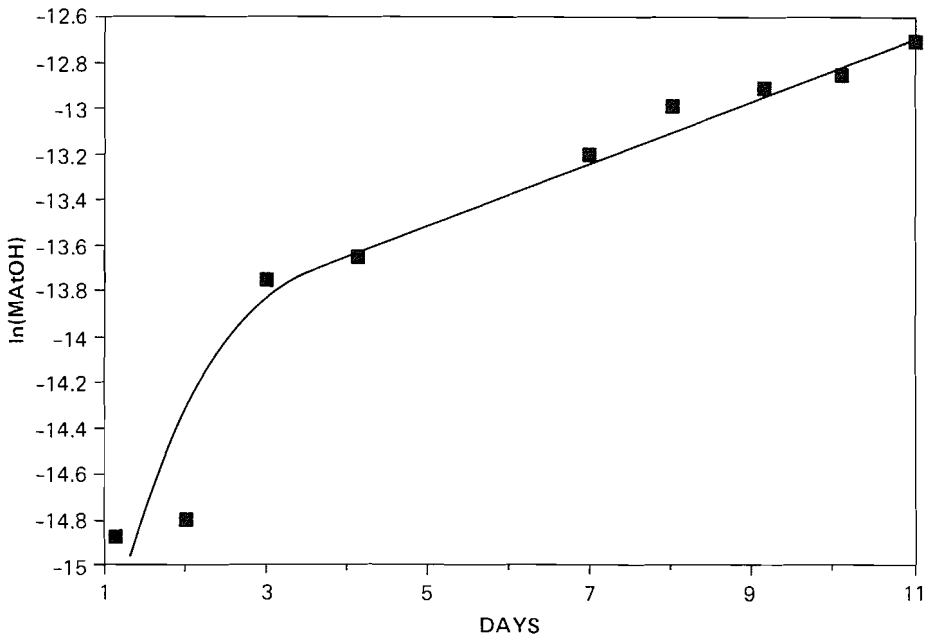

FIG. 8. Hydroxyatrazine in the external solution, as a function of reaction time, at 25.0°C. Sorption equilibrium is seen after 4 days. Sample 4.

TABLE 2. Atrazine sorption equilibrium: $\bar{K}_1$ calculated by partial differentiation[a]

M_{AtOH}	$\bar{K}_1$
0.00×10^{-6}	1.746×10^2
0.60×10^{-6}	1.753×10^2
1.00×10^{-6}	1.787×10^2
2.00×10^{-6}	1.729×10^2
2.60×10^{-6}	1.701×10^2

[a]Average = 1.743×10^2, $\sigma = 0.032 \times 10^2$.

by material balance and because $\bar{K}_2$ has a relatively large error, the hydroxyatrazine coverage was actually calculated by difference. The three sorption curves in Fig. 9 present some very important information. The maximum site coverage was only a few percent of the carboxyl groups. This means that the total range of weak acid K_a values encountered by the sorbed molecules was too small for the sorption equilibrium function to vary to any extent visible outside experimental error. The changes are, however, significant mole percentages of the maximum atrazine sorption. This implies that the experimental data should be calculated with the variable coverage rate laws in

Can. J. Chem. Downloaded from www.nrcresearchpress.com by 196.1.178.254 on 09/07/12
For personal use only.

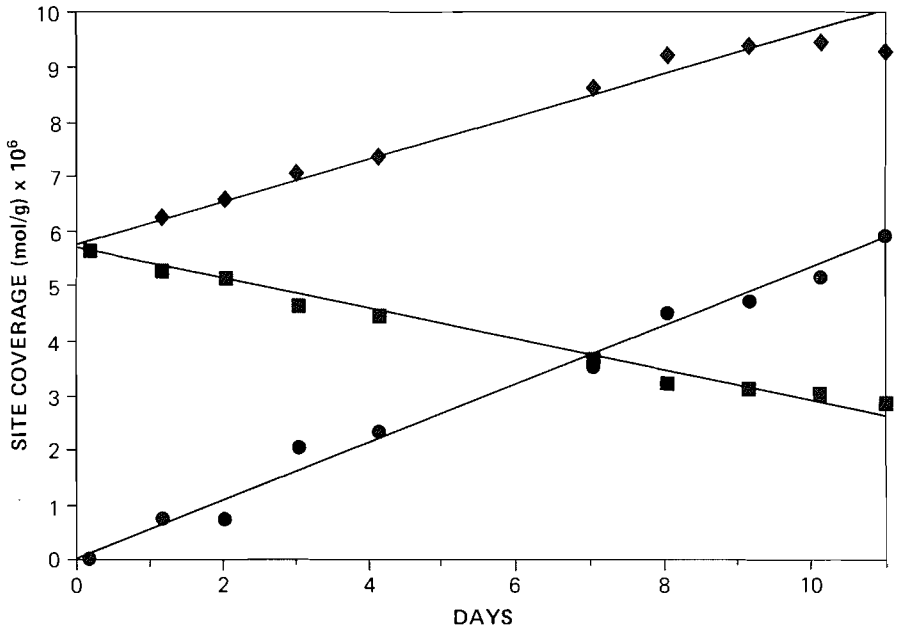

FIG. 9. The coverage of sorption sites at 25.0°C, as a function of reaction time. Sample 4. ■, atrazine; ●, hydroxyatrazine; ◆, total.

TABLE 3. Hydroxyatrazine sorption equilibrium: $\bar{K}_2$ calculated by partial differentiation[a]

M_{At}	$\bar{K}_2$
3.00×10^{-5}	5.914×10^2
2.10×10^{-5}	6.586×10^2
1.90×10^{-5}	8.386×10^2
1.70×10^{-5}	11.34×10^2
1.50×10^{-5}	11.73×10^2
1.30×10^{-5}	7.058×10^2
1.10×10^{-5}	8.790×10^2

[a]Average = 8.54×10^2, $\sigma = 2.27 \times 10^2$.

eqs. [15] and [22]. If the changes in site coverage are neglected, then the pseudo first order rate constants for hydroxyatrazine is not obtained.

B. Apparent rate constants in the solution phase

The apparent rate constant k_{r1} for the disappearance of atrazine from solution was calculated from the slopes of linear least squares fits, using eq. [15]. The apparent rate constant k_{p1}, for the appearance of hydroxyatrazine in solution, was more difficult to calculate. It was necessary to rearrange eq. [22] for least squares fitting, and to numerically evaluate the integral on the right hand side.

C. Tests for parameters against theory

The ratios (k_{p1}/k_{r1}) and $(\bar{K}_2/\bar{K}_1)$ were used for testing experimental results against theory, in accordance with eq. [24]. The calculated values and test results have been tabulated in Table 4. The relative amounts of humic acid and reaction solution are also indicated for the samples, since the observed values of k_{r1} and k_{p1} depend on them. The experimental results are consistent with theory, within the limits of the estimated experimental error. The errors are contributed by at least two factors. One is that the quantity and quality of the hydroxyatrazine data are not as good as those for atrazine. The measurements are more difficult to make. The other factor is that the partial derivative calculations for $\bar{K}_1$ and $\bar{K}_2$ tend to produce systematic errors from the original errors of measurement. Once the validity of the experimental parameters k_{r1} and k_{r2} had been tested, the final step was their use for the calculation of k_{r2}, the pseudo first order rate constant for hydrolysis on the catalytic sorption sites.

D. Calculation of pseudo first order rate constants

Three different methods were found for calculating k_{r2}, the pseudo first order rate constant for hydrolysis on the catalytic sorption sites. (*a*) The k_{r1} values obtained from atrazine measurements were used with eq. [25], for each of several chemical kinetics samples. (*b*) The k_{p1} values obtained from the slopes of fitted hydroxyatrazine measurements as previously described, were used with eq. [26] for various chemical kinetics samples. (*c*) The intercepts of fitted hydroxyatrazine measurements from various chemical kinetics samples were used in accordance with eq. [21] and the rearranged form of eq. [22].

The best quality k_{r2} data have been obtained from the atrazine calculations (*a*), and these have been tested and tabulated in Tables 4 and 8 for future use.[4] The hydroxyatrazine calculations (*b*) and (*c*) gave k_{r2} values of similar quality, which was inferior to that of the atrazine values. The hydroxyatrazine slope and intercept values have been listed in Table 9 for comparison with the atrazine slope values in Fig. 10 and Table 8. The hydroxyatrazine values for k_{r2} are too scattered for useful correlations, but within the limits of experimental error they are consistent with the atrazine data. This judgement takes into account the fact that they are averages whose numerical values are weighted by the spectrum of K_a values of the sorption sites covered.

Figure 9 documents the competition between atrazine and hydroxyatrazine for the catalytic sorption sites. No indication of a sorption limit was found, and without site saturation the atrazine sorption and hydroxyatrazine sorption are not additive. None the less, the more strongly sorbed hydroxyatrazine selectively preempts the most strongly catalytic sites. The anticipated "catalyst poisoning" is seen as a decrease in the k_{r2} in the experimental results of Fig. 11. This is also consistent with Brönsted acid catalysis theory.

Can. J. Chem. Downloaded from www.nrcresearchpress.com by 196.1.178.254 on 09/07/12
For personal use only.

TABLE 4. Solution phase changes: pseudo first order rate constants at 25.0°C[a]

Sample No.	Days^{-1} Atrazine disappearance k_{r1}	Hydroxyatrazine appearance k_{p1}	(k_{p1}/k_{r1})	(g Humic Acid/L) (W_{HA}/V_s)
10(a)	6.68×10^{-2}			0.9501
10(b)	6.83×10^{-2}	6.79×10^{-1}	9.93	0.9843
9	8.15×10^{-2}			1.026
8	8.59×10^{-2}			0.9828
7	8.64×10^{-2}			0.9921
6	8.88×10^{-2}	3.93×10^{-1}	4.43	1.004
4	9.11×10^{-2}	9.22×10^{-1}	10.1	1.045
3	1.04×10^{-1}			1.032
2	9.73×10^{-2}	7.49×10^{-1}	7.70	1.025
1	1.17×10^{-1}	6.69×10^{-1}	5.72	1.003

[a]Average $(k_{p1}/k_{r1}) = 6.82$; $\sigma = 2.93$; $(K_2/K_1) = 4.90$, $\sigma = 1.39$.

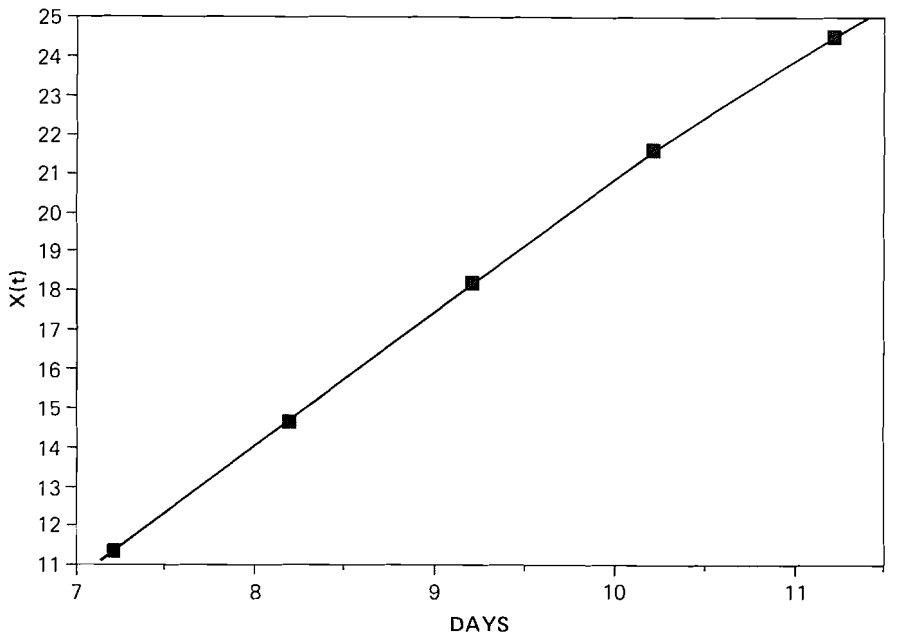

FIG. 10. The hydroxyatrazine site coverage function, $X(t) = (\theta_c/M_{At})$. See eq. [72]. Sample 4.

In practice it was found, however, that the change in site coverage during a kinetics run was not sufficiently great relative to the number and precision of the measurements, for any change in the rate constant to be detected. The expected dependence shows up instead when a chord plot is made with a whole set of kinetics runs, as has been done in Fig. 11. There are several conclusions to be drawn from this chord plot. (*1*) The rate constant k_{r2} decreases with decreasing acid strength of carboxyl groups, as predicted by Brönsted acid catalysis theory (39). (*2*) The k_{r2} values obtained are no better than ±20%, and improved data sets should be available before any attempt is made to calculate correlations between k_{r2} and the K_a values of a humic carboxyl groups. (*3*) Correlations of k_{r2} vs. K_a will continue to require the use of chord plots because changes in k_{r2} will not be detected within individual kinetics run. (*4*) Future correlations of k_{r2} vs. K_a should be calculated with two or three times as many chords. Each of these should have a statistically sound set of data points confined to chords that are only 1/3 to 1/2 the lengths of those in Fig. 10. This would require two or three times as many kinetics samples, each run for 1/3 to 1/2 the length of time. (*5*) The emergence of chord plots implies that the k_{r2} value obtained from each kinetics run is some sort of average value, corresponding to a set of occupied carboxyl groups that has a range of K_a values. Assuming that the carboxyl groups have a continuum of K_a values, then there should be a corresponding continuum of k_{r2} values. From the point of view of future modelling, it would be useful to know this continuous k_{r2} spectrum. Its calculation from the experimental averages would require, however, more and better data.

Calculated values for the pseudo first order rate constant, k_{r2}, are listed for future use, in the Depository of Unpublished Data.[4]

E. The comparison of humic acid and fulvic acid catalysts

An equation has been published for fulvic acid solutions, which describes the atrazine hydrolysis rate constant in terms of

Can. J. Chem. Downloaded from www.nrcresearchpress.com by 196.1.178.254 on 09/07/12
For personal use only.

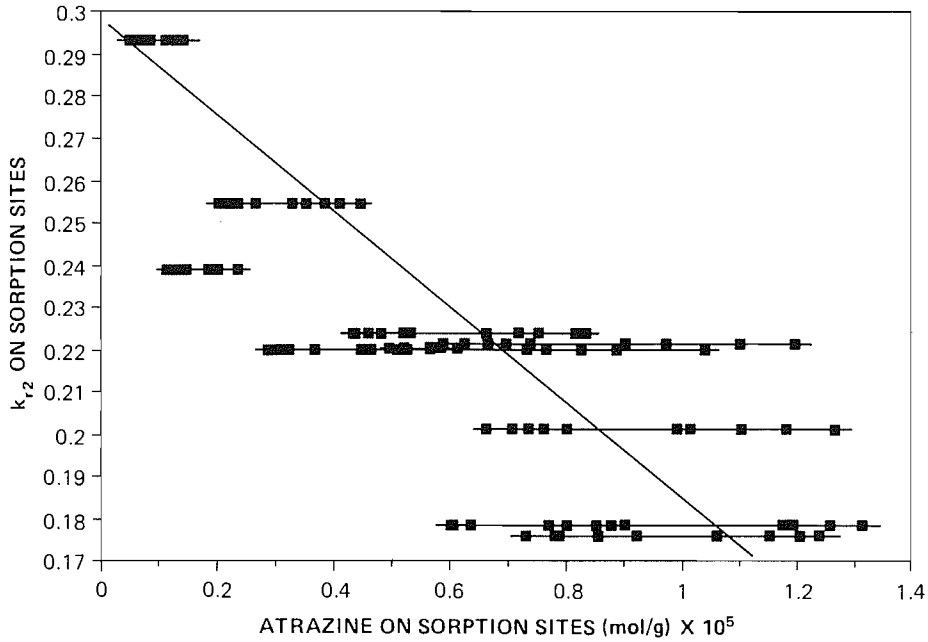

FIG. 11. Pseudo first order reaction rate constant on the catalytic sorption sites, vs. site coverage by atrazine. 25.0°C. Sample 4.

Can. J. Chem. Downloaded from www.nrcresearchpress.com by 196.1.178.254 on 09/07/12
For personal use only.

both pH and the molarity of protonated carboxyl groups. If one assumes that the ion exchange particles of the aqueous humic acid suspension have internal gel solutions (52, 53), then it should be possible to compare k_{r2} with the rate constants in equivalent fulvic acid solutions.

Catalysed hydrolysis reactions are commonly expected to be fast. This expectation must be qualified, however, by a consideration of the number of catalytically active binding sites occupied, and their catalytic activities. This has been demonstrated by the solution phase fulvic acid catalysis of atrazine (45, 58).

While it was not possible to determine the spectrum of K_a values for the Chernozem humic acid used here, the carboxyl groups of a typical humic acid would have K_a values in about the range of 1.0×10^{-4} to 1.0×10^{-5}. Considering that peat soils quite commonly contain 80 wt% water, it seems reasonable to assume this value for the Chernozem humic acid. Using these values and the measured value for the carboxyl content, a corresponding range of k_{r2} values can be calculated for the internal gel solution. The calculations allow for the constraint on the movement of H^+, imposed by the Donnan potential in the absence of inorganic salts. For the internal gel solution, $K_A = 1.0 \times 10^{-4}$ gives $M_{AH} = 0.138\,M$ and pH = 2.46. Likewise, $K_A = 1.0 \times 10^{-5}$ gives $M_{AH} = 0.140\,M$ and pH = 2.94. The published fulvic acid equation predicts $k_{r2} = 1.1\ day^{-1}$ over this whole range. This is four to six times larger than the values actually found for the Chernozem humic acid. The difference between humic acid and fulvic acid primarily reflects the fact that humic acids generally have more weakly acidic carboxyl groups than fulvic acids do.

It is conventional practice to calculate rate constants from initial rates for the following types of experiments: (*a*) those complicated by a back reaction; (*b*) those which do not permit the estimation of equilibrium constants and site coverages for both reactant and product during the course of a kinetics run; (*c*) those which must relate to practical systems in which only the most strongly catalytic sorption sites will be occupied by the reactants.

As shown, none of these conditions applies to the present work.

Conclusions

Hydroxyatrazine is more strongly sorbed than atrazine is, and this caused the sorption equilibria to shift during the course of chemical kinetics runs. The reaction rate laws must account for this effect in order for correct rate constants to be calculated. The apparent rate constants for the disappearance of atrazine from solution and for the appearance of hydroxyatrazine in solution are different from each other and from the pseudo first order rate constant for the hydrolysis reaction on the catalytic sorption sites. The apparent rate constants are only empirical experimental parameters that depend directly on experimental conditions. Because they have no direct chemical meaning, they cannot be used for comparing experiments or samples, and cannot be used for the modelling of practical field problems. Any attempts to use these parameters in this way would cause serious misjudgements and general confusion. Health risks or crop damage could result. The correct chemical kinetics reaction rate constant can be calculated, however, for future use in comparisons, predictions, and modelling. The correct rate constant depends on the acid strength of catalytically active carboxyl groups as predicted by the Brönsted acid catalysis theory. The quantitative investigation of this effect would make an important contribution to future modelling.

Acknowledgement

Mr. A. D. Gordon produced the large number of potentiometric H^+ measurements for the humic acid calibration, as well as conducting the heterogeneous catalysis experiments with large numbers of HPLC analyses.

1. P. S. C. RAO and J. M. DAVIDSON. Retention and transformations of selected pesticides and phosphorus in soil–water systems: A critical review. Project Summary, Research and Development EPA – 600/S3 – 82 – 060 Sept. 1982. United States Environmental Protection Agency.
2. F. J. STEVENSON. J. Environ. Qual. **1**, 333 (1972).

Can. J. Chem. Downloaded from www.nrcresearchpress.com by 196.1.178.254 on 09/07/12
For personal use only.

3. T. H. SHEETS, A. S. CRAFTS, and H. R. DREVER. J. Agr. Food Chem. **10**, 485 (1962).
4. R. P. UPCHURCH, F. L. SELMAN, D. D. MASON, and E. J. KAMPRATH. Weeds, **14**, 42 (1966).
5. J. D. SULLIVAN, JR. and G. T. FELBECK, JR. Soil Sci. **106**, 42 (1968).
6. R. GROVER. Can. J. Soil Sci. **53**, 307 (1973).
7. G. G. BRIGGS. A simple relationship between soil adsorption of organic chemicals and their control/water partition coefficients. Proceedings 7th British Insecticide and Fungicide Conference. 1973.
8. R. D. CARRINGER, J. B. WEBER, and T. J. MONACO. J. Agr. Food Chem. **23**, 568 (1975).
9. R. GROVER, J. B. BANTING, and P. M. MORSE. Weed Res. **19**, 363 (1979).
10. S. W. KARICKHOFF, D. S. BROWN, and T. A. SCOTT. Water Res. **13**, 241 (1979).
11. C. T. CHIOU, L. J. PETERS, and V. H. FREED. Sci. **206**, 831 (1979).
12. M. S. SHAROM, J. R. W. MILES, C. R. HARRIS, and F. L. MCEWEN. Water Res. **14**, 1095 (1980).
13. C. W. CARTER and I. H. SUFFET. Environ. Sci. Technol. **16**, 735 (1978).
14. J. HANCE. Weed Res. **9**, 108 (1969).
15. B. WEBER, S. B. WEED, and T. M. WARD. Weed Sci. **17**, 417 (1969).
16. R. E. GRICE and M. H. B. HAYES. Proc. 10th British Weed Control Conf. **3**, 1089 (1970).
17. M. B. H. HAYES. Residue Rev. **32**, 131 (1970).
18. J. T. GILMOUR and N. T. COLEMAN. Soil Sci. Soc. Am. Proc. **35**, 256 (1971).
19. J. A. BEST, J. B. WEBER, and S. B. WEED. Soil Sci. **114**, 444 (1972).
20. G. C. LI and G. R. FELBECK, JR. Soil Sci. **113**, 140 (1972).
21. I. G. BURNS, M. H. B. HAYES, and M. STACEY. Pestic. Sci. **4**, 629 (1973).
22. I. G. BURNS, M. H. B. HAYES, and M. STACEY. Weed Res. **13**, 79 (1973).
23. I. G. BURNS, M. H. B. HAYES, and M. STACEY. Pestic. Sci. **4**, 201 (1973).
24. R. E. GRICE, M. H. B. HAYES, P. R. LUNDIE, and M. H. CARDEW. Chem. Ind. (Lond.) 233 (1973).
25. S. U. KHAN. Can. J. Soil Sci. **53**, 199 (1973).
26. I. G. BURNS and M. H. B. HAYES. Residue Rev. **52**, 117 (1974).
27. S. U. KHAN. Residue Rev. **52**, 1 (1974).
28. S. B. WEED and J. B. WEBER. Pesticide – organic matter in soil and water. *Edited by* W. D. Guenzi. Soil Sci. Soc. America, Inc., Madison, WI. 1974.
29. D. C. NEARPASS. Soil Sci. **121**, 272 (1976).
30. S. U. KHAN. The interaction of organic matter with pesticides. *In* Soil organic matter. *Edited by* M. Schnitzer and S. U. Khan. 1987. p. 137.
31. P. GAILLARDON, R. CALVERT, and J. C. GAUDRY. Weed Res. **20**, 201 (1980).
32. N. SENESI and C. TESTINI. Soil Sci. **130**, 314 (1980).
33. P. J. ISACCSON and M. H. B. HAYES. J. Soil Sci. **35**, 79 (1984).
34. D. E. ARMSTRONG and G. CHESTERS. Environ. Sci. Technol. **2**, 683 (1968).
35. R. TURSKI and A. STEINBRICH. Polish J. Soil Sci. **4**, 119 (1971).
36. N. SENESI and C. TESTINI. Geoderma, **28**, 129 (1982).
37. R. A. CHAPMAN and C. M. COLE. J. Environ. Sci. Health, B**17**(5), 487 (1982).
38. C. W. CARTER and I. H. SUFFET. *In* Fate of chemicals in the environment. *Edited by* R. L. Swann and A. Eschroeder. Am. Chem. Soc. Sympo. Ser. 225, Washington, D.C. Chap. 11.
39. E. M. PERDUE. Association of organic pollutants with humic substances: partitioning equilibria and hydrolysis kinetics. *In* Aquatic and terrestrial humic materials. *Edited by* Russel F. Christman and Egil T. Gjessing. Ann Arbor Science, Ann Arbor, MI. 1983. Chap. 22.
40. R. E. TALBERT and O. H. FLETCHALL. Weeds, **13**, 46 (1965).
41. M. D. MCGLAMERY and F. W. SLIFE. **14**, 237 (1966).
42. D. S. GAMBLE, M. I. HANIFF, and R. H. ZIENIUS. Anal. Chem. **54**, 732 (1986).
43. D. S. GAMBLE, M. I. HANIFF, and R. H. ZIENIUS. Anal. Chem. **54**, 727 (1986).
44. M. I. HANIFF, R. H. ZIENIUS, C. H. LANGFORD, and D. S. GAMBLE. J. Environ. Sci. Health, B**20**, 215 (1985).
45. D. S. GAMBLE and S. U. KHAN. Can. J. Soil Sci. **65**, 435 (1985).
46. D. S. GAMBLE. Can. J. Chem. **50**, 2680 (1972).
47. D. S. GAMBLE. Can. J. Chem. **48**, 2662 (1970).
48. W. T. MCGEORGE. Ariz. Agri. Exp. Sta. Bull. **30**, 181 (1930).
49. J. T. GILMOUR and N. T. COLEMAN. Soil Sci. Soc. Am. Proc. **35**, 710 (1971).
50. A. M. POSNER. Titration curves of humic acid. Vol. III. 8th International Congress of Soil Sci. Bucharest, Romania. 1964. p. 161.
51. A. M. POSNER. J. Soil Sci. **17**, 65 (1966).
52. V. MERLE and J. A. MARINSKY. Talanta, (1983).
53. J. A. MARINSKY. Interpretation of ion exchange phenomena. *In* Ion exchange. Vol. 1. *Edited by* J. A. Marinsky. Marcel Dekker, New York. 1966. Chap. 9.
54. F. HELFFERICH. Ion exchange. McGraw-Hill, New York. 1962.
55. R. D. BURCH, C. H. LANGFORD, and D. S. GAMBLE. Can. J. Chem. **56**, 1196 (1978).
56. D. S. GAMBLE. Can. J. Chem. **58**, 2150 (1980).
57. D. S. GAMBLE. Can. J. Chem. **59**, 1630 (1981).
58. D. S. GAMBLE, S. U. KHAN, and O. S. TEE. Pestic. Sci. **14**, 537 (1983).
59. K. GHOSH and M. SCHNITZER. J. Soil Sci. **30**, 735 (1979).
60. K. GHOSH and M. SCHNITZER. Can. J. Chem. **60**, 373 (1980).
61. E. P. DUNIGAN and T. H. MCINTOSH. Weed Sci. **19**, 279 (1971).
62. S. U. KHAN. Soil Sci. **112**, 401 (1971).
63. S. U. KHAN. Geochim. Cosmochim. Acta, **36**, 745 (1972).
64. S. J. PLUST, J. R. LOEHE, F. J. FEHER, J. H. BENEDICT, and H. F. HERBRANDSON. J. Org. Chem. **46**, 3661 (1981).
65. S. U. KHAN and M. SCHNITZER. Israel J. Chem. **9**, 667 (1971).
66. M. SCHNITZER and J. S. DESJARDIN. Soil Sci. Am. Proc. **26**, 362 (1962).

Excess properties of mixtures of some *n*-alkoxyethanols with organic solvents. V. Excess enthalpies of 2-butoxyethanol with normal alkanes at 298.15 K[1]

JOSE CARLOS COBOS, ISAIAS GARCIA, AND CARLOS CASANOVA
Departamento de Física Aplicada II, Universidad de Valladolid, 47071-Valladolid, Spain

Received March 3, 1988

JOSE CARLOS COBOS, ISAIAS GARCIA, and CARLOS CASANOVA. Can. J. Chem. **66**, 2618 (1988).

The excess molar enthalpy H^E has been determined as a function of mole fraction x at 298.15 K and atmospheric pressure for five (2-butoxyethanol + *n*-alkane) mixtures. The *n*-alkanes were *n*-heptane, *n*-octane, *n*-decane, *n*-dodecane, and *n*-tetradecane. The mixtures show positive and unsymmetrical H^E, skewed towards low mole fractions of 2-butoxyethanol, and whose value increases with the chain length n of the alkane.

JOSE CARLOS COBOS, ISAIAS GARCIA et CARLOS CASANOVA. Can. J. Chem. **66**, 2618 (1988).

Opérant à 298,15 K et à pression atmosphérique, on a mesuré l'enthalpie molaire en excès, H^E, de cinq mélanges (butoxy-2 éthanol + *n*-alcane) en fonction de la fraction molaire, x. Parmi les *n*-alcanes, on a utilisé le *n*-heptane, le *n*-octane, le *n*-décane, le *n*-dodécane et le *n*-tétradécane. Avec une augmentation de la longueur de la chaîne n de l'alcane, tous les mélanges présentent un H^E qui est à la fois positif, asymétrique et déplacé vers les basses fractions molaires de butoxy-2 éthanol.

[Traduit par la revue]

Introduction

The study of alkoxyalkanols is of interest not only because of their wide use as industrial solvents, but also from the more theoretical point of investigating the effect of the simultaneous presence of etheric and hydroxyl groups on the interactions of such molecules.

In spite of the potential applications of *n*-alkoxyethanols there are relatively few experimental thermodynamics studies on this class of substances with organic solvents; the most studied medium is water (1). In particular, for mixtures with *n*-alkanes, to our knowledge, data only exist for excess enthalpies and isobaric vapor–liquid equilibria of 2-ethoxyethanol + *n*-octane (2); isobaric vapor–liquid equilibria of 2-butoxyethanol + *n*-octane (3); isobaric vapor–liquid equilibria of 2-ethoxyethanol + *n*-hexane (4); mutual solubilities of alkanes and 2-methoxyethanol (5); infinite-dilution activity coefficients of *n*-heptane with 2-methoxyethanol (6); excess volumes and isentropic compressibilities of 2-ethoxyethanol + *n*-heptane (7); heats of solutions of some poly-alkoxyalkanols with *n*-dodecane (8); excess enthalpies of 2-butoxyethanol + *n*-heptane (9), and excess enthalpies of some alkoxyalkanols with *n*-heptane (10). Therefore there is no systematic study on the behaviour of *n*-alkoxyethanols where the chain length of the *n*-alkanes is varied.

In this paper we extend our previous investigations on the excess molar functions (H^E, V^E, and C_p^E) of binary liquid mixtures of *n*-alkoxyethanols with organic solvents (11–15) to the excess molar enthalpies of 2-butoxyethanol (1) + *n*-alkane (2) mixtures. Measurements with *n*-heptane, *n*-octane, *n*-decane, *n*-dodecane, and *n*-tetradecane at 298.15 K and atmospheric pressure are reported.

Experimental

Liquid components

All chemicals used were from Fluka. *n*-Heptane (puriss p.a., with purity >99.5 mol%), *n*-octane (purum olefin-free, with purity >99 mol%), *n*-decane (purum olefin-free, with purity >99 mol%), *n*-dodecane (purum olefin-free, with purity >98 mol%), and *n*-tetradecane (puriss olefin-free, with purity >99 mol%), were used without further purification. 2-Butoxyethanol (purum, stated purity >98 mol%), was fractionally distilled many times in a glass 100 theoretical plates column, at a reflux ratio of approximately 25:1 at 3 kPa of reduced pressure, until no measurable impurities were observed in a vapor-phase chromatography trace analysis. The final purity was estimated to be 99.9%. Prior to the experimental measurements, all liquids were carefully dried over molecular sieves beads (Union Carbide type 4A) from Fluka.

Excess enthalpy measurements

A standard Calvet type microcalorimeter, equipped with a batch mixing cell with small (<2%) gas phase and the experimental technique of Paz Andrade *et al.* (16) was used to determine the excess molar enthalpies over the entire mole fraction range, x, of 2-butoxyethanol. Details of the experimental technique and of the accuracy attainable have been described previously (11, 12, 17).

Binary mixtures were prepared by mass. All weighings were corrected for buoyancy effects, and the error on the final mole fraction is estimated to be less than 0.0001. Conversion to molar quantities is based on the relative atomic mass table of 1975, issued by IUPAC.

Results

Experimental densities and refractive indices at 298.15 K of the pure *n*-alkanes were in good agreement with published values (18, 19). For the purified 2-butoxyethanol our observed density at 298.15 K $\rho = 896.0\ \mathrm{kg\ m^{-3}}$, determined in a SODEV densimeter (Model 02D), is in good agreement with available literature values (9, 20).

The results of our measurements of H^E as a function of x at 298.15 K and atmospheric pressure are summarized in Table 1. An equation of the type:

$$[1]\quad H^E(\mathrm{J\ mol^{-1}}) = x(1-x)\sum_{i=0}^{n} A_i(x)^{i/2}$$

was fitted to each set of results by least-squares regression with all points weighted equally. The coefficients A_i and the corresponding standard deviations $s(H^E)$ are given in Table 2. For all mixtures $s(H^E)/H^E(\mathrm{max}) < 0.01$, where $H^E(\mathrm{max})$ denotes the maximum value of the excess molar enthalpy with respect to mole fraction x, in accord with the precision attainable with the instrument used. A graphical representation of the experimental points together with the smoothing curves is shown in Fig. 1.

For mixtures with *n*-heptane our results differ by less than 1% in the range $0.3 < x < 0.7$ from those of the Kimura *et al.* (10), who used an isothermal displacement calorimeter. Their experi-

[1]For paper IV, see ref. 15.

Printed in Canada / Imprimé au Canada

Can. J. Chem. Downloaded from www.nrcresearchpress.com by 196.1.178.254 on 09/07/12
For personal use only.

TABLE 1. Excess molar enthalpy, H^E, for 2-butoxyethanol (x) + n-alkane ($1 - x$) mixtures at 298.15 K

n-Heptane		n-Octane		n-Decane		n-Dodecane		n-Tetradecane	
x	H^E (J mol^{-1})	x	H^E (J mol^{-1})	x	H^E (J mol^{-1})	x	H^E (J mol^{-1})	x	H^E (J mol^{-1})
0.0548	495	0.0241	287	0.0570	536	0.0491	483	0.0566	546
0.0907	648	0.0555	506	0.0957	717	0.0802	675	0.0993	778
0.0999	663	0.0976	683	0.1557	904	0.1052	792	0.1456	969
0.1137	705	0.1481	803	0.2012	975	0.1617	973	0.1879	1077
0.1499	782	0.2067	895	0.2424	1034	0.2003	1046	0.2508	1189
0.1737	807	0.2579	946	0.2992	1080	0.2490	1116	0.3004	1235
0.1965	849	0.3046	970	0.3593	1097	0.3072	1163	0.3413	1275
0.2018	842	0.3558	991	0.3933	1091	0.3579	1191	0.3807	1284
0.2374	889	0.4166	997	0.4515	1091	0.3963	1195	0.4250	1293
0.2419	892	0.4511	977	0.4843	1078	0.4578	1182	0.4463	1287
0.2876	918	0.5033	967	0.5344	1046	0.4993	1161	0.4925	1273
0.3232	927	0.5540	928	0.5941	1007	0.5044	1167	0.5387	1255
0.3462	936	0.6027	895	0.6533	938	0.5557	1137	0.5891	1218
0.3931	931	0.6536	819	0.7027	864	0.6069	1091	0.6548	1139
0.3940	931	0.7037	747	0.7453	791	0.6591	1035	0.6887	1084
0.4322	935	0.7531	661	0.7995	661	0.6953	976	0.7572	952
0.4420	931	0.8029	553	0.8411	559	0.7534	866	0.8032	833
0.4901	908	0.8459	451	0.8963	391	0.7997	751	0.8503	693
0.5332	889	0.8989	309	—	—	0.8573	591	0.8990	508
0.5618	860					0.8989	445		
0.5997	828								
0.6572	757								
0.6951	701								
0.7520	599								
0.8020	501								
0.8422	414								
0.8825	323								
0.9341	166								

TABLE 2. Coefficients, $A_i \times 10^2$ (J mol^{-1}), and standard deviations, $s(H^E)$ (J mol^{-1}), for least-squares representations of H^E by eq. [1]

x $C_4H_9OCH_2CH_2OH$	A_0	A_1	A_2	A_3	$s(H^E)$
+ $(1 - x)$ n-C_7H_{16}	186.7	−530.9	639.8	−268.5	6
+ $(1 - x)$ n-C_8H_{18}	186.1	−511.7	600.9	−243.4	5
+ $(1 - x)$ n-$C_{10}H_{22}$	177.4	−422.6	426.4	−138.3	5
+ $(1 - x)$ n-$C_{12}H_{26}$	167.1	−343.6	286.5	−58.4	4
+ $(1 - x)$ n-$C_{14}H_{30}$	158.3	−283.5	190.7	−6.1	4

mental values, those that do not appear in the ref. 10, may be found in ref. 21. Outside this range of mole fraction the differences are slightly greater. On the other hand, the results of Villamañán *et al.* (9) measured with a Picker microcalorimeter are 5% lower than ours for $x < 0.7$; showing better agreement at high concentrations of 2-butoxyethanol. For other systems there are no available literature data for comparison.

Discussion

For all the mixtures studied H^E is positive over the whole composition range and as expected the endothermic mixing shows a higher intensity as the chain length of the n-alkane increases. This increase is approximately linear at equimolecular composition, $x = 0.5$, and can be estimated to be of the order of 50 J/mol for each —CH_2— group added to the n-alkane, beginning with n-heptane.

Both previous ir and microwave spectroscopic (23–29) and calorimetric (8, 10, 30) studies indicate that the molecules of n-alkoxyethanol are self-associated and form intermolecular and, more interesting, intramolecular hydrogen bonds. This second possibility is due to the simultaneous presence of both oxygen and hydroxyl groups in the same molecule, and it can be used to study the intramolecular heteroproximity effect in theoretical models of liquid mixtures based on the method of group contributions.

Our present results confirm this behaviour on the n-alkoxyethanol molecules and allow us to rationalize the results of the previous studies. Firstly, they suggest that the 2-butoxyethanol molecules form intermolecular H-bonds as in the alkanols. In fact, we observed similar characteristics between the data reported here and the data on mixtures formed with n-alkanols and solvents like alkanes or ethers (21, 22): large positive value and unsymmetrical excess enthalpy, skewed towards low mole fractions of 2-butoxyethanol or n-alkanol. Our previous work on mixtures of n-alkoxyethanols with ethers (9, 12) are in agreement at this point.

Secondly, the significantly higher H^E values found here on 2-butoxyethanol + n-alkane mixtures in comparison with the well-known values for homomorphic mixtures of n-alkanol + n-alkane (21) suggest that the intermolecular self-association of the n-alkoxyethanols are lower than those of n-alkanols. This may be due to the possible existence of intramolecular H-bonds in these molecules, which effectively decreases the alcohol self-association capability. Previous data of H^E on n-alkoxyalkanol + n-heptane mixtures (10), and the large excess molar

Can. J. Chem. Downloaded from www.nrcresearchpress.com by 196.1.178.254 on 09/07/12
For personal use only.

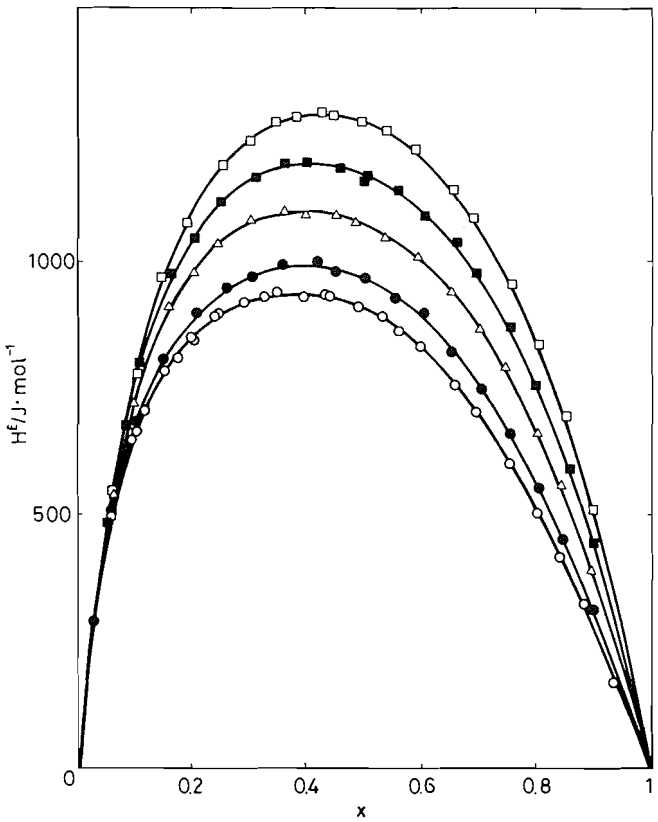

FIG. 1. Experimental excess molar enthalpies, H^E, for $x C_4H_9O(CH_2)_2OH + (1 - x)C_nH_{2n+2}$ at 298.15 K: (○), $n = 7$; (●), $n = 8$; (△), $n = 10$; (■), $n = 12$, and (□), $n = 14$. Full curves represent the smoothing eq. [1] with the coefficients of Table 2.

volume V^E of 2-ethoxyethanol + *n*-heptane (7), also confirm that the hydroxyl terminal group into 2-butoxyethanol becomes hindered by possible formation of intramolecular H-bonds.

On the other hand, it is important to note which dipole moments of the *n*-alkoxyethanols are greater than those of the *n*-alkanols (18, 31). Although in this work we were able to measure H^E for mixtures of 2-butoxyethanol with long *n*-alkanes without any signs of partial miscibility, it is well-known (5, 6, 32) that other *n*-alkoxyethanols have upper critical solution temperatures (UCST) when mixed with linear and cyclic alkanes at temperatures over 298.15 K, and that the UCST of 2-butoxyethanol with long alkanes are near 282 K.

These large UCST compared with those of homomorphic *n*-alkanol mixtures using the same alkanes can be interpreted in terms of a smaller intermolecular self-association. The existence of intramolecular H-bonds in *n*-alkoxyethanols may enhance the dipolar interactions between the more anisotropic molecules. In this work we can see this effect in the composition dependence of H^E. This dependence is unsymmetrical and skewed towards low mole-fractions of 2-butoxyethanol, but less than that in the corresponding *n*-alkanol + *n*-alkane mixtures.

One last remark is on the H^E values of the *n*-alkoxyethanols in mixtures with non-polar but polarizable solvents such as benzene or ethylbenzene (2, 30). These H^E values are lower than those with *n*-alkanes. This contrasts with the behaviour of *n*-alkanols, where the H^E values of benzene mixtures are greater than those of *n*-alkanes.

1. J. WISNIAK and A. TAMIR. Mixing and excess thermodynamic properties. A literature source book. Elsevier, Amsterdam. 1978; Supplement 1. Elsevier, Amsterdam. 1982; Supplement 2. Elsevier, Amsterdam. 1986.
2. P. S. MURTI and M. VAN WINKLE. A.I.Ch.E.J. **3**, 517 (1957).
3. P. S. PRABHU and M. VAN WINKLE. J. Chem. Eng. Data, **8**, 14 (1963).
4. Y. S. SURYANARAYANA and M. VAN WINKLE. J. Chem. Eng. Data, **11**, 7 (1966).
5. A. LANDAUER, R. N. LICHTENTHALER, and J. M. PRAUSNITZ. J. Chem. Eng. Data, **25**, 152 (1980).
6. G. M. LOBIEN and J. M. PRAUSNITZ. Ind. Eng. Chem. Fundam. **21**, 109 (1982).
7. G. C. BENSON, C. J. HALPIN, and A. J. TRESZCZANOWICZ. J. Chem. Thermodyn. **13**, 1175 (1981).
8. T. MIURA and M. NAKAMURA. Bull. Chem. Soc. Jpn. **50**, 2528 (1977).
9. M. A. VILLAMAÑÁN, C. CASANOVA, A. H. ROUX, and J.-P. E. GROLIER. J. Chem. Eng. Data, **27**, 89 (1982).
10. F. KIMURA, S. MURAKAMI, R. FUJISHIRO, and Y. TOSHIYASU. Bull. Chem. Soc. Jpn. **50**, 791 (1977).
11. J. C. COBOS and C. CASANOVA. Fluid Phase Equilibr. **20**, 155 (1985).
12. J. C. COBOS and C. CASANOVA. J. Chem. Thermodyn. **19**, 751 (1987).
13. J. C. COBOS, C. CASANOVA, G. ROUX-DESGRANGES, and J.-P. E. GROLIER. J. Chem. Thermodyn. **19**, 791 (1987).
14. J. C. COBOS, I. GARCIA, C. CASANOVA, G. ROUX-DESGRANGES, and J.-P. E. GROLIER. Thermochim. Acta, **131**, 73 (1988).
15. J. C. COBOS, I. GARCIA, C. CASANOVA, G. ROUX-DESGRANGES, and J.-P. E. GROLIER. Thermochim. Acta. In press.
16. M. I. PAZ ANDRADE, E. JIMENEZ, and C. HERNANDEZ. Anal. Real Soc. Esp. Fis y Quim. Quím. **68**, 33 (1972).
17. J. C. COBOS, M. A. VILLAMAÑÁN, and C. CASANOVA. J. Chem. Thermodyn. **16**, 861 (1984).
18. J. A. RIDDICK and W. B. BUNGER. Organic solvents, techniques of organic chemistry. Vol. II. *Edited by* A. Weissberger. Wiley-Interscience, New York. 1970.
19. TRC thermodynamics tables – hydrocarbons. Thermodynamic Research Center. The Texas A&M University System, College Station, TX.
20. I. A. MCLURE, F. GUZMAN-FIGUEROA, and I. L. PEGG. J. Chem. Eng. Data, **27**, 398 (1982).
21. J. J. CHRISTENSEN, R. W. HANKS, and R. M. IZATT. Handbook of heats of mixing. John Wiley & Sons, Inc., New York. 1982. p. 794.
22. M. A. VILLAMAÑÁN, C. CASANOVA, A. H. ROUX, and J.-P. E. GROLIER. J. Chem. Thermodyn. **14**, 251 (1982).
23. L. P. KUHN. J. Am. Chem. Soc. **74**, 2492 (1952).
24. L. P. KUHN and R. A. WIRES. J. Am. Chem. Soc. **86**, 2161 (1964).
25. P. J. KRUEGER and H. D. METTEE. J. Mol. Spectrosc. **18**, 131 (1965).
26. P. BUCKLEY and M. BROCHU. Can. J. Chem. **50**, 1149 (1972).
27. W. CAMINATI and E. B. WILSON. J. Mol. Spectrosc. **81**, 356 (1980).
28. L. S. PRABHUMIRASHI. J. Chem. Soc. Faraday Trans. 2, **74**, 1567 (1978).
29. S. N. VINOGRADOV and R. H. LINNELL. Hydrogen bonding. Van Nostrand Reinhold, New York. 1971. pp. 136, 141.
30. J. VALERO, M. GRACIA, and C. GUTIERREZ LOSA. J. Chem. Thermodyn. **11**, 1101 (1979).
31. A. L. MCCLELLAN. Tables of experimental dipole moments. Freeman, San Francisco. 1963; Tables of experimental dipole moments. Vol. II. Rahara Enterprises, El Cerrito. 1974.
32. A. W. FRANCIS. Ind. Eng. Chem. **36**, 764 (1944).

Can. J. Chem. Downloaded from www.nrcresearchpress.com by 196.1.178.254 on 09/07/12
For personal use only.

Structural studies of organoboron compounds. XXXII.[1] 5,5-Difluoro-2,2-pentamethylene-1,4,6-trioxa-3*a*-azonia-5-borata-1,2,3,4,5,6-hexahydrobenzo[*h*]azulene and 2,2-pentamethylene-5,5-diphenyl-1,4,6-trioxa-3*a*-azonia-5-borata-1,2,3,4,5,6-hexahydrobenzo[*h*]azulene

WOLFGANG KLIEGEL AND MAHMOOD TAJERBASHI

Institut für Pharmazeutische Chemie, der Technischen Universität Braunschweig, Beethovenstraße 55, 3300 Braunschweig, Bundesrepublik Deutschland

AND

STEVEN J. RETTIG AND JAMES TROTTER

Department of Chemistry, University of British Columbia, 2036 Main Mall, Vancouver, B.C., Canada V6T 1Y6

Received May 5, 1988

WOLFGANG KLIEGEL, MAHMOOD TAJERBASHI, STEVEN J. RETTIG, and JAMES TROTTER. Can. J. Chem. **66**, 2621 (1988).

Details of the syntheses, physical properties, and crystal structures of the title compounds are reported. Crystals of 5,5-difluoro-2,2-pentamethylene-1,4,6-trioxa-3*a*-azonia-5-borata-1,2,3,4,5,6-hexahydrobenzo[*h*]azulene are triclinic, a = 6.1576(3), b = 11.2651(3), c = 10.8118(3) Å, α = 109.747(3), β = 105.807(4), γ = 92.976(4)°, Z = 2, space group $P\bar{1}$, and those of 2,2-pentamethylene-5,5-diphenyl-1,4,6-trioxa-3*a*-azonia-5-borata-1,2,3,4,5,6-hexahydrobenzo[*h*]azulene are monoclinic, a = 9.8549(6), b = 10.9242(6), c = 41.263(2) Å, β = 92.717(6)°, Z = 8, space group $P2_1/n$. Both structures were solved by direct methods and were refined by full-matrix least-squares procedures to R = 0.045 and 0.042 for 2344 and 4248 reflections with $I \geq 3\sigma(I)$, respectively. The molecules were both found to possess a seven-membered chelate structure, the *O,O*-chelating ligand being strongly bound to the X_2B moiety. Two conformational isomers of the X = Ph compound were found in the solid state. The 2-oxazoline *N*-oxide moieties present in both compounds are the first to be structurally characterized. Important mean libration-corrected bond lengths are: O—B = 1.491 and F—B = 1.387 Å for X = F; O—B = 1.511 and C—B = 1.620 Å for X = Ph.

WOLFGANG KLIEGEL, MAHMOOD TAJERBASHI, STEVEN J. RETTIG et JAMES TROTTER. Can. J. Chem. **66**, 2621 (1988).

On rapporte les détails relatifs à la synthèse, aux propriétés physiques et à la structure cristalline des composés mentionnés dans le titre. Les cristaux du difluoro-5,5 pentaméthylène-2,2 trioxa-1,4,6 azonia-3*a* borata-5 hexahydro-1,2,3,4,5,6 benzo[*h*]azulène sont tricliniques, avec a = 6,1576(3), b = 11,2651(3) et c = 10,8118(3) Å, α = 109,747(3), β = 105,807(4) et γ = 92,976(4)°, Z = 2 et groupe d'espace $P\bar{1}$ alors que ceux du pentaméthylène-2,2 diphényl-5,5 trioxa-1,4,6 azonia-3*a* borata-5 hexahydro-1,2,3,4,5,6 benzo[*h*]azulène sont monocliniques avec a = 9,8549(6), b = 10,9242(6) et c = 41,263(2) Å, β = 92,717(6)°, Z = 8 et groupe d'espace $P2_1/n$. On a résolu les deux structures par des méthodes directes et on les a affinées par les méthodes des moindres carrés (matrice entière) jusqu'à des valeurs respectives de R = 0,045 et 0,042 pour 2344 et 4248 réflexions avec $I \geq 3\sigma(I)$. On a trouvé que les deux molécules possèdent des structures comportant un chélate à sept chaînons dans lesquels le ligand qui se chélate en *O,O* est fortement lié à la portion X_2B. A l'état solide, on a observé les deux isomères conformationnels du composé avec X = Ph. Les portions *N*-oxyde de l'oxazoline-2 qui sont présentes dans chacun des composés sont les premiers à être caractérisés d'un point de vue structural. Les longueurs de liaison moyennes corrigées pour la libration sont les suivantes : O—B = 1,491 et F—B = 1,387 Å dans le composé avec X = F; O—B = 1,511 et C—B = 1,620 Å pour le composé avec X = Ph.

[Traduit par la revue]

Introduction

In the course of our investigations of the formation, structure, and reactivity of *N*-substituted hydroxamic acids (1–4) we attempted to synthesize the difluoroboron chelate **2** by reaction of the β-hydroxyalkylated salicylhydroxamic acid **1** with trifluoroborane in diethyl ether solution. A crystalline reaction product was obtained which not only possesses the expected difluoroboron group (as a result of HF elimination), but has also lost a water molecule as shown by elemental analysis and ir and nmr spectroscopy. There are no OH bands in the ir spectrum nor are any OH signals present in the ^{1}H nmr spectrum that could arise from alcoholic, phenolic, or hydroxamic hydroxyl groups.

The condensation product could be an intramolecular alkylation product derived from an intermediate **2** by the formation of the cyclic ether **3** which features the BF_2 hydroxamate grouping. The alkylation of phenols with alkanols in the presence of Lewis acids like BF_3 is well documented (5). Less probable, but not excludable spectroscopically, are the alternative structures **4**, featuring a seven-membered BF_2 chelate ring containing a bidentate *N*-(2-hydroxyalkyl)amide ligand, and **5**, with a phenolic hydroxyl oxygen atom and an amide carbonyl oxygen atom as ligands in a six-membered chelate ring system. Structure **4** would require the formation of a 3-hydroxy-1,2-benzisoxazole ring by cyclodehydration, possible in the presence of BF_3. Comparable cyclocondensations of 2-hydroxybenzohydroxamic acids have been conducted with thionyl chloride (6) or carbonyldiimidazole (7) as dehydrating reagents. A ring closure to the four-membered oxazetidine system in **5** seems very unfavorable under the applied conditions. An intramolecular alkylation of the hydroxamic acid function by the *N*-(2-hydroxyalkyl) group is more likely. This would lead to the structure **6** with boron being chelated by the phenolic and hydroxylamine oxygen atoms. The seven-membered difluoroboron chelate **6** with a B—O—N—C—C—C—O ring system resembles the difluoroboron chelates of salicylaldehyde nitrones **7** (8).

[1]Previous paper in this series: ref. 29.

Printed in Canada / Imprimé au Canada

Can. J. Chem. Downloaded from www.nrcresearchpress.com by 196.1.178.254 on 09/07/12
For personal use only.

Can. J. Chem. Downloaded from www.nrcresearchpress.com by 196.1.178.254 on 09/07/12
For personal use only.

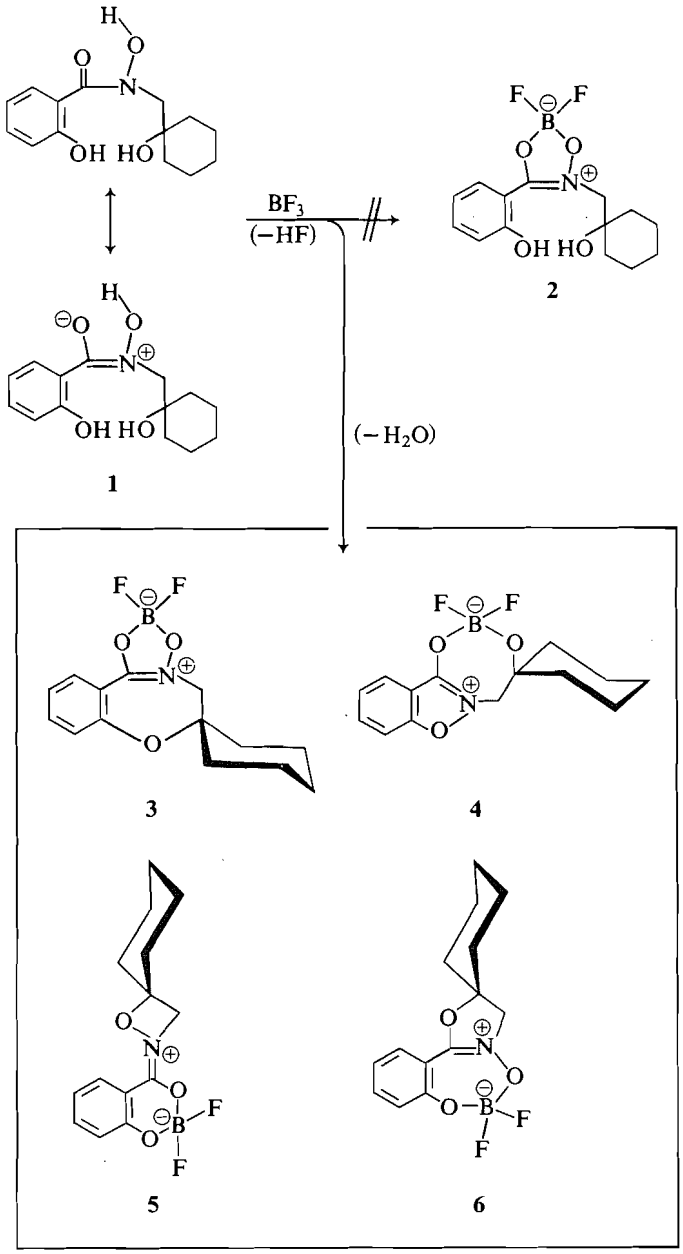

For further elucidation of the chelate structure and of the chelate formation pathway, **1** was also reacted with oxybis(diphenylborane), a well-suited reagent for trapping hydroxamic acid ligands (2–4). A crystalline condensation product was obtained which contains a diphenylboron grouping and as in the reaction of **1** with BF_3, a water molecule has been eliminated. The crystal structures of both of these condensation products have been determined.

Experimental

N-Hydroxy-N-(1-hydroxycyclohexyl)methyl-salicyloylamide, 1

Compound **1** was prepared by an acylating method reported for *N*-phenylsalicylhydroxamic acid (9) with slight modifications (10). Melting point 155°C (crystallized from diethyl ether). *Anal.* calcd. for $C_{14}H_{19}NO_4$ (fw 265.3): C 63.38, H 7.22, N 5.28; found: C 63.16, H 7.55, N 5.22. Infrared (KBr): 3600–2400 (broad O—H), 1610 cm^{-1} (C=O). ^1H nmr (d_6-DMSO/TMS): δ (ppm) = 1.0–2.1 (m, 10 H of $—(CH_2)_5—$), 3.65 (s, CH_2N), 4.11 (s, broad, exchangeable, alkyl OH), 6.7–7.5 (m, C_6H_4), 9.79 (s, broad, exchangeable, N—OH and aryl OH).

5,5-Difluoro-2,2-pentamethylene-1,4,6-trioxa-3a-azonia-5-borata-1,2,3,4,5,6-hexahydrobenzo[h]azulene, 6

1 (0.30 g, 1.13 mmol) and diethyl ether – trifluoroborane (0.32 g, 2.26 mmol) were dissolved in 70 mL dry diethyl ether and refluxed for 20–30 min. During evaporation of the solvent *in vacuo*, boric acid (32 mg) precipitated and was separated. The remaining oil was treated with diethyl ether until crystallization began after 2 days at room temperature. Yield: 0.22 g (66%) of colorless crystals, mp 150°C (from ether). *Anal.* calcd. for $C_{14}H_{16}BF_2NO_3$: C 56.98, H 5.46, N 4.75; found: C 56.94, H 5.60, N 4.64. Infrared (KBr): 1660 cm^{-1} (C=N). ^1H nmr (d_6-DMSO/TMS): δ (ppm) = 1.20–2.25 (m, 10 H of $—(CH_2)_5—$), 4.23 (s, CH_2N), 6.8–7.7 (m, C_6H_4). Crystals suitable for X-ray analysis were obtained by recrystallization from diethyl ether.

2,2-Pentamethylene-5,5-diphenyl-1,4,6-trioxa-3a-azonia-5-borata-1,2,3,4,5,6-hexahydrobenzo[h]azulene, 8

1 (0.53 g, 2 mmol) and oxybis(diphenylborane) (0.35 g, 1 mmol) were refluxed in 80 mL of benzene for 15 min. After evaporation of the solvent and the addition of diethyl ether, crystallization started. Yield: 0.50 g (60%) of colorless crystals, mp 159–160°C (from ether). *Anal.* calcd. for $C_{26}H_{26}BNO_3$: C 75.92, H 6.36, N 3.40; found: C 76.30, H 6.52, N 3.42. Infrared (KBr): 1645 cm^{-1} (C=N). ^1H nmr ($CDCl_3$/TMS): δ (ppm) = 1.2–2.0 (m, 10 H of $—(CH_2)_5—$), 3.89 (s, CH_2N), 6.6–7.6 (m, 14 H of Ph_2B and C_6H_4). The substance gives a blue color reaction with diphenylcarbazone (11) in methanolic solution, indicating the presence of a Ph_2B moiety. Crystals suitable for X-ray analysis were obtained by recrystallization from diethyl ether.

X-ray crystallographic analyses of 6 and 8

Crystallographic data for the two compounds are presented in Table 1. Unit-cell parameters were refined by least-squares on 2 sin θ/λ values for 25 carefully centered reflections with 2θ = 80–96° for **6** and 50–92° for **8**. The intensities of three standard reflections, measured each hour of X-ray exposure time throughout the data collections,

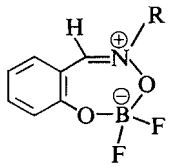

7

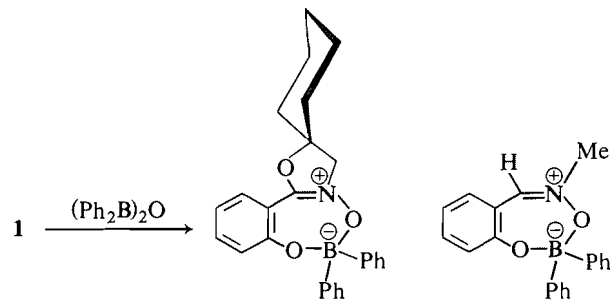

8 **9**

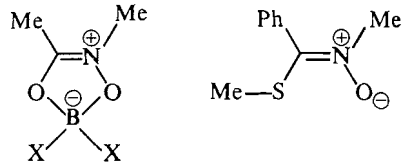

10 (X = F, Ph) **11**

TABLE 1. Crystallographic data[a]

Compound	**6**	**8**
Formula	$C_{14}H_{16}BF_2NO_3$	$C_{26}H_{26}BNO_3$
fw	295.09	411.31
Crystal system	Triclinic	Monoclinic
Space group	$P\bar{1}$	$P2_1/n$
a (Å)	6.1576(3)	9.8549(6)
b (Å)	11.2651(3)	10.9242(6)
c (Å)	10.8118(5)	41.263(2)
α (deg)	109.747(4)	
β (deg)	105.807(4)	92.717(6)
γ (deg)	92.976(4)	
V (Å^3)	670.55(5)	4437.2(4)
Z	2	8
ρ_c (g/cm^3)	1.461	1.231
$F(000)$	308	1744
μ(Cu-K$_\alpha$) (cm^{-1})	9.78	5.93
Crystal dimensions (mm)	0.28 × 0.40 × 0.44	0.20 × 0.36 × 0.45
Transmission factors		0.786–0.901
Scan type	ω–2θ	ω–2θ
Scan range (deg in ω)	0.80 + 0.14 tan θ	0.75 + 0.14 tan θ
Scan speed (deg/min)	1.3–10.0	1.3–10.0
Data collected	$+h, \pm k, \pm l$	$+h, +k, \pm l$
$2\theta_{max}$ (deg)	150	150
Crystal decay	negligible	negligible
Unique reflections	2764	7945
Reflections with $I \geq 3\sigma(I)$	2344	4248
Number of variables	255	560
R	0.045	0.042
R_w	0.059	0.045
S	1.438	0.752
Mean Δ/σ (final cycle)	0.01	0.004
Max Δ/σ (final cycle)	0.04	0.03
Residual density (e/Å^3)	−0.20 to +0.41	−0.17 to +0.22

[a]Temperature 295 K, Enraf-Nonius CAD4-F diffractometer, Cu-K$_\alpha$ radiation (λK_{α_1} = 1.540562, λK_{α_2} = 1.544390 Å), nickel filter, takeoff angle 2.7°, aperture (2.0 + tan θ) × 4.00 mm at a distance of 173 mm from the crystal, scan range extended by 25% on both sides for background measurement, $\sigma^2(I) = C + 2B + [0.04(C - B)]^2$ (C = scan count, B = normalized background count), function minimized: $\Sigma w(|F_o| - |F_c|)^2$ where $w = 1/\sigma^2(F)$, $R = \Sigma||F_o| - |F_c||/\Sigma|F_o|$, $R_w = (\Sigma w(|F_o| - |F_c|)^2/\Sigma w|F_o|^2)^{1/2}$, $S = (\Sigma w(|F_o| - |F_c|)^2/(m - n))^{1/2}$. Values given for R, R_w, and S are based on those reflections with $I \geq 3\sigma(I)$.

showed only small random variations. The data were reduced[2] and, for **8**, corrected for absorption (numerical integration). No absorption correction was applied for **6** due to irregularity of the crystal surface. Both structures were solved by direct methods, the positions of all non-hydrogen atoms being determined from E-maps and those of the hydrogen atoms from subsequent difference Fourier syntheses. The non-hydrogen atoms were refined with anisotropic thermal parameters. Hydrogen atoms in **6** were refined with isotropic thermal parameters and those in **8** were fixed in calculated positions with C(sp^2)—H = 0.97, C(sp^3)—H = 0.98 Å, and $U_H \propto U_{\text{bonded atom}}$. Neutral atom scattering factors for all atoms and anomalous dispersion corrections (F, O, N, and C) were taken from ref. 12. Isotropic Type I extinction corrections were applied (13–15), the final values of g being 0.36(4) × 10^4 for **6** and 0.73(9) × 10^4 for **8**. Final positional and anisotropic thermal parameters appear in Tables 2 and 7[3], respectively. Measured and calculated structure factors have been placed in the Depository of Unpublished Data.[3]

The thermal motion in both structures has been analysed in terms of the TLS model (16). The rms errors in the temperature factors U_{ij} (derived from the least-squares analyses) are 0.0009 and 0.0020 Å^2 for **6** and **8**, respectively. Analyses of the entire molecules indicated significant independent motion. The structural subunits O_2BF_2, O(3)C(3)—C(8), O(1)C(1)C(2)C(10)—C(14), and O(1)O(2)NC(2)-C(8)C(9) (Fig. 1) were separately analysed for **6** (rms ΔU_{ij} = 0.0011–0.0018 Å^2); and for each of the two independent molecules of **8** the subunits PhB, O(3)C(3)—C(9), O(1)C(1)C(2)C(10)—C(14), and the fused-ring systems were analysed (rms ΔU_{ij} = 0.0019–0.0040 Å^2). The appropriate bond distances have been corrected for libration (16, 17), using shape parameters q^2 of 0.08 for all atoms involved. Corrected bond lengths appear in Table 3 along with the uncorrected values; bond angles appear in Table 4 and intra-annular torsion angles in Table 5. Hydrogen atom parameters (Table 6), bond lengths and angles involving hydrogen, and a complete listing of torsion angles (Tables 8–10) have been deposited.[3]

[2]The computer programs used include locally written programs for data processing and locally modified versions of the following: MULTAN 80, multisolution program by P. Main, S. J. Fiske, S. E. Hull, L. Lessinger, G. Germain, J. P. Declercq, and M. M. Woolfson; AGNOST, absorption corrections, by J. A. Ibers; ORFLS, full-matrix least-squares, and ORFFE, function and errors, by W. R. Busing, K. O. Martin, and H. A. Levy; FORDAP, Patterson and Fourier syntheses, by A. Zalkin; ORTEP II, illustrations, by C. K. Johnson.

[3]Supplementary material mentioned in the text may be purchased from the Depository of Unpublished Data, CISTI, National Research Council of Canada, Ottawa, Ont., Canada K1A 0S2.

Can. J. Chem. Downloaded from www.nrcresearchpress.com by 196.1.178.254 on 09/07/12
For personal use only.

Can. J. Chem. Downloaded from www.nrcresearchpress.com by 196.1.178.254 on 09/07/12
For personal use only.

TABLE 2. Final positional (fractional × 10^4) and isotropic thermal parameters ($U \times 10^3$ Å^2) with estimated standard deviations in parentheses*

Atom	x	y	z	U_{eq}
		6		
F(1)	−1518(2)	1042(1)	4187(2)	72
F(2)	538(3)	2729(1)	6057(1)	67
O(1)	3638(2)	512(1)	1684(1)	41
O(2)	2541(2)	1460(1)	4830(1)	44
O(3)	36(3)	2724(2)	3825(2)	60
N	2742(3)	790(1)	3563(2)	40
C(1)	3179(3)	−813(2)	1691(2)	37
C(2)	2918(4)	−565(2)	3123(2)	47
C(3)	1699(3)	3322(2)	3561(2)	42
C(4)	1716(4)	4601(2)	3707(2)	51
C(5)	3323(4)	5217(2)	3374(2)	52
C(6)	4925(4)	4582(2)	2842(2)	51
C(7)	4894(3)	3302(2)	2642(2)	44
C(8)	3300(3)	2675(2)	3005(2)	37
C(9)	3248(3)	1331(2)	2776(2)	37
C(10)	5186(3)	−1471(2)	1449(3)	47
C(11)	4708(4)	−2863(2)	1305(3)	56
C(12)	2497(5)	−3561(2)	178(3)	60
C(13)	500(4)	−2872(2)	393(3)	55
C(14)	984(3)	−1480(2)	533(2)	48
B	332(4)	1996(2)	4721(2)	43
		8 ($z \times 10^5$)		
O(1)	1241(2)	1633(2)	32949(4)	51
O(2)	1215(2)	585(2)	24962(4)	45
O(3)	1580(2)	−1537(2)	26640(4)	46
N	1104(2)	1202(2)	27808(5)	42
C(1)	476(3)	2677(3)	31423(6)	43
C(2)	700(3)	2488(3)	27801(7)	45
C(3)	2070(3)	−1422(3)	29694(6)	41
C(4)	2749(3)	−2448(3)	30979(7)	52
C(5)	3275(3)	−2461(3)	34101(8)	63
C(6)	3149(4)	−1456(3)	36112(7)	63
C(7)	2506(3)	−450(3)	34933(7)	56
C(8)	1988(3)	−386(3)	31684(7)	43
C(9)	1437(3)	781(3)	30693(7)	44
C(10)	−980(3)	2515(3)	32279(7)	52
C(11)	−1836(3)	3563(3)	30992(8)	64
C(12)	−1271(4)	4780(3)	32224(8)	70
C(13)	223(4)	4929(3)	31512(8)	66
C(14)	1063(3)	3852(3)	32782(7)	55
C(15)	−866(3)	−693(3)	26558(6)	44
C(16)	−1309(3)	−1632(3)	28507(7)	59
C(17)	−2612(4)	−1651(4)	29648(8)	77
C(18)	−3503(4)	−731(4)	28934(9)	82
C(19)	−3106(3)	225(4)	27006(9)	69
C(20)	−1813(3)	231(3)	25830(7)	53
C(21)	485(2)	−1110(3)	21193(6)	39
C(22)	188(3)	−292(3)	18675(7)	45
C(23)	13(3)	−676(3)	15466(7)	52
C(24)	106(3)	−1890(4)	14696(7)	57
C(25)	389(3)	−2736(3)	17145(8)	58
C(26)	582(3)	−2341(3)	20340(7)	46
B	606(3)	−695(3)	24944(8)	41
O(1′)	4320(2)	962(2)	56325(5)	59
O(2′)	5771(2)	1939(2)	49215(4)	55
O(3′)	8008(2)	1168(2)	51034(4)	50
N′	4980(2)	1699(2)	51770(6)	49
C(1′)	3270(3)	1903(3)	55373(7)	57
C(2′)	3687(3)	2311(3)	52007(8)	61
C(3′)	7698(3)	302(3)	53126(7)	46
C(4′)	8709(3)	−565(3)	53855(7)	55
C(5′)	8549(4)	−1473(3)	56078(8)	64
C(6′)	7345(4)	−1560(3)	57703(8)	65
C(7′)	6322(3)	−749(3)	57005(7)	56
C(8′)	6456(3)	184(3)	54713(7)	45
C(9′)	5291(3)	963(3)	54157(7)	48
C(10′)	3415(3)	2915(3)	57849(8)	72
C(11′)	3010(4)	2529(4)	61204(9)	85
C(12′)	1599(4)	1976(5)	61090(9)	100
C(13′)	1523(4)	903(4)	58763(9)	93
C(14′)	1906(3)	1271(4)	55353(8)	79
C(15′)	7204(3)	3221(3)	53373(7)	43
C(16′)	7908(3)	3035(3)	56321(7)	50
C(17′)	7869(4)	3868(4)	58848(7)	65
C(18′)	7119(4)	4916(4)	58486(9)	75
C(19′)	6412(4)	5152(3)	55594(10)	73
C(20′)	6474(3)	4311(3)	53098(8)	61
C(21′)	7865(3)	2946(3)	47188(6)	47
C(22′)	7376(3)	2781(4)	44062(8)	85
C(23′)	7941(4)	3369(5)	41435(8)	99
C(24′)	9004(4)	4132(4)	41937(9)	75
C(25′)	9525(4)	4308(4)	44966(9)	82
C(26′)	8952(4)	3733(4)	47550(7)	76
B′	7237(3)	2313(3)	50300(8)	46

*U_{eq} = (1/3) trace of diagonalised U.

Results and discussion

The structure analyses confirm the boron chelate structures **6** and **8**. Surprisingly, in both cases the hydroxamic acid function does not serve as a bidentate ligand but rather has been transformed into an imidate *N*-oxide group by intramolecular alkylation. This imidate *N*-oxide function is bound to the boron atom only via the *N*-oxide oxygen atom, the second donor atom of the resulting bidentate chelating ligand being the phenolate oxygen atom.

The cyclocondensation of the *N*-(2-hydroxyalkyl)hydroxamic acid, leading to a 2-oxazoline *N*-oxide, is obviously not only possible in the presence of BF_3 but also proceeds under the influence of diphenylborinic anhydride, $(Ph_2B)_2O$, which should be a poorer acceptor (18) and therefore act as a weaker Lewis acid. Syntheses of 2-oxazolines by the cyclocondensation of *N*-(2-hydroxyalkyl)amides are well-known (19), whereas 2-oxazoline *N*-oxides have been reported only sporadically in the recent literature, prepared either by *N*-oxidation of the corresponding 2-oxazoline (20) or by condensation of *N*-(2-hydroxyalkyl)hydroxylamines and *ortho*-esters/amides (21).

The crystal structures of **6** and **8** both consist of discrete molecules, the shortest intermolecular distances between non-hydrogen atoms being F(1)···C(9) ($x - 1, y, z$) = 3.254(2) Å for **6** and O(1)···C(25) ($1/2 - x, 1/2 + y, 1/2 - z$) = 3.394(4) Å for **8**. Molecules are associated in the solid state by possible weak interactions: C(10)—H(10b)···F(1) ($1 + x, y, z$) and C(2)—H(2b)···O(2) ($1 - x, -y, 1 - z$) for **6** and C(4)—H(4)···O(2) ($1/2 - x, y - 1/2, 1/2 - z$) for **8** (H···O/F = 2.56(3), 2.51(3), and 2.54 Å; C···O/F = 3.371(3), 3.487(3), and 3.451(3) Å; C—H···O/F = 145(2), 168(2), and 156°, respectively). The two crystallographically independent molecules of **8** are, in fact, conformational isomers; in the unprimed molecule O(1) occupies an equatorial position of the cyclohexane ring while in the primed molecule O(1′) is in an

TABLE 3. Bond lengths (Å) with estimated standard deviations in parentheses

Bond	Length		Bond	Length	
	Uncorr.	Corr.		Uncorr.	Corr.
			6		
F(1)—B	1.372(3)	1.390	C(1)—C(14)	1.515(3)	1.524
F(2)—B	1.367(3)	1.384	C(3)—C(4)	1.395(3)	1.398
O(1)—C(1)	1.508(2)	1.512	C(3)—C(8)	1.402(2)	1.409
O(1)—C(9)	1.320(2)	1.323	C(4)—C(5)	1.372(3)	1.378
O(2)—N	1.366(2)	1.369	C(5)—C(6)	1.386(3)	1.392
O(2)—B	1.508(2)	1.518	C(6)—C(7)	1.381(3)	1.385
O(3)—C(3)	1.342(2)	1.347	C(7)—C(8)	1.394(3)	1.400
O(3)—B	1.449(3)	1.464	C(8)—C(9)	1.446(2)	1.450
N—C(2)	1.457(2)	1.460	C(10)—C(11)	1.527(3)	1.531
N—C(9)	1.292(2)	1.294	C(11)—C(12)	1.514(4)	1.523
C(1)—C(2)	1.533(3)	1.538	C(12)—C(13)	1.518(3)	1.525
C(1)—C(10)	1.512(2)	1.520	C(13)—C(14)	1.528(3)	1.532
			8		
O(1)—C(1)	1.491(3)	1.495	O(1′)—C(1′)	1.498(4)	1.507
O(1)—C(9)	1.337(3)	1.339	O(1′)—C(9′)	1.340(3)	1.343
O(2)—N	1.363(2)	1.365	O(2′)—N′	1.367(3)	1.370
O(2)—B	1.521(4)	1.523	O(2′)—B′	1.547(4)	1.550
O(3)—C(3)	1.334(3)	1.338	O(3′)—C(3′)	1.327(3)	1.331
O(3)—B	1.481(4)	1.482	O(3′)—B′	1.487(4)	1.489
N—C(2)	1.460(3)	1.462	N′—C(2′)	1.446(4)	1.448
N—C(9)	1.304(3)	1.306	N′—C(9′)	1.297(4)	1.300
C(1)—C(2)	1.535(3)	1.540	C(1′)—C(2′)	1.533(4)	1.538
C(1)—C(10)	1.505(4)	1.514	C(1′)—C(10′)	1.507(4)	1.519
C(1)—C(14)	1.505(4)	1.513	C(1′)—C(14′)	1.511(4)	1.521
C(3)—C(4)	1.397(4)	1.400	C(3′)—C(4′)	1.397(4)	1.400
C(3)—C(8)	1.402(4)	1.407	C(3′)—C(8′)	1.421(4)	1.427
C(4)—C(5)	1.365(4)	1.370	C(4′)—C(5′)	1.365(4)	1.370
C(5)—C(6)	1.385(4)	1.389	C(5′)—C(6′)	1.393(4)	1.399
C(6)—C(7)	1.348(4)	1.351	C(6′)—C(7′)	1.363(4)	1.366
C(7)—C(8)	1.414(4)	1.418	C(7′)—C(8′)	1.401(4)	1.406
C(8)—C(9)	1.438(4)	1.440	C(8′)—C(9′)	1.439(4)	1.442
C(10)—C(11)	1.503(4)	1.509	C(10′)—C(11′)	1.519(4)	1.524
C(11)—C(12)	1.520(5)	1.527	C(11′)—C(12′)	1.515(5)	1.526
C(12)—C(13)	1.524(4)	1.532	C(12′)—C(13′)	1.514(5)	1.526
C(13)—C(14)	1.517(4)	1.523	C(13′)—C(14′)	1.528(5)	1.534
C(15)—C(16)	1.386(4)	1.396	C(15′)—C(16′)	1.387(4)	1.396
C(15)—C(20)	1.398(4)	1.407	C(15′)—C(20′)	1.393(4)	1.402
C(15)—B	1.625(4)	1.630	C(15′)—B′	1.612(4)	1.617
C(16)—C(17)	1.389(4)	1.394	C(16′)—C(17′)	1.386(4)	1.391
C(17)—C(18)	1.358(5)	1.374	C(17′)—C(18′)	1.368(5)	1.376
C(18)—C(19)	1.380(5)	1.394	C(18′)—C(19′)	1.377(5)	1.387
C(19)—C(20)	1.385(4)	1.390	C(19′)—C(20′)	1.384(4)	1.389
C(21)—C(22)	1.391(4)	1.397	C(21′)—C(22′)	1.367(4)	1.390
C(21)—C(26)	1.395(4)	1.401	C(21′)—C(26′)	1.376(4)	1.395
C(21)—B	1.612(4)	1.616	C(21′)—B′	1.608(4)	1.612
C(22)—C(23)	1.392(4)	1.396	C(22′)—C(23′)	1.398(5)	1.402
C(23)—C(24)	1.368(4)	1.374	C(23′)—C(24′)	1.347(5)	1.365
C(24)—C(25)	1.388(4)	1.394	C(24′)—C(25′)	1.342(4)	1.367
C(25)—C(26)	1.392(4)	1.396	C(25′)—C(26′)	1.381(4)	1.385

axial position at C(1′). In **6**, only the equatorial conformer is present (see Fig. 1).

In the formation of the boron chelates, **6** and **8**, the seven-membered chelate ring system is preferred over a five-membered (like **3**) or a six-membered chelate system (like **5**), in spite of the fact that five- and six-membered boron chelates are very stable and frequently reported. Seven-membered boron chelates are rare in the literature (8). The boron chelates of salicylaldehyde nitrones like **7** or **9**, however, do possess the same seven-membered ring skeleton as observed for **6** and **8** (8, 22). The structural dimensions of the chelate ring BONCCCO of **9**, established by X-ray analysis (22), are strikingly similar to those observed for **6** and **8** (especially so for the latter as expected). The seven-membered chelate ring in **8** has a distorted envelope-like conformation very similar to that observed for **9** while that in **6** has a different conformation, best described as a "twist-envelope" (see Table 5). The bulkier phenyl substituents at boron and the longer intracyclic B—O

Can. J. Chem. Downloaded from www.nrcresearchpress.com by 196.1.178.254 on 09/07/12
For personal use only.

TABLE 4. Bond angles (deg) with estimated standard deviations in parentheses

Bonds	Angle (deg)	Bonds	Angle (deg)
		6	
C(1)—O(1)—C(9)	108.15(13)	C(6)—C(7)—C(8)	120.0(2)
N—O(2)—B	112.10(14)	C(3)—C(8)—C(7)	120.9(2)
C(3)—O(3)—B	126.6(2)	C(3)—C(8)—C(9)	119.2(2)
O(2)—N—C(2)	122.20(14)	C(7)—C(8)—C(9)	119.9(2)
O(2)—N—C(9)	123.04(15)	O(1)—C(9)—N	112.7(2)
C(2)—N—C(9)	113.39(15)	O(1)—C(9)—C(8)	122.40(15)
O(1)—C(1)—C(2)	103.30(13)	N—C(9)—C(8)	124.8(2)
O(1)—C(1)—C(10)	107.58(14)	C(1)—C(10)—C(11)	109.8(2)
O(1)—C(1)—C(14)	106.67(14)	C(10)—C(11)—C(12)	111.8(2)
C(2)—C(1)—C(10)	114.3(2)	C(11)—C(12)—C(13)	111.6(2)
C(2)—C(1)—C(14)	112.5(2)	C(12)—C(13)—C(14)	111.3(2)
C(10)—C(1)—C(14)	111.6(2)	C(1)—C(14)—C(13)	110.0(2)
N—C(2)—C(1)	100.75(14)	F(1)—B—F(2)	110.5(2)
O(3)—C(3)—C(4)	119.4(2)	F(1)—B—O(2)	111.3(2)
O(3)—C(3)—C(8)	122.3(2)	F(1)—B—O(3)	107.5(2)
C(4)—C(3)—C(8)	118.0(2)	F(2)—B—O(2)	103.7(2)
C(3)—C(4)—C(5)	120.6(2)	F(2)—B—O(3)	112.8(2)
C(4)—C(5)—C(6)	121.3(2)	O(2)—B—O(3)	111.1(2)
C(5)—C(6)—C(7)	119.2(2)		
		8	
C(1)—O(1)—C(9)	109.0(2)	C(1′)—O(1′)—C(9′)	109.3(2)
N—O(2)—B	114.3(2)	N′—O(2′)—B′	112.8(2)
C(3)—O(3)—B	125.8(2)	C(3′)—O(3′)—B′	127.0(2)
O(2)—N—C(2)	120.5(2)	O(2′)—N′—C(2′)	120.0(2)
O(2)—N—C(9)	125.8(2)	O(2′)—N′—C(9′)	125.6(3)
C(2)—N—C(9)	113.5(2)	C(2′)—N′—C(9′)	114.4(3)
O(1)—C(1)—C(2)	102.4(2)	O(1′)—C(1′)—C(2′)	103.0(2)
O(1)—C(1)—C(10)	106.2(2)	O(1′)—C(1′)—C(10′)	106.5(2)
O(1)—C(1)—C(14)	108.5(2)	O(1′)—C(1′)—C(14′)	106.9(3)
C(2)—C(1)—C(10)	113.3(2)	C(2′)—C(1′)—C(10′)	112.3(3)
C(2)—C(1)—C(14)	114.0(2)	C(2′)—C(1′)—C(14′)	113.9(3)
C(10)—C(1)—C(14)	111.5(2)	C(10′)—C(1′)—C(14′)	113.2(3)
N—C(2)—C(1)	100.3(2)	N′—C(2′)—C(1′)	101.6(2)
O(3)—C(3)—C(4)	115.4(3)	O(3′)—C(3′)—C(4′)	116.1(3)
O(3)—C(3)—C(8)	126.9(3)	O(3′)—C(3′)—C(8′)	126.5(3)
C(4)—C(3)—C(8)	117.7(3)	C(4′)—C(3′)—C(8′)	117.4(3)
C(3)—C(4)—C(5)	121.3(3)	C(3′)—C(4′)—C(5′)	122.2(3)
C(4)—C(5)—C(6)	121.1(3)	C(4′)—C(5′)—C(6′)	120.1(3)
C(5)—C(6)—C(7)	118.9(3)	C(5′)—C(6′)—C(7′)	119.5(3)
C(6)—C(7)—C(8)	121.7(3)	C(6′)—C(7′)—C(8′)	121.5(3)
C(3)—C(8)—C(7)	119.2(3)	C(3′)—C(8′)—C(7′)	119.2(3)
C(3)—C(8)—C(9)	125.5(3)	C(3′)—C(8′)—C(9′)	124.8(3)
C(7)—C(8)—C(9)	115.4(3)	C(7′)—C(8′)—C(9′)	116.0(3)
O(1)—C(9)—N	110.6(3)	O(1′)—C(9′)—N′	110.9(3)
O(1)—C(9)—C(8)	119.0(2)	O(1′)—C(9′)—C(8′)	118.8(3)
N—C(9)—C(8)	130.4(3)	N′—C(9′)—C(8′)	130.3(3)
C(1)—C(10)—C(11)	110.7(3)	C(1′)—C(10′)—C(11′)	113.2(3)
C(10)—C(11)—C(12)	111.0(3)	C(10′)—C(11′)—C(12′)	111.3(3)
C(11)—C(12)—C(13)	111.7(3)	C(11′)—C(12′)—C(13′)	110.2(3)
C(12)—C(13)—C(14)	111.6(3)	C(12′)—C(13′)—C(14′)	111.9(3)
C(1)—C(14)—C(13)	109.8(2)	C(1′)—C(14′)—C(13′)	112.0(3)
C(16)—C(15)—C(20)	115.7(3)	C(16′)—C(15′)—C(20′)	115.6(3)
C(16)—C(15)—B	123.3(3)	C(16′)—C(15′)—B′	124.9(3)
C(20)—C(15)—B	120.9(3)	C(20′)—C(15′)—B′	119.4(3)
C(15)—C(16)—C(17)	122.0(3)	C(15′)—C(16′)—C(17′)	122.2(3)
C(16)—C(17)—C(18)	120.9(3)	C(16′)—C(17′)—C(18′)	120.1(3)
C(17)—C(18)—C(19)	119.2(3)	C(17′)—C(18′)—C(19′)	120.0(3)
C(18)—C(19)—C(20)	119.7(3)	C(18′)—C(19′)—C(20′)	118.8(3)
C(15)—C(20)—C(19)	122.5(3)	C(15′)—C(20′)—C(19′)	123.2(3)
C(22)—C(21)—C(26)	116.4(3)	C(22′)—C(21′)—C(26′)	115.0(3)
C(22)—C(21)—B	122.7(3)	C(22′)—C(21′)—B′	124.4(3)
C(26)—C(21)—B	120.7(3)	C(26′)—C(21′)—B′	120.6(3)

Can. J. Chem. Downloaded from www.nrcresearchpress.com by 196.1.178.254 on 09/07/12
For personal use only.

TABLE 4 (*concluded*)

Bonds	Angle (deg)	Bonds	Angle (deg)
C(21)—C(22)—C(23)	122.0(3)	C(21′)—C(22′)—C(23′)	122.4(3)
C(22)—C(23)—C(24)	120.4(3)	C(22′)—C(23′)—C(24′)	120.0(3)
C(23)—C(24)—C(25)	119.4(3)	C(23′)—C(24′)—C(25′)	119.5(3)
C(24)—C(25)—C(26)	119.8(3)	C(24′)—C(25′)—C(26′)	120.1(3)
C(21)—C(26)—C(25)	122.0(3)	C(21′)—C(26′)—C(25′)	123.0(3)
O(2)—B—O(3)	108.8(2)	O(2′)—B′—O(3′)	107.3(2)
O(2)—B—C(15)	110.9(2)	O(2′)—B′—C(15′)	109.7(2)
O(2)—B—C(21)	106.0(2)	O(2′)—B′—C(21′)	105.8(2)
O(3)—B—C(15)	112.2(2)	O(3′)—B′—C(15′)	112.7(2)
O(3)—B—C(21)	107.2(2)	O(3′)—B′—C(21′)	108.2(2)
C(15)—B—C(21)	111.5(2)	C(15′)—B′—C(21′)	112.8(3)

Can. J. Chem. Downloaded from www.nrcresearchpress.com by 196.1.178.254 on 09/07/12
For personal use only.

distances in **8**, relative to those in **6**, are believed to be primarily responsible for the differences between the chelate ring conformations.

The C(9)—N bond distances[4] of 1.294(2) Å in **6** and an average of 1.303(4) Å in **8** are comparable to the C=N$^+$ double bond length of 1.290(2) Å in **9** (22) and demonstrate the iminium salt character within the *B*,*N*-betaine structure of **6** and **8**. A typical iminium salt like *N*,*N*-dimethylisopropylidenimminium perchlorate (23) shows an uncorrected C=N$^+$ bond length of 1.302 ± 0.043 Å. Similar C=N$^+$ distances have been observed in difluoroboron (X = F) and diphenylboron (X = Ph) chelates of *N*-methylacetohydroxamic acid **10** (1, 2), which are also best described as cyclic *B*,*N*-betaines (24). To our knowledge no imidate *N*-oxide groups have been structurally characterized by X-ray analysis. The 2-oxazoline *N*-oxide moieties in **6** and **8** therefore represent the first such examples. The structure of a thioimidate *N*-oxide **11** has recently been reported (25) and shows an uncorrected C=N$^+$ bond distance of 1.303 Å, essentially the same as that observed for the functionally related imidate *N*-oxide group in **8**.

In both compounds, **6** and **8**, the (sp^2)C—O single bonds C(9)—O(1) and C(3)—O(3) are relatively short (1.323(2)–1.347(2), mean 1.337 Å) with an estimated π-bond order (26) of about 0.35, indicative of an interaction with the adjacent π-bond systems. The significant difference between the C(9)—O(1) bond lengths in **6** (1.323(2) Å) and **8** (mean 1.341(3) Å) might result from distortions of the 2-oxazole ring. The sum of the C(9)—O(1) and O(1)—C(1) bonds in both compounds is nearly identical (~2.835 Å). The C(3)—O(3) bond distances correspond to similar phenolate C—O bonds in chelates like **9** (22) or corresponding salicylaldoxime derivatives (27, 28). The N—O bond distances in **6** and **8** (1.369(2) and 1.368(4) Å, respectively) are similar to that observed for the nitrone group in **9** (1.364(3) Å) and, as mentioned above for the nitrone C=N$^+$ bond in **9** (22), indicate the increased iminium salt character of the imidate *N*-oxide group within the *B*,*N*-betaine complexes **6** and **8**.

As in other boron chelates with one *N*-oxide and one phenolate (or alcoholate) ligand (ref. 22 and references therein), the two O—B bond lengths in **6** and **8** are significantly different from one another. As is generally the case, the O—B bonds to the *N*-oxide oxygen atoms are longer than those to the phenolate (or alcoholate) oxygen atoms. The shorter O—B distances in **6** (average 1.491 Å) compared with those in **8** (average 1.511 Å) demonstrate both the better acceptor qualities of the chelated difluoroborenium ion (BF_2^+) relative to the diphenylborenium ion (BPh_2^+) and the dependence of the boron covalent radius on the electronegativity of its substituents. These effects have been noted for the difluoroboron chelate **10** (X = F) (1) and its diphenylboron analog **10** (X = Ph) (2) with average O—B distances of 1.497 and 1.550 Å, respectively. For "Ph_2BO_2" compounds such as **8** the ratio of the average C—B and O—B bond lengths is a good indicator of the overall binding strength of the *O*,*O*-chelating ligand with respect to the "BPh_2^+" moiety (29). These mean C—B/mean O—B ratios range from 1.039 to 1.093 with an average value of 1.061 for 16 "Ph_2BO_2" compounds having six-, seven-, and eight-membered chelate rings (ref. 29 and references therein). The values of 1.080 and 1.063 observed for the two independent molecules of **8** are both indicative of above average binding strength for the ligand. The difference between the bond length ratios for the two molecules of **8**, which are conformational isomers (see above), is a result of significantly longer O—B and shorter C—B distances in the primed molecule (O(1′)-axial isomer). It is possible that the equatorial isomer is a slightly better donor than the axial isomer, consistent with the fact that only the former is observed in the structure of **6**. Differences in mean bond length ratios of up to 0.008 have been noted earlier for conformational isomers, structural polymorphs, and essentially equivalent crystallographically independent molecules (ref. 29 and references therein). The only other "Ph_2BO_2" compound having a seven-membered chelate ring, **9** (22), has a bond length ratio of 1.054.

The uncorrected O—B and F—B distances in **6** lie within the ranges 1.439–1.526 (mean 1.489 Å) and 1.314–1.401 (mean 1.366 Å) observed for "F_2BO_2" compounds having the boron atom in a six-membered ring (30). Compound **6** is the first example of a compound of this type having a seven-membered chelate ring. The ratios of the mean F—B and mean O—B distances in the six-membered "F_2BO_2" chelates range from 0.884 to 0.949 with an average value of 0.915. The value of 0.930 observed for **6** represents a relatively strong ligand binding to the "F_2B^+" moiety, as was also noted for the diphenylboron analog **8**.

The cyclohexane rings in **6** and **8** all have nearly undistorted chair conformations while the oxazoline rings display flattened C(1)-envelope conformations (see Table 5). The oxazoline rings, qualitatively, are nearly planar, the largest deviation from the mean plane being 0.140(3) Å for C(1) of **8**. The

[4]Libration corrected bond lengths (esd's assumed equal to those of the uncorrected values) are employed in the discussion and are compared with similarly treated (16) distances unless otherwise stated.

Can. J. Chem. Downloaded from www.nrcresearchpress.com by 196.1.178.254 on 09/07/12
For personal use only.

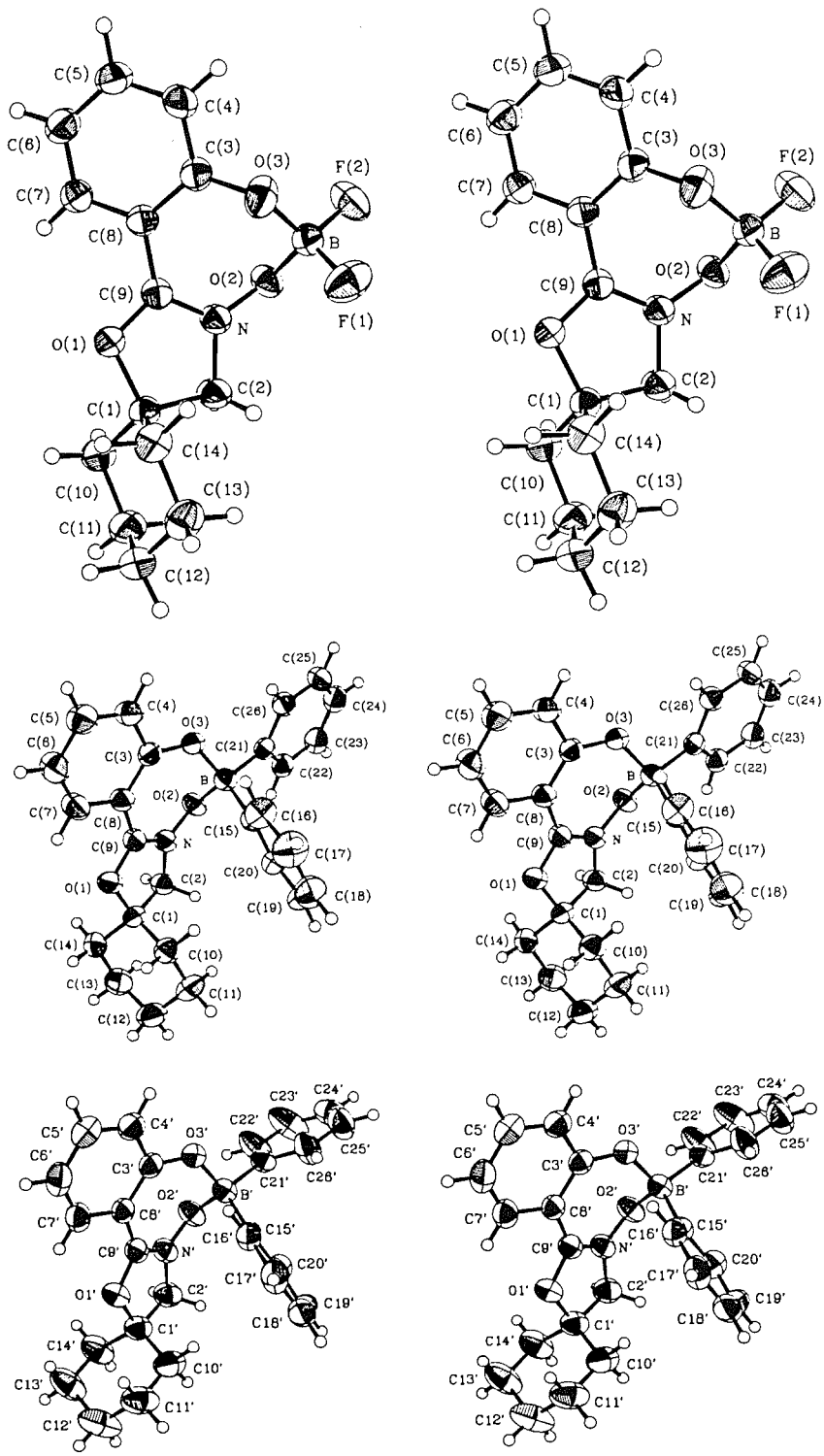

FIG. 1. Stereoscopic views of **6** (top) and the two independent molecules of **8** (middle and bottom); 50% probability thermal ellipsoids are shown for the non-hydrogen atoms.

TABLE 5. Intra-annular torsion angles (deg) standard deviations in parentheses

Atoms	Value (deg)
6	
B—O(2)—N—C(9)	75.8(2)
O(2)—N—C(9)—C(8)	−10.6(3)
C(3)—C(8)—C(9)—N	−35.7(3)
O(3)—C(3)—C(8)—C(9)	−3.4(3)
B—O(3)—C(3)—C(8)	57.8(3)
C(3)—O(3)—B—O(2)	−26.2(3)
N—O(2)—B—O(3)	−52.7(2)
C(14)—C(1)—C(10)—C(11)	−57.7(2)
C(1)—C(10)—C(11)—C(12)	55.5(3)
C(10)—C(11)—C(12)—C(13)	−54.3(3)
C(11)—C(12)—C(13)—C(14)	54.3(3)
C(12)—C(13)—C(14)—C(1)	−55.7(2)
C(10)—C(1)—C(14)—C(13)	58.1(2)
C(9)—O(1)—C(1)—C(2)	−10.6(2)
O(1)—C(1)—C(2)—N	12.3(2)
C(9)—N—C(2)—C(1)	−11.2(2)
C(2)—N—C(9)—O(1)	5.0(2)
C(1)—O(1)—C(9)—N	4.0(2)
8	
N—O(2)—B—O(3)	−79.6(3)
C(3)—O(3)—B—O(2)	58.1(3)
B—O(3)—C(3)—C(8)	−13.5(4)
O(3)—C(3)—C(8)—C(9)	−4.8(5)
C(3)—C(8)—C(9)—N	−11.9(5)
O(2)—N—C(9)—C(8)	0.2(5)
B—O(2)—N—C(9)	49.6(3)
C(14)—C(1)—C(10)—C(11)	59.0(3)
C(1)—C(10)—C(11)—C(12)	−56.0(3)
C(10)—C(11)—C(12)—C(13)	53.6(4)
C(11)—C(12)—C(13)—C(14)	−53.5(4)
C(12)—C(13)—C(14)—C(1)	55.1(3)
C(10)—C(1)—C(14)—C(13)	−58.1(3)
C(9)—O(1)—C(1)—C(2)	−18.8(3)
O(1)—C(1)—C(2)—N	19.0(2)
C(9)—N—C(2)—C(1)	−15.0(3)
C(2)—N—C(9)—O(1)	3.6(3)
C(1)—O(1)—C(9)—N	10.3(3)
N′—O(2′)—B′—O(3′)	81.5(3)
C(3′)—O(3′)—B′—O(2′)	−56.6(3)
B′—O(3′)—C(3′)—C(8′)	11.0(4)
O(3′)—C(3′)—C(8′)—C(9′)	3.6(5)
C(3′)—C(8′)—C(9′)—N′	17.7(5)
O(2′)—N′—C(9′)—C(8′)	−3.3(5)
B′—O(2′)—N′—C(9′)	−51.6(4)
C(14′)—C(1′)—C(10′)—C(11′)	49.4(4)
C(1′)—C(10′)—C(11′)—C(12′)	−53.2(4)
C(10′)—C(11′)—C(12′)—C(13′)	56.6(5)
C(11′)—C(12′)—C(13′)—C(14′)	−57.2(4)
C(12′)—C(13′)—C(14′)—C(1′)	53.3(4)
C(10′)—C(1′)—C(14′)—C(13′)	−49.0(4)
C(9′)—O(1′)—C(1′)—C(2′)	8.3(3)
O(1′)—C(1′)—C(2′)—N′	−8.0(3)
C(9′)—N′—C(2′)—C(1′)	5.8(3)
C(2′)—N′—C(9′)—O(1′)	−0.7(4)
C(1′)—O(1′)—C(9′)—N′	−5.2(3)

aromatic rings in both compounds are either planar to within experimental error or are nearly so, and show the expected substituent-induced geometrical distortions (31).

Acknowledgments

We thank the Natural Sciences and Engineering Research Council of Canada and the Fonds der Chemischem Industrie, Frankfurt am Main, for financial support and the University of British Columbia Computing Centre for assistance.

1. S. J. RETTIG, J. TROTTER, W. KLIEGEL, and D. NANNINGA. Can. J. Chem. **55**, 1 (1977).
2. S. J. RETTIG, J. TROTTER, W. KLIEGEL, and D. NANNINGA. Can. J. Chem. **56**, 1676 (1978).
3. W. KLIEGEL and D. NANNINGA. Chem. Ber. **116**, 2616 (1983).
4. W. KLIEGEL, D. NANNINGA, S. J. RETTIG, and J. TROTTER. Can. J. Chem. **61**, 2493 (1983).
5. (*a*) A. V. TOPCIEV, S. V. ZAVGORODNIJ, and J. M. PAUSKIN. Borfluorid und seine verbindungen als katalysatoren in der organischen chemie. Berlin. 1962. p. 159; (*b*) D. KASTNER. Neuere methoden der praparativen organischen chemie. Vol. 1. *Edited by* W. Foerst. Weinheim. 1963. p. 431.
6. (*a*) H. BOSHAGEN. Chem. Ber. **100**, 954 (1967); (*b*) U. R. KALKOTE and D. D. GOSWAMI. Austr. J. Chem. **30**, 1847 (1977).
7. R. FRIARY and B. R. SUNDAY. J. Heterocycl. Chem. **16**, 1277 (1979).
8. W. KLIEGEL and D. NANNINGA. J. Organomet. Chem. **243**, 373 (1983).
9. U. R. KALKOTE and D. D. GOSWAMI. J. Indian Chem. Soc. **54**, 519 (1977).
10. W. KLIEGEL and M. TAJERBASHI. Unpublished results.
11. R. NEU. Z. Anal. Chem. **176**, 334 (1960); B. FRIESE and F. UMLAND. Anal. Chim. Acta, **96**, 303 (1978).
12. International tables for X-ray crystallography. Vol. IV. Kynoch press, Birmingham. 1974. pp. 99–102 and 149.
13. P. J. BECKER and P. COPPENS. Acta Crystallogr. Sect. A, **30**, 129 (1974); **30**, 148 (1974); **31**, 417 (1975).
14. P. COPPENS and W. C. HAMILTON. Acta Crystallogr. Sect. A, **26**, 71 (1970).
15. F. R. THORNLEY and R. J. NELMES. Acta Crystallogr. Sect. A, **30**, 748 (1974).
16. V. SCHOMAKER and K. N. TRUEBLOOD. Acta Crystallogr. Sect. B, **24**, 63 (1968).
17. D. W. J. CRUICKSHANK. Acta Crystallogr. **9**, 747 (1956); **9**, 754 (1956); **14**, 896 (1961).
18. M. F. LAPPERT. The chemistry of boron and its compounds. *Edited by* E. L. Muetterties. New York. 1967. p. 528; T. ONAK. Organoborane chemistry. New York. 1975. p. 153.
19. J. A. FRUMP. Chem. Rev. **71**, 483 (1971); G. V. BOYD. Comprehensive heterocyclic chemistry. *Edited by* A. R. Katritzky and C. W. Rees. Oxford. 1984. p. 228.
20. J. W. F. KEANA and T. D. LEE. J. Am. Chem. Soc. **97**, 1273 (1975); T. D. LEE and J. W. F. KEANA. J. Org. Chem. **41**, 3237 (1976); J. B. HENDRICKSON and D. A. PEARSON. Tetrahedron Lett. **24**, 4657 (1983).
21. S. P. ASHBURN and R. M. COATES. J. Org. Chem. **49**, 3127 (1984); **50**, 3076 (1985).
22. W. KLIEGEL, U. LAUTERBACH, S. J. RETTIG, and J. TROTTER. Can. J. Chem. **65**, 1457 (1987).
23. L. M. TREFONAS, R. L. FLURRY, R. MAJESTE, E. A. MEYERS, and R. F. COPELAND. J. Am. Chem. Soc. **88**, 2145 (1966).
24. W. KLIEGEL. Organomet. Chem. Rev. Sect. A, **8**, 153 (1972).
25. R. M. COATES and S. J. FIRSAN. J. Org. Chem. **51**, 5198 (1986).
26. G. HAFELINGER. Chem. Ber. **103**, 2941 (1970).

Can. J. Chem. Downloaded from www.nrcresearchpress.com by 196.1.178.254 on 09/07/12
For personal use only.

27. S. J. RETTIG and J. TROTTER. Can. J. Chem. **61**, 206 (1983).
28. W. KLIEGEL, S. J. RETTIG, and J. TROTTER. Can. J. Chem. **62**, 1363 (1984).
29. W. R. CULLEN, S. J. RETTIG, J. TROTTER, and E. B. WICKENHEISER. Can. J. Chem. **66**, 2007 (1988).
30. A. W. HANSON and E. W. MACAULAY. Acta Crystallogr. Sect. B, **28**, 1961 (1972); O. P. ANDERSON and J. C. MARSHALL. Inorg. Chem. **17**, 1258 (1978); R. R. GAGNE, J. L. ALLISON, and G. C. LISENSKY. Inorg. Chem. **17**, 3563 (1978); P. G. LENHERT, C. M. LUKEHART, and L. T. WARFIELD. Inorg. Chem. **19**, 2343 (1980); O. P. ANDERSON and A. B. PACKARD. Inorg. Chem. **19**, 2941 (1980); F. S. STEPHENS and R. S. VAGG. Inorg. Chim. Acta, **43**, 77 (1980); M. W. MCCOOL, R. E. MARSH, D. M. INGLE, and R. R. GAGNE. Acta Crystallogr. Sect. B, **37**, 935 (1981); D. E. BERRY, G. W. BUSHNELL, and K. R. DIXON. Inorg. Chem. **21**, 957 (1982); H. BINDER, W. MATHEIS, H.-J. DOISEROTH, and HAN FU-SON. Z. Naturforsch. Teil B, **38**, 554 (1983); R. C. F. JONES and G. E. PETERSON. Tetrahedron Lett. **24**, 4757 (1983); F. S. STEPHENS and R. S. VAGG. Inorg. Chim. Acta, **89**, 47 (1984); H. BINDER, W. MATHEIS, G. HECKMANN, H.-J. DOISEROTH, and HAN FU-SON. Z. Naturforsch. Teil B, **40**, 934 (1985); P. G. LENHERT, C. M. LUKEHART, and L. A. SACKSTEDER. J. Am. Chem. Soc. **108**, 793 (1986); D. AFZAL, P. G. LENHERT, C. M. LUKEHART, and R. SRINIVASAN. Inorg. Chem. **25**, 710 (1986); M. S. HUSSAIN, M. Z. EL-FAER, A. KHAN, and E. O. SCHLEMPER. Inorg. Chim. Acta, **128**, 81 (1987).
31. A. DOMENICANO, P. MURRAY-RUST, and A. VACIAGO. Acta Crystallogr. Sect. B, **39**, 457 (1983) and references therein.

Can. J. Chem. Downloaded from www.nrcresearchpress.com by 196.1.178.254 on 09/07/12
For personal use only.

Charge distributions and chemical effects. XLV. Graphite

ANDREA PELUSO AND SÁNDOR FLISZÁR

Département de Chimie, Université de Montréal, C.P. 6128, Succ. A, Montréal (Qué.), Canada H3C 3J7

Received February 11, 1988

ANDREA PELUSO and SÁNDOR FLISZÁR. Can. J. Chem. **66**, 2631 (1988).

The zero point energy of graphite, ZPE = $(2/3)R\theta_{\parallel} + (1/4)R\theta_{\perp}$, is deduced from Debye's theory by separating the lattice vibrations into two approximately independent parts, with Debye temperatures $\theta_{\parallel}$ (in plane) and $\theta_{\perp}$ (perpendicular). A balanced evaluation gives ZPE $\simeq$ 3.68 kcal mol^{-1}. The bond energies of graphite in its potential minimum are derived from those of polynuclear benzenoïd hydrocarbons using a formula describing bond energies in terms of the charges at the bond-forming atoms. These energies plus a consideration of (*i*) van der Waals interactions between layers ($\sim$1.2 kcal mol^{-1}), (*ii*) ZPE = 3.68, and (*iii*) the experimental heat content, $H_T - H_0$ = 0.25 kcal mol^{-1}, lead to a theoretical enthalpy of atomization, $\Delta H_a(298.15)$ = 174.6, which is $\sim$2% larger than its experimental counterpart, 170.9 kcal mol^{-1}. Exploiting the fact that the carbon atoms are electroneutral in graphite and not so in benzenoïd hydrocarbons, the results obtained for graphite support the approximate validity of bond energies deduced for polynuclear benzenoïd hydrocarbons and of the net charge, 14.8 $\times$ 10^{-3} e, deduced for the carbon atom of benzene.

ANDREA PELUSO et SÁNDOR FLISZÁR. Can. J. Chem. **66**, 2631 (1988).

On a déduit l'énergie au point zéro du graphite, EPZ = $(2/3)R\theta_{\parallel} + (1/4)R\theta_{\perp}$, à l'aide de la théorie de Debye en séparant les vibrations du réseau en deux parties approximativement indépendantes avec les températures de Debye $\theta_{\parallel}$ (dans le plan) et $\theta_{\perp}$ (perpendiculaire au plan). Une évaluation balancée conduit à une valeur de EPZ de 3,68 kcal mol^{-1}. On a déduit les énergies de liaison du graphite à son potentiel minimum à partir de celles d'hydrocarbures benzénoïdes polynucléaires et en faisant appel à une formule décrivant les énergies de liaison en fonction des charges au niveau des atomes conduisant à la formation de liaisons. Ces énergies prises de concert avec (*i*) les interactions de van der Waals entre les couches ($\sim$1,2 kcal mol^{-1}), (*ii*) une valeur de EPZ de 3,68 et (*iii*) l'enthalpie expérimentale, $H_T - H_0$, de 0,25 kcal mol^{-1}, conduit à une enthalpie théorique d'atomisation, $\Delta H_a(298,15)$ = 174,6, qui est environ 2% plus élevée que sa contrepartie expérimentale, 170,9 kcal mol^{-1}. En exploitant le fait que les atomes de carbone sont électriquement neutres dans le graphite alors qu'ils ne le sont pas dans les hydrocarbures benzénoïdes, les résultats qui sont obtenus pour le graphite apportent donc un support à l'hypothèse établissant une validité approximative des énergies de liaison déduites d'hydrocarbures benzénoïdes polynucléaires et de la charge nette de 14,8 $\times$ 10^{-3} e qui a été déduite pour l'atome de carbone du benzène.

[Traduit par la revue]

Introduction

Here we submit an energy analysis of graphite covering (*i*) its vibrational energy and (*ii*) its energy when all the atoms are stationary in their equilibrium positions. Neither aspect is trivial. The first centers, in essence, on an estimate of the zero point energy while the second involves a calculation of bond energies. A comparison with experiment sheds light on the approximate validity of the two components evaluated in this analysis. The final result is instructive as regards the nature of the carbon–carbon bonds in benzenoïd hydrocarbons.

Zero point energy, ZPE

A crystal containing N atoms can be considered as a giant oscillating molecule with $3N$ normal modes of vibration, each with its own frequency, ν_i, and

$$\text{ZPE} = \frac{1}{2}\sum_{i=1}^{3N} h\nu_i$$

Since the frequencies are many and close together, this sum is conveniently replaced by the integral

$$[1] \qquad \text{ZPE} = \frac{1}{2}\int_0^{\nu_{max}} h\nu\rho(\nu)d\nu$$

where $\rho(\nu)d\nu$ is the number of frequencies in the range ν to $\nu + d\nu$ and ν_{max} is the highest allowable frequency. The problem thus rests with the evaluation of the density of states, $\rho(\nu)$.

Our approach follows Debye's model (1, 2) although, in spite of its success in numerous applications, it is unclear how it would perform in the evaluation of ZPE. The point is that the density of states function is not smooth, particularly in the region of high frequencies, as it exhibits occasional peaks corresponding to modes with different polarizations and velocities.[1] With these reservations in mind, we examine as follows the possibility of retrieving an acceptable estimate of ZPE in a simple manner.

Graphite has a layer-like structure. Each carbon is bonded to three other carbon atoms forming a framework of planar benzenoïd rings, with bond distances of 1.42 Å. The planes are separated by $\sim$3.4 Å. The atomic displacements perpendicular to a plane have restoring forces which are much weaker than for displacements in the plane. Briefly, the forces between the atoms in graphite are extremely anisotropic: high frequencies correspond to displacements in a plane, whereas modes in which the basal planes move essentially as rigid units have low frequencies. It is thus reasonable to separate the lattice vibrations into two approximately independent parts (5–16), with distinct Debye temperatures $\theta_{\parallel}$ (in plane) and $\theta_{\perp}$ (perpendicular) (Table 1).

Applying Debye's arguments to a graphite crystal containing N = Avogadro's number of atoms, we obtain after normalization (Appendix) the following expressions for the density of states:

$$[2] \qquad \rho_{\parallel}(\nu) = \frac{4N}{\nu_{max\parallel}^2}\nu$$

[1]Lattice dynamics (and a reasonable sampling of representative frequencies in the first Brillouin zone) gives access to $\rho(\nu)$ (3). This approach is plagued by errors largely due to force constants which, even in refined theoretical calculations, are usually overestimated by up to 20% (4) — a circumstance which would impair any definite assessment regarding the precision of the final result deduced in this way.

Can. J. Chem. Downloaded from www.nrcresearchpress.com by 196.1.178.254 on 09/07/12
For personal use only.

TABLE 1. Debye temperatures of graphite (K)

Method	$\theta_\parallel$	$\theta_\perp$	Reference
Calorimetry	2280	760	6
Calorimetry	2300	800	9
LEED	2300	780	10
LEED	2046	774	14
X-ray		700	11
Lattice dynamics	2500	950	8
Semi-continuum theory	2480		16*a*, *b*

$$[3] \qquad \rho_\perp(\nu) = \frac{N}{\nu_{\max\perp}}$$

where $\rho_\parallel$, $\nu_{\max\parallel}$ refer to the modes in the plane and $\rho_\perp$, $\nu_{\max\perp}$ to the perpendicular modes, with

$$[4] \qquad \theta_\parallel = \frac{h\nu_{\max\parallel}}{k} \qquad \theta_\perp = \frac{h\nu_{\max\perp}}{k}$$

Finally, it follows from eqs. [1]–[4] that

$$[5] \qquad \mathrm{ZPE} = \tfrac{3}{8}R\theta_\parallel + \tfrac{1}{4}R\theta_\perp$$

where $R = Nk$ is the gas constant.

Our description of $\rho_\parallel(\nu)$ is just an alternate form of a result given earlier by Komatsu and Nagamiya (16*a*), deduced from a semi-continuum treatment of graphite. Its quality is difficult to assess, however; $\rho_\parallel(\nu)$ is certainly not as smooth a function as suggested by eq. [2]. On the other hand, our $\rho_\parallel(\nu)$ benefits from a normalization offsetting at least part of the error due to the neglect of local departures from eq. [2]. Supporting evidence is offered by the following result due to Komatsu and Nagamiya. The force constants between the carbon atoms of benzene, determined by infrared and Raman spectroscopy, were used with appropriate modifications to permit a reasonable estimate of those of a graphite layer. On this basis, the authors arrive at $\theta_\parallel = 2440°$, which is realistic (Table 1). The point is that eq. [2] is part of this evaluation. Thus we may infer that eq. [2], if not taken on a point-by-point basis, behaves like an acceptable approximation in problems involving its use to cover the entire range from 0 to $\nu_{\max\parallel}$.

The distribution function for the vibrations perpendicular to the layers, eq. [3], differs from Komatsu's results (16*a*, *b*) only in the low frequency range, $\nu < \nu_z' = 3.76 \times 10^{12}\ \mathrm{s}^{-1}$, i.e., below $\theta_z' = h\nu_z'/k \simeq 180$ K. While these low frequencies play a leading role in the calculation of specific heats, they contribute little to the "perpendicular part" of ZPE. As a consequence, the error introduced by using eq. [3] in the entire range 0 to $\nu_{\max\perp}$ is minimal, all the more as the overall contribution of perpendicular vibrations represents only ~10% of the total ZPE.

Hence, within the framework of a simple Debye approach applied to a non-isotropic system, eq. [5] emerges as a reasonably viable first approximation. Of course, the difficulty now rests with the selection of the appropriate Debye temperatures. For internal consistency, we select $\theta_\parallel = 2480$ K, which is Komatsu's revised result (16*b*) obtained from his semi-continuum theory, and (somewhat arbitrarily) $\theta_\perp = 800$ K (Table 1). Our estimate is thus

$$\mathrm{ZPE} = 3.68\ \mathrm{kcal\ mol^{-1}}$$

which is tentatively used in the forthcoming analysis involving the enthalpy of atomization of graphite.

Bond energies of vibrationless graphite

For a molecule in its hypothetical vibrationless state we apply the energy formula (17)

$$[6] \qquad \epsilon_{ij} = \epsilon_{ij}^0 + a_{ij}\Delta q_i + a_{ji}\Delta q_j$$

where ϵ_{ij}^0 is for a bond formed by atoms i and j whose net charges are q_i^0 and q_j^0, respectively, and ϵ_{ij} for the same bond with charges $q_i = q_i^0 + \Delta q_i$ and $q_j = q_j^0 + \Delta q_j$. The a_{ij} and a_{ji} parameters measure the effect of unit charge variations at atom i (bonded to j) and atom j (bonded to i), respectively. This equation was successfully applied to a variety of organic systems (17), namely benzenoïd hydrocarbons (18), in calculations of their atomization energies, $\Delta E_a^* \simeq \Sigma\epsilon_{ij}$. Here we apply eq. [6] in a straightforward manner by treating graphite as a giant polycyclic aromatic system and temporarily postpone the discussion of imperfections associated with this simplified model. We use the theoretical a_{CC} value determined earlier (18) for benzenoïd hydrocarbons, namely $a_{CC} = -0.358\ \mathrm{kcal\ mol^{-1}\ me^{-1}}$ (1 me = 10^{-3} e), and the reference net charge, $q_C^0 = 14.8$ me, of the benzene carbon atom. The graphite carbon atoms being electroneutral, it follows that $\Delta q_C = -14.8$ me and, from eq. [6],

$$\epsilon_{CC} = \epsilon_{CC}^0 + 10.60\ \mathrm{kcal\ mol^{-1}}$$

The construction of the carbon skeleton of a planar polynuclear benzenoïd hydrocarbon, leaving all carbons with $q_C^0 = 14.8$ me, involves two types of ϵ_{CC}^0 energies. The aromatic carbon–carbon bond, $\epsilon^0(\mathrm{C}\cdots\mathrm{C}) = 114.21\ \mathrm{kcal\ mol^{-1}}$, represents, so to speak, the average between a single and a double bond as they are found in benzenoïd structures: it is the CC bond of benzene. This type of bond occurs twice as often as the number of double bonds one can write using classical Kékulé structures (e.g., six times in benzene, ten times in naphthalene, etc.). In addition, except for benzene, there is a number of single CC bonds "in excess" (e.g., 1 in naphthalene, 2 in anthracene, etc.) which are treated as such, i.e., as $C(sp^2)$—$C(sp^2)$ single bonds with $\epsilon^0(\mathrm{C—C}) = 91.56\ \mathrm{kcal\ mol^{-1}}$ (18). With zero net charges we thus obtain $\epsilon(\mathrm{C}\cdots\mathrm{C}) = 124.81$ and $\epsilon(\mathrm{C—C}) = 102.16\ \mathrm{kcal\ mol^{-1}}$.

In graphite, each carbon atom is engaged in one double and two single bonds, i.e., two bonds with energy 124.81 and one bond with energy 102.16, for a total of $351.78\ \mathrm{kcal\ mol^{-1}}$. The cleavage of these three bonds frees two carbon atoms. The atomization energy of graphite in its potential minimum at 0 K is thus

$$\Delta E_a^*(\mathrm{graphite}) = \tfrac{1}{2}\Sigma\epsilon_{CC} = 175.89\ \mathrm{kcal\ mol^{-1}}$$

This theoretical result can now be compared with experiment.

Discussion

The energy of atomization at $T = 298.15$ K, $\Delta E_a = \Delta H_a - RT$ (where ΔH_a is the corresponding enthalpy), is deduced from ΔE_a^* by subtracting ZPE as well as the heat content, $H_T - H_0$, gained between 0 and T and by adding the translational energy, $(3/2)RT$, of the carbon atoms formed during the atomization of graphite, i.e.,

$$[7] \qquad \Delta H_a = \Delta E_a^* - \mathrm{ZPE} - (H_T - H_0) + \tfrac{5}{2}RT$$

Using the experimental result (7), $H_T - H_0 = 0.25\ \mathrm{kcal\ mol^{-1}}$ (which consists, in essence, of thermal vibrational energy), our calculation gives

$$\Delta H_a(\mathrm{graphite}, 298.15) = 173.44\ \mathrm{kcal\ mol^{-1}}$$

The commonly accepted experimental value is $170.9\ \mathrm{kcal\ mol^{-1}}$

Can. J. Chem. Downloaded from www.nrcresearchpress.com by 196.1.178.254 on 09/07/12
For personal use only.

Can. J. Chem. Downloaded from www.nrcresearchpress.com by 196.1.178.254 on 09/07/12
For personal use only.

(19). Although our calculation appears to be in reasonable accord with the latter, the discrepancy is unusually large in comparison with what is generally obtained from eq. [6] (17, 18). Moreover, our model neglects the interactions between layers — a circumstance which adds approximately 1.2 kcal mol^{-1} to the error (20).

At best, only a minor part of the discrepancy can be blamed on possible errors associated with our evaluation of ZPE. The bond energies are certainly overestimated. Let us first examine the $a_{CC}\Delta q_C$ part of eq. [6]. In the evaluation of ΔE_a^*, a total of $\frac{1}{2}(3 \times 10.60) = 15.90$ kcal mol^{-1} comes from the charge neutralization, $\Delta q_C = -14.8$ me. This Δq_C is based on the carbon net charge in benzene, 14.8 ± 1 me (18). Hence, if the discrepancy in the calculation of ΔH_a (of the order of 3.7 kcal mol^{-1}) was to be *entirely* attributed to a misrepresentation of the benzene carbon, the charge of the latter should be reduced to ~11.4 me. This extreme, however, is probably not justified, as suggested by an examination of the ϵ_{CC}^0's. Those used here are for CC bonds with carbons 1.40 Å apart (18). In graphite, the bond distances are 1.42 Å (21). Our simple model cannot account for this change in geometry but it should be anticipated that longer bonds correspond to smaller bond energies. It is thus reasonable to advocate that at least a good part of the error made in our calculation should be blamed on too large ϵ_{CC}^0 reference energies.

Graphite represents a severe test for the simple approach describing bond energies in terms of the charges of the bond-forming atoms, eq. [6], and provides a fresh insight into the approximate validity of the charge, 14.8 ± 1 me, estimated for the benzene carbon atom. The results vividly support the approximate validity of the energies associated with the two types of carbon–carbon bonds occurring in polynuclear benzenoïd structures.

Acknowledgements

We thank the Authorities of the Italian National Institute ENICHEM, Milano, in particular Drs. L. Costa and A. Mezzadra, for the support given to A.P. Financial assistance given by the Natural Sciences and Engineering Research Council of Canada is gratefully acknowledged.

1. P. Debye. Ann. Phys. **39**, 789 (1921).
2. O. K. Rice. Statistical mechanics, thermodynamics and kinetics. W. H. Freeman and Co., San Francisco, CA. 1967.
3. J. M. Ziman. Principles of the theory of solids. Cambridge University Press, Cambridge. 1972; A. Yoshimori and Y. Kitano. J. Phys. Soc. Jpn. **11**, 352 (1956); J. A. Young and J. U. Koppel. J. Chem. Phys. **42**, 357 (1965); R. Nicklow, N. Wakabayashi, and H. G. Smith. Phys. Rev. B**5**, 4951 (1972); E. de Rouffignac, G. P. Alldredge, and F. W. de Wette. Phys. Rev. B**23**, 4208 (1981).
4. P. Pulay. *In* Modern theoretical chemistry. Vol. 4. *Edited by* H. F. Schaefer. Plenum Press, New York, NY. 1977. p. 153.
5. W. Nernst. Ann. Phys. **36**, 395 (1911).
6. A. Magnus. Ann. Phys. **70**, 303 (1923).
7. W. DeSorbo and W. W. Tyler. J. Chem. Phys. **21**, 1660 (1953).
8. J. Krumhansl and H. Brooks. J. Chem. Phys. **21**, 1663 (1953).
9. W. C. Morgan. Carbon, **10**, 73 (1972).
10. G. Albinet, J. P. Biberian, and M. Bienfait. Phys. Rev. B**3**, 2015 (1971).
11. G. E. Bacon. Acta Crystallogr. **5**, 492 (1952).
12. J. P. Biberian, M. Bienfait, and J. B. Theeten. Acta Crystallogr. A**29**, 221 (1973).
13. R. Chen and P. Trucano. Acta Crystallogr. A**34**, 979 (1978).
14. B. Firey, F. W. de Wette, E. de Rouffignac, and G. P. Alldredge. Phys. Rev. B**28**, 7210 (1983).
15. N. Y. Wu, V. Kumykov, and A. Ignatiev. Surf. Sci. **163**, 51 (1985).
16. (*a*) K. Komatsu and T. Nagamiya. J. Phys. Soc. Jpn. **6**, 438 (1951); (*b*) K. Komatsu. J. Phys. Soc. Jpn. **10**, 346 (1955); (*c*) K. Komatsu. J. Phys. Chem. Solids, **25**, 707 (1964).
17. S. Fliszár. Charge distributions and chemical effects. Springer-Verlag, Heidelberg, New York, NY. 1983; S. Fliszár. J. Am. Chem. Soc. **102**, 6946 (1980).
18. S. Fliszár, G. Cardinal, and N. A. Baykara. Can. J. Chem. **64**, 404 (1986).
19. D. R. Stull and G. C. Sinke. Adv. Chem. Ser. **18**, (1956).
20. D. D. Richardson. J. Phys. C. Sol. State Phys. **10**, 3235 (1977); E. Santos and A. Villagrá. Phys. Rev. B**6**, 3134 (1972); R. J. Good, L. A. Girifalco, and G. Kraus. J. Phys. Chem. **62**, 1418 (1958).
21. D. E. Gray (*Editor*). American Institute of Physics Handbook. 3rd ed. McGraw-Hill, New York, NY. 1972. p. 905.

Appendix

Debye's approximation (1, 2) is based on a consideration of $\rho(\nu)$ at low frequencies and an extrapolation therefrom. Whether a given wave can persist, and hence be included among the normal oscillations, depends on whether it reinforces itself upon reflection from the surfaces of the solid. Reinforcement depends on the relation between the wavelength and the dimensions of the solid, only certain wavelengths being permitted. The wave velocity u may, for long wavelengths, be taken as constant for any type of wave. Since the wavelength λ and the frequency ν are related by the relation

[A1] $$u = \lambda\nu$$

this will determine the allowed frequencies. For a three-dimensional wave, with a slab of lengths a, b, and c, we have

[A2] $$\frac{\lambda}{\cos\alpha} = \frac{2a}{k_x} \qquad \frac{\lambda}{\cos\beta} = \frac{2b}{k_y} \qquad \frac{\lambda}{\cos\gamma} = \frac{2c}{k_z}$$

where k_x, k_y, and k_z are integers. The number of frequencies in any given range of frequencies is given by the number of integral triplets k_x, k_y, and k_z in that range; $\cos\alpha$, $\cos\beta$, and $\cos\gamma$ are the direction cosines of the direction of propagation in the directions of space.

Treating the problem of two-dimensional vibrations in a layer just as in Debye's theory of a three-dimensional continuum, it follows that (16*a*)

[A3] $$\rho_{\parallel}(\nu) = 2\pi ab\left(\frac{1}{u_l^2} + \frac{1}{u_t^2}\right)\nu$$

where u_l and u_t are the velocities of the longitudinal and transverse waves, respectively. Similarly, assuming parallel propagation and polarization vectors, we obtain for the perpendicular vibrations that $\lambda = u'/\nu = 2c/k_z$, i.e., $k_z = 2c\nu/u'$, and

[A4] $$\rho_{\perp}(\nu) = 2c/u'$$

Equations [A3] and [A4] are conveniently simplified with the introduction of the following normalizations

[A5] $$\int_0^{\nu_{\max\parallel}} \rho_{\parallel}(\nu)\,d\nu = 2N$$

[A6] $$\int_0^{\nu_{\max\perp}} \rho_{\perp}(\nu)\,d\nu = N$$

Equation [2] is obtained from eqs. [A3] and [A5], whereas eqs. [A4] and [A6] give eq. [3].

Molecular conformation of 2′-deoxy-3′,5′-di-*O*-acetyl guanosine. Crystal structure and high resolution proton nuclear magnetic resonance investigations

LEO H. KOOLE[1] AND HENK M. BUCK

Department of Organic Chemistry, Eindhoven University of Technology, P.O. Box 513, 5600 MB Eindhoven, The Netherlands

AND

JAN A. KANTERS AND ARIE SCHOUTEN

Laboratory of Crystal and Structural Chemistry, State University of Utrecht, Utrecht, The Netherlands

Received November 6, 1987[2]

LEO H. KOOLE, HENK M. BUCK, JAN A. KANTERS, and ARIE SCHOUTEN. Can. J. Chem. **66**, 2634 (1988).

2′-Deoxy-3′,5′-di-*O*-acetyl guanosine crystallizes in the triclinic space group $P1$ (C_1^1, No. 1), and the cell dimensions are $a = 8.643(1)$ Å, $b = 10.122(1)$ Å, $c = 10.391(1)$ Å, $\alpha = 87.04(1)°$, $\beta = 73.58(1)°$, $\gamma = 72.37(1)°$, $V = 830.4(2)$ Å^3; $Z = 2$ molecules per cell. Least-squares refinement converged at $R = 0.031$ for 3450 observed reflections. The asymmetric unit consists of two independent molecules. The guanine bases are linked via N(1)—H...N(7) and N(2)—H...O(6) hydrogen bonds to form a virtually planar system. Moreover, the conformational preferences of the title compound in DMSO-d_6 solution have been determined with 300 MHz ^{1}H NMR. It is found that the X-ray structure and the solution conformation are essentially similar. The C(4′)—C(5′) linkage resides in the *gauche*$^+$ (g^+) or *trans* (t) rotamers in the solid state, while an approximately equal distribution over g^+, t, and *gauche*$^-$ is found in solution.

LEO H. KOOLE, HENK M. BUCK, JAN A. KANTERS et ARIE SCHOUTEN. Can. J. Chem. **66**, 2634 (1988).

La désoxy-2′ di-*O*-acétyl-3′,5′ guanosine cristallise dans le groupe d'espace triclinique $P1$ (C_1^1, No. 1) avec $a = 8,643(1)$, $b = 10,122(1)$ et $c = 10,391(1)$ Å, $\alpha = 87,04(1)$, $\beta = 73,58(1)$ et $\tau = 72,37(1)°$, $V = 830,4(2)$ Å^3 et $Z = 2$. La structure a été résolue par la méthode des moindres carrés (matrice entière) jusqu'à une valeur de R de 0,031 pour 3450 réflexions observées. L'unité asymétrique comporte deux molécules indépendantes. Les bases guanines sont liées par le biais de liaisons hydrogènes N(1)—H...N(7) et N(2)—H...O(6) et elles forment un système virtuellement plan. De plus, opérant en solution dans le DMSO-d_6 et faisant appel à la RMN du ^{1}H à 300 MHz, on a déterminé les préférences conformationnelles du composé mentionné dans le titre. On a trouvé que la structure déterminée par diffraction des rayons-X possède essentiellement la même conformation qu'en solution. A l'état solide, la liaison C(4′)—C(5′) se retrouve dans les rotamères *gauche*$^-$ (g^+) ou *trans* (t); en solution, on retrouve une distribution approximativement égale des rotamères g^+, t et *gauche*$^-$.

[Traduit par la revue]

Introduction[3]

Recent literature covers a substantial number of X-ray crystallographic studies on acetylated DNA or RNA nucleosides (1–9). The interest in these compounds stems primarily from their remarkable structural features. It has been found that acetylated nucleosides can serve as unique models to study different modes of hydrogen-bonded base pairing, which must be considered as alternatives for the conventional antiparallel coupling of complementary bases according to the Watson and Crick (10) model (adenine (A) – thymine (T), or guanine (G) – cytosine (C)). For example, it was found that 3′,5′-di-*O*-acetyl thymidine crystallizes in a *parallel* base-paired conformation, in which the T bases are linked via two N(3)—H...O(4) hydrogen bonds (6, 11, 12). We have recently shown that the possibility of parallel T–T base-pair formation may have a more general significance. Exclusive methylation of the phosphate groups in the mononucleotide d(pTp), and in the oligonucleotides d(T_2), d(T_3), d(T_4), d(T_6), and d(T_8) results in the formation of a remarkably slim parallel double helical structure in aqueous solution (11–13). The parallel strands in this structure are linked via T–T base pairs as first observed in the crystal structure of 3′,5′-di-*O*-acetyl thymidine. Very recent UV hyperchromicity experiments with unmodified d(T_8) have provided preliminary evidence for the formation of an analogous double helix, if one equivalent of the cationic protein polylysine is present (13). Most likely, complexation of polylysine with the negatively charged phosphodiester groups in d(T_8) leads to a substantial reduction of the effective negative charge on the phosphate groups. This is essential for the formation of T–T base pairs (11–13).

To investigate self association of the other DNA bases, we have previously studied the structure of 2′-deoxy-3′,5′-di-*O*-acetyl adenosine (1). It was observed that the A base does not form parallel A–A base pairs but, instead, any array of one-dimensional ribbons in which the bases are linked via two crystallographically-independent hydrogen bonds: N(6)—H...N(1) and N(6)—H...N(7). A highly comparable hydrogen bonding scheme was found by Wilson *et al.* for the crystal structure of the acetylated RNA counterpart structure, 2′,3′,5′-tri-*O*-acetyl adenosine (3).

In this paper we wish to report a structural study on the acetylated DNA nucleoside 2′-deoxy-3′,5′-di-*O*-acetyl guanosine (Fig. 1). The X-ray structure reveals that the asymmetric unit consists of two independent molecules, **I** and **II**. The planar guanine fragments of **I** and **II** are connected via N(1)—H...N(7) and N(2)—H...O(6) hydrogen bonds to form a nearly planar system with the two guanine rings at an angle of 5.0(1)°. Furthermore, a comparison is made of the X-ray data of the title compound, and the solution conformation as determined with 300 MHz ^{1}H NMR spectroscopy.

Experimental section

Preparation

Acetic anhydride (1.83 g, 17.92 mmol) was added to a stirred suspension of dry 2′-deoxyguanosine (2.00 g, 7.49 mmol) and

[1]To whom all correspondence should be addressed.

[2]Revision received May 31, 1988.

[3]Nomenclature in this work follows the IUPAC-IUB recommendations on nucleotide conformational nomenclature. See: "Abbreviations and symbols for the description of conformation of polynucleotide chains", Recommendations 1982. Eur. J. Biochem. **131**, 9 (1983).

Printed in Canada / Imprimé au Canada

Can. J. Chem. Downloaded from www.nrcresearchpress.com by 196.1.178.254 on 09/07/12
For personal use only.

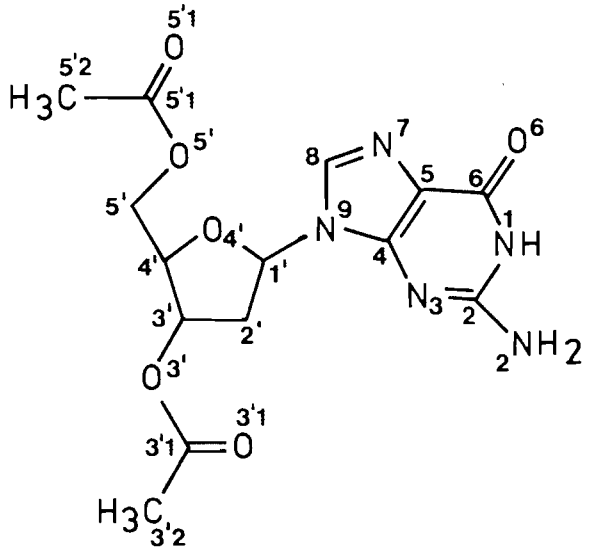

FIG. 1. Structural formula and atomic labelling of the 2′-deoxy-3′,5′-di-*O*-acetyl guanosine molecule.

4-*N*,*N*′-dimethylaminopyridine (0.15 g, 1.23 mmol) in a mixture of dry acetonitrile (100 mL) and 2.00 g (19.71 mmol) of triethylamine (14). After 2 h, methanol (2 mL) was added, and stirring was continued for 5 min. The reaction mixture was then filtered. 2′-Deoxy-3′,5′-di-*O*-acetyl guanosine was obtained as a white powder, which was purified by washing with ethanol and diethylether. Yield: 2.55 g (96%). Recrystallization from ethanol yielded plate-shaped colorless crystals. ^{1}H NMR (DMSO-d_6): δ 1.94 (3H, s, CH_3), 1.97 (3H, s, CH_3), 2.33 (1H, m, H(2″)), 2.81 (1H, m, H(2′)), 4.11 (2H, m, H(4′/5″), 4.15 (1H, m, H(5′)), 5.19 (1H, m, H(3′)), 6.03 (1H, dd, H(1′)), 6.40 (2H, bs, NH_2), 7.80 (1H, s, H(8)).

Crystallographic measurements and structure resolution

$C_{14}H_{17}N_5O_6$ fw = 351.32

Triclinic, a = 8.643(1) Å, b = 10.122(1) Å, c = 10.391(1) Å, α = 87.04(1)°, β = 73.58(1)°, γ = 72.37(1)°, V = 830.4(2) Å^3, Z = 2, D_c = 1.405 g cm^{-3}, λ(MoKα) = 0.71073 Å, t = 20°C, μ(MoKα) = 1.21 cm^{-1}, F(000) = 368; space group $P\bar{1}$ (C_i^1, No. 1).

A plate-shaped colorless crystal with dimensions (mm) 1.3 × 0.4 × 0.3 was mounted on a Nonius CAD4 diffractometer. Unit-cell dimensions were determined by least-squares refinement of the setting angles of 25 reflections in the θ range 17.1–22.0°. Intensities of 3795 reflections were measured within the sphere of reflection limited by 2θ = 55° and $-11 \leq h \leq 11$, $-12 \leq k \leq 12$, and $0 \leq l \leq 13$, using Zr-filtered MoKα radiation. The ω/2θ scan technique was applied with ω = (0.60 + 0.35 tan θ)°. The intensities of three reference reflections (014, 104, and 140), measured every 60 reflections, showed an average deviation less than 1% during the duration of the data collection. The intensities were corrected for Lorentz polarization effects, but not for absorption. A total of 3450 reflections that satisfied the criterion $I \geq 2.5\sigma(I)$ were retained for the structure determination and refinement. $\sigma(I)$ was derived from counting statistics. The structure was solved with the direct methods program of SHELXS84 (15), the coordinates of all non-hydrogen atoms being determined from an *E*-map. The hydrogen atoms were located on subsequent difference maps. The overall thermal parameter of the non-methyl hydrogen atoms refined to 0.054(4) Å^2. The hydrogen atoms of the methyl groups were placed at idealized positions (C—H 1.00 Å, H—C—H 109.5°). In the refinement the hydrogen atoms of the methyl groups were riding on their bonded atoms. The overall thermal parameter of the hydrogen atoms of the methyl groups refined to 0.14(1) Å^2. Anisotropic blocked full-matrix refinement (8 blocks) on F of 552 parameters converged at R = 0.031 and R_w = 0.034 with $w = 2.6552/\sigma^2(F_o) + 0.00012F_o^2$. The quantity minimized was $\Sigma w\Delta F^2$, the goodness of fit $s = \Sigma w\Delta F^2/(m - n)^{1/2}$, was 2.21 and the average and maximal shift to error ratio's 0.01 and 0.08, respectively. A final ΔF showed maximal fluctuations of +0.14 and −0.14 e Å^{-3}. Scattering factors were those of Cromer and Mann (16), and for hydrogen of Stewart, Davidson, and Simpson (17). Programs used include SHELX76 (18) (refinement) and EUCLID (19) (geometry and illustrations).

Nuclear magnetic resonance spectroscopy

One-dimensional spectra were recorded in the FT mode at 300.1 MHz on a Bruker CXP 300 NMR spectrometer, interfaced with an ASPECT 2000 computer (NMR facility at the Eindhoven University of Technology). An internal $(CD_3)_2SO$ field-frequency lock, and a spectral window of 3000 Hz (16 K data points) were used. Prior to Fourier transformation, the spectra were zero-filled to 32 K, and resolution enhanced by an appropriate Gaussian multiplication. A computer simulation-iteration routine was used in order to accurately extract chemical shifts and *J*-coupling constants. This proved to be of great value, especially for the non-first order pattern that corresponds to the nearly isochronous protons H(4′), H(5′), and H(5″) (*vide infra*).

Results and discussion

Crystal structure[4]

The fractional coordinates, along with equivalent isotropic temperature factors are summarized in Table 1. Bond distances between non-hydrogen atoms are given in Table 2. Table 3 lists bond angles between non-hydrogen atoms for the molecules **I** and **II**. Table 4 contains a selected set of torsion angles, describing the geometry of the furanose ring, the acetylated backbone, as well as the conformation around the glycosidic (C(1′)—N(9)) bond.

Furanose and backbone conformation

The 2′-deoxyribofuranose rings in the molecules **I** and **II** are found in the C(2′)-*endo* puckered form. A more precise description of the sugar ring conformations can be given with the pseudorotation concept (20), which relates the five endocyclic torsion angles mathematically to a phase angle of pseudorotation (P), which actually indicates which part of the ring is bent, and a puckering amplitude (ν_{max}), which identifies the deviation from planarity of the ring. For the title compound, P values of 167° and 164° are found for **I** and **II**, respectively. The puckering amplitudes amount to 30.6° and 35.6° for **I** and **II**, respectively. The bond distances and angles within the furanose unit are in agreement with other known C(2′)-*endo* puckered nucleosides (21, 23). The ring C—O bond distances are unequal, in such a way that C(4′)—O(4′) is approximately 0.03 Å longer than C(1′)—O(4′) (molecule **I**: C(1′)—O(4′) = 1.408(3) Å, C(4′)—O(4′) = 1.432(3) Å; molecule **II**: C(1′)—O(4′) = 1.415(2) Å, C(4′)—O(4′) = 1.442(2) Å). The difference in observed bond length is due to the anomeric effect, which is known to cause a slight shortening of C(1′)—O(4′) in nucleosides (22). The anomeric effect essentially stems from the proclivity of the heterocyclic base ring, as transmitted through N(9). The conformation around the exocyclic C(4′)—C(5′) bond shows a marked difference for molecules **I** and **II**. The *trans* (*t*) conformation (*trans* location of O(5′) and C(3′)) with γ(O(5′)—C(5′)—C(4′)—C(3′)) = 165.7(2)° is found for **I**. The C(4′)—C(5′) conformation is *gauche*$^+$ (g^+) (O(5′) *gauche* with respect to O(4′) and C(3′)), for **II**, γ = 57.8(2)°. The acetyl geometries are as previously noted (1–9), showing short C=O bonds. For molecule **I**, it is found that

[4]Tables of structure factor amplitudes, anisotropic temperature factors of non-hydrogen atoms, hydrogen atom coordinates, and the internal geometry may be purchased from the Depository of Unpublished Data, CISTI, National Research Council of Canada, Ottawa, Ont., Canada K1A 0S2.

Can. J. Chem. Downloaded from www.nrcresearchpress.com by 196.1.178.254 on 09/07/12
For personal use only.

Can. J. Chem. Downloaded from www.nrcresearchpress.com by 196.1.178.254 on 09/07/12
For personal use only.

TABLE 1. Refined fractional coordinates of non-hydrogen atoms, and equivalent isotropic temperature factors U_{eq} (Å^2)[a]; estimated standard deviations are given in parentheses

	x		y		z		U_{eq}	
Atom	Molecule **I**	Molecule **II**	Molecule **I**	Molecule **II**	Molecule **I**	Molecule **II**	Molecule **I**	Molecule **II**
C(1′)	−0.0117(2)	−0.0123(2)	0.2796(2)	1.2572(2)	0.1771(2)	−0.3847(2)	0.0397(5)	0.0406(5)
C(2′)	−0.0332(2)	0.0570(3)	0.1892(2)	1.3408(2)	0.0758(2)	−0.3109(2)	0.0431(6)	0.0461(6)
C(3′)	0.1291(2)	0.0473(3)	0.0705(2)	1.4705(2)	0.0452(2)	−0.3908(2)	0.0412(5)	0.0421(5)
C(4′)	0.2583(2)	0.0806(2)	0.1359(2)	1.4166(2)	0.0652(2)	−0.5335(2)	0.0392(5)	0.0403(5)
C(5′)	0.3578(3)	0.2590(3)	0.1761(3)	1.3930(2)	−0.0665(2)	−0.6212(2)	0.0509(6)	0.0475(6)
C(3′1)	0.2241(4)	−0.1546(3)	−0.1606(3)	1.6931(2)	0.1082(3)	−0.3809(3)	0.0700(10)	0.0624(8)
C(3′2)	0.1880(6)	−0.3294(4)	−0.2618(4)	1.7809(3)	0.2138(5)	−0.3063(4)	0.1050(20)	0.0850(10)
C(5′1)	0.5085(3)	0.5247(3)	0.3380(2)	1.2257(2)	−0.1361(3)	−0.6383(2)	0.0625(6)	0.0562(6)
C(5′2)	0.5734(4)	0.6310(4)	0.4391(3)	1.1301(3)	−0.0881(4)	−0.5634(4)	0.0910(10)	0.0800(10)
C(2)	−0.4383(2)	−0.1644(2)	0.5694(2)	0.9757(2)	0.4505(2)	−0.0832(2)	0.0368(5)	0.0360(5)
C(4)	−0.2302(2)	−0.0011(2)	0.5095(2)	1.0294(2)	0.2626(2)	−0.2716(2)	0.0381(5)	0.0363(5)
C(5)	−0.2622(2)	0.1125(2)	0.6401(2)	0.8982(2)	0.2107(2)	−0.2983(2)	0.0438(5)	0.0428(5)
C(6)	−0.3996(3)	0.0848(3)	0.7495(2)	0.7915(2)	0.2872(2)	−0.2091(2)	0.0459(6)	0.0423(5)
C(8)	−0.0487(3)	0.2013(3)	0.5126(2)	1.0206(2)	0.0662(2)	−0.4582(2)	0.0512(6)	0.0530(6)
O(3′)	0.1063(2)	−0.1232(2)	−0.0345(2)	1.5618(1)	0.1411(2)	−0.3387(2)	0.0555(5)	0.0524(4)
O(4′)	0.1635(2)	0.0393(2)	0.2581(2)	1.2879(1)	0.1488(2)	−0.5217(1)	0.0560(5)	0.0428(4)
O(5′)	0.4429(2)	0.3729(2)	0.2666(2)	1.2956(2)	−0.0347(2)	−0.5571(1)	0.0562(5)	0.0500(4)
O(3′1)	0.3399(3)	−0.0530(3)	−0.1823(2)	1.7301(2)	0.0092(2)	−0.4654(3)	0.0970(10)	0.0889(8)
O(5′1)	0.5115(3)	0.5655(2)	0.3178(2)	1.2417(2)	−0.2503(2)	−0.7570(2)	0.0845(6)	0.0808(6)
O(6)	−0.4487(2)	0.1687(2)	0.8717(1)	0.6685(1)	0.2597(2)	−0.2161(2)	0.0654(5)	0.0549(5)
N(1)	−0.4823(2)	−0.0613(2)	0.7020(2)	0.8416(2)	0.4075(2)	−0.1023(2)	0.0438(5)	0.0406(4)
N(2)	−0.5308(2)	−0.2966(2)	0.5451(2)	1.0038(2)	0.5704(2)	0.0266(2)	0.0497(5)	0.0452(5)
N(3)	−0.3113(2)	−0.1396(2)	0.4672(2)	1.0760(2)	0.3803(1)	−0.1665(2)	0.0384(4)	0.0374(4)
N(7)	−0.1460(2)	0.2387(2)	0.6402(2)	0.8945(2)	0.0873(2)	−0.4170(2)	0.0538(5)	0.0532(5)
N(9)	−0.0930(2)	0.0571(2)	0.4277(2)	1.1077(2)	0.1682(2)	−0.3755(2)	0.0419(5)	0.0443(5)

[a] U_{eq} = (1/3)(trace of orthogonalized U_{ij} tensor).

TABLE 2. Bond distances (Å)

	Length			Length	
Bonds	Molecule **I**	Molecule **II**	Bonds	Molecule **I**	Molecule **II**
O(6)—C(6)	1.227(2)	1.230(2)	N(7)—C(5)	1.388(3)	1.390(3)
O(3′)—C(3′)	1.438(3)	1.447(3)	N(7)—C(8)	1.300(3)	1.300(3)
O(3′)—C(3′1)	1.358(4)	1.349(2)	N(9)—C(4)	1.373(3)	1.376(3)
O(4′)—C(1′)	1.408(3)	1.415(2)	N(9)—C(8)	1.373(3)	1.370(3)
O(4′)—C(4′)	1.432(3)	1.442(2)	N(9)—C(1′)	1.461(3)	1.458(3)
O(5′)—C(5′)	1.437(3)	1.449(3)	C(4)—C(5)	1.380(3)	1.378(3)
O(5′)—C(5′1)	1.336(3)	1.344(3)	C(5)—C(6)	1.424(3)	1.418(3)
O(3′1)—C(3′1)	1.190(4)	1.188(4)	C(1′)—C(2′)	1.514(3)	1.515(3)
O(5′1)—C(5′1)	1.206(4)	1.200(3)	C(2′)—C(3′)	1.510(3)	1.510(3)
N(1)—C(6)	1.395(3)	1.400(3)	C(3′)—C(4′)	1.524(3)	1.525(3)
N(1)—C(2)	1.368(3)	1.368(3)	C(4′)—C(5′)	1.506(3)	1.507(3)
N(2)—C(2)	1.333(3)	1.337(3)	C(3′1)—C(3′2)	1.495(5)	1.506(4)
N(3)—C(2)	1.321(3)	1.327(3)	C(5′1)—C(5′2)	1.473(4)	1.475(4)
N(3)—C(4)	1.347(2)	1.349(3)			

C(3′1)—O(3′1) = 1.190(4) Å, C(5′1)—O(5′1) = 1.206(4) Å, and for **II**, C(3′1)—O(3′1) = 1.188(4) Å, C(5′1)—O(5′1) = 1.200(4) Å.

Geometry and orientation of the base

The glycosyl bond length C(1′)—N(9) and bond angle O(4′)—C(1′)—N(9) are 1.461(3) Å, 107.9(2)° for **I**, and 1.458(3) Å, 107.0(2)° for **II**. The guanine rings are approximately planar, the r.m.s. deviation of the 9 atoms from the least-squares plane is 0.010(4) Å, for **I** and **II**. The orientation of the base falls in the *anti* range, with values of χ(O(4′)—C(1′)—N(9)—C(4)) of −130.3(2)° for **I**, and −159.4(2)° for **II**. These data are indicated as spokes *1* and *2* in the conformational wheel of Fig. 2, showing the distribution of the glycosidic torsion angle χ in the crystal structures of acetylated nucleosides. Figure 2 clearly indicates that the χ values for acetylated nucleosides have a bimodal distribution. Nine *anti* conformations occur in the range χ = −148 ± 33°, and three *syn* conformations have been found in the range χ = 63 ± 11°. The favored *anti* and *syn* domains of acetylated nucleosides

TABLE 3. Bond angles (deg)

Bonds	Angle Molecule I	Angle Molecule II	Bonds	Angle Molecule I	Angle Molecule II
C(3′)—O(3′)—C(3′1)	114.9(2)	116.7(2)	C(2′)—C(1′)—O(4′)	106.1(2)	105.8(2)
C(1′)—O(4′)—C(4′)	111.3(2)	109.8(1)	C(2′)—C(1′)—N(9)	113.9(2)	113.4(2)
C(5′)—O(5′)—C(5′1)	116.1(2)	116.0(1)	O(4′)—C(1′)—N(9)	107.9(2)	107.0(2)
C(2)—N(1)—C(6)	125.7(2)	125.4(2)	C(3′)—C(2′)—C(1′)	103.5(2)	102.6(2)
C(4)—N(3)—C(2)	112.0(2)	111.8(2)	O(3′)—C(3′)—C(2′)	108.0(2)	106.2(2)
C(5)—N(7)—C(8)	104.5(2)	104.5(2)	O(3′)—C(3′)—C(4′)	111.1(2)	112.1(2)
C(1′)—N(9)—C(4)	125.9(2)	125.6(2)	C(2′)—C(3′)—C(4′)	103.5(2)	102.8(2)
C(1′)—N(9)—C(8)	127.6(2)	127.6(2)	O(4′)—C(4′)—C(3′)	106.2(2)	106.6(2)
C(4)—N(9)—C(8)	106.5(2)	106.4(2)	O(4′)—C(4′)—C(5′)	109.2(2)	109.6(2)
N(3)—C(2)—N(1)	123.7(2)	123.8(2)	C(3′)—C(4′)—C(5′)	111.2(2)	115.1(2)
N(9)—C(4)—N(3)	125.8(2)	125.7(2)	C(4′)—C(5′)—O(5′)	106.7(2)	108.4(2)
N(9)—C(4)—C(5)	105.2(2)	105.4(2)	O(3′)—C(3′1)—O(3′1)	122.8(3)	122.3(2)
N(3)—C(4)—C(5)	129.0(2)	128.9(2)	O(3′)—C(3′1)—C(3′2)	110.5(3)	111.1(2)
C(4)—C(5)—C(6)	118.5(2)	118.9(2)	O(3′1)—C(3′1)—C(3′2)	126.7(3)	126.6(2)
C(4)—C(5)—N(7)	110.7(2)	110.5(2)	O(5′1)—C(5′1)—O(5′1)	122.1(2)	122.8(2)
C(6)—C(5)—N(7)	130.8(2)	130.6(2)	O(5′)—C(5′1)—C(5′2)	110.0(2)	111.8(2)
N(1)—C(6)—C(5)	111.1(2)	111.1(2)	O(5′1)—C(5′1)—C(5′2)	126.9(3)	125.4(3)
N(1)—C(6)—O(6)	120.2(2)	119.9(2)	N(1)—C(2)—N(2)	116.7(2)	116.5(2)
C(5)—C(6)—O(6)	128.8(2)	128.9(2)	N(3)—C(2)—N(2)	119.6(2)	119.8(2)
N(7)—C(8)—N(9)	113.1(2)	113.2(2)			

TABLE 4. Selected torsion angles (deg)

Bonds	Torsion angle Molecule I	Torsion angle Molecule II
C(4′)—O(4′)—C(1′)—C(2′)	−16.2(2)	−20.3(2)
O(4′)—C(1′)—C(2′)—C(3′)	28.7(2)	33.7(2)
C(1′)—C(2′)—C(3′)—C(4′)	−29.8(2)	−33.4(2)
C(2′)—C(3′)—C(4′)—O(4′)	21.0(2)	22.3(2)
C(2′)—C(3′)—C(4′)—C(5′)	−97.8(2)	−99.4(2)
C(1′)—O(4′)—C(4′)—C(3′)	−3.1(2)	−1.4(2)
C(3′1)—O(3′)—C(3′)—C(2′)	164.8(2)	170.2(2)
C(3′)—O(3′)—C(3′1)—C(3′2)	−179.6(3)	−172.9(2)
C(3′)—O(3′)—C(3′1)—O(3′1)	1.7(4)	6.4(4)
C(3′)—C(4′)—C(5′)—O(5′)	165.7(2)	57.8(2)
C(5′1)—O(5′)—C(5′)—C(4′)	−166.0(2)	157.3(2)
C(5′)—O(5′)—C(5′1)—C(5′2)	173.0(2)	179.7(2)
C(5′)—O(5′)—C(5′1)—O(5′1)	−7.2(4)	0.0(3)
C(8)—N(9)—C(1′)—O(4′)	49.4(3)	28.5(3)
C(1′)—N(9)—C(8)—N(7)	179.9(2)	173.9(2)
C(5)—N(7)—C(8)—N(9)	−0.1(3)	−0.8(3)
C(8)—N(7)—C(5)—C(4)	0.6(2)	0.7(2)
N(9)—C(4)—C(5)—N(7)	−0.8(2)	−0.3(2)
C(8)—N(9)—C(4)—C(5)	0.7(2)	−0.1(2)
C(2)—N(3)—C(4)—C(5)	0.5(3)	−1.7(3)
C(4)—N(3)—C(2)—N(1)	0.5(3)	0.1(3)
C(6)—N(1)—C(2)—N(3)	−1.5(3)	1.3(3)
C(2)—N(1)—C(6)—C(5)	1.3(3)	−0.9(3)
C(4)—C(5)—C(6)—N(1)	−0.3(3)	−0.6(3)
C(2)—N(1)—C(6)—O(6)	−178.9(2)	179.7(2)
C(4)—N(3)—C(2)—N(2)	−179.4(2)	−179.9(2)
C(6)—N(1)—C(2)—N(2)	178.4(2)	−178.8(2)
C(4)—C(5)—C(6)—O(6)	179.9(2)	178.7(2)

are in close agreement with the structural data set of Altona *et al.* (21).

Hydrogen bonding and molecular stacking

The N—H and NH_2 groups of the purine fragment of molecules **I** and **II** are hydrogen-bond donors in seven intermolecular hydrogen bonds (Table 5). Two hydrogen bonds between molecules **I** and **II** form a dimer-type ribbon typical for guanosine derivatives. These bonds, N(1)...N(7) and N(2)...O(6), connect molecules **II** and **I**, and the same interaction exists between molecule **I** and a translationally related molecule **II** at $(-1 + x, y, 1 + z)$. This repeated pattern gives rise to an infinite chain of paired bases running in the $\bar{1}\,0\,1$ direction. Each molecule has an additional hydrogen bond between the NH_2 group and O(5′1) of the acetyl group at C(5′) of a translationally related molecule, also at $(-1 + x, y, 1 + z)$. The seventh hydrogen bond is between the NH_2 group of **II** and the ester oxygen $O_{5'}$ of the acetyl group at $C_{5'}$ of **I** at $(-1 + x, 1 + y, z)$. This implies that one N—H bond of the NH_2 group of **II** is involved in a bifurcate interaction, which is planar as follows from the sum of angles (359.5°), having the H atom as apex. The bifurcation results in weak hydrogen bonds as may be seen from their geometries (Table 5). Like in other acetylated pyrimidine and purine nucleosides (1–9), the acetyl groups play an important role in the stacking, in that the polar carbonyl group is oriented toward the base ring of neighbouring molecules. As Table 4 shows, the two carbonyl oxygen atoms O(3′1) and O(5′1) of both **I** and **II** have close contacts with atoms of the guanosine ring. The greater part of these contacts and also the shortest ones involve the carbonyl groups of molecule **II**.

Conformation in solution

The set of experimental *J*-coupling constants, determined at 298 K, are summarized in Table 6. The data refer to the solvent DMSO-d_6, since 2′-deoxy-3′,5′-di-*O*-acetyl guanosine was found to be virtually insoluble in D_2O. An iterative computer simulation procedure was used in order to obtain accurate NMR spectral data (Fig. 4). The structure of the 2′-deoxyribose ring can be described in terms of a rapid C(2′)-*endo* ⇄ C(3′)-*endo* conformational equilibrium (25, 26):

$$x(\text{C(2′)-}endo) = (17.8 - J(1'2'') - J(2''3''))/10.9 = 0.88$$

A similar preference for the C(2′)-*endo* conformation is

Can. J. Chem. Downloaded from www.nrcresearchpress.com by 196.1.178.254 on 09/07/12
For personal use only.

TABLE 5. Intermolecular hydrogen bond geometry and structural details of acetyl-base-stacking[a]

Donor	Acceptor	$D....A$ (Å)	H....A (Å)	D—H....A (deg)
N(1,I)—H(1)	N(7,IIA)	2.823(3)	2.06(3)	178(3)
N(2,I)—H(2)	O(6,IIA)	2.879(3)	2.06(3)	147(3)
N(2,I)—H(3)	O(5'1,IA)	2.886(3)	2.05(3)	155(3)
N(1,II)—H(1)	N(7,I)	2.872(3)	1.93(3)	176(3)
N(2,II)—H(2)	O(6,I)	2.883(3)	2.09(3)	156(3)
N(2,II)—H(3)	O(5'1,IIA)	3.095(3)	2.42(2)	139(2)
N(2,II)—H(3)	O(5',IB)	3.092(3)	2.45(3)	134(2)
Acetyl-base stacking (Å)				
O(3'1,I) —	C(6,IIC)	3.650(4)	O(3'1,II)	—C(6,IIE) 3.363(4)
O(5'1,I) —	N(3,IID)	3.555(3)	O(3'1,II)	—C(5,IIE) 3.338(3)
O(3'1,II) —	O(6,IIE)	3.562(3)	O(5'1,II)	—N(3,IF) 3.324(3)
O(3'1,II) —	N(7,IIE)	3.567(3)	O(5'1,II)	—C(4,IF) 3.697(3)

[a]I and II refer to molecules **I** and **II**, respectively. Symmetry code: (A) $-1 + x, y, 1 + z$; (B) $-1 + x, 1 + y, z$; (C) $x, -1 + y, z$; (D) $1 + x, -1 + y, z$; (E) $x, 1 + y, z$; (F) $1 + x, 1 + y, -1 + z$.

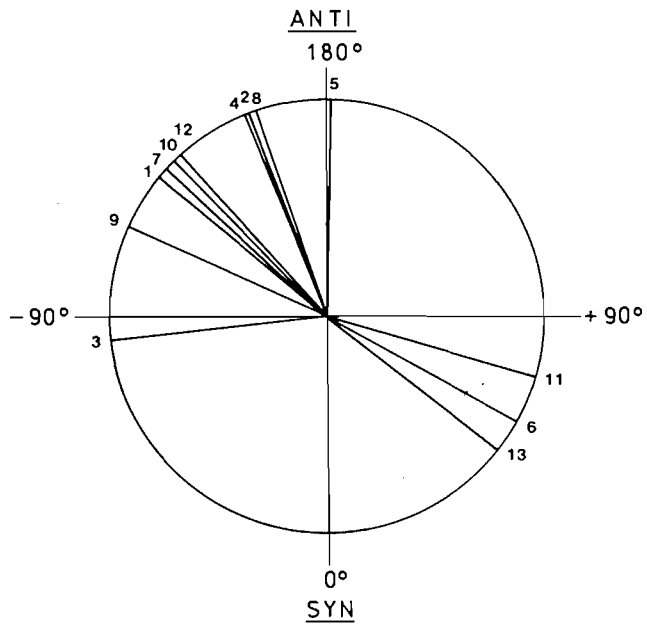

FIG. 2. Conformational wheel representing the glycosidic torsion angles for backbone-acetylated nucleosides (χ(O(4')—C(1')—N(9)—C(4)) for purine, and χ(O(4')—C(1')—N(9)—C(2) for pyrimidine structures). *1*, *2*: $\chi = -130°$ and $-159°$, 2'-deoxy-3',5'-di-*O*-acetyl guanosine (this work); *3*: $\chi = -84°$, 2'-deoxy-3',5'-di-*O*-acetyl adenosine (ref. 1); *4*, *5*: $\chi = -158°$ and 179°, 2',3',5'-tri-*O*-acetyl guanosine (orthorhombic form, ref. 2); *6*: $\chi = 61°$, 2',3',5'-tri-*O*-acetyl adenosine (ref. 3); *7*: $\chi = -133°$, 1/1 complex of 2'-deoxy-3',5'-di-*O*-acetyl-5-bromo uridine and 2'-deoxy-3',5'-di-*O*-acetyl-5-iodo uridine (ref. 4); *8*: $\chi = -161°$, 2',3',5'-tri-*O*-acetyl guanosine (ref. 5); *9*, *10*: $\chi = -115°$ and $-136°$, 3',5'-di-*O*-acetyl thymidine (refs. 6, 11); *11*: $\chi = 74°$, 2',3',5'-tri-*O*-acetyl uridine (ref. 7); *12*: $\chi = -138°$, 2'-deoxy-3',5'-di-*O*-acetyl-5-iodo uridine (ref. 8); *13*: $\chi = 52°$, 2'-deoxy-3'-*O*-acetyl adenosine (ref. 9).

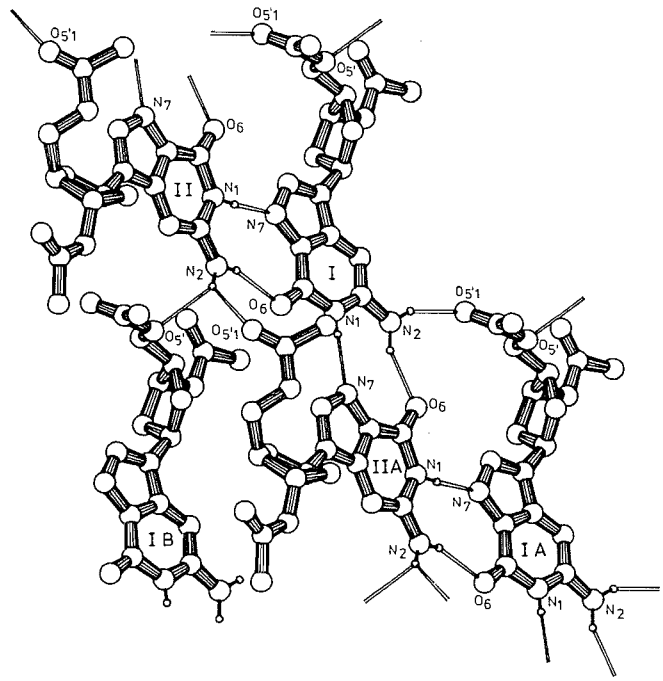

FIG. 3. Projection of a part of the structure showing the hydrogen bond network as seen approximately perpendicular the (1 2 0) plane. Only N and O atoms involved in hydrogen bonds have been labelled. A and B denote molecules **I** and **II** at positions $-1 + x, y, 1 + z$ and $-1 + x, 1 + y, z$, respectively. Hydrogen atoms not involved in hydrogen bonds have been omitted for clarity.

commonly encountered for 2'-deoxyribo nucleotides, including 3',5'-di-*O*-acetyl thymidine and 2'-deoxy-3',5'-di-*O*-acetyl adenosine (1, 12, 24).

The conformation around the exocyclic C(4')—C(5') bond was characterized on the basis of $J(4'5')$ and $J(4'5'')$ (1, 25, 26). From the experimental data one calculates: $x(g^+) = 0.31$, $x(t) = 0.40$, $x(gauche^-) = 0.29$, i.e., only a slight preference

TABLE 6. Vicinal coupling constants (in Hz) between the protons of the backbone and the 2'-deoxyribofuranose ring, measured in DMSO-d_6 at 20°C

Parameter	Value	Parameter	Value
$J(1'2')$	8.4	$J(3'4')$	2.0
$J(1'2'')$	5.8	$J(4'5')$	4.9
$J(2'2'')$	−14.0	$J(4'5'')$	5.7
$J(2'3')$	6.4	$J(5'5'')$	−11.9
$J(2''3')$	2.4		

Can. J. Chem. Downloaded from www.nrcresearchpress.com by 196.1.178.254 on 09/07/12
For personal use only.

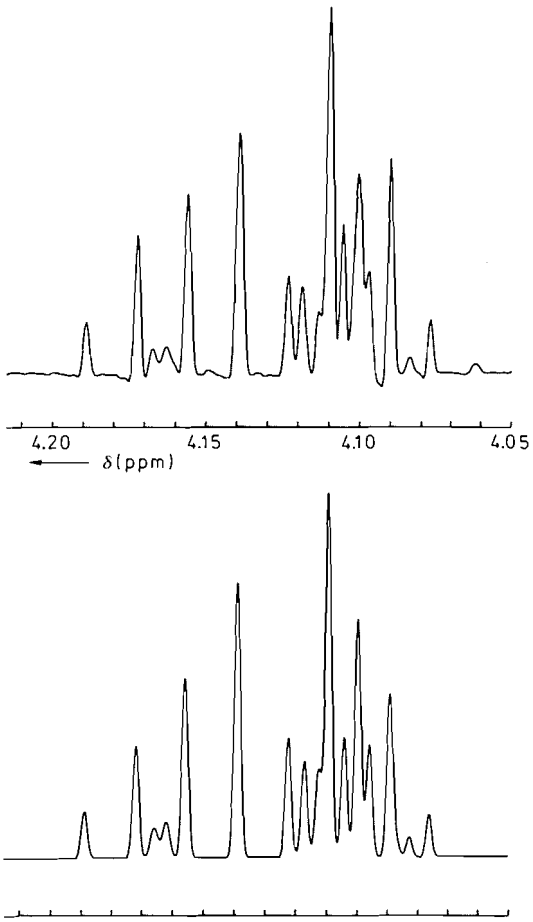

FIG. 4. Upper trace: expansion of the H(4′)/H(5′)/H(5″) pattern (non-first order) in the 300 MHz ^{1}H NMR spectrum. Lower trace: computer simulation.

for *t* over g^+ and *gauche*$^-$ (g^-) is observed. It should be noted that 3′,5′-di-*O*-acetyl thymidine and 2′-deoxy-3′,5′-di-*O*-acetyl adenosine exhibit a clear preference for g^+ in solution.

Conclusion

The crystal structure of 2′-deoxy-3′,5′-di-*O*-acetyl guanosine consists of two independent molecules **I** and **II** in the asymmetric unit. The guanine bases are connected via two N(1)—H...N(7), and two N(2)—H...O(6) hydrogen bonds. The hydrogen donating base in this structure in fact mimics the C base in the Hoogsteen C—G base pair (27). Two hydrogen bonds N(2)—H...O(5′1) connect pairs of molecule **I** and pairs of molecule **II**. An additional N(2)—H...O(5′) interaction between **I** and **II** gives rise to a bifurcate hydrogen bond. Highly comparable hydrogen bonding patterns (except for the bifurcated hydrogen bond) have been found for the acetylated RNA counterpart structure 2′,3′,5′-tri-*O*-acetyl guanosine, both in the monoclinic (5) and orthorhombic (2) form. The conformational properties of the furanose unit and the acetylated backbone show a close correspondence between the solid state and the DMSO solution. The molecules **I** and **II** both have C(2′)-*endo* type furanose rings in the solid state, while a clear preference for C(2′)-*endo* is also observed in solution. With respect to the C(4′)—C(5′) conformation, it is found that an approximately equal distribution over the rotamers g^+, *t*, and g^- exists in solution. Both *t* (molecule **I**) and g^+ (molecule **II**) are encountered in the crystal structure. The crystal structure of 2′-deoxy-3′,5′-di-*O*-acetyl guanosine differs substantially from the structures of other acetylated DNA nucleosides, i.e., 2′-deoxy-3′,5′-di-*O*-acetyl adenosine (in which the A bases are linked in one-dimensional chains via N(6)—H...N(1) and N(6)—H...N(7) hydrogen bonds), and 3′,5′-di-*O*-acetyl thymidine, for which a parallel T–T base pair was found. Work is in progress to solve the X-ray structure of the fourth acetylated DNA nucleoside, 2′-deoxy-3′,5′-di-*O*-acetyl cytidine.

1. L. H. KOOLE, H. M. BUCK, J. A. KANTERS, and A. SCHOUTEN. Can. J. Chem. **65**, 326 (1987).
2. J. N. LOW, P. TOLLIN, C. C. WILSON, and S. H. SCRIMGEOUR. Acta Crystallogr. Sect. C, **42**, 700 (1986).
3. C. C. WILSON, P. TOLLIN, and R. A. HOWIE. Acta Crystallogr. Sect. C, **42**, 697 (1986).
4. C. C. WILSON and P. TOLLIN. Acta Crystallogr. Sect. C, **41**, 465 (1985).
5. C. C. WILSON, J. N. LOW, and P. TOLLIN. Acta Crystallogr. Sect. C, **41**, 1123 (1985).
6. C. C. WILSON, J. N. LOW, P. TOLLIN, and H. R. WILSON. Acta Crystallogr. Sect. C, **40**, 1712 (1984).
7. J. N. LOW and C. C. WILSON. Acta Crystallogr. Sect. C, **40**, 1030 (1984).
8. C. C. WILSON, J. N. LOW, and D. W. YOUNG. Acta Crystallogr. Sect. C, **39**, 1103 (1983).
9. S. T. RAO and M. SUNDARALINGAM. J. Am. Chem. Soc. **92**, 4963 (1970).
10. J. D. WATSON and F. H. C. CRICK. Nature (London), **171**, 173 (1953).
11. L. H. KOOLE, M. H. P. VAN GENDEREN, H. FRANKENA, H. J. M. KOCKEN, J. A. KANTERS, and H. M. BUCK. Proc. Kon. Ned. Akad. Wet. Ser. B, **89**, 51 (1986); communicated by H. M. Buck at the meeting of November 25, 1985.
12. L. H. KOOLE, M. H. P. VAN GENDEREN, and H. M. BUCK. J. Am. Chem. Soc. **109**, 3916 (1987).
13. M. H. P. VAN GENDEREN, L. H. KOOLE, and H. M. BUCK. Proc. Kon. Ned. Akad. Wet. Ser. B, 181 (1987); communicated by H. M. Buck at the meeting of June 22, 1987.
14. A. MATSUDA, M. SHINOZAKI, M. SUZUKI, K. WATANABE, and T. MIYASAKA. Synthesis, 385 (1986).
15. G. M. SHELDRICK. SHELXS 84. Program for crystal structure solution. Univ. of Göttingen, Federal Republic of Germany.
16. D. T. CROMER and J. B. MANN. Acta Crystallogr. Sect. A, **24**, 321 (1968).
17. R. F. STEWART, E. R. DAVIDSON, and W. T. SIMPSON. J. Chem. Phys. **42**, 3175 (1965).
18. G. M. SHELDRICK. SHELXS 76. Program for crystal structure determination. Univ. of Cambridge, England.
19. A. L. SPEK. EUCLID. Computational crystallography. *Edited by* D. Sayre. Clarendon Press, Oxford, England. 1982. p. 528.
20. C. ALTONA and M. SUNDARALINGAM. J. Am. Chem. Soc. **94**, 8205 (1972).
21. H. P. M. DE LEEUW, C. A. G. HAASNOOT, and C. ALTONA. Isr. J. Chem. **20**, 108 (1980).
22. A. J. KIRBY. The anomeric effect and related stereo-electronic effects at oxygen. Springer Verlag, Berlin. 1983.
23. U. THEWALT, C. E. BUGG, and R. E. MARSH. Acta Crystallogr. Sect. B, **26**, 1089 (1970).
24. D. B. DAVIES. *In* Progress in nuclear magnetic resonance spectroscopy. *Edited by* J. W. Emsley, J. Feeney, and L. H. Sutcliffe. Pergamon Press, Oxford, England. 1978.
25. C. A. G. HAASNOOT, F. A. A. M. DE LEEUW, H. P. M. DE LEEUW, and C. ALTONA. Recl. Trav. Chim. Pays-Bas, **98**, 576 (1979).
26. C. ALTONA. Recl. Trav. Chim. Pays-Bas, **101**, 413 (1982).
27. K. HOOGSTEEN. Acta Crystallogr. **16**, 907 (1963).

Can. J. Chem. Downloaded from www.nrcresearchpress.com by 196.1.178.254 on 09/07/12
For personal use only.

Transfer of divalent metal ions into the organic phase of the systems water–chloroform–$ZnCl_2$–$CdCl_2$–$HgCl_2$–NaOH–(NaCl)–*n*-alkyltri(oxyethylene) carboxylic acid

JERZY STRZELBICKI[1] AND WITOLD CHAREWICZ

Institute of Inorganic Chemistry and Metallurgy of Rare Elements, Technical University of Wroclaw, 50-370 Wroclaw, Poland

AND

JORG BEGER AND LUTZ HINZ

Chemistry Section, Bergakademie Freiberg, 9200 Freiberg, GDR

Received April 28, 1988

JERZY STRZELBICKI, WITOLD CHAREWICZ, JORG BEGER, and LUTZ HINZ. Can. J. Chem. **66**, 2640 (1988).

The influence of the length of an *n*-alkyl chain incorporated into the molecule of an *n*-alkyltri(oxyethylene) carboxylic acid of a general formula $C_nH_{(2n+1)}(OCH_2CH_2)_3OCH_2CO_2H$ (n = 6, 8, 10, and 12, respectively) on transfer of the zinc group element ions into chloroform was investigated. Metal ions were transferred from the aqueous solutions of $ZnCl_2$, $CdCl_2$, and $HgCl_2$ at initial concentrations of 0.835 m*M* and 1.67 m*M* with, and without, added NaCl. From the aqueous solutions to which no NaCl was added, the selectivity of transfer of divalent metal ions into the organic phase was low.

The selectivity of transfer of the divalent metal ions improved remarkably when NaCl was added to the aqueous phase due to the chemical equilibria involving complexation of the divalent metal ions by Cl^-, OH^-, and *n*-alkyltri(oxyethylene) carboxylic acid. In most systems (with NaCl added), Zn(II) was separated from Cd(II) and Hg(II). Less lipophilic *n*-alkyltri(oxyethylene) carboxylic acids (with a shorter *n*-alkyl chain incorporated) exhibited higher selectivity and efficiency as divalent metal ion carriers.

JERZY STRZELBICKI, WITOLD CHAREWICZ, JORG BEGER et LUTZ HINZ. Can. J. Chem. **66**, 2640 (1988).

On a étudié l'influence de la longueur de la chaîne *n*-alkyle, incorporée dans des molécules d'acide *n*-alkyl(oxyéthylène) carboxylique de formule générale $C_nH_{(2n+1)}(OCH_2CH_2)_3OCH_2CO_2H$ (n = 6, 8, 10 et 12 respectivement), sur le transfert des ions des éléments du groupe du zinc vers le chloroforme. On a examiné le transfert des ions métalliques à partir de solutions aqueuses de $ZnCl_2$, de $CdCl_2$ et de $HgCl_2$ à des concentrations initiales de 0,835 et 1,67 m*M* avec, et sans, addition de NaCl. Pour des solutions aqueuses auxquelles on n'a pas ajouté de NaCl, la sélectivité pour le transfert des ions métalliques bivalents vers la phase organique est faible.

Cette sélectivité augmente considérablement lorsqu'on ajoute du NaCl à la phase aqueuse; cette différence est dûe à l'équilibre chimique impliquant la complexation des ions métalliques bivalents par les ions Cl^- et OH^- ainsi que par l'acide *n*-alkyltri(oxyéthylène)carboxylique. Dans la plupart des systèmes (lorsque du NaCl a été additionné), on a pu séparer le Zn(II) du Cd(II) et du Hg(II). Les acides *n*-alkyltri(oxyéthylène) carboxyliques moins lipophiles (incorporant des chaînes *n*-alkyles plus courtes) présentent une plus grande sélectivité et une plus grande efficacité comme transporteurs d'ions métalliques bivalents.

[Traduit par la revue]

Introduction

The open chain polyethylene glycols (OCPGs) and their derivatives have been found to be capable of forming complexes with different metal cations in organic solvents in a manner similar to the macrocyclic polyethers. Due to their complexing abilities and relative inexpensiveness these compounds are of increasing interest in various areas of chemistry. The metal complexes of OCPGs and their derivatives have been mostly studied in homogenous systems (e.g. alcoholic solvents) or/and the crystal structure of these complexes has been investigated (1, 2). Much less is known about OCPGs and their derivatives as metal ion carriers from an aqueous solution into and/or through an organic phase (3–12), in particular, in systems containing transition and posttransition metal ions (5, 8, 12).

In the previous paper (12), we have reported the results on extraction of Zn(II), Cd(II), and Hg(II) using a series of dodecyloligo(oxyethylene) carboxylic acids. When NaCl was not added to the aqueous phase, the extractability of Hg(II) increased with an increasing number of oxyethylene units incorporated into the molecule of an extractant. For Zn(II) and Cd(II) no ionic size polyoxyethylene chain length dependence was found and the selectivity of extraction was low in those systems.

The selectivity of extraction of Zn(II), Cd(II), and Hg(II) improved dramatically in the extraction systems with NaCl added to the aqueous solution. The extractability of Hg(II) was always very low. The region of the high extractability of Cd(II) was shifted into the more basic region of the pH compared to that of Zn(II). The selectivity was apparently produced by the chemical equilibria involving divalent metal ions complexation by Cl^- and OH^- anions in the aqueous phase and by the dodecyloligo(oxyethylene) carboxylic acid in the organic phase.

Above pH 8, concentration of the divalent metal in the organic phase decreased as the pH was raised, and the precipitates of $Zn(OH)_2$ and/or $Cd(OH)_2$ appeared. This finding was in contrast with earlier reported results on extraction of Co(II) and Ni(II) by the dodecyltetra(oxyethylene)oxyacetic acid (8) because these metal ions were transferred efficiently into the chloroform phase also in the basic region of the pH.

The $M(OE)_2$ type of stoichiometry (OE = dodecyloligo(oxyethylene carboxylate anion) has been anticipated for the extraction complex (12).

The complexing abilities and extractabilities of crown carboxylic acids have been found as strongly dependent on an alkyl chain (or an aromatic component) incorporated into the molecule of a complexone (8, 13–15). Also, complexation of metal ions by neutral OPGs depends strongly on the end-group substitutions in the molecule of a complexone and the lipophilicity of a complexone (4, 10, 11, 16).

In this paper, the results on transfer of the divalent metal ions

[1]Author to whom correspondence may be addressed.

Printed in Canada / Imprimé au Canada

Can. J. Chem. Downloaded from www.nrcresearchpress.com by 196.1.178.254 on 09/07/12
For personal use only.

TABLE 1. Physical properties, elemental analysis data, yields, and spectral data for *n*-alkyltri(oxyethylene) carboxylic acids

Compd no.	Boiling point, °C/Pa	Molecular formula, molecular weight n_D^{20}	Elemental analysis theory/found C	H	Yield, %	^{1}H NMR spectra (80 MHz), ppm[a]
1	160/ 26.6	$C_{14}H_{28}O_6$ 292.36 1.4442	57.51 57.78	9.65 9.58	50	0.81 (t, 3H) 1.10–1.50 (m, 8H) 3.3 (t, 2H) 3.38–3.68 (m, 12H) 4.00 (s, 2H) 10.55 (s, 1H)
2	215– 217/92	$C_{16}H_{32}O_6$ 320.42 1.4526	59.98 60.01	10.07 9.92	55	0.78 (t, 3H) 0.95–1.25 (m, 12H) 3.38 (t, 2H) 3.42–3.78 (m, 12H) 4.08 (s, 2H) 10.13 (s, 1H)
3	195– 200/20	$C_{18}H_{36}O_6$ 348.47 1.4548	62.04 62.31	10.41 10.50	60	0.80 (t, 3H) 1.00–1.40 (m, 16H) 3.30 (t, 2H) 3.30–3.62 (m, 12H) 3.98 (s, 2H) 8.33 (s, 1H)

[a]Measured in $CDCl_3$.

into chloroform in the water-chloroform systems containing $ZnCl_2$, $CdCl_2$, $HgCl_2$, NaOH (the pH regulator), NaCl (in two series of experiments), and an acyclic polyether carboxylic acid (the complexone) are described. A series of *n*-alkyltri(oxyethylene) carboxylic acids **1**–**4** was used to check the influence of an *n*-alkyl chain length on transfer of the divalent metal ions into chloroform.

$C_nH_{(2n+1)}(OCH_2CH_2)_3OCH_2CO_2H$

$n = 6$ **1**

$n = 8$ **2**

$n = 10$ **3**

$n = 12$ **4**

Experimental

Apparatus

Concentrations of metals in aqueous and organic phases were determined radiometrically (^{65}Zn, ^{115m}Cd, and ^{203}Hg) with a Nuclear Data Inc. (Model 1200) multichannel spectrometer and a Canberra Industries (Model 7228) Ge/Li γ-radiation semiconductor probe. Measurements of the equilibrium pH in the aqueous phases were made with an ELPO (Model N-512) pH-meter and an Energopomiar (Model SAgP-209W) glass body combination electrode. ^{1}H NMR spectra were determined with a Tesla BC 487 nuclear magnetic resonance spectrometer. Melting points, which were corrected, were measured using a Carl Zeiss Jena micromelting point Boethius apparatus.

Reagents

Radioisotopes were from the isotope Production and Reactor Center of the Institute of Atomic Energy, Swierk, Poland (^{65}Zn, ^{115m}Cd), and from the Central Institute of Nuclear Research, Dresden, GDR (^{203}Hg). Reagent grade sodium, hydrochloric acid, sulphuric acid, $ZnCl_2$, $CdCl_2$, $HgCl_2$, NaCl, NaOH, sodium chloroacetate, diethyl-ether, *n*-hexane, xylene, and chloroform were obtained from POCh (Gliwice, Poland). $ZnCl_2$, $CdCl_2$, and $HgCl_2$ were first dried at 120°C and then kept in a desiccator containing a drying agent. 1-Bromohexane, 1-bromooctane, 1-bromodecane, and triethylene glycol were obtained from Fluka (FRG). Glycol was converted into the corresponding α-alkyl-ω-hydroxytri(oxyethylene) according to published procedure (17). The procedure of the synthesis of *n*-dodecyltri(oxyethylene) carboxylic acid (**4**) was described previously (12). The synthetic routes to *n*-alkyltri(oxyethylene) carboxylic acids **1**–**3** were analogous. Physical properties, elemental analysis data, yields, and spectral data for **1**–**3** are presented in Table 1.

Procedure

The phases were equilibrated at room temperature (19–21°C). The organic phase (5 mL) was a solution of an oligoether carboxylic acid in chloroform and the aqueous phase (5 mL) was an aqueous solution of zinc, cadmium, and mercury chlorides (labelled with ^{65}Zn, ^{115m}Cd, and ^{203}Hg radioisotopes), NaOH (pH regulator), and NaCl (in two series of experiments).

Both organic and aqueous phases were placed in a separatory funnel and shaken vigorously for 15 min. Usually, the phases separated just after shaking was stopped (in particular, in the systems with acidic or neutral aqueous solutions) or they could be separated by centrifuging for several minutes (15–20 min) in case if an emulsion appeared (usually in the systems with the basic aqueous solution). However, most often the separatory funnel was allowed to stand for 18 h to provide complete separation of the organic and aqueous phases. Samples (1.0 mL of 2.0 mL) from each phase were removed for the γ-spectrometric determination of metal ion concentrations. The metal concentrations were determined only in the clear organic and aqueous phases. Finally, the equilibrium pH of the aqueous phase was measured.

To determine the complexing agent concentration in the chloroform phase after the equilibration, the organic phase was shaken with equal volume of 1.0 *M* aqueous hydrochloric acid to remove metal ions. After stripping, the organic phase (1 mL) was diluted to 5 mL with methanol and titrated, using a 5.0 m*M* methanolic solution of NaOH, to the phenolphthalein end point.

Can. J. Chem. Downloaded from www.nrcresearchpress.com by 196.1.178.254 on 09/07/12
For personal use only.

Can. J. Chem. Downloaded from www.nrcresearchpress.com by 196.1.178.254 on 09/07/12
For personal use only.

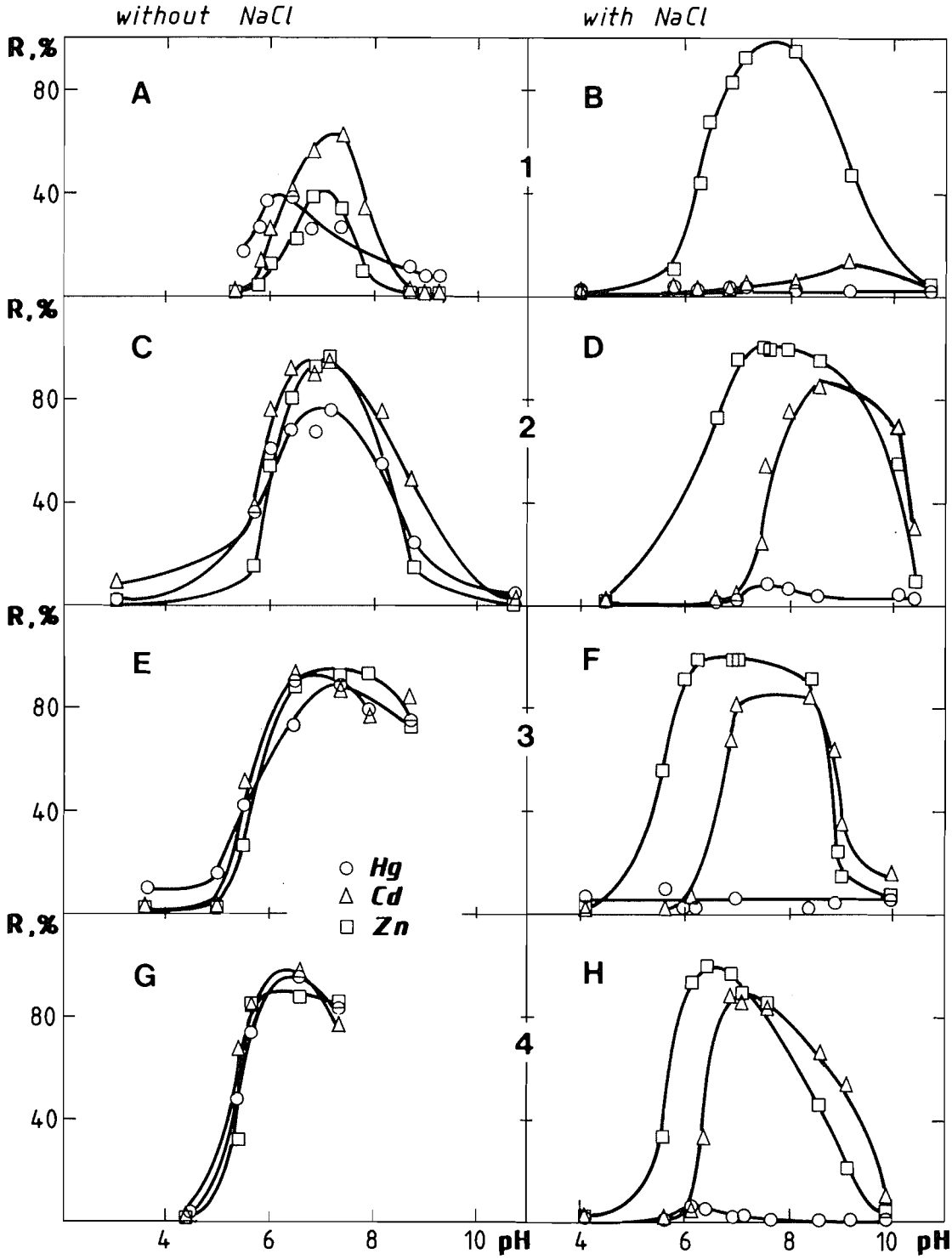

FIG. 1. Fraction of metal ions transferred (R) from aqueous solutions of 0.835 m*M* $ZnCl_2$, $CdCl_2$, and $HgCl_2$ (each) (*A*, *C*, *E*, *G*) and from aqueous solutions of 0.835 m*M* $ZnCl_2$, $CdCl_2$, and $HgCl_2$ (each) and 1.17 *M* NaCl (*B*, *D*, *F*, *H*) into 10 m*M* solutions of **1** (*A*, *B*), **2** (*C*, *D*), **3** (*E*, *F*), and **4** (*G*, *H*) (12) in chloroform vs. equilibrium pH of the aqueous phase.

At high equilibrium pH of the aqueous phase, an emulsion was formed and was often so stable that separation of the phases was impossible even by centrifuging. The results of experiments are presented only for those regions of the equilibrium pH of the aqueous phase, in which the organic and aqueous phases could be well separated and clear, before metal ion concentrations were determined. Thus, the end of the extraction curves in the figures indicates the pH values for which the emulsification process was too strong to continue experiments (Figs. 1*E*, *G* and 2*B*, *D*).

In the basic region of the equilibrium pH, Zn(II) and/or Cd(II) hydroxides precipitates appeared in the systems. Because the metal ion concentrations were determined in the clear organic and aqueous phases after the phases were fully equilibrated, the experimental data are included in the paper.

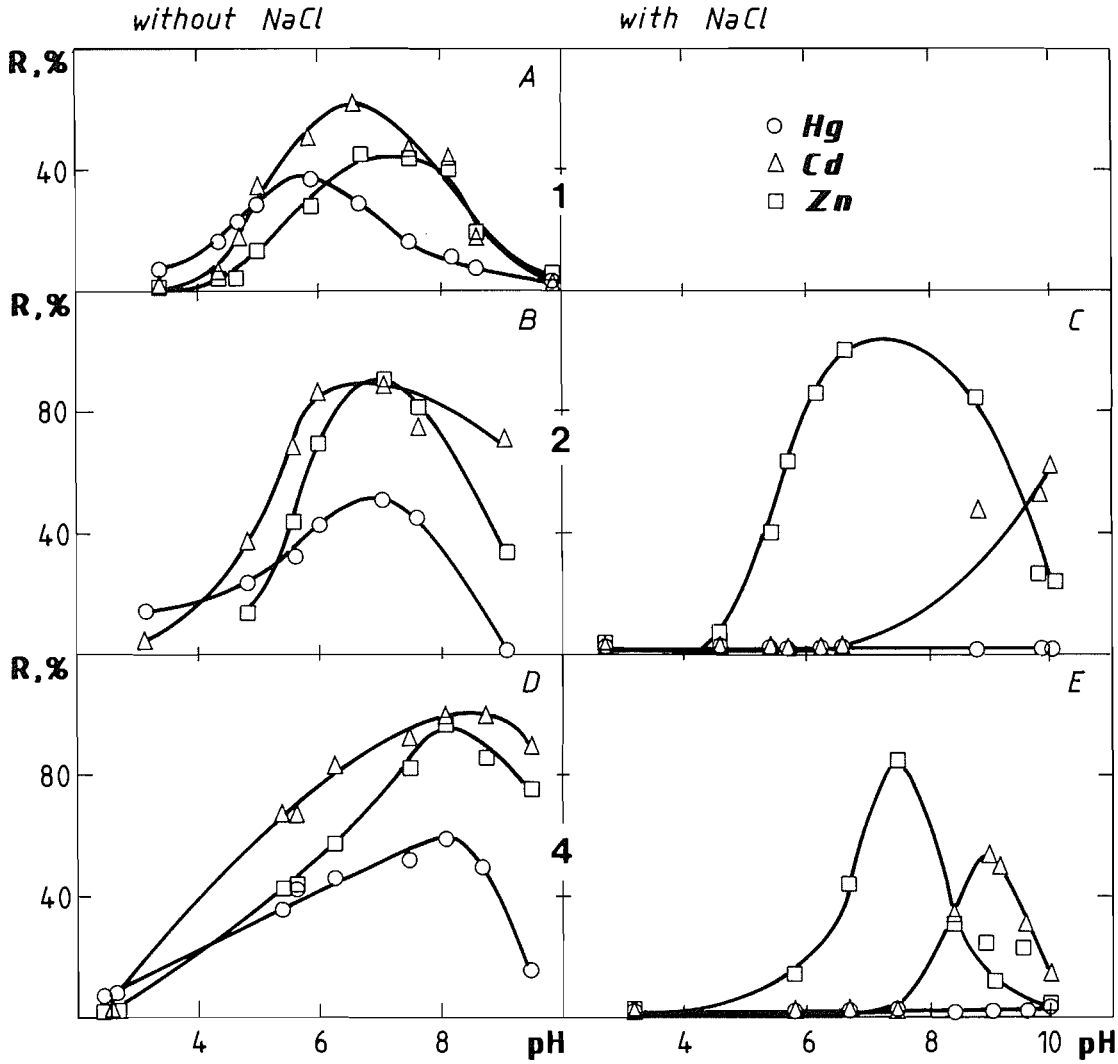

FIG. 2. Fraction of metal ions transferred (R) from aqueous solutions of 1.67 m*M* $ZnCl_2$, $CdCl_2$, and $HgCl_2$ (each) (*A*, *B*, *D*) and from aqueous solutions of 1.67 m*M* $ZnCl_2$, $CdCl_2$, and $HgCl_2$ (each) and 2.34 *M* NaCl (*C*, *E*) into 10 m*M* solutions of **1** (*A*), **2** (*B*, *C*), and **4** (*D*, *E*) (12) in chloroform vs. equilibrium pH of the aqueous phase.

Results and discussion

The results of experiments on transfer of Zn(II), Cd(II), and Hg(II) from aqueous solutions of $ZnCl_2$, $CdCl_2$, and $HgCl_2$ at an initial concentrations of 0.835 m*M* into a 10 m*M* solution of oligoether carboxylic acids **1**–**4** in chloroform are presented in Fig. 1 and Table 2. Two series of experiments were done, without (Figs. 1*A*, *C*, *E*, *G*), and with (Figs. 1*B*, *D*, *F*, *H*), added NaCl (at a concentration of 1.17 *M*). The results of experiments on transfer of Zn(II), Cd(II), and Hg(II) from 1.67 m*M* initial aqueous solutions of divalent metal chlorides into a 10 m*M* chloroform solution of **1**, **2**, and **4** are presented in Fig. 2 and Table 3. Experiments were done without (Figs. 2*A*, *B*, *D*), and with (Figs. 2*C*, *E*), added NaCl (at a concentration of 2.34 *M*). The sodium concentration in the initial aqueous solutions, which resulted from the pH regulation using a NaOH solution, did not exceed 20 m*M* (for the highest pH values).

Transfer of the divalent metal cations into chloroform was enhanced when the equilibrium pH of the aqueous phase increased up to pH of about 7. In the acidic pH region, there were "clean" solvent extraction systems composed of two liquid phases containing metal ions and/or their complexes with a complexing agent. Further increase of the pH usually produced a decrease of concentrations of the divalent metal ion in the organic phase and the precipitates of Zn(II) and/or Cd(II) hydroxides appeared (Tables 2 and 3). Hg(II) formed a precipitate (presumably Hg(II) oxide) usually at pH above 8.5. When precipitation occurs, there is not "clean" solvent extraction but yet the basic region of the equilibrium pH values in the systems under investigation is interesting because: (*i*) Formation of metal hydroxides approximately indicates the stability of complexes of the zinc group element with an *n*-alkyltri(oxyethylene) carboxylic acid. In the basic region of the pH, hydroxides were formed since they were thermodynamically more stable than complexes of the metal ion with an alkyltri(oxyethylene) carboxylic acid. (*ii*) Formation of hydroxide precipitates and a decrease of the metal ion concentrations in the organic phase provide possibility of removing the divalent metal ions from the organic phase in contact with the basic aqueous phase, without contamination of the aqueous phase with the divalent metal ions. (*iii*) The experimental data

Can. J. Chem. Downloaded from www.nrcresearchpress.com by 196.1.178.254 on 09/07/12
For personal use only.

TABLE 2. Percentage of metal ions forming precipitates and percentage of the complexing agent lost from the organic phase after equilibration (the initial aqueous phase: 0.835 m*M* $ZnCl_2$, $CdCl_2$, $HgCl_2$ (each), NaOH (the pH regulator), and 1.17 *M* NaCl (in the systems with NaCl added); the initial organic phase: a 10 m*M* chloroform solution of an *n*-alkyltri(oxyethylene) carboxylic acid

Systems without NaCl					Systems with NaCl				
Complexing agent and pH	% of metal Zn	Cd	Hg	% of complexing agent lost	Complexing agent and pH	% of metal Zn	Cd	Hg	% of complexing agent lost
1					**1**				
5.5, 5.8	—	—	—	—	4.0, 5.8	—	—	—	—
6.0	—	—	—	7	6.3	—	—	—	11
6.5	—	—	—	17	6.5	—	—	—	15
6.6	—	—	—	29	6.9	—	—	—	18
7.4	22	—	—	30	7.1	—	—	—	25
7.8	69	34	—	34	8.1	—	—	—	31
8.7	78	80	—	43	9.2	50	—	—	45
9.0	82	87	18	47	10.8	93	98	9	42
9.3	93	90	20	51					
2					**2**				
3.1–6.9	—	—	—	—	4.5–7.5	—	—	—	—
7.2	—	—	—	18	7.6	—	—	—	15
8.2	29	13	—	26	8.0	—	—	—	12
8.8	55	38	—	37	8.6	—	—	—	14
10.1	60	57	—	46	10.1	An emulsion in			13
10.9	67	60	—	46	10.4	the aqueous phase			13
					11.0	"			13
3					**3**				
3.7–6.5	—	—	—	—	4.2–8.4	—	—	—	—
7.4	—	10	—	—	8.9	75	4	23	—
7.9	—	12	—	—	9.0	79	36	43	—
8.8	3	13	—	—	10.0	86	80	42	—
4					**4**				
4.4–6.6	—	—	—	—	4.1–6.8	—	—	—	—
7.4	3	20	—	—	7.6	15	10	10	—

points in the basic region of the pH values also indicate how "clean" solvent extraction systems function in that pH region.

Transfer of the divalent metal ions from the aqueous solutions in the systems to which no NaCl was added

The results of experiments are presented in Figs. 1*A*, *C*, *E*, *G*, and Table 2 (for the initial aqueous solution of 0.835 m*M* $ZnCl_2$, $CdCl_2$, and $HgCl_2$), and in Figs. 2*A*, *B*, *D* and Table 3 (for the initial aqueous solution of 1.67 m*M* $ZnCl_2$, $CdCl_2$, and $HgCl_2$).

The divalent metal ions investigated were complexed and transferred into the organic phase unselectively, in particular from a 0.835 m*M* aqueous solution of divalent metal chlorides (Figs. 1*A*, *C*, *E*, *G*). It indicated that the stabilities of Zn(II), Cd(II), and Hg(II) complexes with alkyltri(oxyethylene) carboxylic acids were the same or very similar. The selectivity of transfer of the metal ions improved slightly in the systems with a 1.67 m*M* solution of divalent metal chlorides (Figs. 2*A*, *B*, *D*). The Hg(II) concentration in the organic phase decreased, probably due to higher concentration of Cl^- and formation of chloride complexes of Hg(II).

The effectiveness of transfer of the metal ions into the organic phase by **1** was the lowest (Figs. 1*A* and 2*A*) due to low lipophilicity of that complexone and its solubility in the slightly acidic, neutral, and basic aqueous solutions (Table 2). The maximal divalent metal ion concentrations in the organic phase raised, when **2** was employed as the complexone, though its solubility in the aqueous phase was still high (Table 2). Thus, an overall lipophilicity of metal ion complexes with **2** was higher than those with **1**. It can be understood taking into account that in case of the $M(OE)_2$ type of complexes (12), the complex molecule formed by **1** contained two methylene units less than the complex molecule formed by **2**.

3 and **4** were highly lipophilic complexones and they were not lost from the organic phase even in contact with the very basic aqueous solutions. Also, the maximal divalent metal ion concentrations in the organic phase in the system with **3** and **4** were high (Figs. 1*E*, *G*).

For **4**, the $M(OE)_2$ stoichiometry type of complexes transferred into the organic phase was reported (12). When **2** was employed as the complexone, the total metal and the complexone concentrations ratio in the highest loaded organic phase was 2.6 (equilibrium pH 7.1, Fig. 2*B*). This ratio in the system with **1** was even higher — 4.4 (equilibrium pH 6.6 — Fig. 2*A*). Therefore, other stoichiometries of the extraction complex are possible depending on a complexone.

Can. J. Chem. Downloaded from www.nrcresearchpress.com by 196.1.178.254 on 09/07/12
For personal use only.

TABLE 3. Percentage of metals forming a precipitates after equilibration (the initial aqueous phase: 1.67 m*M* $ZnCl_2$, $CdCl_2$, $HgCl_2$ (each), NaOH (the pH regulator), and 2.34 *M* NaCl (in the systems with NaCl added); the initial organic phase: a 10 m*M* chloroform solution of an *n*-alkyltri(oxyethylene) carboxylic acid

Systems without NaCl				Systems with NaCl			
	% of metal in				% of metal in		
Complexing agent and pH	Zn	Cd	Hg	Complexing agent and pH	Zn	Cd	Hg
1				**1**			
3.4–5.8	—	—	—	2.6–9.0	An emulsion in the organic phase		
6.7	8	—	—				
7.5	42	33	—				
8.2	52	38	—				
8.6	73	78	22				
9.9	87	93	22				
2				**2**			
3.2–7.1	—	—	—	2.7–6.6	—	—	—
7.6	11	20	—	8.8	13	2	—
9.1	60	22	—				
9.8	68	41	—				
11.0	94	88	—				
4				**4**			
2.5–8.1	—	—	—	3.3–6.7	—	—	—
8.8	4	—	3	7.45	—	6	—
9.5	10	7	6	8.4	58	9	—
				9.0	64	24	—
				9.2	75	30	6
				9.6	80	49	10

*Transfer of the divalent metal ions from aqueous solutions containing 0.835 m*M *$ZnCl_2$, $CdCl_2$, $HgCl_2$ and 1.17* M *NaCl*

The results of experiments are presented in Figs. 1*B*, *D*, *F*, *H* and Table 2.

The selectivity of transfer of the zinc group element ions into chloroform improved remarkably when NaCl was added to the aqueous phase. Due to formation of very stable chloride complexes of Hg(II) (18, 19), Hg(II) was not transferred into the organic phase or the percentage of Hg(II) transferred was very low (no more than 12%). In the system with **1**, also the percentage of Cd(II) transferred into chloroform was very low (the maximal amount was 14% at pH 9.2 — Fig. 1*B*). It indicated that chloride complexes of Cd(II) and Cd(II) hydroxide were enough stable to prevent complexation of Cd(II) by **1** and its transfer into chloroform. Thus, only Zn(II) was transferred efficiently by **1** into the organic phase and good separation of Zn(II) from other divalent metal ions was achieved in that phase. In the pH region of 5.8–7.1, 11 to 94% of Zn(II), respectively, was transferred by **1** into chloroform while transfer of Cd(II) and Hg(II) did not exceed 3% (Fig. 1*B*).

In the system with **2** employed as the complexone, also good separation of Zn(II) from Cd(II) and Hg(II) was found. In the pH region of 6.6–7.0, 74 to 97% of Zn(II), respectively, was transferred into the organic phase while transfer of Cd(II) and Hg(II) did not exceed 2.5% (Fig. 1*D*). When the pH was raised above 7.0, transfer of Cd(II) into chloroform by **2** increased and reached its maximal value (87%) at pH 8.6. Thus, **2** (with the *n*-octyl chain incorporated into the molecule) was a stronger complexone of Cd(II) than **1** (with the *n*-hexyl chain incorporated).

The curve portions illustrating concentrations of Zn(II) and Cd(II) in the organic phase in the acidic pH region were closer to each other if a complexone with a longer *n*-alkyl chain incorporated into the molecule was used (Figs. 1*D*, *F*, *H*). Thus, a difference in complexation of Zn(II) and Cd(II) decreased when lipophilicity of the complexone was raised. In other words, higher lipophilic *n*-alkyltri(oxyethylene) carboxylic acids were less selective.

*Transfer of the divalent metal ions from aqueous solutions containing 1.67 m*M *$ZnCl_2$, $CdCl_2$, $HgCl_2$, and 2.34* M *NaCl*

The results of experiments are presented in Figs. 2*C*, *E* and Table 3.

No metal concentrations were measured in the system with **1** because a stable emulsion was formed in chloroform in the pH region of 2.6–9.0.

In the system with **2**, good separation of Zn(II) from Cd(II) and Hg(II) was found. In the pH region of 4.6–6.6, 9.7 to 100% of Zn(II) was transferred into chloroform, respectively, while Cd(II) and Hg(II) remained entirely in the aqueous phase (Fig. 2*C*).

In the system with **4**, the efficiency of transfer of Zn(II) was lower (Fig. 2*E*) than in case of **2** (Fig. 2*C*). Only 83.5% (the maximal amount) of Zn(II) was transferred by **4** at pH 7.45. However, still good separation was achieved in that system because neither Cd(II) nor Hg(II) were transferred into chloroform in the pH region of 3.3–7.45 (Fig. 2*E*).

Again, less lipophilic **2** was found to be a better (more selective and more efficient) ion carrier than **4** which has two more methylene units incorporated into its molecule.

n-*Alkyloligo(oxyethylene) carboxylic acids (APOs) as selective complexones of the zinc group element ions*

APOs were found to be selective complexones of the zinc group metal ions when NaCl was added to the aqueous phase. In fact, the selectivity of separation was produced by the chemical equilibria involving complexation of those metal ions by Cl^-, OH^-, and an APO. Thus, the separation was strongly dependent on the aqueous phase composition.

The selectivity and efficiency of separation of the zinc group metal ions by APOs depend on the length of a poly(oxyethylene) chain (12) and on the length of a *n*-alkyl chain incorporated into their molecule.

The complexing abilities of APOs improved gradually when more oxyethylene units were incorporated into their molecule (12). This was in contrast with complexing abilities of poly(oxyethylene) dicarboxylic acids toward alkaline-earth cations because their selectivities changed remarkably but disorderly when a poly(oxyethylene) chain was lengthened (11).

Less lipophilic APOs (with a shorter poly(oxyethylene) chain incorporated into their molecule) were more selective and efficient carriers of the zinc group metal ions. This time, it was in contrast with the properties of both crown carboxylic acids and poly(oxyethylene) dicarboxylic acids because complexing abilities (the selectivity among them) of those compounds usually improved if their lipophilicity was raised (9, 13, 20).

Concentrations of the zinc group metal ion in the organic phase decreased in the basic region of the equilibrium pH of the aqueous phase due to formation of Zn(II) and Cd(II) hydroxides

Can. J. Chem. Downloaded from www.nrcresearchpress.com by 196.1.178.254 on 09/07/12
For personal use only.

and Hg(II) oxide precipitates, even if an APO was enough highly lipophilic to remain entirely in the aqueous phase. Apparently, these hydroxides were thermodynamically more stable than complexes of the metal ion with an APO.

At high Cl^- concentration, chloride complexes of Hg(II) were also enough strong to prevent Hg(II) complexation by an APO and its transfer into chloroform.

Acknowledgement

We express our appreciation to Mrs. Aleksandra Kotecka of the IICMRE, Technical University of Wroclaw, for her assistance in the experiments described in this paper.

1. F. VOGTLE and E. WEBER. Angew. Chem. Int. Ed. Engl. **18**, 753 (1979).
2. J. SMID. Angew. Chem. Int. Ed. Engl. **11**, 112 (1972).
3. N. YAMAZAKI, S. NAKAHAMA, A. HIRAO, and S. NEGI. Tetrahedron Lett. 2429 (1978).
4. N. YAMAZAKI, A. HIRAO, and S. NAKAHAMA. J. Macromo. Sci.-Chem. A**13**, 321 (1979).
5. M. DELCANALE, R. MARCHELLI, A. MANGIA, A. DOSSENA, and G. CASNATI. Angew. Chem. Int. Ed. Engl. **2**, 563 (1983).
6. K. HIRATANI, H. SUGIHARA, K. TAGUCHI, and K. IIO. Chem. Lett. 1657 (1983).
7. K. TAGUCHI, K. HIRATANI, and H. SUGIHARA. Chem. Lett. 1457 (1984).
8. J. STRZELBICKI, W. CHAREWICZ, J. BEGER, and L. HINZ. Extraction of nickel and cobalt by ionizable polyethers. 6th International Symposium on High Purity Materials in Science and Technology — Preparation, Characterization, and Application of Well-Defined Materials. Dresden, GDR. May 1985. Poster Abstracts. pp. 144, 145.
9. S. I. KANG, A. CZECH, B. P. CZECH, L. E. STEWART, and R. A. BARTSCH. Anal. Chem. **57**, 1713 (1985).
10. W. J. MCDOWELL, G. N. CASE, R. A. BARTSCH, and B. CZECH. Solvent Extraction Ion Exchange. **4**, 411 (1986).
11. W. WALKOWIAK, L. E. STEWART, H. K. LEE, B. P. CZECH, and R. A. BARTSCH. Anal. Chem. **58**, 188 (1986).
12. J. STRZELBICKI, W. CHAREWICZ, J. BEGER, and L. HINZ. Can. J. Chem. In press.
13. J. STRZELBICKI and R. A. BARTSCH. Anal. Chem. **53**, 1894 (1981).
14. J. STRZELBICKI and R. A. BARTSCH. Anal. Chem. **53**, 2247 (1981).
15. J. STRZELBICKI and R. A. BARTSCH. J. Membrane Sci. **10**, 35 (1982).
16. L. TOKE, G. T. SZABO, and K. ARANYOSI. Acta Chim. Acad. Hung. **100**, 257 (1979).
17. T. GIBBSON. J. Org. Chem. **45**, 1095 (1980).
18. L. G. SILLEN and A. E. MARTELL. Stability constants of metal-ions complexes. Special Publication No. 17. The Chemical Society, Burlington House, London. 1964. pp. 292, 293.
19. L. G. SILLEN and A. E. MARTELL. Stability constants of metal-ions complexes. Special Publication No. 25. The Chemical Society, Burlington House, London. 1971. pp. 181, 182.
20. J. STRZELBICKI and R. A. BARTSCH. Anal. Chem. **53**, 2251 (1981).

Can. J. Chem. Downloaded from www.nrcresearchpress.com by 196.1.178.254 on 09/07/12
For personal use only.

$(Ph_3P)_2Rh(SPCy_2)$: A complex containing a side-on bonded η^2-secondary phosphine sulfide anion

LUCIO GELMINI[1] AND DOUGLAS W. STEPHAN[2]

Department of Chemistry and Biochemistry, University of Windsor, Windsor, Ont., Canada N9B 3P4

Received March 29, 1988

LUCIO GELMINI and DOUGLAS W. STEPHAN. Can. J. Chem. **66**, 2647 (1988).

The reaction of $Cp_2Zr(SPCy_2)_2$ with either $(Ph_3P)_3RhH(CO)$ or $(Ph_3P)_4RhH$ led not to the expected heterobimetallic species but rather to a novel Rh species $(Ph_3P)_2Rh(SPCy_2)$, **4**. The $^{31}P\{^1H\}$ NMR spectrum of this complex is an ABCX pattern. The molecular geometry of **4** was confirmed by a crystallographic study. Compound **4** crystallizes in the space group $P2_1/c$ with $a = 10.912(1)$ Å, $b = 12.335(2)$ Å, $c = 32.346(7)$ Å, $\beta = 96.17(1)°$, $V = 4328(1)$ Å^3, and $Z = 4$. The coordination sphere about Rh in **4** is pseudo-square planar, containing three phosphorus and a sulfur atom from the two coordinated phosphines and a side-on bonded $SPCy_2$ moiety. This structural study confirms that the secondary phosphine chalcogenide is bonded to Rh in an η^2 fashion. The complex **4** is only the fourth example in which this mode of binding has been crystallographically confirmed and is the first such species to involve one of the Pt group metals.

LUCIO GELMINI et DOUGLAS W. STEPHAN. Can. J. Chem. **66**, 2647 (1988).

La réaction du $Cp_2Zr(SPCy_2)_2$ avec soit le $(Ph_3P)_3RhH(CO)$ ou le $(Ph_3P)_4RhH$ ne conduit pas aux espèces hétérobimétalliques attendues mais plutôt à une nouvelle espèce de Rh, le $(Ph_3P)_2Rh(SPCy_2)$, **4**. Le spectre rmn du $^{31}P\{^1H\}$ de ce complexe se présente sous la forme d'un arrangement ABCX. On a confirmé la géométrie moléculaire du composé **4** par une étude cristallographique. Le composé **4** cristallise dans le groupe d'espace $P2_1/c$ avec $a = 10{,}912(1)$, $b = 12{,}335(2)$ et $c = 32{,}345(7)$ Å, $\beta = 96{,}17(1)°$, $V = 4328(1)$ Å^3 et $Z = 4$. La sphère de coordination autour du Rh dans le composé **4** est pseudo plan carré et elle contient trois phosphores et un atome de soufre provenant de deux phosphines coordonnées et une portion de $SPCy_2$ liée sur le côté. Cette étude structurale permet de confirmer que la phosphine chalcogène secondaire est liée au Rh d'une façon η^2. Le complexe **4** n'est que le quatrième exemple dans lequel ce mode de liaison a pu être confirmé d'une façon cristallographique et il s'agit de la première espèce de ce type à incorporer un des métaux du groupe du Pt.

[Traduit par la revue]

Can. J. Chem. Downloaded from www.nrcresearchpress.com by 196.1.178.254 on 09/07/12
For personal use only.

Introduction

Our interest in early/late heterobimetallics (1–12) has led us to investigate the use of functionalized early transition metal complexes as metalloligands for later transition metals. In a recent paper we described syntheses, structures and chemistry of some Ti, Zr, and Hf complexes of secondary phosphine sulfides and selenides (9). In these Ti, Zr, and Hf complexes, bonding of XPR_2 anions through chalcogenide was observed. However, secondary phosphine chalcogenides or their conjugate bases are known to exhibit at least six different bonding modes (Fig. 1) (13–35). One of these modes involves bonding in which the chalcogen and phosphorus nuclei are bound to different metal atoms (Fig. 1(*e*)); however, this type of ligand system has not been employed to synthesize mixed metal species. Thus, the complex $Cp_2Zr(SPCy_2)_2$, **1**, seemed a suitable synthon for the preparation of Zr/M heterobimetallics. In this paper, we describe some initial investigations that show that reactions of **1** with two Rh-hydride species result in the cleavage of the Zr—S bond, yielding the monometallic species $(Ph_3P)_2Rh(SPCy_2)$, **4**. The species, **4**, has been characterized crystallographically. The results show that the secondary phosphine sulfide moiety is side-on bonded in an η^2 fashion. Although this form of binding is known, this report is only the fourth in which this form of bonding has been structurally confirmed.

Experimental section

All preparations were done under an atmosphere of dry, O_2-free N_2. Solvents were reagent grade, distilled from the appropriate drying agents under N_2, and degassed by the freeze–thaw method at least three times prior to use. $^{31}P\{^1H\}$ NMR spectra were recorded on a Bruker AC-200 spectrometer, using external 85% H_3PO_4 as the reference. The chemical shifts are reported in ppm relative to this reference. Melting points are reported uncorrected. The complex $Cp_2Zr(SPCy_2)_2$, **1**, $(Ph_3P)_3RhH(CO)$, **2**, and $(Ph_3P)_4RhH$, **3**, were prepared by published methods (9, 36).

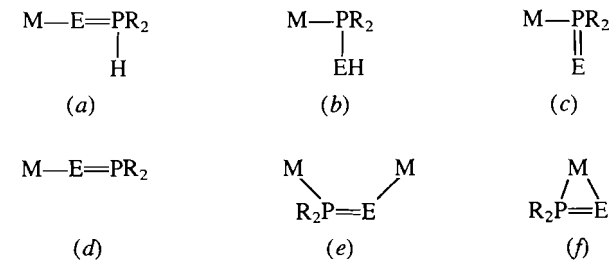

FIG. 1. Bonding modes of secondary phosphine chalcogenides.

Preparation of $(Ph_3P)_2Rh(SPCy_2)$, 4

To a benzene solution (5 mL) of 38 mg of **1** was added 50 mg of **2** in 5 mL of benzene. The solution was stirred for 12 h. The product precipitated from solution upon addition of hexane. The orange–red crystalline material was recrystallized from benzene/hexane. Replacement of **2** with an equivalent of **3** also affords the isolation of **4** via an identical work up procedure. Yield 35 mg (75%). ^1H NMR (δ, C_6D_6): 7.1–7.4 (m, 30 H), 2.2–2.8 (m, 22 H). $^{31}P\{^1H\}$ NMR (C_6H_6, δ, J (Hz)): 40.80 (P3, d of d of d, 1P), 48.20 (P2, d of d of d, 1P), 87.38 (P1, d of d of d, 1P), $|J_{P1—Rh}| = 87.9$, $|J_{P2—Rh}| = 215.6$, $|J_{P3—Rh}| = 168.7$, $|J_{P1—P2}| = 28.4$, $|J_{P1—P3}| = 231.6$, $|J_{P2—P3}| = 30.1$.

X-ray data collection and reduction

Orange–red crystals of **1** were obtained by vapour diffusion of hexane into a benzene solution of **2**. Diffraction experiments were performed on a four-circle Syntex $P2_1$ diffractometer with graphite-monochromatized Mo Kα radiation. The initial orientation matrix was obtained from 15 machine-centred reflections selected from a rotation photograph. These data were used to determine the crystal system. Partial rotation photographs around each axis were consistent with a monoclinic crystal system. Ultimately, 37 reflections ($4.7° < 2\theta <$

[1]Present address: Department of Chemistry, University of California, Berkeley, CA, U.S.A.

[2]To whom correspondence should be addressed.

Can. J. Chem. Downloaded from www.nrcresearchpress.com by 196.1.178.254 on 09/07/12
For personal use only.

TABLE 1. Crystallographic parameters

Formula	$C_{48}H_{52}P_3SRh$
Crystal colour, form	Orange–red blocks
a (Å)	10.912(1)
b (Å)	12.335(2)
c (Å)	32.346(7)
β (deg)	96.17(1)
Crystal system	Monoclinic
Space group	$P2_1/c$
Volume (Å^3)	4328(1)
Density (g cm^{-3})	1.31
Z	4
Crystal dimensions (mm)	0.40 × 0.30 × 0.40
Absorption coefficient, μ (cm^{-1})	5.10
Radiation λ, (Å)	Mo Kα (0.71069)
Temperature (°C)	24
Scan speed (deg/min)	2.0–5.0 (θ/2θ scan)
Scan range (deg)	1.0 below $K\alpha_1$ 1.0 below $K\alpha_2$
Background/scan time ratio	0.5
Data collected	3002
No. of unique data $F_o^2 > 3\sigma(F_o^2)$	2088
No. of variables	166
R (%)	4.53
R_w (%)	5.32
Largest Δ/σ in the final least squares cycle	0.001
Maximum residual electron density (e/Å^3) (atom associated)	0.49 (C84—C85)

25°) were used to obtain the final lattice parameters and the orientation matrix. Machine parameters, crystal data, and data collection parameters are summarized in Table 1. The observed extinctions were consistent with the space group $P2_1/c$. All $\pm h$, $+k$, $+l$ data were collected in one shell ($4.5° < 2\theta < 35.0°$) and three standard reflections were recorded every 197 reflections. Their intensities showed no statistically significant change over the duration of the data collection. The data were processed using the SHELX-76 program package on the computing facilities at the University of Windsor. A total of 3002 reflections with $F_o^2 > 3\sigma F_o^2$ were used in the refinement. The absorption coefficient was small (μ = 5.10 5.10 cm^{-1}) and thus no absorption correction was applied to the data.

Structure solution and refinement

Non-hydrogen atomic scattering factors were taken from the literature tabulations (37–39). The Rh atom position was determined using the heavy atom (Patterson) method. The remaining non-hydrogen atoms were located from successive difference Fourier map calculations. The initial refinements were carried out by using full-matrix least-squares techniques on F, minimizing the function $\Sigma w(|F_o| - |F_c|)^2$ where the weight, w, is defined as $4F_o^2/\sigma^2(F_o^2)$ and F_o and F_c are the observed and calculated structure factor amplitudes. In the final cycles of refinement the Rh, P and S atoms were assigned anisotropic temperature factors. The carbon atoms of the phenyl and cyclohexyl rings were described by isotropic thermal parameters. The phenyl ring geometries were constrained to that of a hexagon with a carbon–carbon distance of 1.39 Å. Hydrogen atom positions were calculated and allowed to ride on the carbon to which they are bonded, assuming a C—H bond length of 0.95 Å. Hydrogen atom temperature factors were fixed at 1.10 times the isotropic temperature factor of the carbon atom to which they are bonded. In all cases the hydrogen atom contributions were calculated, but not refined. The final values of R and R_w are given in Table 1. The maximum Δ/σ on any of the parameters in the final cycles of the refinement and the location of the largest peaks in the final difference Fourier map calculation are also given in Table 1. The residual electron densities were of no chemical significance. The following data are tabulated: positional parameters (Table 2) and selected bond distances and angles (Table 3). Thermal parameters (Table S1), hydrogen atom parameters (Table S2), bond distances and angles associated with the cyclohexyl rings (Table S3) and values of $10|F_o|$ and $10|F_c|$ (Table S4) have been deposited as supplementary material.[3]

Results and discussion

The reaction of **1** with either $(Ph_3P)_3RhH(CO)$ or $(Ph_3P)_4RhH$ resulted in the immediate formation of an orange–red product, **4**. This material exhibits a ^1H NMR spectrum that shows only phenyl and cyclohexyl proton resonances, indicating the loss of the Cp_2Zr fragment. The $^{31}P\{^1H\}$ NMR spectrum contains three distinct resonances each comprised of a doublet of doublets of doublets. This ABCX spectrum (Fig. 2) is consistent with three inequivalent phosphorus nuclei about a pseudo-square planar Rh atom. The resonances were assigned to P1 (the phosphorus of the $SPCy_2$ moiety), P2 (the phosphorus of the PPh_3 *cis* to P1) and P3 (the phosphorus of the PPh_3 *trans* to P1) on the basis of chemical shifts and coupling constants. The expectation of square planar coordination geometry for Rh suggests that the S of the $SPCy_2$ moiety is also bound to Rh. This is consistent with either a monometallic species containing an η^2 bound secondary phosphine sulfide, **4**, a dimeric, **5**, or an oligomeric

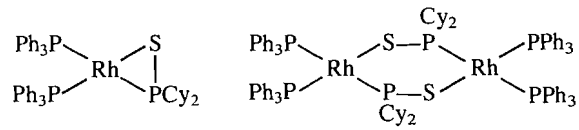

4 **5**

complex. The magnitude of the P1—Rh coupling constant suggests the incorporation of P1 in a three-membered ring, thus suggesting a monometallic species (15, 29). Such η^2 binding of SPR_2 moieties to Rh has been previously postulated on the basis of spectroscopic data (17, 29) and is herein confirmed by X-ray crystallography (*vide infra*). This mode of binding of a secondary phosphine sulfide has also been confirmed for Mo (15, 35) and Fe (34) complexes. Complexes in which SPR_2 moieties are bound in a η^2 fashion have been postulated as intermediates in a number of reactions and are generally considered to be unstable (19–21, 26, 27, 34).

The mechanism of formation of **4** is not known nor is the nature of the Zr-containing product. It is clear, however, that cleavage of a Zr—S bond must occur in the process of the formation of **4**. Such lability of Zr—S bonds has been noted in other Zr—S chemistry (9).

Structure description

The crystallographic investigation of **4** revealed that the unit cell is monoclinic with a single discrete molecule in the asymmetric unit. The closest non-bonded distance between discrete molecules is 2.380 Å (H15B---H73). An ORTEP drawing of the molecule is shown in Fig. 3. The coordination sphere of Rh is pseudo-square planar containing three phos-

[3]A complete set of data, including thermal parameters (Table S1), hydrogen atom parameters (Table S2), and bond distances and angles associated with the cyclohexyl rings (Table S3) (6 pages); values of $10|F_o|$ and $10|F_c|$ (Table S4) (8 pages), may be purchased from the Depository of Unpublished Data, CISTI, National Research Council of Canada, Ottawa, Ont., Canada K1A 0S2.

TABLE 2. Positional parameters[a]

Atom	x	y	z	Atom	x	y	z
Rh	3592(1)	1398(1)	3778(1)	S	4826(2)	1353(2)	4438(1)
P1	4325(2)	−56(2)	4143(1)	P2	2309(2)	826(2)	3243(1)
P3	3394(2)	3244(2)	3750(1)	C11	5705(8)	−809(8)	4037(3)
C12	6485(9)	−145(8)	3761(3)	C13	7650(9)	−739(9)	3668(3)
C14	8411(10)	−1075(9)	4074(3)	C15	7659(10)	−1772(9)	4339(4)
C16	6491(9)	−1194(8)	4432(3)	C21	3494(8)	−924(7)	4480(3)
C22	3283(9)	−2079(8)	4308(3)	C23	2684(9)	−2803(8)	4618(3)
C24	1454(9)	−2312(8)	4711(3)	C25	1599(10)	−1125(9)	4860(4)
C26	2247(9)	−446(8)	4555(3)	C31	2626(6)	1009(5)	2697(2)
C32	3469(6)	1800(5)	2604(2)	C33	3703(6)	1967(5)	2193(2)
C34	3093(6)	1343(5)	1875(2)	C35	2250(6)	553(5)	1968(2)
C36	2017(6)	386(5)	2378(2)	C41	743(6)	1383(5)	3250(2)
C42	338(6)	1501(5)	3642(2)	C43	−799(6)	1984(5)	3682(2)
C44	1532(6)	2348(5)	3329(2)	C45	1128(6)	2229(5)	2937(2)
C46	10(6)	1747(5)	2897(2)	C51	2032(5)	−655(5)	3231(2)
C52	3026(5)	−1322(5)	3166(2)	C53	2869(5)	−2444(5)	3144(2)
C54	1719(5)	−2898(5)	3187(2)	C55	726(5)	−2231(5)	3252(2)
C56	882(5)	−1109(5)	3274(2)	C61	4740(5)	3955(6)	4011(2)
C62	4602(5)	4880(6)	4250(2)	C63	5640(5)	5406(6)	4444(2)
C64	6815(5)	5008(6)	4400(2)	C65	6953(5)	4083(6)	4161(2)
C66	5916(5)	3556(6)	3967(2)	C71	2152(6)	3746(5)	4040(2)
C72	1954(6)	3158(5)	4395(2)	C73	1013(6)	3462(5)	4631(2)
C74	271(6)	4353(5)	4512(2)	C75	469(6)	4941(5)	4157(2)
C76	1410(6)	4637(5)	3921(2)	C81	3137(5)	3967(5)	3251(2)
C82	1981(5)	3919(5)	3021(2)	C83	1813(5)	4359(5)	2622(2)
C84	2799(5)	4847(5)	2453(2)	C85	3954(5)	4895(5)	2683(2)
C86	4123(5)	4455(5)	3083(2)				

[a]Multiplied by 10^4.

TABLE 3. Selected bond distances (Å) and angles (deg)

Bond	Distance	Bond	Distance	Bond	Distance
Rh—P1	2.248(3)	Rh—P2	2.219(3)	Rh—P3	2.287(3)
Rh—S	2.399(3)	P1—S	2.028(4)	P1—C11	1.833(9)
P1—C21	1.836(9)	P2—C31	1.853(7)	P2—C41	1.844(7)
P2—C51	1.854(7)	P3—C61	1.838(8)	P3—C71	1.837(7)
P3—C81	1.837(7)				

Bonds	Angle	Bonds	Angle	Bonds	Angle
S—Rh—P1	51.6(1)	S—Rh—P2	158.8(1)	P1—Rh—P2	108.4(1)
S—Rh—P3	95.8(1)	P1—Rh—P3	147.3(1)	P2—Rh—P3	103.6(1)
Rh—S—P1	60.3(1)	Rh—P1—S	68.0(1)	C11—P1—C21	106.5(4)
C31—P2—C41	103.6(3)	C31—P2—C51	98.4(3)	C41—P2—C51	102.5(3)
C61—P3—C71	101.6(3)	C61—P3—C81	102.2(3)	C71—P3—C81	103.5(3)

phorus atoms and a sulfur atom. The Rh—P1 bond distance is 2.248(3) Å. In comparison, the Rh—P bonds involving the PPh_3 moieties are 2.219(3) and 2.287(3) Å. All of these Rh—P distances are typical of those seen in other Rh–phosphine complexes (39). The Rh—P3 distance is longer than the Rh—P2 distance reflecting the *trans* influence of the basic phosphorus atom of the $SPCy_2$ moiety. The Rh—S bond distance of 2.399(3) Å is slightly longer than the Rh—S distance found in $[Rh(MeSCH_2CH_2PPh_2)_2]BF_4$ (2.353(3) and 2.342(3) Å) (40). Poorer donor ability of the sulfur of a $SPCy_2$ anion compared to that of the thioether sulfur of $MeSCH_2CH_2PPh_2$ may arise from the presence of P—S multiple bonding. In addition, the strain associated with the three-membered ring may result in poor orbital overlap between S and Rh.

The P1—Rh—P2 and P3—Rh—S angles of 108.4(1) and 95.8(1)° are consistent with the pseudo-square planar geometry about Rh. The P2—Rh—P3 angle of 103.6(1)° compares with the angle of 92.9(1)° found between the phosphine groups in $[Rh(COD)(PPh_2(C_4H_4S))_2]^+$ (40). Steric interactions between the phenyl rings on P2 with the cyclohexyl groups on P1 are apparently minimized by the orientation of the rings, such that only ring 5 (C51—C56) is directed towards the cyclohexyl groups. Steric interactions with the phenyl rings on P2 with

Can. J. Chem. Downloaded from www.nrcresearchpress.com by 196.1.178.254 on 09/07/12
For personal use only.

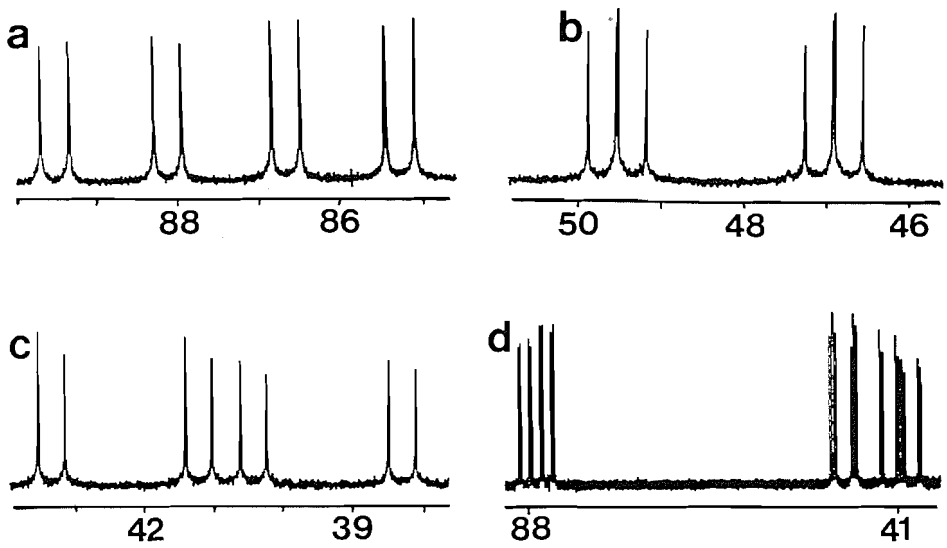

FIG. 2. $^{31}P\{^{1}H\}$ NMR Spectrum of **4**, scales are given in ppm. Expansion of the signals arising from P1, P2, and P3 are shown in (*a*), (*b*), and (*c*) respectively; (*d*) full spectrum.

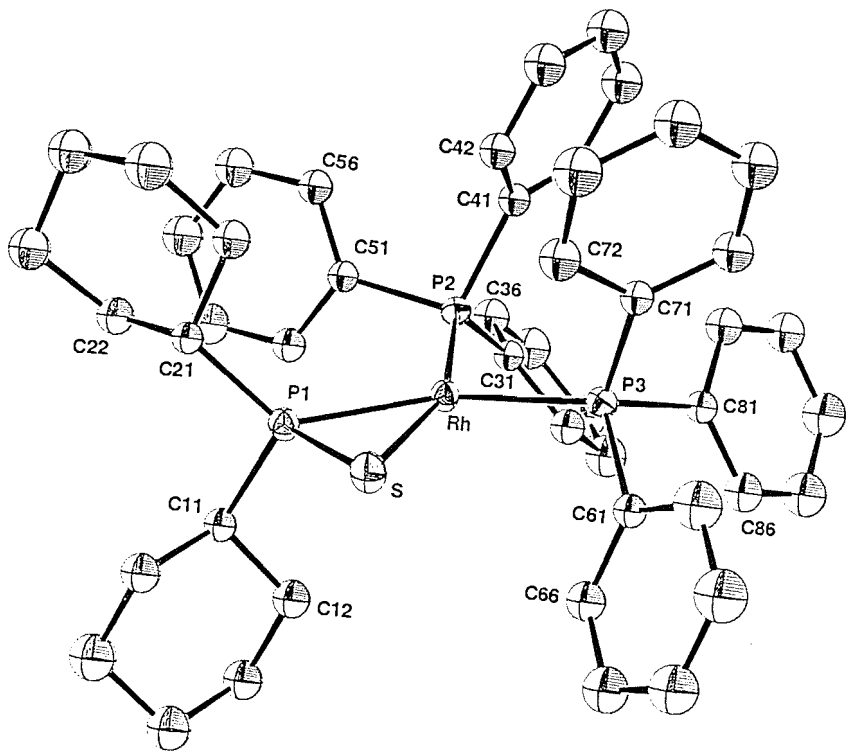

FIG. 3. ORTEP drawing of **4**, hydrogen atoms are omitted for clarity, 30% thermal ellipsoids are shown.

those on P3 are relived by the relatively large P2—Rh—P3 angle. These steric constraints are also reflected in the fact that the S—Rh—P3 angle (95.8(1)°) is smaller than the P1—Rh—P2 angle (108.4(1)°). The P1—Rh—S angle is 51.6(1)°. This is similar to the P—Fe—S angle of 51.13(3)° found in $(C_3F_7)Fe(CO)_3(SPEt_2)$, **6**, (34) and in contrast to the P—Mo—S angles of 47.11(5) and 46.91(5)° found in $Mo(CO)_2(PPh_3)(SPPh_2)_2$, **7** (15) and 47.5(1)° found in $(MeC_5H_4)Mo(CO)_2(\eta^2\text{-}SPPh_2)$, **8** (35). The larger angle at the metal center in **4** is consistent with the shorter M—P and M—S distances.

The P1—S bond distance of 2.028(4) Å is considerably longer than the typical P—S double bond length of 1.95 Å and shorter than P—S single bond lengths of 2.18 Å (15). The observed P—S distance in **4** is comparable to the P—S bond distances in the complexes containing η^2-bound SPR_2 units **6** (2.011(1) Å) (34), **7** (2.008(2), 2.013(2) Å) (15), and **8** (2.003(2) Å) (35). Thus, the P—S bond distance reflects a considerable degree of π bonding between phosphorus and sulfur.

Summary

The reaction of **1** with two Rh hydrides does not lead to the formation of stable heterobimetallics. Rather, the monometallic species **4** is formed. The structural study described herein, confirms the η^2 bonding mode of the secondary phosphine

Can. J. Chem. Downloaded from www.nrcresearchpress.com by 196.1.178.254 on 09/07/12
For personal use only.

sulfide anion. The complex **4** is only the fourth example in which this mode of binding has been crystallographically confirmed and is the first such species to involve one of the Pt group metals.

Acknowledgements

Natural Sciences and Engineering Research Council of Canada is thanked for financial support of this work. L.G. is grateful for the award of an NSERC of Canada postgraduate scholarship.

1. L. GELMINI, L. C. MATASSA, and D. W. STEPHAN. Inorg. Chem. **24**, 2585 (1985).
2. L. GELMINI and D. W. STEPHAN. Inorg. Chem. **25**, 1222 (1986).
3. L. GELMINI and D. W. STEPHAN. Inorg. Chim. Acta, **111**, L17 (1986).
4. S. J. LÖEB, H.-A. TAYLOR, L. GELMINI, and D. W. STEPHAN. Inorg. Chem. **25**, 1977 (1986).
5. G. S. WHITE and D. W. STEPHAN. Inorg. Chem. **24**, 1499 (1985).
6. T. A. WARK and D. W. STEPHAN. Inorg. Chem. **26**, 363 (1987).
7. G. S. WHITE and D. W. STEPHAN. Organometallics, **6**, 2169 (1987).
8. T. A. WARK, G. S. WHITE, J. S. TSE, and D. W. STEPHAN. Unpublished results.
9. L. GELMINI and D. W. STEPHAN. Organometallics, **6**, 1515 (1987).
10. G. S. WHITE and D. W. STEPHAN. Organometallics. **7**, 903 (1988).
11. L. GELMINI and D. W. STEPHAN. Organometallics. **7**, 849 (1988).
12. W. ZHENG and D. W. STEPHAN. Inorg. Chem. **27**, 2386 (1988).
13. O. J. SCHERER, H. JUNGMANN, C. KRUGER, and G. WOLMERSCHAUSER. Chem. Ber. **117**, 2382 (1984).
14. E. LINDNER, F. BOUACHIR, and S. HOEHNE. Chem. Ber. **116**, 45 (1983).
15. H. P. M. AMBROSIUS, J. H. NOORDIK, and G. J. A. ARIAANS. J. Chem. Soc. Chem. Commun. 832 (1980).
16. W. MALISCH, R. MAISCH, I. J. COLQUHOUN, and W. MCFARLANE. J. Organomet. Chem. **220**, C4 (1981).
17. V. MARSALA, F. FARAONE, and P. PIRAINO. J. Organomet. Chem. **133**, 301 (1977).
18. E. LINDNER, F. BOUACHIR, and W. HILLER. J. Organomet. Chem. **210**, C37 (1981).
19. E. LINDNER, A. RAU, and S. HOEHNE. Angew. Chem. Int. Ed. Engl. **20**, 787 (1981).
20. E. LINDNER, A. RAU, and S. HOEHNE. Chem. Ber. **114**, 3281 (1981).
21. E. LINDNER and W. P. MEIER. J. Organomet. Chem. **114**, 67 (1976).
22. G. J. KRUGER, S. LOTZ, L. LINFORD, M. VAN DYK, and H. G. RAUBENHEIMER. J. Organomet. Chem. **280**, 241 (1985).
23. E. LINDNER and C. P. KRIEG. J. Organomet. Chem. **269**, 65 (1984).
24. W. KLAUI, K. SCHMIDT, A. BOCKMAN, P. HOFMANN, H. R. SCHMIDT, and P. STAUFFERT. J. Organomet. Chem. **286**, 407 (1985).
25. E. LINDNER, K. AUCH, W. HILLER, and R. FAWZI. Angew. Chem. Int. Ed. Engl. **23**, 320 (1984).
26. E. LINDNER, C. P. KRIEG, W. HILLER, and R. FAWZI. Chem. Ber. **118**, 1398 (1985).
27. E. LINDNER, C. P. KRIEG, W. HILLER, and D. HUBNER. Chem. Ber. **117**, 489 (1984).
28. B. WALTHER, B. MESSBAUER, and H. MEYER. Inorg. Chim. Acta, **37**, L525 (1979).
29. D. H. M. W. THEWISSEN. J. Organomet. Chem. **192**, 115 (1980).
30. K. P. WAGNER, R. W. HESS, P. M. TRIECHEL, and J. C. CALABRESE. Inorg. Chem. **14**, 1121 (1975).
31. B. MESSBAUER, H. MEYER, B. WALTHER, M. J. HEEG, A. F. M. M. RAHMAN, and J. P. OLIVER. Inorg. Chem. **22**, 272 (1983).
32. B. WALTHER. Coord. Chem. Rev. **60**, 67 (1984).
33. J. R. WASSON, G. M. WOLTERMANN, and H. J. STOKLOSA. Top. Curr. Chem. **35**, 65 (1973).
34. E. LINDNER, C. P. KRIEG, W. HILLER, and R. FAWZI. Angew. Chem. Int. Ed. Engl. **23**, 523 (1984).
35. H. ALPER, F. W. B. EINSTEIN, F. W. HARTSTOCK, and R. H. JONES. Organometallics, **6**, 829 (1987).
36. G. WILKINSON. Inorg. Synth. **13**, 126 (1972).
37. D. T. CROMER and J. B. MANN. Acta Crystallogr. Sect. A: Cryst. Phys., Diffr., Theor. Gen. Crystallogr. A**24**, 324 (1968).
38. D. T. CROMER and J. B. MANN. Acta Crystallogr. Sect. A: Cryst. Phys., Diffr., Theor. Gen. Crystallogr. A**24**, 390 (1968).
39. D. T. CROMER and J. T. WABER. International tables for X-ray crystallography. Kynoch Press, Birmingham, England. 1974.
40. D. G. DICK and D. W. STEPHAN. Can. J. Chem. **64**, 1870 (1986).

Can. J. Chem. Downloaded from www.nrcresearchpress.com by 196.1.178.254 on 09/07/12
For personal use only.

Anodic oxidation of lead in aqueous carbonate solutions. I. Film formation and dissolution at pH = 12

D. W. SHOESMITH[1] AND M. G. BAILEY

Fuel Waste Technology Branch, Atomic Energy of Canada Limited, Whiteshell Nuclear Research Establishment, Pinawa, Man., Canada R0E 1L0

Received November 16, 1987[2]

D. W. SHOESMITH and M. G. BAILEY. Can. J. Chem. **66**, 2652 (1988).

The anodic oxidation of lead has been studied using rotating disk electrodes, under voltammetric and potentiostatic conditions, in aqueous carbonate solutions at pH = 12. The solid films formed on the electrode surface have been identified by X-ray diffractometry. Two distinct surface layers are formed: a compact layer composed of two separate phases, plumbonacrite ($Pb_{10}O(OH)_6(CO_3)_6$) and hydrocerussite ($Pb_3(OH)_2(CO_3)_2$); and a more dispersed layer of hydrocerussite. The plumbonacrite in the compact layer is formed directly on the electrode surface by a solid-state growth process. The hydrocerussite component of this compact layer appears to form by conversion of the outer layers of plumbonacrite. The dispersed layer is formed by deposition from solution. The extent of deposition is controlled by the rate of transport of soluble Pb^{2+} species to the bulk of solution.

D. W. SHOESMITH et M. G. BAILEY. Can. J. Chem. **66**, 2652 (1988).

Opérant dans des solutions aqueuses de carbonate, à un pH de 12, dans des conditions voltamétriques ainsi que potentiostatiques et faisant appel à des électrodes à disque tournant, on a étudié l'oxydation anodique du plomb. Utilisant la diffraction des rayons-X, on a identifié les films solides qui se forment à la surface de l'électrode. À cette surface, il se forme deux couches distinctes : une couche compacte composée de deux phases séparées, de la plumbonacrite (Pb_{10})$(OH)_6(CO_3)_6$) et de l'hydrocérussite ($Pb_3(OH)_2(CO_3)_2$) ainsi qu'une couche plus dispersée d'hydrocérussite. La plumbonacrite présente dans la couche compacte se forme directement sur la surface de l'électrode par un processus de croissance à l'état solide. Il semble que la composante hydrocérussite de cette couche compacte se forme par la conversion des couches extérieures de plumbonacrite. La couche dispersée se forme par une déposition à partir de la solution. Le taux de déposition est contrôlé par la vitesse de transport des espèces Pb^{2+} à partir de la solution.

[Traduit par la revue]

Can. J. Chem. Downloaded from www.nrcresearchpress.com by 196.1.178.254 on 09/07/12
For personal use only.

Introduction

The proposed Canadian method for the disposal of high-level nuclear waste, in the form of either irradiated fuel or reprocessed waste, is to bury it 1 km below the surface of a stable rock formation (1). A number of engineered barriers have been suggested to prevent access of groundwater to the wasteform and to impede the subsequent release of radionuclides. One proposal is that the wasteform be invested in lead and placed inside a titanium canister. The corrosion performance of titanium has been studied in detail (2) but little work has been done on lead (3).

Besides acting as a corrosion barrier, there appear to be a number of other chemical advantages in having lead present: (*a*) The lead could act as a redox scavenger by removing dissolved oxidants from the groundwater, thereby slowing down the oxidative dissolution of the uranium dioxide fuel (4). (*b*) The corrosion of lead could lead to the formation of basic lead compounds with a number of anions expected in the groundwater (5). The solubility of such compounds is generally low, and the anion concentration in the groundwater would be significantly reduced. This would be of particular advantage in the case of carbonate that strongly complexes UO_2^{2+}, the product of UO_2 dissolution ($UO_2(CO_3)_2^{2-}$, $UO_2(CO_3)_3^{4-}$), thereby increasing its solubility and accelerating the dissolution process (6, 7).

To evaluate the efficacy of lead as a barrier, it is necessary to have a good understanding of the chemical processes occurring under the redox and chemical conditions possible in a nuclear waste repository. The interaction of lead oxide (PbO, litharge) with aqueous carbonate solutions has been studied in detail (8), and the stability fields for a number of solids in the $PbO–CO_2–H_2O$ system have been determined. The infrared and Raman spectra for the various solids have been published (9). In this paper, we present results on the electrochemistry of lead in aqueous carbonate solutions. Since the Pb^{4+} state will not be achieved under natural corrosion conditions, we have concentrated on the study of the Pb/Pb^{2+} system.

Experimental

Experiments were performed in a conventional three-electrode cell, degassed with nitrogen. Solutions were made up with Fisher Scientific certified reagents. The lead was supplied by the Canadian Metal Company and was 99.99% pure. The electrodes were constructed as rotating disks with an exposed surface area of 1.6 cm^2. Electrodes were polished with wet 600 grit SiC, and washed with triply distilled water. The results were found to be very dependent on electrode preparation, and the preparation used gave reproducible results. Unless otherwise stated, all experiments were conducted in 1.0 mol L^{-1} potassium carbonate. All potentials are quoted against the saturated calomel electrode (vs. SCE).

Electrochemical experiments were performed using an EG and G model 173 potentiostat/galvanostat coupled to a model 179 coulometer and a model 175 Universal programmer. Electrodes were rotated using a Pine Instrument Company ASR rotator. Data were recorded using a Phillips model PM 8132 XY recorder.

The phases formed on the electrode surface were identified using a Philips PW-1150 diffractometer with Cu K_α radiation and a diffracted beam monochromator. The relative amounts of the different phases present were measured by comparing the heights of single diffraction peaks for the various phases. The particular peaks used were chosen so that they were of comparable intensities and did not significantly overlap with other peaks in the X-ray pattern. Thus, the peaks used for the various phases were as follows: plumbonacrite (*d*-spacing = 3.36 Å); hydrocerussite (3.29 Å); cerussite (3.498 Å); litharge (3.115 Å). Such a comparison is only semiquantitative.

[1]Author to whom correspondence may be addressed.

[2]Revision received June 13, 1988.

Can. J. Chem. Downloaded from www.nrcresearchpress.com by 196.1.178.254 on 09/07/12
For personal use only.

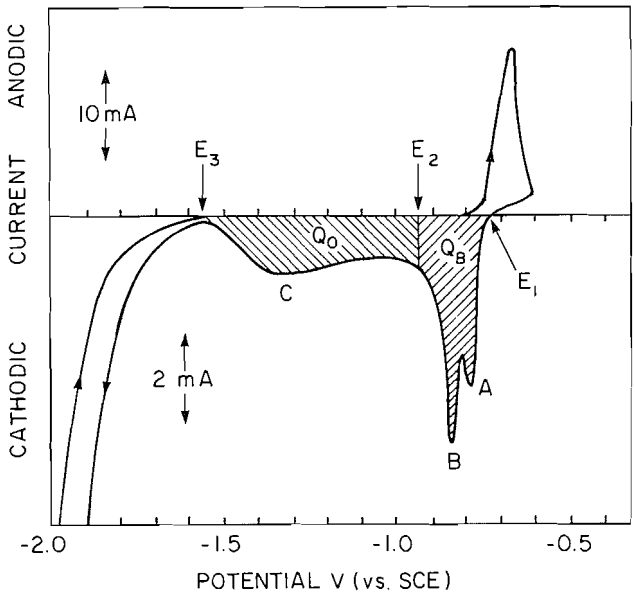

FIG. 1. Cyclic voltammogram recorded in 1.0 mol L^{-1} K_2CO_3 (pH = 12.0) at v = 20 mV s^{-1} and ω = 1.67 Hz. The various cathodic peaks are marked A, B, and C. The hatched areas show the sections of the plots integrated to obtain the charges Q_B and Q_O.

Results

Cyclic voltammetry

Figure 1 shows a cyclic voltammogram recorded in 1.0 mol L^{-1} K_2CO_3 (pH = 12) on a rotating disk electrode (ω = 1.67 Hz) at a scan rate of 20 mV s^{-1}. A single anodic peak is observed around −0.660 V (vs. SCE) with a shoulder at more negative potentials (~ −0.700 V). If the potential scan is reversed immediately after the main anodic peak, Fig. 1, three distinct reduction peaks (A, B, and C) are observed on the reverse cathodic scan. The existence of three reduction peaks suggests that three distinct films or phases are formed on the anodic scan. The sharpness, symmetry, and position of peaks A and B indicate the reduction of two compact adherent films. The broadness of peak C suggests that the second process (around E = ~ −1.300 V) is the reduction of a more dispersed film. If the process occurring at peak C is the reduction of an outer layer of deposit, it will be taking place on a possibly porous metal layer formed by the reduction of the base layer at peaks A and B. Further justification for our claim that peak C is due to the reduction of a deposited outer layer is offered below.

Figure 2 shows a series of voltammograms reversed at various anodic limits. The electrode rotation rate (ω) is an order of magnitude greater than for Fig. 1. The effect of this increase is to reduce the extent of formation of the film reduced at peak C. Potential scans limited to the cathodic side of the anodic peak show that the film reduced at peak B is formed in this region. This is clearly demonstrated by the data of Fig. 7, to be discussed below. The film reduced at peak A forms at more positive potentials, and becomes dominant as the scan progresses down the anodic side of the peak. Both peaks grow as the scan progresses to more positive potentials in the passive region beyond the main anodic peak. Although not shown in Fig. 2, the film reduced at peak C forms on the cathodic side of the anodic peak, and does not thicken significantly as the scan progresses to more positive potentials.

Figure 3 shows the effect of potential scan rate (to an anodic limit of −610 mV) on the anodic and cathodic charges, Q_A and

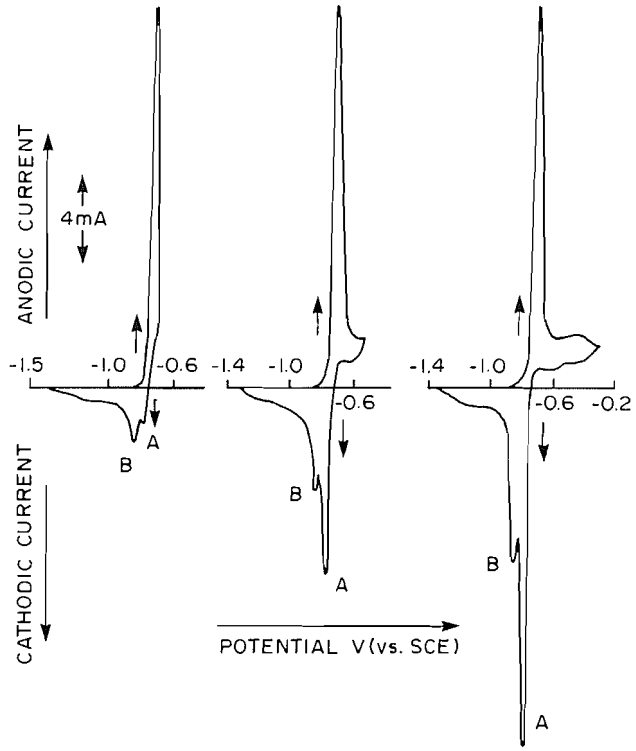

FIG. 2. Voltammetric scans to various anodic limits recorded in 1.0 mol L^{-1} K_2CO_3 (pH = 12.0) at v = 20 mV s^{-1} and ω = 16.7 Hz.

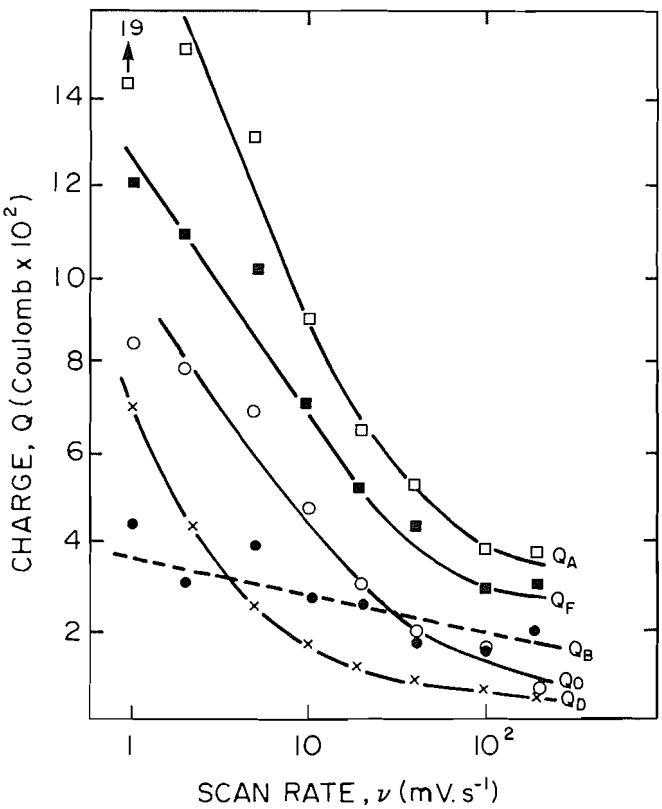

FIG. 3. Anodic and various cathodic charges, as a function of the scan rate (v), obtained by integration of voltammetric scans (to an anodic limit of −610 mV) recorded in 1.0 mol L^{-1} K_2CO_3 (pH = 12.0) at ω = 1.67 Hz; Q_A, Q_F, and Q_D are defined by eqs. [1] and [2] of the text, and Q_B and Q_O are defined in Fig. 1.

Q_F, and on the distribution of charges between base-layer formation (Q_B), outer-layer formation (Q_O), and the charge, Q_D, given by the expression

[1] $Q_D = Q_A - Q_F$

with

[2] $Q_F = Q_B + Q_O$

The charges are obtained by the integration of voltammograms of the form shown in Fig. 1: Q_A is the total anodic charge consumed during the anodic scan plus the small amount consumed at the start of the reverse scan; Q_F is the total charge measured by integration of the current between potentials E_1 and E_3 (Fig. 1), and is taken as the charge due to the reduction of all films; Q_B and Q_O are obtained by integration of the current between E_1 and E_2, and E_2 and E_3, respectively; Q_D is taken to be the charge due to dissolution to Pb^{2+} species.

By contrast, the charge associated with the reduction of the base layer, Q_B, changes only slightly with scan rate. This behaviour suggests that the thickness of the base layer is determined by kinetic parameters that are potential dependent, but large enough to be independent of scan rate. The passivating nature of this layer is the cause of the anodic peak observed in Fig. 1 and the rapid fall in current at potentials positive to the peak. By contrast to Q_B, both Q_A and Q_F decrease as the scan rate increases. This can be attributed to decreases in the extent of dissolution (Q_D) and in the thickness of the deposited layer (proportional to Q_O). As the scan rate increases, the potential spends less time in the potential region where dissolution occurs, i.e., less time on the cathodic side of the peak. Consequently, less dissolution and deposition are observed.

The parallel decrease in the thickness of the outer layer (Q_O) and the extent of dissolution (Q_D) indicate that these two processes are related. It is possible that the extent of dissolution determines the thickness of the outer layer, suggesting that this layer is formed by deposition of dissolved Pb^{2+} species. As discussed above, this deposited layer only forms on the cathodic side of the anodic peak.

Figure 4 shows the effect of electrode rotation speed on the form of the cyclic voltammograms. The height of the anodic peak is increased, but the size of the cathodic peaks is reduced. The major impact is on the size of peak C, which almost disappears at high electrode rotation rates. The relative heights of reduction peaks A and B do not vary consistently with changes in rotation rate.

Figures 5A and 5B show the effect of electrode rotation rate (ω) on the various charges, calculated as described above. The total anodic charge increases by ~40% over the range of rotation rates investigated (0.83–33.3 Hz), attributable to an increase in the extent of dissolution (Q_D). The extent of film formation (Q_F), Fig. 5B, decreases with increasing rotation rate. The thickness of the base layer (proportional to Q_B) is almost independent of rotation rate. However, there is a redistribution of charge between dissolution (Q_D), which increases, and film deposition (Q_O), which decreases. This redistribution demonstrates that the dissolution and deposition processes are competing for the same soluble material, and confirms that the outer layer of film is formed by deposition from solution. The extent of formation of this film is determined by the concentration of dissolved Pb^{2+} species close to the electrode surface. This concentration will decrease as the electrode rotation rate increases and the rate of transport of soluble species away from the electrode increases. In this manner, the solution transport and deposition processes compete for the soluble Pb^{2+} species, with transport predominating at higher electrode rotation rates. The Pb^{2+} species lost to the bulk of solution are not reduced on the subsequent cathodic scan. Hence, Q_F ($= Q_A - Q_D$, eq. [1]) decreases with increasing electrode rotation rate.

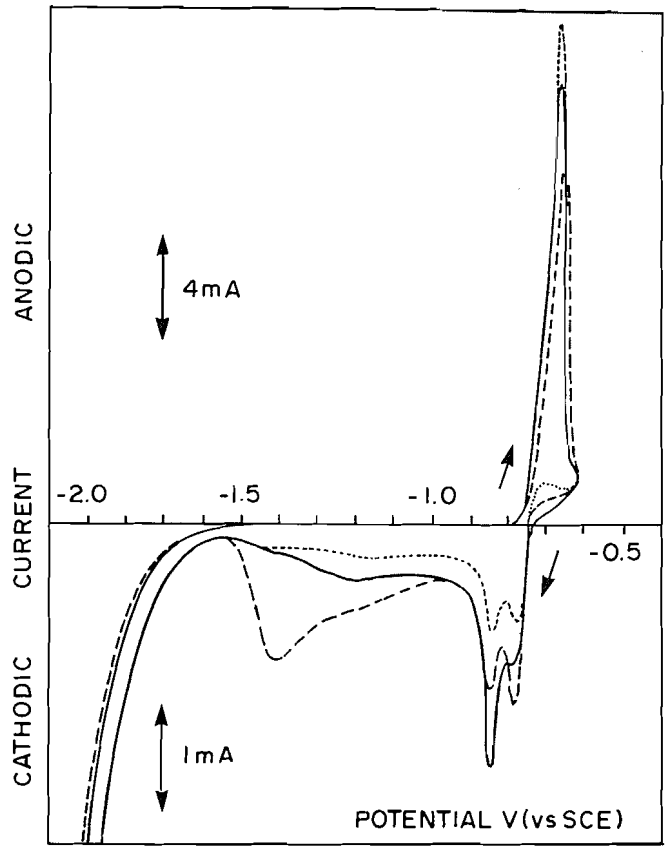

FIG. 4. Voltammetric scans recorded in 1.0 mol L^{-1} K_2CO_3 (pH = 12.0) at 20 mV s^{-1} and various electrode angular velocities (ω, in Hz); (---) 1.67 Hz; (—) 16.7 Hz; (····) 50 Hz.

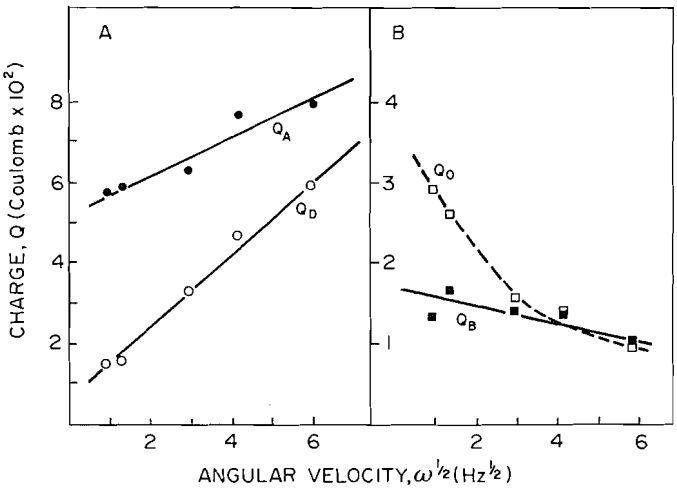

FIG. 5. Anodic and various cathodic charges, as a function of angular velocity (ω), obtained by integration of voltammetric scans recorded in 1.0 mol L^{-1} K_2CO_3 (pH = 12.0) at $v = 20$ mV s^{-1}; Q_A and Q_D are defined by eqs. [1] and [2] of the text, and Q_B and Q_O are defined in Fig. 1.

Can. J. Chem. Downloaded from www.nrcresearchpress.com by 196.1.178.254 on 09/07/12
For personal use only.

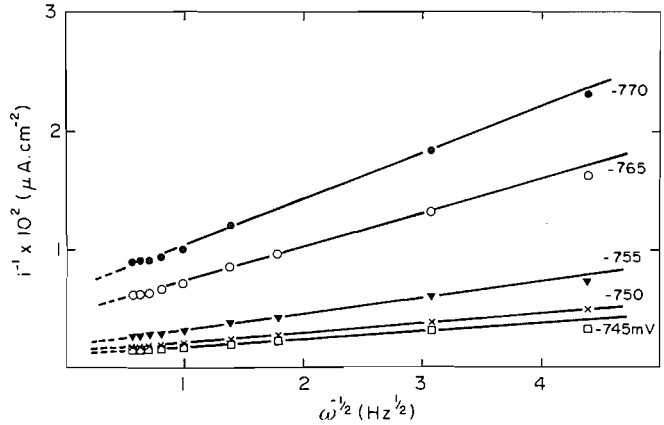

FIG. 6. Plot of steady-state currents (as i^{-1}) against $\omega^{-1/2}$ (Hz) recorded under potentiostatic conditions at various potentials in 1.0 mol L^{-1} K_2CO_3 (pH = 12.0).

Potentiostatic experiments

A series of potentiostatic experiments was performed under stagnant conditions ($\omega = 0$) at potentials in the vicinity of the foot of the main anodic peak (−0.790 to −0.740 V). Rapidly falling transients were obtained with the current (i) decreasing from >1 mA cm^{-2} to <15 $\mu A \cdot cm^{-2}$ in times (t) from 20 to 30 s. Steady-state currents were achieved after ~6–7 min. The form of the current (i) versus time (t) plot was dependent on electrode preparation. No consistent linear relationship between i and t was obtained. Also, no peak was observed in the current transient, indicating that a phase nucleation and growth process was not involved.

The steady-state currents are dependent on electrode rotation rate (ω) and are plotted according to the Levich theory (6) in Fig. 6. Extrapolation of these plots to infinite rotation speeds ($\omega^{-1/2} \rightarrow 0$) yields values for the dissolution current free from transport, confirming that the dissolution process is under mixed electrochemical/transport control. Further analysis according to this theory (6) did not yield consistent results.

From these data it can be concluded that a surface film is formed at potentials as negative as −0.790 V, and that there appears to be no potential region where dissolution of Pb^{2+} species occurs from a clean metal surface. Dissolution of this surface film occurs via a field-assisted process partially controlled by transport of Pb^{2+} species away from the electrode surface. Since the maximum Pb^{2+} concentration in equilibrium with hydrocerussite, the predominant surface phase, is $<10^{-3}$ mol L^{-1}, control by OH^- (10^{-2} mol L^{-1}) or carbonate (1.0 mol L^{-1}) transport to the electrode surface is ruled out.

XRD analyses of potentiostatically grown films

A series of potentiostatic oxidations was performed for various durations at different potentials. The films formed were subsequently analyzed by X-ray diffraction (XRD), or cathodically stripped using a voltammetric scan (CSV) from the oxidation potential to −2.0 V.

Figure 7 shows a series of cathodic stripping voltammograms (CSVs) recorded after oxidations at −0.726 V, a potential negative to the shoulder on the main anodic oxidation peak, Fig. 1. The XRD data obtained on a second series of experiments at this potential are shown in Fig. 8. For short oxidations, Fig. 7A, only peak B is observed. A corresponding XRD analysis detects only plumbonacrite, $Pb_{10}O(OH)_6(CO_3)_6$. After 10 min of oxidation, peak C is observed in the CSV, Fig. 7B, but, again,

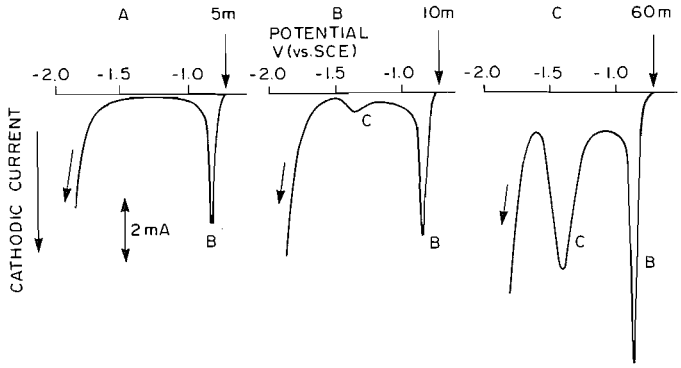

FIG. 7. Cathodic stripping voltammograms recorded after potentiostatic oxidation at −0.726 V (vs. SCE) for various times in 1.0 mol L^{-1} K_2CO_3 (pH = 12.0) at $v = 20$ mV s^{-1} and $\omega = 1.67$ Hz.

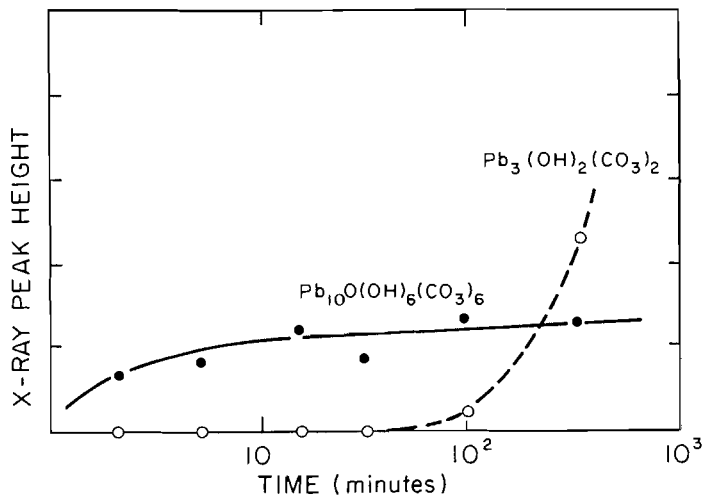

FIG. 8. X-ray peak heights for plumbonacrite and hydrocerussite recorded on electrodes oxidized at −0.726 V for various times in 1.0 mol L^{-1} K_2CO_3 (pH = 12.0) at $\omega = 1.67$ Hz.

only plumbonacrite is detected by XRD. At longer times of oxidation, Fig. 7C, peak C predominates in the CSV and hydrocerussite ($Pb_3(OH)_2(CO_3)_2$) is the dominant phase, Fig. 8. Since an XRD analysis and a CSV cannot be performed on the same sample it proved difficult to demonstrate unequivocably that peak B is due to the reduction of plumbonacrite and peak C is due to the reduction of hydrocerussite. However, repeating these two series of experiments four times showed that hydrocerussite was never observed by XRD when only peak B was present in the CSV, and after long times of oxidation, when peak C was much larger than peak B, hydrocerussite always predominated in the XRD pattern. These observations give us some confidence in our assignment of peaks B and C. Our results over a wider pH range help substantiate this claim.[3]

The amount of plumbonacrite required to yield a detectable XRD signal appears to be much smaller than for hydrocerussite, suggesting an enhanced X-ray sensitivity for plumbonacrite. An examination of the diffraction patterns for the two phases shows: (*i*) no evidence of a preferred orientation for the plumbonacrite layer that would confer an enhanced X-ray sensitivity; (*ii*) no evidence for a lower degree of crystallinity

[3]D. W. Shoesmith, M. G. Bailey, and P. Taylor. Unpublished results.

Can. J. Chem. Downloaded from www.nrcresearchpress.com by 196.1.178.254 on 09/07/12
For personal use only.

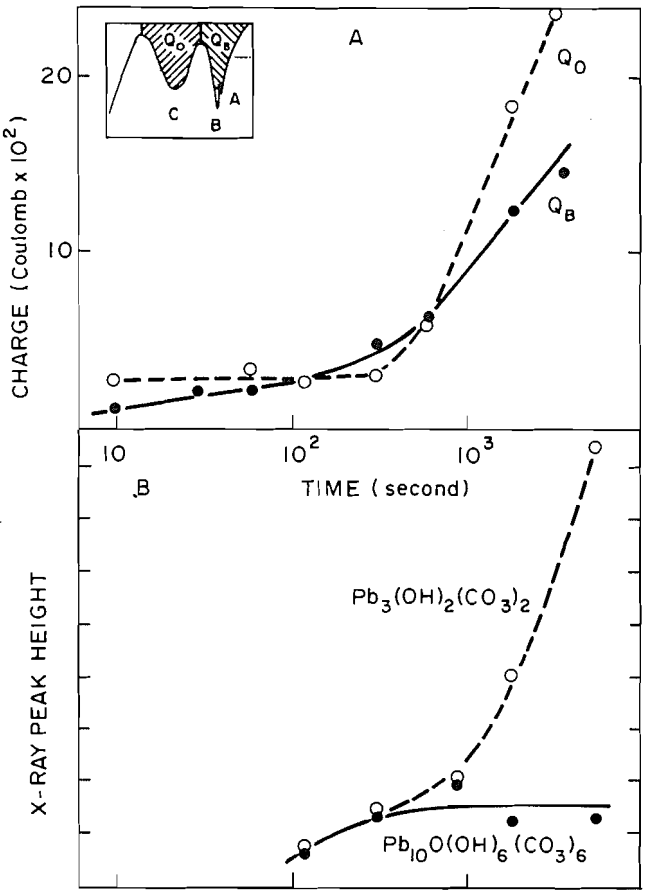

FIG. 9. (A) Charges Q_B and Q_O (obtained as indicated in the inset and outlined in Fig. 1) as a function of the time of potentiostatic oxidation at −0.640 V (vs. SCE) in 1.0 mol L^{-1} K_2CO_3 (pH = 12.0) at ω = 1.67 Hz. (B) X-ray peak heights for plumbonacrite and hydrocerussite as a function of the time of oxidation at −0.640 V (vs. SCE) in 1.0 mol L^{-1} K_2CO_3 (pH = 12.0) at ω = 1.67 Hz.

in hydrocerussite (as opposed to plumbonacrite) that would confer on this phase a lower sensitivity.

A possible explanation for this apparent difference in sensitivity is that the hydrocerussite is formed at local sites on the plumbonacrite surface and does not form a complete, coherent surface layer. Such a situation is consistent with the deposition of hydrocerussite from the solution, a process that would be expected to involve nucleation and growth at widely dispersed sites on the surface.

When oxidation is performed at −0.640 V (i.e., anodic to the main oxidation peak of Fig. 1), we obtain the data of Fig. 9. The charges due to reduction of the two layers (peaks A + B, Q_B, and peak C, Q_O), obtained by integration of the CSVs, increase with the duration of oxidation. Also the peak in the CSV for the reduction of the base layer contains both peaks A and B (as indicated in the inset to Fig. 9A), even for the shortest oxidation (10 s). The XRD results, Fig. 9B, show that plumbonacrite and hydrocerussite are both formed at short oxidation times. As the two films thicken, Fig. 9A, the amount of hydrocerussite increases substantially, whereas the XRD peak height for plumbonacrite levels off at approximately the same value as observed at −0.726 V. This behaviour suggests that both phases are formed initially, but the thickening of both layers involves mainly hydrocerussite formation. We conclude that the base layer formed at −0.640 V is composed of two

TABLE 1. Phases observed on a lead electrode by X-ray diffraction after potentiostatic oxidation in 1.0 mol L^{-1} K_2CO_3 (pH = 12, ω = 1.67 Hz) for 30 min at various potentials

E, V (vs. SCE)	Phase
−0.74	P only
−0.72	P > HC
−0.68	P ~ HC
−0.64	HC > P

P = Plumbonacrite ($Pb_{10}O(OH)_6(CO_3)_6$); HC = Hydrocerussite ($Pb_3(OH)_2(CO_3)_2$).

phases: plumbonacrite, reduced at peak B, and hydrocerussite, reduced at peak A. Again, peak C is attributed to hydrocerussite deposited from solution.

This conclusion is supported by the data of Table 1, which shows the nature of the predominant phase (based on XRD) after oxidations for 30 min at four separate potentials within the anodic peak region. The composition of the surface film changes from totally plumbonacrite, at the foot of the anodic peak, to mainly hydrocerussite on the anodic side of the peak. The presence of PbO was not detected in any of our diffractograms.

Discussion

The electrochemical and XRD data show that two distinct layers are formed: a base layer composed of two separate phases, plumbonacrite and hydrocerussite (depending on the potential), and a deposited layer of hydrocerussite. Our evidence for the formation of a deposited layer is supported by the response of the reduction peak C to variations in scan rate and, in particular, electrode rotation rate. The decrease in size of peak C with increasing electrode rotation rate demonstrates that the extent of formation of this film is determined by the concentration of Pb^{2+} species close to the electrode surface. Solution transport and deposition processes compete for soluble Pb^{2+} with film deposition predominating at the lower electrode rotation rates.

The formation of a dual-phase base layer was also claimed by Buchanan *et al.* (10) for lead oxidation in 0.1 mol L^{-1} $Na_2B_4O_7$ at pH = 9.0. The nature of these phases was not determined, but lead metaborate ($Pb(BO_2)_2$) and lead tetraborate (PbB_4O_7) were mentioned as two possibilities. The formation of a deposited layer was not observed. For potentials anodic to the peak shown in Fig. 2 of their paper, these authors observed a rise in the current on the anodic scan and a third reduction peak on the reverse scan, at a potential more positive than peak A. This peak was attributed to the reduction of PbO, identified as tetragonal PbO by photocurrent spectroscopy. We observed a slight rise in current for potentials greater than −600 mV, Fig. 2, but no corresponding reduction peak was observed.

The falling current transients observed at potentials around the foot of the main anodic peak (Fig. 1) show that the base layer is rapidly formed at all potentials ≥ −790 mV. There does not appear to be a potential region within which reversible dissolution of Pb^{2+} occurs from a film-free surface. The XRD results of Fig. 8, and the CSVs of Fig. 7, show that this base layer is plumbonacrite. The fact that the thickness of this layer, as determined from Q_B, is almost independent of scan rate (Fig. 3) and electrode rotation rate (Fig. 5B) indicates direct, solid-state growth on the electrode surface.

Can. J. Chem. Downloaded from www.nrcresearchpress.com by 196.1.178.254 on 09/07/12
For personal use only.

Can. J. Chem. Downloaded from www.nrcresearchpress.com by 196.1.178.254 on 09/07/12
For personal use only.

At potentials in the range $-790 < E < -740$ mV, the base layer thickens but remains plumbonacrite. The appearance of hydrocerussite at longer times (reduced at peak C, Fig. 7) indicates a slow conversion of this plumbonacrite base layer. This process appears to involve dissolution and reprecipitation, since the extent of hydrocerussite formation is very dependent on the electrode rotation rate. This is demonstrated for voltammetric conditions by the data of Fig. 5, which showed that there is competition for the dissolved Pb^{2+} between the deposition of hydrocerussite and transport to the bulk of solution.

The conversion of plumbonacrite to hydrocerussite has been shown to occur rapidly under the conditions of our experiment (8). The fact that the conversion to hydrocerussite, the thermodynamically stable phase under our conditions, is not accompanied by the disappearance of plumbonacrite, indicates that the plumbonacrite base layer is maintained by further anodic oxidation of the lead. The process can be represented by the following sequence of reactions:

[3] $10Pb + 8OH^- + 6CO_3^{2-} \xrightarrow{k_1(E)} Pb_{10}O(OH)_6(CO_3)_6 + H_2O + 20e$

[4] $Pb_{10}O(OH)_6(CO_3)_6 + H_2O + 7OH^- + 4CO_3^{2-} \xrightarrow{k_2(E)} 5\{Pb(OH)_3^-\}_{surf} + 5\{Pb(CO_3)_2^{2-}\}_{surf}$

[5] $2\{Pb(OH)_3^-\}_{surf} + \{Pb(CO_3)_2^{2-}\}_{surf} \xrightarrow{k} Pb_3(OH)_2(CO_3)_2 + 4OH^-$

[6] $\{Pb(OH)_3^-\}_{surf} + \{Pb(CO_3)_2^{2-}\}_{surf} \xrightarrow{\beta_T} \{Pb(OH)_3^-\}_{sol'n} + \{Pb(CO_3)_2^{2-}\}_{sol'n}$

In reactions [3]–[6], $k_1(E)$ and $k_2(E)$ represent potential-dependent rate constants for the solid-state growth of the base layer and its field-assisted dissolution, respectively; k is the potential-independent constant for the deposition process; β_T is a mass-transport constant and is given by D/δ under rotating disk conditions, where D is the diffusion coefficient for the dissolved Pb^{2+} species[4] and δ is the thickness of the diffusion layer ($\propto \omega^{-1/2}$); $\{\ \}_{surf}$ and $\{\ \}_{sol'n}$ designate surface and bulk concentrations, respectively. Since the electric field will be across the base layer on the electrode surface, the driving force for dissolution is the transport of Pb^{2+} species across this film.

Obviously, reactions [3]–[6] summarize a more detailed, but undetermined, series of reactions. The species $Pb(OH)_3^-$ and $Pb(CO_3)_2^{2-}$ are used because these are the predominant solution species present in 1.0 mol L^{-1} carbonate at pH = 12 (8). Reaction [4] is written as involving equal amounts of these species because they will be present in approximately equal concentrations in our solutions.

At higher potentials, around the maximum of the anodic peak in Fig. 1 (~ -700 mV), a second phase, hydrocerussite, is formed as part of the base layer. Since this layer is reduced at peak A, before the reduction of plumbonacrite at peak B, it is probably present as a layer on top of the initially formed plumbonacrite. The close crystallographic similarity between these two phases (8) may promote the epitaxial crystallization of hydrocerussite on plumbonacrite. Since this layer is, in effect, a continuation of the base-layer growth process, it can be considered a primary oxidation product of the lead, its growth being supported by the transport of Pb^{2+} species through the underlying plumbonacrite layer under the influence of the large electric field; i.e.,

[7] $3Pb + 2OH^- + 2CO_3^{2-} \rightarrow Pb_3(OH)_2(CO_3)_2 + 6e$

The presence of plumbonacrite directly on the electrode surface suggests this phase is stabilized by the high rate of supply of Pb^{2+} species.

[4] $D_{Pb(OH)_3^-}$ and $D_{Pb(CO_3)_2^{2-}}$ may have slightly different values.

Acknowledgements

We are grateful to P. Taylor and A. M. Duclos for help with the recording and interpretation of the X-ray diffraction patterns, and for many fruitful discussions throughout the course of this work.

1. T. E. Rummery and E. L. J. Rosinger. *In* Proc. Int. Conf. Nucl. Fuel Waste Management, Winnipeg, Man. Sept. 1982. Canadian Nuclear Society, Toronto, Ont. 1982. p. 6.
2. B. M. Ikeda and C. F. Clarke. *In* Proc. 2nd Int. Conf. Nucl. Fuel Waste Management, Winnipeg, Man. Sept. 1986. Canadian Nuclear Society, Toronto, Ont. 1986. p. 605.
3. P. Mani Mathew. *In* Proc. 2nd Int. Conf. Nucl. Fuel Waste Management, Winnipeg, Man. Sept. 1986. Canadian Nuclear Society, Toronto, Ont. 1986. p. 558.
4. D. W. Shoesmith and M. G. Bailey. *In* The corrosion performance of nuclear fuel waste containers. Atomic Energy of Canada Limited Technical Record, TR-340, July 1985. p. 95.
5. A. M. Beccaria, E. D. Mor, G. Bruno, and G. Poggi. Br. Corros. J. **17**, 87 (1982).
6. V. G. Levich. Physicochemical hydrodynamics. Prentice Hall, Englewood Cliff, NJ. 1966.
7. D. W. Shoesmith, S. Sunder, M. G. Bailey, and D. G. Doern. *In* Passivity of metals and semiconductors. Proc. 5th Int. Symp. Passivity, Bombannes, France. 1983. *Edited by* M. Froment. Elsevier, Amsterdam. 1983. p. 125.
8. P. Taylor and V. J. Lopata. Can. J. Chem. **62**, 395 (1984).
9. M. H. Brooker, S. Sunder, P. Taylor, and V. J. Lopata. Can. J. Chem. **61**, 494 (1983).
10. J. S. Buchanan, N. P. Freestone, and L. M. Peter. J. Electroanal. Chem. **182**, 383 (1985).

A tensammetric study of polyacrylamides, including their determination

TRUIS SMITH-PALMER,[1] BYRON R. WENTZELL, AND JOHN C. DONINI[2]
Chemistry Department, Saint Francis Xavier University, Antigonish, N.S., Canada B2G 2E2

AND

ROBERT J. JERRARD
Mathematics Department, Saint Francis Xavier University, Antigonish, N.S., Canada B2G 2E2

Received August 25, 1987[3]

TRUIS SMITH-PALMER, BYRON R. WENTZELL, JOHN C. DONINI, and ROBERT J. JERRARD. Can. J. Chem. **66**, 2658 (1988).

Phase-sensitive tensammetry is shown to be a convenient and useful way to analyse polyacrylamides and associated derivatives (pams) in dilute aqueous solutions. Standard curves were obtained with ranges varying from 9 to 25 ppm and limits of detection varying from 0.7 to 2 ppm. Ways to change the range and sensitivity are discussed and demonstrated. Typical interferences and their effects are tabulated, and the analysis of pams in coal washings is discussed. The analysis of certain mixtures of polyacrylamides is shown to be possible.

TRUIS SMITH-PALMER, BYRON R. WENTZELL, JOHN C. DONINI et ROBERT J. JERRARD. Can. J. Chem. **66**, 2658 (1988).

On a démontré que la tensamétrie sensible à la phase est une méthode appropriée et utile d'analyser des solutions aqueuses diluées de polyacrylamides et des dérivés qui leur sont associés (pams). On a obtenu des courbes standards pour des concentrations allant de 9 à 25 ppm et des L.D.D allant de 0,7 à 2 ppm. On discute des méthodes qui permettraient de modifier la limite de détection ainsi que la sensibilité et on en fait la démonstration. On présente un tableau résumant les interférences typiques ainsi que leurs effets et on discute de l'analyse des pams dans les lavages de charbon. On démontre que l'analyse de certains mélanges de polyacrylamides est possible.

[Traduit par la revue]

Introduction

Polyacrylamides and polyacrylic-based polymers (pams) in ppm concentrations are widely used as flocculating agents in coal and other mineral washing operations. It would be of interest to be able to determine the residual levels of these polymers after flocculation has occurred. A fast analytical technique would also aid research into the mode of interaction of polyacrylamides with particles and salts, a poorly understood phenomenon.

We recently reported the determination of several polyacrylamide-based polymers by polarographic maximum suppression in mercury (II) solutions (1). The main disadvantage of this method is that it is non-specific; it cannot be used to analyse one pam in the presence of other pams, or in the presence of other types of surfactant. The clean-up step that is required prior to analysis is not a problem when determining anionic or neutral pams, but the loss of cationic pams during chromatography on cation exchange resins and Sephadex is significant.

Leung *et al.* (2) have reported a method of analysis of pams in coal washings involving ultrafiltration followed by HPLC. The method is rather involved and time-consuming, it produces a low percentage of recovery, and its applicability to cationic pams is not clear.

A second electrochemical method that has been used in the determination of surfactants is tensammetry. The general shape of the capacitive current–potential (tensammetric) curves is largely dependent on the anions present. In the absence of specific adsorption at the electrode surface U-shaped curves are observed with the minimum centred at the potential of zero charge (pzc). When there is specific adsorption of anions such as chloride, capacitance humps are observed. The sizes and shapes of these humps have been related to the structure and polarizability of the anion (3, 4). The capacitive current is lowered by the adsorption of surfactants such as sodium dodecyl sulphate (S.D.S.) onto the hanging mercury drop electrode (HMDE). On either side of this dip resulting from the lowering of the surface current, adsorption/desorption peaks are observed. Presumably the hydrocarbon tails of S.D.S. can "squeeze out" water molecules at the electrode surface, thus lowering the capacitance. Most analytical work using tensammetry has involved the analysis of similar detergent-type surfactants.

Dunsch *et al.* reported that polyacrylamide adsorption in aqueous solution had little effect on double layer capacitance (5). The absence of a marked depression of the capacitive current can be explained in terms of the structure of pams. On every second carbon of the polyacrylamide backbone there is a polar amide group which can interact with water molecules, thus preventing them from forming a condensed film and explaining the absence of a marked depression of the capacitive current.

However, contrary to Dunsch, Itoh found that polyacrylamide changed the size of the capacitance hump for perchlorate (6) and this suggested a way for us to analyse pam concentrations.

Tensammetric curves can be examined without interference from faradaic processes by means of a phase-selective detector (7–9). Most surface-active substances are adsorbed only over a small range of potentials, and this suggested a way of distinguishing different components of a mixture.

In this paper, we describe the use of phase-sensitive tensammetry to analyse pam concentrations in clean water and in coal washings, to study the adsorption of pams onto coal tailings and to investigate the analysis of pams in mixtures.

Experimental

Polarograms were obtained using a Princeton Applied Research Model 174A Polarographic Analyzer and a Model 303 static mercury drop electrode (SMDE) in conjunction with a PAR Model 174/50 AC

[1]To whom all correspondence should be addressed.

[2]Present address: Devon Coal Research Centre, P.O. Bag 1280, Devon, Alta., Canada T0C 1E0.

[3]Revision received June 13, 1988.

Can. J. Chem. Downloaded from www.nrcresearchpress.com by 196.1.178.254 on 09/07/12
For personal use only.

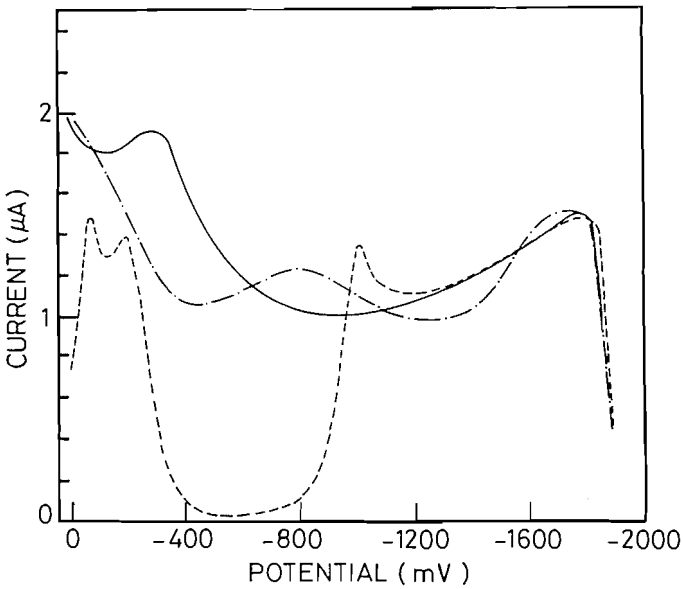

FIG. 1. Tensammetric current–potential curves for — 0.1 *M* KCl, --- 20 ppm S.D.S. in 0.1 *M* KCl, ····· 40 ppm polyacrylamide in 0.1 *M* KCl.

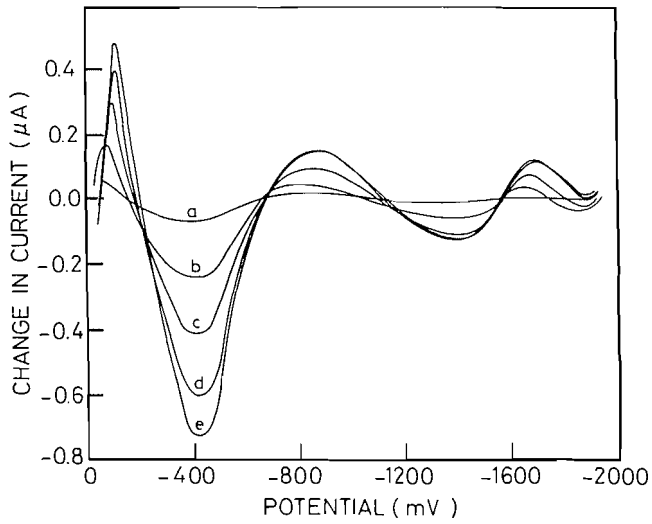

FIG. 2. Change in capacitive current versus potential for the following concentrations of polyacrylamide in 0.25 *M* KCl: (*a*) 1 ppm, (*b*) 4 ppm, (*c*) 8 ppm, (*d*) 12 ppm, (*e*) 16 ppm.

Polarographic Analyzer Interface and a PAR Model 122 Lock-In Amplifier. The analog output of the polarograph was digitized using an Apple IIe microcomputer with Interactive Microware software (Lab Data Manager, Scientific Plotter) and hardware (ADALAB Interface Card, ADA-AMP Instrumentation Amplifier). A modulation amplitude of 10 mV (p-p) at 200 Hz was used. The phase of the lock-in amplifier's phase-sensitive detector was adjusted to be 135 degrees away from the phase of the reference modulation to minimize faradaic currents. The HMDE and a scan rate of 5 mV/s were used.

Tensammetric curves were initially run scanning from 0 V. However, standard curves were normally obtained from scans starting at −600 mV, after a chosen hold time. Variations on this procedure are discussed in the next section. All potentials reported are relative to a silver – silver chloride reference electrode containing KCl (saturated).

Polyacrylic acid was purchased from Aldrich Chemical Company Inc., Milwaukee, WI. The polyacrylamides (1), polyalkylamine (10), and thickener feed were provided by the Coal Research Lab, Energy, Mines and Resources, Edmonton. Coal washings were prepared from four different raw coal samples as described previously (1).

Limits of detection (LOD) were calculated by taking three times the standard deviation of the blank. The range was considered to be the maximum concentration of pam that could be analysed.

Results and discussion

The tensammetric curve for chloride shows a hump centred at −300 mV because of specific adsorption of the chloride ions (Fig. 1*a*). A typical surfactant such as S.D.S. gives the curve shown in Fig. 1*b*. There is no chloride hump but rather a deep well indicating a decrease in capacitance as discussed in the Introduction. Although polyacrylamide cannot squeeze out the water molecules from the electrode surface and thus does not show a deep well in its tensammetric curve (Fig. 1*c*), it can displace adsorbed chloride ions and thus the chloride hump is absent from the curve. However, unlike the tensammetric curve for S.D.S., the curve for polyacrylamide has no adsorption/ desorption peaks; these are the usual way to measure concentration. Although for KCl and S.D.S. identical tensammetric curves were obtained using a dropping mercury electrode (DME) or a HMDE, this was not the case for polyacrylamide. The chloride hump was still present in the tensammetric curve for polyacrylamide obtained using a DME, even with high concentrations of polymer. Use of the HMDE is thus mandatory for the analysis of pams. A difference tensammetric curve (Fig. 2), obtained by subtracting the curve for KCl from the curve for polyacrylamide alone, shows up the effects of the polyacrylamide on the capacitance more clearly. The broad peak at −800 mV may be attributed to reorientation of the adsorbed molecules as the charge on the electrode changes. The curves in Fig. 2 were each obtained in two portions by scanning from −600 mV after a 2 min hold time. This potential is close to that used by Bednarkiewicz *et al.* and is in the potential region where maximum absorption occurs (8). These curves demonstrate the effect of concentration. Reading the change in the capacitive current at −350 mV, where the differences were large, enabled the standard curve shown in Fig. 3 to be constructed. The LOD was 0.8 ppm and the range was 16 ppm (0.8–16 ppm). The difference tensammetric curve obtained for a non-ionic polymer, Praestol 2810/73, was almost identical to that for polyacrylamide and a standard curve could be obtained in the same way (0.8–16 ppm). The difference tensammetric curve for an anionic pam with about 25% charge density, Praestol 2900/73, had the same general shape as that of the non-ionic polymers, but the troughs and humps were slightly shifted to less negative potentials. A standard curve could be constructed in the same way (0.7–9 ppm). Tensammetric curves were also obtained in acidic (0.1 *M* KCl, 0.01 *M* HCl) and basic (0.1 *M* KCl, 0.01 *M* KOH) solutions to determine the effect of ionization of the carboxyl groups. The peaks shifted somewhat and the difference tensammetric curve for the acidic solution showed a much larger trough at −400 mV, attributed to stronger adsorption of the unionized groups. In the difference tensammetric curve of the basic solution there was a pronounced hump at −700 mV. The tensammetric curves for polyacrylic acid, which could be classified as an anionic pam with a charge density of 100% (although with much smaller molecular weight than the other pams used), were even more affected by pH. At pH 6 the tensammetric curve for a 20 ppm polyacrylic acid solution resembled that of the supporting electrolyte alone, indicating that the polymer had little surface activity. This is no doubt due to its high solubility in the ionized state. At pH 3 the tensammetric curve for polyacrylic acid was that of a typical strongly adsorbed surfactant, with a marked depression in

Can. J. Chem. Downloaded from www.nrcresearchpress.com by 196.1.178.254 on 09/07/12
For personal use only.

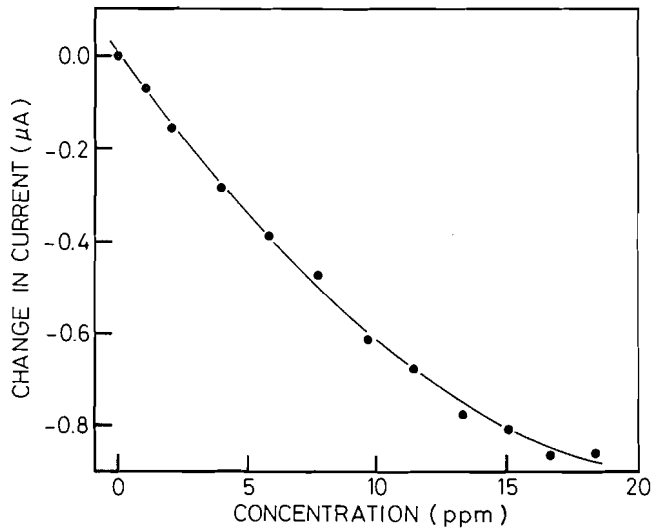

FIG. 3. Standard curve (change in current versus concentration) for polyacrylamide. Held at −600 mV for 2 min then scanned and the current read at −350 mV.

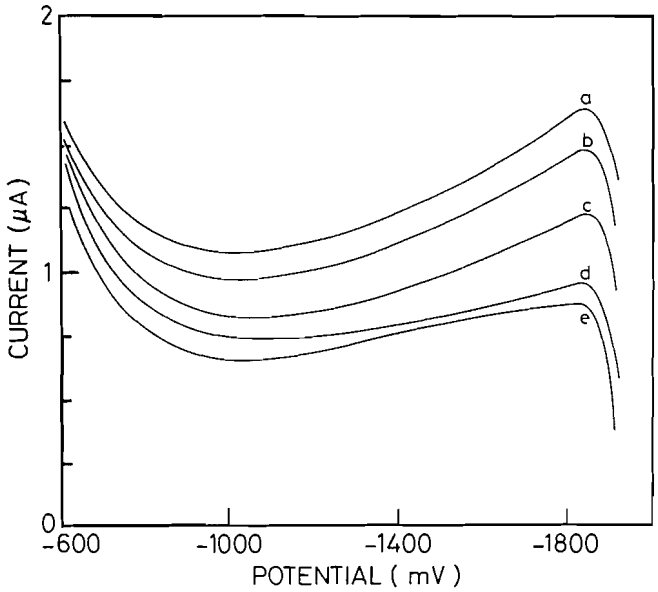

FIG. 4. Capacitive current versus potential curves for the following concentrations of Praestol 444k: (*a*) 0 ppm, (*b*) 2 ppm, (*c*) 6 ppm, (*d*) 9.5 ppm, (*e*) 13 ppm.

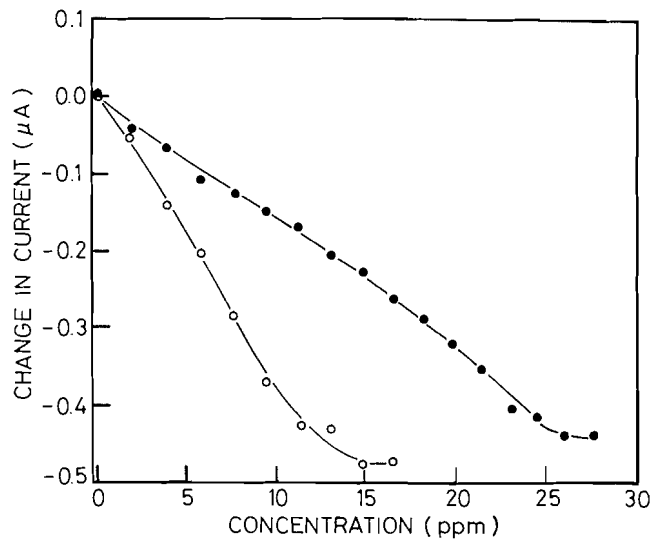

FIG. 5. Standard curves (change in current versus concentration) for Praestol 444k. ○ Held at −600 mV for 2 min, then scanned and the current read at −1600 mV. ● Scanned from −1200 mV with no hold and the current read at −1600 mV.

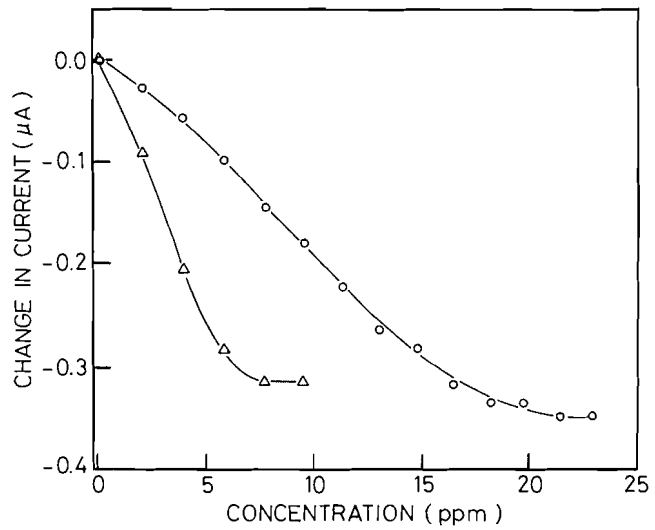

FIG. 6. Standard curves (change in current versus concentration) for Praestol 534k: ○ Held at −600 mV for 2 min, then scanned and the current read at −1450 mV. △ Held at −600 mV for 1 min with stirring, let sit for 0.5 min, then scanned and the current read at −1450 mV.

capacitive current from −400 to −1200 mV and a sharp desorption peak at −1400 mV. Itoh has reported a similar pH dependence for polyacrylic acid in ClO_4^- (6).

Since cationic polymers are more strongly adsorbed at negatively, rather than positively, charged electrodes; they yield curves which are distinctly different to the above. Thus the chloride capacitance hump was largely unaffected by the cationic polymers, while the capacitive current was lowered at voltages negative with respect to the pzc. Typical tensammetric curves are shown in Fig. 4 for a cationic pam with close to 100% charge density, Praestol 444k. A standard curve was plotted using the difference current measured at −1600 mV after a 2 min hold time at −600 mV and is shown in Fig. 5 (0.7–11 ppm). Similar standard curves were able to be plotted for cationic pams of lesser charge densities, but the slope of the curves decreased with the charge density of the pam in question (compare Figs. 5 and 6), affecting the LOD's and the ranges. The slope of the curves also changed as the amount of preconcentration of pam onto the Hg drop was changed. The preconcentration was decreased (and thus the slope decreased) by decreasing the hold time and/or the length of the scan. For example, in Fig. 5 the range of the standard curve, and therefore of the analytical method, was increased from 11 to 23 ppm by not using a hold time and by starting the scan at −1200 mV rather than −600 mV. However, this is at the expense of the sensitivity and the LOD (increased to 1.3 ppm). The preconcentration was increased by using a hold time before a scan was started, and even more by stirring the solution during the hold time. This is shown in Fig. 6 for a cationic pam with around 70% charge density, Praestol 534k. The LOD went from 2 to 0.5 ppm as the range went from 20 to 7 ppm. For this polymer, the difference current was measured at −1450 mV rather than

Can. J. Chem. Downloaded from www.nrcresearchpress.com by 196.1.178.254 on 09/07/12
For personal use only.

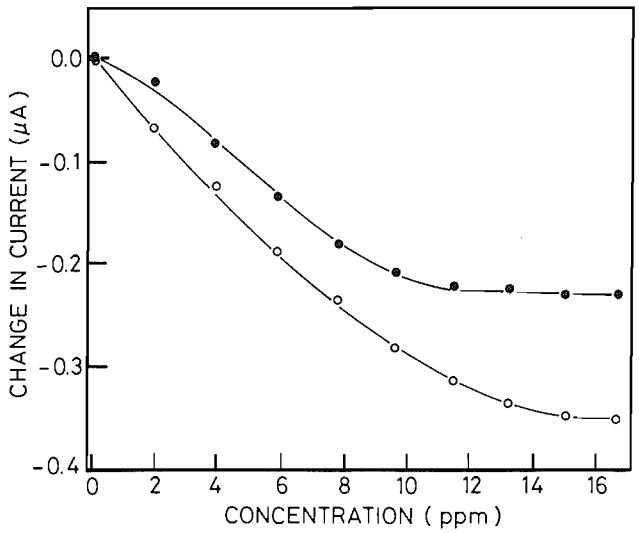

FIG. 7. Standard curves (change in current versus concentration) for a polyalkylamine after scanning from −600 mV with no hold time. ● Current read at −1450 mV; ○ current read at −1100 mV.

TABLE 1. Interferences for Praestol 2810/73* determination

Substance	Concentration	Apparent [P 2810/73] (ppm)
KCl	5.0 m*M*	5.0
K_2SO_4	4.0 m*M*	5.0
K_2HPO_4	5.0 m*M*	5.0
Fe^{2+}	10 ppm	4.1
Cu^{2+}	10 ppm	3.3
Humic acid	1 ppm	10.8
S.D.S.	0.2 ppm	9.9
Triton X-100	0.2 ppm	9.8

*5.0 ppm in 0.25 *M* KCl; initial voltage = −600 mV; hold time of 2 min; current measured at −350 mV.

−1600 mV because the differences were slightly larger at that voltage. The tensammetric curves for a polyalkylamine (10) were of the same basic shape but were generally shifted to more positive potentials. A standard curve was plotted using the current difference at −1100 mV (0.7 to 15 ppm); reading the difference at −1450 mV leads to a less useful curve (2 to 11 ppm) (Fig. 7). Thus it can be seen that the analytical parameters can be changed to alter the range and LOD of an analysis, depending on the levels of polymer being analyzed. The LOD and precision depend on the reproducibility of current measurements, and the capillary needs to be cleaned and siliconized regularly especially when using cationic pams. A typical precision of 0.3 ppm at the 95% confidence level was obtained for P534 (1 min stirring before analysis). Using a phase angle of 90° increases the sensitivity by increasing the size of the measured current by $\sqrt{2}$. However, at this angle there is also some contribution from faradaic current, thus leading to problems of interferences if reducible species are in solution with the polymer. Some species, particularly those that are surface-active, can interfere with the analysis even at the 135° phase angle. Tables 1–3 show the effect of a variety of salts and surfactants on the analysis of three pams (non-ionic, anionic, and neutral, respectively). These interferences were removed using chromatography on small precolumns before the tensammetric analysis. Recoveries are excellent for anionic and neutral

TABLE 2. Interferences for Praestol 2900/73* determination

Substance	Concentration	Apparent [P 2810/73] (ppm)
KCl	5.0 m*M*	5.0
K_2SO_4	4.0 m*M*	5.0
K_2HPO_4	5.0 m*M*	5.0
$CaCl_2$	5.0 m*M*	5.0
Zn^{2+}	5 ppm	5.0
Fe^{2+}	10 ppm	2.7
Cu^{2+}	10 ppm	0.9
Humic acid	1 ppm	12.3
S.D.S.	0.2 ppm	11.4
Triton X-100	0.2 ppm	8.7

*5.0 ppm in 0.25 *M* KCl; initial voltage = −600 mV; hold time of 2 min; current measured at −350 mV.

TABLE 3. Interferences for Praestol 444k* determination

Substance	Concentration	Apparent [P 444k] (ppm)
KCl	10 m*M*	5.0
K_2HPO_4	5 m*M*	5.0
Zn^{2+}	5 ppm	5.0
Fe^{2+}	10 ppm	2.3
Humic acid	5 ppm	4.5
	10 ppm	0.0
S.D.S.	1 ppm	4.3
	2 ppm	0.6
Triton X-100	0.1 ppm	6.4
	0.2 ppm	10.3

*5.0 ppm in 0.25 *M* KCl; initial voltage = −600 mV; hold time of 2 min; current measured at −1600 mV.

pams but lower for cationic pams (1). However, potential interferences generally had less effect on cationic analyses (compare Tables 1, 2, and 3), and in many cases of real samples of interest to us, no pretreatment was necessary before the analysis of cationic pams. For example, the tensammetric curves for four coal washings, a thickener feed supernatant and tap water containing humic acid were run, and only those for the Lingan coal washings showed interferences in the region used for analysis of cationic pams. (The Lingan coal washings were very acidic and contained high levels of iron.) The standard curves for cationic pams prepared in the other waters mentioned were identical to those prepared in pure water. Interferences were found in the region of these curves that are used for the analysis of anionic and neutral pams, but removal of these was quick and efficient. Thus for many coals, tensammetry provides a quick and facile method with which to analyse for pams in wash and waste waters. To demonstrate an application of this method, we include results obtained from a study of the absorption of cationic polymers onto thickener feed (mostly coal fines and clay). The solids in the slurry are generally negatively charged and thus the binding capacity of the slurry for cationic polymers is high. The binding increased linearly (slope = 0.8) with the amount of pam added, but the experiment was stopped before a binding maximum was reached (Fig. 8).

The tensammetric curves for mixtures of polyacrylamides were examined to see if it would be possible to distinguish the individual components. The difference tensammetric curves for a solution of 5 ppm Praestol 2810/73 and one containing

Can. J. Chem. Downloaded from www.nrcresearchpress.com by 196.1.178.254 on 09/07/12
For personal use only.

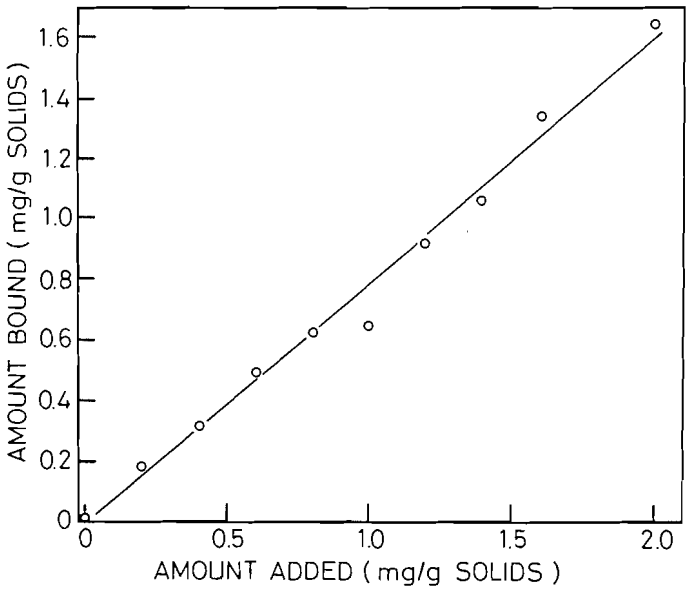

FIG. 8. Amount of Praestol 444k bound to thickener feed versus the amount of Praestol 444k added.

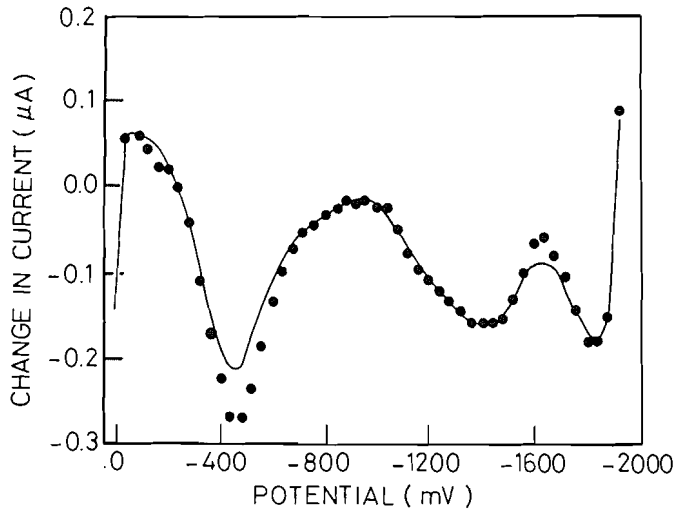

FIG. 9. Difference polarograms (change in current versus potential for 5 ppm Praestol 2810/73 (---) and for 5 ppm Praestol 444k (—).

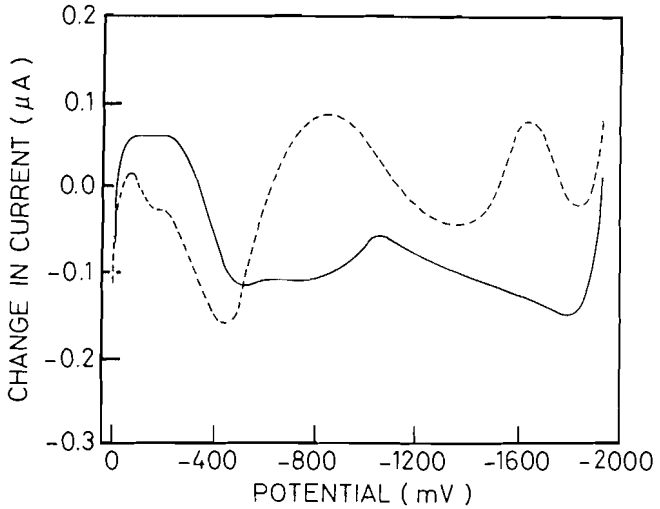

FIG. 10. Measured (—) and calculated (●) difference polarograms for a solution containing 5 ppm Praestol 2810/73 + 5 ppm Praestol 444k.

TABLE 4. Comparison between prepared and experimentally determined concentrations

Prepared concentrations (ppm)			Experimentally determined concentrations (ppm)		
P2810	P2900	P444k	P2810	P2900	P444k
7.9		1.5	7.0		1.2
6.0		2.0	5.4		1.3
5.9		4.0	5.4		3.2
4.0		2.0	3.1		1.3
4.0		4.0	3.9		3.5
4.0		6.0	3.8		5.4
2.0		2.0	2.5		2.0
2.0		8.0	3.0		8.2
4.0	5.0		2.9	6.5	
3.9	9.9		3.7	10.3	
6.9	6.9		6.2	6.2	
6.9	4.0		6.9	4.0	
9.9	4.0		10.5	4.0	

*Initial voltage = −600 mV; no hold time.

5 ppm Praestol 444k were added arithmetically and the resulting tensammetric curve was found to be almost identical to the experimentally determined difference tensammetric curve for a solution containing both (Fig. 9). Since the tensammetric curves of the individual components were quite different (Fig. 10), it should be possible to resolve the two components of the mixture mathematically. With higher concentrations of polymers (enough to completely cover the electrode) the tensammetric curves of mixtures were not additive and only the more strongly adsorbed component of a mixture was adsorbed. For a solution containing 40 ppm Praestol 2810/73 plus 40 ppm Praestol 444k the difference tensammetric curves resembled that of the non-ionic polymer where the electrode was positively charged (between 0 and approximately −500 mV), whereas at more negative voltages the tensammetric curves resembled that of the cationic polymer. Thus as the voltage was scanned past the potential of zero charge on the electrode the cationic polymer displaced the nonionic one at the electrode surface.

Similarly the effects of Praestol 2810/73 and Praestol 2900/73 were additive at low concentrations, and the difference tensammetric curves of the individual polymers showed distinctive differences at potentials between −1000 mV and −1900 mV. This suggested that mixtures of these should also be able to be resolved mathematically.

To demonstrate this, various prepared mixtures were run and experimental and actual concentrations were compared (Table 4). Measurements of the change in capacitive current at two potentials (−350 mV and −1340 mV for mixtures of P2810 and P2900, and −350 mV and −1600 mV for mixtures of P2810 and P444k) were used to prepare standard curves for each polymer, and then the concentration of each polymer was determined by solving the appropriate simultaneous equations. The potentials were chosen so that the difference current at at least one potential would be chiefly due to only one component. Standard curves obtained by tensammetric analysis are generally not linear, but for the concentration ranges over which mixtures of pams are additive, linear concentration curves were obtained (0–14 ppm for P2810, 0–12 ppm for P2900 and

Can. J. Chem. Downloaded from www.nrcresearchpress.com by 196.1.178.254 on 09/07/12
For personal use only.

P444k). Thus the solving of the simultaneous equations was trivial.

The difference tensammetric curve of a solution containing 5 ppm Praestol 2900/73 and 5 ppm Praestol 444k and the tensammetric curve calculated as the sum of the two individual curves were quite different. The actual measured capacitive current changes were much less than those calculated. This agreed with our maximum suppression experiments (1) which found that interaction between oppositely charged polymers reduced their surface activity.

Conclusions

Phase-sensitive tensammetry is a useful method of analysis for pams even in many dirty systems. The parameters used to run the tensammetric curves (hold time, stirring or lack thereof, initial potential, and the potential at which the difference current is read) can influence the slope and range of the standard curves, and thus these can be optimized for particular analytical requirements.

The shape of the tensammetric curve yields information on the nature of the charge of the pam being studied, and at low concentrations the curves of all except oppositely charged polymers are additive.

Acknowledgement

This work was supported in part by a grant from Energy, Mines and Resources, Canada.

1. B. R. WENTZELL, T. SMITH-PALMER, and J. C. DONINI. Can. J. Chem. **65**, 557 (1987).
2. R. W. M. LEUNG, R. N. PANDEY, and B. S. DAS. Environ. Sci. Technol. **21**, 476 (1987).
3. M. A. V. DEVANTHAN and B. V. K. S. R. A. TILAK. Chem. Rev. **65**, 635 (1965).
4. D. C. GRAHAME. Chem. Rev. **41**, 441 (1947).
5. L. DUNSCH, U. FEIST, and J. MORGENSTERN. Acta Polym. **34**, 73 (1983).
6. N. ITOH. Bull. Soc. Sci. Photogr. Jpn. No. **16**, 24 (1966).
7. B. COSOVIC and V. VOJVODIC. Limnol. Oceanogr. **27**, 361 (1982).
8. E. BEDNARKIEWICZ, M. DONTEN, and Z. KUBLIK. J. Electroanal. Chem. **127**, 241 (1981).
9. H. JEHRING and W. STOLLE. Collect. Czech. Commun. **33**, 1670 (1968).
10. C. W. ANGLE and H. A. HAMZA. *In* Flocculation in biotechnology and separation systems. *Edited by* Y. A. Attia. Elsevier, Amsterdam. 1987.

Can. J. Chem. Downloaded from www.nrcresearchpress.com by 196.1.178.254 on 09/07/12
For personal use only.

Equilibria between Bi_2O_3 and Bi_5O_7I in aqueous solutions at 10–60°C, and in oxygen atmospheres at 550–800°C[1]

PETER TAYLOR[2] AND VINCENT J. LOPATA

Research Chemistry Branch, Atomic Energy of Canada Limited, Whiteshell Nuclear Research Establishment, Pinawa, Man., Canada R0E 1L0

Received February 24, 1988

PETER TAYLOR and VINCENT J. LOPATA. Can. J. Chem. **66**, 2664 (1988).

Equilibria between Bi_5O_7I and Bi_2O_3 have been measured with the solids in contact with aqueous solutions at 10–60°C, and with low-pressure oxygen (0.2–100 kPa) at 550–800°C. In the aqueous systems, iodide activities were measured as functions of pH and temperature. In the dry system, iodine partial pressures were measured spectrophotometrically while varying the temperature and oxygen partial pressure. The standard enthalpy of formation and entropy of α-Bi_5O_7I were derived from these measurements, and values for BiOI were also estimated. The results combine to give a self-consistent account of phase relations between Bi_5O_7I and Bi_2O_3 up to 800°C. Some equilibria involving BiOI are discussed briefly.

PETER TAYLOR et VINCENT J. LOPATA. Can. J. Chem. **66**, 2664 (1988).

On a mesuré l'équilibre entre le Bi_5O_7I et le Bi_2O_3 alors que les solides étaient en contact avec des solutions aqueuses, à 10–60°C ou de l'oxygène à basse pression (0,2 à 100 kPa), à des températures allant de 550 à 800°C. Dans les systèmes aqueux, on a mesuré les activités de l'iode en fonction du pH et de la température. Dans le système sec, on a fait appel à des méthodes spectrophotométriques pour mesurer les pressions partielles de l'iode tout en faisant varier la température ainsi que la pression partielle de l'oxygène. A l'aide de ces mesures, on a calculé l'enthalpie standard de formation ainsi que l'entropie du α-Bi_5O_7I et on a évalué les valeurs correspondantes pour le BiOI. On peut combiner les résultats pour obtenir une évaluation auto-cohérente des relations de phase entre le Bi_5O_7I et le Bi_2O_3, jusqu'à 800°C. On discute brièvement de quelques équilibres impliquant le BiOI.

[Traduit par la revue]

I. Introduction

The phase assemblage α-Bi_2O_3 + α-Bi_5O_7I has been considered as a candidate material for immobilizing radioactive iodine-129 (1, 2). This combination of solids can buffer the dissolved iodide activity, $\{I^-\}$, at low levels in non-acidic aqueous solutions, in accordance with equilibrium [1].

[1] $$Bi_5O_7I(s) + OH^-(aq) \rightleftharpoons (5/2)Bi_2O_3(s) + I^-(aq) + (1/2)H_2O(l)$$

$$K_1 = \{I^-\}/\{OH^-\} = K_{10} \text{ of ref. 1}$$

$$\log_{10} K_1 = -3.39 \pm 0.20 \text{ at } 25°C \text{ (1)}.$$

whence

$$\log_{10} \{I^-\} = -17.39 + pH$$

This equilibrium can not be sustained at pH < 6, because of the high solubility of Bi_2O_3 in acidic solution (3). In addition, α-Bi_5O_7I has reasonably high thermal stability; it decomposes in air above about 550°C (1, 2, 4, 5) by reaction [2].

[2] $$2Bi_5O_7I(s) + \tfrac{1}{2}O_2(g) \rightarrow 5Bi_2O_3(s) + I_2(g)$$

The purpose of the present work was to examine the relationship between K_1 and temperature, and to obtain more quantitative information on reaction [2]. Specifically, we wished to see if reaction [2] is reversible and, if so, determine K_2.

[3] $$K_2 = p(I_2)/[p(O_2)]^{1/2}$$

The fact that equilibria [1] and [2] involve the same pair of solid phases permits us to compare and interrelate measurements of K_1 and K_2. Note that $p(I_2)$ and $p(O_2)$ represent partial pressures, whereas pI and pOH represent the negative logarithms of aqueous ion activities (cf. pH).

Hereafter, the formulae Bi_2O_3 and Bi_5O_7I refer to the α forms, unless otherwise specified. The name bismuth oxide refers to Bi_2O_3 in the generic sense.

II. Experimental

(a) Preparative work

We previously found (1) that partial conversion of Bi_2O_3 to Bi_5O_7I gave a product that equilibrated with aqueous solutions in subsequent experiments more rapidly than a simple mixture of the two solids, presumably because the oxyiodide crystals had grown in intimate contact with the oxide. We have also found that Bi_2O_3 powder is sometimes contaminated with basic bismuth carbonates, $(BiO)_2CO_3$ and $(BiO)_4(OH)_2CO_3$ (6), probably from reaction with atmospheric CO_2 and moisture.

For the present study, we used Bi_2O_3 that was 20% converted to Bi_5O_7I. The Bi_2O_3 (BDH, reagent grade) was first washed with concentrated NaOH (~10 mol dm^{-3}) for 16 h, to eliminate traces of carbonate, then washed repeatedly with freshly deionized, distilled water, and contacted with the appropriate amount of KI solution (~10^{-2} mol dm^{-3}) for 16 h. At much lower iodide concentrations, formation of Bi_5O_7I is sometimes delayed, while other solid products are formed at higher concentrations. These aspects are discussed in a separate publication (7).

(b) Aqueous equilibrium measurements

In the following discussion, all activities of aqueous ions refer to an ideal standard state of unit molality. We have used the approximation that pH = $-\log \{H^+\}$, where pH is measured according to the normal operational definition for measurements with a glass electrode. Solutions were sufficiently dilute that molarity and molality could be considered identical at ambient temperatures, within the limits of accuracy of our measurements. Standard solutions were therefore prepared volumetrically. Activity corrections for standard iodide solutions were made using the Davies equation.

(i) Isothermal experiments

Measurements of K_1 at different temperatures followed essentially the same procedure as described in ref. 1. The Bi_2O_3 + Bi_5O_7I was suspended with stirring in nitrogen-purged, distilled deionized water in a thermostatted vessel (±0.5°C). Successive aliquots of NaOH were added, and the pH and iodide activity were monitored using ion-selective electrodes. These values typically stabilized within

[1] Issued as Atomic Energy of Canada Ltd. Report No. AECL-9647.
[2] Author to whom correspondence may be addressed.

Can. J. Chem. Downloaded from www.nrcresearchpress.com by 196.1.178.254 on 09/07/12
For personal use only.

15–30 min at 25°C, and 5 min or less at 55°C. Equilibration "from above", i.e., after addition of iodide rather than hydroxide, was much slower. Therefore, only a few such additions were made, to assure that the experimental measurements did indeed represent close approach to equilibrium. Each titration was terminated when the hydroxide concentration reached about 10^{-2} mol kg^{-1}, then the solid was filtered and washed, and at least one further titration was run.

Since these experiments each lasted 1–3 days, there was some drift in electrode response during each run (typically 5–10 mV, corresponding to 0.1–0.2 units of pH or pI). Iodide activity and pH measurements were based on the average of calibrations at temperature before and after each run. Reliable calibration is difficult with iodide solutions more dilute than 10^{-5} mol kg^{-1}, so it was necessary to extrapolate the iodide calibration line. Similarly, pH measurements were based on standard buffers with pH of 6.86 and 9.18 at 25°C, using standard pH values at each experimental temperature. In our experience, such extrapolations give reliable measurements (±0.1) of pI and pH up to about 7 and 11.5, respectively (1).

(ii) Variable-temperature experiment at constant pOH

The Bi_2O_3 + Bi_5O_7I was first allowed to equilibrate with dilute NaOH (pH ≃ 11.3), then the pH and iodide electrodes were monitored as the temperature was changed in the following sequence: 25, 35, 45, 55, 25, 60, 50, 40, 30, 25, 10, 15, 20, 25°C. The four measurements at 25°C showed little drift of either electrode during this experiment. Since the hydroxide activity remained constant (see below), the pH electrode was calibrated only at 25°C; the iodide electrode was calibrated at six temperatures between 10 and 55°C.

(c) Gas–solid equilibrium measurements

To investigate reaction [2] in detail, we constructed a simple low-resolution, dual-beam, single-detector spectrophotometer, with the sample beam passing through a tube furnace. In this instrument, light from a tungsten lamp was first passed through a manual monochromator, then split into a sample and reference beam. The reference beam passed outside, and parallel to, the furnace tube through which the sample beam was directed. The reference beam was deflected back across the sample beam by a fixed mirror, and a movable mirror allowed either the sample or reference beam to be directed to the photomultiplier – tube detector. Filters could be introduced between this last mirror and the detector, as described below (III(*b*)(*i*)).

The spectrophotometric cells were constructed of fused silica tubing (2-cm O.D., 10-cm path length), with the solid samples held in a side-arm outside the optical path. Previous calibration had shown that the cells would be contained within the central plateau of the furnace tube's temperature profile. The cells were filled with a known partial pressure of oxygen (up to ~30 kPa) on a vacuum line at ambient temperature (23 ± 1°C), and flame-sealed. Iodine vapor densities, and hence partial pressures, were determined from optical density measurements, as described below (III(*b*)(*ii*)).

III. Results and discussion

(a) Aqueous equilibria

(i) Isothermal experiments

Measurements of K_1, as a function of pH, at 25, 35, 45, and 55°C, are shown in Fig. 1; the 25°C data are taken from ref. 1. In all cases there is a slight systematic decrease in apparent K_1 with increasing pH. This most likely arises from residual calibration errors, or perhaps interference from dissolved O_2 or CO_2; if real, it would imply a deviation from the stated solid stoichiometries. The 45°C data deviate more at pH < 9.5 as the iodide electrode approaches its detection limit. We therefore used only the data obtained within the pH range 9.5–11.5 to calculate K_1 at each temperature, as shown in Table 1. Some deterioration in the quality of data is evident at 55°C.

These results confirm that the system behaved in accordance with eq. [1] at each temperature and indicate that $\log_{10} K_1$ increases by about 0.6 between 25 and 55°C. This corresponds to an enthalpy of reaction, $\Delta_r H^0$, of about 40 kJ mol^{-1}.

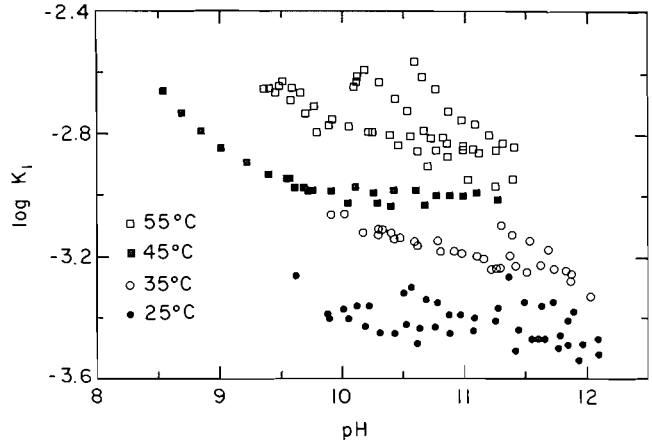

FIG. 1. Experimental measurements of $\log_{10} K_1$ (pK_w − pI − pH) in isothermal experiments at 25°C (from ref. 1), 35°C, 45°C, and 55°C vs. pH.

TABLE 1. Experimental measurements of K_1 at 10–60°C

T(°C)	$\log_{10} K_1$[a]	$\log_{10} K_1$[b]
10		−3.65
15		−3.59
20		−3.47
25	−3.39 ± 0.20[c]	−3.31, −3.27, −3.28, −3.34
30		−3.16
35	−3.16 ± 0.20	−3.04
40		−2.87
45	−2.99 ± 0.15	−2.75
50		−2.60
55	−2.76 ± 0.30	−2.47
60		−2.36

[a]Isothermal experiments; uncertainty limits are estimated accuracy.
[b]Variable temperature experiments; estimated precision ±0.07.
[c]From ref. 1.

(ii) Variable temperature experiment

The variable temperature experiment was designed to improve the precision of $\log_{10} K_1$ measurements, and hence the accuracy of the derived enthalpy of reaction, in three ways: (*a*) The experiment was shorter, reducing the opportunity for electrode drift, and allowing more accurate calibration; (*b*) Any variation arising from differences in sample history, or any other differences between isothermal runs at different temperatures, was eliminated; and (*c*) The hydroxide activity was sufficiently high to be effectively constant, eliminating the need for pH calibration at more than one temperature.

Four measurements at 25°C yielded an average pH value of 11.35 ± 0.05. The corresponding pOH of 2.65 ± 0.05 was used in the calculations at all temperatures, because the hydroxide concentration is much greater than the amount consumed or released by the adjustment of equilibrium [1] to temperature changes (<10^{-5} mol kg^{-1}). There is no other plausible cause for significant reversible variation of pOH with T (such as changes in speciation of bismuth (3)). The sequence of pH measurements at 25°C did not reveal any irreversible consumption of hydroxide by glass corrosion or absorption of CO_2.

Results of this experiment are presented in Table 1 and Fig. 2. The observation of a substantial, reversible variation of K_1 with temperature, without detectable hysteresis, indicates that equilibrium was achieved at each temperature. Linear regression

Can. J. Chem. Downloaded from www.nrcresearchpress.com by 196.1.178.254 on 09/07/12
For personal use only.

TABLE 2. Summary of thermodynamic data for bismuth oxyiodides at 298.15 K, 0.1 MPa

Parameter	Value			
	α-Bi_5O_7I		BiOI	
	Robie[a]	NBS[b]	Robie[a]	NBS[b]
Δ_fG^0, kJ mol^{-1}	−1266.1 ± 5.7[c]	−1266.5[c]	−247.8 ± 2.8[c]	−247.7[c]
Δ_fH^0, kJ mol^{-1}	−1453.8 ± 6.6	−1452.1	(est. −275 ± 6)	
S^0, J mol^{-1} K^{-1}	430 ± 44	437	(est. 127 ± 10)	

[a]Internally consistent with Robie *et al.* (8).
[b]Internally consistent with Wagman *et al.* (9).
[c]Based on equilibrium data from ref. 1.

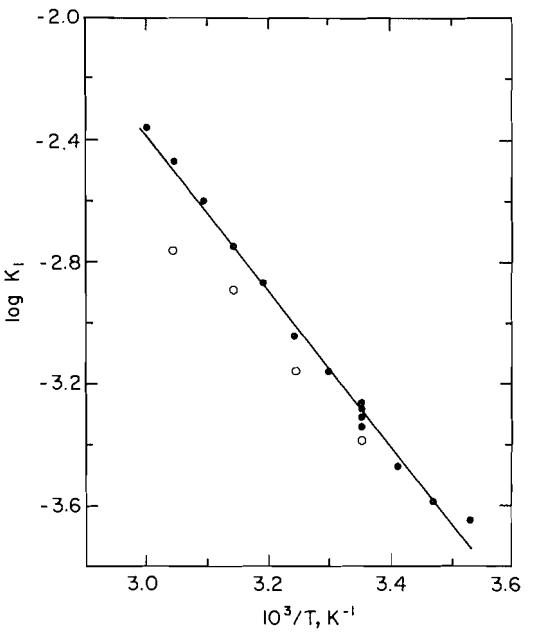

FIG. 2. Experimental measurements of $\log_{10} K_1$ (pOH − pI) from variable temperature experiment. Open circles represent mean values from isothermal experiments.

gave a relationship between $\log_{10} K_1$ and reciprocal absolute temperature.

[4] $$\log_{10} K_1 = (-3.082 \pm 0.010) - (2573 \pm 128)\left(\frac{1}{T} - 0.003275\right)$$

The slope, −2573 ± 128, corresponds to $\Delta_rH^0 = 49.3 \pm 2.5$ kJ mol^{-1} for reaction [1]. When combined with enthalpy data for Bi_2O_3, OH^-, I^-, and H_2O from ref. 8 (Table 3), this yields the enthalpy of formation of α-Bi_5O_7I.

[5] $$\Delta_fH^0(\alpha\text{-}Bi_5O_7I, s, 298\ K) = -1453.8 \pm 6.6\ kJ\ mol^{-1}$$

Using the previously reported Gibbs energy of formation, $\Delta_fG^0 = -1266.1 \pm 5.8$ kJ mol^{-1}, we then obtain the entropy of formation.

[6] $$\Delta_fS^0(\alpha\text{-}Bi_5O_7I, s, 298) = -630 \pm 42\ J\ mol^{-1}\ K^{-1}$$

whence

$$S^0_{298}(\alpha\text{-}Bi_5O_7I, s) = 430 \pm 45\ J\ mol^{-1}\ K^{-1}$$

These values are internally consistent with refs. 1 and 7. Alternative values, derived from the NBS thermodynamic database (9), are included in Table 2. The principal discrepancy between refs. 8 and 9 is in the enthalpy of formation of I^-(aq); the resulting difference in enthalpies for Bi_5O_7I (Table 2) is only a quarter of the experimental uncertainty.

The relationship between K_1 and T, expression [4], does not take into account any systematic bias in the variable temperature experiment. (This bias will include the slight discrepancy between pH and $-\log_{10}\{H^+\}$.) We have therefore combined the temperature dependence obtained here with the 25°C equilibrium data from ref. 1 ($\log K_1 = -3.39 \pm 0.20$). This combination is approximated by expression [7].

[7] $$\log_{10} K_1 = 5.24 - \frac{2573}{T} \pm 0.24 \quad (283 < T < 333\ K)$$

(b) Gas–solid equilibria

(i) Spectral measurements

The spectrophotometer was tested by measuring the spectrum of a fixed quantity of iodine vapour at various temperatures up to 780°C. The monochromator was manually scanned from 400 to 650 nm in increments of 5 or 10 nm. The resulting low-resolution peak profile was in broad agreement with published high-resolution spectra (10, 11), but, of course it lacked the fine structure displayed in the latter. The absorption feature extends from 420 to 650 nm, with a peak at about 510 nm and a shoulder near 545 nm.

The low-resolution spectrum of a fixed quantity of I_2 in an evacuated cell was insensitive to temperature changes up to 500°C, but it was difficult to measure at higher temperatures because of interference from furnace glow. We did not have sufficiently accurate control of $p(I_2)$ to measure the extinction coefficient, so partial pressure calculations were based on spectroscopic data in ref. 10, as detailed below.

The visible spectrum of I_2 vapor at ambient temperature has two distinct regions: a smooth continuum between 420 and 500 nm, and a region with vibrational fine structure between 500 and 650 nm (10, 11). Extinction coefficients vary considerably with total pressure within the latter region, but are insensitive to pressure in the former region (10, 11). Therefore, for the partial-pressure measurements, we removed the monochromator and introduced a narrow-band-pass filter at the receiving end (Andover Corporation filter: peak wavelength 481.8 nm; band width at half height, 9.4 nm). This had the added advantage of virtually eliminating interference from furnace glow.

The effective extinction coefficient, ϵ_{eff}, of iodine was calculated from the transmission profile of the filter and the corresponding portion of the I_2 spectrum. We obtained $\epsilon_{eff} = 335$ L mol^{-1} cm^{-1}, based on $\epsilon_{500} = 578$ L mol^{-1} cm^{-1} from

Can. J. Chem. Downloaded from www.nrcresearchpress.com by 196.1.178.254 on 09/07/12
For personal use only.

Can. J. Chem. Downloaded from www.nrcresearchpress.com by 196.1.178.254 on 09/07/12
For personal use only.

ref. 12, as recommended in ref. 10. Because ϵ varies by a factor of two across the filter band, the integrated absorbance shows a slight deviation from Beer's law; this amounts to less than 2% for absorbances below 1.0. The stated value of ϵ_{eff} refers to an overall absorbance of 0.3, which represents the mid-range of our data. This treatment is essentially in agreement with the spectra depicted in ref. 11.

(ii) Equilibrium measurements

Preliminary measurements showed that iodine was released reversibly from the mixture of bismuth oxide and oxyiodide in an oxygen atmosphere, between about 550 and 800°C. Typical equilibration times were of the order of tens of minutes. Therefore, we could readily measure $p(I_2)$ as a function of both T and $p(O_2)$.

For partial-pressure calculations, ϵ_{eff} was converted to units of equivalent ideal-gas partial pressure at 298 K.

$$[8] \quad \epsilon' = 1.35 \times 10^{-4}\ \text{Pa}^{-1}\ \text{cm}^{-1}$$

The value of $p(I_2)$ at given T is then determined from the absorbance, A, in a 10-cm path-length cell.

$$[9] \quad p(I_2) = \frac{A}{10\epsilon'} \times \frac{T}{298}$$

The corresponding oxygen partial pressure is given by eq. [10], which includes a minor correction for oxygen consumed by the reaction (eq. [2]).

$$[10] \quad p(O_2)_T = \left[p(O_2)_{296} \times \frac{T}{296} \right] - 0.5p(I_2)$$

Here, $p(O_2)_{296}$ is the partial pressure of oxygen originally loaded in the cell at 296 K. Substituting expressions [9] and [10] into eq. [3], we obtain K_2 at a given T. Iodine partial pressure measurements made at two values of $p(O_2)_{296}$ (26.7 and 3.3 kPa) are shown in Fig. 3. Experimental values of K_2, obtained in two runs at each of six starting partial pressures of oxygen, are presented in Fig. 4.

A break in the slope of the plots of $\log_{10} K_2$ vs. $1/T$, near 700°C, can be attributed to the α–δ phase transition of bismuth oxide (13–15). There is evidence of hysteresis on cooling below this transition, i.e., data obtained while running the temperature down lie on a metastable extension of the δ-Bi_2O_3/α-Bi_5O_7I equilibrium line. In several cases this persisted into the second heating stage of the run. There is also greater scatter in the data obtained at lower temperatures, reflecting the poorer accuracy of low absorbance measurements.

The apparent iodine partial pressures, and hence the values of K_2, obtained at the lowest oxygen partial pressure ($p(O_2)_{296}$ = 0.13 kPa (1 Torr)), and also some of the measurements at 1.3 kPa, were higher than expected, for several possible reasons. (*i*) Inaccurate oxygen metering at low pressures. (*ii*) Sublimation of bismuth oxide at low total pressures caused some fogging of the cell windows, and hence a positive bias in measured absorbances. (*iii*) Some other decomposition product (e.g. BiI_3) may have interfered with the spectrophotometric measurement. Bismuth oxyiodides have been reported to decompose by sequential loss of BiI_3 in a non-oxidizing atmosphere (4). Equilibrium measurements of BiI_3 vapor pressure over BiOI + $Bi_7O_9I_3$ have been reported by Klimakov *et al.* (16). (*iv*) One or both solids may deviate from ideal stoichiometry at low oxygen partial pressures. Substoichiometric bismuth oxides are known (13).

Excluding these measurements at $p(O_2)_{296}$ = 0.13 kPa, our data are consistent with equilibrium [2]. Figure 3 shows that measured iodine partial pressures varied with the square root of oxygen partial pressure at a given temperature, as required by eqs. [2] and [3].

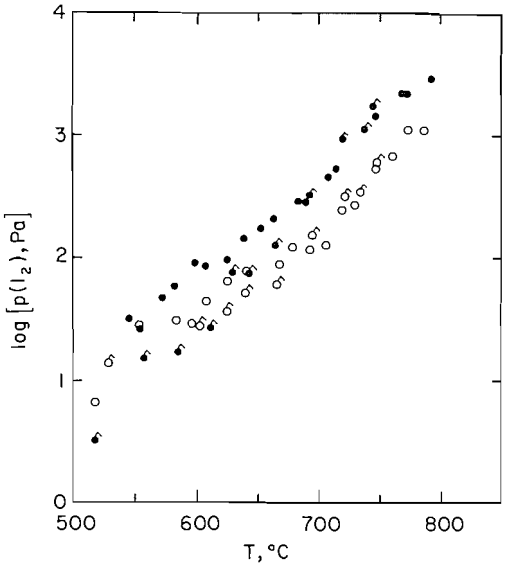

FIG. 3. Experimental measurements of iodine partial pressure vs. T, at initial oxygen pressures (296 K) of 26.7 kPa (●) and 3.3 kPa (○). Expected separation of the two data sets is 0.45 log units of $p(I_2)$. Flagged data points were obtained while running temperature down.

Enthalpies of reaction [2] above and below the phase transition were obtained by linear regression of data measured above and below 700°C, respectively. Below 700°C, we only included data from the heating half of the temperature cycle. We also omitted data that showed strong evidence of persistent hysteresis (i.e., persistence of δ-Bi_2O_3 into the second heating cycle). The resulting enthalpies are given in Table 3. From these, we estimate that $\Delta_r H^0$ for reaction [2] is 219 ± 29 kJ mol^{-1} above the phase transition temperature, and 97 ± 28 kJ mol^{-1} below. From the intersections of the five pairs of regression lines, we estimate a transition temperature of 698 ± 10°C, and a corresponding value of $\log_{10} K_2$ = 0.1 ± 0.3. Reported values for the transition temperature range from 701 to 730°C (14).

Our best estimate of the relationship between K_2 and T, based on the value at the transition temperature and the enthalpies of reaction above and below, is given by eqs. [11] and [12]:

$$[11] \quad \log_{10} K_2 = (0.1 \pm 0.3) + (11400 \pm 1500)\left[\frac{1}{971} - \frac{1}{T}\right] \qquad \text{(above 971 K)}$$

$$[12] \quad \log_{10} K_2 = (0.1 \pm 0.3) + (5100 \pm 1500)\left[\frac{1}{971} - \frac{1}{T}\right] \qquad \text{(below 971 K)}$$

The enthalpy change associated with the Bi_2O_3 phase transition, 122 ± 57 kJ mol^{-1}, lies at the high end of the range of reported values (30–117 kJ mol^{-1}) (14)). This suggests that some additional endothermic reaction may occur near the transition temperature. X-ray diffraction of quenched samples confirmed the presence of δ-Bi_2O_3 and also showed some diminution of Bi_5O_7I peaks above 700°C; a solid solution of Bi_5O_7I in δ-Bi_2O_3 may therefore have been formed. Differential thermal analysis showed a well-defined endotherm near 700°C,

Can. J. Chem. Downloaded from www.nrcresearchpress.com by 196.1.178.254 on 09/07/12
For personal use only.

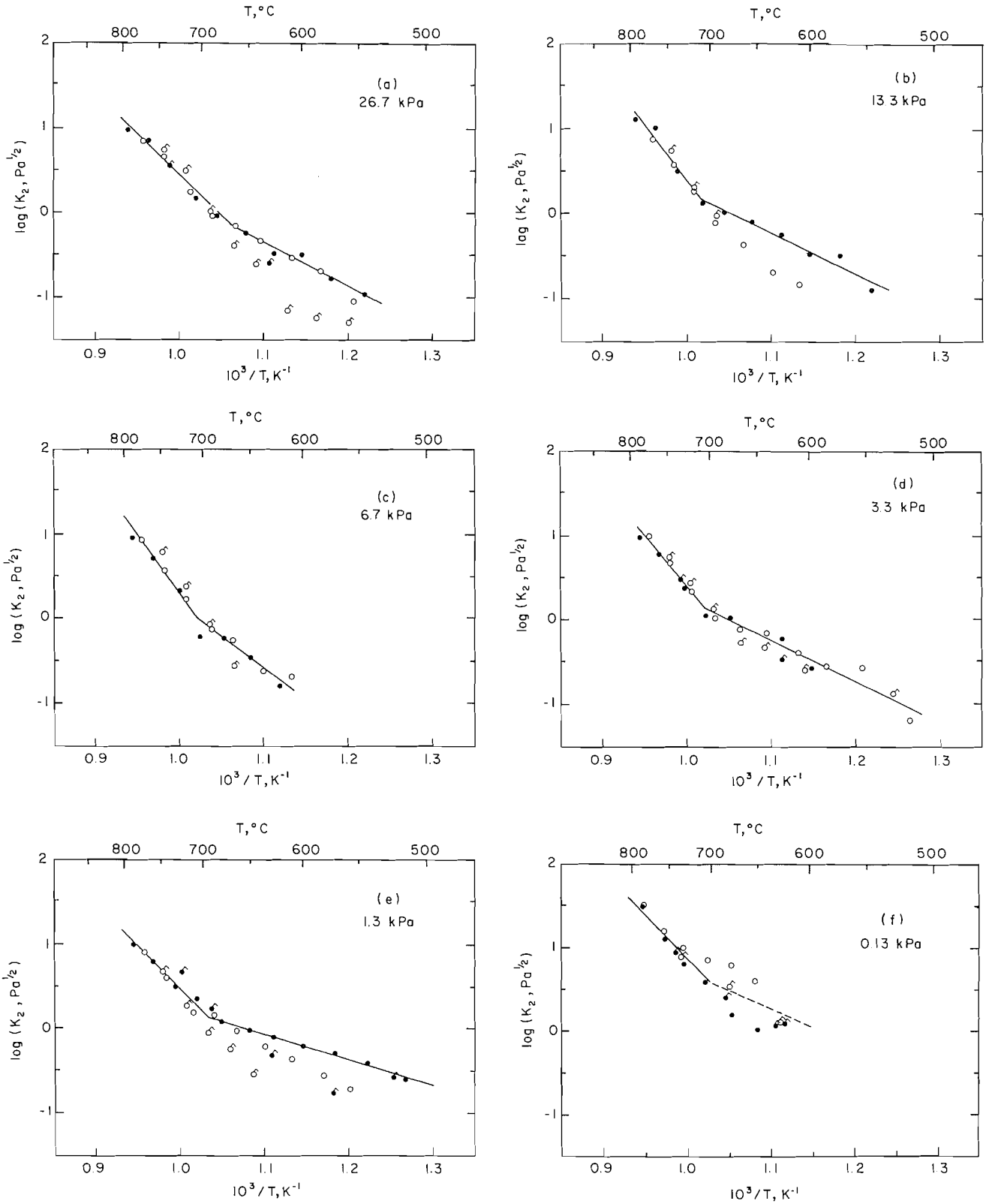

FIG. 4. Experimental measurements of $\log_{10} K_2$ at six different initial oxygen pressures (296 K): (*a*) 26.7 kPa; (*b*) 13.3 kPa; (*c*) 6.7 kPa; (*d*) 3.3 kPa; (*e*) 1.3 kPa; (*f*) 0.13 kPa. Closed and open circles represent successive runs with the same sample (different samples were used at each temperature). Flagged data points were obtained while running temperature down.

with evidence of a second feature at slightly higher temperature. Solid solubility between δ-Bi_2O_3 and Bi_5O_7I is reported in the phase-diagram study by Klimakov *et al.* (15). They report a eutectoidal decomposition of the δ-Bi_2O_3/Bi_5O_7I solid solution to α-Bi_2O_3 + Bi_5O_7I at 700 ± 5°C. This agrees well with our estimated transition temperature of 698 ± 10°C. A host of other oxides form compounds or solid solutions with bismuth oxide (13); this is partly responsible for the wide range of reported transition temperatures and enthalpies (14). Also, we can not rule out the possibility of some reaction with the silica sample

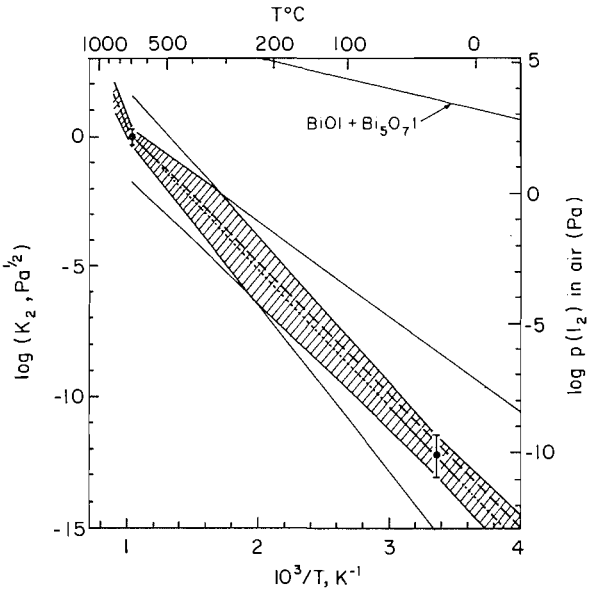

FIG. 5. Relationship between $\log_{10} K_2$ and T, based on measurements of the aqueous system at 10–60°C (eq. [13]), and the solid–gas system at 550–800°C (eqs. [11] and [12]). The hatched area represents estimated uncertainty limits on K_2 throughout the temperature range up to 800°C.

tubes in our own experiments. We have seen no evidence of β-Bi_5O_7I (17) in these experiments.

(c) Comparison of aqueous and anhydrous equilibria

It is desirable to integrate the equilibrium data obtained from the wet and dry experiments. We therefore derived a 25°C value of K_2 and its temperature dependence from the aqueous equilibrium data.

From the Gibbs energies of formation of Bi_2O_3 and Bi_5O_7I (Table 2), we obtain $\Delta_r G^0 = 84.3 \pm 4.3$ kJ mol^{-1} for reaction [2] at 25°C (standard state pressure = 10^5 Pa), whence $\log_{10} K_2 = -12.3 \pm 0.8$ (pressures in Pa). From the corresponding enthalpies of formation, we obtain $\Delta_r H^0 = 101 \pm 7$ kJ mol^{-1} at 25°C, in good agreement with the value of 97 ± 28 kJ mol^{-1}, determined directly at 700°C; the temperature dependence of this enthalpy is expected to be small. Many other reactions of the same general type, iodide + $(1/2)O_2 \rightleftharpoons$ oxide + I_2, have enthalpy changes of 100–120 kJ mol^{-1} (based on data in refs. 7 and 8).

From the experimental enthalpy of reaction, 101 ± 7 kJ mol^{-1}, we obtain the relationship between $\log_{10} K_2$ and T (K):

$$[13] \quad \log_{10} K_2 = (-12.3 \pm 0.8) + (5280 \pm 370)\left[\frac{1}{298} - \frac{1}{T}\right]$$

Figure 5 shows the relationship between K_2 and reciprocal temperature, derived from the anhydrous and aqueous experiments. Given the good mutual agreement of the two extrapolations, we can define K_2 over the range 0–800°C, with an uncertainty that varies between 0.3 and 1.3 orders of magnitude.

Reported thermogravimetric measurements on Bi_5O_7I (1, 4, 5), and those made by E. R. Vance (private communication) all show the onset of measurable decomposition in air near 550°C, which accelerates up to about 650°C and reaches completion around 750–800°C. These observations are qualitatively consistent with the magnitude of $p(I_2)$ values at these temperatures, as shown in Fig. 5.

(d) Further thermochemical estimates

Finally it is useful to compare the entropy of Bi_5O_7I, obtained from our aqueous equilibrium data, with values estimated from the principle of additivity (18). Using values recommended by Latimer (18) for Bi, O^{2-}, and I^- in inorganic solids, we obtain $S^0_{298} = 393.3$ J mol^{-1} K^{-1}, in agreement with our value of 430 ± 45 J mol^{-1} K^{-1}. Much closer agreement is obtained if we substitute the actual entropy of Bi_2O_3 (Table 2) into expression [14].

$$[14] \quad S^0(Bi_5O_7I) = 2.5S^0(Bi_2O_3) + S^0(I^-) - 0.5S^0(O^{2-})$$
$$= 429.9 \text{ J mol}^{-1} \text{ K}^{-1} \quad (!)$$

The same approach yields an estimate for the entropy of BiOI.

$$[15] \quad S^0(BiOI) = 0.5S^0(Bi_2O_3) + S^0(I^-) - 0.5S^0(O^{2-})$$
$$= 127.0 \text{ J mol}^{-1} \text{ K}^{-1}$$

whence $\Delta_f S^0(BiOI) = -90.4$ J mol^{-1} K^{-1}. Combining this with the Gibbs energy of formation of BiOI from ref. 1, and assuming an uncertainty of ±10 J mol^{-1} K^{-1} in the entropy, we then estimate the enthalpy of formation.

$$\Delta_f H^0(BiOI) = -275 \pm 6 \text{ kJ mol}^{-1}$$

We can now estimate the equilibrium constant for reaction [16] as a function of temperature:

$$[16] \quad (5/2)BiOI(s) + (1/2)O_2(g) \rightleftharpoons (1/2)Bi_5O_7I(s) + I_2(g)$$

$$K_{16} = p(I_2)/[p(O_2)]^{1/2}$$

$$\log_{10} K_{16} = 1.5 \pm 1.2 \text{ at } 25°C$$

(from Gibbs energies of formation; pressures in Pa)

$$\Delta_r H^0_{298} = 23 \pm 15 \text{ kJ mol}^{-1};$$

$$d(\log_{10} K_{16})/d(1/T) = -1200 \pm 800$$

These estimates are included in Fig. 5 and illustrate the much lower thermal stability of BiOI than Bi_5O_7I in air. Thermogravimetric analysis (1, 4, 5) has previously shown that reaction [16] proceeds quantitatively to the right near 300°C in air, in an open system. Using the spectrophotometric method described above, we have observed irreversible evolution of I_2 from BiOI above about 100°C.

We can also estimate the temperature dependence of equilibrium [17]:

$$[17] \quad (5/4)BiOI(s) + OH^-(aq) \rightleftharpoons (1/4)Bi_5O_7I(s) + I^-(aq) + (1/2)H_2O(l)$$

$$\Delta_r H^0_{298} \simeq 10 \text{ kJ mol}^{-1}$$

$$\log_{10} K_{17} = \{I^-\}/\{OH^-\} = 3.5 \pm 0.2 \text{ at } 25°C \text{ (from ref. 1)}$$

$$d(\log_{10} K_{17})/d(1/t) \simeq 550$$

Although this is a very rough estimate, it does indicate that

TABLE 3. Enthalpy data derived from anhydrous experiments

$p(O_2)_{296}$ (kPa)	$\Delta_r H(2)^a$ kJ mol^{-1} >700°C	$\Delta_r H(2)^a$ kJ mol^{-1} <700°C	Transition temperature,^{b} T_t	log $K_2{}^b$ at T_t
26.7	185	99	669	−0.12
13.3	248	92	711	0.21
6.7	264	144	706	0.04
3.3	229	95	707	0.18
1.3	193	57	695	0.17
0.13	196	—	~700	(~0.6)
Mean	219 ± 29	97 ± 28	698	0.10

[a]Enthalpy of reaction [2] from regression lines in Fig. 4.
[b]Intersection of regression lines for data measured above and below 700°C.

Can. J. Chem. Downloaded from www.nrcresearchpress.com by 196.1.178.254 on 09/07/12
For personal use only.

the temperature dependence of log K_{17} is only about one-fifth that of log K_1.

Acknowledgements

We are grateful to R. MacFarlane and A. C. Vikis for information and advice on the photometric detection of iodine vapor, and to N. H. Sagert and P. P. S. Saluja for helpful comments on the manuscript. Differential thermal analyses were run by E. R. Vance.

1. P. Taylor and V. J. Lopata. Can. J. Chem. **64**, 290 (1986).
2. P. Taylor, V. J. Lopata, and D. D. Wood. *In* Proceedings of ASTM 4th International Hazardous Waste Symposium, Atlanta, GA. May 1987.
3. C. F. Baes and R. E. Mesmer. The hydrolysis of cations. Wiley-Interscience, New York. 1976. p. 382.
4. M. Schulte-Kellinghaus and V. Krämer. *In* Angewandte Chemische Thermodynamik und Thermoanalytik. *Edited by* E. Marti, H. R. Oswald, and H. G. Wiedemann. Birkhäuser Verlag, Basel. 1979.
5. A. Rulmont. Rev. Chim. Miner. **14**, 277 (1977).
6. P. Taylor, S. Sunder, and V. J. Lopata. Can. J. Chem. **62**, 2863 (1984).
7. P. Taylor, D. D. Wood, and V. J. Lopata. Atomic Energy of Canada Limited Report No. AECL-9554. 1988.
8. R. A. Robie, B. S. Hemingway, and J. R. Fisher. U.S. Geol. Surv. Bull. 1452 (reprinted with corrections, 1979).
9. D. D. Wagman, W. H. Evans, V. B. Parker, R. H. Schumm, I. Halow, S. M. Bailey, K. L. Churney, and R. L. Nuttall. J. Phys. Chem. Ref. Data, **11**, Supp. 2 (1982).
10. L. C. Glasgow. Ph.D. Thesis, Univ. of Wisconsin. 1971. Available from University Microfilms, Inc., Ann Arbor, MI.
11. J. G. Calvert and J. N. Pitts, Jr. Photochemistry. Wiley, New York. 1966. p. 184.
12. R. L. Strong. Ph.D. Thesis, Univ. of Wisconsin. 1954.
13. J. Medernach and R. L. Snyder. J. Am. Ceram. Soc. **61**, 494 (1978).
14. S. C. Schaefer. U.S. Bur. Mines Rept. of Investigations No. 8906. 1984.
15. A. M. Klimakov, B. A. Popovkin, and A. V. Novoselova. Russ. J. Inorg. Chem. **19**, 1394 (1974) (Zh. Neorg. Khim. **19**, 2553 (1974)).
16. A. M. Klimakov, B. A. Popovkin, and A. V. Novoselova. Russ. J. Inorg. Chem. **22**, 928 (1977) (Zh. Neorg. Khim. **22**, 1711 (1977)).
17. J. Ketterer, E. Keller, and V. Kramer. Z. Krist. **172**, 63 (1985).
18. W. M. Latimer. Oxidation potentials. 2nd ed. Prentice-Hall, Englewood Cliffs, NJ. 1952. p. 359.

Can. J. Chem. Downloaded from www.nrcresearchpress.com by 196.1.178.254 on 09/07/12
For personal use only.

James P. Johnson, Michael Murchie, Jack Passmore, Mahmoud Tajik, Peter S. White, and Chi-Ming Wong. Can. J. Chem. **65**, 2744 (1987). The preparation of SeI_3SbF_6 and TeI_3SbF_6; the X-ray crystal structures of SBr_3AsF_6, SeI_3AsF_6, SeI_3SbF_6, and TeI_3SbF_6; some considerations of the energetics of the formation of SBr_3AsF_6 and SeI_3AsF_6.

Page 2744. The middle initial of Michael P. Murchie was omitted from his name in the title and in refs. 9 and 25.

Can. J. Chem. Downloaded from www.nrcresearchpress.com by 196.1.178.254 on 09/07/12
For personal use only.

REVIEW/SYNTHÈSE

Solvent effects in organic chemistry — recent developments

MICHAEL H. ABRAHAM[1] AND PRISCILLA L. GRELLIER
Department of Chemistry, University of Surrey, Guildford, Surrey, GU2 5XH, United Kingdom

JOSE-LUIS M. ABBOUD
Consejo Superior de Investigaciones Cientificas, Instituto de Quimica Fisica Rocasolano Serrano, Madrid 119-28006, Spain

RUTH M. DOHERTY
Naval Surface Weapons Center, White Oak Laboratory, Silver Spring, MD 20910, U.S.A.

AND

ROBERT W. TAFT
Department of Chemistry, University of California, Irvine, CA 92717, U.S.A.

Received May 20, 1988

MICHAEL H. ABRAHAM, PRISCILLA L. GRELLIER, JOSE-LUIS M. ABBOUD, RUTH M. DOHERTY, and ROBERT W. TAFT. Can. J. Chem. **66**, 2673 (1988).

Solvent effects on a number of different processes have been surveyed, and results of the application of multiple linear regression analysis are discussed. The processes examined include examples of solubility of gases or vapours, distribution coefficients of solutes between water and a series of solvents, and solvent effects on conformational equilibria, on keto–enol tautomerism, and on reaction rates. It is shown that two particular equations, that due to Koppel and Palm and extended by Makitra and Pirig, and that due to Abraham, Kamlet, and Taft, can cope quite satisfactorily with solvent effects on these various processes. It is pointed out that interpretation of parameters obtained from equations that involve macroscopic quantities such as $\Delta G^{\ddagger}$ or ΔG^0 is not necessarily straightforward, and that some model is needed in order to interpret these macroscopic quantities in terms of microscopic quantities that can characterise, for example, solute–solvent interactions.

MICHAEL H. ABRAHAM, PRISCILLA L. GRELLIER, JOSE-LUIS M. ABBOUD, RUTH M. DOHERTY et ROBERT W. TAFT. Can. J. Chem. **66**, 2673 (1988).

On a évalué les effets de solvant sur un certain nombre de processus et on discute des résultats de l'application de l'analyse de regression linéaire multiple. Les processus étudiés comportent des exemples de solubilité des gaz ou des vapeurs, des coefficients de distribution des solutés entre l'eau et une série de solvants ainsi que des effets de solvant sur l'équilibre conformationnel, sur la tautomérie céto–énolique et sur les vitesses de réaction. On démontre que deux équations particulières, celle de Koppel et Palm qui a été étendue par Makitra et Pirig ainsi que celle d'Abraham, Kamlet et Taft, peuvent rendre compte d'une façon satisfaisante des effets de solvant sur ces divers processus. On note que l'interprétation des paramètres obtenus à l'aide de ces équations qui impliquent des quantités macroscopiques comme le $\Delta G^{\ddagger}$ ou le ΔG^0 ne sont pas simples; des modèles sont nécessaires pour interpréter ces quantités macroscopiques en fonction de quantités microscopiques qui peuvent caractériser, par exemple, les interactions soluté–solvant.

[Traduit par la revue]

Introduction

The first experimental observation to show that "inert" solvents could affect the rate of a chemical reaction was provided by Berthelot and Saint-Gilles (1). However, it was the classic paper of Menschutkin (2) in 1890 that initiated the widespread investigations on solvent effects that have characterised a large area of physical organic chemistry. Menschutkin (2) showed that rate constants for the reaction of triethylamine with ethyl iodide at 373 K were highly dependent on the solvent, there being factors of up to 700 between rate constants in hexane and acetophenone. Since the work of Menschutkin, there have been published a host of papers on solvent effects in organic chemistry, mainly dealing with reaction rates but also on equilibria.

At the outset, it is useful to consider the objectives of studies of solvent effects on reaction rates and other processes. In principle, there are two main objectives, (*a*) the prediction of rate constants in other solvents, and (*b*) to reach some understanding of the various influences that might affect reaction rates. The first objective is certainly important as regards testing theoretical models in the Popperian sense, but practically has been but little used. In the few recorded instances in which rate constants have been estimated for some particular purpose, rather simple procedures have been used. Thus log *k* values for the solvolysis of *t*-butyl bromide or *t*-butyl iodide in aqueous organic media can be estimated from corresponding values for *t*-butyl chloride, cf. the well-known Grunwald–Winstein *mY* equation. Again, rate constants for the Et_3N/EtI reaction can be estimated from corresponding values for the related Pr_3N/MeI reaction, and vice versa, if required. By far the greatest use of solvent effect studies has been in developing an understanding of the factors that influence reaction rates, that is to probe the reaction at a microscopic level in order to obtain information on the nature of any solute–solvent interactions, etc., that may be set up.

Unfortunately, there is no direct logical connection between

[1]To whom correspondence should be addressed.

Printed in Canada / Imprimé au Canada

Can. J. Chem. Downloaded from www.nrcresearchpress.com by 196.1.178.254 on 09/07/12
For personal use only.

Can. J. Chem. Downloaded from www.nrcresearchpress.com by 196.1.178.254 on 09/07/12
For personal use only.

the macroscopic solvent parameters that are used in studies of solvent effects, and microscopic details of reaction processes. In order to establish such a connection, it is necessary to construct a "link", usually based on some theoretical model. As an example we can take the effect of solvent dielectric constant (ϵ) on reaction rate constants. It is quite well known that for a restricted range of solvents, usually aliphatic non-halogenated, non-hydroxylic solvents, there is often a quite good correlation between rate constants (as log k or $\Delta G^{\ddagger}$) and functions such as $1/\epsilon$ or $(\epsilon - 1)/(2\epsilon + 1)$. Steiner and Huisgen (3*a*) found for the addition of tetracyanoethylene (TCNE) to butylvinylether a correlation of the type,[2]

$$[1] \quad \Delta G^{\ddagger} = -16.1(\epsilon - 1)/(2\epsilon + 1) + \text{constant}$$

Such a correlation, by itself, leads to no information whatsoever of a microscopic nature. The "link" or model, in this case, was provided by Kirkwood (4) who showed that the electrostatic part of the Gibbs energy of a species was given by eq. [2], if the species could be regarded as a dipole of moment μ in a sphere of radius r. In eq. [2], ΔG_E is in kcal mol^{-1}, μ in Debyes, and r in Å.

$$[2] \quad \Delta G_E = -14.4\frac{(\epsilon - 1)}{(2\epsilon + 1)}\frac{\mu^2}{r^3}$$

Laidler and Eyring (5, 6) then combined eq. [2] with the transition state theory, to yield eq. [3] for the effect of solvent dielectric constant on rate constants, as $\Delta G^{\ddagger}$.

$$[3] \quad \Delta G^{\ddagger} - \Delta G_0^{\ddagger} = 14.4\frac{(\epsilon - 1)}{(2\epsilon + 1)}\left(\frac{\mu_A^2}{r_A^3} + \frac{\mu_B^2}{r_B^3} - \frac{\mu_{\ddagger}^2}{r_{\ddagger}^3}\right) + \Delta\phi$$

The total nonelectrostatic effect is denoted as $\Delta\phi$, and A, B and the symbol $\ddagger$ stand for reactants A and B and the transition state. If $\Delta\phi$ is zero or constant, then a plot of $\Delta G^{\ddagger}$ against $(\epsilon - 1)/(2\epsilon + 1)$ will yield a line from whose slope the term in the square parentheses can be evaluated. Then knowing μ_A, r_A, μ_B, and r_B, the term $\mu_{\ddagger}^2/r_{\ddagger}^3$ can be deduced. If $r_{\ddagger}$ can be estimated, the microscopic quantity $\mu_{\ddagger}$ can be obtained. Steiner and Huisgen (3) carried out these calculations and found a reasonable value of 10.3 D for $\mu_{\ddagger}$. They also calculated a dipole moment of 17 D for the zwitterionic intermediate, so that the transition state seems reasonably close to the intermediate.

[4] $(CN)_2C{=}C(CN)_2 + H_2C{=}CH{-}OBu \rightarrow [Tr]^{\ddagger}$

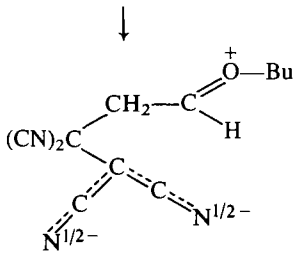

We have dealt with this in some detail, because it is a very simple example of how a model or "link" can be set up in order to connect microscopic details of reaction mechanisms with bulk solvent properties. Other cycloaddition reactions were considered by Steiner and Huisgen (3),[3] and Abraham (7) has listed a number of transition-state dipole moments obtained via the Kirkwood equation [3]. More sophisticated reaction-field equations have been applied to the Et_3N/EtI reaction and to the heterolysis of *t*-butyl chloride (8, 9) leading also to transition-state dipole moments. Volumes of activation can also be correlated with the pressure derivative of the Kirkwood function to yield the microscopic quantities $\mu_{\ddagger}^2/r_{\ddagger}^3$ and hence $\mu_{\ddagger}$, as shown by McCabe and Eckert (10). Activation entropies can similarly be correlated with the temperature derivative of the Kirkwood function to give the same microscopic quantities (11).

Application of the Kirkwood function and its derivatives has mostly been to a series of pure organic solvents. Indeed, following Menschutkin, for many years studies on mixed solvents were rather uncommon. The advent of the Winstein–Grunwald equation (12, 13) specifically designed to apply to solvolyses in aqueous organic media brought about a radical change. Since that time, there have been a very large number of studies using such mixed solvents, usually in terms of the original mY equation [5] or some variant.

$$[5] \quad \log k/k_0 = mY = m \log (k/k_0)^{t\text{-BuCl}}$$

Here k and k_0 denote rate constants in a solvent and in the standard solvent of 80% aqueous ethanol, and m is defined as unity for the solvolysis of *t*-butyl chloride. The difficulty with the Winstein–Grunwald equation is that no link is provided between the macroscopic quantities in eq. [5] and microscopic parameters characteristic of the reaction or transition-state. Hence from eq. [5] it is impossible to deduce any such microscopic parameters.

Quite recently, however, there has been an interesting new approach to the study of medium effects in highly aqueous solutions. Blandamer, Engberts, and co-workers (14) have shown that by assuming a specific solvation model for the transition state, it is possible to apply pairwise group interaction parameters to reactant/solvent and transition-state/solvent interactions and hence to explain the effect of additives to aqueous media. They have carried out such an analysis for the hydrolysis of 4-methoxyphenyl dichloroacetate in aqueous solutions of urea and alkyl-ureas, and extension to other systems is eagerly awaited.

Multiple linear regression analysis

We now turn to processes in pure organic solvents. As far as rate constants are concerned, it is now quite clear that there is no single solvent parameter that will satisfactorily correlate log k values for a variety of widely differing reactions (15). Hence there has developed considerable interest into correlations by the method of multiple linear regression analysis (MLRA). The first general system of analysis by MLRA was devised by Koppel and Palm (16, 17), specifically for the correlation of rate constants. They argued that a number of solvent influences could be specified on general chemical grounds, and put forward their well-known equation [6]:

$$[6] \quad \log k = \log k_0 + g.f(\epsilon) + p.f(\eta) + c.E + b.B$$

Here $f(\epsilon)$ is a dielectric constant function, usually taken as $(\epsilon - 1)/(2\epsilon + 1)$, $f(\eta)$ is the refractive index function $(\eta^2 - 1)/(\eta^2 + 2)$, and E and B are measures of solvent electrophilic solvation ability and nucleophilic solvation ability,

[2]We shall deal in this paper not only with rate constants but with Gibbs energies. In order that the constants in various regression equations are all compatible, we shall transform any equations in log k into equation in $\Delta G^{\ddagger}$/kcal mol^{-1}, using the factor -1.36425 at 298 K.

[3]For a recent article, see ref. 3*b*.

Can. J. Chem. Downloaded from www.nrcresearchpress.com by 196.1.178.254 on 09/07/12
For personal use only.

respectively. Although Koppel and Palm did not explicitly set out a model to link the macroscopic quantities in eq. [6] with microscopic quantities, their approach is not too dissimilar to that of Abraham, Kamlet, and Taft and their co-workers (18–22) who have devised a more general equation based on a cavity theory of solution. In this approach, the solution of a solute in a solvent may be broken down conceptually into a number of stages, (*a*) the creation of a cavity of suitable size in the solvent, (*b*) reorganisation of solvent molecules around the cavity, and (*c*) introduction of the solute into the cavity, to set up various solvent–solute interactions. The endothermic or endoergic term (*a*) depends on the forces holding the solvent molecules together and on the size of the cavity. A measure of the solvent forces is the Hildebrand cohesive energy density, $(\delta_H^2)_1$, defined as the enthalpy of vaporisation of the solvent at 298 K per unit volume:

$$[7] \quad (\delta_H^2)_1 = (\Delta H_v^0 - RT)/\overline{V}_1$$

To a first approximation, the cavity size can be taken as proportional to the solute volume V_2; note that solvent properties are denoted by the subscript 1 and solute properties by the subscript 2. The reorganisation energy is probably not important, at least in terms of Gibbs energy, but the final term (*c*) will involve a number of exothermic or exoergic interactions, depending on the nature of the solvent and solute. Acid–base interactions will be set up if the solvent is a hydrogen-bond acid (α_1) and the solute a hydrogen-bond base (β_2), or if the solvent is the base (β_1) and the solute the acid (α_2). In addition there may be dipolar interactions of the dipole–dipole and dipole – induced dipole type, proportional to the dipolarity (π^x) of solvent and solute ($\pi_1^x \pi_2^x$).. A full equation for the solution of a solute in a solvent will therefore be given by eq. [8].

$$[8] \quad \Delta G^0 = \Delta G_0^0 + A\pi_1^x.\pi_2^x + B\alpha_1.\beta_2 + C\beta_1.\alpha_2 + D(\delta_H^2)_1.V_2$$

If we consider only the case of a single solute in a series of solvents, all the solute parameters are constant to leave an equation for the effect of solvents only:[4]

$$[9] \quad \Delta G^0 = \Delta G_0^0 + d.\delta + s.\pi_1^x + a.\alpha_1 + b.\beta_1 + h.(\delta_H^2)_1$$

Equation [9], the AKT equation, can be applied not only to the solubility of a single species, but to equilibrium constants, rate constants (as $\Delta G^{\neq}$), etc.[5] Values of the solvent parameters π_1^x, α_1, and β_1 have been listed for a wide range of solvents (23). Some of these, together with a number of cohesive energy densities, are given in Table 1. Whenever possible, the latter have been calculated from calorimetrically-determined ΔH_v^0 values at 298 K. Because the original Koppel–Palm equation [5] contains no parameter that can deal with a cavity term, it is restricted to processes in which cavity effects largely cancel out, i.e. to correlations of rate constants where initial-state and transition-state cavity contributions do, indeed, in general cancel. Makitra and Pirig (24, 25), however, have added the δ_H^2 cavity term to the Koppel–Palm equation giving a more general equation [10] that covers the same range of applicability as the AKT equation [9].[6]

$$[10] \quad \Delta G^0 = A_0 + A_1.f(\eta) + A_2.f(\epsilon) + A_3.\delta_H^2 + A_4.B + A_5.E$$

Equations [9] and [10] have both been applied to numerous solubility-related phenomena, generally with rather good results. The equations clearly closely resemble each other in the identification of the various solvent properties that will influence solvent–solute interactions, viz. solvent dipolarity as π_1^x or $f(\epsilon)$, solvent hydrogen-bond acidity or electrophilicity as α_1, or E, and solvent hydrogen-bond basicity or nucleophilicity as β_1 or B. Both equations have their disadvantages. The AKT equation [9] suffers in that there is no parameter directly related to solvent–solute dispersion interactions, and that for solvents with δ not equal to zero, it is not so easy to interpret the $d.\delta/s.\pi_1^x$ terms. On the other hand, the modified Koppel–Palm equation [10], includes a solvent basicity term B that is directly derived from the change in the OH infrared stretching frequency of phenol with the solvent, when both phenol and solvent are present in dilute solution in CCl_4 (26). Thus the B-scale is actually a *solute* scale and is not a solvent scale at all. Although a solute B-scale can probably be used as a solvent B-scale for nonassociated compounds, it is most unlikely that basicities of associated bulk solvents can be matched to those of monomeric solute species.[7]

There have been numerous applications of eqs. [6], [9], and [10], and we shall review these by taking examples from a variety of processes. It is as well, however, to point out a number of conditions that should be obeyed in such applications. Firstly, the solvent parameters in any given data set must not be colinear. If any two parameters are colinear over the given data set, incorporation of both of the parameters into eqs. [6], [9], or [10] may lead to meaningless coefficients. Secondly, parameters must be available for enough data points; usually five data points per each explanatory variable would be regarded as the minimum number. Thirdly, some statistical procedure, based on Student's *t*-test or the *F*-statistic, must be used to avoid the accumulation of extra unnecessary variables. In the equations that follow, we shall either exclude all parameters for which the confidence level (CL) is less than 95%, or else show these parameters specifically. Fourthly, and very importantly, results of application of equations based on some chemical model must make general chemical sense. Thus if *solvent* hydrogen-bond acidity (α_1) seems to be important in a process that does not involve any *solute* hydrogen-bond bases, the resulting equation cannot be taken seriously.

Similarly, for a process in which there is no, or little, volume change with respect to the species involved, the cavity contributions should cancel out, and the term in δ_H^2 should be redundant. This must certainly be the case for spectroscopic transitions that obey the Frank–Condon principle. However, we shall not discuss these here, since they have already been examined in detail (23, 27).

Application of MLRA to equilibria

There are a number of equilibria in which the cavity term (in δ_H^2) should cancel between reactants and products, especially

[4]The term $d.\delta$ in eq. [9] is a polarisability correction term, with δ taken as 0.5 for polyhalogenated solvents, 1.0 for aromatic solvents, and zero for all others.

[5]Note that in the first papers of AKT on this subject, the parameter δ_H was used (18, 19) rather than the better parameter δ_H^2.

[6]Makitra and Pirig (24, 25) use a log K term rather than ΔG^0 in eq. [10].

[7]The original Koppel–Palm equation [6] used ν(MeOD) in pure solvents as the basis of the B-parameter, but Koppel and Paju (26) suggested the alternative ν(PhOH) solute scale because of practical difficulties over the ν(MeOD) solvent scale. Koppel and Paju were well aware of the assumption involved in using a solute scale for a solvent scale, but concluded (26) that it was a satisfactory approximation.

TABLE 1. Some solvent parameters used in this work[a]

No.	Solvent	δ	π_1^*	α_1	β_1	$(\delta_H^2)_1$
3351	Water	0	1.09	1.17	0.18	549.0
3352	Methanol	0	0.60	0.93	0.62	205.2
3353	Ethanol	0	0.54	0.83	0.77	162.1
3354	1-Propanol	0	0.52	0.78	0.83	143.2
3355	2-Propanol	0	0.48	0.76	0.95	133.1
3356	1-Butanol	0	0.47	0.79	0.88	129.5
3359	*t*-Butanol	0	0.41	0.68	1.01	111.9
3360	1-Pentanol	0	0.44	0.70	0.92	119.8
3362	3-Methylbutanol	0	0.45	0.78	0.90	116.3
3368	1-Hexanol	0	0.41	0.67	0.94	113.1
3389	1-Heptanol	0	0.39	0.64	0.96	108.4
3405	1-Octanol	0	0.37	0.62	0.97	103.3
3460	Ethylene glycol	0	0.92	0.90	0.52	274.0
2501	Formamide	0	0.97	0.71	0.60	361.7
3497	Trifluoroethanol	0	0.73	1.51	0	137.1
3499	Hexafluoro-2-propanol	0	0.65	1.96	0	89.3
2952	Acetic acid	0	0.64	1.12	0.45	203.5
3520	Benzyl alcohol	1	0.98	0.80	0.50	148.4
2241	Benzonitrile	1	0.90	0	0.37	122.9
2140	Nitrobenzene	1	1.01	0	0.30	122.2
1750	Acetophenone	1	0.90	0	0.49	103.7
1251	Iodobenzene	1	0.81	0	0.05	100.6
1201	Bromobenzene	1	0.79	0	0.06	97.4
1001	Chlorobenzene	1	0.71	0	0.07	93.6
1450	Anisole	1	0.73	0	0.22	92.9
1922	Ethyl benzoate	1	0.74	0	0.41	91.7
1451	Phenetole	1	0.69	0	0.20	84.3
751	Benzene	1	0.59	0	0.10	83.8
752	Toluene	1	0.54	0	0.11	79.4
753	*o*-Xylene	1	0.47	0	0.12	80.8
754	*m*-Xylene	1	0.47	0	0.12	77.8
755	*p*-Xylene	1	0.43	0	0.12	80.0
2701	Pyridine	1	0.87	0	0.64	111.3
1993	Propylene carbonate	0	0.83	0	0.40	176.9
3630	Dimethyl sulphoxide	0	1.00	0	0.76	168.8
2101	Nitromethane	0	0.85	0.22	0.25	158.5
2503	Dimethylformamide	0	0.88	0	0.69	138.9
2201	Acetonitrile	0	0.75	0.19	0.37	137.8
2854	*N*-Methylpyrrolidinone	0	0.92	0	0.77	127.6
2102	Nitroethane	0	0.82	0	0.25	126.9
2509	Dimethylacetamide	0	0.88	0	0.76	116.6
2202	Proprionitrile	0	0.71	0	0.37	113.0
1421	Dioxan	0	0.55	0	0.37	100.0
1708	Cyclohexane	0	0.76	0	0.53	98.0
1651	Propanone	0	0.71	0.08	0.48	90.6
1418	Tetrahydrofuran	0	0.58	0	0.55	86.4
1652	Butanone	0	0.67	0.06	0.48	86.0
1861	Ethyl acetate	0	0.55	0	0.45	79.2
366	Decalin	0	0.09	0	0	75.4
1864	Butyl acetate	0	0.50	0	0.45	74.9
1867	Pentyl acetate	0	0.45	0	0.45	74.0
4355	HMPA	0	0.87	0	1.05	73.4
1376	1,2-Dimethoxyethane	0	0.53	0	0.41	67.2
287	Cyclohexane	0	0	0	0	67.2
192	Hexadecane	0	0.08	0	0	64.1
1355	Di-*n*-butylether	0	0.24	0	0.46	59.6
126	Decane	0	0.03	0	0	59.7
72	Octane	0	0.01	0	0	57.0
1352	Diethylether	0	0.27	0	0.47	56.2
1354	Di-isopropylether	0	0.27	0	0.47	55.7
63	Heptane	0	−0.02	0	0	55.3
58	Hexane	0	−0.08	0	0	52.8
55	Pentane	0	−0.08	0	0	49.9
86	Iso-octane	0	0	0	0	49.5

Can. J. Chem. Downloaded from www.nrcresearchpress.com by 196.1.178.254 on 09/07/12
For personal use only.

TABLE 1 (*concluded*)

No.	Solvent	δ	π_1^x	α_1	β_1	$(\delta_H^2)_1$
557	1,2-Dichloroethane	0.5	0.81	0	0	98.3
560	1,1,2,2-Tetrachloroethane	0.5	0.95	0	0	97.8
552	Dichloromethane	0.5	0.82	0.30	0	97.7
553	Trichloromethane	0.5	0.58	0.44	0	88.7
587	1,1,2,2-Tetrachloroethylene	0.5	0.28	0	0	86.5
586	1,1,2-Trichloroethylene	0.5	0.53	0	0	84.8
616	1-Bromobutane	0.5	0.48	0	0	75.5
632	1-Bromoheptane	0.5	0.48	0	0	74.7
554	Tetrachloromethane	0.5	0.28	0	0	73.8
558	1,1,1-Trichloroethane	0.5	0.49	0	0	71.5
584	*cis*-1,2-Dichloroethylene	0.5	0.44	0	0	44.0

[a]For an extensive list of π_1^x, α_1, and β_1 see ref. 23. Cohesive energy densities are in kcal dm^{-3} as calculated from ΔH_V^0 values at 298 K.

conformational equilibria where reactants and products will have almost exactly the same intrinsic volume. Although there have been numerous studies on solvent effects on conformational equilibria (28), only in very few cases have sufficient solvents of a wide variety been examined. In one study, Abraham (29) measured the nmr coupling constant, J, between the C_1 and C_2 protons in 1,1,2-trichloroethane in 22 aprotic solvents as 10% solutions. Solvent parameters are available for nineteen of these solvents, Table 2, and an analysis through eq. [9] leads to:

$$[11]\quad J = (6.27 \pm 0.05) + (0.25 \pm 0.10)\delta - (0.70 \pm 0.09)\pi_1^x - (0.45 \pm 0.12)\beta_1$$
$$n = 19, \quad \text{sd} = 0.10, \quad r = 0.967$$

Abraham and Bretschneider (28), and also Chen *et al.* (30), calculated ΔG^0 values for equilibrium [12] from the original (29) J-values. The two sets of ΔG^0 values are not the same, due to different assumptions over the absolute values for the conformers (I) and (II), and so we have correlated both sets of results, with ΔG^0 in kcal mol^{-1}, eqs. [13], [14].

[12] 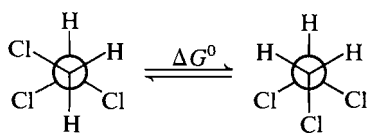

(I) (II)

$$[13]\quad \Delta G^0(28) = (1.22 \pm 0.05) + (0.29 \pm 0.11)\delta - (1.13 \pm 0.10)\pi_1^x - (0.30 \pm 0.13)\beta_1$$
$$n = 19, \quad \text{sd} = 0.10, \quad r = 0.978$$

$$[14]\quad \Delta G^0(30) = (0.60 \pm 0.03) + (0.18 \pm 0.07)\delta - (0.58 \pm 0.06)\pi_1^x - (0.34 \pm 0.08)\beta_1$$
$$n = 19, \quad \text{sd} = 0.07, \quad r = 0.974$$

As expected, the term in δ_H^2 is not significant, and the main factor influencing the equilibrium is solvent dipolarity. Since (**II**) will have a larger dipole moment than (**I**), any increase in π_1^x should decrease ΔG^0, exactly as observed in all three correlations. An unexpected observation is that solvent basicity also favours (**II**) over (**I**). Now in (**II**) the acidic C_1 proton is *trans* to the C_2 chlorine atom, and hence will be slightly more acidic than the C_1 proton in (**I**), so that an increase in basicity should favour (**II**), as observed. Although the absolute values

TABLE 2. Parameters for the conformational equilibrium of 1,1,2-trichloroethane[a]

Solvent	J(29)	ΔG^0(28)	ΔG^0(30)
Pentane	6.25	1.25	0.62
Hexane	6.21	1.24	0.57
Decalin	6.17	1.17	0.53
Tetrachloromethane	6.17	1.14	0.53
Benzene	5.94	0.63	0.30
1,1,2-Trichloroethylene	6.13	0.92	0.48
Di-isopropylether	6.04	0.84	0.39
Diethylether	6.05	0.79	0.40
Trichloromethane	6.03	0.75	0.39
1-Bromoheptane	5.99	0.71	0.35
Dichloromethane	5.93	0.52	0.30
1,2-Dichloroethane	5.87	0.46	0.25
Butanone	5.53	0.27	0.00
Propanone	5.52	0.24	−0.01
Acetonitrile .	5.52	0.08	−0.01
Nitromethane	5.51	0.07	−0.01
Dimethylformamide	5.34	0.05	−0.13
Dimethylacetamide	5.28	0.04	−0.16
Dimethylsulphoxide	5.17	−0.04	−0.24
Carbon disulphide	6.13	1.03	0.48
1,1,2-Trichloroethane[b]	5.92	0.58	0.30
Mesityl oxide	5.64	0.32	0.08
Sulpholane	5.31	−0.02	−0.15

[a]All values of J obtained as 10% solutions, except where shown.
[b]Bulk pure solvent.

of the coefficients in eqs. [13] and [14] differ, the general interpretation remains the same. However, the calculated ΔG^0 value in the gas phase is not the same; if we take $\delta = 0$, $\beta_1 = 0$ and, from Abboud *et al.* (31), $\pi_1^x = -1.1$, then on eq. [13] ΔG^0 (gas phase) = 2.46 kcal mol^{-1} and on eq. [14] ΔG^0 (gas phase) = 1.24 kcal mol^{-1}. Abraham and Bretschneider (28) gave a range of possible values from 1.7 to 2.7 kcal mol^{-1} with a "best" value of 1.9 kcal mol^{-1}, whereas Chen *et al.* (30) using their own values of ΔG^0 extrapolated a value of 0.81 kcal mol^{-1}.

Interestingly, Abraham and co-workers (32) suggested a much lower value of −0.44 for the gas phase value of π_1^x, and this lower value yields ΔG^0 (gas phase) as 1.72 from eq. [13] and 0.86 from eq. [14], in much better agreement with the extrapolations given (28, 30).

Another equilibrium that involves conformers which differ in

Can. J. Chem. Downloaded from www.nrcresearchpress.com by 196.1.178.254 on 09/07/12
For personal use only.

dipole moment is that given as eq. [15]. Abraham and Griffiths (33) obtained ΔG^0 values in 13 non-hydroxylic solvents from which we have calculated equation [16]. The fit is not very good, but we have included all the solvents studied, including CCl_4 that the authors felt was anomalous. General chemical sense is maintained in that the δ_H^2 term is not significant, and that an increase in solvent dipolarity favours the more polar conformer (**IV**).

[15] 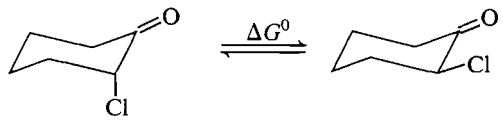

(**III**) μ = 3.17 D (**IV**) μ = 4.32 D

[16] $\Delta G^0 = (0.88 \pm 0.07) + (0.53 \pm 0.14)\delta - (1.56 \pm 0.10)\pi_1^x$

$n = 13$, sd = 0.13, $r = 0.982$

A gas phase value of 1.5 kcal mol^{-1} was suggested (33), as compared to one of 1.57 kcal mol^{-1} calculated from eq. [16] if $\pi_1^x = -0.44$ for the gas phase (32), but no less than 2.60 if π_1^x is taken as -1.1 for the gas phase.[8]

Another, much studied, equilibrium that might also be uninfluenced by solvent cohesive energy density is the well-known keto $\rightleftharpoons$ enol equilibrium. A recent study by Emsley and Freeman (35) has yielded ΔG^0 values from results at zero concentration in 21 protic and aprotic solvents for pentane-2,4-dione, eq. [17].

[17] 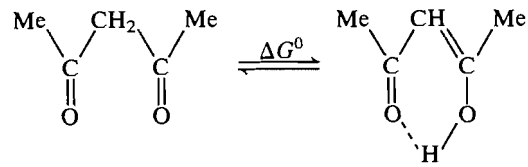

Of the 21 solvents, parameters were not available for formic acid or diglyme, but the remaining 19 solvents yielded eqs. [18] and [19]. The %CL for the α_1 term in eq. [18] is 96.7, so that this parameter is just about significant; ΔG^0 is in kcal mol^{-1}.

[18] $\Delta G^0 = (-2.24 \pm 0.14) + (2.39 \pm 0.21)\pi_1^x + (0.32 \pm 0.14)\alpha_1$

$n = 19$, sd = 0.26, $r = 0.953$

[19] $\Delta G^0 = (-2.22 \pm 0.16) + (2.54 \pm 0.23)\pi_1^x$

$n = 19$, sd = 0.29, $r = 0.936$

As suggested by Emsley and Freeman (35), polar solvents markedly favour the more polar keto form. Hydroxylic solvents are not anomalous and so the enol hydrogen-bond must remain intact, again as pointed out by Emsley and Freeman. There is a possibility, eq. [18], that solvents that are hydrogen-bond acids may stabilise the keto form preferentially. The keto form should be more basic than the enol form, certainly, but the effect is quite small. Emsley and Freeman (35) also gave results for 3-ethylpentane-2,4-dione in 6 solvents and for 3-methylpentane-2,5-dione in 12 solvents, but in neither case are there really enough solvents for MLRA to be carried out rigorously, although the dominant effect can still be seen to be that of solvent dipolarity.

One of the first processes to be investigated by either the extended Koppel–Palm equation [10] or the AKT equation was that of solubility. Various parameters can be used to express solubility, for example, the Ostwald solubility coefficient L, the Henry's law constant K^H, or ΔG^0, the standard Gibbs energy of solution based on some particular standard states. To avoid confusion over the sign of the coefficients in regression equations, we shall either set out equations in terms of ΔG^0, or when equations have been cast in terms of log K values, we shall recast these as equations in ΔG^0. Naturally, this does not affect any "goodness-of-fit" as denoted by the correlation coefficient.

On the cavity theory of solution, solubility of a solute in a series of solvents (or transfer of a solute from one solvent to another) should be inhibited by increase in cohesive energy density so that in any regression on ΔG^0, the δ_H^2 coefficient should be positive. Any solute-interaction that is set up will aid solution and hence the coefficients of terms in $f(\epsilon)$, $f(\eta)$, E, and B in eq. [10] or terms in π_1^x, α_1, and β_1 in eq. [9] should correspondingly all be negative. These considerations must be kept in mind when assessing any particular application, see the fourth condition, above.

Makitra and Pirig and their co-workers have applied eq. [10] to the solubility of a number of gases in a series of solvents (24, 25, 36–41). For example, the solubility of Freon-22 ($CHClF_2$) in 15 solvents is given by eq. [20] where N is the mole fraction solubility at 293 K (40):

[20] $\log N(CHClF_2) = 0.838 - 0.41\delta_H^2/100 + 0.00281B - 0.053E$

$n = 15$, sd = 0.161, $r = 0.966$

To be consistent with our other equations, we can simply transform eq. [20] into [21], where ΔG_S^0 is the standard Gibbs energy of solution in kcal mol^{-1} for the transfer from the gas phase to solution:

[21] $\Delta G_S^0(CHClF_2) = -1.13 + 0.56\delta_H^2/100 - 0.0038B + 0.072E$

$n = 15$, sd = 0.22, $r = 0.966$

Makitra and Pirig (40) point out that the two main factors influencing solution are solvent basicity which favours solution and solvent cohesive energy density which inhibits solution. The solvent electrophilicity, E, also seems to inhibit solution, but for the 15 solvents examined, the correlation coefficient between δ_H^2 and E is no less than 0.749, so that δ_H^2 and E are no longer independent parameters. With the exclusion of solvent THF, Makitra and Pirig (40) obtained the more sensible correlation,[9]

[22] $\Delta G_S^0(CHClF_2) = -1.05 + 0.84\delta_H^2/100 - 0.0042B$

$n = 14$, sd = 0.27, $r = 0.952$

The problem of parameter colinearity still exists if the AKT equation is applied to the solution of $CHClF_2$ since for the 14 solvents for which we have available values there is a marked

[8]The gas phase value of -1.1 has been obtained from gas phase spectrophotometric data (31) whereas that of -0.44 is an indirect value from the known gas phase ΔG^0 value for the 1,2-dibromo-4-*t*-butylcyclohexane conformational equilibrium (32). Suppan (34) has suggested that gas phase spectrophotometric shifts should not be compared with those in solution, and it is possible that for chemical processes the value of -0.44 is better.

[9]Note that Makitra and Pirig list δ_H^2 values as $\delta_H^2/1000$ when δ_H^2 is in kcal dm^{-3} (Table 1). In addition, many of the δ_H^2 values of Makitra and Pirig differ substantially from those that we consider to be the "best" values.

Can. J. Chem. Downloaded from www.nrcresearchpress.com by 196.1.178.254 on 09/07/12
For personal use only.

TABLE 3. Correlations of ΔG_t^0, kcal mol^{-1} at 298 K on the mole fraction scale, from methanol of some ion-pairs and pairs of dissociated ions, through the AKT equation [9][a]

Solute	Coefficients						
	ΔG_0^0	$s.\pi_1^x$	$a.\alpha_1$	$h(\delta_H^2/100)_1$	n	r	sd
Me_4NI	10.9	−15.6	−6.2	2.2	18	0.997	0.3
Me_4NBr	15.1	−18.8	−10.4	2.8	18	0.996	0.5
Me_4NCl	18.3	−20.0	−13.3	2.9	17	0.997	0.6
Et_4NI	10.9	−14.9	−6.8	2.4	18	0.997	0.4
Et_4NBr	15.4	−18.0	−11.4	3.1	16	0.997	0.5
Et_4NCl	18.2	−18.9	−14.2	3.1	15	0.997	0.6
Pr_4NI	9.5	−14.8	−8.0	3.3	11	0.990	0.5
$Me_4\overset{+}{N} + I^-$	28.2	−42.0	−16.4	6.3	14	0.988	1.1
$Me_4\overset{+}{N} + \bar{Br}$	32.8	−44.5	−20.7	6.7	13	0.993	0.9
$Me_4\overset{+}{N} + \bar{Cl}$	36.2	−45.5	−23.9	6.8	13	0.994	0.9
$Et_4\overset{+}{N} + I^-$	26.6	−39.3	−16.3	6.3	14	0.981	1.2
$Et_4\overset{+}{N} + \bar{Br}$	31.2	−41.9	−20.6	6.7	13	0.988	1.1
$Et_4\overset{+}{N} + \bar{Cl}$	34.7	−42.8	−23.7	6.8	13	0.992	1.0

[a]All solvents are aliphatic with $\delta = 0$, and in all cases the term in β_1 is statistically not significant, see ref. 44 and also Table 4.

correlation between δ_H^2 and α_1 ($r = 0.722$); we have had to exclude tributylphosphate for which we have no reliable δ_H^2 value. With the exclusion of any term in α_1, the best equation is,

$$[23]\quad \Delta G_S^0(CHClF_2) = 0.31 - 1.14\beta_1 + 0.78\delta_H^2/100$$
$$n = 14, \quad \text{sd} = 0.15, \quad r = 0.967$$

Both eqs. [22] and [23] lead to a chemically sensible interpretation, namely that the endoergic cohesive energy density term is counterbalanced by an exoergic solute–solvent interaction term that arises through hydrogen bonding between the somewhat acidic $CHClF_2$ molecule, and basic solvents.

The above discussion shows the difficulty of MLRA when explanatory variables are not independent. Other difficulties may arise if general chemical sense is not maintained. Abraham, Kamlet, and Taft (42) used a truncated version of eq. [9] to account for the solution of a number of solutes into a set of 22 solvents that were all non-acidic ($\alpha_1 = 0$), using just the π_1^x and (δ_H) terms. Makitra and Pirig (41) re-examined this work and showed that for two solutes, trimethylamine and 4-nitrobenzyl chloride, the truncated version of the AKT equation did not apply when the solvent set was extended to cover hydrogen-bond acidic solvents. They concluded, obviously erroneously, that the AKT equation was not satisfactory. Clearly, for solutes that are hydrogen-bond bases, a term in α_1 must be included in the regression equation. If this is done, then for all 15 solvents mentioned by Makitra and Pirig (41) the best equation for transfer Gibbs energies (43) from a standard solvent, in kcal mol^{-1} is given as:

$$[24]\quad \Delta G_t^0(Me_3N) = -0.34 - 0.55\delta - 2.40\alpha_1 + 1.03\delta_H^2/100$$
$$n = 15, \quad \text{sd} = 0.17, \quad r = 0.974$$

This compares very favourably with the corresponding correlation using the five parameter extended Koppel–Palm equation for which $r = 0.905$ for the same 15 solvents. Makitra and Pirig (41) do not give the resulting equation for these 15 solvents, but after the exclusion of chloroform find eq. [25]:

$$[25]\quad \Delta G_t^0(Me_3N) = 4.66 - 7.94f(\eta) + 7.24f(\epsilon) - 0.0042B - 0.112E$$
$$n = 14, \quad \text{sd} = —, \quad r = 0.958$$

The coefficients in eq. [24] make general chemical sense. Thus the (δ_H^2) term shows that increase in cohesive energy density inhibits solvation, exactly as expected on a cavity theory of solution, whilst increase in solvent hydrogen-bond acidity considerably aids solution, again exactly as expected for a solute that is a strong base. On the other hand, the reported (41) coefficients in eq. [25] make little general chemical sense — there is no apparent effect of solvent cohesive energy density, increase in solvent polarity as $f(\epsilon)$ *retards* solution, and an increase in solvent basicity B *aids* solution of the basic trimethylamine. This is an example of how application of the regression eqs. [9] and [10] must be carried out in accord with general chemical principles as well as with statistical ones.

The number of possible applications of eqs. [9] and [10] to the solubility of solutes is almost limitless, but we give possibly the most complicated example studied to date, that of the solubility (as transfer Gibbs energies) of tetra-alkylammonium halides and ion-pairs (44) using results for up to 18 aliphatic aprotic and hydroxylic solvents for which δ in eq. [8] is zero. For compounds of type $R_4\overset{+}{N}\bar{X}$ or ($R_4\overset{+}{N} + X^-$) it would be expected that solvent dipolarity and hydrogen-bond acidity would greatly reduce the value of ΔG_t^0, and that solvent cohesive energy density would considerably increase ΔG_t^0 through the endoergic cavity term. This is exactly as found, see ref. 44 and a summary of the regression equations in Table 3. What is somewhat unexpected is that solvents that are hydrogen-bond bases, all of which have lone pairs of electrons, seem to have no effect at all on ΔG_t^0. The coefficient in the $b.\beta_1$ term is always statistically insignificant, see also Table 4, and hence there can be no interaction between these basic solvents and the quaternary ammonium positive centre. The unit positive charge, even in the dissociated ions, must be almost completely shielded from the solvent. Inspection of Table 3 shows that the coefficients of π_1^x and α_1 very with solute in a chemically sensible way. Both the $s.\pi_1^x$ and the $a.\alpha_1$ term become more

Can. J. Chem. Downloaded from www.nrcresearchpress.com by 196.1.178.254 on 09/07/12
For personal use only.

TABLE 4. Correlations of ΔG_t^0, kcal mol^{-1} at 298 K on the mole fraction scale from methanol of some ion-pairs through the AKT equation[9][a]

Solute	Coefficients									% CL[b]				
	ΔG_0^0	$d.\delta$	$s.\pi_1^x$	$a.\alpha_1$	$b.\beta_1$	$h(\delta_H^2/100)_1$	n	r	sd	δ	π_1^x	α_1	β_1	δ_H^2
Me_4NI	10.79		−16.02	−6.61	0.50	2.35	18	0.998	0.34		100	100	66	100
Me_4NBr	15.30		−19.28	−10.89	0.59	2.96	18	0.997	0.54		100	100	52	100
Me_4NCl	18.50		−19.50	−12.79	−0.56	2.68	18	0.997	0.62		100	100	43	100
Et_4NI	10.80		−15.25	−7.07	0.37	2.55	18	0.997	0.35		100	100	51	100
Me_4NI	11.02	2.59	−15.88	−6.41	0.12	2.25	23	0.995	0.50	100	100	100	13	100
Me_4NBr	15.69	3.87	−19.09	−10.51	−0.06	2.79	23	0.995	0.67	100	100	100	5	100
Me_4NCl	18.96	3.53	−19.33	−12.40	−1.26	2.49	22	0.995	0.75	100	100	100	73	100
Et_4NI	11.06	2.16	−15.10	−6.81	−0.07	2.43	23	0.995	0.48	100	100	100	8	100
Et_4NI	11.12	1.90	−14.72	−6.29	−0.40	2.23	29	0.989	0.60	100	100	100	56	100

[a]Solvents in the first set, $n = 18$, are aliphatic with $\delta = 0$.
[b]Percentage CL. The entry "100" denotes CL > 99.999%.

Can. J. Chem. Downloaded from www.nrcresearchpress.com by 196.1.178.254 on 09/07/12
For personal use only.

negative (exoergic) along the series I^-, Br^-, and Cl^- both for the R_4NX and $(R_4N^+ + X^-)$ solutes, leading to increasing stabilisation of the chlorides by dipolar and by hydrogen-bond acid solvents. The $h.\delta_H^2$ term becomes more positive (endoergic) from Me_4N^+ to Et_4N^+ for the ion-pairs, but not so for the dissociated ions. Furthermore, the increase in $h.\delta_H^2$ is always in the order $I^- < Br^- < Cl^-$, the reverse of the order of ionic radius. It was suggested (44) that solvent electrostriction and possible solvent reorganisation around the ions or ion-pairs may play a significant role.

One difficulty over the reported (44) regression is that for the 18 solvents examined (Table 3) there is a non-negligible correlation between π_1^x and δ_H^2 ($r = 0.585$) and between α_1 and δ_H^2 ($r = 0.641$), so that extension to a wider set of solvents would be of interest. Results are available (45) for five other solvents (nitrobenzene, benzonitrile, chlorobenzene, benzene, and tetrachloromethane) with several of the ion-pairs, and for an extra eleven solvents for Et_4NI (the five given, plus ethyl benzoate, 1,1,2,2-tetrachloroethane, dichloromethane, 1,2-dichloroethane, anisole, and bromobenzene) and so we have applied eq. [9] to an extended solvent set. Unfortunately, this still does not resolve the problem of colinearity ($r = 0.435$ and 0.658) for the two above cases over the full 29 solvents, but if the equations in Table 3 are artificial, then incorporation of a different set of solvents should alter the magnitude of the coefficients considerably.[10] In Table 4 are details of regressions for ion-pairs, where now the $d.\delta$ term has had to be included. We give also the $b.\beta_1$ term, just to show how insignificant it is. Results in Tables 3 and 4 are very similar, as are the results in the two sections of Table 4. Hence we can conclude that the original equations (44) in Table 3 are, indeed "robust".

A process closely related to solubility is that of the distribution of a solute between solvent phases. Indeed, since the distribution, or partition, coefficient K_p is defined by eq. [26]

$$[26] \quad K_p = A_s/A_w$$

where A_s and A_w are the activities of the solute in solvent (s) and water (w), K_p is simply the ratio of the solubilities in the two phases, provided that the ratio of the secondary medium activity coefficients is unity. Thus for distribution of a given solute between water and a number of solvents, $\log K_p$ or ΔG_p^0 might

[10]This is quite a good test of the "robust" character of a regression — namely that the coefficients should remain the same for various subsets of data.

TABLE 5. Carbonyl compounds used in extraction experiments (46)

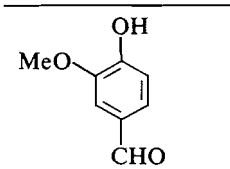	Vanillin
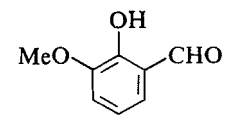	Orthovanillin
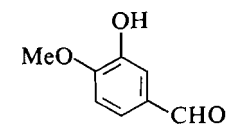	Isovanillin
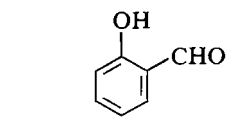	Salicylaldehyde
$CH_3COCH_2COCH_3$	Acetylacetone
$PhCOCH_2COCH_3$	Benzoylacetone

be expected to depend on $(\delta_H^2)_1$ and on parameters that reflect the various solute–solvent interactions in the solvent phases. Makitra and Pirig (46) have applied the extended Koppel–Palm equation [10] to the distribution of several carbonyl compounds between water and a number of solvents. Because the chosen solvents must be immiscible with water, the solvent variation is, perforce, limited. Furthermore, all the distributions refer to the water-saturated solvents and not the normal, dry, solvents, so that correlations using parameters for dry solvents would be expected to be not as good as usual. For a number of the carbonyl compounds, there are too few data points available, but for those shown in Table 5, we give the best regressions obtained using the AKT equation [9]; as usual we have transformed the given (46) K_p values into ΔG_p^0 values in kcal mol^{-1}. Results are in Table 6 for six carbonyl compounds. By and large, the regression coefficients make general chemical sense. Thus distribution is hindered by the endoergic $(\delta_H^2)_1$

TABLE 6. Application of the AKT equation [9] to ΔG_p^0 values for extraction of some carbonyl compounds[a]

Solute	ΔG_0^0	π_1^x	α_1	β_1	$(\delta_H^2/100$	n	r	sd
Vanillin	−2.18 ± 0.67	−5.29 ± 0.63	−2.21 ± 0.56	−1.71 ± 0.15	5.06 ± 1.16	16	0.975	0.29
Orthovanillin	−2.74 ± 0.48	−3.97 ± 0.45	−1.28 ± 0.38	—	2.93 ± 0.82	16	0.974	0.20
Isovanillin	−1.61 ± 0.65	−4.95 ± 0.61	−1.75 ± 0.55	−1.45 ± 0.35	4.35 ± 1.13	16	0.974	0.27
Salicylaldehyde	−1.94 ± 0.08	−1.61 ± 0.15	—	—	—	18	0.936	0.19
Acetylacetone	−1.30 ± 0.35	−2.41 ± 0.35	−2.00 ± 0.38	+0.93 ± 0.63	1.95 ± 0.63	20[b]	0.943	0.19
Benzoylacetone	−3.94 ± 0.38	−2.81 ± 0.42	−1.75 ± 0.33	+0.89 ± 0.23	1.71 ± 0.72	20[b]	0.981	0.15

[a]Results for solvents no. 1–26 in Table 2 of ref. 46 after conversion to ΔG^0.
[b]Excluding solvent tri-*n*-butylphosphate for which no reliable value of $(\delta_H^2)_1$ was available.

TABLE 7. A summary of the "best" regressions reported[a] for distribution of some carbonyl compounds, in terms of ΔG_p^0

Carbonyl compound	Constant	$f(n)$	$f(\epsilon)$	E	B	$\delta_H^2/100$	n	sd	r
Vanillin	4.07	−9.86	—	0.17	−0.01	−1.70	13	0.31	0.971
Orthovanillin	3.62	−19.19	—	0.13	−0.01	—	12	0.22	0.966
Isovanillin	4.41	−10.44	—	0.18	−0.01	−1.75	12	0.31	0.964
Salicylaldehyde	0.85	−4.34	1.68	0.08	—	−3.54	16	0.18	0.958
Acetylacetone	3.47	−16.20	—	0.08	—	0.64	15	0.14	0.960
Benzoylacetone	0.84	−12.57	−2.03	−0.09	—	−0.65	11	0.14	0.988

[a]From Makitra and Pirig (46), after conversion by the factor −1.364.

term, and favoured by the various other terms that reflect exoergic solute–solvent interactions. The only exceptions are the small, but statistically significant endoergic β_1 terms for acetylacetone and benzoylacetone and the lack of any term in $(\delta_H^2)_1$ for salicylaldehyde. All distributions are favoured by increase in solvent π_1^x, as expected and are usually favoured by increase in solvent α_1 value, the latter arising no doubt through solute (base) – solvent (acid) interactions. The one marked exception, salicylaldehyde, is internally hydrogen-bonded and hence unable to interact with external hydrogen-bond acids. That is, the intramolecular hydrogen-bond competes effectively with any intermolecular hydrogen-bond.

It is rather difficult to compare results in Table 6 with those of Makitra and Pirig, since these workers give several "best" equations, all obtained after removing one or more solvents. We give in Table 7 the coefficients for some of these equations, after multiplication by −1.364 in order to transform them into coefficients related to ΔG^0. There is very little chemical sense to be made out of these coefficients — thus increase in dispersion hinders partition, whilst increase in solvent cohesive energy density actually aids partition into the solvent.

In truth, there are neither enough solvents nor a sufficiently varied collection of solvents to obtain "robust" MLRA equations for the distributions. We have considered these processes, however, because Makitra and Pirig (46) have used them as examples of the extended Koppel–Palm equation [10].

Application of MLRA to kinetics

The first comprehensive application of MLRA to kinetic phenomena was that of Koppel and Palm (17) who listed regression constants for the simple Koppel–Palm equation [6], for various processes. Shorter and co-workers (47) have applied correlation analysis to solvent effects on the reaction between diazodiphenylmethane and carboxylic acids, but one particular reaction that has been studied by several workers is the unimolecular decomposition of *t*-butyl chloride at 298 K. The "best" equation obtained by Koppel and Palm when a variety of solvents, including aprotic and hydroxylic, was considered is,[11]

$$[27]\quad \Delta G^{\ddagger}(\mathrm{Bu^tCl}) = (2.713 \pm 1.01) - (18.27 \pm 2.76)f(\epsilon) - (18.36 \pm 4.88)f(\eta) - (0.52 \pm 0.04)E$$
$$n = 23, \quad \mathrm{sd} = —, \quad r = 0.982$$

More recently, Dvorko and co-workers (48) applied the extended Koppel–Palm equation to 28 aprotic and hydroxylic solvents:

$$[28]\quad \Delta G^{\ddagger}(\mathrm{Bu^tCl}) = 24.83 - 9.63f(\epsilon) - 22.65f(\eta) - 0.400E - 0.651\delta_H^2/100$$
$$n = 28, \quad \mathrm{sd} = 0.91, \quad r = 0.960$$

As Dvorko and co-workers point out, both eq. [27] and eq. [28] lead to the conclusion that $\Delta G^{\ddagger}$ is reduced by solvent electrophilicity (E) and to a lesser extent by solvent polarity. Very significantly, solvent nucleophilicity (B) seems to play no part, in contrast to the conclusion of Fawcett and Krygowski (49). Abraham, Taft, and Kamlet (50) also examined the *t*-butyl chloride reaction using a truncated version of the AKT equation [9], without the $(\delta_H^2)_1$ variable. For a variety of aliphatic aprotic and hydroxylic solvents they obtained,

$$[29]\quad \Delta G^{\ddagger}(\mathrm{Bu^tCl}) = 20.54 - 9.47\pi_1^x - 7.30\alpha_1$$
$$n = 15, \quad \mathrm{sd} = —, \quad r = 0.995$$

Although the explanatory variables in eq. [29] are different to those in eqs. [27] and [28], the conclusions are very similar, namely that solvent polarity and hydrogen-bond acidity (or electrophilicity) reduce $\Delta G^{\ddagger}$ and hence increase log k.

The corresponding *t*-butyl bromide and *t*-butyl iodide reactions have also been examined by Dvorko and co-workers (48) and Abraham, Kamlet, and Taft (50), but the most recent set of

[11]Note that in eq. [27], $f(\epsilon) = (\epsilon - 1)/(2\epsilon + 1)$, and that the original equation was given in terms of log k.

Can. J. Chem. Downloaded from www.nrcresearchpress.com by 196.1.178.254 on 09/07/12
For personal use only.

TABLE 8. Application of AKT equation [9] to the *t*-butyl halide reactions (51)[a]

	Coefficients								CL%[b]			
	$\Delta G_0^{\ddagger}$	π_I^x	α_1	β_1	$(\delta_H^2)_I/100$	n	r	sd	π_I^x	α_1	β_1	$(\delta_H^2)_I/100$
$\Delta G^{\ddagger}$(Bu^{t}Cl)	19.92	−6.96	−5.70	−0.99	−0.65	21[c]	0.9973	0.33	100	100	99.6	100
$\Delta G^{\ddagger}$(Bu^{t}Br)	16.33	−7.87	−4.31	−0.63	−0.43	21[c]	0.9947	0.38	100	100	92	99.8
$\Delta G^{\ddagger}$(Bu^{t}I)	13.37	−8.28	−3.32	0.46	−0.04	21[c]	0.9905	0.42	100	100	76	24
$\Delta G^{\ddagger}$(Bu^{t}Cl)[d]	19.62	−6.49	−5.45	−0.83	−0.73	30	0.9863	0.68	100	100	83	99.9
$\Delta G^{\ddagger}$(Bu^{t}Br)[d]	16.45	−8.06	−4.00	−0.75	−0.45	30	0.9799	0.68	100	100	84	97.4

[a]Converted from log k regressions to $\Delta G^{\ddagger}$ in kcal mol^{-1}.
[b]Where the value 100 is used, the CL% > 99.999.
[c]A variety of aliphatic aprotic and hydroxylic solvents.
[d]Reference 57; the coefficients of δ are 1.30 and 1.77 for the Bu^{t}Cl and Bu^{t}Br reactions, respectively.

Can. J. Chem. Downloaded from www.nrcresearchpress.com by 196.1.178.254 on 09/07/12
For personal use only.

correlations is due to Abraham and co-workers (51). Details are given in Table 8. The solvents studied are a number of aliphatic aprotic and hydroxylic solvents, so that the $d.\delta$ term is zero, cf. eq. [29]. Although the regression coefficients in Table 8 are numerically smaller than those in eq. [29], for π_I^x and α_1, the general chemical sense is the same. As now seems clear from a number of different regressions, eqs. [27] to [29] and Table 8, the two main factors influencing the reaction are solvent dipolarity and solvent electrophilicity (or hydrogen-bond acidity). This is chemically quite reasonable because the transition-state seems to behave as a dipolar species of dipole moment around 8 D, with a substantial negative charge on the leaving chlorine atom. Transition states (**V**) and (**VI**) have previously been suggested (52), both of which would be stabilised by solvents with large π_I^x and α_1 values.

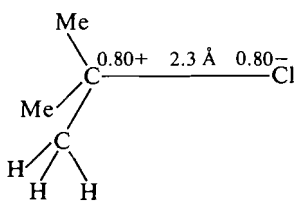

(**V**) μ = 8.80 D

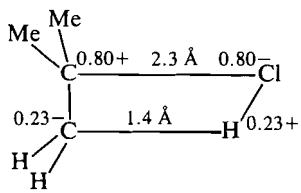

(**VI**) μ = 7.29 D

Results in Table 8 show that there are minor accelerating effects of solvent cohesive energy density (suggested to be due to electrostriction of solvent by the dipolar transition state) and solvent hydrogen-bond basicity, β_1. Now since solvents that are hydrogen-bond bases are also nucleophiles, it follows that solvent nucleophilicity plays but a very minor rôle in stabilising (**V**) or (**VI**). Bentley (52) has quite correctly pointed out that the identification of solvent hydrogen-bond basicity, β_1, with solvent nucleophilicity is only an assumption. However, it can be shown (53) that there is a reasonable connection between the nucleophilic solvent parameter Y^+ of Kevill and Anderson (54) and solvent β_1 values,

$$[30] \quad Y^+ = 0.38 - (0.61 \pm 0.08)\beta_1$$
$$n = 8, \quad \text{sd} = 0.08, \quad r = 0.946$$

There seems little doubt, therefore, that solvent dipolarity and electrophilicity are the dominant factors that determine the magnitude of $\Delta G^{\ddagger}$ and hence log k for the unimolecular heterolysis of *t*-butyl chloride. Because solvent nucleophilicity and electrophilicity are colinear over many of the hydroxylic solvents used in solvolysis studies, it has been difficult to determine their individual contributions. The studies discussed here (51, 53) as well as other recent work (55, 56) has finally enabled the extent of nucleophilic and electrophilic assistance to be established.

It might be thought somewhat odd that the positive centre in transition state (**V**) and (**VI**), carrying some 0.8 units of charge, is not stabilised by nucleophilic solvents. However, we already know that R_4N^+ centres are completely unaffected by solvent nucleophilicity (as β_1), see Table 3 and especially Table 4. The very small nucleophilic assistance to the *t*-butyl chloride reaction is therefore quite consistent with effects on R_4NCl and $(R_4N^+ + Cl^-)$ solutes.

In Table 8 are given also regression coefficients for the *t*-butyl bromide and *t*-butyl iodide reactions (51). Nucleophilic assistance is not statistically significant in either case. The variation in the coefficients of π_I^x and β_1 is as expected on general chemical grounds. Along the series RCl, RBr, and RI the transition states will probably become slightly more dipolar, but much less susceptible to electrophilic assistance, hence the order of π_I^x coefficients in $\Delta G^{\ddagger}$ is numerically RCl < RBr < RI but for α_1 the order is RCl > RBr > RI. More recently, Abraham and co-workers (57) have extended results to cover aromatic and polyhalogenated solvents as well as the aliphatic solvents examined before (51). Although the fits are not as good as for the 21 aliphatic solvents, the various regression coefficients agree very well with those for the aliphatic solvent set, and the general conclusions based on the 21 solvent set remain unchanged.

One of the difficulties with MLRA is not only that quite a large number of solvents are needed, but also that there must be a wide variety of solvents. A number of Menschutkin reactions have been studied over a very wide range of solvents, and Koppel and Palm (17) have examined that between tri-*n*-propylamine and methyl iodide,

$$[31] \quad Pr_3N + MeI \rightarrow Pr_3NMe^+I^-$$

For 28 aprotic solvents, eq. [32] was found, but the correlation coefficient decreased markedly when the solvent set was extended to include hydroxylic solvents, eq. [33].

$$[32] \quad \Delta G^{\ddagger}(Pr_3N/MeI) = 12.27 - 12.52f(\epsilon) - 18.84f(\eta) - 0.47E$$
$$n = 28, \quad \text{sd} = —, \quad r = 0.945$$

$$[33] \quad \Delta G^{\ddagger}(Pr_3N/MeI) = 10.11 - 14.09f(\epsilon) - 13.22f(\eta) + 0.06E$$
$$n = 32, \quad \text{sd} = —, \quad r = 0.798$$

Can. J. Chem. Downloaded from www.nrcresearchpress.com by 196.1.178.254 on 09/07/12
For personal use only.

Both equations indicate that solvent dipolarity and polarisability greatly reduce $\Delta G^{\neq}$ and hence increase $\log k$. However, on eq. [32] solvent electrophilicity is important but on eq. [33] it is statistically not significant (CL < 80%).

The related reaction between triethylamine and ethyl iodide has recently been examined by Abraham and co-workers (58) who find for 33 aprotic and hydroxylic solvents,[12]

$$[34]\quad \Delta G^{\neq}(Et_3N/EtI) = 5.41 + 1.29\delta - 7.31\pi_1^x + (0.111\alpha_1) + (0.222\beta_1) + 0.543(\delta_H^2)_1/100$$
$$n = 33, \quad sd = 0.35, \quad r = 0.980$$

According to eq. [34] the over-riding factor influencing the reaction rate is solvent dipolarity, with solvent hydrogen-bond acidity and basicity being statistically not significant. Presumably the stabilisation of the leaving iodide ion in the transition state by electrophilic assistance is exactly counterbalanced by stabilisation of triethylamine in the initial state.

If the leaving halide is altered, but the incoming amine is kept constant, then on the above suggestion, the effect of solvent electrophilicity will be to stabilise the transition state in the order RI < RBr < RCl and hence to lower $\Delta G^{\neq}$ in the same order, since a leaving chloride will be electrophilically solvated better than a leaving bromide or iodide. Auriel and Hoffmann (59) have studied the reaction of 1,4-diazabicyclo[2.2.2]octane, or Dabco, with 2-chloro-, 2-bromo-, and 2-iodoethylbenzene using a wide variety of aprotic and hydroxylic solvents. The best equations are given below:

$$[35]\quad \Delta G^{\neq}(Dabco/Cl) = 1.00 + 1.01\delta - 5.20\pi_1^x$$
$$n = 27, \quad sd = 0.40, \quad r = 0.927$$

$$[36]\quad \Delta G^{\neq}(Dabco/Br) = -2.12 + 1.00\delta - 4.90\pi_1^x + 0.74\alpha_1$$
$$n = 27, \quad sd = 0.35, \quad r = 0.946$$

$$[37]\quad \Delta G^{\neq}(Dabco/I) = -3.05 + 1.04\delta - 4.85\pi_1^x + 1.54\alpha_1$$
$$n = 27, \quad sd = 0.32, \quad r = 0.964$$

In all eqs. [35]–[37] terms in β_1 and $(\delta_H^2)_1$ were not significant. Exactly as found for the Et_3N/EtI reaction, the main solvent influence is dipolarity, stabilising the transition state and increasing $\log k$. For all three reactions, the initial-state effect of solvent hydrogen-bond acidity will be the same, and hence the variation in the $a.\alpha_1$ term must be due to variation in transition-state property. As suggested above, the largest stabilising effect will be on the Dabco/Cl transition state, just counteracting the effect on the dibasic Dabco amine. But for the bromide and more so for the iodide, the stabilisation effect on the transition state is less, leading to more positive $a.\alpha_1$ coefficients and hence to a retarding effect on the rate.

The coefficients of π_1^x for the various Menschutkin reactions are all large and negative in eqs. [34]–[37], reflecting stabilisation of the dipolar transition states, a lowering of $\Delta G^{\neq}$, and an increase in $\log k$. Other studies (15) have yielded a dipole moment of 7.6 D for the Et_3N/EtI transition state and a charge separation of around 0.4 units, so that there is considerable independent evidence for transition-state structure. This is not necessarily so for other reactions that have been somewhat less studied, and we give as a final example the thermal *cis–trans* isomerisation of azobenzenes. Whitten and co-workers (60) determined rate constants for the isomerisation of *cis*-4-diethylamino-4′-nitroazobenzene (*cis*-DENAB) in a number of aprotic and hydroxylic solvents and correlated $\Delta G^{\neq}$ separately with π_1^x and α_1. We have applied the MLRA equation [9] to as many solvents as we had parameters for. The parameters β_1 and $(\delta_H^2)_1$ are not statistically significant, and the best regression equation is,

$$[38]\quad \Delta G^{\neq}(cis\text{-DENAB}) = 20.87 + 2.02\delta - 7.11\pi_1^x - 2.23\alpha_1$$
$$n = 22, \quad sd = 0.53, \quad r = 0.971$$

with all three parameters being significant at ≥99.99% CL. Such an equation suggests that the transition state is stabilised by dipole–dipole interactions and by hydrogen-bond interactions between acidic solvents and the nitro group in the rotational transition state, which may be close to the valence bond structure (**VII**). The lack of any stabilisation of the $=\overset{+}{N}R_2$

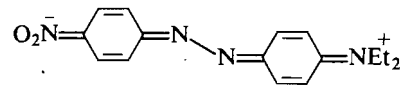

(**VII**)

centre (no β_1 effect) is not surprising in view of our previous discussion on R_4N^+ compounds. Whitten and co-workers (60) also examined the π, π^x transition of *trans*-DENAB for which we find,

$$[39]\quad E_{max}(trans\text{-DENAB}) = 62.97 - 6.36\pi_1^x - 0.77\alpha_1 - 0.92\beta_1$$
$$n = 22, \quad sd = 0.39, \quad r = 0.976$$

with %CL of >99.9999 (π_1^x), 95 (α_1), and 99 (β_1). Consideration of the Frank–Condon principle suggests that *trans*-DENAB itself is but marginally hydrogen-bonded. Presumably this is also the case for *cis*-DENAB, so that the transition state for isomerisation is preferentially stabilised by hydrogen-bonded acidic solvents. It follows from the coefficient of π_1^x in eqs. [38] and [39] that the dipolarity of the Frank–Condon excited state and the isomerisation transition state must be very similar, as pointed out by Whitten and co-workers (60). The latter suggest dipole moments of 8.0 D for *trans*-DENAB, 25 D for the excited state and 20.5 D for the transition state. From comparisons of the $s.\pi_1^x$ term in eqs. [38] and [39] with those in, for example, eqs. [34] to [37] and Table 8, it seems as though the dipolarity of the DENAB transition state is no more than that of the *t*-butyl chloride transition state (μ = 8.80 or 7.29 D). Possibly the degree of charge separation in the transition state is a determining factor, rather than the actual dipole moment.

Asano and Okada (61) studied the isomerism of the related compound *cis*-4-dimethylamino-4′-nitroazobenzene (*cis*-DMNAB) in a different set of aprotic plus hydroxylic solvents, leading to

$$[40]\quad \Delta G^{\neq}(cis\text{-DMNAB}) = 3.51 + 3.05\delta - 6.48\pi_1^x - 1.94\alpha_1$$
$$n = 18, \quad sd = 0.53, \quad r = 0.981$$

in good agreement with eq. [38]. Asano and Okada (61) showed also that for a number of other 4- or 4,4′-substituted azobenzenes there was very little solvent effect on the rate of isomerisation, e.g. for the ratio $k(MeOH)/k(hexane)$ they found 2.30 (4-nitro), 1.44 (4-*N*,*N*-diethylamino), 1.88 (4-*N*,*N*-dimethylamino-4′-chloro), and 1.08 (2,4-dinitro) as against a ratio of 25 500 for *cis*-DMNAB itself. Clearly, a push–pull mechanism leading to a rotational transition state close to (**VII**)

[12]Note in eq. [34], $\Delta G^{\neq}$ is calculated with respect to solvent DMF.

is favored only by the specific combination of a +R and −R substituent in the 4 and 4′ positions.

Although we have mostly dealt with solvent effects in terms of the AKT equation rather than the Koppel–Palm equation, both equations when properly used give results that are generally reasonable. Sometimes the AKT equation leads to statistically better fits, as we have seen in many of the examples discussed above, but sometimes a better fit is obtained using the Koppel–Palm equation. Zhong-yuan *et al.* (62) have applied several regression equations to the substitution of 2,4-dinitrofluorobenzene by the ethyl ester of tyrosine and find for the 11 solvents studied that the Koppel–Palm equation in B, E, and $f(\epsilon)$ leads to the best fit of the log k values. For a general discussion of solvent effects, especially on kinetic processes, the excellent book of Reichardt (63) is highly recommended.

The application of MLRA to chemical kinetics is clearly limited only by the number of reactions that have been studied in a wide variety of solvents and we have given but a selection of such processes. It must be kept in mind, however, that just as kinetic data relate only to differences between transition state and initial state, so do all the regressions based on log k or $\Delta G^{\ddagger}$ values. Although we have analysed regression equations in terms, especially, of transition-state effects, this can only be done through "chemical intuition", there being no logical connection whatsoever between any log k, $\Delta G^{\ddagger}$, or regression constant and a transition-state effect. In order to establish such a connection, solvent effects on log k or $\Delta G^{\ddagger}$ must first be broken down into initial-state and transition-state contributions; we deal briefly with this aspect of solvent effects in the next section.

Initial-state and transition-state effects and MLRA

The separation of solvent effects on rate constants (as log k or $\Delta G^{\ddagger}$ values) into initial-state and transition-state contributions is now a well-known technique in physical organic chemistry, see for example a number of reviews (7, 15, 64). Values of $\Delta G^{\ddagger}$ are rather more convenient to use than log k values, a general equation for the separation being (7),

$$[41] \quad \Delta G_t^0(\mathrm{Tr}) = \Delta G_t^0(\mathrm{Reactants}) + \Delta G_B^{\ddagger} - \Delta G_A^{\ddagger}$$

where ΔG_t^0 represents the Gibbs energy of transfer of a species from a standard reference solvent (A) to any other solvent (B). Values of ΔG_t^0(reactants) can be found by conventional thermodynamic methods (7) and are combined with kinetic measurements of $\Delta G_B^{\ddagger}$ and $\Delta G_A^{\ddagger}$ to give the resulting effect on the transition state, $\Delta G_t^0(\mathrm{Tr})$. It is not our intention to discuss the various applications of eq. [41], or equivalent equations that can be set up using any thermodynamic parameter such as H, S, V, etc., but only to deal with one specific recent advance, as follows.

Suppose that eq. [41] can be applied to a given reaction, using quite a large number of different solvents. It is then possible to apply the method of multiple linear regression analysis, not only to $\Delta G^{\ddagger}$ values but also to values of $\Delta G_t^0(\mathrm{Tr})$. In this way, the exact origin of all the terms in an equation such as the AKT equation [9] can be determined, without recourse to chemical intuition. Unfortunately, application of this method, known as the "unified method" (15), requires the availability of a very large quantity of experimental data, both kinetic and thermodynamic, and but few examples are known to date. We discuss now, the one complete published analysis on these lines — that of the *t*-butyl halide reactions carried out by Abraham and co-workers (57).

These workers first studied the 21 aliphatic solvents previously investigated (51). Values of $\Delta G_t^0(\mathrm{Bu^tX})$ were obtained and combined with $\Delta G^{\ddagger}$ values to yield the corresponding transition-state values via eq. [42]. The standard solvent was DMF.

$$[42] \quad \Delta G_t^0(\mathrm{Tr}) = \Delta G_t^0(\mathrm{Bu^tX}) + \Delta G_B^{\ddagger} - \Delta G_{\mathrm{DMF}}^{\ddagger}$$

It is then possible to apply the AKT equation [9] to $\Delta G_t^0(\mathrm{Tr})$, $\Delta G_t^0(\mathrm{Bu^tX})$ and $\delta\Delta G^{\ddagger} = \Delta G_B^{\ddagger} - \Delta G_{\mathrm{DMF}}^{\ddagger}$ and then to see exactly how each term in the equation originates. Details are in Table 9 for the case of Bu^{t}Cl and Bu^{t}Br. Inspection of the coefficients for the Bu^{t}Cl reaction shows very clearly that the π_I^x term in $\Delta G^{\ddagger}$ arises almost exclusively through a transition-state effect, as indeed does the α_1 term as well. The rather small β_1 term is again a transition-state effect, showing that a small amount of nucleophilic participation may take place. However, the negative δ_H^2 term in the $\Delta G^{\ddagger}$ equation can now be shown to arise through two positive endoergic effects on initial state and transition state that do not quite cancel out.

Effects on the Bu^{t}Br reaction for the same 21 solvents are very similar, but in this case the effect of nucleophilic participation is even smaller as judged by the β_1 term. Abraham and co-workers (57) also carried out an analysis using a further set of solvents that included aromatic and polyhalogenated ones as well as the original (53) 21 aliphatic solvents. Although a $d.\delta$ term is now required, the remaining coefficients are very close to those obtained for the 21 solvent set, compare Tables 9 and 10. However, the β_1 term in both $\delta\Delta G^{\ddagger}$ and $\Delta G_t^0(\mathrm{Tr})$ is rather less significant in the 30 solvent set, Table 10.

The only other reaction for which there are sufficient results to apply this "unified" method is the Menschutkin reaction of triethylamine and ethyl iodide. Abraham (15) has given a preliminary account of work on these lines, but since a more extensive and detailed account is in preparation (58) we refrain from an analysis until a later date.

Although it is unlikely ever to be applied to a great many reactions, we feel that it is important to use the unified method for the analysis of typical organic reactions. In the way, not only can solvent effects on $\Delta G^{\ddagger}$ be broken down into individual interactions, but it is then possible to assign exactly these interactions to initial-state and transition-state effects.

Summarising discussion

We have devoted much of this review to showing how the method of MLRA can be applied to various phenomena in organic chemistry and can lead to some understanding of solvent effects. As with all linear free energy relationships, equations such as [9] and [10] are based on the assumption that individual effects act independently and can be summed to yield an overall effect. Considering the complicated nature of solvents and solution, especially those involving solvents such as water and alcohols, it is remarkable that equations based on such an assumption hold over a wide range of processes and solvents. No doubt there will be situations in which this basic assumption breaks down, but it certainly seems to lead to chemically reasonable results for the processes we have considered.

There are, of course, other approaches to the study of solvent effects, notably factor analysis (FA) and principal component analysis (PCA). Factor analysis itself has been used in two quite different ways. Chastrette and Carretto (65) applied FA to several solvent properties and obtained four factors, or parameters, that were simply regarded as abstract factors, although it was shown, for example, that the first factor was strongly

Can. J. Chem. Downloaded from www.nrcresearchpress.com by 196.1.178.254 on 09/07/12
For personal use only.

TABLE 9. Application of the AKT equation [9] to initial-state and transition-state contributions in the *t*-butyl halide reactions for 21 aliphatic solvents at 298 K (57)

	Coefficients						CL%				
	ΔG_0	π_1^*	α_1	β_1	$(\delta_H^2)_1/100$	r	sd	π_1^*	α_1	β_1	$(\delta_H^2)_1/100$
ΔG_t^0(Tr)[a]	7.39	−7.50	−5.72	−1.29	0.48	0.9925	0.45	100	100	99.5	99.7
ΔG_t^0(Bu^{t}Cl)	−0.86	−0.54	−0.03	−0.31	1.13	0.9856	0.23	85	22	84	100
$\delta\Delta G^{\neq}$	8.25	−6.96	−5.70	−0.99	−0.65	0.9973	0.33	100	100	99.6	100
ΔG_t^0(Tr)[b]	7.75	−8.40	−4.27	−0.91	0.73	0.9882	0.43	100	100	96.8	100
ΔG_t^0(Bu^{t}Br)	−0.91	−0.53	0.04	−0.28	1.16	0.9871	0.23	85	27	81	100
$\delta\Delta G^{\neq}$	8.66	−7.87	−4.31	−0.63	−0.43	0.9947	0.38	100	100	92	99.8

[a]For the Bu^{t}Cl reaction.
[b]For the Bu^{t}Br reaction.

TABLE 10. Application of the AKT equation [9] to initial-state and transition-state contributions in the *t*-butyl halide reactions for 30 solvents at 298 K (57)

	Coefficients								CL%					
	ΔG_0	π_1^*	δ	α_1	β_1	$(\delta_H^2)_1/100$	r	sd	π_1^*	δ	α_1	β_1	$(\delta_H^2)_1/100$
ΔG_t^0(Tr)[a]	7.22	−7.34	1.19	−5.46	−1.21	0.42	0.9805	0.66	100	99	100	97.5	96.5
ΔG_t^0(Bu^{t}Cl)	−0.73	−0.85	−0.09	−0.01	0.38	1.15	0.9633	0.32	95	32	8	87	100
$\delta\Delta G^{\neq}$	7.95	−6.49	1.28	−5.45	−0.83	−0.73	0.9863	0.68	100	99	100	88	99.9
ΔG_t^0(Tr)[b]	7.55	−8.23	1.59	−3.96	0.81	0.66	0.9672	0.66	100	99.8	100	88	99.8
ΔG_t^0(Bu^{t}Br)	−1.24	−0.16	−0.18	0.04	−0.06	1.11	0.9771	0.26	36	69	27	23	100
$\delta\Delta G^{\neq}$	8.78	−8.06	1.77	−4.00	−0.75	−0.45	0.9799	0.68	100	99.9	100	84	97.4

[a]For the Bu^{t}Cl reaction.
[b]For the Bu^{t}Br reaction.

correlated with solvent dipole moment and $f(\epsilon)$, etc. Svoboda *et al.* (66) also analysed solvent properties (35 properties for 85 solvents or a restricted set of 20 properties for 51 solvents) and showed that a minimum number of four abstract factors were required. They then rotated these factors to yield four orthogonal factors to which were ascribed a physical significance: *AP* (electrophilic solvation), *BP* (nucleophilic solvation), *EP* (polar solvation), and *PP* (dispersion solvation), and then set out a multiple linear regression equation,

[43] $A = A_0 + a.AP + b.BP + c.EP + d.PP$

where A is the dependent parameter (log k, $\Delta G^{\neq}$, etc.) and A_0, a, b, c, d are constants to be found by MLRA. Application of eq. [43] is no different in principle to the multiple linear regression equations we have already discussed. Whether eq. [43] is more general, or leads to better fits of the data, than the AKT equation [9] or the Koppel–Palm–Makitra–Pirig equation [10] could be decided by the simple, although lengthy procedure of comparing the three equations as applied to as many sets of data as possible. This is quite beyond the scope of this review, but since Svoboda *et al.* (66) list regressions for a large number of kinetic and spectroscopic processes, some idea of the relative success of the various MLRA equations can be obtained. Thus for some S_N1 reactions in hydroxylic and aprotic solvents, eq. [43] leads to good fits, with $r = 0.972$ and 0.990, compare the AKT eq. [9] where r ranges from 0.980 to 0.997, Table 8, and the simple Koppel–Palm equation [6] where values of r 0.982 and 0.985 are obtained (17). On the other hand, for S_N2 reactions of the Menschutkin type, the same "all-solvent" correlations by eq. [43] results in correlation coefficients between 0.764 and 0.846 as compared to values by the AKT equation [10] of 0.927 to 0.980, eqs. [34] and [37], and a value of 0.798 using the Koppel–Palm equation, see eq. [33]. At the moment, there does not seem to be any advantage of eq. [43] over the previous eqs. [9] and [10].

Wold and co-workers (67) take a rather different view. From a PC analysis of ^{13}C NMR shifts of indenyl-lithium, they derived two principal components, θ_1 and θ_2. Although θ_1 could be correlated with solvent parameters such as π_1^*, the second component θ_2 seemed to be system-specific. It can then be argued (68) that the appearance of system-specific parameters precludes the use of MLRA, because the latter is based on the assumption that *general* solvent parameters can be used in the correlation of solvent effects on various processes. In principle, Wold and co-workers (67, 68) are no doubt correct. The complicated nature of solvents and solvent–solute interactions must give rise ultimately to system-specific factors. However, in practice, it appears that MLRA can be applied to a reasonably wide range of processes, and, as we have seen, can yield coefficients in equations such as the AKT equation [9] that make general chemical sense.

Our conclusion is therefore that if MLRA is properly applied, with due consideration given to matters such as colinearity of explanatory variables, etc., it is possible to derive equations that can be interpreted in a chemically sensible way, and that can lead to further understanding of a rather large range of thermodynamic, kinetic, and spectroscopic processes.

1. M. BERTHELOT and L. PÉAN DE SAINT-GILLES. Ann. Chim. (3 me Ser), **65**, 385 (1862); **66**, 5 (1862); **68**, 225 (1863).
2. N. A. MENSCHUTKIN. Z. Phys. Chem. **5**, 589 (1890).
3. (*a*) G. STEINER and R. HUISGEN. J. Am. Chem. Soc. **95**, 5056 (1973); (*b*) M. ESSEFAR, M. EL MOUHTADI, D. LIOTARD, and J.-L. M. ABBOUD. J. Chem. Soc. Perkin Trans. 2, 143 (1988).

Can. J. Chem. Downloaded from www.nrcresearchpress.com by 196.1.178.254 on 09/07/12
For personal use only.

4. J. G. KIRKWOOD. J. Chem. Phys. **2**, 351 (1934).
5. K. J. LAIDLER and H. EYRING. Ann. N.Y. Acad. Sci. **39**, 303 (1940).
6. S. GLASSTONE, K. J. LAIDLER, and H. EYRING. The theory of rate processes. McGraw-Hill, New York. 1944.
7. M. H. ABRAHAM. Prog. Phys. Org. Chem. **11**, 1 (1974).
8. M. H. ABRAHAM and R. J. ABRAHAM. J. Chem. Soc. Perkin Trans. 2, 47 (1974).
9. M. H. ABRAHAM and R. J. ABRAHAM. J. Chem. Soc. Perkin Trans. 2, 1677 (1975).
10. J. R. MCCABE and C. A. ECKERT. Acc. Chem. Res. **7**, 251 (1974).
11. H. KWART and T. H. LILLEY. J. Org. Chem. **43**, 2374 (1978).
12. E. GRUNWALD and S. WINSTEIN. J. Am. Chem. Soc. **70**, 846 (1948).
13. S. WINSTEIN, E. GRUNWALD, and H. W. JONES. J. Am. Chem. Soc. **73**, 2700 (1951).
14. W. BLOKZIJL, J. B. F. N. ENGBERTS, J. JAGER, and M. J. BLANDAMER. J. Phys. Chem. **91**, 6022 (1987).
15. M. H. ABRAHAM. Pure Appl. Chem. **57**, 1155 (1985).
16. I. A. KOPPEL and V. A. PALM. Org. React. USSR, **8**, 291 (1971).
17. I. A. KOPPEL and V. A. PALM. *In* Advances in linear free energy relationships. *Edited by* N. B. Chapman and J. Shorter. Plenum Press, London. 1972.
18. M. J. KAMLET, P. W. CARR, R. W. TAFT, and M. H. ABRAHAM. J. Am. Chem. Soc. **103**, 6062 (1981).
19. M. H. ABRAHAM, M. J. KAMLET, and R. W. TAFT. J. Chem. Soc. Perkin Trans. 2, 923 (1982).
20. R. W. TAFT, M. H. ABRAHAM, R. M. DOHERTY, and M. J. KAMLET. J. Am. Chem. Soc. **107**, 3105 (1985).
21. M. J. KAMLET, R. M. DOHERTY, J.-L. M. ABBOUD, M. H. ABRAHAM, and R. W. TAFT. Chemtech. 566 (1986).
22. M. H. ABRAHAM, R. M. DOHERTY, M. J. KAMLET, and R. W. TAFT. Chem. Brit. **22**, 551 (1986).
23. M. J. KAMLET, J.-L. M. ABBOUD, M. H. ABRAHAM, and R. W. TAFT. J. Org. Chem. **48**, 2877 (1983).
24. R. G. MAKITRA, YA. N. PIRIG, A. M. ZELIZNYI, M. A. DANIEL DE AGUAR, V. L. MIKOLAJEV, and V. A. RAMANOV. Org. React. USSR, **14**, 421 (1977).
25. R. G. MAKITRA and YA. N. PIRIG. Org. React. USSR, **16**, 535 (1979).
26. I. A. KOPPEL and A. I. PAJU. Org. React. USSR, **11**, 121 (1974).
27. R. W. TAFT, J.-L. M. ABBOUD, M. J. KAMLET, and M. H. ABRAHAM. J. Soln. Chem. **14**, 153 (1985).
28. R. J. ABRAHAM and E. BRETSCHNEIDER. *In* Internal rotation in molecules. *Edited by* W. J. Orville-Thomas. Wiley, London. 1974.
29. R. J. ABRAHAM. J. Phys. Chem. **73**, 1192 (1969).
30. J.-S. CHEN, R. B. SHIRKS, and W.-C. LIN. J. Phys. Chem. **90**, 4970 (1986).
31. M. ESSFAR, G. GUIHENEUF, and J.-L. M. ABBOUD. J. Am. Chem. Soc. **104**, 6786 (1982).
32. M. H. ABRAHAM, L. E. XODO, M. J. COOK, and R. CRUZ. J. Chem. Soc. Perkin Trans. 2, 1503 (1982).
33. R. J. ABRAHAM and L. GRIFFITHS. Tetrahedron, **37**, 575 (1981).
34. P. SUPPAN. Chem. Phys. Lett. **94**, 272 (1983).
35. J. EMSLEY and N. J. FREEMAN. J. Mol. Struct. **161**, 193 (1987).
36. R. G. MAKITRA and YA. N. PIRIG. Org. React. USSR, **15**, 547 (1978).
37. R. G. MAKITRA, YA. N. PIRIG, T. I. POLITANSKAYA, and F. B. MOIN. Org. React. USSR, **15**, 561 (1978).
38. R. G. MAKITRA, YA. N. PIRIG, T. I. POLITANSKAYA, and F. B. MOIN. Org. React. USSR, **16**, 549 (1979).
39. R. G. MAKITRA, YA. N. PIRIG, and T. I. POLITANSKAYA. Zhur. Priklad. Khim. **54**, 54 (1981).
40. R. G. MAKITRA, YA. N. PIRIG, T. I. POLITANSKAYA, and F. B. MOIN. Zhur. Fiz. Khim. **55**, 758 (1981).
41. R. G. MAKITRA and YA. N. PIRIG. Zhur. Obshchei Khim. **56**, 2657 (1986).
42. M. H. ABRAHAM, M. J. KAMLET, and R. W. TAFT. J. Chem. Soc. Perkin Trans. 2, 923 (1982).
43. M. H. ABRAHAM. J. Chem. Soc. B, 299 (1971).
44. R. W. TAFT, M. H. ABRAHAM, R. M. DOHERTY, and M. J. KAMLET. J. Am. Chem. Soc. **107**, 3105 (1985).
45. M. H. ABRAHAM. J. Chem. Soc. Perkin Trans. 2, 1343 (1972).
46. R. G. MAKITRA and YA. N. PIRIG. Org. React. USSR, **16**, 535 (1979).
47. D. MATHER and J. SHORTER. J. Chem. Soc. Perkin Trans. 2, 1179 (1983) and previous papers.
48. G. F. DVORKO, E. A. PONOMAREVA, and N. I. KULIK. Usp. Khim. **53**, 948 (1984); Engl. Trans. p. 547.
49. W. F. FAWCETT and T. M. KRYGOWSKI. Austral. J. Chem. **28**, 2115 (1975).
50. M. H. ABRAHAM, R. W. TAFT, and M. J. KAMLET. J. Org. Chem. **46**, 3053 (1981).
51. M. H. ABRAHAM, R. M. DOHERTY, M. J. KAMLET, J. M. HARRIS, and R. W. TAFT. J. Chem. Soc. Perkin Trans. 2, 913 (1987).
52. T. W. BENTLEY. Am. Chem. Soc. Ser. **215**, 255 (1987).
53. M. H. ABRAHAM, R. M. DOHERTY, M. J. KAMLET, J. M. HARRIS, and R. W. TAFT. J. Chem. Soc. Perkin Trans. 2, 1097 (1987).
54. D. N. KEVILL and S. W. ANDERSON. J. Am. Chem. Soc. **108**, 1579 (1986).
55. R. M. DOHERTY, M. H. ABRAHAM, J. M. HARRIS, R. W. TAFT, and M. J. KAMLET. J. Org. Chem. **51**, 4872 (1986).
56. J. M. HARRIS, S. P. MCMANUS, M. R. SEDAGHAT-HERATI, N. NEAMATI-MAZRAEY, R. M. DOHERTY, R. W. TAFT, and M. H. ABRAHAM. Am. Chem. Soc. Ser. **215**, 247 (1987).
57. M. H. ABRAHAM, P. L. GRELLIER, A. NASEHZADEH, and R. A. C. WALKER. J. Chem. Soc. Perkin Trans. 2, 1717 (1988).
58. M. H. ABRAHAM, P. L. GRELLIER, and A. NASEHZADEH. Unpublished work.
59. M. AURIEL and E. DE HOFFMANN. J. Am. Chem. Soc. **97**, 7433 (1975).
60. K. S. SCHANZE, T. F. MATTOX, and D. G. WHITTEN. J. Org. Chem. **48**, 2808 (1983).
61. T. ASANO and T. OKADA. J. Org. Chem. **49**, 4387 (1984).
62. Z. ZHONG-YUAN, S. CHENG-E, and H. TE-KANG. J. Chem. Soc. Perkin Trans. 2, 929 (1985).
63. C. REICHARDT. Solvent effects in organic chemistry. Verlag Chemie, Weinheim, New York. 1974.
64. E. BUNCEL and H. WILSON. Acc. Chem. Res. **12**, 42 (1979).
65. M. CHASTRETTE and J. CARRETTO. Tetrahedron, **38**, 1615 (1982).
66. P. SVOBODA, O. PYTELA, and M. VECERA. Coll. Czech. Chem. Commun. **48**, 3287 (1983).
67. B. ELIASSON, D. JOHNELS, S. WOLD, and U. EDLUND. Acta. Chem. Scand. B**36**, 155 (1982).
68. S. WOLD and M. SJOSTROM. Acta. Chem. Scand. B**40**, 270 (1986).

Can. J. Chem. Downloaded from www.nrcresearchpress.com by 196.1.178.254 on 09/07/12
For personal use only.

MMPEP: Development and evaluation of peptide parameters for Allinger's MMP2(85) programme, including calculations on crambin and insulin

SAUL WOLFE,[1] DONALD FREDRIC WEAVER, AND KIYULL YANG
Department of Chemistry, Queen's University, Kingston, Ont., Canada K7L 3N6

Received September 22, 1987[2]

SAUL WOLFE, DONALD FREDRIC WEAVER, and KIYULL YANG. Can. J. Chem. **66**, 2687 (1988).

Allinger's MMP2(85) program has been converted to an IBM environment, and the dimensions expanded to a current maximum of 999 atoms. Substantial additional expansion will be possible. An all-atom set of parameters, which permit Allinger's comprehensive force field to be applied to the molecular mechanics treatment of peptides, has been determined. These parameters, termed MMPEP, contain 21 atom types: 5 for carbon, 6 for hydrogen, 5 for nitrogen, 4 for oxygen, and 1 for sulfur, and are based on crystallographic heavy atom bond lengths and bond angles, vibrational and microwave spectra, and *ab initio* calculations. To minimize the conformational energy of a peptide from an initial starting geometry, all internally stored parameters are released, and replaced by PEPCON, a 360-line external file containing the MMPEP parameters.

The ability of the MMPEP parameterization of MM85 to reproduce experimental crystal structures has been tested on several peptides and polypeptides, and the use of a dielectric constant $\varepsilon = 78.5$ D leads to the following results: Ala-Ala-Gly (rms = 0.261); Gly-Gly-Val (rms = 0.349); glutathione (rms = 0.417); crambin (327 heavy atoms; rms = 0.310 for all heavy atoms); insulin (389 heavy atoms; rms = 0.646 for all heavy atoms); the origins of deviations can be interpreted. No problems have been encountered in the application of the Newton–Raphson minimization procedure to such large molecules as crambin and insulin, even though all possible nonbonded interactions have been retained. On the IBM 3081 computer, real time minimization of tripeptides requires 1–2 min, crambin requires 250 min, and insulin 200 min. Since hydrogen bonding in Allinger's force field is a natural result of electrostatic and van der Waals interactions, in MMPEP hydrogen bonding is taken into account through the large number of hydrogen atom types and their different bond moments and van der Waals radii.

SAUL WOLFE, DONALD FREDRIC WEAVER et KIYULL YANG. Can. J. Chem. **66**, 2687 (1988).

On a transformé le programme d'Allinger MMP2(85) pour un environnement IBM et on en a étendu les dimensions pour inclure actuellement un maximum de 999 atomes. Des expansions supplémentaires importantes sont possibles. On a déterminé un ensemble de paramètres couvrant tous les atomes; on pourra ainsi appliquer le champ de force global d'Allinger au traitement des peptides par la mécanique moléculaire. Ces paramètres, que l'on a appelé MMPEP, contiennent 21 types d'atomes : 5 pour le carbone, 6 pour l'hydrogène, 5 pour l'azote, 4 pour l'oxygène et 1 pour le soufre et ils sont basés sur des longueurs de liaisons et des angles de liaisons déterminées par des méthodes cristallographiques aux atomes lourds, sur des spectres de vibration et de micro-ondes et sur des calculs *ab initio*. Afin de minimiser l'énergie conformationnelle d'un peptide à partir d'une géométrie initiale, on remplace tous les paramètres conservés d'une façon interne par PEPCON, une filière externe de 360 lignes contenant les paramètres MMPEP.

Afin de vérifier les possibilités du programme MM85 incorporant les paramètres MMPEP de reproduire les structures cristallines expérimentales, on a utilisé plusieurs peptides et polypeptides; utilisant une constante diélectrique $\varepsilon = 78{,}5$ D, on obtient les résultats suivants : Ala-Ala-Gly (rms = 0,261); Gly-Gly-Val (rms = 0,349); glutathion (rms = 0,417); crambine (327 atomes lourds; rms = 0,310 pour tous les atomes lourds); insuline (389 atomes lourds; rms = 0,646 pour les atomes lourds); on peut interpréter les causes des déviations. On n'a pas rencontré de problèmes dans l'application de la méthode de minimisation de Newton–Raphson à des molécules de la taille de la crambine et l'insuline, même si toutes les interactions non-liées ont été conservées. Sur un ordinateur IBM 3081, le temps réel de minimisation des tripeptides est de 1 à 2 min; celui de la crambine est de 250 min et celui de l'insuline est de 200 min. Dans le champ de force d'Allinger, les liaisons hydrogènes sont un résultat naturel des interactions électrostatiques et de van der Waals; dans le MMPEP, on tient compte des liaisons hydrogènes par le biais de plusieurs types d'atomes d'hydrogène ainsi que par leurs moments de liaison et leurs rayons de van der Waals qui sont différents.

[Traduit par la revue]

Introduction

In the course of an investigation into the interaction of the anticonvulsant drug 5,5-diphenylhydantoin (DPH) with its receptor (1), it became necessary to study some properties of a hexapeptide containing two terminal cysteines (2). The four internal amino acids of this peptide had to be selected in such a manner that, in its oxidized cyclic form (**1**), the compound

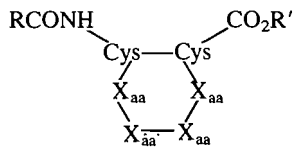

1

would have a cavity with a diameter of 4.6 Å (3), five heteroatoms directed inwards, and the ability to complex sodium ions selectively. In addition, it was required that the complexation of sodium ions be inhibited by DPH, but not by biologically inactive analogs of this drug, e.g., 5,5-dibenzylhydantoin.

This kind of design problem has usually been solved (4) by trial and error, through the syntheses and experimental evaluation of many candidate structures. Since such a labour-intensive approach was not feasible for us, we decided to examine an alternative design strategy, based on molecular mechanics (5), that would allow three-dimensional structures to be viewed *prior* to synthesis. An essential requirement for this strategy was the development of the parameters of a force field for peptides that could be employed in conjunction with an accessible and well-documented computational procedure, e.g., MM2 (6).

[1]Author to whom correspondence may be addressed.
[2]Revision received March 25, 1988.

Can. J. Chem. Downloaded from www.nrcresearchpress.com by 196.1.178.254 on 09/07/12
For personal use only.

Can. J. Chem. Downloaded from www.nrcresearchpress.com by 196.1.178.254 on 09/07/12
For personal use only.

The use of empirical potential energy functions to describe peptide conformations (7) began with the work of Sasisekharan and Ramachandran (8), Scheraga (9), Lifson and co-workers (10), Gelin and Karplus (11), Hagler (12), and Levitt (13). The early work initially employed a hard sphere model, which was gradually improved to include van der Waals and electrostatic interactions, and a cosine term for torsional interactions (14, 15). The computational procedure ECEPP (Empirical Conformation Energy Program for Peptides) (16) was then documented and distributed by Scheraga. In its use of fixed bond lengths and bond angles, the ECEPP force field exemplifies a "first-generation" molecular mechanics procedure. Other first-generation peptide force fields assume a united atom model, in which methyl, methylene, and methine groups are treated as spheres, or assume purely harmonic potential functions (17) for bond lengths and bond angles.

Programmes that implement these and other force fields exist (for a discussion, see ref. 18), but are not as accessible as ECEPP, and the FORTRAN source codes of these programmes are normally not made available. It is, therefore, difficult to accommodate modifications or extensions that may be needed to treat specific problems. For this reason, mainly, we chose the second-generation force field of MM2 (6) as the basis of our own work. The present article is concerned with the development of MMPEP, an all-atom parameterization of MM2 for peptides. The following article (19) describes modifications to ECEPP, which allow this latter programme to serve as a very convenient starting point for the application of MMPEP to the conformational analysis of peptides. Full details of these programming changes will be provided free of charge to all authorized users of MMP2 (85).

The MMPEP force field

The force field to be parameterized is given by eq. [1]:

$$[1] \quad E_{TOT} = \sum_{BL} E1 + \sum_{BA} E2 + \sum_{DA} E3 + \sum_{VDW} E4 + \sum_{EI} E5$$

where

$$[2] \quad E_1 = \frac{1}{2}K_1(l - l_0)^2 + K_1'(l - l_0)^3$$

$$[3] \quad E_2 = \frac{1}{2}K_2(\theta - \theta_0)^2 + K_2'(\theta - \theta_0)^4$$

$$[4] \quad E_3 = \frac{V_1}{2}(1 + \cos\omega) + \frac{V_2}{2}(1 - \cos 2\omega) + \frac{V_3}{2}(1 + \cos 3\omega)$$

$$[5] \quad E_4 = (2.90 \times 10^5)\varepsilon e^{-12.5(r_0/r)} - 2.25\varepsilon\left(\frac{r_0}{r}\right)^6$$

$$[6] \quad E_5 = \frac{\mu_i\mu_i}{Dr_{ij}^3}(\cos\chi - 3\cos\alpha_i\cos\alpha_j)$$

In eqs. [2]–[6], E_1 represents bond length energies, E_2 bond angle energies, E_3 dihedral angle energies, E_4 van der Waals interactions, and E_5, electrostatic interactions. All variables and constants are defined in subsequent discussions.

Atom types of MMPEP

The basis of a force field is the allocation of atom types, i.e., the selection of atoms that are sufficiently alike in a chemical sense to be treated identically in the molecular mechanics refinement. MMPEP employs 21 atom types for its description of amino acids and peptides (Table 1). Although the sp^3 atom types are straightforward, a variety of sp^2 types was necessary to improve geometrical precision. The number of atom types employed in MMPEP is considered to represent the minimum required for an accurate representation and concurrent avoidance of problems associated with excessive parameterization.

TABLE 1. Atom types used in MMPEP

Element	Atom type	Description of atom type
C	1	C_{sp^3}: CH_2, CH_3 (e.g., leucine side chain)
C	2	C_{sp^2}: 6-membered ring (e.g., phenylalanine)
C	3	C_{sp^2}: carbonyl, C=O (e.g., peptide backbone)
C	4	C_{sp^2}: 5-membered ring (e.g., histidine)
C	27	C_{sp^2}: junction between 5- and 6-membered rings
N	8	N_{sp^3}: amine nitrogen
N	9	N_{sp^2}: amide nitrogen
N	13	N_{sp^3}: ammonium nitrogen
N	19	Nitrogen in guanidino group (e.g., arginine)
N	26	Nitrogen in 5-membered ring (e.g., histidine)
H	5	Hydrogen attached to a carbon
H	14	Hydrogen attached to an amide nitrogen
H	23	Hydrogen attached to a non-amide nitrogen
H	21	Alcohol hydrogen (e.g., serine, tyrosine)
H	24	Carboxylic acid hydrogen, COOH
H	25	Hydrogen attached to sulfur
O	6	Alcohol oxygen, OH (e.g., serine)
O	7	Carbonyl oxygen, C=O
O	11	Oxygens in carboxylate, COO^-
O	12	Hydroxyl oxygen in carboxylic acid, COOH
S	15	Sulfur (e.g., methionine, cysteine)

Bond length parameters of MMPEP

While first-generation calculations treated bond lengths as constants, for many peptides bond energies vary significantly and require the introduction of a bond stretching potential function. Although it is possible to represent bond stretching with the harmonic potential of a Hooke's Law function (17), deviations from this harmonic potential for large bond length deformations dictate the introduction of an anharmonic correction. This correction may be approximated with the cubic term of a truncated Taylor series expansion (eq. [2]), in which l_0 is an ideal bond length, l is the bond length of interest, and K_1 and K_1' are stretching force constants.

In the parameterization of MMPEP, extensive use was made of experimental data. The X-ray and neutron diffraction bond lengths of all of the amino acids as well as a number of peptides were used to establish the strainless bond lengths for MMPEP (20–51). The ideal bond lengths used in MMPEP are listed in Table 2, and are the average of at least 10 experimental values in each case. All hydrogen atoms are considered explicitly. Since X-ray crystallography is limited in its ability to locate these atoms, the MMPEP values for X—H bond lengths were obtained from STO-3G calculations, using GAUSSIAN 80 (52). Schåfer has reported that the 4-21G C—H bond length is within 0.001 Å of spectroscopic values (53). Extensive peptide calculations by Peters and Peters (54–64) and by Kollman and co-workers (65*a*) suggest that an STO-3G basis set is also acceptable.

Can. J. Chem. Downloaded from www.nrcresearchpress.com by 196.1.178.254 on 09/07/12
For personal use only.

TABLE 2. Bond lengths used in MMPEP

Bond type (by number)		Bond type (by element)		Bond length (Å)
1	1	C	C	1.525
1	2	C	C	1.504
1	3	C	C	1.526
1	4	C	C	1.504
1	5	C	H	1.081
1	6	C	O	1.425
1	8	C	N	1.461
1	9	C	N	1.452
1	13	C	N	1.472
1	15	C	S	1.815
1	19	C	N	1.460
2	2	C	C	1.382
2	5	C	H	1.101
2	6	C	O	1.381
2	8	C	N	1.331
2	19	C	N	1.331
2	27	C	C	1.400
3	5	C	H	1.103
3	6	C	O	1.330
3	7	C	O	1.229
3	9	C	N	1.330
3	11	C	O	1.250
3	12	C	O	1.328
4	4	C	C	1.371
4	5	C	H	1.101
4	26	C	N	1.394
4	27	C	C	1.459
6	21	O	H	0.968
8	23	N	H	1.015
9	14	N	H	0.991
12	24	O	H	0.972
13	23	N	H	1.023
15	15	S	S	2.024
15	25	S	H	1.354
19	23	N	H	1.007
23	26	H	N	1.010
26	27	N	C	1.380
27	27	C	C	1.419

TABLE 3. Stretching force constants used in MMPEP

Bond type (by number)		Bond type (by element)		Stretching force constant (mdyn/Å)
1	1	C	C	4.40
1	2	C	C	4.48
1	3	C	C	4.75
1	4	C	C	4.40
1	5	C	H	4.60
1	6	C	O	5.36
1	8	C	N	5.10
1	9	C	N	5.47
1	13	C	N	5.15
1	15	C	S	3.21
1	19	C	N	5.27
2	2	C	C	9.60
2	5	C	H	4.60
2	6	C	O	6.20
2	8	C	N	5.10
2	19	C	N	5.10
2	27	C	C	6.51
3	5	C	H	4.80
3	6	C	O	5.05
3	7	C	O	10.01
3	9	C	N	7.74
3	11	C	O	5.11
3	12	C	O	5.05
4	4	C	C	7.19
4	5	C	H	4.60
4	26	C	N	5.69
4	27	C	C	5.39
6	21	O	H	4.60
8	23	N	H	6.10
9	14	N	H	5.78
12	24	O	H	7.20
13	23	N	H	6.03
15	15	S	S	3.10
15	25	S	H	3.80
19	23	N	H	5.95
23	26	H	N	6.05
26	27	N	C	5.94
27	27	C	C	6.21

The N—H bond lengths of MMPEP were obtained from the optimized STO-3G structures of methylamine and formamide. Based on these calculations, the *8–23* and *9–14* type bond lengths of MMPEP have values of 1.015 and 0.991 Å respectively. Additional STO-3G calculations on 2-aminoethanol and acetic acid were used to obtain the O—H bond lengths of an alcohol and a carboxylic acid. Based on these calculations, the *6–21* and *12–24* type bond lengths are 0.968 and 0.972 Å, respectively. An STO-3G optimization of propane was used to obtain C—H (type *1–5*) bond lengths for the side chains of amino acids such as valine and leucine. Finally, a 3-21G* optimization of 2-mercaptoethanol provided the S—H (type *15–25*) bond length of cysteine.

The harmonic bond stretching force constants K_1 were assigned from a variety of data. Although desirable, the purely experimental determination of force constants tends to be a difficult task. Theoretical determinations by gradient calculations represent an alternative. Since the potential surface governing the nuclear movement is given, in the Born–Oppenheimer approximation, by the electronic energy of the molecule (as a function of the displacement coordinates), the theoretical calculation of force constants requires the calculation of the second derivatives of the molecular energy as obtained from the electronic Schrödinger equation. The development of analytical derivative techniques has made theoretical determination of force constants meaningful and accessible (66–70).

The force constants (K_1) used in MMPEP are listed in Table 3. The values for the peptide backbone have been adopted from model calculations with a 4-31G basis set (71). The force constants of the alkyl side chains of amino acids (e.g., leucine, isoleucine, valine) were based on examination of the molecular mechanics literature. For example, the C–C (type *1–1*) stretching constant is given as 4.40, 4.40, 4.40, and 4.48 mdyn/Å by Allinger, Schleyer, Lifson, and Boyd, respectively (72–75). The C–H (type *1–5*) constants are given as 4.60, 3.85, 4.60, 4.54, and 4.70 mdyn/Å by Allinger, Schleyer and co-workers,

TABLE 4. Bond angles and bending force constants used in MMPEP[a]

Angle type (by number)			Angle type (by element)			Bond angle (deg)	Bending force constant (mdyn Å/rad^2)
1	1	1	C	C	C	110.30	0.45
1	1	1	C	C	C	111.20	0.45
1	1	1	C	C	C	112.40	0.45
1	1	2	C	C	C	114.00	0.58
1	1	3	C	C	C	107.80	0.67
1	1	3	C	C	C	110.80	0.67
1	1	3	C	C	C	112.20	0.67
1	1	4	C	C	C	113.10	0.71
1	1	5	C	C	H	109.39	0.36
1	1	6	C	C	O	109.10	0.56
1	1	6	C	C	O	104.10	0.56
1	1	6	C	C	O	109.40	0.56
1	1	8	C	C	N	109.47	0.57
1	1	9	C	C	N	109.40	0.56
1	1	9	C	C	N	109.60	0.56
1	1	9	C	C	N	111.10	0.85
1	1	13	C	C	N	111.20	0.90
1	1	15	C	C	S	108.80	0.63
1	1	19	C	C	N	111.20	0.75
1	2	2	C	C	C	121.40	0.55
1	2	5	C	C	H	118.20	0.36
1	3	7	C	C	O	120.60	0.86
1	3	9	C	C	N	116.40	0.78
1	3	11	C	C	O	117.00	0.64
1	3	12	C	C	O	115.00	0.70
1	4	4	C	C	C	129.80	0.80
1	4	26	C	C	N	121.70	0.80
1	4	27	C	C	C	128.60	0.80
1	6	21	C	O	H	108.40	0.35
1	8	23	C	N	H	109.50	0.48
1	9	1	C	N	C	111.90	0.45
1	9	2	C	N	C	123.20	0.75
1	9	3	C	N	C	120.60	0.49
1	9	3	C	N	C	121.70	0.35
1	9	14	C	N	H	124.00	0.54
1	13	23	C	N	H	109.50	0.40
1	15	1	C	S	C	97.60	0.78
1	15	15	C	S	S	103.90	1.17
1	15	25	C	S	H	96.00	0.48
1	19	2	C	N	C	123.20	0.56
1	19	23	C	N	H	118.40	0.38
2	1	5	C	C	H	109.40	0.36
2	2	2	C	C	C	120.00	0.43
2	2	5	C	C	H	120.00	0.36
2	2	6	C	C	O	121.00	0.75
2	2	27	C	C	C	120.00	0.96
2	6	21	C	O	H	113.00	0.35
2	8	23	C	N	H	120.00	0.50
2	9	23	C	N	H	120.00	0.50
2	19	23	C	N	H	120.00	0.38
2	27	4	C	C	C	134.90	0.90
2	27	26	C	C	N	132.80	0.35
2	27	27	C	C	C	122.70	0.90
3	1	5	C	C	H	107.90	0.37
3	1	8	C	C	N	110.74	0.82

TABLE 4 (*continued*)

Angle type (by number)			Angle type (by element)			Bond angle (deg)	Bending force constant (mdyn Å/rad^2)
3	1	9	C	C	N	110.00	0.44
3	1	9	C	C	N	109.70	0.47
3	1	9	C	C	N	110.80	0.56
3	1	13	C	C	N	110.74	0.90
3	2	1	C	C	C	110.2	0.47
3	9	14	C	N	H	122.50	0.50
3	12	24	C	O	H	106.10	0.74
4	1	5	C	C	H	109.50	0.38
4	4	5	C	C	H	126.30	0.36
4	4	26	C	C	N	107.90	0.80
4	4	27	C	C	C	106.40	0.43
4	26	4	C	N	C	106.30	0.80
4	26	23	C	N	H	126.40	0.40
4	26	27	C	N	C	111.60	0.80
4	27	27	C	C	C	108.80	0.95
5	1	5	H	C	H	109.40	0.32
5	1	6	H	C	O	103.10	0.43
5	1	8	H	C	N	108.80	0.46
5	1	9	H	C	N	109.39	0.36
5	1	9	H	C	N	109.41	0.36
5	1	9	H	C	N	110.00	0.36
5	1	13	H	C	N	108.80	0.50
5	1	15	H	C	S	112.00	0.36
5	1	19	H	C	N	109.00	0.38
5	2	27	H	C	C	120.00	0.36
5	3	7	H	C	O	112.0	0.37
5	3	9	H	C	N	122.3	0.40
5	4	26	H	C	N	120.00	0.36
7	3	9	O	C	N	124.10	0.85
7	3	12	O	C	O	124.50	1.13
8	2	19	N	C	N	120.00	0.80
11	3	11	O	C	O	126.00	0.85
14	9	14	H	N	H	120.00	0.50
19	2	19	N	C	N	120.00	0.80
23	8	23	H	N	H	106.80	0.50
23	19	23	H	N	H	120.00	0.50
23	13	23	H	N	H	109.50	0.50
23	26	27	H	N	C	124.20	0.40
26	4	26	N	C	N	110.90	0.90
26	27	27	N	C	C	104.40	0.90
	3	11		C	O	[b]	0.80
	3	12		C	O	[b]	0.80
	9	14		N	H	[b]	0.05
	2	27		C	C	[b]	0.05
	2	1		C	C	[b]	0.05
	2	2		C	C	[b]	0.05
	2	5		C	H	[b]	0.05
	2	6		C	O	[b]	0.05
	2	8		C	N	[b]	0.05
	2	19		C	N	[b]	0.05
	3	1		C	C	[b]	0.80
	3	5		C	H	[b]	0.80
	3	7		C	O	[b]	0.80
	3	9		C	C	[b]	0.80
	9	1		N	C	[b]	0.05
	9	3		N	C	[b]	0.05

Can. J. Chem. Downloaded from www.nrcresearchpress.com by 196.1.178.254 on 09/07/12
For personal use only.

TABLE 4 (*concluded*)

Angle type (by number)		Angle type (by element)		Bond angle (deg)	Bending force constant (mdyn Å/rad^2)
4	26	C	N	[b]	0.05
4	4	C	C	[b]	0.05
27	27	C	C	[b]	0.05
27	2	C	C	[b]	0.05
27	4	C	C	[b]	0.05
26	27	N	C	[b]	0.05
4	1	C	C	[b]	0.05
4	5	C	H	[b]	0.05
4	27	C	C	[b]	0.05
27	26	C	N	[b]	0.05

[a]Where more than one angle is given for a particular angle type (e.g., 1–1–1, 3–1–9), the first value is for angles of the type X–CH_2–X, the second value is for angles of the type X–CHR–X, and the third is for angles of the type X–CR_2–X.

[b]Out-of-plane bending.

Ermer and Lifson, Boyd and co-workers, and Fitzwater and Bartell, respectively (72–76). MMPEP uses constants of 4.40 and 4.60 mdyn/Å for the *1–1* and *1–5* bond types.

Experimental force constants for carboxylic acids have been reported by Brooks and Haas and these have been used for residues bearing acidic side chains (e.g., glutamate, aspartate) (77). Experimental spectroscopic data also were used to obtain force constants for amino acids possessing alcohol groups (e.g., serine, tyrosine) (78). The stretching constants for amines, required for residues such as lysine, were taken from the experimental literature (79). The force constants necessary to calculate cysteine and cystine also were obtained from the experimental literature (80).

Lastly, the value of K_1' was assigned. The cubic term of eq. [2] represents an anharmonic modification of the Hooke's law function. As suggested by Allinger, the value of K_1' has been set at 2.0 mdyn/Å (5).

Bond angle parameters of MMPEP

It is known from X-ray crystallography (81) and vibrational spectroscopy (82) that bond angles exhibit a greater variability than bond lengths, and are thus of greater import for precise conformational analysis. The potential energy functions used to describe bond angle deformations are, in general, harmonic, but corrections for anharmonicity are again necessary (83–85). In MMPEP, the potential function for bond angle deformation is given by eq. [3].

As with bond lengths, both theoretical and experimental values may be employed for parameter selection. The strainless bond angles used in MMPEP are listed in Table 4. All heavy atom bond angles were taken from X-ray and neutron diffraction data (20–51), and are the average of at least 10 experimental values in each case. Angles containing hydrogen atoms were taken either from microwave data or from theoretical calculations. For angles of the type CNH, HNH, and NCH, microwave data on model molecules such as methylamine and dimethylamine were examined (86, 87). For hydroxyl groups, microwave data on methanol and dimethyl ether were employed (88). Microwave data on methanethiol and ethanethiol were used to describe the angles of the cysteine side chain (89). The amide hydrogen angles and the angles of carboxyl groups were obtained from STO-3G optimizations of formamide and acetic acid.

The harmonic bending force constants (K_2) are listed in Table 4, and, as with K_1, were derived from both experimental and theoretical data. The force constants for the peptide backbone were adopted from model peptide calculations with a 4-31G basis set (71). The force constants for alkyl side chains of amino acids (e.g., leucine, isoleucine, valine) were based on examination of the molecular mechanics literature. For example, the C–C–C (type *1–1–1*) bending constant is given as 0.450, 0.629, 0.570, 0.647, and 0.800 mdyn Å/rad^2 by Allinger, Schleyer, Lifson, Boyd, and Bartell respectively (72–76). Similarly, the C–C–H (type *1–1–5*) constants are 0.360, 0.322, 0.400, 0.521, and 0.608 mdyn Å/rad^2 and the H–C–H (type *5–1–5*) constants are 0.320, 0.350, 0.330, 0.549, and 0.508 mdyn Å/rad^2 (72–76). In MMPEP, values of 0.450, 0.360, and 0.320 mdyn Å/rad^2 are employed for the *1–1–1*, *1–1–5*, and *5–1–5* bond angle types.

Experimental spectroscopic data were used to provide force constants for carboxylate groups (e.g., glutamic acid, aspartic acid), alcohol groups (e.g., serine, tyrosine), and amines (e.g., lysine) (77–80).

Lastly, the value of K_2' was set at 7×10^{-8} mdyn Å/rad^2, as suggested by Allinger (5).

Table 5 compares a number of the bond lengths, bond angles, and force constants employed in the force fields of AMBER (65*a*), CHARMM (65*b*), MMP2(85), and MMPEP.

Torsional parameters of MMPEP

The explicit incorporation of torsional terms is necessary for the consideration of atom pairs that are separated by a chain of three bonds. An evaluation of the torsional energy about a single C_{sp^3}—C_{sp^3} bond can be made by study of one or more of the nine torsional angles defined for such a bond. Since symmetry problems arise with branched carbon skeletons when less than nine torsional angles are used, the MMPEP approach requires parameters for all possible dihedral angles.

In MMPEP the torsional potential function is represented as a Fourier series expansion, eq. [4]. Positive V_1 and V_3 terms destabilize eclipsed forms, while a positive V_2 term represents a minimum at 0° and 180°. The low periodicity (V_1 and V_2) terms tend to dominate in systems carrying heteroatoms; thus, the planarity of formamide is well described by a V_2 term. Hydrocarbons, on the other hand, have threefold symmetry requiring a V_3 term. Pople and co-workers have demonstrated the value of a Fourier expansion to interpret calculated torsional energy changes (90).

As described earlier, extensive use of STO-3G calculations has been made to determine bond length and bond angle parameters. Calculations of comparable quality were used to determine torsional parameters. This was done by computation of the torsional energy profile of the moiety of interest, followed by calculation of the Fourier expansion parameters by means of a least-squares fit.

The peptide backbone was evaluated first. The amide bond of a peptide is most stable in the planar *trans* form. This has been established by many X-ray and neutron diffraction studies, and more recently by gas-phase electron diffraction (91–93). In addition, the theoretical rotational barriers of amide bonds have been studied extensively. The available results include extended Hückel computations on model peptides (94, 95), and CNDO studies of N-substituted amides (96), formamide (97), various

Can. J. Chem. Downloaded from www.nrcresearchpress.com by 196.1.178.254 on 09/07/12
For personal use only.

TABLE 5. A comparison of the stretching and bending parameters employed to describe the moiety C1—N2(H5)—C3(O6)—C4 in the force fields of AMBER, CHARMM, MMP2(85), and MMPEP

Bond or bond angle	AMBER[a]		CHARMM[b]		MMP2(85)[c]		MMPEP[d]	
	Value	Force constant	Value	Force constant	Value	Force constant	Value	Force constant
1–2	1.449[e]	4.93[f]	1.45	5.86	1.470	3.52*[g]	1.452	5.47
2–3	1.335	6.81	1.33	6.54	1.385	6.40*	1.330	7.74
3–4	1.522	4.65	1.53	5.63	1.509	4.40	1.526	4.75
2–5	1.010	6.03	0.98	5.63	1.022	5.90*	0.991	5.78
3–6	1.229	7.92	1.23	8.06	1.208	10.80	1.229	10.01
1–2–5	118.4°	0.53[h]	120.°	0.49	124.0°	0.44*	124.0°	0.54
1–2–3	121.9°	0.69	120.°	1.11	117.0°	0.76*	120.6°	0.49
5–2–3	119.8°	0.49	120.°	0.42	119.42°	0.42*	122.5°	0.50
2–3–4	116.6°	0.97	117.5°	0.28	114.0°	0.66*	116.4°	0.78
2–3–6	122.9°	1.11	121.0°	0.90	124.7°	0.67*	124.1°	0.85
4–3–6	120.4°	1.11	121.5°	1.18	122.5°	0.46	120.6°	0.86

[a]Reference 65*a*.
[b]Reference 65*b*.
[c]From the MMP2(85) manual.
[d]Present work.
[e]In Ångstroms.
[f]Units are mdyn/Å.
[g]Asterisked force constants and values are not yet firmly established.
[h]Units are mdyn Å/rad^2.

methylated amides (98), and *N*-methylacetamide (99). *Ab initio* computations have been carried out on formamide (100–102), *N*-methylformamide, and acetamide (103). These *ab initio* studies suggest that the C—N rotational barrier in formamide is 20.3 kcal/mol. This compares to proton nmr results that yield a value of 19.7 kcal/mol for the Arrhenius activation energy (104). The calculated C—N rotational barrier in *N*-methylformamide is 21.1 kcal/mol, with the *trans* isomer more stable by 1.8 kcal/mol.

To reflect the torsional behaviour about the amide bond, MMPEP employs the values $V_1 = 1.8$, $V_2 = 6.49$, $V_3 = 0$ kcal/mol. This choice leads to a rotational barrier of 19.9 kcal/mol, and ensures the relative stability of the planar *trans* form.

Although the amide bond is the conformationally dominant feature of the peptide backbone, the ϕ (N—C_α) and ψ (C′—C_α) dihedral angles must also be considered. These angles exhibit a high degree of conformational variation, and are responsible for the overall flexibility of a peptide (105). In harmony with early work by Scott and Scheraga (106), Levitt (107) and Gelin and Karplus (108) have used rotational barriers of 0.6 and 0.2 kcal/mol for the ϕ and ψ dihedral angles, respectively. Kollman and co-workers initially set both of these torsional barriers at zero to maximize conformational freedom (17). Scheraga has argued that, provided the barriers lie between 0 and 1.0 kcal/mol, the results are essentially equivalent (109). Brant and Flory used values of 1.5 and 1.0 kcal/mol for ϕ and ψ, respectively, but noted that their results were not sensitive to these values (110); de Santis *et al.* neglected these barriers altogether (111). However, in a study of 22 globular proteins, Kolaskar and Prashanth concluded that non-zero torsional potential functions for ϕ and ψ are indeed necessary to account for the absence of the left-handed α-helix ($\psi = 60°$) and the high occurrence of dihedral angles in which $\psi = 0°$ (112).

Theoretical studies on small molecules provide further insight. *Ab initio* calculations on the barrier to rotation about the C_{sp^3}—C_{sp^2} bond in acetaldehyde gave a value of 0.38 kcal/mol (113). In CH_3—NH_3^+, which simulates the ϕ dihedral angle of a zwitterionic amino acid, the calculated barrier is 0.36 kcal/mol (114). A series of calculations on model dipeptides at the 4-21G level revealed that the ϕ and ψ torsional angles have relatively shallow minima as well as flat areas of potential energy (115). For example, a change of 3° in the optimized ψ dihedral angle causes an energy change of only 0.05 kcal/mol while a simultaneous 10° change in both ϕ and ψ is accompanied by an energy change of only 0.5 kcal/mol.

On the basis of these data MMPEP assumes a ψ rotational barrier of 0.30 kcal/mol. This is a threefold barrier, with minima at 0°, 120°, and 240° and maxima at 60°, 180°, and 300°. For the ϕ dihedral angle, a rotational barrier of 0.36 kcal/mol has been incorporated. Minima occur when the N—H bond is staggered with respect to the bonds C_α—H, C_α—R, and C_α—C′.

Just as the amide bond dominates the peptide backbone, the C_α—C_β (χ_1) torsional angle dominates the side chain. The χ_1 dihedral angle is C_{sp^3}–C_{sp^3} in form and is usually assigned a barrier of 2.7 kcal/mol. Calculations of the barrier to rotation in ethane support this choice (116).

Although χ_1 has been considered to be purely threefold in the work of Karplus, Kollman, Levitt, and Scheraga (11, 17, 107, 109), when polar atoms are attached to C_β a significantly asymmetrical environment is created and simple rotational behaviour, in which $V_1 = V_2 = 0$ and $V_3 = 2.7$, is no longer reasonable. Moreover, amino acids such as arginine, aspartic acid, glutamine, glutamic acid, histidine, leucine, lysine, methionine, phenylalanine, tryptophan, and tyrosine (Case 1), which have single branching distal to the β carbon must be differentiated from amino acids such as isoleucine, threonine, and valine (Case 2), which have double branching. Chuman and Momany have suggested the following equations to describe

Can. J. Chem. Downloaded from www.nrcresearchpress.com by 196.1.178.254 on 09/07/12
For personal use only.

Can. J. Chem. Downloaded from www.nrcresearchpress.com by 196.1.178.254 on 09/07/12
For personal use only.

these two cases (117):

[7] Case 1 $E = 0.5(1 + \cos 3x) + 0.2(1 + \cos x) + 0.75(1 + \cos (x - 120))$

[8] Case 2 $E = 0.5(1 + \cos 3x) + 0.3(1 + \cos x) + 0.4(1 + \cos (x - 120)) + 0.2(1 + \cos (x + 120))$

Accordingly, the Fourier expansion of MMPEP was modified to give eqs. [9] and [10].

[9] Case 1 $E = 0.13(1 + \cos \omega) + 0.49(1 - \cos 2\omega) + 0.77(1 + \cos 3\omega)$

[10] Case 2 $E = 0.28(1 + \cos \omega) + 0.29(1 - \cos 2\omega) + 0.67(1 + \cos 3\omega)$

Although V_3 remains numerically the most significant term, the contributions from V_1 and V_2 serve to destabilize the 0° and 90° conformations.

The remainder of the side-chain torsional angle parameters have been assigned by consideration of individual amino acids. For the alkyl-substituted amino acids (e.g., valine, leucine, isoleucine) and the alkyl chains of amino acids such as lysine, the usual approach has been to use a symmetrical threefold barrier with a height of about 2 kcal/mol to describe C_{sp^3}–C_{sp^3} dihedral angles (11, 17, 107, 109). This approach has been modified in MMPEP, because there seemed no *a priori* reason to eliminate one- and twofold torsional terms (118). Following Pople's Fourier treatment of torsional potentials (90), Bartell and Allinger found that better accuracy could be achieved by use of one-, two-, and threefold terms (118–120). MMPEP uses this procedure to treat alkyl side chains. In lysine, for example, the C_γ–C_δ torsional angle is represented by a Fourier series deconvolution in which $V_1 = 0.20$, $V_2 = 0.27$, and $V_3 = 2.13$ kcal/mol.

The rotational barriers of the hydroxyl groups in serine and threonine have been determined from a variety of sources. Kollman, Scheraga, and Allinger and Chung have represented this torsional angle with V_3 terms of 0.6, 0.81, and 1.0 kcal/mol, respectively (17, 109, 121). Molecular orbital calculations of the rotational barrier in methanol give variable results: extended Hückel, 0.4 kcal/mol (122); CNDO, 0.78 kcal/mol (123); *ab initio*, 0.95 kcal/mol (124). In MMPEP the rotational barrier of the hydroxyl group has been assigned the value $V_3 = 0.9$ kcal/mol.

The rotational barrier for the terminal ammonium group of lysine was determined analogously. For this χ_5 angle, Scheraga and Kollman have assigned V_3 terms of 1.8 and 2.8 kcal/mol, respectively (17, 109), while Profeta and Allinger's V_3 term is 1.8 kcal/mol for similar torsional angles (125). A variety of rotational barriers have been calculated for methylamine, ranging from 1.57 kcal/mol (CNDO) (126) to 2.02 kcal/mol (*ab initio*) (127). Spectroscopic measurements lead to a rotational barrier of 1.98 kcal/mol (128). A V_3 term of 1.8 kcal/mol has been selected for MMPEP.

Arginine has four torsional angles requiring different parameterizations. For the C_δ—N_ε bond, Kollman and Scheraga suggested $V_3 = 0$, thereby neglecting the intrinsic torsional term associated with this angle (17, 109). Low rotational barriers are expected for this angle, because the rotational barriers of methyl groups attached to planar conjugated groups are generally in the range 0–1.0 kcal/mol (129). A V_3 term of 0.5 kcal/mol has been included in MMPEP. The guanidino group of arginine is nearly planar, indicating high rotational barriers for χ_5, $\chi_{6.1}$, and $\chi_{6.2}$. Calculations (CNDO/2) give 18–20 kcal/mol barriers for each of these torsional angles (109). To achieve both planarity and a barrier of 18 kcal/mol, the value $V_2 = 18.0$ kcal/mol has been incorporated into MMPEP for these three torsional angles.

Torsional barriers are required for the carboxylic acid groups of aspartic acid and glutamic acid. Because of π-electron delocalization, the hydroxyl group tends to remain in the plane of the carbonyl group, and hydrogen bonding places the hydroxyl hydrogen *syn* to the carbonyl oxygen. Experimental results show that the *syn* conformation is more stable than the *anti* by 2–4 kcal/mol, and a value of 4.73 kcal/mol is calculated at the STO-3G level (130). In MMPEP, Allinger's MM2 values for carboxylic acids have been used directly (130). Experimental and theoretical estimates indicate that the rotational barrier about X—C—O—H (*X–3–12–24*) is 8.1, 10.9, and 13.4 kcal/mol (131–133). To reproduce these experimental and theoretical values for formic acid, Allinger determined that the HCOH dihedral angle should have $V_1 = 0.6$ and $V_3 = 6.3$ kcal/mol (130). These values have been incorporated in MMPEP. Microwave studies on acetic acid suggest a methyl rotational barrier of less than 0.5 kcal/mol (134, 135). Accordingly, a rotational barrier of 0.4 kcal/mol has been used for the *X–1–3–X* dihedral angle in MMPEP. For asparagine and glutamine, the side-chain amides have been treated as planar and have been given the same values as the peptide bond.

Aromatic amino acids are considered as a group. In accord with available experimental data, MMPEP uses a rotational barrier of 0.4 kcal/mol for χ_2 (136). In phenylalanine and tyrosine, the rotational barrier about the conjugated bonds of the aromatic ring has been set at 34 kcal/mol to agree with *ab initio* (137) and experimental studies (138). For histidine and tryptophan, the C—N conjugated double bonds have been assigned rotational barriers of 20 kcal/mol, as suggested by Kollman (17, 65). Since the experimental barrier to rotation of the hydroxyl group in phenol is 3.5 kcal/mol (136), an intrinsic torsional term $V_2 = 3.5$ kcal/mol has been adopted for MMPEP.

Finally, parameters were developed for the sulfur containing amino acids. The χ_3 and χ_4 dihedral angles of methionine are conformationally controlled by C–S torsion (type: *1–15*). Examination of applicable experimental data suggests that the C—S bond in dimethyl sulfide has a threefold rotational barrier of 2.1 kcal/mol while diethyl sulfide has a threefold barrier of 1.75 kcal/mol (136). The value $V_3 = 2.1$ kcal/mol provides MMPEP with the necessary threefold barrier of appropriate height. In the side chain of cysteine S—H replaces the —CH_2—S—CH_3 group of methionine. Experimental data for rotational barriers on relevant model compounds are 1.27 kcal/mol (methanethiol), 1.64 kcal/mol (ethanethiol), and 1.36 kcal/mol for 2-methyl-2-propanethiol (136). Calculations on methanethiol yield a C—S rotational barrier of 0.94 kcal/mol (CNDO), and 1.17 kcal/mol (*ab initio*) (139). MMPEP employs a threefold torsional barrier of 1.2 kcal/mol in its representation of this torsional angle. This value is 20% lower than the value $V_3 = 1.5$ kcal/mol used initially by Scheraga and later by Kollman.

MMPEP has also been parameterized for cystine, thereby permitting examination of disulfide linkages. Although it has been extensively discussed in the literature, the nature of the R—S—S—R torsional barrier remains uncertain. Experimental estimates vary, depending on the method used. A barrier height of 7.29 kcal/mol has been obtained from infrared data

TABLE 6. Torsional parameters of MMPEP

Angle type				Parameters (kcal/mol)		
				V_1	V_2	V_3
1	1	1	1	0.20	0.27	0.09
1	1	1	3	0.26	0.00	0.06
1	1	1	5	0.00	0.00	0.27
1	1	1	8	0.00	0.00	0.06
1	1	1	9	0.00	0.00	0.06
1	1	1	13	0.00	0.00	0.40
1	1	1	15	0.00	0.00	0.80
1	1	1	19	0.00	0.00	0.60
1	1	2	2	0.00	0.00	0.10
1	1	3	7	0.00	0.00	−0.04
1	1	3	9	0.00	0.00	−0.04
1	1	3	11	0.00	0.00	−0.09
1	1	3	12	0.00	0.00	−0.20
1	1	4	4	0.00	0.00	0.10
1	1	4	26	0.00	0.00	0.10
1	1	4	27	0.00	0.00	0.10
1	1	6	21	0.00	0.00	0.30
1	1	8	23	0.00	0.00	0.30
1	1	9	1	0.00	0.00	0.12
1	1	9	3	0.00	0.00	0.06
1	1	9	14	0.00	0.00	0.06
1	1	13	23	0.00	0.00	0.20
1	1	15	1	0.00	0.00	0.70
1	1	15	15	0.00	0.00	0.80
1	1	15	25	0.00	0.00	0.20
1	1	19	2	0.00	0.00	0.05
1	1	19	23	0.00	0.00	0.05
1	2	2	2	0.00	3.50	0.00
1	2	2	5	0.00	3.50	0.00
1	3	9	1	1.80	6.49	0.00
1	3	9	14	0.00	2.66	0.00
1	3	12	24	0.60	0.00	3.20
1	4	4	5	−0.30	3.80	0.00
1	4	4	26	0.00	3.50	0.00
1	4	26	4	0.00	5.00	0.00
1	4	26	23	0.00	5.00	0.00
1	4	27	2	−0.30	3.80	0.00
1	4	27	27	0.00	3.50	0.00
1	9	1	3	0.00	0.00	0.12
1	9	1	5	0.00	0.00	0.12
1	9	3	7	0.00	7.19	0.00
1	15	1	5	0.00	0.00	0.70
1	15	15	1	0.00	−7.60	1.70
1	19	2	8	0.00	4.50	0.00
1	19	2	19	0.00	4.50	0.00
2	1	1	3	0.26	0.00	0.06
2	1	1	5	0.00	0.00	0.27
2	1	1	8	0.00	0.00	0.06
2	1	1	9	0.00	0.00	0.06
2	1	1	13	0.00	0.00	0.06
2	1	3	7	0.00	0.00	−0.35
2	1	3	9	0.00	−0.50	−1.70
2	2	1	3	0.00	0.00	0.90
2	2	1	5	0.00	0.00	0.05
2	2	2	2	−0.30	3.80	0.00
2	2	2	5	0.00	3.50	0.00
2	2	2	6	0.00	3.80	0.00
2	2	2	27	−0.30	3.80	0.00
2	2	6	21	0.00	1.80	0.00
2	2	27	4	0.00	3.50	0.00
2	2	27	26	0.00	3.50	0.00
2	2	27	27	−0.30	3.80	0.00

TABLE 6 (*continued*)

Angle type				Parameters (kcal/mol)		
				V_1	V_2	V_3
2	19	1	5	0.00	0.00	0.05
2	27	4	4	0.00	3.50	0.00
2	27	26	4	0.00	5.00	0.00
2	27	26	23	0.00	5.00	0.00
2	27	27	2	−0.30	3.80	0.00
2	27	27	4	0.00	3.50	0.00
2	27	27	26	0.00	3.50	0.00
3	1	1	3	0.26	0.00	0.06
3	1	1	4	0.26	0.00	0.06
3	1	1	5	0.00	0.00	0.16
3	1	1	6	0.26	0.00	0.06
3	1	1	8	0.00	0.00	0.06
3	1	1	9	0.00	0.00	0.08
3	1	1	13	0.00	0.00	0.06
3	1	1	15	0.26	0.00	0.06
3	1	8	23	0.00	0.00	0.30
3	1	9	3	0.00	0.00	0.06
3	1	9	14	0.00	0.00	0.06
3	1	13	23	0.00	0.00	0.30
3	9	1	5	0.00	0.00	0.06
4	1	1	5	0.00	0.00	0.27
4	1	1	8	0.00	0.00	0.06
4	1	1	9	0.00	0.00	0.06
4	1	1	13	0.00	0.00	0.06
4	4	1	5	0.00	0.00	0.10
4	4	26	4	0.00	5.00	0.00
4	4	26	23	0.00	5.00	0.00
4	4	26	27	0.00	5.00	0.00
4	4	27	27	−0.30	3.80	0.00
4	26	4	5	0.00	5.00	0.00
4	26	4	26	0.00	5.00	0.00
4	26	27	27	0.00	5.00	0.00
4	27	2	5	−0.30	3.80	0.00
4	27	27	26	−0.30	3.80	0.00
5	1	1	5	0.00	0.00	0.24
5	1	1	6	0.00	0.00	0.50
5	1	1	8	0.00	0.49	0.16
5	1	1	9	0.00	0.49	0.16
5	1	1	13	0.00	0.00	0.40
5	1	1	15	0.00	0.00	0.40
5	1	1	19	0.00	0.00	0.30
5	1	3	7	0.00	0.00	−0.04
5	1	3	9	0.00	0.00	−0.04
5	1	3	11	0.00	0.00	−0.09
5	1	3	12	0.00	0.00	−0.06
5	1	4	26	0.00	0.00	0.10
5	1	4	27	0.00	0.00	0.10
5	1	6	21	0.00	0.00	0.30
5	1	8	23	0.00	0.00	0.30
5	1	9	14	0.00	0.00	0.06
5	1	13	23	0.00	0.00	0.20
5	1	15	15	0.00	0.00	0.80
5	1	15	25	0.00	0.00	0.50
5	1	19	23	0.00	0.00	0.05
5	2	2	5	−0.30	3.80	0.00
5	2	2	6	−0.30	3.80	0.00
5	2	2	27	0.00	3.50	0.00
5	2	27	27	0.00	3.50	0.00
5	2	27	26	0.00	3.50	0.00
5	3	9	14	0.00	2.33	0.00
5	4	4	26	0.00	3.50	0.00
5	4	4	27	0.00	3.50	0.00

Can. J. Chem. Downloaded from www.nrcresearchpress.com by 196.1.178.254 on 09/07/12
For personal use only.

TABLE 6 (*concluded*)

Angle type				Parameters (kcal/mol) V_1	V_2	V_3
5	4	26	23	0.00	5.00	0.00
5	4	26	27	0.00	5.00	0.00
6	1	1	8	0.00	0.00	0.06
6	1	1	9	0.00	0.00	0.06
6	1	1	13	0.00	0.00	0.06
7	3	1	8	0.00	0.00	−0.04
7	3	1	9	0.00	0.00	−0.04
7	3	1	13	0.00	0.00	−0.04
7	3	9	14	0.00	2.66	0.00
7	3	12	24	0.00	0.00	3.10
8	1	1	15	0.00	0.00	0.06
8	1	3	9	0.00	0.00	−0.09
8	1	3	11	0.00	0.00	−0.09
8	1	3	12	0.00	0.00	−0.06
8	2	19	23	0.00	4.50	0.00
9	1	1	15	0.00	0.00	0.06
9	1	3	9	0.00	0.00	−0.04
9	1	3	11	0.00	0.00	−0.09
9	1	3	12	0.00	0.00	−0.06
9	3	1	13	0.00	0.00	−0.06
11	3	1	13	0.00	0.00	−0.09
12	3	1	13	0.00	0.00	−0.06
13	1	1	15	0.15	0.00	0.10
19	2	8	23	0.00	4.50	0.00
19	2	19	23	0.00	4.50	0.00
23	26	4	26	0.00	5.00	0.00
23	26	27	27	0.00	5.00	0.00
26	4	4	26	−0.30	3.80	0.00
26	4	4	27	−0.30	3.80	0.00

(140) while Raman spectroscopy has produced values of 9.5 kcal/mol and 13.2 kcal/mol (141) for dimethyl disulfide and diethyl disulfide, respectively. Extended Hückel calculations on dimethyl disulfide suggest a *cis* barrier of 7.0 kcal/mol, (142, 143) and *ab initio* calculations on H_2S_2 give values of 7.7 and 7.4 kcal/mol (144, 145). At the 3-21G and 3-21G* levels, disulfides gave rotational barriers of 6–9 kcal/mol (146). This complicated torsional potential cannot be represented by a simple twofold term, but requires a minimum of two terms, both twofold and threefold. Allinger's disulfide torsional parameters give minima at ±90° and S—S rotational barriers of approximately 7.0 kcal/mol; consequently, they have been incorporated into MMPEP (147).

Table 6 lists the dihedral angle parameters of MMPEP.

van der Waals parameters of MMPEP

The Lennard–Jones equation is a general form of a nonbonded interaction potential for neutral, nonpolar molecules. The Buckingham potential, which has an exponential repulsive function, is also in common use (148). The Hill equation, (eq. [6]), used in MMPEP, is a specific example of the Buckingham potential (149). Hill showed that this equation provides a description for many simple molecules that reduces the problem of nonbonded interactions to the selection of two parameters, the van der Waals parameters, r_0 and ε. In this approach, atoms are regarded as distensible spheres of radius r_0 and hardness ε.

The selection of these van der Waals parameters is a difficult part of the parameterization process. Estimates of these parameters are available if one uses experimentally determined van der Waals potentials of rare gas atoms (150), and the fact that atomic radii increase across the periodic table. However, the final parameters must be derived empirically by a fitting of observed quantities. Allinger has employed such a procedure for a variety of amines, carboxylic acids, hydrocarbons, and sulfides, and the MMPEP values for r_0 and ε are based on MM2.

TABLE 7. van der Waals parameters of MMPEP

Atom type	Atom number	r_0 (Å)	ε (kcal/mol)
C	1	1.900	0.044
C	2	1.940	0.044
C	3	1.940	0.044
C	4	1.940	0.044
H	5	1.500	0.047
O	6	1.740	0.050
O	7	1.740	0.066
N	8	1.820	0.055
N	9	1.820	0.055
O	11	1.780	0.066
O	12	1.740	0.050
N	13	1.900	0.030
H	14	0.930	0.017
S	15	2.110	0.202
N	19	1.820	0.055
H	21	1.200	0.036
H	23	1.325	0.034
H	24	0.900	0.015
H	25	1.250	0.036
N	26	1.820	0.055
C	27	1.940	0.044

The van der Waals characteristics of a hydrogen attached to the oxygen of a carboxyl group have been made "small" and "soft" (151). The amide hydrogen, which is involved extensively in the hydrogen bonding process, has been treated analogously. The van der Waals parameters for sulfur require comment. For this atom, as for oxygen and nitrogen, the lone pairs are not considered explicitly (152, 153). Allinger and Hickey's molecular mechanics calculations on alkanethiols and thiaalkanes (154) suggest that this assumption may be acceptable.

The van der Waals parameters used in MMPEP are listed in Table 7.

Electrostatic parameters of MMPEP

Electrostatic interactions are of utmost importance in the consideration of nonbonded interactions (155, 156). In classical electrostatic theory the interaction energy between diffuse charge clouds is calculated by a series expansion. For interactions between point charges, the Coulomb potential is the leading term; for interactions between dipoles, the dipole/dipole interaction energy is the leading term, and can be calculated by Jeans' formula (157–160). Thus, there are two possible approaches for the treatment of electrostatic interactions: the point charge model, in which the charges are treated as geometric points placed at the atomic nuclei; and the dipole model, in which bond moments are assigned to every bond in the molecule. After evaluation of a number of different calculations, Allinger concluded that the two approaches are

Can. J. Chem. Downloaded from www.nrcresearchpress.com by 196.1.178.254 on 09/07/12
For personal use only.

TABLE 8. Bond moments used in MMPEP

Bond type		Bond moment (D)	Bond type		Bond moment (D)
1	1	0.000	3	7	3.010
1	2	0.100	3	9	3.320
1	3	−1.020	3	11	3.950
1	4	−0.180	3	12	1.850
1	5	0.000	4	4	0.000
1	6	2.530	4	5	0.000
1	8	3.980	4	26	2.120
1	9	2.650	4	27	1.120
1	13	1.720	6	21	−1.960
1	15	−0.671	8	23	−1.410
1	19	2.058	9	14	−1.810
2	2	0.000	12	24	0.000
2	5	−0.058	13	23	−1.350
2	6	0.810	15	15	0.000
2	8	4.524	15	25	0.000
2	19	3.260	19	23	−2.270
2	27	−0.700	23	26	1.430
3	5	0.000	26	27	−1.030
3	6	0.000	27	27	0.000

equivalent (5). Although the point charge model is used by Kollman and Scheraga (17, 109), MMPEP employs the dipole model to exploit the computational versatility and flexibility of the MM2 force field.

To use the dipole model, bond moments were assigned to all possible peptide bond types. In accord with Smyth's definition, a bond moment is a vector quantity acting in the line of the bond (161). This vector has a charge at each end and a length equal to the bond length. Accordingly, the bond moment is equal to the product of charge difference and the bond length,

$$[11] \quad \mu = 2.385 l_0 (Q_1 - Q_2)$$

where $Q_1 > Q_2$ and 2.385 is a scalar multiplier which converts μ to debye units when l_0 is in Å and charge is expressed in units of electrons.

Bond lengths (l_0) have been discussed earlier. Charge densities were determined from STO-3G calculations after the method of Kollman (17, 65). For the atoms of the peptide backbone calculations were performed on the dipeptide glycylglycine. The charge densities for the side-chain atoms were determined from calculations on the *N*-acetyl amides (CH_3—CO—NH—CHR—CO—NH_2) of all 20 amino acids. The MMPEP values are listed in Table 8.

Modifications to MM2 to allow the use of MMPEP

Conversion of MMP2(85) from VAX to IBM environments

The MM2 and MMP2 programmes are dimensioned for a maximum of 100 atoms. These versions of the programme therefore allow the MMPEP parameters to be used for calculations on peptides containing up to six amino acid residues. Although this was adequate for our original design problem (1), for several reasons we wished to expand these dimensions. Since the 1985 version (MMP2(85)) had been expanded to 255 atoms, and the details of this expansion were documented (162), we began with MMP2(85), which was available in a VAX version.

The FORTRAN source code of MMP2(85) was, for the most part, ANSI standard Fortran-77. The programme was system independent, except for a few functions that interacted with the operating system; an acquiescent conversion to the VS operating system of the Queen's University IBM 3081 computer was, therefore, feasible.

The VAX version contained two routines, CPUTIM and IDATE, which provide information concerning timing and current date. These routines were modified with the aid of Queen's Subroutine Library (SUBLIB), specifically QTIME, to provide current date, current time, and virtual and total CPU time. In the IBM-VS version, timing was handled in two ways: one, which remained unchanged from the VAX version, related to total CPU time; the other made use of real time. The latter proved more important, especially for large molecules whose CPU time requirements were difficult to predict. Programme termination could then be initialized within the real time limitations imposed by the operating system (999 min).

A second problem related to the use of equivalence statements in the VAX version. The IBM-VS FORTRAN disallows equivalence of numeric integer and Hollerith type integer variables, as found in the VAX version. To overcome this restriction in the VS environment, routines were added to translate information stored in integer variables to character variables, and conversely.

Expansion of MMP2(85) to 999 atoms

The MMP2(85) programme makes extensive use of Include and Parameter FORTRAN statements to define and dimension most of the arrays. Redimensioning of these arrays was, therefore, relatively simple. However, an increase in the maximum number of atoms affected the dimensions of many interrelated arrays and, where applicable, their compile time initializations.

More serious problems were encountered in the integer packing function and unpacking subroutines, which were used to represent bond connectivity, especially the four atom numbers that describe a torsional angle. The packing routine of MMP2(85) used a 32-bit primary integer to store four secondary integers uniquely. This allowed 8 bits for each non-overlapping secondary integer, and thereby imposed a range of 0–255 ($2^8 - 1$) for each secondary integer. It became clear that more than 32 bits would be required to correct this problem. Accordingly, a 64-bit double precision real variable was used for the value of the packing functional. In such a configuration 8 bits are used to represent the exponent, leaving 56 bits to represent the mantissa. An artificial limit of 999 was imposed on the four secondary integers to be packed into the real, yielding the implementation of eq. [12],

$$[12] \quad \text{(Packed value) } P = \sum_{i=0}^{3} (I_i \times 10^{3i})$$

where I_i ($i = 0, \ldots 3$) are double precision floated representations of the secondary integers. The unpacking of such a packing scheme is straightforward.

Although packing and unpacking are normally accomplished by bit manipulating intrinsic functions, leading to faster schemes, these operate only on 32-bit integers, and were unwieldy for the present application.

Modification of MMP2(85) to accept the MMPEP parameters

The MMP2(85) programme contains partially filled arrays, to which additional parameters can be added. The atom types corresponding to such additional parameters must have been previously undefined. A failure to appreciate this point can lead

Can. J. Chem. Downloaded from www.nrcresearchpress.com by 196.1.178.254 on 09/07/12
For personal use only.

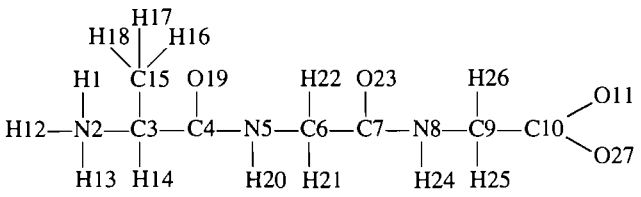

FIG. 1. Numbering scheme for Ala-Gly-Gly.

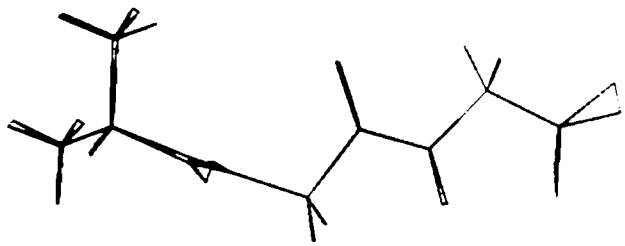

FIG. 2. Superposition of the calculated and X-ray structures of Ala-Gly-Gly.

to erroneous results, which would not be detected by internal error-trapping procedures. For our purposes, the unfilled space proved to be insufficient to accommodate all of the atom types used in MMPEP. Accordingly, all internal parameters were released and replaced by information read in from an external file (PEPCON), which contained the MMPEP parameters. This approach has several advantages: it facilitates updating or expansion of the MMPEP parameters, and it can be applied readily to the treatment of other classes of compounds for which an external file can be created. PEPCON will be provided upon request.

Testing the MMPEP parameters

Any projected application of MMPEP to the theoretical conformational analysis of peptides has two prerequisites: the parameterization must be seen to provide geometries compatible with experiment; and procedures must be developed for the preliminary scanning of the conformational hyperspace of a general peptide, and the creation of an MMP2(85) input file. The question of strategy is examined in the following paper (19). Here we present tests of the parameters, performed on experimental crystal structures of several peptides and proteins.

The Newton–Raphson minimization is employed in MMP2(85); this is guaranteed to lead to the bottom of the energy well in which the initial structure is located, provided that the geometry of this structure is already close to the minimum (163). Although the conformation that crystallizes need not correspond to the global minimum, because of the effects of crystal packing and incorporation of solvent molecules, the coordinates of an X-ray structure are normally a reliable description of the geometry at a particular energy minimum. Thus, to the extent that intermolecular crystal packing forces are not severe, the use of crystal coordinates as input for a Newton–Raphson minimization should not alter the structure, if the force field and its parameterization are valid. Therefore, MMPEP was tested by comparison of minimized structures with crystal structures, starting with the X-ray coordinates, and a dielectric constant of 78.5. The consequences of this choice will be examined later.

Ala-Gly-Gly (44)

Figure 1 shows the numbering scheme employed for this peptide. Table 9 compares the calculated and experimental dihedral angles, and Fig. 2 is a superposition of the two structures, using SNOOPI.[3] The rms deviation, i.e., the root mean square fit in Å, compared to the coordinates of the starting crystal structure, is 0.261.

TABLE 9. Calculated[a,b] and crystallographic[c] dihedral angles of Ala-Gly-Gly

Dihedral angle				Calculated (deg)	Found (deg)
1	2	3	4	−178	180
1	2	3	14	−61	−61
1	2	3	15	58	56
2	3	4	5	154	160
2	3	15	16	62	60
2	3	15	18	−58	−60
3	4	5	6	176	172
4	3	15	16	−63	−62
4	5	6	7	−80	−83
5	4	3	15	−81	−78
5	6	7	8	164	170
5	6	7	23	−16	−10
6	5	4	19	−3	−8
6	7	8	9	180	175
7	8	9	10	177	171
8	9	10	11	−15	−5
8	9	10	27	166	175
12	2	3	15	−61	−63
14	3	15	17	−60	−62

[a]Using the MMPEP parameters.
[b]See Fig. 1 for numbering scheme.
[c]Reference 44.

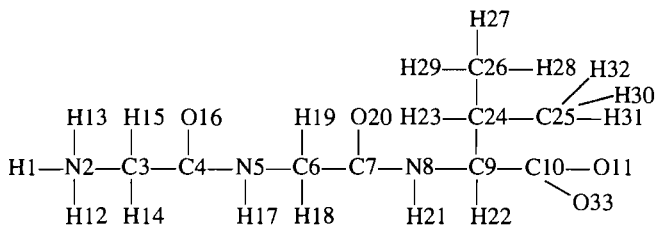

FIG. 3. Numbering scheme for Gly-Gly-Val.

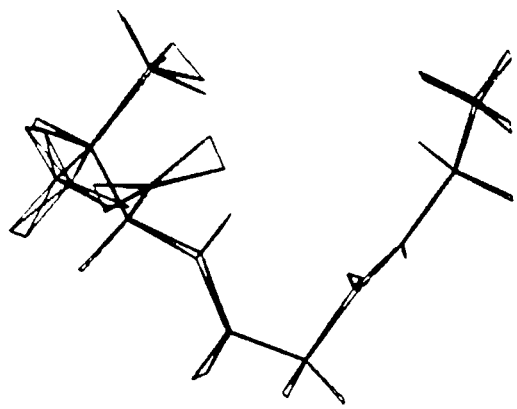

FIG. 4. Superposition of the calculated and X-ray structures of Gly-Gly-Val.

[3]The authors thank Dr. Keith Davies for permission to use this option of CHEMGRAF, and Professor A. S. Cameron (Dalhousie University) and I. Kucirec (Perkin–Elmer Canada) for the Perkin–Elmer version of the programme.

Can. J. Chem. Downloaded from www.nrcresearchpress.com by 196.1.178.254 on 09/07/12
For personal use only.

TABLE 10. Calculated[a,b] and crystallographic[c] dihedral angles of Gly-Gly-Val

Dihedral angle				Calculated (deg)	Found (deg)
1	2	3	4	−61	−60
2	3	4	5	−158	−155
3	4	5	6	180	−176
4	5	6	7	−67	−77
5	4	3	14	80	82
5	6	7	8	−26	−23
6	7	8	9	179	−178
7	8	9	10	−77	−81
8	9	10	11	−47	−50
8	9	24	23	−178	−176
10	9	24	23	57	61
12	2	3	14	179	−179
13	2	3	14	60	61
14	3	4	16	−97	−97
15	3	4	16	142	145
16	4	5	17	180	−176
22	9	24	23	−62	−59

[a]Using the MMPEP parameters.
[b]See Fig. 2 for numbering scheme.
[c]Reference 39.

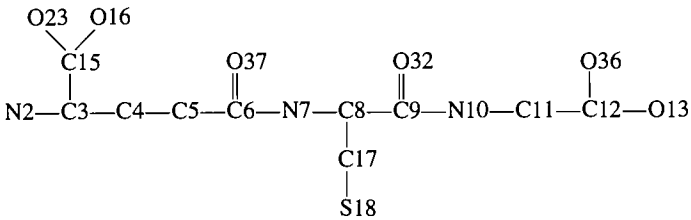

FIG. 5. Numbering scheme for glutathione.

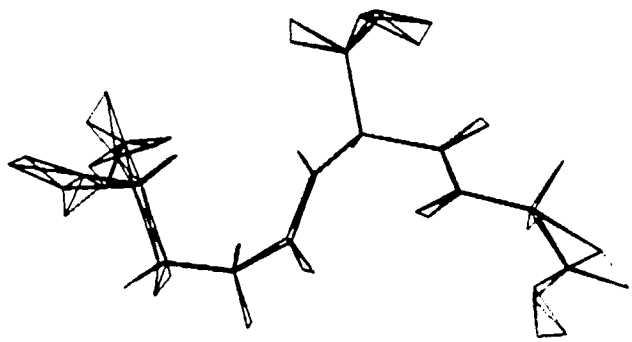

FIG. 6. Superposition of the calculated and X-ray structures of glutathione.

Gly-Gly-Val (39)

Figure 3 is the numbering system for this peptide, and Fig. 4 is a superposition of the calculated and experimental structures. Table 10 compares the calculated and experimental dihedral angles. The rms deviation is 0.349.

Glutathione (164)

Figure 5 is the numbering system for this peptide, and Fig. 6 is a superposition of the calculated and experimental structures. Table 11 compares the calculated and experimental dihedral angles. The rms deviation is 0.417.

TABLE 11. Calculated[a,b] and crystallographic[c] dihedral angles of glutathione

Dihedral angle				Calculated (deg)	Found (deg)
2	3	4	5	−69	−70
2	3	15	16	171	170
2	3	15	23	−9	−11
4	5	6	7	103	102
6	7	8	9	−90	−88
6	7	8	17	145	147
7	8	17	18	65	69
7	8	9	10	−8	−4
8	9	10	11	180	−177
9	10	11	12	−77	−84
10	11	12	13	0	13
10	11	12	36	−180	−162

[a]Using the MMPEP parameters.
[b]See Fig. 3 for numbering scheme.
[c]Reference 164.

Crambin (165)

This polypeptide contains 46 residues, 327 heavy atoms, and 636 atoms including hydrogens. The published structure (165) includes diffraction data to 1.5 Å. A structure refined to 0.945 Å (166) has been used as the starting point for calculations with the united atom force field of AMBER (17). In these calculations (166), over 70 conjugate gradient minimizations were performed, with systematic variation of the electrostatic potential energy, the dielectric constant, the nonbonding cutoff, the van der Waals radii, the protein environment, and the presence or absence of α hydrogens. The best fit (rms = 0.245) was achieved with Jorgensen's van der Waals radii (167), a distance dependent dielectric constant of $4.0r$, and a 6.0-Å residue-based or a 9.0-Å atom-based nonbonding cutoff. Explicit inclusion of solvent or large portions of the crystal environment did not improve the fit sufficiently to justify the additional computational time.

In the present work, hydrogens were added to the heavy atoms of the 1.5 Å structure (162), and Newton–Raphson minimization was performed. The resulting rms deviation was 0.291 for the heavy atoms of the backbone, and 0.310 for all heavy atoms. Figure 7 shows a superposition of the calculated and experimental structures.[4]

Insulin (168)

The zinc complex of des-Phe B1 bovine insulin has been refined to 2.5 Å (168). The crystallographic asymmetric unit consists of two molecules, each containing two chains (A + B, and C + D). The two molecules are aggregated as a hexamer, with the dimers related by threefold rotational symmetry. In the hexamer, zinc atoms are coordinated to three symmetry-related imidazole rings of the 10 histidines. The monomer has 51 residues, 389 unique heavy atoms, and 756 atoms including hydrogens. The coordinates of A + B were used for the calculations, and led to a structure with rms = 0.511 for backbone atoms and 0.646 for all heavy atoms.[4] The superposition of the calculated and experimental structures is shown in Fig. 8.

[4]Copies of the calculated output will be provided upon request (BITNET: WOLFES@QUCDN).

Can. J. Chem. Downloaded from www.nrcresearchpress.com by 196.1.178.254 on 09/07/12
For personal use only.

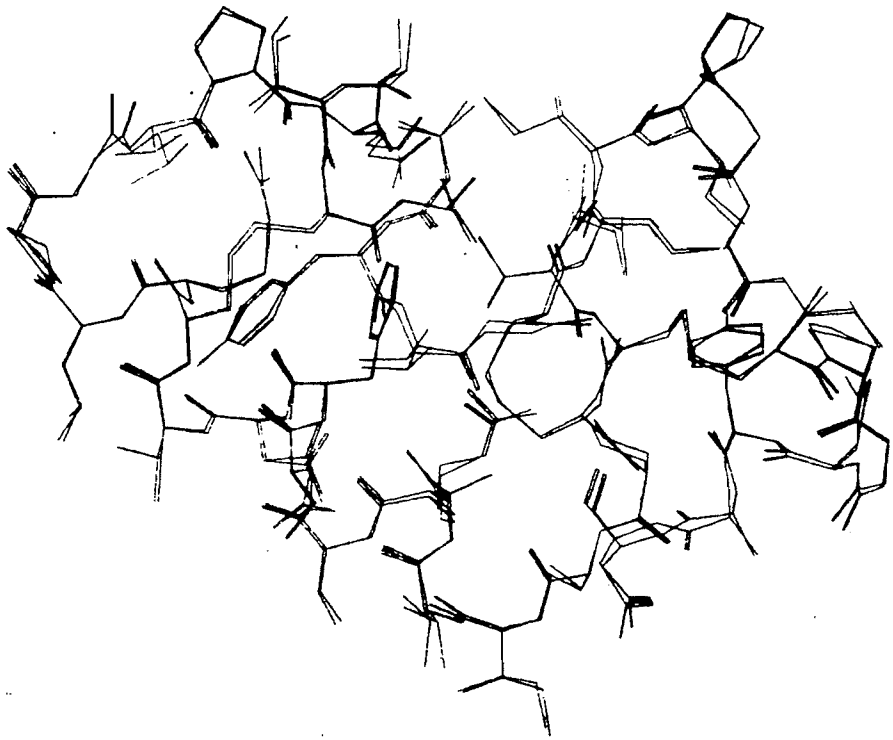

FIG. 7. Superposition of the calculated and X-ray structures of crambin (heavy atoms).

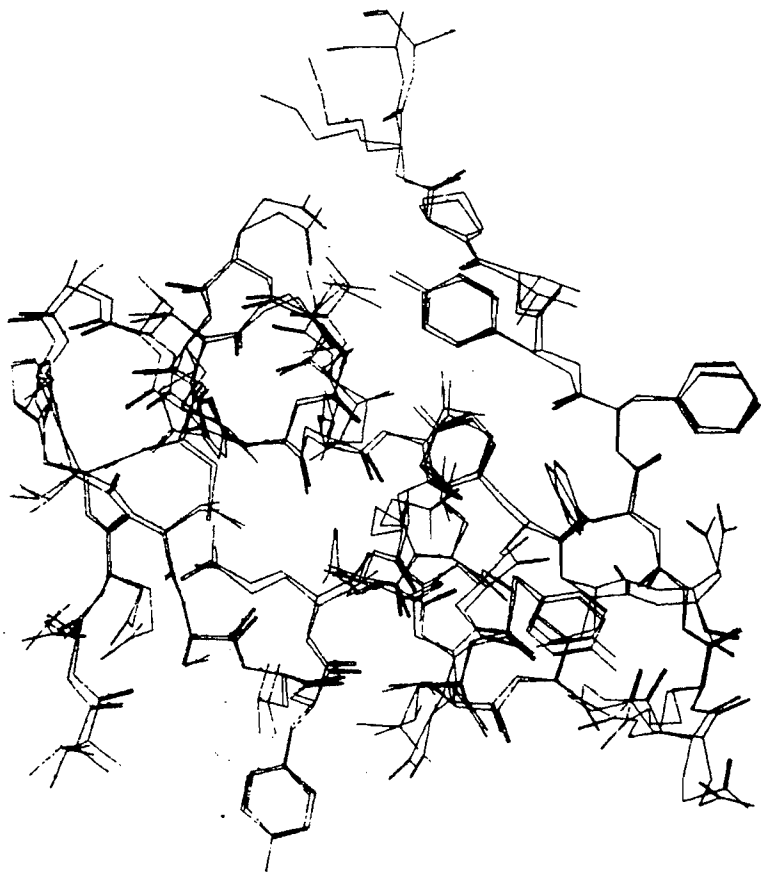

FIG. 8. Superposition of the calculated and X-ray structures of insulin (heavy atoms).

Can. J. Chem. Downloaded from www.nrcresearchpress.com by 196.1.178.254 on 09/07/12
For personal use only.

Can. J. Chem. Downloaded from www.nrcresearchpress.com by 196.1.178.254 on 09/07/12
For personal use only.

Porcine insulin, resolved to 1.5 Å (404 heavy atoms) has been examined by Kollman, using both the united atom (17) and all-atom (65*a*) force fields of AMBER. With a distance dependent dielectric constant ($\varepsilon = R_{ij}$) and a 9.0-Å or 8.0-Å cutoff distance for evaluation of nonbonded interactions, rms = 0.43 (17) and 0.44 (65*a*).

Summary and conclusions

At the outset of our work we believed that Allinger's force field and the MMP2(85) programme constituted the most thoroughly tested and documented framework for the practical implementation of a molecular mechanics calculation. A reliable parameterization of the force field for peptides could, therefore, make the theoretical conformational analysis of such compounds generally accessible.

Some workers have argued that the Newton–Raphson minimization procedure that is implemented in MMP2(85) is too slow to be applied routinely to a force field that treats all nonbonded interactions of all atoms of a complex molecule. This has not been our experience. On the IBM 3081 computer, real time minimization of each of the tripeptides was achieved in 1–2 min, crambin in 250 min, and insulin in 200 min, starting with the geometries of the crystal structures. In the tripeptides, the deviations seen in Figs. 2, 4, and 6 occur at the charged ends of the molecules, and are considered to reflect the consequences of intermolecular interactions in the experimental structures. In crambin, deviations are found at residues 7 and 25, which exhibit conformational heterogeneity in the crystal structure, and at residue 22, which exhibits compositional heterogeneity. In view of these results, it is tempting to consider that the calculation of the insulin monomer provides a reasonable description of the structure that binds to the insulin receptor.

It is noteworthy that the use of a standard dielectric constant $\varepsilon = 78.5$ in MMPEP leads to acceptable agreement with experimental crystal structures in each case. Although more work is needed on this point, and on additional test examples, we believe that it will be possible to generate meaningful structures by one full Newton–Raphson minimization.

In contrast to the force fields of AMBER (17, 65*a*) and CHARMM (65*b*), the MMPEP parameterization of Allinger's force field contains no specific hydrogen bonding term. As noted by Allinger (5), hydrogen bonding in the MM2 force field occurs as a result of the electrostatic and van der Waals interactions. Similar views have been expressed by Lifson, Hagler, and co-workers for intermolecular interactions in amides (169) and carboxylic acids (170). The use of six different atom types for hydrogen in MMPEP, with different bond moments and different van der Waals radii, seems to be sufficient. For example, the van der Waals radii of H—NH— and H—N—CO are 1.320 and 0.930, respectively. The reduced radius of the amide N—H permits a short contact distance in a N—H...O=C interaction, and increases the electrostatic interaction between these groups.

The five nitrogen atom types of MMPEP permit a greater degree of geometric precision in the descriptions of the guanidine group of arginine and the five-membered rings of tryptophan and histidine. Finally, the use of low and high periodicity terms in the treatment of dihedral angles permits these to be shaped with a high degree of accuracy. It is thus possible to differentiate the χ_1 angles of amino acids such as valine and isoleucine, which have double branching distal to the β carbon atom, from other single branched residues.

Acknowledgements

The authors thank the Natural Sciences and Engineering Research Council of Canada for financial support, the Medical Research Council of Canada for the award of a Graduate Fellowship, and Queen's University for generous allocation of computer time. We are most grateful to Dr. George Birnbaum for encouragement and many helpful discussions, as well as the retrieval of many peptide crystal structures, including crambin and insulin, and the generation of the data shown in Figs. 7 and 8. We also acknowledge a helpful discussion with Michael Zucker on the subject of rms differences.

1. S. Wolfe, R. J. Bowers, H. S. Shin, C.-K. Sohn, D. F. Weaver, and K. Yang. Can. J. Chem. **66**, 2751 (1988).
2. M. Raban, J. Greenblatt, and F. Kandil. J. Chem. Soc. Chem. Commun. 1409 (1983).
3. M. Dobler. Ionophores and their structures. Wiley–Interscience, New York. 1981.
4. Yu. A. Ovchinnikov, V. T. Ivanov, and A. M. Shkrob. Membrane-active complexones. Elsevier, Amsterdam. 1974.
5. U. Burkert and N. L. Allinger. Molecular mechanics. American Chemical Society, Washington. 1982.
6. N. L. Allinger and Y. Yuh. QCPE, **12**, 395 (1980).
7. E. D. Bergmann and B. Pullman (*Editors*). Conformation of biological molecules and polymers. The Israel Academy of Sciences and Humanities, Jerusalem. 1973.
8. G. N. Ramachandran and V. Sasisekharan. Adv. Protein Chem. **23**, 283 (1968).
9. H. A. Scheraga. Adv. Phys. Org. Chem. **6**, 103 (1968).
10. A. Warshel, M. Levitt, and S. Lifson. J. Mol. Spectrosc. **33**, 84 (1970).
11. B. R. Gelin and M. Karplus. J. Am. Chem. Soc. **97**, 6996 (1975).
12. A. T. Hagler. *In* Conformation in biology and drug design. *Edited by* V. R. Hruby. Academic Press, New York. 1985. p. 213.
13. M. Levitt. J. Mol. Biol. **170**, 723 (1983).
14. E. Ralston and J. L. De Coen. J. Mol. Biol. **83**, 393 (1974).
15. S. S. Zimmerman. *In* Conformation in biology and drug design. *Edited by* V. R. Hruby. Academic Press, New York. 1985. p. 165.
16. ECEPP/2. QCPE No. 454.
17. S. J. Weiner, P. A. Kollman, D. A. Case, U. C. Singh, C. Ghio, G. Alagona, S. Profeta, Jr., and P. Weiner. J. Am. Chem. Soc. **106**, 765 (1984).
18. N. C. Cohen. Adv. Drug Res. **14**, 41 (1985).
19. S. Wolfe, S. Bruder, D. F. Weaver, and K. Yang. Can. J. Chem. **66**, 2703 (1988).
20. M. S. Lehmann, T. F. Koetzle, and W. C. Hamilton. J. Am. Chem. Soc. **94**, 2657 (1972) (alanine).
21. M. S. Lehmann, J. J. Verbist, W. C. Hamilton, and T. F. Koetzle. J. Chem. Soc. Perkin Trans. 2, 133 (1973) (arginine).
22. J. J. Verbist, M. S. Lehmann, T. F. Koetzle, and W. C. Hamilton. Acta Crystallogr. Sect. B: Struct. Crystallogr. Cryst. Chem. **28**, 3006 (1972) (asparagine).
23. D. S. Eggleston, E. J. Valente, and D. J. Hodgson. Acta Crystallogr. Sect. B: Struct. Crystallogr. Cryst. Chem. **37**, 1428 (1981) (aspartyl-glycine).
24. K. A. Kerr and J. P. Ashmore. Acta Crystallogr. Sect. B: Struct. Crystallogr. Cryst. Chem. **29**, 2124 (1973) (cysteine).
25. D. D. Jones, I. Bernal, M. N. Frey, and T. F. Koetzle. Acta Crystallogr. Sect. B: Struct. Crystallogr. Cryst. Chem. **30**, 1220 (1974) (cystine).
26. T. F. Koetzle, M. N. Frey, M. S. Lehmann, and W. C. Hamilton. Acta Crystallogr. Sect. B: Struct. Crystallogr. Cryst. Chem. **29**, 2571 (1973) (glutamine).
27. D. S. Eggleston, E. J. Valente, and D J. Hodgson. Acta

Can. J. Chem. Downloaded from www.nrcresearchpress.com by 196.1.178.254 on 09/07/12
For personal use only.

Crystallogr. Sect. B: Struct. Crystallogr. Cryst. Chem. **37**, 1430 (1981) (glutamyl-glycine).
28. T. J. KISTENMACHER, D. J. HUNT, and R. E. MARSH. Acta Crystallogr. Sect. B: Struct. Crystallogr. Cryst. Chem. **28**, 3352 (1972) (*N*-acetylhistidine).
29. K. TORII and Y. IITAKA. Acta Crystallogr. Sect. B: Struct. Crystallogr. Cryst. Chem. **27**, 2237 (1971) (isoleucine).
30. L. GOLIC and W. C. HAMILTON. Acta Crystallogr. Sect. B: Struct. Crystallogr. Cryst. Chem. **28**, 1265 (1972) (leucine).
31. T. F. KOETZLE, M. S. LEHMANN, J. J. VERBIST, and W. C. HAMILTON. Acta Crystallogr. Sect. B: Struct. Crystallogr. Cryst. Chem. **28**, 3207 (1972) (lysine).
32. C. CHEN and R. PARTHASARATHY. Acta Crystallogr. Sect. B: Struct. Crystallogr. Cryst. Chem. **33**, 3332 (1977) (*N*-formylmethionine).
33. A. R. AL-KARAGHOULI and T. F. KOETZLE. Acta Crystallogr. Sect. B: Struct. Crystallogr. Cryst. Chem. **31**, 2461 (1975) (phenylalanine).
34. I. TANAKA, T. KOZIMA, T. ASHIDA, N. TANAKA, and M. KAKUDO. Acta Crystallogr. Sect. B: Struct. Crystallogr. Cryst. Chem. **33**, 116 (1977) (carbobenzoxyglycyl-proline).
35. M. N. FREY, T. F. KOETZLE, M. S. LEHMANN, and W. C. HAMILTON. J. Chem. Phys. **58**, 2547 (1973) (tyrosine).
36. M. N. FREY, M. S. LEHMANN, T. F. KOETZLE, and W. C. HAMILTON. Acta Crystallogr. Sect. B: Struct. Crystallogr. Cryst. Chem. **29**, 876 (1973) (serine).
37. V. S. YADAVA and V. M. PADMANABHAN. Acta Crystallogr. Sect. B: Struct. Crystallogr. Cryst. Chem. **29**, 854 (1973) (glycine-threonine).
38. T. F. KOETZLE, L. GOLIC, M. S. LEHMANN, J. J. VERBIST, and W. C. HAMILTON. J. Chem. Phys. **60**, 4690 (1974) (valine).
39. V. LALITHA, E. SUBRAMANIAN, and J. BORDNER. Int. J. Pept. Protein Res. **24**, 437 (1984) (glycyl-glycyl-valine).
40. K. N. GOSWAMI, V. S. YADAVA, and V. M. PADMANABHAN. Acta Crystallogr. Sect. B: Struct. Crystallogr. Cryst. Chem. **33**, 1280 (1977) (leucyl-glycyl-glycine).
41. V. PATTABHI, K. VENKATESAN, and S. A. HALL. J. Chem. Soc. Perkin Trans. 2, 1722 (1974) (glycyl-leucine).
42. F. BENEDETTI, V. PAVONE, C. TONIOLO, G. BONORA, and M. PALUMBO. Macromolecules, **10**, 1350 (1977).
43. R. E. MARSH, M. R. N. MURTHY, and K. VENKATESAN. J. Am. Chem. Soc. **99**, 1251 (1977) (Boc-glycyl-proline).
44. E. SUBRAMANIAN and V. LALITHA. Biopolymers, **22**, 833 (1983) (alanyl-glycyl-glycine).
45. S. CAPASSO, C. A. MATTIA, L. MAZZARELLA, and A. ZAGARI. Int. J. Pept. Protein Res. **24**, 85 (1984) (Boc-aminosuccinyl-glycyl-glycine methyl ester).
46. D. F. DETAR and N. P. LUTHRA. J. Am. Chem. Soc. **99**, 1232 (1977) (proline).
47. A. ARNONE, C. BIER, F. COTTON, V. DAY, and J. RICHARDSON. J. Biol. Chem. **246**, 2302 (1971).
48. D. M. BLOW. Biochem. J. **112**, 261 (1969).
49. R. E. DICKERSON, T. TAKANO, D. EISENBERG, O. KALLAI, L. SAMPSON, and A. COOPER. J. Biol. Chem. **246**, 1511 (1971).
50. F. S. MATHEWS, M. LEVINE, and P. ARGOS. J. Mol. Biol. **64**, 449 (1972).
51. C. NOCKOLDS, R. KRETSINGER, C. COFFEE, and R. BRADSHAW. Proc. Natl. Acad. Sci. U.S.A. **69**, 581 (1972).
52. J. S. BINKLEY, R. A. WHITESIDE, R. KRISHNAN, R. SEEGER, D. J. DEFREES, H. B. SCHLEGEL, S. TOPIOL, L. R. KAHN, and J. A. POPLE. QCPE, **13**, 406 (1981).
53. K. SIAM, V. J. KLIMKOWSKI, J. D. EWBANK, C. VAN ALSENOY, and L. SCHÄFER. J. Mol. Struct. **110**, 171 (1984).
54. D. PETERS and J. PETERS. J. Mol. Struct. **50**, 133 (1978).
55. D. PETERS and J. PETERS. J. Mol. Struct. **53**, 103 (1979).
56. D. PETERS and J. PETERS. J. Mol. Struct. **62**, 229 (1980).
57. D. PETERS and J. PETERS. J. Mol. Struct. **64**, 103 (1980).
58. D. PETERS and J. PETERS. J. Mol. Struct. **68**, 243 (1980).
59. D. PETERS and J. PETERS. J. Mol. Struct. **68**, 255 (1980).
60. D. PETERS and J. PETERS. J. Mol. Struct. **69**, 249 (1980).
61. D. PETERS and J. PETERS. J. Mol. Struct. **85**, 107 (1981).
62. D. PETERS and J. PETERS. J. Mol. Struct. **85**, 257 (1981).
63. D. PETERS and J. PETERS. J. Mol. Struct. **85**, 267 (1981).
64. D. PETERS and J. PETERS. Biopolymers, **24**, 491 (1985).
65. (*a*) S. J. WEINER, P. A. KOLLMAN, D. T. NGUYEN, and D. A. CASE. J. Comput. Chem. **7**, 230 (1986); (*b*) B. R. BROOKS, R. E. BRUCCOLERI, B. D. OLAFSON, D. J. STATES, S. SWAMINATHAN, and M. KARPLUS. J. Comput. Chem. **4**, 187 (1983).
66. H. B. SCHLEGEL. Ph.D. thesis, Queen's University, 1975.
67. G. FOGARASI and P. PULAY. Ann. Rev. Phys. Chem. **35**, 191 (1984).
68. G. FOGARASI and P. PULAY. *In* Vibrational spectra and structure. Vol. 14. *Edited by* J. R. Durig. Elsevier, New York. 1985. pp. 126–219.
69. P. PULAY. *In* Applications of electronic structure theory. *Edited by* H. F. Schaefer III. Plenum, New York. 1977. pp. 153–185.
70. P. PULAY. *In* The force concept in chemistry. *Edited by* B. M. Deb. Van Nostrand Reinhold, New York. 1981.
71. Y. SUGAWARA, A. Y. HIRAKAWA, and M. TSUBOI. J. Mol. Spectrosc. **108**, 212 (1984).
72. N. L. ALLINGER. Adv. Phys. Org. Chem. **13**, 1 (1976).
73. E. M. ENGLER, J. D. ANDOSE, and P. VON R. SCHLEYER. J. Am. Chem. Soc. **95**, 8005 (1973).
74. O. ERMER and S. LIFSON. J. Am. Chem. Soc. **95**, 4121 (1973).
75. S. CHANG, D. MCNALLY, S. SHARY-TEHRANY, M. J. HICKEY, and R. H. BOYD. J. Am. Chem. Soc. **92**, 3109 (1970).
76. S. FITZWATER and L. S. BARTELL. J. Am. Chem. Soc. **98**, 5107 (1976).
77. W. V. F. BROOKS and C. M. HAAS. J. Phys. Chem. **71**, 650 (1967).
78. R. G. SNYDER and G. ZERBI. Spectrochim. Acta, **23**, 391 (1967); P. LABARBE, M. T. FOREL, and G. BESSIS. Spectrochim. Acta, **24**, 2165 (1968).
79. G. DELLEPIANE and G. ZERBI. J. Chem. Phys. **48**, 3573 (1968); A. Y. HIRAKAWA, M. TSUBOI, and T. SHIMANOUCHI. J. Chem. Phys. **57**, 1236 (1972).
80. D. W. SCOTT and M. Z. EL-SABBAN. J. Mol. Spectrosc. **31**, 362 (1969); D. W. SCOTT and J. P. MCCULLOUGH. J. Mol. Spectrosc. **6**, 372 (1961).
81. J. P. TOLLENAERE, H. MOEREELS, and L. A. RAYMAEKERS. Atlas of the three-dimensional structure of drugs. Elsevier/North-Holland Biomed. Press, Amsterdam. 1979.
82. D. H. WILLIAMS and I. FLEMING. Spectroscopic methods in organic chemistry. 2nd ed. McGraw–Hill, Toronto. 1973.
83. J. C. WILLIAMS, P. J. STANG, and P. VON R. SCHLEYER. Ann. Rev. Phys. Chem. **19**, 531 (1968).
84. C. ALTONA and D. FABER. Top. Curr. Chem. **45**, 1 (1974).
85. A. WARSHEL and S. LIFSON. J. Chem. Phys. **53**, 582 (1970).
86. D. C. MCKEAN. J. Chem. Soc. Chem. Commun. 1373 (1971).
87. G. ERLANDSSON and W. GORDY. Phys. Rev. **106**, 513 (1957).
88. R. M. LEES and J. G. BAKER. J. Chem. Phys. **48**, 5299 (1968).
89. T. KOJIMA. J. Phys. Soc. Jpn. **15**, 1284 (1960).
90. L. RADOM, W. J. HEHRE, and J. A. POPLE. J. Am. Chem. Soc. **94**, 2371 (1972).
91. O. KENNARD and D. G. WATSON. Mol. Struct. Dimens. **1**, 343 (1970).
92. M. KITANO, T. FUKUYAMA, and K. KUCHITSU. Bull. Chem. Soc. Jpn. **46**, 384 (1973).
93. M. KITANO and K. KUCHITSU. Bull. Chem. Soc. Jpn. **46**, 3048 (1973).
94. J. F. YAN, F. A. MOMANY, R. HOFFMAN, and H. A. SCHERAGA. J. Phys. Chem. **74**, 420 (1970).
95. G. GOVIL. J. Chem. Soc. A, 386 (1971).
96. C. N. R. RAO, K. G. RAO, and D. BALASUBRAMANIAN. J. Chem. Soc. A, 3077 (1971).
97. K. N. SHAW and L. W. REEVES. Chem. Phys. Lett. **10**, 89 (1971).

Can. J. Chem. Downloaded from www.nrcresearchpress.com by 196.1.178.254 on 09/07/12
For personal use only.

98. F. A. MOMANY, R. F. MCGUIRE, J. F. YAN, and H. A. SCHERAGA. J. Phys. Chem. **74**, 2424 (1970).
99. G. N. RAMACHANDRAN, A. V. LAKSHMINAYANAN, and A. S. KOLASKOV. Biochim. Biophys. Acta, **303**, 8 (1973).
100. T. J. ZIELINSKI, R. A. POIRIER, M. R. PETERSON, and I. G. CSIZMADIA. J. Comput. Chem. **3**, 477 (1982).
101. G. FOGARASI, P. PULAY, F. TÖRÖK, and J. BOGGS. J. Mol. Struct. **57**, 259 (1979).
102. D. H. CHRISTENSEN, R. N. KORTZEBORN, B. BAK, and J. J. LED. J. Chem. Phys. **53**, 3912 (1970).
103. M. PERICAUDEL and A. PULLMAN. Int. J. Pept. Protein Res. **5**, 99 (1973).
104. T. DRAKENBERG and S. FORSÉN. J. Phys. Chem. **74**, 1 (1970).
105. G. SCHULTZ and R. SCHIRMER. Principles of protein structure. Springer-Verlag, New York. 1979.
106. R. A. SCOTT and H. A. SCHERAGA. J. Chem. Phys. **45**, 2091 (1966).
107. M. LEVITT. J. Mol. Biol. **82**, 393 (1974).
108. B. R. GELIN and M. KARPLUS. Biochemistry, **18**, 1256 (1979).
109. F. A. MOMANY, R. F. MCGUIRE, A. W. BURGESS, and H. A. SCHERAGA. J. Phys. Chem. **79**, 2361 (1975).
110. D. A. BRANT and P. J. FLORY. J. Am. Chem. Soc. **87**, 2791 (1965).
111. P. DE SANTIS, E. GIGLIO, A. LIQUORI, and A. RIPAMONTI. Nature, **206**, 456 (1965).
112. A. S. KOLASKAR and D. PRASHANTH. Int. J. Pept. Protein Res. **14**, 88 (1979).
113. H. VEILLARD and B. REES. Chem. Phys. Lett. **8**, 267 (1971).
114. A. C. HOPKINSON and I. G. CSIZMADIA. Theor. Chim. Acta, **34**, 93 (1974).
115. J. N. SCARSDALE, C. VAN ALSENOY, V. J. KLIMKOWSKI, L. SCHÄFER, and F. A. MOMANY. J. Am. Chem. Soc. **105**, 3438 (1983).
116. J. A. POPLE and G. A. SEGAL. J. Chem. Phys. **44**, 3289 (1966); R. D. BROWN and R. D. HARCOURT. Aust. J. Chem. **16**, 737 (1963); R. N. DIXON. Mol. Phys. **12**, 83 (1967); M. PELISSIER, A. SERAFINI, J. DEVANNEAUX, J. F. LABARRE, and J. F. TOCANNE. Tetrahedron, **27**, 3271 (1971); R. HOFFMAN. J. Chem. Phys. **40**, 2745 (1964); N. C. BAIRD and M. J. S. DEWAR. J. Chem. Phys. **50**, 1262 (1969); C. A. COULSON and H. C. LONGUET-HIGGINS. Proc. R. Soc. London, A: **191**, 39 (1947); R. D. BROWN and M. L. HEFFERNAN. Aust. J. Chem. **12**, 319 (1959).
117. H. CHUMAN and F. A. MOMANY. Int. J. Pept. Protein Res. **24**, 249 (1984).
118. N. L. ALLINGER, D. HINDMAN, and H. HÖNIG. J. Am. Chem. Soc. **99**, 3282 (1977).
119. N. L. ALLINGER. J. Am. Chem. Soc. **99**, 8127 (1977).
120. L. S. BARTELL. J. Am. Chem. Soc. **99**, 3279 (1977).
121. N. L. ALLINGER and D. Y. CHUNG. J. Am. Chem. Soc. **98**, 6798 (1976).
122. B. P. VAN EIJCK. Recl. Trav. Chim. Pays-Bas, **85**, 1129 (1966).
123. M. S. GORDON. J. Am. Chem. Soc. **91**, 3122 (1969).
124. C. W. KERN, R. M. PITZER, and O. J. SOVERS. J. Chem. Phys. **60**, 3583 (1974).
125. S. PROFETA, JR. and N. L. ALLINGER. J. Am. Chem. Soc. **107**, 1907 (1985).
126. W. ENGLAND and M. S. GORDON. J. Am. Chem. Soc. **93**, 4649 (1971).
127. L. PEDERSEN and K. MOROKUMA. J. Chem. Phys. **46**, 3941 (1967).
128. T. NISHIKAWA, T. ITOH, and K. SHIMODA. J. Chem. Phys. **23**, 1735 (1955).
129. A. VEILLARD. Small molecules and inorganic compounds. *In* Quantum mechanics of molecular conformations. *Edited by* B. Pullman. Wiley–Interscience, Toronto. 1976.
130. N. L. ALLINGER and S. H. M. CHANG. Tetrahedron, **33**, 1561 (1977).
131. T. MIYAZAWA and K. S. PITZER. J. Chem. Phys. **30**, 1076 (1959).
132. P. ROS. J. Chem. Phys. **49**, 4902 (1968).
133. D. L. BERNITT, K. O. HARTMAN, and I. C. HISATSUNE. J. Chem. Phys. **42**, 3553 (1965).
134. W. T. TABOR. J. Chem. Phys. **27**, 974 (1957).
135. L. C. KRISHER and E. SAEGEBARTH. J. Chem. Phys. **54**, 4553 (1971).
136. J. P. LOWE. Prog. Phys. Org. Chem. **6**, 1 (1968).
137. S. D. PEYERIMHOFF and R. J. BUENKER. J. Chem. Phys. **51**, 2528 (1969).
138. V. BUSS, R. GLEITER, and P. VON R. SCHLEYER. J. Am. Chem. Soc. **93**, 3927 (1971).
139. M. S. GORDON and L. NEUBAUER. J. Am. Chem. Soc. **96**, 5690 (1974).
140. M. Z. EL-SABBAN and D. SCOTT. Bull. U.S. Bur. Mines, No. 654. 1970.
141. D. W. SCOTT, H. L. FINKE, M. E. GROSS, G. B. GUTHRIE, and H. M. HUFFMAN. J. Am. Chem. Soc. **72**, 2424 (1950); D. W. SCOTT, H. L. FINKE, J. P. MCCULLOUGH, M. E. GROSS, R. E. PENNINGTON, and G. WADDINGTON. J. Am. Chem. Soc. **74**, 2478 (1952).
142. D. B. BOYD. J. Am. Chem. Soc. **94**, 8799 (1972).
143. D. B. BOYD. Theor. Chim. Acta, **30**, 137 (1973).
144. I. H. HILLIER, V. R. SAUNDERS, and J. F. WYATT. Trans. Faraday Soc. **66**, 2665 (1970).
145. M. E. SCHWARTZ. J. Chem. Phys. **51**, 4182 (1969).
146. T.-K. HA. J. Mol. Struct. (Theochem), **122**, 225 (1985).
147. N. L. ALLINGER, M. J. HICKEY, and J. KAO. J. Am. Chem. Soc. **98**, 2741 (1976).
148. D. FITTS. Ann. Rev. Phys. Chem. **17**, 59 (1966).
149. T. L. HILL. J. Chem. Phys. **16**, 399 (1948).
150. J. O. HIRSCHFELDER and W. J. MEATH. Adv. Chem. Phys. **12**, 3 (1967).
151. G. GOVIL and R. V. HOSUR. Conformation of biological molecules, new results from NMR. *In* NMR: basic principles and progress. Vol. 20. *Edited by* P. Diehl, E. Fluck, and R. Kosfeld. Springer-Verlag, New York. 1982.
152. U. BURKERT. Tetrahedron, **33**, 2237 (1977).
153. S. MELBERG and K. RASMUSSEN. J. Mol. Struct. **57**, 215 (1979).
154. N. L. ALLINGER and M. J. HICKEY. J. Am. Chem. Soc. **97**, 5167 (1975).
155. R. G. C. ARRIDGE and C. G. CANNON. Proc. R. Soc. London, A: **278**, 91 (1964).
156. D. A. BRANT and P. J. FLORY. J. Am. Chem. Soc. **87**, 663 (1965).
157. J. H. JEANS. Mathematical theory of electricity and magnetism. 5th ed. Cambridge University Press, London. 1933.
158. C. P. SMYTH, R. W. DORNTE, and E. B. WILSON. J. Am. Chem. Soc. **53**, 4242 (1931).
159. J. M. LEHN and G. OURISSON. Bull. Soc. Chim. 1113 (1963).
160. E. L. ELIEL, N. L. ALLINGER, S. J. ANGYAL, and G. A. MORRISON. Conformational analysis. Wiley–Interscience, New York. 1965.
161. C. P. SMYTH. Dielectric behaviour and structure. McGraw–Hill, Toronto. 1955.
162. N. L. ALLINGER. MMP2(85). Quantum Chemistry Program Exchange, Bloomington, IN.
163. O. ERMER. Struct. Bonding (Berlin), **27**, 161 (1976).
164. W. B. WRIGHT. Acta Crystallogr. **11**, 632 (1958).
165. W. A. HENDRICKSON and M. M. TEETER. Nature (London), **290**, 107 (1981).
166. M. WHITLOW and M. M. TEETER. J. Am. Chem. Soc. **108**, 7163 (1986).
167. W. L. JORGENSEN. J. Am. Chem. Soc. **103**, 335 (1981).
168. G. D. SMITH, W. L. DUAX, E. J. DODSON, G. G. DODSON, R. A. G. DE GRAAF, and C. D. REYNOLDS. Acta Crystallogr. Sect. B: Struct. Crystallogr. Cryst. Chem. **38**, 3028 (1982).
169. A. T. HAGLER, E. HULER, and S. LIFSON. J. Am. Chem. Soc. **96**, 5319 (1974); A. T. HAGLER and S. LIFSON. J. Am. Chem. Soc. **96**, 5327 (1974).
170. S. LIFSON, A. T. HAGLER, and P. DAUBER. J. Am. Chem. Soc. **101**, 5111 (1979); A. T. HAGLER, S. LIFSON, and P. DAUBER. J. Am. Chem. Soc. **101**, 5122 (1979).

Theoretical conformational analysis of peptides. Evolution of a strategy and its application to cholecystokinin analogs

SAUL WOLFE,[1] STEPHEN BRUDER, DONALD FREDRIC WEAVER, AND KIYULL YANG
Department of Chemistry, Queen's University, Kingston, Ont., Canada K7L 3N6

Received September 22, 1987[2]

SAUL WOLFE, STEPHEN BRUDER, DONALD FREDRIC WEAVER, and KIYULL YANG. Can. J. Chem. **66**, 2703 (1988).

Scheraga's ECEPP program has been used to determine the relationship between one-point energies and the energies minimized by a quadratic procedure, for different sized (ϕ, ψ, χ_1) dihedral angle grid searches of simple peptides. Based on these trials, a new subroutine, INIT, has been written and incorporated into the program. This subroutine calculates the one-point ECEPP energies of up to 200,000 random permutations of (ϕ, ψ) = 0, ±90, 180 and (χ_1) = −60, 180 with all $\omega = \chi_{\neq 1} = 180$; after each 40,000 permutations, the structures having the 10 lowest energies are ordered and selected for minimization. The ECEPP program has been modified further to provide an MMP2(85) input file as part of its normal output. This allows structures located by INIT to be minimized automatically, and then refined by the Newton–Raphson minimization and MMPEP parameters of MMP2(85).

During the development of this protocol, it has been found that MMPEP correctly reproduces the C_7 conformational preference of the alanyl dipeptide in nonpolar media, and also the experimentally observed shift to α_R and P_{II} conformations in polar solvents, when the dielectric constant $\varepsilon = 78.5$ D. This dielectric constant has, therefore, been selected for a conformational analysis, using INIT/MMPEP, of the peptides Gly-Trp-Met-Asp-Phe-NH_2 (GLMAP), Gly-D-Trp-Met-Asp-Phe-NH_2 (GDMAP), and Gly-Gly-Met-Asp-Phe-NH_2 (GGMAP); GLMAP is CCK-5, a cholecystokinin fragment possessing anticonvulsant activity, which is found in the brain. The analogs GDMAP and GGMAP are not active, or much less so than GLMAP. One strongly preferred structure has been found, in each case, for GLMAP (GLMAP3) and GDMAP (GDMAP39). These structures are very similar, in the nature of the edge-to-face stacking of their Trp and Phe aromatic rings, but the C-terminal regions differ. The conformation of the C-terminal tetrapeptide of GLMAP3 is identical to a previously calculated structure of CCK-4. A comparison of the C-terminal regions of GLMAP3 and GDMAP39 with the structure of 5,5-diphenylhydantoin suggests that the mechanisms of anticonvulsant action of phenytoin and CCK-5 are not the same. In the absence of an aromatic–aromatic interaction, no clear-cut conformational preference is found for GGMAP. The structure of GGMAP whose C-terminal region is the same as that of GLMAP3 (GGMAP20) is 1.51 kcal/mol higher in energy than the lowest energy structure, and lacks the hydrophobic wall provided by the Trp residue of GLMAP3.

SAUL WOLFE, STEPHEN BRUDER, DONALD FREDRIC WEAVER et KIYULL YANG. Can. J. Chem. **66**, 2703 (1988).

On a utilisé le programme ECEPP de Scheraga pour déterminer la relation qui existe entre les énergies ponctuelles et les énergies minimisées par une méthode quadratique, pour diverses grilles de recherches d'angles dièdres (ϕ, ψ, χ_1) de peptides simples. Sur la base de ces essais, on a développé une nouvelle sous-routine, INIT, et on l'a incorporée dans le programme. Cette sous-routine calcule les énergies ponctuelles ECEPP de 200,000 permutations au hasard de (ϕ, ψ) = 0, ±90, 180 et (χ_1) = −60, 180 avec $\omega = \chi_{\neq 1} = 180$; après avoir examiné 40,000 permutations, les structures possédant les 10 énergies les plus basses sont ordonnées et choisies pour une minimisation. On a encore modifié le programme ECEPP de façon à obtenir un ensemble de données que le programme MMP2(85) peut utiliser normalement dans son cheminement. Cette possibilité permet de minimiser automatiquement des structures localisées par INIT et de les raffiner ensuite à l'aide de la méthode de minimisation de Newton–Raphson et des paramètres MMPEP du programme MMP2(85).

Au cours du développement de ce protocole, on a trouvé que MMPEP reproduit correctement la préférence conformationnelle du C_7 du dipeptide de l'alanyle dans des milieux non-polaires ainsi que le déplacement observé expérimentalement vers les conformations α_R et P_{II} dans des solvants polaires, lorsque $\varepsilon = 78{,}5$ D. On a donc choisi cette constante diélectrique pour une analyse conformationnelle, utilisant le programme INIT/MMPEP, des peptides Gly-Trp-Met-Asp-Phe-NH_2 (GLMAP), Gly-D-Trp-Met-Asp-Phe-NH_2 (GDMAP) et Gly-Gly-Met-Asp-Phe-NH_2 (GGMAP); le GLMAP est le CCK-5, un fragment cholécystokinine possédant une activité contre les convulsions et qui est retrouvé dans le cerveau. Les analogues GDMAP et GGMAP ne sont pas actifs ou beaucoup moins que le GLMAP. Dans chacun des ces du GLMAP (GLMAP3) et du GDMAP (GDMAP39), on a trouvé une structure qui est fortement privilégiée. Ces structures sont très voisines par la nature de l'empilement côté à face de leurs cycles Trp et Phe aromatique; toutefois, les régions C-terminales diffèrent. La conformation du tétrapeptide C-terminal du GLMAP3 est identique à celle calculée antérieurement pour la structure du CCK-4. Une comparaison des régions C-terminales du GLMAP3 et du GDMAP39 avec la structure de la diphényl-5,5 hydantoïne suggère que les mécanismes d'action contre les convulsions de la phénytoïne et du CCK-5 ne sont pas les mêmes. En l'absence d'une interaction aromatique–aromatique, on ne trouve pas de préférence conformationnelle marquée pour le GGMAP. L'énergie de la structure du GGMAP, dont la région C-terminale est identique à celle du GLMAP3 (GGMAP20), est 1,51 kcal/mol plus élevée que celle de la structure de plus basse énergie; de plus, elle ne possède pas le mur hydrophobe qui est fourni par le résidu Trp du GLMAP3.
[Traduit par la revue]

Introduction

The preceding article (1) has described the development of an all-atom peptide parameterization of Allinger's MMP2(85) programme (2). The MMPEP parameters provide calculated geometries of peptides in agreement with experimental crystal structures, when the Cartesian coordinates of these crystal structures are supplied as input for the block-diagonal Newton–Raphson minimization of MMP2(85).

This minimization procedure is most reliable for a function of many variables when the initial structure already lies near the bottom of its energy well (3), as is the case for the conformation that crystallizes. Therefore, any projected application of MMPEP to the search for other conformations of peptides,

[1]Author to whom correspondence may be addressed.
[2]Revision received March 25, 1988.

Can. J. Chem. Downloaded from www.nrcresearchpress.com by 196.1.178.254 on 09/07/12
For personal use only.

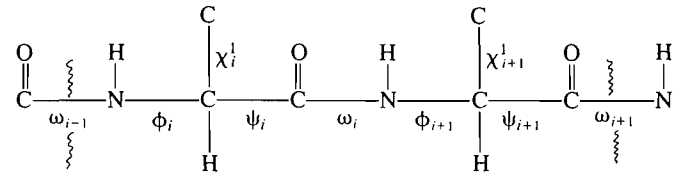

FIG. 1. Nomenclature used for the (i) and (i + 1) residues of a general peptide.

including conformations in solution, or conformations lower in energy than that of the crystal structure, would require initial geometries comparable in quality to those of X-ray structures. One possible approach is to proceed from the crystal structure to other minima by the use of successive dihedral drives. However, such a strategy does not seem practical, because of the large number of dihedral angles that would have to be examined for any peptide containing more than two or three residues.

The present work is concerned with the development and evaluation of a protocol for peptide conformational analysis based on the use of ECEPP (4) to obtain Cartesian coordinates suitable for the Newton–Raphson minimization of MMPEP. As described by Scheraga and co-workers (5), ECEPP (Empirical Conformational Energy Program for Peptides) is a molecular mechanics procedure whose force field assumes fixed bond lengths and bond angles. The input to ECEPP consists of a sequence of amino acids, together with two end groups and a set of backbone and side-chain dihedral angles. The output includes the Cartesian coordinates of all atoms, but in a format different from that required by MMP2(85). One of the features of the combined ECEPP/MMPEP analysis described herein is a routine that converts ECEPP output into a structure, analyzes this structure to obtain connected and attached atom lists, determines the atom types on the basis of connectivities, reformats the Cartesian coordinates, and creates an input file for MMPEP (see Appendix 1).

The application of this subroutine to the coordinates generated by a one-point ECEPP calculation with an arbitrary set of dihedral angles would be inappropriate, because these coordinates would normally describe a structure that is far from a minimum. Consequently, minimization of the initial ECEPP structure is necessary. Following Scheraga (5), we have incorporated into ECEPP a quadratic minimization procedure (6) that treats dihedral angles consecutively and iteratively.

Coordinates generated following the application of this procedure are suitable for MMPEP, but the structure thus obtained refers to the energy well reached in the quadratic minimization, and depends upon the choices of the initial dihedral angles and the step size. A central problem, therefore, is to preselect these initial angles according to criteria or search procedures that are sufficiently objective to be reproducible from one laboratory to another.

Figure 1 shows the (i) and (i + 1) residues of a general peptide in the standard convention (7). In the native conformation of a globular protein, peptide segments are folded so as to take advantage of intramolecular hydrogen bonding. These hydrogen bonds lead, *inter alia*, to α-helices, parallel or antiparallel β-pleated sheets, or β-bends (8). Each of these encompasses a specific number of residues, and a specific range of (ϕ,ψ) within a residue. In most cases, ω_i is ca. 180°, and the most common value of χ_1 observed in crystal structures is ca. −60° (9). Values of (ϕ,ψ) that reflect different folding patterns include (10): right-handed α-helix, (−57, −47); antiparallel β-pleated sheet ($\equiv C_5$ bend) (−139, +135); parallel β-pleated sheet (−119, +113); C_7 bend, (−80, +80); collagen (−75, +150).

The existence of trends in the crystal structures of peptides and proteins has led to the development of empirical rules to predict the probable secondary structure adopted by an amino acid that occupies a specific position within the molecule (11). These rules are undergoing continuous refinement (12), and it is presently considered that the statistical accuracy of a three-state definition of secondary structure (helix, sheet, loop/turn) is about 60%.

A proper appeal to such methods would constitute one possible criterion for the selection of the initial ECEPP structure(s). However, this strategy would be incomplete, for several reasons: (*i*) the single structure reached following minimization would retain any uncertainty in the secondary structure prediction; (*ii*) the search for other low energy structures would remain undefined; (*iii*) rules derived from crystal structures of globular proteins may not be applicable to shorter, conformationally flexible, peptides.

These considerations led us to examine the application of more generalized sampling methods to scan the conformational hyperspace of a peptide. Since, for any residue, the specification of the initial values of (ϕ, ψ, χ_1) is most important, an initial survey could reasonably be based on $\omega^i = \chi^i_{\neq 1} = 180°$, and the selection of a set of possible values of (ϕ^i, ψ^i, χ^i_1). An initial decision concerning these values was made on the basis of the following representative series of computations: (*i*) one-point ECEPP calculations were performed on the alanyl dipeptide (Ac-L-Ala-NHMe, **1**), and on Ac-D-Ala-D-Ala-OH (**2**), for all possible permutations of (ϕ,ψ) = 0, ±60, ±120, 180°, and all possible permutations of (ϕ,ψ) = 0, ±90, 180°; (*ii*) each of these structures was minimized, using a maximum step size of 0.5 radian; (*iii*) all of the structures found for **1**, and the 10 lowest energy structures found for **2**, were subjected to a Newton–Raphson minimization, using MMPEP.

The following observations were made: (*a*) the same set of low energy structures resulted, after minimization of ECEPP, whether the increment in (ϕ,ψ) was 60° or 90°; (*b*) the lowest energy ECEPP structure, after minimization, corresponded to one of the structures having the lowest one-point energy in the case of **1**, and also in the case of **2**, although some crossovers were seen with other structures; (*c*) energy differences, and some relative energies, were altered when the ECEPP structures were refined using MMPEP; (*d*) the lowest energy structure of **1**, after MMPEP minimization with the dielectric constant ε = 1.5, has the C_7^{eq} conformation (Fig. 2), and is 1.13 kcal/mol more stable than the crystal structure (ϕ,ψ) = (−88, 155) (13), whose P_{II} conformation is stabilized by *inter*molecular hydrogen bonding; (*e*) with a dielectric constant of 78.5, corresponding to water solvent, the C_7^{eq} conformation and the crystal structure of **1** have the same energy, but the global minimum is α_R (ϕ,ψ = −67, −47); (*f*) the lowest energy structure of **2**, after MMPEP minimization with a dielectric constant of 78.5, has a C_7 bend (Fig. 3) (ϕ,ψ = 79, −76; ϕ_2,ψ_2 = 76, 41), and is 11.0 kcal/mol more stable than the crystal structure (14) (ϕ_1,ψ_1 = 81, −152; ϕ_2,ψ_2 = 70, 40).

There have been many previous calculations on the alanyl dipeptide, the most commonly discussed minimum dipeptide unit (15). As summarized in Table 1, all calculations, including our own, find the C_7^{eq} conformation to be preferred under nonpolar conditions. This is also the experimental conclusion reached by Madison and Kopple (16), based on cd and nmr

Can. J. Chem. Downloaded from www.nrcresearchpress.com by 196.1.178.254 on 09/07/12
For personal use only.

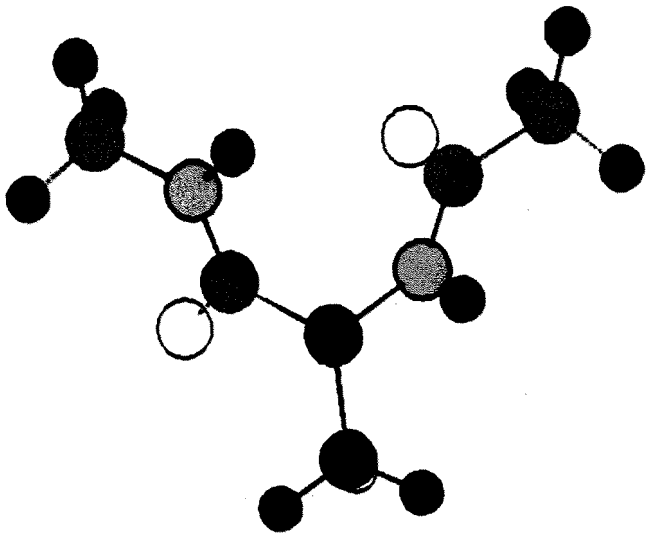

FIG. 2. Global minimum of the alanyl dipeptide (**1**), for a dielectric constant of 1.5.

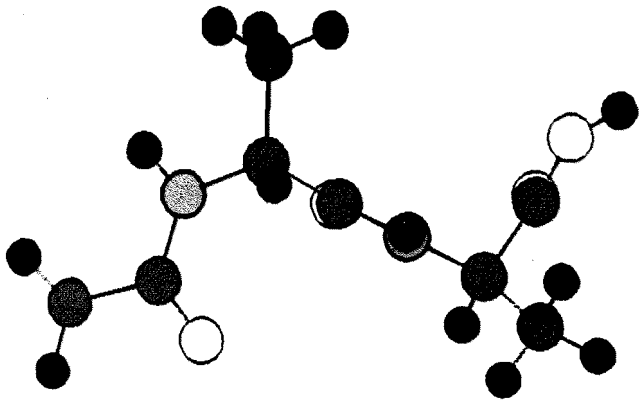

FIG. 3. Global minimum of Ac-NH-D-Ala-D-Ala-OH for a dielectric constant of 78.5.

measurements in chloroform solvent. These latter workers also find (16) that the conformation shifts from C_7-predominant to α_R and polyproline II (P_{II}) in water solvent; any C_5 conformation remains approximately constant in the two solvents. Inspection of Table 1 suggests that only the present calculations, using MMPEP and a dielectric constant of 78.5, reproduce these solvent-induced conformational changes. This is an encouraging result. It suggests that the MMPEP parameterization of MMP2(85) is valid not only for the calculation of geometries but also for the calculation of relative energy differences in water solvent. All subsequent MMPEP calculations were, therefore, performed using $\varepsilon = 78.5$.

The MMPEP results summarized in Table 1 are representative of many such calculations, starting with ECEPP, and it was concluded that a generalized search procedure could begin with one-point ECEPP calculations for permutations of $(\phi,\psi) = 0, \pm 90, 180°$, followed by ECEPP minimization of a sufficient number of the low energy structures thus identified.

This strategy would require 4^{2n} one-point calculations for a complete search of the (ϕ,ψ) space, where n is the number of residues in the peptide. Since the total number of such calculations rapidly becomes astronomical for $n > 5$, if χ_1 is not varied, and for $n > 4$ if χ_1 is allowed values of -60, 180°, some reduction of the problem was necessary. For this to be meaningful, it was essential that the selection be uniform, a condition that defines a problem in random number generation (see Appendix 2). This problem was approached in stages.

In the first stage, χ_1 was fixed at $+60$, -60, or 180°, and one-point energies were calculated for random permutations of (ϕ,ψ) generated using the integers 0, 1, 2 to code for the angles 90, 180, 270 ($\equiv -90°$) as a 60-digit base-three number. This allowed the treatment of peptides containing up to 28 amino acid residues, i.e., $2'(28 + 2'') = 60$, where $2''$ refers to end groups and $2'$ refers to the (ϕ,ψ) of each residue. In this first stage, a maximum of 6600 permutations was allowed for each seed value of the random number generator, and only the 60-digit number coding for the lowest energy structure was printed. This number was then decoded to create an ECEPP input file, and the structure was minimized.

The procedure just described was tested on peptides containing 4–28 amino acid residues, with χ_1 fixed successively at -60, $+60$, and 180°. In all cases, the one-point energies of the single structure found in a given search were $\chi_1^{60} >> \chi_1^{180} > \chi_1^{-60}$. After minimization, the energies were found to be $\chi_1^{60} >> \chi_1^{180} \sim \chi_1^{-60}$. These results strongly suggested that $\chi_1^i \neq 60°$.

In the second stage, a 90-digit base-four number was used to code a maximum of 28 amino acid residues as $3(28 + 2)$, where the 2 refers to end groups; the first two entries of the 3 refer to $(\phi,\psi) = 0, 90, 180, 270$, coded as 0, 1, 2, 3; the third entry of the 3 refers to $\chi_1 = -60$, 180, coded as 1, 2, with 0 used in the case of glycine, or when all χ_1 were fixed at $-60°$ or at 180°. In this second stage, the maximum number of permutations was expanded to 25,000, and only the lowest energy structure was again retained. The tests at this stage suggested that χ_1 be allowed to vary ($\chi_1 = -60$, 180).

In the next stage, the maximum number of permutations was increased to 40,000, and the *ten* lowest energy structures were retained and minimized. Table 2 summarizes the results thus obtained for the octapeptide H-Gly-Asn-Thr-Ile-Val-Ala-Val-Glu-OH (**3**). These results, which are typical, suggested that for complex peptides there is no obvious correlation between one-point energies and minimized energies, within the first few low energy structures, and that at least 10 such structures should be examined.

Accordingly, in the strategy that has been used to obtain the results discussed below, the maximum number of permutations was increased to 200,000, and, after each 40,000 permutations, the 10 lowest energy structures were retained. All of this is accomplished via a new subroutine, INIT, which has been incorporated into ECEPP. This strategy leads to the identification of 50 structures for examination by ECEPP/MMPEP.

The cholecystokinins: endogenous anticonvulsant peptides?

Cholecystokinin (CCK) was discovered as a gastrointestinal mediator of digestive function and feeding behaviour, and was subsequently found also to be present in high concentrations in several regions of the brain (for general reviews, see ref. 17). The peptide pro-CCK contains 95 residues, and is converted by human plasma enzymes into CCK-58, CCK-39, CCK-33, CCK-12, CCK-8, CCK-5, and CCK-4 (18). Of these fragments, CCK-33 and CCK-8 are the major forms present in gut and brain, respectively; CCK-5 is also present in large amounts in the brain (19), and is active in binding to brain receptors (20).

The C-terminal peptapeptide of CCK (CCK-5) has the

Can. J. Chem. Downloaded from www.nrcresearchpress.com by 196.1.178.254 on 09/07/12
For personal use only.

Can. J. Chem. Downloaded from www.nrcresearchpress.com by 196.1.178.254 on 09/07/12
For personal use only.

TABLE 1. Calculated relative energies[a] and (ϕ,ψ) of the alanine dipeptide using different computational and solvation strategies

	Relative energies (ϕ,ψ)						
Conformation	Vacuum[b,c]	$\varepsilon = 78.5$[b,c]	Vacuum[d]	Vacuum[e]	ECEPP[f]	Solvated[e]	$\varepsilon = R_{ij}$[d,g]
C_7^{eq}	0.00 (−87, 89)	0.21 (−69, 126)	0.0 (−76, 69)	0.0 (−67, 65)	0.0 (−84, 79)	0.0 (−65, 69)	0.0 (−76, 66)
α_R	0.67 (−62, −46)	0.00 (−67, −47)	4.7 (−60, −34)		1.1 (−74, −45)	2.0 (−69, −48)	3.6 (−61, −41)
α'	0.82 (−152, −70)	0.26 (−157, −57)			1.6 (−158, 58)		
C_5	0.85 (−149, 133)	0.46 (−156, 155)	4.0 (−158, 169)	3.6 (−172, 171)	0.4 (−154, 153)	1.1 (−176, 172)	3.2 (−161, 169)
P_{II}	1.13 (−67, 159)	0.23 (−71, 151)				0.4 (−55, −176)	
α_L	1.24 (53, 52)	0.62 (55, 51)	5.7 (54, 37)		2.3 (54, 57)	1.3 (64, 61)	4.3 (54, 42)
C_7^{ax}	1.33 (74, −82)	0.97 (58, −105)	1.1 (69, −67)	1.1 (63, −62)	8.8 (78, −64)	1.1 (62, −65)	0.6 (69, −64)

[a]In kcal/mol.
[b]Present work.
[c]No additional low energy structures were found in an 18 × 18 grid search of (ϕ,ψ) using the Dihedral Drive option of MM85.
[d]Reference 15*c*.
[e]Reference 15*d*.
[f]Reference 15*a*.
[g]Distance-dependent dielectric constant.

TABLE 2. One-point energies, minimized ECEPP energies, and final MMPEP energies of 10 structures of **3** from a random search of 40,000

Number	One-point energy[a]	Relative minimized energy[a]	
		ECEPP	MMPEP
1	441	26.35	6.09
2	456	19.02	6.66
3	581	18.69	3.65
4	603	16.92	12.06
5	2543	48.60	12.13
6	2564	0.00	0.00
7	2673	21.82	6.39
8	3781	20.56	7.98
9	5272	49.49	10.61
10	5298	59.73	7.30

[a]In kcal/mol.

constitution H-Gly-Trp-Met-Asp-Phe-NH_2, and is identical to the C-terminus of gastrin, whose terminal tetrapeptide moiety H-Trp-Met-Asp-Phe-NH_2 (≡ CCK-4) constitutes the minimum requirement for physiological activity in the mammalian gut (21). However, the gastrin gene is not expressed in the cerebral cortex (19), and brain receptors for CCK fragments are distinctly different from the receptors for the same fragments in the pancreas and gallbladder (22).

Our interest in C-terminal CCK fragments was stimulated by reports (23) that these fragments possess potent anticonvulsant activity in several chemical convulsant models, including picrotoxin-induced seizures. Some workers speculate that CCK may function as an endogenous anticonvulsant, and that convulsive disorders can arise from an abnormal function of CCK-like peptides in the brain (23–26). The mechanism of the CCK anticonvulsant activity is uncertain, but is known to differ from that of diazepam (24). Structure–activity studies (25–31) suggest that a terminal Phe-NH_2, a side chain resembling Asp, and Trp (but not its D epimer) are necessary for anticonvulsant activity.

The requirement for a terminal aromatic amino acid amide is reminiscent of the conclusions of quantitative structure–activity relationships of hydantoin anticonvulsants (32), whose most important member is 5,5-diphenylhydantoin (DPH). In the case of DPH, the activity is associated with the presence of a conformationally constrained phenylacetamide (PhCHCONH) moiety. 5-Benzyl-substituted hydantoins, which contain a benzylacetamide ($PhCH_2CHCONH$) moiety, are inactive, because the aromatic ring lies over the hydantoin ring, and restricts access to the important amide bond (32). If it is assumed that a structural and mechanistic relationship exists between DPH and CCK, the presence of a benzylacetamide moiety (Phe-NH_2) in active CCK fragments would require that the role of L-Trp is to cause the phenyl group to be rotated away from the terminal amide bond in the biologically active conformation.

The nature of aromatic–aromatic interactions in peptides and proteins has received considerable recent attention (33). In contrast to expectations based on considerations of orbital interactions, edge-to-face stacking of aromatic rings is preferred energetically when the centroids are separated by 4.5–7 Å. The stabilization amounts to 1–2 kcal/mol, and is thought (34) to play an important role in the adoption of biologically active conformations. For example, constraint of somatostatin, which

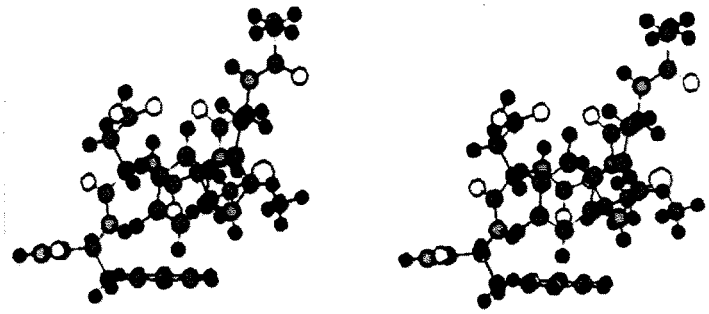

FIG. 4. Diastereoscopic view of GLMAP3.

Can. J. Chem. Downloaded from www.nrcresearchpress.com by 196.1.178.254 on 09/07/12
For personal use only.

contains a perpendicular Phe...Phe interaction, by incorporation of a cystine moiety in place of the two phenylalanines, leads to a biologically active analog (35).

Other aromatic–X interactions have also been identified in the crystal structures and solution conformations of peptides (36). In particular, the sulfur atoms of *methionine* residues express an affinity for the *edges* of aromatic rings.

Roques and co-workers (37) have studied the ^{1}Hmr spectra and fluorescence transfer of various CCK fragments in DMSO-d_6 and D_2O, as a function of pH and temperature. They find that CCK-4, but not CCK-5, exhibits stacking of Trp and Phe, mainly on the basis of the pH dependence of chemical shifts. However, the pH-dependent conformational changes proposed by these workers are not associated with large variations of vicinal coupling constants. Roques and co-workers suggest that CCK-5 prefers a cyclic structure, in which there is close contact between the N-terminal amino group and the carboxyl group of aspartic acid. In DMSO-d_6, the CCK-4 analog H-Trp-Nle-Asp(O-*t*Bu)-Phe-NH_2 has a random structure, which transforms to a stacked conformation in 2,2,2-trifluoroethanol (38).

In view of these various findings, and as a test of our proposed strategy for peptide conformational analysis, we have carried out calculations on three variations of CCK-5: the parent structure H-Gly-Trp-Met-Asp-Phe-NH_2 (GLMAP), and the two analogs H-Gly-Gly-Met-Asp-Phe-NH_2 (GGMAP) and H-Gly-D-Trp-Met-Asp-Phe-NH_2 (GDMAP). In GGMAP, the biologically significant Trp residue is replaced by a conformationally flexible Gly; in GDMAP, the Trp residue is replaced by its less active D epimer. All calculations were performed on the uncharged molecules.

It was hoped that the calculations would provide information concerning (*i*) the relative energies of stacked and cyclic structures in GLMAP and GDMAP; (*ii*) the geometrical nature of Ar...Ar stacking; (*iii*) the role of Ar–sulfur interactions; (*iv*) the possible accessibility to a receptor of the Asp side chain and the terminal amide bond; (*v*) the relationship, if any, between CCK conformations and the active region of DPH.

Structures were examined, using the SNOOPI option of CHEMGRAF,[3] after the ECEPP minimizations, and again after the final MMPEP minimizations. It was quickly established that the use of the default dielectric constant ($\varepsilon = 2$) for the preliminary ECEPP search led to a pronounced energetic preference for cyclic structures, which did not remain cyclic following MMPEP refinement with $\varepsilon = 78.5$. Accordingly, all subsequent computations were performed using $\varepsilon = 78.5$ at all stages. With this dielectric constant, cyclic structures located in the ECEPP search remained cyclic after the final MMPEP refinement.

TABLE 3. Relative MMPEP energies[a] of 50 structures of GLMAP located following an initial search of 200,000 structures

Number	1–10	11–20	21–30	31–40	41–50
1	1.91	2.19	4.73	6.08	2.13
2	1.70	6.13	5.48	3.26	2.94
3	0.00	5.86	3.07	4.05	2.80
4	5.53	3.80	4.17	5.95	5.99
5	7.83	8.36	8.69	7.65	5.22
6	4.63	9.00	7.20	6.17	8.03
7	4.25	4.47	8.52	8.35	6.70
8	6.62	5.79	5.72	5.76	4.15
9	5.83	6.26	7.46	8.41	7.30
10	5.01	6.67	8.09	8.37	7.09

[a]In kcal/mol.

GLMAP

Table 3 lists the final MMPEP energies of 50 structures, located following a one-point initial search of 200,000 structures and ECEPP minimization of the 50 lowest energy structures thus identified. No structure lower in energy than GLMAP3 was found in a second search of 200,000 initial structures. The first search located only six structures within 3 kcal/mol of GLMAP3; the second search located an additional four structures within this energy range.

Figure 4 shows a diastereoscopic view of GLMAP3. The structure appears identical, in the region of the terminal tetrapeptide, to the structure calculated by Abillon *et al.* (39) for the gastrin tetrapeptide (CCK-4) (see also ref. 40), which is shown as Fig. 5 (41). Figure 6 is a space-filling view of GLMAP3, and the following observations are made: (*i*) the structure is not cyclic; (*ii*) there is a perpendicular stacking of the two aromatic rings; (*iii*) there is also an interaction between the sulfur atom of methionine and the edges of both aromatic rings; (*iv*) the aromatic–aromatic interaction creates a hydrophobic wall around two sides of the molecule; (*v*) the terminal amide bond and the side chain of Asp are jointly accessible to a potential receptor, on one side of the molecule.

[3]The authors thank Dr. Keith Davies for permission to use this option of CHEMGRAF, and Professor A. S. Cameron (Dalhousie University) and I. Kucirec (Perkin–Elmer Canada) for the Perkin–Elmer version of the programme.

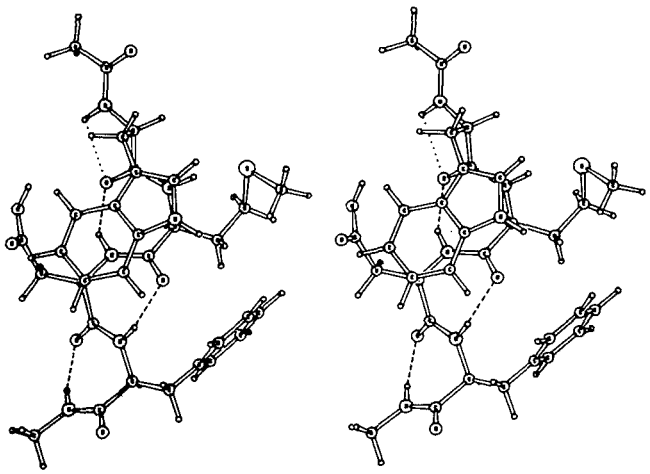

FIG. 5. Structure calculated for the gastrin tetrapeptide (CCK-4). Adapted from ref. 41.

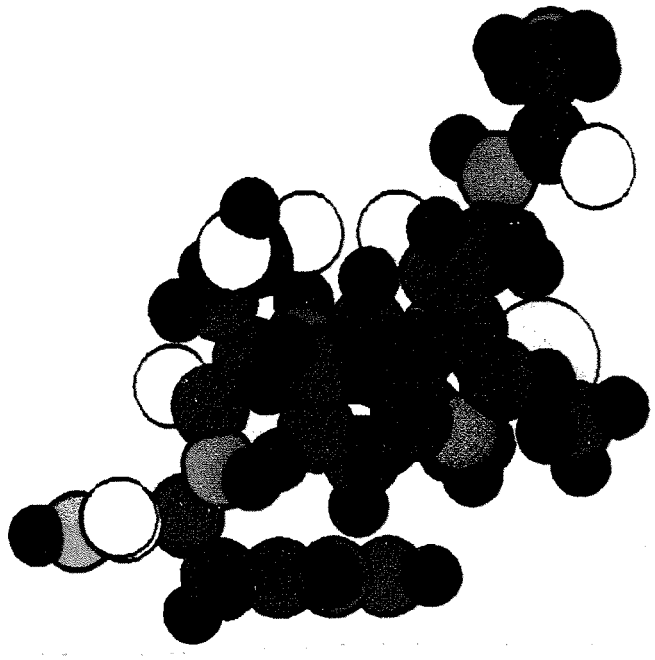

FIG. 6. Space-filling view of GLMAP3.

The finding that edge-to-face aromatic–aromatic and aromatic–sulfur interactions are present in GLMAP3 is of interest, because no specific parameterization of such effects is incorporated in ECEPP or MMPEP. We suggest that these interactions are dipole–dipole in nature and are, therefore, located by force fields in which the dipole–dipole term is properly taken into account.

Of the 10 other low energy GLMAP structures, only GLMAP41, which is 2.13 kcal/mol higher in energy than GLMAP3, is cyclic; in this structure, the terminal amide and the carboxyl group of Asp are on opposite sides of the molecule. In four of the structures, the terminal amide lies under one of the aromatic rings, or is buried within the molecule; in another three structures there is no aromatic–aromatic interaction. In GLMAP43 (Fig. 7), which is 2.8 kcal/mol higher in energy

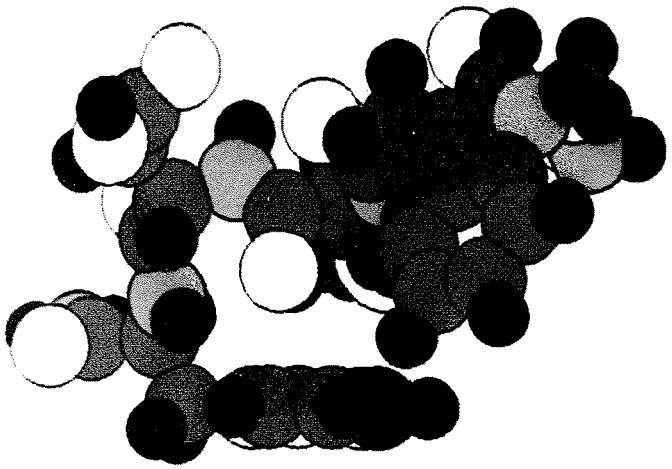

FIG. 7. Space-filling view of GLMAP43.

than GLMAP3, there is a phenyl–S interaction, but the hydrophobic wall is absent, and the terminal amide is rotated from its orientation in the lowest energy structure.

GDMAP

Table 4 lists the MMPEP energies of 50 structures located following a single search of 200,000 initial structures, in the usual manner. One of these structures, GDMAP39, is strongly preferred, and is shown in Fig. 8. Seven other structures are about 3 kcal/mol higher in energy and, in each of these seven structures, the terminal amide is buried within the interior of the molecule.

A comparison of Fig. 8 with Fig. 6 reveals numerous similarities in the structures of GDMAP39 and GLMAP3. Thus, in GDMAP39: (*i*) the structure is not cyclic; (*ii*) there is a perpendicular stacking of the two aromatic rings; (*iii*) the aromatic–aromatic interaction creates a hydrophobic wall around two sides of the molecule, but the sulfur atom is more exposed on one of these sides than in GLMAP3; (*iv*) the terminal amide bond and the side chain of Asp are jointly accessible to a potential receptor, on one side of the molecule.

The most significant difference between the two structures is observed in the relative orientations of the terminal amide moieties, which differ by ca. 180°. The difference is seen more clearly in Figs. 9 and 10, which show, respectively, the C-termini of GDMAP39 and GLMAP3 and their relationship to **4**, the active region of 5,5-diphenylhydantoin (32). If

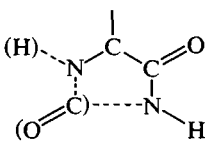

4

GDMAP39 and GLMAP3 were biologically significant conformations of the epimeric CCKs it is evident that only the *less active* epimer resembles DPH. This would imply that the mechanisms of the anticonvulsant activities of CCK-5 and DPH are not the same. We plan to check this point experimentally in our biomimetic model of DPH activity (42).

GGMAP

For GLMAP, the random number search covered 2%, and

Can. J. Chem. Downloaded from www.nrcresearchpress.com by 196.1.178.254 on 09/07/12
For personal use only.

Can. J. Chem. Downloaded from www.nrcresearchpress.com by 196.1.178.254 on 09/07/12
For personal use only.

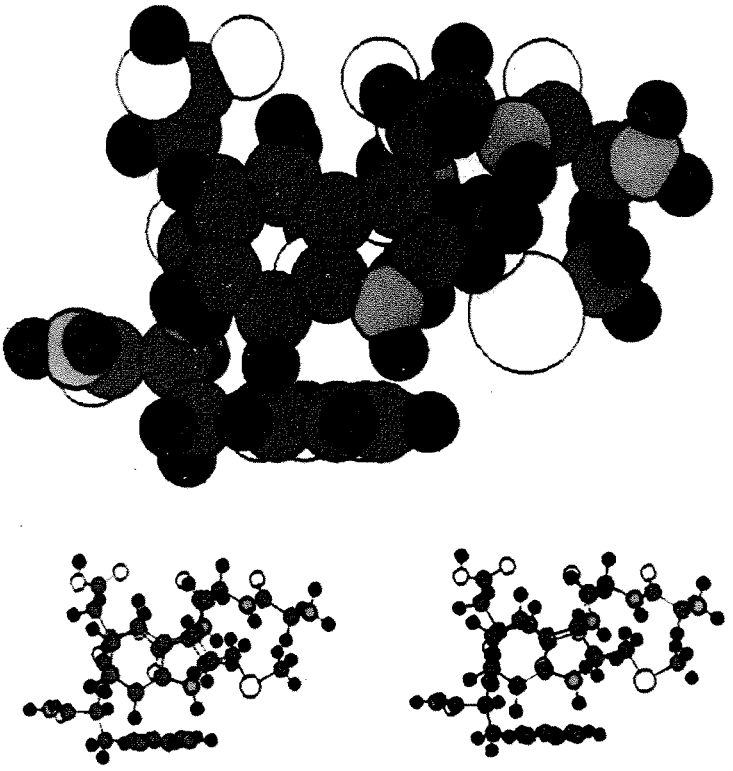

FIG. 8. Calculated structure of GDMAP39.

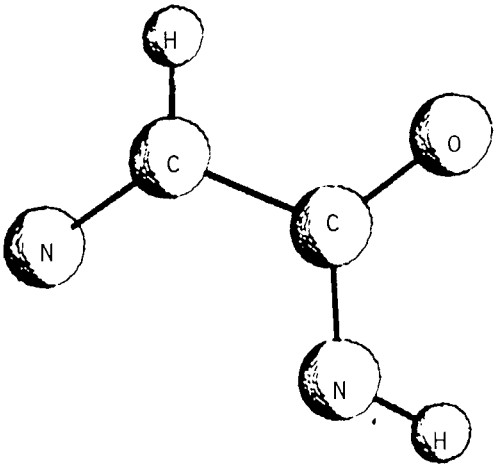

FIG. 9. The C-terminus of GDMAP39 (see **4**).

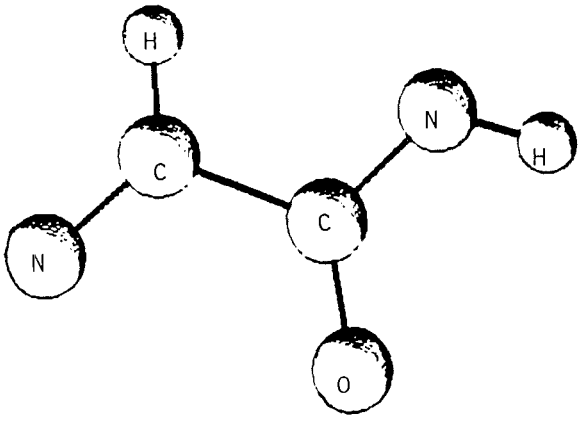

FIG. 10. The C-terminus of GLMAP3 (see **4**).

for GDMAP, 1% of the total (ϕ, ψ, χ_1) space. An analogous structure is found in each case, and there is a significant energetic preference for this structure. Much more work would be needed to support a claim that the magnitudes of such energetic preferences signal the presence of *global* minima. In any event, we have no information concerning the nature of the anticonvulsant receptor for CCK, and it is, therefore, not established that GLMAP3 and GDMAP39 are biologically relevant.

Table 5 lists the MMPEP energies of 50 GGMAP structures located following a search of 200,000 initial structures. This represents 2% of the total space. In contrast to GLMAP and GGMAP, 12 structures are within 1.5 kcal/mol of the lowest energy structure, GGMAP1. This may reflect a failure to locate a global minimum or, more significantly, the consequences of the removal of the stabilizing Ar...Ar interaction, and the conformational flexibility introduced with the Gly-Gly unit.

The structure that corresponds most closely to GLMAP3, in the relationships of the terminal amide and the side chain of Asp to the single aromatic ring, is GGMAP20, shown in Fig. 11.

Can. J. Chem. Downloaded from www.nrcresearchpress.com by 196.1.178.254 on 09/07/12
For personal use only.

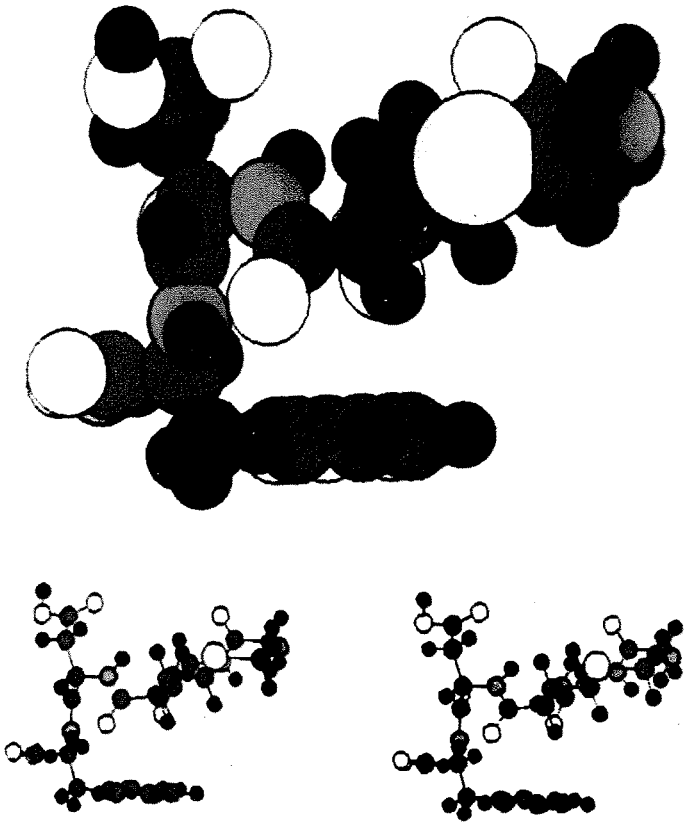

FIG. 11. Space-filling view of GGMAP20.

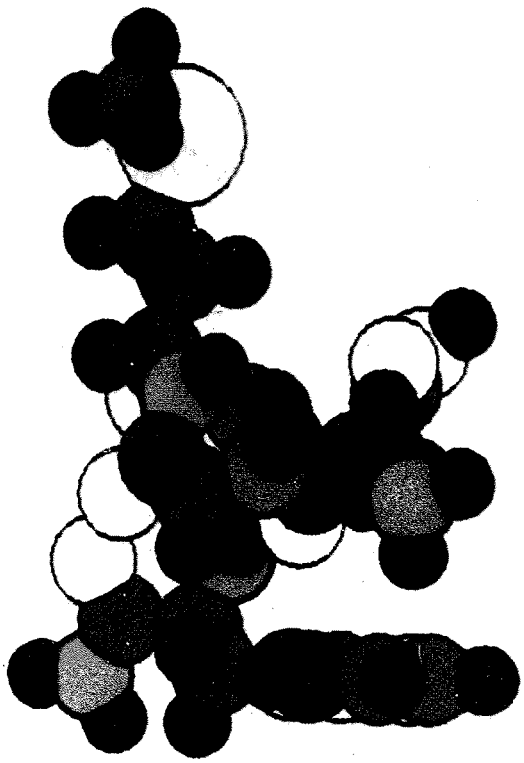

FIG. 12. Space-filling view of GGMAP1.

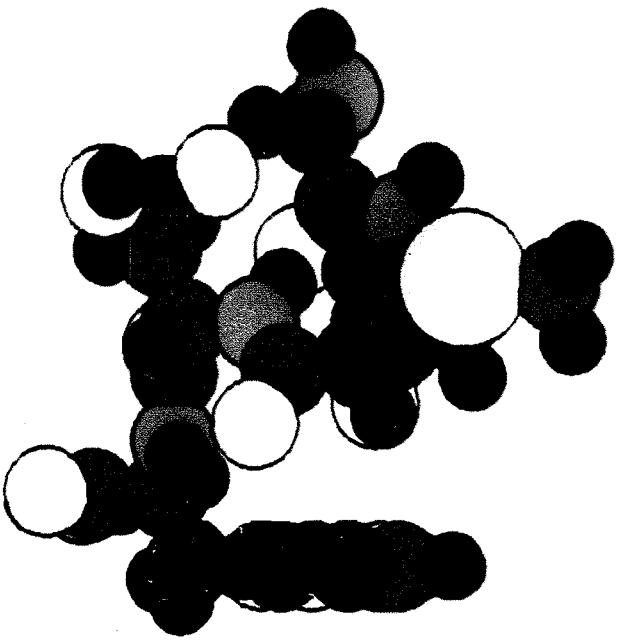

FIG. 13. Space-filling view of GGMAP10.

TABLE 4. Relative MMPEP energies[a] of 50 structures of GDMAP located following an initial search of 200,000 structures

Number	1–10	11–20	21–30	31–40	41–50
1	7.61	6.73	5.49	5.50	2.77
2	9.06	4.70	7.66	6.09	2.95
3	10.77	8.80	7.80	10.33	7.59
4	8.59	2.66	3.04	4.38	7.80
5	9.29	6.32	4.27	9.54	6.72
6	4.68	10.23	5.60	6.41	8.58
7	7.17	9.24	8.54	5.68	7.00
8	7.13	5.48	10.39	6.92	4.97
9	2.98	5.59	3.98	0.00	5.97
10	3.59	7.00	3.13	7.24	7.36

[a]In kcal/mol.

TABLE 5. Relative MMPEP energies[a] of 50 structures of GGMAP located following an initial search of 200,000 structures

Number	1–10	11–20	21–30	31–40	41–50
1	0.00	1.81	0.54	0.53	0.93
2	3.15	1.39	2.34	1.08	2.30
3	2.79	3.30	2.04	2.45	2.40
4	2.49	2.75	3.31	1.03	0.97
5	1.54	2.28	2.21	3.02	3.30
6	2.54	3.17	5.10	1.63	1.09
7	1.54	2.22	3.30	2.52	1.67
8	1.70	3.41	4.30	2.96	2.68
9	0.40	2.96	4.98	2.16	0.93
10	0.49	1.51	3.23	3.55	0.86

[a]In kcal/mol.

TABLE 6. A comparison of the (ϕ,ψ,χ_1) dihedral angles of GLMAP3, GDMAP39, and GGMAP20

	GLMAP3			GDMAP39			GGMAP20		
Residue	ϕ	ψ	χ_1	ϕ	ψ	χ_1	ϕ	ψ	χ_1
Gly	−59	−76		180	−59		−60	−117	
Trp(D-Trp,Gly)	−158	153	177	65	38	−74	−91	66	
Met	−84	88	−69	−83	105	−63	168	−21	−60
Asp	−74	94	−69	−76	99	−68	−87	80	−63
Phe	−77	140	−63	−74	−47	−53	−75	140	−60

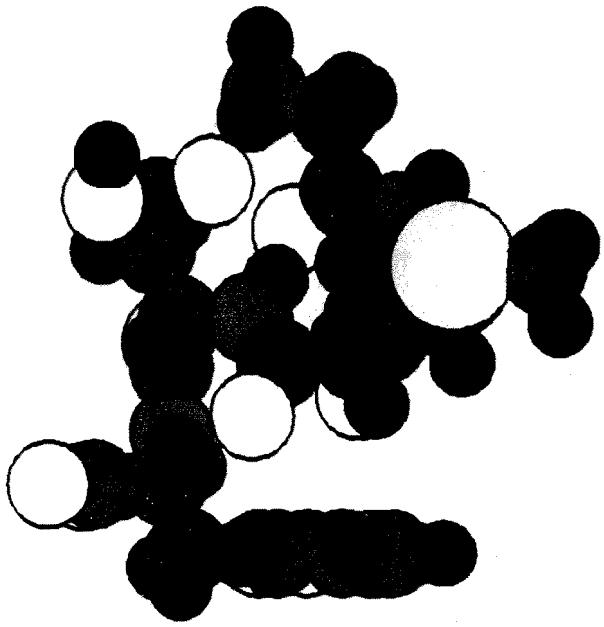

FIG. 14. Space-filling view of GGMAP49.

This is 1.51 kcal/mol higher in energy than GGMAP1, shown in Fig. 12. In GGMAP20, the N-terminus is superimposable on that of GLMAP3, but one of the hydrophobic walls has been replaced by a series of heteroatoms. In GGMAP1, the terminal amide and the side chain of Asp are on opposite sides of the molecule. Other structures of interest are GGMAP10 (Fig. 13) and GGMAP49 (Fig. 14), which resemble GGMAP20 in the N-terminal region, but are cyclic.

Table 6 summarizes the dihedral angles of GLMAP3, GDMAP39, and GGMAP20.

Concluding remarks

The principal objective of this work was the development of a protocol that could be applied generally to the theoretical conformational analysis of peptides, and be accessible through the use of the well-documented programmes ECEPP and MMP2(85). A first requirement, the parameterization of MMP2(85) for peptides (MMPEP), has been published, along with a description of the expansion of the dimensions of the programme (1). A new, energy-based, subroutine, INIT, which searches 200,000 initial structures, has been written and incorporated into ECEPP. Programmes to decode the results of INIT and to create an input file for MMP2(85) have also been written for the IBM-VS operating system. These are described in the appendices; their FORTRAN source codes will be made available upon request.

In the course of the establishment of the INIT variables, we have found that the MMPEP parameterization of MMP2(85) is valid not only to reproduce the geometries of crystal structures, but also to achieve proper ordering of energy differences. The use of the dielectric constant ε = 78.5 D appears to be appropriate. With this choice, the entire strategy becomes fixed, except for the selection of a seed value for the random number generator of INIT.

It is not yet clear how many searches of 200,000 structures should be performed in any given case, although there is a suggestion, in the results obtained with GLMAP and GDMAP, that a strong energetic preference for one structure is meaningful. For each of the examples presented here, the entire protocol, leading to 50 MMPEP structures, can be carried out in less than 1 day. In the case of the 28-residue atrial natriuretic factor, cardionatrin (43), an INIT search of 40,000 structures required 6 h, and the subsequent ECEPP + MMPEP minimization of the 10 structures identified in this search required 2–3 h in each case.[4]

As noted during the presentation of the CCK results, the conclusions that can be reached from theoretical calculations are permissive, if not compelling. Ideally, calculations should be performed not only on a biologically active peptide, and its receptor (if known), but on the complex formed between them. Our first attempt in this direction is described elsewhere (45).

Since the subject of active site conformational analysis of receptors is still in a primitive state (46), it seems that the proper place for the type of work presented here will continue to be in biomimetic design (42), or as part of a multidisciplinary approach, which includes the synthesis and biological evaluation of conformationally constrained analogs and simpler structures suggested by theory.

Acknowledgements

The authors thank the Natural Sciences and Engineering Research Council of Canada for financial support, the Medical Research Council of Canada for the award of a Graduate Fellowship, and Queen's University for generous allocation of computer time.

1. S. WOLFE, D. F. WEAVER, and K. YANG. Can. J. Chem. **66**, 2687 (1988).
2. N. L. ALLINGER. MMP2(85). Quantum Chemistry Program Exchange, Bloomington, IN.

[4]S. Wolfe and K. Yang. Unpublished results.

Can. J. Chem. Downloaded from www.nrcresearchpress.com by 196.1.178.254 on 09/07/12
For personal use only.

Can. J. Chem. Downloaded from www.nrcresearchpress.com by 196.1.178.254 on 09/07/12
For personal use only.

3. T. CLARK. A handbook of computational chemistry. Wiley–Interscience, New York, NY. 1985.
4. ECEPP. Quantum Chemistry Program Exchange No. 454, Bloomington, IN.
5. F. A. MOMANY, R. F. MCGUIRE, A. W. BURGESS, and H. A. SCHERAGA. J. Phys. Chem. **79**, 2361 (1975); C. POTTLE, M. S. POTTLE, R. W. TUTTLE, R. J. KINCH, and H. A. SCHERAGA. J. Comput. Chem. **1**, 46 (1980); G. NÉMETHY, M. S. POTTLE, and H. A. SCHERAGA. J. Phys. Chem. **87**, 1883 (1983).
6. M. J. D. POWELL. Quantum Chemistry Program Exchange No. 60, Bloomington, IN; J. L. KUESTER and J. H. MIZE. Optimization techniques with fortran. McGraw–Hill, New York, NY. 1973. p. 331.
7. IUPAC–IUB Commission on Biochemical Nomenclature. Pure Appl. Chem. **56**, 596 (1984).
8. P. Y. CHOU and G. D. FASMAN. Ann. Rev. Biochem. **47**, 251 (1978).
9. J. JANIN, S. WODAK, M. LEVITT, and B. MAIGRET. J. Mol. Biol. **125**, 357 (1978).
10. M. LEVITT. J. Mol. Biol. **170**, 723 (1983).
11. J. A. SMITH and L. G. PEASE. Crit. Rev. Biochem. **8**, 315 (1980).
12. V. I. LIM. J. Mol. Biol. **88**, 873 (1974); P. Y. CHOU and G. D. FASMAN. Adv. Enzymol. Relat. Areas Mol. Biol. **47**, 45 (1978); J. M. LEVIN, B. ROBSON, and J. GARNIER. FEBS Lett. **205**, 303 (1986); W. KLABSCH and C. SANDER. FEBS Lett. **155**, 179 (1983).
13. Y. HARADA and Y. IITAKA. Acta Crystallogr. Sect. B: Struct. Crystallogr. Cryst. Chem. **30**, 1452 (1974).
14. E. BENDETTI, B. DIBLASIO, V. POVONE, C. PEDONE, C. TONIOLO, and G. M. BONORA. J. Biol. Chem. **256**, 9229 (1981).
15. (*a*) S. S. ZIMMERMAN, M. S. POTTLE, G. NÉMETHY, and H. A. SCHERAGA. Macromolecules, **10**, 1 (1977); (*b*) J. N. SCARSDALE, C. VAN ALSENOY, V. J. KLIMKOWSKI, L. SCHÄFER, and F. A. MOMANY. J. Am. Chem. Soc. **105**, 3438 (1983); (*c*) S. J. WEINER, U. S. SINGH, T. J. O'DONNELL, and P. A. KOLLMAN. J. Am. Chem. Soc. **106**, 6243 (1984); (*d*) B. M. PETTITT and M. KARPLUS. Chem. Phys. Lett. **121**, 194 (1985); (*e*) M. MEZEI, P. K. MEHROTRA, and D. L. BEVERIDGE. J. Am. Chem. Soc. **107**, 2239 (1985), and references cited therein; (*f*) G. RAVISHANKER, M. MEZEI, and D. L. BEVERIDGE. J. Comput. Chem. **7**, 345 (1986).
16. V. MADISON and K. D. KOPPLE. J. Am. Chem. Soc. **102**, 4855 (1980).
17. J. DE BELLEROCHE and G. J. DOCKRAY (*Editors*). Cholecystokinin (CCK) in the nervous system. Verlag Chemie, Weinheim, FRG. 1984; J.-J. VANDERHAEGHEN and J. N. CRAWLEY (*Editors*). Neuronal cholecystokinin. Ann. N.Y. Acad. Sci. **448** (1985); J. E. MORLEY and A. S. LEVINE. Handbook of Neurochemistry. **8**, 115 (1985).
18. J. F. REHFELD. Acta Pharmacol. Toxicol. **41**, 24 (1977); J. F. REHFELD, N. GOLTERMAN, L.-I. LARSON, P. M. EMSON, and C. M. LEE. Fed. Proc. **38**, 2325 (1979); V. E. EYSSELEIN, G. A. EBERLEIN, M. SCHÄFER, J. R. REEVE, JR., and H. GOEBELL. Gastroenterology, **88**, 1376 (1985).
19. J. F. REHFELD and H. F. HANSEN. J. Biol. Chem. **261**, 5832 (1986).
20. R. B. INNIS and S. H. SNYDER. Proc. Natl. Acad. Sci. U.S.A. **77**, 6917 (1980).
21. R. A. GREGORY. Bioorg. Chem. **8**, 497 (1979).
22. J. A. WILLIAMS, K. A. GRYSON, and D. J. MCCHESNEY. Peptides, **7**, 293 (1986).
23. G. ZETLER. Eur. J. Pharmacol. **65**, 297 (1980).
24. J. G. BAJOREK, R. J. LEE, and P. LOMAX. Adv. Neurol. **44**, 489 (1986).
25. T. KADAR, A. PESTI, G. TÓTH, B. PENKE, and G. TELEGDY. *In* Neuropeptides and psychosomatic processes. *Edited by* E. Endroczi, L. Angelucci, U. Scapagnini, and D. DeWied. Akadémiai Kiadó, Budapest, Hungary. 1983. p. 231.
26. M.-F. LIGNON, M.-C. GALAS, M. RODRIGUEZ, J. LAUR, A. AUMELAS, and J. MARTINEZ. J. Biol. Chem. **262**, 7226 (1987).
27. T. KADAR, B. PENKE, A. PESTI, and G. TELEGDY. Peptides, **6**, 1009 (1985).
28. B. PENKE, F. HAJNAL, J. LONOVICS, G. HOLZINGER, T. KADAR, and G. TELEGDY. J. Med. Chem. **27**, 845 (1984).
29. T. KÁDÁR, A. PESTI, B. PENKE, G. TÓTH, M. ZARAŃDI, and G. TELEGDY. Neuropharmacology, **22**, 1223 (1983).
30. G. ZETLER. Peptides, **3**, 701 (1982).
31. D. C. HORWELL, A. BEEBY, C. R. CLARK, and J. HUGHES. J. Med. Chem. **30**, 729 (1987).
32. D. F. WEAVER. Ph.D. thesis, Queen's University, Kingston, Ont. 1986.
33. (*a*) B. H. ARISON, R. HIRSCHMANN, W. J. PALEVEDA, S. F. BRADY, and D. F. VEBER. Biochem. Biophys. Res. Commun. **100**, 1148 (1981); (*b*) S. K. BURLEY and G. A. PETSKO. Science, **229**, 23 (1985); (*c*) J. SINGH and J. M. THORNTON. FEBS Lett. **191**, 1 (1985); (*d*) T. BLUNDELL, J. SINGH, J. M. THORNTON, S. K. BURLEY, and G. A. PETSKO. Science, **234**, 1005 (1986); (*e*) F. J. BERMEJO, M. RICO, J. SANTORO, J. HERRANZ, E. GALLEGO, and J. L. NIETO. J. Mol. Struct. **142**, 339 (1986).
34. S. K. BURLEY and G. A. PETSKO. J. Am. Chem. Soc. **108**, 7995 (1986).
35. D. F. VEBER, F. W. HOLLY, W. J. PALEVEDA, R. F. NUTT, S. J. BERGSTRAND, M. TORCHIANA, M. S. GLITZER, R. SAPERSTEIN, and R. HIRSCHMANN. Proc. Natl. Acad. Sci. U.S.A. **75**, 2636 (1979).
36. R. S. MORGAN, C. E. TATSCH, R. H. GUSHARD, J. M. MCADON, and P. K. WARME. Int. J. Pept. Protein Res. **11**, 209 (1978); R. S. MORGAN and J. M. MCADON. Int. J. Pept. Protein Res. **15**, 177 (1980); K. S. C. REID, P. F. LINDLEY, and J. M. THORNTON. FEBS Lett. **190**, 209 (1985); M. LEBL, E. E. SUGG, and V. R. HRUBY. Int. J. Pept. Protein Res. **29**, 40 (1987).
37. M. C. FOURNIÉ-ZALUSKI, J. BELLENEY, C. DURIEUX, G. GACEL, B. P. ROQUES, D. BÉGUÉ, I. MENANT, B. LUX, and D. GERARD. *In* Neuropeptides and psychosomatic processes. *Edited by* E. Endroczi, L. Angelucci, U. Scapagnini, and D. DeWied. Akadémiai Kiadó, Budapest, Hungary. 1983. p. 598; M. C. FOURNIÉ-ZALUSKI, J. BELLENEY, B. LUX, C. DURIEUX, D. GERARD, G. GACEL, B. MAIGRET, and B. P. ROQUES. Biochemistry, **25**, 3778 (1986); C. DURIEUX, J. BELLENEY, J.-Y. LALLEMAND, B. P. ROQUES, and M.-C. FOURNIÉ-ZALUSKI. Biochem. Biophys. Res. Commun. **114**, 705 (1983); M. C. FOURNIÉ-ZALUSKI, C. DURIEUX, B. LUX, J. BELLENEY, P. PHAM, D. GÉRARD, and B. P. ROQUES. Biopolymers, **24**, 1663 (1985).
38. S. MAMMI, M. GOODMAN, E. PEGGION, M. T. FOFFANI, L. MORODER, and E. WUENSCH. Int. J. Pept. Protein Res. **27**, 145 (1986).
39. E. ABILLON, P. P. VAN CHUONG, and P. FROMAGEOT. Int. J. Pept. Protein Res. **17**, 480 (1981).
40. S. MIYAMOTO and Y. YOSHIMITO. Chem. Pharm. Bull. **34**, 694 (1986).
41. A. T. HAGLER. *In* The peptides. Vol. 7. *Edited by* V. J. Hruby. Academic Press, New York, NY. 1985. p. 213.
42. S. WOLFE, R. J. BOWERS, H.-S. SHIN, C.-K. SOHN, D. F. WEAVER, and K. YANG. Can. J. Chem. **66**, 2751 (1988).
43. A. DE BOLD. Science, **230**, 767 (1985).
44. D. E. KNUTH. The art of computer programming. Vol. 3. Addison–Wesley, New York, NY. 1973.
45. S. WOLFE, K. YANG, and M. KHALIL. Can. J. Chem. **66**, 2733 (1988).
46. P. J. GOODFORD. J. Med. Chem. **27**, 557 (1984); G. V. NIKIFOROVICH. J. Mol. Struct. (Theochem), **134**, 325 (1986).
47. I. W. HUNTER and R. E. KEARNEY. Biol. Cybern. **47**, 141 (1983).
48. M. SAUNDERS. J. Am. Chem. Soc. **109**, 3150 (1987).
49. D. E. KNUTH. The art of computer programming. Vol. 2. Addison–Wesley, New York, NY. 1981.

50. V. A. DYCK, J. D. LAWSON, and J. A. SMITH. Fortran 77, an introduction to structured problem solving. Reston Publishing Company, New York, NY. 1984.
51. W. J. KENNEDY and J. E. GENTLE. Statistical coupling. Marcel Dekker, Inc., New York, NY. 1980.
52. H. LORIN. Sorting and sort systems. The system programming series. Addison–Wesley, New York, NY. 1975.

Appendix 1

Conversion of ECEPP output into an MMP2(85) input file

The conversion by hand of the Cartesian coordinates generated in an ECEPP calculation to an acceptable input file for MMP2(85) is a tedious, error-prone task. The method introduced here creates the file from an ECEPP calculation as part of its output.

An MMP2(85) input file requires the specification of lists of connected and attached atoms, and the Cartesian coordinates of all of the atoms. Structure **5** illustrates a numbering scheme that might be employed for the zwitterionic tripeptide Gly-Gly-Val by following the instructions in the MMP2(85) manual. However, the ECEPP Cartesian coordinates are listed in a standard peptide format, with each residue presented consecutively.

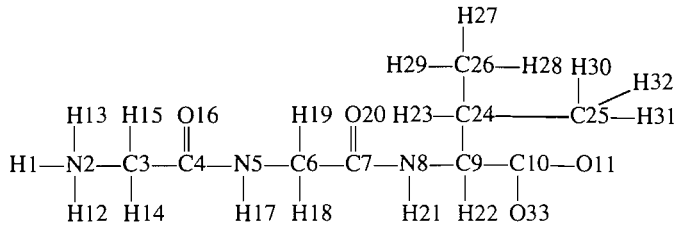

5

Accordingly, a standard reference set of amino acid residues was constructed, which contained connected and attached atom lists for each amino acid and the various end groups normally encountered in ECEPP. This reference set contained relative numbering schemes for each group or residue, based on the ECEPP numbering scheme.

The sequence of amino acids, together with the two end groups, is processed by a table look-up method. This entails the concatenation of the relative connected and attached atom lists, from a knowledge of the total number of atoms in any group. The numbers of the next group are then offset accordingly. Structure **6** shows the numbering scheme that results for Gly-Gly-Val.

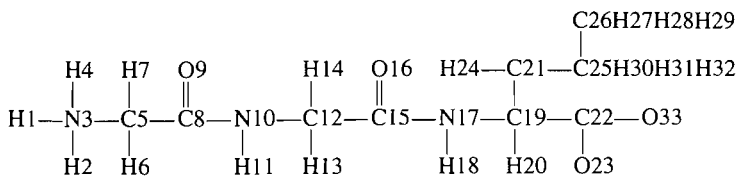

6

Appendix 2

Random number generation of initial structures (47, 48)

It is required to generate a set of "l" matrices

$$\mathbf{A}_p \in \mathbf{S}^{j\times 3} = \begin{vmatrix} a^p_{11} & a^p_{12} & a^p_{13} \\ a^p_{21} & a^p_{22} & a^p_{23} \\ \cdot & \cdot & \cdot \\ \cdot & \cdot & \cdot \\ a^p_{j1} & a^p_{j2} & a^p_{j3} \end{vmatrix}$$

where

$$p \in [1, \ldots, l], \quad j \in [1, \ldots, 30], \quad a_{ji} \in I^1$$

(the set of integers)

such that the distribution function $f_{\mathbf{A}_p}(a^p_{11}, a^p_{12}, \ldots, a^p_{j3})$ is jointly uniform, and

$$E\{\mathbf{A}_p\mathbf{A}_q^{\mathrm{T}}\} = \mathbf{B} \text{ (a matrix of constants)}, \quad \text{for all } p = q$$
$$= \mathbf{0} \text{ (null matrix)}, \quad \text{otherwise}$$

An intuitive rationalization of the above is to consider the $a^p_{11}, a^p_{12}, \ldots, a^p_{j3}$ ($3j$ elements) as the coordinates of the pth point in the $3j$ dimensional space $\mathbf{S}^{j\times 3}$. The "l" points should then be distributed uniformly over the space, in a random manner.

In practice, realization of the above protocol becomes, at best, forbiddingly abstruse. A less computationally demanding approach involves use of three sequential generators to obtain the values of the corresponding three columns of the $\mathbf{A}_p$ matrix, and thereby allow the desired joint distribution and sequential correlation characteristics.

For the practical implementation under consideration here, the maximum value of "l" was set at 200,000, and required the generation of up to 1.8×10^7 random variates in total.

Mixed congruential recursive generation techniques allow a pseudorandom variate to be produced from a preceding variate, with as little as one (floating point) multiplication and addition. The statistical characteristics of such generators are well documented (49–51), and are normally represented as

$$z_{i+1} = [az_i + c] \bmod m$$

where $z_1 \in [0, \ldots, m]$, and m, a, and c are integer constants. Extensive empirical studies (49) have led to the determination of strategies for the selection of a, c, and m to obtain desirable statistical properties, such as minimum serial correlation, and uniformity of distribution. The mod m arithmetic is performed automatically by most finite length computers. In the case of a 32-bit word computer (IBM), m becomes $2^{31} - 1$.

The main drawback to the application of a mixed congruential generation method to the required application is the phenomenon of clustering of successive sets of k points in the sequence on planes in k-dimensional space.

Once each $\mathbf{A}_p$ matrix has been generated, it is used to represent part of the geometry of the molecule. This information is optimally encoded, and stored in five 32-bit integers; the energy of this structure is stored via a 32-bit real variable.

Can. J. Chem. Downloaded from www.nrcresearchpress.com by 196.1.178.254 on 09/07/12
For personal use only.

Up to 40,000 randomly generated geometries and their energies are stored in this manner, with a requirement of less than 1 megabyte, and are then sorted to find the geometries that correspond to the 10 lowest energies. To obtain a relatively short ordered list, it is known (44, 52) that the average number of comparisons for an Insertion type sort is the smallest of the generally available methods (including a Quick sort). Therefore, to locate the 10 lowest energies from a list of 40,000, an Insertion type sorting technique, which uses a binary search rather than a linear search, was implemented. Once these 10 lowest energies are obtained, the 50 corresponding integers are decoded to generate 10 starting geometries for minimization.

Can. J. Chem. Downloaded from www.nrcresearchpress.com by 196.1.178.254 on 09/07/12
For personal use only.

MMPEN: Development and evaluation of penicillin parameters for Allinger's MMP2(85) programme

SAUL WOLFE,[1] MAGED KHALIL, AND DONALD FREDRIC WEAVER
Department of Chemistry, Queen's University, Kingston, Ont., Canada K7L 3N6
Received September 22, 1987[2]

SAUL WOLFE, MAGED KHALIL, and DONALD FREDRIC WEAVER. Can. J. Chem. **66**, 2715 (1988).

A set of parameters, termed MMPEN, has been determined for the bicyclic nucleus of penicillin, which, in conjunction with the appropriate parameters from MMPEP and the internally stored parameters of the program, allow Allinger's force field and MMP2(85) program to be applied to the molecular mechanics treatment of penicillins. The MMPEN parameters are based on crystallographic heavy atom bond lengths and bond angles, vibrational spectra, and molecular orbital calculations. The parameters reproduce the experimental crystal structures of several penicillins, including penicillin G and penicillin V, with an average deviation of 0.005 Å in bond lengths, 0.5° in bond angles, and 3° in dihedral angles. Conformational analyses of penicillin G and penicillin V, for a dielectric constant $\epsilon = 78.5$ D, suggest that neither penicillin retains the crystal structure in solution. In both cases, the global minima have the C3-carboxyl group antiperiplanar to the 2β-methyl group in the thiazolidine ring, and the side chains are oriented so that the amide N-H occupies the convex face of the molecule. The predicted conformations of the methyl esters of penicillin G and bisnorpenicillin G, for a dielectric constant of 4.8 D, are consistent with the nuclear magnetic resonance spectra obtained for these compounds in chloroform solvent.

SAUL WOLFE, MAGED KHALIL et DONALD FREDRIC WEAVER. Can. J. Chem. **66**, 2715 (1988).

On a déterminé un ensemble de paramètres, apelés MMPEN, pour le noyau bicyclique de la pénicilline qui, utilisés de concert avec les paramètres appropriés de MMPEP ainsi que les paramètres emmagasinés d'une façon interne, permettent d'appliquer le champ de force d'Allinger et le programme MMP2(85) à l'étude des pénicillines par mécanique moléculaire. Les paramètres MMPEN sont basés sur des longueurs et des angles de liaisons d'atomes lourds, sur des spectres de vibration ainsi que sur des calculs d'orbitales molèculaires. Les paramètres reproduisent les structures cristallines expérimentales de plusieurs pénicillines, y compris les pénicillines G et V, avec une déviation moyenne de 0,005 Å pour les longueurs des liaisons, de 0,5° pour les angles de liaison et de 3° pour les angles dièdres. Des analyses conformationnelles sur les pénicillines G et V, pour une constante diélectrique $\epsilon = 78,5$ D, suggèrent que ni l'une ni l'autre des pénicillines ne retient sa structure cristalline en solution. Dans chacun des cas, les valeurs minimales d'une façon globale correspondent à des structures comportant un groupement carboxyle en C3 qui est antipériplanaire par rapport au groupement méthyle en 2β du noyau thiazolidine et des chaînes latérales qui sont orientées d'une façon telle que le N-H de l'amide occupe la face convexe de la molécule. Les conformations prévues pour les esters méthyles de la pénicilline G et de la bisnorpénicilline G, pour une constant diélectrique $\epsilon = 4,8$ D, sont en accord avec les spectres en résonance magnétique nucléaire obtenus pour des solutions chloroformiques de ces composés.

[Traduit par la revue]

Can. J. Chem. Downloaded from www.nrcresearchpress.com by 196.1.178.254 on 09/07/12
For personal use only.

Introduction

We have recently described MMPEP, a set of all-atom peptide parameters for use with Allinger's versatile and well-documented MMP2(85) programme (1, 2). Using MMPEP, the structures obtained following minimization are in excellent agreement with experimental crystal structures of peptides, when the Cartesian coordinates of these X-ray structures are supplied as input. More importantly, in conjunction with protocols for secondary structure prediction (3), and (or) the use of Scheraga's ECEPP (Empirical Conformation Energy Program for Peptides) (4) for a preliminary mapping of large portions of the conformational hypersurface, MMPEP leads to "global minima" compatible with experiment in a number of cases (5), as well as other low energy structures. Conformations lower in energy than the crystal structures can also be found, and reasons for their computational existence identified.

Penicillins and cephalosporins are formed biosynthetically by oxidative transformations of a peptide precursor (6). The peptide origin of these antibiotics suggested that parameters to describe the fused thiazolidine– and dihydrothiazine–azetidinone ring systems, together with the appropriate parameters from MMPEP, would allow MMP2(85) to be applied to the conformational analysis of these antibiotics. The present work is concerned with the development and evaluation of MMPEN, an all-atom parameterization of MMP2(85) for penicillins.

TABLE 1. Atom types used in MMPEN[a]

Element	Atom	Type	Number
C	C_{sp^3}	C2, C3 of penam nucleus	16
C	C_{sp^3}	C6 of penam nucleus	20
C	C_{sp^3}	C5 of penam nucleus	22
C	C_{sp^2}	C7 of penam nucleus	31
N		β-lactam nitrogen	32
O		β-lactam oxygen	28
O[b]		OH of CO_2H	29
O[c]		Oxygen of CO_2^-	30
S		Sulfur	15

[a]This list supplements those used in MMP2(85) and MMPEP.
[b]Same as atom type 12 of MMPEP.
[c]Same as atom type 11 of MMPEP.

Penicillins (**1**) contain a fused β-lactam–thiazolidine nucleus, and an acylamino side chain. The nucleus, 6-aminopenicillanic acid (6-APA, **2**), originates from the amino acids L-cysteine and D-valine. The thiazolidine ring of 6-APA, and of penicillins generally, is flexible. It can exist in two principal conformations, **3***a* and **3***b*, that are interconvertible via the pseudorotation associated with S1—C2—C3—N4 torsion, which causes the C2-methyl substituents and the C3-carboxyl

[1]Author to whom correspondence may be addressed.
[2]Revision received March 25, 1988.

Can. J. Chem. Downloaded from www.nrcresearchpress.com by 196.1.178.254 on 09/07/12
For personal use only.

TABLE 2. Bond lengths of various penam compounds

Bond (Å)	Pen G	Pen V	Oxacillin	Cloxacillin	Ampicillin	Amoxicillin	Bacmecillinam	Methicillin	Average
S1—C2	1.80	1.87	1.89	1.850	1.849	1.843	1.861	1.843	1.851
S1—C5	1.84	1.82	1.83	1.807	1.811	1.775	1.796	1.804	1.810
C2—C3	1.59	1.57	1.58	1.553	1.551	1.559	1.562	1.554	1.565
C3—N4	1.47	1.46	1.47	1.458	1.465	1.456	1.460	1.449	1.476
N4—C5	1.48	1.52	1.50	1.475	1.456	1.492	1.467	1.485	1.484
C5—C6	1.50	1.58	1.57	1.555	1.532	1.575	1.564	1.551	1.553
C6—C7	1.50	1.55	1.49	1.557	1.518	1.515	1.547	1.536	1.527
N4—C7	1.34	1.46	1.42	1.392	1.385	1.381	1.382	1.389	1.393

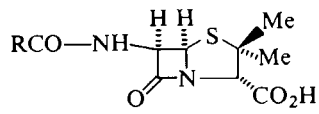

1

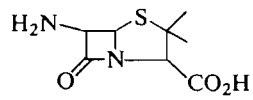

2

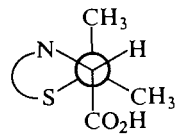

3a

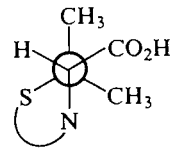

3b

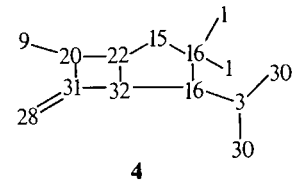

4

group to move synchronously. In **3***a*, the 2β and 3α substituents are pseudoaxial (7) in the five-membered ring, and C3 is out of the plane of an envelope conformation (8); in **3***b*, these substituents are pseudoequatorial (7), and sulfur is out of the plane of the envelope conformation (8). Both types of conformation have been encountered crystallographically (for reviews, see refs. 9 and 10), but only the pseudoequatorial conformation is observed in aqueous solution at pH 4.0–4.6, in the presence of the lanthanides La^{III}, Pr^{III}, Eu^{III}, and Gd^{III} (11). Since these lanthanides are thought to bind to the C3-carboxyl group (12), it is not clear whether the conclusions of ref. 11 also apply to the uncomplexed antibiotics (13). Further, although the different conformations observed in the solid state have been implicated in structure–activity studies (9, 10), it is noteworthy that the potassium salt of penicillin G crystallizes in the pseudoaxial conformation **3***a*, but the procaine salt of this penicillin crystallizes in the pseudoequatorial conformation **3***b* (14).

The force field (15, 16)

Atom types

Taking the view that penicillins are modified peptides, MMPEN incorporates several of the atom types of MMPEP. However, the description of the bicyclic nucleus is based on a unique set. These are indicated in **4**, and are summarized in Table 1.

Bond lengths

The required standard bond lengths were obtained from crystallographic data (7, 8, 17–24), as the average of four representative pseudoaxial (17–19, 22) and four representative pseudoequatorial (8, 20, 21, 23) structures (Table 2). The X—H bond lengths were taken from MMPEP.

Stretching force constants for the thiazolidine ring and 2-azetidinone were taken from experimental infrared (25) and Raman data (26). The complete list of bond length parameters is collected in Table 3.

Bond angles

Crystallographic data for eight representative penicillins were again used to obtain heavy atom bond angles (Table 4) (8, 17–23). An angle of particular interest is C5—S1—C2, which correlates with the conformation of the thiazolidine ring. In a pseudoequatorial penicillin this angle is ca. 90°; in a pseudoax-

TABLE 3. Stretching parameters of MMPEN

Bond types		Force constant (mdyn/Å)	Bond length (Å)
1	16	5.26	1.525
3	16	4.45	1.550
3	30	10.01	1.240
5	16	4.60	1.070
5	20	4.39	1.080
5	22	4.38	1.090
8	20	5.10	1.510
9	20	5.47	1.449
12	20	3.23	1.793
13	20	2.30	1.926
15	16	3.98	1.847
15	22	3.98	1.818
16	16	4.50	1.570
16	32	4.30	1.470
20	22	2.56	1.560
20	31	2.58	1.517
22	32	4.30	1.454
28	31	8.65	1.210
31	32	4.79	1.380

ial penicillin, this angle is ca. 96°. MMPEN employs a value of 93°. As will be seen, this value allows the trends in the C5—S1—C2 angles to be reproduced.

The angles associated with the hydrogen atoms at C3, C5, and C6 were determined with the MMP2(85) programme (1), which has the ability to place a hydrogen on any atom, and to minimize the resulting structure.

Bending force constants were taken from refs. 25 and 26. Table 5 contains the complete list of bond angle parameters.

van der Waals parameters

The values of ϵ and r_e for the atom types of MMPEN have been taken from MMP2(85), and are collected in Table 6.

Electrostatic parameters

The MMP2(85) force field incorporates the electrostatic potential as a dipole–dipole term, expressed by Jeans' equation (eq. [1]).

$$[1] \quad E_{ES} = (\mu_i\mu_j/Dr_{ij}^3)\,(\cos\chi - 3\cos\alpha_i\cos\alpha_j)$$

In eq. [1], D is the effective dielectric constant, χ is the angle between the dipoles μ_i and μ_j, and α_i and α_j are the angles formed by the dipoles with the vector connecting them.

The bond moments required for the dipole–dipole term were obtained from the net atomic charges (Q_i) of STO-3G calculations (27) on thiazolidine and 2-azetidinone, using eq. [2]. In eq. [2], the units of Q_i and Q_j are electrons, l_0 is the length of the bond, and 2.385 is a scalar multiplier that converts the bond moment to debye units. The calculated atomic charges are collected in Table 7, and the bond moments of MMPEN are provided in Table 8.

$$[2] \quad \text{Bond moment} = 2.385 l_0\,(Q_i - Q_j)$$

Torsional parameters

These refer to the V_1, V_2, and V_3 terms of the Fourier expansion, eq. [3], in which ϕ is the A/D dihedral angle in a moiety A-B-C-D. When energy is calculated as a function of ϕ by both molecular orbital (MO) and molecular mechanics (MM) methods, E_ϕ can be estimated using eq. [4], where P_{MO} (ϕ) is

TABLE 4. Bond angles of various penam compounds

Angle (deg)	Pen G	Pen V	Oxacillin	Cloxacillin	Ampicillin	Amoxicillin	Bacmecillinam	Methicillin	Average
S1—C2—C3	108	105	104	106	103	104	102	103	104.3
C2—C3—N4	103	104	107	105	106	106	107	107	105.7
C3—N4—C5	118	120	117	117	118	117	117	123	117.4
N4—C5—S1	106	103	104	105	104	103	105	103	104.1
C5—S1—C2	95	96	97	95	91	90	90	90	93.2
C3—N4—C7	124	129	130	126	126	128	123	123	126.1
S1—C5—C6	121	122	121	119	119	119	119	117	119.5
N4—C5—C6	87	88	87	88	89	87	88	88	87.5
N4—C7—C6	91	96	92	91	92	93	92	92	92.2
C5—C6—C7	87	83	87	85	86	85	85	84	85.2
C5—N4—C7	95	92	92	94	94	93	95	92	93.4

Can. J. Chem. Downloaded from www.nrcresearchpress.com by 196.1.178.254 on 09/07/12
For personal use only.

Can. J. Chem. Downloaded from www.nrcresearchpress.com by 196.1.178.254 on 09/07/12
For personal use only.

TABLE 5. Bending parameters of MMPEN

Angle types			Force constant (mdyn Å/rad^2)	Angle (deg)	
1	6	2	0.77	117.00	
1	8	20	0.63	110.00	
1	16	1	0.45	110.90	1[a]
1	16	1	0.45	111.20	2[b]
1	16	1	0.45	112.40	3[c]
1	16	5	0.36	109.40	
1	16	15	0.63	109.80	
1	16	16	0.45	110.30	1
1	16	16	0.45	111.20	2
1	16	16	0.45	112.40	3
3	1	6	0.70	106.00	
3	9	20	0.49	121.20	
3	16	5	0.37	107.90	
3	16	16	0.67	113.90	
3	16	32	0.44	111.30	
5	1	16	0.36	109.40	
5	16	15	0.36	112.00	
5	16	16	0.36	113.36	
5	16	32	0.50	100.00	
5	20	8	0.36	98.90	
5	20	9	0.36	98.90	
5	20	22	0.33	113.50	
5	20	31	0.63	113.50	
5	22	15	0.36	112.00	
5	22	20	0.45	119.30	
5	22	32	0.37	112.40	
6	3	16	0.65	107.10	
7	3	16	0.86	110.60	
8	20	22	0.56	117.30	
8	20	31	0.56	115.00	
9	20	22	0.56	118.70	
9	20	31	0.56	116.50	
12	20	13	1.03	111.11	
12	20	22	0.35	115.30	
12	20	31	0.35	114.70	
13	20	22	0.36	117.70	
13	20	31	0.36	110.50	
14	9	20	0.54	137.90	
15	16	16	0.95	104.10	
15	22	20	0.63	119.50	
15	22	32	0.95	104.10	
16	3	30	0.64	116.50	
16	15	22	1.10	93.00	
16	16	32	0.95	105.70	
16	32	22	0.70	117.40	
16	32	31	0.95	126.10	
4[d]	20	22	32	0.27	87.50
4	20	31	32	0.52	92.20
20	31	28	0.02	136.80	
4	22	20	31	0.30	85.20
4	22	32	31	0.35	93.40
30	3	30	0.85	127.00	
32	31	28	1.59	130.60	
	3	16	0.80		
	3	30	0.80		
	9	20	0.05		
	20	31	0.80		
	31	32	0.80		

[a]This value is used when the central atom has no attached hydrogens.
[b]This value is used when the central atom has one attached hydrogen.
[c]This value is used when the central atom has two attached hydrogens.
[d]This angle is part of a 4-membered ring.

TABLE 6. Van der Waals parameters of MMPEN

Atom type	ϵ (kcal/mol)	r_e(Å)
16	0.044	1.920
20	0.044	1.920
28	0.066	1.740
31	0.044	1.920
32	0.055	1.820

TABLE 7. Net atomic charges (STO-3G basis set)

Atom	Number	Net charge
S	15	0.315
C2	16	−0.698
C3	16	−0.072
N4	32	−0.734
C5	22	−0.528
C6	20	−0.132
C7	31	0.295
O8	28	−0.238
O20	6	−0.147

TABLE 8. Electrostatic parameters of MMPEN

Bond type		Bond moment (D)
1	16	0.000
3	16	5.872
3	30	3.950
5	16	0.000
5	20	0.000
5	22	0.000
8	20	3.980
9	20	0.000
12	20	1.940
13	20	1.790
15	16	4.464
15	22	3.653
16	16	0.000
16	32	2.304
20	22	−0.062
20	31	1.547
22	32	0.712
31	32	2.280
28	31	−1.533

an MO energy, and $P_{MM}(\phi)$ is an MM energy (28).

[3] $E_\phi = \frac{1}{2}V_1(1 + \cos\phi) + \frac{1}{2}V_2(1 - \cos 2\phi) + \frac{1}{2}V_3(1 + \cos 3\phi)$

[4] $E_\phi = P_{MO}(\phi) - P_{MM}(\phi)$

For a given A-B-C-D moiety of interest, the A/D dihedral angle was varied step by step and, at each angle, one-point calculations were performed using CNDO/2 and also the internally stored parameters of MMP2(85). Each pair of energies was then subjected to eq. [4], to provide an estimate of E_ϕ as a function of ϕ, and the Fourier components V_1, V_2, and

Can. J. Chem. Downloaded from www.nrcresearchpress.com by 196.1.178.254 on 09/07/12
For personal use only.

TABLE 9. Torsional parameters of MMPEN

Torsional angle type				Parameters (kcal/mol)		
				V_1	V_2	V_3
1	3	9	20	1.80	6.49	−6.23
1	6	2	2	3.53	2.30	−2.53
1	6	3	7	−1.66	8.98	0.00
1	6	3	16	−2.50	1.39	0.00
1	8	20	5	0.00	0.00	0.52
1	8	20	22	−0.20	0.73	0.80
1	8	20	31	0.00	0.00	0.00
1	16	1	5	0.00	0.00	0.27
1	16	15	22	−1.00	3.01	1.86
1	16	16	3	−0.26	1.00	−0.80
1	16	16	5	0.00	0.00	−0.90
1	16	16	32	−0.26	0.70	−0.06
2	1	3	9	0.00	−0.50	−1.70
2	2	1	3	0.00	0.00	0.50
2	2	2	6	0.00	3.80	0.00
2	6	1	3	0.00	0.00	−0.60
2	6	1	5	0.00	0.00	0.53
3	6	1	6	−1.00	−5.00	0.00
3	9	20	5	0.00	0.00	0.51
3	9	20	22	0.00	0.00	0.01
3	9	20	31	−3.50	−0.05	−4.30
3	16	16	15	−1.75	0.30	1.50
3	16	32	22	−1.00	−0.80	0.40
3	16	32	31	−1.00	−0.53	1.13
5	1	16	15	0.00	0.00	0.40
5	1	16	16	0.00	0.00	0.27
5	2	2	6	−0.30	3.80	0.00
5	16	3	6	0.00	0.00	−0.02
5	16	3	7	0.00	0.00	−0.04
5	16	3	29	0.00	0.00	−0.04
5	16	3	30	0.00	0.00	−0.09
5	16	16	15	0.00	0.00	−0.80
5	16	32	22	0.00	0.00	0.40
5	16	32	31	0.00	0.00	0.04
5	20	9	14	0.00	0.00	0.00
5	20	22	5	0.00	0.00	1.30
5	20	22	15	0.00	0.00	0.04
5	20	22	32	0.00	0.00	0.10
5	20	31	32	0.00	0.00	−0.09
5	20	31	28	0.00	0.00	0.21
5	22	15	16	0.00	0.00	0.00
5	22	20	8	0.00	0.00	0.20
5	22	20	9	0.00	0.00	0.20
5	22	20	12	0.00	3.00	0.40
5	22	20	13	0.00	5.00	0.20
5	22	20	31	0.00	0.00	0.87
5	22	32	16	0.00	0.00	0.00
5	22	32	31	0.00	0.00	0.98
6	1	3	7	0.00	0.00	−0.04
6	1	3	9	0.00	0.00	−0.04
6	3	16	16	0.40	−0.30	−0.07
6	3	16	32	0.00	0.00	0.50
7	3	9	20	0.00	7.19	0.00
7	3	16	16	0.00	0.00	−0.04
7	3	16	32	0.00	0.00	−0.04
8	20	22	32	0.00	0.00	0.40
8	20	31	32	−4.30	5.00	−1.50
8	20	31	28	−3.50	3.00	8.00
9	20	22	15	0.50	0.00	1.00
9	20	22	32	0.00	0.00	0.40
9	20	31	32	−4.30	5.00	−1.50
9	20	31	28	−3.50	3.00	8.00
	12	20	22	15	0.00	0.00	0.04
	12	20	22	32	0.00	0.00	0.50
	12	20	31	32	0.00	0.00	−0.09
	12	20	31	28	0.00	0.00	0.21
	13	20	22	15	0.50	−2.75	3.00
	13	20	22	32	0.00	0.00	1.40
	13	20	31	32	−4.30	5.00	−1.50
	13	20	31	28	−1.50	5.00	8.00
	14	9	20	22	0.00	0.00	0.01
	14	9	20	31	0.00	0.00	0.01
	15	16	16	32	−0.75	2.00	−0.90
	15	22	20	31	0.00	1.00	1.00
	15	22	32	16	−3.00	7.00	0.00
	15	22	32	31	0.00	1.00	0.30
	16	15	22	20	−2.50	3.60	−3.00
	16	15	22	32	−2.50	3.00	−1.00
	16	16	3	29	0.00	0.00	−0.20
	16	16	3	30	0.00	0.00	−0.09
	16	16	15	22	0.00	2.50	0.40
	16	16	32	32	−1.00	−2.50	0.40
	16	16	32	31	−0.50	0.50	2.50
	16	32	22	20	0.00	1.00	−0.50
	16	32	31	20	−4.00	3.00	0.40
	16	32	31	28	−1.00	3.00	2.00
4[a]	20	22	32	31	1.50	10.00	1.00
4	20	31	32	22	−1.00	8.50	5.00
4	22	20	31	32	−1.00	9.00	3.00
	22	20	31	28	0.20	3.50	−2.50
	22	32	31	28	0.20	8.00	−4.70
4	31	20	22	32	−2.65	6.10	0.20
	32	16	3	29	0.00	0.00	−0.06
	32	16	3	30	0.00	0.00	−0.09

TABLE 9 (*concluded*)

[a]This torsional angle is part of a four-membered ring.

V_3 were identified by a least-squares fit, using the programme provided in the appendix of ref. 28.

For example, to obtain the parameters for torsion about S1—C5, calculations were performed on CH_3S–CH_2NH_2. Other appropriate model structures, corresponding to fragments of the penicillin nucleus, were treated analogously, and the resulting parameters were introduced into the force field.

An initial force field, which contained torsional parameters arrived at in this manner, did not give acceptable results when applied to penicillin G. Thus, for the C5—C6—C7—O8 dihedral angle, MMPEN yielded 154°, compared to 169° in the crystal structure. The discrepancy was traced to the highly constrained torsion that exists in a fused ring system, which causes the use of normal, unconstrained, torsional parameters to be inappropriate for the problem.

Since inspection of molecular models suggested that the maximum torsion about S1—C2—C3—N4 is ±60°, a second set of calculations for the fragments of the thiazolidine ring was performed, and was restricted to this range of dihedral angles. The resulting parameters, with additional minor modifications by trial and error (29), proved acceptable. Table 9 lists the torsional parameters of MMPEN.

TABLE 10. Comparison of the crystallographic and calculated dihedral angles of penicillin G[a]

Dihedral angle	Calcd. (deg)	Obs. (deg)	Dihedral angle	Calcd. (deg)	Obs. (deg)
1-2-3-4	−36	−28	4-3-11-13	−139	−142
1-2-3-11	88	94	4-5-6-7	6	5
1-5-4-3	−18	−20	4-5-6-14	124	121
1-5-4-7	116	114	4-7-6-5	−6	−6
1-5-6-7	−102	−109	4-7-6-14	−125	−124
1-5-6-14	17	15	5-4-3-11	−90	−91
			5-6-7-8	170	169
2-1-5-4	−5	0	5-4-7-6	6	6
2-1-5-6	94	97	5-6-14-15	165	169
2-3-4-5	37	32	6-14-15-16	169	176
2-3-4-7	−79	−86	7-4-3-11	154	149
2-3-11-12	−79	−79	7-6-14-15	−96	−94
2-3-11-13	101	100	9-2-3-11	−30	−26
3-2-1-5	24	16	10-2-3-11	−153	−149
3-4-5-6	−140	−140	14-15-16-17	8	5
3-4-7-6	133	137	15-16-17-18	84	84
4-3-11-12	41	40	15-16-17-22	−95	−91

[a]See **5** for numbering.

Minimization

The block-diagonal Newton–Raphson procedure, which is standard in MMP2(85), leads reliably to the minimum of the potential well that contains the initial structure. However, when this geometry is far from the minimum of the well, convergence of the Newton–Raphson procedure can be slow and unreliable (30).

Testing the MMPEN parameters

Calculations were performed on the anions of penicillin G (**5**) and penicillin V (**6**), on the zwitterion **7**, and on the ester **8**. The heavy atom Cartesian coordinates of the crystal structures of potassium penicillin G (18), penicillin V (17), **7** (31), and **8** (32) were supplied as input, hydrogen atoms were added as necessary (1), and one-point energies were computed, followed by minimization, using a dielectric constant of 78.5. In each case, minimization proceeded rapidly, and was achieved within 25 iterations. Since each of **5** – **8** crystallizes in the pseudoaxial conformation, and minimization with MMPEN did not change the initial conformation of the thiazolidine ring, C5—S1—C2 bond angles of 96° resulted in each case. Tables 10–13 contain comparisons of the crystallographic and calculated dihedral angles, after minimization.

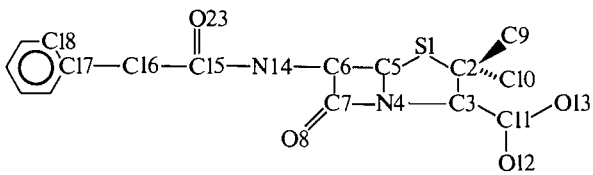

5

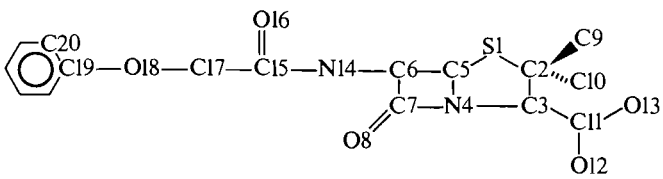

6

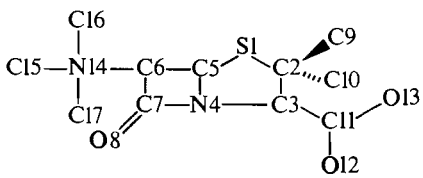

7

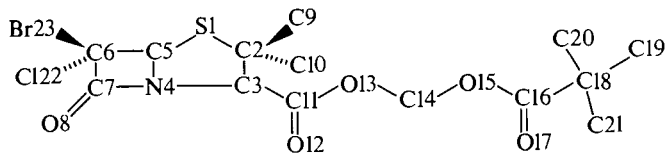

8

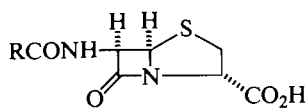

9

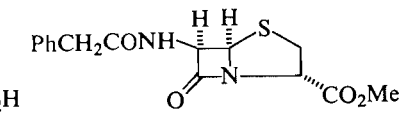

10

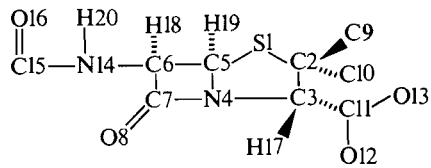

11

For the more than 300 dihedral angles compared in Tables 10–13, the average deviation between the calculated and experimental values is less than 3°. Only the angles associated with the carboxyl group of penicillin V and the β-lactam carbonyl oxygen atom of **7** show significant deviation. In the latter case, this deviation can be traced to an unusually short C=O bond length of 1.15 Å in the crystal structure, compared to the calculated value of 1.21 Å. This longer C=O bond length is observed experimentally in penicillin G, penicillin V, and **8**.

It can be concluded that the MMPEN parameterization is

Can. J. Chem. Downloaded from www.nrcresearchpress.com by 196.1.178.254 on 09/07/12
For personal use only.

TABLE 11. Comparison of the crystallographic and calculated dihedral angles of penicillin V[a]

Dihedral angle	Calcd. (deg)	Obs. (deg)	Dihedral angle	Calcd. (deg)	Obs. (deg)
1-2-3-4	−36	−34	4-5-6-14	121	120
1-2-3-11	88	89	4-7-6-5	−4	−6
1-5-4-3	−17	−18	4-7-6-14	−123	−120
1-5-4-7	118	117	5-1-2-9	−94	−94
1-5-6-7	−103	−101	5-1-2-10	146	144
1-5-6-14	14	13	5-4-3-11	−91	−88
2-1-5-4	−6	−5	5-4-7-6	4	6
2-1-5-6	92	96	5-4-7-8	−169	−173
2-3-4-5	36	36	5-6-7-8	169	173
2-3-4-7	−80	−79	5-6-14-15	154	156
2-3-11-12	99	85	6-5-4-7	−4	−6
1-2-11-13	−82	−94	6-14-15-16	8	8
3-2-1-5	25	24	6-14-15-17	−170	−170
3-4-5-6	−139	−141	7-4-3-11	153	158
3-4-7-6	132	134	7-6-14-15	−108	−111
3-4-7-8	−42	−45	8-7-6-14	50	59
4-3-2-9	83	83	9-2-3-11	−153	−154
4-3-2-10	−154	−151	10-2-3-11	−28	−28
4-3-11-12	−141	−157	14-15-17-18	−3	−5
4-3-11-13	39	24	15-17-18-19	−165	−161
4-5-6-7	4	6	17-18-19-20	162	168

[a]See **6** for numbering.

appropriate for the molecular mechanics treatment of penam compounds.[3]

Conformational analysis of penicillin G

Figure 1 shows a stereoscopic view (along the N4—C5 bond) of penicillin G in the calculated conformation of the crystal structure. Three aspects of this structure are of particular interest: (*i*) the carboxylate anion and the 2β-methyl group are antiperiplanar in the thiazolidine ring, illustrative of the pseudoaxial conformation; (*ii*) the carbonyl oxygen of the side chain is directed towards the convex face of the molecule; (*iii*) the aromatic ring is directed towards the concave face of the bicyclic ring system, leading to a compact structure.

Figure 2 shows, in more detail, the relationship between the aromatic ring and the sulfur atom. In this figure, the view is from the C5—S1—C2 plane to the benzene ring, and it can be seen that the *p*-type nonbonding orbital of sulfur is directed approximately perpendicular to C17, the ipso carbon atom. This kind of orientation is characteristic of the aromatic–S interaction found in the crystal structures of globular proteins (33), in which the sulfur atoms of cyst(e)ine and methionine residues express an affinity for the edges of aromatic rings.

The conformational analysis of penicillin G proceeded in three stages. In the first, the acylamino side chain was optimized by successive dihedral drives along C6—N14, C15—C16, and C16—C17; these were performed in 20° increments from +180° to −180°, and in each case the lowest energy structure was minimized fully before proceeding to the next dihedral angle. Although two complete cycles were performed, the second did not lead to a lower energy structure. In the second stage of the conformational analysis, the thiazolidine ring was inverted from the pseudoaxial to the pseudoequatorial conformation; this was done by driving the S1—C2—C3—N4 dihedral angle in increments from its optimized value (ca. −36°) to −0.1°, manually changing the Cartesian coordinates of these four atoms to obtain a positive dihedral angle, and then proceeding with the dihedral drive. The lowest energy pseudoequatorial structure was then minimized fully. In the final stage of the conformational analysis the acylamino side chain of the pseudoequatorial structure was reoptimized, by successive dihedral drives, as before.

The optimization of the acylamino side chain led to a structure, displayed in Fig. 3, which is calculated to be

[3]Referees have questioned the need to create a unique set of parameters for the bicyclic nucleus of penicillin, and argue that this detracts from the utility of the molecular mechanics approach. Our view is that, for the method to be credible, *every* class of compound examined with MMP2(85) must be described in a manner compatible with all available experimental and (or) theoretical data for that compound. In the present case, it seemed obvious that the β-lactam ring is a unique entity; it was also clear, from our examination of the crystal structures of penicillins, that the bond lengths and bond angles associated with the sulfur atom are conformation-dependent, and require special treatment. The need for caution in the uncritical use of asterisked (i.e., not fully determined) parameters of MMP2(85) and its predecessors has been emphasized repeatedly by Allinger; these programmes will also run with unknown torsional parameters set at $V_1 = V_2 = V_3 = 0$. It is not clear to us how such restrictions can be compatible with claims that quantitative conformational analyses are being performed. To illustrate these points, we attempted to perform calculations on penicillin G, using the parameters of MMPEP, and also the parameters of MMP2(85). The MMPEP parameters led to 27 error messages; the MMP2(85) parameters led to 31 error messages, corresponding to structural features of this compound that are unknown in these force fields. One of the aspects of the modified and expanded version of MMP2(85) described in ref. 2 is an ability to release all internal parameters, and replace these by an external file for the molecule of interest. We will provide the required source code to all authorized users of MMP2(85). There is no doubt that reliable, fully documented parameters are central to the application of molecular mechanics to quantitative conformational analysis. Accordingly, in subsequent papers we plan to describe novel strategies for the relatively rapid establishment of parameters.

Can. J. Chem. Downloaded from www.nrcresearchpress.com by 196.1.178.254 on 09/07/12
For personal use only.

TABLE 12. Comparison of the crystallographic and calculated dihedral angles of the zwitterion **7**

Dihedral angle	Calcd. (deg)	Obs. (deg)	Dihedral angle	Calcd. (deg)	Obs. (deg)
1-2-3-4	−31	−30	4-3-11-13	−140	−146
1-2-3-11	92	90	4-5-6-7	13	12
1-5-4-3	−24	−28	4-5-6-14	136	133
1-5-4-7	112	111	4-7-6-5	−13	−12
1-5-6-14	30	28	4-7-6-14	−141	−139
2-1-5-4	2	6	5-1-2-9	139	137
2-1-5-6	99	102	5-1-2-10	−101	−103
2-3-4-5	38	40	5-4-3-11	−88	−83
2-3-4-7	−81	−84	5-4-7-6	14	13
2-3-11-12	−80	−81	5-4-7-8	−177	−164
2-3-11-13	101	96	5-6-7-8	179	164
3-2-1-5	18	14	5-6-14-15	174	175
3-4-5-6	−150	−152	6-5-4-7	−14	−13
3-4-7-6	144	146	7-4-3-11	153	153
3-4-7-8	−47	−31	7-6-14-15	−81	−79
4-3-2-9	−149	−147	8-7-6-14	51	37
4-3-2-10	88	86	9-2-3-11	−26	−27
4-3-11-12	40	38	10-2-3-11	−149	−154

TABLE 13. Comparison of the crystallographic and calculated dihedral angles of **8**

Dihedral angle	Calcd. (deg)	Obs. (deg)	Dihedral angle	Calcd. (deg)	Obs. (deg)
1-2-3-4	−31	−33	4-5-6-22	−106	−109
1-2-3-11	95	89	4-5-6-23	114	116
1-5-4-3	−22	−23	4-7-6-5	−100	−100
1-5-4-7	116	118	4-7-6-22	141	139
1-5-6-7	−100	−101	4-7-6-23	−91	−87
1-5-6-22	148	144	5-1-2-9	8	7
1-5-6-23	8	10	5-1-2-10	−171	−172
2-1-5-4	0	1	5-4-3-11	171	172
2-1-5-6	98	97	5-4-7-6	−8	−7
2-3-4-5	36	38	5-4-7-8	147	149
2-3-4-7	−86	−86	5-6-7-8	171	172
2-3-11-12	−86	−87	6-5-4-7	50	54
2-3-11-13	92	91	7-4-3-11	−147	−152
3-2-1-5	18	18	8-7-6-22	−23	−28
3-4-5-6	−146	−148	8-7-6-23	85	86
3-4-7-6	140	138	9-2-3-11	3	1
3-4-7-8	−39	−40	10-2-3-11	73	78
3-11-13-14	−176	−177	11-13-14-15	−4	−5
4-3-2-9	88	86	12-11-13-14	175	174
4-3-2-10	−149	−150	13-14-15-16	164	163
4-3-11-12	35	33	14-15-16-17	−7	−6
4-3-11-13	−147	−149	14-15-16-18	108	109
4-5-6-7	7	6	15-16-18-20	−129	−124

3.10 kcal/mol *lower* in energy than the crystal structure. This is the global minimum of penicillin G for a dielectric constant of 78.5. The fully optimized pseudoequatorial structure, shown in Fig. 4, is 1.93 kcal/mol *higher* in energy than the global minimum.

In the pseudoequatorial structure (Fig. 4) the C5—S1—C2 angle is calculated to be 93°, significantly smaller than the corresponding angle in the pseudoaxial structure (96°). This trend is consistent with experiment, and offers additional support for the validity of the MMPEN parameters.

The orientation of the side chain of the global minimum differs significantly from that in the crystal structure. Although the aromatic ring is still folded under the bicyclic ring system, retaining the compact shape of the molecule, and an aromatic–S interaction is still present (Fig. 5), the *amide hydrogen* of the acylamino side chain now resides on the convex face of the molecule. We note that, in the crystal structure, the H6—O23 distance is 2.40 Å, significantly less than the sum of the van der Waals radii of these two atoms (3.4 Å).

The conformational analysis of penicillin G, if correct, is of some importance in relation to the significance of structure –activity studies based on crystallographic data (9, 10, 34). It

Can. J. Chem. Downloaded from www.nrcresearchpress.com by 196.1.178.254 on 09/07/12
For personal use only.

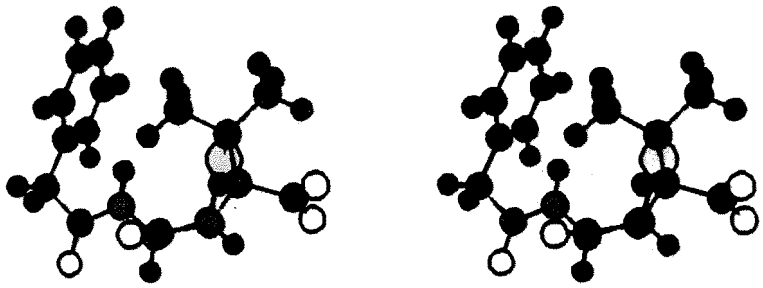

FIG. 1. The crystal structure of penicillin G, viewed along N4—C5.

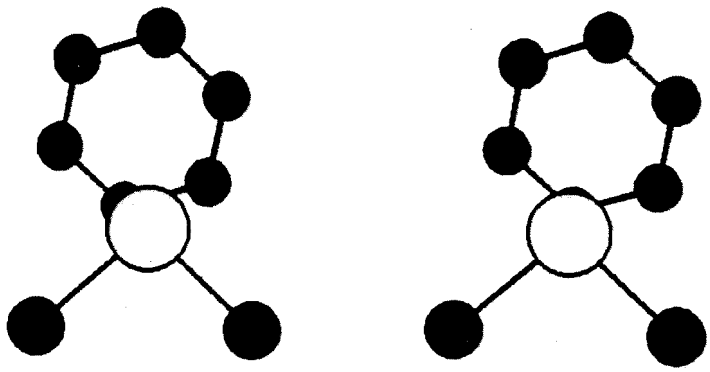

FIG. 2. Aromatic–S interaction in the crystal structure of penicillin G.

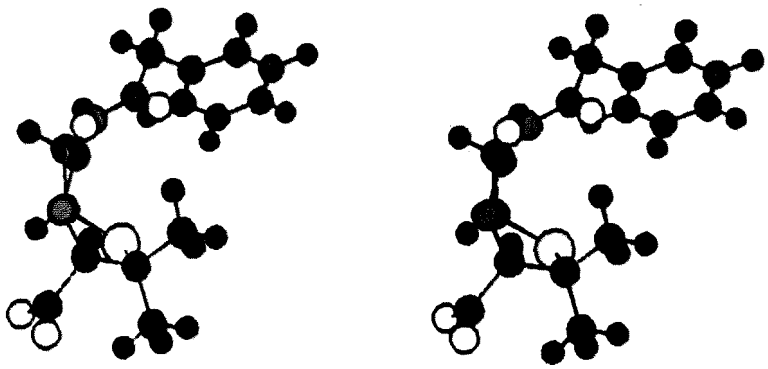

FIG. 3. Calculated global minimum (pseudoaxial) of penicillin G.

was, therefore, desirable to compare results obtained theoretically using MMPEN to the results of experimental measurements in solution.

Experimental tests of the MMPEN strategy for conformational analysis. The methyl esters of penicillin G and bisnorpenicillin G

Osborne has described an efficient sequence for the conversion of a penicillin into its bisnor derivative **9** (35). In such compounds the conformation of the thiazolidine ring can be determined from measurements of the vicinal H2–H3 coupling constants. In addition, in chloroform solvent, the orientation of the side chain can be probed by determination of the H-N-C6-H coupling constant, and by nOe measurements. Accordingly, **10**, the methyl ester of bisnorpenicillin G was synthesized,[4]

[4]R.Z. Sterzycki and S. Wolfe. Unpublished results.

Can. J. Chem. Downloaded from www.nrcresearchpress.com by 196.1.178.254 on 09/07/12
For personal use only.

Can. J. Chem. Downloaded from www.nrcresearchpress.com by 196.1.178.254 on 09/07/12
For personal use only.

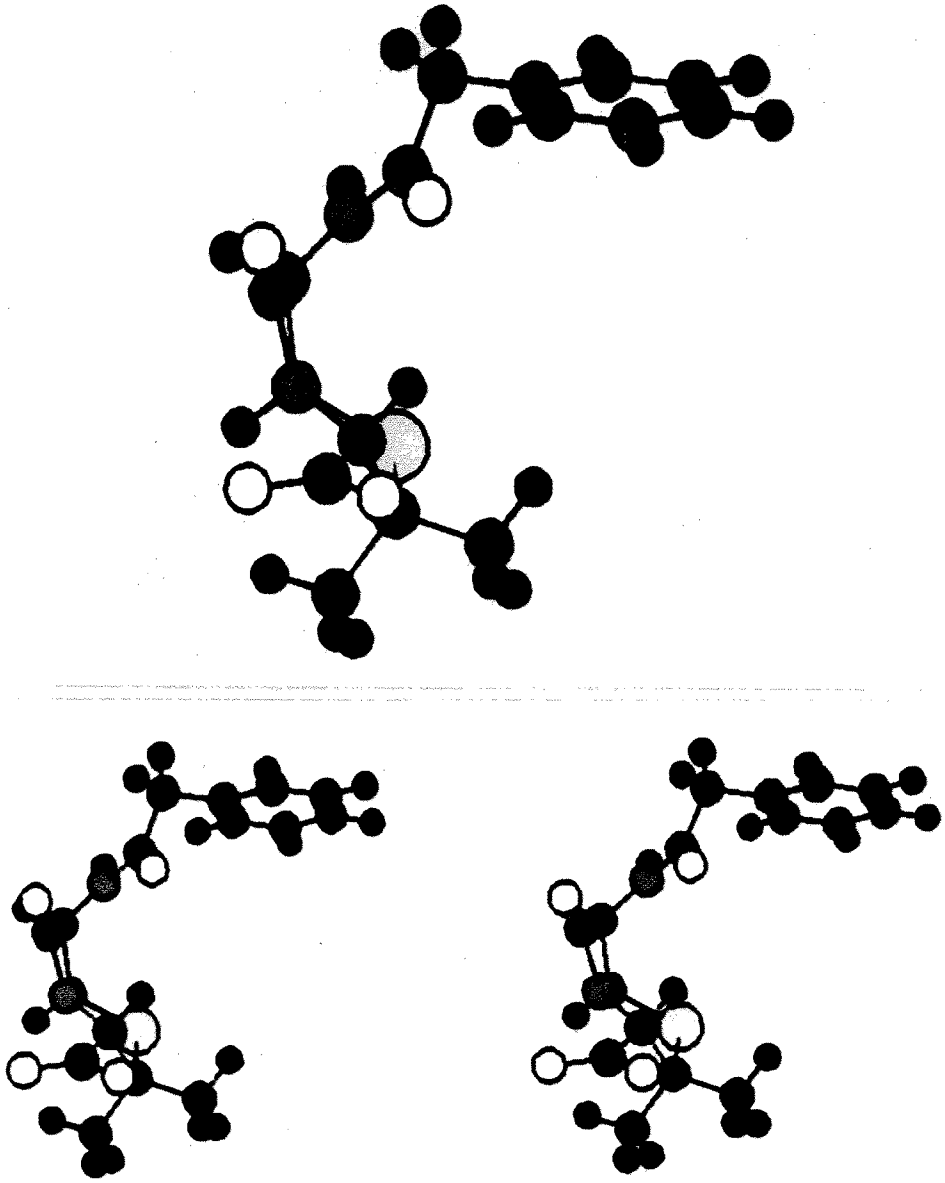

FIG. 4. Calculated pseudoequatorial conformation of penicillin G.

and its 400 MHz ^{1}Hmr spectrum was measured in chloroform. Concurrently, a conformational analysis of methyl bisnorbenzylpenicillanate was undertaken, using MMPEN, with a dielectric constant of 4.8, corresponding to chloroform solvent.

The theoretical conformational analysis began with the coordinates of the global minimum of penicillin G, with deletion of the C2-methyl groups and their replacement by hydrogens, and the attachment of a methyl group to the carboxyl. The pseudoaxial and pseudoequatorial conformations were then optimized, as already described. Figure 6 shows the optimized pseudoaxial structure; the optimized pseudoequatorial structure is shown in Fig. 7. The two structures have the same energy.

Table 14 compares the calculated H2β—C2—C3—H3, H2α—C2—C3—H3, and H—N—C6—H6 dihedral angles of the pseudoaxial and pseudoequatorial conformations to the experimentally determined vicinal coupling constants. The observed H2–H3 coupling constants are consistent only with a pseudoequatorial conformation of the thiazolidine ring. This is compatible with the calculations. The H-N-C-H coupling

TABLE 14. Calculated dihedral angles and observed vicinal coupling constants[a] in methyl bisnorbenzylpenicillanate

Dihedral angle	Value (deg)		Coupling constant (Hz)
	Pseudoaxial	Pseudoequatorial	
H2β—C2—C3—H3	−27	46	8.0
H2α—C2—C3—H3	97	169	12.7
H—N—C6—H6	−60	−30	7.5

[a]In $CDCl_3$.

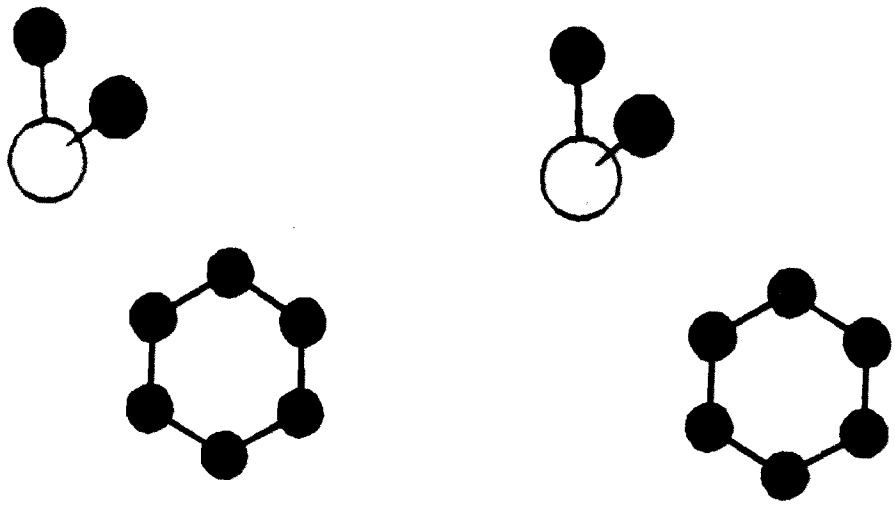

FIG. 5. Aromatic–S interaction in the calculated global minimum of penicillin G.

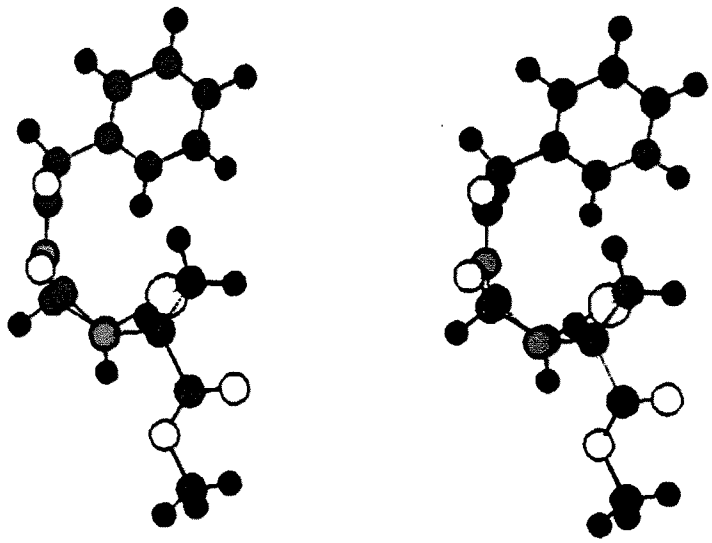

FIG. 6. Pseudoaxial conformation of **10**.

Can. J. Chem. Downloaded from www.nrcresearchpress.com by 196.1.178.254 on 09/07/12
For personal use only.

constant is consistent either with an *endo* N-H, as in the crystal structure of penicillin G, or with an *exo* N-H, as in Fig. 7. As can be seen from Fig. 7, an *endo* N-H should exhibit a nuclear Overhauser effect with H3, if the thiazolidine ring has the pseudoequatorial conformation. This nOe was not observed.

In a second test of the computational strategy, the methyl ester of penicillin G was calculated for a dielectric constant of 4.8, and the pseudoaxial conformation, shown in Fig. 8, was found to be 2.2 kcal/mol lower in energy than the pseudoequatorial conformation (not shown). The observed H-N–C-H coupling constant, in chloroform-*d* solvent, is 7.5 Hz, and is again consistent with either an N-H *endo* or an N-H *exo* conformation. No nOe is observed[5] between H5 and the methyl hydrogens, or between N-H and the methyl hydrogens. The absence of an nOe between H5 and methyl hydrogens has been taken as evidence for a pseudoaxial conformation in CCl_4 solvent in the case of the methyl ester of penicillin V (36). The absence of an nOe between N-H and methyl hydrogens is consistent with the structure shown in Fig. 8.

Conformational analysis of penicillin V

Figure 9 shows the crystal structure of penicillin V, and Fig. 10 displays the relationship between the aromatic ring and the sulfur atom in this crystal structure. Several points may be noted: (*i*) the thiazolidine ring has a pseudoaxial conformation; (*ii*) the amide bond of the side chain is orientated as in the crystal structure of penicillin G, with the carbonyl oxygen directed towards the convex face of the molecule; (*iii*) the aromatic–S interaction is absent. In the case of (*iii*), it is observed in Figs. 7

[5]The authors thank Professors B.K. Hunter and B.M. Pinto for these nOe measurements, details of which will be published elsewhere.

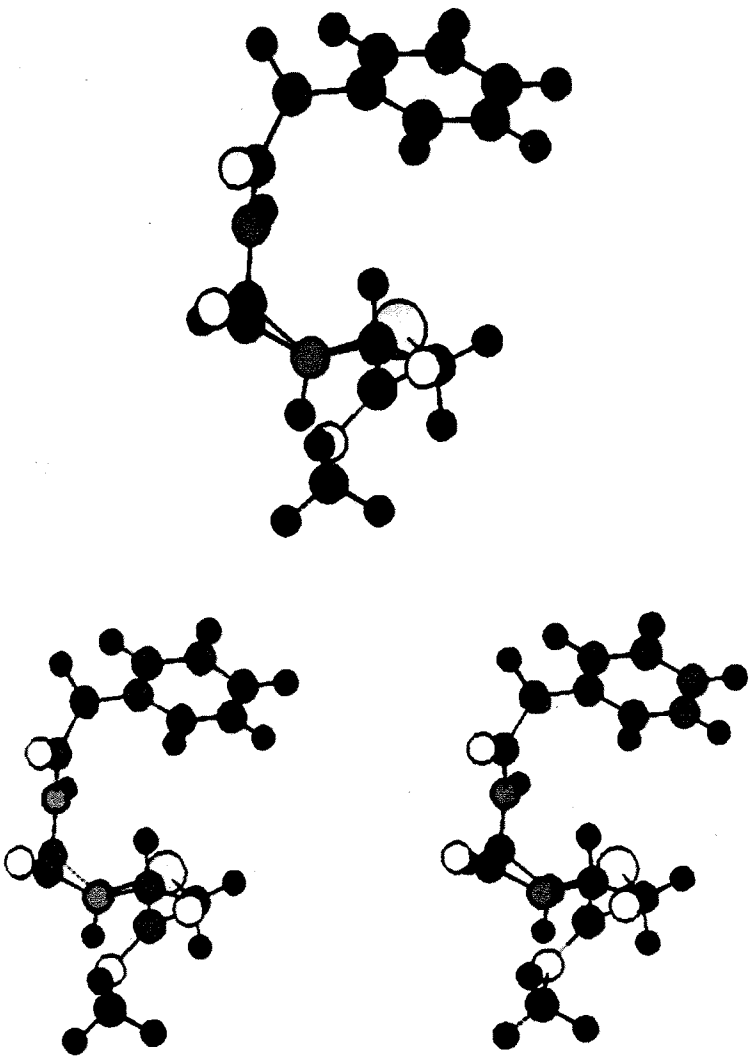

FIG. 7. Pseudoequatorial conformation of **10**.

and 8 of ref. 17 that crystal packing of penicillin V emphasizes *inter*molecular aromatic–aromatic interactions, rather than an intramolecular aromatic–*S* interaction.

The conformational analysis of penicillin V was performed as described for penicillin G, and led to a pseudoequatorial structure 2.52 kcal/mol lower in energy than the crystal structure, with a C5—S1—C2 angle of 93°, and a pseudoaxial structure 4.22 kcal/mol lower in energy than the crystal structure. This latter structure is shown as Fig. 11, and its aromatic–S interaction is seen in Fig. 12.

The calculated global minimum of penicillin V, like that of penicillin G, is compact, because of the enforcement of the aromatic–S interaction in solution, and the orientation of the side-chain amide bond is again opposite to that observed in the crystal structure. The amide oxygen is found on the concave face of the molecule, and the amide nitrogen is on the convex face.

The implications of these findings concerning the side chains of penicillins are extended and examined in more detail in the accompanying paper (37).

Conformational analysis of the penam derivatives 7 and 8

Figure 13 shows the pseudoaxial (crystal) structure of the zwitterion **7** and Fig. 14 displays the calculated pseudoequatorial structure of this compound. The pseudoaxial structure is 1.80 kcal/mol more stable.

Figures 15 and 16 refer to the pseudoaxial and pseudoequatorial structures of the ester **8**, respectively. In this case, the pseudoequatorial conformation is lower in energy, by 1.53 kcal/mol.

Summary and concluding remarks

A major incentive for this work has been the desire to have a convenient, accessible, and reproducible procedure for the theoretical conformational analysis of penicillins. Allinger's force field is well established, and versions of the MM2 programme are available for many types of computers. Thus, it seemed reasonable to believe that a standardized molecular mechanics approach to penicillins, based on MM2, could be devised, whose results would be as reproducible as the description of a synthesis or the report of an *ab initio* calculation

Can. J. Chem. Downloaded from www.nrcresearchpress.com by 196.1.178.254 on 09/07/12
For personal use only.

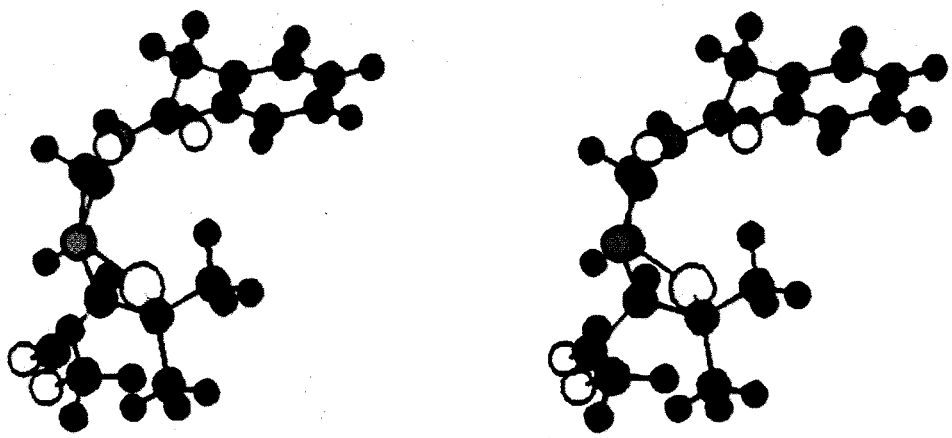

FIG. 8. Global minimum (pseudoaxial) of the methyl ester of penicillin G.

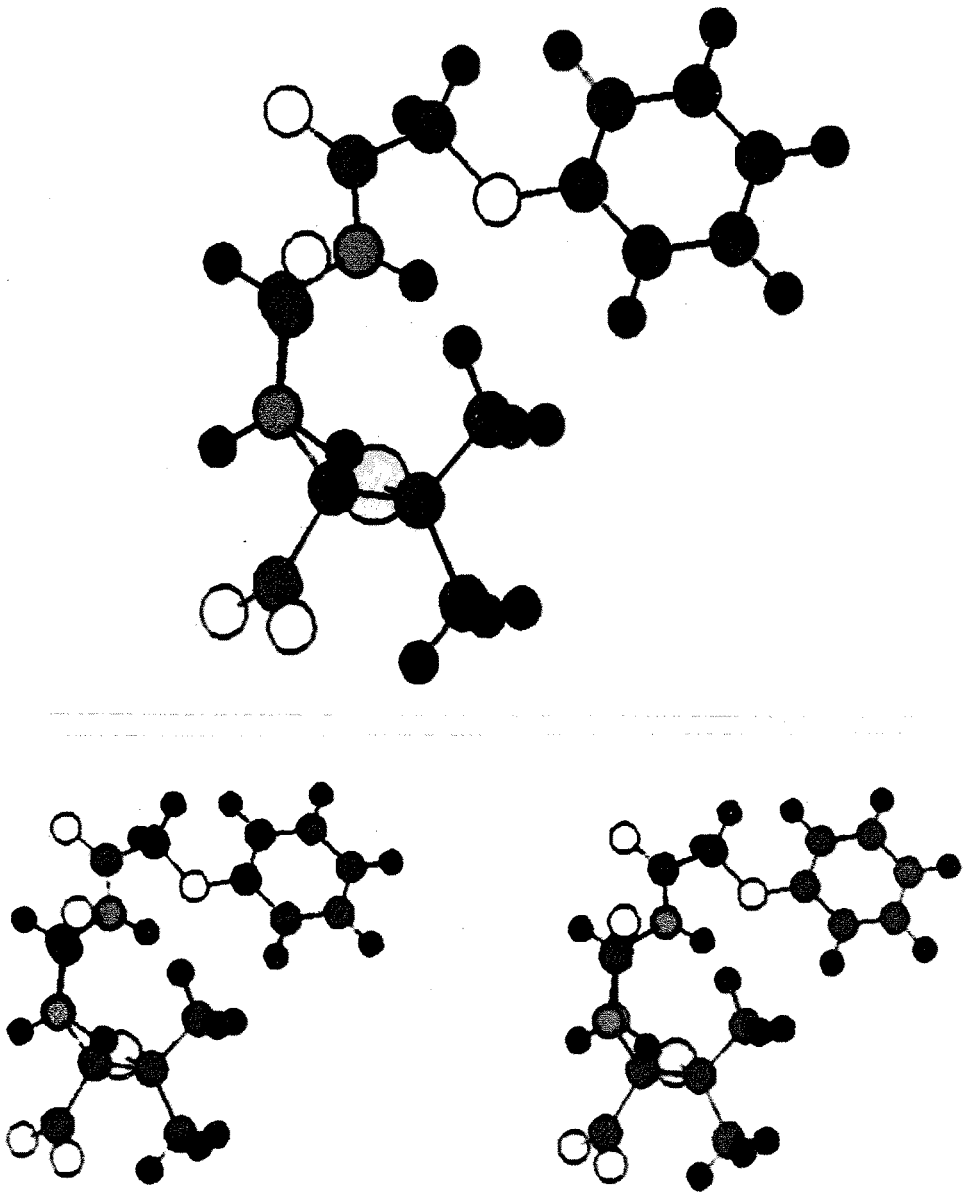

FIG. 9. Crystal structure of penicillin V.

Can. J. Chem. Downloaded from www.nrcresearchpress.com by 196.1.178.254 on 09/07/12
For personal use only.

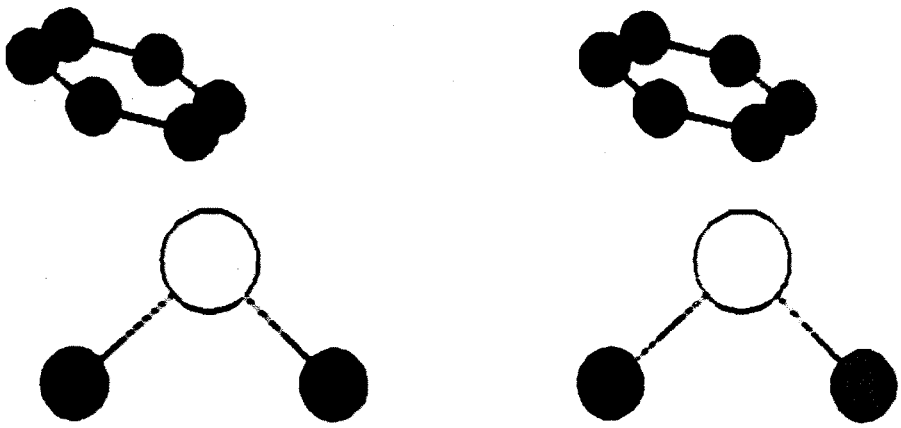

FIG. 10. Aromatic–S relationship in the crystal structure of penicillin V.

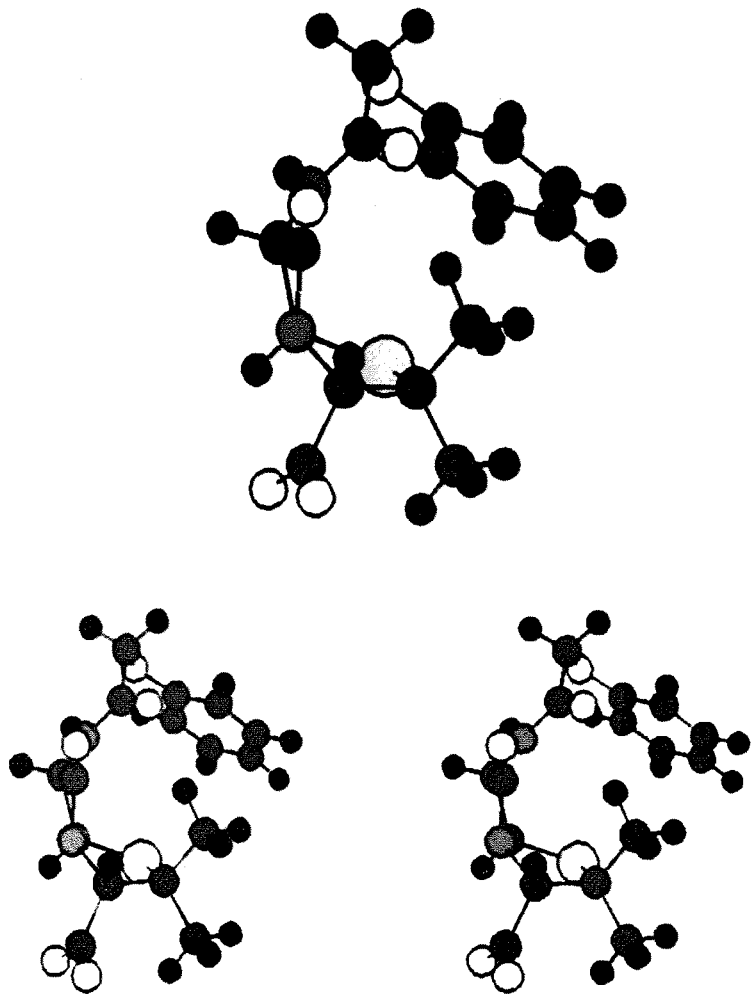

FIG. 11. Calculated global minimum (pseudoaxial) of penicillin V.

Can. J. Chem. Downloaded from www.nrcresearchpress.com by 196.1.178.254 on 09/07/12
For personal use only.

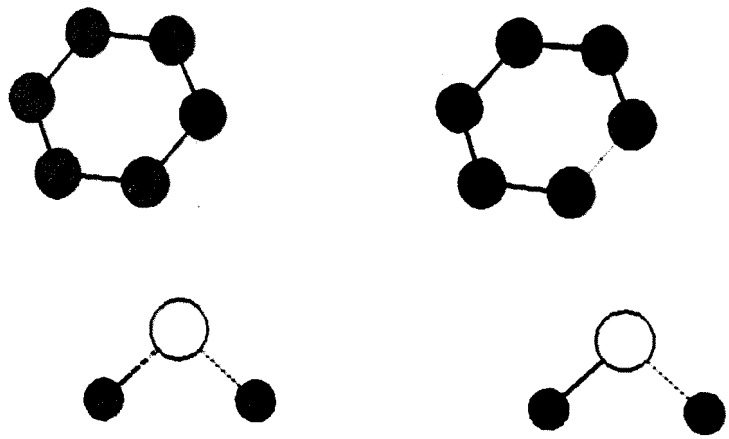

FIG. 12. Aromatic–S relationship in the global minimum of penicillin V.

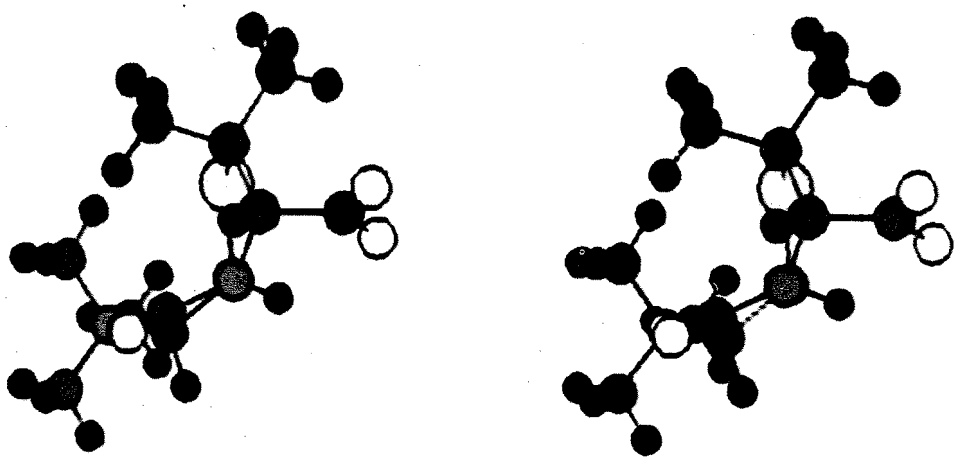

FIG. 13. Crystal structure of **7**.

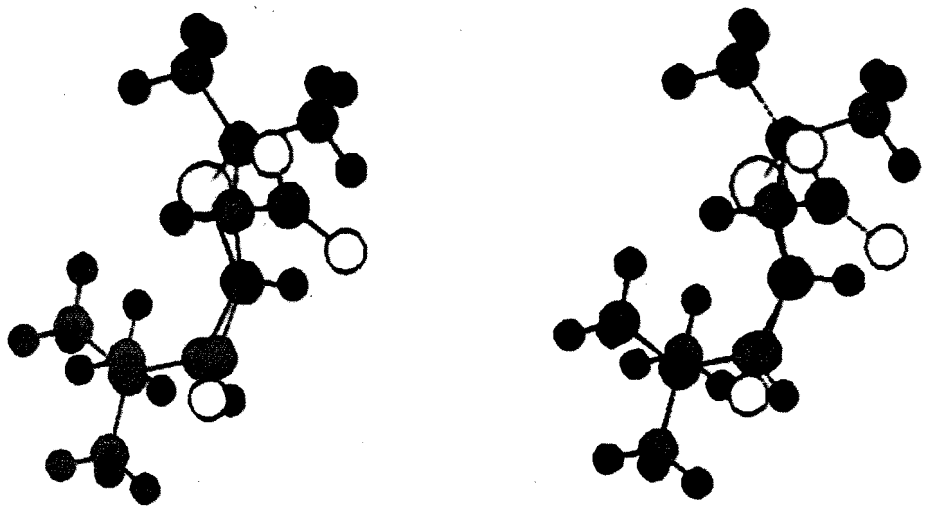

FIG. 14. Calculated pseudoequatorial structure of **7**.

Can. J. Chem. Downloaded from www.nrcresearchpress.com by 196.1.178.254 on 09/07/12
For personal use only.

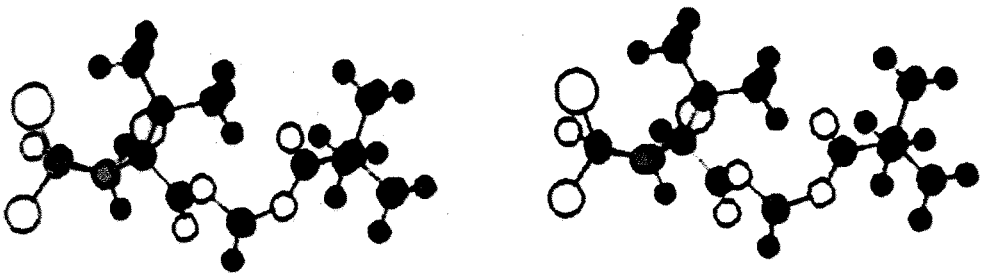

FIG. 15. Crystal structure of **8**.

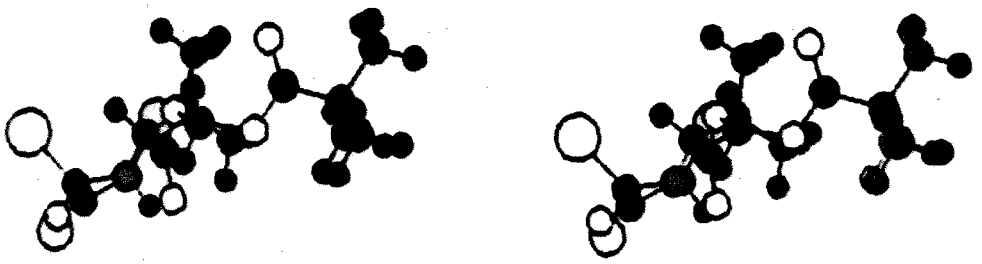

FIG. 16. Calculated pseudoequatorial structure of **8**.

Can. J. Chem. Downloaded from www.nrcresearchpress.com by 196.1.178.254 on 09/07/12
For personal use only.

TABLE 15. Atom types and cartesian coordinates for a general pseudoaxial conformation (see **11**)

Atom	*x*	*y*	*z*	Type
S(1)	0.05328	−5.08984	−1.15244	(15)
C(2)	−0.54700	−6.18771	0.23449	(16)
C(3)	−2.11113	−6.26009	0.04131	(16)
N(4)	−2.48575	−4.96297	−0.57241	(32)
C(5)	−1.57234	−4.41653	−1.60274	(22)
C(6)	−2.01328	−2.99362	−1.16436	(20)
C(7)	−2.57283	−3.71103	0.06439	(31)
O(8)	−3.10203	−3.39837	1.09747	(28)
C(9)	0.15673	−7.55205	0.11179	(1)
C(10)	−0.19419	−5.57040	1.60170	(1)
C(11)	−2.65058	−7.46505	−0.78990	(3)
O(12)	−2.57321	−7.38404	−2.02561	(30)
O(13)	−3.11964	−8.41858	−0.14877	(30)
N(14)	−1.06007	−1.88918	−1.15691	(9)
C(15)	−0.53170	−1.43848	−0.01049	(3)
O(16)	−0.55713	−2.07676	1.01573	(7)
H(17)	−2.68440	−6.18329	0.94411	(5)
H(18)	−1.79410	−4.74091	−2.62118	(5)
H(19)	−2.78482	−2.54345	−1.77593	(5)
H(20)	−0.86708	−1.26311	−1.91147	(14)

TABLE 16. Atom types and cartesian coordinates for a general pseudoequatorial conformation (see **11**)

Atom	*x*	*y*	*z*	Type
S(1)	−0.11908	−5.09198	−1.52952	(15)
C(2)	−0.58463	−6.39189	−0.26826	(16)
C(3)	−1.54759	−5.59457	0.69290	(16)
N(4)	−2.30150	−4.69198	−0.20764	(32)
C(5)	−1.77431	−4.36146	−1.55428	(22)
C(6)	−2.11253	−2.88589	−1.17641	(20)
C(7)	−2.80393	−3.42355	0.08145	(31)
O(8)	−3.39412	−3.01862	1.04596	(28)
C(9)	−1.32998	−7.56083	−0.93975	(1)
C(10)	−0.68446	−6.89802	0.43611	(1)
C(11)	−2.48187	−6.44929	−1.60225	(3)
O(12)	−3.64752	−6.62229	−1.21353	(30)
O(13)	−1.98682	−6.89152	−2.65076	(30)
N(14)	−1.07298	−1.85934	−1.16645	(9)
C(15)	−0.56055	1.41466	−0.01015	(3)
O(16)	−0.62932	−2.04747	−1.01807	(7)
H(17)	−1.03750	−4.90483	1.33789	(5)
H(18)	−2.38959	−4.84803	−2.31426	(5)
H(19)	−2.78023	−2.40087	−1.87628	(5)
H(20)	−0.82918	−1.25283	−1.92242	(14)

with a standard basis set. The MMPEN parameterization reported herein is a first step towards this objective. To facilitate the use of MMPEN, Tables 15 and 16 contain Cartesian coordinates of the pseudoaxial and pseudoequatorial conformations of **11**.

There have been many previous theoretical studies on β-lactam compounds, including penicillins (38). Since the antibacterial activities of β-lactam compounds are known to be the result of acylation of the active site serines of a group of serine proteases (39), the majority of the molecular orbital

Can. J. Chem. Downloaded from www.nrcresearchpress.com by 196.1.178.254 on 09/07/12
For personal use only.

calculations have focused on properties of azetidinone rings, including the charge distribution in the N—CO region, and the pyramidality of the nitrogen atom.

It is not surprising that β-lactam antibiotics do not exhibit unusual reactivities or hydrolysis mechanisms (40). The antibacterial activity of a penicillin must depend not only on the intrinsic chemical reactivity of its β-lactam ring, but on the ability of the compound to reach its site of action and bind to it. This binding involves the action of the entire molecule, and not just that portion that undergoes the chemical change. With this view, an ability to treat the conformation of the entire molecule may be useful.

Studies towards this goal have been initiated by Rao (38), and by Cohen (10). Rao's approach is based on a first generation molecular mechanics strategy. A hard sphere model is employed, methyl groups are treated as united atoms, and a single threefold torsional term is used. Side chains are minimized, but with the amide bond oriented as in the crystal structure of penicillin G. Cohen focuses on the pseudoaxial–pseudoequatorial relationship, using a combination of crystal structures and the molecular modelling system SCRIPT (41). Side chains are not considered.

Although the conclusions reached by Rao and by Cohen may be valid, we do not know how to reproduce their results, because of the limited documentation of the procedures used. This lack of documentation obviously inhibits the ability of other groups to contribute to these problems. We hope that this apparent absence of (published) activity can be overcome by the development and publication of MMPEN. Extensions of the MMPEN approach to other classes of β-lactam antibiotics are currently in progress.

Acknowledgements

The authors thank the Natural Sciences and Engineering Research Council of Canada for financial support, the Medical Research Council of Canada and the Province of Ontario for the award of Graduate Fellowships, Queen's University for generous allocation of computer time, and Dr. Keith Davies for permission to use the SNOOPI option of CHEMGRAF.

1. N. L. ALLINGER. MMP2(85). Quantum Chemistry Program Exchange, Bloomington, In.
2. S. WOLFE, D. F. WEAVER, and K. YANG. Can. J. Chem. **66**, 2687 (1988).
3. V. I. LIM. J. Mol. Biol. **88**, 873 (1974); P. Y. CHOU and G. D. FASMAN. Ann. Rev. Biochem. **47**, 251 (1978)-; J. M. LEVIN, B. ROBSON, and J. GARNIER. FEBS Lett. **205**, 303 (1986). W. KLABSCH and C. SANDER. FEBS Lett. **155**, 179 (1983).
4. F. A. MOMANY, R. F. MCGUIRE, A. W. BURGESS, and H. A. SCHERAGA. J. Phys. Chem. **79**, 2361 (1975); G. NÉMETHY, M. S. POTTLE, and H. A. SHERAGA. J. Phys. Chem. **87**, 1883 (1983).
5. S. WOLFE, S. BRUDER, D. F. WEAVER, and K. YANG. Can. J. Chem. **66**, 2703 (1988).
6. S. WOLFE, A. L. DEMAIN, S. E. JENSEN, and D. W. S. WESTLAKE. Science, **226**, 1386 (1984).
7. P. BLANPAIN and F. DURANT. Cryst. Struct. Commun. **6**, 711 (1977).
8. M. O. BOLES, R. J. GIRVEN, and P. A. C. GANE. Acta Crystallogr. Sect B: Struct. Crystallogr. Cryst. Chem. **34**, 461 (1978); R. M. SWEET. *In* Cephalosporins and penicillins. *Edited by* E. H. Flynn. Academic Press, New York. 1972. p. 281.
9. A. BALSAMO, P. DOMIANO, B. MACCHIA, F. MACCHIA, and M. NARDELLI. Eur. J. Med. Chem. **15**, 559 (1980).
10. N. C. COHEN. Actual. Chim. (5), 7 (1983); J. Med. Chem. **26**, 259 (1983).
11. C. M. DOBSON, L. O. FORD, S. E. SUMMERS, and R. J. P. WILLIAMS. J. Chem. Soc. Faraday Trans 2, **71**, 1145 (1975).
12. B. A. LEVINE and R. J. P. WILLIAMS. Proc. R. Soc. London, A: **345**, 5 (1975).
13. F. FRANKS, J. R. HALL, D. E. IRISH, and K. NORRIS. Carbohydrate Res. **157**, 53 (1986).
14. D. D. DEXTER and J. M. VAN DER VEEN. J. Chem. Soc. Perkin Trans. 1. 185 (1978).
15. U. BURKERT and N. L. ALLINGER. Molecular mechanics. American Chemical Society, Washington, DC. 1982.
16. S. J. WEINER, P. A. KOLLMAN, D. A. CASE, U. CHANDRA SINGH, C. GHIO, G. ALAGONA, S. PROFETA, JR., and P. WEINER. J. Am. Chem. Soc. **106**, 765 (1984).
17. S. ABRAHAMSSON, D. CROWFOOT HODGKIN, and E. N. MASLEN. Biochem. J. **86**, 514 (1963).
18. G. J. PITT. Acta Crystallogr. 770 (1952).
19. P. BLANPAIN and F. DURANT. Cryst. Struct. Commun. **5**, 83 (1976).
20. M. O. BOLES and R. J. GIRVEN. Acta Crystallogr. Sect. B: Struct. Crystallogr. Cryst. Chem. **32**, 2279 (1976).
21. P. BLANPAIN, M. MELEBECK, and F. DURANT. Acta Crystallogr. Sect. B: Struct. Crystallogr. Cryst. Chem. **33**, 580 (1977).
22. P. BLANPAIN, G. LAURENT, and F. DURANT. Bull. Soc. Chim. Belg. **85**, 767 (1977).
23. T. B. PALM and I. CSÖREGH. Acta Crystallogr. Sect. B: Struct. Crystallogr. Cryst. Chem. **34**, 138 (1978).
24. F. M. LOVELL and N. A. PERKINSON. Cryst. Struct. Commun. **7**, 7 (1978).
25. K. HANAI, Y. MAKI, and A. KUWAE. Bull. Chem. Soc. Jpn. **58**, 1367 (1985).
26. M. GUILLIANO, G. MILLE, T. AVIGNON, and J. CHOUTEAU. J. Raman Spectrosc. **7**, 214 (1978).
27. T. HIRANO and E. OSAWA. Croat. Chem. Acta, **57**, 1633 (1984).
28. A. J. HOPFINGER and R. A. PEARLSTEIN. J. Comput. Chem. **5**, 486 (1984).
29. D. H. WERTZ and N. L. ALLINGER. Tetrahedron, **35**, 3 (1975).
30. T. CLARK. Handbook of computational chemistry. John Wiley, New York. 1985.
31. P. J. COX, J. MCCLURE, and G. A. SIM. J. Chem. Soc. Perkin Trans. 2, 360 (1974).
32. D. U. BELINZONI, O. A. MASCARETTI, P. M. ALZARI, G. PUNTE, C. FAERMAN, and A. PODJARNY. Can. J. Chem. **63**, 3177 (1985).
33. R. S. MORGAN, C. E. TATSCH, R. H. GUSHARD, J. M. MCADON, and P. K. WARME. Int. J. Pept. Protein Res. **11**, 209 (1978); R. S. MORGAN and J. M. MCADON. Int. J. Pept. Protein Res. **15**, 177 (1980); K. S. C. REID, P. F. LINDLEY, and J. M. THORNTON. FEBS Lett. **190**, 209 (1985); M. LEBL, E. E. SUGG, and V. R. HRUBY. Int. J. Pept. Protein Res. **29**, 40 (1987).
34. N. J. CLAYDEN, C. M. DOBSON, L-Y. LIAN, and J. M. TWYMAN. J. Chem. Soc. Perkin Trans. 2, 1933 (1986).
35. N. F. OSBORNE. J. Chem. Soc. Perkin Trans. 1, 150 (1980).
36. R. D. G. COOPER, P. V. DEMARCO, J. C. CHENG, and N. D. JONES. J. Am. Chem. Soc. **91**, 1408 (1969).
37. S. WOLFE, K. YANG, and M. KHALIL. Can. J. Chem. **66**, 2733 (1988).
38. W. C. TOPP and B. G. CHRISTENSEN. J. Med. Chem. **17**, 342 (1974); D. B. BOYD, R. B. HERMANN, D. E. PRESTI, and M. MARSH. J. Med. Chem. **18**, 408 (1975); H.-D. HÖLTJE. Arch. Pharm. **309**, 26 (1976); D. B. BOYD. Proc. Natl. Acad. Sci. U.S.A. **74**, 5239 (1977); R. VIRUDACHALAM and V. S. R. RAO. Int. J. Pept. Protein Res. **10** 51 (1977); N. V. JOSHI, R. VIRUDACHALAM, and V. S. R. RAO. Curr. Sci. **47**, 933 (1978); D. B. BOYD. J. Med. Chem. **22**, 533 (1979); C. PETRONGOLO, G. RANGHINO, and R. SCORDAMAGLIA. Chem. Phys. **45**, 279 (1980); C. PETRONGOLO, E. PESCATORI, G. RANGHINO, and R. SCORDAMAGLIA. Chem. Phys. **45**, 291 (1980); C. PETRONGOLO and G.

RANGHINO. Theor. Chim. Acta, **54**, 239 (1981); T. K. VASUDEVAN and V. S. R. RAO. Biopolymers, **20**, 865 (1981); D. B. BOYD. Ann. N.Y. Acad. Sci. **367**, 531 (1981); C. GLIDEWELL and G. S. M. MOLLISON. J. Mol. Struct. **72**, 203 (1981); N. V. JOSHI and V. S. R. RAO. J. Biosci. **4**, 209 (1982); T. K. VASUDEVAN and V. S. R. RAO. Curr. Sci. **51**, 402 (1982); T. K. VASUDEVAN and V. S. R. RAO. Int. J. Biol. Macromol. **4**, 347 (1982); T. VASUDEVAN and V. S. R. RAO. Int. J. Biol. Macromol. **4**, 219 (1982); V. S. R. RAO and T. K. VASUDEVAN. CRC Crit. Rev. Biochem. **14**, 173 (1983); S. VISHVESHWARA and V. S. R. RAO. J. Mol. Struct. (Theochem), **92**, 19 (1983); V. S. R. RAO. *In* The target of penicillin. *Edited by* R. Hackenbeck, J.-V. Höltje, and H. Labischinski. Walter de Gruyter, Berlin. 1983. p. 359.

39. L. VARETTO, J.-M. FRÈRE, M. NGUYEN-DISTÈCHE, J.-M. GHUYSEN, and C. HOUSSIER. Eur. J. Biochem. **162**, 525 (1987), and references cited therein.
40. M. I. PAGE. Acc. Chem. Res. **17**, 144 (1984).
41. N. C. COHEN, P. COLIN, and G. LEMOINE. Tetrahedron, **37**, 1711 (1981).

Can. J. Chem. Downloaded from www.nrcresearchpress.com by 196.1.178.254 on 09/07/12
For personal use only.

Conformation–activity relationships and the mechanism of action of penicillin

SAUL WOLFE,[1] KIYULL YANG, AND MAGED KHALIL
Department of Chemistry, Queen's University, Kingston, Ont., Canada K7L 3N6
Received September 22, 1987[2]

SAUL WOLFE, KIYULL YANG, and MAGED KHALIL. Can. J. Chem. **66**, 2733 (1988).

Using the MMPEN parameters of Allinger's MMP2(85) force field, a conformational analysis has been performed on four biologically active penicillins: D-ampicillin, L-α-phenoxyethylpenicillin, penicillin G, and penicillin V, and on five biologically inactive or much less active penicillins: L-ampicillin, D-α-phenoxyethylpenicillin, *N*-methylpenicillin G, 6α-methylpenicillin G, and bisnorpenicillin G. Antibacterial activity is found to be associated with the existence of a global minimum having a compact structure, whose convex face is accessible to a penicillin binding protein (PBP), with the C3-carboxyl group and the side-chain N-H exposed on this face. Using the MMPEP parameters of MMP2(85), a conformational analysis has been performed on phenylacetyl-D-Ala-D-Ala-O^-, a peptide model of the normal substrate of a PBP. Labischinski's global minimum has been reproduced, along with structures that correspond to Tipper and Strominger's proposal that the N4—C7 bond of a penicillin corresponds to the Ala–Ala peptide bond, and to Hasan's proposal that the N4—C5 bond of penicillin corresponds to the peptide bond. For both models, conformations of the peptide related to the pseudoaxial and pseudoequatorial conformations of the thiazolidine ring of penicillin G have been examined. It is concluded that penicillin is not a structural analog of the global minimum of the peptide; however, comparisons based on unbound conformations of PBP substrates are unable to determine which model is more appropriate, or which conformation of penicillin G is the biologically significant one. Using the ECEPP/MMPEP strategy, a model of the active site of a PBP has been obtained, following a search of 200,000 structures of the peptide Ac-NH-Val-Gly-Ser-Val-Thr-Lys-NH-Me. This peptide contains the sequence at the active site of a PBP of *Streptomyces* R61, for which it is also known that the C3-carboxyl group of penicillin binds to the ε-amino group of lysine, and the β-lactam reacts chemically with the serine OH. The lysine and serine side chains and the C-terminal carbonyl group are found to occupy the concave face of the active site model.

A strategy for the docking of penicillins or peptides to this model, with full minimization of the conformational energies of the complexes, has been devised. All active penicillins bind through strong hydrogen bonds to the C3-carboxyl group and the side-chain N-H, and with a four-centered relationship between the O-H of serine and the (O)C-N of the β-lactam ring. The geometrical parameters of this relationship are reminiscent of those found in the *gas phase* transition state of *neutral* hydration of a carbonyl group. When the energies of formation and geometries of the pseudoaxial and pseudoequatorial penicillin G complexes are examined, there is now a clear preference for the binding of the *pseudoaxial* conformation, which is the global minimum of the uncomplexed penicillin in this case. A similar examination of the peptide complexes reveals that only the conformation of the peptide that corresponds to Tipper and Strominger's model, and is based on the pseudoaxial conformation of penicillin G, can form a complex with a geometry and energy comparable to those of a biologically active penicillin.

SAUL WOLFE, KIYULL YANG et MAGED KHALIL. Can. J. Chem. **66**, 2733 (1988).

Utilisant les paramètres MMPEN du champ de force MMP2(85) d'Allinger, on a effectué une analyse conformationnelle sur quatre pénicillines biologiquement actives (D-ampicilline, L-α-phénoxyéthylpénicilline, pénicilline G et pénicilline V) et sur cinq pénicillines inactives ou beaucoup moins actives (L-ampicilline, D-α-phénoxyéthylpénicilline, *N*-méthylpénicilline, méthyl-6α pénicilline G et bisnorpénicilline G). On a trouvé que l'activité antibactérienne est associée à l'existence d'un minimum global possédant une structure compacte, dont la face convexe est accessible à une protéine pouvant lier une pénicilline (PLP) et qui porte sur cette face un groupement carboxyle en C3 ainsi qu'une chaîne latérale du N-H qui est exposée. Utilisant les paramètres MMPEP du MMP2(85), on a effectué une analyse conformationnelle sur le phénacetyl-D-Ala-D-Ala-O^-, un peptide modèle du substrat normal d'une PLP. On a pu reproduire le minimum global de Labischinski ainsi que les structures qui correspondent à la proposition de Tipper et Strominger concernant le fait que la liaison N4—C7 d'une pénicilline correspond à la liaison Ala–Ala du peptide et à la proposition de Hasan à l'effet que la liaison N4—C5 de la pénicilline correspond à la liaison peptidique. Pour chaçun des modèles, on a examiné les conformations du peptide qui sont reliées aux conformations pseudo-axiale et pseudo-équatoriale du cycle thiazolidine de la pénicilline G. On en conclut que la pénicilline n'est pas un analogue de structure du minimum global du peptide; toutefois, des comparaisons basées sur les conformations qui ne sont pas liées de substrats de PLP ne permettent pas de déterminer quel modèle est le plus approprié ou quelle conformation de la pénicilline G est la plus importante d'un point de vue biologique. Utilisant la stratégie ECEPP/MMPEP et après avoir fait une recherche parmi 200,000 structures du peptide Ac-NH-Val-Gly-Ser-Val-Thr-Lys-NH-Me, on a obtenu un modèle du site actif d'une PLP. Ce peptide contient la séquence du site actif d'une PLP du *Streptomyces* R61 pour lequel on sait aussi que le groupement carboxyle en C3 de la pénicilline se lie au groupement ε-amino de la lysine et que le β-lactame réagit d'une façon chimique avec le OH de la sérine. On a trouvé que les chaînes latérales lysine et sérine ainsi que le groupement carbonyle du terminus-C occupent la face concave du modèle du site actif.

On a mis au point une stratégie d'arrimage des pénicillines ou des peptides à ce modèle; elle comporte une minimisation complète des énergies conformationnelles des complexes. Toutes les pénicillines actives forment des liaisons hydrogènes importantes avec le groupement carboxyle en C3 et avec la chaîne latérale du N-H et aussi, par une relation à quatre centres, entre le O-H de la sérine et le (O)C-N du cycle du β-lactame. Les paramètres géométriques de cette relation ressemblent à ceux qu'on retrouve dans l'état de transition en *phase qazeuse* de l'hydration *neutre* d'un groupement carbonyle. Lorsqu'on examine les énergies de formation et les géométries des complexes pseudo-axial et pseudo-équatorial de la pénicilline G, on observe

---

[1]Author to whom correspondence may be addressed.
[2]Revision received March 29, 1988.

Can. J. Chem. Downloaded from www.nrcresearchpress.com by 196.1.178.254 on 09/07/12
For personal use only.

qu'il existe une préférence marquée pour une liaison de la conformation *pseudo-axiale* qui, dans ce cas, correspond au minimum global de la pénicilline qui n'est pas complexée. Un examen semblable des complexes du peptide révèle que seule la conformation du peptide qui correspond au modèle de Tipper et Strominger et qui est basée sur la conformation pseudo-axiale de la pénicilline G peut former un complexe avec une géométrie et une énergie qui se comparent à celles d'une pénicilline qui est active d'un point de vue biologique.

[Traduit par la revue]

Introduction

β-Lactam compounds manifest their antibacterial activity through an ability to interfere with the biosyntheses of bacterial cell walls (1). This is accomplished, at the molecular level, by covalent binding (2) (see **1**) to the active sites of one or more of a

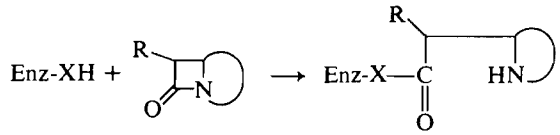

1

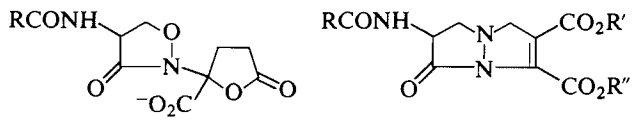

4 **5**

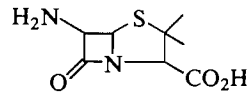

7

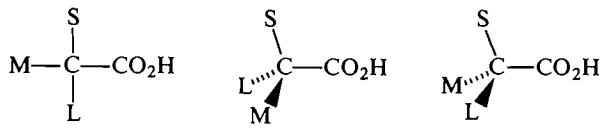

8 **9a** **9b**

group of enzymes termed penicillin binding proteins (PBPs) (3). The PBPs are transpeptidases and (or) carboxypeptidases, whose function in the cytoplasmic membrane (4) is to complete cell wall synthesis by a cross-linking of peptidoglycan chains. The peptide segments of these chains terminate in the sequence R-X-D-Ala-D-Ala (most commonly X = L-Lys or *meso*-diaminopimelate), and the simplest model substrate for PBPs is Ac_2-L-Lys-D-Ala^1-D-Ala^2 (5).

The cross-linking reaction mediated by PBPs, and inhibited by β-lactam antibiotics, is R-X-D-Ala-D-Ala + $H_2NR' \rightarrow$ R-X-D-Ala-NHR′ + D-Ala, where R and R′ belong to different chains. This was discovered, initially for the case of penicillins, in 1965 (6), and Tipper and Strominger proposed that penicillin is a structural analog of *N*-acyl-D-Ala^1-D-Ala^2 (**2**). In their view (Model A), the N4—C7 bond of penicillin corresponds to the D-Ala^1-D-Ala^2 peptide bond, as depicted in **3***a*.

Although Model A has survived for more than 20 years (7), the stereochemical problems that it raises (8) remain unresolved. Thus, C6 of penicillin, which has the L configuration, must correspond to the asymmetric centre of Ala^1, which has the D configuration. However, 6-epipenicillins (8) are inactive (9), and Ac_2-L-Lys-L-Ala-D-Ala is not a substrate for PBPs (10). Since the orientation and nature of the acylamino side chain are critical to the activity of penicillin, a structural analogy between penicillin and **2** based on Model A therefore requires that the Ala^1 methyl group correspond to H6 of penicillin in the

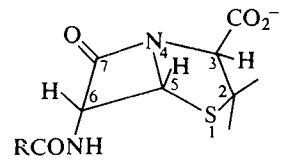

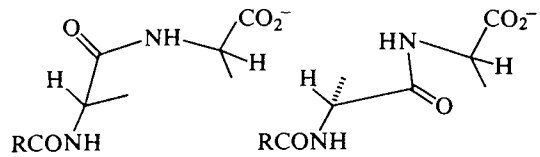

3*a* **3***b*

conformations that bind to the active site of PBP. This point was recognized by Strominger and Tipper (11), who suggested that 6α-methylation of penicillin (see Fig. 5) would improve the structural analogy. The required compounds were synthesized in 1971 (12), and found to be inactive.

The caveats expressed in ref. 8 led (13) to an alternative proposal (Model B) (see **3***b*), in which the N4—*C5* bond of penicillin corresponds to the D-Ala–D-Ala peptide bond, and C6—C7 corresponds to C_α-CH_3 of Ala^1. The effect of Model B is to interchange the oxidation levels of the atoms of **2** that correspond to C5 and C7 of penicillin in the comparison of the two structures. This overcomes the stereochemical problem and, at the same time, maintains similar spatial arrangements of the two side chains.

Two features of Model B were of particular interest (13): (*i*) the *sulfur* atom of penicillin corresponds spatially to the *oxygen* atom of the D-Ala^1–D-Ala^2 peptide bond. This observation suggested that replacement of the sulfur atom by oxygen would improve the analogy, and it stimulated work on synthetic approaches to oxapenicillins and oxacephalosporins (14), which led ultimately to the discovery of Latamoxef, a clinically important antibiotic (15); (*ii*) *the presence of the β-lactam ring is not essential for the structural analogy*; the covalent bonding depicted in **1** only becomes possible after the β-lactam ring has been positioned over X in the primary complex.

Very recently, two non β-lactam structures consistent with (*ii*) have been discovered; lactivicin (**4**, R = CH_3), a natural product (16); and pyrazolidinone **5** (R = *t*-BOC), a synthetic compound (17). Both **4** and **5** inhibit the action of PBPs, and are potent antibacterial agents when R is a side chain known to confer high activity upon penicillins (18).

Although Model B continues to be permissive, we felt that it could not be tested properly until it became possible to carry out detailed analyses of the conformations of penicillins, **2**, and the putative binding site of a PBP in water solvent.

The problems associated with these requirements have now been largely overcome. Thus, the nature of the binding sites of several PBPs has become known in some detail (19); in addition, in several accompanying papers (20), we have described and evaluated procedures for the conformational analysis of peptides and penicillins in water solvent. The theoretical procedures are based on successful parameteriza-

Can. J. Chem. Downloaded from www.nrcresearchpress.com by 196.1.178.254 on 09/07/12
For personal use only.

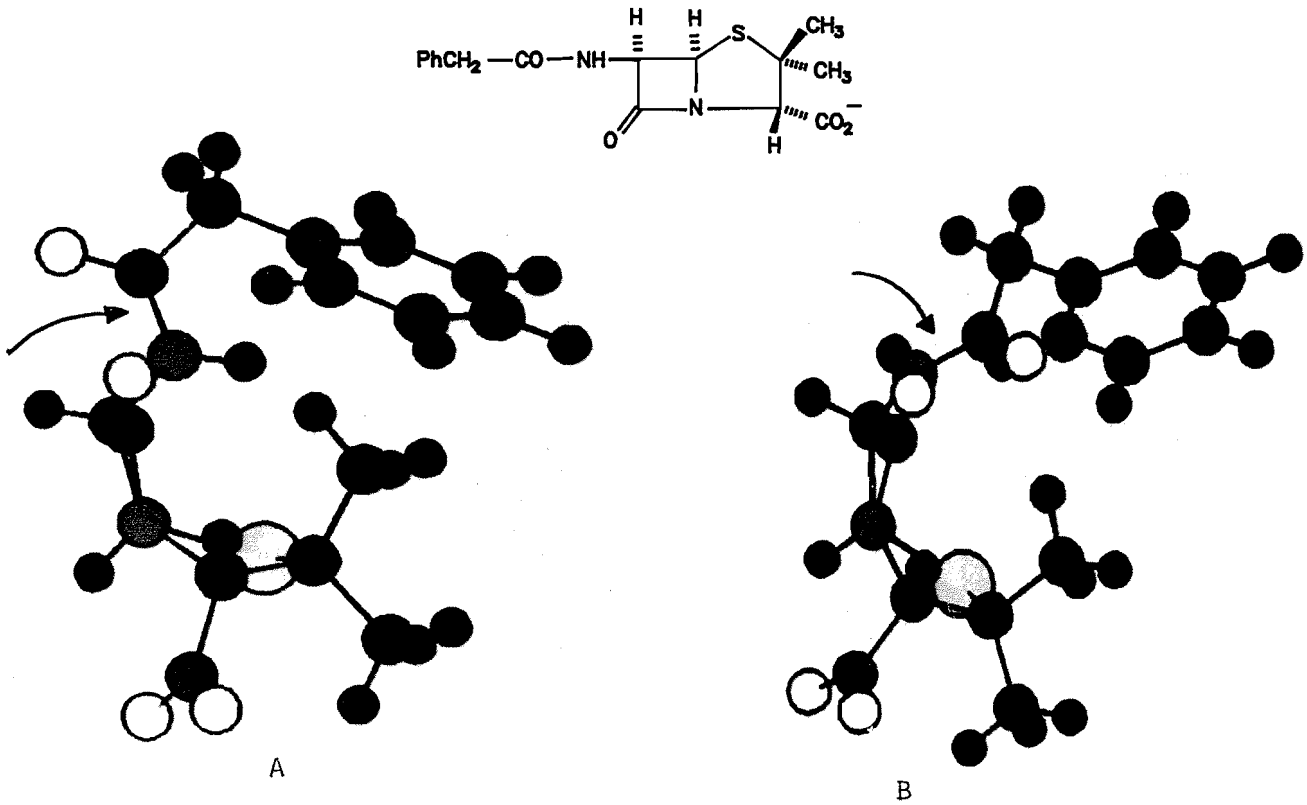

FIG. 1. (A) Crystal structure of penicillin G; (B) Calculated global minimum of penicillin G.

tions of Allinger's well-tested molecular mechanics force field (21, 22) for peptides and penicillins, and the use of MMP2(85) (23) in the computations. The objectives of the present work are, therefore, as follows: (*a*) to examine the conformations of active and inactive penicillin derivatives, in order to map out intramolecular relationships associated with activity; (*b*) to generate, from the coordinates of the global minimum of penicillin G, conformations of $PhCH_2CONH$-D-Ala-D-Ala (**6**) that correspond to Models A and B, to examine the "fit" of the resulting structures to the parent penicillin, and to compare the energies of these conformations of **6** to those obtained in a more general search; (*c*) to carry out a conformational analysis of a hexapeptide that contains the active site of the PBP of *Streptomyces* R61 (24); (*d*) to examine the intermolecular complexes formed between different conformations of penicillin G and the calculated active site, taking into account known experimental features of these complexes (25); (*e*) to determine which calculated conformation of **6** exhibits the best fit to the calculated active site of the PBP.

All calculations were performed with a dielectric constant $\epsilon = 78.5$ (20).

Conformational analysis of active and inactive penicillin derivatives

Figures 1A and 1B recall, respectively, the crystal structure and the calculated global minimum of penicillin G (20*c*). The most important difference is in the orientation of the amide moiety of the side chain (see arrows). In the crystal structure, oxygen is on the convex face and hydrogen on the concave face of the molecule (< H6—C6—N—H = −156°.) The locations of these two atoms are reversed in the calculated structure (< H6—C6—N—H = −36°). The calculated higher energy pseudoequatorial conformation of penicillin G (20*c*) resembles the global minimum in the orientation of its —CO—NH— moiety.

The crystal structure and the calculated structures of penicillin V differ in the same way (20*c*). As will be seen, most of the calculated structures of acylaminopenicillins examined in the present work resemble penicillin G and penicillin V in this respect. On the other hand, the *oxygen–exo* orientations seen in the crystal structures of penicillin G and penicillin V also appear to be general (26). Since the —CO—NH— orientation found in X-ray structures has been assumed in all previous structure–activity studies and comparisons of penicillin with *N*-acyl-D-Ala-D-Ala (26, 27), it is not surprising that the orientation of the amide N-H or, indeed, of the side chain itself, have received only limited attention (28).

However, it has long been known (29) that not only C6-alkylation, but also N-alkylation of penicillin (see Fig. 2) abolishes its antibacterial activity. It is also found (30) that the diastereomeric penicillins formed by acylation of 6-aminopenicillanic acid (**7**) with a carboxylic acid of type **8**, in which S, M, and L refer to small, medium, and large substituents, differ greatly in antibacterial activity; the penicillin formed from **9***a* is significantly more active. Thus, in the case of ampicillin and related penicillins (see Fig. 3), only the D epimers (**9***a*: S = H, M = NH_2, L = Ar) are clinically useful, whereas in the case of α-substituted penicillin V analogs, e.g., α-phenoxyethylpenicillin (see Fig. 4), only the L epimers (**9***a*: S = H, M = alk, L = OAr) are of clinical value. It was clear in

Can. J. Chem. Downloaded from www.nrcresearchpress.com by 196.1.178.254 on 09/07/12
For personal use only.

Can. J. Chem. Downloaded from www.nrcresearchpress.com by 196.1.178.254 on 09/07/12
For personal use only.

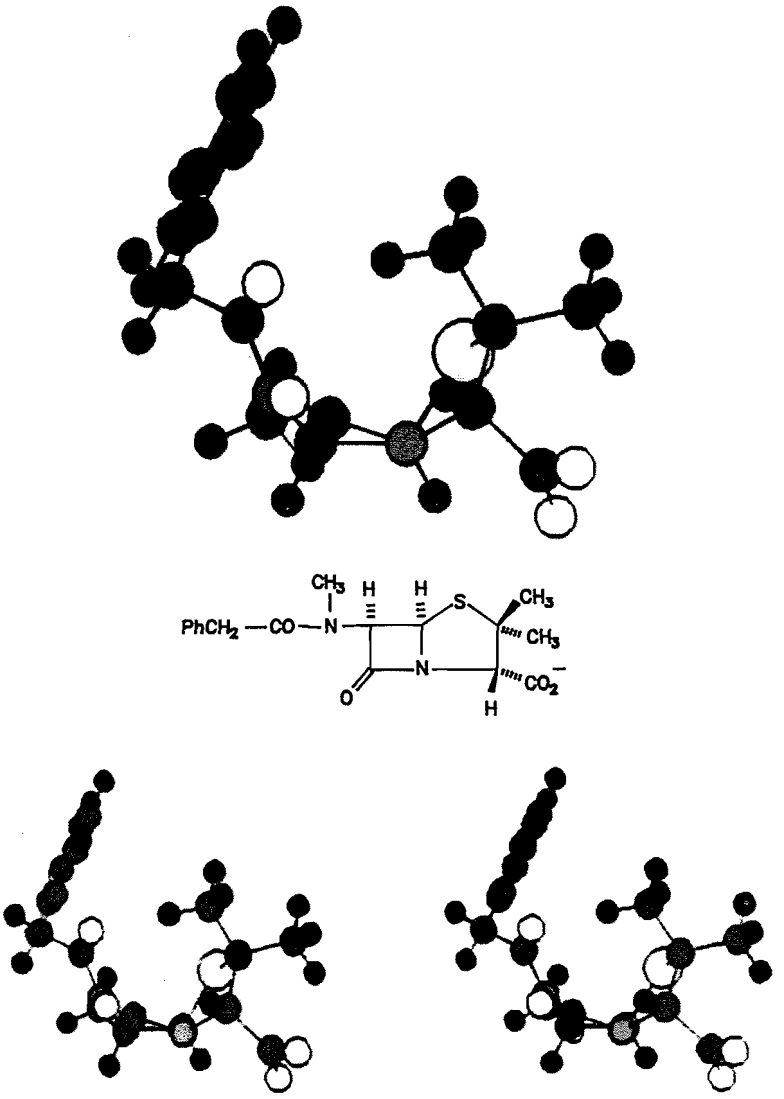

FIG. 2. Calculated structure of *N*-methylpenicillin G.

1961 (30) that such differences in properties must reflect subtle three-dimensional differences in the abilities of side-chain epimers to interact with the penicillin receptor; however, the information and techniques needed to pursue this point did not exist at that time.

Figure 2 shows the calculated structure of *N*-methylpenicillin G. The structure is virtually identical to that found for penicillin G itself: the thiazolidine ring has a pseudoaxial conformation, and the benzyl moiety is folded towards the concave face, leading to a compact molecule. But, whereas in the active compound, penicillin G, N-H points towards a putative receptor, in the inactive *N*-methyl derivative, N-CH_3 occupies the same relative position.

Figures 3A and 3B show, respectively, the calculated structures of D- and L-ampicillin. The D isomer is compact; the L isomer is not (31). In both cases, the amide N-H is on the convex face of the molecule (see arrows in Figs. 3A,B). Interestingly, both epimers have a pseudoequatorial conformation of the thiazolidine ring, as is observed in the crystal structure of D-ampicillin (32).

Figures 4A and 4B show, respectively, the calculated structures of L- and D-α-phenoxyethylpenicillin. In this case, the L isomer is compact and the D isomer is not. Both epimers have a pseudoaxial conformation of the thiazolidine ring and, in both cases, the amide N-H is on the convex face of the molecule (see arrows in Figs. 4A,B)

Significantly, the conformational differences found for these active and inactive penicillin epimers are expressed within the side chains and not within the nuclei. It is difficult to avoid the conclusion that whether the thiazolidine ring is pseudoaxial or pseudoequatorial is less important than has been suggested previously (26).

In both D- and L-ampicillin, the C_α—N and amide N—H bonds are *syn*-periplanar (**10***a,b*). This is the dominant conformational effect, and it causes Ar to reside on the concave face of the molecule in the D isomer, and on the convex face in the L isomer. On the other hand, in both L- and D-α-phenoxyethylpenicillin, the C_α—H and amide C=O bonds are eclipsed (**11***a,b*). This causes Ar to reside on the concave face in the L isomer, and on the convex face in the D isomer.

Can. J. Chem. Downloaded from www.nrcresearchpress.com by 196.1.178.254 on 09/07/12
For personal use only.

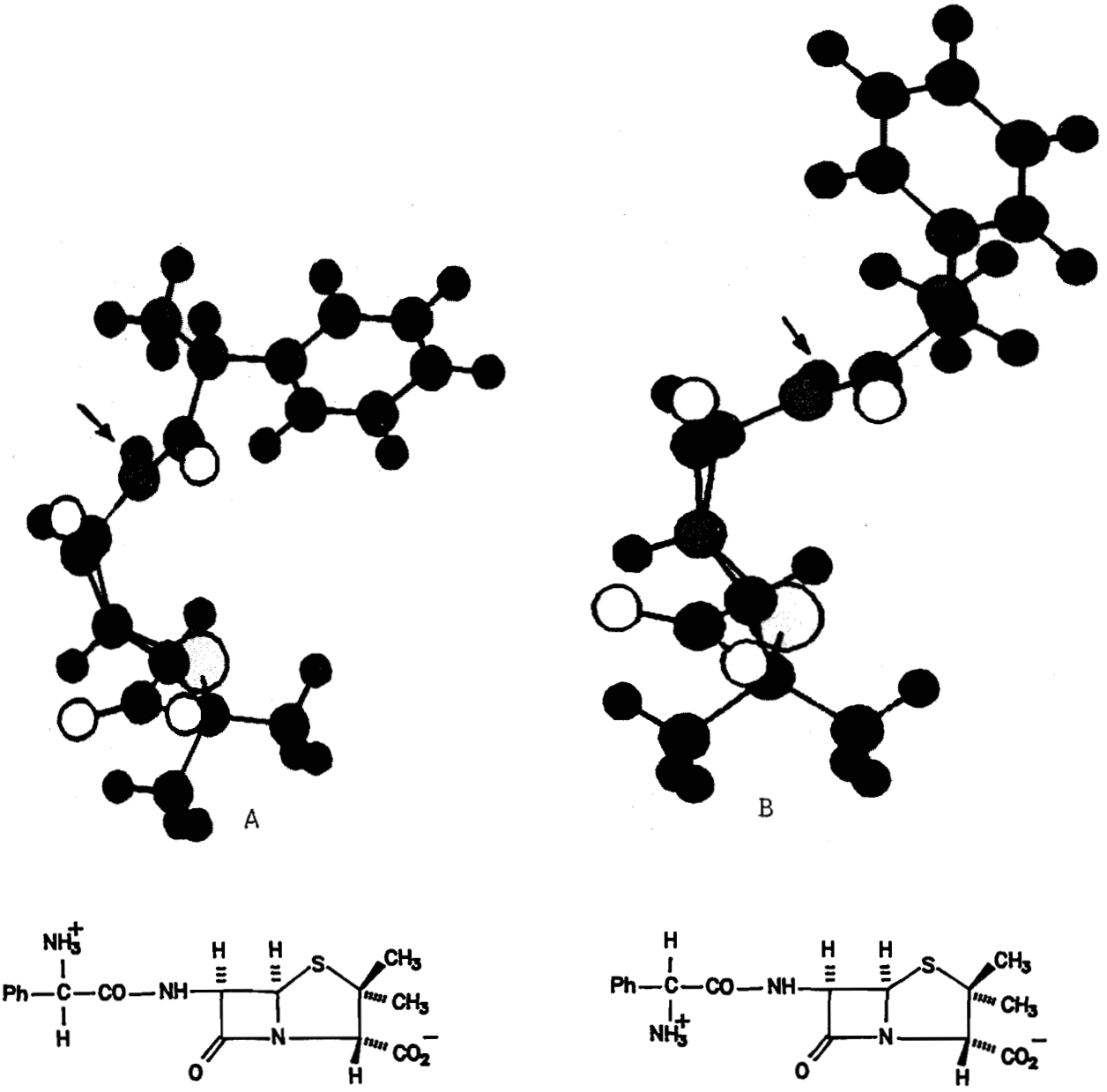

FIG. 3. (A) Calculated structure of D-ampicillin; the amide N-H is indicated by the arrow. (B) Calculated structure of L-ampicillin; the amide N-H is indicated by the arrow.

All of these results are consistent with the hypotheses that the convex face of penicillin is presented to its receptor, and that the carboxyl group and the *amide N-H* are involved in the bonding to this receptor. Since 6-aminopenicillanic acid (**7**), whose amino group is a hydrogen bonding donor at pH 7, is not active, acylation must be necessary to create a hydrogen bonding *acceptor* at this position (33). It is noteworthy that sulfonamide (34), sulfinamide (35), and phosphonamide (36) isosteres of penicillins are active, but the carbon, sulfur, and oxygen isosteres of the NH moiety are not (37).

Figure 5 shows the structure calculated for the biologically inactive 6α-methylpenicillin G. The introduction of the methyl group on the convex face of the molecule causes a significant increase in the dihedral angle with the amide N-H, from −36° in the parent compound to −69° in the derivative. This amide hydrogen has moved towards the concave face of the molecule.

The bisnorpenicillins (**12**; see Fig. 6) comprise a family of penicillin derivatives whose low activity (38) is not understood. Figure 6 is the structure calculated for bisnorpenicillin G. The structure resembles that of penicillin G in several respects: (*i*) the thiazolidine ring has a pseudoaxial conformation; (*ii*) the benzene ring is folded on the concave face of the molecule; (*iii*) the β-lactam nitrogen is significantly nonplanar. The sum of the angles at this nitrogen atom is 334.4°, compared to 335.8° in penicillin G. *However, the orientation of the amide N-H is significantly different.* In bisnorpenicillin G, the

Can. J. Chem. Downloaded from www.nrcresearchpress.com by 196.1.178.254 on 09/07/12
For personal use only.

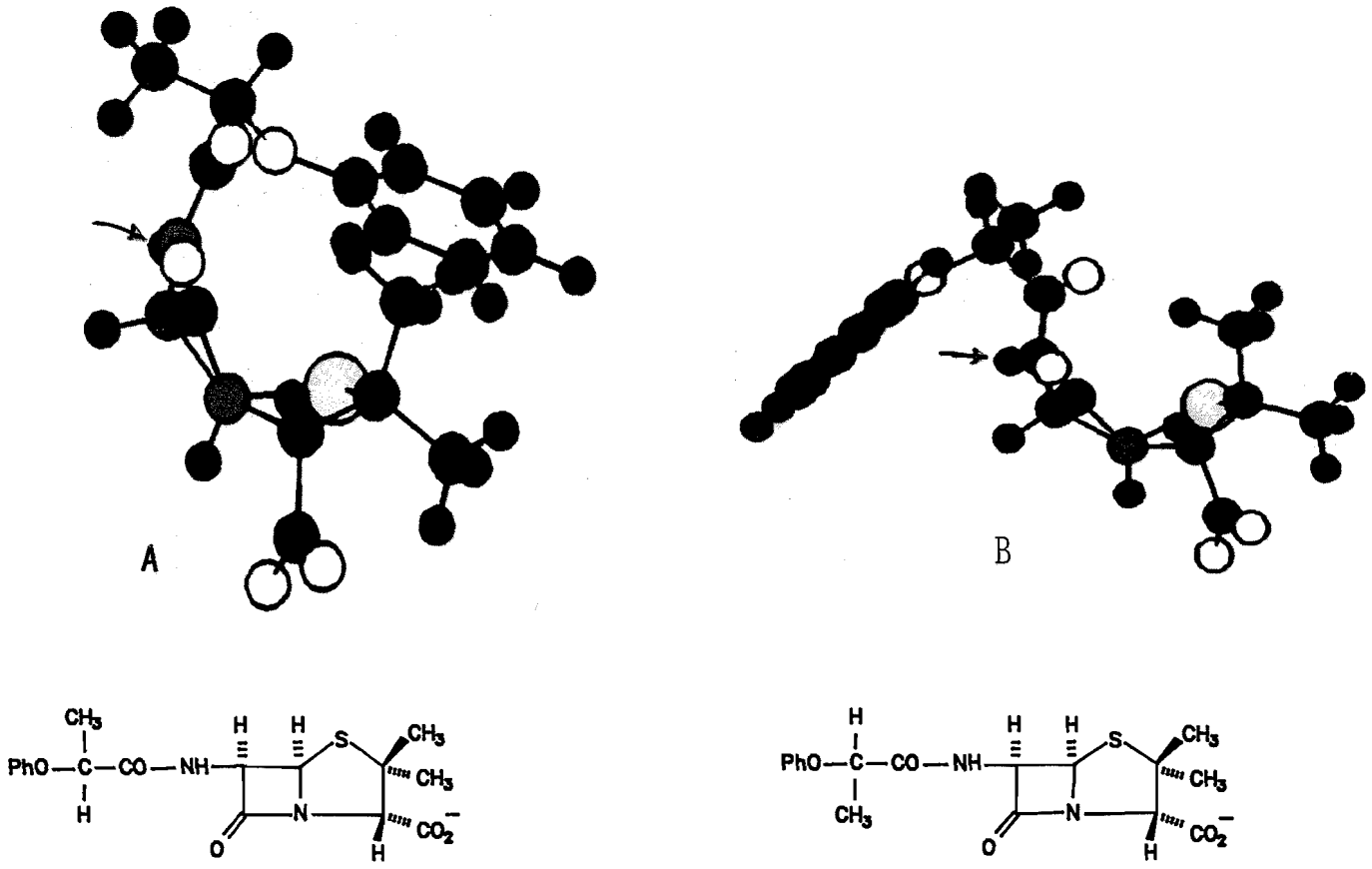

FIG. 4. (A) Calculated structure of L-α-phenoxyethylpenicillin; the amide N-H is indicated by the arrow. (B) Calculated structure of D-α-phenoxyethylpenicillin; the amide N-H is indicated by the arrow.

H—N—C6—H6 dihedral angle has increased from −36° to −60°. As in 6α-methylpenicillin G, the amide hydrogen has moved towards the concave face of the molecule.

All of these results continue to be consistent with the view that the amide N-H of the penicillin side chain participates in binding to the penicillin receptor.

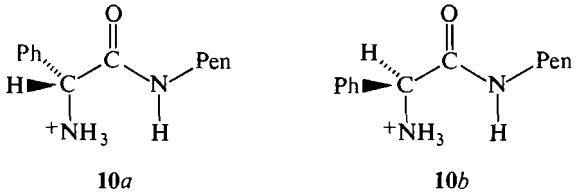

10*a*

10*b*

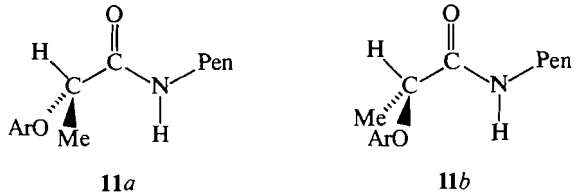

11*a*

11*b*

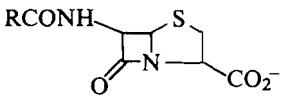

12

Conformational analysis of phenylacetyl-D-alanyl-D-alanine

Labischinski *et al.* (27) have carried out a conformational analysis on the non-ionized form of **6**, using ECEPP (39). Their calculations, presumably with a dielectric constant $\epsilon = 2.0$ D, identified 55 low energy conformations within 3 kcal/mol of their lowest energy structure, here termed **6*L***, and shown in Fig. 7. This structure was reproduced, within the MMPEP parameterization of MM85 (20*a*), in the following manner: (*i*) a one-point ECEPP calculation was performed on Ac-NH-D-Ala-D-Ala-O$^-$ with a dielectric constant $\epsilon = 78.5$ D (20*b*), using the (ϕ,ψ) dihedral angles of **6*L*** (ϕ_1,$\psi_1 = 75,42$; ϕ_2,$\psi_2 = 154,-164$); (*ii*) from the resulting MM85 input file (20*b*), six starting geometries of **6** were generated by replacement of acetyl methyl hydrogens by a phenyl group in two possible orientations (23); (*iii*) each of these six was minimized, using MMPEP and a dielectric constant $\epsilon = 78.5$ D (20*b*). One of the six minimized structures, **6*LA***, was significantly lower in energy than the others. This structure has (ϕ_1,ψ_1) = (56,42) and (ϕ_2,ψ_2) = (159,−120) (see Fig. 7). As shown in Fig. 8, **6*LA*** corresponds to **6*L*** (Fig. 7), except for the orientation of the terminal carboxylate group. The carboxyl orientation of **6*L*** is not a minimum in **6*LA***.

The skeleton of **6*LA*** does not have the conformation that seems to be associated with antibacterial activity in a penicillin.

Can. J. Chem. Downloaded from www.nrcresearchpress.com by 196.1.178.254 on 09/07/12
For personal use only.

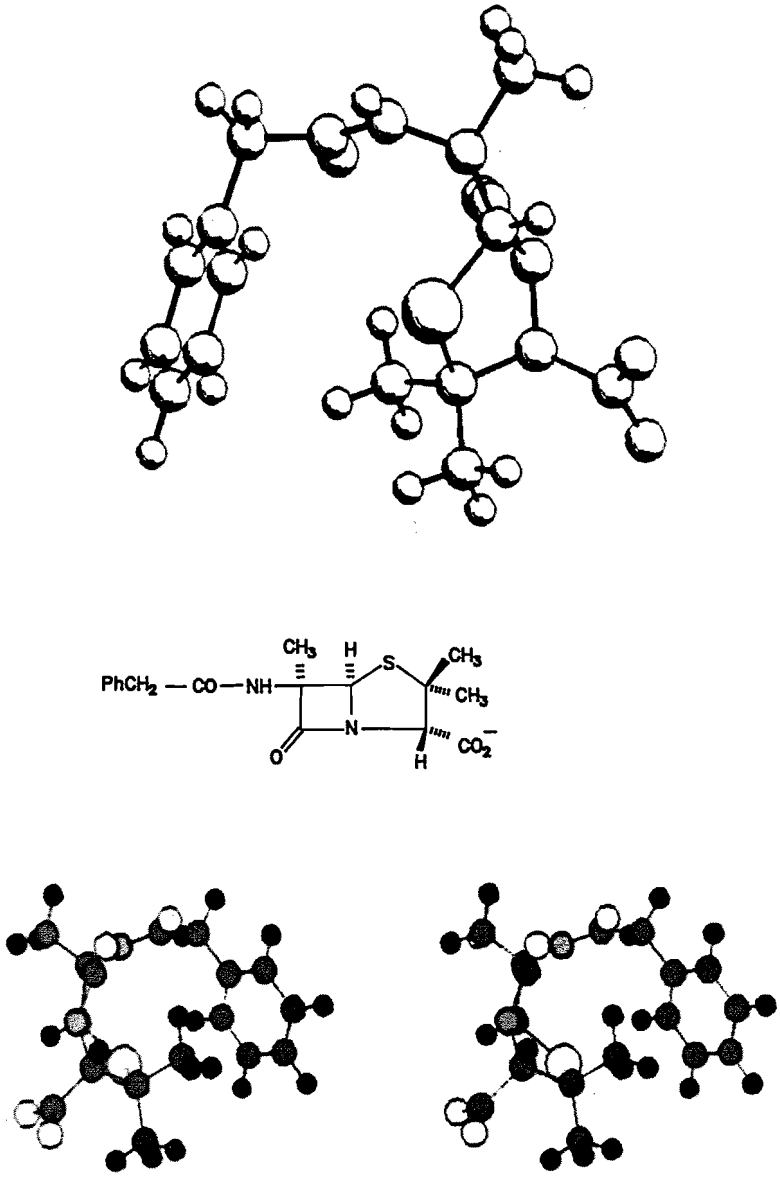

FIG. 5. Calculated structure of 6α-methylpenicillin G.

In particular, the H—N—C—H dihedral angle of **6***LA* that mimics H—N—C6—H6 of penicillin is +121° compared to −36°.

To obtain conformations of **6** that correspond more closely to the essential portions of the penicillin skeleton, we began with the Cartesian coordinates of the pseudoaxial and pseudoequatorial conformations of penicillin G. These were truncated, to obtain initial geometries appropriate for Model A and for Model B. As shown in Scheme 1, to simulate Model A, the two conformations of penicillin G were truncated to **13**. The atom type of H_A was then changed from *5* to *1* (to correspond to the sp^3 carbon), and hydrogens were added to this carbon, and at B, C, and D, to give $\mathbf{6}A_{ax}$ and $\mathbf{6}A_{eq}$. To simulate Model B, the two conformations of penicillin G were truncated to **14**, C_A was changed to atom type *1*, and C_B to atom type *3*; a carbonyl oxygen was then added at B, and hydrogens at A, C, and D, to give $\mathbf{6}B_{ax}$ and $\mathbf{6}B_{eq}$. Each of $\mathbf{6}A_{ax}$, $\mathbf{6}A_{eq}$, $\mathbf{6}B_{ax}$, and $\mathbf{6}B_{eq}$ was then minimized, using MMPEP and $\epsilon = 78.5$ D.

Table 1 summarizes the relative energies and dihedral angles of the five conformations of **6** examined in this work. Figures 9 and 10 show, respectively, superpositions of $\mathbf{6}A_{ax}$ and $\mathbf{6}B_{ax}$ on the pseudoaxial conformation of penicillin G. Close inspection of these diastereoscopic views reveals that the methyl group of Ala^1 projects onto the convex face of penicillin in the case of $\mathbf{6}A_{ax}$, but is perpendicular to this face in $\mathbf{6}B_{ax}$. For a more quantitative evaluation of the fits, the coordinates of **15** and **16** were generated from the pseudoaxial, and also from the pseudoequatorial conformations of penicillin G, and the rms deviations between **15** and the corresponding atoms of $\mathbf{6}A_{ax}$ and $\mathbf{6}A_{eq}$, and between **16** and the corresponding atoms of $\mathbf{6}B_{ax}$ and $\mathbf{6}B_{eq}$, were calculated. These are included in Table 1.

The data of Table 1 allow several tentative conclusions at this

Can. J. Chem. Downloaded from www.nrcresearchpress.com by 196.1.178.254 on 09/07/12
For personal use only.

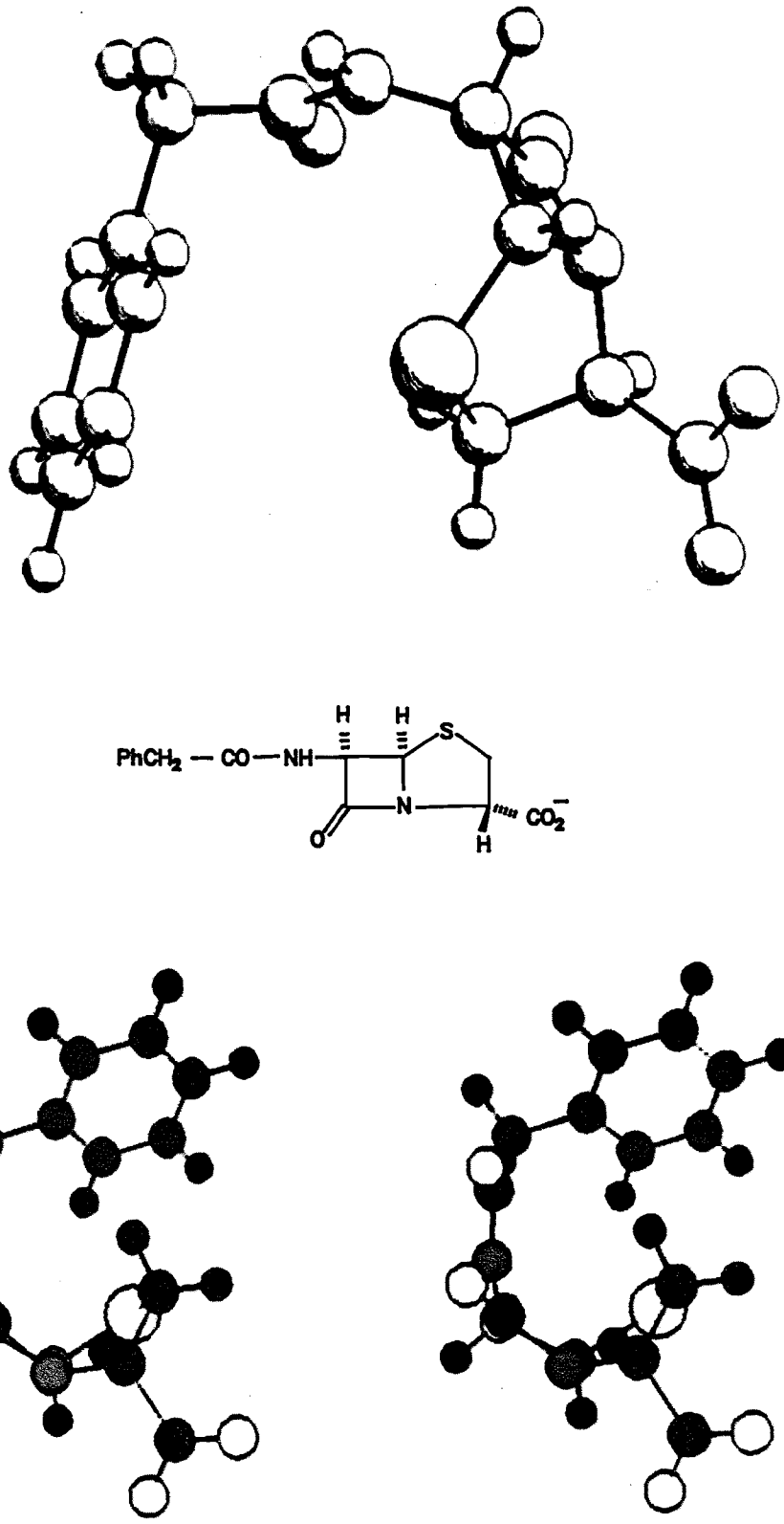

FIG. 6. Calculated structure of bisnorpenicillin G.

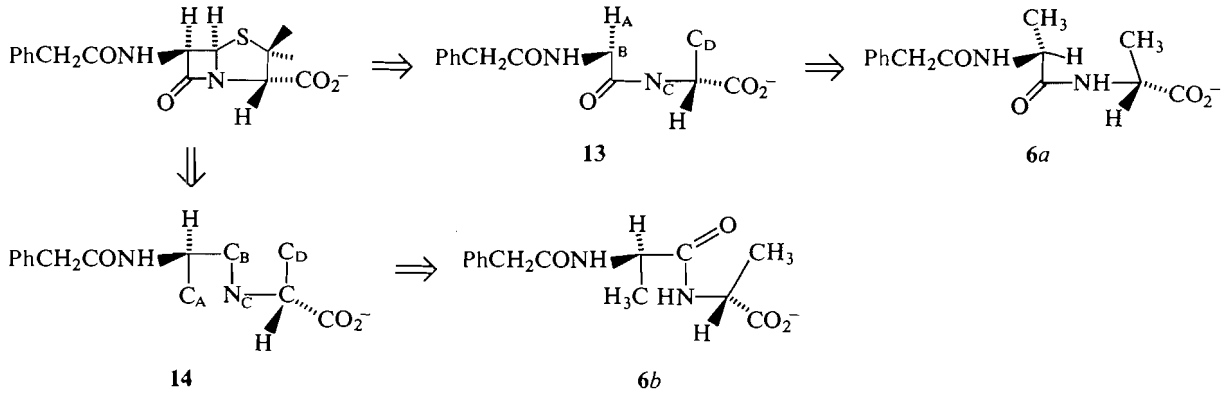

13 6a

14 6b

SCHEME 1

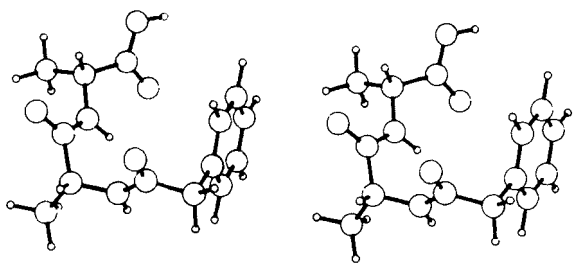

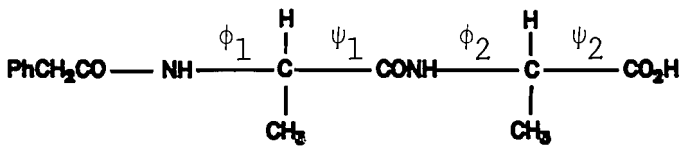

FIG. 7. Lowest energy structure of $PhCH_2CONH$-D-Ala-D-Ala-OH (from ref. 27).

TABLE 1. Relative energies (kcal/mol) and (ϕ,ψ) dihedral angles of various conformations of **6**

Conformation	Relative energy	Dihedral angles (deg) $\phi1$	$\psi1$	$\phi2$	$\psi2$	RMS[a]
6*LA*[b]	0.00	56	42	159	120	
6*A*$_{ax}$[c]	2.07	59	−151	153	−131	0.87
6*B*$_{eq}$[d]	2.56	−52	150	165	−127	0.71
6*B*$_{ax}$[e]	2.92	−62	146	−60	−60	0.95
6*A*$_{eq}$[f]	2.88	46	−127	61	−135	0.74

[a]Refers to the root-mean-square fit, in Å, between the coordinates of the peptide and the coordinates of the corresponding atoms of penicillin G (see text).
[b]Corresponds to the lowest energy structure of ref. 27.
[c]Corresponds to Model A, from pseudoaxial penicillin G.
[d]Corresponds to Model B, from pseudoequatorial penicillin G.
[e]Corresponds to Model B, from pseudoaxial penicillin G.
[f]Corresponds to Model A, from pseudoequatorial penicillin G.

stage: (*i*) the conformation of **6** of which penicillin is a structural analog is not the global minimum of this peptide; (*ii*) based on their structural analogy to the appropriate atoms of penicillin G, Models A and B are equally valid; (*iii*) it is not yet possible to state which conformation of the thiazolidine ring is bound to the penicillin receptor. Additional insights require information concerning the active site of a penicillin binding protein.

Modeling the active site of a penicillin-binding protein

The PBPs have been defined (3) as those bacterial proteins that bind penicillins and other β-lactam antibiotics covalently. For any organism, these are numbered 1,2,..., in order of decreasing molecular weight. The higher molecular weight PBPs of *E. coli* (PBPs 1a, 1b, 2, 3) are essential to the cell, and are the killing sites of the antibiotics (40). The lower molecular weight PBPs (PBPs 4, 5, 6) are D-alanine carboxypeptidases.

Regardless of their origin or molecular weight, each of the PBPs whose sequence and (or) active site region have so far been determined has been found to contain a unique serine residue that reacts with penicillin G (see **1**), and is followed in the sequence by X-X-Lys (41, 42).

The active site serine D-alanyl carboxypeptidase-transpeptidase of *Streptomyces* R61 (M_r 38,000) has been crystallized with incorporation of β-lactam compounds (19, 24), and the crystal structure has been partially solved. The pH dependence of the same enzyme has also been examined (25). Both kinds of studies strongly suggest that the carboxyl group of a penicillin is closely associated with the protonated ε-amino group of the lysine residue of X-X-Lys. The X-ray structure confirms that, in the complex, the β-lactam ring of penicillin is in close proximity to the active site serine; the pH-dependence study rules out involvement of a histidine residue in the chemical process, in

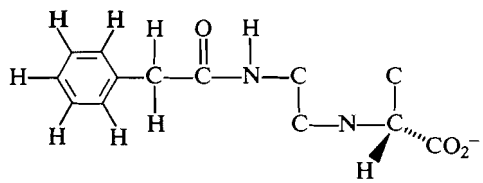

15

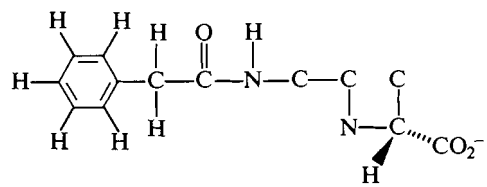

16

Can. J. Chem. Downloaded from www.nrcresearchpress.com by 196.1.178.254 on 09/07/12
For personal use only.

Can. J. Chem. Downloaded from www.nrcresearchpress.com by 196.1.178.254 on 09/07/12
For personal use only.

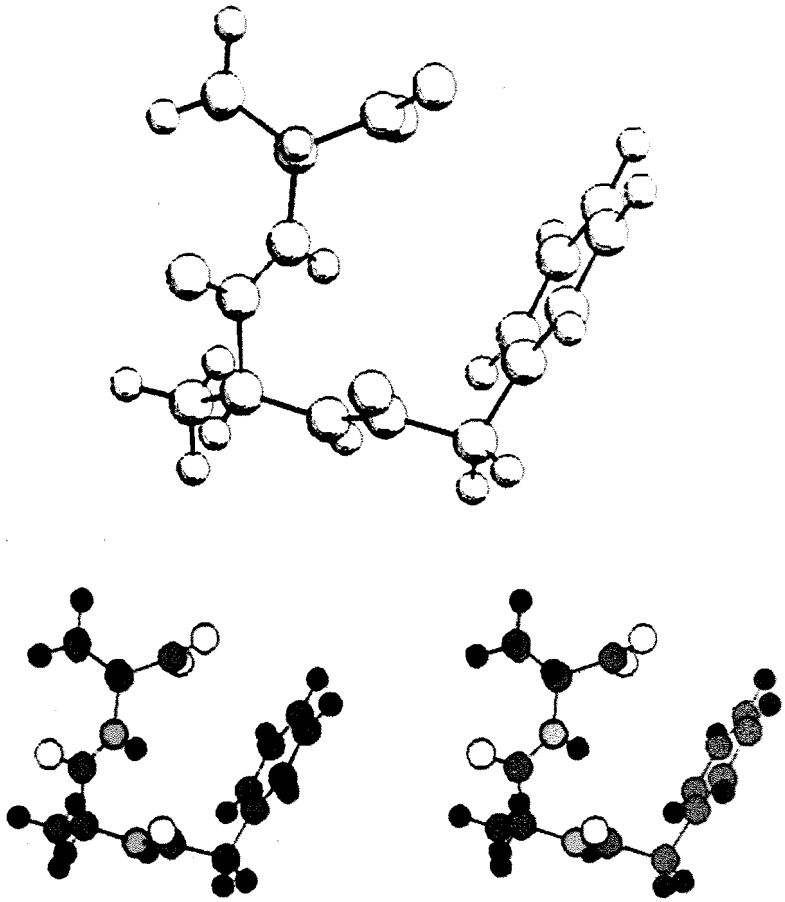

FIG. 8. Structure of **6***LA* corresponding to the structure of ref. 27.

contrast to the behaviour of chymotrypsin and related serine peptidases.

These observations suggest that, even in the absence of published atomic coordinates for this enzyme, it might be possible to obtain a valid model of the active site solely in terms of the amino acids that surround the unique serine residue, viz., Val-Gly-Ser-Val-Thr-Lys. Accordingly, the peptide Ac-HN-Val-Gly-Ser-Val-Thr-Lys-NH-Me was subjected to a theoretical conformational analysis at $\epsilon = 78.5$ D, using an initial ECEPP search of 200,000 structures (20*b*), followed by MMPEP refinement (20*a*,*b*) of 50 low energy structures identified in this search. Attention was focused, especially, on conformations that placed the serine and lysine side chains in proximity. One such structure, ca. 1.0 kcal/mol higher in energy than the lowest energy structure, was found. This structure (**17**), after further dihedral drive refinement of the serine and lysine side chains and the N-terminus, is shown in Fig. 11. The dihedral angles of **17** are summarized in Table 2.

Structure **17** has several features of interest. The convex face is mainly hydrophobic, and the concave face, which includes the serine and lysine side chains, is mainly hydrophilic. The concave face also contains the amide oxygen of the N-terminal acetyl group. The existence of a lock-and-key relationship (43) between the concave face of **17** and the convex face of a penicillin seems inherently appealing and, in terms of such a relationship, the role of the amide N-H of the penicillin side chain becomes clear: there is an N—H...O=C hydrogen bond between this hydrogen of penicillin and the N-terminal carbonyl oxygen of **17**.

We therefore wish to examine a supermolecule in which **17** is docked (44) to a penicillin or peptide through $-NH_3^+ \ldots {}^-O_2C-$ and N—H...O=C interactions. The MMPEP (20*a*) and MMPEN (20*c*) parameterizations of MMP2(85) allow Allinger's complete force field to be applied to the minimization of the energy of such a supermolecule, provided that a set of initial Cartesian coordinates can be specified.

A solution to such problems has been devised that obviates a requirement for sophisticated real-time computer graphics. The method, a full account of which will be given separately,[3] may be summarized as follows. Let A refer to a receptor molecule containing N_1 atoms and B a substrate molecule containing N_2 atoms, which is to be docked to A. We assume that the geometries of A and B are known in Cartesian coordinates or in internal coordinates, and that transformation between the two types of coordinate systems is possible. In this case, we begin with $(3N_1-6)$ and $(3N_2-6)$ predetermined internal coordi-

[3]K. Yang and S. Wolfe. To be published.

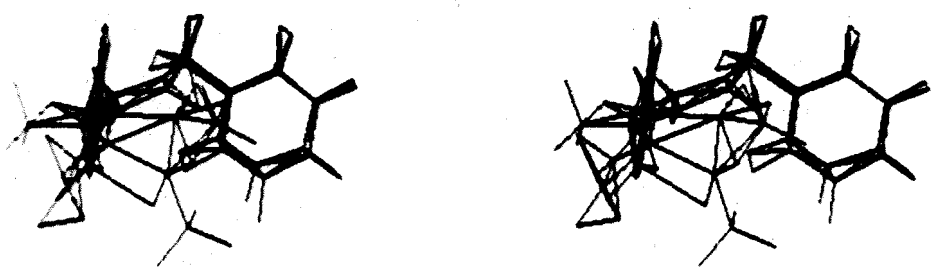

FIG. 9. Superposition of $\mathbf{6}A_{ax}$ on the pseudoaxial conformation of penicillin G.

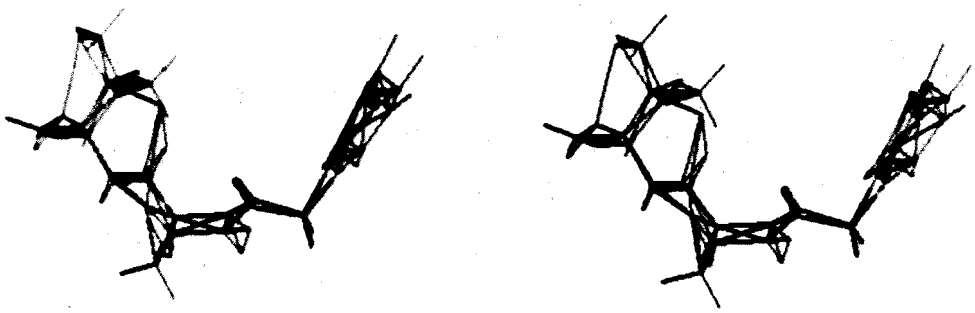

FIG. 10. Superposition of $\mathbf{6}B_{ax}$ on the pseudoaxial conformation of penicillin G.

Can. J. Chem. Downloaded from www.nrcresearchpress.com by 196.1.178.254 on 09/07/12
For personal use only.

nates. To describe the geometry of the supermolecule containing $(N_1 + N_2)$ atoms requires 3 $(N_1 + N_2) - 6$ internal coordinates, i.e., six additional internal coordinates must be determined. These comprise, typically, one bond length, two bond angles, and three dihedral angles, and they may be termed "intermolecular" internal coordinates.

A variety of procedures can be employed (46) to minimize an unconstrained, multivariable nonlinear function $F(r, \theta_1, \theta_2, \phi_1, \phi_2, \phi_3)$, but are unnecessary in the present case, in which contact between $-NH_3^+$ and $^-O_2C-$, and between N—H and C=O is desired. Accordingly, we select one of these interactions, e.g., (N—H...O=C), and set $r_{H...O}$ = 1.7–2.5 Å, a typical intermolecular hydrogen bonding distance. Initial values are then given to the five remaining variables, and the energy is minimized, using eq. [1], with $r_{NH_2—H^+...^-O—CO}$ as a probe. The geometry of the resulting supermolecule, now expressed in Cartesian coordinates, is considered appropriate for MMPEP/MMPEN refinement when the minimization leads to $r_{NH_3^+...^-O_2C}$ = 1.7–2.5 Å.

$$[1] \quad E_{INT} = \Sigma(2.9 \times 10^5 \epsilon e^{-12.5}(r_0/r) - 2.25\epsilon(r_0/r)^6) + \Sigma 332.0 q_i q_j / r_{ij}$$

Equation [1] consists of the electrostatic and van der Waals terms of Allinger's force field (21, 23).

Binding of penicillins to the PBP model *17*

Figure 12 shows the structure obtained when the pseudoaxial conformation of penicillin G is docked to **17** by the procedure just described. Although this is not a fully optimized structure, some remarkable features are already evident. The assumption that the carboxyl group and the amide N-H of the penicillin side chain engage in primary interactions with the receptor leads to a fit in which the hydroxyl group of the unique serine is almost perfectly positioned for attack upon the β-lactam carbonyl group. In this structure the Ser-O...C=O distance is 3.59 Å, and the O...C=O angle is 108.8.° (47).

TABLE 2. Dihedral angles of **17**, the model of the active site of the PBP of *Streptomyces* R61

	Dihedral angle (deg)							
Residue	ϕ	ψ	ω	χ1	χ2	χ3	χ4	χ5
Ac			180					
Val	−72	121	180	−60	178	180		
Gly	160	−179	178					
Ser	79	−62	−177	−55	62			
Val	72	−86	177	−52	180	180		
Thr	−71	152	176	−172	176	−179		
Lys	−69	−47	179	−179	62	176	180	180

Minimization of the structure of Fig. 12 leads to **18**, shown in Fig. 13. In **18** the O...C=O distance is 3.93 Å, the O...C=O angle is 113.0°, and the geometrical parameters of the N—H...O=C hydrogen bond are $r_{H...O}$ = 2.25 Å; < N—H...O = 149.3° (48).

Figure 14 shows a closer view of the relationship in **18** between the C—O—H of serine and the N—C=O of the β-lactam ring. This geometry is reminiscent of the cyclic transition structures found by Schowen and co-workers for the addition of water and methanol to formaldehyde in the gas phase

Can. J. Chem. Downloaded from www.nrcresearchpress.com by 196.1.178.254 on 09/07/12
For personal use only.

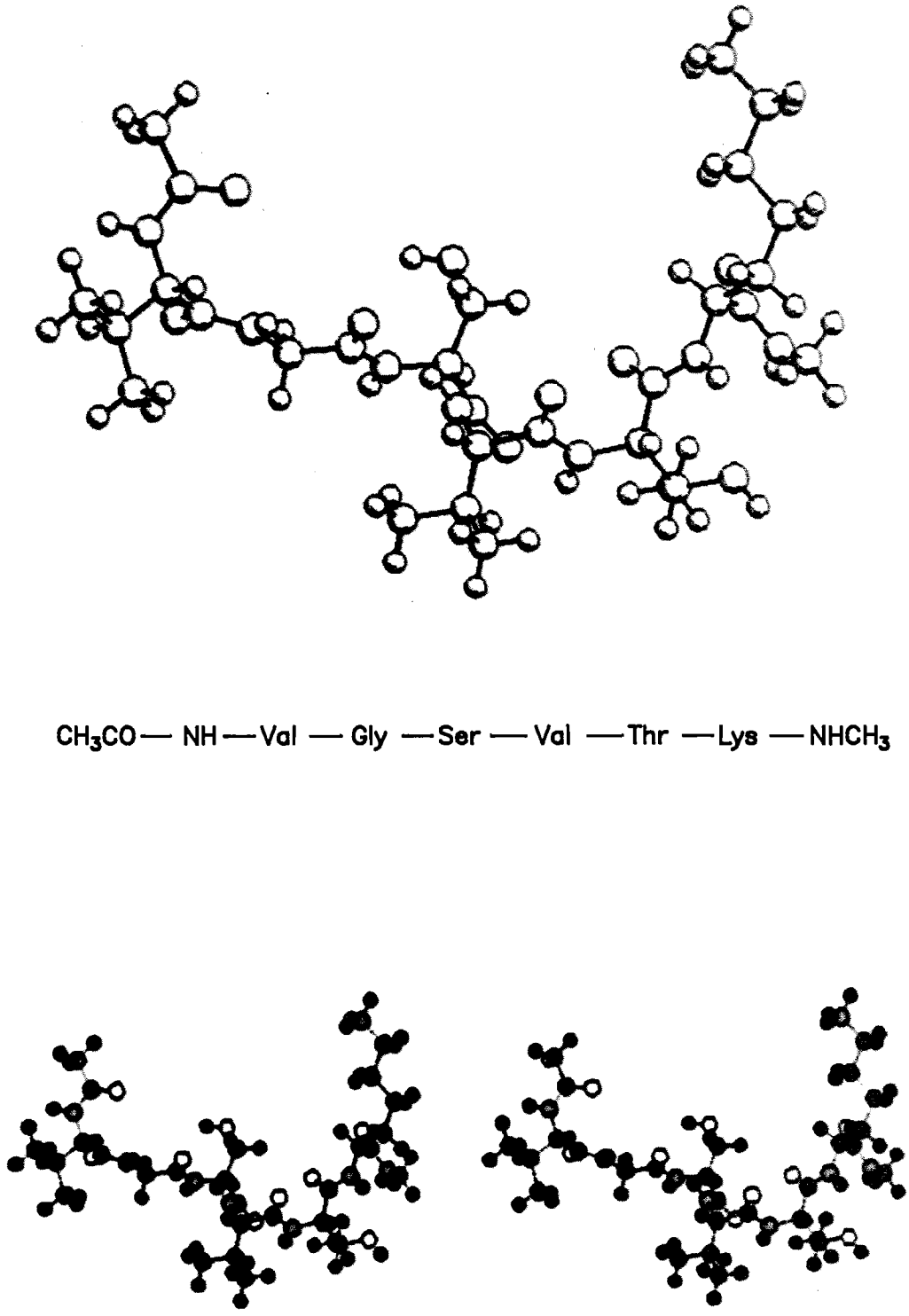

FIG. 11. Calculated structure (**17**) of the binding site of penicillin.

(49). Significantly, such structures do not persist in water solvent (50), and are not found in anionic addition to formaldehyde or formamide, either in the gas phase or in water solvent (51).

Structure **18** is, therefore, compatible not only with the observation (25) that a histidine residue does not participate in the chemical reaction between the serine residue of a PBP and penicillin G, but also with the notion (52) that the environment in which this reaction occurs must be essentially water-free. In terms of this model, the convex face of penicillin is the site of the chemical reaction, in part because there is proton transfer to the pyramidal β-lactam nitrogen in the transition structure (53).

These views appear to be consistent with those of Pauling (54) and Wolfenden (55), i.e., that the function of an enzyme is

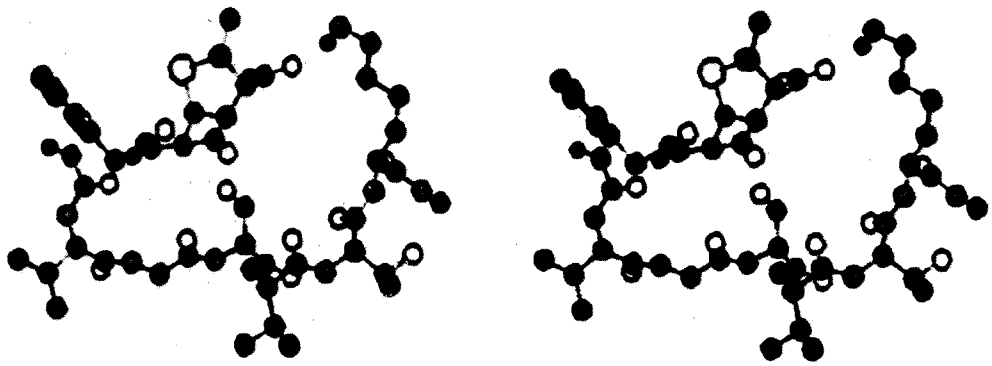

FIG. 12. Structure obtained following docking of pseudoaxial penicillin G to **17** (before final minimization).

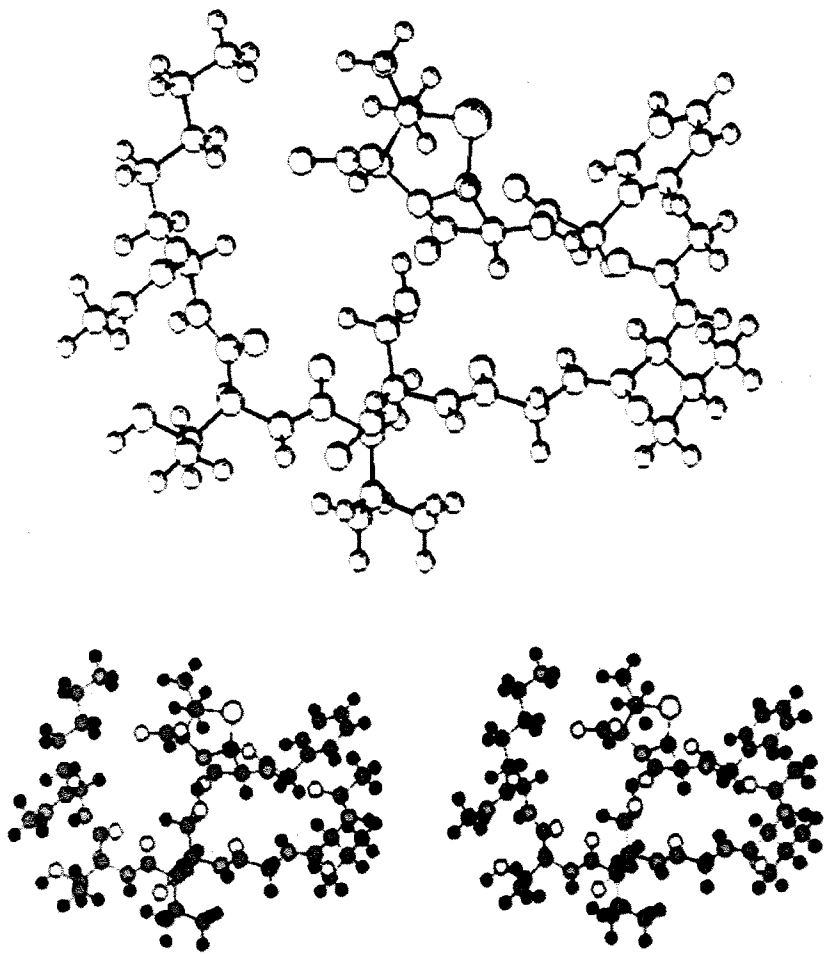

FIG. 13. Structure (**18**) obtained following full minimization of the structure of Fig. 12.

to encourage the formation of a transition state; this is evident in **18**. As will be seen in the following section, the complexes formed between the PBP model **17** and phenylacetyl-D-Ala-D-Ala are closely analogous to **18** in this respect, so that it does not seem necessary to postulate (56) that penicillin itself is a conformational analog of the tetrahedral transition state of peptide hydrolysis.

It should be possible eventually to relate the energetics of formation and the geometry of **18** and its analogs quantitatively to experimental kinetic data, and to antibacterial activity. This

Can. J. Chem. Downloaded from www.nrcresearchpress.com by 196.1.178.254 on 09/07/12
For personal use only.

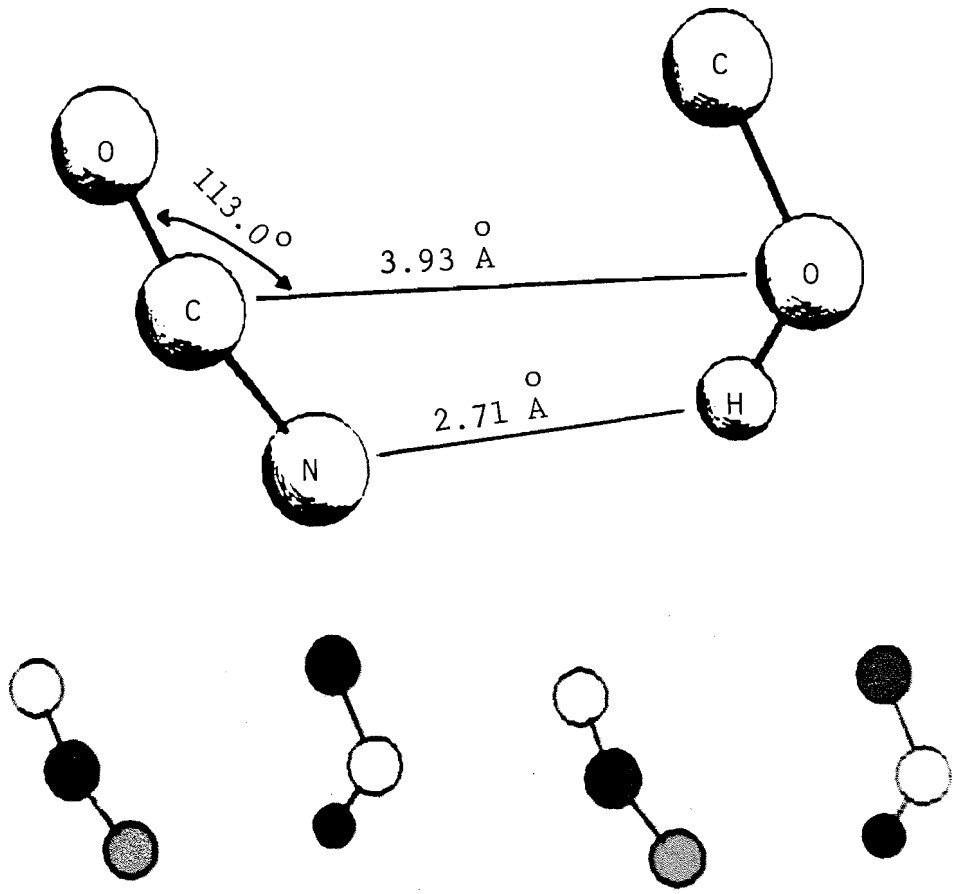

FIG. 14. A closeup view of the geometrical relationship in **18** between the C—O—H atoms of serine and the N—C=O atoms of the β-lactam ring.

Can. J. Chem. Downloaded from www.nrcresearchpress.com by 196.1.178.254 on 09/07/12
For personal use only.

will require: (*i*) that the conformational energies now calculated with MMPEP/MMPEN be expressed as heats of formation and, preferably, as free energies of formation; (*ii*) knowledge of the precise geometry of the transition state for neutral alcoholysis of a β-lactam. Although (*i*) and (*ii*) are not yet available, the properties of **18**, relative to those of other penicillin and peptide complexes with the PBP model **17**, can be compared at this stage.

Table 3 summarizes the results obtained following full minimization of the complexes of **17** with pseudoequatorial penicillin G, 6α-methylpenicillin G, and bisnorpenicillin G, in the manner already described for **18**. In each case, the H...N distance between the hydroxyl hydrogen of serine and the β-lactam nitrogen is less than the O...C distance between the serine oxygen and the carbonyl carbon of the β-lactam. The pseudoaxial and pseudoequatorial conformations of penicillin G bind with very similar geometries, but the energies of the two complexes differ by 2.73 kcal/mol. Since these are conformational isomers, the Curtin–Hammett principle applies (57), and only this energy difference is needed. It follows that *the pseudoaxial conformation of penicillin G is bound preferentially to* ***17***.

Bisnorpenicillin G binds to **17** with a geometry similar to that of penicillin G in the region of the β-lactam, but the N—H...O=C hydrogen bond is poorly formed, and the energy of complexation is less than that of penicillin G by 2.90 kcal/mol. In the case of 6α-methylpenicillin G, the energy of complexation is lower than that of penicillin G, the geometry of the serine–β-lactam interaction is poor, and the N—H...O=C hydrogen bond is poorly formed.

There is thus a one-to-one correspondence between the properties of these complexes and the relative antibacterial activities of the penicillins concerned. We hope that the quantitative nature of the correspondence will become clearer when (*i*) and (*ii*) above have been clarified.

Binding of the peptide 6 to the PBP model 17

Table 4 summarizes the results obtained following minimization of the complexes of **17** with the five conformations of **6** determined earlier. Figure 15 is the complex with $\mathbf{6}A_{ax}$. This figure shows that, in the complex, the serine hydroxyl group has the same relationship to the carbonyl group of the Ala–Ala peptide bond as to the β-lactam group of a penicillin, and the face of the carbonyl group that is attacked by serine corresponds to the convex face of penicillin G (cf Figs. 13 and 15). The steric effect of the Ala[1] methyl group (8) can be seen in Fig. 15 in the contact between this carbon and the oxygen atom of serine; this may be responsible for the decrease in the O...C=O angle, from 109.4° in the penicillin G complex to 99.5° in the peptide complex.

Can. J. Chem. Downloaded from www.nrcresearchpress.com by 196.1.178.254 on 09/07/12
For personal use only.

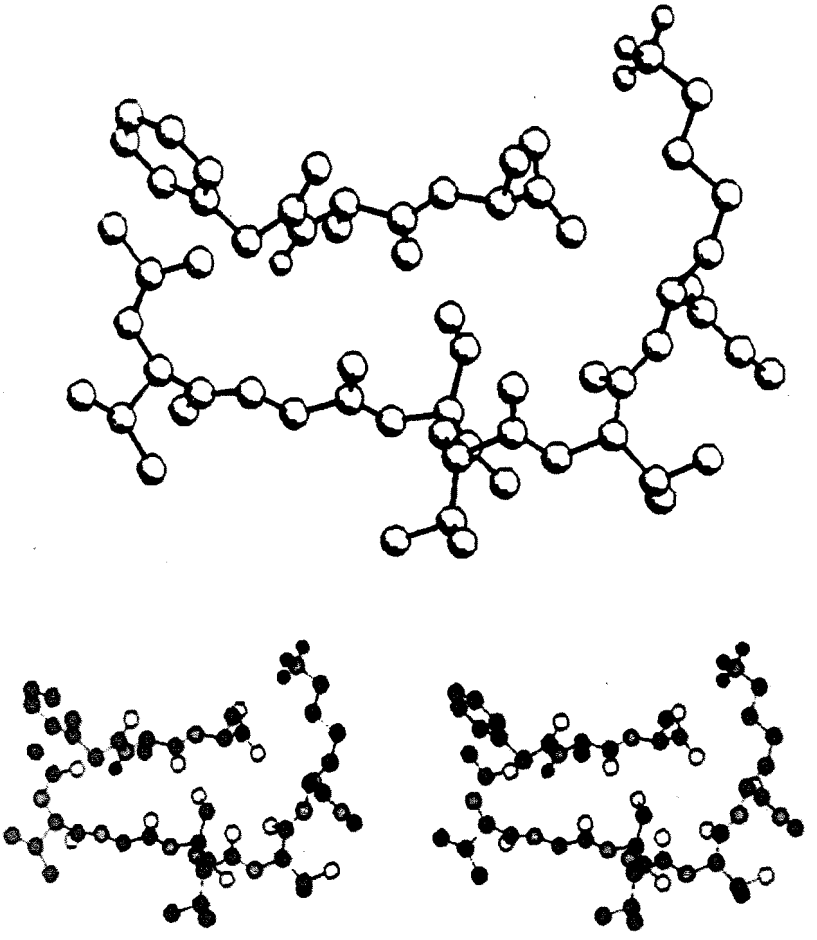

FIG. 15. Structure obtained following full minimization of the complex formed between $\mathbf{6}A_{ax}$ and **17**.

TABLE 3. Properties of the complexes formed between **17** and various penicillins

Penicillin	ΔE (kcal/mol)	$r_{O\cdots C}$[a]	< OCO[b]	$r_{H\cdots N}$[c]	$r_{H\cdots O}$[d]	< NHO[e]
G_{axial}[f]	0.00	3.93	113.0	2.71	2.25	148.4
$G_{equatorial}$[g]	2.73	3.58	105.9	3.01	2.10	157.7
6α-Methyl[h]	0.72[i]	4.36	75.3	4.27	2.65	106.5
Bisnor[j]	2.90[i]	3.83	113.7	2.95	2.28	114.0

[a]Refers to the Ser-O...C=O distance, in Å.
[b]Refers to the Ser-O...C=O angle, in degrees.
[c]Refers to the Ser-O—H... β-lactam nitrogen distance, in Å.
[d]Refers to the H...O distance (Å) in the N—H...O=C hydrogen bond.
[e]Refers to the N—H...O angle (deg) in the N—H...O=C hydrogen bond.
[f]Pseudoaxial conformation of penicillin G.
[g]Pseudoequatorial conformation of penicillin G.
[h]6α-Methylpenicillin G.
[i]Calculated from the difference in E_{INT}, where $E_{INT} = E_{COMPLEX} - (E_{17} + E_{SUBST})$.
[j]Bisnorpenicillin G.

Can. J. Chem. Downloaded from www.nrcresearchpress.com by 196.1.178.254 on 09/07/12
For personal use only.

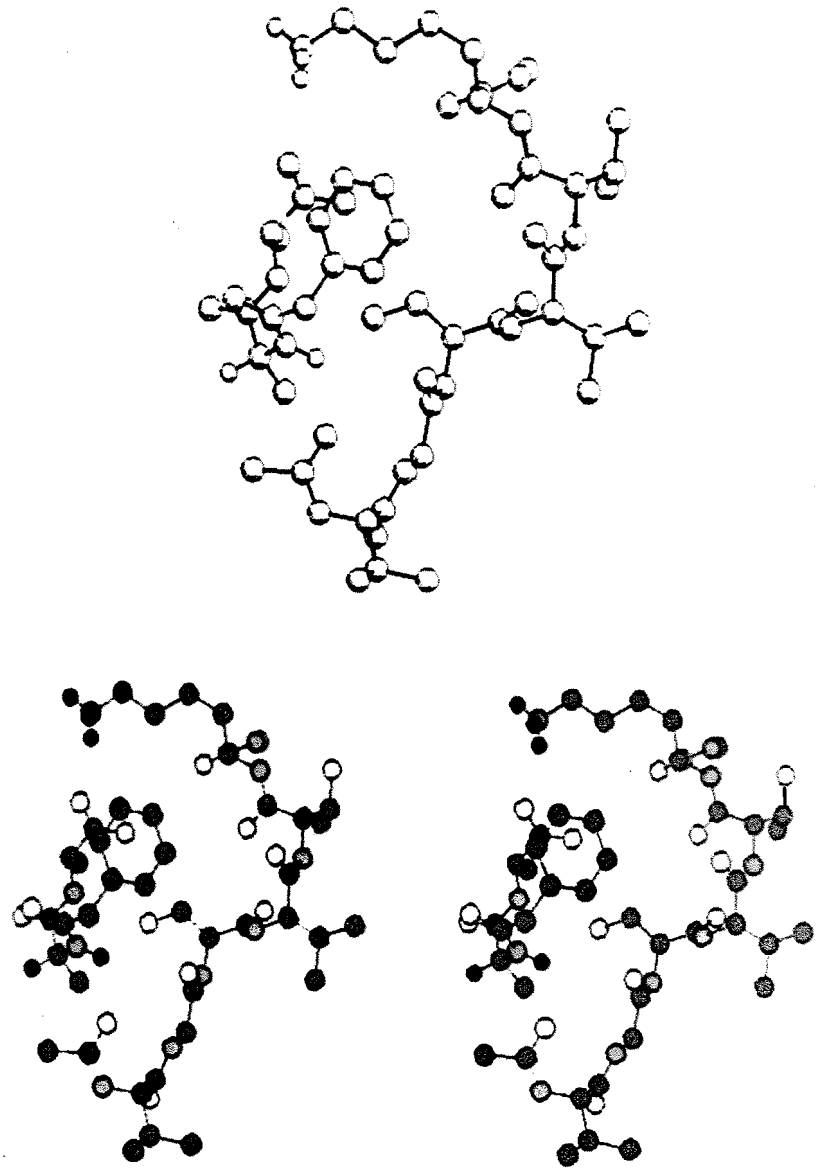

FIG. 16. Structure obtained following full minimization of the complex formed between **6***LA* and **17**.

Figure 16 is the complex of **17** with **6***LA*, the lowest energy conformation found for the peptide. The energy of this complex is higher than that of the $\mathbf{6}A_{ax}$ complex and the geometrical parameters are not as good. Most importantly, comparison of Fig. 13 and 16 reveals *that the face of the Ala^1 carbonyl group of* **6***LA that is attacked by the serine hydroxyl group corresponds to the concave face of penicillin.*

With these specific comments, it is clear that the data of Table 4 permit the following conclusions: (*i*) Strominger's 1965 model is most appropriate representation of the relationship between the skeleton of a penicillin and that of a peptide which serves as a substrate for a PBP; (*ii*) conclusion (*i*) is valid only when the peptide is compared to the pseudoaxial conformation of penicillin. The study of the complexes of **17** with penicillins and with **6** therefore leads to the consistent conclusion that the pseudoaxial conformation of penicillin G, which is the global minimum in this case, is the biologically active conformation.

Summary and concluding remarks

In this work we have employed the MMPEP (20*a*) and MMPEN (20*c*) parameterizations of Allinger's molecular mechanics force field (21, 23) to analyze the conformational factors that are associated with antibacterial activity of penicillins, and to determine the conformations of phenylacetyl-D-Ala-D-Ala that can be compared to appropriate regions of the conformationally constrained penicillin skeleton. In conjunction with a strategy for peptide conformational analysis (20*b*), the work has allowed a model for the active region of a penicillin binding protein to be proposed. A method has been developed to determine the minimized structures and conformational

TABLE 4. Properties of the complexes formed between **17** and various conformations of **6**[a]

Conformation	ΔE^b	r_{O-C}	< OCO	R_{H-N}	R_{H-O}	< NHO
$\mathbf{6}A_{ax}$	0.00	3.81	99.5	2.91	2.39	128.2
$\mathbf{6}A_{eq}$	1.14	4.02	59.2	3.93	2.55	112.2
$\mathbf{6}LA$	1.98	4.04	134.1	2.47	2.56	117.0
$\mathbf{6}B_{eq}$	2.17	4.95	159.1	3.40	2.76	96.0
$\mathbf{6}B_{ax}$	2.37	3.89	103.0	3.77	2.75	87.4

[a]See footnotes to Table 3 for definitions of the geometrical parameters.
[b]Relative energy of the complex, in kcal/mol.

energies of the complexes formed between penicillins or peptide substrates and the putative active site. The origin of antibacterial activity can thus be traced to the formation of a complex in which the hydroxyl group of a unique serine residue is positioned over the convex face of the β-lactam ring in a geometry close to that of the gas-phase transition state of the chemical process of alcoholysis of this ring (45).

The model of the active site has been deduced without access to the coordinates of the crystal structure of a penicillin binding protein, and may require revision when these coordinates become available. Nevertheless, it seems clear at this stage that the nature of the lock-and-key relationships between β-lactam compounds and PBPs can be treated in some detail by the methods of molecular mechanics. We plan to extend the approach described here and in ref. 20*c* to other classes of β-lactam antibiotics, and to non-β-lactam compounds, including lactivicin (**4**) and pyrazolidinones (**5**).

Acknowledgements

The authors thank the Natural Sciences and Engineering Research Council of Canada for financial support, the Province of Ontario for the award of a Graduate Fellowship, Dr. Keith Davies for permission to use the SNOOPI option of CHEMGRAF, and Dr. K.A. Kerridge for a computer search of the patent literature.

1. J. P. DUGUID. Edinburgh Med. J. **53**, 401 (1946); J. LEDERBURG. J. Bacteriol. **73**, 144 (1957); J. T. PARK and J. L. STROMINGER. Science, **125**, 99 (1957).
2. P. D. COOPER. Bacteriol Rev. **20**, 28 (1956); H. J. ROGERS. Biochem. J. **103**, 90 (1967); P. M. BLUMBERG and J. L. STROMINGER. Bacteriol. Rev. **38**, 291 (1974); J.-M. FRÈRE and B. JORIS. CRC Crit. Rev. Microbiol. **11**, 299 (1985).
3. D. J. WAXMAN and J. L. STROMINGER. Ann. Rev. Biochem. **52**, 825 (1983).
4. J.-M. GHUYSEN, J.-M. FRÈRE, M. LEYH-BOUILLE, and O. DIDEBERG. *In* β-lactam antibiotics. Mode of action, new developments, and future prospects. *Edited by* M. R. J. Salton and G. D. Shockman. Academic Press, New York, NY. 1981. p. 127.
5. J. M. GHUYSEN, M. LEYH-BOUILLE, R. BONALY, M. NIETO, H. R. PERKINS, K. H. SCHLEIFER, and O. KANDLER. Biochemistry, **9**, 2955 (1970); M. LEYH-BOUILLE, J. COYETTE, J. M. GHUYSEN, J. IDCZAK, H. R. PERKINS, and M. NIETO. Biochemistry, **10**, 2163 (1971); M. LEYH-BOUILLE, M. NAKEL, J. M. FRÈRE, K. JOHNSON, J. M. GHUYSEN, M. NIETO, and H. R. PERKINS. Biochemistry, **11**, 1290 (1972).
6. E. M. WISE and J. T. PARK. Proc. Natl. Acad. Sci. U.S.A. **54**, 75 (1965); D. J. TIPPER and J. L. STROMINGER. Proc. Natl. Acad. Sci. U.S.A. **54**, 1133 (1965).
7. J. LAMOTTE-BRASSEUR, G. DIVE, and J.-M. GHUYSEN. Eur. J. Med. Chem. **19**, 319 (1984).
8. S. WOLFE and W. S. LEE. Chem. Commun. 242 (1968).
9. D. A. JOHNSON, D. MANIA, C. A. PANETTA, and H. H. SILVESTRI. Tetrahedron Lett. 1903 (1968); D. A. JOHNSON and D. MANIA. Tetrahedron Lett. 267 (1969).
10. J.-L. DE COEN, J. LAMOTTE-BRASSEUR, J.-M. GHUYSEN, J.-M. FRÈRE, and H. R. PERKINS. Eur. J. Biochem. **121**, 221 (1981).
11. J. L. STROMINGER and D. J. TIPPER. Am. J. Med. **39**, 708 (1965).
12. E. H. W. BÖHME, H. E. APPLEGATE, B. TOEPLITZ, J. E. DOLFINI, and J. Z. GOUGOUTAS. J. Am. Chem. Soc. **93**, 4324 (1971).
13. S. K. HASAN. PhD thesis, Queen's University, Kingston, Ont. 1969.
14. S. WOLFE. *In* Current trends in organic synthesis. *Edited by* H. Nozaki. Pergamon Press, New York, NY. 1983. p. 101.
15. W. NAGATA. Stud. Org. Chem. **6**, 95 (1981).
16. Y. NOZAKI, N. KATAYAMA, H. ONO, S. TSUBOTANI, S. HARADA, H. OKAZAKI, and Y. NAKAO. Nature, **325**, 179 (1987).
17. L. N. JUNGHEIM, S. K. SIGMUND, and J. W. FISHER. Tetrahedron Lett. **28**, 285 (1987).
18. L. N. JUNGHEIM, S. K. SIGMUND, N. D. JONES, and J. K. SWARTZENDRUBER. Tetrahedron Lett. **28**, 289 (1987); H. NATSUGARI, Y. KAWANO, A. MORIMOTO, K. YOSHIOKA, and M. OCHIAI. J. Chem. Soc. Chem. Commun. **62** (1987).
19. J. A. KELLY, P. C. MOEWS, J. R. KNOX, J.-M. FRÈRE, and J.-M. GHUYSEN. Science, **218**, 479 (1982); O. DIDEBERG, P. CHARLIER, G. DIVE, B. JORIS, J. M. FRÈRE, and J.-M. GHUYSEN. Nature, **299**, 469 (1982).
20. (*a*) S. WOLFE, D. F. WEAVER, and K. YANG. Can. J. Chem. **66**, 2687 (1988); (*b*) S. WOLFE, S. BRUDER, D. F. WEAVER, and K. YANG. Can. J. Chem. **66**, 2703 (1988); (*c*) S. WOLFE, M. KHALIL, and D. F. WEAVER. Can. J. Chem. **66**, 2715 (1988).
21. U. BURKERT and N. L. ALLINGER. Molecular mechanics. American Chemical Society, Washington, DC. 1982.
22. G. K. LIPKOWITZ, A. M. NAYLOR, and W. B. MELCHIOR. Tetrahedron Lett. **25**, 2297 (1984).
23. N. L. ALLINGER. MMP2(85). Quantum Chemistry Program Exchange, Bloomington, IN.
24. J. A. KELLY, J. R. KNOX, P. C. MOEWS, G. J. HITE, J. B. BARTOLONE, H. ZHAO, B. JORIS, J.-M. FRÈRE, and J.-M. GHUYSEN. J. Biol. Chem. **260**, 6449 (1985).
25. L. VARETTO, J.-M. FRÈRE, M. NGUYEN-DISTÈCHE, J.-M. GHUYSEN, and C. HOUSSIER. Eur. J. Biochem. **162**, 525 (1987).
26. A. BALSAMO, P. DOMIANO, B. MACCHIA, F. MACCHIA, and M. NARDELLI. Eur. J. Med. Chem. **15**, 559 (1980); V. S. R. RAO and T. K. VASUDEVAN. CRC Crit. Rev. Biochem. **14**, 173 (1983); N. C. COHEN. J. Med. Chem. **26**, 259 (1983).
27. H. LABISCHINSKI, G. BARNICKEL, D. NAUMANN, W. RÖNSPECK, and H. BRADACZEK. Biopolymers, **24**, 2087 (1985).
28. R. VIRUDACHALAM and V. S. R. RAO. Int. J. Pept. Protein Res. **10**, 51 (1977); T. K. VASUDEVAN and V. S. R. RAO. Int. J. Biol. Macromol. **4**, 347 (1982).
29. T. LEIGH. J. Chem. Soc. 3616 (1965).
30. A. GOUREVITCH, S. WOLFE and J. LEIN. Antimicrob. Agents Chemother. 576 (1961).

Can. J. Chem. Downloaded from www.nrcresearchpress.com by 196.1.178.254 on 09/07/12
For personal use only.

31. V. S. R. RAO. *In* The target of penicillin. *Edited by* R. Hakenbeck, J.-V. Höltje, and H. Labischinski. Walter de Gruyter, Berlin. 1983. p. 359.
32. P. BLANPAIN and F. DURANT. Cryst. Struct. Commun. **6**, 711 (1977).
33. W. P. JENCKS. Catalysts in chemistry and enzymology. McGraw–Hill, New York, NY. 1969.
34. K. E. PRICE. *In* Structure–activity relationships among the semisynthetic antibiotics. *Edited by* D. Perlman. Academic Press, New York, NY. 1977.p. 1.
35. P. W. HENNINGER, P. WOLFGANG, V. DER DRIFT, and J. KAREL. Ger. Offen. DE 2235390 (1973); A. NUDELMAN and R. J. MCCAULLY. U.S. Patent 3894013 (1973); H. MURAI, S. MATSUMURA, M. KISE, M. OZAKI, M. KITANO, and T. TOMITA. Japan Kokai 53/25591 (1978).
36. S. I. HONG, C. S. KIM, and Y. J. KIM. Bull. Kor. Chem. Soc. **4**, 171 (1983).
37. J. C. SHEEHAN, E. CHACKO, T. J. COMMONS, Y. S. LO, D. R. PONZI, A. SCHWABACHER, N. SOLOMON, and A. L. DEMAIN. J. Antibiot. **37**, 1441 (1984).
38. N. F. OSBORNE. J. Chem. Soc. Perkin Trans. 1, 150 (1980).
39. ECEPP. Quantum Chemistry Program Exchange No. 454, Bloomington, IN.
40. B. G. SPRATT. J. Gen. Microbiol. **129**, 1247 (1983).
41. R. A. NICHOLAS, J. L. STROMINGER, H. SUZUKI, and Y. HIROTA. J. Bacteriol. **164**, 456 (1985).
42. J.-M. GHUYSEN, J.-M. FRÈRE, M. LEYH-BOUILLE, M. NGUYEN-DISTÈCHE, and J. COYETTE. Biochem. J. **235**, 159 (1986).
43. E. FISCHER. Ber. Dtsch. Chem. Ges. **27**, 2985 (1894).
44. N. PATTABIRAMAN, M. LEVITT, T. E. FERRIN and R. LANGRIDGE. J. Comput. Chem. **6**, 432 (1985).
45. M. J. S. DEWAR. Proc. Natl. Acad. Sci. U.S.A. **82**, 2225 (1985).
46. J. L. KUESTER and J. H. MIZE. Optimization techniques with FORTRAN. McGraw–Hill, New York, NY. 1973.
47. H. B. BÜRGI, J. D. DUNITZ, and E. SHEFTER. J. Am. Chem. Soc. **95**, 5066 (1973); H. B. BÜRGI and J. D. DUNITZ. Acc. Chem. Res. **16**, 153 (1983).
48. G. C. PIMENTEL and A. L. MCCLELLAN. The hydrogen bond. I.W.H. Freeman and Company, San Francisco, CA. 1960; S. N. VINOGRADOV and R. H. LINNELL. Hydrogen bonding. Van Nostrand Reinhold, New York, NY. 1971.
49. I. H. WILLIAMS, D. SPANGLER, G. M. MAGGIORA, and R. L. SCHOWEN. J. Am. Chem. Soc. **107**, 7717 (1985).
50. I. H. WILLIAMS, D. SPANGLER, D. A. FEMEC, G. M. MAGGIORA, and R. L. SCHOWEN. J. Am. Chem. Soc. **105**, 31 (1983); J. D. MADURA and W. L. JORGENSEN. J. Am. Chem. Soc. **108**, 2517 (1986).
51. S. J. WEINER, U. C. SINGH, and P. A. KOLLMAN. J. Am. Chem. Soc. **107**, 2219 (1985).
52. R. WOLFENDEN. Science, **222**, 1087 (1983).
53. M. I. PAGE. Acc. Chem. Res. **17**, 144 (1984).
54. L. PAULING. Chem. Eng. News, **24**, 1375 (1946).
55. R. WOLFENDEN. Acc. Chem. Res. **5**, 10 (1972).
56. B. LEE. J. Mol. Biol. **61**, 463 (1971); D. B. BOYD. Proc. Natl. Acad. Sci. U.S.A. **74**, 5239 (1977); D. B. BOYD. J. Med. Chem. **22**, 533 (1979).
57. J. I. SEEMAN. J. Chem. Educ. **63**, 42 (1986).

Can. J. Chem. Downloaded from www.nrcresearchpress.com by 196.1.178.254 on 09/07/12
For personal use only.

Phenceptin: a biomimetic model of the phenytoin receptor

SAUL WOLFE,[1] RAYMOND JOHN BOWERS, HEE-SOOK SHIN, CHANG-KOOK SOHN, DONALD FREDRIC WEAVER, AND KIYULL YANG

Department of Chemistry, Queen's University, Kingston, Ont., Canada K7L 3N6

Received September 22, 1987[2]

SAUL WOLFE, RAYMOND JOHN BOWERS, HEE-SOOK SHIN, CHANG-KOOK SOHN, DONALD FREDRIC WEAVER, AND KIYULL YANG. Can. J. Chem. **66**, 2751 (1988).

5,5-Diphenylhydanytoin (phenytoin) is the most widely used anticonvulsant drug, but has many side effects. Although its chemical mode of action is unknown, phenytoin is believed to function primarily by interference with the transport of sodium ions across the neuronal membrane. Structure–activity and lipophilicity–activity studies suggest that the drug interacts with its receptor through hydrogen bonding to the N3—C4 amide bond, and an aromatic–aromatic interaction with the C5 substituent. Since sodium channels are cysteine-rich peptides, whose function depends upon the cysteine⇄cystine redox process, it has been hypothesized that the action of the phenytoin receptor may be mimicked by a properly designed cyclodepsipeptide containing a cystinyl moiety, a cavity lined with five oxygen atoms oriented in the trigonal-bipyramidal manner appropriate for selective transport of sodium ions, and a site for the binding of phenytoin. A computer programme and strategy were developed to permit the three-dimensional structures of potential target molecules to be viewed, prior to synthesis. Use of this programme led to the discovery of Boc-L-cystinyl-glycyl-L-prolyl-glycyl-L-prolyl-L-cystine-$OCHPh_2$. This compound, termed phenceptin, was synthesized from a linear precursor containing *tert*-butoxycarbonyl protection at the N-terminus, benzhydryl ester protection at the C-terminus, and trityl protection at sulfur. Detritylation and cyclization to phenceptin were accomplished with iodine in methanol–pyridine. Using an *n*-octanol membrane to study the kinetics of ion transport, phenceptin was found to transport sodium ions selectively, but only in its oxidized, cyclic form. This transport was inhibited significantly by one mol-equiv. of phenytoin, and not at all by biologically inactive analogs of the drug. The nature of the binding of phenytoin to phenceptin was examined by nuclear magnetic resonance, in *n*-C_8D_{17}-OH solvent, and found to involve hydrogen bonding of the drug to a glycine residue whose oxygen atom is involved in complexation to sodium ions.

SAUL WOLFE, RAYMOND JOHN BOWERS, HEE-SOOK SHIN, CHANG-KOOK SOHN, DONALD FREDRIC WEAVER ET KIYULL YANG. Can. J. Chem. **66**, 2751 (1988).

La diphényl-5,5 hydantoïne (phénytoïne) est le médicament le plus utilisé comme anticonvulsivant; toutefois, il provoque de nombreuses réactions secondaires. Même si son mode d'action chimique est inconnu, on croit que la phénytoïne agit principalement par interférence avec le transport des ions sodium à travers les membranes neuronales. Des études de structure/activité et caractère liphophilique/activité suggèrent que la drogue interagit avec son récepteur par le biais de liaisons hydrogènes avec la liaison amide N3—C4 et par une interaction aromatique/aromatique avec le substituant en C5. Puisque les canaux du sodium sont des peptides riches en cystéine dont la fonction dépend du processus redox cystéine/cystine, il a été suggéré que l'on pourrait répliquer l'action du récepteur de la phénytoïne à l'aide d'un cyclodepsipeptide approprié contenant une portion cystinyle, une cavité contenant cinq atomes d'oxygène orientés d'une façon trigonale/bipyramidale appropriée au transport sélectif d'ions sodium et d'un site pour la liaison de la phénytoïne. On a mis au point un programme d'ordinateur et une stratégie qui permettent de voir les structures tri-dimensionnelles des molécules cibles potentielles avant d'en réaliser la synthèse. L'utilisation de ce programme a conduit a la découverte du Boc-L-cystinyl-glycyl-L-prolyl-L-cystine-$OCHP_2$. On a synthétisé ce composé, appelé phenceptine, à partir d'un précurseur linéaire contenant le groupement protecteur *tert*-butoxycaronyle sur l'acide portant le N-terminal, un groupement protecteur ester benzhydryle sur l'acide du C-terminal et une protection trityle sur le soufre. On a réalise la détritylation et la cyclisation de la phenceptine à l'aide d'iode dans un mélange de méthanol et de pyridine. Utilisant un membrane de *n*-octanol pour étudier la cinétique du transport ionique, on a trouvé que la phenceptine transporte sélectivement les ions sodium uniquement dans sa forme oxydée, cyclique. Ce transport subit une inhibition importante par un équivalent molaire de phénytoïne; les analogues biologiquement inactifs de la drogue ne causent toutefois pas d'inhibition. Opérant dans le *n*-C_8H_{17}-OH comme solvant et faisant appel à la résonance magnétique nucléaire, on a examiné la nature de la liaison de la phénytoïne à la phenceptine; on a trouvé que celle-ci implique une liaison hydrogène de la drogue avec un résidu glycine dont l'atome d'oxygène est impliqué dans la complexation avec les ions sodium.

[Traduit par la revue]

Introduction

The epilepsies are a group of diverse disorders with a common central nervous system manifestation, the occurrence of seizures (convulsions). An accurate epidemiology of the illness is difficult, but various studies suggest an overall incidence of 1% in the general population (1). Ten times this number of persons require medical attention at some time during their lives as the result of a seizure.

A seizure is primarily an electrical event: a high voltage discharge of an assemblage of brain cells (neurons), and aberrant neuronal excitability is associated mainly with the ion transport behaviour of sodium channels (2). As these open and close sequentially throughout the cerebral cortex, an electrical discharge spreads from an initial focus, and the symptoms of the epileptic state become manifest.

Treatment of epilepsy is imperative, because brain damage and (or) death are not infrequent sequelae of untreated abnormal electrical activity. Any successful drug therapy for the control of seizures must function by interference with the development and propagation of this activity.

The most important drug for the control of seizures is 5,5-diphenylhydantoin (**1**), known in medicine as Dilantin or phenytoin (3). However, phenytoin and all other anticonvulsant drugs have deficiencies associated with their use: only 60% of epileptic patients can be controlled adequately (5) and each of the drugs exhibits many side effects.

Consequently, there is a need to develop new drugs for the

[1]Author to whom correspondence may be addressed.

[2]Revision received May 31, 1988.

Can. J. Chem. Downloaded from www.nrcresearchpress.com by 196.1.178.254 on 09/07/12
For personal use only.

Can. J. Chem. Downloaded from www.nrcresearchpress.com by 196.1.178.254 on 09/07/12
For personal use only.

treatment of epilepsy, a point emphasized repeatedly in the medical literature (4, 5). The present work is concerned with the development and experimental evaluation of a biomimetic model of the activity of phenytoin. This is the first stage of a programme that, it is hoped, will eventually allow the design of novel anticonvulsants, whose activity is based on the mechanism of action of phenytoin.

Structure–activity and lipophilicity–activity relationships of phenytoin analogs

A search of the literature yielded data for over 800 analogs of phenytoin, about one quarter of which had been evaluated comparably using maximal electroshock techniques. Structure–activity studies have led to the view (6) that the phenytoin receptor interacts with the drug primarily through the formation of intermolecular hydrogen bonds, but also possesses a hydrophobic pocket that interacts with the C5 substituent. In addition, within the hydantoin ring, an unsubstituted N3—C4 amide bond is the most important, one phenyl group or a bulky aliphatic group is necessary at C5, and the introduction of one or more benzyl substituents at C5 causes loss of activity.

Conformational studies on 5-phenyl and 5-benzyl substituted hydantoins provide insight into the origin of the benzyl effect. In phenytoin, the phenyl groups are approximately perpendicular to the hydantoin ring (7); in 5-benzylhydantoin the phenyl group is approximately parallel to the hydantoin ring (8), in harmony with an early suggestion (9) concerning the existence of aromatic–amide interactions in phenylalanyl-containing peptides. To probe this point further, 3-ethyl-5-phenyl- (**2**) and 3-ethyl-5-benzyl-hydantoin (**3**) were synthesized (see Experimental), and their ^{1}Hmr spectra examined. In the 5-benzyl compound, both the methylene and the methyl hydrogens of the 3-ethyl group are shifted upfield by 0.3 ppm, as expected for a structure in which the aromatic ring lies over the ethyl group.

The existence of an aromatic–N3C4 amide interaction in a 5-benzylhydantoin would have two consequences: access by a receptor to the N3—C4 amide bond would be impaired; and the aromatic ring would no longer possess the proper orientation for interaction with the hydrophobic pocket of the receptor (cf. Fig. 12 of ref. 7).

It is also necessary that the drug reach this receptor, and this capability will depend upon the lipophilicity of the hydantoin (10, 11). Our examination of the literature (12) suggests that, although the contribution of lipophilicity cannot be ignored (13), the anticonvulsant activity of a hydantoin depends primarily upon its ability to bind to the phenytoin receptor. Any attempt to model this process requires information concerning the nature of this receptor and its chemical constitution.

Phenytoin and the sodium channel

The anticonvulsant activity of phenytoin can be ascribed to a single demonstrable primary event: the specific inactivation of sodium channels (14, 15).

Recent studies (see ref. 16 for a review) have demonstrated that sodium channels are glycoproteins, containing up to 36% by weight of carbohydrate, principally sialic acid (7). Studies of the function of these channels suggest that the carbohydrate portion is directed extracellularly, and the peptide portion is directed intracellularly; the movement of ions occurs through a fixed pore or channel, rather than as part of a larger membrane macromolecule, and is selective for sodium. A model of the ion-selectivity filter, i.e., the narrowest region of the ion-conducting pore of the sodium channel, has been proposed (18).

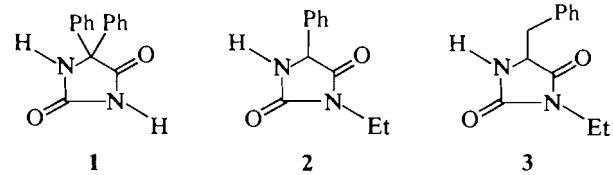

1 **2** **3**

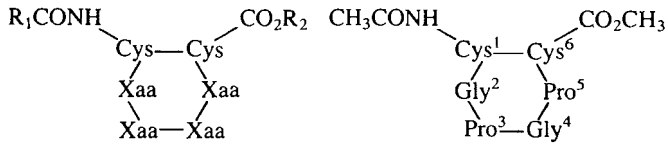

4 **5**

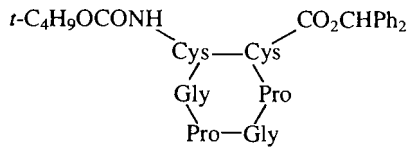

6

This consists of a 3 × 5 Å orifice *lined by oxygen atoms* (italics added).

All sodium channels contain a ca. 260 kD unit, and the primary structure of the peptide portion of this unit (M_r 208,321) in the electric eel, *Electrophorus electricus*, has been determined by Noda *et al.* (19). The peptide contains 36 cysteine residues, and shows sequence homology to the corresponding peptide of rat brain (20).

Hypothesis

Noda *et al.* (19) and Kosower (21) have developed models for the sodium channel of *Electrophorus electricus*, based on slightly different analyses of the structure of the 180-residue protein. In both models, the sodium binding site consists of a series of negatively charged (−) residues (Asp^-, Glu^-), and is surrounded by a series of positively charged (+) residues (Arg^+, Lys^+). Opening (activation) and closing (inactivation) of the channel is determined by conformational motion of side chains, e.g., (−, −, −, −) (open) ⇄ (−, −, −, +) (closed). In Kosower's model, possible (−) residues are Asp-908, Asp-910, Glu-943, and Glu-944; possible (+) residues are Arg-210, Arg-657, and Arg-1417.

If we accept such models as plausible representations of the chemical events associated with normal electrical behaviour, is it possible that aberrant behaviour is the result of the creation of additional sodium binding sites?

A number of reagents have been found to slow or prevent sodium channel inactivation, including *N*-bromoacetamide, *N*-chlorosuccinimide, *N*-bromosuccinimide, and *N*-chloro-*p*-toluenesulfonamide (chloramine-T) (22). All of these are mild oxidants; in a molecule containing an abundance of cysteine residues, the primary effect of such reagents must be to maintain the cysteine–cystine couple in its oxidized form. Significantly, sulfhydryl-specific reagents, such as *N*-ethylmaleimide and 5,5′-dithiobis-2-nitrobenzoic acid, neither slow nor prevent inactivation of sodium channels (22).

The simplest reagent for the oxidation of a mercaptan to a disulfide is O_2 (23), and it is known that hyperventilation (24) or hyperbaric oxygen (25) precipitate seizures, which can be suppressed with phenytoin.

We are, therefore, led to the hypothesis that the opening of

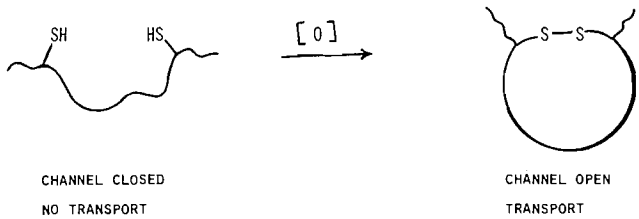

FIG. 1. Hypothesis of the present work: the opening and closing of sodium channels associated with abnormal electrical behaviour is a redox process.

sodium channels that initiates a seizure corresponds chemically to the creation of a sodium-selective *cyclodepsipeptide ionophore* (26), by an oxidative process, as depicted schematically in Fig. 1.[3]

The concept of "redox-switched" ionophores is not new. Shinkai and co-workers (28) and Raban *et al.* (29) have reported the syntheses of α,ω-dimercapto polyoxy compounds, which behave as pro-ionophores. In their reduced forms these compounds are poor ionophores; oxidation generates effective crown ether ionophores, whose cation selectivity depends on ring size. The oxidation reaction exhibits a marked template effect (28), and it has been argued (29) that "chemically switchable pro-ionophore–ionophore couples can serve as models for biological "ion gates", structures in which ion transport is initiated by an external stimulus."[3]

Phenceptin: design[4]

To convert the concept of Fig. 1 into a biomimetic model of the phenytoin receptor required a peptide containing two terminal cysteines. The number, nature, and sequence of the internal amino acids of this peptide had to be selected so that, in its reduced form, the compound would not behave as an ionophore. In its oxidized, cyclic form it was necessary that (*i*) the substance be sodium-selective; (*ii*) the transport of sodium ions be blocked by phenytoin; (*iii*) biologically inactive phenytoin analogs, e.g., 5,5-dibenzylhydantoin, have no effect on sodium transport.

Many cyclopeptides behave as ionophores (30), but none exhibits selectivity for sodium ions. The structures of cyclodepsipeptide ionophores and their complexes are also well established (26, 31), but none of these ionophores possesses the desired redox-switching feature, or selectivity for sodium. Although both natural (32) and synthetic (33) peptides containing the cysteine–cystine couple are known, their transport properties have not been studied.

Nevertheless, the dimensions of the cavity (3 × 5 Å) of the cyclic target were clear from the properties, already discussed, of the ion-selectivity filter of the sodium channel (18). These correspond closely to the hole size observed in the crystal structures of sodium-selective *crown ether* ionophores (26, 34), whose cavities have a ca. 4.6 Å diameter. The complexation of sodium ions is accomplished, in such cases, by a trigonal-bipyramidal arrangement of five oxygens.

[3]For an alternative model of a receptor channel, see ref. 27.

[4]The authors thank Professor Morton Raban and his co-workers for helpful discussions during the formative stages of this design project, including prepublication information concerning ref. 29, and its potential implications for our own work.

TABLE 1. Dihedral angles of **5**

Residue	Angle (deg)			
	ϕ^a	ψ^b	ω^c	$\chi_1{}^d$
Cys^1	−83	−12	173	−128
Gly^2	−61	−66	173	
Pro^3	−75	−180	178	
Gly^4	79	−166	−180	
Pro^5	−68	−30	174	
Cys^6	−67	143	178	−174

[a]$N-C_\alpha$ dihedral angle.
[b]$C_\alpha-C'$ dihedral angle.
[c]$N-C'$ dihedral angle.
[d]$C_\alpha-C_\beta$ dihedral angle.

Examination of molecular models suggested that a cyclohexadepsipeptide would be the simplest system potentially containing these features (cf. ref. 35). This redefined the design problem to a structure of type **4**.

For the case of valinomycin, the best-known cyclodepsipeptide ion carrier (26, 31, 36), selection and syntheses of analogs (31, 37) have been conducted mainly by trial and error. This labour-intensive process was not feasible for us, and it was necessary to devise a theoretical strategy to screen candidate structures *prior* to synthesis. This strategy is based on molecular mechanics (38), and it has been documented fully (39).

Attention was focused, especially, on the use of proline and glycine residues. Proline residues were expected to reside on the exterior of the molecule, and enhance the lipophilicity required to maintain the ionophore in a membrane environment. In addition, the presence of this amino acid should inhibit transannular hydrogen bonding and excessive conformational lability (40). Glycine was expected to fit into a tightly turned cyclic peptide structure, promote cyclization (41), and reduce the possibility of steric interactions between amino acid side chains and a putative phenytoin binding site.

Figure 2 is the lowest energy structure calculated for the cyclohexadepsipeptide **5**, which contains a Gly-Pro-Gly-Pro sequence (42). The strategy consisted of a preliminary ECEPP search (39*b*, 43) of 200,000 structures, followed by final refinement of the 50 low energy structures identified in this search, using the peptide parameters (39*a*) of Allinger's MMP2(85) programme (44). Table 1 summarizes the dihedral angles of **5**.[5]

Inspection of Fig. 2 reveals that six carbonyl oxygens are directed towards the interior of the molecule, and that a trigonal-bipyramidal arrangement can be achieved from apical carbonyl oxygens of Cys^1 and Gly^4, whose separation is 5.56 Å, and equatorial carbonyl oxygens from three of CH_3CO, Gly^2, Pro^3, Cys^6. Three of the latter are amide carbonyls, and the fourth (Cys^6) is an ester carbonyl. The carbonyl oxygens of Gly^2, Pro^3, and Cys^6 form an equilateral triangle, and the diameter of the circumscribed circle is 3.63 Å.

In the potassium complex of valinomycin, the cation is bound

[5]Other peptides examined analogously led to low energy structures whose cavities did not contain the number and orientation of oxygen atoms considered necessary for complexation of sodium ions. For example, with Gly-Gly-Gly-Gly, Ala-Pro-Ala-Pro, and Pro-Pro-Pro-Pro as the four internal amino acids, substantial conformational changes appeared to be necessary to achieve a backbone structure analogous to **5**.

Can. J. Chem. Downloaded from www.nrcresearchpress.com by 196.1.178.254 on 09/07/12
For personal use only.

Can. J. Chem. Downloaded from www.nrcresearchpress.com by 196.1.178.254 on 09/07/12
For personal use only.

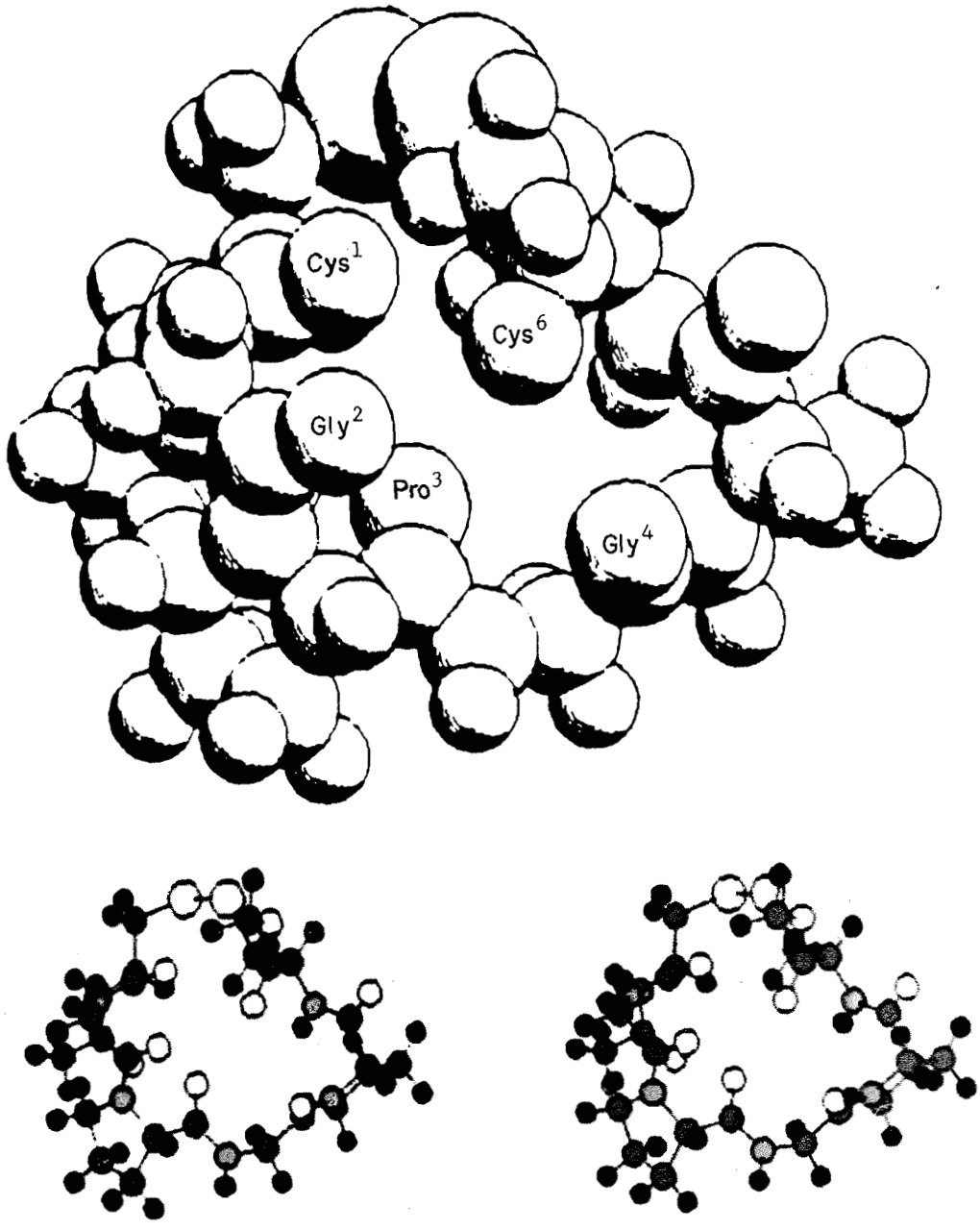

FIG. 2. The lowest energy structure calculated for the cyclohexadepsipeptide **5**. The atoms labelled Cys^1, Gly^2, ... are the carbonyl oxygens of these residues. The lower view of **5** requires a diastereoscopic viewer.

octahedrally to six ester carbonyl oxygens (26). In the potassium complex of enniatin B, three amide carbonyl and three ester carbonyl oxygens bind to the cation (26). Thus, binding to both ester and amide carbonyl oxygens is known.

Compound **6** was selected for synthesis and experimental evaluation as a biomimetic model of the phenytoin receptor. In **6**, the replacement of CH_3CO by *t*-BuOCO was expected to reduce the basicity of this carbonyl oxygen, and promote the formation of a trigonal-bipyramidal cation complex. According to Fig. 2, the C-terminal ester methyl group lies over the carbonyl oxygens of Gly^2 and Gly^4; if one of these oxygens were to serve as a phenytoin binding site, aromatic–aromatic interactions would be promoted by the attachment of one or more phenyl substituents to the methyl carbon. The choice of benzyhydryl at this position meets this requirement, and simplifies the synthesis.

The cyclohexadepsipeptide **6** has been named "phenceptin" (*phen*ytoin re*cept*or).

Phenceptin: synthesis

The synthesis of phenceptin was carried out from Boc-glycine (**7**), the benzyl ester of L-proline (**8**), Boc-*S*-trityl-L-cysteine (**9**), and the benzhydryl ester of *S*-trityl-L-cysteine (**10**).

As summarized in Scheme 1, coupling of **7** with **8** afforded **11**, fully protected Gly-Pro. This was O-deprotected by hydro-

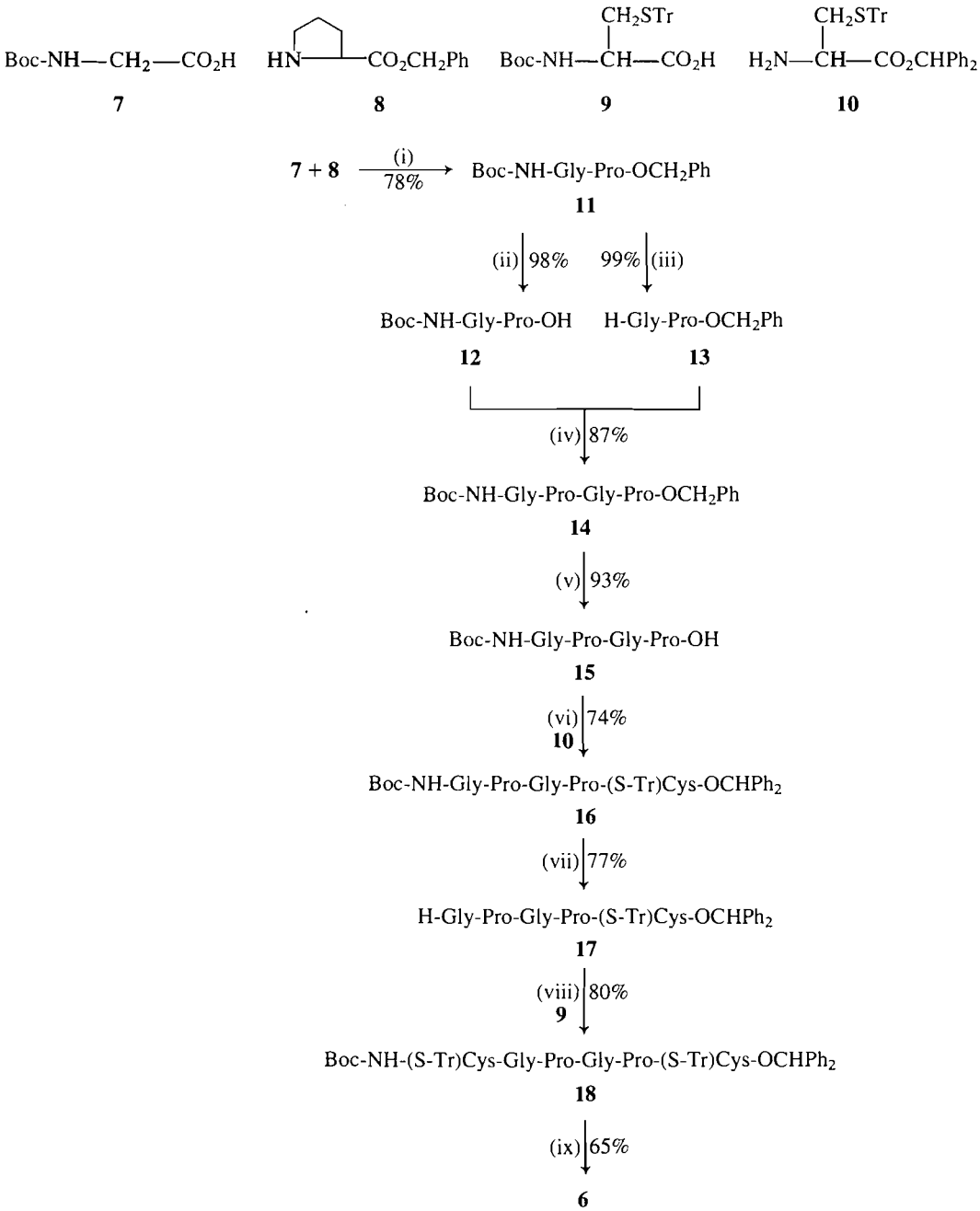

Reagents: (i) EEDQ; (ii) 10% Pd/C; (iii) HCl; (iv) EEDQ; (v) 10% Pd/C; (vi) EEDQ; (vii) HCO_2H; (viii) EEDQ; (ix) I_2-MeOH–pyridine

SCHEME 1

genolysis to **12**, and N-deprotected with HCl to **13**. Coupling of **12** with **13** gave **14**, fully protected Gly-Pro-Gly-Pro. Hydrogenolysis of **14** exposed the terminal carboxyl group (**15**), and coupling with **10** yielded the fully protected pentapeptide **16**, Gly-Pro-Gly-Pro-Cys. This was deprotected selectively at the N-terminus, using anhydrous formic acid (45), and the product (**17**) was coupled with **9** to form the acyclic, fully protected hexapeptide Cys-Gly-Pro-Gly-Pro-Cys (**18**). Removal of the *S*-trityl protecting groups, and cyclization to phenceptin were accomplished by treatment of **18** with iodine, in a mixture of methanol and pyridine (46).

Phenceptin was obtained in analytically pure form as an amorphous solid, which has not yet been crystallized. Although the compound is homogeneous on thin-layer chromatography in several systems, its 400 MHz ^{1}Hmr spectrum (in $CDCl_3$) is temperature dependent and suggests a 4:1 mixture of two conformations.[6] Comparison of the spectrum of phenceptin with those of the intermediates of the synthesis allowed assignment of proton resonances associated with the different residues (see Experimental).

[6]S. Wolfe and R. J. Bowers. To be published.

Can. J. Chem. Downloaded from www.nrcresearchpress.com by 196.1.178.254 on 09/07/12
For personal use only.

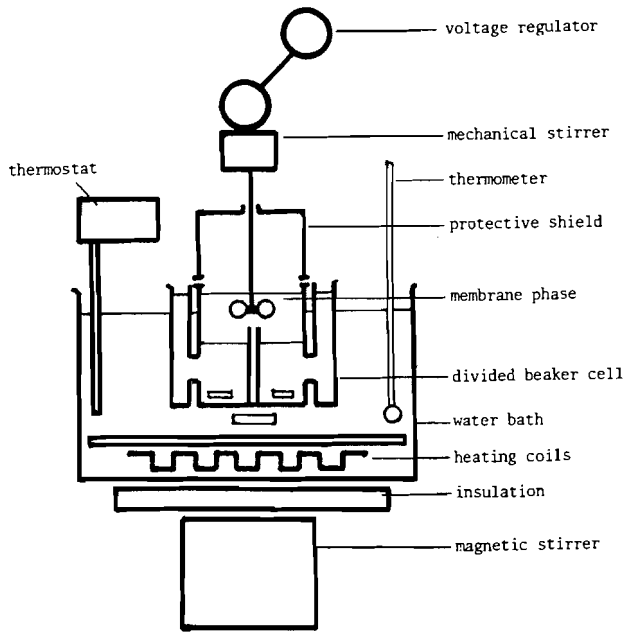

FIG. 3. Divided beaker cell for kinetic studies of cation transport through a 1-octanol membrane.

Cation transport through an *n*-octanol membrane

Most workers employ a U-tube to model the process of ion transport across a liquid membrane. In such an apparatus, water occupies each of the arms, and an organic solvent denser than water, e.g., chloroform, is placed in the base. If a salt is added to one of the arms and the organic solvent is stirred, no transport to the second arm is observed until a water-insoluble ionophore is added to the system. When an ionophore is present, the movement of salt from one arm to the other represents a biomimetic model of transport from an extracellular phase, through a membrane, to an intracellular phase.

This system did not seem biologically appropriate for an examination of the properties of phenceptin, for several reasons: (*i*) chloroform is not a proper model of a cell membrane; (*ii*) the membrane employed in a typical U-cell is too thick, averaging 8–10 cm between the two aqueous phases; (*iii*) the area of surface contact between each aqueous phase and the membrane is typically of the order of 1.15 cm^2.

The selection of 1-octanol as the membrane phase seemed more meaningful. It has been known for many years (48) that pharmacological activity can be related to octanol–water partition coefficients.

This choice necessitated a modification of the usual apparatus, because 1-octanol is less dense than water. Figure 3 shows the "divided beaker" transport cell devised for this purpose. This apparatus minimizes the separation of the intracellular and extracellular aqueous phases, and increases the area of surface contact between the membrane phase and each aqueous phase to 39.3 cm^2. All phases are stirred continuously to minimize effects of concentration gradients upon solute distribution; a series of voltage regulators control the stirring devices, and promote experimental reproducibility. All kinetic measurements were performed at 37.0 ± 0.1°C.

To evaluate the capabilities of the apparatus, an initial set of experiments was performed, using as ionophores the crown ethers 12-crown-4, 15-crown-5, and 18-crown-6. In a typical run the ionophore was dissolved in the octanol layer at a concentration of 150 μM. The extracellular aqueous phase contained an inorganic salt at a concentration of 20 mM, and the intracellular aqueous phase consisted of redistilled water.

The transport rate was determined through periodic sampling of the intracellular phase, and measurement of the concentration of the anion that migrates concomitantly with the cation to preserve electrical neutrality. With thiocyanate as the counter-anion, 12-crown-4 prefers Li^+ over Na^+, 18-crown-6 prefers K^+ over Na^+, and 15-crown-5 is selective for Na^+ (cf. refs. 26 and 31).

The behaviour of 15-crown-5 was studied more fully. The role of the counter-anion was examined using sodium chloride, sodium thiocyanate, and sodium picrate. This was found to be picrate ≈ thiocyanate ≫ chloride. Evidently the weakly hydrated picrate and thiocyanate anions are transported more rapidly than the small, spherical, strongly hydrated chloride anion. This trend is well established for chloroform membranes (49).

Chloride is obviously more appropriate than picrate for use in a biomimetic process, but this choice would have led to inconveniently slow transport rates. The problem might, in principle, be overcome by measurement of junction potentials (50) in place of transport rates, but it was considered that this was not essential at this stage. Thiocyanate was selected as a compromise, and all subsequent work was performed with this anion.

Further studies demonstrated that the transport of sodium thiocyanate is first order in the concentration of ionophore, as is observed in a U-cell with a chloroform membrane (51), and second order in the concentration of sodium thiocyanate (data not shown); this has also been observed with a chloroform membrane (25). Thus, replacement of the standard chloroform membrane with a biologically more appropriate 1-octanol membrane does not appear to alter the mechanism of the transport process when 15-crown-5 is employed as the membrane carrier. It can be concluded that the divided beaker cell is suitable for experimental studies with phenceptin.

Phenceptin is a redox-switched sodium selective ionophore with specific phenytoin binding capability

Figure 4 compares the transport behaviour of phenceptin and 15-crown-5. Under the conditions [NaSCN] = 20 mM, [Ionophore] = 150 μM, the transport rates are 0.347 μM/h with phenceptin, and 0.435 μM/h with 15-crown-5.

Reduction of phenceptin with dithiothreitol gave the acyclic compound **19**. Neither this peptide nor the phenceptin precursor **18** transported sodium ions at a measurable rate.

Replacement of NaSCN by KSCN led to the transport of potassium ions at a rate of 0.204 μM/h (Fig. 4). The selectivity for sodium ions is, therefore, 1.7. This compares to the Na^+/K^+ selectivity of 5.9 found with 15-crown-5, and the Na^+/K^+ selectivity of 12.5 observed in a functioning sodium channel (16).

These experiments demonstrate phenceptin to be a redox-switched sodium selective ionophore, as required for our biomimetic model of the sodium channel.

The effect of phenytoin on the behaviour of various membrane carriers could now be examined. Preliminary experiments were performed with the 15-crown-5/NaSCN and 18-crown-6/NaSCN systems. For these studies, the cell was operated initially for 4 h, to ensure that sodium transport was occurring. Then 1.0 mol-equiv. of phenytoin was injected into the extracellular phase. There was no change in the transport rate. The same result was obtained in subsequent experiments in which 0.5,

Can. J. Chem. Downloaded from www.nrcresearchpress.com by 196.1.178.254 on 09/07/12
For personal use only.

Can. J. Chem. Downloaded from www.nrcresearchpress.com by 196.1.178.254 on 09/07/12
For personal use only.

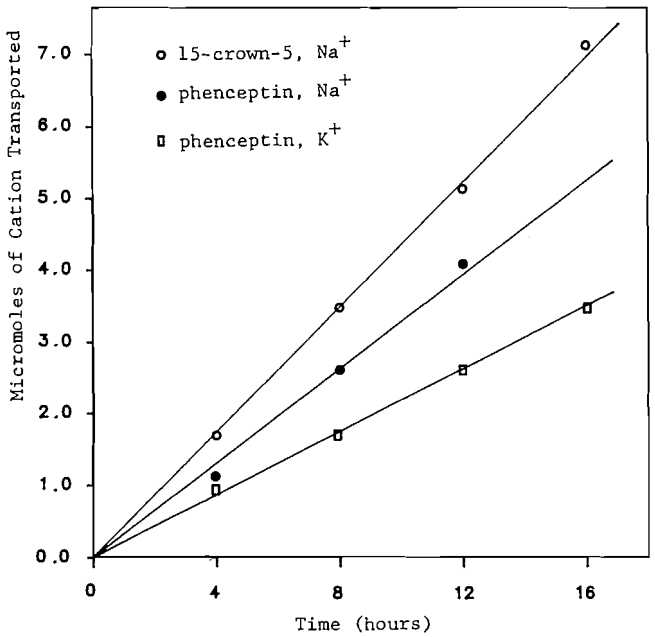

FIG. 4. Transport of sodium thiocyanate by 15-crown-5 (open circles) and by phenceptin (closed circles), and transport of potassium thiocyanate by phenceptin (squares). All data refer to experiments at 37.0°C, with cation and ionophore concentrations of 20 mM and 150 μM, respectively.

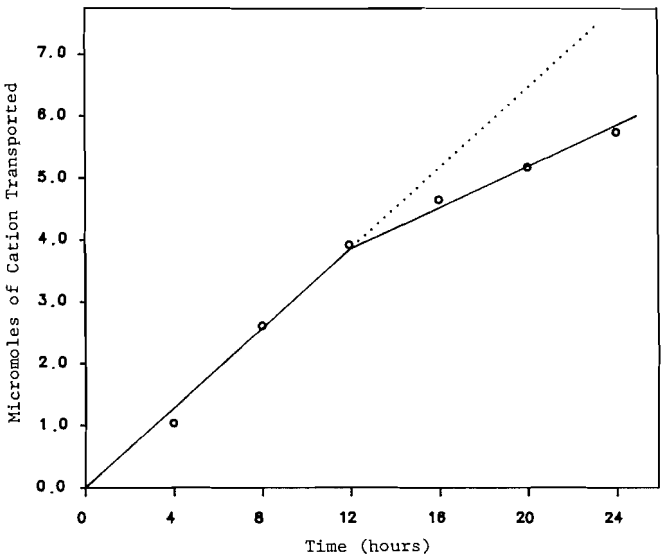

FIG. 5. Effect of addition of 5,5-diphenylhydantoin (one molar-equivalent) upon sodium ion transport by phenceptin. The hydantoin was added after 12 h, using the conditions of Fig. 4.

2.0, and 1000 mol-equiv. of phenytoin were injected after 4 h. It is clear that phenytoin has no effect on sodium ion transport by crown ether ionophores.

An entirely different result is obtained when these experiments are repeated with the phenceptin/NaSCN system. Figure 5 shows the effect of an injection of *1 mol-equiv.* of phenytoin after 12 h of sodium transport under the usual conditions. There is an immediate reduction in the rate of transport, which then continues at 40% of the original rate (60% inhibition).

However, when the *biologically inactive* 5,5-dibenzylhydantoin is substituted for phenytoin in such an experiment (Fig. 6), there is a very slight *increase* in the transport rate.

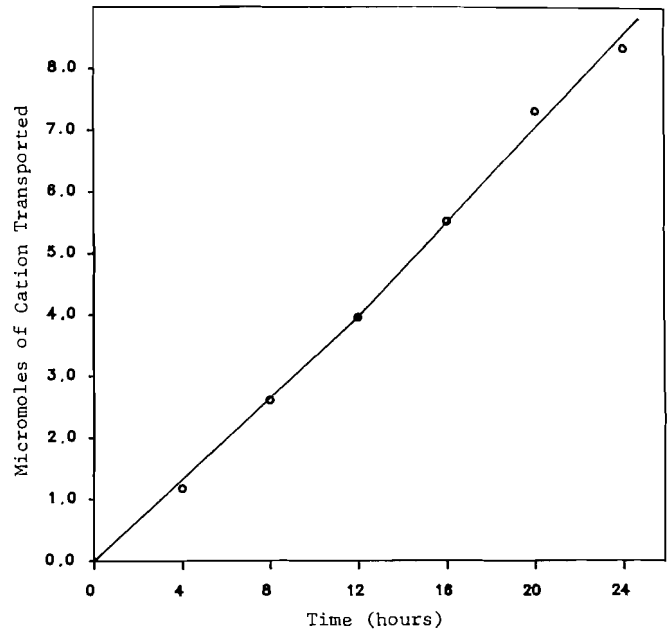

FIG. 6. Effect of addition of 5,5-dibenzylhydantoin (one molar-equivalent) upon sodium ion transport by phenceptin. The hydantoin was added after 12 h, using the conditions of Fig. 4.

Phenceptin is, therefore, a valid biomimetic model of a sodium channel phenytoin receptor.

Nature of the interaction between phenytoin and phenceptin

The inhibition of sodium ion transport by phenceptin was found to be linear in the concentration of added phenytoin, up to a 1:1 [phenytoin]/[phenceptin] ratio. Further increases in the phenytoin concentration did not increase the inhibition beyond the 60% observed with the 1:1 mixture. These observations suggested that the inhibition of sodium ion transport is achieved through the formation of a 1:1 complex.

The structure of this complex was studied by 400 MHz ^{1}Hmr at 37°C, using *n*-C_8D_{17}-OH as the solvent. Figure 7A shows the aromatic region of phenceptin in this solvent; addition of one mol-equiv. of phenytoin (Fig. 7B) leads to a significant change in the chemical shift differences of the aromatic protons of phenceptin. An aromatic–aromatic interaction (53) is suggested by these changes, but the data do not allow the nature of this interaction to be specified with certainty.

The effect of phenytoin upon the methylene protons of Gly^4 of phenceptin is more interesting, and can be interpreted. Figure 8A shows this region of the spectrum for a solution of phenceptin in *n*-C_8D_{17}-OH; Fig. 8B is the spectrum obtained immediately after addition of 1 mol-equiv. of phenytoin; Fig. 8C is the spectrum that results when the solution of 8B is shaken overnight with D_2O.

The glycine methylene protons are anisochronous because of the asymmetric environment, but coupling to the adjacent N—H is not observed in the hydroxylic solvent as a result of rapid exchange with the O—H protons. Addition of phenytoin must lead to the formation of a fairly strong complex with the glycyl amide hydrogen, because coupling of N—H to adjacent methylene protons is now observed. That this is the correct explanation of Fig. 8B is seen by the restoration of the original spectrum (Fig. 8C) following exchange of N—H with D_2O.

These observations can be understood by reference to the calculated phenceptin structure of Fig. 2. Only the N—H and

Can. J. Chem. Downloaded from www.nrcresearchpress.com by 196.1.178.254 on 09/07/12
For personal use only.

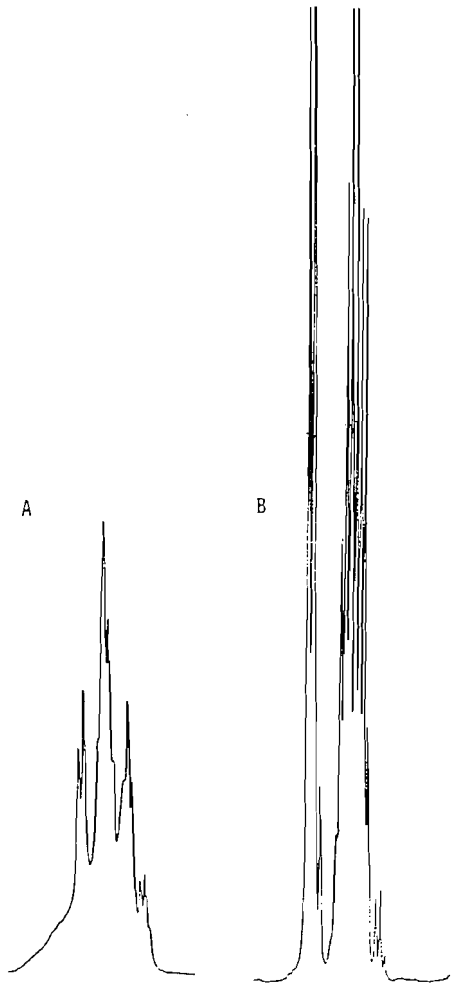

FIG. 7. (A) Aromatic region of the ^{1}Hmr spectrum of phenceptin in n-C_8D_{17}-OH solvent; (B) after addition of phenytoin (1 mol-equiv.).

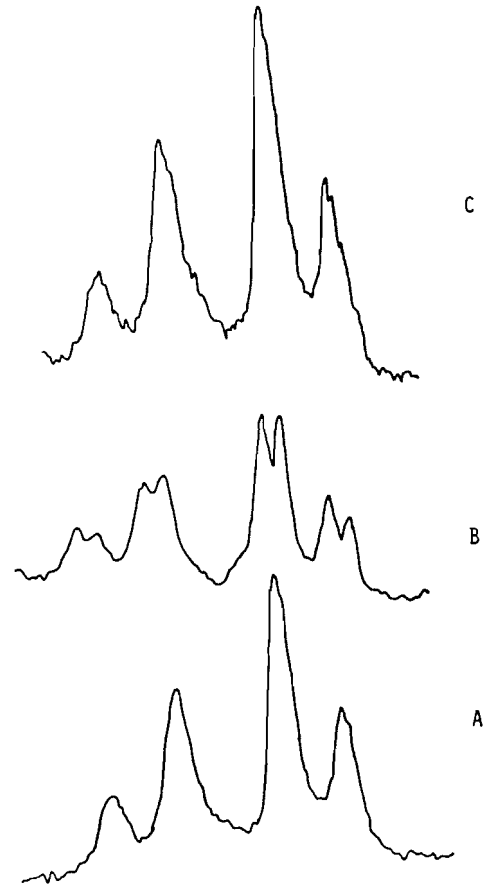

FIG. 8. (A) Glycine region of the ^{1}Hmr spectrum of phenceptin in n-C_8D_{17}-OH solvent; (B) after addition of phenytoin (1 mol-equiv.); (C) after shaking the solution of B overnight with D_2O.

C=O of Gly^4 possess orientations capable of complexation to an amide bond of phenytoin. This is shown schematically in Fig. 9, which provides an explanation for the inhibition of sodium ion transport by phenytoin, if the carbonyl oxygen of Gly^4 is also a cation binding site. The experimental and theoretical studies suggested by Fig. 9 have been completed, and will be published separately (47).

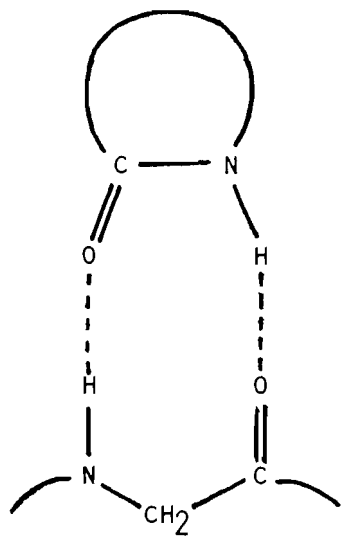

FIG. 9. Proposed interaction between Gly^4 of phenceptin and phenytoin.

Experimental

A. Syntheses

General

All solvents (Fisher or Anachemia, reagent grade) were purified before use, by standard methods (55–57). Several reagents were also purified before use. 2-*tert*-Butoxycarbonyloxyimino-2-phenylacetonitrile (BOC-ON) (Aldrich) was recrystallized from warm methanol. 1-Ethoxycarbonyl-2-ethoxy-1,2-dihydroquinoline (EEDQ) (Aldrich, 97% pure) was recrystallized from methylene chloride – ethyl ether. Diphenylhydantoin (Aldrich, Gold Label) was recrystallized twice from ethanol. Boc-glycine (Sigma) and L-proline benzyl ester hydrochloride (Sigma) were used as received.

Proton nmr spectra of hydantoins were obtained at 60 MHz on Varian T60 or EM360 spectrometers. Proton nmr spectra of peptides were recorded at 400 MHz on a Bruker AM400 spectrometer. Chemical shifts are reported in δ values relative to tetramethylsilane or 2,2-dimethyl-2-sila-pentane-5-sulfonate as internal standards. Infrared (ir) spectra were taken on a Perkin–Elmer 180 spectrometer. Absorption spectroscopy readings were made on a Bausch and Lomb Spectronic 20 spectrophotometer. Melting points were determined on a Meltemp apparatus and are uncorrected. Thin-layer chromatography (tlc) was performed on precoated Brinkmann silica gel 60F-254 plates with aluminium backing; spots were visualized with ninhydrin, palladium chloride, iodine vapour, or ultraviolet light.

Can. J. Chem. Downloaded from www.nrcresearchpress.com by 196.1.178.254 on 09/07/12
For personal use only.

Hydantoins

3-Ethyl-5-phenylhydantoin (2): L-Phenylglycine (Aldrich, 1.97 g, 0.013 mol) was dissolved in water (6.0 mL) containing potassium hydroxide (Fisher, 0.91 g, 0.016 mol), and ethyl isocyanate (Aldrich, 1.07 g, 0.015 mol) was added dropwise with stirring, during 3 h. The mixture was stirred overnight, filtered, and the filtrate acidified to pH 1.0. The *N*-ethylhydantoic acid was collected, dried, and cyclized by refluxing for 3 h with 6 N HCl (10.0 mL). The product crystallized upon cooling and was recrystallized from ethanol, 1.98 g (74%); mp 138°C; ir (Nujol): 1710, 1760 cm^{-1}; ^{1}Hmr ($CDCl_3$): 1.22 (3H, t), 3.60 (2H, q), 5.03 (1H, s), 6.80 (1H, s), 7.37 (5H, m); tlc: R_f 0.56 (methylene chloride: acetone: acetic acid 100.0: 100.0: 0.5), R_f 0.61 (ethanol: acetic acid 20:1), R_f 0.84 (methylene chloride: methanol 5:2).

3-Ethyl-5-benzylhydantoin (3): The synthesis was carried out as for **2**, except that L-phenylalanine (Sigma, 2.15 g, 0.013 mol) was used in place of phenylglycine. The product was recrystallized twice from ethanol to give 2.13 g (75%), mp 145°C; ir (Nujol): 1708, 1758 cm^{-1}; ^{1}Hmr ($CDCl_3$): 0.90 (3H, t), 3.02 (2H, q), 3.30 (2H, q), 4.19 (1H, t), 5.90 (1H, s), 7.37 (5H, m); tlc: R_f 0.57 (methylene chloride: acetone: acetic acid 100.0: 100.0: 0.5), R_f 0.63 (ethanol: acetic acid 20:1), R_f 0.85 (methylene chloride: methanol 5:2).

5,5-Dibenzylhydantoin: 1,3-Diphenyl-2-propanone (Aldrich, 4.10 g, 0.02 mol), potassium cyanide (Fisher, 2.5 g, 0.039 mol), and ammonium carbonate (Fisher, 7.4 g, 0.077 mol) were mixed with 50% aqueous ethanol (80.0 mL) and heated at 60°C for 15 h, to give a clear yellow solution. A slush of crystals formed rapidly when this solution was cooled. This crude product was dissolved in 5% sodium hydroxide (50.0 mL), filtered, treated with decolourizing carbon, and reprecipitated by the addition of an excess of concentrated hydrochloric acid. The product was recrystallized twice from 60% aqueous ethanol to give 3.92 g (70%) of material, mp 304–306°C, (lit. (58) mp 305°C); ir (Nujol): 1705, 1720, 1754 cm^{-1}; ^{1}Hmr (CD_3OD): 2.94 (2H, d, 15 Hz), 3.23 (2H, d, 15 Hz), 7.24 (10H, m); tlc: R_f 0.66 (methylene chloride: acetone: acetic acid 100.0: 100.0: 0.5), R_f 0.69 (ethanol: acetic acid 20:1), R_f 0.83 (methylene chloride: methanol 5:2).

Synthesis of phenceptin

N-Boc-S-trityl-L-cysteine dicyclohexylamine salt (9): *S*-Trityl-L-cysteine (8.74 g, 24.1 mmol) was suspended in dichloromethane (50.0 mL) and dicyclohexylamine (Aldrich, 5.3 mL, 26.5 mmol) was added, followed by BOC-ON (6.48 g, 26.4 mmol). The solution was stirred at room temperature for 24 h. Removal of the solvent under reduced pressure yielded a yellow foam, to which was added anhydrous ether (200 mL). The product crystallized after storage at −20°C for 15 h, and it was collected, dried, and recrystallized from absolute methanol. 13.0 g, mp 215–216°C, (lit. (46) mp 211–212°C).

S-Trityl-L-cysteine benzhydryl ester (10): A mixture of benzophenone (Aldrich, 25.2 g, 0.138 mol), hydrazine hydrate (BDH, 10.0 g, 0.2 mol), and absolute ethanol (15 mL) was refluxed for 10 h. Benzophenone hydrazone was recrystallized from 95% ethanol to give long pale brown needles: 22 g (80%), mp 96–98°C (lit. (59) mp 98°C). A solution of benzophenone hydrazone (5.8 g, 30 mmol), anhydrous magnesium sulfate (Anachemia, 3.0 g), and methylene chloride (60.0 mL) was stirred rapidly in an ice-bath. To this was added activated manganese dioxide (Aldrich, 9.2 g) in one portion. Stirring was continued for 2 h at 0°C and for 1 h at room temperature. Removal of the solvent gave a dark purple oil, which, upon storage at −16°C, afforded red needles of diphenyldiazomethane: 5.2 g (88%), mp 33–34°C (lit. (60) mp 35°C).

S-Trityl-L-cysteine (11.0 g, 30.3 mmol), diphenyldiazomethane 11.74 g, 60.6 mmol), methanol (100 mL), and methylene chloride (150 mL) were mixed, yielding a suspension, which was stirred at room temperature. After 12 h a pink solution had formed. Evaporation of the solvent gave an oil, which was dissolved in a minimum of acetone and treated with *p*-toluenesulfonic acid (Eastman, 5.76 g, 30.3 mmol); The acetone was evaporated, and subsequent trituration with hexane produced an amorphous solid, 21.33 g (98%); $[\alpha_D]$ 70.7 (*c* 1.35, methanol); tlc (free base); R_f 0.78 (methylene chloride: ethyl acetate 9:1). The compound gave a single spot, which was visualized with ninhydrin and with palladium chloride spray.

N-Boc-glycyl-L-proline benzyl ester (11): A solution of *N*-Boc-glycine (8.76 g, 50 mmol) and EEDQ (Aldrich, 13.6 g, 55 mmol) in methylene chloride (120 mL) was stirred for 5 min. Then L-proline benzyl ester hydrochloride (12.08 g, 50 mmol), triethylamine (Anachemia, 5.16 g, 51 mmol), and additional methylene chloride (40 mL) were added. Stirring was continued at room temperature for 20 h. The reaction mixture was washed successively with 10% aqueous potassium bisulfate (5 × 160 mL), saturated brine (1 × 160 mL), saturated sodium bicarbonate (3 × 160 mL), and brine (1 × 160 mL), dried over anhydrous magnesium sulfate, and evaporated to give a viscous oil. This was dissolved in warm ethyl acetate (15 mL), and hexane was added to the cloud-point (100 mL). After overnight storage at 4°C, the product crystallized, and was recrystallized twice from ethyl acetate – hexane to give colourless needles, 14.24 g (78%), mp 77–78°C (lit. (61) mp 76–77°C); ^{1}Hmr ($CDCl_3$): 1.47 (9H, s, *t*-Bu), 2.02 (3H, m, Pro β- + γ-CH_2), 2.20 (1H, m, Pro β- + γ-CH_2), 3.47 (1H, m, Pro δ-CH_2), 3.60 (1H, m, Pro δ-CH_2), 3.92 (1H, dd, 7, 18 Hz, Gly CH_2), 4.02 (1H, dd, 7, 18 Hz, Gly CH_2), 4.59 (1H, q, 5.0, 7.5 Hz, Pro α-H), 5.44 (1H, br s, urethane N-H), 7.37 (5H, d, aromatic), tlc: R_f 0.43 (methylene chloride: ethyl acetate, 9:1), R_f 0.86 (methylene chloride: methanol 5:2), one spot, ninhydrin negative.

N-Boc-glycyl-L-proline (12): *N*-Boc-glycyl-L-proline benzyl ester (14.0 g, 38.7 mmol) was dissolved in methanol (300 mL), and 10% palladium on carbon (Aldrich, 1.01 g) was added under nitrogen. The reaction vessel was purged three times with nitrogen and three times with hydrogen, and the mixture was then stirred for 4 h under hydrogen at atmospheric pressure. The catalyst was removed by filtration through diatomaceous earth (Fisher, Celite), and the filtrate was evaporated to a viscous oil. After trituration with ethyl acetate – ethyl ether (50 mL ethyl acetate, 50 mL ethyl ether), a white crystalline solid formed, 9.75 g (98%), mp 145–146°C; ^{1}Hmr ($CDCl_3$): 1.45 (9H, s, Boc), 2.08 (3H, m, Pro β- + γ-CH_2), 2.26 (1H, m, Pro β- + γ-CH_2), 3.48 (1H, m, Pro δ-CH_2), 3.58 (1H, m, Pro δ-CH_2), 3.94 (1H, q, 5, 20 Hz, Gly CH_2), 4.08 (1H, q, 6, 20 Hz, Gly CH_2), 4.60 (1H, q, 6, 8 Hz, Pro α-H), 5.51 (1H, br, urethane N-H), 9.13 (1H, br s, CO_2H); tlc: R_f 0.41 (methylene chloride: methanol 5:2), one spot, ninhydrin negative. The compound became ninydrin positive after pretreatment with formic acid.

Glycyl-L-proline benzyl ester hydrochloride (13): *N*-Boc-glycyl-L-proline benzyl ester (13.91 g, 38.4 mmol) was dissolved in dry ethyl acetate (360 mL). The solution was cooled to 0°C in an ice-bath, and anhydrous hydrogen chloride gas (Matheson Gas Products) was bubbled into the solution for 25 min. Stirring was continued at 0°C for 1 h, and then at room temperature for an additional 30 min. The solvent was then removed at 26°C to yield a white foam, which was crystallized from ethanol (20 mL) and ether (200 mL), 11.21 g (100%), mp 108–113°C; ^{1}Hmr ($CDCl_3$): 1.90 (3H, br, Pro β- + γ-CH_2), 2.12 (1H, br, Pro β- + γ-CH_2), 3.54 (2H, br, Pro δ-CH_2), 4.03 (1H, d, 17.5 Hz, gly CH_2), 4.17 (1H, d, 17.5 Hz, Gly CH_2), 4.60 (1H, d, 7 Hz, Pro α-H), 5.11 (1H, d, 14 Hz, CH_2Ph), 5.18 (1H, d, 14 Hz, CH_2Ph), 7.35 (5H, d, Ph), 8.36 (3H, br, NH_3^+); tlc: R_f 0.46 (methylene chloride: methanol 5:2). The compound gave one spot which was ninhydrin positive.

N-Boc-glycyl-L-prolyl-glycyl-L-proline benzyl ester (14): A solution of *N*-Boc-glycyl-L-proline (9.71 g, 38 mmol) and EEDQ (Aldrich, 10.32 g, 42 mmol) in methylene chloride (250 mL) was stirred at room temperature for 5 min, and glycyl-L-proline benzyl ester hydrochloride (11.10 g, 38 mmol) and triethylamine (BDH, 3.84 g, 38 mmol) were then added. The resulting solution was stirred at room temperature for 20 h and then washed successively with 10% aqueous potassium bisulfate (3 × 250 mL), saturated brine (2 × 250 mL), saturated sodium bicarbonate (3 × 250 mL), saturated brine (1 × 250 mL), dried over anhydrous sodium sulfate, and evaporated to a white amorphous solid. This was crystallized from ethyl acetate – hexane, and then recrystallized from acetone (25 mL) and hexane (50 mL), 16.23 g (87%), mp 162–164°C (lit. (42) mp 162–163°C); ^{1}Hmr ($CDCl_3$): 1.47 (9H, s, Boc), 2.04 (4H, m, Pro CH_2), 2.20 (4H, m, Pro CH_2), 3.46 (2H, m, Pro δ-CH_2), 3.60 (2H, m, Pro δ-CH_2), 3.90–4.16 (4H, m, glycine CH_2), 4.60 (2H, m, Pro α-H), 5.16 (1H, d, 12 Hz, benzyl), 5.22 (1H, d, 12 Hz, benzyl), 5.49 (1H, br, urethane N-H), 7.21 (1H,

Can. J. Chem. Downloaded from www.nrcresearchpress.com by 196.1.178.254 on 09/07/12
For personal use only.

br, NH), 7.38 (5H, br d, aromatic), tlc: R_f 0.38 (methylene chloride: acetone: acetic acid 100.0: 100.0: 0.5), R_f 0.81 (methylene chloride: methanol 5:2), one spot, ninhydrin negative.

N-Boc-glycyl-L-prolyl-glycyl-L-proline (15): *N*-Boc-glycyl-L-prolyl-glycyl-L-proline benzyl ester (5.0 g, 9.6 mmol) was dissolved in methanol (350 mL), and 10% palladium on carbon (Alfa, 800 mg) was added under nitrogen. The reaction vessel was purged three times with nitrogen and three times with hydrogen, and the mixture was then stirred vigorously for 5 h under hydrogen at atmospheric pressure. The catalyst was removed by filtration through diatomaceous earth (Fisher, Celite) and the filtrate was evaporated to dryness under reduced pressure to give a white foam, which crystallized from ethyl acetate. Three recrystallizations from ethyl acetate gave 3.83 g (93%), mp 191–193°C; $[\alpha_D]$ −135° (*c* 1.5, methanol); ^{1}Hmr ($CDCl_3$): 1.46 (9H, s, *tert*-butyl), 1.94–2.32 (8H, m, Pro β- + γ-CH_2), 3.45–3.62 (4H, m, Pro δ-CH_2), 3.69–4.26 (4H, m, overlapping Gly CH_2), 4.52 (1H, m, Pro α-H), 4.60 (1H, m, Pro α-H), 5.60 (1H, br, urethane NH), 7.51 (1H, br, NH). *Anal.* calcd. for $C_{19}H_{30}N_4O_7$: C 53.46, H 7.03, N 13.13; found: C 53.54, H 7.31, N 12.95.

N-Boc-glycyl-L-prolyl-glycyl-L-prolyl-S-trityl-L-cysteine benzhydryl ester (16): A solution of *N*-Boc-glycyl-L-prolyl-glycyl-L-proline (7.0 g, 16.63 mmol) and EEDQ (Aldrich, 4.52 g, 18.3 mmol) in methanol (200 mL) was stirred for 5 min, and *S*-trityl-L-cysteine benzhydryl ester *p*-toluenesulfonate (11.67 g, 16.63 mmol) and triethylamine (1.68 g, 16.63 mmol) were then added. The solution was stirred for 44 h, and then evaporated to an oily residue. This was dissolved in ethyl acetate (170 mL) and washed successively with 10% potassium bisulfate (5 × 170 mL), saturated brine (1 × 170 mL), saturated sodium bicarbonate (3 × 170 mL), and brine (1 × 170 mL), dried over anhydrous sodium sulfate, and evaporated under reduced pressure. The residue was converted to a foam by addition of methylene chloride (50 mL) and removal of the solvent, followed by repetition of this process twice more. This foam crystallized from ethyl acetate (26 mL) and hexane (130 mL), (11.75 g (75%), mp 110–120°C; $[\alpha_D]$ −55.8° (*c* 1.25, methanol); ^{1}Hmr ($CDCl_3$): 1.44 (9H, s, *tert*-butyl), 1.92 (6H, m, Pro β- and γ-CH_2), 2.21 (2H, m, Pro β- and γ-CH_2), 2.66 (2H, m, Cys CH_2), 3.30–3.52 (4H, m, Pro δ-CH_2), 3.83–4.16 (4H, m, Gly CH_2), 4.47 (1H, m, Cys α-H), 4.54 (2H, m, Pro α-H), 5.45 (1H, br, urethane NH), 6.80 (1H, s, benzhydryl), 7.12 (1H, d, 12 Hz, NH), 7.28 (25H, m, aromatic); tlc: R_f 0.51 (methylene chloride: acetone: acetic acid 100.0: 100.0: 0.5), R_f 0.81 (methylene chloride: methanol 5:2). The compound gave a single spot, which was ninhydrin negative but readily visualized with palladium chloride spray.

Glycyl-L-prolyl-glycyl-L-prolyl-S-trityl-L-cysteine benzhydryl ester (17): *N*-Boc-glycyl-L-prolyl-glycyl-L-prolyl-*S*-trityl-L-cysteine benzhydryl ester (2.0 g, 2.13 mmol) was dissolved in formic acid (BDH, 100%, AnalR grade, 200 mL) that had been precooled to 10°C. The resulting solution was stirred at 10.0 ± 0.1°C for 25 min and then frozen using liquid nitrogen. The formic acid was quickly removed by freeze-drying to leave an amorphous white solid. This was dissolved in ethyl acetate, and the solution was washed with saturated sodium bicarbonate (3 × 100 mL), dried over anhydrous sodium sulfate, and evaporated. Two treatments with methylene chloride, followed by reevaporation, yielded a white foam, 1.36 g (77%); $[\alpha_D]$ −61.9° (*c* 1.1, methanol); ^{1}Hmr ($CDCl_3$): 1.63 (2H, br, NH_2), 1.91 (6H, m, Pro β- + γ-CH_2), 2.22 (2H, m, Pro β- + γ-CH_2), 2.60 (1H, q, 5, 12 Hz, Cys CH_2), 2.69 (1H, q, 8, 12 Hz, Cys CH_2), 3.28 (2H, m, Pro δ-CH_2), 3.38 (1H, d, 15 Hz, Gly CH_2), 3.40 (1H, d, 15 Hz, Gly CH_2), 3.50 (2H, m, Pro δ-CH_2), 3.92 (1H, q, 5, 15 Hz, Gly CH_2), 4.08 (1H, q, 5, 15 Hz, Gly CH_2), 4.44 (1H, m, Cys α-H), 4.54 (2H, d, 7 Hz, Pro α-H), 6.78 (1H, s, benzhydryl), 7.21 (1H, d, 7 Hz, N-H), 7.35–7.50 (26H, aromatic + N-H); tlc: R_f 0.77 (methyl ethyl ketone: acetic acid: water 4:1:1). The compound gave a single spot and was ninhydrin positive.

N-Boc-S-trityl-L-cysteinyl-glycyl-L-prolyl-glycyl-L-prolyl-S-trityl-L-cysteine benzhydryl ester (18): *N*-Boc-*S*-trityl-L-cysteine dicyclohexylammonium salt (1.05 g, 1.63 mmol) was partitioned between ethyl acetate (50 mL) and 10% citric acid (50 mL). The organic phase was separated, washed with 10% citric acid (2 × 30 mL) and brine (1 × 30 mL), dried over anhydrous sodium sulfate, and evaporated to yield 780 mg of material. This was dissolved in ethyl acetate (15 mL), and EEDQ (Aldrich, 0.443 g, 1.77 mmol) was added. The solution was stirred for 10 min, and a solution of glycyl-L-prolyl-glycyl-L-prolyl-*S*-trityl-L-cysteine benzhydryl ester (1.36 g, 1.63 mmol), in ethyl acetate (25 mL), was added. Stirring was continued for 20 h, and the cloudy reaction mixture was then filtered. The filtrate was washed successively with 10% potassium bisulfate (4 × 100 mL), brine (1 × 100 mL), saturated sodium bicarbonate (3 × 100 mL), brine (1 × 100 mL), dried over anhydrous sodium sulfate, and evaporated. Two treatments with methylene chloride yielded a white foam, 895 mg (80%); ^{1}Hmr ($CDCl_3$): 1.40 (9H, s, *tert*-butyl), 1.84 (3H, m, Pro β- and γ-CH_2), 1.95 (3H, m, Pro β- and γ-CH_2), 2.13 (1H, m, Pro β- and γ-CH_2), 2.22 (1H, m, Pro β- and γ-CH_2) 2.50–2.71 (4H, overlapping AB of ABX, Cys CH_2), 3.34 (2H, m, Pro δ-CH_2), 3.50 (2H, m, Pro δ-CH_2), 3.82–4.10 (4H, overlapping Gly CH_2), 4.43 (1H, d, Cys α-H), 4.48 (1H, d, Pro α-H), 4.53 (1H, d, Pro α-H), 4.87 (1H, d, Cys α-H), 4.98 (1H, br, urethane NH), 6.77 (1H, s, benzhydryl), 6.94 (2H, br, NH), 7.08 (1H, d, 6 Hz, NH), 7.17–7.35 (30 H, m, aromatic), 7.40 (10 H, d, aromatic); tlc: R_f 0.89 (dichloromethane: methanol 5:2). The compound gave one spot, which was ninhydrin negative.

Phenceptin (N-Boc-L-cystinyl-glycyl-L-prolyl-glycyl-L-prolyl-L-cysteine benzhydryl ester): *N*-Boc-*S*-trityl-L-cysteinyl-glycyl-L-prolyl-glycyl-L-prolyl-*S*-trityl-L-cysteine benzhydryl ester (2.5 g, 2.27 mmol) was dissolved in a mixture of methanol (500 mL) and methylene chloride (500 mL), and the solution was added dropwise, with stirring, to an ice-cold solution prepared from iodine (1.15 g, 2 equiv.) and pyridine (2 mL, 10 equiv.), in methanol (1 L). When the addition was complete (4.5 h), the ice-bath was removed and stirring was continued for 2 h, by which time tlc (methylene chloride – acetone, 1:1) showed that the starting material had been consumed. The methanol solvent was removed under reduced pressure to give a dark brown oil. This was dissolved in methylene chloride (500 mL), and the solution was washed successively with 10% potassium bisulfate (1 × 400 mL), 10% sodium bisulfate (2 × 300 mL), and water (3 × 300 mL), dried over anhydrous sodium sulfate, and evaporated. The white foam was triturated with hexane (3 × 50 ML) and filtered to give 1.811 g of material, which was chromatographed on silica gel (35 g) using acetone as eluant and a flow rate of 5 mL/min, yielding 1.18 g (65%) of phenceptin. The analytical sample was prepared by repetition of the column chromatography. $[\alpha_D]$ −1.29 (*c* 1.15, methanol); ^{1}Hmr ($CDCl_3$, 273 K, major conformation): 2.01 (6H, m, Pro β- + γ-CH_2), 2.16 (2H, m, Pro β- + γ-CH_2), 2.72 (2H, q, 4, 16 Hz, Cys CH_2), 3.08 (2H, q, 7, 16 Hz, Cys CH_2), 3.19 (2H, br, CH_2 of Gly^2), 3.47 (2H, m, Pro δ-CH_2), 3.59 (2H, m, Pro δ-CH_2) 3.92 (1H, q, 4, 18 Hz, CH of Gly^4), 4.09 (1H, q, 4, 18 Hz, CH of Gly^4), 4.42 (1H, m, Cys α-H), 4.53 (1H, m, Cys α-H), 4.66 (1H, m, Pro α-H), 4.94 (1H, m, Pro α-H), 6.20 (1H, d, 9 Hz, urethane N-H), 6.93 (1H, s, benzhydryl), 7.14 (2H, d, 7 Hz, N-H), 7.35 (11H, m, Ar + N-H); tlc: R_f 0.65 (methylene chloride: methanol 5:2), R_f 0.87 (methyl ethyl ketone: acetic acid: water 4:1:1). The peptide gave a single spot on tlc, which was not visualized with ninhydrin but became ninhydrin positive after pretreatment with formic acid. *Anal.* calcd. for $C_{38}H_{48}N_6O_9S_2 \cdot H_2O$: C 56.01, H 6.18, N 10.31, S 7.85; found: C 56.18, H 6.07, N 10.13, S 8.61.

B. Transport studies

General

The divided beaker cell was sealed with a protective shield, to minimize loss of solvent, and immersed in a water bath maintained at 37.0 ± 0.1°C, using a Haake temperature controller. The extracellular phase contained a salt (20 mM) in water (80.0 mL). The membrane phase contained the ionophore (150 μmol/L) in 1-octanol (50.0 mL). The intracellular phase was water (80.0 mL). All phases were stirred simultaneously at constant, reproducible rates. Periodic sampling of the intracellular phase allowed determination of transport rates. Experiments were repeated several times to ensure reproducibility. Blank runs were always used as controls. At no time did the divided beaker cell "leak" ions into the intracellular phase in the absence of an ionophore.

Analytical methods

Transport rates were quantified by determination of the concentration of the counter-anion in the intracellular phase. For studies involving thiocyanate as the counter-anion, the anion concentration was determined spectrophotometrically at 480 nm. Aliquots (0.50 mL) of the intracellular phase were mixed with 0.005 M ferric chloride (5.00 mL), which was made 0.18 M in perchloric acid and the thiocyanate concentration was determined from a Beer's Law plot. A new calibration curve was determined prior to each kinetic run.

When picrate was the counter-anion, the extracellular phase contained picric acid (50 mM) and HEPES buffer (10 mM) at pH 7.0. The appearance of the yellow picrate anion in the intracellular phase was determined spectrophotometrically at 355 nm.

When chloride was the counter-anion, the concentration was determined indirectly by the Volhard method (54).

Can. J. Chem. Downloaded from www.nrcresearchpress.com by 196.1.178.254 on 09/07/12
For personal use only.

Acknowledgements

The authors are grateful to the Natural Sciences and Engineering Research Council of Canada for financial support, the Medical Research Council of Canada for the award of a Graduate Fellowship, and Queen's University for generous allocation of computer time. In addition to Professor Morton Raban, mentioned in the text, the authors thank Professor John Page (Queen's University) for many helpful discussions on the subject of electrochemical aspects of ion transport, Professor Louis Ramaley (Dalhousie University) for a helpful discussion concerning redox properties of hydantoins, Robert Campbell for construction of the transport cell, and Susan Blake for assistance with the nmr measurements.

1. G. H. GLASER. The epilepsies. *In* Cecil's textbook of medicine. 15th ed. *Edited by* P. Beeson. W.B. Saunders, Toronto. 1979; D. ROSENBLOOM and A. UPTON. Can. Med. Assoc. J. **128**, 261 (1983); W. LENNOX and M. LENNOX. Epilepsy. Little, Brown, and Co., Boston. 1960.
2. B. HILLE. Ionic channels of excitable membranes. Sinauer Associates Inc., Sunderland, MA. 1984.
3. H. H. MERRITT and T. J. PUTNAM. Arch. Neurol. Psychiatry, **39**, 1003 (1938).
4. J. BRUNI. Can. Med. Assoc.J. **120**, 817 (1979).
5. R. D. ADAMS and M. VICTOR. Principles of neurology. 3rd ed. McGraw–Hill, Toronto. 1985.
6. J. H. POUPAERT, D. VANDERVORST, P. GUIOT, M. M. M. MOUSTAFA, and P. DUMONT. J. Med. Chem. **27**, 76 (1984); S. CORTES, Z-K LIAO, D. WATSON, and H. KOHN. *J. Med. Chem.* **28**, 601 (1985).
7. M. G. WONG, J. A. DEFINA, and P. R. ANDREWS. J. Med. Chem. **29**, 562 (1986).
8. D. F. WEAVER. PhD thesis, Queen's University, Kingston, Ont. 1986.
9. D. R. ROBINSON and W. P. JENCKS. J. Am. Chem. Soc. **87**, 2470 (1965).
10. C. HANSCH. Drug design. Volume 1. *Edited by* E. J. Ariens. Academic Press, New York. 1971; C. HANSCH, R. MUIR, P. MALONEY, F. GEIGER, and M. STREICH. J. Am. Chem. Soc. **85**, 2817 (1963).
11. C. HANSCH and T. FUJITA. J. Am. Chem. Soc. **86**, 1616 (1964); A. LEO, P. JOW, C. SILIPO, and C. HANSCH. J. Med. Chem. **18**, 865 (1975); M. PLEISS and G. GRUNEWALD. J. Med. Chem. **26**, 1760 (1983); E. J. LIEN, R. C. H. LIAO, and H. G. SNINOUDA. J. Pharm. Sci. **68**, 463 (1979).
12. J. A. VIDA and E. H. GERRY. Cyclic ureides. *In* Anticonvulsants: medicinal chemistry. Vol. 15. *Edited by* J. A. Vida. Academic Press, New York. 1977; W. J. CLOSE and M. A. SPIELMAN. Med. Chem. (N.Y.), **5**, 1 (1961).
13. E. J. LIEN. J. Med. Chem. **13**, 1189 (1970); C. YANAGAMI, H. TAKAMI, Y. YAMAMOTO, and N. TAKAO. Chem. Pharm. Bull. **32**, 4994 (1984).
14. D. M. WOODBURY. *In* Antiepileptic drugs: mechanisms of action. *Edited by* G. H. Glaser, J. K. Penry, and D. M. Woodbury. Raven Press, New York. 1980. p. 305.
15. (*a*) J. G. PERRY, L. MCKINNEY, and P. DE WEER. Nature, **272**, 271 (1978); (*b*) M. WILLOW, and W. A. CATTERALL. Mol. Pharmacol. **22**, 627 (1982); (*c*) M. WILLOW, E. A. KUENZEL, and W. A. CATTERALL. Mol. Pharmacol. **25**, 228 (1984); (*d*) R. L. MACDONALD and M. J. MCLEAN. Adv. Neurol. **44**, 713 (1986); (*e*) W. A. CATTERALL. Trends Pharm. Sci. **8**, 57 (1987).
16. W. A. CATTERALL. Ann. Rev. Biochem. **55**, 953 (1986).
17. D. J. MESSNER and W. A. CATTERALL. J. Biol. Chem. **260**, 10597 (1985).
18. B. HILLE. J. Gen. Physiol. **58**, 599 (1971); J. Gen. Physiol. **59**, 637 (1972).
19. M. NODA, S. SHIMIZU, T. TANABE, T. TAKAI, T. KAYANO, T. IKEDA, H. TAKAHASHI, H. NAKAYAMA, Y. KANAOKA, N. MINAMINO, K. KANGAWA, H. MATSUO, M. A. RAFTERY, T. HIROSE, M. NOTAKE, S. INAYAMA, H. HAYASHIDA, T. MIYATA, and S. NUMA. Nature, **312**, 121 (1984).
20. V. AULD, J. MARSHALL, A. GOLDIN, A. DOWSETT, W. CATTERALL, N. DAVIDSON, and R. DUNN. J. Gen. Physiol. **86**, 10a (1985).
21. E. M. KOSOWER. FEBS Lett. **182**, 234 (1985).
22. G. S. OXFORD, C. H. WU, and T. NARAHASHI. J. Gen. Physiol. **71**, 227 (1978); W. NONNER, B. C. SPALDING, and B. HILLE. Nature, **284**, 360 (1980); G. K. WANG. J. Physiol. **346**, 127 (1984); Biophys. J. **46**, 121 (1984).
23. A. OHNO and S. OAE. *In* Organic chemistry of sulfur. *Edited by* S. Oae. Plenum Press, New York. 1977. p. 119.
24. R. H. MATTSON, G. R. HENIGEB, B. B. GALLAGHER, and G. H. GLASER. Neurology, **20**, 407 (1970).
25. L. K. WEAVER. Ann. Emerg. Med. **12**, 38 (1983).
26. M. DOBLER. Ionophores and their structures. Wiley–Interscience, New York. 1981; B. C. PRESSMAN, E. J. HARRIS, W. S. JAGGER, and J. H. JOHNSON. Proc. Natl. Acad. Sci. U.S.A. **58**, 1949 (1967).
27. H. R. GUY. Biophys. J. **45**, 249 (1984).
28. T. MINAMI, S. SHINKAI, and O. MANABE. Tetrahedron Lett. **23**, 5167 (1982); S. SHINKAI, K. INUZUKA, O. MIYAZAKI, and O. MANABE. J. Am. Chem. Soc. **107**, 3950 (1985).
29. M. RABAN. J. GREENBLATT, and F. KANDIL. J. Chem. Soc. Chem. Commun. 1409 (1983).
30. (*a*) T. SHIMIZU, Y. TANAKA, and K. TSUDA. Bull. Chem. Soc. Jpn. **55**, 3817 (1982); (*b*) S. KIMURA and Y. IMANISHI. Biopolymers, **22**, 2383 (1983); (*c*) Biopolymers, **23**, 563 (1984); (*d*) F. BEHM, D. AMMANN, W. SIMON, K. BRUNFELDT, and J. HALSTRØM. Helv. Chim. Acta, **68**, 10 (1985); (*e*) T. SHIMIZU, Y. TANAKA, and K. TSUDA. Bull. Chem. Soc. Jpn. **58**, 3436 (1985).
31. YU. A. OVCHINNIKOV, V. T. IVANOV, and A. M. SHKROB. Membrane active complexones. Elsevier, Amsterdam. 1974.
32. A. J. DE BOLD. Science, **230**, 767 (1985).
33. H. I. MOSBERG and J. R. OMNAAS. J. Am. Chem. Soc. **107**, 2986 (1985); A. RAVI and P. BALARAM. Tetrahedron, **40**, 2577 (1984).
34. D. F. MAYERS and D. W. URRY. J. Am. Chem. Soc. **94**, 77 (1972).
35. J. LEJEUNE. Ann. Génét. **22**, 108 (1979).
36. (*a*) B. C. PRESSMAN. Ann. Rev. Biochem. **45**, 501 (1976); (*b*) R. W. ROESKE and S. V. KENNEDY. *In* Chem. Biochem. of Amino Acids, Pept. Proteins, **7**, 205 (1983); (*c*) D. W. URRY. Top. Curr. Chem. **128**, 175 (1985).
37. B. F. GISIN and R. B. MERRIFIELD. J. Am. Chem. Soc. **94**, 6165 (1972); D. BARON, L. G. PEASE, and E. R. BLOUT. J. Am. Chem. Soc. **99**, 8299 (1977); J. P. DEGELAEN, P. P. PHAM, and E. R. BLOUT. J. Am. Chem. Soc. **106**, 4882 (1984).
38. U. BURKERT and N. L. ALLINGER. Molecular mechanics. American Chemical Society, Washington. 1982.

39. (*a*) S. WOLFE, D. F. WEAVER, and K. YANG. Can. J. Chem. **66**, 2687 (1988); (*b*) S. WOLFE, S. BRUDER, D. F. WEAVER and K. YANG. Can. J. Chem. **66**, 2703 (1988).
40. C. M. DEBER, V. MADISON, and W. R. BLOUT. Acc. Chem. Res. **9**, 106 (1976).
41. P. Y. CHOU and G. D. FASMAN. J. Mol. Biol. **115**, 135 (1977).
42. C. M. DEBER and E. R. BLOUT. Isr. J. Chem. **12**, 15 (1974).
43. ECEPP. Quantum Chemistry Program Exchange No. 454, Bloomington, IN.
44. N. L. ALLINGER. MMP2(85). Quantum Chemistry Program Exchange, Bloomington, IN.
45. S. WOLFE, R. J. BOWERS, S. K. HASAN, and P. M. KAZMAIER. Can. J. Chem. **59**, 406 (1981).
46. S. WOLFE and M. G. JOKINEN. Can. J. Chem. **57**, 1388 (1979); S. E. JENSEN, D. W. S. WESTLAKE, R. J. BOWERS, C. F. INGOLD, M. JOUANY, L. LYUBECHANSKY, and S. WOLFE. Can. J. Chem. **62**, 2712 (1984).
47. S. WOLFE, R. J. BOWERS, H.-S. SHIN, C.-K. SOHN, and K. YANG. Heterocycles. In press.
48. K. MEYER. Arch. Exp. Pathol. Pharmacol. **42**, 109 (1899); E. OVERTON. Studien über die narkose. Jena, 1901; V. A. LEVIN. J. Med. Chem. **23**, 682 (1980).
49. J. J. CHRISTENSEN, J. D. LAMB, S. R. IZATT, S. E. STARR, G. WEED, and B. D. STITT. J. Am. Chem. Soc. **100**, 3219 (1978).
50. A. J. BARD and L. R. FAULKNER. Electrochemical methods. Fundamentals and applications. John Wiley, New York. 1980.
51. C. F. REUSCH and E. L. CUSSLER. A. I. Ch. E. J. **19**, 736 (1973).
52. J. D. LAMB, J. J. CHRISTENSEN, S. R. IZATT, K. BEDKE, M. S. ASTIN, and R. M. IZATT. J. Am. Chem. Soc. **102**, 3399 (1980).
53. S. K. BURLEY and G. A. PETSKO. Science, **229**, 23 (1985); S. K. BURLEY and G. A. PETSKO. J. Am. Chem. Soc. **108**, 7995 (1986).
54. D. A. SKOOG and D. M. WEST. Fundamentals of analytical chemistry. 3rd ed. Holt, Rinehart and Winston, Toronto. 1976.
55. B. S. FURNISS, A. J. HANNAFORD, V. ROGERS, P. W. G. SMITH, and A. R. TATCHELL. Vogel's textbook of practical organic chemistry. 4th ed. Longman, New York. 1978.
56. D. D. PERRIN, W. L. F. ARMAREGO, and D. R. PERRIN. Purification of laboratory chemicals. Pergamon, Oxford. 1966.
57. L. F. FIESER and M. FIESER. Reagents for organic synthesis. Vols. 1–5. Wiley–Interscience, New York. 1967–1975.
58. K. H. SLOTTA and G. SZYSKA. Ber. Dtsch. Chem. Ges. B: **67**, 1529 (1934).
59. J. B. MILLER. J. Org. Chem. **24**, 560 (1959).
60. H. REIMLINGER. Chem. Ber. **97**, 3493 (1954).
61. C. M. DEBER, F. A. BOVEY, J. P. CARVER, and E. R. BLOUT. J. Am. Chem. Soc. **92**, 6191 (1970).

Can. J. Chem. Downloaded from www.nrcresearchpress.com by 196.1.178.254 on 09/07/12
For personal use only.

Pressure effects on the rate of electron transfer between tris(1,10-phenanthroline)iron(II) and -(III) in aqueous solution and in acetonitrile

HIDEO DOINE AND THOMAS WILSON SWADDLE[1]

Department of Chemistry, The University of Calgary, Calgary, Alta., Canada T2N 1N4

Received May 25, 1988

HIDEO DOINE and THOMAS WILSON SWADDLE. Can. J. Chem. **66**, 2763 (1988).

Proton nmr line-broadening experiments at ambient and elevated (to 215 MPa) pressures show that the rate of electron transfer between $Fe(phen)_3^{2+}$ and $Fe(phen)_3^{3+}$ as bisulfates in D_2O/D_2SO_4 is represented by the activation parameters (at ionic strength $I \sim 0.4$ mol kg^{-1}) $\Delta H^{\ddagger} = 1.6 \pm 0.5$ kJ mol^{-1}, $\Delta S^{\ddagger} = -102.2 \pm 1.6$ J K^{-1} mol^{-1}, $k(276\text{ K}) = 1.31 \times 10^7$ kg mol^{-1} s^{-1}, and (at $I \sim 0.3$ mol kg^{-1} and a mean pressure of 100 MPa) $\Delta V^{\ddagger} = -2.2 \pm 0.1$ cm^3 mol^{-1}. For the same reaction of the perchlorate salts (total [Fe] 0.046–0.065 mol kg^{-1}) in CD_3CN, $\Delta H^{\ddagger} = 11.0 \pm 1.0$ kJ mol^{-1}, $\Delta S^{\ddagger} = -72.5 \pm 3.6$ J K^{-1} mol^{-1}, $k(277\text{ K}) = 8.0 \times 10^6$ kg mol^{-1} s^{-1}, and $\Delta V^{\ddagger} = -5.9 \pm 0.5$ cm^3 mol^{-1}. For water as solvent, $\Delta V^{\ddagger}$ is satisfactorily accounted for by a classical theory of the Stranks–Hush–Marcus type. Volumes of activation for electron self-exchange are shown to provide criteria for non-adiabaticity and for dominance of (non-aqueous) solvent reorganization dynamics; on this basis, it is seen that neither of these factors is important in the title reactions.

HIDEO DOINE et THOMAS WILSON SWADDLE. Can. J. Chem. **66**, 2763 (1988).

Des expériences d'élargissement de raies dans les spectres rmn du proton, effectuées à la pression ambiante et à des pressions allant jusqu'à 215 MPa, permettent de démontrer que la vitesse de transfert d'électron, entre les ions $Fe(phen)_3^{2+}$ et le $Fe(phen)_3^{3+}$ qui existent sous la forme de bisulfates dans une solution de D_2O/D_2SO_4, peut être représentée par les paramètres d'activation suivants : (à une force ionique de $I \sim 0{,}4$ mol kg^{-1}), $\Delta H^{\ddagger} = 1{,}6 \pm 0{,}5$ kJ mol^{-1}, $\Delta S^{\ddagger} = -102{,}2 \pm 1{,}6$ J K^{-1} mol^{-1}, $k(276\text{ K}) = 1{,}31 \times 10^7$ kg mol^{-1} s^{-1} et (à $I = 0{,}3$ mol kg^{-1} et une pression moyenne de 100 MPa) $\Delta V^{\ddagger} = -2{,}2 \pm 0{,}1$ cm^3 mol^{-1}. Pour la même réaction des perchlorate ([Fe] totale de 0,046 à 0,065 mol kg^{-1}) dans le CD_3CN $\Delta H^{\ddagger} = 11{,}0 \pm 1{,}0$ kJ mol^{-1}, $\Delta S^{\ddagger} = -72{,}5 \pm 3{,}6$ J K^{-1} mol^{-1}, $k(277\text{ K}) = 8{,}0 \times 10^6$ kg mol^{-1} s^{-1} et $\Delta V^{\ddagger} = -5{,}9 \pm 0{,}1$ cm^3 mol^{-1}. Lorsque l'eau est le solvant, on peut facilement expliquer la valeur du $\Delta V^{\ddagger}$ par une théorie classique du type Stranks–Hush–Marcus. On démontre que les volumes d'activation pour l'auto-échange des électrons fournissent des critères pour expliquer les propriétés non-adiabatiques ainsi la dominance de la dynamique de réorganisation des solvants non-aqueux; sur cette base, on peut comprendre pourquoi aucun de ces facteurs n'est important dans les réactions mentionnées dans le titre.

[Traduit par la revue]

Introduction

A continuing theme in the work of our laboratory has been the quantitative prediction, tested by experimental measurement, of the effects of pressure on the rates of inorganic reactions in solution (1–5). Outer-sphere electron transfer reactions are particularly attractive subjects in this respect, since the Stranks–Hush–Marcus ("SHM") theory (6) allows one, in principle, to calculate the effect of pressure on the rate constant k (expressed as the volume of activation $\Delta V^{\ddagger} = -RT(\partial \ln k/\partial P)_T$) from basic physical properties of the reactants and the solvent. The initial apparent success (6) of simple SHM theory for self-exchange reactions of metal complexes in aqueous solution, however, has been shown to have been fortuitous (7, 8), and we have therefore undertaken a re-evaluation of this approach.

Our early considerations (4) suggested that, subject to some minor modifications (notably the treatment of the separation σ between the reacting metal–ion centres as a pressure-sensitive variable), the SHM theory might prove adequate for self-exchange reactions of transition metal complexes containing large ligands with extended π-electron systems. In such cases, fully adiabatic electron transfer (*i.e.*, electronic transmission coefficient $\varkappa_{el} \sim 1$) might be expected, and the solvent should be adequately represented as a continuous dielectric with relative permittivity equal to the bulk value D throughout. Indeed, Braun and van Eldik (9) reported that $\Delta V^{\ddagger}$ for electron transfer between $Co(terpy)_2^{2+}$ and $Co(bipy)_3^{3+}$ in water comes close to the predictions of simple SHM theory (this is, however, a *net reaction* rather than self-exchange).

An appropriate test case is the self-exchange reaction of tris(1,10-phenanthroline)iron(II) and -(III)

[1] $$Fe(phen)_3^{2+} + Fe(phen)_3^{3+} \rightleftharpoons Fe(phen)_3^{3+} + Fe(phen)_3^{2+}$$

the ambient-pressure kinetics of which were mapped out for various solvents by Wahl and co-workers with ^{1}H nmr line-broadening (10, 11). We report here a high-pressure study of this system in water and acetonitrile, in addition to refinements of some of the measurements of Larsen and Wahl (10, 11). An attractive feature of this widely-used couple is that the Fe—N bond lengths are identical in the oxidized and reduced species (12), so that the contributions of internal reorganization $\Delta V_{IR}^{\ddagger}$ and $\Delta G_{IR}^{\ddagger}$ to $\Delta V^{\ddagger}$ and the free energy of activation $\Delta G^{\ddagger}$, respectively, should be negligible, thereby permitting simplification of the theoretical calculations.

Experimental

Preparation of materials

$[Fe(phen)_3](ClO_4)_2$ and $[Fe(phen)_3](ClO_4)_3$ were made by the methods of Chan and Wahl (11). $[Fe(phen)_3]SO_4 \cdot 9H_2O$ was prepared by dissolving $FeSO_4 \cdot 7H_2O$ (0.9 g) in 15 mL water to which phen$\cdot H_2O$ (3 g) was added. The mixture was stirred for 1 h in the dark and then filtered; to the filtrate, 200 mL acetone was added. The combined precipitates were recrystallized twice from ethanol–acetone. All complex salts were shown spectrophotometrically to be >99% pure, and were stored *in vacuo* over P_2O_5.

For the kinetic studies in aqueous media, $Fe(phen)_3^{3+}$ could not be introduced as a solid salt (the sulfate could not be obtained pure, and the perchlorate caused precipitation of $[Fe(phen)_3](ClO_4)_2$) and was therefore generated in solution by oxidation of $[Fe(phen)_3]SO_4$ in aqueous sulfuric acid with the stoichiometric amount of ammonium hexanitratocerate(IV) (G. Frederick Smith Chemical Co., 99.98%). It was shown by spectrophotometric titration that the oxidation was quantitative in the time required for solution preparation, and further-

[1]To whom all correspondence should be addressed.

Can. J. Chem. Downloaded from www.nrcresearchpress.com by 122.72.124.2 on 09/07/12
For personal use only.

Can. J. Chem. Downloaded from www.nrcresearchpress.com by 122.72.124.2 on 09/07/12
For personal use only.

more that $Fe(phen)_3^{3+}$ was stable enough in solution in aqueous sulfuric acid (0.1 mol L^{-1}) below 5°C for completion of a cycle of pressurized nmr experiments (ca. 8 h); significant decomposition of the iron(III) complex in solution, however, precluded reliable kinetic measurements under pressure at higher temperatures (cf. refs. 11 and 13). In acetonitrile, on the other hand, $[Fe(phen)_3](ClO_4)_3$ proved to be very stable even at room temperature.

Nuclear magnetic resonance measurements

All nmr spectra were taken on a Bruker WH-90 spectrometer with quadrature detection. The spectra of the separate $Fe(phen)_3^{2+}$ and $Fe(phen)_3^{3+}$ complexes in solution were in good agreement with those in the literature (11, 13). The required quantities were the full widths W at half height and chemical shifts δ of the protons in the 2 and 9 positions on the phenanthroline ligands. Temperature dependence studies were made with a standard Bruker ^1H probehead, and spectra at elevated pressures (to 215 MPa) were obtained with the pressurizable assembly described previously (5). For measurements on aqueous systems, the solutions were prepared from $[Fe(phen)_3]SO_4 \cdot 9H_2O$ and D_2SO_4 (Sigma, 98 atom%) in D_2O (Aldrich, 99.8 atom%). Ammonium hexanitratocerate(IV) in D_2O/D_2SO_4 was used to produce $Fe(phen)_3^{3+}$, and DSS (sodium 3-(trimethylsilyl)propanesulfonate; MSD) was introduced as an internal standard. For measurements in acetonitrile, the requisite amounts of $[Fe(phen)_3](ClO_4)_2$ and $[Fe(phen)_3](ClO_4)_3$ were dissolved in CD_3CN (Aldrich, 99 atom%) which had been dried over a 4A molecular sieve.

Results

Aqueous solutions at variable temperature

The rate constant k for reaction [1] was obtained from the "fast exchange" expression (5, 11)

$$[2] \quad k = 4\pi f_P(1 - f_P)(\Delta\nu)^2/\{W_{DP} - (1 - f_P)W_D - f_P W_P\}[Fe]_T$$

where f_P is the fraction of the total iron concentration $[Fe]_T$ corresponding to the paramagnetic Fe^{III} species (calculated as in ref. 5), $\Delta\nu$ is the difference in chemical shift between the 2,9-proton resonances of the Fe^{II} and Fe^{III} complexes in separate solutions, and W_{DP}, W_D, and W_P are respectively the linewidths of these resonances in the reaction mixture, in a corresponding solution containing the Fe^{II} complex without Fe^{III}, and in a solution containing the Fe^{III} complex without Fe^{II}. Equation [2] is applicable only in the "fast exchange limit" and is appropriate here because the criterion $k[Fe]_T/2\pi\Delta\nu \gg 1$ was satisfied in all the experiments reported in this paper. At 11.2°C, $\Delta\nu$ = 5055 and W_P = 298.5 Hz; at 1.0°C, the corresponding values were 5244 and 309.6 Hz. Thus, W_P follows Curie's law. Values of $\Delta\nu$ and W_P for other temperatures were obtained by interpolation. The assumption implicit in eq. [2], that the effects on W of coupling of the 2,9 with the 3,8 and 4,7 protons can be neglected, was shown to be valid; like Chan and Wahl (11), we calculated that this contribution to W would in no case exceed 10%.

Measurements were made with $[Fe]_T$ ranging from 0.0608 to 0.1485, $[D_2SO_4]$ from 0.100 to 0.201, and ionic strength I from 0.22 to 0.48 mol kg^{-1}. Surprisingly, the twenty values of k so obtained, calculated from eq. [2] and subject to an estimated error of less than ±5%, ranged only from 1.26×10^7 to 1.37×10^7 mol kg^{-1} s^{-1} over the accessible temperature range −2.4 to +11.2°C and showed no discernable dependence on I. Full details are given in the Supplementary Tables,[2] but values of k are well represented by the Eyring equation

$$[3] \quad k = (\varkappa k_B T/h) \exp((\Delta S^{\ddagger}/R) - (\Delta H^{\ddagger}/RT))$$

where $\Delta H^{\ddagger}$ = 1.6 ± 0.5 kJ mol^{-1}, $\Delta S^{\ddagger}$ = −102.2 ± 1.6 J K^{-1} mol^{-1}, transmission coefficient $\varkappa$ = 1 (assumed), and the other symbols have their unusual meanings.[3] At 25°C, the extrapolated value of k is 1.49×10^7 kg mol^{-1} s^{-1}. Chan and Wahl reported $k = (3.6 \pm 1.0) \times 10^7$ and $(4.9 \pm 1.5) \times 10^7$ L mol^{-1} s^{-1} for reaction [1] at 5 and 17°C, respectively, but the counterion in their experiments was chloride rather than HSO_4^-, and the rate data may have been affected by decomposition of the Fe^{III} complex (11).

Acetonitrile solutions at variable temperature

In acetonitrile, the perchlorate salts of $Fe(phen)_3^{2+}$ and $Fe(phen)_3^{3+}$ were used, as they are both sufficiently soluble and stable at room temperature. The quantities $\Delta\nu$ and W_P in eq. [2] had the values 5105 and 239 Hz at 19°C, and 5564 and 261 Hz at −5.1°C, respectively, in good agreement with previous reports (11, 12). Thus, they conformed to Curie's law, and values for other temperatures were obtained by interpolation. Determinations of the rate constant k were made from eq. [3] for five temperatures ranging from −8.9 to +15.9°C for three different solutions ($[Fe]_T$ = 0.0646, 0.0651, 0.0463 mol kg^{-1}; I = 0.19, 0.20, 0.14 mol kg^{-1}) but the results were independent of concentration within the experimental error. The data (Supplementary Tables[2]) are represented by $\Delta H^{\ddagger}$ = 11.0 ± 1.0 kJ mol^{-1} and $\Delta S^{\ddagger}$ = −72.5 ± 3.6 J K^{-1} mol^{-1} if $\varkappa$ = 1, so that $k = 1.20 \times 10^7$ kg mol^{-1} s^{-1} at 25°C. These agree satisfactorily with the results of Chan and Wahl (11) for reaction [1] in CD_3CN with perchlorate as counterion (note different concentration units and $[Fe]_T$).

Aqueous solutions at variable pressure

Here, the anions were again HSO_4^- and SO_4^{2-}. It was not possible to determine accurately the effect of pressure on the contact shifts and line widths of the pure paramagnetic Fe^{III} species, since the high pressure probehead is relatively insensitive and because small amounts of the Fe^{II} complex tended to form, with consequent exchange broadening, on the longer timescale of the high pressure experiments. The Debye equation, however, suggests that W_P should be proportional to the viscosity η of the solvent at a given temperature (14). Water is an anomalous fluid in that η is only slightly affected (it is actually *decreased* and then increased (15, 16)) by rising pressure under the conditions of our experiments (3.0°C, 0.1–215 MPa), so that the pressure dependences of $\Delta\nu$ and W_P in aqueous solutions can be safely neglected.

Values of the rate constant k obtained for reaction [1] at various pressures P at 3.0 ± 0.3°C are given in the Supplementary Material and are summarized in Fig. 1. There is no evidence of any dependence of k on concentrations or ionic strength ($I \sim 0.17$–0.32 mol kg^{-1}), and the ln k vs. P plot can be regarded as linear within the experimental error, giving $\Delta V^{\ddagger} = -2.2 \pm 0.1$ cm^3 mol^{-1} for the mean conditions P = 100 MPa, I = 0.3 mol kg^{-1}, and T = 3.0°C; $k_{P=0} = 1.29 \times 10^7$ kg mol^{-1} s^{-1}, in excellent agreement with the variable-temperature result. Data obtained at the lower $[Fe]_T$ are less precise and hence more scattered in Fig. 1.

Acetonitrile solutions at variable pressure

The perchlorate salts of the complexes were used. In

[2] Supplementary tables S1–S5 may be purchased from the Depository of Unpublished Data, CISTI, National Research Council of Canada, Ottawa, Ont., Canada K1A 0S2.

[3] Except where otherwise indicated, uncertainties cited in this paper are standard deviations.

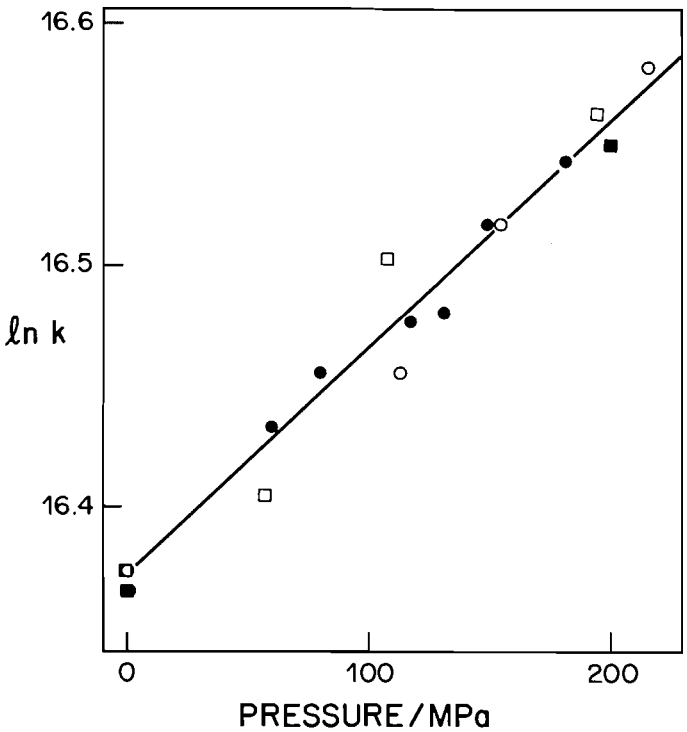

FIG. 1. Pressure dependence of the rate of reaction [1] in aqueous acidic (D_2O/D_2SO_4) solution at 3.0°. Filled circles: $[Fe]_T = 0.0352$, $[D_2SO_4] = 0.1001$, $I = 0.17$ mol kg^{-1}. Filled squares: $[Fe]_T = 0.0621$, $[D_2SO_4] = 0.1351$, $I = 0.26$ mol kg^{-1}. Open circles: $[Fe]_T = 0.0706$, $[D_2SO_4] = 0.1351$, $I = 0.28$ mol kg^{-1}. Open squares: $[Fe]_T = 0.1050$, $[D_2SO_4] = 0.1001$, $I = 0.32$ mol kg^{-1}.

acetonitrile, $Fe(phen)_3^{3+}$ is sufficiently stable that the pressure dependence of the linewidth W_P could be measured, and the results over the range 0.1–205 MPz at 3.8°C and [Fe] = 0.042 mol kg^{-1} are represented adequately by

$$[4] \quad \ln W_P = 5.548 + 0.00168P$$

where P is in MPa. This type of relationship reflects the behavior of acetonitrile as a normal fluid (5). There was no detectable variation of $\Delta\nu$ with pressure (5380 ± 60 Hz).

The data (Supplementary Tables[2]) are summarized in Fig. 2. The scatter is worse than for the acidic aqueous systems, but again there is no discernable concentration effect over the admittedly limited range $[Fe]_T = 0.0468$ to 0.0677 mol kg^{-1}. The ln k vs. P plot may be taken to be linear within the experimental uncertainty, giving $\Delta V^{\ddagger} = -5.9 \pm 0.5$ cm^3 mol^{-1} and $k_{P=0} = 8.1 \times 10^6$ kg mol^{-1} s^{-1} (*cf.* 7.9×10^6 kg mol^{-1} s^{-1} from the temperature dependence study) at 3.8°C and $I \sim 0.18$ mol kg^{-1}.

Discussion

Three models were considered in interpreting the above kinetic data for reaction [1]: (*a*) a two-sphere, weakly adiabatic, continuous-dielectric model of the SHM type, developed elsewhere (3–5) from principles laid down by Sutin (17); (*b*) an adaptation of model (*a*) with allowance for possible non-adiabaticity (3); and (*c*) following recent developments (18–22), a model in which solvent reorganization dynamics are important.

(a) Adiabatic continuous-dielectric model

In this case, the rate coefficient k is given by

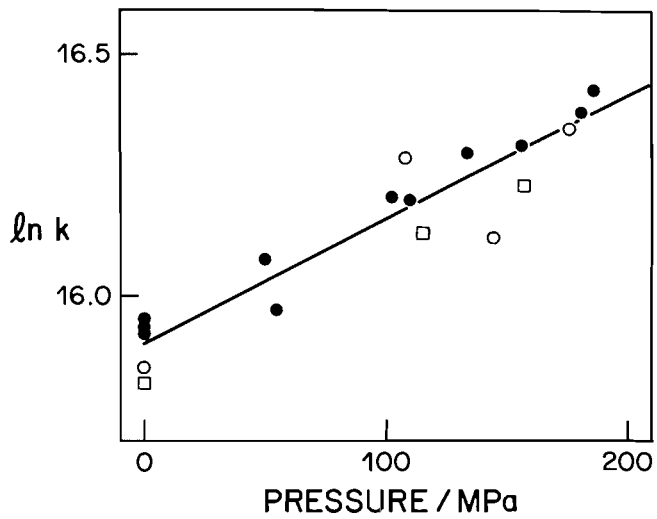

FIG. 2. Pressure dependence of the rate of reaction [1] in acetonitrile (counterion: perchlorate) at 3.8°C. Open circles: $[Fe]_T = 0.0468$ mol kg^{-1}. Open squares: $[Fe]_T = 0.0668$ mol kg^{-1}. Filled circles: $[Fe]_T = 0.0677$ mol kg^{-1}.

$$[5] \quad k = (K_A \varkappa_{el} \nu_n) \exp[-(\Delta G_{IR}^{\ddagger} + \Delta G_{OS}^{\ddagger})/RT]$$

where K_A is the formation constant for the precursor assembly $\{Fe(phen)_3^{2+}, Fe(phen)_3^{3+}\}$, ν_n is the nuclear frequency factor, and $\Delta G_{IR}^{\ddagger}$ and $\Delta G_{OS}^{\ddagger}$ are the contributions to the free energy $\Delta G^{\ddagger}$ of activation from reorganization within the reactants and from the surrounding solvent, respectively, in the activation process. For reaction [1], $\Delta G_{IR}^{\ddagger}$ will be negligible because neither the Fe—N bond lengths (12) nor the stretching frequencies (23) change significantly on going from Fe^{II} to Fe^{III}. The formation of the precursor assembly involves exponential factors $\Delta G_{COUL}^{\ddagger}$ and $\Delta G_{DH}^{\ddagger}$ representing the Coulombic work and Debye–Hückel effects, respectively, which can be combined with the solvent reorganization term $\Delta G_{SR}^{\ddagger}$ to give $\Delta G^{\ddagger}$ while K_A is replaced by $4000\pi N\sigma^3/3$ (in L mol^{-1} s^{-1}, for σ in metres) where σ is the Fe—Fe separation and N is Avogadro's number (17). For consistency with transition state theory (eq. [3]), ν_n may be set equal to $k_B T/h$. We have, in SI units and symbols,

$$[6] \quad \Delta G_{SR}^{\ddagger} = (Ne^2/16\pi\varepsilon_0)(r^{-1} - \sigma^{-1})(n^{-2} - D^{-1})$$

where r is the effective radius of the reactant ions approximated to spheres (here, r is the same for each), n is the refractive index of the solvent (for convenience, taken to be the Na-D-line value commonly tabulated), and D is the relative permittivity (dielectric constant) of the solvent. If a is the distance of closest approach of the reactant cations (charges z_1 and z_2) to the counter-ions, we have

$$[7] \quad \Delta G_{COUL}^{\ddagger} = (Nz_1z_2e^2/4\pi\varepsilon_0)/D\sigma$$

$$[8] \quad \Delta G_{DH}^{\ddagger} = -2RTz_1z_2CI^{1/2}/(1 + BaI^{1/2})$$

where B and C are the usual Debye–Hückel parameters.

The approximation of $Fe(phen)_3^{x+}$ to a sphere is obviously crude, but values of $r \sim 700$ pm and $a \sim 900$ pm seem reasonable (11, 12), and in any event it turns out that the calculated values of k are not very sensitive to these choices. Similarly, although σ is to be regarded as variable (4, 17), it transpires that k changes very little as σ is allowed to vary from 1.0 to 1.8 nm; for $\sigma = 2r = 1.4$ nm, $k = 8.2 \times 10^{10}$ kg mol^{-1} s^{-1}, $\Delta G_{SR}^{\ddagger} = 13.7$, $\Delta G_{COUL}^{\ddagger} = 6.9$, and

Can. J. Chem. Downloaded from www.nrcresearchpress.com by 122.72.124.2 on 09/07/12
For personal use only.

Can. J. Chem. Downloaded from www.nrcresearchpress.com by 122.72.124.2 on 09/07/12
For personal use only.

$\Delta G_{DH}^{\ddagger} = -6.6$ kJ mol^{-1} in water at 3°C, 0.1 MPa and $I = 0.3$ kg mol^{-1}. In view of the simplicity of the model, the discrepancy between the calculated and the observed value of k (1.3×10^7 kg mol^{-1} s^{-1}) is not excessive. It may be noted that the coulombic and Debye–Hückel terms tend to cancel at the ionic strengths used in this study.

For acetonitrile as the solvent with the same choices of r, σ, and a, but with $I = 0.2$ mol kg^{-1} and $T = 25.0$°C, eqs. [5]–[8] predict $k = 2 \times 10^{11}$ kg mol^{-1} s^{-1}, with $\Delta G_{SR}^{\ddagger} = 13.1$, $\Delta G_{COUL}^{\ddagger} = 16.4$, and $\Delta G_{DH}^{\ddagger} = -16.2$ kJ mol^{-1}. Although the latter two terms are much larger than for aqueous solution, once again they cancel at the relevant ionic strength, and indeed the measured k, though 10^4-fold smaller than predicted, is almost the same in the two solvents because $\Delta G_{SR}^{\ddagger}$ is little affected. Our failure to detect the acceleration of reaction [1] in acetonitrile by the perchlorate counter-ion as reported by Chan and Wahl (11) may mean that $Fe(phen)_3^{3+}$–ClO_4^- pairing was approaching saturation in our concentration range (which, however, was narrow). Indeed, recent measurements by Schmid *et al.* (24) indicate that $Fe(phen)_3^{3+}$–ClO_4^- pairing would be about 90% complete in our acetonitrile solutions at 25°C.

The prediction of k from eqs. [5]–[8] is clearly subject to errors from the numerous assumptions and simplifications, but at least some of these should cancel out in taking the pressure derivative of $\ln k$ to obtain $\Delta V^{\ddagger}$. Thus, a model which gives only rough predictions of k may estimate $\Delta V^{\ddagger}$ quite accurately. Differentiation of eqs. [5]–[8] with respect to pressure gives the following expressions for the volume of activation in the adiabatic two-sphere continuous-dielectric model (3); β is the isothermal compressibility of the solvent, and, for reaction [1], $\Delta V_{IR}^{\ddagger}$ is zero.

$$[9]\quad \Delta V^{\ddagger} = \Delta V_{IR}^{\ddagger} + \Delta V_{OS}^{\ddagger} + \beta RT = \Delta V_{IR}^{\ddagger} + (\Delta V_{SR}^{\ddagger} + \Delta V_{COUL}^{\ddagger} + \Delta V_{DH}^{\ddagger}) + \beta RT$$

$$[10]\quad \Delta V_{SR}^{\ddagger} = (Ne^2/16\pi\varepsilon_0)[(r^{-1} - \sigma^{-1}) \times (\partial(n^{-2} - D^{-1})/\partial P)_T - (n^{-2} - D^{-1})\beta/3\sigma]$$

$$[11]\quad \Delta V_{COUL}^{\ddagger} = (Nz_1z_1e^2/4\pi\varepsilon_0\sigma)[(\partial D^{-1}/\partial P)_T + \beta/3D]$$

$$[12]\quad \Delta V_{DH}^{\ddagger} = [RTz_1z_2CI^{1/2}/(1 + BaI^{1/2})^2] \times [(\partial \ln D/\partial P)_T(3 + 2BaI^{1/2}) - \beta]$$

Parameters such as $(\partial n/\partial P)_T$, $(\partial D/\partial P)_T$, and β are themselves pressure dependent, with the result that $|\Delta V^{\ddagger}|$ must decrease with rising pressure (i.e., a plot of $\ln k$ vs. P will be a curve tending towards the horizontal) (3–5). This anticipated curvature, however, is often lost within the experimental uncertainty of k, as is the case here (Figs. 1 and 2), and it is then expedient to treat the $\ln k$ vs. P plot as linear, giving a mean $\Delta V^{\ddagger}$ that would be representative of the mid-point of the pressure range — here, 100 MPa. We have therefore evaluated eqs. [9]–[12] for water at 100 MPa, 3.0°C, $I = 0.3$ mol kg^{-1}, $r = 700$ pm, $a = 900$ pm, and $\sigma = 1.4$ nm: $\Delta V_{SR}^{\ddagger} = -4.18$, $\Delta V_{COUL}^{\ddagger} = -1.81$, $\Delta V_{DH}^{\ddagger} = +2.56$, $\beta RT = +0.88$, and $\Delta V^{\ddagger} = -2.5$ cm^3 mol^{-1}. This last is in close agreement with the observed value of -2.2 cm^3 mol^{-1}. The calculations are not significantly affected by the choice of r, and, if σ is varied from 1.0 to 1.8 nm with $r = 700$ pm, opposing trends in $\Delta V_{SR}^{\ddagger}$ and $\Delta V_{COUL}^{\ddagger}$ result in a very small change in $\Delta V^{\ddagger}$ (from -3.0 to -2.3 cm^3 mol^{-1}). For $I = 0.4$ mol kg^{-1}, the calculated $\Delta V^{\ddagger}$ is -2.2 cm^3 mol^{-1}.

It is not possible at present to evaluate eqs. [9]–[12] for acetonitrile, since the pressure dependence of its refractive index is not known, and furthermore there are indications (11) that anion–cation association influences the reaction rate.

(b) Possibility of non-adiabaticity

Since eqs. [5]–[8] overestimate k, the possibility should be considered that reaction [1] is non-adiabatic with $\varkappa_{el} \sim 10^{-4}$. If non-adiabaticity applies at Fe–Fe separations σ greater than a certain value σ_{ad}, a semi-classical approach (17) can be adopted, noting that $\Delta G_{IR}^{\ddagger}$ is negligible for reaction [1]. The electronic coupling factor H_{AB} is given approximately by

$$[13]\quad H_{AB} = H_{AB}^0 \exp[-\alpha(\sigma - \sigma_{ad})]$$

whence, if the distance scaling factor α is known, $\varkappa_{el}$ is calculable from

$$[14]\quad \varkappa_{el} = 2[1 - \exp(-\nu_{el}/2\nu_n)]/[2 - \exp(\nu_{el}/2\nu_n)]$$

where the electronic frequency ν_{el} is given by

$$[15]\quad \nu_{el} = (H_{AB}^2/h)(\pi^3/RT\Delta G_{OS}^{\ddagger})^{1/2}$$

Thus, from eq. [5], we have

$$[16]\quad \ln k = \ln(4000\pi N\sigma^3/3h) + 2\ln H_{AB} + [\ln(\pi^3/RT)]/2 - (\ln \Delta G_{OS}^{\ddagger})/2 - \Delta G_{OS}^{\ddagger}/RT$$

and hence, proceeding as above and in ref. 3, with the assumptions that H_{AB}^0, σ_{ad}, and α are independent of P, the non-adiabatic volume of activation $\Delta V_{NON}^{\ddagger}$ is given by

$$[17]\quad \Delta V_{NON}^{\ddagger} = -RT(\partial \ln k/\partial P)_T = \beta RT - (2\alpha\beta\sigma RT/3) + (RT\Delta V_{OS}^{\ddagger}/2\Delta G_{OS}^{\ddagger}) + \Delta V_{OS}^{\ddagger}$$

For reaction [1] in water, α is not known, but is probably in the usual range 6 to 25 nm^{-1} (17), in which case $\Delta V_{NON}^{\ddagger}$ lies between -8 and -23 cm^3 mol^{-1} for $T = 3.0$°C, $P = 100$ MPa, $I = 0.3$ mol kg^{-1}, $a = 900$ pm, and $\sigma = 2r = 1.4$ nm. Clearly, this range is quite inconsistent with the observed value of -2.2 cm^3 mol^{-1}, and it may be confidently concluded that reaction [1] in water is fully adiabatic, as Taube (25) and Chan and Wahl (11) have suggested.

Thus, in favorable cases (such as when the components of eq. [9] are all quite small), the pressure effect on the rate of a self-exchange redox reaction can be diagnostic of its adiabaticity. It will be noted that σ_{ad} and H_{AB}^0 need not be known for this purpose; either the reaction is fully adiabatic because $\sigma < \sigma_{ad}$, in which case eq. [9] should account for the observed $\Delta V^{\ddagger}$, or it is non-adiabatic and eq. [17] applies.

(c) Solvent-dynamical models

Grampp *et al.* (19) have analyzed adiabatic electron exchange processes in which solvent reorganization dynamics are dominant. Consider a solvent of viscosity η, molar volume V_M, high frequency dielectric constant D_∞ ($\sim n^2$) and longitudinal relaxation time τ_L. If the Ovchinnikova condition (19, 26)

$$[18]\quad [\Delta G_{IR}^{\ddagger}/(\Delta G_{IR}^{\ddagger} + \Delta G_{SR}^{\ddagger})]^{1/2}\nu_{IR}\exp(-\Delta G_{IR}^{\ddagger}/RT) > \tau_L^{-1}$$

is satisfied, the pre-exponential part of eq. [5] becomes solvent dependent; for reaction [1] in water at 3°C and acetonitrile at 25°C, this requires $\Delta G_{IR}^{\ddagger} \leq 200$ and 100 J mol^{-1} respectively, and these conditions could be met, in view of the insensitivity of the Fe—N bond lengths and stretching frequencies to the oxidation state of the iron (12, 23). If $\Delta G_{IR}^{\ddagger}$ is negligible, the solvent frequency ν_S

[19] $\nu_S = DRT(\Delta G_{SR}^{\ddagger}/4\pi RT)^{1/2}/3V_M\eta D_\infty$

can be used directly to predict values of k for reaction [1]

[20] $k = (4000\pi N\sigma^3/3)\nu_S \exp(-\Delta G_{OS}^{\ddagger}/RT)$

of 1.2×10^{10} and 1.8×10^{10} kg mol^{-1} s^{-1} for water (3°C) and acetonitrile (25°C), respectively. Thus, regardless of whether condition [18] is met, this approach gives essentially the same result as model (*a*).

A solvent-dynamical treatment of pressure effects on k (in the case where $\Delta G_{IR}^{\ddagger}$ is negligible) involves the replacement of eq. [9] by

[21] $\Delta V^{\ddagger} = \Delta V_{IR}^{\ddagger} + \Delta V_{OS}^{\ddagger} + \beta RT - RT(\partial \ln \nu_S/\partial P)_T$
$= \Delta V_{OS}^{\ddagger} + \Delta V_{SD}^{\ddagger}$

where

[22] $\Delta V_{SD}^{\ddagger} = RT[(2/n)(\partial n/\partial P)_T + (\partial \ln \eta/\partial P)_T - (\partial \ln D/\partial P)_T - (\Delta V_{SR}^{\ddagger}/2\Delta G_{SR}^{\ddagger})]$

For water at 3°C, it can be estimated (16) that $RT(\partial \ln \eta/\partial P)_T$ ranges from -2.9 to $+1.2$ cm^3 mol^{-1} on going from 0.1 to 200 MPa, and is zero near 120 MPa. Thus, the mean calculated $\Delta V^{\ddagger}$ on the basis of eqs. [10], [11], [12], [21], and [22] for water at 3°C and $I = 0.3$ mol kg^{-1} is about -4.7 cm^3 mol^{-1}, which is 2.5 cm^3 mol^{-1} too negative. The discrepancy is not large, but model (*a*) gives a closer prediction.

For "normal" liquids, η rises monotonically and roughly exponentially with pressure, often doubling between 0.1 and 100 MPa (15, 27). Consequently, for non-aqueous solutions, the term $RT(\partial \ln \eta/\partial P)_T$ will typically make a large (20 cm^3 mol^{-1} or more) *positive* contribution to $\Delta V^{\ddagger}$ where solvent reorganization dynamics are dominant. Since the volumes of activation generated by models (*a*) and (*b*), and by refinements of these (3), are generally in the range 0 to -20 cm^3 mol^{-1}, the observation of a markedly positive $\Delta V^{\ddagger}$ for outer-sphere electron transfer in a non-aqueous system may be taken as evidence for dominance of solvent dynamics. Clearly, reaction [1] in acetonitrile is not such a case.

Acknowledgement

We thank the Natural Sciences and Engineering Council of Canada for financial support.

1. T. W. SWADDLE. Inorg. Chem. **22**, 2663 (1983).
2. H. DOINE, K. ISHIHARA, H. R. KROUSE, and T. W. SWADDLE. Inorg. Chem. **26**, 3240 (1987).
3. L. SPICCIA and T. W. SWADDLE. Inorg. Chem. **26**, 2265 (1987).
4. T. W. SWADDLE. *In* Inorganic high pressure chemistry. *Edited by* R. van Eldik. Elsevier, Amsterdam. 1986. Chap. 5.
5. H. DOINE and T. W. SWADDLE. Inorg. Chem. **27**, 665 (1988).
6. D. R. STRANKS. Pure Appl. Chem. **38**, 303 (1974).
7. S. WHERLAND. Inorg. Chem. **22**, 2349 (1983).
8. L. SPICCIA and T. W. SWADDLE. J. Chem. Soc. Chem. Commun. 67 (1985).
9. P. BRAUN and R. VAN ELDIK. J. Chem. Soc. Chem. Commun. 1349 (1985).
10. D. W. LARSEN and A. C. WAHL. J. Chem. Phys. **43**, 3765 (1965).
11. M.-S. CHAN and A. C. WAHL. J. Phys. Chem. **82**, 2542 (1978).
12. B. B. BRUNSCHWIG, C. CREUTZ, D. H. MACARTNEY, T. K. SHAM, and N. SUTIN. Faraday Discuss. Chem. Soc. **74**, 113 (1982).
13. R. DESIMONE and R. S. DRAGO. J. Am. Chem. Soc. **92**, 2343 (1970).
14. J. JONAS. Annu. Rev. Phys. Chem. **26**, 167 (1975).
15. P. W. BRIDGMAN. The physics of high pressure. G. Bell and Sons, London. 1931. p. 346.
16. K. E. BETT and J. B. CAPPI. Nature, **207**, 620 (1965).
17. N. SUTIN. Prog. Inorg. Chem. **30**, 441 (1983).
18. G. E. MCMANIS, M. N. GOLOVIN, and M. J. WEAVER. J. Phys. Chem. **90**, 6563 (1986).
19. G. GRAMPP, W. HARRER, and W. JAENICKE. J. Chem. Soc. Faraday Trans. **83**, 161 (1987).
20. X. ZHANG, H. YANG, and A. J. BARD. J. Am. Chem. Soc. **109**, 1916 (1987).
21. J. T. HYNES. Annu. Rev. Phys. Chem. **36**, 573 (1985).
22. H. FRAUENFELDER and P. WOLYNES. Science, **229**, 337 (1985).
23. Y. SAITO, J. TAKEMOTO, B. HUTCHINSON, and K. NAKAMOTO. Inorg. Chem. **11**, 2003 (1972).
24. R. SCHMID, K. KIRCHNER, and F. L. DICKERT. Inorg. Chem. **27**, 1530 (1988).
25. H. TAUBE. Adv. Chem. Ser. **162**, 127 (1977).
26. M. YA. OVCHINNIKOVA. Theor. Exp. Chem. **17**, 507 (1981).
27. N. S. ISAACS. Liquid phase high pressure chemistry. J. Wiley and Sons, Toronto. 1981. pp. 102–107.

Can. J. Chem. Downloaded from www.nrcresearchpress.com by 122.72.124.2 on 09/07/12
For personal use only.

On chemical relaxation modes in homogeneous chemical systems

F. PALOMARES, J. VEGUILLAS, AND M. A. DIAZ

Universidad del Pais Vasco, Facultad de Ciencias, Departamento de Química-Física, apartado 644, Bilbao, Spain

Received November 12, 1987[1]

F. PALOMARES, J. VEGUILLAS, and M. A. DIAZ. Can. J. Chem. **66**, 2768 (1988).

We study the compatibility between the linearized phenomenological equations of an homogeneous chemical gaseous system, and the theoretical ones obtained with the aid of the kinetic theory of gases. Our discussion is based on the concept of chemical relaxation mode. The theoretical description is provided by a reactive Boltzmann equation for each component of the system. Then, we show the conditions under which the linearized phenomenological equations can be reproduced.

F. PALOMARES, J. VEGUILLAS et M. A. DIAZ. Can. J. Chem. **66**, 2768 (1988).

On a effectué une comparaison entre l'étude de compatibilité des équations phénoménologiques linéarisées d'un système chimique gazeux homogène et les équations théoriques obtenues à l'aide de la théorie cinétique des gaz. Notre discussion est basée sur le concept du mode de relaxation chimique. On fait l'hypothèse que l'on peut obtenir une description théorique à l'aide d'une équation de Boltzmann réactive pour chacune des composantes du système. On présente alors les conditions permettant de reproduire les équations phénoménologiques linéarisées.

[Traduit par la revue]

1. Introduction

In dilute gases, the microscopic foundations of chemical reactions are mostly based on the use of Boltzmann equations, generalized to include reactive collisions. Such generalizations have been postulated "ad hoc" (1–21), although can be derived using different formalisms (see, for instance, refs. 22–29).

The homogeneous reacting systems have been studied for the first time by Prigogine and co-workers (1, 2) and independently by Curtiss (3), in the case of bimolecular reactions in which the reaction products were ignored. They have obtained the expression of the reaction rate using a modification of the Chapman–Enskog perturbation method for transport processes, by considering the reactive cross sections smaller than the elastic ones. Subsequently, many other authors (4–21) have given a more definitive form to the theory of these systems, analysing the deviation produced by the chemical reaction on the Maxwellian distribution function and calculating the reaction rates and rate coefficients by a Chapman–Enskog or a moment method. For this, they have considered the momentum relaxation time of all gaseous species very short compared with the chemical relaxation time.

One of the most interesting questions in connection with the preceding systems is to know the conditions under which a microscopic description is compatible with the macroscopic description furnished by linear thermodynamics (30). In this way, Snider and Ross (15) have discussed in detail, for the exchange reaction

$$[1.1] \qquad A + B \rightleftharpoons C + D$$

the compatibility between the microscopic description and the phenomenological equation

$$[1.2] \qquad -\frac{dn_A}{dt} = K_f n_A n_B - K_r n_C n_D$$

where the rate constants are independent of composition and time, and verify the mass action law

$$[1.3] \qquad K = \frac{K_f}{K_r}$$

K being the equilibrium constant. They have shown that this compatibility holds in linear cases when one of the components is present in a large excess or when the chemical reaction is a slow process. In their paper, Snider and Ross have only considered an isothermal system in which all molecules maintain translational equilibrium.

On the other hand, in refs. 1–21, the problem of the deduction of the phenomenological equations from the kinetic theory in the most general situation (nonisothermal case) has not been studied.

The purpose of this paper is to study, using the kinetic theory, the chemical relaxation of a nonisothermal homogeneous reacting system from a perturbed initial equilibrium state to final equilibrium state. This study permits us to obtain the microscopic expression of the phenomenological equations which govern such an evolution and to establish their range of validity. Indeed, the chemical relaxation provides a method (31) to measure reaction rates. In this method, one starts from a system which is already at chemical equilibrium and a small perturbation, either transient or stationary, is applied to it. The system will then relax to a new equilibrium, and from the knowledge of the relaxation time and the equilibrium constant, one finds the value of the rate constants. In the transient case, the perturbation is usually a sudden change of some parameter, such as the temperature, the pressure or, in special cases, the electric or magnetic field. For the stationary measurements, the sound absorption and dispersion method is the most widely used (32).

We will consider that the system is a dilute gas consisting of four components that participate in a reaction of the type [1.1], and whose statistical evolution is described by a reactive Boltzmann equation. We will see that, for a system in which the reactive collisions are much less probable than the elastic ones, there exists a microscopic expression for the phenomenological equation from which we obtain rate coefficients that satisfy the mass action law. This analysis will be based on the extension, for reacting systems, of the concept of hydrodynamical modes introduced by Résibois (33–35) and on a generalization of the method introduced by Theodosopulu, Grecos, and Prigogine (36, 37) in the microscopic derivation of the linearized transport equations for a simple fluid.

The present paper is organized as follows. In the next section, we establish the phenomenological equations and we introduce the concept of the chemical relaxation mode. The

[1]Revision received June 21, 1988.

Can. J. Chem. Downloaded from www.nrcresearchpress.com by 196.1.178.254 on 09/07/12
For personal use only.

Can. J. Chem. Downloaded from www.nrcresearchpress.com by 196.1.178.254 on 09/07/12
For personal use only.

derivation of the microscopic expressions of the phenomenological equations is given in third section. Finally, in the fourth section the main results of this paper are discussed.

2. Phenomenological equations

In this section, we establish the phenomenological equations for an uniform and isolated multi-component reacting system characterized by the reaction

[2.1] $A + B \rightleftharpoons C + D$

and we introduce the concept of chemical relaxation mode.

The basic variables to describe a multi-component system are the total density ρ, the concentration γ_i of each component defined as the mass fraction ρ_i/ρ, the momentum density $\boldsymbol{g}$ and the energy density U (30). As this system is uniform, it is not necessary to consider the evolution equations of the total density and momentum density. Therefore, in the absence of external forces, the conservation equations may be written in the form

[2.2] $$\rho \frac{\partial \gamma_i}{\partial t} = \bar{\nu}_i m_i J \qquad (i = 1, 2, 3 \equiv \text{A, B, C})$$

[2.3] $$\rho \frac{\partial U}{\partial t} = 0 \qquad \text{(uniform and isolated system)}$$

where $\bar{\nu}_i$, m_i, and J are the stoichiometric coefficients, the molecular mass of the i-component, and the chemical reaction rate, respectively.

The system of equations [2.2], [2.3] can be reduced to a system of two equations if we introduced the parameter, ξ, called degree of advancement of the reaction, defined by (30),

[2.4] $$\xi(t) = \frac{\gamma_i(t) - \gamma_i(0)}{\bar{\nu}_i m_i}$$

Thus, from [2.2]–[2.4] we get

[2.5] $$\rho \frac{\partial \xi}{\partial t} = J$$

[2.6] $$\rho \frac{\partial U}{\partial t} = 0$$

Assuming the system is very close to equilibrium, it is possible to consider a linear relation among the fluxes and thermodynamic forces (30). Thus, we may write the chemical reaction rate as

[2.7] $$J = -\frac{l_{rr}}{T} A = -\epsilon A$$

A being the chemical affinity of the reaction [2.1], defined by means of the chemical potentials μ_k (k = A, B, C, and D) (30)

[2.8] $$A = m_C\mu_C + m_D\mu_D - m_A\mu_A - m_B\mu_B$$

ϵ is a scalar phenomenological coefficient related with the rate coefficients, K_f and K_r, of the forward and reversal reactions, by the expression

[2.9] $$\epsilon = K_r\left(\frac{\gamma_C\gamma_D}{k_B T}\right) = K_f\left(\frac{\gamma_A\gamma_B}{k_B T}\right)$$

or, in function of the degree of advancement of the reaction

[2.10] $$\epsilon = K_r\left(\frac{\xi^2\bar{\nu}_C\nu_D m_C m_D}{k_B T}\right) = K_f\left(\frac{\xi^2\bar{\nu}_A\bar{\nu}_B m_A m_B}{k_B T}\right)$$

When the state of the system is very close to equilibrium, we can write all the variables in the following way

[2.11] $$\varphi(t) = \varphi^e + \delta\varphi(t): \frac{|\delta\varphi(t)|}{\varphi^e} \ll 1$$

φ^e being the equilibrium value of $\xi(t)$, $U(t)$, and $A(t)$ (in this particular case $A^e = 0$).

Now, we will assume that the Gibbs thermodynamic relation remains valid for our system

[2.12] $$\delta U = C_v\delta T + \left[\frac{P}{\rho^2} - \frac{T}{\rho^2}\left(\frac{\partial P}{\partial T}\right)_{\rho\xi}\right]\delta\rho + \left\{\sum_{i=1}^{3}\left[\mu_i - T\left(\frac{\partial\mu_i}{\partial T}\right)_{\rho\xi}\right]\bar{\nu}_i m_i\right\}\delta\xi$$

where C_v is the specific heat at constant volume and μ_i (i = 1, 2, and 3) denotes the differences among the chemical potentials; $\mu_1 = \mu_A - \mu_D$, $\mu_2 = \mu_B - \mu_D$, and $\mu_3 = \mu_C - \mu_D$. Thus by expressing δA in function of $\delta\xi$ and δT,

[2.13] $$\delta A = \left(\frac{\partial A}{\partial T}\right)_{\rho\xi}\delta T + \left(\frac{\partial A}{\partial \xi}\right)_{\rho T}\delta\xi$$

from eqs. [2.5]–[2.7] and [2.11]–[2.13], we arrive at the following linear phenomenological equations

[2.14] $$\frac{\partial\delta\xi}{\partial t} = -\frac{\epsilon}{\rho}\left(\frac{\partial A}{\partial T}\right)_{\rho\xi}\delta T - \frac{\epsilon}{\rho}\left(\frac{\partial A}{\partial\xi}\right)_{\rho T}\delta\xi$$

[2.15] $$\frac{\partial\delta T}{\partial t} = -\frac{T\epsilon}{\rho C_v}\left(\frac{\partial A}{\partial T}\right)^2_{\rho\xi}\delta T - \frac{T\epsilon}{\rho C_v}\left(\frac{\partial A}{\partial\xi}\right)_{\rho T}\left(\frac{\partial A}{\partial T}\right)_{\rho\xi}\delta\xi$$

Equations [2.14]–[2.15] constitute a system of ordinary differential equations, which may be written in the compact form

[2.16] $$\frac{\partial\Psi(t)}{\partial t} = \hat{\mathbf{M}}\cdot\Psi(t)$$

where we have used a two-dimensional space, $\Psi(t)$ being the vector

[2.17] $$\Psi(t) = \begin{bmatrix}\delta\xi\\ \delta T\end{bmatrix}$$

The matrix elements of $\hat{\mathbf{M}}$ are the thermodynamic coefficients which appear in eqs. [2.14]–[2.15]. $\hat{\mathbf{M}}$ is an hermitian matrix and its eigenvalue problem

[2.18] $$\hat{\mathbf{M}}\cdot\chi_i = \omega_i\cdot\chi_i$$

has two linearly independent solutions. Thus, any vector Ψ can be written as

[2.19] $$\Psi = \sum_{i=1}^{2} C_i(0)\exp(\omega_i t)\chi_i$$

with

[2.20] $$C_i(0) = \langle\chi_i|\Psi(0)\rangle$$

The eigenvalues ω_i are the solutions of the secular determinant

[2.21] $$\|\hat{\mathbf{M}} - \omega_i\mathbf{U}\| = 0$$

(here $\mathbf{U}$ represents the unit matrix in a two-dimensional space), from which we get

[2.22] $$\omega_1 = -\frac{\epsilon}{\rho}\left(\frac{\partial A}{\partial\xi}\right)_{\rho T} - \frac{T\epsilon}{\rho C_v}\left(\frac{\partial A}{\partial T}\right)^2_{\rho\xi}$$

[2.23] $\omega_2 = 0$

Hence, from these results the Ψ vector becomes

[2.24] $\Psi(t) = C_1(0) \exp(\omega_1 t)\chi_1 + C_2(0)\chi_2$

The time-dependent term of the right hand side is called chemical relaxation mode; it determines the evolution of the system to equilibrium state, with a relaxation time equal to $(-\omega_1^{-1})$, and describes the dissipation due to the chemical reaction.

The thermodynamic stability of the system requires ω_1 to be negative. In order to show this fact, we take into account that ϵ is positive as a consequence of the positive character of the entropy production (30), and that

[2.25] $$\left(\frac{\partial A}{\partial \xi}\right)_{\rho T} = \left(\frac{\partial^2 F}{\partial \xi^2}\right)_{\rho T} > 0$$

is a positive derivative because the Helmholtz free energy, F, has a minimum in the equilibrium at constant density and temperature. Therefore, under these considerations, we conclude that ω_1 must be negative. This result insures the stability of the system.

3. Microscopic derivation of the phenomenological equations

As our system is a dilute gas, it is reasonable to assume that its statistical time evolution is given by the Boltzmann equation, which in absence of external forces takes the form

[3.1] $$\frac{\partial f_A}{\partial t} = \sum_S \int d\upsilon_s\, d\Omega' \sigma_{AS}^{(e)} g_{AS}[f_A' f_S' - f_A f_S] + \int d\upsilon_B\, d\Omega' \sigma_{AB}^{(r)} g_{AB}[f_C f_D - f_A f_B]$$

where S = A, B, C, and D; υ_s is the velocity of S-particle; Ω' the solid angle into which the particles are scattered in a particular collision event; $\sigma_{AS}^{(e)}$ and $\sigma_{AB}^{(r)}$ are the differential elastic and reactive cross sections, respectively; g_{AS} is the relative velocity and f_S is the singlet distribution function. Similar equations hold for B, C, and D. Now, we assume the separation between the fundamental internal level and the first excited one to be sufficiently large, to avoid the inelastic collisions; later, this situation will be analysed.

As we consider that the gas is only slightly perturbed away from absolute equilibrium, we can write the distribution function in the form

[3.2] $$f_S(t) = f_S^e(\upsilon_s) + \delta f_S^e(\upsilon_s; t); \frac{|\delta f_S|}{f_S^e} \ll 1$$

$f_S^{(e)}$ being the Maxwell–Boltzmann distribution function and δf_S the deviation of f_S from its equilibrium value. Introducing this expression into [3.1] yields a linearized Boltzmann equation

[3.3] $$\frac{\partial \delta f_A}{\partial t} = \sum_S \int d\upsilon_s\, d\Omega' \sigma_{AS}^{(e)} g_{AS} f_A^e f_S^e \times \left[\left(\frac{\delta f_A}{f_A^e}\right)' + \left(\frac{\delta f_S}{f_S^e}\right)' - \left(\frac{\delta f_A}{f_A^e}\right) - \left(\frac{\delta f_S}{f_S^e}\right)\right] + \int d\upsilon_B\, d\Omega' \sigma_{AB}^{(r)} g_{AB} f_A^e f_B^e \times \left[\left(\frac{\delta f_C}{f_C^e}\right)' + \left(\frac{\delta f_D}{f_D^e}\right)' - \left(\frac{\delta f_A}{f_A^e}\right) - \left(\frac{\delta f_B}{f_B^e}\right)\right]$$

This equation may also be written as

[3.4] $$\frac{\partial \delta f_A}{\partial t} = \sum_S \hat{C}_{AS}^{(e)} \delta f_S + \sum_S \hat{C}_{AS}^{(r)} \delta f_S$$

where $\hat{C}_{AS}^{(e)}$ = operators come from the linearized elastic collision terms and $\hat{C}_{AS}^{(r)}$ = operators from the linearized reactive ones.

Similar equations hold for the other components of the system. This allows us to express the statistical evolution of our system by means of a matrix equation

[3.5] $$\frac{\partial}{\partial t}\begin{bmatrix}\delta f_A\\ \delta f_B\\ \delta f_C\\ \delta f_D\end{bmatrix} = \hat{C}^{(e)}\cdot\begin{bmatrix}\delta f_A\\ \delta f_B\\ \delta f_C\\ \delta f_D\end{bmatrix} + \hat{C}^{(r)}\cdot\begin{bmatrix}\delta f_A\\ \delta f_B\\ \delta f_C\\ \delta f_D\end{bmatrix}$$

If δf means

[3.6] $$\delta f \equiv \begin{bmatrix}\delta f_A\\ \delta f_B\\ \delta f_C\\ \delta f_D\end{bmatrix}$$

then expression [3.5] becomes

[3.7] $$\frac{\partial \delta f}{\partial t} = (\hat{C}^{(e)} + \hat{C}^{(r)})\cdot\delta f$$

$\hat{C}^{(e)}$ and $\hat{C}^{(r)}$ being matrix operators which will be called "elastic and reactive collision operators", respectively. These linear operators are characterized by a set of useful mathematical properties. Thus with the aid of the following scalar product

[3.8] $$\langle F|G\rangle = \sum_S \int d\upsilon_s [f_s^e(\upsilon_s)]^{-1} F_s^*(\upsilon_s) G_s(\upsilon_s)$$

where

[3.9] $$F \equiv \begin{bmatrix}F_A(\upsilon_A)\\ F_B(\upsilon_B)\\ F_C(\upsilon_C)\\ F_D(\upsilon_D)\end{bmatrix};\quad G \equiv \begin{bmatrix}G_A(\upsilon_A)\\ G_B(\upsilon_B)\\ G_C(\upsilon_C)\\ G_D(\upsilon_D)\end{bmatrix}$$

the operators $\hat{C}^{(e)}$ and $\hat{C}^{(r)}$ are hermitian. Hence, their corresponding eigenvalues $\lambda_j^{(e)}$ and $\lambda_j^{(r)}$ are real. Moreover, it can be easily shown that these eigenvalues are non-positive.

Assuming that the set of eigenfunctions $\{|\phi_j\rangle\}$ of the operator $(\hat{C}^{(e)} + \hat{C}^{(r)})$ is a complete set, the solution of [3.7] will be given by

[3.10] $$\delta f(t) = \sum_j a_j(0) \exp(\lambda_j t)\phi_j$$

with

[3.11] $$a_j(0) = \langle \phi_j|\delta f(0)\rangle$$

On the other hand, we shall assume as it is habitual that reactive collisions are less frequent than elastic ones. Therefore, we shall treat $\hat{C}^{(r)}$ as a perturbation with respect to $\hat{C}^{(e)}$. This assumption allows us to simplify the complex equation [3.10]. In fact, for non-reacting systems (where $\hat{C}^{(r)} \equiv \mathbf{0}$) there exist eight eigenfunctions corresponding to the eigenvalue zero ($\lambda_\alpha^{(e)} = 0$, $\alpha = 1, \ldots, 8$) (see Appendix 1). This is a consequence of the eight collisional invariants associated to the non-

Can. J. Chem. Downloaded from www.nrcresearchpress.com by 196.1.178.254 on 09/07/12
For personal use only.

Can. J. Chem. Downloaded from www.nrcresearchpress.com by 196.1.178.254 on 09/07/12
For personal use only.

reactive collisions. The eigenvalues $\lambda_j^{(e)}$ ($j \geq 9$) measure the rate of approach to equilibrium by means of elastic collisions. We introduce the elastic relaxation times, $\tau_{rel,j}^{(e)}$, through (39),

$$[3.12] \quad \tau_{rel,j}^{(e)} = -(\lambda_j^{(e)})^{-1} > 0; \qquad j = 9, 10, \ldots$$

We shall assume that the spectrum of $\hat{C}^{(e)}$ is discrete and has no accumulation point. In particular, this implies that there exists a finite positive number μ such that

$$[3.13] \quad \lambda_j^{(e)} < -\mu; \qquad j = 9, 10, \ldots$$

This has been shown (40) for repulsive r^{-n} ($n > 2$) potentials and we shall assume that it remains valid even when we deal with forces that are not strictly repulsive (35). Consequently, the eigenvalue $\lambda_9^{(e)}$, closest to zero will be separated from the origin by a finite maximum elastic relaxation time, $\tau_{rel,9}^{(e)}$, that fixes the duration of the elastic relaxation towards equilibrium. This time is the so-called elastic relaxation time and will be denoted by $\tau_{rel}^{(e)}$.

For times, $t \gg \tau_{rel}^{(e)}$, and for a non-reacting system, we have

$$[3.14] \quad \delta f \simeq \sum_{\alpha=1}^{8} a_\alpha^{(e)}(0)\phi_\alpha^{(e)}$$

Therefore, for the reacting system considered in the present section, a similar equation to [3.14] holds

$$[3.15] \quad \delta f(t) = \sum_{\alpha=1}^{8} a_\alpha(0) \exp(\lambda_\alpha t)\phi_\alpha$$

Precisely, if we assume the eigenvalues λ_α to be evaluated by a perturbation theory, there will be eight eigenvalues vanishing when the reactive cross section tends to zero, the other remaining finite. Hence, only the corresponding eight terms survive in eq. [3.10] for times longer than the elastic relaxation time. In fact, for reacting systems (where $\hat{C}^{(r)} \neq \mathbf{0}$) the chemical species are not independent of each other since reaction [1.1] imposes the constraint that every time a molecule A (or B) disappears a molecule C (or D) must appear. For that, there exist only seven eigenfunctions of the $\hat{C}$ operator for the zero eigenvalue ($\lambda_\alpha = 0$, $\alpha = 1, \ldots, 7$) (see Appendix I). Of course, this is a consequence of the seven collisional invariants associated to the reactive collisions (the eighth invariant is destroyed by the constraint imposed by the chemical reaction). Consequently, the goal must be to find the remaining non-zero eigenvalue and its associated eigenfunction.

Thus, in order to solve the eigenvalue problem associated to the operator $(\hat{C}^{(e)} + \hat{C}^{(r)})$, we can utilise a perturbation calculus expanding λ_α and ϕ_α according to

$$[3.16] \quad \lambda_\alpha = \lambda_\alpha^{(1)} + \lambda_\alpha^{(2)} + \lambda_\alpha^{(3)} + \ldots$$

$$[3.17] \quad \phi_\alpha = \varphi_\alpha + \phi_\alpha^{(1)} + \phi_\alpha^{(2)} + \ldots$$

Introducing these expansions in the eigenvalue problem

$$[3.18] \quad (\hat{C}^{(e)} + \hat{C}^{(r)})|\phi_\alpha\rangle = \lambda_\alpha|\phi_\alpha\rangle$$

and using the projection operators P and Q, defined as

$$[3.19] \quad P = \sum_{\alpha=1}^{8} |\varphi_\alpha\rangle\langle\varphi_\alpha|; \qquad Q = \sum_{k\neq\{\alpha\}} |\phi_k^{(e)}\rangle\langle\phi_k^{(e)}|, \{\alpha\} = \{1, \ldots, 8\}$$

that satisfy the properties

$$[3.20] \quad P + Q = \mathbf{1}, \qquad P\hat{C}^{(e)} = \hat{C}^{(e)}P = \mathbf{0}$$

we get (Appendix I)

$$[3.21] \quad \lambda_\alpha^{(1)} = 0, \lambda_\alpha^{(2)} = 0, \lambda_\alpha^{(3)} = 0 \qquad (\alpha = 1, \ldots, 7)$$

$$[3.22] \quad \lambda_8^{(1)} = \left[\frac{2}{3n}\left(\frac{\Delta E}{k_B T}\right)^2 + \sum_{i=A,B,C,D} n_i^{-1}\right]\Lambda$$

$$[3.23] \quad \lambda_8^{(2)} = \left[\frac{2}{3n}\left(\frac{\Delta E}{k_B T}\right)^2 + \sum_{i=A,B,C,D} n_i^{-1}\right] \times \langle\Psi|Q\hat{C}^{(e)-1}Q|\Psi\rangle$$

$$[3.24] \quad \lambda_8^{(3)} = \left[\frac{2}{3n}\left(\frac{\Delta E}{k_B T}\right)^2 + \sum_{i=A,B,C,D} n_i^{-1}\right] \times \{-\lambda_8^{(1)}\langle\Psi|Q\hat{C}^{(e)-1}Q\hat{C}^{(e)-1}Q|\Psi\rangle + \langle\Psi|Q\hat{C}^{(e)-1}Q\hat{C}^{(r)}Q\hat{C}^{(e)-1}Q|\Psi\rangle\}$$

The results [3.21]–[3.24] show, according to [3.15] that the δf function may be expressed as

$$[3.25] \quad \delta f(t) = \sum_{\alpha=1}^{7} a_\alpha(0)\phi_\alpha + a_8(0) \exp(\lambda_8 t)\phi_8$$

Defining the chemical relaxation time, $\tau_{rel}^{(r)}$ as

$$[3.26] \quad \tau_{rel}^{(r)} = (-\lambda_8)^{-1}$$

the solution [3.25] holds for times, $t \gg \tau_{rel}^{(r)}$, but for times $t \gg \tau_{rel}^{(r)}$, the second term of this solution (associated with the so-called reactive mode) will decay, driving the system towards a new equilibrium state characterized by the distribution function (35)

$$[3.27] \quad f^e = f_{in}^e + \delta f^e$$

f_{in}^e being the distribution of the initial equilibrium state.

From eq. [3.25] we can obtain all the variables which describe the system. For instance (41),

$$[3.28] \quad \delta T = T\sqrt{\frac{2}{3n}}\langle\phi_8^{(e)}|\delta f\rangle = T\sqrt{\frac{2}{3n}}\left[\sum_{\alpha=1}^{7} a_\alpha(0)\langle\phi_8^{(e)}|\phi_\alpha\rangle + a_8(0) \exp(\lambda_8 t)\langle\phi_8^{(e)}|\phi_8\rangle\right]$$

$\phi_8^{(e)}$ being the eighth eigenfunction of $\hat{C}^{(e)}$ for $\lambda_j^{(e)} = 0$.

If we compare [3.28] with its macroscopic expression obtained of the fourth component of Ψ in eq. [2.24], we find

$$[3.29] \quad \lambda_8 = \omega_1$$

Taking into account the standard formula for the affinity of a dilute reacting gas (30)

$$[3.30] \quad A = -\frac{3}{2}k_B T \ln\left(\frac{m_C m_D}{m_A m_B}\right) + \Delta E + k_B T \ln\left(\frac{n_C n_D}{n_A n_B}\right)$$

eq. [2.22] becomes

$$[3.31] \quad \omega_1 = -\epsilon k_B T\left\{\frac{2}{3n}\left(\frac{\Delta E}{k_B T}\right)^2 + \sum_{S=A,B,C,D} n_S^{-1}\right\}$$

Hence, the coefficient ϵ is given by

Can. J. Chem. Downloaded from www.nrcresearchpress.com by 196.1.178.254 on 09/07/12
For personal use only.

[3.32] $$\epsilon = -\frac{1}{k_B T\left\{\frac{2}{3n}\left(\frac{\Delta E}{k_B T}\right)^2 + \sum_{S=A,B,C,D} n_S^{-1}\right\}} \times \{\lambda_8^{(1)} + \lambda_8^{(2)} + \lambda_8^{(3)}\}$$

From here, one can obtain immediately K_f and K_r by using [2.9]

[3.33] $$K_r = \frac{1}{\gamma_C \gamma_D}\left\{\int dv_C\, dv_D\, d\Omega'\, \sigma_{CD}^{(r)} g_{CD} f_C^e f_D^e + \langle\Psi|Q\hat{C}^{(e)-1}Q|\Psi\rangle + \lambda_8^{(1)}\langle\Psi|Q\hat{C}^{(e)-1}Q\hat{C}^{(e)-1}Q|\Psi\rangle - \langle\Psi|Q\hat{C}^{(e)-1}Q\hat{C}^{(r)}Q\hat{C}^{(e)-1}Q|\Psi\rangle\right\}$$

[3.34] $$K_f = \frac{1}{\gamma_A \gamma_B}\left\{\int dv_A\, dv_B\, d\Omega'\, \sigma_{AB}^{(r)} g_{AB} f_A^e f_B^e + \langle\Psi|Q\hat{C}^{(e)-1}Q|\Psi\rangle + \lambda_8^{(1)}\langle\Psi|Q\hat{C}^{(e)-1}Q\hat{C}^{(e)-1}Q|\Psi\rangle - \langle\Psi|Q\hat{C}^{(e)-1}Q\hat{C}^{(r)}Q\hat{C}^{(e)-1}Q|\Psi\rangle\right\}$$

In expressions [3.32]–[3.34], all the terms are expressed in function of equilibrium properties. This is a consequence of the fact that the considered reference state is the absolute equilibrium. Thus, the two rate coefficients are constants and satisfy the mass action law.

The first term of the rate coefficients, coming from the first correction $\lambda_8^{(1)}$ to the eigenvalue λ_8, represents the equilibrium contribution of the coefficients, whereas the other terms represent the non-equilibrium contributions.

Now, we will deduce the microscopic expressions of the phenomenological equations from the distribution function.

Using the linearized expressions of density, the degree of advancement of the reaction and temperature (41), i.e.,

[3.35] $$\delta\rho = \langle I|\delta f\rangle$$
$$|I\rangle = m_A n_A^{1/2}|\phi_1^{(e)}\rangle + m_B n_B^{1/2}|\phi_2^{(e)}\rangle + m_C n_C^{1/2}|\phi_3^{(e)}\rangle + m_D n_D^{1/2}|\phi_4^{(e)}\rangle$$

[3.36] $$\delta\xi = \langle II|\delta f\rangle$$
$$|II\rangle = \frac{m_B n_A^{1/2} n_B^{1/2}}{\rho^2}[n_A^{1/2}|\phi_2^{(e)}\rangle - n_B^{1/2}|\phi_1^{(e)}\rangle] + \frac{m_C n_A^{1/2} n_C^{1/2}}{\rho^2}[n_A^{1/2}|\phi_3^{(e)}\rangle - n_C^{1/2}|\phi_1^{(e)}\rangle] + \frac{m_D n_A^{1/2} n_D^{1/2}}{\rho^2}[n_A^{1/2}|\phi_4^{(e)}\rangle - n_D^{1/2}|\phi_1^{(e)}\rangle]$$

[3.37] $$\delta T = \langle III|\delta f\rangle$$
$$|III\rangle = T\sqrt{2/3n}\,|\phi_8^{(e)}\rangle$$

one can deduce the following general evolution equation

$$\frac{\partial\delta\omega}{\partial t} = \sum_{\alpha=1}^{8}\langle\beta|Z|\phi_\alpha^{(e)}\rangle\langle\phi_\alpha^{(e)}|\delta f\rangle$$

[3.38] $$\beta = I, II, III$$
$$\delta\omega = \delta\rho, \delta\xi, \delta T$$

where

[3.39] $$Z = \lambda_8|\phi_8\rangle\langle\phi_8|$$

If we consider the property,

[3.40] $$\hat{C}^{(r)}|\varphi_\alpha\rangle = 0 \qquad (\alpha = 1, \ldots, 7)$$

then

[3.41] $$\langle\varphi_\alpha|\phi_\beta^{(1)}\rangle = (\lambda_\alpha^{(1)} - \lambda_\beta^{(1)})^{-1}\langle\varphi_\alpha|\hat{C}^{(r)}Q\hat{G}^{-1}Q\hat{C}^{(r)}|\varphi_\beta\rangle = 0$$

and similar results are found for $\phi_\beta^{(n)}$ $(n > 1)$. In this case Z becomes

[3.42] $$Z = \lambda_8|\varphi_8\rangle\langle\varphi_8|$$

Calculating the matrix elements $\langle\beta|Z|\phi_\alpha^{(e)}\rangle$ and taking into account,

[3.43] $$\langle\phi_1^{(e)}|\delta f\rangle = \frac{n_A^{1/2}}{\rho}\delta\rho - \frac{\rho}{n_A^{1/2}}\delta\xi$$

[3.43] $$\langle\phi_2^{(e)}|\delta f\rangle = \frac{n_B^{1/2}}{\rho}\delta\rho - \frac{\rho}{n_B^{1/2}}\delta\xi$$

[3.45] $$\langle\phi_3^{(e)}|\delta f\rangle = \frac{n_C^{1/2}}{\rho}\delta\rho + \frac{\rho}{n_C^{1/2}}\delta\xi$$

[3.46] $$\langle\phi_4^{(e)}|\delta f\rangle = \frac{n_D^{1/2}}{\rho}\delta\rho + \frac{\rho}{n_D^{1/2}}\delta\xi$$

we arrive at the microscopic expressions of the phenomenological equations

[3.47] $$\frac{\partial\delta\rho}{\partial t} = 0$$

[3.48] $$\frac{\partial\delta\xi}{\partial t} = \frac{\lambda_8\sum_{S=A,B,C,D} n_S^{-1}}{\left\{\frac{2}{3n}\left(\frac{\Delta E}{k_B T}\right)^2 + \sum_{S=A,B,C,D} n_S^{-1}\right\}}\delta\xi - \frac{\lambda_8\left(\frac{\Delta E}{k_B T}\right)}{\rho T\left\{\frac{2}{3n}\left(\frac{\Delta E}{k_B T}\right)^2 + \sum_{S=A,B,C,D} n_S^{-1}\right\}}\delta T$$

[3.49] $$\frac{\partial\delta T}{\partial t} = -\frac{\lambda_8\left(\frac{2\rho T}{3n}\right)\left(\frac{\Delta E}{k_B T}\right)\sum_{S=A,B,C,D} n_S^{-1}}{\left\{\frac{2}{3n}\left(\frac{\Delta E}{k_B T}\right)^2 + \sum_{S=A,B,C,D} n_S^{-1}\right\}}\delta\xi + \frac{\lambda_8\left(\frac{2}{3n}\right)\left(\frac{\Delta E^2}{k_B T}\right)}{\left\{\frac{2}{3n}\left(\frac{\Delta E}{k_B T}\right)^2 + \sum_{S=A,B,C,D} n_S^{-1}\right\}}\delta T$$

Since for a dilute gas the following relations are verified

$$\left(\frac{\partial A}{\partial\xi}\right)_{\rho T} = -\rho k_B T\sum_{S=A,B,C,D} n_S^{-1}$$

[3.50] $$\left(\frac{\partial A}{\partial T}\right)_{\rho\xi} = -\frac{\Delta E}{T}$$

$$C_v = \frac{3k_B n}{2\rho}$$

eqs. [3.48], [3.49] can be compared with the phenomenological

Can. J. Chem. Downloaded from www.nrcresearchpress.com by 196.1.178.254 on 09/07/12
For personal use only.

eqs. [2.14], [2.15]. This comparison permits us to identify the phenomenological coefficient ϵ, recovering eq. [3.32].

Until this point, we have considered, for simplicity, a system in which there exist no inelastic collisions. Even if there are inelastic collisions, we can make the same analysis by considering each internal state as a new component of the system. For instance, whenever the component A appears in the states A_1 and A_2 (characterized by the energies E_{A_1} and E_{A_2}, respectively) the following reactive collisions

[3.51] $A_1 + B \rightleftharpoons C + D$

[3.52] $A_2 + B \rightleftharpoons C + D$

could be possible.

If we assume that the elastic and inelastic collisions are more probable than the reactive ones, the matrix kinetic equation may be written as follows

$$[3.53] \quad \frac{\partial \delta f}{\partial t} = (\hat{C}' + \hat{C}^{(r)})\delta f$$

where $\hat{C}'$ is the collision operator associated with the elastic and inelastic collisions, $\hat{C}^{(r)}$ the collision operator associated with the reactive ones [3.51], [3.52], and now δf means

$$[3.54] \quad \delta f \equiv \begin{bmatrix} \delta f_{A_1} \\ \delta f_{A_2} \\ \delta f_B \\ \delta f_C \\ \delta f_D \end{bmatrix}$$

Therefore, eq. [3.53] can be resolved by a perturbation method assuming $\hat{C}^{(r)}$ as a small perturbation of $\hat{C}'$. Proceeding in this way, it is possible to arrive at the microscopic expressions of the phenomenological eqs. [2.14], [2.15], where now

$$[3.55] \quad \epsilon = \frac{1}{k_B T}\left\{\sum_{j=1,2}\int dv_{A_j}\, dv_B\, d\Omega' \sigma^{(r)}_{A_jB} g_{A_jB} f^e_{A_j} f^e_B + \langle \Psi | Q\hat{C}^{-1}Q|\Psi\rangle + \ldots\right\}$$

and

$$[3.56] \quad \Psi \equiv \begin{bmatrix} \sum_{j=1,2}\int dv_B\, d\Omega' \sigma^{(r)}_{A_jB} g_{A_jB} f^e_{A_j} f^e_B \\ \int dv_{A_1}\, d\Omega' \sigma^{(r)}_{A_1B} g_{A_1B} f^e_{A_1} f^e_B \\ \int dv_{A_2}\, d\Omega' \sigma^{(r)}_{A_2B} g_{A_2B} f^e_{A_2} f^e_B \\ -\int dv_D\, d\Omega' \sigma^{(r)}_{CD} g_{CD} f^e_C f^e_D \\ -\int dv_C\, d\Omega' \sigma^{(r)}_{CD} g_{CD} f^e_C f^e_D \end{bmatrix}$$

4. Discussion

In the present paper, we have discussed, using the kinetic theory of fluids, the derivation of macroscopic evolution equations for a non-isothermal homogeneous reacting system. This study has been achieved for a system characterized by a bimolecular reaction like [2.1]. Such an analysis has also permitted the identification of true non-equilibrium rate constants in terms of equilibrium quantities and microscopic properties of the particles and verification of the mass action law. We have assumed that reactive collisions are less probable than elastic ones and the study has been achieved in the framework of the method introduced by Résibois (33–35), Theodosopulu, Grecos, and Prigogine (36, 37). We must point out that this method, based on a standard perturbation calculus, consists of assuming the system only slightly perturbed away from absolute equilibrium, according to [3.2]. Indeed, when the system is deviated from equilibrium state, it experiments a relaxation process and reaches a new equilibrium state described by

$$[4.1] \quad f^e = f^e_{in} + \delta f^e$$

This state is perfectly defined by the collision invariants which characterize the reacting system. Precisely, this feature of the method enables us to write non-equilibrium properties, like the rate coefficients, as functions of equilibrium quantities.

Nevertheless, the deviation from equilibrium state is defined by the collision invariants and by the relaxation modes. The relaxation modes decay exponentially and as $t \to \infty$, such modes vanish. In this way, $\delta f(t)$ becomes exclusively defined by the collision invariants. The relaxation modes are dependent on the type of system under consideration. Therefore, for systems as the ones considered in section 3, all the relaxation modes except one are fundamentally elastic, i.e., the more important contribution associated with such modes comes from elastic collisions; the other mode being characterized by a reactive collision frequency, λ_8 (to which we have associated the chemical relaxation time, $\tau^{(r)}_{rel}$) has been called "chemical relaxation mode".

We have seen that for times satisfying the condition, $t \geqslant \tau^{(r)}_{rel}$, the equilibrium established by elastic collisions is perturbed by the presence of the reactive ones; this occurs because, the reaction introduces a constraint which reduces the number of collision invariants. This fact removes partially the initial degeneration of the $\hat{C}^{(e)}$ operator (from eight eigenfunctions to seven for the zero eigenvalue). Calculating λ_8, by considering the $\hat{C}^{(r)}$ operator as a small perturbation of $\hat{C}^{(e)}$ operator, we have derived the microscopic expressions of the phenomenological equations.

We must point out that the procedure used for solving the eigenvalue equation [3.18], i.e., to consider $\hat{C}^{(r)}$ as a perturbation with regards to $\hat{C}^{(e)}$ permits to establish the time scale

$$[4.2] \quad \tau^{(e)}_{rel} \ll \tau^{(r)}_{rel}$$

Obviously, eq. [3.7] has a different solution for each of the following conditions: $\tau^{(r)}_{rel} > t \geqslant \tau^{(e)}_{rel}$, $t \geqslant \tau^{(r)}_{rel}$, or $t \gg \tau^{(r)}_{rel}$. In the first case, the evolution of the system is described by a set of infinite relaxation modes. In the last case, the system does not experiment an evolution because it has already reached the absolute equilibrium. Nevertheless, in the second case (the most important here) the evolution of the system is described by a single mode, the chemical relaxation mode. Of course, we are interested in this case because we must analyse the system at times in which the chemical reaction occurs ($t \geqslant \tau^{(r)}_{rel}$). Hence, for times of the order of the chemical relaxation time, $\tau^{(r)}_{rel}$, the chemical relaxation mode, associated with λ_8, is sufficient for describing the macroscopic behaviour of the system.

The comparison of both sets of equations has permitted us to identify the rate coefficients as true constants, which verify the mass action law. At this point, we want to detach that their first

Can. J. Chem. Downloaded from www.nrcresearchpress.com by 196.1.178.254 on 09/07/12
For personal use only.

correction represents the equilibrium contribution, while the other corrections represent non-equilibrium contributions, but expressed by means of the equilibrium values of the variables.

Finally, we point out that the present study can be extended for non-uniform systems, by incorporating to the Boltzmann equations the flux term and assuming a slow local dependance of the distribution function. We are working on the subject.

1. I. PRIGOGINE and E. XHROUET. Physica (Utrecht), **15**, 913 (1949).
2. I. PRIGOGINE and M. MATHIEU. Physica (Utrecht), **16**, 51 (1950).
3. C. F. CURTISS. University of Wisconsin Report CM-476. 1948.
4. K. TAKAYANAGI. Prog. Theoret. Phys. (Kyoto), **6**, 486 (1951).
5. M. A. ELIASON and J. O. HIRSCHFELDER. J. Chem. Phys. **30**, 1426 (1959).
6. R. D. PRESENT. J. Chem. Phys. **31**, 747 (1959); J. Chem. Phys. **48**, 4875 (1968).
7. J. ROSS and P. MAZUR. J. Chem. Phys. **35**, 19 (1961).
8. B. M. MORRIS and R. D. PRESENT. J. Chem. Phys. **51**, 4862 (1969).
9. B. MAHAN. J. Chem. Phys. **32**, 362 (1960).
10. M. D. KOSTIN. J. Chem. Phys. **46**, 1316 (1967); J. Chem. Phys. **43**, 2679 (1965).
11. C. W. PYUN. J. Chem. Phys. **48**, 1306 (1968).
12. B. WIDOM. Science, **148**, 1555 (1965).
13. O. K. RICE. J. Phys. Chem. **65**, 1972 (1961); J. Phys. Chem. **67**, 1733 (1963).
14. N. S. SNIDER. J. Chem. Phys. **42**, 548 (1965).
15. N. S. SNIDER and J. ROSS. J. Chem. Phys. **44**, 1087 (1966).
16. C. W. PYUN and J. ROSS. J. Chem. Phys. **40**, 2572 (1964).
17. B. SHIZGAL and M. KARPLUS. J. Chem. Phys. **52**, 4262 (1970); J. Chem. Phys. **54**, 4345 (1971); J. Chem. Phys. **54**, 4357 (1971).
18. B. SHIZGAL. J. Chem. Phys. **55**, 76 (1971); J. Chem. Phys. **69**, 5355 (1978).
19. G. W. FORD. Phys. Fluids, **11**, 515 (1968).
20. K. KUMAR. Ann. Phys. **37**, 113 (1966).
21. S. HUDSON and J. ROSS. J. Stat. Phys. **14**, 469 (1975).
22. J. T. LOWRY and R. F. SNIDER. J. Chem. Phys. **61**, 2320 (1974).
23. R. F. SNIDER and J. T. LOWRY. J. Chem. Phys. **61**, 2330 (1974).
24. B. C. EU. J. Chem. Phys. **63**, 303 (1975).
25. C. I. IVANOV. Physica A, **94**, 571 (1978).
26. D. K. HOFFMAN, D. J. KOURI, and Z. H. TOP. J. Chem. Phys. **70**, 4640 (1979).
27. J. VEGUILLAS and M. RIVAS. Mol. Phys. **47**, 1429 (1982).
28. J. VEGUILLAS, M. A. DÍAZ, and A. M. GUTIERREZ. Can. J. Chem. **60**, 2151 (1982).
29. J. VEGUILLAS, M. A. DÍAZ, and F. PALOMARES. Mol. Phys. **50**, 403 (1983).
30. S. R. DEGROOT and P. MAZUR. Nonequilibrium thermodynamics. North-Holland, Amsterdam. 1962.
31. M. EIGEN and L. DE MAEYER. Techniques of organic chemistry. Vol. 8. *Edited by* S. J. Friess, E. S. Lewis, and A. Weissberg. 2nd ed. Part 2. New York, Interscience. p. 895.
32. S. FLUGGE. Acoustics. Hand. der Physic. Vol. XI/1. Springer Verlag, Berlin. 1961.
33. P. RÉSIBOIS. J. Stat. Phys. **2**, 21 (1970).
34. G. VASU and P. RÉSIBOIS. Physica, **63**, 209 (1972).
35. P. RÉSIBOIS and M. DE LEENER. Classical kinetic theory of fluids. J. Wiley. 1977.
36. M. THEODOSOPULU and A. P. GRECOS. Physica, **95**, 35 (1979).
37. M. THEODOSOPULU, A. P. GRECOS, and I. PRIGOGINE. Proc. Natl. Acad. Sci. USA, **75**, 1632 (1978).
38. P. L. BHATNAGAR, E. P. GROSS, and M. KROOK. Phys. Rev. **94**, 511 (1954).
39. R. BALESCU. Equilibrium and nonequilibrium statistical mechanics. J. Wiley. 1975.
40. Y. PAO. Commun. Pure Appl. Math. **27**, 407 (1974).
41. S. CHAPMAN and T. G. COWLING. The mathematical theory of non-uniform gases. Cambridge University Press. 1970.

Appendix I

In this appendix we show the eigenfunctions of the zero eigenvalue for $\hat{C}^{(e)}$. We provide too, a detailed perturbation calculus of the eigenvalue λ_8 of the operator $\hat{C} = (\hat{C}^{(e)} + \hat{C}^{(r)})$.

We can obtain the eigenfunctions $\{\phi_\alpha^{(e)}\}$ of $\hat{C}^{(e)}$ taking into account that in a system composed of four components there exist eight collision invariants associated with the elastic collisions (35). Thus, using the orthogonality condition

$$[I.1] \qquad \langle \phi_\alpha^{(e)} | \phi_\beta^{(e)} \rangle = \delta_{\alpha\beta}^{kr}$$

we easily get, for instance

$$|\phi_1^{(e)}\rangle = \begin{bmatrix} n_A^{-1/2} f_A^e \\ 0 \\ 0 \\ 0 \end{bmatrix}; \quad |\phi_2^{(e)}\rangle = \begin{bmatrix} 0 \\ n_B^{-1/2} f_B^e \\ 0 \\ 0 \end{bmatrix};$$

$$|\phi_3^{(e)}\rangle = \begin{bmatrix} 0 \\ 0 \\ n_C^{-1/2} f_C^e \\ 0 \end{bmatrix}; \quad |\phi_4^{(e)}\rangle = \begin{bmatrix} 0 \\ 0 \\ 0 \\ n_D^{-1/2} f_D^e \end{bmatrix} \qquad [I.2]$$

$$|\phi_i^{(e)}\rangle = (\rho k_B T)^{-1/2} \begin{bmatrix} m_A v_{A,i} f_A^e \\ m_B v_{B,i} f_B^e \\ m_C v_{C,i} f_C^e \\ m_D v_{D,i} f_D^e \end{bmatrix};$$

$$(i = 5, 6, 7 \equiv X, Y, Z)$$

$$|\phi_8^{(e)}\rangle = \sqrt{\frac{2}{3n}} \begin{bmatrix} \left(\frac{m_A v_A^2}{2k_B T} - \frac{3}{2}\right) f_A^e \\ \left(\frac{m_B v_B^2}{2k_B T} - \frac{3}{2}\right) f_B^e \\ \left(\frac{m_C v_C^2}{2k_B T} - \frac{3}{2}\right) f_C^e \\ \left(\frac{m_D v_D^2}{2k_B T} - \frac{3}{2}\right) f_D^e \end{bmatrix}$$

In a similar way, it is possible to find the eigenfunctions $\{\phi_\alpha^{(r)}\}$ of $C^{(r)}$, but considering that in a reactive collision there are only seven collision invariants (one invariant disappears because of the constraint imposed by the chemical process).

Whenever $\hat{C}^{(r)}$ may be considered as a small pertubation of $\hat{C}^{(e)}$, the following relations can be derived from [3.16]–[3.18]

$$[I.3] \qquad \hat{C}^{(e)} |\varphi_\alpha\rangle = 0$$

$$[I.4] \qquad \hat{C}^{(r)} |\varphi_\alpha\rangle + \hat{C}^{(e)} |\phi_\alpha^{(1)}\rangle = \lambda_\alpha^{(1)} |\varphi_\alpha\rangle$$

$$[I.5] \qquad \hat{C}^{(r)} |\phi_\alpha^{(1)}\rangle + \hat{C}^{(e)} |\phi_\alpha^{(2)}\rangle = \lambda_\alpha^{(1)} |\phi_\alpha^{(1)}\rangle + \lambda_\alpha^{(2)} |\varphi_\alpha\rangle$$

$$[I.6] \qquad \hat{C}^{(r)} |\phi_\alpha^{(2)}\rangle + \hat{C}^{(e)} |\phi_\alpha^{(3)}\rangle = \lambda_\alpha^{(1)} |\phi_\alpha^{(2)}\rangle + \lambda_\alpha^{(2)} |\phi_\alpha^{(1)}\rangle + \lambda_\alpha^{(3)} |\varphi_\alpha\rangle$$

Equation [I.3] allows us to express

$$[I.7] \qquad |\varphi_\alpha\rangle = \sum_{\alpha'=1}^{8} C_{\alpha\alpha'}^0 |\phi_{\alpha'}^{(e)}\rangle$$

By using the projection operators P and Q defined in [3.19], we find

[I.8] $P\hat{C}^{(r)}P|\varphi_\alpha\rangle = \lambda_\alpha^{(1)}|\varphi_\alpha\rangle$

showing that $|\varphi_\alpha\rangle$ and $\lambda_\alpha^{(1)}$ are the eigenfunctions and eigenvalues of the $P\hat{C}^{(r)}P$ operator. Multiplying by the bra $\langle\phi_\beta^{(e)}|$, we get the set of equations

[I.9] $$\sum_{\alpha'=1}^{8} C^0_{\alpha,\alpha'}[\langle\phi_\beta^{(e)}|\hat{C}^{(r)}|\phi_{\alpha'}^{(e)}\rangle - \lambda_\alpha^{(1)}\delta^{K_r}_{\beta\alpha'}] = 0$$

having solution whenever the following determinant vanishes

[I.10] $$\|\langle\phi_\beta^{(e)}|\hat{C}^{(r)}|\phi_\alpha^{(e)}\rangle - \lambda_\alpha^{(1)}\delta^{K_r}_{\beta\alpha'}\| = 0$$

from which, the corrections of first order $\lambda_\alpha^{(1)}$ can be obtained. Taking into account that the matrix elements,

[I.11] $$C^{(r)}_{i,j} \equiv \langle\phi_i^{(e)}|\hat{C}^{(r)}|\phi_j^{(e)}\rangle \qquad (i, j = 1, \ldots, 8)$$

vanish except for

$$C^{(r)}_{1,1} = n_A^{-1}\Lambda, \quad C^{(r)}_{2,2} = n_B^{-1}\Lambda, \quad C^{(r)}_{3,3} = n_C^{-1}\Lambda, \quad C^{(r)}_{4,4} = n_D^{-1}\Lambda$$
$$C^{(r)}_{1,2} = C^{(r)}_{2,1} = n_A^{-1/2}n_B^{-1/2}\Lambda, \quad C^{(r)}_{1,3} = C^{(r)}_{3,1} = -n_A^{-1/2}n_C^{-1/2}\Lambda, \quad C^{(r)}_{1,4} = C^{(r)}_{4,1} = -n_A^{-1/2}n_D^{-1/2}\Lambda$$
[I.12] $$C^{(r)}_{2,3} = C^{(r)}_{3,2} = -n_B^{-1/2}n_C^{-1/2}\Lambda, \quad C^{(r)}_{2,4} = C^{(r)}_{4,2} = -n_B^{-1/2}n_D^{-1/2}\Lambda, \quad C^{(r)}_{3,4} = C^{(r)}_{4,3} = n_C^{-1/2}n_D^{-1/2}\Lambda$$
$$C^{(r)}_{1,8} = C^{(r)}_{8,1} = \sqrt{\frac{2}{3nn_A}}\left(\frac{\Delta E}{k_BT}\right)\Lambda, \quad C^{(r)}_{2,8} = C^{(r)}_{8,2} = \sqrt{\frac{2}{3nn_B}}\left(\frac{\Delta E}{k_BT}\right)\Lambda, \quad C^{(r)}_{3,8} = C^{(r)}_{8,3} = -\sqrt{\frac{2}{3nn_C}}\left(\frac{\Delta E}{k_BT}\right)\Lambda$$
$$C^{(r)}_{4,8} = C^{(r)}_{8,4} = -\sqrt{\frac{2}{3nn_D}}\left(\frac{\Delta E}{k_BT}\right)\Lambda, \quad C^{(r)}_{8,8} = \frac{2}{3n}\left(\frac{\Delta E}{k_BT}\right)^2\Lambda$$

where

[I.13] $$\Lambda = -\int dv_A\, dv_B\, d\Omega' \sigma^{(r)}_{AB} g_{AB} f^e_A f^e_B, \qquad \Delta E = E_C + E_D - E_A - E_B$$

takes the form

[I.14] $$\lambda_\alpha^{(1)} = 0, \qquad \alpha = 1, \ldots, 7$$
$$\lambda_8^{(1)} = \left[\frac{2}{3n}\left(\frac{\Delta E}{k_BT}\right)^2 + \sum_{i=A,B,C,D} n_i^{-1}\right]\Lambda$$

Now we can calculate the φ_α functions by solving [I.9]. So, it results

[I.15] $$|\varphi_1\rangle = |\phi_5^{(e)}\rangle$$

[I.16] $$|\varphi_2\rangle = |\phi_6^{(e)}\rangle$$

[I.17] $$|\varphi_3\rangle = |\phi_7^{(e)}\rangle$$

[I.18] $$|\varphi_4\rangle = \frac{1}{\sqrt{1 + \frac{3n}{2}\left(\frac{k_BT}{\Delta E}\right)^2 n_A^{-1}}}\left[|\phi_1^{(e)}\rangle - \sqrt{\frac{3n}{2n_A}}\left(\frac{k_BT}{\Delta E}\right)|\phi_8^{(e)}\rangle\right]$$

[I.19] $$|\varphi_5\rangle = \frac{1}{\sqrt{\left[1 + \frac{3n}{2}\left(\frac{k_BT}{\Delta E}\right)^2 n_A^{-1}\right]\cdot\left[1 + \frac{3n}{2}\left(\frac{k_BT}{\Delta E}\right)^2 \sum_{S=A,B} n_S^{-1}\right]}}\left\{-\frac{3n}{2\sqrt{n_An_B}}\left(\frac{k_BT}{\Delta E}\right)^2|\phi_1^{(e)}\rangle\right.$$
$$\left. + \left[1 + \frac{3n}{2}\left(\frac{k_BT}{\Delta E}\right)^2 n_A^{-1}\right]|\phi_2^{(e)}\rangle - \sqrt{\frac{3n}{2n_B}}\left(\frac{k_BT}{\Delta E}\right)|\phi_8^{(e)}\rangle\right\}$$

[I.20] $$|\varphi_6\rangle = \frac{1}{\sqrt{\left[1 + \frac{3n}{2}\left(\frac{k_BT}{\Delta E}\right)^2 \sum_{S=A,B} n_S^{-1}\right]\cdot\left[1 + \frac{3n}{2}\left(\frac{k_BT}{\Delta E}\right)^2 \sum_{S=A,B,C} n_S^{-1}\right]}}\left\{\frac{3n}{2\sqrt{n_An_C}}\left(\frac{k_BT}{\Delta E}\right)^2|\phi_1^{(e)}\rangle\right.$$
$$\left. + \frac{3n}{2\sqrt{n_Bn_C}}\left(\frac{k_BT}{\Delta E}\right)^2|\phi_2^{(e)}\rangle + \left[1 + \frac{3n}{2}\left(\frac{k_BT}{\Delta E}\right)^2 \sum_{S=A,B} n_S^{-1}\right]|\phi_3^{(e)}\rangle + \sqrt{\frac{3n}{2n_C}}\left(\frac{k_BT}{\Delta E}\right)|\phi_8^{(e)}\rangle\right\}$$

[I.21] $$|\varphi_7\rangle = \frac{1}{\sqrt{\left[1 + \frac{3n}{2}\left(\frac{k_BT}{\Delta E}\right)^2 \sum_{S=A,B,C} n_S^{-1}\right]\cdot\left[1 + \frac{3n}{2}\left(\frac{k_BT}{\Delta E}\right)^2 \sum_{S=A,B,C,D} n_S^{-1}\right]}}\left\{\frac{3n}{2\sqrt{n_An_D}}\left(\frac{k_BT}{\Delta E}\right)^2|\phi_1^{(e)}\rangle\right.$$
$$+ \frac{3n}{2\sqrt{n_Bn_D}}\left(\frac{k_BT}{\Delta E}\right)^2|\phi_2^{(e)}\rangle - \frac{3n}{2\sqrt{n_Cn_D}}\left(\frac{k_BT}{\Delta E}\right)^2|\phi_3^{(e)}\rangle + \left[1 + \frac{3n}{2}\left(\frac{k_BT}{\Delta E}\right)^2 \sum_{S=A,B,C,D} n_S^{-1}\right]|\phi_4^{(e)}\rangle$$
$$\left. + \sqrt{\frac{3n}{2n_D}}\left(\frac{k_BT}{\Delta E}\right)|\phi_8^{(e)}\rangle\right\}$$

Can. J. Chem. Downloaded from www.nrcresearchpress.com by 196.1.178.254 on 09/07/12
For personal use only.

$$[I.22]\quad |\varphi_8\rangle = \frac{1}{\sqrt{\frac{2}{3n}\left(\frac{\Delta E}{k_B T}\right)^2 + \sum_{S=A,B,C,D} n_S^{-1}}} \left\{ n_C^{-1/2}|\phi_3^{(e)}\rangle + n_D^{-1/2}|\phi_4^{(e)}\rangle - n_A^{-1/2}|\phi_1^{(e)}\rangle - n_B^{-1/2}|\phi_2^{(e)}\rangle - \sqrt{\frac{2}{3n}}\left(\frac{\Delta E}{k_B T}\right)|\phi_8^{(e)}\rangle \right\}$$

The functions φ_i ($i = 1, \ldots, 8$) are a linear combination of the set $\phi_i^{(e)}$ ($i = 1, \ldots, 8$) and hence, are eigenfunctions with zero eigenvalue of $\hat{C}^{(e)}$. However, it is the eigenfunction φ_8 that must be singled out, since this is the only linear combination of the elastic collisional invariants that gets a non-zero eigenvalue in a reacting system. Indeed, in the presence of reactive collisions, we could have started the study of the reacting system from the set φ_i ($i = 1, \ldots, 8$). From this point of view, our goal should be to evaluate the eigenvalue associated with φ_8 becoming non-zero for existing reactive collisions.

Introducing P and Q in formula [I.4], we have

$$[I.23]\quad \hat{C}^{(r)}|\varphi_\alpha\rangle + \hat{C}^{(e)}Q|\phi_\alpha^{(1)}\rangle = \lambda_\alpha^{(1)}|\varphi_\alpha\rangle$$

and by applying the Q operator we express $Q|\phi_\alpha^{(1)}\rangle$ as a function of $|\varphi_\alpha\rangle$,

$$[I.24]\quad Q|\phi_\alpha^{(1)}\rangle = -\hat{G}^{-1}Q\hat{C}^{(r)}|\varphi_\alpha\rangle$$

$\hat{G}$ being the $Q\hat{C}^{(e)}Q$ operator.

Multiplying eq. [I.5] by the bra $\langle\varphi_\alpha|$, we have

$$[I.25]\quad \langle\varphi_\alpha|\hat{C}^{(r)}|\phi_\beta^{(1)}\rangle = \lambda_\beta^{(1)}\langle\varphi_\alpha|\phi_\beta^{(1)}\rangle + \lambda_\beta^{(2)}\delta_{\alpha\beta}^{K_r}$$

and inserting the identity resolution, $\mathbf{1} = P + Q$, in the left hand side of the [I.25], we get

$$[I.26]\quad \langle\varphi_\alpha|P\hat{C}^{(r)}P|\phi_\beta^{(1)}\rangle + \langle\varphi_\alpha|\hat{C}^{(r)}Q|\phi_\beta^{(1)}\rangle = \lambda_\beta^{(1)}\langle\varphi_\alpha|\phi_\beta^{(1)}\rangle + \lambda_\beta^{(2)}\delta_{\alpha\beta}^{K_r}$$

As

$$[I.27]\quad \langle\varphi_\alpha|P\hat{C}^{(r)}P|\phi_\beta^{(1)}\rangle = \lambda_\alpha^{(1)}\langle\varphi_\alpha|\phi_\beta^{(1)}\rangle$$

with the help of [I.24], formula [I.26] becomes

$$[I.28]\quad \lambda_\alpha^{(1)}\langle\varphi_\alpha|\phi_\beta^{(1)}\rangle - \langle\varphi_\alpha|\hat{C}^{(r)}Q\hat{G}^{-1}Q\hat{C}^{(r)}|\varphi_\beta\rangle = \lambda_\beta^{(1)}\langle\varphi_\alpha|\phi_\beta^{(1)}\rangle + \lambda_\beta^{(2)}\delta_{\alpha\beta}^{K_r}$$

This relation is verified for all the functions $|\varphi_\alpha\rangle$, since the functions $\{|\varphi_\alpha\rangle\}_{\alpha=1}^{7}$ are the eigenfunctions of $\hat{C}^{(r)}$ for the zero eigenvalue

$$[I.29]\quad \hat{C}^{(r)}|\varphi_\alpha\rangle = 0 \qquad (\alpha = 1, \ldots, 7)$$

Thus the residual degeneration corresponding to the first correction does not cause any problematical situation. This permits us to calculate the second correction with the aid of the following formula

$$[I.30]\quad \lambda_\alpha^{(2)} = -\langle\varphi_\alpha|\hat{C}^{(r)}Q\hat{G}^{-1}Q\hat{C}^{(r)}|\varphi_\alpha\rangle$$

It can be easily shown from [I.30] that

$$[I.31]\quad \lambda_\alpha^{(2)} = 0 \qquad (\alpha = 1, \ldots, 7)$$

$$\lambda_8^{(2)} = -\left[\frac{2}{3n}\left(\frac{\Delta E}{k_B T}\right)^2 + \sum_{S=A,B,C,D} n_S^{-1}\right] \times \langle\Psi|Q\hat{C}^{(e)-1}Q|\Psi\rangle$$

where Ψ means

$$[I.32]\quad \begin{bmatrix} \int dv_B\, d\Omega'\, \sigma_{AB}^{(r)} g_{AB}\, f_A^e f_B^e \\ \int dv_A\, d\Omega'\, \sigma_{AB}^{(r)} g_{AB}\, f_A^e f_B^e \\ -\int dv_D\, d\Omega'\, \sigma_{CD}^{(r)} g_{CD}\, f_C^e f_D^e \\ -\int dv_C\, d\Omega'\, \sigma_{CD}^{(r)} g_{CD}\, f_C^e f_D^e \end{bmatrix}$$

Analogously, higher corrections can be found. For instance

$$[I.33]\quad \lambda_\alpha^{(3)} = 0 \qquad (\alpha = 1, \ldots, 7)$$

$$\lambda_8^{(3)} = \left[\frac{2}{3n}\left(\frac{\Delta E}{k_B T}\right)^2 + \sum_{S=A,B,C,D} n_S^{-1}\right] \times \{-\lambda_8^{(1)}\langle\Psi|Q\hat{C}^{(e)-1}Q\hat{C}^{(e)-1}Q|\Psi\rangle + \langle\Psi|Q\hat{C}^{(e)-1}Q\hat{C}^{(r)}Q\hat{C}^{(e)-1}Q|\Psi\rangle\}$$

From the results [I.14]–[I.22], [I.31], and [I.33] we must point out that the initial degeneration has been very partially eliminated. Initially, there were eight eigenfunctions $\phi_\alpha^{(e)}$ of $\hat{C}^{(e)}$ for the zero eigenvalue and when the perturbation $\hat{C}^{(r)}$ is applied only one function arises with an eigenvalue different from zero. This is a logical result because there are seven collision invariants associated with reactive collisions (the chemical reaction is a restriction that eliminates one invariant), and for that the operator $\hat{C} = (\hat{C}^{(e)} + \hat{C}^{(r)})$ owns seven eigenfunctions for the zero eigenvalue. Indeed, the introduction of the perturbation $\hat{C}^{(r)}$ has allowed us to get the first non-zero eigenvalue λ_8 of $\hat{C}$ and its eigenfunction (at least in the zero order approximation φ_8).

Can. J. Chem. Downloaded from www.nrcresearchpress.com by 196.1.178.254 on 09/07/12
For personal use only.

Structural investigation of water-hyacinth (*Eichhornia crassipes*) polysaccharides. Part I. Water-soluble polysaccharides

MOHAMADY A. ISSA
Agricultural Chemistry Department, Faculty of Agriculture, El Minia University, El-Minia, Egypt

Received May 4, 1988

MOHAMADY A. ISSA. Can. J. Chem. **66**, 2777 (1988).

A galactomannan and a branched (1→3)-β-D-glucan were isolated from the water hyacinth plant. The galactomannan, purified from the cold water extract, is composed of D-galactose and D-mannose in a ratio of 1.0:2.8. It has a (1→4)-linked D-mannose backbone, one out of three D-mannose residues being substituted with a single α-D-galactosyl unit. The branched (1→3)-β-D-glucan isolated from the hot water extract has a main chain composed of β-(1→3)-linked D-glucopyranosyl residues, and two single β(1→6)-D-glucopyranosyl groups attached as side chains to, on average, every 5 sugar units of the main chain. In addition, the branching of the β-glucan occurs regularly at O-6 of the β-(1→3)-linked backbone.

MOHAMADY A. ISSA. Can. J. Chem. **66**, 2777 (1988).

On a isolé un galactomannane ainsi qu'un β-D-glucane portant une chaîne (1→3) à partir de plants de jacinthes d'eau (*Eichornia*). Le galactomannane, purifié à partir des produits extraits à l'eau froide, se compose de D-galactose et de D-mannose dans un rapport de 1,0 à 2,8. Il possède un squelette de D-mannoses liés en (1→4) et un résidu D-mannose sur trois est substitué par une seule unité α-D-galactosyle. Le β-D-glucane portant une chaîne (1→3) a été isolé par de l'eau chaude et il possède une chaîne principale formée de résidus D-glucopyrannosyles liés en β-(1→3) ainsi que deux groupements β-(1→6) D-glucopyrannosyles attachés individuellement comme chaînes latérales à, en moyenne, cinq unités de sucre de la chaîne principale. De plus, il se produit régulièrement une ramification du β-glucane au niveau du O-6 du squelette lié en β-(1→3).
[Traduit par la revue]

Introduction

The water hyacinth (*Eichhornia crassipes*) is known as the most noxious weed in the River Nile streams. The rapid growth of this plant causes a great deal of water loss as well as danger of blocking the streams. Many attempts have been made to use this plant as animal feed, e.g., forage for cattle (1–3). A considerable number of reports (4–6) reveal that it could be used as a source of fermentable sugars and in the manufacture of paper and pressed boards. As well, reports on the effect of different extracts as growth regulators have been published (7–10).

The chemical composition of the water hyacinth has been studied by many investigators (1, 11–13); however, no reports on its polysaccharides have been published.

This work was conducted to study the possible structural features of water-soluble polysaccharides isolated from the water hyacinth, as revealed by methylation fragmentation analysis and enzymatic degradation as well as by ^{13}C nmr spectra.

Discussion

Fractionation and chemical constitution of water-soluble polysaccharides of the water hyacinth

The dried water hyacinth (*Eichhornia crassipes*) flour was first defatted and the polysaccharides in this study were extracted successively with phosphate-buffered saline (PBS) at 2–4°C, hot water at 85°C, and again at 100°C. This fractionation afforded the following polysaccharide fractions: the cold water extractable fraction (Fr. CW) and the hot water extractable fraction (Fr. HW). The polysaccharide in each fraction was purified and lyophilized.

The water-soluble polysaccharides so obtained were hydrolyzed with acid and their sugar constituents were examined. Table 1 lists their yields and compositions.

Structural characterization of the polysaccharides

Galactomannan

As shown in Table 1, the water-soluble neutral polysaccharide isolated from the PBS extract was a galactomannan, composed of D-galactose and D-mannose in a molar ratio of 1.0:2.8 as analyzed by glc. It had a molecular weight of 5.0×10^5, as determined by hplc. Its negative specific optical rotation $[\alpha]_D^T -10.2°$ (*c* 1.0, 0.5 M NaOH) and an absorption band at 875 cm^{-1} in the infrared spectrum suggest that most sugar residues are of the β configuration (14).

TABLE 1. Water-soluble polysaccharide fractions of water-hyacinth and their chemical composition

Polysaccharide fraction	Yield (%)[a]	Carbohydrate component (%) Glc	Man	Gal
PBS extract (CW) (galactomannan)	3.0	—	73	27
Hot water extract (HW) (branched β-glucan)	2.1	100	—	—

[a]Values were on dry defatted basis.

To obtain information on the mode of glycosidic linkages of the sugar constituents of galactomannan and their sequential arrangements, the galactomannan was subjected to methylation followed by acid hydrolysis and to partial acid hydrolysis. Acid hydrolysis of methylated galactomannan gave 2,3,4,6-tetra-*O*-methyl-D-galactose, in a quantity equivalent to all the galactose present, and 2,3,6-tri-*O*-methyl- and 2,3-di-*O*-methyl-D-mannose in a molar ratio of 1.0:1.9:1:1 (Table 2) as analyzed by glc–ms. This result indicates that the galactomannan contains a backbone of (1→4)-linked D-mannose residues and one out of three D-mannose residues is substituted at the O-6 atom (branching point) with a single D-galactose residue as a side chain. This was confirmed by partial acid hydrolysis of the polysaccharide (see experimental section). The hydrolyzate contained a mixture of two di- and trisaccharides as well as two tetrasaccharides (Fig. 1), separable first by chromatography on an activated charcoal column and then on a

Can. J. Chem. Downloaded from www.nrcresearchpress.com by 196.1.178.254 on 09/07/12
For personal use only.

β-D-Manp(1 → 4)-D-Manp
(**1**)

α-D-Galp(1 → 6)-D-Manp
(**2**)

β-D-Manp(1 → 4) β-D-Manp(1 → 4)-D-Manp
(**3**)

β-D-Manp(1 → 4)-D-Manp
6
↑
1
(**4**) α-D-Galp

β-D-Manp(1 → 4)-β-D-Manp(1 → 4)-β-D-Manp(1 → 4)-D-Manp
(**5**)

β-D-Manp(1 → 4)-β-D-Manp(1 → 4)-D-Manp
6
↑
1
α-D-Galp
(**6**)

FIG. 1. Structural formulas of oligosaccharides.

TABLE 2. Molar ratios of methyl sugar components of the methylated galactomannan and β-glucan

O-Methyl sugar (alditol acetate)	Mode of linkage	Molar ratio	
		Galactomannan	β-glucan
O-Methyl-D-galactose			
2,3,4,6-tetra	(Gal)1→	1.0	
O-Methyl-D-mannose			
2,3,6-tri-	→4(Man)1→	1.9	
2,3-di-	→4(Man)1→ ↑ 6	1.1	
O-Methyl-D-glucose			
2,3,4,6-tetra-	(Glc)1→		1.00
2,4,6-tri-	→3(Glc)1→		1.48
2,4-di-	→6(Glc)1→ ↑ 3		0.99

Bio-gel P-2 column. Each oligosaccharide was further purified by tlc and its structure was examined by methylation analysis. As shown in Table 3, the two disaccharides were characterized as 4-*O*-β-D-mannopyranosyl-D-mannose (**1**) and 6-*O*-α-D-galactopyranosyl-D-mannose (**2**) respectively.

The trisaccharide (**3**) was shown to contain three D-mannose units linked β-(1→4) whereas the trisaccharide (**4**) was shown to contain two nonreducing terminal D-mannose and D-galactose residues, and the doubly substituted D-mannose (third unit) at the O-4 and O-6 positions. In addition, two tetrasaccharides (**5** and **6**) were isolated and their possible structural features were elucidated on the basis of results of methylation analysis (Table 3).

Characteristic ^{13}C chemical shifts for sugar residues of the polysaccharides are given in Table 4. The chemical shift of C-1 at 93.80 ppm should be attributed to α-D-galactopyranose residues at the nonreducing ends, and that at 102.3 ppm to (1→4)-linked β-D-mannopyranose residues, by comparison with previous data (15, 16). The chemical shift at 69.81 should be due to the O-substituted C-6 of β-(1→4) D-mannose residues, and the peak at 75.52 ppm could be assigned as the C-4 of β-(1→4) D-mannopyranose residues, as deduced from the data for β-(1→4)-linked D-glucan (17).

Periodate oxidation revealed galactomannan consumed ca. 1 mol of oxidant per mol of hexose residue without liberation of formic acid. This and the absence of D-galactose or D-mannose in the hydrolyzate of the periodate-oxidized polysaccharide indicated that the galactomannan contained substituted sugar units at neither the O-2 nor O-3 positions.

Thus, the most probable structure of the galactomannan is as shown in Fig. 2.

Galactomannan occurs in most leguminous seeds (18) having a chain of D-mannose units linked β(1→4) with single side chains of α-D-galactopyranosyl linked α-(1→6) to one or more D-mannose units, but differing from each other in yield, optical rotatory power, mannose/galactose ratio, and degree of polymerization. Sometimes the galactosyl stubs are more than one unit long (18, 19) and occasionally there are linkages other than (1→4) between D-Manp residues (20–22). In general, the galactomannan found in this study was structurally quite similar to leguminous seed galactomannans.

Branched (1→3) glucan

The water-soluble glucan, isolated from the hot water extract (HW) in 2.1% yield, was composed solely of D-glucose residues (Table 1), as shown by pc (paper chromatography) of the hydrolyzate, by glc of the alditol acetate prepared from the hydrolyzate. It had a negative specific rotation $[\alpha]_D^{25}$ −13.5° (*c* 1.5, 1 M NaOH) and showed a characteristic ir absorption at 892 cm^{-1}, indicating the presence of β-D-glycosidic linkages (23). It had a molecular weight of 6.5×10^5 as measured by hplc (water system). The glucan was methylated, followed by acid hydrolysis. The partially methylated sugars were analyzed as the alditol acetate derivatives by glc and glc–ms, and identified by comparing their retention times in glc and their mass spectra with those of authentic samples, or with the values reported in the literature (24). As shown in Table 2, the methylation analysis indicated the presence of 2,3,4,6-tetra-, 2,4,6-tri-, and 2,4-di-*O*-methyl-D-glucose in a molar ratio of 1.00:1.48:0.99.

Periodate oxidation showed that the β-glucan consumed 0.58 mol of IO_4^- with liberation of 0.28 mol of formic acid per anhydrous glucose residue. The values were in good agreement with those computed from the results of the methylation analysis, namely, 0.58 and 0.29 mol (Table 2). The oxidized polysaccharide was reduced with $NaBH_4$ and the resultant polyalcohol was hydrolyzed. The hydrolyzate (containing the Smith degradation product) was analyzed by glc as the alditol acetate derivatives, and glycerol and glucose were detected in a

Can. J. Chem. Downloaded from www.nrcresearchpress.com by 196.1.178.254 on 09/07/12
For personal use only.

TABLE 3. Hydrolysis products of methylated oligosaccharides isolated from partial hydrolyzate of the galactomannan

Oligosaccharide	Yield[a] (mg)	R_{Glc}[b]	*O*-Methyl sugar	Molar ratio
(**1**) Disaccharide	8.6	0.55	2,3,4,6-Tetra-*O*-methyl-D-mannose	1.2
			2,3,6-tri-*O*-methyl-D-mannose	1.0
(**2**) Disaccharide	6.1	0.63	2,3,4,6-Tetra-*O*-methyl-D-galactose	1.3
			2,3,4-Tri-*O*-methyl-D-mannose	1.0
(**3**) Trisaccharide	12.5	0.44	2,3,6-Tri-*O*-methyl-D-mannose	2.3
			2,3,4,6-Tetra-*O*-methyl-D-mannose	1.0
(**4**) Trisaccharide	6.0	0.49	2,3,4,6-Tetra-*O*-methyl-D-galactose	1.3
			2,3,4,6-Tetra-*O*-methyl-D-mannose	1.2
			2,3-Di-*O*-methyl-D-mannose	1.0
(**5**) Tetrasaccharide	5.0	0.24	2,3,6-Tri-*O*-methyl-D-mannose	3.1
			2,3,4,6-Tetra-*O*-methyl-D-mannose	1.0
(**6**) Tetrasaccharide	4.0	0.22	2,3,4,6-Tetra-*O*-methyl-D-mannose	1.2
			2,3,4,6-Tetra-*O*-methyl-D-galactose	1.1
			2,3,6-Tri-*O*-methyl-D-mannose	1.1
			2,3-Di-*O*-methyl-D-mannose	1.0

[a]The galactomannan (1.2 g) was partially hydrolyzed with 0.5 M TFA at 100°C for 3 h.
[b]Paper-chromatographic mobility to that of D-glucose (solvent a).

TABLE 4. Representative ^{13}C chemical shifts for nuclei of polysaccharides in dimethyl sulfoxide-d_6

^{13}C Galactomannan	δ (ppm)	^{13}C Branched β-glucan	δ (ppm)
Gal, C-1	93.80	Glc, C-1	103.56
Man, C-1	102.30	Glc, C-2	72.76
Man, C-2	71.20	O-subst, Gal, C-3	86.76
Man, C-3	74.50	Glc, C-4	68.62
Man, C-4	68.40	Glc, C-5	76.42
Man, C-6	62.60	Glc, C-6	61.43
O-subst, Man, C-4	75.52	O-subst, Glc, C-6	70.65
O-subst, Man, C-6	69.81		

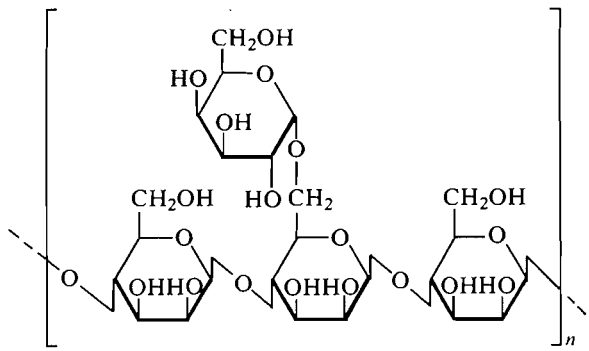

FIG. 2. Possible structure of the repeating unit of galactomannan.

molar ratio of 1.00:2.57. The glycerol must have arisen from the terminal D-glucose residues, and the occurrence of glucose must be due to the presence of oxidation-resistant D-glucose such as (1→3)-linked residues. These results were in good agreement with those from the methylation analysis.

The β-glucan was incubated with *exo*-(1→3)-β-D-glucanase (Lysing Enzymes) from Basidiomycetes, in 0.1 M acetate buffer (see experimental section). Each enzymic degradation product was subjected to gel filtration on Bio-Gel P-2; only two peaks, corresponding to the mono- and di-saccharide, were observed. The products recovered from the eluates at 5 and 48 h were analyzed by pc, or by glc as the trifluoroacetyl derivative of the disaccharide-alditol (25). Consequently, in each case, glucose and gentiobiose were detected. The molar ratio of gentiobiose to glucose was almost constant, that is, 0.68 at 5 h and 0.63 at 48 h, vs. 0.67 expected from the methylation analysis (Table 2).

The foregoing data indicate that glucan, isolated from the hot water extract of the water hyacinth, has a main chain composed of (1→3)-β-D-glucopyranosyl residues, and has as side chains two single β-(1→6)-linked D-glucopyranosyl groups attached, on average, to every five sugar residues of the main chain as shown in Fig. 3. Furthermore, from the results of the enzymic hydrolysis it was indicated that the branching of β-glucan occurs regularly at O-6 of the β(1→3)-linked backbone.

Such a branched structure of (1→6)-branched (1→3)-β-D-glucan was supported by its ^{13}C nmr, as shown in Table 4, including characteristic peaks of chemical shifts of C-1 (103.56 ppm), O-substituted C-3 (86.79 ppm), and O-substituted C-6 (70.65 ppm).

β-D-Glucans made up of (1→3) and (1→4)-linked pyranosyl residues are found usually in small amounts, but widely spread throughout, in the seed of Gramineae. These β-D-glucans are linear polymers in which (1→3) and (1→4) linkages are interspersed (26–29). It is interesting that the β-D-glucan obtained in this study has a quite different structure from cereal β-D-glucans.

Experimental

Materials

Water hyacinth plants were collected from the River Nile at the front of El-Minia city, Egypt. In this study the air-dried whole plant of the water hyacinth was used. Carbohydrates and Lysing Enzymes were purchased from Sigma, and Tsk G-500 PW for hplc, ECNSS-M, and Gas Chromosorb W (80–100 mesh) from Applied Science Laboratories. OV-225 coated on Gas Chrom Q (100–120 mesh) was obtained from Supelco Inc. Standard pullulan fractions having definite molecular weights, P-800, P-400, and P-200, for hplc were from Worthington Biochemicals, Bio-Gel P-2 was purchased from Bio-Rad Laboratories, and Sephadex LH-20 from Pharmacia Fine Chemicals. Other chemicals were commercially available.

Can. J. Chem. Downloaded from www.nrcresearchpress.com by 196.1.178.254 on 09/07/12
For personal use only.

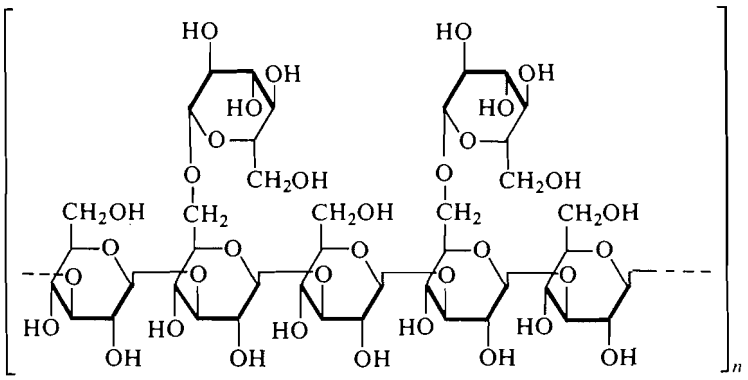

FIG. 3. Possible structure of repeating unit of β-glucan.

General analytical method

All evaporations and concentrations of solutions were conducted under diminished pressure at temperatures not exceeding 35–40°C. Specific optical rotations were measured at room temperature with a Perkin–Elmer automatic digital polarimeter, model 141. Paper chromatography (pc) was performed by the double-descending technique on Whatman No. 1 filter paper using the following solvent systems (v/v): (a) *n*-butanol–pyridine–water (6:4:3) for unsubstituted sugars; (b) benzene–ethanol–water (38:10:1) for methylated sugars, and (c) ethyl acetate – pyridine–water (8:2:1) for oligosaccharides. Sugars were located on the paper by alkaline silver nitrate and *p*-anisidine–HCl. Thin-layer chromatography (tlc) was carried out on precoated glass plates (0.25 mm) of silica gel 60F-254 (E. Merck, Darmstadt, FRG) using the solvent (d): benzene–ethanol – acetic acid – water (200:47:15:1, v/v) for further purification of oligosaccharides. Their spots were detected by spraying the plates with 20% H_2SO_4 in ethanol, with heating. Quantitative determination of the total carbohydrate content was generally done by the phenol – sulfuric acid colorimetric method (30) using D-glucose or D-mannose as a standard. Gas–liquid chromatography (glc) of neutral sugars and their methyl derivatives was usually performed after conversion into their corresponding alditol acetates, using a Hewlett Packard 5720 A chromatograph equipped with a flame-ionization detector at a gas flow rate of 35–40 mL of N_2/min and a glass column (0.3 × 175 cm) packed with 3% ECNSS-M on Gas Chrom Q at 200°C and 190°C for free sugars and methyl sugars respectively. The ir spectra were recorded with a Perkin–Elmer 457 grating spectrophotometer. Gas–liquid chromatography – mass spectrometry (gs–ms) of the alditol acetates of methylated sugars was carried out on a Shimadzu LKB-9000BGC mass spectrometer with a column packed with 3% ECNSS on Gas Chromosorb W or 3% OV-225 on Gas Chrom Q, at temperatures programmed from 120°C to 180°C at 1°C/min. For identification of sugar constituents, a sample of polysaccharide (ca. 10 mg) was heated, first with 90% formic acid (1 mL) at 100°C for 10 h in screw-capped tubes, and after evaporation the residue was heated further with 2 M trifluoroacetic acid (TFA, 0.5 mL) for 8 h. After removing TFA by repeated evaporation with H_2O, the sugars in the hydrolyzate were analyzed by glc or pc. The molecular weights of the polysaccharides were estimated by hplc using a Hitachi liquid chromatograph model 635 with a TSK G-5000 PW column and water as the carrier system (31).

Isolation of polysaccharides

Generally, pure polysaccharide fractions were obtained by repeated ethanol precipitations followed by lyophilization. The insoluble residue after each step was washed thoroughly with distilled H_2O.

Lipids and pigments were first extracted from dried water hyacinth flour (100 g) in a Soxhlet apparatus, by successive treatments with $CHCl_3$–MeOH (2:1, v/v) and MeOH–H_2O (4:1, v/v). After air-drying, the defatted flour (75.5 g) was homogenized in phosphate-buffered saline (3 litres, PBS, 0.01 M, pH 7.1) with a Waring blender, and stirred at 2–4°C overnight. The insoluble material was collected by centrifugation. The supernatant was concentrated to small volume, which gave a negative starch/iodine reaction, and then added to 3 volumes of ethanol to give precipitation of PBS-extractable polysaccharide (Fr. CW yield 2.3 g, ca. 3.0% on dry defatted basis). After extraction with PBS, the residue was suspended in 3.5 L of distilled H_2O and heated to 85°C for 5 h with constant stirring. The insoluble residue was collected by centrifugation and heated again at 100°C for 1 h. After centrifugation the insoluble residue was kept for further study elsewhere. The hot water extracts were combined and concentrated; they gave a weak positive starch/iodine reaction, and were treated, first, with a mixture of α- and β-amylases (Sigma) overnight at 37°C in phosphate buffer (pH 5.8) to remove contaminating starch and then with cetylpyridinium chloride to remove any uronic-acid polysaccharide according to ref. 32. After such treatments, the extract was dialyzed, giving no colouration with I_2/KI solution, and then the H_2O-soluble protein was removed by the method of Sevag (33). The hot water-soluble neutral-polysaccharide protein-free extract was concentrated and poured into 3 volumes of ethanol to give hot water extractable neutral polysaccharide (Fr. HW yield 1.6 g, 2.1% on dry defatted basis).

Methylation analysis

The polysaccharide (10 mg, dissolved in dry DMSO under nitrogen atmosphere) was methylated by the method of Hakomori (34) with fresh methylsulfinyl carbanion and methyl iodide. The methylation was repeated until the product showed no absorption attributable to hydroxyl in its ir spectrum. The fully methylated product was hydrolyzed with 90% formic acid (1 mL) for 13 h at 105°C and then with 2 M TFA (1 mL) for 4 h. After removal of the acids as before, the methylated sugars in the hydrolyzate were converted into their corresponding alditol acetates (35) and analyzed by glc (36) and glc–ms (37).

Isolation of oligosaccharides obtained by partial acid hydrolysis of galactomannan

The native polysaccharide (1.2 g) was partially hydrolyzed by heating with 0.5 M TFA (125 mL) for 3 h at 100°C. After evaporation of the acid, the residue was put on an active charcoal column (2 × 30 cm), the column being washed first with water until monosaccharides are removed (650 mL) and then with 75% ethanol (650 mL) to give a mixture of oligosaccharides (340 mg). The oligosaccharide fraction was fractionated using a Bio-gel P-2 column (2 × 175 cm), by elution with water. Each of the five fractions obtained by the above procedure (elution volume ~350 mL) was further purified by tlc to isolate each oligosaccharide.

Structural analysis of oligosaccharides

The oligosaccharides (3–5 mg, each) were hydrolyzed with 2 M TFA for 5 h at 100°C. After evaporation of the acid, the monosaccharides in the hydrolyzate were converted into the alditol acetates and analyzed by glc. Methylation of the oligosaccharide was done by

Can. J. Chem. Downloaded from www.nrcresearchpress.com by 196.1.178.254 on 09/07/12
For personal use only.

the method of Hakomori. The methylated oligosaccharide was purified on a Sephadex LH-20 column (1 × 25 cm) by elution with dichloromethane. The pure methylated oligosaccharide was hydrolyzed successively with 90% formic acid and 2 M TFA as described previously and then converted into the alditol acetate for analysis by glc.

Periodate oxidation

A 10-mg sample of the polysaccharide was dissolved in 15 mL of 0.3 M $NaIO_4$ and periodate uptake at room temperature in the dark was estimated, as described in ref. 38, at intervals until constant (40 and 96 h for galactomannan and β-glucan respectively). The formic acid liberated was determined by titration with 5 mM NaOH (39). In a separate experiment the polysaccharide (100 mg) was oxidized with periodate (40) for 50 h at room temperature. The excess periodate was destroyed by addition of ethylene glycol and the solution was dialyzed against tap water for 72 h. The non-dialyzed material was recovered by concentration and hydrolyzed with 1 N H_2SO_4. The hydrolyzate was neutralized with $BaCO_3$, filtered, and concentrated for examination by pc.

Smith degradation

A sample of β-glucan (100 mg) was treated with 0.3 M $NaIO_4$ (100 mL) at room temperature. After 7 days, a few drops of ethylene glycol were added to the reaction mixture and it was dialyzed against tap water to remove $NaIO_3$. The polyaldehyde was reduced with a 10-fold molar excess of $NaBH_4$ at room temperature overnight. Addition of ice-cold 4 N acetic acid to chilled polyalcohol (final pH, 5.5) was used to terminate the reaction, and the solution was again dialyzed and lyophilized (yield, 50.2 mg glucan polyol). For complete Smith degradation, 1% solutions of polyalcohol were successively treated with 90% formic acid for 3 h at 100°C as before and then with 0.5 N H_2SO_4 for 8 h at 100°C. The hydrolyzate was made neutral with $BaCO_3$ in the usual way and the hydrolysis product was analyzed by glc, after $NaBH_4$ reduction followed by acetylation.

Enzymic hydrolysis

β-Glucan (6 mg) was treated with *exo*-(1→3)-β-D-glucanase (Lysing Enzymes, 2.5 mg) in 0.1 M acetate buffer, pH 5.0 (15 mL), and incubated at 37°C; half of the reaction mixture was taken at 5 h and the residual portion was allowed to react for 48 h. Each enzymic degradation product, prepared according to ref. 41, was subjected to gel filtration on a column of Bio-Gel P-2, and two peaks were revealed. The products recovered were analyzed by pc (solvent c) and two spots, corresponding to glucose and gentiobiose (R_{glc} 0.63), were detected. The gentiobiose was further identified by glc as the trifluoroacetate of the disaccharide-alditol as previously reported (41). The molar ratio of the sugars was calculated from the peak in gel filtration on Bio-Gel P-2.

^{13}C nuclear magnetic resonance spectroscopy

The ^{13}C nmr spectra of the polysaccharides were determined at 25 MHz with a Bruker WP-200 spectrometer. All spectra were recorded for solutions in dimethyl sulfoxide-d_6 at a concentration of 6% at 60°C using 8K data points and a spectral width of 5K/3 Hz.

Acknowledgment

Most of the analyses were conducted in the laboratory of Professor Dr. D. Horton, Ohio State University. I wish to express my appreciation to him for the use of his facilities during the peace fellowship program.

1. G. Minano. Indian J. Anim. Sci. **8**, 377 (1938).
2. C. E. Boyd. J. Anim. Sci. **40**, 968 (1968).
3. G. E. Combs. J. Anim. Sci. **42**, 961 (1970).
4. K. H. Sen, P. P. Patit, and G. B. Sindhu. J. Indian Chem. Soc. **6**, 673 (1929).
5. A. M. Azam. Sci. Cult. **6**, 656 (1941).
6. M. A. Gloor and P. R. Gloor. Australian, **138**, 426 (1950); Chem. Abstr. **47**, 12816g (1953).
7. M. S. Sircar and M. Kundu. Sci. Cult. **24**, 332 (1959).
8. M. S. Sircar and M. Kundu. Plant. **13**, 56 (1960).
9. M. S. Sircar and R. Chakravaty. Curr. Sci. **30**, 428 (1961).
10. M. S. Sircar and R. Chakravaty. J. Plant Physiol. **5**, 257 (1962).
11. K. O. Sreemannarayana, K. T. Nambiar, and V. Satchidanandam. Indian J. Anim. Sci. **43**, 545 (1973).
12. K. R. Datta, R. P. Chadrabarty, C. B. Guha, and J. J. Ghosh. Sci. Cult. **32**, 247 (1966).
13. A. M. R. Afify. Biochemical studies on water-hyacinth. M.Sc. thesis, University of Cairo, Cairo, Egypt. 1978.
14. H. Spedding. Adv. Carbohydr. Chem. **19**, 23 (1964).
15. K. Book and C. Pederson. Adv. Carbohydr. Chem. Biochem. **41**, 27 (1983).
16. E. Barreto-Bergter and P. A. J. Gorin. Adv. Carbohydr. Chem. Biochem. **41**, 67 (1983).
17. P. Colson, H. J. Jennings, and I. C. P. Smith. J. Am. Chem. Soc. **96**, 8081 (1974).
18. I. C. M. Dea and A. Morrison. Adv. Carbohydr. Chem. Biochem. **31**, 241 (1975).
19. J.-E. Courtois and P. Le Dizet. Carbohydr. Res. **3**, 141 (1966).
20. A. M. Unrau and Y. M. Choy. Carbohydr. Res. **14**, 151 (1970).
21. A. M. Unrau and Y. M. Choy. Can. J. Chem. **48**, 1123 (1970).
22. V. P. Kapoor and S. Mukherijee. Phytochemistry, **10**, 655 (1971).
23. S. A. Barker, E. J. Bourne, and D. H. Whiffen. Methods Biochem. Anal. **3**, 213 (1956).
24. H. Björndal, C. G. Hellerovist, B. Lindberg, and S. Svensson. Angew. Chem. Int. Ed. Engl. **9**, 610 (1970).
25. H. Nakamura and Z. Tamura. Chem. Pharm. Bull. **18**, 2314 (1970).
26. F. Smith and R. Montgomery. The chemistry of plant gums and mucilages. Van Nostrand – Reinhold, Princeton, NJ. 1959.
27. A. Bacic and B. A. Stone. Carbohydr. Res. **82**, 372 (1980).
28. N. Shibuya and A. Mizaki. Agric. Biol. Chem. **42**, 2267 (1978).
29. G. M. Ballance and D. J. Manners. Carbohydr. Res. **61**, 107 (1978).
30. M. Dubois, K. A. Gilles, J. K. Hamilton, P. A. Rebers, and F. Smith. Anal. Chem. **28**, 350 (1956).
31. A. Misaki, K. Kawaguchi, M. Miyaji, H. Nagae, S. Hokkoku, M. Kakuta, and T. Sasaki. Carbohydr. Res. **129**, 209 (1984).
32. Y. Sone, M. Kakuta, and A. Misaki. Agric. Biol. Chem. **42**, 417 (1978).
33. M. G. Sevag. Biochem. Z. **273**, 419 (1934).
34. S. Hakomori. J. Biochem. **5**, 205 (1964).
35. J. H. Sloneker. Methods Carbohydr. Chem. **6**, 20 (1972).
36. H. Björndal, B. Lindberg, and S. Svensson. Carbohydr. Res. **5**, 433 (1967).
37. P. V. Salinath, R. N. Tharanathan, J. Weckesser, and H. Mayer. Eur. J. Biochem. **144**, 227 (1984).
38. R. L. R. Whistler and J. L. Hickson. J. Am. Chem. Soc. **76**, 1671 (1954).
39. A. R. S. El-Hanafy and M. I. Taha. J. Org. Chem. **28**, 1559 (1963).
40. G. A. Adams. Can. J. Chem. **38**, 280 (1960).
41. C. Hara, T. Tiho, and S. Ukai. Carbohydr. Res. **117**, 201 (1983).

Can. J. Chem. Downloaded from www.nrcresearchpress.com by 196.1.178.254 on 09/07/12
For personal use only.

Stereochemical assignment of *erythro* and *threo* isomers of 2-aryloxy-1-(2-piperidyl)ethanol by phase sensitive homocorrelation nuclear magnetic resonance experiments

M. FELIZ[1]

Departament de Química Orgànica, Facultat de Química, Universitat de Barcelona, Martí i Franqués 1, 08028-Barcelona, Spain

AND

D. MAULEÓN AND C. MINGUILLÓN

Unitat de Química Farmacèutica, Departament de Farmacologia i Química Terapèutica, Facultat de Farmàcia, Universitat de Barcelona, Avd. Diagonal s/n, 08028-Barcelona, Spain

Received March 8, 1988

M. FELIZ, D. MAULEÓN, and C. MINGUILLÓN. Can. J. Chem. **66**, 2782 (1988).

The stereochemical assignment as *erythro* and *threo* for two pairs of 2-(aryloxy)-1-(2-piperidyl)ethanols **1** and **2** is described. Their CHO–CHN coupling constants were measured on the phase sensitive $^1H-^1H$ homocorrelation spectra (DQF–COSY), optimized by means of the LAOCOON-3 program, and compared with the calculated values from an MM2 conformational analysis. The experimental constants were $J_{erythro}$ = 3.3/3.8 Hz and J_{threo} = 6.4/6.8 Hz, whereas the calculated values were 2.5 and 5.4 Hz, respectively. ^{13}C nuclear magnetic resonance steric shielding of the C(3) carbon atom in the *erythro* diastereomers confirms the results of the conformational analysis.

M. FELIZ, D. MAULEÓN et C. MINGUILLÓN. Can. J. Chem. **66**, 2782 (1988).

On décrit l'attribution des stéréoisoméries *érythro* et *thréo* aux deux paires d'(aryloxy)-2 (pipéridyl-2)-1 éthanols **1** et **2**. On a mesuré leurs constantes de couplage CHO–CHN dans la portion sensible à la phase du spectre d'homocorrélation $^1H-^1H$ (DQF–COSY), on les a optimisées à l'aide d'une programme LAOCOON-3, et on les a comparées aux valeurs calculées à l'aide d'une analyse conformationnelle MM2. Les valeurs expérimentales sont $J_{érythro}$ = 3,3/3,8 Hz et $J_{thréo}$ = 6,4/6,8 Hz alors que les valeurs calculées sont respectivement 2,5 et 5,4 Hz. Le blindage stérique de l'atome de carbone C(3) dans le spectre en résonance magnétique nucléaire du ^{13}C des diastéréomères *érythro* confirme les résultats de l'analyse conformationnelle.

[Traduit par la revue]

Introduction

As a part of our work directed to the synthesis of β-adrenergic agents, we became interested in the new 2-aryloxy-1-(2-piperidyl)ethanol structure, which can be considered as a cyclic analogue of the classic aryloxypropanolamine drugs. Thus, we separately obtained (1) the *erythro* and *threo* isomers of compounds **1** and **2**, which were *O*-debenzylated to the corresponding phenols **3** and **4**. These are cyclic analogues of the β-adrenergic agonist prenalterol (2) and of its *meta* isomer.

Since it has been established (3) that a difference in the stereochemistry of α-substituted aryloxypropanolamines markedly affects their β-adrenergic properties, the unequivocal assignment of the *erythro* and *threo* **1–4** diastereomers was imperative. This paper deals with this stereochemical assignment, carried out mainly through the measurement of ^1H nmr coupling constants by a two-dimensional technique.

Results and discussion

The assignment of *erythro* and *threo* stereoisomers in the structurally related aryl 2-piperidyl methanols has usually been carried out from the C*H*OH–C*H*N coupling constant values, which are 3–6 Hz greater in the *threo* compounds than in the *erythro* isomers. However, the ^1H nmr spectra of aryloxy derivatives **1–4** are very complex and the C*H*OH proton appears as a multiplet, overlapped with the -OCH_2- signals. This complexity precluded the direct measurement of the CHO–CHN coupling, as well as the complete assignment of signals in the spectra. Although the use of $^1H-^1H$ homocorrelation spectra (COSY), in absolute value, allows the determination of chemical shifts, these experiments also have some drawbacks. Among them, a lack of sensitivity (4), low resolution, and a loss of information about coupling constant values can be noted. These problems have been recently overcome through the development of two-dimensional experiments directed to obtain phase sensitive homocorrelation spectra (5).

Figure 1 shows the correlation map (positive signals) of the phase sensitive double quantum filter spectrum (DQF–COSY,

TABLE 1. The ^1H nmr chemical shifts and coupling constants for compounds *erythro* and *threo* **1** and **2**

	Chemical shifts (ppm)			
Assignment	*erythro*-**1**	*threo*-**1**	*erythro*-**2**	*threo*-**2**
C(2)H	2.84	2.62	2.83	2.70
C(6)Ha	2.65	2.62	2.68	2.61
$C(6)H_e$	3.13	3.11	3.12	3.10
CH–OH	3.94	3.74	3.95	3.70
$ArOCH_2$	4.00	3.95/4.02	4.00	3.95/4.05
$PhCH_2O$	5.00	4.99	5.02	5.02
	Coupling constants (Hz)			
Coupling	*erythro*-**1**	*threo*-**1**	*erythro*-**2**	*threo*-**2**
C(2)H–CHOH	3.3	6.4	3.8	6.8
$C(2)H-C(3)H_a$	10.5	10.4	10.8	10.5
$C(2)H-C(3)H_e$	2.8	2.7	2.8	2.8
$C(6)H_a-C(6)H_e$	−12.0	−12.0	−11.5	−12.8
$C(6)H_a-C(5)H_a$	11.5	10.8	11.2	10.7
$C(6)H_a-C(5)H_e$	3.0	2.9	2.6	3.2
$CHOH-OCH_2$	3.4/7.0	3.4/5.9	3.8/6.7	3.7/3.7

[1]Author to whom correspondence may be addressed.

Can. J. Chem. Downloaded from www.nrcresearchpress.com by 196.1.178.254 on 09/07/12
For personal use only.

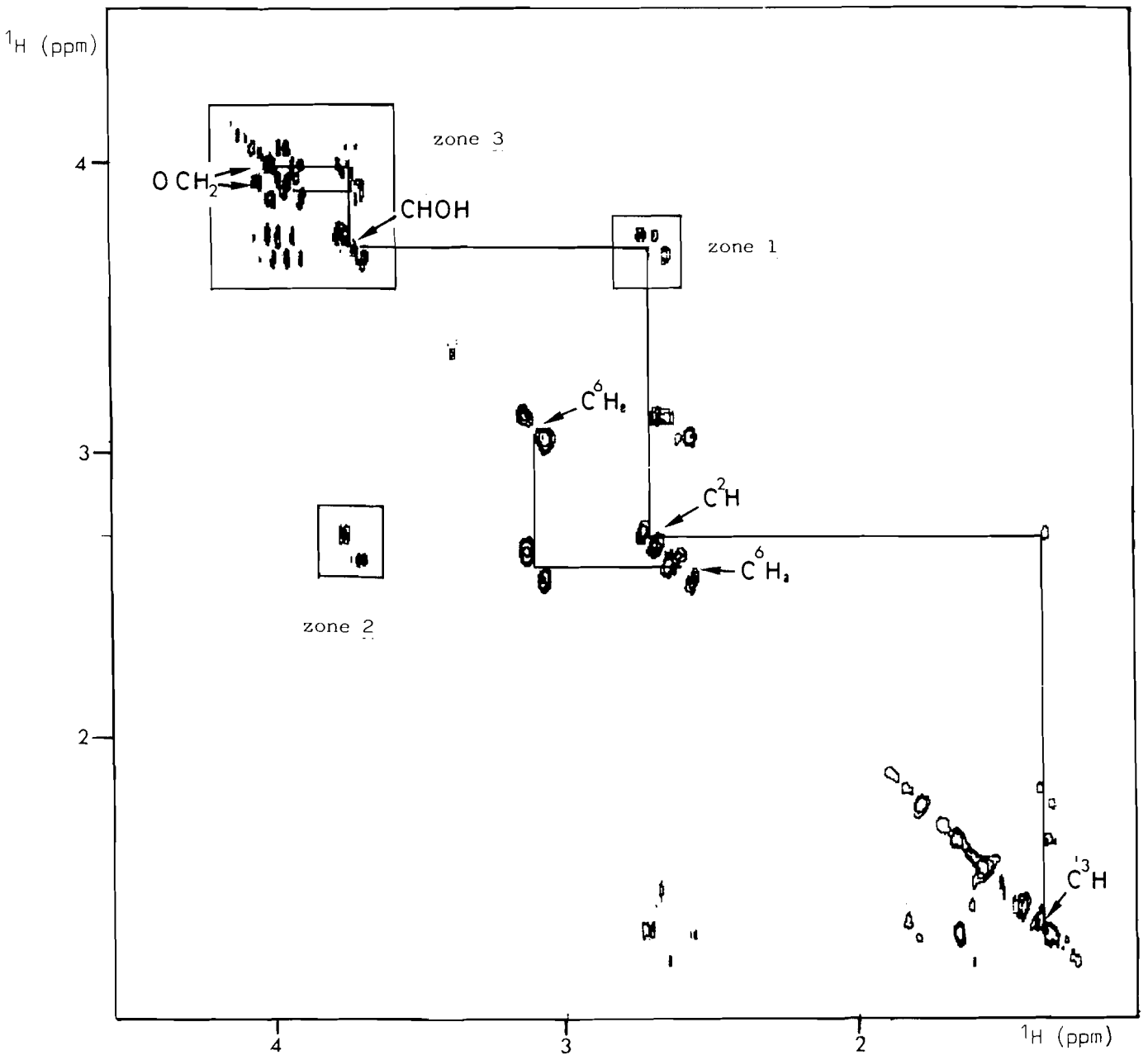

FIG. 1. Contour plot (positive levels) of a phase-sensitive DQF–COSY spectrum of compound *threo*-**1**.

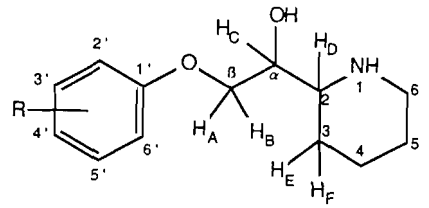

1 R = 4'-OCH$_2$C$_6$H$_5$
2 R = 3'-OCH$_2$C$_6$H$_5$
3 R = 4'-OH
4 R = 3'-OH
5 R = H

SCHEME 1

ref. 6) for *threo*-**1**. Coupling patterns of the non-aromatic protons are indicated by means of connectivity lines between diagonal peaks and cross peaks. The correlation blocks used to perform a first measurement of coupling constants are enclosed in squares. Measurements were performed on expanded plots, along the f_2 dimension that has the higher digital resolution (0.4 Hz) and using the cross peaks from both sides of the diagonal.

Figure 2 is an expansion of the zone 1 (Fig. 1) in which couplings have been indicated. We could measure the H_C/H_D coupling constant, as the active constant (i.e., the coupling that generates the cross peak). Furthermore, two passive constants between H_D and each of the two C(3)H_2 (H_E and H_F) protons are also observed. The corresponding signals on the other side of the diagonal (zone 2, Fig. 1) allowed us to measure the same H_C/H_D coupling, as well as two passive constants between H_C and the -OCH_2- protons H_A and H_B. Finally, in zone 3 (Fig. 1) we could verify the H_B/H_C and H_A/H_B coupling constants previously measured.

The above measurement procedure was also applied to the phase sensitive DQF–COSY spectra of *erythro*-**1**, *erythro*-**2**,

Can. J. Chem. Downloaded from www.nrcresearchpress.com by 196.1.178.254 on 09/07/12
For personal use only.

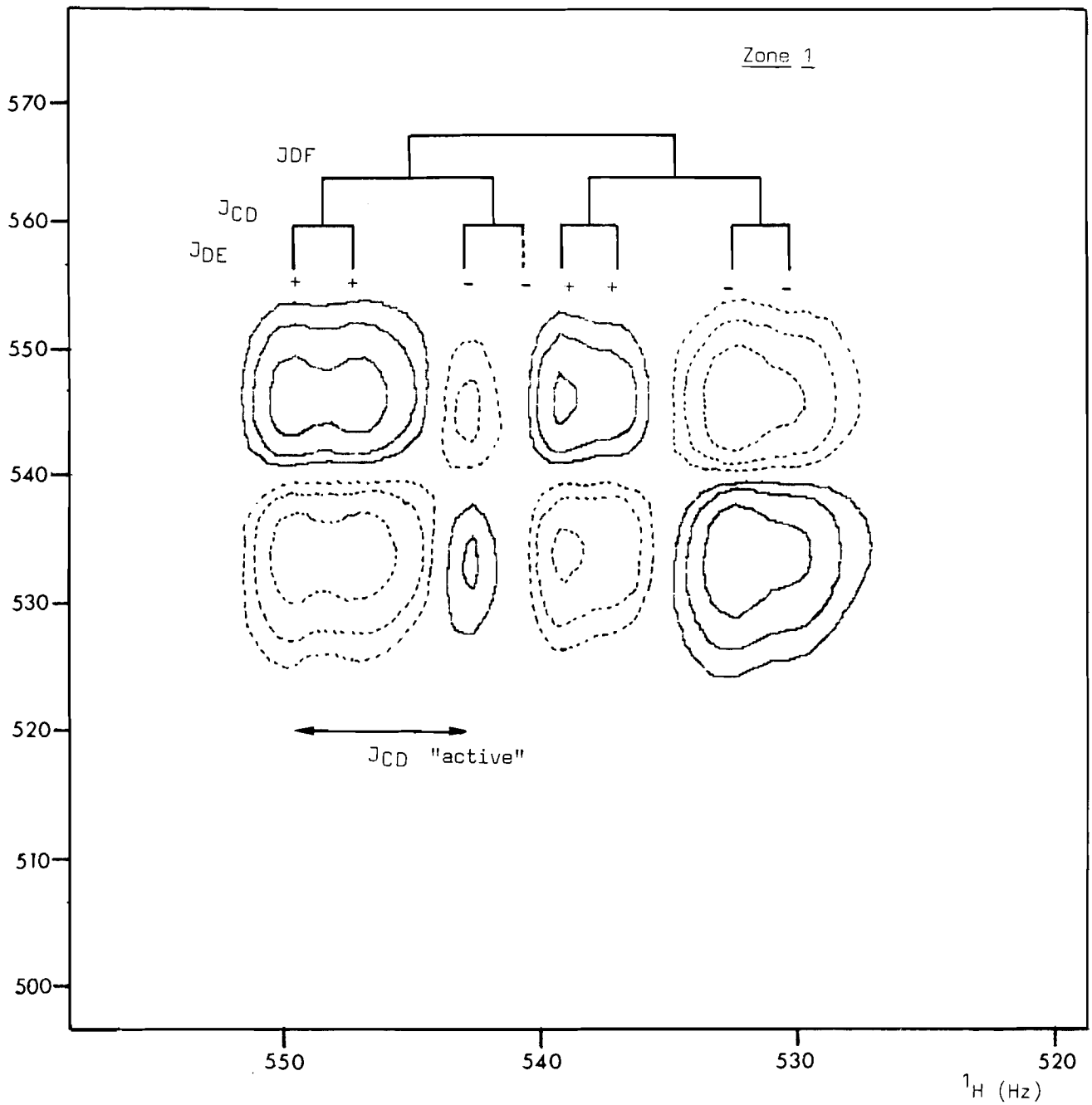

FIG. 2. Expansion of correlation signal between H_C and H_D (zone 1, see Fig. 1).

and *threo*-**2**. The resulting sets of chemical shifts and coupling constants were optimized by means of the LAOCOON-3 program, until a good superposition between real and theoretical monodimensional spectra was achieved. The final values are collected in Table 1.

As expected, the most important difference between the spectral parameters of *erythro* and *threo* diastereomers was the magnitude of the CHO–CHN coupling (J_{CD}). The observed increment of $J_{threo} - J_{erythro} = 3$ Hz can be explained in conformational terms. The reported interpretations in the aryl(2-piperidyl)methanol series (7) only take into account the OH...N hydrogen bond, which stabilizes the O/N *gauche* conformers. However, in the 2-aryloxy-1-(2-piperidyl)ethanols **1** and **2**, three different intramolecular hydrogen bonding interactions can occur (OH...N, NH...OH, and OH...OAr) and thus the conformational preferences could be different from those found in the piperidylmethanols. Therefore, we decided to perform a theoretical conformational analysis of two model structures, *erythro*-**5** and *threo*-**5**, by means of the MM2 force field program (8). A set of 72 conformers for each diastereomer was considered;[2] the resulting most stable conformations *erythro*-**5***a–e* and *threo*-**5***a–d* are depicted in Scheme 2. All the

[2]These correspond to three values (60°C, 180°, and 300°) for each of the O—CH_2—CHOH—C(2) and CH_2—CHOH—C(2)—N dihedral angles, two piperidine chair forms, the equatorial and axial disposition of the NH group, and the O—H...N and N—H...O directed hydrogen bonds ($3 \times 3 \times 2 \times 2 \times 2 = 72$ conformers). After location of the minima, these were optimized by rotation of the aromatic ring plane.

Can. J. Chem. Downloaded from www.nrcresearchpress.com by 196.1.178.254 on 09/07/12
For personal use only.

TABLE 2. MM2 calculated geometries and coupling constants for *erythro-* and *threo-***5**

Conformer	Relevant geometric parameters: N-H disposition	Hydrogen bonds	Dihedral angles: 1,2,α,β	2,α,β,O	β,O,1′,2′	H,α,2,H	Relative energy (kcal/mol)	Relative population (percent)	Calculated* $J_{CHO-CHN}$ (Hz)
*erythro-***5***a*	eq	NH..OH/OH..OAr	−55	180	8	64	0	59.5	2.5
*erythro-***5***b*	ax	NH..OH/OH..OAr	168	180	9	−69	0.6	21.7	1.3
*erythro-***5***c*	ax	NH..OAr/OH..N	−68	60	3	54	1.0	11.1	3.5
*erythro-***5***d*	ax	NH..OH/OH..OAr	173	75	7	−63	1.5	4.8	1.7
*erythro-***5***e*	ax	OH..OAr	57	180	2	178	1.8	2.9	9.1
*threo-***5***a*	eq	NH..OH/OH..OAr	177	180	7	−178	0	54.6	9.0
*threo-***5***b*	ax	NH..OH/OH..OAr	59	180	7	63	0.4	27.9	1.1
*threo-***5***c*	eq	NH..OAr/OH..N	60	−60	7	63	0.8	14.3	1.1
*threo-***5***d*	ax	NH..OH/OH..OAr	61	−73	1	62	1.7	3.2	1.2

*Calculated from H,α,2,H dihedrals by means of the Karplus–Altona equation (ref. 10).

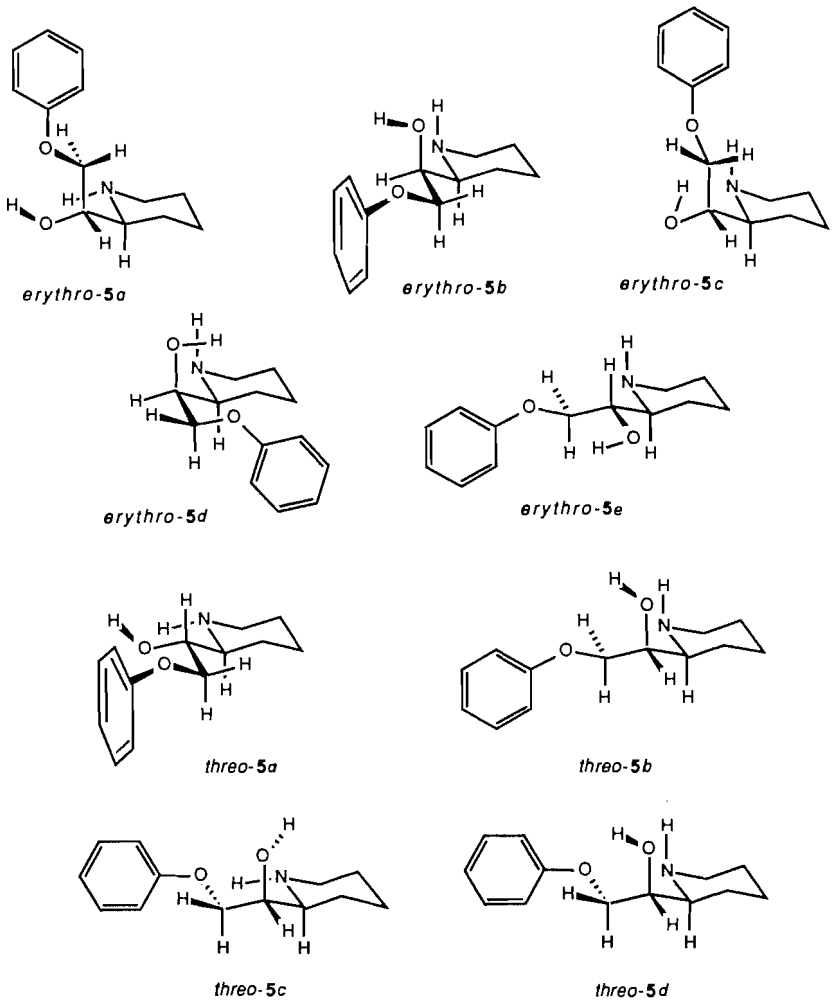

SCHEME 2

remaining conformers have energies >2 kcal/mol above the absolute minima **5***a* and their population contributions are negligible.

Relevant geometric parameters, relative energies, and relative populations for the above conformers are collected in Table 2, together with the individual CHO–CHN coupling constants, calculated from the corresponding dihedral angles by means of the Karplus–Altona equation (9). From these J_i values and the percent populations P_i, two average $J_{erythro}$ and J_{threo} constants were calculated, through the equation:

$$J_{avg} = \Sigma_i(J_i, P_i)/100$$

The resulting mean values ($J_{erythro}$ = 2.5 Hz and J_{threo} = 5.4 Hz) are in good agreement with the experimental coupling constants.

The above stereochemical assignment is also in accordance

Can. J. Chem. Downloaded from www.nrcresearchpress.com by 196.1.178.254 on 09/07/12
For personal use only.

TABLE 3. The ^{13}C nmr chemical shifts (ppm) for compounds **1** and **2**

Carbon atom	*erythro*-**1**	*threo*-**1**	*erythro*-**2**	*threo*-**2**
C(2)	58.65	58.40	58.78	58.21
C(3)	25.44	28.40	26.59	28.95
C(4)	23.28	24.02	24.55	24.30
C(5)	25.44	25.67	27.25	26.24
C(6)	46.41	46.22	47.05	46.39
C-OH	71.15	72.55	72.57	72.81
ArO-C	69.63	70.70	69.36	70.02
Ph-C-O	70.85	70.52	70.03	70.02
C(1′)	153.00*	153.06*	159.89*	159.93*
C(2′)	115.58#	115.59#	102.01	102.03
C(3′)	116.02#	115.89#	160.04*	160.02*
C(4′)	153.30*	153.29*	107.18#	107.14#
C(5′)	116.02#	115.89#	129.93	129.91
C(6′)	115.58#	115.59#	107.48#	107.46#
C(1″)	137.25	137.26	136.93	136.92
C(2″) + C(6″)	127.57§	127.44§	127.46§	127.45§
C(3″) + C(5″)	128.60§	128.53§	128.56§	128.55§
C(4″)	128.00	127.88	127.94	127.93

The signals marked with *, #, and § symbols are interchangeable.

with ^{13}C nmr spectral data (Table 3). The *erythro* and *threo* isomers of **1** and **2** gave very similar spectra, except for the signals of the piperidine C(3) carbon atoms, which are shielded in the *erythro* diastereomers. The $\Delta\delta$ = 2.5–3 ppm can be explained by considering that conformations *erythro*-**5***b* and *erythro*-**5***d* have greater steric interactions between the lateral chain and the C(3) hydrogen atoms than the remaining stable conformers (Scheme 2). Thus, from the MM2 conformational analysis we could expect a greater steric shielding for C(3) in the *erythro* diastereomers than in the *threo* ones, as was experimentally observed.

Experimental

The nmr spectra were recorded on a Varian XL-200 spectrometer operating at 200 MHz (^1H) or 50.3 MHz (^{13}C). For ^1H nmr spectra, 15 mg of sample were dissolved in 0.7 mL of $CDCl_3$ and introduced in 5-mm tubes. The ^{13}C nmr spectra were obtained from 150–200 mg of sample, dissolved in $CDCl_3$, in 10-mm tubes. Chemical shifts were directly measured from TMS.

The DQF–COSY spectra were recorded using the sequence written by Dr. J. Keeler and software developed by him for phase sensitive acquisition, using a V77-200 data system on a Varian XL-200 instrument (10).[3] In all cases, 32 transients were accumulated for 256 values of the evolution period, with a spectral width of 700 Hz in both dimensions. The recycle time was 4 s and the acquisition time, AT, was 1.45 s. A 2048 × 1024 data matrix was used. Processing: Lorentz to Gauss with RE = 1, AF = 0.87 and RE = 1, AF = 0.06 in f_2 and f_1, respectively. The 90° pulse widths were 12.5 μs for ^{13}C and 8 μs for ^1H.

Acknowledgements

We are grateful to the CAICYT for financial support of this research. We warmly thank Dr. Miquel Pons for helpful discussions.

1. D. MAULEÓN, C. MINGUILLÓN, and M. D. PUJOL. J. Heterocycl. Chem. In press.
2. E. CARLSSON, C.-G. DAHLÖF, A. HEDBERG, H. PERSSON, and B. TANGSTRAND. Arch. Pharmacol. **300**, 101 (1977).
3. R. HOWE. J. Med. Chem. **12**, 642 (1969).
4. A. BAX. Two dimensional NMR in liquids. Delft Univ. Press, Delft, The Netherlands. 1982.
5. (*a*) D. J. STATES, R. A. HABERKORN, and D. J. REUBEN. J. Magn. Reson. **48**, 286 (1982); (*b*) D. MARION and K. WÜTHRICH. Biochem. Biophys. Res. Commun. **113**, 967 (1982).
6. M. RANCE, O. W. SØRENSEN, G. BODENHAUSEN, C. WAGNER, R. R. ERNST, and K. WÜTHRICH. Biochem. Biophys. Res. Commun. **117**, 479 (1983).
7. (*a*) J. BOSCH, R. GRANADOS, R. LLOBERA, D. MAULEÓN, and J. TUR. An. Quim. **77C**, 166 (1981); (*b*) M. K. MEILAHN, C. N. STATHAM, J. MCMANAMAM, and M. E. MUNK. J. Org. Chem. **40**, 3553 (1975).
8. V. BURKERT and N. L. ALLINGER. Molecular mechanics. ACS Monograph 177, Washington, DC. 1982.
9. C. A. G. HAASNOOT, F. A. A. M. LEEUW, and C. ALTONA. Tetrahedron, **36**, 2783 (1980).
10. J. KEELER and D. NEUHAUS. J. Magn. Reson. **63**, 454 (1985).

[3]Also, J. Keeler, private communication.

Can. J. Chem. Downloaded from www.nrcresearchpress.com by 196.1.178.254 on 09/07/12
For personal use only.

Glycosides from *Muscari armeniacum* and *Muscari botryoides*. Isolation and structure of Muscarosides G–N

MATTEO ADINOLFI,[1] GASPARE BARONE, MARIA MICHELA CORSARO, AND LORENZO MANGONI
Dipartimento di Chimica Organica e Biologica, Università di Napoli, Via Mezzocannone 16, 80134 Napoli, Italy

AND

ROSA LANZETTA AND MICHELANGELO PARRILLI
Istituto di Chimica, Università della Basilicata, Via Nazario Sauro 85, 85100 Potenza, Italy

Received March 31, 1988

MATTEO ADINOLFI, GASPARE BARONE, MARIA MICHELA CORSARO, LORENZO MANGONI, ROSA LANZETTA, and MICHELANGELO PARRILLI. Can. J. Chem. **66**, 2787 (1988).

Eight novel oligoglycosides, Muscarosides G–N **3–10**, have been isolated from the bulbs of *Muscari armeniacum* and *Muscari botryoides*, in addition to known Muscarosides A–C **12–14** and scillascilloside D-1 **11**. Their structure was elucidated mainly by spectral analysis (FAB–MS and 1D- and 2D-nmr spectroscopy) and, in some cases, degradative chemical study. The aglycone of **3–10** is the spirocyclic nortriterpenoid **1** or **2**. The monose units of their di-, tri-, tetra-, or hexasaccharide chain are β-D-glucopyranose, α-L-arabinopyranose, α-L-rhamnopyranose, β-D-galactopyranose, α-L-arabinofuranose, and β-D-apio-D-furanose.

MATTEO ADINOLFI, GASPARE BARONE, MARIA MICHELA CORSARO, LORENZO MANGONI, ROSA LANZETTA et MICHELANGELO PARRILLI. Can. J. Chem. **66**, 2787 (1988).

À partir des bulbes du *Muscari armeniacum* ainsi que du *Muscari botryoides*, on a isolé huit nouveaux oligoglycosides, les muscarosides G–N, **3–10**, en plus des muscarosides A–C, **12–14**, et du scillascilloside D-1, **11**, déjà connus. Afin d'élucider leurs structures, on a principalement fait appel à des analyses spectrales (SM–FAB ainsi que spectroscopie rmn en 1D et 2D) et, dans quelques cas, à des études impliquant une dégradation chimique. L'aglycone des composés **3–10** est le nortriterpénoïde spirocyclique **1** ou **2**. Les unités de monose de leurs chaînes di-, tri-, tétra- ou hexasaccharides sont formées de β-D-glucopyrannose, de α-L-arabinopyrannose, de α-L-rhamnopyrannose, de β-D-galactopyrannose, de α-L-arabinofurannose et de β-D-apio-D-furannose.

[Traduit par la revue]

The bulbs of *Muscari comosum* Miller (Liliaceae) have been shown (1–4) to contain six oligoglycosides, named Muscarosides A–F. Their spirocyclic nortriterpenoid aglycones belong to the eucosterol group and the glycone moieties are constituted by four to six units of glucose, arabinose, and rhamnose or apiose. This study was extended to bulbs of other *Muscari* species, namely *M. armeniacum* Leicht and *M. botryoides* Miller, affording the isolation and structure elucidation of eight novel glycosides, Muscarosides G–N, all of them structurally related to Muscarosides A–F. In particular, Muscarosides G **3**, J **6**, K **7**, L **8**, and M **9** (see Chart 1) were obtained from *M. armeniacum*, in addition to known Muscarosides A **12** and B **13**, whereas Muscarosides H **4**, I **5**, and N **10** were isolated from *M. botryoides*, besides the known Muscarosides A **12** (1), B **13** (2), and C **14** (3) and scillascilloside D-1 **11**, already found (5) in the bulbs of another Liliacea, *Scilla scilloides*.

The structures of the novel Muscarosides G–N were elucidated by spectral analysis (^{1}H and ^{13}C nmr spectroscopy and fast atom bombardment mass spectrometry) with the aid of chemical work, whenever a sufficient amount of material was available. The known glycosides **11–14** were identified by comparison of their spectral data with those reported in refs. 1–5.

In the upfield part of the ^{1}H spectra (Table 1) of Muscarosides G **3**, H **4**, J **6**, and L **8** the signals of four tertiary, one secondary, and one primary methyl group are observed. In addition, the signals of one methylene group appear centered at δ 2.43–2.47 as four lines of the A_2 part of an A_2X_3 system, correlated by scalar coupling with the primary methyl group, and the signals of a second methylene group appear centered at δ 2.37–2.39 and δ 3.03–3.05 as an AB quartet. The close similarity between these ^{1}H nmr data and those (see Table 1) obtained for the aglycone of Muscaroside B **13** indicated that Muscarosides G **3**, H **4**, J **6**, and L **8** also possess eucosterol **1** as their aglycone moiety. This was confirmed by comparison of the ^{13}C nmr shifts of the aglycone carbons of Muscarosides G **3**, H **4**, J **6**, and L **8** with the ^{13}C data for eucosterol **1**, both free and linked in Muscaroside B **13** (Table 2). Analogously, the presence, in the ^{1}H nmr spectrum, of the signals of three tertiary, one secondary, and one primary methyl group, as well as the signals of one methylene group at δ 2.50–2.51 as four lines of the A_2 part of an A_2X_3 system, and the absence of an AB quartet at δ 2.3–3.2 indicated, by comparison with the nmr data for the aglycone protons of Muscaroside C **14** that (23*S*)-17,23-epoxy-3β, 30,31-trihydroxy-27-nor-5α-lanost-8-en-24-one **2** was the aglycone moiety of Muscarosides I **5**, K **7**, H **9**, and N **10**. The ^{13}C data (Table 2) were in accordance with this conclusion.[2]

The negative-ion FAB–MS spectrum (Scheme 1) of Muscaroside G **3** exhibited an ion peak at m/z 1367 $(M - H)^-$,

[1]Author to whom correspondence may be addressed.

[2]In a previous paper (3), the chemical shifts of the aglycone carbons of Muscaroside C **14** in pyridine-d_5 were compared to those of **2** in chloroform-d_1, on the assumption, supported by literature (7), that the different solvents did not affect the chemical shifts of Muscaroside aglycones highly. The observed differences between **14** and **2** for carbons 5 and 30 were therefore ascribed to glycosidation, whereas they are mainly due to solvent effect, since they almost completely disappear if the spectrum of **2** in pyridine-d_5 (6) (Table 2) is considered. On the other hand, the 8-ppm upfield shift of the carbon 30 of free **2** on going from pyridine-d_5 to chloroform-d_1 is hardly explained and deserves investigation.

Can. J. Chem. Downloaded from www.nrcresearchpress.com by 122.72.124.2 on 09/07/12
For personal use only.

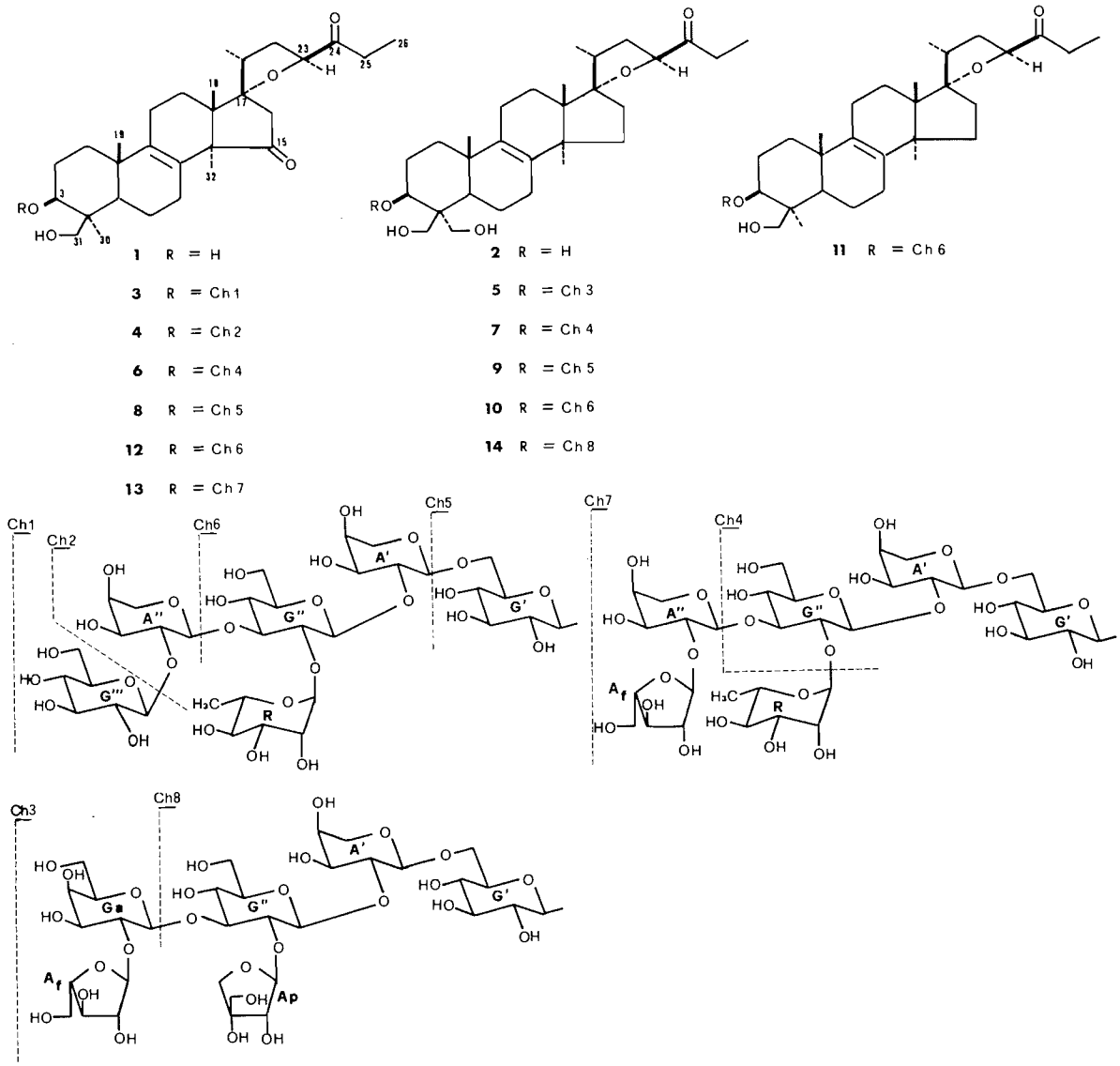

CHART 1.

which, together with ^{13}C and ^{1}H nmr data, suggested the molecular formula $C_{63}H_{100}O_{32}$. The corresponding molecular weight of 1368 daltons was confirmed by the presence of the peak at m/z 1391, formed by cationization of the molecule with Na^+, in the positive-ion spectrum.

Acid hydrolysis (7% H_2SO_4) of Muscaroside G **3** gave rhamnose, arabinose, and glucose, identified by tlc and hplc of the water-soluble fraction of the hydrolysate through comparison with authentic samples of the monosaccharides. A 1:2:3 molar ratio of the monoses was established on calibration of the hplc peak integrated areas against known concentrations. The monose-containing water-soluble fraction of the hydrolysate was perbenzoylated with benzoyl chloride and pyridine and the pure perbenzoates (α-anomers (8)) of rhamnose, glucose, and arabinose were isolated by hplc. Identity in chirality and amplitude of their circular dichroism (cd) curves with those of the perbenzoates (α-anomers) obtained from authentic samples of L-rhamnose, D-glucose, and L-arabinose established the absolute configuration D of all three glucopyranose units and the absolute configuration L of both arabinopyranose units and of the rhamnopyranose unit in the sugar chain of Muscaroside G **3**.

The comparison of the ^{13}C chemical shifts of Muscaroside G (Table 3) with those of reference methyl glycosides revealed the attachment position in the sugar chain (through the glycosidation shifts) and the configuration at the anomeric centres. Thus, the glycone moiety of Muscaroside G was found to consist of one terminal α-rhamnopyranose unit (1, 12), one terminal β-glucopyranose unit, one nodal β-glucopyranose unit linked at its positions 2 and 3, one inner β-glucopyranose unit linked at its position 6, and two inner α-arabinopyranose units, both linked at their position 2 (1, 13, 14). The glycosidation shift (+9.0, Table 2) observed for the C-3 carbon of the aglycone moiety showed that the sugar chain was linked at this carbon. The values of the coupling constants $^{3}J_{H\text{-}1,H\text{-}2}$ listed in Table 1 were in accordance with the configuration of the anomeric centres as determined from the ^{13}C data.

The determination of the glycone sequence was arrived at mainly on the basis of the negative-ion FAB–MS data (Scheme 1). The peak at m/z 633, due to the loss of two hexoses, two pentoses, and rhamnose, indicated that the inner glucose is directly linked to the aglycone. The peak at m/z 765 (= 633 + 132) shows that one inner arabinose is linked to this

Can. J. Chem. Downloaded from www.nrcresearchpress.com by 122.72.124.2 on 09/07/12
For personal use only.

TABLE 1. ^{1}H nuclear magnetic resonance chemical shifts of Muscarosides **3**–**10** and **13**–**14** in pyridine-d_5[a]

Proton	**3**	**4**	**6**	**8**	**13**[b]	**5**	**7**	**9**	**10**	**14**[c]
18-H_3	0.90[d] s	0.91[d] s	0.93[d] s	0.92[d] s	0.93[d] s	0.91 s	0.91 s	0.90 s	0.91 s	0.92 s
19-H_3	0.91[d] s	0.93[d] s	0.94[d] s	0.93[d] s	0.95[d] s	1.04 s	1.02 s	1.04 s	1.03 s	1.04 s
21-H_3	1.03 d	1.03 d	1.05 d	1.05 d	1.05 d	1.00 d	1.00 d	1.02 d	1.01 d	1.02 d
	J = 6.7	J = 6.6	J = 7.0	J = 7.0	J = 6.6	J = 6.3	J = 6.6	J = 6.6	J = 6.8	J = 6.6
30-H_3	1.54 s	1.53 s	1.55 s	1.49 s	1.55 s	—	—	—	—	—
32-H_3	1.69 s	1.68 s	1.69 s	1.64 s	1.70 s	1.46 s	1.45 s	1.41 s	1.47 s	1.47 s
25-H_2	2.43 q	2.44 q	2.47 q	2.46 q	2.46 q	2.51 q	2.50 q	2.51 q	2.51 q	2.52 q
	J = 7.3	J = 7.3	J = 7.4	J = 7.4	J = 7.3	J = 7.3	J = 7.3	J = 7.5	J = 7.4	J = 7.3
26-H_3	1.00 t	1.02 t	1.02 t	1.03 t	1.03 t	1.02 t	1.02 t	1.03 t	1.00 t	1.03 t
	J = 7.3	J = 7.3	J = 7.4	J = 7.4	J = 7.3	J = 7.3	J = 7.3	J = 7.5	J = 7.4	J = 7.3
16-H_2	2.37, 3.03 ABq,	2.37, 3.05 ABq	2.39, 3.03 ABq,	2.39, 3.05 ABq	2.38, 3.06 ABq	—	—	—	—	—
	J = 18.9	J = 18.7	J = 19.0	J = 19.0	J = 19.0					
R-6-H_3	1.78 d	1.72 d	—	—	1.75 d	—	—	—	1.75 d	—
	J = 6.2	J = 6.3			J = 6.1				J = 6.1	
G′-1-H	4.95 d	4.94 d	5.04[e] d	4.96 d	4.98 d	5.16 d	5.19 d	5.15 d	5.17 d	5.14 d
	J = 7.7	J = 8.1	J = 8.1	J = 8.1	J = 7.7	J = 7.9	J = 7.7	J = 7.7	J = 8.0	J = 7.8
A′-1-H	5.27 d	5.28 d	5.12 d	4.94 d	5.29[e] d	5.09 d	5.07 d	4.94 d	5.33 d	5.18 d
	J = 3.3	J = 3.7	J = 5.5	J = 7.0	J = 4.4	J = 2.8	J = 4.8	J = 6.6	J = 3.3	J = 4.1
G″-1-H	5.16 d	5.17 d	5.07[e] d	—	5.21 d	4.98 s	5.05 d	—	5.10 d	5.07 d
	J = 7.7	J = 7.3	J = 7.7		J = 7.2	J = 7.9	J = 7.7		J = 7.3	J = 7.3
R-1-H	6.30 bs	6.20 d	—	—	5.98 d	—	—	—	6.34 bs	—
		J = 1.5			J = 1.8					
Ap-1-H	—	—	—	—	—	6.26 d	—	—	—	6.40 d
						J = 2.9				J = 2
A″-1-H	5.04 d	4.83 d	—	—	5.18[e] d	—	—	—	—	—
	J = 5.8	J = 7.3			J = 6.1					
Ga-1-H	—	—	—	—	—	5.32 d	—	—	—	—
						J = 8.1				
A_f-1-H	—	—	—	—	6.05 d	6.20 bs	—	—	—	—
					J = 1.5					
G‴-1-H	5.16 d	—	—	—	—	—	—	—	—	—
	J = 7.7									

[a]Chemical shift values are given in δ relative to TMS. Coupling constants are given in Hz and were inferred from pertinent decoupling experiments.
[b]Reference 2.
[c]Reference 3.
[d,e]Interchangeable values.

glucose unit. The subsequent unit is nodal glucose, as indicated by the very low intensity, due to secondary fragmentation, of the peak at m/z 927, corresponding to the loss of the terminal rhamnose, the terminal glucose, and the remaining inner arabinose unit. The peaks at m/z 1073 $[M - H - (162 + 132)]^-$ and m/z 1221 $[M - H - 146]^-$ may be explained only by locating the second inner arabinose between the terminal and the nodal glucoses. Finally, the small value (+2.9, Table 3) of the glycosidation shift of the 2-carbon of the nodal glucose confirmed that rhamnose is linked to this unit, and identified that carbon as its attachment position (15). Consequently, the linkage location of the other branch of the chain was established at carbon 3. The structure **3** for Muscaroside G was also supported by comparison of the ^{13}C data with those of Muscaroside B **13**, which differs from **3** only in having a terminal arabinofuranose in place of a terminal glucopyranose in its sugar chain.

Muscaroside H **4**, positive-ion FAB–MS m/z 1229 $(M + Na)^+$, negative-ion FAB–MS m/z 1205 $(M - H)^-$, was shown, upon application of the chemical procedure and the cd method already used for **3**, to possess a sugar chain constituted by one L-rhamnose, two D-glucose, and two L-arabinopyranose units. This was confirmed by comparison of the negative-ion FAB mass spectra of the two Muscarosides (see Scheme 1), which accorded with a glycone chain for the former identical to that of the latter, apart from the lack of the terminal hexose. Support to the structure **4** thus assigned to Muscaroside H was given by comparison of the ^{13}C spectrum with those of **12** and **3** (Table 3), which particularly confirmed the positions of the interglycosidic linkages, and by analysis of the ^{1}H nmr spectrum (Table 1). The assignment of the nmr resonances of the anomeric carbons of **4** was confirmed through the use of 2D-heteronuclear carbon–proton shift correlation.

Muscaroside I **5** is unique in having a galactopyranose unit in its chain, as shown by the result of acid hydrolysis of the glycoside, which afforded that carbohydrate as well as glucose, arabinose, and apiose with the molar ratio 1:2:2:1. The negative-ion FAB mass spectrum of Muscaroside I showed peaks at m/z 1355 $(M - H)^-$, 1223 $(M - H - 132)^-$, 1091 $[M - H - (2 \times 132)]^-$ (very low relative intensity), 1061 $[M - H - (132 + 162)]^-$, 929 $[M - H - ((2 \times 132) + 162)]^-$ (very low relative intensity), 767 $[M - H - ((2 \times 132) + (2 \times 162))]^-$, and 635 $[M - H - ((3 \times 132) + (2 \times 162))]^-$, which indicated a branched-chain hexasaccharide moiety, -hex-

Can. J. Chem. Downloaded from www.nrcresearchpress.com by 122.72.124.2 on 09/07/12
For personal use only.

TABLE 2. ^{13}C nuclear magnetic resonance chemical shifts in pyridine-d_5 of nortriterpenes **1** and **2** and of aglycone moieties of Muscarosides **3–10**, **13**, and **14**[a]

Carbon	3	4	6	8	13[b]	1[b]	5	7	9	10	14[c]	2[d]
1	35.7	35.6	35.8	35.6	35.6	35.9	35.8	35.8	35.6	35.8	35.8	35.7
2	27.4	27.4	27.4	27.5	27.3	29.0	27.3	27.3	27.3	27.3	27.3	28.7
3	89.0[e]	88.8[e]	88.8[e]	88.8[e]	88.8[e]	80.0	82.2[e]	82.1[e]	82.5[e]	83.1[e]	82.2[e]	73.9
4	44.4	44.4	44.4	44.5	44.3	43.2	48.2[f]	48.2[f]	48.2[f]	48.3[f]	48.2[f]	46.9
5	51.3	51.2	51.5	51.2	51.2	51.3	43.6	43.6	43.6	43.6	43.6	44.1
6	18.5	18.7	18.7	18.7	18.7	18.9	18.8	18.7	18.7	18.8	18.8	19.0
7	27.5	27.5	27.4	27.3	27.3	27.3	26.7	26.6	26.6	26.6	26.6	26.5
8	133.2	133.0	133.3	132.9	132.8	133.1	134.8	135.0	134.8	135.0	134.8	134.6
9	136.6	136.5	136.7	136.5	136.2	136.4	135.9	136.0	135.8	135.8	135.8	135.1
10	37.2	37.2	37.3	37.2	37.2	37.7	36.8	36.7	36.6	36.8	36.8	37.0
11	20.8	20.8	20.8	20.8	20.8	20.9	21.3	21.2	21.1	21.2	21.2	21.1
12	23.2	23.2	23.3	23.2	23.1	23.3	25.4	25.4	25.3	25.3	25.4	25.3
13	47.7	47.7	47.8	47.7	47.6	47.6	49.0[f]	49.0[f]	48.9[f]	49.0[f]	49.0[f]	48.7
14	58.0	58.0	58.2	58.0	58.0	58.0	50.9	50.9	50.8	50.9	50.9	50.7
15	215.2	215.3	215.5	216.0	215.1	215.2	32.2	32.1	32.1	32.2	32.2	32.0[f]
16	52.0	51.9	52.0	51.9	51.1	52.0	39.8	39.8	39.7	39.8	39.8	39.6
17	91.4	91.2	91.4	91.2	91.2	91.3	97.2	97.2	97.1	97.1	97.2	96.9
18	20.5	20.4	20.6	20.5	20.4	20.4	19.4	19.4	19.3	19.4	19.4	19.3
19	19.4	19.4	19.5	19.4	19.4	20.0	19.7	19.6	19.6	19.7	19.7	19.9
20	43.4	43.3	43.4	43.3	43.3	43.4	43.8	43.7	43.7	43.7	43.8	43.6
21	17.1	17.1	17.1	17.1	17.1	17.2	17.3	17.3	17.2	17.3	17.3	17.2
22	36.8	36.9	36.9	36.9	36.9	36.9	37.0	37.0	36.9	37.0	36.9	36.8
23	81.8	81.2	81.9	81.9	81.8	81.9	81.7	81.7	81.6	81.8	81.7	81.4
24	211.8	211.8	212.0	211.8	211.3	211.9	212.6	212.7	212.6	212.6	212.5	211.9
25	32.3	32.3	32.3	32.3	32.3	32.4	32.4	32.3	32.3	32.2	32.4	32.2[f]
26	7.5	7.6	7.7	7.7	7.6	7.6	7.8	7.7	7.7	7.8	7.7	7.7
30	23.1	23.2	23.1	23.1	23.1	23.4	61.4	61.2	61.3	61.3	61.2	62.9[g]
31	63.1	62.9	63.2	63.2	63.1	64.4	62.7	62.7	62.6	62.6	62.7	63.3[g]
32	24.1	24.2	24.2	24.2	24.1	24.1	26.4	26.3	26.2	26.4	26.3	26.2

[a]Chemical shift values are given in δ relative to TMS.
[b]Reference 2.
[c]Reference 3.
[d]Reference 6.
[e]Glycosidation shifts: **3**, +9.0; **4**, +8.8; **5**, +8.3; **6**, +8.8; **7**, +8.2; **8**, +8.8; **9**, +8.6; **10**, +9.2; **13**, +8.8; **14**, +8.3.
[f,g]Interchangeable values.

Can. J. Chem. Downloaded from www.nrcresearchpress.com by 122.72.124.2 on 09/07/12
For personal use only.

ose-pentose-hexose(-pentose)-hexose-pentose. The comparison between the glycone-carbon chemical shifts of Muscaroside I and those of known **13** and **14** (Table 3) suggested the chain ara·*p*(1→2)-gal·*p*(1→3)(api·*f*(1→2))-glu·*p*(1→2)-ara·*p*(1→6)-glu·*p*-. The mode of galactopyranose linkage in Muscaroside I **5** was regarded as β on the basis of the $^3J_{H\text{-}1,H\text{-}2}$ (8.1 Hz) for the anomeric proton.

The sugar chain of both Muscaroside J and Muscaroside K was immediately established as constituted by one pentose and two hexose units from the positive-ion FAB–MS spectra, which displayed the (aglycone + (2 × 162) + 132 + Na)$^+$ peak at *m/z* 951 and *m/z* 953, respectively. The ^{13}C nmr data for the sugar moieties of Muscarosides J and K were almost identical (Table 3) and were consistent with a trisaccharide chain glu·*p*(1→2)-ara·*p*(1→6)-glu·*p*-, which, on the other hand, constitutes the sequence of the first three monoses linked to the aglycone in all so-far isolated Muscarosides, both those from *M. comosum* (1, 4) and those from *M. armeniacum* and *M. botryoides*. Structures **6** and **7** for Muscaroside J and K, respectively, were also supported by ^1H nmr data (Table 1).

Structures **8** and **9** with a disaccharide ara·*p*(1→6)-glu·*p*-chain were attributed to Muscarosides L and M quite similarly, consistent with the pseudomolecular-ion (aglycone + 132 + 162 + H)$^+$ peak at *m/z* 767 and *m/z* 769, respectively, exhibited by the positive-ion FAB mass spectra, and with the ^{13}C and ^1H nmr data listed in the tables.

Muscaroside N was identified as having a rha·*p*(1→2)-glu·*p*(1→2)-ara·*p*(1→6)-glu·*p*- chain identical with that of Muscaroside A **12** on the basis of the positive-ion FAB mass spectrum (pseudomolecular-ion peak at *m/z* 1099 (M + Na)$^+$) and of the ^{13}C nmr data for the sugar moiety (Table 3), which were quite similar to those of **12**.

Experimental[3]

The ^1H (270 MHz) and ^{13}C (67.88 MHz) nmr spectra were taken on a Fourier transform Bruker instrument WH270 with an Aspect 2000 computer with 48K memory (32K data). Two-dimensional carbon–proton shift correlations for Muscaroside H **4** were performed by choosing polarization transfer delays equal to average one-bond couplings of *J*(CH) = 140 Hz. Exponential multiplication in the ^{13}C domain and Gaussian resolution enhancement in the ^1H domain were applied to a 256 × 1024 data matrix prior to Fourier transformation.

Mass spectra were recorded with a Kratos MS50 instrument

[3]With the assistance of Italo Giudicianni.

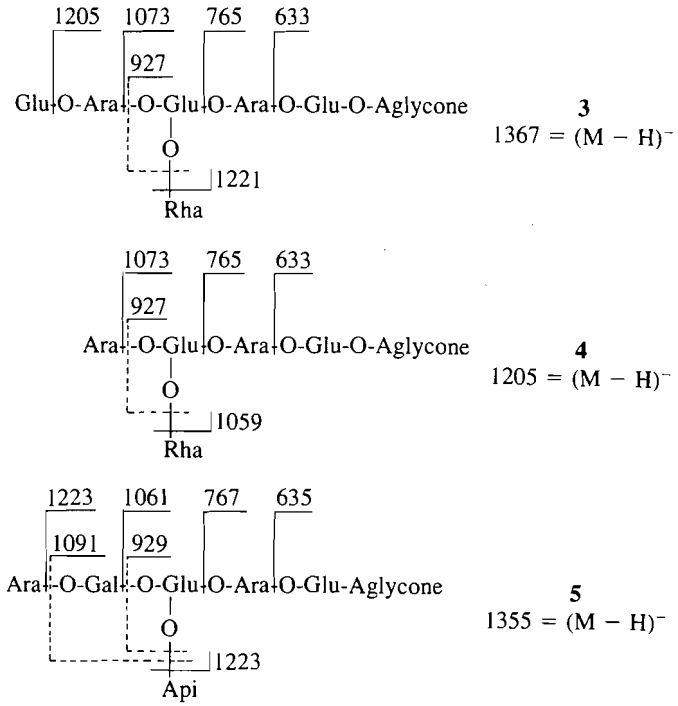

SCHEME 1. Negative FAB–MS fragmentation (— primary, --- secondary) patterns of Muscarosides G **3**, H **4**, and **15**.

equipped with a FAB source. The circular dichroism curves were recorded with a JASCO A500 dichrograph. The hplc was performed with a Varian 5060 instrument using a Waters R401 differential refractometer as the detector. The preparative and the thin-layer chromatography were carried out on precoated silica gel plates (Merck F_{254}, 2 mm and 0.25 mm, respectively). Merck silica gel 60 H was used for column chromatography.

Isolation of Muscarosides

Fresh bulbs (18 kg) of *Muscari armeniacum* Leicht (purchased from Stassen Italiana, Como, Italy, and authenticated by the Botanical Garden of the University of Naples) were homogenized in a mechanical stirrer, freeze-dried, and extracted in a Soxhlet with light petrol (12 h), ethyl ether (12 h), and with methanol (12 h). The methanol extract was evaporated (40 g), dissolved in water (600 mL), and chromatographed on an Amberlite XAD-2 (800 g) column. Elution with methanol gave a crude glycoside mixture (9 g).

A similar procedure was adopted to obtain the crude glycoside mixture (3 g) from fresh bulbs (2 kg) of *Muscari botryoides* Miller (collected in May 1985 near Formia, Italy, and authenticated by the Botanical Garden of the University of Naples).

The glycoside mixtures were fractionated as detailed in Chart 2.

The spectral data (negative and (or) positive FAB–MS, ^1H and ^{13}C nmr spectroscopy) of novel Muscarosides G–N, **3**–**10**, are reported in the text, in Scheme 1, and in Tables 1–3. The known Muscarosides A **12**, B **13**, and C **14** were identified by comparison (^1H and ^{13}C nmr spectra, tlc, hplc) with authentic samples (1, 3). Glycoside **11** was recognized to be the known scillascilloside D-1, isolated from *Scilla scilloides*, as it exhibited ^1H and ^{13}C nmr data that were practically identical with those reported in ref. 5.

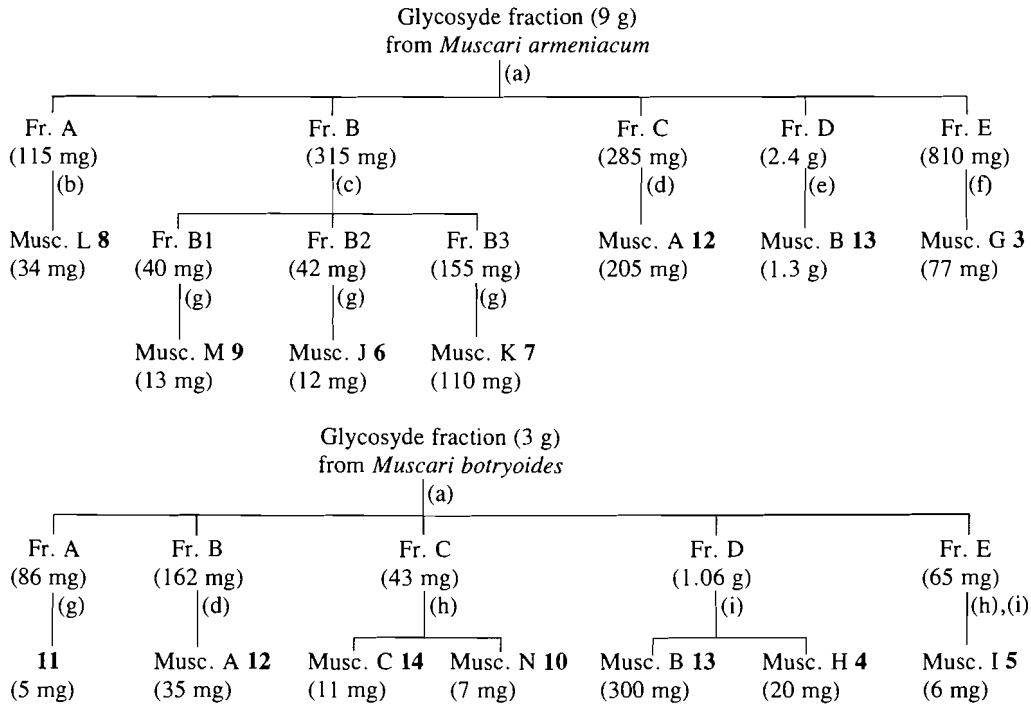

(a) Silica gel column chromatography on a Chromatospac Prep10 apparatus (Jobin Yvon); solvent: 7:3 chloroform–methanol.
(b) Preparative hplc on a Lichrosorb RP-18 (7 μm) column, 3:2 methanol–water, 5 mL min^{-1}.
(c) Preparative chromatography on silica gel plates (2 mm); solvent: 13:7:1 chloroform–methanol–water (3 runs).
(d) Preparative hplc on a Lichrosorb RP-18 (7 μm) column, 3:1 methanol–water, 5 mL min^{-1}.
(e) Crystallization from 95% ethanol.
(f) Preparative hplc on a Lichrosorb RP-18 (7 μm) column, 7:3 methanol–water, 5 mL min^{-1}.
(g) Preparative hplc on a Lichrosorb RP-18 (7 μm) column, 2:1 methanol–water, 5 mL min^{-1}.
(h) Flash chromatography on silica gel; solvent: 6:1 methanol–water.
(i) Dry column chromatography on silica gel; solvent: 14:6:1 chloroform–methanol–water.

CHART 2. Isolation of Muscarosides from *Muscari armeniacum* and from *Muscari botryoides*.

Can. J. Chem. Downloaded from www.nrcresearchpress.com by 122.72.124.2 on 09/07/12
For personal use only.

TABLE 3. ^{13}C nuclear magnetic resonance chemical shifts and glycosidation shifts (in parentheses) of muscaroside sugar moieties in pyridine-d_5[a]

Carbon	Reference substance[b]	Monose unit	3	4	12[c]	5	13[d]	14[e]
1	A 105.4	G′	106.1	106.1	106.1	105.6	106.2	105.5
2	74.8		75.4	75.3	75.4	75.6	75.3	75.5
3	78.1		78.2	78.2	78.2	79.0	78.2	78.3
4	71.4		71.5	71.6	71.5	72.4	71.8	72.6
5	78.1		75.7 (−2.4)	75.6 (−2.5)	75.5 (−2.6)	75.1 (−3.0)	75.6 (−2.5)	75.5 (−2.6)
6	62.5		68.7 (+6.2)	68.6 (+6.1)	68.7 (+6.2)	68.9 (+6.4)	68.8 (+6.3)	68.8 (+6.3)
1	B 105.9	A′	101.3 (−4.5)	101.1 (−4.8)	101.2 (−4.7)	101.5 (−4.4)	101.4[f]	101.3 (−4.6)
2	72.2		78.6 (+6.4)	77.8 (+5.6)	79.3 (+7.1)	79.7 (+7.5)	79.4 (+7.2)	79.6 (+7.4)
3	74.4		72.4 (−2.0)	72.2 (−2.4)	72.3 (−2.1)	72.1 (−2.3)	72.3 (−2.1)	72.1 (−2.3)
4	69.1		66.8	66.8	66.5	67.2	67.0	66.9
5	66.6		64.8	63.1	64.2	63.8	63.2	63.2
1	A 105.4	G″	102.5 (−2.9)	102.5 (−2.9)	103.1 (−2.3)	103.6 (−1.8)	102.8[f]	103.7 (−1.7)
2	74.8		77.7 (+2.9)	77.6 (+2.8)	78.3 (+3.5)	81.7 (+6.9)	76.2 (+1.4)	79.8 (+5.0)
3	78.1		86.3 (+8.2)	87.5 (+9.4)	77.7 (−0.4)	88.2 (+10.1)	87.3 (+9.2)	77.6 (−0.5)
4	71.4		69.0 (−2.4)	69.0 (−2.4)	71.5	68.9 (−2.5)	68.9 (−2.5)	71.2
5	78.1		77.7	77.8	78.3	77.6	77.7	78.2
6	62.5		62.0	61.7	62.7	61.9	61.8	63.2
1	C 102.4	R	102.4	102.3	102.2	—	102.4	—
2	71.9		72.0	72.2	72.7	—	71.9	—
3	72.5		72.5	72.6	72.7	—	72.9	—
4	73.6		74.0	74.0	74.3	—	73.9	—
5	69.4		70.0	70.0	69.5	—	70.2	—
6	18.4		18.6	18.8	18.7	—	18.7	—
1	D 111.2	Ap	—	—	—	111.0	—	111.2
2	78.1		—	—	—	77.9	—	77.9
3	80.4		—	—	—	80.2	—	80.4
4	75.3		—	—	—	75.5	—	75.4
5	65.5		—	—	—	65.5	—	66.0
1	B 105.9	A″	101.7 (−4.2)	105.4	—	—	102.6[f]	—
2	72.2		81.6 (+9.4)	72.6	—	—	77.8 (+5.6)	—
3	74.4		73.3 (−1.1)	74.4	—	—	72.5 (−1.9)	—
4	69.1		68.1	69.4	—	—	68.1	—
5	66.6		66.1	67.7	—	—	65.7	—
1	E 106.1	Ga	—	—	—	102.8 (−3.3)	—	—
2	72.5		—	—	—	77.0 (+4.5)	—	—
3	75.2		—	—	—	74.8 (−0.4)	—	—
4	70.1		—	—	—	70.0	—	—
5	76.8		—	—	—	76.1	—	—
6	62.3		—	—	—	61.1	—	—
1	F 110.4	A_f	—	—	—	110.0	110.0	—
2	83.0		—	—	—	82.2	81.8	—
3	78.5		—	—	—	78.4	78.7	—
4	85.5		—	—	—	85.1	85.3	—
5	62.7		—	—	—	62.7	62.5	—
1	A 105.4	G‴	106.2	—	—	—	—	—
2	74.8		75.8	—	—	—	—	—
3	78.1		78.1	—	—	—	—	—
4	71.4		70.6	—	—	—	—	—
5	78.1		77.8	—	—	—	—	—
6	62.5		62.9	—	—	—	—	—

Carbon	Reference substance[b]	Monose unit	6	7	8	9	10
1	A 105.4	G′	106.0	105.8	106.2	105.3[f]	105.2
2	74.8		75.8	75.6	75.5	75.4	75.1
3	78.1		78.6	78.3	78.7	78.5	77.9
4	71.4		71.9	73.0	72.0	72.2[g]	72.5
5	78.1		76.3 (−1.8)	76.0 (−2.1)	77.1 (−1.0)	76.8 (−1.3)	75.1 (−3.0)

Can. J. Chem. Downloaded from www.nrcresearchpress.com by 122.72.124.2 on 09/07/12
For personal use only.

TABLE 3 (*concluded*)

Carbon	Reference substance[b]	Monose unit	6	7	8	9	10
6	62.5		69.3 (+6.8)	69.2 (+6.7)	69.9 (+7.4)	69.0 (+6.5)	68.6 (+6.1)
1	B 105.9	A′	102.5 (−3.4)	102.3 (−3.6)	105.7	105.7[f]	100.5 (−5.4)
2	72.2		81.0 (+8.8)	80.9 (+8.7)	72.3	71.8[g]	81.3 (+9.1)
3	74.4		73.1 (−1.3)	72.0 (−2.4)	74.5	74.3	73.5 (−0.9)
4	69.1		67.9	67.8	69.3	69.5	66.0
5	66.6		65.1	64.9	66.8	66.3	64.3
1	A 105.4	G″	105.8	105.5	—	—	102.8 (−2.6)
2	74.8		75.5	75.7	—	—	79.1 (+4.3)
3	78.1		78.1	78.4	—	—	77.4 (−0.7)
4	71.4		71.3	71.0	—	—	71.1
5	78.1		78.3	78.6	—	—	78.1
6	62.5		62.4	62.0	—	—	62.6
1	C 102.4	R	—	—	—	—	101.6
2	71.9		—	—	—	—	72.0
3	72.5		—	—	—	—	72.5
4	73.6		—	—	—	—	73.9
5	69.4		—	—	—	—	69.5
6	18.4		—	—	—	—	18.6

[a]Chemical shift values are given in δ relative to TMS.
[b]Reference substances: A = methyl β-D-glucopyranoside (9); B = methyl α-L-arabinopyranoside (9); C = methyl α-L-rhamnopyranoside (9); D = methyl β-D-apio-D-furanoside (10); E = methyl β-D-galactopyranoside (9); F = methyl α-L-arabinofuranoside (11).
[c]Reference 1.
[d]Reference 2.
[e]Reference 3.
[f,g]Interchangeable values.

Acid hydrolysis of Muscaroside G **3**

A sample of Muscaroside G **3** was hydrolyzed with 7% H_2SO_4 and the water-soluble fraction of the hydrolysate was analyzed by tlc and hplc following the procedure described in ref. 4, establishing the presence of rhamnose, arabinose, and glucose in a 1:2:3 molar ratio.

Perbenzoylation of the hydrolysate from Muscaroside G **3**

Perbenzoylation of the water-soluble fraction of the above hydrolysate, isolation of pure perbenzoates of rhamnose, arabinose, and glucose, and measurement of the amplitudes (−12, +71, and +12, respectively) of their circular-dichroism split curves were carried out following the procedure described in ref. 4.

Acid hydrolysis of Muscaroside I **5**

A sample of Muscaroside I **5** was hydrolyzed with 7% H_2SO_4 and the water-soluble fraction of the hydrolysate was analyzed by tlc and hplc following the procedure described in ref. 4, establishing the presence of galactose, glucose, arabinose, and apiose in a 1:2:2:1 molar ratio.

Acknowledgments

We thank Professor H. Egge, Institut für Physiologische Chemie, Bonn, for the FAB–MS spectra, the Centro Interdipartimentale di Metodologie Chimico-Fisiche, Università di Napoli, for the 270/67.88 MHz nmr spectra, and the Ministero della Pubblica Istruzione, Roma, for financial support of this work.

1. M. ADINOLFI, G. BARONE, R. LANZETTA, G. LAONIGRO, L. MANGONI, and M. PARRILLI. Can. J. Chem. **61**, 2633 (1983); *addenda* **62**, 1228 (1984).
2. M. ADINOLFI, G. BARONE, R. LANZETTA, G. LAONIGRO, L. MANGONI, and M. PARRILLI. Can. J. Chem. **62**, 1223 (1984).
3. R. LANZETTA, G. LAONIGRO, M. PARRILLI, and E. BREITMAIER. Can. J. Chem. **62**, 2874 (1984).
4. M. ADINOLFI, G. BARONE, M. M. CORSARO, R. LANZETTA, L. MANGONI, and M. PARRILLI. Can. J. Chem. **65**, 2317 (1987).
5. M. SHOLICHIN, K. MIYAHARA, and T. KAWASAKY. Chem. Pharm. Bull. **33**(4), 1756 (1985).
6. M. SHOLICHIN, K. MIYAHARA, and T. KAWASAKY. Heterocycles, **17**, 251 (1982).
7. K. YAMASAKY, H. KOHDA, T. KOBAYASHI, R. KASAI, and O. TANAKA. Tetrahedron Lett. 1005 (1976).
8. H. LIU and K. NAKANISHI. Tetrahedron, **38**, 513 (1982).
9. S. SEO, Y. TOMITA, K. TORI, and Y. YOSHIMURA. J. Am. Chem. Soc. **100**, 3331 (1978).
10. H. ISHII, K. TORI, T. TOZIO, and Y. YOSHIMURA. Chem. Pharm. Bull. **26**, 674 (1978).
11. R. ENCARNATION, L. KENNE, G. SAMUELSSON, and F. SANDBERG. Phytochemistry, **20**, 1939 (1981).
12. R. KASAI, M. OKIHARA, J. ASAKAWA, K. MIZUTANI, and O. TANAKA. Tetrahedron, **35**, 1427 (1979).
13. H. ISHII, I. KITAGAWA, K. MATSUSHITA, K. SHIRAKAWA, K. TORI, T. TOZYO, M. YOSHIKAWA, and Y. YOSHIMURA. Tetrahedron Lett. 1529 (1981).
14. K. MIZUTANI, A. HAYASHI, R. KASAI, O. TANAKA, N. YOSHIDA, and T. NAKAJIMA. Carbohydr. Res. **126**, 177 (1984).
15. S. B. MAHATO, N. P. SAHU, A. N. GANGULY, R. KASAI, and O. TANAKA. Phytochemistry, **19**, 2017 (1980).

Can. J. Chem. Downloaded from www.nrcresearchpress.com by 122.72.124.2 on 09/07/12
For personal use only.

Influence of cyclodextrins on the photo-Fries rearrangement of acetanilide

MIRTHA NASSETTA AND RITA H. DE ROSSI[1]

Instituto de Investigaciones en Físico Química de Cordoba (INFIQC), Departamento de Química Orgánica, Facultad de Ciencias Químicas, Universidad Nacional de Cordoba, Suc 16, CC 61, 5016 Cordoba, Argentina

AND

JUAN J. COSA

Departamento de Química y Física, Universidad Nacional de Rio Cuarto, 5800 Rio Cuarto, Argentina

Received February 28, 1988

MIRTHA NASSETTA, RITA H. DE ROSSI, and JUAN J. COSA. Can. J. Chem. **66**, 2794 (1988).

The effect of α-, β-, and γ-cyclodextrins on the quantum yield for the formation of *o*- and *p*-aminoacetophenone from the photolysis of acetanilide at 254 nm was determined. There is an increase in the ratio of *o*/*p* products when cyclodextrins are added and the total quantum yield is about the same as in water in the presence of γ-CD, higher with β-CD, and lower with α-CD. The association constants between acetanilide and CD were determined and the values are 22.7 M^{-1} and 30.7 M^{-1} for α- and β-CD respectively. The quantum yields for the formation of *o*- and *p*-aminoacetophenone were measured. The rearrangement occurs in water and in the included acetanilide. The quantum yields for the formation of *o*-aminoacetophenone and *p*-aminoacetophenone from the included substrate could be calculated for α- and β-cyclodextrin. Comparing these values with those obtained in water, it is concluded that there is some steric inhibition for rearrangement at the *para* position when α-cyclodextrin is the host, whereas with β-cyclodextrin the less polar microsolvent effect is responsible for the increase in the total quantum yield relative to water.

MIRTHA NASSETTA, RITA H. DE ROSSI et JUAN J. COSA. Can. J. Chem. **66**, 2794 (1988).

On a déterminé l'influence des α-, β- et γ-cyclodextrines sur les rendements quantiques des réactions conduisant à la formation des *o*- et *p*-amino acétophénones, par photolyse de l'acétanilide à 254 nm. Lorsqu'on ajoute des cyclodextrines, on observe une augmentation du rapport des produits *o*/*p* et le rendement quantique global est pratiquement le même que celui observé dans l'eau en présence de γ-CD, plus élevé qu'avec de la β-CD et plus faible qu'avec de l'α-CD. On a déterminé les constantes d'association de l'acétanilide avec les CD et on a obtenu des valeurs de 22,7 M^{-1} et 30,7 M^{-1} respectivement pour l'α- et la β-CD. On a mesuré les rendements quantiques pour la formation des *o*- et *p*-amino acétophénones. La transposition se produit dans l'eau ainsi qu'avec de l'acétanilide inclus. On peut calculer les rendements quantiques pour la formation des *o*- et *p*-amino acétophénones à partir de substrats inclus dans l'α- ainsi que la β-cyclodextrine. Lorsqu'on compare ces données avec celles obtenues dans l'eau, on peut conclure que, lorsque l'α-cyclodextrine est l'hôte, il existe une certaine inhibition stérique à la transposition vers la position *para*; par ailleurs, lorsqu'on utilise de la β-cyclodextrine, l'effet de microsolvant moins polaire est responsable de l'augmentation de rendement quantique par rapport à l'eau.

[Traduit par la revue]

Introduction

Cyclodextrins are cyclic oligomers of α-D-glucose with 6, 7, or 8 glucose units (α-, β-, or γ-cyclodextrins) and are able to form inclusion complexes with a great variety of organic as well as inorganic compounds (1). As a result of the interaction, the reactivity of the included substrate changes and, when parallel reactions take place, the presence of the host may change the proportion of the various products formed (2).

Some examples are the halogenation of anisole (3) and the iodination (4), carboxylation (5), or formylation of phenoxide ion (6). It has been reported that in the photo-Fries rearrangement of acetanilide in the presence of β-cyclodextrin there is a significant increase in the *para* relative to the *ortho* product (7), and that there is an increase in the yield of rearrangement products. The change in selectivity was attributed to steric inhibition for the reaction at the *ortho* position. On the other hand, a very high *ortho* selectivity was recently reported for the photo-rearrangement of phenyl esters and anilides in solution and in the solid state, for reactions carried out in the presence of α- and β-cyclodextrins (8).

We considered it of interest to carry out a kinetic study of the photo-rearrangement of acetanilide in the presence of α-, β-, and γ-cyclodextrins to determine whether the change in product ratio was due to a decrease in reactivity at the *ortho* position or to an increase in reactivity at the *para* position. We were surprised to find that in the presence of α- and β-cyclodextrin there is an increase in the *ortho* rather than in the *para* product, but we believe that our results are consistent with what is known about the mechanism of photo-Fries reactions (*vide infra*).

[1]Author to whom correspondence may be addressed.

Results and discussion

The photolysis of acetanilide has been extensively studied in protic as well as in non-protic solvents (9). The main photolysis products are *o*- and *p*-aminoacetophenone. The quantum yield of these products is not affected by oxygen, piperylene, initial concentration of reactants, and radiation intensity. These results suggest that the excited state responsible for the photorearrangement is a singlet (9*a*). The absorption band of acetanilide centered at 239 nm suffers a small bathochromic shift when α- or β-CD is added, indicating some type of association (10). No changes in the spectra are observed with γ-CD. A similar shift in the wavelength maximum is observed when the solvent is changed from water to dioxane, indicating that the acetanilide is in a less polar environment.

From the changes in the optical density at the λ_{max} of the difference spectrum, the equilibrium constant for the association was determined (11). The values obtained are 22.7 ± 0.1 and 30.7 ± 0.1 M^{-1} for α- and β-CD, respectively. The value for the equilibrium constant for the association of acetanilide and α-CD is in good agreement with that obtained by other authors by nmr (12), namely 20 M^{-1}.

In the presence of α-, β-, or γ-CD the ratio of quantum

Can. J. Chem. Downloaded from www.nrcresearchpress.com by 196.1.178.254 on 09/07/12
For personal use only.

TABLE 1. Effect of α-cyclodextrin on the quantum yield for the formation of *ortho*- and *para*-aminoacetophenone[a]

$[CD] \times 10^3$, M[b]	$\phi^p_{exp} \times 10^3$ [c]	$\phi^o_{exp} \times 10^3$ [d]	$[o]/[p]$[e]
	2.0[f]	5.0[f]	2.71
4.0	1.82	4.73	2.81
7.0	1.58	4.13	2.85
11	1.53	4.16	2.95
14	1.51	4.38	3.14
18	1.48	4.46	3.27
20	1.45	4.42	3.31

[a] T = 25°C. Solvent, water. $[Substrate]_0 = 3 \times 10^{-4}$ M.
[b] Initial concentration of α-cyclodextrin. Conversion was kept below 3%. Quantum yields are calculated using a solution of acetanilide as actinometer.
[c] Observed quantum yield for the formation of *para* product.
[d] Observed quantum yield for the formation of *ortho* product.
[e] Ratio of concentration of *ortho*- and *para*-aminoacetophenone.
[f] Calculated using ferrioxalate as actinometer.

yields for the formation of *ortho*- and *para*-aminoacetophenone increases. But there is not a big change in the total quantum yield of product formation (the data are summarized in Tables 1–3). In one reaction, in the presence of β-CD, the solution was photolyzed up to 40% and was analyzed by gas chromatography to determine whether any aniline was formed. Within the limits of the detection of our instrument (~1%), aniline was not formed. In the same reaction we compared the yield of *ortho*- and *para*-aminoacetophenone, determined spectrophotometrically and by gas chromatography, and we found the same value within experimental error (see experimental section).

We also carried out an experiment using similar concentrations of acetanilide and β-cyclodextrin as those reported in a previous work (7) and we found that the concentrations of *ortho* and *para* products are similar to those obtained in water (see last run in Table 2). The measured ratio of concentrations of *o*- and *p*-aminoacetophenone is similar to that reported by Chenevert and Raymond (7). We believe that the reason for their interpretation, that β-cyclodextrin increased the amount of the *para* product relative to the *ortho*, is that they obtained a value of 3.8 for the *o*/*p* ratio in water. This value is larger than that previously reported in the literature (9, 13) and than our own values (Tables 1–3).

Similar results were obtained when degassed solutions were used. The changes observed in quantum yields in the presence of cyclodextrins are not large, but it is important to note that the association constants are quite weak and, due to solubility limitations for the host, the fraction of complexed substrates under extreme conditions is less than 30%. Therefore, the photochemical reaction must be taking place in both environments. The kinetic scheme may be represented as in eq. [1],

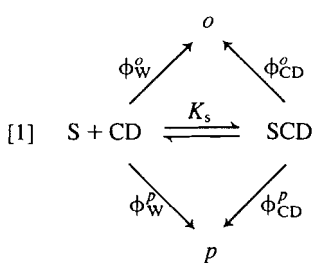

where S is acetanilide, CD is the cyclodextrin, SCD is the inclusion complex, *o* is *o*-aminoacetophenone, *p* is *p*-aminoacetophenone, ϕ^o_W, ϕ^p_W and ϕ^o_{CD}, ϕ^p_{CD} are the quantum yields for the formation of products in water and in CD respectively, and K_s is the binding constant for acetanilide.

The observed quantum yields for *ortho* ϕ^o_{exp} or *para* ϕ^p_{exp} products are described in eq. [2] (14, 15), where ϵ_c/ϵ_w is an approximate correction factor for the differences in light absorption by the complexed and uncomplexed acetanilide. This value is 1.2 for α- and β-CD and was determined from the absorbance at 254 nm of solutions of acetanilide in the presence of the appropriate cyclodextrin and from the calculated fraction of complexed substrate.

$$[2] \quad \phi^{o(p)}_{exp} = \frac{\phi^{o(p)}_w + (\epsilon_c/\epsilon_w)\phi^{o(p)}_{CD} K_s[CD]}{1 + K_s[CD]}$$

Equation [2] can be rearranged to eq. [3]:

$$[3] \quad \frac{1}{\phi^{p(o)}_W - \phi^{o(p)}_{exp}} = \frac{1}{\phi^{o(p)}_W - \epsilon_c/\epsilon_w \phi^{o(p)}_{CD}} + \frac{1}{[\phi^{o(p)}_W - \epsilon_c/\epsilon_w \phi^{o(p)}_{CD}] K_s[CD]}$$

In Table 1 it can be observed that while ϕ^o_{exp} remains approximately constant, ϕ^p_{exp} decreases when the concentration of α-CD increases. A plot (not shown) of the left-hand side of eq. [3] vs. $[CD]^{-1}$ for the *p*-aminoacetophenone yields a straight line. From the intercept of this plot, $\phi^p_{CD} = (0.3 \pm 0.4) \times 10^{-3}$ is calculated. The ratio of slope over intercept yields $K_s = (37 \pm 18)$ M^{-1}, in fair agreement with the spectrophotometric value.

Alternatively, eq. [2] can be rearranged to eq. [4]:

$$[4] \quad \phi^{o(p)}_{exp} = \phi^{o(p)}_W + \left[\frac{\epsilon_c}{\epsilon_w}\phi^{o(p)}_{CD} - \phi^{o(p)}_W\right] \frac{K_s[CD]}{1 + K_s[CD]}$$

From a plot of ϕ^p_{exp} vs. the fraction of complexed acetanilide (using the spectrophotometric value of K_s), ϕ^p_{CD} is calculated as $(0.2 \pm 0.2) \times 10^{-3}$. Although in both cases the error in the calculated value is quite high, it is smaller in the latter treatment. Since there is not a marked trend in the values of ϕ^o_{exp}, we estimated ϕ^o_{CD} using eq. [2] for each experimental point. The average value is $(1.9 \pm 0.8) \times 10^{-3}$.

In Table 2 the data for the reactions in the presence of β-CD are shown. It can be seen that there is a change in the product ratio mainly due to changes in the quantum yield for the formation of the *ortho* product. We attempted to fit the data using eq. [3] but there was a poor linear correlation; however, the value of K_s that can be estimated from the ratio of the slope and the intercept is similar to that determined spectrophotometrically. We estimated ϕ^o_{CD} and ϕ^p_{CD} for each experiment from eq. [2] using the K_s determined spectrophotometrically and the value $\epsilon_c/\epsilon_w = 1.2$. These values show that the quantum yield for the formation of the *para* product is somewhat lower in the included substrate than in water, whereas the quantum yield for the formation of the *ortho* product in the substrate included in CD is about 50% higher than in water.

The experimental *o*/*p* ratios for the reactions in the presence of γ-CD (Table 3) show a tendency to behave similarly to those for β-CD but, since the equilibrium constant for the association could not be determined and the changes in $\phi^{o(p)}_{exp}$ with the concentration of γ-CD are barely outside the experimental error, it was not possible to calculate ϕ^o_{CD} and ϕ^p_{CD}.

Can. J. Chem. Downloaded from www.nrcresearchpress.com by 196.1.178.254 on 09/07/12
For personal use only.

TABLE 2. Effect of β-cyclodextrin on the quantum yield for the formation of *o*- and *p*-aminoacetophenone[a]

[CD] × 10^3, M[b]	$\phi^p_{exp} \times 10^3$ [c]	$\phi^p_{CD} \times 10^3$ [d]	$\phi^o_{exp} \times 10^3$ [e]	$\phi^o_{CD} \times 10^3$ [d]	$[o]/[p]$[f]
	2.0[g]		5.0[g]		2.43
4.23	1.9	1.0	5.3	6.3	2.67
6.70	2.0	1.6	5.6	6.9	2.73
8.14	2.0	1.7	5.9	8.1	2.85
10.7	2.2	2.2	6.3	8.3	2.83
14.2	1.9	1.3	5.9	6.7	3.03
	Average:	1.6 ± 0.4		7.4 ± 0.8	
0.5[h]					2.50

[a] T = 25°C. Solvent, water. $[Substrate]_0 = 3 \times 10^{-4}$ M. Conversion was kept below 3%. Quantum yields are calculated using a solution of acetanilide as actinometer.
[b] Initial concentration of β-cyclodextrin.
[c] Observed quantum yield for the formation of *p*-aminoacetophenone.
[d] Calculated from eq. [2] using K_s = 30.7 M and $\epsilon_c/\epsilon_w = 1.2$
[e] Observed quantum yield for the formation of *o*-aminoacetophenone.
[f] Ratio of yield of *o*- and *p*-aminoacetophenone.
[g] Calculated using ferrioxalate as actinometer.
[h] $[Substrate]_0 = 1 \times 10^{-2}$.

TABLE 3. Effect of γ-cyclodextrin on the quantum yield for the formation of *o*- and *p*-aminoacetophenone[a]

[CD] × 10^3, M[b]	$\phi^p_{exp} \times 10^3$ [c]	$\phi^o_{exp} \times 10^3$ [d]	$[o]/[p]$[e]
	2.0[f]	5.0	2.59
4.0	1.8	4.5	2.57
7.5	1.8	4.5	2.66
12.6	1.8	4.8	2.78
16.0	2.0	5.3	2.79
18.8	1.8	5.0	2.87

[a] T = 25°C. Solvent, water. $[Substrate]_0 = 3 \times 10^{-4}$ M.
[b] Initial concentration of γ-cyclodextrin.
[c] Observed quantum yield for the formation of *p*-aminoacetophenone.
[d] Observed quantum yield for the formation of *o*-aminoacetophenone.
[e] Ratio of yields of *o*- and *p*-aminoacetophenone.
[f] Calculated using ferrioxalate as actinometer.

It has been reported that the mechanism of the photo-Fries rearrangement of acetanilide may be described in Scheme 1, where S_0, S_1, and T_1 represent the ground state, first singlet, and first triplet excited state respectively.

The total quantum yield is highly dependent on the hydrogen-bonding ability of the solvent with the substrate (16).

Equation [9] is accepted as the initial process of the photo-Fries reaction, followed by rearrangement of the radical pair within the solvent cage (Scheme 2) (9*b*).

We assume that the photophysical and photochemical primary processes of acetanilide, given in Scheme 1, are not appreciably altered by association with CD, and we have no reason to believe they are. To explain the observed changes in quantum yields in the reactions that occur inside the cavity of the cyclodextrins or in the bulk solution (Table 4), we must consider the various factors that may induce changes in quantum yields. These are (*a*) hydrogen bonding, (*b*) steric hindrance for migration of the acetyl radical to the *ortho* and *para* positions, (*c*) escape of radicals from the solvent cage (this is not an important reaction under our experimental conditions since we could not detect aniline), (*d*) back recombination of the geminate radical pair to regenerate acetanilide.

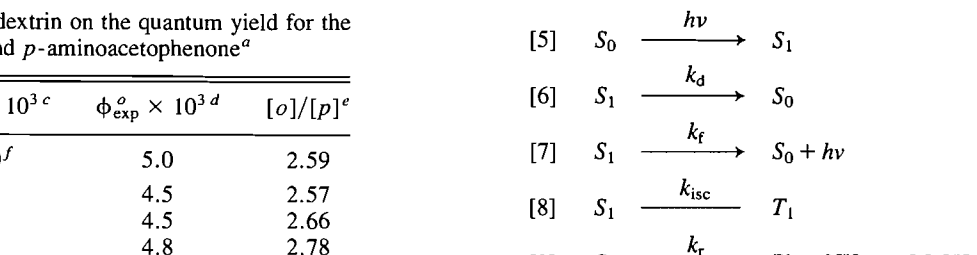

SCHEME 1

It is known that reaction [9] is strongly dependent on the hydrogen bonding ability of the solvent (9). The quantum yield of products decreases when the hydrogen bonding ability of the solvent increases. For instance, the total quantum yield is 7×10^{-3} in water, 3.1×10^{-2} in ethanol, and 8×10^{-2} in ethyl ether. On the other hand, the *ortho*/*para* ratio increases from 1.2 in ethyl ether to 2.5 in water (9*a*).

Our results show that the total quantum yield of products is about the same as in water in the presence of γ-CD (Table 3), somewhat higher with β-CD (Table 2), and somewhat lower with α-CD (Table 1).

The changes observed in the uv spectra of solutions of acetanilide in the presence of α- and β-CD indicate that acetanilide is in a less polar microenvironment; therefore under these conditions the quantum yield of product formation should be larger, whereas the *ortho*/*para* ratio should be lower, than in water.

It was determined that in the complex of acetanilide with α-CD, the benzene ring penetrates the cavity and the *ortho* positions are sterically hindered due to interactions with the cyclodextrin ring system (12). In this way, it is possible to explain the decrease in the ϕ^o_{CD} for the reactions carried out in the presence of α-CD. The larger decrease in the value of ϕ^p_{CD} can also be explained on the basis of steric inhibition for the migration of the acetyl group to the *para* position. We suggest that the decrease in total quantum yield is due to an increase in the rate of the back reaction. The phenomenon of "cage combination" is well known (17). This effect is observed in systems involving two radicals simultaneously produced in

Can. J. Chem. Downloaded from www.nrcresearchpress.com by 196.1.178.254 on 09/07/12
For personal use only.

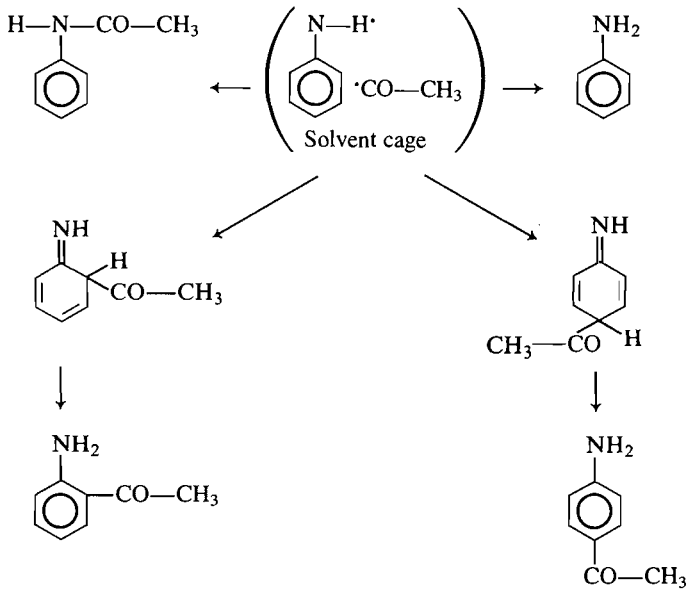

SCHEME 2

solution at the same location and is strongly dependent on the solvent viscosity. The cavity of the α-CD may present an increased microviscosity and therefore the migration of the acetyl radical is somehow impeded. On the other hand, studies regarding the location of substituted benzene derivatives in the cavity of β-CD (18) indicate that the aromatic ring does not penetrate the cavity very deeply, so that the *ortho* position may not be sterically hindered for reaction, while we would expect some steric inhibition for migration of the acetyl radical to the *para* position, consistent with the value of $\phi^p_{CD}/\phi^p_W = 0.8$. The observed $\phi^o_{CD}/\phi^o_W = 1.5$ may be due to the less polar microenvironment where the reaction is taking place.

In Table 4 the values for the quantum yield for the formation of *ortho* and *para* aminoacetophenone in the presence of cyclodextrins are summarized. Although the values have a considerable error, the results indicate that there is a significant increase in the formation of the *ortho* product relative to the *para* product, when the rearrangement takes place in the cavity of α- and β-CD. The lack of a comparable effect upon the addition of γ-CD is reasonable if it does not bind acetanilide, as suggested by the absorption spectrum, or if γ-CD allows several water molecules to share the cavity with acetanilide.

Experimental

Photolysis methods

A set of reactions was carried out in a quartz reactor where solutions of acetanilide 2×10^{-4} M in water, with or without cyclodextrin, were irradiated with an immersion type low-pressure mercury lamp (254 nm) during 120 min. The yield of products was determined spectrophotometrically as indicated below. Bubbling nitrogen through the solution did not change the results.

A solution containing 6×10^{-4} M acetanilide and 1.5×10^{-2} M β-CD and one without β-CD were photolyzed up to 40% conversion. The solutions were analyzed spectrophotometrically, giving 31.56% of *ortho* and 10.06% of *para* aminoacetophenone for the former and 26.77% of *ortho* and 10.41% of *para* aminoacetophenone for the latter. Then they were extracted three times with 10-mL portions of ether. The combined ether extracts were dried with calcium chloride, concentrated, and analyzed by gas chromatography. The gc analysis was performed on a Varian Aerograph series 1400 instrument using a 1.5 mts, OV 101 on 3% Chromosorb GHP column, using β-naphthol as internal standard giving 32.16% and 11.04% of *o*- and *p*-aminoacetophenone respectively for the former and 28.00% and 12.41% of *o*- and *p*-aminoacetophenone respectively for the latter. No aniline was detected in this analysis. In all cases the photoproducts were compared to those of known mixtures of authentic samples.

TABLE 4. Association constants of acetanilide with cyclodextrins, and calculated quantum yields for the formation of *o*- and *p*-aminoacetophenone from the complexed acetanilide

Cyclodextrin	K_s, M^{-1} [a]	$\phi^o_{CD} \times 10^3$	$\phi^p_{CD} \times 10^3$
α[b]	22.7 ± 0.1	1.9 ± 0.8	0.2 ± 0.2
β[c]	30.7 ± 0.1	7.4 ± 0.8	1.6 ± 0.4
γ[d]		5	2
Water		5.0 ± 0.2	2.0 ± 0.1

[a]All determinations were done at 25°C in water. $[\text{Acetanilide}]_0 = 3 \times 10^{-4}$ M.
[b]Concentration range $(4–20) \times 10^{-3}$ M.
[c]Concentration range $(2–14) \times 10^{-3}$ M.
[d]Concentration range $(4–18) \times 10^{-3}$ M.

Quantum yield determinations

Aqueous solutions of 3×10^{-4} M acetanilide and the required amount of CD contained in square quartz cuvettes were placed in a merry-go-round apparatus and irradiated with a low-pressure mercury lamp (254 nm). Every 20 minutes the lamp was covered to stop irradiation and the spectra of the solutions were taken. The yield of photoproducts was determined by measuring the absorption at 312 and 357 nm, which are the λ_{max} of *o*- and *p*-aminoacetophenone respectively. In all cases the conversion was below 10%. To calculate the yield we use eqs. [10] and [11]:

$$[10] \quad C_1 = A_1 \frac{\epsilon_{22}}{\epsilon_{11}\epsilon_{22} - \epsilon_{12}\epsilon_{21}} + A_2 \frac{-\epsilon_{21}}{\epsilon_{11}\epsilon_{22} - \epsilon_{12}\epsilon_{21}}$$

$$[11] \quad C_2 = A_1 \frac{-\epsilon_{12}}{\epsilon_{11}\epsilon_{22} - \epsilon_{12}\epsilon_{21}} + A_2 \frac{\epsilon_{11}}{\epsilon_{11}\epsilon_{22} - \epsilon_{12}\epsilon_{21}}$$

where ϵ_{11} and ϵ_{21} are the extinction coefficients at 357 nm of *p*- and *o*-aminoacetophenone respectively; ϵ_{12} and ϵ_{22} are the extinction coefficients at 312 nm of *p*- and *o*-aminoacetophenone; A_1 and A_2 are the observed values of the absorbance at these two wavelengths; and C_1 and C_2 are the observed values of concentration of *p*- and *o*-aminoacetophenone. The concentration so calculated was plotted vs. time, and the ratios of the slopes for the *o*- and *p*-aminoacetophenone are the values of the *o*/*p* ratio reported in Tables 1–3.

The quantum yields were determined using the solution of acetanilide in water as acetinometer. The quantum yield for the acetanilide solution was checked using the ferrioxalate actinometer (19). The value obtained is the same as that reported in the literature (9, 13).

Equilibrium constant determinations

The spectrum of solutions containing 1.4×10^{-4} M acetanilide and variable concentrations of α- or β-CD was run and the spectrum of the cyclodextrin and that of acetanilide were subtracted. This difference spectrum has its maximum at 230 nm. The equilibrium constant for the association was determined from the measurement of the change in optical density as a function of cyclodextrin concentration (11).

Acknowledgments

This work was supported in part by the Consejo Nacional de Investigaciones Cientificas y Tecnicas (CONICET) and the Consejo de Investigaciones Cientificas y Tecnologicas de la Provincia de Cordoba (CONICOR).

1. M. L. BENDER and M. KOMIYAMA. Cyclodextrin chemistry. Springer Verlag, New York. 1977; W. SAENGER. Angew. Chem. Int. Ed. Engl. **19**, 344 (1980); C. SIRLIN. Bull. Soc. Chim. Fr. II-5 (1984); I. TABUSHI and Y. KURODA. Adv. Catal. **32**, 417 (1983).

Can. J. Chem. Downloaded from www.nrcresearchpress.com by 196.1.178.254 on 09/07/12
For personal use only.

2. I. TABUSHI. Acc. Chem. Res. **15**, 66 (1982); M. KOMIYAMA, I. SUGIURA, and H. HIRAI. J. Inclusion Phenom. **2**, 823 (1984).
3. R. BRESLOW and P. CAMPBELL. J. Am. Chem. Soc. **91**, 3085 (1969); Biorg. Chem. **1**, 140 (1971).
4. A. VEGLIA and R. H. DE ROSSI. J. Org. Chem. In press.
5. M. KOMIYAMA and H. HIRAI. J. Am. Chem. Soc. **106**, 174 (1984).
6. M. KOMIYAMA and H. HIRAI. J. Am. Chem. Soc. **105**, 2018 (1983).
7. R. CHENEVERT and P. RAYMOND. Can. J. Chem. **61**, 1092 (1983).
8. V. RAMAMURTHY. Tetrahedron, **42**, 5753 (1987).
9. (*a*) H. SHISUKA and I. TANAKA. Bull. Chem. Soc. Jpn. **41**, 2343 (1968); (*b*) H. SHISUKA. Bull. Chem. Soc. Japan. **42**, 52 (1969).
10. R. L. SCHILLER, S. F. LINCOLN, and J. H. COATES. J. Chem. Soc. Faraday Trans. 1, **82**, 2123 (1986).
11. F. CRAMER, W. SAENGER, and H. SPATZ. J. Am. Chem. Soc. **89**, 14 (1967).
12. R. CHENEVERT and G. AMPLEMAN. Can. J. Chem. **65**, 307 (1987).
13. J. J. COSA, H. MENEZ, and C. PREVITALI. Anal. Asoc. Quim. Argentina, **70**, 1 (1982).
14. J. H. FENDLER. Membrane mimetic chemistry. Wiley, New York. 1982. p. 293.
15. J. H. LIU and R. G. WEISS. Isr. J. Chem. **25**, 228 (1985).
16. D. BELLUS. Adv. Photochem. **8**, 109 (1971).
17. G. DOBIS, J. M. PEARSON, and M. SZWARC. J. Am. Chem. Soc. **90**, 278 (1968).
18. Y. WANG and D. F. EATON. Chem. Phys. Lett. **120**, 441 (1985).
19. (*a*) S. L. MUROV. Handbook of photochemistry. Marcel Dekker, Inc., New York. 1973; (*b*) C. G. HATCHARD and C. A. PARKER. Proc. R. Soc. London, A: **235**, 518 (1956).

Can. J. Chem. Downloaded from www.nrcresearchpress.com by 196.1.178.254 on 09/07/12
For personal use only.

Crenuladial, an antimicrobial diterpenoid from the brown alga *Dilophus ligulatus*

C. TRINGALI,[1] G. ORIENTE, AND M. PIATTELLI
Dipartimento di Scienze Chimiche, Viale A. Doria 6, I-95125 Catania, Italy

C. GERACI AND G. NICOLOSI
Istituto del CNR per lo studio delle Sostanze Naturali di Interesse Alimentare e Chimico-farmaceutico, Viale A. Doria 6, I-95125 Catania, Italy

AND

E. BREITMAIER
Institute für Organische Chemie und Biochemie, Gerhard-Domagk-Str. 1, D-53 Bonn 1, West Germany

Received April 26, 1988

C. TRINGALI, G. ORIENTE, M. PIATTELLI, C. GERACI, G. NICOLOSI, and E. BREITMAIER. Can. J. Chem. **66**, 2799 (1988).
From the brown alga *Dilophus ligulatus* a new secondary metabolite with antimicrobial activity, crenuladial **4**, has been isolated and its structure determined.

C. TRINGALI, G. ORIENTE, M. PIATTELLI, C. GERACI, G. NICOLOSI et E. BREITMAIER. Can. J. Chem. **66**, 2799 (1988).
À partir de l'algue brune *Dilophus ligulatus*, on a isolé un nouveau métabolite secondaire qui possède une activité antimicrobienne. Il s'agit du crénuladial **4** dont on a déterminé la structure.

[Traduit par la revue]

Can. J. Chem. Downloaded from www.nrcresearchpress.com by 196.1.178.254 on 09/07/12
For personal use only.

Marine brown algae belonging to the family Dictyotaceae are known to be a rich source of bioactive terpenoids that possibly act as feed deterrent against herbivorous marine animals. Previous work on *Dilophus ligulatus* (Kütz.) Feldm. (Syn. *D. Spiralis* (Montagne) Hamel) has afforded diterpenoids **1**–**3** (1–3), one of which (**2**) possesses antibiotic properties (4). A further secondary metabolite, crenuladial **4**, active against *Aeromonas hydrophila*, *Staphylococcus aureus*, and *Micrococcus luteus*, has been now isolated from the more polar fractions of the chloroform extract of this alga.

Crenuladial **4** was obtained as an optically active oil, $[\alpha]_D$ +27.3°. Its elemental composition was established as $C_{22}H_{34}O_5$ by combustion analysis. In the mass spectrum the molecular ion was not discernible, the ion at highest mass being observed at *m/z* 360 ($M^+ - H_2O$). Diagnostically important fragments were observed at *m/z* 342 ($M^+ - (H_2O \times 2)$), 318 ($M^+ - CH_3COOH$), 300 ($M^+ - H_2O - CH_3COOH$), 282 ($M^+ - (H_2O \times 2) - CH_3COOH$), 109 ($C_8H_{13}$), and 69 ($C_5H_9$); the last two ions were considered to be strongly suggestive, based on the known fragmentation of diterpenoids from Dictyotaceae seaweeds (5, 6), of the 1,5-dimethyl-4-hexen-1-yl side chain. The ir spectrum showed intense hydroxyl (3400 cm^{-1}) and ester (1740 cm^{-1}) absorptions. In both ^1H and ^{13}C nmr spectra of **4** the majority of signals were broadened and ill-defined; the few sharp ones were readily assigned to the terminal portion of the side chain (1.70, s, 3H; 1.61, s, 3H; 5.10, t, 1H; 25.7, q (C-15); 17.7, q (C-16); 131.9, s (C-14); 124.6, d (C-13); 32.0, d (C-10); 25.6, t (C-12)). Signal broadening was substantially affected neither by acetylation (which afforded triacetate **5**, $C_{26}H_{38}O_7$, in the ir spectrum of which the OH absorption had disappeared) nor by measuring the spectra at low (−40°C) or high (100°C) temperature. Also, 2D nmr techniques (H,H and H,C correlations) were moderately informative.

As elucidation of the structure of **4** by spectroscopic means appeared unfeasible, the possibility of chemical correlation to known compounds was considered. The tricyclic nature of **4**, deduced from the molecular formula and ^{13}C nmr data, together with the probable presence of a cyclopropane ring (broad signals at δ 0.01 (H-8a) and 0.92 (H-7), and 8.5 ppm (C-8)) suggested a close relationship with a group of marine diterpenoids (crenulides and crenulacetals (5–8)) isolated from brown algae of the family Dictyotaceae as well as from sea hares that presumably feed on them. That two of these compounds, namely crenulacetals C and D (6), also show severe broadening of the nmr signals due to "mobility" of the conformations of the ring system lent support to the conjecture that crenuladial could be structurally related to them.

Sodium borohydride reduction of **4** gave compound $C_{22}H_{36}O_4$, which exhibited well-defined ^1H and ^{13}C nmr spectra (Tables 1 and 2), interpretable in terms of structure **6**. During the chromatographic purification of **6** on Si gel the formation of a small amount of a dehydration product, **7**, was observed. Definite confirmation of the structure of diol **6** was obtained by acetylation, which afforded triacetate **8**. Identification is based on comparison of ^1H nmr data with those reported in the literature (partial) for a semisynthetic compound obtained from acetoxycrenulide **9**, by reduction ($LiAlH_4$) followed by acetylation (8). This correlation definitely settled the gross structure of **6**, while its stereochemistry remained undefined since the value of the optical rotation of **8** has not been reported. To solve the question, **6** was treated with MnO_2 to give a compound that had physical properties (ms, ir, uv, ^1H and ^{13}C nmr) identical with those of acetoxycrenulide **9** (7, 8). The optical rotation was +21.5°, which closely compares with the value (+20.5°) reported for semisynthetic acetoxycrenulide obtained from the natural 1,9-dihydroxycrenulide by $NaBH_4$ reduction followed by acetylation (8), and therefore the stereochemistry at C-3, -4, -6, -7, and -9 was assumed to be the same.

In the light of the above results, the ^1H and ^{13}C nmr features of **4** could be interpreted as summarized in Tables 1 and 2, and the new algal metabolite described as the cyclic monohydrate of the hypothetical dialdehyde, **10**, that has been proposed as the precursor of crenulacetals (6). The isolated material, although homogeneous in many different chromatographic systems, is actually a mixture of isomers, possibly in equilibrium through the free aldehyde **10**, differing in the stereochemistry at

[1]Author to whom correspondence may be addressed.

Can. J. Chem. Downloaded from www.nrcresearchpress.com by 196.1.178.254 on 09/07/12
For personal use only.

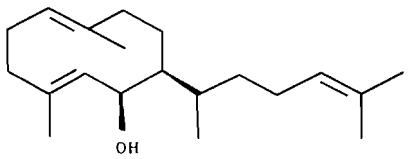

1

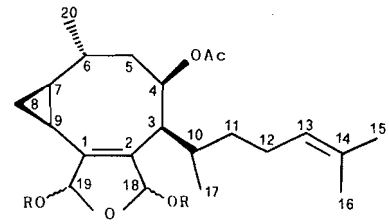

4 R = H

5 R = Ac

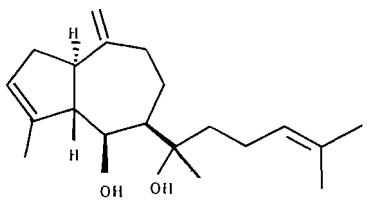

2

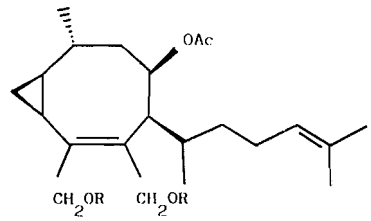

6 R = H

8 R = Ac

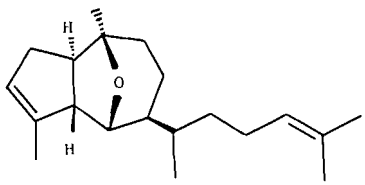

3

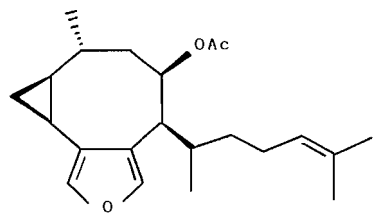

7

C-18 and C-19, as indicated by the presence in the ^{13}C nmr spectrum of no less than four hemiacetal resonances in the range 102–105 ppm.

Experimental

Mass spectral measurements were obtained at 70 eV with a Kratos MS-50S spectrometer. The ir and uv spectra were obtained using Perkin–Elmer 330 and Perkin–Elmer 684 spectrophotometers respectively. Optical rotations were taken on a Beckman DB-GT polarimeter. The alga was collected in February 1986 off the south coast of Sicily (Portopalo).

Isolation of compound 4

Freeze-dried alga (200 g) was extracted three times with CH_2Cl_2. Evaporation of the solvent afforded an oily residue (12 g), which was chromatographed on Si gel (5 × 100 cm; increasing concentrations of Et_2O in C_6H_{14} as the eluent). Fractions of 100 mL were collected and pooled according to their tlc profiles. Compound **4**, eluted in fractions 40–45, was purified by successive chromatographies on LiChroprep Si 60, using as solvent Et_2O–C_6H_{14}, 3:2 vol/vol and then Me_2CO–C_6H_{14}, 1:4 vol/vol, to give 300 mg of pure **4**.

Crenuladial (**4**): $[\alpha]_D$ ($CHCl_3$) +27.3°; ir ν(CCl_4): 3400, 2930, 1740, 1450, 1360, 1250, 1115, 1030, 835 cm^{-1}; hrms, *m/z* calcd. for $C_{22}H_{32}O_4$: 360.2300; found: 360.2305 ($M^+ - H_2O$, 6%); ms, *m/z* (rel. int.): 342 ($M^+ - (H_2O \times 2)$, 2%), 318 ($M^+ - CH_3COOH$, 16%), 300 ($M^+ - CH_3COOH - H_2O$, 13%), 285 ($M^+ - CH_3COOH - H_2O - CH_3$, 13%), 282 (6%), 275 (8%), 257 (11%), 244 (7%), 228 (9%), 218 (28%), 202 (10%), 189 (49%), 176 (18%), 173 (15%), 161 (26%), 159 (16%), 147 (21%), 145 (30%), 133 (24%), 131 (16%), 123 (14%), 121 (15%), 119 (20%), 109 (50%), 105 (26%), 95 (26%), 93 (20%), 91 (33%), 82 (35%), 79 (28%), 69 (100%). *Anal.* calcd. for $C_{22}H_{34}O_5$: C 69.81, H 9.05; found: C 69.85, H 9.08. The ^1H and ^{13}C nmr data are given in Tables 1 and 2.

Acetylation of 4 to give 5

Acetylation (Ac_2O/Py) of **4** (100 mg) and conventional work-up afforded, after chromatographic purification (LiChroprep Si 60, Et_2O/C_6H_{14}, 3:7 vol/vol, as the eluent), 110 mg of triacetate **5**;

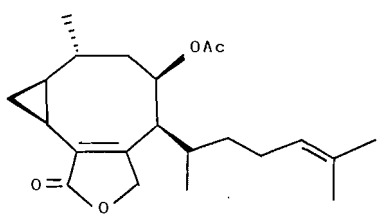

9

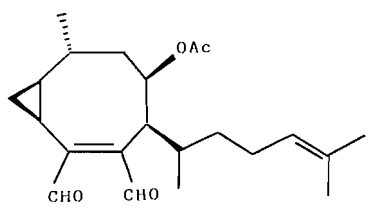

10

TABLE 1. ^{1}H nuclear magnetic resonance data for compounds **4**–**8**[a]

Position	**4**[b]	**5**[b]	**6**[c]	**7**[c]	**8**[c]
3	2.81	3.18	3.12 (d, 11)	2.80 (d, 9)	3.20 (d, 11)
4	5.56	6.00	5.49 (t, 3.5)	5.36 (t, 3.5)	5.36 (t, 3.5)
5a				1.68 (m[e])	[d]
5b			1.75 (dd, 12, 3.5)	1.82 (dd, 15, 3.5)	1.78 (dd, 15, 3.5)
6			1.36 (qdd, 7, 8, 6)	0.89 (m[e])	1.30 (m[e])
7	0.92	0.84	0.85 (m)	0.90 (m[e])	0.88 (m)
8a	0.01	0.02	0.46 (td, 5, 4.6)	0.24 (q, 5)	0.11 (q, 5)
8b			0.76 (td, 9, 4)	0.75 (m)	0.76 (td, 9, 5)
9			1.66 (m[e])	1.62 (m[b])	1.60 (m)
10a			1.56 (m)	1.70 (m[e])	1.68 (m[e])
11a			1.12 (m)	1.13 (m)	0.95 (m[e])
11b				1.45 (m)	1.35 (m[e])
12a	1.85–1.95	1.85–1.95	1.75–1.85 (m[e])	1.65 (m[e])	1.65 (m[e])
12b				1.85 (m)	1.80 (m)
13	5.10 (bt, 7)	5.00 (bt, 7)	5.01 (bt, 7)	5.02 (bt, 7)	5.02 (bt, 7)
15	1.70 (s)	1.62 (s)	1.66 (s)	1.64 (s)	1.66 (s)
16	1.61 (s)	1.53 (s)	1.55 (s)	1.53 (s)	1.57 (s)
17	1.03	0.94	1.04 (d, 7)	1.05 (d, 7)	1.03 (d, 7)
18a	5.51–5.97	6.48–6.82	3.90	7.08 (d, 2)	4.53[f] (bs)
18b			4.26 (AB syst., 12)[f]		
19a	5.51–5.97	6.48–6.82	4.09	7.20 (dd, 2, 1.5)	4.64[f] (bs)
19b			4.35 (AB syst., 12)[f]		
20	1.03	0.94	0.97 (d, 7)	0.91 (d, 7)	0.96 (d, 7)
4-OAc	2.06	1.98 (s)	2.08 (s)	1.94 (s)	1.97 (s)
18-OAc		2.04 (s)			2.03 (s)
19-OAc		2.06 (s)			2.04 (s)

[a]Measured in $CDCl_3$; chemical shifts are δ values, TMS as internal standard. *J* values are given in Hz in parentheses.
[b]Owing to severe broadening and overlapping, only part of the peaks have been assigned.
[c]Assignments were aided by 2D nmr methods.
[d]Chemical shifts could not be determined.
[e]Overlapped with other signals.
[f]Interchangeable.

Can. J. Chem. Downloaded from www.nrcresearchpress.com by 196.1.178.254 on 09/07/12
For personal use only.

ir $\nu(CCl_4)$: 2910, 1740, 1445, 1215, 1175, 1080, 1025, 1000, 965, 925 cm^{-1}; hrms, *m/z* calcd. for $C_{26}H_{38}O_7$: 462.2602; found: 462.2609 (M^+, 0.4%); ms, *m/z* (rel. int.): 402 ($M^+ - CH_3COOH$, 3%), 362 (10%), 342 ($M^+ - (CH_3COOH \times 2)$), 318 (12%), 300 (13%), 283 (22%), 282 (20%), 257 (8%), 245 (8%), 239 (8%), 227 (9%), 218 (16%), 191 (20%), 176 (14%), 161 (13%), 145 (10%), 109 (30%), 105 (12%), 95 (12%), 91 (14%), 69 (75%), 67 (18%), 55 (30%), 43 (100%), 41 (51%). The ^{1}H and ^{13}C nmr data are given in Tables 1 and 2.

*Reduction of **4** to give **6** and **7***

$NaBH_4$ (50 mg) was added to a solution of **4** (50 mg) in EtOH (2 mL) and the mixture kept at room temperature for 4 h. H_2O (2 mL) was added and the solution extracted with Et_2O. The ether extract was evaporated to give a crude product that was purified by chromatography (LiChroprep, Et_2O/C_6H_{14}, 2:3 vol/vol), thus affording 30 mg of pure **6**. In the course of the chromatographic purification of **6** formation of small amounts of the less polar compound **7** was observed.

*Compound **6***: ms, *m/z* (rel. int.): 304 ($M^+ - CH_3COOH$, 2%), 286 ($M^+ - CH_3COOH - H_2O$, 8%), 271 ($M^+ - CH_3COOH - H_2O - CH_3$, 11%), 255 (13%), 243 (10%), 213 (17%), 201 (22%), 175 (58%), 159 (38%), 145 (42%), 133 (41%), 121 (32%), 119 (42%), 109 (100%), 95 (34%), 82 (27%), 69 (61%). The ^{1}H and ^{13}C nmr data are given in Tables 1 and 2.

Compound 7: ms, *m/z* (rel. int.): 344 (M^+, 18%), 302 (4%), 284 ($M^+ - CH_3COOH$, 32%), 269 ($M^+ - CH_3COOH - CH_3$, 24%), 241 (44%), 213 (20%), 202 (100%), 187 (58%), 173 (64%), 159 (40%), 147 (44%), 131 (26%), 119 (26%), 109 (28%), 105 (20%), 101 (22%), 95 (24%), 88 (36%), 81 (22%), 69 (30%). The ^{1}H and ^{13}C nmr data are given in Tables 1 and 2.

*Acetylation of **6** to give **8***

Acetylation (Ac_2O/Py) of **6** (20 mg) gave, after chromatography on LiChroprep Si 60 (Et_2O–C_6H_{14}, 2:3 vol/vol), 18 mg of pure **8**; ms, *m/z* (rel. int.): 328 ($M^+ - (CH_3COOH \times 2)$, 3%), 286 (16%), 271 (11%), 268 (41%), 255 (23%), 253 (47%), 243 (22%), 225 (34%), 215 (20%), 213 (53%), 211 (28%), 200 (30%), 199 (48%), 197 (22%), 189 (26%), 186 (42%), 175 (70%), 173 (52%), 171 (40%), 161 (28%), 159 (70%), 157 (57%), 149 (19%), 147 (37%), 145 (53%), 143 (28%), 133 (33%), 131 (30%), 121 (19%), 119 (37%), 109 (100%), 107 (29%), 105 (27%), 95 (20%), 93 (18%), 82 (24%), 69 (33%), 43 (14%). The ^{13}C nmr data and a full set of ^{1}H nmr data are given in Tables 1 and 2 because those reported in the literature are insufficient.

*MnO_2 oxidation of **6** to give **9***

MnO_2 (60 mg) was added to a solution of **6** (40 mg) in C_6H_{14} (3 mL) and the suspension was stirred overnight at room temperature. The precipitate was filtered off and the solution was evaporated to give 40 mg of residue, which was purified by chromatography (Lichroprep Si 60, Et_2O/C_6H_{14}, 3:7 vol/vol) to give 30 mg of a compound, identified by comparison of its physical properties (uv, ir, ms, ^{1}H and ^{13}C nmr) with those reported in the literature for acetoxycrenulide (**9**); $[\alpha]_D$ +21.5° ($CHCl_3$) (lit. (7) $[\alpha]_D$ +13.0°; (8) $[\alpha]_D$ +13.4°, +20.5°).

Proton and carbon nuclear magnetic resonance spectra

The nmr spectra were recorded at 200 MHz (^{1}H) and 50 MHz (^{13}C), respectively, using a Bruker AC-200 instrument equipped with a carbon-13–proton dual probe head, an Aspect 3000 data system, and a 160 MByte Disk cartridge. One-dimensional proton and carbon-13 Fourier transform nmr spectra with sweep widths and transmitter frequencies optimized for the lowest possible digital resolution

TABLE 2. ^{13}C nuclear magnetic resonance data for compounds **4–8**[a]

Carbon	4	5[b]	6	7	8
1	141.3[c]		142.4[c]	126.4	137.1
2	141.4[c]		142.9[c]	124.7	138.6
3	45.8	47.3	50.0	44.0	50.2
4	74.5	72.2	74.1	70.6	73.0
5	44.5	44.5	45.0	44.3	44.7
6	29.5	31.5[c]	29.2	27.7	29.3
7	26.7[d]		28.7	24.3	28.4
8	8.5	9.0	7.3	10.4	9.4
9	12.9	12.6	20.4	9.8	19.5
10	32.0	32.5[c]	32.7	35.2	32.7
11	34.9	35.5	34.9	35.6	35.0
12	25.6[d]	29.7	24.5	25.3	24.8
13	124.6	124.1	124.3	124.6	124.5
14	131.9	132.0	131.8	131.5	131.5
15	25.7	25.7	25.7	25.7	25.7
16	17.7	17.7	17.6	17.6	17.7
17	16.7	19.4	18.2	17.7	18.1
18	102.2[e] 103.9[e]	101.3[d]	59.9	140.4	61.7
19	104.1[e] 104.7[e]	102.0[d]	64.1	141.0	64.5
20	23.7	23.4	23.3	24.0	23.3
$OCOCH_3$	171.4	169.9	170.0	170.7	170.6
$OCOCH_3$		170.1 (2C)			170.9 (2C)
$OCOCH_3$	21.5	21.2	21.3	21.4	21.0
$OCOCH_3$		21.3			21.3 (2C)
$OCOCH_3$		21.5			

[a]Measured in $CDCl_3$; chemical shifts (δ) are reported in ppm, TMS as internal standard.

[b]Owing to severe broadening, only part of the peaks have been assigned.

[c,d]Values with identical superscript within each column may be interchanged.

[e]At least four discernible peaks are observed in the 102–105 ppm region, attributable to C-18 and C-19 resonances for different stereoisomers.

(Hz/data point) were obtained for 32 K free induction decay signals. Gaussian resolution enhancements for proton nmr and exponential multiplication for carbon-13 nmr were applied before performing Fourier transformations; LB (line broadening) constants were adapted to the digital resolution. Two-dimensional proton–proton shift correlations were performed using the commercially available microprogram COSY without delay. Sine-squared shaping functions without shifts were applied before Fourier transformations in both dimensions. Two-dimensional carbon-13–proton shift correlations were performed using the commercially available microprogram XHCORR by polarization transfer via J_{CH}. Relaxation delays were 0.8 s; incremented delays were adapted to the individual proton chemical shift ranges of each sample, optimized as described above. Polarization transfer delays ($1/2J_{CH}$ = 0.0036 s and $1/2^{2,3}J_{CH}$ = 0.07 s) were adapted to the expected averages of one-bond couplings (J_{CH} = 150 Hz) for CH correlation and two- or three-bond couplings ($^{2,3}J_{CH}$ = 7.5 Hz) for long-range CH correlations. 1024 × 256 data matrices were applied for the carbon-13 and proton chemical shift domains. Shifted ($\pi/4$) sine-squared shaping functions were applied prior to Fourier transformations in both domains.

Antimicrobial activity

In the course of fractionation, antimicrobial activity was followed by the paper disc – agar diffusion assay using *Staphylococcus aureus* as test organism. The minimum inhibitory concentrations (MICs, μg/mL) against *S. aureus* (75), *Micrococcus luteus* (75), and *Aeromonas hydrophyla* (>100) were determined by the conventional agar dilution method for compounds **4–8**. Compounds **5–8** were totally inactive. All test strains were grown in Mueller Hinton medium incubated at 37°C for 18 h.

Acknowledgements

Thanks are due to NATO Scientific Affairs Division (Brussels) and the Ministero della Pubblica Istruzione (Roma) for financial support. We are grateful to Professor L. Mayol (Dipartimento di Sostanze Naturali, Universitá di Napoli) for helpful discussions during this study, and to Mrs. C. Rocco for skilful technical assistance.

1. V. AMICO, G. ORIENTE, M. PIATTELLI, C. TRINGALI, E. FATTORUSSO, S. MAGNO, and L. MAYOL. J. Chem. Soc. Chem. Commun. 1024 (1976).
2. B. DANISE, L. MINALE, R. RICCIO, V. AMICO, G. ORIENTE, M. PIATTELLI, C. TRINGALI, E. FATTORUSSO, S. MAGNO, and L. MAYOL. Experientia, **33**, 413 (1977).
3. V. AMICO, G. ORIENTE, M. PIATTELLI, and C. TRINGALI. Phytochemistry, **18**, 1895 (1979).
4. V. AMICO, R. CHILLEMI, G. ORIENTE, M. PIATTELLI, S. SCIUTO, and C. TRINGALI. Atti del convegno delle Unitá Operative afferenti ai sottoprogetti Risorse Biologiche e Inquinamento Marino. CNR, Rome. 1982. p. 267.
5. M. ISHITSUKA, T. KUSUMI, H. KAKISAWA, Y. KAWAKAMI, Y. NAGAI, and T. SATO. Tetrahedron Lett. **24**, 5117 (1983).
6. T. KUSULI, D. MUANZA-NKONGOLO, M. GOYA, M. ISHITSUKA, T. IWASHITA, and H. KAKISAWA. J. Org. Chem. **51**, 384 (1986).
7. H. H. SUN, F. J. MCENROE, and W. FENICAL. J. Org. Chem. **48**, 1903 (1983).
8. S. L. MIDLAND, R. M. WING, and J. J. SIMS. J. Org. Chem. **48**, 1906 (1983).

Can. J. Chem. Downloaded from www.nrcresearchpress.com by 196.1.178.254 on 09/07/12
For personal use only.

A new dihydrofusarubin O-ethyl ether produced by the fungus *Nectria haematococca* (Berk. and Br.) Wr.

MICHEL BARBIER[1] AND MICHEL DEVYS
Institut de chimie des substances naturelles, Centre national de la recherche scientifique, 91190 Gif sur Yvette, France

AND

DENISE PARISOT
Laboratoire de cryptogamie, Bâtiment 400, Faculté des sciences, 91405, Orsay, France

Received May 5, 1988

MICHEL BARBIER, MICHEL DEVYS, and DENISE PARISOT. Can. J. Chem. **66**, 2803 (1988).

A dihydrofusarubin O-ethyl ether from a strain of the fungus *Nectria haematococca* (Berk. and Br.) Wr. is reported. On the basis of spectrographic data, the stereochemistry **4** is proposed for the pyran ring of this new substance, which thus represents an isomeric form of the previously reported O-ethyl ether **3***b*.

MICHEL BARBIER, MICHEL DEVYS et DENISE PARISOT. Can. J. Chem. **66**, 2803 (1988).

Un éther éthylique de la dihydrofusarubine a été obtenu à partir d'une souche du champignon *Nectria haematococca* (Berk. and Br.) Wr. Sur la base des données spectrographiques, la stéréochimie **4** est proposée pour le cycle pyrannique de cette nouvelle substance qui représente ainsi un isomère de l'éther éthylique précédemment décrit **3***b*.

Can. J. Chem. Downloaded from www.nrcresearchpress.com by 196.1.178.254 on 09/07/12
For personal use only.

Introduction

Nectria haematococca (Berk. and Br.) Wr., the teleomorph of the fungus *Fusarium solani*, produces in vitro a wide series of naphthoquinone pigments related to fusarubin **1**. Over the last six years, we have isolated and identified 12 of these metabolites from selected mutants or the wild strain. Six were new compounds, namely, nectriafurone (1) (the first reported naturally occurring isofuranonaphthoquinone), anhydrofusarubin lactone (1), 5-deoxyfusarubin, 5-deoxyanhydrofusarubin (2), 13-hydroxynorjavanicin (3), and fusarubinoic acid (4). Biosynthetic experiments on 5-deoxyfusarubin and the corresponding anhydro derivative, from *Nectria haematococca*, have shown that these two compounds, and probably the others also, are derived from a heptaketide (2). Indeed, as fusarubinoic acid is probably the initial product arising from cyclization of the heptaketide, it seems likely that it is a common intermediate in the formation of the other metabolites, a hypothesis requiring experimental verification.

Pyranonaphthoquinones of the fusarubin type **1** are typical pigments of *Fusarium* species (5–8) and have shown interesting antibiotic (5–7), insecticidal (9), and phytotoxic (6, 10, 11) activities.

In the present publication, we report on the isolation and properties of a new dihydrofusarubin O-ethyl ether (7, 8, 12) from *Nectria haematococca*.

Results

A new dihydrofusarubin O-ethyl ether was discovered by chance, when anhydrofusarubin epoxide was prepared from an anhydrofusarubin **2** sample previously obtained from *Nectria haematococca*.

Examination by tlc of the product from the reaction between *m*-chloroperbenzoic acid and crude anhydrofusarubin revealed the presence of another metabolite with the same R_f value, which fluoresced in the uv at 366 nm, and was now visible because anhydrofusarubin had been converted to a derivative with different chromatographic behaviour. The epoxidation reaction was unfortunately required for the isolation of the new metabolite, because attempts to separate it from anhydrofusarubin by tlc using a wide variety of solvent systems were unsuccessful. The new substance was obtained in crystalline form, and its structure established through the usual spectrographic methods. The ms spectrum is consistent with the presence of an O-ether group. The molecular ion at m/z 336 is accompanied by characteristic fragments at $M - OCH_2CH_3^+$ and $M - CH_3CH_2OH^+$ (base peak). The uv spectrum is identical to that reported for a dihydrofusarubin O-ethyl ether previously obtained from *Fusarium martii*, and the appearance of signals for the methylene protons for the new substance at 3.50 ppm instead of 5.00 ppm was the only significant difference in their proton nmr spectra. That the newly found dihydrofusarubin O-ethyl ether was different from the previously reported substance was finally confirmed by the rotatory power, determined in the same solvent as published (found, +67 instead of +125).

The agreement between the proton chemical shifts and spin–spin coupling constants for H-3, H-4, H-13, and H-14 of metabolites **4** and **3***b* (7) indicates that the substituents attached to C-4 and C-13 of compound **4** have the same relative configurations as in **3***b*. This and other structural features of the dihydrofusarubins, including evidence that the tetrahydropyran ring exists in a chair conformation, have been reported in detail in previous communications (7, 8). Furthermore, the structural similarity of compounds **4** and **3***b* as established by nmr, combined with the observation that their specific rotations have the same sign but differ in magnitude, indicates that the compounds are diastereoisomers. From the nmr evidence it can be readily deduced that the substituents attached to the ketal centre in compounds **4** and **3***b* have different configurations, thereby establishing structure **4** for the new metabolite.

Experimental

The melting points were determined under the microscope of a Kofler apparatus and are corrected. The ^1H nmr spectrum was obtained with a Bruker 400 MHz apparatus and the ms with an AEI MS 50 spectrometer. The rotatory power was determined with an automatic polarimeter (Perkin–Elmer) and the uv spectrum with a Lambda-5 uv spectrophotometer (Perkin Elmer). Thin-layer chromatography was carried out on Schleicher–Schüll SiO_2 fluorescent films for analytical purposes, and on 20 × 20 cm plates, 1 mm thickness, for preparative

[1]Author to whom correspondence may be addressed.

Printed in Canada / Imprimé au Canada

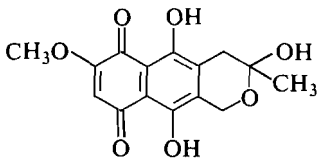

1

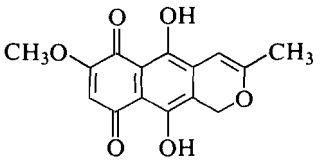

2

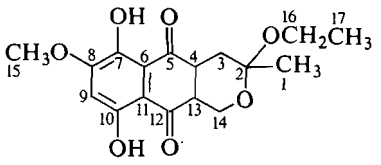

3*a*

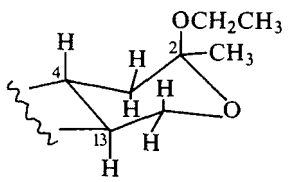

3*b*

rest as in 3*a*

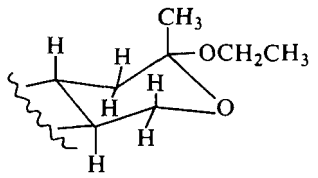

4

use; chromatograms were examined under a Desaga uv lamp at 336 nm in the dark, and the substance was isolated from the scraped SiO_2 layer by extraction with ethyl acetate.

Isolation of the new dihydrofusarubin O-ethyl ether

The "*58*-red" mutant of *Nectria haematococca* was grown at 26°C in the dark for 12 days on synthetic agar medium as previously (1) reported. The agar medium was extracted with acetone and the concentrate reextracted with ethyl acetate according to the method of Bell *et al.* (13). The ethyl acetate residue dissolved in chloroform was applied to a Sephadex LH-20 column packed in $CHCl_3$–MeOH, 49:1, and the pigments were eluted with this same solvent (1). The first fraction to be eluted was a violet product containing anhydrofusarubin (**2**) as the major compound. The new dihydrofusarubin O-ethyl ether was isolated from this fraction after epoxidation. One hundred milligrams of isolated fraction **2** were dissolved in 5 mL anhydrous $HCCl_3$ and 150 mg of *m*-chloroperbenzoic acid in 2 mL $CHCl_3$ were added. The reaction mixture was kept at 0°C and the epoxidation was followed by tlc (hexane–CH_2Cl_2–MeOH 29:29:2), starting anhydrofusarubin R_f 0.60. The reaction was found to be complete after 6 h, showing the presence of a fluorescent spot in uv at the R_f of the now absent violet anhydrofusarubin **2**. (The corresponding epoxide, ms *m/z* 304, was found at R_f 0.30 as a red product.) After this reaction, the dihydrofusarubin O-ethyl ether was isolated by preparative tlc in the same solvent system; yield 4 mg (representing 4% of the mixture).

Physical properties of the isolated substance

The orange product was crystallized from CH_2Cl_2, giving small orange-red prisms, mp 137–141°C (2 mg); uv ($CHCl_3$), λ_{max}, nm (log ε): 242 (4.2), 275 (3.70), 305 (3.65), 390 (3.70), with shoulders at 370 and 415; ^1H nmr ($CDCl_3$, TMS reference), δ ppm: 1.47 (CH_3, C-1, 3H, s), 2.40 (H-C3, 1H, dd, $J_{ax} - J_{eq}$ 15 Hz, $J_{ax} - J_{H\text{-}C4}$ 12 Hz), 1.80 (H-C3, dd, $J_{eq} - J_{H\text{-}C4}$ 4 Hz), 3.50 (H-C4, 1H, ddd, $J_{H\text{-}C4}/J_{H\text{-}C13}$ 13 Hz), 12.0 (phenolic proton at C-7, 1H, s), 3.95 (OCH_3 at C-8, 3H, s), 6.60 (H-C9, 1H, s), 12.10 (phenolic proton at H-C10, 1H, s), 2.97 (H-C13, 1H, ddd), 3.80 (H-C14, 1H, dd, $J_{ax} - J_{eq}$ 13 Hz, $J_{ax}/J_{H\text{-}C13}$ 7 Hz, $J_{eq}/J_{H\text{-}C13}$ 5 Hz), 4.20 (H-C14, 1H, dd, $J_{eq}/J_{H\text{-}C13}$ 5 Hz), 3.50 (q, 2H, CH_2 at C-16, $J_{H\text{-}C16}/J_{H\text{-}C17}$ 6 Hz), 1.20 (t, 3H, CH_3 at C-17, $J_{H\text{-}C17}/J_{H\text{-}C16}$ 6 Hz. ms *m/z*: 336, 8%, M^+ ($C_{17}H_{20}O_7$); 291 $(M - OC_2H_5)^+$, 46%; 290 $(M - C_2H_5OH)^+$, 100%.

The minute amounts of substance that we were able to isolate did not permit determination of the ^{13}C nmr spectra.

The numbering system used in this publication corresponds to the natural (heptaketide) origin of the molecule.

Acknowledgements

Thanks are due to Drs. B. C. Das and C. Girard for mass spectrometric determinations, and to Mrs. M. Maugin (Orsay) and L. Quaino (Gif sur Yvette) for their expert technical assistance.

1. D. Parisot, M. Devys, J. P. Férézou, and M. Barbier. Phytochemistry, **22**, 1301 (1983).
2. D. Parisot, M. Devys, and M. Barbier. Phytochemistry, **24**, 1977 (1985).
3. D. Parisot, M. Devys, and M. Barbier. Microbios Lett. **36**, 129 (1987).
4. D. Parisot, M. Devys, and M. Barbier. Phytochemistry, **27**, 3002 (1988).
5. H. R. V. Arnstein, A. H. Cook, and M. S. Lacey. Nature, **157**, 333 (1946).
6. H. Kern. Ann. Phytopathol. **10**, 327 (1978).
7. I. Kurobane, N. Zaita, and A. Fukuda. Antibiot. **39**, 205 (1986).
8. I. Kurobane, L. C. Vining, A. G. McInnes, and D. G. Smith. Can. J. Chem. **56**, 1593 (1978).
9. N. Claydon, J. F. Grove, and M. Pople. J. Invertebr. Pathol. **30**, 216 (1977).
10. R. A. Baker, J. H. Tatum, and S. Nemec, Jr. Phytopathology, **71**, 951 (1981).
11. J. Marcinkowska, J. M. Kraft, and L. Y. Marquis. Can. J. Plant Sci. **62**, 1027 (1982).
12. I. Kurobane, L. C. Vining, A. G. McInnes, and N. N. Gerber. J. Antibiot. **33**, 1376 (1980).
13. A. A. Bell, R. D. Stipanovic, and J. E. Puhalla. Tetrahedron, **32**, 1353 (1976).

Can. J. Chem. Downloaded from www.nrcresearchpress.com by 196.1.178.254 on 09/07/12
For personal use only.

Synthesis of cedranoid sesquiterpenes. V. The biotols[1]

PETER YATES,[2] RUPINDER S. GREWAL, PETER C. HAYES, AND JEFFERY F. SAWYER
Lash Miller Chemical Laboratories, University of Toronto, Toronto, Ont., Canada M5S 1A1

Received April 7, 1988

PETER YATES, RUPINDER S. GREWAL, PETER C. HAYES, and JEFFERY F. SAWYER. Can. J. Chem. **66**, 2805 (1988).

Reduction of dimethyl 3-hydroxy-4,4,8-trimethyl-6-oxo-*cis*-bicyclo[3.3.0]octa-2,7-diene-1,2-dicarboxylate (**8**) with lithium and ammonia gives dimethyl 3-hydroxy-4,4,*exo*-8-trimethyl-6-oxo-*cis*-bicyclo[3.3.0]oct-2-ene-1,2-dicarboxylate (**9**), which on acetylation, reduction with sodium borohydride, and methanolysis gives dimethyl 3,*exo*-6-dihydroxy-4,4,*exo*-8-trimethyl-*cis*-bicyclo[3.3.0]oct-2-ene-1,2-dicarboxylate (**12**). This on 2-decarbomethoxylation followed by treatment with lithium acetylide in the presence of cerium trichloride gives methyl 3-ethynyl-3,*exo*-6-dihydroxy-4,4,*exo*-8-trimethyl-*cis*-bicyclo[3.3.0]octane-1-carboxylate (**21**), which on hydration, diacetylation, and treatment with tri-*n*-butyltin hydride and azoisobutyronitrile is converted to methyl *exo*-6-acetoxy-3-acetyl-4,4,*exo*-8-trimethyl-*cis*-bicyclo[3.3.0]octane-1-carboxylate (**31**). Methanolysis of **31**. *tert*-butyldimethylsilylation, and reaction with potassium *tert*-butoxide in *tert*-butyl alcohol gives *exo*-4-*tert*-butyldimethylsilyloxy-*exo*-2,6,6-trimethyl[5.3.1^{1,5}]undecane-8,10-dione (**35**). This on treatment with lithium aluminum hydride followed by oxidation and hydrogenation provides the corresponding 10-deoxo compound, **39**. Reaction of this with methyllithium, dehydration, and desilylation with hydrogen fluoride in acetonitrile gives a mixture of (±)-α-biotol (**1**) and (±)-β-biotol (**2**); desilylation with hydrogen chloride in methanol gives solely (±)-**1**.

PETER YATES, RUPINDER S. GREWAL, PETER C. HAYES et JEFFERY F. SAWYER. Can. J. Chem. **66**, 2805 (1988).

La réduction de l'hydroxy-3 triméthyl-4,4,8 oxo-6 bicyclo[3.3.0]octadiène-2,7 dicarboxylate-1,2 de diméthyle *cis* (**8**) par le lithium et l'ammoniac conduit à l'hydroxy-3 triméthyl-4,4,8-*exo* oxo-6 bicyclo[3.3.0]octène-2 dicarboxylate-1,2 de diméthyle *cis* (**9**) qui, par une acétylation suivie d'une réduction par le borohydrure de sodium et d'une méthanolyse, conduit au dihydroxy-3,6-*exo* triméthyl-4,4,8-*exo* bicyclo[3.3.0]octène-2 dicarboxylate-1,2 de diméthyle *cis* (**12**). Ce composé, par une décarboxyméthylation en 2 suivie d'un traitement par l'acétylure de lithium en présence de trichlorure cérique, fournit l'éthynyl-3 dihydroxy-3,6-*exo* triméthyl-4,4,8-*exo* bicyclo[3.3.0]octane carboxylate-1 de méthyle (**21**) qui, par une hydration suivie d'une diacétylation et d'un traitement par l'hydrure de tri-*n*-butylétain et l'azoisobutyronitrile, est transformé en acétoxy-6-*exo* acétyl-3 triméthyl-4,4,8-*exo* bicyclo[3.3.0]octane carboxylate-1 de méthyle (**31**). La méthanolyse du produit **31**, suivie d'une *tert*-butyldiméthylsilylation et d'une réaction avec le *tert*-butylate de potassium dans l'alcool *tert*-butylique, fournit le *tert*-butyldiméthylsilyloxy-4-*exo* triméthyl-2-*exo*-6,6 [5.3.1^{1,5}]undécanedione-8,10 (**35**). Ce composé, soumis à un traitement par l'hydrure double de lithium et d'aluminium, puis à une oxydation et une hydrogénation, conduit au composé désoxo-10 correspondant, **39**. La réaction du composé **39** avec le méthyllithium, suivie d'une déshydratation et d'une désilylation par le fluorure d'hydrogène dans l'acétonitrile, livre un mélange des (±)-α-biotol (**1**) et (±)-β-biotol (**2**); une désilylation par le chlorure d'hydrogène dans le méthanol ne conduit qu'au (±)-**1**.

[Traduit par la revue]

Can. J. Chem. Downloaded from www.nrcresearchpress.com by 196.1.178.254 on 09/07/12
For personal use only.

Introduction

α-Biotol (**1**) and β-biotol (**2**), the *exo*-4-hydroxy derivatives of the prototypical cedranoid sesquiterpenes, α-cedrene (**3**) and β-cedrene (**4**), respectively (3), were isolated in 1968 from the alcoholic portion of the essential oil of the wood of *Biota orientalis* (4). These alcohols are minor components of the oil, cedrol (**5**) being one of the major components. Their gross structures were assigned on the basis of chemical and spectroscopic methods (4). To establish the relative stereochemistry at C-4, α-biotone (**6**), formed by oxidation of **1**, was reduced with sodium borohydride to a mixture of **1** and 4-epi-α-biotol (**7**).

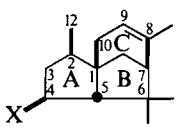

1 X = OH
3 X = H

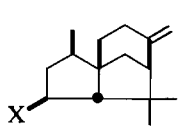

2 X = OH
4 X = H

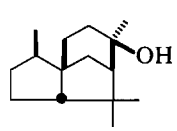

5

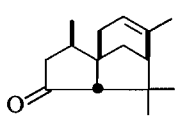

6

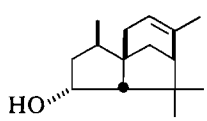

7

[1]For paper IV, see ref. 1; for a preliminary communication concerning part of this work, see ref. 2.

[2]Author to whom correspondence may be addressed.

Comparison of the ^{1}H nmr chemical shifts for the C-12 methyl group in the two epimeric alcohols with that for α-cedrene suggested the configurations at C-4 in **1** and **7** to be those shown.

Four partial syntheses of **1** or **7** have been reported (5–9), but there have been no previous total syntheses of the biotols. We describe here total syntheses of (±)-α- and (±)-β-biotol by a route that we have designed for the synthesis of cedranoid sesquiterpenes of various levels of oxidation — a pathway that we have earlier used in a new synthesis of α-cedrene (10).

Results and discussion

Rings A and B. Construction of bicyclo[3.3.0]octanone 13

The key step in our route to the bicyclo[3.3.0]octane system of rings A and B is the photosensitized oxa-di-π-methane rearrangement of a bicyclo[2.2.2]octanone to a tricyclo [3.2.1.0^{2,8}]octanone. The utilization of this reaction in the synthesis of the bicyclo[3.3.0]octanone **8** has been reported earlier from these Laboratories (11).

Compound **8** was converted to the ketol **13** by the route shown in Scheme 1; the gross structural assignments for compounds **9**–**13** were corroborated by their ir, ^{1}H nmr, and ^{13}C nmr spectra[3] (see Experimental). Reduction of **8** with lithium/ammonia gave the dihydro compound **9**. The ^{1}H and ^{13}C nmr spectra of this product showed that it exists in solution in $CDCl_3$

[3]The ^{13}C nmr spectroscopic assignments will be discussed elsewhere.

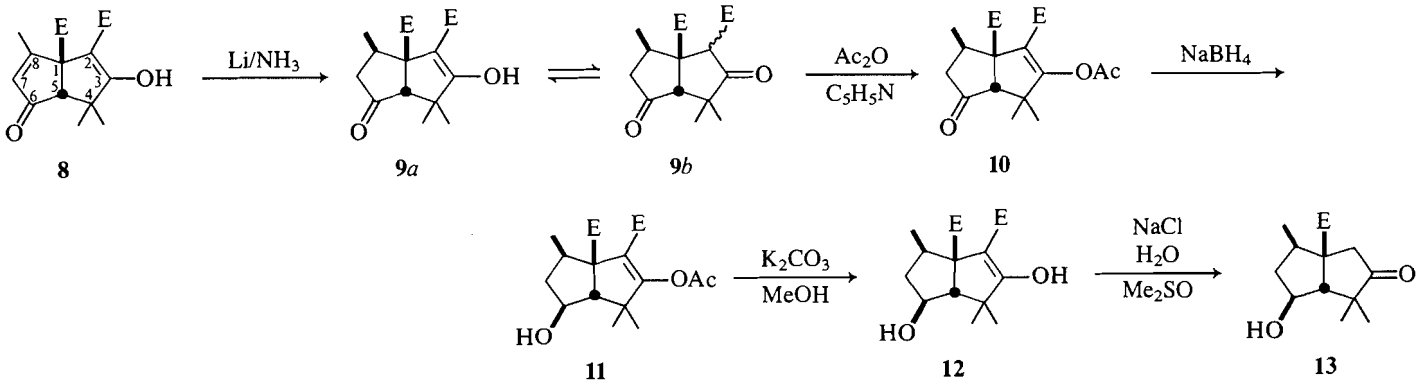

SCHEME 1

as a mixture of the enol and keto tautomers **9***a* and **9***b*, with the latter predominating. This is uncommon, since we have usually observed in the cases of related dimethyl 3-oxobicyclo[3.3.0]octane-1,2-dicarboxylates prepared in this and earlier work (10, 11) that the enol forms are so predominant that the keto forms cannot be detected spectroscopically.

Compound **9** was converted with acetic anhydride and pyridine to the enol acetate **10** to protect the C-3 carbonyl group so that the C-6 carbonyl group could be reduced selectively. This reduction was carried out with sodium borohydride in methanol to give a single product **11** in quantitative yield. Compound **11** in methanol was treated with potassium carbonate to give **12**, whose ^{1}H nmr spectrum showed the presence of the enol tautomer alone. Monodecarbomethoxylation of **12** with sodium chloride and wet dimethyl sulfoxide (12) gave hydroxy keto ester **13**.

The relative configuration of compound **13**, and thus the relative configurations of compounds **8**–**12** also, was established by X-ray crystallography (1). The *exo* disposition of the C-8 methyl group was expected on the basis of our earlier work (11). However, the *exo* disposition of the C-6 hydroxyl group was not anticipated. This showed that the sodium borohydride reduction of **10** gave a product with an *exo* hydroxyl group. In general, such reactions of bicyclo[3.3.0]octan-2-ones proceed with preferential attack on the *exo* face of the ketone to give the *endo* alcohol (13). The exclusive formation of the *exo* product in the case of **10** may result from two factors: (*i*) reduced steric hindrance to *endo* attack because of an increased fold angle between the rings resulting from the presence of the ethylenic bond, and (*ii*) increased hindrance to *exo* attack because of the *exo* C-8 methyl group (1). These factors apply only if this methyl group has a pseudoaxial disposition and the *endo* geminal methyl group a pseudoequatorial disposition, as shown in **14**.

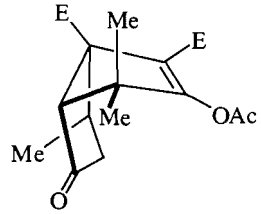

14

For spectroscopic comparison, we converted **13** to its C-6 epimer **15** by treatment with triphenylphosphine, benzoic acid, and diethyl azodicarboxylate (14) followed by methanolysis (Scheme 2). The ir and ^{1}H nmr spectra of **13** and **15** may be

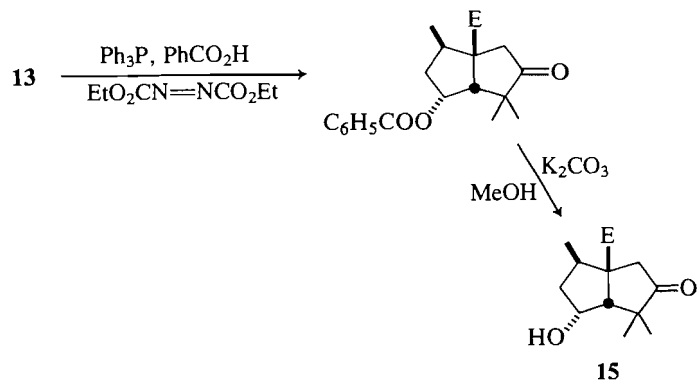

SCHEME 2

compared with those of the *endo*-6-hydroxy-*endo*-8-methyl isomer **18**, which was obtained previously (11) by the route shown in Scheme 3. It may be noted that in this case sodium borohydride reduction of the α,β-unsaturated ketone **16** (carried out in the presence of cerium trichloride (15)) gave alcohol **17**. This diastereomer, whose relative configuration was established by an X-ray crystallographic determination of the relative configuration of **18** (1), was the only product detected. The contrasting stereochemical course of this reduction reaction relative to the stereochemical course of the sodium borohydride reduction of **10** is attributable to the planarity of the enone ring in **16**.

Comparison of the ^{1}H nmr spectra of **13** and **15** shows that the C-6 proton signal of **13** appears at higher field than that in **15** ($\Delta\delta = 0.33$). This is analogous to the case of the *exo* and *endo* bicyclo[3.3.0]octan-2-ols, **19** and **20** (13*b*), where the signal of the *endo*-2 proton of **19** appears at δ 3.73 while that of the *exo*-2 proton of **20** appears at δ 4.09 ($\Delta\delta = 0.36$).

Construction of ring C. Synthesis of the tricyclic β-diketone 35

Our next aim was to add a two-carbon chain at C-3 in the hydroxy ketone **13** that would permit closure of ring C in the biotols. This was first attempted with lithium acetylide as in the synthesis of α-cedrene (10); however, only starting material was recovered. Lithium acetylide – ethylenediamine complex (16) was also without effect. It is considered that these reactions were unsuccessful because of the formation of the lithium enolate of **13**, which returned the starting material upon work-up.

Recent observations by Imamoto *et al.* (17) have provided a solution to problems encountered during attempted nucleophilic addition to readily enolizable ketones. They found that organocerium reagents react cleanly with easily enolizable ketones to

Can. J. Chem. Downloaded from www.nrcresearchpress.com by 196.1.178.254 on 09/07/12
For personal use only.

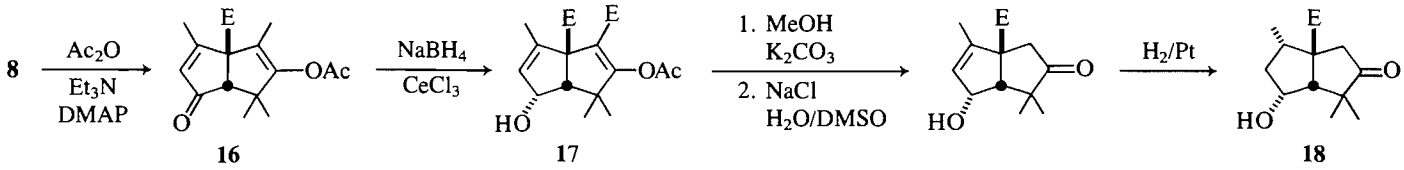

SCHEME 3

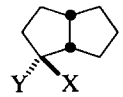

19 X = OH, Y = H
20 X = H, Y = OH

afford addition products. In the present case the organocerium reagent was prepared by reaction of lithium acetylide (prepared from *n*-butyllithium and acetylene) with anhydrous cerium(III) chloride at −78°C in tetrahydrofuran. Reaction of this with hydroxy ketone **13** gave the propargylic alcohol **21** in 73% yield. At least two equivalents of the reagent had to be used since the hydroxyl substituent reacts with one equivalent. The structure of this product was established by comparison of its ir and ^{1}H nmr spectra with those of the analogous propargylic alcohol **23**, which was an intermediate in the synthesis of α-cedrene (10) (Table 1).

The relative configuration at C-3 in **21** was not established. It is thought to involve the *exo* placement of the ethynyl group, resulting from attack of acetylide on the *exo* face of the bicyclic system. However, this is of no consequence insofar as the final synthetic goals are concerned. Terashima and co-workers (18) have used 2-trimethylsilylethynylcerium(III) to synthesize propargylic alcohols from ketones and we investigated its use in the present case. However, treatment of **13** with this reagent gave the *bis* adduct **22** rather than the (trimethylsilyl)ethynyl analogue of **21** (Scheme 4).

The identity of compound **22** was established from its composition, $C_{22}H_{36}O_3Si_2$, and its spectra. Its ir spectrum shows a hydroxyl-stretching band at 3.15 μm and a weak band at 4.68 μm attributable to the acetylenic-stretching vibration. It also exhibits a carbonyl-stretching band at 5.76 μm. However, there was no signal corresponding to a methoxyl group in either the ir or nmr spectra. The ^{1}H nmr spectrum of **22** shows two distinct nine-hydrogen singlets at δ 0.15 and 0.16, indicating the presence of two trimethylsilyl groups. Three signals corresponding to the C-methyl groups appear at δ 1.04 (s), 1.18 (s), and 1.30 (d, J = 6.8 Hz). Two broad one-proton singlets at δ 1.56 and 3.70 are attributable to two hydroxyl protons, as

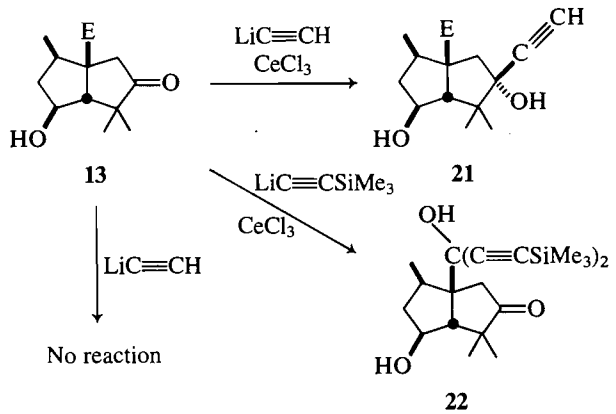

SCHEME 4

TABLE 1. The ir and ^{1}H nmr spectra of compounds **21** and **23**

	21	**23**[b]
λ_{max} ($CHCl_3$)		
	3.11 (m)	2.79 (m)
	5.80 (s)	5.81 (s)
$^H\delta$($CDCl_3$)[a]		
H-2	1.95 (d, 14.8)	2.03 (d, 14)
	2.72 (d, 14.8)	2.18 (d, 14)
H-5	2.45 (d, 7.7)	1.2–2.3 (m)
H-6	4.52 (m)	
H-7	1.5–2.2 (m)	
H-8		
CH	2.49 (s)	2.47 (s)
CH_3(4)	0.98 (s), 1.21 (s)	1.00 (s), 1.07 (s)
CH_3(8)	0.85 (d, 6.9)	0.87 (d, 7)
OCH_3	3.69 (s)	3.67 (s)
OH(3)	*c*	*c*
OH(6)	*c*	—

[a]The nmr spectra were recorded at 200 or 400 MHz unless otherwise indicated; their signals have relative areas in accord with the assignments; J values are given in Hz.
[b]The nmr spectrum of **23** was recorded at 60 MHz (10).
[c]The OH proton signals overlap with the CH multiplets at δ ~ 2.

confirmed by their absence after deuterium exchange. The ^{13}C nmr spectrum shows 18 signals; the SFORD spectrum includes quartets at δ −0.4 and −0.5 ppm, attributable to the methyl groups of the two trimethylsilyl groups, and four singlets at δ 89.8, 90.8, 104.6, and 105.7, assignable to the four acetylenic carbons.

This product must result from attack of the cerium reagent at the carbonyl group of the ester, followed by further attack of the reagent on the resulting acetylenic ketone (an excess of the reagent was used). It is interesting to find that this reagent, unlike lithium acetylide, attacks the ester group, although both reactions were carried out under similar conditions. The reason for the preferred attack at the ester rather than the ketone group is uncertain; it may involve prior complexation of the silicon atom with the oxygen atom of the ketonic carbonyl or the methoxyl group.

Our next aim was to convert the propargylic alcohol **21** to the methyl ketone **32** preparatory to closure of ring C. In our synthesis of α-cedrene (10) the analogous transformation of **23** to **25** had been carried out by the route shown in Scheme 5. However, this route is made unattractive by the low yield in the conversion of **23** to **24**, which results from competing methyl migration. We therefore adopted an alternative route in which **21** was converted to **26** by mercuric oxide-catalyzed hydration, which in turn was acetylated with acetic anhydride/DMAP to give the diacetate **27** (with acetic anhydride/pyridine, **26** gave

Can. J. Chem. Downloaded from www.nrcresearchpress.com by 196.1.178.254 on 09/07/12
For personal use only.

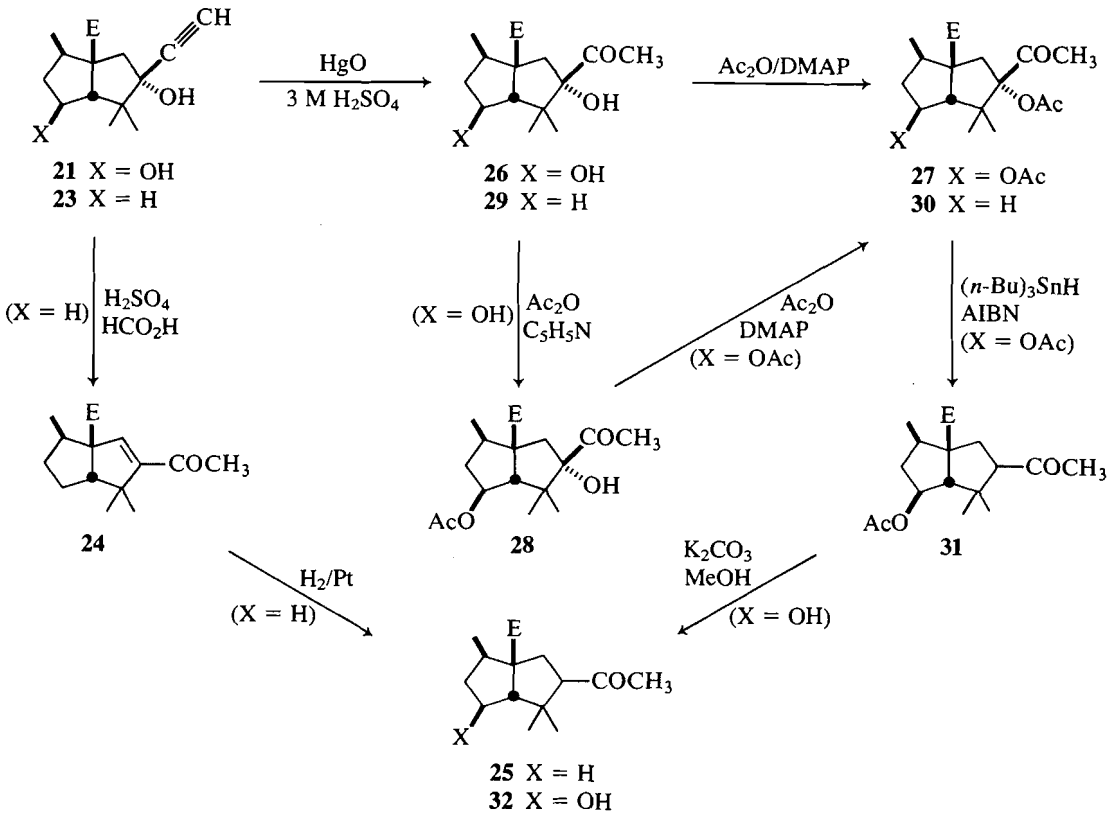

SCHEME 5

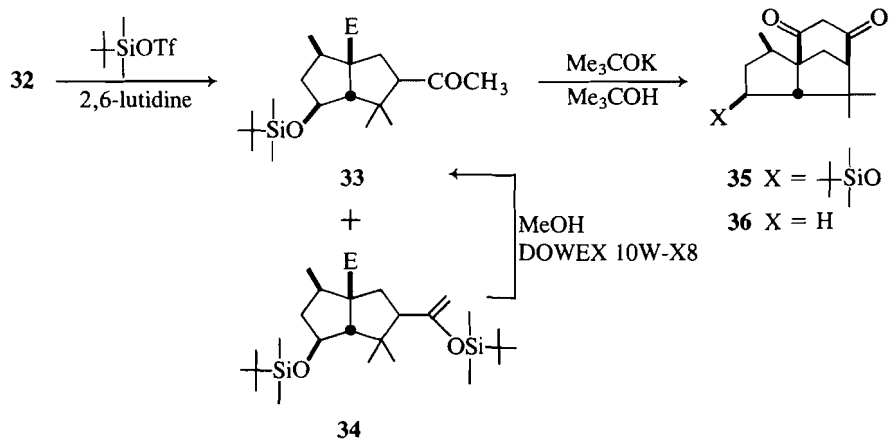

SCHEME 6

the monoacetate **28**; this could be converted to **27** with acetic anhydride/DMAP).

It was next necessary to remove selectively the 3-acetoxyl group of **27**. We had previously unsuccessfully attempted to carry out in the α-cedrene series (10, 19) an analogous transformation of **30**, the acetate of **29**, the hydration product of **23**. Treatment of **30** with a variety of reducing agents had been tried, including zinc and acid and chromous salts. In the case of **27**, amalgamated zinc and calcium/ammonia (20) were tried with equal lack of success. However, treatment of **27** with tri-*n*-butyltin hydride in the presence of azoisobutyronitrile (AIBN) in boiling toluene (21) gave the desired reduction product **31** in high yield, which was converted to the corresponding alcohol **32**.

The gross structures assigned to compounds **26**–**28** and **31** and **32** are confirmed by their ir and ^{1}H nmr spectra and their ^{13}C nmr spectra[3] and the relationship of these to the spectra of compounds **29** and **30** (Tables 2 and 3). Their relative configurations follow from that assigned to their precursor **13** (*vide supra*). No assignment of stereochemistry is made at C-3 in compounds **31** and **32**, but as will be seen from the sequel this is not critical.

It was planned to close ring C via a base-catalyzed intramolecular Claisen condensation involving the δ-keto ester system of **32**, as utilized originally by Stork and Clarke (22) and later by Yates and Stevens (10) in the synthesis of α-cedrene. However, it seemed wise to protect first the hydroxyl groups of **32**; this was done by treatment with *tert*-butyldimethylsilyl triflate and

Can. J. Chem. Downloaded from www.nrcresearchpress.com by 196.1.178.254 on 09/07/12
For personal use only.

TABLE 2. The ir and ^{1}H nmr spectra of compounds **26–29**

	26	**27**	**28**[b]	**29**[b]
λ_{max} ($CHCl_3$)				
	3.06 (w)		3.04 (w)	2.94 (m)
	5.84 (s), 5.92 (s)	5.79 (s)	5.79 (s)	5.85 (s), 5.90 (sh)
$^H\delta(CDCl_3)$[a,c]				
H-2	1.72 (d, 14.6)	1.6–2.2 (m)*	1.6–2.3 (m)*	1.82 (d, 14.5)
	3.02 (dd, 14.6, 1.7)	3.35 (d, 16.2)	3.05 (d, 14.8)	3.14 (dd, 14.5, 1.5)
H-5	2.35 (d, 7.3)	2.83 (d, 8.1)	2.67 (d, 6.4)	
H-6	4.58 (m)	4.91 (ddd, 10.3, 8.3, 6.1)	5.50 (m)	
H-7	1.2–2.0 (m)	1.6–2.2 (m)	1.6–2.3 (m)*	1.45–2.7 (m)
H-8				
CH_3(4)	0.89 (s)	0.81 (s)	0.99 (s)	0.92 (s)
	1.02 (s)	1.17 (s)	1.07 (s)	0.96 (s)
CH_3(8)	0.82 (d, 6.9)	0.90 (d, 6.7)	0.87 (d, 6.4)	0.90 (d, 7.0)
$COCH_3$	2.23 (s)	2.16 (s)	2.26 (s)	2.27 (s)
$OCOCH_3$	—	2.07 (s)	2.02 (s)	—
		2.11 (s)		
OCH_3	3.69 (s)	3.74 (s)	3.73 (s)	3.70 (s)
OH(3)	3.49 (d, 1.7)	—	1.6–2.3 (m)*	3.38 (d, 1.5)
OH(6)	1.57 (br s)	—	—	—

[a]See footnote *a* in Table 1.
[b]The nmr spectra of **28** and **29** were recorded at 60 MHz (10).
[c]Overlapping signals are marked with asterisks.

TABLE 3. The ir and ^{1}H nmr spectra of compounds **30–33**

	30[b]	**31**	**32**[b]	**33**[c]
λ_{max} ($CHCl_3$)				
			3.13 (w)	
	5.82 (s)	5.79 (s)	5.82 (s)	5.80 (s)
$^H\delta(CDCl_3)$[a]				
H-2	2.16 (d, 16)	1.5–1.7 (m)*	1.5–2.0 (m)*	1.5–1.9 (m)*
	3.41 (d, 16)			
H-3	—	2.45–2.7 (m)	2.5–2.7 (m)	2.55–2.65 (m)
H-5	2.6–3.1 (m)			
H-6		4.91 (ddd, 10.3, 8.3, 5.8)	4.07 (m)	3.99 (ddd, 9.9, 7.7, 5.9)
H-7	1.4–2.2 (m)	1.5–1.7 (m)*	1.5–2.0 (m)*	1.5–1.9 (m)*
H-8				
CH_3(4)	0.79 (s)	0.74 (s)	0.84 (s)	0.78 (s)
CH_3(4)	1.16 (s)	1.07 (s)	1.31 (s)	1.22 (s)
CH_3(8)	0.90 (d, 6.5)	0.86 (d, 6.8)	0.92 (d, 6.0)	0.90 (d, 6.7)
$COCH_3$	2.11 (s)	1.98 (s)	2.17 (s)	2.15 (s)
$OCOCH_3$		2.08 (s)	—	—
OCH_3	3.71 (s)	3.65 (s)	3.71 (s)	3.70 (s)
OH	—	—	1.5–2.0 (m)*	—

[a]See footnotes *a* and *c* in Table 2.
[b]The nmr spectra of **30** (10) and **32** were recorded at 60 MHz.
[c]For $(CH_3)_2Si$ and $(CH_3)_3CSi$, δ = 0.06 (s) and 0.87 (s), respectively.

2,6-lutidine at 0°C to give **33**,[4] whose spectra are compared with those of **32** in Table 3. Reaction of **33** with potassium *tert*-butoxide in *tert*-butyl alcohol gave the tricyclic β-diketone **35** (Scheme 6), whose ir and ^{1}H nmr spectra are given in Table 4. These show that **35** exists in deuterochloroform as the unenolized form, giving rise in its ^{1}H nmr spectrum to two doublets for the two nonequivalent protons on the α-methylene group of the β-diketone system. The analogous β-diketone **36** prepared in the synthesis of α-cedrene similarly exists in the unenolized form, but in this case the analogous methylene

[4]When the reaction was carried out at room temperature a mixture of **33** and the disilyloxy compound **34** was obtained; the latter could be converted to **33** by methanolysis.

Can. J. Chem. Downloaded from www.nrcresearchpress.com by 196.1.178.254 on 09/07/12
For personal use only.

TABLE 4. The ir and ^1H nmr spectra of compounds **35**, **39**, and **40**

	35	**39**	**40**
λ_{max} ($CHCl_3$)			
	5.78 (s), 5.85 (s)	5.88 (s)	3.08 (w)
$^H\delta(CDCl_3)$[a]			
H-2	1.9–2.0 (m)*		
		1.8–1.9 (m)*	1.6–1.75 (m)*
H-3	1.88 (ddd, 12.4, 10.4, 9.6)		
	2.08 (dt, 10.4, 5.2)	2.07 (dt, 11.2, 5.6)	1.93 (dt, 10.4, 5.2)
H-4	4.23 (ddd, 9.6, 7.8, 5.4)	4.13 (ddd, 9.2, 8.0, 5.2)	4.01 (ddd, 9.3, 8.1, 5.3)
H-5	2.16 (d, 7.8)	1.96 (d, 8.0)	1.72 (d, 8.3)
H-7	2.61 (d, 3.7)	2.31 (d, 4.2)	1.6–1.75 (m)*
H-9	3.19 (d, 21.3)	2.38 (m)	
	3.29 (d, 21.3)	2.47 (dd, 18.3, 7.8)	
H-10	—	1.5–1.7 (m)	1.35–1.5 (m)
H-11	1.9–2.0 (m)*		
	2.21 (d, 13.4)	1.8–1.9 (m)*	
CH_3(2)	1.29 (d, 6.8)	0.95 (d, 7.1)	0.87 (d, 7.6)
CH_3(6)	1.09 (s), 1.21 (s)	1.06 (s), 1.12 (s)	1.09 (s), 1.23 (s)
CH_3(8)	—	—	1.35 (s)
$(CH_3)_2Si$	0.05 (s), 0.07 (s)	0.05 (s), 0.08 (s)	0.03 (s), 0.06 (s)
$(CH_3)_3CSi$	0.86 (s)	0.88 (s)	0.86 (s)
OH	—	—	1.55 (br s)

[a]See footnotes *a* and *c* in Table 2.

protons give rise to a singlet (10), presumably because of a greater rate of exchange.

It may be noted that the formation of such a product is possible, whatever the configuration at C-3 in **33**, since equilibration of the *trans* acetyl ester to the *cis* acetyl ester can occur under the reaction conditions.

Manipulation of Ring C. Synthesis of the biotols

Following the procedure of Stork and Clarke (22) in the cedrene series, we treated **35** with lithium aluminum hydride in boiling ether and were happy to find that the somewhat unusual course of reduction observed by these workers in the case of **36** was duplicated, giving a mixture of the allylic and saturated alcohols, **37** and **38**, respectively (Scheme 7). Oxidation of this mixture with chromium trioxide – pyridine followed by hydrogenation gave the single saturated ketone **39**. This was treated with methyllithium to give the cedrol analogue **40**. The relative configuration at C-8 was assigned as shown, based on analogy with previously observed conversion of **36** to cedrol (**5**) itself by this route (22).

Dehydration of **40** with thionyl chloride and pyridine gave a mixture of the endocyclic and exocyclic alkenes **41** and **42**, which upon desilylation with hydrogen fluoride in acetonitrile gave a 2:1 mixture of (±)-α-biotol (**1**) and (±)-β-biotol (**2**) (Scheme 8). These were separated by chromatography on silica and the identity of (±)-**1** was established by direct comparison of its ir and ^1H nmr spectra (Table 5) and ^{13}C nmr spectrum with those of a sample of (−)-**1** of natural provenance.[5] The spectra of (±)-**2** were in accord with those published (4) for natural β-biotol (**2**). When the mixture of **41** and **42** was desilylated with hydrogen chloride in methanol, isomerization of the double bond also occurred and the only product obtained was (±)-**1** (Scheme 9).

Oxidation of (±)-**1** gave (±)-α-biotone (**6**), which on reduction with lithium aluminum hydride gave a 1:1 mixture of (±)-**1** and (±)-4-epi-α-biotol (**7**). These were separated by

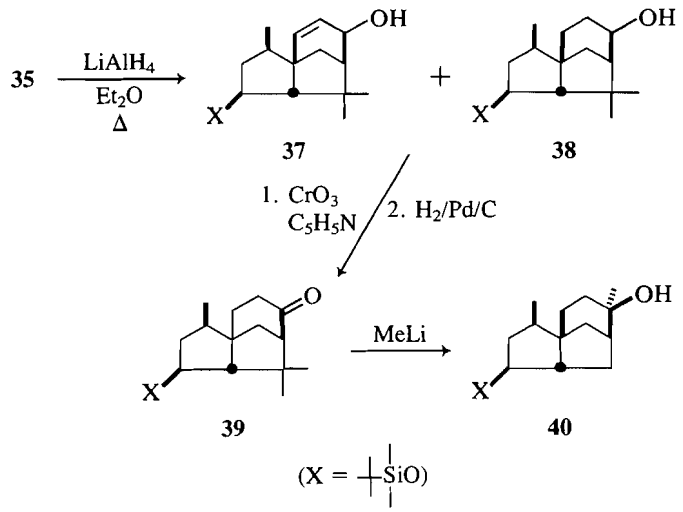

SCHEME 7

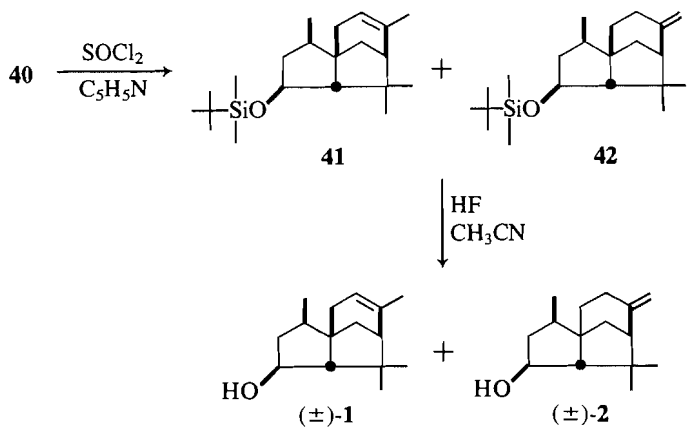

SCHEME 8

Can. J. Chem. Downloaded from www.nrcresearchpress.com by 196.1.178.254 on 09/07/12
For personal use only.

TABLE 5. The ir and ^{1}H nmr spectra of α-biotol (**1**), epi-α-biotol (**7**), and β-biotol (**2**)

	1	**7**	**2**
λ_{max} ($CHCl_3$)			
	3.00 (m)	2.94 (m)	2.99 (m), 6.09 (m)
$^H\delta(CDCl_3)$[a]			
H-2	1.7–1.8 (m)	1.95–2.05 (m)*	1.65–1.75 (m)*
H-3	1.5–1.6 (m)*	1.63 (m)	1.3–1.6 (m)**
	2.08 (dt, 10.6, 5.3)	1.95–2.05 (m)*	2.07 (dt, 11.4, 5.7)
H-4	4.08 (ddd, 8.6, 7.6, 5.4)	4.42 (m)	4.10 (ddd, 9.5, 8.2, 5.3)
H-5	1.62 (d, 8.6)	1.7–1.8 (m)**	1.69 (d, 8.2)
H-7	1.75 (d, 3.4)		2.19 (d, 4.5)
H-9	5.20 (m)	5.20 (m)	2.3 (m)
H-10	1.86 (d, 16.4)[b]	1.7–1.8 (m)**	1.3–1.6 (m)**
	2.20 (dt, 16.4, 2.5)	2.12 (dt, 16.9, 2.3)	
H-11	1.44 (d, 10.6)	1.47 (d, 10.8)	1.25 (d, 11.5)
	1.5–1.6 (m)*	1.81 (ddd, 10.8, 4.0, 0.9)	1.65–1.75 (m)*
CH_3(2)	0.92 (d, 7.1)	0.87 (d, 7.1)	0.89 (d, 7.1)
CH_3(6)	1.06 (s), 1.10 (s)	1.11 (s), 1.29 (s)	1.00 (s), 1.10 (s)
CH_3(8)	1.65 (d, 2.5)[b]	1.65 (d, 1.7)[b]	—
$=CH_2$(8)	—	—	4.50 (s)[b]
			4.58 (s)[b]
OH	1.54 (br s)	1.53 (br s)	1.54 (br s)

[a]See footnotes *a* and *c* in Table 2.
[b]With additional fine splitting.

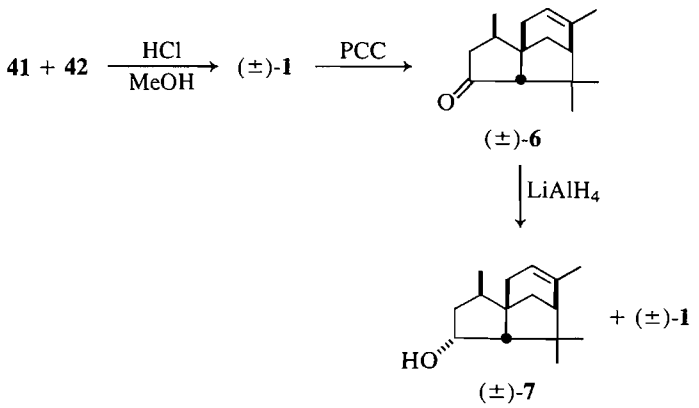

SCHEME 9

chromatography on silica and their identity was established by direct comparison of their ir and ^{1}H nmr spectra (Table 5) and ^{13}C nmr spectrum with those of the corresponding naturally occurring compounds.[5]

These syntheses of the biotols and our earlier syntheses of α-cedrene (10) and bicyclo[3.3.0]octane intermediates with a carboxy substituent at the carbon destined to become C-2 in the derived cedranoids (24) give promise of the attainment of our goal of a general synthetic route for cedranoids of various levels of oxidation.

Experimental

Melting points (mp) were taken on a Fisher–Johns melting point apparatus and are uncorrected.

Analytical thin-layer chromatography was performed with silica gel plates (0.25-mm thickness) from Merck. Preparative thin-layer chromatography was performed on 20 × 20-cm plates coated with 0.25, 1.0, or 2.0 mm of Silica Gel 60 containing a fluorescent indicator (Merck). Bands were scraped off the plate and stirred with ethyl acetate and the extracts were filtered and concentrated. Column chromatography was carried out on silica gel (Grace Davison, grade 923, 100–200 mesh). Flash chromatography was performed on 40–60 μm silica gel (Merck, grade 60, 230–400 mesh, 60 Å mean pore diameter).

Unless otherwise specified, infrared (ir) of solutions in chloroform were recorded on a Perkin–Elmer 137 or 337 spectrometer or a Nicolet 5DX Fourier transform spectrometer. Band positions in microns (μm) are reported relative to the 6.24-μm band of polystyrene. The intensities of the bands are denoted as strong (s), medium (m), or weak (w).

Proton magnetic resonance (^{1}H nmr) spectra of deuterochloroform solutions (unless otherwise specified) were recorded on a Varian T-60 spectrometer; spectra reported at 200 and 400 MHz were recorded on Varian XL-200 and XL-400 spectrometers, respectively. Signal positions are reported on the delta (δ) scale in parts per million (ppm) downfield from tetramethylsilane as an internal standard. Spectra run at 200 and 400 MHz were referenced to either the chloroform signal at 7.24 ppm or the tetramethylsilane signal at δ 0.00 ppm. Signal multiplicities are denoted as singlet (s), broad singlet (br s), doublet (d), triplet (t), quartet (q), multiplet (m), doublet of doublets (dd), doublet of triplets (dt), and doublet of doublet of doublets (ddd). Coupling constants (*J*) are given in hertz (Hz). Carbon-13 magnetic resonance (^{13}C nmr) spectra of deuterochloroform solutions were recorded on a Varian CFT-20 Fourier transform spectrometer or a Varian XL-200 or XL-400 spectrometer. The chemical shifts are reported on the delta (δ) scale in ppm and are referenced to the signal for the middle line of deuterochloroform at 77.0 ppm. Signal multiplicities were determined from single-frequency off-resonance decoupled (SFORD) spectra or from APT or DEPT (25) experiments. In the cases where an APT spectrum was obtained, the chemical shifts are denoted as "e" (no or two attached protons) or "o" (one or three attached protons) (26).

Low resolution mass spectra (ms) were obtained either at 60 eV on a Bell and Howell CEC 21-490 single focussing mass spectrometer or a VG 70-2505 mass spectrometer. Peaks are reported in mass-to-charge units (*m*/*z*) and the relative abundances in parentheses. Exact mass measurements were determined from high resolution mass spectra

[5]We are most grateful to Dr. Pierre Brun, Université d'Aix-Marseille, for providing these spectra and a preprint of his comprehensive paper on the ^{13}C nmr spectra of cedrane derivatives (23).

Can. J. Chem. Downloaded from www.nrcresearchpress.com by 196.1.178.254 on 09/07/12
For personal use only.

Can. J. Chem. Downloaded from www.nrcresearchpress.com by 196.1.178.254 on 09/07/12
For personal use only.

obtained on either an AE1 MS-3074 double focussing mass spectrometer with a DS-50 Data System or a VG 70-250S mass spectrometer.

*Dimethyl 3-hydroxy-4,4,*exo*-8-trimethyl-6-oxo-*cis*-bicyclo[3.3.0]oct-2-ene-1,2-dicarboxylate (**9**)*

Lithium (304 mg, 43.8 mg-atom) was added to a stirred solution of **8** (11) (4.00 g, 13.6 mmol) in dry tetrahydrofuran (60 mL) and liquid ammonia (distilled from sodium; 200 mL) at −78°C under an argon atmosphere. After 15 min the reaction mixture was treated with solid ammonium chloride (2.5 g) and the ammonia was allowed to evaporate. Water (20 mL) was added and the mixture was extracted with ethyl acetate (3 × 30 mL). The combined organic extracts were washed with saturated aqueous sodium chloride (20 mL) and dried over anhydrous sodium sulfate. The solvent was removed and the residue was chromatographed on a silica gel column with ethyl acetate/hexanes (1:3) as eluent to give **9** (1.64 g, 41%) as a clear, colorless oil; ir λ_{max}: 5.77 (s), 6.01 (m), 6.16 (m) μm; ^{1}H nmr (200 MHz) spectrum includes signals at "δ": 1.01, 1.04, 1.07, 1.09, 1.23, 1.25, 3.69 (s), 3.70 (s), 3.82 (s), and 10.9 (br s); ^{13}C nmr spectrum inclues signals at δ: 14.6, 16.7, 21.8, 23.0, 27.3, 29.7, 36.0, 38.7, 43.7, 45.4, 47.3, 49.0, 51.1, 51.6, 52.5, 61.3, 61.4, 61.6, 63.0, 167.5, 170.1, 171.7, 173.4, 181.2, 212.5, 214.4, 215.0; ms *m/z*: 296 (15), 194 (100). *Exact Mass* calcd. for $C_{15}H_{20}O_6$: 296.1260; found: 296.1251.

*Dimethyl 3-acetoxy-4,4,*exo*-8-trimethyl-6-oxo-*cis*-bicyclo[3.3.0]oct-2-ene-1,2-dicarboxylate (**10**)*

A mixture of compound **9** (2.20 g, 7.42 mmol), freshly distilled acetic anhydride (17 mL), and dry pyridine (1.7 mL) was stirred at room temperature for 19 h under argon. The acetic anhydride and pyridine were evaporated and the residue was dissolved in dichloromethane (25 mL). This solution was washed with saturated aqueous sodium bicarbonate (15 mL), followed by water (15 mL). The aqueous layer was reextracted with dichloromethane (3 × 25 mL). The combined organic solutions were dried over anhydrous magnesium sulfate and the solvent was evaporated. The residue was passed through a short silica gel column with ethyl acetate/hexanes (1:3) as solvent and eluent to give **10** (2.40 g, 96%) as a clear, colorless oil; ir (NaCl) λ_{max}: 5.67 (s), 5.80 (s), 6.06 (m) μm; ^{1}H nmr (200 MHz) δ: 1.01 (s, 3H), 1.16 (d, *J* = 7.0 Hz, 3H), 1.23 (s, 3H), 2.23 (s, 3H), 2.25–2.38 (m, 1H), 2.58 (dd, *J* = 15.7, 7.8 Hz, 1H), 2.87 (s, 1H), 3.02 (dd, *J* = 15.7, 7.2 Hz, 1H), 3.70 (s, 3H), 3.74 (s, 3H); ^{13}C nmr δ: 16.4 (o), 20.3 (o), 21.6 (o), 27.7 (o), 37.5 (o), 45.9 (e), 47.3 (e), 51.1 (o), 51.8 (o), 61.5 (o), 63.1 (e), 117.6 (e), 161.5 (e), 163.5 (e), 166.9 (e), 172.5 (e), 214.5 (e); ms *m/z*: 338 (4), 296 (26), 237 (100). *Exact Mass* calcd. for $C_{15}H_{20}O_6$ (M − C_2H_2O): 296.1260; found: 296.1268.

*Dimethyl 3-acetoxy-*exo*-6-hydroxy-4,4,*exo*-8-trimethyl-*cis*-bicyclo[3.3.0]oct-2-ene-1,2-dicarboxylate (**11**)*

Sodium borohydride (0.35 g, 9.25 mmol) was added to ketone **10** (2.40 g, 7.09 mmol) in methanol (120 mL) at 0°C. After the mixture had been stirred at 0°C for 20 min the solution was neutralized with 5% hydrochloric acid (20 mL). Methanol was removed and the residue was extracted with dichloromethane (3 × 40 mL). The combined organic extracts were washed with water (15 mL) and dried over anhydrous magnesium sulfate. Evaporation gave alcohol **11** (2.41 g, 100%) as a colorless, viscous oil; ir (NaCl) λ_{max}: 2.86 (m), 5.65 (s), 5.78 (s), 6.02 (m) μm; ^{1}H nmr (400 MHz) δ: 1.10 (s, 3H), 1.16 (d, *J* = 6.7 Hz, 3H), 1.18 (s, 3H), 1.63–1.73 (m, 1H), 2.04–2.10 (m, 1H), 2.26 (s, 3H), 2.26–2.34 (m, 1H), 2.37 (br s, 1H, absent after treatment with deuterium oxide), 2.55 (d, *J* = 9.0 Hz, 1H), 3.69 (s, 3H), 3.71 (s, 3H), 4.13 (m, 1H); ^{13}C nmr δ: 16.0 (q), 18.7 (q), 20.6 (q), 28.2 (q), 39.8 (d), 43.6 (t), 44.3 (s), 51.0 (q), 51.7 (q), 62.2 (s), 63.8 (d), 73.3 (d), 118.5 (s), 163.5 (s), 163.8 (s), 167.5 (s), 174.9 (s); ms *m/z*: 341 (10), 239 (100). *Exact Mass* calcd. for $C_{17}H_{25}O_7$: 341.1600; found: 341.1628.

*Dimethyl 3-*exo*-6-dihydroxy-4,4,*exo*-8-trimethyl-*cis*-bicyclo[3.3.0]oct-2-ene-1,2-dicarboxylate (**12**)*

A solution of alcohol **12** (2.41 g, 7.08 mmol) in methanol (80 mL) was treated with potassium carbonate (0.96 g) and the mixture was stirred at room temperature for 2.5 h under an argon atmosphere. Dilute hydrochloric acid (5%; 20 mL) was added and the methanol was evaporated. The residue was extracted with dichloromethane (3 × 40 mL). The combined organic extracts were dried over anhydrous sodium sulfate and the solvent was removed to give **12** (2.10 g, 99%) as an oil; ir λ_{max}: 3.09 (w), 5.76 (s), 6.02 (s), 6.15 (m) μm; ^{1}H nmr δ: 1.12 (s, 3H), 1.12 (d, *J* = 6.4 Hz, 3H), 1.30 (s, 3H), 1.43–2.27 (m, 4H), 2.51 (d, *J* = 9.2 Hz, 1H), 3.70 (s, 3H), 3.80 (s, 3H), 4.11 (m, 1H), 10.80 (br s, 1H); ^{13}C nmr δ: 16.0 (q), 18.9 (q), 28.3 (q), 40.7 (t), 43.8 (d), 44.2 (s), 51.1 (q), 51.6 (q), 61.0 (s), 64.8 (d), 73.9 (d), 102.5 (s), 170.8 (s), 175.7 (s), 180.5 (s); ms *m/z*: 298 (3). *Exact Mass* calcd. for $C_{15}H_{22}O_6$: 298.1410; found: 298.1434.

Methyl exo*-6-hydroxy-4,4,*exo*-8-trimethyl-3-oxo-*cis*-bicyclo[3.3.0]octane-1-carboxylate (**13**)*

A mixture of compound **12** (2.10 g, 7.04 mmol), sodium chloride (1.18 g, 20.2 mmol), and distilled water (4 mL) in reagent grade dimethyl sulfoxide (75 mL) was heated at 85°C for 19 h under argon. Dimethyl sulfoxide was removed under high vacuum and water (10 mL) was added to the residue. The resulting mixture was extracted with dichloromethane (3 × 40 mL). The combined organic extracts were washed with water (2 × 15 mL) and dried over anhydrous sodium sulfate, and the solvent was removed. The residue was chromatographed on silica gel with a 1:2 mixture of ethyl acetate and hexanes as eluent to give **13** (1.04 g, 62%) as a colorless viscous oil, which was crystallized from a 1:3 mixture of ethyl acetate and hexanes to give **13** as colorless rhombs, mp 63.5–64.0°C; ir λ_{max}: 3.03 (w), 5.75 (s) μm; ^{1}H nmr (400 MHz) δ: 0.98 (d, *J* = 6.6 Hz, 3H), 1.07 (s, 3H), 1.14 (s, 3H), 1.68–1.83 (m, 2H), 2.19 (d, *J* = 19.2 Hz, 1H), 2.18 (m, 1H), 2.55 (br s, 1H, absent after treatment with deuterium oxide), 2.67 (d, *J* = 6.6 Hz, 1H), 3.25 (d, *J* = 19.2 Hz, 1H), 3.78 (s, 3H), 4.04 (m, 1H); ^{13}C nmr δ: 14.9 (o), 19.1 (o), 28.3 (o), 43.1 (e), 44.2 (o), 44.9 (e), 48.1 (e), 52.2 (o), 55.2 (e), 63.7 (o), 74.1 (o), 176.3 (e), 219.9 (e); ms *m/z*: 240 (10), 140 (100). *Anal.* calcd. for $C_{13}H_{20}O_4$: C 64.98, H 8.39; found: C 64.85, H 8.49.

Methyl endo*-6-hydroxy-4,4,*exo*-8-trimethyl-3-oxo-*cis*-bicyclo[3.3.0]octane-1-carboxylate (**15**)*

To a solution of hydroxy ketone **13** (29 mg, 0.119 mmol), triphenylphosphine (96.5 mg, 0.368 mmol), and benzoic acid (30.9 mg, 0.253 mmol) in dry tetrahydrofuran (3 mL) under argon was added diethyl azodicarboxylate (42.0 mg, 0.241 mmol). The mixture was stirred at room temperature for 48 h. Removal of tetrahydrofuran under reduced pressure afforded the crude product, which was chromatographed on a silica gel plate with 1:3 ethyl acetate/hexanes as eluent to give *methyl* endo*-6-benzoyloxy-3-oxo-4,4-*exo*-8-trimethyl-3-oxo-*cis*-bicyclo[3.3.0]octane-1-carboxylate* (27.8 mg, 68%) as a solid, which was recrystallized from hexanes to give crystals, mp 136–138°C; ir λ_{max}: 5.77 (s), 5.82 (s) μm; ^{1}H nmr (400 MHz) δ: 0.96 (s, 3H), 1.00 (d, *J* = 7.1 Hz, 3H), 1.08 (s, 3H), 1.76 (dt, *J* = 2.8, 13.5 Hz, 1H), 2.20 (dd, *J* = 13.5, 5.7 Hz, 1H), 2.36 (m, 1H), 2.37 (d, *J* = 19.8 Hz, 1H), 3.18 (d, *J* = 4.2 Hz, 1H), 3.65 (d, *J* = 19.8 Hz, 1H), 3.78 (s, 3H), 5.48 (m, 1H), 7.40–7.82 (m, 5H); ^{13}C nmr δ: 15.4 (o), 18.3 (o), 26.7 (o), 41.8 (e), 47.0 (o), 47.6 (e), 47.9 (e), 52.3 (o), 55.3 (e), 61.1 (o), 78.0 (o), 128.7 (o), 129.5 (o), 129.7 (e), 133.3 (o), 165.8 (e), 176.2 (e), 218.8 (e); ms *m/z*: 344 (1), 140 (80), 105 (100). *Exact Mass* calcd. for $C_{20}H_{24}O_5$: 344.1624; found: 344.1633.

A mixture of this product (21.6 mg, 0.0627 mmol) and potassium carbonate (14.9 mg) in methanol (2 mL) was stirred at room temperature for 48 h under argon. Methanol was evaporated and water (2 mL) was added to the residue. The mixture was extracted with dichloromethane (3 × 15 mL) and the extracts were dried over anhydrous sodium sulfate. After evaporation, the residue was chromatographed on a silica gel plate with ethyl acetate/hexanes (1:3) as solvent and eluent to give hydroxy ketone **15** (13.9 mg, 92%) as a colorless oil; ir λ_{max}: 3.03 (w), 5.76 (s), 5.81 (s) μm; ^{1}H nmr (400 MHz) δ: 0.87 (s, 3H), 0.99 (d, *J* = 7.1 Hz, 3H), 1.23 (s, 3H), 1.58 (br s, 1H, absent after treatment with deuterium oxide), 1.61 (dt, *J* = 2.5, 13.0 Hz, 1H), 1.88 (dd, *J* = 13.0, 6.1 Hz, 1H), 2.26 (d, *J* = 19.6 Hz, 1H), 2.50 (m, 1H), 2.85 (d, *J* = 3.7 Hz, 1H), 3.45 (d, *J* = 19.6 Hz, 1H), 3.72 (s, 3H), 4.37 (m, 1H); ^{13}C nmr δ: 15.9 (o), 18.8 (o), 26.5

Can. J. Chem. Downloaded from www.nrcresearchpress.com by 196.1.178.254 on 09/07/12
For personal use only.

(o), 45.2 (e), 46.6 (o), 47.8 (e), 47.9 (e), 52.0 (o), 55.0 (e), 62.5 (o), 73.6 (o), 176.5 (e), 219.3 (e); ms *m/z*: 240 (3), 140 (33), 82 (100). *Exact Mass* calcd. for $C_{13}H_{20}O_4$: 240.1362; found: 240.1333.

*Methyl 3-ethynyl-3-*exo*-6-dihydroxy-4,4,*exo*-8-trimethyl-*cis*-bicyclo[3.3.0]octane-1-carboxylate (**21**)*

Acetylene was bubbled into a solution of *n*-butyllithium in hexanes (2.00 M; 10.0 mL, 20.0 mmol) in anhydrous tetrahydrofuran (45 mL) at −78°C for 1 h. This solution was added to a suspension of anhydrous cerium(III) chloride in tetrahydrofuran at −78°C (cerium(III) chloride heptahydrate (7.44 g, 20.0 mmol) was heated with stirring at 140°C under reduced pressure (0.1 Torr; 1 Torr = 133.3 Pa) for 3 h and then cooled; dry tetrahydrofuran (50 mL) was added with stirring under argon and stirring was continued overnight at room temperature). The resulting organocerium reagent was stirred at −78°C for 0.5 h and then a solution of hydroxy ketone **13** (0.890 g, 3.70 mmol) in dry tetrahydrofuran (12 mL) was added. The mixture was stirred at −78°C for 4 h and then saturated aqueous ammonium chloride (18 mL) was added. The mixture was allowed to warm to room temperature and filtered through Celite, and the resultant solids were washed with dichloromethane. The combined organic solutions were dried over anhydrous sodium sulfate and the solvent was evaporated. Trituration of the residue with hexanes containing 5–10% ethyl acetate gave propargylic alcohol **21** (0.72 g, 73%) as a solid. Recrystallization from a 1:3 mixture of ethyl acetate and hexanes gave white needles, mp 159–160°C; ^{13}C nmr δ: 14.5 (q), 16.8 (q), 29.0 (q), 42.6 (d), 43.4 (t), 47.1 (t), 47.9 (s), 51.7 (q), 60.8 (s), 67.1 (d), 73.5 (d), 74.9 (d), 81.6 (s), 84.5 (s), 177.0 (s). *Anal.* calcd. for $C_{15}H_{22}O_4$: C 67.65, H 8.33; found: C 67.63, H 8.37.

exo*-6-Hydroxy-1-[1-(1-hydroxy-1-(2-(trimethylsilyl)-1-ethynyl))-3-(trimethylsilyl)-2-propynyl]-4,4,*exo*-8-trimethyl-*cis*-bicyclo[3.3.0]octan-3-one (**22**)*

Anhydrous cerium(III) chloride (prepared by heating cerium(III) chloride heptahydrate (934 mg, 2.51 mmol) as above for 4 h) was suspended in dry tetrahydrofuran (10 mL) and the suspension was stirred overnight at room temperature under argon. A solution of 2-trimethylsilylethynyllithium, which was prepared by adding *n*-butyllithium in hexanes (2.00 M; 1.25 mL, 2.50 mmol) to a solution of trimethylsilylacetylene (308.2 mg, 3.139 mmol) in tetrahydrofuran (8 mL) at −78°C, was stirred at −78°C for 15 min. This solution was added to the suspension of cerium(III) chloride at −78°C with a cannula. The mixture was stirred at −78°C for 1 h, giving a solution of 2-trimethylsilylethynylcerium(III) chloride. Then a solution of hydroxy ketone **13** (197 mg, 0.819 mmol) in dry tetrahydrofuran (4 mL) was added at −78°C. The mixture was stirred at −78°C for 3 h, and then treated with water (10 mL). The mixture was extracted with dichloromethane (3 × 40 mL). The combined extracts were dried over anhydrous sodium sulfate and concentrated. Chromatography of the residue on a silica gel plate with ethyl acetate/hexanes (1:3) as solvent and eluent gave **22** (201.5 mg, 61%) as a solid. Recrystallization from hexanes gave a white solid, mp 77.5–79.0°C; ir λ_{max}: 3.10 (w), 4.68 (w), 5.76 (s) μm; ^{1}H nmr (400 MHz) δ: 0.15 (s, 9H), 0.16 (s, 9H), 1.04 (s, 3H), 1.18 (s, 3H), 1.30 (d, *J* = 6.8 Hz, 3H), 1.56 (br s, 1H, absent after treatment with deuterium oxide), 1.72–1.90 (m, 2H), 2.20–2.35 (m, 1H), 2.35 (d, *J* = 18.1 Hz, 1H), 2.87 (d, *J* = 18.1 Hz, 1H), 2.88 (br s, 1H), 3.70 (br s, 1H, absent after treatment with deuterium oxide), 4.28 (m, 1H); ^{13}C nmr δ: −0.5 (q), −0.4 (q), 15.1 (q), 22.3 (q), 27.8 (q), 44.2 (d), 45.5 (t), 47.1 (t), 47.8 (s), 57.8 (s), 64.6 (d), 69.3 (s), 73.0 (d), 89.8 (s), 90.8 (s), 104.6 (s), 105.7 (s), 221.6 (s); ms *m/z*: 404 (1), 134 (100). *Anal.* calcd. for $C_{22}H_{36}O_3Si_2$: C 65.29, H 8.97; found: C 65.10, H 8.98.

*Methyl 3,*exo*-6-dihydroxy-4,4,*exo*-8-trimethyl-3-(1-oxoethyl)-*cis*-bicyclo[3.3.0]octane-1-carboxylate (**26**)*

A mixture of propargylic alcohol **21** (0.72 g, 2.70 mmol), mercuric oxide (0.16 g, 0.74 mmol), and sulfuric acid (3 M; 10.7 mL) in tetrahydrofuran (20 mL) was stirred at room temperature for 4 days under argon. Solid sodium bicarbonate was added until the solution had a pH of 8, and the solvent was evaporated. Water (15 mL) was added and the mixture was extracted with ethyl acetate (3 × 40 mL). The combined organic extracts were dried over anhydrous sodium sulfate and the solvent was removed to give dihydroxy ketone **26** (0.72 g, 94%) as a solid. This was recrystallized from 10% ethyl acetate in hexanes to give white needles, mp 175–176°C; ^{13}C nmr δ: 14.5 (q), 16.9 (q), 28.0 (q), 28.7 (q), 41.9 (t), 42.1 (d), 43.1 (t), 48.5 (s), 51.8 (q), 61.1 (s), 68.8 (d), 74.8 (d), 90.9 (s), 177.3 (s), 211.6 (s); ms *m/z*: 284 (5), 163 (100). *Anal.* calcd. for $C_{15}H_{24}O_5$: C 63.36, H 8.51; found: C 63.33, H 8.53.

*Methyl 3,*exo*-6-diacetoxy-4,4,*exo*-8-trimethyl-3-(1-oxoethyl)-*cis*-bicyclo[3.3.0]octane-1-carboxylate (**27**)*

A solution of diol **26** (0.686 g, 2.41 mmol), 4-(dimethylamino)pyridine (1.19, 9.74 mmol), and freshly distilled acetic anhydride (2.20 mL) in dichloromethane (20 mL) was stirred at room temperature for 20 h under argon. The mixture was washed with saturated aqueous sodium bicarbonate (15 mL) and saturated aqueous sodium chloride (15 mL). The aqueous layers were reextracted with dichloromethane (3 × 20 mL). The combined organic solutions were dried over anhydrous sodium sulfate and the solvent was evaporated. The residue was chromatographed on silica gel column with ethyl acetate/hexanes (1:3) as solvent and eluent. The diacetate **27** (0.58 g, 65%) was obtained as a clear, colorless oil; ^{13}C nmr δ: 14.7 (o), 17.6 (o), 21.2 (o), 21.3 (o), 26.8 (o), 26.9 (o), 39.1 (e), 39.4 (e), 43.8 (o), 46.1 (e), 51.9 (o), 58.5 (e), 64.9 (o), 75.8 (o), 97.4 (e), 170.3 (e), 170.7 (e), 176.1 (e), 203.3 (e); ms *m/z*: 337 (3), 223 (100). *Exact Mass* calcd. for $C_{18}H_{25}O_6$ (M − OCH_3): 337.1651; found: 337.1656.

Methyl exo*-6-acetoxy-3-hydroxy-4,4,*exo*-8-trimethyl-3-(1-oxoethyl)-*cis*-bicyclo[3.3.0]octane-1-carboxylate (**28**)*

A solution of diol **26** (48.8 mg, 0.172 mmol), distilled acetic anhydride (1 mL), and pyridine (0.08 mL) in dichloromethane (3 mL) was stirred at room temperature for 20 h under argon. The mixture was washed with saturated aqueous sodium bicarbonate (10 mL) and saturated aqueous sodium chloride (10 mL). The aqueous layers were reextracted with dichloromethane (3 × 25 mL). The combined organic solutions were dried over anhydrous sodium sulfate and the solvent was evaporated to give **28** (56.0 mg, 100%) as a viscous oil; ^{13}C nmr δ: 14.4 (q), 16.8 (q), 21.2 (q), 27.9 (q), 28.2 (q), 39.4 (t), 42.0 (t), 42.4 (d), 48.2 (s), 51.8 (q), 60.0 (s), 64.8 (d), 76.6 (d), 90.8 (s), 170.6 (s), 176.9 (s), 210.9 (s); ms *m/z*: 327 (50), 223 (100), 163 (95). *Exact Mass* calcd. for $C_{17}H_{26}O_6$: 326.1729; found: 326.1718.

This monoacetate was converted to diacetate **27** under conditions analogous to those used for the formation of **27** from **26**.

Methyl exo*-6-acetoxy-4,4,*exo*-8-trimethyl-3-(1-oxoethyl)-*cis*-bicyclo[3.3.0]octane-1-carboxylate (**31**)*

A solution containing diacetate **27** (304 mg, 0.826 mmol), azoisobutyronitrile (36.7 mg, 0.223 mmol), tri-*n*-butyltin hydride (0.42 g, 1.44 mmol), and dry toluene (10 mL) was boiled under reflux under argon for 6 h. The solvent was removed and the residue was chromatographed on silica gel with ethyl acetate/hexanes (1:3) as solvent and eluent to give monoacetate **31** (233 mg, 91%) as a clear, colorless oil. Crystallization from hexanes gave white crystals, mp 75.0–75.5°C; ^{13}C nmr δ: 14.6 (q), 21.2 (q), 23.0 (q), 24.2 (q), 31.7 (q), 35.5 (t), 38.5 (t), 42.9 (d), 43.3 (s), 51.7 (q), 58.4 (s), 58.6 (d), 64.1 (d), 75.0 (d), 170.5 (s), 175.9 (s), 208.1 (s); ms *m/z*: 311 (60), 147 (100). *Anal.* calcd. for $C_{17}H_{26}O_5$: C 65.78, H 8.44; found: C 65.73, H 8.47.

Methyl exo*-6-hydroxy-4,4,*exo*-8-trimethyl-3-(1-oxoethyl)-*cis*-bicyclo[3.3.0]octane-1-carboxylate (**32**)*

A mixture of monoacetate **31** (315.5 mg, 1.016 mmol) and potassium carbonate (145.8 mg, 1.055 mmol) in methanol (20 mL) was stirred at room temperature for 17 h under argon. The methanol was evaporated and water (15 mL) was added to the residue. The resulting mixture was extracted with dichloromethane (4 × 25 mL) and the combined organic extracts were dried over anhydrous magnesium sulfate. The solvent was removed to give alcohol **32** (273 mg, 100%) as a solid, which was recrystallized from 10% ethyl acetate in hexanes to give white needles, mp 95.5–96.0°C; ^{13}C nmr δ: 14.5 (q), 23.2 (q),

Can. J. Chem. Downloaded from www.nrcresearchpress.com by 196.1.178.254 on 09/07/12
For personal use only.

24.6 (q), 31.6 (q), 35.3 (t), 42.1 (t), 42.4 (d), 43.4 (s), 51.6 (q), 58.8 (d), 59.3 (s), 67.9 (d), 73.9 (d), 176.9 (s), 209.3 (s); ms *m/z*: 268 (2), 147 (100). *Exact Mass* calcd. for $C_{15}H_{24}O_4$: 268.1674; found: 268.1669. *Anal.* calcd. for $C_{15}H_{24}O_4$: C 67.14, H 9.01; found: C 67.07, H 9.00.

Methyl exo-*6-(*tert-*butyldimethylsilyloxy)-4,4,*exo-*8-trimethyl-3-(1-oxoethyl)-*cis-*bicyclo[3.3.0]octane-1-carboxylate (33) and methyl* exo-*6-(*tert-*butyldimethylsilyloxy)-3-[1-(*tert-*butyldimethylsilyloxy)ethenyl]-4,4,*exo-*8-trimethyl-*cis-*bicyclo[3.3.0]-octane-1-carboxylate (34)*

(*i*) A solution containing alcohol **32** (161 mg, 0.601 mmol), 2,6-lutidine (175.0 mg, 1.633 mmol), and *tert*-butyldimethylsilyl triflate (179.8 mg, 0.680 mmol) in dry dichloromethane (10 mL) was stirred at 0°C for 3 h under argon. Saturated aqueous sodium bicarbonate (10 mL) was added and the layers were separated. The aqueous layer was reextracted with dichloromethane (3 × 25 mL) and the combined organic solutions were dried over anhydrous magnesium sulfate. The residue, after evaporation, was chromatographed on a silica gel column with ethyl acetate/hexanes (1:3) as solvent and eluent to give silyl ether **33** (225.5 mg, 98%) as a solid. The silyl ether was recrystallized from hexanes to give a crystalline solid, mp 75.0–76.5°C; ^{13}C nmr δ: −4.9 (q), −3.7 (q), 14.5 (q), 17.6 (s), 23.6 (q), 24.5 (q), 25.7 (q), 31.4 (q), 35.4 (t), 42.2 (t), 42.4 (d), 43.5 (s), 51.4 (q), 58.5 (s), 58.9 (d), 68.0 (d), 74.3 (d), 176.6 (s), 208.9 (s); ms *m/z*: 325 (100). *Anal.* calcd. for $C_{21}H_{38}O_4Si$: C 65.92, H 10.01; found: C 66.19, H 10.09.

(*ii*) A solution containing alcohol **32** (60 mg, 0.965 mmol), dry 2,6-lutidine (258.5 mg, 2.41 mmol), and *tert*-butyldimethylsilyl triflate (383 mg, 1.45 mmol) in dry dichloromethane (10 mL) was stirred at room temperature for 3 h under argon. Work-up and chromatography as in (*i*) gave the silyl ether **33** (169 mg, 46%) and its silyl enol ether **34** (208.4 mg, 43%) as oils. The disilyloxy compound has ir λ_{max}: 5.80 (s), 6.18 (w) μm; ^{1}H nmr δ: 0.07 (s, 6H), 0.18 (s, 6H), 0.76 (s, 3H), 0.90 (s, 9H), 0.93 (d, 3H), 0.96 (s, 9H), 1.07 (s, 3H), 1.20–1.26 (m, 7H), 3.67 (s, 3H), 4.07 (m, 3H). When a solution of this product (208 mg, 0.419 mmol) in methanol was passed through a Dowex 10W-X8 plug it gave **33** (overall yield 85%).

exo-*4-(*tert-*Butyldimethylsilyloxy)-*exo-*2,6,6-trimethyltricyclo[5.3.1.0^{1,5}]undecane-8,10-dione (35)*

Keto ester **33** (165 mg, 0.431 mmol) in dry *tert*-butyl alcohol (8 mL) was treated with potassium *tert*-butoxide (0.77 g, 6.9 mmol). This mixture was heated under reflux for 1.5 h. *tert*-Butyl alcohol was evaporated. Water (2 mL) and dichloromethane (15 mL) were added. The resulting emulsion was passed through Celite and the solution was dried over anhydrous magnesium sulfate. The residue left after evaporation of dichloromethane was passed through a short silica gel column with ethyl acetate as solvent and eluent to give solid dione **35** (144.5 mg, 96%), which was recrystallized from 5–10% ethyl acetate in hexanes to give a crystalline solid, mp 152–153°C; ^{13}C nmr δ: −5.0 (q), −3.9 (q), 14.6 (q), 17.7 (s), 25.6 (q), 25.9 (q), 28.1 (q), 36.4 (t), 39.6 (d), 42.0 (s), 46.9 (t), 52.3 (t), 65.1 (s), 66.7 (d), 67.1 (d), 73.5 (d), 204.9 (s), 207.8 (s); ms *m/z*: 335 (3), 293 (100). *Exact Mass* calcd. for $C_{16}H_{25}O_3Si$ (M − $C(CH_3)_3$): 293.1573; found: 293.1565.

exo-*4-(*tert-*Butyldimethylsilyloxy)-*exo-*2,6,6-trimethyltricyclo[5.3.1.0^{1,5}]undec-9-en-8-ol (37) and* exo-*4-(*tert-*butyldimethylsilyloxy)-*exo-*2,6,6-trimethyltricyclo[5.3.1.0^{1,5}]undecan-8-ol (38)*

A mixture of dione **35** (118 mg, 0.335 mmol) and lithium aluminum hydride (69.5 mg, 1.83 mmol) in dry ether (40 mL) was boiled under gentle reflux for 20 h. Saturated aqueous sodium sulfate (2 mL) was added and then the mixture was dried with anhydrous sodium sulfate. The mixture was filtered and the resulting solids were washed with ethyl acetate. The combined organic solutions were concentrated to give a mixture of alcohols **37** and **38** (111 mg, 98%) as an oil; ir λ_{max}: 2.97 (w), 6.18 (w) μm; ^{1}H nmr spectrum of the mixture includes signals at δ: 0.05 (s), 0.92 (s), 3.52–4.25 (m), 4.67 (m), 5.40 (m), 6.12 (m).

exo-*4-(*tert-*Butyldimethylsilyloxy)-*exo-*2,6,6-trimethyltricyclo[5.3.1.0^{1,5}]undecan-8-one (39)*

Chromic anhydride (98 mg, 0.98 mmol) was added to cold, dry pyridine (6.7 mL) under argon. The mixture was stirred at room temperature for 10 min and the mixture of alcohols **37** and **38** (111 mg, ~0.33 mmol) in pyridine (1 mL) was added and the mixture was stirred for 20 h at room temperature. The pyridine was evaporated, water (10 mL) and ethyl acetate (25 mL) were added, and the layers were separated. The aqueous layer was reextracted with ethyl acetate (3 × 25 mL) and the combined organic solutions were dried over anhydrous sodium sulfate. Evaporation and passage of the residue through a silica gel plug with ethyl acetate as solvent and eluent gave a mixture of exo-*4-(*tert-*butyldimethylsilyloxy)-*exo-*2,6,6-trimethyltricyclo[5.3.1.0^{1,5}]undec-9-en-8-one and* exo-*4-(*tert-*butyldimethylsilyloxy)-*exo-*2,6,6-trimethyltricyclo[5.3.1.0^{1,5}]undecan-8-one* (94 mg, 85%) as an oil; ir λ_{max}: 5.86 (m), 5.97 (s) μm. The ^{1}H nmr spectrum of the mixture includes signals at δ: 0.06 (s), 0.88 (s), 4.10 (m), 5.73 (d, *J* = 10 Hz), 7.47 (d, *J* = 10 Hz).

The mixture (94 mg, ~0.28 mmol) in absolute ethanol (15 mL) containing 10% palladium on carbon (35.5 mg) was hydrogenated for 1 h at room temperature. Filtration and evaporation gave crude ketone **39**. Chromatography on a silica gel plate with ethyl acetate/hexanes (1:3) as solvent and eluent gave **39** (83 mg, ~89%) as a clear, colorless oil. The overall yield from diketone **35** was 74%. Compound **39** has ^{13}C nmr δ: −4.9 (q), −3.8 (q), 15.2 (q), 17.8 (s), 25.5 (q), 25.8 (q), 26.2 (q), 32.0 (t), 36.2 (t), 39.1 (d), 41.5 (s), 41.8 (t), 46.5 (t), 52.0 (s), 65.6 (d), 67.8 (d), 73.4 (d), 213.8 (s); ms *m/z*: 336 (5), 279 (100). *Exact Mass* calcd. for $C_{20}H_{36}O_2Si$: 336.2484; found: 336.2476.

exo-*4-(*tert-*Butyldimethylsilyloxy)-*exo-*2,6,6,*endo-*8-tetramethyltricyclo[5.3.1.0^{1,5}]undecan-*exo-*8-ol (40)*

To a solution of ketone **39** (83 mg, 0.247 mmol) in dry ether (10 mL) was added methyllithium in hexanes (1.4 M; 6.0 mL), 8.4 mmol) under argon. The mixture was heated under reflux for 5 h. Water (10 mL) was added and the layers were separated. The aqueous layer was reextracted with ethyl acetate (3 × 25 mL) and the combined organic solutions were dried over anhydrous sodium sulfate. The solvent was evaporated and the residue was chromatographed on silica with ethyl acetate as eluent to give alcohol **40** (83 mg, 95%) as a solid, mp 65.0–67.0°C; ^{13}C nmr δ: −4.9 (q), −3.7 (q), 15.3 (q), 17.8 (s), 25.8 (q), 27.8 (q), 28.3 (q), 30.0 (q), 31.6 (t), 34.7 (t), 38.6 (d), 42.5 (s), 42.7 (t), 46.5 (t), 51.8 (s), 61.6 (d), 64.8 (d), 73.6 (d), 75.0 (s); ms *m/z*: 335 (16), 295 (100). *Exact Mass* calcd. for $C_{21}H_{39}OSi$ (M + H − H_2O): 335.2766; found: 335.2780.

exo-*4-(*tert-*Butyldimethylsilyloxy)-*exo-*2,6,6,8-trimethyltricyclo[5.3.1.0^{1,5}]undec-8-ene (41) and* exo-*4-(*tert-*butyldimethylsilyloxy)-*exo-*2,6,6-trimethyl-8-methylenetricyclo[5.3.1.0^{1,5}]undecane (42)*

Thionyl chloride (0.16 mL) was added to a cold (0°C) solution of alcohol **40** (38 mg, 0.107 mmol) in pyridine (2 mL) under argon. The reaction mixture was stirred for 1.5 h at 0°C. Water (10 mL) was added and the mixture was extracted with ethyl acetate (3 × 25 mL). The combined extracts were dried over anhydrous sodium sulfate and the solvent was evaporated. The residue was passed through a short silica gel column with ethyl acetate as solvent and eluent to give a 2:1 mixture of **41** and **42** (29 mg, 81%) as an oil; ir λ_{max}: 6.08 (w) μm. The ^{1}H nmr (400 MHz) spectrum of **41** includes signals at δ: 0.00 (s), 0.02 (s), 0.84 (s), 0.91 (d, *J* = 7.6 Hz), 1.01 (s), 1.06 (s), 1.64 (m, vinyl methyl), 4.00 (ddd, *J* = 7.9, 6.9, 5.5 Hz), 5.19 (m) and the ^{1}H nmr (400 MHz) spectrum of **42** includes signals at δ: 0.01 (s), 0.05 (s), 0.86 (s), 0.88 (d, *J* = 7.6 Hz), 0.96 (s), 1.05 (s), 4.04 (ddd, *J* = 9.3, 8.1, 5.5 Hz), 4.48 (m), 4.56 (m).

(±)-α-Biotol (1)

The mixture of compounds **41** and **42** (20.0 mg, 0.060 mmol) was treated with a solution (6 mL) of 5% hydrogen chloride in methanol under argon and this mixture was stirred at room temperature for 2 h. Saturated aqueous sodium bicarbonate (10 mL) was added and the mixture was extracted with ethyl acetate (3 × 25 mL). The extracts

were dried over anhydrous sodium sulfate and the solvent was evaporated. The residue was chromatographed on a silica gel plate with 25% ethyl acetate in hexanes as solvent and eluent to give (±)-α-biotol (**1**) (9.1 mg, 69%), mp 68–70°C; ^{13}C nmr δ: 15.8 (q), 24.7 (q), 25.8 (q), 27.9 (q), 38.8 (t), 39.6 (d), 41.0 (t), 46.5 (t), 46.6 (s), 52.6 (s), 55.6 (d), 68.9 (d), 73.8 (d), 118.6 (d), 140.4 (s).

*(±)-α-Biotol (**1**) and (±)-β-biotol (**2**)*

A solution of 5.2% hydrofluoric acid in acetonitrile was prepared from a standard solution of 52% aqueous hydrofluoric acid. The former solution (7 mL) was added to a mixture of silyl ethers **41** and **42** (14.0 mg, 0.0418 mmol) under argon. The solution was stirred at 0°C for 1.75 h and then allowed to warm to room temperature during 15 min. Saturated aqueous sodium bicarbonate (10 mL) was added and the mixture was extracted with ethyl acetate (3 × 10 mL). The combined extracts were dried over anhydrous sodium sulfate and the solvent was evaporated. The residue was chromatographed on a silica gel plate with 1:3 ethyl acetate/hexanes as solvent and eluent to give (±)-α-biotol (**1**) (4.5 mg) and (±)-β-biotol (**2**) (2.2 mg) in a combined yield of 77%. (±)-β-Biotol has mp 95–97°C; ^{13}C nmr δ: 14.9 (q), 26.2 (q), 26.3 (q), 29.0 (t), 33.7 (t), 39.5 (d), 41.1 (s), 45.5 (t), 46.6 (t), 53.1 (s), 61.1 (d), 65.1 (d), 73.6 (d), 108.1 (t), 151.0 (s).

*(±)-α-Biotone (**6**)*

To a suspension of pyridinium chlorochromate (31.1 mg, 0.144 mmol) in dichloromethane (1.5 mL), was added (±)-α-biotol (**1**) (13.2 mg, 0.0599 mmol) in dichloromethane (1.5 mL). The mixture was stirred at room temperature for 3 h. Water was added and the mixture was extracted with dichloromethane (3 × 10 mL). The combined extracts were dried over anhydrous sodium sulfate and passed through Celite to give (±)-α-biotone (**6**) (13.1 mg, 100%) as an oil; ir λ_{max}: 5.78 (s) μm; ^{1}H nmr δ: 0.93 (d, J = 8.0 Hz, 3H), 1.00 (s, 3H), 1.20 (s, 3H), 1.70 (m, 3H), 1.50–3.00 (m, 9H), 5.20 (m, 1H).

*(±)-α-Biotol (**1**) and (±)-4-epi-α-biotol (**7**)*

(±)-α-Biotone (**6**) (9.9 mg, 0.045 mmol) and lithium aluminum hydride (11.6 mg, 0.306 mmol) in dry ether (5 mL) were heated under reflux for 5 h under argon. Saturated aqueous sodium sulfate (0.5 mL) was added and the solution was dried with anhydrous sodium sulfate. The mixture was filtered and the solids were washed with ethyl acetate. The combined filtrates were concentrated and the residue was chromatographed on a silica gel plate with ethyl acetate/hexanes (1:3) as solvent and eluent to give (±)-α-biotol (**1**) (3.2 mg) and (±)-4-epi-α-biotol (**7**) (3.3 mg) in a total yield of 65%. (±)-4-Epi-α-biotol (**7**) has mp 57–59°C; ^{13}C nmr δ: 15.8 (q), 24.7 (q), 27.4 (q), 28.7 (q), 37.3 (d), 38.7 (t), 41.7 (t), 44.7 (t), 49.7 (s), 53.1 (s), 56.5 (d), 62.1 (d), 73.7 (d), 119.1 (d), 140.3 (s).

Acknowledgment

We thank the Natural Sciences and Engineering Research Council of Canada for support of this work.

1. D. J. Burnell, V. J. Freer, R. S. Grewal, P. C. Hayes, J. F. Sawyer, and P. Yates. Acta Crystallogr. Sect. C: Cryst. Struct. Commun. **C44**, 296 (1988).
2. R. S. Grewal, P. C. Hayes, J. F. Sawyer, and P. Yates. J. Chem. Soc. Chem. Commun. 1290 (1987).
3. P. Yates. Structure determination. W. A. Benjamin, Inc., New York, NY. 1967. Chap. 1.
4. B. Tomita, Y. Hirose, and T. Nakatsuka. Tetrahedron Lett. 843 (1968).
5. E. Trifilieff, B. Luu, and G. Ourisson. Tetrahedron Lett. 4307 (1975).
6. B. Luu and G. Ourisson. Tetrahedron Lett. 1881 (1975).
7. M.-J. Shiao, J. L. Lin, Y.-H. Kuo, and K.-S. Shih. Tetrahedron Lett. **27**, 4059 (1986).
8. Y. H. Kuo, I. C. Yang, C. S. Chen, and Y. T. Lin. Experientia, **32**, 686 (1976).
9. P. Brun. Tetrahedron Lett. 2269 (1977).
10. P. Yates and K. E. Stevens. Tetrahedron, **37**, 4401 (1981).
11. P. Yates, D. J. Burnell, V. J. Freer, and J. F. Sawyer. Can. J. Chem. **65**, 69 (1987).
12. A. P. Krapcho and A. J. Lovey. Tetrahedron Lett. 957 (1973); A. P. Krapcho. Synthesis, 805 (1982); 893 (1982).
13. (*a*) B.-W. Au-Yeung and I. Fleming. J. Chem. Soc. Chem. Commun. 81 (1977); K. Kojima and K. Sakai. Tetrahedron Lett. 3743 (1978); K. Tatsuta, K. Akimoto, and M. Kinoshita. J. Am. Chem. Soc. **101**, 6116 (1979); G. Mehta and A. V. Reddy. J. Chem. Soc. Chem. Commun. 756 (1981); P. Callant, D. De Wilde, and M. Vandewalle. Tetrahedron, **37**, 2079 (1981); (*b*) I. Tabushi, K. Fujita, and R. Oda. J. Org. Chem. **35**, 2383 (1970).
14. O. Mitsunobu and M. Yamada. Bull. Chem. Soc. Jpn. **40**, 2380 (1967); O. Mitsunobu and E. Masahiko. Bull. Chem. Soc. Jpn. **44**, 3427 (1971); T. Sano, M. Wada, and O. Mitsunobu. Bull. Chem. Soc. Jpn. **46**, 2833 (1973); A. K. Bose, B. Lal, W. A. Hoffman, and M. S. Manhas. Tetrahedron Lett. 1619 (1973); K. Mitsonobu. Synthesis, 1 (1981).
15. A. L. Gemal and J.-L. Luche. J. Am. Chem. Soc. **103**, 5454 (1981).
16. O. F. Beumel and R. F. Harris. J. Org. Chem. **29**, 1872 (1964).
17. T. Imamoto, Y. Sugiura, and N. Takiyama. Tetrahedron Lett. **25**, 4233 (1984); T. Imamoto, N. Takiyama, and K. Nakamura. Tetrahedron Lett. **26**, 4763 (1985).
18. M. Suzuki, Y. Kimura, and S. Terashima. Chem. Lett. 1543 (1984).
19. K. E. Stevens. Ph. D. thesis, University of Toronto (1980).
20. S. P. Douglas, J. F. Sawyer, and P. Yates. Tetrahedron Lett. **26**, 5955 (1985); P. Yates, S. P. Douglas, S. K. Datta, and J. F. Sawyer. Can. J. Chem. **66**, 2268 (1988).
21. H. Redlich, H.-J. Neumann, and H. Paulsen. Chem. Ber. **110**, 2911 (1977).
22. G. Stork and F. H. Clarke, Jr. J. Am. Chem. Soc. **83**, 3114 (1961).
23. P. Brun, J. Casanova, M. S. Raju, B. Waegell, E. Wenkert, and J. P. Zahra. Magn. Reson. Chem. **25**, 619 (1987).
24. P. Yates and K. E. Stevens. Can. J. Chem. **60**, 825 (1982).
25. R. Benn and H. Gunther. Angew. Chem. Int. Ed. Engl. **22**, 350 (1983).
26. S. A. Hardinger and P. L. Fuchs. J. Org. Chem. **52**, 2739 (1987).

Can. J. Chem. Downloaded from www.nrcresearchpress.com by 196.1.178.254 on 09/07/12
For personal use only.

Confirmation of the polyketide origin of kotanin by incorporation of [1,2-$^{13}C_2$]acetate[1,2]

J. B. STOTHERS
Department of Chemistry, University of Western Ontario, London, Ont., Canada N6A 5B7
AND
ALBERT STOESSL
Agriculture Canada, London Research Centre, 1400 Western Road, London, Ont., Canada N6G 2V4

Received May 31, 1988

J. B. STOTHERS AND ALBERT STOESSL. Can. J. Chem. **66**: 2816 (1988).

Incorporation experiments with [1,2-$^{13}C_2$]acetate establish that the biosynthesis of kotanin, a dimeric 5-methylcoumarin, proceeds through a polyketide pathway and, therefore, represents an exception to Turner's rule regarding the relative lengths of the uncyclized residues of polyketide chains. The previous ^{13}C signal assignments are also revised.

J. B. STOTHERS ET ALBERT STOESSL. Can. J. Chem. **66** 2816 (1988).

Des expériences d'incorporation du acétate [$^{13}C_2$-1,2] ont permis de démontrer que la biosynthèse de la kotanine, un dimère de la méthyl-5 coumarine, se produit par le biais d'un polycétide et qu'elle correspond donc à une exception à la régle de Turner concernant les longueurs relatives des résidus non-cyclisés des chaines polycétides. On a aussi revisé les attributions antérieures des signaux relatifs au ^{13}C.

[Traduit par la revue]

Can. J. Chem. Downloaded from www.nrcresearchpress.com by 196.1.178.254 on 09/07/12
For personal use only.

Fungal metabolites whose structures are in real or apparent breach of Turner's rule (1) that "the uncyclized residues from the methyl ends of polyketide chains are never shorter than residues from the carboxyl end of the chain" include marticin (**1**) from *Fusarium martii* (2), colletruncoic acid methyl ester (**2**) from *Colletotrichum truncatum* (3), kotanin (**3**) and demethyl kotanin (**4**) from *Aspergillus clavatus* (4, 5), orlandin (**5**) from *A. niger* (6), siderin (**6**), the monomer of kotanin, from *A. variecolor* (7, 8), and the desertorins A, B, and C (**7–9**, respectively) from *Emericella desertorum* (*A. nidulans* group) (9). Another group of compounds comprises the benzoisochromane quinones, such as actinorhodin (10) and granaticin (11), whose relevant structural moieties (12) have been shown to be of polyketide origin by extensive biosynthetic studies (10, 11). The latter compounds, however, are metabolites of actinomycetes, that is, prokaryotic organisms which may not be encompassed by the rule. Of the true fungal metabolites marticin has been proven (2, 12) to be of mixed polyketide and tricarboxylic acid cycle origin, which accounts for the apparent anomaly. Of the others, only siderin (**6**) has been the subject of an experimental biosynthetic study. It was found (7) that *A. variecolor* cultures incorporated sodium [2-$^{14}C_1$]acetate into **6** with 0.75% efficiency. Kuhn–Roth degradation of the labelled siderin placed 25.8% of its total radioactivity into the 5-methyl group and the excess, over the expected result of uniform incorporation (20% at each of 5 sites), was very plausibly ascribed to the starter effect as frequently seen in polyketide biosynthesis. Unfortunately, lack of material precluded further degradative experiments that could have rendered this conclusion certain. Alternative interpretations of the data, therefore, could not be entirely discounted. For instance, it might be envisaged that the coumarin nucleus is derived from shikimate, while non-uniform incorporation of acetate via formate into the C- and the two O-methyl groups could account for the activity data.

To test these concepts, we undertook an incorporation study with the readily available *A. niger*, applying [1,2-$^{13}C_2$]acetate together with L-[1-$^{14}C_1$]phenylalanine as potential precursors, in the expectation of isolating orlandin (**5**) as the labelled product. In a preliminary cold run, however, chromatography of the culture extract furnished crystalline kotanin (**3**) in good yield. This compound had not been reported previously as a metabolite of *A. niger*. Other fractions from the chromatogram were complex and, in the absence of an authentic specimen, orlandin could not be detected in them with certainty. Further work on this aspect seemed unnecessary because it was clearly advantageous, in subsequent runs, to add diazomethane to the crude extracts to convert any **4** and **5** into **3**. In fact, in the final incorporation experiment described below, kotanin was present only in small amounts before, but was isolated in good yield after, methylation.

Our ^{13}Cmr spectrum of natural kotanin agreed well with that originally reported (6) but the specific signal assignments required reconsideration in the light of a comparison of the proton-coupled and decoupled spectra together with the results reported earlier for siderin and related coumarins (13). These data led to reassignment of six of the nine skeletal carbon signals, each arising from fully substituted carbons. In the coupled spectrum, the signals at δ_C 153.5 and 163.0 remain as singlets, albeit slightly broadened, which is indicative of the absence of vicinal $^{13}C-^1H$ coupling and consistent with their assignment to C-9 and C-2, respectively. In contrast, the signals at δ_C 107.4 and 108.5 appear as multiplets in the coupled spectrum, the former as a broadened doublet, J = 5.5 Hz, and the latter as a nine-line pattern, $\nu_{\frac{1}{2}}$ = 22.5 Hz. It follows that the 107.4-ppm signal arises from C-8 with one vicinal $^{13}C-^1H$ coupling to H-6 and the δ_C 108.5 pattern is that of C-10 exhibiting vicinal coupling with H-3, H-8, and the 5-methyl protons. The carbons bearing methoxyl groups at δ_C 159.5 and 169.8 each gave rise to a doublet of quartets in the coupled spectrum through geminal coupling to the neighbouring proton and vicinal coupling with the methoxyl protons; these signals were not unequivocally assigned until the spectrum of the labelled sample was recorded. While our work was in progress a different assignment of the kotanin spectrum was reported (9), which also requires revision.

An attempt to achieve incorporation of labelled precursors into **3** on the shredded wheat medium of Cutler *et al.* (6) was abortive. Several fully liquid media were therefore compared as to the kotanin yield and the most promising, Czapek–Dox

[1]Part 137 of ^{13}Cmr studies; for Part 136 see ref. 15, for Part 135, ref. 16.

[2]Contribution No. 1074 from the Research Centre.

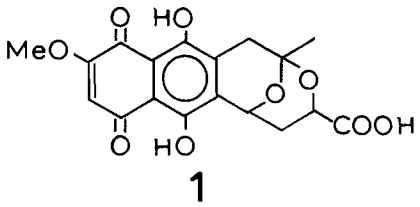

1

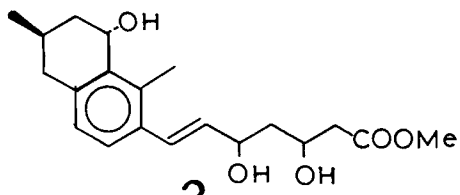

2

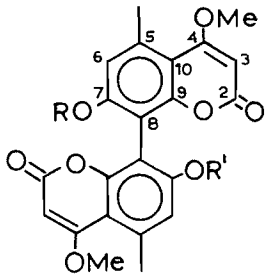

3 R=R'=Me

4 R=H, R'=Me

5 R=R'=H

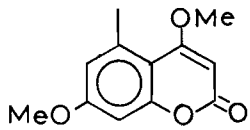

6

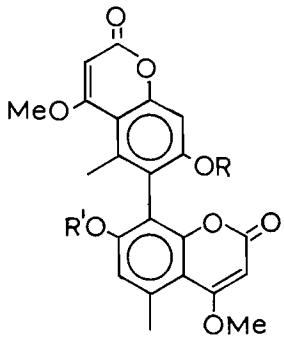

7 R=R'=H

8 R=H, R'=Me

9 R=R'=Me

solution modified by the addition of corn steep liquor, was chosen for the critical experiment. The crystalline kotanin isolated therefrom gave a ^{13}C spectrum in which each of the original signals was flanked by a pair of weak satellite peaks indicative of incorporation of five intact acetate units, since the separations of the satellite peaks readily permitted pairing of each of the 10 signals in an unequivocal manner as shown in **10**, in which the J_{CC} values are given in Hz in parentheses. The relative intensities of the satellite peaks and the central signals showed that the specific enrichment level was very low, 0.18 ± 0.01%, but the labelling pattern of intact acetate units is unequivocal evidence that the metabolite is generated through a polyketide pathway as shown in Fig. 1.

An additional complication arose, however, because the ^{13}C-labelled sample of kotanin also exhibited low levels of radioactivity, which reached a constant value, 4 ± 2 dpm/mg, on repeated recrystallization. This corresponds to a specific incorporation rate of about 0.05% at each of two sites and an incorporation efficiency of 0.003%. For comparison, the specific enrichment of 0.18% ^{13}C, at each of 20 sites as determined from the ^{13}Cmr spectrum, represents an incorporation efficiency of 0.01%. The incorporation of radioactivity from phenylalanine could be due to its breakdown by fungal agency to acetic acid with subsequent incorporation into kotanin. Another similar experiment gave analogous results. The activity of the available kotanin was much too low (ca. 50 dpm in the total recrystallized sample) to allow verification of this surmise by degradative studies. In contrast, the labelling pattern revealed by the ^{13}C spectrum is consistent only with a polyketide origin of kotanin, in accord with the earlier conclusion of Holker and co-workers (7) with respect to siderin

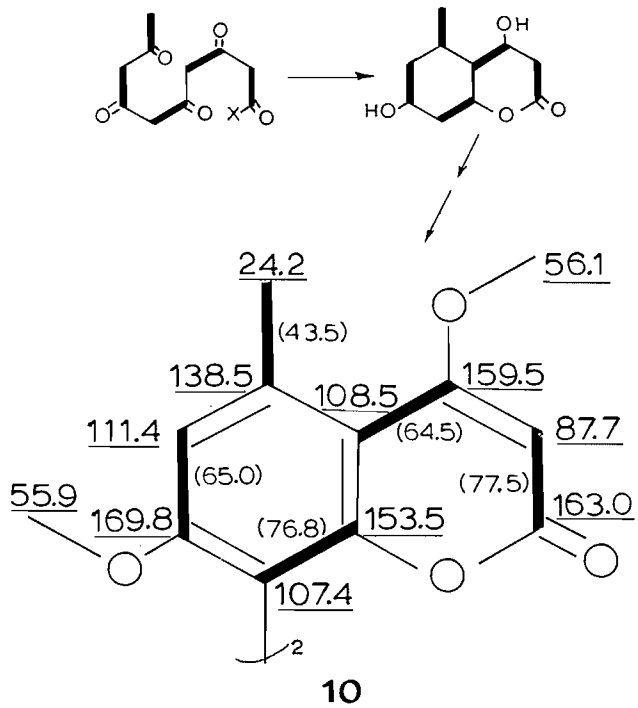

10

FIG. 1. Probable biosynthetic route to kotanin.

biosynthesis in *A. variecolor*. However, siderin and many other 5-methylcoumarins are also known as metabolites of higher plants (14). It would be highly interesting to determine whether the polyketide route is also operative in these cases.

Can. J. Chem. Downloaded from www.nrcresearchpress.com by 196.1.178.254 on 09/07/12
For personal use only.

Can. J. Chem. Downloaded from www.nrcresearchpress.com by 196.1.178.254 on 09/07/12
For personal use only.

Experimental

General purpose solvents were redistilled before use. Evaporations were done at the reduced pressure of the water aspirator. Thin-layer chromatography (tlc) was done on precoated sheets of silica gel (Macherey–Nagel Polygram Sil G/UV_{254}, 0.25 mm) with MeOH/$CHCl_3$ (2:98 v/v) as solvent and uv light (254 nm) and (or) vanillin (0.5% in 60% phosphoric acid) for detection. Column chromatography was performed as described by Cutler *et al.* (6). Melting points were determined on a Kofler hot stage and are uncorrected. Optical rotations were measured with a Perkin–Elmer 241 photoelectric polarimeter. Radioactivities were determined on a Beckman LS 9000 scintillation counter utilizing an Omnifluor (New England Nuclear, Boston, MA; 4 g in toluene (1 L) and ethylene glycol monomethyl ether (800 mL)) scintillation cocktail. Ultraviolet spectra were recorded in 96% EtOH with a Shimadzu UV 240 spectrophotometer. A Varian XL-200 instrument was used to obtain the ^{1}Hmr spectra in $CDCl_3$ solution with TMS as internal reference. The ^{13}Cmr spectra were recorded on a Varian XL-300 system using the same solutions. The coupled spectrum of **3** was obtained with the gated decoupling technique.

Aspergillus niger, accession number ATCC 36626, was purchased from the American Type Culture Collection, Rockville, MD, and routinely maintained on potato-dextrose agar in Petri dishes at 20–24°C. Preparative culture media were inoculated by direct transfer of spores, with a needle, from stock cultures. All operations with viable fungal cells were done aseptically in a biohazard cabinet type IIA. Sodium [1,2-$^{13}C_2$]acetate, 99.1% ^{13}C, was obtained from Isotec Inc., Miamisburg, OH, and L-[1-$^{14}C_1$]phenylalanine from New England Nuclear, Boston, MA.

Preliminary experiments were carried out as described by Cutler *et al.* (6) with a cake (25 g) of shredded wheat (Nabisco) and nutrient solution (50 mL, ref. 6) per flask (Erlenmeyer, 500 mL). On column chromatography (6) of the product from one flask, crystalline kotanin (30 mg) was obtained by concentration of fractions 35–40 (50 mL each, EtOAc/C_6H_6, 3:2). After recrystallization (H_2O/HOAc), the compound had mp > 350°C; $\lambda_{max}(\epsilon)$: 316(19 000 sh), 306(23 450), 296(19 400 sh), 235(18 800 sh), 207(52 400); ^{1}Hmr ($CDCl_3$) δ: 6.72(s, 1H, H-6), 5.51(s, 1H, H-3), 3.93(s, 3H, OMe), 3.80(s, 3H, OMe), 2.71(s, 3H, 5-Me); ^{13}Cmr (see text).

The experiment was repeated with 6 cultures of *A. niger* on medium supplemented with sodium [1,2-$^{13}C_2$]acetate (42 mg, 99.1% ^{13}C) and L-[1-$^{14}C_1$]phenylalanine (41.5 mg, 3.4×10^6 dpm) in each 50 mL of nutrient solution. On extraction after 9 days growth, the cultures afforded only 9.3 mg of crystalline **3** on chromatography of the methylated extract (see below); there was no evidence of ^{13}C satellite signals in its ^{13}C spectrum and its radioactivity (347 dpm/mg) decreased to 42 dpm/mg after two recrystallizations.

Further preliminary experiments with several completely liquid media indicated that the best yields of **3** were realized on a Czapek–Dox medium amended with corn steep liquor ($NaNO_2$, 1.5 g; KCl, 0.3 g; $MgSO_4 \cdot 7H_2O$, 0.3 g; $FeSO_4 \cdot 7H_2O$, 0.006 g; K_2HPO_4, 0.6 g; $CuSO_4$, 0.002 g; $ZnSO_4 \cdot 7H_2O$, 0.006 g; sucrose, 120.0 g; corn steep liquor (Sigma, St. Louis, MO), 12 mL; H_2O to 600 mL), as estimated by two-dimensional tlc (MeOH/$CHCl_3$, 1:10, and EtOAc/toluene/HCOOH, 3:6:1 v/v). However, the rate of kotanin production in these experiments, as determined after methylation, was found to be variable and not a reliable guide for the planned incorporation experiment.

Main experiment

A batch of Delong flasks (250 mL), each containing 40 mL of amended Czapek–Dox medium, were inoculated and monitored, by extraction of one flask at a time, until a distinct spot for kotanin was first observed on tlc of the methylated extract (day 8). Twelve of the cultures were then treated with 4 mL/flask of a solution containing, in 100 mL, sodium (1,2-$^{13}C_2$]acetate (420 mg, 99.1 at.% ^{13}C), L-phenylalanine (413 mg), and L-[1-$^{14}C_1$]phenylalanine (0.006 mg, 2 μCi). The treatment was repeated (4 mL/flask) on day 10 and growth was terminated by the addition of MeOH (100 mL/flask) on day 11. After standing for two days, the supernatant was decanted from the mycelia, which were extracted twice more by steeping in MeOH. The combined supernatants were concentrated until aqueous (ca. 300 mL) and then extracted with $CHCl_3$ (3 × 100 mL). The extracts were combined, evaporated, redissolved in MeOH (20 mL), and treated with ethereal diazomethane (3 × 5 mL, added over 1 h). The product was chromatographed as before to yield crystalline **3** (12.5 mg), which gave the ^{13}C spectrum discussed in the text. On successive recrystallizations from MeOH/$CHCl_3$, the apparent specific radioactivity decreased from 24 dpm/mg to a constant value of 4 ± 2 dpm/mg.

Acknowledgements

We are grateful for the financial support provided by the Natural Sciences and Engineering Research Council of Canada and for the excellent technical assistance of G. L. Rock and S. Wilson.

1. W. B. Turner. Fungal metabolites. Academic Press Inc., London and New York, 1971. p. 198.
2. J. E. Holenstein, A. Stoessl, H. Kern, and J. B. Stothers. Can. J. Chem. **62**: 1971 (1984).
3. A. Stoessl and J. B. Stothers. Z. Naturforsch. C: Biosci. **41C**: 677 (1986).
4. G. Buchi, D. H. Klaubert, R. C. Shank, S. M. Weinreb, and G. N. Wogan. J. Org. Chem. **36**: 1143 (1971).
5. G. Buchi, G., K. C. Luk, B. Kobbe, and J. M. Townsend. J. Org. Chem. **42**: 244 (1977).
6. H. G. Butler, F. G. Crumley, R. H. Cox, O. Hernandez, R. J. Cole, and J. W. Dorner. J. Agric. Food Chem. **27**: 592 (1979).
7. K. K. Chexal, C. Fouweather, and J. S. E. Holker. J. Chem. Soc. Perkin Trans. 1, 554 (1975).
8. A. W. Dunn, R. A. W. Johnstone, T. J. King, L. Lessinger, and B. Sklarz. J. Chem. Soc. Perkin Trans. 1, 2113 (1979).
9. K. Nozawa, H. Seyea, S. Nakajima, S. Udagawa, and K. Kawai. J. Chem. Soc. Perkin Trans. 1, 1735 (1987).
10. C. P. Gorst-Allman, B. A. M. Rudd, C. Chang, and H. G. Floss. J. Org. Chem. **46**: 455 (1981).
11. X. He, C. C. Chang, C. Chang, J. C. Vederas, A. G. McInnes, J. A. W[illiams]ter, and H. G. Floss. Z. Naturforsch. C: Biosci. **41C**: 215 (19[86]).
12. A. St[oessl], and J. B. Stothers. *In* Biologically active natural products. *Edited by* K. Hostettmann and P. J. Lea. Annu. Proc. Phytochem. Soc. Eur. **27**: 1 (1988).
13. R. D. Lapper. Tetrahedron Lett. 4293 (1974).
14. R. D. H. Murray, J. Mendez, and S. A. Brown. The natural coumarins. J. Wiley and Sons, Chicester, England. 1982.
15. A. N. Starratt, J. B. Stothers, and E. W. B. Ward. J. Chem. Soc. Chem. Commun. 590 (1988).
16. A. Stoessl, G. L. Rock, J. B. Stothers, and R. C. Zimmer. Can. J. Chem. **66**: 1084 (1988).

Some aspects of the alkylation of epoxides of 1,6-anhydropyranoses[1]

LEON MAGDZINSKI[2] AND BERT FRASER-REID[3]
Department of Chemistry, University of Maryland, College Park, MD 20742, U.S.A.
and
Department of Chemistry, Paul M. Gross Chemical Laboratory, Duke University, Durham, NC 27706, U.S.A.
Received March 18, 1987[4]

L. MAGDZINSKI and B. FRASER-REID. Can. J. Chem. **66**, 2819 (1988).

The formation of *C*-alkyl derivatives from 1,6:2,3-dianhydro-*manno*-pyranose precursors has been examined. Regioselectivity at C2 is excellent when the C4 substituent is benzyloxy. However, with CH_3, reaction at C2 and C3 occurs, although the ratio of products can be altered substantially depending on the nature of the nucleophile and the reaction conditions.

L. MAGDZINSKI et B. FRASER-REID. Can. J. Chem. **66**, 2819 (1988).

On a examiné la possibilité de former des dérivés *C*-alkylés à partir du dianhydro-1,6:2,3 *manno*-pyrannose. La régiosélectivité au niveau C2 est excellente lorsque le substituant en C4 est un benzyloxy. Avec un substituant CH_3, la réaction se produit toutefois en C2 et en C3; le rapport des produits peut être modifié d'une façon importante en faisant varier la nature du nucléophile ainsi que les conditions de la réaction.

[Traduit par la revue]

The use of 2,4-di-*C*-methyl-pyranose derivatives (e.g., **II**) as chirons (1) in the synthesis of propionate-derived natural products represented by **I** was pioneered by Hanessian *et al.* in their seminal approach to the synthesis of erythronolide (2). Several related contributions have appeared since then (3–8) and among these, 1,6-anhydro sugars (e.g., **III**), first exploited by Kelly and Roberts (6), and Kochetkov *et al.* (7), have been found to be particularly appealing (see for example ref. 8). Thus, the unique topological properties of these derivatives usually engender high stereoselectivities, a fact that had been established previously by the extensive studies of Cerny and Stanek (9).

In the early approaches to the fragment **I**, the anomeric center of **II** was invariably a site for chain elongation (i.e., C1a of **I**) via attachment of the group R. In an alternative approach, we have disconnected the C2 site of **I** differently, in that the C2-CH_3 group is derived from the anomeric carbon (path b), chain elongation being pendant to the ring, as in **V**. This simple change in strategy facilitated the development of the concept of pyranosidic homologation, which we have described elsewhere (10, 11) as a method for assembling multiple contiguous chiral centers with predictable stereoselectivity and easily verified configurations. For this plan, 1,6-anhydro derivatives (e.g., **V**) could serve as intermediates in which the substituent at C2 would need to be more complex than CH_3. In this manuscript, we describe some of our work directed at such chirons.

Epoxide **2** is readily available from levoglucosan, **1**, in two steps (12), and its copper-induced reactions with allyl Grignard reagents had been described by Kelly and Roberts (6) prior to our own work. Accordingly, reaction of **2** with methylmagnesium chloride and cuprous iodide in tetrahydrofuran at 0°C gave **3** in 91% yield.

However, the presence of a functionalized alkyl substituent at C4 was deemed worthy of exploration because of the number of synthetic options that would be opened thereby. Unfortunately, reactions of **2** with a variety of sodium, lithium, or aluminum alkyls were either sluggish or gave complex mixtures probably due to cleavage of the sulfonyl ester, and isomerization to the more stable 2,3-epoxide, **4** (9). Indeed, derivatives of **4** were isolated from some of these reactions.

The sulfonyl group in **2** was therefore removed by sodium–ammonia reduction and the product **5** (13) was treated with ethylvinyl ether to give the α-ethoxyethyl derivative **6**. Reaction of the latter with excess 2-lithio-1,3-dithiane required 11 days and gave **7***a* in only 38% yield. Fortunately, the reaction of **6** with excess bis-diethyl-(trimethylsilylalkynyl)-alane (14) for 30 min at 80°C gave **8***a* in the excellent yield of 96%.

The feasibility of introducing a second alkyl group at C2 of the compounds in Scheme 1 was next considered and, for this purpose, the 4-*C*-methyl product **3** was the most available substrate. Reaction of the latter with sodium methoxide afforded the 2,3-*manno*-epoxide **9** in 86% yield after distillation. Treatment of **9** with methylmagnesium chloride in the presence of cuprous iodide did give the dimethyl compound **10** in 66% yield.

In contrast to this encouraging result, the reactions of **9** with more functionalized nucleophiles proved to be more complex, the regioselectivity and yields being found to be vey dependent on the reaction conditions. For example, reaction with the Grignard reagent **11***c* (prepared from the silylated propargyl ether **11***b*) gave epoxide ring opening at C2 and C3, the products **12***a* and **13***a* being formed quantitatively in 3:2 ratio. The alkynyl alane that had worked so well to give **8** (Scheme 1) was next examined, but several modifications had to be made before optimum selectivity and yields were achieved. For example, reaction of *tert*-butyldimethylsilylpropargyl ether **11***b* with butyllithium, followed by 3 equivalents of diethylaluminum chloride, generated a mixture that reacted with **9** at 80°C in 24 h to give **12***a* and **13***a* in a 2:3 ratio with an excellent total yield of 94%. Further experimentation showed that the ratio of **12***a* and **13***a* could be changed to 7:1 by using equimolar amounts of the alkynyl alane and increasing the temperature to 110°C. Unfortunately, the yield in the latter reaction was also reduced.

Attempts at rationalizing the selectivity at C2 or C3 in reactions of *manno*-2,3-epoxides (e.g., **9**) have been advanced by Cerny and Stanek on the basis of HASB arguments (9). More polarizable "soft" bases (e.g., I^-) attack these substrates predominantly at C3, while "hard" bases (e.g., OH^-) attack at

[1]Taken from Ph.D. thesis of L.M., University of Maryland, 1983.
[2]Present Address: Domtar Research Centre, Senneville, Quebec, Canada H9X 3L7.
[3]Author to whom correspondence may be addressed at Duke University.
[4]Revision received March 4, 1988.

Can. J. Chem. Downloaded from www.nrcresearchpress.com by 196.1.178.254 on 09/07/12
For personal use only.

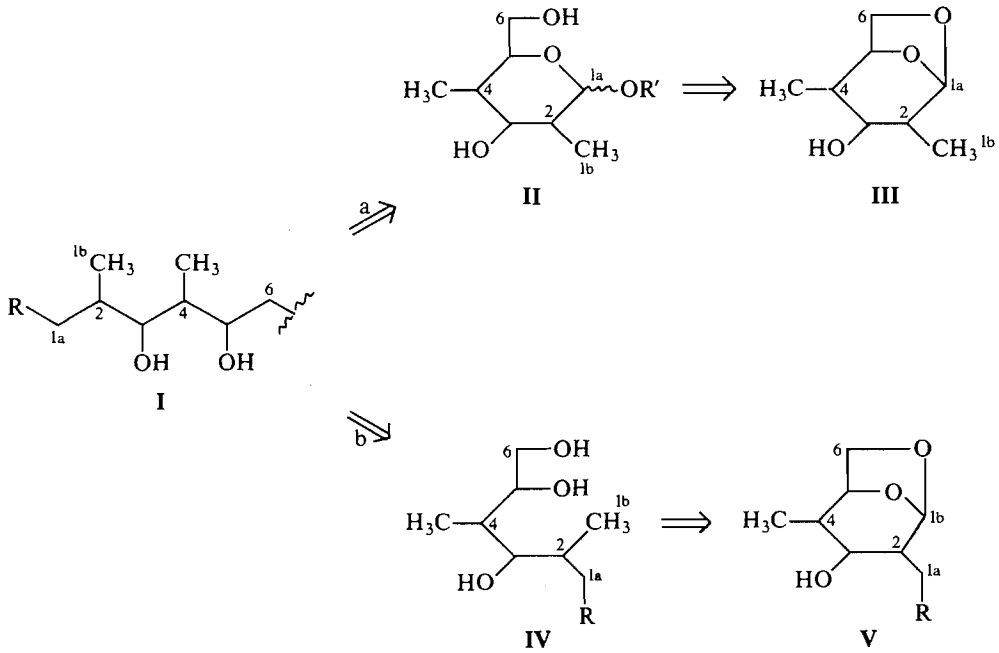

CHART 1

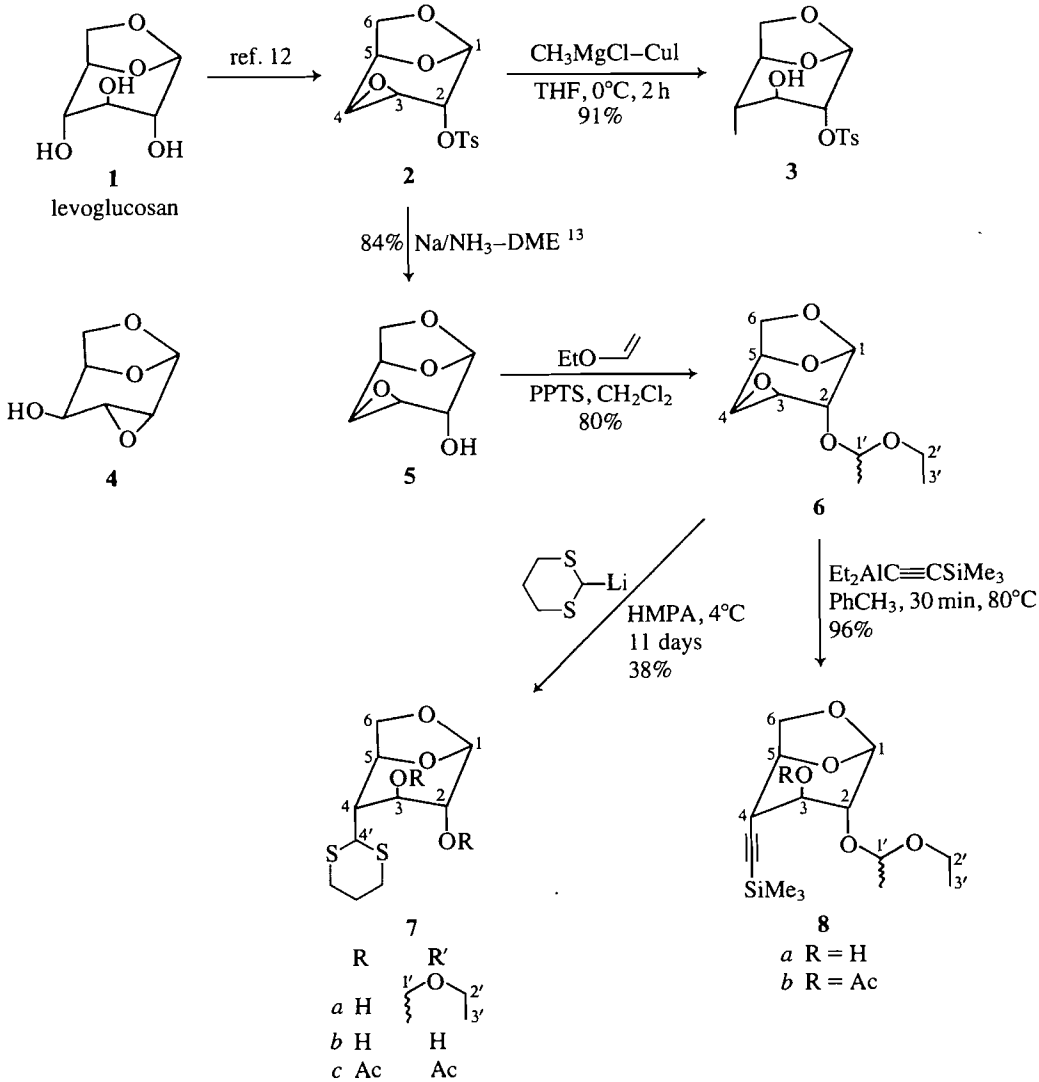

SCHEME 1

Can. J. Chem. Downloaded from www.nrcresearchpress.com by 196.1.178.254 on 09/07/12
For personal use only.

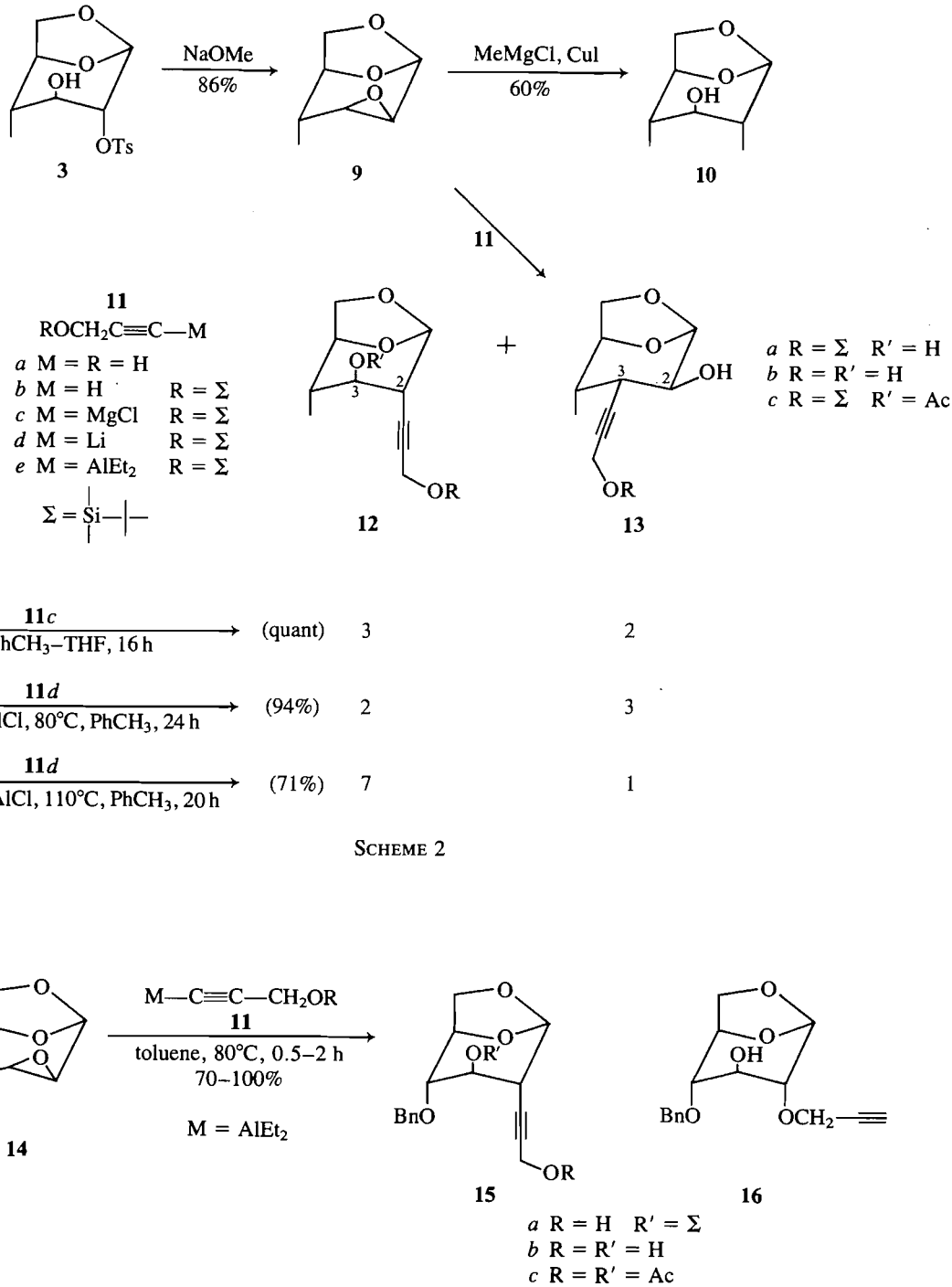

SCHEME 2

SCHEME 3

C2, leading to *trans*-diaxial openings. Copper catalyzed addition of methyl magnesium bromide occurred exclusively at C2; however, the regioselectivity in organometallic reactions is dependent on the metal. This is clear with the magnesium and aluminum propargyl derivatives in Scheme 2.

The effect of the C4 substituent on regioselectivity was apparent when the reaction of the *O*-benzyl analog **14** (12*a*) was examined (Scheme 3). Thus, reaction with alane **11***e* in toluene at 80°C for 2 h gave **15***a* in quantitative yields. Similarly, the unprotected propargyl derivative **11***a* (M = $AlEt_2$) also reacted stereoselectively, but the product was a mixture of **15***b* and **16** in 71 and 7% yields, respectively. However, in both cases reaction was observed only at C2, and in both cases the reaction was much more rapid than in the 4-*C*-methyl derivative. These differences in rate and stereoselectivity in the reactions of **9** and **14** with the same alkynyl alane can be rationalized by evoking electronic influence by the C4 oxygen of **14**.

Data from ^1H nmr and ^{13}C nmr for selected compounds, shown in Tables 1 and 2, were very helpful in making structural assignments. The rigid bicyclic framework allows many long-range couplings, including through-the-ring-oxygens (J_{14}, J_{15}, J_{16}, and J_{25}). These long-range couplings, in addition to the small diequatorial pyranosidic proton couplings, support the triaxial assignments at C2, C3, and C4 encountered in most of the 1,6-anhydro-β-D-glucopyranoses shown in Table 1 (9). In addition, the J_{23} = 10.0 Hz coupling seen in **13** independently

Can. J. Chem. Downloaded from www.nrcresearchpress.com by 196.1.178.254 on 09/07/12
For personal use only.

Can. J. Chem. Downloaded from www.nrcresearchpress.com by 196.1.178.254 on 09/07/12
For personal use only.

TABLE 1. ^{1}H nuclear magnetic resonance parameters of some *C*-alkyl-1,6-anhydro pyranoses

Proton	**15***c*	**12***c*	**13***c*	**10**	**3**	**8***a*	**7***c*	**16**
H1	5.58	5.52	5.36	5.28	5.31	5.32 5.36	5.32	5.47
H2	2.81	2.73	4.78	2.89	4.21	3.4	5.40	3.42
H3	5.18	4.78	3.10	3.30	3.64	3.8	4.55	3.82
H4	3.29	1.84	1.93	2.87	1.81	2.78	2.0	3.29
H5	4.59	4.32	4.32	4.22	4.31	4.25	4.98	4.51
H6x	3.73	3.78	3.80	3.68	3.72	3.46	3.73	3.62
H6n	3.98	4.15	3.82	4.11	4.08	3.86	4.04	3.80
C-CH_3		1.37	1.27	(2) 1.20 (4) 1.07	1.30		(H2′) 4.14	
Coupling constant								
J_{12}	1.0	1.0	1.0	1.0	1.0	~0	1	1.0
J_{23}	1.3	1.2	10.0	0	1.0		1	4.0
J_{34}	1.3	1.2	4.5	1.0	1.0	1	2	4.3
J_{45}	1.0	0	2.0	1.0	0	1	1	1.0
J_{56x}	5.5	5.2	5.3	5.0	5.0	4.8	5.0	5.3
J_{56n}	1.0	1.0	1.0	0.8	0	1.0	0	0
J_{66}	7.2	7.0	7.0	7.2	7.6	7.0	7.0	7.5
J_{13}	1.3	1.2		1.0	1.0			
J_{14}	1.0	1.0	1.0					
J_{16}	1.0							
J_{24}					1.0			
J_{25}	1.0	1.0						
J_{35}	1.0	1.2		1.0	1.0			
J_{15}	1.3		1.0	1.0				
$J_{1'2'}$								
$J_{1'2'}$							(2′4) 10.0	

TABLE 2. ^{13}C nuclear magnetic resonance parameters of some *C*-alkyl-1,6-anhydro pyranoses

Carbon	**15***c*	**12***c*	**13***c*	**10**	**3**
C1	100.8	100.9	99.4	104.4	99.9
C2	36.8	36.6	71.9	42.3	79.2
C3	69.9	73.5	30.7	74.6	72.1
C4	75.3	37.8	37.2	40.4	38.8
C5	74.8	76.1	77.2	76.8	76.8
C6	65.2	67.7	68.3	67.9	68.4
C1′	96.3	82.4	82.0		
C2′	82.7	81.2	82.3		
C3′	52.5	51.7	51.6		
ϕCH_2	71.3				
C=O	170.0 169.5	169.5	169.8		
$AcCH_3$	21.0 20.6	21.2	20.8		
C4-CH_3		17.6	14.2	18.5	17.5
CH_3				(C2) 15.9	Ts (21.6)

confirms its structure and is consistent with "diequatorial" epoxide ring opening of **9**. The ^{13}C nmr data (Table 2) indicated that C5 was very sensitive to substitution at C4. The assignments were verified by off-resonance broad-band decoupling of both sides of the proton spectrum.

Experimental

General

Melting points were determined in capillary tubes using a Buchi model 510 melting point apparatus and are uncorrected. Elemental analyses were performed by Dr. F. Kasler, University of Maryland. The ir spectra were recorded on a Perkin–Elmer model 298 instrument using sodium chloride plates for thin films of liquids, syrups, or solids in Nujol mulls. Optical rotations were detemined at the sodium D line using a Perkin–Elmer 241 polarimeter. The ^{1}H nmr spectra were determined on the following spectrometers: Varian EM-360 A, Varian XL-100, or Varian XL 200. Unless otherwise stated, the solvent used was $CDCl_3$ with internal tetramethylsilane or $CHCl_3$ as the standard. The coupling constants were verified by homonuclear decoupling experiments. For the purpose of ^{1}H nmr interpretation, compound structures have been numbered in the schemes. Low resolution mass spectra were obtained using a Varian MAT-CM7 or a Bell and Howell 21-492 instrument and high resolution mass spectra (hrms) were performed at the Research Triangle Park, North Carolina, with a VG707OF instrument. The progress of all reactions was monitored by thin-layer chromatography (tlc), which was performed on aluminum plates precoated with silica gel HF-254 (0.2-mm layers) containing a fluorescent indicator (Merck, 5539), with detection by uv (254 nm), charring with sulfuric acid spray. Flash chromatography was performed using Kieselgel 60 (230–400 mesh, E. Merck).

*1,6-Anhydro-4-deoxy-4-*C*-methyl-2-*O*-p-toluenesulfonyl-*β*-*D*-glucopyranose, 3*

To a mixture of purified (15) cuprous iodide (800 mg, 0.4 mmol) and methylmagnesium chloride (2.9 M in THF, 60 mL, 160 mmol) in dry THF (200 mL) at −44°C under argon was added solid **2** (12) (12.0 g, 40 mmol). After 2 h at 20°C, the reaction was complete and the mixture was cooled to 0°C, diluted with ether (400 mL), and poured slowly onto 5 M NH_4Cl (400 mL). The ether–THF layer was washed with a 10% ammonium hydroxide, NH_4Cl solution, dried ($MgSO_4$), filtered, and evaporated to yield a yellow semisolid, which was recrystallized from ether – petroleum ether to give the title compound as white plates, mp 91.5–92.0°C, 11.4 g (91%); $[\alpha]_D^{25}$ −54.2° (*c* 1.00, $CHCl_3$); ^{1}H nmr

Can. J. Chem. Downloaded from www.nrcresearchpress.com by 196.1.178.254 on 09/07/12
For personal use only.

(200 MHz), δ: 1.30 (d, J = 7.5 Hz, 3H, C4-CH_3), 1.81 (bq, J = 7.5 Hz, 1H, H4), 2.30 (bs, 1H, OH, D_2O ex), 2.50 (s, 3H, φCH_3), 3.64 (quintet, J = 1.0 Hz, 1H, H3), 3.72 (dd, J = 7.6, 5.0 Hz, 1H, H6x), 4.08 (d, J = 7.6 Hz, 1H, H6n), 4.21 (q, J = 1.0 Hz, 1H, H2), 4.31 (bd, J = 5.0 Hz, 1H, H5), 5.31 (bs, 1H, H1), 7.82 and 7.37 (2 × d, J = 2.3 Hz, 4H, φH); ^{13}C nmr (200 MHz), δ: 145.2 (φC1), 133.8 (φC4), 130.0 (φC2 and φC5), 127.9 (φC3 and φC4), 99.1 (C1), 79.2 (C2), 76.8 (C5), 72.1 (C3), 68.4 (C6), 38.8 (C4), 21.6 (φCH_3), and 17.5 (C4-CH_3); ms: 314 (M, 0.5), 297 (0.5), 279 (1), 243 (2), 227 (7), 159 (70), 155 (60), 113 (32), 101 (58), 91 (70), 85 (69), 71 (42), 55 (75), and 43 (100). *Anal.* calcd. for $C_{14}H_{18}O_6S$: C 53.49, H 5.77, S 10.20; found: C 53.65, H 5.98, S 10.50.

*1,6:3,4-Dianhydro-2-*O*-α-ethoxyethyl-*β*-D-galactropyranose (**6**)*

To an *efficiently* stirred solution of the sulfonate **2** (1.0 g, 2.1 mmol) in dry DME (100 mL) and liquid ammonia (100 mL) at −78°C was added just enough sodium (in 20-mg pieces) to produce a persistent blue color. The addition and stirring were at such a rate as not to allow any large accumulation of sodium metal. At the first sign of the blue color, excess solid ammonium chloride was added. The mixture was diluted with dry ether, refluxed for 5 min, and filtered through Celite 503 (Celite, Baker). The Celite was washed with DME (20 mL) and the combined organic phases evaporated to give compound **5** as white prisms (0.340, 72%); mp 69.0–70.5°C (lit. (13) mp 67–69°C); $[\alpha]_D^{25}$ −83.3° (c 1.46, H_2O) (lit. (13) $[\alpha]_D$ −80°). Treatment of the epoxy alcohol **5** (2.0 g, 13.9 mmol) with ethyl vinyl ether (10 mL, 100 mmol), and pyridinium p-toluenesulfonate (0.1 g) (16) in dry CH_2Cl_2 (20 mL) gave a new material (R_f 0.50, 50% EtOAc – petroleum ether). The mixture was washed successively with sodium bicarbonate solution, water, and brine, dried (K_2CO_3), processed, and chromatographed (30% EtOAc – petroleum ether) to afford the title compound, **6**, as a colorless liquid, bp 100°C/0.06 Torr (1 Torr = 133.3 Pa); 2.4 g (80%); $[\alpha]_D^{25}$ −53.6° (c 0.81, $CHCl_3$); ^1H nmr (200 MHz), δ: 5.28 and 5.19 (2 s, 1:1, 1H, H1), 4.83 (m, 2H, H5 and H1′), 4.00 (d, J = 7.0 Hz, 1H, H6n), 3.78 (s, 1H, H2), 3.63 (m, 3H, H4 and H1″), 3.51 (dd, J = 7.0, 3.4 Hz, 1H, H6x), 3.16 and 3.09 (2 × d, J = 2.5 Hz, 1:1, 1H, H3), 1.40 (d, J = 6.6 Hz, 3H, H2′), and 1.26 (t, J = 6.8 Hz, 3H, H2″). *Anal.* calcd. for $C_{10}H_{16}O_5$: C 55.54, H 7.45; found: C 55.34, H 7.64.

*1,6-Anhydro-4-deoxy-2-*O*-α-ethoxyethyl-4-*C*-(2-trimethylsilyleth-1-ynyl)-*β*-D-glucopyranose (**8**a)*

To a stirred solution of trimethylsilylacetylene (707 mg, 7.2 mmol) in dry toluene (20 mL) at −78°C was added dropwise a solution of n-butyllithium (6.6 mmol). After warming to 20°C, THF (ca. 0.2 mL) was added to dissolve a gelatinous precipitate, the reaction was recooled to −78°C, and Et_2AlCl (6 mmol) was added. The mixture was warmed to 20°C for 45 min, causing a thick white precipitate to form. The temperature was raised to 80°C and epoxide **6** added. After 30 min, tlc (2% MeOH–CH_2Cl_2) indicated completion, and the product was isolated by usual work-up procedures. Column chromatography (60% EtOAc – petroleum ether) gave the title compound (**8***a*) as a colorless liquid, bp 100°C/0.06 Torr; 588.6 mg (96%); $[\alpha]_D^{25}$ −30.5° (c 1.12, $CHCl_3$). Acetylation gave **8***b* as a colorless liquid, bp 80°C/0.06 Torr; $[\alpha]_D^{25}$ −21° (c 0.39, $CHCl_3$); ^1H nmr (60 MHz), δ: 5.52 and 5.46 (2 × d, J = 2.0 Hz, 1H, H1), 5.10 (m, 1H, H3), 4.50 (m, 2H), 4.10 (m, 1H, H2), 3.95 (d, J = 7.0 Hz, 1H, H6n), 3.60 (m, 4H), 2.07 (s, 3H, Ac), 1.30 (m, 6H), and 0.15 (s, 9H, $SiCH_3$). *Anal.* calcd. for $C_{17}H_{28}O_6Si$: C 57.28, H 7.92; found: C 57.29, H 8.14.

*1,6-Anhydro-2-*O*-α-ethoxyethyl-4-deoxy-4-*C*-(1,3-dithian-2-yl)-*β*-D-glucopyranose (7*a*)*

Reaction of epoxide **6** (250 mg, 1.6 mmol) with 1,3-dithianyllithium (5 mmol) in 10 mL dry HMPA at 4°C for 11 days gave a new material (tlc R_f 0.27, 50% EtOAc – petroleum ether; NBS–fluorescein (17) spray positive for thioether) and residual starting **6** (R_f 0.55). The mixture was diluted with ether, washed with water, dried ($MgSO_4$), filtered, evaporated, and chromatographed to yield the title compound (**7***a*) as a pale yellow syrup. The α-ethoxyethyl group was removed by treatment with 80% acetic acid at 60°C for 16 h and the resulting diol, **7***b*, was acetylated to the diacetate **7***c* as a pale yellow syrup, 172.0 mg; $[\alpha]_D^{25}$ −7.6 (c 1.18, $CHCl_3$); ^1H nmr (60 MHz), δ: 5.40 (bt, J = 1.0 Hz, 1H, H2), 5.32 (bs, 1H, H1), 4.98 (bd, J = 5.0 Hz, 1H, H5), 4.55 (bs, 1H, H3), 4.14 (d, J = 10.0 Hz, 1H, H2′), 4.04 (d, J = 7.0 Hz, 1H, H6n), 3.73 (dd, J = 7.0, 5.0 Hz, 1H, H6x), 2.78 (m, 4H, H4′ and H6′), 2.12 (d, J = 10.0 Hz, 1H, H4), 2.04 (s, 6H, Ac), and 1.98 (m, 2H, H5′). *Mol. Wt.* (hrms) calcd. for $C_{14}H_{20}O_6{}^{32}S_2$: 348.0701; found: 348.0703.

*1,6:2,3-Dianhydro-4-deoxy-4-*C*-methyl-*β*-D-mannopyranose (**9**)*

Treatment of **3** (11.4 g, 36.4 mmol) with sodium methoxide (4.0 g) in 30 mL dry MeOH and 300 mL $CHCl_3$ for 16 h produced a clean product (tlc R_f 0.45, 2% MeOH–CH_2Cl_2). After diluting with $CHCl_2$ (600 mL), the organic phase was washed with water, dried ($MgSO_4$), filtered, and evaporated. The resulting pale yellow liquid was distilled to give the title compound (**9**) as a colorless liquid, bp 90°/0.1 Torr; $[\alpha]_D^{25}$ −24.6° (c 1.57, $CHCl_3$); ^1H nmr (100 MHz), δ: 5.68 (d, J = 1.8 Hz, 1H, H1), 4.13 (m, J = 4.2, 22, 1.0, 0.5 Hz, 1H, H5), 3.76 (m, 2H, H6), 3.38 (dt, J = 1.8, 1.8, 0.5 Hz, 1H, H2), 2.88 (dd, J = 1.8, 1.0 Hz, 1H, H3), 2.11 (bq, J = 7.5 Hz, 1H, H4), and 1.23 (d, J = 7.5 Hz, 3H, CH_3); ^{13}C nmr (100 MHz), δ: 97.8 (C1), 73.3 (C2), 68.3 (C6), 53.5 (C2), 51.3 (C3), 34.2 (C4), and 16.4 (CH_3). *Anal.* calcd. for $C_7H_{10}O_3$: C 59.14, H 7.09; found: C 58.58, H 7.24.

*1,6-Anhydro-2,4-dideoxy-2,4-di-*C*-methyl-*β*-D-glucopyranose (**10**)*

To a solution of methylmagnesium chloride (2.9 M in THF, 8.5 mL, 25 mmol) and cuprous iodide (100 mg, 0.5 mmol) in 10 mL dry THF was added epoxide **9** (1.5561 g, 3.9 mmol) at −44°C. After 5 h, tlc (2% MeOH–CH_2Cl_2) showed that reaction was complete. Work-up as for **3** and chromatography (50% EtOAc – petroleum ether) provided the title compound **10** as a colorless liquid, bp 60°/0.06 Torr; 407.0 mg (66%); $[\alpha]_D^{25}$ −62.4° (c 0.82, $CHCl_3$); ^1H nmr (200 MHz), δ: 5.28 (bs, 1H, H1), 4.22 (bd, J = 5.0 Hz, 1H, H5), 4.11 (dd, J = 7.2, 0.8 Hz, 1H, H6n), 3.68 (dd, J = 7.2, 5.0 Hz, 1H, H6x), 3.30 (bd, 1H, H3), 2.50 (bs, 1H, OH, D_2O ex), 2.89 (H2), and 2.87 (H4) (2 × bq, J = 7.5 Hz, 2H), and 1.20 (C2-CH_3) and 1.07 (C4-CH_3) (2 × d, J = 7.5 Hz, 6H); ^{13}C nmr (100 MHz), δ: 104.4 (C1), 76.8 (C5), 74.6 (C3), 67.9 (C6), 42.2 (C2), 40.4 (C4), 18.5 (C4-CH_3), and 15.9 (C2-CH_3). *Mol. Wt.* (hrms) calcd. for $C_8H_{14}O_3$: 158.0942; found: 158.0945.

tert-*Butyldimethylsilyl propargyl ether (**11**b)*

To a solution of propargyl alcohol **11***a* (22.5 g, 0.4 mol), imidazole (60 g, 0.88 mol), and 4-dimethylaminopyridine (2 g) in dry CH_2Cl_2 (500 mL) at 0°C was slowly added *tert*-butyldimethylsilyl chloride (64 g, 0.4 mol). After stirring for 18 h at 25°C, the mixture was poured into water and the CH_2Cl_2 phase washed with water and bicarbonate solution, then dried (Na_2SO_4), filtered, and evaporated. The pale yellow liquid was distilled and the fraction boiling at 155–165°C redistilled through glass rings to give *tert*-butyldimethylsilyl propargyl ether (**11***b*) as a colorless liquid, 51.7 g (76%), bp 161–163°/760 Torr; ^1H nmr (60 MHz), δ: 4.25 (d, J = 2.0 Hz, 2H), 2.32 (t, J = 3.0 Hz, 1H), 0.86 (s, 9H), and 0.03 (s, 6H). *Anal.* calcd. for $C_9H_{18}OSi$: C 63.43, H 10.66; found: C 62.56, H 11.06.

*1,6-Anhydro-2,4-dideoxy-4-*O*-methyl-2-*C*-(3-*tert*-butyldimethylsilyloxyprop-1-nyl)-*β*-D-glycopyranose (**12**a) and 1,6-anhydro-3,4-dideoxy-4-*C*-methyl-3-(3-*tert*-butyldimethylsilyloxyprop-1-ynyl)-*β*-D-altropyranose (**13**a)*

To a stirred solution of TBDMS-propargyl ether **11***a* (4.66 g, 27.4 mmol), in 40 mL dry toluene at −78°C under argon, was added dropwise n-BuLi (27.4 mmol). After warming to 20°C for 30 min, the solution was cooled to −78°C, and 1.3 M Et_2AlCl (6.0 mmol) was added. After stirring for 16 h at 20°C, the epoxide **9** (780 mg, 5.47 mmol), dissolved in 15 mL toluene, was added to the white mixture and the mixture was heated to 100°C. After 20 h, the starting material **9** was completely converted to new material and the mixture was cooled to 0°C and poured into concentrated NH_4Cl solution. EtOAc and Celite were added and the mixture was filtered and washed well with EtOAc. Customary work-up and column chromatography (50% EtOAc – petroleum ether) provided a colorless liquid containing a 7:1 mixture of compounds **12***a* and **13***a*. The major isomer, **12***a*, could be purified by removal of the TBDMS group with fluoride and chromatography (EtOAc) to give the diol **12***b* as a pale yellow syrup,

bp 125°/0.1 Torr; 704.9 mg (65.7% from **9**); $[\alpha]_D^{25}$ +29.5° (*c* 0.43, $CHCl_3$); ^1H nmr (200 MHz), δ: 5.56 (s, 1H, H1), 4.33 (bd, J = 5.0 Hz, 1H, H5), 4.26 (d, J = 2.0 Hz, 2H, H3′), 4.20 (d, J = 7.5 Hz, 1H, H6n), 3.25 (m, 2H, H3 and H6x), 2.76 (bs, 1H, H2), 1.93 (bq, J = 7.0 Hz, 1H, H4), 1.60 (bs, 2H, OH, D_2O ex), and 1.32 (d, J = 7.0 Hz, 3H, C4-CH_3); ms, *m/e*: 198 (*M*, 0.2). *Anal.* calcd. for $C_{10}H_{14}O_4$: C 60.59, H 7.12; found: C 59.95, H 7.00. The regioisomers could be separated by column chromatography (30% EtOAc – petroleum ether) after acetylation to give the corresponding acetates as syrups:

(*a*) **12***c*: ^1H nmr (100 MHz), δ: 5.52 (bs, 1H, H1), 4.78 (quintet, J = 1.2 Hz, 1H, H3), 4.34 (d, J = 2.0 Hz, 2H, H3′), 4.32 (bd, J = 5.2 Hz, 1H, H5), 4.15 (d, J = 7.0 Hz, 1H, H6n), 3.78 (dd, J = 7.0, 5.3 Hz, 1H, H6x), 2.73 (bs, 1H, H2), 1.07 (s, 3H, Ac), 1.84 (bq, J = 7.5 Hz, 1H, H4), 1.37 (d, J = 7.5 Hz, 3H, C4-CH_3), 0.92 (s, 9H, 6Bu), and 0.12 (s, 6H, $SiCH_3$); ^{13}C nmr (100 MHz), δ: 169.5 (C=O), 100.9 (C1), 82.4 (C2′), 81.2 (C1′), 76.1 (C5), 73.5 (C3), 67.7 (C6), 51.7 (C3′), 37.8 (C4), 36.6 (C3), 25.7 (*t*$BuCH_3$), 21.2 ($AcCH_3$), 18.2 (*t*BuC), 17.6 (C4-CH_3), and −5.1 ($SiCH_3$).

(*b*) **13***c*: ^1H nmr (200 MHz), δ: 5.36 (bs, 1H, H1), 4.78 (dd, J = 10.0, 1.0 Hz, 1H, H2), 4.32 (bd, J = 5.3 Hz, 1H, H5), 4.25 (d, J = 2.0 Hz, 2H, H3′), 3.82 (d, J = 7.0 Hz, 1H, H6n), 3.80 (dd, J = 7.0, 5.3 Hz, 1H, H6x), 3.10 (dd, J = 10.0, 4.5 Hz, 1H, H3), 2.07 (s, 3H, Ac), 1.93 (m, 1H, H4), 1.27 (d, J = 7.5, 3H, H4-CH_3), 0.92 (s, 9H, *t*Bu), and 0.12 (s, 6H, $SiCH_3$); ^{13}C nmr (100 MHz), δ: 16.95 (C=O), 99.4 (C1), 82.3 (C2′), 82.0 (C1′), 77.2 (C5), 71.9 (C2), 68.3 (C6), 51.6 (C3′), 37.2 (C4), 82.0 (C1′), 77.2 (C5), 71.9 (C2), 68.3 (C6), 51.6 (C3′), 37.2 (C4), 30.7 (C3), 25.7 (*t*$BuCH_3$), 20.8 ($AcCH_3$), 18.2 (*t*BuC), 14.2 (C4-CH_3), and −5.1 ($SiCH_3$).

*1,6-Anhydro-4-*O*-benzyl-2-deoxy-2-*C*-(3-*tert*-butyldimethylsilyloxy-prop-1-nyl)-β-*D*-glucopyranose (**15**a)*

To a stirred solution of freshly distilled TBDMS-propargyl ether **11***b* (29.0 g, 170.8 mmol), in dry toluene (300 mL) at −78°C under argon, was added dropwise *n*-butyllithium (170.8 mmol). The solution was warmed to 0°C for 1 h. On cooling to −78°C, Et_2AlCl (106.8 mmol) was added to the dark yellow solution. After stirring for 36 h at 25°C, the light yellow mixture was warmed to 80°C and the epoxide **14** (18) (9.90 g, 42.25 mmol) was added as a solid. After 45 min, a new compound (R_f 0.48, 2% MeOH–CH_2Cl_2) had formed. The mixture was cooled to 0°C, 5 M NH_4Cl (30 mL) was carefully added, followed by Celite (30 g) and EtOAc (400 mL). The resulting mixture was filtered through Celite, the solid washed with EtOAc, and the combined organic phases evaporated and chromatographed to remove residual **11***b* (25% EtOAc–petroleum ether). The title compound, **15***a*, was obtained as a pale yellow liquid, bp >150°C/0.06 Torr; 16.9 g (99.1%); $[\alpha]_D^{25}$ +38.8° (*c* 2.36, $CHCl_3$); ^1H nmr (200 MHz); δ: 7.30 (m, 5H, ϕ), 5.52 (bs, 1H, H1), 4.52 (ABq, J = 12.5, Δδ = 0.09 ppm, 2H, CH_2ϕ), 4.54 (bd, J = 5.5 Hz, 1H, H5), 4.27 (d, J = 2.5 Hz, 2H, C3′), 3.94 (dd, J = 7.5, 0.5 Hz, H6x), 3.92 (ddd, J = 7.0, 2.5, 2.0 Hz, 1H, H3), 3.63 (dd, J = 7.5, 5.5 Hz, 1H, H6x), 3.32 (ddd, J = 2.5, 1.5, 1.0 Hz, 1H, H4), 2.67 (bt, J = 2.5 Hz, 1H, H2), 2.49 (d, J = 7.0 Hz, OH, D_2O ex), 0.82 (s, 9H, *t*Bu), and 0.03 (s, 6H, $SiCH_3$); ^{13}C nmr (200 MHz) δ: 139.0, 128.4, 127.7 (aromatic carbons), 101.8 (C1), 82.3 (C2′), 81.3 (C1′), 80.0 (C4), 75.2 (C5), 71.6 (ϕCH_2), 70.4 (C3), 66.0 (C6), 52.0 (C3′), 39.9 (C2), 25.9 (*t*Bu, CH_3), 19.7 (*t*Bu, C), and −5.0 ($SiCH_3$).

*Preparation of 1,6-anhydro-4-*O*-benzyl-2-deoxy-2-*C*-(3-hydroxypropynyl)-β-*D*-glucopyranose **15**b and 1,6-anhydro-4-*O*-benzyl-2-*O*-(prop-2-ynyl)-β-*D*-glucopyranose **16***

To a stirred solution of propargyl alcohol **11***a* (0.20 mL, 280 mg, 5 mmol) in 20 mL dry toluene was added dropwise a solution of *n*-butyllithium in hexane (1.0 M, 10 mL, 10 mmol) at −78°C under argon. The mixture was warmed to 20°C for 30 min until a transparent solution developed. It was sometimes necessary to add a few drops of tetrahydrofuran to redissolve a precipitate. On recooling to −78°C, a solution of diethylaluminum chloride in hexane (1.4 M, 4.5 mL, 6.3 mmol) was added and the resulting white mixture warmed to 20°C. After 18 h, this mixture was heated to 80°C and a solution of the epoxide **14** (18) (234 mg, 1 mmol) in 5 mL toluene was added. After 2 h, the reaction was cooled to 20°C, poured onto 5 M NH_4Cl (30 mL), diluted with 30 mL EtOAc, and filtered through Celite. The solid residue was washed with EtOAc and the aqueous phase extracted with EtOAc. The combined organic phases were dried over magnesium sulfate, filtered, and evaporated. Column chromatography on silica gel provided:

(*a*) (50% EtOAc–petroleum ether) **16** as a colorless oil, bp 110°C/0.1 Torr; 20.6 mg (7%); $[\alpha]_D^{25}$ −23.2° (*c* 1.56, $CHCl_3$); ir: 34.80 (sb), 2120 cm^{-1}; ^1H nmr (200 MHz), δ: 7.34 (m, 5H, PhH), 5.47 (bs, 1H, H1), 4.65 (ABq, J_{AB} = 12 Hz, Δδ = 0.04 ppm, 2H, CH_2Ph), 4.51 (bd, J = 5 Hz, 1H, H5), 4.28 (d, J = 2.0 Hz, 2H, H1′), 3.82 (m, 1H, H3), 3.80 (d, J = 7.5 Hz, 1H, H6n), 3.62 (dd, J = 7.5, 5.3 Hz, 1H, H6x), 3.42 (d, J = 4.0 Hz, 1H, H2), 3.29 (d, J = 4.3 Hz, 1H, H4), 2.46 (bs, 1H, OH, D_2O ex), and 2.42 (t, J = 2.0 Hz, H3′); ms, *m/e* (%): 290 (M^+, 0.5).

(*b*) (5% isopropanol–EtOAc) **15***a* as a colorless syrup, bp 130°C/0.1 Torr; 204 mg (71%); $[\alpha]_D^{25}$ +60.1° (*c* 2.37, $CHCl_3$); ^1H nmr (100 MHz), δ: 7.35 (m, 5H, PhH), 5.53 (s, 1H, H1), 4.65 (ABq, J = 12.0 Hz, Δδ = 1.0 ppm, 2H, CH_2, Ph), 4.54 (d, J = 5.5 Hz, 1H, H5), 4.20 (d, J = 2.0 Hz, 2H, H3′), 4.00 (m, 2H, H3 and H6n), 3.65 (dd, J = 7.0, 5.5 Hz, 1H, H6x), 3.34 (t, J = 1.5 Hz, 1H, H4), 2.75 (bm, 2H, OH's, D_2O ex), and 2.70 (bs, 1H, H2). *Anal.* calcd. for $C_{16}H_{18}O_5$: C, 66.20, H, 6.25; found: C, 65.98, H, 6.25.

Acetylation of **15***a* gave **15***c* as a colorless syrup, bp 130°C/0.06 Torr; $[\alpha]_D^{25}$ +63.1° (*c* 2.82, $CHCl_3$); ir: 1739 (s) and 1233 (s) cm^{-1}; ^1H nmr (200 MHz), δ: 7.37 (m, 5H, PhH), 5.58 (bs, 1H, H1), 5.18 (quintet, J = 1.3 Hz, 1H, H3), 4.77 (ABq, J = 12.1 Hz, Δδ = 0.17 ppm, CH_2Ph), 4.70 (d, J = 2.0 Hz, 2H, H3′), 4.59 (bd, J = 5.5 Hz, 1H, H5), 3.98 (dd, J = 7.2, 1.0 Hz, 1H, H6n), 3.73 (dd, J = 7.2, 5.5 Hz, 1H, H6x), 3.29 (bs, 1H, H4), 2.81 (bs, 1H, H2), and 2.09 and 2.07 (2 × s, 6H, OAc's); ^{13}C nmr (200 MHz), δ: 170.0 and 169.5 (C=O's), 137.9, 128.4, 127.9, 127.8 (aromatic carbons), 100.8 (C1), 96.3 (C1′), 82.7 (C2′), 75.3 (C4), 74.8 (C5), 71.3 ($PhCH_2$), 69.9 (C3), 65.2 (C6), 52.5 (C3′), 36.8 (C2), and 21.0 and 20.6 ($AcCH_3$). *Mol. Wt.* (hrms) calcd. for $C_{20}H_{22}O_7$: 374.1365; found: 374.1368.

Acknowledgements

We are grateful to the National Science Foundation (CHE 8304283) and the University of Maryland for financial support.

1. S. Hanessian. *In* Total synthesis of natural products: The "chiron" approach. Pergamon Press, New York. 1983.
2. S. Hanessian and G. Rancourt. Can J. Chem. **55**, 111 (1977); S. Hanessian, G. Rancourt, and Y. Guidon. Can J. Chem. **55**, 1843 (1978).
3. T. Mukaiyama and R. Noyori. Kagaku Zokan (Kyoto), **91**, 101 (1981).
4. T. D. Inch. Tetrahedron, **40**, 3161 (1984).
5. I. Patterson and M. M. Mansuri. Tetrahedron, **41**, 3569 (1985).
6. A. G. Kelly and J. S. Roberts. J. Chem. Soc. Chem. Commun. 228 (1980).
7. N. K. Kochetkov, A. F. Sviridov, and M. S. Ermolenko. Tetrahedron Lett. **22**, 4315 (1981); **22**, 4319 (1981).
8. M. P. Edwards, S. V. Ley, S. G. Lister, B. D. Palmer, and D. J. Williams. J. Org. Chem. **49**, 3507 (1984); S. Challenger and G. Proctor. Tetrahedron Lett. **27**, 391 (1985); T. Wakamatsu, H. Nakamura, Y. Nishikimi, K. Yoshida, T. Noda, and M. Taniguchi. Tetrahedron Lett. **27**, 6071 (1986).
9. M. Cerny and J. Stanek. Adv. Carbohydr. Chem. Biochem. **34**, 23 (1977).
10. B. F. Molino, L. Magdzinski, and B. Fraser-Reid. Tetrahedron Lett. **24**, 5819 (1983). L. Magdzinski, B. Cweiber, and B. Fraser-Reid. Tetrahedron Lett. **24**, 5823 (1983).
11. B. Fraser-Reid, L. Magdzinski, and B. Molino. J. Am. Chem. Soc. **106**, 731 (1984).

Can. J. Chem. Downloaded from www.nrcresearchpress.com by 196.1.178.254 on 09/07/12
For personal use only.

12. (*a*) M. CERNY, V. GUT, and J. PACAK. Collect. Czech. Chem. Commun. **26**, 2542 (1961); (*b*) R. W. JEANLOZ, A. M. C. RAPIN, and S. I. HAKOMORI. J. Org. Chem. **26**, 3939 (1961).
13. M. CERNY, I. BUBEN, and J. PACAK. Collect. Czech. Chem. Commun. **28**, 1569 (1963).
14. C. G. CHAVDARIAN, S. L. WOO, R. D. CLARK, and C. H. HEATHCOCK. Tetrahedron Lett. 1769 (1976).
15. (*a*) G. B. KAUFFMAN and L. A. TETER. Inorg. Synth. **7**, 9 (1963); (*b*) G. LINSTRUMMELLE, J. K. KREIEGER, and G. M. WHITESIDES. Org. Synth. **55**, 103 (1976).
16. M. MIYASHITA, A. YOSHIKOSHI, and P. A. GRIECO. J. Org. Chem. **42**, 3772 (1977).
17. *In* Dyeing reagents for thin layer and paper chromatography. E. Merck, Darmstadt. 1976.
18. T. TRAHA and M. CERNY. Collect. Czech. Chem. Commun. **36**, 2216 (1971).

Can. J. Chem. Downloaded from www.nrcresearchpress.com by 196.1.178.254 on 09/07/12
For personal use only.

Natural amino acids as chiral auxiliaries in asymmetric Diels–Alder reactions

MARIA P. BUENO, CARLOS CATIVIELA,[1] AND JOSÉ A. MAYORAL
Departamento de Química Orgánica, Instituto de Ciencia de los Materiales de Aragón, Universidad de Zaragoza, 50009 Zaragoza, Spain
ALBERTO AVENOZA, PAULA CHARRO, AND MIGUEL A. ROY
Departamento de Química Orgánica, Colegio Universitario de la Rioja, Logroño, Spain
AND
JOSÉ M. ANDRÉS
Instituto de Carboquímica, C.S.I.C., Zaragoza, Spain

Received June 10, 1988

MARIA P. BUENO, CARLOS CATIVIELA, JOSÉ A. MAYORAL, ALBERTO AVENOZA, PAULA CHARRO, MIGUEL A. ROY, and JOSÉ M. ANDRÉS. Can. J. Chem. **66**, 2826 (1988).

To test whether α-amino acids can be efficient chiral auxiliaries in asymmetric Diels–Alder reactions, the chiral dienophile *N*-acryloyl-L-phenylalanine methyl ester was made to react with cyclopentadiene. Diastereofacial selectivity is to a great extent dependent on the Lewis acid used to promote the reaction; whereas moderate excesses of the (1*R*, 2*R*)-cycloadduct were achieved with $AlCl_3$, the reaction did not show diastereofacial selectivity when titanium catalysts were used. Moreover, with $Ti(^iPrO)_4$ a transesterification reaction, which leads to the isopropyl ester and competes with the Diels–Alder reaction, was observed. In spite of the structural similarity of this dienophile to the acrylate of (*S*)-ethyl lactate, it behaved very differently in the titanium-catalyzed reactions.

MARIA P. BUENO, CARLOS CATIVIELA, JOSÉ A. MAYORAL, ALBERTO AVENOZA, PAULA CHARRO, MIGUEL A. ROY et JOSÉ M. ANDRÉS. Can. J. Chem. **66**, 2826 (1988).

Afin de déterminer si les acides α-aminés peuvent être des auxiliaires chiraux efficaces dans des réactions de Diels–Alder asymétriques, on a fait réagir le cyclopentadiène avec le dièNophile chiral suivant: l'ester méthylique de la *N*-acryloyl-L-phénylalanine. La sélectivité diastéréofaciale dépend beaucoup de l'acide de Lewis utilisé pour promouvoir la réaction; alors que le $AlCl_3$ nous permet d'obtenir de légers excès du cycloadduit-(1*R*, 2*R*), on n'a pas détecté de sélectivité diastéréofaciale lorsqu'on a utilisé des catalyseurs de titane. De plus, avec le Ti(i-PrO)$_4$, on a observé une réaction de transestérification qui entre en compétition avec la réaction de Diels–Alder et qui conduit à la formation de l'ester isopropylique. D'un point de vue structural, ce dièNophile ressemble beaucoup à l'acrylate du (*S*)-lactate d'éthyle; malgré ces ressemblances, les deux se comportent très différemment au cours de réactions catalysées par le titane.

[Traduit par la revue]

Can. J. Chem. Downloaded from www.nrcresearchpress.com by 196.1.178.254 on 09/07/12
For personal use only.

High levels of diastereofacial selectivity have been achieved in asymmetric Diels–Alder additions of prochiral 1,3-dienes to dienophiles with a removable, chiral-directing auxiliary (1). However, it is interesting to test whether chiral reagents, both enantiomers of which are inexpensive and easily available, can be efficient chiral auxiliaries in this kind of reaction. In this context, reactions of acrylates (2) and fumarates (3) of several derivatives of chiral hydroxy acids with cyclopentadiene are reported to proceed with good selectivity, mainly when $TiCl_4$ is used to promote the reaction. The results obtained are explained by the formation of a dienophile–$TiCl_4$ chelate complex, which amplifies diastereofacial discrimination (4). Also several *N*-acryloyl and *N*-crotonyl compounds, such as the *N*-acyloxazolidones (5) and the *N*-acylsultams (6) derived from camphor, have been used as chiral dienophiles.

In spite of their availability, inexpensive natural α-amino acids, which have been used in a lot of asymmetric reactions (7), have not been tested as chiral auxiliaries in asymmetric Diels–Alder reactions. In view of that, we have studied the reaction between cyclopentadiene and *N*-acryloyl-L-phenylalanine methyl ester (**1**).

The chiral dienophile was easily obtained by reaction of L-phenylalanine with acryloyl chloride (8), followed by methylation with BF_3–MeOH complex. *N*-acryloyl-L-phenylalanine methyl ester **1** was made to react with cyclopentadiene under several conditions, using a molar relationship dienophile: diene = 1:6 (Scheme 1). The results of the reactions were determined by hplc and are shown in Table 1.

No significant solvent effect was found for the reaction of cyclopentadiene with dienophile *N*-acryloyl-L-phenylalanine methyl ester **1**, the slight changes in *endo*/*exo* selectivity conforming to the pattern found by Berson *et al.* (9) for reactions of acrylates with cyclopentadiene.

As expected, the use of $AlCl_3$ as a catalyst caused a remarkable increase in both the reaction rate and *endo*/*exo* selectivity. When the reaction temperature was lowered the *endo*/*exo* ratio increased, but diastereofacial selectivity was not noticeably modified for reaction temperatures below 0°C.

Helmchen and co-workers have previously reported (2*a*) that the use of $TiCl_4$ to promote the reaction between cyclopentadiene and the acrylate of (*S*)-ethyl lactate causes a high diastereofacial differentiation, mainly with 0.75 equiv. of Lewis acid. In spite of the structural similarity between the dienophile used by these authors and *N*-acryloyl-L-phenylalanine methyl ester **1**, in our case this catalyst gave low diastereofacial selectivity for all tested molar ratios of catalyst:dienophile.

To increase diastereofacial selectivity, a less effective titanium catalyst, $Ti(^iPrO)_4$, was tested. The relationship between the areas of the hplc peaks corresponding to the *endo* products **2***a*:**2***b* followed an unexpected pattern, since it increased with increasing reaction temperatures. A careful analysis showed that the peak corresponding to **2***a* was contaminated by a new product, which was obtained by reaction of *N*-acryloyl-L-phenylalanine methyl ester with $Ti(^iPrO)_4$ and identified as

[1]Author to whom correspondence may be addressed.

Printed in Canada / Imprimé au Canada

Can. J. Chem. Downloaded from www.nrcresearchpress.com by 196.1.178.254 on 09/07/12
For personal use only.

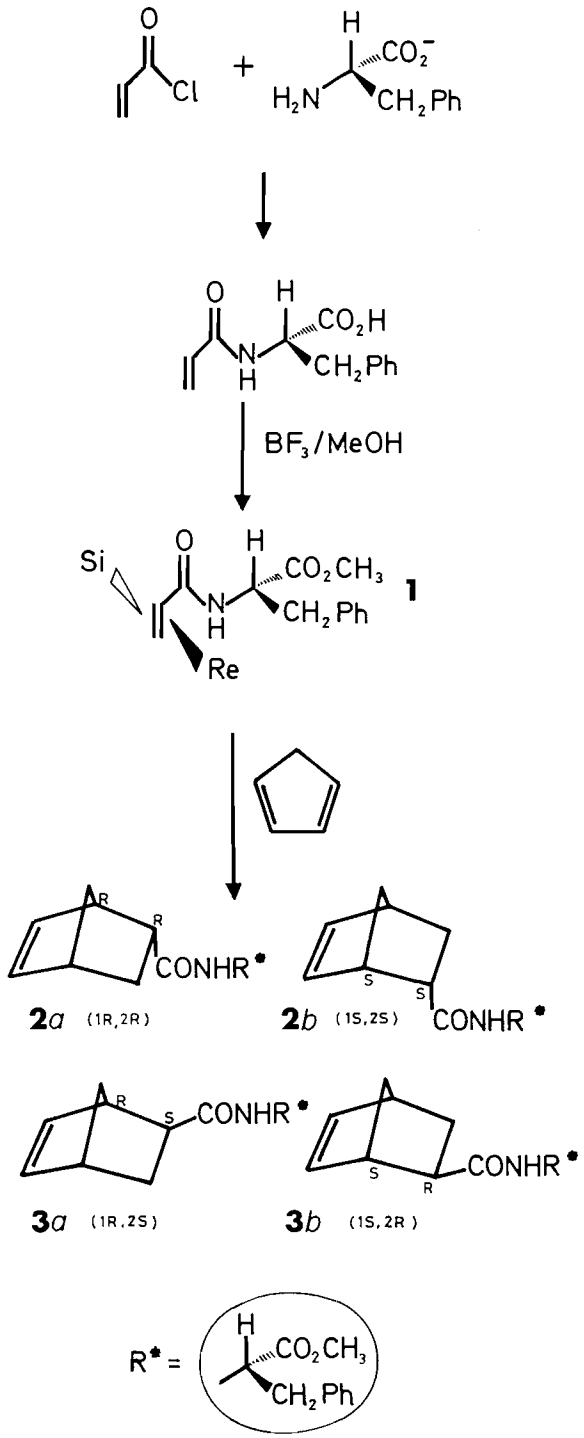

SCHEME 1

N-acryloyl-L-phenylalanine isopropyl ester **4**. The proportion of this product increases with the reaction time and temperature (Scheme 2).

When the reaction was carried out at −25°C the formation of the isopropyl ester **4** was minimized, and the ratio of **2***a*:**2***b* approached that obtained with $TiCl_4$. Neither the Diels–Alder reaction nor ester formation occurred at still lower reaction temperatures.

N-Acryloyl-L-phenylalanine isopropyl ester **4** was made to react, in CH_2Cl_2 at −40°C, with 6 equiv. of cyclopentadiene using 1.1 equiv. of $AlCl_3$ to promote the reaction. In comparison to the reaction between *N*-acryloyl-L-phenylalanine methyl

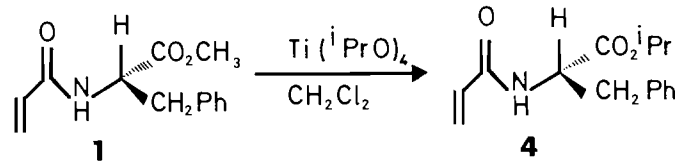

T (°C)	Time (h)	Ratio **4** : **1**
25	19	79
0	66	91

SCHEME 2

ester **1** and cyclopentadiene under the same conditions, a similar *endo*/*exo* ratio (35.4:1) but a lower diastereofacial selectivity (54:46) were obtained.

The low diastereofacial selectivities obtained with titanium catalysts suggest that the coordination of **1** with this kind of catalyst does not lead to a chelate complex, similar to that postulated by Helmchen *et al.* for the acrylate of (*S*)-ethyl lactate – $TiCl_4$ complex. However, the formation of *N*-acryloyl-

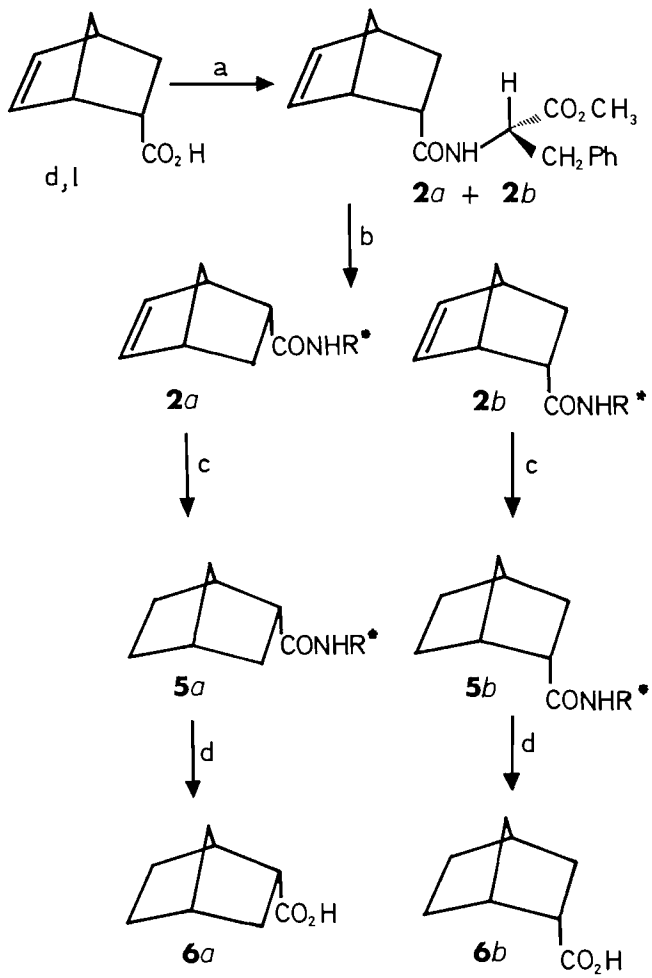

(a) $SOCl_2$, followed by L-$H_2NCH(CO_2^-)CH_2Ph$ and BF_3/MeOH (b) Column Chromatography on Silica gel using n-Hexane/Et_2O (1/3) as eluting agent; (c) H_2, Pd/C; (d) HCl 6N.

SCHEME 3

TABLE 1. Diels–Alder reactions of cyclopentadiene with *N*-acrylolyl-L-phenylalanine methyl ester (**2**)

Lewis acid (equiv.)	Solvent[a]	*T* (°C)	Time (h)	Yield (%)[b]	*endo*/*exo* ratio of **2**:**3**[b]	Ratio of **2***a*:**2***b*[b]
—	CH_2Cl_2	25	70	63	2.8:1	52:48
—	Toluene	25	70	49	2.0:1	55:45
$AlCl_3$ (1.1)	CH_2Cl_2	25	5	99	7.3:1	60:40
$AlCl_3$ (1.1)	Toluene	25	5	99	4.5:1	57:43
$AlCl_3$ (1.1)	CH_2Cl_2	0	20	80	15.9:1	70:30
$AlCl_3$ (1.1)	CH_2Cl_2	−25	25	95	29.0:1	68:32
$AlCl_3$ (1.1)	CH_2Cl_2	−40	50	93	31.3:1	71:29
$AlCl_3$ (1.1)	CH_2Cl_2	−60	55	76	42.8:1	65:35
$TiCl_4$ (0.75)	CH_2Cl_2	25	20	95	14.9:1	51:49
$TiCl_4$ (0.75)	CH_2Cl_2	−15	65	91	12.5:1	51:49
$TiCl_4$ (1.1)	CH_2Cl_2	−15	65	86	3.0:1	49:51
$TiCl_4$ (1.7)	CH_2Cl_2	−15	65	86	4.0:1	52:48
$Ti(^iPrO)_4$ (1.1)	CH_2Cl_2	−25	65	40	5.1:1[c]	58:42[c]
$Ti(^iPrO)_4$ (1.1)	CH_2Cl_2	−40	190	—	—	—

[a]Twenty-five millilitres.

[b]Determined by hplc. Column, 5 μm silica Hypersil[R]. Eluent, ethanol–hexane, gradient 1 to 5% of ethanol in 1 min. Flow rate, 2 mL/min. Detection, 215 nm, $\epsilon_1:\epsilon_{2a}:\epsilon_{2b}:\epsilon_{3a+3b}$ = 1.686:1.034:1.000:1.030.

[c]The peak corresponding to **2***a* is contaminated by a small amount of *N*-acrylolyl-L-phenylalanine isopropyl ester **4**.

L-phenylalanine isopropyl ester **4** indicates that, in spite of the greater basicity of the amide moiety, there may be some degree of coordination to the ester moiety.

To determine the absolute configuration of the major product, *endo*- and *exo*-5-norbornen-2-carboxylic acids, which were prepared by reaction of acrylic acid with cyclopentadiene followed by iodolactone separation, were used to prepare *endo* and *exo* cycloadducts **2** and **3**. The *endo* mixture was separated into its components by means of column chromatography on silica gel, using n-C_6H_{14}/Et_2O (1:3) as eluting agent. By treatment of **2***a* or **2***b* with 20% aqueous NaOH only the ester moiety was hydrolysed and, after 2 h, partial epimerization was observed. Treatment of **2***a* and **2***b* with aqueous mineral acids led to a complex mixture of products, probably due to Wagner–Meerwein type rearrangements (10). In view of this, **2***a* and **2***b* were hydrogenated and converted without epimerization into both enantiomers of the *endo*-norbornan-2-carboxylic acid, **6***a* and **6***b*, by acid hydrolysis. The absolute configurations of these acids were determined by comparing their specific rotations with those given in the literature (11). Under these conditions **2***a* gave (1*S*, 2*R*, 4*R*) norbornan-2-carboxylic acid and **2***b* (1*R*, 2*S*, 4*S*) norbornan-2-carboxylic acid, with optical rotations $[\alpha]_D^{26}$ (EtOH) of +30° (*c* 1.2) and −30° (*c* 1.2) respectively (Scheme 3).

In all cases the Diels–Alder reaction led predominantly to the (1*R*, 2*R*)-*endo* diastereomer **2***a*, which comes from the attack of the cyclopentadiene on the Si face of the dienophile **1**. This result can be explained on the basis of reactive conformer **1**, with antiplanar enoate conformation, which is similar to those postulated for complexes (**7**) of "classical" chiral acrylates with only one center capable of coordination (1*a*) (Scheme 4). The preferential attack on the Si face of the dienophile **1** suggests a possible electronic effect of the phenyl group (12).

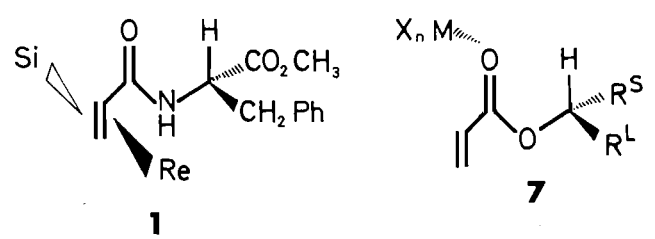

1 **7**

SCHEME 4

Experimental

The ^1H nmr spectra were recorded at 80 MHz with a Bruker model WP 80 CW spectrometer and at 200 MHz with a Varian model XL 200 spectrometer in $CDCl_3$ with Me_4Si as internal standard. High pressure liquid chromatography was performed using a Hewlett–Packard model 1090 M chromatograph; specific rotations were measured with a Perkin–Elmer model 241-MC polarimeter. Melting points were determined on a Buchi 510 apparatus and are uncorrected.

The chiral dienophile **1** was easily obtained by reaction of L-phenylalanine with acryloyl chloride (8) followed by methylation with BF_3–MeOH complex.

A. Diels–Alder reactions

1. Without a catalyst

One millimole of **1** and 6 mmol of cyclopentadiene were stirred under nitrogen in 25 mL of the appropriate solvent and at the temperature specified (Table 1). After the corresponding time the solvent was removed under reduced pressure and the residue was dissolved in methanol. The solution was filtered and evaporated under reduced pressure to give a solid, which was analyzed by hplc.

2. With a catalyst

One millimole of **1** and the corresponding amount of the catalyst were stirred in 20 mL of dry CH_2Cl_2 under nitrogen at the appropriate temperature for 1 h. A solution of cyclopentadiene (6 mmol) in 5 mL of dry CH_2Cl_2 at the same temperature was then added. The mixture was stirred for the adequate time (Table 1) and treated with a cold 10% aqueous NaOH solution in the case of $AlCl_3$ or 15% aqueous NaOH solution in the case of titanium catalyst. The organic layer was dried with anhydrous sodium sulfate, filtered, and evaporated under reduced pressure to give a solid, which was analyzed by hplc.

B. Synthesis of N*-acryloyl-L-phenylalanine isopropyl ester 4*

One millimole of **1** and 1.1 mmol of $Ti(^iPrO)_4$ were stirred in 25 mL of dry CH_2Cl_2 under nitrogen at the appropriate temperature for the chosen time. The mixture was then treated with a 15% NaOH solution and the organic layer was dried with anhydrous sodium sulfate, filtered,

Can. J. Chem. Downloaded from www.nrcresearchpress.com by 196.1.178.254 on 09/07/12
For personal use only.

and evaporated under reduced pressure to give a solid, which was analyzed by hplc.

To obtain an analytically pure sample of **4**, the reaction was carried out with 2 mmol of $Ti(^iPrO)_4$ at room temperature for 72 h, and the solid obtained after the treatment was recrystallized from diethyl ether/*n*-hexane; mp 81–83°C; nmr ($CDCl_3$) δ: 1.12 (d, 3H), 1.22 (d, 3H), 3.12 (dd, 2H), 4.9 (m, 2H), 5.5 (dd, 1H), 6.1 (m, 3H), 7.25 (m, 5H). *Anal.* calcd. for $C_{15}H_{19}NO_3$: C 68.94, H 7.33, N 5.36; found: C 69.29, H 7.07, N 5.43.

C. Alternative synthesis of methyl-N-(endo-*bicyclo[2.2.1]hept-2-carbonyl)-L-phenylalaninates* **2**a *and* **2**b

Ten millimoles of *endo*-bicyclo[2.2.1]hept-5-en-2-carboxylic acid and 15 mmol of thionyl chloride in dry chloroform were refluxed for 3 h. After this time the solution was evaporated under reduced pressure and the residue was distilled at 14 Torr (1 Torr = 133.3 Pa) to give 80% of the corresponding acyl chloride. This compound was dripped into a solution of 8 mmol of L-phenylalanine in 10 mL of 10% aqueous sodium hydroxide previously cooled in an ice bath (if a precipitate appeared, a little more water was added). After 3 h the stirred solution was acidified with 6 N hydrochloric acid; the precipitate was filtered and recrystallized from water to give a 65% yield of *N*-(*endo*-bicyclo[2.2.1]hept-5-en-2-carbonyl)-L-phenylalanine. Five millimoles of this compound were refluxed with BF_3–MeOH complex for 2 h. The solution was washed with sodium acid carbonate solution and extracted several times with ether. The organic layer was separated and dried over anhydrous sodium sulfate. After removing the organic solvent a white oil appeared (yield 90%), which was passed through a chromatographic column of silica gel, using *n*-hexane/Et_2O = 1:3 as eluting agent, to give both diastereoisomers. These were recrystallized from *n*-hexane to give analytically pure samples of methyl-*N*-(*endo*-bicyclo[2.2.1]hept-5-en-2-carbonyl)-L-phenylalaninate **2***a* and **2***b*. mp (**2***a*) 114–116°C; nmr (**2***a*) ($CDCl_3$) δ: 1.23–1.40 (m, 3H), 1.88 (m, 1H), 2.82–2.89 (m, 2H), 3.00–3.20 (m, 3H), 3.73 (s, 3H), 4.85 (m, 1H), 5.74 (m, 1H), 6.18 (m, 1H), 7.08–7.32 (m, 5H). *Anal.* calcd. for $C_{18}H_{21}NO_3$: C 72.22, H 7.07, N 4.68; found: C 71.96, H 7.20, N 4.93. For **2***b*: mp 80–82°C; nmr ($CDCl_3$) δ: 1.24–1.45 (m, 3H), 1.92 (m, 1H), 2.81–2.90 (m, 2H), 3.00–3.20 (m, 3H), 3.73 (s, 3H), 4.83 (m, 1H), 5.85 (m, 1H), 6.18 (m, 1H), 7.06–7.38 (m, 5H). *Anal.* found: C 72.52, H 7.33, N 4.21.

Two millimoles each of **2***a* and **2***b* in 20 mL of methanol were hydrogenated at room temperature and atmospheric pressure using 10% Pd/C as catalyst until completion of the reaction (tlc). In 1 h the hydrogenation was completed, the catalyst filtered off, and the solvent removed under reduced pressure to give white solids, **5***a* and **5***b*, in quantitative yield. *Anal.* calcd. for $C_{18}H_{23}NO_3$: C 71.73, H 7.69, N 4.65; found for **5***a*: C 71.54, H 7.99, N 4.15; found for **5***b*: C 71.45, H 7.96, N 4.28.

To identify the major product in the Diels–Alder reaction, 1 millimole each of **5***a* and **5***b* in 5 mL of 6 N hydrochloric acid were refluxed for 24 h. After this time the solution was extracted with ether and the organic layer was dried over anhydrous sodium sulfate and evaporated to give both *endo* bicyclo[2.2.1]heptan-2-carboxylic acids **6***a* and **6***b* whose specific rotations were measured, $[\alpha]_D^{26}$ (**6***a*) +30° (*c* 1.2, EtOH) and $[\alpha]_D^{26}$ (**6***b*) −30° (*c* 1.2, EtOH), and compared with the literature value, $[\alpha]_D$ 30.6° (*c* 1.2, EtOH) (11).

Acknowledgements

This research was made possible by the generous financial support of the Comisión Asesora de Investigación Científica y Técnica (project number PB85-0335). María P. Bueno would like to express her gratitude to the Diputación General de Aragón and Paula Charro to the Instituto de Estudios Riojanos for a grant.

1. (*a*) W. OPPOLZER. Angew. Chem. Int. Ed. Engl. **23**, 876 (1984); (*b*) Tetrahedron, **43**, 1969 (1987); (*c*) L. A. PAQUETTE. *In* Asymmetric synthesis. Vol. 3. *Edited by* J. D. Morrison: Academic Press, New York. 1984.
2. (*a*) T. POLL, G. HELMCHEN, and B. BAUER. Tetrahedron Lett. **25**, 2191 (1984); (*b*) T. POLL, A. SOBCZAK, H. HARTMANN, and G. HELMCHEN. Tetrahedron Lett. **26**, 3095 (1985).
3. H. HARTMANN, A. F. A. HADY, K. SARTOR, J. WEETMAN, and G. HELMCHEN. Angew. Chem. Int. Ed. Engl. **26**, 1143 (1987).
4. T. POLL, J. O. METTER, and G. HELMCHEN. Angew. Chem. Int. Ed. Engl. **24**, 112 (1985).
5. D. A. EVANS, K. T. CHAPMAN, and J. BISAHA. J. Am. Chem. Soc. **106**, 4261 (1984).
6. W. OPPOLZER, C. CHAPUIS, and G. BERNARDINELLI. Helv. Chim. Acta, **67**, 1397 (1984).
7. (*a*) K. DRAUZ, A. KLEEMAN, and J. MARTENS. Angew. Chem. Int. Ed. Engl. **21**, 584 (1982); (*b*) G. M. COPPOLA and H. F. SCHUSTER. Asymmetric synthesis. John Wiley and Sons, New York. 1987.
8. R. K. KULKARNI and H. MORAWETZ. J. Polym. Sci. **54**, 491 (1961).
9. J. A. BERSON, Z. HAMLET, and W. A. MUELLER. J. Am. Chem. Soc. **84**, 297 (1962).
10. M. NAKAZAKI, K. NAEMURA, and H. KADOWAKI. J. Org. Chem. **43**, 4947 (1978).
11. (*a*) J. A. BERSON and D. A. BEN-EFRAIM. J. Am. Chem. Soc. **81**, 4083 (1959); (*b*) J. A. BERSON, J. S. WALIA, A. REMANICK, S. SUZUKI, P. REYNOLDS-WARNHOFF, and D. WILLNER. J. Am. Chem. Soc. **83**, 3986 (1961).
12. D. A. EVANS, K. T. CHAPMAN, D. TAN HUNG, and A. T. KAWAGUCHI. Angew. Chem. Int. Ed. Engl. **26**, 1184 (1987).

Can. J. Chem. Downloaded from www.nrcresearchpress.com by 196.1.178.254 on 09/07/12
For personal use only.

Étude de la flash thermolyse du méthyl-5 azido-2 thiadiazole-1,3,4 par spectroscopie photoélectronique (HeI) et calculs quantiques[1]

I. B'Shary, C. Guimon, M. Grimaud et G. Pfister-Guillouzo
Université de Pau et des Pays de l'Adour, Laboratoire de physico-chimie moléculaire, Unité Associée 474, Avenue de l'Université, 64000 Pau, France

Reçu le 11 mars 1988

I. B'Shary, C. Guimon, M. Grimaud et G. Pfister-Guillouzo. Can. J. Chem. **66**, 2830 (1988).

La flash thermolyse du méthyl-5 azido-2 thiadiazole-1,3,4 sous pression réduite (10^{-2} mbar) a été suivie par spectroscopie photoélectronique ultraviolette (HeI). Elle conduit à l'obtention du thiocétène $H_2C{=}C{=}S$ accompagné d'acide cyanhydrique HCN et d'azote N_2. La formation de ces molécules montre que le thiadiazolo-nitrène instable subit une ouverture de cycle pour donner une thione linéaire **4** qui se réarrange thermiquement dans les produits finals. Ce dernier réarrangement est analysé théoriquement à l'aide de la méthode semi-empirique MNDO.

I. B'Shary, C. Guimon, M. Grimaud, and G. Pfister-Guillouzo. Can. J. Chem. **66**, 2830 (1988).

The flash thermolysis of 5-methyl 2-azido 1,3,4-thiadiazole (vapour phase: 10^{-2} mbar) was studied by ultraviolet photoelectron spectroscopy (HeI). The products detected ($H_2C{=}C{=}S$, HCN, and N_2) suggest that the unstable thiadiazole-nitrene undergoes a ring opening to form a linear thione **4**, which generates the thiocetene $H_2C{=}C{=}S$. This step was theoretically analysed by the MNDO method.

Can. J. Chem. Downloaded from www.nrcresearchpress.com by 196.1.178.254 on 09/07/12
For personal use only.

Les azotures sont utilisés depuis de nombreuses années comme précurseurs de molécules à courte durée de vie aussi bien par photolyse que par thermolyse car, perdant relativement facilement une molécule d'azote, ils génèrent un nitrène instable qui se réarrange aussitôt en composés stables ou métastables

$$R{-}N_3 \xrightarrow{\Delta \text{ ou } h\nu} R{-}\ddot{N}{:} + N_2 \rightarrow ? + N_2$$

Dans le cadre d'une étude des réarrangements thermiques de nitrènes en série hétérocyclique en particulier sur le pyridino-nitrène-2 (1) et triazolo-1,2,4 nitrène-3 (2), nous avons examiné l'évolution du méthyl-5 thiadiazolo-2 nitrène **2** issu de la thermolyse éclair du méthyl-5 azido-2 thiadiazole-1,3,4 en phase vapeur et sous pression réduite ($\sim 10^{-2}$ mbar) :

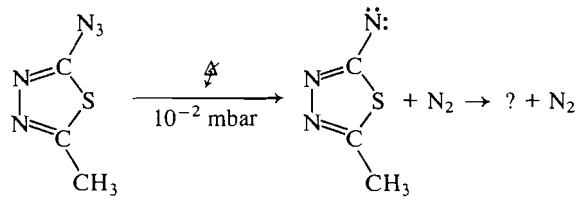

1 **2**

Si d'une part on admet la validité de l'hypothèse de la conservation de spin (3–5) (réaction se déroulant entièrement à l'état singulet) et si d'autre part on ne considère que les réactions monomoléculaires du fait de la faible pression, trois processus de réarrangement sont généralement proposés (3).

(a) L'extension de cycle déjà observée à basse température dans le cas des cycles à six chaînons (6, 7) conduit à un cycle de structure mésoionique à six chaînons **3**, très instable dans nos conditions opératoires, qui pourrait alors s'ouvrir pour donner le composé linéaire **4** :

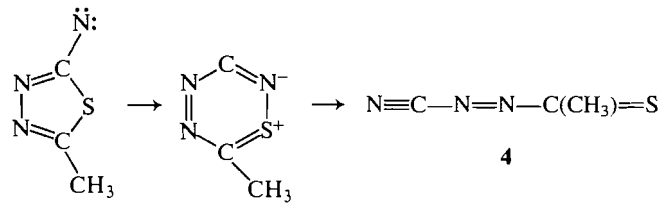

2 **3** **4**

(b) La contraction de cycle a également été mise en évidence dans le cas des cycles à six chaînons du type pyridine ou pyrimidine (1, 3, 8–10) pour lesquels on obtient des cycles à 5 chaînons. Dans notre cas, ce processus conduit à un cycle à quatre chaînons **5** évidemment beaucoup moins stable :

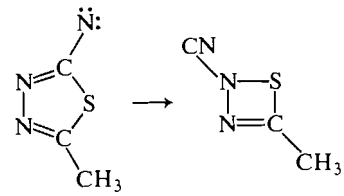

2 **5**

(c) L'ouverture de cycle a été postulée dans la décomposition d'azotures hétérocycliques du même type que **1** tel que l'azido-5 triazole-1,2,4 (11) et l'azido pyrazole (12, 13). Ici, comme l'extension de cycle, ce processus conduit au composé **4** :

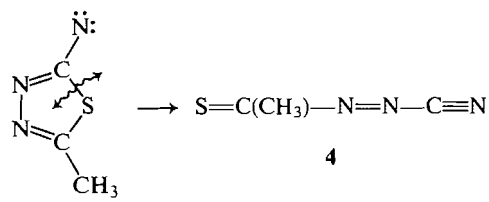

2 **4**

Les composés métastables issus de ces réarrangements peuvent eux mêmes évoluer en produits plus stables thermodynamiquement. Ainsi, nous montrons dans ce travail que la

1. Partie 36 de «Application de la spectroscopie photoélectronique aux propriétés moléculaires». Partie 35, ref. 2.

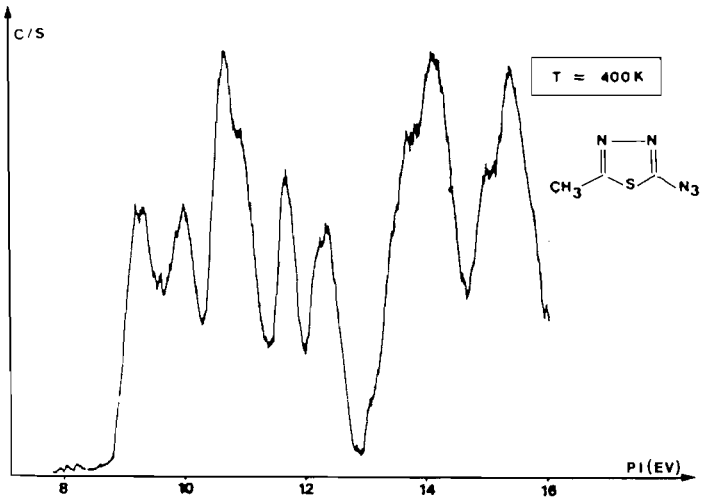

FIG. 1. Spectre photoélectronique du méthyl-5 azido-2 thiadiazole-1,3,4 avant thermolyse (400 K).

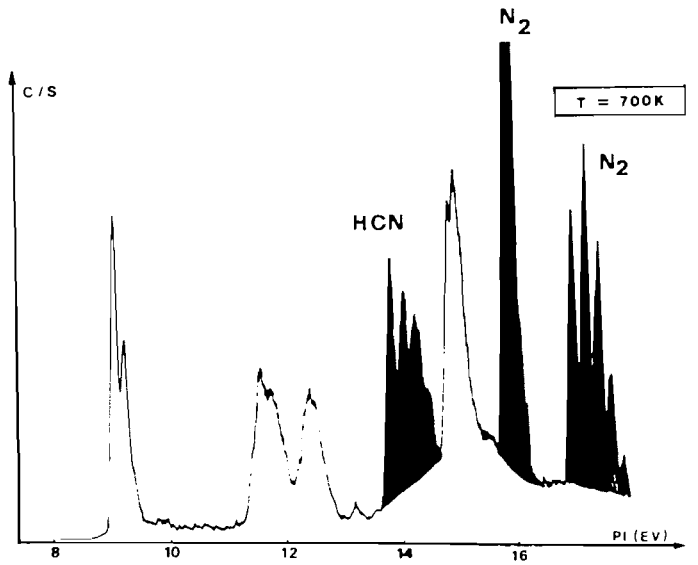

FIG. 2. Spectre photoélectronique du méthyl-5 azido-2 thiadiazole-1,3,4 après thermolyse (700 K). Les parties noires sont les bandes de HCN et de N_2.

décomposition thermique du méthyl-5 azido-2 thiadiazole-1,3,4 conduit à l'obtention du thiocétène en deux étapes principales (ouverture du cycle pour former **4**, puis décomposition de **4** en $CH_2{=}C{=}S + N_2 + HCN$). Ce chemin de réaction a été analysé à l'aide de la méthode semi-empirique MNDO.

Résultats expérimentaux

Le méthyl-5 azido-2 thiadiazole-1,3,4 dont le spectre photoélectronique (HeI) est présenté dans la figure 1, commence à se décomposer à partir de 600 K pour donner le thiocétène **5** $CH_2{=}C{=}S$, l'acide cyanhydrique HCN et l'azote N_2 (bandes hachurées dans la figure 2). Ce spectre reste inchangé jusqu'à 1200 K où l'on observe l'apparition de CS_2.

Ces dernières années la structure du thiocétène déterminée par spectrométrie microondes (14–18) et son spectre infrarouge (17–19) ont intéressé de nombreux auteurs. En général sa synthèse a été effectuée soit par photolyse, soit par pyrolyse du thiadiazole-1,2,3 non substitué. Outre le thiocétène, ce précurseur est susceptible de donner également le thiirène

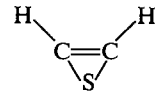

et l'éthényl mercaptan $HC{\equiv}C{-}SH$ (17, 20) qui sont cependant moins stables que leur homologue allénique (21–24).

Le spectre photoélectronique (figure 2) du thiocétène est tout à fait en accord avec celui réalisé par Bock *et al.* (21). La séquence des états ioniques donnée par le calcul d'interaction de configurations (cf. partie théorique) confirme l'ordre des valeurs propres du calcul SCF donné par la méthode MNDO (tableau 1). Contrairement au cas des molécules ne comprenant que des atomes de la seconde période ou même celui de composés comme l'iminosilylène et l'iminogermylène (26), le calcul d'interaction de configurations (CIPSI) donne des résultats relativement distants des valeurs expérimentales (sous estimation de 0,2 à 0,6 eV selon les potentiels d'ionisation). Cette observation avait déjà été relevée lors de plusieurs études concernant des composés sulfurés (27, 28). Il avait alors été montré que l'origine se situait dans un effet de base puisque l'élargissement de celle-ci améliorait considérablement les résultats quantitatifs. Nos résultats présentent toutefois une fiabilité qualitative certaine aussi bien au niveau de l'ordre des premiers états ioniques que de leur caractère. Ils montrent en particulier que les deux premiers d'entre eux $^2B_1$ et $^2B_2$ ainsi que le quatrième $^2A_1$ (dans une moindre mesure toutefois) sont relativement purs puisque issus à près de 90% d'une seule configuration correspondant au départ d'un électron respectivement des orbitales b_1 ($n_S - \pi_{C=C}$), b_2 ($\pi'_{C=S}$) et a_1 (σ_{CCS}). Par contre le troisième état ionique $^2B_1$, s'il a une configuration majoritaire (~70%) associée à l'orbitale monooccupée b_1 ($\pi_{CC} + n_S$), montre un mélange de configurations plus prononcé, les deux plus importantes (14% et 5%) correspondant à des effets de corrélation spécifique de l'ion, c'est-à-dire des déterminants décrivant des monoexcitations du premier état ionique. Les deux configurations suivantes (3% et 1%) correspondent à un effet de polarisation (déterminants décrivant des simples et des doubles excitations de l'état ionique étudié).

Ces deux effets ayant tendance à abaisser la valeur des potentiels d'ionisation calculés, il faut toutefois remarquer que ces calculs semblent les surestimer puisque toutes les valeurs théoriques sont inférieures aux valeurs expérimentales, celle se rapprochant le plus (0,27 eV) étant la valeur du deuxième potentiel pour lequel les effets électroniques ont le moins d'importance (0,51 eV d'écart entre $-\epsilon_i$ et le potentiel calculé après IC).

Chemin de reaction

Si, comme nous l'avons précisé dans l'introduction, nous admettons que, du fait de la faible pression ambiante, les réactions de réarrangement sont unimoléculaires et sont favorisées par un mouvement nucléaire minimal, l'obtention du thiocétène n'est explicable que par la formation intermédiaire du composé **4**. Ceci implique qu'à la suite du départ de N_2 et de la formation du nitrène, la première étape, très rapide, correspond à une ouverture du cycle. En général, cette ouverture demande moins d'énergie que la scission du groupement azido qui est l'étape déterminante au niveau énergétique et qui détermine la température pour laquelle commence le processus de dégradation thermique (2, 29). Cette température est d'ailleurs sensiblement plus basse dans ce type d'hétérocycles

Can. J. Chem. Downloaded from www.nrcresearchpress.com by 196.1.178.254 on 09/07/12
For personal use only.

TABLEAU 1. Potentiels d'ionisation (eV) calculés dans le cadre de l'approximation de Koopmans (PI = $-\epsilon_i$) (25) par les méthodes MNDO et HONDO (base 4.31G*) pour les deux premières colonnes et après interaction de configurations (3^e colonne) comparés aux valeurs expérimentales (4^e colonne).

État ionique	$-\epsilon_i$ (MNDO)	O.M.	$-\epsilon_i$ (HONDO)	PI (CIPSI)	PI (exp)
$^2B_1$	9,23	$n_S - \pi_{C=C}$	8,76	8,24	8,89
$^2B_2$	11,67	$\pi'_{C=S}$	11,56	11,05	11,32
$^2B_1$	13,15	$\pi_{C=C} + n_S$	13,68	11,67	12,14
$^2A_1$	15,19	σ_{CCS}	16,05	14,07	14,55

(entre 600 et 700 K) que dans les azotures linéaires saturés (26, 30) (entre 800 et 1100 K) et est voisine des azotures linéaires insaturés comme l'azoture de vinyle (31) (650 K). Il semble donc que la conjugaison fragilise ce groupement tout en stabilisant le nitrène résultant. Nous nous sommes plus particulièrement intéressés aux processus de réorganisation du nitrène présentés dans l'introduction.

Les calculs ont été effectués à l'aide de la méthode MNDO à laquelle a été ajoutée une recherche du col (point selle) le plus bas reliant deux minima de l'hypersurface de potentiel (cf. partie théorique). Dans l'optimisation énergétique des minima (matrice des dérivées secondes avec aucune valeur propre négative) et des points selles (une seule valeur propre négative) ont été pris en compte tous les paramètres géométriques.

Nous avons tout d'abord vérifié le mode d'ouverture du cycle. Comme nous l'avons noté, cette ouverture peut soit passer par l'intermédiaire cyclique à six chaînons **3**, soit être directe. Dans ce but nous avons effectué d'une part un calcul MNDO sur ce cycle intermédiaire **3** et d'autre part la recherche du col reliant le nitrène **2** au composé linéaire **4**.

Le calcul (figure 3) montre que ce cycle est de type mésoionique avec un atome de soufre très positivé (charge nette de 0,54 e$^-$) et un atome d'azote négatif. De plus l'analyse théorique (figure 5) met en évidence que l'ouverture directe du nitrène est favorisée. En effet l'énergie d'activation de la réaction d'ouverture (différence énergétique entre le col et le nitrène de départ) est de 75 kJ mol^{-1} alors que le cycle à six chaînons **3** est moins stable que le nitrène de 96 kJ mol^{-1} et donc à 21 kJ au dessus du col direct entre **2** et **4**.

D'après les calculs MNDO, la forme stable de **4** n'est pas plane, le soufre et le groupement méthyl se trouvant de part et d'autre (angle dièdre de 76°) du plan formé par le reste du squelette (N≡C—N=N—C) (figure 4). Il n'est cependant pas exclu que ce résultat soit du à un artefact de la méthode de calcul.

Les deux formes correspondant aux configurations où les doubles liaisons N=N et C=S se trouvent en position *syn* ou *anti* sont en fait des points selles et sont respectivement à 11,6 et 30,6 kJ mol^{-1} au dessus du minimum (figure 5). Il semble donc que l'ouverture du cycle nitrène **2** débute dans le plan (allant vers la forme *syn* de **4**) puis qu'il y ait rotation autour de la simple liaison N—C. Or, l'analyse de l'hypersurface de potentiel associée aux mouvements nucléaires de **4** pour former les composés observés expérimentalement (CH_2=C=S, HC≡N, N_2) a montré que le chemin de réaction passe par la forme *anti* de **4** (figure 5). À partir de ce point, tous les atomes lourds restent dans le plan moléculaire. Nous montrons dans la figure 6 la structure de l'état de transition ET dont l'énergie totale indique une barrière d'activation conséquente de 382 kJ mol^{-1}. La hauteur de cette barrière s'explique par la scission de trois liaisons et en particulier celle de C—H. En effet, la

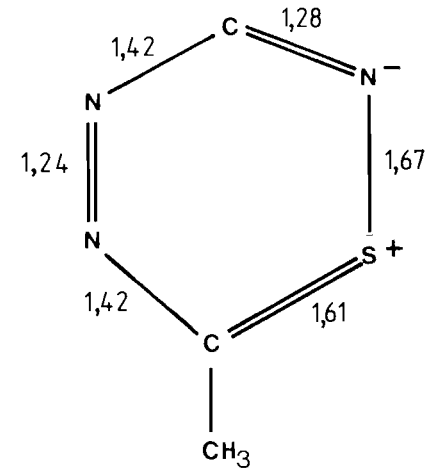

FIG. 3. Structure calculée (MNDO) du composé **3**.

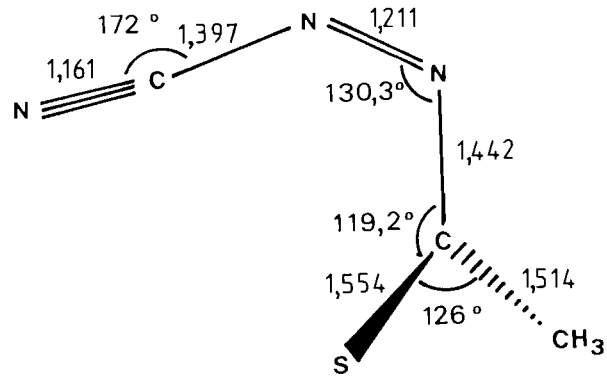

FIG. 4. Structure calculée (MNDO) du composé **4**.

structure de ET montre une pré-formation de HCN et seulement étirement des liaisons C—N. La seconde partie de cette étape (allant vers les trois molécules séparées) consiste en l'éloignement progressif de N_2 alors que les entités HCN et H_2CCS aboutissent à une structure stable (H—C≡N et H_2C=C=S) principalement par une évolution des angles définis par leurs liaisons.

Nous avons examiné en outre le chemin décrivant un processus non concerté. Celui-ci comprend plusieurs étapes, à savoir la coupure radicalaire d'une liaison C—N (→ $H_3CCS^\cdot$ + $NNCN^\cdot$), puis une seconde scission générant une molécule d'azote ($NNCN^\cdot \rightarrow N_2 + CN^\cdot$) et enfin une réaction radicalaire pour former le thiocétène ($H_3CCS^\cdot + CN^\cdot \rightarrow HCN + H_2CCS$). Il s'avère que ce processus n'est pas favorisé énergétiquement par rapport à la réaction concertée, du fait essentiellement de la très haute instabilité des radicaux et en particulier de $CN^\cdot$. En

Can. J. Chem. Downloaded from www.nrcresearchpress.com by 196.1.178.254 on 09/07/12
For personal use only.

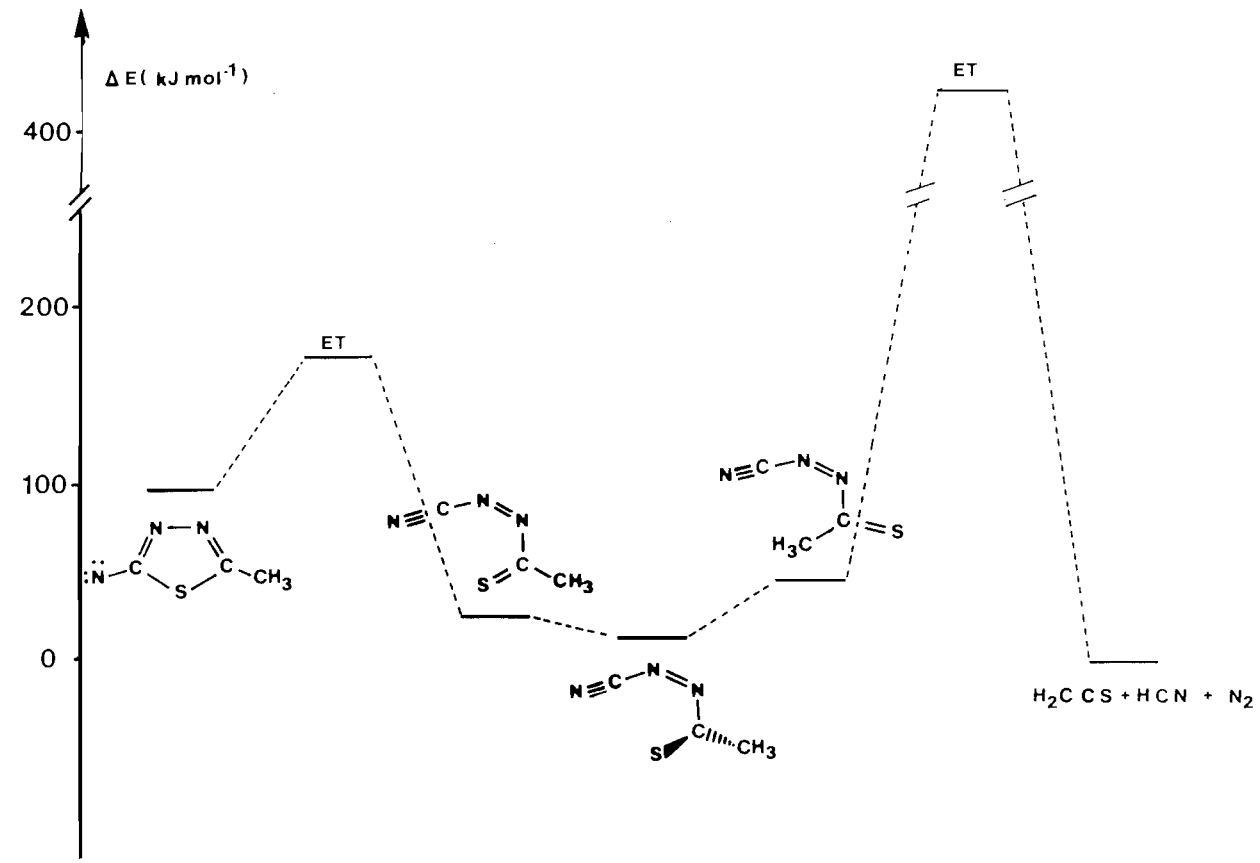

FIG. 5. Profil énergétique de la réaction de décomposition thermique de **4**.

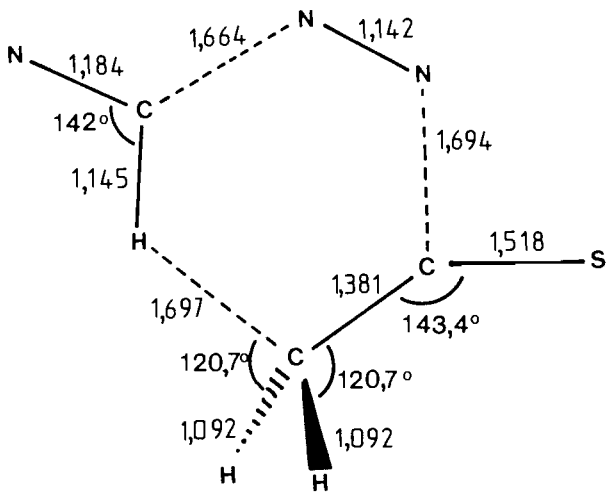

FIG. 6. Structure (MNDO) de l'état de transition ET entre **4** et $CH_2{=}C{=}S + HCN + N_2$.

outre, il est vraisemblable que ce type de réaction donnerait des produits parasites que nous n'avons jamais observés.

Conclusion

Lors de ce travail, nous avons montré que la décomposition thermique du méthyl-5 azido-2 thiadiazole-1,3,4 aboutissait à la formation de thiocétène accompagné d'azote et d'acide cyanhydrique. Après l'analyse des états ioniques de cette molécule, nous avons analysé le processus de cette réaction. Seul un mécanisme d'ouverture du cycle après formation initiale du thiadiazolonitrène peut rendre compte des produits observés expérimentalement. La thione linéaire ainsi formée se réarrange spontanément à la température de la pyrolyse (~700 K) par départ de N_2 intracyclique et migration d'un hydrogène du groupement méthyl sur le carbone du groupement cyano.

Partie expérimentale et théorique

L'azido-2 méthyl-5 thiadiazole-1,3,4 a été synthétisé suivant une variante de la méthode de Claramunt *et al.* (32):

formation à −10°C, à partir de l'amino-2 méthyl-5 thiadiazole-1,3,4, du phosphate de diazonium correspondant

obtention de l'azido-2 méthyl-5 thiadiazole-1,3,4 par action sur le phosphate de diazonium, de l'azoture de sodium

purification par chromatographie sur colonne de silice et recristallisation dans la chlorure de méthylène ($t°_{fus}$ = 93,5°C)

caractérisation par absorption dans l'infrarouge ($\nu_{as}N_3$ = 2145 cm^{-1}) en solution dans CH_2Cl_2.

Les spectres photoélectroniques ont été enregistrés sur un spectromètre modèle 0078 de « Photo Electron Spectrometer Laboratories Ltd » et calibrés à l'aide des doublets $^2P_{1/2}$ et $^2P_{3/2}$ du xénon et de l'argon. Pour réaliser la flash pyrolyse nous avons utilisé une sonde à « température variable » (33) permettant de chauffer la vapeur jusqu'à 1300 K pendant quelques fractions de seconde dans un tube de céramique situé à proximité immédiate de la chambre d'ionisation. Cette distance très courte permet d'obtenir le spectre photoélectronique de composés à courte durée de vie (~0.1 s) ou des produits issus de réarrangements moléculaires.

Les chemins de réaction décrivant le passage d'un minimum de l'hypersurface de potentiel à un autre (matrice des dérivés seconde à 0 valeur propre négative) ont été calculés par la méthode MNDO (34) qui présente l'avantage de donner, pour un coût raisonnable, une qualité des résultats qui s'approche de celle des méthodes *ab initio* (double

Can. J. Chem. Downloaded from www.nrcresearchpress.com by 196.1.178.254 on 09/07/12
For personal use only.

zeta) (35, 36) plus élaborées. De plus dans le cas particulier des nitrènes hétérocycliques une étude parallèle (à paraître) effectué sur la décomposition thermique du tétrazole nous a montré que les résultats MNDO étaient quantitativement proches et qualitativement similaires aux résultats *ab initio* avec interaction de configurations. Pour ces calculs nous avons utilisé un algorithme de recherche de point selle (37–39) qui nous permet de trouver le col le plus bas situé sur le chemin reliant deux minima de l'hypersurface de potentiel.

Les données spectroscopiques ont été comparées aux valeurs des potentiels d'ionisation pris comme la différence énergétique entre les divers états ioniques et l'état fondamental. À la suite du calcul SCF effectué grâce au programme HONDO (40) sur une base de type 4.31G* (orbitales *d* de polarisation sur le soufre), une interaction de configuration, conduite sur l'état fondamental du thiocetene ainsi que sur ses premiers états ioniques, a été réalisée à partir d'un programme (41) utilisant l'algorithme CIPSI (42).

Une fonction variationnelle d'ordre zéro est construite à partir d'une sélection itérative des déterminants les plus importants, les autres étant pris en considération au travers d'une perturbation au second ordre de Möller–Plesset. Le nombre de déterminants entrant dans la fonction d'onde variationnelle est de 60, celui généré dans le calcul perturbationnel étant compris entre 6×10^5 et 10^6.

La structure moléculaire utilisée pour ces calculs est tirée d'une optimisation de l'énergie totale prenant en compte tous les paramètres géométriques grâce à un processus de minimisation à métrique variable avec évaluation du gradient selon l'algorithme de Broyden–Fletcher–Goldfard–Shanno (43) inclus dans le programme « Monstergauss » (44, 45), la base choisie étant identique aux calculs précédents.

1. C. Guimon, S. Khayar, G. Pfister-Guillouzo, R. M. Claramunt et J. Elguero. Spectrosc. Lett. **15**, 435 (1982).
2. I. B'Shary, C. Guimon, M. Grimaud, G. Pfister-Guillouzo et D. Liotard. Can. J. Chem. **66**, 2123 (1988).
3. C. Wentrup. Top. Curr. Chem. **62**, 176 (1976) et réferences citées; React. Intermed. (Plenum), **1**, 263 (1980) et références citées.
4. G. Herzberg. Molecular spectra and molecular structure. I. Spectra of diatomic molecules. 2ème ed. Van Nostrand, Princeton, NJ. 1950.
5. S. Khayar. Thèse, Pau, France. 1982.
6. W. D. Crow et C. Wentrup. Tetrahedron Lett. 6149 (1968).
7. C. Wentrup. Bull. Soc. Chim. Belg. **91**, 997 (1982).
8. W. D. Crow et C. Wentrup. Chem. Commun. 1082 (1968); 1387 (1969).
9. C. Wentrup et W. D. Crow. Tetrahedron, **27**, 361 (1971).
10. T. Sasaki, K. Kanematsu et M. Murata. J. Org. Chem. **36**, 446 (1971).
11. P. A. S. Smith, L. O. Krbecher et W. Resemann. J. Am. Chem. Soc. **86**, 2025 (1963).
12. P. A. S. Smith, G. J. W. Breen, M. K. Hajek et D. V. C. Awang. J. Org. Chem. **35**, 2215 (1970).
13. P. A. S. Smith et H. Dounchis. J. Org. Chem. **38**, 2958 (1973).
14. K. Georgiu, H. W. Kroto et B. M. Landsberg. J. Chem. Soc. Chem. Commun. 739 (1974); J. Mol. Spectrosc. **77**, 365 (1979).
15. B. Bak, O. J. Nielsen, H. Svanholt, A. Holm, N. H. Toubroka. Krantz, et J. Laureni. Acta Chem. Scand. Ser. A: **33**, 161 (1979).
16. M. Winnewisser et E. Schafer. Z. Naturforsch. A: Phys. Phys. Chem. Kosmophys. **35A**, 483 (1980).
17. A. Krantz et J. Laureni. J. Am. Chem. Soc. **96**, 6768 (1974); **103**, 486 (1981).
18. M. E. Jacox. J. Phys Chem. Ref. Data, **13**, 1013 (1984).
19. H. W. Kroto et D. McNaughton. J. Mol. Spectrosc. **114**, 473 (1985).
20. A. Krantz et J. Laureni. J. Am. Chem. Soc. **99**, 4842 (1976).
21. H. Bock, B. Solouki, G. Bert et P. Rosmus. J. Am. Chem. Soc. **99**, 1663 (1976).
22. P. Rosmus, B. Solouki et H. Bock. Chem. Phys. **22**, 453 (1977).
23. O. P. Strausz, R. K. Gosavi, F. Bernardi, P. G. Mezey, J. D. Goddard et I. G. Csizmadia. Chem. Phys. Lett. **53**, 211 (1978).
24. R. K. Gosavi et O. P. Strausz. Can. J. Chem. **61**, 2596 (1983).
25. T. Koopmans. Physica, **1**, 104 (1934).
26. C. Guimon et G. Pfister-Guillouzo. Organometallics, **6**, 1387 (1987).
27. W. Von Niessen, L. S. Cederbaum, W. Domcke et G. H. F. Diercksen. J. Chem. Phys. **66**, 4893 (1977).
28. C. Lafon. Thèse, Pau, France. 1987.
29. I. B'Shary. Thèse, Pau, France. 1988.
30. H. Bock, R. Dammel et L. Horner. Chem. Ber. **114**, 220 (1981).
31. H. Bock, R. Dammel et S. Aygen. J. Am. Chem. Soc. **105**, 7681 (1983).
32. R. M. Claramunt, J. Elguero, A. Fruchier et M. J. Nye. Afinidad, **34**, 550 (1977).
33. H. J. Lempka. Helectros Developments, Beaconsfield, England.
34. M. J. S. Dewar et W. Thiel. J. Am. Chem. Soc. **99**, 4899 (1977).
35. H. L. McKee. J. Am. Chem. Soc. **107**, 1900 (1985).
36. S. Chroder et W. Thiel. J. Am. Chem. Soc. **107**, 4422 (1985).
37. D. Liotard. Thèse, Pau, France. 1979.
38. D. Liotard et J. P. Penot. J. Chim. Phys. R**11**, 77 (1980).
39. D. Liotard et J. P. Penot. *Dans* Numerical methods in the study of critical phenomena. *Éditeurs* : J. Dellarosa, J. Demongeot et B. Locolle. 1981. p. 213.
40. M. Dupuis, J. Rys et H. F. King. J. Chem. Phys. **65**, 111 (1976).
41. M. Pelissier. Thèse, Toulouse, France. 1980.
42. B. Huron, J. P. Malrieu et P. Rancurel. J. Chem. Phys. **58**, 5745 (1973).
43. R. Fletcher. Comput. J. **13**, 317 (1970).
44. M. Peterson et R. Poirier. Univ. of Toronto, Toronto, Ontario.
45. W. C. Davidon et L. Nazareth. Argonne Natl. Lab. Tech. Memos, 303, 306. Argonne, IL. 1981.

Can. J. Chem. Downloaded from www.nrcresearchpress.com by 196.1.178.254 on 09/07/12
For personal use only.

Computational study of heterocyclic thione ligands. Part I. Five-membered heteroatomic thiones possessing an α-nitrogen heteroatom

GEORGE S. KAPSOMENOS AND PERICLES D. AKRIVOS

Department of General and Inorganic Chemistry, P.O.B. 135, GR-540 06 Thessaloniki, Faculty of Chemistry, Aristotelian University of Thessaloniki, Greece

Received September 30, 1987[1]

GEORGE S. KAPSOMENOS and PERICLES D. AKRIVOS. CAN. J. CHEM. **66**, 2835 (1988).

A SCF-MNDO study is made of the equilibrium between the "thiol" and "thione" tautomers of four species possessing a five-membered heterocyclic ring, where nitrogen and oxygen or sulfur are the α-heteroatoms. Based on the computationally derived $\Delta(\Delta H_f)$ values for each pair of forms, evidence is presented for the possibility of co-occurrence of the two forms in solution. The tautomerism is particularly interesting in this class of compounds, since it offers the possibility for a sulfur, nitrogen, or sulfur and nitrogen coordination. The nucleophilicity of each specific site in both forms is discussed in terms of net atomic charges and the HOMO constitution of the molecules. Results concerning the study of metal complexes are generally in accordance with these considerations, since the preference for a specific donation scheme is governed by an HSAB criterion.

GEORGE S. KAPSOMENOS et PERICLES D. AKRIVOS. CAN. J. CHEM. **66**, 2835 (1988).

On étudie par la méthode SCF-MNDO l'équilibre entre les tautomères thioniques et thioliques des quatre espèces possédant un anneau hétérocyclique penta atomique avec des atomes d'azote, d'oxygène ou de soufre en position α. On met en évidence la possibilité de coexistence des deux formes en solution, basée sur un calcul des valeurs $\Delta(\Delta H_f)$ pour chaque couple de formes. La tautomérie est particulièrement intéressante dans cette classe des composés parce qu'elle offre la possibilité de coordination par l'intermédiaire de l'atome de soufre, d'azote ou d'azote et soufre en même temps. On discute le charactère nucléophile de chaque coté spécifique pour les deux formes en termes des charges atomiques nettes et de la constitution HOMO des molécules. Les resultats concernant l'étude des complexes métalliques sont géneralement en accord avec ces considérations parce qu'un critère HSAB gouverne la préférence pour un schema particulier de coordination.

Can. J. Chem. Downloaded from www.nrcresearchpress.com by 196.1.178.254 on 09/07/12
For personal use only.

Introduction

Heterocyclic thiones possessing α-heteroatoms show a variety of bonding modes toward different metal ions; this coordination behaviour has been reviewed quite recently (1). In particular, five-membered heterocyclic thiones with N in the α-position reveal a coordination potential, which is affected by several factors, predominantly by prototropic tautomerism occurring in the ligand, and in particular, which tautomer–(Fig. 1) is present in solution immediately prior to the metal-ligand bond formation (2). Though structural analysis (3) and ^{1}H NMR results concerning the free ligands account for the predominance of the thione form (Fig. 1*a*), the NMR studies of complexes (4) indicate the presence of —SH groups and therefore support a through nitrogen coordination (i.e. ligand structure as in Fig. 1*b*). This is the case of benzo-1,3-thiazoline-2-thione, benz-1,3-oxazoline-2-thione and a series of related ligands (5).

Thus, the suggested prototropic migration taking place between heterocyclic N and exocyclic S gains importance considering the plethora of bonding schemes toward different metal centres. An equilibrium in solution between the "thiol" and "thione" forms or the predominance of one of them would possibly account for the aforementioned observations.

Therefore, a quantum chemical calculation of the energy stabilization of one form relative to the other would be of interest since evidence should be provided for the possibility of coexistence of both forms in solution. The need for such a determination has led to the proposition of several empirical models, among which that of Duus (6), where the percent occurrence of each form emerges from an analysis of the UV–Vis and EPR spectra of the studied compounds.

Furthermore, in a series of analogous compounds, the role of a second heteroatom may be investigated along with the influence of substitutions such as a double bond or a delocalized π-system on the "thionic" character of the compounds under discussion.

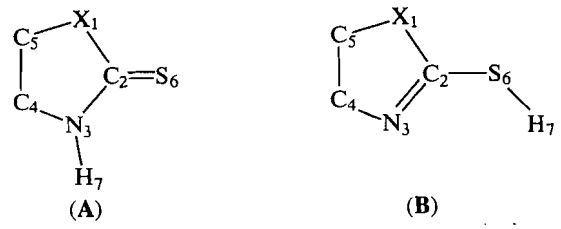

FIG. 1. The atomic numbering scheme in the five-membered heterocyclic ring for the "thione" (**A**) and the "thiol" (**B**) tautomers discussed.

Computational details

The results presented and discussed in this report emerged by carrying out MNDO-SCF calculations (7) as implemented in the MNDOC ensemble of programs (8). The parameters used for sulfur were those proposed by Dewar and McKee (9*b*). These were recently revised by Dewar and Reynolds (9*d*), but their improved set is particularly important when dealing with compounds having SS bonds and will not alter the main conclusions herein obtained, as will be discussed presently. The approximation used has proved to be effective in studies analogous to the present one (9, 10), giving, in general, results comparable or parallel to those of *ab initio* studies, which if used in the present case, would have been impractical.

The relevant internal coordinates of the studied compounds have been fully optimized by means of the DFP algorithm included in the above mentioned package. Table 1 includes all the final internal coordinates, whereas Fig. 1 presents the numbering scheme of the basic five-membered ring in both tautomeric forms considered. The only structural constraint used in the case of the benzo-derivatives, is the assumption of an ideal benzene ring.

[1]Received March 22, 1988.

Printed in Canada / Imprimé au Canada

TABLE 1. Optimized bond lengths (in Å) and bond angles (in deg) of the compounds **1**–**8**. The compounds are numbered according to the notation used in Fig. 2 (experimental values in brackets)

	Distance							
Bond	**1**	**2**	**3**	**4**	**5**	**6**	**7**	**8**
X(1)—C(2)	1.365	1.368	1.708	1.703	1.385	1.399	1.718 [1.75]	1.663
C(2)—N(3)	1.403	1.341	1.390	1.319	1.396	1.317	1.388	1.330
N(3)—C(4)	1.410	1.398	1.414	1.412	1.405	1.403	1.380 [1.39]	1.434
C(4)—C(5)	1.384	1.400	1.367	1.379	1.375	1.374	1.375 [1.42]	1.376
C(2)—S(6)	1.572	1.672	1.560	1.672	1.566	1.664	1.555 [1.60]	1.685
N(3)—H(7)	0.997	—	1.000	—	0.996	—	1.002	—
S(6)—H(7)	—	1.309	—	1.310	—	1.311	—	1.310 [1.34]

	Angle							
Bonds	**1**	**2**	**3**	**4**	**5**	**6**	**7**	**8**
X(1)—C(2)—N(3)	125.9	122.1	126.1	123.9	125.0	120.9	125.2 [136.0]	121.3
X(1)—C(2)—S(6)	106.6	113.0	108.1	114.7	105.2	108.2	107.0 [96.0]	112.8
C(2)—N(3)—C(4)	109.4	105.1	114.8	110.2	109.6	109.2	116.4	113.3
N(3)—C(4)—C(5)	105.1	107.9	111.5	113.6	107.8	107.0	112.0	111.5
C(2)—N(3)—H(7)	124.6	—	122.7	—	124.9	—	121.3	—
C(2)—S(6)—H(7)	—	100.7	—	100.0	—	99.1 [96.5]	—	101.4

Discussion

Calculations on the thione forms of the discussed compounds directly taken from crystallographic data (3, 11) led to unrealistic $\Delta(\Delta H_f)$ compared to theoretical data (10, 12) and also to experimental suggestions (1), so the comparison will be made between the optimized structures.

Table 1 presents in brackets the experimental values (16) for the geometries of some of these compounds. The main conclusion is a general underestimation of bond distances, a result also noted by Dewar *et al.* (9*b*, *d*). Thus, in the lengths of SH and SC bonds the errors are ca. 0.027 and 0.045 Å, respectively.

Regarding the effect of the second heteroatom on the thionic character of the exocyclic group, substitution of O by S generally leads to shorter SC bonds as can be seen from the results also contained in Table 1. This is apparently a consequence of the more electronegative character of O relative to S. Thus, oxygen "attracts" electron density from the neighbouring carbon atom, subsequently enhancing the polarity of the SC bond. The atomic net and p_π charges presented in Fig. 2 indicate, as expected, that this electron withdrawing is associated with the σ-rather than the π-system of the molecules. Further evidence for this charge withdrawing ability of oxygen relative to sulfur is the case of **2** and **4** (hereafter, each specific molecule will be referred to by using the notation used in Fig. 2) and the π-system involving C(2), N(3), C(4), and C(5) in each of them. The bond distances and atomic p_π charges associated with these systems strongly suggest an enhanced electron donating character for sulfur. The additional charge provided to C(5) in **4**, certainly provokes a stronger C(5)—N(4) p_π overlap and in an indirect way a weaker N(4)—N(3) and a stronger N(3)–C(2) one.

The concept of coordination to a metal ion, is generally understood in terms of the net atomic charges and the partitioning of the HOMO of the ligands. The net charges (Fig. 2) are indicative for a preference for nitrogen donation in the case of thiol forms while in the thione ones, the thioketo sulfur atom possesses a negative charge comparable, though less than that of nitrogen. The effect of the second heteroatom on the charge resident on N may be readily explained in a qualitative way, based on the same arguments as in the dependence of the SC bond character on the same factor (*vide supra*). The effect of the substituent at the 4- and 5-position of the heterocyclic ring on the nitrogen atom on going from the thiol to the thione tautomers is a depression in the amount of its net charge. This effect is less pronounced in the case of the benzo-compounds, thus providing grounds for the argument that the N charge reduction is related to the capacity of the system to transform the CN bond from a single one in the thione tautomer to a double one in the thiol one. Apparently this capacity is rather limited in the case of the benzo-compounds owing to the fact that the C(5)—C(4) bond possesses only partial double bond character.

The enhanced role of the thioketo S atom in the coordination of the thione tautomeric forms is also indicated by the constitution of the HOMOs of the ligands under study, which

Can. J. Chem. Downloaded from www.nrcresearchpress.com by 196.1.178.254 on 09/07/12
For personal use only.

TABLE 2. HOMO eigenvalues and coefficients of the p_π AOs of the exocyclic sulfur (S), heterocyclic nitrogen (N), and the second α-heteroatom (X, X = S, O) in this MO

	1	2	3	4	5	6	7	8
E_{HOMO} (eV)	−9.141	−9.472	−9.220	−9.680	−9.269	−9.399	−9.170	−9.365
S	0.691	0.458	0.633	0.503	0.640	0.327	0.558	0.330
N	0.384	0.284	0.371	0.255	0.390	0.347	0.381	0.343
X	0.274	0.132	0.402	0.238	0.243	0.102	0.311	0.128

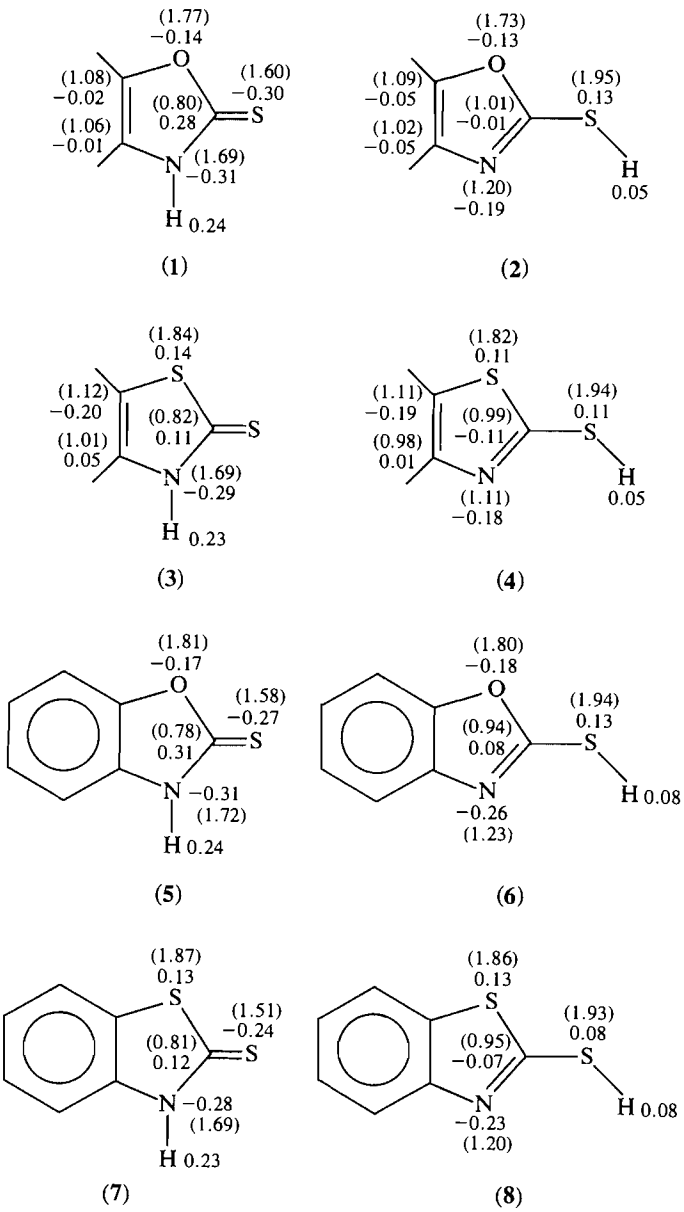

FIG. 2. The atomic net and p_π charges (in parentheses) for compounds **1**–**8**.

are responsible for the electron donation to the metal ions. It is quite evident that in the thione tautomers, sulfur donation is the main phenomenon, while in the thiol ones, nitrogen participation in the HOMOs gains in importance and in the benzo-compounds exceeds even that of sulfur. In every case, the HOMO is extensively delocalized over the entire molecule, especially in the region of the double bond or the aromatic system. The HOMO eigenvalues presented in Table 2, along with the coefficients by which N and S participate in them, suggest, as would have been expected, that the thiol tautomers are harder (13) than their thione counterparts, i.e. **2** will preferably attack an electrophilic metal site via the nitrogen atom, whereas **1** would most probably adopt a through-sulfur coordination scheme. Of course, in such a limited series of compounds, with the HOMO eigenvalues lying within a rather small energy margin, one cannot propose a strict classification according to the HSAB (14, 15) criterion, but only discuss the relative hardness or softness of the compounds. Nevertheless, the relative hardness of the thiols with respect to the corresponding thiones, as it follows from their HOMO eigenvalues is in accordance with the more significant nitrogen participation in their HOMOs relative to that of their thione analogues.

TABLE 3. Heats of formation (corrected) and their difference for the the tautomeric forms of the studied compounds in kJ mol^{-1}

1	2	3	4
−16.83	27.13	146.02	202.84
43.96		56.82	
5	**6**	**7**	**8**
42.81	107.43	190.44	284.22
64.62		57.78	

Moreover, the question arises whether the ligands discussed will act toward metal centres in their thiol or thione forms. To go into such a question we present in Table 3 the difference in the energies of formation of the tautomeric forms. The $\Delta(\Delta H_f)$ values computed for the discussed compounds are presented in Table 3.

The thione form should be the prevailing one for benz-1,3-oxazoline-2-thione, since it is more stable than its tautomeric form by 64.6 kJ mol^{-1}. The preference for the thione form should be lower in the case of benzo-1,3-thiazoline-2-thione, since the thione forms are calculated to be more stable than their thiol counterparts by 57.8 and 56.8 kJ mol^{-1}, respectively. Some larger amounts of "thiol" should be present in the case of 1,3-oxazoline-2-thione as the thione is favoured by only 43.9 kJ mol^{-1}. Based on the above results, one would expect the compounds to ligate through the exocyclic sulfur atom, while the benzo-derivatives may also act in a bridging fashion through both S and N atoms as has been argued in a few instances.

The mean error in enthalpies of formation calculated by the MNDO method is ca. 44 kJ mol^{-1}, as pointed out by Dewar and McKee (9*b*). However, this is the case when the complete list of molecules presented by these authors is considered. This list contains molecules with SS bonds as well as molecules for which one must, probably, include *d* functions in the basis set. If we exclude such molecules, the average error is much smaller (ca. 12.5 kJ mol^{-1}) and our conclusions still apply. It must also

Can. J. Chem. Downloaded from www.nrcresearchpress.com by 196.1.178.254 on 09/07/12
For personal use only.

be noticed that for the final enthalpies we have applied the corrections proposed by the above authors.

Thus, it could be suggested that the thione form of the compounds prevails initially in solution. A hard metal site could, however, provoke a prototropic migration from nitrogen to sulfur forcing the ligand to coordinate mainly through nitrogen, while a soft metal would coordinate to the thioketo sulfur atom of the thione form. Complexes that have been prepared in neutral media express bonding modes that are in accordance with these MNDO predictions, but the NH hydrogen atom is very labile and even in slightly alkaline media will be eliminated in favour of the corresponding anionic species which have attracted much more interest than the neutral ones.

Acknowledgement

The authors wish to express their thanks to Professor Dr. W. Thiel for his useful comments regarding the use of the MNDOC package of programs.

1. E. S. RAPER. Coord. Chem. Rev. **61**, 115 (1985).
2. A. P. KATRITZKY and J. M. LAGOWSKI. Advances in heterocyclic chemistry. Vol. I. 1961; Vol. II. 1963.
3. J. P. CHESICK and J. DONOHUE. Acta Crystallogr. B**27**, 1441 (1971).
4. R. F. WILSON and P. MERCHANT. J. INORG. NUCL. CHEM. **29**, 1993 (1967).
5. P. MURA, B. G. OLBY, and S. D. ROBINSON. Inorg. Chim. Acta, **97,** 45 (1985).
6. F. DUUS. J. Am. Chem. Soc. **108,** 630 (1986).
7. M. J. S. DEWAR and W. THIEL. J. Am. Chem. Soc. **99,** 4899 (1977); **99,** 4907 (1977).
8. QCPE program No 438, Indiana University, Bloomington, IN.
9. (*a*) M. CONTI, D. W. FRANCO, and M. TRSIC. Inorg. Chim. Acta, **113,** 71 (1986); (*b*) M. J. S. DEWAR and M. L. MCKEE. J. Comp. Chem. **4,** 84 (1983); (*c*) A. JAWORSKI, J. S. KWIATKOWSKI, and B. LESYNG. Int. J. Quantum Chem. QBS **12,** 209 (1986); (*d*) M. J. S. DEWAR and C. H. REYNOLDS. J. Comp. Chem. **7**, 140 (1986).
10. (*a*) A. MONTRAGON and A. O. BLAKE. Int. J. Quantum Chem. **22**, 89 (1982); (*b*) M. H. PALMER, W. J. ROSS, J. S. KWIATKOWSKI, AND B. LESYNG. Theochem. **9,** 283 (1983); (*c*) A. BUDA AND A. SYGULA. Theochem **9,** 255 (1983); **9,** 267 (1983).
11. P. GROTH, K. DAVIDKOV, and D. SIMOV. Acta Chem. Scand. **26,** 1931 (1972).
12. P. FRIEDMAN and L. C. ALLEN. Int. J. Quantum Chem. **29,** 1503 (1986).
13. G. KAPSOMENOS and P. AKRIVOS. Can. J. Chem **64,** 2225 (1986).
14. S. AHRLAND, J. CHATT, and N. R. DAVIES. Q. REV. **12,** 265 (1958).
15. R. G. PEARSON. (*a*) J. Chem. Educ. **45,** 581 (1968); (*b*) J. Am. Chem. Soc. **85,** 3533 (1963).
16. Interatomic distances supplement. Special Publication 18. The Chemical Society, London. 1965.

Can. J. Chem. Downloaded from www.nrcresearchpress.com by 196.1.178.254 on 09/07/12
For personal use only.

Structure and reactivity in highly halogenated ketazines

ELLEN C.K. LAI, DONALD MACKAY,[1] NICHOLAS J. TAYLOR, AND KENNETH N. WATSON[2]

The Guelph–Waterloo Centre for Graduate Work in Chemistry, Department of Chemistry, University of Waterloo, Waterloo, Ont., Canada N2L 3G1

Received July 21, 1987[3]

ELLEN C.K. LAI, DONALD MACKAY, NICHOLAS J. TAYLOR, and KENNETH N. WATSON. Can. J. Chem. **66**, 2839 (1988).

The azines of acetophenone and its mono- and di-chlorinated derivatives show a bathochronic shift in the yellow region, but the azine of trichloroacetophenone is colorless. Similar trends are observed in the brominated analogs and in the chlorinated propiophenone azines. The colorless tetrachloropropiophenone azine (**13**) is shown by X-ray analysis to be nonplanar at the azine atoms (N—N torsion angle, 126.7°). Hexachloroacetophenone azine (**9**) undergoes displacement of all its chlorines with NaOMe to give the hexamethoxy compound **16**, also colorless. With acid, **16** gives the yellow planar (X-ray) ketazine diester **20**. These reactions appear to be general for the trichloromethyl group in azines, but not for the α,α-dichloroalkyl group, attempts at the sequence **13** to **28** proving unsuccessful.

ELLEN C.K. LAI, DONALD MACKAY, NICHOLAS J. TAYLOR et KENNETH N. WATSON. Can. J. Chem. **66**, 2839 (1988).

Les azines de l'acétophénone et de ses dérivés mono- et di-chlorés présentent un effet bathochrome vers la région jaune; toutefois, l'azine de la trichloroacétophénone est incolore. Des tendances semblables ont été observés avec les analogues bromés ainsi qu'avec les azines de la propiophénone chlorée. Faisant appel à la diffraction des rayons-X, on a démontré que, au niveau des atomes de l'azine (angle de torsion N—N de 126,7°), l'azine incolore de la tétrachloropropiophénone (**13**) n'est pas plane. Sous l'influence du NaOMe, tous les atomes de chlore de l'azine de l'hexachloroacétophénone (**9**) subissent des réactions de substitution qui conduisent au composé hexaméthoxy, **16**, qui est aussi incolore. En milieu acide, le composé **16** conduit au cétazine diester, **20**, qui est jaune et plan (diffraction des rayons-X). Ces réactions semblent générales pour le groupement trichlorométhyle des azines. Toutefois, ce n'est pas le cas pour les groupements α,α-dichloroalkyles; en effet, des essais effectués en vue de transformer le composé **13** en **28** se sont avérés infructueux.

[Traduit par la revue]

In conjunction with our studies on conjugatively unsaturated azo compounds (1, 2), we became interested in the halogenation of azines as potential routes to the terminally unsubstituted 3,4-diazatrienes **1** (methylene analogs of azodiacyls), e.g. as in Scheme 1.

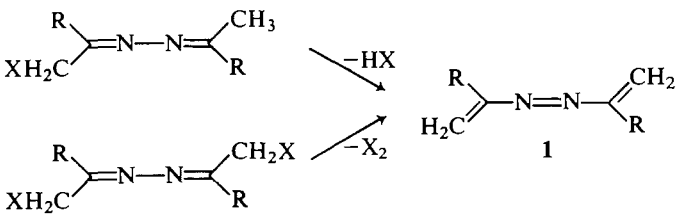

SCHEME 1

Compounds of type **1** have so far not been described though the fully substituted examples **2** and **3** have been prepared (3, 4). We chose acetophenone azine **4** as a starting point for this chemistry.

Both α-chloro (**5**) and α,α′-dichloroacetophenone azine (**6**) have been observed in the mixture obtained when the parent azine is treated with one equivalent of Cl_2 in CCl_4 (5), but neither has been characterized. We attempted to synthesize **5** by reaction of acetophenone hydrazone and chloroacetophenone and obtained only a mixture of **4**, **5**, and **6**. Azine formation is clearly reversible under these conditions. The dichloro-azine **6** was made in a modest yield by the acid-catalyzed reaction of α-chloroacetophenone and hydrazine (2:1). The dibromo analogue **7** is available from the known reaction of acetophenone azine with Br_2 in methanol (6), conditions which give only coupling products in the analogous reaction with Cl_2 (7).

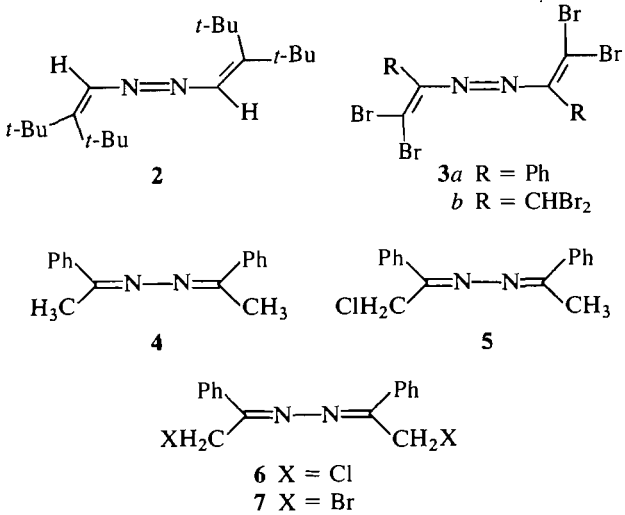

Attempts to dehalogenate **6** or **7** or to dehydrohalogenate **5** (as in Scheme 1) to 2,5-diphenyl-3,4-diaza-1,3,5-triene (**1**, R=Ph) have so far been unsuccessful, but some of the physical and chemical properties of the halogenated acetophenone azine and propiophenone azine are of sufficient interest to warrant reporting on here.

The chlorination of these azines has been studied in some detail (5). In the case of acetophenone azine either 1,4-addition to give the azo compound **8**, or substitution, occurs cleanly, depending on solvent and temperature (Scheme 2). One equivalent (5), or an excess, of Cl_2 in methylene chloride at −70°C gives **8**. In carbon tetrachloride only substitution is observed, 6 equivalents of Cl_2 giving the hexachloro compound **9** at room temperature (5). Lower levels of Cl_2 gave the expected mixtures of partially chlorinated azines. One equivalent gave mainly **5** and **6**, but also starting material and small

[1]Author to whom correspondence may be addressed.

[2]Polysar Limited, South Vidal Street, Sarnia, Ont., Canada N7T 7M2.

[3]Revision received June 21, 1988.

Can. J. Chem. Downloaded from www.nrcresearchpress.com by 196.1.178.254 on 09/07/12
For personal use only.

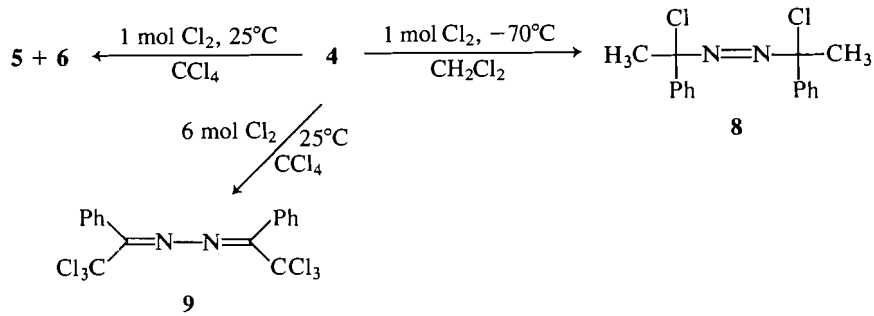

SCHEME 2

TABLE 1. Ultraviolet–visible and phenyl ^{1}H nmr absorptions of representative azines,[a]

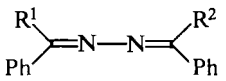

Compound	R^1	R^2	Melting point (°C)	Color	Ultraviolet (cyclohexane) λ_{max} (nm)	Ph ^{1}H nmr ($CDCl_3$) (ppm)
4	CH_3	CH_3	120–121	Yellow	271,290	7.3–7.4(3H,m), 7.8–8.0(2H,m)
5[b]	CH_2Cl	CH_3	90–91	Yellow	275,300	7.2–7.5(3H,m), 7.8–8.0(2H,m)
6	CH_2Cl	CH_2Cl	138–139	Yellow	278,309	7.4–7.6(3H,m), 8.0–8.2(2H,m)
7	CH_2Br	CH_2Br	151–152	Orange	286,318	7.4–7.6(3H,m), 7.9–8.1(2H,m)
9	CCl_3	CCl_3	108–109	Colorless	244	7.2–7.4(5H,brs)
12[c]	CBr_3	CBr_3	170(dec.)	Pale yellow	sh 220,266	7.45(5H,sharp s)
16	$C(OMe)_3$	$C(OMe)_3$	81–82	Colorless	238	7.30(5H, s)
20	CO_2Me	CO_2Me	140–141	Yellow	308	7.4–7.6(3H,m), 7.7–7.9(2H,m)
	CH_2CH_3	CH_2CH_3	64.5–66.5	Deep yellow	273,301	7.3–7.6(3H,m), 7.8–8.0(2H,m)
13	CCl_2CH_3	CCl_2CH_3	56–57	Colorless	211,sh240	7.40(s)

[a]The related data for the colorless azo compound **8** are λ_{max} 222 nm; δ 7.3–7.4.
[b]Prepared in this laboratory by C. Leo.
[c]Reference 4.

amounts of more highly chlorinated products; for example methine absorption is observed in the ^{1}Hmr spectrum ($CDCl_3$) at δ 7.2, possibly due to compound **10**, as well as peaks for the other expected symmetric and unsymmetric products.

Two spectroscopic trends concerning acetophenone azine and its symmetrically chlorinated derivatives intrigued us. The yellow color of acetophenone azine (λ_{max}, cyclohexane, 290 nm) deepens on dichlorination (compound **6**: λ_{max}, 309 nm). We could not purify the tetrachloro derivative **10** from the mixture of chlorinated isomers, but solutions rich in it were yellow; it has been described, without details, as a yellow product obtained by the photolysis of *N*,*N*-dichloro-α-phenylethylamine (8). The fully chlorinated compound **9**, however, is *colorless* (λ_{max}, 244 nm). The bromo derivatives, inherently deeper in color, show the same trend: the dibromo compound **7** is orange, the tetrabromo compound **11** has not been prepared, and the hexabromo compound **12** is pale yellow. The absorption spectroscopy data for all these and related azines are given in Table 1.

Propiophenone azine is yellow, but its tetrachloro derivative **13** (5) is colorless. The α,α′-dichloropropiophenone azine has not been reported.

The second feature of note was found in the phenyl region of the ^{1}Hmr spectra. In both acetophenone azine and propiophenone azine, and in all but their fully halogenated derivatives, the *ortho* protons appeared downfield of and fully resolved from the *meta* and *para* protons, the expected pattern in a phenyl group attached to a conjugatively electron-withdrawing group. By contrast, in the fully halogenated azines **9**, **12**, and **13** separation of the *o* peaks from the others was very much less (the phenyl peak of **12** was a singlet); their Ph nmr absorptions are also given in Table 1. A similar collapse of the ring aryl protons to a singlet has been observed in the spectrum of α,α-dichloroalkylarylketimines (9).

The abrupt change in both these properties with the introduction of the last halogen atoms made us wonder whether in fact structures **9** and **13** were correct, and if instead a profound structural change had occurred at this last step. For example, in the case of tetrachloroacetophenone azine a final 1,4-addition followed by oxidative cyclization would give the cyclic hexachloro azo compound **14**, which, like **8**, would be colorless. The latter has only a very slight separation of the *o* from the *m* + *p* protons in its nmr spectrum.

An alternative possibility was that the extended conjugation responsible for the yellow color in the azines **5**–**7**, **10**, and **11** was destroyed in the fully halogenated azines **9**, **12**, and **13**, by twisting of the two halves around the N—N bond. This in fact appears to be the case.

Can. J. Chem. Downloaded from www.nrcresearchpress.com by 196.1.178.254 on 09/07/12
For personal use only.

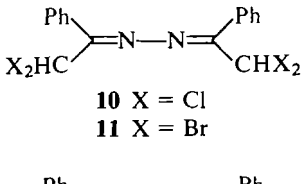

10 X = Cl
11 X = Br

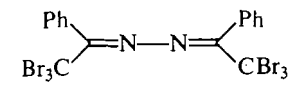

12

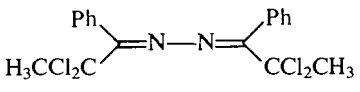

13

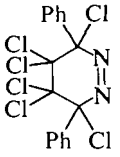

14

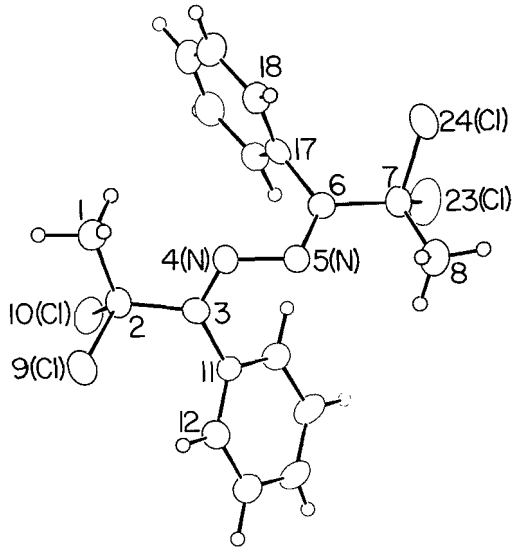

FIG. 1. ORTEP drawing of tetrachloropropiophenone azine, **13**.

The X-ray crystallographic analysis of the propiophenone azine derivative **13** (Fig. 1, ORTEP II plot, C.K. Johnson, Oak Ridge National Laboratory, Oak Ridge, TN, 1976) shows it to have the *E,E* configuration with an N—N torsion angle of 126.5(5)°. Bond lengths and angles are shown in Table 2. As expected from the space group of the crystal (See Table 5, experimental section) the molecule has no symmetry element, and differences exist between corresponding angles and distances on either side of the N to N bond. For example the torsion angles for C(2)C(3)N(4)N(5) and C(7)C(6)N(5)N(4) are 178.6(5)° and 179.1(5)° respectively, and for C(11)C(3)N(4)N(5) and C(17)C(6)N(5)N(4) they are 175.2(5)° and 176.9(5)°.

A search of the X-ray crystallographic literature shows that of six ketazines on record (10–14),[4] all of them colored, three have a locally planar arrangement around the C=N—N=C portion (10–12). C to N and N to N bond lengths and the N—N torsion angle of these six ketazines and of **13** are shown in Table 3. We expected that in the planar azines delocalization through the C=N—N=C system would lead to longer C to N and shorter N to N bonds than in the twisted azines. There is in fact no such discernible pattern. From bond length data at least, the evidence for delocalization between the two halves of a planar azine is much weaker than it is from ultraviolet–visible spectroscopy.

One of the planar ketazines cocrystallizes in a red modification along with one of the nonplanar ketazines that is yellow (10, 15). They are both *E,E* forms of the lactone derived azines **15**,

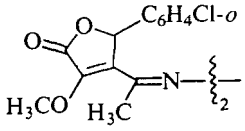

15

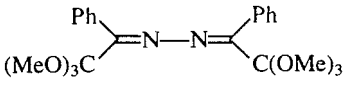

16

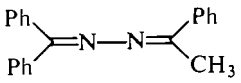

17

and are alleged to differ structurally only in the torsion angle at N—N, despite their non-identical ^{1}Hmr and solution ir and uv spectra (15). In fact the crystal structure diagrams of these show them to be stereoisomers (chiral ring carbon), the red compound being the *meso* and the yellow the *racemic*. Both of these have extended conjugation in each separate half of the molecule, accounting for the yellow color in the nonplanar form. One of the other two nonplanar azines, that of benzylidene acetone (13), likewise has extended conjugation. The remaining nonplanar ketazine, that of 4,4′-dihydroxyacetophenone, which is described as pale yellow (14), has a hydrogen-bonded water molecule in the crystal; the origin of the color is not obvious.

While trichloroacetophenone gives the haloform reaction with aqueous NaOH (to benzoate ion), or with NaO-*t*-Bu in cyclohexene (to *tert*-butyl benzoate) (16), its azine **9** proved remarkably resistant to alkali, being largely recovered after a 10-h reflux.

With NaOMe in refluxing MeOH, substitution of all six chlorines in **9** occurred to give the hexamethoxy compound **16**. The conversion of CCl_3 into $C(OR)_3$ is a venerable reaction when the reacting carbon is part of a locally saturated system (17), but examples are also known where the reacting carbon is next to a conjugatively electron-withdrawing function, for example in the conversion of 2-trichloromethylimidazoles into the imidazole ortho esters (18, 19). In related cases conversion of CCl_2OR into $C(OR)_3$ adjacent to ester groups leads to trialkoxyacetate esters (hemiorthooxalates) (20–24), and from them trialkoxyacetamide derivatives (22, 23).

We tried with ^{1}Hmr spectroscopy to monitor the sequence of introduction of the MeO groups into **9**, using a range of NaOMe concentrations and reaction times. Twelve different methoxy shifts are possible in principle in the mixture of nine products formed when **9** is substituted one to six times with MeO

[4]A total of 22 azine crystal structures (three for benzaldehyde azine) were found in the CRYSTOR database as of August 1986. Those not referenced here consist of azines in which either or both of the nitrogen attached groups are derived from aldehydes or from less common carbonyl derivatives (e.g., thio- or chloro-carbonyl). We thank Dr. S.R. Gough, Services Coordinator, Scientific and Technical Information, Ottawa, for undertaking this search for us.

Can. J. Chem. Downloaded from www.nrcresearchpress.com by 196.1.178.254 on 09/07/12
For personal use only.

TABLE 2. Bond lengths (Å) and angles (°) for azine **13** with standard deviations in parentheses

Bond	Length (Å)	Bond	Length (Å)
C(1)—C(2)	1.518(9)	C(2)—C(3)	1.530(7)
C(2)—Cl(9)	1.800(6)	C(2)—Cl(10)	1.793(6)
C(3)—N(4)	1.271(6)	C(3)—C(11)	1.477(7)
N(4)—N(5)	1.397(6)	N(5)—C(6)	1.275(6)
C(6)—C(7)	1.509(7)	C(6)—C(17)	1.490(7)
C(7)—C(8)	1.493(10)	C(7)—Cl(23)	1.808(6)
C(7)—Cl(24)	1.787(6)	C(11)—C(12)	1.384(7)
C(12)—C(13)	1.399(9)	C(13)—C(14)	1.374(10)
C(14)—C(15)	1.374(9)	C(15)—C(16)	1.381(9)
C(16)—C(11)	1.394(8)	C(17)—C(18)	1.397(9)
C(18)—C(19)	1.406(9)	C(19)—C(20)	1.386(12)
C(20)—C(21)	1.367(12)	C(21)—C(22)	1.394(9)
C(22)—C(17)	1.399(9)		
C(1)—H(1A)	0.88(6)	C(1)—H(1B)	1.08(6)
C(1)—H(1C)	1.01(7)	C(8)—H(8A)	0.96(6)
C(8)—H(8B)	1.01(6)	C(8)—H(8C)	0.97(5)
C(12)—H(12)	0.97(5)	C(13)—H(13)	1.05(5)
C(14)—H(14)	0.83(5)	C(15)—H(15)	1.05(7)
C(16)—H(16)	1.02(5)	C(18)—H(18)	0.96(6)
C(19)—H(19)	1.15(9)	C(20)—H(20)	0.96(7)
C(21)—H(21)	0.94(7)	C(22)—H(22)	1.01(5)

Angle	(°)	Angle	(°)
C(1)—C(2)—C(3)	115.8(3)	C(1)—C(2)—Cl(9)	107.7(3)
C(1)—C(2)—Cl(10)	108.4(3)	C(3)—C(2)—Cl(9)	110.2(2)
C(3)—C(2)—Cl(10)	106.8(2)	Cl(19)—C(2)—Cl(10)	107.8(1)
C(2)—C(3)—N(4)	111.9(3)	C(2)—C(3)—C(11)	121.6(3)
N(4)—C(3)—C(11)	126.2(3)	C(3)—N(4)—N(5)	117.7(3)
N(4)—N(5)—C(6)	112.6(3)	N(5)—C(6)—C(7)	115.3(3)
N(5)—C(6)—C(17)	122.9(3)	C(7)—C(6)—C(17)	121.8(3)
C(6)—C(7)—C(8)	115.5(4)	C(6)—C(7)—Cl(23)	107.1(2)
C(6)—C(7)—Cl(24)	108.9(2)	C(8)—C(7)—Cl(23)	109.1(3)
C(8)—C(7)—Cl(24)	109.8(3)	Cl(23)—C(7)—Cl(24)	106.0(1)
C(3)—C(11)—C(12)	122.3(3)	C(3)—C(11)—C(16)	120.3(3)
C(16)—C(11)—C(12)	117.4(3)	C(11)—C(12)—C(13)	120.9(4)
C(12)—C(13)—C(14)	120.1(4)	C(13)—C(14)—C(15)	120.1(4)
C(14)—C(15)—C(16)	119.5(4)	C(15)—C(16)—C(11)	122.0(3)
C(6)—C(17)—C(18)	118.2(3)	C(6)—C(17)—C(22)	121.3(3)
C(22)—C(17)—C(18)	120.3(4)	C(17)—C(18)—C(19)	119.5(4)
C(18)—C(19)—C(20)	118.8(4)	C(19)—C(20)—C(21)	122.2(4)
C(20)—C(21)—C(22)	119.6(4)	C(21)—C(22)—C(17)	119.6(4)

groups.[5] The nmr spectra were complex under all conditions and we were unable to analyze them. Methoxy absorptions occurred in three regions, representing mono- (near δ 4.0), di- (near δ 3.4), and tri- (near δ 3.0; δ 3.05 for **16**) substitution on a given carbon (Cl thus has a more deshielding effect than MeO on a geminal MeO group); each of these regions has a possible maximum of four peaks.

To try to simplify the problem we synthesized the mixed azine **17** (25) and chlorinated it (3–4 equivalent Cl_2 at room temperature) to **18**, a colorless, rather unstable, solid. Replacement of the chlorines (3–4 equivalents MeO^- in refluxing MeOH) proceeded smoothly to the oily **19**. Low levels of MeO^- (one equivalent) produced rapid buildup (Scheme 3) of the mono- (δ 3.99) but much less of the di- and tri-methoxy derivatives (δ 3.25, 3.09; ratio ca. 8:2:3). In a reaction with 3 equivalents of NaOMe, growth of the trimethoxy derivatives was very rapid and the amount of di- was always less than that of the mono-methoxy derivative (ca. 6:1:10 after 3 h reflux). These results suggest that both k_1 and k_3 are considerably larger than k_2. This may simply reflect a mechanistic change (e.g., S_N2 to S_N1) between the first and third steps, but no detailed kinetic studies were carried out, and we can only assume that the same relative rate effects pertain to both ends of the hexachloro compound **9**.

The solid colorless **16**, which like **13** presumably has a significant torsional angle round the N—N bond, is the azine of methyl benzoylorthoformate. As expected for an orthoformate (26), it was rapidly converted in acidic MeOH into a yellow crystalline solid, $C_{18}H_{16}N_2O_4$, mp 140–141°C, which showed

[5]This number is that predicted for the *E,E* azine only. In none of this work did we have evidence for the presence of any other stereoisomer.

Can. J. Chem. Downloaded from www.nrcresearchpress.com by 196.1.178.254 on 09/07/12
For personal use only.

TABLE 3.[a] C to N and N to N bond lengths and N—N torsion angles in known symmetrical ketazines

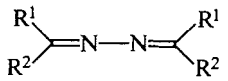

R^1	R^2	Color	Bond lengths (Å) C=N	Bond lengths (Å) N—N	Torsion angle (°)	Reference
Ph	CCl_2CH_3	Colorless	1.271(6) 1.275(6)	1.397(6)	126.7	This work
Ph	CH_3	Yellow	1.30[b] 1.29	1.38	137	13
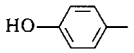	CH_3	Pale yellow	1.278(7) 1.282(7)	1.417(7)	148	14
(±) 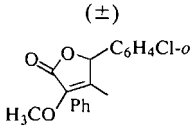	CH_3	Yellow	1.274(4) 1.282(4)	1.376(4)	115	10
meso		Red	1.296(5)	1.379(5)	180	10
Ph	CO_2CH_3	Yellow	1.283(2)	1.406(2)	180	This work
	CH_3	Yellow	1.27(1) 1.288(7)	1.41(1)	180	11
	CH_3	Yellow	1.293(7)	1.390(7)	180	12

[a]See footnote 4.
[b]The R value was 0.17 (ref. 13).

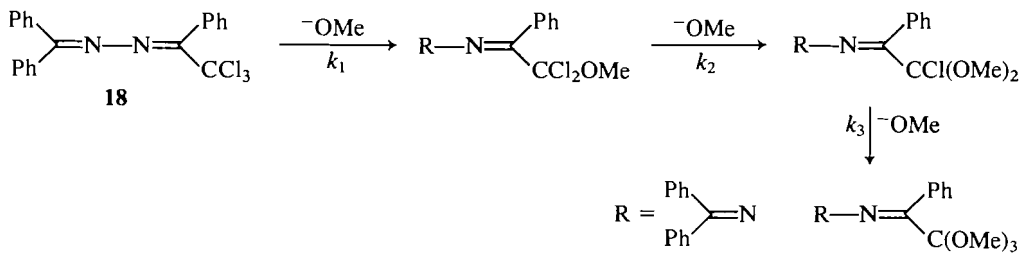

SCHEME 3

equivalent MeO groups at δ 4.00 and strong and weak bands at 1746 and 1609 cm^{-1} in its ir spectrum (CCl_4), attributed to C=O and C=N. An X-ray crystal structure determination showed this compound to be the planar *Z,Z* diester **20** (Fig. 2), the azine of methyl benzoylformate. Its imine stereochemistry is opposite to that found in **13**. Selected bond lengths and angles are shown in Table 4 (see also Table 3). Molecular dimensions are identical in both halves of the molecule, which has an inversion centre. The C to N and N to N bond lengths in this planar azine are not significantly different than those in the twisted azine **13**.

The functional groups found in **16** and **20**, the azine of an α-keto orthoester and of its derived carboxylate ester, are to the best of our knowledge the first examples of their kind in the literature. The closest analogies to **16** are the aforementioned imidazole (18, 19), ester, and carboxamate (20–24) derivatives and, in particular, α-imino ortho esters synthesized from the hydrazonium salts of pyruvaldehyde acetal (27).

The trimethoxy azine **19** similarly gave the yellow ester **21**, mp 118–118.5°C, on treatment with acidic MeOH.

Treatment of **16** with acidic EtOH rapidly gave a mixture of the diesters **20** and **22** (ca. 0.5:1). There was no evidence of the mixed diester **23** in the nmr spectrum (unless its alkoxy peaks coincided with the corresponding ones in **20** and **22**), a surprising result. The diester **22** was formed directly from **16**, and not by way of **20**, which was stable to these conditions over a long time. An authentic sample of **22** was made by transesterification of **20** with NaOEt in EtOH.

Hydrazone exchange could be effectively used to liberate the

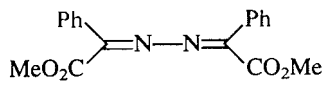

20

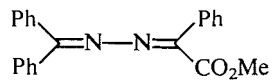

21

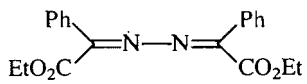

22

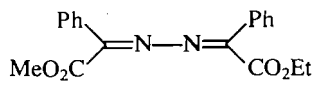

23

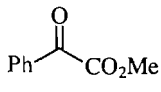

24

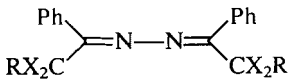

25 X = halogen
26 X = OMe
27 X, X = O

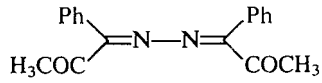

28

Can. J. Chem. Downloaded from www.nrcresearchpress.com by 196.1.178.254 on 09/07/12
For personal use only.

TABLE 4. Bond lengths (Å) and angles (°) for azine **20** with standard deviations in parentheses

Bond	Length (Å)	Bond	Length (Å)
O(1)—C(2)	1.195(2)	C(2)—C(3)	1.510(2)
C(2)—O(5)	1.372(2)	C(3)—N(4)	1.283(2)
C(3)—C(7)	1.470(2)	N(4)—N(4)′	1.406(2)
O(5)—C(6)	1.453(3)	N(7)—C(8)	1.389(2)
C(8)—C(9)	1.386(2)	C(9)—C(10)	1.376(3)
C(10)—C(11)	1.378(3)	C(11)—C(12)	1.375(2)
C(12)—C(7)	1.395(2)		

Angle	(°)	Angle	(°)
O(1)—C(2)—C(3)	123.61(8)	O(1)—C(2)—O(5)	125.66(8)
C(3)—C(2)—O(5)	110.71(7)	C(2)—C(3)—N(4)	120.65(8)
C(2)—C(3)—C(7)	118.88(8)	N(4)—C(3)—C(7)	120.46(8)
C(3)—N(4)—N(4)′	111.69(8)	C(2)—O(5)—C(6)	115.48(13)
C(3)—C(7)—C(8)	120.55(9)	C(3)—C(7)—C(12)	120.46(8)
C(12)—C(7)—C(8)	118.98(9)	C(7)—C(8)—C(9)	120.03(9)
C(8)—C(9)—C(10)	120.43(10)	C(9)—C(10)—C(11)	119.74(10)
C(10)—C(11)—C(12)	120.52(10)	C(11)—C(12)—C(7)	120.28(9)

Bond	Length (Å)	Bond	Length (Å)
C(6)—H(6A)	0.96(3)	C(6)—H(6B)	1.00(3)
C(6)—H(6C)	0.94(3)	C(8)—H(8)	0.95(2)
C(9)—H(9)	0.98(2)	C(10)—H(10)	0.99(2)
C(11)—H(11)	0.98(2)	C(12)—H(12)	0.97(2)

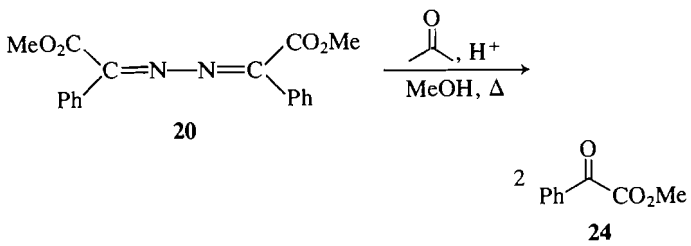

SCHEME 4

keto ester **24** from its azine **20**, by refluxing the latter in acetone in the presence of MeOH containing HCl (Scheme 4). Attempts to reconvert **24** into **20** using hydrazine (0.5 equivalents) showed that the azine was only one of several products that could not be readily separated.

In the general case of a perhalogenated phenyl alkyl ketone, the sequence analogous to **9** → **16** → **20** would result in the formation of the azine of an α-diketone, **25** → **26** → **27** (Scheme 5). With tetrachloropropiophenone azine (**13**), however, reaction with NaOMe–MeOH was very complex. The product mixture had a larger number of MeO peaks in it, and it was not particularly simplified on addition of dilute acid. There was no clear evidence of the presence of the expected azine of phenylmethylglyoxal, **28**. Related chemistry describing the reactions of α,α-dichloroalkylarylketimines with NaOMe–MeOH was similarly complex, mixtures of unsaturated halogenated and methoxylated ketones being produced (9). In light of the well-established synthesis of ketones by reaction of Grignard reagents with simple ortho esters ($RC(OEt)_3 + R'MgX \rightarrow RC(R')(OEt)_2 \rightarrow RCOR'$) an alternative route to **28** from the trimethoxy compound **16** seemed feasible. The latter, however, proved quite inert to an excess of either methylmagnesium iodide or methyllithium.

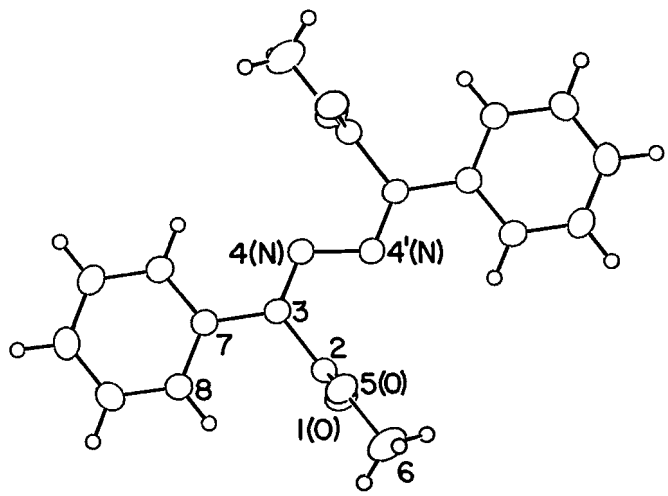

FIG. 2. ORTEP drawing of methyl benzoylformate azine, **20**.

Experimental

The following spectrometers were used: for infrared, a Perkin Elmer 983, samples being run in Nujol mulls or in solution in CCl_4 or $CHCl_3$; for ultraviolet, a Unican SP 800 with cyclohexane as solvent; for ^1H and ^{13}C nmr, a Bruker WP 80 or AM 250 ($CDCl_3$ as solvent). Melting points are uncorrected. Elemental analyses were done by Guelph Chemical Laboratories, Guelph, Ontario.

Magnesium sulfate was used as drying agent for solutions in organic solvents. The uv and ^1Hmr data for compounds **4–7**, **9**, **12**, **13**, **16**, and **20** are listed in Table 1. Hexachloroacetophenone azine (**9**) and tetrachloropropiophenone azine (**13**) were prepared as described by Malament and McBride (5), and dibromoacetophenone azine by the method of Tsuge *et al.* (6).

Attempted synthesis of α-chloroacetophenone azine (5)

Acetophenone hydrazone (4.4 g, 32.5 mmol) and α-

Can. J. Chem. Downloaded from www.nrcresearchpress.com by 196.1.178.254 on 09/07/12
For personal use only.

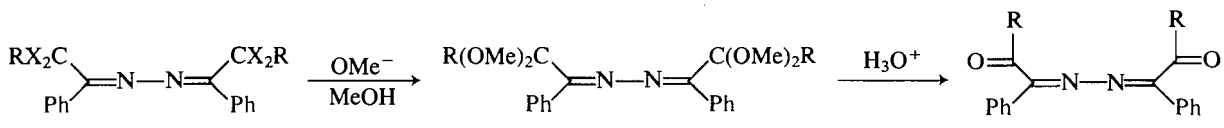

25
X = Cl, Br

26

27

SCHEME 5

chloroacetophenone (5.0 g, 32.5 mmol) were dissolved in EtOH (50 mL) and the solution cooled in ice over 3 h. Colorless crystals (an inorganic salt, probably hydrazine hydrochloride) were filtered off. The filtrate was kept overnight, and evaporated to a small volume to give a precipitate (2.0 g), consisting of a mixture of acetophenone azine, and the symmetrical and unsymmetrical azines **6** and **5**.

α,α′-Dichloroacetophenone azine (6)

α-Chloroacetophenone (10 g, 65 mmol), freshly distilled anhydrous hydrazine (1.0 g, 33 mmol), and 12 M hydrochloric acid (2.7 mL, 33 mmol) were dissolved in ethanol (50 mL), and kept for 12 h in the dark. The crystalline **6** was filtered off and recrystallized from ethanol (5.4 g, 55%), mp 138–139°C: ν (Nujol): 1603 (C=N) cm^{-1}; ^{1}Hmr, δ: 4.67 (4H, s, CH_2), 7.27–8.07 (10H, m, 2Ph). *Anal.* calcd. for $C_{16}H_{14}Cl_2N_2$: C 62.97, H 4.62, N 9.18, Cl 23.23; found: C 63.21, H 4.59, N 9.22, Cl 23.45%.

Stability of hexachloroacetophenone azine to aqueous alkali

To solid chlorinated azine **9** (0.15 g, 0.34 mmol) was added 2 M aqueous NaOH (2 mL, 4 mmol) and the whole was refluxed. The azine (mp 108–109°C) became semisolid. After 10 h, the mixture was cooled, cold carbon tetrachloride (1 mL) was added down the condenser, and the organic phase separated and dried. The ^{1}Hmr spectrum of the residue obtained on evaporation was that of **9** only. Chloroform was not present.

Hexamethoxyacetophenone azine (16)

To a solution of hexachloroacetophenone azine (**9**) (5.0 g, 11.3 mmol) in MeOH (50 mL) was added NaOH (5.5 g, 136 mmol, 12 equiv.). The whole was heated to a clear solution and refluxed for 17 h. The residue upon evaporation was treated with water and methylene chloride and the water layer shaken out with further methylene chloride. The combined organic extracts were dried and evaporated to give an oil, which crystallized on addition of hexane. Recrystallization from hexane gave colorless **16** (64%), mp 81–82°C: ν (Nujol): 1624 (C=N) cm^{-1}; λ_{max} (cyclohexane): 238 nm; ^{1}Hmr, δ: 3.05 (18H, s, MeO), 7.25–7.35 (10H, br s, 2 Ph); ^{13}Cmr, δ: 49.5 (CH_3), 112.5, 127.3, 128.2, 128.7 (Ph), 132.6 (C=N), 149.9 ($C(OMe)_3$). *Anal.* calcd. for $C_{22}H_{28}N_2O_6$: C 63.44, H 6.78, N 6.73; found: C 63.59, H 7.15, N 6.63%.

NaOH dissolved in a large excess of MeOH is mostly converted into NaOMe. In smaller scale preparations of **16** sodium dissolved in MeOH was used.

Reaction of hexachloroacetophenone azine with a limited amount of NaOMe

The azine **9** (0.30 g, 0.67 mmol) was kept at room temperature in 0.1 M NaOMe in MeOH (7.6 mL, 1.1 equiv.). Aliquots were taken periodically, evaporated, and their residues shaken out with water and methylene chloride. The contents of the organic layer were examined by ^{1}Hmr spectroscopy. The product from a half-hour reaction showed (as well as a large amount of unreacted **9**) MeO peaks at δ 2.90 and 3.40; after 18 h, peaks at δ 2.95, 3.36, 3.45, 3.49, 3.72, 3.98. These very likely represent an increasing degree of MeO substitution with increasing field, i.e., δ 2.95 and 3.98 are MeO resonances for a tri- and mono-methoxy substituted carbon. Detailed assignments were not possible.

Mixed azine 17

Benzophenone hydrazone (28) (5.0 g, 26 mmol) and acetophenone (3.05 g, 26 mmol) were stirred together in chloroform (10 mL) at room temperature for 5 h. Evaporation and crystallization of the residue from hexane gave long yellow needles, mp 103.5–105°C (lit. (25) mp 105°C); ^{1}Hmr, δ: 2.40 (3H, s, CH_3), 7.26–7.80 (15H, m, 3Ph).

Trichloroazine 18

The mixed azine **17** (0.50 g, 1.7 mmol) in CCl_4 (5 mL) was treated dropwise and with stirring with a solution of Cl_2 (0.49 g, 6.8 mmol, 4 equiv.) in CCl_4 (20 mL). After 1 h the solvent was removed and the colorless solid residue was recrystallized from pentane giving needles of **18** (63%), mp 73–75°C; ν (Nujol): 1590 (C=N) cm^{-1}; ^{1}Hmr, δ: 7.22–7.42 (15H, m, 3 Ph). This compound was rather unstable and slowly discolored at room temperature.

Trimethoxyazine 19

The trichloro compound **18** (0.50 g, 1.2 mmol) was refluxed in a solution of 0.10 M NaOMe in MeOH (48 mL, 4 equiv.) for 30 h. Evaporation, addition of ether and water, and an ether extraction work-up gave the product as a pale yellow oil; ^{1}Hmr, δ: 3.10 (9H, s, 3 OCH_3), 7.02–7.55 (15H, m, 3 Ph).

It was used directly in the synthesis of the ester **21**.

Reaction of trichloroazine 18 with limited amounts of NaOMe

A refluxing solution of **18** (0.20 g, 0.50 mmol) in 0.10 M NaOMe in MeOH (4.8 mL, 1 equiv.) was sampled at intervals, aliquots being evaporated and the residues shaken out with water and ether. The ^{1}Hmr spectra of the residue were taken. Typical result: at 2 h 35 min, δ 3.09, 3.25, 3.99, possibly due to $C(OMe)_3$, $CCl(OMe)_2$, $CCl_2(OMe)$ in a ratio of ca. 8:2:3; at 4 h 20 min the peaks at 3.09 and 3.25 had disappeared (after consumption of base the solution probably becomes slightly acidic, causing formation of the ester **21**, whose absorption is not readily distinguishable from the peak at 3.99. The latter may be more stable to acid than the di- or tri-methoxy compounds).

In a similar experiment compound **18** (0.60 g, 1.49 mmol) was refluxed in 0.10 M NaOMe in MeOH (44.3 mL, 3 equiv.) and the reaction monitored before completion, as above. The growth of the trimethoxy compound was very rapid after the initial stages. The dimethoxy compound was the least abundant component at all times. After 3 h, work-up of a sample led to the mono-, di-, and trimethoxy compounds in a molar ratio of ca. 6:1:10.

Methyl benzoylformate azine (20)

One drop of 1 M HCl was added to a solution of hexamethoxyacetophenone azine (0.134 g, 0.32 mmol) in MeOH (2 mL). The colorless solution immediately became deep yellow, and the yellow azine separated within minutes. Evaporation and recrystallization of the residue from MeOH gave large deep yellow prisms (0.094 g, 90%), mp 140–141°C: ν (CCl_4) 1746 (C=O), 1609 (C=N) cm^{-1}; λ_{max} (cyclohexane): 308 nm; ^{1}Hmr, δ: 4.00 (6H, s, OCH_3), 7.40–7.85 (10H, m, 2 Ph); ^{13}Cmr, δ: 52.2 (CH_3), 128.2, 129.0, 131.4, 132.3 (Ph), 162.5 (C=N), 165.9 (C=O). *Anal.* calcd. for $C_{18}H_{16}N_2O_4$: C 66.66, H 4.97, N 8.64; found: C 66.74, H 5.26, N 8.50%.

Mixed azine ester 21

The oily trimethoxyazine **19**, prepared as described above (0.10 g, 0.26 mmol), was dissolved in MeOH (2 mL) and acidified with 1 drop of 12 M HCl. The solid that precipitated was recrystallized from MeOH as yellow prisms (88%), mp 118–118.5°C; ν (Nujol): 1720 (C=O), 1650 (C=N) cm^{-1}; ^{1}Hmr, δ: 3.97 (3H, s, OCH_3), 7.3–7.5, 7.5–7.9 (15H, two multiplets, 3 Ph); m/e 342 (M^+). *Anal.* calcd. for $C_{22}H_{18}N_2O_2$: C 77.19, H 5.26, N 8.19; found: C 77.30, H 5.36, N 8.10%.

Can. J. Chem. Downloaded from www.nrcresearchpress.com by 196.1.178.254 on 09/07/12
For personal use only.

TABLE 5. Crystal data

Parameter	**13**	**20**
Molecular formula	$C_{18}H_{16}Cl_4N_2$	$C_{18}H_{16}N_2O_4$
Molecular weight	402.15	324.34
Space group	$P2_12_12_1$	$P2_1/c$
a, Å	5.911(2)	8.972(1)
b, Å	17.641(5)	11.617(1)
c, Å	18.197(5)	8.097(1)
β, deg	—	101.94(1)
V, Å^3	1898(1)	825.7(2)
Z	4	2
ρ_c, g cm^{-3}	1.408	1.304
$F(000)$	824	340
μ(MoKα), cm^{-1}	6.24	1.01
Crystal size, mm	0.28 × 0.28 × 0.30	0.33 × 0.34 × 0.36
Transmission factors	0.79–0.87	0.95–0.97
Scan method	θ–2θ	θ–2θ
Scan speed, deg min^{-1}	3.91–29.30	3.45–29.30
Scan width, deg	1.0° below $K\alpha_1$ to 1.0° above $K\alpha_2$	
2θ Range, deg	45	54
Standard reflections (every 100 measurements)	132	302;20$\bar{4}$
Standard variation, %	±2	±2
Number of measured reflections	1516	1816
Number of observed reflections, $I \geq 3\sigma(I)$	1114	1267
Secondary extinction correction	0.694×10^{-7}	0.248×10^{-6}
Final R, Rw	0.033, 0.038	0.034, 0.037
Largest shift/error in final cycle, Δ/σ	0.04	0.02
Weighting scheme $w^{-1} = A - B\lvert F_o\rvert + C\lvert F_o\rvert^2$	A 2.02 B 0.025 C 0.00067	2.70 0.075 0.0055
Maximum and minimum residual electron density, e Å^{-3}	0.29; −0.13	0.13; −0.10
$[\Sigma w(\lvert F_o\rvert - \lvert F_c\rvert)^2/(NO-NV)]^{1/2}$	0.668	0.197

*Conversion of hexamethoxy compound **16** into the dimethyl and the diethyl esters (**20**+**22**)*

The hexamethoxy compound **16** (0.40 g, 0.96 mmol) dissolved in ethanol (5 mL) was treated with 2 drops of 12 M HCl. The solution, which immediately turned yellow, was kept at room temperature for 0.5 h and evaporated. The residue (93%) was shown by ^{1}Hmr spectroscopy to consist of **20** and **22** in a ratio of 1:2. This mixture was converted as described below into the pure diethyl ester **22**.

*Stability of dimethyl ester **20** to acidic ethanol*

The ester **20** (0.10 g, 0.31 mmol) was dissolved in ethanol (60 mL) and 2 drops of 12 M HCl were added. The solution was kept at room temperature and monitored over 4 days, by work-up and nmr analysis of samples. There was no reaction.

*Transesterification of dimethyl ester **20***

The ester (50 mg, 0.15 mmol) was kept at room temperature for 1 h in 1 M NaOEt in ethanol (2 mL). Evaporation and extraction of the residue with water – methylene chloride gave from the dried organic layer a mixture shown by ^{1}Hmr spectroscopy to be starting material **20** and the diethyl ester **22** in a ratio of about 1:1.

The 1:2 mixture (0.10 g), prepared as described above in acidic ethanol, was stirred at room temperature for 6 days in ethanol (3 mL) containing a catalytic amount of NaOEt (5 drops of 0.1 M in ethanol). Evaporation and a water – methylene chloride work-up gave a yellow solid whose ^{1}Hmr spectrum showed ethoxy peaks only. Recrystallization from ethanol gave **22** as yellow prisms, mp 135–137°C: ν (CCl_4): 1743 (C=O), 1609 (C=N) cm^{-1}; ^{1}Hmr, δ: 1.45 (6H, t, J = 7.1 Hz, CH_3), 4.50 (4H, q, OCH_2), 7.39–7.86 (10H, m, 2 Ph). *Anal.* calcd. for $C_{20}H_{20}N_2O_4$: C 68.18, H 5.68, N 7.95; found: C 68.60, H 5.91, N 8.01%.

*Hydrazone exchange of diester **20** with acetone*

To a solution of **20** (0.10 g, 0.31 mmol) in acetone (3 mL) were added MeOH (0.02 g, 0.62 mmol) and 12 M HCl (0.07 mL, 0.62 mmol), and the whole was refluxed for 2 h. Evaporation gave a pale yellow oil (55%; considerable ester loss by volatilization) whose ^{1}Hmr spectrum was the same as that of an authentic sample of methyl benzoylformate: δ: 3.98 (3H, s, OCH_3), 7.48–8.10 (5H, m, Ph).

*Attempted synthesis of diester **20** from methyl benzoylformate*

Methyl benzoylformate (0.40 g, 2.4 mmol) and 95% hydrazine (0.040 mL, 1.2 mmol) were kept in MeOH (1 mL) for 24 h, with periodic monitoring of the reaction by thin-layer chromatography. This showed **20** to be one of several products. Evaporation gave a yellow oil whose ^{1}Hmr spectrum confirmed the presence of **20** as a minor product.

*Attempted synthesis of phenylmethylglyoxal azine (**28**) from **16***

The hexamethoxy compound **16** (45 mg, 0.11 mmol) in ether (5 mL) was treated with a large excess of ethereal methylmagnesium iodide. After 1 h, the solution was filtered and worked up to give only the starting material.

A similar reaction using methyllithium led also to the recovery of **16**.

X-ray analyses

Crystals of both **13** and **20** were grown from methanol. Details of the crystal data, intensity collection, and refinement are given in Table 5. The intensity data were collected on a Syntex $P2_1$ diffractometer using graphite monochromated MoKα radiation. Accurate cell constants for

Can. J. Chem. Downloaded from www.nrcresearchpress.com by 196.1.178.254 on 09/07/12
For personal use only.

Can. J. Chem. Downloaded from www.nrcresearchpress.com by 196.1.178.254 on 09/07/12
For personal use only.

TABLE 6(*a*). Atomic coordinates (fractional, × 10^4) and U_{eq}[a] (× 10^3) for **13** with standard deviations in parentheses

Atom	*x*	*y*	*z*	U_{eq}
C(1)	−1629(15)	1760(4)	473(4)	69
C(2)	−278(10)	1029(3)	476(3)	48
C(3)	493(10)	748(3)	1232(3)	45
N(4)	−308(8)	1152(2)	1749(2)	50
N(5)	309(8)	967(2)	2467(2)	46
C(6)	1120(9)	1530(3)	2818(3)	43
C(7)	1789(10)	1370(3)	3603(3)	53
C(8)	1209(18)	598(4)	3881(4)	79
Cl(9)	−1956(3)	313.3(9)	28.2(9)	72
Cl(10)	2229(3)	1169.3(9)	−62.0(8)	65
C(11)	2161(10)	130(3)	1311(3)	44
C(12)	1821(12)	−581(3)	1010(3)	59
C(13)	3437(13)	−1154(4)	1093(3)	64
C(14)	5362(13)	−1022(3)	1496(4)	66
C(15)	5745(11)	−319(3)	1796(3)	60
C(16)	4154(11)	247(3)	1705(3)	54
C(17)	1473(10)	2288(3)	2476(3)	46
C(18)	−284(12)	2816(3)	2517(3)	57
C(19)	−73(14)	3514(4)	2150(4)	71
C(20)	1868(17)	3653(4)	1744(3)	76
C(21)	3598(15)	3141(4)	1701(3)	72
C(22)	3424(12)	2451(3)	2071(3)	55
Cl(23)	4815(3)	1506(1)	3665(1)	88
Cl(24)	552(4)	2074(1)	4184.5(8)	80

[a] $U_{eq} = \sqrt[3]{U_{11}U_{22}U_{33}}$.

TABLE 6(*b*). H atom coordinates (fractional, × 10^3) and U_{iso} (× 10^3) for **13** with standard deviations in parentheses

Atom	*x*	*y*	*z*	U_{iso}
H(1A)	−291(11)	166(3)	70(3)	70(20)
H(1B)	−181(12)	193(3)	−10(3)	96(22)
H(1C)	−81(12)	220(4)	72(4)	101(26)
H(8A)	162(11)	57(3)	439(3)	77(20)
H(8B)	187(12)	19(4)	355(3)	103(26)
H(8C)	−42(9)	53(3)	386(2)	37(15)
H(12)	47(9)	−69(2)	73(2)	37(14)
H(13)	319(9)	−169(3)	87(3)	53(16)
H(14)	629(9)	−137(3)	147(3)	54(18)
H(15)	723(13)	−22(4)	209(3)	93(23)
H(16)	447(9)	76(3)	193(2)	43(15)
H(18)	−167(10)	270(3)	277(3)	44(16)
H(19)	−173(15)	385(4)	220(4)	137(32)
H(20)	210(15)	412(4)	150(4)	122(28)
H(21)	505(12)	323(4)	151(3)	80(24)
H(22)	469(8)	206(2)	209(2)	31(13)

each were determined using 15 general reflections ($23 < 2\theta < 30°$) well distributed in reciprocal space. Intensities were measured by the θ–2θ scan technique with background counts being made at the beginning and end of each scan for a total of half the scan time. The stability of the crystals was checked by monitoring the intensities of standard reflections every 100 measurements. Only minor variations were observed. The data were corrected for Lorentz and polarization effects but not for absorption. Both structures were solved by direct methods (MULTAN80) and refined by full-matrix least-squares methods; the function minimized was $\Sigma w\|F_o|-|F_c\|^2$. All hydrogen atoms were located in difference Fourier syntheses and included in the refinement in unconstrained isotropic form. In the final cycles of refinement, empirical weighting schemes of the form $A\text{-}B|F_o|+C|F_o|^2$ were applied to give constant error in the various ranges of F_o, the coefficients being derived from Ranger.

TABLE 7. Atomic coordinates (fractional, × 10^4, for H × 10^3) and U_{iso} or U_{eq}[a] (× 10^3) for **20** with standard deviations in parentheses

Atom	*x*	*y*	*z*	U_{iso} or U_{eq}
O(1)	1463(1)	142(1)	−966(1)	58.4
C(2)	2377(2)	−382(1)	38(2)	46.2
C(3)	3711(2)	174(1)	1210(2)	40.9
N(4)	5009(1)	255(1)	790(1)	46.1
O(5)	2353(1)	−1507(1)	313(2)	60.7
C(6)	1128(3)	−2135(2)	−770(4)	89.6
C(7)	3488(2)	644(1)	2827(2)	41.2
C(8)	2143(2)	441(2)	3374(2)	51.4
C(9)	1971(2)	848(2)	4933(2)	62.7
C(10)	3116(2)	1470(2)	5936(2)	58.6
C(11)	4443(2)	1691(1)	5385(2)	52.6
C(12)	4642(2)	1276(1)	3856(2)	46.0
H(6A)	19(3)	−188(2)	−51(3)	128(10)
H(6B)	116(3)	−196(2)	−197(4)	132(11)
H(6C)	138(3)	−291(3)	−52(3)	139(11)
H(8)	134(2)	2(1)	267(2)	57(5)
H(9)	102(2)	68(2)	531(2)	70(5)
H(10)	301(2)	175(2)	705(2)	68(5)
H(11)	525(2)	214(1)	610(2)	58(5)
H(12)	558(2)	140(1)	347(2)	52(4)

[a] $U_{eq} = \sqrt[3]{U_{11}U_{22}U_{33}}$.

Atomic coordinates for **13** and **20** are listed in Tables 6 and 7 respectively. Anisotropic thermal parameters and structure factors for **13**, and anisotropic thermal parameters and structure factors for **20** are provided as supplementary material in Tables S1–S4 respectively.[6]

1. D. MACKAY, C. W. PILGER, and L. WONG. J. Org. Chem. **38**, 2043 (1973); J. A. CAMPBELL, I. HARRIS, D. MACKAY, and T. D. SAUER. Can. J. Chem. **53**, 1973 (1975); W. G. BARRETT and D. MACKAY. J. Chem. Soc., Perkin Trans. 1, 1046 (1975); D. MACKAY, D. D. MCINTYRE, N. J. TAYLOR, and L. L. WONG. Can. J. Chem. **61**, 1213 (1983); D. MACKAY, N. J. TAYLOR, and I. D. WIGLE. J. Org. Chem. **52**, 1288 (1987).
2. K. N. WATSON. Ph.D. thesis, University of Waterloo (1983).
3. W. AHRENS and A. BERNDT. Agnew. Chem. Int. Ed. Engl. **12**, 655 (1973).
4. D. S. MALAMENT and N. LEVI. J. Org. Chem. **40**, 3285 (1975).
5. D. S. MALAMENT and J. M. MCBRIDE. J. Am. Chem. Soc. **92**, 4586 (1970).
6. O. TSUGE, M. TASHIRO, and K. KAMATA. Org. Prep. Proced. Int. **3**, 289 (1971).
7. S. GOLDSCHMIDT and B. ACKSTEINER. Liebigs Ann. Chem. **618**, 173 (1958).
8. S. SUGIMORI. Nippon Kagaku Zasshi, **92**, 528 (1971); Chem. Abstr. **76**, 58609r (1972).
9. N. DEKIMPE, R. VERHE, L. DE BUYCK, S. TUKIMAN, and N. SCHAMP. Tetrahedron, **35**, 789 (1979).
10. T. ISHIDA, M. INOUE, K. NASU, and T. KURIHARA. Acta Crystallogr. **39**, 470 (1983).
11. M. R. CIAJOLO, A. SIRIGU, and A. TUZI. Acta Cryst. C: Cryst. Struct. Commun. **41**, 483 (1985).
12. J. FAYOO, M. MARTINEZ-RIPOLL, M. C. GARCIA-MINA, J. GONZALEZ-MARTINEZ, and F. ARRESE. Acta Crystallogr. Sect. B: Struct. Crystallogr. Cryst. Chem. **36**, 1952 (1980).

[6]These tables may be purchased from the Depository of Unpublished Data, CISTI, National Research Council of Canada, Ottawa, Ont., Canada K1A 0S2.

13. J. BERTHOU, R. JAQUIER, A. LAURENT, C. MARZIN, B. RERAT, C. RERAT, and Y. UESU. C.R. Seances Acad. Sci. Ser. C: **271**, 802 (1970).
14. M. C. GARCIA-MINA, F. ARRESE, M. MARTINEZ-RIPOLL, S. GARCIA-BLANCO, and J. L. SERRANO. Acta Crystallogr. Sect. B: Struct. Crystallogr. Cryst. Chem. **38**, 2726 (1982).
15. T. KURIHARA, Y. SAKAMOTO, M. MORI, and T. SAKAKI. Heterocycles, **9**, 1041 (1978).
16. H. DAHL, F. NERDAL, and P. WEYERSTAHL. Liebigs Ann. Chem. **755**, 40 (1972).
17. A. W. WILLIAMSON and G. KAY. Ann. Chem. **92**, 346 (1854).
18. G. HOLAN, E. L. SAMUEL, B. C. ENNIS, and R. W. HINDE. J. Chem. Soc. C: 20 (1967).
19. B. C. ENNIS, G. HOLAN, and E. L. SAMUEL. J. Chem. Soc. C: 30 (1967).
20. Y. N. IVASHCHENKO and S. D. MOSHCHITSKII. Zh. Obshch. Khim. **33**, 1412 (1963).
21. Y. N. IVASHCHENKO and S. D. MOSHCHITSKII. Zh. Obshch. Khim. **33**, 3825 (1963).
22. A. V. KIRSANOV and V. P. MOLOSNOVA. Zh. Obshch. Khim. **29**, 1684 (1959).
23. R. ANSCHUTZ and STIEPEL. Ann. Chem. **306**, 8 (1899).
24. R. G. JONES. J. Am. Chem. Soc. **73**, 5168 (1951).
25. T. H. CURTIUS and F. RAUTERBERG. J. Prakt. Chem. **44**, 192 (1891).
26. R. H. DE WOLFE. Carboxylic ortho acid derivatives. Academic Press, New York. 1970. Chap. 2.
27. K. R. HENERY-LOGAN and T. L. FRIDINGER. J. Am. Chem. Soc. **89**, 5724 (1967).
28. L. I. SMITH and K. L. HOWARD. Org. Synths. Coll. Vol. **III**, 352 (1955).

Can. J. Chem. Downloaded from www.nrcresearchpress.com by 196.1.178.254 on 09/07/12
For personal use only.

Interlayer ammine complexes of metal uranyl phosphates

RAFAELA POZAS-TORMO, SEBASTIÁN BRUQUE GAMEZ, MARÍA MARTINEZ-LARA, AND LAUREANO MORENO-REAL[1]

Dpto. Quimica Inorgánica, Universidad de Málaga, Apartado 59, E-29071 Malaga, Spain

Received April 22, 1988

RAFAELA POZAS-TORMO, SEBASTIÁN BRUQUE GAMEZ, MARÍA MARTINEZ-LARA, and LAUREANO MORENO-REAL. Can. J. Chem. **66**, 2849 (1988).

The solids derived from HUP by substituting metallic ions for protons, take up Lewis base molecules (like NH_3 and $C_4H_9NH_2$) in the interlamellar space. The diffractograms of these inclusion compounds indicate that the host crystallinity was preserved.

The infrared spectroscopy of the Ni, Co, Cu, Zn, and Cd intercalates revealed that part of the sorbate was protonated in the interlaminar space while the other part displaced the water in their coordination spheres. However, in the Mn derivative, no coordinated or free Lewis base could be detected: it was all in the protonated form.

RAFAELA POZAS-TORMO, SEBASTIÁN BRUQUE GAMEZ, MARÍA MARTINEZ-LARA et LAUREANO MORENO-REAL. Can. J. Chem. **66**, 2849 (1988).

On peut insérer des molécules de bases de Lewis (comme le NH_3 et le $C_4H_9NH_2$) dans l'espace interlamellaire des solides que l'on obtient lorsqu'on remplace les protons des HUP par des ions métalliques. Les diffractogrammes de ces composés d'inclusion indiquent que la cristallinité de l'hôte est préservée.

Les spectres infrarouges des produits intercalés comportant du Ni, du Co, du Cu, du Zn ou du Cd révèlent que, dans l'espace interlamellaire, une portion du sorbate est protonée alors que l'autre portion a déplacé l'eau de ses sphères de coordination. Toutefois, dans les dérivés du Mn, on n'a pas pu détecter de base de Lewis soit libre ou coordonnée; elles étaient toutes sous la forme protonée.

[Traduit par la revue]

1. Introduction

$H_3OUO_2PO_4.3H_2O$ (HUP) is a member of the large family of uranium–mica compounds with the general formula $M^{n+}(UO_2PO_4)_n^{n-}.zH_2O$, where M may be a mono-, di-, or trivalent cation. HUP crystallizes in the tetragonal system in which the interlayer distance is 8.8 Å. In electrochemical studies, uranyl hydrogen phosphate was shown to have a high protonic conductivity ($0.4\ \Omega^{-1}\ m^{-1}$ at 290 K). The solids derived from HUP by substituting metallic ions for protons show lower conductivity (1). Other authors have systematically studied the effect that certain chemical substitutions of HUP have on its luminescence (2, 3).

Recently we prepared some *d* and *f* metal derivatives of HUP by ion-exchange topotactic reactions (4, 5). All the resulting solids were isostructural and their tetragonal lattices remained intact during the cationic substitution. The structure of metal uranyl phosphates consists of negatively charged layers of $(UO_2PO_4)_n^{n-}$ separated by sheets of water containing the compensating cations. The environments of these cations are compatible with their corresponding hexaaquocations and their electronic spectra show the vibronic transition bands of the UO_2 moiety in addition to the electronic absorption bands of the metal ions (4). All of the intercalation reactions, ionic exchange, solvation or neutralization, modified the photoluminescent properties (2, 3) and the proton conductivities of these solids (1).

These layered compounds are suitable systems to study changes in optical properties based on different coordination around the interlaminar cations. Some basic substances like ammonia and butylamine modify the system of the intracrystalline space and change the observed behavior of their diffuse reflectance spectra. The processes occurring within the solid during intercalation of the above molecules have elements of similarity with the formation of complex cations in aqueous media.

2. Experimental

The metal uranylphosphates $M(H_2O)^n[UO_2PO_4]_2$ (M = Mn^{2+}, Ni^{2+}, Co^{2+}, Cu^{2+}, Cd^{2+}, and Zn^{2+}) (MUP) were prepared according to the method described by Pozas Tormo *et al.* (4). Table 1 gives the composition, M:U:P molar ratio, and the color of these solids.

The intercalation complexes were prepared by exposing MUP to a saturated atmosphere of: (*1*) *n*-butylamine vapour (NBA), and (*2*) a concentrated solution of aqueous ammonia (24% w/w) in a desiccator for 2 weeks. The products were then evacuated at room temperature and kept for 3 to 5 days in a desiccator containing H_2SO_4 (98%) to remove the physically adsorbed basic molecules. The prepared samples were stored in an atmosphere of controlled humidity (H_2SO_4 40% w/w).

The composition of the intercalates was determined: nitrogen by Kjeldahl microanalysis and water content by thermal analysis.

The new materials were characterised by (*1*) infrared spectroscopy using the KBr disk method in a Perkin Elmer 883 instrument; (*2*) X-ray diffraction with CuKα monochromated radiation in a Siemens D-501 powder diffractometer; (*3*) thermogravimetric analysis in a Rigaku Thermoflex apparatus with a heating rate of 10 K/min in air and using calcined Al_2O_3 as reference; and (*4*) visible diffuse reflectance spectroscopy using barium sulfate as white reference in a Kontron UVIKON 810 instrument fitted with an integrating sphere attachment.

3. Results

The metal uranyl phosphates retained ammonia and *n*-butylamine (NBA) when they were exposed to the above mentioned Lewis base vapours. The sorption of NH_3 and NBA diminishes the degrees of hydration of the host solids and this suggests that the observed retention of the nitrogenated species in each case occurred by displacement of interlaminar water. Details of the composition of the new materials are given in Table 2.

Under the experimental conditions employed, no more than two molecules of NBA were retained by each metallic cation, but in the complexes containing NH_3, the retention was observed to be greater, possibly because the size of the NH_3 molecule is smaller than that of the NBA so that less energy was required for its interlaminar diffusion and at the same time the process was faster.

[1]To whom correspondence should be addressed.

Printed in Canada / Imprimé au Canada

Can. J. Chem. Downloaded from www.nrcresearchpress.com by 196.1.178.254 on 09/07/12
For personal use only.

TABLE 1. Composition and color of metal uranyl phosphates

Compound	Colour	P (%)	U (%)	M (%)	M:U:P*
$Ni(UO_2PO_4)_2 \cdot 9H_2O$	Pale green	6.5	50.3	6.12	1.0:1.9:1.9
$Co(UO_2PO_4)_2 \cdot 9H_2O$	Pale orange	6.4	50.2	6.25	1.0:2.0:2.0
$Zn(UO_2PO_4)_2 \cdot 9.5H_2O$	Yellow	6.4	49.6	6.70	1.0:2.0:2.0
$Cu(UO_2PO_4)_2 \cdot 10H_2O$	Blue green	6.5	48.9	6.46	1.0:2.0:2.1
$Cd(UO_2PO_4)_2 \cdot 7H_2O$	Yellow	6.4	48.9	11.51	1.0:2.0:2.0
$Mn(UO_2PO_4)_2 \cdot 9.5H_2O$	Yellow	6.5	49.1	5.41	1.0:2.1:2.1

*Molar ratio.

TABLE 2. Color and stoichiometric formulas of the intercalated solids

$M(NH_3)_x(H_2O)_y[UO_2PO_4]_2$				$M(NBA)_x(H_2O)_y[UO_2PO_4]_2$			
M	x	y	Color	M	x	y	Color
Ni	3.7	3.6	Pale green	Ni	1.0	6.2	Pale green
Co	3.2	4.2	Emerald green	Co	2.0	2.4	Emerald
Zn	3.0	1.3	Yellow	Zn	1.7	3.7	Yellow
Cu	3.6	3.8	Mallow	Cu	1.8	3.0	Green
Cd	2.3	1.7	Yellow	Cd	1.2	3.2	Yellow
Mn	2.0	6.0	Brown	Mn	2.0	5.0	Brown

X-ray diffraction data

The sorption of NH_3 or $C_4H_9NH_2$ vapours by the layered MUP host lattices took place in the interlaminar spaces because the $00l$ and hkl reflections were modified while those of $hk0$ remained unchanged. This indicated a topotactic intercalation.

The d_{002} interlaminar distances of the MUP + NH_3 complexes (Fig. 1*B*) are smaller than those of the starting phosphates (Fig. 1*A*) (4). Although the substitution of H_2O by NH_3 (both molecules are similar in size) should not produce noticeable variations in the basal spacings, the observed contraction in *ca.* 1 Å, is due to the smaller number of sorpted molecules (see Tables 1 and 2). On the other hand, as Fig. 1*C* shows, the MUP + NBA derivatives displayed mixtures of phases around 14.5 and 9 Å; the latter possibly due to the unchanged MUP phases in which the NBA did not penetrate, or to phases in which the amine intercalated with the carbonated chain parallel to the $[UO_2PO_4]_n^{n-}$ layers. In every case, the 9 Å reflection is of much lower intensity than that at 14.5 Å. The 14.5 Å phase is the consequence of the presence of the NBA alkyl chain being oriented perpendicularly to the laminar plane, similarly to that which occurs in $C_4H_9NH_3UO_2PO_4 3H_2O$, described by us (4).

Tables 3 and 4 display a selection of the most intense reflections and the corresponding Miller indices of the MUP + NH_3 and MUP + NBA derivatives.

The diffractograms of the MUP + NBA complexes (Fig. 1*C*), in contrast to those of MUP + NH_3, are rather diffuse in the 2θ high angle zone, probably due to stacking disorder. The pattern shown in Fig. 1*C* indicates a well-defined *c*-spacing and ***ab*** plane, because the $00l$ and $hk0$ reflection lines are sharp. Nevertheless, the effect of defective stacking on the pattern provokes a widening of certain diffraction lines in a characteristic fashion, as is reported for layered silicates (6).

Thermal analysis

Two or three endothermic effects were observed in the thermograms of the MUP + NH_3 complexes. In the TG these were accompanied by weight loss between room temperature and 200°C. This corresponds to the elimination of the water molecules or the NH_3 coordinated to the cation, or both. Between 200 and 700°C two endothermic effects were observed which were similar to those reported by Schaekers (7) for the decomposition of ammonium uranyl phosphate; they are consistent with the following reactions of the $NH_4UO_2PO_4$ component of the complexes:

[1] $NH_4UO_2PO_4 \rightarrow HUO_2PO_4 + NH_3$

[2] $HUO_2PO_4 \rightarrow (UO_2)P_2O_7 + H_2O$

The DTA–TG recording of the $Co(NH_3)_{3.2}(H_2O)_{4.2}[UO_2PO_4]$ complex is shown in Fig. 2*A*.

The MUP + NBA derivatives exhibited similar behaviour, but in these cases, between 200–500°C, the elimination of amine was accompanied by an exothermic effect, the result of the combustion of organic residues (Fig. 2*B*).

Infrared ir spectra

The infrared spectroscopy gave valuable information about the shapes adopted by the guest species. The first remarkable characteristic of the infrared spectra (Fig. 3 and Tables 5 and 6) was the appearance of bands at 1400 and 1470 cm^{-1} that indicate the unequivocal presence of the NH_4^+ ion in all MUP + NH_3 compounds. Baran and Botto (8) assign these to the $\nu_4(\delta_S)$ deformation vibrations of the NH_4^+ group in the ammonium uranyl phosphates. The MUP + NBA intercalates displayed a similar picture; bands due to the deformation vibrations of the NH_3^+ group were observed between 1495 and 1575 cm^{-1} in the spectra of all the samples and this fact confirms the existence of the alkylammonium species.

The presence of the coordinated NH_3 species was also detected in the infrared spectra of all intercalates, except the Mn derivative, by the bending vibrations (symmetric (δ_S), towards 1260 cm^{-1}; degenerate (δ_d) at 1620 cm^{-1}; and rocking (ρ_r) between 600 and 750 cm^{-1}). The first of these was very sensitive to the coordination of ammonia to the metallic ions because the frequencies at which this vibration appeared in this type of complex was in the order of 300 cm^{-1} higher than in the free molecule (9). Moreover, the presence of a band assignable to the ρ_r (NH_3) mode confirms the existence of the ammine complexes because this band is not present in the free NH_3 molecule. The vibration band towards 1620 cm^{-1} (δ_d of the ammonia) is not diagnostic, because the δHOH band of the water present in the compound overlaps it.

Diffuse reflectance

The replacement of the water molecules by NH_3 or NBA around the metallic ions displaces the bands produced by the *d–d* transitions to higher frequencies. Only the intercalates of Co^{2+}, Ni^{2+}, and Cu^{2+} exhibit this phenomenon; the other intercalates (Mn^{2+}, Zn^{2+}, and Cd^{2+}) have complete, or semi-

Can. J. Chem. Downloaded from www.nrcresearchpress.com by 196.1.178.254 on 09/07/12
For personal use only.

Can. J. Chem. Downloaded from www.nrcresearchpress.com by 196.1.178.254 on 09/07/12
For personal use only.

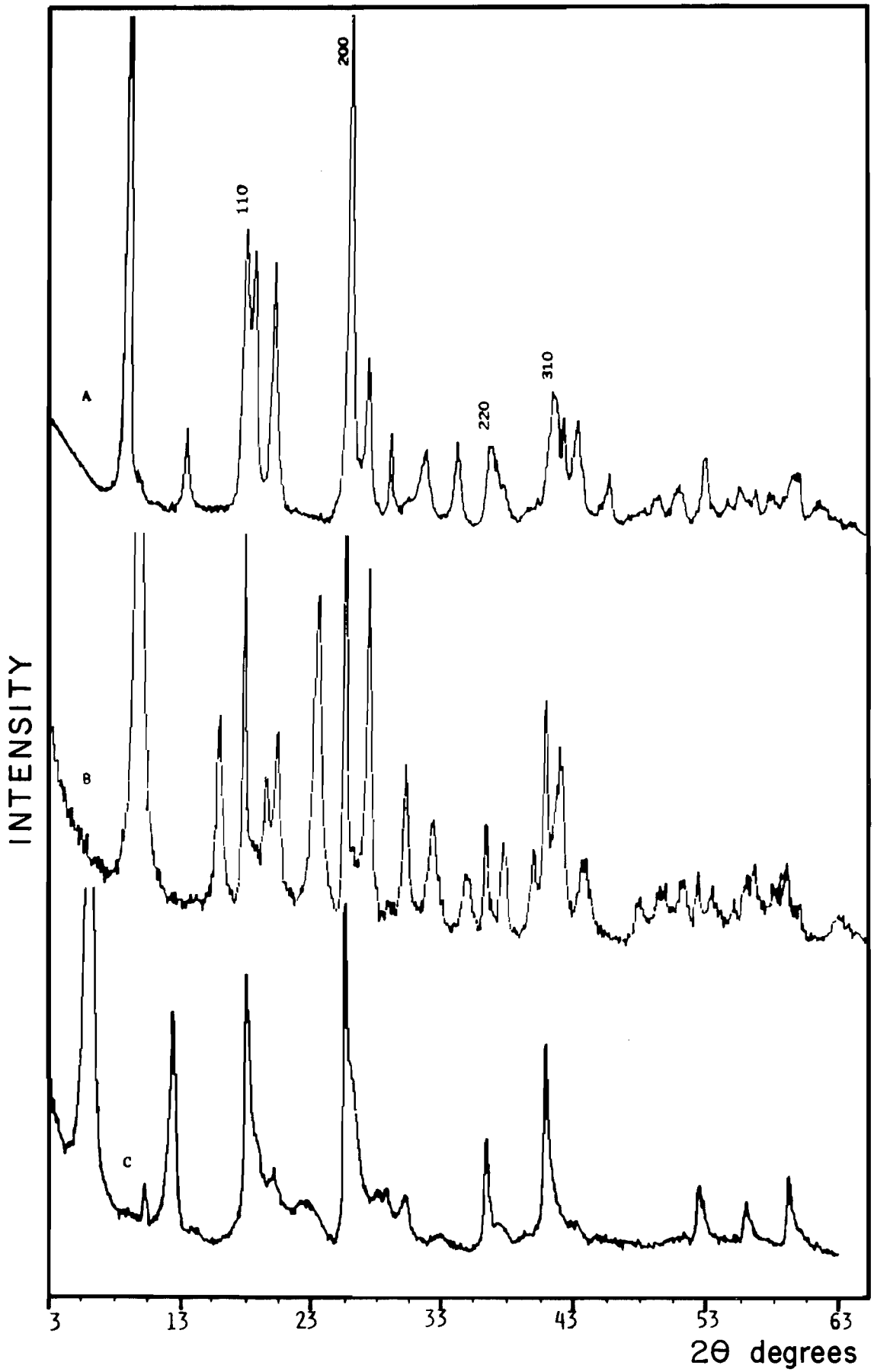

FIG. 1. X-ray powder patterns of (*A*) $Co(UO_2PO_4)_2 \cdot 9H_2O$, (*B*) $Co(NH_3)_{3.2}(H_2O)_{4.2}[UO_2PO_4]_2$, and (*C*) $Co(NBA)_2(H_2O)_{2.4}[UO_2PO_4]_2$.

TABLE 3. The most intense reflections (in Å) and their corresponding Miller indices of $M(NH_3)_x(H_2O)_y[UO_2PO_4]_2$

	Reflection intensity								
M	002	004	110	104	200	202	122	220	310
Ni	8.895	4.440	4.960	3.754	3.499	3.257	2.960	2.473	2.219
Co	9.095	4.534	4.963	3.806	3.507	3.273	2.963	2.476	2.216
Zn	9.046	4.530	4.957	3.813	3.487	3.265	2.959	2.472	2.214
Cu	8.945	4.456	4.973	3.763	3.498	3.268	2.963	2.475	2.218
Cd	9.060	4.540	4.962	3.804	3.487	3.284	2.958	2.474	2.214
Mn	9.084	4.528	4.966	3.806	3.495	3.274	2.964	2.481	2.219

TABLE 4. The most intense reflections (in Å) and their corresponding Miller indices of $M(NBA)_x(H_2O)_y[UO_2PO_4]_2$

	Reflection intensity							
M	002	004	002′	004′	110	200	220	310
Ni	*14.770*	7.340	9.951	4.940	4.920	3.497	2.470	2.208
Co	*14.666*	7.280	9.045	4.445	4.910	3.495	2.468	2.209
Zn	*14.537*	7.271	9.000	—	4.922	3.499	2.471	2.211
Cu	*14.000*	—	8.910	—	4.929	3.493	2.470	2.209
Cd	*14.670*	7.420	8.953	4.580	4.919	3.494	2.471	2.211
Mn	*14.699*	7.254	8.843	4.416	4.911	3.490	2.469	2.210

Can. J. Chem. Downloaded from www.nrcresearchpress.com by 196.1.178.254 on 09/07/12
For personal use only.

complete outer shells and so *d–d* transitions are forbidden by Laporte and spin rules. Consequently, these bands do not appear in the visible spectrum.

Narrow bands due to vibronic transitions of a UO_2^{2+} moiety were observed in the 300–500 nm region (10). However, these were not seen in the manganese intercalates because the MnUP + RNH_2 solids (R = Bu or H) have strong absorption in all regions of the visible spectrum: they are almost black. Figure 4 shows the diffuse reflectance spectra of the nickel derivatives.

4. Discussion

The sorption of the Lewis base molecules may be produced by (*1*) The presence of ions by transition metals with water in the coordination sphere which may be replaced by relatively stronger ligands (R—NH_2; R = Bu or H) in the spectrochemical series, in an anation process and (*2*) The strong acidity of the interlaminar coordinated water produced by the polarizing action of two electrostatic fields, that of the M^{2+} cation, and that of the $[UO_2PO_4]_n^{n-}$ layer.

These two effects might produce (*a*) the partial substitution of water by R—NH_2 (R = Bu or H)

[3] $[M(OH_2)_n]^{2+} + NH_3 \rightarrow [M(OH_2)_{n-1}NH_3]^{2+} + H_2O$

and (*b*) the insertion of R—NH_2 and its subsequent protonation to form RNH_3^+ ions (R = Bu or H) via dissociation of the water and protonation of the Lewis base. The latter reaction involves a decrease of the charge on the metallic cation and the appearance of additional RNH_3^+ ions as compensators of the layer charge, according to the following reaction:

[4] $[M(OH_2)_n]^{2+} + NH_3 \rightarrow [M(OH_2)_{n-1}OH]^+ + NH_4^+$

However, reactions [3] and [4] could be coupled to give

[5] $[M(OH_2)_n]^{2+} + zNH_3 \rightarrow [M(OH_2)_{n-z}(NH_3)_{z-1}OH]^+ + NH_4^+$

The reactions with $C_4H_9NH_2$ occur in a way similar to that of NH_3.

The cations $[M(OH_2)_{n-z}(NH_3)_z]^{2+}$ and $[M(OH_2)_{n-z}(NH_3)_{z-1}OH]^+$ should show a similar electronic spectrum to those of the aqueous cations. The R—NH_2 ligand (R = H, C_4H_9) is somewhat stronger than water in the spectrochemical series so that the bands must be displaced to lower wavelengths. This effect may be partially compensated by the presence of OH^- in the coordination sphere. Nevertheless, in the diffuse reflectance spectra of CuUP + NH_3, there is a net shift of the 675 nm band (transition $^2E \leftarrow {}^2B_{1g}$; aqueous cation) to 540 nm (ammine complexes). In the case of nickel uranylphosphate, the shift is from 650 nm to 625 nm (Fig. 4). These facts, together with the color changes observed, support the existence of ligand molecules, different from water, in the proximity of the metallic ions.

Although the techniques employed do not permit an exact estimate of the coordination symmetry, the slight changes in the spectra and the very small numbers of nitrogenated molecules detected suggest that the octahedrical conformation established in the aquation process persists (4, 11).

Infrared spectroscopy of the Ni, Co, Cu, Zn, and Cd intercalates revealed that part of the sorbate was protonated in the interlaminar space while the other part displaced the water in their coordination spheres. However, in the Mn derivative, no coordinated or free Lewis base could be detected: it was all in the protonated form.

When the manganese uranyl phosphate absorbs RNH_2 (R = H, or C_4H_9) it forms a very dark brown product and this suggests that the interlaminar cation is oxidised, as occurs in basic solutions of Mn^{2+} when exposed to air. As the manganese ammine complexes are usually only slightly stable in humid atmospheres, the insertion of RNH_2 might create the basic medium required for oxidation, according to the following

TABLE 5. Assignments of the most significant bands of the ir spectra of $M(NH_3)_x(H_2O)_y[UO_2PO_4]_2$ (refs. 4, 5, 8, 9)

M	δ_dOPO	$\rho_r NH_3$	$\nu_s UO_2$	$\nu_{as} UO_2$	ν_sPO	ν_{as}PO	$\delta_S NH_3$	$\delta_S NH_4(\nu_4)$	$\delta_d NH_3 + \delta$HOH	νNH + νOH
Ni	550	600, 655	820	916	1010	1115	1265	1400, 1475	1630	3200, 3300 3380, 3450
Co	550	610, 640	820	925	1000	1125	1260	1400, 1470	1640	3200, 3450
Zn	544	635, 685	814	915	996	1118	1270	1400, 1466	1620	2900, 2950 3200, 3300 3375, 3475
Cd	542	625, 700	810	911	1011	1116	1220	1400, 1466	1610	3184, 3277 3358, 3476
Cu	545	603, 750	803	908	991	1113	1245	1400, 1460	1620	3200, 3360 3450
Mn	545	—	816	921	997	1117	—	1400, 1470	1650	3200, 3354 3440

Can. J. Chem. Downloaded from www.nrcresearchpress.com by 196.1.178.254 on 09/07/12
For personal use only.

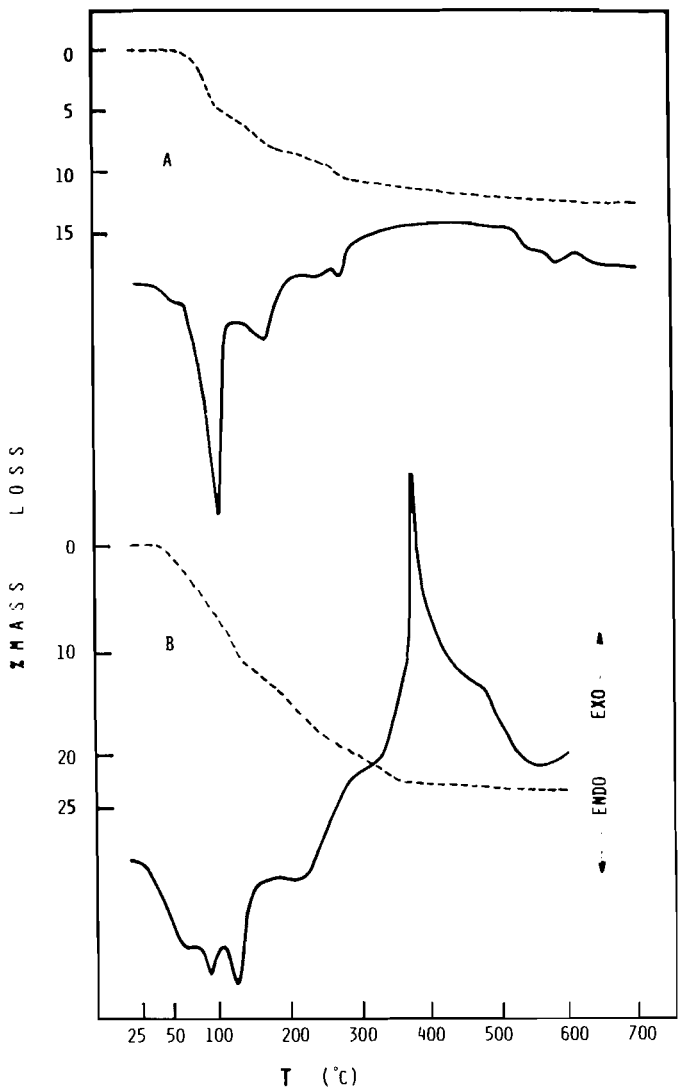

FIG. 2. Thermal analyses (TGA dashed curve and DTA solid curve) of (*A*) $Co(NH_3)_{3.2}(H_2O)_{4.2}[UO_2PO_4]_2$ and (*B*) $Co(NBA)_2(H_2O)_{2.4}[UO_2PO_4]_2$.

reactions:

[6] $2[M(OH_2)_n]^{2+} + 4RNH_2 \rightarrow 2Mn(OH)_2(n-2)H_2O + 4RNH_3^+$

[7] $2Mn(OH)_2(n-2)H_2O + (1/2)O_2 \rightarrow 2MnOOH(n-2)H_2O + H_2O$

black

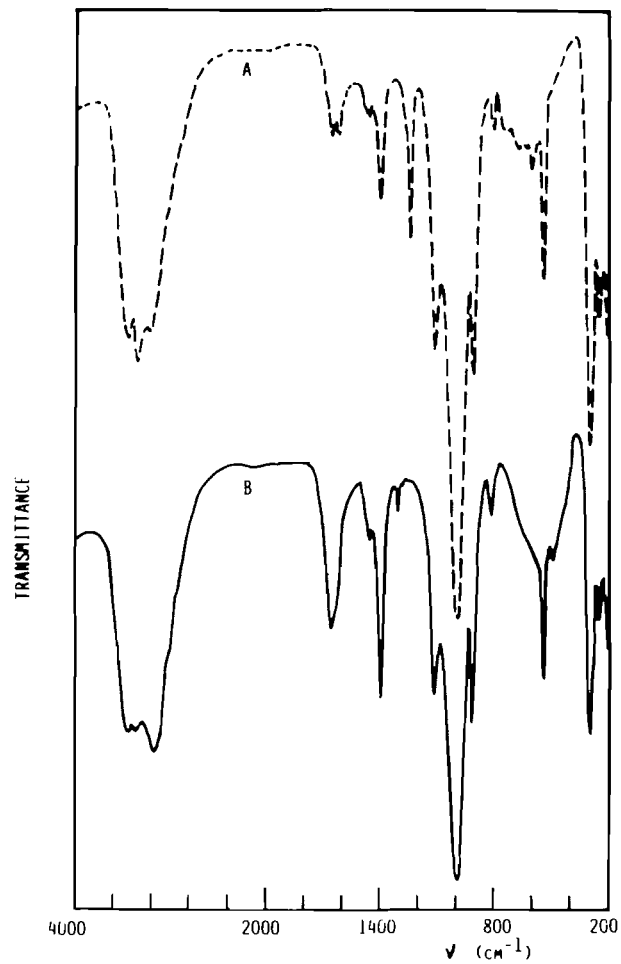

FIG. 3. Infrared spectra of (*A*) $Cu(NH_3)_{3.6}(H_2O)_{3.8}[UO_2PO_4]_2$ and (*B*) $Mn(NH_3)_2(H_2O)_6[UO_2PO_4]_2$.

Reactions [6] and [7] are thermodynamically more favourable than [3] and [4] so that the formation of the complex is hindered. Consequently, in the ir spectra, the bands due to the δ_s and ρ_r of the NH_3 united to the cation are absent (Fig. 3*B*). The stoichiometries determined for MnUP + NH_3 and MnUP + NBA reactions lend support to the above hypothesis, in the sense that two molecules of either NH_3 or NBA were absorbed for each manganese ion as required for reactions [6] and [7].

The above argument means that the resultant product of the retention of NH_3 or NBA by $Mn(H_2O)_n[UO_2PO_4]_2$ should be

TABLE 6. Assignments of the most significant bands of the ir spectra of $M(NBA)_x(H_2O)_y[UO_2PO_4]_2$ (refs. 4, 5, 8, 9)

M	ρCH_2	δCH_2, δCH_3	δNH_3^+	δH_2O, δNH_2	$\nu_s CH_3$	$\nu_s CH_2$	$\nu_{as} CH_3$
Ni	1400	1470	1500	1640	2880	2940	2965
Co	1390	1470	1510	1645	2900	2950	2970
Zn	1390	1470	1500	1610, 1635	2900	2950	2970
Cu	1400	1465	1575	1620, 1640	2870	2950	2970
Cd	1400	1470	1495	1625, 1650	2870	2930	2970
Mn	1400	1470	1490	1650	2870	2950	2970

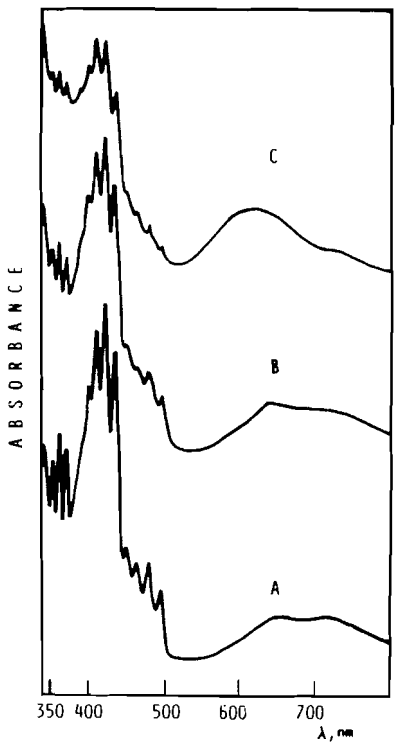

FIG. 4. Diffuse reflectance spectra of (*A*) $Ni(UO_2PO_4)_2 \cdot 9H_2O$, (*B*) $Ni(NBA)(H_2O)_{6.2}[UO_2PO_4]_2$, and (*C*) $Ni(NH_3)_{3.7}(H_2O)_{3.6}[UO_2PO_4]_2$.

considered an inclusion compound of Mn(III) oxohydroxide in a matrix of $RNH_3\ UO_2PO_4$ (R = H or C_4H_9). The diffractograms of these inclusion compounds were surprisingly well defined, indicating that the host crystallinity was preserved. However, the insertion of a mono-layer between the matrix layers prevented the intended diffractometric examination of $MnOOH \cdot H_2O$ because the necessary three-dimensional regularity no longer existed. *The ESR spectra showed poorly defined broad lines due to spin–lattice and spin–spin interactions. For this reason, it was impossible to confirm the existence of Mn(III) in the compounds. However, the XPS data show the existence of manganese in oxidation states greater than +2.*

Acknowledgements

The authors thank both referees for helpful comments. We are grateful to Mr. David Schofield for reviewing the English version and the Dirección General de Investigación Científica y Técnica (Spain) (PB 86/0244) for financial support.

1. C. M. JOHNSON, M. G. SHILTON, and A. T. HOWE. J. Solid State Chem. **36**, 3 (1981).
2. M. M. OLKEN, R. N. BIAGIONI, and A. B. ELLIS. Inorg. Chem. **22**, 4128 (1983).
3. M. M. OLKEN, C. M. VERSCHOOR, and A. B. ELLIS. Inorg. Chem. **25**, 80 (1986).
4. R. POZAS TORMO, L. MORENO REAL, M. MARTINEZ LARA, and S. BRUQUE GAMEZ. Can. J. Chem. **64**, 30 (1986).
5. R. POZAS TORMO, L. MORENO REAL, M. MARTINEZ LARA, and S. BRUQUE GAMEZ. Inorg. Chem. **26**, 1442 (1987).
6. G. W. BRINDLEY and G. BROWN. Crystal structures of clay minerals and their X-ray identification. Monograph No. 5, Mineralogical Society, London. 1980.
7. J. M. SCHAEKERS. J. Thermal Anal. **6**, 145 (1974).
8. E. J. BARAN and I. L. BOTTO. Monatsch. Chem. **108**, 781 (1987).
9. K. NAKAMOTO. Infrared and Raman spectra of inorganic and coordination compounds. 4th ed. Wiley, New York. 1986.
10. H. D. BURROWS and T. J. KEMP. J. Chem. Soc. Rev. **3**, 139 (1974).
11. B. J. HATHAWAY and D. E. BILLING. Coord. Chem. Rev. **5**, 143 (1970).

Can. J. Chem. Downloaded from www.nrcresearchpress.com by 196.1.178.254 on 09/07/12
For personal use only.

Kinetics and mechanism of the hexacyanomanganate(IV)–arsenic(III) redox reaction in acidic medium

GUILLERMO LÓPEZ-CUETO[1]

División de Química Analítica, Facultad de Ciencías, Universidad de Alicante, Apdo. 99, 03080 – Alicante, Spain

AND

CARLOS UBIDE

Departamento de Química Aplicada, Facultad de Química, Universidad del País Vasco, Apdo. 1072, 20080 – San Sebastián, Spain

Received March 24, 1988

GUILLERMO LÓPEZ-CUETO and CARLOS UBIDE. Can. J. Chem. **66**, 2855 (1988).

The reaction between hexacyanomanganate(IV) and arsenic(III), in acidic media, proceeds with a stoichiometry $\Delta[Mn(IV)]/\Delta[As(III)] = 1$. The reaction in sulfuric acid media has been followed spectrophotometrically at 387 nm, where the Mn(IV) cyanide complex has an absorption maximum, and shows a first-order dependence on the hexacyanomanganate(IV) concentration, viz., $-d[Mn(IV)]/dt = k[Mn(IV)]$, the value of k being dependent on the acidity and the arsenic(III) concentration. At As(III), 0.1 *M*; H^+, 0.16 *M*; ionic strength, 2.0; and *T*, 30°C, the value of the rate constant was found to be $k = (1.04 \pm 0.06) \times 10^{-5}$ s^{-1}. The proposed mechanism, through three parallel pathways, explains satisfactorily the experimental results observed.

GUILLERMO LÓPEZ-CUETO et CARLOS UBIDE. Can. J. Chem. **66**, 2855 (1988).

La réaction de l'hexacyanomanganate(IV) et l'arsenic(III), en milieu acide, se produit avec une stoechiométrie de $\Delta[Mn(IV)]/\Delta[As(III)] = 1$. Opérant dans un milieu d'acide sulfurique, on a suivi la réaction par spectrophotométrie à 387 nm, la longueur d'onde d'absorption maximale du complexe de cyanure de Mn(IV); on a observé que la réaction est du premier ordre par rapport à la concentration d'hexacyanomanganate(IV), soit $-d[Mn(IV)]/dt = k[Mn(IV)]$ dans laquelle k dépend de l'acidité ainsi que de la concentration en arsenic(III). A une concentration de As(III) de 0,1 *M*, de H^+ de 0,16 *M*, une force ionique de 2,0 et une *T* de 30°C, on a observé que la valeur de la constante de vitesse est égale à $k = (1{,}04 \pm 0{,}06) \times 10^{-5}$ s^{-1}. Le mécanisme proposé, impliquant trois voies parallèles, explique correctement les données expérimentales obtenues.

[Traduit par la revue]

Introduction

Manganese(IV) is a strong Lewis acid and in aqueous solutions is only soluble in the form of coordination compounds (1). In aqueous solutions, the relatively few Mn(IV) known complexes have a strong tendency to hydrolyze in neutral as well as acidic media (2–5). On the other hand, transient soluble species of Mn(IV) have been detected on the permanganate oxidations in neutral or basic media (6–8). Kinetic and mechanistic studies with soluble species of Mn(IV) in acidic media are rather scarce in the literature (9).

Hexacyanomanganate(IV) is produced in acidic solutions by disproportionation of hexacyanomanganate(III) (10) ($Mn(H_2O)_6^{2+}$ and HCN are also produced). At room temperature the reaction is quite fast and quantitative, and the hexacyanomanganate(IV) formed is a relatively inert complex in acidic media, but slowly decomposes to yield Mn(II) and $(CN)_2$. The kinetics of the latter reaction has been studied and a mechanism has been proposed (11). In acidic media, arsenic(III) reduces hexacyanomanganate(IV), the reaction rate being slow. In this paper the kinetics of this reaction is studied and a mechanism is proposed.

Experimental

Apparatus

A Shimadzu UV-260 spectrophotometer with 1.0-cm fused-silica cells was used for the kinetic measurements. A water bath circulator Selecta Tectron Digiterm was used for the cells' temperature control. When pH measurements were required, a Radiometer PHM 82 pH-meter with a combined glass – silver chloride electrode was used.

Reagents

All chemicals were of analytical reagent grade (Merck or Riedel-de-Haën) and doubly distilled water was used throughout. Potassium hexacyanomanganate(III) was prepared and characterized as described previously (11); hexacyanomanganate(IV) was formed in the reaction mixture by the disproportionation of hexacyanomanganate(III), this reaction proceeding to completion in less than three minutes under the reaction conditions. A 0.4 *M* solution of sulfuric acid (standardized with Na_2CO_3) was used to adjust the H^+ concentration. Solid $NaAsO_2$ (99.0% against MnO_4^- previously standardized with As_2O_3) and $NaNO_3$ were used as received.

Stoichiometry measurements

The stoichiometry of the reaction was determined by means of the following procedure: in a 250 mL volumetric flask, a measured amount of arsenic(III) between 0.990 and 1.423 mmol was dissolved with 30 mL of 0.15 *M* H_2SO_4, two drops of 10^{-2} *M* KI were added as a catalyst and finally 0.08 g of $K_3Mn(CN)_6$ (accurately weighed) were added with the aid of 20 mL of 0.15 *M* H_2SO_4 (whenever $K_3Mn(CN)_6$ is taken into acidic solution HCN is produced, so *care* should be taken). After the reaction had proceeded to completion — and no colour was detected (10–15 min) — 15 mL of 6 *M* HCl and one drop of 0.002 *M* KIO_3 were added; finally, the remaining arsenic(III) was determined by titration with a 0.02 *M* MnO_4^- standard solution.

Kinetic measurements

Solutions were prepared in a dark 250 mL standard flask by mixing the required amounts of sodium arsenite, sodium nitrate (to adjust the ionic strength), 0.4 *M* sulfuric acid and water up to 220–230 mL. The resulting solution was kept in a thermostatic bath for 30 min; the required amount of $K_3Mn(CN)_6$ was then added with stirring and the volume was quickly adjusted with water to 250 mL. The solution was stirred again ($K_3Mn(CN)_6$ dissolves very quickly) and transferred to a spectrophotometric cell. The kinetic curve at 387 nm (where the $Mn(CN)_6^{2-}$ shows an absorption maximum) was recorded for about 60 min using water as a reference.

The temperature in the cell was kept constant within ±0.2°C during each run.

[1]To whom correspondence should be addressed.

Can. J. Chem. Downloaded from www.nrcresearchpress.com by 196.1.178.254 on 09/07/12
For personal use only.

The value of the observed rate constant (k_{obs}) was calculated by plotting ln A vs. time ($A_\infty = 0$) and by applying linear regression analysis. This value includes the decomposition reaction constant (k_{dec}) (11); when the value of the rate constant for the Mn(IV)–As(III) reaction (k) had to be calculated, the rate constant for the decomposition — estimated or known from previous work (11) — was subtracted. With the exception of the variable studied the initial conditions were Mn(IV), 2.5×10^{-4} M; As(III), 0.1 M; H^+, 0.16 M; I, 2.0; T, 30°C (customary working conditions).

Results and discussion[2]

Stoichiometry

Because the reaction between hexacyanomanganate(IV) and arsenic(III) proceeds slowly and, at the same time, hexacyanomanganate(IV) decomposes at a comparable rate, the stoichiometry of the Mn(IV)–As(III) reaction can be determined only in the presence of a suitable catalyst.

We have found that iodide notably accelerates the reaction. In the presence of iodide concentrations as low as 2×10^{-5} M the reaction rate is high enough to render the hexacyanomanganate(IV) decomposition negligible. Concentrations of iodide higher than 2×10^{-5} M were not allowed as significant amounts of Mn(IV) are reduced. The reaction stoichiometry was determined by using excess arsenic(III). Varying the [As(III)]/[Mn(IV)] initial ratio from 8.00 to 11.48, the stoichiometry was found to be $\Delta[Mn(IV)]/\Delta[As(III)] = 1.01 \pm 0.01$ (six determinations). The oxidation products were not positively identified, but no spectral evidence was found of Mn(II)–As(III) associations and a flat spectrum is obtained at equilibrium;[3] therefore, the reaction can probably be represented by the equation

$$[1] \quad Mn(CN)_6^{2-} + H_3AsO_3 + 4H_3O^+ + 3H_2O = Mn(H_2O)_6^{2+} + H_3AsO_4 + 6HCN$$

Effect of hexacyanomangate(IV) concentration. Reaction order

Plots of ln A vs. time were linear for at least three half lives, the slope being independent of the initial concentration of $Mn(CN)_6^{2-}$. This shows a first order dependence on the hexacyanomanganate(IV) concentration. Decomposition of $Mn(CN)_6^{2-}$, which takes place simultaneously, is also a pseudo-first order reaction (11), and hence, the rate law below must be followed:

$$[2] \quad \text{Rate} = -\frac{d[Mn(IV)]}{dt} = k_{obs}[Mn(IV)] = (k_{dec} + k)[Mn(IV)]$$

From the slope values, k_{obs} can be evaluated. Under the customary working conditions and for Mn(IV) concentrations ranging from 1 to 3×10^{-5} M, it has been found that $k_{obs} = (7.68 \pm 0.05) \times 10^{-5}\ s^{-1}$ (five runs). The experimental value for k_{dec} under these conditions is $(6.64 \pm 0.03) \times 10^{-5}\ s^{-1}$ (6 runs), and the rate constant for the Mn(IV)–As(III) reaction will be

$$k = (1.04 \pm 0.06) \times 10^{-5}\ s^{-1}$$

The rate constant is independent of the Mn(II) concentration, at least at the concentration levels in which it is produced during the reaction.

Effect of the ionic strength on k_{obs}

In the range of ionic strength from 0.3 to 2.8 a very slight positive primary salt effect was found for the whole reaction, but no attempt was made to obtain conclusions about the Mn(IV)–As(III) reaction because the decomposition reaction shows a similar effect.

Effect of the As(III) concentration and acidity

In Fig. 1 values of k_{obs} have been plotted versus the arsenic(III) concentration for different H_3O^+ concentrations. The effects of both variables can be represented as follows: for [As(III)] from 3×10^{-2} to 0.20 M (maximum concentration tested), plots of k_{obs} vs. [As(III)] were linear and showed positive slopes (m) and intercepts (b) both of whose values decrease as the acidity increases. Figures 2 and 3 show the linear dependence of both m and b with respect to the reciprocal of the H_3O^+ concentration; for $[As(III)] < 3 \times 10^{-2}$ M, k_{obs} rapidly decreases and approaches the value of k_{dec} measured in the absence of As(III). The following equation

$$[3] \quad k_{obs} = k_{dec} + A[As(III)] + B\frac{[As(III)]}{[H_3O^+]} + \frac{C[As(III)]}{(1 + D[As(III)])[H_3O^+]}$$

represents satisfactorily the results observed for both high and low As(III) concentrations. Thus, at very low As(III) concentrations, k_{obs} approaches k_{dec} and, at zero As(III) concentration

$$[4] \quad k_{obs} = k_{dec}$$

On the other hand, when [As(III)] is high enough

$$[5] \quad k_{obs} = k_{dec} + A[As(III)] + B\frac{[As(III)]}{[H_3O^+]} + \frac{E}{[H_3O^+]}$$

where $E = C/D$.

From Figs. 2 and 3 the values for A, B, and E can be estimated. For $T = 30$°C and $I = 2$, $A = 9.2 \times 10^{-5}\ s^{-1}\ M^{-1}$, $B = 3.9 \times 10^{-7}\ s^{-1}$, and $E = 2.4 \times 10^{-7}\ s^{-1}\ M$.

Values of k_{obs} were calculated from eq. [5] and compared with the experimental ones, the mean of the quotient k_{calc}/k_{obs} being 1.006 and the standard deviation 0.031 (24 runs).

Reaction mechanism

According to eq. [3], the hexacyanomanganate(IV)–arsenic(III) reaction must proceed through three parallel pathways. The following reaction scheme is proposed to explain the kinetic results:

$$[6] \quad Mn(CN)_5(CNH)^- + H_2O \overset{K_a}{\rightleftharpoons} Mn(CN)_6^{2-} + H_3O^+$$

$$[7] \quad Mn(CN)_5(CNH)^- + As(OH)_3 \xrightarrow{k_1} [Mn(CN)_4(CNH)—CN—As(OH)_3]^-$$

$$[8] \quad Mn(CN)_6^{2-} + As(OH)_3 \xrightarrow{k_2} [Mn(CN)_5—CN—As(OH)_3]^{2-}$$

$$[9] \quad Mn(CN)_6^{2-} \underset{k_{-3}}{\overset{k_3}{\rightleftharpoons}} Mn(CN)_6^{2-}*$$

$$[10] \quad Mn(CN)_6^{2-}* + As(OH)_3 \xrightarrow{k_4} [Mn(CN)_5—CN—As(OH)_3]^{2-}$$

[2]Tables of observed and calculated rate constants, and the effect of ionic strength and temperature on rate constants may be purchased from the Depository of Unpublished Data, CISTI, National Research Council of Canada, Ottawa, Ont., Canada K1A 0S2.

[3]Nevertheless, when pH is higher than 3 a change in the uv spectrum seems to be produced, and above pH 7 the spectrum is clearly different, the solution shows an orange–pink colour and no precipitate is observed. This can probably be due to some kind of manganese–arsenic association in these less acidic solutions.

Can. J. Chem. Downloaded from www.nrcresearchpress.com by 196.1.178.254 on 09/07/12
For personal use only.

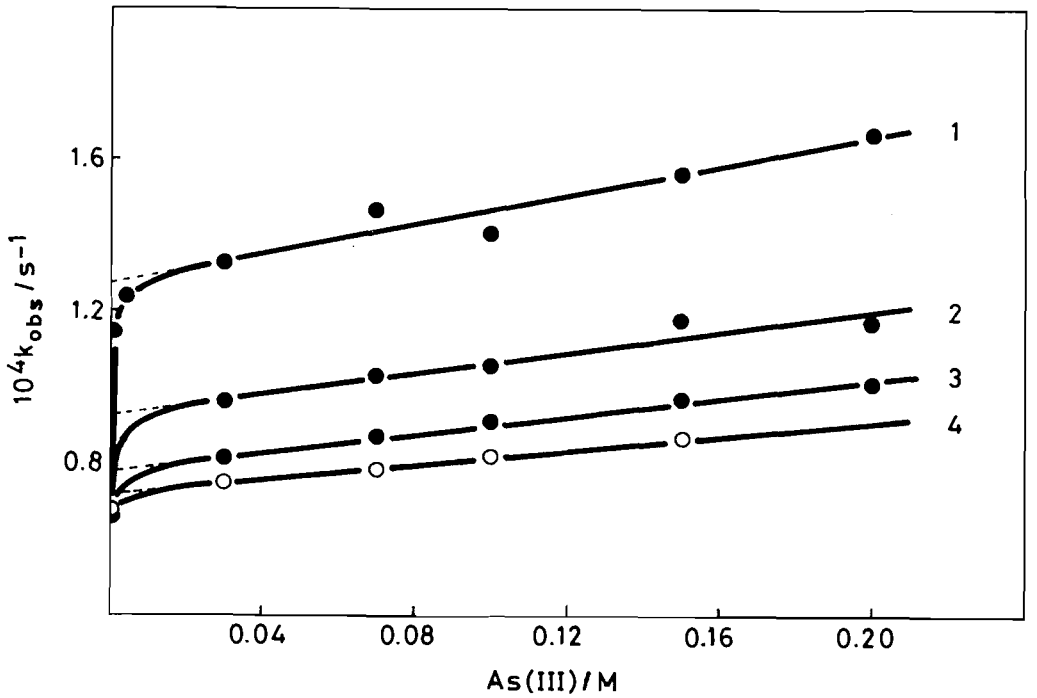

FIG. 1. Plots of k_{obs} vs. [As(III)] for different values of $[H_3O^+]$. Mn(IV), 2.5×10^{-4} *M*; *I*, 2; *T*, 30°C; H_3O^+, *M*: (*1*), 4×10^{-3}; (*2*), 8.3×10^{-3}; (*3*), 1.67×10^{-2}; (*4*), 0.16.

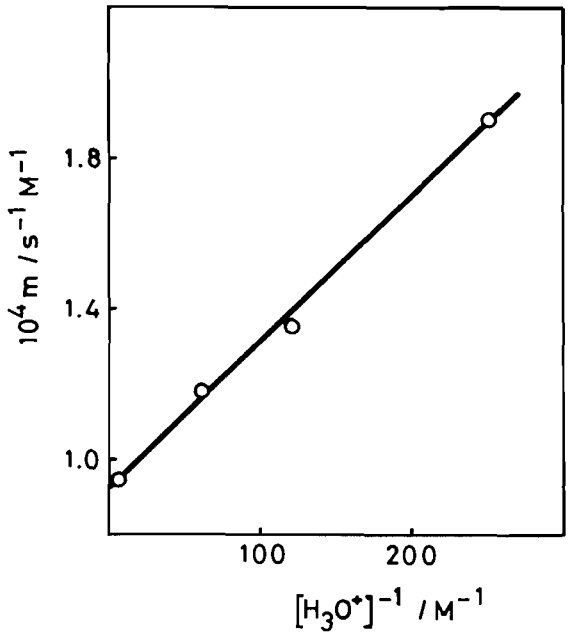

FIG. 2. Plot of the slope, *m*, vs. the reciprocal of $[H_3O^+]$ (see text).

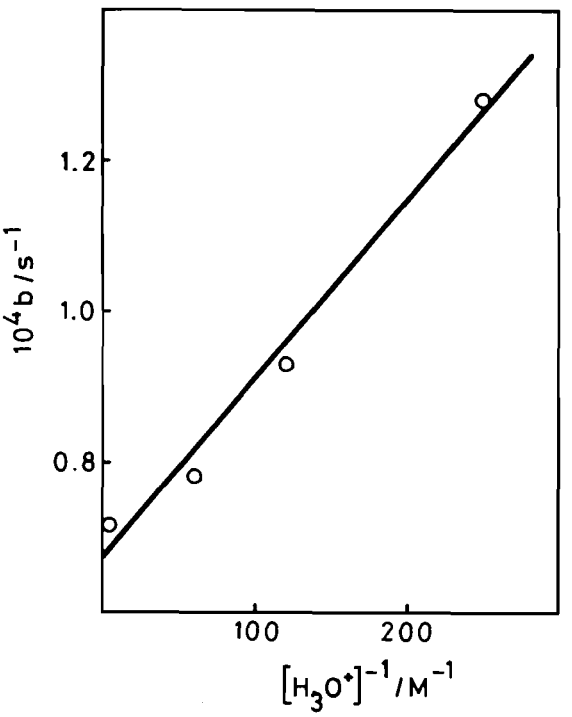

FIG. 3. Plot of the intercept, *b*, vs. the reciprocal of $[H_3O^+]$ (see text).

[11] $[Mn(CN)_4(CNH)—CN—As(OH)_3]^- + 3H_3O^+ + 4H_2O \xrightarrow{fast} Mn(H_2O)_6^{2+} + 6HCN + H_3AsO_4$

[12] $[Mn(CN)_5—CN—As(OH)_3]^{2-} + 4H_3O^+ + 3H_2O \xrightarrow{fast} Mn(H_2O)_6^{2+} + 6HCN + H_3AsO_4$

$Mn(CN)_5(CNH)^-$ is a species partially protonated on the nitrogen of one of the coordinated cyano groups, as previously reported (11) and stated for some other cyano complexes (12). Reactions [7] and [8] follow the equilibrium step [6] and they are the limiting steps of two of the three aforementioned parallel pathways. They correspond to bimolecular interactions of $As(OH)_3$ (which is proposed as predominant species rather than $HAsO_2$ in line with previous work (13)) with both the protonated and the deprotonated species of the Mn(IV) cyano complex. They would probably originate binuclear cyanide-bridged species, previous to the transfer of two electrons, that

Can. J. Chem. Downloaded from www.nrcresearchpress.com by 196.1.178.254 on 09/07/12
For personal use only.

would be accompanied by a CN^+ group transfer.[4] The oxidation reactions of As(III) may take place through either one or two electron steps. The former case is quite usual with one electron oxidizing agents, including cerium(IV) (14) and some cyanocomplexes as octacyanomolybdate(V) (15), hexacyanoferrate(III) (16) and octacyanotungstate(V) (17); arsenic(IV) is then produced as an intermediate species. On the other hand, two-electron steps are not so common as one-electron steps. We have not found in the literature two-electron oxidations of arsenic(III) with cyanocomplexes, but they can be found when the stable oxidation states of the oxidant are two units apart, as it happens with the platinum(IV)–arsenic(III) reaction (18).

The kinetics of the third pathway depends on reactions [9] and [10]. We have not found spectral evidence on the existence of the intermediate $Mn(CN)_6^{2-}$ * in step [9], but the formation of such an intermediate has been postulated in order to explain the experimental results. Stanghellini *et al.* (19) proposed a step as [9] to interpret the kinetics of the reaction between bis(cyclopentadienylcarbonylnickel) with diphenylacetylene. In that work, the intermediate proposed was a complex in which a $\pi \rightarrow \sigma$ conversion of some ligand–metal bonds was produced. In our reaction, the species $Mn(CN)_6^{2-}$ * would be an intermediate in which the charge transfer from CN^- to Mn(IV) would not have completely taken place.

Reactions [11] and [12] are fast and therefore none of them exert influence on the rate law. These two reactions will probably proceed through consecutive bimolecular steps.

From the proposed mechanism, and by applying the steady-state assumption for the $Mn(CN)_6^{2-}$ * species, the following rate law is derived:

$$[13]\quad \text{Rate} = -\frac{d[Mn(IV)]}{dt} = \left\{ k_1 \frac{[As(III)]}{1 + \frac{K_a}{[H_3O^+]}} + k_2 \frac{[As(III)]}{1 + \frac{[H_3O^+]}{K_a}} + \frac{k_3 k_4 [As(III)]}{(k_{-3} + k_4[As(III)])\left(1 + \frac{[H_3O^+]}{K_a}\right)} \right\} [Mn(IV)]$$

and, if we consider that Mn(IV) cyanide complex predominates as the monoprotonated form,[5] that is to say $K_a \ll [H_3O^+]$, eq. [13] reduces to

$$[14]\quad \text{Rate} = \left\{ k_1[As(III)] + k_2 K_a \frac{[As(III)]}{[H_3O^+]} + \frac{k_3 \frac{k_4}{k_{-3}} K_a [As(III)]}{\left(1 + \frac{k_4}{k_{-3}}[As(III)]\right)[H_3O^+]} \right\} [Mn(IV)]$$

where the pseudo first-order constant is

$$[15]\quad k = k_a + k_b + k_c = k_1[As(III)] + k_2 K_a \frac{[As(III)]}{[H_3O^+]} + \frac{k_3 \frac{k_4}{k_{-3}} K_a [As(III)]}{\left(1 + \frac{k_4}{k_{-3}}[As(III)]\right)[H_3O^+]}$$

This equation, in which k_a, k_b, and k_c are the pseudo first-order constants of the three parallel pathways, agrees with the experimental results found for the Mn(IV)–As(III) reaction, where $A = k_1$, $B = k_2 K_a$, $C = k_3 k_4 K_a / k_{-3}$, and $D = k_4 / k_{-3}$. The third term will take two limiting forms depending on the value of the As(III) concentration:

(*i*) For $(k_4/k_{-3})[As(III)] \gg 1$

$$[16]\quad k_c = \frac{k_3 K_a}{[H_3O^+]}$$

That is to say, k_c will be independent of the As(III) concentration. This takes place for $[As(III)] \geq 3 \times 10^{-2}$. Step [10] is rapid and the reaction rate is limited by the rate of formation of the intermediate (step [9]).

(*ii*) For $(k_4/k_{-3})[As(III)] \ll 1$

$$[17]\quad k_c = k_3 \frac{k_4}{k_{-3}} K_a \frac{[As(III)]}{[H_3O^+]}$$

From this, at low As(III) concentrations ($[As(III)] < 3 \times 10^{-2}\ M$), k_c will depend linearly on the As(III) concentration. In these conditions, step [10] is slow (rate determining).

Effect of temperature on k_{obs}

A plot of ln k_{obs} vs. $1/T$ between 20 and 50°C gives an apparent activation energy of 76.1 ± 1.4 kJ mol^{-1}. For the decomposition reaction, E_a = 74.9 kJ mol^{-1}; hence, a value higher than 76.1 kJ mol^{-1} can probably be estimated for the Mn(IV)–As(III) reaction, but attempts to calculate it more accurately were unsuccessful owing to decomposition of hexacyanomanganate(IV). When a plot of ln (k_{obs}/T) vs. $1/T$ was made, the apparent activation enthalpy and entropy were found to be 78.6 ± 1.5 kJ mol^{-1} and 30.4 ± 4.8 J mol^{-1} K^{-1}, respectively.

[4]We are indebted to one of the reviewers for pointing out the possibility of a CN^+ group transfer, what is more convincing than our original proposition.

[5]In an earlier paper (11) on the decomposition of the hexacyanomanganate(IV) we assumed the predominant species of Mn(IV) to be $Mn(CN)_6^{2-}$. The inconsistency is only apparent, because we could have supposed that the $Mn(CN)_5(CNH)^-$ species was predominant in the decomposition reaction, without changing the deduced rate law, by considering the equilibrium reaction:

$$Mn(CN)_5(CNH)^- + H_3O^+ \overset{K}{\rightleftharpoons} Mn(CN)_4(CNH)_2 + H_2O$$

instead of

$$Mn(CN)_6^{2-} + H_3O^+ \overset{K}{\rightleftharpoons} Mn(CN)_5(CNH)^- + H_2O$$

Can. J. Chem. Downloaded from www.nrcresearchpress.com by 196.1.178.254 on 09/07/12
For personal use only.

1. K. S. YAMAGUCHI and D. T. SAWYER. Isr. J. Chem. **25**, 164 (1985).
2. C. M. FLYNN JR. and M. T. POPE. J. Am. Chem. Soc. **92**, 85 (1970).
3. S. R. COOPER and M. CALVIN. J. Am. Chem. Soc. **99**, 6623 (1977).
4. K. D. MAGERS, C. G. SMITH, and D. T. SAWYER. Inorg. Chem. **17**, 515 (1978).
5. F. A. COTTON and G. M. WILKINSON. Advanced inorganic chemistry. 4th ed. Interscience, New York. 1980. pp. 745, 746.
6. L. I. SIMÁNDI, M. JÁKY, F. FREEMAN, C. O. FUSELIER, and E. M. KARCHEFSKI. Inorg. Chim. Acta, **31**, L457 (1978).
7. F. FREEMAN, C. O. FUSELIER, C. R. ARMSTEAD, C. E. DALTON, P. A. DAVIDSON, E. M. KARCHEFSKI, D. E. KROCHMAN, M. N. JOHNSON, and N. K. JONES. J. Am. Chem. Soc. **103**, 1154 (1981).
8. A. M. QURESHI and S. A. ZUBAIRI. J. Chem. Soc. Pak. **6**, 83 (1984).
9. M. JÁKY, L. I. SIMÁNDI, and V. YA. SHAFIROVICH. Inorg. Chim. Acta, **90**, L39 (1984).
10. G. TRAGESER and H. H. EYSEL. Inorg. Chim. Acta, **26**, L56 (1978).
11. G. LÓPEZ-CUETO and C. UBIDE. Can. J. Chem. **64**, 2301 (1986).
12. R. J. GILLESPIE and R. HULME. J. Chem. Soc. Dalton, 1261 (1973).
13. T. M. LOEHR and R. A. PLANE. Inorg. Chem. **7**, 1708 (1968).
14. P. A. RODRIGUEZ and H. L. PARDUE. Anal. Chem. **41**, 1369 (1969).
15. J. G. LEIPOLDT, L. D. C. BOK, and C. R. DENNIS. J. Inorg. Nucl. Chem. **38**, 1655 (1976).
16. D. MOHAN, D. GUPTA, and Y. K. GUPTA. Inorg. Chem. **16**, 1026 (1977).
17. J. G. LEIPOLDT, L. D. C. BOK, A. J. VAN WYK, and C. R. DENNIS. J. Inorg. Nucl. Chem. **39**, 2019 (1977).
18. K. K. SEN GUPTA and P. KUMAR SEN. J. Inorg. Nucl. Chem. **40**, 1657 (1978).
19. P. L. STANGHELLINI, R. ROSSETTI, O. GAMBINO, and G. CETINI. Inorg. Chem. **10**, 2672 (1971).

Can. J. Chem. Downloaded from www.nrcresearchpress.com by 196.1.178.254 on 09/07/12
For personal use only.

Steric effects in the diastereoselective reduction of β-ketosulfones[1,2]

J. Stuart Grossert, H. Ranjith W. Dharmaratne, T. Stanley Cameron, and Beverly R. Vincent
Department of Chemistry, Dalhousie University, Halifax, N.S., Canada B3H 4J3

Received November 18, 1987[3]

J. Stuart Grossert, H. Ranjith W. Dharmaratne, T. Stanley Cameron, and Beverly R. Vincent. Can. J. Chem. **66**, 2860 (1988).

The stereochemical course of the reduction of ketones adjacent to a chiral center normally shows some diastereoselectivity (described by Cram's rule), the degree of which is dependent on the structure of the ketone and on the reaction conditions; the selectivity in acyclic species is often not very great. In this paper, we describe the sodium borohydride reduction of four acyclic β-ketosulfones, containing a chiral center at the α position, in which the products are formed with high diastereoselectivity. Reasons for this selectivity became apparent when we were able to show that these ketosulfones apparently exist predominantly in the same conformation in solution as in the solid state. This conformation requires that the preferred trajectory for nucleophilic attack on the carbonyl group leads to reaction on the *re* face, to yield the *threo* diastereomer of the β-hydroxysulfone. The results that led to these conclusions were obtained from structural studies by X-ray crystallography, as well as by detailed ^{1}H and ^{13}C nuclear magnetic resonance spectroscopy. In some cases, the latter spectra were run both in solution and in the solid state.

J. Stuart Grossert, H. Ranjith W. Dharmaratne, T. Stanley Cameron et Beverly R. Vincent. Can. J. Chem. **66**, 2860 (1988).

La degré de diastéréosélectivité (décrit par la règle de Cram) de la réduction de cétones adjacentes d'un centre chiral dépend de la structure de la cétone ainsi que des conditions de la réaction; la sélectivité des espèces acycliques est souvent faible. Dans ce travail, on décrit la réduction par le borohydrure de sodium de quatre β-cétosulfones acycliques, contenant un centre chiral en position α, qui donnent lieu à une haute diastéréosélectivité. Les raisons de cette sélectivité sont devenues apparentes lorsqu'on a pu montrer que la conformation principale de ces cétosulfones est la même à l'état solide qu'en solution. Cette conformation implique que l'attaque nucléophile sur le groupement carbonyle se produit préférentiellement selon une trajectoire d'attaque sur la face *re* qui conduit au diastéréoisomère *thréo* de la β-hydroxysulfone. Les résultats qui ont permis de proposer cette conclusion ont été obtenus à l'aide d'études de structures par diffraction des rayons-X ainsi que par résonance magnétique nucléaire du ^{1}H et du ^{13}C. Dans quelques cas, on a déterminé ces derniers spectres tant en solution qu'à l'état solide.

[Traduit par la revue]

Introduction

The fact that the two π faces of a carbonyl group adjacent to a chiral center are diastereotopic and hence that a nucleophilic attack on the carbonyl group will lead to an excess of one diastereomer in the product was first reported by Fischer in 1894 (1). The phenomenon is much more familiar when described by Cram's rule, which is well documented (2, 3).

Stereoselectivity is not usually very high in the case of normal acyclic molecules in which the energy barriers to carbon–carbon bond rotation are low, and in which the effects are simply steric. However, selectivity can be markedly improved in the case of α-hydroxy ketones, or similar molecules in which two adjacent groups can chelate with a cation. The carbonyl group is now part of a cyclic system, and the stereoelectronic requirements for the addition of a nucleophile to the carbonyl group (4–7) are such that much greater stereoselectivity is possible (8–10). Indeed, the correct choice of nucleophile, solvent, and substrate can give reactions with either chelation or nonchelation control leading to diastereomeric excesses of better than 95:5. By contrast, when the chiral center is located at a distance from the carbonyl group, even in a vinylogous manner, stereoselectivity is not observed (11).

In the absence of chelation or some other situation that constrains the carbonyl group, it is not easy to interpret and predict the direction of the diastereoselectivity during the addition of a nucleophile to an acyclic carbonyl group. Indeed, Cram's rule is based on the assumption that a particular conformation of the chiral carbonyl compound will predominate in solution and that addition to the carbonyl is favoured from a particular direction, based on steric grounds (cf. **1***a*). Other explanations, such as that due to Felkin and co-workers (cf. **1***b*) (12), have been offered and have been discussed at length (2, 4, 7, 8). One major difficulty in assessing the reactivity of acyclic carbonyl compounds is to decide what is the major conformer in solution. Even if this conformer can be identified, the Curtin–Hammett principle may apply, which renders predictions hazardous, if not useless.

In connection with other work,[4] we had occasion to prepare the *acyclic* β-hydroxysulfone **5** and we report here that it can be obtained, with remarkable diastereoselectivity, by reduction of the corresponding β-ketosulfone **4**. This led us to carry out the physical measurements on the structures of these and related molecules, with the result that we are able to present in this paper a plausible rationale for this unusual behaviour of acyclic molecules.

Results and discussion

Preparation of the molecules

The preparation of the ketosulfone **2** (see Scheme 1) is unremarkable, and can be effected from readily available starting materials. The alkylation reaction, **6** → **2** was found to be somewhat sluggish, but could be done effectively under phase-transfer conditions, especially using an ultrasonic bath to assist with the stirring (13). Preparation of the analogous *tert*-butylsulfonyl compound **8** proceeded similarly via **7**, care being needed in temperature control during the oxidation step

[1]Part 4 in a series on the chemistry of β-ketosulfones; for part 3, see ref. 16.

[2]General communications regarding this paper may be addressed to J.S.G.; address communications regarding crystallographic details to T.S.C.

[3]Revision received June 23, 1988.

[4]J. S. Grossert, S. Sotheeswaran, H. R. W. Dharmaratne, and T. S. Cameron, following paper.

Can. J. Chem. Downloaded from www.nrcresearchpress.com by 196.1.178.254 on 09/07/12
For personal use only.

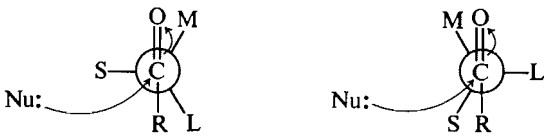

1a **1b**

(S = small, M = medium, L = large)

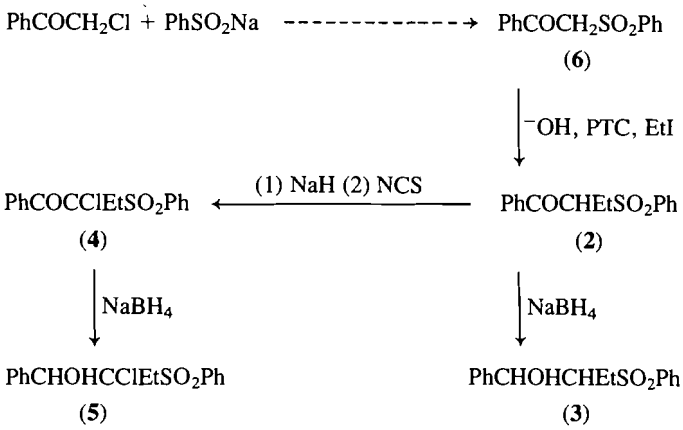

SCHEME 1

leading to **7** (eq. [1]). The chlorination steps **2** → **4** and **8** → **10** were readily accomplished by the modification of an earlier procedure (14).

[1] $PhCOCH_2Cl \xrightarrow[2.\ H_2O_2 + cat., in MeOH]{1.\ Bu^tSH,\ ^-OH,\ PTC} PhCOCH_2SO_2Bu^t$ (7)

Reduction of the ketones **2**, **4**, **8**, and **10** was carried out in a mixed solvent system, containing a mildly acidic buffer that was essential in the case of **4** to prevent the base-catalyzed cleavage of the α-chloro-β-ketosulfones (15, 16). Otherwise, **5** was found to be contaminated with benzyl alcohol, from which purification was difficult. When **2** was reduced, we were able to observe the presence of *only* the *threo* diastereomer (3); in the case of **4** the ratio of stereoisomers produced was reproducibly at least 19:1 in favour of the *threo* form, for **8**, 9:1, and for **10**, ca. 5:2.

Structural and spectroscopic features

Structural features of the compounds **2–11** were readily apparent from standard spectroscopic techniques but, desiring an unequivocal proof of the stereochemistry in **5**, we resorted to X-ray crystallography. Crystal data for the compounds **2–5** are recorded in Table 1, selected bond lengths and angles in Table 2, and selected torsion angles in Table 3.[5] Figures 1–4 contain stereoscopic drawings to show the geometry of these four molecules.[6]

[5]Sets of positional parameters and isotropic thermal parameters (Tables 5–8), of the complete anisotropic thermal parameters (Tables 9–12), of the structure factor tables (Tables 13–16), and full details of distances, bond angles, and torsion angles (Tables 17–20) and the structure determinations (Tables 21–24) may be purchased from the Depository of Unpublished Data, CISTI, National Research Council of Canada, Ottawa, Ont., Canada K1A 0S2.

Crystal data and bond lengths and angles for these compounds have also been deposited with the Cambridge Crystallographic Data Centre, and can be obtained on request from the Director, Cambridge Crystallographic Data Centre, University Chemical Laboratory, Lensfield Road, Cambridge CB2 1EW, U.K.

[6]The stereoscopic drawings were produced by the SNOOPI program, a part of the CHEMGRAF system (Chemical Designs, Oxford, U.K.).

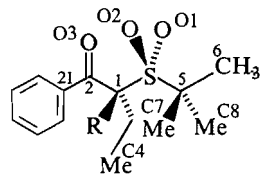

8, R = H (H11) **10**, R = Cl

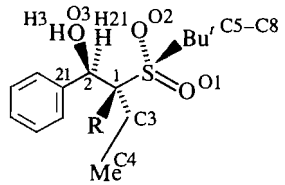

9, R = H (H11) **11**, R = Cl (*a* = *threo*; *b* = *erythro*)

Examination of the structures reveals that most features of the molecules **2–5** are unexceptional, apart from a few details worthy of comment. For instance, the two S—O bond lengths in both **2** and **3** are significantly different. Normally, the S—O bond lengths in a sulfone are equivalent (17–19), with a few cases being known in which they are significantly different (18–20), the differences generally being ascribed to factors that are not clearly understood.

An understanding of these factors is not readily achieved. For example, when the structures of known sulfones are considered, there does not appear to be evidence to support electrostatic forces due to adjacent polar bonds (18), or to implicate π–π interactions between a carbonyl group or a phenyl ring and the sulfonyl group (18, 20). An attempt to shed light on the phenomenon by examining the infrared stretching frequencies of the relevant functional groups is hampered by the fact that both the S—O symmetric and antisymmetric stretching vibrations are not obviously assignable to bands in the normally accepted wave-number ranges (21) for most of the molecules described in this paper. However, it is interesting to examine the C=O stretching frequencies in **2**, **4**, **7**, **8**, and **10**. These range from 1670 cm^{-1} in **10** to 1688 cm^{-1} in **8**, which can be compared with the frequencies found in other benzoyl derivatives. Thus, alkyl phenyl ketones absorb between 1684 and 1695 cm^{-1}, and the wave number increases with adjacent, inductive, electron-withdrawing groups to about 1710 cm^{-1} in $PhCOCHCl_2$ (22). By contrast, the β-ketosulfones show bathochromic shifts, characteristic of conjugation and a weaker C=O bond. X-ray crystal data show no unequivocal lengthening of these bonds, but any possible lengthening could be masked by uncertainties in the bond lengths. A definitive explanation of this phenomenon awaits further work.

In the case of **3**, a more straightforward explanation is available: the S—O(2) bond is the longer bond, and this oxygen atom is only 2.5 Å away from H(3) of the hydroxyl group, which is typical of a very weak hydrogen bonding interaction (23). Hydrogen bonding to sulfonyl groups is not common (24), although evidence for its presence has been observed previously (25). Again, the infrared spectrum was not especially helpful since it shows a strong band at 1142 cm^{-1}, close to the region for the sulfone S—O symmetrical stretch, but there is no obviously assignable band for the antisymmetric stretch, at the normally expected frequency just above 1350 cm^{-1} (21). However, the hydroxyl proton is coupled to a vicinal methine proton, the implications of which are discussed below.

In the case of **4**, the X-ray results show that there are two nonidentical molecules in each unit cell, but the differences

Can. J. Chem. Downloaded from www.nrcresearchpress.com by 196.1.178.254 on 09/07/12
For personal use only.

TABLE 1. Crystal data for compounds **2–5**

Parameter	Compound 2	3	4	5
Formula weight	288.36	290.38	322.80	324.82
a (Å)	5.395(2)	5.896(2)	13.210(6)	9.379(3)
b (Å)	15.254(7)	7.201(2)	9.401(3)	7.039(7)
c (Å)	17.936(12)	33.862(7)	24.740(9)	12.430(6)
α, deg	90.0	90.0	90.0	92.70(8)
β, deg	90.0	90.0	98.02(3)	109.54(3)
γ, deg	90.0	90.0	90.0	86.60(5)
Z	4	4	8	2
V (Å^3)	1476(1)	1437.7(7)	3042(2)	771.7(9)
d_c, g cm^{-3}*	1.298(1)	1.342(1)	1.410(1)	1.398(1)
Space group	$P2_12_12_1$ (no. 19)	$P2_12_12_1$ (no. 19)	$P2/c$ (no. 13)	$P\bar{1}$ (no. 2)
F(000), e$^-$	608	616	1344	340
μ, cm^{-1} †	2.229	2.292	3.926	3.872
Reflections:				
counted	1276	1388	5385	2854
unique	1216	1168	4748	2350
used (>3 esd)	1098	906	3627	1814
R	0.0561	0.0732	0.0492	0.0498
R_w	0.0551	0.0896	0.0497	0.0542

*Calculated density.
†MoK_{α_1} (λ = 0.70926 Å).

TABLE 2. Selected bond lengths and angles for compounds **2–5**

Bond length (Å) or angle (°)	Compound 2	3	4	5
S1—O1	1.411(6)	1.422(6)	1.427(3)	1.441(3)
S1—O2	1.464(6)	1.482(6)	1.435(3)	1.425(4)
S1—C1	1.785(6)	1.814(10)	1.859(4)	1.843(4)
C1—C3	1.502(9)	1.500(10)	1.537(6)	1.538(6)
C3—C4	1.525(11)	1.52(2)	1.527(6)	1.518(8)
C1—C2	1.547(9)	1.497(13)	1.559(6)	1.549(6)
C1—H11	1.079(4)*	1.080(2)*	—	—
C1—Cl1	—	—	1.776(4)	1.783(4)
C2—O3	1.223(8)	1.411(13)	1.203(4)	1.418(6)
C2—H21	—	1.080(2)*	—	1.02(4)
Cl1—S1—C1	104.6(3)	108.3(5)	107.0(3)	112.4(2)
O1—S1—O2	120.8(4)	118.8(5)	118.4(2)	118.5(2)
S1—C1—C2	105.8(5)	111.1(7)	105.1(3)	110.2(3)
S1—C1—C3	112.2(5)	109.5(7)	109.2(3)	107.7(3)
C3—C1—C2	113.4(6)	116.4(9)	110.6(4)	113.7(4)
Cl1—C1—C2	—	—	114.6(3)	110.6(3)
Cl1—C1—C3	—	—	109.4(3)	107.5(4)
C1—C2—O3	116.6(7)	108.7(8)	115.4(4)	106.1(4)
C1—C2—C21	121.5(6)	111.5(8)	124.1(4)	113.7(4)
O3—C2—C21	121.8(7)	110.6(8)	120.5(4)	112.0(4)

*Constrained during refinement.

between them are not sufficient to warrant their inclusion in Table 2; complete details are given in the tables that have been deposited.[5]

Apart from the cases discussed above, the infrared spectrum for each molecule showed the expected absorption bands. The mass spectra are consistent with the various structures. Fragmentation of the molecular ions formed in the mass spectra of all the β-ketosulfones is characterized by a very facile cleavage of these ions. In the cases of **2** and **4** the cleavage processes are simple and as expected (16, 18). In the cases of the *tert*-butylsulfonyl compounds, **7**, **8**, and **10**, another major fragmentation pathway appears, viz. migration of a hydrogen atom (presumably in a McLafferty rearrangement), followed by loss of a total of 120 daltons, which corresponds to $Me_2C{=}CH_2$ + SO_2 (i.e., the *tert*-butylsulfonyl group). The resulting radical cation then fragments further in expected pathways. These three molecules also show a prominent ion at 57 daltons.

The fragmentation patterns of the β-hydroxysulfones are

Can. J. Chem. Downloaded from www.nrcresearchpress.com by 196.1.178.254 on 09/07/12
For personal use only.

TABLE 3. Selected torsion angles for compounds **2–5**

Torsion angle (°)*	Compound				
	2	**3**	**4**	**4′**	**5**
O1—S1—C1—C2	52(2)	166(1)	−60(1)	−55(1)	−172(1)
O1—S1—C1—H11	−62(5)	−80(4)	—	—	—
O1—S1—C1—Cl1	—	—	177(2)	−177(2)	68(1)
O2—S1—C1—C3	45(2)	−93(2)	−174(2)	−167(2)	79(1)
O2—S1—C1—C2	−79(2)	37(2)	67(2)	73(2)	−45(2)
Cl1—S1—C1—C3	−68(2)	149(2)	−57(2)	−51(2)	−162(1)
S1—C1—C2—O3	85(2)	59(1)	87(2)	91(2)	−54(1)
S1—C1—C2—C21	−98(2)	−179(1)	−92(2)	−89(2)	−178(1)
C3—C1—C2—O3	−39(2)	−175(2)	−31(2)	−27(2)	−175(2)
H11—C1—C2—C21	16(5)	51(4)	—	—	—
Cl1—C1—C2—C21	—	—	26(2)	29(2)	−60(1)
H11—C1—C3—H31	−64(7)	77(8)	—	—	—
H11—C1—C3—H32	178(7)	−41(8)	—	—	—
C2—C1—C3—C4	−64(2)	−59(1)	−62(2)	−61(2)	64(2)

*A positive rotation is anticlockwise from atom 1, when viewed from atom 3 to atom 2.

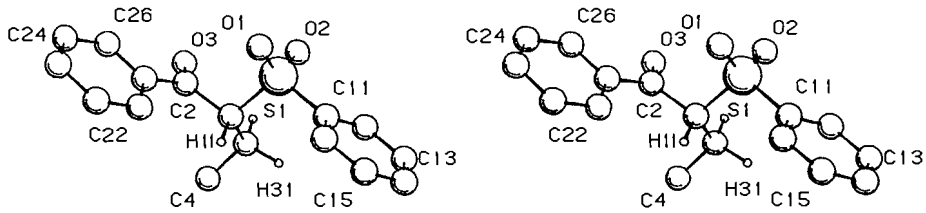

FIG. 1. A stereoscopic view of the crystal structure of 2-phenylsulfonyl-1-phenylbutanone (**2**).

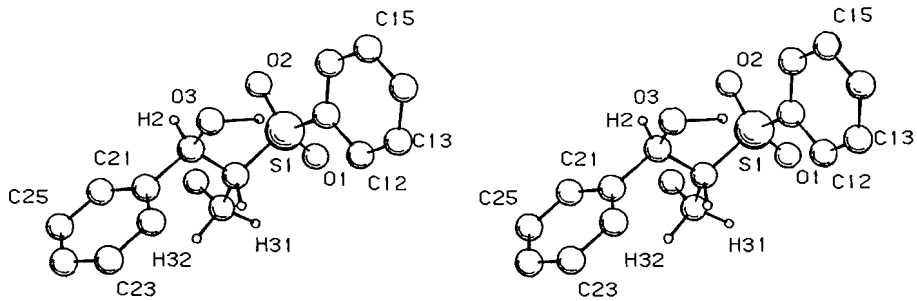

FIG. 2. A stereoscopic view of the crystal structure of 2-phenylsulfonyl-1-phenylbutanol (**3**).

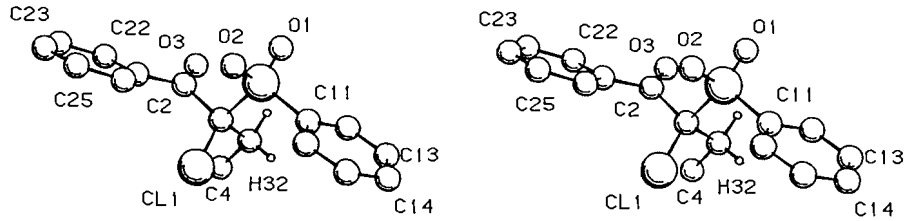

FIG. 3. A stereoscopic view of the crystal structure of 2-chloro-2-phenylsulfonyl-1-phenylbutanone (**4**).

much more complex, with major fragmentation pathways of the molecular ions from **3** and **5** being outlined in Scheme 2. The molecular ions from **9** and **11** fragment similarly in some ways, although not with the loss of $Bu^tSO_2^{\bullet}$; rather, a major fragmentation pathway appears to involve the sequential loss of the elements of $Me_2C{=}CH_2$, SO_2, and H_2O. However, due to the complex nature of the fragmentations, it is not possible to make a detailed assessment of their pathways using a low-resolution spectrum and the intensities of isotope peaks, even with the observation of some metastable peaks. This assessment must await further study.

We have carried out detailed nmr studies on the four

Can. J. Chem. Downloaded from www.nrcresearchpress.com by 196.1.178.254 on 09/07/12
For personal use only.

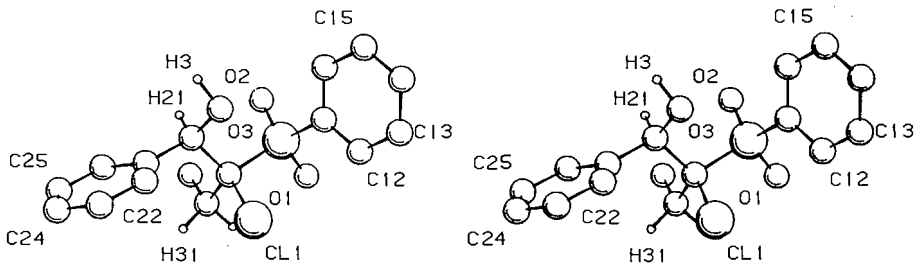

FIG. 4. A stereoscopic view of the crystal structure of 2-chloro-2-phenylsulfonyl-1-phenylbutanol (**5**).

TABLE 4. Nuclear magnetic resonance spectral parameters for compounds **2–5**

	^{1}H spectra		^{13}C spectra		
Compound	Atom: (ppm)*	J (Hz)†	Atom:	Solution	Solid (ppm)
2	H41: 0.889	H41–H31: 7.42	C4:	11.2	10.6
	H42: 0.889	H31–H32: −13.22	C3:	21.7	22.4
	H31: 2.061	H31–H11: 10.98	C1:	71.0	68.3
	H32: 2.174	H32–H11: 3.58	C2:	192.4	191.8
	H11: 5.010		C11/C21:	136.4/137.1 (soln)	
3	H41: 0.533	H41–H31: 7.50	C4:	11.9	10.3
	H31: 1.349	H31–H32: −15.06	C3:	20.2	19.2
	H32: 1.615	H31–H11: 5.71	C1/C2:	72.1	69.3
	H11: 3.277	H32–H11: 4.86	C2/C1:	73.3	72.7
	H3: 4.363	H11–H21: 8.79			
	H21: 5.035	H3–H21: 1.62			
4	H41: 0.964	H41–H31: 7.18	C4:	8.8	9.7
	H31: 2.072	H31–H32: −13.70	C3:	31.5	34.0
	H32: 2.864		C1:	93.7	br, m
			C2:	192.9	189.3
5	H41: 0.706	H41–H31: 7.35	C4:	9.1	9.6
	H31: 1.852	H31–H32: −14.94	C3:	29.2	29.3
	H32: 1.961	H3–H21: 3.86	C1:	92.8	br, m
	H3: 3.814		C2:	74.6	71.7
	H21: 5.544				

*Estimated precision = ±0.002 ppm.
†Estimated precision = ±0.05 Hz.

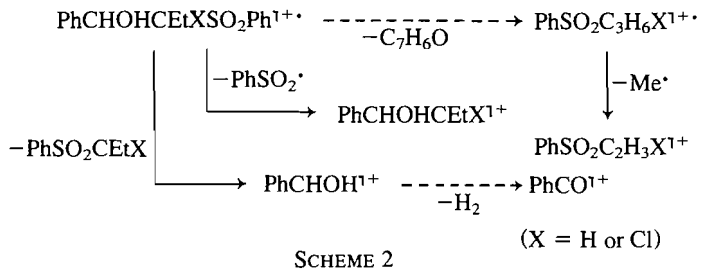

SCHEME 2

molecules, **2–5**. These include proton nmr spectra in solution, and carbon-13 nmr spectra in solution and in the liquid phase. Relevant results are presented in Table 4. Solution nmr spectral data for **8–11** are presented in Table 5. All molecules also showed appropriate resonances for the aromatic protons and carbon atoms, in the expected chemical shift ranges; these could not be correlated with any structural properties of the molecules that are relevant to the work reported here, and are therefore not included in this paper. The first point to note is that the chemical shifts in both the solution and the solid-state carbon-13 spectra are very similar in the case of **2** and not quite so similar in the case of **4**. This suggests that these molecules exist largely in the same conformations in these two states. Also, the proton–proton coupling constants of **8** and **9** are remarkably similar to those of **2** and **3**, thus suggesting very similar solution conformations for these four molecules.

The H31–H11 and H32–H11 coupling constants in **2** are typical of those for *anti* and *gauche* conformations (26), respectively, which is evidence that only one conformer about the C1—C3 bond is predominant in solution. The torsion angles for these atoms from the X-ray crystal structure are 178(7)° and 64(7)°; although these are imprecise, they confirm that the solution conformation of this bond is very similar to the solid-state conformation. Since only one conformer of the ethyl group (C1—C3 bond) is appreciably populated, it is likely that the same will be true for the C11—S1—C1—C2—C21 backbone of the molecule and, given the bulky and polar substituents about this part of the molecule, that it will be subject to bond rotation barriers. A modified form of the Karplus–Conroy equation given by Günther (eq. [2]) (26) can

$$[2] \quad \cos\phi = [1 + (40^3J - 79)^{0.5}]/20$$

be used to correlate the torsion angle (ϕ) with vicinal proton coupling constants. The experimental values of these constants give torsion angles of 2° and 63°, which are within the error limits of the angles found from the X-ray determinations.

Can. J. Chem. Downloaded from www.nrcresearchpress.com by 196.1.178.254 on 09/07/12
For personal use only.

TABLE 5. Nuclear magnetic resonance spectral parameters for compounds **8–11**

Compound*	^{1}H spectra Atom: (ppm)‡	^{1}H spectra J (Hz)§	^{13}C spectra† Atom: (ppm)
8	H41: 0.945	H41–H31: 7.50	C4: 11.78
	H31: 2.258	H31–H32: −13.76	C3: 22.83
	H32: 2.508	H31–H11: 3.55	C5: 63.25
	H61: 1.414	H32–H11: 11.33	C6,7,8: 23.92
	H11: 4.883		C1: 66.52
			C2: 192.77
9	H41: 0.622	H41–H31: 7.44	C4: 11.80
	H31: 1.520	H31–H32: −15.23	C3: 21.24
	H32: 1.794	H31–H11: 5.77	C5: 61.51
	H61: 1.448	H32–H11: 4.50	C6,7,8: 23.50
	H11: 3.376	H11–H21: 9.08	C1: 65.79
	H3: 4.433	H3–H21: 3.16	C2: 72.95
	H21: 5.047		C11: 139.75
10	H41: 0.978	H41–H31: 7.17	C4: 8.76
	H31: 2.444	H31–H32: −14.18	C3: 32.27
	H32: 3.081		C5: 69.91
	H61: 1.542		C6,7,8: 25.90
			C1: 97.26
			C2: 193.15
11*a*	H41: 0.642	H41–H31: 7.50	C4: 9.3
	H31: 2.063	H31–H32: −15.20	C3: 30.0
	H32: 2.180	H3–H21: 3.54	C5: 70.3
	H61: 1.668		C6,7,8: 26.2
	H3: 4.364		C1: 96.2
	H21: 5.406		C2: 75.3
11*b*	H41: 1.096	H41–H31: 7.40	C4: 10.3
	H31: 2.342	H31–H32: −15.17	C3: 26.0
	H32: 2.543	H3–H21: 2.41	C5: 70.5
	H61: 1.717		C6,7,8: 26.4
	H3: 4.430		C1: 93.4
	H21: 5.550		C2: Obscured

*The numbering of atoms is given on the structures and is analogous to that for compounds **2–5**.

†Assignments were based on the multiplicities of each resonance in the gated ^{13}C nmr spectrum.

‡Estimated precision = ±0.002 ppm.

§Estimated precision = ±0.05 Hz.

Alternatively, the Altona equation (eq. [3]) for 3 substituents (27) takes into account both substituent electronegativity and orientation; it has been used successfully to describe the conformations of acyclic methylsulfonyl compounds in solution (28).

$$[3]\quad {}^3J_{HH} = 13.22\cos^2\phi - 0.99\cos\phi + \Sigma\Delta\chi_i\{0.87 - 2.46\cos^2(\xi_i\phi + 19.9|\Delta\chi_i|)\}^7$$

Application of this equation to a molecule such as **2** presents difficulties because of uncertainties in the values of group electronegativities, χ_i, especially for sulfones. For example, published group electronegativities for the phenylsulfonyl group are 2.9 (29), 4.10 (30), or 3.014 (31), whereas the methylsulfonyl group is given as 2.83 (28), 3.1 (29), or 2.998 (31) and the benzoyl group as 3.42 (30) or 2.681 (31). Clearly, the $PhSO_2$ group is more electronegative than an $MeSO_2$ group, since the pK_a values of $PhSO_2Me$ and $MeSO_2Me$ are 29.0 and 31.1, respectively (32); furthermore, Creary *et al.* (33) have recently shown that the $PhSO_2$ group is strongly electron-withdrawing, in an inductive manner. We have therefore chosen to use Langler's electronegativities (30) in the Altona equation for describing coupling constants in **2** (as outlined in footnote 7, even though these are probably too large relative to other electronegative functional groups, such as CF_3), from which we obtained torsion angles of 175° and 59°, which again agree with the X-ray results. The use of the electronegativities from ref. 31 gave torsion angles of 166° and 59°, which are in poorer agreement with, but still close to, the results for the solid state. Presumably, a similar solution conformation pertains in the case of the chloroketosulfone, **4**. Application of the Altona equation [3] to the C1—C3 bond in **8** presented further difficulties when χ values of 3.4 (PhCO) and 3.1 (Bu^tSO_2) (values from refs. 29 and 30) were used, as the equation then did not yield a large enough value for the *trans* coupling constant (only 11.15 Hz, whereas the experimental value is 11.33 Hz). The use of the group electronegativities due to Inamoto and Masuda (31), assuming that a *tert*-butylsulfonyl group has a similar electronegativity to a methylsulfonyl group, leads to torsion angles of 56° and 170° for the coupling constants of 3.55 and 11.33 Hz, respectively. This discussion serves to illustrate the difficulties that are encountered when attempts are made to quantify the electronic properties of sulfonyl groups; the values suggested for the above torsion angles must be considered to be approximate.

It is reasonable to expect that the β-hydroxysulfones **3**, **5**, **9**, and **11** will be more likely to experience bond rotations in solution, as restrictions to rotations will now be mostly steric, since these molecules have lost the electronic conjugation effects associated with the benzoyl groups of **2**, **4**, **8**, and **10**. Application of the Altona equation for four substituents (27) to the coupling constant between H11 and H21 in **3** (χ = 4.02 for $PhSO_2$, other values from ref. 29) provided a torsion angle of 177°, which compares favourably with the angle derived from the X-ray data, viz. 172(5)°. A similar application of this equation for the value obtained from **9** (χ = 3.05 for Bu^tSO_2) leads to a torsion angle of 176°. Thus, the conformation of the C2—C1—S1 backbone in these four β-hydroxysulfones is probably similar in solution to what it is in the solid state. The coupling constants between H11 and H21 and the chemical shifts of H21 in **3** and **9** are quite similar to the values given for the *threo* diastereomer of PhCHOHCHMeTs prepared by Truce and Klinger (34), using a condensation between a sulfonyl-stabilized carbanion and benzaldehyde.

The vicinal coupling constants of 5.71 and 4.86 Hz between H11 and H31,32 could not be related using eq. [3] to the approximately 60° torsion angles obtained from the X-ray structure of **3**. Rather, it became apparent that the relationship between the coupling constants was that which would be expected from a mixture of the three possible conformers arising from rotation about the C1—C3 bond. Depending on how the coupling constants were assigned, the proportions of the conformers are 37:25:38 or 40:32:28, the first number representing the conformer present in the solid state. Application of a similar procedure to the same coupling constants from **8** leads to a conformer population of 53:17:30. These proportions must be regarded as qualitative. Comparison of the solution and solid-state ^{13}C nmr spectra of **3** (Table 4) reveals only slight differences between the resonances, differences of a similar order of magnitude to those in the case of **2**. These examples

[7]The following values for the substituents $PhSO_2$, PhCO, and Me were used: χ_i = 4.1, 3.4, 2.3; ξ_i = +1, −1, +1, respectively, with the substituents in the given order, when applying this equation to coupling constants from **2**.

Can. J. Chem. Downloaded from www.nrcresearchpress.com by 196.1.178.254 on 09/07/12
For personal use only.

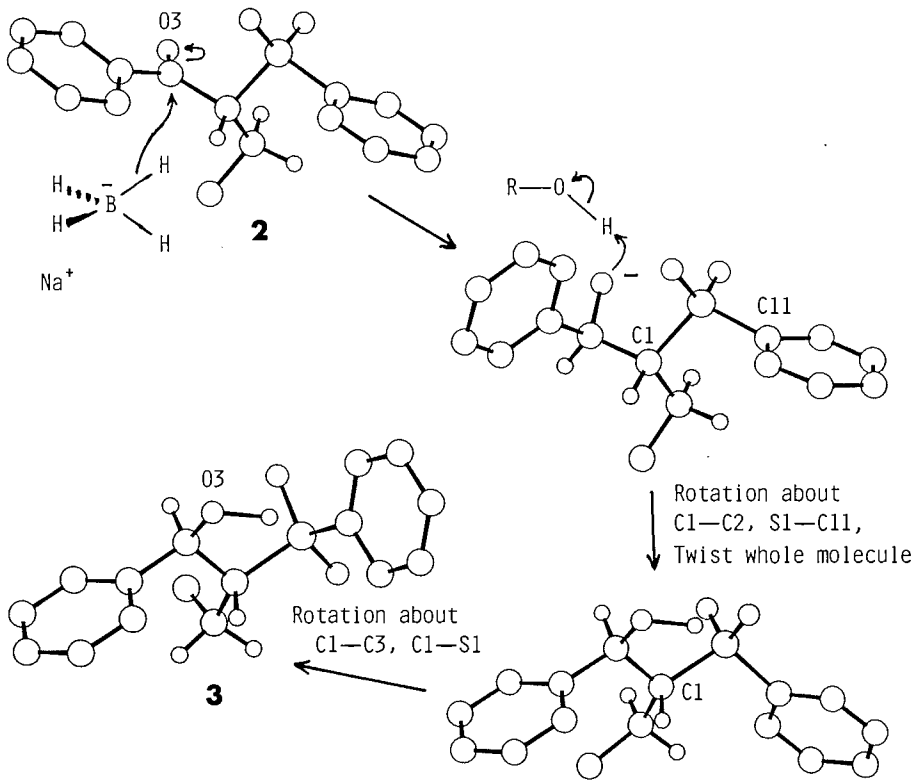

FIG. 5. A simulation of the step-by-step geometry changes required in the conversion of **2** into **3**.

serve as a further example that care must be taken when attempting to draw conclusions from comparisons between nmr spectra in these two phases (35).

A further point of interest is that the nmr spectra of **3**, **5**, **9**, and **11***a*,*b* showed coupling between the hydroxyl and the carbinol protons. In **3**, the splitting is shown unequally on the two proton resonances that are somewhat broadened, implying that the hydroxyl proton is undergoing slow exchange. However, in the other molecules, the resonances are sharply defined and the vicinal coupling constant of 3.86 Hz in **5** implies that the relationship between H3 and H21 is primarily *gauche* (36). It is likely that the greater population of this *gauche* orientation is due to weak hydrogen bonding between the hydroxyl proton and one of the sulfonyl oxygen atoms (25).

The solid-state spectra of **4** and **5** both show their resonance for Cl as a complex multiplet of relatively broad lines. This is due to a phenomenon of dipolar coupling between the carbon-13 and the two chlorine isotopes. The phenomenon is the subject of continuing interest.[8]

Mechanistic aspects of the reduction reaction

We are aware of four other reports in which diastereoselectivity in the reduction of β-ketosulfones has been observed. Bordwell and co-workers have reported (37) that the carbonyl group of 2-benzenesulfonylcyclohexanone is stereoselectively reduced by sodium borohydride; similarly, Bohlmann and Haffer (38) found that reduction of an acyclic methyl sulfone ($PhCOCMeClSO_2Me$) gives a mixture of chlorohydrins in a 7:3 ratio. More recently, Julia *et al.* (39), in a search to improve the Julia olefin synthesis (40–42), have studied the reduction of the acyclic β-ketosulfones, **12**, with three hydride-type reducing agents. Sodium borohydride gave high yields, but was relatively nonstereoselective (55–74%), lithium tri-*sec*-butylborohydride gave rather lower yields, but in some case better stereoselectivity (38–100%), and lithium aluminum hydride gave somewhat better yields and quite good selectivity (72–91%).

$RCOCHR'SO_2R''$ R = Ph or Bu^t; R′,R″ = alkyl
(12)

Interestingly, only in the case of **12**, R = Bu^t, R′ = R″ = Me, was the reduction fully stereoselective, and only by using the tributylborohydride. The authors do not provide full details in their note, nor do they provide a rationalization for the stereoselectivity that they found. The fourth report (43) is concerned with the reduction of cycloalkanones that contain a 3-arylsulfonyl group, and the reductions are only partially stereoselective.

The results discussed in this paper show quite clearly that when the carbonyl and sulfonyl groups are sufficiently proximate, the polar electronic fields about them interact to cause one conformer about the CO—C—SO_2 bonds to be predominant. When the β-ketosulfone includes both a benzoyl group and a phenylsulfonyl group, as in **2** and **4**, extra conjugation or polar effects are imposed; rotation about this bond is then probably completely hindered (at room temperature). Furthermore, in **2** and **4**, one of the sulfonyl oxygen atoms is located close enough to the trajectory normally followed by a nucleophile adding to the *si* face of the carbonyl group so that this reaction is kinetically disfavoured. The preferred reaction path is thus attack at the *re* face, leading to the *threo* diastereomer.[9]

It was intriguing to find that the actual conformation of the products (**3** or **5**) from reduction of **2** or **4**, respectively, can be

[8]R. E. Wasylishen and M. McKinnon, to be published.

[9]Alternatively, **3** can be described as the *RS*(1*l*,2*u*) diastereomer, whereas **5** is *RS*(1*l*,2*l*) (44).

Can. J. Chem. Downloaded from www.nrcresearchpress.com by 196.1.178.254 on 09/07/12
For personal use only.

arrived at quite simply by assuming the hydride attack on the *re* face of the carbonyl (which includes a rehybridization of the carbonyl carbon atom), followed by partial rotations about three C—C bonds. This view of the reaction can be simulated using molecular models, or by the molecular drawing properties of the CHEMGRAF system, as shown in Fig. 5. Although we recognize that this approach is speculative and that it cannot suggest the order in which the events might have happened, the structures in Fig. 5 represent a plausible representation for the reaction pathway of the stereoselective reduction at the carbonyl group.

Conclusions

The stereoselective reduction of these β-ketosulfones can be described by the Felkin modification of Cram's Rule (4, 7). It is not readily apparent whether the stereoselectivity is due to a low-lying σ* orbital from the adjacent C—SO_2 bond (7), or whether the effect is simply a steric control on the reagent trajectory, arising from the particular conformation adopted by these β-ketosulfones.

We suggest that the diastereoselectivity shown by this reaction system has significant synthetic potential as a stereoselective synthesis of heavily substituted styrenes, using the Julia synthesis (40–42). We are exploring the potential of such a synthesis.

Experimental

General

Thin-layer chromatography was carried out on E. Merck or Brinkmann silica sheets with fluorescent indicator, which were developed with dichloromethane. Aqueous solutions were worked up by extraction with the requisite organic solvent, which was washed two or three times with water, dried over anhydrous sodium sulfate, and rotary evaporated using a water-aspirator vacuum. The compounds were all purified by recrystallization from the solvent given. Melting points were taken with a Fisher–Johns apparatus and are uncorrected. Infrared spectra were run as KBr pellets on a Perkin–Elmer model 283 spectrophotometer. Mass spectra were recorded on a CEC 21-104 magnetic sector spectrometer, equipped with a modified scan system (45) and IBM-PC control and data system,[10] at 70 eV, source temperature of ca. 150°C, using a glass direct-injection probe.

Proton nmr spectra were run in $CDCl_3$ solutions, referenced to TMS, on a Nicolet 360 NB nmr spectrometer typically using a spectral window of 4000 Hz, an acquisition time of 4–8 s, and transformed using 32- or 64K data points. Carbon-13 nmr spectra for **2**–**5** were recorded in $CDCl_3$ solutions, referenced to TMS, on a Varian CFT-20 spectrometer, using 35° pulses, a spectral window of 4505 Hz, an acquisition time of 0.5 ms, and were processed using 8K data points. The ^{13}C solution nmr spectra for **8**–**11** were recorded on the Nicolet spectrometer with SW = 20 000 Hz, AT = 400 ms, and a 16K Fourier transform. All lines observed in each spectrum could be interpreted in terms of the structure of the molecule. Solid-state carbon-13 nmr spectra were recorded on powdered samples (ca. 0.4 g) packed into cylindrical rotors made from alumina, using a Bruker MSL-200 spectrometer operating at 50.3 MHz while the sample was spun (magic-angle) at 4.5–5 kHz. Cross polarization was accomplished using the Hartmann–Hahn match with 90° pulses of about 4 μs and contact times of 2–3 ms. Data tables of 8K points were collected over a sweep width of 13.5 kHz and spectra were signal-averaged for at least 100 transients using recycle times of 2–3 s. A sensitivity enhancement corresponding to 15 Hz of line broadening was applied before Fourier transformation. The chemical shifts were referenced with respect to external adamantane, which has shifts of 29.50 ppm (*C*H) and 38.56 ppm (CH_2) with respect to TMS (46). All the nmr data are recorded in Tables 4 and 5.

[10]B. Millier and J. S. Grossert, unpublished work in this department.

Details by which data for the X-ray crystal structure determinations were acquired have been published recently (17); all structures were refined using the CRYSTALS system (issue V).

Preparation of 2-phenylsulfonyl-1-phenylethanone, 6

Sodium benzenesulfinate and phenacyl chloride were refluxed in absolute ethanol and worked up to give **6** as colourless needles (95% ethanol, >80% yield), mp 91–92°C (lit. (47) mp 96°C).

Preparation of 2-phenylsulfonyl-1-phenylbutanone, 2

A mixture of **6** (5.20 g, 20 mmol), iodoethane (16 mL, 200 mmol), benzyltriethylammonium bromide (0.7 g), sodium hydroxide (1.60 g, 40 mmol), dichloromethane (40 mL), and water (20 mL) was stirred in an ultrasonic bath for 4.5 h. After cooling, dichloromethane (100 mL) was added and the mixture worked up to give **2** as white needles (95% ethanol, 3.5 g, 60%), mp 91–92°C; ir ν_{max}: 1667 (s), 1448 (m), 1305 (m, br), 1267 (s), 1145 (s), 745 (s), 679 (m), 559 (s) cm^{-1}; ms *m/z*: 288 ($M^{+\cdot}$, 3.2), 260 (2.4), 224 (6.4), 147 (3.4), 146 (6.4), 105 (100), 91 (2.3), 77 (32) daltons.

Preparation of 2-phenylsulfonyl-1-phenylbutanol, 3

A mixture of **2** (1.10 g, 3.82 mmol), NaH_2PO_4 (0.360 g, 3 mmol), $NaBH_4$ (0.152 g, 4.02 mmol), dimethoxyethane (15 mL), and water (3 mL) was stirred for 1 h at room temperature, after which it was poured into 10% NH_4Cl solution (25 mL) and extracted with diethyl ether. Regular work-up gave **3** as fine white needles (1:1 hexane–dichloromethane, 0.82 g, 74%), mp 135–137°C; ir ν_{max}: 3500 (s), 1449 (m), 1283 (s), 1142 (s), 759 (s), 729 (s), 692 (s), 628 (m) cm^{-1}; ms *m/z*: 292 (2.25), 291 (6.38), 290 ($M^{+\cdot}$, 33.8), 184 (100), 169 (93), 149 (17), 148 (32), 107 (35), 105 (14), 91 (32), *m** at 117.0, 146.5, 155.5 daltons.

Preparation of 2-chloro-2-phenylsulfonyl-1-phenylbutanone, 4

A solution of **2** (1.19 g, 4.13 mmol) in dry toluene (40 mL) was dropped on to NaH while stirring (0.20 g of 50% oil dispersion, oil removed by washing with dry ligroin, 4.17 mmol) and the mixture was then heated under nitrogen for 5 h (90°C oil bath). At this point, *N*-chlorosuccinimide (0.70 g, 5.2 mmol) was added in one portion, and heating continued for a further 5 h, after which the mixture was allowed to stand at room temperature overnight before being worked up with diethyl ether and water to give **4** as brilliant colourless prisms (1:1 hexane – diethyl ether, 1.30 g, 97%), mp 58–60°C; ir ν_{max}: 1678 (m), 1450 (m), 1315 (m), 1232 (s), 1153 (s), 763 (s), 682 (s), 568 (s) cm^{-1}; ms *m/z*: 324 ($M^{+\cdot}$, 1.00), 322 (2.52), 183 (2.13), 181 (6.39), 141 (1), 125 (1), 117 (1), 115 (1), 105 (100), 77 (33) daltons.

Preparation of threo*-2-chloro-2-phenylsulfonyl-1-phenylbutanol, 5*

A mixture of **4** (3.26 g, 10.1 mmol), NaH_2PO_4 (1.152 g, 9.6 mmol), $NaBH_4$ (0.384 g, 10.2 mmol), dimethoxyethane (48 mL), and water (10.6 mL) was reacted and worked up as for **3** (above) to give **5** as fine white needles (1:1 diethyl ether – dichloromethane, 2.90 g, 88%), mp 130–133°C; ir ν_{max}: 3495 (s), 1448 (m), 1303 (s), 1285 (s), 1148 (s), 1062 (s), 731 (s), 555 (s) cm^{-1}; ms *m/z*: 326 (5.75), 324 ($M^{+\cdot}$, 14.9), 220 (22.3), 218 (60.1), 205 (11.4), 203 (30), 185 (4.4), 183 (12.8), 147 (37), 143 (21), 125 (10), 119 (12), 107 (100), 105 (36), 91 (63), 79 (30), 78 (23), 77 (67), *m** at 189.5 daltons.

Preparation of 2-tert*-butylsulfonyl-1-phenylbutanone, 8*

Phase-transfer condensation of phenacyl chloride (15.4 g, 0.1 mol) and *tert*-butylthiol (9.0 g, 0.1 mol) in an analogous manner to that described for the preparation of **2** gave relatively clean *tert*-butyl phenacyl sulfide (20.6 g), part of which was recrystallized to give needles, mp 143–145°C (from ethanol), ms *m/z* 208 ($M^{+\cdot}$, 11), 152 (23), 105 (100) daltons. A methanolic solution of the sulfide (5.0 g, 24 mmol) was oxidized with excess 30% H_2O_2 in the presence of ammonium molybdate catalyst following the method of Schultz *et al.* (48) to give crude 2-*tert*-butylsulfonyl-1-phenylethanone (**7**). This was purified by recrystallization from absolute ethanol to form **7** as needles (4.2 g, 73%), mp 77–78°C; ir ν_{max}(KBr): 1681 (s), 1452 (s), 1339 (m), 1238 (s), 1017 (m), 710 (s), 704 (s), 576 (s) cm^{-1}; ^1H nmr δ($CDCl_3$): 1.4 (s, 9H), 4.5 (s, 2H), 6.9–8.0 (m, 5H); ms *m/z*:

Can. J. Chem. Downloaded from www.nrcresearchpress.com by 196.1.178.254 on 09/07/12
For personal use only.

240 ($M^{+\cdot}$, 0.6), 184 (0.9), 176 (5), 120 (100), 118 (3), 105 (19), 91 (9), 78 (6), 77 (14), 57 (94), *m** at 150, 92.0, 82.2, 46.9 daltons.

Ethylation of **7** (2.8 g, 11.6 mmol) was carried out by phase-transfer condensation with iodoethane (3.6 g, 23 mmol), as described above for **2**, to give crude **8**; several recrystallizations (ethanol) gave **8** as white needles, mp 188–189°C (1.63 g, 55%); ir ν_{max}(KBr): 2980 (m), 1688 (s), 1287 (s), 1269 (s), 1217 (s), 1110 (s), 747 (s), 685 (s) cm^{-1}; ms *m/z*: 150 (0.77), 149 (11.4), 148 (100, $M^{+\cdot} - 64 - 56$), 147 (17), 133 (36), 120 (5), 105 (49), 91 (3), 77 (28), 57 (70), *m** 97.5 daltons.

Preparation of threo-*2*-tert-*butylsulfonyl-1-phenylbutanol, **9***

A mixture of **8** (420 mg, 1.57 mmol), NaH_2PO_4 (138 mg, 1.15 mmol), and $NaBH_4$ (60 mg, 1.57 mmol) in EtOH–Et_2O–water (11 mL, 5:5:1) was stirred vigorously for 1 h, at room temperature. Regular work-up with water and Et_2O gave homogeneous (by tlc) material, which by ^1H and ^{13}C nmr was a mixture (ca. 9:1) of the *threo* and *erythro* diastereomers (400 mg, 95%). Recrystallization (CH_2Cl_2–hexane, 1:1) gave **9** as white prisms, mp 67–69°C; ir ν_{max}: 3500 (s), 2990 (m), 1470 (m), 1271 (s), 1239 (s), 1100 (s), 697 (s), 555 (s) cm^{-1}; ms *m/z*: 270 ($M^{+\cdot}$, 3.4), 214 (0.25), 205 (0.1), 187 (0.1), 164 (9), 150 (2.5), 149 (19), 148 (22), 147 (2), 133 (10), 132 (45), 131 (7), 117 (23), 108 (38), 107 (22), 105 (7), 91 (24), 79 (9), 77 (11), 57 (100), *m** at 146.0, 104.0 daltons.

Preparation of 2-tert-*butylsulfonyl-2-chloro-1-phenylbutanone, **10***

A sample of **8** (2.0 g, 7.46 mmol) was chlorinated with NaH and NCS, as for the preparation of **4**, to give **10** as colourless needles (Et_2O–hexane, 1:1, 1.55 g, 68%), mp 74–75°C; ir ν_{max}(KBr): 2985 (m), 1670 (s), 1308 (s), 1301 (s), 1236 (s), 1121 (s), 759 (s), 618 (s) cm^{-1}; ms *m/z*: 302 ($M^{+\cdot}$, 0.28), 184 (26), 183 (11), 182 (77), 169 (8), 167 (23), 147 (6), 131 (4), 105 (100), 77 (45), 57 (80), *m** at 153.6, 119.0 daltons.

Preparation of 2-tert-*butylsulfonyl-2-chloro-1-phenylbutanol, as a diastereomeric mixture, **11**a + b*

A mixture of **10** (800 mg, 2.65 mmol), NaH_2PO_4 (250 mg, 2.17 mmol), and $NaBH_4$ (127 mg, 3.4 mmol) was reacted in the usual way in DME (10 mL) and water (1 mL) to give **11** as a crystalline mixture (785 mg, 97%); ir ν_{max}(KBr): 3450 (s), 2930 (m), 1457 (s), 1285 (s), 1120 (s), 1095 (s), 1085 (s), 1048 (s), 697 (s), 660 (s), 555 (s) cm^{-1}; ms *m/z*: 306 (1.2), 304 ($M^{+\cdot}$, 3.3), 200 (1), 198 (3), 185 (1), 183 (4), 168 (7), 166 (21), 148 (10), 147 (13), 142 (15), 131 (11), 107 (26), 105 (20), 91 (19), 77 (16), 57 (100) daltons.

Acknowledgements

The authors gratefully acknowledge financial support from NSERC of Canada in the form of operating grants (to J.S.G. and T.S.C.), an infrastructure grant (to T.S.C.), and a graduate fellowship (to B.R.V.). The Izaak Walton Killam Memorial Trust kindly awarded a predoctoral fellowship (to B.R.V.) and the authors thank Drs. D. L. Hooper and R. E. Wasylishen for their kindness in providing the high-field solution and solid-state nmr spectra, by means of the facilities at the Atlantic Region Magnetic Resonance Center, Halifax, N.S. Kalyani Paramasigamani and Cheryl L. Wallace provided technical assistance for some parts of the work.

1. E. Fischer. Ber. Dtsch. Chem. Ges. **27**, 3189 (1894).
2. E. L. Eliel. *In* Asymmetric synthesis. Vol. 2. Stereodifferentiating reactions. *Edited by* J. D. Morrison. Academic Press, New York, NY. 1983. pp. 125–155.
3. Y. Izumi and A. Tai. Stereodifferentiating reactions. Kodansha, Tokyo. 1977. pp. 124–136, 178–211.
4. P. Deslongchamps. Stereoelectronic effects in organic chemistry. Pergamon, Oxford. 1983. pp. 32–33, 209–211, 234.
5. S. M. Bachrach and A. Streitwieser, Jr. J. Am. Chem. Soc. **108**, 3946 (1986).
6. R. R. Fraser and M. Stanciulescu. J. Am. Chem. Soc. **109**, 1580 (1987).
7. E. P. Lodge and C. H. Heathcock. J. Am. Chem. Soc. **109**, 3353 (1987), and references therein.
8. M. T. Reetz. Angew. Chem. Int. Ed. Engl. **23**, 556 (1984).
9. T. Oishi and T. Nakata. Acc. Chem. Res. **17**, 338 (1984).
10. G. R. Brown and A. J. Foubister. J. Chem. Soc. Chem. Commun. 455 (1985); M. Fujita and T. Hiyama. J. Am. Chem. Soc. **107**, 8294 (1985).
11. I. Fleming, H. Kühne, and K. Takaki. J. Chem. Soc. Perkin Trans. 1, 725 (1986).
12. M. Cherest, H. Felkin, and N. Prudent. Tetrahedron Lett. 2199 (1968).
13. J. Ezquerra and J. Alvarez-Builla. J. Chem. Soc. Chem. Commun. 54 (1984).
14. J. S. Grossert, J. Hoyle, and D. L. Hooper. Tetrahedron, **40**, 1135 (1984).
15. D. Scholz. Chem. Ber. **114**, 909 (1981); J. Ficini and G. Stork. Bull. Soc. Chim. Fr. 723 (1964).
16. J. S. Grossert, P. K. Dubey, and T. Elwood. Can. J. Chem. **63**, 1263 (1985).
17. J. S. Grossert, J. Hoyle, T. S. Cameron, S. P. Roe, and B. R. Vincent. Can. J. Chem. **65**, 1407 (1987).
18. J. S. Grossert, P. K. Dubey, G. H. Gill, T. S. Cameron, and P. A. Gardner. Can. J. Chem. **62**, 798 (1984), and references therein.
19. R. J. Boyd and J. P. Szabo. Can. J. Chem. **60**, 730 (1982).
20. G. D. Andreetti, G. Bocelli, and P. Sgarabotto. Cryst. Struct. Commun. **6**, 89 (1977).
21. L. J. Bellamy. The infrared spectra of complex molecules. 3rd ed. Chapman and Hall, London. 1975. Table 22.
22. C. J. Pouchert. The Aldrich library of infrared spectra. 3rd ed. Aldrich Chemical Co., Milwaukee, WI. 1981.
23. R. Taylor and O. Kennard. Acc. Chem. Res. **17**, 320 (1984).
24. J. S. Grossert. *In* The chemistry of sulphoxides and sulphones. *Edited by* S. Patai, Z. Rappoport, and C. J. M. Stirling. Wiley, Chichester. 1988. p. 925.
25. S. J. Shafer and W. D. Closson. J. Org. Chem. **40**, 889 (1975).
26. H. Günther. NMR spectroscopy. Wiley, New York, NY. 1980. pp. 106–113.
27. C. A. G. Haasnoot, F. A. A. M. de Leeuw, and C. Altona. Tetrahedron, **36**, 2783 (1980).
28. E. Brunet, J. L. García-Ruano, J. H. Rodríguez, and F. Alcudia. Tetrahedron, **40**, 4433 (1984); E. Brunet, M. T. Gallego, J. L. García-Ruano, and F. Alcudia. Tetrahedron, **42**, 1423 (1986).
29. J. E. Huheey. J. Phys. Chem. **70**, 2086 (1966).
30. J. R. Hancock, W. R. Hardstaff, P. A. Johns, R. F. Langler, and W. S. Mantle. Can. J. Chem. **61**, 1472 (1983).
31. N. Inamoto and S. Masuda. Chem. Lett. 1003 (1982).
32. W. S. Matthews, J. E. Bares, J. E. Bartmess, F. G. Bordwell, F. J. Cornforth, G. E. Drucker, Z. Margolin, R. J. McCallum, G. J. McCollum, and N. R. Vanier. J. Am. Chem. Soc. **97**, 7006 (1975).
33. X. Creary, M. E. Mehrsheikh-Mohammadi, and M. D. Eggers. J. Am. Chem. Soc. **109**, 2435 (1987).
34. W. E. Truce and T. C. Klingler. J. Org. Chem. **35**, 1834 (1970).
35. J. O. Friedrich and R. E. Wasylishen. Can. J. Chem. **64**, 2132 (1986).
36. R. R. Fraser, M. Kaufman, P. Morand, and G. Govil. Can. J. Chem. **47**, 403 (1969); C. P. Rader. J. Am. Chem. Soc. **91**, 3248 (1969).
37. J. Weinstock, R. G. Pearson, and F. G. Bordwell. J. Am. Chem. Soc. **78**, 3468 (1956).
38. F. Bohlmann and G. Haffer. Chem. Ber. **102**, 4017 (1969).
39. M. Julia, M. Launay, J.-P. Stacino, and J.-N. Verpeaux. Tetrahedron Lett. **23**, 2465 (1982).
40. M. Julia and J. M. Paris. Tetrahedron Lett. 4833 (1973).
41. M. Julia, H. Lauron, J.-P. Stacino, J.-N. Verpeaux, Y. Jeannin, and Y. Dromzee. Tetrahedron, **42**, 2475 (1986).

Can. J. Chem. Downloaded from www.nrcresearchpress.com by 196.1.178.254 on 09/07/12
For personal use only.

42. P. J. KOCIENSKI. Chem. Ind. 548 (1981); P. KOCIENSKI and M. TODD. J. Chem. Soc. Chem. Commun. 1078 (1982).
43. I. ROTHBERG, B. SUNDORO, G. BALANIKAS, and S. KIRSCH. J. Org. Chem. **48**, 4345 (1983).
44. J. H. BREWSTER. J. Org. Chem. **51**, 4751 (1986).
45. L. RAMALEY, C. M. ROPER, and J. S. GROSSERT. Anal. Instrum. **13**, 231 (1984–1985).
46. W. L. EARL and D. L. VANDERHART. J. Magn. Reson. **48**, 35 (1982).
47. E. H. HOLST and W. C. FERNELIUS. J. Org. Chem. **23**, 1881 (1958); J. TRÖGER and O. BECK. J. Prakt. Chem. [2] **87**, 295 (1913).
48. H. S. SCHULTZ, H. B. FREYERMOUTH, and S. R. BUC. J. Org. Chem. **28**, 1140 (1963).

Can. J. Chem. Downloaded from www.nrcresearchpress.com by 196.1.178.254 on 09/07/12
For personal use only.

Stereochemical studies on the formation of α,β-epoxysulfones using α-chloro-β-hydroxysulfones of known configuration

J. Stuart Grossert,[1] Subramanian Sotheeswaran,[2] H. Ranjith W. Dharmaratne, and T. Stanley Cameron[1]

Department of Chemistry, Dalhousie University, Halifax, N.S., Canada B3H 4J3

Received November 18, 1987[3]

J. Stuart Grossert, Subramanian Sotheeswaran, H. Ranjith W. Dharmaratne, and T. Stanley Cameron. Can. J. Chem. **66**, 2870 (1988).

Substitution reactions adjacent to sulfonyl groups are known to proceed with difficulty, and there is evidence to suggest that these may not necessarily proceed by an S_N2 pathway. The mechanism of these reactions could be studied in principle by using the conversion of α-chloro-β-hydroxysulfones of known configuration into α,β-epoxysulfones of known configuration. This paper describes results in which this has been attempted. However, the stereochemical aspects of the epoxide formation could not be assigned unequivocally because of the intervention of a very facile "retro-aldol" process when the chlorohydrins are subjected to treatment with bases, although the experimental results do suggest that the reaction does proceed in a regular S_N2-like manner, with inversion at carbon. The X-ray crystal structures of two highly substituted α,β-epoxysulfones are presented, thus putting the structures, including stereochemistry, of a range of these compounds on firm ground.

J. Stuart Grossert, Subramanian Sotheeswaran, H. Ranjith W. Dharmaratne et T. Stanley Cameron. Can. J. Chem. **66**, 2870 (1988).

Il est connu que les réactions de substitution sur des carbones voisins de groupements sulfonyles ne se produisent qu'avec difficulté et il existe des données suggérant que ces réactions ne procèdent pas nécessairement par une voie S_N2. En principe, on peut étudier le mécanisme de ces réactions en utilisant la transformation d'α-chloro β-hydroxysulfones de configurations connues en α,β-époxysulfones de configurations connues. Dans ce travail, on décrit les résultats de telles études. Toutefois, dû au fait qu'un processus «rétro-aldolique» facile intervient lorsque les chlorohydrines sont soumises à un traitement par les bases, on n'a pas pu attribuer sans équivoque les aspects stéréochimiques de la formation de l'époxyde même si les résultats expérimentaux suggèrent que la réaction se produit de fait par le biais d'une réaction régulière S_N2, avec inversion au niveau du carbone. On présente les structures cristallines déterminées par diffraction des rayons-X de deux α,β-époxysulfones fortement substituées; on établit donc avec certitude les structures, y compris leur stéréochimie, d'un large éventail de ces composés.

[Traduit par la revue]

Introduction

Substitution reactions adjacent to sulfones are known to be both difficult and complex in mechanism. Generally, the reactions occur when thiolate nucleophiles attack α-chloro- or bromosulfones (eq. [1]) (1–6), whereas most other nucleophiles give rise to reductive dehalogenation rather than to substitution reactions (eq. [2]) (1, 4, 7–11). This being the

[1] $RCHClSO_2R' + R''S^- \rightarrow RCHSR''SO_2R' + Cl^-$

[2] $RCHClSO_2R' + Nu^- + HA \rightarrow RCH_2SO_2R' + NuCl + A^-$

case, it is possible to envisage an alternative pathway for the substitution reactions to occur, as outlined in eq. [3] (4, 12, 13), although possible difficulties with this concept have been pointed out (4). We have been able to show that this pathway is indeed operative when thiolate anions attack an α-halo-β-ketosulfone in tetrahydrofuran solutions (14). Both we and Hendrickson have suggested that a similar pathway could be operative in the Ramberg–Bäcklund reaction (15). So far as we are aware, there is clear experimental evidence for an S_N2 reaction process only in the case of reactions involving regular types of nucleophiles, such as halide ions, and triflate or N_2^+ leaving groups (cf. eq. [4]) (16, 17).

[3] $RCHClSO_2R' + R''S^- \rightarrow R^-CHSO_2R' + R''SCl \rightarrow RCHSR''SO_2R' + Cl^-$

[4] $ArSO_2CH_2OSO_2CF_3 + Nu:^- \rightarrow ArSO_2CH_2Nu$

By contrast, a small group of reactions that result in an intramolecular expulsion of chloride or bromide ions are well known to be facile. The first is the Ramberg–Bäcklund reaction, which has been thoroughly reviewed (18, 19). A second group of reactions is those in which an internal oxygen or sulfur nucleophile displaces a chlorine or bromine atom α to a sulfonyl group, the products being 5-membered rings with two or more heteroatoms. The recorded examples (20–22) proceed relatively easily and efficiently.

The final reaction in this group concerns the formation of α,β-epoxysulfones from the corresponding chlorohydrins (23) and is the basis of the work described in this paper. Bohlmann and Haffer prepared a diastereomeric mixture of sulfonyl chlorohydrins, **1** and **2**, and found that these could be converted into a mixture of epoxysulfones **3** and **4**. The major diastereomer (**1**) could be crystallized out of the mixture, and converted into the major epoxysulfone, **3**. These authors assigned a configuration to this epoxysulfone from the chemical shifts of groups in its proton nmr spectrum. Then, from the above conversion, the authors assigned the configurations of the chlorohydrins (23): "Da 15 aus 12 entsteht, ist damit auch die Konfiguration der epimeren Chlorhydrine geklärt, denn die Bildung von 15 dürfte zweifellos als innere S_N2-Reaktion mit Inversion ablaufen". This argument is not necessarily flawless, since the configuration of the epoxysulfone **3** is in fact not readily determined by correlation of chemical shift values with stereochemistry. Furthermore, in the light of the results from work done (*vide supra*, 11–13) since Bohlmann and Haffer wrote this sentence, it is no longer so clear-cut that the formation of the epoxysulfones, **3** and **4**, *necessarily* proceeds from **1** and **2** via an internal S_N2 process.

In parallel with the work by Bohlmann and Haffer, Vogt and

[1] Address general communications regarding this paper to J.S.G., and those regarding crystallographic details to T.S.C.

[2] Visiting professor from the University of Peradeniya, current address at the University of the South Pacific, Suva, Fiji.

[3] Revision received June 23, 1988.

Can. J. Chem. Downloaded from www.nrcresearchpress.com by 196.1.178.254 on 09/07/12
For personal use only.

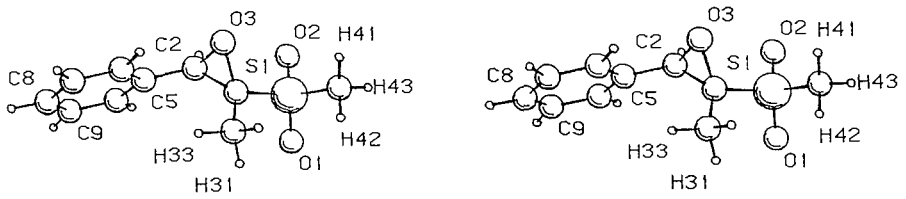

FIG. 1. A stereoscopic view of the crystal structure of *E*-1,2-epoxy-2-methylsulfonyl-1-phenylpropane (**3**).

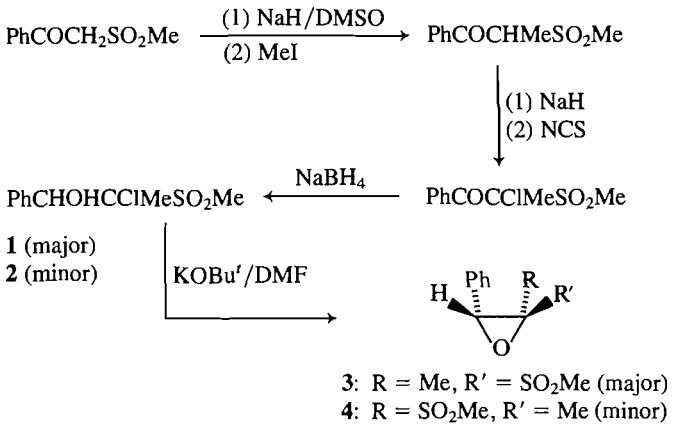

SCHEME 1

Tavares synthesized α,β-epoxysulphones, **5**, by a Darzens-type of condensation and found that only the *trans* stereoisomer was formed (24). Their assignment of stereochemistry was based on known vicinal proton–proton coupling constants in oxiranes, but the differences in these constants between the *cis* and *trans* isomers are in fact too small to permit unambiguous assignments (25), and caution is required. Since this time, the Darzens type reaction has been extended by the use of phase-transfer conditions (26), but no further work has apparently been done to confirm the stereochemistry of the oxirane rings.

We have demonstrated that it is possible to prepare highly substituted α-chloro-β-hydroxysulfones (27) of known stereochemistry. The purpose of the work described here was to take these and other chlorohydrins and convert them into α,β-epoxysulfones, at the same time determining unambiguously the stereochemistry of the relevant species by the use of ^{1}H nmr spectroscopy and X-ray crystallography. From this stereochemical knowledge, it should then be possible to describe the mechanism of displacement reactions α to the sulfonyl group as occurring with inversion or with retention of configuration, the former being required by an S_N2-type process, the latter by a process as outlined in eq. [3].

Results and discussion

The preparation and structures of the chlorohydrins and epoxysulfones

To gain an understanding of the reactions involved, as well as to take advantage of modern spectroscopic and structural techniques, we repeated the preparations of a few key compounds. Thus Bohlmann's diastereomeric mixture of chlorohydrins **1** and **2** (23) was prepared by a different reaction sequence, as outlined in Scheme 1. The reactions used in this synthesis are directly analogous to those described in the previous paper (27). Treatment of these molecules with potassium *tert*-butoxide in DMF solution gave an oily mixture from which the *E*-epoxysulfone, **3**, could be recovered. Its physical properties agreed with those found by Bohlmann and Haffer (23), and we resorted to X-ray crystallography to determine its stereochemistry unambiguously.[4,5] We did not succeed in isolating the *Z* epoxide, **4**, which may have been present in the crude product from the reaction, but this was not isolated by Bohlmann and Haffer either. The result of this determination was to confirm the stereochemistry of **3** (see Fig. 1)[6] that was assigned by Bohlmann and Haffer. It has also given substance to the stereochemistry of a range of other α,β-epoxysulfones, such as **5***a* and *b*, that have been prepared by Vogt and Tavares (24). We prepared **5***c* as an unstable, crystalline material, using

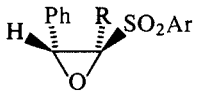

5

a: R = H, Ar = *p*-tolyl
b: R = Me, Ar = *p*-tolyl
c: R = H, Ar = Ph

the phase-transfer-catalyzed technique (26) for the Darzens condensation. A nuclear Overhauser experiment on the two protons directly attached to the epoxide ring showed that these are *trans* to each other, which again confirmed the previous literature assignments of stereochemistry in these epoxysulfones.

Having established that the published stereochemistry of these epoxysulfones was indeed firmly grounded, we turned our attention to the stereochemical relationship between them and their precursor chlorohydrins. We had prepared the *threo* chlorohydrin, **6**, and had established its stereochemistry unequivocally (27). When this was subjected to the same basic

[4]Crystal data for **3**: $C_{10}H_{12}O_3S$, F.W. = 212.35, orthorhombic, a = 15.122(3), b = 10.039(2), c = 6.986(1) Å; Z = 4; V = 1060.5(3) Å^3; d_c = 1.329(1) g cm^{-3}; space group $Pca2_1$; $F(000)$ = 448e; μ = 2.32 cm^{-1}; Mo-K_{α_1} radiation, λ = 0.70926 Å; 1000 unique reflections were collected, of which 846 with $I > 3\sigma(I)$ were used; R = 0.0311, R_w = 0.0313.

[5]Selected bond lengths, bond angles, and torsion angles for compounds **3** and **21** are recorded in Table 3. Sets of positional parameters and isotropic thermal parameters (Tables 5, 6), of the complete anisotropic thermal parameters (Tables 7, 8), of the structure factor tables (Tables 9, 10), and full details of distances, bond angles, and torsion angles (Tables 11, 12) and the structure determinations (Tables 13, 14) may be purchased from the Depository of Unpublished Data, CISTI, National Research Council of Canada, Ottawa, Ont., Canada K1A 0S2.

Crystal data and bond lengths and angles for these compounds have also been deposited with the Cambridge Crystallographic Data Centre, and can be obtained on request from The Director, Cambridge Crystallographic Data Centre, University Chemical Laboratory, Lensfield Road, Cambridge CB2 1EW, U.K.

[6]This stereoscopic drawing was produced by the SNOOPI program, a part of the CHEMGRAF system (Chemical Designs, Oxford, U.K.).

Can. J. Chem. Downloaded from www.nrcresearchpress.com by 196.1.178.254 on 09/07/12
For personal use only.

conditions (including reaction concentration) that Bohlmann and Haffer had used, the exclusive product was the *E*-α,β-epoxysulfone, **7**, as shown in eq. [5].

[5] 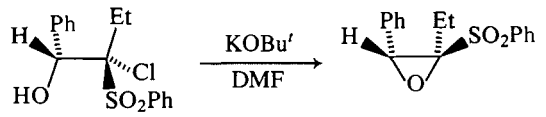

6 (*threo*) **7**

An epoxide with this stereochemistry could not have been formed directly from **6** *by a reaction pathway involving the normal stereoelectronics expected for the conversion of a chlorohydrin into an epoxide (28).* We were unable to produce crystals of **7** of an adequate quality, suitable for an X-ray diffraction experiment, and while its stereochemistry was quite convincingly given by the very similar chemical shifts of the benzylic ring methine proton in **7** and **3**, we wished to obtain as unequivocal as possible a picture of the reactions that were involved in the formation of these epoxysulfones. The fact that the formation of **7** from **6** was not a direct process was readily apparent when we found that it was possible to prepare the *erythro* diastereomer, **10** (see eq. [6]), and we were then able to show that this also could be converted very readily into the same epoxysulfone, **7**, that had been made from **6**. It was thus necessary to obtain clear evidence for the stereochemistry of **7**, or to obtain the stereochemical evidence needed with another chlorohydrin and epoxysulfone pair.

[6] $PhSO_2CHClEt$ (**8**) $\xrightarrow[(2)\ PhCHO,\ cold]{(1)\ Bu^nLi}$ 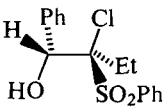 $\xrightarrow[DMF]{KOBu^t}$ **7**

10 (*erythro*)

This was sought in several ways. The compounds **11**, having a methyl in place of the ethyl group in **6** and **10**, could be prepared, but only as an inseparable mixture of diastereomers. We prepared these in two ways. In the first instance, the chlorosulfone **9** (which is readily available from phenyl ethyl sulfide, by chlorination and oxidation) could be condensed with benzaldehyde at low temperatures to yield **11**, which contained an excess of the *erythro* diastereomer, eq. [7].

In the second instance, the β-ketosulfone, **14**, was prepared from propiophenone via **12** and **13**. Reduction of **14** with sodium borohydride again led to a mixture of **11***a* + *b*, but with the *threo* diastereomer, **11***a*, predominating. This sequence of reactions is outlined in Scheme 2.

[7] $PhSO_2CHClMe$ (**9**) $\xrightarrow[(2)\ PhCHO,\ -60°C]{(1)\ Bu^nLi}$ $PhCHOHCClMeSO_2Ph$

(**11***b*, major)
(*erythro*)

Treatment of a diastereomeric mixture of the chlorohydrins, **11**, with potassium *tert*-butoxide, as before, led to a single epoxysulfone, **15**, the nmr spectra of which (Table 2) implied an *E* stereochemistry, the same as that of **3** and **7**. The same epoxysulfone could be prepared by a Darzens condensation, under phase-transfer conditions (26), from the chlorosulfone **9** and benzaldehyde, as in eq. [8].

[8] $PhCHOHCClMeSO_2Ph$ (**11**) $\xrightarrow[DMF]{KOBu^t}$ 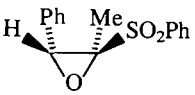

15

P.T.C. ^-OH, PhCHO

$PhSO_2CHClMe$ (**9**)

These reactions and their products showed great similarity to those of the ethyl series, viz. **6** or **10** → **7**. However, they still did not provide unequivocal evidence for the stereochemical path of the reaction leading to formation of the epoxysulfones. The fact that either **6** or **10** could lead to a single product was highly suggestive of a common intermediate, which must involve a cleavage reaction that is the reverse of eq. [7] and involves the intermediacy of a chloroalkyl phenylsulfonyl carbanion, $^-$:CClRSO$_2$Ph. We reasoned that this cleavage reaction could perhaps be disfavoured by employing an alkylsulfonyl residue in place of the phenylsulfonyl moiety (29), and proceeded to explore the chemistry of the equivalent compounds leading to **7** and **15**, but instead incorporating the *tert*-butylsulfonyl group. This was chosen to provide a reasonable degree of steric hindrance around the sulfonyl group so as to afford adequate diastereoselectivity in the reduction of the appropriate β-ketosulfones (27).

The preparation of **18** was straightforward (Scheme 3), starting from 2-chloropropiophenone (**12**), which was condensed with *tert*-butyl mercaptan, followed by oxidation of the β-ketosulfide to the sulfone **16**. This could be chlorinated in the

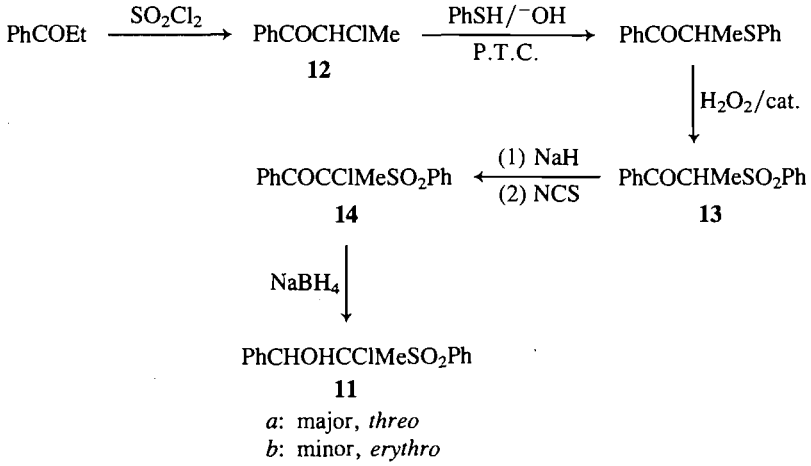

SCHEME 2

Can. J. Chem. Downloaded from www.nrcresearchpress.com by 196.1.178.254 on 09/07/12
For personal use only.

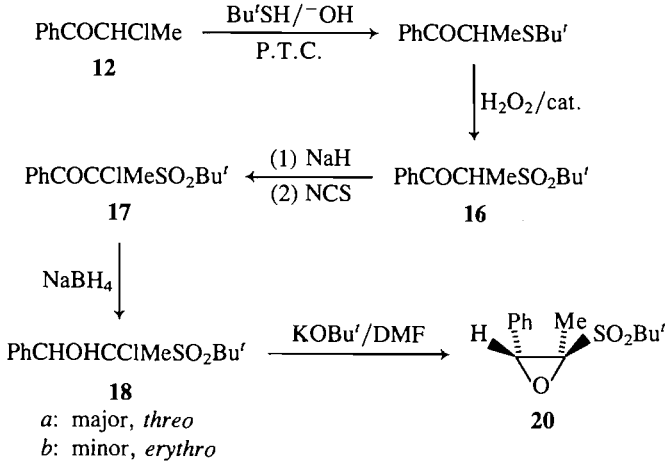

SCHEME 3

usual way to **17**, which on reduction with sodium borohydride gave the chlorohydrin **18** as a mixture of diastereomers, the *threo* form, **18***a*, again being predominant. The corresponding ethyl derivative, **19**, was also prepared (27), again as a mixture of diastereomers. When **18** and **19** were subjected to the regular basic conditions used for epoxide formation, the epoxysulfones **20** and **21**, respectively, were cleanly formed, as outlined in eq. [9].

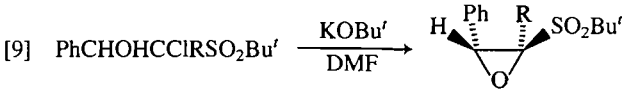

18: R = Me
19: R = Et
20: R = Me
21: R = Et

The structures of these species were apparent from the close similarities of all the nmr spectra as seen in Tables 1 and 2. However, we were successful in growing crystals of **21** that were suitable for X-ray diffraction,[5,7] which confirmed the *E* stereochemical designation for this molecule, as depicted in Fig. 2.[6]

Spectroscopic and structural features

All molecules were carefully characterized by a full range of standard spectroscopic methods. It quickly became apparent that the most useful method for the detection and positive identification of the diastereomeric mixtures of chlorohydrins was high-field proton and carbon-13 nmr spectroscopy. The resonances of each species, as well as of the associated epoxysulfones and the chlorosulfones, such as **8** or **9**, are adequately dispersed about the chemical shift scale so as to permit ready, and positive, observation of significant quantities of any of these species within a given mixture.

An examination of Table 1 shows that the chemical shifts of most protons in the diastereomeric pairs of chlorohydrins show clear-cut differences, characteristic of each diastereomer. For example, the resonance of the carbinol methine proton is downfield in the *threo* diastereomer in each pair, except for **18**. This serves to underline the need for care, and the use of a range of both compounds and structural evaluations in assigning the stereochemistry of these species. Many of the spectral features discussed in detail in the accompanying paper (27) appear in these molecules, except for the epoxysulfones, and thus do not warrant further detailed discussion. The ring stereochemistry of the epoxysulfones **3**, **5***c*, and **21** has been determined unequivocally and an inspection of Table 2 shows that the same stereochemistry must pertain to **3**, **7**, **15**, **20**, and **21**, given the similarities of the chemical shifts of their ring carbons and protons.

Fragmentation patterns in the mass spectra of most stereoisomers are usually quite similar. This is so in the case of the *threo* and *erythro* diastereomers **6** and **10**, with the exception of the ion at *m/z* 142, which is quite insignificant in **6**, yet is a major ion in the spectrum of **10**. A mass spectrum at high resolution is required to identify the composition of this ion,

TABLE 1. Nuclear magnetic resonance spectral parameters for selected chlorohydrins

Compound	Atom/s	^{1}H spectra (ppm)	^{1}H spectra J (Hz)†	^{13}C spectra* (ppm)
1	*Me*–S	3.27	0	37.9
	Me–C	1.53	0	18.5
	C–SO_2	—	—	85.5
	CH–OH	5.35	0	73.9
2	*Me*–S	3.06	0	36.9
	Me–C	1.87	0	16.8
	C–SO_2	—	—	85.2
	CH–OH	5.25	0	73.7
6	CH_3	0.71	^3J = 7.35	9.1
	CH_2	(1.85 (1.96	^2J = −14.94	29.2
	C–SO_2	—	—	92.8
	OH	3.86	J_{CH-OH} = 3.9	—
	CH–OH	5.54	J_{CH-OH} = 3.9	74.6
10	CH_3	1.06	^3J = 7.42	9.7
(*erythro*)	CH_2	(2.22 (2.57	^2J = −15.0	23.8
	C–SO_2	—	—	89.6
	OH	4.21	J_{CH-OH} = 2.2	—
	CH–OH	5.09	J_{CH-OH} = 2.2	76.2
11*a*	CH_3	1.43	0	22.9
(*threo*)	*C*–SO_2	—	—	89.3
	OH	3.95	J_{CH-OH} = 2.5	—
	CH–OH	5.58	J_{CH-OH} = 2.5	75.4
11*b*	CH_3	1.85	0	18.7
(*erythro*)	*C*–SO_2	—	—	87.3
	OH	4.18	J_{CH-OH} ca. 2	—
	CH–OH	5.30	J_{CH-OH} ca. 2	75.3
18*a*	*Me*–CCl	1.60	0	26.0‡
(*threo*)	*Me*(Bu')	1.67	0	26.1
	C(Bu')	—	—	69.7
	C–SO_2	—	0	91.2
	OH	4.39	J_{CH-OH} = 2.4	—
	CH–OH	5.46	J_{CH-OH} = 2.4	75.3
18*b*	*Me*–CCl	1.98	0	19.9‡
(*erythro*)	*Me*(Bu')	1.69	0	26.2‡
	C(Bu')	—	—	69.6
	C–SO_2	—	—	88.3
	OH	4.32	J_{CH-OH} ca. 2	—
	CH–OH	5.58	J_{CH-OH} ca. 2	76.4

*Assignments based on expected chemical shift values, line intensities, and resonance multiplicity in a gated spectrum.
†Resonance observed as a singlet if J = 0 Hz.
‡Resonance could not be assigned unambiguously.

[7]Crystal data for **21**: $C_{14}H_{20}O_3S$, F.W. = 268.37, orthorhombic, a = 7.266(6), b = 19.450(12), c = 20.266(8) Å; Z = 8; V = 2864(3) Å^3; d_c = 1.245(1) g cm^{-3}; space group $Pbca$; $F(000)$ = 1152e; μ = 1.82 cm^{-1}; Mo-K_{α_1} radiation, λ = 0.70926 Å; 1011 unique reflections were collected, of which 617 having $I > 3\sigma(I)$ were used; R = 0.0406, R_w = 0.0406.

Can. J. Chem. Downloaded from www.nrcresearchpress.com by 196.1.178.254 on 09/07/12
For personal use only.

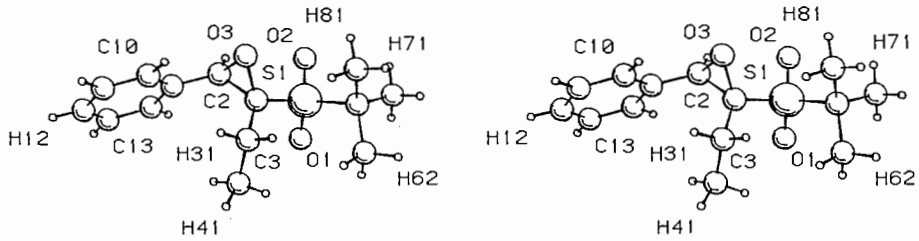

FIG. 2. A stereoscopic view of the crystal structure of *E*-1,2-epoxy-2-*tert*-butylsulfonyl-1-phenylbutane (**21**).

TABLE 2. Nuclear magnetic resonance spectral parameters for selected epoxides*

Compound	Atom	^{1}H spectra (ppm)	^{1}H spectra J (Hz)	^{13}C spectra (ppm)
3	*Me*–S	2.95	0	36.1
	Me–C	1.54	0	10.9
	C–SO_2	—	—	74.2
	CH–O	4.83	0	60.5
5*c*	*CH*–SO_2	4.12	$^3J = 2$	70.8
	CH–O	4.52	$^3J = 2$	57.3
7	CH_3	0.729	$^3J = 7.59$	8.7
	CH_2	(1.625 (1.847	$^2J = -15.20$	18.7
	C–SO_2	—	—	77.0
	CH–O	4.852	0	61.0
15	*Me*–C	1.35	0	10.8
	C–SO_2	—	—	75.0
	CH–O	4.90	0	60.4
20	CH_3	1.58	0	14.2
	Me(Bu^t)	1.54	0	24.4
	C(Bu^t)	—	—	62.6
	C–SO_2	—	—	75.4
	CH–O	4.79	0	59.8
21	CH_3	0.936	$^3J = 7.54$	9.0
	CH_2	(1.878 (2.013	$^2J = -15.20$	21.6
	Me(Bu^t)	1.536	0	24.3
	C(Bu^t)	—	—	62.7
	C–SO_2	—	—	79.0
	CH–O	4.760	0	60.2

*Footnotes as per Table 1.

but it is likely to be $PhSO_2H^{\cdot+}$, which could arise by the interaction of the $PhSO_2$ group and a proximate proton, followed by a cleavage reaction, either from the molecular ion of **10** or from a higher energy daughter ion in the fragmentation process. The relevant proton would be proximate to the sulfonyl group only in the *erythro* diastereomer, and further work on clarification of this interesting reaction is under way.

So far as we are aware, only Bohlmann and Haffer (23) have discussed the mass spectrometry of α,β-epoxysulfones, in which they have produced some interesting speculation for a fragmentation pathway. The spectra of **7** and **21** on the one hand and **15** and **20** on the other are quite similar. The phenylsulfonyl compounds lose m/z 141 ($PhSO_2$), but the *tert*-butyl compounds lose both the elements of $C_4H_8SO_2$ and $C_4H_9SO_2$, probably in two-step processes, transfer of a proton from the *tert*-butyl group in the first case being energetically favourable. Thus, the spectra of both **7** and **21** have strong ions at 147 daltons, which appear to fragment further as outlined in eq. [10]. Evidence for these steps comes from the shape of the

$$[10]\quad \underset{m/z\ 147}{C_{10}H_{11}O^{+}} \xrightarrow[-C_2H_4]{} \underset{119}{C_8H_7O^{+}} \xrightarrow[-CO]{} \underset{91}{C_4H_7^{+}} \rightarrow\rightarrow$$

metastable ions associated with them, the ion at ca. 97.0 daltons being broad, whereas the ion at ca. 69.9 daltons is quite sharp and has a very similar shape to the ion associated with the loss of CO from $PhCO^{+}$, as observed in many benzoyl compounds. These ions have a very similar shape in the spectra of both molecules. The spectra of **15** and **20** are somewhat more complex, although both molecules give m/z $M^{+\cdot}$ – "RSO_2", viz. ions at 133 daltons. These appear to fragment further to ions at 105 and 79 daltons, with metastable ions that appear to support these processes.

All four epoxy sulfones show strong evidence of rearrangements occurring in the molecular ions, in addition to the cleavages described above. The formation of ions at 232 and 231 daltons in the fragmentation of **7** and **15**, and 212 daltons in **20**, is evidence of oxygen-to-carbon migration by the sulfonyl group in the molecular ion. This is confirmed by the presence of significant ions at 125 daltons ($PhSO^{+}$), as these ions are not normally very strong in the mass spectra of regular phenylsulfonyl compounds (14). There is also methyl-to-carbon migration in the molecular ions of **15** and **21**, as shown by the strong ions at 105 daltons in these species, whereas the corresponding ions in the ethyl derivatives **7** and **21** occur at 119 daltons. The fragmentations proposed here can be deduced by a careful examination of low-resolution spectra and accompanying metastable ions. However, the processes are complex and confirmatory evidence will have to be acquired from detailed high-resolution spectra and precursor-ion studies.

As far as we have been able to determine, the structures of the two α,β-epoxysulfones, **3** and **21**, are the first crystal structures of this particular complex functionality. One bicyclic structure having some similarities has been studied by Sands (30). In fact, even the reported number of *tert*-butylsulfonyl structure determinations is limited, one example being that of a chiral α-chlorosulfone (31). The bond lengths and angles about the key parts of **3** and **21** (see Table 3) are within the normal ranges for the relevant combinations of atoms (32–34). Perhaps the only noteworthy feature of the two structures is the significant difference between the C1—O3 and C2—O3 bond lengths in **3**. There is no obvious explanation for this difference. Compounds **3** and **21** are substituted styrene oxides and their crystal structures are of interest in connection with work in another area,[8] viz. the stereoelectronic effects associated with substitution reactions at a benzylic carbon atom (35). A particular aspect of this reaction concerns the nucleophilic attack on substituted styrene oxides (36), in which it has been shown that phenyl-

[8]We thank Prof. J. F. King for bringing this work to our attention.

Can. J. Chem. Downloaded from www.nrcresearchpress.com by 196.1.178.254 on 09/07/12
For personal use only.

Can. J. Chem. Downloaded from www.nrcresearchpress.com by 196.1.178.254 on 09/07/12
For personal use only.

TABLE 3. Selected bond lengths, bond angles, and torsion angles* for compounds **3** and **21**

Bond length (Å) or angle (°)	Compound 3	Compound 21
S1—C4/C5	1.768(7)	1.814(1)
S1—O1	1.428(2)	1.427(4)
S1—O2	1.428(4)	1.439(7)
S1—C1	1.802(3)	1.822(3)
C1—C3	1.496(7)	1.523(8)
C1—C2	1.471(7)	1.463(1)
C2—H2	0.99(3)†	1.01(6)†
C1—O3	1.422(3)	1.418(4)
C2—O3	1.453(5)	1.429(7)
C2—C5/9	1.481(5)	1.471(4)
C1—S1—C4/5	104.7(2)	110.4(2)
O1—S1—O2	118.8(2)	118.4(3)
S1—C1—C3	114.7(2)	120.0(3)
C1—C2—O3	58.2(2)	59.4(2)
C2—C1—O3	60.3(2)	59.4(2)
H2—C2—C5/9	115.(2)	115.(3)
O1—S1—C1—C2	100.8(5)	−93(1)
O1—S1—C1—O3	166.8(4)	−158(1)
O1—S1—C1—C3	−54.8(4)	59(1)
O2—S1—C1—C2	−28.2(4)	33(1)
O2—S1—C1—C3	176.2(5)	−174(1)
O2—S1—C1—O3	37.8(5)	−32(1)
S1—C1—C2—O3	101.9(4)	−104(1)
S1—C1—C2—C5/9	−153.8(4)	147(1)
O3—C2—C5/9—C6/10	3.7(5)	7(1)

*A positive rotation is anticlockwise from atom 1, when viewed from atom 3 to atom 2.

†Constrained during refinement.

oxirane is significantly less reactive towards nucleophilic attack than is oxirane itself. The preferred regiochemistry for this reaction is β to the phenyl ring, in contrast to the normal reactions of benzylic halides, and the phenomenon has been attributed to conformational preferences of the phenyl ring with respect to the oxirane ring (35, 36). Calculations suggest that the preferred conformation of phenyloxirane has an O—$C_{benzylic}$—C_{ipso}—C_{ortho} torsion angle of 0° (37), whereas the optimum geometry for reactivity towards nucleophiles requires this angle to be about 90°. The equivalent torsion angle is 3.7° and 7° in **3** and **21**, respectively, but is 24° in 4′-nitrophenyloxirane (32); however, the mechanism of nucleophilic attack on this latter oxirane does not appear to have been reported (35).

Mechanistic aspects of the epoxide formation

When we found that either chlorohydrin **6** or **10** could be converted into **7**, it was abundantly clear that this reaction system was not going to provide the answer to the stereochemical question that we had posed, viz., "Does a nucleophilic substitution reaction α to the sulfonyl group proceed with inversion or with retention of configuration at the electrophilic carbon?" We have studied the conversion of these chlorohydrins into **7** under a range of conditions, summarized in Table 4, which leads to the conclusion that the reaction of the chlorohydrins with base in dry *N*,*N*-dimethylformamide must involve more than one reaction process. At higher reaction concentrations, epoxide formation predominates; otherwise the reaction (cf. eqs. [5] or [9]) leads to a substantial quantity of the cleavage products, benzaldehyde and the appropriate α-chlorosulfone. It is remarkable how facile the formation of the epoxysulfones is, when compared to intermolecular displacement reactions adjacent to sulfones, and that even the briefest treatment of **6** or **10** with potassium *tert*-butoxide in DMF leads to complete destruction of the chlorohydrin, such as in entries 1, 2, and 9 (Table 4). The argument made by Bohlmann and Haffer (23) that the configuration of the chlorohydrins **1** and **2** could be deduced from the configuration of the epoxysulfone, **3**, is thus unfounded, although it was quite reasonable at the time when it was made (38).

The fact that the relevant reaction was complicated by a "retro-aldol"-type process, the reverse process of that depicted in eqs. [6] or [7], was proved by carrying out crossover experiments in which the chlorohydrins **6** and **10** were reacted under the regular basic conditions in the presence of *p*-tolualdehyde, as depicted in eq. [11]. The crossover epoxide,

[11] $PhCHOHCClEtSO_2Ph + p\text{-TolCHO} \xrightarrow[DMF]{KOBu^t}$

6 or **10**

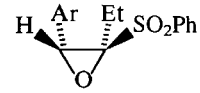

+ $PhSO_2CHClEt$

8

7: Ar = Ph
22: Ar = *p*-tolyl

22, was clearly visible in the product mixture because of its characteristic peaks in both the ^1H nmr and mass spectra. We reasoned that this cleavage process would be facilitated by the phenylsulfonyl group, which would strongly stabilize the carbanion $^-$:$CEtClSO_2Ph$, **23** (29), and that this stabilization would be decreased by the use of a sterically hindered *tert*-butylsulfonyl group. Hence, the two series of compounds, **16**–**21**, were prepared. However, this group must still stabilize the carbanion adequately to permit the retro-aldol process, since the diastereomer mixtures **18** and **19** gave only the *E*-epoxysulfones, **20** and **21**, respectively. We have been able to show that the *erythro* chlorohydrin diastereomer, **10**, could be prepared from reacting the carbanion **23** with benzaldehyde in a relatively nonpolar solvent (THF) at low temperature, and that the proportion of **6** being formed increased at higher temperatures. This observation may be interpreted as the salt of **10** being a kinetic product whereas the salt of **6** is a thermodynamic product. Truce and Klingler (39) have also reported some diastereoselectivity in related addition reactions between non-halogenated α-sulfonyl carbanions and aldehydes, with the *erythro* form being found to be in excess.

The structure of **23** can be depicted as shown in Scheme 4 (34), which illustrates three of the six possible orientations for the aldehyde in the condensation outlined in eq. [6]. It is noteworthy that this orientation appears to describe the least sterically hindered transition state, which in fact leads to **10** after work-up. The intermediate alkoxide should be lithiated in tetrahydrofuran, but is undoubtedly largely ionized in *N*,*N*-dimethylformamide, which would explain why **10** can be isolated from the former solvent, and why the latter favours epoxide formation. Furthermore, deprotonation of **6** in DMF must lead to the equilibria shown in Scheme 5, and we venture to suggest that the actual epoxide formation takes place via the anion of **10**, by means of an internal displacement process that has the stereoelectronics of an S_N2 reaction (28, 38). This

TABLE 4. Reactions of the chlorohydrins **6** and **10** (= **CH**) with various bases, under different reaction conditions

Entry	Base, concentration*	Temperature (°C)	Time (min)	Molar ratio of **CH**:base	Yields (%) or ratio (:) of **7** and **8**
1.	KOBu^t, 0.048 M	−50	10	(**6**) 1:1	75%† —‡
2.	KOBu^t, 0.28 M	0	1	(**6**) 1:1	87%† —‡
3.	KOBu^t, 0.28 M	0	5	(**6**) 1:1	90%† —‡
4.	KOBu^t, 0.28 M	0	10	(**6**) 1:1	86%† —‡
5.	KOBu^t, 0.071 M	0	6	(**6**) 1:1	ca. 1:1 by ^{1}H nmr
6.	KOBu^t, 0.036 M	0	5	(**6**) 2:1	ca. 2:3 by ^{1}H nmr
7.	KOBu^t, 0.15 M	0	5	(**6**) 2:1	ca. 3:2 by ^{1}H nmr
8.	KOBu^t, 0.12 M	0	1	(**6**) 8:1	ca. 3:8 by ^{1}H nmr
9.	KOBu^t, 0.033 M	−50	10	(**10**) 1:1	70%† —‡
10.	KOBu^t, 0.19 M	0	5	(**10**) 1:1	ca. 4:1 by ^{1}H nmr
11.	KOBu^t, 0.12 M	0	5	(**10**) 2:1	ca. 1:2 by ^{1}H nmr
12.	NaH, 0.05 M	20	60	(**6**) 1:1	ca. 5:1 by ^{1}H nmr

*The initial concentration of the base in the reaction mixture, using anhydrous DMF as the solvent. Reactions were carried out in the general manner described for the preparation of **7** from **6**.
†Isolated yield, based on the initial quantity of **CH**.
‡Less than 5% of **8** (traces observed in ^{1}H nmr spectra).

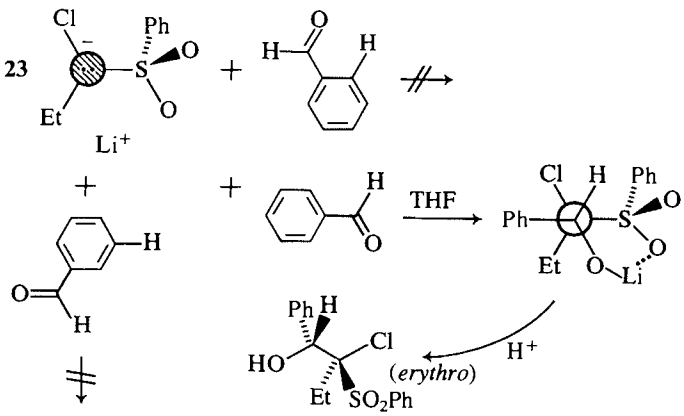

SCHEME 4

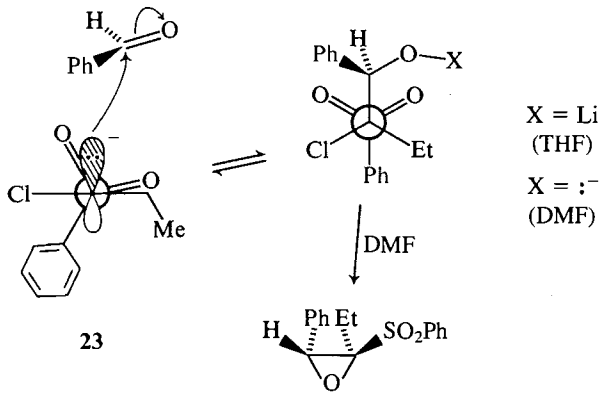

SCHEME 5

reaction would be greatly facilitated by the intramolecular nature of the reaction and the steric crowding about the epoxide ring (40). We also draw the reader's attention to the striking similarities between the crystal structures of the chlorohydrin **6** (27) and the two epoxysulfones, **3** and **21**. If the structure of **10** is indeed similar to that of **6**, but with the chloro and ethyl groups interchanged, the internal nucleophilic displacement process for epoxide formation from these halohydrins appears to be very favourable indeed.

Experimental

General

Most details have been provided previously (27). Proton nmr spectra were run either on a Varian T-60 spectrometer or, when analysis of complex spin systems or reaction mixtures required the extra dispersion, on a Nicolet 360 NB spectrometer, operating at 361.05 MHz. These spectra were analysed using a LAOCOON program, adapted locally to run on an IBM-XT computer. All expected lines were present in the high-field spectra. Carbon-13 nmr spectra were run either on a Varian CFT-20 or the Nicolet 360 NB spectrometers. X-ray crystal structures were determined by collection of data using a Nonius CAD-4 four-circle diffractometer; data were processed by published procedures (34). Chromatography was done using products of the E. Merck Co.; some tlc also was done using Brinkmann silica plates on polyester film. Anhydrous tetrahydrofuran (THF) was prepared by standing it over P_2O_5, distillation from P_2O_5, storage over $NaAlH_4$, and, before use, distillation from $NaAlH_4$ under an N_2 atmosphere. Dry *N,N*-dimethylformamide (DMF) was ACS grade, dried over 4A molecular sieves. Regular work-up procedures were to extract thoroughly the quenched reaction mixture with dichloromethane, or with diethyl ether in the case of any reaction that employed DMF or DMSO as solvents. The organic solvent was washed with dilute acid and (or) base, as appropriate, and water or saturated brine, dried with anhydrous magnesium sulfate, and rotary evaporated under water-aspirator vacuum.

Preparation of 2-chloro-2-methylsulfonyl-1-phenylpropanol as a mixture of diastereomers, 1 and 2

Sodium hydride (50% oil dispersion, 0.97 g, 20 mmol) was washed free of oil with dry ligroin, mixed with a solution of 2-methylsulfonyl-1-phenylethanone (3.6 g, 18 mmol) in dry DMSO, and heated under dry nitrogen for 60 min, using an oil bath at 55°C. The mixture was cooled, methyl iodide (2.7 g, 19 mmol in DMSO, 10 mL) was added carefully, and heating was resumed for a further 250 min, at 60–65°C. Work-up was effected by pouring into excess water, followed by a regular extraction procedure, some residual starting material (0.5 g) being removed by a wash with 2% NaOH solution, to give 2-methylsulfonyl-1-phenylpropanone, 2.1 g, 63%, mp 54–55°C (lit. (41), mp 56–57.5°C), >95% pure, by ^{1}H nmr.

The methylated sulfone prepared above (212 mg, 1 mmol) in dry benzene (5 mL) was added to washed NaH (50 mg of 50% oil

Can. J. Chem. Downloaded from www.nrcresearchpress.com by 196.1.178.254 on 09/07/12
For personal use only.

Can. J. Chem. Downloaded from www.nrcresearchpress.com by 196.1.178.254 on 09/07/12
For personal use only.

suspension, 1 mmol) and the resulting slurry was heated in an oil bath (80°C) for 4 h. Solid *N*-chlorosuccinimide (133 mg, 1 mmol) was added and heating at 90°C was continued for a further 3 h. Regular work-up was done by pouring into water and extraction with ether to give 2-chloro-2-methylsulfonyl-1-phenylpropanone (170 mg), contaminated by some starting material. Preparative tlc gave the pure chloroketosulfone, 120 mg, 48%, mp 68–70°C (lit. (23) mp 72.5–73°C).

Reduction of this chloroketosulfone (120 mg, 0.49 mmol) with $NaBH_4$ in dioxane–water, following the published procedure (23), gave a mixture of chlorohydrins, **1** and **2** (70 mg, 58%), in a ratio of 7:3.

*Preparation of 1,2-epoxy-2-methylsulfonyl-1-phenylpropane, as a mixture of diastereomers **3** and **4***

The diastereomeric mixture of **1** and **2** prepared above (660 mg, 2.66 mmol) in dry DMF (4 mL) was treated with 0.665 M Bu^{t}OK in dry DMF (4.0 mL) at 0°C, as per the procedure of Bohlmann and Haffer (23). The product was an oily mixture of epoxides, from which several recrystallizations (ether–ligroin) gave clean **3**, 130 mg, 23%, mp 111–112°C (lit. (23), mp 112–112.5°C).

Preparation of E-*1,2-epoxy-1-phenyl-2-phenylsulfonylethane, **5**c*

Chloromethyl phenyl sulfone (42) (285 mg, 1.5 mmol), benzaldehyde (191 mg, 1.8 mmol), and dimethylethylhexadecylammonium bromide (30 mg) were dissolved in acetonitrile (0.4 mL) and mixed with NaOH solution (50%, 1 mL). After vigorous stirring for 45 min, the reaction mixture was worked up with ether and water to give crude **5***c* (330 mg, 85%), which was recrystallized (CCl_4–ligroin) to give needles that decomposed with time, mp 104–105°C; for nmr spectra, see Table 2, but the ^{1}H nmr spectrum also showed aromatic resonances at δ: 7.25 (5H, s), 7.32–8.02 (5H, m); irradiation in the range of δ 4.18–4.28 produced a 5% increase in the intensity of the signal at δ 4.52; ms *m/z*: 260 (39), 231 (57), 167 (13), 165 (7), 141 (7), 125 (30), 119 (100), 91 (35), 77 (30) daltons.

Preparation of E-*1,2-epoxy-1-phenyl-2-phenylsulfonylbutane, **7***

A stirred solution of *threo*-2-chloro-1-phenyl-2-phenylsulfonylbutanol, **6**, (27) (324 mg, 1 mmol), under N_2 in dry DMF (3 mL), was cooled in an ice bath and carefully treated with Bu^{t}OK in DMF (0.5 mL of 2.0 M solution), so that the temperature did not rise above 5°C. The mixture was stirred for 5 min and worked up by adding NH_4Cl solution (10 mL of 10%) and extraction with ether. Regular procedures gave **7** as a semisolid that was homogeneous on tlc (248 mg, 86%). Crystalline material, as fine needles, mp 44–46°C (from ether–hexane), was best obtained by passage of this material through a short column of neutral alumina (25% CH_2Cl_2 in ligroin); ir (KBr) ν_{max}: 1322 (m), 1317 (m), 1310 (m), 1143 (s), 1079 (s), 714 (m), 590 (m), 556 (m) cm^{-1}; for nmr spectra, see Table 2; ms *m/z*: 288 ($M^{+\cdot}$, 4), 232 (14), 231 (7), 167 (3), 147 (85), 125 (16), 119 (10), 91 (100), 90 (12), 89 (10), 77 (25), *m** = 96.9, 69.9. *Exact Mass* calcd. for $C_{16}H_{16}O_3$: 288.082; found, for $M^{+\cdot}$ *m/z*: 288.082 daltons.[9]

*Preparation of α-chloropropyl phenyl sulfone, **8***

An ethanolic solution (2 mL) of 2-chloro-1-phenyl-2-phenylsulfonylbutanone (27) (290 mg, 0.9 mmol) was hydrolyzed by the addition of aqueous NaOH (0.5 mL, 2 M solution) and stirring for 60 min at 20°C. The solution was poured into water and worked up in a regular way with ether to give a crude product, from which the pure (tlc) chlorosulfone, **8** (130 mg, 66%), could be obtained as white needles after chromatography (25% CH_2Cl_2 in ligroin on neutral alumina), followed by recrystallization (ether–hexane), mp 57–58°C; ir (KBr) ν_{max}: 1450 (m), 1318 (s), 1151 (s), 1075 (s), 748 (s), 682 (m), 586 (s), 538 (s); ^{1}H nmr δ($CDCl_3$): 1.142 (3H, t of A_3MNX, ^3J = 7.27 Hz), 1.847 (1H, $^2J_{MN}$ = 14.40 Hz), 2.465 (1H), 4.599 (1H, $^3J_{MX}$ = 10.59 Hz, $^3J_{NX}$ = 3.01 Hz); ^{13}C nmr δ($CDCl_3$): 10.7 (CH_3), 24.6 (CH_2), 76.5 (*C*HCl), 129.1, 130.1, 134.5 (*C*H of Ph), 135.5 (*C*S of Ph); ms *m/z*: 220 ($M^{+\cdot}$, 0.6), 218 ($M^{+\cdot}$, 1.6), 143 (97), 142 (78), 141 (9), 125 (15), 94 (17), 79 (14), 78 (98), 77 (100), 51 (45) daltons.

*Preparation of α-chloroethyl phenyl sulfone, **9***

Ethyl phenyl sulfide (2.06 g, 15 mmol) was chlorinated by refluxing for 2 h with freshly distilled SO_2Cl_2 (2.16 g, 15.8 mmol, added slowly) in dichloromethane. Rotary evaporation of the solution at room temperature gave an oil (2.0 g, 78%) that was homogeneous by tlc, and was the α-chloroethyl sulfide by ^{1}H nmr; δ($CDCl_3$): 1.8 (3H, d, *J* = 8 Hz), 5.3 (1H, q), 7.4 (5H, s). A solution of this sulfide (686 mg, 4 mmol) in dry ether was cooled in an ice bath and carefully treated with *m*-chloroperoxybenzoic acid (85%, 1.72 g, 8.5 mmol) so that the temperature did not rise above 5°C. The mixture was stirred (ice bath, 16 h) and then worked up ($NaHSO_3$ and $NaHCO_3$ washes) to give a solid (700 mg, 85%) that was homogeneous on tlc (benzene), and was recrystallized (benzene) to give **9** as fine needles, mp 54–55°C; ir (KBr) ν_{max}: 2967 (m), 1450 (m), 1314 (s), 1150 (s), 1052 (m), 745 (s), 685 (s), 533 (s) cm^{-1}; ^{1}H nmr δ($CDCl_3$): 1.80 (3H, d, *J* = 7 Hz), 4.75 (1H, t, *J* = 7 Hz), 7.6 (5H, m);[10] ms *m/z*: 204 ($M^{+\cdot}$, 6), 160 (3), 141 (100), 125 (29) daltons.

Preparation of erythro-*2-chloro-1-phenyl-2-phenylsulfonylbutanol, **10***

A stirred solution of the chlorosulfone, **8** (335 mg, 1.52 mmol), in dry THF (5 mL) was cooled to −70°C, treated cautiously with *n*-BuLi (0.76 mL of 2.2 M solution), and kept cold for 15 min, after which distilled benzaldehyde (163 mg, 1.53 mmol) in dry THF (3 mL) was added slowly. The reaction was kept for a further 60 min (during which time the temperature was allowed to rise to −50°C), quenched by the addition of ice-cold NH_4Cl solution, and worked up in a regular way using an extraction with ether. The crude, oily solid (470 mg) was a mixture of chlorohydrins **10** and **6** in a ratio of ca. 4:1. Column chromatography with 20% CH_2Cl_2 in hexane gave pure **10** (330 mg, 67%), as fine colourless needles from CH_2Cl_2–hexane, mp 110–112°C; ir ν_{max}(KBr): 3465 (s), 1455 (m), 1305 (s), 1148 (s), 1074 (s), 1057 (s), 700 (m), 579 (s) cm^{-1}; nmr spectra in Table 1; ms *m/z*: 326 (4.8), 324 ($M^{+\cdot}$, 12.4), 220 (20), 218 (52), 205 (11), 203 (29), 185 (3), 183 (8), 153 (6), 147 (32), 143 (38), 142 (20), 129 (8), 125 (14), 119 (11), 107 (97), 106 (21), 105 (49), 91 (46), 79 (32), 78 (50), 77 (100), *m** at 189.5 daltons.

*Preparation of 2-chloro-1-phenyl-2-phenylsulfonylpropanol, **11***

*(a) By condensation reaction from **9***

In a similar way to the previous preparation, the chlorosulfone, **9** (prepared in a similar way to **8**), was reacted with *n*-butyllithium and benzaldehyde on a 0.7-mmol scale, to give the *erythro* hydroxysulfone (**11***b*) as the major product (ca. 3:2, by ^{1}H nmr) of a diastereomer mixture, obtained as needles, mp 148–154°C (from ether–ligroin), nmr spectra in Table 1, ms *m/z*: 312, 310 ($M^{+\cdot}$) daltons.

*(b) From 2-chloropropiophenone, **12***

Propiophenone (26.6 g, 0.2 mol) was chlorinated by stirring with a 20% molar excess of freshly distilled sulfuryl chloride in CH_2Cl_2 for 3 h at room temperature. Removal of the solvent and distillation of the crude product *in vacuo* gave pure **12** (28 g, 83%). A mixture of **12** (13.3 g, 0.079 mol), thiophenol (8.7 g, 0.079 mol), and Bu^t_4NBr (0.5 g) was stirred vigorously for 12 h in CH_2Cl_2 (75 mL) and NaOH solution (75 mL of 1.9 M). Regular work-up gave crude PhCOCHMeSPh (15 g, 78%), 3.0 g (12.4 mmol) of which was oxidized in methanol with excess 30% H_2O_2 in the presence of ammonium molybdate catalyst following the method of Schultz *et al.* (43) to give $PhCOCHMeSO_2Ph$, **13**, as colourless needles, mp 78–79°C (2.8 g, 82%, from CH_2Cl_2–EtOH, 1:9); ^{1}H nmr δ($CDCl_3$): 1.57

[9]We thank Dr. L. Ramaley for this accurate mass measurement.

[10]The *upfield* shift of the methine proton when an α-chloroalkyl sulfide is oxidized to the corresponding sulfone appears to be a general phenomenon: J. S. Grossert and S. Sotheeswaran, Abstract no. A 12.0, Eleventh Int. Symp. Org. Chem. of Sulphur, Lindau, FRG, 1984, and to be published. The phenomenon does not appear to have been described in the chemical literature, and must arise from a shielding cone around the sulfonyl group.

Can. J. Chem. Downloaded from www.nrcresearchpress.com by 196.1.178.254 on 09/07/12
For personal use only.

(3H, d, J = 6.95 Hz), 5.19 (1H, q, J = 6.95 Hz), 7.4–8.0 (10H, m); ^{13}C nmr δ($CDCl_3$): 12.9 (Me, q), 65.0 (*C*H, d), 128–137 (Ar C), 192.2 (C=O); ms m/z: 274 ($M^{+\cdot}$, 4), 210 (8), 141 (1), 133 (1), 116 (2), 106 (7.8), 105 (100), 77 (29) daltons.

A sample of **13** (2.74 g, 10 mmol) was then chlorinated with NaH and NCS (10 mmol each) in dry toluene following a previously described procedure (27) to give crude 2-chloro-1-phenyl-2-phenylsulfonylpropanone, **14** (2.16 g, 96%), which could be purified by chromatography on silica gel (1:1 ligroin in CH_2Cl_2) and recrystallization (ether–hexane) to give **14** as small colourless prisms, mp 62–64°C; ms m/z: 310 (1.0), 308 ($M^{+\cdot}$, 2.6), 169 (1.6), 167 (4.2), 141 (4.9), 139 (6.6), 106 (7.5), 105 (100), 103 (5), 91 (1.0), 89 (2.5), 77 (29) daltons. Reduction of this material (1.6 g, 5.2 mmol) with $NaBH_4$ in DME–water containing NaH_2PO_4, as described previously (27), gave **11** (1.55 g, 95%) as a mixture of diastereomers (*threo*:*erythro*, ca. 9:1 by proton nmr). Recrystallization (ether–CH_2Cl_2) gave pure *threo*, **11***a*, mp 193–194°C; nmr spectra in Table 1; ms m/z: 312 (7.3), 310 ($M^{+\cdot}$, 19), 206 (17), 204 (45), 171 (2.4), 169 (7.6), 143 (14), 141 (4), 139 (9), 133 (29), 125 (6), 115 (5), 107 (100), 105 (43), 79 (22), 78 (17), 77 (37), 53 (15) daltons.

Conversion of the erythro *chlorohydrin, **10**, into the epoxysulfone, **7***

A solution of the chlorohydrin, **10** (72 mg, 0.23 mmol), in dry DMF (1 mL) was treated with a solution of potassium *tert*-butoxide in dry DMF (0.23 mL of 1.0 M solution) as for the conversion of **6** into **7**. The product was a semisolid (65 mg), which by high-field ^{1}H nmr spectroscopy was a mixture of epoxysulfone, **7**, and chlorosulfone, **8** (ca. 4:1). Recrystallization (ether–hexane) gave pure **7** (mp 45–48°C), identical to the substance prepared from **6**, by tlc, ^{1}H nmr, and ms.

*Conversion of the chlorohydrins, **11**, into the epoxysulfone, **15***

A diastereomeric mixture of chlorohydrins, **11** (*erythro*:*threo* = 3:2, 78 mg, 0.25 mmol), was reacted with KOBu^t as in the previous experiment. The residue (50 mg) gave *E*-1,2-epoxy-1-phenyl-2-phenylsulfonylpropane, **15**, as needles, mp 109–110°C (from CCl_4–ligroin); for nmr data, see Table 2. This sample was identical (mp, mmp, ^{1}H nmr) to another sample of **15** that was prepared by a phase-transfer-mediated Darzens condensation, in the way described for the preparation of **5***c*. This sample also had an ms recorded, m/z: 274 ($M^{+\cdot}$, 2), 233 (2), 232 (9), 231 (7), 168 (2), 167 (3), 134 (10.6), 133 (100), 126 (15), 125 (17), 105 (92), 90 (11), 89 (11), 79 (13), 77 (30), m^* = 196.5, 83.6 daltons. *Anal.* calcd. for $C_{15}H_{14}O_3S$: C 65.67, H 5.14%; found: C 65.55, H 5.16%.

*Preparation of 2-*tert*-butylsulfonyl-1-phenylpropanone, **16***

2-Chloropropiophenone (**12**, 14.2 g, 0.84 mol) and *tert*-butylthiol (7.68 g, 0.85 mol) were reacted together under phase-transfer conditions (as described in the previous paper) to yield an oil that, on purification by chromatography over silica gel in 1:1 hexane–dichloromethane, gave 2-*tert*-butylsulfenyl-1-phenylpropanone, oil, (16 g, 88%); ^{1}H nmr δ($CDCl_3$): 1.3 (9H, s), 1.6 (3H, d, J = 7 Hz), 4.3 (1H, q, J = 7 Hz), 7.2–8.0 (5H, m); ms m/z: 222 ($M^{+\cdot}$, 15), 166 (6), 134 (5), 118 (5), 117 (65), 105 (83), 77 (35), 61 (39), 57 (100) daltons. Oxidation of this β-ketosulfide (6.0 g, 27 mmol) with H_2O_2 in MeOH in the presence of ammonium molybdate catalyst (43), as described previously, gave a solid that was recrystallized (CH_2Cl_2–EtOH, 1:9) to give **16** as colourless needles (5.7 g, 83%), mp 119–120°C; ir ν_{max}: 2995 (m), 1685 (s), 1290 (s), 1284 (s), 1245 (s), 1108 (s), 988 (s), 951 (s), 726 (s) cm^{-1}; ^{1}H nmr δ($CDCl_3$): 1.43 (9H, s), 1.74 (3H, d, J = 7.05 Hz), 5.14 (1H, q, J = 7.05 Hz), 7.4–8.1 (5H, m); ^{13}C nmr δ($CDCl_3$): 14.52 (*Me*CH), 24.21 (Me_3C-), 60.27 (*C*HMe), 60.49 (Me_3C-), 128.84, 129.04 (*o*- and *m*-*C* of Ph), 133.82 (*p*-*C*), 136.25 (quart. *C* of Ph), 193.00 (*C*=O); ms m/z: 254 ($M^{+\cdot}$, 0.22), 198 (0.07), 180 (0.15), 135 (10.3), 134 (100), 133 (23), 115 (1), 105 (44), 77 (27), 57 (66), m^* = 132.2, 83.2 daltons.

*Preparation of 2-*tert*-butylsulfonyl-2-chloro-1-phenylpropanone, **17***

Chlorination of **16** (3.0 g) was carried out as described previously (27), which resulted in crude material that after purification by chromatography over silica gel (hexane–CH_2Cl_2, 1:1) gave pure **17** as white needles, mp 67–69°C (1.46 g, 43%, CH_2Cl_2–hexane); ir ν_{max}: 1680 (s), 1668 (s), 1305 (s), 1242 (s), 1228 (s), 1185 (s), 1120 (s), 950 (s), 737 (s), 690 (s), 555 (s) cm^{-1}; ^{1}H nmr δ($CDCl_3$): 1.53 (9H, s), 2.29 (3H, s), 7.4–8.3 (5H, m); ^{13}C nmr δ($CDCl_3$): 25.74 (Me_3C-), 28.36 (*Me*CCl), 69.15 (Me_3C-), 90.17 (MeCCl), 128.04, 130.66 (*o*-and *m*-*C* of Ph), 133.39 (*p*-*C*), 134.81 (quart. *C* of Ph), 193.07 (*C*=O); ms m/z: 288 ($M^{+\cdot}$, 0.21), 232 (0.13), 170 (26.4), 168 (79.6), 139 (3), 105 (67), 103 (8), 92 (5), 90 (14), 77 (33), 57 (100), m^* = 115.0 daltons.

*Preparation of 2-*tert*-butylsulfonyl-2-chloro-1-phenylpropanol, **18***

Reduction of **17** (1.46 g, 5.1 mmol) was carried out in the same way as described for the preparation of **11***a*. Work-up gave crude material (1.4 g) that was chromatographed on silica gel (hexane–CH_2Cl_2, 1:1) to give **18** (953 mg, 65%) as a mixture of diastereomers (*threo*:*erythro* = ca. 7:2, by ^{1}H nmr), needles, mp 72–73°C (ethanol); ir ν_{max}: 3465 (s), 1288 (s), 1116 (s), 1095 (s), 1070 (s), 726 (s), 697 (s), 636 (s) cm^{-1}; nmr spectra in Table 1; ms m/z: 292 (1.3), 290 ($M^{+\cdot}$, 3.4), 184 (2), 169 (2), 154 (5), 152 (15), 134 (5), 133 (9), 130 (5), 128 (13), 107 (29), 105 (13), 79 (8), 77 (9), 57 (100), m^* = 114.5, 84.0 daltons.

*Conversion of the chlorohydrins, **18**, into the epoxide, **20***

The mixture of chlorohydrins **18** (390 mg, 1.0 mmol) was reacted with base as described for the preparation of **7**. Regular work-up gave crude product that was a mixture of **20** and Bu^tSO_2CHClMe (269 mg); repeated recrystallization (ligroin) gave **20** as fine colourless needles, mp 56–58°C; ir ν_{max}: 3010 (m), 2980 (m), 1295 (s), 1120 (s), 874 (s), 760 (s), 690 (s), 578 (s) cm^{-1}; nmr spectra in Table 2; ms m/z: 254 ($M^{+\cdot}$, 0.41), 212 (0.54), 135 (10), 134 (100), 133 (97), 105 (83), 91 (19), 90 (14), 89 (11), 79 (11), 77 (19), 57 (90), m^* = 101.5, 83.3 daltons.

*Conversion of the chlorohydrins, **19**, into the epoxide, **21***

The mixture of chlorohydrins **19** (439 mg, 1.442 mmol) was reacted with base as described for the preparation of **7**. Regular work-up gave crude product that was a mixture of **21** and Bu^tSO_2CHClEt (481 mg); repeated recrystallization (ligroin) gave **21** as fine colourless needles, mp 71–72°C; ir ν_{max}: 2995 (m), 1467 (m), 1458 (m), 1305 (s), 1122 (s), 768 (s), 683 (s), 580 (s) cm^{-1}; nmr spectra in Table 2; ms m/z: 149 (11), 148 (94), 147 (74), 119 (14), 105 (8), 92 (11), 91 (100), 90 (14), 89 (10), 77 (9), 57 (90) daltons.

Conversion of chlorohydrins into epoxides in the presence of p*-tolualdehyde — crossover experiments*

The typical procedure was the same as for the preparation of the epoxysulfone **7** from the chlorohydrins **6** or **10**, with the exception that the one mole equivalent of freshly distilled *p*-tolualdehyde was added to the solution of chlorohydrin in DMF before the KOBu^t was added. After regular work-up, the crude product was filtered through a short column of silica gel using 20% hexane in CH_2Cl_2 and the resulting oil was analyzed by ^{1}H nmr spectroscopy. Two experiments were carried out:

(*a*) Chlorohydrin **6** (150 mg, 0.46 mmol) in DMF (2.0 mL), plus *p*-tolualdehyde (55 mg, 0.46 mmol), plus KOBu^t (0.46 mL of 1.0 M solution in DMF) gave an oil, the ^{1}H nmr spectrum of which clearly showed the presence of three compounds in a mixture, viz. **7**:**22**:**8** in a ratio of ca. 8:5:12; **22** could be distinguished by its resonances at δ 2.35 (s, aryl C*H*$_3$) and 4.82 (s, epoxy ring C*H*). The mass spectrum of the oil varied with time, but clearly showed the required pattern of ions characteristic of **7** and **8**, together with ions at m/z 302, 246, 245, and 161, characteristic of **22**.

(*b*) Chlorohydrin **10** (128 mg, 0.39 mmol in 1.5 mL of DMF) reacted as above, giving a crude product (133 mg) that yielded an oil (70 mg) after chromatography. This oil had essentially the identical ^{1}H nmr spectrum (at 361.05 MHz) to that from the previous experiment, with the ratio of **7**:**22**:**8** = ca. 4:3:8.

Acknowledgements

The authors gratefully acknowledge financial support from NSERC of Canada in the form of operating grants (to J.S.G.

and T.S.C.) and an infrastructure grant (to T.S.C.). Dalhousie University provided financial support (to S.S.) and the Atlantic Region Magnetic Resonance Center in Halifax, N.S. provided high-field nmr spectra through the courtesy of Dr. D. L. Hooper and Mr. B. J. MacDonald. Dr. J.-H. Kim ran the mass spectra, Mrs. Wanda Tacreiter, Mr. Y.-C. Luo, and Dr. A. Linden assisted with the crystal structure determinations, and Mrs. P. V. Turner-Chiapetta carried out some of the initial preparations.

1. W. M. Ziegler and R. Conner. J. Am. Chem. Soc. **62**, 2596 (1940).
2. F. G. Bordwell and G. D. Cooper. J. Am. Chem. Soc. **73**, 5184 (1951).
3. F. G. Bordwell and W. T. Brannen, Jr. J. Am. Chem. Soc. **86**, 4645 (1964).
4. F. G. Bordwell and B. B. Jarvis. J. Am. Chem. Soc. **95**, 3585 (1973).
5. P. Robson, P. R. H. Speakman, and D. G. Stewart. J. Chem. Soc. (C), 2180 (1968).
6. R. F. Langler and J. A. Pincock. Can. J. Chem. **55**, 2316 (1977); D. G. Kay, R. F. Langler, and J. E. Trenholm. Can. J. Chem. **57**, 2185 (1979).
7. H. Hoffmann and H. Förster. Tetrahedron Lett. 1547 (1963).
8. P. del Buttero and S. Maiorana. Gazz. Chim. Ital. **103**, 809 (1973).
9. F. G. Bordwell and E. Doomes. J. Org. Chem. **39**, 2298 (1974).
10. B. B. Jarvis and B. A. Marien. J. Org. Chem. **42**, 2676 (1977), and references therein.
11. N. S. Zefirov and D. I. Makhon'kov. Chem. Rev. **82**, 615 (1982).
12. P. D. Magnus. Tetrahedron, **33**, 2019 (1977).
13. T. Durst. *In* Comprehensive organic chemistry. Vol. 3. *Edited by* D. N. Jones. Pergamon, Oxford. 1979. pp. 197–213.
14. J. S. Grossert, P. K. Dubey, and T. Elwood. Can. J. Chem. **63**, 1263 (1985).
15. J. S. Grossert. Tenth International Symposium on the Organic Chemistry of Sulphur, Bangor, Wales, Abstr. no. B.028 (1982); J. B. Hendrickson, G. J. Boudreaux, and P. S. Palumbo. J. Am. Chem. Soc. **108**, 2358 (1986).
16. B. B. Jarvis and P. E. Nicholas. J. Org. Chem. **45**, 2265 (1980).
17. A. Bruggink, B. Zwanenburg, and J. B. F. N. Engberts. Tetrahedron, **27**, 4571 (1971); K. Hovius and J. B. F. N. Engberts. Tetrahedron Lett. 2477 (1972), and references therein.
18. L. A. Paquette. Org. React. **25**, 1 (1977).
19. E. W. Warnhoff. *In* Rearrangements in ground and excited states. Vol. 1. *Edited by* P. de Mayo. Academic Press, New York, NY. 1980. p. 391.
20. K. Dickoré. Justus Liebig's Ann. Chem. **671**, 135 (1964).
21. U. Jacobsson, T. Kempe, and T. Norin. J. Org. Chem. **39**, 2722 (1974).
22. W. Meichle and H.-H. Otto. Arch. Pharm. (Weinheim, Ger.), **319**, 982 (1986).
23. F. Bohlmann and G. Haffer. Chem. Ber. **102**, 4017 (1969).
24. P. F. Vogt and D. F. Tavares. Can. J. Chem. **47**, 2875 (1969).
25. G. G. Lyle and L. K. Keefer. J. Org. Chem. **31**, 3921 (1966).
26. A. Jonczyk, K. Banko, and M. Makosza. J. Org. Chem. **40**, 266 (1975), and references therein.
27. J. S. Grossert, H. R. W. Dharmaratne, T. S. Cameron, and B. R. Vincent. Can. J. Chem. **66**, 2860 (1988).
28. P. Deslongchamps. Stereoelectronic effects in organic chemistry. Pergamon, Oxford. 1983. pp. 164–173.
29. F. G. Bordwell, J. E. Bares, J. E. Bartmess, G. E. Drucker, J. Gerhold, G. J. McCollum, M. van der Puy, N. R. Vanier, and W. S. Matthews. J. Org. Chem. **42**, 326 (1977).
30. D. E. Sands. Acta Crystallogr. Sect. B: Struct. Crystallogr. Cryst. Chem. **28**, 2463 (1972).
31. G. D. Andreetti, G. Bocelli, and P. Sgarabotto. Cryst. Struct. Commun. **6**, 89 (1977).
32. D. J. Williams, P. Crotti, B. Macchia, and F. Macchia. Tetrahedron, **31**, 993 (1975).
33. M. Willson, F. Mathis, R. Burgada, J. Jaud, and J. Galy. Acta Crystallogr. Sect. B: Struct. Crystallogr. Cryst. Chem. **34**, 2772 (1978).
34. J. S. Grossert, J. Hoyle, T. S. Cameron, S. P. Roe, and B. R. Vincent. Can. J. Chem. **65**, 1407 (1987).
35. J. F. King, G. T. Y. Tsang, M. M. Abdel-Malik, and N. C. Payne. J. Am. Chem. Soc. **107**, 3224 (1985).
36. J. I. Lynas-Gray and C. J. M. Stirling. J. Chem. Soc. Chem. Commun. 483 (1984); Recl. Trav. Chim. Pays-Bas, **105**, 341 (1986).
37. S. Sorriso, F. Stefani, E. Semprini, and A. Flamini. J. Chem. Soc. Perkin Trans. 2, 374 (1976).
38. G. Berti. Top. Stereochem. **7**, 93 (1972).
39. W. E. Truce and T. C. Klingler. J. Org. Chem. **35**, 1834 (1970).
40. E. S. Gould. Mechanism and structure in organic chemistry. Holt, New York, NY. 1959. pp. 561–569.
41. H. O. House and J. K. Larsen. J. Org. Chem. **33**, 61 (1968).
42. O. Exner and J. B. F. N. Engberts. Collect. Czech. Chem. Commun. **44**, 3378 (1979).
43. H. S. Schultz, H. B. Freyermouth, and S. R. Buc. J. Org. Chem. **28**, 1140 (1963).

Can. J. Chem. Downloaded from www.nrcresearchpress.com by 196.1.178.254 on 09/07/12
For personal use only.

Intramolecular sensitization in salicylatotetraammine cobalt(III) complex

LUIS VASQUEZ, CARLOS ANDRADE, AND IRMA CRIVELLI[1]
Department of Chemistry, Faculty of Sciences, Universidad de Chile, Casilla 653, Santiago, Chile

Received October 20, 1987[2]

LUIS VASQUEZ, CARLOS ANDRADE, and IRMA CRIVELLI. Can. J. Chem. **66**, 2880 (1988).

Luminescence studies show that the fluorescence of salicylic acid and its anionic species is quenched when they belong to the coordination sphere of the Co(III) and no new emission appears even in glass at 77 K. The metallic center seems to provide new and efficient non-radiative deactivation paths for the ligand centered states.

Irradiation in the intraligand bands of the complex, in aqueous solution, leads to photoredox reaction generating Co^{2+} species characteristic of the charge transfer cobalt photochemistry. Results are discussed in terms of an efficient intramolecular sensitization or intramolecular energy transfer from states centered in the ligand to LMCT state centered at the metal.

LUIS VASQUEZ, CARLOS ANDRADE et IRMA CRIVELLI. Can. J. Chem. **66**, 2880 (1988).

Des études de luminescence démontrent que la fluorescence de l'acide salicylique et de ses espèces ioniques est piégée lorsqu'ils font partie de la sphère de coordination du Co(III); on n'observe aucune nouvelle émission, même dans un verre à 77 K. Le centre métallique semble fournir des voies de désactivation non-radiactives nouvelles et efficaces pour les états centrés sur le ligand.

L'irradiation, en solution aqueuse, dans les bandes intra-ligands du complexe, provoque une réaction photorédox conduisant à la formation d'espèces Co^{2+} caractéristiques de transferts de charges lors la photochimie du cobalt. On discute des résultats en fonction d'une sensibilization intramoléculaire efficace ou d'un transfert intramoléculaire d'énergie d'états centrés dans le ligand vers l'état LMCT centré au niveau du métal.

[Traduit par la revue]

Introduction

Different reactions result from CTTM and LF excitations in transition metal complexes (1, 2). Particularly, a variety of reaction modes have been observed for Co(III) complexes. There have been different approaches in evolving general patterns of photochemical behaviour, not only from a mechanistic point of view but also from excited state models (2, 3); although it has been recognized that the molecular properties (reactivity, energy, ...) of the excited states and some molecular processes (radiative and non-radiative relaxation, excited state distortions, ...) are relevant, the complete characterization of the excited state manifolds and the communication between excited states is not an easy task (4, 5). The lack of luminescence for cobalt complexes other than Co(III) cyanides (6) has made the access to this kind of information more difficult. Furthermore, Endicott *et al.* (7) with regard to the possibility of a meaningful use of the sensitization technique conclude that "there is no clear way to relate intermolecular energy transfer studies to intrinsic processes which take place within the molecular charge transfer state in coordination compounds."

Intramolecular energy transfer in metalloorganic bichromophore has been reported for some Rh(III) (8) and for heterobimetallic Co(III)–Cr(III) (9) and Ru(II)–Rh(III) complexes (10). In all cases the energy transfer results in metal-centred reactions characteristic of ligand field excited states of Rh(III), Cr(III), and Ru(II)–Rh(III), respectively. Through intramolecular energy transfer processes it is possible to get information about the possibility and competivity of the different inter- and intraconfigurational non-radiative relaxation processes within the excited state manifolds.

The present report is concerned with the intramolecular sensitization of redox reactions characteristic of CTTM excited states in Co(III) complexes, reactions which characterize Co(III) photochemistry.

Experimental

Preparations

Salicylatotetraamminecobalt (III) ion (Complex **I**) was prepared by adding slowly with continuous stirring 8.8 g of $[Co(NH_3)_4CO_3]NO_3$ (11) to a 40°C solution of 19 g salicylic acid in 100 mL of butanol 40%. The reaction mixture was stirred at 40–45°C for 12 h, cooled, and filtered. The solid was washed several times with ethanol to eliminate the excess of salicylic acid and the complex precipitated as salicylate. *Anal.* calcd. for $[Co(NH_3)_4O_2CC_6H_4O]C_6H_4(OH)CO_2$: Co 14.7, N 14, C 42, H 5.2; found: Co 13.5, N 13.97, C 39.22, H 4.99.

Cobalt content was determined gravimetrically (12). The salicylato species present as ligand in the complex was determined by measuring the concentration of the free ligand after a full hydrolysis of the complex (0.1 *M* $HClO_4$) by (*a*) emission, (*b*) spectrophotometrically adding $FeCl_3$ and measuring the absorbance at 515 nm (13).

Tridistilled H_2O was used in the preparation of all solutions. pH was adjusted using $HClO_4$ (Mallinckrodt 70%) and the ionic strength with $NaClO_4$ (Merck) when needed. Salicylic acid (Aldrich gold label) was used without further purification. All other reagents were of adequate grade.

Photolysis procedures

The light source was a water-cooled Phillips HPL-400 W (Hg) mounted in a conventional optical bench with adequate collimating lenses. A UG-11 Schott glass filter and a F-254 interference filter were used for irradiation at the 303 and 235 nm bands of the complex, respectively.

Photolysis were carried out in 0.1 *M* $HClO_4$ solutions, at complex concentrations which provided essentially total light absorption in a 5-cm cylindrical cell. Photolysis experiments were run without deoxygenating the solutions. Concurrent thermal hydrolysis reaction was negligible ($k = 1.09 \times 10^{-5}$ s^{-1}, 60°C, pH = 1, $I = 0.6$ *M* in $NaClO_4$ (14) at the irradiation conditions. Absolute light intensities were determined by ferrioxalate actinometry.

Analytic procedures: The salicyclic acid quantum yields, (ϕ_{sal}) were determined by emission analysis of diluted photolyzed solutions. The corresponding cobalt(II) quantum yields ($\phi_{Co(II)}$) were obtained using a modification of Kitson's method (15): 25 mL of the solution prepared by dissolving 546 g of NH_4SCN in 1 L of 1:5 water/acetone solvent, were added to an appropriate volume of the photolyzed solution, diluted to 50 mL with distilled water and the absorbance recorded at

[1]Author to whom correspondence should be addressed.
[2]Revision received June 27, 1988.

Printed in Canada / Imprimé au Canada

Can. J. Chem. Downloaded from www.nrcresearchpress.com by 196.1.178.254 on 09/07/12
For personal use only.

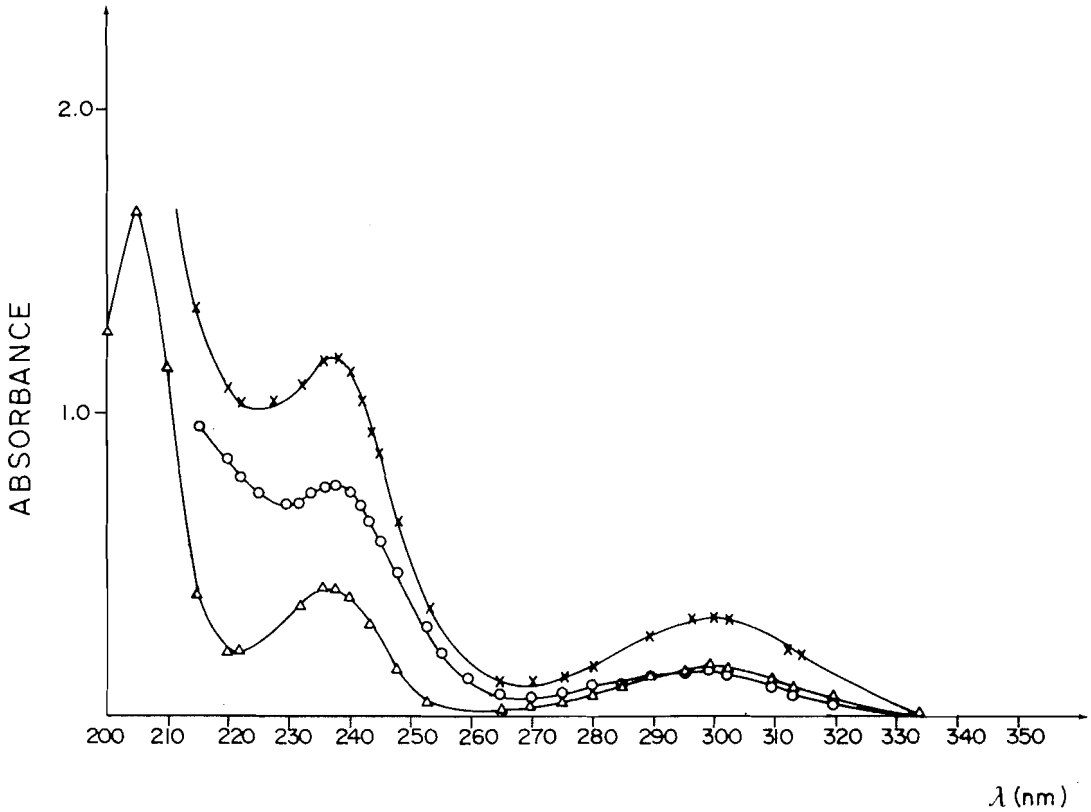

FIG. 1. Ultraviolet absorption spectra for 0.1 *M* $HClO_4$ aqueous solutions 5×10^{-5} *M* of △, free salicylic ligand; ○, $[Co(NH_3)_4OCOC_6H_4O]^+$ ion; ×, $[Co(NH_3)_4OCO_6H_4O]C_6H_4(OH)CO_2$.

625 nm. For quantum yield determinations photolysis were not carried out beyond 15–25% reaction.

Gas chromatography, absorption and emission spectrometry were used for identification of the other products. Cation exchange resin (H^+ form) was used to separate the eventual aquo complex species.

Emission procedures

A Perkin Elmer MPF-2A spectrofluorimeter was used for emission and quenching experiments. The emission properties of the $[Co(NH_3)_4O_2CC_6H_4O]^+$ ion were determined by dissolving the solid in NaAc–HAc buffer (pH = 5) and passing through an anionic exchange resin (Bio-Rad Analytical grade AG:X8 in ClO_4^+ form) to eliminate the salicylate counterion.

The fluorescence quantum yields were measured in modular equipment consisting of 1000 W Hanovia Xe–Hg lamp, a Hilger Monospek 1000 excitation monochromator, a Perkin Elmer E-1 emission monochromator, an EMI 9559 OB photomultiplier tube detector and a power supply from a Perkin Elmer E-11 spectrophotometer, using 9,10-dichloroanthracene as standard reference.

Calculations

Quantum yields of the photolysis products were calculated for each photolysis run since the inner filter effect of the salicylic acid formed as photoproduct, continuously added to the base inner filter effect of the salicylic counterion. The quantum yields reported were obtained by extrapolation to zero irradiation time.

Corrections for partial light absorption were taken into account in calculations where required (particularly UG-11 filter photolysis). Quantum yields of fluorescence were calculated using the original expression (16) corrected by the ratio of the refractive indexes.

Results

Figure 1 shows the absorption spectra of the free salicylic ligand and $[Co(NH_3)_4OCOC_6H_4O]^+$ ion. Electronic absorption spectra of some cobalt amine complexes are given in Table 1. Emission characteristics of the ligand and its anionic species are shown in Table 2. Table 3 summarizes the quantum yields of the main photoproducts obtained when aqueous solution of Complex **I** (0.001 *M*, μ = 0.1 $HClO_4$, pH = 1) is irradiated at 235 and 300 nm bands (F-254 and UG-11 filters, respectively).

The bands of the salicylic acid and the anionic forms are associated with $\pi-\pi^*$ and $n\pi-\pi^*$ transition and the emission is characterized as fluorescence (17). The absorption intraligand bands remain practically unchanged in the salicylic cobalt complex, but the emission of the bound ligand is quenched and new emissions are not observed even at 77 K. It may be seen from Table 1 that the aquo and oxalate complexes present a *d–d* band around 350 nm. A similar ligand field transition may be present in the 300 nm range for Complex **I**; however, the contribution to the total band absorption will be at least two orders of magnitude smaller than the transition observed for the ligand in the same spectral region. Therefore the 300 nm band is dominated by an intraligand band.

The free ligand band at 235 nm is also observed in Complex **I**, on top of the beginning of the ~200 nm band, maintaining the same maximum and minimum, which suggests it to be an intraligand band.

The free salicylic acid, whose quantum yields are given in Table 3 is related to the photoredox process through which Co(II) is formed (i.e., is a consequence of the kinetic lability of the Co(II) formed) since we were not able to find $[Co(NH_3)_4(H_2O)_2]^{3+}$. Although a small amount of CO_2 was found as a photolysis product, the identification of phenol was unsuccessful due to interference by minimum amounts of salicylic acid or its anionic species. The same problem was

Can. J. Chem. Downloaded from www.nrcresearchpress.com by 196.1.178.254 on 09/07/12
For personal use only.

TABLE 1. Electronic absorption spectra of salicylic acid and some tetraammine Co(III) complexes

Species	λ_{max} (nm)	ϵ(lt/mol·cm)
$[Co(NH_3)_4OC_6H_4CO_2]^{+a}$	515; 300; 235; ~200	74.6; 2950; 15 504; ~44 000
$C_6H_4OHCOOH$	300; 235; ~200	3452; 8175; ~34 000
$[Co(NH_3)_4C_2O_4]^{+b}$	508; 350; 265	72.8; 80.4; 10 000
$[Co(NH_3)_4(H_2O)_2]^{3+c}$	510; 350; ~200	45.7; 39.8; 1000

[a]Complex I.
[b]Reference 18.
[c]Reference 22.

TABLE 2. Fluorescence quantum yield of salicylic acid, pH and excitation wavelength dependence

	λ_{exc} = 248 nm		λ_{exc} = 313 nm	
pH	λ_{em} (Å)	ϕ_f[a]	λ_{em} (Å)	ϕ_f
1	4530	4.55×10^{-3}	4530	6.16×10^{-3}
5	4270	0.101	4260	0.206
13	4160	0.031	4170	0.034

[a]Aqueous solution; room temperature.

TABLE 3. Photoproducts quantum yields for $[Co(NH_3)_4OCOC_6H_4O]^{+a}$

$\bar{\phi}$	λ_{exc} 235 nm band (F-254)	λ_{exc} 300 nm band (UG-11)
$\bar{\phi}_{Co^{2+}}$	0.9±0.03	0.4±0.03
$\bar{\phi}_{sal}$	0.34±0.01	0.15±0.01
$\bar{\phi}_{sal}/\bar{\phi}_{Co^{2+}}$	0.38±0.02	0.38±0.05

[a]The values of the ϕ are an average of four determinations and the uncertainty indicated in each value is the largest deviation of the ϕ with respect to $\bar{\phi}$; aqueous percholoric media (pH = 1); room temperature.

faced after separation of the products through an ion exchange column. The irradiation conditions (pH = 1, $HClO_4$) made it impossible to measure any NH_3 production by pH changes. The identification of photolysis product was not pursued further since our main purpose was not mechanistic.

The emission of an aqueous acidic solution of $C_6H_4(OH)CO_2H$ ($\simeq 10^{-3}$–10^{-5} M) was not affected by addition of Co^{2+}, $[Co(NH_3)_4(H_2O)_2]^{2+}$ or $[Co(NH_3)_4O_2CC_6H_4O]^{+}$ ions, at least at the initial irradiation concentrations or at the final concentrations of the photoproducts formed during the reaction.

Discussion

The data of Table 1 and Fig. 1 suggest that the absorbance properties of the two chromophores, $Co(NH_3)_4^{3+}$ and $OC_6H_4CO_2^{2-}$, seem to add to give the spectral characteristics of Complex **I**, without major perturbation, and that the bands at 300 and 235 nm are essentially intraligand bands. A general spectral feature common to Co(III) amine complexes with carboxylate ligands is to show ligand bands around 500 nm ($\epsilon \simeq 100\ M^{-1}\ cm^{-1}$) and intense charge transfer bands ($\epsilon > 5 \times 10^3\ M^{-1}\ cm^{-1}$) in the UV region, therefore possible overlap of intraligand and LMCT absorptions must be analized for the salicylate–Co(III) complex. The only changes observed in the 235 nm centered band, are the relative increase of the absorption in the 245–260 nm range and around the minimum at 225 nm in relation to the spectra of the free ligand. The first change may be explained by an apparent 245–260 nm band, — obtained by Gaussian analysis — having an ϵ(250 nm) $\simeq 3 \times 10^3\ M^{-1}\ cm^{-1}$, and the second considering the overlap with the higher energy band tail. However, the apparent band at 245–260 nm, may just be artificial and the small change only a consequence of a broadening of the complex 235 nm band as compared to the free ligand spectra. The extinction coefficient observed for this apparent band, which is in the region of the CT bands, does not have the right value for a Co(III)–carboxylate CT band. Therefore we believe that the CT band is probably under the 200 nm band, and that the 235 and 300 nm bands appear to be essentially intraligand bands. On other hand, the emission of the $OC_6H_4CO_2^{2-}$ moiety is quenched on coordination to the Co(III) chromophore and Complex **I** is not luminescent. Although this result may be expected, since the lack of luminescent properties of Co(III)d^6 complexes as compared to $3d^3$ and $4d^6$–$5d^6$ complexes is known, the presence of a redox process when the intraligand bands of Complex **I** are irradiated, may give more information about the mechanism which accounts for the lack of luminescence in Co(III) low ligand field complexes. Literature accounts have emphasized the possibility of fast radiationless dissipation of excitation energy through the ligand field states manifold and (or) an inefficient intersystem crossing to the lowest ligand field triplet, the emitting state in luminescent Co(III) complexes (2, 6). The results obtained here suggest that for Complex **I**, the new deactivation non-radiative path provided to the intraligand excited states involves an energy transfer process.

Since the salicylic acid fluorescence (at 295°C and 0.1 M $NaClO_4$) is not modified by the presence of $[Co(NH_3)_4(H_2O)_2]^{3+}$ nor $[Co(NH_3)_4O_2CC_6H_4O]^{+}$ at the experimental irradiation conditions, the intermolecular energy transfer does not seem to be efficient; therefore the energy transfer must be an intramolecular process, or intramolecular sensitization.[3]

Irradiation at 254 and 300 nm bands yields the same products; however, the quantum yield values at 254 nm are greater than at 300 nm; i.e., ϕ_{redox} increasing going from the lower to the higher energy intraligand band. Nevertheless, the $\phi_{sal}/\phi_{Co^{2+}}$ ratio is the same for both bands, suggesting that the energy transfer process populates the same excited state, responsible for the photoreaction which is CT in nature.

[3]Way and Filipescu (18) have assigned a redox process for the $|Co(NH_3)_4C_2O_4|^{+}$ complex to a ligand field band centered at 350 nm with a $\phi_{Co^{2+}} = 0.2$. However ϵ(intraligand)/$\epsilon(d$–$d) \simeq 50$ and $\phi_{Co^{2+}} = 0.4$ (Table 2, 300 nm) for Complex **I**; hence the assumption that a ligand field transition band would be the photochemically active, would require a $\phi_{Co^{2+}} \simeq 20$, after filter effect correction, which is not a reasonable value.

Can. J. Chem. Downloaded from www.nrcresearchpress.com by 196.1.178.254 on 09/07/12
For personal use only.

Can. J. Chem. Downloaded from www.nrcresearchpress.com by 196.1.178.254 on 09/07/12
For personal use only.

Considering that $\phi_{Co^{2+}} > \phi_{sal}$, and the value itself of both quantum yields, it seems that Complex **I** is only in part reduced to Co(II) by the salicylic ligand. Therefore the process should start by two different primary photochemical acts (19). This suggestion does not exclude the possibility that the complete photoreduction mechanism may involve chemical reduction of the complex by radical species derived from the primary act. However, as it was mentioned above, we were unsuccessful to identify other products besides salicylic acid and small amounts of CO_2, thus any mechanistic interpretation of the results would only be speculative. Considering that fluorescence is the only deactivation process observed in the free ligand (20) and that the emission wavelength is independent of the excitation energy, as may be expected from Kasha's rule (21), the energy transfer must take place from the intraligand fluorescent state. Should this occur, not only equal quantum yield ratios would have been observed on irradiation at both λ_{exc} (254 and 300 nm), but also $\phi_{Co^{2+}}$ and ϕ_{sal} independent values should have moved in the same direction of ϕ_f if ϕ_f is dependent on λ_{exc}. Table 2 shows the ϕ_f measured for salicylic acid and the two anionic species; ϕ_f for both, totally protonated and completely ionized species, is constant (the first is at the limit of detection); for the monoprotonated species ϕ_f increases as the λ_{exc} increases, which is in the opposite direction of the products quantum yield changes (Table 3).

The results indicate that the transfer process is in competition with the relaxation processes to the fluorescent state within the intraligand manifold initially populated. Furthermore, they may suggest the existence of several competitive deactivation processes taking place in the CT manifold populated by the energy transfer process.

The possibility of direct excitation contribution to the same intermediate state when the irradiation in made at 254 nm band may be considered; in this case the absolute quantum yields may be expressed as:

$$\phi_{sal,Co(II)} = a\phi^{d(254)}_{sal,Co(II)} + b\phi^{ET(254)}_{sal,Co(II)}$$

where $\phi_{sal,Co(II)}$ is the total quantum yield for salicylic acid or Co(II), $\phi^{d(254)}_{sal,Co(II)}$ the corresponding quantum yield for direct population of the excited state and $\phi^{ET(254)}_{sal,Co(II)}$ is related to the excited population by energy transfer; *a* and *b* are coefficients which express the contribution of the charge transfer and intraligand bands, respectively, to the total absorption ($a + b = 1$).

The spectra of Complex **I** around the 235 nm centered band was examined above and based on it, two possible contribution to $\phi^{d(254)}_{sal,Co(II)}$ may be considered: one is absorption in the region of overlap with the higher energy band tail and the second is absorption in the 250–260 nm zone (apparent band). The first one in negligible on account of: number of intensity of the irradiation lamp lines, the cut-off point of the F-254 filter and the ending point of higher energy band tail. Considering now the absorption in the apparent band region (250–260 nm) and assuming that is in part a LMCT absorption, its contribution is only about 13.5% of the total; taking a limiting unfavorable condition (imply from Table 2), $\phi^{ET(254)}_{Co,sal} = \phi^{ET(300)}_{Co,sal}$, will result that $\phi^{d(254)}_{Co(II)} \simeq 4$ and $\phi^{d(254)}_{sal} \simeq 1.5$ which are unrealistic values for Co(III) photochemistry, even considering free radicals participation (2, 23). Therefore it is unlikely that irradiation through the F-254 filter may involve direct population of a LMCT, or at least will be negligible in our system.

In summary, the fluorescence quenching of the free ligand by the metal when it is coordinated to the $Co(NH_3)_4^{3+}$ chromophore, together with the presence of a redox process when the intraligand bands are irradiated, indicate that the initial intraligand excitation is followed by intramolecular transfer or intramolecular sensitization to a final LMCT state centered at the metal and reveal that for Complex **I** the new deactivation paths for the ligand upon coordination to the metal involve more than fast non-radiative paths through ligand field states to the ground state of the complex, i.e., involves energy tranfer or intramolecular sensitization processes which populate a LMCT state.

The total efficiency (tranfer plus redox processes) seems to be greater when the irradiation is made at the higher energy intraligand band. In this case the results suggest that the energy transfer is in competition with relaxation processes within the intraligand manifold initially populated. The fact that the quenching of the ligand fluorescence by the metallic center results in a redox process instead of a substitutional or new emission agrees with the considerations made by Yamamoto (6) about a possible relation between photochemical behaviour and luminescence in Co(III) complexes.

Acknowledgements

The authors are thankful to the Miss Miriam Pino for the early experiments related to the complex emission and to the Departamento de Investigaciòn y Bibliotecas de la Universidad de Chile by Gran Q-498/855.

1. V BALZANI and V. CARASSITI. Photochemistry of coordination compounds. Academic Press, New York, NY. 1970 and references therein.
2. Concepts of inorganic photochemistry. A. Adamsons and P. Fleischauer (*Editors*). J. Wiley and Sons, New York. 1975. (*a*) Chapt. 4; (*b*) Chapt. 3.
3. J. ENDICOTT and G. FERRAUDI. J. Phys. Chem. **80**, 949 (1976).
4. N. J. TURRO. Modern molecular photochemistry. Benjamin/Cummings, Menlo Park, CA., 1978. Chapts. 5, 6, and 9.
5. K. ROHATGI-MUKHERJEE. Fundamentals of photochemistry. J. Wiley and Sons, New York. 1978. Chapts. 3, 5, and 6.
6. Y. YAMAMOTO. Bull. Chem. Soc. Jpn. **52**, 84 (1979).
7. J. ENDICOTT, G. FERRAUDI, and J. BARBER. J. Am. Chem. Soc. **97**, 219 (1975) and references therein.
8. P. FORD, R. WATTS, and M. BERGKAMP. Inorg. Chem. **20**, 1764 (1981).
9. A. L. HEATHERINGTON, J. S. HALLOCK, J. M. VAUGHT, M. M. ALLEN, and N. A. P. KANE-MAGUIRE. Inorg. Chem. **22**, 3851 (1983).
10. J. D. PETERSEN, H. D. WOHLERS, A. J. STINSON, J. A. GELROTH, J. E. FIGARD, L. LEE, and K. J. MOORE. J. Am. Chem. Soc. **105**, 2274 (1983).
11. G. SCHLESSINGER. Inorganic syntheses. McGraw Hill, New York, **6**, 173 (1960).
12. N. SERPONE and M. HOFFMAN. J. Chem. Educ. **60**, 85 (1983).
13. P. G. FOGG and R. J. HALL. J. Chem. A, 1365 (1971).
14. J. MORA. To be published.
15. R. E. KITSON. Anal. Chem. **22**, 664 (1950).
16. C. A. PARKER. Photoluminescence of solutions. Elsevier Publishing Co., Amsterdam. 1968. p. 262.
17. A. Z. WELLER. Z. Electrochem. **60**, 1144 (1956).
18. H. WAY and N. FILIPESCU. Inorg. Chem. **8**, 1609 (1969).
19. A. W. ADAMSON, A. VOGLER, and I. LANTZKE. J. Phys. Chem. **73**, 4187 (1969).
20. J. CALVERT and J. PITTS. Photochemistry. Wiley, New York, NY. 1966. Chapt. 5.
21. M. KASHA. Discuss. Faraday Soc. **9**, 14 (1950).
22. P. PASCAL. Nouveau traité de chimie minerale. Complexes du fer, du cobalt et du nickel. Vol. XVIII. 1959.
23. A. F. VAUDO, E. R. KANTROWITZ, M. Z. HOFFMAN, E. PAPACONSTANTINOU, and J. F. ENDICOTT. J. Am. Chem. Soc. **94**, 6655 (1972).

The multiphoton spectra of the 1,3-*trans*-butadiene molecule from *AB-initio* and configuration interaction calculations

MARCO ANTONIO CHAER NASCIMENTO

Instituto de Quimica, Departamento de Fisico-Quimica, Universidade Federal do Rio de Janeiro, Rio de Janeiro, RJ 21910, Brasil

Received February 3, 1988

MARCO ANTONIO CHAER NASCIMENTO. Can. J. Chem. **66**, 2884 (1988).

The multiphoton spectra of the 1,3-*trans*-butadiene is investigated using highly correlated wave-functions. On the basis of computed transitions energies, intensities and polarization ratios, assignments are made to the first members of five Rydberg series and to a valence ($\pi \rightarrow \pi^*$) state. The results are in good agreement with the experimental results.

MARCO ANTONIO CHAER NASCIMENTO.Can. J. Chem. **66**, 2884 (1988).

On a étudié la spectre multiphotonique du butadiène-1,3 *trans* en faisant appel à des fonctions d'onde hautement corrélées. Sur la base des énergies et des intensitiés de transition calculées ainsi que des rapports de polarisation, on a fait des attributions aux premiers membres de cinq séries de Rydberg et à un état de valence ($\pi \rightarrow \pi^*$). Les résultats sont en bon accord avec les données expérimentales.

[Traduit par la revue]

Can. J. Chem. Downloaded from www.nrcresearchpress.com by 196.1.178.254 on 09/07/12
For personal use only.

1. Introduction

The electronic spectra of linear polyenes have been the subject of intensive experimental and theoretical studies since they were first prepared in the early 1930's. Recently there has been a revival of interest in the subject, partly because of its relation to the chemistry of visual pigments (1, 2).

The 1,3-*trans*-butadiene molecule (hereafter butadiene), being the first and the smaller of the polyenes, has received the greatest attention of both theoreticians and experimentalists (3). This molecule has now been studied using such techniques as vacuum ultraviolet (4), electron impact (5–7) and multiphoton spectroscopy (8–12), and also *ab-initio* calculations (13–15).

The electronic spectrum of butadiene is very complex and most of the observed peaks have been assigned to Rydberg series. Many of the optically forbidden Rydberg transitions appear as weak vibronic transitions in the one-photon spectra of the molecule, and their correct characterization is difficult. Such dipole forbidden transitions are more easily recognized by variable angle electron impact (5–7) and multiphoton ionization spectroscopy (8–12). The latter method presents the advantage that polarization studies can be conducted to determine the symmetry of the excited states (16).

In this article we present the results of extensive *ab-initio* calculations of transition energies, intensities (for both linear and circularly polarized radiation) and polarization ratios for the first members of the two-photon allowed Rydberg states of butadiene, and also for the $2\ ^1A_g$ ($\pi \rightarrow \pi^*$) valence state. These parameters are then used to assign the observed transitions in the multiphoton spectra of the compound.

2. Computational details

All the calculations were carried out using the Dunning (17) valence double-ζ (DZ) contraction of Huzinaga (18) double-ζ ($9s/5p,4s$) gaussian basis set, augmented with diffuse basis functions of either $3s$, $3d_\sigma$, or $3d_\pi$ ($\zeta_{3s} = 0.023$, $\zeta_{3d} = 0.015$) character on each carbon atom, in order to provide an adequate description of the Rydberg excited states.

With the molecule in the yz plane, we used the experimentally determined ground-state geometry (19) in all the calculations.

To understand the symmetry of the Rydberg states being described, it is important to recall that the molecular designation of the atomic orbitals in butadiene is $3s = a_g$; $3d = a_g\ (\sigma)$, $b_g\ (\pi)$. The two-photon allowed Rydberg states will have the overall symmetries B_g ($\pi\ (1b_g) \rightarrow 3s$, $3d_\sigma$) and A_g ($\pi\ (1b_g) \rightarrow 3d_\pi$).

The ground-state, $X\ ^1A_g$, was solved self-consistently at the GVB(5/PP) (20) level (correlating the three σ and the two π bonds) and the orbitals generated were used for the CI calculations of the ^1A_g valence states.

For the $3s$ Rydberg state, the valence basis set was augmented with a diffuse s basis function on each carbon atom. Using this augmented basis set and the natural orbitals from the ground-state calculation (properly recombined into symmetry orbitals), we performed an improved virtual calculation (IVO, 21) to obtain the starting guess for the $3s$-like excited orbital. Using the first IVO of a_g ($3s$) symmetry, we solved self-consistently for the ^1B_g ($1b_g(\pi) \rightarrow 3s$) Rydberg state.

Similarly, for the $3d_\sigma$ and $3d_\pi$ states, the valence basis set was augmented either with d_σ or d_π -like basis functions, and IVO calculations were performed to obtain the starting excited orbitals for the self-consistent calculations. With the proper IVO's, we solved self-consistently for the ^1B_g ($1b_g(\pi) \rightarrow 3d_\sigma$) state at the HF level, and for the ^1A_g ($1b_g(\pi) \rightarrow 3d_\pi$) state at the GVB(3/PP) level. For the latter state we used, in addition to the IVO orbital, the orbitals corresponding to the GVB(3/PP) of the ground-state, because we do not expect that correlating the σ orbitals will cause any constraints in the description of the π states.

Because the ^1B_g ($3d_\sigma$) and the ^1A_g ($3d_\pi$) Rydberg states are not the lowest states of these particular symmetries, their self-consistent wave-functions will not represent *pure* Rydberg states. Nevertheless, the self-consistent orbitals generated will be adequate to describe diffuse open-shell states. The final description of these Rydberg states is obtained as higher roots of CI calculations.

We have considered two different types of CI calculations, referred as full π-CI and all-valence CI calculations (22). Both calculations follow very closely the ones presented in a previous publication (14). The major difference is that in the latter paper all the Rydberg states were constructed from four off-centre s-like basis functions while in the present calculation they were constructed from s or d basis centered on each carbon atom. Reference 14 should be consulted for a detailed description of these calculations.

As discussed in ref. 14, the correct description of the $2\ ^1A_g$

TABLE 1. Transition energies (ΔE), two-photon transition rates (τ) and polarization ratios (Ω) for some electronic transitions of the 1,3-*trans*-butadiene molecule

State	ΔE(eV)		τ_C^c	τ_I^c	$\Omega(\tau_C/\tau_I)$		
	Theory[a]	Experiment[b]			Predicted[d]	Calculated	Experimental
$3s(^1B_g)$	6.29	6.21	3.15(−49)	2.10(−49)	1.5	1.5	1.4–1.6[e]
$2^1A_g(\pi\rightarrow\pi^*)$	7.06	7.3	2.33(−50)	4.39(−50)	<1	0.53	
$3d_{z2}(^1B_g)$	7.29				1.5		
$3d_{yz}(^1B_g)$	7.40	7.35	2.24(−51)	1.58(−51)	1.5	1.42	
$3d_{xy}(^1A_g)$	7.68	7.61, 7.62[f]	1.85(−50)	7.13(−50)	<1	0.26	0.3[f]
$3d_{xz}(^1A_g)$	7.79				<1		

[a]Transition energies relative to the ground state ($X\ ^1A_g$) energy of −155.01537 hartrees.
[b]Reference 24 if not otherwise specified.
[c]In units of $F^2\ s^{-1}$, where F is the photon flux in photons/cm^2 s.
[d]$\Omega<1$ for $A_g\leftrightarrow A_g$ transitions and 3/2 for $A_g\leftrightarrow B_g$ transitions. See ref. 16.
[e]Reference 9.
[f]Reference 12.

state requires the inclusion of σ correlation, while the Rydberg states can be well described at the full π-CI level. Therefore, the full π-CI results cannot be used for comparison purposes. These calculations have been performed as part of a process to select configurations for the all-valence CI calculations. A selection process is necessary because the number of configurations becomes quite large as we consider singles and doubles excitations in the σ space while simultaneously performing a full CI in the π space.

In the all-valence CI calculations we allowed all but the carbon 1*s*-like orbitals to participate in the treatment. Since the calculation is identical for all the states considered, we limit ourselves to the description of the general strategy used.

The π space, for each state, is the same considered in the π-CI calculations (14). To the σ occupied orbitals from the SCF calculations on each of the states considered we added the respective virtual σ orbitals associated to the C—C and C—H bonds of each state.

Starting from the respective HF or GVB type wave-functions, we considered the lists of configurations used in the π-CI calculations of the various states described above, and selected from the lists those configurations contributing an energy lowering[1] of 0.001 hartrees or more. From these configurations we allowed single excitations in the π space times single + double excitations in the σ space. To the new lists we added the respective lists of configurations used in the π-CI calculations. The final lists were then used to perform the all-valence CI calculations.

Using these all-valence CI wave-functions we computed transition energies and the two-photon transition rates from the expression (16)

$$[1]\quad \tau_{fi} = CF^2(h\nu)^2 \sum_f^{\alpha} \sum_i^{\beta} |\ M_{fi}^{\alpha\beta}|^2$$

considering up to six terms in the expansion. The intermediate virtual states were obtained at the same level of CI treatment. In eq. [1], C is a constant, F^2 the photoionization flux (in photons/cm^2 s) and α and β the degrees of degeneracy of the states $|f>$ and $|i>$, respectively, and M_{fi} is the second order matrix element

$$[2]\quad M_{fi} = \sum_k <f|\hat{e}\cdot r|k><k|\hat{e}\cdot r|i> / (E_{k'} - h\nu)$$

In eq. [2] the summation index runs over all the intermediate states of energy $E_{k'}$ relative to the initial state $|i>$.

We have considered the possibility that configurations which do not contribute appreciably to the variationally determined wave-function energies could still be important when computing the transition moment matrix elements. In order to verify that possibility we have considered calculations, for the $2\ ^1A_g$ and 3*s* states, which included all the configurations contributing a coefficient as small as 10^{-8} in the full π-CI wave-functions. The results of these calculations clearly indicated that the energy-based selection criterium described above could be safely used to compute the two-photon transition rates.

3. Results and discussion

Table 1 shows the results of the calculations at the all-valence CI level. Except for the $2\ ^1A_g$ state (for which σ correlation is very important) the results do not differ appreciably from the ones obtained at the full π-CI level. Table 2 contains information about the number of configurations used in the all-valence CI calculations.

The $3d_\pi$ (^1A_g) states were obtained as higher roots in the respective CI calculations, in order to project out the ground and the $2\ ^1A_g$ valence states. The first root corresponds to a dominantly closed shell valence state, the second root is also dominantly a valence state and exhibits the doubly-excited dominant configuration characteristic of the $2\ ^1A_g$ state.[2] Finally, the third and fourth roots are dominantly single excited diffuse configurations corresponding to the $3d_\pi$ Rydberg states. The designation of these states as $3d_{xz}$ and $3d_{xy}$ follows from the fact that the excited orbitals of the strongly dominant configurations exhibit amplitude plots analogous to the $3d_{xz}$ and $3d_{xy}$ atomic orbitals respectively.

The $3d_\sigma$ (^1B_g) state obtained as second root in the CI calculation for the 3*s* Rydberg state is very similar to the one

[1]We call "energy lowering" of a configuration the energy increase that would result from deleting the configuration from the CI list without readjusting the coefficients of the remaining configurations.

[2]The dominant configuration in the CI calculation of the $2\ ^1A_g$ state, using either localized or delocalized π orbitals (13, 14), exhibits four open shell orbitals with electrons singlet coupled. We have interpreted that (14*a*), using the exciton model, as being the result of a double excitation (one excitation per double bond). In the exciton notation that corresponds to a *TT* state.

Can. J. Chem. Downloaded from www.nrcresearchpress.com by 196.1.178.254 on 09/07/12
For personal use only.

TABLE 2. Number of spatial configurations used in the all-valence CI calculations

State	Number of configurations
$2\,^1A_g$	2176
$3d_{xy}$	3944
$3d_{xz}$	3944
$3s$	1972
$3d_z^2$	2142
$3d_{yz}$	2142

obtained as the second root in the CI calculation of the $3d$ state. On the other hand, the first root of the last calculation is a very poor description of the $3s$ Rydberg state, showing, as expected, that the shape of the $3s$ orbital cannot be well described by d-like functions, except in the core region.

Because of the complexity involved, we restricted the calculations of two-photon transition rates to the $3s$, one $3d_\sigma$ and one $3d_\pi$ Rydberg states, besides the $2\,^1A_g$ valence state. From Table 1 one should, in principle, observe at least six transitions in the MPI spectra in the region 6.2–7.8 eV.

Johnson (8) was the first to examine the MPI spectra of butadiene in the region 5.29–6.79 eV. He observed a single transition in this region, with origin at 6.21 eV, and assigned it tentatively to the $3s$ Rydberg state. Berg *et al.* (9) have also examined the MPI spectra in the region about 6.2 eV. They also detected one single transition, at 6.21 eV, with polarization ratio $\Omega = 1.4$–1.6. Vaida *et al.* (10) recorded the MPI and thermal lensing spectra of the molecule between 6.2 and 6.5 eV and concluded, from pressure broadening studies, that the transition should correspond to a Rydberg state. From the results shown in Table 1 we assign this transition to the $3s$ Rydberg state, because the excellent agreement between the theoretical and experimental results for the transition energy and Ω.

Mallard *et al.* (11) have examined the MPI spectra of butadiene in the region 7.5–9.2 eV. They observed a series of transitions that they assigned to the various members ($4s$–$12s$) of the s (B_g) Rydberg series, converging to the first ionization potential (IP) of the molecule. More recently, Taylor *et al.* (12), based on polarization studies (16), reassigned these transitions. The first one, at 7.62 eV, was assigned to the $3d_\pi$ (^1A_g) state (consistent with $\Omega < 1$) and the others to higher members of this series. Polarization studies conducted for the observed peaks indicated that they should all correspond to states of A_g symmetry. From the results in Table 1, one sees that the only Rydberg states, predicted by the calculations, to occur in this region, are the $3d_\pi$ (^1A_g) states. The first members of the two series are very close in energy and cannot be distinguished by polarization studies since they have the same symmetry. As the principal quantum number increases, the two series become degenerated what definitely prevents the identification of the different components. Once more, there is an excellent agreement between the theoretical and experimental results. Thus, we assigned the observed transitions to the members of the d_π series converging to the first IP.

None of the experimental studies covered the region from 7.0 eV to 7.4 eV, where the $2\,^1A_g$ valence and the $3d_\sigma$ Rydberg states are predicted to occur.

From Table 1, the two-photon intensities of the observed transitions to the $3s$ and $3d_\pi$ states, relative to the intensity of the $2\,^1A_g$ transition, indicate that the last state should be observable once an experiment conducted at the proper energy is performed. Nevertheless, because the MPI spectra involve a two-photon resonance three-photon ionization process, it is possible that the resonant two-photon $2\,^1A_g$ valence state would not leave enough to enable subsequent ionization. Therefore, it is possible that in spite of its intensity the $2\,^1A_g$ state may not be detected by MPI spectroscopy. This state has been observed in the electron impact (EI) spectra of the molecule (5, 6).

On the other hand, one expects the $3d_\sigma$ states to have life-times comparable to the other observed by Rydberg states. However, if we compare the relative intensities, one sees that the two-photon intensities to the ^1A_g ($3d_{xy}$) state relative to the ^1B_g ($3d_{yz}$) state are 8.26 and 45.12 for circularly and linearly polarized light, respectively. Thus, the ^1B_g states should be much more difficult to detect. We encountered a similar situation in the MPI spectra of the 1,3,5-*trans*-hexatriene molecule, where the in-plane $3p_\sigma$ Rydberg states are not observed but the $3p_\pi$ is clearly identified, in agreement with the theoretical calculations (23). The $3d_{yz}$ state has been observed in the EI spectra of the butadiene molecule (5).

Finally it is interesting to notice that while various members of the nd_π series have been observed (12), only the first one of the ns series has been detected. Based on the quantum defect for the $3s$ state, it is easy to show that the higher members of this series should lie very close in energy to the nd_π states. However, the polarization studies (12) clearly indicate that none of the other peaks observed in the MPI spectrum correspond to members of the s series. The reason for not observing the higher members of this series could be that either their lifetimes or their transition rates drop very rapidly with the quantum number. The last possibility goes contrary to the common belief that Rydberg transitions with precursors (ns) should be more intense than the ones without precursors (nd).

4. Conclusions

The results of the calculations indicate that the multiphoton (two-photon resonance three-photon ionization) spectrum of butadiene, below the first IP, consists of a series of Rydberg transitions (ns, nd_σ, nd_π) and possibly of a valence $\pi \rightarrow \pi^*$ ($2\,^1A_g$) state. The $3d_\sigma$ states should be difficult to observe because of their small two-photon transition rates whereas the two-photon resonant $2\,^1A_g$ valence state may be too short-lived to be detected in the MPI experiment. The calculations are in good agreement with the available experimental results.

5. Acknowledgment

The author acknowledges Conselho Nacional de Desenvolvimento Cientifico e Tecnologico (CNPq-Brasil) for financial support.

1. B. HONIG and T. EBREY. Ann. Rev. Biophys. Bioeng. **3**, 151 (1974).
2. D. OESTERHELT. Agnew. Chem. Intern. Ed. **15**, 17 (1976).
3. B. KOHLER, B. HUDSON, and K. SCHULTEN. *In* Excited states. Vol. 6. *Edited by* E. Lim. Academic Press, New York. 1983. p. 11 and references therein.
4. R. MCDIARMID. Chem. Phys. Lett. **34**, 130 (1975); **64**, 514 (1976).
5. O. A. MOSHER, W. M. FLICKER, and A. KUPPERMANN. J. Chem. Phys. **59**, 6502 (1973); W. M. FLICKER, O. A. MOSHER, and A. KUPPERMANN. Chem. Phys. **30**, 307 (1978).
6. J. P. DOERING and R. MCDIARMID. J. Chem. Phys. **73**, 3617 (1980).

Can. J. Chem. Downloaded from www.nrcresearchpress.com by 196.1.178.254 on 09/07/12
For personal use only.

7. R. McDiarmid and J. P. Doering. J. Chem. Phys. **73**, 4192 (1980).
8. P. M. Johnson. J. Chem. Phys. **64**, 4638 (1976).
9. J. O. Berg, D. H. Parker, and M. A. El-Sayed. J. Chem. Phys. **68**, 5661 (1978).
10. V. Vaida, R. E. Turner, J. L. Casey, and S. D. Colson. Chem. Phys. Lett. **54**, 25 (1978).
11. W. G. Mallard, J. H. Miller, and K. C. Smyth. J. Chem. Phys. **79**, 5900 (1983).
12. P. H. Taylor, W. G. Mallard, and K. C. Smyth. J. Chem. Phys. **84**, 1053 (1986).
13. R. J. Buenker, S. Shih, and S. Peyerimhoff. Chem. Phys. Lett. **44**, 385 (1976).
14. M. A. C. Nascimento and W. A. Goddard III. Chem. Phys. **36**, 147 (1979); **53**, 251 (1980).
15. M. Aoyagi, Y. Osamura, and S. Iwata. J. Chem. Phys. **83**, 1140 (1985).
16. M. A. C. Nascimento. Chem. Phys. **74**, 51 (1983).
17. T. H. Dunning and P. J. Hay. *In* Modern theoretical chemistry. Vol. 3. *Edited by* H. F. Schaefer. Plenum Press, New York. 1977. p. 1.
18. S. Huzinaga. J. Chem. Phys. **42**, 1293 (1965).
19. M. Traetteberg. Acta Chem. Scand. **22**, 628 (1968).
20. F. Brobowicz and W. A. Goddard III. *In* Modern theoretical chemistry. Vol. 3. *Edited by* H. F. Scahefer. Plenum Press, New York. 1977. p. 79.
21. W. J. Hunt and W. A. Goddard III. Chem. Phys. Lett. **3**, 414 (1969).
22. F. Bobrowicz. Ph.D. Thesis, California Institute of Technology. 1974.
23. M. A. C. Nascimento. Can. J. Chem. **63**, 1349 (1985).
24. A. Sabljic and R. McDiarmid. J. Chem. Phys. **82**, 2559 (1985).

Can. J. Chem. Downloaded from www.nrcresearchpress.com by 196.1.178.254 on 09/07/12
For personal use only.

Substituent effects on the rate of carbene formation in the pyrolysis of indenyl diazo compounds

S. KAPUR, N. C. MATHUR, K. MCMANUS, A. L. PINCOCK, AND J. A. PINCOCK[1]
Department of Chemistry, Dalhousie University, Halifax, N.S., Canada B3H 4J3

Received August 27, 1987[2]

S. KAPUR, N. C. MATHUR, K. MCMANUS, A. L. PINCOCK, and J. A. PINCOCK. Can. J. Chem. **66**, 2888 (1988).

Rate constants for the pyrolysis of the indenyl diazo compounds, **5***a*–**5***e*, in methanol have been determined and correlated with σ^+, giving a $\rho^+ = -0.76$. The product of this pyrolysis reaction is the methyl ether resulting from trapping at the carbenic centre. The mechanism proposed for this process involves rate-determining unimolecular loss of nitrogen by the allowed nonlinear pathway to form the singlet σ^2 carbene. Evidence presented implies that this singlet state is more stable than the p^2 state despite the difference in aromatic stabilization of the two.

S. KAPUR, N. C. MATHUR, K. MCMANUS, A. L. PINCOCK et J. A. PINCOCK. Can. J. Chem. **66**, 2888 (1988).

Opérant dans le méthanol, on a déterminé les constantes de vitesse pour la pyrolyse des composés diazoindényles, **5***a*–**5***e*, et on a établi une corrélation avec σ^+ conduisant à une valeur de ρ^+ de −0,76. Le produit de cette réaction de pyrolyse est l'éther méthylique provenant d'un piégeage par le centre carbénique. L'étape déterminante du mécanisme proposé pour ce processus implique une perte unimoléculaire d'azote par la voie non-linéaire permise et elle conduit à la formation d'un carbène σ^2 singulet. Des données qui sont présentées impliquent que cet état singulet est plus stable que l'état p^2 malgré la différence de stabilisation aromatique des deux.

[Traduit par la revue]

Introduction

We have recently been studying the thermal chemistry of vinyldiazo compounds as a simple and direct way to learn about the electronic structure of the carbene generated, eq. [1] (1–3).

[1] 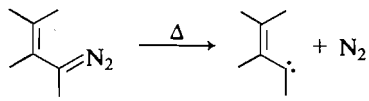

Vinyl carbenes, as singlets and in planar geometry, have three low lying states: **1** (2π or σ^2) (4–6), **2** (4π or p^2), and **3** (3π or p). As well, there is a triplet state corresponding to **3** that

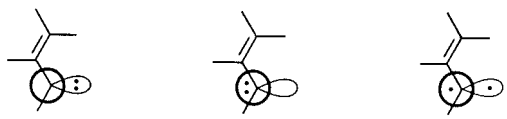

1 **2** **3**

is normally the most stable of all four electronic configurations. Nevertheless, in any given chemical reaction, the triplet state may not be the first formed of the four possibilities. For instance, in the thermal decomposition of vinyldiazo compounds the rate-determining transition state for loss of nitrogen will be energetically a reflection of the structure of the developing singlet state. An examination of substituent effects on these reactions has been particularly revealing.

Rate constants for the pyrolysis of ring substituted diphenyldiazomethanes gave a parabolic-type Hammett plot where all substituted compounds react faster than the unsubstituted case (7, 8). A set of phenyldiazobutenes showed the same effect (2). These results were interpreted in terms of the rate-determining transition state resembling the carbene **1**, which is zwitterionic in the sense that the σ-system is electron rich and the π-system electron deficient. Rotation of the benzene ring at the carbene carbon allows conjugation with either the σ- or π-system. Thus, electron-donating substituents stabilize the transition state by conjugation with the electron deficient σ-system and electron-withdrawing ones with the electron rich π-system. These studies do not rule out the possibility that the transition state resembles carbene **2** since the same arguments can be applied.

Loss of nitrogen from a diazo carbon is analogous to the cheletropic reactions described by Woodward and Hoffmann (9) in which there are two geometrically different modes. The linear mode leads directly to the carbene **2** (3) and, since **2** is not the ground state singlet, this pathway can be described as thermally forbidden. If the restriction on a linear dissociation geometry is removed then the starting material can proceed directly by a nonplanar transition state to the carbene **1** and this pathway is thermally allowed. A test of these two pathways is possible and proves that the nonlinear pathway is preferred (3). Thus pyrolysis of the set of ring substituted compounds, **4**, showed a linear Hammett plot with a $\rho^+ = -0.84$. The substituents can only conjugate with the π-system at the carbene center because of restricted rotation in the rigid ring system. The negative ρ value and correlation with σ^+ confirms the formation of carbene **1**.

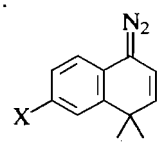

4

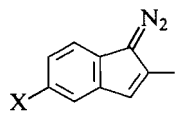

5*a* (X = CH_3O)
5*b* (X = CH_3)
5*c* (X = H)
5*d* (X = Br)
5*e* (X = NO_2)

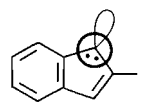

6

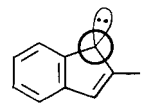

7

We were interested in examining the magnitude of the preference for this nonlinear pathway and here report on the thermal kinetics for the loss of nitrogen from a series of 1-diazoindenes, **5***a*–**5***e*. This set of diazo compounds was chosen with the idea that the transition state for carbene formation might reflect the generation of **6** (analogous to **2**) rather than **7** (analogous to **1**) and thus the linear pathway would

[1]Author to whom correspondence may be addressed.
[2]Revision received July 6, 1988.

Can. J. Chem. Downloaded from www.nrcresearchpress.com by 196.1.178.254 on 09/07/12
For personal use only.

Can. J. Chem. Downloaded from www.nrcresearchpress.com by 196.1.178.254 on 09/07/12
For personal use only.

be preferred. This suggestion is based on the fact that **6** has aromatic stabilization because it is a 10π-electron system whereas **7** has only 8π electrons.

Results and discussion

Synthesis of diazoindenes

The diazo compounds were prepared by pyrolysis of the corresponding sodium salts of the tosylhydrazones, **8***a*–**8***e*, in refluxing hexane, eq. [2]. This proved to be easier than

[2] 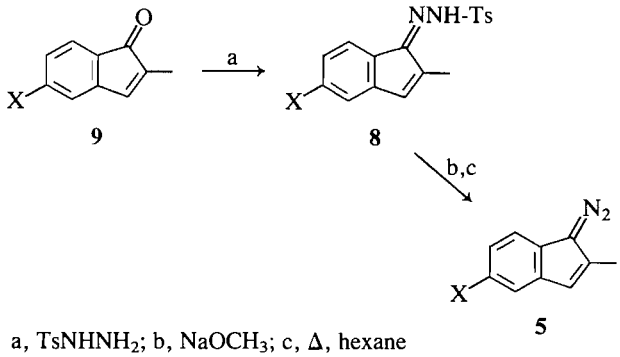

a, $TsNHNH_2$; b, $NaOCH_3$; c, Δ, hexane

the previous cases examined (1–3) because the diazoindenes formed are somewhat more stable thermally and decompose only very slowly at this temperature. The tosylhydrazones were prepared from the corresponding 2-methylindenones, **9***a*–**9***e*, eq. [2]. The 2-methyl derivatives were chosen in preference to the unsubstituted indenones because of the known tendency towards polymerization of unsubstituted indenones (10, 11) and because a convenient synthetic route to **9***a*–**9***d* is available (11). Thus, **9***c* is known and **9***a*, **9***b*, and **9***d* were prepared by the same method, eq. [3]. The nitro compound, **9***e*, could not

[3] 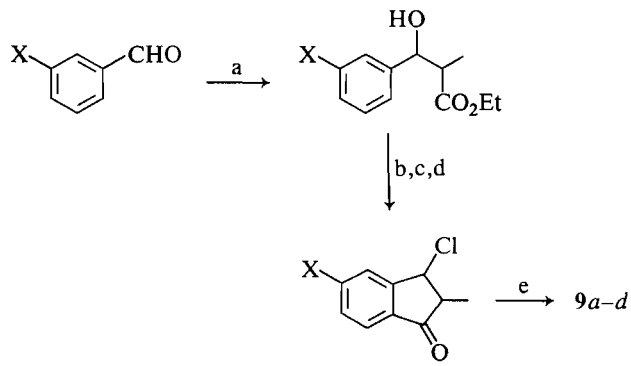

a, $Zn/CH_3CHBrCO_2Et$; b, NaOH; c, $SOCl_2$; d, $AlCl_3$; e, C_5H_5N

[4] 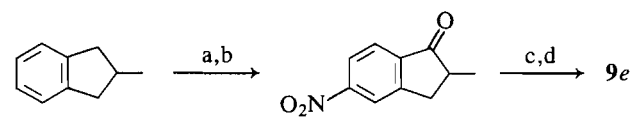

10

a, $Cu(NO_3)_2$; b, CrO_3; c, Br_2; d, $LiBr/LiCO_3/DMF$

be prepared this way because Friedel–Crafts cyclizations are unsuccessful for strongly deactivated rings. However, nitration (12) and oxidation of 2-methylindane gave a mixture of nitroindanones from which the 5-nitro isomer **10** could be obtained in low yield after careful chromatography, eq. [4]. The structure of this isomer was confirmed by nmr spectral comparison with the closely related indanones that do not have the methyl group at C-2. Thus, even at 60 MHz, **10** could be seen to have an identical ^1H nmr spectrum in the aromatic region to the known 5-methylindanone (13) and quite different from that of the 6-methyl isomer (14). Bromination followed by dehydrobromination then gave **9***e*. Details of the syntheses are given in the experimental section.

Products of the thermal decomposition of diazoindene, 5c (X = H)

Samples from the pyrolysis of **5***c* (X = H) at 110°C in 5% pyridine in methanol were analyzed by gc/ms. These samples were identical to those used for infinity values in kinetic runs (see below). The major product was the methyl ether, **11**, as expected based on the usual trapping of the carbene by methanol (1–3) as shown in eq. [5]. Isolation of this ether from these very

[5] 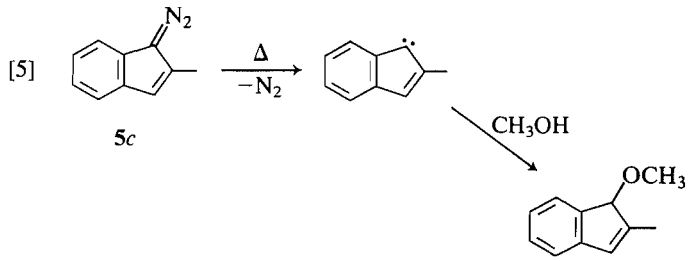

11

dilute samples was impossible but its structure was confirmed by independent synthesis as in eq. [6].

[6] 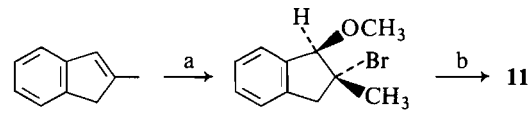

12

a, Br_2/CH_3OH; b, $LiBr/LiCO_3/DMF$

Thus, bromination of 2-methylindene in methanol gave the dibromide and the bromoether, **12**, both as single stereoisomers that are probably (although not confirmed) the ones resulting from *anti* addition. Bromination of indene itself in methanol gives exclusively *anti* addition (15). Dehydrobromination then gave **11**, which had a retention time and mass spectrum identical to the kinetic sample. Details are given in the experimental section.

In addition to the ether, **11**, a minor component observable in the gc/ms scans of samples from the pyrolysis of **5***c* was a compound of molecular weight 207 corresponding to the carbene plus pyridine. That pyridine is a good trap for carbenes has been suggested from recent flash photolysis experiments where an ylid was formed by reaction of naphthylmethyl carbene with the pyridine nitrogen (16). If sodium methoxide (1.8×10^{-2} M) was used as the base instead of pyridine, the only observable product was the ether, **11**. The rate constant of decomposition of **5***c* (see below) was very similar for these two conditions: $7.8 \pm 0.3\ s^{-1}$ in 5% pyridine/methanol and $6.5 \pm 0.3\ s^{-1}$ with 1.8×10^{-2} M $NaOCH_3$ in methanol.

Rates of the thermal decomposition of the diazoindenes

The rates of thermal decomposition of **5***a*–**5***e* in 5% pyridine/methanol were monitored spectrophotometrically as described in the experimental section. The pyridine was added to the methanol to quench, as described previously (1), any possible acid catalysis. The reactions all exhibited good first-order kinetics and plots of $\log(A - A_\infty)$ versus time gave the following rate constants and mean deviations ($s^{-1} \times 10^5$) at 110°C: **5***a*, 22.9 ± 0.3; **5***b*, 9.8 ± 0.2; **5***c*, 7.8 ± 0.3; **5***d*, 5.12 ± 0.06; **5***e*, 1.39 ± 0.05.

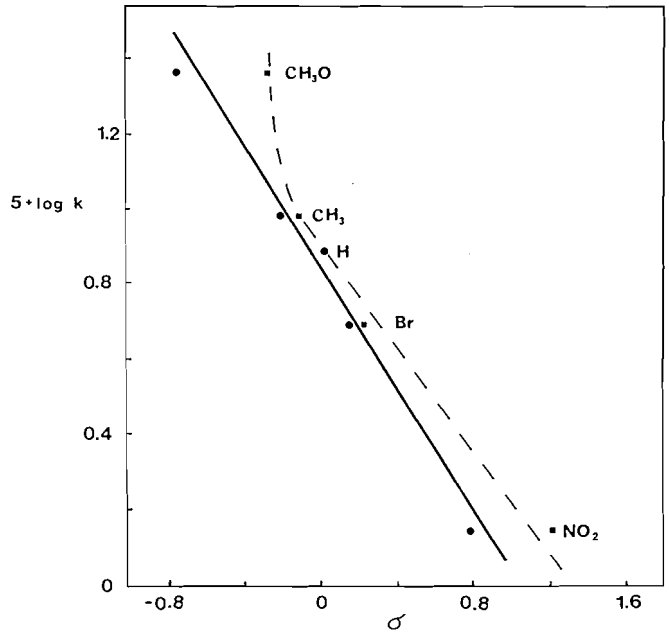

FIG. 1. Hammett plots for the rate constants for the thermal decomposition of the diazoindenes, **5***a*–**5***e*, in methanol at 110°C. ● are for σ^+ values and ■ for σ^-.

In this and our previous studies, we have assumed that rate constants such as these are measuring the rate of unimolecular decomposition of the diazo compound to the singlet carbene and are not complicated by some bimolecular component from the solvent system that would not be detected kinetically. The product information above supports this assumption since the rate of decomposition of the diazo compound, **5***c*, is similar with either pyridine or sodium methoxide as the base, even though the product composition changes. Moreover, measurement of the rate constant of decomposition as a function of temperature for **5***c* (104°C, 4.18×10^{-5} s^{-1}; 116°C, 13.5×10^{-5} s^{-1}; 123°C, 31.1×10^{-5} s^{-1}) gave the following activation parameters: $\Delta H^{\ddagger} = 30 \pm 1$ kcal/mol and $\Delta S^{\ddagger} = 1 \pm 4$ eu. We have also measured the activation parameters for the decomposition in 6% triethylamine/methanol for the diazotetralin, **4** (X = H), described previously (3): $\Delta H^{\ddagger} = 26 \pm 1$ kcal/mol and $\Delta S^{\ddagger} = 3 \pm 2$ eu. The low entropy of activation values are similar to all those reported previously for unimolecular diazo compound decompositions (1, 2, 17, 18) and point out that these decomposition rates are controlled almost entirely by enthalpy effects.

As expected for a process where a dipolar but neutral starting material like **5** proceeds to a carbene (also neutral), substituent effects are small. The total rate spread in going from **5***a* (X = CH_3O) to **5***e* (X = NO_2) is only a factor of 16. Analysis of these substituent effects may therefore be difficult although there is no doubt that electron-donating substituents favor the reaction.

Hammett plots for these kinetic results versus σ^+ and σ^-, the two substituent constants that allow direct resonance interaction with the reaction site, are shown in Fig. 1. The σ^+ plot is clearly better, giving a $\rho^+ = -0.76 \pm 0.06$ ($r = 0.990$). The σ^- plot gives a similar $\rho = -0.70 \pm 0.12$ ($r = 0.955$) but a much lower correlation coefficient. The line on the graph for σ^- is not the least-squares line but rather a line that emphasizes the deviation of the point for **5***a* (X = CH_3O).

The main objective of this work was to analyze substituent effects for the rate-determining transition state and to compare

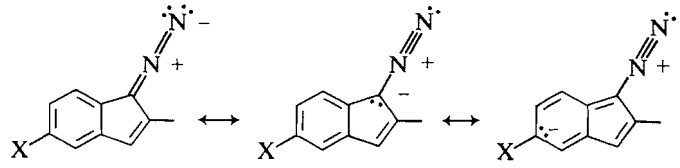

the results for these indenyl compounds with those for the related tetralin derivatives, **4**, which were correlated with a $\rho^+ = -0.84$. The two are remarkably similar and suggest that the two sets of compounds have very similar mechanisms for thermal loss of nitrogen.

In the analysis of systems of this type there has been concern that ground-state substituent effects play an important role in the linear free energy correlations and that these effects might be as important as, or more important than, the transition state effects (2, 3, 7, 8). An examination of important resonance contributors that describe the charge distribution in these indenyl diazo compounds, **5**, shows why this is a concern. Obviously, electron-withdrawing groups should stabilize **5**. This should make **5***e* (X = NO_2) the least reactive, as observed. This ground-state stabilizing effect should be correlated with σ^-; however, in both this and the previous rigid system studied (3) the rate data correlate better with σ^+.

One way of examining the importance of ground-state resonance delocalization of this type is by measurement of the ^{13}C chemical shift of the diazo carbon (8). Although we have been unable to prepare enough material to do this for the very weak signal observed for the quaternary carbon of the set of indenyldiazo compounds, **5**, we have done so for the set of diazo tetralins, **4**. Thus ^{13}C chemical shifts (8) in CD_3CN relative to TMS for the diazo carbons in **4** are as follows: X = CH_3O, 61.4; X = CH_3, 61.7; X = H, 61.9; X = Br, 62.2; X = NO_2, 64.3 ppm. They obviously follow the expected deshielding order and, in fact, correlate with σ^-, giving $\rho^- = 1.85$ ($r = 0.997$). A very similar correlation has been observed for substituted diphenyldiazomethanes (8). The fact that ground-state delocalization is well accounted for by such a ρ^- correlation and that the rate constants for thermal decomposition are not fitted well by σ^- increases our confidence that analysis of the kinetic results for thermal decomposition is a useful way of assessing the transition state structure.

The σ^+ correlation for these thermal reactions is then best rationalized by increasing positive charge in the π orbital at the diazo carbon, and therefore the transition state is a reflection of the indenyl carbene being initially generated in the σ^2 configuration, **7**. Therefore, either the aromatic p^2 configuration, **6**, is less stable than the σ^2 one, **7**, or the driving force for nonlinear loss of nitrogen is large. Note that this discussion is only concerned with the rate-determining transition state for these pyrolysis reactions. The ground state of indenyl carbene is a σp triplet (19) but it can be trapped as a singlet using high concentrations of alkenes (20).

An estimate of the energy required to convert **6** and **7** can be made from some related ground-state chemistry. The destabilizing antiaromatic effect of having a positive charge in an indenyl ring system can be approximated by the solvolysis of **13** and **14**, which have estimated relative rates of 10^5 in favor of **13** forming the more stable cation (21). This corresponds to a free energy difference at 25°C of 6.8 kcal/mol. In contrast, the energetic advantage of having a negative charge in an indenyl ring system can be evaluated from the pK value (= 20.1) of indene, resulting in an estimated aromatic stabilization energy of 20 kcal/mol (22). Thus, approximately 27 kcal/mol of

Can. J. Chem. Downloaded from www.nrcresearchpress.com by 196.1.178.254 on 09/07/12
For personal use only.

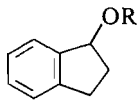

13

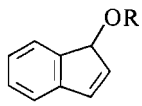

14

π-energy are lost as a pair of electrons is removed from the π-system.

Opposed to this loss of energy as **6** (p^2) is converted to **7** (σ^2) is the gain in energy resulting from putting that pair of electrons in the more stable orbital. An estimate of this value is available from MO calculations on methylene itself (23). The vertical excitation energy from the $1'A_1$ to the $2'A_1$ state (analogous to excitation from **7** to **6**) is dependent on the H—C—H angle but increases from about 55 kcal/mol at 130°C, 72 kcal/mol at 120°C, to 105 kcal/mol at 100°C. This suggests that the energetic advantage of having the electron pair in the more stable σ orbital overcomes any disadvantage resulting from aromaticity factors. Supporting this estimate are calculations, including CI, on cyclopentadienylidene, which indicate that the 4π electronic configuration at a geometry with two localized π-bonds is 33 kcal/mol more stable than the 6π configuration at a geometry of an equilaterial pentagon (24). From these considerations, the apparent conclusion is that the ground-state singlet of indenyl carbene has the σ^2 configuration, **7**.

The conclusion as to the mechanism of the thermal decomposition of the indenyldiazo compounds **5** in methanol is that the reaction proceeds by rate-determining unimolecular loss of nitrogen by the allowed nonlinear pathway to form the carbene **7**. Substituent effects reflect the increased positive charge in the π-system during the conversion from starting material to transition state. The carbene is then trapped in a rapid second step to yield the methyl ether, **11**.

Experimental

The 60-MHz nmr spectra were recorded on either a Varian T-60 or EM-360 spectrometer using TMS as the internal standard. The 360-MHz nmr spectra were recorded on a Nicolet spectrometer. The ir spectra were recorded on a Perkin–Elmer 283B spectrometer using the 1620 cm^{-1} polystyrene absorption as a calibration. Mass spectra (70 eV) were recorded on a Dupont CEC-21-104 mass spectrometer and are reported as *m/e* (relative intensity). Except for the molecular ion peak, only peaks greater in intensity than 10% of the base peak are reported. The uv spectra were recorded on a Varian Carey 219 spectrometer. Melting points were taken on a Fisher–John apparatus and are uncorrected.

Combustion analyses were performed by Canadian Microanalytical Service Ltd., New Westminster, BC.

Preparation of 2-methylindenones, **9**a, **9**b, **9**c, *and* **9**d was by the method of Floyd and Allen (11): **9***a* (X = CH_3O), 25% based on 3-methoxybenzaldehyde; **9***b* (X = CH_3), 6% based on 3-methylbenzaldehyde; **9***c* (X = H), 18% based on benzaldehyde, mp 41–43°C (lit. (11) mp 45–47°C); **9***d* (X = Br), 28% based on 3-bromobenzaldehyde.

Preparation of 5-nitro-2-methylindenone, **9**e

2-Methylindanone was prepared as described previously (12) in 55% yield based on propiophenone, bp 91–92°C at 2.5 Torr (lit. (12) bp 65–66°C at 0.6 Torr) (1 Torr = 133.3 Pa). *2-Methylindane* was prepared by Clemmenson reduction of the ketone. To 67 g of amalgamated zinc in 310 mL of concentrated hydrochloric acid was added 35.0 g (0.24 mol) of 2-methylindanone and the mixture refluxed for 18 h. The mixture was then filtered and the filtrate extracted with ether. The ether layer was washed with water and saturated $NaHCO_3$ solution and then dried ($MgSO_4$), evaporated, and distilled to give 29 g (0.22 mol, 91%) of 2-methylindane, bp 200–202°C (lit. (12) bp 66–68° at 11 Torr).

2-Methyl-5-nitroindane and 2-methyl-4-nitroindane (12): A solution of 5.7 g (43 mmol) of 2-methylindane in 350 mL of acetic anhydride was cooled to 0°C and 7.5 g of $Cu(NO_3)_2 \cdot 3H_2O$ was added. The mixture was stirred for 1 h at 0°C and then for 3 h at ambient temperature. The mixture was poured into 500 mL of ice water and left stirring overnight. The mixture was then extracted with chloroform and the extract washed with water and then saturated $NaHCO_3$, dried over $MgSO_4$, and concentrated to give 6.9 g of crude nitroindanes. These indanes could be separated in low yield by flash chromatography using benzene eluant and silica gel. The faster eluting component (R_f 0.20) was assigned as the 4-nitro isomer and the second (R_f 0.16) as the 5-nitro isomer based on the observation of one lowfield aromatic hydrogen for the 4-nitro (δ 7.8–8.1) and two (δ 7.8–8.0) for the 5-nitro case. Because of the difficulty in this separation the mixture was oxidized before separation.

2-Methyl-5-nitroindanone, ***10***: To a solution of 0.93 g (5.3 mmol) of the mixed nitroindanes in 8.4 mL of acetic acid and 1.0 mL of water was added dropwise a solution of 2.5 g of chromium trioxide in 6.7 mL of acetic acid. The mixture was stirred at room temperature for 60 h, and was then poured into water and extracted with chloroform. The extract was washed with water and saturated $NaHCO_3$, dried over $MgSO_4$, and concentrated to give 1.3 g of crude nitroindanones and starting nitroindanes. Material of this type was chromatographed on a gravity column using silica gel and dichloromethane to separate the nitroindanones (795 mg) from the rest. This material could be recrystallized from methanol to give 195 mg (1.03 mmol, 19%) of pure 2-methyl-5-nitroindanone, mp 104–105°C; nmr ($CDCl_3$), δ: 1.4 (3H, d, J = 8 Hz), 2.7–3.2 (2H, m), 3.3–3.9 (1H, dd, J = 18 Hz, 8 Hz), 7.9 (1H, d, J = 8 Hz), 8.15–8.45 (2H, m).

2-Bromo-2-methyl-5-nitroindanone: To a solution of 75 mg (0.43 mmol) of the nitroindanone in 1 mL of CCl_4 was added 0.062 mL of bromine in 1 mL of CCl_4. This reaction can be monitored by titration to the faint end-point red colour of bromine. Evaporation of the CCl_4 gave 105 mg (0.41 mmol) of the bromoketone that was pure enough to use in the next step directly; nmr ($CDCl_3$), δ: 2.03 (3H, s), 3.4–4.3 (2H, dd, J = 19 Hz), 7.9–8.5 (3H, m).

2-Methyl-5-nitroindenone, **9**e: A mixture of 95 mg of LiBr, 82 mg of $LiCO_3$, and 160 mg (0.62 mmol) of the bromoindanone in 1.4 mL of DMF was heated to 130–140°C under a nitrogen atmosphere for 3 h. The mixture was then poured into 13 mL of water and extracted with 2 × 6 mL of ether. The extract was washed with 2 × 10 mL of water, dried over $MgSO_4$, and concentrated to give 46 mg (0.27 mmol, 43%) of **9***e*, which was used directly for the preparation of the tosylhydrazone; nmr ($CDCl_3$), δ: 1.97 (3H, s), 7.33 (1H, s), 7.47 (1H, d, J = 8 Hz), 7.82 (1H, s), 8.13 (1H, d, J = 8 Hz).

5-Nitroindanone: This compound was prepared by chromic acid oxidation of 5-nitroindane as described in the literature (13), mp 133–134°C (lit. (13) mp 131–133°C); nmr (360 MHz, $CDCl_3$), δ: 2.84 (m, 2H), 3.28 (m, 2H), 7.90 (d plus extensive long-range coupling, J = 8.4 Hz, H7), 8.23 (d plus extensive long-range coupling, J = 8.4 Hz, H6), 8.35 (complex multiplet H4).

6-Nitroindanone: This compound was prepared by nitration of indanone as described in the literature (14), mp 72–74°C (lit. (14) mp 74°C); nmr (360 MHz, $CDCl_3$), δ: 2.84 (m, 2H), 3.28 (m, 2H), 7.66 (dd, J = 8.4 Hz, 0.6 Hz, H4), 8.45 (dd, J = 8.4 Hz, 2.3 Hz, H5), 8.58 (dd, J = 2.3 Hz, 0.6 Hz, H7).

Preparation of tosylhydrazones **8**a, **8**b, **8**c, **8**d, *and* **8**e

The indenones were all relatively unstable (polymerization?) and were best converted directly to the tosylhydrazones. The procedure was the same for each and an example is given for **8***c*. To 1.10 g (8.2 mmol) of the indenone and 1.51 g of tosylhydrazine in 40 mL of methanol were added 5 drops of concentrated hydrochloric acid. The mixture was left to stand at 5°C overnight and the precipitate (1.4 g, 6.9 mmol,

Can. J. Chem. Downloaded from www.nrcresearchpress.com by 196.1.178.254 on 09/07/12
For personal use only.

84%) collected. Pure samples could be obtained by recrystallization from methanol.

8*a* (X = CH_3O); mp 155–156°C; ir ($CHCl_3$): 3700, 1625, 1603, 1468, 1340, 1163, 1108, 1090, 860 cm^{-1}; uv (CH_3OH): 339 (12 300), 281 (10 400) nm; nmr (360 MHz, $CDCl_3$), δ: 1.98 (3H, s), 2.43 (3H, s), 3.81 (3H, s), 6.46 (H3, s), 6.55 (H6, dd, J = 8.2 Hz, 0.9 Hz), 6.61 (H4, d, J = 0.9 Hz), 7.32 (2H, d, J = 8 Hz), 7.50 (H7, J = 8.1 Hz), 7.91 (2H, d, J = 8 Hz), 8.10 (NH, s); mass spectrum: 342 (2), 314 (12), 311 (14), 159 (16), 188 (11), 156 (21), 138 (13), 114 (14), 92 (17), 91 (30). *Anal.* calcd. for $C_{18}H_{18}N_2O_3S$: C 63.14, H 5.30, N 8.18; found: C 63.12, H 5.26, N 8.14.

8*b* (X = CH_3); mp 169.5–170°C; ir ($CHCl_3$): 3700, 1622, 1605, 1382, 1333, 1165, 1092, 850 cm^{-1}; uv (CH_3OH): 329 (13 700), 293 (10 900) nm; nmr (360 MHz, $CDCl_3$), δ: 1.98 (3H, s), 2.31 (3H, s), 2.42 (3H, s), 6.48 (H3, s), 6.86 (H4, s), 6.90 (H6, d, J = 7 Hz), 7.32 (2H, d, J = 8 Hz), 7.44 (H7, d, J = 7 Hz), 7.91 (2H, d, J = 8 Hz), 8.25 (NH, s); mass spectrum: 326 (24), 171 (74), 170 (33), 156 (22), 143 (23), 142 (100), 141 (66), 139 (15), 128 (12), 115 (26), 92 (14), 91 (31). *Anal.* calcd. for $C_{18}H_{18}N_2O_2S$: C 66.24, H 5.56, N 8.58; found: C 66.08, H 5.55, N 8.59.

8*c* (X = H); mp 152–153°C; ir ($CHCl_3$): 3700, 1602, 1460, 1380, 1360, 1348, 1165, 907, 865 cm^{-1}; uv (CH_3OH): 345 (2540), 321 (3110), 286 (2160) nm; nmr (360 MHz, $CDCl_3$), δ: 2.00 (3H, s), 2.43 (3H, s), 6.54 (H3, s), 7.05 (H4, d, J = 7.1 Hz), 7.12 (1H, t), 7.23 (1H, t), 7.33 (2H, d, J = 8 Hz), 7.56 (H7, d, J = 7 Hz), 7.92 (2H, d, J = 8 Hz), 8.31 (NH, s); mass spectrum: 312 (17), 157 (25), 156 (41), 129 (46), 128 (100), 127 (18), 102 (12), 92 (13), 91 (25). *Anal.* calcd. for $C_{17}H_{16}N_2O_2S$: C 65.36, H 5.16, N 8.97; found: C 65.45, H 5.10, N 8.97.

8*d* (X = Br); mp 170–171°C; ir ($CHCl_3$): 3700, 1603, 1451, 1390, 1360, 1330, 1167, 1071, 887, 850 cm^{-1}; uv (CH_3OH): 366 (14 420), 333 (17 800), 297 (13 200) nm; nmr (360 MHz, $CDCl_3$), δ: 2.00 (3H, s), 2.43 (3H, s), 6.49 (H3, s), 7.19 (H4, s), 7.25 (H6, d, J = 8.1 Hz), 7.33 (2H, d, J = 8.3 Hz), 7.43 (H7, d, J = 8.1 Hz), 7.91 (2H, d, J = 8.3 Hz), 8.30 (NH, s); mass spectrum: 392 (6), 390 (6), 236 (28), 235 (10), 234 (28), 209 (75), 208 (81), 207 (75), 206 (73), 156 (32), 139 (28), 128 (40), 127 (100), 126 (23), 115 (15), 107 (11), 101 (11), 92 (30), 91 (59). *Anal.* calcd. for $C_{17}H_{15}BrN_2O_2S$: C 52.18, H 3.86, N 7.16; found: C 52.16, H 3.84, N 7.17.

8*e* (X = NO_2); mp 168–169°C; uv (CH_3OH): 337 (16 400), 298 (20 000) nm; nmr (360 MHz, $CDCl_3$), δ: 2.06 (3H, s), 2.44 (3H, s), 6.65 (H3, s), 7.36 (2H, d, J = 8.0 Hz), 7.71 (H7, d, J = 8.2 Hz), 7.87 (H4, d, J = 2.0 Hz), 7.93 (2H, d, J = 8.0 Hz), 8.04 (H6, dd, J = 8.2 and 2.0 Hz), 8.52 (NH, s); mass spectrum: 278 (26), 201 (59), 190 (18), 174 (27), 173 (100), 156 (44), 155 (28), 139 (65), 127 (86), 126 (33), 123 (17), 115 (36), 107 (14), 108 (12), 101 (16), 92 (39), 91 (98). *Anal.* calcd. for $C_{17}H_{15}O_4SN_3$: C 57.13, H 4.23; found: C 57.56, H 4.43.

2-Bromo-1-methoxy-2-methylindane, ***12***

To 0.5 g (3.9 mmol) of 2-methylindene (12) in 10 mL of methanol was added dropwise 0.2 mL of bromine until the colour of unreacted bromine persisted. The solution was concentrated *in vacuo* to give a residue that, by nmr analysis, was a mixture containing 1,2-dibromo-2-methylindane (50%) and 2-bromo-1-methoxy-2-methylindane (50%). Flash chromatography on silica gel using hexane as eluant gave 0.42 g (43%) of the bromoether; nmr, δ: 1.80 (s, 3H), 3.27 (s, 2H), 3.40 (s, 3H), 4.77 (s, 1H), 7.0–7.2 (m, 4H).

3-Methoxy-2-methylindene, ***11***

The bromoether **12**, 0.42 g, was dissolved in 5 mL of dry DMF; 0.169 g of lithium bromide and 0.144 g of lithium carbonate were added and the reaction heated to 140°C for 3 h. The mixture was then poured into 100 mL of water, extracted with 2 × 100 mL of ether, and the extracts washed with 2 × 100 mL of water, dried over $MgSO_4$, and concentrated to give 0.12 g (44%) of crude **11**, which could be purified by bulb-to-bulb distillation: nmr, δ: 2.01 (d, J = 1 Hz, 3H), 3.00 (s, 3H), 4.80 (s, 1H), 6.33 (bs, 1H), 6.9–7.3 (m, 4H); mass spectrum: 160 (255), 146 (39), 145 (382), 130 (64), 129 (48), 128 (78), 117 (192), 116 (83), 115 (332), 102 (45), 91 (97), 89 (82), 86 (22), 79 (36), 78 (24). This compound had gc/ms identical to infinity samples from kinetic runs.

Preparation of diazoindenes ***5***a, ***5***b, ***5***c, ***5***d, *and* ***5***e

The procedure used was the same for all and an example is given for **5***c*. The tosylhydrazone, **8***c* (400 mg, 1.28 mmol), was dissolved in 8 mL of dichloromethane and 0.22 g (4.0 mmol) of sodium methoxide was added. The mixture was stirred for 15 min and then the dichloromethane was evaporated under vacuum and 40 mL of hexane was added. After refluxing for 4 h the mixture was filtered and the hexane evaporated under vacuum to give 0.13 g (0.83 mmol, 65%) of 1-diazo-2-methylindene **5***c*; ir: 2055 cm^{-1}; nmr ($CDCl_3$), δ: 2.35 (3H, s), 6.10 (1H, s), 7.1–7.6 (4H, m).

Spectral data for the other diazoindenes are as follows: **5***a*; ir: 2050 cm^{-1}; nmr ($CDCl_3$), δ: 2.33 (3H, d, J = 1 Hz), 3.85 (3H, s), 6.07 (H3, q, J = 1 Hz), 6.77 (H6, dd, J = 8 Hz, 2 Hz), 7.03 (H4, d, J = 2 Hz), 7.29 (H7, d, J = 8 Hz); **5***b*; ir: 2050 cm^{-1}; nmr ($CDCl_3$), δ: 2.33 (3H, d, J = 1 Hz), 2.40 (3H, s), 6.07 (H3, q, J = 1 Hz), 6.95 (H5, d, J = 8 Hz), 7.17–7.42 (H4, H7, m); **5***d*; ir: 2060 cm^{-1}; nmr ($CDCl_3$), δ: 2.35 (3H, d, J = 1 Hz), 6.05 (H3, q, J = 1 Hz), 7.15–7.55 (3H, m); **5***e*; ir: 2055 cm^{-1}; nmr (360 MHz, $CDCl_3$), δ: 2.41 (3H, d, J = 1.3 Hz), 6.26 (H3, q, J = 1.3 Hz), 7.44 (H7, d, J = 8.6 Hz), 8.03 (H6, dd, J = 8.6 Hz, 2.1 Hz), 8.30 (H4, d, J = 2.1 Hz).

Kinetics of the thermal decomposition of diazoindenes ***5***a, ***5***b, ***5***c, *and* ***5***e

The concentration of the diazoindenes in 5% pyridine in methanol was adjusted to give an absorbance near 1.0 at the maximum: **5***a*, 338 nm; **5***b*, 326 nm; **5***c*, 322 nm; **5***d*, 328 nm; and **5***e*, 300 nm. Samples were then purged with nitrogen, sealed in ampoules wrapped with aluminum foil, and placed in a constant temperature bath. Kinetic samples were withdrawn and quenched by immersion in an ice bath. Rate constants were obtained from the slope of the linear log ($A - A_\infty$) versus time plots and the values are reported in the text.

Acknowledgements

This research was supported by a grant from the Natural Sciences and Engineering Research Council of Canada. We also thank the Dalhousie Faculty of Graduate Studies for an award to N. Mathur and NSERC of Canada for a Summer Scholarship to S. Kapur. We thank P. R. Redden for preparing samples and obtaining spectra of the diazoindenes. Part of this work was completed at the University of Texas in Austin and the Pincocks thank M. A. Fox for her hospitality.

1. J. A. Pincock and K. P. Murray. Can. J. Chem. **57**, 1403 (1979).
2. J. A. Pincock and N. C. Mathur. J. Org. Chem. **47**, 3699 (1982).
3. N. C. Mathur, M. S. Snow, K. M. Young, and J. A. Pincock. Tetrahedron, **41**, 1509 (1985).
4. R. Hoffmann, G. D. Zeiss, and G. W. Van Dine. J. Am. Chem. Soc. **90**, 1485 (1968).
5. J. H. Davis, W. A. Goddard III, and R. G. Bergman. J. Am. Chem. Soc. **99**, 2427 (1977).
6. N. Honjou, J. Pacansky, and M. Yoshimine. J. Am. Chem. Soc. **107**, 5332 (1985).
7. R. J. Miller, L. S. Yang, and H. Shechter. J. Am. Chem. Soc. **99**, 938 (1977).
8. R. J. Miller and H. Shechter. J. Am. Chem. Soc. **100**, 7920 (1978).
9. R. B. Woodward and R. Hoffmann. The conservation of orbital symmetry. Verlag Chemie, Weinheim, Germany. 1970. p. 152.
10. H. D. House, V. Paragamian, R. S. Ro, and D. Wluka. J. Am. Chem. Soc. **82**, 1452 (1960).
11. M. B. Floyd and G. R. Allen. J. Org. Chem. **35**, 2647 (1970).
12. H. Sternerup. Acta Chem. Scand. Ser. B: **B28**, 969 (1974).

Can. J. Chem. Downloaded from www.nrcresearchpress.com by 196.1.178.254 on 09/07/12
For personal use only.

13. C. A. PANETTA and S. C. BUNCE. J. Org. Chem. **26**, 4859 (1961).
14. C. K. INGOLD and H. A. PIGGOTT. J. Chem. Soc. 1469 (1923).
15. G. E. HEASLEY, T. R. BOWER, K. W. DOUGHARTY, J. C. EASDON, V. L. HEASLEY, S. ARNOLD, T. L. CARTER, D. B. YEAGER, B. T. GIPE, and D. F. SHELLHAMER. J. Org. Chem. **45**, 5150 (1980).
16. R. L. BARCUS, L. M. HADEL, L. J. JOHNSTON, M. S. PLATZ, T. G. SAVINO, and J. C. SCAIANO. J. Am. Chem. Soc. **108**, 3928 (1986).
17. D. BETHELL, D. WHITTAKER, and J. D. CALLISTER. J. Chem. Soc. 2466 (1965).
18. G. MURGULESCU and T. ONCESCU. J. Chim. Phys. **58**, 508 (1961).
19. E. WASSERMAN, L. BARASH, A. M. TROZZOLO, R. W. MURRAY, and W. A. YAGER. J. Am. Chem. Soc. **86**, 2304 (1983).
20. R. A. MOSS and C. M. YOUNG. J. Am. Chem. Soc. **105**, 5859 (1983).
21. E. C. FRIEDRICH and D. B. TAGGART. J. Org. Chem. **43**, 805 (1978).
22. F. G. BORDWELL, G. E. DRUCKER, and H. E. FRIED. J. Org. Chem. **46**, 632 (1981).
23. J. ROMELT, J. D. PEYERIMHOFF, and R. J. BURENKER. Chem. Phys. **54**, 147 (1981).
24. R. SHEPARD and J. SIMONS. Int. J. Quantum Chem. Quantum Chem. Symp. **14**, 349 (1980).

Can. J. Chem. Downloaded from www.nrcresearchpress.com by 196.1.178.254 on 09/07/12
For personal use only.

A further view on the calculation of the enthalpy of cavity formation in liquids. The influence of the cavity size and shape

JOAQUIM J. MOURA-RAMOS[1] AND MADALENA S. DIONÍSIO
Centro de Química Física Molecular (INIC), Complexo I, IST, Av. Rovisco Pais, 1096 Lisboa Codex, Portugal

RAQUEL C. GONÇALVES
CECUL (INIC), Calçada Bento Rocha Cabral 14, 1200 Lisboa, Portugal

AND

HERMÍNIO P. DIOGO
Centro de Química Estrutural (INIC), Complexo I, IST, Av. Rovisco Pais, 1096 Lisboa Codex, Portugal

Received March 31, 1988

JOAQUIM J. MOURA-RAMOS, MADALENA S. DIONÍSIO, RAQUEL C. GONÇALVES, and HERMÍNIO P. DIOGO. Can. J. Chem. **66**, 2894 (1988).

A reformulation of the Sinanoglu–Reisse semi-empirical approach to describe the cavity formation process in liquids is proposed. The energy of cavity formation is regarded as a strictly potential energy corrected for short range order effects in the liquid state. Deviations from the Corresponding States Principle quantified by the Pitzer acentric factor are considered to describe these short range order effects.

The influence of the cavity shape on the calculation of its energetics is emphasized as well as the need for a realistic description of the dependence of the microscopic surface tension on the size and shape of the cavities. The proposed method is successfully applied to binary mixtures of *n*-alkanes at infinite dilution.

JOAQUIM J. MOURA-RAMOS, MADALENA S. DIONÍSIO, RAQUEL C. GONÇALVES et HERMÍNIO P. DIOGO. Can. J. Chem. **66**, 2894 (1988).

On propose une nouvelle formulation de l'approche semi-empirique de Sinanoglu–Reisse pour décrire le processus de formation de cavités dans des liquides. L'énergie de formation de la cavité est considérée strictement comme une énergie potentielle corrigée pour les effets d'ordre à courte distance dans l'état liquide. Les déviations par rapport au Principe des Etats Correspondants sont quantifiées par le facteur acentrique de Pitzer et sont utilisées sous cette forme pour décrire ces effets d'ordre à courte distance.

On démontre l'importance de la forme de la cavité sur le calcul de son énergie ainsi que la nécessité de posséder une description réaliste de la relation entre la tension superficielle microscopique et la taille et la forme des cavités. La méthode proposée a été appliquée avec succès à l'étude de mélanges binaires de *n*-alcanes à dilution infinie.

[Traduit par la revue]

Can. J. Chem. Downloaded from www.nrcresearchpress.com by 196.1.178.254 on 09/07/12
For personal use only.

The importance of the energetics of cavity formation to elucidate the solvent effect on chemical processes has been strongly emphasized (1–3). The thermodynamic parameters ΔX associated with a chemical process A $\rightarrow$ B at infinite dilution are, in principle, solvent dependent and we may write $\Delta X_0 = \bar{X}_{BO} - \bar{X}_{AO}$ in the solvent S_0 and $\Delta X = \bar{X}_B - \bar{X}_A$ in the solvent S. The $\bar{X}$ are partial molar quantities at infinite dilution. Since $(\bar{X}_B - \bar{X}_A) - (\bar{X}_{BO} - \bar{X}_{AO}) = (\bar{X}_B - \bar{X}_{BO}) - (\bar{X}_A - \bar{X}_{AO})$,

$$[1] \qquad \delta(\Delta X) = \Delta(\delta \bar{X})$$

The operators δ (solvent effect) and Δ (process) are thus permutable (4). Equation [1] shows the relationship which exists between the solvent effect on ΔX and the thermodynamic transfer quantities $\delta \bar{X}$, and is at the origin of a generalised use of these transfer quantities in order to interpret the observed solvent effects (5–7). Nevertheless, $\delta \bar{X}$ are complex quantities, which reflect both solute–solvent and solvent–solvent interactions. To obtain information about the molecular structure of a solute it would be necessary to accede directly to the solute–solvent interaction and this is an important point when solvent effect studies are carried on in order to characterise short-lived species like electronic excited states or transition states.

The thermodynamic quantity $\delta \bar{X}_A$ for the transfer of a solute A from one solvent, S_0, to another, S, at infinite dilution, may be described as a sum of at least two terms[2]

$$\delta \bar{X}_A = (\delta \bar{X}_A)_c + (\delta \bar{X}_A)_i$$

where $(\delta \bar{X}_A)_c$ is a cavity contribution which depends on the size and shape of the solute A but reflects only the cohesive forces of the solvents (solvent–solvent interactions), and $(\delta \bar{X}_A)_i$ is a solute–solvent interaction contribution which depends on the polarity and the polarizability of the solute and of the solvent molecules. Only the last term gives information about the structure of the solute. Since thermodynamic transfer quantities are generally easy to obtain experimentally, the calculation of the energetics of cavity formation would make it possible to accede directly to the solute–solvent interaction term, and that is why this is an important feature in the context of solvent effect studies.

Two different methods are available in the literature for calculating the energetics of cavity formation in liquids: the Scaled Particle Theory (SPT) and a semi-empirical method based on the concept of microscopic surface tension of the solvent. The SPT is a statistical theory of liquids based on a hard

[1]Author to whom correspondence should be addressed.

[2]We neglect here an eventual contribution from the reorganization of the solvent in the cosphere of the solute. This contribution should be taken into account when structured solvents (particularly water) are involved. We also assume that the separation term, which describes the dispersion of the solute molecules in the solvent, is a pure solute property and does not depend on the solvent.

Can. J. Chem. Downloaded from www.nrcresearchpress.com by 196.1.178.254 on 09/07/12
For personal use only.

sphere potential, which was developed by Reiss *et al.* (8, 9) and applied to solubility problems by Pierotti (10–12). The second approach, which describes the cavity formation process as a work against the surface forces of the solvent, was qualitatively proposed a long time ago by Uhlig (13) and Eley (14) and has been quantitatively developed by Sinanoglu (3, 15) and Reisse *et al.* (2, 16). Since both methods have been criticized on different grounds (17, 18), we decided to reinvestigate this problem. In this paper we reconsider the thermodynamic formulation of the Sinanoglu–Reisse approach and we propose a new method for the calculation of the enthalpy of cavity formation.

The enthalpy of cavity formation: the basic equation

If the cavity formation process is described as a work against the surface forces of the liquid, $dW = \sigma_0 dS$, where dW is the infinitesimal work to create the infinitesimal surface dS[3] and σ_0 is the macroscopic surface tension of the liquid. This generalised work is a Gibbs energy if the process takes place at constant temperature and pressure so that the enthalpy of cavity formation can be obtained by derivation using the Gibbs–Helmholtz relationship. We thus have

$$[2] \quad H_c = N_A \sigma_0 A_0 S$$

with

$$[3] \quad A_0 = 1 - T\left(\frac{1}{\sigma_0}\frac{d\sigma_0}{dT} + \frac{2}{3}\alpha_0\right)$$

where N_A is the Avogadro's number, α_0 the solvent isobaric thermal expansion coefficient (see comment on p. 311 of ref. 3), S the surface of the cavity, and H_c the molar enthalpy of cavity formation.[4]

The cavities we are dealing with in this context are microscopic cavities (cavities of molecular size). As shown by Tolman (19), Kirkwood and Buff (20), and Koenig (21), the surface tension at the curved surfaces of these cavities is different from the macroscopic surface tension. To take into account the high curvature of these cavities we must multiply $\sigma_0 A_0$ (the enthalpy part of the surface tension) by a corrective factor K_h which depends on the size and the shape of the cavity. Then eq. [2] becomes

$$[4] \quad H_c = N_A \sigma_0 A_0 S K_h$$

This basic equation shows different forms according to the shape of the cavity. For spherical cavities $S = 4\pi r^2$, where r is the radius. If we take $V = N_A 4\pi r^3/3$, where V is the molar volume, we have

$$[5] \quad H_c/\text{J mol}^{-1} = 40.84 \sigma_0 A_0 V^{2/3} K_h$$

The factor 40.84 contains constants and unit conversion factors in order to obtain H_c in J mol^{-1} by introducing σ_0 in dyn cm^{-1} and V in cm^3 mol^{-1}. Since the relationship between the surface of a cylinder, S_{cyl}, and that of a sphere with the same volume, S_{sph}, is

$$[6] \quad \frac{S_{cyl}}{S_{sph}} = 0.4897\frac{V^{1/3}}{r} + 0.9266\frac{r^2}{V^{2/3}}$$

where r is the radius of the cylinder in Å and V is expressed in cm^3 mol^{-1}, the enthalpy of cavity formation for cylindrical cavities will be given by:

$$[7] \quad H_c/\text{J mol}^{-1} = 40.84 \sigma_0 A_0 K_h\left(\frac{0.4897V}{r} + 0.9266r^2\right)$$

An equivalent equation can be easily obtained for disc-shaped cavities.

The microscopic surface tension and its dependence on the size and shape of the cavity

The surface tension of spherical interfaces was studied by Tolman (19) based on Gibbs theory and a quasi-thermodynamic approach to the interface. He showed that the curvature dependence of the surface tension is appreciable for droplets and bubbles smaller than 10^{-6} cm radius, and obtained for this dependence the following equation:

$$[8] \quad \ln K = \ln\frac{\sigma(r)}{\sigma} = \int_{\infty}^{r} \frac{\left(\frac{2\delta}{r^2}\right)\left(1 + \frac{\delta}{r} + \frac{1}{3}\frac{\delta^2}{r^2}\right)}{1 + \left(\frac{2\delta}{r}\right)\left(1 + \frac{\delta}{r} + \frac{1}{3}\frac{\delta^2}{r^2}\right)} dr$$

where $\sigma(r)$ is the surface tension at the curved surface, σ_0 the macroscopic surface tension, r the radius of the sphere, and δ is the difference between the radius of the equimolar surface (for which adsorption is zero) and the radius of the surface of tension.[5,6] This equation was also obtained by Kirkwood and Buff (20) using the radial distribution function method, and by Ahn *et al.* (23) from the liquid partition function derived from the Significant Structure Theory. It is doubtful that the value of δ remains constant and independent of the radius of curvature for droplets and bubbles so small that r is of the same order as δ. Since δ is an unknown function of r, it is usual to consider it as a constant (24–26). If δ lies between 3 and 5 Å (and this is the case for most organic liquids (26–28)), the calculation of the Tolman integral leads to a curvature dependence which can be described by the equation

$$[9] \quad K = 1 + \left(\frac{V_0}{V}\right)^{2/3}(K_0 - 1)$$

previously proposed by Sinanoglu (15). We will consider this equation to describe the variation of K_h with the size of spherical cavities.[5]

As pointed out by different authors (25, 27), the Tolman integral (calculated assuming δ constant) underestimates K for small (molecular sized) cavities. To calculate K and K_h a semi-empirical method was thus proposed (2, 16, 29, 30). According to this method attention is focused on a reference cavity which corresponds to that occupied by a single molecule in the pure liquid. For the reference cavity we may write

$$[10] \quad H_{c0}/\text{J mol}^{-1} = 40.84 \sigma_0 A_0 V_0^{2/3} K_{h0}$$

[3] If the volume of the system changes during the process of creation of the new surface there will be a volume work which must be added to the surface work. Nevertheless, this volume work can be neglected at moderate pressures.

[4] From now on subscript zero indicates a solvent property; quantities without subscript are solute properties.

[5] This corrective factor K which may be used in Gibbs energy calculations is not the same as K_h (the corrective factor for the enthalpy part of the surface tension, $\sigma_0 A_0$). Nevertheless, it can be shown that both exhibit the same dependence on the curvature of the cavity (22).

[6] The δ value is positive for a droplet and negative for a bubble.

Can. J. Chem. Downloaded from www.nrcresearchpress.com by 196.1.178.254 on 09/07/12
For personal use only.

if spherical and

$$[11]\quad H_{c0}/\mathrm{J\ mol^{-1}} = 40.84\sigma_0 A_0 K_{h0}\left(\frac{0.4897V_0}{r} + 0.9266r^2\right)$$

if cylindrical.

To obtain K_{h0} it was suggested to identify H_{c0}, the reference cavity formation enthalpy, with the vaporization enthalpy of the pure liquid, H_{v0} (2, 16, 29, 30):

$$[12]\quad H_{c0} = H_{v0}$$

In this context the energy required to bring a molecule from the bulk to the surface (cavity formation) is considered to be the same as the one required to bring the molecule from the surface to the vapour phase (vaporization) (31, 32). The idea underlying this statement is that a given molecule has, at the surface, a number of nearest neighbours which is half the neighbours it has in the bulk.

The model developed by Prigogine and Saraga (33, 34) in which not all the surface lattice sites are occupied by molecules, the density at the surface being less than that in the underlying liquid, seems to confirm this approach. This modification of the cell model named incomplete-monolayer model gives good agreement between calculated and experimental surface tension if 30% of empty surface lattice sites are considered. Since for a compact structure (for example, a face-centered cubic lattice) the number of nearest neighbours is twelve in the bulk and nine at the surface of maximum compacity (six in the surface monolayer and three in the adjacent one), the Prigogine and Saraga results support the idea that the number of nearest neighbours in the bulk is approximately the double of that at the surface. (See appendix for another approach of this problem.)

Although this is an important point we must realise that the cavity formation process and the vaporization process are apparently very different in nature. During the cavity formation process molecules remain in the liquid state, while in the vaporization process molecules undergo a phase transition in which the molecular degrees of freedom are strongly changed: the liberational or quasi-vibronic modes of movement in the liquid change to translational degrees of freedom in the gas and the internal rotations, as well as the other contributions to the energy of molecules, can be dramatically changed in the phase transition.[7] Since the specific heat at constant volume, C_v, is a measure of the degrees of freedom of the molecules in a macroscopic assembly (35), the quantity $T\Delta C_v = T(C_{vg} - C_{vl})$ (where g and l refer to the gas and the liquid, respectively) may be taken as the contribution of the change of the degrees of freedom to the vaporization energy. In this context $H_v - T\Delta C_v$ would be the potential energy of vaporization (the enthalpy associated with the break of intermolecular interactions which takes place in the vaporization process) and consequently this is the quantity, and not H_v itself, that should be compared with the enthalpy of cavity formation.[8]

The influence of the molecular shape on thermodynamic properties is another debatable matter as regards the identification of the cavity formation and vaporization processes. The success of the Prigogine–Flory–Patterson theory to predict the thermodynamic excess properties of liquid mixtures containing hydrocarbon molecules of different sizes and shapes is well known. However, some inconsistencies are observed for mixtures containing long-chain *n*-alkanes which can be explained by postulating the existence in these liquids of a short range order or a correlation of molecular order (37). This correlation of molecular order is broken in the vaporization process but remains in the reference cavity formation process. Long chain *n*-alkanes strongly deviate from the Corresponding States Principle (CSP) (38, 39), and the short range order is certainly at the origin of these deviations. The CSP states that the variation of the reduced saturated pressure as a function of the reduced temperature is expressed by a single curve for a large number of substances. This means that liquids complying with the CSP have the same vaporization enthalpy at the same reduced temperature. Deviations from the CSP can be quantified by using the so-called Pitzer acentric factor, ω (38, 40). Originally ω was proposed to represent the acentricity of the shape or the nonsphericity of the molecules. Nevertheless, ω rises also with polarity. At present the acentric factor is widely used as a parameter which is a measure of the short range order in liquids and this short range may be caused by the anisotropy of the molecular shape or by the dipole correlation.

We will show now that the quantity $H_v/(1 + \omega) = H_v^*$ represents the vaporization enthalpy that a substance would have if it complied with the CSP (if correlation of molecular order effects were absent). Assuming a constant vaporization enthalpy, the integrated Clapeyron–Clausius equation in reduced variables takes the form

$$[13]\quad \ln p_r = \frac{H_v}{RT_c}\left(1 - \frac{1}{T_r}\right)$$

where T_c is the critical temperature and p_r and T_r are, respectively, the reduced vapour pressure and the reduced temperature. The fact that this simple equation holds for many fluids depends on a fortunate coincidence that errors from assuming a constant heat of vaporization and ideal gas behaviour tend to cancel each other (39). For fluids complying with the CSP the reduced vapour pressure curve is the same so that the quantity H_v/RT_c has the same value for these substances: 5.3650 according to the Rowlinson equation (41). For substances deviating from the CSP it is necessary to introduce a third parameter in order to account for their properties. The parameter which has been most extensively studied is the Pitzer acentric factor, ω, defined as (38)

$$[14]\quad \omega = [1 - \log_{10} p_r]_{T_r = 0.7}$$

and, hence, eq. [13] becomes

$$[15]\quad \ln p_r = \frac{H_v}{(1 + \omega)RT_c}\left(1 - \frac{1}{T_r}\right)$$

[7] In order to relate the energy of cavity formation with the vaporization energy Sinanoglu (29) considers a term named ΔE_{idf} which describes the change in the internal degrees of freedom (idf) of the molecules associated with the vaporization process. He is thus conscious of the different nature of the two processes (vaporization and cavity formation). Nevertheless he does not suggest any method for estimating this term and in practical applications he always neglects it.

[8] This has some analogy with Ben-Naim's preoccupation (36) of defining the solvation process of a solute in a solvent as the process of transferring the solute from a fixed position in the gas phase into a fixed position in the liquid solution at constant temperature and pressure.

Can. J. Chem. Downloaded from www.nrcresearchpress.com by 196.1.178.254 on 09/07/12
For personal use only.

The comparison between eqs. [15] and [13] suggests that the quantity $H_v/(1 + \omega) = H_v^*$ may be regarded as the vaporization enthalpy a substance would have if it complied with the CSP.

As the process of making a reference cavity takes place with no short range molecular order change in the liquid, we propose the use of the CSP vaporization enthalpy, H_v^*, instead of H_v, to calculate the reference cavity formation enthalpy. Thus eq. [12] must be replaced by:

$$[16] \quad H_{c0} = H_{v0}^* - T\Delta C_{v0}$$

The combination of eq. [16] with [10] or [11] enables us to calculate K_{h0} from the experimental properties of the pure liquids:

$$[17] \quad K_{h0} = \frac{H_{v0}^* - T\Delta C_{v0}}{40.84\sigma_0 A_0 V_0^{2/3}}$$

for spherical reference cavities, and

$$[18] \quad K_{h0} = \frac{H_{v0}^* - T\Delta C_{v0}}{40.84\sigma_0 A_0 \left(\frac{0.4897 V_0}{r} + 0.9266 r^2\right)}$$

for cylindrical reference cavities. Having this reference value for K_h and postulating some dependence of K_h on the size of the cavity (for example, eq. [9] for spheres) K_h values for any cavity may be obtained. The dependence of K_h on the size of cavity is an important problem which has been oversimplified in the literature dealing with the energetics of cavity formation. In fact, eq. [9] has been used for all cavities independently of their shape. Nevertheless, most of the organic molecules are not spherical. The molecules of *n*-alkanes in the liquid state, for instance, are in extended conformations such that the cavities occupied by each molecule are much more like cylinders than like spheres. Furthermore, the reference cavities for *n*-alkanes will differ in length but should have similar radii. These are relevant features because the difference between the surface area of the *n*-alkanes and that of a sphere of equal volume would increase rapidly (42) with the lengthening of the hydrocarbon chain. In addition, since the cylinders are of similar radii, the cavities of *n*-alkanes must have similar curvatures and thus similar values of K_h.

To use eqs. [7], [11], and [18] for cylindrical cavities we must choose the value of r, the radius of the cylinder. For *n*-alkane molecules we assumed $r = 3.5$ Å[9] and hence:

$$[19] \quad H_c/\text{J mol}^{-1} = 40.84\sigma_0 A_0 K_h(0.140V + 11.3509)$$

$$[20] \quad H_{c0}/\text{J mol}^{-1} = 40.84\sigma_0 A_0 K_{h0}(0.140V + 11.3509)$$

$$[21] \quad K_{h0} = \frac{H_{v0}^* - T\Delta C_{v0}}{40.84\sigma_0 A_0(0.140V_0 + 11.3509)}$$

[9]The value of r could be obtained from the plot of the molecular volume, v, against the molecular surface area, s, since between these quantities we have the relationship $v = (sr/2) - \pi r^3$. If we use the Bondi method (43) to calculate the Van der Waals volume and the Valvani method (44) to calculate the molecular surface area we obtain for *n*-alkanes $r = 1.9$ Å. Nevertheless, this is a very strong underestimation. As pointed out by A. Y. Meyer in his beautiful paper on the size of molecules (45), "This choice (of Van der Waals volumes) makes molecules as small as conceivably admissible". In fact, a Van der Waals *n*-alkane has a volume which is nearly one half the volume the molecule really occupies in the liquid at room temperature. The value of 3.5 Å seems reasonable if we compare it with the radius calculated from molar volumes of small molecules for which the spherical shape approximation is valid: acetone, $r = 3.1$ Å at 25°C; propane, $r = 3.1$ Å at the boiling point; *n*-butane, $r = 3.4$ Å at the boiling point; *n*-pentane, $r = 3.6$ Å at 25°C; neopentane, $r = 3.7$ Å at 25°C.

Table 1 lists the selected physical properties of the pure liquid *n*-alkanes required for the calculations. Table 2 shows the K_h values for reference cavities in these liquids calculated from eq. [21]. It is interesting to note that K_{h0} is nearly constant in the *n*-alkane series which means that the curvature of the cylindrical reference cavities does not change with the size of *n*-alkane molecules as predicted. This physically founded behaviour was not observed when previous methods of calculating K_{h0} (15, 16) were used. It is also interesting to observe that the K_{h0} values for *n*-alkane are not very different from the value $K_{h0} = 0.57$ we obtain for cyclohexane using the spherical approximation (eq. [17]). Thus if, for example, cyclohexane is dissolved in hexadecane the use of eq. [9] to estimate the microscopic surface tension of the solute cyclohexane cavity would lead to a strong underestimation of K_h. A better solution for this situation would be to consider $K_h = K_{h0}$. The previous comments emphasize how important it is to recognize the variation of the microscopic surface tension with the size and shape of the cavity in order to calculate the energetics of cavity formation.

The effect of the solute and solvent molecular size and shape of H_c

With respect to the K_h dependence on the size and the shape of the cavity, we will consider essentially two different situations: (*1*) eq. [9] describes the variation of K_h with the size of the cavity for spherical cavities in spherical solvents; (*2*) K_h will be taken as independent of the size of the cavity so that $K_h = K_{h0}$ for cylindrical cavities and for moderate sized spherical cavities in large cylindrical solvents. This leads to several alternative formulations to calculate the enthalpy of cavity formation:

(*a*) Spherical cavity in a spherical solvent. If we substitute eqs. [9] and [17] in [5] the result is:

$$[22] \quad H_c/\text{J mol}^{-1} = 40.84\sigma_0 A_0(V^{2/3} - V_0^{2/3}) + H_{v0}^* - T\Delta C_{v0}$$

(*b*) Spherical cavity in a cylindrical solvent. Substituting [21] in [19] yields:

$$[23] \quad H_c/\text{J mol}^{-1} = \frac{0.140V + 11.3509}{0.140V_0 + 11.3509}(H_{v0}^* - T\Delta C_{v0})$$

(*c*) Cylindrical cavity in a spherical solvent. From eqs. [17] and [19] one obtains:

$$[24] \quad H_c/\text{J mol}^{-1} = \frac{0.140V + 11.3509}{V_0^{2/3}}(H_{v0}^* - T\Delta C_{v0})$$

K_h for the cylindrical cavity was taken as being equal to K_{h0} for the spherical reference cavity of the solvent. This kind of choice must be discussed in each particular case.

(*d*) Spherical cavity in a cylindrical solvent. If we consider K_h varying according to eq. [9], from [5] and [21] we obtain:

$$[25] \quad H_c/\text{J mol}^{-1} = 40.84\sigma_0 A_0(V^{2/3} - V^{2/3}) + \frac{V_0^{2/3}}{0.140V + 11.3509}(H_{v0}^* - T\Delta C_{v0})$$

TABLE 1. Physical properties of *n*-alkanes at 25°C

n-Alkane	H_v[a] (kJ mol^{-1})	ω[b]	σ[c] (dyn cm^{-1})	A[d]	V[e] (cm^3 mol^{-1})	$\alpha \times 10^4$[f] (K^{-1})	$\beta \times 10^4$[g] (MPa^{-1})	ΔC_p[h] (J K^{-1} mol^{-1})	ΔC_v[i] (J K^{-1} mol^{-1})
n-Pentane	26.7	0.2510	15.48	2.712	116.290	15.61[s]	21.80[o]	−47.12[s]	−16.68
n-Hexane	31.5	0.2957	17.91	2.426	131.608	13.87[m]	17.04[m]	−52.38[s]	−16.39
n-Heptane	36.6	0.3506	19.80	2.227	147.468	12.56[n]	14.61[n]	−58.58[s]	−19.42
n-Octane	41.5	0.3942	21.14	2.111	163.543	11.64[n]	13.02[n]	−64.48[s]	−22.05
n-Nonane	46.4	0.4437	22.38	2.032	179.684	10.74[l]	11.77[n]	−72.68[s]	−28.49
n-Decane	51.4	0.4902	23.37	1.965	195.920	10.51[n]	11.10[n]	−79.87[s]	−30.05
n-Undecane	56.3	0.5349	24.34	1.886	211.230	10.28[j]	10.31[p]	−84.72[j]	−28.48
n-Dodecane	61.3	0.5622	24.91	1.864	228.597	9.60[n]	9.88[n]	−91.58[t]	−36.32
n-Tridecane	66.7[j]	0.6231	25.69	1.822	244.924	9.43[j]	9.48[p]	−103.86[u]	−43.50
n-Tetradecane	71.1[k]	0.6797	26.26	1.793	261.301	9.22[j]	9.13[q]	−107.84[t]	−43.62
n-Pentadecane	76.2[j]	0.7060	26.74	1.769	277.691	9.02[j]	8.82[p]	−121.09[u]	−53.03
n-Hexadecane	81.4	0.7418	27.22	1.753	294.068	8.98[m]	8.57[r]	−123.70[t]	−49.51

[a] Vaporization enthalpies from ref. 46 except if otherwise stated.
[b] Acentric factors from ref. 40.
[c] Surface tensions from ref. 47.
[d] Calculated from eq. [3] with data from ref. 47.
[e] Molar volumes from ref. 47.
[f] Thermal expansion coefficient at constant pressure.
[g] Isothermal compressibility.
[h] Difference of molar heat capacity at constant pressure between the gas and the liquid.
[i] ΔC_v values have been calculated from ΔC_p using the relation $\Delta C_v = \Delta C_p - R + VT\alpha^2/\beta$.
[j] From ref. 47.
[k] From ref. 48.
[l] From ref. 49.
[m] From ref. 50.
[n] From ref. 51.
[o] From ref. 52.
[p] From ref. 53.
[q] From ref. 54.
[r] From ref. 55.
[s] From ref. 56.
[t] From refs. 47 and 57.
[u] From refs. 47 and 58.

Can. J. Chem. Downloaded from www.nrcresearchpress.com by 196.1.178.254 on 09/07/12
For personal use only.

As discussed before, the description which is implicit in eq. [25] does not fit many real systems. In some cases, $K_h = K_{h0}$ was found to be the most appropriate. H_c is then given by:

$$[26] \quad H_c/\text{J mol} = \frac{V^{2/3}}{0.140V_0 + 11.3509}(H^*_{v0} - T\Delta C_{v0})$$

To test the adequacy of eqs. [22]–[26] we decided to focus our attention on binary mixtures of *n*-alkanes at infinite dilution (the next paragraphs should clarify the reasons for this option). Among these apolar molecules in such conditions there are neither solute–solute interactions nor directional or specific solute–solvent interactions. We must note, however, that particularly in the higher alkanes we can find strong deviations from CSP.

As enthalpy is a state function, the dissolution enthalpy at infinite dilution, H_d, of a liquid solute in a solvent can be factorised as:

$$[27] \quad H_d = H_s + H_c + H_i$$

where H_s corresponds to the enthalpy associated with the separation (or dispersion) of the solute molecules in the solvent, H_c is the enthalpy of cavity formation (which depends on the solute size and shape, but reflects only the solvent–solvent interactions), and H_i is the solute–solvent interaction enthalpy. We neglect here a reorganization term which would be present in structured solvents (particularly in water) and which would describe a change of the solvent structure in the cybotactic region of the solute. For a pure liquid $H_c = -H_i/2$ since H_c and H_i are potential energies and, as pointed out earlier, the number of nearest neighbours of a given molecule in the bulk is twice this number at the surface. For a binary mixture this will also be true provided the solute and the solvent interaction potentials are similar. Alkane–alkane mixtures are the systems which can most probably fulfill this condition as confirmed by different approaches (37, 59). Thus, we may write:

$$[28] \quad H_s - H_d = H_c$$

If the solute and the solvent are the same (dissolution of a liquid in itself) H_d will be zero and eq. [28] becomes $H_{s0} = H_{c0}$ suggesting that the so-called separation process and the cavity formation proess are energetically equivalent processes. This is reasonable since in the dispersion of the solute molecules in the solvent, as well as in the cavity formation process, there is no phase transition: both processes involve only changes in the potential interaction energy of the molecules. For the separation process we can thus write $H_s = H^*_v - T\Delta C_v$ and eq. [28] becomes

$$[29] \quad H^*_v - H^*_{v0} - T\Delta C_v + T\Delta C_{v0} - H_d = H_c - H^*_{v0} + T\Delta C_{v0}$$

In eq. [29] all quantities except H_c are obtained experimentally. H_c can be calculated by eqs. [22]–[26] or by the scaled particle theory. Experimental H_d values for different *n*-alkane/*n*-alkane systems are presented in Table 3. Figure 1 presents the results obtained by calculating H_c from eq. [22].

TABLE 2. The corrective factor, K_{h0}, which takes into account the curvature of microscopic reference cavities in *n*-alkanes

n-Alkane	K_{h0}[a]
n-Pentane	0.56
n-Hexane	0.55
n-Heptane	0.57
n-Octane	0.58
n-Nonane	0.60
n-Decane	0.60
n-Undecane	0.59
n-Dodecane	0.61
n-Tridecane	0.62
n-Tetradecane	0.60
n-Pentadecane	0.62
n-Hexadecane	0.60

[a] K_{h0} calculated from eq. 21.

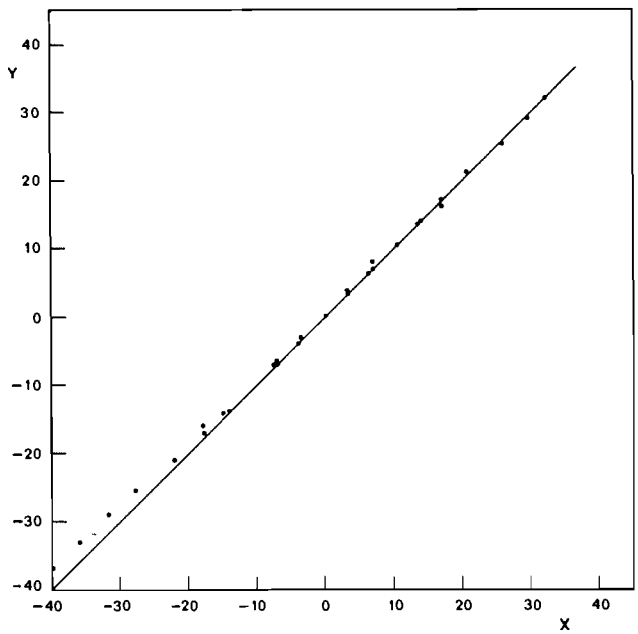

FIG. 1. Comparison between the calculated points and the theoretically predicted behaviour (line). The H_c values have been calculated from eq. [22]. Y and X are in kJ mol^{-1}.

Figure 2 shows similar results obtained by calculating H_c using different equations from [23] to [26].

In these figures Y (the ordinate) corresponds to the left-hand side of eq. [29] and X to the right-hand side, the straight-line representing the theoretical behaviour predicted by this equation.

From Figs. 1 and 2 we observe that calculated points are closely correlated with predicted behaviour (straight line). From Fig. 1 we conclude that eq. [22] (spherical approximation with K_h varying according to eq. [9]) is a good approach to H_c except for systems in which the solute is small compared with the solvent. The small but systematic deviations observed in these cases are due, as explained before, to an underestimation of K_h. Figure 2 shows that eqs. [23], [24], and [26] also lead to good values of H_c when realistically applied to particular systems. We may also note that the systematic deviations observed in

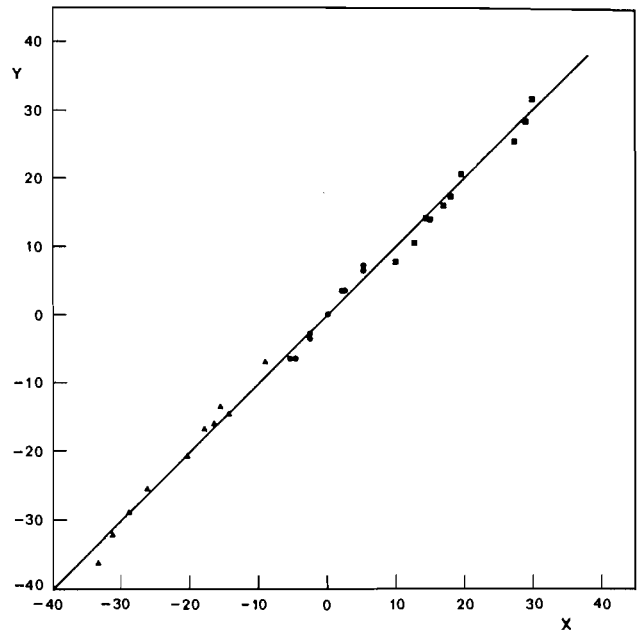

FIG. 2. Comparison between the calculated points and the theoretically predicted behaviour (line). The H_c values have been calculated by eqs. [26] (triangles), [23] (discs), and [24] (squares). Y and X are in kJ mol^{-1}.

Fig. 1 are now vanished. On the left-hand side of Fig. 2, the triangles correspond to the solution of the smaller *n*-alkane in the long *n*-alkane solvents and eq. [26] was used to calculate H_c (spherical cavity in cylindrical solvent). The squares on the right-hand side of the same figure represent systems composed of large solutes dissolved in the smaller *n*-alkane solvents and eq. [24] was used to calculate H_c (cylindrical cavity in a spherical solvent). The intermediate points correspond to systems well described by the eq. [23] (cylindrical cavity in a cylindrical solvent). Figure 2 shows a close correlation between the calculated points and the predicted behaviour.

It is interesting to compare our results with the ones obtained by the scaled particle theory. According to this theory the heat, H_c, involved in creating a cavity in a liquid to accommodate the solute molecule is related to the hard-sphere diameters, σ, of the solute and the solvent molecules. There are several methods proposed in the literature to estimate these hard-sphere diameters. In Table 4 we list the σ values for *n*-alkanes obtained by Reiss *et al.* (9) from vaporization enthalpies and by Wilhelm and Battino (68) from gas solubility data. The two sets of σ values are indeed very similar but the calculated enthalpies of cavity formation are very different when we use one set or the other. This strong dependence of H_c on the hard-sphere diameters of the solute and the solvent has been emphasized before (17) and it is illustrated in Figs. 3 and 4. In these figures Y and X have the same meaning as in the previous figures but now H_c has been calculated by the scaled particle theory. The points in the Fig. 3 correspond to H_c values from hard-sphere diameters in ref. 68. To obtain the points of Fig. 4 H_c has been calculated with the hard-sphere diameter values from ref. 9. The discrepancy between the results obtained with the two sets of σ values is large, particularly when the solute is small compared with the solvent. On the other hand, some methods of estimation of σ (for example, the use of the Stearn and Eyring equation (69)) yield results which are not physically acceptable, leading to H_c values which decrease with the size of cavity in the same

Can. J. Chem. Downloaded from www.nrcresearchpress.com by 196.1.178.254 on 09/07/12
For personal use only.

TABLE 3. Solution enthalpies at infinite dilution at 25°C (in J mol^{-1}) of liquid *n*-alkanes in *n*-alkane solvents

Solute	Solution enthalpy when solvent is						
	n-C_6	*n*-C_7	*n*-C_8	*n*-C_{10}	*n*-C_{11}	*n*-C_{12}	*n*-C_{16}
n-Pentane	0[a]	84[i]					1322[l]
n-Hexane	0	3[b,c]	10[b,d]	64[b,e]	111[b,f]	160[b,g]	418[m]
n-Heptane	1[b,g]	0				117[b,j]	410[b,k]
n-Octane	4[b,d]	0[i]	0			77[b,j]	320[b,k]
n-Nonane		42[i]					
n-Decane	44[b,e]	0[i]		0		20[b,j]	126[m]
n-Undecane	81[b,f]				0		
n-Dodecane	131[b,g]	126[i]	79[b,j]	21[b,j]		0	
n-Hexadecane	540[h]	460[i]	320[b,k]				0

[a]From ref. 60.
[b]Solution enthalpies at infinite dilution calculated from the H^E curves for binary mixtures by $\lim_{x_1 \to 1} H^E/x_1x_2$ where x_1 is the solvent mole fraction.
[c]From ref. 61.
[d]From ref. 62.
[e]From ref. 63.
[f]From ref. 64.
[g]From ref. 50.
[h]From ref. 60.
[i]From ref. 65.
[j]From ref. 51.
[k]From ref. 66.
[l]From ref. 67.
[m]From ref. 70.

TABLE 4. Hard-sphere diameters, σ, for *n*-alkanes

n-Alkane	σ/Å[a]	σ/Å[b]
n-Pentane	5.48	5.59[c]
n-Hexane	5.87	5.92
n-Heptane	6.23	6.25
n-Octane	6.55	6.54
n-Nonane	6.86	6.83
n-Decane	7.12	7.08
n-Undecane	7.35	7.34[c]
n-Dodecane	7.62	7.58
n-Tetradecane	8.05	8.00
n-Hexadecane	8.45	8.36[c]

[a]From the enthalpy of vaporization, according to the equation given by Reiss *et al.* (9).
[b]From ref. 68.
[c]Extrapolated or interpolated value from: $\sigma/Å = 3.697 + 0.4196n - 8.019 \times 10^{-3} n^2$ where *n* is the number of carbon atoms, using hard-sphere diameters from ref. 68.

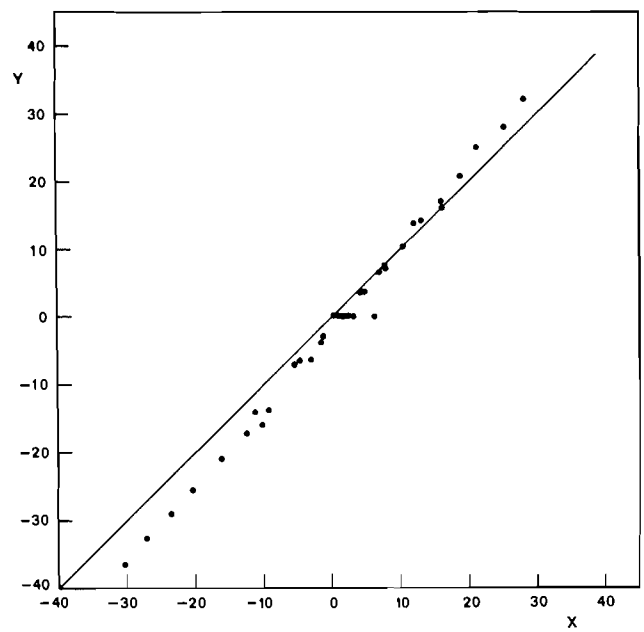

FIG. 3. Comparison between the calculated points and the theoretically predicted behaviour (line). The H_c values have been calculated from the scaled particle theory using hard-sphere diameters from ref. 68. *Y* and *X* are in kJ mol^{-1}.

solvent. It is difficult to assess the reliability limits of the scaled particle theory application. It has been pointed out before (17) that the application of the scaled particle theory is restricted to systems with no orientational molecular correlations or, otherwise stated, to systems composed of nearly spherical and apolar molecules. Nevertheless, using hard-sphere diameters from ref. 68, the discrepancies observed relative to the behaviour predicted by eq. [29] are not very large and they could probably be minimised by a suitable choice of the hard-sphere diameter values. It is obvious that this high sensitivity of H_c on the σ values is a strong handicap of the scaled particle theory. The semi-empirical method we propose here to calculate the energetics of cavity formation is more promising since it does not present this kind of sensitivity to molecular parameters and it allows a detailed description of the system under study (the shape of the solute cavity and of the reference cavity, the curvature of the surface cavities, ...).

Can. J. Chem. Downloaded from www.nrcresearchpress.com by 196.1.178.254 on 09/07/12
For personal use only.

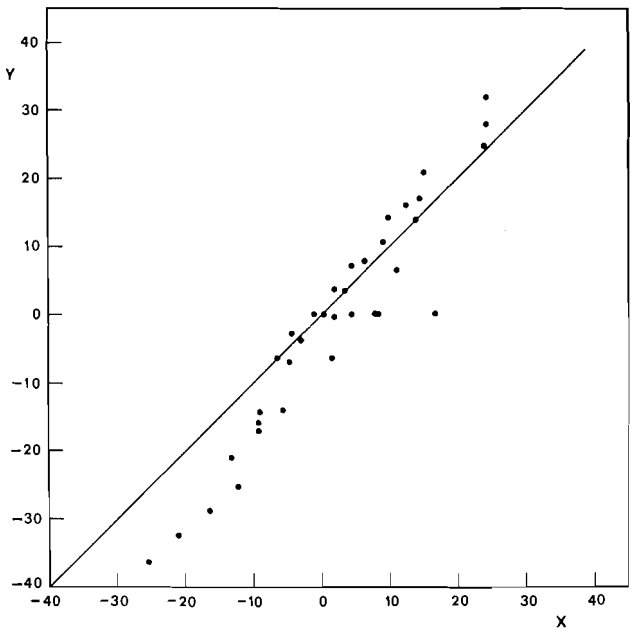

FIG. 4. Comparison between the calculated points and the theoretically predicted behaviour (line). The H_c values have been calculated from the scaled particle theory using hard-sphere diameters from ref. 9. Y and X are in kJ mol^{-1}.

Conclusions

The new method we proposed to calculate the enthalpy of cavity formation is based, as previous methods suggested in the literature, on a comparison between the vaporization process and the reference cavity formation process. Nevertheless, we showed that the identification of these two processes is not correct due to their different physical nature. The vaporization enthalpy is viewed as being composed of different contributions:

$$H_v = H_p + H_k + H_0$$

(*1*) a potential energy contribution, $H_p = H_v - T\Delta C_v$, due to the break of intermolecular interactions between neighbouring molecules; (*2*) a kinetic energy contribution, H_k, due to the change in the degrees of freedom of molecules in the vaporization process. (*3*) an order contribution $H_0 = H_v - H_v/(1 + \omega)$ which describes the destruction of the short-range order in the vaporization process of liquids deviating from the Corresponding States Principle. The reference cavity enthalpy formation H_{c0} is taken as a strictly potential energy corrected for order effects when they are present:

$$H_{c0} = H_p - H_0 = \frac{H_v}{1 - \omega} - T\Delta C_v$$

We emphasized the importance of taking into account the molecular shape of the solute and the solvent for calculating the energetics of cavity formation. We also emphasized the importance of describing correctly the dependence of the microscopic surface tension on the size and the shape of the solute cavities. In this context, we deduced different equations for calculating the enthalpy of cavity formation for real systems.

By applying these equations to binary mixtures of *n*-alkanes at infinite dilution we think that our new method for calculating the enthalpy of cavity formation constitutes a considerable improvement when compared with the other methods proposed in the literature.

1. J. J. MOURA-RAMOS, M. L. STIEN, and J. REISSE. Chem. Phys. Lett. **42**, 373 (1976).
2. J. J. MOURA-RAMOS, M. LEMMERS, R. OTTINGER, M. L. STIEN, and J. REISSE. J. Chem. Res. (M), 0655 (1977).
3. T. HALICIOGLU and O. SINANOGLU. Ann. N.Y. Acad. Sci. **158**, 308 (1969).
4. J. E. LEFFLER and E. GRUNWALD. Rates and equilibria of organic reactions. John Wiley and Sons, New York. 1963. p. 23.
5. P. HABERFIELD. J. Am. Chem. Soc. **96**, 6526 (1974).
6. M. H. ABRAHAM. J. Chem. Soc. Perkin II, 1343 (1972).
7. P. HABERFIELD, P. M. BLOCK, and M. S. LUX. J. Am. Chem. Soc. **97**, 5804 (1975).
8. H. REISS, H. L. FRISCH, and J. L. LEBOWITZ. J. Chem. Phys. **31**, 369 (1959).
9. H. REISS, H. L. FRISCH, E. HELFAND, and J. L. LEBOWITZ. J. Chem. Phys. **32**, 119 (1960).
10. R. A. PIEROTTI. J. Phys. Chem. **67**, 1840 (1963).
11. R. A. PIEROTTI. J. Phys. Chem. **69**, 281 (1965).
12. R. A. PIEROTTI. Chem. Rev. **76**, 717 (1976).
13. H. H. UHLIG. J. Phys. Chem. **41**, 1215 (1937).
14. D. D. ELEY. Trans. Faraday Soc. **35**, 1281 (1939); **35**, 1421 (1939).
15. O. SINANOGLU. *In* Molecular association in biology. *Edited by* B. Pullman. Academic Press, New York. 1968. p. 427.
16. J. J. MOURA-RAMOS and J. REISSE. Rev. Port Quim. **26**, 61 (1984).
17. N. MOREL-DESROSIERS and J. P. MOREL. Can. J. Chem. **59**, 1 (1981).
18. B. N. SOLOMONOV, I. S. ANTIPIN, V. V. GORBACHUK, and A. I. KONOVALOV. J. Gen. Chem. USSR, **52**, 1917 (1983).
19. R. C. TOLMAN. J. Chem. Phys. **17**, 333 (1949).
20. J. G. KIRKWOOD and F. P. BUFF. J. Chem. Phys. **17**, 338 (1949); **18**, 991 (1950).
21. F. D. KOENIG. J. Chem. Phys. **18**, 449 (1950).
22. J. J. MOURA-RAMOS. Doctoral Dissertation, Science Faculty, University of Brussels. 1977.
23. W. S. AHN, M. S. JHON, H. PAK, and S. CHANG. J. Colloid Interface Sci. **38**, 605 (1972).
24. J. SCHMELZER and R. MAHNKE. J. Chem. Soc. Faraday Trans. 1, **82**, 1413 (1986).
25. A. I. RUSANOV and E. N. BRODSKAYA. J. Colloid Interface Sci. **62**, 542 (1977).
26. D. S. CHOI, M. S. JHON, and H. EYRING. J. Chem. Phys. **53**, 2608 (1970).
27. H. WAKESHIMA. J. Phys. Soc. Jpn. **16**, 6 (1961).
28. R. S. SCHECHTER, W. H. WADE, and J. A. WINGRAVE. Preprints of the 48th National Colloid Symposium, Austin, Texas, June 24–26, 1974. p. 150.
29. O. SINANOGLU. *In* Molecular interactions. Vol. 3. *Edited by* H. Ratajczak and W. J. Orville-Thomas. John Wiley. 1982. p. 283.
30. O. SINANOGLU and A. FERNANDEZ. Biophys. Chem. **21**, 157 (1985).
31. J. STEFAN. Wied. Ann. **29**, 655 (1886).
32. H. EYRING. J. Chem. Phys. **4**, 283 (1936).
33. I. PRIGOGINE and L. SARAGA. J. Chim. Phys. **49**, 399 (1952).
34. R. DEFAY and I. PRIGOGINE. Surface tension and absorption. Longmans, Green and Co., London. 1966. Chap. XI.
35. E. A. MOELWYN-HUGHES. Physical chemistry. Pergamon Press, Oxford. 1965. Chap. XVI.
36. A. BEN-NAIM. J. Phys. Chem. **89**, 3791 (1985).
37. H. WAGNER and R. W. LICHTENTHALER. Thermochim. Acta, **94**, 67 (1985).
38. R. C. REID, J. M. PRAUSNITZ, and B. E. POLING. The properties of gases and liquids. 4th ed. McGraw-Hill, New York. 1987.
39. T. W. LELAND, JR. and P. S. CHAPPELEAR. Ind. Eng. Chem. **60**, 15 (1968).
40. C. A. PASSUT and R. P. DANNER. Ind. Eng. Chem. Process Des. Develop. **12**, 365 (1973).

Can. J. Chem. Downloaded from www.nrcresearchpress.com by 196.1.178.254 on 09/07/12
For personal use only.

41. J. S. ROWLINSON. Liquids and liquid mixtures. 2nd ed. Butterworths, London. 1971. p. 278.
42. J. T. EDWARD, P. G. FARREL, and F. SHAHIDI. J. Phys. Chem. **82**, 2310 (1978).
43. J. T. EDWARDS. J. Chem. Ed. **47**, 261 (1970).
44. S. C. VALVANI, S. H. YALKOWSKY, and G. L. AMIDON. J. Phys. Chem. **80**, 829 (1976).
45. A. Y. MEYER. J. Chem. Soc. Rev. **15**, 449 (1986).
46. J. D. COX and G. PILCHER. Thermochemistry of organic and organometallic compounds. Academic Press, London. 1970.
47. N. B. VARGAFTIK. Tables on the thermophysical properties of liquids and gases. Hemisphere Publishing Co., 1975.
48. P. P. S. SALUJA, T. M. YOUNG, R. F. RODEWALD, F. H. FUCHS, D. KOHLI, and R. FUCHS. J. Am. Chem. Soc. **99**, 2949 (1977).
49. J. A. RIDDICK and W. B. BUNGER. Organic solvents. *In* Techniques of chemistry. *Edited by* A. Weissberger. Wiley, Interscience. 1970.
50. S. E. M. HAMAN, M. K. KUMARAN, and G. C. BENSON. J. Chem. Thermodyn. **16**, 537 (1984).
51. M. K. KUMARAN and G. C. BENSON. J. Chem. Thermodyn. **18**, 993 (1986).
52. A. J. RICHARD, K. T. MCCRICKARD, and P. B. FLEMING. J. Chem. Thermodyn. **11**, 93 (1979).
53. E. AICART, G. TARDAJOS, and M. DIAZ PENA. J. Chem. Thermodyn. **13**, 783 (1981).
54. E. AICART, G. TARDAJOS, and M. DIAZ PENA. J. Chem. Eng. Data, **26**, 22 (1981).
55. M. DIAZ PENA, G. TARDAJOS, R. L. ARENOSA, and C. MENDUINA. J. Chem. Thermodyn. **11**, 951 (1979).
56. Physical constants of hydrocarbons C_1 to C_{10}, ASTM Data Series, Publication DS 4A, 1971.
57. E. WILHELM, A. LAINEZ, A. H. ROUX, and J. P. E. GROLIER. Thermochim. Acta, **105**, 101 (1986).
58. M. LURIA and S. W. BENSON. J. Chem. Eng. Data, **22**, 90 (1977).
59. W. SCHRÖER, W. D. DOMKE, K. H. NAUMANN, and E. LIPPERT. *In* Organic liquids. *Edited by* A. D. Buckingham, E. Lippert, and S. Bratos. John Wiley. 1978.
60. B. N. SOLOMONOV, I. S. ANTIPIN, V. V. GORBACHUK, and A. I. KONOVALOV. Dokl. Akad. Nauk SSSR, **243**, 1499 (1978).
61. F. KIMURA, G. C. BENSON, and G. J. HALPIN. Fluid Phase Equilibr. **11**, 245 (1983).
62. S. E. M. HAMAN, M. K. KUMARAN, and G. C. BENSON. Fluid Phase Equilibr. **18**, 147 (1984).
63. S. E. M. HAMAN and G. C. BENSON. J. Chem. Eng. Data, **31**, 45 (1986).
64. K. N. MARSH, J. B. OTT, and A. E. RICHARDS. J. Chem. Thermodyn. **12**, 897 (1980).
65. R. FUCHS and W. R. STEPHENSON. Can. J. Chem. **63**, 349 (1985).
66. M. BARBE and D. PATTERSON. J. Solution Chem. **9**, 753 (1980).
67. M. H. ABRAHAM. J. Am. Chem. Soc. **104**, 2085 (1982).
68. E. WILHELM and R. BATTINO. J. Phys. Chem. **55**, 4012 (1971).
69. A. E. STEARN and H. EYRING. J. Chem. Phys. **5**, 113 (1937).
70. R. FUCHS, E. J. CHAMBERS, and W. K. STEPHENSON. Can. J. Chem. **65**, 2624 (1987).

Appendix

Consider an assembly of N molecules in the liquid state. N_b of these molecules are in the bulk and $N_s = N - N_b$ are at the surface. Consider also that C_b is the number of nearest neighbours of a molecule in the bulk, C_s is this number at the surface, and that ϕ is the pair potential interaction energy. The total potential energy of the assembly will be:

$$[A1] \quad U = \tfrac{1}{2}(N_b\phi C_b + N_s\phi C_s) = \tfrac{1}{2}\phi[(N - N_s)C_b + N_sC_s] = \tfrac{1}{2}\phi[NC_b + N_s(C_s - C_b)]$$

and the potential energy per molecule will be:

$$u = \frac{U}{N} = \tfrac{1}{2}\phi\left[C_b + \frac{N_s}{N}(C_s - C_b)\right]$$

and the molar potential energy of vaporization will be:

$$[A2] \quad U_m = \tfrac{1}{2}\phi\left[N_AC_b + \frac{N_AN_S}{N}(C_s - C_b)\right]$$

Let us suppose now that $C_s = m + n$ where m is the number of nearest neighbours a surface molecule has on the surface monolayer and n the number of nearest neighbours it has on the adjacent monolayer. If we bring a molecule from the surface to the gas phase, the m neighbours will have now $C_s - 1$ neighbours and the n molecules in the adjacent layer will have $C_b - 1$ neighbours. The potential energy of the assembly after removing the molecule from the surface monolayer will be

$$U' = \tfrac{1}{2}\phi[m(C_s - 1) + n(C_b - 1) + (N_s - m - 1)C_s + (N_b - n)C_b]$$

because $N_s - m - 1$ molecules at the surface and $N_b - n$ molecules in the bulk did not change their number of neighbours. The change of the potential energy associated with the removal of one molecule from the surface to the gas phase will thus be

$$U - U' = C_s\phi$$

and the molar potential energy of vaporization will be:

$$[A3] \quad U_m = N_A(U - U') = N_AC_s\phi$$

Comparing [A2] and [A3] we obtain

$$N_AC_s = \tfrac{1}{2}N_AC_b + \frac{1}{2}\frac{N_AN_s}{N}(C_s - C_b)$$

or

$$[A4] \quad \frac{N_s}{N} = \frac{2C_s - C_b}{C_s - C_b}$$

From [A4] it comes out that $C_s = (1/2)C_b$ if N_s/N is very small, which is the case for a macroscopic system in which the number of molecular monolayers in the bulk is big compared to unity.

Can. J. Chem. Downloaded from www.nrcresearchpress.com by 196.1.178.254 on 09/07/12
For personal use only.

Model studies of competing hydrolysis and epimerization of some tetrapeptides of interest in amino acid racemization studies in geochronology

MICHAEL E. MOIR AND ROBERT J. CRAWFORD
Department of Chemistry, University of Alberta, Edmonton, Alta., Canada T6G 2G2

Received March 23, 1988

MICHAEL E. MOIR AND ROBERT J. CRAWFORD. Can. J. Chem. **66**, 2903 (1988).

The processes of epimerization of individual peptide units in proteins and the concurrent cleavage of peptide bonds are modelled by heating some tetrapeptide and tetrapeptide derivatives to 148.5°C in pH 6.8 phosphate buffer. An excess of D-proline was observed during the heating of L-prolyl-L-leucylglycylglycine. The D/L ratio of proline attains a maximum value of 2.1 after 90 minutes. The excess D-proline is attributed to the formation of a 2.3:1 mixture of diketopiperazines *cyclo*-(D-prolyl-L-leucyl) and *cyclo*-(L-prolyl-L-leucyl). These two species account for most of the leucine and proline in the final mixture after the tetrapeptide is no longer detectable. Only small amounts of prolylleucine can be detected after 50 hours. It is suggested that the above tetrapeptide undergoes internal aminolysis. Leucine in the tetrapeptide glycyl-L-leucylglycylglycine racemizes three times faster than in L-prolyl-L-leucylglycylglycine. This demonstrates that an amino acid residue in a peptide chain does have an effect upon the rate of epimerization of a neighbouring peptide residue. A discussion of the geochemical implications of the results is included.

MICHAEL E. MOIR ET ROBERT J. CRAWFORD. Can. J. Chem. **66**, 2903 (1988).

Afin de développer un modèle des processus d'épimérisation des unités peptidiques de protéines et du clivage apparenté des liaisons peptidiques, on a chauffé des tétrapeptides ainsi que leurs dérivés à 148,5°C, dans un tampon de phosphate, à un pH de 6,8. Lorsqu'on a chauffé le L-prolyl-L-leucylglycylglycine, on a observé la formation d'un excès de D-proline. Le rapport de D/L proline atteint une valeur maximale de 2,1 après 90 minutes. On attribue la formation d'un excès de D-proline à la formation d'un mélange 2,3:1 des dicétopipérazines *cyclo*-(D-prolyl-L-leucyl) et *cyclo*-(L-prolyl-L-leucyl). Ces deux espèces peuvent expliquer la formation de la plus grande partie de la leucine ainsi que de la proline présentes dans le mélange final, même lorsqu'on ne peut plus détecter la présence du tétrapeptide. On ne peut détecter la présence que de faibles quantités de prolylleucine après 50 heures. On suggère que le tétrapeptide utilisé subit une aminolyse interne. La leucine du tétrapeptide glycyl-L-leucylglycylglycine se racémise trois fois plus rapidement que dans le L-prolyl-L-leucylglycylglycine. Ce résultat démontre que le résidu d'acide aminé d'une chaîne peptidique influence la vitesse d'épimérisation du résidu voisin. On présente une discussion des implications géochimiques de nos résultats.

[Traduit par la revue]

Can. J. Chem. Downloaded from www.nrcresearchpress.com by 196.1.178.254 on 09/07/12
For personal use only.

Introduction

Abelson's discovery of amino acids in fossils (1) has led to the use of the pseudo-first-order rate constant for racemization of the amino acids as a geochronometric tool. With the development of chiral phases for capillary column gas chromatography, the analytical technique has become sensitive enough that the enantiometric purity of nanogram quantities of the amino acid derivatives can be assessed. The process of amino acid racemization (slow at ambient temperature) is now widely used for dating fossils (2). Radiocarbon dating also is used often. In its most recent variation (3) it is generally considered to be accurate to between 30 and 50 ky bp. Geological dating by amino acid racemization is in fact peptide unit epimerization, in that generally the reaction occurs at one of the α carbons of a peptide unit, resulting in a peptide diastereomer being produced. Hydrolysis, derivatization, and GC analysis result in the comparison of the amounts of D and L isomers of the individual amino acids. The interconversion depicted in Scheme 1 begins after the death of the organism (except in those tissues which are not repaired) and has a half-life at ambient temperature varying from about 20 to 300 ky depending on the particular amino acid used for dating (4). There is often considerable disagreement between the ages obtained by the $^{14}C/^{13}C$ accelerator mass spectrometry method and those obtained from the analysis of enantiomeric amino acids (5). Despite these difficulties, the ease of sample preparation and the low initial capital cost of the amino acid method make it attractive for large volumes of samples when compared to the accelerator mass spectrometry method. The method does have value for relative dating, i.e., in deciding the relative age of a

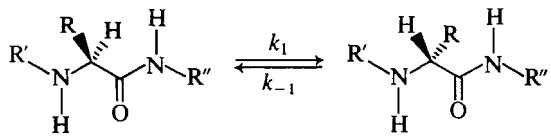

SCHEME 1

series of samples within fossil beds or other deposits (6). In this paper we investigate three of the problems that may cause difficulty in attempting to use the amino acid method to obtain absolute dates. They are (*a*) the possibility of concomitant hydrolysis affecting the peptide epimerization rate, (*b*) the effect of neighbouring peptide units upon the rate of epimerization, and (*c*) the possibility that peptide epimerization rates cannot be calculated in the conventional manner. Equation [1] describes amino acid racemization exactly.

$$[1]\quad \ln\left[\frac{1 - K'[\mathrm{D}]/[\mathrm{L}]}{1 + [\mathrm{D}]/[\mathrm{L}]}\right]_t - \ln\left[\frac{1 - K'[\mathrm{D}]/[\mathrm{L}]}{1 + [\mathrm{D}]/[\mathrm{L}]}\right]_{t=0} = -(k_1 + k_{-1})t$$

For those amino acids which have only one asymmetric centre, $k_1 = k_{-1}$ and thus the right hand side becomes $-2kt$. For those amino acids for which racemization produces diastereomers (epimerization), the value of K' must be determined (for L-isoleucine epimerization of the α carbon produces D-alloisoleucine and $K' = 1.25$ (7)).

The use of amino acids racemization as a tool for geological dating has created the need to understand better the racemization of peptides and proteins. Racemization of a peptide has generally been treated as if it were occurring in discrete amino

acids. For the purpose of geological dating and stratigraphy, the first-order (or pseudo-first-order) rate law has been assumed to be operating for amino acids, peptides, proteins, and protein hydrolysates of changing composition. This simplification minimizes both the asymmetry of the peptides and the competing cleavage of peptide bonds. Since the initiation of our work Mitterer and Kriausakul (8) have demonstrated that the process of epimerization in peptides obeys first-order kinetics by separating the substrate from the hydrolysis mixture for the tripeptide L-Ile-Gly-Gly. The presence of more than one epimerizing centre has not been adequately addressed, particularly with respect to the potential for diastereomer formation from another chiral peptide unit within the protein.[1]

The epimerizations of tetrapeptides and their N-terminal and C-terminal derivatives were studied so as to model the protein situation. By studying model systems some of the properties of peptides that can complicate the interpretation of peptide epimerizations used for geochemical dating may be evaluated. Generally, in model studies, the rate constants have been taken from an examination of the individual amino acids from a protein hydrolysate. With the advent of convenient high performance liquid chromatography (HPLC) systems, it is possible to separate the amino acids from the di-, tri-, and tetrapeptides and thus obtain kinetic data on each species.

Experimental

Materials

Commercial peptides were found to be pure by electrophoresis (3000 V, pH 1.8, 45 min) and HPLC and required no further purification. Benzyl chloroformate, DMSO, *N*-methyl morpholine, isobutylchloroformate, and aniline were purified by distillation *in vacuo*. Ethyl acetate was purified by washing with sodium carbonate, water, and saturated sodium chloride, and then drying with anhydrous potassium carbonate followed by distillation from 3A molecular sieves. The water used for lyophilization was deionized, doubly distilled, and deionized again. Derivatives of peptides were prepared according to Bodanszky (10); examples of the synthetic preparations follow.

N-*Benzyloxycarbonyl-L-proline-L-leucylglycylglycine (1)*

L-Pro-L-Leu-Gly-Gly (**2**) (Bachem, Torrance, CA) (146.2 mg, 0.427 mmol) was dissolved in 20 mL water containing sodium bicarbonate (1.53 g). Benzyl chloroformate (2.0 mL, 14 mmol) was added and the mixture was mechanically stirred for 5 h at room temperature. Reaction times in excess of this caused significant hydrolysis of the starting material. The excess benzyl chloroformate was extracted three times with diethyl ether, the pH adjusted to 4, and the solution was then extracted three times with 25 mL of ethyl acetate. After drying the combined extracts, the solvent was evaporated and the white solid recrystallized from ethyl acetate/petroleum ether to give crystals of **1**, 125 mg (62%), mp 204–205°C. The product was characterized by its ^{1}Hmr and FAB-MS (11).

N-*Benzyloxycarbonyl-L-prolyl-L-prolyl-L-leucylglycylglycine anilide (3)*

A solution of **1** (57.3 mg, 0.12 mmol) in ethyl acetate (25 mL) was cooled to −15°C and enough DMSO was added to keep the solution homogeneous. *N*-Methylmorpholine (15 mL, 0.144 mmol) was added by syringe, followed immediately by isobutylchloroformate (20 L, 0.144 mmol). After 5 min, aniline (15 mL, 0.12 mmol) was added and the mixture was stirred for 1 h at −15°C, followed by additional stirring at room temperature for 6 h. After successive washes with sodium carbonate, water, 1 M HCl, and water, the organic layer was dried over magnesium sulfate. Evaporation of the solvent gave a white solid, which was recrystallized from ethyl acetate/petroleum ether to give 34.5 mg (56%) of **3**, mp 115–118°C. The product was characterized by its ^{1}Hmr and FAB-MS spectra (11).

L-Prolyl-L-leucyl-glycylglycine anilide (4)

A sample of **3** (50.8 mg, 0.919 mmol) was dissolved in 45% HBr in acetic acid (2 mL) and stirred for 30 min. The solution was evaporated to dryness and lyophilized several times with water. Upon dissolution in 1 mL ethanol the derivative was precipitated with methylene chloride and the solid filtered and washed with methylene chloride. This procedure was repeated until the material obtained was white. The anilide **4** was obtained as a white solid, 34.4 mg (87%), mp 160°C (dec.). The product was characterized by its ^{1}Hmr and FAB-MS spectra (11).

Using analogous procedures, *N*-benzyloxycarbonyl glycyl-L-leucylglycylglycine (**5**), mp 140°C, was synthesized from commercially available glycyl-L-leucylglycylglycine (**6**); N-benzyloxycarbonyl glycyl-L-leucylglycylglycine anilide (**7**), mp 160–162°C, was produced from **5**; glycyl-L-leucylglycylglycine anilide (**8**), mp 180°C, was produced from **7**; glycyl-L-prolyl-L-leucylglycine (**9**), mp 183–185°C, was produced from commercially available *N*-benzyloxycarbonyl glycyl-L-prolyl-L-leucylglycine (**10**); *N*-benzyloxycarbonyl glycyl-L-prolyl-L-leucylglycine anilide (**11**), mp 191–193°C, came from **10**; and glycyl-L-prolyl-L-leucylglycine anilide (**12**), mp 160°C, came from **11**. Each of these products was characterized by its ^{1}Hmr and FAB-MS spectra (11).

Procedure for studying reaction kinetics

Kinetic runs were carried out in a phosphate buffer (pH 6.8, 25°C) with a total phosphate concentration of 0.050 N. Two millilitres of ca. 10 mM peptide solution were placed in a glass tube and sealed after five freeze–pump–thaw cycles. The tubes were placed in a thermostated oil bath at a temperature of 148.5 ± 0.05°C. The bath was found to be stable to this precision for a period exceeding the maximum time required for the kinetic runs.

Eight to ten samples were analyzed for the disappearance of substrate peptide, the appearance of new species, and the extent of racemization in these components. Samples were removed from the heating bath at times between 5 and 300 min. The hydrolysis mixture of partially racemized material was separated by TLC or HPLC.

The hydrolysis mixture was separated on silica gel TLC plates (Whatman LK6DF, 250 μm) developed with 4:1:1 *n*-butanol:acetic acid:water. The components in the mixture were visualized with ninhydrin reagent (90 mL of a 0.3 wt.% aqueous solution of ninhydrin, and 10 mL of a solution of 3 g cadmium acetate in 300 mL acetic acid and 150 mL water) or with a UV lamp. The components in the mixture were isolated by scraping off the appropriate section of silica gel followed by extraction with 5.5 M HCl. After filtering the acid extracts (2 μm Metricel) the samples were derivatized and the extent of racemization measured.

Separation of the hydrolysis mixture by HPLC was accomplished using a C-18 reversed phase radial compression column (Waters Associates) connected to a Perkin–Elmer Series 2 liquid chromatograph solvent delivery system. The components of the hydrolysis mixture were detected by UV absorption at 230 nm using a Perkin–Elmer LC-55B UV detector. The separation was performed isocratically using 0.1 M ammonium acetate (pH 7) containing 10% acetonitrile. Ammonium acetate was purified by sublimation. The water used for the separation was deionized and distilled from potassium permanganate. HPLC grade acetonitrile (Caledon) was used untreated. The solvent mixture was degassed by bubbling helium through it for 2 min.

Typically, 1 mL of the reaction mixture was separated by repetitive injections of 100 mL. The hydrolysis fragments were collected manually as they eluted from the column after passing through the UV detector. Six fractions were collected for the hydrolysis and racemization studies of L-prolyl-L-leucylglycylglycine:

1. LL* + DD tetrapeptide
2. DL + LD tetrapeptide

[1]This is not to be confused with those cases wherein a second chiral centre is contained within the peptide unit, e.g., as in isoleucine; such cases have been well described in ref. 9.

Can. J. Chem. Downloaded from www.nrcresearchpress.com by 196.1.178.254 on 09/07/12
For personal use only.

3. LL + DD + DL + LD tetrapeptide[2]
4. DL + LD DKP
5. LL + DD DKP
6. DL + LD + LL + DD DKP[2]

*e.g., DL refers to the sequence D-Pro-L-Leu in the peptide. DKP = diketopiperazine.

In the case of glycyl-L-leucylglycylglycine, three fractions were collected:

1. initial fraction containing dipeptides
2. substrate enantiomers
3. *c*-(gly-L-leu) + *c*-(gly-D-leu)

For all three peptides, a portion of the total hydrolysis mixture was saved to obtain a measurement of racemization of the total hydrolysate. The HPLC solvent was removed from the fraction in a centrifugal biodryer. The identity of the hydrolysis components was determined by FAB-MS and by NMR spectroscopy. The extent of racemization of the separated components was subsequently determined by GC.

The dipeptide Pro-Leu and its diastereomer have similar retention times to the tetrapeptide L-prolyl-L-leucylglycylglycine and its diastereomer. From the measurement of the rate of formation of the DKP's it appeared that the tetrapeptide was hydrolyzing to the DKP with little or no incidence of the dipeptides. However, at long reaction times, the DKP's could be opening to the dipeptides, thus complicating the kinetic picture (12). To test this idea and to determine if the DKP's were in equilibrium with each other, the DKP's were separated from the reaction mixture, heated under the same conditions, and then separated again by HPLC. It was found that the DKP's were in equilibrium with each other and with the dipeptides. The dipeptides were found to be present in the equilibrating mixture to an amount not exceeding ca. 10% of the total. It was assumed that the DKP's were essentially stable to the reactions conditions and that the dipeptides were not significantly affecting the rate constant for hydrolysis derived from the measurement of the disappearance of the substrate. Sample chromatograms and conditions are shown for L-prolyl-L-leucylglycylglycine (Fig. 1).

Identification of hydrolysis products

The dried eluate from chromatography was analyzed by FAB-MS in the case of the peptides or by chemical ionization mass spectroscopy (CI) in the case of the DKP. The absolute configuration of the α carbons of the hydrolysis mixture was determined by GC analysis of the derivatives.

The hydrolysis of L-prolyl-L-leucylglycylglycine yielded three major components. The component having the shortest retention time after the substrate was found to have an $M + 1$ peak at mass 343. GC analysis showed that it consisted of D-proline, L-leucine, and glycine. Although it is tempting to assign the structure D-prolyl-L-leucylglycylglycine to this component, there is a potential complication. The formation of cyclic tetrapeptide(10) from the substrate followed by hydrolysis could in principle yield four isomeric tetrapeptides: Pro-Leu-Gly-Gly, Leu-Gly-Gly-Pro, Gly-Gly-Pro-Leu, or Gly-Pro-Leu-Gly.[3] The sequence of the peptide units was determined by examining the NMR chemical shifts at pH 1.00, 6.40, and 9.18. The removal of charge is predicted to have an effect on the chemical shift of those protons near to the centre of charge (13). A comparison of the change of chemical shift as function of pH for the starting material and the unknown tetrapeptide demonstrates identical behaviour, thus the structure D-prolyl-L-leucylglycylglycine is assigned to this component from the heating experiment.[4] The CI mass spectra of the other two components in the hydrolysis mixture each showed an $M + 1$ peak at mass 211, corresponding to *c*-(prolylleucyl). The component with the shorter retention time was shown by GC analysis to consist of D-proline and L-leucine while the other consisted of L-proline and L-leucine. The proton NMR and MS of authentic *c*-(L-prolyl-L-leucyl) and the latter component were identical. The spectra of the former component was consistent with *c*-(D-prolyl-L-leucyl).

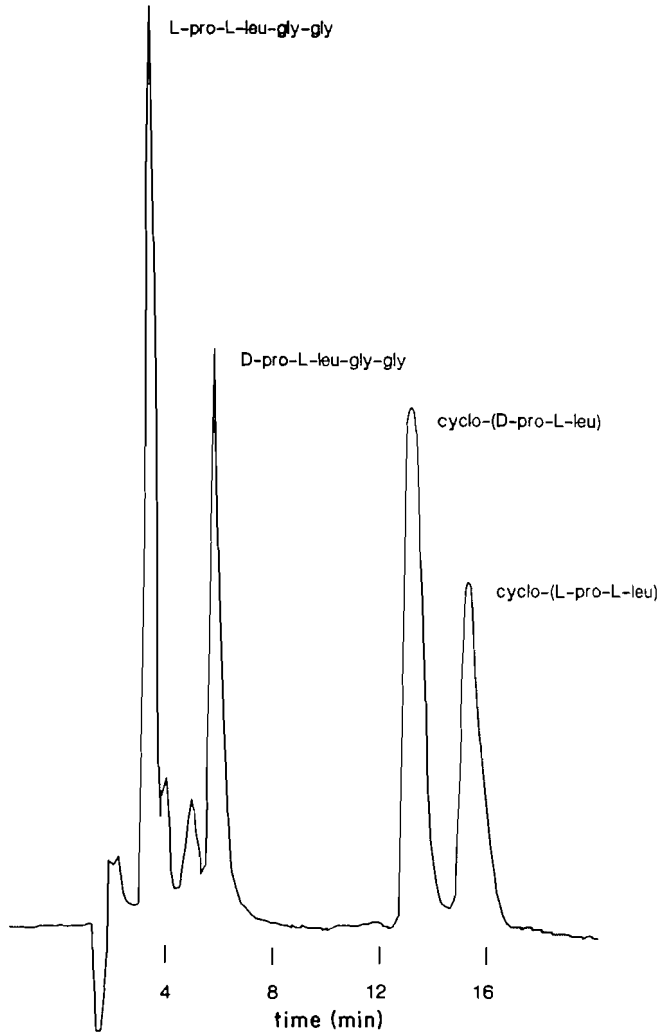

FIG. 1. HPLC trace of the mixture produced after heating L-Pro-L-Leu-Gly-Gly for 30 min at 148.5°C, pH 6.8. Chromatographic conditions: reversed phase C-18 column (Waters), 0.1 M NH_4OCOCH_3, 10% CH_3CN, 1.2 mL/min.

There were also three major components from the heating of L-prolyl-L-leucine, two of which correspond to the DKP's *c*-(D-prolyl-L-leucyl) and *c*-(L-prolyl-L-leucyl) obtained from heating of the tetrapeptide. The CI mass spectrum of the other component eluting after the substrate had an $M + 1$ peak at mass 229. GC analysis of this compound showed that it consisted of D-proline and L-leucine. Again, the sequence of the peptide units is ambiguous and was determined from the pH dependence of chemical shift in the proton NMR (13).

The component with the longest retention time, from the heating experiment with glycyl-L-leucylglycylglycine, gave a CI mass spectrum with an $M + 1$ peak at mass 170. The proton NMR and mass spectra of this compound were identical to the spectra obtained for authentic *c*-(glycyl-L-leucyl). The proton NMR spectrum of the least retained component indicated that it was a mixture. The composition was tentatively assigned to a mixture of glycine and leucine containing dipeptides.

[2]Fractions 3 and 6 were obtained by combining the column effluent from fractions 1 and 2 and fractions 4 and 5 respectively.

[3]It is assumed that the peptide Pro-Gly-Leu-Gly is not possible. The formation of this peptide requires the breaking of the Pro-Leu and Gly-Gly peptide bonds followed by the condensation of Pro, Gly, and Leu-Gly. This seems highly improbable.

[4]The nonobservance of any tripeptide is noteworthy. Presumably this is due to the preferential formation of diketopiperazines by internal aminolysis rather than peptide hydrolysis to yield a tripeptide.

Can. J. Chem. Downloaded from www.nrcresearchpress.com by 196.1.178.254 on 09/07/12
For personal use only.

TABLE 1. D/L ratios from components isolated from TLC[a] of peptide hydrolysate, 148.5°C, pH 6.8, 270 min

Peptide[b]	Component No.	R_f	D/L val	leu	glu	phe	ala	pro
Val-Leu-Ser-Glu-Gly	1	0.36	0.50	0.40	0.03			
	2	0.29	1.13	1.01	0.04			
	3*	0.17		0.05	0.15			
	4	0.14			1.27			
	5	0.11	0.50	0.40	0.003			
Gly-Leu-Gly-Gly	1	0.25		0.66				
	2*	0.18		0.43				
Ala-Phe-Pro-Ala-β-Naphth	1	0.38					0.20	
	2*	0.35				0.03	1.15	0.085
	3	0.28				0.04	0.90	0.00
	4	0.16					0.49	
Z-Gly-Pro-Leu-Gly[c]	1*	0.27		0.02				0.00
	2	0.21		0.34				0.78
	3	0.18		0.22				
	4	0.16		0.02				0.77
Gly-Gly-Pro-Ala	1	0.061					0.020	
	2*	0.036					0.07	0.09
Pro-Leu-Gly-Gly	1	0.27		0.40				0.73
	2	0.22		0.18				1.04
	3*	0.12		0.04				2.03

[a]Stationary phase: silica gel (Whatman LK6DF 250 μm). Mobile phase: *n*-butanol/acetic acid/water, 4:1:1.
[b]Substrate marked by *.
[c]Z = $C_6H_5CH_2OCO$.

Results and discussion

To determine the effect of neighbouring peptide units on the rate of epimerization of a peptide, it is necessary to separate the peptide from the mixture of products from hydrolysis. In an exploratory experiment thin-layer chromatography was used to attempt to separate the components of the mixture after heating a buffered aqueous solution of the model peptides. Extensive cleavage of the starting tetrapeptide occurs before any significant degree of epimerization of the reactant occurs. This last point underscores the limitation of studies that focus on the racemization of the total hydrolysis mixture. The assignment of the experimentally determined rate constant to the substrate accounts for only a small amount of the material in the hydrolysis mixture, if amino acid chirality is the parameter being measured.

Separation of the hydrolysis mixture is also not without hazards. In the case of a peptide with several chiral centres, there could be several separable diastereomers of the original peptide. Analysis of the component having the same retention time as the original peptide will likely result in a rate of epimerization that will certainly be lower than the rate of epimerization for all of the diastereomers combined. Therefore, it is important to be sure that the substrate and its diastereomers are not separated from each other or that they can be identified in the chromatogram. For experimental purposes, especially for determining epimerization rate constants for a protein, it is far better to try to achieve the former situation.

Despite the problems associated with separation, conclusions are possible from heating experiments on model peptides using TLC as the separation technique. The data in Table 1 were collected by isolating a fraction from the TLC plate having the same R_f as the substrate. Aside from the substrate, the identity of each spot on the TLC is not known. The important observation is the large variation in the D/L ratios in the components from the hydrolysis of peptides containing more than one chiral centre.

The one peptide that cannot suffer from the problems of diastereomers is the tetrapeptide containing only one chiral centre, glycyl-L-leucylglycylglycine. The tetrapeptide was heated at 148.5°C at pH 6.8 and the hydrolysis mixture separated by TLC. Five distinct components were detected (Table 2); that corresponding to the substrate was isolated and its D/L ratio measured. Equation [1] ($K' = 1.00$) is appropriate if there are no reversible processes, other than racemization, involving the substrate. Figure 2 shows the quality of fit obtained, demonstrating that the racemization process does follow pseudo-first-order kinetics described by eq. [1]. Similarly we observed that the other TLC spots that contained leucine had D/L ratios greater than that of the original substrate, and thus any rate constant derived from an analysis of the total sample would yield a rate constant faster than that of the tetrapeptide (Table 3).

Racemization and disappearance of L-prolyl-L-leucylglycylglycine

A goal of this work was to model the racemization of protein, using peptides having more than one chiral centre. Separation by TLC was incapable of resolving the complex hydrolysis mixture from peptides of this type. HPLC was considered to be the analytical method of choice since the experimental parameters could be controlled better than for TLC. For subsequent studies, HPLC was used exclusively for separation of peptide decomposition[5] mixtures.

The predominant feature of the racemization of L-prolyl-L-

[5]The generic term "decomposition" will be used to describe both the hydrolysis and cyclization.

Can. J. Chem. Downloaded from www.nrcresearchpress.com by 196.1.178.254 on 09/07/12
For personal use only.

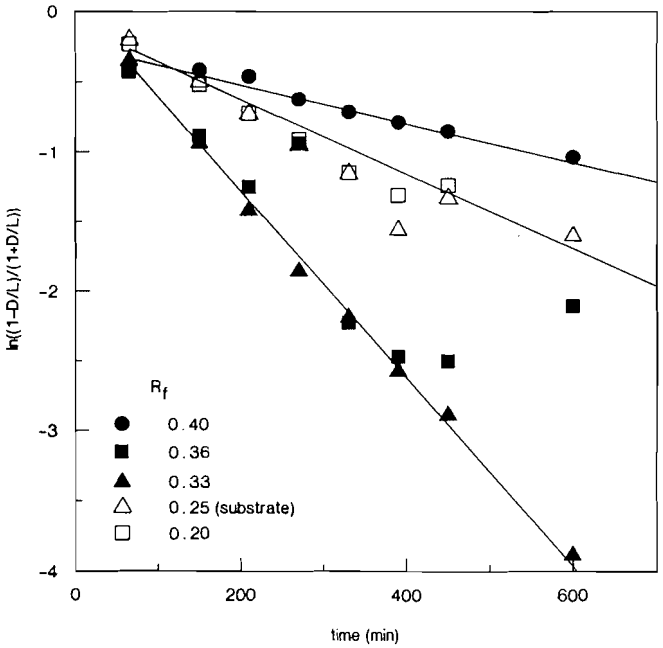

FIG. 2. Racemization of the leucine peptide unit in components isolated by TLC during the decomposition of Gly-L-Leu-Gly-Gly, 148.5°C, pH 6.8, 7.71 mM. The solid lines were produced for the components having R_f values of 0.40, 0.33, and 0.25. See Table 2.

TABLE 2. Racemization[a] (D/L) of leucine peptide unit in components isolated by TLC during the decomposition of glycyl-L-leucyl-glycyl-glycine (148.5°C, pH 6.8, 7.71 mM)

	D/L ratios of components in mixture				
Time (min)	1 (0.40)[b]	2 (0.36)	3 (0.33)	4 (0.25)	5 (0.20)
65	0.205	0.213	0.173	0.101	0.118
150	0.205	0.418	0.437	0.244	0.255
210	0.234	0.556	0.610	0.350	0.349
270	0.302	0.440	0.729	0.444	0.430
330	0.344	0.806	0.799	0.522	0.522
390	0.375	0.844	0.859	0.654	0.576
450	0.401	0.849	0.895	0.582	0.553
600	0.476	0.784	0.960	0.665	—

[a]Separation performed on Whatman LK6DF 250 μm silica gel. Mobile phase, *n*-butanol:acetic acid:water, 4:1:1.

[b]R_f values of each component in parentheses; see Table 3 for identification of each component.

leucylglycylglycine is the occurrence of an excess of D-proline in the total hydrolysate and in the diketopiperazine isolated during the decomposition of the substrate (Fig. 3). Excess D-proline has been observed in similar systems. For example *N*-benzyloxycarbonyl-L-alanyl-L-phenylalanyl-L-proline treated with acetic anhydride and sodium acetate gives *N*-(*N*-benzyloxycarbonyl-L-alanyl)-*c*-(L-phenylalanyl-D-prolyl) (**13**) (14). Also, phenylacetyl- L-alanyl-L-phenylalanyl-L-prolyl-*p*-nitrophenyl ester treated with NaH in DMF at 0°C for 2 h gives **14**, *N*-(phenylacetyl-L-alanyl)-*c*-(L-phenylalanyl-D-prolyl) (15). Earlier, a 90:10 ratio of *c*-(L-Phe-D-Pro):*c*-(L-Phe-L-Pro) was formed by treating *c*-(L-Phe-L-Pro) with 0.5 N NaOH at room temperature for 15 min (16), see Scheme 3. In the early studies of ergot alkaloids (17), D-proline was isolated from the alkaline hydrolysate in the form *c*-(D-prolyl-X) (X = Leu, Phe,

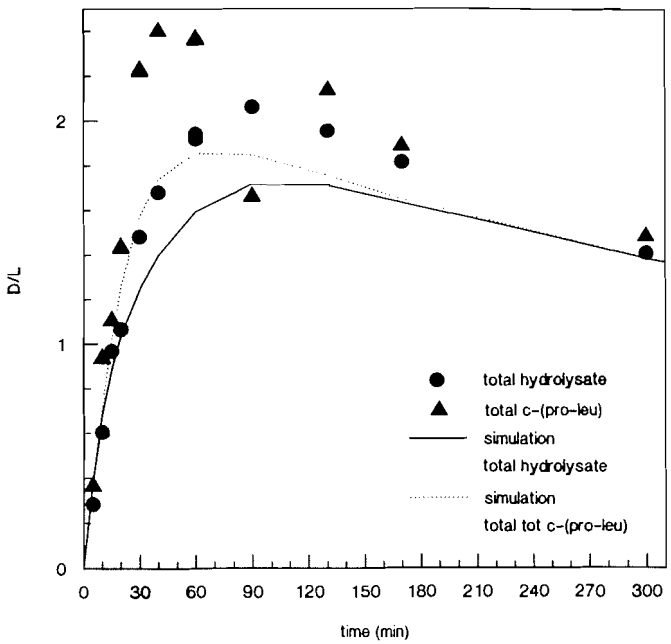

FIG. 3. Racemization of the proline peptide unit in the total hydrolysate and total *c*-(Pro-Leu) isolated during the decomposition of L-Pro-L-Leu-Gly-Gly, 148.5°C, pH 6.8, 8.45 mM. The *N*-pentafluoropropionyl isopropyl esters of D- and L-proline could not be baseline resolved by GC. Immediately after a sample run, a standard D/L proline derivative mixture having a D/L ratio close to that of the sample was injected into the GC. The observed D/L ratio for the sample was subsequently adjusted. The dotted and solid lines show the computer simulation produced for total *c*(-Pro-Leu) and total hydrolysate respectively using the experimentally derived rate constants (Table 4). The details of the assumptions used to obtain the rate constants are given in the text. The computer simulation is based on the pathways given in Scheme 2.

TABLE 3. Leucine epimerization rate constants for components isolated by TLC[a] during the decomposition of glycyl-L-leucyl-glycycl-glycine (148.5°C, pH 6.8, 7.71 mM)

Component (R_f)	10^5 k (s^{-1})
Leucine (0.40±0.03)	1.10±0.08
Glycylleucine (0.36±0.03)	4.93±0.79[b]
Glycylleucylglycine (0.33±0.03)	5.45±0.10
Glycylleucylglycylglycine (0.25±0.02)[c]	2.30±0.33
Glycylleucylglycylglycine (0.20±0.03)[c]	2.40±0.15

[a]Separation performed on Whatman LK6DF 250 μm silica gel. Mobile phase, *n*-butanol:acetic acid:water, 4:1:1.

[b]Only the first seven points (of the data in Table 2) were used to calculate the rate constant.

[c]Both the leading and trailing edge of this spot were sampled.

Val). This caused confusion regarding the stereochemistry of proline in these alkaloids (18). It was later discovered that in the alkaloids, proline was in the L form. By using only 1 equivalent of base to hydrolyze the alkaloids, the DKP containing L-proline can be obtained. Addition of more base epimerizes the DKP to the thermodynamically more stable *c*-(L-leucyl-D-prolyl) (18).

Scheme 2 shows the pathways consistent with our observations of L-prolyl-L-leucylglycylglycine. There is sufficient information available to estimate the 10 rate constants, eight of

Can. J. Chem. Downloaded from www.nrcresearchpress.com by 196.1.178.254 on 09/07/12
For personal use only.

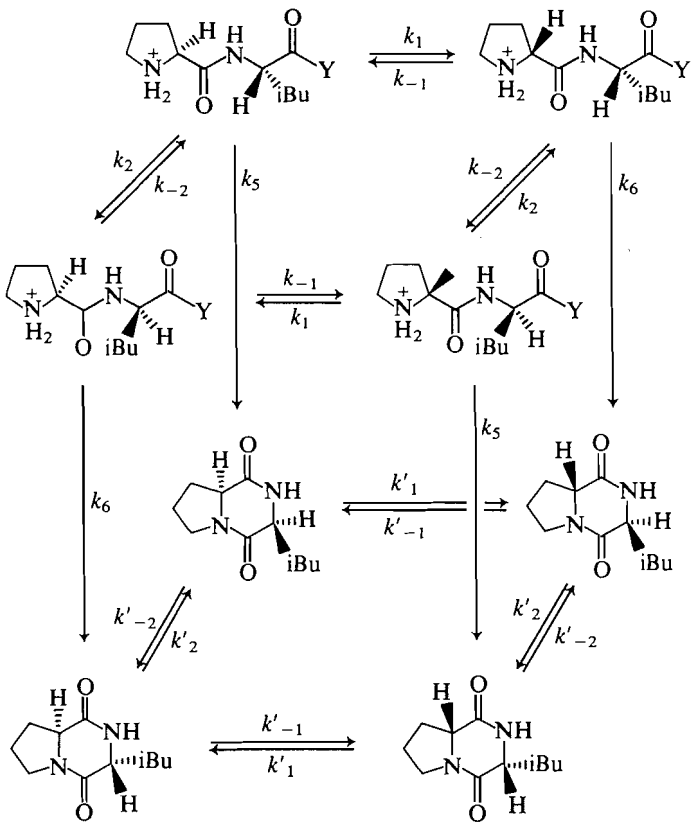

Pro-Leu-Gly-Gly; Y = 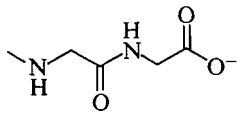

Pro-Leu; Y = O^-

SCHEME 2

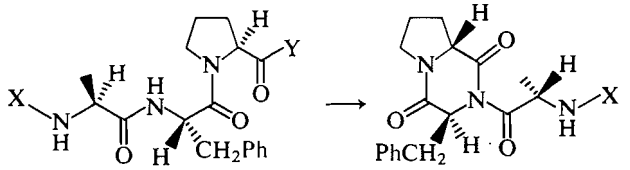

13 X = $PhCH_2OCO$; Y = −OH
14 X = $PhCH_2CO$; Y = $pNO_2C_6H_4O^-$

SCHEME 3

which are independent. The disappearance of L-prolyl-L-leucylglycylglycine and its diastereomer D-prolyl-L-leucylglycylglycine and the appearance of *c*-(L-prolyl-L-leucyl) and its diastereomer *c*-(D-prolyl-L-leucyl) are shown in Fig. 4. The rate constants k_5 and k_6 (Scheme 2) can be seen from Fig. 4 to be equal since, after approximately 20 min, the diastereomers are disappearing at the same rate. The facile formation of DKP is not unexpected. Dipeptide esters and amides are known to cyclize, especially when one of the peptide units is proline or N-methylated (19). Adding together the concentrations of the diastereomers of prolylleucylglycylglycine and plotting the natural logarithm of the concentration versus time should yield a straight line with slope $-k_5$ or $-k_6$ (Fig. 5). A similar

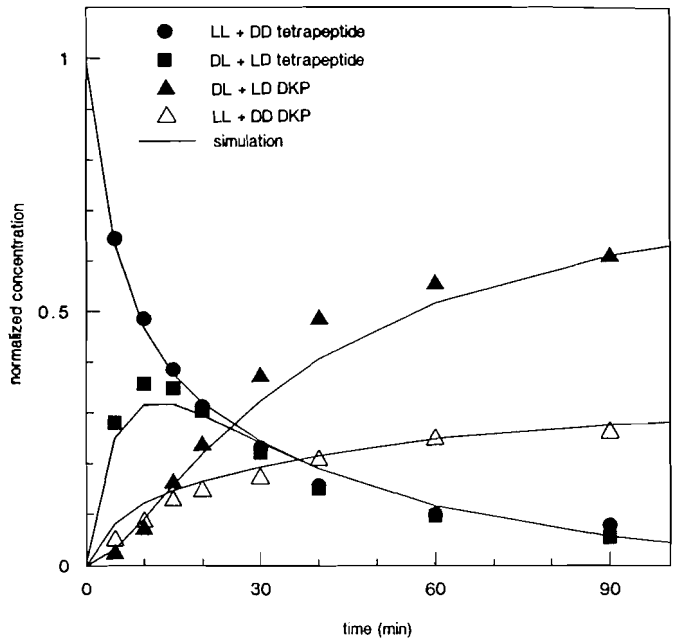

FIG. 4. Decomposition of L-Pro-L-Leu-Gly-Gly, 148.5°C, pH 6.8, 8.45 mM. As in Fig. 3, the solid line shows the result of the computer simulation.

treatment[6] of the data for the DKP's yields the same rate constant if there is no competing hydrolysis of the tetrapeptide.[7]

Figure 4 shows that the diastereomers L-prolyl-L-leucylglycylglycine and D-prolyl-L-leucylglycylglycine achieved the same concentration after 20 min. This phenomenon can be expressed as

$$[2] \quad \frac{\text{DL} + \text{LD}}{\text{DD} + \text{LL}} = 1.0$$

and requires that $k_{-1} = k_1$ and $k_2 = k_{-2}$, where, for example, DL refers to the concentration of D-prolyl-L-leucylglycylglycine. The D/L ratio for the proline of the tetrapeptide unit never exceeded unity (Fig. 6). The fact that $k_5 = k_6$, $k_1 = k_{-1}$, and $k_2 = k_{-2}$ significantly simplifies the extraction of the rate constants depicted in Scheme 2. The procedure for extracting the rate constants can be summarized as follows:

1. Since there is no evidence for a preferred diastereomer in the recovered tetrapeptides, k_1 and k_2 can be obtained from the appropriate plots using eq. [1].

[6]The complete derivation of the kinetics applicable to Scheme 2 and Fig. 5, and an appropriate computer program written in Microsoft Basic Version 3.2 may be purchased from the Depository of Unpublished Data, CISTI, National Research Council of Canada, Ottawa, Ont., K1A 0S2.

[7]There are two pieces of evidence to support this: (1) A test sample of L-prolyl-L-leucylglycylglycine (2.99 mg/mL) was extracted with 3 × 5 mL CH_2Cl_2 after 60 min of heating at 148.5°C. Material weighing 3.2 ± 0.2 mg was isolated, having the same 200-MHz ^{1}Hmr spectrum as the DKP and with mass 210 (M + 1 in CI mass spectrum). This constituted an 86 ± 5% yield in good agreement with the expected result. (2) The total eluate from the HPLC up to the elution of L-prolyl-L-leucylglycylglycine (the first major peak) was collected. By GC analysis this was found to contain mostly glycine, with a Gly/Pro/Leu ratio of 1:0.06:0.01. The relative amount of glycine is larger than this since the derivatization/analysis procedure depletes the glycine derivative more than it does Pro or Leu.

Can. J. Chem. Downloaded from www.nrcresearchpress.com by 196.1.178.254 on 09/07/12
For personal use only.

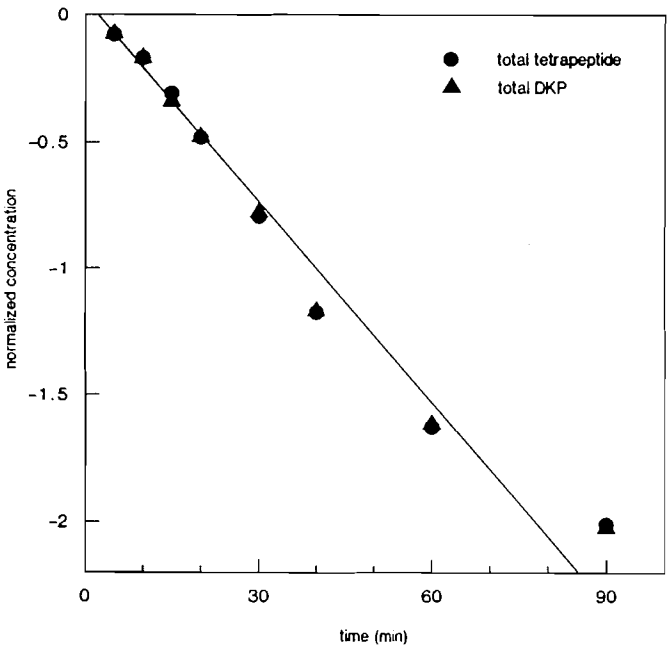

FIG. 5. Decomposition of L-Pro-L-Leu-Gly-Gly, 148.5°C, pH 6.8, 8.45 mM. For Pro-Leu-Gly-Gly the ordinate is $-\ln(c)$ where c is the normalized concentration of total tetrapeptide. For c-(Pro-Leu) the ordinate is $-\ln(1-c)$ where c is the normalized concentration of diketopiperazine. The solid line was produced by linear regression analysis.

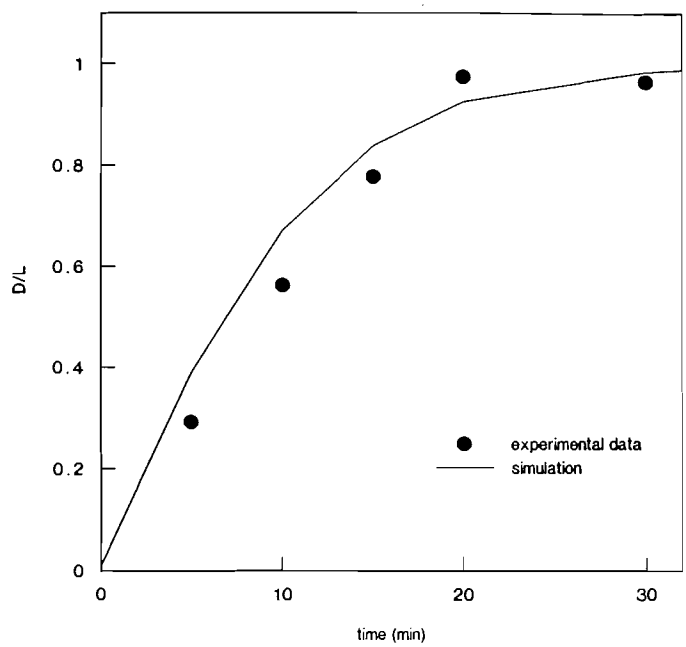

FIG. 6. Racemization of the proline peptide unit in the total tetrapeptide isolated during the decomposition of L-Pro-L-Leu-Gly-Gly, 148.5°C, pH 6.8, 8.45 mM. As in Fig. 3, the solid line shows the result of the computer simulation.

2. Obtain k'_1/k'_{-1} by measuring (DL + LD)/(DD + LL) at long reaction times.
3. Plot $\ln((1\text{-D/L})/(1 + \text{D/L}))$ versus time for the peptide unit undergoing epimerization to yield $k'_1 + k'_{-1}$.
4. Plot $\ln((1\text{-D/L})/(1 + \text{D/L}))$ versus time for the other racemizing centre. Using the slope, m, of this plot, k'_2 can be obtained from eq. [3]:

$$[3] \quad k'_2 = \frac{-m(m + k'_1 + k'_{-1})}{1 + K + 4k'_1}$$

k'_{-2} is obtained from $k'_{-2} = k'_2K$.

There are two weaknesses to this method; firstly, accuracy of $k'_1 + k'_{-1}$ is sensitive to the precision of the data and the number of data points taken around time zero. Also, the determination of "around time zero" and "long reaction times" is somewhat arbitrary. Secondly, a choice must be made between using a small number of data points and the precision of the individual data point. For example, using data at time 5, 10, and 15 min will yield a value of $k'_1 + k'_{-1}$ that will be less than the true value and probably less than that obtained from the first two data points. It is also a better approximation of the true average slope.

The experimentally determined rate constants for L-prolyl-L-leucylglycylglycine are given in Table 4. The consistency of the kinetic model was tested by substituting the experimental values in a computer program simulating Scheme 2. Overall the agreement is quite good (11). As expected, the major discrepancy is associated with the rate constant for epimerization of the proline peptide unit ($k'_1 + k'_{-1}$) in the DKP. The computer simulations using the experimentally determined values are superimposed on the experimental data in Figs. 3, 4, and 6.

TABLE 4. Experimentally determined rate constants for L-Pro-L-Leu-Gly-Gly and L-Pro-L-Leu (148.5°C, pH 6.8)

Rate constant	L-Pro-L-Leu-Gly-Gly[a] (10^4 s^{-1})	L-Pro-L-Leu[b] (10^4 s^{-1})
$k_1=k_{-1}$	13.4±0.8[d]	3.58±0.15
$k_2=k_{-2}$	0.083±0.015	0.0046±?
$k_5=k_6$	4.03±0.30	1.72±0.06
k'_1	10.4±1.0	13.9±1.5
k'_{-1}	4.52±0.45	6.97±0.66
k'_2	0.202±0.015[c]	0.235±0.030
k'_{-2}	0.436±0.036	0.540±0.069

[a]Rate constants k_1, k_{-1}, k_2, and k_{-2} refer to the tetrapeptide; k'_1, k'_{-1}, k'_2, and k'_{-2} refer to the diketopiperazine.
[b]Rate constants k_1, k_{-1}, k_2, and k_{-2} refer to the dipeptide; k'_1, k'_{-1}, k'_2, and k'_{-2} refer to the diketopiperazine.
[c]From $m = (5.60 \pm 0.43) \times 10^{-5}$ s^{-1} leucine epimerization, eq. [3]; $(5.65 \pm 1.12) \times 10^{-5}$ s^{-1} including proline epimerization.
[d]The rate constants are quoted as averages of several measurements. The error is reported at the 95% confidence level.

The maximum D/L ratio of the proline predicted using the experimentally determined rate constants is about 1.86 (at 40 min)) Fig. 3). If the decomposition of the tetrapeptide was instantaneous (i.e., the starting condition was pure c-(L-prolyl-L-leucyl)) the maximum predicted is 1.92 (at 50 min). Therefore an underestimate of the rate constant k'_1 or k'_{-1} cannot be completely responsible for the discrepancy in $k'_1 + k'_{-1}$. The most likely source of error lies with the model used to extract the rate constant (Scheme 2) for it does not account for the presence of species other than the tetrapeptide and the diketopiperazine. Other species in the mixture that yield D-proline could account for the discrepancy in $k'_1 + k'_{-1}$ and the maximum D/L ratio observed for the diketopiperazine and the total hydrolysate. The dipeptide L-prolyl-L-leucine was thought to be a logical candi-

Can. J. Chem. Downloaded from www.nrcresearchpress.com by 196.1.178.254 on 09/07/12
For personal use only.

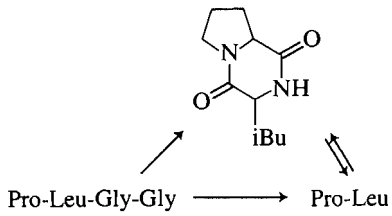

SCHEME 4

date for another species that could be found in the hydrolysis mixture from L-prolyl-L-leucylglycylglycine since it could be formed according to Scheme 4.

Figure 7 shows a plot of the D/L ratio of the proline peptide units at various reaction times when a sample of L-prolyl-L-leucine is used as the reactant, and the D/L ratio of both the total reaction mixture and that of the DKP isolated from the reaction mixture are measured. The rate constants were extracted in a similar manner as for L-prolyl-L-leucylglycylglycine above and are given in Table 4. A computer simulation using these values was performed and the agreement is shown in Fig. 7 and in a plot of the L-prolyl-L-leucine decomposition data (Fig. 8). A comparison of the rate constants for L-prolyl-L-leucylglycylglycine and for L-prolyl-L-leucine shows three noteworthy features:

1. The rate of cyclization (dehydration) of L-prolyl-L-leucine to the corresponding DKP is slower than the rate of production of the DKP from L-prolyl-L-leucylglycylglycine.
2. Proline racemization is slower for L-prolyl-L-leucine than for L-prolyl-L-leucylglycylglycine. These two observations indicate that the dipeptide cannot be giving rise to the underestimate of $k'_1 + k'_{-1}$ in the DKP.
3. Leucine racemization in the dipeptide is at least an order of magnitude slower than in the tetrapeptide. Removal of the proton at the asymmetric centre of the dipeptide may be inhibited by the electrostatic repulsion between the carboxylate anion and the developing negative charge in **15**.

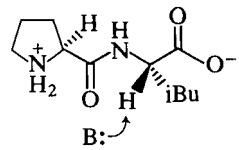

15

To probe the influence of ring-opening of the DKP to prolylleucine, pure *c*-(L-prolyl-L-leucyl) was epimerized under the decomposition reaction conditions. The rate constant was found to be $2.03 \times 10^{-3}\,s^{-1}$, essentially the same value obtained from both L-prolyl-L-leucylglycylglycine and L-prolyl-L-leucine. These results suggest that the rate-determining step in the racemization of proline from L-prolyl-L-leucylglycylglycine is at the DKP stage and that the cyclization of the L-prolyl-L-leucine can be ignored. This implies that the DKP is, in this instance, arising directly from the tetrapeptide.

Racemization of glycyl-L-leucylglycylglycine

A time study of the racemization and hydrolysis behaviour of glycyl-L-leucylglycylglycine was carried out for comparison with the study on L-prolyl-L-leucylglycylglycine. The species in the hydrolysis mixture are the substrate, glycyl-L-leucylglycylglycine, the DKP *c*-(glycylleucyl), and at least two other components. Spiking the mixture with authentic dipeptides indicated that these components were probably Gly-Leu, Leu-Gly, and Gly-Gly.

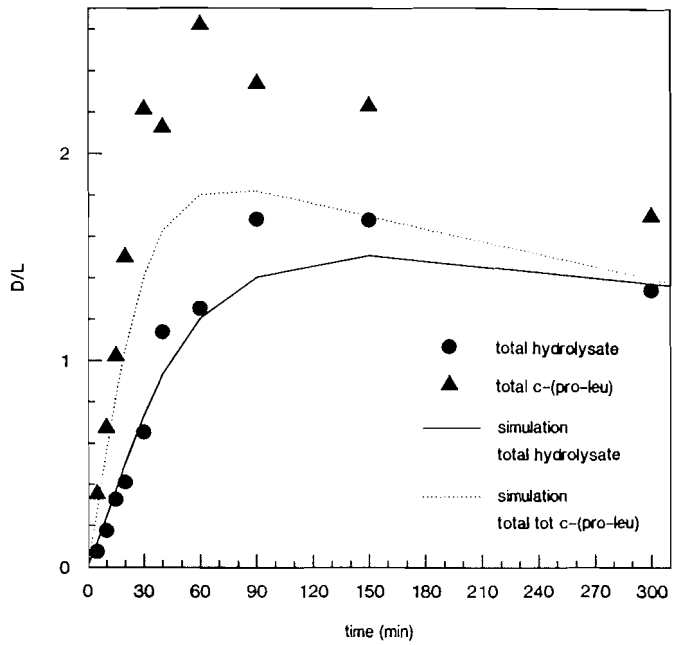

FIG. 7. Racemization of the proline peptide unit in the total hydrolysate and total *c*-(Pro-Leu) isolated during the decomposition of L-Pro-L-Leu, 148.5°C, pH 6.8, 9.01 mM. As in the case of L-Pro-L-Leu-Gly-Gly, the proline D/L ratios were corrected (see Fig. 3). The dotted and solid lines show the computer simulation produced for total *c*-(Pro-Leu) and total hydrolysate respectively using the experimentally derived rate constants (Table 4). The details of the assumptions used to obtain the rate constants are given in the text. The computer simulation is based on the pathways given in Scheme 2.

The source of DKP in this experiment is ambiguous since in the early stages there is more dipeptide than DKP.[8] Some of the DKP must ultimately come from the dipeptides arising from hydrolysis of the tetrapeptide.

There are three important findings from this experiment. First, a DKP is formed during the heating of another tetrapeptide. Second, the racemization rate of the substrate $(2.57 \pm 0.08) \times 10^{-5}\,s^{-1}$ does not resemble that of the total hydrolysis mixture $(4.53 \pm 0.11) \times 10^{-5}\,s^{-1}$ (Figs. 9 and 10). This further demonstrates that the epimerization rate constant of a peptide cannot be measured by the initial slope of a plot using eq. [1]. Third, the racemization of glycyl-L-leucylglycylglycine is about three times faster than the rate of epimerization of the leucine peptide unit in L-prolyl-L-leucylglycylglycine. This demonstrates that neighbouring peptide units have a significant effect on epimerization rates, and that such factors must be considered in using amino acid racemization rates as a geochronometric tool.

Racemization of peptide derivatives

In several previous studies (20), attempts have been made to explain the way in which the position of the peptide unit along the peptide chain affects the rate of racemization. It has been suggested that proximity to the termini increased the rate of racemization. By use of the N-terminal *N*-benzyloxycarbonyl and C-terminal anilide derivatives of the tetrapeptides glycyl-L-leucylglycylglycine, L-prolyl-L-leucylglycylglycine, and glycyl-L-prolyl-L-leucylglycine, this idea was tested. Tetrapeptides were considered to be better protein models than di- or

[8]Glycyl-L-leucylglycylglycine decomposes with a first-order rate constant of $(1.8 \pm 0.4) \times 10^{-4}\,s^{-1}$.

Can. J. Chem. Downloaded from www.nrcresearchpress.com by 196.1.178.254 on 09/07/12
For personal use only.

Can. J. Chem. Downloaded from www.nrcresearchpress.com by 196.1.178.254 on 09/07/12
For personal use only.

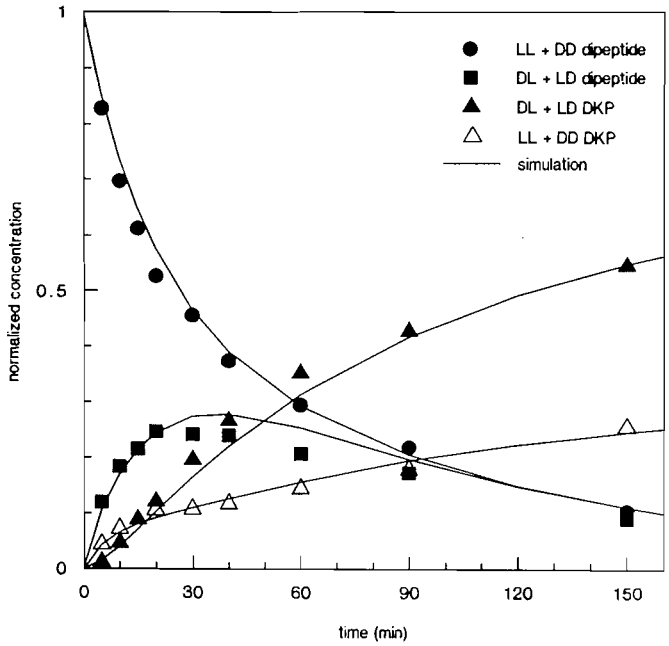

FIG. 8. Decomposition of L-Pro-L-Leu, 148.5°C, pH 6.8, 9.01 mM. As in Fig. 7, the solid line shows the result of the computer simulation.

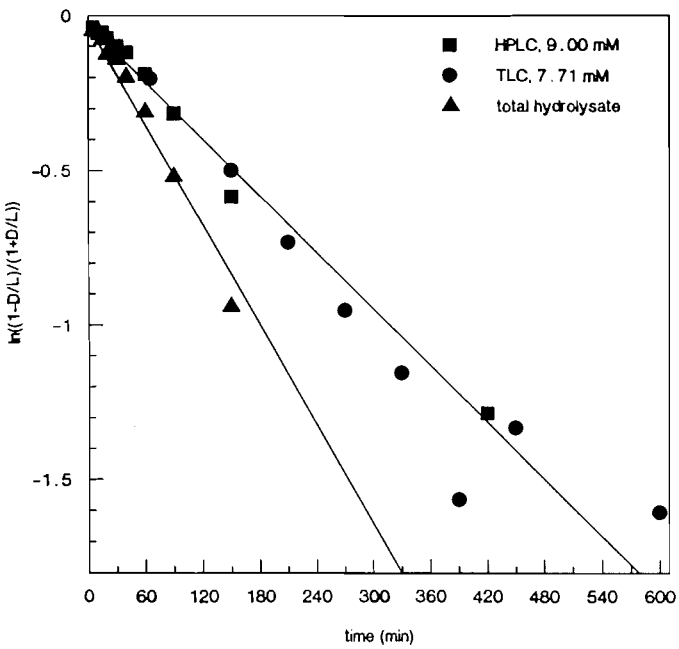

FIG. 9. Racemization of the leucine peptide unit in Gly-Leu-Gly-Gly isolated during the decomposition of Gly-L-Leu-Gly-Gly, 148.5°C, pH 6.8, 9.00 mM. Data from the separation by TLC and HPLC are combined in this plot. The solid line was produced from the HPLC data by linear regression analysis.

tripeptides. Also, the N-, C-, and N- and C-blocked peptides were taken to model the C-terminal, N-terminal, and interior portions of the peptide respectively.

The compounds were heated under the same conditions used in the time studies (Table 5). Since hydrolysis consumes the unblocked parent peptides quite rapidly, the degree of observed racemization is small in some cases.

Assuming that the epimerization follows eq. [1], the rate constants can be estimated. Placing a *N*-benzyloxycarbonyl

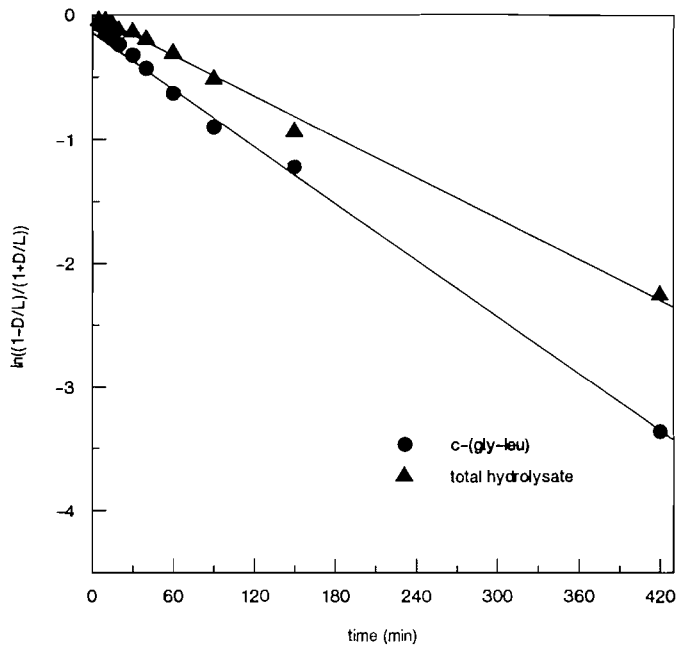

FIG. 10. Racemization of the leucine peptide unit in *c*-(glycyl-leucyl) isolated during the decomposition of Gly-L-Leu-Gly-Gly, 148.5°C, pH 6.8, 9.00 mM. The solid lines were produced by linear regression analysis.

TABLE 5. Leucine epimerization in recovered substrates (148.5°C, pH 6.8, 150min)

Peptide	(D/L)	$(D/L)_{t=0}$	$10^5\ k\ (s^{-1})^b$
Pro-Leu-Gly-Gly[a]	0.0841	0.0105	1.4±0.2
Z-Pro-Leu-Gly-Gly[a]	0.0249	0.0110	0.26±0.20
Z-Pro-Leu-Gly-Gly-NHPh[a]	0.0405	0.0116	0.53±0.18
Pro-Leu-Gly-Gly-NHPh[a]	0.0944	0.0119	1.5±0.1
Gly-Pro-Leu-Gly	0.126	0.0176	1.2±0.2
Z-Gly-Pro-Leu-Gly	0.0282	0.0187	0.1±0.1
Z-Gly-Pro-Leu-Gly-NH-Ph	0.05317	0.0201	0.37±0.12
Gly-Pro-Leu-Gly-NH-Ph	0.184	0.0222	1.8±0.1
Gly-Leu-Gly-Gly	0.3489	0.0194	3.8±0.1
Z-Gly-Leu-Gly-Gly	0.0579	0.0189	0.43±0.12
Z-Gly-Leu-Gly-Gly-NHPh	0.0736	0.0177	0.62±0.12
Gly-Leu-Gly-Gly-NHPh	0.270	0.0156	2.9±0.1

[a]Ninety minutes.
[b]Calculated using eq. [1].

group on the N-terminus decreases the rate of epimerization of the leucine peptide unit. N-Benzyloxycarbonyl has the added effect of reducing hydrolysis. Conversely, addition of a C-anilide has little effect. It does not significantly change the rate of epimerization of leucine nor does it prevent hydrolysis. The results for proline as shown in Table 6 are essentially the same as for leucine. The rate decreases caused by the *N*-benzyloxycarbonyl group can be explained in three ways:

1. Free NH_2 can act as a base in **14**. When blocked with the *N*-benzyloxycarbonyl group, the nitrogen is not so readily able to remove the proton from the asymmetric centre of either the adjacent peptide or a peptide unit of another molecule. Since peptides are present at neutral pH as zwitterions there would be very little free NH_2. It would be tempting to eliminate the above pathway for this reason. However, since DKP formation

TABLE 6. Proline epimerization in recovered substrates (148.5°C, pH 6.8)

Peptide	(D/L)	$(D/L)_{t=0}$	$10^5\ k\ (s^{-1})^b$
Pro-Leu-Gly-Gly[a]	0.0956	0.0081	1.6±0.2
Z-Pro-Leu-Gly-Gly	0.0181	0.0131	0.09±0.1
Z-Pro-Leu-Gly-Gly-NHPh	0.0256	0.081	0.32±0.10
Pro-Leu-Gly-Gly-NHPh	0.174	0.0094	3.1±0.2
Gly-Pro-Leu-Gly	0.252	0.0145	2.7±0.2
Z-Gly-Pro-Leu-Gly	0.0284	0.0142	0.16±0.12
Z-Gly-Pro-Leu-Gly-NH-Ph	0.0241	0.1611	0.88±0.12
Gly-Pro-Leu-Gly-NH-Ph	0.314	0.0182	3.42±0.15

[a]Ninety minutes for Pro-Leu-Gly-Gly and derivatives, 150 min for Gly-Pro-Leu-Gly and derivatives.
[b]Calculated using eq. [1].

requires an unprotonated amino function **15** and since DKP formation is so predominant, elimination of the above pathway is not justified. Indeed, the ability to cyclize to give a DKP may be reflected by an enhanced rate of racemization.

2. The removal of the positive charge from nitrogen by substitution eliminates the inductive stabilization of the incipient carbanion.

3. The presence of the hydrophobic *N*-benzyloxycarbonyl group disrupts the solvation shell so that the approach of water, acting as a base to remove the chiral proton, is impeded. When the N-terminus is not blocked, racemization may be aided by more tightly packed solvent molecules.

Since the anilide derivatives are amines, at pH 6.8 they will be predominantly in the protonated form (21). Therefore, it is not surprising that the anilide derivative behaves in the same way as the parent tetrapeptide, giving both relatively rapid racemization and a large amount of DKP. The derivatives can then be grouped according to their racemization behaviour. Those derivatives that racemize relatively quickly have positively charged nitrogen termini. The derivatives with blocked nitrogen termini racemize more slowly regardless of the charge on the C-terminus. The derivative with a protected nitrogen terminus (e.g., *N*-benzyloxycarbonyl-L-prolyl-L-leucylglycylglycine) will be mostly in the form of an anion (19).

Since the anion on the C-terminus does not appear to increase the rate of racemization, the anion cannot be acting as a base. It is noteworthy that the presumed increase in solvation of the anion (compared with the uncharged derivative) is also ineffective in promoting racemization. On the contrary, the leucine peptide unit of derivatives blocked only at the C-terminus racemizes more slowly than those derivatives having both termini blocked (Table 5). It appears that the presence of a carboxylate anion inhibits formation of an anion at the asymmetric centre. This is consistent with the slower rate of racemization observed for L-prolyl-L-leucine compared with L-prolyl-L-leucylglycylglycine.

The racemization of the peptide units in the total hydrolysate is given in Table 7 for leucine and in Table 8 for proline. The behaviour is the same as the substrates with one exception. The D/L ratio for the proline peptide in the total hydrolysate reaches a value of 1.97 for L-prolyl-L-leucylglycylglycine and 1.94 for L-prolyl-L-leucylglycylglycine anilide. This indicates that L-prolyl-L-leucylglycylglycine anilide is decomposing by internal aminolysis to give the DKP, *c*-(L-prolyl-L-leucyl). The DKP then epimerizes to the thermodynamically preferred diastereomer *c*-(D-prolyl-L-leucyl) (22).

The above experiments demonstrate that proximity to a protonated nitrogen enhances the rate of racemization. Conversely, proximity to a carboxylate anion decreases the rate of racemization. This does not mean that the rate of racemization for the individual peptide units in a peptide or peptide chain will increase monotonically from the C-terminus to the N-terminus. It is not justified to ignore possible rate enhancement/retardation by a nearby charge centre that is not a terminus (e.g. $-NH_3^+$ of lysine or $-CO_2^-$ of glutamic acid). Further complicating the picture, a uniform distribution of water along the peptide chain should not be assumed. Hare observed little racemization in bones heated at 157°C for 3 days under anhydrous conditions, while there was essentially complete racemization in the presence of water (22). By analogy, a lower rate of racemization is expected for peptide units in a region of peptide where water is excluded. Clearly, because of the individual structural characteristics of each protein, it is difficult to generalize protein racemization behaviour based on any one model study.

TABLE 7. Leucine epimerization in total hydrolysate of tetrapeptides (148.5°C, pH 6.8)

Peptide	(D/L)	$(D/L)_{t=0}$
Pro-Leu-Gly-gly[a]	0.0841	0.0105
Z-Pro-Leu-Gly-Gly[a]	0.249	0.0110
Z-Pro-Leu-Gly-Gly-NHPh[a]	0.0405	0.0116
Pro-Leu-Gly-Gly-NHPh[a]	0.0944	0.0119
Gly-Pro-Leu-Gly	0.126	0.0176
Z-Gly-Pro-Leu-Gly	0.0282	0.0187
Z-Gly-Pro-Leu-Gly-NH-Ph	0.05317	0.0201
Gly-Pro-Leu-Gly-NH-Ph	0.184	0.0222
Gly-Leu-Gly-Gly	0.3489	0.0194
Z-Gly-Leu-Gly-Gly	0.0579	0.0189
Z-Gly-Leu-Gly-Gly-NHPh	0.0736	0.0177
Gly-Leu-Gly-Gly-NHPh	0.270	0.0156

[a]Ninety minutes for Pro-Leu-Gly-Gly and derivatives, 150 min for all others.

TABLE 8. Proline epimerization in total hydrolysate of tetrapeptides (148.5°C, pH 6.8)

Peptide	(D/L)	$(D/L)_{t=0}$
Pro-Leu-Gly-Gly[a]	1.966	0.0081
Z-Pro-Leu-Gly-Gly[a]	0.164	0.0131
Z-Pro-Leu-Gly-Gly-NHPh[a]	0.275	0.0081
Pro-Leu-Gly-Gly-NHPh[a]	1.942	0.0094
Gly-Pro-Leu-Gly	0.252	0.0145
Z-Gly-Pro-Leu-Gly	0.0219	0.0143
Z-Gly-Pro-Leu-Gly-NH-Ph	0.110	0.0161
Gly-Pro-Leu-Gly-NH-Ph	1.0722	0.0185

[a]Ninety minutes for Pro-Leu-Gly-Gly and derivatives, 150 min for Gly-Pro-Leu-Gly and derivatives.

Summary

The general goal of this work was to investigate some of the unique properties of peptides that can complicate the interpretation of peptide racemization measurements used for dating fossils. It was found that the leucine peptide unit in glycyl-L-leucylglycylglycine racemizes about three times faster than in L-prolyl-L-leucylglycylglycine. The result helps to explain the variation in the D/L ratio in fossils of the same radiocarbon age

Can. J. Chem. Downloaded from www.nrcresearchpress.com by 196.1.178.254 on 09/07/12
For personal use only.

but of different species. The range of reported D/L ratios in fossil shells spans at least a factor of two (23).

Peptide derivatives blocked at the nitrogen terminus were observed to racemize 6 to 25 times more slowly than the unblocked parent peptides. This suggests that interior peptide units racemize more slowly than terminal units and that the racemization rate is dependent on the proximity to the nitrogen terminus.

D/L ratios of greater than unity were observed. The occurrence of this phenomenon is a major deviation from the pseudo-first-order kinetics found for amino acids and assumed previously to be operating for proteins (20). Anomalously high D/L ratios (but not greater than unity) have been reported for alanine, glutamic acid, and aspartic acid and this is attributed to the addition of D-alanine and D-glutamic acid from the peptidoglycan from the cell wells of bacteria (24). Preferential epimerization of one peptide unit provides another mechanism for high D/L ratios.

Amino acid dating has the potential to be an important tool for geologists because of its simplicity and speed of analysis. The uncertainty in age determination is thought to be primarily due to an unknown temperature history (25) but this work has shown that there is uncertainty in the chemistry as well. The utility of the method may lie in restricting the kinds of peptide units used for analysis, namely, the peptide units in the interior of the protein. If rapid preferential epimerization is confined to DKP's, and provided that it occurs in only DKP's and near nitrogen termini, the chemical variability could potentially be controlled by judicious selection of the higher molecular weight fraction of the protein hydrolysate.

Acknowledgments

We wish to thank Dr. Nathaniel Rutter of the Department of Geology for his continued interest, the Natural Sciences and Engineering Research Council of Canada for a grant in aid, and the University of Alberta for financial support.

1. P. H. ABELSON. Year Book, Carnegie Inst. Washington. **53**, 97 (1954).
2. P. E. HARE and R. M. MITTERER. Year Book, Carnegie Inst. Washington. **67**, 205 (1968).
3. L. A. CURRIE (*Editor*). Nuclear and chemical dating techniques: Interpreting the environmental record. American Chemical Society, Washington, DC. 1982.
4. P. E. HARE, T. C. HOERING, and K. KING, JR. (*Editors*). Biogeochemistry of amino acids. John Wiley and Sons, New York, NY. 1980.
5. R. E. TAYLOR, L. A. PAYEN, and P. J. SLATER, JR. Nucl. Instrum. Methods. Phys. Res. Sect. B: **233**, 312 (1984).
6. N. W. RUTTER, R. J. CRAWFORD, and R. D. HAMILTON. Geoscience Canada, **17**, 1559 (1979).
7. J. F. WEHMILLER, P. E. HARE, and G. KUJALA.Geochim. Cosmochim. Acta, **40**, 763 (1960).
8. R. M. MITTERER and N. KRIAUSAKUL, Org. Geochem. **7**, 91 (1984).
9. P. E. HARE and R. M. MITTERER. Year Book, Carnegie Inst. Washington, **65**, 362 (1967).
10. M. BODANSZKY. Peptide synthesis. Wiley Interscience, New York, NY. 1976.
11. M. E. MOIR. PhD. thesis, University of Alberta, 1985.
12. J. L. BADA and S. M. STEINBURG. J. Org. Chem. **48**, 2295 (1983).
13. M. STEINBLATT. J. Am. Chem. Soc. **88**, 2845 (1966); D. L. RABENSTEIN. J. Am. Chem. Soc. **95**, 2797 (1973); D. L. RABENSTEIN and T. L. SAYER. Anal Chem. **48**, 1141 (1976); D. L. RABENSTEIN, M. S. GREENBERG, and C. A. EVANS. Biochemistry, **16**, 977 (1977).
14. G. LUCENTE, F. PINNEN, G. ZANOTTI S. CERRINI, and F. MAZZA. J. Chem. Soc. Perkin Trans. **1**, 1499 (1980).
15. G. LUCENTE, F. PINNEN, A. ROMEO, G. ZANOTTI, S. CERRINI, and F. MAZZA. J. Chem. Soc. Perkin Trans. **1**, 1127 (1983).
16. H. OTT, A. J. FREY, and A. HOFMANN. Tetrahedron, **19**, 1675 (1963).
17. S. SMITH and G. M. TIMMINS. J. Chem. Soc. 396 (1937).
18. A. STOLL, A. HOFMANN, and B. BECKER. Helv. Chim. Acta, **26**, 1602 (1943).
19. J. E. PURDIE and N. L. BENOITON. J. Chem. Soc., Perkin Trans. 2, 1845 (1973).
20. N. KRIAUSAKUL and R. M. MITTERER. Science, **201**, 1011 (1978); Geochim. Cosmochim. Acta, **44**, 753 (1980); Geochim. Cosmochim. Acta, **47**, 963 (1983); G. G. SMITH and B. S. DE SOL. Science, **207**, 765 (1980); G. G. SMITH and R. BAUM. J. Org. Chem. **52**, 2248 (1987); R. BAUM and G. G. SMITH. J. Am. Chem. Soc. **108**, 7325 (1986); G. G. SMITH, R. C. EVANS, and R. BAUM. J. Am. Chem. Soc. **108**, 7327 (1986).
21. R. C. WEAST (*Editor*). Handbook of biochemistry. 2nd ed. The Chemical Rubber Co., Cleveland, OH. 1970. p. J-59.
22. P. E. HARE. Year Book, Carnegie Inst. Washington. **73**, 571 (1974).
23. K. KING, JR. *In* Biogeochemistry of amino acids. *Edited by* P. E. Hare, T. C. Hoering, and K. KING, JR. John Wiley and Sons, New York, NY. 1980. pp. 377–391.
24. G. E. POLLOCK, C-N. CHENG, and S. E. CRONIN. Anal. Chem. **49**, 2 (1977); G. DUNGWORTH, J. A. TH. VRENKER, and A. W. SCHWARTZ. Comp. Biochem. Physiol. B: **51B**, 331 (1975); D. H. G. CROUT. *In* International review of science: Organic chemistry, Series Two. Vol. 6. *Edited by* H. N. RYDON. Butterworth, London. 1976. pp. 231–234.
25. K. M. WILLIAMS and G. G. SMITH. Origins Life, **8**, 91 (1977).

Can. J. Chem. Downloaded from www.nrcresearchpress.com by 196.1.178.254 on 09/07/12
For personal use only.

Strong cooperative protonation of a small tris-urea cryptand[1]

PIERRE G. POTVIN[2] AND MAN HUNG WONG
Department of Chemistry, York University, 4700 Keele Street, North York, Ont., Canada M3J 1P3

Received June 6, 1988

PIERRE G. POTVIN and MAN HUNG WONG. Can. J. Chem. **66**, 2914 (1988).

A small bicyclic cryptand **3** bearing urea groups along the 7-atom bridges was synthesized in 22% yield by a novel tripod–tripod coupling procedure. Protonation and complexation studies are reported and compared with results with polyoxa-[2]-cryptands and [3]-cryptand **6**. These show that **3** is a moderate base, a weak metal ion binder, but a two-proton binder exhibiting strong positive cooperativity ($pK_{a_2} > pK_{a_1}$) and fast proton exchange kinetics. As demonstrated by molecular mechanics calculations, an inward rotation of the carbonyl groups to form hydrogen bonds to cryptated protons was invoked to explain the cooperativity.

PIERRE G. POTVIN et MAN HUNG WONG. Can. J. Chem. **66**, 2914 (1988).

On décrit la synthèse, par une nouvelle méthode de couplage tripode–tripode avec un rendement de 22%, du cryptand bicyclique **3** portant le long des bras des groupements urées. On rapporte les résultats d'études de protonation et de complexation de ce cryptand, comparés à ceux obtenus avec les polyoxa-[2]-cryptands et le macrotricycle **6**. Il résulte que **3** est une base peu forte qui lie faiblement les ions métalliques, mais qui lie réversiblement et en échange rapide deux protons avec une coopérativité prononcée ($pK_{a_2} > pK_{a_1}$). Ce phénomène de coopérativité est expliqué par une rotation des groupements carbonyles vers l'intérieur de la cavité pour former des liaisons hydrogènes avec les protons complexés, tel que demontré par des calculs de mécanique moléculaire.

[Traduit par la revue]

Introduction

In protonations of simple diamines, the second protonation step is more difficult than the first ($pK_{a_2} < pK_{a_1}$), with the difference depending on the distance between the two protonation sites. The polyoxa-[2]-cryptands (1), each possessing tertiary amino sites at the bridgehead positions, also obey this rule but display a form of cooperative proton binding in that the pK_{a_2} values increase with decreasing cavity size in spite of increasing electrostatic repulsions between the bridgeheads in the diprotonated forms. In this report, we describe a small cryptand, to our knowledge the first polyurea-[2]-cryptand, that appears to not obey this rule and display strongly cooperative binding (i.e., $pK_{a_2} > pK_{a_1}$). Its synthesis is a novel one-step macrobicyclization from acyclic precursors. With the help of molecular mechanical calculations, we can rationalize the observed cooperativity in terms of protonation-induced conformational changes involving the carbonyl groups.

Experimental

General

DMF was dried (anhydrous $MgSO_4$) and distilled before use. CH_2Cl_2 was hplc grade and used without further purification. 1,1′-Carbonyl diimidazole (CDI), from Aldrich, was recrystallized from THF. Tris(2-aminoethyl)amine **1**, 98% pure from Aldrich, was dried under high vacuum at room temperature for 3 h before use.

Melting points were determined on a Fisher–Johns apparatus and are uncorrected. Infrared (ir) spectra were run on a Unicam SP 3-200 ir spectrometer. Nuclear magnetic resonance (nmr) spectra were run either in $CDCl_3$ with $CHCl_3$ as internal reference (at 7.26 ppm in ^1H spectra, and at 77.00 ppm for ^{13}C spectra), or in D_2O with *t*-BuOH as internal reference (at 1.20 ppm in ^1H spectra and 30.07 ppm in ^{13}C spectra). The instrument, a Bruker AM-3000, operated at 300.13 MHz (^1H) or 75.5 MHz (^{13}C). *J*-resolved ^1H–^{13}C correlation spectroscopy was used to establish signal assignments. Analyses were performed by Guelph Chemical Laboratories Ltd.

pH-Metric titrations

Titrations were run in a jacketted flask at 25°C on 4 mL of titrate solutions. Titrant was added via a Metrohm 635 automatic burette under control of a Metrohm 636 Titroprocessor equipped with a micro combination glass electrode (Metrohm). The electrode was standardized with buffer solutions at pH 4, 7, and 10 (Fisher). The delivery of titrant was programmed to allow 20 s between increments and full stabilization of the electrode emf before recording the pH directly. The increment size was programmed to decrease with increasing slope of the pH vs. volume curve to obtain a maximum point density within a reasonable amount of time. Titrant was carbonate-free 0.10004 N NaOH prepared by dilution of a packaged concentrated solution (BDH) and standardized with potassium acid phthalate. Acids used in the titrate were 0.09977 N HCl (similarly prepared by dilution of a packaged concentrate) or 0.09843 N $HClO_4$, and both were standardized with the NaOH solution.

The recorded titrant volume vs. pH data were treated using a locally modified version of the program BEST (2). The major differences from the original are that the measure of "fit" used in the refinement was the standard deviation between calculated and experimental pH curves, that duplicate titrations were treated together to obtain a single set of protonation constants and a single standard deviation, and that a Gauss–Newton iteration algorithm was used.

Molecular mechanics calculations

The program MACROMODEL (W. C. Still, Columbia University), version 1.5 with the MM2 force field, was used to calculate minimum energy structures for **3** and its protonated forms. Using constraints at input on the urea geometries and on the orientation of the bridgehead lone pairs or added protons in all possible combinations, the (local) minimum energies were calculated for each possible conformer associated with a minimum, and the lowest of these was retained as the (global) minimum energy conformer. Refinement was considered complete if the drop in energy between iterations was ≤ 1 kJ mol^{-1}. All *in,out* combinations (conformers) were associated with shallow or nonexistent local minima, i.e., were so unstable that the refinement routine converted them to a more stable form (usually *in,in*). For the hypothetical Li^+ and Na^+ complexes of **3**, *in,in* all-*Z,Z* structures were created with the facilities of MACROMODEL, then reformatted for calculation by MMX, version 87.1 with the MM2 and MMP1 force fields, with the program MODEL (both due to K. Gilbert, Serena Software, P.O. Box 3076, Bloomington, Indiana), defining the M—O and M—N bonds as dative and the metals as coordinatively unsaturated. The force field was modified to define Li^+ and Na^+ as monopositive hard spheres (bond stretching force constants were set to

[1]Dedicated to Professor Jean-Marie Lehn to mark his becoming a Nobel Laureate.

[2]Author to whom correspondence may be addressed.

Can. J. Chem. Downloaded from www.nrcresearchpress.com by 196.1.178.254 on 09/07/12
For personal use only.

Can. J. Chem. Downloaded from www.nrcresearchpress.com by 196.1.178.254 on 09/07/12
For personal use only.

1000) with radii 0.68 and 1.00 Å, respectively. Standard bond lengths (Li—O, 2.08 Å; Li—N, 2.18 Å; Na—O, 2.40 Å; Na—N, 2.50 Å) were assumed, and all bending and torsional force constants were set to 0. Refinement was considered complete when the drop in total energy was ≤ 1 kcal mol^{-1}.

1,4,6,9,12,14,19,21-Octaaza-5,13,20-trioxobicyclo[7,7,7]eicosatriane (3)

Tris(2-aminoethyl)amine **1** (0.50 mL, 3.34 mmol) was dissolved in DMF (10 mL) in a volumetric flask. A 5-mL aliquot of this solution was added to a stirred solution of CDI (0.8 g, 4.93 mmol) in DMF (2 mL) over a period of 5 min. This reaction mixture was then transferred into another 10-mL volumetric flask and topped up with DMF to total 10 mL. The remaining triamine solution in the former volumetric flask was also diluted with DMF to make 10 mL total volume. Both solutions were transferred into two 10-mL syringes each fitted with a 12-in. needle of identical bore. These were then mounted on a syringe pump, and the needles were inserted through side arms of a dry, Ar-flushed three-neck flask and under the surface of a volume of fresh DMF (200 mL). The pumping rate was preset to 0.135 mL min^{-1} (ca. 1 drop s^{-1}) and vigorous magnetic stirring was maintained during the addition. After completion, the solvent was removed on a rotatory evaporator, leaving an amber oil that was then heated at 70°C under high vacuum for 4 h to sublime away most of the imidazole side-product. The residue was partially purified, first by chromatography on a short column of Al_2O_3 (eluting with CH_3OH), then by precipitation from a methanolic solution with Et_2O. The solid product was then recrystallized from EtOH to afford 136 mg of **3** (22% yield), mp 292°C; ir (KBr): 1570 (C=O), 1530 (asym N–H bend), 1470 (sym N—H bend) cm^{-1}; ^1H nmr ($CDCl_3$): 5.84 (bs, 1H, NH), 3.18 (bm, 2H, CH_2CH_2NHCO), 2.54 (t, 2H, $J = 4.9$ Hz, CH_2CH_2NHCO); ^1H nmr (D_2O, in square brackets with excess D_3PO_4): 3.07 [3.49] (t, 2H, $J = 5.0$ Hz, CH_2CH_2NHCO), 2.52 [3.35] (t, 2H, $J = 5.11$ Hz, CH_2CH_2NHCO) ppm; ^{13}C nmr (D_2O, in square brackets with excess D_3PO_4): 161.26 [161.69] (s, CO), 51.42 [58.89] (t, $J = 133.0$ Hz, CH_2CH_2NHCO), 37.51 [35.33] (t, $J = 138.7$ Hz, CH_2CH_2NHCO) ppm. *Anal.* calcd. for $C_{15}H_{30}N_8O$: C 48.63, H 8.16, N 30.25; found: C 48.98, H 8.37, N 30.37%. ms (*m/e*): 370 (M^+), 371 (MH^+).

Titrated solutions were 1.28×10^{-2} M in **3**, 3.74×10^{-2} M in $HClO_4$, and 0.101 M in $NaClO_4$, or 1.02×10^{-2} M in **3**, 2.95×10^{-2} M in $HClO_4$, and 0.116 M in KBr.

Tris(5-ethyl-3,5-diaza-4-oxo-heptyl)amine 4

Diethylamine (1.99 mL, 19.2 mmol) was added to a stirred solution of CDI (3.11 g, 19.2 mmol) in CH_2Cl_2 (30 mL). The reaction mixture was stirred at room temperature for 15 min, then triamine **1** (0.96 mL, 6.41 mmol) was combined with the above mixture. After 2 h, solvent and imidazole were removed as before. The residue was purified as before, and was treated with decolourizing charcoal. The product **5** (yield 1.54 g, 65.90%) was obtained as a light amber solid that resisted attempts at recrystallization; ir (KBr disk): 3350 (N–H str), 1650 (C=O), 1600 (N–H bend) cm^{-1}; ^1H nmr ($CDCl_3$): 3.14 (m, 6H, CH_2CH_3, CH_2CH_2NHCO), 2.58 (t, 2H, $J = 7.0$ Hz, CH_2CH_2NHCO), 1.07 (t, 18H, $J = 7.0$ Hz, CH_2CH_3) ppm; ^{13}C nmr ($CDCl_3$): 157.45 (s, CO), 54.90 (t, $J = 134.9$ Hz, CH_2CH_2NHCO), 40.75 (t, $J = 136.1$ Hz, CH_2CH_3), 38.48 (t, $J = 137.7$ Hz, CH_2CH_2NHCO), 13.50 (q, $J = 126.5$ Hz, CH_2CH_3) ppm; ms (*m/e*): 444 (MH^+), 443 (M^+).

Tritrated solutions were 6.31×10^{-3} M in **4**, 2.00×10^{-2} M in HCl, and 0.150 M in KNO_3.

1,9-Dimethyl-1,4,6,9,12,14,19,21-octaaza-5,13,20-trioxobicyclo-[7,7,7]eicosatrianium diiodide 5

Cryptand **3** (24.6 mg, 66 μmol) was treated with CH_3I (2 mL) in DMF (3 mL) and CH_2Cl_2 (2 mL), then allowed to reflux overnight. Solvents were then removed and the residue washed with CH_2Cl_2 (10 mL) to afford 31.7 mg of a pale yellowish hygroscopic solid (73% yield); ^1H nmr (D_2O): 3.49 (bt, 6H, CH_2CH_2NHCO), 3.36 (bt, 6H, CH_2CH_2NHCO), 3.22 (s, 6H, NCH_3) ppm; ^{13}C nmr (D_2O): 162.07 (CO), 58.93 (CH_2CH_2NHCO), 55.77 (NCH_3), 34.67 (CH_2CH_2NHCO) ppm.

Results

The addition of one part of tris(2-aminoethyl)amine **1** to three parts of carbonyl diimidazole (CDI) cleanly provided the tris(carbamylimidazole) **2**, as made evident by nmr spectra. In a one-pot preparation, simple addition of a second equivalent of **1** provided cryptand **3** in 11% yield. With a high dilution apparatus, where syringes containing equimolar DMF solutions of preformed **2** and of **1** were slowly pumped into a volume of pure DMF such that the initial concentrations of the first aliquots were ca. 4×10^{-6} M or lower (the needle tips were held in the solution), the yield improved to 22%. The cryptand **3** was crystalline and soluble in organic solvents and H_2O.

Compound **4**, a model for the first protonation site of **3**, was prepared in two steps by the reaction of equal parts of diethylamine and CDI, followed by treatment of the resulting nonisolated intermediate with one-third equivalent of **1**. The dimethiodide salt **5** of **3** was prepared as a model for the *out,out* diprotonated form of **3**, by overnight reflux of **3** with excess CH_3I in a mixture of DMF and CH_2Cl_2.

The nmr, ir, and mass spectra of **3**, **4**, and **5** were entirely in accord with the assigned structures. Interestingly, the upfield CH_2 resonance of **3** correlated with the downfield CH_2 resonance, and was displaced further upfield upon diprotonation or dimethylation. The nmr spectra of **5** in D_2O were not significantly different from those of **3** in the presence of excess D_3PO_4.

pH-Metric base titrations were performed on acidic solutions of **3** at 25°C and μ 0.15 M, using $NaClO_4$ or KBr as background electrolytes. The calculated values for pK_{a_1} and pK_{a_2} with the former salt (7.81 and 7.96, respectively) were very similar to those with the latter salt (7.84 and 7.92, respectively), indicating the absence of complexation of Na^+. The pK_a of **4**, obtained by similar titration, was found to be 7.64 (with KNO_3 as background electrolyte). Additionally, titrations of **3** in the

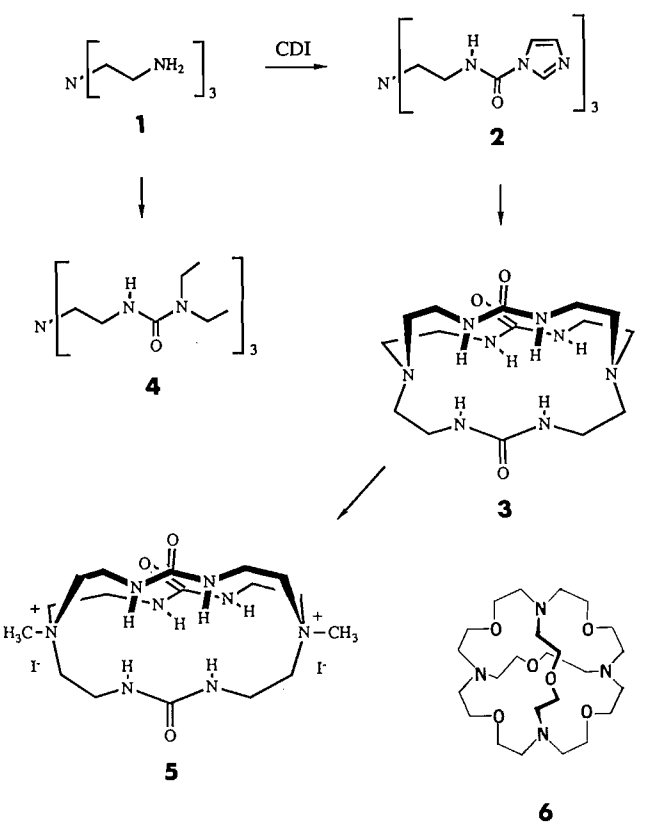

Can. J. Chem. Downloaded from www.nrcresearchpress.com by 196.1.178.254 on 09/07/12
For personal use only.

presence of various salts revealed that complexation of Li^+, Na^+, and F^- was very weak or nonexistent in H_2O.

Molecular mechanical calculations were performed on **3** and both of its protonated forms, exploring all possible conformations of the urea groups in combination with *in* or *out* bridgehead electron pairs or attached protons. The minimum energy form of **3** (see Fig. 3A), the *in,in Z,Z;Z,Z;E,Z* form, had three close contacts (≤2 Å) between oxygen on one bridge and urea NH on another bridge, while, in comparison, the next most stable conformer (some 43.5 kJ mol^{-1} more energetic), the *in,in* all-*Z,Z* form, had only two, and the *out,out* analogue of the latter (some 101 kJ mol^{-1} more energetic) had none. The minimum energy form of $(\mathbf{3}\cdot H)^+$ was *in,in* all-*Z,Z* with one such close contact and two others between oxygens and the added proton. In contrast, the *out,out* analogue had none of either kind. In the minimum energy form of $(\mathbf{3}\cdot H_2)^{+2}$, also *in,in* all-*Z,Z*, all six distances between oxygens and added protons were ≤1.95 Å.

The largest inscribed spherical cavity (radius 0.98 Å) was defined by the carbonyl carbons in the minimum energy form of **3**, and the interbridgehead distance was 5.65 Å. These values were larger for *in,in* or *out,out* all-*Z,Z* forms, reflecting the looser networks of hydrogen bonds in these structures. As expected, the protonated forms were compressed along the C_3 axes (down to 4.42 Å interbridgehead distance in $(\mathbf{3}\cdot H_2)^{+2}$) and expanded at the midsections.

Calculations were also attempted on hypothetical Li^+ and Na^+ inclusion complexes of *in,in* all-*Z,Z* **3**. In the resulting structures, the interbridge hydrogen bonding networks were broken as the cavities were compressed along the C_3 axes, and expanded at the midsections. Interbridgehead distances decreased to 4.50 Å with Na^+ and to 4.30 Å with Li^+, shorter than the sums of the appropriate radii (5.00 Å for Na^+ and 4.36 Å for Li^+). As the with the free ligand, the carbonyl groups were still largely tangent to the cavities and the largest inscribed spherical cavities were again enclosed by the carbonyl carbons instead of the oxygens, indicating poor alignment of the carbonyls with the metals. The shortest Li—O distance (2.66 Å, avg. 3.02 Å) indicated poor contact, while better contact was made with Na^+ (shortest Na—O distance 2.40 Å, avg. 2.78 Å).

Discussion

In our synthesis of **3**, the key formation of the necessary intermediate **2** amounted to a transformation of a triamine into a tris-electrophile, to our knowledge the first such transformation. This proceeded well with CDI, without intramolecular cyclization into ureas, but not with oxalyl 1,1′-diimidazole (ODI) (3). Both reagents were known to produce acylimidazoles in reaction with carboxylic acids, the latter with fragmentation and elimination of CO as well as CO_2 (3), but we obtained symmetrical diamides in reaction of either reagent with two equivalents of 2-phenylethylamine (4). Unfortunately, a DMF-insoluble gum was produced in reaction of ODI with one-third equivalent of **1**, undoubtedly containing intra- and intermolecular oxalyldiamide linkages. Presumably, the individual imidazole substitution steps proceeded at very different rates with CDI, but at similar rates with ODI. This was confirmed in an experiment using millimolar $CDCl_3$ solutions of 2-phenylethylamine and of CDI, monitoring the reaction by ^1H nmr spectroscopy. The first imidazole substitution step was essentially complete upon mixing, while the second reaction with a second equivalent of 2-phenylethylamine required 1.5–2 h for completion (4). Further, an asymmetric tris-urea, compound **4**, could be prepared by taking advantage of that difference in rates, while only a symmetric oxalyldiamide could be formed.

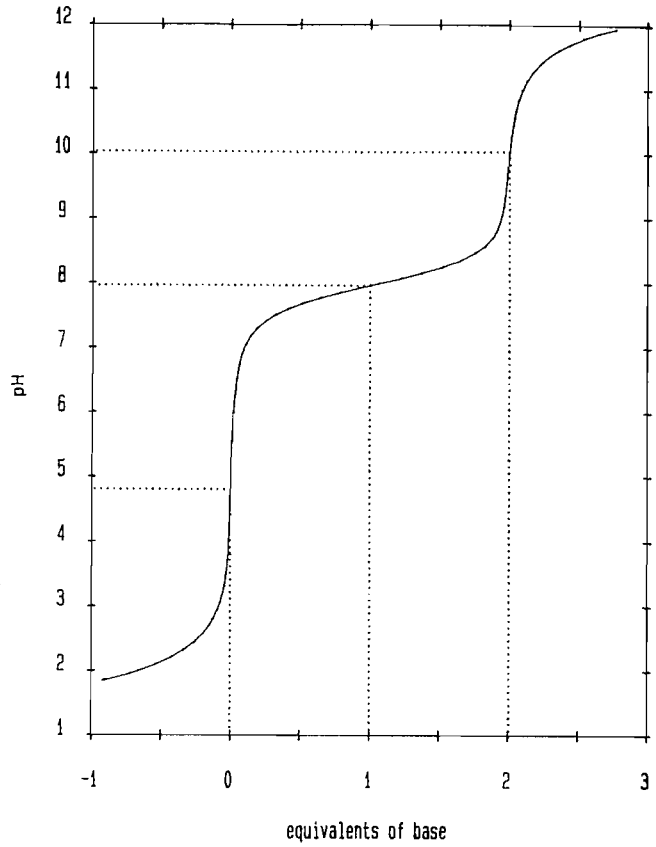

FIG. 1. Titration of 4 mL of 1.28×10^{-2} M **3** and 3.74×10^{-2} M $HClO_4$ with 0.10004 N NaOH. Plot of pH vs. added equivalents of base measured from the point where the excess acid (0.92 equiv.) was fully titrated.

The coupling of **2** and **1** proceeded well even when no special precautions were taken, and in surprisingly high yield for a non-templated tripod–tripod coupling reaction.[3] Even with very slow addition of dilute solutions ("high dilution conditions"), it is unlikely that high dilutions were maintained throughout the addition, as the reaction was probably too slow to have reached completion between increments. Nevertheless, a significant gain in yield resulted.

The cryptand **3** is a small cage molecule whose cavity size was expected to be intermediate between those of the polyoxa-[2]-cryptands [1.1.1] and [2.2.2]. Like these, **3** can be expected to have the bridgehead lone pairs *in* or *out* and to form inclusion complexes. As the former formed a weak complex with Li^+ (pK_{Li^+} ca. 2.2) (6), and as the latter formed a strong complex with K^+ (1), we sought evidence of Li^+ or Na^+ binding by **3**. However, the ^1H and ^{13}C nmr spectra in D_2O of **3** changed little in the presence of a large excess of LiCl. pH-Metric titrations in the presence of excess Na^+ or Li^+ confirmed this lack of binding, although complexation may occur in organic solvents. However, strongly cooperative protonation was clearly evident in the shape of the titration curve (Fig. 1), where, from the point where excess acid had been titrated (near pH 4.9), no further inflection occurred until two equivalents of base had been added (near pH 10). The cryptand therefore behaves as two equiva-

[3]For an example of a Cs^+-templated tripod–tripod coupling, see ref. 5.

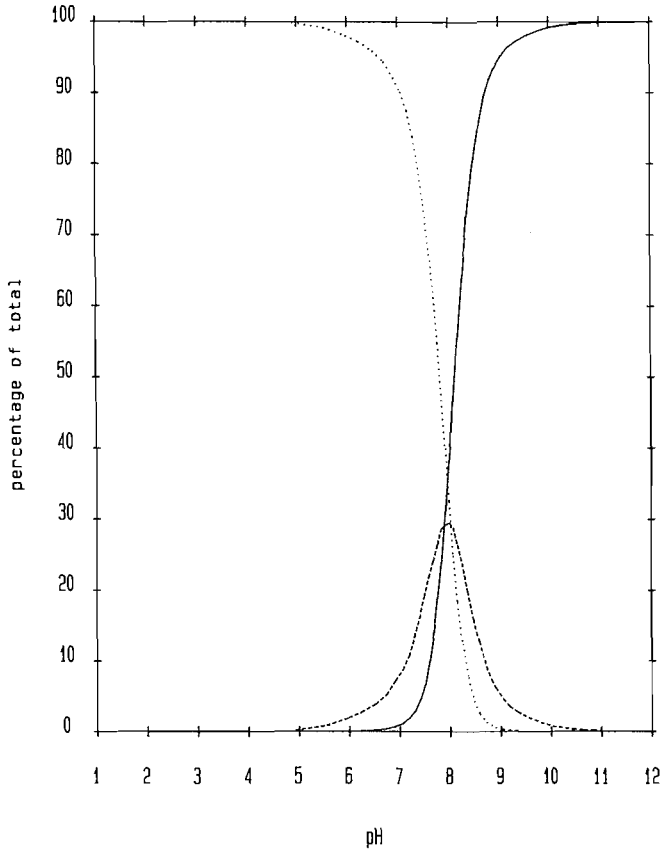

FIG. 2. Plots of the concentrations of **3** (solid line), $(\mathbf{3}\cdot H)^+$ (dashed line), and $(\mathbf{3}\cdot H_2)^{2+}$ (dotted line) against pH, calculated using pK_a values obtained with $NaClO_4$ as background electrolyte (see experimental section).

lents of a monobasic ligand of pK_a near 8 (half-titration point). Both pK_a's were indeed calculated to be near 8, but the pK_{a_2} values were in fact slightly larger than the pK_{a_1} values. The differences (0.15 log units with $NaClO_4$ as background electrolyte, 0.08 with KBr) were significant, as the pH-metric titration technique is usually considered to provide binding and protonation constants accurate to ±0.05 log units (1). The pH profile of the calculated species concentrations (Fig. 2) revealed that the monoprotonated species, $(\mathbf{3}\cdot H)^+$, was minor throughout the pH range and maximal at pH near 8. Normally, the calculated formation constants for minor species are considered suspect, since the pH calculated therefrom at all titration points and the standard deviation over the whole data set are little affected by errors in the concentrations of minor species arising from errors in their formation constants. Therefore, it was possible that the minority status of $(\mathbf{3}\cdot H)^+$ introduced calculational uncertainty in the values of pK_{a_1}. However, these were close to the pK_a measured for **4** (7.64), which we considered to be a good model for the first protonation site in **3**. Indeed, **4** could be expected to be less basic than **3** because it is less rigid and less preorganized for hydrogen bonding, and because *in,in* orientation of the bridgehead lone pairs of **3** would increase the electron density in its cavity. Hence, the calculated pK_a values of **3** appeared reasonable.

This kind of positive cooperativity could also be inferred from the protonation behaviour of the polyoxa-[2]-cryptands (1). In this series, the values for pK_{a_1} increase with decreasing cavity size (see Table 1). At the extremes, the smallest member

TABLE 1. Protonation constants for polyoxa-[2]-cryptands (ref. 1). (25°C, μ 0.05 M, H_2O)

Cryptand	pK_{a_1}	pK_{a_2}
[3.3.3]	7.70	6.96
[3.3.2]	8.16	7.31
[3.2.2]	8.50	7.33
[2.2.2]	9.60	7.28
[2.2.1]	10.53	7.50
[2.1.1]	10.64	7.85

of the series ([1.1.1]) is an extraordinarily strong base whose pK_{a_1} value could not be measured in aqueous solution (7), and the largest member ([3.3.3]) has pK_{a_1} (7.70) near those of the monoprotonation models *N*-ethylmorpholine (7.62, ref. 8*a*) and triethanolamine (7.8, ref. 8*b*). Increasingly rigid and progressively smaller cryptand cavities become more and more basic through increasing electron density within the cavity, and better stabilize the protonated forms through hydrogen bonding with the ether oxygens. But such hydrogen bonding also orients the ether oxygen lone pairs inward, and this adds more and more electron density near the second bridgehead as the cavity size decreases. There is therefore an increasingly efficient preorganization of the second protonation site as a result of the first protonation step and the values for pK_{a_2} also increase with decreasing cavity size (at least for the cryptands of Table 1), in spite of increasing Coulombic repulsion between the protonated bridgeheads. However, the increased basicity in the second protonation site never fully overcomes the Coulombic repulsion and pK_{a_2} remains much smaller than pK_{a_1}, unlike the values for **3**.

A more dramatic instance of protonation cooperativity ($pK_{a_1} - pK_{a_2} = 0.7$ with slow exchange) was witnessed with spheroidal [3]-cryptand **6** (9). ^{17}O nuclear magnetic resonance studies indicated that the diprotonated macrotricycle formed a water cryptate in its all-*in* form, with a tetrahedral array of hydrogen bonds. Thus, both the first proton and water are effectors in this case, and the diprotonated form is stabilized by the complexed water molecule (10). However, it is unlikely that the same be true of **3** because of the small cavity.

Rather, a conformational change similar to that occurring in the polyoxa[2]-cryptands can be invoked to explain the cooperativity observed in the protonation of **3**, involving the carbonyl oxygens as the only possible sources of new electron density. Indeed, the carbonyls must not be contributing much electron density at the first protonation site of the free ligand since **3** (pK_{a_1} 7.81) is considerably less basic than [2.2.2] (pK_{a_1} 9.60, ref. 1), the closest polyoxa analogue. Yet they must contribute more new electron density at the second site in $(\mathbf{3}\cdot H)^+$ than the ether oxygens in $([2.2.2]\cdot H)^+$ since $(\mathbf{3}\cdot H)^+$ is more basic (pK_{a_2} 7.96) than $([2.2.2]\cdot H)^+$ (pK_{a_2} 7.28, ref. 1) or even the lower homologues $([2.2.1]\cdot H)^+$ (pK_{a_2} 7.50, ref. 1) or $([2.1.1]\cdot H)^+$ (pK_{a_2} 7.85, ref. 1), probably as a result of inward orientation enforced by H-bonding to the first added proton held *in*. Hydrogen-bonding of *in* $N\text{-}H^+$ to the carbonyl oxygens of **3**, forming seven-membered rings, is likely geometrically less favourable than to the ether oxygens of the polyoxa-cryptands, forming five-membered rings, but electronically more favourable since the carbonyls are stronger dipoles and, in any case, evidently more effective at increasing the basicity of the second site.

Such a conformational change would not be likely were

Can. J. Chem. Downloaded from www.nrcresearchpress.com by 196.1.178.254 on 09/07/12
For personal use only.

protonation to have occurred *out,out* since H-bonding with the carbonyls would then be impossible. We therefore sought experimental confirmation of this change by looking for conformational differences, through nmr spectral differences, between *in,in* and *out,out* diprotonation, using salt **5** as a model for *out,out* $(\mathbf{3}\cdot H_2)^{+2}$. Unfortunately, this was inconclusive, as the spectral displacements upon diprotonation (presumed to occur *in,in*) were in the same directions and of similar magnitudes as upon dimethylation (presumed to occur exclusively *out,out*).

However, molecular mechanical calculations of the minimum energy structures of **3**, $(\mathbf{3}\cdot H)^+$, and $(\mathbf{3}\cdot H_2)^{+2}$ (presented in cross-sectional views in Fig. 3) were in agreement with the proposed conformational change. In the least energetic form of the free ligand (Fig. 3A), the bridgehead lone pairs were both *in* and the urea groups lay tangent to the cavity, not well preorganized for H-bonding. This explains the similarity in basicity between **3** and **4**. The preferred geometries of the urea groups (two were *Z,Z* and one was *E,Z*) seemed determined by the number and the strengths of the interbridge hydrogen bonds that could be achieved. As expected, the calculated interbridgehead distance (5.6 Å) was intermediate between those in [2.2.2] (6.87 Å, ref. 11) and [1.1.1] (estimated at 3.5 Å, ref. 7). The calculated radius of the largest enclosed sphere was 0.98 Å, large enough for Li^+, and perhaps for Na^+ with lengthwise compression of the cavity. Indeed, calculations on the hypothetical Li^+ and Na^+ complexes revealed that the interbridgehead distance did diminish, but that the carbonyl groups could not turn sufficiently inwards for good alignment of the dipoles with the cationic spheres.

In both $(\mathbf{3}\cdot H)^+$ and $(\mathbf{3}\cdot H_2)^{+2}$, the bridgehead lone pair or the added protons were *in* and all three urea groups had *Z,Z* geometries. Importantly, two of the carbonyl groups of $(\mathbf{3}\cdot H)^+$ (Fig. 3B) were found twisted inward, forming two hydrogen bonds with the *in* $N-H^+$ and one with the urea N–H on the third bridge. In $(\mathbf{3}\cdot H_2)^{+2}$ (Fig. 3C), all three carbonyl groups were similarly twisted inward, forming six hydrogen bonds with both *in* $N-H^+$ groups. In so doing, the cavity was compressed along its length, making the cavity more spherical for more room for the carbonyl oxygens. In contrast, the *out,out* analogues of $(\mathbf{3}\cdot H)^+$ and $(\mathbf{3}\cdot H_2)^{+2}$ underwent no such change.

Solvation effects could not be taken into account in these calculations, and would be expected to somewhat affect the structural picture painted above, particularly with regard to the preferred geometries of the urea groups when these are not involved in hydrogen bonds to cryptated protons. However, the hydrogen bonding patterns found in the protonated species should not be significantly altered by the inclusion of solvent effects, since bulk or partially included H_2O molecules could not compete with the more strongly dipolar carbonyls, internal hydrogen bonding is entropically favoured, and the cooperativity cannot satisfactorily be explained by solvation effects. Also, it must also be cautioned that, although the structures of Fig. 3 appear reasonable, the number of possible conformers involved is likely very large, and it is difficult to ensure that the global minimum has been found without refinement of a large number of trial structures, a very laborious task, or without dihedral angle drivers (12) or a stochastic procedure such as that of Saunders (13).

Four other features of **3** are worthy of comparison with other proton cryptands ([1.1.1], **6**, and 1,6-diazabicyclo[4.4.4]tetradecane, a catapinand synthesized by Alder *et al.* (14, 15)): **3** is much more easily synthesized and a milder base; it excludes

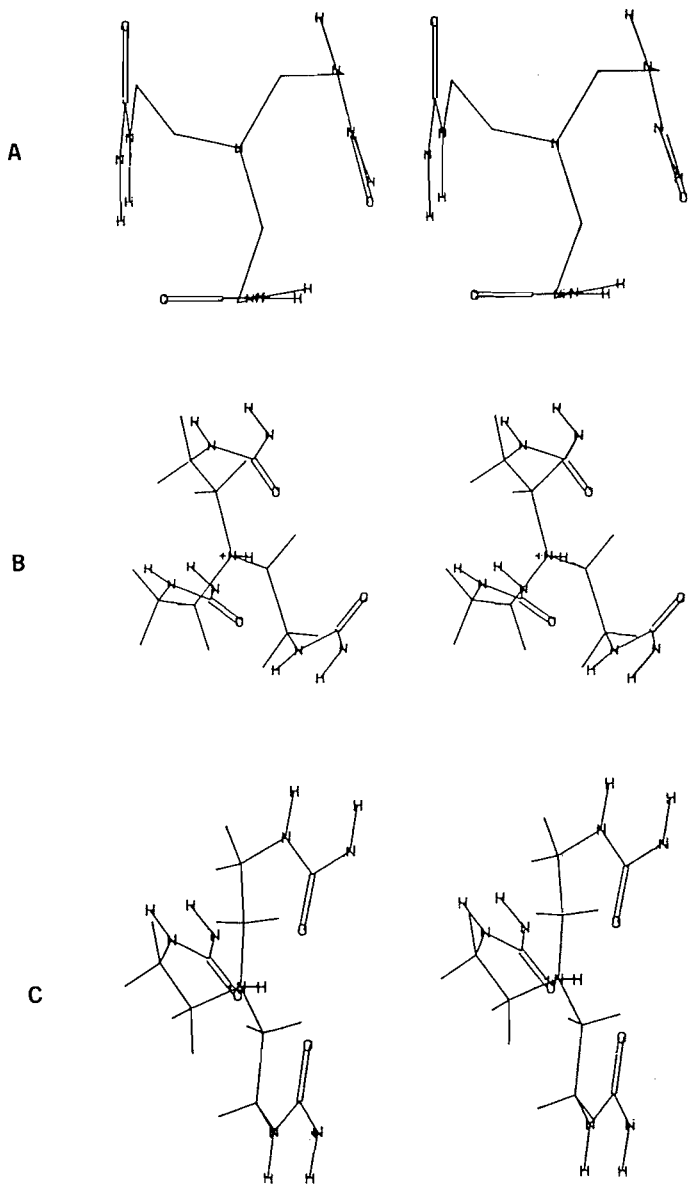

FIG. 3. Calculated minimum energy structures of (A) **3**, (B) $(\mathbf{3}\cdot H)^+$, and (C) $(\mathbf{3}\cdot H_2)^{2+}$ shown as stereoviews of cross sections of the cavities. Labels for methylene hydrogens and some C—H bonds have been omitted for clarity.

metal ions, and there was no evidence of slow proton exchange kinetics with **3** (i.e., protonation was easily reversed). In conclusion, compound **3** appears to be the first of a new class of proton cryptand. We are currently exploring its possible application in the selective transport or detection of one or another isotope of hydrogen, and are applying the bicyclization method to the preparation of larger polycarbonyl cryptands.

Acknowledgements

We thank Miss Sangeeta Sharma for performing the titrations of **4**, and Professor Michael Brook for invaluable help and advice on the use of the computing facilities of McMaster University, which were generously made available to us. We thank Professor Lehn for bringing to our attention the unusual protonation behaviour of **6**, and a reviewer for helpful comments. We are also indebted to the Natural Sciences and Engineering Research Council of Canada for a University

Can. J. Chem. Downloaded from www.nrcresearchpress.com by 196.1.178.254 on 09/07/12
For personal use only.

Research Fellowship awarded to P.G.P. and to the Research Corporation for a Cottrell Research Grant in support of this work.

1. J.-M. LEHN and J.-P. SAUVAGE. J. Am. Chem. Soc. **97**, 6700 (1975).
2. R. J. MOTEKAITIS and A. E. MARTELL. Can. J. Chem. **60**, 2403 (1982).
3. S. MURATA. Chem. Lett. 1819 (1983).
4. M. H. WONG. M.Sc. thesis, York University. 1988 (in preparation).
5. B. DIETRICH, M. W. HOSSEINI, and J.-M. LEHN. Helv. Chim. Acta, **68**, 289 (1985).
6. J. CHENEY, J.-P. KINTZINGER, and J.-M. LEHN. Nouv. J. Chim. **2**, 411 (1978).
7. J. CHENEY and J.-M. LEHN. J. Chem. Soc. Chem. Commun. 487 (1972).
8. (*a*) A. E. MARTELL and R. M. SMITH. (*Editors*). Critical stability constants. Vol. 5. Plenum Press, New York. 1975. p. 436; (*b*) Vol. 2. p. 118.
9. E. GRAF. Thèse de Doctorat, Université Louis Pasteur, Strasbourg, France. 1979.
10. J.-M. LEHN. Pure Appl. Chem. **50**, 871 (1978); Acc. Chem. Res. **11**, 49 (1978); Angew. Chem. Intl. Ed. Engl. **27**, 89 (1988).
11. B. METZ, D. MORAS, and R. WEISS. J. Chem. Soc. Perkin Trans. 2, 423 (1976).
12. K. B. WIBERG and R. H. BOYD. J. Am. Chem. Soc. **94**, 8426 (1972); F. A. L. ANET and J. KRANE. Tetrahedron Lett. 5029 (1973).
13. M. SAUNDERS. J. Am. Chem. Soc. **109**, 3150 (1987).
14. R. W. ALDER and R. B. SESSIONS. J. Am. Chem. Soc. **101**, 3651 (1979).
15. R. W. ALDER, A. CASSON, and R. B. SESSIONS. J. Am. Chem. Soc. **101**, 3652 (1979); R. W. ALDER, R. J. ARROWSMITH, A. CASSON, R. B. SESSIONS, E. HEILBRONNER, B. KOVAC, H. HUBER, and M. TAAGEPERA. J. Am. Chem. Soc. **103**, 6137 (1981).

Can. J. Chem. Downloaded from www.nrcresearchpress.com by 196.1.178.254 on 09/07/12
For personal use only.

Light-promoted catalytic hydrogenation of olefins with nickel complexes: the formation of nickel hydrides from the reaction of Ni(I) complexes with hydrogen

YUAN L. CHOW, HUALI LI, AND MENG-SU YANG
Department of Chemistry, Simon Fraser University, Burnaby, B.C., Canada V5A 1S6

Received April 5, 1988

CHOW, Y. L., LI, H., and YANG, M-S. Can. J. Chem. **66**, 2920 (1988).

The conditions pertaining to triplet excited state ketone-sensitized photoreduction of $Ni(acac)_2$ under hydrogen were shown to serve as a method for light-promoted hydrogenation of olefins with clean chemospecificity. For example, the double bond in the bicyclic system was preferentially hydrogenated over the other double bond in dicyclopentadiene and in 5-methylenebicyclo-[2.2.1]heptene. This photohydrogenation could be run under a wide range of conditions and was apparently a homogeneous catalytic process; in a late stage of photohydrogenation, concurrence of heterogeneous catalytic processes was not ruled out. The Ni(I) complexes of tetrahydrofuran and olefins generated from the photoreduction of $Ni(acac)_2$ were shown to react with hydrogen to give nickel hydride complexes. By analogy with the generally accepted reaction pattern, coordinated olefins in these nickel hydride complexes probably spontaneously undergo intramolecular addition to give Ni–alkyl complexes. It is suggested that these Ni–alkyl complexes are photoexcited to generate a vacant coordination site so that the reaction with hydrogen can proceed to give products and regenerate a nickel hydride catalyst.

CHOW, Y. L., LI, H., et YANG, M-S. Can. J. Chem. **66**, 2920 (1988).

On a démontré que les conditions permettant d'effectuer la photoréduction du $Ni(acac)_2$, sensibilisée par l'état excité triplet de la cétone et effectuée sous l'influence de l'hydrogène, peuvent servir de méthode pour effectuer des hydrogénations d'oléfines amorcées par la lumière et présentant une grande chémospécificité. Par exemple, on a pu effectuer l'hydrogénation préférentielle de la double liaison du système bicyclique par rapport à l'autre double liaison du dicyclopentadiène et du méthylène-5 bicyclo[2,2,1]heptène. Cette photohydrogénation, qui est apparemment un processus catalytique homogène, peut être réalisée dans diverses conditions expérimentales; dans la dernière portion de la photohydrogénation, il est possible que des processus catalytiques hétérogènes interviennent d'une façon concurrente. On a démontré que les complexes du Ni(I) avec le tétrahydrofuranne et les oléfines qui sont produits lors de la photoréduction du $Ni(acac)_2$ réagissent avec l'hydrogène pour donner des complexes d'hydrure de nickel. Par analogie avec le processus généralement accepté pour cette réaction, on croit que les oléfines coordonnées aux complexes d'hydrure de nickel subissent spontanément une addition intramoléculaire conduisant à des complexes de Ni–alkyle. On suggère que ces complexes de Ni–alkyle sont photoexcités pour générer un site de coordination vacant qui permet à la réaction avec l'hydrogène de procéder pour donner les produits et pour régénérer un catalyseur d'hydrure de nickel.

[Traduit par la revue]

Can. J. Chem. Downloaded from www.nrcresearchpress.com by 196.1.178.254 on 09/07/12
For personal use only.

Introduction

We have described the sensitized photoreduction of $Ni(acac)_2$ by triplet excited state ketones to give Ni(I) complexes and acetylacetone (acacH) and proposed a mechanism to explain the observations (1). The basic reaction pattern involves an interaction of a triplet excited ketone with $Ni(acac)_2$ to generate a coordinatively unsaturated Ni(I) complex with 17-electrons in the bonding shell and concurrent oxidation of a H-atom donor by radical pathways. Transient Ni(I) complexes decompose to metallic nickel or to Ni(0) complexes in the presence of a suitable ligand. It has been shown (2) that reduction conditions could be varied considerably as long as a ketone sensitizer with high triplet energy (e.g. acetone, xanthone, or benzophenone, etc) and a H-atom donor are present in an irradiated solution.

$$Ni(acac)_2 + RCH_2OH \xrightarrow[L]{\text{Xanthone, } h\nu} L_2Ni(acac) + RCHO + CH_3COCH_2COCH_3$$

$$\downarrow$$

$$NiL_4 + Ni(acac)_2$$

We have reported in a preliminary communication (3) that hydrogen can act as a H-atom donor not only in the photoreduction but also in the interaction with transient Ni(I) complexes to give nickel–hydride (Ni–H) complexes. We wish to report that the photoreduction conditions under slow purging of H_2 also serves as catalytic hydrogenation of simple olefins. Among metal catalysed olefin reactions (4–8), Ni–H complexes are good homogeneous catalysts for skeletal rearrangements (9, 10), isomerization (11–13), oligomerization (14–18), and hydrogenation (19, 20) of olefins under moderate pressure and temperature. Examples of light-promoted catalysis with other metal complexes in hydrogenation of olefins are also known and nicely summarized in recent reviews (7, 8).

Results

Irradiation of a benzene solution containing $Ni(acac)_2$ and xanthone (as a sensitizer) under hydrogen through a Pyrex filter caused reduction as shown by the disappearance of the 630 nm band of $Ni(acac)_2$ and by the change of the green solution to a yellow photolysate. Similar irradiation of solutions containing 10–50 fold excess of a simple olefin caused the photoreduction and concurrent hydrogenation of the olefin. Interruption of irradiation stopped the hydrogenation process and the conversion of photolysate to the original green colour occurred if air was leaked in. The percentage yields of hydrogenation products were determined quantitatively by GC analysis against an internal standard (Table 1). The structures of these products were either obtained by direct comparison with authentic samples or deduced from their spectral data. The sensitized photohydrogenation could be run in any kind of apparatus with a variety of configuration ranging from a Hanovia photocell to a test tube. Unoptimized results using various configurations of apparatus under different conditions are summarized in Table 1.

While unconjugated dienes with straight chains were hydrogenated without selectivity, 5-methylenebicyclo[2.2.1]heptene

TABLE 1. Photohydrogenation of olefins in benzene in the presence of $Ni(acac)_2$ and xanthone[a] under H_2

	Olefins (mmol)	$Ni(acac)_2$ (mmol)	Time (h)	Products (%)
1	Octa-1,7-diene (1.8)	0.34[b]	6	Octa-1,7-diene (59) 1-Octene (26) Octane (16)
2	Hexa-1,5-diene (0.8)	0.34[b,c]	6	Hexa-1,5-diene (50) 1-hexene (21) Hexane (15)
3	Octa-1-en-3-ol (4.0)	1.0	4	Octa-1-en-3-ol (25) 3-octanol (72)
4	Cyclooctene (0.17)	0.74[b]	6	COE (18) COA (74)
5	Norbornene (6.0)	1.0	>8	Norbornene (6) Norbornane (77)
6	**1** (6.0)	1.0	6	**1** (4) **2** (74)
7	**4** (6.0)	1.0	6	**4** (54) **5** (18) **6** (16)

[a] Xanthone, as a sensitizer, was added at the level of a 50% excess of $Ni(acac)_2$ concentrations that are in the range of 0.004–0.007 *M*.

[b] These experiments use Method II; others use Method I and ordinary Hanovia photolysis apparatus.

[c] Use toluene as solvent to avoid the overlap of GC peaks in benzene.

(**1**) and dicyclopentadiene (**4**) were selectively reduced at the bicyclic olefinic bond exclusively and hydrogenation of the other olefinic bonds (i.e. those of **2** and **5**) did not occur before the dienes **1** and **4** were consumed. The caged hydrocarbon **6** was shown to be formed from **4** by the competing sensitized photocycloaddition (21). Indeed, it was found that the caged product **6** could be prepared by acetone- or xanthone-sensitized photocyclization which occurred even more efficiently by benzene-sensitized process using a Corex filter. During the photohydrogenation of Oct-1-en-3-ol, no 3-octanone was detected; 3-octanone was unaffected under the conditions. Amides, nitriles, carboxylates, and aldehydes were also shown to resist hydrogenation under these conditions. As a control experiment, when similar ingredients in benzene 2-propanol (9:1 v/v ratio) were photolysed under nitrogen, $Ni(acac)_2$ was photoreduced to Ni(0) metal but olefins were not hydrogenated.

For those experiments with a total product yield of less than 100%, oxetanes from the photocycloaddition of triplet excited xanthone to olefins could be detected by GC–MS analysis; these oxetanes were not isolated. In photohydrogenation of **1** (Table 1), a higher concentration of $Ni(acac)_2$ retarded the oxetane formation but the formation of hydrogenation products also became slower. It was obvious that triplet excited state xanthone preferentially interacted with $Ni(acac)_2$ in the initial phase to generate hydrogenation catalysts and thus prevented the alternative oxetane formation.

$Ni(acac)_2$ was rapidly reduced in a mixture of acetone and 2-propanol where the former was sensitizer and the latter a H-atom donor (1). Similar solutions containing an excess of either norbornene or **4** underwent photohydrogenation rapidly under hydrogen, but not under nitrogen, to give the expected products shown in Table 1. However, under these conditions, black precipitates of metallic nickel started to form rapidly as hydrogenation proceeded and was particularly rapid and severe

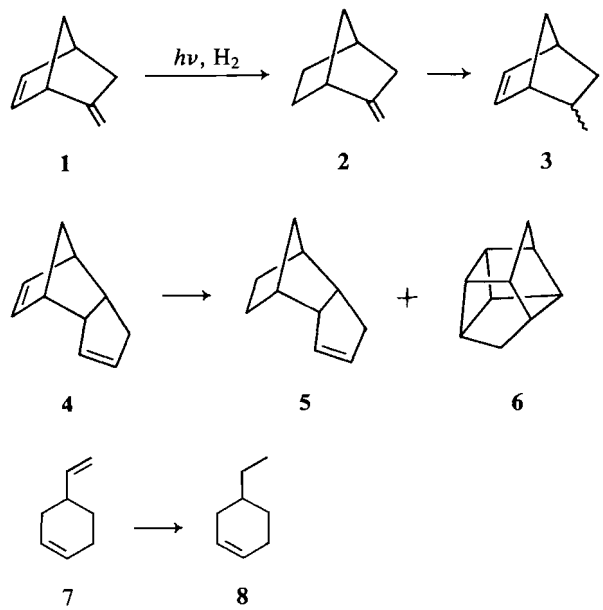

for 2-propanol concentrations higher than 25% (by volume) in 2-propanol–acetone mixtures. When benzone was added as a cosolvent in acetone–2-propanol mixtures, the deposition of metallic nickel was delayed in proportion to the benzene concentration. Typical results of the photohydrogenation of olefins in acetone–2-propanol–benzene mixtures are shown in Table 2. The photohydrogenation of 4-vinylcyclohexene (**7**) cleanly gave ethylcyclohexene (**8**) as shown by GC–MS analysis.

Dicyclopentadiene **4** was used as a model compound to study suitable conditions for photohydrogenation in acetone 2-propanol–benzene mixtures. The hydrogenation product **5** was contaminated by the sensitized photocycloaddition product **6**,

Can. J. Chem. Downloaded from www.nrcresearchpress.com by 196.1.178.254 on 09/07/12
For personal use only.

TABLE 2. Photohydrogenation of olefins with acetone as the sensitizer[a]

Olefins (*M*)	$[Ni(acac)_2]$ (*M*)	Solvent	Time	% Conversion	% $(+H_2)$[a]
1,7-octadiene (0.05 *M*)	0.005	(3:1:2)[b]	5	70	49[d]
1 (0.057 *M*)	0.005	(2:2:1)[b]	5	84	61[e]
4 (0.03 *M*)	0.003	(4:1:8)[b]	2	67	58[f]
7 (0.05 *M*)	0.005	(2:2:1)[b]	6	58	56
Norbornene (0.05 *M*)	0.005	(4:1)[c]	10	79	79
1 (0.032 *M*)	0.005	(4:1)[c]	3	98	93
4 (0.035 *M*)	0.006	(4:1)[c]	8	76	73[g]
7 (0.04 *M*)	0.004	(4:1)[c]	7	94	91

[a] Solutions (25 mL) in a flat cell was irradiated with a 200 watt Hanovia lamp through a Pyrex filter. The dihydro-products are those shown in Table 1.
[b] The ratios of acetone, 2-propanol, and benzene (A:I:B) by volume are shown.
[c] The ratio of acetone to tetrahydrofuran (A:T) by volume is shown.
[d] Octane was also isolated in 21%.
[e] The corresponding oxetanes (6%) were also detected by GC–MS.
[f] The caged product **6** was obtained in 15%.
[g] **6** was obtained in ~1%.

TABLE 3. The effects of $Ni(acac)_2$ concentrations on hydrogenation of dicyclopentadiene (**4**)[a]

	Percentage yields					
[**4**]	A:I:B (12:3:10)[b]			A:T (4:1)[b]		
$[Ni(acac)_2]$	**4**	**5**	**6**	**4**	**5**	**6**
1:1	99	0	~2	98	0	<1
1:0.5	99	0	~2	97	~1	<1
1:0.2	68	27	4	34	64	~1
1:0.1	59	35	8	23	76	~2
1:0.04	54	39	9	—	—	—
1:0.02	41	44	17	0	92	~2[c]

[a] Solutions containing **4** (0.052 *M*) and necessary amounts of $Ni(acac)_2$ was saturated with H_2 under a septum. The solutions were irradiated for 6 h with a 200 watt Hanovia lamp at ca. 18°C.
[b] The ratios of acetone (A), 2-propanol (I), benzene (B), and tetrahydrofurane (T) by volume.
[c] The saturated dicyclopentadiene (tetrahydro-**4**) was obtained in 5%.

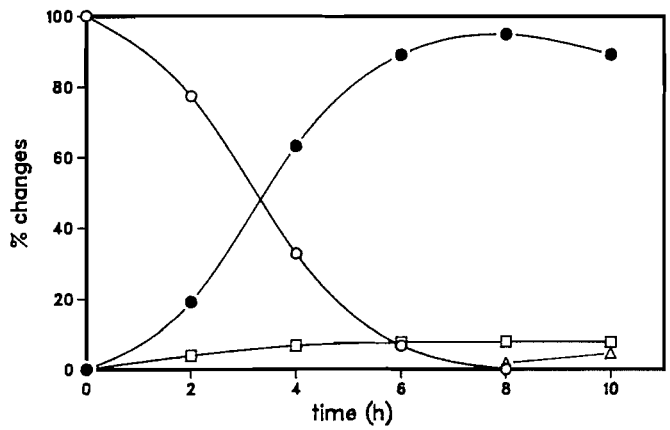

FIG. 1. Photohydrogenation of dicyclopentadiene **4** (0.029 *M*) and $Ni(acac)_2$ (0.0056 *M*) in a mixture of acetone, 2-propanol, and benzene (12:3:10 by volume): (Δ)% yields of tetrahydro-**4**.

particularly in the low concentration range of $Ni(acac)_2$ (Table 3). At a relatively high concentration of $Ni(acac)_2$, the formation of **6** was suppressed but the photohydrogenation of **4** to **5** was also retarded in the initial stage since triplet state acetone was preferentially intercepted by $Ni(acac)_2$. The photohydrogenation pattern under optimum conditions (Fig. 1) indicated that the photohydrogenation of **5** commenced at the point where **4** was totally consumed and that caged product **6** was formed in the initial stage.

Similar photohydrogenation of **4** in acetone–THF (4:1 by volume) remedied these problems; only a trace amount of **6** was formed (Table 3) and the precipitation of Ni(0) metal was much slower, occurring only in a much later stage of prolonged photolysis. The secondary hydrogenation of **5** started only when all **4** was consumed (Fig. 2). The interruption of irradiation caused the cessation of the photohydrogenation which restarted immediately on resumption of irradiation as shown in Fig. 3. Undoubtedly, irradiation was a necessary ingredient for the present catalytic hydrogenation. The long induction period required (see Figs. 2 and 3) indicated that the photoreduction of $Ni(acac)_2$ must precede and was obviously much more efficient than the photohydrogenation. The photohydrogenation of some bisolefins in acetone THF solution gave monohydrogenated products cleanly (Table 2) with only traces of side-products such as **6** and oxetanes.

Taking advantage of transient isotropic ESR signals exhibited by Ni(I) complexes in solution (1, 22–27), the xanthone-

Can. J. Chem. Downloaded from www.nrcresearchpress.com by 196.1.178.254 on 09/07/12
For personal use only.

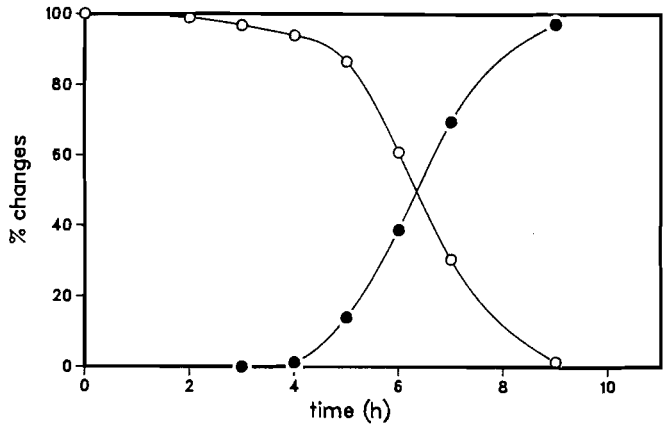

FIG. 2. Photohydrogenation of dicyclopentadiene **4** (0.051 *M*) and $Ni(acac)_2$ (0.001 *M*) in a mixture of acetone–THF (4:1 by volume): (Δ)% yield of tetrahydro-**4**.

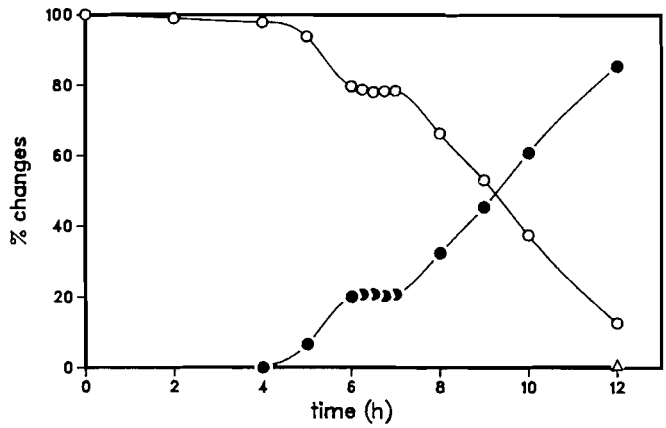

FIG. 3. The same conditions as in Fig. 2 except the dark reaction at the 6–7 h period.

sensitized photoreduction of $Ni(acac)_2$ was investigated with ESR spectroscopy. Photolysis of a solution of $Ni(acac)_2$, xanthone, and tri-*n*-butylphosphine, $P(n\text{-}Bu)_3$, in benzene 2-propanol (19:1 v/v) in the ESR cavity gave a signal at $g = 2.155$, $\Delta H_{pp} = 35$ gauss whether the solution was saturated with hydrogen or nitrogen. In pure benzene (without 2-propanol), photolysis of a similar solution under hydrogen gave a similar signal (Fig. 4) but that under nitrogen gave neither a signal nor photoreduction. Similar solutions in toluene were photolysed either under hydrogen of nitrogen to give a comparable signal, $g = 2.158$, $\Delta H_{pp} = 31$ gauss. These experiments clearly established that hydrogen could act as a H-atom donor in the photoreduction of $Ni(acac)_2$. However, hydrogen at the saturation concentration in benzene was a less efficient H-atom donor than alcohols or toluene since the estimated time required to reach a photostationary state in Fig. 4 was at least 2.5 times longer than those of other cases.

In the absence of $P(n\text{-}Bu)_3$, xanthone-sensitized photoreduction of $Ni(acac)_2$ in a benzene–2-propanol (19:1) mixture or in toluene under nitrogen generated a broad signal of colloidal nickel, $g = 2.286$, $\Delta H_{pp} = 920$ gauss (Fig. 5) (28): these photolysates soon deposited nickel metal. Similar photoreductions in benzene-2-propanol either in the presence of an olefin or hydrogen exhibited neither ESR signals of colloidal nickel nor those of Ni(I) complexes: the photolysate was bleached and remained clear for considerable times. This indicated that through ligation with an olefin and/or reaction with hydrogen some kinds of soluble nickel complexes were maintained in the solution.

The Ni(I) complexes generated in the sensitized photoreduction of $Ni(acac)_2$ decomposed rapidly as shown by the decays of their ESR signals reported previously (1). Because of the proportional variations of the Ni(I) ESR signal (i.e. the peak-to-peak line widths are the same, see Fig. 4), the concentrations of Ni(I) complexes, or their ESR intensities, are proportional to the peak-to-peak amplitudes of the first derivative waves (29). Thus signal heights can be monitored with respect to times at the peak position to represent the formation by photolysis and decay of Ni(I) complexes in the dark as shown in Fig. 6. For a solution placed in the ESR cavity, such generation and decay curves could be repeated several times.

The decay curves of Ni(I) ESR signals were analysed as a double exponential pattern, i.e., a mixture of bimolecular and unimolecular reactions on the basis of our previous findings (1); that is,

$$-(dA/dt) = k_1A + k_2A^2$$

where dA is the decreases of signal heights during time dt, and k_1 and k_2 are the first and second order rate constants. Its integrated form is

$$\ln [(k_1 + k_2A)A_0/(k_1 + k_2A_0)A] = k_1t$$

or

$$A = A_0k_1/[(k_1 + k_2A_0) \exp (k_1t) - k_2A_0]$$

Using computer best fit to simulate the data points of decay curves, k_1 and k_2 are obtained (Table 4). Under N_2, the first-order rate constants are negligibly small showing that the decay curves are dominated by the second order kinetics. Indeed when these curves are analysed with single second order kinetics, the values (values in parentheses in Table 4) are very close to those obtained by the double exponential analysis. The first order rate constants of the decay curves in THF under hydrogen show substantial increases from those under nitrogen and also the dependency on the amount of hydrogen present in the sealed tubes. These k_1 values should represent a bimolecular reaction of Ni(I) complexes and hydrogen; because the concentration of hydrogen (7×10^{-3} *M*) (30) must be orders of magnitude higher (30) than the concentration of the former, a first order pattern is obtained. It should be mentioned that k_2 values in these experiments are not absolute values since the concentration of Ni(I) complexes could not be determined and ESR signal amplitudes varied from one series of experiments to the other according to ESR settings.

Xanthone-sensitized photolysis of $Ni(acac)_2$ in C_6D_6 under hydrogen showed a weak signal at −15.2 ppm which was assigned to Ni–H resonance by reference to the published ^1H NMR data of known Ni–H complexes (31–34).

Discussion

We have established that sensitized photoreduction of $Ni(acac)_2$ with triplet excited state ketones under hydrogen can serve as a system to cause catalytic hydrogenation of olefins added *in situ*. The efficiency of this photohydrogenation is necessarily dependent, among other factors, on the rate of photon input. Eventual precipitations of metallic nickel further complicate quantitative studies of this process and prevent the measurements of quantum yields and turn over rates. The method is simple and shows chemospecificity toward unconjugated olefins; it can also

Can. J. Chem. Downloaded from www.nrcresearchpress.com by 196.1.178.254 on 09/07/12
For personal use only.

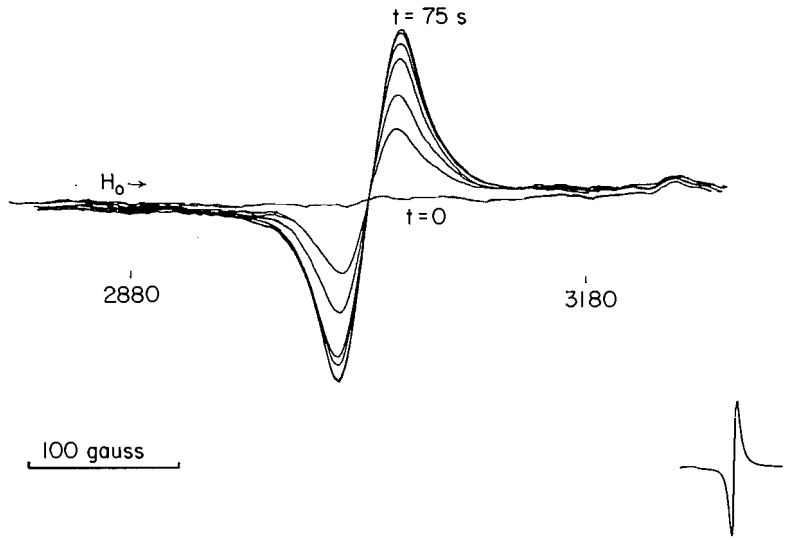

FIG. 4. ESR spectra recorded at every 15 s intervals in irradiation of benzene solution containing $Ni(acac)_2$ (0.010 *M*), xanthone (0.015 *M*), and $P(n\text{-}Bu)_3$ (0.050 *M*) saturated with hydrogen.

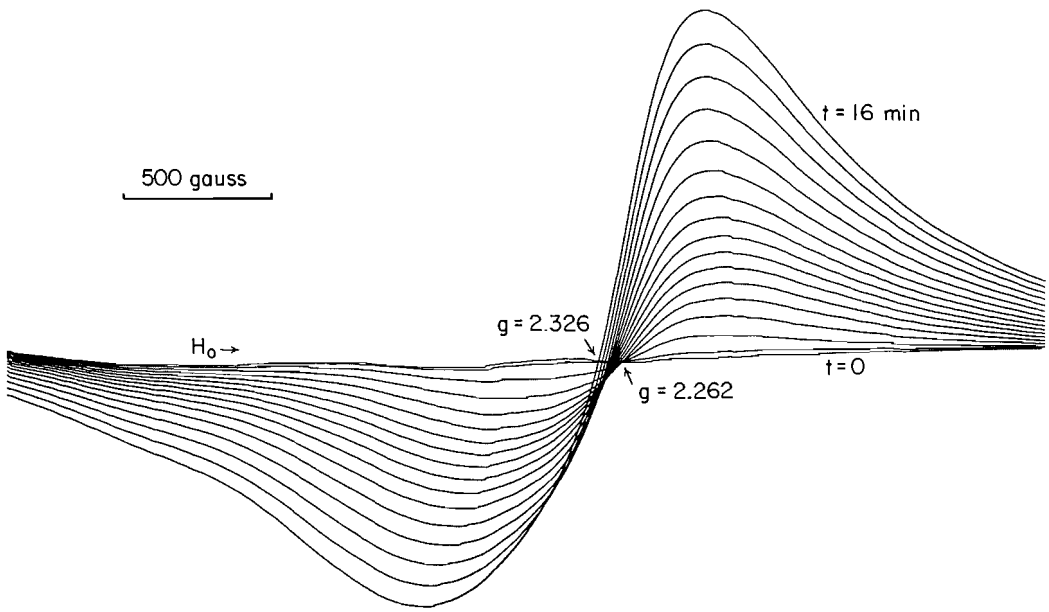

FIG. 5. ESR spectra recorded at one minute intervals in irradiation of $Ni(acac)_2$ (0.010 *M*) and xanthone (0.015 *M*) in benzene 2-propanol (19:1 v/v) under nitrogen.

tolerate many functional groups that do not interact with triplet excited states of ketones.

The overall reaction can be divided into three inter-related consecutive chemical events for mechanistic discussions. First of all, a triplet excited ketone promotes the sensitized photoreduction of $Ni(acac)_2$ in the presence of a H-atom donor and a ligand to give Ni(I) complexes, $Ni(acac)L_2$. Second, $Ni(acac)L_2$, being complexes with the 17-electron valence shell configuration, react with hydrogen rapidly to form monohydridonickel complexes, $H\text{–}Ni(acac)L_2$, that should have a stable 18-electron configuration. Third, light promotes hydrogenation of olefins using Ni–H complexes as catalytic vehicles.

The basic mechanism of sensitized reduction has been described in our previous publication (1). In this study, hydrogen is shown to be a H-atom donor to the proposed charge transfer complex either by H-atom transfer to acetylacetonyl radicals, or by other mechanisms mediated by the Ni-atom. The high H—H bond energy of 104 kcal/mol in comparison to much lower C—H bond energy (35) suggests that the latter pathway is more likely to be involved. Acetone possesses a high triplet excited state energy (78 kcal/mol) and a high volatility, making it an acceptable sensitizer; its drawback are low absorptivity in the >300 nm region and self-quenching reaction of its triplet state ($k_{sq} = 3 \times 10^6\ M^{-1}\ s^{-1}$) (36). The low reactivity to form the corresponding oxetanes with olefins under the photohydrogenation conditions (see Table 2) is an added advantage for the present purpose.

Many transient Ni(I) complexes have been identified in a variety of reductions of divalent nickel species in the presence of phosphines (22–27), and some stable Ni(I) complexes have been isolated and analysed by spectroscopy and X-ray crystallography (37, 38). The Ni(I) species generated in this sensitized photoreduction are sufficiently stabilized by good coordinating ligands, such as phosphines, THF, and diglyme, to permit the

Can. J. Chem. Downloaded from www.nrcresearchpress.com by 196.1.178.254 on 09/07/12
For personal use only.

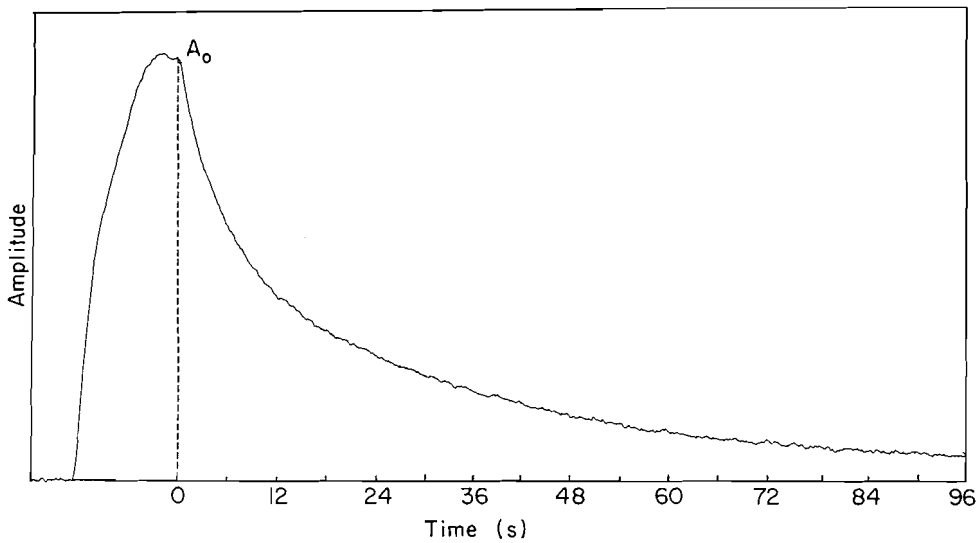

FIG. 6. The formation and decay curve of the Ni(I) ESR signal generated by irradiation of $Ni(acac)_2$ (0.010 *M*), xanthone (0.015 *M*), and $P(n\text{-}Bu)_3$ in benzene under nitrogen.

TABLE 4. Decay kinetics of Ni(I) ESR signals[a]

Conditions	Rate constants: k_2 component[b] $\times 10^3$ (unit $^{-1}$ s^{-1})	Rate constants: k_1 component $\times 10^3$ (s^{-1})
C_6H_6-2-PrOH(19:1), N_2 $P(n\text{-}Bu)_3$, 0.05 *M*	5.7 ± 1.2 (6.0 ± 0.2)[c]	0.5 ± 0.8
C_6H_6-2-PrOH(19:1), H_2 $P(n\text{-}Bu)_3$, 0.05 *M*	5.1 ± 0.5 (5.1 ± 0.3)[c]	0.8 ± 1.0
THF, N_2	34 ± 2 (36 ± 2)[c]	0.3 ± 0.2[c]
THF, H_2	19 ± 2 (21 ± 2)[c]	6.3 ± 0.2[c]
THF, H_2[d]	17 ± 2 (19 ± 2)	4.1 ± 0.5

[a] Solutions containing $Ni(acac)_2$ (0.010 *M*), xanthone (0.015 *M*) with or without additional ligand were irradiated at the cavity temperature of 24 ± 1°C.

[b] The rate constants in the parentheses were calculated on the assumption of purely second order reactions for entire decay curves. Since the absolute concentrations of Ni(I) complexes are unknown, they are represented by the unit of ESR spectra.

[c] These rate constants are averages of several determinations; others are standard deviations from best fit calculations.

[d] This kinetic determination was carried on the above sample preirradiated for 10 min.

detection by ESR spectroscopy; by analogy with the well established Ni(I) complexes reported (22–27, 37–38), these are assumed to have molecular formula of $Ni(acac)L_2$. The photoreduction in the presence of an olefin (using ethene C_2H_4 as a model) obviously also forms a soluble Ni(I) complex, $Ni(acac)_2(C_2H_4)_2$ (**9**), since colloidal nickel is not formed and a clear photolysate is maintained. The lack of the corresponding Ni(I) ESR signals probably means that such complexes are not as stable as those of phosphines and possess lifetimes too short to be detected under the ESR conditions. Acetone, alcohols, and benzene are weak ligands and probably form unstable Ni(I) complexes that are rapidly decomposed thermally or photolytically to give Ni(0) precipitates.

Although interactions with hydrogen to form nickel hydrides should be a key step in hydrogenation and other related processes, the present case (eq. [2]) is the first unambiguous proof of the reaction between Ni(I) complexes and hydrogen. Some Ni–H complexes appear to have remarkable stability and

[1] $Ni(acac)_2 + CH_2{=}CH_2 \xrightarrow[SH]{h\nu} Ni(acac)(C_2H_4)_2 + acacH$ (**9**)

[2] $Ni(acac)(C_2H_4)_2 + H_2 \longrightarrow H{-}Ni(acac)(C_2H_4)_2$ (**9** → **10**)

[3] $H{-}Ni(acac)(C_2H_4)_2$ (**10**) $\rightleftharpoons$ $CH_3CH_2{-}Ni(acac)(C_2H_4)$ (**11**), $h\nu(?)$; **10** → C_2H_6; **11** → $H_2 + C_2H_4$

their formations from Ni(II) or Ni(0) complexes by other methods are also known (31–34). Since $Ni(acac)L_2$ complexes have the 17-electron configuration, their reaction with hydrogen as in eq. [2] is expected to be spontaneous and to generate 18-electron Ni–H complexes, although the mechanism remains unknown. The failure of $Ni(acac)L_2$, where L = phosphines, to react with hydrogen supports the presence of steric hindrance since certain Ni(I) complexes with bulky phosphine ligands are stable enough to be isolated.

The bimolecular reaction of Ni(I) complexes as demonstrated by kinetic ESR studies (Table 4) is proposed to be the disproportionation shown in eq. [4]. Indeed, a freshly bleached $Ni(acac)_2$ solution in benzene 2-propanol regains the faint green color under nitrogen when irradiation is stopped. Equation [5]

[4] $2Ni(acac)L_2 \rightarrow NiL_4 + Ni(acac)_2$

[5] $NiL_4 + acacH \rightarrow H{-}Ni(acac)L_2 + 2L$

[6] $NiL_4 \rightarrow$ "Colloidal Ni" $\rightarrow$ "Ni metal"

shows an alternative route to form Ni–H complexes and has analogies in the prototropic generation of Ni–H bonds from Ni(0) complexes (37, 38); $Ni(1,5\text{-}COD)_2$ is known to react with acetylacetone to give a compound analogous to **11**, (η^1,η^2-cyclooctenyl) (acetylacetonato)nickel(II), either directly or via **10** (17, 18). The decomposition of NiL_4 to form colloidal and

Can. J. Chem. Downloaded from www.nrcresearchpress.com by 196.1.178.254 on 09/07/12
For personal use only.

Can. J. Chem. Downloaded from www.nrcresearchpress.com by 196.1.178.254 on 09/07/12
For personal use only.

metallic nickel may compete under the irradiation conditions. As the photohydrogenation proceeds smoothly while the photolysate remains clear, and shows ESR isotropic signals as well as H NMR signals, it appears to occur in the homogeneous phase where soluble Ni complexes **9**–**11** are probably involved and photoexcitation is required. However, we have not excluded the possibility that metallic and colloidal nickel, formed in the processes, may also act as heterogeneous catalysts in hydrogenation concurrently. The question on heterogeneous *versus* homogeneous catalysis, particularly for hydrogenation, has become a current interest (39–42) as catalytic reactions of transition metal and their derivatives figure more prominently in chemical industry. Although in recent years, several proposals have been put forward to differentiate homogeneous *versus* heterogeneous reaction processes (39–42), characterization and identification of colloidal metals (or metal sols) in reaction mixtures are not straightforward. Regardless of heterogeneous or homogeneous processes, the present photohydrogenation method works and is useful in some specific applications with excellent chemical selectivity. Leaving this question aside for future investigation, we continue to discuss the photohydrogenation as a homogeneous catalytic reaction.

The catalytic cycle of homogeneous photohydrogenation with nickel monohydride complexes is depicted in eq. [3] by analogy with the commonly accepted (4, 5) intramolecular addition of the Ni–H bond across a coordinated olefinic bond and hydrogenolysis to regenerate Ni–H complex **10**. Elimination of a Ni–H moiety in Ni–alkyl complexes, such as **11**, is apparently facile at ambient temperature or even lower (10–20): such processes are the source of Ni–H catalysed isomerization of olefins (9–12). The hydrogenolysis of **11** requires a vacant coordination site to accommodate oxidative addition of hydrogen followed by reductive elimination to give products and the regeneration of **10**. Without elaborating the mechanistic details, the role played by light energy is assigned to the photoexcitation of **11**, either by a direct or sensitized route, to promote the **11**—**10** transformation.

On the basis of the proposed mechanisms, the observed chemoselectivity of hydrogenation can be explained: (*i*) any functional groups possessing weak coordination properties with Ni(I) centers scarcely have a chance to undergo reduction (e.g., carbonyl, ester, cyano, amide groups), and (*ii*) better coordinating carbon–carbon double bonds should be preferentially hydrogenated; e.g., norbornene type vs. other olefinic bonds in intramolecular competitions in **1** and **4**. The latter point is further confirmed from an observation that the hydrogenation of dicyclopentadiene (**4**) is completely stopped in the presence of four equivalents of P(*n*-Bu)$_3$. Obviously, P(*n*-Bu)$_3$, being a better coordinating ligand, has displaced the olefin from **9** and/or **10**; a probable Ni(I) complex, Ni(acac)[P(*n*-Bu)$_3$]$_2$ (corresponding to **9**) reacts feebly with hydrogen in benzene as shown in Table 4. The observed clean chemoselectivity in the present photohydrogenation is the consequence of a complex overall effect consisting of various factors, such as the ability of olefins to coordinate, the facility of nickel complex **11** to undergo hydrogenolysis, and other steric and excitation factors. Furthermore, the addition of a Ni–H bond to an unsymmetrical olefinic bond should be regioselective by analogy with catalysed oligomerization of terminal olefins (14–17). This question will not be considered as it does not show in the products.

The present photohydrogenation depends on acetone-sensitized photoprocess as the key step to pump the reaction. Any substrates that can quench triplet excited ketone efficiently, say with $k_q \geq 10^9\ M^{-1}\ s^{-1}$, are not suitable substrates since they can compete efficiently to retard the processes of generating catalytic species **10** and **11**. Conjugated dienes and α,β-unsaturated carbonyl compounds are among those substrates that could not be used because of low triplet excited state energy (43). However, it is known that the former can be reduced to monoolefins by a thermal catalytic process of Ni–H complexes (20). It is interesting to note that **4** can be sensitized to undergo photocyclization to give caged compound **6** and that benzene is the most efficient sensitizer. Furthermore, triplet excited state acetone preferentially interacts with Ni(acac)$_2$ in THF even in the presence of **4** as shown in Table 3 and Fig. 2. This may arise from modifications of Ni complexes through loose coordination with solvent molecules.

Experimental

General conditions and materials

The experimental conditions and apparatus were the same as those described in ref. 1. The olefins (Aldrich) were distilled and stored under N_2. Reagent grade solvents were distilled.

Photolysis methods

Hanovia medium pressure mercury lamp 450 or 200 watts placed on a Pyrex Hanovia type cooling unit was used as the source.

Method I: A common Hanovia type irradiation cell was used to accommodate about 200 mL photolysates.

Method II: Solution was placed in a flat round cell (30–50 mL) with side arms for a gas tube inlet and an outlet connected to a condenser. The cell is placed facing the lamp housing in a running water bath.

Method III: A Pyrex test tube (10–20 mL) containing a solution was capped with a septum. A long needle extending to the bottom served as a gas inlet and a short needle extending to the upper space served as a leak. The tube was placed close to the lamp housing in upright position. Both of them were immersed in a running water bath.

Electron spin resonance spectra and signal decays

A solution necessary for photolysis was placed in a quartz ESR tube, up to 2 cm height (ca. 1.5 mL), which was capped with a septum at the top. The solution was purged with H_2 or N_2 with two needles. On removal of needles, the septum was sealed with wax paper. The cavity temperature in an equilibrated state was 24 ± 1°C.

For signal decay studies, the magnetic field was set at the maximum height of the first derivative wave, and scanned against time at the cavity temperature 24 ± 1°C. While the pen was running at a fixed speed, irradiation began until the signal reached the stationary state in 10–15 s. The irradiation beam was blocked to commence the decay as shown in Fig. 6. The data points read from these decay curves were analysed as follows: (*1*) according to a pure first or second order reaction by means of the "MINITAB" program of the MTS Computing System of SFU, and (2) according to double exponential decays of first and second order reactions on the bases of eq. [2], using the "MINUIT" program of Professor P. Percival (Chemistry Department, Simon Fraser University).

Photohydrogenation

Photohydrogenation of olefins was run with one of the apparatus described above. Aliquots of samples (2 mL) were removed at intervals and filtered through a short basic alumina (ca. 4 g) column, which was washed with benzene (2 mL). The filtrate was mixed with an internal standard solution of methylenedioxybenzene (0.05 *M*, 1.0 mL) and was brought to exactly 5 mL. This solution was injected in GC for quantitative analysis.

In the preparative photohydrogenation of **1** and **4**, the products **2**, **5**, and **6** were isolated with preparative GC (10% Carbowax 20 M on Anakrom Q, 0.25 in × 3 ft). Their physical data were as follows: **2** (45): MS *m/e*(%) 110(10, M^+), 95(4), 82(32), 67(86), 54(54), and 41(100); ^{1}H nmr($CDCl_3$), 4.82(s, $J_{\frac{1}{2}}$ = 0.7 Hz, 1H) 4.57(s, J = 0.7 Hz. 1H), 2.68(d, J = 1.2 Hz, 1H), 2.35(d, J = 1.2 Hz, 1H), 2.16 (d, J = 17.3 Hz, 1H), 1.90 (d, J = 17.3 Hz, 1H), 1.58(m, 2H), and 1.28(m,

4H) ppm. **5**: MS, *m/e*(%), 134(5, M^+), 66(100), 65(40); ^{1}H nmr; 5.60 (AB quartet and further coupling, J = 7, 2H), 2.99(m, 1H), 2.53(m, 1H), 2.27(m, 1H), 2.20(m, 2H), 2.12(m, 1H), 1.46 (AB quartet and further coupling, J = 8 Hz, 2H) and 1.20(m, 4H) ppm. **6**: MS, *m/e*(%), 132(8, M^+), 117(48), and 66(100); ^{1}H nmr, 2.75(m, 2H), 2.55(m, 4H), 2.47(m, 2H), 1.62(d, J = 11.3 Hz, 2H), and 1.23(d, J = 11.3, 2H) ppm.

In a prolonged irradiation, the fully hydrogenated product from **1** and **4** were not isolated but were identified by GC–MS to show the molecular ion peaks at *m/e* 112 and 136, respectively.

For photohydrogenation of hexa-1.5-diene, oeta-1,7-diene, octa-1-en-3-ol, and norbonene, the products 1-hexene, hexane, 1-octene, octane, norbornene, and 3-octanol were identified from their GC–MS spectra and co-injection in GC analysis with authentic samples.

Ethylcyclohexene (**8**) was isolated as a sample containing 15% 4-vinylcyclohexene (**7**) by preparative GC. This sample showed typical olefinic protons at 5.6 ppm (m, 2H) but no ABX system of the vinyl group at 5.9 and 5.0 ppm, and MS spectral pattern as follow (45); *m/e*(%) 110(M^+, 20), 95(17), 81(100), 67(30), 54(40), and 41(25).

Acknowledgement

We thank the Natural Sciences and Engineering Research Council of Canada, Ottawa, for generous financial support.

1. Y. L. Chow, G. E. Buono-Core, C. W. B. Lee, and J. C. Scaiano. J. Am. Chem. Soc. **108**, 7620 (1986); Y. L. Chow and G. E. Buono-Core. J. Chem. Soc. Chem. Commun. 592 (1985).
2. H. Li. Ph.D. Thesis. Simon Fraser University, Burnaby, B.C. 1988.
3. Y.L. Chow and H. Li. Can. J. Chem. **64**, 2229 (1986).
4. G. W. Parshall. Homogeneous catalysis. Wiley-Interscience, New York. 1980. Chapt. 3.
5. (*a*) B. R. James. *In* Comprehensive organometallic chemistry. Vol. 8. *Edited by* G. Wilkinson, F. G. A. Stone, and E. Abel. Academic Press, New York. 1982. p. 285; (*b*) B. R. James. Homogeneous hydrogenation. Wiley, New York. 1973.
6. P. W. Jolly and G. Wilke. The organic chemistry of nickel. Vol. II. Academic Press, New York. 1975. Chapt. 1.
7. R. G. Solomon. Tetrahedron, **39**, 485 (1983).
8. L. Moggi, A. Juris, D. Sandrini, and M. F. Manfrin. Rev. Chem. Interm. **4**, 171 (1981).
9. R. G. Miller, P. A. Pinke, R. D. Stauffer, H. J. Golden, and D. J. Baker. J. Am. Chem. Soc. **96**, 4211 (1974); **96**, 4221 (1974); **96**, 4229 (1974).
10. L. W. Gosser and G. W. Parshall. Tetrahedron Lett. 2555 (1971).
11. M. J. D'Aniello, Jr. and E. K. Barefield. J. Am. Chem. Soc. **100**, 1474 (1978).
12. (*a*) H. Kanai, K. Kushi, K. Sakanoue, and N. Kishimoto. Bull. Chem. Soc. Jpn. **53**, 2711 (1980); (*b*) H. Kanai, M. Sakagami, and S. Kishimoto. Shokubai, **16**, 403 (1974).
13. H. Takaya, T. Suzuki, Y. Kumagai, M. Yamakawa, and R. Noyori. J. Org. Chem. **46**, 2846 (1981).
14. P. W. Jolly. *In* Comprehensive organometallic chemistry. Vol. 8. *Edited by* G. Wilkinson, F. G. A. Stone, and E. Abel. Academic Press, New York. 1982. pp. 613, 615, 649, and 671.
15. W. Keim, A. Behr, and M. Röper. *In* Comprehensive organometallic chemistry. Vol. 8. *Edited by* G. Wilkinson, F. G. A. Stone, and E. Abel. Academic Press, New York. 1982. p. 371.
16. B. Bogdanovic, M. Kröner, and G. Wilke. Liebigs Ann. **699**, 1(1966).
17. W. Keim, B. Hoffmann, R. Lodewick, M. Peuckert, G. Schmitt, J. Fleischhauer, and U. Meier. J. Mol. Catal. **6**, 79 (1979).
18. W. Keim, A. Behr, and G. Kraus. J. Organomet. Chem. **251**, 377 (1983).
19. H. Itatani, and J. C. Bailar, Jr. Ind. Eng. Chem. Prod. Res. Develop. **11**, 146 (1972).
20. M. Sakai, F. Harada, Y. Sakakibara, and N. Uchino. Bull. Chem. Soc. Jpn. **55**, 343 (1982).
21. G. O. Schenck and R. Steinmetz. Chem. Ber. **96**, 520 (1963): Esso Research and Engineering Co. British Patent, 842, 140. 1960.
22. N. Tanaka, T. Ogata, and S. Niizuma. Inorg. Nucl. Chem. Lett. **8**, 965 (1972).
23. H. C. Budnikov and O. Yu. Kargina. J. Electroanal. Chem. **169**, 195 (1984).
24. F. V. Lovecchio, E. S. Gore, and D. H. Busch. J. Am. Chem. Soc. **96**, 3109 (1974).
25. G. A. Bowmaker, P. D. W. Boyd, and G. K. Campbell. Inorg. Chem. **21**, 2043 (1982).
26. P. Maruthamuthu, L. K. Patterson, and G. Ferraudi. Inorg. Chem. **17**, 3157 (1978).
27. N. Jubran, G. Ginzburg, H. Cohen, Y. Koresh, and D. Meyerstein. Inorg. Chem. **24**, 251 (1985).
28. A. Tkáč and A. Staško. Coll. Czech. Chem. Commun. **37**, 573 (1972).
29. J. E. Wertz. Electron spin resonance. McGraw-Hill Book Co., New York. 1972.
30. H. Stephens and T. Stephens. Solubilities of inorganic and organic compounds I. McMillan, New York. 1963.
31. M. L. H. Green and T. Saito. Chem. Commun. 208, (1969); M. L. H. Green, H. Munakata, and T. Saito. J. Chem. Soc. A, 469 (1971).
32. K. Jonas and G. Wilke. Angew. Chem. Internat. Edit. **8**, 519 (1969).
33. M. L. H. Green, T. Saito, and P. J. Tanfield. J. Chem. Soc. A, 152 (1971).
34. H. Bönnemann. Angew. Chem. Internat. Edit. **9**, 736 (1970).
35. D. M. Golden and S. W. Benson. Chem. Rev. **69**, 125 (1969).
36. I. Naito and W. Schnabel. Bull. Chem. Soc. Jpn. **57**, 771 (1984).
37. R. A. Schunn. Inorg. Chem. **9**, 394 (1970).
38. W. C. Drinkard, D. R. Eaton, J. P. Jesson, and R. V. Lindsey, Jr. Inorg. Chem. **9**, 392 (1970).
39. G. M. Whitesides, M. Hackett, R. L. Brainard, J-P. P. M. Lavalleye, A. F. Sowinski, A. N. Izumi, S. S. Moore, D. W. Brown, and E. M. Staudt. Organometal, **4**, 1819 (1985).
40. D. R. Anton and R. H. Crabtree. Organometal. **2**, 855 (1983).
41. J. P. Collman, K. M. Mosydar, M. Bressan, W. Lamanna, and T. Garret. J. Am. Chem. Soc. **106**, 2569 (1984).
42. J. E. Hamlin, K. Hirai, A. Millan, and P. M. Maitlis. J. Mol. Catal. **7**, 543 (1980).
43. N. J. Turro. Modern molecular photochemistry. The Benjamin-/Cummings, Menlo Park, CA. Chapt. 9.
44. A. K. Colter and R. A. Reith. J. Org. Chem. **44**, 3529 (1979).
45. S. R. Heller and G. W. A. Milne. EPA/NIH Mass Spectral Data Base. Vol. 1. U.S. Government Printing Office, Washington, DC. 1978. p. 125.

Can. J. Chem. Downloaded from www.nrcresearchpress.com by 196.1.178.254 on 09/07/12
For personal use only.

Minor metabolites of the cold water soft coral *Gersemia rubiformis*

DAVID E. WILLIAMS[1] AND RAYMOND J. ANDERSEN[2]
Department of Chemistry and Oceanography, University of British Columbia, Vancouver, B.C., Canada V6T 1W5
AND
JOHN F. KINGSTON[3] AND ALEX G. FALLIS[4]
Department of Chemistry, Memorial University, St. Johns, Nfld., Canada A1B 3X7

Received May 13, 1988

DAVID E. WILLIAMS, RAYMOND J. ANDERSEN, JOHN F. KINGSTON, and ALEX G. FALLIS. Can. J. Chem. **66**, 2928 (1988).

The minor metabolites of both Pacific and Atlantic Ocean specimens of the cold water soft coral *Gersemia rubiformis* have been investigated. Pacific coast animals yielded two new pseudopterane diterpenoids, isogersemolides A (**11**) and B (**12**), and four new cembrane diterpenoids, isoepilophodiones A (**13**), B (**14**), and C (**15**) and rubifol (**16**). Atlantic coast animals yielded 3-acetoxy-β-cubebene (**17**). The proposed structures of all the new metabolites are based on spectroscopic analysis and chemical interconversions.

DAVID E. WILLIAMS, RAYMOND J. ANDERSEN, JOHN F. KINGSTON et ALEX G. FALLIS. Can. J. Chem. **66**, 2928 (1988).

On a examiné les métabolites mineurs d'échantillons, provenant de l'océan Atlantique ainsi que de l'océan Pacifique, du corail mou vivant en eau froide *Gersemia rubiformis*. Les animaux du Pacifique ont fourni deux nouveaux diterpénoïdes du pseudoptérane, les isogersémolides A (**11**) et B (**12**) ainsi que quatre nouveaux diterpénoïdes du cembrane, les isoépilophodiones A (**13**), B (**14**) et C (**15**) ainsi que le rubifol (**16**). Les animaux de l'Atlantique ont fourni de l'acétoxy-3 β-cubébène (**17**). Les structures qui sont proposées pour les métabolites sont toutes basées sur des analyses spectroscopiques ainsi que sur des interconversions chimiques.

[Traduit par la revue]

Can. J. Chem. Downloaded from www.nrcresearchpress.com by 196.1.178.254 on 09/07/12
For personal use only.

Tropical reef environments, particularly in the Indo-Pacific, are populated by a large variety of soft corals. In contrast to the tropical diversity of soft corals, the cold waters off both the eastern and western Canadian coasts harbour an extremely limited number of soft coral species (1).

Gersemia rubiformis, commonly referred to as the "sea raspberry", is one soft coral that can be collected in abundance from Canadian waters. Our previous chemical studies on *G. rubiformis* revealed that Atlantic specimens have entirely different chemistry than Pacific specimens. Atlantic Ocean samples of *G. rubiformis*, collected off the shores of Newfoundland, contained the two pregnane derivatives **1** and **2** (2) as well as the two C26 steroids **3** and **4** (3). Pacific Ocean collections of *G. rubiformis*, acquired off the northern end of Vancouver Island, yielded the cembrane diterpenoids rubifolide (**5**) and epilophodione (**6**), the pseudopterane diterpenoid gersemolide (**7**) (4), the gersolane diterpenoid gersolide (**8**) (5), and the cuprane sesquiterpenoids tochuinyl acetate (**9**) and dihydrotochuinyl acetate (**10**) (6). Our continuing investigations of the minor metabolites of both east and west coast specimens of *G. rubiformis* have resulted in the isolation of six new diterpenoids, **11**–**16**, from the Pacific animals, and one new sesquiterpenoid, **17**, from the Atlantic animals. We now wish to report the structures of these new *G. rubiformis* metabolites.

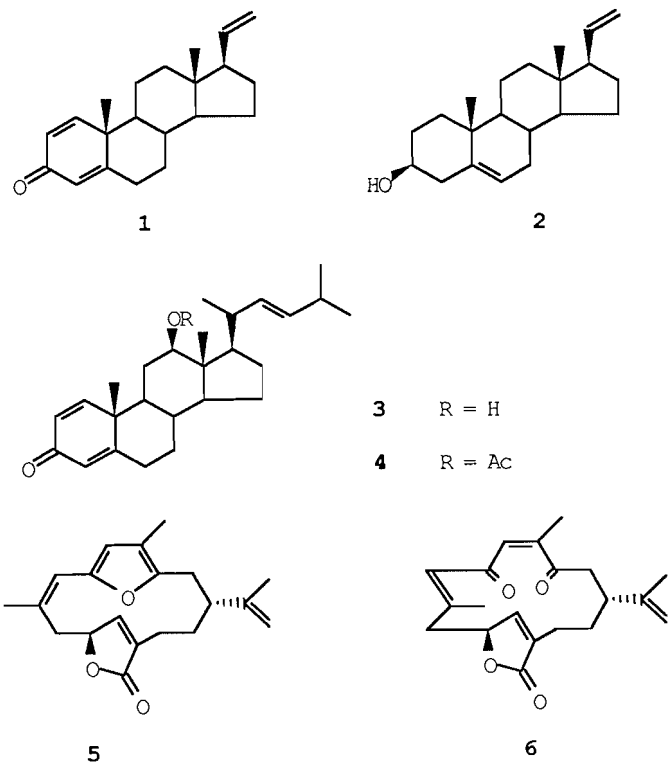

Pacific coast specimens

Samples of *G. rubiformis* were collected by hand using SCUBA (−5 to −15 m) around the Gordon Islands off the northern tip of Vancouver Island. Freshly collected soft coral was immediately immersed in methanol and extracted at room temperature for 2–3 days. The organic soluble portion of the methanol extract was fractionated by sequential application of silica gel flash, silica gel preparative thin-layer (tlc), radial thin-layer, and normal and reverse phase high performance (hplc) chromatographies to give pure metabolites.

Isogersemolide A (**11**) was obtained from methanol as colourless needles (mp 121–124°C). It showed a parent ion in the HREIMS at 328.1669 daltons appropriate for a molecular formula of $C_{20}H_{24}O_4$ (ΔM = −0.6 mmu), identical to that of gersemolide (**7**). The ^{13}C nmr spectrum of **11** (Table 2) showed resonances that could be assigned to eight olefinic carbons, two ketone carbonyls, and one lactone carbonyl. Six of the olefinic carbons and all three of the carbonyl carbons could be accounted

[1]Present address: Department of Chemistry, University of Hawaii, Honolulu, HA 96822.

[2]Author to whom correspondence may be addressed.

[3]Present address: CIL Inc., McMasterville, P.Q.

[4]Present address: Ottawa–Carleton Chemistry Institute, Department of Chemistry, University of Ottawa, Ottawa, Ont., K1N 9B4.

Can. J. Chem. Downloaded from www.nrcresearchpress.com by 196.1.178.254 on 09/07/12
For personal use only.

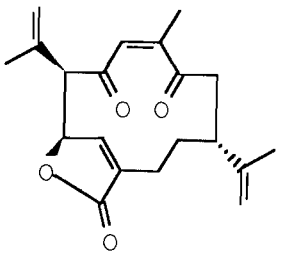

7

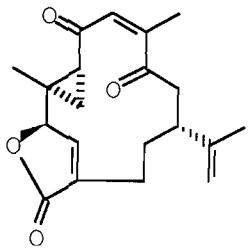

8

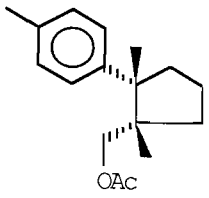

9

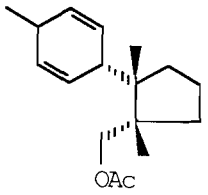

10

for by methyl substituted enedione (^{1}H nmr δ: 2.08 (d, J = 1.2 Hz, 3H), 6.21 (q, J = 1.2 Hz, 1H), α,β-unsaturated-γ-lactone (^{1}H nmr δ: 7.02 (dd, J = 0.6, 0.6 Hz, 1H) and 5.92 (d, J = 0.6 Hz, 1H)), and isopropenyl (^{1}H nmr δ: 1.72 (bs, 3H), 4.76 (bs, 1H), and 4.86 (bs, 1H)) residues similar to those found in gersemolide (**7**) (4). The two remaining olefinic carbon atoms and two additional olefinic methyl resonances apparent in the ^{1}H nmr of **11** (δ 2.01, s, 3H; 2.06, s, 3H) were assigned to a C7—C17 double bond and carbons 18 and 19 of the second isopropyl residue of a pseudopterane diterpene. Irradiation of the methyl resonance at δ 2.08 (C16) failed to induce an observable nOe (nuclear Overhauser enhancement) in the H5 olefinic resonance (δ 6.21), suggesting that the C4—C5 olefin had the *E* configuration. The chiral centers at C1 and C8 in isogersemolide A (**11**) were assigned the same relative configurations as the corresponding centers in gersemolide (**7**).

Isogersemolide B (**12**), also isolated as colorless needles (<1.5 mg), gave a parent ion at 328.1684 daltons in the HREIMS, indicating that it had a molecular formula of $C_{20}H_{24}O_4$ (ΔM = +0.9 mmu) as well. The ^{1}H nmr data for **12** showed a strong resemblance to those displayed by isogersemolide A (**11**) (Table 1), suggesting that the two metabolites had the same constitution but that they differed in some stereochemical sense. This hypothesis was confirmed by treatment of **11** with a catalytic amount of iodine in benzene/ethyl acetate, resulting in the formation of a 3:1 mixture of the geometric isomers **11** and **12**, as evidenced by ^{1}H nmr and tlc analysis. The assignment of the *Z* configuration to the C4—C5 alkene in isogersemolide B (**12**) was based on the observation of an nOe between H5 (δ 6.11) and the C16 methyl protons (δ 2.14), and on the observation of a 1.6-Hz allylic coupling between H5 and the C16 methyl protons in **12** and a 1.2-Hz allylic coupling between the same protons in **11**. It is generally observed that *cis* allylic coupling is larger than *trans* allylic coupling (7).

Isogersemolides A (**11**) and B (**12**) are formally related to gersemolide (**7**) by combinations of an allylic rearrangement and geometric isomerism. These interrelationships could be demonstrated by gently refluxing gersemolide (**7**) in formic acid/ethyl acetate to give a mixture of **7**, **11**, and **12** (30:20:3), as indicated by ^{1}H nmr and tlc.

Isoepilophodione A (**13**) was isolated as a pale yellow oil that gave a parent ion at 328.1686 daltons in the HREIMS appropriate for a molecular formula of $C_{20}H_{24}O_4$ (ΔM +1.1 mmu). Examination of the ^{1}H and ^{13}C nmr spectra (Tables 1 and 2) of **13** indicated the presence of the α,β-unsaturated-γ-lactone, methyl substituted enedione, trisubstituted olefin, and isopropenyl substructures found in epilophodione (**6**) (4). The strong similarity in the spectral data of **13** and **6** suggested that they were simply stereoisomers of each other, differing in the configuration of either one or both of the C4—C5 and C7—C8 olefins. Treatment of epilophodione (**6**) with iodine in benzene/ethyl acetate gave a mixture of **6**, **13**, and **14**, confirming that isoepilophodione A (**13**) and epilophodione (**6**) were geometric isomers of each other. The observation of a strong nOe between H7 (δ 6.07) and the C19 methyl protons (δ 1.99) established the *Z* configuration for the C7—C8 olefin in **13**. There was no demonstrable nOe between H5 (δ 6.68) and the C18 methyl protons (δ 2.16), implying that the C4—C5 olefinic configuration was *E*. Epilophodione (**6**) and isoepilophodione A (**13**), therefore, have the same relationship to each other as do the previously reported metabolites lophodione (**23**) and isolophodione (**24**) (8).

Isoepilophodione B (**14**) was isolated as a pale yellow oil that was shown by HREIMS (M^+ 328.1670; ΔM −0.5 mmu) to possess the same $C_{20}H_{24}O_4$ molecular formula as epilophodione and isoepilophodione A. Many of the resonances in the room temperature ^{1}H nmr spectrum of **14** were very broad, making it impossible to extract much structural information. Fortunately, however, isomerization of either epilophodione (**6**) or isoepilophodione A (**13**) with iodine in benzene/ethyl acetate gave

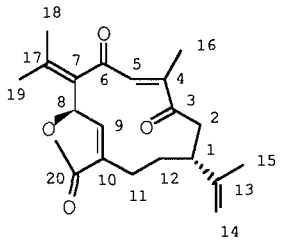

11

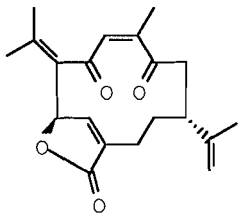

12

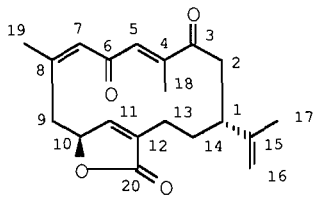

13

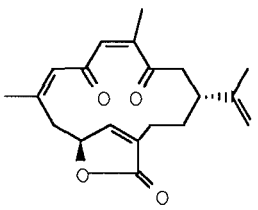

14

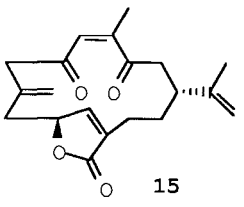

15

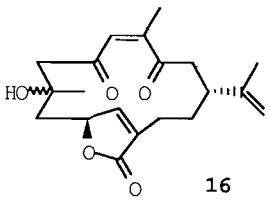

16

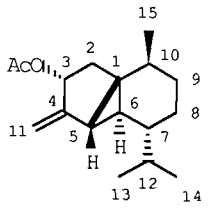

17

TABLE 1. The ^{1}H nmr assignments for diterpenoids **6** and **7** (4) and **11**–**16**. Spectra

Proton on carbon no.	7	11	12	6
1	2.26(m)	2.33(m)	1.95–2.06(m)	2.20–2.47(m)
2	2.38(dd, J = 15.1, 9.5 Hz)	2.49–2.57(m)	2.31–2.49(m)	2.51(m, 2H)
	2.53(dd, J = 15.1, 4.5 Hz)	2.71(dd, J = 14.0, 5.7 Hz)	2.72(dd, J = 13.6, 3.8 Hz)	
5	6.33(q, J = 1.2 Hz)	6.21(q, J = 1.2 Hz)	6.11(q, J = 1.6 Hz)	6.38(q, J = 1.6 Hz)
7	3.29(d, J = 0.6 Hz)	—	—	6.12(bs)
8	5.38(m)	5.92(d, J = 0.6 Hz)	5.93(bs)	—
9	7.12(bs)	7.02(dd, J = 0.6, 0.6 Hz)	7.10(bs)	2.67(dd, J = 13.3, 4.5 Hz)
				2.82(dd, J = 13.3, 4.8 Hz)
10	—	—	—	5.27(m)
11	2.01(m)	2.17(m)	2.31–2.49(m, 2H)	7.15(bd, J = 0.9 Hz)
	2.32–2.45(m)	2.49–2.57(m)		
12	1.28(m, 2H)	1.26–1.41(m)	1.18(m)	—
13	—	—	—	2.20–2.47(m)
14	5.20(bs)	4.76(bs)	4.94(m)	1.38(m)
	5.47(bs)	4.86(q, J = 0.9 Hz)	5.07(bs)	1.86(m)
15	1.73(bs)	1.72(bs)	1.73(bs)	—
16	1.83(d, J = 1.2 Hz)	2.08(d, J = 1.2 Hz)	2.14(d, J = 1.6 Hz)	4.92(m, 2H)
17	—	—	—	1.61(bs)
18	4.76(m, 2H)	2.01(s)	1.85(s)	1.91(d, J = 1.6 Hz)
19	1.64(bs)	2.06(s)	1.93(s)	2.19(d, J = 1.2 Hz)

isoepilophodione B (**14**) as one component of the equilibrium mixture. Thus, isoepilophodione B (**14**) had to be one of the remaining geometric isomers of epilophodione, i.e., with the C4—C5 and C7—C8 double bonds in either the *E,E* or *Z,Z* configurations. Irradiation of the C19 methyl protons at δ 2.06 induced an nOe into the H7 olefinic proton at δ 6.25, and irradiation of the C18 methyl protons at δ 1.88 induced an nOe into the H5 proton at δ 6.21, demonstrating that both double bonds in **14** had the *Z* configuration.

The broadening of several resonances in the ^{1}H nmr spectrum of isoepilophodione B (**14**) was attributed to the slow interconversion of two low energy conformations of the molecule. Heating the nmr sample to 50°C failed to resolve the problem and it resulted in partial decomposition of the metabolite. Cooling the nmr sample to −40°C froze out two distinct conformations in a ratio of 4:1, producing sharp signals that could be assigned to both conformers.

Isoepilophodione C (**15**), isolated as a clear oil, was also shown by HREIMS (M^+ 328.1671, $C_{20}H_{24}O_4$; ΔM −0.4 mmu) to be isomeric with epilophodione. Methyl substituted ene dione, α,β-unsaturated-γ-lactone, and isopropenyl residues were again readily apparent in the ^{1}H and ^{13}C nmr spectra of **15** (Tables 1 and 2). Additional ^{13}C nmr resonances at δ 125.3 and 143.7, and ^{1}H nmr resonances at δ 5.90 and 6.08 were tentatively assigned to a C8—C19 exocyclic methylene functionality. A pair of SINEPT experiments (9), optimized for polarization transfer through two- and three-bond ^{1}H,^{13}C couplings of 7 Hz, confirmed the placement of the C8—C19 double bond and aided the assignment of the ^{13}C nmr spectrum (Table 2). Application of a selective pulse to the ^{1}H resonance at δ 3.73, assigned to one of the C7 methylene protons, gave polarization transfer into carbon resonances at δ 128.3 (C5), 143.7 (C8), and 196.9 (C6). Irradiation of the exocyclic methylene proton resonating at δ 5.90 (H19a) gave polarization transfer into carbon resonances at δ 48.3 (either C7 or C9) and 143.7 (C8). A strong nOe between H5 and the C18 methyl protons established the *Z* stereochemistry for the C4—C5 double bond. Additional decoupling and nOe experiments were completely consistent with the proposed structure and they facilitated complete assignment of the ^{1}H nmr spectrum (Table 1). Isoepilophodione A (**13**) gave isoepilophodione C (**15**) as one component of an equilibrium mixture upon treatment with refluxing formic acid/ethyl acetate.

Rubifol (**16**) ($C_{20}H_{26}O_5$; HREIMS M^+ 346.1785, ΔM +0.4 mmu) was isolated as colorless needles from methanol. As was the case with the other *G. rubiformis* cembranoid diterpenes, the ^{1}H and ^{13}C nmr spectra (Tables 1 and 2) of **16** clearly revealed the presence of the methyl substituted ene dione, α,β-unsaturated-γ-lactone, and isopropenyl fragments common to these metabolites. Clearly absent from the nmr data of **16** were resonances that could be assigned to a C7—C8 or C8—C19 olefin. Instead there was a new resonance at δ 80.7(C) in the ^{13}C nmr spectrum and a methyl singlet at δ 1.20 in the ^{1}H nmr spectrum of **16** that could be assigned to a tertiary carbinol carbon (C8) bearing a methyl substituent (C19). An alcohol stretching band at 3509 cm^{-1} in the ir spectrum of **16** supported the presence of the alcohol functionality. The alcohol accounted for the fifth oxygen atom in the molecular formula of rubifol. Irradiation of the C19 methyl protons at δ 1.20 induced nOe's into both H7a (δ 2.47) and H7B (δ 3.37). Irradiation of H7b (δ 3.37) in turn induced nOe's in H5 (δ 6.31) as well as H7a (δ 2.47) and the C19 methyl protons (δ 1.20). Decoupling and nOe experiments also demonstrated the expected connectivity from H9a and H9b continuously around the ring to H2a and H2b. It was not possible to unambiguously determine the relative configuration at C8 from the nOe data. We have assumed that the relative configurations at C1 and C10 in rubifol (**16**) and in the other new cembranoid metabolites **13**, **14**, and **15** are the same as the relative configurations of the corresponding centers in gersemolide (**7**) and gersolide (**8**). The relative stereochemis-

Can. J. Chem. Downloaded from www.nrcresearchpress.com by 196.1.178.254 on 09/07/12
For personal use only.

were recorded in $CDCl_3$. Chemical shifts are reported in ppm from internal TMS

13	14	15	16
2.33–2.45(m)	2.20–2.62(m)	—	3.34(bd, J = 10.7 Hz)
2.50(m, 2H)	2.20–2.62(m)	—	2.09–2.19(m)
	2.68–2.92(m)	2.21–2.37(m)	
6.68(q, J = 1.2 Hz)	6.21(m)	6.29(q, J = 1.2 Hz)	6.31(bs)
6.07(bs)	6.25(bs)	3.08(d, J = 15.0 Hz)	2.47(d, J = 17.3 Hz)
		3.73(d, J = 15.0 Hz)	3.37(d, J = 17.3 Hz)
—	—	—	—
2.98(ddm, J = 13.5, 5.1 Hz)	2.68–2.92(m)	2.14(m)	2.59(dd, J = 10.8, 3.9 Hz)
3.04(ddm, J = 13.5, 4.5 Hz)	4.03(m)	3.05(dd, J = 11.1, 1.8 Hz)	3.91(dd, J = 10.8, 10.8 Hz)
5.23(m)	5.27(m)	5.06(m)	4.83(m)
7.19(bs)	7.16	6.79(d, J = 1.8 Hz)	6.64(d, J = 0.6 Hz)
—	—	—	—
2.33–2.45(m)	2.20–2.62(m)	—	2.09–2.19(m)
			2.21–2.37(m)
2.06(m)	1.41(m)	—	1.67–1.77(m)
?	?		1.82(dd, J = 10.7, 10.7 Hz)
—	—	—	—
4.54(bs)	4.64(m)	4.69(bs)	4.82(bs)
4.76(q, J = 0.6 Hz)	4.83(m)	4.81(bs)	4.84(bs)
1.66(bs)	1.70(bs)	1.16(bs)	1.70(bs)
2.16(d, J = 1.2 Hz)	1.88(bs)	1.95(d, J = 1.2 Hz)	2.06(bs)
1.99(bs)	2.06(m)	5.90(d, J = 0.9 Hz)	1.20(s)
		6.08(s)	

TABLE 2. ^{13}C nuclear magnetic resonance data. Spectra were recorded in $CDCl_3$. Chemical shifts are reported in ppm from internal TMS

Carbon no.	6	7	11[a]	13[a]	15[b]	16[a]
1	41.8	41.2	43.5*	41.5*	35.7*	40.7
2	45.5	44.9	44.3*	42.8*	41.7*	39.3*
3	205.5	208.3*	203.3#	202.6	202.0	217.3#
4	143.9*	156.2	150.0&	149.8#	154.3#	155.2&
5	133.5	123.8	130.8&	132.3	128.3	126.3
6	192.1	197.6*	193.8#	194.6	196.9	202.9
7	127.1	62.4	145.3&	130.2	48.3*	50.2*
8	151.8	79.0	77.6	140.0#	143.7#	80.7
9	43.6	150.0	148.1&	38.9*	41.6*	37.6*
10	78.4	134.2#	135.1&	78.1	80.0	78.3
11	148.1	22.0	23.1@	147.8	148.0	147.2
12	136.2	31.4	28.4	134.1	132.9	132.3
13	21.0	146.4#	147.3&	22.1&	21.2&	21.3
14	33.5	112.3@	112.7	29.0	27.6	26.6
15	145.4*	19.8&	21.9@	144.9#	145.8#	145.2&
16	115.6	21.9&	23.8@	113.2	113.0	112.9
17	17.2	138.1#	131.4&	14.3	18.1	18.2
18	21.1#	116.1@	14.2@	18.3&	27.3&	26.7@
19	22.3#	23.1&	18.4@	23.4&	125.3	24.9@
20	173.6	173.7	172.4	172.2	173.9	173.6

*, &, #, @ Values within a column may be interchanged.

[a]Assignments are based on comparisons to related compounds and must be considered tentative.

[b]Assignments are based on SINEPT experiments and comparisons to related compounds and must be considered tentative.

tries of **7** and **8** were determined by X-ray diffraction analysis (4, 5).

Atlantic coast specimens

East coast samples of *G. rubiformis* were collected by hand using SCUBA at Admiral's Cove and Bay Bulls, Newfoundland. Freshly collected specimens were immediately frozen and stored at −5°C until needed. Thawed material was homogenized in a Waring blender with methanol and the resulting homogenate was kept at room temperature for up to 3 days. The organic soluble portion of the methanol extract was fractionated by sequential application of silica gel flash, normal phase, and reverse phase high performance chromatographies to give pure samples of the known steroids **1**–**4** (2,3) and the new sesquiterpenoid **17**.

3-Acetoxy-β-cubebene (**17**) was obtained as a clear oil that failed to give a parent ion in the EI mass spectrum. The ^{13}C nmr spectrum of **17** showed resonances for 17 carbons (Table 3). An APT experiment (10) demonstrated that the molecule contained three quaternary, six methine, four methylene, and four methyl carbons and therefore 26 protons attached to carbon. An ir absorption at 1732 cm^{-1}, ^{13}C nmr resonances at δ 21.6(CH_3), 76.1(CH), and 170.4(C═O) (Table 3), and ^1H nmr resonances at δ 5.39 (d, J = 8.0 Hz, 1H) and 2.01 (s, 3H) (Table 3) all indicated the presence of a secondary acetate functionality in **17**. There was no spectral evidence for additional heteroatom containing functionalities, leading to the conclusion that **17** had a molecular formula of $C_{17}H_{26}O_2$ requiring five units of unsaturation. A strong fragment ion at m/z 202.1713 daltons ($C_{15}H_{22}$; ΔM −0.9 mmu) in the mass spectrum of **17**, corresponding to the facile loss of acetic acid from the parent molecule, confirmed the molecular formula. Evidence for four methyl residues, in addition to the acetate methyl, was apparent in the ^1H nmr spectrum of **17** (three methyl doublets, and one exocyclic methylene), indicating that the molecule was a sesquiterpene acetate.

Two other structural fragments could be readily recognized from the spectral data of **17**. A shielded one-proton multiplet at δ 0.58 in the ^1H nmr spectrum suggested a cyclopropyl ring. The base peak observed at m/z 159 daltons in the mass spectrum of **17** corresponded to a loss of acetic acid followed by a loss of a

Can. J. Chem. Downloaded from www.nrcresearchpress.com by 196.1.178.254 on 09/07/12
For personal use only.

TABLE 3. Nuclear magnetic resonance data for the sesquiterpenoid **17**. Spectra were recorded in $CDCl_3$. Chemicals shifts are reported in ppm from internal TMS

Carbon no.	^1H	^{13}C
1	—	37.4
2	2.38(dd, J = 14.4, 8.0 Hz) 1.55–1.67(m)	38.9*
3	5.39(d, J = 8.0 Hz)	76.1
4	—	152.8
5	—	44.2#
6	0.58(m)	34.6#
7	—	33.5#
8	—	31.1*
9	—	31.2*
10	—	30.4#
11	5.01(bs) 5.05(bs)	109.0
12	1.74(m)	26.5#
13	0.92(d, J = 7 Hz)*	18.8&
14	0.94(d, J = 7 Hz)*	19.8&
15	0.96(d, J = 7 Hz)*	20.0&
Ac (CH_3)	2.01(s)	170.4
Ac (CO)	—	21.6&

*, &, #, @ Values may be interchanged.

TABLE 4. Comparison of the partial ^{13}C nmr data for the model compounds **20**, **21**, and **22** with that for **17**. All spectra were recorded in $CDCl_3$

Carbon no.	**17**	**20** (11)	**21** (12)	**22** (13)
13[a]	18.8	19.1	18.7	18.9
14[a]	19.8	19.8	19.6	19.5
15[a]	20.0	20.0	20.0	20.0

[a]The assignments may be interchanged.

C_3H_7 fragment. That observation, coupled with the presence of three methyl doublets in the ^1H nmr spectrum, provided evidence for an isopropyl residue.

The cubebene sesquiterpenoid structure **17** effectively accommodated all the identified structural fragments and observed spectral features of the metabolite. In concert with the proposed structure, irradiation of the carbinol methine proton at δ 5.39 (H3) sharpened the two exocyclic methylene resonances at δ 5.01 (H11a) and 5.05 (H11b) and simplified H2a (δ 2.38) to a doublet (J = 14.4 Hz). Irradiation of H2a (δ 2.38) collapsed the carbinol methine (H3, δ 5.39) to a broad singlet and also collapsed H2b (δ 1.54) to a singlet.

3-Acetoxy-β-cubebene (**17**) decomposed to give a complex mixture of very polar compounds when it was exposed to nmr solvents or subjected to routine laboratory manipulations. Hydrogenation of **17** gave an inseparable mixture of two stable dihydro epimers **18** and **19** in a ratio of 4:1. Decoupling and nOe experiments (see Experimental) conducted on the major isomer of the mixture supported the constitution of **17** and established that the relative stereochemistry at C3, C5, and C6 was as shown. A comparison of the ^{13}C nmr data for **17** with those reported for the related compounds **20** (11) and **21** (12) and with those which we recorded for the synthetic model compound **22** (13) showed excellent agreement (Table 4). In particular, the

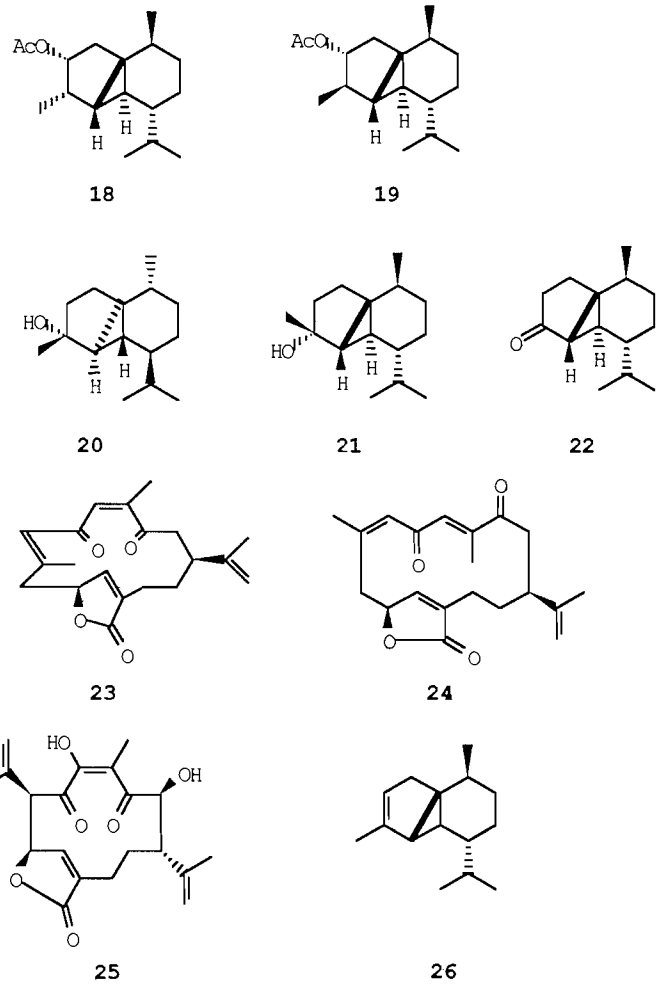

resonances assigned to the methyl groups at C13, C14, and C15 have virtually identical chemical shifts in all three molecules, supporting our stereochemical assignments for C7 and C10.

The ^1H nmr resonance assigned to H6 (δ 0.58) in **17** displayed a complex coupling pattern that could not be readily explained on the basis of its vicinal proximity to only two other protons. The resonance assigned to H6 in the ^1H nmr spectrum of the model compound **22** showed an identical coupling pattern. Presumably the additional splittings observed in the H6 multiplets are the result of long-range scalar couplings facilitated by the strain and rigidity of the cubene ring system.

Discussion

Tropical soft corals and gorgonians are well known to be a very rich source of novel terpenoid metabolites (14). Our examination of the chemistry of *G. rubiformis* has shown that cold water soft corals are equally capable of elaborating a wide spectrum of interesting terpenes that are structurally related to those found in their tropical relatives. For example, two of the diterpenes found in Pacific specimens of *G. rubiformis*, gersemolide (**7**) and epilophodione (**6**), are close structural analogues of kallolide C (**25**) (15) and lophodione (**23**) (8) isolated from the tropical gorgonians *Pseudopterogorgia kallos* and *Lophogorgia alba*. Similarly, 3-acetoxy-β-cubebene (**17**), isolated from Atlantic specimens of *G. rubiformis*, is closely related to α-cubebene (**26**) isolated from several tropical gorgonians belonging to the genus *Pseudoplexaura* (16). The major difference between the tropical and cold water coelenterates is the observed concentration of the terpenoids. Rubifolide (**5**), the most abundant metabolite in *G. rubiformis*, is

Can. J. Chem. Downloaded from www.nrcresearchpress.com by 196.1.178.254 on 09/07/12
For personal use only.

present at a concentration of 2×10^{-4}% dry weight, while kallolide A, the most abundant metabolite of *P. kallos*, is present at a concentration of 3×10^{-1}% dry weight (15). The lower concentration of secondary metabolites in *G. rubiformis* appears to be typical of most cold water organisms.

The co-occurrence of cembrane, pseudopterane, and gersolane diterpenoids in the Pacific specimens of *G. rubiformis* suggests that all three carbon skeletons share a common biogenetic origin. Fenical has suggested that the pseudopterane skeleton is formed via a ring contraction of cembrane precursor (17) and it seems likely that the pathway to the gersolane skeleton also passes through a cembrane intermediate.

Pacific Ocean specimens of *G. rubiformis* contain secondary metabolites that are completely different than the metabolites present in Atlantic Ocean specimens. The reason for the difference is unclear; however, a reexamination of the taxonomy of *G. rubiformis*, taking into account the chemical information now available, is a necessary starting point in the quest for an explanation.

Experimental

The nmr spectra were recorded on Varian XL 300 and Bruker WH-400 spectrometers. Deutero chloroform was used as a solvent for recording all nmr spectra and Me_4Si was used as an internal standard. Low resolution mass spectra were recorded on an AEI MS902 spectrometer and high resolution mass spectra were recorded on an AEI MS50 spectrometer. The ir spectra were recorded on a Perkin Elmer 1710 Fourier transform spectrometer. The uv spectra were recorded on a Bausch and Lomb Spectronic 2000 instrument. Optical rotation measurements were recorded on a Perkin Elmer 141 polarimeter. A Fish–Johns apparatus was used to determine melting points and the reported vaues are uncorrected.

Merck silica gel (230–400 mesh) was used for flash chromatography and Merck silica gel 60 PF-254 with $CaSO_4 \cdot 1/2H_2O$ was employed in radial tlc (Harrison Research Chromatotron model 7924). Whatman Magnum-9 Partisil 10 or Whatman Magnum 9 Partisil 10 ODS-3 columns were used for preparative hplc.

Collection data

Specimens of *G. rubiformis* were collected by hand using SCUBA around exposed rocky reefs (−1 to −5 m) located within the Gordon Group of Islands, British Columbia, and at Admiral's Cove, Cape Broyle, and Bulls Bay, Newfoundland.

Isolation of metabolites from British Columbia specimens

Freshly collected animals (1.5 kg dry wt.) were homogenized with methanol in a Waring blender and left at room temperature for up to 3 days. The homogenized material was filtered through Celite and the solids were reextracted twice with fresh methanol. Evaporation of the combined methanol extracts *in vacuo* gave an aqueous suspension (1 L) that was sequentially extracted with hexanes (4 × 250 mL), dichloromethane (2 × 250 mL), and ethyl acetate (2 × 250 mL). The organic extracts were dried over sodium sulfate, combined, and evaporated *in vacuo* to give a dark red oil (33 g). Silica gel flash chromatography, employing a step gradient from 1:20 ethyl acetate/hexanes to 1:10 methanol/ethyl acetate, was used to separate the red oil into Fraction A (2.1 g, eluted with 1:20 ethyl acetate/hexanes), Fraction B (3.3 g, eluted with 1:4 ethyl acetate/hexanes), Fraction C (2.3 g, early part of material eluted with ethylacetate), and Fraction D (2.2 g, late part of material eluted with ethyl acetate).

Preparative silica gel tlc of Fraction C (5% methanol/dichloromethane) gave a series of close running uv active bands (R_f's 0.71–0.83) that were collected as a group to give a mixture (485 mg total) of gersemolide (**7**), isogersemolides A (**11**) and B (**12**), isoepilophodiones A (**13**), B (**14**), and C (**15**), rubifol (**16**), and gersolide (**8**). Radial tlc separation of the mixture (two-step gradient: (*i*) 1:1 dichloromethane/hexanes; (*ii*) 1:1:1 diethyl ether/hexanes/dichloromethane) gave fraction 1 (314 mg) containing **7**, **11**, **12**, **14**, **15**, and **16** and fraction 2 (24 mg) containing only **13** and fat. Normal phase hplc (3:3:1 diethyl ether/hexanes/dichloromethane) and reverse phase hplc (3:2 methanol/water) were used to separate fraction 1 into pure isogersemolide A (**11**) (3 mg), isogersemolide B (**12**) (1 mg), isoepilophodione B (**14**) (78 mg), isoepilophodione C (**15**) (17 mg), and rubifol (**16**) (8 mg). Reverse phase hplc (3:2 methanol/water) was used to obtain pure isoepilophodione A (**13**) (9 mg) from fraction 2.

Isolation of 3-acetoxy-β-cubebene (17) from Newfoundland specimens

Freshly collected Atlantic specimens of *G. rubiformis* (250 g dry wt.) were frozen and stored at −5°C until needed. Defrosted animals were homogenized with methanol in a Waring blender and the homogenized material was left at room temperature for 3 days before being filtered through Celite. The solids were reextracted twice with fresh methanol. Evaporation of the combined methanol filtrates *in vacuo* gave an aqueous suspension (300 mL) that was partitioned between brine (200 mL) and ethyl acetate (6 × 175 mL). The combined ethyl acetate layers were dried over sodium sulfate and concentrated *in vacuo* to give a dark orange-brown oil (4 g). Fractionation of the oil by silica gel flash (1:20 ethyl acetate/hexanes), normal phase hplc (1:40 ethyl acetate/hexanes), and reverse phase hplc (8:1:1 methanol/water/dichloromethane) gave pure 3-acetoxy-β-cubebene (**17**) (5 mg).

Isogersemolide A (11): colorless needles (MeOH), mp 121–124°C; $[\alpha]_D^{25}$ −225° (*c* 0.37, CH_2Cl_2); R_f 0.77 (silica gel, 1:20 MeOH/CH_2Cl_2); uv (MeOH) λ_{max}: 205 (ε 4700), 242(sh) nm; ir (CH_2Cl_2): 3017, 2960, 2930, 2855, 1761, 1695, 1672, 1645, 1607, 1458, 1379, 1175, 1045, and 871 cm^{-1}; ^1H nmr, see Table 1; ^{13}C nmr, see Table 2; LRMS, *m/z* (rel. intensity): 328 (M^+, 30), 310(10), 300(15), 283(27), 67(100).

Isogersemolide B (12): colorless needles (1:1 Et_2O/MeOH); $[\alpha]_D^{25}$ −27° (*c* 0.02, CH_2Cl_2); R_f 0.75 (silica gel, 1:20 MeOH/CH_2Cl_2); uv (MeOH) λ_{max}: 218 (ε 3050), 237(sh) nm; ^1H nmr, see Table 1; LRMS, *m/z* (rel. intensity): 328(M^+, 100), 310(25), 283(60), 201(38), 189(38), 173(50).

Isomerization of isogersemolide A (11) with iodine

To a stirred room temperature solution of isogersemolide A (**11**) (2 mg) in ethyl acetate (2 mL) was added 5 drops of a solution prepared by adding one crystal of iodine to 10 mL of benzene. The reaction was quenched after 16 h by adding 5 mL of an aqueous sodium bisulfite solution followed by repeated extraction with ethyl acetate (3 × 5 mL). Evaporation of the combined ethyl acetate layers *in vacuo* gave 1.3 mg of an oil that contained a 3:1 mixture of isogersemolide A (**11**) and isogersemolide B (**12**), as evidenced by ^1H nmr and tlc analysis.

Isomerization of gersemolide (7) with formic acid

A solution of gersemolide (**7**) (2 mg), ethyl acetate (4 mL), and formic acid (3 drops) was gently refluxed for 16 h under nitrogen. The cooled reaction mixture was neutralized with 5% sodium bicarbonate solution (10 mL) and extracted with ethyl acetate (2 × 5 mL). Evaporation of the ethyl acetate fraction *in vacuo* gave 1.5 mg of an oil that contained a 30:20:3 mixture of gersemolide (**7**), isogersemolide A (**11**), and isogersemolide B (**12**), as evidenced by ^1H nmr and tlc analysis.

Isoepilophodione A (13): pale yellow oil; $[\alpha]_D^{25}$ +138° (*c* 0.55, CH_2Cl_2); R_f 0.71 (silica gel, 1:20 MeOH/CH_2Cl_2); uv (MeOH) λ_{max}: 246 (ε 12 800), 208 (ε 16 200) nm; ir (CH_2Cl_2): 3070, 2985, 2936, 2845, 1761, 1681, 1648, 1619, 1605, 1445, 1380, 1276, 1065, and 1026 cm^{-1}; ^1H nmr, see Table 1; ^{13}C nmr, see Table 2; LRMS *m/z* (rel. intensity): 328(M^+, 4), 310(3), 178(21), 151(26), 135(25), 121(28), 107(30), 82(100).

Isoepilophodione B(14): pale yellow oil; $[\alpha]_D^{25}$ +298° (*c* 0.40, CH_2Cl_2); R_f 0.77 (silica gel, 1:20 MeOH/CH_2Cl_2); uv (MeOH) λ_{max}: 267 (ε 14 400), 212 (ε 13 100) nm; ir (CH_2Cl_2): 2982, 2935, 2875, 1758, 1683, 1643, 1620, 1610, 1443, 1381, 1260, 1120, 1105, 1064, 1026, and 882 cm^{-1}; ^1H nmr, see Table 1; ^{13}C nmr, see Table 2; LRMS *m/z* (rel. intensity): 328(M^+, 11), 82(100).

Isoepilophodione C(15): clear oil; $[\alpha]_D^{25}$ −170° (*c* 0.26, CH_2Cl_2); R_f 0.75 (silica gel, 1:20 MeOH/CH_2Cl_2); uv (MeOH) λ_{max}: 230 (ε 2500) nm; ir (CH_2Cl_2): 2982, 2942, 2868, 1756, 1689, 1643, 1614, 1441, 1380, 1335, 1102, 1091, 1042, and 948 cm^{-1}; ^1H nmr, see Table 1; ^{13}C nmr, see Table 2; LRMS *m/z* (rel. intensity): 328(M^+, 8), 310(6), 150(100), 121(27), 109(28), 82(60).

Can. J. Chem. Downloaded from www.nrcresearchpress.com by 196.1.178.254 on 09/07/12
For personal use only.

Rubifol (16): colorless needles (MeOH), mp 127–130°C; $[\alpha]_D^{25}$ −41° (*c* 0.38, CH_2Cl_2); R_f 0.76 (silica gel, 1:20 MeOH/CH_2Cl_2); uv (MeOH) λ_{max}: 230 (ε 6700), 207 (ε 10 300) nm; ir (CH_2Cl_2): 3509, 2980, 2934, 2869, 1756, 1700, 1671, 1644, 1610, 1447, 1382, 1338, 1200, 1094, and 1042 cm^{-1}; ^1H nmr, see Table 1; ^{13}C nmr, see Table 2; LRMS *m/z* (rel. intensity): 346(M^+, 2), 328(5), 151(89), 140(45), 133(33), 109(54), 91(62), 82(100).

Isomerization of epilophodione (6) and isoepilophodione A (13) with iodine

Epilophodione (**6**) (7 mg) and isoepilophodione A (**13**) (3 mg) were independently isomerized with iodine according to the procedure described above for the isomerization of isogersemolide A (**11**). The reaction with epilophodione (**6**) gave a 2:1:4:1 mixture of epilophodione (**6**), isoepilophodione A (**13**), isoepilophodione B (**14**), and an unidentified compound, as evidenced by tlc and ^1H nmr analysis. Isomerization of isoepilophodione A (**13**) gave a 1:3:2 mixture of **6**, **13**, and **14**.

Isomerization of epilophodione A (13) with formic acid

Eilophodione A (**13**) was isomerized with formic acid according to the procedure described above for gersemolide (**7**). The reaction gave a 3:1:1 mixture of isoepilophodione A (**13**), isoepilophodione B (**14**), and isoepilophodione C (**15**), as evidenced by tlc and ^1H nmr analysis.

3-Acetoxy-β-cubebene (17): clear oil; $[\alpha]_D^{25}$ +29° (*c* 0.24, CH_2Cl_2); R_f 0.34 (silica gel, 1:20 EtOAc/hexane); uv (MeOH) λ_{max}: 207 (ε 6100) nm; ir (CH_2Cl_2): 3057, 2962, 2934, 2875, 1732, 1609, 1464, 1374, 1246, and 1023 cm^{-1}; ^1H nmr, see Table 3, ^{13}C nmr, see Table 3; LRMS *m/z* (rel. intensity): 202(M^+ − 60, 18), 159(100), 157(74), 142(38), 131(59), 117(50), 105(56), 91(69), 77(38), 69(29), 60(26), 54(41).

Hydrogenation of 3-acetoxy-β-cubebene (17)

The fractions from the flash chromatography of a crude Newfoundland *G. rubiformis* extract that contained 3-acetoxy-β-cubebene (**17**) (75 mg) were added to methanol (10 mL) containing a catalytic amount of palladium on charcoal. The solution was stirred for 13 h at room temperature under balloon pressure of hydrogen gas. The palladium catalyst was removed via sintered glass filtration and the methanol was evaporated to give a crude mixture of the epimers **18** and **19**, fats, and steroids. The crude mixture was fractionated by normal phase hplc (1:40 EtOAc/hexanes) to give a fraction that contained only the inseparable epimers **18** and **19** (5 mg); ^1H nmr ($CDCl_3$, major isomer **18** only) δ: 0.54 (m, 1H), 083 (m, 1H), 0.88 (d, *J* = 7 Hz, 3H), 0.94 (d, *J* = 7 Hz, 3H), 1.03 (d, *J* = 7 Hz, 3H), 2.01 (s, 3H), 5.12 (t, *J* = 7 Hz, 1H); LRMS *m/z* (rel. intensity, of mixture): 264(M^+, 1), 204(12), 161(100), 133(10), 119(30), 105(50), 91(23), 81(24).

Nuclear Overhauser enhancement (nOe) experiments on the dihydro compound 18:

Proton irradiated	Observed nOe's
H2b(δ 2.33)	H3(δ 5.12), Me15(δ 0.94)
H3(δ 5.12)	H2b(δ 2.33), H4(δ 2.47)
H4(δ 2.47)	H3(δ 5.12), H5(δ 0.83), Me11(δ 0.97)

Acknowledgements

The authors would like to thank M. LeBlanc and D. Hooper for assisting the collection of *G. rubiformis*. Financial support was provided by NSERC grants to A.G.F. and R.J.A. and a National Cancer Institute of Canada grant to R.J.A.

1. W. C. Austin. An annotated checklist of marine invertebrates in the cold temperate Northeast Pacific. Kyotan Marine Laboratory, Cowichan Bay, B.C. 1985.
2. (*a*) J. F. Kingston, B. Gregory, and A. G. Fallis. Tetrahedron Lett. 4261 (1977); (*b*) J. Chem. Soc. Perkin Trans. 1, 2064 (1979).
3. (*a*) J. F. Kingston. Tetrahedron Lett. **21**, 4295 (1980); (*b*) J. F. Kingston and A. G. Fallis. Can. J. Chem. **60**, 820 (1982).
4. D. E. Williams, R. J. Andersen, G. D. Van Duyne, and J. Clardy. J. Org. Chem. **52**, 332 (1987).
5. D. E. Williams, R. J. Andersen, L. Parkanyi, and J. Clardy. Tetrahedron Lett. **28**, 5079 (1987).
6. D. E. Williams and R. J. Andersen. Can. J. Chem. **65**, 2244 (1987).
7. L. M. Jackman and S. Sternhall. *In* Applications of nuclear magnetic resonance spectroscopy in organic chemistry. Pergamon Press, New York, NY. 1969. p. 316.
8. M. M. Bandurraga, B. McKittrick, W. Fenical, E. Arnold, and J. Clardy. Tetrahedron, **38**, 305 (1982).
9. A. Bax. J. Magn. Reson. **57**, 314 (1984).
10. S. L. Patt and J. N. Shoolery. J. Magn. Reson. **46**, 535 (1982).
11. M. Suzuki, N. Kowata, and E. Kurosawa. Bull. Chem. Soc. Jpn. **54**, 2366 (1981).
12. B. F. Bowden, J. C. Coll, and D. M. Tapiolis. Aust. J. Chem. **36**, 211 (1983).
13. E. W. Piers, R. W. Britton, and W. deWaal. Can. J. Chem. **49**, 12 (1971).
14. (*a*) D. J. Faulkner. Nat. Prod. Rep. **1**, 551 (1984), (*b*), **3**, 1 (1986); (*c*) **4**, 539 (1987).
15. S. A. Look, M. T. Burch, W. Fenical, Q. Zheng, and J. Clardy. J. Org. Chem. **50**, 5741 (1985).
16. L. Ciereszko and T. K. B. Karns. *In* Biology and geology of coral reefs. Vol. II. *Edited by* O. A. Jones and R. Endean. Academic Press, New York, NY. 1973. Chap. 6. p. 193.
17. W. Fenical. J. Nat. Prod. **50**, 1001 (1987).

Can. J. Chem. Downloaded from www.nrcresearchpress.com by 196.1.178.254 on 09/07/12
For personal use only.

Coordination compounds of indium. Part 44. The oxidation of indium(I) halides by tetrahalogeno-*ortho*-quinones

THEODORE A. ANNAN AND DENNIS G. TUCK[1]

Department of Chemistry and Biochemistry, University of Windsor, Windsor, Ont., Canada N9B 3P4

Received May 6, 1988

THEODORE A. ANNAN and DENNIS G. TUCK. Can. J. Chem. **66**, 2935 (1988).

The reaction of indium(I) halides (InX; X = Cl, Br, I) with tetrahalogeno-*ortho*-quinones ($Y_4C_6O_2$; Y = Cl, Br) gives the oxidative addition product $Y_4C_6O_2InX$. These compounds have been isolated as adducts with neutral bidentate donor ligands (*N*,*N*,*N'*,*N'*-tetramethylethanediamine (tmen), 1,10-phenanthroline) or as salts of the anionic complexes $[Y_4C_6O_2InCl_2]^-$ or $[Y_4C_6O_2In(Cl)Br]^-$. The number of coordinated tmen molecules, and hence the structure, depends on the method of preparation. Infrared, ^1H NMR, and ^{13}C NMR spectroscopy all confirm that these products are all substituted-catecholato derivatives of indium(III), and the structure of these various neutral or anionic derivatives is discussed. The temperature dependence of the ^{13}C NMR spectra shows that the dynamic behaviour of these compounds (in d_6-dmso) is similar to that observed in previous studies of indium(III) chelate complexes.

THEODORE A. ANNAN et DENNIS G. TUCK. Can. J. Chem. **66**, 2935 (1988).

La réaction des halogénures d'indium(I) (InX; X = Cl, Br, I) avec des tétrahalogéno *o*-quinones ($Y_4C_6O_2$; Y = Cl, Br) conduit à des produits d'addition oxydative $Y_4C_6O_2InX$. On a isolé ces composés sous la forme d'adduits avec des ligands donneurs bidentates neutres (*N*,*N*,*N'*,*N'*-tétraméthyléthanediamine (tmen), phénanthroline-1,10) ou sous la forme de sels de complexes anioniques $[Y_4C_6O_2InCl_2]^-$ ou $[Y_4C_6O_2In(Cl)Br]^-$. Le nombre de molécules de tmen qui se coordonnent et, en fin de compte, la structure dépendent de la méthode de préparation. Les spectres infrarouges ainsi que rmn du ^1H et du ^{13}C confirment tous que ces produits sont tous des dérivés catécholato-substitués de l'indium(III); on discute des structures de ces divers dérivés neutres ou anioniques. La variation des spectres rmn du ^{13}C avec la température démontre que le comportement dynamique de ces composés (dans le dmso-d_6) est semblable à celui observé au cours d'études antérieures sur des complexes de l'indium(III) chélaté.

[Traduit par la revue]

Introduction

The oxidation of indium(I) compounds by various inorganic or organic substrates has been demonstrated in a number of studies. For example, the oxidative addition of various alkyl halides to indium(I) iodide or bromide yields the appropriate $RInX_2$ compounds (1–6), whilst oxidation of cyclopentadienylindium(I) (CpIn) by iodine gives $CpInI_2$ (7). Both CpIn (8) and indium(I) halides (9) react with 1,2-bis(trifluoromethyl)dithiete by cleavage of the S—S bond, forming indium(III) derivatives containing a C_2S_2In ring. A related type of M—M cleavage involves the reaction of InX with $Co_2(CO)_8$ to give $XIn[Co(CO)_4]_2$ (10), and similar reactions with dimeric manganese and iron carbonyls have also been reported (11, 12). The discovery that indium(I) halides have significant solubility in mixtures of aromatic solvents and neutral bases (13) allowed the range of these oxidative reactions to be extended. The overall mechanism which was proposed to explain the reaction, or absence of reaction, between InX and various M—M or M—X bonded compounds (14–16) involves the lone pair of electrons on indium(I) being donated to M to form the appropriate M—In bond, with a concomitant rearrangement and transfer of the remaining ligands.

The use of *ortho*-quinones for the oxidation of transition metal ions has been the subject of many publications, but few analogous studies with Main Group metals have been reported. In a recent paper (17), we showed that the oxidation of stannous halides (SnX_2) by tetrahalogeno-*ortho*-quinones ($Y_4C_6O_2$: Y = Cl, Br) gives the corresponding tin(IV) catecholates $Y_4C_6O_2SnX_2$. The present paper demonstrates that solutions of indium(I) halides in organic solutions containing strong donors react with these same substituted *ortho*-quinones to give indium(III)-catecholato compounds, which have been isolated as adducts with neutral bidentate or anionic donors.

[1]To whom all correspondence should be addressed.

Experimental

General

Indium(I) halides were prepared as in earlier work (13). Tetrahalogeno-*o*-quinones, *N*,*N*,*N'*,*N'*-tetramethylethanediamine (tmen), 2,2'-bipyridine (bpy), and 1,10-phenanthroline (phen) were used as supplied. Solvents were dried by conventional methods, and stored over drying agents. All reactions were carried out in an atmosphere of dry nitrogen.

Indium analysis were by atomic absorption spectrophotometry using an IL 251 instrument, and microanalysis was carried out by Guelph Chemical Laboratory. The presence of the strongly coloured *o*-quinone in acidified aqueous solution prevented the use of the Volhard method for halogen analysis. Proton nmr spectra were recorded on a Varian EM 360 instrument, and ^{13}C spectra on a Bruker AC 300L instrument. Infrared spectroscopy involved the use of samples in KBr discs with a Nicolet 5DX instrument. Conductivity measurements were made with a YSI Model 31 bridge, and a conventional cell calibrated with aqueous KCl solution.

Preparation of adducts of $Y_4C_6O_2InX$ (Y = Cl, Br; X = Cl, Br, I)

(*i*) With tmen. The same general method was used throughout for the initial reactions, followed by isolation procedures which varied depending on the particular system. In a typical experiment, 3 mmol of InX (X = Cl, Br, I) was suspended in 25 mL of toluene/methylene chloride (1:1, v/v) and the mixture cooled to about −40°C. When tmen (ca. 2 mL, 13 mmol) was syringed in, the characteristic reddish colour of solutions of InX in such systems was observed. With the temperature still at ca. −40°C, an equimolar amount of tetrachloro-*ortho*-quinone in the same toluene/methylene chloride mixture (25 mL) was added dropwise over a period of 1 h. Stirring was continued for an hour, and the solution was then allowed to warm up slowly to room temperature, with further stirring for another 1 h. The resultant clear red–wine solution was filtered and the volume of the filtrate reduced by 60% *in vacuo*; addition of diethyl ether or petroleum ether then yielded

Can. J. Chem. Downloaded from www.nrcresearchpress.com by 196.1.178.254 on 09/07/12
For personal use only.

Can. J. Chem. Downloaded from www.nrcresearchpress.com by 196.1.178.254 on 09/07/12
For personal use only.

a brown precipitate for X = Cl or Br. With X = I, an oily material was obtained at this stage, and a solid product was formed only after lengthy trituration with cold petroleum ether. All products were washed twice with either petroleum ether or diethyl ether (20 mL), and dried *in vacuo*, and identified as $Cl_4C_6O_2InX.n$tmen (n = 1.5, 2) (see Table 1 for analytical results).

(*ii*) Since it seemed probable that the use of excess tmen in the above procedure affected the composition of the final adduct, a different preparative approach was investigated. Indium(I) halide (InX, ca. 3 mmol) was suspended in a solution of tetrahalogeno-*ortho*-quinone (3 mmol) in 50 mL of a toluene/methylene chloride mixture (1:1, v/v) at room temperature. The red colour of the *o*-quinone was discharged after stirring for ca. 6 h, with complete consumption of the indium monohalide. At this stage, tmen (0.45 mL, 3 mmol) was syringed into the reaction mixture, and stirring continued for 1 h, after which the now light yellow solution was filtered to remove any traces of solid impurity. The isolation procedure was that described above. The final products were the 1:1 adducts $Y_4C_6O_2InX$.tmen.

(*iii*) Equimolar amounts (ca. 3 mmol) of InX and tetrahalogeno-*ortho*-quinones were stirred together in methylene chloride at room temperature; complete reaction occurred over a period of 4–6 h. Addition of an equimolar amount of 1,10-phenanthroline quantitatively precipitated the 1:1 adduct $Y_4C_6O_2InX$.phen.

(*iv*) Anionic derivatives of $Y_4C_6O_2InX$ were also prepared. Equimolar quantities of InCl and $Y_4C_6O_2$ (ca. 3 mmol) were stirred together in tetrahydrofuran (thf) at room temperature for 3 h. The resultant solution was filtered to remove traces of unreacted material, and the filtrate run into a solution of either Ph_4PCl or Et_4NBr (3 mmol) in methanol (5 mL). The resultant mixture was stirred (3 h), and the solvents were removed *in vacuo* to yield a dark brown oily residue, which was redissolved in the minimum amount of acetonitrile (5–10 mL). Addition of diethyl ether (100 mL) produced an oily deposit, which on trituration over several days at room temperature gave a colorless solid, $Ph_4P[Y_4C_6O_2InCl_2]$ or $Et_4N[Y_4C_6O_2In(Cl)Br]$, which was collected and dried *in vacuo*.

(*v*) An alternative route to these anionic species involved formation of the $Y_4C_6O_2^{2-}$ anion by treating a solution of *o*-$Br_4C_6(OH)_2$ (2.0 g, 4.7 mmol) in thf (20 mL) with a suspension of NaH (0.22 g, 9.2 mmol) in the same solvent. Evolution of hydrogen occurred. The resultant light brown solution was treated dropwise with a solution of $InCl_3$ (1.05 g, 4.7 mmol) in thf (25 mL), and the mixture refluxed gently for 1 h. The white precipitate of NaCl was removed by filtration, and the filtrate treated with equimolar quantities of Ph_4PCl or Et_4NBr. The products were isolated as in (*iv*) above.

In each case, the products were characterized by elemental analysis, and by ir and nmr spectroscopy, and in the case of the anionic species by molar conductivity measurements.

Results and discussion

Preparative

The compounds listed in Table 1 are all neutral or anionic adducts of substituted-catecholato-indium(III) halides species, which themselves are formed in the redox reaction.

[1] 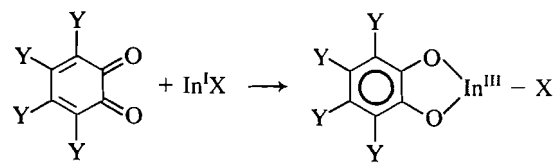

This process is exactly analogous to that identified in the reaction of SnX_2 with these same tetrahalogeno-*o*-quinones, producing the tin(IV) compounds $Y_4C_6O_2SnX_2$ (17). Both reactions are formally oxidative addition processes, involving the transfer of a pair of electrons. A study of the reaction of SnX_2 with 3,5-di-*tert*-butyl-*ortho*-quinone (TBQ) has revealed clear evidence from electron spin resonance spectroscopy that such reactions actually involve two distinct one-electron transfers via the appropriate semiquinone (18), and we have found that the pale yellow solutions observed in the synthesis (e.g., method (*ii*) of Preparation above) are also esr-active, although these systems are not as conveniently investigated as are those with TBQ.

TABLE 1. Analytical results for indium(III)–catecholato derivatives

Compound	Method	In (%)
$Cl_4C_6O_2InCl.2tmen.\frac{1}{2}Et_2O$	*i*	17.3(17.3)[a]
$Cl_4C_6O_2InBr.2tmen$	*i*	17.0(17.1)[b]
$Cl_4C_6O_2InI.1.5tmen$	*i*	17.3(17.4)[c]
$Cl_4C_6O_2InCl.tmen$	*ii*	22.0(22.4)
$Cl_4C_6O_2InBr.tmen$	*ii*	21.0(20.6)
$Cl_4C_6O_2InI.tmen$	*ii*	18.7(19.0)
$Br_4C_6O_2InCl.tmen$	*ii*	16.6(16.6)
$Br_4C_6O_2InBr.tmen$	*ii*	15.7(15.6)
$Br_4C_6O_2InI.tmen$	*ii*	14.5(14.7)
$Cl_4C_6O_2InCl.phen$	*iii*	19.9(19.9)
$Cl_4C_6O_2InBr.phen$	*iii*	18.4(18.5)
$Cl_4C_6O_2InI.phen$	*iii*	17.2(17.2)[d]
$Br_4C_6O_2InCl.phen$	*ii*	15.2(15.2)
$Br_4C_6O_2InBr.phen$	*iii*	14.4(14.4)
$Br_4C_6O_2InI.phen$	*iii*	13.6(13.6)
$Ph_4P[Cl_4C_6O_2InCl_2]$	*iv*,*v*	15.0(14.9)
$Et_4N[Cl_4C_6O_2In(Cl)Br]$	*iv*,*v*	18.8(18.1)
$Ph_4P[Br_4C_6O_2InCl_2]$	*iv*,*v*	12.6(12.1)
$Et_4N[Br_4C_6O_2In(Cl)Br]$	*iv*,*v*	14.8(14.6)

[a]C 35.6 (36.1); H 6.0 (5.9); N 8.6 (8.4)%.
[b]C 32.3 (32.1); H 4.9 (4.8); N 8.1 (8.3)%.
[c]C 27.9 (27.2); H 4.1 (4.0); N 6.5 (6.4)%.
[d]C 32.5 (32.4); H 1.4 (1.2); N 4.0 (4.2)%.

The adducts prepared with equimolar quantities of phen or tmen can be readily formulated as the five-coordinate species **1**

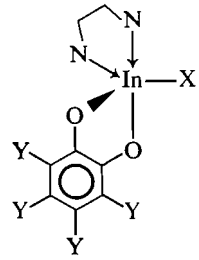

1

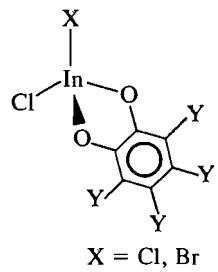

X = Cl, Br

2

and this is in keeping with the spectroscopic evidence (see below). This coordination state has been established for a number of indium(III) compounds, and must now be regarded as one of the standard stereochemical forms of the element. Relevant examples include Ph_3SnInX_2.tmen (16), $InCl_3.2Ph_3P$ (19), $(R_2E)_2InX.L_2$ (E = S, Se) (15), $EtInX_2$.tmen (20), L_2InX (L = 2-[(dimethylamino)methyl]phenyl ligand) (21), $In^{III}(dthz)_3$ (dthz = dithizone) (22), Me_2InCl (23), $(MeInCl_2)_2$ (24), and Me_2InBr (25). Unlike the higher adducts of tmen (see below), these compounds typically have low conductivities in *N*,*N*′-dimethylformamide (dmf) (see Table 2), in keeping with the neutral formulation shown.

It is also possible to prepare anionic derivatives of $Y_4C_6O_2InX$, in which indium(III) is four-coordinate (structure **2**); many such complexes are known. The structure of these particular complexes is confirmed by their synthesis via the disodium salt of the tetrahalogeno-catechol as shown in Scheme 1.

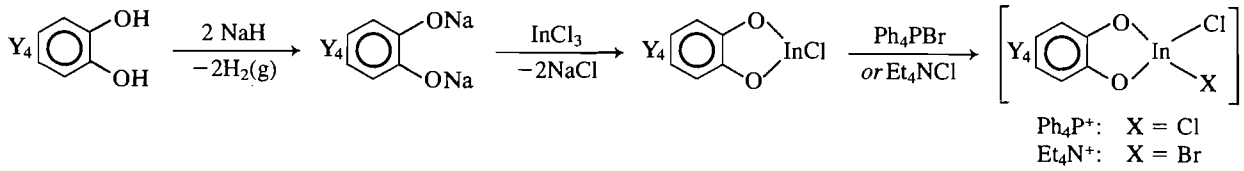

SCHEME 1

TABLE 2. Molar conductivities of some indium(II)–catecholato derivatives

Compound	Solvent[a,b]	Molar conductivity ($ohm^{-1}\,cm^2\,mol^{-1}$)
$Cl_4C_6O_2InCl.tmen$	dmf	18
$Cl_4C_6O_2InBr.tmen$	dmf	19
$Cl_4C_6O_2InI.tmen$	dmf	20
$Cl_4C_6O_2InCl.phen$	dmf	15
$Cl_4C_6O_2InBr.phen$	dmf	22
$Cl_4C_6O_2InI.phen$	dmf	17
$Br_4C_6O_2InI.phen$	dmf	29
$Cl_4C_6O_2InCl.2tmen$	$C_6H_5NO_2$	35
$Cl_4C_6O_2InBr.2tmen$	$C_6H_5NO_2$	29
$Cl_4C_6O_2InI.1.5tmen$	$C_6H_5NO_2$	34
$Ph_4P[Cl_4C_6O_2InCl_2]$	dmf	80
$Et_4N[Cl_4C_6O_2In(Cl)Br]$	dmf	84
$Ph_4P[Br_4C_6O_2InCl_2]$	dmf	79
$Et_4N[Br_4C_6O_2In(Cl)Br]$	dmf	86

[a] m*M* concentration.

[b] The expected range for 1:1 electrolytes in dmf is 65–90 $ohm^{-1}\,cm^2\,mol^{-1}$ and in $C_6H_5NO_2$ 20–40 $ohm^{-1}\,cm^2\,mol^{-1}$ (36).

Complexes obtained by this route were identical in all respects with those synthesised from InX + *ortho*-quinone. Anionic indium(III) catecholates have been previously prepared in aqueous media by Bevillard (26), and were characterized as anionic complexes, e.g., $[In(O_2C_6H_5)_3]^{3-}$. Investigations by Srivastava and Mohan (27) with aqueous solutions of indium(III) nitrate showed that it is possible to isolate compounds in which the indium:catecholate ratio is 1:1, 1:2, or 1:3, depending on the pH of the reaction mixture. The present work appears to be the first preparation of catecholato–halogeno mixed ligand anionic complexes.

Finally we note that the use of excess tmen in the $Cl_4C_6O_2$/InX reaction gives rise to the compounds $Cl_4C_6O_2InX.n$tmen (X = Cl, Br, n = 2; X = I, n = 1.5). The conductivities of these complexes in nitrobenzene identify them as 1:1 electrolytes in solution, and we therefore propose the structures **3** and **4**.

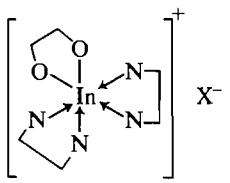

3, X = Cl, Br

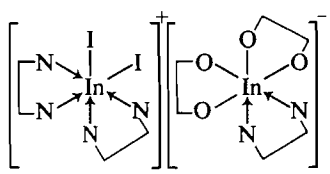

4

The structure of indium(III) species isolated from solution frequently depend upon the solution conditions (28), and the present results are in keeping with this observation. Structures similar to that shown in **4** have been proposed to explain the behaviour of the indium(III) halide adducts $InX_3.1.5$bpy (X = Cl, Br, I) (29).

Vibrational spectroscopy

A comparison of the infrared spectra of the indium(III)–catecholato complexes with those of the parent *ortho*-quinones and the corresponding diols shows marked changes in the ν(C=O) and ν(C—O) regions. The substituted tetrahalogeno-*ortho*-quinones have strong absorptions at 1670 and 1641 cm^{-1} while in the corresponding diol *o*-$Br_4C_6(OH)_2$, ν(C—O) is at 1445 and 1270 cm^{-1}. The complexes typically show strong absorptions in the 1440 cm^{-1} region, supporting the identification of these products as catecholato derivatives.

TABLE 3. Far infrared spectra of some indium(III)–catecholato complexes (in cm^{-1})

Compound	ν(In—N)	ν(In—O)	ν(In—X)
$Cl_4C_6O_2InCl.tmen$	480(m)	400(w)	270(s,br)
	454(m)		
$Cl_4C_6O_2InCl.2tmen$	476(m)	426(m)	—
	458(m)		
$Cl_4C_6O_2InI.1.5tmen$	482(m)	428(m)	177(s,br), 152(m)
	454(m)		
$Cl_4C_6O_2InCl.phen$	[a]	424(m)	290(s,br)
$Cl_4C_6O_2InBr.phen$	288(m)	422(m)	208(s,br)
$Cl_4C_6O_2InI.phen$	290(m)	424(m)	175(s,br)
$Br_4C_6O_2InI.phen$	290(s)	424(s)	185(s)

[a] ν(In—N) obscured by broad In—Cl band.

The vibrational spectra in the far infrared region are presented in Table 3. The tmen adducts have weak to medium bands between 450 and 520 cm^{-1}, readily assigned to ν(In—N) from earlier work (30), while the ν(In—N) absorptions of the phenanthroline adducts are in good agreement with reported values for $InX_3.1.5$phen (X = Cl, Br, I), which fall in the range 270–220 cm^{-1} (29). The assignment of ν(In—X) and ν(In—O) follows the analysis of the spectra of $InX_2(acac)L_2$ (X = Cl, Br, I, L = phen, bpy) (31), and the ν(In—X) values are in general agreement with those reported for other indium(III) halides (32). The identification of ν(In—O) has been the subject of discussion, with frequencies between 450 cm^{-1} and 180 cm^{-1} being proposed; in the present work, a band at ca. 420 cm^{-1} is observed in all the compounds prepared, and is tentatively assigned to this mode.

The tmen adducts $Cl_4C_6O_2InX.2$tmen do not show any infrared absorption in the ν(In—X) region, in agreement with the ionic structure **3** proposed, while the compound $Cl_4C_6O_2InI.1.5$tmen has two bands in the far ir spectrum at 177 and 152 cm^{-1}, assigned as ν_{as}(In—I) and ν_s(In—I). The presence of two ν(In—I) modes supports the structure **4**, rather than a mononuclear structure.

Nuclear magnetic resonance spectroscopy

The ^1H nmr spectra, some typical examples of which are presented in Table 4, serve to confirm the presence of the coordinated bidentate ligand (phen or tmen), and also establish that the species in question are diamagnetic. The resolution of the spectra of the 1,0-phenanthroline adducts was hampered by their low solubility in dimethyl sulphoxide, but the proton

Can. J. Chem. Downloaded from www.nrcresearchpress.com by 196.1.178.254 on 09/07/12
For personal use only.

TABLE 4. ^{1}H NMR spectra of indium(III)–catecholate complexes (in d_6-dmso)

Compound[a]	Chemical shift[b]	Assignment
$Y_4C_6O_2InX.tmen$	2.50(s,12H)	$(CH_3)_2N$
	2.86(s,4H)	NC_2H_4N
$Cl_4C_6O_2InCl.2tmen.\frac{1}{2}Et_2O$	2.48(s,48H)	$(CH_3)_2N$
	2.87(s,16H)	NC_2H_4N
	1.20(t,3H) }	$(CH_3CH_2)_2O$
	3.64(q,2H) }	
$Y_4C_6O_2InI.phen$	9.24(m,2H)	C2,C9 (phen)
	7.90(m,2H)	C3,C8
	8.15(m,2H)	C5,C6
	8.60(m,2H)	C4,C7
$Ph_4P[Y_4C_6O_2InCl_2]$	7.7–8.1(m)	C_6H_5
$Et_4N[Y_4C_6O_2In(Cl)Br]$	1.12(t,3H)	CH_3
	3.15(q,2H)	CH_2

[a]Y = Cl, Br; X = Cl, Br, I. There were no significant differences between individual members of any given group of these compounds.
[b]In ppm, relative to Me_4Si.

resonances are typical of those observed in related phen complexes.

The ^{13}C NMR spectra also proved to have considerable diagnostic value. Table 5 shows the relevant features of some typical compounds; comparisons with previously published values for the tetrahalogeno-*o*-quinones, the analogous diols and the neutral bidentate ligands (17) again confirm the assignments proposed.

As in the tin(IV) compounds, there are substantial shifts from (say) the *o*-quinone $Cl_4C_6O_2$ (C1, C2 168.8; C3, C6 143.7; C4, C5 131.9 ppm) to the various indium(III) complexes, for which the values are close to those in *o*-$Cl_4C_6(OH)_2$ (C1, C2 143.0; C3, C6 122.5; C4, C5 119.5 ppm). These results then confirm the identification of these products, and again establish the change from *o*-quinone to *o*-catecholate on reaction with InX. There are small but significant differences between the present results and those for the analogous tin(IV) species. The C1, C2 resonances are approximately 4 ppm higher in the indium(III) compounds, while C3, C6 and C4, C5 are 2–3 ppm lower, and similarly the ^{13}C resonances of tmen are 2–3 ppm higher in the indium(III) complexes than in the tin(IV) analogues.

These spectra also serve to identify the structures of the species present in dimethyl sulphoxide solution. We consider first the molecule $Cl_4C_6O_2InCl.tmen$, which is formulated from infrared and conductivity results as the five-coordinate monomeric neutral species.

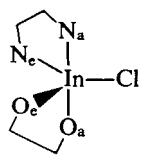

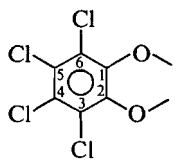

The room temperature (295 K) spectrum showed double resonances for each of the three pairs of the carbons on the catecholato ring, at 158.4 and 157.7 (C1, C2), 120.4 and 120.3 (C3, C6), and 119.4 and 118.9 (C4, C5) ppm from Me_4Si. These values are significantly different in frequency from those quoted in Table 5, due to (*i*) the presence of tmen rather than phen as the neutral ligand and (*ii*) the different coordination number at indium(III) (see below). As the solution warmed up, these signals coalesced, and the coalescence temperatures and other derived kinetic data are shown in Table 6. The $\Delta G^{\ddagger}$ values obtained from the three sets of results by standard methods (33) are essentially identical, at 70.3 kJ mol^{-1}. Before considering the mechanistic implications of this temperature dependence, it is worth noting that the tmen region is too complicated to allow a similar analysis. There are two pairs of diastereotopic CH_3 groups on the different nitrogen atoms of the bidentate ligand (51.9, 49.4 ppm) and similarly these are two

TABLE 5. ^{13}C NMR of some typical indium(III)–catecholato derivatives (in d_6-dmso)

Compound	Chemical shift[a]	Assignment
$Cl_4C_6O_2InCl.2tmen.\frac{1}{2}Et_2O$	114.0	C4,C5
	114.8	C3,C6
	152.4	C1,C2
	43.8, 47.1 } tmen	CH_3
	53.5, 54.1 } tmen	C_2H_4
	22.0 } Et_2O	CH_3CH_2
	63.5 } Et_2O	CH_3CH_2
$Cl_4C_6O_2InI.1.5tmen$	112.6	C4,C5
	114.0	C3,C6
	153.2	C1,C2
	43.7, 47.1 } tmen	CH_3
	53.1, 54.7 } tmen	C_2H_4
$Cl_4C_6O_2InI.phen$	114.5	C4,C5
	115.6	C3,C6
	152.2	C1,C2
	126.2 } phen	C5,C6
	127.6 } phen	C4a,C6a
	129.3 } phen	C4,C7
	135.6 } phen	C3,C8
	141.3 } phen	C4b,C6b
	147.9 } phen	C2,C9
$Ph_4P[Cl_4C_6O_2InCl_2]$	113.4	C4,C5
	114.8	C3,C6
	153.2	C1,C2
	117.1 } Ph_4P^+	
	118.2 } Ph_4P^+	
	130.6 } Ph_4P^+	
	134.6 } Ph_4P^+	
$Et_4N[Cl_4C_6O_2In(Cl)Br]$	112.5	C4,C5
	114.0	C3,C6
	153.2	C2
	154.0	C1
	7.2 } Et_4N^+	CH_3CH_2
	51.6 } Et_4N^+	CH_3CH_2
$Ph_4P[Br_4C_6O_2InCl_2]$	106.5	C4,C5
	108.8	C3,C6
	155.2	C1,C2
	[b]	
$Et_4N[Br_4C_6O_2In(Cl)Br]$	106.4	C4,C5
	108.5	C3,C6
	155.1	C2
	155.7	C1
	[c]	

[a]In ppm, relative to Me_4Si.
[b]Cation resonances identical to those in tetrachloro compound.
[c]Cation resonances identical to those in tetrachloro compound

Numbering system:

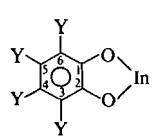

$Y_4C_6O_2^{2-}$

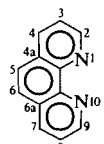

phen

Can. J. Chem. Downloaded from www.nrcresearchpress.com by 196.1.178.254 on 09/07/12
For personal use only.

TABLE 6. Temperature dependence of ^{13}C NMR spectrum of $Cl_4C_6O_2InCl.tmen$

Sites	ν (Hz)	$\Delta\nu$	K_c (s^{-1})	T_c (K)	$\Delta G^{\ddagger}$ (kJ mol^{-1})
C1	7968.6	32.7	145.3	≥353	≥70.3
C2	7935.9				
C3	6058.9	6.6	29.1	333	70.6
C6	6052.3				
C4	6006.5	21.2	93.9	343	69.5
C5	5985.4				

CH_2 resonances (60.3, 59.4 ppm). All these signals show the appropriate coalescence behaviour, but it was not possible to assign the resonances to the individual CH_3 (or CH_2) groups unambiguously, so that a detailed analysis of these results has not been attempted. An approximate treatment shows that here again $\Delta G^{\ddagger} \approx 65 \pm 10$ kJ mol^{-1}.

The most probable mechanism for the dynamic nmr involves the breaking of an N → In bond to give a quasi-tetrahedral species.

[2] 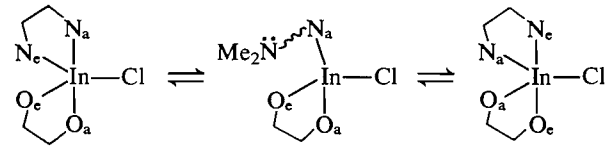

$\mathbf{A_1}$ $\mathbf{B}$ $\mathbf{A_2}$

A similar mechanism has been established for indium(III) derivatives of the 2-[(dimethylamino)methyl]phenyl ligand (34), and for ligand exchange between InL_3 and HL (HL = various β-diketones) (35). In fact, the $\Delta G^{\ddagger}$ values of 70.3 kJ mol^{-1} deduced above is close to the values found in the latter work, where the rate-controlling process to which this relates was identified as the rotation of a monodentate β-diketonate ligand coordinated to indium. The analogous process in the present work would be the motion of the monodentate tmen ligand in the four-coordinate intermediate B, thus leading to the transformation $\mathbf{A_1} \rightleftarrows \mathbf{A_2}$, so that 70.3 kJ mol^{-1} is the rearrangement energy of this intermediate.

The spectra reported in Table 5 do not show any temperature dependence, which is also in keeping with the proposed structures. The spectra of the anionic complexes $[Y_4C_6O_2InCl_2]^-$ give singlets for the C1 + C2, C3 + C6, and C4 + C5 sites, so that the catecholate ligand is symmetrical within experimental error, while in the $[Y_4C_6O_2In(Cl)Br]^-$ series C1 and C2 are separated by ca. 1 ppm. Given the strong donor properties of the solvent dimethyl sulphoxide, it seems likely that the species in solution in both cases is a five-coordinate solvate. The relative electronegativities of the ligating atoms are in the order O > Cl > Br, but in arriving at the most probable structure one must allow the catecholate ligand to span equatorial and axial sites of a trigonal bipyramid, given that the O—In—O bite angle must be close to the value of 81.5(2)° in the analogous tin system (17). Given the usual arguments of VSEPR theory, the most probable structure for the solvated $[Y_4Cl_6O_2In(Cl)Br]^-$ anion is **5**.

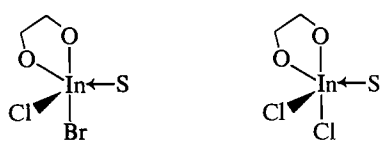

5 **6** S = dmso

All forms of **5** must produce a stereotopic distinction between C1 and C2 of the catecholate, so that rapid solvent exchange cannot make these sites degenerate. For the solvate of $[Y_4C_6O_2InCl_2]^-$, rapid solvent exchange would render C1 and C2 homotopic, as they are in the four-coordinate parent anions of both **5** and **6**. The effect is a short-range one, being confined to C1 and C2, as shown by the results in Table 5.

Finally we note that those compounds which are 1:1 electrolytes in nitrobenzene (Table 2) (i.e., $Cl_4C_6O_2InX.2tmen$, X = Cl, Br, and $Cl_4C_6O_2InI.1.5tmen$) show only single resonances for all related pairs of carbon atoms in both the catecholate and tmen ligands. We assume that these compounds are also dissociated in dmso into the ionic species shown earlier as **3** and **4**. For the six-coordinate cation $[Cl_4C_6O_2In(tmen)_2]^+$ of species **3**, a process in which one of the tmen ligand undergoes uncoupling and recoupling via a five-coordinate intermediate cannot change the NMR spectrum irrespective of the rates involved.

[3] 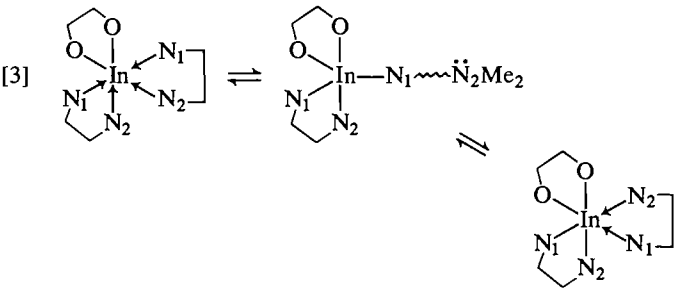

Both initial and final stages are identical, so that the NMR spectra reveal nothing about this exchange process. Similar arguments apply to the ions proposed for the iodo complex **4**.

In sum then, the ^{13}C NMR spectra of these complexes examined are in good agreement with the structures proposed from the vibrational spectra, and are also in keeping with earlier results on the rearrangement processes for indium(III) complexes in solution.

Acknowledgement

This work was supported in part by Operating Grants (to D.G.T.) from the Natural Sciences and Engineering Research Council of Canada. Professor J. M. McIntosh is thanked for helpful discussions of ^{13}C NMR spectroscopy.

1. L. G. WATERWORTH and I. J. WORRALL. Chem. Commun. 569 (1971).
2. M. J. S. GYNANE and I. J. WORRALL. Inorg. Nucl. Chem. Lett. **8**, 547 (1972).
3. M. J. S. GYNANE, L. G. WATERWORTH, and I. J. WORRALL. J. Organomet. Chem. **43**, 257 (1972).
4. J. S. POLAND and D. G. TUCK. J. Organomet. Chem. **42**, 315 (1972).
5. L. G. WATERWORTH and I. J. WORRALL. J. Organomet. Chem. **81**, 23 (1974).
6. M. J. S. GYNANE, L. G. WATERWORTH, and I. J. WORRALL. Inorg. Nucl. Chem. Lett. **9**, 543 (1973).
7. J. G. CONTRERAS and D. G. TUCK. J. Organomet. Chem. **66**, 405 (1974).
8. A. F. BERNIAZ and D. G. TUCK. J. Organomet. Chem. **51**, 113 (1973).
9. A. F. BERNIAZ, G. HUNTER, and D. G. TUCK. J. Chem. Soc. A, 3254 (1971).
10. D. J. PATMORE and W. A. G. GRAHAM. Inorg. Chem. **5**, 1586 (1966).
11. J. HOYANO, D. J. PATMORE, and W. A. G. GRAHAM. Inorg. Nucl. Chem. Lett. **4**, 201 (1968).

Can. J. Chem. Downloaded from www.nrcresearchpress.com by 196.1.178.254 on 09/07/12
For personal use only.

12. A. T. T. HSIEH and M. J. MAYS. Inorg. Nucl. Chem. Lett. **7**, 223 (1971).
13. C. PEPPE, D. G. TUCK, and L. VICTORIANO. J. Chem. Soc. Dalton Trans. 2165 (1982).
14. C. PEPPE and D. G. TUCK. Can. J. Chem. **62**, 2793 (1984).
15. C. PEPPE and D. G. TUCK. Can. J. Chem. **62**, 2798 (1984).
16. T. A. ANNAN and D. G. TUCK. J. Organomet. Chem. **325**, 83 (1987).
17. T. A. ANNAN, R. K. CHADHA, D. G. TUCK, and K. D. WATSON. Can. J. Chem. **65**, 2670 (1987).
18. T. A. ANNAN, R. K. CHADHA, B. R. MCGARVEY, A. OZAROWSKI, and D. G. TUCK. J. Chem. Soc. Dalton Trans. In press.
19. M. V. VEIDIS and G. J. PALENIK. Chem. Commun. 1182 (1970).
20. M. A. KHAN, C. PEPPE, and D. G. TUCK. J. Organomet. Chem. **280**, 17 (1985).
21. M. A. KHAN, R. S. STEEVENSZ, D. G. TUCK, J. G. NOLTES, and P. W. R. CORFIELD. Inorg. Chem. **19**, 3407 (1980).
22. J. M. HARROWFIELD, C. PAKOWATCHAI, and A. H. WHITE. J. Chem. Soc. Dalton Trans. 1109 (1983).
23. H. D. HAUSEN, K. MERTZ, E. VEIGEL, and J. WEIDLEIN. Z. Anorg. Chem. **410**, 156 (1974).
24. K. MERTZ, W. SCHWARTZ, F. ZETTLER, and H. D. HAUSEN. Z. Naturforsch. Teil B, **30**, 159 (1975).
25. H. D. HAUSEN, K. MERTZ, J. WEIDLEIN, and W. SCHWARTZ. J. Organomet. Chem. **93**, 291 (1975).
26. P. BEVILLARD. Compt. Rendus. **240**, 1776 (1955).
27. T. N. SRIVASTAVA and G. MOHAN. Z. Anorg. Chem. **379**, 82 (1970).
28. D. G. TUCK. Pure Appl. Chem. **55**, 1477 (1983).
29. (*a*) B. F. G. JOHNSON and R. A. WALTON. Inorg. Chem. **5**, 49 (1966); (*b*) R. A. WALTON. J. Chem. Soc. A, 61 (1969).
30. M. J. TAYLOR, D. G. TUCK, and L. VICTORIANO. Can. J. Chem. **60**, 691 (1982).
31. J. G. CONTRERAS and D. G. TUCK. J. Chem. Soc. Dalton Trans. 1249 (1974).
32. J. E. DRAKE, J. L. HENCHER, L. N. KHASROU, D. G. TUCK, and L. VICTORIANO. Inorg. Chem. **19**, 34 (1980).
33. H. S. GUTOWSKY and C. H. HOLM. J. Chem. Phys. **25**, 1228 (1956).
34. J. H. B. H. JASTRZEBSKI, G. VAN KOTEN, D. G. TUCK, H. A. MEINEMA, and J. G. NOLTES. Organometallics, **1**, 1492 (1982).
35. G. T. TANNER, D. G. TUCK, and E. J. WELLS. Can. J. Chem. **50**, 3950 (1972).
36. W. J. GEARY. Coord. Chem. Rev. **7**, 81 (1971).

Can. J. Chem. Downloaded from www.nrcresearchpress.com by 196.1.178.254 on 09/07/12
For personal use only.

Anodic oxidation of lead in aqueous carbonate solutions. II. Film formation and dissolution in the pH range 9 to 14

D. W. SHOESMITH, M. G. BAILEY, and P. TAYLOR

Geochemistry and Waste Immobilization Division, Whiteshell Nuclear Research Establishment, Pinawa, Man., Canada R0E 1L0

Received May 2, 1988

D. W. SHOESMITH, M. G. BAILEY, and P. TAYLOR. Can. J. Chem. **66**, 2941 (1988).

The anodic oxidation of lead has been studied in aqueous carbonate solutions at pH values in the range $9 \leq pH \leq 14$. The solid films formed on the electrode surface have been identified by X-ray diffractometry. The dissolution and film formation processes have been studied by a number of electrochemical techniques at rotating disk electrodes. The anodic oxidation process can be divided into two distinct regions. In the main anodic oxidation process, a variety of surface phases is formed. The nature of the phase formed is pH-dependent. Plumbonacrite ($Pb_{10}O(OH)_6(CO_3)_6$) formation is observed at all pH values and predominates at $pH \geq 13$. At $pH < 11$, cerussite ($PbCO_3$) is the predominant phase, whereas at intermediate pH values, hydrocerussite ($Pb_3(OH)_2(CO_3)_2$) predominates. The dissolution rate of Pb^{2+} species from the electrode surface is directly proportional to the solubility of the predominant phase present. At more positive potentials, a reactivation, involving increased dissolution and a further stage of film formation, is observed. Litharge (PbO) is observed to grow underneath the initially formed basic lead carbonates. Dissolution occurs either by the field-assisted dissolution of the base-layer on the electrode or by metal dissolution through faults in the base-layer.

D. W. SHOESMITH, M. G. BAILEY et P. TAYLOR. Can. J. Chem. **66**, 2941 (1988).

Opérant dans des solutions aqueuses de carbonate et à des pH allant de 9 à 14, on a étudié l'oxydation anodique du plomb. On a utilisé la diffraction des rayons-X pour identifier les films solides qui se forment à la surface de l'électrode. Faisant appel à un certain nombre de techniques électrochimiques impliquant des électrodes à disque tournant, on a étudié les processus de formation et de dissolution du film. On peut diviser les processus d'oxydation anodique en deux régions distinctes. Dans le processus principal d'oxydation anodique, il se forme une grande variété de phases superficielles. La nature de la phase qui se forme dépend du pH. On observe la formation de la plumbonacrite ($Pb_{10}O(OH)_6(CO_3)_6$) à tous les pH; cette formation prédomine à un $pH \geq 13$. A un $pH \leq 11$, la cérusite ($PbCO_3$) est la phase prédominate alors qu'à des pH intermédiaires, l'hydrocérusite ($Pb_3(OH)_2(CO_3)_2$) prédomine. La taux de dissolution des espèces Pb^{2+} à partir de la surface de l'électrode est directement proportionnel à la solubilité de la phase prédominate qui est présente. A des potentiels plus positifs, on observe une réactivation impliquant une dissolution accrue ainsi qu'un autre stage de formation de film. On a observé que du litharge (PbO) se forme sous la couche de carbonates basiques de plomb qui se forment au départ. La dissolution se produit soit par une dissolution, aidée par le champ, de la couche de base de l'électrode soit par une dissolution du métal à travers les défauts de la couche de base.

[Traduit par la revue]

Introduction

Lead carbonates occur (or are expected) as corrosion products on artifacts as diverse as wine-bottle tops (1), bullets used in the American Civil War (2), water pipes (3, 4), and nuclear waste containers (5). Surprisingly little is known, however, about the electrochemistry of lead in carbonate solutions. As part of a program to understand the corrosion behaviour of lead in aqueous carbonate solutions, we have been studying its oxidation under electrochemical conditions. In a previous paper (6), we presented our results on the anodic oxidation of lead in 1.0 mol L^{-1} potassium carbonate solutions at pH = 12. Experiments were confined to the potential range where Pb^{2+} species were formed. The formation of higher oxidation states was not considered because oxidation does not proceed to these states under natural corrosion conditions.

We have extended our electrochemical and X-ray diffraction studies to cover the region $9 \leq pH \leq 14$. Also, our measurements of the corrosion potential (E_{CORR}) of lead in carbonate solutions (5) yielded values in the range $-0.540\ V < E_{CORR} < -0.350\ V$. Consequently, we have studied the dissolution and film formation processes occurring on lead at potentials up to 0 mV (vs. SCE). This value is over 0.600 V more positive than our previous anodic limit (6).

Experimental

Details of our electrochemical and X-ray diffraction (XRD) procedures have been described previously (6). All the experiments were performed at rotating disk electrodes of surface area ~1.6 cm^2. All potentials were measured, and are quoted, against the saturated calomel electrode. Unless otherwise stated, all experiments were performed in 1.0 mol L^{-1} potassium bicarbonate solutions. All solutions were originally made up with bicarbonate and the pH adjusted to the desired value with potassium hydroxide.

Results

(a) Cyclic voltammetry

Figure 1 compares the form of the voltammograms recorded at pH = 9.8 (A) and pH = 13.9 (B) at an electrode rotation rate (ω) of 16.7 Hz. The form of these voltammograms is similar to that observed at pH = 12, shown in Fig. 1 of ref. 1. The shoulder, observed on the negative side of the main anodic peak at pH = 12, is not so prominent at pH = 9.8 and is apparently absent at pH = 13.9. At pH = 9.8, two peaks are observed on the cathodic sweep, corresponding to the reduction of a base-layer (peak X) and a deposited-layer (peak Y). This assignment of peaks X and Y was discussed in ref. 7. At pH = 9.8, peak X shows no tendency to split into two, as observed at pH = 12; this suggests the base-layer is composed of a single phase. At pH = 13.9, the main anodic peak occurs at a more negative potential. Only peak X, corresponding to reduction of a single-phase base-layer, is observed on the reverse cathodic scan. The absence of reduction peak Y at pH = 13.9 shows that dissolution to form Pb^{2+} species is not accompanied by redeposition of an upper-layer on the electrode surface.

At pH = 13.9, the current passes through a minimum and rises again for potentials (E) > −0.6 V, eventually forming a

Can. J. Chem. Downloaded from www.nrcresearchpress.com by 196.1.178.254 on 09/07/12
For personal use only.

Can. J. Chem. Downloaded from www.nrcresearchpress.com by 196.1.178.254 on 09/07/12
For personal use only.

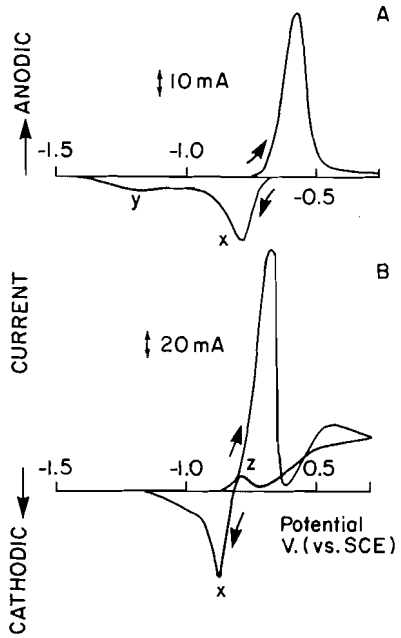

FIG. 1. Cyclic voltammograms recorded in 1.0 mol L^{-1} K_2CO_3 at a scan rate of 20 mV s^{-1}: (*A*) pH = 9.8, (*B*) pH = 13.9.

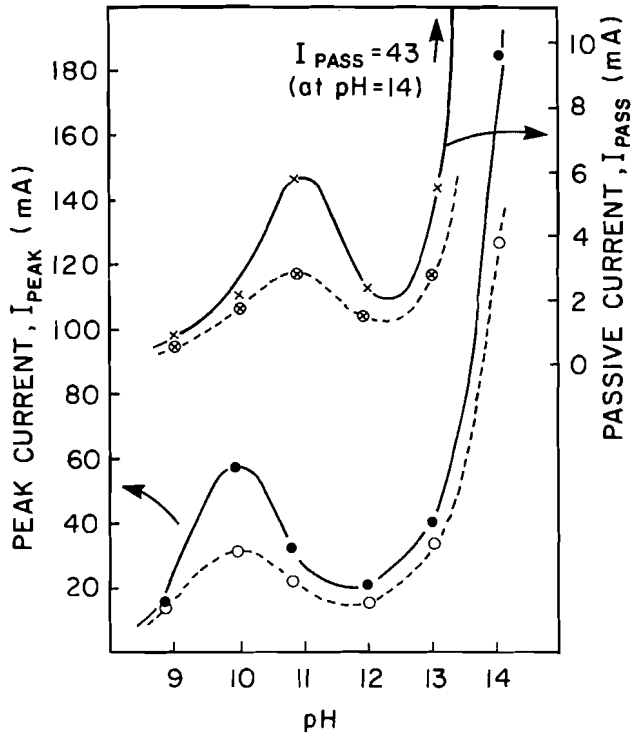

FIG. 2. Peak current (I_{PEAK}) and the passive current (I_{PASS} at −0.250 V), taken from voltammograms recorded at 20 mV s^{-1}, plotted as a function of pH: —, ω = 16.7 Hz; --- ω = 1.67 Hz.

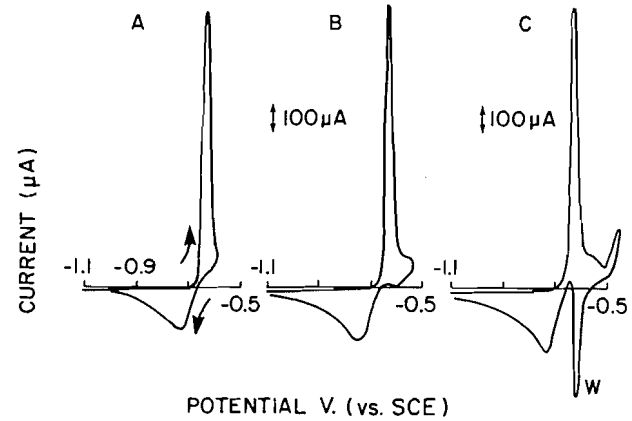

FIG. 3. Cyclic voltammograms, from −2.0 V to various anodic limits, recorded at 1.0 mV s^{-1} in 0.1 mol L^{-1} $NaClO_4$ plus 5×10^{-3} mol L^{-1} K_2CO_3 (pH = 10).

second, very broad peak at ~ −0.45 V. On the reverse cathodic scan, the current remains anodic and yields a small anodic peak (*Z* in Fig. 1*B*) at ~ −0.79 V. This anodic current and peak Z are symptomatic of a reactivation process, whereby the film formed at the main anodic peak is partially dissolved at more anodic potentials.

Figure 2 shows the peak current, I_{PEAK}, for the main anodic peak, and the current at −0.25 V, I_{PASS}, plotted as functions of the pH at which the voltammogram was recorded. The solid and dashed lines show the values obtained at ω = 16.7 and 1.67 Hz, respectively. A maximum in I_{PEAK} occurs around pH = 10, when the current is most sensitive to ω. For I_{PASS}, a similar peak occurs at pH ~11, again when the current is most sensitive to ω. Both I_{PEAK} and I_{PASS} increase substantially at pH > 13.

At lower carbonate concentrations, the size of the main anodic peak in the voltammogram (I_{PEAK}) is reduced by over two orders of magnitude. Figure 3 shows a series of scans, to various anodic limits, recorded in 0.1 mol L^{-1} $NaClO_4$ plus 5×10^{-3} mol L^{-1} K_2CO_3 (pH = 9.9), at ω = 33.3 Hz. When the anodic limit of the scan is extended into the reactivation region ($E > -0.5$ V), an additional, very sharp cathodic peak (W) appears in the reverse scan, Fig. 3 (*B* and *C*). The voltammograms of Fig. 3 were recorded at a scan rate of 1 mV s^{-1}, because peak W is most prominent at slow scan rates. Peak W can be attributed to the reduction of a further surface film formed in the activation region. This dependence on scan rate suggests the extent of formation of this layer is determined by the time spent in the reactivation region, $E > -0.5$ V.

(b) X-ray diffraction of anodically formed films

Figure 4 shows the identity of the phases formed after 60 min of potentiostatic oxidation at a potential on the positive side of the main anodic peak. This potential varies from −0.680 V at pH = 13.9 to −0.600 V at pH = 9. The vertical lines in Fig. 4 represent the stability boundaries between the indicated phases (7). Because the formation of the individual phases is compared on the basis of the height of a single diffraction peak for each phase, the data of Fig. 4 can only be considered semi-quantitative. The formation of plumbonacrite ($Pb_{10}O(OH)_6(CO_3)_6$) is observed over the whole potential range and it is the only detectable phase formed at pH > 13. The amount formed varies very little over the range 9 ≤ pH ≤ 12. Cerussite ($PbCO_3$) is formed at pH < 11, but is replaced by hydrocerussite ($Pb_3(OH)_2(CO_3)_2$) in the range 11 ≤ pH ≤ 13. Some hydrocerussite was also formed at pH = 10. Around pH = 12 to 13, traces of massicot/litharge (PbO) are observed, and traces of another phase, possibly $KOH{\cdot}2PbCO_3$ (8) are obtained around pH = 10 to 11. The same distribution of products is observed at more positive potentials around the current minimum after the main peak, i.e., in the potential range −0.600 to −0.450 V. Both hydrocerussite and cerussite predominate in the pH ranges within which they are the stable phases (7).

If the anodically formed films are stripped from the electrode

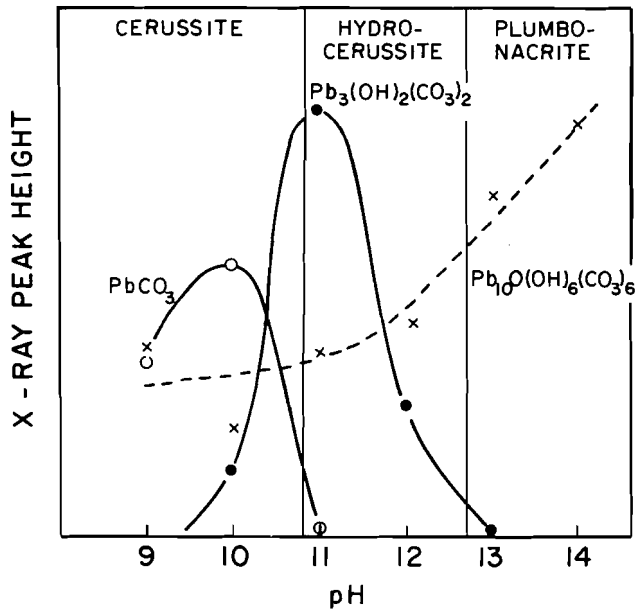

FIG. 4. Nature of the phases formed, determined from X-ray peak heights (6) as a function of pH after potentiostatic oxidation on the positive side of the main anodic peak (Fig. 1) for 60 min in 1.0 mol L^{-1} K_2CO_3; the vertical lines represent the stability boundaries between the basic lead carbonate phases.

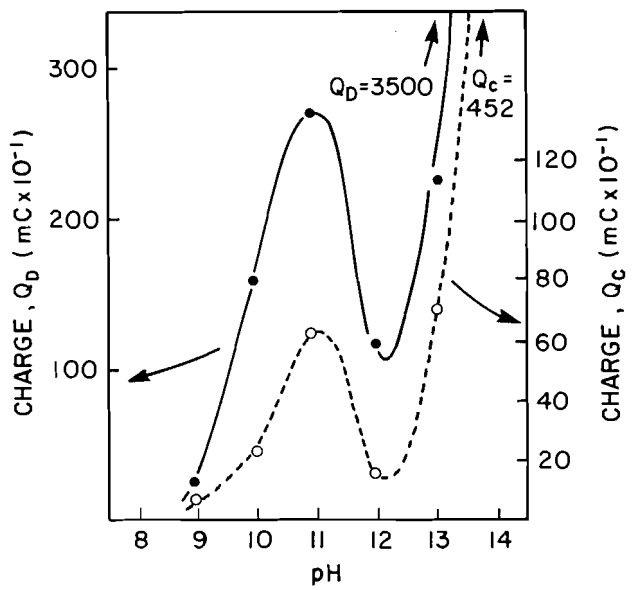

FIG. 5. The charge due to dissolution (Q_D) and the charge due to film formation (Q_C) as functions of potential for oxidation under the conditions given in the legend to Fig. 4. The Q_D and Q_C values noted on the figure are the respective values achieved at pH = 14.

surface by cathodic stripping voltammetry two cathodic reduction peaks are observed at all pH values below 13. The form of the cathodic stripping voltammograms (CSVs) is similar to the cathodic sections of the voltammograms obtained at pH = 12 (Fig. 1 of ref. 1) and is consistent with the voltammograms of Fig. 1, which show the reduction of both a base-layer (peak X) and a recrystallized layer (peak Y) at pH = 9.8, but only the reduction of a base-layer at pH = 13.9. Apparently no recrystallization is observed at pH $\geq$ 13, consistent with the rapid increase in lead solubility at pH values above 13 (see below).

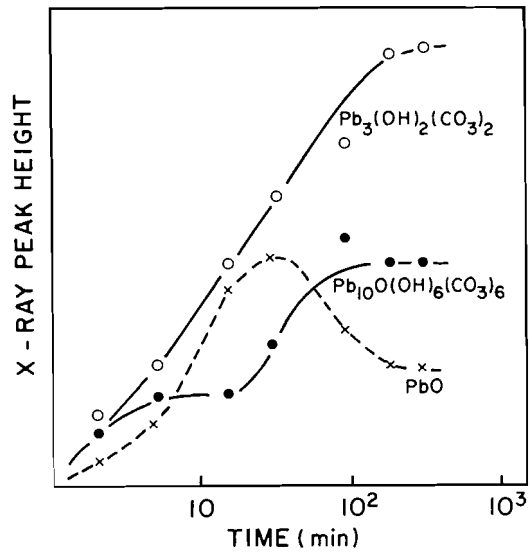

FIG. 6. Distribution of phases, expressed as X-ray peak heights (6), as a function of the duration of potentiostatic oxidation at 0 V in 1.0 mol L^{-1} K_2CO_3 at pH = 12.

This evidence confirms that plumbonacrite constitutes the base-layer over the whole pH range, and that it is formed via a solid-state reaction directly on the electrode but not by deposition from solution. When deposition occurs at pH < 13, it leads to the formation of hydrocerussite and/or cerussite.

Figure 5 shows the charge due to dissolution, Q_D, and the charge due to film formation, Q_C, for a one-hour oxidation at the same potentials used to record the data of Fig. 4. The value of Q_C was obtained by integration of the CSV recorded after completion of oxidation. The total anodic charge consumed, Q_A, was obtained by integration of the current recorded during oxidation, and Q_D is given by the difference, $Q_A - Q_C$. Both Q_D and Q_C possess a maximum around pH = 11, a minimum around pH = 12, and very large values at high pH.

At more positive potentials in the reactivation region, i.e., $E > -0.5$ V, more complex behaviour is observed. This is illustrated by the distribution of phases, as a function of the duration of oxidation at 0 V (pH = 12), shown in Fig. 6. Three phases are observed: plumbonacrite and hydrocerussite, which were observed at more negative potentials (6); and litharge (PbO), a phase not observed in significant amounts at lower potentials. After 16 h, hydrocerussite is the predominant phase. The formation of litharge is initially as extensive as hydrocerussite formation, but the amount present decreases after about 20 min. Plumbonacrite forms in two stages, the second stage coinciding with the disappearance of litharge.

Figure 7 shows the extent of plumbonacrite formation for three different potentials. The data for −0.720 and −0.640 V are taken from ref. 7, and for 0 V, from Fig. 6. The common curve for all three potentials at short times is consistent with the rapid formation of a plumbonacrite base-layer. The second stage of plumbonacrite formation observed at 0 V is distinct from this initial process, suggesting a different mechanism for its formation.

(c) Potentiostatic oxidation in the reactivation region

The current in the potential region positive to the main anodic peak (i.e., $E > -0.5$ V) is dependent on the electrode rotation speed, but independent of potential. This is demonstrated by the data of Figs. 8 and 9.

Can. J. Chem. Downloaded from www.nrcresearchpress.com by 196.1.178.254 on 09/07/12
For personal use only.

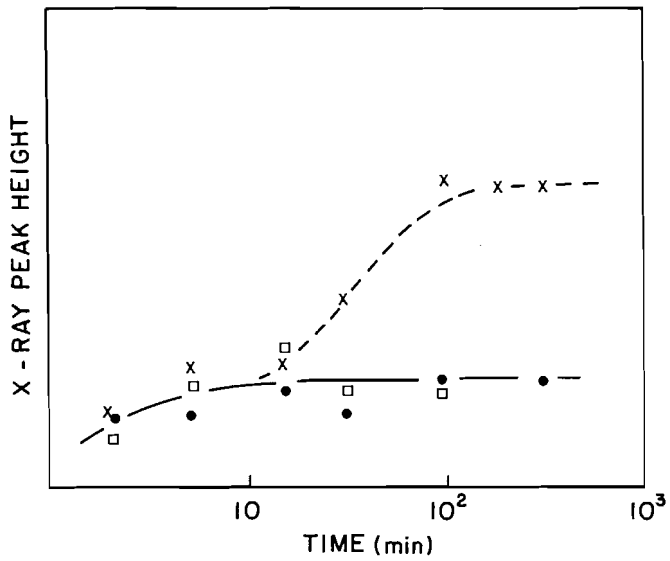

FIG. 7. The extent of plumbonacrite ($Pb_{10}O(OH)_6(CO_3)_6$) formation (as X-ray peak height) as a function of the duration of oxidation at three different poentials: ○, −0.726 V; □, −0.640 V; ×, 0 V.

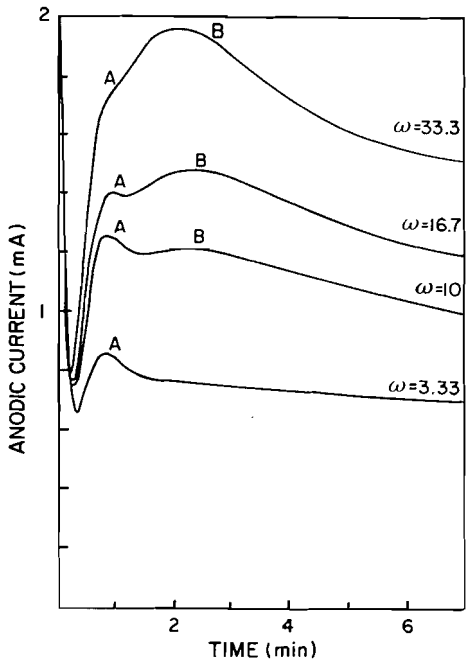

FIG. 8. Current–time plots recorded at a potential of −0.480 V in 1.0 mol L^{-1} K_2CO_3 (pH ~ 10) for various values of electrode rotation speed (ω).

Figure 8 shows a series of current–time curves recorded at $E = -0.480$ V, in 1.0 mol L^{-1} K_2CO_3 at a pH of 9.96, for various values of ω. The current for times < 20 s is large, but falls rapidly with time and is almost independent of the electrode rotation rate. This is consistent with the rapid growth of a base-layer on the electrode surface. No attempt was made to investigate the form of the current at such short times. At more negative potentials, $-0.740 \leq E \leq -0.700$ V, however, a peak is observed in the current transient, suggesting base-layer formation may be a nucleation and growth process.

For ω = 3.3 Hz, a peak (A in Fig. 8) is observed at $t \sim 60$ s; subsequently, the current falls slightly, eventually achieving a

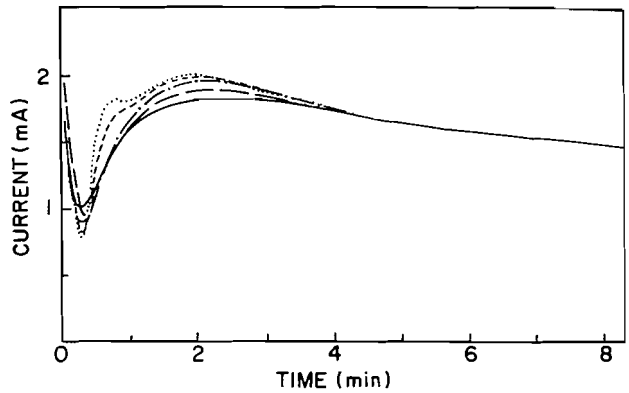

FIG. 9. Current–time plots recorded at ω = 33.3 Hz in 1.0 mol L^{-1} K_2CO_3 (pH ~ 10) for various values of potential in the reactivation region: —, −0.60 V; – –, −0.550 V; -·-·-, 0.525 V; ---, −0.48 V; ····, −0.46 V.

constant value for $t \geq 420$ s. The size and position of this peak are independent of ω. Peak A, however, is eventually swamped, at higher values of ω, by a second, much broader peak, B, as shown in Fig. 8. Peak A becomes sharper at more positive potentials, but is not observed at more negative potentials, Fig. 9. This behaviour is consistent with the nucleation and growth of a film for potentials greater than ~ −0.500 V. Peak B, however, is independent of potential (Fig. 9) as expected for a film breakdown process.

For all values of ω, the current eventually levels off at a constant value for $t > 420$ s, Fig. 9. These steady-state currents are plotted according to the Levich relationship for a system jointly controlled by transport and surface reaction kinetics (9, 10) in Fig. 10. These data confirm that the current in this potential region (-0.650 V $\leq E \leq -0.480$ V) is potential-independent but rotation-rate (ω) dependent. Similar data, exhibiting the same trends, were obtained for other pH values in the range $9 \leq$ pH ≤ 14. When the currents are compared at the same value of ω for various values of pH, a plot identical in form to that obtained voltammetrically for I_{PASS} (Fig. 2) is obtained.

Using the relationships developed previously (11) and estimating solubility values from the calculations of Taylor and Lopata (7), we can calculate a value for the average diffusion coefficient (D_{AVER}) for Pb^{2+} species from the slope of Fig. 10. If we assume that the deposited cerussite layer present at pH = 10, Fig. 4, controls the dissolution rate, we obtain a value for D_{AVER} of $\sim 4 \times 10^{-2}$ cm^2 s^{-1}. If we assume that an underlying base-layer of plumbonacrite or litharge controls dissolution, then a minimum value for D_{AVER} of $\sim 3 \times 10^{-4}$ cm^2 s^{-1} is obtained. Both these values are too large to be meaningful; the maximum expected value for solution-transport of dissolved Pb^{2+} species is $\sim 10^{-5}$ cm^2 s^{-1}. This suggests that dissolution in this region is not controlled by the solubility of the basic carbonate phases present on the electrode surface.

(d) Solubility and stability relationships

Figure 11 shows the computed equilibrium dissolved lead activities for the four individual phases observed on our electrodes, at a constant total carbonate activity of 1.0 mol L^{-1}. This figure was calculated from the thermodynamic data compilation of Taylor and Lopata (7), according to which the solution species $Pb(OH)_3^-$ and $Pb(CO_3)_2^{2-}$ dominate the solubility over the pH range $8 \leq$ pH ≤ 14 in 1 mol L^{-1} carbonate/bicarbonate solution.

Ferri *et al.* (12) have recently redetermined the speciation of

Can. J. Chem. Downloaded from www.nrcresearchpress.com by 196.1.178.254 on 09/07/12
For personal use only.

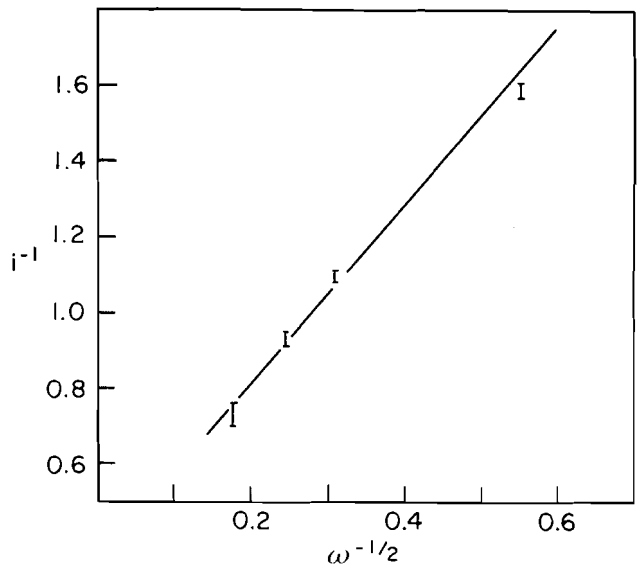

FIG. 10. Steady-state currents (i) under potentiostatic oxidation conditions as a function of electrode rotation rate (ω) plotted according to the Levich equation. Each data bar contains a data point for four different potentials in the range −0.650 V to −0.480 V in 1.0 mol L^{-1} K_2CO_3 (pH ~ 10).

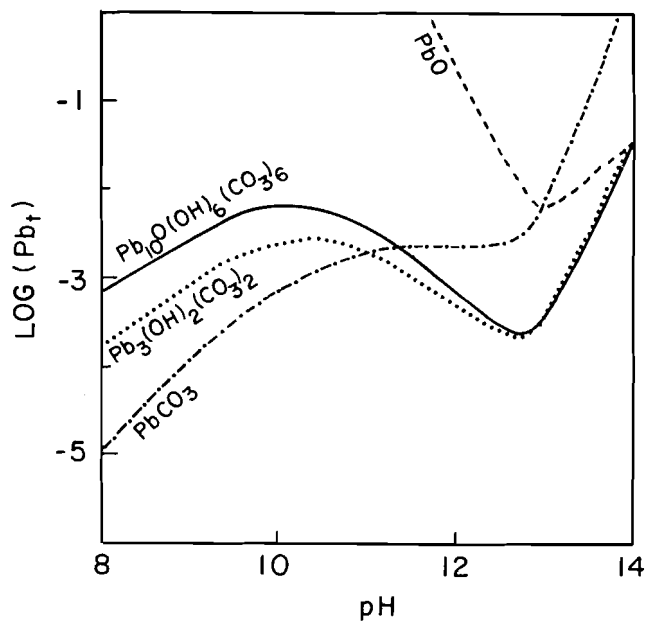

FIG. 11. Computed equilibrium dissolved lead activities, $\{Pb(CO_3)_2^{2-}\}$ + $\{Pb(OH)_3^-\}$, as a function of pH for the four phases shown, at a total dissolved carbonate activity of 1 mol L^{-1} (derived from ref. 7).

lead in alkaline carbonate solutions. Their stability constants for $Pb(CO_3)_2^{2-}$ and $Pb(OH)_3^-$ are in good agreement with earlier work (as summarized in ref. 7), but they detected an additional species, $Pb(OH)(CO_3)^-$. Their data were obtained at high ionic strength, and so are not readily incorporated into Fig. 11, which is based on Gibbs energies and refers to a hypothetical standard state of zero ionic strength. In 1 mol L^{-1} carbonate solution, $Pb(OH)(CO_3)^-$ is a major species only between pH 12 and 13, exceeding $Pb(OH)_3^-$ and $Pb(CO_3)_2^{2-}$ combined by no more than a factor of two (12). Its inclusion would therefore result in somewhat shallower minima in the dissolved lead activity curves for PbO and the basic lead carbonates, and a less pronounced inflection for $PbCO_3$, than in Fig. 11. The following discussion is based only on solubility trends, and so is not substantially affected.

Discussion

The voltammograms of Fig. 1 show that the anodic oxidation process can be divided into two distinct regions: (*i*) the main anodic oxidation region for $E \leq -0.5$ V; and (*ii*) a reactivation region at more positive potentials, where increased dissolution of the electrode occurs. The pH dependence of the current I_{PASS} (reactivation region), Fig. 2, has the same general form as the solubility curve, Fig. 11. The maximum in the value of I_{PEAK} (Fig. 2), however, does not coincide with that in the solubility curve. This indicates the value of I_{PEAK} is determined, at least in part, by processes other than dissolution. Potentiostatic transients recorded at potentials on the negative side of the main anodic peak have a form suggesting film formation by a nucleation and growth process. Consequently, it is possible that, under voltammetric conditions, the position and height of the main anodic peak (I_{PEAK}) is determined as much by film formation as by dissolution processes.

The distribution of phases with pH, Fig. 4, at potentials in the vicinity of the main anodic peak is similar to that predicted thermodynamically, and the extent of dissolution (Q_D, Fig. 5) varies with pH in a similar manner to the solubility, Fig. 11. Thus, we can claim that the dissolution rate in this potential region is directly proportional to the solubility of the predominant surface phase present. The similarity in Q_D (the extent of dissolution) and Q_C (the extent of film formation) as a function of pH shows that dissolution and film formation are directly related at a constant electrode rotation speed, i.e., under constant convective conditions. In the CSV obtained after potentiostatic oxidation both peak X, for the reduction of a base-layer, and peak Y for the reduction of a redeposited layer (see Fig. 1) are observed. The predominance of peak Y indicates that the majority of the film is present in the recrystallized form. Consequently, as the dissolution rate increases, the rate of redeposition/recrystallization back onto the electrode surface increases. As demonstrated previously at pH = 12, recrystallization competes with solution transport for the soluble Pb^{2+} species produced by dissolution. The extent of recrystallization decreases as the rate of transport of soluble Pb^{2+} species to the lead-free bulk of solution is increased by increases in electrode rotation rate.

The peak in the plot of Q_C versus pH (Fig. 5) coincides with the predominance of hydrocerussite ($Pb_3(OH)_2(CO_3)_2$) and/or cerussite ($PbCO_3$) on the electrode surface. Hence, we can conclude that both these phases are formed by recrystallization from solution. Film formation in this manner is more likely to yield the thermodynamically stable phase because its formation will be independent of the electrochemically applied field. It is not possible to decide which of these two phases forms directly from solution. The interconversion of these two phases has been shown to be fast and reversible (7). Consequently, our observation that the thermodynamically stable phase is present is not surprising.

For pH > 13, plumbonacrite is the thermodynamically stable phase, and the only phase observed experimentally. Its formation at lower pH values (8 to 13) and its identification with the base-layer reduction process are consistent with our claim in ref. 1 that plumbonacrite is formed directly on the electrode surface. It appears to be kinetically stabilized by the high rate of anodic formation of Pb^{2+} species. The potentiostatic transients indicate

Can. J. Chem. Downloaded from www.nrcresearchpress.com by 196.1.178.254 on 09/07/12
For personal use only.

Can. J. Chem. Downloaded from www.nrcresearchpress.com by 196.1.178.254 on 09/07/12
For personal use only.

that its formation may be controlled by a nucleation and growth process. A similar mechanism of formation has been demonstrated for lead sulphate (13) and lead chloride (14) films. Plumbonacrite appears to be kinetically stabilized by the anodic injection of Pb^{2+} species from the underlying metal into the surface film.

It is interesting that at pH = 12 (6), the base-layer appears to possess a sandwich structure with hydrocerussite growing on top of an initially formed layer of plumbonacrite. This dual structure was explained on the basis of the close crystallographic relationship between these two phases which allows epitaxial growth of one phase on the other. Also, the curves of Fig. 11 show that, for pH $\geq$ 12, there is almost no difference in solubility between these two phases. For more alkaline pH values ($\geq$ 13), only plumbonacrite is formed, Fig. 4, despite the observed closeness in solubility, Fig. 11. This suggests that hydrocerussite formation is inhibited when the OH^-/CO_3^{2-} concentration ratio increases.

The potentiostatic transients of Fig. 8 show that the behaviour in the reactivation region is complex. The potential and electrode rotation rate dependencies of peaks A and B suggest that breakdown of the film grown at short times is accompanied by the formation of a further film (peak A) and the eventual establishment of a steady-state involving dissolution and continued recrystallization. The broad peak B can be attributed to film breakdown, leading to a surge in current due to dissolution. The slow decrease in current to an eventual steady-state after approximately 7 min can be attributed to further growth of the porous deposited layer. The data of Fig. 6 show that the additional film formed is litharge and the continued growth at longer times can be attributed to deposition of hydrocerussite from solution.

The formation of litharge could be explained as follows. When rupture of the initially formed plumbonacrite/hydrocerussite film occurs, presumably as a result of stress in this rapidly formed layer, the subsequent metal dissolution process will be extremely rapid. Hence, the local concentration of dissolved Pb^{2+} in the faults in the base-layer will be high. If the transport of CO_3^{2-} into the fault is limited, perhaps because of the presence of the upper-layer of hydrocerussite, then the carbonate concentration at the electrode surface will be much lower than the bulk concentration. If carbonate depletion is sufficiently large, then PbO could be stabilized with respect to plumbonacrite (7).

This explanation is supported by the voltammogram of Fig. 3, which shows a further stage of film formation at low carbonate concentrations. This film is reduced on the reverse cathodic scan before the main anodic film, Fig. 3*C*, indicating that it is formed under the basic lead carbonate layer. A similar peak was observed by Buchanan *et al.* (15) in borate solutions at pH = 9; and was attributed to the reduction of a tetragonal PbO (litharge) layer formed in the reactivation region. These authors confirmed their claim by photocurrent spectroscopy.

When litharge formation becomes extensive, Fig. 6, the outer areas of the film will be exposed to more concentrated carbonate solutions. Under these conditions, the oxide becomes unstable with respect to plumbonacrite and converts, at least partially, to the latter phase (see Fig. 6) as shown by Taylor and Lopata (7):

$$10PbO + 9H_2O + 6CO_3^{2-} \rightarrow Pb_{10}O(OH)_6(CO_3)_6 + 12OH^-$$

This reaction would explain the second stage of plumbonacrite formation only observed at very positive potentials, Fig. 6. This stage is distinct from the initial formation of this phase as a base-layer which occurs at all potentials over the range −0.726 to 0 V.

The analysis of the steady-state currents in the reactivation region shows that they are not proportional to the solubility of the phases present. The independence of the currents on potential, Fig. 9, suggests a constant field across the dissolving film. This is consistent with a film thickness (x) that increases with potential (E) and maintains the electric field ($\Delta E/\Delta x$) in the film constant. The dependence of the currents on electrode rotation rate confirms that transport processes are important. Reasonable values for the diffusion coefficient of Pb^{2+} species can only be obtained if we assume the surface films are more soluble than indicated by thermodynamic calculations. Such values can be explained by a dissolution process involving either (*a*) a field-assisted dissolution of the plumbonacrite (or litharge) base-layer or (*b*) metal dissolution through pores, or other faults, in the base-layer.

Acknowledgement

We are grateful to A. M. Duclos for recording the X-ray diffractograms.

1. C. M. Wai, C. R. Knowles, and J. F. Keely. Bull. Environm. Contam. Toxicol. **21**, 4 (1979).
2. R. S. Mitchell. Rocks Miner. **52**, 5 (1977).
3. R. M. Harrison and D. P. H. Laxen. Nature, **286**, 791 (1980).
4. E. L. Schmeling and B. Röschenbleck. Korrosion, **12**, 83 (1960).
5. D. W. Shoesmith and M. G. Bailey. *In* The corrosion performance of nuclear fuel waste containers. Atomic Energy of Canada Limited Technical Record, TR-340. July 1985. p. 95.
6. D. W. Shoesmith and M. G. Bailey. Can. J. Chem. **66**, 2652 (1988).
7. P. Taylor and V. J. Lopata. Can. J. Chem. **62**, 395 (1984).
8. M. H. Brooker, S. Sunder, P. Taylor, and V. J. Lopata. Can. J. Chem. **61**, 494 (1983).
9. V. G. Levich. Physicochemical hydrodynamics. Prentice Hall, Englewood Cliff, NJ. 1966.
10. R. D. Armstrong and G. H. Bulman. J. Electroanal. Chem. **25**, 121 (1970).
11. R. G. Barradas, K. Belinko, and D. W. Shoesmith. Electrochim. Acta, **121**, 357 (1976).
12. D. Ferri, I. Grenthe, S. Hietanen, and F. Salvatone. Acta. Chem. Scand. **A41**, 349 (1987).
13. G. Archdale and J. A. Harrison. J. Electroanal. Chem. **34**, 21 (1972).
14. J. Ambrose, R. G. Barradas, K. Belinko, and D. W. Shoesmith. J. Coll. Interfac. Sci. **47**, 441 (1974).
15. J. S. Buchanan, N. P. Freestone, and L. M. Peter. J. Electroanal. Chem. **182**, 383 (1985).

Fragmentation of alkoxide ions following collisional activation. An energy-resolved study

ROGER S. MERCER and ALEX G. HARRISON
Department of Chemistry, University of Toronto, Toronto, Ont., Canada M5S 1A1

Received December 31, 1987[1]

ROGER S. MERCER and ALEX G. HARRISON. Can. J. Chem. **66**, 2947 (1988).

The collisionally activated dissociation reactions of the C_2 to C_5 alkoxide ions have been studied for collisons occurring at 8 keV kinetic energy and also over the range 5 to 100 eV kinetic energy. The alkoxide ions fragment by 1,2-elimination of H_2 and/or an alkane. Thus, primary alkoxide ions fragment by elimination of H_2 only, secondary alkoxide ions show elimination of H_2 and alkane molecules, while tertiary alkoxide ions show elimination of alkanes only. In alkane elimination, loss of CH_4 is much more facilie than loss of larger alkanes. For secondary alkoxide ions, where more than one elimination reaction occurs, the energy dependence of fragmentation has been explored over the collision energy range 5 to 100 eV. The results are interpreted in terms of a step-wise mechanism involving formation of an anion-carbonyl compound ion–dipole complex, followed by proton abstraction by the H^- or alkyl anion leading to the final products. The relative importance of the reaction channels is determined by the relative stabilities of these ion–dipole complexes.

ROGER S. MERCER et ALEX G. HARRISON. Can. J. Chem. **66**, 2947 (1988).

On a étudiée les réactions de dissociation des ions alcoolates C_2 à C_5 activées par des collisions se produisant à une énergie cinétique de 8 keV ainsi qu'à des énergies cinétiques allant de 5 à 100 eV. Les ions alcoolates se fragmentent par une élimination-1,2 de H_2 et/ou d'alcane. Ainsi, les ions alcoolates primaires se fragmentent uniquement par une élimination de H_2; par ailleurs, les ions alcoolates secondaires présentent de l'élimination de H_2 ainsi que celle de molécules d'alcanes alors que les ions alcoolates tertiaires ne présentent que de l'élimination d'alcanes. Lors de l'élimination d'alcanes, la perte de CH_4 est beaucoup plus facile que celle des alcanes plus volumineux. Dans le cas des alcoolates secondaires où il se produit plus d'une élimination, on a évalué la relation qui existe entre l'énergie de collision (de 5 à 100 eV) et le type de fragmentation. On interprète les résultats en fonction d'un mécanisme par étape impliquant la formation d'un complexe ion–dipôle d'un composé anion-carbonyle, suivie par l'enlèvement d'un proton par un H^- ou par un anion alkyle, conduisant aux produits. On a déterminé l'importance relative des diverses voies réactionnelles en se basant sur les stabilités relatives de ces complexes ion–dipôles.
[Traduit par la revue]

Introduction

Studies of the fragmentation of gaseous ions have long been invaluable sources of information concerning the structures and chemistry of such species (1, 2). This information is even more useful if the internal energy of the fragmenting ions is known and can be varied in a controlled fashion; such energy-resolved studies permit the establishment of break-down graphs expressing the variation of fragment ion yields with internal energy. Energy-resolved data for odd-electron molecular cations can be obtained with high precision by photoelectron/photoion coincidence (PEPICO) experiments (3–5) and, with reduced precision, by charge exchange experiments (6–8). Energy-resolved data, not restricted to molecular cations, also can be obtained from mass-resolved studies of the single-photon photodissociation of gaseous ions by varying the wavelength of the incident photons (9, 10). More qualitative data on the energy dependence of ionic fragmentation reactions can be obtained from energy-resolved (ERMS) collisional experiments (11–13), from angle-resolved (ARMS) collisional experiments (13, 14), and from field ionization kinetics (FIK) measurements (15, 16), the latter also being limited to odd-electron molecular cations. With this extensive armoury of techniques, the study of the energy dependence of the fragmentation of organic cations is a well-established field.

However, the same cannot be said for the study of the energy dependence of the fragmentation of organic anions. Techniques such as PEPICO and FIK are not applicable to anions, while charge exchange methods have not been developed. It should be possible to obtain energy-resolved data for anions by single-photon laser photodissociation experiments, however, such studies have not been reported. Angle-resolved collisional mass spectrometry (ARMS) requires specialized equipment not readily available; in addition, there have been some questions raised concerning the interpretation of the results (17, 18). Thus, the simplest, and most accessible, method of obtaining at least qualitative data on the energy dependence of the fragmentation reactions of gaseous anions appears to be low, variable collision energy collisional mass spectrometry (ERMS). In such studies the collision-induced dissociation (CID) mass spectra of the ions of interest are recorded as a function of collision energy over the range from ~2 to 100 or 200 eV. It is clear from positive ion studies that, at these low collision energies, the kinetic energy transformed into internal energy increases with increasing collision energy (13, 19–23), although the relationship between collision energy and mean internal energy is unknown and appears to vary from system to system and the kinetic to internal energy transfer appears to reach a maximum at higher collision energies (22, 23). A recent communication from this laboratory (24) has reported such an ERMS study for the fragmentation of a number of simple ester enolates and has compared the results obtained with the energy-resolved results obtained earlier (25), over the collision energy range 0 to 150 eV, using Fourier-transform mass spectrometric methods. The present paper reports an energy-resolved study of the collision-induced dissociation of simple alkoxide ions. Boand *et al* (26) have recorded the 8 keV CID mass spectra of a few alkoxide ions. They observed elimination of H_2 and/or small alkanes from the activated alkoxide ions; from limited isotopic labelling they concluded that specific 1,2-eliminations were responsible for the fragmentation reactions occurring. This conclusion is supported by the more recent isotopic labelling studies of Bowie and co-workers (27, 28) who also concluded, from *ab initio* calculations and a study of isotope effects, that the elimination reactions proceeded by a step-wise mechanism involving intermedi-

[1]Revision received July 11, 1988.

Can. J. Chem. Downloaded from www.nrcresearchpress.com by 196.1.178.254 on 09/07/12
For personal use only.

TABLE 1. Collision-induced dissociation of alkoxide ions at 8 keV and 30 eV collision energies

	Reaction		Product abundance at 8 kev	Product abundance at 30 eV
[1]	$CH_3Ch_2O^-$	$\rightarrow CH_2$—$CHO^- + H_2$	100	100
[2]	$CH_3CH_2CH_2O^-$	$\rightarrow CH_3CH + CHO^- + H_2$	100	100
[3]	$(CH_3)_2CHO^-$	$\rightarrow CH_2$—$C(CH_3)O^- + H_2$	71	47
		$\rightarrow CH_2$—$CHO^- + CH_4$	29	53
[4]	$CH_3(CH_2)_3O^-$	$\rightarrow CH_3CH_2CH$—$CHO^- + H_2$	100	100
[5]	$CH_3CH(CH_3)CH_2O^-$	$\rightarrow CH_3C(CH_3)$—$CHO^- + H_2$	100	92
		$\rightarrow C_3H_5O^- + CH_4$	0	8
[6]	$CH_3CH_2CH(CH_3)O^-$	$\rightarrow C_4H_7O^- + H_2$	76	65
		$\rightarrow CH_3CH$—$CHO^- + CH_4$	24	30
		$\rightarrow CH_2$—$CHO^- + C_2H_6$	0	5
[7]	$(CH_3)_3CO^-$	$\rightarrow CH_2$—$C(CH_3)O^- + CH_4$	100	100
[8]	$CH_3(CH_2)_4O^-$	$\rightarrow CH_3(CH_2)_2CH$—$CHO^- + H_2$	100	100
[9]	$CH_3CH_2CH(CH_3)CH_2O^-$	$\rightarrow CH_3CH_2C(CH_3)$—$CHO^- + H_2$	100	100
[10]	$CH_3CH(CH_3)CH_2CH_2O^-$	$\rightarrow CH_3CH(CH_2)CH$—$CHO^- + H_2$	100	100
[11]	$CH_3CH_2CH_2CH(CH_3)O^-$	$\rightarrow C_5H_9O^- + H_2$	78	61
		$\rightarrow CH_3CH_2CH$—$CHO^- + CH_4$	22	28
		$\rightarrow CH_2$—$CHO^- + C_3H_8$	0	9
[12]	$(CH_3)_2CH$-$CH(CH_3)O^-$	$\rightarrow C_5H_9O^- + H_2$	52	37
		$\rightarrow (CH_3)_2C$—$CHO^- + CH_4$	24	47
		$\rightarrow CH_2$—$CHO^- + C_3H_8$	12	4
		$\rightarrow CH_3^- + ?$	12	12
[13]	$CH_3CH_2C(CH_3)_2O^-$	$\rightarrow CH_3CH$—$C(CH_3)O^- + CH_4$	85	95
		$\rightarrow CH_2$—$C(CH_3)O^- + C_2H_6$	15	5
[14]	$(CH_3CH_2)_2CHO^-$	$\rightarrow CH_3CH$—$C(C_2H_5)O^- + H_2$	100	92
		$\rightarrow CH_3CH$—$CHO^- + C_2H_6$	0	8

ate formation of a long-lived complex of H^-/CH_3^- and a carbonyl compound. The conclusions that the elimination reactions are specifically 1,2-eliminations and that they occur in a stepwise fashion are in agreement with the conclusions reached by Brauman and co-workers (29–31) from a study of the infrared multiphoton dissociation of a variety of alkoxide ions. Base on this evidence we have interpreted the results obtained in the present work for larger alkoxide ions in terms of specific 1,2-elimination reactions.

The multi-photon photodissociation experiments (29–31) explore threshold fragmentation reactions while our low energy collisional experiments explore higher energy fragmentation reactions as well, thus probing the energy dependence of possible competing fragmentation reactions. We also have determined the CID mass spectra following activation by 8 keV collisions; the comparison of the results obtained with the low energy CID mass spectra provides information on the relative internal energies achieved by the two methods of activation.

Experimental

Experiments were carried out using a VG Analytical ZAB-2FQ mass spectrometer, which has been described in detail previously (32). In brief, the ZAB-2FQ is of BEQQ geometry in which a reversed-geometry (BE) double-focussing mass spectrometer precedes a third stage consisting of a deceleration lens system, an r.f.-only quadrupole collision cell and a quadrupole mass analyzer. The instrument also contains a collision cell in the second field free region (between the magnetic and electric sectors) which allows high energy CID experiments to be carried out.

In all cases, the alkoxide ions were prepared by reaction of the appropriate alcohol with $[OH]^-$ in a chemical ionization source operating at 200°C. The $[OH]^-$ was produced by electron impact on a $10\%N_2O/90\%CH_4$ mixture at a pressure of $\sim 1.5 \times 10^{-5}$ Torr as read by an ionization gauge on the pumping line from the ion source region. The alcohols were commercial samples of high purity and were used as received. They were admitted through a heated capillary inlet system held at 130°C.

Low energy collisional experiments were performed by mass selecting the appropriate ion using the double focussing (BE) portion of the instrument, decelerating the ion beam from 8 keV to the desired collision energy (5–100 eV) and allowing the ion beam to undergo collision with N_2 gas in the r.f.-only quadrupole at a pressure $\sim 1.5 \times 10^{-7}$ Torr as indicated by the ionization gauge situated on the pumping line for the quadrupole region. Spectra were obtained as a function of collision energy by varying the potential of the r.f.-only quadrupole with respect to the ion source and scanning the analyzer quadrupole in a mass selective fashion.

For the high energy collisional experiments the ion of interest was selected by the magnetic sector and underwent collision, at 8 keV kinetic energy, with He in a collision cell located between the magnetic and electric sectors. The ionic fragmentation products were analyzed by their kinetic energy by scanning the voltage applied to the electric sector. The He pressure, as measured by an ionization gauge on the pumping lead for the region, was $\sim 1.5 \times 10^{-7}$ Torr, which gave ~50% attenuation of the main beam, although a significant part of this apparent reduction may correspond to collisional electron detachment.

Results and Discussion

Table 1 compares the CID mass spectra observed after collision with He at 8 keV collision energy and after collision with N_2 at 30 eV collision energy for the C_2 through C_5 alkoxide ions. With one exception, the primary alkoxide ions show only loss of H_2 in both the high and low energy CID mass spectra. The exception is *i*-butoxide (entry 5) where a minor loss of CH_4 is observed in the low energy CID mass spectra; Bowie and co-workers (28) also reported loss of H_2 and CH_4 from this alkoxide ion following 8 keV excitation, although the relative importance of the two reactions was not indicated. Fragmentation of the

Can. J. Chem. Downloaded from www.nrcresearchpress.com by 196.1.178.254 on 09/07/12
For personal use only.

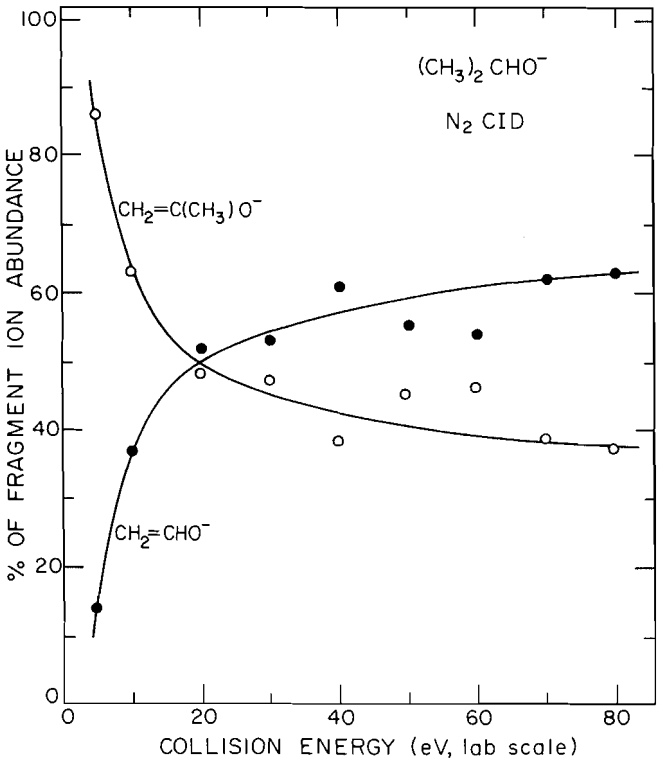

FIG. 1 Breakdown graph for *i*-propoxide (*m/z* 59).

$CH_3CD_2O^-$ anion resulted in elimination of HD only, in agreement with results of Hayes *et al.* (28) and with a specific 1,2-elimination reaction.

In contrast to the primary alkoxide ions, secondary alkoxide ions show more than one fragmentation pathway. The simplest of the secondary ions is isopropoxide (entry 3) which shows elimination of both H_2 and CH_4 in both the low energy and high energy CID mass spectra. These two fragmentation reactions were reported by Bowie and co-workers (28), although their relative importance was not indicated. They also reported that CD_3H was eliminated from $(CD_3)_2CHO^-$, a reaction inconsistent with the proposed 1,2-elimination. We observe elimination of CD_4 (and HD) from $(CD_3)_2CHO^-$, consistent with a specific 1,2-elimination reaction. In contrast with the collisional studies, Brauman and co-workers (30) have reported that the infrared multiphoton photodissociation of isopropoxide results in elimination of H_2 only. Figure 1 shows the dependence of fragmentation of isopropoxide ions on collision energy over the range 5 to 80 eV, laboratory scale. At the lowest collision energies elimination of H_2 is the dominant fragmentation reaction indicating that this reaction has the lower critical reaction energy and will be the channel observed when threshold reactions are probed by multiphoton activation. However, with increasing collision energy (and presumably, increasing energy deposition in the ion) elimination of CH_4 increases rapidly in importance up to ~40 eV collision energy beyond which there is little change in relative yields.

Scheme 1 summarizes the possible fragmentation reactions of the *i*-propoxide ion and gives for each possible set of products the enthalpy relative to the reactant ion. The scheme has been constructed on the basis of the step-wise mechanism proposed by Bowie and co-workers (27, 28) and Brauman and co-workers (29–31). Although the simple bond fission products (H^- and CH_3^-) were not observed they are included in this and following

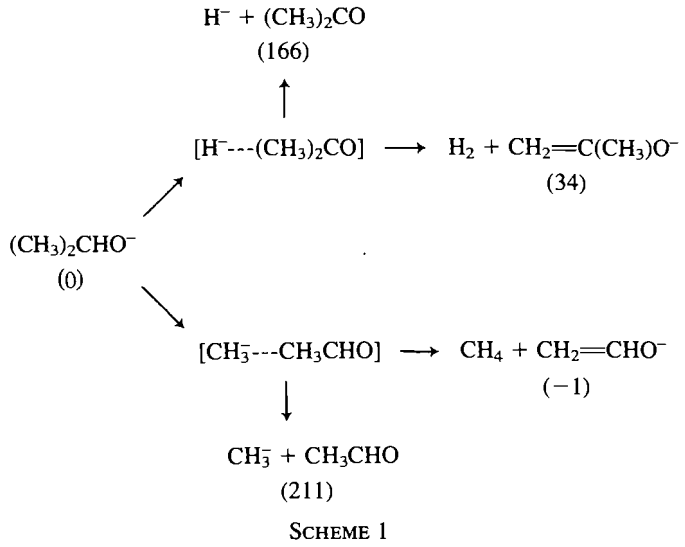

SCHEME 1

TABLE 2. Thermochemical data (kJ mol^{-1})

A—H	$\Delta H_f^0(AH)^a$	$\Delta H_{acid}^0(AH)^b$	$\Delta H_f^0(A^-)$
H—H	0.	1675	139
CH_3—H	−74.9	1743	133
C_2H_5—H	−84.5	1761[c]	141
$(CH_3)_2CHO$—H	−272.8	1565	−244
$CH_3CH_2CH(CH_3)O$—H	−292.8	1556[d]	−272
$(C_2H_5)_2CHO$—H	−314.6	1556[d]	−294
$CH_3CH_2CH_2CH(CH_3)O$—H	−314.6	1556[d]	−294
$CH_3CH(CH_3)CH(CH_3)O$—H	−315.3	1556[d]	−295
$OCHCH_2$—H	−166.2	1533	−169
$OCHCH(CH_3)$—H	−190.2	1531	−195
$OCHCH(C_2H_5)$—H	−204.8	1531	−209
$OCHC(CH_3)_2$—H	−204.8	1529[d]	−211
CH_3COCH_2—H	−217.1	1543	−210
$CH_3COCH(CH_3)$—H	−238.6	1537	−237
$CH_3CH_2COCH_2$—H	−238.6	1541[d]	−233
$CH_2CH_2COCH(CH_3)$—H	−257.9	1537	−256
$CH_3COCH(C_2H_5)$—H	−259.1	1536[d]	−259
$C_3H_7COCH_2$—H	−259.1	1540[d]	−255
$CH_3COC(CH_3)_2$—H	−262.6	1535	−263
$(CH_3)_2CCOCH_2$—H	−262.6	1540[d]	−258

[a]From ref. 37.
[b]From ref. 38, unless otherwise noted.
[c]From ref. 34.
[d]Estimated from ΔH_{acid}^0 of related compounds

schemes because they provide information relevant to the energies of the intermediate ion–dipole complexes. The necessary thermochemical data used in deriving the relative enthalpies in the schemes are summarized in Table 2. As shown in the scheme, elimination of CH_4 is the thermochemically favoured reaction (indeed it is essentially thermoneutral), however, both the present results and the earlier photo-dissociation results (30) indicate that elimination of H_2 is the favoured reaction energetically, presumably because the intermediate ion–dipole complex $[H^-\text{---}(CH_3)_2CO]$ is lower in energy than the ion–dipole complex $[CH_3^-\text{---}CH_3CHO]$ (the site of the negative charge in these complexes and those shown in later schemes is uncertain. The available evidence (28, 30) favours the structure shown). The stabilization of these complexes, relative to the separated products $H^- + (CH_3)_2CO$ and $CH_3^- + CH_3CHO$, should arise

Can. J. Chem. Downloaded from www.nrcresearchpress.com by 196.1.178.254 on 09/07/12
For personal use only.

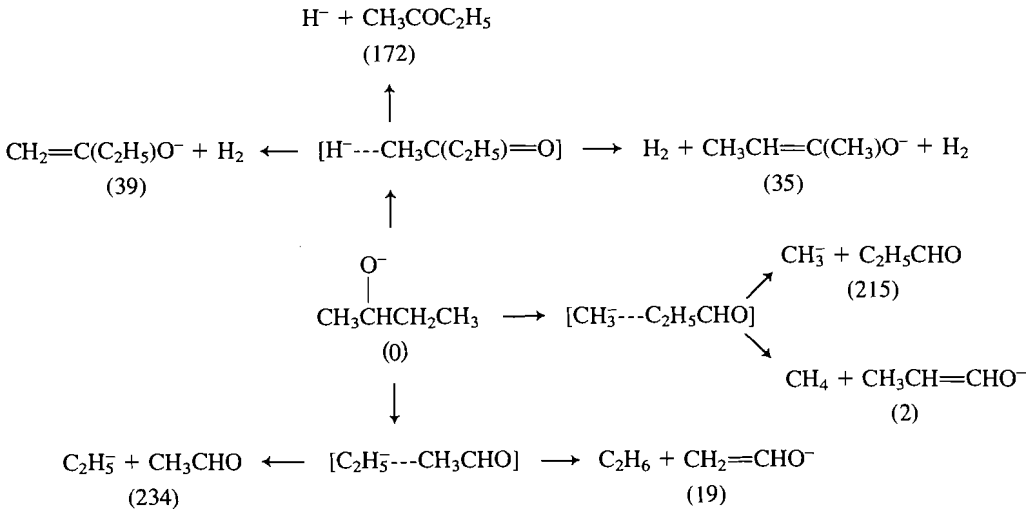

SCHEME 2

primarily from ion–dipole interactions and, since the dipole moments (33) of $(CH_3)_2CO$ (μ = 2.89 D) and CH_3CHO (μ = 2.72 D) are similar, the stabilization energies should be similar. (This should be true for all ion/dipole complexes discussed in this work since all the carbonyl compounds have similar dipole moments.) Thus, since H^- + $(CH_3)_2CO$ is lower in energy than CH_3^- + CH_3CHO, the [H^----$(CH_3)_2CO$] complex should be the lower energy ion–dipole complex. However, in view of the rapid rise in importance of the CH_4 elimination reaction with increasing collision energy, it appears that the critical energy for CH_4 elimination must be only slightly greater than that for H_2 elimination; in addition there may be entropic effects which favour CH_4 elimination.

The *s*-butoxide ion (entry 6) also fragments by more than one channel, exhibiting elimination of H_2, CH_4, and C_2H_6 in the low energy CID and the former two in the high energy CID. Boand *et al.* (26), in high energy CID experiments, have observed H_2, CH_4 and, in low yield, C_2H_6 elimination. Figure 2 shows the dependence of the fragmentation of *s*-butoxide on collision energy over the range 5–80 eV, while Scheme 2 presents a fragmentation scheme giving the enthalpy of products relative to the *s*-butoxide ion. Although elimination of H_2 is the least favourable reaction thermochemically, it clearly is the most favourable reaction energetically. Two H_2-elimination products are possible and are of similar final enthalpies; the present work provides no information on the relative importance of these two reactions. Although elimination of methane is an essentially thermoneutral reaction, the [CH_3^- --- C_2H_5CHO] complex is less stable than that leading to H_2 elimination and CH_4 elimination is less important than H_2 elimination at all collision energies; it is not clear why CH_4 elimination is not as important in this system as in the *i*-propoxide system. Elimination of C_2H_6 is of only minor importance at all collision energies despite the fact that the ΔH for the reaction is only ~19 kJ mol^{-1}. There is no reliable evidence that alkyl anions other than CH_3^- are stable gas phase species. Indeed DePuy and co-workers (34) have estimated a gas-phase acidity for C_2H_6 of 761 kJ mol^{-1}, which leads to an electron affinity of −37.7 kJ mol^{-1} for C_2H_5. For comparison, the electron affinity of CH_3 is 7.5 kJ mol^{-1} (35). Using the $\Delta H°$ acid for C_2H_6, the enthalpy of the hypothetical products [$C_2H_5^-$ + CH_3CHO] is calculated to be ~234 kJ mol^{-1} relative to the *s*-butoxide ion; thus, assuming equal ion–dipole stabilization in the intermediate complexes, the [$C_2H_5^-$---CH_3CHO] complex will be the highest in energy in agreement with the low yield of C_2H_6 + CH_2=CHO^-.

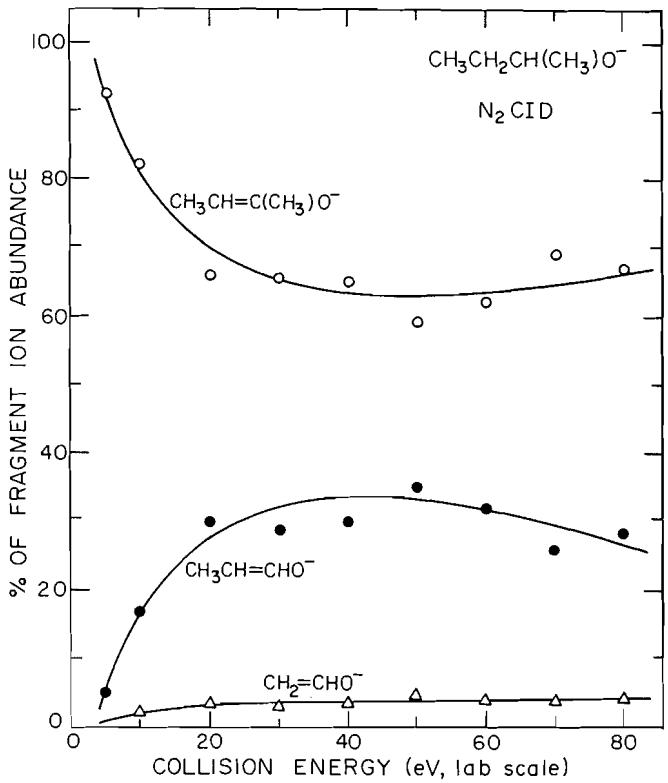

FIG. 2 Breakdown graph for *s*-butoxide (*m/z* 75).

The same arguments apply for the 3-pentoxide ion (entry 14, Table 1) where C_2H_6 elimination is of only minor importance relative to H_2 elimination over the entire collision energy regime (Fig. 3) even though elimination of C_2H_6 is the more favourable reaction thermochemically (Scheme 3). An interesting observation is the low yield of CH_2=CHO^- (*m/z* 43) at high collision energies corresponding to elimination of C_3H_8 from the 3-pentoxide ion.

Fragmentation of the 2-pentoxide anion (entry 11) involves elimination of H_2, CH_4 and, in low yield, C_3H_8; the breakdown

Can. J. Chem. Downloaded from www.nrcresearchpress.com by 196.1.178.254 on 09/07/12
For personal use only.

Can. J. Chem. Downloaded from www.nrcresearchpress.com by 196.1.178.254 on 09/07/12
For personal use only.

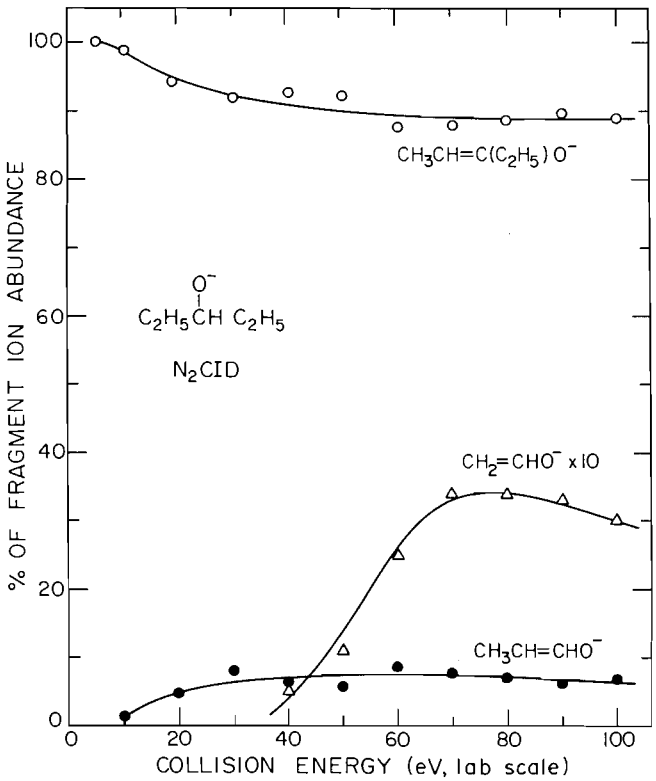

FIG. 3 Breakdown graph for 3-pentoxide (*m/z* 87).

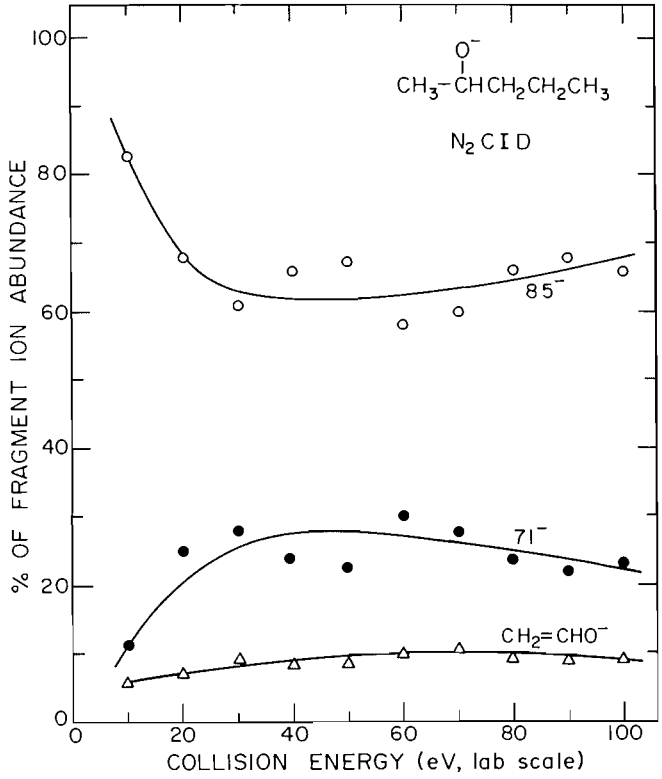

FIG. 4 Breakdown graph for 2-pentoxide (*m/z* 87).

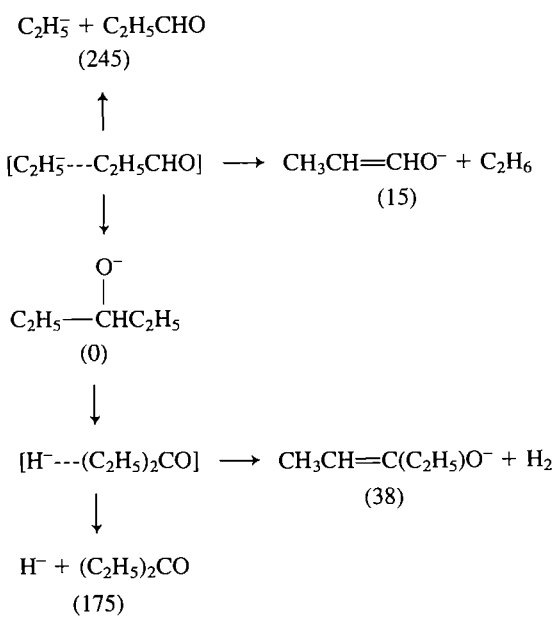

SCHEME 3

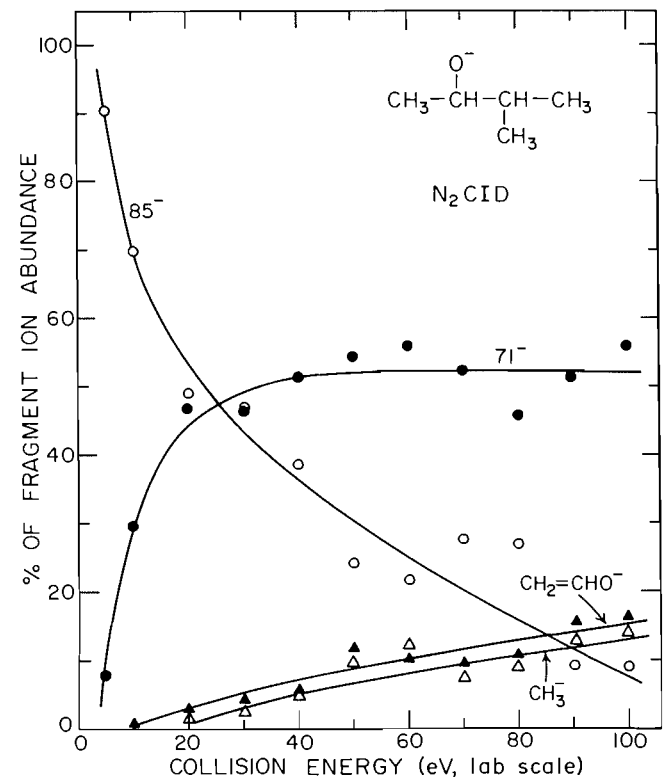

FIG. 5 Breakdown graph for 3-methyl-2-butoxide (*m/z* 87).

graph is shown in Fig. 4 while the thermochemical data are summarized in Scheme 4. Clearly elimination of H_2 is the favoured reaction at low internal energies and must have the lowest critical reaction energy even though it is the least favourable reaction thermochemically. This is in agreement with the expected energies of the intermediate ion–dipole complexes. By analogy with other alkyl anions (34) $(CH_3)_2CH^-$ is not expected to be stable and the intermediate $[(CH_3)_2CH^-$---$CH_3CHO]$ complex will be quite high in energy leading to only minor reaction by this mode. One should note that H_2 elimination can lead to two products of similar stability; the present work provides no information on the relative importance of these two channels (Scheme 5).

In contrast to the 2-pentoxide ion, collision-induced dissociation of the 3-methyl-2-butoxide ion (entry 12, Fig. 5) results in

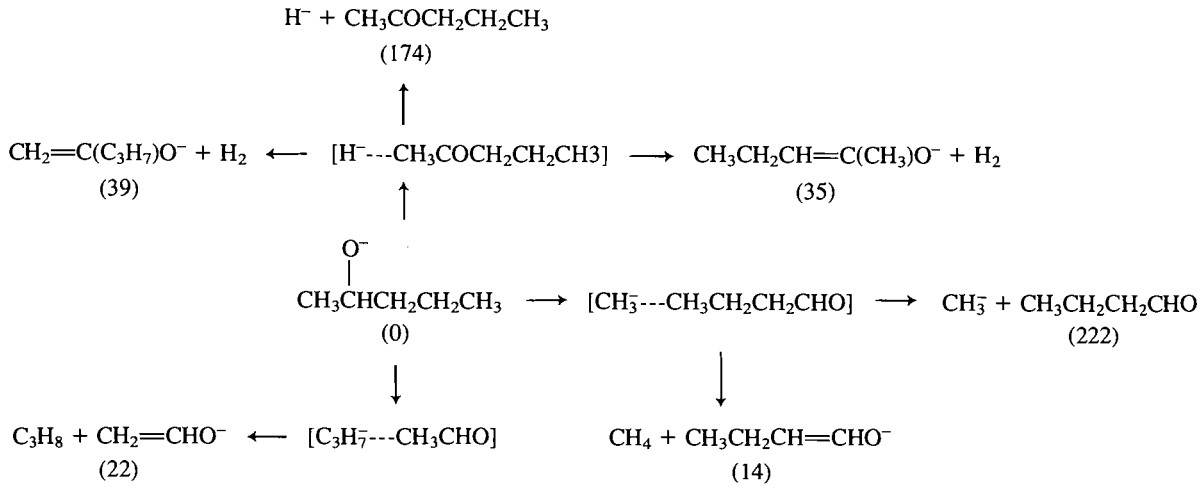

SCHEME 4

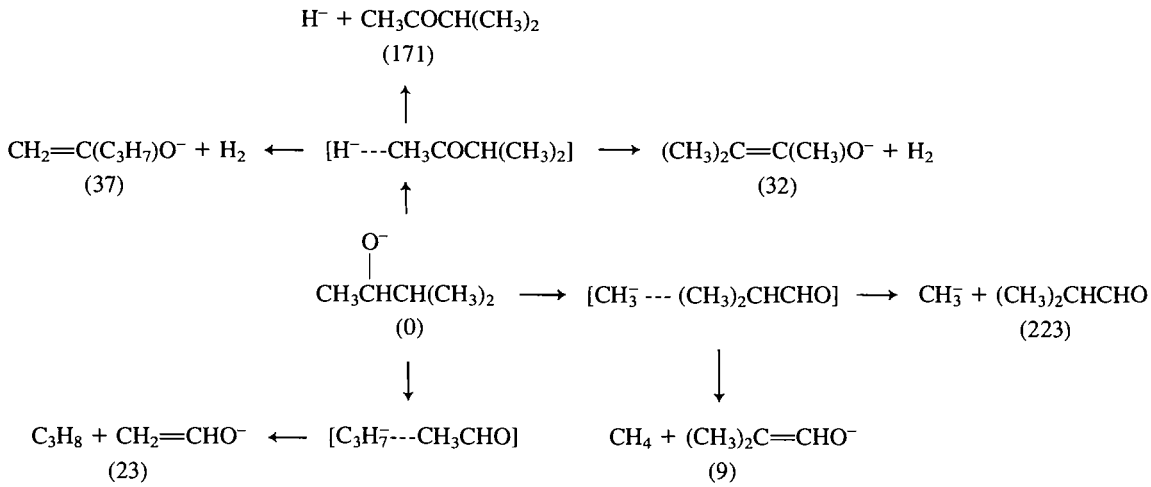

SCHEME 5

much more significant elimination of CH_4 although elimination of H_2 is the favoured reaction at low internal energies. The increased importance of CH_4 elimination may result from the fact that the final step involves abstraction of a tertiary hydrogen; the *ab initio* calculations suggest (28) that either step may be rate determining. This is the only system where formation of CH_3^- is observed in significant yield. We do not believe that this product arises by primary fragmentation of the alkoxide ion, but rather that it arises by further fragmentation of the ion formed by H_2 elimination, viz.

The evidence, admittedly weak, for this proposal is the continual decrease in relative intensity of the *m/z* 85⁻ ion with increasing collision energy, in contrast to the other systems studied.

1,2-Elimination from tertiary alkoxide ions must result in alkane elimination. Thus as reported previously (28, 29, 31), *t*-butoxide (entry 7) eliminates CH_4, while the *t*-pentoxide ion (entry 13) shows elimination of CH_4 and, in minor yield, C_2H_6.

Comparison of the results in Table 1 for the 8 keV collision-induced dissociation reactions with the low energy CID results, particularly the breakdown graphs, leads to the conclusion that, on the whole, in the high energy system those ions which fragment to form detectable products are of lower internal energy than those fragmenting after 30 eV or higher energy collisions. Similar conclusions were reached in the study of ester enolate ions (24). It is likely that the alkoxide ions receiving higher internal energies in the 8 keV collisions suffer electron detachment since high energy collisional activation is believed (36) to involve electronic excitation.

Acknowledgements

We are indebted to the Natural Sciences and Engineering Research Council of Canada for financial support. R.S.M. gratefully acknowledges support in the form of University of Toronto Open Fellowships while A.G.H. is indebted to the Canada Council for the award of a Killam Fellowship (1985–1987).

1. K. LEVSEN. Fundamental aspects of mass spectrometry. Verlag Chemie, New York. 1978.
2. J. L. HOLMES. Org. Mass Spectrom. **20**, 169 (1985).
3. J. H. D. ELAND. *In* Mass spectrometry. Special Periodical Report, Vol. 5. The Chemical Society, London. 1979.

Can. J. Chem. Downloaded from www.nrcresearchpress.com by 196.1.178.254 on 09/07/12
For personal use only.

4. T. BAER. *In* Ionic processes in the gas phase. *Edited by* M. A. Almoster Ferreira. Reidel, Dordrecht. 1984.
5. J. DANNACHER. Org. Mass Spectrom. **19**, 253 (1984).
6. E. LINDHOLM. *In* Ion–molecule reactions in the gas phase. *Edited by* P. Ausloos. Am. Chem. Soc. Washington. 1966.
7. E. LINDHOLM. *In* Ion–molecule reactions. Vol. 2. *Edited by* J. L. Franklin. Plenum Press, New York. 1972.
8. A. G. HARRISON. *In* Ionic processes in the gas phase. *Edited by* M. A. Almoster Ferreira. Reidel, Dordrecht. 1984.
9. F. M. HARRIS and J. H. BEYNON. *In* Gas phase ion chemistry. Vol. 3. *Edited by* M. T. Bowers. Academic Press, Orlando. 1984.
10. R. C. DUNBAR. *In* Gas phase ion chemistry. Vol. 3. *Edited by* M. T. Bowers. Academic Press, Orlando. 1984.
11. S. L. MCLUCKEY, G. L. GLISH, and R. G. COOKS. Int. J. Mass Spectrom. Ion Phys. **39**, 219 (1981).
12. D. D. FETTEROLF and R. A. YOST. Int. J. Mass Spectrom. Ion Phys. **44**, 37 (1982).
13. S. A. MCLUCKEY and R. G. COOKS. *In* Tandem mass spectrometry. *Edited by* F. W. McLafferty. Wiley, New York. 1983.
14. J. A. LARAMEE, J. J. CARMODY, and R. G. COOKS. Int. J. Mass Spectrom. Ion Phys. **31**, 333 (1979).
15. H. D. BECKEY. Principles of field ionization and field desorption mass spectrometry. Pergamon Press, Oxford. 1977.
16. P. J. DERRICK. *In* Mass spectrometry. Special Periodical Report, Vol. 4. The Chemical Society, London. 1977.
17. P. J. TODD, R. J. WARMACK, and E. H. MCBAY. Int. J. Mass Spectrom. Ion Phys. **50**, 299 (1983).
18. R. K. BOYD, E. E. KINGSTON, A. G. BRENTON, and J. H. BEYNON. Proc. R. Soc. London, Ser. A, **392**, 59 (1984).
19. D. J. DOUGLAS. J. Phys. Chem. **86**, 185 (1982).
20. P. H. DAWSON. Int. J. Mass Spectrom. Ion Phys, **50**, 287 (1983).
21. P. H. DAWSON and W.-F. SUN. Int. J. Mass Spectrom. Ion Phys. **44**, 51 (1982).
22. S. NACSON and A. G. HARRISON. Int. J. Mass Spectrom. Ion Processes, **63**, 325 (1985).
23. J. J. ZWINSELMAN, S. NACSON, and A. G. HARRISON. Int. J. Mass Spectrom. Ion Processes, **67**, 93 (1985).
24. A. B. YOUNG and A. G. HARRISON. Org. Mass Spectrom, **22**, 622 (1987).
25. S. W. FROELICHER, R. E. LEE, R. R. SQUIRES, and B. S. FREISER. Org. Mass Spectrom. **20**, 4 (1985).
26. G. BOAND, R. HOURIET, and T. GÄUMANN. Lecture Notes Chem., **31**, 195 (1982).
27. R. N. HAYES, J. C. SHELDON, J. H. BOWIE, and D. E. LEWIS. J. Chem. Soc. Chem. Commun. 1431 (1984).
28. R. N. HAYES, J. C. SHELDON, J. H. BOWIE, and D. E. LEWIS. Aust. J. Chem. **38**, 1197 (1985).
29. W. TUMAS, R. F. FOSTER, M. J. PELLERITE, and J. I. BRAUMAN. J. Am. Chem. Soc. **105**, 7464 (1983).
30. W. TUNAS, R. F. FOSTER, M. J. PELLERITE, and J. I. BRAUMAN. J. Am. Chem. Soc. **106**, 4053 (1984).
31. W. TUMAS, R. F. FOSTER, M. J. PELLERITE, and J. I. BRAUMAN. J. Am. Chem. Soc. **109**, 961 (1987).
32. A. G. HARRISON, R. S. MERCER, E. J. REINER, A. B. YOUNG, R. K. BOYD, R. E. MARCH, and C. J. PORTER. Int. J. Mass Spectrom. Ion Processes, **74** 13 (1986).
33. R. C. WEAST (*Editor*), Handbook of chemistry and physics. 45th ed. Chemical Rubber Co. Cleveland. 1964.
34. C. H. DEPUY, V. M. BIERBAUM, and R. DAMRAUER. J. Am. Chem. Soc. **106**, 4051 (1984).
35. G. B. ELLISON, P. C. ENGELKING, and W. C. LINEBURGER. J. Am. Chem. Soc. **100**, 2556 (1978).
36. P. J. TODD and F. W. MCLAFFERTY. *In* Tandem mass spectrometry. *Edited by* F. W. McLafferty. Wiley, New York. 1983.
37. J. D. COX and G. PILCHER. Thermochemistry of organic and organometallic compounds. Academic Press, New York. 1970.
38. J. E. BARTMESS and R. T. MCIVER, JR. *In* Gas phase ion chemistry. Vol. 2. *Edited by* M. T. Bowers. Academic Press, New York. 1979.

Can. J. Chem. Downloaded from www.nrcresearchpress.com by 196.1.178.254 on 09/07/12
For personal use only.

A redetermination of the ultraviolet photoelectron spectrum of (*Z*)-2-methyl-1,3-pentadiene; evidence that twisted conformers predominate in the gas phase

NICK HENRY WERSTIUK AND GEORGE TIMMINS

Department of Chemistry, McMaster University, Hamilton, Ont., Canada L8S 4M1

Received May 11, 1988

NICK HENRY WERSTIUK and GEORGE TIMMINS. Can. J. Chem. **66**, 2954 (1988).

A redetermination of the ultraviolet photoelectron spectrum of (*Z*)-2-methyl-1,3-pentadiene (**1***a*) has resulted in a correction of the spectrum published by Masclet and co-workers. MMX and AM1 calculations on **1***a* predict that twisted *s-cis* conformations should be populated preferentially in the gas phase; this is in keeping with the experimentally determined π_-, π_+ splitting of 1.55 ± 0.05 eV.

NICK HENRY WERSTIUK et GEORGE TIMMINS. Can. J. Chem. **66**, 2954 (1988).

On a redéterminé le spectre photoélectronique ultraviolet du méthyl-2 pentadiène-1,3-(*Z*) (**1***a*) et il en résulte que l'on doit corriger le spectre publié antérieurement par Masclet et ses collaborateurs. En se basant sur des calculs MMX et AM1 effectués sur la molécule **1***a*, on peut prédire que, en phase gazeuse, les conformations *s-cis* croisées sont privilégiées; ces prédictions sont en accord avec le couplage π_-, π_+ de 1,55 ± 0,05 eV qui a été déterminé expérimentalement.

[Traduit par la revue]

Can. J. Chem. Downloaded from www.nrcresearchpress.com by 196.1.178.254 on 09/07/12
For personal use only.

We have undertaken a systematic study of the effect of methyl and ethyl substituents on butadiene conformation by ultraviolet photoelectron spectroscopy (UPS) and the computational methods MMX and AM1. Our aim is to carry out conformational analysis of dienes computationally by calculating the heats of formation as a function of the 2—3—4—5 dihedral angle — we chose to use MMX and AM1 initially because of their ease of usage and the low computational costs — to calculate the π_-, π_+ splittings for the predicted preferred conformations and the *s-trans* planar conformers and to compare these values to the experimentally obtained splittings. Through such comparisons, we hope to establish whether or not a combination of UPS-AM1/MMX will be useful generally for studying conformational isomerism of alkyl-substituted polyenes in the gas phase. Since structure determines conformational behaviour, it may be possible also in certain cases to use this methodology to elucidate the structure of highly substituted dienes and polyenes. In this connection, when we reviewed the photoelectron (pe) spectroscopy of the pentadienes, we were surprised to find that Masclet and co-workers (1)[1] reported that the lowest three ionization energies of (*Z*)-2-methyl-1,3-pentadiene (**1***a*) and (*E*)-2-methyl-1,3-pentadiene (**1***b*) are identical within experimental error; this is not what would be expected on the basis of the results of MMX calculations.[2] Figures 1(*A*) and 1(*B*) show ΔH_f as a function of the C1—C2—C3—C4 dihedral angle calculated by MMX for **1***a* and **1***b*, respectively. AM1 yields similar data.[3] Both computational methods predict that the (*Z*)-diene should exist in twisted conformations in gas phase at ambient temperature. For this reason and the fact that there is renewed interest (3,4) in the conformation of dienes, a topic which occupied the attention of experimentalists and theoreticians for several decades,[4] we undertook to redetermine the pe spectra of **1***a* and **1***b*.

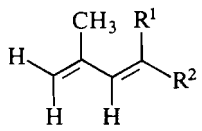

1

a, $R^1 = CH_3$; $R^2 = H$

b, $R^1 = H$; $R^2 = CH_3$

In addition to the MMX study,[5] which shows that planar *s-trans* **1***a* is 20 kJ higher in energy than *s-trans* **1***b* (Fig. 1), AM1 calculations also established that planar *s-trans* **1***b* is 12.5–16.5 kJ higher in energy than planar *s-trans* **1***b* depending on the conformations of the =CH—CH_3 units. This difference must be due mostly to a 1,3-CH_3,CH_3 steric interaction. On the assumption that $\Delta\Delta S \simeq 0$ for rotation about C2—C3, according to MMX twisted *s-cis* conformers should predominate over twisted *s-trans* conformers by approximately 4:1. Since the planar *s-trans* conformer is expected to be the stablest structure of (*E*)-isomer **1***b* — the results of MMX calculations summarized in Fig. 1(*B*) are in accord with this expectation — the spectra of **1***a* and **1***b* should be different; the π_-, π_+ splitting of (*Z*)-isomer **1***a* should be less than the splitting of (*E*)-isomer **1***b*.

[1]The authors reported only the three lowest ionization energies of **1***a* (8.43, 10.49, and 11.53 eV) and **1***b* (8.42, 10.46, and 11.50 eV).

[2]MMX, Version 87.200 of PCMODEL: A molecular mechanics package including MM2 (Allinger-QCPE 395), MMP1 Pi (Allinger-QCPE 318), MODEL parameters (Still) plus more atoms and constants by K.E. Gilbert and J.J. Gajewski, Indiana University. Available from Dr. K.E. Gilbert, Serena Software, P.O. Box 3096, Bloomington, IN, 47402.

[3]AM1 of AMPAC; Austin Method 1 Package (QCPE 506) (2).

[4]See ref. 3 for a comprehensive list of pertinent references.

[5]The C1—C2—C3—C4 dihedral angle was incremented and the geometry was optimized at each stage. The heats of formation were reproducible to ±0.4 kJ/mol regardless of the increment (15° or 30°) or the starting dihedral angle (0° or 180°). MMX87.200 predicts the difference in energy between planar *s-trans*-1,3-butadiene and the planar *s-cis* conformer (calcd. 10.0 kJ/mol, obsd. 10.4 to 12.9 kJ (5,6)) and the barrier to rotation (calcd. 24.4 kJ/mol, obsd. 16.3 to 19.6 kJ (5,6)) with better accuracy than AM1 (3.4 and 9.0 kJ, respectively).

Can. J. Chem. Downloaded from www.nrcresearchpress.com by 196.1.178.254 on 09/07/12
For personal use only.

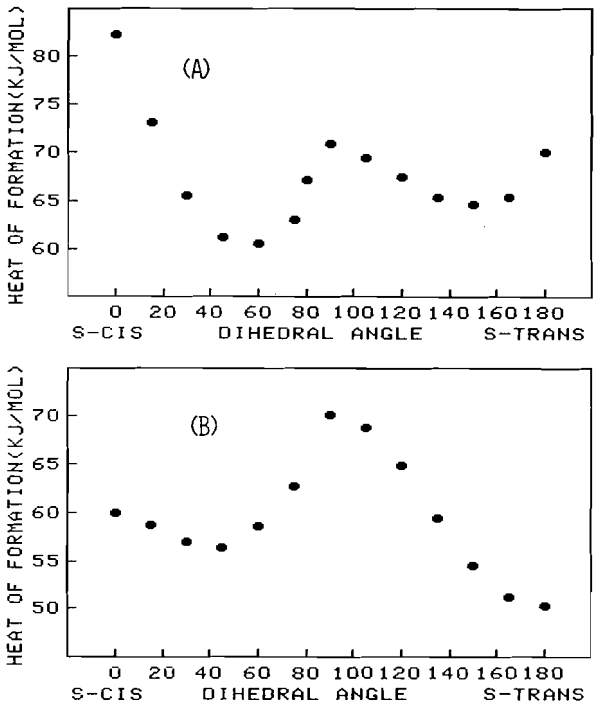

FIG. 1. Heat of formation (ΔH_f) as a function of C1—C2—C3—C4 dihedral angle: (*A*), **1***a*; (*B*), **1***b*.

Nevertheless, the pe spectrum of a sample of what supposedly was the (*Z*)-diene **1***a* obtained from Aldrich Chemical Co.,[6] did indeed exhibit bands at 8.42, 10.46, and 11.50 eV, identical within experimental error to the values for **1***a* and **1***b* reported by Mascalet and co-workers (1); however, the 500 MHz ^{1}H nmr spectrum of the major component of this commercial material[6] corresponded closely to the ^{1}H nmr spectrum of the (*E*)-diene. That the major component is, in fact, the (*E*)-isomer was established by the fact that it was photochemically isomerized to **1***a*, which turns out to be the *minor* component (~2%) of the commercial material.[6,7,8,9] Photoisomerization of (*E*)-dienes to (*Z*)-dienes is well documented in the literature (7). The correct pe spectra of the (*Z*)- and (*E*)-pentadienes **1***a* and **1***b* are given in Fig. 2(*A*) and 2(*B*), respectively. As expected (*vide supra*), the spectra are different; the MMX and AM1 predictions are supported by these experimental results. The difference between the maxima of the lowest ionization energy bands of **1***a* (8.65 ± 0.025 and 10.20 ± 0.025 eV) is 1.55 ± 0.05 eV. This splitting correlates well with the difference of 1.50 eV between the eigenvalues of π_- and π_+ calculated by AM1[10] for a *s-cis* conformer twisted by 40°. It should be pointed out that it is conceivable that MMX and AM1 overestimate the 1,3-CH_3,CH_3 steric interaction and underestimate the "resonance" stabilization; if this is the case, then twisted *s-trans* conformers would predominate. That the π_+, π_- splitting calculated by AM1 for a *s-trans* conformer twisted

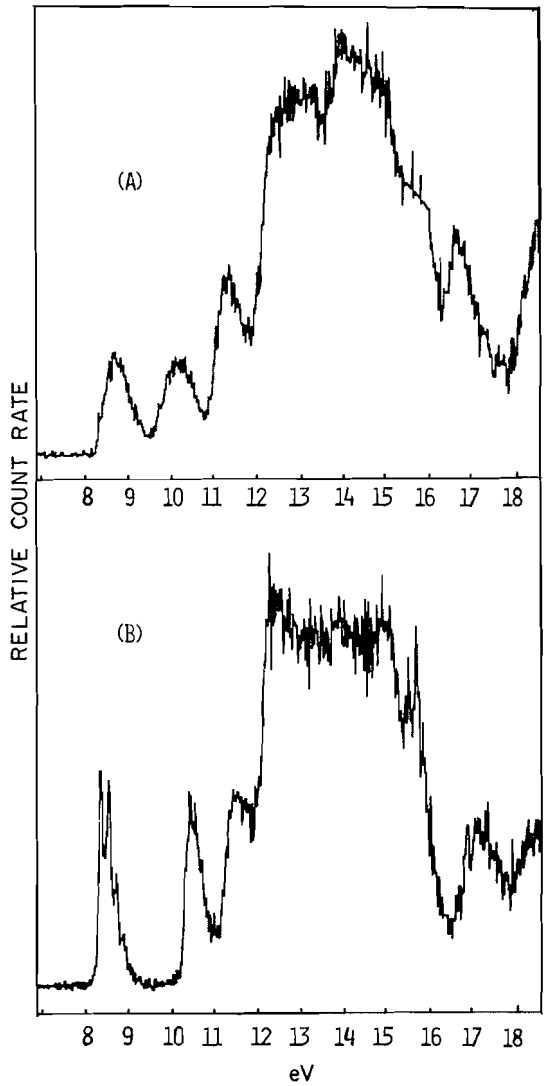

FIG. 2. Ultraviolet photoelectron spectra: (*A*), **1***a*; (*B*), **1***b*.

[6]The commercial sample was described as a mixture of 80% of (*Z*)-diene **1***a* and 20% of (*E*)-diene **1***b*. Analysis by gc at ambient temperature on a 1,2,3-tris (2-cyanoethoxy)propane (TCEP) column, known to be especially useful for separating alkenes, established that three components with relative retention times of 1:1.40:1.55 were present in a ratio of 1:39:10. The major components were isolated by preparative gc on a TECP column. High-field ^{1}H nmr spectroscopy along with analytical gc analysis on the TCEP column established that the dienes were >95% pure.

[7]The commercial sample was dissolved in pentane (0.1 *M*), containing acetophenone (0.01 *M*), the solution was degassed with nitrogen and photolyzed at 300 nm in a Rayonet reactor. After 9 h, the ratio of the areas of the three peaks corresponding to the starting components[4] was 1:1.84:0.87. The dienes were isolated by preparative gc on a TCEP column and shown to be >95% pure by analytical gc using a TCEP column and by high-field ^{1}H nmr. The component of lowest retention time is the (*Z*)-diene **1***a*. The component of longest retention time which was supposedly the (*E*)-diene was identified as 4-methyl-1, 3-pentadiene by its mass spectrum, its 500 MHz ^{1}H nmr spectrum, and by its pe spectrum. The component of intermediate retention time is **1***b*.

[8]We thank Dr. W. Leigh for suggesting photochemical isomerization of **1***b* as a route to **1***a*.

[9]We have notified Aldrich Chemical Co. of our findings.

[10]AM1 accurately predicts the splittings for planar *s-trans* dienes. The splittings (2.35, 2.53, 2.46, and 2.43 eV) calculated for (*Z*),(*Z*)-2,4-hexadiene, (*E*),(*E*)-2,4-hexadiene, (*E*),(*Z*)-2,4-hexadiene, and 2,5-dimethyl-2,4-hexadiene which are *s-trans* and planar, correlate very well with the experimental values (2.35, 2.47, 2.42, 2.46 eV) (1).

by 40° is similar to the splitting for the *s-cis* conformer twisted by 40° indicates that this possibility must be considered and eventually excluded. However, we presently favour our initial interpretation because MMX accurately predicts the barrier to rotation and the difference in energy between the planar *s-trans* and *s-cis* conformers of butadiene.[3] The π_-, π_+ ionization energy bands of **1***a* are broad, unlike the corresponding bands of **1***b*; this is in keeping with our view that a wider range of conformers (twisted *s-cis* and twisted *s-trans*) are populated at ambient temperature for **1***a* than for **1***b* as predicted by MMX and AM1. AM1 predicts a splitting of 2.14 eV for planar *s-trans*-**1***a*. A π_-, π_+ splitting of 2.04 eV for the (*E*)-isomer which turns out to be the major component of the commercial material is consistent with a planar *s-trans* structure; AM1 predicts a splitting of 2.09 eV for this conformer.

We will report on other examples of the application of UPS-AM1/MMX to the structure elucidation of alkyl-substituted dienes in the near future.

Acknowledgement

We thank the Natural Science and Engineering Research Council of Canada for financial support.

1. P. Masclet, G. Mouvier, and J. F. Bocquet. J. Chim. Phys. **78**, 99 (1981).
2. Dewar Research Group and J. P. Stewart. QCPE Bull. **6**, 2 (1986).
3. J. J. Fisher and J. Michl. J. Am. Chem. Soc. **109**, 1056 (1987).
4. M. E. Squillacote, T. C. Semple, and P. W. Mui. J. Am. Chem. Soc. **107**, 6842 (1985).
5. M. E. Squillacote, R. S. Sheridan, O. L. Chapman, and F. A. L. Anet. J. Am. Chem. Soc. **101**, 3657 (1979) and references therein.
6. P. W. Mui and E. Grundwald. J. Am. Chem. Soc. **104**, 6562 (1982).
7. J. Saltiel and J. L. Charlton. *In* Rearrangements in ground and excited states. *Edited by* P. De Mayo. Academic Press. New York. Vols. 3, 25, and references cited therein.

Can. J. Chem. Downloaded from www.nrcresearchpress.com by 196.1.178.254 on 09/07/12
For personal use only.

Selenium coronands. A novel conformational pair

B. Mario Pinto,[1] Blair D. Johnston, Raymond J. Batchelor, Frederick W. B. Einstein,[1] and Ian D. Gay[1]

Department of Chemistry, Simon Fraser University, Burnaby, B.C., Canada V5A 1S6

Received March 31, 1988

B. Mario Pinto, Blair D. Johnston, Raymond J. Batchelor, Frederick W. B. Einstein, and Ian D. Gay. Can. J. Chem. **66**, 2956 (1988).

The synthesis and characterization of the novel selenium coronands, 1,3,7,9-tetraselenacyclododecane **1***a*, 1,3,7,9,13,15-hexaselenacyclooctadecane **2***a*, the corresponding β-*gem*-dimethyl derivatives **1***b*, **2***b*, and 1,5,9,13-tetraselenacyclohexadecane **3**, and 1,5,9,13,17,21-hexaselenacyclotetracosane **4** are described. X-ray crystallographic analysis of **1***a* reveals three independent molecules that exist in two distinct conformations, one molecule having approximate two-fold symmetry together with two molecules (of similar conformation) each having crystallographic $\bar{1}$ symmetry. The conformations are denoted as [3333] or [66]. Whereas one resembles that of cyclododecane and tetrathia-12-crown-4 with respect to torsion angles, the other resembles that of tetraoxa-12-crown-4. The solid state CP-MAS ^{77}Se and ^{13}C nmr spectra are interpreted in light of the crystallographic information. Crystal structure: formula $Se_4C_8H_{16}$; fw = 428.05; monoclinic, $P2_1/c$; $Z = 8$; $a = 15.823(2)$ Å, $b = 5.534(1)$ Å, $c = 27.962(5)$ Å, $\beta = 92.26(1)°$; $V = 2446.6$ Å^3; $T = 200$ K; $R = 0.027$ for 2162 observed data ($I \geq 2.5\sigma(I)$).

B. Mario Pinto, Blair D. Johnston, Raymond J. Batchelor, Frederick W. B. Einstein et Ian D. Gay. Can. J. Chem. **66**, 2956 (1988).

On décrit la synthèse et la caractérisation de nouveaux coronands du sélénium, le tétraséléna-1,3,7,9 cyclododécane, **1***a*, l'hexaséléna-1,3,7,9,13,15 cyclooctadécane, **2***a*, et les dérivés correspondants portant des groupements *gem*-diméthyles en β, **1***b* et **2***b*, ainsi que le tétraséléna-1,5,9,13 cyclohexadécane, **3**, et l'hexaséléna-1,5,9,13,17,21 cyclotétracosane, **4**. Une analyse cristallographique à l'aide de rayons-X effectuée sur le composé **1***a* révèle que trois molécules indépendantes existent sous deux conformations distinctes, l'une possédant une symétrie approximativement binaire alors que les deux autres (de conformation semblable) possèdent une symétrie cristallographique de $\bar{1}$. On dénote les conformations par [3333] ou [66]. Alors que, par rapport aux angles de torsion, l'une ressemble à celle du cyclododécane et du tétrathia-12-couronne-4, l'autre ressemble à celle de la tétraoxa-12-couronne-4. A la lumière des informations cristallographiques, on peut facilement interpréter les spectres rmn CP-MAS à l'état solide du ^{77}Se et du ^{13}C. Structure cristalline: formule $Se_4C_8H_{16}$; MF = 428,05; monoclinique, $P2_1/c$; $Z = 8$; $a = 15,823(2)$ Å, $b = 5,534(1)$ Å, $c = 27,962(5)$ Å, $\beta = 92,26(1)°$; $V = 2446,6$ Å^3; $T = 200$ K; $R = 0,027$ pour 2162 données observées avec $I \geq 2.5\sigma(I)$.

[Traduit par la revue]

The study of synthetic ionophores such as crown ethers, coronands, cryptands, and podands is of current interest (1), both from a structural viewpoint as well as a means of modelling the more complex natural host–guest complexes present in antibiotics and membrane transport systems. While macrocyclic polyoxaethers (the crown ethers) have been extensively studied, and investigation of the corresponding polythiaethers is also well documented (2), extension of this type of chemistry to the corresponding third-row analogues is virtually unknown.[2] We now

[1]Authors to whom correspondence may be addressed.

[2]The only large ring selenides reported to date are cyclic oligomers of selenaformaldehyde (3), diselenacyclophanes (4), and a selenium porphyrin derivative (5).

by 40° is similar to the splitting for the *s-cis* conformer twisted by 40° indicates that this possibility must be considered and eventually excluded. However, we presently favour our initial interpretation because MMX accurately predicts the barrier to rotation and the difference in energy between the planar *s-trans* and *s-cis* conformers of butadiene.[3] The π_-, π_+ ionization energy bands of **1***a* are broad, unlike the corresponding bands of **1***b*; this is in keeping with our view that a wider range of conformers (twisted *s-cis* and twisted *s-trans*) are populated at ambient temperature for **1***a* than for **1***b* as predicted by MMX and AM1. AM1 predicts a splitting of 2.14 eV for planar *s-trans*-**1***a*. A π_-, π_+ splitting of 2.04 eV for the (*E*)-isomer which turns out to be the major component of the commercial material is consistent with a planar *s-trans* structure; AM1 predicts a splitting of 2.09 eV for this conformer.

We will report on other examples of the application of UPS-AM1/MMX to the structure elucidation of alkyl-substituted dienes in the near future.

Acknowledgement

We thank the Natural Science and Engineering Research Council of Canada for financial support.

1. P. Masclet, G. Mouvier, and J. F. Bocquet. J. Chim. Phys. **78**, 99 (1981).
2. Dewar Research Group and J. P. Stewart. QCPE Bull. **6**, 2 (1986).
3. J. J. Fisher and J. Michl. J. Am. Chem. Soc. **109**, 1056 (1987).
4. M. E. Squillacote, T. C. Semple, and P. W. Mui. J. Am. Chem. Soc. **107**, 6842 (1985).
5. M. E. Squillacote, R. S. Sheridan, O. L. Chapman, and F. A. L. Anet. J. Am. Chem. Soc. **101**, 3657 (1979) and references therein.
6. P. W. Mui and E. Grundwald. J. Am. Chem. Soc. **104**, 6562 (1982).
7. J. Saltiel and J. L. Charlton. *In* Rearrangements in ground and excited states. *Edited by* P. De Mayo. Academic Press. New York. Vols. 3, 25, and references cited therein.

Can. J. Chem. Downloaded from www.nrcresearchpress.com by 196.1.178.254 on 09/07/12
For personal use only.

Selenium coronands. A novel conformational pair

B. Mario Pinto,[1] Blair D. Johnston, Raymond J. Batchelor, Frederick W. B. Einstein,[1] and Ian D. Gay[1]

Department of Chemistry, Simon Fraser University, Burnaby, B.C., Canada V5A 1S6

Received March 31, 1988

B. Mario Pinto, Blair D. Johnston, Raymond J. Batchelor, Frederick W. B. Einstein, and Ian D. Gay. Can. J. Chem. **66**, 2956 (1988).

The synthesis and characterization of the novel selenium coronands, 1,3,7,9-tetraselenacyclododecane **1***a*, 1,3,7,9,13,15-hexaselenacyclooctadecane **2***a*, the corresponding β-*gem*-dimethyl derivatives **1***b*, **2***b*, and 1,5,9,13-tetraselenacyclohexadecane **3**, and 1,5,9,13,17,21-hexaselenacyclotetracosane **4** are described. X-ray crystallographic analysis of **1***a* reveals three independent molecules that exist in two distinct conformations, one molecule having approximate two-fold symmetry together with two molecules (of similar conformation) each having crystallographic $\bar{1}$ symmetry. The conformations are denoted as [3333] or [66]. Whereas one resembles that of cyclododecane and tetrathia-12-crown-4 with respect to torsion angles, the other resembles that of tetraoxa-12-crown-4. The solid state CP-MAS ^{77}Se and ^{13}C nmr spectra are interpreted in light of the crystallographic information. Crystal structure: formula $Se_4C_8H_{16}$; fw = 428.05; monoclinic, $P2_1/c$; $Z = 8$; $a = 15.823(2)$ Å, $b = 5.534(1)$ Å, $c = 27.962(5)$ Å, $\beta = 92.26(1)°$; $V = 2446.6$ Å^3; $T = 200$ K; $R = 0.027$ for 2162 observed data ($I \geq 2.5\sigma(I)$).

B. Mario Pinto, Blair D. Johnston, Raymond J. Batchelor, Frederick W. B. Einstein et Ian D. Gay. Can. J. Chem. **66**, 2956 (1988).

On décrit la synthèse et la caractérisation de nouveaux coronands du sélénium, le tétraséléna-1,3,7,9 cyclododécane, **1***a*, l'hexaséléna-1,3,7,9,13,15 cyclooctadécane, **2***a*, et les dérivés correspondants portant des groupements *gem*-diméthyles en β, **1***b* et **2***b*, ainsi que le tétraséléna-1,5,9,13 cyclohexadécane, **3**, et l'hexaséléna-1,5,9,13,17,21 cyclotétracosane, **4**. Une analyse cristallographique à l'aide de rayons-X effectuée sur le composé **1***a* révèle que trois molécules indépendantes existent sous deux conformations distinctes, l'une possédant une symétrie approximativement binaire alors que les deux autres (de conformation semblable) possèdent une symétrie cristallographique de $\bar{1}$. On dénote les conformations par [3333] ou [66]. Alors que, par rapport aux angles de torsion, l'une ressemble à celle du cyclododécane et du tétrathia-12-couronne-4, l'autre ressemble à celle de la tétraoxa-12-couronne-4. A la lumière des informations cristallographiques, on peut facilement interpréter les spectres rmn CP-MAS à l'état solide du ^{77}Se et du ^{13}C. Structure cristalline: formule $Se_4C_8H_{16}$; MF = 428,05; monoclinique, $P2_1/c$; $Z = 8$; $a = 15,823(2)$ Å, $b = 5,534(1)$ Å, $c = 27,962(5)$ Å, $\beta = 92,26(1)°$; $V = 2446,6$ Å^3; $T = 200$ K; $R = 0,027$ pour 2162 données observées avec $I \geq 2.5\sigma(I)$.

[Traduit par la revue]

The study of synthetic ionophores such as crown ethers, coronands, cryptands, and podands is of current interest (1), both from a structural viewpoint as well as a means of modelling the more complex natural host–guest complexes present in antibiotics and membrane transport systems. While macrocyclic polyoxaethers (the crown ethers) have been extensively studied, and investigation of the corresponding polythiaethers is also well documented (2), extension of this type of chemistry to the corresponding third-row analogues is virtually unknown.[2] We now

[1]Authors to whom correspondence may be addressed.

[2]The only large ring selenides reported to date are cyclic oligomers of selenaformaldehyde (3), diselenacyclophanes (4), and a selenium porphyrin derivative (5).

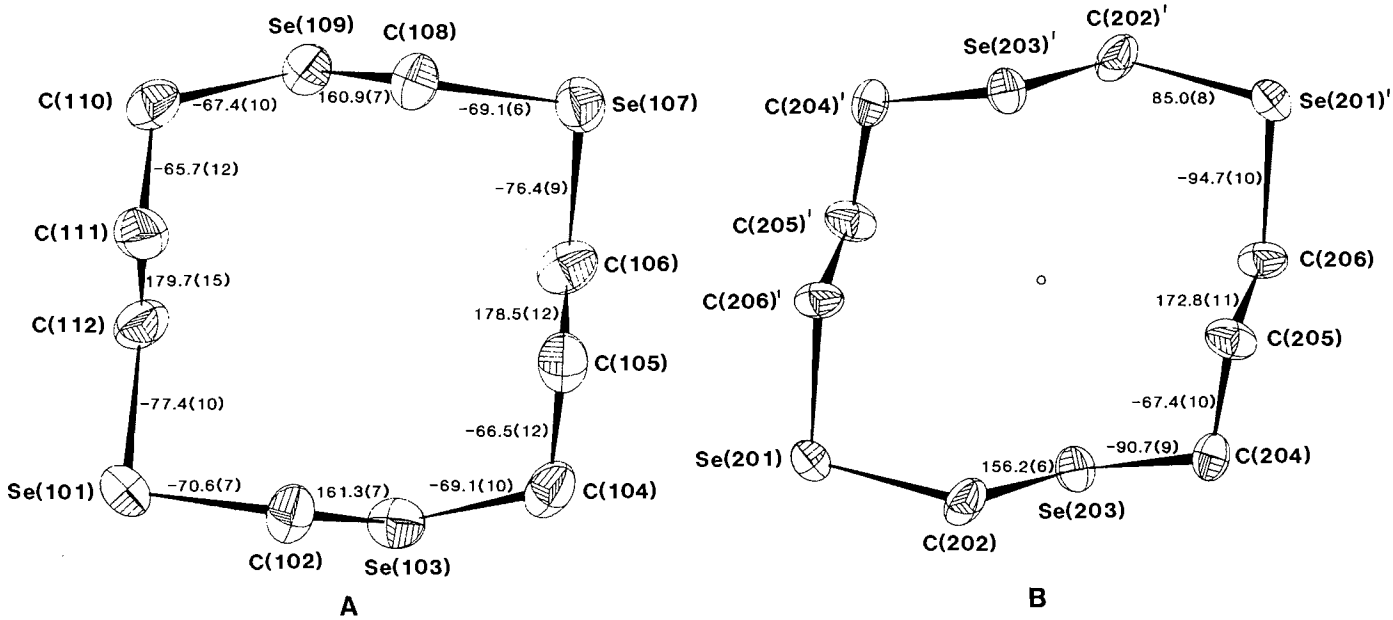

FIG. 1. Thermal ellipsoid (50% probability) drawings of rings A (left) and B (right) of **1***a* each projected on its molecular plane. The torsion angles (deg) about each bond are shown.

report the first examples of a novel class of selenium coronands, namely, 1,3,7,9-tetraselenacyclododecane **1***a*, 1,3,7,9,13,15-hexaselenacyclooctadecane **2***a*, the corresponding *gem*-dimethyl derivatives **1***b* and **2***b*, and 1,5,9,13-tetraselenacyclohexadecane **3**, and 1,5,9,13,17,21-hexaselenacyclotetracosane **4**.

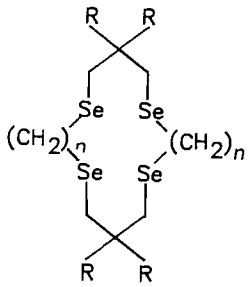

1*a* $n = 1$, R = H
1*b* $n = 1$, R = Me
3 $n = 3$, R = H

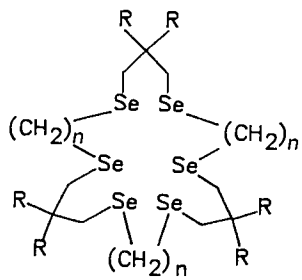

2*a* $n = 1$, R = H
2*b* $n = 1$, R = Me
4 $n = 3$, R = H

Reaction of propane-1,3-bisselenolate **5** in liquid ammonia and THF with dibromomethane gave, in addition to 1,3-diselenane (10%), **1***a* (10%), and **2***a* (5%) as colorless solids, and similar treatment of 2,2-dimethylpropane-1,3-bisselenolate yielded crystalline **1***b* and **2***b*.[3] Extension of this approach to the preparation of coronands containing only three-carbon bridges was more successful.[4] Thus, treatment of **5** with 1,3-dibromopropane afforded, in one step, **3** (40%), **4** (15%), and 1,5-diselenacyclooctane **6** (17%).[3] The structures of **1**–**4** were deduced by mass spectrometry and by ^1H and ^{13}C nmr spectroscopy.[3,5]

Selenium coronands **1**–**4**, in addition to their potential as agents for complexing transition metals,[6] are interesting candidates for conformational analysis.[7] By way of example, we present herein the conformational analysis of **1***a* in the solid state. It is noteworthy that the solid state conformations of sulfur coronands show significant differences from those of their oxygen counterparts (7).

Interestingly, the structure of **1***a*[8] contains three crystallographically independent molecules that exist in two distinct conformations. Whereas ring A has no crystallographic symmetry but has an approximate two-fold axis normal to the molecular plane, rings B and C lie on centres of inversion and have similar conformations. Figure 1 illustrates the different ring types. Ring A has corners formed by two consecutive *gauche* torsion angles of the same sign as in cyclododecane (8) and 1,4,7,10-tetrathia-12-crown-4 **7** (7), and can be denoted as [3333] in Dale's notation (9). In contrast, ring B (and C) has two such torsional sequences at opposite corners (with C as the pivotal atom) while the remaining corners (with Se as the pivotal atom) are formed by consecutive *gauche* torsion angles of opposite sign as in 1,4,7,10-tetraoxa-12-crown-4 **8** (10), and is denoted as [66] in Dale's notation (9). An additional feature of interest in the conformations of **1***a* is the location of the selenium atoms at both side and corner positions of the quadrilateral. In contrast, the oxygen analog, 1,3,7,9-tetraoxacyclododecane, has been shown

[3]A complete set of data may be purchased from the Depository of Unpublished Data, CISTI, National Research Council of Canada, Ottawa, Ont., Canada K1A 0S2.

[4]Similar attempts to synthesize two-carbon bridged analogues were totally unsuccessful, the reactions being complicated by the extrusion of ethylene.

[5]All compounds gave satisfactory combustion microanalysis (C, H) data. The actual structures were confirmed by simulation of the isotopic clusters for parent ions in the isobutane CI mass spectra.

[6]For the preparation of acyclic oligoselena ethers and their complexes with transition metals, see ref. 6.

[7]**1** and **2** contain an additional conformational feature of interest, the Se—CH_2—Se anomeric effect (Pinto *et al.* (13)).

[8]$Se_4C_8H_{16}$; monoclinic, $P2_1/c$; $T = 200$ K; $a = 15.823(2)$ Å, $b = 5.534(1)$ Å, $c = 27.962(5)$ Å, $\beta = 92.26(1)°$; $Z = 8$; $\rho_c = 2.324$ g cm^{-3}; $\lambda = 0.71069$ Å; μ(Mo K_α) = 118.3 cm^{-1}; Crystal size 0.21 × 0.48 × 0.11 mm; Transmission 0.075–0.330, corrected analytically; 2θ: 2–48°; Data $I \geq 2.5\sigma(I)$, 2162. Refined parameters, 313; $R = \Sigma||F_o|-|F_c||/\Sigma|F_o| = 0.027$; max. |shift/error| 0.08 (non-hydrogen variables); bond distances: Se—C 1.935(10)–1.974(11) Å, C—C 1.479(15)–1.536(15) Å; average bond angles: C—Se—C 98.0°, Se—C—Se 111.1°, C—C—Se 113.7°, C—C—C 112.6°.

Can. J. Chem. Downloaded from www.nrcresearchpress.com by 196.1.178.254 on 09/07/12
For personal use only.

by nmr spectroscopy to exist in solution preferentially in a [3333] conformation with the oxygen atoms occupying side positions across corners (11). The preference of the selenium atoms for the corner positions in **1***a* is similar to that of the sulfur atoms in **7** but contrasts with the preference of oxygen for the side positions in **8**.

The asymmetric unit of **1***a* is comprised of 8 Se and 16 C atoms. The solid state CP-MAS ^{77}Se nmr spectrum[3] consists of six resolved resonances (δ 209–130) of relative intensity 1:1:1:2:1:2, some of which exhibit Se–Se coupling. The linewidth of the peak at highest field is such that the individual unresolved resonances must be of considerably larger linewidth than the others. We note that Se(101) and Se(107) show the largest thermal motion, and assign the highest field peak to these atoms (12). The solid state CP-MAS ^{13}C nmr spectrum of **1***a*[3] is also consistent with the proposed structure. The resonances at δ 19.8, 17.6, and 11.2, of intensities 1:1:2, are assigned to the carbons of the four independent Se—CH_2—Se units. The high-field shifts appear to be characteristic of this structural unit (13). Structurally, each of these four atoms has one *gauche* and one *anti* Se—C*—Se—C arrangement, the atoms being distinguished by differences in the torsion angles. The angles for C*(102) and C*(108) are not significantly different, suggesting the assignment of the peak at δ 11.2 to these atoms. Finally, we note the implications of the magnitudes of the *gauche* torsion angles and the carbon chemical shifts in Se—C—Se units for the study of selenium anomeric interactions.

Acknowledgement

We thank the Natural Sciences and Engineering Research Council of Canada for financial support.

1. E. VOGTLE (*Editor*). Top. Curr. Chem. Host Guest Complex Chemistry I, **98** (1981); II, **101** (1982); III, **121** (1984). Springer-Verlag, Berlin; E. VOGTLE and E. WEBER (*Editors*). Host–guest complex chemistry — macrocycles — synthesis, structures, applications. Springer-Verlag, Berlin. 1985.
2. A. J. BLAKE, R. O. GOULD, A. J. LAVERY, and M. SCHRODER. Angew. Chem. Int. Ed. Engl. **25**, 274 (1986); I. R. YOUNG, L. A. OCHRYMOWYCZ, and D. B. RORABACHER. Inorg. Chem. **25**, 2576 (1986); L. L. DIADDARIO, JR., E. R. DOCKAL, M. D. GLICK, L. A. OCHRYMOWYCZ, and D. B. RORABACHER. Inorg. Chem. **24**, 356 (1985); V. B. PETT, L. L. DIADDARIO, JR., E. R. DOCKAL, P. W. CORFIELD, C. CECCARELLI, M. D. GLICK, L. A. OCHRYMOWYCZ, and D. B. RORABACHER. Inorg. Chem. **22**, 3661 (1983); P. W. R. CORFIELD, C. CECCARELLI, M. D. GLICK, I. WEI-YU MOY, L. A. OCHRYMOWYCZ, and D. B. RORABACHER. J. Am. Chem. Soc. **107**, 2399 (1985); S. C. RAWLE and S. R. COOPER. J. Chem. Soc. Chem. Commun. 308 (1987); S. C. RAWLE, J. R. HARTMAN, D. J. WATKIN, and S. R. COOPER. J. Chem. Soc. Chem. Commun. 1083 (1986); J. R. HARTMAN, E. J. HINTSA, and S. R. COOPER. J. Chem. Soc. Chem. Commun. 386 (1984); E. J. HINTSA, J. R. HARTMAN, and S. R. COOPER. J. Am. Chem. Soc. **105**, 3738 (1983); J. R. HARTMAN and S. R. COOPER. J. Am. Chem. Soc. **108**, 1202 (1986); J. R. HARTMAN, E. J. HINTSA, and S. R. COOPER. J. Am. Chem. Soc. **108**, 1208 (1986).
3. V. E. WEISSFLOG. Z. Anorg. Allg. Chem. **488**, 60 (1982).
4. H. HIGUCHI and S. MISUMI. Tetrahedron Lett. **23**, 5571 (1982); H. HIGUCHI, K. TANA, T. OTSUBO, Y. SAKATA, and S. MISUMI. Bull. Chem. Soc. Jpn. **60**, 4027 (1987); R. H. MITCHELL. Can. J. Chem. **58**, 1398 (1980); R. H. MITCHELL, K. S. WEERAWARNA, and G. W. BUSHNELL. Tetrahedron lett. **28**, 5119 (1987).
5. A. ULMAM, J. MANASSEN, F. FROLOW, and D. RABINOVICH. Tetrahedron Lett. 167 (1978).
6. D. J. GULLIVER, E. G. HOPE, W. LEVASON, S. G. MURRAY, D. M. POTTER, and G. L. MARSHALL. J. Chem. Soc. Perkin Trans. II. 429 (1984) and references therein; E. G. HOPE, W. LEVASON, S. G. MURRAY, and G. L. MARSHALL. J. Chem. Soc. Dalton Trans. 2185 (1985).
7. R. E. WOLF, JR., J. R. HARTMAN, J. M. E. STOREY, B. M. FOXMAN, and S. R. COOPER. J. Am. Chem. Soc. **109**, 4328 (1987).
8. J. D. DUNITZ and H. M. M. SHEARER. Helv. Chim. Acta, **43**, 18 (1960).
9. J. DALE. Isr. J. Chem. **20**, 3 (1980).
10. P. GROTH. Acta Chem. Scand. A**32**, 279 (1978).
11. G. BORGEN and J. DALE. J. Chem. Soc. Chem. Commun. 484 (1974).
12. D. SUWELACK, W. P. ROTHWELL, and J. S. WAUGH. J. Chem. Phys. **73**, 2559 (1980).
13. B. M. PINTO, B. D. JOHNSTON, and R. NAGELKERKE. Heterocycles. In press.

Can. J. Chem. Downloaded from www.nrcresearchpress.com by 196.1.178.254 on 09/07/12
For personal use only.

A study of thermodynamic acidities of carbon acids by AM1

NICK HENRY WERSTIUK
Department of Chemistry, McMaster University, Hamilton, Ont., Canada L8S 4M1

Received May 17, 1988

NICK HENRY WERSTIUK. Can. J. Chem. **66**, 2958 (1988).

Monocyclic carbon acids **1–8** have been studied by the semiempirical computational method AM1 in an attempt to develop a methodology for estimating p*K*s. The results indicate that there is a good correlation between $[\Delta H_f(R^-) - \Delta H_f(R\text{-}H)]$ obtained computationally and the p*K*s measured in DMSO. The p*K*s of **9***a*, **9***b*, **10**, **11** (tetronic acid), and the dioxolane dione **12** are predicted on the basis of this correlation.

NICK HENRY WERSTIUK. Can. J. Chem. **66**, 2958 (1988).

Dans le but de développer une méthodologie appropriée à l'évaluation des p*K*, on a utilisé la méthode de calculs semi-empiriques AM1 pour étudier les acides carboniques monocycliques **1–8**. Les résultats indiquent qu'il existe une bonne corrélation entre la valeur $[\Delta H_f(R^-) - \Delta H_f(R\text{-}H)]$ obtenue par calculs et les valeurs de p*K* mesurés dans le DMSO. Utilisant cette corrélation, on a pu prédire correctement les valeurs des p*K* des composés **9***a*, **9***b*, **10**, **11** (acide tétronique) ainsi que de la dioxolanedione **12**.

[Traduit par la revue]

by nmr spectroscopy to exist in solution preferentially in a [3333] conformation with the oxygen atoms occupying side positions across corners (11). The preference of the selenium atoms for the corner positions in **1***a* is similar to that of the sulfur atoms in **7** but contrasts with the preference of oxygen for the side positions in **8**.

The asymmetric unit of **1***a* is comprised of 8 Se and 16 C atoms. The solid state CP-MAS ^{77}Se nmr spectrum[3] consists of six resolved resonances (δ 209–130) of relative intensity 1:1:1:2:1:2, some of which exhibit Se–Se coupling. The linewidth of the peak at highest field is such that the individual unresolved resonances must be of considerably larger linewidth than the others. We note that Se(101) and Se(107) show the largest thermal motion, and assign the highest field peak to these atoms (12). The solid state CP-MAS ^{13}C nmr spectrum of **1***a*[3] is also consistent with the proposed structure. The resonances at δ 19.8, 17.6, and 11.2, of intensities 1:1:2, are assigned to the carbons of the four independent Se—CH_2—Se units. The high-field shifts appear to be characteristic of this structural unit (13). Structurally, each of these four atoms has one *gauche* and one *anti* Se—C*—Se—C arrangement, the atoms being distinguished by differences in the torsion angles. The angles for C*(102) and C*(108) are not significantly different, suggesting the assignment of the peak at δ 11.2 to these atoms. Finally, we note the implications of the magnitudes of the *gauche* torsion angles and the carbon chemical shifts in Se—C—Se units for the study of selenium anomeric interactions.

Acknowledgement

We thank the Natural Sciences and Engineering Research Council of Canada for financial support.

1. E. VOGTLE (*Editor*). Top. Curr. Chem. Host Guest Complex Chemistry I, **98** (1981); II, **101** (1982); III, **121** (1984). Springer-Verlag, Berlin; E. VOGTLE and E. WEBER (*Editors*). Host–guest complex chemistry — macrocycles — synthesis, structures, applications. Springer-Verlag, Berlin. 1985.
2. A. J. BLAKE, R. O. GOULD, A. J. LAVERY, and M. SCHRODER. Angew. Chem. Int. Ed. Engl. **25**, 274 (1986); I. R. YOUNG, L. A. OCHRYMOWYCZ, and D. B. RORABACHER. Inorg. Chem. **25**, 2576 (1986); L. L. DIADDARIO, JR., E. R. DOCKAL, M. D. GLICK, L. A. OCHRYMOWYCZ, and D. B. RORABACHER. Inorg. Chem. **24**, 356 (1985); V. B. PETT, L. L. DIADDARIO, JR., E. R. DOCKAL, P. W. CORFIELD, C. CECCARELLI, M. D. GLICK, L. A. OCHRYMOWYCZ, and D. B. RORABACHER. Inorg. Chem. **22**, 3661 (1983); P. W. R. CORFIELD, C. CECCARELLI, M. D. GLICK, I. WEI-YU MOY, L. A. OCHRYMOWYCZ, and D. B. RORABACHER. J. Am. Chem. Soc. **107**, 2399 (1985); S. C. RAWLE and S. R. COOPER. J. Chem. Soc. Chem. Commun. 308 (1987); S. C. RAWLE, J. R. HARTMAN, D. J. WATKIN, and S. R. COOPER. J. Chem. Soc. Chem. Commun. 1083 (1986); J. R. HARTMAN, E. J. HINTSA, and S. R. COOPER. J. Chem. Soc. Chem. Commun. 386 (1984); E. J. HINTSA, J. R. HARTMAN, and S. R. COOPER. J. Am. Chem. Soc. **105**, 3738 (1983); J. R. HARTMAN and S. R. COOPER. J. Am. Chem. Soc. **108**, 1202 (1986); J. R. HARTMAN, E. J. HINTSA, and S. R. COOPER. J. Am. Chem. Soc. **108**, 1208 (1986).
3. V. E. WEISSFLOG. Z. Anorg. Allg. Chem. **488**, 60 (1982).
4. H. HIGUCHI and S. MISUMI. Tetrahedron Lett. **23**, 5571 (1982); H. HIGUCHI, K. TANA, T. OTSUBO, Y. SAKATA, and S. MISUMI. Bull. Chem. Soc. Jpn. **60**, 4027 (1987); R. H. MITCHELL. Can. J. Chem. **58**, 1398 (1980); R. H. MITCHELL, K. S. WEERAWARNA, and G. W. BUSHNELL. Tetrahedron lett. **28**, 5119 (1987).
5. A. ULMAM, J. MANASSEN, F. FROLOW, and D. RABINOVICH. Tetrahedron Lett. 167 (1978).
6. D. J. GULLIVER, E. G. HOPE, W. LEVASON, S. G. MURRAY, D. M. POTTER, and G. L. MARSHALL. J. Chem. Soc. Perkin Trans. II. 429 (1984) and references therein; E. G. HOPE, W. LEVASON, S. G. MURRAY, and G. L. MARSHALL. J. Chem. Soc. Dalton Trans. 2185 (1985).
7. R. E. WOLF, JR., J. R. HARTMAN, J. M. E. STOREY, B. M. FOXMAN, and S. R. COOPER. J. Am. Chem. Soc. **109**, 4328 (1987).
8. J. D. DUNITZ and H. M. M. SHEARER. Helv. Chim. Acta, **43**, 18 (1960).
9. J. DALE. Isr. J. Chem. **20**, 3 (1980).
10. P. GROTH. Acta Chem. Scand. A**32**, 279 (1978).
11. G. BORGEN and J. DALE. J. Chem. Soc. Chem. Commun. 484 (1974).
12. D. SUWELACK, W. P. ROTHWELL, and J. S. WAUGH. J. Chem. Phys. **73**, 2559 (1980).
13. B. M. PINTO, B. D. JOHNSTON, and R. NAGELKERKE. Heterocycles. In press.

Can. J. Chem. Downloaded from www.nrcresearchpress.com by 196.1.178.254 on 09/07/12
For personal use only.

A study of thermodynamic acidities of carbon acids by AM1

NICK HENRY WERSTIUK
Department of Chemistry, McMaster University, Hamilton, Ont., Canada L8S 4M1

Received May 17, 1988

NICK HENRY WERSTIUK. Can. J. Chem. **66**, 2958 (1988).

Monocyclic carbon acids **1–8** have been studied by the semiempirical computational method AM1 in an attempt to develop a methodology for estimating p*K*s. The results indicate that there is a good correlation between $[\Delta H_f(R^-) - \Delta H_f(R\text{-}H)]$ obtained computationally and the p*K*s measured in DMSO. The p*K*s of **9***a*, **9***b*, **10**, **11** (tetronic acid), and the dioxolane dione **12** are predicted on the basis of this correlation.

NICK HENRY WERSTIUK. Can. J. Chem. **66**, 2958 (1988).

Dans le but de développer une méthodologie appropriée à l'évaluation des p*K*, on a utilisé la méthode de calculs semi-empiriques AM1 pour étudier les acides carboniques monocycliques **1–8**. Les résultats indiquent qu'il existe une bonne corrélation entre la valeur $[\Delta H_f(R^-) - \Delta H_f(R\text{-}H)]$ obtenue par calculs et les valeurs de p*K* mesurés dans le DMSO. Utilisant cette corrélation, on a pu prédire correctement les valeurs des p*K* des composés **9***a*, **9***b*, **10**, **11** (acide tétronique) ainsi que de la dioxolanedione **12**.

[Traduit par la revue]

Can. J. Chem. Downloaded from www.nrcresearchpress.com by 196.1.178.254 on 09/07/12
For personal use only.

Our interest in the synthesis and homoenolization of monoketones and diketones has led to a number of significant contributions to the area of carbanion chemistry (1–7). For studies of this type, it would be useful to have an economical, easy-to-use, graphics-based computational methodology to probe the thermodynamic acidities of carbon acids. This would greatly facilitate the design of unusually acidic polycyclic multicarbonyl compounds and their thione analogues. A combination of the MM2-based molecular modelling packages MACROMODEL (8) and MODEL (9) and the semiempirical computational package AMPAC (10, 11) meets these requirements. MACROMODEL and MODEL provide an interactive graphics environment to generate good input geometries for optimizations using the AM1 or MNDO Hamiltonian of AMPAC; MODEL also has the facility to interconvert MODEL and MACROMODEL geometry files, to generate input files for AMPAC, and to read geometries from AM1/MNDO output files. In principle then, fairly large molecules can be studied with minimum effort at a reasonable cost. The pKs of a wide range of carbon acids are documented in the chemical literature. This communication reports the results of an AM1 study of a series of monocyclic compounds **1**–**13**; Meldrum's acid (MDA) (**1**), which exhibits an enhanced acidity, has been the subject of a number of studies recently (12–14).

The enthalpy change for ionization of a carbon acid in the gas phase (eq. [1]) is given by eqs. [2] and [3].

[1] $\mathrm{R{-}H \rightarrow R^- + H^+}$

[2] $\Delta H = [\Delta H_f(R^-) + \Delta H_f(H^+)] - \Delta H_f(\text{R-H})$

[3] $\Delta H = [\Delta H_f(R^-) - \Delta H_f(\text{R-H})] + \Delta H_f(H^+)$

If a series of structurally similar substrates are studied, then $[\Delta H_f(R^-) - \Delta H_f(\text{R-H})]$ and ΔH should correlate with the solution pK of R-H if the entropy of ionization in solution (ΔS_i) and the degree of ion-pairing remain essentially constant through the series. $\Delta H_f(R^-)$ and $\Delta H_f(\text{R-H})$ (Table 1) were obtained computationally using AM1,[1] and $\Delta H_f(H^+)$ was taken as 364.2 kcal/mol, the sum of one half the H_2 bond energy and the hydrogen atom ionization energy. Figure 1 shows a plot of ΔH versus pK for the series **1**–**8** measured in DMSO (12). The correlation, which spans nearly 20 pK units, establishes that this methodology may be useful generally for estimating thermodynamic acidities. The equation[2] for this line (—) is given in eq. [4]. While the pKs as a whole deviate from the

[4] $\Delta H = 1.75\ \mathrm{p}K + 315.0$

least-squares line, the correlation (----) involving the cyclic lactones **1** (MDA), **2**, **3**, **4**, and **5** is excellent.

Based on the correlation developed herein, bis-lactone **9***a*, the unsubstituted analogue of MDA that could not be prepared by Arnett and Harrelson (12), should exhibit a pK of 5.8. This result provides support for Arnett's analysis that the enhanced

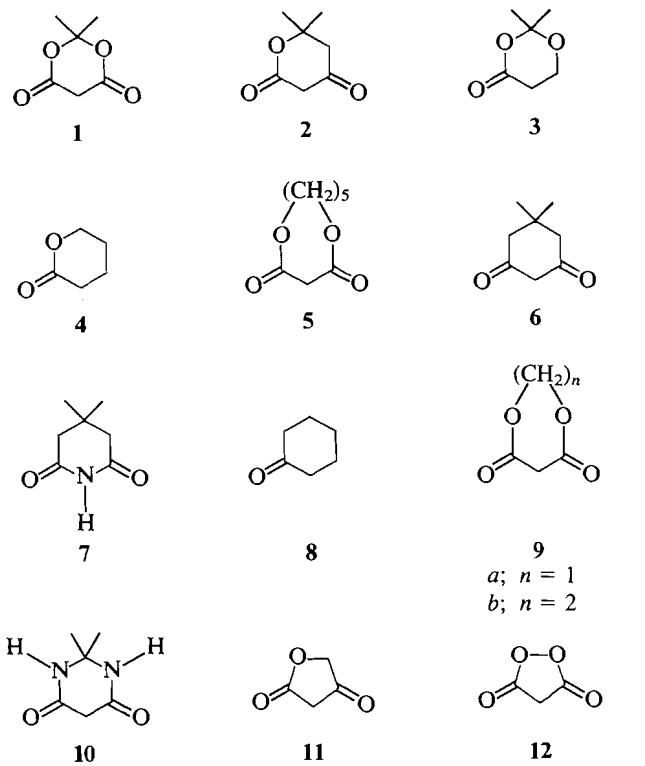

TABLE 1. Heats of formation (kcal/mol) and thermodynamic acidities

Substrate	$\Delta H_f(R^-)$	ΔH_f(R-H)	ΔH^a	pK^b obsd.	pK^b est.
1	−203.8	−166.4	326.8	7.32	
2	−159.8	−127.6	332.0	10.50	
3	−148.8	−136.6	352.1	23.25	
4	−104.8	−98.0	357.4	25.22	
5	−199.2	−170.9	335.9	12.99	
6	−120.6	−93.8	337.4	11.24	
7	−112.1	−97.3	349.3	17.28	
8	−63.9	−63.3	363.6	26.25	
9*a*	−200.2	−161.1	325.1	—	5.8
9*b*	−190.8	−155.0	328.5	—	7.7
10	−95.6	−73.9	342.5	—	15.7

[a] $\Delta H_f(H^+) = BE(H_2)/2 + IE(H\cdot)$.
[b] See ref. 12.

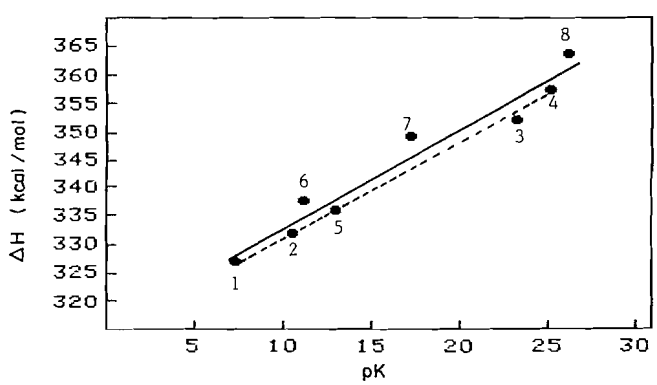

FIG. 1. Plot of ΔH versus pK of carbon acids **1**–**8**.

[1] All structures were generated using MACROMODEL and the geometries were optimized using the MM2 force field of this package. The MACROMODEL files were converted to MODEL files, which were used to generate the AMPAC input files. The geometries of the carbon acids and the corresponding anions were fully optimized using the AM1 Hamiltonian of AMPAC. All computations were carried out on a VAX 11/780 computer.

[2] The pK can be related to ΔG_i^0 ($\Delta G_i^0 = 2.303RT - (\mathrm{p}K + \log 14)$) according to the equation described by Arnett and Venkatasubramaniam (15).

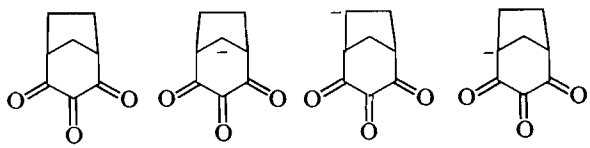

13

ΔH_f(kcal/mol)	−92.5	−90.2	−83.4	−84.9

FIG. 2. ΔH_f of **13** and isomeric anions.

acidity of MDA—the stablest conformation is the boat—is not due to buttressing of the axial hydrogen at C5 by the axial methyl at C2. Furthermore, the seven-membered bis-lactone **9***b*, which also could not be prepared by Arnett (12), is predicted to have a pK of 7.7 in DMSO. According to MM2 of MACROMODEL and AM1, the stablest structure of **9***b* is a boat conformation. Bis-amide **10**, the diaza analogue of MDA, is predicted to have a pK of 15.7.

Based on a study of cyclopentanone, cyclopentane-1,3-dione, 2-methylcyclopentane-1,3-dione, 2-oxotetrahydrofuran (γ-butyrolactone), and tetrahydrofuran-2,4-dione (tetronic acid) (**11**), **11** is predicted to be more acidic (estimated $pK^{DMSO} = 5$) than MDA.[3] The accuracy of this value is established by the relative acidities of MDA and **11** in aqueous solution; MDA exhibits a pK of 4.83 (12) and **11** exhibits a pK of 3.76 (17). It is noteworthy that replacement of a *single* methylene of cyclopentane-1,3-dione by an oxygen yields a stronger acid than MDA. Perhaps this is an indication that additional factors, other than those already proposed (12–14), are important in determining the acidity of multicarbonyl heterocycles such as MDA. According to AM1, 1,2-dioxolone-3,5-dione (**12**) should be unusually acidic and should exhibit a pK of approximately −1.5; in this case the anion may be aromatic.

The results of a study of the isomeric anions derived from bicyclo[3.2.1]octane-2,3,4-trione (**13**) illustrate the potential utility of this methodology for studying homoenolizations. According to AM1 (the ΔH_fs are shown in Fig. 2), **13** should homoenolize faster at C8 than at C7. In fact, based on $[\Delta H_f(R^-) - \Delta H_f(R\text{-}H)]$, the p$K$ of **13** at C8 should be ~30.

AM1 studies of other series of carbon acids including hydrocarbons are planned. Tetronic acid (**11**), **12**, and the corresponding anions will be studied at the *ab initio* level to accurately determine the electron populations (18, 19) and the σ and π densities (20).

[3]Cyclopentanone (ΔH, 365.3; pK^{DMSO} = 25.6 (15)) and cyclopentane-1,3-dione (ΔH, 339.9; pK^{DMSO} = 10 estimated from the pK of 2-methylcyclopentane-1,3-dione (16)) were used as reference points for a plot for the 5-membered ring compounds. These points define a line that is parallel to the plot for the 6-membered ring series, but the intercept (323.6 kcal) is displaced upward by 8.6 kcal from the intercept (315.0 kcal) for the 6-membered ring series. An initial study of 1-methylcyclohexene, 1-methylcyclopentene, 1-methylcyclobutene, and the corresponding exocyclic isomers indicates that AM1 overestimates the strain in endocyclic cycloalkenes as ring size decreases. The upward displacement of the plot may be due to a computational differential destabilization of the 5-membered ring enolates. Using an intercept of 323.6 and a slope of 1.75, the pKs of γ-butyrolactone (ΔH, 360.1), **11** (ΔH, 332.3), and **12** (ΔH, 320.9) are predicted to be 20.8, 5.0, and −1.5, respectively.

Acknowledgement

The author thanks the Natural Sciences and Engineering Research Council of Canada for financial support and Dr. M. Brook for assistance in running MACROMODEL and MODEL. We thank Professor Still for a copy of MACROMODEL and Professor Steliou for a copy of MODEL.

1. N. H. WERSTIUK. Can. J. Chem. **53**, 2211 (1975).
2. N. H. WERSTIUK, R. TAILLEFER, and S. BANERJEE. Can. J. Chem. **56**, 1148 (1978).
3. N. H. WERSTIUK and S. YEROUSHALMI. Can. J. Chem. **58**, 1601 (1980).
4. N. H. WERSTIUK and S. YEROUSHALMI. Can. J. Chem. **58**, 1603 (1980).
5. N. H. WERSTIUK, S. YEROUSHALMI, and G. TIMMINS. Can. J. Chem. **61**, 2403 (1983).
6. N. H. WERSTIUK and G. TIMMINS. Can. J. Chem. **63**, 526 (1985).
7. N. H. WERSTIUK, G. I. WADE, and P. J. J. MARTIN. Can. J. Chem. **63**, 2582 (1985).
8. W. C. STILL. MACROMODEL. 1.5. Department of Chemistry, Columbia University, New York, NY 10027, U.S.A.
9. W. C. STILL. MODEL. Columbia University. *Modified by* K. Steliou (Version 2.9). Départment de Chimie, Université de Montréal, C.P. 6128 Succursale A, Montréal (Qué.), Canada H3C 3J7.
10. M. J. S. DEWAR, E. G. ZOEBISH, E. F. HEALEY, and J. P. STEWART. J. Am. Chem. Soc. **107**, 3902 (1985).
11. AMPAC; Austin Method 1 Package (QCPE 506). Dewar Research Group and J. P. Stewart. QCPE Bull. **6**, 2 (1986).
12. E. M. ARNETT and J. A. HARRELSON, JR. J. Am. Chem. Soc. **109**, 809 (1987).
13. X. WANG and K. N. HOUK. J. Am. Chem. Soc. **110**, 1870 (1988).
14. K. B. WIBERG and K. E. LAIDIG. J. Am. Chem. Soc. **110**, 1872 (1988).
15. E. M. ARNETT and K. G. VENKATASUBRAMANIAM. J. Org. Chem. **48**, 1569 (1983).
16. E. M. ARNETT, S. G. MAROLDO, S. L. SCHILLING, and J. A. HARRELSON. J. Am. Chem. Soc. **106**, 6759 (1984).
17. W. D. KUMLER. J. Am. Chem. Soc. **60**, 859 (1938).
18. F. W. BEIGLER-KONIG, R. F. W. BADER, and T.-H. TANG. Comput. Chem. **3**, 317 (1982).
19. R. F. W. BADER, T.-H. TANG, and F. W. BEIGLER-KONIG. J. Am. Chem. Soc. **104**, 946 (1982).
20. K. B. WIBERG and J. J. WENDOLOWSKI. J. Proc. Natl. Acad. Sci. U.S.A. **78**, 6561 (1981).

Can. J. Chem. Downloaded from www.nrcresearchpress.com by 196.1.178.254 on 09/07/12
For personal use only.

The correspondence between Hückel theory and *ab initio* atomic charges in allyl ions

TOM S. SLEE[1] AND PRESTON J. MACDOUGALL[2]
Department of Chemistry, McMaster University, Hamilton, Ont., Canada L8S 4M1

Received July 4, 1988

TOM S. SLEE and PRESTON J. MACDOUGALL. Can. J. Chem. **66**, 2961 (1988).

Atomic charges for the allyl cation and anion are reported, as defined by the quantum theory of atoms in molecules. An interesting feature of these charges is that they differ considerably from expectations based on simple π orbital models. The reasons for the difference are investigated and it is shown that the charges are both compatible with and understandable in terms of simple orbital models.

TOM S. SLEE et PRESTON J. MACDOUGALL. Can. J. Chem. **66**, 2961 (1988).

On rapporte les charges atomiques des cations allyles et des anions telles que définies par la théorie quantique des atomes dans les molécules. Une caractéristique intéressante de ces charges réside dans le fait qu'elles diffèrent considérablement des valeurs prévues à partir des modèles d'orbitale π simple. On étudie les raisons de cette différence et on montre que la nature des deux charges la justifie. Les modèles d'orbitale simple permettent de comprendre ce fait.

[Traduit par la revue]

Can. J. Chem. Downloaded from www.nrcresearchpress.com by 196.1.178.254 on 09/07/12
For personal use only.

Atomic charges for the allyl cation and anion are reported, as defined by the quantum theory of atoms in molecules. An interesting feature of these charges is that they differ considerably from expectations based on simple π orbital models. The reasons for the difference are investigated and it is shown that the charges are both compatible with and understandable in terms of simple orbital models.

The theory of atoms in molecules defines an atom in a molecule from quantum mechanics (1), and has been recently reviewed (2). An atom is defined as the union of a nucleus and its basin. An atomic basin is just the region of space traversed by all paths of steepest ascent in the total charge density, which terminate at a given nucleus. Any two bonded atoms share, and are separated by, an interatomic surface. They are also linked by a ridge of charge density, or bond path, which exhibits a minimum at the point of intersection with the interatomic surface. This is called the bond critical point.

Integrations of the total charge density and the density of all π molecular orbitals (where molecular symmetry permits) over this basin yield average atomic electron populations, $N(A)$, and their π components, $N_\pi(A)$, respectively (3). Although the π component of an atom's average electron population is definable only within the context of molecular orbital theory (unlike the total population), it is found here to be extremely useful in establishing a correspondence between simple orbital models and the total charge distribution. The total charge on an atom is defined as $q(A) = Z(A) - N(A)$. The π charge on a formally sp^2 carbon is defined as $q_\pi(A) = 1 - N_\pi(A)$, to correspond with the Hückel model.

The total charges and π charges for the allyl cation and anion are shown in Table 1, along with the positions of the bond critical points. The charges are obtained using a 6-31G** basis set (4) augmented by diffuse *s* and *p* functions on carbon, which provides a good description of the electron distribution in such systems (5). Predictions made on the basis of the Hückel model are in remarkable agreement with the π charges in these systems, with the terminal CH_2 groups each having a π charge of +0.50 in the cation and −0.53 in the anion. The total atomic charges illustrate the consequences of the Hückel model's neglecting the σ orbital contributions to the atomic charge.

The relationship between π charges and total charges can be qualitatively understood using an approach described in detail elsewhere (6). Perturbations of electron distributions affect the charges of atoms in two ways (to first order). The "basin" contribution is the change in the density evaluated over the volume of the *unperturbed* atom, while the "surface" contribution arises from the change in volume of the atom as it is perturbed, and can be approximated by the product of the total charge in the surface $N(S)$ and the distance through which the bond point moves, δx_c.

$$[1] \quad \delta N(A) = \delta N(A^0) + N(S)\delta x_c$$

Changes in the π distribution contribute directly to the change in the total population only through the basin term. The surface term is determined by the bond point position, which in turn is dictated by the σ density (7). It is this surface term which is largely responsible for the discrepancy between the π and total atomic charges.

The large π charge on the terminal CH_2 groups in the allyl cation will increase their electronegativity, and hence they will withdraw σ electrons from the central CH group. The polarisation of the CC σ bond produces a large shift in the bond point position towards the central carbon atom, and so the surface contribution to the net change in population is substantial. Thus, the *total* charge on the terminal CH_2 groups will be considerably more negative than π orbital models predict, and the total charge on the central CH group will be correspondingly more positive. Table 1 verifies these predictions. The total charges in the allyl anion can be explained in exactly the same manner, although the simple Hückel model does not predict the slight positive π charge on the central CH group.

The charges on the formally positive carbons of simple alkyl cations can be explained in an identical manner to the allyl ions, and are reported in Table 2 (8). Simple orbital models correctly predict that in the methyl cation the central carbon will have a π charge of +1.0, and that as hydrogens are replaced by methyl groups this positive π charge will decrease in magnitude. The total charge on the formally positive carbon is determined partly by the π contribution, but also by the changes induced in the σ distribution (partially due to the electronegativity difference between sp^2 and sp^3 carbons in this case) which modify the positions of the bond points. The slightly non-planar CH_2 group in the ethyl cation leads to a contamination of the "π" orbital,

[1]Present address: Inorganic Chemistry Laboratory, University of Oxford, 25 South Parks Road, Oxford, 0X1 3Q4, U.K.
[2]Author to whom all correspondence should be addressed.

TABLE 1. Net atomic charges and bond point positions in the allyl cation and anion

Numbering	Atom	$C_3H_5^+$ q(A)	$C_3H_5^+$ q_π(A)	$C_3H_5^+$ R_{bp}(C—C)[a]	$C_3H_5^-$ q(A)	$C_3H_5^-$ q_π(A)	$C_3H_5^-$ R_{bp}(C—C)[a]
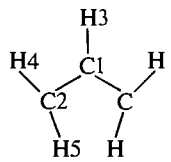	C1	+0.219	+0.032	1.175	+0.024	+0.096	1.393
	C2	+0.087	+0.520	1.421	−0.162	−0.378	1.229
	H3	+0.086	−0.026		−0.127	−0.038	
	H4	+0.143	−0.010		−0.148	−0.080	
	H5	+0.118	−0.012		−0.137	−0.070	
	$-CH_2$	+0.348	+0.498		−0.447	−0.528	

[a]R_{bp} is the distance from the nucleus to the bond critical point in au, 1 au = 0.5292 Å.

TABLE 2. Net atomic charges and bond point positions in alkyl cations

Cation	$q(C^+)$	$q_\pi(C^+)$	R_{bp}(C—C) au
$[CH_3]^+$	+0.244	+1.000	1.402 (C—H)
$[CH_3CH_2]^+$	+0.090	+0.698[a]	1.604
$[(CH_3)_2CH]^+$	−0.010	+0.690	1.594
$[(CH_3)_3C]^+$	−0.098	+0.632	1.580

[a]Complete separation of σ and π not possible.

and a consequent uncertainty in the value of the "π" charge in this group. All other species are planar around the central carbon.

The quantum theory of atoms in molecules also allows the calculation of π charges and total charges in heteroatomic systems. For example, in difluoromethylene (singlet) the π population on carbon is 0.152, and the total charge is +1.552, showing that the inductive electron withdrawing effect of fluorine far outweighs its weak π donating ability (9). The greater π donating ability of the amino group compared to fluorine is shown by the π population of 0.232 on the carbon in aminomethylene (singlet). The weaker inductive electron withdrawing ability is reflected in the total charge on the amino group, which is −0.598.

In conclusion, it has been shown that the apparently counter-intuitive total atomic charges in allyl ions and other related systems are understandable in terms of simple orbital models, as long as the correspondence between the two is treated properly. The verification of Hückel theory expectations by *ab initio* π orbital charges emphasises the importance of the σ framework in determining the total atomic charges in unsaturated hydrocarbons (7).

Acknowledgement

We would like to thank Professor R. F. W. Bader for supplying us with the π charges for the alkyl cations, and for helpful discussions.

1. R. F. W. BADER and T. T. NGUYEN-DANG. Adv. Quantum Chem. **14**, 63 (1981).
2. R. F. W. BADER. Acc. Chem. Res. **18**, 9 (1985).
3. F. W. BIEGLER-KÖNIG, R. F. W. BADER, and T.-H. TANG. J. Comput. Chem. **13**, 317 (1982); K. B. WIBERG and J. J. WENDOLOSKI. Proc. Natl. Acad. Sci. USA, **78**, 6561 (1981).
4. J. S. BINKLEY, R. A. WHITESIDE, R. KRISHNAN, R. SEEGER, D. J. DEFREES, H. B. SCHLEGEL, S. TOPIO, L. R. KAHN, and J. A. POPLE. GAUSSIAN 80. Carnegie-Mellon University.
5. A. J. DUKE. Chem. Phys. Lett. **21**, 275 (1973); A. J. DUKE and R. F. W. BADER. Chem. Phys. Lett. **10**, 631 (1971); J. CHANDRASEKAR, J. G. ANDRADE, and P. V. R. SCHLEYER. J. Am. Chem. Soc. **103**, 5609 (1981).
6. T. S. SLEE. J. Am. Chem. Soc. **108**, 7541 (1986).
7. T. S. SLEE. J. Am. Chem. Soc. **108**, 606 (1986).
8. R. F. W. BADER. Can. J. Chem. **64**, 1036 (1986).
9. P. J. MACDOUGALL and R. F. W. BADER. Can. J. Chem. **64**, 1496 (1986).

Can. J. Chem. Downloaded from www.nrcresearchpress.com by 196.1.178.254 on 09/07/12
For personal use only.

Martine Taran et Bernard Delmond. Obtention de nouveaux squelettes diterpéniques lors de l'isomérisation d'époxydes diterpéniques sur alumine active. Can. J. Chem. **66**, 1558 (1988).

Page 1561. À la neuvième ligne du haut, première colonne, «une configuration γ» devrait être remplacé par «une configuration β».

Can. J. Chem. Downloaded from www.nrcresearchpress.com by 196.1.178.254 on 09/07/12
For personal use only.

Phosphoranylation de polyols : Voie d'accès aux phosphates d'intérêt biologique. I. Cas du myo-inositol

BRIGITTE DUTHU, DOURAID HOUALLA[1] ET ROBERT WOLF

Université Paul Sabatier de Toulouse, Unité associée au Centre national de la recherche scientifique n° 454, 118 route de Narbonne, 31062 Toulouse CEDEX, France

Reçu le 26 janvier 1988

BRIGITTE DUTHU, DOURAID HOUALLA et ROBERT WOLF. Can. J. Chem. **66**, 2965 (1988).

Nous décrivons une méthode originale de phosphorylation du myo-inositol non protégé, qui fournit plusieurs myo-inositol phosphates à la fois. Le schéma réactionnel comporte une phosphoranylation totale ou partielle du cyclitol, à l'aide de l'aminobicyclophosphane **8**, suivie d'une oxydation des bicyclophosphoranes à liaison P—H obtenus et d'une hydrolyse acide des phosphates neutres qui en résultent. Dans le cas de la tris-phosphoranylation nous avons identifié, parmi les fractions séparées par HPLC, le myo-inositol-1,2(cycl) phosphate **22**, le myo-inositol-1 phosphate **23** et le myo-inositol-2 phosphate **24**.

BRIGITTE DUTHU, DOURAID HOUALLA, and ROBERT WOLF. Can. J. Chem. **66**, 2965 (1988).

An original method for the phosphorylation of an unprotected myo-inositol is described, which yields several myo-inositol phosphates at the same time. The reaction proceeds via a partial or complete phosphoranylation of the cyclitol by means of the aminobicyclophosphane **8**, followed by oxidation of the resulting bicyclophosphoranes bearing a P—H bond and acid hydrolysis of the neutral phosphates thus formed. In the case of the tris-phosphoranylation we identified, among the HPLC fractions, the myo-inositol-1,2-(cycl)phosphate **22**, the myo-inositol-1-phosphate **23**, and the myo-inositol-2-phosphate **24**.

Introduction

Des polynucléotides aux phospholipides, les constituants et métabolites du système biologique que l'on peut considérer comme des phosphates de polyols se comptent par centaines, ce qui explique l'intérêt que les chimistes et biochimistes portent au problème de la phosphorylation des polyols.

Schématiquement la phosphorylation d'un alcool a été réalisée jusqu'à présent essentiellement par deux voies :

1. Voie de Khorana et coll. (1) : Action d'un dérivé du phosphore tétracoordonné possédant déjà le groupement phosphoryle P=O :

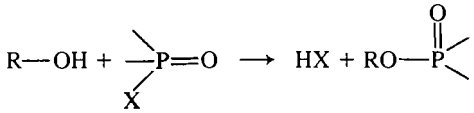

X étant un groupement nucléofuge: Cl, OR, -OH, $(RO)_2P(O)$

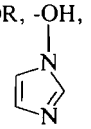

etc. ...

2. Voie de Caruthers (2) : Action d'un dérivé du phosphore tricoordonné, suivie d'une oxydation :

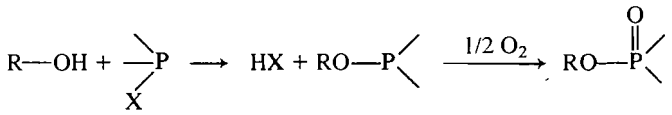

X = Cl, NR_2, RC(O)O-

Les phosphates biologiquement intéressants sont des monoesters ou diesters auxquels on accède par hydrolyse des phosphates neutres obtenus par ces deux procédés.

Appliquées aux polyols, chacune de ces deux méthodes a ses avantages et inconvénients.

Le myo-inositol **1** voit son intérêt renouvelé depuis la mise en évidence du rôle du D-myo-inositol-1,4,5 tris-phosphate **2** et d'autres myo-inositol phosphates, comme les dérivés **3** et **4**, dans le mécanisme de régulation du calcium intracellulaire (3–5).

1. Auteur à qui adresser toute correspondance.

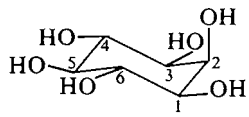

1

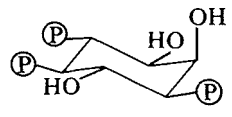

2

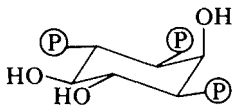

3

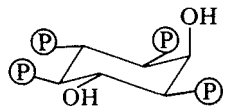

4

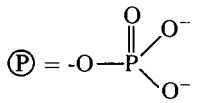

Le D-myo-inositol-1,4,5 tris-phosphate, ainsi qu'un certain nombre de myo-inositol phosphates, sont extraits du cerveau de bovins par voie enzymatique (6). Quelques-uns sont disponibles, depuis peu, dans le commerce à des prix forts élevés (7). La synthèse chimique de tels composés en fournissant des quantités relativement importantes de produits et surtout en permettant l'accès à des dérivés marqués ou modifiés, revêt par conséquent une importance considérable. Une dizaine de synthèses ont été décrites récemment. Elles nécessitent toutes l'obtention préalable du myo-inositol protégé, optiquement actif ou non, la phosphorylation étant faite soit par la méthode de Khorana (8–12) soit par celle de Caruthers (13–17).

Nous décrivons une méthode originale et générale de phosphorylation des polyols, appliquée à l'obtention de différents phosphates de myo-inositol. Elle s'appuie sur l'aptitude exceptionnelle des bicyclophosphanes **5**[2] à additionner les alcools pour donner des alcoxybicyclophosphoranes à liaison P—H stables **6** (18) :

2. La nomenclature de ces composés est la suivante : **5**, 2,8-dioxa 5-aza 1-phospha^{III} bicyclo[3,3,0]octane; **6**, 1-alcoxy 2,8-dioxa 5-aza 1-phospha^{V} bicyclo[3,3,0]octane. Pour des raisons de commodité, nous les appellerons bicyclophosphanes pour **5** et bicyclophosphoranes pour **6**.

Printed in Canada / Imprimé au Canada

Can. J. Chem. Downloaded from www.nrcresearchpress.com by 122.72.124.2 on 09/07/12
For personal use only.

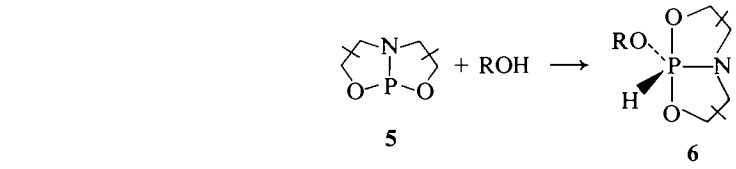

5 6

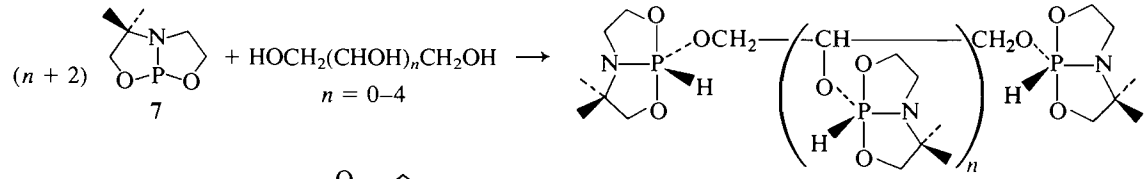

7 6′

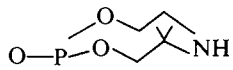

6″

Nous avons montré avec une série d'alditols (HO—CH_2—(CHOH)$_n$—CH_2OH (n = 0, 1, 2, 3, 4)) qu'on peut facilement introduire autant de groupes bicyclophosphoranes qu'il y a de fonctions alcool dans le polyol et que les per-bicyclophosphoranes **6′** obtenus sont en équilibre avec des entités dans lesquelles le groupe phosphorane est passé sous sa forme tautomère phosphite **6″** (19).

Nous nous sommes alors attachés à réaliser la phosphorylation du myo-inositol sans protection préalable, en effectuant une phosphoranylation totale ou partielle de ce dernier, suivie d'une oxydation des bicyclophosphoranes obtenus et d'une hydrolyse acide des esters neutres qui en résultent. Les produits de la réaction sont séparés par HPLC.

Résultats et discussion

Ces expériences ont été conduites avec, comme agent de phosphoranylation, le bicyclophosphane **8** qui se distingue de son analogue **7** par la présence de deux substituants CH_3 sur chacun des carbones 3 et 7 au lieu de deux groupes CH_3 sur le seul carbone 6. L'intérêt de cette substitution apparaîtra par la suite.

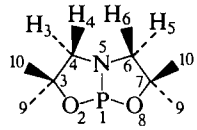

8

1. Per-phosphoranylation

La per-phosphoranylation du myo-inositol a été effectuée soit dans le toluène (phase hétérogène), soit dans le diméthyl sulfoxyde (DMSO) (phase homogène).

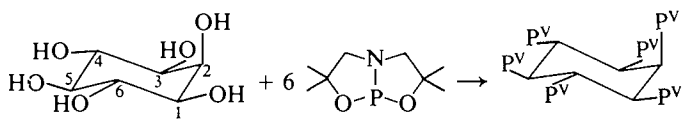

1 8 9

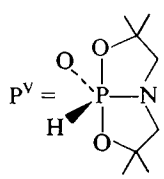

Elle nécessite 6–14 h de chauffage à 80°C dans le premier cas, 1/2 h d'agitation à la température ambiante dans le second.

En outre, nous avons vérifié à l'aide de la RMN ^{31}P que dans ces conditions le DMSO n'oxyde pas les dérivés phosphorés obtenus (20).

La formation du per-phosphorane **9** est attestée par (*i*) la disparition, dans le spectre de RMN ^{31}P du mélange réactionnel, du singulet correspondant au bicyclophosphane **8** (δ = 163 ppm) et son remplacement par un ensemble de doublets entre −38 et −46 ppm avec un couplage $^1J_{P-H}$ de l'ordre de 800 Hz (figure 1); (*ii*) l'absence dans le spectre infrarouge de toute absorption de vibration OH; (*iii*) la présence dans le spectre de masse (désorption de champ) d'un pic à M^+ = 1314, correspondant à l'addition de 6 molécules de bicyclophosphane **8** (masse moléculaire = 189) sur le myo-inositol.

Du point de vue stéréochimique, la présence dans le myo-inositol d'un plan de symétrie passant par les carbones C_2 et C_5 se traduit par l'existence dans le per-phosphorane **9** de quatre sites de phosphoranylation différents (P_1 P_3), P_2, (P_4 P_6) et P_5. En fait, le spectre de RMN ^{31}P comporte au moins cinq pics identifiables au lieu des quatre attendus (figure 1). Cela traduit l'existence d'équilibres tautomères phosphorane–phosphite, comparable à ce qui a été observé avec les polyols linéaires (19) et qui donne ipso-facto des phosphoranes originaux. On détecte dans le spectre du produit **9** (figure 1) un signal peu intense (inférieur à 10%), situé à 134 ppm, qui correspond à la résonance du noyau de phosphore des phosphites (21). La formation de ces phosphites est également attestée par la présence dans le spectre infrarouge de deux absorptions à 3235 cm^{-1} et 3450 cm^{-1}, attributables à ν_{N-H} associé et ν_{N-H} libre.

2. Phosphoranylation partielle

Comme exemple de phosphoranylation partielle du myo-inositol, nous avons choisi la tris-phosphoranylation. Celle-ci a été réalisée de deux manières :

1. Action du bicyclophosphane **8** sur le myo-inositol en solution dans le DMSO. À la fin de la réaction le spectre de

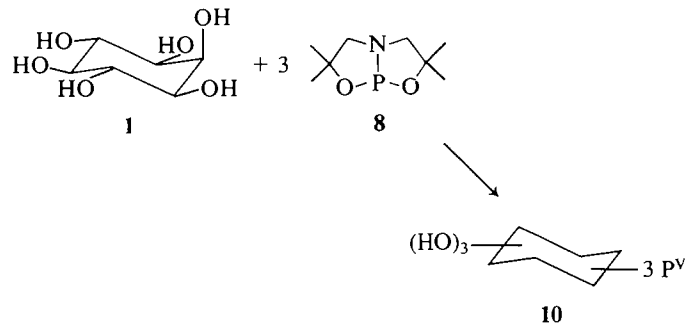

1 8 10

Can. J. Chem. Downloaded from www.nrcresearchpress.com by 122.72.124.2 on 09/07/12
For personal use only.

Can. J. Chem. Downloaded from www.nrcresearchpress.com by 122.72.124.2 on 09/07/12
For personal use only.

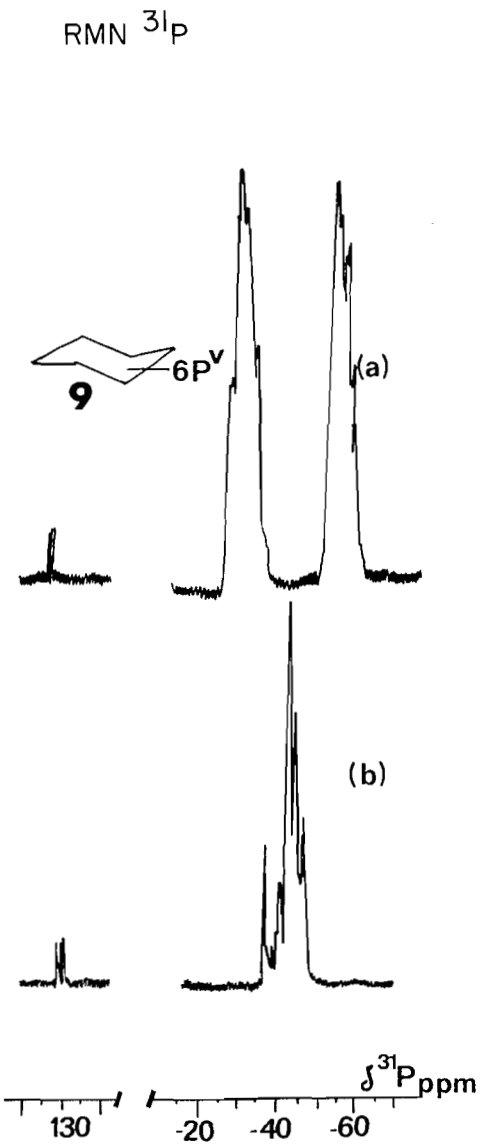

FIG. 1. Spectre de RMN ^{31}P, (a) proton non découplé; (b) proton découplé du per-phosphorane de myo-inositol **9**.

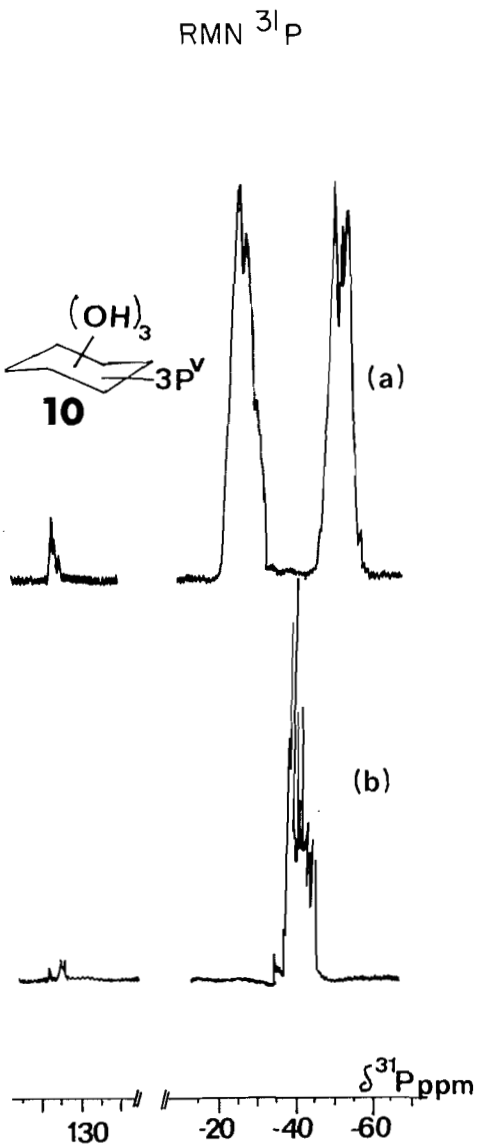

FIG. 2. Spectre de RMN ^{31}P, (a) proton non découplé; (b) proton découplé du myo-inositol tris-phosphorane **10**.

RMN ^{31}P comporte à -40 ppm un ensemble de doublets ($^1J_{P-H}$ = 815 Hz) qui, par irradiation du proton, donnent naissance à 16 pics identifiables. Notons là également, la présence d'un signal peu intense (~10%) à 134 ppm, attribuable aux phosphites tautomères (figure 2).

La complexité de ce spectre s'explique par des considérations stéréochimiques. La fixation de trois atomes de phosphore sur le myo-inositol donne naissance à 12 stéréoisomères identifiables par RMN qui comportent 32 noyaux de phosphore différents. Ce nombre peut encore être augmenté par la présence de phosphites tautomères. Bien plus, on ne peut exclure dans cette réaction la formation d'entités correspondant à la fixation d'un nombre d'atomes de phosphore différent de 3 (1, 2, 4, 5, 6) ce qui ajoute à la complexité du spectre.

2. Méthanolyse du per-phosphorane **9**. En effet, nous avons préalablement montré que l'action du méthanol sur l'isopropyl-

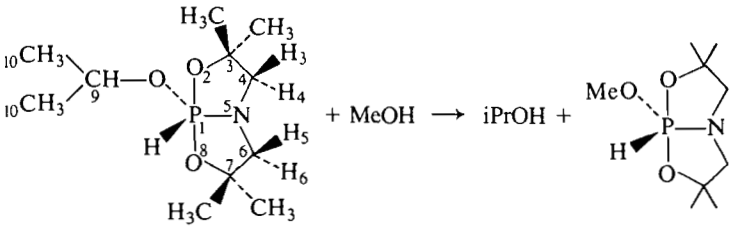

11
$\delta^{31}P = -37{,}3$ ppm
$^1J_{P-H} = 791{,}5$ Hz

12
$\delta^{31}P = -36{,}9$ ppm
$^1J_{P-H} = 798$ Hz

Can. J. Chem. Downloaded from www.nrcresearchpress.com by 122.72.124.2 on 09/07/12
For personal use only.

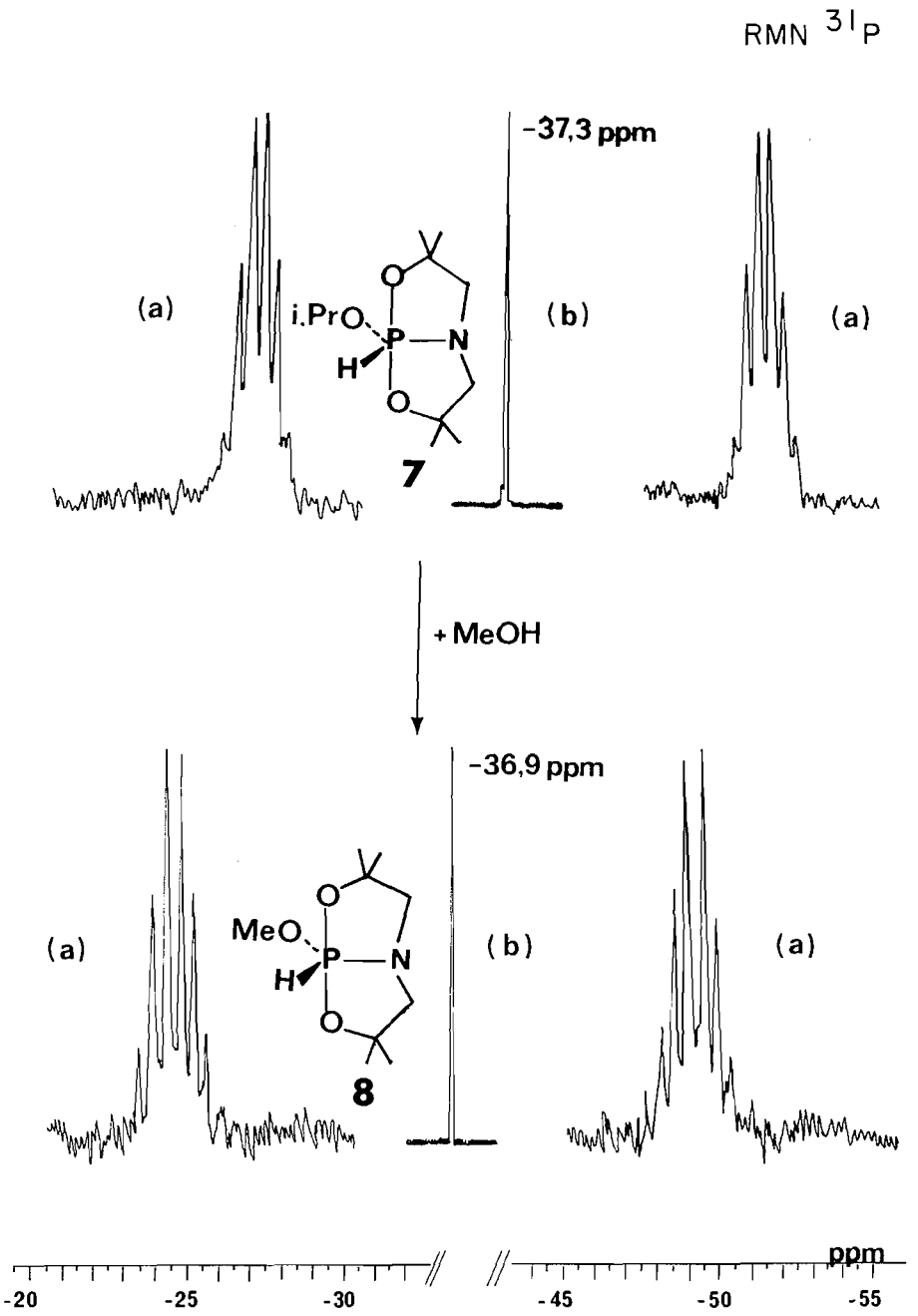

FIG. 3. La méthanolyse de **11** conduit exclusivement au méthoxy bicyclophosphorane **12**. Spectre de RMN ^{31}P de **11** et **12**, (a) proton non découplé; (b) proton découplé.

oxybicyclophosphorane **11**, spécialement préparé pour cette expérience, conduit exclusivement au méthoxybicyclophosphorane **12** (figure 3). La méthanolyse du per-phosphorane **9** est attestée par l'apparition dans le spectre de RMN ^{31}P $\{^1H\}$ d'un signal à $\delta = -35{,}2$ dû au méthoxybicyclophosphorane **12** (la variation de la valeur de $\delta^{31}P$ est due au changement de milieu) et la multiplication attendue des signaux des phosphoranes de myo-inositol (figure 4). On notera que l'aptitude du bicyc-

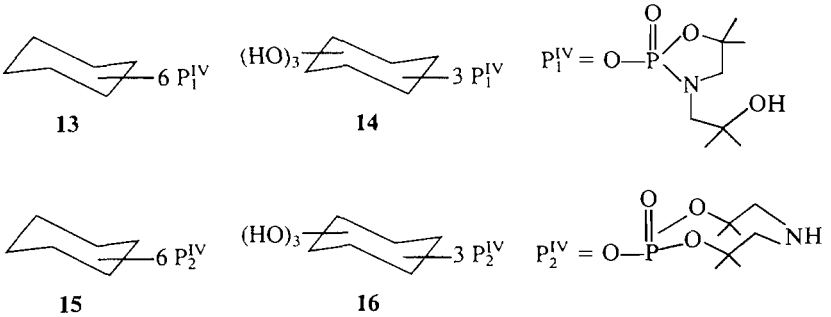

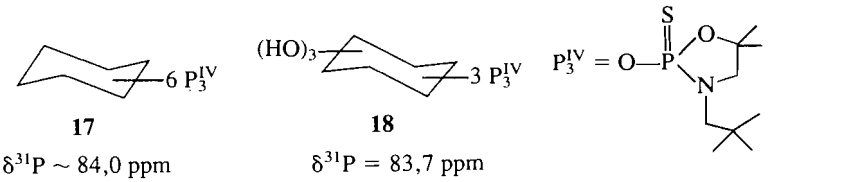

17

$\delta^{31}P \sim 84{,}0$ ppm

18

$\delta^{31}P = 83{,}7$ ppm

19

$\delta^{31}P \sim 52{,}0$ ppm

20

$\delta^{31}P = 51{,}0$ ppm

lophosphane à se fixer sur le myo-inositol et à en être retiré lui confère des caractéristiques d'un bon groupement protecteur.

3. Oxydation – sulfuration

L'oxydation par le tertiobutylhydroperoxyde (22) des phosphoranes **9** et **10** en solution dans le DMSO a été effectuée à la température ambiante. Dans les deux cas, les spectres de RMN $^{31}P\{^1H\}$ des mélanges réactionnels montrent la disparition totale des signaux des phosphoranes et phosphites tautomères et leur remplacement par un groupe majeur situé entre 10 et 20 ppm, attribuable aux composés **13** et **14** (23), et un groupe mineur, situé entre −16 et 0 ppm, attribuable aux dérivés **15** et **16** (23). Bien entendu, le nombre de pics représentant les produits d'oxydation est bien plus grand dans le cas du produit **10** que dans celui du dérivé **9**, ce qui traduit le fait que le composé **9** est un isomère unique possédant quatre noyaux de phosphore différents alors que le dérivé **10** peut représenter un mélange de 12 isomères comportant au total 32 noyaux de phosphore différents.

Nous avons montré ensuite que l'action du soufre élémentaire transforme quantitativement les phosphoranes **9** et **10** en deux types de dérivés thiophosphorylés : les produits majeurs **17** et **18** d'une part et les produits mineurs **19** et **20** d'autre part, dont les paramètres de RMN ^{31}P sont tout à fait comparables à ceux de composés analogues relevés dans la littérature (23, 24).

4. Hydrolyse

L'hydrolyse des phosphates neutres a pour but d'accéder aux monoesters selon la réaction :

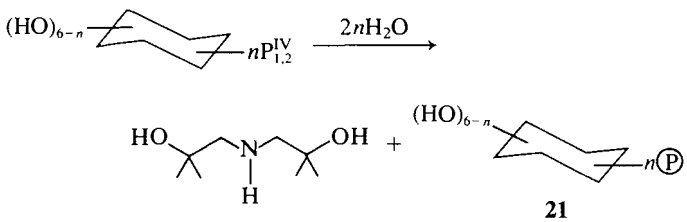

21

L'hydrolyse acide conduisant à un alcool tertiaire étant plus rapide que celle conduisant à un alcool secondaire (25), l'utilisation du bicyclophosphane **8** permet de réduire le taux de déphosphorylation du myo-inositol.

Nous avons effectué cette réaction sur les produits d'oxydation **14** et **16** des tris-phosphoranes **10**. À la température ambiante, la réaction est quasi-instantanée. Le spectre de RMN ^{31}P du mélange réactionnel continue à présenter deux groupes de signaux, entre −16 et 0 ppm d'une part et entre 10 et 16 ppm d'autre part, mais ce dernier groupe n'est plus aussi prédominant comme dans le spectre des produits de départ. En outre les déplacements chimiques sont sensiblement différents de ceux pointés dans le spectre du mélange des produits **14** + **16.**

Ce mélange réactionnel a été soumis à une séparation par chromatographie liquide à haute performance (HPLC) sur une résine échangeuse d'anions dans les conditions expérimentales d'Irvine *et al.* (26). Celles-ci permettent, par la modification de la force ionique à l'aide d'un gradient de formiate d'ammonium, de séparer les phosphates du myo-inositol en fonction du nombre de leurs atomes de phosphore qui est en relation directe avec la concentration du formiate d'ammonium. On conclut que les fractions 1–16 correspondent surtout aux molécules à un atome de phosphore, les fractions 17–22 aux molécules à deux atomes de phosphore et les fractions suivantes aux molécules à trois atomes de phosphore. Nous avons collecté au total 48 fractions et enregistré leurs spectres de RMN ^{31}P (pH = 3,5).

L'étude de ces spectres montre que seules les 22 premières fractions contiennent des molécules phosphorées, ce qui veut dire que les entités séparées contiennent seulement un ou deux atomes de phosphore. L'hydrolyse ne s'est donc pas limitée aux liaisons P—O—C et P—N—C, liant le phosphore au reste

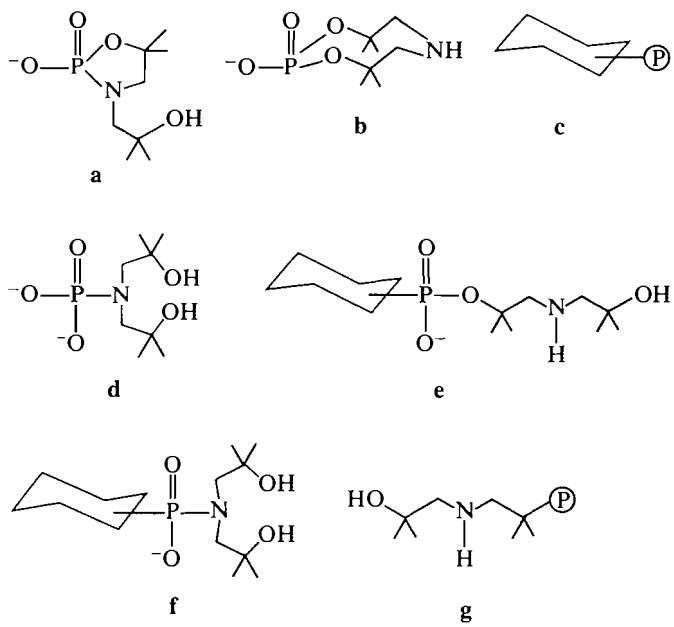

a **b** **c** **d** **e** **f** **g**

≪aminodiol≫, mais elle a également touché les liaisons P—O—C inositol. Dans ces conditions, l'hydrolyse partielle des phosphates **14** et **16** peut conduire à 7 types de molécules (**a**–**g**) qui se distinguent par l'allure du signal de résonance du phosphore : singulet pour **b** et **g**, doublet pour **c** et **e** et multiplet pour **a**, **d** et **f**. Les fractions recherchées sont celles qui correspondent aux entités **c**. Nous en avons relevé trois :

Fraction 5

Le spectre de RMN ^{31}P (figure 5) comporte un doublet qui se

Can. J. Chem. Downloaded from www.nrcresearchpress.com by 122.72.124.2 on 09/07/12
For personal use only.

Can. J. Chem. Downloaded from www.nrcresearchpress.com by 122.72.124.2 on 09/07/12
For personal use only.

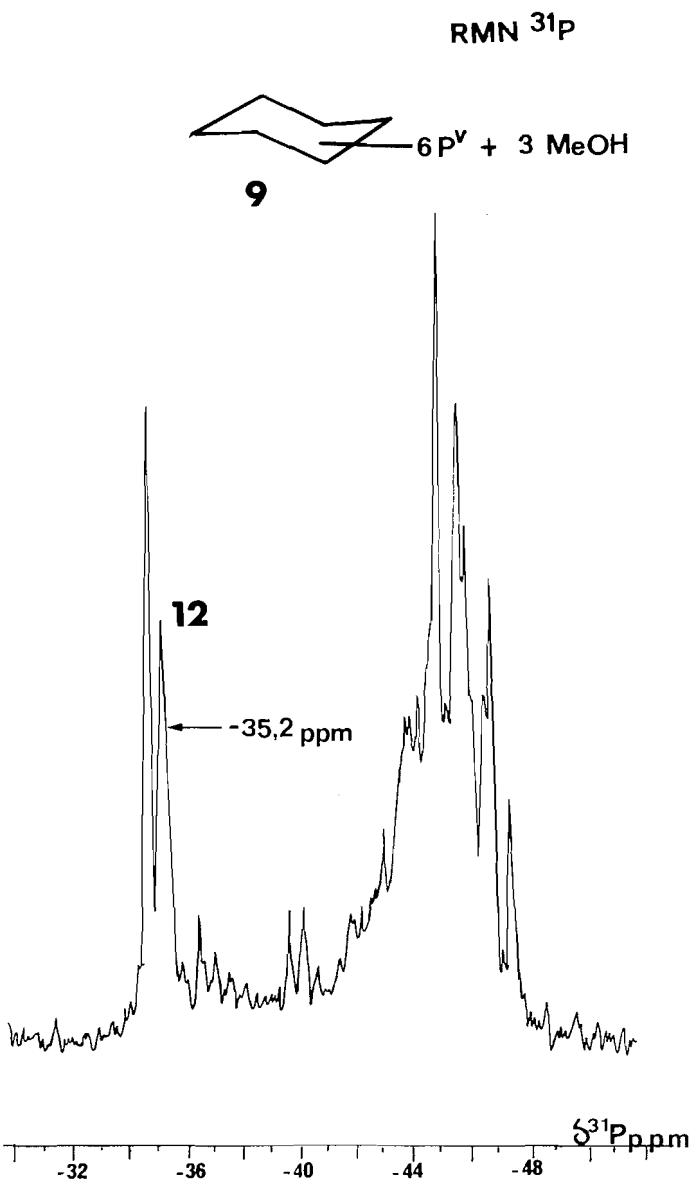

FIG. 4. La méthanolyse du per-phosphorane de myo-inositol **9** conduit à une augmentation du nombre de phosphoranes de myo-inositol (voir fig. 1) et à la formation du méthoxybicyclophosphorane **12** : $\delta = -35,2$ ppm valeur légèrement différente de celle lue sur la figure 3 en raison de la modification du milieu.

transforme en singulet par découplage des protons : $\delta^{31}P$, 15,8 ppm; $^3J_{P—O—C—H}$, 20,1 Hz. Ces paramètres sont quasi identiques à ceux du myo-inositol-1,2(cycl) phosphate **22** : $\delta^{31}P$, 16,5 ppm; $^3J_{P—O—C—H}$, 20 Hz (27). L'identification est parachevée en comparant le spectre de RMN ^1H de cette fraction (figure 6) à celui d'un échantillon authentique du produit **22**, récemment publié dans la littérature (28).

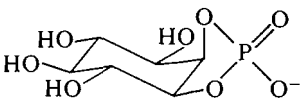

22

Fraction 7

Le spectre de RMN ^{31}P (figure 7) comporte un signal unique: $\delta^{31}P$, 0,20 ppm; $^3J_{P—O—C—H}$, 7,6 Hz; cette fraction a été

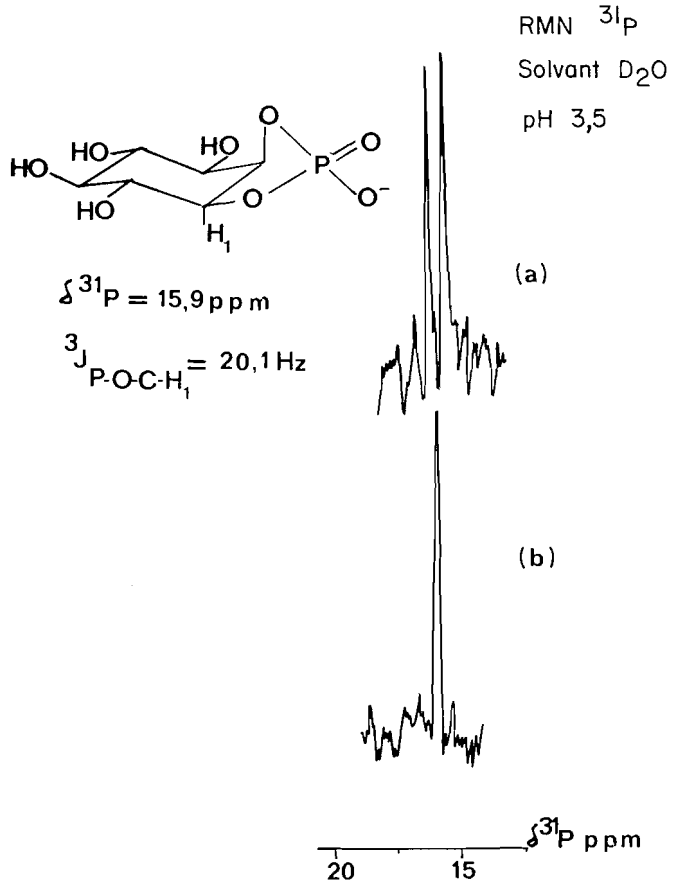

FIG. 5. Spectre de RMN ^{31}P, (a) proton non découplé; (b) proton découplé de la fraction 5 obtenue lors de la séparation par HPLC des produits d'hydrolyse de phosphates **14** et **16**. Nombre d'accumulations : 104.

identifiée comme étant le myo-inositol-1 phosphate **23** en comparant son spectre de RMN ^1H à celui d'un échantillon authentique (28) (figure 8).

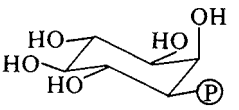

23

La valeur de $\delta^{31}P$: 0,20 ppm à pH 3,5 diffère de celle relevée dans la littérature : 4,75 ppm à pH 8. Toutefois la différence est conforme à ce qui a été généralement observé dans les phosphates de myo-inositol : un blindage quand la valeur du pH diminue (29). En revanche, les constantes de couplage $^3J_{P—O—C—H}$ 7,6 Hz et 7,3 Hz (littérature) sont quasiment identiques.

Le spectre de résonance ^{13}C de cette fraction 7 est reproduit en figure 9. Il montre que les six noyaux de carbone sont devenus tous différents par suite de la fixation du groupe phosphate sur le carbone 1 (ou sur le carbone 3 suivant l'énantiomère considéré). Par comparaison avec les déplacements chimiques des noyaux de carbone du myo-inositol[3] d'une part et compte tenu de l'effet bien connu de déblindage du noyau de carbone touché par la phosphorylation (29, 30), le spectre peut être

3. Dans le myo-inositol, les noyaux de ^{13}C ont les déplacements chimiques suivants : $C_1C_3 = 72,4_4$ ppm, $C_2 = 72,1_8$ ppm, $C_4C_6 = 71,1_5$ ppm, $C_5 = 74,3_5$ ppm (solvant D_2O) (ce travail).

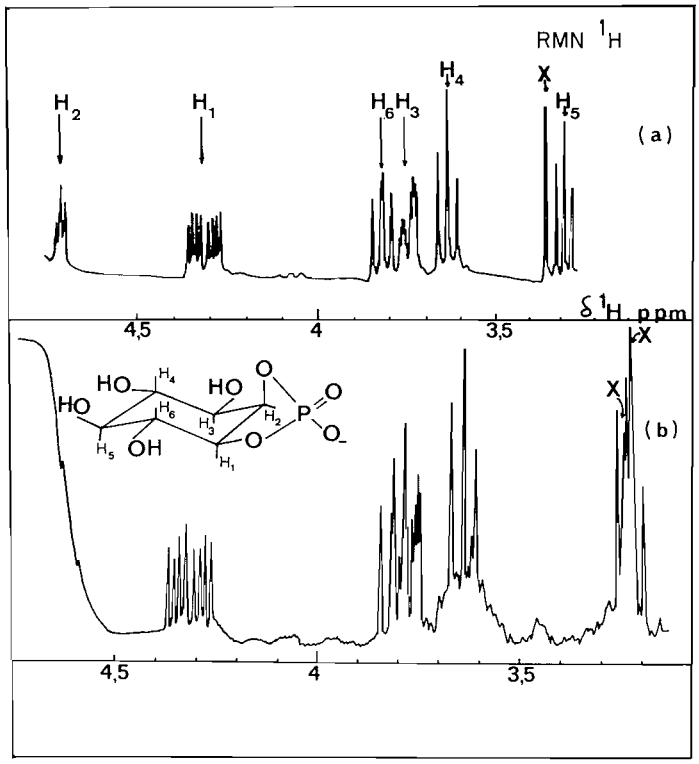

FIG. 6. Spectres de RMN ^{1}H, (a) d'un échantillon authentique de myo-inositol-1,2(cycl)phosphate publié par Cerdan *et al.* (28); (b) de la fraction 5 obtenue lors de la séparation par HPLC des produits d'hydrolyse des phosphates **14** et **16**. Nombre d'accumulations : 16. Le signal du proton H_2 est masqué par le signal OH de H_2O, $\delta > 4,5$ ppm. × = impureté.

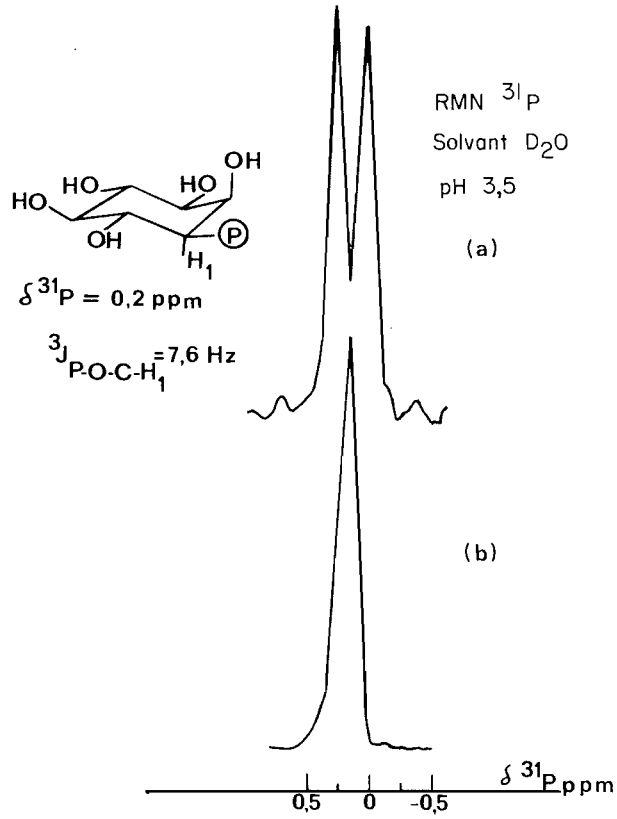

FIG. 7. Spectre de RMN ^{31}P, (a) proton non découplé; (b) proton découplé de la fraction 7 obtenue lors de la séparation par HPLC des produits d'hydrolyse des phosphates **14** et **16**. Nombre d'accumulations : 64.

analysé de la façon suivante : le doublet à δ 75,5$_7$ ppm, $^2J_{C\text{-}P}$ 5,8 Hz, correspond au carbone C_1; le doublet à δ 74,0$_5$ ppm, avec un écart de 0,8 Hz entre ses branches, est attribué au carbone C_5 présentant un couplage à travers quatre liaisons avec le phosphore : $^4J_{C\text{—}C\text{—}C\text{—}O\text{—}P}$ 0,8 Hz ; les singulets à δ 72,3 ppm et δ 70,8 ppm sont attribuables respectivement aux carbones C_3 et C_4; le doublet à δ 71,6 ppm, $^3J_{C\text{—}P}$ 5,8 Hz, peut être attribué aussi bien au carbone C_2 qu'au carbone C_6. Il en est de même du doublet à δ 71,2$_5$, $^3J_{C\text{—}P}$ 1,6$_5$ Hz.

Cette ambiguïté peut être levée en tenant compte d'une part du fait que les variations des constantes de couplage $^3J_{C\text{—}C\text{—}O\text{—}P}$ en fonction des angles dièdres C—C—O—P suivent une loi (31) comparable à celle qui existe pour les constantes de couplage $^3J_{H\text{—}C\text{—}O\text{—}P}$ (32) et, d'autre part, en considérant la valeur non nulle du couplage $^4J_{C5\text{-}P}$. Cette dernière donnée implique en effet que les quatre liaisons C_5—C_6, C_6—C_1, C_1—O et O—P sont dans le même plan (règle du M), ce qui entraîne un empêchement à la rotation autour de la liaison C_1—O. Ceci peut résulter d'une liaison hydrogène intramoléculaire entre le groupement phosphoryle P=O et l'hydroxyle porté par le carbone C_6 ou C_2. La liaison O—P peut donc être soit du côté du carbone C_6 soit du côté du carbone C_2 par rapport au plan perpendiculaire au plan moyen du cycle et passant par C_1 et C_4. L'examen d'un modèle moléculaire montre que dans le premier cas ((**A**): projection de Newman suivant O—C_1), l'angle dièdre C_6—C_1—O—P serait presque nul et l'angle dièdre C_2—C_1—O—P voisin de 120°, alors que dans le second (**B**) les valeurs des mêmes angles dièdres seraient voisines de 180° et 60° respectivement. Seule cette dernière situation rend bien compte des

A **B**

valeurs expérimentales des constantes de couplage. L'attribution définitive est donc : $\delta^{13}C_2$ 71,2$_5$ ppm, $^3J_{C2\text{-}P}$ 1,6$_5$ Hz ; $\delta^{13}C_6$ 71,6 ppm, $^3J_{C6\text{-}P}$ 5,8 Hz.

Fraction 8

Le spectre de cette fraction (figure 10) comporte deux doublets d'inégale intensité : δ ^{31}P 1,9 ppm, $^3J_{P\text{—}O\text{—}C\text{—}H}$ 7,5 Hz ; δ ^{31}P 0,38 ppm, $^3J_{P\text{—}O\text{—}C\text{—}H}$ 7,2 Hz. L'analyse de son spectre de RMN ^{1}H montre qu'elle est constituée d'un mélange de myo-inositol-1 phosphate **23** et de myo-inositol-2 phosphate **24**. On y

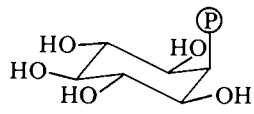

24

relève, en effet, les deux signaux caractéristiques du proton H_2 de ces deux entités (cf. réf. 28) : un triplet à δ 4,08 ppm correspondant au proton H_2 de **23**, un doublet de triplet à δ 4,35 ppm correspondant au proton H_2 de **24**.

Le spectre de RMN ^{13}C de cette fraction (figure 11) confirme la présence de ces deux entités. Il est facile d'y reconnaître les six signaux (ombrés) correspondant aux noyaux de carbone de **23**. Le reste du spectre comporte quatre signaux dont les intensités relatives sont comme 1.1.2.2. Cette allure est celle prévue

Can. J. Chem. Downloaded from www.nrcresearchpress.com by 122.72.124.2 on 09/07/12
For personal use only.

Can. J. Chem. Downloaded from www.nrcresearchpress.com by 122.72.124.2 on 09/07/12
For personal use only.

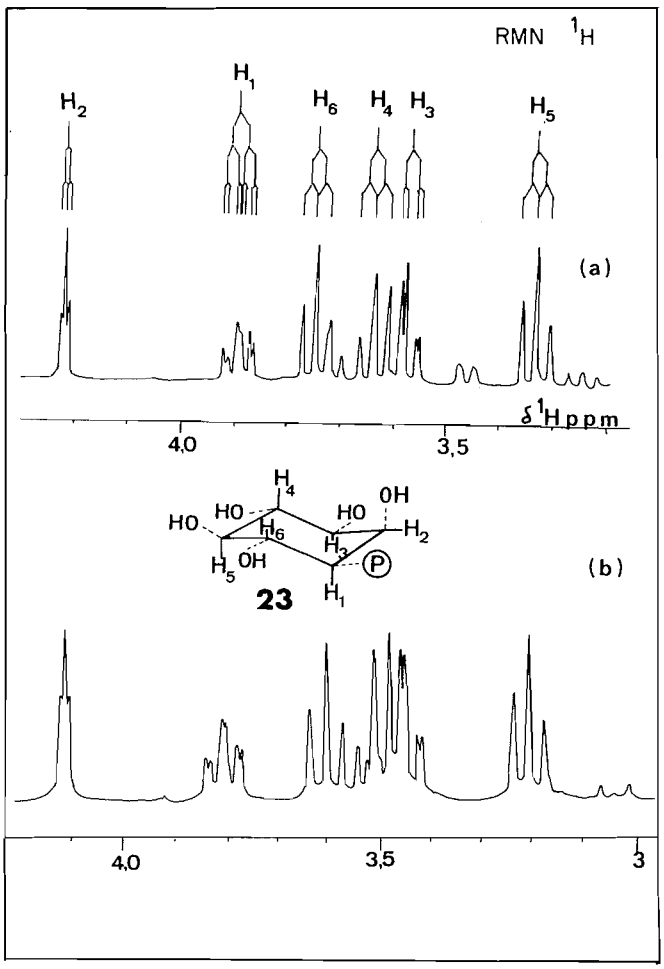

FIG. 8. Spectres de RMN ^{1}H, (a) d'un échantillon authentique de myo-inositol-1 phosphate **23** publié par Cerdan *et al.* (28); (b) de la fraction 7 obtenue lors de la séparation par HPLC des produits d'hydrolyse des phosphates **14** et **16**. Nombre d'accumulations : 16.

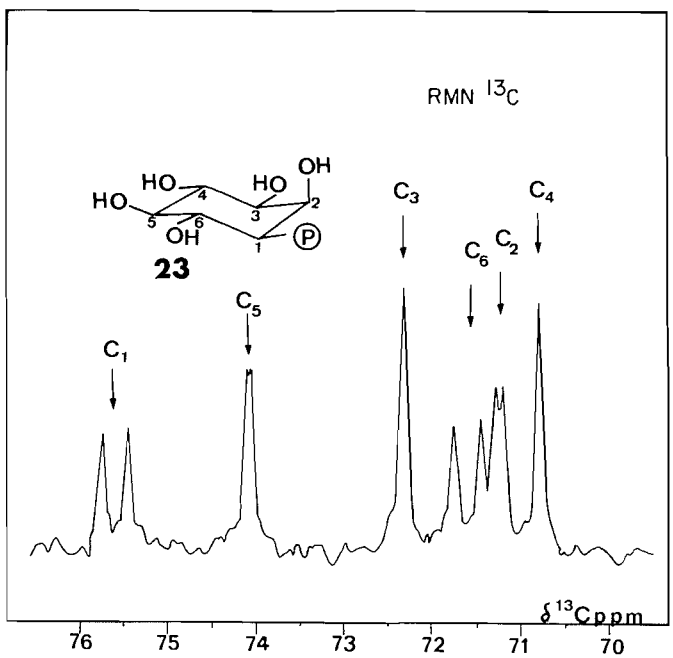

FIG. 9. Spectre de RMN ^{13}C (20,15 MHz) de la fraction 7 obtenue lors de la séparation par HPLC des produits d'hydrolyse des phosphates **14** et **16**. Nombre d'accumulations : 4480.

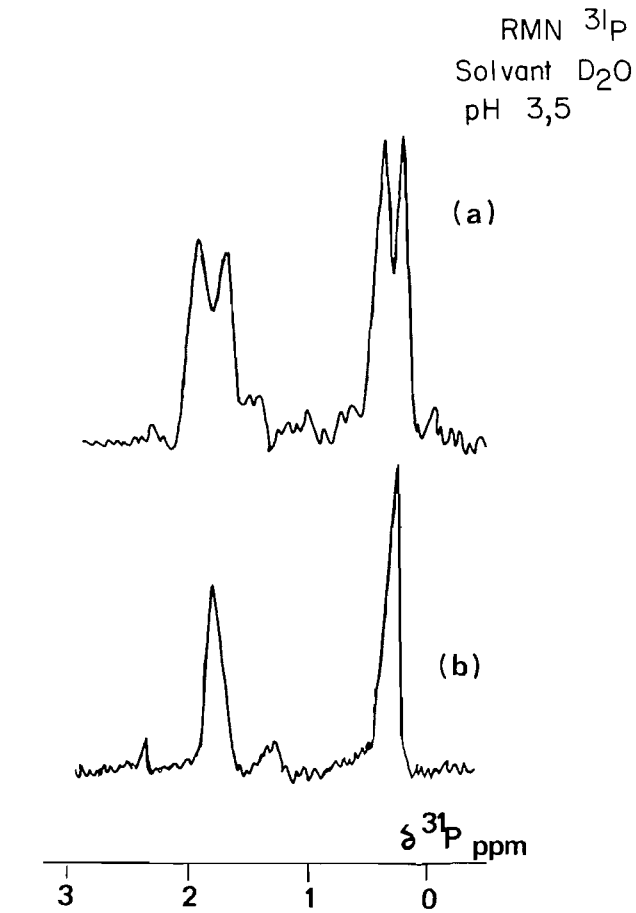

FIG. 10. Spectre de RMN ^{31}P, (a) proton non découplé; (b) proton découplé de la fraction 8 obtenue lors de la séparation par HPLC des produits d'hydrolyse des phosphates **14** et **16**. Nombre d'accumulations : 240.

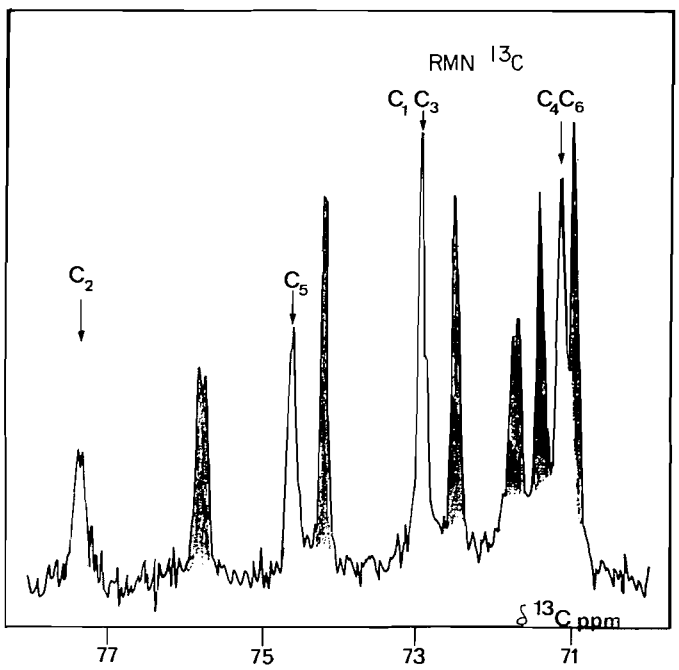

FIG. 11. Spectre de RMN ^{13}C (62,97 MHz) de la fraction 8 obtenue lors de la séparation par HPLC des produits d'hydrolyse des phosphates **14** et **16**. Nombre d'accumulations : 4970. Les signaux ombrés appartiennent au myo-inositol-1 phosphate **23**, les autres au myo-inositol-2 phosphate **24**.

Can. J. Chem. Downloaded from www.nrcresearchpress.com by 122.72.124.2 on 09/07/12
For personal use only.

pour les signaux ^{13}C du myo-inosotol-2 phosphate **24**. Tout comme le myo-inositol, ce dernier admet comme plan de symétrie le plan perpendiculaire au plan moyen du cycle et passant par C_2 et C_5. Ainsi les paramètres de RMN ^{13}C de **24** sont les suivants : C_1C_3, δ 72,8_4; C_2, δ 77,4_5, $^2J_{C2-P}$ 5,8 Hz; C_4C_6, δ 71,1_1; C_5, δ 74,5_2.

La séparation de ces monophosphates dans l'ordre que nous venons de décrire concorde avec les résultats récemment publiés par Binder *et al.* (33). Ainsi, parmi les produits à un atome de phosphore obtenus dans cette réaction, nous avons caractérisé trois myo-inositol monophosphates qui peuvent avoir un intérêt biologique. L'analyse des fractions à deux atomes de phosphore dans le but de détecter des myo-inositol bis-phosphates se poursuit actuellement.

Conclusion

Nous avons mis au point une méthode de phosphorylation du myo-inositol qui diffère de toutes celles rapportées dans la littérature (8–17, 35) par le fait qu'elle n'exige pas la protection préalable du myo-inositol.

Ce procédé à trois étapes seulement : phosphoranylation du myo-inositol, oxydation des phosphoranes et hydrolyse des phosphates neutres ainsi obtenus, permet d'accéder en une seule préparation à plusieurs phosphates de myo-inositol, ce qui est illustré par l'obtention des myo-inositol phosphates **22**, **23** et **24** en partant des tris-phosphoranes **10**. L'obtention, toujours en une seule opération, d'autres phosphates de myo-inositol biologiquement intéressants, comme les tris ou les tetrakis-phosphates, devient ainsi concevable moyennant une adéquation du degré de phosphoranylation du myo-inositol et une recherche de conditions d'hydrolyse qui protègeraient la liaison P—O de l'inositol. C'est ce que nous nous proposons d'étudier dans un proche avenir.[4]

Partie expérimentale

Méthodes spectroscopiques

Les spectres de RMN ^1H, ^{13}C et ^{31}P ont été enregistrés avec différents appareils Bruker : W.P 60, A.C 80, W.H. 90, W.M. 250 et A.M. 300 WB.

Les déplacements chimiques, exprimés en parties par million du champ inducteur (ppm) sont mesurés avec une précision de ±0,02 ppm pour ^1H, ±0,03 ppm pour ^{31}P et ^{13}C (références : TMS pour ^1H et ^{13}C, H_3PO_4 à 85% pour ^{31}P). Les constantes de couplage, exprimées en Hz, sont mesurées avec une précision de ±0,2 Hz.

Les spectres IR ont été enregistrés à l'aide d'un spectrographe Bruker I.F.S. 110 fonctionnant en transformée de Fourier (cuves de 200–1000 μm, 50–1000 accumulations). Résolution ±0,5 cm^{-1}.

Préparations

1. Le bicyclophosphane 8

Le 3,3,7,7-tetramethyl 2,8-dioxa 5-aza 1-phospha^{III} bicyclo [3,3,0]octane (bicyclophosphane *8*) a été obtenu selon une procédure que nous avons décrite précédemment (18, 34).

L'oligomérisation bien connue de ce composé a été réduite en mélangeant les solutions des réactifs goutte à goutte et non en une seule fois, comme c'était le cas précédemment. La pureté du produit obtenu a été vérifiée par RMN ^{31}P, ^1H et ^{13}C. Elle se situe en général entre 95 et 100%. Rdt, 45%. RMN ^{31}P (32, 44 MHz, toluène-d_8) : s 163 ppm; ^1H (80 MHz, C_6D_6): 1,21_6 ppm (s, 6H, CH_3), 1,30_8 ppm (s, 6H, CH_3), 2,73 et 2,99 ppm (2 quadruplets AB, 4H, $H_3H_4H_5H_6$, $^2J_{H3H4} = {}^2J_{H5H6} = -11,5$ Hz; $|{}^3J_{H3P}| = |{}^3J_{H5P}| = 8$ Hz; $|{}^3J_{H4P}|\,|{}^3J_{H6P}| = 9,3$ Hz); $^{13}C\{^1H\}$ (20,15 MHz, toluène-d_8): 28,5 (s, C_9), 30,5_2 (d, C_{10}, $^3J_{CP} = 3,2$ Hz)[5]; 64,20 (d, C_4, C_6, $^2J_{C—N—P} = 3,8$ Hz), 82,0_7 (d, C_3, C_7 $^2J_{C—O—P} = 10,5$ Hz) ppm.

2. Phosphoranes de myo-inositol

Les per-phosphoranes ainsi que les tris-phosphoranes de myo-inositol ont été préparés selon le même protocole expérimental dont voici un exemple. Une solution de 14,4 mg (0.08×10^{-3} mol) de myo-inositol dans 5 mL de DMSO est ajoutée en une fois à 90,7 mg ($0,48 \times 10^{-3}$ mol) de bicyclophosphane **8** (45,8 mg soit $0,24 \times 10^{-3}$ mol dans le cas de la tris-phosphoranylation). Au bout d'une dizaine de minutes d'agitation à la température ambiante, l'examen du spectre de RMN ^{31}P du mélange réactionnel montre que la réaction est terminée (voir Résultats et discussion).

*3. Le 3,3,7,7-tétraméthyl-1 isopropyloxy-2,8 dioxa-5 aza-1 phospha^V [3,3,0] bicyclooctane **11***

Une solution de 30 mg ($0,5 \times 10^{-3}$ mol) d'isopropanol, fraîchement distillé, dans 0,25 mL de toluène a été ajoutée en une fois à une solution de 94,5 mg ($0,5 \times 10^{-3}$ mol) du bicyclophosphane **8** dans 0,25 mL du même solvant. Le spectre de RMN ^{31}P enregistré 10 min après le mélange des réactifs montre que la réaction est terminée. Le produit n'a pas été isolé. Il a été caractérisé par RMN ^1H, ^{31}P et ^{13}C. RMN ^{31}P (32,44 MHz, toluène-d_8) : −37,27 ppm (d, $^1J_{P-H} = 791,5$ Hz); $^{31}P\{^1H\}$: −37,23 ppm (s); ^1H (300 MHz, toluène-d_8) : 1,18_5 ppm (d, 6H, CH_3 (10), $^3J_{H—C—C—H} = 6,2$ Hz), 1,21 ppm (s, 6H, CH_3 (11 ou 12)), 1,28_5 ppm (s, 6H, CH_3 (12 ou 11)), 2,49_7 et 2,56_6 ppm (2 quadruplets AB, 4H, H_3, H_4, H_5, H_6, $^2J_{H3H4} = {}^2J_{H5H6} = -8,2$ Hz; $|{}^3J_{H3\text{ ou }H_4P}| = 15$ Hz; $|{}^3J_{H4\text{ ou }H3P}| = 12,8$ Hz), 4,59_4 ppm (m, 1H H_9, $^3J_{H—C—O—P} = 10,7$ Hz); $^{13}C\{^1H\}$ (20,1_5 MHz, toluène-d_8) : 24,1_7 (d, C_{10}, $^3J_{C—C—O—P} = 5,9$ Hz), 29,1_7 (s, C_{11}), 29,6_3 (d, C_{12}, $^3J_{CP} = 5$ Hz), 55,5_9 (d, C_4, C_6, $^2J_{C—N—P} = 19$ Hz), 68,5_9 (d, C_9, $^2J_{C—O—P} = 6,4$ Hz), 70,0_8 (d, C_3, C_7, $^2J_{C—O—P} = 5,8$ Hz) ppm.

4. Oxydation

Au mélange réactionnel issu de la per-phosphoranylation (105,1 mg ($0,08 \times 10^{-1}$ mol) du composé **9** en solution dans 5 mL de DMSO) on ajoute 43,20 mg ($0,48 \times 10^{-3}$ mol) de tertiobutylhydroperoxyde, t-C_4H_9OOH, fraîchement redistillé (Eb_{10} = 28°C). Une agitation pendant 2 h à la température ambiante suffit pour conduire au mélange des phosphates neutres **13** et **15**. Le mélange des phosphates **14** et **16** est obtenu par le même procédé. Seule la quantité de tertiobutylhydroperoxyde est divisée par 2.

5. Sulfuration

Une solution de 131,4 mg ($0,1 \times 10^{-3}$ mol) du per-phosphorane de myo-inositol **9** dans 5 mL de DMSO est mélangée à 19,2 mg ($0,075 \times 10^{-3}$ mol) de fleur de soufre S_8. La dissolution de ce dernier dans le mélange réactionnel nécessite un chauffage à 40°C pendant 20–30 min. Un contrôle par RMN de ^{31}P montre que la sulfuration est terminée. Dans le cas des tris-phosphoranes **10** la quantité de fleur de soufre est réduite de moitié.

*6. Hydrolyse des phosphates neutres **13** + **15** ou **14** + **16***

L'addition à la température ambiante de la quantité stoechiométrique d'une solution d'acide chlorhydrique 1 N au mélange réactionnel des produits **13** + **15** ou **14** + **16** en solution dans le DMSO conduit à une solution dont le pH est égal à 5. À ce pH, la réaction est lente; au bout de 6 h, les modifications du spectre de RMN ^{31}P sont quasiment nulles. Nous avons vérifié qu'en diminuant le pH par addition de quantité

4. Pendant le temps qui s'est écoulé entre l'envoi du manuscrit et la réception des avis des rapporteurs, nous avons identifié, parmi les fractions à 2 atomes de phosphore, le myo-inositol-1,4 bis-phosphate. Cette identification a été réalisée en comparant le spectre de RMN ^1H de la fraction séparée à celui d'un échantillon authentique publié dans la littérature (28).

5. L'étude conformationnelle des bicyclophosphanes de ce type nous montre que la molécule se présente comme un toit à deux pentes, les doublets libres du phosphore et de l'azote étant sur le toit. Les cycles pentagonaux adoptent une conformation enveloppe bloquée, les atomes de carbone C_3 et C_7 étant à la pointe des rabats, lesquels sont orientés en *trans* par rapport aux doublets libres du phosphore et de l'azote (géométrie *endo–endo* (34)). L'existence d'une relation de type Karplus (31) pour le couplage $^3J_{P\text{-}O\text{-}C\text{-}C}$ explique l'existence ou non d'un couplage détectable entre le phosphore et les carbones C_9 et C_{10}. Pour le premier l'angle dièdre P—O—C_9 est voisin de 90°, alors que l'angle dièdre P—O—C—C_{10} est voisin de 150°.

croissante de solution d'acide chlorhydrique, la réaction est accélérée. À pH 2 elle est quasiment instantanée. Aussi les hydrolyses de ces phosphates ont été effectuées en portant directement à 2 la valeur du pH de la solution par addition de la quantité nécessaire de solution d'acide chlorhydrique 1 N.

7. Séparation par HPLC

Le mélange réactionnel de l'hydrolyse des phosphates neutres est évaporé à sec sous 10^{-2} Torr (1 Torr = 133.3 Pa). Le résidu est repris par un minimum d'eau puis filtré sur 0,22 μm millipore.

La séparation HPLC est réalisée sur colonne échangeuse d'anion Whatman Partisil Sax 10. Le gradient employé est analogue à celui de Irvine *et al.* (26). Le pH des solutions tampons est ajusté à 3,5 avec l'acide chlorhydrique et non de l'acide orthophosphorique pour permettre le contrôle par RMN. Tout au long de la séparation, le débit est de 3 mL/min et les fractions sont collectées toutes les minutes.

Remerciements

Les auteurs tiennent à remercier les responsables et personnels techniques des services spécialisés du Groupe régional de mesures physiques de Toulouse : Mme Bon, MM. Commenges, Dall'ava, Pelletier, Servin et Tran le Trang (RMN), Mme Bouissou (IR) et M. Roussel (spectrométrie de masse) pour l'enregistrement des spectres qui ont servi au cours de ce travail. Ils tiennent également à remercier Mme et Monsieur Cavadore du Centre de recherche de biochimie macromoléculaire du C.N.R.S. à Montpellier qui ont apporté une contribution décisive à la mise au point des séparations chromatographiques.

1. K. L. Agarwal, A. Yamazaki, P. T. Cashion et M. G. Khorana. Angew. Chem. Int. Ed. Engl. **11**, 457 (1972).
2. M. H. Caruthers. Science, **230**, 281 (1985).
3. (*a*) H. Streb, R. F. Irvine, M. J. Michell et I. Schule. Nature, **306**, 67 (1983); (*b*) M. J. Berridge et R. F. Irvine. Nature, **312**, 315 (1984).
4. R. J. Michell. Nature, **318**, 176 (1986).
5. A. A. Abdel-Latif. Pharmacolol. Rev. **38**, 227 (1986).
6. (*a*) C. Grado et C. E. Ballou. J. Biol. Chem., **236**, 54 (1961); (*b*) R. V. Tomlinson et C. E. Ballou. J. Biol. Chem. **236**, 1902 (1961).
7. Catalogue Boehringer, Mannheim, République fédérale d'Allemagne. 1987. pp. 158–160.
8. S. Ozaki, Y. Watanabe, T. Ogasawara, Y. Kondo, N. Shiotani, H. Nishi et T. Matsuki. Tetrahedron Lett. **27**, 3157 (1986).
9. D. C. Billington, R. Baker, J. J. Kulagowski et I. M. Mawer. J. Chem. Soc. Chem. Commun. 314 (1987).
10. D. C. Billington et R. Baker. J. Chem. Soc. Chem. Commun. 1011 (1987).
11. (*a*) J. P. Vacca, S. Jane de Solmes et J. R. Huff. J. Am. Chem. Soc. **109**, 3478 (1987); (*b*) Tetrahedron Lett. **28**, 4503 (1987).
12. Y. Watanabe, H. Nakahira, M. Bunya et S. Ozaki. Tetrahedron Lett. **28**, 4179 (1987).
13. M. R. Hamblin, B. V. L. Potter et R. Gigg. J. Chem. Soc. Chem. Commun. 626 (1987).
14. C. B. Reese et J. G. Ward. Tetrahedron Lett. **28**, 2309 (1987).
15. (*a*) A. M. Cooke, B. V. L. Potter et R. Gigg. Tetrahedron Lett. **28**, 2305 (1987). (*b*) M. Cooke, R. Gigg et B. V. L. Potter. J. Chem. Soc. Chem. Commun. 1525 (1987).
16. (*a*) Y. Watanabe, T. Ogasawara, N. Shiotani et S. Ozaki. Tetrahedron Lett. **28**, 2607 (1987); (*b*) S. Ozaki, Y. Kondo, H. Nakahira, S. Yamauka et Y. Watanabe. Tetrahedron Lett. **28**, 4691 (1987).
17. (*a*) M. R. Hamblin, J. S. Flora et B. V. L. Potter. Biochem. J. **246**, 771 (1987); (*b*) K. L. Yu et B. Fraser-Reid. Tetrahedron Lett. **29**, 979 (1988); (*c*) J. L. Meek, F. Davidson et F. W. Hobbs, Jr. J. Am. Chem. Soc. **110**, 2317 (1988).
18. D. Houalla, F. H. Osman, M. Sanchez et R. Wolf. Tetrahedron Lett. **35**, 3041 (1977).
19. (*a*) D. Houalla, A. Munoz, H. Ramdame et R. Wolf. Tetrahedron Lett. **26**, 2003 (1985); (*b*) B. Duthu, D. Houalla, M. C. Duriez et R. Wolf. Phosphorus Sulfur, **30**, 319 (1987).
20. (*a*) E. H. Amondo-Neizer, S. K. Ray, R. A. Shaw et B. C. Smith. J. Chem. Soc. 4296 (1965); (*b*) M. Dreux, Y. Leroux et P. Savignac. Synthesis, 506 (1974); (*c*) A. Munoz, M. Gallagher, A. Klaebe et R. Wolf. Tetrahedron Lett. 673 (1976); (*d*) J. Dabrowiez, T. Numata et S. Oae. Org. Prep. Proced. Int. **9**, 63 (1977).
21. J. M. Socol et J. G. Verkade. Inorg. Chem. **23**, 3487 (1984).
22. K. Taira et D. G. Gorenstein. Tetrahedron, **40**, 3215 (1984).
23. V. Mark, C. H. Dungan, M. M. Crutchfield et J. R. Van Wazer. Topics in phosphorus chemistry. Interscience Publishers, New-York, NY. 1967. Chap. 4.
24. J. Devillers. Thèse de l'Université Paul Sabatier de Toulouse. 1972.
25. J. P. Cox et M. G. Newton. J. Org. Chem. **34**, 2600 (1969).
26. R. F. Irvine, E. E. Anggard, A. Letcher et C. P. Downes. Biochem. J. **229**, 505 (1985).
27. R. A. Graham, R. A. Meyer, B. S. Szwergold et T. R. Brown. J. Biol. Chem. **262**, 35 (1987).
28. S. Cerdan, C. A. Hansen, R. Johanson, T. Inubushi et J. R. Williamson. J. Biol. Chem. **261**, 14676 (1986).
29. L. R. Isbrandt et R. P. Oertel. J. Am. Chem. Soc. **102**, 3144 (1980).
30. J. C. Lindon, D. J. Baker, R. D. Farrant et J. M. Williams. Biochem. J. **233**, 275 (1986).
31. D. G. Gorenstein. Phosphorus 31 NMR — Principles and applications. Academic Press, New York, NY. 1984. pp. 43–51.
32. (*a*) M. Karplus. J. Am. Chem. Soc. **85**, 2870 (1963); (*b*) W. J. Jung, R. E. Marsh et M. Kainosho. J. Am. Chem. Soc. **99**, 5471 (1977); (*c*) Y. Y. Samitov, A. A. Musina, R. M. Aminova, M. A. Pudovik, A. I. Khayarov et M. D. Medvedeva. Org. Magn. Reson. **13**, 162 (1980); (*d*) P. P. Lankhorst, C. A. G. Haasnoot, C. Erkelens et C. Altona, J. Biomol. Struct. Dyn. **1**, 1387 (1984).
33. H. Binder, P. C. Weber et W. Siess. Anal. Biochem. **148**, 220 (1985).
34. C. Bonningue, D. Houalla, M. Sanchez, R. Wolf et F. H. Osman. J. Chem. Soc. Perkin Trans. 2, 19 (1981).
35. (*a*) F. L. Pizer et C. E. Ballou. J. Am. Chem. Soc. **81**, 915 (1959); (*b*) T. Posternak. Helv. Chim. Acta, **42**, 390 (1959).

Can. J. Chem. Downloaded from www.nrcresearchpress.com by 122.72.124.2 on 09/07/12
For personal use only.

A new synthesis of 2,5-anhydro-D-mannose derivatives[1]

JUAN A. LÓPEZ SASTRE,[2] JOSÉ MOLINA MOLINA,[3] DOLORES PORTAL OLEA, AND CRISTINA ROMERO-AVILA[2]
Departamento de Quimica Orgánica, Universidad de Granada, 18071 Granada, Spain

Received August 17, 1987[4]

JUAN A. LÓPEZ SASTRE, JOSÉ MOLINA MOLINA, DOLORES PORTAL OLEA, and CRISTINA ROMERO-AVILA. Can. J. Chem. **66**, 2975 (1988).

Penta-*O*-acetyl-D-glucose diethyl dithioacetal monoxide **3** was obtained by oxidation of penta-*O*-acetyl-D-glucose diethyl dithioacetal **2** with 3-chloroperbenzoic acid. By reaction of **3** with sodium methoxide in methanol and further acetylation, 3,4,6-tri-*O*-acetyl-2,5-anhydro-D-mannose-diethyl dithioacetal monoxide **8** and the reduction product 3,4,6-tri-*O*-acetyl-2,5-anhydro-1,1-bis(ethylthio)-1-deoxy-D-arabino-hex-1-enitol **4** were obtained. Reduction of **8** yielded the corresponding dithioacetal derivative **9**, which was converted to 3,4,6-tri-*O*-acetyl-2,5-anhydro-D-mannose diethyl acetal **11**.

JUAN A. LÓPEZ SASTRE, JOSÉ MOLINA MOLINA, DOLORES PORTAL OLEA et CRISTINA ROMERO-AVILA. Can. J. Chem. **66**, 2975 (1988).

L'oxydation du diéthyl dithioacétal du penta-*O*-acétyl-D-glucose **2** par l'acide chloro-3 perbenzoïque conduit au monoxyde du diéthyl dithioacétal penta-*O*-acétyl-D-glucose **3**. La réaction du composé **3** avec le méthanolate de sodium dans le méthanol, suivie d'une acétylation, conduit au monoxyde du diéthyl dithioacétal tri-*O*-acétyl-3,4,6 déhydro-2,5 D-mannose **8** et au produit de réduction, le tri-*O*-acétyl-3,4,6 anhydro-2,5 bis-éthylthio-1,1 déoxy-1 D-arabino-hexène 1 itol **4**. La réduction du composé **8** conduit au dérivé dithioacétal correspondant **9** que l'on transforme en diéthyl acétal tri-*O*-acétyl-3,4,6 anhydro-2,5 D-mannose.
[Traduit par la revue]

Introduction

One of the best-known methods to obtain 2,5-anhydro aldehydo sugars is the nitrous acid deamination of 2-amino-2-deoxy-D-glucose to yield 2,5-anhydro-D-mannose **1** (1). However, because of the nature of **1**, the utility of this method is seriously diminished; nevertheless the crystalline 2,5-anhydro-D-mannitol was obtained (2) by a reduction procedure, although this compound lacks the potentiality of a carbonyl group. In our laboratories this synthesis was modified by *in situ* protection of the aldehyde group, preparing several 2,5-anhydro-D-mannose dithioacetal derivatives (3), and using them in a further synthesis of C-nucleoside analogues (4).

In the literature the oxidation of dialkyl dithioacetal sugar derivatives with peracid yields the corresponding sulfoxides and sulfones, and on some occasions the unsaturated product from the elimination between C-1 and C-2 is isolated (5). From disulfone derivatives of aldose diethyldithioacetals, the formation of side products of 2,6-anhydro hexose and heptose and of 2,5-anhydro pentose derivatives has been postulated (6). However, those anhydro derivatives have not been fully characterized or used in synthesis.

In this work we present a new method of obtaining 2,5-anhydro-D-mannose derivatives from D-glucose. At the same time, 2,5-anhydro-D-gluco- or manno-ketene dithioacetal derivatives are isolated.

Results and Discussion

Oxidation of penta-*O*-acetyl-D-glucose diethyl dithioacetal **2** with 3-chloroperbenzoic acid yields penta-*O*-acetyl-D-glucose diethyl dithioacetal monoxide **3** as a mixture of isomers. During the reaction, two new chiral centers are formed.

By reaction of **3** with an excess of sodium methoxide in methanol and subsequent acetylation of the reaction mixture;

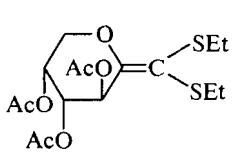

5

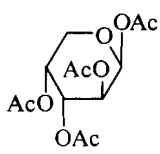

6

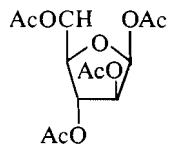

7

two products are isolated by column chromatography with a large R_f (tlc) difference (R_{f1} 0.75; R_{f2} 0.25 (hexane:ether 1:1)).

The first product is identified as 3,4,6-tri-*O*-acetyl-2,5-anhydro-1-deoxy-1,1-bis(ethylthio)-D-arabino-hex-1-enitol **4**.

Firstly, we concentrated our attention on the structural determination of the ring size of **4**. To solve this question we used both ^1H and ^{13}C nmr data, and molecular mechanics calculations.

Molecular models for a six-membered ring in the $^4C_1$ conformation show that the H-5,6 and H-5,6′ angles are 180° and 80° approximately. These angles must show a large and a small coupling constant, respectively. However, in the $^1C_4$ conformation, the H-5,6 and H-5,6′ angles are the same, about 60°, but the H-3,4 angle is 180°. The coupling constant $J_{3,4}$ must be large. Molecular models for a five-membered ring show that the C-3,4 and C-4,5 angles are 90°, therefore $J_{3,4}$ and $J_{4,5}$ must be small. Molecular mechanics calculations have been performed for a related compound of **4**, compound **16** (see Fig. 1). The reason for choosing this compound is the structural similarity between **4** and **16**, and the impossibility for doing such a calculation on **4**, due to the lack of parameterization on the S—C_{sp^2}—S group. Molecular mechanics calculations show angles for H—C3—C4—H and H—C4—C5—H of 94.6° and −91.4° respectively. Theoretical $^3J_{HH}$ calculations show $J_{3,4} = -0.12$ and $J_{4,5} = 0.47$ Hz. The final conformation obtained by molecular mechanics is shown in Fig. 1, and the atomic Cartesian coordinates in Appendix 1. Experimentally (see experimental part) the compound **4** shows $J_{3,4}$ and $J_{4,5}$ as less than 1 Hz.

Similarly, we can obtain inferential data from the ^{13}C nmr spectra. As can be seen, both structures **4** and **5** show close analogies to 1,2,3,4-tetra-*O*-acetyl-β-D-arabino furanose **7** and 1,2,3,4-tetra-*O*-acetyl-β-D-arabino pyranose **6**, respectively; therefore we can compare the 2,3,4, and 5 carbon ^{13}C nmr absorptions in structures **6** and **7** with those corresponding to

[1]This research was supported in part by two grants from the CAICYT, numbers 1236/81 and G 165/85.

[2]Departamento de Quimica Orgánica, E.T.S. Ingenieros Industriales, Universidad de Valladolid, 47071 Valladolid, Spain.

[3]Author to whom correspondence may be addressed.

[4]Revision received August 5, 1988.

Can. J. Chem. Downloaded from www.nrcresearchpress.com by 122.72.124.2 on 09/07/12
For personal use only.

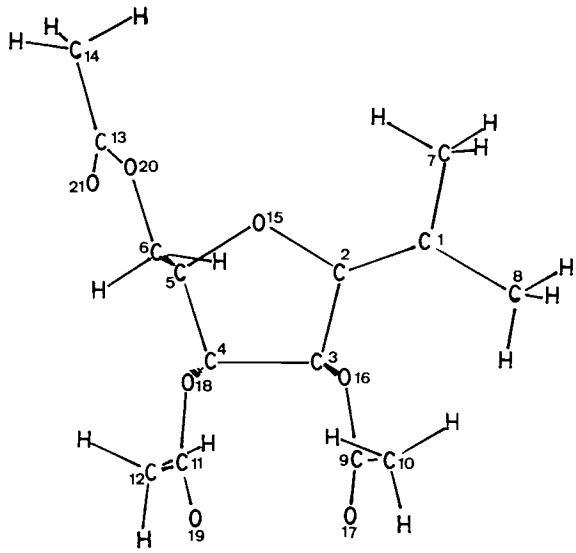

FIG. 1. Final conformation for **16**, obtained by molecular mechanics calculations.

TABLE 1. Carbon-13 nmr data

Compound	C—2	C—3	C—4	C—5	Reference
6	67.3	68.7	66.9	62.9	7
7	75.4	74.8	79.7	64.5	7

carbons 3,4,5, and 6 in structures **5** and **4**, respectively, as shown in Table 1.

The experimental data obtained for these compounds are C-3: 76.3; C-4: 74.7; C-5: 84.6; and C-6: 62.1, in complete accordance with those of compound **7** and in agreement with a five-membered ring structure.

The synthesis of **4** from **3** implies a reduction of the ethylsulfinyl to a ethylthio group. We explain this formation, as shown in Scheme 2.

Oxidation of C-2 could be an internal Moffatt oxidation upon treatment with acetic anhydride in pyridine (8); posterior cyclization leads to the hemiacetal and, after acetylation and acetic acid elimination, product **4** was formed.

The second product was 3,4,6-tri-*O*-acetyl-2,5-anhydro-D-mannose diethyl dithioacetal monoxide **8**. Its ^{1}H nmr shows the existence of three acetyl groups and two methyl groups from ethylthio groups. The above data are consistent with the existence of a ring. After several, very careful column chromatographic separations, only one pure compound could be isolated (yield 1.3%). Its spectroscopic and physical data are in agreement with one isomer of structure **8**; from the ^{1}H and ^{13}C nmr data we can conclude its structure: in ^{1}H nmr only two peaks appear, corresponding to two methines bonded to acetate groups (H-3 and H-4). The methylene at C-6 appears as a doublet, and is located at very low field, in agreement with having a five-membered ring and being bonded to an acetate group. It is also possible to say that one of the sulfur atoms is oxidized to a sulfoxide group; the signals corresponding to both methyls, in the ethylthio and ethylsulfinyl groups, appear at different field as two triplets, and the two H's of the methylene of the ethylsulfinyl group are diastereotopic, appearing as two sets of signals at different field. All the above arguments can be confirmed using ^{13}C nmr data. The methyls from the ethylthio and ethylsulfinyl groups appear at 14.96 and 7.13 ppm respectively, and the methylenes from the same groups at 28.06 and 43.19 ppm respectively. The absorptions of C-3, C-4, and C-5 appear at values in accordance with compound **7** (see Table 1), in agreement with a five-membered ring.

From the above-mentioned column chromatographic separation, fractions consisting of mixtures of several isomers of **8** in different yields could be obtained, except for the compound mentioned (**8**). The hplc separation of these fractions shows that they are mixtures of four different compounds, representing more than 90% of the mixture. The retention times (RT) and the yields from **3** are as follows: (a) 7.5 min, 22.3%; (b) 8 min, 13.3%; (c) 8.8 min, 9.8%; (d) 11 min, 7.1%. The compound isolated by column chromatography corresponds to an RT of 8 min.

Reduction of **8** yields 3,4,6-tri-*O*-acetyl-2,5-anhydro-D-mannose diethyl dithioacetal **9**. Its structure could be determined chemically as follows: hydrolysis of **9** yields 3,4,6-tri-*O*-acetyl-2,5-anhydro-D-mannose **10**, which, without purification, was treated with triethyl orthoformate in ethanol to yield 3,4,6-tri-*O*-acetyl-2,5-anhydro-D-mannose diethyl acetal **11**.

We obtained **11** by the following unequivocal method: acetylation of 2,5-anhydro-D-mannose di-*n*-propyl dithioacetal **12** yields the triacetate derivative **13**, which upon hydrolysis and subsequent reaction with ethyl orthoformate produces a compound with spectroscopic values identical to **11**.

Compound **8** can be formed by an intramolecular nucleophilic attack of OH at C-5 on the double bond between C-1 and C-2, as shown in Scheme 2. This double bond in **14** is activated by the presence of the sulfoxide group (9).

The above conclusions have been confirmed by reaction of **3**

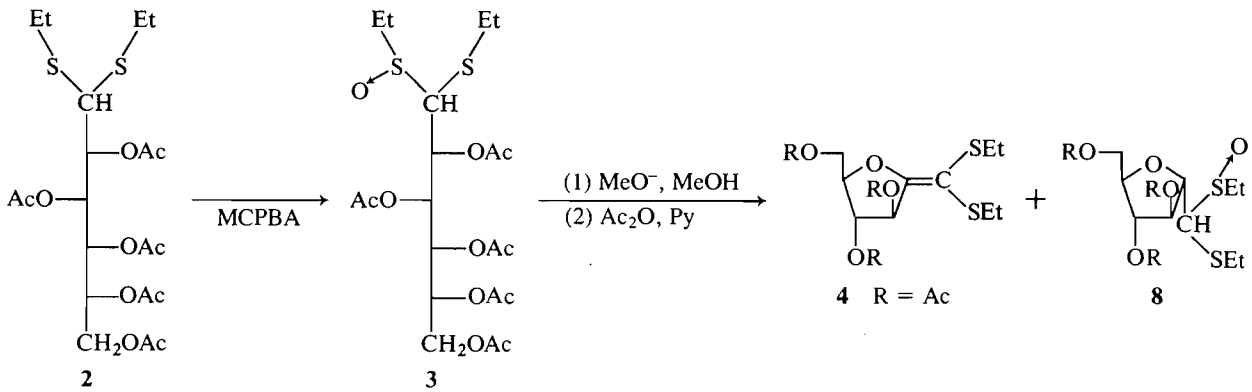

2 **3** **4** R = Ac **8**

SCHEME 1

Can. J. Chem. Downloaded from www.nrcresearchpress.com by 122.72.124.2 on 09/07/12
For personal use only.

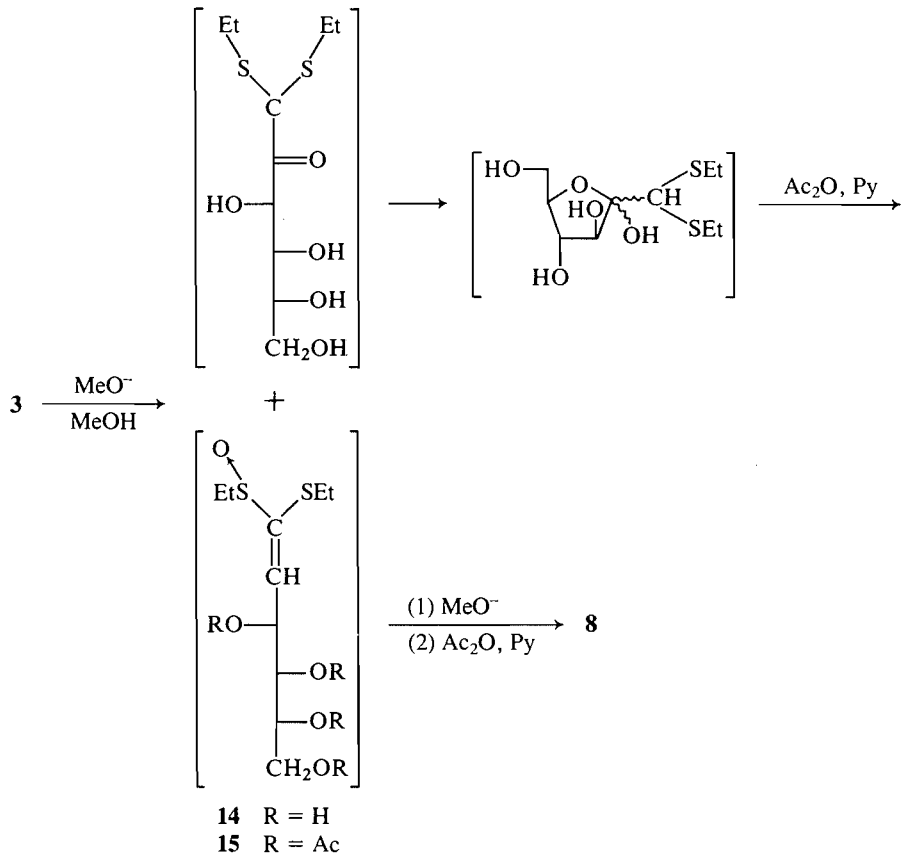

SCHEME 2

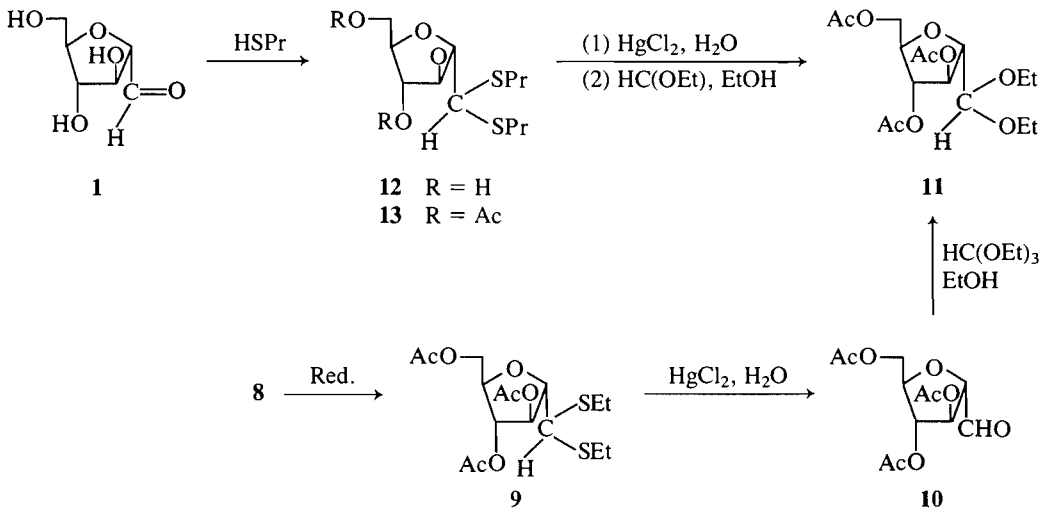

SCHEME 3

with potassium *tert*-butoxide to yield 3,4,5-tri-*O*-acetyl-1,2-dideoxy-1-ethylthio-1-ethylsulfinyl-hex-1-enitol **15**.

Integration of the ^{1}H nmr spectrum of **15** shows four acetyl groups and a vinyl proton, which is in accordance with a linear molecule. When **15** is treated with sodium methoxide, followed by acetylation and reduction, a mixture of **4** and **9** is obtained.

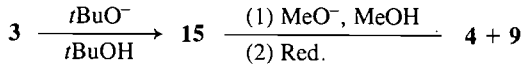

SCHEME 4

The presence of **4** in the reaction mixture can be explained by addition of the methoxide ion to the double bond and subsequent oxidation and elimination in a mechanism similar to the one shown in Scheme 2.

Experimental

General methods

Organic solutions were dried over anhydrous $MgSO_4$. Solvents were evaporated under diminished pressure below 40°C. Column chromatography was carried out on Silica Gel 60 (Merck, 70–230 mesh, ASTM). Optical rotations were measured with a Perkin–Elmer 141

Can. J. Chem. Downloaded from www.nrcresearchpress.com by 122.72.124.2 on 09/07/12
For personal use only.

Can. J. Chem. Downloaded from www.nrcresearchpress.com by 122.72.124.2 on 09/07/12
For personal use only.

automatic polarimeter. The ^1H nmr and ^{13}C nmr spectra were recorded for solutions in $CDCl_3$ (internal Me_4Si), using a Bruker WP-80-SY or a Bruker AM-300, and ir spectra with a Perkin–Elmer 983-G spectrometer. Elemental analyses were realized on a Perkin–Elmer 240C or on a Carlo Erba 1106. The hplc separations were carried out on a Waters-501, using a Pyrkle IA column, with 80:20 isopropanol–hexane as a mobile phase at 0.8 mL/min, monitoring at 230 nm.

Calculations

The energetic minimizations were performed by an MMPM program from Serena Software.[5] The inputs for the MMPM program were carried out using the STRP program.[5] A value of 10 for the effective dielectric constant has been chosen. Theoretical $^3J_{HH}$ calculations were performed by application of the generalized Karplus equation (10), using the program from Osawa and Jaime (11).

*2,3,4,5,6-Penta-*O*-acetyl-*D*-glucose diethyl dithioacetal* **2**

Ethanethiol (50 mL) was added dropwise to a stirred solution of D-glucose (50 g) in hydrochloric acid (43 mL) at room temperature. After 30 min ice was added up to precipitation of the corresponding dithioacetal. The solid was filtered and washed with ice-water, $NaHCO_3$ solution, and ethanol. A white solid (69 g) was obtained. After acetylation in the usual manner with acetic anhydride and pyridine, 2,3,4,5,6-penta-*O*-acetyl-D-glucose diethyl dithioacetal **2** (197 g) was obtained (12).

*2,3,4,5,6-Penta-*O*-acetyl-*D*-glucose diethyl dithioacetal monoxide* **3**

A solution of 3-chloroperbenzoic acid (4.34 g) in CH_2Cl_2 (70 mL) was added dropwise to a solution of penta-*O*-acetyl-D-glucose diethyl dithioacetal (9.92 g) in CH_2Cl_2 (100 mL), stirred at −10°C for 20 min. The reaction mixture was treated with $NaHCO_3$ and water, dried, and the solvent removed to leave 2,3,4,5,6-penta-*O*-acetyl-D-glucose diethyl dithioacetal monoxide **3** (10.5 g) as a mixture of the possible diasteromers observed by the ^1H nmr spectrum. It was not possible to resolve this mixture after several attempts using column chromatography.

Reaction of **3** *with sodium methoxide*

Sodium methoxide in methanol was added dropwise, until pH was basic, to a solution of 2,3,4,5,6-penta-*O*-acetyl-D-glucose diethyl dithioacetal monoxide **3** (1.3 g) in methanol (15 mL), stirred for 1 h at room temperature. After 30 min, acid Amberlite IR-45 resin was added until pH 7, and the mixture stirred for 1 h. This mixture was filtered and the solvent evaporated to leave a syrup, which, upon acetylation (acetic anhydride and pyridine), produced a mixture (1.29 g). After purification by column chromatography (hexane:ethyl acetate 3:1 to ethyl acetate and to ethyl acetate:acetone 9:1) two products were obtained:

(*i*) 3,4,6-Tri-*O*-acetyl-2,5-anhydro-1,1-bis-ethylthio-1-deoxyhex-1-enitol **4** (100 mg); $[\alpha]_D$ +17.1(*c* 0.4, Cl_3CH); ir ν_{max} (cm^{-1}): 1747, 1620, 1448, 1369, and 1227; ^1H nmr, δ(ppm): 6(s, 1H, H-3), 5.05 (dd, 1H, $J_{3,4} = J_{4,5} < 1$ Hz, H-4), 4.56 (dt, 1H, H-5), 4.34 (dd, 1H, $J_{6,6'} = 12$ Hz, $J_{5,6} = 6$ Hz, H-6), 4.24 (dd, 1H, $J_{5,6'} = 5$ Hz, H-6′), 2.5–2.9 (m, 4H, 2S—CH_2—CH_3), 2.14 (s, 3H, COCH_3), 2.10 (s, 6H, 2COCH_3), 1.25 (t, 3H, $J = 7$ Hz, SCH_2CH_3), and 1.20 (t, 3H, $J = 7$ Hz, SCH_2CH_3); ^{13}C nmr, δ(ppm): 170, 169.3, and 168.7 ($3COCH_3$), 158.3 (C-2), 104.5 (C-1), 84.6, 76.3, and 74.7 (3CH, C-5, 3, and 4, respectively), 62.1 (CH_2, C-6), 27 and 26.6 ($2CH_2$, SCH_2CH_3), 20.5 and 20.4 ($3CH_3$, $COCH_3$), 14.4 and 14.1 ($2CH_3$, SCH_2CH_3). *Anal.* calcd. for $C_{16}H_{24}O_7S_2$: C 48.96, H 6.16; found: C 48.92, H 6.30.

(*ii*) 3,4,6-Tri-*O*-acetyl-2,5-anhydro-D-mannose diethyl dithioacetal monoxide **8** (539 mg). After several and very careful column chromatography separations using hexane–ether as eluent, a fraction with only one pure isomer (17 mg) could be isolated. Liquid, $[\alpha]_D$ +13.7 (*c* = 1.1, $CHCl_3$); ir ν_{max} (cm^{-1}): 2968, 2933, 1740, 1447, 1371, 1229, 1047, 970, and 908; ^1H nmr, δ(ppm): 5.59 (dd, 1H, $J_{2,3} = 6.59$, $J_{3,4} = 4.52$ Hz,H-3), 5.31(t, 1H, $J_{4,5} = 4.54$ Hz, H-4), 4.65 (dd, 1H, $J_{1,2} = 1.78$ Hz, H-2), 4.29(q, 1H, $J_{5,6} = J_{5,6'} = 4.23$ Hz, H-5), 4.21 (d,2H, H-6 and H-6′), 3.89 (d, 1H, H-1), 3.2–3.04 (m, 1H, H-a of the methylene in the ethylsulfinyl group), 2.9–2.68 (m, 3H, H-b of the methylene of the ethylsulfinyl group and the methylene of ethylthio group), 2.06, 2.07, and 2.09 (3s, 9H, 3CO—CH_3), 1.39 (t, 3H, $J = 7.49$ Hz, CH_3—CH_2—SO), 1.29 (t, 3H, $J = 7.45$ Hz, CH_3—CH_2—S); ^{13}C nmr, δ (ppm): 170.72, 170.32 (3C, *CO*—CH_3), 80.56, 78.69, 78.58, and 77.83 (4CH, C-2, C-3, C-4, and C-5), 67.62 (CH, C-1), 63.14 (CH_2, C-6), 43.19 (CH_2, SO—CH_2—CH_3), 28.06 (CH_2, S—CH_2—CH_3), 20.85 and 20.71 ($3CH_3$, CO—CH_3), 14.56 (CH_3, CH_3—CH_2—S), and 7.13 (CH_3, CH_3—CH_2—SO).

The remaining fractions were mixtures of different isomers.

*Reduction of 3,4,6-tri-*O*-acetyl-2,5-anhydro-*D*-mannose diethyl dithioacetal monoxide* **8**

$TiCl_4$ (0.25 mL) was added to a stirred and cooled suspension of powdered Zn (273.7 mg) in anhydrous diethyl ether (2 mL). After 2 min a solution of **8** (539 mg) in CH_2Cl_2 (2 mL) was added. The reaction mixture was poured into water and extracted twice with diethyl ether. The combined organic layers were dried over $MgSO_4$ and the solvent removed to leave a mixture that was purified by column chromatography (hexane:ether 10:1 to 2:1), giving 3,4,6-tri-*O*-acetyl-2,5-anhydro-D-mannose diethyl dithioacetal **9** (151 mg); $[\alpha)_D$ +41.3 (*c* 1.01, Cl_3CH); ir, ν_{max} (cm^{-1}): 1745, 1451, 1370, 1225, 1045, and 900; ^1H nmr, δ(ppm): 5.55 (dd, 1H, $J_{2,3} = 5$ *Hz*, $J_{3,4} = 4$ Hz, H-3), 5.12 (t, 1H, H-4), 4.37–4.12 (m, 4H, H-2, 5, 6, and 6′), 4.00 (d, 1H, $J = 6$ Hz, H-1), 2.7 (q, 4H, $J = 7$ Hz, SCH_2CH_3), 2.05 (s, 9H, COCH_3), 1.25 (t, 6H, SCH_2CH_3); ^{13}C nmr, δ (ppm): 170.3, 169.8, 169.6 (3C, $COCH_3$), 85.4, 80.53, 79.2, and 78.02 (4CH, C-2, 5, 3, and 4, respectively), 62.8 (CH_2, C-6), 52.8 (CH, C-1), 25.02 and 24.8 ($2CH_2$, SCH_2CH_3), 20.05 ($3CH_3$, $COCH_3$), 14.25 ($2CH_3$, SCH_2CH_3). *Anal.* calcd. for $C_{16}H_{26}O_7S_2$: C 48.71, H 6.64; found: C 48.58, H 6.74.

*Hydrolysis of 3,4,6-tri-*O*-acetyl-2,5-anhydro-q2d-mannose diethyl dithioacetal* **9**

A mixture of **9** (199 mg), acetone (2 mL), water (0.15 mL), HgO (344 mg), and $HgCl_2$ (344 mg) was stirred for 2 h at room temperature. Then the solvent was removed, $CHCl_3$ (50 mL) was added, and the mixture was filtered through Celite. The chloroform solution was washed with a solution of KI and water, dried, and the solvent removed to leave 3,4,6-tri-*O*-acetyl-2,5-anhydro-aldehydro-D-mannose **10** (145 mg); ^1H nmr, δ (ppm): 9.67 (s, H, aldehyde). This compound was used without further purification.

*3,4,6-Tri-*O*-acetyl-2,5-anhydro-*D*-mannose diethyl acetal* **11**

Ethyl orthoformate (0.5 mL) and Amberlite IR-45 resin were added to a solution of **10** (145 mg) in ethanol (1 mL) and stirred at room temperature for 24 h. The reaction mixture was filtered and solvent removed to leave a syrup that was purified by column chromatography (ethyl ether:hexane 2:1) to give 3,4,6-tri-*O*-acetyl-2,5-anhydro-D-mannose diethyl acetal **11** (106 mg); $[\alpha]_D$ +24.85 (*c* 1.02, Cl_3CH); ir, ν_{max} (cm^{-1}): 2985, 1746, 1370, 1230, and 1060; ^1H nmr, δ (ppm): 5.36 (t, 1H, $J_{3,2} = J_{3,4} = 4$ Hz, H-3), 5.05 (m, 1H, H-4), 4.51 (d, 1H, $J_{1,2} = 5$ Hz, H-1), 4.10–4.25 (m, 3H, H-5, 6, and 6′), 4.02 (dd, 1H, H-2), 3.85–3.30 (m, 4H, OCH_2CH_3), 2.02 (s, 9H, CH_3CO), 1.15 and 1.16 (2t, 6H, $J = 7$ Hz, OCH_2CH_3); ^{13}C nmr, δ(ppm): 170.4, 169.7, and 169.5 (3C, $COCH_3$), 111.5 (CH, C-1), 82.63, 80.93, 78.3, and 77.9 (4CH, C-2, 5, 3, and 4, respectively), 63.6, 63.08, and 62.3 ($3CH_2$, C-6 and OCH_2), 20.6 (CH_3, $COCH_3$), and 15.08 (CH_3, OCH_2CH_3). *Anal.* calcd. for $C_{16}H_{26}O_9$: C 53.03, H 7.23; found: C 52.97, H 7.29.

*Synthesis of 2,5-anhydro-*D*-mannose di-*n*-propyl dithioacetal* **12**

Treatment of 2,5-anhydro-D-mannose **1** with *n*-propanethiol as described for the synthesis of 2,5-D-mannose dialkyl dithioacetal (3) produces **12**. Solid, mp 64–65°C; $[\alpha]_D$ +51.9 (*c* 1, $CHCl_3$); ir, ν_{max} (cm^{-1}): 3400, 3000, 2900, and 1060; ^1H nmr, δ (ppm): 3.8–3.5 (br, 2H, 2OH), 3.35–3.1 (m, 1H, OH), 3.0–2.25 (7H, H-1, 2, 3, 4, 5, 6,

[5]MMPM is an addition to MM2 (Allinger, QCPE 395) and MMP1 (Allinger, QCPE 318), by K. E. Gilbert and J. J. Gajewski, Indiana University. STRP is used to generate an input file.

and 6′), 1.15–0.9 (m, 4H, $2CH_3$—CH_2—CH_2), 0.9–0.65 (t, 6H, $2CH_3$). *Anal.* calcd. for $C_{12}H_{24}O_4S_2$: C 48.64, H 8.17; found: C 48.99, H 8.17.

*Synthesis of 3,4,6-tri-*O*-acetyl-2,5-anhydro-*D*-mannose diethyl acetal **11** from 2,5-anhydro-q2d-mannose di-*n*-propyl dithioacetal **12***

2,5-Anhydro-D-mannose di-*n*-propyl dithioacetal **12** was acetylated by the usual procedure (pyridine – acetic anhydride). The reaction mixture was purified by column chromatography (hexane:ether) to give **13** in quantitative yield. Hydrolysis of **13** following the same procedure as for **9** gave the corresponding aldehyde **10**; ^{1}H nmr, δ(ppm): 9.67 (s, H, aldehyde). Treatment of this aldehyde, without any purification, with triethyl orthoformate and ethanol under the same conditions as above, after column chromatography yielded a product with the same physical and spectroscopic properties as those presented by **11**.

*Reaction of **3** with potassium* tert-butoxide

Potassium *tert*-butoxide (218 mg) in *tert*-butanol was added dropwise to a stirred solution of **3** (1 g) in *tert*-butanol (40 mL), and refluxed for 10 min. Then Amberlite IR-45 resin was added until acid pH. The solution was filtered and the solvent evaporated to give a mixture that, upon acetylation by the usual method and after column chromatography (ethyl ether), rendered **15** (510 gmg) as a mixture of the possible isomers; ^{1}H nmr, δ (ppm): 6.65 and 6.60 (2d, $J_{2,3}$ = 8 Hz, H-2), 6.25 (dd, 1H, $J_{3,4}$ = 2 Hz, H-3), 5.50–5.20 (m, 2H, H-4 and 5), 4.3–4.1 (m, 2H, H-6 and 6′), 3.25–2.5 (m, 4H, SCH_2CH_3 and $SOCH_2CH_3$), 2.1–1.9 (m, 12H, $4COCH_3$), 1.45–1.00 (m, 6H, SCH_2CH_3 and $SOCH_2CH_3$).

*Reaction of **15** with sodium methoxide in methanol*

Sodium methoxide in methanol was added dropwise until permanent basic pH to a solution of **15** (510 mg) in methanol (15 mL), which was then stirred for 30 min at room temperature. Amberlite IR-45 resin was added until pH 7. This was filtered and evaporated, giving a mixture that was acetylated in the usual manner. The acetylated mixture (335 mg) was reduced with $TiCl_4$ and Zn, under the same conditions as **8**, yielding, after purification by column chromatography, a mixture of **4** and **9**.

Acknowledgements

The authors thank José Macario Funes Tovar for his cooperation in the English translation of this text, and also thank both referees for helpful comments.

1. G. LEDDERHOUSE. Z. Physiol. Chem. **4**, 139 (1880); E. FISCHER and F. TIEMANN. Ber. **27**, 138 (1884).
2. B. C. BERA, A. B. FOSTER, and M. STACEY. J. Chem. Soc. 4531 (1956); D. HORTON and K. B. PHILLIPS. Carbohydr. Res. **30**, 367 (1975).
3. J. A. LÓPEZ SASTRE, J. ISAC GARCIA, J. MOLINA MOLINA, and C. ROMERO-AVILA. An. Quim. Ser. C: **79**, 283 (1983).
4. F. J. LÓPEZ APARICIO, J. A. LÓPEZ SASTRE, J. MOLINA MOLINA, and C. ROMERO-AVILA. An. Quim. Ser. C: **77**, 348 (1981).
5. D. L. MCDONALD and H. O. L. FISCHER. J. Am. Chem. Soc. **74**, 2087 (1952).
6. L. HOUGH and T. J. TAYLOR. Chem. Ind. (London), 1018 (1954); J. Chem. Soc. 970 (1956); R. BARKER and D. L. MCDONALD. J. Am. Chem. Soc. **82**, 2297 (1960); A. FARRINGTON and L. HOUGH. Carbohydr. Res. **16**, 59 (1971); L. D. HALL, L. HOUGH, S. H. SHUTE, and T. J. TAYLOR. J. Chem. Soc. 1154 (1965); B. COXON and L. HOUGH. J. Chem. Soc. 1643 (1961).
7. B. L. KAM, J. L. BARASCUT, and J. L. IMBACH. Carbohydr. Res. **69**, 135 (1979); K. BOCK and C. PEDERSEN. Acta. Chem. Scand. Ser B: **B29**, 258 (1975).
8. A. J. MANCUSO and D. SWERN. Synthesis, 164 (1981).
9. A. MARTINEZ DE ARAGÓN. Tesis de Licenciatura, Universidad de Granada. 1985.
10. C. A. G. HAASNOOT, F. A. A. M. DE LEEUW, and C. ALTONA. Tetrahedron, **36**, 2783 (1980).
11. E. OSAWA and C. JAIME. QCPE, 461 (1983).
12. E. FISCHER. Ber. **27**, 673 (1894).

Appendix 1

Final atomic coordinates and bonded atom table for compound **16**

Atom	X	Y	Z	Type	Bound to atoms
C(1)	−0.50503	0.64118	−0.25524	(2)	2 7 8
C(2)	−1.82832	0.40030	−0.22653	(2)	1 3 15
C(3)	−2.44255	−0.97638	−0.18719	(1)	2 4 16 40
C(4)	−3.91833	−0.66108	−0.48504	(1)	3 5 18 41
C(5)	−4.07475	0.80527	−0.05128	(1)	4 6 15 42
C(6)	−4.52452	0.95537	1.41117	(1)	5 20 27 28
C(7)	0.04097	2.04703	−0.3116	(1)	1 22 29 30
C(8)	0.54840	−0.43852	−0.23552	(1)	1 23 31 32
C(9)	−2.37890	−2.85245	1.26685	(3)	10 16 17
C(10)	−2.15111	−3.21308	2.71959	(1)	9 24 33 34
C(11)	−4.43644	−1.91497	−2.43652	(3)	12 18 19
C(12)	−4.67696	−1.74654	−3.92194	(1)	11 25 35 36
C(13)	−5.13548	2.66554	2.91997	(3)	14 20 21
C(14)	−5.17592	4.17231	3.06455	(1)	13 26 37 38
O(15)	−2.79532	1.38864	−0.22597	(6)	2 5 43
O(16)	−2.29036	−1.51640	1.11357	(6)	3 9 44
O(17)	−2.59469	−3.64967	0.38401	(7)	9
O(18)	−4.15462	−0.71817	−1.88364	(6)	4 11 39
O(19)	−4.49966	−2.96647	−1.84315	(7)	11
O(20)	−4.66104	2.33571	1.70135	(6)	6 13 45
O(21)	−5.46554	1.87924	3.77752	(7)	13
H(22)	0.66807	2.24442	0.59758	(5)	7
H(23)	1.15406	−0.40352	−1.16916	(5)	8
H(24)	−2.15704	−4.31862	2.85480	(5)	10

Can. J. Chem. Downloaded from www.nrcresearchpress.com by 122.72.124.2 on 09/07/12
For personal use only.

Appendix 1 (*Concluded*)

Final atomic coordinates and bonded atom table for compound **16**

Atom	*X*	*Y*	*Z*	Type	Bound to atoms
H(25)	−4.96381	−2.71800	−4.38516	(5)	12
H(26)	−5.53605	4.45921	4.07843	(5)	14
H(27)	−5.51111	0.45240	1.55775	(5)	6
H(28)	−3.76871	0.52686	2.11046	(5)	6
H(29)	0.67312	2.18245	−1.20779	(5)	7
H(30)	−0.75403	2.82557	−0.33117	(5)	7
H(31)	1.23207	−0.28462	0.62975	(5)	8
H(32)	0.14038	−1.46831	−0.14097	(5)	8
H(33)	−1.16520	−2.82701	3.06597	(5)	10
H(34)	−2.95636	−2.78042	3.35632	(5)	10
H(35)	−5.50155	−1.01970	−4.10279	(5)	12
H(36)	−3.75236	−1.38213	−4.42524	(5)	12
H(37)	−4.15681	4.60203	2.92473	(5)	14
H(38)	−5.86556	4.61742	2.31222	(5)	14
LH(39)	−3.64927	−0.53098	−2.14907	(20)	18
H(40)	−1.98126	−1.64936	−0.94852	(5)	3
H(41)	−4.64689	−1.32761	0.03633	(5)	4
H(42)	−4.78504	1.35359	−0.71637	(5)	5
LP(43)	−2.68169	1.70160	0.27372	(20)	15
LP(44)	−2.73664	−1.28864	1.44335	(20)	16
LP(45)	−5.06526	2.55013	1.31109	(20)	20

Can. J. Chem. Downloaded from www.nrcresearchpress.com by 122.72.124.2 on 09/07/12
For personal use only.

Structure-activity studies of β-carbolines. 4. Crystal and molecular structures of *t*-butyl β-carboline-3-carboxylate and 2-(methoxycarbonyl)canthine-6-one

PENELOPE W. CODDING,[1] MARIA B. SZKARADZINSKA, ALEKSANDER W. ROSZAK,[2] and LORRAINE J. AHA
Departments of Chemistry and of Pharmacology and Therapeutics, University of Calgary, Calgary, Alta., Canada T2N 1N4

AND

TIMOTHY J. HAGEN and JAMES M. COOK
Department of Chemistry, University of Wisconsin-Milwaukee, WI 53201, U.S.A.

Received April 22, 1988.

PENELOPE W. CODDING, MARIA B. SZKARADZINSKA, ALEKSANDER W. ROSZAK, LORRAINE J. AHA, TIMOTHY J. HAGEN, and JAMES M. COOK. Can. J. Chem. **66**, 2981 (1988).

The crystal and molecular structures of two ligands for the benzodiazepine (BZ) receptor, *t*-butyl β-carboline-3-carboxylate, **I** ($C_{16}H_{16}N_2O_2$), and 2-(methoxycarbonyl)canthin-6-one, **II** ($C_{16}H_{10}N_2O_3$), are reported. The *t*-butyl β-carboline compound has high affinity for the receptor and is an antagonist; in contrast, the canthin-6-one has a 10-fold lower affinity for the receptor and no determinable *in vivo* activity. The space group for **I** is $P2_1/c$ with $a = 11.756(1)$, $b = 11.2324(8)$, $c = 11.964(1)$ Å, and $\beta = 105.99(1)°$. For **II**, the space group is also $P2_1/c$ with $a = 9.317(1)$, $b = 7.964(1)$, $c = 17.180(3)$ Å, and $\beta = 104.173(7)°$. The orientation of the alkyl-carboxylate side chain is different in the two molecules and may be related to the difference in affinity and *in vivo* activity of the ligands. In addition, the packing arrangements in the two structures are dominated by π-stacking interactions; and, in the case of the *t*-butyl compound, by hydrogen bonding.

PENELOPE W. CODDING, MARIA B. SZKARADZINSKA, ALEKSANDER W. ROSZAK, LORRAINE J. AHA, TIMOTHY J. HAGEN et JAMES M. COOK. Can. J. Chem. **66**, 2981 (1988).

On rapporte les structures cristallines et moléculaire de deux ligands du récepteur de la benzodiazépine (BZ) : la β-carboline carboxylate-3 de *tert*-butyle, **I**, ($C_{16}H_{16}N_2O_2$) et la (methoxycarbonyle)-2 canthinone-6, **II**, ($C_{16}H_{10}N_2O_3$). Le composé β-carboline de tert-butyle a une grande affinité pour le récepteur et son antagoniste; la canthinone-6, au contraire a une affinité 10 fois plus faible pour le récepteur et son activité in vivo n'est pas décelable. Le composé **I** appartient au groupe d'espace $P2_1/c$ avec $a = 11,756(1)$, $b = 11,2324(8)$, $c = 11,964(1)$ Å et $\beta = 105.99(1)°$. Le composé **II** appartient également au groupe d'espace $P2_1/c$ avec $a = 9,317(1)$, $b = 7,964(1)$, $c = 17,180(1)$ Å, et $\beta = 104,173(7)°$. L'orientation de la chaine latérale alkyle-carboxylate est différente dans les deux molécules et peut être reliée à la différence d'affinité et d'activité in vivo des ligands. De plus des interactions π-entassement domine l'entassement des deux structures; et, dans le cas du composé *tert*-butyle ce sont des liaisons hydrogènes.qui dominent.

[Traduit par la revue]

Introduction

The benzodiazepine receptor found in brain tissue mediates anticonvulsant, anxiolytic, hypnotic, and sedative effects (1). This receptor is part of a macromolecular complex that includes both the γ-aminobutyric acid (GABA) receptor and the chloride anion channel (2, 3). Ligands for the benzodiazepine receptor exert their action by modulating the apparent potency of GABA at the GABA receptor. Ligands which interact with the benzodiazepine receptor demonstrate effects that range, in a continuous fashion, from full agonists to inverse agonists. Antagonists are in the center of this continuum of effects, while partial agonists and partial inverse agonists lie to either side of the midpoint (4). Agonists reduce anxiety and convulsions, antagonists elicit no biological response, and inverse agonists promote anxiety and convulsions (5). In essence, inverse agonists enhance neuronal firing while agonists decrease it.

Many compounds other than the 1,4-benzodiazepines have affinity and biological effect at the benzodiazepine receptor. Derivatives of the β-carbolines span the entire range of biological actions. Indeed, minor changes in the alkyl group on the 3-carboxylate substituent are known to modify the activity from inverse agonist for a methyl group to antagonist for a propyl group (6). A bulky alkyl group, as in the *t*-butyl compound presented herein, also produces an antagonist; the *t*-butyl compound has high affinity for the receptor (K_i = 10 n*M*) and antagonizes the anticonvulsant and anti-punishment effects of diazepam (7).

Two models for the recognition of and the differential response to ligands that are as dissimilar as benzodiazepines and β-carbolines have been derived from the pharmacological data. In one model, a conformational difference in the receptor site is assumed, such that in one conformation the agonist ligand binds more tightly and has the effect of increasing GABA transmission; in the other conformation, inverse agonists bind preferentially and decrease the efficacy of GABA (5, 8). Following this reasoning, antagonists would bind to either conformation and cause no shift in the latent response to GABA. In the other model, some photolabeling studies have been interpreted in terms of two separate but interacting sites, one that recognizes benzodiazepines (agonists) and one that recognizes antagonists and β-carboline inverse agonists (9).

Since no experiment has, as yet, actually established which of these explanations is correct, studies of the structures of ligands for the benzodiazepine receptor have been done in several laboratories (10–12) to attempt to find a structural discrimination between these two models. Thus far, the structural information has led to proposals for the differences between agonists and non-agonists (10), to a model containing two interacting sites (11), and, recently, to a description of the recognition site for inverse agonist ligands (13 *a* and *b*). Three features of the β-carbolines have been invoked as key to receptor recognition. The first is a requirement for a planar aromatic system (14) and

[1]Author to whom correspondence should be addressed.
[2]On leave from the Institute of Chemistry, N. Copernicus University, Torun, Poland.

Printed in Canada / Imprimé au Canada

Can. J. Chem. Downloaded from www.nrcresearchpress.com by 122.72.124.2 on 09/07/12
For personal use only.

Can. J. Chem. Downloaded from www.nrcresearchpress.com by 122.72.124.2 on 09/07/12
For personal use only.

TABLE 1. Crystal data

Compound	I	II
Formula	$C_{16}H_{16}N_2O_2$	$C_{16}H_{10}N_2O_3$
fw	268.31	278.27
System and space group	Monoclinic, $P2_1/c$	Monoclinic, $P2_1/c$
a (Å)	11.756(1)	9.317(1)
b (Å)	11.2324(8)	7.964(1)
c (Å)	11.964(1)	17.180(3)
β(°)	105.99(1)	104.173(7)
V (Å^3)	1518.7(3)	1236.0(3)
Z	4	4
ρ_c(g/cm^3)	1.173	1.495
μ (cm^{-1})	6.43	8.87
Color of crystal	Colorless	light brown/orange
Crystal dimensions (mm)	0.48 × 0.22 × 0.18	0.38 × 0.26 × 0.08
h, k, l ranges	0,14; 0,13; −14,14	0,11; 0,9; −20,20
Max (sin θ) /λ (Å^{-1})	0.609	0.609
No. of unique reflections	2866	2335
No. of observed reflections ($I > 2.5\ \sigma\ (I)$)	2172	1879
No. of reflections used in refinement*	2625	2154
No. of parameters refined	209	230
Weighting scheme	$w^{-1}=\sigma^2(F)+0.0004F^2$	$w^{-1}=\sigma^2(F)+0.0001F^2$
Final $R = \Sigma \lvert \lvert F_o \rvert - \lvert F_c \rvert \rvert / \Sigma \lvert F_o \rvert$	0.053 (2625 refls.)	0.040 (2154 refls.)
$R_w = ((\Sigma\omega(\lvert F_o \rvert - \lvert F_c \rvert)^2/\Sigma\omega F_o^2)^{1/2}$	0.072	0.045
S(stand. dev. of obs. of units wt.) =	1.02	1.23
Maximum shift/error (final cycle)	0.006	0.004
Maximum residual density in ΔF map (e Å^{-3})	0.23	0.15
Minimum residual density in ΔF map (e Å^{-3})	−0.18	−0.22

*The reflections used in the refinement included the observed reflections and those unobserved reflections for which $F_c^2 > 2.5\sigma(I_o)$.

near coplanarity of the 3-carboxylate group (15). Also, two hydrogen bonding groups have been implicated in activity: the indole N—H function as a donor and either the pyridyl N atom or the carbonyl O atom of the side chain (or both) as an acceptor (10, 13*a*, *b*). In the crystal, inverse agonist β-carbolines have similar conformations which place the carbonyl O atom *cis* to the N atom of the pyridyl ring. In contrast, a similar 3-substituted β-carboline which is an antagonist, the 3-(methoxycarbonyl) amino β-carboline (12), has the opposite conformation.

The β-carbolines presented in this work are the high affinity antagonist, *t*-butyl ester (**I**), and 2-(methoxycarbonyl)canthin-6-one (**II**) which has an affinity similar to clinically useful benzodiazepines, i.e., K_i = 100 n*M* (16). The structure of **I** was determined to gain more information regarding the side chain conformation common to antagonist ligands. The canthin-6-one structure was undertaken to look for a structural explanation for the fact that this compound has receptor affinity even though the N—H indole function is blocked. Comparison of both of these structures to those of other known receptor ligands will help to further characterize the recognition site and to define the differences for recognition of inverse agonists vs. antagonists.

Experimental

Samples were prepared in the Wisconsin laboratory and recrystallized in the Calgary laboratory from pyridine (**I**) and from a chloroform–methanol mixture (**II**) by a slow evaporation. X-ray intensity data were collected at room temperature on an Enraf-Nonius CAD-4F automated diffractometer with Ni-filtered CuKα radiation, λ(CuKᾱ = 1.54178 Å), using an ω/2θ scan mode. The cell parameters and orientation matrix were determined by least-squares refinements of the angular positions of 25 reflections with θ values in the range 16–45° for **I** and 22–28° for **II**. During the data collection the intensities of three reflections were measured every 2000 s of exposure of the crystal to X-ray radiation; these reflections showed no significant variation in intensity. The crystal data are given in Table 1. Lorentz and polarization corrections were applied; absorption corrections were not deemed necessary. The intensities were converted into normalized structure factors (E values) by application of a K-curve.

Both structures were solved by direct methods using MULTAN78 (17); the most probable phase sets were used to calculate E maps that revealed the positions of all but two of the non-hydrogen atoms of **I** and all of the non-hydrogen atoms of **II**. The remaining atoms of **I** were located in a difference Fourier synthesis calculated from the phases of the partial structure. After isotropic refinement of the parameters of the non-hydrogen atoms, most of the hydrogen atoms were located in difference Fourier syntheses. All hydrogen atoms were included in the model at idealized positions. The parameters varied in the final refinement cycles consisted of the coordinates of all the atoms, the anisotropic thermal parameters of the non-hydrogen atoms, and the isotropic thermal parameters of the hydrogen atoms except for those in methyl groups. The methyl hydrogen atoms were held in fixed positions with U_{iso} equal to 120% of the U_{eq} of the C atoms to which they were bonded. All calculations were done with the XRAY76 system of programs (18) implemented on a Honeywell computer. The atomic scattering factors used were those of Cromer and Mann (19) for the non-H atoms and of Stewart *et al.* (20) for the hydrogen atoms.

The atomic coordinates[3] for **I** are given in Table 2 and for **II** are given in Table 3, with the atoms labeled as in Figs. 1 and 2, respectively. The bond distances and bond angles are given in Table 4.

[3]The anisotropic thermal parameters, the hydrogen atom parameters, least squares planes data, the lists of observed and calculated structure factors, and the REFCODES from the Database search may be purchased from the Depository of Unpublished Data, CISTI, National Research Council of Canada, Ottawa, Ont., Canada K1A 0S2.

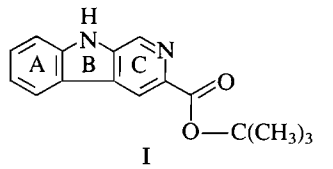

I

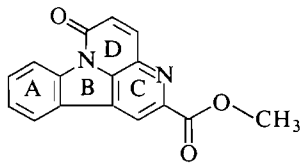

II

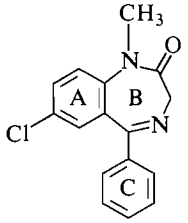

III

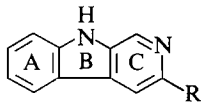

IV R = —C(=O)—N(H)—CH_2CH_3

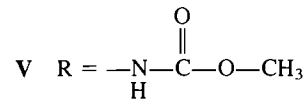

V R = —N(H)—C(=O)—O—CH_3

Results

The β-carboline portion of **I** and the canthin-6-one portion of **II** are both planar: the standard deviations for the planes are 0.022 Å for 13 atoms in **I** and 0.022 Å for 16 atoms in **II**.[3] Also, in both structures, the ester side chains are in extended conformations and are nearly coplanar with the aromatic systems. In **I**, the angle between the plane of the β-carboline and the plane containing C(3), C(31), O(34), O(32), and C(33) is 10.5(3)°; in **II**, the angle between the canthin-6-one and the corresponding atoms of the ester side chain is 6.1(2)°. These conformations facilitate the formation of an extended π system over the side chain and the polycycle. Such extended systems have been found in all 3-substituted β-carbolines (21–24) except the 3-(methoxycarbonyl) amino β-carboline (12).

The major difference between these two structures is in the orientation of the ester side chain. In the canthin-6-one (**II**) structure, the side chain is oriented so that the ester carbonyl oxygen atom is *trans* to the pyridine N atom: the N(2)—C(3)—C(31)—O(34) torsion angle is 173.9(2)°. In **I**, the side chain is in the opposite orientation (*cis*) so that the carbonyl oxygen atom is adjacent to the pyridine N atom: the torsion angle N(2)—C(3)—C(31)—O(34) is −9.0(3)°. Muir and Codding (21) examined the orientation of ester side chains to pyridine rings by surveying the conformations found in 18 similar molecular fragments tabulated in the Cambridge Crystallographic Database (25). The eighteen examples consisted of 10 with *cis* conformations and 8 with the *trans* conformation found in the canthin-6-one crystal structure reported here. The approximately equal populations of the two conformers suggest that the two forms have similar potential energies. Interestingly, the *cis* arrangement for the side chain has been found in all of the ester-containing benzodiazepine receptor ligands except the canthin-6-one. The *cis* compounds include R015-1788 (10), an

TABLE 2. The fractional coordinates ($\times 10^4$) and equivalent isotropic vibration parameters, B_{eq}, ($A^2 \times 10^2$) for the non-hydrogen atoms of *t*-butyl β-carboline-3-carboxylate, **I**

Atom	*x/a*	*y/b*	*z/c*	B_{eq}†
C(1)	5336(2)	5659(2)	2327(2)	564
N(2)	5942(1)	6673(1)	2521(1)	565
C(3)	6844(1)	6822(2)	2026(2)	544
C(4)	7146(2)	5982(2)	1313(2)	570
C(5)	7245(2)	3471(2)	−262(2)	693
C(6)	7033(2)	2351(3)	−759(2)	789
C(7)	6177(3)	1618(3)	−527(2)	750
C(8)	5489(2)	1964(2)	175(2)	657
N(9)	5118(1)	3659(2)	1379(1)	569
C(10)	5610(1)	4759(2)	1651(1)	498
C(11)	6528(1)	4919(2)	1117(1)	510
C(12)	6566(2)	3844(2)	475(2)	544
C(13)	5696(2)	3088(2)	673(1)	538
C(31)	7456(2)	7985(2)	2298(2)	644
O(32)	8432(1)	8022(1)	1948(2)	809
C(33)	9197(2)	9083(2)	2093(3)	922
O(34)	7110(1)	8786(1)	2781(2)	962
C(35)	10198(3)	8671(3)	1628(5)	1639
C(36)	9679(3)	9347(4)	3394(4)	1408
C(37)	8544(4)	10098(4)	1472(5)	1607

†$B_{eq} = {}^8/_3\pi^2 \Sigma_i \Sigma_j U_{ij} a_i^* a_j^* \mathbf{a}_i \cdot \mathbf{a}_j$

TABLE 3. The fractional coordinates ($\times 10^4$) and equivalent isotropic vibration parameters, B_{eq}, ($A^2 \times 10^2$) for the non-hydrogen atoms of 2-(methoxycarbonyl)canthin-6-one, **II**

Atom	*x/a*	*y/b*	*z/x*	B_{eq}†
C(1)	27495(17)	−8369(19)	94000(10)	308
N(2)	35211(15)	216(17)	89610(8)	330
C(3)	39010(18)	16094(20)	91893(10)	322
C(4)	35713(18)	24440(21)	98420(10)	330
C(5)	22600(2)	31919(22)	115161(11)	367
C(6)	16354(21)	30150(24)	121633(12)	413
C(7)	9705(22)	15204(25	123017(12)	442
C(8)	8849(20)	1522(23)	117912(11)	393
N(9)	16254(14)	−8379(16)	105439(8)	319
C(10)	23927(16)	−753(19)	100492(9)	295
C(11)	27841(17)	15643(19)	102965(10)	298
C(12)	22093(17)	18383(20)	110020(10)	310
C(13)	15136(17)	3361(20)	111473(10)	310
C(14)	11219(18)	−24873(2)	104141(11)	345
C(15)	14918(21)	−32966(22)	97202(12)	391
C(16)	22562(2)	−25526(21)	92459(11)	375
O(17)	4428(15)	−31521(15)	108582(8)	481
C(31)	47480(19)	25803(22)	87003(11)	369
O(32)	51426(13)	16602(14)	81451(7)	419
C(33)	58534(27)	25509(30)	76043(14)	477
O(34)	50394(18)	40484(18)	88097(9)	634

†$B_{eq} = ({}^8/_3)\pi^2 \Sigma_i \Sigma_j U_{ij} a_i^* a_j^* \mathbf{a}_i \cdot \mathbf{a}_j$

Can. J. Chem. Downloaded from www.nrcresearchpress.com by 122.72.124.2 on 09/07/12
For personal use only.

TABLE 4. Bond distances and bond angles for the non-hydrogen atoms of **I** and **II**

Compound **I**		Compound **II**	
Bond	Distance (Å)	Bond	Distance (Å)
C(1) —N(2)	1.330(3)	C(1) —N(2)	1.349(2)
C(1) —C(10)	1.387(3)	C(1) —C(10)	1.380(2)
N(2) —C(3)	1.359(3)	C(1) —C(16)	1.445(2)
C(3) —C(4)	1.382(3)	N(2) —C(3)	1.345(2)
C(3) —C(31)	1.484(3)	C(3) —C(4)	1.401(3)
C(4) —C(11)	1.383(3)	C(3) —C(31)	1.500(3)
C(5) —C(6)	1.385(4)	C(4) —C(11)	1.385(3)
C(5) —C(12)	1.407(3)	C(5) —C(6)	1.383(3)
C(6) —C(7)	1.387(4)	C(5) —C(12)	1.387(2)
C(7) —C(8)	1.373(4)	C(6) —C(7)	1.389(3)
C(8) —C(13)	1.389(3)	C(7) —C(8)	1.389(3)
N(9) —C(10)	1.365(2)	C(8) —C(13)	1.380(3)
N(9) —C(13)	1.378(3)	N(9) —C(10)	1.378(2)
C(10)—C(11)	1.409(3)	N(9) —C(13)	1.419(2)
C(11)—C(12)	1.438(3)	N(9) —C(14)	1.394(2)
C(12)—C(13)	1.400(3)	C(10)—C(11)	1.394(2)
C(31)—O(32)	1.326(3)	C(11)—C(12)	1.456(3)
C(31)—O(34)	1.199(3)	C(12)—C(13)	1.412(2)
O(32)—C(33)	1.474(3)	C(14)—C(15)	1.469(3)
C(33)—C(35)	1.507(6)	C(14)—O(17)	1.224(2)
C(33)—C(36)	1.531(6)	C(15)—C(16)	1.344(3)
C(33)—C(37)	1.458(5)	C(31)—O(32)	1.324(2)
		C(31)—O(34)	1.205(2)
		O(32)—C(33)	1.451(3)

Bonds	Angle (deg)	Bonds	Angle (deg)
N(2) —C(1) —C(10)	121.8(2)	N(2) —C(1) —C(10)	119.7(1)
C(1) —N(2) —C(3)	118.3(2)	N(2)—C(1) —C(16)	124.5(2)
N(2) —C(3) —C(4)	123.3(2)	C(10)—C(1) —C(16)	115.8(2)
N(2) —C(3) —C(31)	113.7(2)	C(1) —N(2) —C(3)	116.9(1)
C(4) —C(3) —C(31)	123.0(2)	N(2) —C(3) —C(4)	125.9(2)
C(3) —C(4) —C(11)	118.7(2)	N(2) —C(3) —C(31)	117.3(2)
C(6) —C(5) —C(12)	118.3(2)	C(4) —C(3) —C(31)	116.9(1)
C(5) —C(6) —C(7)	120.5(3)	C(3) —C(4) —C(11)	117.5(2)
C(6) —C(7) —C(8)	122.5(3)	C(6) —C(5) —C(12)	118.5(2)
C(7) —C(8) —C(13)	117.2(2)	C(5) —C(6) —C(7)	121.2(2)
C(10)—N(9) —C(13)	108.6(2)	C(6) —C(7) —C(8)	121.6(2)
C(1) —C(10)—N(9)	130.4(2)	C(7) —C(8) —C(13)	116.9(2)
C(1) —C(10)—C(11)	120.1(2)	C(10)—N(9) —C(13)	107.6(1)
N(9) —C(10)—C(11)	109.6(2)	C(10)—N(9)—C(14)	121.4(1)
C(4) —C(11)—C(10)	117.8(2)	C(13)—N(9) —C(14)	131.0(2)
C(4) —C(11)—C(12)	136.3(2)	C(1) —C(10)—N(9)	124.7(1)
C(10)—C(11)—C(12)	106.0(2)	C(1) —C(10)—C(11)	124.2(2)
C(5) —C(12)—C(11)	133.7(2)	N(9) —C(10)—C(11)	111.2(1)
C(5) —C(12)—C(13)	119.5(2)	C(4) —C(11)—C(10)	115.9(2)
C(11)—C(12)—C(13)	106.7(2)	C(4) —C(11)—C(12)	138.3(1)
C(8) —C(13)—C(9)	128.9(2)	C(10)—C(11)—C(12)	105.8(1)
C(8) —C(13)—C(12)	121.9(2)	C(5) —C(12)—C(11)	133.2(2)
N(9) —C(13)—C(12)	109.2(2)	C(5) —C(12)—C(13)	119.4(2)
C(3) —C(31)—O(32)	111.6(2)	C(11)—C(12)—C(13)	107.4(1)
C(3) —C(31)—O(34)	123.9(2)	C(8) —C(13)—N(9)	129.6(2)
O(32)—C(31)—O(34)	124.5(2)	C(8) —C(13)—C(12)	122.3(2)
C(31)—O(32)—C(33)	122.8(2)	N(9) —C(13)—C(12)	108.1(2)
O(32)—C(33)—C(35)	102.8(2)	N(9) —C(14)—C(15)	114.0(2)
O(32)—C(33)—C(36)	108.6(3)	N(9) —C(14)—O(17)	120.8(2)
O(32)—C(33)—C(37)	110.7(2)	C(15)—C(14)—O(17)	125.2(2)
C(35)—C(33)—C(36)	109.1(3)	C(14)—C(15)—C(16)	124.3(2)
C(35)—C(33)—C(37)	114.0(4)	C(1) —C(16)—C(15)	119.8(2)
C(36)—C(33)—C(37)	111.2(3)	C(3) —C(31)—O(32)	113.1(1)
		C(3) —C(31)—O(34)	122.8(2)
		O(32)—C(31)—O(34)	123.9(2)
		C(31)—O(32)—C(33)	116.2(1)

Can. J. Chem. Downloaded from www.nrcresearchpress.com by 122.72.124.2 on 09/07/12
For personal use only.

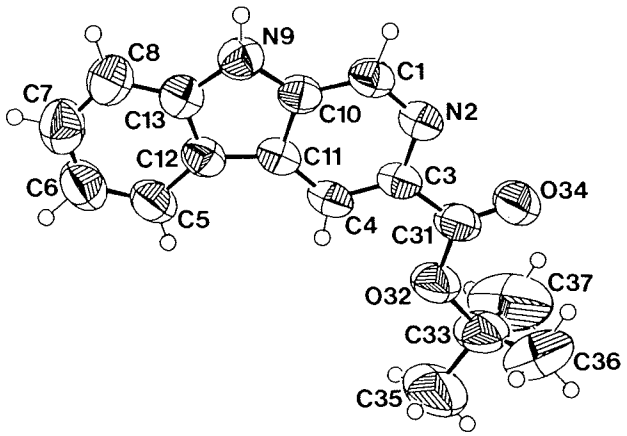

Fig. 1. The molecular conformation and atomic labelling scheme for *t*-butyl β-carboline-3-carboxylate, **I**. The drawing was made with the computer program ORTEP (34).

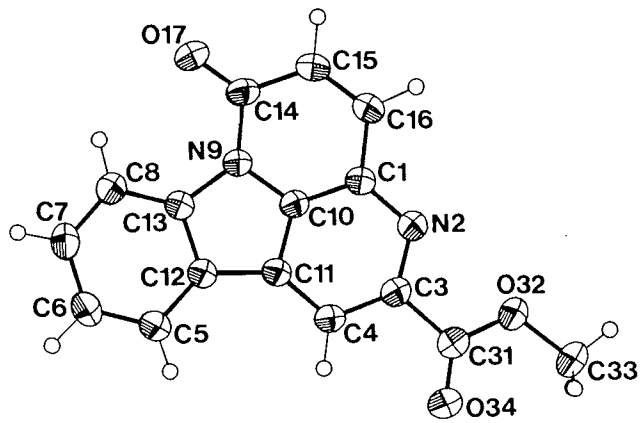

FIG. 2. The molecular conformation and atomic labelling scheme for 2-(methoxycarbonyl)cathin-6-one, **II**. The drawing was made with the computer program ORTEP (34).

antagonist which forms no hydrogen bonds in the crystal, and several ligands which form three-center hydrogen bonds, including the antagonist, 6-*N*-benzyl-β-carboline methyl ester (22), and the inverse agonists, β-carboline methyl ester (21) and β-carboline ethyl ester (23).

The two molecules reported in this paper have different crystal packing arrangements. The packing in the *t*-butyl β-carboline ester is determined by the formation of three-center H-bonds. Similar hydrogen bonding patterns have been found in both the methyl- (21) and ethyl- (23) ester crystal structures. The unique feature of the *t*-butyl packing arrangement is the formation of closely stacked dimers which facilitates strong π–π interactions. In the dimers, the entire polycyclic ring system is stacked such that the two molecules face in opposite directions and are aligned **A** ring over **C** ring with a dimer–dimer separation of 3.422(6) Å. Neither of the inverse agonist β-carboline esters (21, 23) show such extensive π interactions; however, both esters show partial π stacking which involves the **A** ring. Such interactions involving the **A** ring are postulated to be important to receptor binding (10, 11). The only other type of π-stacking observed in β-carboline crystals involved stacking of the side chain over the five-membered ring: this was observed for the low affinity *N*-ethyl-3-carbamoyl-β-carboline (24).

In contrast to the H-bonding found in the β-carboline esters, the packing of the canthin-6-one molecules is determined solely by π-stacking interactions. The canthin-6-one molecules are stacked in columns that are aligned to form sheets held together by van der Waals interactions. The distances between adjacent molecules in the stacks are 3.453(5) Å and 3.472(5) Å for the two molecules related by the centers of symmetry: 0,0,0 and 1/2,0,0, respectively. Molecules in a single sheet are aligned so that there are two types of van der Waals interactions, one between interleaved ester side chains and the other between the edges of the **A** and **D** rings. Although there are no hydrogen bonding interactions in the lattice of **II** because there are no hydrogen bond donors in the crystal, such interactions are found in the other crystal structure of a canthin-6-one, amarorine hydrate (26). The π-stacking in the amarorine crystals is similar to that found in crystals of **II**; in addition, a water molecule serves as a hydrogen donor and the acceptor atom is the pyridyl N atom (the N(2) atom in **II**), an atom that is held to be important for interactions with the benzodiazepine receptor (10, 11, 13*a*, *b*).

Discussion

Intermolecular contacts that are observed in crystals have been used as models for the interactions of receptors with ligands (10, 11, 27). The three-center hydrogen bond found in the crystal lattice of the *t*-butyl β-carboline is found in the structures of all β-carboline-3-carboxylate ester crystal structures and has been invoked as a model for the interaction of the pyridyl-ester portion of the molecule with the benzodiazepine receptor (10, 13*a*, *b*, 21). A novel feature of the three-center hydrogen bond is that the position of the donor, relative to the two acceptors: the pyridyl N atom and the carbonyl O atom, can vary over a wide range of values. Indeed, the bonding possibilities range from a two-center H bond to the N atom, through a range of positions that form a three-center H bond, finally to a two-center H bond to the carbonyl O atom. The variation in H bond geometries observed in the β-carbolines is shown in Table 5. Although these are all three-center bonds, they range from a bond that is stronger to the N(2) atom than to O(34) in the case of the 6-*N*-benzyl structure, to a bond that is stronger to the carbonyl O atom, as evidenced by shorter O(34)···N(9) distances than N(2)···N(9) distances, in the methyl and ethyl esters. The *t*-butyl β-carboline forms the most symmetrical three-center bond.

According to models for the interaction of the ligand with the receptor (10, 11, 13*a*, *b*), this H-bond donor position determines the distance between two postulated recognition points on the receptor: one that binds an aromatic ring, the **A** ring of the β-carboline or benzodiazepine(III), and a second that donates a hydrogen atom to a H-bond acceptor on the ligand. Previously (10, 23), the separation between the two recognition points on the ligands has been found to lie in the range 4.72–4.95 Å for benzodiazepine agonists. This value for agonist ligands is much shorter than that for the antagonist and inverse agonist β-carbolines, imidazobenzodiazepines, and pyrazoloquinolinones. If, for the ester ligands, both the *cis* conformation and the position of the H-bond acceptor as the midpoint of the N(2)···O(34) group are assumed, the separation between recognition points on the ligand varies from 6.06(1) Å for RO15-1788 to an average of 6.50(5) Å for the β-carboline esters. The analogous separation for an inverse agonist pyrazoloquinolinone, CGS-8216 (23), is 6.10(1) Å. Unfortunately, the variability in the position of the H-bond acceptor point obscures any determination of a specific distance between ligand features that would distinguish inverse agonists from antagonists. It is clear,

Can. J. Chem. Downloaded from www.nrcresearchpress.com by 122.72.124.2 on 09/07/12
For personal use only.

TABLE 5. Geometry of the three-center hydrogen bonds of the β-carboline crystal structures. The compounds are the *t*-butyl ester (this work), the methyl ester (17), the ethyl ester (20), and the 6-*N*-benzyl methyl ester (19); all crystal lattices contain two unique molecules except for the *t*-butyl structure reported herein

N(2)···N(9) (Å)	O(34)···N(9) (Å)	N(2)···H(9) (Å)	O(34)···N(9) (Å)	N(2)···H(9)—N(9) (deg)	O(34)···H(9)—N(9) (deg)	
3.028(2)	3.056(3)	2.22(3)	2.24(3)	142(2)	143(2)	(this work)
3.637(5)	2.819(4)	2.91(2)	2.04(2)	144(2)	150(2)	(17)
3.317(3)	2.919(4)	2.54(2)	2.27(2)	154(2)	134(2)	(17)
3.16(2)	3.06(2)	2.26	2.14	139	142	(20)
3.26(2)	3.05(2)	2.49	2.17	132	145	(20)
3.018(3)	3.200(3)	2.21(2)	2.58(2)	160(2)	131(2)	(19)
2.998(3)	3.066(3)	2.18(2)	2.44(3)	155(3)	129(2)	(19)

however, that the receptor can recognize ligands of different size and that size may, at least, be important to distinguishing between agonist or inverse agonist activity.

The *trans* conformation of the ester side chain that was found in the canthin-6-one crystal has also been observed in two non-ester benzodiazepine receptor ligands: the *N*-ethyl-3-carbamoyl-β-carboline **IV** (24), which has low benzodiazepine receptor affinity (28), and 3-(methoxycarbonyl)amino-β-carboline **V** (12), which produces 50% antagonism of diazepam (**III**) binding at a concentration of 71 n*M* (29). Because our examination (24) of the tabulated geometries of pyridyl–carbamoyl fragments showed that *trans* is the only observed conformation, and because the carbamoyl-β-carboline has low receptor affinity (28), we have proposed (24) that this *trans* conformation is not the binding conformation. Thus, models for the receptor–ligand interaction have assumed a *cis* conformation for the ester side chain (9, 13*a*, *b*). For this proposal to be valid, the side chains of both the canthin-6-one, **II**, and the methoxycarbonylamino compound **V** must have alternative conformations to those found in the crystal structures.

To evaluate the conformational freedom of the pyridyl-methoxycarbonyl amino fragment; the Cambridge Crystallographic Database (25) was searched for the variety of conformations found for the fragment. Like the ester side chain (21, *vide infra*), the methoxycarbonyl amino side chain is found in both *cis* and *trans* conformers: of the nine fragments found in the database, six were *trans* as found in the β-carboline crystal structure (12) and three were *cis* (the REFCODES for this search are in the deposited information[3]). However, unlike the ester case, in the methoxycarbonyl amino search all of the *cis* conformers were stabilized by molecular interactions: either by an intramolecular hydrogen bond or by complexation to a metal ion. This finding suggests that the *cis* conformer of the methoxycarbonyl amino side chain is less stable than the *trans* form. To determine the energy required to stabilize the *cis* conformer, the GAUSSIAN86 molecular orbital program (31) was used to calculate the difference in energy between the *cis* and *trans* forms of the β-carboline (**V**). The *cis* conformer is 4.8 kcal/mol less stable than the *trans* form. This energy would be required to convert the observed (12) *trans* conformer to a *cis* conformer which could form a three-center hydrogen bond at the receptor site; such energies are available from the formation of the three-center H-bond. Therefore, the higher affinities of the canthin-6-one (**II**) and the methoxycarbonylamino compound (**V**) over that of the carbamoyl compound (**IV**) may be due to the facile formation of the *cis* conformer that, it is assumed (9, 13*a*, *b*, 30), binds to the receptor site.

Alternatively, these molecules could retain the *trans* conformation and bind in a different orientation from that proposed for the *cis* β-carboline esters. This possibility is most likely for the canthin-6-one because the usual binding orientation, i.e., N(2) and O(34) as acceptors and N(9)—H as donor, causes the **D** ring to interfere with the hypothesized (9, 13*a*, *b*) N—H donor position and, indeed, places a group of opposite polarity (the carbonyl O(17) atom) in the position normally occupied by the N—H. Thus, the **D** ring in the canthin-6-one may select for binding to the receptor in an "opposite" orientation by using the observed *trans* conformation and the carbonyl O atom, O(34), as the sole hydrogen bond acceptor. To assess this possibility, the overall shapes of the *t*-butyl β-carboline antagonist (**I**) and of the canthinone (**II**) were compared to the shape of the potent, 1,4-benzodiazepine antagonist, RO15-1788(10). Comparisons of the fit of the canthin-6-one in this "opposite" orientation and the *t*-butyl β-carboline ester in a normal orientation, both to RO15-1788, are shown in Fig. 3*a* and *b*. The separation between the midpoint of the **A** ring of the canthin-6-one and O(34) is 6.749(2) Å which is ca. 0.25 Å longer than the separation between the **A** ring and the midpoint between N(2) and O(32), the binding point of a "normal" β-carboline orientation. In either orientation, this ligand cannot form a H-bond to the receptor through the indole N—H; this interaction is thought to be necessary for inverse agonist activity (13*a*, *b*).

Neither of the other two *trans* ligands, *N*-ethyl-3-carbamoyl-β-carboline (**IV**) or 3-(methoxycarbonyl)amino-β-carboline (**V**), have good superpositions in the "opposite" orientation. In addition to poor fit in the side chain region, another difference is that this alternative orientation places the indole N—H function of the β-carbolines in the same position as the carbonyl oxygen atom, O(21), of RO15-1788. In contrast, the canthin-6-one superposition shown in Fig. 3*a* places two similar functionalities, the two carbonyl O atoms, O(21) from RO15-1788 and O(17) from the canthin-6-one, in the same position. Thus, the canthin-6-one may be unique in its ability to bind in either of the *trans* or *cis* conformations.

The canthin-6-one, **II**, was screened in whole animal studies (32) and did not demonstrate potent *in vivo* activity: the canthin-6-one did not antagonize the anticonvulsant effects of diazepam, nor did it show any inverse agonist activity. The lack of *in vivo* activity may be due either to a low *in vivo* affinity so that the biological effect is small or to an inability of the compound to reach the benzodiazepine receptor via the blood–brain barrier. This latter argument is supported by the results of a CNDO (33) calculation of the electronic properties of both the *t*-butyl ester β-carboline and the canthin-6-one. These calculations indicate

Can. J. Chem. Downloaded from www.nrcresearchpress.com by 122.72.124.2 on 09/07/12
For personal use only.

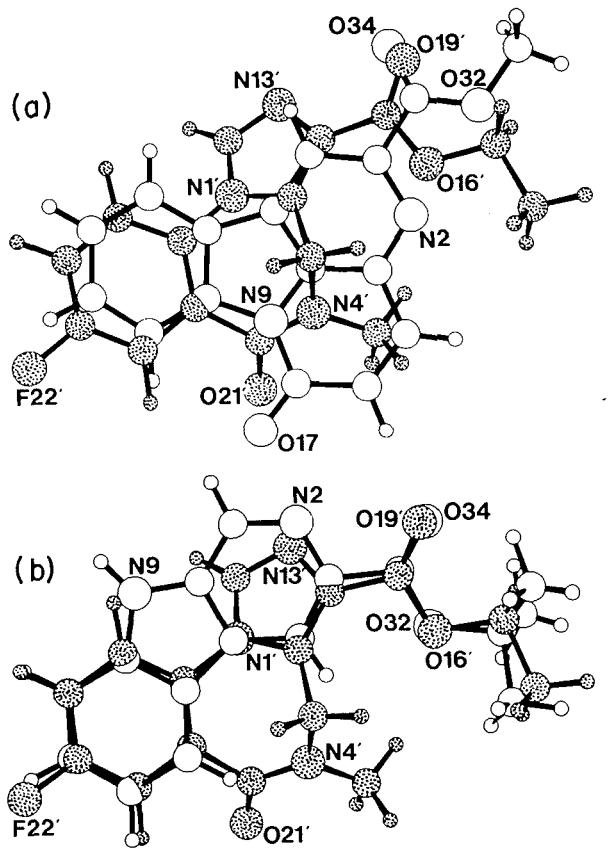

FIG. 3. (*a*) Superposition of the structure of compound **II** (open circles) in the "opposite" orientation with the structure of the antagonist, RO15-1788 (stippled circles, 10). (*b*) Superposition of compound **I** (open circles) in the normal orientation with RO15-1788 (stippled circles). In both drawings, the points of overlap were the **A** rings and the carbonyl O atoms. The least squares superpositions of the molecules were calculated with the program PROFIT (35) and the drawings were made with the program PLUTO (36).

that, while the individual atomic charges are similar in the two structures, the dipole moments are quite different. The β-carboline ester has a large dipole moment of 4.46 debye while the canthin-6-one is much less polar with a dipole moment of 1.38 debye. This difference in relative polarity may indicate that the biological transport characteristics of the two ligands are quite different or that electrostatic orientation of the two ligands in the binding site could be different.

In summary, the structure of the *t*-butyl ester, **I**, supports the hypothesis that the presence of a hydrogen bond acceptor site on the ligand (the pyridyl N atom) is an important criterion for receptor affinity (10, 11, 13*a*, *b*, 30) and that substituents and conformations that enhance the acceptor function enhance affinity. The *cis* conformation of the ester side chain, which will enhance the proposed hydrogen bond formation between N(2) and the receptor by forming a three-center H-bond involving the carbonyl O atom as a secondary hydrogen acceptor, has been found in **I** and in another antagonist, 6-N-benzyl methyl ester (22) as well as in the inverse agonist esters (21, 23), all high affinity ligands. The methoxycarbonyl amino β-carboline antagonist (12), which crystallized with a *trans* side chain conformation, is shown to have an accessible *cis* conformation (*vide infra*); thereby supporting the hypothesized importance of the proposed *cis* interaction. Comparison of the inverse agonist β-carboline esters with the structure of the antagonist, **I**, indicates that the difference between ligands which elicit different biological effects is mainly a difference in molecular volume. The larger size of the antagonist compounds may preclude complete occupation of the inverse agonist site, in the case of the two interacting site model, or preclude the complete conformational change to the inverse agonist-elicited receptor shape in the case of the induced conformation model. Taken together, these two features, the similar hydrogen bonding patterns and the different sizes, suggest that inverse agonists and antagonists can occupy, if somewhat differently, a common binding site (10, 13*a*, *b*).

The affinity of the canthin-6-one may be due to the highly planar aromatic system, a feature that is known to be necessary for binding (14, 15). The low polarity of the molecule may either affect transport or may preclude proper orientation in the binding site so that the molecule simply occupies the binding pocket without forming specific hydrogen bonds and, therefore, without eliciting any biological response. Interestingly, the canthin-6-one fits the current structural models for the recognition site better in a reversed orientation rather than in the orientation adopted by ligands that do have *in vivo* activity.

In summary, the structures presented here support the hypotheses that size and the formation of specific H-bonds are important criteria for receptor affinity (10, 11, 13*a*, *b*) and activity; however, they do not clearly discriminate between the two models for the benzodiazepine receptor. Further characterization of benzodiazepine receptor ligands is underway to define the geometric and electrostatic characteristics of the recognition site, particularly as to the discrimination between inverse agonists and agonists.

Acknowledgements

This work was supported by the Medical Research Council of Canada (grant MA-8087 to P.W.C.), by the Alberta Heritage Foundation for Medical Research (fellowship to A.R. and scholarship to P.W.C.), and by a grant of computer time from the University of Calgary.

1. C. BROWN, I. MARTIN, B. JONES, and N. O'OAKLEY. Eur. J. Pharmacol. **103**, 139 (1984).
2. S. H. SNYDER. J. Med. Chem. **26**, 1667 (1983).
3. W. HAEFLEY and P. POLC. Receptor biochemistry and methodology. Vol. 5. Alan R. Liss, Inc. 1986. p. 97.
4. T. M. BARE, J. F. RESCH, and J. B. PATEL. Ann. Rep. Med. Chem. **22**, 11 (1987).
5. C. BRAESTRUP and M. NIELSEN. Ann. Rep. Med. Chem. 167 (1986).
6. J. H. SKERRITT, G. A. R. JOHNSTON, and C. BRAESTRUP. Eur. J. Pharmacol. **86**, 299 (1983); C. BRAESTRUP. J. Neurochem. **37**, 333 (1981).
7. H. E. SHANNON, F. GUZMAN, and J. M. COOK. Life Sci. **35**, 2227 (1984).
8. F. J. EHLERT, P. RAGAN, A. CHEN, W. R. ROESKE, and H. I. YAMAMURA. Eur. J. Pharmacol. **78**, 249 (1982).
9. J. F. TALLMAN. Receptor biochemistry and methodology. Vol. 5. Alan R. Liss, Inc. 1986. p. 275.
10. P. W. CODDING and A. K. S. MUIR. Mol. Pharmacol. **28**, 178 (1985).
11. P. A. BOREA, G. GILLI, V. BERTOLASI, and V. FERRETTI. Mol. Pharmacol. **31**, 334 (1987).
12. R. H. DODD, C. OUANNÈS, A. CHIARONI, C. RICHE, G. POISSONNET, J. ROSSIER, G. DEVAUX, and P. POTIER. Mol. Pharmacol. **31**, 74 (1987).
13. (*a*) T. J. HAGEN, M. TRUDELL, S. LIFER, C. TAN, M. ALLEN, P. SKOLNICK, P. W. CODDING, J. M. COOK, Abstr. 214, 43rd

Can. J. Chem. Downloaded from www.nrcresearchpress.com by 122.72.124.2 on 09/07/12
For personal use only.

Southwest Regional Meeting of the American Chemical Society, Little Rock, Ark., Dec. 1987; (*b*) M. S. ALLEN, T. J. HAGEN, M. L. TRUDELL, P. W. CODDING, P. SKOLNICK, and J. M. COOK. J. Med. Chem. **31**, 1854 (1988).
14. M. CAIN, R. WEBER, F. GUZMANN, J. M. COOK, S. A. BAKER, K. C. RICE, P. SKOLNICK. J. Med. Chem. **25**, 1081 (1982).
15. P. W. CODDING. Can. J. Chem. **61**, 529 (1983).
16. F. GUZMANN, M. CAIN, P. LARSCHEID, T. HAGEN, J. M. COOK, M. SCHWERI, P. SKOLNICK, and S. M. PAUL. J. Med. Chem. **27**, 564 (1984).
17. P. MAIN, S. E. HALL, L. LESSINGER, G. GERMAIN, J.-P. DECLERCQ, and M. M. WOOLFSON. MULTAN78. A system of computer programs for the automatic solution of crystal structures from X-ray diffraction data. Universities of York, England and Louvain, Belgium. 1978.
18. J. M. STEWART. The X-ray system of crystallographic programs. Computer Science Center, University of Maryland, College Park, MD. 1976.
19. D. T. CROMER and J. B. MANN. Acta Crystallogr. Sect. A, **24**, 321 (1968).
20. R. F. STEWART, E. R. DAVIDSON, and W. T. SIMPSON. J. Chem. Phys. **42**, 3175 (1968).
21. A. K. S. MUIR and P. W. CODDING. Can. J. Chem. **63**, 2752 (1985).
22. P. W. CODDING and M. B. SZKARADZINSKA. 14th International Congress of Crystallography, Perth, Australia, Abstract 03.1-4, August 1987.
23. A. K. S MUIR. Ph.D Thesis. University of Calgary, Calgary, Alta. 1985.
24. A. K. S. MUIR and P. W. CODDING. Can. J. Chem. **62**, 1803 (1984).
25. F. H. ALLEN, S. BELLARD, M. D. BRICE, B. A. CARTWRIGHT, A. DOUBLEDAY, H. HIGGS, T. HUMMELINK, B. G. HUMMELINK-PETERS, O. KENNARD, W. D. S. MOTHERWELL, J. R. RODGERS, and D. G. WATSON. Acta Crystallogr. Sect. B, **35**, 2331 (1979).
26. P. J. CLARKE, K. JEWERS, and H. F. JONES. J. Chem. Soc. Perkin I, 1614 (1980).
27. P. MURRAY-RUST and J. P. GLUSKER. J. Am. Chem. Soc. **106**, 1018 (1984).
28. R. A. LOCOCK, G. B. BAKER, R. G. MICETISH, R. T. COUTTS, and A. BENDERLY. Prog. Neuro-Psychopharmacol. Biol. Psychiat. **6**, 407 (1982).
29. R. H. DODD, C. OUANNES, L. P. DE CARVALDO, A. VALIN, P. VENAULT, G. CHAPOUTHIER, J. ROUSSIER, and P. POTIER. J. Med. Chem. **28**, 824 (1985).
30. G. LOEW, J. NIENOW, J. A. LAWSON, L. TOLL, and E. T. UYENO. Mol. Pharmacol. **28**, 17 (1985).
31. M. J. FRISCH, J. S. BRINKLEY, H. S. SCHLEGEL, K. RAGHAVACHARI, C. F. MELIUS, R. L. MARTIN, J. P. STEWART, F. W. BOBROWICZ, C. M. ROHLFING, L. R. KAHN, D. J. DEFREES, R. SEEGER, R. A. WHITESIDE, D. J. FOX, E. M. FLEUDER, and J. A. POPLE. GAUSSIAN86, Carnegie-Mellon Quantum Chemistry Publishing Unit, Pittsburgh, PA. 1984.
32. J. M. COOK. Unpublished results.
33. J. A. POPLE and G. A. SEGAL. J. Chem. Phys. **44**, 3289 (1966).
34. C. K. JOHNSON. ORTEP-II. Report ORNL-5138, Oak Ridge National Laboratory 1976.
35. G. D. SMITH. PROFIT. A molecular fitting program. Medical Foundation of Buffalo, Buffalo, NY. 1983.
36. S. MOTHERWELL. PLUTO. University Chemical Laboratory, Cambridge, England. 1979.

Can. J. Chem. Downloaded from www.nrcresearchpress.com by 122.72.124.2 on 09/07/12
For personal use only.

Naphthaloyl group: a new selective amino protecting group for deoxynucleosides in oligonucleotide synthesis

ARCHANA DIKSHIT, MANJULA CHADDHA, R. K. SINGH, AND KRISHNA MISRA[1]

Nucleic Acids Research Laboratory, Department of Chemistry, University of Allahabad, Allahabad-211 002, India

Received November 18, 1987[2]

ARCHANA DIKSHIT, MANJULA CHADDHA, R. K. SINGH, and KRISHNA MISRA. Can. J. Chem. **66**, 2989 (1988).

The naphthaloyl group has been found to be a selective amino protecting group for deoxycytidine, deoxyadenosine, and deoxyguanosine in oligodeoxyribonucleotide synthesis. All three protected monomers obtained (78–85%), being six-membered cyclic imides, were fairly stable. These protected monomers were used successfully for the preparation of dimers (phosphodiester approach) and tetramers (phosphotriester approach) in solution as well as solid phase, respectively. The group acted as a purification tool due to its high lipophilicity. No adverse effect has been observed either on the glycosidic bond (depurination) or the internucleotidic bond during its removal. The monomeric units were characterized by UV, NMR, and elemental analyses whereas the tetramers were characterized by enzymatic hydrolyses with snake venom phosphodiesterase followed by alkaline phosphatase.

ARCHANA DIKSHIT, MANJULA CHADDHA, R. K. SINGH, et KRISHNA MISRA. Can. J. Chem. **66**, 2989 (1988).

On a trouvé que le groupe naphtaloyle constitue un groupe protecteur sélectif de la fonction amine de la déoxycytidine, de la déoxyadénosine et de la déoxyguanosine dans la synthèse de l'oligodéoxyribonucléotide. Les trois monomères protégés obtenus (78–85%) sont des imides cycliques à six chainons assez stables. On a utilisé avantageusement ces trois monomères protégés dans la préparation des dimères (approche phosphodiester) et des tétramères (approche phosphotriesters) en solution aussi bien qu'en phase solide respectivement. La grande lipophilicité de ce groupe en fait un outil de purification. On n'a pas observé d'effets contraires ni sur la liaison glycosidique (dépurination) ni sur la liaison internucléotidique lors de la déprotection. On a caractérisé les unités monomères par ultraviolet, par résonance magnétique nucléaire et par analyse élémentaire tandis que l'hydrolyse enzymatique par le phosphodiestérase du venin de serpent suivie d'une phosphatase alcaline ont permis de caractériser les tétramères.

[Traduit par la revue]

Can. J. Chem. Downloaded from www.nrcresearchpress.com by 122.72.124.2 on 09/07/12
For personal use only.

Introduction

The importance of synthetic oligodeoxyribonucleotides in molecular biology (1–5) has long attracted attention to the refining of chemical synthetic methods. The most important aspect of chemical syntheses of oligodeoxyribonucleotides is the selective protection of different nucleophilic sites of the monomer building blocks, and amino protection is one of them. The amino protecting groups remain in place throughout the course of the synthesis and, therefore, are extremely important. Several groups have been used for the protection of the amino function (5–10) but selective protection of the amino group, despite repeated attempts, is still a challenging and important problem. Notable success has been achieved only in the case of deoxycytidine (11–14). We have now successfully used naphthaloyl as a new selective amino protecting group for the protection of all three deoxynucleosides, i.e., dA, dG, and dC. The protected monomers are found to be compatible with conditions for the synthesis of oligodeoxyribonucleotides, as evidenced by good yields of dimers and tetramers synthesized in solution phase and solid phase, respectively.

Experimental

Nucleosides, nucleotides, dimethoxytrityl chloride, 5′-*O*-dimethoxytritylthymidine-3′-*O*-chlorophenyl phosphate (triethylammonium salt), mesitylenesulfonyl-3-nitro-1,2,4-triazole, triisopropylbenzene sulfonyl chloride (TPSCl), 1,1,3,3-tetramethylguanidine, 4-nitrobenzaldoxime, 1-methylimidazole, DCC, Fmoc-glycine, ninhydrin, and acenaphthene were purchased from Fluka, Sigma, and Cruachem Chemical Co. The enzymes, snake venom phosphodiesterase (EC 3.1.4.1., *Crotalus durissus*) and alkaline phosphatase (EC 3.1.3.1., *Escherichia coli*), were purchased from Sigma Chemical Co. Naphthalic anhydride was prepared by dichromate oxidation of acenaphthene (15). Composite polydimethylacrylamide/kieselguhr support was used for solid phase synthesis, which was carried out on a dual column DNA bench synthesizer (OMNIFIT Ltd., Cambridge). HPLC separations were made on an LKB Ultrapac TSK DEAE-35W column (7.5 × 150 mm) and UV absorption was measured on a Hitachi 220 S spectrophotometer. Elemental analyses were carried out using a Carlo Erba 1106 analyser.

All the tlc analyses were done on silica gel G (Merck) using solvent system *a* (CH_2Cl_2/CH_3OH ; 9:1,v/v) or *b* (CH_2Cl_2/CH_3OH ; 9.5:0.5, v/v).

General preparation of N-*napthaloyldeoxynucleosides (N-nph-dNS)*

Each deoxynucleoside (1 mmol) was dried by evaporation *in vacuo* with pyridine (3 mL), twice. It was then suspended in dry pyridine (10 mL) and naphthalic anhydride (1 mmol) was added. Triethylamine (0.02 mL) was used as a catalyst. The flask was sealed and shaken in the dark at 70°C for 7 h, the mixture was evaporated to a gum *in vacuo*, poured into water (10 mL), and extracted with dichloromethane (4×5 mL). The organic layer was backwashed with water, dried over Na_2SO_4, and filtered. This organic part yielded 55, 55, and 50% of the N-protected derivatives of dC, dA, and dG, respectively. The aqueous layer was repeatedly coevaporated to dryness with pyridine, the residue reacted with naphthalic anhydride (1 mmol), and, after an appropriate time, it was extracted with dichloromethane. The combined dichloromethane solution was evaporated to dryness *in vacuo* and the residue was subjected to silica gel column chromatography. Elution was done with CH_2Cl_2/ CH_3OH of increasing polarity (Scheme 1). Data obtained are given in Table 1.

Conditions for removal of naphthaloyl group

Conditions for the removal of the naphthaloyl group were worked out by treating the N-protected derivatives with 40% ammonia at 30, 50, and 70°C. Reaction was quenched after 1, 2, 3, 4, 5, and 6 h duration. After hydrolysis, the mixtures were analysed for deprotected 2′-deoxynucleosides by preparative tlc and subsequent estimation by UV spectroscopy. Ammonia (40%) at 50°C for 4 h showed the best result and was taken to be the optimal condition for removal of the group, although the initial rate of hydrolysis varied in each case (Table 2).

[1]Author to whom correspondence may be addressed.

[2]Revision received August 3, 1988.

TABLE 1. Yield and characterization of naphthaloyl protected dC, dA, and dG

Compound	Yield (%)	R_f	UV (CH_2Cl_2) λ_{max} (nm)	UV (CH_2Cl_2) λ_{min} (nm)	^1H NMR ($CDCl_3$) (ppm)	Elemental analysis
N^4-nph-dC	85	0.30 (*a*)	290 302 310	285	8.25 (d,2H), 8.68 (d,2H), 7.92 (t,2H), 7.32 (d,1H), 7.54 (d,1H), 3.20–3.48 (sugar protons, 4H), 5.18 (m,1H)*	$C_{21}H_{17}N_3O_6$ (407) Calcd.: C61.94, H4.17, N10.32 Found: C61.88, H4.19, N10.35
N^6-nph-dA	82	0.35 (*b*)	270–272	258	8.25 (d,2H), 8.68 (d,2H), 7.92 (t, 2H), 9.0 (s,1H), 5.20 (m,1H,N-CH), 4.2–4.4 (sugar protons), 5.82 (m,1H)*	$C_{22}H_{17}O_5N_5$ (431) Calcd.: C61.25, H3.94, N16.24 Found: C61.39, H3.91, N16.30
N^2-nph-dG	78	0.31 (*b*)	258–262	250	8.25 (d,2H), 8.68 (d,2H), 7.92 (t,2H), 9.81 (s,1H, N-H), 5.20 (m,1H, N-CH), 3.30–3.6 (sugar protons 4H), 5.08 (m,1H)*	$C_{22}H_{17}N_5O_6$ (447) Calcd.: C59.05, H3.83, N15.65 Found: C59.11, H3.79, N15.62

a and *b* refer to solvent systems (see text), and * indicates anomeric protons.

TABLE 2. Percentage deprotection with 40% ammonia

Temperature (°C)	Time (h)	N^4-nph-dC	N^6-nph-dA	N^2-nph-dG
30	1	9.0	7.5	7.0
	2	17.2	16.1	15.3
	3	23.4	21.3	20.3
	4	30.1	27.2	28.0
	5	32.8	32.6	30.6
	6	42.0	41.6	40.0
50	1	10.8	10.2	9.8
	2	45.0	45.0	41.0
	3	83.2	80.6	79.1
	4	100	100	100
	5	100	100	100
	6	100	100	100
70	1	15.0	14.2	13.6
	2	60.1	58.2	56.8
	3	93.0	92.4	90.0
	4	100	100	100
	5	100	100	100
	6	100	100	100

General preparation of 5′-O-dimethoxytrityl-N-naphthaloyl-deoxynucleosides (5′-O-DMTr-N-nph-dNS)

The corresponding trityl derivatives were prepared by treating dried N-nph-dNS (1 mmol) with DMTrCl (1.2 mmol) in pyridine (10 mL) at room temperature (25–30°C) (Table 3). After completion of the reaction (as checked by tlc), the clear solution was evaporated to a gum *in vacuo*. Ice-cooled water (10 mL) was added and it was extracted with ethyl acetate (3×10 mL). The organic layer was dried over Na_2SO_4, concentrated, and applied to an alumina column, eluting with CH_2Cl_2/CH_3OH of increasing polarity. Yield, R_f, and λ_{max} of different derivatives are shown in Table 3.

General method for preparation of N,3′-diacetyldeoxyadenosine-5′-phosphate (pdA-N,3′-O-Ac_2)

Deoxyadenosine-5′-phosphate (1 mmol) was dried by evaporation *in vacuo* three times with dry pyridine (2 mL). The residue was placed in dry pyridine (5 mL), acetic anhydride (5 mL) added, and the solution stirred at room temperature. After 3 h, the reaction was checked for completion, by tlc, and methanol (5 mL) was added. The reaction mixture was evaporated to a gum. The gum was dissolved in a minimum amount of water, which was washed with ether. The aqueous solution was evaporated to a gum. The process of evaporation was repeated twice with 10% aqueous pyridine. The residue thus obtained was dissolved in dry pyridine, concentrated, and added dropwise to dry ether (5 times the volume of concentrated pyridine solution); the white precipitate was filtered, washed with ether, and dried under vacuum (yield, 90%; λ_{max} 272 nm).

TABLE 3. Preparation and characterization of 5′N-protected units

	Reaction time (h)	Yield (%)	R_f	λ_{max} (nm)
5′-O-DMTr-N^4-nph-dC	3	90	0.42 (*a*)	292,303,312
5′-O-DMTr-N^6-nph-dA	2	94	0.47 (*b*)	271–273
5′-O-DMTr-N^2-nph-dG	1.5	95	0.45 (*b*)	262–264

a and *b* refer to solvent systems (see text).

General procedure for dimer preparation

All three 5′-O-DMTr-N-naphthaloyldeoxynucleosides (1 mmol) and N,3′-diacetylated-5′-phosphates of dA (2 mmol) were evaporated *in vacuo* three times with dry pyridine and suspended in pyridine (5 mL). Triisopropyl benzenesulfonyl chloride (4 mmol) was added and the mixture stirred. After 4 h at room temperature (22–25°C), water (5 mL) was added while cooling the flask in an ice-bath (Scheme 2).

Purification of dimers

Purification of dimers was carried out on a DEAE cellulose (HCO_3^-) ion-exchange column. Elution was done by tris-HCl buffer (pH 8.3, 0.1 M) using a linear gradient of NaCl (0.05–0.15 M) and columns were monitored at 300, 270, and 260 nm in the case of CpA, ApA, and GpA, respectively. The desired fractions were pooled and evaporated to dryness *in vacuo*.

Dry residue dissolved in concentrated ammonia (40%) was kept sealed at 50°C for 4 h. It was then evaporated carefully, *in vacuo*, to dryness. Acetic acid (80%) was added to the flask and left at 25–30°C for 30 min. Acid was evaporated *in vacuo* and the residue dissolved in a minimum amount of water, diluted to twice the initial volume, and extracted four times with ether. The aqueous layer was lyophilized and stored under dry conditions. The dimers were obtained in 62–68% yield.

Can. J. Chem. Downloaded from www.nrcresearchpress.com by 122.72.124.2 on 09/07/12
For personal use only.

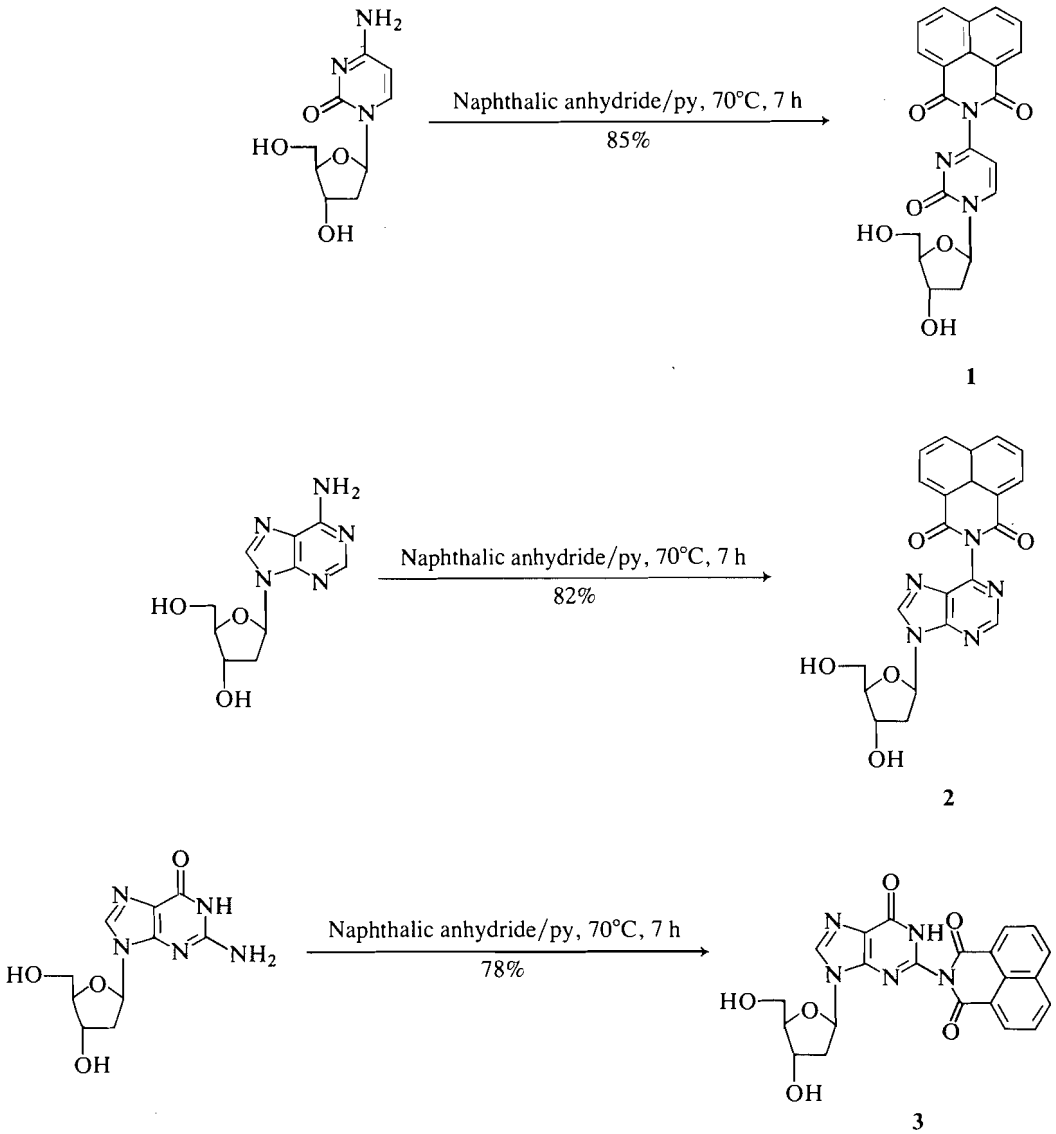

SCHEME 1. Preparation of cyclic imides of deoxynucleosides (dC, dA, and dG).

Preparation of 5'-O-DMTr-N-nph-dNS-3'-O-succinate

To 5'-O-DMTr-N-nph-dNS (0.5 mmol) dissolved in pyridine (2.5 mL) were added triethylamine (0.2 mL) and succinic anhydride (0.55 mmol). The reaction mixture was worked up as usual (14) to give the final product. Yield, 70–75%.

Preparation and purification of tetramers d(TTTC), d(TTTA), and d(TTTG)

5'-O-DMTr-N-nph-dNS-3'-O-succinate was linked to the support (kieselguhr/polydimethylacrylamide, 500 mg) with the help of the spacer, i.e., ethylenediamine and two glycine units, using Gait's procedure (16). Loading was estimated to be 68, 65, and 57 μmol g^{-1} in the case of dC, dA, and dG, respectively.

This functionalized resin (100 mg each) was placed in the column of the DNA bench synthesizer and allowed to stand in DMF for 5 min. Synthesis, deprotection, and purification of the tetramers were carried out by the usual procedure (14) (Fig. 1). Yield of d(TTTC), d(TTTA), and d(TTTG) was 72.6, 70.0, and 66.4%, respectively (Scheme 3).

Enzymatic hydrolysis of tetramers

Each tetramer (0.4 A_{260} units) dissolved in 0.1 M Tris-HCl buffer, pH 8.5 (0.5 mL), was first digested with snake venom phosphodiesterase (5 μg, 37°C, 2 h) and then incubated with alkaline phosphatase (5 μg, 37°C, 1 h). The nucleosides thus obtained were separated (Fig. 2) using 0.1 M triethylammonium acetate, pH 7.0 (A), and acetonitrile (B). A gradient elution using 6% B over 20 min at a flow rate of 0.5 mL min^{-1} was achieved. After separation, quantification was made at 260 nm on the basis of peak areas and extinction coefficients of the nucleosides (E_{260} : dT, 8800; dC, 7300; dA, 15 400; and dG, 11 700).

Results and discussion

The naphthaloyl group has been used for protection of the exocyclic amino function of all three deoxynucleosides, i.e., dA, dG, and dC, when cyclic imides were obtained (Scheme 1). These cyclic imides have been well characterized by elemental analyses, and by their UV and NMR spectra. There was no indication of any free -NH or -COOH group.

The absolute selectivity observed during protection under controlled experimental conditions for all three deoxynucleosides is of utmost importance. It eliminates the two-step procedure of protection whereby, first, a fully protected derivative is formed that on subsequent and selective hydrolysis gives the desired product (Khorana's procedure) (17), and it also avoids the need for prior silylation (Jones' procedure) (18). This selectivity may be explained as most probably due to the formation of stable cyclic imides, which drives the reaction predominantly in this direction.

Can. J. Chem. Downloaded from www.nrcresearchpress.com by 122.72.124.2 on 09/07/12
For personal use only.

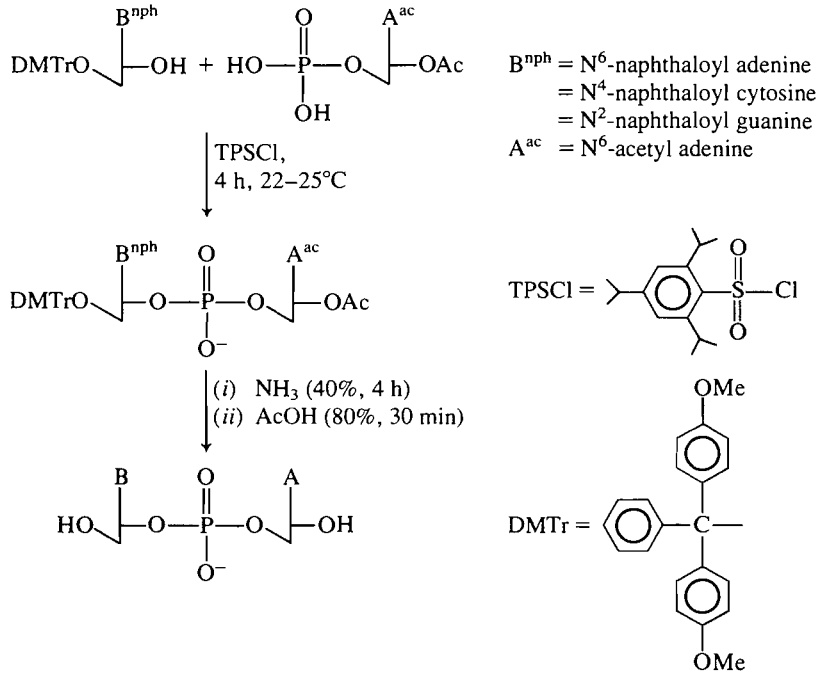

SCHEME 2. Preparation of dimer in solution phase.

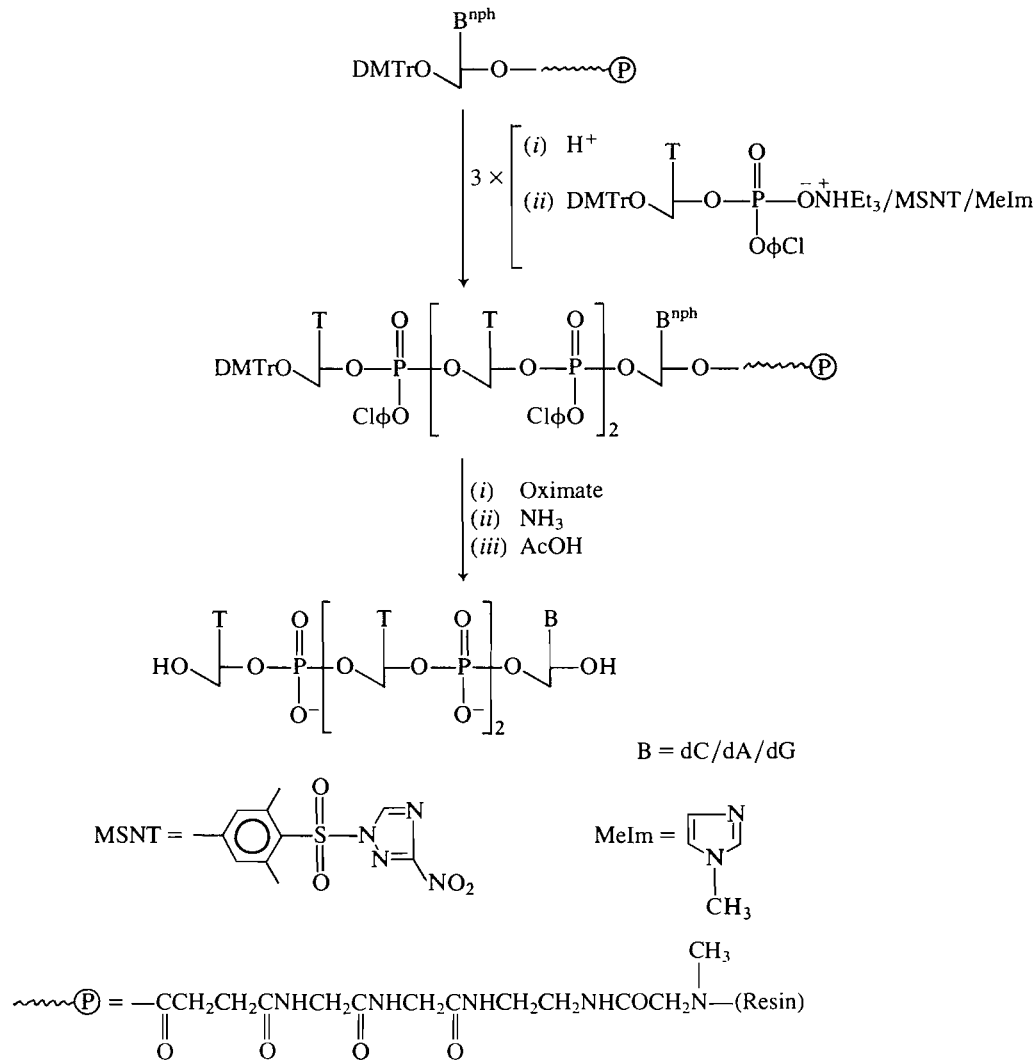

SCHEME 3. Synthesis of tetramer on solid support.

Can. J. Chem. Downloaded from www.nrcresearchpress.com by 122.72.124.2 on 09/07/12
For personal use only.

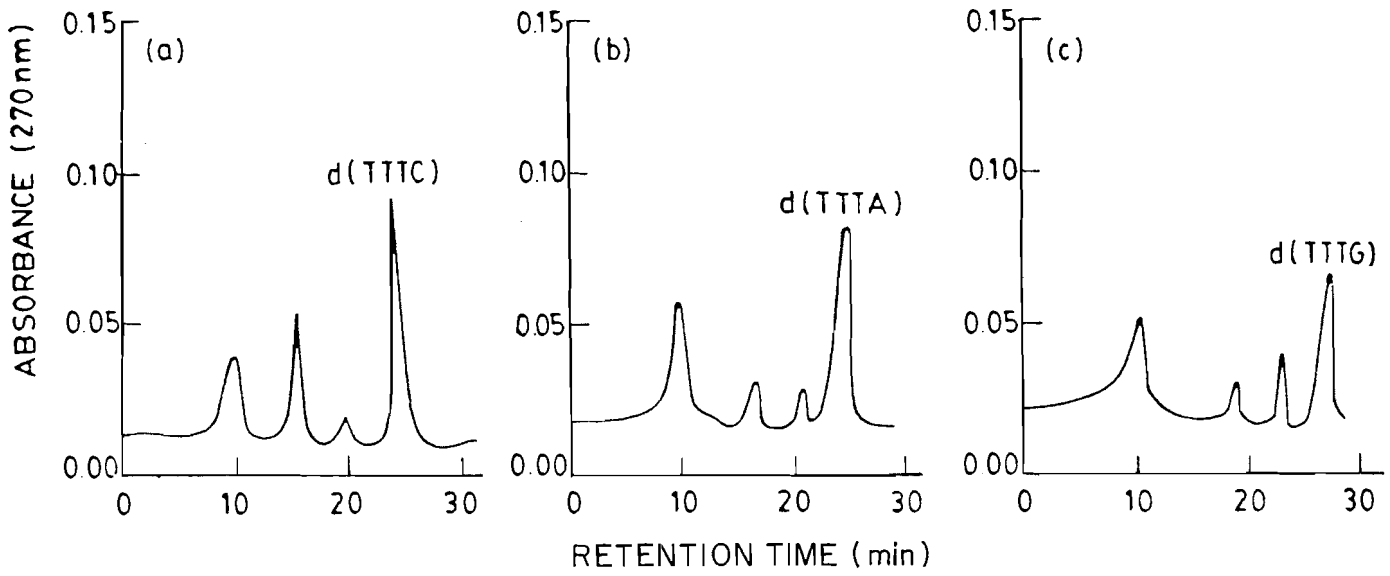

FIG. 1. Ion-exchange HPLC of tetramers, gradient 0–70% buffer B, 40 min, temperature 25°C.

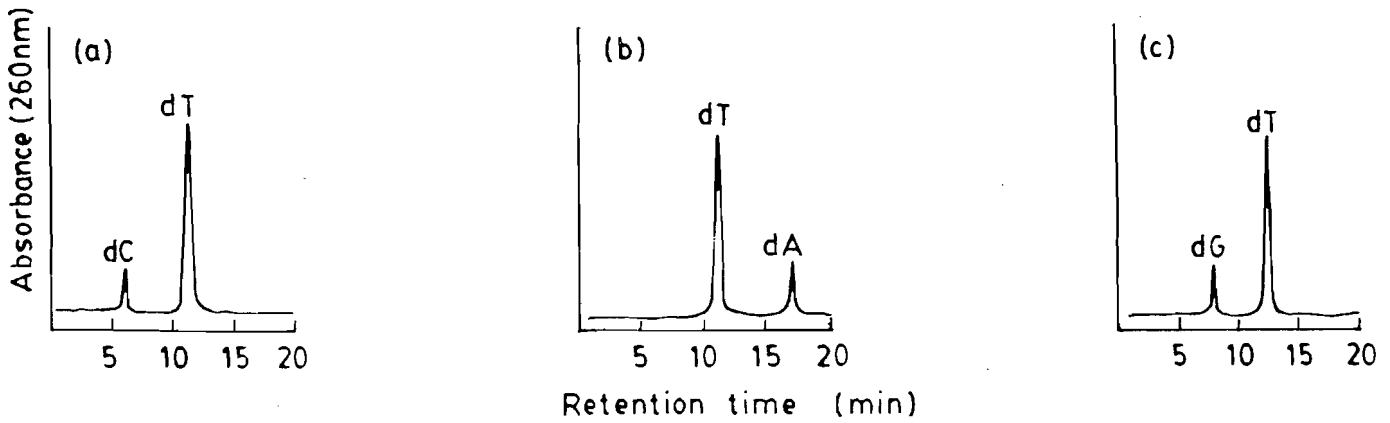

FIG. 2. Reversed phase HPLC of enzymatically hydrolyzed tetramers, 6% buffer B over 20 min, flow rate 0.5 mL min^{-1}.

A literature survey reveals that, so far, acid chlorides have been employed for acylation of the exocyclic amino function of deoxynucleosides. Because of the slow reaction between anhydride and amino function (cf. chloride and amino function), more selectivity can be observed. Thus, the use of anhydride is certainly advantageous, due also to its stable nature and easy storage. Furthermore, use of acid chlorides is well known to yield isomeric imides, while anhydrides are reported to exclude the formation of any such isomers (19). In this respect the use of the naphthaloyl group is more advantageous and convenient as compared to the phthaloyl group.

Other advantages envisaged for this group are its bulkier nature and higher lipophilicity. These are important considerations for N-acyl protecting groups. The naphthaloyl group has found extensive use in preparation of smaller blocks via solution phase methodology where column purification of those fully protected blocks after each condensation step is necessary. Because of high lipophilicity, the group helps in purification. It has been observed that phosphodiester oligomers have a tendency to become less soluble in organic solvents with increasing chain length due to polar effects (20). This can make experimental procedure difficult in connection with solvent extractions and adsorption chromatographic methods. However, naphthaloyl derivatives are highly soluble in organic solvents due to the hydrophobic nature of the group and are, therefore, well suited for adsorption chromatography as well as for purification of protected oligonucleotides by reversed phase HPLC (21). Thus, the group acts as a purification handle.

The protected monomer units have been found sufficiently stable. In the case of adenosine, the imidazole ring opened when the phthaloyl group was used for amino protection, under the reaction conditions of oligonucleotide synthesis (7), and thus many problems were created. But in the present case no ring opening was observed. This, in all probability, was due to the formation of a more stable six-membered ring in the cyclic imides in place of a five-membered ring as in the case of phthaloyl derivatives.

Conditions for removal of the naphthaloyl group are comparatively milder and speed of reaction is faster. It can be removed by concentrated ammonia (40%) at 50°C in 4 h (cf. the benzoyl group, 40% ammonia, 50°C, 5 h), although the initial rate of hydrolysis is different in the case of different nucleosides.

To adjudge the efficiency of the group in preparation of small blocks and oligonucleotides by solution and solid phase methods, different dimers and tetramers have been prepared by the phosphodiester and triester approach, respectively. An overall yield of 62–68% in the case of dimers and 66–72% in the case of tetramers was obtained, which is almost comparable

Can. J. Chem. Downloaded from www.nrcresearchpress.com by 122.72.124.2 on 09/07/12
For personal use only.

to the yields reported in the literature, thereby indicating the suitability of the group in both approaches, viz., solution and solid phase.

To confirm the structure of the tetramers, enzymatic hydrolysis with snake venom phosphodiesterase followed by alkaline phosphatase was carried out. After HPLC analysis, the cleavage pattern of the tetramers clearly indicated the presence of deoxynucleosides in a 3:1 ratio in each case (Fig. 2). The peak assignment, based on the retention time, was confirmed by direct comparison with authentic samples of deoxynucleosides. HPLC analyses clearly showed the absence of any base modification.

Acknowledgement

The authors are grateful to the C.S.I.R., Government of India, for financial assistance.

1. K. Itakura, T. Hirose, R. Crea, A. D. Riggs, H. L. Heyneker, F. Bolivar, and H. W. Boyer. Science, **198**, 1056 (1977).
2. A. C. Herington, H. J. Cornbell, and A. D. Kulfer. Int. J. Biochem. **15**, 1201 (1983).
3. Z. Laron. Ergeb. Inn. Med. Kinderheilkd. **51**, 117 (1984).
4. F. Wengenmayer. Angew. Chem. Int. Ed. Engl. **22**, 842 (1983).
5. M. Gouy and C. Gautier. Nucleic Acids Res. **10**, 7055 (1982).
6. Y. Lapidot and H. G. Khorana. J. Am. Chem. Soc. **85**, 3857 (1963).
7. A. Kume, M. Sekine, and T. Hata. Tetrahedron Lett. **23**, 4365 (1982).
8. B. C. Froehler and M. D. Matteucci. Nucleic Acids Res. **11**, 8031 (1983).
9. Y. Hayakawa, N. Kato, M. Uehiyama, H. Kajino, and R. Noyori. J. Org. Chem. **51**, 2400 (1986).
10. F. Benseler and L. W. McLaughlin. Synthesis, 45 (1986).
11. I. Butula, L. Curkovie, M. Prostenie, V. Vela, and F. Zorko. Synthesis, 704 (1976).
12. H. Frank and P. Wolfgang. Tetrahedron Lett. **24** 3583 (1983).
13. J. Igolen and M. Morin. J. Org. Chem. **45**, 4802 (1980).
14. R. K. Mishra and K. Misra. Nucleic Acids Res. **14**, 6197 (1986).
15. Encyclopedia of organic chemistry. Vol. 12B. Elsevier, Amsterdam. 4700.
16. M. J. Gait, H. W. D. Matthes, M. Singh, B. S. Sproat, and R. C. Titmas. Nucleic Acids Res. **10**, 6243 (1982).
17. H. Schaller, G. Weimann, B. Lerch, and H. G. Khorana. J. Am. Chem. Soc. **85**, 3821 (1963).
18. G. S. Ti, B. L. Gaffney, and R. A. Jones. J. Am. Chem. Soc. **104**, 1316 (1982).
19. E. V. Ganin, V. F. Makarov, and V. I. Nikitin. J. Org. Chem. USSR, **21**, 2209 (1985).
20. C. B. Reese. Tetrahedron, **34**, 3143 (1978).
21. R. F. Jones, H. J. Fritz, and H. G. Khorana. Biochemistry, **17**, 1268 (1978).

Can. J. Chem. Downloaded from www.nrcresearchpress.com by 122.72.124.2 on 09/07/12
For personal use only.

Modelling the binding step in dopamine receptor–antagonist interactions

ALAIN BOUDON, JAN SZYMONIAK, JACQUES R. CHRÉTIEN,[1] and JACQUES-EMILE DUBOIS

Institut de Topologie et de Dynamique des Systèmes de l'Université Paris VII, associé au CNRS, 1 rue Guy de la Brosse, 75005 Paris, France, and Laboratoire de Chimiométrie, Université d'Orléans, B.P. 6759, 45067 Orleans Cedex 2, France

Received July 5, 1988

ALAIN BOUDON, JAN SZYMONIAK, JACQUES R. CHRÉTIEN, and JACQUES-EMILE DUBOIS. Can. J. Chem. **66**, 2995 (1988).

Modelling of the binding step in dopamine receptor–antagonist interactions was undertaken using sixteen antagonists belonging to the following five chemical series: phenothiazines, thioxanthenes, butyrophenones, benzamides, and benzisoxazoles. The Lower Unoccupied Molecular Orbitals (LUMOs) of the antagonists used for these interactions were compared using a similarity τ_{ij} index, which enabled us to define the characteristic orbital forms of the active molecules. The result of the intersection of these representative orbital forms was the form common to the antagonists' LUMOs. This form corresponds to the orbital form of the indole's Higher Occupied Molecular Orbital (HOMO), and thus suggests that the aromatic binding site of the dopamine receptor is part of a tryptophan type structure.

ALAIN BOUDON, JAN SZYMONIAK, JACQUES R. CHRÉTIEN et JACQUES-EMILE DUBOIS. Can. J. Chem. **66**, 2995 (1988).

La modélisation de l'étape de liaison des interactions récepteur dopaminergique–antagoniste est entreprise sur seize antagonistes appartenant à cinq séries chimiques: les phénothiazines, les thioxanthènes, les butyrophénones, les benzamides et les benzisoxazoles. Une comparaison des orbitales moléculaires vacantes les plus basses (LUMO) des antagonistes mises en jeu lors de l'interaction, est effectuée à l'aide de l'indice de similitude τ_{ij}. Elle permet de préciser les formes des orbitales caractéristiques des molécules actives. L'intersection de ces formes orbitales représentatives aboutit à la forme commune des LUMO des antagonistes. Cette forme commune correspond à la forme de l'orbitale HOMO de l'indole; elle suggère que le site de liaison aromatique du récepteur dopaminergique fait partie de la structure de type tryptophane.

Introduction

Neuroleptic compounds, which are dopamine receptor–antagonists, include a wide variety of chemical series: phenothiazines, thioxanthenes, butyrophenones, benzamides, benzisoxazoles... Despite this structural diversity each antagonist contains an aromatic ring linked to an alkyl amine chain with three or four nodes betwen the nitrogen atom and the aromatic ring. The antagonists act on two primary sites of the dopamine receptor (1), whose exact structure has not yet been determined.

Several studies stress that the proper positioning of the chain's nitrogen atom in relation to the aromatic ring is essential for a strong affinity between the antagonist and the receptor. In the case of the rigid molecules in the butaclamol series, a slight modification of the positioning of the ring eliminates activity (2). Receptor mapping studies provided the receptors' topography, most importantly the three-dimensional location of the zones corresponding to the two primary sites (3, 4). The superposition of the pharmacophores (N atom-chain – aromatic ring) — corresponding to the antagonists with flexible chains and belonging to a different series — was accomplished with only slight modifications of the chain's conformation (5). Comparative conformational analysis allows us to locate the nitrogen orbital's vectoral position relative to the orbital of the aromatic system (6). Geometric models of the receptor obtained from such research do not, however, inform us about the nature of the interactions.

Recently it was demonstrated that the energy of the lower unoccupied molecular orbital (ϵ_{LUMO}) was correlated with the biological activity for different series of antagonists (7, 8); biological activity increases with the decrease of the LUMO energy. An excellent correlation exists, for example, between activity (C_1) and the ϵ_{LUMO} for sixteen 2-substituted phenothiazines belonging to three series: promazine, perazine, and phenazine (8). These results have been formalized in terms of the LUMO antagonist – HOMO receptor (L_a–H_r) principle, which denotes the participation of the antagonist's aromatic ring LUMO and the receptor's aromatic binding site HOMO in the complex formation.

The L_a–H_r principle led us to examine more closely the role played by the antagonist's LUMO, with the object of modelling the interactions of the antagonists with the dopamine receptor.

Our investigations are based on several primary assumptions. First, the factors relating to drug transport play a minor role so the activity differences reflect essentially events occurring at the receptor. The validity of this assumption is confirmed by several studies (9, 10). Second, the charge-transfer interactions are an important feature in stabilizing the drug–receptor complex. Third, the antagonist's unoccupied orbital (LUMO) acts as an electron acceptor in charge-transfer interactions. Since the receptor has not been isolated, the latter two assumptions cannot be verified through direct experimentation at the present time. However, these conditions seem to prevail in the current study, in light of theoretical considerations.

If a major portion of the stabilization energy ΔW for the drug–receptor complex is provided by charge-transfer interactions (11) in which the drug acts as an electron acceptor, ΔW may be expressed approximately by the Mulliken equation (12)

$$\Delta W = Q - \kappa/(\epsilon_a - \epsilon_d - \lambda)$$

where Q is the energy of interaction between the drug and receptor exclusive of charge-transfer, $\epsilon_a - \epsilon_d$ is the energy gap between the donor (receptor) Φ_d and acceptor Φ_a molecular orbitals, and λ is a term which depends upon the degree of overlap between Φ_d and Φ_a. Significant charge-transfer contributions to ΔW exist only when Φ_d and Φ_a exhibit complementary features in the overlap region with regard to local symmetry and density distribution. If this were not the case, k would become negligible (12). If the distribution of density in the critical regions of the pharmacophore remained essentially constant for a given series of drug molecules, the values of Q, k, and λ would not be expected to change greatly. As a result, the stability of the drug–receptor complex appears to depend pri-

[1]To whom correspondance should be addressed.

Printed in Canada / Imprimé au Canada

Can. J. Chem. Downloaded from www.nrcresearchpress.com by 122.72.124.2 on 09/07/12
For personal use only.

marily on the energy (ϵ_a) of the molecular orbital Φ_a. This stability is enhanced if Φ_a is a low-energy unoccupied molecular orbital and Φ_d is a high-energy occupied molecular orbital.

Consider a homogeneous group of 2-substituted phenithiazine molecules which will orientate in the same way according to the field of the receptor and where the contribution of the second interaction on the side of the chain's nitrogen atom is weighed: a very good correlation exists between ϵ_{LUMO} and antagonist activity (8). This correlation is characterized by a negative slope. It therefore fulfills the conditions of a $\Delta W = f(\epsilon_a)$ relationship, and is consistent with the expectation that a reduction of the energy of the orbital acceptor stabilizes the drug–receptor complex when charge-transfer interactions play an important role (13).

The relationship between activity and the single ϵ_{LUMO} for the aromatic binding site interaction indicates only a slight variation of the overlap factor. This lets us assume that the LUMOs corresponding to the aromatic rings of active phenothiazines have similar characteristics with regard to local symmetry and density distribution. This supposed similarity among the LUMOs (Φ_a) of the active phenothiazines related to the HOMO (Φ_d) of the receptor's aromatic binding site also assures conditions favorable for a significant contribution by charge-transfer interactions to ΔW.

The activity of the non-phenothiazine series of antagonists also increases with the reduction in LUMO's energy (8). It could be assumed that LUMOs corresponding to these antagonists show a likeness to LUMOs of the phenothiazines, just as it may be assumed that they resemble each other. We may now ask, what is the extent and content of this similarity in the case of a group of structurally heterogeneous antagonists?

In the present work we would like to focus attention on the dopamine receptor–antagonist MOs' overlap factor. We will study the distribution of the LUMO density among the aromatic parts of a series of antagonists, while assuming that the LUMO acts as an electron acceptor in charge-transfer interactions dominating the stabilization of the complex.

Because of the rudimentary nature of our model (assumption that the contribution of the N-atom interaction is constant for the non-variable alkyl-chain analogues, approximation of the frontier orbital approach, limitations imposed by the quality of the biological data ...) we did not attempt to establish a quantitiative structure–activity relationship. The reasoning and final conclusions remain semi-quantitative.

In order to systematize our approach, the following procedure was taken. A preliminary comparison of the LUMO density distributions was carried out using a τ_{ij} similarity index. This methodology applied by Cheney *et al.* (14, 15) in studies on drug–receptor charge-transfer interactions using frontier MOs was adopted for our ends. Applying these results as a point of departure, we conducted a more extensive analysis, seeking, above all, to determine the characteristics shared by the antagonists' LUMOs. Moreover a comparison of the series of antagonists was always preceded by an analysis of the LUMO density distribution of the homogeneous series of phenothiazines.

We examined the overlap factor to determine the shape of the aromatic binding site of the dopamine receptor (HOMO) through an indirect approach of receptor mapping.

Methods

Calculations were performed on a VAX-11/780 computer under VMS. Wave functions and electron densities were calculated by the Gaussian 80 program (QCPE 446) operating in the

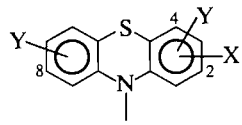

I

Ia: X = H, Y = H
Ib: X = 2-Cl, Y = H
Ic: X = 3-Cl, Y = H
Id: X = 4-Cl, Y = H
Ie: X = 2-OCH_3, Y = H
If: X = 2-Cl, Y = 4-Cl
Ig: X = 2-Cl, Y = 8-CF_3
Ih: X = 2-CF_3, Y = H

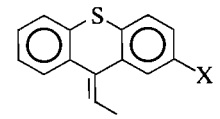

II

IIa: X = H
IIb: X = Cl

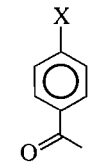

III

IIIa: X = H
IIIb: X = Cl

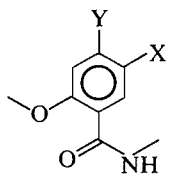

IV

IVa: X = SO_2NH_2, Y = H
IVb: X = Cl, Y = NH_2

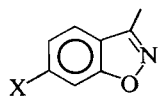

V

Va: X = F
Vb: X = MeO

SCHEME 1

STO-3G* minimal basis set. As in our previous investigation, standard bond lengths and valency angles (16) were used. No geometrical optimiztions were performed. Molecular orbitals are written as linear combinations of the basis functions, using the following equation:

$$[1] \quad \Phi_i = \sum_r^N C_{ri}\Psi_r$$

N is the number of basis function Ψ_r, and C_{ri} is an expansion coefficient on atom r. Optimization of the molecular wave function was performed using a standard self-consistent field (SCF) procedure (17, 18).

The similarity τ_{ij} index (14) is used to express the correlation between MOs from two molecules, A and B.

$$[2] \quad \tau_{ij} = \left|\sum_r^n C_{rI}^A \times C_{rj}^B\right|$$

C_{ri}^A represents the coefficient of Ψ_r in the ith MO (LUMO in this case) of molecule A (**I** to **V**, Scheme 1). In this case, only corresponding structural moieties in molecules A and B, i.e., C atoms of the aromatic rings are taken into account and give rise to significant terms in eq. [2]. If Φ_r in the aromatic part of molecule A has no counterpart in the aromatic part of molecule B, the value of C_{rj}^B is considered to be zero. The τ_{ij} similarity index (Table 1) is calculated for two different molecules (A ≠ B), with respect to only the density contribution made by the aromatic ring. The value of τ_{ij} then varies from 0 to 1, depending on the degree of similarity between the density distribution over

Can. J. Chem. Downloaded from www.nrcresearchpress.com by 122.72.124.2 on 09/07/12
For personal use only.

Can. J. Chem. Downloaded from www.nrcresearchpress.com by 122.72.124.2 on 09/07/12
For personal use only.

TABLE 1. Matrix of the similarity index (τ_{ij}) indicating the degree of similarity between the aromatic part of the LUMO orbital forms of sixteen model compounds **I**–**V** (Scheme 1). The substituted aromatic rings were considered for compounds **I** and **II** (CF_3-substituted ring for **Ig**). The τ_{ij} values are separated into three zones: phenothiazine/phenothiazine correlations (PP), phenothiazine/non-phenothiazine correlations (PN), and non-phenothiazine/non-phenothiazine correlations (NN). The diagonal of the τ_{ij} matrix gives electron density values for the substituted aromatic rings for compounds **I**–**V** (LED).

	Ia	Ib	Ic	Id	Ie	If	Ig	Ih	IIa	IIb	IIIa	IIIb	IVa	IVb	Va	Vb	
LED	0.49	0.55	0.56	0.20	0.39	0.38	0.48	0.55	0.33	0.40	0.48	0.48	0.44	0.51	0.23	0.20	Ia
		0.81	0.56	0.61	0.27	0.76	0.65	0.81	0.24	0.32	0.40	0.40	0.25	0.41	0.03	0.07	Ib
			0.70	0.05	0.53	0.29	0.51	0.55	0.44	0.52	0.63	0.62	0.63	0.67	0.41	0.37	Ic
				0.92	0.21	0.85	0.42	0.63	0.15	0.12	0.13	0.12	0.36	0.15	0.53	0.55	Id
					0.47	0.01	0.28	0.25	0.38	0.44	0.53	0.52	0.59	0.56	0.46	0.44	Ie
PP						0.89	0.56	0.77	0.02	0.08	0.10	0.11	0.10	0.10	0.34	0.38	If
							0.53	0.65	0.25	0.32	0.39	0.39	0.29	0.40	0.06	0.03	Ig
								0.82	0.23	0.31	0.38	0.38	0.24	0.40	0.04	0.09	Ih
PN									0.33	0.38	0.46	0.45	0.50	0.48	0.39	0.37	IIa
										0.44	0.53	0.52	0.56	0.56	0.43	0.40	IIb
											0.64	0.64	0.68	0.68	0.51	0.48	IIIa
												0.63	0.67	0.67	0.51	0.48	IIIb
NN													0.78	0.73	0.64	0.62	IVa
														0.72	0.55	0.52	IVb
															0.62	0.61	Va
																0.61	Vb

Can. J. Chem. Downloaded from www.nrcresearchpress.com by 122.72.124.2 on 09/07/12
For personal use only.

the corresponding carbon atoms of two aromatic rings.[2] However, in the case of a comparison within the ring itself (**I***a*–**I***a*, etc.) τ_{ij} is not calculated with respect to the ring (for this would invariably give a τ_{ij} value of 1) but rather to the electron density of the whole molecule. In this event, τ_{ij} expresses the absolute value of the aromatic ring's LUMO density. The electron density values for sixteen model compounds are then given in the diagonal of the τ_{ij} matrix in Table 1.

Determination of the common LUMO form was done by intersecting the LUMOs previously defined by τ_{ij} analysis. Intersections were constructed on corresponding atoms of comparative aromatic rings starting from the carbon atom linked to the aliphatic fragment. The wave function Φ was calculated in a plane parallel to the aromatic ring at a distance of 0.5 Å (~1 Bohr). The intersection Λ yielded the smallest common Φ value.

Supposing that Φ_A and Φ_B are wave functions calculated at any point on the plane,

$$\text{If } \Phi_A \times \Phi_B > 0$$

then

$$\Lambda = \min(|\Phi_A|, |\Phi_B|)$$

otherwise

$$\Lambda = 0$$

The results of the intersections in graphic terms are given in Fig. 1, indicating points on the plane for which $|\Phi| \geq 0.06$.

The chlorpromazine index C_l is the relative measure of the phenothiazines' neuroleptic activity ($C_l = 1$ for the chlorpromazine). The C_l values of the antiapomorphine test for the promazine analogues, corresponding to model phenothiazines **I***a*–*h* (Scheme 1), were derived from ref. 19. They are as follows: $C_l = 0.03$ for **I***a*, 1.0 for **I***b*, 0.25 for **I***c*, 0.01 for **I***d*, 0.25 for **I***e*, 1 for **I***f*, 0.20 for **I***g*, 4.0 for **I***h*. The C_l values for the promazine chain analogues of model thioxanthenes **II***a* and **II***b* are 0.06 for **II***a* and 1.0 for **II***b* (19). Binding test values for the active analogues of model series **III**–**V** are given in the text.

Results and discussion

In order to study the distribution of the LUMO density among the aromatic fragments of a series of antagonists, we chose sixteen model compounds from the following five chemical series: phenothiazines (**I**), thioxanthenes (**II**), butyrophenones (**III**) benzamides (**IV**), and benzisoxazoles (**V**). They are aromatic (tricyclic) parts corresponding to the non-variable alkyl-chain analogues of different levels of activity (see Methods). The eight phenothiazines (**I***a*–**I***h*) differ by the nature of their substituents and positions. The influence of the disubstitution in the same aromatic ring (**I***f*) or both aromatic rings (**I***g*) will be observed. The four non-phenothiazine series (**II**–**V**) are each represented by two differently substituted compounds.

As already explained (see Methods), the τ_{ij} index and the intersection procedure require an equivalence of carbon atoms in the two aromatic rings compared. In fact, it may be assumed that the location of the antagonist's aromatic ring in relation to the corresponding site on the receptor does not vary much at the time of the binding interaction. This supposition follows from geometric constraints related to the second simultaneous interaction, that of the alkyl chain's nitrogen atom (see Introduction). More precisely, doing away with the equivalence of carbon atoms in the compared aromatic rings amounts to rotating one ring at least 60 degrees, which corresponds to the displacement of one atom, or a C_1–$C_{2'}$ interaction instead of a C_1–$C_{1'}$. Even this minimum rotation would bring about significant conformational constraints in the chain, due to the nitrogen atom's fixed position to the aromatic ring (2–6).

The LUMO electron density

The LUMO electron density is a localized electronic property whose role in the interaction of the antagonists' aromatic ring with the aromatic binding site of the dopamine receptor will be considered. The values for the sixteen model compounds are given in the diagonal of the τ_{ij} matrix in Table 1. The LUMO electron density is generally concentrated at the aromatic rings, to the detriment of the heteroatoms S and N for the phenothiazines. Thus the LUMO electron density values are 0.49 for each of the two aromatic rings of *N*-methylphenothiazine **I***a*, which represents 98% of the total density. Substitution of the aromatic ring by an electroacceptor (**I***b*, **I***c*, **I***d*, **I***h*) strongly increases its electron density.

Two groups of compounds will be examined. The first group is composed of compounds with high electron densities ranging from 0.63 to 0.92. This group includes five phenothiazines (**I***b*, **I***c*, **I***d*, **I***f*, **I***h*) and all of the butyrophenones, benzamides, and benzisoxazoles. The second group, which contains compounds with low electron densities ranging from 0.34 to 0.53, includes the other three phenothiazines (**I***a*, **I***e*, **I***g*) and the two thioxanthenes.

It is not possible to establish a close relationship between activity and electron density to the exclusion of other important parameters like the ϵ_{LUMO} (8). Nevertheless, the biological activity of the first group's phenothiazines was generally greater than that of the second, except for the inactive 4-Cl-*N*-methylphenothiazine **I***d*. This compound's low activity is undoubtedly due to a very unfavorable overlap factor which will be discussed further on.

The important role played by the electron density is demonstrated by 2-Cl,8-CF_3-*N*-methylphenothiazine **I***g* of the second group. Compound **I***g* has a chlorpromazine index ($C_l = 0.20$) (19) corresponding to a relatively low activity, though a favorably low ϵ_{LUMO} (8) was observed (5.97 eV). The lowering of the activity of compound **I***g* is explained by the fact that its electron density is distributed between the two substituted rings, giving values of 0.53 for the CF_3-substituted ring (Table 1) and 0.41 for the Cl-substituted ring. Indeed, when compared to the electron density of the monosubstituted phenothiazine ring as in active compound **I***b* (0.81), the relatively lower values of the electron densities of the two aromatic rings weaken the potential interactions with the receptor's aromatic binding site. The other two phenothiazines of the second group (**I***a* and **I***e*) have similarly low electron densities which contribute to decreased activity. The difference in activity for these two compounds (C_l **I***a* = 0.03; C_l **I***e* = 0.25) are probably due to the favorable orientation vector of 2-MeO-*N*-methylphenothiazine **I***e* as already observed.

Degrees of similarity of the LUMO form

The distribution of the LUMO density of an aromatic ring will be referred to as the orbital form. The similarity index τ_{ij} (Table 1) indicates the degree of orbital form similarities for any two molecules. Comparison of τ_{ij} of sixteen molecules **I**–**V** (Scheme 1) serves to screen the LUMO having the characteristic form of active antagonists. For clarity, the τ_{ij} data of Table 1

[2]For tricyclic molecules **I** and **II** the substituted aromatic ring is considered.

Can. J. Chem. Downloaded from www.nrcresearchpress.com by 122.72.124.2 on 09/07/12
For personal use only.

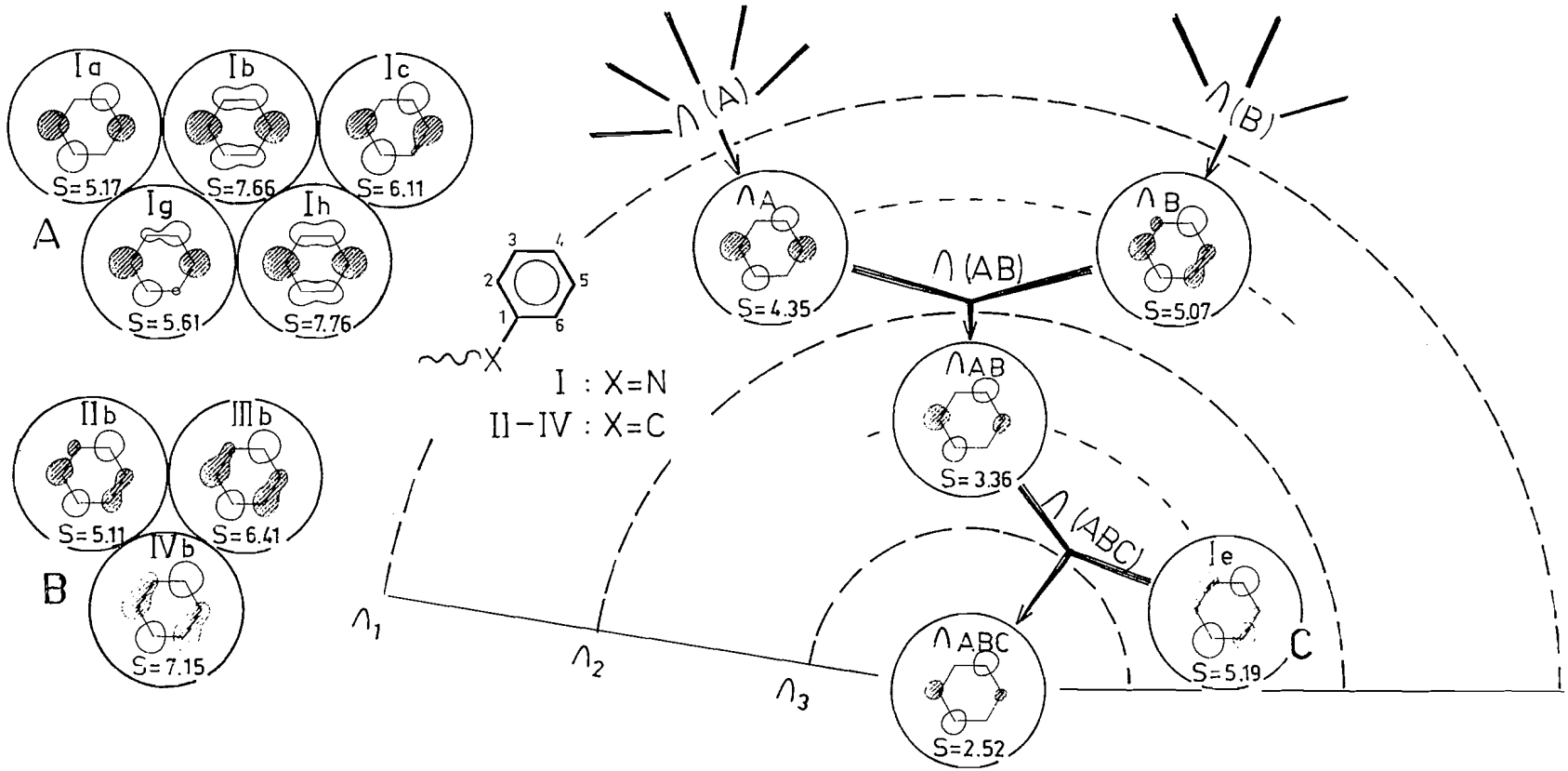

FIG. 1. Graphic representation of the intersections of the dopamine antagonist LUMO orbital forms. The intersections are made on the corresponding carbon atoms of the aromatic rings (where the C_1-atom of the ring is linked to the aliphatic fragment —×~). A represents the LUMO orbital forms of phenothiazines, B the LUMO orbital forms of the non-phenothiazine antagonists, and Λ_{ABC} the orbital form common to all four antagonist series. The S surfaces (Å^2) are indicated in a plane 0.5 Å (~1 Bohr) above the aromatic ring.

Can. J. Chem. Downloaded from www.nrcresearchpress.com by 122.72.124.2 on 09/07/12
For personal use only.

should be separated into three correlating zones: orbital forms for phenothiazine/phenothiazines (PP), orbital forms for phenothiazine/non-phenothiazines (PN), and orbital forms for non-phenothiazine/non-phenothiazines (NN). It is important to note that the orbital form of a phenothiazine may be better, equally or less well correlated with the orbital form of other phenothiazines (zone PP) than with the orbital forms of non-phenothiazine compounds (zone PN).

In other words, the two zones PP and PN of the τ_{ij} values which characterize the orbital forms of phenothiazines may exhibit the following three trends: (*1*) $\tau_{ij\,(PP)} \simeq \tau_{ij(PN)}$, (*2*) $\tau_{ij\,(PP)} > \tau_{ij\,(PN)}$, (*3*) $\tau_{ij\,(PP)} < \tau_{ij\,(PN)}$.

The first trend is represented by three phenothiazines, *N*-methylphenothiazine, 3-Cl-, and 2-Cl,8-CF_3-*N*-methylphenothiazine (**I***a*, **I***c*, **I***g*) showing a homogenous dispersion of their τ_{ij} values in the PP and PN zones. Generally, relatively high τ_{ij} values ($\tau_{ij} \simeq 0.4$–0.6) are observed for these compounds. Contrary to this general tendency, low τ_{ij} values are observed for **I***a* when compared with phenothiazine **I***d*, as well as with benzisoxazoles **V***a* and **V***b*, compound **I***c* when compared with phenothiazines **I***d* and **I***f*, and compound **I***g* when compared with benzisozazoles **V***a* and **V***b*.

In the second trend, there is a better correlation of the orbital forms between phenothiazines (as represented by **I***b*, **I***h*, and **I***f*) than between phenothiazines and non-phenothiazines. For 2-Cl-*N*-methylphenothiazine **I***b* and 2-CF_3-*N*-methylphenothiazine **I***h*, τ_{ij} values of the PP zone are only moderately higher than those of the PN zone. However, for 2,4-dichloro-*N*-methylphenothiazine **I***f*, the discrepancy increases with values ranging from 0.3 to 0.8 in the PP zone, and from 0.02 to 0.1 in the PN zone, with the exception of benzisoxazoles **V***a* and **V***b*.

The third trend, $\tau_{ij\,(PP)} < \tau_{ij\,(PN)}$, deals with the orbital forms of the phenothiazines which are less well correlated with other phenothiazines than with the non-phenothiazine compounds. This is illustrated by 2-MeO-*N*-methylphenothiazine **I***e* whose relatively high τ_{ij} values (~0.3–0.6) are nevertheless slightly lower in the PP zone than in the PN zone.

In general, the differences of the τ_{ij} of phenothiazines for zones PP and PN are weak (**I***b*, **I***h*, **I***e*) or nonexistent (**I***a*, **I***c*, **I***g*), with the exception of only two 4-substituted chlorinated compounds: 4-chloro- and 2,4-dichloro-*N*-methylphenothiazine (**I***d* and **I***f*, respectively). It must be noted that the virtually inactive phenothiazine **I***d* exhibits low τ_{ij} values (0.1–0.2) with most of the other model compounds. Only three of the fifteen τ_{ij} values, corresponding to compounds **I***b*, **I***h*, and **I***f* with heavy orbital density, present τ_{ij} values greater than 0.6. The relatively good correlation of **I***d* with the orbital form of the benzisoxazoles ($\tau_{ij} \simeq 0.5$) is obviously related to the special properties of their LUMOs.

Search for a LUMO form common to the dopamine antagonits

The LUMO form is only one of the parameters responsible for antagonist activity related to the interaction at the aromatic binding site. Therefore the selection of optimal LUMO forms — those that best resemble the hypothetical HOMO form of the receptor's binding site — cannot be made merely by distinguishing the active and inactive molecules. Another important parameter, ϵ_{LUMO}, must also be taken into account. Indeed the orbital forms of molecules demonstrating very low activity cannot be considered as representative of the optimal form, just as the LUMO forms of two molecules of comparable, medium activity are not necessarily representative to the same degree. It was in view of the complexity of this problem that the preliminary τ_{ij} analysis was carried out by comparing the similarity of the orbital forms. This quantitative comparison of each LUMO form with all of the others (corresponding to phenothiazine and non-phenothiazine antagonists with different levels of activity) was made in order to facilitate selecting the optimal orbital forms. It is important to note that the orbital forms corresponding to active antagonists of different chemical series show a strong resemblance. This justifies delineating a characteristic shape common to all of them. The contribution of phenothiazine and/or non-phenothiazine antagonists to this common form is demonstrated in a step-by-step approach (Fig. 1) in which three groups (A, B, and C) are considered.

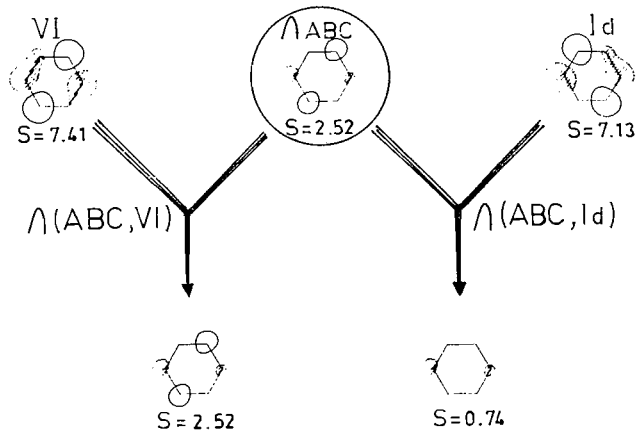

FIG. 2. Graphic representation of the intersections of the LUMO orbital form common to the antagonists (Λ_{ABC}) with the LUMO orbital forms of **I***d* and **VI**. The Λ_{ABC} is as different from the LUMO orbital form of the inactive **I***d* as it is similar to that of the active compound **VI**, which does not belong to the **I–V** series (Scheme 1).

Group A includes five of the eight phenothiazines studied (**I***a*, **I***b*, **I***c*, **I***g*, and **I***h*). In this group the phenothiazine orbital forms correlate well with both the other phenothiazines and the non-phenothiazines.

Two phenothiazines, **I***d* and **I***f*, are considered as non-representative of the optimal form. 4-Cl-*N*-Methylphenothiazine **I***d* is inactive ($C_I = 0.01$ for the promazine analogue) and it is significant that its orbital form is poorly correlated with the orbital forms of the active antagonists (preceding section). The activity of the promazine analogue of 2,4-dichloro-*N*-methylphenothiazine **I***f* is comparable to that of the analogue of 2-chloro-*N*-methylphenothiazine **I***b* (chlorpromazine, $C_I = 1$). However, its LUMO energy ($\epsilon_{LUMO} = 6.0$ eV) is appreciably lower and therefore, more favourable than the LUMO energy of **I***b* ($\epsilon_{LUMO} = 6.5$ eV) (8). We can assume that the favorable effect of **I***'s* ϵ_{LUMO} *is offset by its orbital form which is less representative than that of* **I***b*. This assumption is all the more probable when considering the fact that τ_{ij} are scattered for compound **I***f*. The degree of similarity between **I***f*'s LUMO form and the active non-phenothiazine antagonists' LUMO forms is clearly lower than that of compound **I***f* and the phenothiazines.

2-MeO-*N*-Methylphenothiazine **I***e* behaves as a distinctive phenothiazine compound in that, as indicated above, its orbital form displays a better likeness to that of the non-phenothiazine antagonists than to that of the phenothiazines (see Table 1). It is for this reason that it is considered separately as belonging to Group C.

Group B includes three non-phenothiazine antagonists which belong to three different chemical series: thioxanthene **II***b*,

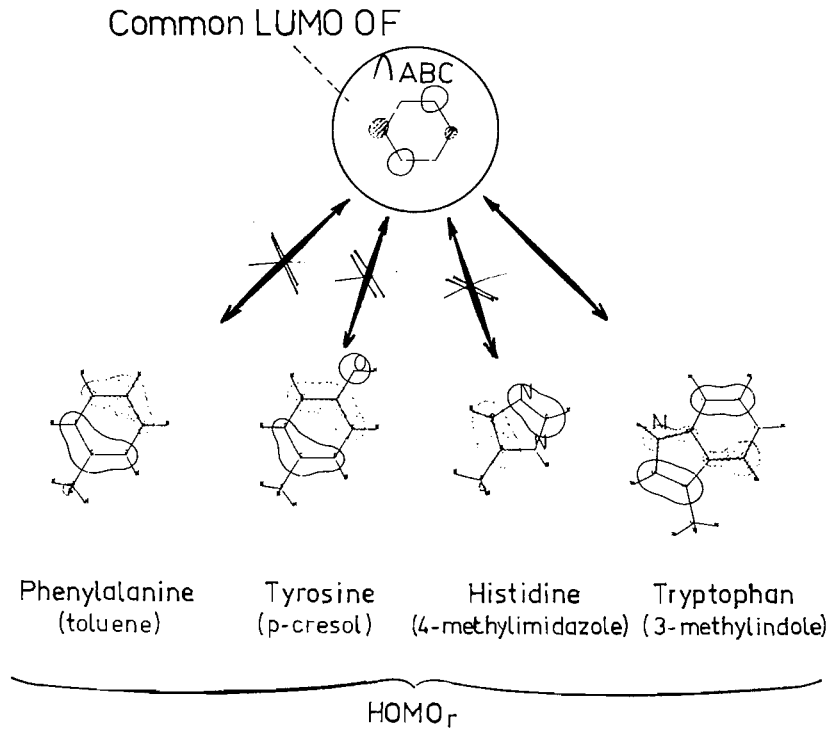

FIG. 3. Comparison of the LUMO orbital form common to the antagonists Λ_{ABC} with the HOMO orbital forms of the amino acid aromatic residues, phenylalanine, tyrosine, histidine, and tryptophan. Only the HOMO orbital form of the indolic part of the tryptophan ressembles Λ_{ABC}.

Can. J. Chem. Downloaded from www.nrcresearchpress.com by 122.72.124.2 on 09/07/12
For personal use only.

benzamide **IV***b*, and butyrophenone **III***b*. Compound **II***b* corresponds to a promazine analogue that is more active (C_l = 1) (19) than **II***a* (C_l = 0.06). As would be expected from its greater activity, **II***b*'s τ_{ij} values are generally higher than **II***a*'s (Table 1). Similarly, **IV***b*, which corresponds to a more active analogue (metoclopramide [^3H] spiperone IC_{50} = 57) (1) than **IV***a* (sulpriride, [^3H] spiperone IC_{50} = 570), is characterized by higher τ_{ij} values with the phenothiazines than **IV***a*. 4-*F*-Butyrophenone **III***b*'s analogue (haloperidol) is only slightly more active ([^3H] haloperidol IC_{50} = 8.5) (1) than the non-substituted **III***a*'s analogue ([^3H] haloperidol IC_{50} = 7.7). **III***b* is characterized by a slightly lower ϵ_{LUMO} (ϵ_{LUMO} **III***b* = 5.7) (8) than **III***a* (ϵ_{LUMO} **III***a* = 5.9), but the two have practically the same τ_{ij} values. Either of these forms — that of **III***a* or **III***b* — could therefore be used. The orbital form of **III***b*, a 4-*F*-substituted derivative whose analogues are frequently found among the neuroleptics, was chosen. The two benzisoxazoles, 6-*F*-benzisoxazole **V***a*, whose analogue is an active compound (IC_{50} = 6.7), and 6-MeO-benzisoxazole **V***b*, whose analogue is practically inactive (IC_{50} = 2800) (20), have similar τ_{ij} values. These values are often more elevated with inactive than with active molecules (for example, τ_{ij} values of **V***a* and **V***b* are 0.03 and 0.07, respectively, with the active phenothiazine **I***b*, but 0.53 and 0.55 with the inactive phenothiazine **I***d*). Furthermore, ϵ_{LUMO} of **V***a* is only slightly lower (ϵ_{LUMO} **V***a* = 5.5 eV) (8) than that of **V***b* (ϵ_{LUMO} = 5.57 eV). Unlike LUMOs of **V***a* and **V***b* with their unusual properties, the orbitals Next to LUMO (NLUMO) demonstrate a strong resemblance to LUMOs of the active molecules of series **I–IV**. It is assumed that in the case of benzisoxazoles, the NLUMO participates in the interaction with the aromatic binding site of the receptor. For the sake of coherence, these orbital forms are not considered in the comparison with LUMO forms **I–IV**. The LUMOs of the benzisoxazoles, however, are disregarded in the search for a common LUMO form of active antagonists.

Looking at the progressive contribution of the groups in Fig. 1, the intersections Λ of the orbital forms of groups A and B are represented by the forms Λ_A and Λ_B, respectively. These common forms are very close to the original orbital forms as indicated by their surface areas. Area $S(\Lambda_A)$ = 4.35 Å^2 is quite similar to the minimal area corresponding to the orbital form of compound **I***a* (S_{Ia} = 5.17 Å^2) and area $S(\Lambda_B)$ = 5.07 Å^2 is close to the minimal value S_{IIb} = 5.11 Å^2 for compound **II***b*. The two common forms Λ_A and Λ_B differ by their orbital density at carbon atoms 3 and 6, which equal zero in the common phenothiazine form Λ_A. Form Λ_B exhibits a lower density at carbon atom 5 than form Λ_A.

In the second step Λ_2, the intersection Λ(AB) between forms Λ_A and Λ_B yields their common form as Λ_{AB}. Its surface S_{AB} is only 28% weaker than the average surface of its predecessors ($S_{A/B} = S_A + S_B/2$. In fact Λ_{AB} retains the essential characteristics of Λ_A and Λ_B, and in particular, a strong orbital density at atoms 1 and 4. Comparison of the orbital form of 2-MeO-*N*-methylphenothiazine **I***e* Λ_C) with forms Λ_B and Λ_{AB} confirms the distinctiveness of this molecule. The orbital form of **I***e*, intermediate between the orbital form of the phenothiazines (A) and the non-phenothiazines (B), becomes a step closer to the latter.

The intersection Λ_3 between forms Λ_{AB} and Λ_C ends with the form Λ_{ABC}. This form, which retains between 35 to 50% of the LUMO density of each of the nine molecules belonging to the four different chemical series, will be considered representative of all the antagonists studied. Λ_{ABC} is characterized by a strong orbital density at atoms 1 and 4, and by a weaker density at atoms 2 and 5. It is noteworthy that a structurally analogous but inactive molecule, 4-Cl-*N*-methylphenothiazine **I***d*, has a very

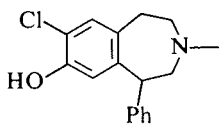

VI

different LUMO form than the proposed common Λ_{ABC} form (Fig. 2). On the other hand, SCH-23390 **VI**, the D-1 selective antagonist (21) which does not belong to the four series in question, is characterized by the orbital form similar to the common Λ_{ABC} form.

Conclusion

It has been observed that the LUMO form of the dopaminergic antagonists, aside from its energy ϵ_{LUMO}, is an important parameter of the binding step, that is to say, of the antagonist activity vis-a-vis the dopamine receptor. A common orbital form of the antagonists has been proposed, Λ_{ABC}, which insures the maximum overlap between the frontier orbitals, the antagonist's LUMO (L_a) and the receptor's HOMO (H_r). Λ_{ABC} may be used in view of a non-classic DRUG DESIGN, which is not only unlimited to a homogenous and known series of compounds, but is also a means of "receptor mapping". In fact, sticking to the L_a–H_r principle (7, 8), the form of the HOMO receptor should have characteristics similar to the common Λ_{ABC} form.

Assuming that the aromatic binding site is an aromatic residue of the amino acid fragment of the polypeptide chain (22), the HOMO orbital form which corresponds to the aromatic fragments most likely to be the aromatic binding site (phenylalanine (Phe), tyrosine (Tyr), histidine (His) and tryptophan (Try)) has been examined. As shown in Fig. 3 only the HOMO orbital form of the indolic fragment (Try) is suitably superimposed on the commor antagonist form Λ_{ABC} to the exclusion of all other forms different from Λ_{ABC}. Thus the aromatic part corresponding to the aromatic binding site of the dopamine receptor is assumed to have a tryptophan structure.

Acknowledgement

The authors wish to thank the D.R.E.T. for its financial support.

1. M. TITELER. Multiple dopamine receptors. M. Dekker, New York. 1983.
2. A. H. PHILIPP, L. G. HUMBER, and K. VOITH. J. Med. Chem. **22**, 768 (1979).
3. L. G. HUMBER, F. T. BRUDERLEIN, A. H. PHILIPP, M. GOTZ, and K. VOITH. J. Med. Chem. **22**, 761 (1979).
4. G. L. OLSON, H. C. CHEUNG, K. D. MORGAN, J. F. BLOUNT, L. TODARO, and L. BERGER. J. Med. Chem. **24**, 1026 (1981).
5. J. P. TOLLENAERE, H. MOEREELS, and L. A. RAYMAEKERS. *In* Drug design. Vol. X *Edited by* E. J. Ariens. Academic Press, New York. 1980. chap. 2.
6. J. P. TOLLENAERE, H. MOERREELS, and M. H. J. KOCH. Eur. J. Med. Chem. **12**, 199 (1977).
7. J. SZYMONIAK, J. R. CHRETIEN, A. BOUDON, and J.-E. DUBOIS. C. R. Acad. Sci. Paris, **302/II**, 1057 (1986).
8. J. SZYMONIAK, A. BOUDON, J. R. CHRETIEN, and J.-E. DUBOIS. Eur. J. Med. Chem. **22**, 101 (1987).
9. F. BARBATO, M. RECANATINI, C. SILIPPO, and A. VITTORIA. Eur. J. Med. Chem. **17**, 229 (1982).
10. J. P. TOLLENAERE and H. MOEREELS. Eur. J. Med. Chem. **11**, 293 (1976).
11. R. S. MULLIKEN. Rec. Trav. Chim. Pays-Bas, **75**, 845 (1956).
12. R. S. MULLIKEN and W. B. PERSON. Molecular complexes. Wiley, New York. 1969.
13. H. WEINSTEIN and R. OSMAN. Int. J. Quantum Chem. QBS. **4**, 253 (1977).
14. B. V. CHENEY, D. J. DUCHAMP, and R. E. CHRISTOFFERSEN. J. Med. Chem. **26**, 719 (1983).
15. B. V. CHENEY, J. SZMUSZKOVICS, R. A. LAHTI, and D. A. ZICHI. J. Med. Chem. **28**, 1853 (1985).
16. R. C. WEAST (*Editor*). CRC handbook of chemistry and physics, 67th ed. CRC Press, Boca Raton, FL. 1986.
17. C. C. J. ROOTHAAN. Rev. Mod. Phys. **23**, 69 (1951).
18. G. G. HALL. Proc. R. Soc. London, Ser. A, **205**, 541 (1951).
19. C. L. ZIRKLE and C. KAISER. *In* Medicinal chemistry. *Edited by* A. Burger. J. Wiley, New York. 1970.
20. J. T. STRUPCZEWSKI, R. C. ALLEN, B. A. GARDNER, B. L. SCHMID, U. STACHE, E. J. GLAMKOWSKI, M. C. JONES, D. B. ELLIS, F. P. HUGER, and R. W. DUNN. J. Med. Chem. **28**, 761 (1985).
21. L. TORIO, A. BARNETT, F. LEITZ, V. HOUSER, and C. KORDUBA. J. Pharmacol. Exp. Ther. **226**, 462 (1983).
22. H. D. HÖLTJE and L. B. KIER. J. Med. Chem. **17**, 814 (1974).

Can. J. Chem. Downloaded from www.nrcresearchpress.com by 122.72.124.2 on 09/07/12
For personal use only.

$Fe(CO)_3$ and Rh(acac) complexes of ergosteryl and 7-dehydrocholesteryl acetates: A high field nuclear magnetic resonance study

RICHARD E. PERRIER and MICHAEL J. MCGLINCHEY[1]
Department of Chemistry, McMaster University, Hamilton, Ont., Canada L8S 4M1

Received May 17, 1988

RICHARD E. PERRIER and MICHAEL J. MCGLINCHEY. Can. J. Chem. **66**, 3003 (1988).

The 500 MHz ^1H and 125 MHz ^{13}C spectra of ergosteryl and 7-dehydrocholesteryl acetate were recorded in C_6D_6 and $CDCl_3$ and assigned using two-dimensional NMR techniques. It is shown that incorporation of an $Fe(CO)_3$ or a Rh(acac) moiety onto the ring B diene system affects the chemical shifts of neighbouring protons and carbons. These changes are discussed in terms of the anisotropic properties of the organometallic fragments.

RICHARD E. PERRIER et MICHAEL J. MCGLINCHEY. Can. J. Chem. **66**, 3003 (1988).

Les spectres rmn ^1H et ^{13}C de l'ergostéryle et de l'acétate de déhydro-7-cholestéryle ont été obtenus dans différents solvants deutérés: C_6D_6 et $CDCl_3$. Les spectres rmn ^1H ont été enregistré sur un spectromètre 500 MHz et les spectres rmn ^{13}C sur un spectromètre 125 MHz. Les techniques de la rmn à 2 dimensions ont été employées pour l'étude de ces molécules. Dans cette publication, nous montrons que l'incorporation d'une unité $Fe(CO)_3$ ou Rh(acac) dans le système cyclique du diène B affecte les déplacements chimiques des protons et des carbons voisins. Puis, nous tentons d'établir une corrélation entre ces changements de déplacements chimiques et les propriétés anisotropiques des fragments organométalliques.

Can. J. Chem. Downloaded from www.nrcresearchpress.com by 122.72.124.2 on 09/07/12
For personal use only.

Introduction

With the advent of high field NMR spectrometers and the ease of applicability of two-dimensional NMR techniques, it is now possible to completely and unambiguously assign all the protons and carbons of complex molecules. These new techniques have facilitated the determination of the structure of numerous biologically important molecules in solution without having to resort to X-ray crystallographic techniques. Typically, steroidal systems provide a plethora of protons and carbons which, in principle, can provide a wealth of structural information.

For years, the only unequivocal assignments one could obtain from the ^1H spectra of steroids were limited to methyl, olefinic, or other protons whose signals were significantly deshielded relative to TMS because of substitution. The rest of the spectrum was often complicated by severe peak overlap as the remaining protons were distributed in a narrow spectral range (0.5 to 2.5 ppm). It was not until Hall and Sanders (1, 2) undertook an exhaustive study using a combination of ^1H 2D *J*-resolved spectroscopy and nOe difference measurements at high field that the overlapping problem was overcome. Since this initial paper, numerous other reports of the ^1H spectra of steroids have appeared in the literature (3–16). In contrast, the ^{13}C NMR spectra of steroids have been exhaustively studied and excellent compilations are now available (17, 18).

Another aspect of steroid chemistry which has gained prominence recently has been the incorporation of organometallic moieties onto the steroidal framework. For example, the $Fe(CO)_3$ fragment coordinates to the C(5)—C(6)—C(7)—C(8) diene unit of ergosterol esters, **1**; this cheap and readily available organometallic moiety has been utilized as a temporary protecting agent in order to synthesize modified steroids which would have been difficult to prepare by normal methods (19, 20). Allyl palladium complexes (21, 22) and $Cr(CO)_3$ moieties (23, 24) have also been exploited for synthetic purposes. The potential of inorganic salts, such as $RhCl_3$, or of organometallic reagents, e.g., $Cr(CO)_6$, to bring about the selective migration of double bonds in ergosterol has been noted by Barton (25, 26). Finally, in the bio-organometallic field, Jaouen and colleagues have demonstrated that steroidal hormones labeled with metal carbonyls can be used to assay receptor sites (27); this latter discovery promises to have an enormous impact on the early detection and treatment of breast cancer.

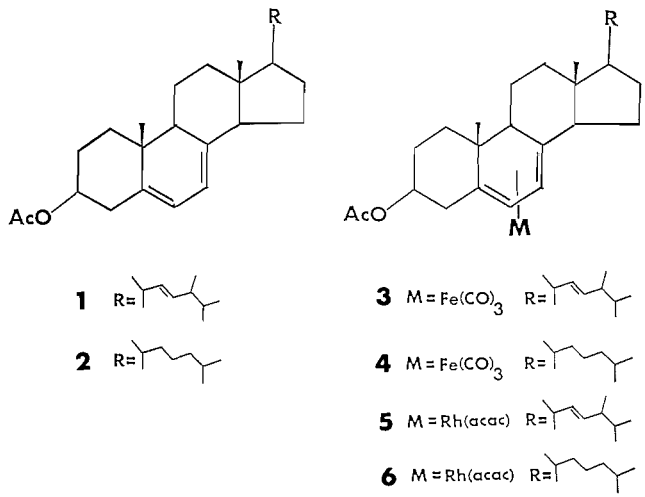

In this paper, we report the ^1H and ^{13}C NMR spectra for 3β-acetoxyergosta-5,7,22 triene (ergosteryl acetate), **1**, and for the closely related steroid, 3β-acetoxycholesta-5,7 diene (7-dehydrocholesteryl acetate), **2**; we also present the spectra of their $Fe(CO)_3$ and Rh(acac) derivatives **3** through **6**. The aim of this work was to investigate the effects induced by the organometallic moiety on the neighbouring protons and carbons of the steroid skeleton. Such effects are not limited merely to steric interactions which can alter the conformation of the steroid but can also include diamagnetic anisotropic contributions to the chemical shifts of proximate nuclei.

Results and discussion

In our earlier studies on organometallic derivatives of steroidal hormones, we were able to incorporate a tricarbonylchromium group into the aromatic A ring of estradiol and a series of related estrogenic steroids (28). The $Cr(CO)_3$ unit can complex either on the α or β face of the hormone and by using high field NMR spectroscopy, we were able to show that the two diastereomers **7***a* and **7***b* could be distinguished. More recently, we have prepared organometallic tetrahedral clusters of the type

[1]To whom all correspondence should be addressed.

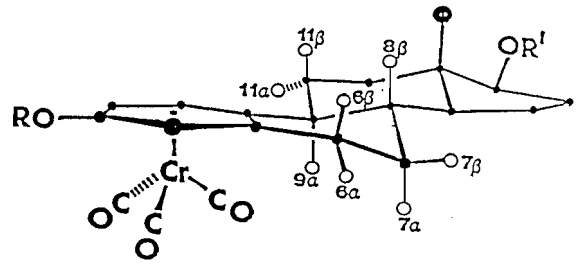

7a

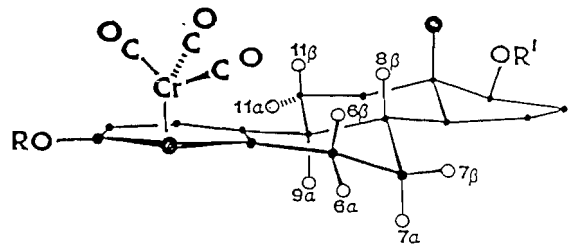

7b

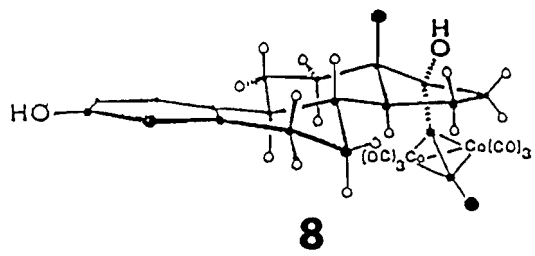

8

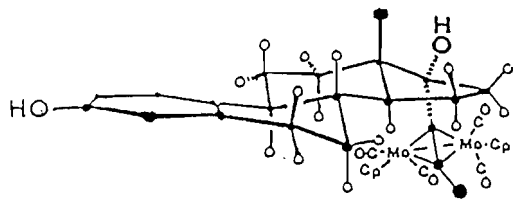

9

$(RC{\equiv}CR')Co_2(CO)_6$, **8**, and $(RC{\equiv}CR')Cp_2Mo_2(CO)_4$, **9**, where the R group is steroidal (29). In those cases, the hormonal steroids used were the commercially available mestranol and an isomer 17α-propynylestradiol. Once again, by using a high field spectrometer, it was possible to show that the effects brought about by the incorporation of these organometallic fragments were localized primarily on protons of the C and D rings. Continuing in this vein, we prepared the $Fe(CO)_3$ complexes of ergosteryl acetate and 7-dehydrocholesteryl acetate with the goal of determining the influence of diamagnetic anisotropy of metal carbonyl ligands on the neighbouring ^1H and ^{13}C nuclei of the steroidal skeleton. In addition, the analogous Rh(acac) complexes were synthesized since the detection of coupling to ^{103}Rh ($I=1/2$) could help to resolve any ambiguities in assignments.

As pointed out by others (3–16, 30), it is still not trivial to assign all the proton resonances in complex steroids even taking advantage of the full armamentarium of 2D techniques currently available. Since there are over 40 protons in each of the compounds and the ^{13}C NMR spectra of the 3β-acetate esters of ergosterol and of 7-dehydrocholesterol were already known (17, 31), the initial phase of our investigation involved the measurement of heteronuclear ^1H–^{13}C shift correlated spectra (32). These experiments were performed in conjunction with APT (33) (Attached Proton Test) spectra to distinguish between C or CH_2 and CH or CH_3 resonances. Figure 1 illustrates the result of such an experiment with correlations between carbons and their attached protons presented as contours; thus methine carbons, such as C-14, exhibit a single contour peak while methylene carbons, for example C-4, show correlations to both of the protons attached to the same carbon atom.

The ^1H assignments were further determined using the ^1H–^1H COSY experiment (32) which enabled the ^1H–^1H connectivities to be established through the scalar couplings between protons. Figure 2 shows the result of a COSY experiment and is presented as a contour plot; the one-dimensional spectrum lies along the diagonal and coupling between two spins is manifested by off-diagonal contours. However, the ^1H–^1H COSY experiment does not directly distinguish between α and β protons in a given methylene group. This distinction can be achieved using nOe difference spectroscopy measurements, allylic couplings (e.g., H-4β/H-6), and the observation of couplings between particular protons and other substituents whose position is unambiguously known. Typically, H-12α shows a clear correlation in the COSY spectrum with the 18-methyl group which is situated anti-periplanar to it. These data, together with the magnitude of the coupling constants and the usual Karplus considerations (34, 35) led to the assignments listed in Tables 1 and 2.

Not surprisingly, the ^1H assignments for 7-dehydrocholesteryl acetate, **2**, are rather similar to those of **1** until one reaches the sidechain which lacks the double bond present in ergosteryl acetate, as well as the C-28 methyl group. Thus the ^{13}C resonances for C-22 and C-23 appear at ≈36 and 24 ppm, respectively, in 7-dehydrocholesteryl acetate rather than at 135 and 132 ppm, as in **1**. These differences are also manifested in the ^1H spectrum whereby the vinylic and allylic hydrogens at C-20 through C-24 in **1** are now more typical of the alkane environments in **2**.

The data were obtained in benzene-d_6 as well as in deuteriochloroform not merely in an attempt to place different protons in environments with less spectral overlap but also to investigate an ingenious proposal advanced by Ustynyuk *et al.* (36). They had suggested the possibility of differentiating protons in a methylene pair situated proximate to an organometallic fragment by recording the spectrum in an isotropic medium and in one which could exhibit the aromatic solvent induced shift (ASIS) effect (37). They reasoned that the bulk of the metal and its associated ligands would hinder the approach of the anisotropic solvent to the complexed face of the molecule. Hence, one might be able to deduce the site of complexation of the metal because the protons proximal to it would not experience the ASIS effect. For the non-complexed steroids, as shown in Table 1, there are indeed some noticeable changes in the spectra of **1** and **2** when they are recorded in $CDCl_3$ and C_6D_6. In benzene

Can. J. Chem. Downloaded from www.nrcresearchpress.com by 122.72.124.2 on 09/07/12
For personal use only.

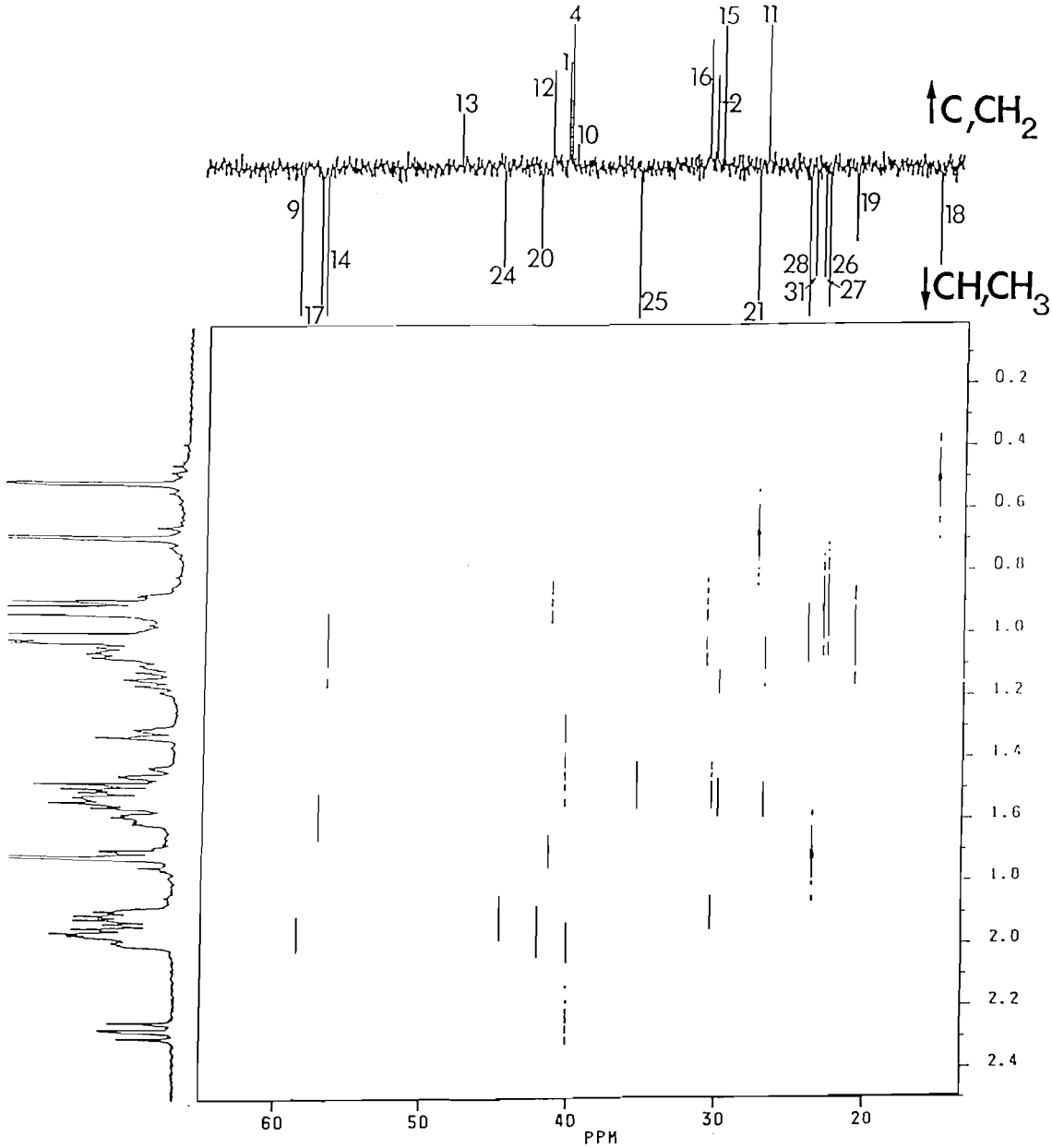

FIG. 1. A section of the 2-D heteronuclear chemical shift correlated spectrum of **3**, recorded in C_6D_6.

one observes a general tendency for the protons attached to carbons 1, 2, 9, and 11 to be shielded relative to their resonance positions in chloroform. In contrast, the protons in the sidechain are generally more shielded when dissolved in $CDCl_3$.

Generally, our assignments for the protons and carbons in the molecules **1** through **6** are in good agreement with the shifts reported in the literature for related systems (30). Figure 3 shows the high field region of the 500 MHz ^1H NMR spectra of ergosteryl acetate, **1**, and of its $Fe(CO)_3$ and Rh(acac) complexes, **3** and **5**, respectively. It is readily apparent from Table 1 and Fig. 3 that the protons which experience the greatest shifts upon complexation are those of the diene unit, viz., H-6 and H-7; their ^1H signals move upfield by as much as 1 ppm. Such large shifts to low frequency are entirely typical of coordinated olefinic systems and provide unequivocal evidence of the site of complexation. One would expect the $Fe(CO)_3$ and Rh(acac) moieties to coordinate onto the α face of the steroid and thus avoid any steric problems with the methyl substituent at C-10. This scenario has been verified by the X-ray crystal structure determination of the $Fe(CO)_3$ complex of 7-dehydrocholesteryl acetate, **4** (results forthcoming), which shows (see Fig. 4) that the metal is attached to the α face of the steroid.

It is noticeable that in $CDCl_3$ solution the 4α hydrogens in both of the $Fe(CO)_3$ complexes, **3** and **4**, are markedly shielded relative to their absorption positions in their precursors **1** and **2**, respectively, while their 4β counterparts are but little affected. Furthermore, we see that, when the solvent is changed to benzene-d_6, the 4α proton positions are actually deshielded as are their 4β partners; apparently, the ASIS effect does not seem to have manifested itself in these particular systems. We have previously noted that protons sited close to metal carbonyl fragments can exhibit sizeable upfield shifts. The carbonyl ligand resembles the alkyne or nitrile linkage in that its cylindrical symmetry and multiple bond character gives rise to a marked diamagnetic anisotropy. Protons which are positioned along, or close to, the multiple bond axis lie in the shielding

Can. J. Chem. Downloaded from www.nrcresearchpress.com by 122.72.124.2 on 09/07/12
For personal use only.

Can. J. Chem. Downloaded from www.nrcresearchpress.com by 122.72.124.2 on 09/07/12
For personal use only.

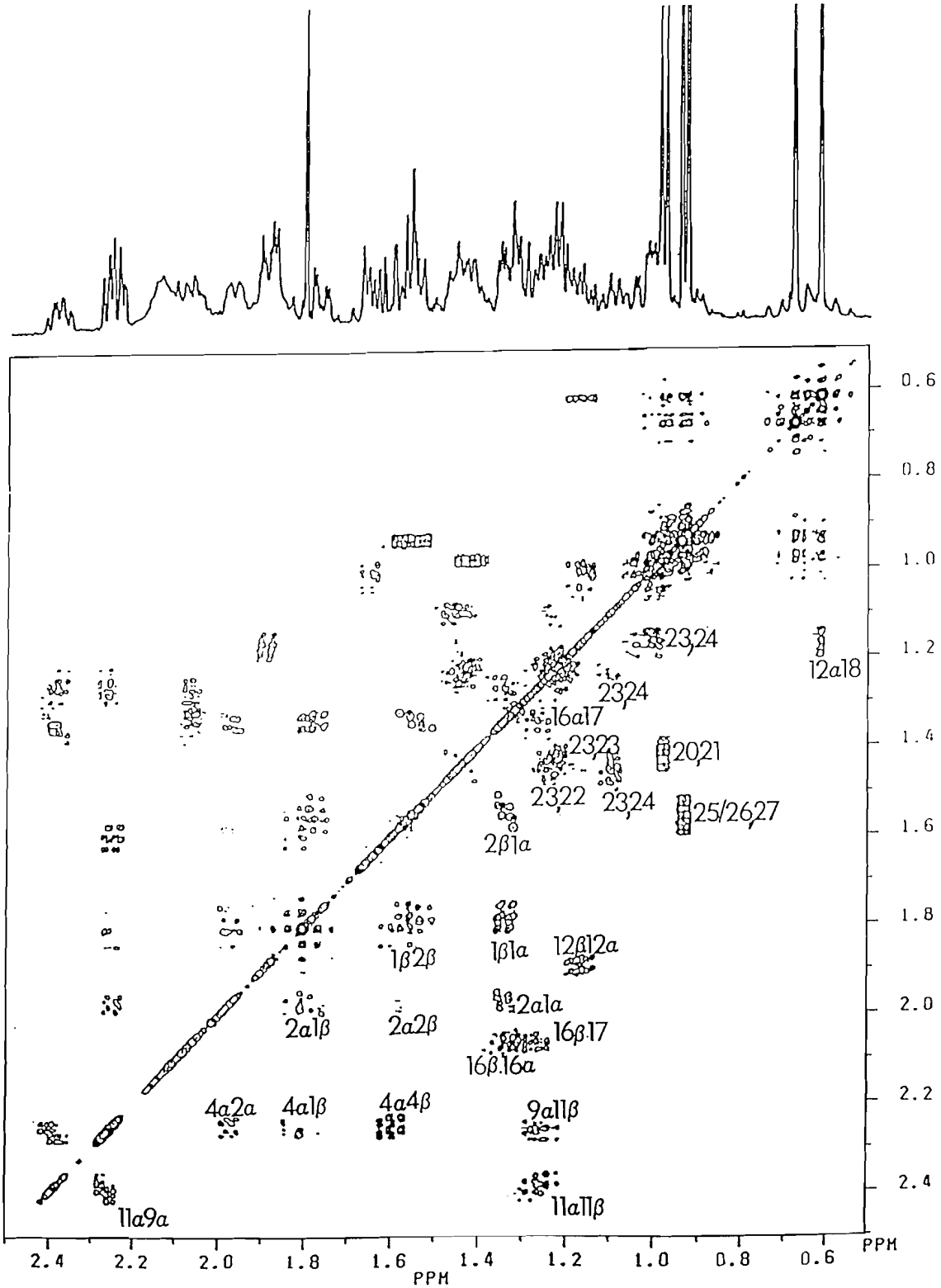

FIG. 2. 500 MHz 2-D NMR spectrum of **6** recorded in C_6D_6. Expanded contour plot of a portion of the matrix for a COSY 45 experiment. The matrix has been symmetrized.

zone while nuclei sited close to the plane perpendicular to the triple bond are deshielded (38, 39). Since we have recently obtained crystallographic data on **4** this allows the correlation of the chemical shift changes observed upon complexation with the geometric relationships between the proton positions and the cones of anisotropy of the metal carbonyl ligands. From these data we have determined that both the 4α and 4β protons are positioned within the shielding zone of a terminal CO ligand, thus their ^1H signals should move to low frequency relative to their resonance positions in the uncomplexed ligand.

When the Rh(acac) moiety is bonded to the diene unit, the effects are again localized primarily to the protons proximate to

TABLE 1. ^{1}H NMR chemical shifts for ergosteryl acetate, **1**, 7-dehydrocholesteryl acetate, **2**, and their $Fe(CO)_3$ and Rh(acac) complexes

	1		**3** (Fe)		**5** (Rh)		**2**		**4** (Fe)		**6** (Rh)	
Proton	$CDCl_3$	C_6D_6	$CDCl_3$	C_6D_6	$CDCl_3$	C_6D_6	$CDCl_3$	C_6D_6	$CDCl_3$	C_6D_6	$CDCl_3$	C_6D_6
1α	1.35	1.15	1.22	1.31	1.59	1.35	1.30	1.18	1.34	1.28	1.57	1.33
1β	1.87	1.62	1.38	1.45	1.82	1.78	1.79	1.66	1.50	1.52	1.80	1.75
2α	1.90	1.92	1.75	1.90	1.95	1.92	1.89	1.83	1.92	1.88	1.87	2.00
2β	1.58	1.55	1.40	1.50	1.50	1.57	1.53	1.50	1.47	1.47	1.25	1.55
3α	4.68	4.84	4.72	5.05	5.32	5.80	4.62	4.86	4.65	5.05	5.35	5.83
4α	2.50	2.62	1.70	2.00	1.95	2.20	2.43	2.60	1.80	1.99	1.90	2.23
4β	2.35	2.40	2.15	2.27	1.52	1.60	2.28	2.40	2.28	2.27	1.55	1.63
6	5.54	5.59	5.20	4.75	4.66	4.53	5.48	5.57	5.16	4.75	4.70	4.54
7	5.35	5.46	4.88	4.45	4.42	4.21	5.31	5.45	4.82	4.45	4.45	4.20
9α	2.02	1.93	1.95	1.95	2.03	2.25	1.93	1.87	2.06	1.96	2.05	2.28
11α	1.68	1.60	1.43	1.55	1.95	2.35	1.60	1.61	1.56	1.57	2.00	2.38
11β	1.58	1.40	1.13	1.08	1.15	1.25	1.49	1.39	1.24	0.97	1.21	1.24
12α	1.23	1.15	1.06	0.95	1.28	1.18	1.13	1.11	1.14	0.93	1.28	1.16
12β	2.08	1.98	1.77	1.70	1.89	1.82	2.00	2.01	1.95	1.76	1.94	1.93
14α	1.88	1.85	1.48	1.60	1.67	1.67	1.83	1.83	1.61	1.62	1.67	1.68
15α	1.60	1.63	1.52	1.55	1.70	2.06	1.63	1.70	1.26	1.04	1.68	2.08
15β	1.37	1.42	1.10	1.15	1.17	1.86	1.33	1.47	1.09	0.92	1.21	1.90
16α	1.24	1.37	1.18	1.08	1.30	1.46	1.29	1.50	1.21	1.10	1.46	1.35
16β	1.74	1.79	0.98	0.90	1.90	1.97	1.91	1.86	1.83	1.64	1.86	2.04
17α	1.31	1.21	1.09	1.05	1.35	1.33	1.09	1.13	1.16	1.00	1.35	1.32
18Me	0.62	0.68	0.70	0.50	0.65	0.61	0.54	0.64	0.65	0.50	0.61	0.61
19Me	0.95	0.92	0.90	1.03	0.78	0.69	0.86	0.90	0.83	0.89	0.90	0.67
20	2.03	2.05	1.80	1.93	2.02	2.03	1.31	1.42	1.31	1.32	1.32	1.40
21Me	1.02	1.11	0.99	0.70	1.00	1.08	0.87	1.00	0.85	0.67	1.10	0.98
22	5.18	5.22	5.17	5.17	5.15	5.23	1.04 0.95	1.33 1.06	1.18 0.95	1.32 1.06	1.20 1.00	1.22 1.06
23	5.21	5.26	5.17	5.25	5.18	5.28	1.28 1.03	1.45 1.22	1.29 1.05	1.36 1.21	1.32 1.15	1.45 1.18
24	1.84	1.90	1.68	1.90	1.83	1.84	1.00	1.20	1.02	1.19	1.10	1.12
25	1.48	1.50	1.30	1.52	1.51	1.51	1.45	1.56	1.44	1.56	1.50	1.53
26Me	0.81	0.91	0.82	0.91	0.85	0.92	0.79	0.91	0.80	0.93	0.83	0.93
27Me	0.81	0.91	0.80	0.92	0.85	0.92	0.80	0.92	0.81	0.94	0.83	0.93
28Me	0.92	1.00	0.89	1.00	0.92	1.03	—	—	—	—	—	—
30Me	2.05	1.78	1.85	1.71	2.02	1.80	1.96	1.74	1.95	1.71	2.00	1.80
acac-CH	—	—	—	—	5.29	5.23	—	—	—	—	5.35	5.24
acac-Me	—	—	—	—	1.97	1.80	—	—	—	—	1.98	1.80

the metal. This time there are some rather dramatic shifts. Thus the 4α and 4β protons suffer upfield shifts in excess of 0.5 ppm while the 1α and 11α hydrogens are deshielded by somewhat smaller amounts. One might speculate that these effects are rationalizable on the basis of a pseudo-aromatic ring current induced in the planar Rh–acac ring. It is well established that metal–acetylacetonate complexes are susceptible to electrophilic attack by, for example, bromine at the γ-H position. If the plane of the Rh–acac ring approximately bisects the C-6 C-7 bond then this would place the 4α and 4β protons in the shielding zone while the H-11α proton would be deshielded just like the aromatic protons in benzene itself. These results suggest that the Rh(acac) fragment is bound in a π fashion to the C(6)—C(7) double bond and σ bond formation occurs to C(5) and C(8), rather than the usual interaction of square planar rhodium with the π-donating C(5)—C(6) and C(7)—C(8) double bonds. We hope to resolve this point crystallographically.

Turning now to the ^{13}C NMR data for the molecules **1** through **6**, the effect of coordination is once again localized to carbons of the diene system, namely C-5, C-6, C-7, and C-8. In all cases, the organometallic moiety induces a very large upfield shift (≈ 40–60 ppm) in their ^{13}C signals while the other remaining ^{13}C signals are relatively unchanged. These observations are not unprecedented, as Butler and co-workers (40) have reported that the resonances of the arene ring carbons in estradiol and estrone 3-methyl ether are shifted upfield upon complexation to a $Cr(CO)_3$ group. Figure 5 shows the vinylic sections of the 125 MHz ^{13}C NMR spectra of **1**, **3**, and **5**. In these APT spectra (33) the carbon atoms with directly bonded hydrogens, viz., C-6 and C-7, have negative phase while the unsubstituted carbons at C-5 and C-8 have positive phase. The very dramatic low frequency shifts of the coordinated carbons are clearly evident. For the Rh complexes, it was gratifying to observe the appropriate Rh coupling (≈ 15 Hz) in the ^{1}H decoupled ^{13}C spectrum.

To conclude, we report the complete ^{1}H and ^{13}C NMR assignments for ergosteryl acetate, 7 dehydrocholesteryl acetate and their respective $Fe(CO)_3$ and Rh(acac) derivatives. In future reports we shall describe the reactions of these steroids and their metal complexes with alkynes to yield initially Diels–Alder adducts and ultimately ansa steroids.

Experimental

Nuclear magnetic resonance spectra were recorded on a Bruker AM 500 spectrometer. The 500 MHz ^{1}H and 125.7 MHz ^{13}C spectra were

Can. J. Chem. Downloaded from www.nrcresearchpress.com by 122.72.124.2 on 09/07/12
For personal use only.

Can. J. Chem. Downloaded from www.nrcresearchpress.com by 122.72.124.2 on 09/07/12
For personal use only.

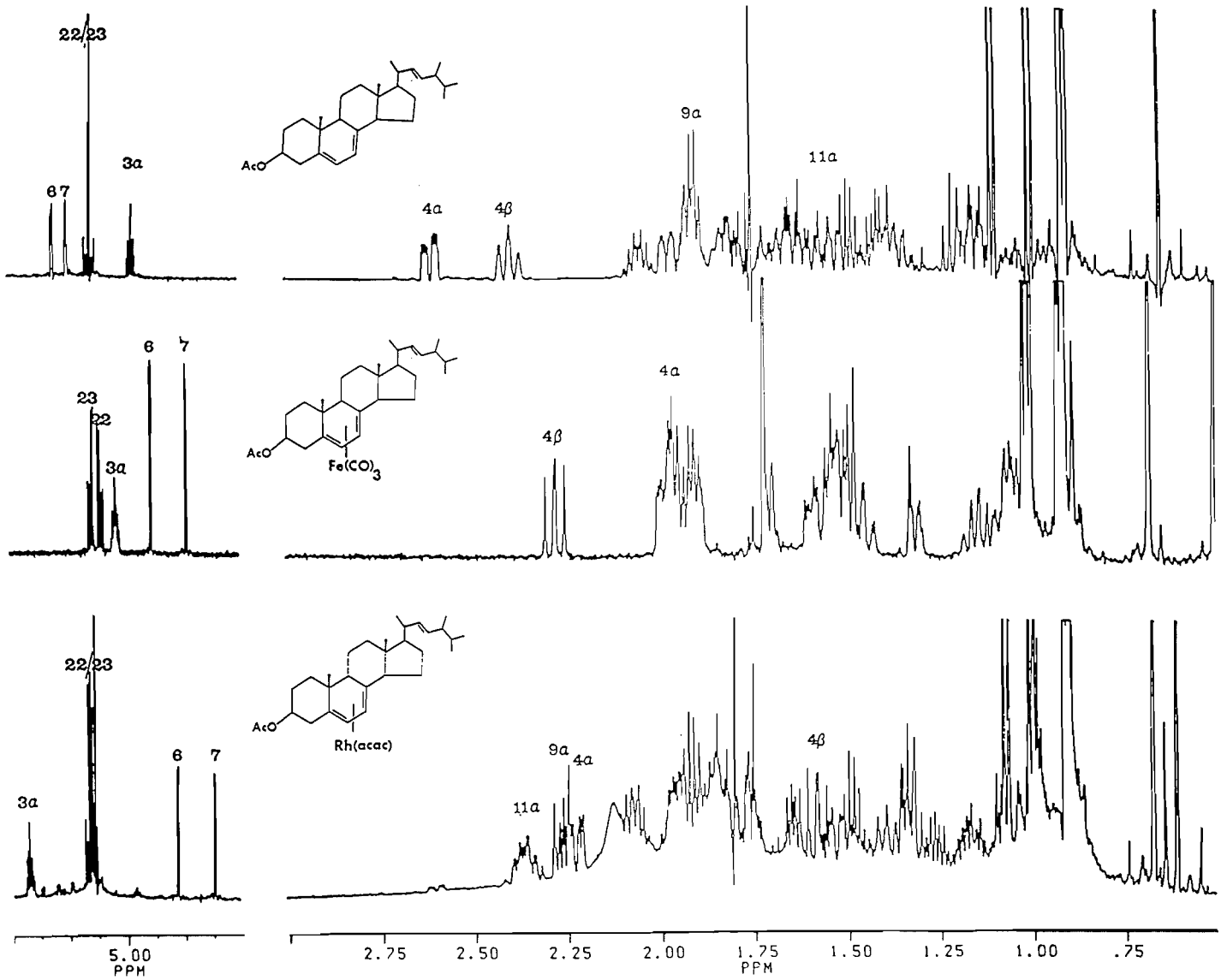

FIG. 3. Sections of the 500-MHz ^{1}H NMR spectra of molecules **1**, **3**, and **5**.

acquired using a 5 mm dual frequency ^{1}H/^{13}C probe. The samples were dissolved in C_6D_6 and $CDCl_3$ to a final volume of 0.6 mL which resulted in concentrations of approximately 0.09 *M*. Chemical shifts are reported relative to tetramethylsilane using the residual C_6H_6 signal (7.15 ppm) and $CHCl_3$ signal (7.24 ppm) as internal references. Proton spectra were acquired in 16 scans over a 3000 Hz spectral width in 32K data points, processed using Gaussian multiplication for line enhancement and zero filled to 64K before transformation.

Homonuclear chemical shift correlation (COSY) experiments were carried out in the absolute value mode by using the pulse sequence: delay – (π/2, ^{1}H) – t_1 – (π/4, ^{1}H) – acquisition. A 2-s relaxation delay was used: the π/2 pulse was 18 μs. The spectra were acquired in 8 scans for each of 256 FID's which contained 1024 data points in f_2. The data were zero filled once in the t_2 domain and yielded a 512 × 512 matrix after transformation. The transformed matrix was symmetrized.

Heteronuclear chemical shift correlated spectra were obtained by using the pulse sequence: delay – (π/2, ^{1}H) – (t_1/2) – (π, ^{13}C) – (t_1/2) – Δ_1 – (π/2, ^{1}H; π/2, ^{13}C) – Δ_2 – acquisition with decoupling. A 2-s relaxation delay was used and the delay times $\Delta_1 = \frac{1}{2}J$ and $\Delta_2 = \frac{1}{4}J$ were calculated from a compromise value of ^1J(C,H) = 125 Hz. The π/2, ^{1}H pulse was 18 μs and π/2, ^{13}C pulse was 7.3 μs. The spectral width in the t_2(carbon) domain was 17857 Hz (140 ppm) and in the t_1(proton) domain was 3000 Hz. The spectra were acquired containing 4K data points in f_2 for each of 256 FID's. Zero filling twice in f_2, followed by 2-D transformation created a 2K × 512 data matrix. Gaussian enhancement of the data was applied.

Ergosterol and 7-dehydrocholesterol were purchased from Aldrich and converted into their corresponding acetates using the procedures described by Stansbury (41). Their $Fe(CO)_3$ complexes were prepared via literature procedures (20). All syntheses were carried out under an atmosphere of nitrogen and all solvents were dried using standard procedures.

*Synthesis of ergosteryl acetate Rh(acac), **5**, and 7-dehydrocholesteryl acetate, **6***

Bis[(chloro)(ergosteryl acetate)rhodium(I)] and bis[(chloro)(7-dehydrocholesteryl acetate)rhodium(I)] were prepared according to the procedure of Barton (25). To the appropriate RhCl dimer (0.5 g) in Et_2O (25 mL) was added acetylacetone (0.1 mL). The solution was cooled to −20°C in an ice–salt water bath and 6 *M* KOH (1 mL) was added. After stirring for 1 h, the solution was warmed to room temperature and extracted with Et_2O (2 × 25 mL). The orange Et_2O layer was concentrated and dried over $MgSO_4$. After filtration, the solution was cooled to −78°C (dry ice – acetone) and a light yellow precipitate was

TABLE 2. ^{13}C NMR chemical shifts for ergosteryl acetate, **1**, 7-dehydrocholesteryl acetate, **2**, and their $Fe(CO)_3$ and Rh(acac) complexes

	1		**3** (Fe)		**5** (Rh)		**2**		**4** (Fe)		**6** (Rh)	
Proton	$CDCl_3$	C_6D_6	$CDCl_3$	C_6D_6	$CDCl_3$	C_6D_6	$CDCl_3$	C_6D_6	$CDCl_3$	C_6D_6	$CDCl_3$	C_6D_6
1	38.13	37.94	39.78	38.42	38.39	38.42	37.89	38.12	38.37	38.67	37.88	38.38
2	28.36	28.37	27.58	28.11	28.19	27.88	27.95	28.45	27.55	28.10	27.32	28.38
3	73.00	72.60	73.46	73.33	72.10	72.45	72.80	72.87	73.47	73.55	71.91	72.10
4	36.87	36.97	37.89	38.69	35.05	34.76	37.03	37.15	37.86	38.47	34.21	35.04
5	138.76	138.50	81.22	81.66	74.85	75.39	138.44	138.65	81.22	81.69	74.89	74.81
6	120.40	120.65	83.31	83.41	73.95	74.13	120.19	120.86	83.31	83.39	73.60	73.95
7	116.51	116.91	78.43	78.75	73.35	73.55	116.25	117.06	78.37	78.69	73.02	73.26
8	141.68	140.96	88.05	87.95	79.24	80.58	141.49	141.27	88.27	88.17	80.13	79.32
9	46.29	46.12	57.93	58.06	54.46	56.69	46.02	46.94	57.82	58.00	53.67	56.82
10	37.33	37.10	[a]	38.09	36.84	36.92	[a]	37.30	[a]	36.87	36.35	36.84
11	21.23	21.09	24.16	24.40	21.57	21.41	22.50	21.31	24.15	24.42	20.86	21.68
12	39.26	39.19	38.40	39.82	40.36	40.22	39.11	39.55	39.89	39.87	39.80	40.50
13	43.15	42.83	46.40	46.41	45.23	45.47	42.85	43.15	46.51	46.59	45.05	45.40
14	54.74	54.63	56.13	56.54	56.17	54.18	54.42	54.75	56.24	56.51	55.01	54.48
15	23.19	23.20	27.32	27.62	26.00	26.08	22.98	23.41	23.67	24.20	25.60	27.33
16	28.45	28.54	28.38	28.57	28.59	28.26	28.05	28.56	27.09	27.34	27.72	28.38
17	55.96	55.78	56.25	56.11	56.91	56.12	55.87	56.27	56.15	56.28	56.10	56.51
18	12.29	12.01	11.81	11.81	12.38	12.43	11.76	12.00	11.51	11.55	11.61	12.11
19	16.41	16.03	17.56	17.94	21.44	23.00	16.10	16.24	18.75	19.00	22.29	22.73
20	40.61	40.68	40.34	40.63	40.99	40.70	36.09	36.50	35.88	36.19	35.88	36.58
21	21.31	20.78	24.95	24.92	21.68	21.49	18.81	19.09	24.90	24.97	18.64	19.17
22	135.75	135.94	135.17	135.79	136.25	135.88	36.60	36.59	35.88	36.27	35.84	36.58
23	132.20	132.13	132.33	132.42	132.29	132.55	23.84	24.39	28.43	28.62	23.67	24.45
24	43.05	43.14	42.80	43.40	43.32	43.13	39.46	39.92	39.43	39.96	39.28	39.90
25	33.32	33.26	33.06	33.42	35.50	33.37	27.95	28.38	27.98	28.42	27.66	28.21
26	20.13	20.01	19.63	20.23	19.92	20.23	22.98	22.99	22.75	23.00	22.55	23.02
27	19.87	19.70	19.95	19.92	20.23	19.82	22.76	22.74	22.50	22.77	22.46	22.73
28	17.81	17.76	21.07	21.34	17.95	17.98	—	—	—	—	—	—
29	170.60	170.06	170.18	170.58	169.98	170.46	170.50	169.15	170.12	169.17	169.50	169.41
30	21.60	21.20	21.33	20.89	22.76	21.74	21.33	20.97	21.30	20.88	21.21	21.14
$Fe(CO)_3$		—	213.97	213.01	—	—	—	—	212.40	213.49	—	—
CH(acac)		—	—	—	100.16	100.18	—	—	—	—	100.16	100.16
Me(acac)		—	—	—	27.33	27.50	—	—	—	—	26.93	24.45

[a]Quaternary carbons not observed due to peak overlap at C-4.

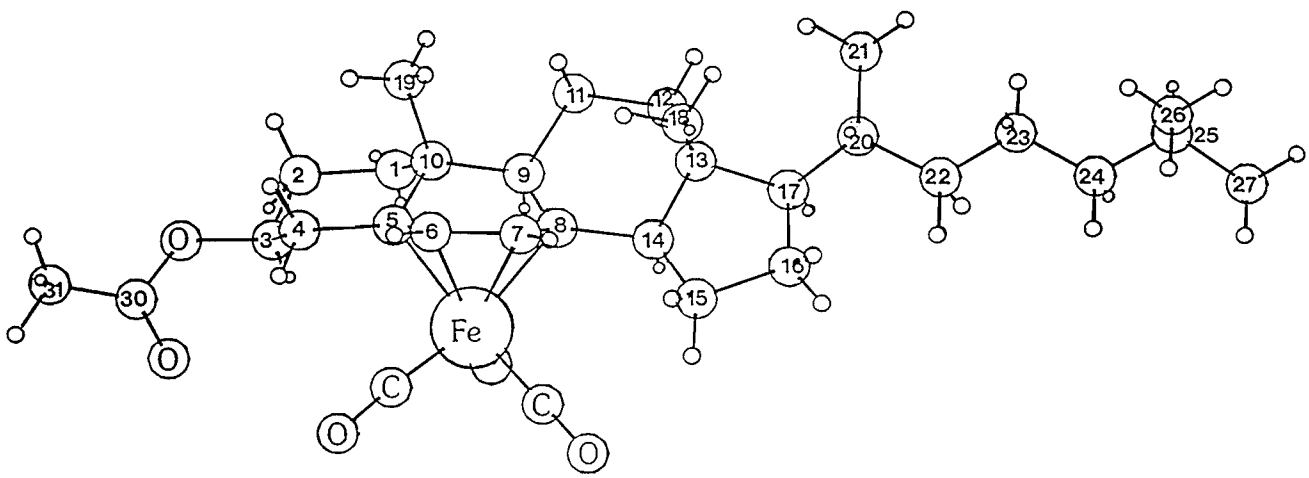

FIG. 4. CHEM-X representation of the crystal structure of 7-dehydrocholesteryl acetate $Fe(CO)_3$.

Can. J. Chem. Downloaded from www.nrcresearchpress.com by 122.72.124.2 on 09/07/12
For personal use only.

Can. J. Chem. Downloaded from www.nrcresearchpress.com by 122.72.124.2 on 09/07/12
For personal use only.

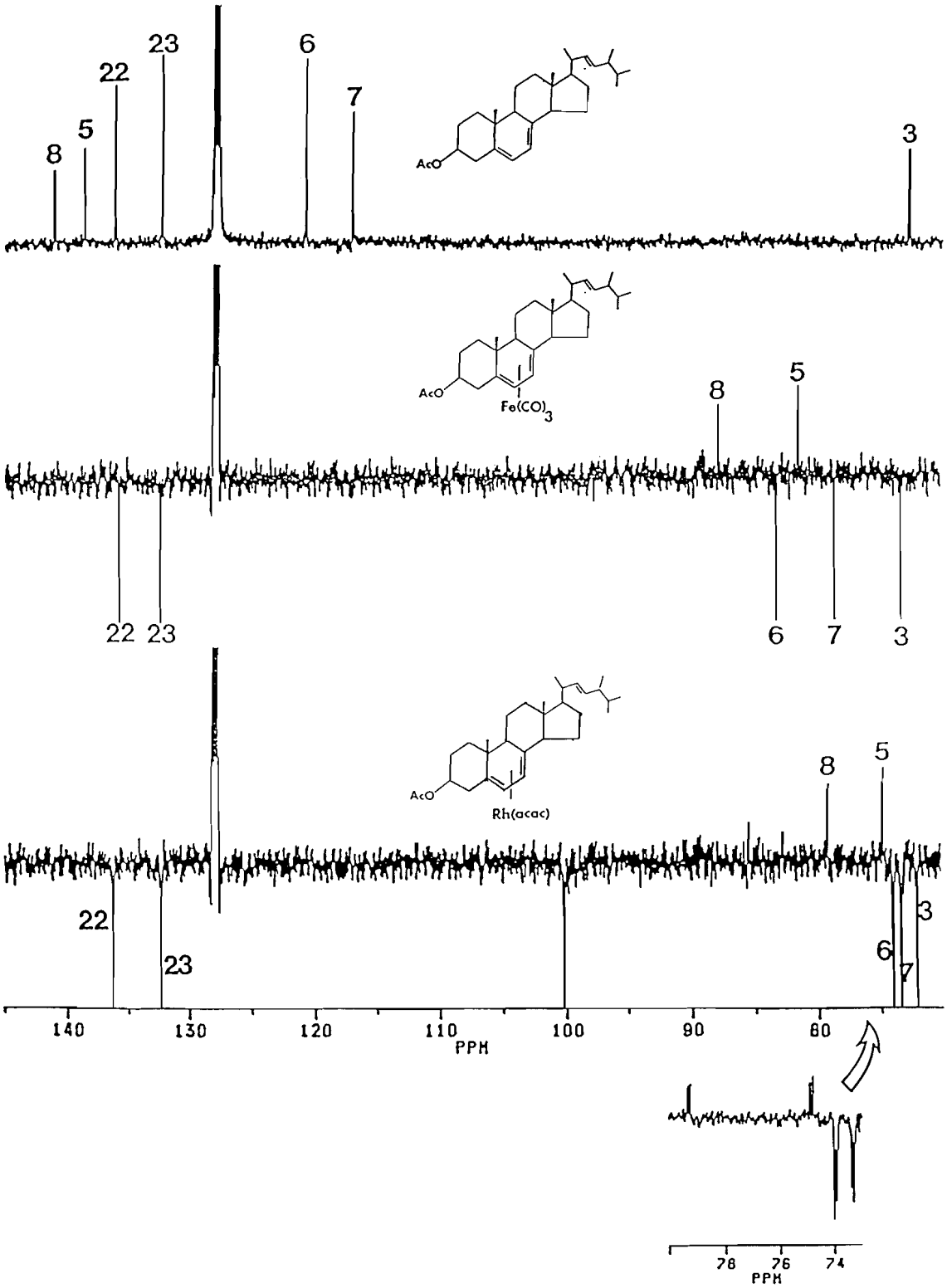

FIG. 5. Sections of the APT ^{13}C NMR spectra of **1**, **3**, and **5**.

deposited. This was filtered off and dried under vacuum to yield: (*i*) **5**, 0.17 g (62%) mp 200°C decomp. *Anal.* calcd. for $C_{35}H_{53}O_4Rh$: C 65.61, H 8.34; found: C 64.17, H 8.18; and (*ii*) **6**, 0.15 g (53%) mp 180°C decomp. *Anal.* calcd. for $C_{34}H_{53}O_4Rh$: C 64.96, H 8.50; found: C 64.28, H 8.24.

Acknowledgments

Financial support from the donors of the Petroleum Research Fund, administered by the American Chemical Society, and from the Natural Sciences and Engineering Research Council of Canada is gratefully acknowledged. We thank B. G. Sayer and Dr. D. W. Hughes for many helpful conversations on 2-D NMR techniques.

1. L. D. HALL and J. K. M. SANDERS. J. Am. Chem. Soc. **102**, 5703 (1980).
2. L. D. HALL and J. K. M. SANDERS. J. Org. Chem. **46**, 1132 (1981).

3. D. LEIBFRITZ, R. HAUPT, M. FEIGEL, W. E. HULL, and D. W. WEBER. Leibigs Ann. Chem. 1971 (1982).
4. M. W. BARRETT, R. D. FARRANT, D. N. KIRK, J. D. MERSH, J. K. M. SANDERS, and W. L. DUAX. J. Chem. Soc. Perkins Trans II. 105 (1982).
5. T. C. WONG, V. RUTAR, and J. S. WANG. J. Am. Chem. Soc. **106**, 7046 (1984).
6. T. C. WONG and V. RUTAR. J. Am. Chem. Soc. **106**, 7380 (1984).
7. A. G. J. SEDEE, G. M. J. BEIJERSBERGEN VAN HENEGOUWEN, W. GUIJT, and C. A. G. HAASNOOT. J. Chem. Soc. Perkin Trans. II. 1755 (1984).
8. H. J. SCHNEIDER, U. BUCHHEIT, N. BECKER, G. SCHMIDT, and U. SIEHL. J. Am. Chem. Soc. **107**, 7027 (1985).
9. A. G. J. SEDEE, G. M. J. BEIJERSBERGEN VAN HENEGOUWEN, M. E. DE VRIES, and C. ERKELENS. Steroids, **45**, 101 (1985).
10. H. DUDDECK, D. ROSENBAUM, M. HANI, A. ELGAMAL, and M. B. E. FAYEZ. Magn. Reson. Chem. **24**, 999 (1986).
11. V. J. ROBINSON, A. D. BAIN, and C. A. RODGER. Steroids, **48**, 267 (1986).
12. K. MARAT, J. F. TEMPLETON, and V. P. SASHI KUMAR. Magn. Reson. Chem. **25**, 25 (1987).
13. N. PLATZER, N. GOASDOUE, and D. DAVOUST. Magn. Reson. Chem. **25**, 312 (1987).
14. K. MARAT, J. F. TEMPLETON, R. K. GUPTA, and V. P. SASHI KUMAR. Magn. Reson. Chem. **25**, 730 (1987).
15. K. BISCHOFBERGER, J. R. BULL, and A. A. CHALMERS. Magn. Reson. Chem. **19**, 780 (1987).
16. D. W. HUGHES. Magn. Reson. Chem. **26**, 214 (1988).
17. W. B. SMITH. Ann. Rep. Nucl. Magn. Reson. Spectrosc. **8**, 199 (1978).
18. J. W. BLUNT, and J. B. STOTHERS. Org. Magn. Reson. **9**, 439 (1977).
19. D. H. R. BARTON, A. A. L. GUNATILIKA, T. NAKANISHI, H. PATIN, D. A. WIDDOWSON, and B. R. WORTH. J. Chem. Soc. Perkin Trans. I. 821 (1976).
20. G. EVANS, B. F. G. JOHNSON, and J. LEWIS. J. Organomet. Chem. **102**, 507 (1975).
21. B. M. TROST and T. VERHOEVEN. J. Am. Chem. Soc. **100**, 3435 (1978).
22. D. J. COLLINS, W. R. JACKSON, and R. N. TIMMS. Aust. J. Chem. **30**, 2167 (1977).
23. S. TOP, A. VESSIERES, J. P. ABJEAN, and G. JAOUEN. J. Chem. Soc. Chem. Commun. 428 (1984).
24. G. JAOUEN, S. TOP, A. LACONI, D. COUTURIER, and J. BROCARD. J. Am. Chem. Soc. **106**, 2207 (1984).
25. J. ANDRIEUX, D. H. R. BARTON, and H. PATIN. J. Chem. Soc. Perkins Trans. I, 359 (1977).
26. D. H. R. BARTON, S. G. DAVIES, and W. B. MOTHERWELL. Synthesis, 265 (1979).
27. G. JAOUEN. Pure Appl. Chem. **58**, 597 (1986).
28. S. TOP, G. JAOUEN, A. VESSIERES, J. P. ABJEAN, D. DAVOUST, C. A. RODGER, B. G. SAYER, and M. J. MCGLINCHEY. Organometallics. **4**, 2143 (1985).
29. M. SAVIGNAC, G. JAOUEN, C. A. RODGER, R. E. PERRIER, B. G. SAYER, and M. J. MCGLINCHEY. J. Org. Chem. **51**, 2328 (1986).
30. J. DREW, J. R. BRISSON, P. MORAND, and A. G. SZABO. Can. J. Chem. **65**, 1784 (1987).
31. W. B. SMITH. Orgn. Magn. Reson. **9**, 644 (1977).
32. (*a*) R. R. ERNST, G. BODENHAUSEN, and A. WOKAUN. Principles of nuclear magnetic resonance in one and two dimensions. Oxford Science Publications, Oxford. 1987; (*b*) A. E. DEROME. Modern NMR techniques for chemistry research. Pergamon Press, Oxford. 1986; (*c*) J. K. M. SANDERS and B. K. HUNTER. Modern NMR spectroscopy — A guide for chemists. Oxford University Press, Oxford. 1987; (*d*) R. BENN and H. GÜNTHER. Angew. Chem. Int. Ed. Engl. **22**, 350 (1983).
33. S. L. PATT and J. N. SHOOLERY. J. Magn. Reson. **46**, 535 (1982).
34. M. KARPLUS (*a*) J. Chem. Phys. **30**, 11 (1959); (*b*) J. Am. Chem. Soc. **85**, 2870 (1963).
35. A. A. BOTHNER-BY. Adv. Magn. Reson. **1**, 195 (1965).
36. N. A. USTYNYUK, L. N. NOVIKOVA, U. K. BEL'SKII, YU. F. OPRUNENKO, S. G. MALYUGINA, O. I. TRIFONOVA, and YU. A USTYNYK. J. Organomet. Chem. **294**, 31 (1985).
37. E. M. ENGLER and P. LASZLO. J. Am. Chem. Soc. **93**, 1317 (1971).
38. A. AGARWAL and M. J. MCGLINCHEY. Can. J. Chem. **56**, 959 (1978).
39. M. J. MCGLINCHEY, R. C. BURNS, R. HOFER, S. TOP, and G. JAOUEN. Organometallics, **5**, 104 (1986).
40. G. POUSKOULELI, I. S. BUTLER, and J. P. HICKEY. J. Inorg. Nucl. Chem. **42**, 1059 (1980).
41. H. A. STANSBURY. J. Am. Chem. Soc. **65**, 1243 (1943).

Can. J. Chem. Downloaded from www.nrcresearchpress.com by 122.72.124.2 on 09/07/12
For personal use only.

The photochemical nucleophile–olefin combination, aromatic substitution reaction (Part 2): methanol – cyclic olefins, 1,4-dicyanobenzene[1]

DONALD R. ARNOLD[2] AND MILES S. SNOW
Department of Chemistry, Dalhousie University, Halifax, N.S., Canada B3H 4J3

Received May 10, 1988

DONALD R. ARNOLD and MILES S. SNOW. Can. J. Chem. **66**, 3012 (1988).

Direct irradiation of acetonitrile–methanol (3:1) solutions of 1,4-dicyanobenzene and the cyclic olefins, cyclohexene, 1-methylcyclohexene, norbornene, and 2-methylnorbornene, leads to formation of regio- and stereoisomers of the 1:1:1 (alcohol:olefin:aromatic) adducts. This reaction can be photosensitized by electron transfer; addition of electron donors, biphenyl or phenanthrene, to the irradiation mixture generally increases the efficiency and yield of adduct formation. The efficiency of the reaction and the ratio of isomeric adducts are also affected by the addition of salts, particularly magnesium perchlorate. All of the possible regio- and stereoisomers from cyclohexene and 1-methylcyclohexene have been identified, two from cyclohexene and four from 1-methylcyclohexene. Three of the four possible isomers from norbornene were characterized; the *endo,endo* isomer was not detected. There are eight possible isomers from 2-methylnorbornene; six were detected and five have been isolated and identified. The two sterically hindered isomers, those having both the 4-cyanophenyl and the methoxy groups in the *endo* position, and *exo*-3-(4-cyanophenyl)-*endo*-2-methoxy-*exo*-2-methylnorbornane, were not characterized. The structures of the products were established largely on the basis of the ^{1}H and ^{13}C nuclear magnetic resonance spectra. The mechanism of the reaction is discussed, with emphasis on those factors that may affect the product ratio. The most striking observation is that the reaction is regioselective when magnesium perchlorate is added to the irradiation mixture.

DONALD R. ARNOLD et MILES S. SNOW. Can. J. Chem. **66**, 3012 (1988).

L'irradiation directe du dicyano-1,4 benzène et des oléfines cycliques : le cyclohexène, le méthyl-1 cyclohexène, le norbornène et le méthyl-2 norbornène en solution dans le mélange acétonitrile–méthanol (3:1) conduit à la formation des régioisomères et des stéréoisomères des adduits 1:1:1 (alcool : oléfine : aromatique). Cette réaction peut-être photosensibilisée par transfert d'électrons; l'addition de donneurs d'électrons : le biphényle ou le phénantrène, au mélange irradié augmente généralement l'efficacité et le rendement de la formation d'adduits. L'addition de sels, le perchlorate de magnésium en particulier, affecte l'efficacité de la réaction et le rapport des adduits isomères. On a identifié tous les régioisomères et les stéréoisomères possibles du cyclohexène et du méthyl-1 cyclohexène, deux pour le cyclohexène et quatre pour le méthyl-1 cyclohexène. On a caractérisé trois des quatre isomères possibles du norbornène; on n'a pas décelé l'isomère *endo,endo*. Le méthyl-2 norbornène a huit isomères possibles; on en a décelé six, et cinq d'entre eux ont pu être isolés et identifiés. On n'a pas caractérisé les deux isomères stériquement encombrés, ceux ayant les deux groupes cyano-4 phényle et méthoxy en position *endo* et le (cyano-4 phényle)-3-*exo*-méthoxy-2-*endo*-méthyl-2-*exo* norbornane. On a établi les structures des produits en se basant essentiellement sur les spectres de résonance magnétique nucléaire du ^{1}H et du ^{13}C. On discute du mécanisme de la réaction en mettant l'accent sur les facteurs qui peuvent affecter le rapport des produits. La régiosélectivité de la réaction due à l'addition de perchlorate de magnésium dans le mélange irradié constitue l'observation la plus remarquable.

[Traduit par la revue]

Introduction

When a solution of 1,4-dicyanobenzene (**1**) and 2,3-dimethyl-2-butene (**2**) in acetonitrile–methanol (3:1) is irradiated, the 1:1:1 (alcohol:olefin:aromatic) adduct (**3**) is obtained in good yield (70%) (reaction [1]). This reaction and some similar reactions involving 1,2-dicyanobenzene and 2-methylpropene (**5**) (Table 1, reactions [2] and [3]) reported at the same time (2) were among the first examples of photochemical nucleophile–olefin combination, aromatic substitution (photo-NOCAS) (3).[3] Two new chemical bonds are formed during this process, which in one simple operation yields a more complex, bifunctional product from readily available starting materials. This reaction will have significant synthetic utility, particularly if it is general and if the product is formed (or can be made to form) regio- and stereoselectively.

Our previous work has shown that this reaction occurs not only upon direct irradiation of **1**, but in some cases also upon photosensitization (electron transfer). Phenanthrene (**4**) and biphenyl (**8**) have been used as photosensitizers.

The proposed mechanism is shown in Scheme 1, where steps 1–5 indicate the events that occur upon direct irradiation (2), and steps 6 and 7 occur instead of step 2 when the reaction is photosensitized (electron transfer) by an additional electron donor (2, 4, 5). Competing with product formation is deactivation by back electron transfer from the radical anion to the radical cation (steps 2d and 8).

Another variation in reaction conditions involves the addition of salts to the irradiation mixture. Salts, particularly magnesium salts, are known to have a profound effect on photosensitized (electron transfer) reactions; they extend the lifetime of radical ions generated in this way (6). Apparently, the magnesium cation forms a complex with the radical anion, which slows down the deactivating back electron transfer from the radical anion to the radical cation (6*b*).

Consideration of each step in this sequence provides an initial basis for predicting the scope, the limitations, and the regio- and stereoselectivity of this reaction. For example, the free-energy for the electron transfer process (step 2b or b′) must be negative (or less than ca. 5 kcal mol^{-1} endergonic) to allow a significant formation of radical ions. Involvement of step 3 directs the regioselectivity of the process in that the olefin will be attached to the aromatic at the more heavily substituted site. Step 4 requires the reduction potential of the intermediate radical to be greater (more negative) than the reduction potential of the

[1]This is also part 20 of the series Radical Ions in Photochemistry. Preceding publications in these series are given in refs. 1 and 2.

[2]Author to whom correspondence may be addressed.

[3]A similar 1:1:1 adduct is formed upon irradiation of a methanol solution of 1,4-dicyanobenzene and phenylcyclopropane (3).

Can. J. Chem. Downloaded from www.nrcresearchpress.com by 122.72.124.2 on 09/07/12
For personal use only.

Reaction [1] (ref. 2)

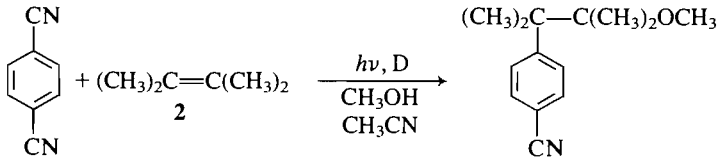

1 **3** (70%)

D = phenanthrene (**4**)

Reaction [6]

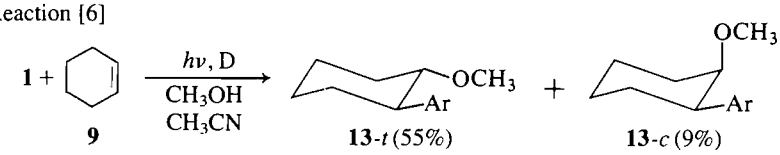

9 **13**-*t* (55%) **13**-*c* (9%)

D = biphenyl (**8**)

Reaction [9]

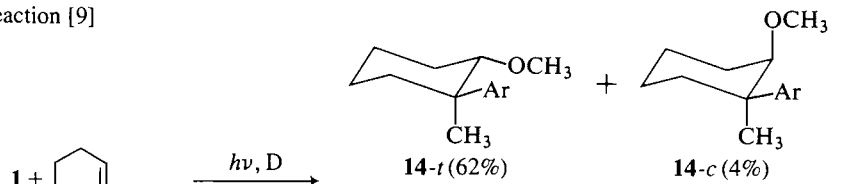

10 **14**-*t* (62%) **14**-*c* (4%)

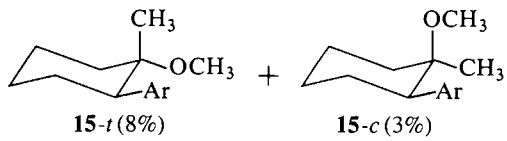

15-*t* (8%) **15**-*c* (3%)

D = biphenyl (**8**)

Reaction [17]

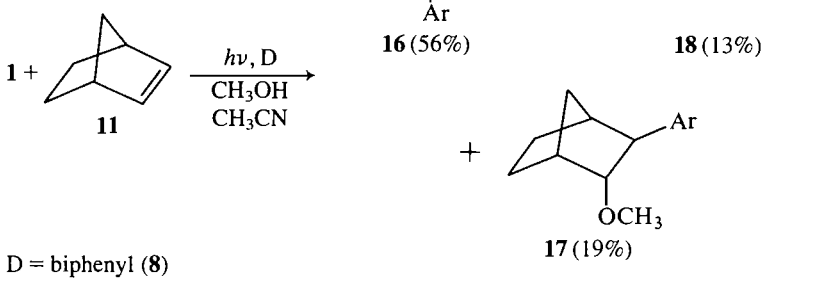

11 **16** (56%) **18** (13%) **17** (19%)

D = biphenyl (**8**)

Reaction [21]

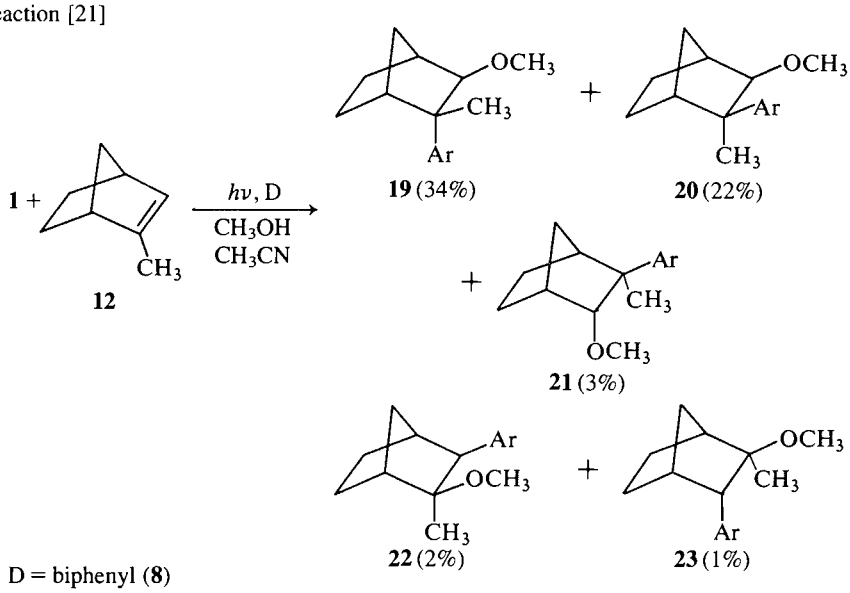

12 **19** (34%) **20** (22%) **21** (3%) **22** (2%) **23** (1%)

D = biphenyl (**8**)

Can. J. Chem. Downloaded from www.nrcresearchpress.com by 122.72.124.2 on 09/07/12
For personal use only.

TABLE 1. The photochemical nucleophile–olefin combination, aromatic substitution reaction: methanol–olefin, dicyanobenzene[a]

Reaction	Olefin	Product(s) (Yield)[b]
[1][c,d]	2,3-Dimethyl-2-butene (**2**)	3-(4-Cyanophenyl)-2-methoxy-2,3-dimethylbutane (**3**) (70%)
[2][c,d,e]	**2**	3-(2-Cyanophenyl)-2-methoxy-2,3-dimethylbutane (45%)
[3][d,f]	2-Methylpropene (**5**)	2-(4-Cyanophenyl)-1-methoxy-2-methylpropane (**6**) (5%)
[4][g]	**5**	**6** (52%); 1-(4-cyanophenyl)-2-methoxy-2-methylpropane (**7**) (2%)
[5][f]	Cyclohexene (**9**)	*cis*-2-(4-Cyanophenyl)-1-methoxycyclohexane (**13**-*c*) (9%); *trans*-2-(4-Cyanophenyl)-1-methoxycyclohexane (**13**-*t*) (46%)
[6][g]	**9**	**13**-*c* (9%); **13**-*t* (55%)
[7][h]	**9**	**13**-*c* (6%); **13**-*t* (34%)
[8][i]	**9**	**13**-*c* (6%); **13**-*t* (24%)
[9][g]	1-Methylcyclohexene (**10**)	*cis*-2-(4-Cyanophenyl)-2-methyl-1-methoxycyclohexane (**14**-*c*) (4%); *trans*-2-(4-Cyanophenyl)-2-methyl-1-methoxycyclohexane (**14**-*t*) (62%); *cis*-2-(4-Cyanophenyl)-1-methyl-1-methoxycyclohexane (**15**-*c*) (3%); *trans*-2-(4-Cyanophenyl)-1-methyl-1-methoxycyclohexane (**15**-*t*) (8%)
[10][c]	**10**	**14**-*c* (4%); **14**-*t* (51%); **15**-*c* (3%); **15**-*t* (6%);
[11][f]	**10**	**14**-*c* (4%); **14**-*t* (50%) **15**-*c* (4%); **15**-*t* (8%)
[12][i]	**10**	**14**-*c* (2%); **14**-*t* (14%)
[13][j]	**10**	**14**-*c* (5%); **14**-*t* (61%) **15**-*c* (4%); **15**-*t* (3%)
[14][k]	**10**	**14**-*c* (4%); **14**-*t* (59%); **15**-*c* (4%); **15**-*t* (6%)
[15][f]	Norbornene (**11**)	*endo*-3-(4-Cyanophenyl)-*exo*-2-methoxynorbornane (**16**) (51%); *exo*-3-(4-Cyanophenyl)-*endo*-2-methoxynorbornane (**17**) (39%); *exo*-3-(4-Cyanophenyl)-*exo*-2-methoxynorbornane (**18**) (10%)
[16][c]	**11**	**16** (62%); **17** (21%); **18** (14%)
[17][g]	**11**	**16** (56%); **17** (19%); **18** (13%)
[18][h]	**11**	**16** (3%); **17** (32%); **18** (2%)
[19][i]	**11**	**16** (9%); **17** (20%); **18** (4%)
[20][f]	2-Methylnorbornene (**12**)	*endo*-3-(4-Cyanophenyl)-*exo*-2-methoxy-*exo*-3-methylnorbornane (**19**) (30%); *exo*-3-(4-Cyanophenyl)-*exo*-2-methoxy-*endo*-3-methylnorbornane (**20**) (15%); *exo*-3-(4-Cyanophenyl)-*endo*-2-methoxy-*endo*-3-methylnorbornane (**21**) (3%); *exo*-3-(4-Cyanophenyl)-*exo*-2-methoxy-*endo*-2-methylnorbornane (**22**) (3%); *endo*-3-(4-Cyanophenyl)-*exo*-2-methoxy-*endo*-2-methylnorbornane (**23**) (3%)
[21][g]	**12**	**19** (34%); **20** (22%); **21** (3%); **22** (2%); **23** (1%)
[22][c]	**12**	**19** (30%); **20** (22%); **21** (2%); **22** (2%); **23** (1%)
[23][h]	**12**	**19** (6%); **20** (5%); **21** (6%)
[24][i]	**12**	**19** (6%); **20** (5%); **21** (5%)

[a]Irradiations were carried out in acetonitrile–methanol (3:1) solution. 1,4-Dicyanobenzene (**1**) was used unless otherwise indicated.
[b]Yields, based upon dicyanobenzene, were estimated by quantitative gas chromatography (gc/fid) and are not optimized. In most cases the conversion was at least 80%.
[c]Photosensitized by phenanthrene (**4**).
[d]Reference 2.
[e]Using 1,2-dicyanobenzene.
[f]Direct irradiation.
[g]Photosensitized by biphenyl (**8**).
[h]Direct irradiation, with added magnesium perchlorate.
[i]Photosensitized by **8**, with added magnesium perchlorate.
[j]Photosensitized by **8**, with added lithium perchlorate.
[k]Photosensitized by **8**, with added tetraethylammonium perchlorate.

aromatic; otherwise, electron transfer from the aromatic radical anion to the radical will occur and addition of methanol to the olefin will result instead of aromatic substitution.

We have begun a detailed study of this reaction to test these predictions and to determine which nucleophiles, olefins, and aromatic compounds can participate. This report describes the reaction of methanol and 1,4-dicyanobenzene (**1**) with several cyclic olefins (cyclohexene (**9**), 1-methylcyclohexene (**10**), norbornene (**11**), and 2-methylnorbornene (**12**)). These olefins were specifically chosen so that the regio- and stereoselectivity of each of the key steps of the overall process could be determined.

A question of particular interest in these experiments is whether the ratio of isomeric products is dependent upon the alternative modes of activation, direct or photosensitized (electron transfer), or upon the presence of added salts. If upon direct irradiation the combination of methanol with the olefin occurs at the exciplex or radical ion pair stage, specific interactions resulting from the associated 1,4-dicyanobenzene (**1**) or the dicyanobenzene radical anion ($\mathbf{1}^{\bullet-}$), with the olefin or the olefin

Can. J. Chem. Downloaded from www.nrcresearchpress.com by 122.72.124.2 on 09/07/12
For personal use only.

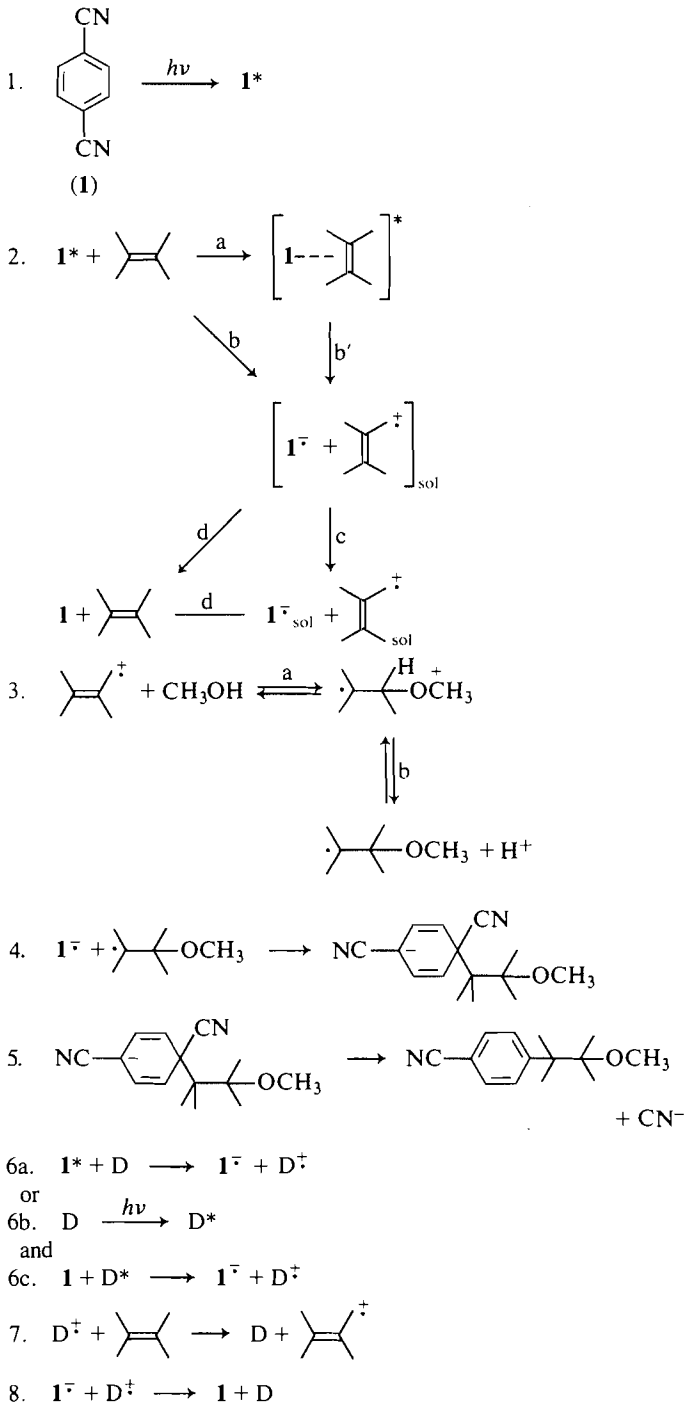

D = Phenanthrene (**4**) or biphenyl (**8**).

SCHEME 1. The mechanism (abbreviated) for the photo-NOCAS reaction. Electron-donating photosensitizers, D in steps 6–8, are phenanthrene (**4**) or biphenyl (**8**).

radical cation, may influence the regio- and stereoselectivity of this and subsequent steps. On the other hand, combination of methanol with the olefin radical cation formed by photosensitization (electron transfer) presumably involves either the freely solvated olefin radical cation, or the olefin radical cation complexed with the photosensitizer. This difference could be reflected in the ratio of regio- and stereoisomeric products.

Another facet to be considered is the addition of salts to the irradiation mixture, which might increase the relative amount of products resulting from reaction of the solvated radical cation. Furthermore, the regio- and stereoselectivity of the radical – radical anion coupling step (step 4) might now reflect the fact that the radical anion is complexed with the added cation.

Results

The irradiation and product isolation procedures were straightforward and operationally simple. A solution of 1,4-dicyanobenzene (**1**) and an excess of the olefin in acetonitrile–methanol (3:1) was irradiated through a Pyrex filter with a mercury vapor lamp. For the photosensitized (electron transfer) reactions an additional electron donor, phenanthrene (**4**) or biphenyl (**8**), was added to the solution. The effect of added salt was tested by dissolving the salt (0.3 M), magnesium perchlorate, lithium perchlorate, or tetraethylammonium perchlorate, in the solution. Some of these solutions were also irradiated after the addition of photosensitizer.

Progress of the reaction was followed by gas chromatography with a mass selective detector (gc/ms). The products were isolated by column chromatography. The yields of photo-NOCAS products, reported in Table 1, were determined by gas chromatography with a flame ionization detector (gc/fid). They are based upon dicyanobenzene, the limiting reagent, when the reaction was more than 80% complete. The error in the tabulated yields may be as much as 10% of the value listed. The ratios of products, on the other hand, are more accurate, less than 5% error. The ratio of products was not dependent upon the extent of conversion and agreed with the ratio obtained upon isolation. Structural assignments were based primarily on a detailed analysis of the nuclear magnetic resonance (^{1}H and ^{13}C nmr) spectra, which are described in the next section.

The only previous report (2) of regioselectivity in the photo-NOCAS reaction was the result of the addition of methanol to 2-methylpropene (**5**) followed by substitution on 1,4-dicyanobenzene (**1**). Direct irradiation gave a low yield of 2-(4-cyanophenyl)-1-methoxy-2-methylpropane (**6**) (Table 1, reaction [3]), the *anti*-Markovnikov adduct.[4] The other regioisomer, 1-(4-cyanophenyl)-2-methoxy-2-methylpropane (**7**), was not detected. We now find that biphenyl (**8**) is an effective photosensitizer for this reaction; the efficiency of the reaction and the yield of adduct(s) are much improved. Under these conditions (reaction [4]) the Markovnikov adduct (**7**) was formed as a minor product (3% of the photo-NOCAS products). Such a small amount of **7** would have gone undetected in the earlier work when the yield of photo-NOCAS product(s) was low.

The reaction that combines methanol with cyclohexene (**9**) and substitutes on 1,4-dicyanobenzene (**1**) was carried out by direct irradiation and also was photosensitized by biphenyl (**8**) (Table 1, reactions [5] and [6]). Phenanthrene (**4**) was not effective as a photosensitizer for this reaction. Product formation was more efficient upon photosensitization with **8**; the required irradiation time was greatly reduced. The *trans* isomer was favoured over the *cis* isomer under both irradiation conditions. The ratio of *cis* to *trans* isomers was essentially independent of mode of activation (**13**-*c*:**13**-*t*, 1:5 direct; 1:6 photosensitized).

The effect of added magnesium perchlorate on the ratio of

[4]The designation of adducts **7** as Markovnikov and **6** as *anti*-Markovnikov is based upon the original definition; by the Markovnikov rule of orientation for the addition of hydrogen halides to olefins, the anion (methanol in this case) combines with the less hydrogenated of the ethenoid carbon atoms (7). No mechanistic information is implied.

Can. J. Chem. Downloaded from www.nrcresearchpress.com by 122.72.124.2 on 09/07/12
For personal use only.

Can. J. Chem. Downloaded from www.nrcresearchpress.com by 122.72.124.2 on 09/07/12
For personal use only.

stereoisomers formed upon both direct and sensitized (**8**) irradiation was also small (**13**-*c*:**13**-*t*, 1:5.5. direct; 1:4 photosensitized) (Table 1, reactions [7] and [8]). The most obvious effect of the addition of magnesium perchlorate to the irradiation mixture was the greatly decreased yield of photo-NOCAS products. The major reactions under these conditions were addition of methanol to the cyclohexene (8), and the allylic radical substitution (2). Reaction [8] gave a 70% yield of 3-(4-cyanophenyl)cyclohexene.

Reaction with 1-methylcyclohexene (**10**) was carried out by both direct irradiation and by photosensitization with phenanthrene (**4**) and with biphenyl (**8**) (Table 1, reactions [9], [10], and [11]). The yield of photo-NOCAS products was 66% (combined yield of isomers) upon direct irradiation and was highest (77%) when **8** was used as a photosensitizer. All four isomeric adducts were obtained under all of these irradiation conditions. The product ratio from the photosensitized reactions was essentially independent of the sensitizer (**4** or **8**) used.

The reaction was somewhat more regioselective upon sensitized irradiation, favouring the *anti*-Markovnikov adducts ((**15**-*c* plus *t*):(**14**-*c* plus *t*), 1:4 direct; 1:6 photosensitized). The stereoselectivity of the reaction favours the *trans* isomer of both of the regioisomers upon both modes of activation. While the *cis*:*trans* isomer ratio of the *anti*-Markovnikov adduct was essentially independent of mode of activation (**14**-*c*:**14**-*t*, 1:12 direct; 1:16 photosensitized), the ratio of isomeric Markovnikov adducts (**15**) varied. Sensitized irradiation led to relatively more of the *cis* isomer although the effect was not large (**15**-*c*:**15**-*t*, 1:3 direct; 1:2 photosensitized).

The addition of magnesium perchlorate to the sensitized (**8**) irradiation had a profound effect on the product ratio. *Adduct formation was regioselective*; neither of the Markovnikov adducts was detected. The stereoselectivity for formation of the *anti*-Markovnikov adducts was also affected by the addition of this salt (**14**-*c*:**14**-*t*, 1:7 with added salt and 1:15 without). Again in this case, the overall yield of photo-NOCAS products decreased upon the addition of magnesium perchlorate to the irradiation mixture. The major competing reaction was formation of the methylcyclohexene allylic radical substitution products.

In marked contrast to the results obtained upon addition of magnesium perchlorate, the addition of lithium or tetraethylammonium perchlorate to the sensitized (**8**) irradiation had little effect on the product ratio. The overall yield of photo-NOCAS products was also relatively unaffected by the addition of these salts. In fact, the addition of lithium perchlorate increased the yield of photo-NOCAS adducts.

In the case of norbornene (**11**) (Table 1, reactions [15]–[19]), three of the four possible stereoisomeric adducts have been identified; the most sterically hindered *endo,endo* isomer was not detected. The ratio of stereoisomers was dependent upon mode of activation. While the isomer bearing the methoxy group in the *exo* position and the 4-cyanophenyl group in the *endo* position (**16**) was the major product under both conditions, direct irradiation and photosensitized, the other *trans* isomer (**17**) was a significant product and the *cis* isomer (**18**) was a relatively minor product upon direct irradiation (**18**:**17**:**16**, 1:3.9:5.1 direct irradiation; 1:1.5:4.4 photosensitized (**8**)).

Addition of magnesium perchlorate to both the direct and sensitized (**8**) irradiation mixtures led to relatively more of the *exo*-(4-cyanophenyl)-*endo*-methoxy isomer; **17** was the major photo-NOCAS product obtained upon direct irradiation when magnesium perchlorate had been added (**18**:**17**:**16**, 1:16:2). The overall yield of photo-NOCAS products was again lower than that obtained upon irradiation in the absence of added salt.

Methylnorbornene (**12**) is not commercially available. Several procedures for the syntheses of this compound were tried; the method eventually chosen was the cuprous ion promoted oxidative bis-decarboxylation of 2-methylbicyclo[1.2.2]heptane-2,3-dicarboxylic acid (9, 10).

The photo-NOCAS reaction could conceivably yield eight isomeric adducts with 2-methylnorbornene; six have been detected (gc/ms) and the five major products, those formed in greater than 1% yield, were isolated and characterized (Table 1, reactions [20]–[24]). Neither of the sterically hindered isomers, those having both the methoxy and the 4-cyanophenyl groups in the *endo* position, were among the isolated products. The other missing isomer was the *trans*-Markovnikov adduct with the methoxy group in the *endo* position.

The five relatively abundant isomeric adducts were formed in a ratio that was again dependent upon mode of activation. The major product under all conditions was the *trans anti*-Markovnikov adduct with the 4-cyanophenyl group in the *endo* position (**19**). The next most abundant isomer was the *cis exo-anti*-Markovnikov adduct **20**; photosensitization using either **4** or **8** (Table 1, reactions [21] and [22]) led to relatively more of this isomer (**19**:**20**, 2:1 direct irradiation; 1.5:1 photosensitized). Again in this case, as with 1-methylcyclohexene (**10**), the reaction was more regioselective upon photosensitization, favouring the *anti*-Markovnikov adducts ((**22** + **23**) : (**19** + **20** + **21**), 1:8 upon direct irradiation; 1:20 photosensitized).

The addition of magnesium perchlorate to the irradiation mixture had an effect on this reaction similar to that observed with 1-methylcyclohexene. The Markovnikov products, **22** and **23**, were missing from the photolysis mixture when magnesium perchlorate had been added. There was also an effect upon the ratio of the isomeric *anti*-Markovnikov products (**21**:**20**:**19**, 1:5:10 direct irradiation; 1:0.8:1 with added salt). The yield of photo-NOCAS products again was decreased by the addition of this salt.

The photo-NOCAS adducts were major products from all of these reactions. There were other products, from competing reactions, that are not listed in the table. These products were not isolated and completely characterized in every case; however, tentative structural assignments, based on gc/ms (retention time and mass spectrum), were made for several of them.

The ethers (e.g., methoxycyclohexane and 1-methoxy-2-methylcyclohexane), resulting from addition of methanol to the olefin, were usually detected. Formation of these products is not reflected in the reported yields because the yields are based upon the consumption of **1** and the olefins were present in excess. Yields based upon olefin were generally poor (<25%). No systematic effort was made to improve this yield; however, there was significantly less of these ether side products when phenanthrene (**4**) was used as photosensitizer. For example, the yield of photo-NOCAS products, based upon 1-methylcyclohexene (**10**), was 8% in reaction [11] involving direct irradiation, and 15% in reaction [10], which was photosensitized with **4**.

The dicyanobenzene–olefin one-to-one adducts (e.g., 3-(4-cyanophenyl)cyclohexene), resulting from substitution of the allylic radical of the olefin on the dicyanobenzene radical anion, were also formed in significant amounts in the reactions involving cyclohexene and 1-methylcyclohexene.

Can. J. Chem. Downloaded from www.nrcresearchpress.com by 122.72.124.2 on 09/07/12
For personal use only.

The product formally resulting from the addition of hydrogen cyanide to phenanthrene (9-cyano-9,10-dihydrophenanthrene) was usually observed when **4** was used as photosensitizer, and 2-cyano- and 4-cyanobiphenyl were detected when **8** was used. The photo-NOCAS products incorporating cyanide ion instead of methanol (e.g., 1-cyano-2-(4-cyanophenyl)cyclohexane) were usually produced in small amounts. The products formally resulting from the addition of the cyanomethyl radical to the olefin, followed by substitution on the dicyanobenzene radical anion (the isomeric 2-cyanomethyl-3-(4-cyanophenyl)norbornanes), were produced in significant amounts in the reactions involving the norbornenyl ring system. The product resulting from the addition of acetonitrile, that is, involving the intermediate cyanomethyl radical, to the olefin was a major product in the case of norbornene (2-*exo*-(cyanomethyl)norbornane). Details concerning the characterization of these minor products are given in the experimental section.

Structural assignments

The structural assignments for the photo-NOCAS products were based largely on an analysis of the ^1H and ^{13}C nmr spectra (11, 12). For the cyclohexene adducts the assignments were straightforward. Using accepted chemical shift correlations, the peak in the region of 3.3 ppm can be assigned to the hydrogen on the cyclohexane ring and adjacent to the methoxy group; the benzylic hydrogen will adsorb at lower frequency, near 2.6 ppm. From the established conformational free-energy values of these substituents (*A* values: methoxy, 0.60; phenyl, 2.9 (13)), the more bulky 4-cyanophenyl ring will adopt the equatorial position. The relationship of the benzylic hydrogen and the hydrogen adjacent to the methoxy group, C*H*—OCH_3, will be axial–axial in the *trans* adduct and axial–equatorial in the *cis* adduct. Vicinal hydrogen axial–axial coupling (8–13 Hz) is significantly larger than axial–equatorial coupling (2–6 Hz) and the configuration of substituted cyclohexanes can be assigned using this criterion.

For the isomer assigned the *cis* configuration (**13**-*c*), the vicinal couplings of the benzylic hydrogen at 2.70 ppm are 12.9, 3.5, and 2.9 Hz, corresponding to one axial–axial and two axial–equatorial couplings. The methoxy group must be axial; the configuration is therefore *cis*. Coupling of the signal due to the hydrogen adjacent to the methoxy group at 3.47 ppm was unresolved.

The isomer assigned the *trans* configuration (**13**-*t*) shows the methine hydrogen adjacent to the methoxy group as a multiplet at 3.26 ppm. The observed vicinal couplings of this hydrogen are 10.4, 10.4, and 4.1 Hz. This hydrogen must be axial with two axial–axial couplings and one axial–equatorial coupling. The couplings of this hydrogen to the benzylic hydrogen at 2.59 ppm is 10.4 Hz, axial–axial. Therefore, both the 4-cyanophenyl and the methoxy group are equatorial, that is, *trans*.

The structural assignments for the methylcyclohexene adducts were somewhat more involved. The regiochemistry was initially assigned on the basis of the chemical shift of the low-field aliphatic hydrogen adjacent to either the 4-cyanophenyl or the methoxy group. The adducts resulting from Markovnikov addition must have a benzylic hydrogen; this structure was assigned to those isomers having multiplets at higher field, at 2.45 and 2.85 ppm. The isomers with the lower-field multiplets, at 3.38 and 3.43 ppm, indicative of hydrogen adjacent to the methoxy group, are taken to be the *anti*-Markovnikov adducts.

In both of the Markovnikov adducts the vicinal couplings of the benzylic hydrogens are axial–axial and axial–equatorial (*cis* (**15**-*c*), 12.8 and 3.4 Hz; *trans* (**15**-*t*), 12.1 and 4.2 Hz), which indicates the 4-cyanophenyl group is equatorial.

The distinction between the *cis* and *trans* Markovnikov adducts (**15**-*c* and **15**-*t*) was made on the basis of the magnitude of the vicinal coupling constants ($^3J_{C-H}$) between the benzylic hydrogen (axial) and the carbon of the methyl group, as determined from the coupled ^{13}C nmr spectra (one of the central lines of the quartet). This coupling ($^3J_{C-H}$) follows a Karplus relationship similar to that pertaining to vicinal hydrogen–hydrogen coupling ($^3J_{H-H}$), dependent on the dihedral angle of the coupled nuclei (14). In general, the magnitude of $^3J_{C-H}$ is ca. 0.6 that of the analogous $^3J_{H-H}$.

In the ^{13}C nmr coupled spectrum of the isomer assigned the *cis* Markovnikov structure (**15**-*c*), the observed couplings were determined from one of the central lines of the quartet that is centered at 23.37 ppm. The width of this line at half-height was approximately 5 Hz. This could only result from several small couplings, e.g., two axial–equatorial and one equatorial–equatorial. Reasonable values for these couplings would be 2–3 Hz.

Analysis of the ^{13}C nmr spectrum provides additional support for the regiochemical assignment, that is, the Markovnikov structure **15**-*c*. The resonance due to the benzylic carbon at 55.28 ppm is a doublet ($^1J_{C-H}$, 123 Hz) and the signal due to the quaternary carbon (the carbon bearing the methyl and methoxy group) is a singlet at 74.10 ppm.

The structural assignment for the *trans* Markovnikov adduct (**15**-*t*) was more obvious because of the larger $^3J_{C-H}$ couplings. Selected proton resonance frequencies were irradiated and the ^{13}C nmr was observed. The axial–axial coupling of the methyl carbon, at 16.66 ppm, to the benzylic hydrogen, at 2.85 ppm, was found to be 5 Hz; the other axial–axial coupling was 6 Hz. An additional 3-Hz coupling was found for the remaining axial–equatorial hydrogen interaction.

Again, an analysis of the ^{13}C nmr spectrum supports the Markovnikov structural assignment of this isomer (**15**-*t*). The signal due to the benzylic carbon at 51.89 ppm is a doublet ($^1J_{C-H}$ coupling of 126.5 Hz). This is a typical coupling constant for an sp^3 carbon bearing alkyl substituents.

Similar reasoning was used to establish the stereochemical assignments for the *anti*-Markovnikov adducts. In the ^1H nmr spectra of one of these isomers the peak due to the hydrogen adjacent to the methoxy group at 3.38 ppm is an apparent triplet with a relatively small 4.4-Hz splitting. This coupling pattern must be due to an axial–equatorial and an equatorial–equatorial interaction, both of which are small and coincidentally identical in this case. This is the expected pattern for the hydrogen adjacent to the methoxy group of the *cis anti*-Markovnikov adduct **14**-*c*.

In the other *anti*-Markovnikov adduct, the 3.43-ppm peak for the hydrogen adjacent to the methoxy group is observed as a doublet of doublets with coupling constants of 10 and 4 Hz. This is indicative of the large axial–axial and a smaller axial–equatorial hydrogen–hydrogen interaction expected of the *trans anti*-Markovnikov adduct **14**-*t*.

Analysis of the coupled ^{13}C nmr spectra of these isomers supports these assignments. Consider first the spectrum of the isomer assigned the *cis anti*-Markovnikov structure (**14**-*c*). The width, at half-height, of one of the central lines of the quartet assigned to the methyl carbon at 27.12 ppm is 12 Hz. This broad

TABLE 2. The calculated free energy change for the electron transfer process with the singlet excited state of 1,4-dicyanobenzene (**1**) as acceptor

Olefin	$E^{ox}_{1/2}$ (V)[a]	ΔG_{ET} (kcal mol−1)[b]
2,3-Dimethyl-2-butene (**2**)	1.62[c]	−23.4
2-Methylpropene (**5**)	2.64[c]	+0.14
Cyclohexene (**9**)	2.31[c] (2.14)[d]	−7.5
1-Methylcyclohexene (**10**)	1.93 (1.70)[d] (1.77)[e]	−16.2
Norbornene (**11**)	2.19 (2.02)[d] (1.95)[f]	−10.2
2-Methylnorbornene (**12**)	1.82	−18.7

[a]Oxidation potentials measured at a platinum electrode relative to the saturated calomel electrode (SCE) using tetraethylammonium perchlorate (0.1 M TEAP) as electrolyte in acetonitrile.

[b]Based upon the Weller equation (ref. 15); $E_{0,0}$(**1**) 97.6 kcal mol^{-1}, $E^{red}_{1/2}$ (**1**) −1.66 V, the Coulombic attraction term was taken to be 1.29 kcal mol^{-1} (2).

[c]Reference 2. The potentials reported in this paper, versus silver/silver nitrate (Ag/0.1 M $AgNO_3$) were related to SCE by adding 0.34 V.

[d]Reference 16. Lithium perchlorate (0.1 M $LiClO_4$) was used as the electrolyte in these determinations.

[e]Reference 8.

[f]Reference 17. Lithium perchlorate (0.1 M $LiClO_4$) was used as the electrolyte in these determinations.

peak is the result of the overlap of lines split by the 5-, 3-, and 3-Hz couplings of the axial–axial and two axial–equatorial vicinal hydrogen–carbon interactions present in this isomer. The chemical shift of the quaternary benzylic carbon is 43.09 ppm (singlet) and the doublet signal ($^1J_{C-H}$, 136 Hz) due to the carbon adjacent to the methoxy group is at 84.85 ppm.

The ^{13}C nmr spectrum of the isomer assigned the *trans anti*-Markovnikov structure (**14-***t*) shows $^3J_{C-H}$ couplings of the vicinal hydrogens to the methyl group of 6, 6, and 3 Hz. This is similar to the coupling pattern observed for the *trans* Markovnikov adduct **15-***t* and is indicative of an axial methyl group coupled to two axial and one equatorial hydrogens. The signal due to the carbon bearing the methoxy group is a doublet (83.82 ppm, $^1J_{C-H}$ 142.3 Hz) and the benzylic carbon shows up as a singlet (43.43 ppm).

The structures of the three adducts from norbornene (**16**, **17**, and **18**) were established by applying similar reasoning. Analyses of both the ^1H and ^{13}C nmr spectra indicate that the norbornane carbon framework is intact; there was no indication of skeletal rearrangement.

The structural assignment for the *exo–exo* product **18** was based on a vicinal coupling of the hydrogen adjacent to the methoxy group (3.50 ppm), C*H*—OCH_3, and the benzylic hydrogen (2.91 ppm) of 7.0 Hz, typical coupling for *endo–endo* vicinal hydrogen interaction. The $^4J_{H2_{endo}-H7_{anti}}$ is small (1.7–2.6 Hz (11)) and in this case it was not observed.

The assignment of the *endo*-(4-cyanophenyl)-*exo*-methoxy product **16** was also based on the observed coupling of the signal due to the hydrogen adjacent to the methoxy group (3.43 ppm). Couplings of this hydrogen were assigned to an *endo–exo* vicinal (3.5 Hz) and a $^4J_{H2_{endo}-H7_{anti}}$ (1.5 Hz) interaction.

The signal at 3.65 ppm, due to the hydrogen adjacent to the methoxy group on the other *trans* addition product, *exo*-(4-cyanophenyl)-*endo*-methoxy (**17**), also had coupling attributed to an *exo–endo* hydrogen interaction (4.4 Hz). This hydrogen was split further by the $^2J_{H1-H2_{endo}}$ (4 Hz) coupling.

The ^{13}C nmr spectra of all three of these isomers are consistent with these structural assignments.

The methodology used for the structure determination of the adducts of 2-methylnorbornene was a combination of that used for the norbornene and methylcyclohexene adducts. Analyses of both the ^1H and ^{13}C nmr spectra indicate that the norbornane ring system is intact in all five isomers.

The regiochemistry of the major product **19** was established as *anti*-Markovnikov on the basis of chemical shift considerations in both the ^1H and ^{13}C nmr spectra. The low-field signal in the aliphatic region of the ^1H nmr spectrum at 3.47 ppm is indicative of a hydrogen adjacent to the methoxy group, C*H*—OCH_3.

The stereochemistry at this carbon was established as that with the hydrogen in the *endo* position because of the observed four-bond coupling, 1.6 Hz, to the *anti* hydrogen at C7. In the ^{13}C nmr spectrum, the observed line width (one of the central lines of the quartet) of the signal due to the methyl carbon (26.81 ppm) is relatively sharp; the width at half-height is only 6.3 Hz. Such a small combined coupling establishes that this methyl is in the *exo* position.

In the ^{13}C nmr spectrum of this isomer (**19**), the signal due to the carbon adjacent to the methoxy group at 90.85 ppm is a doublet, $^1J_{C-H}$, 142 Hz; the signal due to the benzylic carbon at 54.74 ppm is a singlet.

The structural assignment, *trans-endo*-(4-cyanophenyl)-*exo*-methoxy-*anti*-Markovnilov (**19**), is consistent with both the ^1H and ^{13}C nmr spectra.

The second most abundant isomer (**20**) was also shown to have the *anti*-Markovnikov structure and the hydrogen adjacent to the methoxy group, C*H*—OCH_3, is also *endo*. The chemical shift of this hydrogen is 3.05 ppm and it is coupled to the hydrogen, $H7_{anti}$, by 1.8 Hz in this case. There is, however, a large difference in the coupled carbon spectra of these two major isomers. The observed splitting of one of the central lines of the quartet due to the methyl carbon measures 4.5 Hz in this isomer. The line width at half-height is 11 Hz. This relatively large coupling constant indicates that the methyl group is in the *endo* position and is coupled ($^3J_{C-H}$) to the *endo* hydrogen adjacent to the methoxy group.

One of the remaining minor products was also established as having the *anti*-Markovnikov regiochemistry, *exo*-(4-cyano-

Can. J. Chem. Downloaded from www.nrcresearchpress.com by 122.72.124.2 on 09/07/12
For personal use only.

Can. J. Chem. Downloaded from www.nrcresearchpress.com by 122.72.124.2 on 09/07/12
For personal use only.

phenyl)-*endo*-methoxy (**21**). The low-field signal at 3.68 ppm, due to the hydrogen adjacent to the methoxy group, C*H*—OCH_3, is split by 3.8 Hz. This coupling results from the interaction of this hydrogen, $H2_{exo}$, with the vicinal hydrogen H1.

In the ^{13}C nmr spectrum of this isomer, the lines of the quartet due to the carbon of the methyl group (23.36 ppm) are narrow, less than 1.6 Hz wide at half-height. This observation leads to the conclusion that the methyl group must be *endo*, so that coupling to the hydrogen $H2_{exo}$ is small.

Analysis of the ^{13}C nmr spectrum confirmed the regiochemical assignment of this isomer (**21**). The signal due to the carbon adjacent to the methoxy group at 89.03 ppm is a doublet, coupled by $^1J_{C-H}$ 143.8. Hz. The peak assigned to the benzylic carbon at 48.30 ppm is a singlet.

The two remaining minor products were established as Markovnikov adducts on the basis of the chemical shift of the low-field hydrogen; one occurs at 2.47 ppm and the other at 3.11 ppm. This is in the region expected for a benzylic hydrogen.

One of these adducts was shown to have the *exo*-(4-cyanophenyl)-*exo*-methoxy configuration (**22**). The benzylic hydrogen (2.47 ppm) had a small but observable coupling to the hydrogen in the *anti* position on C7; thus this hydrogen was assigned as *endo*.

In the ^{13}C nmr spectrum of this isomer, the observed splitting of one of the central lines of the quartet due to the carbon of the methyl group (19.39 ppm) was 4.0 Hz. This was attributed to coupling involving $H2_{endo}$ and the carbon of the methyl group in the *endo* position.

Support for the regiochemical assignment comes from the ^{13}C nmr spectrum of this isomer (**22**). The signal due to the carbon adjacent to the methoxy group is a singlet (84.69 ppm), while a doublet peak centered at 61.67 ppm ($^1J_{C-H}$, 129.2 Hz) is observed for the benzylic carbon.

The other Markovnikov adduct was established as the *endo*-(4-cyanophenyl)-*exo*-methoxy isomer (**23**). The signal due to the benzylic hydrogen (3.11 ppm) was split by a 3.4-Hz coupling to the hydrogen at C4, and is therefore in the *exo* position.

The ^{13}C nmr spectrum of this isomer shows the lines of the quartet due to the carbon of the methyl group (19.19 ppm) are relatively sharp (<4.5 Hz) with little coupling and therefore the orientation of the methyl group must be *exo*. The signal due to the carbon adjacent to the methoxy group occurs at 83.50 ppm and is a singlet. The signal due to the benzylic carbon at 58.83 ppm is a doublet, coupled by 126.7 Hz ($^1J_{C-H}$).

The consistent pattern that emerges from analysis of the spectra of all of these isomers gives us confidence in all of the structural assignments.

Discussion

Direct and photosensitized irradiations

Salient features of the mechanism of the photo-NOCAS reaction were introduced in the first paper in this series (2). The new results generally are consistent with that proposal (Scheme 1).

Reactions carried out by direct irradiation, without added donor, involve excitation of the 1,4-dicyanobenzene **1**. The ultraviolet absorption spectrum of **1** extends to 300 nm, beyond the short wavelength cutoff due to absorption of Pyrex (280 nm). Previous studies have shown that the fluorescence of **1** is quenched at nearly the diffusion controlled rate by simple olefins (2). The intersystem crossing process from singlet **1** is relatively slow. It is therefore reasonable that steps 2a and (or) 2b involve the single excited state of **1** upon direct irradiation.

Table 2 is a list of the calculated free-energy change, based upon the Weller equation (15), for the electron transfer process between the excited singlet state of **1** and the olefins studied. Step 2b is significantly exergonic for all of the cyclic olefins studied; the rate of electron transfer will be diffusion controlled. Only with 2-methylpropene (**5**) is the calculated free-energy change for the electron transfer step positive, and the photo-NOCAS reaction is in fact inefficient in this case (2).

The alternative mode of activation, photosensitization (electron transfer), occurs in those reactions in which another donor, phenanthrene (**4**) or biphenyl (**8**), has been added (steps 6 and 7). In the case of added **4**, the major light-absorbing species is the phenanthrene (step 6b). The ultraviolet absorption spectrum of phenanthrene extends to 360 nm. Electron transfer from the singlet excited state of phenanthrene to 1,4-dicyanobenzene is an exergonic process (-7.8 kcal mol^{-1}) and is known to be a rapid (diffusion controlled) process (18). In the case of added biphenyl (**8**), it is the singlet excited state of **1** that accepts an electron from **8** (step 6a). The ultraviolet absorption spectrum of **8** does not extend much beyond 290 nm. Electron transfer from **8** to the excited singlet state of **1** is spontaneous (-19 kcal mol^{-1}).

Of the examples listed in Table 1 several show that the efficiency of the reaction and yield of photo-NOCAS product(s) are greatly improved by the addition of the photosensitizer. In many of these cases, secondary electron transfer from the olefin to the radical cation of the added donor is spontaneous, or only slightly endergonic, and therefore formation of the olefin radical cation should be rapid (step 7) (4, 5).

There are some cases, however, where the reaction is improved in spite of the fact that the oxidation potential of the photosensitizer is significantly less than that of the olefin. For example, reaction [5], where the addition of biphenyl (**8**) to the irradiation mixture improves the reaction with 2-methylpropene (**5**), even though the oxidation potential of **8** is 19 kcal mol^{-1} less than that of **5**, and reaction [16], where phenanthrene (**4**) improves the reaction with norbornene (**11**) even though the oxidation difference ($E_{1/2}$(**11**) $-$ $E_{1/2}$(**4**)) is $+12$ kcal mol^{-1}.

To complete the analysis, there are examples where addition of the photosensitizer does not significantly improve the reaction; in fact, there are some examples where the added donor even quenches the reaction. For example, phenanthrene (**4**) quenches the reaction with 2-methylpropene (**5**); the oxidation potential difference ($E_{1/2}$(**5**) $-$ $E_{1/2}$(**4**)) is 23 kcal mol^{-1} (2). Yet, biphenyl (**8**) improves this reaction (reaction [4]); the oxidation potential difference ($E_{1/2}$(**5**) $-$ $E_{1/2}$(**8**)) is 19 kcal mol^{-1}. And, while the addition of **8** improves the reaction with cyclohexene (**9**) (reaction [6]) (the oxidation potential difference ($E_{1/2}$(**9**) $-$ $E_{1/2}$(**8**) is 11 kcal mol^{-1}), **4** is ineffective (the oxidation potential difference ($E_{1/2}$(**9**) $-$ $E_{1/2}$(**4**)) is 15 kcal mol^{-1}).

From this limited number of examples we conclude that the photosensitizer may improve the reaction even though it has an oxidation potential significantly (as much as 20 kcal mol^{-1}) lower than that of the olefin. As the difference in oxidation potential becomes greater, the effectiveness of photosensitization decreases. The relative oxidation potentials of the olefins and photosensitizers are plotted in Fig. 1.

The fact that an added donor can function as a photosensitizer even though it has an oxidation potential significantly lower than the olefin makes it unlikely that a simple electron transfer, forming the olefin radical cation, is involved. We suggest that there is formation of a bimolecular radical cation complex involving the olefin and the added donor (4*d*). Even though such a complex might have most of the charge and spin density on the

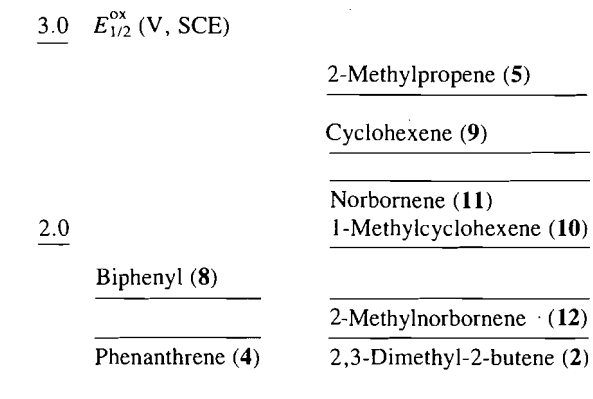

FIG. 1. The relative oxidation potentials of the photosensitizers and olefins studied.

component with the lower oxidation potential, the olefin component could still be reactive toward methanol. The analogous dimeric radical cations of polynuclear aromatic compounds are well known and the radical cation complex of benzene–ethylene has recently been characterized (19).

In those reactions that are more efficient upon photosensitization, the product ratios are essentially the same with both photosensitizers. We make the assumption that under these conditions the olefin radical cation is formed away from the 1,4-dicyanobenzene radical anion ($\mathbf{1}^{\bullet -}$) and is either freely solvated or is involved in a mixed radical cation complex with the donor. In fact, termolecular complexes cannot be ruled out (5). The increased efficiency may be the result of a slower back electron transfer process within the initially formed radical anion – photosensitizer radical cation pair.

The representation of step 3 shown in the scheme is oversimplified in that it only shows reaction of methanol occurring with the olefin radical cation. The extent of the association of the radical cation with the radical anion $\mathbf{1}^{\bullet -}$ or with an added donor is not indicated. In those reactions induced by direct irradiation, along the increasing stages of radical ion pair separation, where does reaction with methanol occur? And, in the photosensitized reactions, does the added donor play a role in this step?

There are small but significant differences in the ratio of isomers formed upon direct irradiation and photosensitized. The most significant, consistent, difference is that the reaction is more regioselective upon photosensitization, favouring the *anti*-Markovnikov adducts. We believe that this is the result of reaction occurring at different stages of radical cation – radical anion pair separation, and that complexation of the olefin radical cation with the added donor is involved.

Let us consider first the possibility that reaction occurs while the radical ion pair is still in an electronic excited state, that is, at the exciplex stage. Formation of the radical ion pair with **1** and 2-methylpropene is endergonic and the photo-NOCAS reaction is very inefficient, and yet the fluorescence of **1** is quenched by 2-methylpropene at nearly the diffusion controlled rate. The quenching process, in this case, may involve formation of an exciplex that does not go on to a reactive radical ion pair stage (2).

The formation (step 2a) and stability of the exciplex is favoured by nonpolar solvents while polar solvents favour the direct formation (step 2b) of the radical ion pair and providc an efficient deactivation pathway for the exciplex to the radical ion pair (step 2b′). The irradiation of cyanoaromatic compounds in the presence of olefins in nonpolar solvents generally leads to cycloadducts (1-azetines and (or) cyclobutanes); this reaction does involve the exciplex (20, 21).

If exciplexes were involved, in the case of norbornene (**11**) and 2-methylnorbornene (**12**), the favoured orientation of the exciplex would have the 1,4-dicyanobenzene (**1**) on the *exo* side. If reaction occurred by bonding within the exciplex, product formation should reflect this structure. While there is, in fact, relatively more of the *exo*-(4-cyanophenyl) isomer (**17**) formed upon direct irradiation in the reaction involving norbornene (**11**), the major isomer in every case has the methoxy group in the *exo* position and the (4-cyanophenyl) group *endo* (**16**, **19**, and **23**).

The evidence is against the exciplex as the reactive intermediate in the photo-NOCAS reaction in polar solvents.

The possibility that coupling between the radical anion and the radical cation within the radical ion pair precedes the addition of methanol should be addressed. This mechanism has been suggested for some related reactions (21*e*, 22). Coupling between the radical anion and the radical cation should lead to the more stable zwitterionic (or diradical) intermediate, and ultimately to the Markovnikov adducts. This mechanism should be more likely upon direct irradiation. The results show that direct irradiation does give relatively more of the Markovnikov adduct(s) in comparison to sensitized irradiation; however, the *anti*-Markovnikov adduct(s) are still the major products. Coupling of the radical anion and the radical cation prior to, or concerted with, reaction with methanol may account for some of the Markovnikov adducts, but this cannot be the dominant mechanism.

The relevant question then becomes, can the rate of reaction of methanol with the olefin radical cation, while still part of the radical ion pair, be fast enough to compete with solvent separation of the pair? The rate of separation of several radical ion pairs, similar to those involved here and also in acetonitrile, has been measured to be ca. 5×10^8 s^{-1} (23). The rate constant for reaction of olefin radical cations with methanol varies with the structure of the olefin. With 1,1-diphenylethylene the rate constant is 1.6×10^9 M^{-1} s^{-1}; more stable and sterically hindered radical cations react more slowly (23). The olefins used here are not stabilized by conjugation with phenyl rings and it is therefore possible that reaction of the radical cation with methanol (ca. 6 M) occurs at the radical ion pair stage, in competition with solvent separation.

Reaction of the olefin radical cation with a nucleophile may appear deceptively simple at first. This is, however, an interesting process that has received relatively little attention. The initial product of step 3 is the β-alkoxy alkyl radical *protonated on the oxygen*, a distonic radical cation. Most of our knowledge of this process comes from electrochemical studies (24) and from studies of ion–molecule reactions in the gas phase (25). Two possible mechanisms have been suggested: direct attack of the nucleophile on the radical cation with covalent bond formation, leading directly to the distonic radical cation, and initial formation of an ion–dipole π-complex. Either of these mechanisms could lead ultimately to the β-alkoxy alkyl radical; however, deprotonation from oxygen may not be fast enough, even in this polar solvent, to compete with reaction with the radical anion. This mechanism would be similar to the termolecular electrophilic addition to olefins (Ad_E3) (26).

A single electron shift from the nucleophile to the radical cation cannot lead directly to nucleophilic addition (27).

The intermediate radical shown as the ultimate result of step 3 is the same as would be obtained upon addition of an alkoxy

Can. J. Chem. Downloaded from www.nrcresearchpress.com by 122.72.124.2 on 09/07/12
For personal use only.

Can. J. Chem. Downloaded from www.nrcresearchpress.com by 122.72.124.2 on 09/07/12
For personal use only.

radical to the neutral olefin. The factors that influence the regioselectivity of radical addition to olefins are well known; both polar and steric effects are important (28). The factors that influence the regioselectivity of the addition of methanol to the radical cation of an unsymmetrical olefin are not yet defined. For example, the regioselectivity may depend upon the extent of separation of the radical ion pair formed upon direct irradiation, and upon the nature of the radical cation complex in the photosensitized reactions.

Methanol adds to the radical cation of 1,1-diphenylethylene to give exclusively the resonance stabilized radical (29). The previously reported photo-NOCAS reaction of methanol combining with 2-methylpropene (**5**) and then substituting on 1,4-dicyanobenzene (**1**) (reaction 3) also implicated the involvement of the more stable radical intermediate. An argument based upon steric factors could also explain these results. Both of these examples involve terminal olefins with large differences in both radical stability and in steric hindrance to approach at the alternate ends of the olefin. It was not clear how regioselective the reaction would be when the difference between the two ends of the olefin was less pronounced than in these earlier examples.

The reactions reported here with 1-methylcyclohexene (**10**) and 2-methylnorbornene (**12**) indicate that addition of methanol to these unsymmetric olefin radical cations, where the intermediate is either a secondary or tertiary radical, is not very regioselective. The reaction is somewhat more regioselective, favouring the *anti*-Markovnikov adducts, upon photosensitization. The largest effect of sensitization is observed in the case of 2-methylnorbornene (**12**) where there is significantly more of the *cis anti*-Markovnikov isomer (**20**) (reaction 21). In this reaction the ratio of *anti*-Markovnikov to Markovnikov adducts is relatively high (20:1). We offer the tentative explanation that it is the initial proximity of the radical anion, in those reactions involving direct irradiation, which leads to relatively more Markovnikov addition.

There is surprisingly little variation in the stereoselectivity as a function of mode of activation. The major differences involve the reactions of norbornene (**11**) and 2-methylnorbornene (**12**); there is relatively more of the *trans* adduct *with the methoxy in the* endo *position* (**17** and **21**) produced upon direct irradiation. This observation can also be explained in terms of reaction of the radical ion pair. The olefin radical cation would be attacked by the methanol on the side opposite from the radical anion; if the radical anion was blocking the preferred *exo* side, the methanol would be forced to attack from the *endo* side.[5]

There is no reason to expect the reaction to be stereoselective if step 4 involves the coupling of the β-alkoxyradical to the 1,4-dicyanobenzene radical anion free from the radical ion pair. Chemical (31) and spectroscopic (32) evidence indicates that "bridging" is of little importance in this type of radical. The suggestion has been made that bridging is more important in the distonic radical cation (25*d*). In these cyclic systems there should be a preference for formation of the *trans* adduct, by coupling of the β-methoxycyclohexyl radical at the less hindered *pseudo-equatorial* position with the methoxy group in the equatorial position. In fact, the *cis*:*trans* ratio of 1:5–6 observed in the case of cyclohexene is comparable to the ratio (1:2.5) of β-chlorocyclohexyl *tert*-butyl ethers obtained upon addition of *tert*-butyl hypochlorite to cyclohexene (33).

If step 4 follows directly after step 3 as a continuation of the reaction of the radical ion pair formed upon direct irradiation, these two reactants are still part of the solvent cage and coupling is likely to occur. If, however, the radical is formed away from the radical anion, the very low concentration of both of these species, and the fact that they are reactive (particularly for coupling and disproportionation of the radical), might make the required encounter improbable. Small amounts of the radical coupling and disproportionation products are in fact among the side products. It therefore seems likely that the high yield of the photo-NOCAS products results from a buildup of the relatively stable radical anion $\mathbf{1}^{\bullet -}$, to the point where the probability of an encounter with the reactive radical becomes significant. This is an example of a reaction controlled by "internal suppression of fast modes" (5*i*, 34).

Another interesting aspect of step 4 involves identification of the factors that influence the position, on the radical anion, at which coupling occurs. The results support the hypothesis that coupling occurs at the position of greatest spin density. This is also the position that minimizes the localization energy in the resulting anion (2, 20).

The driving force for step 5 is the rearomatization of the phenyl ring. If step 4 occurs at a position on the aromatic ring other than that bearing the cyano group, or if the driving force for rearomatization is insufficient, as in polynuclear aromatics, then the anion can be protonated and addition will occur instead of substitution (2, 21*a*, 21*e*).

A minor product under most irradiation conditions was the photo-NOCAS product incorporating cyanide ion, instead of methanol, as the nucleophile. Presumably this product arises from the addition of cyanide ion, generated in the final aromatization step (step 5), in competition with methanol in step 3 of the scheme.

The effects of added salts

The addition of salts (0.3 M), particularly magnesium perchlorate, has a profound effect on both the yield and the ratio of photo-NOCAS products. The yield is adversely affected; the amount of ethers resulting from addition of methanol to the radical cation of the olefin is increased. The amount of the allylic radical substitution products is also increased. *The photo-NOCAS reaction is regioselective when magnesium perchlorate has been added; only the* anti-*Markovnikov products are formed*. Both of these effects may result from a stabilization of the radical anion by the magnesium cation, causing a decrease in reactivity and increased selectivity.

Flash photolysis studies have shown that the lifetime of radical cations can be significantly increased by the addition of magnesium cation. The explanation given was that stabilization of the radical anion inhibits the deactivating back electron transfer (6*b*). Other cations were not as effective.

The reaction of methanol with the olefin radical cation may occur without any influence being exerted by the 1,4-dicyanobenzene radical anion $\mathbf{1}^{\bullet -}$ when it is stabilized by the magnesium cation. This would imply that the uncomplexed radical anion $\mathbf{1}^{\bullet -}$ is involved in the step that determines the regiochemistry in the absence of magnesium cations. Involvement of $\mathbf{1}^{\bullet -}$ directs the addition in favour of the Markovnikov adduct(s). This is consistent with the conclusion reached earlier: in the absence of added salts there is an addition step that is analogous to the Ad_E3 mechanism, resulting in an increase in the relative amount of Markovnikov addition. When magnesium salt is added to the irradiation mixture the radical anion is deactivated, the reaction becomes analgous to the Ad_E2 mechanism, and the reaction is regioselective, i.e., *anti*-Markovnikov.

[5]There is still some debate over the cause of the generally preferred *exo* attack on norbornene (see ref. 30, and the references therein).

Can. J. Chem. Downloaded from www.nrcresearchpress.com by 122.72.124.2 on 09/07/12
For personal use only.

The addition of other salts (lithium perchlorate and tetrabutylammonium perchlorate) had much less effect. Lithium perchlorate had a noticeable effect in some cases, increasing the yield of photo-NOCAS products incorporating methanol (reaction 13). Formation of the side product involving cyanide addition was greatly reduced when lithium perchlorate was added to the irradiation mixture; hence, the yield of the methanol adducts was increased. This may result from lithium cation scavenging the cyanide anion.

Perspective

Not too many years ago the major (only) reaction considered to be generally useful in a synthetic strategy for alkylation of an aromatic ring would have involved the electrophilic aromatic substitution mechanism (S_E2Ar). Recent years have seen a significant increase in our understanding of the mechanism, if not the routine application, of several alternative methods for achieving this objective. Some of these newer methods involve radical ions, both the radical cation and the radical anion, of the aromatic compound (35).[6]

It is already obvious from these few examples that the photo-NOCAS reaction will also have significant synthetic utility. The limitations of the reaction, many of which are now predictable in terms of the mechanism, are no more severe or restrictive than those imposed by the S_E2Ar mechanism. The differences observed in the ratio of regio- and stereoisomeric products, as a function of mode of activation and complexation, encourage us to predict that ways will be found to control this aspect of the reaction as well.

Experimental

General Information

The ^1H and ^{13}C nmr spectra were recorded on a Nicolet 360 NB nmr spectrometer coupled to an Oxford Instruments superconducting magnet and a Nicolet 192 kword data acquisition system, a Varian CFT-20, or an EM-360L spectrometer, and are reported in parts per million to high frequency from TMS. Coupling constants are reported as absolute values; the signs of the couplings were not determined. Infrared spectra (ir) were recorded on an air-purged Perkin–Elmer 180 grating infrared spectrometer or a Pye Unican SP3-200 and are reported in wavenumbers relative to the 1601.4 cm^{-1} absorption of polystyrene. Mass spectra (ms) were recorded on a Hewlett–Packard 5970 series mass selective detector and are reported as *m/z* (relative intensity). Exact mass determinations were done on a Du Pont CEC 21-110B mass spectrometer. Elemental analyses were performed by Canadian Microanalytics Services Inc. The melting points were determined using a Cybron Corporation Thermolyne melting point apparatus and are corrected.

Product analyses were determined by gas chromatography (gc) using either a Hewlett–Packard (HP) 5890 gc, fitted with a 5% phenyl methyl silicone fused silica WCOT column (25 m × 0.20 mm, 0.33-μm film thickness), coupled to an HP 5970 mass selective detector (ms), or a Hewlett–Packard 5890 gc, fitted with a DB-1701 or DB-225 fused silica WCOT column (30 m × 0.25 mm, 0.25-μm film thickness), with a flame ionization detector (fid). The digital signal from the fid was transmitted to a HP 3392A integrator and the data were acquired by software developed at the Department of Chemistry, Dalhousie University, using a Commodore PC-II.

Compounds that were obtained as liquids were purified prior to analysis by preparative gas chromatography using a Varian Aerograph 90-P and a 3/8 in. × 10 ft aluminum column, column "A". Column A was packed with 5% SE-52 on Chromosorb A 60/80 NAW. Column "B" was used for the purification of the olefins for the electrochemistry experiments; it was a 3/8 in. × 10 ft aluminum column packed with 40% SE-30 on Chromosorb W 60/80 NAW. Preparative medium-pressure liquid chromatography (mplc) was carried out using a 2.5 cm × 1 m column packed with tlc grade silica gel (without binder) (Merck) at 15 psi (helium) (1 psi = 6.9 kPa). The chromatograms were developed with a hexanes – methylene chloride linear gradient and the eluant was monitored, collected by a uv spectrometer-fraction collector.

Materials

Solvents were fractionally distilled. Acetonitrile (Fisher ACS grade) was distilled successively from sodium hydride and phosphorus pentoxide, and was then passed through a column of basic alumina, refluxed over calcium hydride for 24 h (under a nitrogen atmosphere), and fractionally distilled. The 1,4-dicyanobenzene (**1**) (Aldrich) was purified by treatment with Norite in methylene chloride, followed by sublimation and recrystallization from 95% ethanol. Tetraethylammonium perchlorate (TEAP) (Aldrich) was recrystallized (three times) from 95% ethanol and dried in a vacuum oven (12 h, 80°C, 10 Torr (1 Torr = 133.3 Pa)) before use.

Irradiations

Irradiations were carried out using a CGE 1-kW medium-pressure mercury vapor lamp contained in a water cooled quartz immersion well. The temperature was maintained at 10°C. The solvent was acetonitrile–methanol (3:1) at a typical concentration of **1** of 0.1 M, and olefin of 0.2 M. The concentration of photosensitizer (electron transfer) was 0.02 M. Solutions were placed in 2 cm i.d. Pyrex tubes (large scale) or 5 mm Pyrex nmr tubes, flushed with dry nitrogen, and sealed. Reaction mixtures (large scale) were chromatographed by mplc, taking ca. 10-mL fractions. For quantitative studies, changes of the ratio between starting material and products were followed by gc/fid. Variation in the fid response was taken into account (37).

Cyclic voltammetric measurements

Oxidation potentials were obtained by cyclic voltammetry using an apparatus similar to that previously described (*1a*). The working electrode was a platinum sphere (1 mm diameter), while the counter electrode was a platinum wire. The reference electrode was a saturated calomel electrode (SCE), which was connected to the solution by a Luggin capillary. The electrolyte was TEAP (0.1 M) and the solvent was acetonitrile. Substrate concentrations were typically 0.005 M. If the anodic wave was not reversible, the half-wave potential was taken as 0.028 V before the anodic peak potential (38).

2-Methylbicyclo[2.2.1]heptane-2,3-dicarboxylic acid

This dicarboxylic acid was prepared by the method of Beckmann and Schaber (9). Freshly distilled cyclopentadiene (108 g, 1.63 mol) was dissolved in 500 mL of ethyl acetate at 0°C. To this solution was added 112 g (1 mol) of citraconic anhydride (Aldrich) in 5-mL aliquots. The reaction was kept at 0°C overnight and was then allowed to warm to room temperature. Gas chromatographic analysis indicated the reaction was 93% complete based on consumed citraconic anhydride.

This solution was added to a 1-L flask containing 2 g of 5% palladium on charcoal (Engelhard). The flask was evacuated and charged with hydrogen. This mixture was stirred for 5 days; reaction was complete. The reaction mixture was filtered through Celite 545 and the solvent was evaporated. The residue was added to 500 mL 15% KOH. After 12 h, tricyclo[5.2.1.$0^{2,6}$]decane was removed by filtration. Concentrated hydrochloric acid was added to the filtrate until pH 2. The product, 2-methylbicyclo[2.2.1]heptane-2,3-dicarboxylic acid, precipitated and was isolated by filtration, washed with water, and dried.

Yield 190 g (96%), mp 142–144°C (lit. (9) mp 143°C).

*2-Methylnorborn-2-ene (**12**)*

The 2-methylnorborn-2-ene was prepared by oxidative bis-decarboxylation of 2-methylbicyclo[2.2.1]heptane-2,3-dicarboxylic acid using a procedure developed by Paquette and co-workers (10). To a 250-mL round bottom flask, equipped for distillation with a receiver in Dry Ice and under a nitrogen atmosphere, was added 9.9 g (0.05 mol) of 2-methylbicyclo[2.2.1]heptane-2,3-dicarboxylic acid, 15.6 g (0.10

[6]An analogous reaction, the photochemical electrophile–olefin combination, aromatic substitution (photo-EOCAS) reaction, might also be developed into a useful synthetic procedure (36).

Can. J. Chem. Downloaded from www.nrcresearchpress.com by 122.72.124.2 on 09/07/12
For personal use only.

mol) 2,2′-dipyridyl (Aldrich), 15.0 g (0.10 mol) red cuprous oxide, 3 g powdered glass, and 75 mL of distilled quinoline. The stirred mixture was heated at 140°C for 1.5 h, and then the temperature was increased to 180°C for 72 h. The distillate was purified by washing, first with 10% hydrochloric acid, then with water, and was dried with magnesium sulphate. The yield of **12** was 2.54 g (47%) as a colourless liquid. Analysis of this product by gc indicated the purity was 97% (impurity, 2-methylenenorbornane). The reactor was recharged repeatedly with the original quantity of 2-methylbicyclo[2.2.1]heptane-2,3-dicarboxylic acid and one quarter of the amount of cuprous oxide (0.05 mol) with little effect on the overall yield.

Infrared (SP3-200) ν: 2940(vs), 2840(m), 1430(m), 790(m); ^{1}H nmr (60 MHz, $CDCl_3$) δ: 5.5(s, 1H), 2.75(s, 1H), 2.6(s, 1H), 1.75(d, 3H, ^4J=2 Hz), 1.70–0.9(m, 6H); ^{13}C nmr (20 MHz, $CDCl_3$) δ: 145.3, 128.2, 48.2, 46.5, 42.4, 26.9, 24.2, 15.0; ms *m/z*: 108(20), 91(12), 80(100), 79(73), 77(21). The ^{1}H nmr spectra of **12** has been reported (39).

Formation of the cyclohexene adducts

A solution of 3.30 g (0.04 mol) cyclohexene (**9**), 3.00 g (0.02 mol) biphenyl (**8**), and 2.50 g (0.02 mol) 1,4-dicyanobenzene (**1**) in 200 mL acetonitrile–methanol (3:1) was degassed with nitrogen for 15 min and irradiated for 90 h. The volatile components of the photolysate, removed by distillation, included unreacted **9** and methoxycyclohexane (analyzed by gc/ms). The nonvolatile residue (8.50 g) was partially separated by standard column chromatography using hexanes as the eluent; **8** was recovered in 97% yield. The solvent was changed to diethyl ether, which eluted the photo-NOCAS isomers as a mixture of yellow oil and crystals (5.79 g). This mixture was separated by mplc.

Fraction no. 140–157: 482 mg of 3-(4-cyanophenyl)cyclohexene (2); ir (PE-180) ν : 3020(w), 2930(s), 2860(m), 2840(w), 2220(s), 1600(s), 1500(m), 830(s); ^{1}H nmr (60 MHz, $CDCl_3$) δ: 7.6–7.1(dd, 4H), 6.1–5.5(m, 2H), 3.6–3.3(m, 1H), 2.3–1.5(m, 6H).

Fraction no. 161–175: 80 mg of a 1:1 mixture of 2- and 4-cyanobiphenyl. The 4-cyanobiphenyl (mp 87°C) was identified by comparison with an authentic sample prepared by the reaction of the diazonium salt of 4-cyanoaniline with benzene in the presence of base (40). The other product, with similar retention time and fragmentation pattern (gc/ms), was assigned the structure *ortho*-cyanobiphenyl; ^{1}H nmr (361.08 MHz, $CDCl_3$) δ: 7.76–7.24(m); ms *m/z*:179(100), 178(25), 152(5), 151(5), 77(3).

Fraction no. 200–208: 150 mg of *cis*-2-(4-cyanophenyl)-1-methoxycyclohexane (**13**-*c*); ir (SP3-200) ν : 2930(vs), 2860(m), 2830(w), 2230(s), 1605(m), 1500(w), 1445(m), 1190(m), 1085(vs), 830(s); ^{1}H nmr (361.08 MHz, $CDCl_3$) δ: 7.56(d, 2H, ^3J=8.3 Hz, H's *ortho* to cyano group), 7.40(d, 2H, ^3J=8.3 Hz, H's *ortho* to alkyl group), 3.47(ddd, 1H, H on carbon with methoxy substituent), 3.10(s, 3H, methoxy), 2.70(ddd, 1H, $^3J_{2,3(a,a)}$ = 12.9 Hz, $^3J_{2,3(a,e)}$ = 3.5 Hz, $^3J_{1,2(e,a)}$ = 2.9 Hz, benzylic), 2.15–2.11 (bd, 1H), 2.04–1.95(qd, 1H), 1.90–1.80(bd, 1H), 1.65–1.35(m, 5H); ^{13}C nmr (90.80 MHz, $CDCl_3$) δ: 150.59(d, 5.3 Hz), 131.64(dd, 4.8 Hz, 164.2 Hz), 128.88(dd, 5 Hz, 161.5 Hz), 119.19(s), 109.67(t, 8.7 Hz), 79.01(d, 143.2 Hz), 56.61(q, 139.6 Hz), 48.30(d, 122.9 Hz), 28.71(t, 126.8 Hz), 26.04(t, 126 Hz), 26.00(t, 126 Hz), 19.50(t, 124.0 Hz); ms *m/z* : 215(10), 183(13), 155(25), 116(20), 71(100). *Anal.* calcd. for $C_{14}H_{17}NO$: C 78.10, H 7.96, N 6.51; found: C 78.39, H 8.01, N 6.57.

Fraction no. 209–222: 241 mg of a mixture of the *cis* and *trans* isomers **13**-*c* and **13**-*t*.

Fraction no 223–270: 1.08 g of *trans*-2-(4-cyanophenyl)-1-methoxycyclohexane (**13**-*t*), mp 50.8–51.0°C; ir PE-180) ν: 2905(vs), 2820(m), 2220(s), 1445(m), 1355(m), 1190(s), 1100(vs), 820(s); ^{1}H nmr (361.08 MHz, $CDCl_3$) δ: 7.55(d, 2H, *J*=8.2 Hz), 7.33(d, 2H, *J*=8.2 Hz), 3.26(ddd, 1H, *J*=4.1 Hz, 10.4 Hz, 10.4 Hz), 3.09(s, 3H), 2.59(m, 1H), 2.28(m, 1H), 1.80(m, 3H), 1.35(m, 4H); ^{13}C nmr (90.80 MHz, $CDCl_3$) δ: 150.37(d, 4.3 Hz), 131.72(d, 163.9 Hz), 128.18(d, 160.0 Hz), 118.84(s), 109.52(t, 8.9 Hz), 82.37(d, 141.4 Hz), 56.10(q, 139.3 Hz), 50.97(d, 129.3 Hz), 33.62(t, 129.4 Hz), 30.82(t, 126.2 Hz), 25.64(t, 126.4 Hz), 24.50(t, 127.3 Hz); ms *m/z*: 215(47), 183(50), 155(57), 71(100). *Anal* . calcd. for $C_{14}H_{17}NO$: C 78.10, H 7.96, N 6.51; found: C 77.73, H 7.93, N 6.56.

*Formation of the 1-methylcyclohexene (**10**) adducts*

Dicyanobenzene (**1**) (2.50 g, 20 mmol) and biphenyl (**8**) (1.80 g, 12 mmol) were dissolved in 200 mL of acetonitrile–methanol (3:1). This solution was distributed between six Pyrex irradiation tubes and degassed. To each tube was added 1-methylcyclohexene (**10**) (0.65 mL in each (33 mmol total)). After irradiation for 20 h, gc analysis indicated that **10** was essentially consumed. The volatile components were removed by distillation leaving a mixture (6.74 g) of yellow-orange oil and some crystals. The distillate contained a small amount of unreacted **10**, *cis*- and *trans*-1-methoxy-2-methylcyclohexane, and 1-methoxy-1-methylcyclohexane. These ethers were identified by direct comparison (gc/ms) with authentic samples prepared from the corresponding alcohols (Aldrich). The nonvolatile residue was filtered through glass wool to yield a yellow-orange oil containing the photo-NOCAS products; the crystalline material was unreacted **1** (200 mg). The oil was partially separated by column chromatography; **8** (1.30 g) was eluted with hexane and the photo-NOCAS products (2.96 g) came off in methylene chloride. The photo-NOCAS products were isolated by mplc.

Fraction no. 153–189: 195 mg of allylic radical substitution products. These products were identified on the basis of gc/ms (retention time and fragmentation pattern) in comparison with the analogous products from **9**.

Fraction no. 190–207: 100 mg of a mixture of the radical substitution products and **15**-*c*.

Fraction no. 208–216: 42 mg pure **15**-*c*.

Fraction no. 217–241: 600 mg of a mixture of **14**-*t* and **14**-*c*.

Fraction no. 242–258: 828 mg pure **14**-*t*.

Fraction no. 259–272: 310 mg of a mixture of **14**-*t* and **15**-*t*.

Fraction no. 273–288: 205 mg pure **15**-*t*.

Fraction no. 289–310: 180 mg of impure **15**-*t*.

cis-*2-(4-Cyanophenyl)-1-methyl-1-methoxycyclohexane (**15**-c)*

Infrared (PE-180) ν: 2940(s), 2865(m), 2835(w), 2235(s), 1605(s), 1500(m), 1460(m), 1415(w), 1370(m), 1260(w), 1155(s), 1075(ws), 895(w), 810(s); ^{1}H nmr (361.08 MHz, $CDCl_3$) δ: 7.54–7.51 (d, 2H), 7.43–7.41 (d, 2H), 3.11 (s, 3H), 2.48–2.43 (dd, 1H, ^3J=12.8 Hz, 3.4 Hz), 2.10–2.05 (m, 2H), 1.85–1.78 (bd, 1H), 1.57–1.45 (m, 3H), 1.39–1.30 (m, 1H), 1.22–1.14 (m, 1H), 0.87 (s, 3H); ^{13}C nmr (90.80 MHz, $CDCl_3$) δ: 149.60, 131.24, 130.37, 119.33, 109.62, 74.10(s), 55.28(d, 123 Hz), 48.23(q, 142 Hz), 33.79(t, 123 Hz), 28.90(t, 129 Hz), 26.33(t, 125 Hz), 23.37(q, 124 Hz), 21.41(t, 125 Hz); ms *m/z* : 229(5), 155(21), 85(100), 72(35), 55(21), 43(28). *Anal.* calcd. for $C_{15}H_{19}NO$: C 78.50, H 8.35, N 6.11; found: C 78.66, H 8.39, N 6.15.

cis-*2-(4-Cyanophenyl)-2-methyl-1-methoxycyclohexane (**14**-c)*

Fraction no. 217–240 was rechromatographed to provide a pure sample of **14**-*c*; ir (PE-180) ν : 2940(vs), 2870(m), 2830(w), 2220(s), 1605(m), 1505(m), 1460(m), 1445(m), 1380(w), 1180(w), 1095(vs), 1020(w), 830(s); ^{1}H nmr (361.08 MHz, $CDCl_3$) δ: 7.65–7.53(m, 4H), 3.42–3.36(t, 1H, *J*=4.4 Hz), 3.18(s, 3H), 2.23–2.13(m, 1H), 1.8–1.35(m, 7H), 1.24(m, 3H), ^{13}C nmr (90.80 MHz, $CDCl_3$) δ: 154.42, 131.65, 127.35, 119.21, 109.02, 84.85(d, 136 Hz), 56.93(q), 43.09(s), 32.89(t), 27.12(q), 24.47(t), 21.58(t), 21.34(t); ms *m/z*: 229(13), 169(25), 154(31), 71(100), 58(25), 41(29). *Anal.* calcd. for $C_{15}H_{19}NO$: C 78.50, H 8.35, N 6.11; found: C 78.14, H 8.32, N 6.17.

trans-*2-(4-Cyanophenyl)-2-methyl-1-methoxycyclohexane (**14**-t)*

Infrared (PE-180) ν : 2980(w), 2940(vs), 2860(m), 2820(w), 2230(s), 1600(s), 1500(m), 1450(m), 1440(m), 1190(w), 1145(w), 1090(s), 1020(w), 910(w), 815(s); ^{1}H nmr (361.08 MHz, $CDCl_3$) δ: 7.60(d, 2H, *J*=8.7 Hz), 7.53(d, 2H, *J*=8.6 Hz), 3.43(dd, 1H, *J*=10 Hz, 4 Hz), 3.16(s, 3H), 1.95–1.88(m, 1H), 1.88–1.77(m, 1H), 1.75–1.62(m, 2H), 1.60–1.47(m, 3H), 1.38–1.25(m, 4H); ^{13}C nmr (90.80 MHz, $CDCl_3$) δ: 155.01(s), 131.71(dd, 164.9 Hz, 6.1 Hz), 126.9(dd, 160.1 Hz, 6.6 Hz), 119.07(s), 109.22, 83.82(d, 143.2 Hz), 56.77(q, 140.75 Hz), 43.43(s), 37.97(t, 124.2 Hz), 25.65(t, 129.2 Hz), 23.73(t, 123.8 Hz), 21.57(t, 126.2 Hz), 18.83(qm, 127.9 Hz, 6 Hz, 6 Hz, 3Hz); ms *m/z*: 229(13), 169(23), 154(40), 116(23), 71(100), 58(33), 41(40). *Anal.* calcd. for $C_{15}H_{19}NO$: C 78.50, H 8.35, N 6.11; found: C 78.52, H 8.41, N 6.18.

trans-*2-(4-Cyanophenyl)-1-methyl-1-methoxycyclohexane (**15**-t)*

Infrared (PE-180) ν : 2980(w), 2920(vs), 2850(m), 2820(w), 2230(s), 1605(m), 1500(m), 1445(m), 1370(m), 1115(s), 1065(s), 955(w), 815(s); ^{1}H nmr (361.08 MHz, $CDCl_3$) δ: 7.55–7.53 (d, 2H, J=8.3 Hz), 7.33–7.30 (d, 2H, J=8.3 Hz), 3.13 (s, 3H), 2.86–2.82 (dd, 1H, J=4.2 Hz, 12.1 Hz), 2.00–1.97 (bd, 1H), 1.86–1.74 (m, 4H), 1.56–1.45 (m, 1H), 1.42–1.34 (m, 2H), 0.99 (s, 3H); ^{13}C nmr (90.80 MHz, $CDCl_3$) δ: 148.49(s), 131.02(d, 165.4 Hz), 130.22(d, 162.7 Hz), 119.23(s), 109.71(s), 76.65(s), 51.89(d, 126.5 Hz), 48.40(q, 140.4 Hz), 36.82(t, 127.4 Hz), 29.16(t, 125.7 Hz), 26.15(t, 126.9 Hz), 23.68(t, 127.2 Hz), 16.66(qm, 125.1 Hz, 5 Hz, 6 Hz, 3 Hz); ^{13}C nmr (90.80 MHz, C_6D_6) δ: 148.21, 130.97, 130.49, 119.26, 110.39, 76.41, 52.22, 48.15, 36.95, 29.02, 26.36, 23.85, 16.35; ms *m/z* : 229(6), 155(25), 85(100), 72(40), 55(24), 43(25). *Anal.* calcd. for $C_{15}H_{19}NO$: C 78.50, H 8.35, N 6.11; found: C 78.86, H 8.42, N 6.27

*Formation of adducts with norbornene (**11**)*

A solution of 1,4-dicyanobenzene (**1**) (2.5 g, 20 mmol), norbornene (**11**) (9.0 g, 96 mmol), and biphenyl (**8**) (1.8 g, 12 mmol) in 250 mL of acetonitrile–methanol (3:1) was purged with nitrogen and irradiated (60 h). The volatile components of the reaction mixture were distilled. Analaysis of the distillate by gc/ms indicated that *endo-* and *exo*-2-methoxynorbornane were present. The nonvolatile components were partially separated by flash chromatography using a 40 cm × 2 cm silica gel column, eluting with methylene chloride (100-mL fractions). Fraction no. 4 (1.35 g) was mainly **8** with some 2-(cyanomethyl)norbornane; fraction no. 5 (1.38 g) was pure 2-(cyanomethyl)norbornane; fraction no. 6–13 contained the photo-NOCAS products. The yield of photo-NOCAS isomers was 2.20 g. When the amount of recovered **1** was taken into account, the yield was 78%. Fractions no. 5–13 were combined and the products were partially separated by mplc using the hexanes – methylene chloride gradient.

Fraction no. 57–64; trace of **8**.

Fraction no. 155–175; 124 mg of 2-cyanomethylnorbornane.

Fraction no. 220–244; 794 mg of a mixture of **16**, **17**, **18**, and **1**.

Fraction no. 245–257; 548 mg of pure **16**.

Fraction no. 258–290; traces of the isomeric 2-(cyanomethyl)-3-(4-cyanophenyl)norbornanes. Structures were tentatively assigned on the basis of gc/ms (retention time and fragmentation pattern).

The structure of *exo*-2-(cyanomethyl)bicyclo[2.2.1]heptane was established by comparison with an authentic sample prepared by refluxing a solution of acetonitrile, norbornene, and dibenzoyl peroxide for 4 days. This is a known compound (41); ir (PE-180) ν: 2950(s), 2870(m), 2240(m), 1460(m), 1425(m); ^{1}H nmr (361.08 MHz, $CDCl_3$) δ: 2.29–2.12(m, 4H), 1.88–1.78(m, 1H), 1.63–1.45(m, 3H), 1.34–1.27(m, 1H), 1.27–1.07(m, 4H); ms *m/z*: 135(2), 95(79), 68(100), 67(100).

Fraction no. 220–244 was rechromatographed (mplc) using methylene chloride as eluent. Traces of unreacted **1** were separated in earlier fractions, then a mixture of **18** and **17** was eluted, followed by a mixture of **18** and **16**, and finally some pure **16**. Pure **17** was obtained from an enriched fraction by preparative gc using column A.

endo-*3-(4-Cyanophenyl)*-exo-*2-methoxynorbornane (**16**)*

Infrared (PE-180) ν: 2960(vs), 2865(s), 2820(w), 2220(s), 1605(s), 1505(m), 1455(m), 1368(w), 1295(w), 1180(w), 1117(m), 1090(vs), 845(m), 810(s), 765(m); ^{1}H nmr (361.08 MHz, $CDCl_3$) δ: 7.61–7.58 (m, 2H), 7.32–7.29 (m, 2H), 3.44–3.43 (dd, 1H, $^3J_{endo,exo}$ = 3.5 Hz, $^4J_{endo,\ H7a}$ = 1.5 Hz), 3.30 (s, 3H), 2.99 (s, 1H), 2.48–2.45 (m, 2H), 1.86–1.82 (d, 1H), 1.65–1.60 (m, 1H), 1.41–1.37 (d, 1H), 1.29–1.28 (m, 1H), 1.10–1.05 (m, 2H); ^{13}C nmr (90.80 MHz, $CDCl_3$) δ: 147.53(s), 131.94(dd, 5.9 Hz, 164.2 Hz), 128.68(d, 164.2 Hz), 118.97(s), 109.83(s), 88.06(d, 143 Hz), 56.47(q, 141.2 Hz), 56.23(d, 129.7 Hz), 41.27(d, 140.9 Hz), 40.75(d, 141.8 Hz), 37.14(t, 133.8 Hz), 25.10(t, 132.2 Hz), 22.19(t, 131.7 Hz); ms *m/z*: 41(82), 71(98), 85(59), 116(100), 180(53), 227(73). *Anal.* calcd. for $C_{15}H_{17}NO$: C 79.26, H 7.54, N 6.16; found: C 79.30, H 8.75, N 6.22.

exo-*3-(4-Cyanophenyl)*-endo-*2-methoxynorbornane (**17**)*

^{1}H nuclear magnetic resonance (361.08 MHz, $CDCl_3$) δ: 7.59–7.57 (d, 2H, J=8.0 Hz), 7.44–7.32 (d, 2H, J=8.2 Hz), 3.65 (m, 1H, J=4.4 Hz, 4.0 Hz), 3.27 (s, 3H), 2.64 (s, 1H), 2.45(s, 1H), 2.37 (s, 1H), 1.87–1.80 (m, 1H), 1.73–1.61 (m, 2H), 1.51–1.39 (m, 3H); ^{13}C nmr (90.80 MHz, $CDCl_3$) δ: 153, 132.24, 127.59, 110, 90.10, 57.16, 54.66, 42.20, 39.24, 35.30, 30.96, 19.55; ms *m/z*: 227(73), 180(48), 116(79), 85(57), 71(100), 41(72).

exo-*3-(4-Cyanophenyl)*-exo-*2-methoxynorbornane (**18**)*

Spectral assignments were made by subtracting the spectra due to the other isomer (**17**) in the mixture; ^{1}H nmr (361.08 MHz, $CDCl_3$) δ: 7.53(d, 2H, J=8.3 Hz), 7.32(d, 2H, J=8.3 Hz), 3.50(d, 1H, J=7.0 Hz), 2.99(s, 3H), 2.91(d, 1H, J=7.0 Hz), 2.45(m, 1H), 2.36(m, 1H), 1.92(d, 1H, J=12 Hz), 1.70–1.44(m, 3H), 1.27(d, 1H, J=12 Hz), 1.15(m, 1H); ^{13}C nmr (90.80 MHz, $CDCl_3$) δ: 147.02, 129.66, 127.57, 119.27, 109.35, 87.09, 57.56, 54.29, 41.51, 39.81, 34.79, 30.51, 23.97; ms *m/z* : 227(77), 180(52), 116(94), 85(74), 71(100), 41(84).

*Formation of adducts from 2-methylnorbornene (**12**)*

A solution of 2-methylnorbornene (**12**) (3.0 g, 27.8 mmol), 1,4-dicyanobenzene (**1**) (3.9 g, 30.6 mmol), and biphenyl (**8**) (2.5 g, 16.2 mmol) in 200 mL acetonitrile–methanol (3:1) was degassed with nitrogen and irradiated for 20 h. The solvent and volatile products were removed by distillation leaving a residue (8.91 g). The distillate contained isomeric 2-methoxy-3-methylnorbornanes (structures were assigned on the basis of retention times and fragmentation patterns, gc/ms). The residue was partially separated by chromatography, using hexanes eluted (**8**) (2.3 g). Methylene chloride was used to elute the photo-NOCAS products. The resulting mixture was separated by mplc (hexanes – methylene chloride gradient).

Fraction no. 245–247; 17 mg of pure **21**.

Fraction no. 248–258; 75 mg of a mixture of **21** and **19**.

Fraction no. 259–268; 273 mg of **19**.

Fraction no. 269–274; 570 mg of a mixture of **19**, **20**, **22**, and **1**.

Fraction no. 275–278, 85 mg of a mixture of **20** and **1**.

Fraction no. 279–290; 45 mg of a mixture of **20** and **23**.

exo-*3-(4-Cyanophenyl)*-endo-*2-methoxy*-endo-*3-methylnorbornane (**21**)*

Infrared (SP3-200) ν : 2960(vs), 2890(s), 2830(w), 2230(s), 1610(m), 1505(m), 1200(w), 1120(s), 1100(vs), 1075(m), 840(s); ^{1}H nmr (361.08 MHz, $CDCL_3$) δ: 7.59–7.57 (d, 2H, ^3J=8.4 Hz), 7.48–7.46 (d, 2H, ^3J=8.4 Hz), 3.68 (d, 1H, ^3J=3.8 Hz, CH—O—CH_2), 3.36 (s, 3H, OCH_3), 2.69 (bs, 1H, H_4), 2.17 (bs, 1H, H_1), 1.85–1.68 (m, 2H), 1.57–1.47 (m, 1H, $H5_{exo}$), 1.28–1.22 (m, 3H), 1.12 (s, 3H, CH_3); ^{13}C nmr (90.80 MHz, C_6D_6) δ: 88.87, 56.90, 48.54, 44.27, 40.86, 34.73, 24.79, 23.68, 18.96; ^{13}C nmr (90.80 MHz, $CDCl_3$) δ: 158.76 (s), 132.07 (dd, 5.5 Hz, 164.9 Hz), 126.87 (dd, 5.8 Hz, 160.0 Hz), 119.06 (s), 108.97 (t, 8.1 Hz), 89.03 (d, 143.8 Hz), 57.14 (q, 140.6 Hz), 48.33 (s), 44.05 (dm, 139.0 Hz), 40.49 (dm, 140.9 Hz), 34.54 (tt, 7.4 Hz, 133.3 Hz), 24.37 (t, 128.7 Hz), 23.36 (q, 128.2 Hz), 18.59 (t, 133.0 Hz); ms *m/z*: 241(24), 209(51), 194(56), 168(31), 156(26), 154(28), 130(42), 116(48), 85(74), 71(100). *Exact Mass* calcd. for $C_{16}H_{19}NO$: 241.147; found: 241.147.

endo-*3-(4-Cyanophenyl)*-exo-*2-methoxy*-exo-*3-methylnorbornane (**19**)*

Infrared (PE-180) ν : 2970(vs), 2880(m), 2820(w), 2230(s), 1610(m), 1510(m), 1450(m), 1380(w), 1200(m), 1105(vs), 1070(m), 970(m), 830(s); ^{1}H nmr (361.08 MHz, $CDCl_3$) δ: 7.61–7.58 (d, 2H, J=8.44 Hz, H's *ortho* to CN), 7.35–7.33 (d, 2H, J=8.39 Hz, H's *ortho* to alkyl), 3.47 (s, 4H, OCH_3 and CH—OCH_3), 2.42–2.37 (d, 2H, H1, H4), 2.04–1.98 (d, 1H, H7s, J=10.6 Hz), 1.56–1.46 (m, 1H, J=12 Hz, 3.8 Hz), 1.44–1.33 (m, 1H, J=4.5 Hz, 4.3 Hz, 12.3 Hz), 1.29–1.24 (d, 1H, H7a, J=10.6 Hz), 1.23–1.16 (m and s, 4H), 0.09–0.81 (m, 1H, J=5.0 Hz, 7.5 Hz, 11.6 Hz); ^{1}H nmr (361.08 MHz, C_6D_6) δ: 7.42–7.35 (d, 2H, adjacent to CN, 9.1 Hz), 7.17–7.11 (d, 2H, H's adjacent to alkyl, 7.6 Hz), 3.28–3.20 (d, 1H, CH—OCH_3, 1.6 Hz), 3.13(s, 3H, O—CH_3), 2.21–2.15 (d, 1H, H1, J=5.5 Hz), 2.05–2.02 (s, 1H, H4), 1.97–1.92 (d, 1H, H7s, J=9.2 Hz), 1.32–1.20 (m, 1H, $H6_{exo}$), 1.20–1.08 (m and s, 4H, $H5_{exo}$ and CH_3), 1.05–0.95 (d, and m, 2H, H7 and $H5_{endo}$, J=9.2 Hz), 0.70–0.55 (m, 1H, $H6_{endo}$); ^{13}C nmr (90.80 MHz, $CDCl_3$) δ: 155.30 (d, 4.3 Hz,

Can. J. Chem. Downloaded from www.nrcresearchpress.com by 122.72.124.2 on 09/07/12
For personal use only.

quaternary aromatic with alkyl sub), 131.89 (dd, 3.8 Hz, 164.1 Hz, carbon adjacent to cyano), 127.99 (dd, 5.3 Hz, 158.6 Hz, carbon adjacent to alkyl group), 119.06 (s, CN), 108.95 (s, quaternary aromatic with cyano substituent), 90.85 (d, 142.3 Hz, CH—OCH_3), 57.85 (q, 137.8 Hz, O—CH_3), 54.76 (s, quaternary), 45.90 (d, 141.4 Hz, bridgehead), 39.90 (d, 144.6 Hz, bridgehead), 34.22 (td, 4.5 Hz, 133.8 Hz, CH_2), 26.83 (q, 129 Hz, CH_3), 25.63 (t, 130 Hz, CH_2), 24.49 (t, 130 Hz, CH_2); ms *m/z*: 241(41), 209(74), 194(75), 168(36), 154(37), 130(44), 116(39), 85(88), 71(100). *Exact Mass* calcd. for $C_{16}H_{19}NO$: 241.147; found: 241.147. *Anal.* calcd.: C 79.63, H 7.94, N 5.80; found: C 80.13, H 7.71, N 5.83.

exo-*3-(4-Cyanophenyl)*-exo-*2-methoxy*-endo-*3-methylnorbornane* ***(20)***

Infrared (PE-180) ν : 2960(vs), 2860(m), 2805(w), 2220(s), 1600(m), 1500(m), 1450(m), 1100(vs), 975(w), 835(s); ^{1}H nmr (361.08 MHz, $CDCl_3$) δ: 7.54–7.52 (d, 2H, J=8.6 Hz, H's adjacent to cyano), 7.47–7.44 (d, 2H, J=8.6 Hz, H's adjacent to alkyl), 3.22 (s, 3H, OCH_3), 3.05 (d, 1H, J=1.8 Hz, CH—OCH_3 ($H2_{endo}$)), 2.64 (d, 1H, 2.2 Hz, H4), 2.35(d, 1H, 4.2 Hz, H1), 1.75–1.65 (m, 3H), 1.45–1.57 (m, 1H), 1.30–1.35 (s, 4H, CH_3 and H7a), 1.15–1.25 (m, 1H); ^{1}H nmr (361.08 MHz, C_6D_6) δ: 7.17–7.14 (d, 2H, J=8.4 Hz, H's adjacent to cyano), 7.04–7.00 (d, 2H, J=8.4 Hz, H's adjacent to alkyl), 2.88 (s, 3H, OCH_3), 2.71 (d, 1H, J=1.4 Hz, CH—OCH_3 ($H2_{endo}$)), 2.23 (d, 1H, J=1.9 Hz, H4), 2.11 (d, 1H, J=4.4 Hz, H1), 1.64 (d, 1H, J=9.7 Hz, H7s), 1.50–1.40 (m, 2H, $H6_{exo}$ and $_{endo}$), 1.30–1.17 (m, 1H, $H5_{exo}$), 1.07–1.02 (s, and d, 4H, CH_3 and H7a), 0.95–0.85 (m, 1H, $H5_{endo}$); ^{13}C nmr (90.80 MHz, C_6D_6) δ: 150.74 (s, quaternary aromatic with alkyl sub), 130.53 (dd, 5 Hz, 165 Hz, carbon adjacent to cyano), 129.70 (dd, 5.6 Hz, 161.3 Hz, carbon adjacent to alkyl), 119.35 (s, CN), 109.54 (s, quaternary carbon with cyano substituent), 93.62 (d, 148.2 Hz, CH—OCH_3), 57.19 (q, 140.5 Hz, OCH_3), 51.34 (s, quaternary), 43.63 (d, 139.4 Hz, bridgehead), 41.07 (d, 141.7 Hz, bridgehead), 36.77 (tm, 134 Hz, bridging methylene), 27.87 (q, 126.0 Hz, 4.5 Hz), 25.05 (tm, 127.8 Hz, CH_2), 24.51 (tm, 128 Hz, CH_2); ms *m/z*: 241(74), 209(98), 194(100), 154(49), 130(49), 116(49), 85(83), 71(98). *Exact Mass* calcd. for $C_{16}H_{19}NO$: 241.147; found: 241.147. *Anal.* calcd.: C 79.63, H 7.94, N 5.80; found: C 79.98, H 7.76, N 5.80.

exo-*3-(4-Cyanophenyl)*-exo-*2-methoxy*-endo-*2-methylnorbornane* ***(22)***

Fraction no. 275–278 was rechromatographed to provide a pure sample of **22**, mp 74.8–76.2°C; ir (SP3-200) ν : 2960(vs), 2880(m), 2830(w), 2230(s), 1605(s), 1500(m), 1375(m), 1305(m), 1180(m), 1140(s), 1100(vs), 1075(vs), 1060(m), 835(m); ^{1}H nmr (361.08 MHz, $CDCl_3$) δ: 7.53–7.51 (d, 2H, J=8.2 Hz), 7.29–7.26 (d, 2H, J=8.7 Hz), 2.91 (s, 3H), 2.47 (s, 1H, $H3_{endo}$), 2.43 (s, 1H), 2.33 (s, 1H), 2.19 (dd, 1H, J=9.7 Hz, 1.6 Hz), 1.68–1.23 (m, 8H); ^{13}C nmr (90.80 MHz, $CDCl_3$) δ: 147.69 (s, quaternary aromatic with alkyl sub), 131.20 (d, 5.28 Hz, 160 Hz), 129.42 (d, 160 Hz), 119.43 (s), 109.12 (s), 84.69 (s), 61.67 (d, 129.2 Hz), 49.69 (q, 140.4 Hz), 42.83 (d, 140 Hz), 42.67 (d, 140 Hz), 36.63 (tm, 134.3 Hz), 31.10 (t, 130.5 Hz), 23.23 (t, 128.4 Hz), 19.39 (q, 4.0 Hz, 128.1 Hz); ms *m/z*: 241(100), 209(94), 181(72), 180(100), 140(60), 116(60), 85(82). *Anal.* calcd. for $C_{16}H_{19}NO$: C 79.63, H 7.94, N 5.80; found: C 79.43, H 7.96, N 5.63.

endo-*3-(4-Cyanophenyl)*-exo-*2-methoxy*-endo-*2-methylnorbornane* ***(23)***

Fraction no. 279–290 was rechromatographed to provide a pure sample of **23**; ir (SP3-200) ν : 2980(vs), 2880(m), 2840(w), 2240(s), 1610(m), 1510(m), 1380(m), 1140(m), 1100(vs), 1070(s), 920(m), 850(m); ^{1}H nmr(361.08 MHz, $CDCl_3$) δ: 7.56 (d, 2H, J=8.3 Hz), 7.36 (d, 2H, J=8.3 Hz), 3.24 (s, 3H), 3.11 (d, 1H, J=3.4 Hz), 2.59 (bs, 1H, H1), 2.51 (bs, 1H, H4), 1.91 (d, 1H, J=10.5 Hz), 1.61–1.40 (m, 3H), 1.38–1.31 (m, 2H), 1.01 (s, 3H); ^{13}C nmr (90.80 MHz, $CDCl_3$) δ: 146.22 (d, 7.5 Hz), 131.43 (dd, 165.9 Hz, 6.4 Hz), 129.81 (d, 5.5 Hz, 162.1 Hz), 119.16 (s), 109.42 (t), 83.50 (s), 58.83 (d, 126.9 Hz), 49.76 (q, 140.4 Hz), 44.47 (d, 140.1 Hz), 40.22 (d, 140.3 Hz), 37.14 (t, 134.1 Hz), 24.50 (t, 133.6 Hz), 21.43 (t, 135 Hz), 19.19 (q, 125.9 Hz); ms *m/z*: 241(5), 209(30), 181(100), 180(33), 173(6), 140(25), 116(15), 85(8). *Exact Mass* calcd. for $C_{16}H_{19}NO$: 241.147; found: 241.147.

Acknowledgments

This work was supported by grants from the Natural Sciences and Engineering Research Council of Canada and from the Petroleum Research Fund administered by the American Chemical Society. We thank Dr. D. L. Hooper at the Atlantic Regional Magnetic Resonance Centre at Dalhousie University for the high-field nmr spectra and for help in the preparation of the manuscript. We are also grateful to Mr. B. M. Millier for developing the data acquisition system interfaced with the gc/fid and to Dr. L. Ramaley for the exact mass determinations.

1. (*a*) A. Okamoto, M. S. Snow, and D. R. Arnold. Tetrahedron, **42**, 6175 (1986); (*b*) D. R. Arnold and S. A. Mines. Can. J. Chem. **65**, 2312 (1987); (*c*) D. R. Arnold, B. J. Fahie, L. J. Lamont, J. Wierzchowski, and K. M. Young. Can. J. Chem. **65**, 2734 (1987).
2. R. M. Borg, D. R. Arnold, and T. S. Cameron. Can. J. Chem. **62**, 1785 (1984).
3. (*a*) V. R. Rao and S. S. Hixson. J. Am. Chem. Soc. **101**, 6458 (1979); (*b*) K. Mizuno, J. Ogawa, and Y. Otsuji. Chem. Lett. 741 (1981).
4. (*a*) C. Pac, A. Nakasone, and H. Sakurai. J. Am. Chem. Soc. **99**, 5806 (1977); (*b*) J. Majima, C. Pac, A. Nakasone, and H. Sakurai. J. Am. Chem. Soc. **103**, 4499 (1981); (*c*) T. Asanuma, T. Gotoh, A. Tsuchida, M. Yamamoto, and Y. Nishijima. J. Chem. Soc. Chem. Commun. 485 (1977); (*d*) T. Majima, C. Pac, and H. Sakurai. Chem. Lett. 1133 (1979).
5. (*a*) H. Beens and A. Weller. Chem. Phys. Lett. **2**, 140 (1968); (*b*) D. Creed, R. A. Caldwell, H. Ohta, and D. C. DeMarco. J. Am. Chem. Soc. **99**, 277 (1977); (*c*) B. T. Lim, S. Okajima, A. K. Chandra, and E. C. Lim. J. Chem. Phys. **77**, 3902 (1982); (*d*) H. Horita, T. Otsubo, and S. Misumi. Chem. Lett. 1309 (1977); (*e*) T. Mimura, M. Itoh, T. Ohta, and T. Okamoto. Bull. Chem. Soc. Jpn. **50**, 1665 (1977); (*f*) C. R. Jones, B. J. Allman, A. Mooring, and B. Spahic. J. Am. Chem. Soc. **105**, 652 (1983); (g) G. C. Calhoun and G. B. Schuster. J. Am. Chem. Soc. **106**, 6870 (1984); (*h*) Tetrahedron Lett. **27**, 911 (1986); (*i*) J. Y. Lan and G. B. Schuster. Tetrahedron Lett. **27**, 4261 (1986).
6. (*a*) B. E. Goodson and G. B. Schuster. J. Am. Chem. Soc. **106**, 7254 (1984); (*b*) Tetrahedron Lett. **27**, 3123 (1986); (*c*) K. Mizuno, N. Ichinose, T. Tamai, and Y. Otsuji. Tetrahedron Lett. **26**, 5823 (1985); (*d*) K. Mizuno, N. Ichinose, and Y. Otsuji. Chem. Lett. 701 (1985); (*e*) R. J. Hartley and L. R. Faulkner. J. Am. Chem. Soc. **107**, 3436 (1985); (*f*) C. Pac, T. Fukunaga, Y. Go-an, T. Saae, and S. Yanagida. Photochem. Photobiol. A: Chem. **41**, 37 (1987).
7. C. K. Ingold. Structure and mechanism in organic chemistry: Cornell Univ. Press, Ithaca, NY. 1953. p. 646.
8. P. G. Gassman and K. J. Bottorff. Tetrahedron Lett. **28**, 5449 (1987).
9. S. Beckmann and R. Schaber. Liebigs Ann. Chem. **585**, 154 (1954).
10. R. A. Snow, C. R. Degenhardt, and L. A. Paquette. Tetrahedron Lett. 4447 (1976).
11. L. M. Jackman and S. Sternhell. Applications of nuclear magnetic resonance spectroscopy in organic chemistry. 2nd ed. Pergamon Press, New York, NY. 1969.
12. J. B. Stothers. Carbon-13 NMR spectroscopy. Academic Press, New York, NY. 1972.
13. (*a*) J. A. Hirsch. Top. Stereochem. **1**, 199 (1967); (*b*) E. L. Eliel and M. Manoharan. J. Org. Chem. **46**, 1959 (1981).
14. J. L. Marshall. Carbon–carbon and carbon–proton NMR coupling: Application to organic stereochemistry and conformational

Can. J. Chem. Downloaded from www.nrcresearchpress.com by 122.72.124.2 on 09/07/12
For personal use only.

analysis. Verlag Chemie International, Deerfield Beach, FL. 1983.
15. D. REHM and A. WELLER. Isr. J. Chem. **8**, 259 (1970).
16. T. SHONO, A. IKEDA, J. HAYASKI, and S. HAKOZAHI. J. Am. Chem. Soc. **97**, 4261 (1978).
17. P. G. GASSMAN, R. YAMAGUCHI, and G. F. KOSER. J. Org. Chem. **43**, 4392 (1978).
18. K. H. GRELLMANN, A. R. WATKINS, and A. WELLER. J. Phys. Chem. **76**, 469 (1972).
19. (*a*) A. TERAHARA, H. OHYA-NISHIGUCHI, N. HIROTA, and A. OKU. J. Phys. Chem. **90**, 1564 (1986); (*b*) O. W. HOWARTH and G. K. FRAENKEL. J. Chem. Phys. **52**, 6258 (1970); (*c*) T. BALLY, K. ROTH, and R. STRAUB. J. Am. Chem. Soc. **110**, 1639 (1988).
20. D. R. ARNOLD, P. C. WONG, A. J. MAROULIS, and T. S. CAMERON. Pure Appl. Chem. **52**, 2609 (1980).
21. (*a*) J. MATTAY. Angew. Chem. Int. Ed. Engl. **26**, 825 (1987); (*b*) J. MATTAY. Tetrahedron, **41**, 2393, 2405 (1987); (*c*) J. J. MCCULLOUGH, R. C. MILLER, D. FUNG, and W.-S. WU. J. Am. Chem. Soc. **97**, 5942 (1975); (*d*) J. J. McCullough and W. S. WU. J. Chem. Soc. Chem. Commun. 1136 (1972); (*e*) J. J. MCCULLOUGH, R. C. MILLER, and W.-S. WU. Can. J. Chem. **55**, 2909 (1977); (*f*) F. D. LEWIS and R. J. DEVOE. Tetrahedron, **38**, 1069 (1982); (*g*) K. MIZUNO, C. PAC, and H. SAKURAI. J. Am. Chem. Soc. **96**, 2993 (1974); (*h*) S. TAMADA, Y. KIMURA, and M. OHASHI. J. Chem. Soc. Chem. Commun. 667 (1977); (*i*) T. S. CANTRELL. J. Org. Chem. **42**, 4238 (1977); (*j*) N. C. YANG, B. KIM, W. CHIANG, and T. HAMADA. J. Chem. Soc. Chem. Commun. 729 (1976).
22. P. H. MAZZOCCHI and G. FRITZ. J. Am. Chem. Soc. **108**, 5362 (1986).
23. (*a*) S. L. MATTES and S. FARID. Org. Photochem. **6**, 233 (1983); (*b*) J. Am. Chem. Soc. **104**, 1454 (1982); (*c*) J. Am. Chem. Soc. **108**, 7356 (1986).
24. (*a*) O. HAMMERICH and V. D. PARKER. Adv. Phys. Org. Chem. **20**, 55 (1984); (*b*) V. D. PARKER. Acc. Chem. Res. **17**, 243 (1984); (*c*) A. J. BARD, A. LEDWITH, and H. SHINE. Adv. Phys. Org. Chem. **13**, 156 (1976).
25. (*a*) B. F. YATES, W. J. BOUMA, and L. RADOM. J. Am. Chem. Soc. **106**, 5805 (1984); (*b*) J. L. HOMES, F. P. LOSSING, J. K. TERLOUW, and P. C. BURGERS. Can. J. Chem. **61**, 2305 (1983); (*c*) K. L. BUSCH, W. B. NIXON, and M. M. BURSEY. J. Am. Chem. Soc. **100**, 1621 (1978); (*d*) B. T. GOLDING and L. RADOM. J. Am. Chem. Soc. **98**, 6331 (1976); (*e*) J. FASSEY and J.-Y. NEDELEC. Tetrahedron, **37**, 2967 (1981).
26. (*a*) R. C. FAHEY, M. W. MONAHAN, and C. A. MCPHERSON. J. Am. Chem. Soc. **92**, 2810 (1970); (*b*) R. C. FAHEY and M. W. MONAHAN. J. Am. Chem. Soc. **92**, 2816 (1970); (*c*) R. C. FAHEY and C. A. MCPHERSON. J. Am. Chem. Soc. **93**, 2445 (1971).
27. A. PROSS. J. Am. Chem. Soc. **108**, 3537 (1986).
28. (*a*) J. M. TEDDER and J. C. WALTON. Tetrahedron, **36**, 701 (1980); (*b*) J. M. TEDDER. Angew. Chem. Int. Ed. Engl. **21**, 401 (1982); (*c*) B. GIESE. Angew. Chem. Int. Ed. Engl. **22**, 53 (1983); (*d*) K. N. HOUK, M. N. PADDON-ROW, D. C. SPELLMEYER, N. G. RONDAN, and S. NAGASE. J. Org. Chem. **51**, 2874 (1986).
29. R. A. NEUNTEUFEL and D. R. ARNOLD. J. Am. Chem. Soc. **95**, 4080 (1973).
30. M. LAJUNEN and R. HIUKKA. J. Org. Chem. **51**, 1522 (1986).
31. P. S. SKELL and K. J. SHEA. *In* Free radicals. Vol. II. *Edited by* J. K. Kochi. Wiley-Interscience, New York, NY. 1973. Chap. 26.
32. P. J. KRUSIC and J. K. KOCHI. J. Am. Chem. Soc. **93**, 846 (1971).
33. (*a*) C. WALLING and W. THALER. J. Am. Chem. Soc. **83**, 3877 (1961); (*b*) C. WALLING and R. T. CLARK. J. Am. Chem. Soc. **96**, 4530 (1974); (*c*) R. T. CLARK. Ph.D. thesis, University of Utah, Salt Lake City, UT. 1973.
34. H. FISCHER. J. Am. Chem. Soc. **108**, 3925 (1986).
35. (*a*) K. L. KIM and J. F. BUNNETT. J. Am. Chem. Soc. **92**, 7463, 7464 (1970); (*b*) R. G. SCAMEHORN and J. F. BUNNETT. J. Org. Chem. **42**, 1449 (1977); (*c*) L. EBERSON and L. JOENSSON. J. Chem. Soc. Chem. Commun. 1187 (1980); (*d*) L. EBERSON, L. JOENSSON, and L. G. WISTRAND. Tetrahedron, **38**, 1087 (1982); (*e*) Z. V. TODRES. Tetrahedron, **41**, 2771 (1985).
36. (*a*) M. OHASHI, Y. TANAKA, and S. YAMADA. Tetrahedron Lett. 3629 (1977); (*b*) M. OHASHI, Y. TANAKA, and S. YAMADA. J. Chem. Soc. Chem. Commun. 800 (1976); (*c*) N. AL-JALAL and A. GILBERT. J. Chem. Res. (S), 266 (1983).
37. J. A. PERRY. Introduction to gas chromatography: History, principles and practice. Vol. 14. Chromatographic Science Series. Marcel Dekker, Inc., New York, NY. 1981.
38. R. S. NICHOLSON and I. SHAIN. Anal. Chem. **36**, 706 (1964); **37**, 178 (1965).
39. R. A. FINNEGAN and R. S. MCNEES. J. Org. Chem. **29**, 3234 (1964).
40. M. GOMBERG and W. E. BACHMANN. J. Am. Chem. Soc. **46**, 2339 (1924).
41. J. W. BRUNO, T. J. MARKS, and F. D. LEWIS. J. Am. Chem. Soc. **104**, 5580 (1982).

Can. J. Chem. Downloaded from www.nrcresearchpress.com by 122.72.124.2 on 09/07/12
For personal use only.

Hydrolysis of *p*-nitrophenyl alkanoates in aqueous organic solvent mixtures. The dispersal of aggregates and the uncoiling of *n*-alkyl chains

OSWALD S. TEE[1] AND JOHN A. ENOS[2]

Department of Chemistry, Sir George Williams Campus, Concordia University, Montréal, P.Q., Canada H3G 1M8

Received May 14, 1988

OSWALD S. TEE and JOHN A. ENOS. Can J. Chem. **66**, 3027 (1988).

Rate constants have been measured for the hydrolysis of six *p*-nitrophenyl alkanoates (C2, C4, C6, C8, C10, and C12) in basic aqueous media containing up to 80% (v/v) of the cosolvents: ethylene glycol (EG), 2-methoxyethanol (2ME), 1,2-dimethoxyethane (DME, glyme), bis(2-methoxyethyl) ether (diglyme), or DMSO. Addition of these cosolvents reduces and ultimately removes hydrophobic aggregation and coiling of the longer chain alkanoates, with the ether-type solvents (2ME, DME, and diglyme) being more efficient than EG or DMSO. Once the rate-lowering effects of aggregation and coiling have been removed by addition of a cosolvent, the rates of hydrolysis of the C4–C12 esters are all virtually the same, in a given medium. Thus, the apparent "steric size" of the C4–C12 (and even C16) acyl chains does not differ significantly in basic *p*-nitrophenyl ester hydrolysis. Addition of DMSO brings about rate increases that are greater in a carbonate buffer (pH 10.48) than those in 0.05 M NaOH solution, and these increases are larger than those observed for ethyl acetate in 0.05 M NaOH solution. None of the rate increases rise as quickly as the enhanced basicity of aqueous DMSO media.

OSWALD S. TEE et JOHN A. ENOS. Can J. Chem. **66**, 3027 (1988).

On a mesuré les constantes de vitesse pour l'hydrolyse de six alcanoates de *p*-nitrophényle (C2, C4, C6, C8, C10 et C12) en milieu aqueux basique contenant jusqu'à 80% (v/v) de cosolvants : l'éthylène glycol (EG), le méthoxy-2 éthanol (2ME), le diméthoxy-1,2 éthane (DME, glyme), l'éther bis-(méthoxy-2 éthyle) (diglyme), ou le DMSO. L'addition de ces cosolvants réduit et à la limite fait disparaître l'aggrégation hydrophobique et l'enroulement des plus longues chaînes d'alcanoates; les cosolvants de type éther (2ME, DME et diglyme) sont plus efficaces que le EG ou le DMSO. Dès que les cosolvants font disparaître l'aggrégation et l'enroulement, responsables de la diminution des vitesses, les vitesses d'hydrolyse des esters de C4–C12 sont à toutes fins pratiques identiques dans un milieu donné. Ainsi, il n'y a pas de différence significative dans la « dimension stérique » apparente des chaînes acyles de C4–C12 (et même C16) lors de l'hydrolyse basique des esters *p*-nitrophényles. L'addition de DMSO provoque des augmentations de vitesse qui sont supérieures dans un tampon de carbonate (pH 10,48) à celles que l'on note dans une solution de NaOH 0,05 M, et ces augmentations sont supérieures à celles observées pour l'acétate d'éthyle dans une solution de NaOH 0,05 M. Les vitesses n'augmentent pas aussi rapidement que l'accroissement de la basicité du milieu aqueux contenant du DMSO.

[Traduit par la revue]

A change of solvent may affect reaction rates in various ways, depending on the reaction and the species involved (1). Dramatic changes in rate may be seen with reactions that involve heterolytic steps, due to the large free energies for the transfer of ions from hydroxylic solvents to non-hydroxylic solvents (1, 2). Indeed, the effects of ion solvation very often obscure the contributions of more subtle types of solvent–solute interactions (1–3). Thus, when a solvent change involves water, alterations in hydrophobic interactions (4) may be masked by the larger effects of ion solvation (1, 2). On the other hand, in the absence of heterolysis, significant hydrophobic effects may be apparent. Thus, Diels–Alder reactions, which are not generally sensitive to solvent, show large rate enhancements on transfer of the reaction to water because of the tendency of the reactants to aggregate in aqueous solution (5).

Obviously, hydrophobic effects in a heterolytic process may be apparent in a series of substrates in which the reaction centre remains constant, but alkyl groups are varied. Thus, hydrophobic aggregation was established in a long-chain *p*-nitrophenyl alkanoate (PNPA) by comparing, in part, the rates of hydrolysis of the dodecanoate and acetate esters (6). Likewise, the reactions of PNPA esters with nucleophiles can be enhanced by hydrophobic attractions, the effect increasing with lengths of the alkyl chains of the reactants (7).

However, the use of PNPAs in such studies must be exercised carefully because of the aggregation of long-chain esters, even at spectrophotometric concentrations (8). Guthrie showed that the rates of hydrolysis of the C6, C8, and C10 esters are not very different *if* the substrate concentrations are kept low enough to ensure that the esters are in a monomeric state (8). Also, since the reactivities of the monomeric esters decrease (modestly) from C6 to C12, it was concluded that coiling of the alkyl chains occurs in water (8, 9).

Recently, Jiang and co-workers studied the effect of organic cosolvents on the hydrolysis of long-chain PNPAs (10). Their principal intent was to probe the aggregation and coiling of *n*-alkyl chains in an aqueous environment and they have presented a variety of evidence that coiling does occur with longer chains (>C12) (10, 11). Further, the effects of most cosolvents can be related to their lipophilicities (10*b*).

The present study extends the former studies to medium chain lengths (C2–C12), other solvent mixtures, and different reaction conditions.[3] It was designed to provide background for future work on solvent effects on the cleavage of esters by cyclodextrins. These complexing agents bind guests hydro-

[1]Author to whom correspondence may be addressed.

[2]Undergraduate participant.

[3]Jiang *et al.* (10*a*) measured rate constants for the hydrolysis of four PNPA esters (C2, C8, C12, and C16) in 30% (v/v) and 50% (v/v) aqueous organic solvents at 40°C (and *not* at 35°C, as given in the Experimental). A 0.02 M carbonate aqueous buffer (pH 9.65 in water) was *diluted* with organic cosolvent (details supplied by Prof. Jiang). Thus, their buffer concentrations were not constant and were lower than ours. The cosolvents used were *t*-BuOH, MeCOMe, MeCN, EtOH, dioxane, DME, DMF, 2ME, DMSO, and EG. In their most recent work (10*b*) the effects of initial ester concentration were extensively explored and the use of a "critical aggregate concentration" was introduced, similar to, but distinct from, a critical micelle concentration.

Can. J. Chem. Downloaded from www.nrcresearchpress.com by 122.72.124.2 on 09/07/12
For personal use only.

Can. J. Chem. Downloaded from www.nrcresearchpress.com by 122.72.124.2 on 09/07/12
For personal use only.

phobically (12, 13) and they exert varying effects on the cleavage of aryl alkanoates, depending on the aryl group (12, 14, 15) and the length of the alkyl chain (16, 17).[4] In one case a change from water to 60% aqueous DMSO enhances the efficiency of ester cleavage by β-cyclodextrin (18) but the origin and generality of this effect has not been established. Also, we are intrigued by the possibility that coiled *n*-alkyl chains may fit into cyclodextrin cavities better than extended ones.

Results and discussion

We have measured the rates of hydrolysis of *p*-nitrophenyl acetate (C2), butanoate (C4), hexanoate (C6), octanoate (C8), decanoate (C10), and, to a limited extent, the dodecanoate (C12) in basic aqueous media (a carbonate buffer or NaOH solution) containing varying amounts of the following organic cosolvents: dimethyl sulphoxide (DMSO), glyme (1,2-dimethoxyethane, DME), diglyme (bis(2-methoxyethyl) ether), 2-methoxyethanol (2ME), or ethylene glycol (EG).[3]

Table 1 presents rate constants for the hydrolysis of the acetate in a carbonate buffer and in dilute NaOH solution, as a function of DMSO content. For the reaction in buffer the rates rise more steeply than in simple base, but the origin of this difference is not clear. It may be due to the unknown effect of added DMSO on the bicarbonate–carbonate buffer system or to an enhanced contribution from buffer catalysis (7*a*).

In both buffer and NaOH solution the rate increases are quite modest when compared to the effects of DMSO and other dipolar aprotic solvents on simple nucleophilic substitutions (1–3). Likewise, the rate increases with added DMSO are not simply due to elevations of the activity of hydroxide ion since the basicity rises much more quickly (2, 19) than do the rate constants in Table 1. As discussed in detail by others (2, 20), the effects of DMSO on the rates of ester hydrolyses in base are composite; there are significant changes in the solvation energies of the ester *and* of the transition state, as well as of hydroxide ion. Moreover, the magnitude of the changes varies with the structure of the ester (20).

In Table 1 there is also a comparison with data for the hydrolysis of ethyl acetate in aqueous DMSO, taken from the literature (21). As seen there, in 50 mM NaOH the rate increases for *p*-nitrophenyl acetate are greater than for ethyl acetate. This difference may simply reflect solvation differences between the aryl and alkyl esters and their respective transition states (20) but it may also arise from the mechanistic difference between the two esters: with the phenyl ester the rate-limiting step is formation of the tetrahedral intermediate, whereas for the ethyl ester loss of the leaving group is rate limiting (4*a*, 22). Furthermore, there may be differential effects on leaving-group abilities since the effects of DMSO on the pK_as of water, ethanol, and phenols are not the same (ref. 1*a*, p. 300; ref. 2).

Table 2 shows the effects of different solvent mixtures on the cleavage of *p*-nitrophenyl acetate in 0.05 M NaOH. The organic solvents were chosen for their abilities to solvate cations well and their varied abilities to solvate anions. In all cases the rates of hydrolysis are elevated relative to wholly aqueous solution but the increases are quite modest. In the case of the two alcohols (EG and 2ME, both $pK_a = 14.8$ (22*b*)), there may be a contribution to ester cleavage from attack by their anions since the anion of 2ME is six times more reactive than OH^- towards *p*-nitrophenyl acetate in water (22*b*).[5] For our purposes, the data in Table 2 delineate the phenomenological effects of the cosolvents on PNPA ester hydrolysis, devoid of hydrophobic effects such as aggregation or coiling (8–11).

In Table 3 there is a comparison of rate constants for the hydrolysis of the C2, C4, C6, C8, and C10 PNPA esters in a carbonate buffer containing 0 and 40% DMSO. The rates for the C8 and C10 esters in water are somewhat lower, presumably due to coiling and the onset of solute aggregation (8–10).[6] In 40% DMSO both coiling *and* aggregation are removed, apparently, since the C4, C6, C8, and C10 esters all react at much the same rate. Similar behaviour has been observed for the C8 and C12 esters (but not the C16 ester) in 50% DMSO (10).

As a referee has noted, the acetate (C2) ester is more reactive than the others in any given medium (Table 3; see also Tables 4

TABLE 1. Pseudo first-order rate constants for the hydrolysis of *p*-nitrophenyl acetate in aqueous DMSO mixtures

DMSO		Buffer[a]		[NaOH] = 0.05 M		
% (v/v)	mol%[b]	k^{obs} (s^{-1})	rel *k*	k^{obs} (s^{-1})	rel *k*	(rel *k*, EtOAc)[c]
0	0	0.00851[d]	1	0.553	1	1
10	3.8	0.0103	1.21	0.590	1.07	1.12
20	6.2	0.0153	1.80	0.714	1.29	1.22
25		0.0196	2.30			
30		0.0238	2.80			
35		0.0334	3.92			
40	15.0	0.0402	4.72	1.42	2.57	1.39
45		0.0604	7.09			
50				2.03	3.67	
60	28.4	[e]		4.01	7.25	1.81
70	46.8			11.1	20.1	2.37
80	51.0			36.1	65.2	4.50

[a]In a 0.025 M carbonate buffer, having pH = 10.48 in water.
[b]From Tommila and Murto (19).
[c]From rate data of Tommila and Murto, also in 0.05 M NaOH (19).
[d]The value is elevated due to buffer effects (7*a*).
[e]The carbonate buffer is not soluble enough.

TABLE 2. Pseudo first-order rate constants for the hydrolysis of *p*-nitrophenyl acetate in aqueous organic solvent mixtures[a]

	k^{obs} (s^{-1})				
Cosolvent	%(v/v): 20	40	50	60	80
$HOCH_2CH_2OH$	2.54	2.05	1.95	1.85	1.50
$MeOCH_2CH_2OH$	1.66	2.64	3.01	3.66	4.55
$MeOCH_2CH_2OMe$	1.52	2.67	3.10	4.28	[b]
$(MeOCH_2CH_2)_2O$	0.730	0.861	1.78	1.06	[b]
DMSO	0.714	1.42	2.03	4.01	36.1

[a]At 25°C, in 0.05 M NaOH. $[Ester]_0 = 0.05$ mM. In wholly aqueous solution $k^{obs} = 0.553\ s^{-1}$ (Table 1).
[b]Solution slightly turbid due to the insolubility of NaOH.

[4]As well as the 4-carboxy-2-nitrophenyl alkanoates reported in ref. 17, we are also studying the cleavage of 2-carboxy-4-nitrophenyl esters, *m*-nitro and *p*-nitrophenyl alkanoates, and of 4-chloro and 5-chloro aspirin homologues (cf. ref. 15) by α-and β-cyclodextrin.

[5]Such a contribution has been posited for the cleavage of PNPAs in aqueous methanol mixtures (10*b*).

[6]With 4-carboxy-2-nitrophenyl alkanoates C4–C8 there is no diminution in the hydrolysis rates in water (17) nor with their 2-carboxy-4-nitrophenyl isomers (O. S. Tee and X.-X. Du. Unpublished work).

TABLE 3. Pseudo first-order rate constants for the hydrolysis of *p*-nitrophenyl alkanoates in water and in 40% (v/v) aqueous DMSO containing a carbonate buffer[a]

		$10^3 \cdot k^{obs}$ (s^{-1})	
Acyl group	% DMSO:	0	40
C2		8.51	40.2
C4		4.58	15.8
C6		4.70	16.5
C8		2.63	21.0
C10		0.86	20.4

[a]At 25°C, $[ester]_0$ = 0.01–0.05 mM, in a 0.025 M carbonate buffer (pH 10.48 in water).

TABLE 4. Pseudo first-order rate constants for the hydrolysis of *p*-nitrophenyl alkanoates in 50% (v/v) aqueous solvent mixtures[a]

	k^{obs} (s^{-1})				
Solvent	C4	C6	C8	C10	C12
EG	0.930	0.932	0.940	[b]	
2ME	1.23	1.20	1.18	1.22	
DME	1.19	1.11	1.06	1.05	1.02
Diglyme	0.688		0.594	0.611	0.588
DMSO	1.01	0.973	0.983	[b]	

[a]At 25°C, in 0.05 M NaOH. $[Ester]_0$ = 0.05 mM for the C4 and C6 esters; 0.01 mM for the C8, C10, and C12 esters. Analogous data for the C2 ester are presented in Table 2; it reacts 2–3 times faster in any given medium.

[b]Very small absorbance change due to biphasic kinetic behaviour (see Experimental).

and 5). Such behaviour has been observed by other workers (8–10), with other aryl esters (17),[4] and with alkyl esters (23). It is entirely consistent with known steric effects on the hydration of carbonyl groups (ref. 1*a*, p. 663), a reasonable model for hydrolysis via a tetrahedral intermediate (4*a*, 22).

The effects of 50% (v/v) of the cosolvents on the rates of hydrolysis of medium-chain PNPA esters in 0.05 M NaOH solution are presented in Table 4. Where measurable, the rate constants for the C4, C6, C8, C10, and C12 esters in a particular solvent mixture are almost exactly equal. Thus, as seen with the buffer/DMSO data in Table 3 and as anticipated from earlier work (8–11), the addition of large amounts of organic solvents removes the rate-lowering effects of aggregation and coiling. However, the abilities of the various cosolvents differ: the ether-type solvents (2ME, DME, and diglyme), which are, presumably, less hydrophilic than EG or DMSO, are more efficient at removing hydrophobic effects from the C10 and C12 esters (Table 4). Consistent with this view, Jiang *et al.* (10*b*) have recently found that the effects of most cosolvents are related to their lipophilicities.

These results concur with those of Jiang *et al.* (10), to the extent that there is overlap.[3] At the 50% (v/v) level, all of their solvents, except EG and DMSO, reduce hydrophobic interactions such that the C8, C12, and the C16 esters react at the same rates in a given water–solvent mixture (10). Thus, combining the results of our study and theirs, the rates of basic hydrolysis of PNPA esters with acyl chain lengths from C4 to C16 are all virtually the same in aqueous solvent mixtures with sufficient organic cosolvent to remove hydrophobic effects.

TABLE 5. Pseudo first-order rate constants for the hydrolysis of *p*-nitrophenyl alkanoates in aqueous DMSO mixtures[a]

	k^{obs} (s^{-1})				
% DMSO (v/v)	C2	C4	C6	C8	C10
0	0.553	0.339	0.370	0.253[b]	[c]
20	0.714	0.446	0.439	0.430[b]	[c]
40	1.42	0.716	0.677	0.663	0.374
60	4.01	1.82	1.92	1.86	1.67
80	36.1	15.7	14.2	14.8	12.1

[a]At 25°C, in 0.05 M NaOH. $[Ester]_0$ = 0.05 mM for the C2, C4, and C6 esters; 0.01 mM for the C8 and C10 esters.

[b]Small absorbance change, biphasic behaviour (see Experimental).

[c]Very small absorbance change.

Finally, we have studied the effects of different amounts of DMSO on the basic hydrolysis of the PNPAs (Table 5). Provided sufficient DMSO is added to disrupt aggregation and remove biphasic kinetic behaviour (see Experimental), the rate constants for all the esters beyond C2 approach the same value. The minimum amount of DMSO that is sufficient for this purpose increases with the length of the acyl chain, as one might expect.[7]

The present study supplements the findings of earlier workers (8–10) and consolidates their conclusions about the hydrophobic aggregation and coiling of *n*-alkanoate chains. It seems clear that beyond the acetate, and up to at least the C16 case (10), there is no significant increase in the apparent steric effect of the alkyl chain in basic PNPA ester hydrolysis *if* the effects of hydrophobic aggregation *and* coiling are removed by an organic cosolvent (Tables 3–5).[8]

Our results also provide a valuable base of information for further studies of the interactions of alkyl chains with cyclodextrins. Initial work on aryl alkanoate cleavage has already revealed some novel features (17).

Experimental

The PNPA esters were obtained from Sigma Chemical Co., except for the acetate; it was purchased from Aldrich, as were the organic solvents, which were of the highest grade available. Stock solutions (0.01 or 0.10 M) of the esters were prepared in HPLC grade methanol and a few microlitres of these were diluted to the desired strength with the chosen media. The final reacting solutions contained 0.2 or 0.5% (v/v) MeOH.

For the reactions in carbonate buffer, the solution was made from 5 mL of 0.5 M aqueous $NaHCO_3$ and 2 mL of 1.0 M aqueous NaOH to which were added water and DMSO in the amounts required to bring the total volume to 100 mL; the final buffer concentration was 0.025 M. In 100% water the buffer had a pH of 10.48. Reactions were initiated by adding a few microlitres of stock ester solution to a cuvette containing 2 mL of buffer, at 25°C in the cell-holder. Ester concentrations were 0.10–0.01 mM, depending on the chain length.

For the experiments in NaOH solutions, the reactant solutions were prepared just before use. Standard 1.0 M NaOH in water was diluted with water and organic solvent to give a 0.10 M solution in the desired mixture. If the base solution showed any turbidity due to the low solubility of NaOH it was not used. After mixing in the stopped-flow

[7]However, coiling persists with esters having very long chains, even in aqueous DMSO with a high DMSO content (10, 11).

[8]Recently, Menger and Venkataram (24) defined a scale of "Microscopic Hydrophobicity Parameters", based on the disruption of aggregates of the C12 ester by substituted trimethylammonium ions, and using hydrolysis kinetics as the probe.

Can. J. Chem. Downloaded from www.nrcresearchpress.com by 122.72.124.2 on 09/07/12
For personal use only.

apparatus, [NaOH] was 0.05 M and $[ester]_0$ was 0.05 mM or 0.01 mM (for the C8, C10, and C12 esters).

For the slow reactions a conventional uv–visible spectrophotometer was used; the fast reactions in NaOH solutions were followed using a stopped-flow apparatus interfaced to a microcomputer (15). In both cases, the appearance of the *p*-nitrophenolate ion was monitored at 405 nm and the observation cells were kept at 25.0±0.1°C. Whenever possible, the reactions were followed to 80–90% completion and an infinity reading was obtained after 10 half-lives. The pseudo first-order rate constants were evaluated in the normal way (15).

With longer esters, in solutions of high water content, biphasic kinetic behaviour was often observed, as reported by others (8, 10, 24). If the faster process, due to monomeric ester, was dominant, the initial absorbance change was followed as far as its first-order behaviour persisted, and an infinity value was estimated by the Kezdy–Swinbourne method (25). However, when the slower reaction of aggregated ester was more significant, so that the initial "fast" absorbance change was small, the kinetic run was abandoned. The problem of biphasic kinetics[9] diminishes and eventually disappears as more organic cosolvent is added (Tables 4 and 5) (8–10).

Acknowledgements

We thank the Natural Sciences and Engineering Research Council of Canada for an operating grant to O.S.T., and Mr. Bryan Takasaki for initial technical assistance. We are also grateful to Professor X.-K. Jiang (Shanghai Institute of Organic Chemistry) for clarifying experimental details and for bringing his most recent publications to our attention.

1. (*a*) T. H. Lowry and K. S. Richardson. Mechanism and theory in organic chemistry. 3rd. ed. Wiley, New York, NY. 1985, Chap. 4; (*b*) G. W. Klumpp. Reactivity in organic chemistry. 3rd ed. Wiley, New York, NY. 1982. pp. 186–203; (*c*) J. March. Advanced organic chemistry. 3rd ed. Wiley, New York, NY. 1985. p. 316ff; (*d*) A. J. Parker. Adv. Phys. Org. Chem. **5**, 173 (1967); Chem. Rev. **69**, 1 (1969).
2. E. Buncel and H. Wilson. Adv. Phys. Org. Chem. **14**, 133 (1977).
3. J. F. Coetzee and C. D. Ritchie. Solute–solvent interactions. Dekker, New York, NY. Vol. 1, 1969; Vol. 2, 1976.
4. (*a*) W. P. Jencks. Catalysis in chemistry and enzymology. McGraw-Hill, New York, NY. 1969; (*b*) A. Fehrst. Enzyme structure and mechanism. W. H. Freeman, New York, NY. 1977. Chap. 9; (*c*) M. J. Blandamer. Adv. Phys. Org. Chem. **14**, 203 (1977), particularly pp. 248–259; (*d*) C. Tanford. The hydrophobic effect. 2nd ed. Wiley, New York, NY. 1980.
5. D. C. Rideout and R. Breslow. J. Am. Chem. Soc. **102**, 7817 (1980).
6. F. M. Menger and C. E. Portnoy. J. Am. Chem. Soc. **90**, 1875 (1968).
7. (*a*) C. A. Blyth and J. R. Knowles. J. Am. Chem. Soc. **93**, 3017 (1971); **93**, 3021 (1971); (*b*) J. P. Guthrie and Y. Ueda. J. Chem. Soc. Chem. Commun. 991 (1974); (*c*) R. Hershfield and M. L. Bender. J. Am. Chem. Soc. **94**, 1376 (1972).
8. J. P. Guthrie. J. Chem. Soc. Chem. Commun. 897 (1972); Can. J. Chem. **51**, 3494 (1973).
9. Y. Murakami, Y. Aoyama, and M. Kida. J. Chem. Soc. Perkin Trans. 2, 1947 (1977).
10. (*a*) X.-K. Jiang, Y.-Z. Hui, and W.-Q. Fan. Acta Chim. Sin. **42**, 1276 (1984); Eng. Ed. 111 (1985); (*b*) X.-K. Jiang, X.-Y. Li, and B.-Z. Huang. Proc. Indian Acad. Sci. Chem. Sci. **98**, 409 (1987).
11. X.-K. Jiang, Y.-Z. Hui, and W.-Q. Fan. J. Am. Chem. Soc. **106**, 3839 (1984); **106**, 7202 (1984); W.-Q. Fan and X.-K. Jiang. J. Am. Chem. Soc. **107**, 7680 (1985); X.-K. Jiang, Y.-Z. Hui, and Z.-X. Fei. J. Am. Chem. Soc. **109**, 5862 (1987); X.-K. Jiang, X.-Y. Li, and B.-Z. Huang. Proc. Indian Acad. Sci. Chem. Sci. **98**, 423 (1987).
12. M. L. Bender and M. Komiyama. Cyclodextrin chemistry. Springer-Verlag, New York, NY. 1978.
13. (*a*) W. Saenger. Angew. Chem. Int. Ed. Engl. **19**, 344 (1980); Isr. J. Chem. **25**, 43 (1985); (*b*) J. L. Atwood, J. E. D. Davies, and D. D. MacNicol. Inclusion compounds. Vols. 2 and 3. Academic Press, London, England. 1984.
14. Y. Matsui, T. Nishiioka, and T. Fujita. Top. Curr. Chem. **128**, 61 (1985).
15. O. S. Tee and B. K. Takasaki. Can. J. Chem. **63**, 3540 (1985).
16. G. M. Bonora, R. Fornasier, P. Scrimin, and U. Tonellato. J. Chem. Soc. Perkin Trans. 2, 367 (1985).
17. O. S. Tee and X.-X. Du. J. Org. Chem. **51**, 1837 (1988).
18. B. Seigel and R. Breslow. J. Am. Chem. Soc. **97**, 6869 (1975).
19. R. A. Cox and R. Stewart. J. Am. Chem. Soc. **98**, 488 (1976).
20. P. Haberfield, J. Friedman, and M. F. Pinkston. J. Am. Chem. Soc. **94**, 71 (1972); M. Balakrishnan, G. V. Rae, and N. Venkatasubramananian. J. Chem. Soc. Perkin Trans. 2, 6 (1974).
21. E. Tommila and M.-L. Murto. Acta Chem. Scand. **17**, 1947 (1963).
22. (*a*) M. L. Bender. Mechanisms of homogeneous catalysis from protons to proteins. Wiley, New York, NY. 1971; (*b*) D. J. Hupe and W. P. Jencks. J. Am. Chem. Soc. **99**, 451 (1977).
23. R. W. Taft, Jr. *In* Steric effects in organic chemistry. *Edited by* M. S. Newman. Wiley, New York, NY. 1956. Chap. 13; L. P. Hammett. Physical organic chemistry. McGraw–Hill, New York, NY. 1940. pp. 211–212.
24. F. M. Menger and U. V. Venkataram. J. Am. Chem. Soc. **108**, 2980 (1986).
25. E. Swinbourne. Analysis of kinetic data. Nelson, London, England. 1971. pp. 78–84.

[9]The observation of biphasic kinetics emphasizes the danger inherent in basing studies solely on initial rate measurements, when the time course of the reaction and the maintenance of kinetic order to high completion have not been established.

Can. J. Chem. Downloaded from www.nrcresearchpress.com by 122.72.124.2 on 09/07/12
For personal use only.

Nature of the oil/water interface and equilibrium surfactant aggregates in systems exhibiting low tensions

ROBERT AVEYARD,[1] BERNARD P. BINKS,[2] THOMAS A. LAWLESS,[3] AND JEREMY MEAD[4]
School of Chemistry, University of Hull, Hull, England, HU6 7RX

Received January 18, 1988

ROBERT AVEYARD, BERNARD P. BINKS, THOMAS A. LAWLESS, and JEREMY MEAD. Can. J. Chem. **66**, 000 (1988).

Oil/water interfacial tensions are reported for systems containing pure alkane, aqueous sodium chloride, and a pure anionic surfactant, either Aerosol OT or *p*-dihexylbenzene sodium sulphonate (DHBS). Evidence is produced to support the claim that monolayer adsorption at the oil/water interface can produce ultralow tensions ($\sim 1\ \mu N\ m^{-1}$), and that the presence at the interface of a third, surfactant-rich phase is not necessary. The aggregation of DHBS and its distribution between oil and aqueous phases of various salinities have been investigated. It has been confirmed that the behaviour of DHBS in these respects is similar to that of Aerosol OT, as might be expected from its molecular structure. The sizes of microemulsion droplets in equilibrium with planar adsorbed monolayers have been determined, and related to the tensions of the plane oil/aqueous phase interfaces using simple existing theory.

ROBERT AVEYARD, BERNARD P. BINKS, THOMAS A. LAWLESS, et JEREMY MEAD. Can. J. Chem. **66**, 000 (1988).

On rapporte les tensions interfaciales des systèmes huile/eau contenant un alcane pur, une solution aqueuse de chlorure de sodium et un surfactant anionique à l'état pur: l'aérosol OT ou le *p*-dihexylbenzènesulphonate de sodium (DHBS). On fournit des preuves qui confirment le fait que l'adsorption monocouche à l'interface huile/eau peut produire des tensions très faibles ($\sim 1\ \mu N\ m^{-1}$), et qu'il n'est pas nécessaire d'avoir à l'interface une troisième phase riche en surfactant. On étudie l'aggrégation du DHBS et sa répartition entre l'huile et les phases aqueuses dont on fait varier la salinité. On confirme que dans ces conditions, compte tenu de sa structure moléculaire, le comportement du DHBS est analogue à celui de l'aérosol OT. On a déterminé la taille des gouttelettes de microémulsion en équilibre avec les monocouches planes adsorbées et on la relie aux tensions de l'interface plan huile/phase aqueuse en faisant appel à la théorie existante.

[Traduit par la revue]

A number of studies have been made in recent years of systems which contain oil, aqueous electrolyte, and surfactant and which exhibit ultralow oil/water interfacial tensions ($<10^{-2}$ mN m^{-1}), e.g. refs. 1–7. These tensions can often be made to pass through a minimum as the temperature, electrolyte concentration, nature of the oil phase, or the concentration of a further surface-active material (e.g. cosurfactant) is varied (6–8). The minimum in tension occurs under conditions around which a surfactant-rich third or "middle" phase (intermediate in density between oil and aqueous phases) is formed. The tension between the middle phase and one of the other two ("outer") phases is lower than the oil/water tension and appears to be associated with a thick interface (3). Our concern here however is with the nature of the oil/water interface and of the surfactant aggregates which form in oil or aqueous phases at equilibrium.

It has been claimed recently (9), on the basis of data obtained using sodium di-(2-ethylhexyl)sulphosuccinate (AOT) as the surfactant, that ultralow tensions are associated with the presence of a third phase between oil and aqueous phases, and that a single adsorbed monolayer of surfactant does not give rise to very low tensions. Other workers, however, (3, 4, 10) believe that tensions at least as low as 10^{-3} mN m^{-1} can be associated with monolayer adsorption. Here we present evidence supporting the latter view, based on measurements on systems containing alkane, aqueous NaCl, and AOT. We also present new data concerning interfacial tensions, and surfactant distribution and aggregation in systems containing *p*-dihexylbenzene sodium sulphonate (DHBS).

Experimental

Materials

The origins and purities of the samples of alkanes, AOT, water, and sodium chloride used have been described elsewhere (6, 7). The *p*-dihexylbenzene sulphonate preparation was carried out as follows. A Friedel–Crafts arylation of *n*-hexylbenzene with caproyl chloride and anhydrous aluminium chloride catalyst produced a mixture of the *o*- and (mainly) *p*-ketones. These were reduced to dihexylbenzene using amalgamated zinc and concentrated HCl. The product contained 12.5% *o*- and 82.5% *p*-isomers. This was sulphonated at 5°C using chlorosulphonic acid, and neutralised with sodium carbonate. The *o*-isomer carried over unsulphonated and was removed by preparative HPLC. The purified *p*-isomer was >99% pure by HPLC and TLC and the ^1H and ^{13}C nmr spectra were consistent with the required structure. The sulphonation stage and purification were carried out by Dr. N. Stewart at the BP Research Centre, Sunbury.

Methods

Interfacial tensions

Interfacial tensions were measured using a Krüss spinning-drop tensiometer (SITE 04) for low tensions and a Krüss K10 automatic tensiometer (with both Wilhelmy plate and du Nouy ring attachments) for higher tensions (>3 mN m^{-1}), as previously described (6, 7). In addition, low tensions were also determined by a surface laser light-scattering technique (11) at the BP Research Centre, Sunbury, in conjunction with Dr. A. R. Goodall. Aqueous and oil phases were all preequilibrated and pipetted into sample cells. All the interfaces were observed to be mirror-like with no visible sign of the presence of a third phase, even when a third phase was present prior to placing the two outer phases into the cell. Light from a He–Ne laser (λ = 632.8 nm) was passed through the oil phase and the scattered light, which was mixed with light reflected from the glass cell walls, was detected by a photomultiplier. The intensity correlation function was measured using a 64 channel multibit autocorrelator (Malvern Instruments) and analysed using a cumulant expansion that fitted the data to a single exponential (12). The necessary bulk viscosities and densities were measured with Ubbelohde viscometers and a Paar DMA 55 densimeter respectively.

[1]To whom all correspondence should be addressed.
[2]Present address: Laboratoire de Spectroscopie Hertzienne de l'E.N.S., 24, rue Lhomond, 75231 Paris Cedex 05, France.
[3]Present address: Atomic Energy Establishment, Winfrith, Dorchester, Dorset, DT2 8DH.
[4]Present address: Unilever Research, Colworth Laboratory, Bedford, MK44 1LQ.

Printed in Canada / Imprimé au Canada

Can. J. Chem. Downloaded from www.nrcresearchpress.com by 122.72.124.2 on 09/07/12
For personal use only.

Absorbance measurements

These were made on aqueous surfactant solutions in cuvettes with a path length of 1 cm, thermostatted at 25°C, using a Perkin Elmer 550 uv/visible spectrophotometer.

Determination of oil and surfactant concentration in aqueous phases

Analysis for AOT and heptane in aqueous phases in equilibrium with excess heptane phase was made using HPLC. A Waters Novapak C18 column was used in conjunction with a mobile phase containing 95% methanol and 5% water. The AOT concentrations were detected by absorbance at 220 nm (using a Waters 481 uv detector) and heptane concentrations by refractive index (Waters differential refractometer 401). Monitoring of the two detectors and evaluation of peak areas was performed using a Comus Instruments twin channel data acquisition and integration system.

Distribution of DHBS between aqueous and heptane phases

The distribution of DHBS was determined as a function of NaCl concentration in the aqueous phase. Aqueous solutions of NaCl were shaken with heptane; the surfactant was initially in either phase. The resulting emulsions were allowed to separate for several days in a thermostat and then samples were collected from both phases. Surfactant concentrations in each of the phases were determined by titration with hyamine (13). Concentrations of water in heptane were measured using a Baird and Tatlock automatic Karl-Fischer titrator (AF3). Hydrodynamic radii of the water droplets in the heptane phase were determined by photon correlation spectrometry (p.c.s.) as described elsewhere (6) using a Malvern Instruments PCS 100 spectrometer and a Malvern K7027 correlator.

Results and Discussion

Nature of interface exhibiting low tensions

As pointed out by Puig *et al.* (9) AOT at low concentrations in water first aggregates (at the cmc) to form micelles and then, at higher concentrations forms liquid crystals. In the presence of 0.017 and 0.068 *M* NaCl, however, only liquid crystallites appear to form and solutions are visibly turbid. In salt solutions the onset of turbidity occurs for the surfactant concentration at which the slope of the surface tension – ln (concentration) plot changes. Puig *et al.* claim that when a pure hydrocarbon is brought into contact with a turbid surfactant solution the dispersed crystallites in the vicinity of the interface take up oil and form a middle phase, the presence of which produces the observed ultralow interfacial tensions. It is observed that in the absence of salt the aqueous surfactant is optically clear and ultralow tensions are not given at the oil/water interface. Puig *et al.* further report that in systems containing salt there is a "precipitous" drop of interfacial tension (with octane as the oil phase) from about 1 mN m^{-1} at the surfactant solubility limit (~ 0.01 wt.% in 0.068 *M* NaCl) to around 10^{-3} mN m^{-1}, which they say is indicative of a change in the mechanism of tension lowering from monolayer adsorption (at high tension) to lowering by the third phase.

We have prepared aqueous solutions of AOT in 0.017 and 0.068 *M* NaCl by two different methods. In one case (method 1) surfactant was dissolved in water and NaCl added, and in the other (method 2) surfactant was dissolved in an aqueous solution of NaCl. Absorbance values at 600 nm of solutions in 0.068 *M* NaCl made up by each of the methods are shown in Fig. 1. Clearly the method of preparation has a profound effect on the size of the aggregates formed. Absorbances quoted by Puig *et al.* fall between the two extremes shown in Fig. 1. We have found that absorbances of solutions prepared by method 2 decrease over a period of several weeks and become equal to absorbances of similar solutions prepared by method 1.

In systems of current interest, however, the aqueous phases are brought into contact with hydrocarbon. Irrespective of how

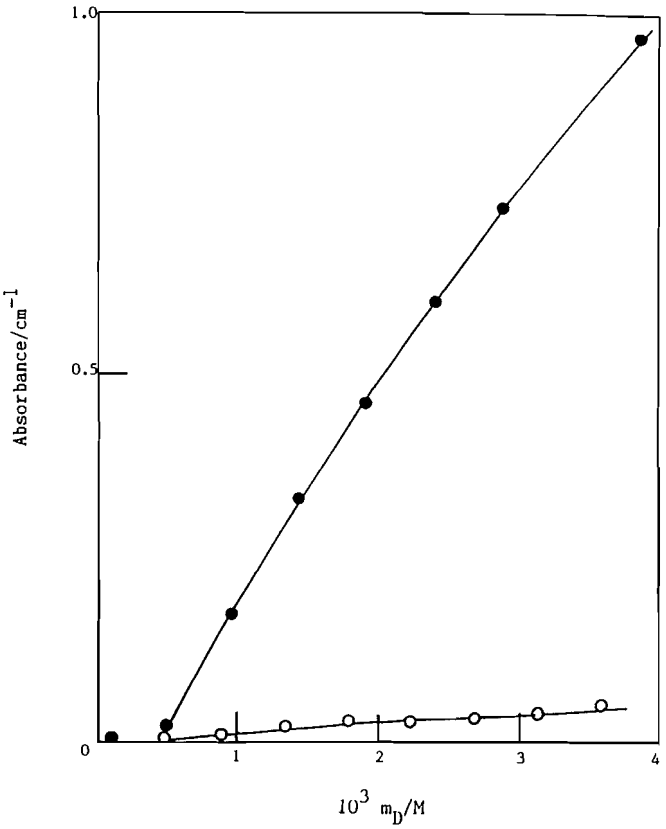

FIG. 1. Absorbance of solutions of AOT, concentration m_D, in 0.0684 *M* aqueous NaCl. Symbols ○ and ● are for solutions prepared by methods 1 and 2, respectively (see text).

the aqueous phases are prepared, when they are shaken with (say and equal volume of) heptane and left to separate, both phases are optically clear with absorbances of less than 0.003 cm^{-1}. Further, we show later (and elsewhere (6)) that the equilibrium aggregates in these systems are microemulsion droplets (oil-in-water or water-in-oil depending on salt concentration) and not liquid crystallites. The droplets themselves are not surface-active; it is found (10) that the oil/water tension is the same in systems containing droplets and those without droplets but otherwise identical.

With regard to the "precipitous" fall in tensions observed around the solubility limit, we have determined tensions in systems containing AOT with heptane and 0.0513 *M* NaCl where tensions range from 25 down to $<10^{-3}$ mN m^{-1}. These data are presented as log (tension, γ) versus ln (surfactant concentration, m_D) in Fig. 2*a*, and plotted in this fashion it does indeed appear that the tensions fall drastically just below the aggregation point. We have however obtained a number of tensions between 1 and 10^{-3} mN m^{-1} and when these data are plotted (as is usual) as γ versus ln m_D a straight line results (Fig. 2*b*). From the slope the area per AOT molecule, obtained by use of the appropriate form of the Gibbs equation (14) is found to be 0.66 ± 0.04 nm^2, in respectable agreement with the value of 0.72 ± 0.02 nm^2 obtained by fitting all the data from tensions of 25 mN m^{-1} down. These areas are consistent with monolayer adsorption down to tensions of at least 5×10^{-2} mN m^{-1}.

As mentioned, at and above the aggregation point the tension remains constant in the range of m_D investigated; we denote this tension γ_c. In Fig. 3 log γ_c is plotted against the salt concentration, m_s, for systems containing AOT, aqueous NaCl,

Can. J. Chem. Downloaded from www.nrcresearchpress.com by 122.72.124.2 on 09/07/12
For personal use only.

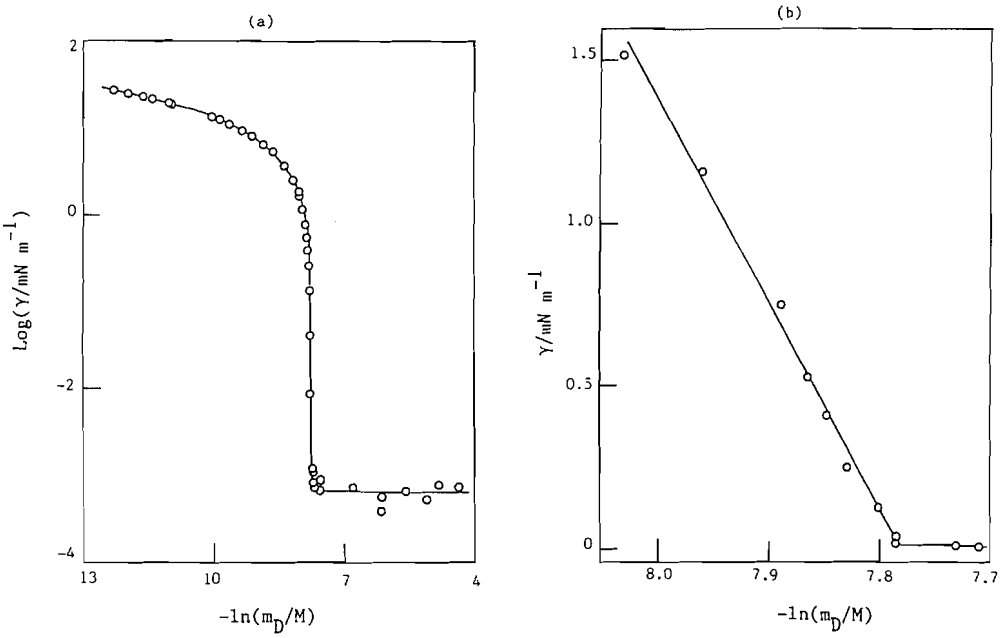

FIG. 2. Variation of tension with surfactant concentration, m_D, in systems containing AOT, heptane, and 0.0513 *M* NaCl at 25°C (*a*) log γ against ln m_D; (*b*) γ against ln m_D for tensions of 1.5 mN m^{-1} and lower.

and heptane at 25°C. Included in the plot are values obtained in three different ways. First, results are shown for systems in which pure heptane was introduced into aqueous surfactant (prepared by methods 1 and 2) which had not previously been equilibrated with the heptane. When $\gamma_c < 0.01$ mN m^{-1} a coating was initially observed to form around the oil drop; the coating was quite fluid and the drop shape responded rapidly to changes in the rotation frequency of the tensiometer capillary. Eventually, the coating became detached from the drop leaving an apparently clean oil/water interface; tensions recorded were those for such clean interfaces. We also prepared equilibrium systems in which heptane was shaken with aqueous NaCl (the AOT being initially in either phase) and left in a thermostat at 25°C to separate. For salt concentrations around 0.05 *M* a third "middle" phase was formed; in such cases the oil and aqueous phases only were removed and introduced into the tensiometer. The tensions so obtained were in close agreement with those for the non-equilibrated systems described above. Thirdly, tensions in equilibrated systems were determined by surface light scattering. The interfaces in these experiments were visibly very clean and completely mirror-like, as mentioned, and the tensions were in good accord with all the other tensions, as seen in Fig. 3.

We conclude from the foregoing that the oil/water interfaces exhibiting low tensions investigated here contain a saturated monolayer of surfactant and not a thick intervening layer of a third phase. It is relevant to note that if a third phase were present the measured tension would presumably be close to the sum of the tensions between the third phase (δ) and the oil phase (α), and the third phase and aqueous phase (β). For such systems at equilibrium Widom (15) has shown that

$$[1] \qquad \gamma_{\alpha\beta} \leq \gamma_{\alpha\delta} + \gamma_{\beta\delta}$$

Thus if the "interface" contained a third phase at equilibrium and the measured tension ($\gamma_{\alpha\delta} + \gamma_{\beta\delta}$) were ultralow it follows from eq. [2] that $\gamma_{\alpha\beta}$ must also be ultralow. Indeed, for systems consisting of sodium dodecyl sulphate, aqueous NaCl, toluene, and butanol Cazabat *et al.* (16) have shown that $\gamma_{\alpha\beta}$ is

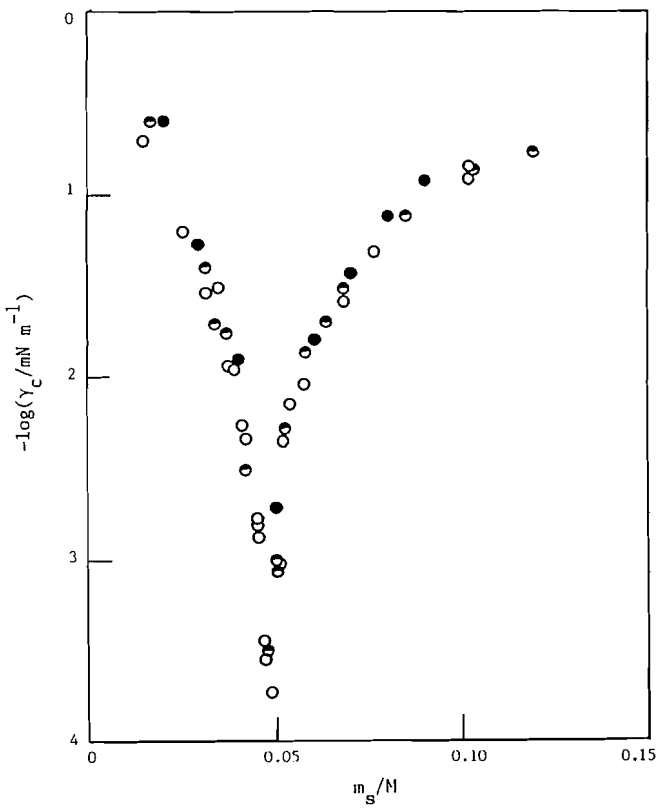

FIG. 3. Variation of γ_c with salt concentration in systems containing AOT, heptane, and aqueous NaCl at 25°C. Symbols ○ are for systems which were not pre-equilibrated prior to introduction into the spinning-drop tensiometer; symbols ◓ represent pre-equilibrated systems. Tensions from light scattering on pre-equilibrated systems are represented by ●.

effectively equal to the higher of $\gamma_{\alpha\delta}$ and $\gamma_{\beta\delta}$, the lower of the two being very low indeed.

We finally mention in this section the recent warnings of Good *et al.* (17, 18) that the spinning-drop method of measuring

Can. J. Chem. Downloaded from www.nrcresearchpress.com by 122.72.124.2 on 09/07/12
For personal use only.

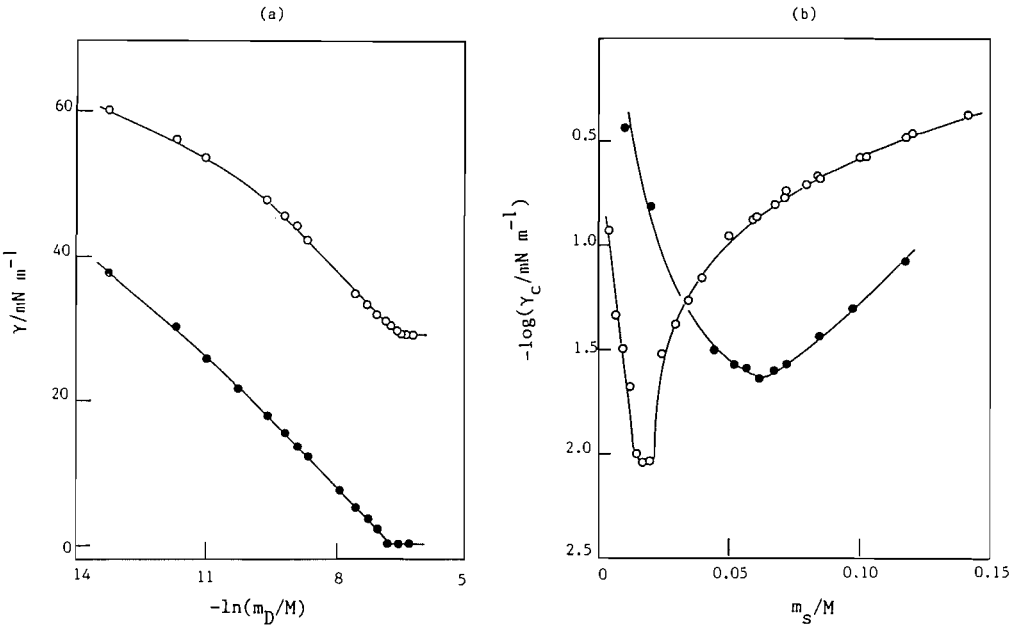

FIG. 4. Interfacial tensions in systems containing DHBS, alkane, and aqueous NaCl at 25°C. (*a*) Variation of γ with surfactant concentration for the air/0.0513 *M* NaCl solution interface (○), and for the heptane/0.0513 *M* NaCl interface (●). (*b*) Variation of γ_c with m_s for the aqueous solution/heptane interface (○) and aqueous solution/dodecane interface (●).

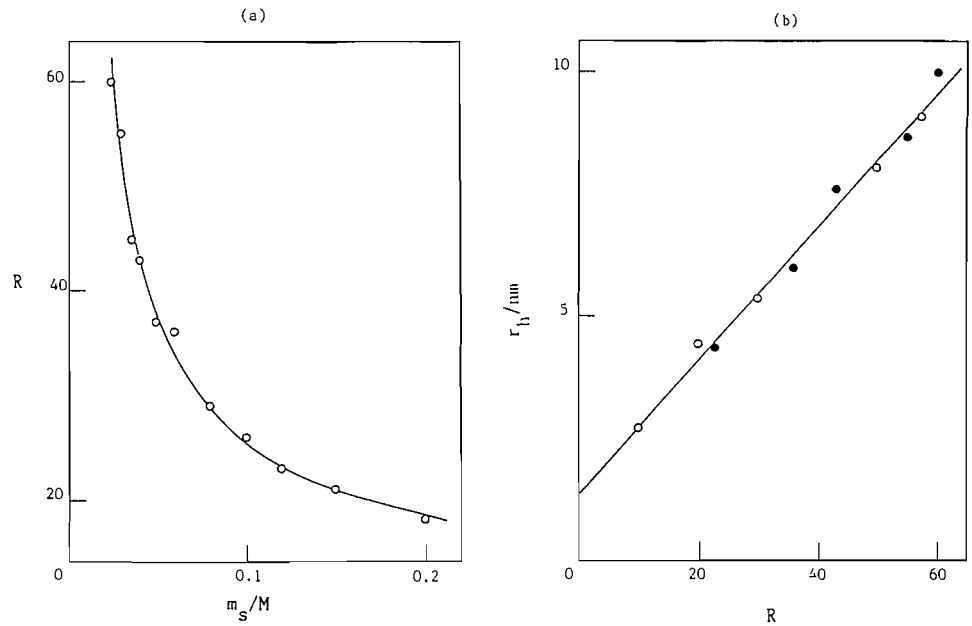

FIG. 5. Variation of R with salt concentration and hydrodynamic radius in systems containing aqueous NaCl, heptane, and DHBS at 25°C. (*a*) *R* as a function of m_s, (*b*) r_h as a function of *R*. Symbols ● are for w/o microemulsions in equilibrium with excess aqueous phase and ○ are for "made-up" w/o microemulsions (see text).

interfacial tensions may not be valid for systems, such as those of present interest, in which one phase is a microemulsion. It is clear however from the level of agreement between tensions measured using the spinning-drop method and those determined by surface light scattering (Fig. 3), that the spinning-drop tensiometer yields correct tensions for the systems studied here.

Tensions and distribution in systems containing DHBS

We briefly summarise here tension and surfactant distribution data for DHBS, which were obtained to confirm that the behaviour resembled that of AOT in otherwise similar systems. Both are twin-tailed anionic surfactants and the origins of the observed behaviour (for AOT) have already been discussed in terms of effective molecular geometry of the surfactant as well as in thermodynamic terms (6).

In Fig. 4*a* are shown tensions for the air/0.0513 *M* NaCl surface and heptane/0.0513 *M* NaCl interface as a function the DHBS concentration, m_D. Tensions become effectively constant (γ_c) at the aggregation point (cmc) and show no minima, consistent with the surfactant sample being free from surface-active impurities. The variation of γ_c for the heptane/solution interface with m_s is shown in Fig. 4*b*, together with results for

Can. J. Chem. Downloaded from www.nrcresearchpress.com by 122.72.124.2 on 09/07/12
For personal use only.

TABLE 1. Tensions, γ_c/mN m^{-1}, and hydrodynamic radii, r_h/nm, in systems containing heptane, aqueous NaCl (molarity m_s), and surfactant at 25°C*

o/w microemulsions containing AOT			w/o microemulsions containing AOT			w/o microemulsions containing DHBS		
m_s	γ_c	r_h	m_s	γ_c	r_h	m_s	γ_c	r_h
0.010	(0.533)	2.4	0.061	0.0178	17.6	0.025	0.030	10.0
0.015	(0.279)	2.3	0.066	0.0234	14.1	0.030	0.042	8.7
0.020	0.252	2.8	0.071	0.0316	13.2	0.040	0.069	7.6
0.025	(0.088)	5.8	0.081	0.0562	11.4	0.050	0.113	(6.4)
0.030	0.054	6.9	0.091	0.0708	9.5	0.060	0.132	6.0
0.035	(0.023)	6.9	0.101	0.0794	8.9	0.080	0.196	(5.3)
0.040	0.012	11.8	0.151	0.269	6.8	0.100	0.267	(4.9)
			0.200	0.468	6.0	0.120	0.344	4.3
			0.252	0.562	5.7	0.150	0.451	(4.2)
			0.300	0.660	5.2	0.200	0.61	(3.9)
			0.400	0.794	4.7			
			0.500	0.871	4.3			

*γ_c in parentheses are interpolated values from data in Fig. 3; r_h in parentheses are interpolated from data in Fig. 5*b*.

the dodecane/solution interface. The γ_c for both interfaces pass through a minimum; as with AOT the minimum for the longer chain alkane is broader, at a higher tension, and at a higher salt concentration ($m_s \sim 0.06$ *M*) than for the shorter chain alkane (where $m_s = 0.02$ *M*). This reflects the stronger penetration of heptane into the chain region of the surfactant monolayer (7). Both minima occur at a lower value of m_s than for AOT, probably resulting from the smaller head group size (relative to the chain cross-sectional area) of the DHBS (7).

We have confirmed that in the heptane + aqueous NaCl system, for $m_s < 0.02$ *M* DHBS resides totally in the aqueous phase and for $m_s > 0.02$ *M*, the surfactant transfers to the oil phase leaving the aqueous phase close to the cmc. A third, surfactant-rich phase forms in the region of $m_s = 0.02$ *M*.

Relation between aggregate size and γ_c

When surfactant is present in the heptane phase, water is also present. If we suppose that the surfactant aggregates consist of monodisperse water droplets (19), radius r_c, coated with an adsorbed monolayer of surfactant, then (6, 20, 21)

$$[2] \qquad r_c = 3R\nu_w A_D^{-1} = r_h - t$$

where $R = ([H_2O]/[DHBS])$ in oil, it being assumed that all the surfactant in the oil is adsorbed at droplet surfaces. The volume of a water molecule in a droplet is ν_w, and A_D is the area occupied by a surfactant molecule at the drop surface. The hydrodynamic radius, r_h, of the droplet differs from r_c by an amount t which is expected to be approximately equal to the surfactant molecular length.

It is seen from Fig. 5*a* that for $m_s > 0.02$ *M* in systems containing DHBS R (and hence by eq. [2] r_h) decrease as m_s increases and (Fig. 4*b*) γ_c increases.

The hydrodynamic radii, r_h, have been determined by photon correlation spectroscopy as described previously (6). According to eq. [2], if A_D and t are independent of drop size a plot of r_h versus R should be linear and A_D and t may be obtained from the slope and intercept, respectively. Such a plot is shown in Fig. 5*b* for the w/o microemulsions containing DHBS in equilibrium with excess aqueous phase (filled circles); some microemulsions of known R were also prepared by addition of water to a solution of DHBS in heptane. The r_h in such "made-up" systems

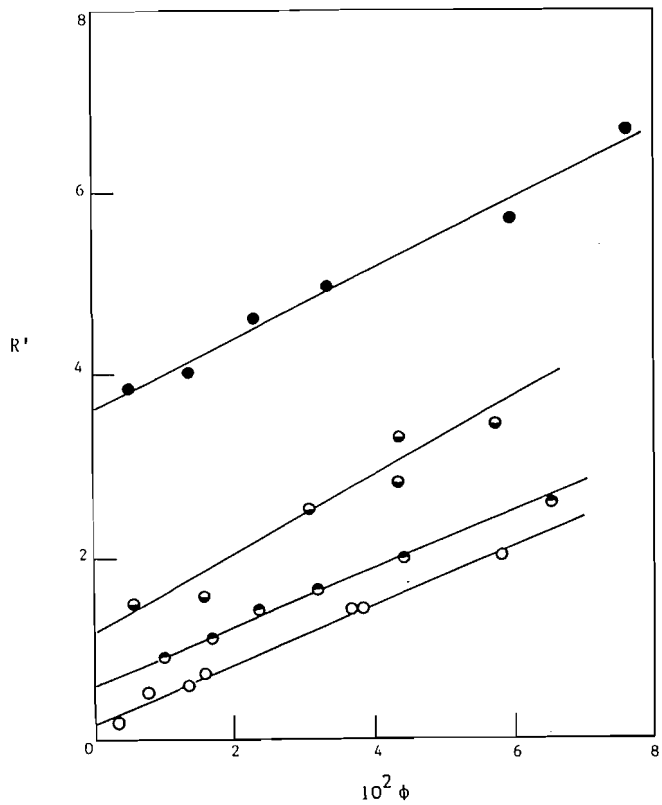

FIG. 6. Variation of R' with droplet volume fraction ϕ for heptane-in-aqueous NaCl microemulsions, stabilised by AOT, for various salt concentrations, m_s. Symbols ○, ◓, ◒, and ● are for m_s of, respectively, 0, 5, 15, and 25 *mM*.

are denoted by open circles. Values of A_D and t of 0.66 ± 0.02 nm^2 and 1.4 ± 0.1 nm respectively were obtained from the plot. The value of A_D is very similar to that, 0.69 nm^2, for the plane interface obtained from the linear part of the graph shown in Fig. 4*a* and the application of the Gibbs equation (14). We list values of r_h of water droplets in oil and corresponding values of γ_c for systems containing AOT and DHBS in Table 1.

In addition to characterising the w/o microemulsions we have

Can. J. Chem. Downloaded from www.nrcresearchpress.com by 122.72.124.2 on 09/07/12
For personal use only.

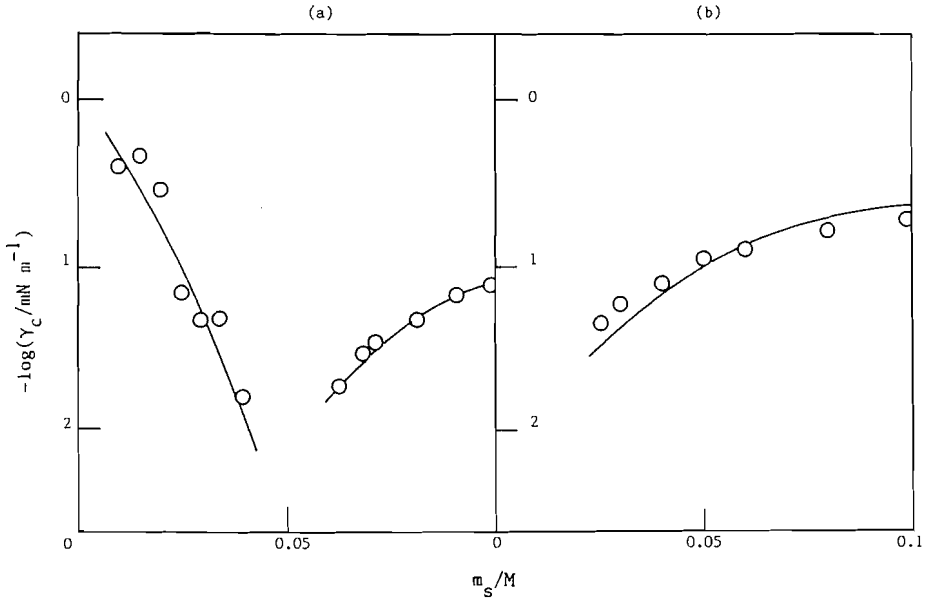

FIG. 7. Tensions γ_c calculated from eq. [3] (○). Full lines represent experimental data. (*a*) Systems containing AOT. Circles on left hand limb (low m_s) obtained using $K/kT = 0.29$, and those on right hand limb using $K/kT = 0.77$. (*b*) Systems containing DHBS. Circles obtained using $K/kT = 0.58$.

also estimated the sizes of oil droplets in heptane/aqueous NaCl microemulsions, stabilised by AOT, in equilibrium with excess heptane. For $m_s < 0.05$ *M* AOT aggregation occurs in the aqueous phase, the heptane phase remaining free of surfactant. Heptane and aqueous NaCl ($m_s < 0.05$ *M*) phases were allowed to come to equilibrium in the presence of AOT above its aggregation point at 25°C. The aqueous phases were then analysed for heptane and AOT using HPLC (see Experimental section). Knowing the cmc at various salt concentrations in the presence of heptane (6) the amount of surfactant at the droplet surfaces can be calculated. The ratios R' (= [heptane]/[aggregated AOT] in aqueous phase) were obtained as a function of AOT concentration (and hence of dispersed phase volume fraction, ϕ) for various salt concentrations. Sample plots of R' against ϕ are shown in Fig. 6. The dependence of R' on ϕ (which presumably arises largely as a result of repulsive forces between the electrical double layers surrounding the droplets) is striking, and in contrast to the situation for w/o microemulsions where R is effectively independent of droplet concentration (6). We will consider here values of R' at infinite dilution of droplets, i.e. the intercepts (R') of plots such as those in Fig. 6. By assuming a value for the area per surfactant molecule at the drop surface (A_D), the core radii have been calculated as $3R'_\infty v_h/A_D$ where v_h is the volume per heptane molecule in the droplets (0.24 nm^3). A value of A_D of 0.52 nm^2 has been used, being that obtained from aggregation numbers determined by a time-resolved fluorescence method (22). The droplet radii, r_h, and the tensions γ_c are listed in Table 1 along with the values for w/o microemulsion systems.

The value of γ_c depends in part on the tendency of the surfactant film to bend, as does the size of the droplets which are in equilibrium with the plane monolayer. It can be appreciated therefore that γ_c and drop radius are related (4). The bending tendency of the film may not be the only important factor in the determination of drop size, however (23, 24). The radius r is perturbed from its spontaneous value r_o as a result of the entropy of mixing the droplets with the medium. This entropy effect favours the formation of a greater number of droplets with radius $< r_o$. At higher volume fractions of dispersed phase, droplet interactions may also modify the drop size and γ_c. In the dilute systems studied here, however, these interactions may be assumed to be negligible. Also we find γ_c is within experimental error independent of surfactant concentration. A possible reason for this is that the effect of the dispersion entropy on γ_c is negligible in our systems. If so the major contributions to γ_c may well be due to the bending energy and we may write as an approximation (4)

$$[3] \qquad \gamma_c \simeq 2K/r^2$$

where K is a rigidity coefficient, having dimensions of energy (25). Equation [3] can only be expected to hold if the interfacial thickness (i.e. t) is considerably smaller than r. Our concern here is to test if the equation predicts the trends in γ_c with radius (and hence m_s) with a reasonable value of K.

Meunier (10) has measured K at plane interfaces directly, using ellipsometry, in systems containing SDS, butanol (cosurfactant), toluene, and aqueous NaCl. Although K is expected to depend on salt concentration Meunier reports that for salinities between 8 and 10%, where w/o microemulsions form with drop radii of between 12 and 18 nm, K/kT only varies between 0.5 and 0.75. We might therefore expect that in the region of the minimum in γ_c (where r is largest) eq. [3] will reasonably represent the trend in experimental data with a single value of K, at least for a given microemulsion type. In what follows we have used hydrodynamic radii in the calculations. The lines in Fig. 7*a* represent the experimental data for AOT (as shown in Fig. 3) and the points are calculated from eq. [3] using values of r_h in Table 1 with $K/kT = 0.29$ for systems containing o/w microemulsions and $k/kT = 0.77$ for those containing w/o microemulsions. Results for DHBS are shown in Fig. 7*b*; points were obtained using $K/kT = 0.58$. These values of K are similar to those quoted by Meunier (for monolayers of SDS + butanol) and agreement between experiment and theory is not unreasonable.

We finally mention that Fletcher (26) has recently considered tensions and drop sizes in more concentrated systems in which γ_c varies with droplet concentration.

Can. J. Chem. Downloaded from www.nrcresearchpress.com by 122.72.124.2 on 09/07/12
For personal use only.

Acknowledgements

The authors are indebted to BP Research (Sunbury) for provision of EMRA funds and a BP Research Studentship to carry out this research.

1. K. S. CHAN and D. O. SHAH. J. Dispersion Sci. Technol. **1**, 55 (1980).
2. E. I. FRANSES, Y. TALMON, L. E. SCRIVEN, H. T. DAVIS, and W. G. MILLER. J. Colloid Interface Sci. **86**, 449 (1982).
3. D. LANGEVIN. Mol. Cryst. Liq. Cryst. **138**, 259 (1986).
4. D. GUEST and D. LANGEVIN. J. Colloid Interface Sci. **112**, 208 (1986).
5. W. H. WADE, J. C. MORGAN, R. S. SCHECHTER, J. K. JACOBSON, and J. L. SALAGER. Soc. Pet. Eng. J. 242 (1978).
6. R. AVEYARD, B. P. BINKS, S. CLARK, and J. MEAD. J. Chem. Soc. Faraday Trans. I, **82**, 125 (1986).
7. R. AVEYARD, B. P. BINKS, and J. MEAD. J. Chem. Soc. Faraday Trans. I, **82**, 1755 (1986).
8. R. AVEYARD, B. P. BINKS, and J. MEAD. J. Chem. Soc. Faraday Trans. I, **84**, 675 (1988).
9. J. E. PUIG, M. T. MARES, W. G. MILLER, and E. I. FRANSES. Colloids Surf. **16**, 139 (1985).
10. J. MEUNIER. J. Phys. Lett. **46**, L-1005 (1985).
11. D. LANGEVIN, J. MEUNIER, and D. CHATENAY. *In* Surfactants in solution. Vol. 3. *Edited by* K. L. Mittal and B. Lindman. Plenum Press, New York. 1984. p. 1991.
12. M. W. KIM, J. S. HUANG, and J. BOCK. Soc. Pet. Eng. J. 203 (1984).
13. V. W. REID, G. F. LONGMAN, and E. HEINERTH. Tenside, **4**, 292 (1967).
14. E. MATIJEVIC and B. A. PETHICA. Trans. Faraday Soc. **54**, 1382 (1958).
15. B. WIDOM. J. Chem. Phys. **62**, 1332 (1975).
16. A. M. CAZABAT, D. LANGEVIN, J. MEUNIER, and A. POUCHELON. Adv. Colloid Interface Sci. **16**, 175 (1982).
17. R. J. GOOD, J. T. HO, G. E. BROERS, and X. YANG. J. Colloid Interface Sci. **107**, 290 (1985).
18. R. J. GOOD, C. J. VAN OSS, G. E. BROERS, and X. YANG. J. Colloid Interface Sci. **110**, 604 (1986).
19. J. TH. G. OVERBEEK. Proc. Kon. Ned. **B89**, 61 (1986).
20. J. D. NICHOLSON and J. H. R. CLARKE. *In* Surfactants in solution. Vol. 3. *Edited by* K. L. Mittal. Plenum Press, New York. 1984. p. 1663.
21. P. D. I. FLETCHER, M. F. GALAL, and B. H. ROBINSON. J. Chem. Soc. Faraday Trans. I, **80** 3307 (1984).
22. P. D. I. FLETCHER. J. Chem. Soc. Faraday Trans. I, **83**, 1493 (1987).
23. J. ISRAELACHVILI. *In* Surfactants in solution. Vol. 4. *Edited by* K. L. Mittal and P. Bothorel. Plenum Press, New York. 1986. p. 3.
24. C. A. MILLER. J. Dispersion Sci. Tech. **6**, 159 (1985).
25. D. LANGEVIN, D. GUEST, and J. MEUNIER. Colloids Surf. **19**, 159 (1986).
26. P. D. I. FLETCHER. Chem. Phys. Lett. **141**, 357 (1987).

Can. J. Chem. Downloaded from www.nrcresearchpress.com by 122.72.124.2 on 09/07/12
For personal use only.

Solvent effect on the solution, ionization, and structure of aminosulfonic acids

ROBERT L. BENOIT, DANIELLE BOULET, AND MONIQUE FRÉCHETTE
Département de Chimie, Université de Montréal, C.P. 6128, Succ. A. Montréal (Qué.), Canada H3C 3J7

Received May 31, 1988

ROBERT L. BENOIT, DANIELLE BOULET, and MONIQUE FRÉCHETTE. Can. J. Chem. **66**, 3038 (1988).

We have determined thermodynamic parameters for the solution and ionization in dimethylsulfoxide and water of four aminosulfonic acids: $NH_2(CH_2)_nSO_3H$ with $n = 0$, 1, and 2, and $NH_2C_6H_4SO_3H$. Potentiometric and calorimetric methods were used. The solubilities of the four acids in Me_2SO are either nearly equal to or lower than in water, but the enthalpies of solution are 15–40 kJ mol^{-1} more exothermic in Me_2SO. The three aliphatic acids are much weaker ($2.1 \leq \Delta pK_a \leq 5.5$) in Me_2SO than in water and their heats of ionization are some 30 kJ mol^{-1} more endothermic in Me_2SO. The discussion of our results is based on comparisons with corresponding data for related substituted amines and ammonium ions, and sulfonic acids and sulfonate ions. We conclude that the four aminosulfonic acids are mostly present as zwitterions in Me_2SO just as in water.

ROBERT L. BENOIT, DANIELLE BOULET et MONIQUE FRÉCHETTE. Can. J. Chem. **66**, 3038 (1988).

On a déterminé des paramètres thermodynamiques pour la dissolution et l'ionisation dans le diméthylsulfoxyde et l'eau de quatre acides aminosulfoniques: $NH_2(CH_2)_nSO_3H$ avec $n = 0$, 1 et 2 et $NH_2C_6H_4SO_3H$. On a utilisé des méthodes potentiométriques et calorimétriques. Les solubilités des quatre acides dans le Me_2SO sont soit voisines soit plus faibles que dans l'eau, mais les enthalpies de solution sont de 15–40 kJ mol^{-1} plus exothermiques dans le Me_2SO. Les trois acides aliphatiques sont nettement plus faibles ($2{,}1 \leq \Delta pK_a \leq 5{,}5$) dans le Me_2SO que dans l'eau et leurs chaleurs d'ionisation sont quelques 30 kJ mol^{-1} plus endothermiques dans le Me_2SO. La discussion de nos résultats est basée sur des comparaisons avec des données correspondantes pour des composés analogues, des amines et ions ammonium substitués et des acides sulfoniques et ions sulfonates. On conclut que les quatre acides aminosulfoniques sont essentiellement présents sous forme de zwitterions dans le Me_2SO comme dans l'eau.

Can. J. Chem. Downloaded from www.nrcresearchpress.com by 122.72.124.2 on 09/07/12
For personal use only.

Introduction

Aminosulfonic acids are bifunctional compounds of general interest because of their structural relation to amino acids. In addition, sulfamic acid, H_2NSO_3H, and particularly some of its N-substituted derivatives (cyclamates) (1) as well as biologically important taurine, $H_2NCH_2CH_2SO_3H$, are of specific interest.

The aminosulfonic (AS) acids are generally regarded as being zwitterionic in the solid state and in aqueous solution (1, 2), just like the amino acids, but little is known about the structure of the acids in non-aqueous solvents (3). In dimethylsulfoxide (Me_2SO) for example, the non-ionic form may prevail since it has been shown that addition of Me_2SO to aqueous solutions of some amino acids shifts the tautomeric equilibrium towards the non-ionic form (4, 5). Some meagre literature data on sulfamic acid in Me_2SO might also be taken as pointing in this direction. First, the pK_a of H_2NSO_3H increases from 1.0 in water (2) to a reported 6.5 in Me_2SO (6). Considering that related CH_3SO_3H, a strong acid in water, has a 1.7 pK_a in Me_2SO, the above 6.5 pK_a value is not incompatible with a non-ionic structure for H_2NSO_3H in Me_2SO. Second, the large pK_a increase from 1.0 to 6.5 for H_2NSO_3H when passing from water to Me_2SO would seem to be at odds with an $^+H_3NSO_3^-$ structure in Me_2SO since the pK_a of substituted ammonium ions ^+H_3NR are nearly the same in both solvents (7). Finally, the very high solubility of H_2NSO_3H both in water and Me_2SO, when contrasted with the high solubility of glycine $H_2NCH_2CO_2H$ in water and near insolubility in Me_2SO, might indicate that Me_2SO solvates the zwitterionic structure $^+H_3NCH_2CO_2^-$ poorly and would then favour a non-ionic structure for H_2NSO_3H.

It would be interesting to ascertain whether AS acids are zwitterionic or not in Me_2SO, and this can be achieved by comparing the solution and ionization thermodynamics of AS acids and simpler analogues in Me_2SO and water. Data for the solution and ionization in water of sulfamic acid, taurine, and sulfanilic acid being already available (2), we have obtained data for aminomethanesulfonic acid in water and for the four AS acids in Me_2SO.

[1]LiA being a strong electrolyte its ΔH_s should be approximately linear in square root of concentration, but because of the low concentrations used this effect is within our experimental errors.

Experimental

Materials

Sulfamic acid (Baker) was dried under vacuum at room temperature for 3.5 h. Aminomethanesulfonic acid and taurine (both from Aldrich) were recrystallized from ethanol–water mixtures. After washing with cold ethanol, the acids were dried at 80°C for 2.5 h. Sulfanilic acid (Fisher) was recrystallized from water and dried under vacuum at 80°C for 2.5 h. Titrations of the acids, in water or Me_2SO, with standard aqueous NaOH indicated a purity of 99.3 ± 0.3% for NH_2SO_3H, 100.0 ± 0.5% for $NH_2CH_2SO_3H$, 100.2 ± 0.3% for $NH_2CH_2SO_3H$, and 99.1 ± 0.2% for $NH_2C_6H_4SO_3H$.

Lithium salts of the acids were prepared. Lithium sulfamate was first obtained by adding solid sulfamic acid to an aqueous 0.1 *M* Li_2CO_3 solution to reach pH 2.98. The salt was recrystallized from methanol–chloroform mixtures and then dried under vacuum at 80°C for 1.5 h. Acidimetric titrations in Me_2SO showed a purity of 98.8 ± 0.2%. Lithium taurinate and lithium sulfanilate were prepared by adding the solid acids to aqueous 0.1 *M* LiOH solutions to reach pH 11.40 and 8.36, respectively. The salts were washed with ethanol and dried under vacuum at 70°C for 3 h. Acidimetric titrations of $NH_2CH_2CH_2SO_3Li$ in water showed a purity of 100.0 ± 0.2%. Purity of $NH_2C_6H_4SO_3Li$ was checked by comparing its UV spectra in aqueous 0.1 *M* HCl and NaOH with the corresponding spectra of pure sulfanilic acid. Results indicated a purity of 88.2 ± 0.7% and Karl Fischer titrations showed that the materials contained 11.9 ± 0.8% water.

Dimethylsulfoxide (Anachemia) was used as received. Trifluoromethanesulfonic acid (Aldrich) was distilled under reduced pressure.

Potentiometry

Potentiometric titrations of Me_2SO solution of the lithium salts (6×10^{-3} to 3×10^{-2} *M*) with standard 0.1 *M* CF_3SO_3H in Me_2SO were carried out at 25.0 ± 0.1°C in a thermostated cell as previously described (8). The glass electrode was calibrated before each run with standard 0.1 *M* CF_3SO_3H to give a 59 ±1 mV slope ($r = 0.9998$) in a

TABLE 1. Solubilities and solution enthalpies of aminosulfonic acids at 25°C (M = mol L^{-1}, m = molality)

Acid	S (M)		ΔH_s^0 (kJ mol^{-1})	
	H_2O	Me_2SO	H_2O	Me_2SO
NH_2SO_3H	2.4 (m)[a]	5.3 (m)	+18.4[b]	−24.2±0.1
$NH_2CH_2SO_3H$	0.22±0.01	0.18±0.01	+25.2±0.4	−4.2±0.8
$NH_2CH_2CH_2SO_3H$	0.84 (m)[b]	0.024±0.001	+24.2[b]	+8.6±0.4
$NH_2C_6H_4SO_3H$	0.083±0.001	0.0084±0.0003	+15.1[b]	−11.2±0.7
$NH_3^+CH_2CO_2^-$ (glycine)	3.3 (m)[c]	Insoluble	+15.0[d]	—

[a]Reference 23.
[b]Reference 2.
[c]Reference 24.
[d]Reference 19.

Can. J. Chem. Downloaded from www.nrcresearchpress.com by 122.72.124.2 on 09/07/12
For personal use only.

ΔE vs. pH plot. Since we were not successful in preparing pure $NH_2CH_2SO_3Li$, we proceeded differently to study the ionization of aminomethanesulfonic acid. First, we carried out a titration of a Me_2SO solution of 0.05 M lithium taurinate with a Me_2SO solution of 0.02 M aminomethanesulfonic acid. Second, we added standard 0.1 M CF_3SO_3H to a Me_2SO solution containing both lithium taurinate and aminomethanesulfonic acid (6×10^{-3} to 1×10^{-2} M).

Calorimetry

The calorimetric work involved the determination at 25.00 ± 0.01°C of heats of solution, heats of protonation of the salts, and heats of deprotonation of the acids using an LKB model 8725-2 isoperibol calorimeter as previously described (8).

The heats of solution of sulfamic acid, lithium sulfamate, and lithium sulfanilate, in Me_2SO and water, as well as those of lithium taurinate and aminosulfonic acid in water, were measured. We also determined the heats of protonation of lithium sulfamate, lithium sulfanilate, and lithium taurinate in 0.1 M CF_3SO_3H in Me_2SO. We obtained as well the heats of deprotonation of sulfamic acid, aminomethanesulfonic acid, taurine, and sulfanilic acid in Me_2SO containing 0.02 M or 0.05 M of a strong base (tetramethylguanidine or lithium taurinate) as well as the heat of solution of aminomethanesulfonic acid in 0.01–0.10 M aqueous NaOH.

The heats of mixing of 0.5–1.0 mL of a standard 0.2 M lithium taurinate solution in Me_2SO with 100 mL of 0.1 M CF_3SO_3H in Me_2SO and with 100 mL of 0.007 M sulfanilic acid in Me_2SO were measured, as well as the heat of mixing of 0.5–1.0 mL of a standard 0.11 M aminomethanesulfonic acid in Me_2SO with 100 mL of 0.05 M lithium taurinate in Me_2SO.

The amounts of acid or salt dissolved or reacted (1×10^{-4} to 6×10^{-3} mol) were deduced from the weights of the glass ampoules. For each determination, three to six separate experiments were made at different concentrations.

Results

Solubilities and solution enthalpies

The solubilities of the AS acids in Me_2SO and water are given in Table 1 and are expressed in molarity (mol L^{-1}) or molality. The heats of solution, Q, of the AS acids and their lithium salts were plotted against the number of moles dissolved. The plots were linear[1] and the least-squares slopes gave the molar enthalpies of solution ΔH_s; in water (ΔH_{sw}) and in Me_2SO (ΔH_{ss}).

[1] $HA(c) = HA(s \text{ or } w)$ $\quad \Delta H_{ss}(HA) \text{ or } \Delta H_{sw}(HA)$

[2] $LiA(c) = A^-(s \text{ or } w) + Li^+(s \text{ or } w)$ $\quad \Delta H_{ss}(LiA) \text{ or } \Delta H_{sw}(LiA)$

Because aminomethanesulfonic acid, taurine, and sulfanilic acid dissolved too slowly in Me_2SO, their heats of solution were obtained indirectly by dissolving the acids in Me_2SO solution of a strong base, B (tetramethylguanidine or lithium taurinate), according to

[3] $HA(c) + B(s) = A^-(s) + BH^+(s)$

We then substracted from these values the enthalpies of protonation of B (−85.8 ± 0.4 kJ mol^{-1} and −67.8 ± 0.7 kJ mol^{-1} for tetramethylguanidine (9) and lithium taurinate, respectively), to obtain the enthalpies for

[4] $HA(c) = H^+(s) + A^-(s)$

Finally, we subtracted from these latter values the enthalpies of ionization for

[5] $HA(s) = H^+(s) + A^-(s)$

to give the enthalpies of solution ΔH_{ss} (eq. [1]).

The heat of solution of lithium taurinate in Me_2SO was also obtained indirectly by subtracting the heat of protonation of the taurinate ion from the heat of protonation of the solid salt in Me_2SO solutions of 0.1 M CF_3SO_3H.

No effect of concentration on ΔH_{ss} or ΔH_{sw} was observed, so that the ΔH_s values were taken as being equal to ΔH_s^0. Our ΔH_s^0 values with their standard deviations are given in Tables 1 and 2.

TABLE 2. Solution enthalpies of lithium aminosulfonates at 25°C

Lithium salt	ΔH_s^0 (kJ mol^{-1})	
	H_2O	Me_2SO
NH_2SO_3Li	+0.79±0.07	−17.5±0.3
$NH_2CH_2CH_2SO_3Li$	−0.55±0.07	−4.3±0.8
$NH_2C_6H_4SO_3Li \cdot 1.34H_2O$	+15.8±0.2	−14.3±0.6

Ionization constants

The ionization constants of the AS acids in Me_2SO were obtained from the potentiometric neutralization data using a program previously described (8). Corrections were made for the effect of ionic strength which varied between 0.005 and 0.025 M. Our pK_a values are given in Tables 3 and 4 together with literature data.

Ionization enthalpies

The heats of protonation of solid lithium sulfamate and lithium sulfanilate in 0.1 M CF_3SO_3H in Me_2SO were plotted against the number of moles dissolved. The least-squares slopes

TABLE 3. Constants and enthalpies of ionization of aliphatic aminosulfonic acids and related compounds at 25°C

Compound	pK_a		ΔH_i^0 (kJ mol^{-1})	
	H_2O	Me_2SO	H_2O	Me_2SO
NH_2SO_3H	1.01[a] (1.04–1.19)[b]	6.56±0.06 (6.5)[b]	+1.0[a]	+30.9±0.9
$NH_2CH_2SO_3H$	5.75[c]	9.12±0.13	+26.0±0.7	+56.7±1.2
$NH_2CH_2CH_2SO_3H$	9.06[a]	11.18±0.06	+41.8[a]	+67.8±0.7
$NH_3^+CH_2CH_3$	10.68[d]	10.90[d]	+57.4[d]	+80.0[d]
CH_3SO_3H	−1.9[e]	1.70[g]	—	≈0[h]
$NH_3^+CH_2CO_2^-$	9.78[f]	—	+44.3[f]	—

[a]Reference 2.
[b]Reference 1.
[c]Reference 25.
[d]Reference 7.
[e]Reference 26.
[f]Reference 27.
[g]Reference 28 and 29.
[h]Unpublished result.

of the linear plots gave the protonation enthalpies of the salts, ΔH_{ps} (LiA), according to [6].

[6] $LiA(c) + H^+(s) = HA(s) + Li^+(s)$

By combining ΔH_{ps}(LiA) with ΔH_{ss}^0(LiA) (eq. [2]), we obtained the ionization enthalpies of the corresponding acids in Me_2SO, ΔH_{is}(HA) according to [5] with

[7] $\Delta H_{is}(HA) = \Delta H_s^0(LiA) - \Delta H_{ps}(LiA)$

The ΔH_{is} of sulfanilic acid was also obtained from the heat of mixing of an Me_2SO solution of lithium taurinate with an Me_2SO solution of sulfanilic acid. These heats were first corrected for the slight ionization of the sulfanilic acid in Me_2SO. Then we subtracted the heat of protonation of the taurinate ion to yield values of $\Delta H_{is} = +23.0 \pm 0.5$ kJ mol^{-1} in fair agreement with the previous value $+24.0 \pm 0.8$.

The ionization enthalpy of taurine in Me_2SO was determined first by dissolving sulfamic acid in an excess of lithium taurinate in Me_2SO. From the resulting heats of reaction, which correspond to eq. [3], we subtracted the heats of solution and of ionization of sulfamic acid to yield the ionization enthalpy of taurine. Second, we added aliquots of a standard Me_2SO solution of lithium taurinate to an excess of 0.1 *M* CF_3SO_3H in Me_2SO. The heat of dilution of the taurinate solution being negligible, we obtained the heat of ionization of taurine directly. The plot of the two series of heats of ionization against the number of moles of taurine ionized was linear and the slope gave the ΔH_{is} of taurine in Table 3.

For aminomethanesulfonic acid, we determined the heats of mixing of aliquots of a standard Me_2SO solution of the acid in an excess of 0.05 *M* lithium taurinate in Me_2SO. The correction for the dilution of the aminomethanesulfonic acid solution was negligible and we subtracted the heat of protonation of the taurinate ion to obtain the ΔH_{is} of aminomethanesulfonic acid.

The heat of ionization of aminomethanesulfonic acid in water was obtained from the heat of solution of the acid in aqueous 0.01 to 0.1 *M* NaOH according to

[8] $HA(c) + OH^-(w) = A^-(w) + H_2O$

Then we added to this value the heat of ionization of water ($\Delta H_i(H_2O) = +55.8$ kJ mol^{-1} (10)) and subtracted the heat of solution of aminomethanesulfonic acid in water. The ionization enthalpy of aminomethanesulfonic acid in water, ΔH_{iw}, was obtained from the slope of the linear plot of the heats against the number of moles of acid ionized.

TABLE 4. Constants and enthalpies of ionization of sulfanilic acid and related compounds at 25°C

Compound	pK_a		ΔH_i^0 (kJ mol^{-1})	
	H_2O	Me_2SO	H_2O	Me_2SO
$NH_2C_6H_4SO_3H$	3.23[a]	3.76±0.03	+17.6[a]	+23.6±0.8
$NH_3^+C_6H_5$	4.60[b]	3.72[b]	+30.1[b]	+30.8[b]
$NH_3^+C_6H_4Cl$	4.05[c]	2.69±0.05[e] (2.66)[c]	+27.9[f]	+24.9±0.5[e]
$C_6H_5SO_3H$	Strong[d]	Strong[e]	—	—

[a]Reference 2.
[b]Reference 30.
[c]Reference 31.
[d]Reference 26.
[e]Unpublished result.
[f]Reference 13.

All our ΔH_i(HA) values are taken to be equal to ΔH_i^0(HA) because no concentration dependence was observed in the concentration range used and because no effect of the ionic strength between 0 and 0.1 *M* was observed for sulfanilic acid and taurine. A small ionic strength effect was observed for aminomethanesulfonic acid, but it was within our experimental error. Our ΔH_i^0 values are given in Tables 3 and 4 with their standard deviations and some literature data.

Enthalpies of transfer from water to Me_2SO

The enthalpies of transfer of the acids from water to Me_2SO, ΔH_{ws}^0(HA), correspond to

[9] $HA(w) = HA(s)$

These values were calculated from

[10] $\Delta H_{ws}^0(HA) = \Delta H_{ss}^0(HA) - \Delta H_{sw}^0(HA)$

The enthalpies of transfer of A^- from water to Me_2SO, $\Delta H_{ws}^0(A^-)$, were calculated by means by eq. [11]:

[11] $\Delta H_{ws}^0(A^-) = \Delta H_{is}^0(HA) - \Delta H_{iw}^0(HA) + \Delta H_{ws}^0(HA) - \Delta H_{ws}^0(H^+)$

Can. J. Chem. Downloaded from www.nrcresearchpress.com by 122.72.124.2 on 09/07/12
For personal use only.

TABLE 5. Enthalpies of transfer from water to Me_2SO of aliphatic aminosulfonates, aminosulfonic acids, and related compounds at 25°C

Compound	ΔH^0_{ws} (kJ mol^{-1})
$NH_3^+SO_3^-$	−42.6
$NH_2SO_3^-$	+12.8
$NH_3^+CH_2SO_3^-$	−29.4
$NH_2CH_2SO_3^-$	+26.8
$NH_3^+CH_2CH_2SO_3^-$	−15.6
$NH_2CH_2CH_2SO_3^-$	+35.9
$NH_3^+CH_3$	−29.7[a]
NH_2CH_3	+18.4[a]
$CH_3SO_3^-$	+28.5[b]

[a]Reference 7.
[b]Unpublished result.

TABLE 6. Enthalpies of transfer from water to Me_2SO of sulfanilic acid, sulfanilate ion, and related compounds at 25°C

	ΔH^0_{ws} (kJ mol^{-1})
$NH_3^+C_6H_4SO_3^-$	−26.3
$NH_2C_6H_4SO_3^-$	+5.2
$NH_3^+C_6H_5$	−37.4[a]
$NH_2C_6H_5$	−11.2[a]
$C_6H_5SO_3^-$	+16.4[b]
C_6H_6	0.3[c]

[a]Reference 30.
[b]Unpublished result.
[c]Reference 32.

The value of $\Delta H^0_{ws}(H^+)$, −25.5 kJ mol^{-1}, is based on the tetraphenylarsonium tetraphenylborate (tatb) extrathermodynamic assumption (11).

The $\Delta H^0_{ws}(A^-)$ values calculated from eq. [11] can be compared to those obtained from data on the solution of lithium salts and eq. [12].

[12] $\Delta H^0_{ws}(A^-) = \Delta H^0_{ss}(LiA) - \Delta H^0_{sw}(LiA) - \Delta H^0_{ws}(Li^+)$

$\Delta H^0_{ss}(LiA)$ and $\Delta H^0_{sw}(LiA)$ are given in Table 2 and $\Delta H^0_{ws}(Li^+)$, the enthalpy of transfer of Li^+, is taken as −27.4 kJ mol^{-1} (12). The values thus obtained for ΔH^0_{sw} of $NH_2SO_3^-$ and $NH_2CH_2CH_2SO_3^-$ are 3.7 kJ mol^{-1} less endothermic than the values obtained through eq. [11]. This difference is not unreasonable considering our experimental errors and those involved in the calculation of ΔH^0_{sw} for H^+ and Li^+ (12). For the sake of consistency we have kept the values obtained through eq. [11]. These ΔH^0_{ws} values for A^- are given in Tables 5 and 6 together with those for HA and related compounds.

Discussion

Solution data

If we first consider the solution in Me_2SO of the three aliphatic acids, the data in Table 1 show a solubility decrease from sulfamic acid to aminomethanesulfonic acid and taurine. The corresponding free energies of solution can only be estimated since there are no data on the activity coefficients of the acids. Such approximate free energies when combined with the solution enthalpies in Table 1 show that the decrease in the acids solubility with the increasing length of the carbon chain is the result of a complex balance between the enthalpy terms becoming less negative and favorable, and entropy terms becoming less negative and unfavorable. The low solubility of sulfanilic acid in Me_2SO is mainly due to a large negative entropy of solution opposing a favorable enthalpy term.

Clearly, in water there is no definite trend in either the solubility or the solution enthalpy data. Since the enthalpy terms are large and positive, there is a large and positive and favorable entropy of solution, thus contrasting the negative entropy of solution in Me_2SO.

It is not possible to gain from our solution data any information on the structure of the AS acids in Me_2SO because of the absence of data in Me_2SO on known zwitterionic compounds, sulfonic acids and substituted ammonium ions as well as on the sublimation of the AS acids.

Ionization data

While we have not tabulated the ionization entropies ΔS^0_{is} and ΔS^0_{iw} which can be calculated from the ionization data in Table 3, it is worth noting that there is a good pK_{aw} (or ΔG^0_{iw}) − ΔH^0_{iw} linear correlation for the three aliphatic AS acids in water so that ΔS^0_{iw} is also linearly related to ΔG^0_{iw} and ΔH^0_{iw}. The corresponding correlation is only fair in Me_2SO. Such linear correlations are often observed for the ionization of structurally related acids (13).

The pK_a data in Tables 3 and 4 show that both in Me_2SO and water the three aliphatic AS acids become progressively weaker when the carbon chain is lengthened, while the ionization becomes more endothermic. The aliphatic acids, but not sulfanilic acid, are also considerably weaker in Me_2SO than in water. Interestingly, the pK_{as} of taurine in Me_2SO, 11.1, is very close to that of ethylammonium ion $NH_3^+CH_2CH_3$, 10.9, and far from that of methanesulfonic acid CH_3SO_3H, 1.7. We can therefore conclude that taurine must be present in Me_2SO as the zwitterion $NH_3^+CH_2CH_2SO_3^-$ and not as non-ionic $NH_2CH_2CH_2SO_3H$. Clearly the electron-attracting effect of the SO_3^- group, 2 carbons away from $—NH_3^+$, must be small, while the electron-donating effect of the $—NH_2$ group, two carbons away from $—SO_3H$, could certainly not account for a pK increase from 1.7 to 11.1.

An argument similar to the previous one can be used to assign the structure $NH_3^+CH_2SO_3^-$ to aminomethanesulfonic acid in Me_2SO. However, for sulfamic acid it is becoming difficult to choose between NH_3^+ SO_3^- and NH_2SO_3H on the strength of a comparison between its pK_{as} 6.30, and those of CH_3SO_3H, 1.70, and $NH_3^+CH_3$, 11.0. Fortunately, the comparison of pK_a of the three aliphatic AS acids in Me_2SO and water helps us to decide on the structure of sulfamic acid in Me_2SO. The plot in Fig. 1 of pK_{as} against pK_{aw} for the three acids gives a good straight line $pK_{as} = (0.57 \pm 0.02)pK_{aw} + (5.95 \pm 0.15)$ (r = 0.9991). This linear correlation makes us conclude that since the AS acids are zwitterionic in water, they must also be so in Me_2SO, the linear correlation reflecting the effect on $—NH_3^+$ of stronger electron-withdrawing substituents when going from $CH_2CH_2SO_3^-$ to $CH_2SO_3^-$ and SO_3^-. It is interesting to note that the slope of the straight line, which is the ratio of the Hammett ρ values for the $—NH_3^+$ series in Me_2SO and water, is unexpectedly lower than 1. For the uncharged acids, substituted benzoic acids (14) and phenols (15) the ρ_s/ρ_w values are, respectively, 2.5 and 2.0, and for substituted anilinium ions ρ_s/ρ_w 1.6. The lower value of ρ_s/ρ_w for the aminosulfonic acids reflects in a complex manner differences in ΔG^0_{ws} of both the zwitterionic acids and the anions. The linear correlation between ΔH^0_{is} and ΔH^0_{iw} (Fig. 1) is not as good as the pK_{as}–

Can. J. Chem. Downloaded from www.nrcresearchpress.com by 122.72.124.2 on 09/07/12
For personal use only.

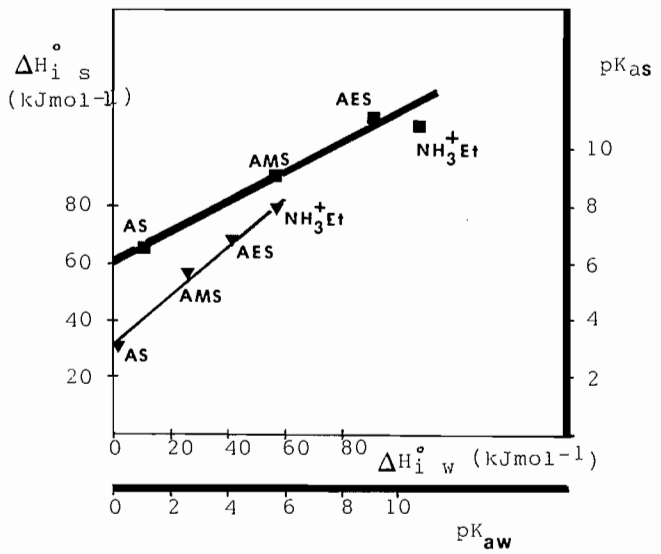

FIG. 1. Correlation between ionization parameters of aminosulfonic acids in Me_2SO and water (AS: sulfamic acid; AMS: aminomethanesulfonic acid; AES: taurine; NH_3^+Et, ethylammonium ion).

pK_{aw} correlation but the point corresponding to $NH_3^+CH_2CH_3$ falls on the line.

As for sulfanilic acid, it comes as no surprise that the ionization data do not follow the correlation for the aliphatic AS acids. Comparing the ionization data in Me_2SO for $NH_2C_6H_4SO_3H$ with those for related $NH_3^+C_6H_5$, $NH_3^+C_6H_4Cl$, and $C_6H_5SO_3H$ (Table 4) strongly suggests that sulfanilic acid is also zwitterionic in Me_2SO. It is worth noting that the $—SO_3^-$ group which is more electron-attracting than —Cl in water, on the basis of pK_{aw} (see also ref. 16) in Table 4, would have a value near 0 in Me_2SO clearly demonstrating the influence of the solvent on a negatively charged substituent.

Transfer parameters

The transfer free energies and enthalpies of HA and A^- are useful parameters to rationalize the change of pK_a (free energies) and enthalpies of ionization when passing from water to Me_2SO. The values can also be compared to thermodynamic functions of transfer of other single ions (11).

The values of the energies of transfer $\Delta G^0_{ws}(HA)$, which are approximate in the absence of activity coefficients data on the AS acids in Me_2SO, are either near 0 or slightly positive (+10 kJ mol^{-1}). Then, the values of $\Delta G^0_{ws}(A^-)$ calculated from an equation similar to [11] are between +40 and +50 kJ mol^{-1} for aliphatic A^- and +25 kJ mol^{-1} for $NH_2C_6H_4SO_3^-$. We conclude from these values that the pK_a increase of the aliphatic AS acids, when passing from water to Me_2SO, is mainly due to a destabilization of A^- in Me_2SO opposed by stabilization of H^+ ($\Delta G^0_{ws}(H^+) = -19.0$ kJ mol^- (11)) and a slight destabilization of $HA^{\pm}$ in Me_2SO. For sulfanilic acid, the much smaller increase of pK_a on going from water to Me_2SO is a consequence of the comparatively smaller destabilization in Me_2SO of $NH_2C_6H_4SO_3^-$ (ΔG^0_{ws} = +25 kJ mol^{-1} instead of +40 – +50 kJ mol^{-1} for aliphatic A^-). This is in line with the known stronger affinity of Me_2SO for aromatic compounds over aliphatic compounds. Our approximate values of $\Delta G^0_{ws}(A^-)$ are comparable to reported values for negative ions such as Cl^- (+40 kJ mol^{-1}), and $CH_3CO_2^-$ (+50 kJ mol^{-1}) (17) which are poorly solvated in Me_2SO because this solvent has no hydrogen bond donor properties.

Turning now to the enthalpies of transfer ΔH^0_{ws} listed in Tables 5 and 6, the data show a strong enthalpy stabilization of aliphatic AS acids in Me_2SO, which however, becomes less pronounced when the length of the carbon chain increases. This stabilization may be attributed to the substituted $—NH_3^+$ structure and the much greater H-bond acceptor properties of Me_2SO compared with water (cf. Taft–Kamlet solvatochromic parameter β: 0.76, Me_2SO; 0.17, H_2O). Conversely, the anions A^- are enthalpy destabilized in Me_2SO and increasingly so from $NH_2SO_3^-$ (+12.8) to $NH_2CH_2SO_3^-$ (+26.8) and $NH_2CH_2CH_2SO_3^-$ (+35.9 kJ mol^{-1}). Although Krishnan and Friedman (18) found small (0.1 kJ mol^{-1}) additive ΔH^0_{ws} terms for the water —Me_2SO transfer of $—CH_2—$ groups in amines and alcohols series, that was only for long carbon chains, if not, terminal polar group interfered as would be the case with our series $NH_2(CH_2)_nSO_3^-$. Attempts were made to determine whether other group additivity rules could be used to estimate ΔH^0_{ws}. Thus, when we add the ΔH^0_{ws} contribution of $CH_3SO_3^-$ (+28.5 kJ mol^{-1}) to those of NH_2CH_3 (+18.4) and $NH_3^+CH_3$ (−29.7), we might obtain approximate values for $NH_2CH_2CH_2SO_3^-$ (+47) and $NH_3^+CH_2CH_2SO_3^-$ (−1). These calculated ΔH^0_{ws} can be contrasted with the experimental values of +35.9 and −15.6 kJ mol^{-1} for $NH_2CH_2SO_3^-$ and $NH_2CH_2CH_2SO_3H$, respectively. The differences between the two sets of values, 13 ± 2 kJ mol^{-1}, could be roughly accounted for by noting that the calculated values include the transfer of two terminal $—CH_3$ groups (ΔH^0_{ws} ($—CH_3$) ~ +5 kJ mol^{-1}) which should be replaced by $—CH_2—$ group with smaller transfer contributions (18). At any rate, and however crude these comparisons may be, they serve to confirm our contention that the three aliphatic AS acids are zwitterionic in Me_2SO. Proceeding similarly with sulfanilic acid, we take $\Delta H^0_{ws}(C_6H_5SO_3^-) = +16.4$ kJ mol^{-1} to which we add for $NH_2C_6H_5$, −11.2 and for $NH_3^+C_6H_5$ −37.4 kJ mol^{-1} to obtain for $NH_2C_6H_4SO_3^-$, +5.2, and for $NH_3^+C_6H_4SO_3^-$, −21.0 kJ mol^{-1} (since $\Delta H^0_{ws}(C_6H_6) \sim 0$ kJ mol^{-1}). The experimental values are +5.2 and −26.3 kJ mol^{-1} for $NH_2C_6H_4SO_3^-$ and $NH_2C_6H_4SO_3H$, respectively. The fair agreement for sulfanilic acid provides us with our strongest argument for the assignment of a zwitterionic structure.

It is clear that our conclusion that the four aminosulfonic acids are present as zwitterions in Me_2SO does not preclude the presence of low concentrations of the non-ionic forms. It is notoriously difficult to determine the equilibrium constant of such tautomeric forms, as is apparent for glycine (19, 20). The selection of the model compounds, whether alkyl esters or $—NR_3^+$ derivatives, and possibly the method used, whether thermodynamic or spectroscopic, may also lead to different results as exemplified in the case of 4-aminobenzoic acid in water (21, 22) where the percentage of zwitterion found varies between 17 and 1%.

NOTE ADDED IN PROOF: Our recent ^{13}C nmr work confirms the ionic structure of three of the four AS acids.

Acknowledgements

The continued financial assistance of the Natural Sciences and Engineering Research Council of Canada and of the Ministère de l'Education is gratefully acknowledged. We thank C. Chabot for her technical assistance.

1. G. A. BENSON and W. J. SPILLANE. Chem. Rev. **80**, 151 (1980).
2. H. P. HOPKINS JR., C. H. WU, and L. G. HEPLER. J. Phys. Chem. **69**, 2244 (1965).
3. E. M. TURNER and P. G. SEARS. J. Inorg. Nucl. Chem. **35**, 2087 (1973) and references therein.

Can. J. Chem. Downloaded from www.nrcresearchpress.com by 122.72.124.2 on 09/07/12
For personal use only.

4. J. C. HALLÉ, C. PICHON, and F. TERRIER. J. Biol. Chem. **259**, 4142 (1984).
5. J. C. HALLÉ and M. P. SIMONNIN. J. Biol. Chem. **256**, 8569 (1981).
6. J. COURTOT-COUPEZ and M. LE DÉMÉZET. Bull. Soc. Chim. Fr. 1033 (1969).
7. A. MUCCI, R. DOMAIN, and R. L. BENOIT. Can. J. Chem. **58**, 953 (1980).
8. R. L. BENOIT, D. BOULET, L. SÉGUIN, and M. FRÉCHETTE. Can. J. Chem. **63**, 1228 (1985).
9. L. BERGERON. Unpublished results.
10. R. W. GOLDBERG and L. G. HEPLER. J. Phys. Chem. **72**, 4654 (1968).
11. R. L. BENOIT and C. LOUIS. The chemistry of non-aqueous solvents. Vol. 5A. *Edited by* J. J. Lagowski. Academic Press, New York. 1978 and references therein.
12. Y. MARCUS. Pure Appl. Chem. **57**, 1103 (1985) and references therein.
13. C. L. LIOTTA, E. M. PERDUE, and H. P. HOPKINS, JR. J. Am. Chem. Soc. **95**, 2439 (1973).
14. C. D. RITCHIE and R. E. USCHOLD. J. Am. Chem. Soc. **90**, 2821 (1968).
15. M. K. CHANTOONI, JR. and I. M. KOLTHOFF. J. Phys. Chem. **80**, 1306 (1976).
16. A. J. HOEFNAGEL, M. A. HOEFNAGEL, and B. M. WEBSTER. J. Org. Chem. **43**, 4720 (1978).
17. Y. MARCUS. Pure Appl. Chem. **55**, 977 (1973).
18. C. V. KRISHNAN and H. L. FRIEDMAN. Solute–solvent interactions. Vol. 2. *Edited by* J. F. Coetzee and C. D. Ritchie. Marcel Dekker, New York. 1976.
19. M. J. LOCKE and R. T. MCIVER, JR. J. Am. Chem. Soc. **105**, 4226 (1983).
20. P. HABERFIELD. J. Chem. Educ. **57**, 346 (1980).
21. B. VAN DE GRAFF, A. J. HOEFNAGEL, and B. M. WEPSTER. J. Org. Chem. **46**, 653 (1981).
22. D. A. LAUFER, R. I. GELB, and L. M. SCHWARTZ. J. Org. Chem. **45**, 691 (1984).
23. P. PASCAL. Nouveau traité de chimie minérale. Tome XIII, fasc. 2. Masson, Paris. 1961. p. 1605.
24. R. C. WEAST. Handbook of chemistry and physics. 66th ed. CRC Press, Cleveland. 1985.
25. R. P. BELL. The proton in chemistry. 2nd ed. Cornell University Press, New York. 1973.
26. J. P. GUTHRIE. Can. J. Chem. **56**, 2342 (1978).
27. R. C. WEAST. Handbook of biochemistry selected data for molecular biology. 2nd ed. CRC Press, Cleveland. 1973.
28. R. L. BENOIT and C. BUISSON. Electrochim. Acta, **18**, 105 (1973).
29. C. MCCALLUM and A. D. PETHYBRIDGE. Electrochim. Acta **20**, 815 (1975).
30. R. L. BENOIT, M. J. MACKINNON, and L. BERGERON. Can. J. Chem. **59**, 1501 (1981).
31. A. G. COOK and C. W. MASON. J. Inorg. Nucl. Chem. **28**, 2579 (1966).
32. R. L. BENOIT and M. FRÉCHETTE. Thermochim. Acta, **127**, 125 (1988).

Can. J. Chem. Downloaded from www.nrcresearchpress.com by 122.72.124.2 on 09/07/12
For personal use only.

Experimental and theoretical investigation of C-nitroso rotation in 2-nitrosoimidazoles

JUDY L. BOLTON, MICHAEL R. PETERSON, AND ROBERT A. MCCLELLAND[1]

Department of Chemistry, University of Toronto, Toronto, Ont., Canada M5S 1A1

Received May 30, 1988

JUDY L. BOLTON, MICHAEL R. PETERSON, and ROBERT A. MCCLELLAND. Can. J. Chem. **66**, 3044 (1988).

1-Methyl-2-nitrosoimidazole exhibits broadened ^1H nuclear magnetic resonance signals at room temperature. The concentration independency of this spectrum as well as the linearity of the 700-nm absorbance with concentration rules out equilibrating nitroso monomer – nitroso dimer. It is suggested that there are equilibrating s-*cis* and s-*trans* nitroso monomer rotational isomers. At −59°C two sets of signals in a 3:1 ratio are observed. Analysis of CH_3 chemical shifts in terms of the magnetic anisotropy of the nitroso group suggests that the s-*trans* is the major isomer. The broadening observed at higher temperatures leads to a barrier for rotation (from the *trans* isomer) of 12.4 kcal mol^{-1}. *Ab initio* calculations with 2-nitrosoimidazole using the 3-21G basis set show that the fully planar s-*cis* and s-*trans* forms are minima, with the s-*trans* more stable by 2.5 kcal mol^{-1}, and a barrier to rotation (from the s-*trans*) of 13.0 kcal mol^{-1}. These results are in good agreement with those from solution phase. Various factors suggest that the π conjugative interaction between the nitroso group and imidazole ring is relatively unimportant.

JUDY L. BOLTON, MICHAEL R. PETERSON et ROBERT A. MCCLELLAND. Can. J. Chem. **66**, 3044 (1988).

Le méthyl-1 nitroso-2 imidazole présente en énlargissement des signaux de résonance magnétique nucléaire du ^1H à la température ambiante. L'absence de relation entre le spectre et la concentration aussi bien que la relation de proportionnalité existant entre la concentration et l'absorption à 700 nm écartent la posibilité d'un équilibre monomère nitroso – dimère nitroso. On suggère qu'il y a un équilibre entre les isomères rotationnels s-*cis* et s-*trans* du monomère nitroso. On observe à −59°C deux groupes de signaux dans un rapport 3:1. L'analyse des déplacements chimiques en fonction de l'anisotropie magnétique du groupe nitroso suggère que l'isomère s-*trans* est majoritaire. L'élargissement des signaux observé à plus haute température conduit à une barrière à la rotation de 12.4 kcal mol^{-1} (pour l'isomère *trans*). Les calculs *ab initio* effectués avec le nitroso-2 imidazole en utilisant l'ensemble de base 3-21G montrent que les formes totalement planes s-*cis* et s-*trans* sont minimales. La forme s-*trans* est plus stable de 2.5 kcal mol^{-1} avec une barrière à la rotation de 13.0 kcal mol^{-1}. Ces résultats s'accordent parfaitement avec ceux obtenus en solution. Divers facteurs suggèrent qu l'interaction π conjuguée entre le groupe nitroso et le cycle imidazole joue un rôle relativement peu important.

[Traduit par la revue]

Extensive studies of the 2-nitroimidazole radiosensitizers have revealed a number of biological and biochemical effects that are associated with reductive metabolism (1–6). The implication is that biological reduction is producing some reactive species that interacts with cellular components. In our investigations into the chemical origins of these effects, we have prepared 1-methyl-2-nitrosoimidazole (7), the two-electron reduction derivative of the model nitroimidazole 1-methyl-2-nitroimidazole. A search of the chemical literature reveals that 2-nitrosoimidazoles are unknown, a small number of 4 (5)-nitroso-5 (4)-phenylimidazoles being the only reported examples of the nitrosoimidazole class (8–11). 1-Methyl-2-nitrosoimidazole is indeed highly cytotoxic *in vitro* and, pending further studies, is a candidate for the biologically active reduction product (7, 12, 13). The compound, a green solid, was isolated in pure form and identified by various methods: C,H,N analysis, mass spectrum, uv–vis spectrum, and ^1H nmr spectrum (7). The latter, when recorded at 60 MHz, showed signals consistent with a substance containing the NCH_3 group and two nonequivalent H4-, H5-imidazole hydrogens. Examination of the 400 MHz spectrum recorded at ambient temperature revealed, however, that these signals were significantly broadened. Our initial assumption was that this was associated with equilibrating nitroso monomers and dimers,

[1] 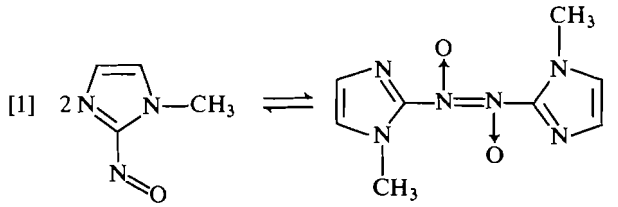

as has been characterized for nitrosobenzenes (14–17). This paper presents our examination of this phenomenon, at both the experimental and theoretical level. As will be shown, our initial premise was incorrect. The nmr broadening is in fact associated with interconverting C—NO rotamers of the monomeric nitrosoimidazole.

Experimental

1-Methyl-2-nitrosoimidazole was prepared as described previously (7). The nmr experiments were carried out at 400 MHz with a Varian XL-400 nmr spectrometer. The uv–visible spectra were recorded with a Varian 2390 spectrophotometer.

Ab initio computations were carried out with the split-valence 3-21G basis set (18) within the Hartree-Fock formalism (19) using the analytic gradient (20) of the SCF energy with respect to the internal geometrical parameters. The Optimally Conditioned (OC) minimization technique (21) was used to determine the optimal geometry at each minimum. The VAO5AD sum of squares technique (22) was used for the transition state optimizations and to confirm the order of the minima obtained with the OC method. The order of a critical point is equal to the number of negative eigenvalues of the Hessian or force constant matrix (second derivatives of the energy with respect to the internal geometrical parameters). The order of minima must be zero, whereas transition states have order one. Optimizations were terminated when the gradient length,

$$\left[|g| = \left(\sum_i^n (\delta E/\delta q_i)^2/n \right)^{1/2} \right]$$

where q_i are the internal parameters and the sum is over the n optimized parameters, was reduced to below 5×10^{-4} mdyn. All computations were performed on the Gould 32/9705 computer system at the University of Toronto with the MONSTERGAUSS *ab initio* program (23).

[1]Author to whom correspondence may be addressed.

Can. J. Chem. Downloaded from www.nrcresearchpress.com by 122.72.124.2 on 09/07/12
For personal use only.

Can. J. Chem. Downloaded from www.nrcresearchpress.com by 122.72.124.2 on 09/07/12
For personal use only.

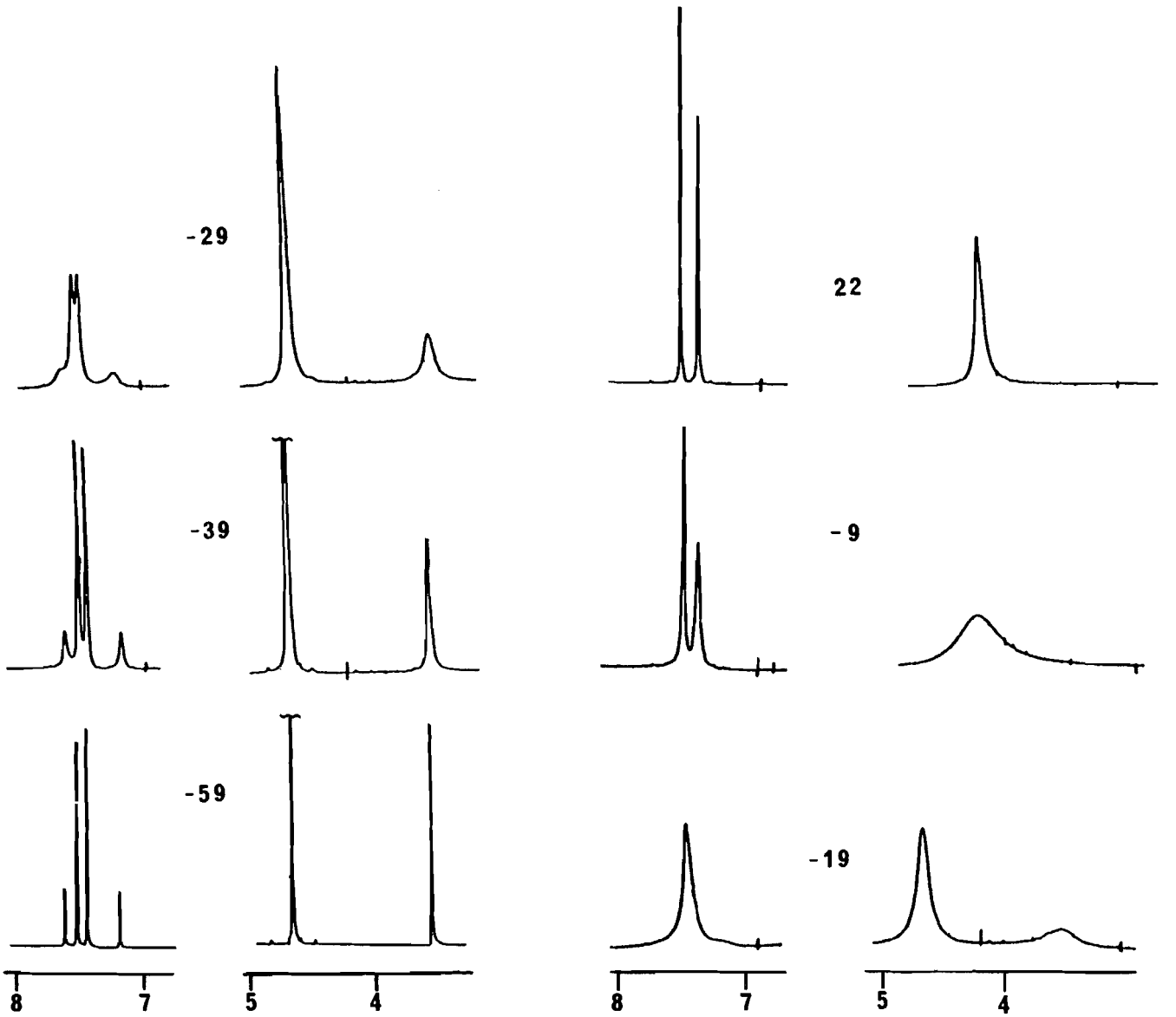

FIG. 1. Temperature dependence of the 400-MHz ^{1}H nmr spectrum of 1-methyl-2-nitrosoimidazole (5 mM) in CD_2Cl_2.

Results and discussion

Monomer–dimer Equilibration

The uv–visible spectrum of 1-methyl-2-nitrosoimidazole in CH_2Cl_2 exhibited three peaks, with λ_{max} at 280 nm ($\epsilon = 2.0 \times 10^3$ M^{-1} cm^{-1}), 355 nm ($\epsilon = 2.0 \times 10^4$ M^{-1} cm^{-1}), and 700 nm ($\epsilon = 45$ M^{-1} cm^{-1}). The weak band around 700 nm is characteristic of monomeric C-nitroso compounds (15), and is obviously the absorption that causes the green color of the solid. Since dimeric C-nitroso compounds lack this visible absorption band, the presence of the dimer in solutions of C-nitroso compounds can be demonstrated by examination of the concentration dependence of the absorption spectra. In particular, as the concentration is increased and the relative amount of dimer at equilibrium increases, the apparent extinction coefficient of the visible band (optical density/concentration) should decrease. With 1-methyl-2-nitrosoimidazole in CH_2Cl_2, however, the optical density at 700 nm is linear in concentration up to 25 mM, the highest concentration investigated. Thus we conclude that this compound exists principally (>90%) as the monomer, at least up to this concentration in this solvent. Similar experiments in methanol and water lead to the same conclusion, although the precision of the optical density measurements is less because the compound is not indefinitely stable in these solvents (7).

The ambient temperature 400 MHz ^{1}H nmr spectrum showing the broadened singlets is shown in one of the panels of Fig. 1. This spectrum was recorded in a 5 mM solution in CD_2Cl_2, where the evidence of the visible absorption spectroscopy is that principally monomer should be present. Increasing the concentration, in this case up to 100 mM, had no effect on the shapes of the peaks in the nmr spectrum. The conclusion therefore is that the broadening is not being caused by equilibrating monomer and dimer.

C-Nitroso rotamers. Variable temperature nuclear magnetic resonance

This leaves as an explanation some form of conformational equilibration. An examination of the structure of this relatively rigid molecule suggests that this would involve rotamers about the C2—NO bond.

[2] 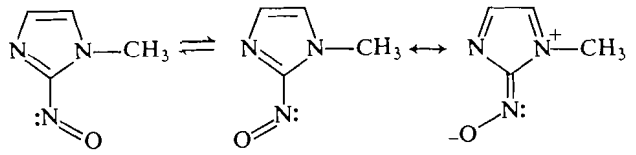

s-*trans* s-*cis*

We define these as s-*cis* and s-*trans* with respect C2=N3 bond as shown in eq. [2]. As indicated by the dipolar resonance contributor of the s-*cis* form, the C2—NO bond is expected to have partial double bond character because of conjugation of the electron-rich imidazole ring and the electron-withdrawing nitroso group. (A similar dipolar contributor can obviously be written for the s-*trans* form.)

The results of a variable temperature nmr investigation are shown in Fig. 1. As the temperature is decreased the signals broaden further, but then there is a separation and, by −59°C, two species are clearly indicated. The major isomer has peaks at δ 7.47 and δ 7.39 corresponding to the imidazole hydrogens and δ 4.65 for the N-methyl, while the minor isomer has signals at δ 7.57, 7.13, and 3.52. The ratio of the major to minor isomer as determined by integration is 3:1.

A tentative assignment of the s-*trans* as the major isomer can be made upon consideration of the magnetic anisotropy of the nitroso group. The major isomer has its methyl signal 1.13 ppm downfield from the corresponding signal of the minor isomer, and it is in the *trans* form, which has the methyl group closer to the nitroso bond, that the hydrogens are most deshielded. Through the use of the appropriate formula for the anisotropy effect with nitroso group parameters (24), we calculated that a freely rotating methyl group has its hydrogens on average deshielded by 0.23 ppm in the *cis* isomer, and by 1.42 ppm in the *trans*. The difference between the two, 1.19 ppm, is remarkably close to the experimental difference.

The ^{13}C nmr spectrum, recorded in $CDCl_3$ at ambient temperature, also showed broadened signals, at 34.4, 126.3, 132.4, and 169.0 ppm. The signal at 169.0 ppm was weak and can be assigned to the quaternary C2 carbon. A proton coupled spectrum revealed that the signal at 126.3 ppm had small coupling to the methyl hydrogens, and this is therefore C5.

The broadening of the separate N—CH_3 signals can be related to the exchange rate constant by the equation $k = \pi(h\text{-}h_0)$ where h is the line width at half-height and h_0 is the linewidth in the absence of exchange (25). The four nmr spectra obtained below the coalescence point (Fig. 1) were analyzed with this equation. The temperature variation in the rate constants was then treated in the normal fashion to give the activation parameters listed in Table 1. The free energy difference between the two isomers also listed in this table was calculated from their 3:1 ratio at −59°C.

Ab initio *computations*

In order to examine the situation at the theoretical level we carried out *ab initio* calculations with the 3-21G basis set, using the simpler parent 2-nitrosoimidazole as the model. The initial

[3] 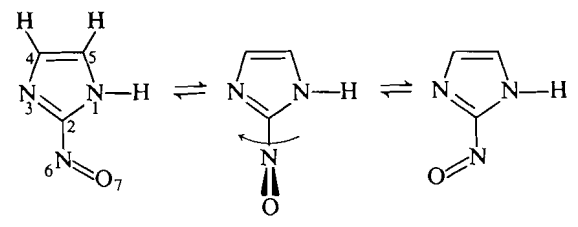

TABLE 1. Activation parameters for nitroso group rotation in 1-methyl-2-nitrosoimidazole

	Major isomer (s-*trans*)	minor isomer (s-*cis*)
$\Delta H‡$, kcal mol^{-1}	12.4	12.2
$\Delta S‡$, cal mol^{-1} K^{-1}	0.1	0.4
$\Delta G‡$ (25°C), kcal mol^{-1}	12.4	12.1
$\Delta G°$ (−59°C), kcal mol^{-1}	0.5	

calculations proceeded with the constraint that the imidazole ring atoms lay in a common plane, and the geometry was optimized in both the s-*cis* and s-*trans* configurations. A check of the critical point order revealed that the calculated geometries did represent true minima (order = 0). The geometry was also optimized for the C—NO torsional transition state. The requirement here is that the critical point order be unity. The results are summarized in Table 2, with the atom numbering corresponding to that given in eq. [3].

Similar calculations were also performed on the non-heterocyclic analog, 2-nitrosoethylene.

[4] 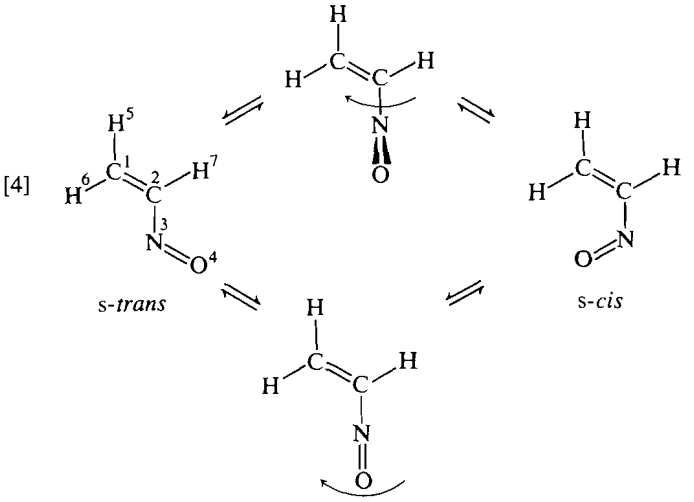

s-*trans* s-*cis*

In this case the transition state for in-plane rotation or nitrogen inversion was also optimized. Results are tabulated in Table 3. Nitrosoalkenes have been isolated, but only when there are bulky substituents at the β-carbon (26). Simple nitrosoalkenes such as nitrosoethylene have only been observed in solution and (or) trapped with various reagents (27, 28). Several theoretical calculations of nitrosoethylenes have been reported (28–30), but none of these have examined the *cis* and *trans* isomerization. *Ab initio* calculations have been carried out at the STO-3G and at the 4-31G level but the geometry was not reported (29). The energies found (−203.99559 hartrees (STO-3G), −206.34914 hartrees (4-31G)) lie on either side of the one calculated in this paper, as is expected for these basis sets.

Considering that the calculations refer to isolated (gas phase) molecules, the nitrosoimidazole results show good correspondence with the experimental results for the 1-methyl derivative. The calculation predicts that the s-*trans* form is the more stable isomer, although the difference in stability, 2.5 kcal mol^{-1}, is larger than that seen experimentally. This discrepancy could be related to solvation differences between the two isomers; there is a slight difference in the calculated dipole moments (see later). Moreover there may be a methyl–nitroso steric interaction in the 1-methylimidazole that would destabilize the s-*trans*

Can. J. Chem. Downloaded from www.nrcresearchpress.com by 122.72.124.2 on 09/07/12
For personal use only.

TABLE 2. 3-21G Optimized parameters for 2-nitrosoimidazole. Bond lengths in angstroms, bond angles (∠) and torsional angles (τ) in degrees. See eq. [3] for atom numbering

Parameters	s-*cis*	Transition state	s-*trans*
N1—C2	1.3661	1.3595	1.3662
C2—N3	1.3003	1.2875	1.3000
N3—C4	1.3781	1.3987	1.3764
C4—C5	1.3640	1.3501	1.3658
C2—N6	1.4063	1.4486	1.4039
N6—O7	1.2211	1.2172	1.2296
N1—H	0.9963	0.9953	0.9962
C4—H	1.0614	1.0614	1.0613
C5—H	1.0626	1.0623	1.0628
∠N1—C2—N3	111.39	112.67	111.52
∠C2—N3—C4	106.11	105.52	106.09
∠N3—C4—C5	109.61	109.70	109.50
∠N1—C2—N6	117.88	121.45	123.50
∠C2—N6—O7	115.14	112.37	112.55
∠C5—C4—H	128.61	129.05	128.57
∠C4—C5—H	131.20	131.86	131.09
∠C5—N1—H	127.67	126.86	128.69
τN3—C4—C5—H	180.00	180.05	180.00
τN1—C5—C4—H	180.00	179.83	180.00
τC2—N3—C4—C5	0.00	−0.42	0.00
τN1—C2—N3—C4	0.00	−0.57	0.00
τC5—N1—C2—N6	180.00	183.13	180.00
τC4—C5—N1—H	180.00	179.92	180.00
τN3—C2—N6—O7	0.00	93.32	180.00
E (hartree)	−351.444114	−351.427262	−351.448054
Δ*E* (kJ/mol)	10.5	54.4	0.0
Δ*E* (kcal/mol)	2.5	13.0	0.0

form relative to the s-*cis* form. The calculated barrier for nitroso rotation, 13.0 kcal mol^{-1} from the s-*trans* form, also shows good agreement with experiment (12.1 kcal mol^{-1}). The calculated transition state has the nitroso group 3° from the perpendicular to the imidazole ring, with the oxygen slightly to the NH side.

The situation with the nitrosoethylene is quite similar. The s-*trans* isomer is again calculated to be more stable. This conformational preference is also observed, both experimentally and theoretically, with 1,3-butadiene (31). One explanation for this trend in the latter case is that the s-*cis* conformation incorporates an unfavorable eclipsed interaction involving the C2 and C3 hydrogens; there is as well van der Waals repulsion between hydrogens at C1 and C4. However, these arguments cannot be applied to either nitrosoethylene or 2-nitrosoimidazole, where such interactions do not exist. An alternative explanation is that there is a diminished electron delocalization in the structures with the s-*cis* double bonds. Evidence for this can be seen in the calculated geometries, which generally have shorter double bonds and longer single bonds for the s-*cis* isomer. Thus, for example, the N=O bond is shorter by 0.0085 Å in s-*cis* nitrosoimidazole, with the difference 0.0017 Å in nitrosoethylene. Elongated C—N single bonds can be observed, the C—NO bond 0.0024 Å longer in s-*cis* nitrosoimidazole than in s-*trans*, and 0.0179 Å in the nitrosoethylene isomers. 1,3-Butadiene also shows similar trends, particularly in the C2—C3 bond, which is 0.0127 Å longer in the s-*cis* form (31).

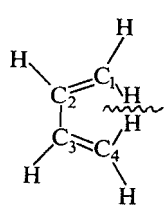

The barrier to nitroso rotation in nitrosoethylene was calculated as 9.5 kcal mol^{-1} (from the s-*trans* isomer). As in the imidazole, the transition state was just slightly off the perpendicular. The barrier to in-plane nitrogen inversion was also computed for the ethylene, and found to be 55.1 kcal mol^{-1}. From this much larger number we conclude that the *trans–cis* isomerization proceeds via rotation. The smaller barrier for the nitrosoethylene as compared to the nitrosoimidazole is not unexpected since the latter should have a stronger π interaction between the nitroso group and adjacent π system. What is perhaps surprising is that the difference between the two is not greater. This may indicate that the nitroso – imidazole π interaction is not that important, and there are in fact several other signs that this may be the case. As shown in Fig. 2, which provides some pertinent bond lengths, the imidazole rings in s-*trans* and s-*cis*-2-nitrosoimidazole are not particularly distorted from imidazole itself. There are some small bond length differences in the direction expected for a nitroso plus imidazole resonance interaction, but these are small, particularly compared to the very large distortions for the imidazole-stabilized nitrenium ion (32) where there is a large delocalization. A comparison of the torsional transition state and the planar forms

Can. J. Chem. Downloaded from www.nrcresearchpress.com by 122.72.124.2 on 09/07/12
For personal use only.

TABLE 3. 3-21G Optimized parameters for nitrosoethylene. Bond lengths in angstroms, bond angles (∠) and torsional angles (τ) in degrees. See eq. [4] for atom numbering

3-21G parameters	s-*trans*	Transition state (rot.)	Transition state (inv.)	s-*cis*
C2—C1	1.3134	1.3087	1.3265	1.3140
N3—C2	1.4420	1.4688	1.3455	1.4599
O4—N3	1.2241	1.2188	1.2131	1.2224
H5—C1	1.0721	1.0712	1.0684	1.0713
H6—C1	1.0710	1.0712	1.0684	1.0709
H7—C2	1.0711	1.0720	1.0752	1.0676
∠N3—C2—C1	118.37	122.39	128.45	123.27
∠O4—N3—C2	112.61	112.92	180.91	114.42
∠H5—C1—C2	120.50	121.74	122.69	120.20
∠H6—C1—C2	121.64	120.97	118.85	121.50
∠H7—C2—C1	125.52	124.31	122.08	124.36
τO4—N3—C2—C1	180.00	94.34		0.00
τH5—C1—C2—N3	0.00	−2.21		0.00
τH6—C1—C2—N3	180.00	177.73	180.00	180.00
τH7—C2—C1—H5	180.00	181.26	180.00	180.00
E (hartree)	−205.500269	−205.487106	−205.412427	−205.496578
Δ*E* (kJ/mol)	0.0	39.8	230.5	9.6
Δ*E* (kcal/mol)	0.0	9.5	55.1	2.3

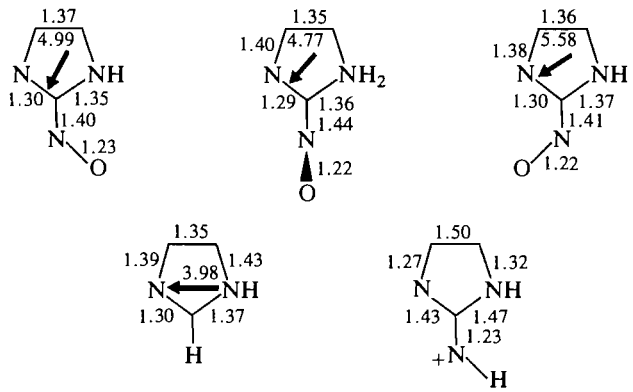

FIG. 2. 3-21G Bond lengths (Å) and dipole moments (debye). Results for imidazole and the imidazole nitrenium ion are from ref. 32.

also exemplifies the point. The former, with the nitroso group perpendicular, can have no conjugative interaction, and yet its geometry is very similar. There are small increases and decreases in bond length during the rotation, in particular a lengthening of the C—NO bond at the transition state, but the changes are small. A final indicator is the direction and magnitude of the dipole moment. Imidazole itself has a significant dipole oriented along the line from N1 to N3. The introduction of the nitroso group shifts the dipole towards this group, but the resultant can in fact be roughly ascribed as the vector sum of the imidazole dipole and C-nitroso dipole. This applies to both the planar and perpendicular forms, leading to the conclusion that π-delocalizations in the former are not causing significant distortions in the electron distribution. It can be noted that *ab initio* calculations with nitrobenzene (33) and various nitroimidazole[2] have pointed to the same conclusion, namely the relative unimportance of a resonance interaction between the nitro group and adjacent ring.

[2]S. F. Farah, R. A. McClelland, M. R. Peterson, and I. G. Csizmadia. Manuscript in preparation.

Acknowledgment

The continued financial support of the Natural Sciences and Engineering Research Council of Canada is gratefully acknowledged.

1. J. B. CHIN, D. M. K. SHEININ, and A. M. RAUTH. Mutat. Res. **58**, 1 (1978).
2. N. J. MCNALLY. Int. J. Radiat. Oncol. Biol. Phys. **8**, 593 (1982).
3. J. M. BROWN. Int. J. Radiat. Oncol. Biol. Phys. **8**, 1491 (1982).
4. E. A. BUMP, Y. C. TAYLOR. and J. M. BROWN. Cancer Res. **43**, 997 (1983).
5. A. M. RAUTH. Int. J. Radiat. Oncol. Biol. Phys. **10**, 1293 (1984).
6. A. R. J. SILVER, P. O'NEILL, and T. C. JENKINS. Biochem. Pharmacol. **19**, 3537 (1985).
7. M. B. NOSS, R. PANICUCCI, R. A. MCCLELLAND, and A. M. RAUTH. Biochem. Pharmacol. **37**, 2585 (1988).
8. S. CUSAMO and G. DIDONNA. Gazz. Chim. Ital. **85**, 208 (1955).
9. M. RUCCIA and G. WEEBER. Atti Accad. Sci. Lett. Arti Palmero Parte 1: **22**, 95 (1961).
10. S. M. BROTHERS and R. A. MCCLELLAND. J. Org. Chem. **52**, 1357 (1987).
11. W. J. ELHARDT, B. B. BEAULIEU, JR., and P. GOLDMAN. J. Med. Chem. **31**, 323 (1988).
12. M. B. NOSS, R. PANICUCCI, R. A. MCCLELLAND, and A. M. RAUTH. Int. J. Radiat. Oncol. Biol. Phys. In press.
13. R. T. MULCAHY, J. J. GIPP, R. PANICUCCI, and R. A. MCCLELLAND. Biochem. Pharmacol. In press.
14. R. R. HOLMES, R. P. BAYER, L. A. ERREDE, H. R. DAVIS, A. W. WIESENFIELD, P. M. BERGMAN, and D. L. NICHOLAS. J. Org. Chem. **30**, 3837 (1965).
15. C. N. R. RAO and K. R. BHASKAN. *In* Chemistry of the functional groups. Vol. 5. Part 1. The chemistry of the nitro and nitroso groups. *Edited by* S. Patai. Wiley–Interscience, New York. 1969. Chap. 3.
16. M. AZOULEY, R. LIPPMANN, and G. WETTERMARK. J. Chem. Soc. Perkin Trans. 2, 256 (1987).
17. C. D. BATICH and D. S. DONALD. J. Am. Chem. Soc. **106**, 2758 (1984).
18. J. S. BINKLEY, J. A. POPLE, and W. J. HEHRE. J. Am. Chem. Soc. **102**, 939 (1980).
19. C. C. J. ROOTHAN. Rev. Mod. Phys. **23**, 69 (1951).

Can. J. Chem. Downloaded from www.nrcresearchpress.com by 122.72.124.2 on 09/07/12
For personal use only.

20. H. B. SCHELGEL. Program FORCE. Ph.D. thesis, Queens University, Kingston, Ont., Canada. 1975.
21. W. C. DAVIDON. Math. Program. **9**, 1 (1975); W. C. DAVIDON and L. NAZARETH. Technical Memos 303 and 306, Applied Mathematics Division, Argonne National Laboratories, Argonne IL, U.S.A.
22. M. J. D. POWELL. Program VA05AD, AERE Subroutine Library, Harwell, Great Britain.
23. M. R. PETERSON and M. A. POIRER. Program MONSTERGAUSS, University of Toronto, Toronto, Ont., Canada. 1981.
24. R. K. HARRIS. *In* Nuclear magnetic resonance spectroscopy, a physicochemical view. Pitman Publishing, New York. 1983. pp. 193–196.
25. R. J. ABRAHAM and P. LOFTUS. *In* Proton and carbon-13 NMR spectroscopy, an integrated approach. Heyden and Son Ltd., London. 1980. Chap. 7. pp. 165–168.
26. W. HOBOLD, U. PRIETZ, and W. PRITZKOW. J. Prakt. Chem. **311** 260 (1968); K. WIESER and A. BERNDT. Agnew. Chem. Int. Ed. Engl. **14**, 70 (1975).
27. R. FARAGHER and T. L. GILCHRIST. J. Chem. Soc. Perkin Trans. 1, **249**, (1979).
28. J. S. BURNIER and W. L. JORGENSEN. J. Org. Chem. **48**, 3923 (1983).
29. S. MARRIOTT and R. D. TOPSOM. Theochem. **106**, 277 (1984).
30. V. BHUJLE, U. P. WILD, H. BAUMANN, and G. WAGNIERE. Tetrahedron, **32**, 467 (1976).
31. C. W. BOCK, P. GEORGE, and M. TRACHTMAN. Theoretica Chim. Acta., **63**, 273 (1983).
32. J. L. BOLTON and R. A. MCCLELLAND. J. Mol. Struct. (Theochem), **165**, 379 (1988).
33. P. POLITZER, P. LANE, K. JAYASURIYA, and L. N. DOMELSMITH. J. Am. Chem. Soc. **109**, 1899 (1987).

Can. J. Chem. Downloaded from www.nrcresearchpress.com by 122.72.124.2 on 09/07/12
For personal use only.

Electron spin resonance study of the structure of some σ* disulfur radical cations

L. BONAZZOLA, J.P. MICHAUT, AND J. RONCIN

Laboratoire de physico-chimie des rayonnements,[1] bat. 350, Université de Paris-Sud, 91405 Orsay CEDEX, France

Received May 30, 1988

L. BONAZZOLA, J.P. MICHAUT, and J. RONCIN. Can. J. Chem. **66**, 3050 (1988).

The radical cations generated by exposure to ^{60}Co γ rays, at 77 K. of dilute solutions of 1,4-dithiane, 1,5-dithiacyclooctane, and thiirane in freon matrices, have been investigated by ESR spectroscopy. The relation between the g_{iso} value and the S—S σ bond length is studied quantitatively.

L. BONAZZOLA, J.P. MICHAUT et J. RONCIN. Can. J. Chem. **66**, 3050 (1988).

Les cations provenant de l'irradiation γ à 77 K de solutions diluées, en matrices de fréons, de 1,4-dithiane, 1,5-dithiacyclooctane et de thiirane, sont étudiés par spectroscopie RPE. La relation entre la valeur de g_{iso} et la longueur de la liaison σ S—S est étudiée quantitativement.

Introduction

It is well known that exposure of dilute solutions of organic sulfides in freon matrices (1, 2) at 77 K to ^{60}Co γ rays gives the parent radical cations. These cations may react with neutral molecules to form dimer cations characterized by an intermolecular sulfur–sulfur σ bond. When a second sulfur is present in the parent molecule, an intramolecular radical cation complex can be observed if it is not prevented by steric factors. From liquid phase studies, it has been shown (3*a*) that the unpaired electron of dithia cations is generally located in an antibonding σ* orbital. Asmus *et al.* (4) found a correlation of optical absorption data in liquid phase with the structure of inter and intramolecular dithia cations: a redshift in the absorption seems to be associated with an increasing distance between the two sulfur atoms. Other liquid phase studies (3*b*, 5) indicate that the *g* factors determined from ESR spectra of the dimer cations $R_2SSR_2^+$ are dependent upon the size of the alkyl substituents. For a given medium and temperature, the *g* factor increases with the bulk of R: for $((CH_3)_2S)_2^+$, $g = 2.0102$: the *g* value becomes 2.0112 for $(Pr_2^iS)_2^+$ and 2.0122 for $(Bu^tSPr^i)_2^+$.

The present work is concerned with the correlation of the *g* values of dithia radical cations with their structure and in particular with the S—S σ bond distance. We focused our attention on two compounds: 1,4-dithiacyclohexane $S(CH_2)_2S(CH_2)_2$ and thiirane $S(CH_2)_2$. The first gives a cation characterized by an intramolecular S—S bond. Its absorption spectrum has been reported by Asmus *et al.* (4); its ESR spectrum in $CFCl_3$ matrix (1) leads to an uncertain g tensor (two of the three principal values are given by the authors). The second compound (thiirane) generates a dimer cation with an intermolecular S—S σ bond. To our knowledge, no data relative to the optical absorption of the dimer cation $((CH_2)_2S)_2^+$ are reported in literature. Nevertheless, the maximum absorptions (9) in liquid phase, of $((CH_3)_2S)_2^+$, $((CH_3CH_2)_2S)_2^+$, and $((CH_2)_4S)_2^+$, occur at the same wavelengths (470 nm). A similar maximum absorption is then expected for the thiirane dimer cation. The *g* value of $((CH_2)_4S)_2^+$ has been measured by Gilbert *et al.* (3*a*) in liquid phase (2.0102). The dimer radical cation of thiirane has been studied by Quin *et al.* (2) in freon matrices. They found a g_{iso} value of 2.0120. This value is unexpectedly high with respect to the values relative to $((CH_3)_2S)_2^+$ (2.0102) (5) and to $((CH_2)_4S)_2^+$ (2.0102). A change for *g* from 2.0102 to 2.0120 means a shift of the center of the spectrum of 3 gauss, which is outside the experimental error. Results concerning 1,5-dithiacyclooctane cation are also given in this paper because some information concerning its structure may be obtained from the comparison of its **g** tensor with those of 1,4-dithiane and thiirane cations.

Experimental

Samples were prepared from commercially available 1,4-dithiane, 1,5-dithiacyclooctane, and ethylene sulfide (Aldrich). Fluorotrichloromethane was purified before use. Dilute solutions (0.3% volume fraction) in freon (1,1,2-trichlorotrifluoromethane, fluorotrichloromethane) were degassed, frozen to 77 K, and then exposed to ^{60}Co γ rays (0.5 Mrads). Electron spin resonance spectra were recorded on a Brucker ER 200 D spectrometer equipped with a RMN gaussmeter. The spectrometer was calibrated with a Hewlett Packard 5342A frequency counter. The experimental spectra were simulated by using a computer program developed in the laboratory.

Results

Figures 1*a* and 2*a* show the spectra obtained from 1,4-dithiane trapped in $CFCl_2CCl_2F$ matrix registered at 80 and 110 K, respectively. The spectra simulated by using the parameters in Table 1 are given in Figs. 1*b* and 2*b*. The spectra in Figs. 1*a* and 2*a* are assigned to 1,4-dithiane radical cation. Warming from 80 to 110 K causes a softening of the matrix and a subsequent reversible spectral change leading to a nonet due to rapid reorientation of the cation. The motion of the cation averages out the g tensor to 2.0118 (spectrum II*a*) which is exactly the value found independently for g_{iso} from the spectrum I*a*. The isotropic coupling constant of 4.4 G (spectrum II*a*) to eight equivalent protons, agrees with the approximate value (1) proposed by Symons *et al.* It has been shown (2) that the radical species generated from thiirane–$CF_2ClCFCl_2$ solutions is the dimer cation, Its spectrum is given in Fig. 3*a*, and is simulated in Fig. 3*b*. It can be seen from the ESR parameters in Table 1 that the *g* and *A* values determined by Quin *et al.* (2) correspond to $A_\perp$ and $g_\perp$ parts of A and g tensors. Our g tensor is in good agreement with measurements in liquid phase (5) for $((CH_2)_4S)_2^+$.

Figure 4*a* shows the spectrum of 1,5-dithiacyclooctane cation trapped in $CFCl_3$ matrix. It indicates coupling to four equivalent protons. The isotropic coupling of 13.8 gauss corresponding to the measured tensor (see Table 1 and simulated spectrum in Fig. 4*b*) does not agree with liquid phase studies by Brown *et al.* (6). The hyperfine couplings observed by these authors are dependent on the method of generation of the

[1]UA 75, associated to CNRS.

Printed in Canada / Imprimé au Canada

Can. J. Chem. Downloaded from www.nrcresearchpress.com by 122.72.124.2 on 09/07/12
For personal use only.

Can. J. Chem. Downloaded from www.nrcresearchpress.com by 122.72.124.2 on 09/07/12
For personal use only.

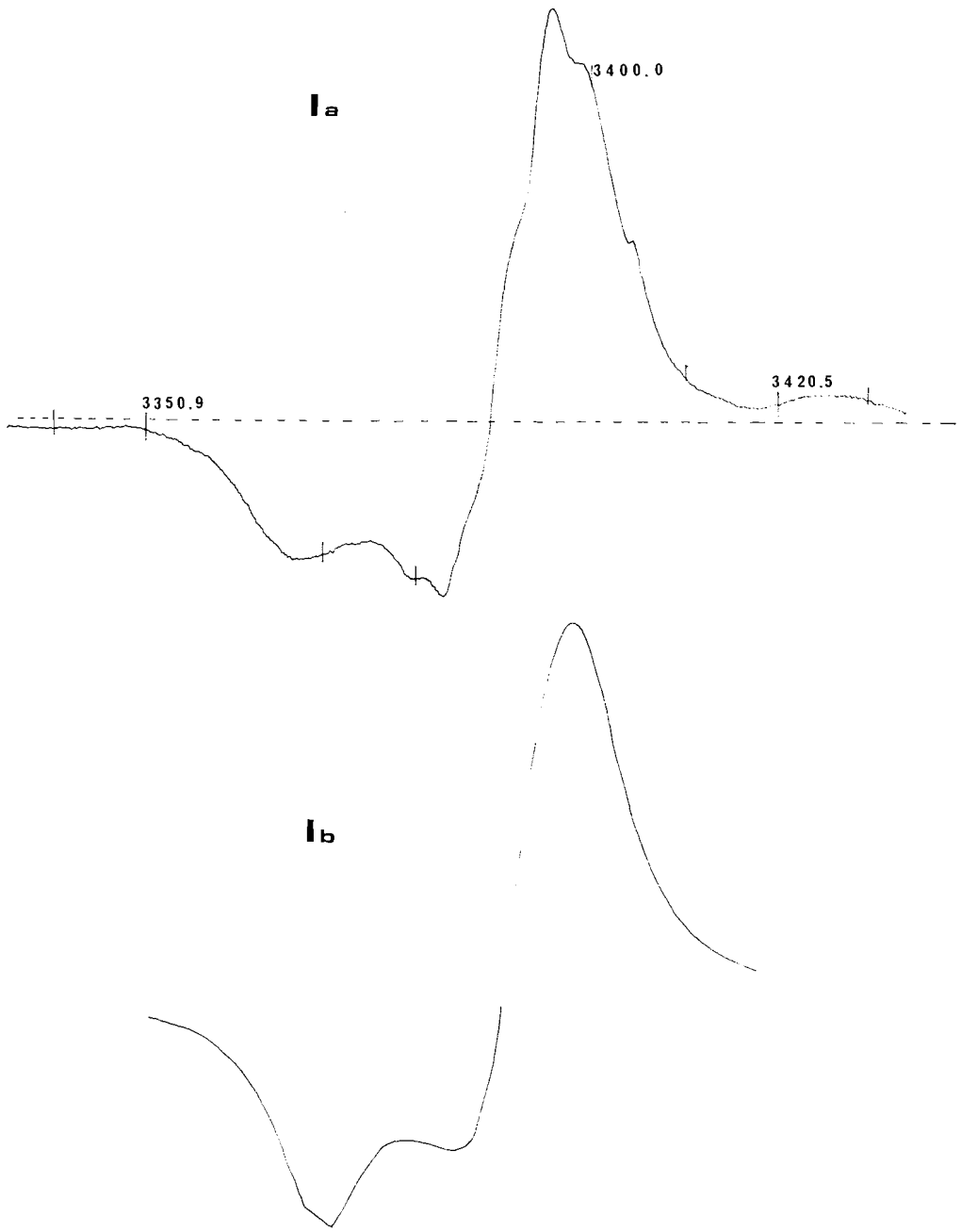

FIG. 1. (*a*) Electron spin resonance spectrum of 1,4-dithiane cation trapped in $CFCl_2CCl_2F$ matrix, registered at 80 K; (*b*) computer simulation of spectrum I*a*.

radical. In H_2SO_4, a five-line spectrum due to four equivalent protons is observed ($A_H = 9.9 \pm 0.2$ G), and in other media, the spectrum is due to the interaction of the unpaired electron with two pairs of equivalent protons ($A_{1H} = 11.2 \pm 0.1$ G; ($A_{2H} = 16.4 \pm 0.1$ G). The coupling of 13.8 gauss to four equivalent protons found in this work is the mean value of the above two couplings. The observed equivalence of the protons is not due to the line width (9.3 G) because the experimental spectrum would have been different: the second line of the spectrum should have been 5 G broader than the first one.

Discussion

As stated by Gara *et al.* (5) and Peterson *et al.* (3*b*), an increase in *g* values for a series of dithia cations is related to an increase of the S—S σ bond length. Optimized geometries for the neutral parent molecule and the radical cation of 1,4-dithiane have been determined by Momose *et al.* (7) (by using an STO 3G basis set and the gradient method for the search of stable conformation). The S—S bond length is found to be of 3.11 Å. The boat structure (7) is confirmed by ESR data: the coupling to eight equivalent protons (spectrum II*a*) would not have been possible with a chair conformation. Then, from our experimental *g* values. the S—S distance in the cation $(S(CH_2)_2)_2^+$ is expected to be less than 3.11 Å. We have performed a geometry optimization of thiirane dimer cation (Fig. 5) with a minimal STO 3G basis set and a minimization procedure using the gradient of the potential energy as described by Iver and Komornicki (8): the calculated value of the S—S bond length is 2.61 Å. Despite the known limitation of minimal basis set calculations, there is a clear trend of increasing

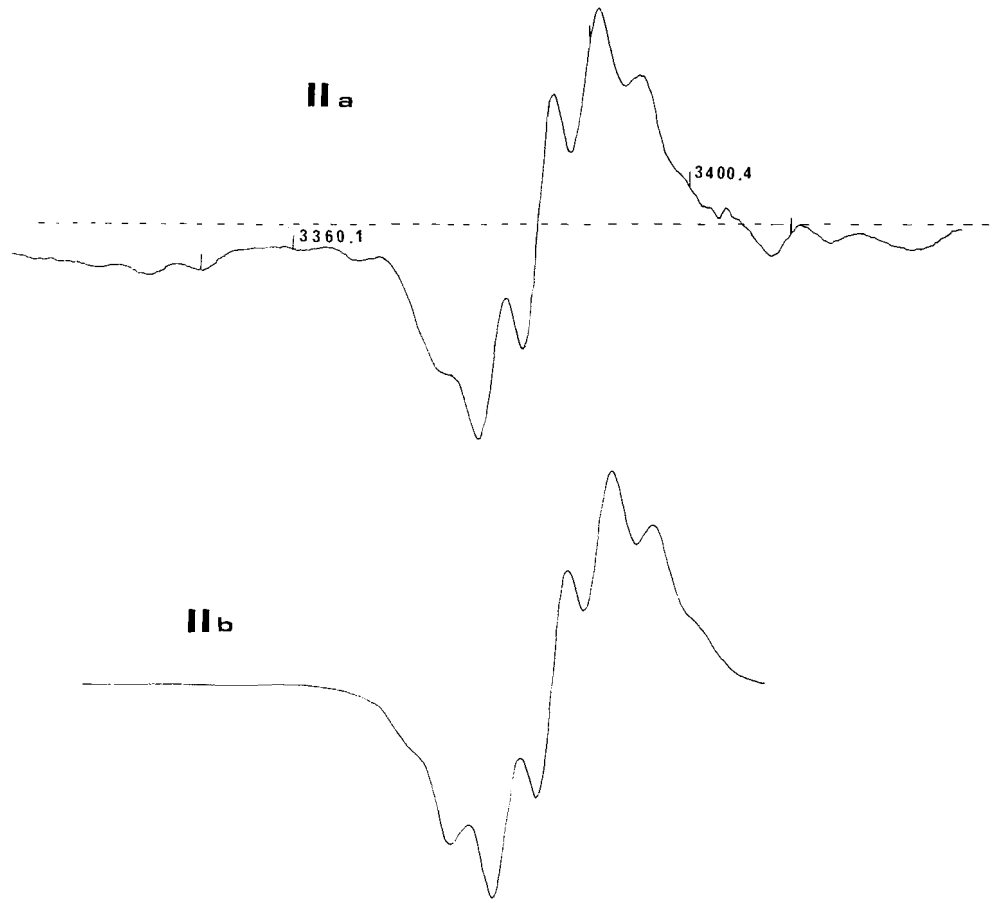

FIG. 2. (*a*) Electron spin resonance spectrum of 1,4-dithiane trapped in $CFCl_2CCl_2F$ matrix registered at 110 K; (*b*) computer simulation of spectrum II*a*.

TABLE 1. Electron spin resonance parameters, maximum optical absorption, and S—S bond distances for some dithia cations with three electron σ* S—S bonds

Radical cation	Matrix or solvent	T/K	g values and g_{iso}		Hyperfine coupling tensor and $a_{H\ iso}$ (G)	Maximum optical absorption (nm)	Calculated SS bond distance (Å)
$[(CH_2)_2S]_2^+$	$CFCl_2CF_2Cl$	100	2.0141 2.0122 2.0029	2.0097	5.0 4.7 5.4 (8H) 3.6		2.61
	$CFCl_3$	90		2.012(2)	5.8(2)		
1,4-Dithiane	$CFCl_2CF_2Cl$	80	2.0215 2.0092 2.0046	2.0118		650(4)	3.11 (7)
		110		2.0118	(8H) 4.4		
	$CFCl_3$	77	2.019 ? 2.001	(1)	4-5 (1)		
1,5-Dithia-cyclaoctane	$CFCl_3$	130	2.0194 2.0158 2.0032	2.0128	13.3 13.8 14.3 (4H) 13.9	400(4)	
	H_2SO_4 other matrix	283		2.012(6) 2.010(6)	(4H) 9.9(6) (2H) 11.2(6) (2H) 16.4(6)		
$[(CH_2)_4S]_2^+$	liquid phase			2.0102 (3)		470(9)	

Can. J. Chem. Downloaded from www.nrcresearchpress.com by 122.72.124.2 on 09/07/12
For personal use only.

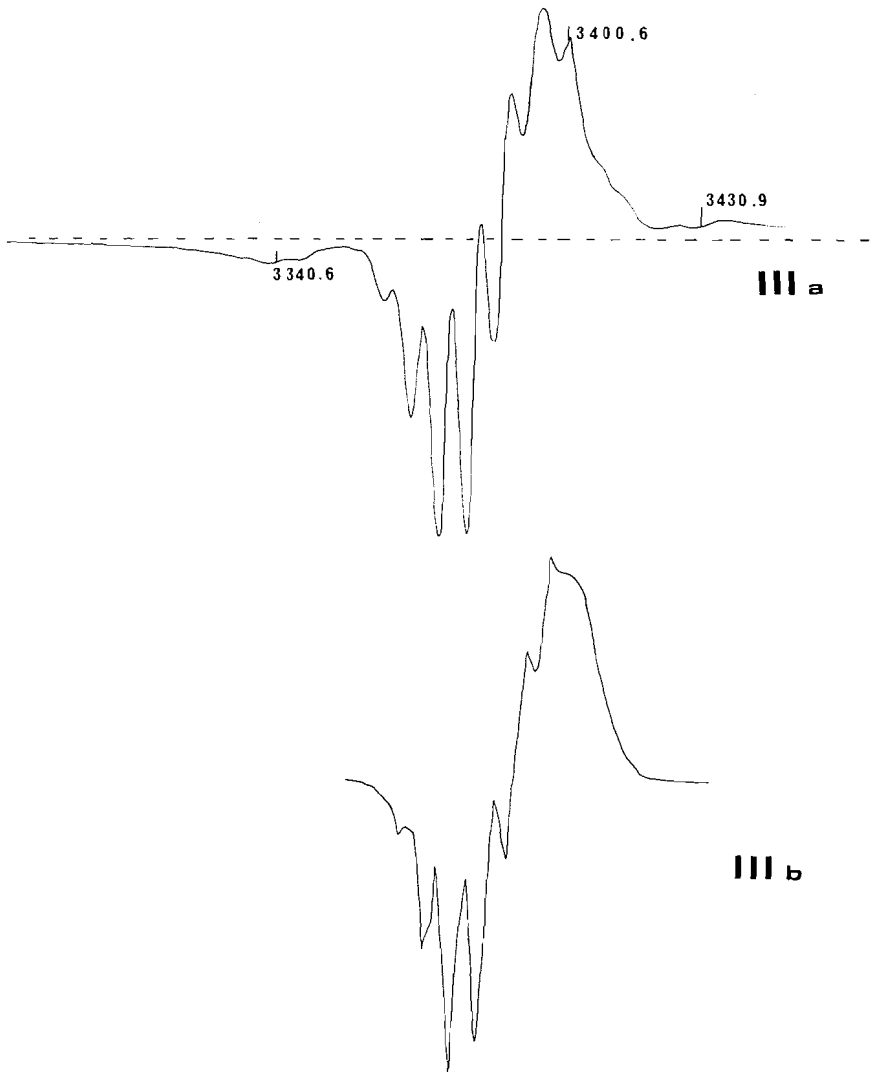

FIG. 3. (*a*) Electron spin resonance spectrum of the dimer radical cation of thiirane in CF_2ClCCl_2F at 77 K; (*b*) computer simulation of spectrum III*a*.

Can. J. Chem. Downloaded from www.nrcresearchpress.com by 122.72.124.2 on 09/07/12
For personal use only.

magnitudes for S—S bond length from thiirane dimer cation to dithiane cation. Similarly, the position of the maximum absorption, reflecting the σ/σ^* energy difference, is expected to increase with S—S distance. To our knowledge the maximum absorption for thiirane dimer cation has not been measured, but it is probably not very different from that of $((CH_2)_4S)_2^+$ cation (470 nm) (9). A λ_{max} value of 650 nm has been found for dithiane cation (4). From the maximum of absorption of 1,5-dithiacyclooctane cation (400 nm) (4), a g_{iso} value inferior to 2.0097 is expected, which disagrees with the value found in this work (2.0128). The many possible conformations of this cation do not allow a geometry optimization because of computational expense. Nevertheless, some information relative to the structure of this cation can be obtained from its ESR spectrum: the coupling of the unpaired electron to four equivalent protons indicates a twist boat–chair conformation with four hydrogens in the plane SSC. For this conformation, a close approach of the two interacting sulfur atoms does not seem possible as in liquid phase (4) where two structurally favorable five-ring systems are established (giving a maximum degree of orbital overlap along S—S coordinate). The most likely structure in liquid phase consists of two *cis*-fused five-membered rings with limited fluxional character (6). The inequivalence of protons in some media may be due to the effect of the counter ions, In solid phase, steric hindrance probably makes the most stable conformation impossible.

Conclusion

Two radical cations exhibiting a S—S three-electron σ intramolecular bond (1,4-dithiane and 1,5-dithiacyclooctane cations) and one radical exhibiting a S—S three-electron intermolecular σ bond (thiirane dimer cation) have been studied by ESR spectroscopy. It appears that a precise measurement of g_{iso} may give a very good indication of the S—S bond length. The chair conformation of the dithiane cation, expected from calculation is confirmed. The equilibrium structure of 1.5-dithiachlorooctane cation in solid phase can be deduced from ESR data.

Can. J. Chem. Downloaded from www.nrcresearchpress.com by 122.72.124.2 on 09/07/12
For personal use only.

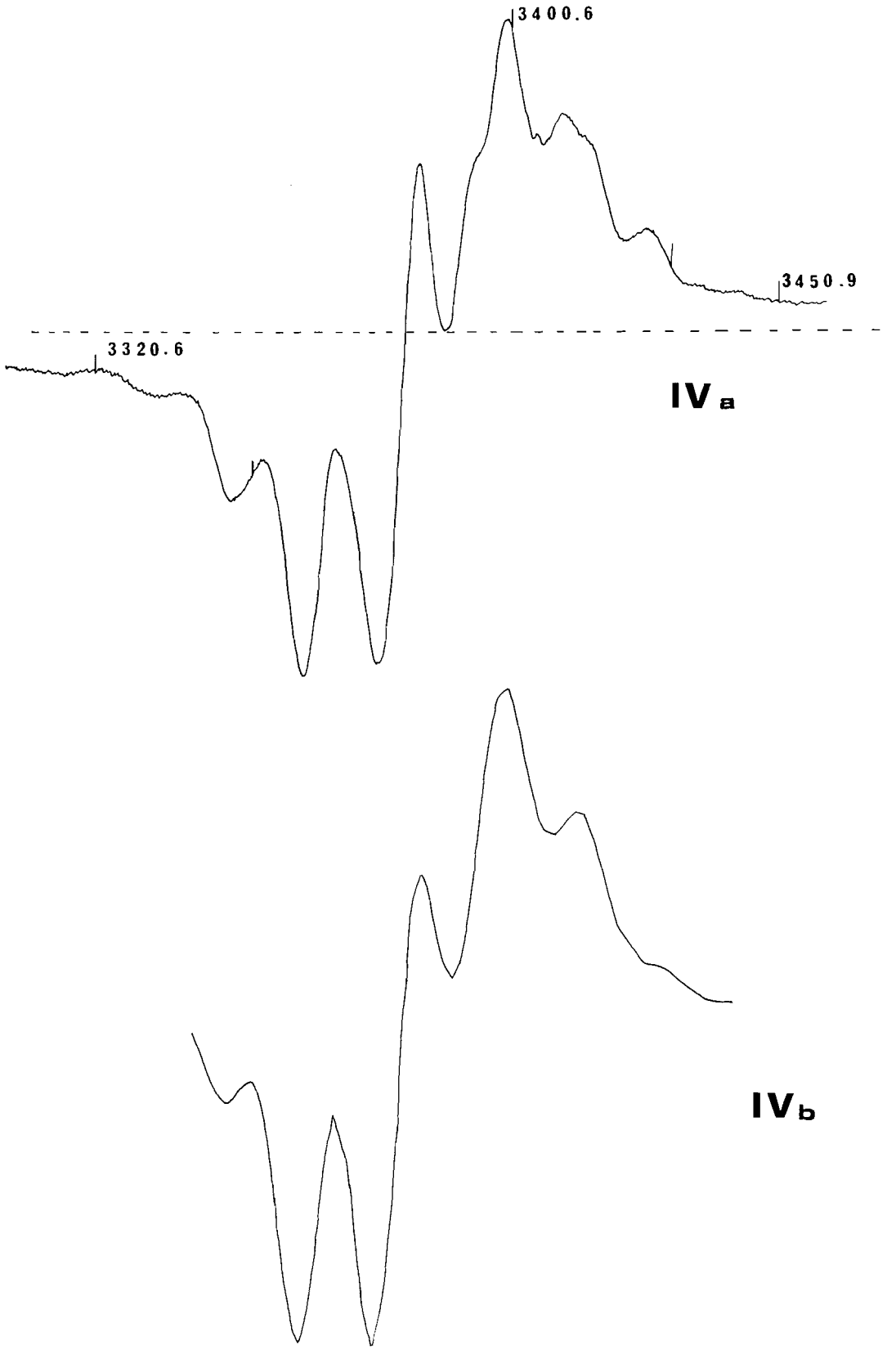

FIG. 4. (*a*) Electron spin resonance spectrum of 1,5-dithiacyclooctane in $CFCl_3$ at 77 K; (*b*) computer simulation of spectrum IV*a*.

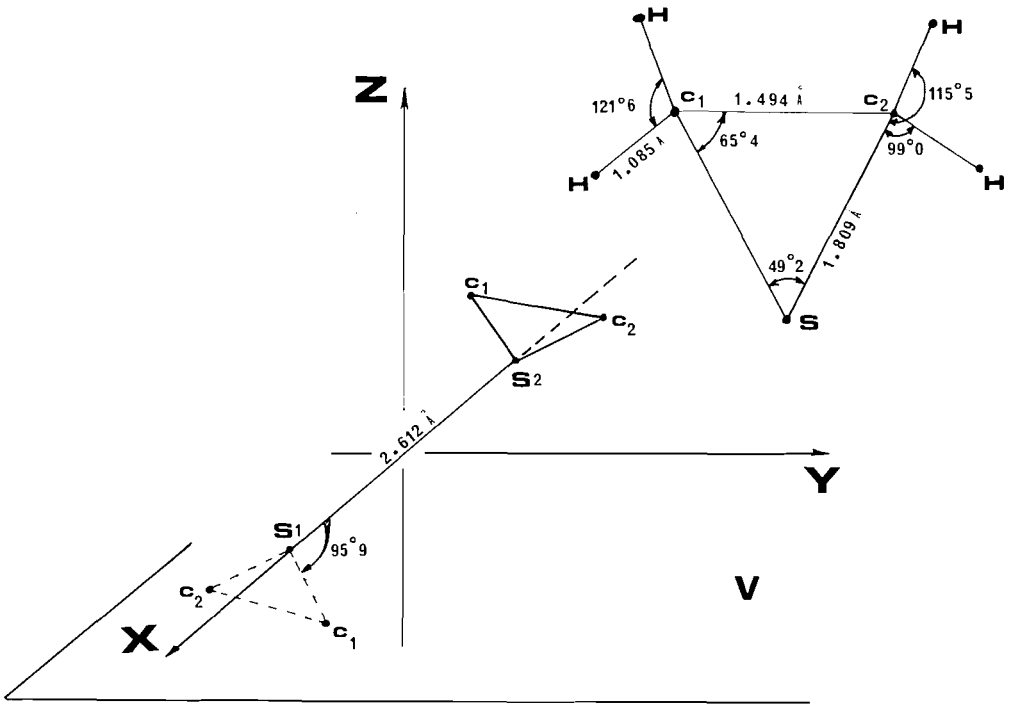

FIG. 5. Equilibrium geometry for thiirane dimer cation.

1. D. N. RAMAKRISHNA RAO, M. C. R. SYMONS, and B. W. WREN. J. Chem. Soc. Perkin Trans. II, 1681, (1984).
2. X. Z. QUIN, Q. C. MENG, and F. WILLIAMS. J. Am. Chem. Soc. **109**, 6778 (1987).
3. (*a*) B. C. GILBERT, D. K. C. HODGEMANN, and R. O. C. NORMANN. J. Chem. Soc. Perkin II, 1748 (1973); (*b*) R. L. PETERSON, D. J. NELSON and M. C. R. SYMONS. J. Chem. Soc. Perkin II, 225 (1978).
4. K. D. ASMUS, D. BAHNEMANN, CH. H. FISCHER, and D. VELTWISH. J. Am. Chem. Soc. **101**, 5322 (1979).
5. W. B. GARA, J. R. M. GILES, and B. P. ROBERTS. J. Chem. Soc. Perkin II, 1444 (1978).
6. TH. G. BROWN, A. S. HIRSCHON, and W. K. MUSKER. J. Phys. Chem. **85**, 3767 (1981).
7. T. MOMOSE, T. SUZUKI, and T. SHIDA. Chem. Phys. Lett. **107**, 568 (1984).
8. J. M. MC IVER and A. J. KOMORNICKI. Phys. Lett. **10**, 303 (1971).
9. M. BONIFACIC, H. MOCKEL, D. BAHNEMANN, and K. D. ASMUS. J. Chem. Soc. Perkin II, 675 (1975).

Can. J. Chem. Downloaded from www.nrcresearchpress.com by 122.72.124.2 on 09/07/12
For personal use only.

Kinetics of hydrolysis of aromatic bicycling disulfonyl dichlorides

PRZEMYSŁAW SANECKI AND EDWARD ROKASZEWSKI
Faculty of Chemistry, I. Lukasiewicz Technical University, 35-959 Rzeszów, Poland

Received July 12, 1988

PRZEMYSŁAW SANECKI and EDWARD ROKASZEWSKI. Can. J. Chem. **66**, 3056 (1988).

Hydrolysis of 16 compounds ClO_2S—Ar—B—Ar—SO_2Cl (B, bridge) in 20% H_2O, 80% v/v CH_3CO_2H, 0.5 mol dm^{-3} CH_3CO_2Na at 298.15 K has been investigated by a polarographic method. From plots of the hydrolysis, pseudo-first-order rate constants for two consecutive reactions $A \xrightarrow{k_1} A_1 \xrightarrow{k_2} A_2$ have been computed and the influence of -SO_2Cl groups, bridges B, and SO_3^- groups on the reactivity of -SO_2Cl groups has been discussed. The ratio of rate constants k_2/k_1 ranges from 0.45 to 30, depending on the structure. Log $(k_1/(2k_H))$ correlated linearly with $\sigma^{m,p}_{B\text{-}C_6H_5}$ and log (k_2/k_1) correlated linearly with ΔpK for the analogous diamine series H_2N—Ar—B—Ar—NH_2.

PRZEMYSŁAW SANECKI et EDWARD ROKASZEWSKI. Can. J. Chem. **66**, 3056 (1988).

Opérant à 298,15 K, en solution dans un mélange 20:80 (v/v) de H_2O/CH_3CO_2H contenant 0,5 mol dm^{-3} de CH_3CO_2Na, et faisant appel à une méthode polarographique, on a étudié l'hydrolyse de 16 composés du type ClO_2S—S—Ar—B—Ar—SO_2Cl (pont, B). À partir des courbes d'hydrolyses, on a calculé les constantes de pseudo-premier ordre des deux réactions consécutives $A \xrightarrow{k_1} A_1 \xrightarrow{k_2} A_2$; on discute de l'influence des groupements -SO_2Cl, des ponts B ainsi que des groupements SO_3^- sur la réactivité des groupements -SO_2Cl. Selon la structure, les rapports des constantes de vitesse k_2/k_1 varient de 0,45 à 30. On a établi une corrélation linéaire entre le log $(k_1/2k_H)$ et le $\sigma^{m,p}_{B\text{-}C_6H_5}$ ainsi qu'entre le log (k_2/k_1) et le ΔpK de la série des diamines analogues H_2N—Ar—B—Ar—NH_2.

[Traduit par la revue]

Introduction

In our previous paper (1) a continuous or semicontinuous polarographic method was applied to the investigation of the hydrolysis kinetics of 10 substituted benzenesulfonyl chlorides X—C_6H_4—SO_2Cl and seven disulfonyl dichlorides $C_6H_{4-n}(CH_3)_n(SO_2Cl)_2$. This method, together with the appropriate computing procedure, made possible the determination of rate constants k_1 and k_2 for the consecutive hydrolysis of disulfonyl compounds. The Hammett correlation was carried out, a reaction mechanism proposed, and the influence of -SO_2Cl and -SO_3^- groups on the reactivity of an unreacted -SO_2Cl group was discussed.

In this paper analogous investigations of a new series of 16 bicyclic disulfonyl dichlorides ClO_2S—Ar—B—Ar—SO_2Cl are reported. Compounds of this type are interesting as monomers for the synthesis of linear polysulfonates (2). The aim of this paper was to determine their reactivities in a model reaction running according to the nucleophilic substitution mechanism. Hydrolyses of some compounds of this type have previously been investigated in a different medium to give a single rate constant k (3).

Experimental

Chemicals

The compounds investigated were synthesized by means of classical methods. Numbers of compounds and their formulas are given in Table 1.

1: mp 128–129°C (lit. (4) mp 128–129°C).

2: mp 152–154°C (CH_3CO_2H); the compound after reduction with $SnCl_2$ + HCl gives dithiol, mp 78–80°C (CH_3OH), identical with dithiol obtained from 4,4′-diaminodiphenyl-2,2-propane by replacement of -NH_2 groups with SH groups; Cl in compound **2**, calcd.: 18.03%; found: 18.10%.[1]

3: mp 146.5–147°C (lit. (5) mp 146°C).

4: mp 126–128°C (lit. (6) mp 126–128°C).

5: mp 209–210°C (CH_3CO_2H) (lit. (3) mp 99–100°C (?); Cl calcd.: 18.695%; found: 18.62%.

6: mp 224–225°C (lit. (7) mp 225–226°C).

7: mp 157–158°C (lit. (8) mp 155–156°C, (9) mp 157–158°C).

8: mp 210–211°C (lit. (10) mp 203°C).

9: mp 218–219°C (lit. (11) mp 218°C).

10: mp 183–184°C; obtained by oxidation of **7** with the stoichiometric amount of $KBrO_3$ in CH_3CO_2H solution at 25°C, Cl calcd.: 17.76%; found: 17.75%.

11: mp 220–221°C (lit. (12) mp 222°C).

12: mp 140.5–141°C (crystallization: twice from CS_2, twice from CCl_4, 5 times from $CHCl_3$ + CCl_4) (lit. (13) mp 134°C).

13: mp 176–177°C (lit. mp 177–178°C);[2] obtained by oxidation of **4** with an excess of $KMnO_4$ in CH_3CO_2H solution at 35°C.

14: mp 185.5–186°C (CH_3CO_2H); obtained by chlorosulfonation of C_6H_5—Se—C_6H_5 with Cl—SO_2OH at 120°C by analogy to chlorosulfonation of C_6H_5—S—C_6H_5; Cl calcd.: 16.48%; found: 16.42%.

15: mp 174–175°C (lit. (9) mp 174–175°C).

16: mp 238–239°C (lit. (3) mp 238°C).

The positions of the -SO_2Cl groups in compound **14** (not described in the literature) as well as **5** and **12** were checked by ir spectroscopy.

Melting points were determined with the use of a Boëtius apparatus. Compounds **1–4** and **6–9** were obtained from the Department of Organic Synthesis, University of Lublin. The other substances were purified as in ref. 1. Apparatus and rate measurements were as in ref. 1.

Kinetic investigations were carried out in 20% H_2O, 80% v/v CH_3CO_2H; $c_{CH_3CO_2Na} = 0.5$ M; $c_{oClO_2S—ArBArSO_2Cl} = 8.5 \times 10^{-4}$ M ($c_{oSO_2Cl} = 1.7 \times 10^{-3}$ M) at 298.15 K.

Kinetics

A system of two irreversible consecutive first-order reactions $A \xrightarrow{k_1} A_1 \xrightarrow{k_2} A_2$ is described by the well-known set of differential equations. Based on the instantaneous concentrations of the -SO_2Cl groups, constants k_1 and k_2 can be determined by means of an iterative computing method (1).

Results and discussion

Hydrolysis of 14 compounds of the ClO_2S—Ar—B—Ar—SO_2Cl type, containing different divalent bridges, as well as of two derivatives with two divalent bridges (in the shape of five-

[1]W. Podkościelny, unpublished data.

[2]W. Podkościelny, private communication.

Printed in Canada / Imprimé au Canada

Can. J. Chem. Downloaded from www.nrcresearchpress.com by 122.72.124.2 on 09/07/12
For personal use only.

TABLE 1. Rate constants of consecutive hydrolysis ($k1$ and k_2) for a series of aromatic bicyclic disulfonyl dichlorides; $k_{C6H5—SO2Cl} = 3.5 \times 10^{-5}\ s^{-1}$ (1)

Compound no.	Formula	$k_1 \times 10^5\ (s^{-1})$	$k_2 \times 10^5\ (s^{-1})$	$r = k_2/k_1$	sd 100% (ref. 1)	$\sigma^{m,p}_{BC_6H_5}$ (refs. 14, 15)
1	4,4′—ClO_2S—C_6H_4—O—C_6H_4—SO_2Cl	6.05± 0.1	121±8	20	1.9	−0.32
2	4,4′—ClO_2S—C_6H_4—$C(CH_3)_2$—C_6H_4—SO_2Cl	6.5 ± 0.1	17.5±1	2.7	3.9	
3	4,4′—ClO_2S—C_6H_4—$(S)_2$—C_6H_4—SO_2Cl	6.5 ± 0.2	4.55± 0.3	0.7	6.0	
4	4,4′—ClO_2S—C_6H_4—CH_2—C_6H_4—SO_2Cl	6.8 ± 0.2	24.±1.5	3.5	5.9	−0.09
5	4,4′—ClO_2S—C_6H_4—$(CH_2)_2$—C_6H_4—SO_2Cl	7.4 ± 0.2	27.±1.8	3.6	4.8	(−0.03)[a]
6	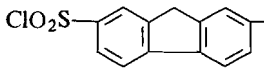	8.0 ± 0.2	240±20	30	2.0	(−0.08)[b]
7	4,4′—ClO_2S—C_6H_4—S—C_6H_4—SO_2Cl	9.5 ± 0.1	285±20	30	3.6	
8	4,4′—ClO_2S—C_6H_4—C_6H_4—SO_2Cl	9.5 ± 0.1	210±15	22	6.9	0.01
9	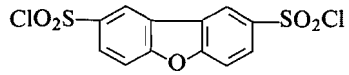	10.3±0.2	8.65±0.56	0.84	2.0	(0.06)[c]
10	4,4′—ClO_2S—C_6H_4—S(O)—C_6H_4—SO_2Cl	15.5±0.3	388±25	25	2.8	
11	4,4′—ClO_2S—C_6H_4—$(N)_2$—C_6H_4—SO_2Cl	17.4±0.3	7.65±0.5	0.45	2.6	0.33
12	3,3′—ClO_2S—C_6H_4—C(O)—C_6H_4—SO_2Cl	17.5±0.4	315±20	18	3.2	0.36
13	4,4′—ClO_2S—C_6H_4—C(O)—C_6H_4—SO_2Cl	20.5±0.3	472±35	23	3.3	0.43
14	4,4′—ClO_2S—C_6H_4—Se—C_6H_4—SO_2Cl	25.5±0.5	765±60	30	2.6	
15	3,3′—ClO_2S—C_6H_4—$S(O)_2$—C_6H_4—SO_2Cl	28.9±0.5	607±40	21	2.5	0.61
16	4,4′—ClO_2S—C_6H_4—$S(O)_2$—C_6H_4—SO_2Cl	44.0±1	790±60	18	2.9	0.70

[a] $\sigma_{CH_2X} = 0.36\ \sigma_X$.
[b] $\sigma_X \cong \sigma^m_{-CH_2—C_6H_5}$.
[c] $\sigma_X \cong \sigma^m_{-C_6H_5}$.

membered rings: compounds **6** and **7**) has been examined (Table 1). All the compounds contain structurally equivalent $-SO_2Cl$ groups and hydrolyze according to the following mechanism (1):

$$-SO_2Cl + CH_3CO_2^- \xrightarrow{k_1 \text{ or } k_2} -SO_2OCOCH_3 + Cl^-$$

$$-SO_2OCOCH_3 + H_2O + CH_3CO_2^- \xrightarrow{\text{fast}} -SO_3^- + 2CH_3CO_2H$$

The reactivity of the first $-SO_2Cl$ group (k_1) depends on the donor or acceptor influence of the bridge -B- and, in contrast, the reactivity of the second $-SO_2Cl$ group (k_2) in the intermediate product ClO_2S—Ar—B—Ar—SO_3^- (A_1) depends additionally on the negative charge localization centre and on the degree of delocalization of the charge in A_1. The numerical order of the compounds in Table 1 corresponds to the order of increase for k_1.

Treating a single bond joining two aromatic rings in the diphenyl derivative (compound **8**) as a standard bridge (B = —) the remaining compounds can be divided into two groups: those with deactivating bridges (**1**–**7**) and those with activating bridges (**9**–**16**). The hydrolysis of compound **8** (diphenyl derivative) is close to that of the unsubstituted compounds C_6H_5—SO_2Cl, if the statistical factor is taken into account:

$$k_{-C_6H_4SO_2Cl(4)} = k_1/2 = 4.25 \times 10^{-5}\ s^{-1}$$

$$k_{C_6H_5—SO_2Cl} = k_H = 3.54 \times 10^{-5}\ s^{-1}$$

After hydrolysis of the first $-SO_2Cl$ group some distinct changes in the hydrolysis rate of the second group can be observed. The ratio of k_1/k_2 changes from 0.45 (-B- = -N=N-) to about 30 (compounds **6**, **7**, **14**). The computing procedure allowed us to distinguish k_1 and k_2 when their ratio is $0.03 < k_1/k_2 < 30$.

With regard to k_2 we get a new series (order of k_2 increase) for the intermediate products ClO_2S—Ar—B—Ar—SO_3^- (A_1), i.e., **3**, **11**, **9**, **2**, **4**, **5**, **1**, **8**,**6**, **7**, **12**, **10**, **13**, **15**, **14**, **16**. The second series differs from the first one in the position of bridges in compounds **1**, **9**, **11** and in the sequence of the neighbouring bridges.

All -B—Ar—SO_2Cl and -B—Ar—SO_3^- groups can be treated as complex substituents for which σ constants are not known. They can be estimated from the previously determined Hammett correlations for mono-ring compounds (1):

[1] $$\log (k_X/k_H) = 1.42\ \sigma_X - 0.087$$
$$n = 13,\ r = 0.9852$$

It was taken into account that

$$\log (k_X/k_H) = \log (k_1/(2k_H)), \quad -X = -B—C_6H_4—SO_2Cl$$

$$\log (k_X/k_H) = \log (k_2/k_H), \quad -X = -B—C_6H_4—SO_3^-$$

For the substituents $-X = -B—C_6H_4—SO_2Cl$, constants σ_X become more and more positive (from 0.01 to 0.62), in the order in which the compounds occur in Table 1. The substituents $-X = -B—C_6H_4—SO_3^-$ are characterized by a wider range of σ_X variation, i.e., 0.14–1.27, and generally $\sigma_{BC_6H_4SO_3^-}$ does not correlate linearly with $\sigma_{BC_6H_4SO_2Cl}$. With a set of literature σ constants for the substituents of type -B—C_6H_5 (14, 15) it is possible to determine an indirect correlation, $\log (k_1/(2k_H)) = f(\sigma_{BC_6H_5})$, to get (Fig. 1):

[2] $$\log (k_1/(2k_H)) = (0.859 \pm 0.143)\ \sigma_{BC_6H_5} + (0.110 \pm 0.056)$$
$$n = 9,\ r = 0.983,\ s_0 = 0.0035, \text{ for } t_{0.05,7}$$

Compounds **6** and **9** with two bridges could be included in this

Can. J. Chem. Downloaded from www.nrcresearchpress.com by 122.72.124.2 on 09/07/12
For personal use only.

Can. J. Chem. Downloaded from www.nrcresearchpress.com by 122.72.124.2 on 09/07/12
For personal use only.

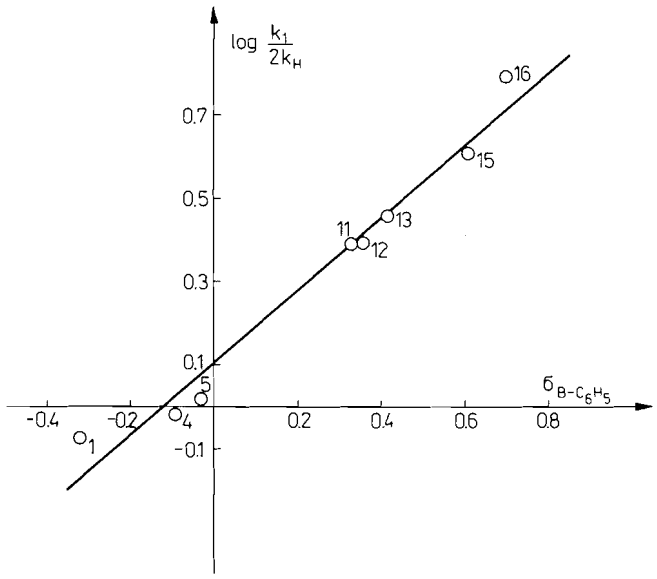

FIG. 1. Relationship of log $(k_1/(2k_H))$, for the first hydrolysis step of disulfonyl dichlorides, to Hammett $\sigma_{BC_6H_5}$ constants—analogous to $\sigma_{BC_6H_5SO_2Cl}$ constants.

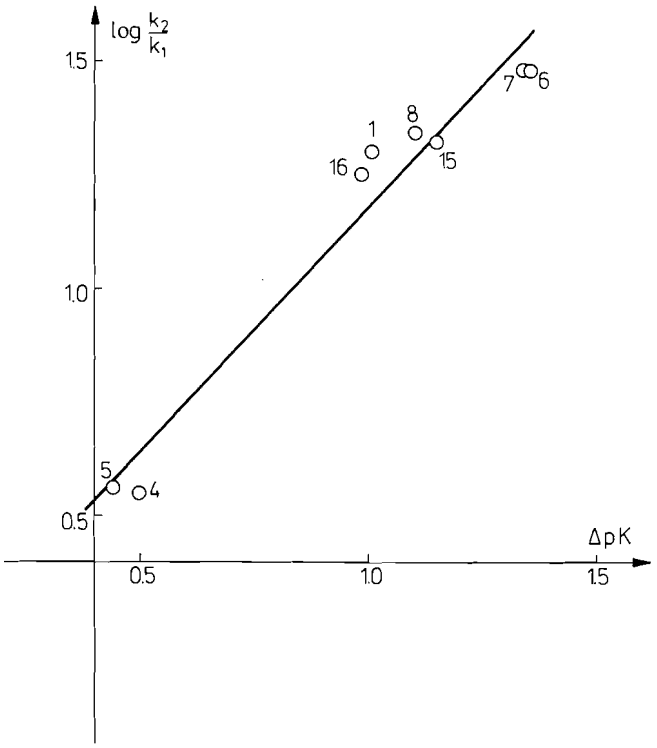

FIG. 2. Relationship of log (k_2/k_1), for the hydrolysis of disulfonyl dichlorides, to $\Delta pK = \log (K_{a_2}/K_{a_1})$ for deprotonation reactions of conjugated acids of analogous diamines (16).

correlation after assuming that the decisive influence is exerted by the bridge situated in the *meta* position in relation to the $-SO_2Cl$ group. This operation corrects only the correlation coefficient. Equation [2] together with [1] give an interstructural correlation [3]:

[3] $\sigma^{m,p}_{BC_6H_4SO_2Cl} = 0.606\ \sigma^{m,p}_{BC_6H_5} + 0.139$

From the data of Table 1 it follows that $\sigma^{p}_{OC_6H_4SO_2Cl} = -0.05$, $\sigma^{p}_{SC_6H_4SO_2Cl} \cong 0.15$, $\sigma^{p}_{SeC_6H_4SO_2Cl} = 0.45$. Equation [3] makes possible the evaluation of $\sigma^{p}_{SC_6H_5} = 0.02$ and $\sigma^{p}_{SeC_6H_5} = 0.52$. The hydrolysis reaction of the first $-SO_2Cl$ group is well described by eq. [2]. The analogous correlation $\log (k_2/k_H) = f(\sigma_{BC_6H_5})$ is fulfilled only for six out of the nine compounds previously taken into consideration. The intermediate products created from the compounds with $-CH_2-$, $-(CH_2)_2$, and $-N=N-$ bridges (**4**, **5** and **11**, respectively), as well as from **9**, do not fulfill the correlation:

[4] $\log (k_2/k_H) = (0.778 \pm 0.173)\cdot\sigma_{BC_6H_5} + (1.762 \pm 0.080)$

$n = 6$, $r = 0.9874$ $s_0 = 0.0539$, for $t_{0.05,4}$

For six intermediate products, A_1 (from compounds **1**, **8**, **12**, **13**, **15**, **16**), two additional structural correlations (eqs. [5] and [6]) are fulfilled:

[5] $\sigma_{BC_6H_4SO_3^-} = 0.548 \cdot \sigma_{BC_6H_5} + 1.302$

[6] $\sigma_{BC_6H_4SO_3^-} = 0.956 \cdot \sigma_{BC_6H_5SO_2Cl} + 1.149$

However, these correlations are not of a general character.

The correlations and abnormalities observed raise the question as to whether all the initial compounds and their intermediates react according to the same mechanism, and if it is possible to determine a more general correlation with regard to where the specific interactions occur. A correlation of this type can be determined by a comparison of relative reactivities of $-SO_2Cl$ groups in A and A_1 with the relative basicities of analogous amines $H_2N—Ar—B—Ar—NH_2$ and $H_2N—Ar—B—Ar—NH_3^+$. Taking into account the acidity constants of the suitable conjugated acids given in ref. 16 we get the following dependence:

[7] $\log (k_2/k_1) = \rho_r \log (K_{a2}/K_{a1}) + \delta_r = \rho_r\, \Delta pK + \delta_r$

where $\Delta pK = pK_{a1} - pK_{a2}$; $\rho_r = 1.073 \pm 0.230$; $\delta_r = 0.100 \pm 0.239$; $n = 8$, $r = 0.9777$, $s_0 = 0.087$, for $t_{0.05,6}$. This is a directly proportional correlation $(k_2/k_1 \cong K_{a2}/K_{a1})$ and it includes compounds **4** and **5** (Fig. 2).

The negative charge of the SO_3^- group changes the reactivity of the unreacted SO_2Cl group in the same way as the positive charge of the protonated amine group changes the acidity of the second protonated amine group in the transition state or the equilibrium state, respectively:

$$[(^-O_3S—)\ ClO_2S—Ar—B—Ar—SO_2Cl \ldots {}^-OCOCH_3]^{\neq} \xrightarrow{(k_1 \text{ or } k_2)} \ldots$$

$$(H_2N\text{-})\ {}^+H_3N—Ar—B—Ar—NH_3^+ + H_2O \xrightleftharpoons{(K_{a1} \text{ or } K_{a2})} \ldots$$

This fact suggests the same hydrolysis mechanism and indirectly confirms the fact that the anion is an intermediate product of hydrolysis A_1 as in ref. 1.

Acknowledgment

The authors wish to express their gratitude to Professor Wawrzyniec Podkościelny for samples of compounds investigated in this paper. The work was supported in part by the MRI-11 and CPBP 01.15 projects.

1. P. SANECKI and E. ROKASZEWSKI. Can. J. Chem. **65**, 2263 (1987).
2. M. PODGÓRSKI and W. PODKOŚCIELNY. J. Appl. Polym. Sci. **34**, 639 (1987).

3. R. V. VIZGERT, I. E. KACHANKO, and V. F. YAVOROVSKAYA. Reakts. Sposobn. Org. Soedin. (Tartu), **3**, 16 (1966).
4. C. S. MARVEL. J. Am. Chem. Soc. **73**, 1097 (1951).
5. E. N. GURJANOVA. Zh. Fiz. Khim. **21**, 411 (1947); **21**, 415 (1947).
6. P. CH. DUTTA and D. J. MANDAL. J. Indian Chem. Soc. **32**, 497 (1955).
7. C. GEOFFROY. C.R. Hebd. Seances Acad. Sci. **178**, 2259 (1924); Beilstein, Vol. 11, II, 125.
8. B. A. HUNTER. U.S. Patent No. 2 626 280 (1953).
9. I. M. TYULENEVA, YU. M. MOSKVICHEV, G. S. MIRONOV, M. I. FARBEROV, G. G. KRYUKOVA, T. S. TITOVA, I. K. CHERNOVA, and F. M. MANDROSOVA. Osnovn. Org. Sint. Neftekhim. No. 2, 93 (1975).
10. J. FELDMAN. Helv. Chem. Acta, **14**, 751 (1931).
11. H. GILMAN, E. W. SMITH and H. J. OATFIELD. J. Am. Chem. Soc. **56**, 1412 (1934).
12. H. LIMPRICHT. Ber. Dtsch. Chem. Ges. **14**, 1357 (1881).
13. A. LAPWORTH. J. Chem. Soc. **73**, 405 (1898).
14. O. EXNER. *In* Advances in linear free energy relationships. *Edited by* N. B. Chapman and J. Shorter. Plenum Press, London and New York. 1972. pp. 28, 29.
15. C. HANSCH and A. LEO. Substituent constants for correlation analysis in chemistry and biology. J. Wiley and Sons, New York. 1979.
16. B. A. KOROLEV, E. V. GERASHCHENKO, and YA. S. VYGOBSKII. Reakts. Sposobn. Org. Soedin. (Tartu), **8**, 681 (1971).

Can. J. Chem. Downloaded from www.nrcresearchpress.com by 122.72.124.2 on 09/07/12
For personal use only.

Crystal chemistry of tetraradial species. Part 2. Crystal structures of Et_4NI, $Ph_4PBr \cdot H_2O$, and $Ph_4PBr \cdot 2H_2O$[1]

BEVERLY R. VINCENT,[2] OSVALD KNOP,[3] ANTHONY LINDEN, T. STANLEY CAMERON, AND KATHERINE N. ROBERTSON

Department of Chemistry, Dalhousie University, Halifax, N.S., Canada B3H 4J3

Received May 26, 1988

BEVERLY R. VINCENT, OSVALD KNOP, ANTHONY LINDEN, T. STANLEY CAMERON, and KATHERINE N. ROBERTSON. Can. J. Chem. **66**, 000 (1988).

The crystal structure of Et_4NI ($I\bar{4}$, a = 8.860(2) Å, c = 6.933(1) Å, Z = 2) has been redetermined and those of $Ph_4PBr \cdot H_2O$ ($P\bar{1}$, a = 10.005(3) Å, b = 10.659(2) Å, c = 10.697(4) Å, α = 102.61(2)°, β = 83.39(3)°, γ = 108.09(3)°, Z = 2) and $Ph_4PBr \cdot 2H_2O$ (*Pnma*, a = 16.255(4) Å, b = 10.810(4) Å, c = 12.667(9) Å, Z = 4) have been determined for the first time. In the Et_4NI structure Et_4N^+ cations in an extended S_4 conformation and I^- anions are arranged in a zincblende-type packing. The two hydrate structures are ionic and very similar. The anion in the monohydrate is a centrosymmetric cyclic dimer $[Br_2(OH_2)_2]^{2-}$; in the dihydrate the anion, which is an almost planar infinite $[Br^-(OH_2)_{4/2}]_\infty$ chain $\| b$, appears to be of a novel type. If the H_2O molecules are not considered, the ion packing in both hydrates may be regarded as of the *anti*-NiAs type. The ion packing in R_4EX structures and the conformation of the Et_4N^+ ion in crystals are discussed in some detail.

BEVERLY R. VINCENT, OSVALD KNOP, ANTHONY LINDEN, T. STANLEY CAMERON et KATHERINE N. ROBERTSON. Can. J. Chem. **66**, 000 (1988).

On a déterminé de nouveau la structure cristalline du composé Et_4Ni ($I\bar{4}$, a = 8,860(2) Å, c = 6,933(1) Å, Z = 2) et on a déterminé pour la première fois les structures cristallines du $Ph_4PBr \cdot H_2O$ ($P\bar{1}$, a = 10,005(3) Å, b = 10,659(2) Å, c = 10,697(4) Å, α = 102,61(2)°, β = 83,39(3)°, γ = 108,09(3)°, Z = 2) et du $Ph_4PBr \cdot 2H_2O$ (*Pnma*, a = 16,255(4) Å, b = 10,810(4) Å, c = 12,667(9) Å, Z = 4). Dans la structure du Et_4NI, les cations Et_4N^+, dans une conformation étendue de type S_4, et les anions I^- sont disposés selon un entassement de type blende. Les deux structures hydrate sont ioniques et sont très voisines. Dans le monohydrate, l'anion est un dimère cyclique centrosymétrique $[Br_2(OH_2)_2]^{2-}$; dans le dihydrate l'anion, qui est quasiment une chaîne plane infinie $[Br^-(OH_2)_{4/2}]_\infty \| b$, semble être d'un nouveau type. Si on ne tient pas compte des molécules d'eau, on peut considérer l'entassement des ions dans les deux hydrates comme étant de type *anti*-NiAs. On discute de l'entassement des ions dans les structures de type R_4EX et de la conformation de l'ion Et_4N^+ dans les cristaux.

[Traduit par la revue]

In this series of investigations we are interested in discovering how the idealized symmetry (T_d or subgroup) of tetraradial[4] $XL_4^{n\pm}$ species is reflected in the crystallographic symmetry when $XL_4^{n\pm}$ is incorporated in a crystal, on its own (n = 0) or in combination with another, not necessarily tetraradial species, and in particular how the packing type is affected by the size and complexity of $XL_4^{n\pm}$ in simple chemical combinations. In the present contribution to the systematic crystal chemistry of such species we report the results of a redetermination of the structure of Et_4NI and of determinations of the structures of $Ph_4PBr \cdot H_2O$ and $Ph_4PBr \cdot 2H_2O$. Although Ph_4PBr rather than its hydrates was originally the compound to be investigated, we were unsuccessful in our attempts to obtain crystals of the anhydrous bromide (see Experimental).[5]

The crystal data of the title compounds are assembled in Table 1. Details of the structure determinations and a list of material deposited will be found under Experimental.

Et_4NI

The structure was partially determined by Wait and Powell (2) from a projection based on visually estimated photographic intensities of 57 independent *hk*0 reflections. The determination utilized the fact that the signs of the $F(hk0)$ were all determined by the contribution from the I atoms and were all positive. With I at 2(*a*) − 000 etc. and N at 2(*d*) − ½0¼ etc. of $I\bar{4}$ they obtained x = 0.633, y = −0.048 for C(1) and x = 0.558, y = −0.190 for C(2) (converted to the setting of Table 2). They did not determine z of either atom, their main concern being with the conformation of the cation skeleton, which they presumed could be derived without this information. The H atoms were not considered.

The present redetermination (Tables 1 and 2) confirms the general features of the structure as reported in ref. 2. However, the coordinates of C(2) given there appear to correspond to C(2) attached to C(1) ($\frac{1}{2} + y, \frac{1}{2} - x, \frac{1}{2} - z$) and not to C(1) with x, y, z of Table 2.

The overall arrangement is shown in Fig. 1. The cation/anion packing is of the 4:4 coordinated, zincblende[6] type, with the cation in an extended S_4 conformation[7] and with the $NC(1)_4$ tetrahedron slightly flattened along the S_4 axis, C(1)NC(1′) = 111.4° (cf. Table 3). Each of the five H atoms has a nearest I neighbour at a distance which ranges from 3.18 to 3.72 Å (Fig. 1). Two of these distances, H(11)···I(1, 0, 0) = 3.18(4) Å and H(22)···I($\frac{1}{2}, \frac{1}{2}, \frac{1}{2}$) = 3.24(4) Å, are slightly but not significantly shorter than the sum of the van der Waals radii, 3.35 Å. The closest H···H approach within the cation is H(11)···H(23) ($\frac{1}{2} + y; \frac{1}{2} - x; \frac{1}{2} - z$) = 2.07(8) Å, with H(11)···H(12) ($\frac{1}{2} - y; x - \frac{1}{2}; \frac{1}{2} - z$) = 2.37(8) Å next. The intercation H···H distances all exceed 2.4 Å, twice the van der Waals radius of the H atom.

$Ph_4PBr \cdot H_2O$

The positional parameters are listed in Table 4 and interatomic distances and bond angles in Table 5.

[1]Reference 1 is considered as Part 1.

[2]Holder of NSERC (1983–1986), Killam (1984–1986), and Sumner (1986–1987) Graduate Fellowships.

[3]To whom correspondence may be addressed.

[4]We use the term "tetraradial" in preference to "tetrahedral", which has also other, quite different connotations.

[5]Much the same difficulty was experienced with Et_4NCl (3, 4). However, the crystal structure of Ph_4PBr was in the meantime determined by Alcock *et al.* (5), who were able to crystallize the anhydrous compounds from mixtures of MeOH and MeCN.

[6]Not wurtzite as stated in ref. 2.

[7]Taking the S_4 axis as the z axis, z(N) = 0, $|z[C(2)]| > |z[C(1)]|$.

Can. J. Chem. Downloaded from www.nrcresearchpress.com by 122.72.124.2 on 09/07/12
For personal use only.

TABLE 1. Crystal data of Et_4NI, $Ph_4PBr \cdot H_2O$, and $Ph_4PBr \cdot 2H_2O$[a]

Parameter	Value		
	Et_4NI	$Ph_4PBr \cdot H_2O$	$Ph_4PBr \cdot 2H_2O$
Formula	$C_8H_{20}IN$	$BrC_{24}H_{22}OP$	$BrC_{24}H_{24}O_2P$
fw	257.16	437.32	455.34
Crystal size, mm^3	$0.2 \times 0.2 \times 0.4$	$0.3 \times 0.3 \times 0.3$	$0.3 \times 0.2 \times 0.5$
Solvent	H_2O	$MeNO_2$	EtOH
θ-range, deg	2–30	2–23	2–23
μ_{Mo}, cm^{-1}	26.9	21.5	20.5
Max/min[b]	1.653/0.787	1.210/0.859	1.163/0.824
a, Å	8.860(2)[c]	10.005(3)	16.255(4)
b, Å	8.860(2)[c]	10.65(2)	10.810(4)
c, Å	6.933(1)[c]	10.697(4)	12.667(9)
α, deg	90	102.61(2)	90
β, deg	90	83.39(3)	90
γ, deg	90	108.09(3)	90
V, $Å^3$	544.2(2)	1057(1)	2226(3)
Z	2	2	4
ρ_c, g/cm^3	1.569(1)[c]	1.374(1)	1.358(2)
Space group	$I\bar{4}$ (no. 82)	$P\bar{1}$ (no. 2)	*Pnma* (no. 62)
F(000), e	256	448	936
Reflections:			
Total measured	490	3119	2202
Unique total	469	2932	1641
Unique used	443[d]	1847[d]	751[e]
$100R$; $100R_w$	2.58; 2.85	3.85; 3.87	3.90; 4.07

[a]Mo $K\alpha_1$, $\lambda = 0.70926$ Å (graphite monochromator).
[b]Max/min empirical absorption corrections, cf. ref. 53.
[c]Reference 2: $a = 8.87(2)$ Å, $c = 6.95(2)$ Å, $\rho_o = 1.56(1)$ g/cm^3.
[d]$I > 3\sigma(I)$.
[e]$I > 2\sigma(I)$.

The structure consists of Ph_4P^+ cations of symmetry C_1 and centrosymmetric cyclic $[Br^-{}_2(OH_2)_2]$ anions (Figs. 2 and 3), and as such it may be viewed as being of a distorted *anti*-CdI_2 packing type, $[Ph_4P^+]_2[Br_2(OH_2)_2]^{2-}$. Alternatively, if the H_2O molecule is disregarded, the packing may be described as a distorted *anti*-NiAs type arrangement, $Ph_4P^+Br^-$. The hydrogen bonding in the cyclic anion is discussed in more detail below.

Comparison of the $Ph_4P^+ \cdots Br^-$ geometry with that of the covalent Ph_4EX (E = Sb, Bi) species (cf. ref. 6) shows that the $P \cdots Br$ distance, 5.821(2) Å, is far in excess of the $Sb \cdots X \sim 3.3$ Å limit for pentacoordination (even though the C(21)PBr angle, 156°, is still acceptable for a distorted trigonal bipyramid with C(21) as the axial and C(11), C(31), and C(41) as the equatorial carbon atoms), and the means of the $C_{ax}PC_{eq}$ and $C_{eq}PC_{eq}$ angles, 110.1(15)° and 108.9(17)°, respectively, are statistically indistinguishable from each other and from the tetrahedral angle. There is thus no doubt that the crystal is ionic.

The internal CCC angles in the phenyl rings are all within 3 esd's of 120°. Specifically, the means of the C(6)C(1)C(2) and C(3)C(4)C(5) angles are 119.7(4)° and 120.0(5)°, respectively, indicating that within the accuracy of the structure determination the rings are undistorted by bonding to the P atom.

$Ph_4PBr \cdot 2H_2O$

The positional parameters are given in Table 6 and interatomic distances and bond angles in Table 7.

This orthorhombic structure also is ionic. The Ph_4P^+ cation is of symmetry C_s, with ring 2 perpendicular to and ring 3 in the mirror plane (Fig. 2). The Br atom is at an inversion centre and coordinated by four oxygens. The $Br^+ \cdots H_2O$ bonds connect the bromide ion and the water molecules to form almost planar infinite $[Br^-(OH_2)_{4/2}]_\infty$ anion chains $\| b$ (Fig. 3); the hydrogen bonding aspects of these chains are discussed below.

The cation/anion packing in the dihydrate is an orthorhombic distortion of the *anti*-NiAs packing if only the Ph_4P^+ and Br^- ions are considered. The $P \cdots Br$ separation, 6.233(3) Å, is 0.4 Å larger than in the monohydrate.

Comparison of $Ph_4PBr \cdot H_2O$ and $Ph_4PBr \cdot 2H_2O$

As is evident from Fig. 2, the two structures are very similar. The main difference is in the linking of the $[Br_2(OH_2)_2]^{2-}$ ions in the monohydrate by the additional water molecule to form the infinite $[Br^-(OH_2)_{4/2}]_\infty$ bands in the dihydrate. In the monohydrate the planes of the anion rings are all parallel, whereas in the dihydrate the orientations of the bands alternate. Similarly, in the monohydrate all the cations are related by parallel translations; in the dihydrate, the cation orientations alternate.

The relationship of the orthorhombic unit cell D of the dihydrate to the triclinic unit cell M of the monohydrate is illustrated in Fig. 2: $2M \rightarrow D$, $\boldsymbol{a}^D \rightarrow \boldsymbol{c}^M - \boldsymbol{a}^M$, $\boldsymbol{b}^D \rightarrow \boldsymbol{b}^M$, $\boldsymbol{c}^D \rightarrow \boldsymbol{c}^M + \boldsymbol{a}^M$. Conversely, M corresponds to a pseudo-hexagonal subcell H of D: $\boldsymbol{a}_1{}^H = \frac{1}{2}(\boldsymbol{c}^D + \boldsymbol{a}^D) \rightarrow \boldsymbol{c}^M$, $\boldsymbol{a}_2{}^H = \frac{1}{2}(\boldsymbol{c}^D - \boldsymbol{a}^D) \rightarrow \boldsymbol{a}^M$, $\boldsymbol{c}^H = \boldsymbol{b}^D \rightarrow \boldsymbol{b}^M$. To take account of the alternating orientations of the ions in the dihydrate in relation to the monohydrate structure, the symmetry of the dihydrate structure may be represented by the dichromatic group $62/448$, $Pn'ma' - Pnma|P2_1/m$, which relates to $P\bar{1}$ of the monohydrate via $P\bar{1} \subset P2_1/m$.

The phenyl rings in the two hydrates are planar to better than $\sigma = 0.005$ Å; ring 3 in the dihydrate is in a mirror plane and hence planar by symmetry. The conformations of the Ph_4P^+

Can. J. Chem. Downloaded from www.nrcresearchpress.com by 122.72.124.2 on 09/07/12
For personal use only.

Can. J. Chem. Downloaded from www.nrcresearchpress.com by 122.72.124.2 on 09/07/12
For personal use only.

TABLE 2. Et_4NI: positional parameters and temperature factors ($\times 10^3$)

Atom	x / y / z	U_{11} / U_{22} / U_{33}	U_{12} / U_{13} / U_{23}
I	0	38.9(1)	0
	0	38.9(1)	0
	0	38.9(1)	0
N	½	30.8(11)	0
	0	30.8(11)	0
	¼	30.8(11)	0
C(1)	632.1(5)	35(1)	2(1)
	−050.5(5)	36(1)	−8(1)
	373.1(7)	34(2)	1(1)
H(11)	726(3)	53(3)*	
	−079(3)		
	279(3)		
H(12)	598(3)	65(3)*	
	−149(3)		
	457(3)		
C(2)	690.3(6)	58(2)	0(2)
	065.7(6)	57(2)	−21(2)
	512.9(17)	51(2)	−3(2)
H(21)	786(3)	62(3)*	
	019(3)		
	592(3)		
H(22)	604(3)	50(3)*	
	102(3)		
	608(3)		
H(23)	733(3)	66(3)*	
	165(3)		
	431(3)		

*U_{iso}.

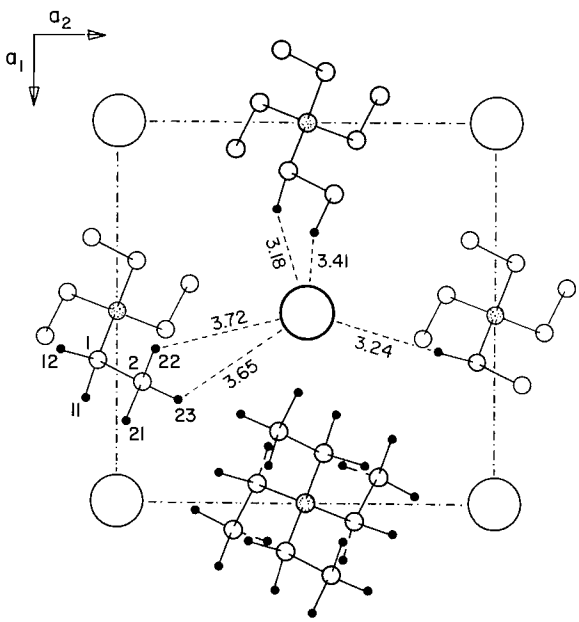

FIG. 1. Et_4NI: projection on (001). Not all the H atoms are shown. Broken lines indicate shortest H···I approaches (Å).

TABLE 3. Et_4NI: interatomic distances (Å) and bond angles (deg)*

Atoms	Distance	Atoms	Angle
N—C(1)	1.516(5)	C(1)—N—C(1′)	111.5(3)
C(1)—C(2)	1.505(10)	C(1)—N—C(1″)	108.5(3)
C(1)···C(1′)	2.506(7)	N—C(1)—C(2)	115.2(4)
C(1)···C(1″)	2.460(7)	C(2)—C(1)—N—C(1′)	−57(1)
N—I	4.757(1)	C(2)—C(1)—N—C(1″)	−177(1)
		C(2)—C(1)—N—C(1‴)	62(1)

*C(1) and C(1′) are related by C_2. C(1′): $1-x, -y, z$. C(1″): $\frac{1}{2}+y, \frac{1}{2}-x, \frac{1}{2}-z$. C(1‴): $\frac{1}{2}-y, x-\frac{1}{2}, \frac{1}{2}-z$.

TABLE 4. $Ph_4PBr\cdot H_2O$: positional parameters and isotropic temperature factors ($\times 10^4$) of the nonhydrogen atoms

Atom	x	y	z	U_{iso}
P	5643(1)	2364(1)	3420(1)	304
C(11)	6041(4)	3652(3)	2479(3)	347
C(12)	7289(4)	3857(4)	1725(4)	473
C(13)	7643(5)	4835(4)	0957(4)	558
C(14)	6742(6)	5565(4)	0943(5)	628
C(15)	5501(5)	5356(4)	1684(5)	619
C(16)	5150(4)	4407(4)	2464(4)	457
C(21)	6948(4)	2848(4)	4578(4)	382
C(22)	7215(4)	1876(4)	5126(4)	496
C(23)	8077(4)	2281(5)	6148(5)	603
C(24)	8646(5)	3631(6)	6625(5)	688
C(25)	8407(5)	4594(5)	6086(5)	658
C(26)	7551(4)	4197(4)	5063(4)	468
C(31)	3967(4)	2175(3)	4281(3)	332
C(32)	3846(4)	2081(4)	5574(4)	452
C(33)	2558(5)	1825(4)	6232(4)	542
C(34)	1373(4)	1663(4)	5608(5)	548
C(35)	1454(4)	1771(4)	4327(4)	501
C(36)	2755(4)	2018(4)	3658(4)	422
C(41)	5649(4)	0802(3)	2370(3)	351
C(42)	4393(4)	−0135(4)	1964(4)	417
C(43)	4419(5)	−1275(4)	1071(4)	527
C(44)	5691(6)	−1488(4)	0583(4)	536
C(45)	6931(5)	−0569(5)	0983(4)	600
C(46)	6928(4)	0582(4)	1887(4)	467
Br	0618.7(5)	2444.7(5)	1223.1(5)	503
O	0676(4)	−0758(4)	1675(3)	768

cations in the two structures are closely similar (Fig. 2), the main difference being that rings 1 and 4 in the dihydrate are related by reflection whereas in the monohydrate they are not, and rings 2 and 3 in the dihydrate are mutually perpendicular whereas in the monohydrate they form an angle of 100°. The P atom is coplanar by symmetry with ring 3 of the dihydrate. In the other cases it is 0.26 Å or less out of the plane of the ring.

Hydrogen bonding

A centrosymmetric cyclic anion dimer of the type $[X_2^-(OH_2)_2]$ (X = Cl, Br), such as that present in the $Ph_4PBr\cdot H_2O$ structure, is not an unusual feature of low hydrates or organic onium halides (e.g. refs. 3, 7, 8), where it occasionally competes with helical or near-planar $[X^-(OH_2)_{2/2}]$ chains (8). However, the infinite flat $[Br^-(OH_2)_{4/2}]_\infty$ anion of $Ph_4PBr\cdot 2H_2O$ appears to be of a hitherto unreported type. It may be regarded (Fig. 3) as a superposition of two planar centrosymmetric zigzag

Can. J. Chem. Downloaded from www.nrcresearchpress.com by 122.72.124.2 on 09/07/12
For personal use only.

TABLE 5. $Ph_4PBr \cdot H_2O$: interatomic distances (Å) and bond angles (deg)

Atoms	Distance	Atoms	Angle
P—C(11)	1.797(5)	C(11)—P—C(21)	108.1(2)
P—C(21)	1/783(5)	C(11)—P—C(31)	112.1(2)
P—C(31)	1.794(5)	C(11)—P—C(41)	108.6(2)
P—C(41)	1.796(4)	C(21)—P—C(31)	107.3(2)
		C(21)—P—C(41)	111.2(2)
C(11)—C(12)	1.391(6)	C(31)—P—C(41)	109.5(2)
C(11)—C(16)	1.377(7)		
C(12)—C(13)	1.402(8)	P—C(11)—C(12)	117.6(4)
C(13)—C(14)	1.365(9)	P—C(11)—C(16)	122.5(3)
C(14)—C(15)	1.378(8)	P—C(21)—C(22)	120.3(3)
C(15)—C(16)	1.386(8)	P—C(21)—C(26)	119.4(4)
		P—C(31)—C(32)	119.6(4)
C(21)—C(22)	1.400(8)	P—C(31)—C(36)	121.1(3)
C(21)—C(26)	1.382(6)	P—C(41)—C(42)	120.3(4)
C(22)—C(23)	1.380(7)	P—C(41)—C(46)	119.4(3)
C(23)—C(24)	1.376(8)		
C(24)—C(25)	1.373(10)	C(11)—C(12)—C(13)	120.0(5)
C(25)—C(26)	1.378(8)	C(12)—C(13)—C(14)	119.4(5)
		C(13)—C(14)—C(15)	120.5(5)
C(31)—C(32)	1.398(6)	C(14)—C(15)—C(16)	120.7(6)
C(31)—C(36)	1.397(7)	C(15)—C(16)—C(11)	119.5(4)
C(32)—C(33)	1.373(6)	C(16)—C(11)—C(12)	119.9(4)
C(33)—C(34)	1.373(8)		
C(34)—C(35)	1.391(8)	C(21)—C(22)—C(23)	119.4(4)
C(35)—C(36)	1.390(6)	C(22)—C(23)—C(24)	119.7(6)
		C(23)—C(24)—C(25)	121.5(5)
C(41)—C(42)	1.386(5)	C(24)—C(25)—C(26)	119.2(5)
C(41)—C(46)	1.392(7)	C(25)—C(26)—C(21)	120.5(5)
C(42)—C(43)	1.377(6)	C(26)—C(21)—C(22)	119.7(4)
C(43)—C(44)	1.385(8)		
C(44)—C(45)	1.365(7)	C(31)—C(32)—C(33)	121.0(5)
C(45)—C(46)	1.388(6)	C(32)—C(33)—C(34)	119.4(5)
		C(33)—C(34)—C(35)	121.2(4)
Br···O	3.569(2)	C(34)—C(35)—C(36)	119.3(5)
Br···O′	3.401(2)	C(35)—C(36)—C(31)	119.9(4)
Br···Br′	5.131(1)	C(36)—C(31)—C(32)	119.1(4)
O···O′	4.721(5)		
Br···P	5.820(2)	C(41)—C(42)—C(43)	119.6(5)
		C(42)—C(43)—C(44)	120.3(4)
Br′ $-x$ $-y$ $-z$		C(43)—C(44)—C(45)	120.3(4)
		C(44)—C(45)—C(46)	120.3(5)
O′ $-x$ $-y$ $-z$		C(45)—C(46)—C(41)	119.4(4)
		C(46)—C(41)—C(42)	120.1(4)
		Br—O—Br′	94.7(1)
		O—Br—O′	85.3(1)
		Br—P—C(21)	156.1(13)

chains, ···Br···O(1)···Br···O(1)··· and ···Br···O(2)···Br···O(2)···, which share the Br atoms; the planes of the two chains form an angle of 11°. The symmetry of these flat bands is almost *pmam* and approaching *pmmm*. The oxygen atoms are located in mirror planes bisecting the HOH angles, so that the symmetry of the water molecules is C_{2v}. Although the H_w atoms have not been located with any accuracy, the BrOBr angles (Table 7) are close to the HOH angle in the free water molecule, which indicates that the O—H_w···Br^- bonds are practically linear.

The O···Br^- distances in both hydrates, between 3.40 and 3.57 Å (Tables 5 and 7), fall in the upper half of the O···Br range observed in hydrates, 3.25–3.58 Å (7–9), and well below the estimated cut-off O···Br distance, 3.92 Å, for O—H···Br interactions (9). The BrOBr angle in the cyclic $[Br_2^-(OH_2)_2]$ anion in the monohydrate is only 94.7°. Whether this rather small angle and the rather long O···Br^- distances are attributable to the bulkiness of the cation cannot be ascertained at present.

TABLE 6. $Ph_4PBr \cdot 2H_2O$: positional parameters and isotropic temperature factors ($\times 10^4$) of the nonhydrogen atoms

Atom	x	y	z	U_{iso}
P	4150(1)	¼	9296(2)	371
C(11)	3598(3)	3851(5)	8880(4)	418
C(12)	3873(3)	4582(6)	8068(6)	675
C(13)	3398(5)	5573(7)	7725(7)	924
C(14)	2668(4)	5796(7)	8160(8)	870
C(15)	2387(4)	5079(7)	8959(7)	825
C(16)	2851(3)	4089(6)	9329(6)	657
C(21)	4197(5)	¼	10 715(7)	460
C(22)	4240(4)	1387(6)	11 249(4)	614
C(23)	4350(4)	1410(7)	12 350(5)	738
C(24)	4398(5)	¼	12 857(8)	664
C(31)	5193(5)	¼	8818(6)	414
C(32)	5851(5)	¼	9536(7)	561
C(33)	6647(5)	¼	9142(8)	586
C(34)	6792(6)	¼	8085(9)	711
C(35)	6156(6)	¼	7388(8)	659
C(36)	5354(5)	¼	7739(7)	540
Br	0	0	0	711
O(1)	1247(4)	¼	0464(6)	702
O(2)	3797(4)	¼	5760(7)	995

Ion packing in $R_4E^+X^-$ structures

Inspection of Fig. 2 reveals two conspicuous gross features present in both Ph_4PBr hydrate structures: the Br^- ions are situated in or close to the $10\bar{1}$ planes of the "orthohexagonal" cells[8] (or the 100 planes of the "hexagonal" cells, i.e. the tabulated triclinic cell M of the monohydrate and the pseudohexagonal subcell H of the dihydrate); and the cations are arranged in columns parallel to b and related, within each column, by inversion or by a 2_1 axis to form infinite cation helices. The $10\bar{1}$ planes confine the cation skeletons to parallel slabs, so that the two structures may be viewed as layer structures, the layers defining in a natural manner the pseudohexagonal cells. These features are strongly reminiscent of the structure of Ph_4SbBr (6), the covalent character of the Sb—Br bond in this compound notwithstanding, and in fact can be shown to be common to a whole family of onium salts and their pro-cation congeners.

In $R_4E^+X^-$ structures all the common AB packing types are represented (Table 8). The occurrence of planes occupied exclusively by anions (or the central atoms of anions) is a natural consequence of the zincblende, CsCl, NiAs, and *anti*-NiAs packing arrangements (Fig. 4). In the two last-named arrangements, which are based on the hexagonal aristotype symmetry $P6_3mc$, the anion planes are $||1\bar{1}00$ or (in *anti*-NiAs) $11\bar{2}0$; they correspond to the anion planes of the two Ph_4PBr hydrates, which accounts for the layer-like character of these structures. Although Ph_4SbBr ($P2_1/n$) is not ionic, the Br atoms (involved

[8]This is the $[\boldsymbol{c}^M - \boldsymbol{a}^M, \boldsymbol{b}^M, \boldsymbol{c}^M + \boldsymbol{a}^M]$ cell of the monohydrate and the D cell of the dihydrate. In the dihydrate the Br^- ions may be described as lying in the $10\bar{1}$ *or* the 101 planes of the D cell.

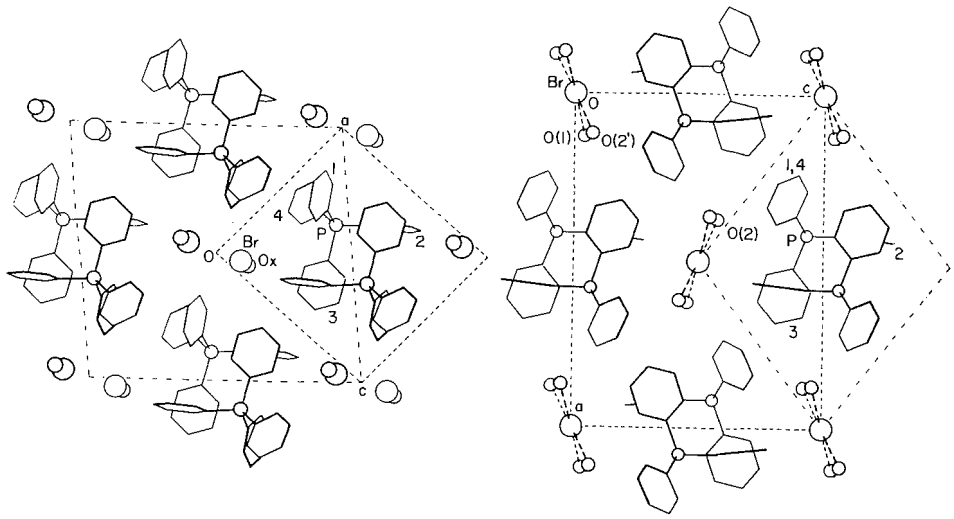

FIG. 2. Structures of the two hydrates of Ph_4PBr. The projections are oriented so as to display the matching features of the two structures. Broken lines, unit cell of Table 1; dash–dot lines, sub- or supercell related to the *anti*-NiAs or *anti*-CdI_2 packing (see text). (*Left*) $Ph_4PBr \cdot H_2O$: projection along *b* on (010). (*Right*) $Ph_4PBr \cdot 2H_2O$: projection on (010). Rings 1 and 4 are related by mirror planes at $y = \pm\frac{1}{4}$, ring 2 is perpendicular to (010), ring 3 is in the mirror plane at $y = \frac{1}{4}$.

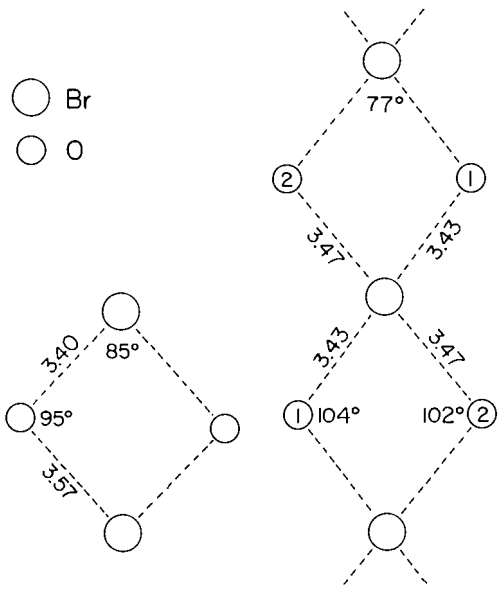

FIG. 3. Hydrogen bonding schemes in the two hydrates of Ph_4PBr. (*Left*) $Ph_4PBr \cdot H_2O$: isolated centrosymmetric $[Br_2(OH_2)_2]^{2-}$ rings. (*Right*) $Ph_4PBr \cdot 2H_2O$: almost planar infinite $[Br^-(OH_2)_{4/2}]_\infty$ anion chains parallel to *b*.

in long Sb—Br bonds) are located almost exactly in the $1\bar{1}00$ planes of the monoclinic, pseudohexagonal unit cell. These planes correspond to the $1\bar{1}00$ planes of the *anti*-NiAs structure and contain only the Br atoms (cf. Fig. 6 of ref. 6), in accord with the view (6) that the Ph_4SbBr structure represents a transitional stage between covalent and ionic R_4EX.

In the wurtzite-type packing ($P6_3mc \subset P6_3/mmc$) the anion planes ($11\bar{2}0$ or $|||100$) in addition accommodate all the cations (or the central atoms of the cations), so that this arrangement lacks the layer-like features. The Me_3SbX_2 ($P\bar{6}2c \subset P6_3/mmc$; X = Cl, Br, I) structure is quite similar in this respect if one allows for the covalent character of the Sb—X bonds (Fig. 4). It is interesting that in Ph_4SbCl (also a covalent structure, cf. ref. 6) the Cl atoms, compared with Ph_4SbBr, are considerably farther away from the $10\bar{1}$ planes of the monoclinic cell than the Br atoms in Ph_4SbBr. In this regard the Ph_4SbCl structure may be viewed as intermediate between the *anti*-NiAs and the wurtzite ion packing; it again represents a transitional stage between covalent and ionic R_4EX structures.

In zincblende-type ion packing in Et_4NI ($I\bar{4}$) and related structures (Table 8) may be compared with the *molecular* packings in, for example (10), $C(SMe)_4(I)$ ($P\bar{4}2_1c$) and $C(CH_2OH)_4$ ($I\bar{4}$). In all three cases the tetragonal bc unit cell can be transformed into a fc setting by a 45° rotation about a tetragonal axis and taking $a\sqrt{2}$ as the base edge of the fc unit cell. The structures can then be formulated as [A][B] = $[Et_4N^+][I^-]$, $[C(SMe)_4][\square]$ (no hydrogen bonding), and $[C(CH_2OH)_4][\square]$ (with intermolecular hydrogen bonding): the octahedral interstices in the fc sublattice of contacting A units are occupied by the smaller ion (I^-) in the case of Et_4NI or are vacant, as in the molecular crystals. The smaller ion thus constitutes "stuffing" in the A framework. The series may be completed by adding $LiNH_2 = [NH_2^-][Li^+]$ ($I\bar{4}$)[9] (10), which represents a reverse of the Et_4NI packing. This classification scheme can be extended to include a variety of other structures containing tetraradial units.

Conformation of the Et_4N^+ (= E) ion in crystals

The highest-symmetry skeletal conformation of $N[C(1)H_2C(2)H_3]_4^+$ not in severe conflict with H–H repulsions would be the flat form of D_{2d} ($z(N) = 0$, $z[C(1)] > 0$, $z[C(2)] \sim 0$; principal axis taken as the *z* axis), but this conformation has so far not been reported, nor has a D_{2d} site symmetry for the N atom of E. Site symmetries at N compatible with possible E geometries will be the subgroup symmetries of D_{2d}, viz. S_4, D_2, C_{2v}, C_2, C_s, and C_1. However, these site symmetries do not necessarily imply an unambiguously positioned single conformation, for they may represent volume- or time-averaged symmetries (or both) or two or more E conformations in orientational disorder. When the crystallographic site symmetry

[9]The $LiNH_2$ structure is related to the zincblende structure through $F\bar{4}2'm' - F\bar{4}2m|F\bar{4}$, $F\bar{4}2m \subset F\bar{4}3m$: $c \sim 2a$, upper and lower half of the unit cell each constitutes a tetragonally distorted ZnS cell.

Can. J. Chem. Downloaded from www.nrcresearchpress.com by 122.72.124.2 on 09/07/12
For personal use only.

TABLE 7. $Ph_4PBr \cdot 2H_2O$: interatomic distances (Å) and bond angles (deg)

Atoms	Distance	Atoms	Angle
P—C(11) 2×	1.793(6)	C(11)—P—C(11′)	109.1(4)
P—C(21)	1.799(9)	C(11)—P—C(21) 2×	108.3(2)
P—C(31)	1.800(8)	C(11)—P—C(31) 2×	111.8(2)
		C(21)—P—C(31)	107.2(4)
C(11)—C(12)	1.371(9)		
C(11)—C(16)	1.366(8)	P—C(11)—C(12)	121.8(7)
C(12)—C(13)	1.390(11)	P—C(11)—C(16)	118.4(5)
C(13)—C(14)	1.329(12)	P—C(21)—C(22)	119.4(4)
C(14)—C(15)	1.356(13)	P—C(31)—C(32)	119.9(6)
C(15)—C(16)	1.391(11)	P—C(31)—C(36)	120.5(6)
C(21)—C(22)	1.382(8)	C(11)—C(12)—C(13)	119.9(6)
C(22)—C(23)	1.407(9)	C(12)—C(13)—C(14)	120.4(8)
C(23)—C(24)	1.344(10)	C(13)—C(14)—C(15)	120.5(8)
		C(14)—C(15)—C(16)	120.6(7)
C(31)—C(32)	1.404(12)	C(15)—C(16)—C(11)	119.2(7)
C(31)—C(36)	1.391(12)	C(16)—C(11)—C(12)	119.5(6)
C(32)—C(33)	1.388(12)		
C(33)—C(34)	1.359(15)	C(21)—C(22)—C(23)	118.4(7)
C(34)—C(35)	1.358(14)	C(22)—C(23)—C(24)	119.8(8)
C(35)—C(36)	1.379(13)	C(23)—C(24)—C(25)	122.5(9)
		C(26)—C(21)—C(22)	121.0(8)
Br···O(1)	3.429(4)		
Br···O(2′)	3.472(4)	C(31)—C(32)—C(33)	118.5(8)
Br···Br′	5.405(2)	C(32)—C(33)—C(34)	121.0(8)
O(1)···O(2′)	4.274(13)	C(33)—C(34)—C(35)	120.6(9)
Br···P′	6.233(3)	C(34)—C(35)—C(36)	120.7(9)
		C(35)—C(36)—C(31)	119.6(8)
		C(36)—C(31)—C(32)	119.6(7)
		Br—O(1)—Br′	104.0(4)
		Br—O(2′)—Br′	102.2(4)
		O(1)—Br—O(2′)	76.5(8)
		Br—P′—C(21′)	150(1)

P′, C(21′):	$\frac{1}{2} - x$	$-\frac{1}{4}$	$z - \frac{1}{2}$
C(11′), C(22′), C(23′):	x	$\frac{1}{2} - y$	z
Br′:	0	$\frac{1}{2}$	0
O(2′):	$x - \frac{1}{2}$	$\frac{1}{4}$	$\frac{1}{2} - z$

C(25) = C(23′), C(26) = C(22′)

is not a subgroup symmetry of D_{2d}, E at such sites is disordered of necessity.

The various observed conformational situations are listed in Table 9. I is seen that a site of S_4 symmetry occupied by a single, uniquely oriented E conformation of S_4 symmetry is found only in EI, although the single E(1) conformation in E_2SnCl_6, at a site of C_2 symmetry, simulates the S_4 symmetry quite closely. In both cases the conformation is of the extended[7] type, as it also is in E_2InCl_5 at the site of symmetry S_4, where an S_4 conformation can occur in either of two equivalent orientations differing in C(1) positions. The flat form deriving from D_{2d} is observed at C_{2v} sites, and D_2 is simulated by E(1) and E(2) in $ECl \cdot H_2O$, at sites of symmetries C_2 and C_1, respectively. The volume-averaged symmetry simulated at an N site can be as high as C_{4h}, D_{2d}, and D_{4h}, and the alternative orientations need not be populated equally (cf. Table 9). In an extreme case of orientational disorder, that in $E_2[W_2Ni_3(CO)_{16}]$ (48), no indication of the atoms of E was observed in electron-density maps, although here the presence of the heavy scatterer W may be partially to blame.

Clearly for a single, uniquely oriented E conformation to occur at a given E site the anion size and shape must not be conducive to producing, at that site, a potential that is flat or contains equivalent minima. The last-named requirement is likely to be in conflict with N being accommodated at special positions of high symmetry, which would explain why ordered single conformations, such as that observed in EI, occur relatively rarely.

Experimental

Material

Et_4NI. Commercial material (Aldrich) was recrystallized from water.

Ph_4PBr. Crystallization of Ph_4PBr from water is reported (49) to give $Ph_4PBr \cdot 2H_2O$, which can be completely dehydrated to a white powder by drying *in vacuo*; no other hydrate or solvate is mentioned in ref. 49. To obtain *crystals* of anhydrous Ph_4PBr, oven-dried commercial Ph_4PBr (Aldrich) was therefore dissolved in (*a*) absolute EtOH, (*b*) dried MeCN, (*c*) dried $MeNO_2$, and the solutions were allowed to crystallize at room temperature by evaporation through pinholes. The good-quality crystals from *a* were shown by structure analysis to be the dihydrate (see below). Solution *b* yielded finer, more powdery dihydrate, unsuitable for single-crystal diffraction. Crystallization from *c* began only when the solvent had almost completely evaporated (similar to *b*) and gave quite large, clear, colourless crystals which turned out to be the hitherto unreported $Ph_4PBr \cdot H_2O$; they did not appear to alter on standing in air. An attempt was therefore made to obtain crystals of the anhydrous salt by refluxing (Dean-Stark trap) the oven-dried commercial material in sodium-dried benzene and subsequent crystallization. However, the bromide did not dissolve in benzene even when the liquid was boiling. In yet another attempt a sample of the dried commercial material was dissolved in a hot mixture of dry acetone and benzene. Crystals separated this time from a *large* volume of solution, but they again proved to be the dihydrate. Finally, a sample was dehydrated in a container which was capped while hot and subsequently opened in a dry-box, the sample was dissolved in dried CH_2Cl_2, and the solution was transferred to a special glass apparatus where the solvent was distilled off slowly in a closed system until crystals appeared. A crystal, visually of very good quality, was mounted in a capillary in a dry-box but turned out to be the dihydrate. After these discouraging results further attempts to obtain crystals of the anhydrous bromide were abandoned.

Infrared spectrum of $Ph_4PBr \cdot 2H_2O$

To gain an idea of the behaviour of the two H_2O molecules in $Ph_4PBr \cdot 2H_2O$ we examined the room-temperature FT-ir spectra of the undeuterated and weakly deuterated compound. The undeuterated dihydrate has OH stretching absorptions at ~3560 (broad shoulder, probably accidental water), 3498(sh), 3473, 3450, and 3427 cm^{-1}, and HOH bending absorptions at 1631(sh) and 1616 cm^{-1}. Since in the spectrum of the weakly deuterated sample only two isotopically isolated ν(OD) absorptions appeared, at 2567.0 and 2550.9 cm^{-1} ($\langle\nu(OH)\rangle/\langle\nu(OD)\rangle$ = 1.353), in accord with the expectation for two nonequivalent H_2O molecules of symmetry C_{2v} (cf. refs. 9 and 50), the complexity of the ν(OH) absorption must be attributed to coupling of the two molecules in the flat $[Br^-(OH_2)_{4/2}]_\infty$ anion chains. The similarity in the hydrogen bonding of the two molecules (cf. Fig. 3) is confirmed by the small difference in the decoupled ν(OD) component frequencies, 16 cm^{-1}. This would correspond, on a rough estimate (9), to a difference of ca. 0.02 Å in the O···Br distances, which is of the same order of magnitude as the difference between the observed O···Br distances (Table 7), 0.04(1) Å. The ν(OD) values are practically the same as those in $SrBr_2 \cdot H_2O$ (51), and the ν(OH) frequencies in the undeuterated sample are similar to those in $SrBr_2 \cdot H_2O$ and $BaBr_2 \cdot H_2O$ at room temperature (51), and about 40 cm^{-1} higher than in $BaBr_2 \cdot 2H_2O$ (52).

Routine low-resolution ir spectra revealed small differences in the

Can. J. Chem. Downloaded from www.nrcresearchpress.com by 122.72.124.2 on 09/07/12
For personal use only.

Can. J. Chem. Downloaded from www.nrcresearchpress.com by 122.72.124.2 on 09/07/12
For personal use only.

TABLE 8. Ion-packing types of $R_4E^+X^-$ (E = N, P, As, Sb, Bi) structures[a]

Coordination 4:4		Coordination 6:6		Coordination 8:8		
ZB	W	NaCl	NiAs	*anti*-NiAs	CsCl	NaTl[b]
eI	maBr	$eFeI_4(I)$	$eGaCII_3$	$msGaCl_4$	mX[c] (X = Cl, Br, I, ClO_4, MnO_4)	$eSbBr_6$ (15)[d]
pBr	Et_3NHX (X = Cl, Br, I) (16)	$eInCII_3$	$eFeI_4(II)$	$eFeCl_4$	$bAuBr_4$[c] (18)	
$bCuX_2$ (X = Cl, Br) (19)		$eTlBr_2I_2$	$pPBr_4$ (17)	$eInCl_4$	$ppBr_3$ (20)	
ppBr (5)		$eTlBrI_3$		$eTlBrI_3$	$paBr_3(II)$ (21)	
ppI (24)		$eTlI_4$		$eInBr_4$	$ppIBr_2$ (23)	
$paBr_3(I)$ (26)		$eWCl_6$ (22)		$eTlBr_4$	paI_3 (25)	
$paHCl_2$ (28)		$bInCl_4$		$eTlBr_3I$	$ppSnX_3$ (X = Cl, Br) (27)	
$ppHg(SCN)_3$ (29)		$bInCl_3Br$		$ppBr \cdot H_2O$[e]	$paAuCl_4$ (30)	
$paClO_4$		$bInClBr_3$		$ppBr \cdot 2H_2O$[e]		
$pbClO_4$		$bInBr_4$				
$paMCl_4$ (M = Ga, Fe, In, Tl)		$bTlCl_4$				
$ppNbBr_6$ (32)		$bTlBr_4$				
		$bTlI_4$				
		ppCl[f] (31)				
		paX[f,g] (33)				

[a]ZB, zincblende, W, wurzite; m, Me_4N; ma, Me_4As; ms, Me_4Sb; e, Et_4N; p, *n*-Pr_4N; b, *n*-Bu_4N; pp, Ph_4P; pa, Ph_4As; pb, Ph_4Bi. Distortions from the aristotype symmetry are not detailed here. For references (where none is given) see refs. 10 and 11. The packing-type classification of bIO_4 ($Pna2_1$) (12) is not obvious. $ppCuCl_3$ and $paCuCl_3$ (13, 14) are in reality $(pp)_2[Cu_2Cl_6]$ and $(pa)_2[Cu_2Cl_6]$, of the *anti*-CdI_2 type.

[b]*B*32 structure type. Actual coordination, (4 + 4):(4 + 4).

[c]Tetragonal. Relation to CsCl: $a(CsCl) \rightarrow a\sqrt{2}$ and $\sim c$.

[d]Tetragonal, $I4_1md \subset I4_1/amd \subset Fd3m$. Relation to NaTl: $a(NaTl) \rightarrow a\sqrt{2}$ and $\frac{1}{2}c \sim a\sqrt{2}$.

[e]If H_2O is disregarded. $[Ph_4P^+]_2[Br_2(OH_2)_2]^{2-}$ may be viewed as *anti*-CdI_2 (see text).

[f]Two interpenetrating NaCl-type lattices.

[g]X = [*cis*-$RuCl_4(H_2O)_2$]$\cdot H_2O$.

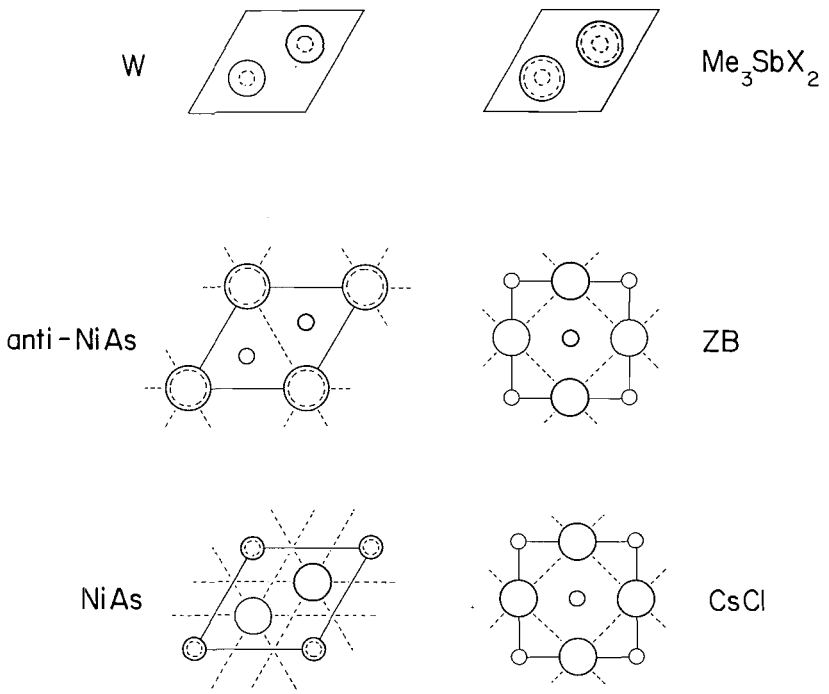

FIG. 4. Schematic representation of the cation/anion packing of the wurtzite (W), *anti*-NiAs, NiAs, Me_3SbX_2, zincblende (ZB) ($a/\sqrt{2}$, $a/\sqrt{2}$, a) and CsCl ($a\sqrt{2}$, $a\sqrt{2}$, a) types (cf. Table 8). Large circles, anions; small circles, cations. Broken lines indicate planes parallel to a (the) principal symmetry axis and containing exclusively anions. Aristotype symmetries: W, NiAs, and *anti*-NiAs, $P6_3mc$; Me_3SbX_2, $P\bar{6}2c$; ZB, $F\bar{4}3m$; CsCl, $Pm3m$; NaTl (not shown), $Fd3m$.

TABLE 9. Stereochemistry of the Et_4N^+ (= E) ion in crystals

s.s	Compound	Reference
$*T_d$	$EFeI_4$(*I*), $EInClI_3$, $ETlBr_2I_2$, $ETlBr_3I$, $ETlI_4$	cf. ref. 11
	E_2PuCl_6 (at 112°C)	34
$*C_{3v}$	$EGaCl_4$, $EInCl_4$, $EInClBr_3$, $EInBr_4$, $ETlBr_4$, $ETlBr_3I$, $EFeCl_4$ (all of the *anti*-NiAs type)	cf. ref. 11
S_4	EI	This work
	E_2InCl_5 (*d*, s.a.s. D_{2d})	35
$*C_4$	E_2InCl_5 (*d*, s.a.s. C_{4h})	35
C_{2v}	$ESbBr_6$ (*d*; C(2) in *m*, s.a.s. D_{2d})	15
	E_2NiCl_4 (*d*; neither C in *m*, s.a.s. D_{2d})	36
$*C_{2h}$	$EGaClI_3$, $EFeI_4$(*II*) (both of the distorted NiAs type)	cf. ref. 11
	EI_7	37
C_2	EI_3(*I*)	38
	$ECl\cdot H_2O$ (E(1), $\sim D_2$)	3
	E_2SnCl_6 (E(1) ordered, $\sim S_4$; E(2), *d*)	39
	E_2MoS_9 (E(1) and E(2) both ordered)	40
$*C_i$	$EWCl_6$	22
	E-μ-ox$(SnCl_4)_2$	41
C_1	$ECl\cdot H_2O$ (E(2), $\sim D_2$)	3
	$ECl\cdot 4H_2O$ ($\sim D_2$)	4
	$EBrCl_2$	42
	EI_3(*II*)	38
	$E[Cr_2(CO)_{10}H]$ (*d*; s.a.s. D_{4h}: C(2) on and C(1) above and below pseudo-*m*)	43
	E(Eu, Np)(*N*,*N*-Et_2dithiocarbamate)	44
	E_2MoS_4 (E(1) ordered; E(2, 3, 4) all *d*, s.a.s. D_{2d})[b]	45
	$E_2[Pt_2Br_6]$	46
	$E_2UO_2Cl_4$ (both E of this symmetry)	47

[a]s.s., observed crystallographic site symmetry; *, s.s. not a subgroup of D_{2d}, E necessarily disorderd; *d*, disordered (where disorder actually demonstrated; disorder may in fact exist in other cases where s.s. $\subset D_{2d}$ but not reported or investigated); s.a.s., average symmetry simulated by the disordered pair.

[b]Alternative positions in the pairs not necessarily equally populated.

Can. J. Chem. Downloaded from www.nrcresearchpress.com by 122.72.124.2 on 09/07/12
For personal use only.

δ(OH) absorption regions of the two hydrates which served for characterization in the preparative work.

Structure determination

The crystals were sealed in glass capillaries. A CAD-4 four-circle diffractometer (ω:2θ scans; 20°C) was used in the data acquisition. Lorentz, polarization, and empirical absorption corrections (53) were applied. Scattering factors for neutral or ionized atoms and corrections for anomalous scattering were taken from ref. 54. The structures were solved using the SHELX (55) and CRYSTALS (56) systems. After the nonhydrogen atoms had been located, full-matrix least-squares ($w\Delta|F| = \min.$) refinement was carried out with isotropic temperature factors until R was reduced to a reasonably low value. The hydrogen atoms were then placed, consistent with the difference maps, and the refinement was continued with anisotropic factors on the nonhydrogen atoms and isotropic factors on the hydrogens. The final difference maps were in all three cases featureless. The anisotropic temperature factor is defined as $T = \exp[-2\pi^2(U_{11}h^2a^{*2} + U_{22}k^2b^{*2} + U_{33}l^2c^{*2} + 2U_{23}klb^*c^* + 2U_{13}hla^*c^* + 2U_{12}hka^*b^*)]$.

Et_4NI. Systematic absences: hkl, $h + k + l$ odd. $R_{merg} = 7.2\%$. Iodine and N atoms placed as in ref. 2. A Fourier map phased with I^- and N revealed the positions of C(1) and C(2), and a difference map after anisotropic refinement of the I, N, and C atoms revealed the positions of the five H atoms. The CH_3 in the final refinement was free. The least-squares weights were $w = 0.0405/(\sigma^2|F| + 0.006F^2)$.

$Ph_4PBr \cdot H_2O$. Systematic absences, none. $R_{merg} = 2.4\%$. The Br and P atoms were located from a Patterson map. A Fourier map revealed the positions of the remaining nonhydrogen atoms. Of the 1860 unique reflections with $I > 3\sigma(I)$ thirteen suffered from extinction and were omitted from further refinement. The H atoms were observable in a difference map and were allowed to refine freely after placement. The least-squares weights were $w^{-1} = \sigma^2|F| + 0.01996F^2$.

$Ph_4PBr \cdot 2H_2O$. Systematic absences: $h00$ and $hk0$, h odd; $0k0$, k odd; $00l$, l odd; $0kl$, $k + l$ odd. $R_{merg} = 2.1\%$. The Br and P atoms were located from a Patterson map and the remaining nonhydrogen atoms from a Fourier map. Only one H_w on each oxygen could be located; the phenyl hydrogens were refined in one cycle and then fixed. Weighting scheme, $w^{-1} = \sigma^2|F| + 0.01F^2$.

Material deposited[10]. The list of tables in the Depository of Unpublished Data is as follows. Table 10. $Ph_4PBr \cdot H_2O$: anisotropic temperature factors ($\times 10^3$) of the nonhydrogen atoms. Table 11. $Ph_4PBr \cdot H_2O$: positional parameters and isotropic temperature factors ($\times 10^3$) of the hydrogen atoms. Table 12. $Ph_4PBr \cdot 2H_2O$: anisotropic temperature factors ($\times 10^3$) of the nonhydrogen atoms. Table 13. $Ph_4PBr \cdot 2H_2O$: positional parameters and isotropic temperature factors ($\times 10^3$) of the hydrogen atoms. Table 14. Best planes through the phenyl ring carbons. Table 15. Observed and calculated structure factors for Et_4NI. Table 16. Observed and calculated structure factors for $Ph_4PBr \cdot H_2O$. Table 17. Observed and calculated structure factors for $Ph_4PBr \cdot 2H_2O$.

Acknowledgments

We thank Dr. N. Burford for an attempt to obtain crystals of anhydrous Ph_4PBr, and Dr. M. Falk for the FT-ir spectra. This investigation was supported by grants from the Natural Sciences and Engineering Research Council of Canada to O.K. and T.S.C.

1. T. S. Cameron, W. J. Chute, and O. Knop. Can. J. Chem. **63**, 586 (1985).
2. E. Wait and H. M. Powell. J. Chem. Soc. 1872 (1958).
3. J. H. Loehlin and Å. Kvick. Acta Crystallogr. B, **34**, 3488 (1978).
4. T. C. W. Mak, H. J. Bruins Slot, and P. T. Beurskens. J. Incl. Phenom. **4**, 295 (1986).
5. N. W. Alcock, M. Pennington, and G. R. Willey. Acta Crystallogr. C, **41**, 1549 (1985).
6. O. Knop, B. R. Vincent, and T. S. Cameron. Can. J. Chem. In press.
7. T. C. W. Mak, S. P. So, C. Chieh, and K. S. Jasim. J. Mol. Struct. **127**, 375 (1985).
8. T. C. W. Mak and Hu Sheng-Zhi. J. Mol. Struct. **156**, 151 (1987).
9. M. Falk and O. Knop. Water: a comprehensive treatise. Vol. 2 *Edited by* F. Franks. Plenum Press, New York. 1973. Chapt. 2.
10. R. W. G. Wyckoff. Crystal structures. 2nd ed. Vol. 5. Interscience, New York – London. 1966.
11. O. Knop, T. S. Cameron, D. Adhikesavalu, B. R. Vincent, and J. A. Jenkins. Can. J. Chem. **65**, 1527 (1987).
12. A. Carpy, M. Goursolle, J.-M. Léger, and E. Nivaud. C.R. **285C**, 311 (1977).
13. M. Textor, E. Dubler, and H. R. Oswald. Inorg. Chem. **15**, 1361 (1974).
14. R. D. Willett and C. Chow. Acta Crystallogr. B, **30**, 207 (1974).
15. M. L. Hackert, R. A. Jacobson, and T. A. Keiderling. Inorg. Chem. **10**, 1075 (1971).
16. M. A. James, T. S. Cameron, O. Knop, M. Neuman, and M. Falk. Can. J. Chem. **63**, 1750 (1985).
17. W. S. Sheldrick, A. Schmidpeter, F. Zwaschka, K. B. Dillon, A. W. G. Platt, and T. C. Waddington. J. Chem. Soc. Dalton, 413 (1981).
18. J. P. Johnson. Acta Crystallogr. A, **37**, C-227 (1981).
19. M. Asplund, S. Jagner, and M. Nilsson. Acta Chem. Scand. A, **37**, 57 (1983).
20. M. P. Bogaard and A. D. Rae. Cryst. Struct. Commun. **11**, 175 (1982).
21. M. P. Bogaard, J. Peterson, and A. D. Rae. Cryst. Struct. Commun. **8**, 347 (1979).
22. W. Eichler and H.-J. Seifert. Z. Anorg. Allg. Chem. **431**, 123 (1977).
23. U. Müller. Z. Naturforsch. **34b**, 1064 (1979).
24. T. L. Khotsyanova and Y. T. Struchkov. Kristallografiya, **1**, 669 (1956).
25. J. Runsink, S. Swen-Walstra, and T. Migchelsen. Acta Crystallogr. B, **28**, 1331 (1972).
26. J. Ollis, V. J. James, D. Ollis, and M. P. Bogaard. Cryst. Struct. Commun. **5**, 39 (1976).
27. U. Müller, N. Mronga, C. Schumacher, and K. Dehnicke. Z. Naturforsch. **37b**, 1122 (1982).
28. U. Müller and H.-D. Dörner. Z. Naturforsch. **37b**, 198 (1982).
29. A. Sakhri and A. L. Beauchamp. Inorg. Chem. **14**, 740 (1975).
30. P. G. Jones, J. J. Guy, and G. M. Sheldrick. Acta Crystallogr. B, **31**, 2687 (1975).
31. J. F. Richardson, J. M. Ball, and P. M. Boorman. Acta Crystallogr. C, **42**, 1271 (1986).
32. U. Müller, R. Dübgen, and K. Dehnicke. Z. Anorg. Allg. Chem. **473**, 115 (1981).
33. T. E. Hopkins, A. Zalkin, D. H. Templeton, and M. G. Adamson. Inorg. Chem. **5**, 1427 (1966).
34. E. Staritzky and J. Singer. Acta Crystallogr. **5**, 536 (1952).
35. D. S. Brown, F. W. B. Einstein, and D. G. Tuck. Inorg. Chem. **8**, 14 (1969).
36. G. D. Stucky, J. B. Folkers, and T. J. Kistenmacher. Acta Crystallogr. **23**, 1064 (1967).
37. E. E. Havinga and E. H. Wiebenga. Acta Crystallogr. **11**, 733 (1958).
38. T. Migchelsen and A. Vos. Acta Crystallogr. **23**, 796 (1967).
39. H. Sowa, U. Drück, and A. Kutoglu. Cryst. Struct. Commun. **10**, 699 (1981).
40. E. D. Simhon, N. C. Baenziger, M. Kanatzidis, M. Draganjac, and D. Coucouvanis. J. Am. Chem. Soc. **103**, 1218 (1981).
41. A. C. Skapski, J.-E. Guerchais, and J.-Y. Calves. C.R. **287C**, 1377 (1974).

[10]Copies can be purchased from the Depository of Unpublished Data, CISTI, National Research Council of Canada, Ottawa, Ont., Canada K1A 0S2.

Can. J. Chem. Downloaded from www.nrcresearchpress.com by 122.72.124.2 on 09/07/12
For personal use only.

42. W. GABES and K. OLIE. Cryst. Struct. Commun. **3**, 753 (1974).
43. L. B. HANDY, J. K. RUFF, and L. F. DAHL. J. Am. Chem. Soc. **92**, 7312 (1970).
44. D. BROWN, D. G. OLAH, and C. E. F. RICKARD. J. Chem. Soc. A, 786 (1970).
45. M. G. KANATZIDIS and D. COUCOUVANIS. Acta Crystallogr. C, **39**, 835 (1983).
46. D. R. RUSSELL, P. A. TUCKER, and C. WHITTAKER. Acta Crystallogr. B, **31**, 2530 (1975).
47. C. BOIS, NGUYEN QUY DAO, and N. RODIER. Acta Crystallogr. B, **32**, 1541 (1976).
48. J. K. RUFF, R. P. WHITE, JR., and L. F. DAHL. J. Am. Chem. Soc. **93**, 2159 (1971).
49. J. DODONOW and H. MEDOX. Ber. Deut. Chem. Ges. **61**, 907 (1928).
50. V. SEIDL, O. KNOP, and M. FALK. Can. J. Chem. **47**, 1361 (1969).
51. H. D. LUTZ and H. CHRISTIAN. J. Mol. Struct. **96**, 61 (1982).
52. H. D. LUTZ, W. POBITSCHKA, B. FRISCHEMEIER, and R. A. BECKER. J. Raman Spectrosc. **7**, 130 (1978).
53. N. WALKER and D. STUART. Acta Crystallogr. A, **39**, 158 (1983).
54. International tables for X-ray crystallography. Vol. IV. The Kynoch Press, Birmingham, England. 1974.
55. G. M. SHELDRICK. SHELX system report. University Chemical Laboratories, Lensfield Road, Cambridge, England. 1976.
56. J. R. CARRUTHERS and D. L. WATKINS. CRYSTALS, issue 5. Chemical Crystallography Laboratory, Oxford, England. 1981.

Can. J. Chem. Downloaded from www.nrcresearchpress.com by 122.72.124.2 on 09/07/12
For personal use only.

Sulfonyl esters 1: The reduction of tribromophenyl sulfonates with mercaptide anions

KATHLEEN ANNE DURKIN, RICHARD FRANCIS LANGLER,[1] AND NANCY ANN MORRISON

Department of Chemistry, Florida Institute of Technology, Melbourne, FL 32901-6988, U.S.A.

Received April 29, 1988

KATHLEEN ANNE DURKIN, RICHARD FRANCIS LANGLER, and NANCY ANN MORRISON. Can. J. Chem. **66**, 3070 (1988).

2,4,6-Tribromophenyl sulfonates have been shown to undergo unusually efficient reduction by mercaptide anions in hexamethylphosphoramide. The reduction products include the sulfinate anion derived from the sulfonate ester and the disulfide derived from the mercaptide anions.

KATHLEEN ANNE DURKIN, RICHARD FRANCIS LANGLER et NANCY ANN MORRISON. Can. J. Chem. **66**, 3070 (1988).

On démontre que les anions mercaptures dans l'hexaméthylphosphoramide provoquent une réduction anormalement efficace des tribromo-2,4,6 sulfonates. Les produits de la réduction comprennent entre autres l'anion sulfinate qui dérive de l'ester sulfonate ainsi que le disulfure provenant des anions mercaptures.

[Traduit par la revue]

Can. J. Chem. Downloaded from www.nrcresearchpress.com by 122.72.124.2 on 09/07/12
For personal use only.

Introduction

Recently, we have observed the sulfonyl transfer reaction shown in eq. [1].

[1] $$CF_3CH_2OSO_2CH_3 + PhCH_2SH \xrightarrow[CH_3OH]{CH_3ONa} CH_3OSO_2CH_3 \longrightarrow PhCH_2SCH_3$$ 27%

Methyl methanesulfonate is an intermediate in this reaction (1). Subsequently, a study of sulfonate esters as reagents for the one-pot condensation of mercaptans and alcohols to furnish sulfone precursors was initiated. Equation [2][2] presents one such reaction.

[2] $$PhOSO_2CH_3 + CH_3C_6H_4SH + CH_3CH_2OH \xrightarrow[HMPA]{NaH} CH_3C_6H_4SCH_2CH_3 \xrightarrow{m\text{CPBA}} CH_3C_6H_4SO_2CH_2CH_3$$ 58% (overall)

Equation [2] presents what has become our routine screening procedure for sulfonate esters, which might be successful in condensing alcohols with mercaptans.

Results and discussion

The first goal in this study was to improve the yield of *p*-tolyl ethyl sulfide (eq. [2]) by modification of the sulfonate ester structure. It seemed likely that the initial transesterification would produce the intermediate ethyl methanesulfonate more efficiently if the phenoxy group were replaced with a better leaving group. An obvious strategy would involve the introduction of electron-withdrawing groups onto the phenoxy phenyl ring. However, as shown in eq. [3], powerful electron-withdrawing groups attached to the phenoxy phenyl ring can promote preferential attack at a ring carbon, thereby suppressing the desired behaviour.

[3] $$O_2NC_6H_4OSO_2CH_3 + CH_3C_6H_4SH + CH_3CH_2OH \xrightarrow[HMPA]{NaH} CH_3C_6H_4SC_6H_4NO_2$$ 50%

$$CH_3C_6H_4SCH_2CH_3$$ 4%

A subsequent experiment examined a sulfonate ester in which the phenoxy ring substituents were somewhat less effective anion stabilizers, in an attempt to suppress nucleophilic attack at the ring carbon.

[4] $$CH_3C_6H_4SH + CH_3CH_2OH + Br_2C_6H_2OSO_2CH_3 \xrightarrow[HMPA]{NaH} (CH_3C_6H_4S)_2 + CH_3C_6H_4SCH_2CH_3$$ 63% 0%

The surprising result presented in eq. [4] (contrast with eqs. [2] and [3]) might be rationalized in the simple ionic terms shown in Scheme 1. While the second step in Scheme 1 invokes a well-documented reaction (2), the first step is questionable. It seems unlikely that such a modest change in sulfonate ester structure would so dramatically alter the propensity for a soft base (RS^-) to attack a hard acid site (sulfonyl sulfur).[3] Despite subsequent examination of a variety of sulfonate esters, the tribromophenoxy systems remain unique in their propensity for clean oxidation of mercaptide anions to disulfides.

Table 1 presents the results of a modest survey of mercaptan dimerization using 2,4,6-tribromophenyl methanesulfonate.

Another feature of the proposed overall transformation pictured in Scheme 1 is the formation of a sulfinate anion. To confirm the presence of methanesulfinate anions in our reaction mixtures, we have carried out the following trapping experiment.

Sulfinate anions may be generated by reduction of sulfonyl chlorides or by reaction of an organometallic reagent with SO_2

[5] $$CH_3C_6H_4SH + Br_2C_6H_2OSO_2CH_3 \text{ (1)} \xrightarrow[(2)\ PhCH_2Cl]{(1)\ NaH} PhCH_2SO_2CH_3$$ 32%

[1]Author to whom correspondence may be addressed.

[2]Equivalent to a conventional 3-step sequence with yields of 83% per step.

[3]"Hardness increases in the order sulfenyl sulfinyl sulfonyl" (3).

Printed in Canada / Imprimé au Canada

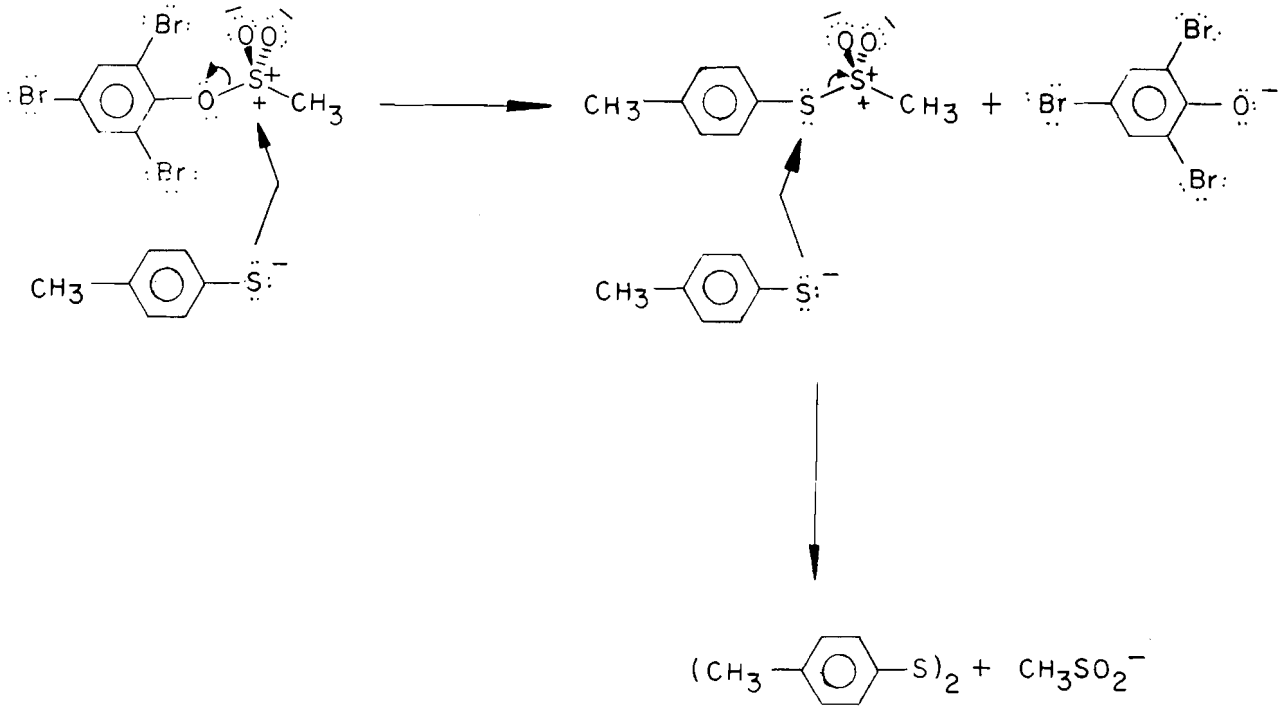

SCHEME 1

TABLE 1. Disulfide formation induced by 2,4,6-tribromophenyl methanesulfonate **1**

Mercaptan	Disulfide	% Yield	Melting or boiling point of disulfide (°C)
1. PhSH	$(PhS)_2$	100[a]	62.5–63.8 (lit. 61)[c]
2. *p*-CH_3PhSH	(*p*-$CH_3PhS)_2$	98[a]	44.5–45.6 (lit. 47)[d]
3. *p*-ClPhSH	(*p*-$ClPhS)_2$	95[a]	69.3–71.1 (lit. 73)[c]
4. $PhCH_2SH$	$(PhCH_2S)_2$	100[a]	67.2–69.7 (lit. 70)[c]
5. $CH_3CH_2CH_2SH$	$(CH_3CH_2CH_2S)_2$	50[b]	100–110/34Torr(195/760Torr)[c]
6. $(CH_3)_2CHSH$	$[(CH_3)_2CHS]_2$	59[b]	75–80/30 Torr (176/760 Torr)[c]
7. $(CH_3)_3CSH$	$[(CH_3)_3CS]_2$	35[b]	85–90/67 Torr (200/760 Torr)

[a]Based on weight of homogeneous (tlc), crystalline crude.
[b]Based on distilled, homogeneous liquid product.
[c]See ref. 4.
[d]See ref. 5.

(6). Commonly, yields are moderate. Consequently, new and mild methodology for the preparation of sulfinate anions might be useful. Since sulfones have proven to be useful and versatile synthetic intermediates, particularly for the production of alkenes and dienes (see ref. 7 for some examples), a preliminary exploration of sulfone preparation via sulfinate anions generated from 2,4,6-tribromosulfonates seemed warranted.

Prior to initiating this series of reactions, we wished to simplify the work-up somewhat. Reactions carried out as outlined in eq. [5] afford substantial amounts of *p*-tolyl disulfide in crude products (see eq. [3] and Table 1). Disulfide isolated in the crude product requires larger chromatography columns to purify products, thereby wasting time and chemicals. After a few trials with thioglycolic acid, *o*-mercaptobenzoic acid, and 3-mercaptopropionic acid, the latter was selected as the routine reducing agent. Work-up is significantly simplified because product disulfide-diacid is conveniently removed by extraction with aqueous base. Equation [6] presents an example of this modified procedure.

[6] $HS(CH_2)_2CO_2H$ + 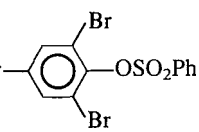 **2**

$$\xrightarrow[(2)\ CH_3I]{(1)\ NaH} PhSO_2CH_3 + [(HO_2C(CH_2)_2S)_2]$$

37%

Table 2 presents the results of our survey of some simple sulfone preparations using this procedure. Although the results in Table 2 might indicate some potential for useful methodology, it is clear that some questions need to be answered to determine whether further improvements can be expected.

The most interesting of these equations concerns the substituent effect exerted by the bromine atoms. *A priori*, two arguments seemed reasonable. Firstly, the *ortho* bromine atoms might crowd the sulfonate-bearing ring carbon, which would

Can. J. Chem. Downloaded from www.nrcresearchpress.com by 122.72.124.2 on 09/07/12
For personal use only.

TABLE 2. Sulfones prepared via sulfinate anions generated from 2,4,6-tribromophenyl sulfonates **1** and **2**

Ester	Mercaptan	Electrophile	Sulfone (% yield)	% Yield per step[a]	Sulfone melting point (°C)
1	*p*-CH_3PhSH	$PhCH_2Cl$	$PhCH_2SO_2CH_3$ (32.6)	57	126.3–127.3 (lit. 127)[b]
2	*p*-CH_3PhSH	CH_3I	$PhSO_2CH_3$ (44)	66	86.9–88.5 (lit. 88)[b]
2	$HO_2C(CH_2)_2SH$	CH_3I	$PhSO_2CH_3$ (40.6)	64	—
2	$HO_2C(CH_2)_2SH$	CH_3CH_2I	$PhSO_2CH_2CH_3$ (41)	64	40.1–41.0 (lit. 42)[b]
2	$HO_2C(CH_2)_2SH$	$PhCH_2Cl$	$PhSO_2CH_2Ph$ (58)	76	148.8–149.8 (lit. 146)[b]

[a]Yield per step assuming a two-step synthesis. This yield is the average yield/step for the actual two-step synthesis, (*i*) sulfonate ester reduction and (*ii*) sulfinate anion alkyation. It also permits convenient comparison with the traditional two-step synthetic approach (*i*) mercaptan alkylation and (*ii*) sulfide oxidation.

[b]See ref. 4.

shift nucleophilic attack to sulfonyl sulfur, leading to disulfide via thiosulfonate intermediacy (vide Scheme 1). Alternatively, the halogens might lower the lowest unoccupied molecular orbital energy sufficiently to facilitate an electron transfer reaction. To distinguish between these possibilities, each of the sulfonate esters **3***a*–**3***c* have been subjected to the reaction conditions shown in eq. [6].

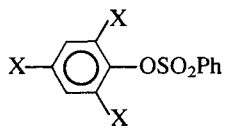

3*a* X = I
3*b* X = CH_3
3*c* X = Cl

The trimethyl system **3***b* gave no phenyl methyl sulfone, suggesting that steric effects do not play a dominant role in these reactions. In contrast, the trichloro ester **3***c* and the triiodo ester **3***a* were successfully transformed into phenyl methyl sulfone, albeit in somewhat poorer yields (32% and 24% respectively). An electron transfer mechanism appears to be a reasonable mechanistic possibility.

The most perplexing of the problems posed by the results disclosed thus far is this: how can the yields of the sulfones (see Table 2) be so much lower than the yields of the disulfides (see Table 1)? Since (*i*) the disulfides are formed in good to excellent yields and (*ii*) little or no starting sulfonate ester is recovered,[4] it seemed likely that near-complete reduction of the sulfonate esters (**1** or **2**) had occurred, producing sulfinate anions in good yield.

It was routine to observe a combined total of less than 10% of (*i*) the tribromophenyl ether derived from tribromophenoxide ions and the electrophile and (or) (*ii*) the disulfide-diester derived from 3-mercaptopropionic acid. Consequently, the eq. [6] reaction was repeated with twice as much electrophile, to ensure that fewer sulfinate anions would be left unreacted.

The results presented in eq. [7] suggest that there are significant amounts of tribromophenoxide ions and biscarboxylate dianions that do not react under normal reaction conditions. However, the eq. [7] sulfone yield (cf. 37% for eq. [6]) suggests that there is *not* a significant pool of unreacted sulfinate anions remaining at the end of a typical run.

The next point addressed was the possibility that there might have been significant air oxidation of sulfinate anions, which

[7] 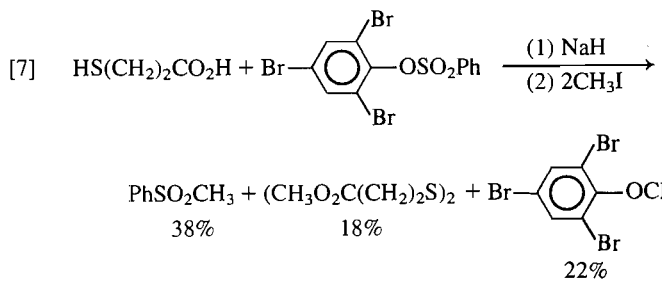

would consume our reagent and produce the corresponding sulfonate anions. The sulfonate anions would be much less nucleophilic[5] and would presumably go unreacted to be lost during the work-up. When carried out under an atmosphere of nitrogen, the eq. [6] reaction furnished the same sulfone yield.

Another possibility involves disproportionation of sulfinate anions as shown in eq. [8].

[8] $3PhSO_2^- \longrightarrow PhS^- + 2PhSO_3^-$

We decided to test for this possibility by using a trap that is specific for mercaptide anions. α-Chlorosulfones have long been known to be very resistant to nucleophilic displacement of chlorine (9). Mercaptide anions are unique in their propensity for accomplishing such substitutions (10). Phenyl mercaptide anions will react with our trap in HMPA, as shown below.

[9] $PhSNa + ClCH_2SO_2CH_3 \xrightarrow[HMPA]{\Delta} PhSCH_2SO_2CH_3$ 57%

The results of an attempt to trap a sulfinate-anion-derived disproportionation product are presented in eq. [10]. Given eqs. [9] and [10], there must be less than 2% disproportionation occurring *at elevated temperature* (100°C). Since these reactions are routinely carried out at ambient temperatures, it is very unlikely that disproportionation is a serious problem here.

[10] 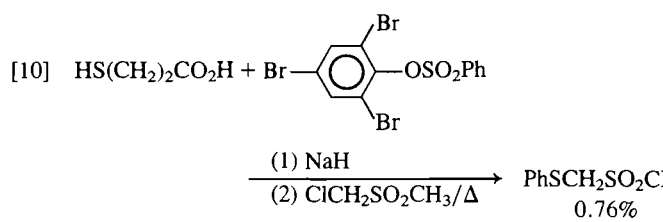

Since sulfinate anions are ambident nucleophiles, we have considered another potential complication in the preparation of sulfones using our scheme. If some sulfinate anions attack the

[4]Any sulfonate ester present in the reaction mixture can be isolated from HMPA nearly quantitatively by our work-up (1).

[5]Sulfonate anions do have some nucleophilicity (8).

Can. J. Chem. Downloaded from www.nrcresearchpress.com by 122.72.124.2 on 09/07/12
For personal use only.

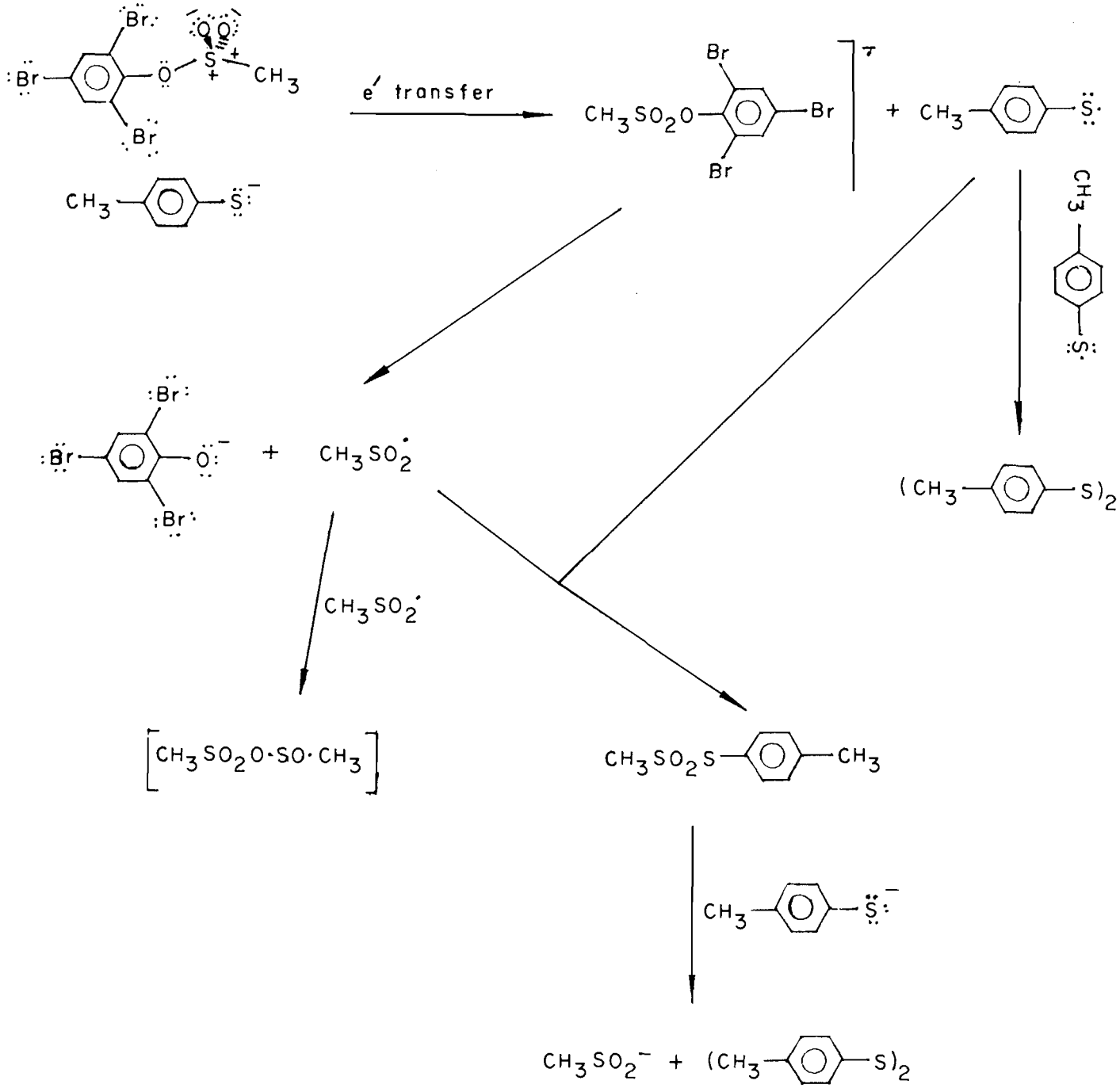

SCHEME 2

electrophile using oxygen rather than sulfur, the product mixture would include a sulfinate ester as well as a sulfone. The sulfinate ester might be hydrolyzed during work-up and lost in the aqueous phase during extraction. Both sulfone and sulfinate ester formation by sulfinate anion alkylation are well-known processes (ref. 3, p. 143). Nucleophilic attack by sulfur is apparently enhanced when reactions are conducted in hydroxylic solvents (11*a*).

The eq. [6] reaction has been repeated with a variation: immediately prior to the addition of methyl iodide, the reaction mixture (50 mL HMPA) was diluted with 10% water in isopropanol (100 mL). After the addition of methyl iodide, the usual work-up afforded phenyl methyl sulfone in 37% yield. Clearly, the hydroxylic solvents did not alter the outcome of the reaction.

If thiosulfonates are indeed principal intermediates in these reactions (see Scheme 1), they must be reduced by mercaptide anions to furnish substantially higher yields of disulfides than sulfinate anions. Experimental confirmation of this conclusion is shown by our results in eq. [11].

$$[11]\quad PhSO_2SPh \xrightarrow[(2)\ CH_3I]{(1)\ PhSNa/HMPA} \underset{57\%}{(PhS)_2} + \underset{30\%}{PhSO_2CH_3}$$

Assuming an electron transfer mechanism as suggested earlier, a reasonable fate for intermediate sulfonyl radicals would be formation of a sulfinate–sulfonate mixed anhydride. Sulfinate–sulfonate mixed anhydrides should not lead to sulfinate anions under our reaction conditions. Sucn anhydrides have been proposed for reactions involving sulfonyl radicals (11*b*,

Can. J. Chem. Downloaded from www.nrcresearchpress.com by 122.72.124.2 on 09/07/12
For personal use only.

11*c*). A complete pathway proposal that accounts for our results is presented in Scheme 2. Presumably, the sulfinate–sulfonate mixed anhydride (or products derived therefrom) would be smoothly hydrolyzed during work-up.

Experimental

General

The ir spectra were recorded on a Perkin–Elmer 237B grating spectrophotometer. Ultraviolet spectra were run on a Beckman DU-2 spectrophotometer. The nmr spectra were obtained on a Varian EM360A instrument using TMS as the internal standard. Melting points were determined on a Mel-Temp capillary melting-point apparatus and are uncorrected.

Preparation of p-*tolyl ethyl sulfone*

A solution of absolute ethanol (0.6317 g, 13.7 mmol) in HMPA (10 mL)[6] was added dropwise to a slurry of NaH (0.672 g, 28.0 mmol) in HMPA (30 mL). The mixture was stirred at ambient temperature for 20 min. A solution of *p*-tolyl mercaptan (1.707 g, 13.7 mmol) in HMPA (10 mL) was added dropwise over 15 min. Upon completion of the addition, the reaction mixture was stirred at ambient temperature to permit complete evolution of H_2. Phenyl methanesulfonate (2.377 g, 13.8 mmol) was added and the reaction mixture stirred at ambient temperature for 2 h.

The reaction mixture was poured into a 2-L Erlenmeyer containing water (400 mL), 10% HCl (5 mL), and diethyl ether (150 mL). The mixture was vigorously shaken and transferred to a separatory funnel. The layers were separated and the aqueous layer washed with diethyl ether (two 100-mL portions).

The combined organic layers were concentrated and the residue poured into a 2-L Erlenmeyer containing water (100 mL) and diethyl ether (100 mL). The layers were separated, the aqueous washed with diethyl ether (two 100-mL portions), and the combined ether layers washed with 2.5% NaOH (100 mL).

The crude product (*p*-tolyl ethyl sulfide) was dissolved in chloroform (100 mL) and the reaction mixture cooled with an ice/water bath. *m*CPBA (85%, 8.500 g) was added in small portions over 2 h. The reaction was permitted to return to ambient temperature while stirring overnight. Chloroform (100 mL) was added and the resultant solution washed with 2.5% NaOH (100-mL aliquots) until the aqueous pH remained basic. The organic layer was dried ($MgSO_4$) and concentrated.

The crude was chromatographed on silica gel (200 g) employing 1:1 methylene chloride/carbon tetrachloride elution (100-mL fractions). Fractions 19–38 were combined and concentrated, affording clean *p*-tolyl ethyl sulfone (1.468 g, 8.08 mmol, 58%), which was identical with authentic material by ir, nmr and double-spotted tlc.

Attempted condensation of p-*tolyl mercaptan and ethanol using* p-*nitrophenyl methanesulfonate*

Sodium hydride (0.678 g, 28.2 mmol), absolute ethanol (0.630 g, 13.7 mmol), *p*-tolyl mercaptan (1.729 g, 13.9 mmol), and *p*-nitrophenyl methanesulfonate (3.001 g, 13.8 mmol) were reacted in hexamethylphosphoramide as described under Preparation of *p*-tolyl ethyl sulfone. The crude product obtained by ether extraction was chromatographed on silica gel (200 g). Thirty fractions (100 mL each) of hexanes followed by 10 fractions of chloroform (100 mL each) were collected.

Fractions 9 and 10 were combined and concentrated, affording *p*-tolyl disulfide (0.048 g, 0.19 mmol). Fractions 12 and 13 were combined and concentrated, yielding clean *p*-tolyl ethyl sulfide (0.070 g, 0.46 mmol).

Fractions 28–35 were combined and concentrated, affording *p*-nitrophenyl *p*-tolyl sulfide (1.307 g, 5.3 mmol, 50%). The nitrosulfide was recrystallized from methanol. It had mp 78–80°C; R_f 0.41 (carbon tetrachloride development); ir ($CHCl_3$): 1520 and 1340 cm^{-1}; uv (CH_3OH): 223(ε 13 706), 257 (s, ε 4826), and 340 nm (ε 13 513); nmr ($CDCl_3$) δ: 8.03 (2H,d), 7.30 (6H,m), and 2.40 (3H,s). *Anal.* calcd. for $C_{13}H_{11}N_2S$: C 63.65, H 4.51; found: C 63.93, H 34.38.

Preparation of 2,4,6-trisubstituted phenyl sulfonates ***1***, ***2***, ***3***a *and* ***3***b

2,4,6-Trisubstituted phenol (15.2 mmol) was dissolved in dry pyridine (25 mL) and triethyl amine (15.2 mmol). The reaction mixture was cooled with an ice/water bath and the appropriate sulfonyl chloride (15 mmol) added dropwise over 5 min. The ice/water bath was removed and the reaction mixture stirred at ambient temperature for 1 h.

Water (50 mL) was added and the resultant mixture washed with chloroform (three 50-mL aliquots). The combined organic layers were extracted with 2.5% HCl (100-mL aliquots) until the aqueous pH remained acidic. The organic layer was dried and concentrated. The residue was recrystallized from methanol.

Recrystallized $Br_3PhOSO_2CH_3$ **1** (62%, mp 80–81°C) had ir ($CHCl_3$): 1385 and 1185 cm^{-1}: nmr ($CDCl_3$) δ: 3.50 (3H,s) and 7.73 (2H,s). *Anal.* calcd. for $C_7H_5Br_3O_3S$: C 20.56, H 1.23; found: C 20.66, H 1.16.

Recrystallized Br_3PhOSO_2Ph **2** (50%,[7] 85.7–86.6°C) had ir ($CHCl_3$): 1190 and 1390 cm^{-1}; nmr ($CDCl_3$) δ: 8.06 (2H,m) and 7.70 (3H,m); ms *m/e*: 474 (1.1%), 472 (3.4%), 470 (3.3%), 468 (1.1%), 141 (12%), and 77 (100%). *Anal.* calcd. for $C_{12}H_7Br_3O_3S$: C 30.60, H 1.49; found: C 30.60, H 1.29.

Recrystallizeed I_3PhOSO_2Ph ***3a*** (44%, mp 120.1–126.6°C) had ir (KBr); 1380 and 1180 cm^{-1}; nmr (DMSO-d_6) δ: 8.20 (2H,s) and 7.80 (5H,m); ms *m/e*: M^+ 612 (95%), 471 (100%), and 77 (77%). *Anal.* calcd. for $C_{12}H_7I_3O_3S$: C 23.55, H 1.15; found: C 23.64, H 1.03.

Crude $(CH_3)_3PhOSO_2Ph$ ***3b*** (5.009 g) was chromatographed on silica gel (400 g) employing 3:2 carbon tetrachloride/methylene chloride (100-mL fractions) for elution. Fractions 13–18 were combined and concentrated, affording clean trimethyl sulfonate ***3b*** (3.206 g, 58%). Recrystallized ***3b*** had mp 48.7–49.6°C; ir ($CHCl_3$): 1370 and 1175 cm^{-1}; nmr ($CDCl_3$) δ: 8.00 (2H,m), 7.65 (3H,m), 6.80 (2H,s), 2.26 (3H,s), and 2.06 (6H,s); ms *m/e*: M^+ 276 (9.8%) and 135 (100%). *Anal.* calcd. for $C_{15}H_{16}O_3S$: C 65.19, H 5.83; found: C 65.47, H 5.85.

Preparation of 2,4,6-trichlorophenyl benzenesulfonate ***3***c

Sodium metal (1.167 g, 50.7 mmol) was dissolved in methanol (250 mL). 2,4,6-Trichlorophenol (10.000 g, 51.0 mmol) was added and the methanol completely evaporated. Acetone (250 mL) was added to the residue. Benzenesulfonyl chloride (9.068 g, 51.5 mmol) was added dropwise to the solution. The reaction mixture was stirred at ambient temperature for 19 h. Chloroform (300 mL) was added and the resultant solution washed with 2.5% sodium hydroxide (100 mL). The organic layer was dried ($MgSO_4$) and concentrated. The residue was recrystallized, affording clean trichlorosulfonate ***3c*** (11.773 g, 69%, mp 64.9–65.8°C). The trichlorosulfonate had ir ($CHCl_3$): 1390 and 1190 cm^{-1}; nmr ($CDCl_3$) δ: 8.00 (2H,m), 7.65 (3H.m), and 7.30 (2H,s). *Anal.* calcd. for $C_{12}H_7Cl_3O_3S$: C 42.69, H 2.08; found: C 42.66, H 1.92.

Reaction of mercaptans with 2,4,6-tribromophenyl methanesulfonate ***1***

The conversion of benzenethiol into diphenyl disulfide will be used to illustrate the procedure that furnished the results in Table 1.

Benzenethiol (1.34 g, 12.1 mmol) in HMPA was added dropwise to a suspension of sodium hydride (0.296 g) in HMPA (25 mL). Upon completion of the addition, the reaction mixture was stirred for 5 min to permit complete evolution of H_2. The tribromomesylate (2.512 g, 6.1 mmol) was added and the reaction mixture stirred at ambient temperature for 0.5 h. The reaction mixture, initially opaque, became a pale yellow homogeneous solution within a minute after adding the mesylate.

The crude was obtained by the same extraction procedure described under "Preparation of *p*-tolyl ethyl sulfone". The crude was crystalline diphenyl disulfide (1.34 g, 6.1 mmol, 100%). After recrystallization

[6]HMPA is hexamethylphosphoramide $[(CH_3)_2N]_3PO$. HMPA is toxic and carcinogenic.

[7]Yield includes second crop.

Can. J. Chem. Downloaded from www.nrcresearchpress.com by 122.72.124.2 on 09/07/12
For personal use only.

Can. J. Chem. Downloaded from www.nrcresearchpress.com by 122.72.124.2 on 09/07/12
For personal use only.

from methanol, the product was shown to be identical to authentic disulfide by mp, mixture mp, tlc, and nmr.

*Reduction of tribromosulfonate **1** with* p*-tolyl mercaptide anions*

A solution of *p*-tolyl mercaptan (4.064 g, 32.7 mmol) in HMPA (10 mL) was added dropwise to a suspension of sodium hydride (0.842 g, 35.1 mmol) in HMPA (30 mL). Upon completion of the addition, the reaction mixture was stirred at ambient temperature for 35 min. The tribromosulfonate **1** (6.552 g, 16.0 mmol) was added and the reaction mixture stirred at room temperature for 1 h. Benzyl chloride (2.078 g, 15.8 mmol) was added dropwise and the reaction mixture stirred at room temperature for 60 h.

The reaction mixture was poured into a 2-L Erlenmeyer containing water (400 mL), 10% HCl (5 mL), and diethyl ether (100 mL). The mixture was vigorously shaken and transferred to a separatory funnel. The layers were separated and the aqueous washed with ether (two 100-mL portions). The combined ether layers were concentrated and poured into water (100 mL). The mixture was washed with diethyl ether (three 100-mL aliquots). The combined organic layers were washed with 2.5% sodium hydroxide (100 mL), dried ($MgSO_4$), and concentrated, affording crude product (5.364 g).

Half of the crude was chromatographed on silica gel (268 g) employing chloroform elution (100-mL fractions). Fractions 13–19 were combined and concentrated, yielding clean benzyl methyl sulfone (0.440 g, 2.58 mmol, overall yield 32.6%). The chromatographed sulfone was recrystallized from methanol and shown to be identical to authentic material by nmr, double-spotted tlc, melting point, and mixture mp.

One-pot sulfone preparations

The conversion of benzyl chloride into benzyl phenyl sulfone will be used to illustrate the procedure that furnished the results presented in Table 2.

A solution of 3-mercaptopropionic acid (0.934 g, 8.8 mmol) in HMPA (10 mL) was added dropwise to a suspension of sodium hydride (0.432 g, 18.0 mmol) in HMPA (30 mL). Upon completion of the addition, the reaction mixture was stirred at ambient temperature for 0.5 h. The tribromosulfonate **2** (2.037 g, 4.3 mmol) was added and the reaction mixture stirred at ambient temperature for 1 h. A solution of benzyl chloride (0.590 g, 4.6 mmol) in HMPA (10 mL) was added dropwise and the reaction mixture stirred at room temperature for 18 h.

Crude product (0.911 g) was obtained using the extraction procedure outlined under "Reduction of tribromosulfonate **1** with *p*-tolyl mercaptide anions". The crude was chromatographed on silica gel (91 g) employing 3:2 carbon tetrachloride/methylene chloride (90-mL fractions). Fractions 7–16 were combined and concentrated, yielding benzyl phenyl sulfone (0.576 g, 2.5 mmol, 57%). Recrystallized product was shown to be identical to authentic material by double-spotted tlc, nmr, mp, and mixture mp.

Preparation of 2,4,6-tribromophenyl methyl ether

A solution of 2,4,6-tribromophenol (1.023 g, 3.09 mmol) in HMPA (25 mL) was added dropwise to a slurry of sodium hydride (0.053 g, 2.21 mmol) in HMPA (15 mL). The reaction mixture was stirred at ambient temperature for 1 h. A solution of methyl iodide (0.325 g, 2.29 mmol) in HMPA (10 mL) was added dropwise to the reaction mixture.

Crude ether (0.6006 g) was obtained using the extraction procedure outlined under "Reduction of tribromosulfonate **1** with *p*-tolyl mercaptide anions." Crude tribromoether was recrystallized from methanol, affording clean ether (0.464 g, 1.34 mmol, 58.5%). The clean ether had mp 87.2–88°C; nmr ($CDCl_3$) δ: 7.66 (2H,s), and 3.85 (3H,s). *Anal.* calcd. for $C_7H_5Br_3O$: C 24.38, H 1.46; found: C 24.59, H 1.44.

Preparation of $(CH_3O_2C(CH_2)_2S)_2$

Sodium metal (2.076 g, 90.2 mmol) was dissolved in methanol (100 mL). A solution of 3-mercaptopropionic acid (4.467 g, 42.1 mmol) in methanol (10 mL) was added dropwise to the reaction mixture. Upon completion of the addition, the reaction mixture was stirred at ambient temperature for 0.5 h. Iodine (5.390 g, 21.2 mmol) was added and the reaction mixture stirred for 10 min. Concentrated sulfuric acid (2.4 mL) was added and the reaction mixture refluxed for 16 h.

The reaction mixture was diluted with chloroform (300 mL) and the resultant solution washed with 2% sodium thiosulfate (100-mL aliquots) until the organic layer became colorless. The organic layer was dried ($MgSO_4$) and concentrated. The residue was rectified at reduced pressure, affording homogeneous disulfide-diester (3.253 g, 13.6 mmol, 64.6%, 134°C/6.5 Torr; 1 Torr = 133.3 Pa). The diester-disulfide had ir ($CHCl_3$); 1740 cm^{-1}; nmr ($CDCl_3$) δ: 3.70 (3H,s), 2.93 (2H,t), and 2.73 (2H,t). *Anal.* calcd. for $C_8H_{14}O_4S_2$: C 40.31, H 5.92; found: C 40.33, H 6.08.

Preparation of phenyl methyl sulfone with excess methyl iodide

A solution of 3-mercaptopropionic acid (1.379 g, 13.0 mmol) in HMPA (10 mL) was added dropwise to a suspension of sodium hydride (0.652 g, 27.1 mmol) in HMPA (30 mL). The reaction mixture was then stirred at room temperature for 0.5 h. The tribromophenyl benzenesulfonate **2** (3.080 g, 6.5 mmol) was added and the reaction mixture stirred for 1 h. A solution of methyl iodide (1.868 g, 13.1 mmol) in HMPA (10 mL) was added dropwise and the reaction mixture stirred overnight.

Crude product (1.629 g) was obtained by employing the extraction procedure outlined under "Reduction of tribromosulfonate **1** with *p*-tolyl mercaptide anions". The crude was recrystallized from methanol. affording clean 2,4,6-tribromophenyl methyl ether (0.351 g). The mother liquor concentrate was chromatographed on silica gel (118 g) employing 3:2 carbon tetrachloride/methylene chloride elution (30 100-mL fractions). Fraction 3 was concentrated, yielding more 2,4,6-tribromophenyl methyl ether (0.157 g). After recrystallization, the tribromophenyl methyl ether (total yield 23%) was shown to be identical to authentic material by nmr, double-spotted tlc, mp, and mixture mp. Fractions 21–36 were concentrated and combined, affording a mixture (0.675 g) that contained phenyl methyl sulfone (0.383 g, 2.45 mmol, 38%) and $(CH_3O_2C(CH_2)_2S)_2$ (0.292 g, 1.22 mmol, 18.7%). The composition of the mixture was determined by nmr using the procedure previously described (12). The identity of the components in the mixture was confirmed by double-spotted tlc and by the addition of authentic samples of each, which caused increases in the intensity of the appropriate nmr signals.

Preparation of $PhSCH_2SO_2CH_3$

A solution of thiophenol (0.473 g, 4.3 mmol) in HMPA (15 mL) was added dropwise to a suspension of NaH (0.101 g, 4.2 mmol) in HMPA (15 mL) over 15 min. The reaction mixture was stirred at ambient temperature for 30 min. A solution of 1-chloro-2-thiapropane-2,2-dioxide (13) (0.509 g, 3.9 mmol) in HMPA (10 mL) was added dropwise to the reaction mixture. The reaction mixture was heated at 100°C for 1.5 h.

Crude product (0.552 g) was obtained with the extraction procedure outlined under "Reduction of tribromosulfonate **1** with *p*-tolyl mercaptide anions". The crude was chromatographed on silica gel (55 g) using chloroform elution (50-mL fractions). Fractions 6–11 were concentrated and combined, affording clean $PhSCH_2SO_2CH_3$ (0.462 g, 2.3 mmd. 57.5%). Upon recrystallization, the product was shown to be identical to authentic sulfone-sulfide (9) by mp, mixture mp, nmr, and double-spotted tlc.

Preparation of $PhSO_2CH_2SO_2CH_3$

A solution of $CH_3SO_2CH_2SPh$ (0.507 g, 2.5 mmol) in chloroform (50 mL) was cooled with an ice/water bath. *m*-Chloroperoxybenzoic acid (1.122 g, 85%) was added in small portions over 15 min. The ice/water bath was removed and the reaction stirred at ambient temperature overnight.

Chloroform (200 mL) was added and the resultant solution washed with 2.5% sodium hydroxide solution (100-mL aliquots) until the aqueous pH remained basic. The organic layer was dried ($MgSO_4$) and concentrated. The crude disulfone (0.316 g) was recrystallized from methanol, affording clean disulfone (0.234 g, 1.0 mmol, 40%), mp 140–143°C. The disulfone had ir ($CHCl_3$): 1340 and 1145 cm^{-1}; nmr ($CDCl_3$) δ: 8.00 (2H,m), 7.70 (3H,m), 4.60 (2H,s), and 3.30 (3H,s);

ms *m/e*: 234 (2.5%), 125 (19.5%), 107 (92%), and 77 (100%). *Anal.* calcd. for $C_8H_{10}O_4S_2$: C 41.01, H 4.30: found C 41.14, H 4.30.

Trapping a disproportionation product

A solution of 3-mercaptopropionic acid (1.884 g, 17.7 mmol) in HMPA (10 mL) was added dropwise to a suspension of sodium hydride (0.792 g, 33.0 mmol) in HMPA (30 mL). The reaction mixture was stirred at ambient temperature for 0.5 h. The tribromobenzenesulfonate **2** (4.049 g, 8.6 mmol) was added and the reaction mixture stirred at ambient temperature for 1 h. A solution of $ClCH_2SO_2CH_3$ (1.120 g, 8.7 mmol) in HMPA (15 mL) was added. The reaction mixture was heated at 90°C for 1.5 h.

Crude product (0.364 g) was obtained by employing the extraction procedure outlined under "Reduction of tribromosulfonate **1** With *p*-tolyl mercaptide anions". The crude was chromatographed on silica gel (25 g) employing chloroform elution (25-mL fractions). Fractions 6 and 7 were combined and concentrated, affording impure sulfone-sulfide (0.055 g). The impure sample contained $PhSCH_2SO_2CH_3$ (0.013 g) and $ClCH_2SO_2CH_3$ (0.042 g) as established by nmr using our previously described procedure (12).

The sulfone-sulfide was converted to disulfone to facilitate removal of the contaminating chlorosulfone. Impure sulfone-sulfide (0.041 g) was dissolved in chloroform (6.5 mL) and cooled with an ice/water bath. *m*-Chloroperoxybenzoic acid (85%, 0.211 g) was added and the reaction mixture stirred overnight.

After base washing, the dried layer was concentrated and chromatographed on silica gel (50 g) employing chloroform elution (50-mL aliquots). Fractions 10–13 were concentrated, combined (0.018 g), and rechromatographed on silica gel (100 g) employing chloroform elution (50-mL fractions). Fractions 25–28 were concentrated and combined, yielding clean $PhSO_2CH_2SO_2CH_3$ (0.012 g, 0.05 mmol). This material was identical to that described in the previous experiment by nmr, ir, mp, and mixture mp.

Reduction of benzenethiosulfonate with phenyl mercaptide anions

A solution of benzene thiol (0.895 g, 8.1 mmol) in HMPA (10 mL) was added dropwise to a slurry of sodium hydride (0.219 g, 9.1 mmol) in HMPA (20 mL) over 10 min. The reaction mixture was stirred at ambient temperature for 1 h. Benzenethiosulfonate (2.030 g, 8.1 mmol) was added and the reaction mixture stirred at room temperature for 1 h. A solution of methyl iodide (1.173 g) in HMPA (10 mL) was added dropwise over 5 min. The reaction mixture was stirred at ambient temperature for 18 h.

Crude product (2.092 g) was obtained using the extraction procedure outlined under "Reduction of tribromosulfonate **1** With *p*-tolyl mercaptide anions". The crude was chromatographed on silica gel (209 g) employing 3:2 carbon tetrachloride methylene chloride (31 100-mL fractions) followed by chloroform (100-mL fractions). Fractions 5–8 were combined and concentrated, yielding diphenyl disulfide (0.504 g, 2.3 mmol, 56.9%). Fractions 9–12 furnished unchanged thiosulfonate (0.073 g). Fractions 27–37 were combined and concentrated, affording phenyl methyl sulfone (0.382 g, 2.4 mmol, 30.1%), which was identical to authentic material by nmr, tlc, and mp.

Acknowledgements

The authors are grateful to the Florida Institute of Technology for financial support. We thank Mr. Jimat Bolhassan for some technical assistance. Mass spectra were obtained at the Midwest Center for Mass Spectrometry, University of Nebraska–Lincoln, which is a National Science Foundation Regional Instrumentation Facility (Grant No. CHE 821164).

1. R. F. LANGLER and N. A. MORRISON. Can. J. Chem. **65**, 2385 (1987).
2. L. FIELD. *In* Organic chemistry of sulfur. *Edited by* S. Oae. Plenum Press, New York, NY. 1977. p. 316.
3. T. L. HO. Hard and soft acids and bases principle in organic chemistry. Academic Press, New York, NY. 1977. p. 144.
4. Z. RAPPOPORT. Handbook of tables for organic compound identification. 3rd ed. The Chemical Rubber Company, Cleveland, OH. 1967.
5. R. C. WEAST. Handbook of chemistry and physics. 50th ed. The Chemical Rubber Company, Cleveland, OH. 1969. p. C-274.
6. S. OAE and N. KUNEIDA. *In* Organic chemistry of sulfur. *Edited by* S. Oae. Plenum Press, New York, NY. 1977. p. 604.
7. (*a*) M. JULIA, A. RIGHINI-TAPIC, and J. N. VERPEAU. Tetrahedron **39**, 3283 (1983); (*b*) L. A. PAQUETTE, R. E. MOERCK, B. HARIRCHIAN, and P. D. MAGNUS. J. Am. Chem. Soc. **100**, 1597 (1978); (*c*) M. YOKOYAMA, K. TSUJI, and T. IMAMOTO. Bull. Chem. Soc. Jpn. **57**, 2954 (1984).
8. I. GALYNKER and W. C. STILL. Tetrahedron Lett. **23**, 4461 (1982).
9. D. G. KAY, R. F. LANGLER, and J. E. TRENHOLM. Can. J. Chem. **57**, 2185 (1979).
10. R. F. LANGLER and J. A. PINCOCK. Can. J. Chem. **55**, 2316 (1977).
11. (*a*) K. SUKATA. Bull. Chem. Soc. Jpn. **57**, 613 (1984). (*b*) C. M. M. DA SILVA CORREA and W. A. WATERS. J. Chem. Soc. (C), 1874 (1968). (*c*) F. FREEMAN. Chem. Rev. **84**, 117 (1984).
12. J. S. GROSSERT and R. F. LANGLER. Can. J. Chem. **55**, 407 (1977).
13. W. R. HARDSTAFF and R. F. LANGLER. Org. Mass Spectrom. **10**, 215 (1975).

Can. J. Chem. Downloaded from www.nrcresearchpress.com by 122.72.124.2 on 09/07/12
For personal use only.

General description of multiple-modulation effects and sideband production in magnetic resonance

HIROKAZU SAKAMOTO, TAKEJI TAKUI, AND KOICHI ITOH

Department of Chemistry, Faculty of Science, Osaka City University, Sugimoto, Sumiyoshi-ku, Osaka 558, Japan

Received November 25, 1987[1]

This paper is dedicated to Professor C. A. McDowell on the occasion of his 70th birthday

HIROKAZU SAKAMOTO, TAKEJI TAKUI, and KOICHI ITOH. Can. J. Chem. **66**, 3077 (1988).

A theory is presented for the sideband structure produced by a general multiple-modulation scheme with arbitrary combination of p-tuple field modulation, q-tuple frequency modulation, and r-tuple amplitude modulation for integral p, q, and r. A general formula describing the multiple-modulation effects is analytically derived using a density matrix formalism under the assumption of negligible saturation; an equivalent result is obtained from the phenomenological Bloch equation. The general formula reveals that field and frequency modulations are equivalent for the sideband production, even in the presence of amplitude modulation. Two particular cases, viz., r-tuple amplitude modulation and double field modulation are dealt with to show the validity and applicability of the general formula.

HIROKAZU SAKAMOTO, TAKEJI TAKUI et KOICHI ITOH. Can. J. Chem. **66**, 3077 (1988).

On présente une théorie pour la structure de bande secondaire produite par un schéma de modulation multiple générale avec une combinaison arbitraire de modulation de champ p-tuple, de modulation de fréquence q-tuple et un modulation d'amplitude r-tuple pour des valeurs entières de p, q et r. On a déduit une formule générale qui décrit les effets de modulation multiple en faisant appel a un formalisme de matrice dense et en supposant une saturation négligeable; on obtient un résultat équivalent à partir de l'équation phénoménologique de Bloch. La formule générale révèle que les modulations de champ et de fréquence sont équivalentes en ce qui a trait à la production de la bande secondaire, même en présence d'une modulation d'amplitude. On a envisagé deux cas particuliers, par exemple la modulation d'amplitude de r-tuple et la modulation de champ double, dans le but de démontrer la validité et l'applicabilité de la formule générale.

[Traduit par la revue]

I. Introduction

Modulation is one of the most useful techniques for improving sensitivity in various branches of spectroscopy. As a time-dependent perturbation to a physical system, modulation is also useful for examining dynamical features of the system, e.g., molecular spin dynamics. It is well known that when a modulation frequency is larger than a spectral linewidth sidebands generally appear. Karplus was the first to propose a quantum mechanical modulation theory for sideband production (1); he treated Stark effect in microwave spectroscopy using a density matrix formalism. This theory has been extended by Smaller to the case of Zeeman modulation in NMR (2), and was later generalized by Macomber and Waugh to cover a wide range of phenomena (3).

Anderson (4) and Haworth and Richards (5) have attempted another approach using the phenomenological Bloch equation for spin systems under the influence of either field or frequency modulation, and they have shown the equivalence of sideband structures induced by the two modulation schemes. Later, Kim (6) re-examined this problem using a density operator method and concluded that field modulation led to the same sideband structure as predicted previously from the Bloch equation (4, 5) while frequency modulation did not. Subsequently, Dulčić ans Rakvin (7) have claimed the equivalence of the two modulations and have pointed out that the answer to the controversy is to be found in the understanding of the detection scheme.

On the other hand, Miyagawa *et al.* (8) have demonstrated that field modulation is an excellent technique for the accurate measurement of the amplitude of a radio-frequency (rf) field applied to a sample in electron–nuclear double resonance (ENDOR) experiments, and they have developed a methodology of the measurement using a first-order time-dependent perturbation theory for isolated spins.

All the theoretical treatments above have been limited to the single modulation. Islam and Miyagawa have recently extended their theory to double-modulation schemes (9); they also obtained the equivalent sideband structures produced by field and frequency modulations. We have independently made a preliminary report on a general theory of sideband production by multiple modulation in magnetic resonance, and have demonstrated, as one of its potential applications, simultaneous measurements of two rf amplitudes at a sample site in electron–nuclear–nuclear triple resonance (TRIPLE) experiments (10). On the experimental side, Ravkin *et al.* (11) have recently reported a new double-modulation spectroscopic technique, observing sharp sidebands with a linewidth equivalent to the individual spin-packet from an inhomogeneously broadened ESR line; this methodology was also applied to the investigation of rotational motions of nitroxide spin-labeled polymers (12).

In this paper we extend the density matrix formalism for a single modulation scheme (6, 13) to the case of simultaneous application of field, frequency, and amplitude modulations, presenting a general theory which interprets multiple-modulation effects on magnetic resonance. It is shown that both the density matrix formalism and the phenomenological Bloch equations predict identical multiple-modulation effects if thermal equilibrium is maintained. The equivalence of field and frequency modulations is re-examined from the view point of general multiple modulation including amplitude modulation. The general formula derived here may serve as a basis for application of multiple modulation to possible new spectroscopic techniques as well

[1]Revision received August 9, 1988.

Printed in Canada / Imprimé au Canada

Can. J. Chem. Downloaded from www.nrcresearchpress.com by 122.72.124.2 on 09/07/12
For personal use only.

as to available spectroscopies, since it has no restriction on the number of modulations or on the types of modulation schemes. Experimental examinations of the theoretical predictions will be presented in a later paper.

II. General expression for sideband production by multiple modulation

A. Modulation fields

To describe a general scheme of multiple modulation, we introduce simultaneous application of three types of modulations: the p-tuple field modulation with the frequencies of ω_1^1 to ω_1^p, the q-tuple frequency modulation with those of ω_2^1 to ω_2^q, and the r-tuple amplitude modulation with those of ω_3^1 to ω_3^r, as defined by the formula

$$[1]\quad \boldsymbol{H}'(t) = H'\left[\boldsymbol{x}\left(1 + \sum_{\gamma=1}^{r} \Omega_3^\gamma \cos \omega_3^\gamma t\right) \cos\left\{\omega t - \sum_{\beta=1}^{q} (\Omega_2^\beta/\omega_2^\beta) \sin \omega_2^\beta t\right\} + \boldsymbol{y}\left(1 + \sum_{\gamma=1}^{r} \Omega_3^\gamma \cos \omega_3^\gamma t\right) \times \sin\left\{\omega t - \sum_{\beta=1}^{q} (\Omega_2^\beta/\omega_2^\beta) \sin \omega_2^\beta t\right\}\right] + \boldsymbol{z}\left(\sum_{\alpha=1}^{p} H_1^\alpha \cos \omega_1^\alpha t\right)$$

Here, the field modulation is applied to a static magnetic field taken to be along the z axis, while the frequency and amplitude modulations to a radiation field (for magnetic resonance) which is rotating in the xy plane with the amplitude H' and the frequency ω; H_1^α denotes the amplitude of the α-th field modulation, Ω_2^β a deviation of the β-th frequency modulation, and Ω_3^γ a degree of the γ-th amplitude modulation. It should be mentioned here that the phases of all these modulations can be neglected, since they have no influence on the sideband structure in our phenomenological treatment. Expressions including the phases and their effects are described in the Appendix.

B. Density matrix approach

We follow the density matrix formalism developed by Abragam (13) for a system with a "simple line" and consider a spin system with a Hamiltonian $\hbar\mathcal{H}_0$ which is not only free from interactions with other spin systems but also weakly coupled to a heat bath (lattice), and to which an rf perturbation $\hbar\mathcal{H}'(t)$ with a frequency ω is applied. Assuming that a pair of its unperturbed states $|a\rangle$ and $|b\rangle$ coupled by $\hbar\mathcal{H}'(t)$ has an energy difference ω_{ab} which is different from any other energy difference $\omega_{\alpha\beta}$ such that $|\omega_{ab} - \omega_{\alpha\beta}| \gg \omega - \omega_{ab}|$ and $|\mathcal{H}'(t)|$, and that the correlation time τ_c of the spin system is short enough to satisfy $|\mathcal{H}'(t)|\tau_c \ll 1$, we can write the equation for the density matrix $\rho(t)$ of this system as

$$[2]\quad d\rho/dt = -i[\mathcal{H}_0 + \mathcal{H}'(t), \rho(t)] - \Gamma(\rho - \rho_{eq})$$

Here, ρ_{eq} is the density matrix of the spin system in thermal equilibrium at a temperature T before the application of the perturbation, and is given by

$$[3]\quad \rho_{eq} = \exp(-\hbar\mathcal{H}_0/kT)/\mathrm{Tr}\,[\exp(-\hbar\mathcal{H}_0/kT)] \sim [1 - \hbar\mathcal{H}_0/kT]/A = 1/A - q\mathcal{H}_0$$

in the high temperature approximation ($kT \gg \hbar\mathcal{H}_0$). Here A is the number of degrees of freedom of the spin system and $q = (\hbar/kT)/A$. The term $-\Gamma(\rho - \rho_{eq})$ in eq. [2], which represents a relaxation of the spin system, is given by

$$[4]\quad [-\Gamma(\rho - \rho_{eq})]_{ab} = -\rho_{ab}/(T_2)_{ab}$$

for a simple line corresponding to the $|a\rangle \leftrightarrow |b\rangle$ transition. Here $(T_2)_{ab}$ stands for the transverse relaxation time characteristic of this transition (13).

When the radiation field given by eq. [1] is applied to the spin system, the time-dependent perturbation $\hbar\mathcal{H}'(t)$ can be written

$$[5]\quad \mathcal{H}'(t) = \left(1 + \sum_{\gamma} \Omega_3^\gamma \cos \omega_3^\gamma t\right)\left[D^- \exp\left[i\left\{\omega t - \sum_{\beta} (\Omega_2^\beta/\omega_2^\beta) \sin \omega_2^\beta t\right\}\right] + D^+ \exp\left[-i\left\{\omega t - \sum_{\beta} (\Omega_2^\beta/\omega_2^\beta) \sin \omega_2^\beta t\right\}\right]\right] + \sum_{\alpha} [F_\alpha \exp(i\omega_1^\alpha t) + F_\alpha^+ \exp(-i\omega_1^\alpha t)]$$

where we define

$$[6]\quad \begin{aligned} &S_\pm = S_x \pm iS_y \\ &D^- = -\gamma_e H' S_-/2,\ D^+ = -\gamma_e H' S_+/2,\ F_\alpha = F_\alpha^+ = -\gamma_e H_1^\alpha S_z/2 \end{aligned}$$

with the abbreviation

$$[7]\quad \langle b|D^-|a\rangle = \langle a|D^+|b\rangle^* = d$$

We introduce a reduced density matrix $\sigma(t) = \rho(t) - \rho_{eq}$ and consider the case where the rf power is low enough so that the two diagonal matrix elements ρ_{aa} and ρ_{bb} have their thermal equilibrium values. Then the departures from these values, σ_{aa} and σ_{bb}, vanish, and eq. [2] can be reduced to the following differential equation for the off-diagonal element σ_{ba} using eqs. [3]–[7]:

$$[8]\quad d\sigma_{ba}/dt + \left[-i\left(\omega_0 + \sum_{\alpha} \Omega_1^\alpha \cos \omega_1^\alpha t\right) + 1/T_2\right]\sigma_{ba} = iq\, d\omega_0\left(1 + \sum_{\gamma} \Omega_3^\gamma \cos \omega_3^\gamma t\right) \exp\left[i\left\{\omega t - \sum_{\beta} (\Omega_2^\beta/\omega_2^\beta) \sin \omega_2^\beta t\right\}\right]$$

where $\omega_0 = -\gamma_e H_0$, $\Omega_1^\alpha = -\gamma_e H_1^\alpha$, and $T_2 = (T_2)_{ab}$. We now look for the solution for eq. [8] of the following form

Can. J. Chem. Downloaded from www.nrcresearchpress.com by 122.72.124.2 on 09/07/12
For personal use only.

Can. J. Chem. Downloaded from www.nrcresearchpress.com by 122.72.124.2 on 09/07/12
For personal use only.

$$[9]\quad \sigma_{ba}(t) = Z(t)\exp\left[i\left\{\omega t + \sum_{\alpha}(\Omega_1^{\alpha}/\omega_1^{\alpha})\sin\omega_1^{\alpha}t\right\}\right]$$

The substitution of eq. [9] into eq. [8] yields the transformed differential equation for $Z(t)$

$$[10]\quad dZ/dt + [i(\omega - \omega_0) + 1/T_2]Z = iq\,d\omega_0\left(1 + \sum_{\gamma}\Omega_3^{\gamma}\cos\omega_3^{\gamma}t\right)\exp\left[-i\left\{\sum_{\alpha}(\Omega_1^{\alpha}/\omega_1^{\alpha})\sin\omega_1^{\alpha}t + \sum_{\beta}(\Omega_2^{\beta}/\omega_2^{\beta})\sin\omega_2^{\beta}t\right\}\right]$$

This equation can be analytically solved to give

$$[11]\quad \sigma_{ba}(t) = (q\,d\omega_0 T_2)\exp(i\omega t)\sum{}'\prod_{\alpha}J_{n_\alpha}(\Omega_1^{\alpha}/\omega_1^{\alpha})\prod_{\alpha'}J_{n_{\alpha'}}(\Omega_1^{\alpha'}/\omega_1^{\alpha'})\prod_{\beta}J_{k_\beta}(\Omega_2^{\beta}/\omega_2^{\beta})$$
$$\times\left\{\frac{\left(\omega - \omega_0 - \sum_{\alpha}n_\alpha\omega_1^{\alpha} - \sum_{\beta}k_\beta\omega_2^{\beta}\right)T_2 + i}{1 + \left(\omega - \omega_0 - \sum_{\alpha}n_\alpha\omega_1^{\alpha} - \sum_{\beta}k_\beta\omega_2^{\beta}\right)^2 T_2^2}\exp\left[i\left(\sum_{\alpha'}n_{\alpha'}\omega_1^{\alpha'} - \sum_{\alpha}n_\alpha\omega_1^{\alpha} - \sum_{\beta}k_\beta\omega_2^{\beta}\right)t\right] + \sum_{j=\pm1}\sum_{\gamma}\frac{\Omega_3^{\gamma}}{2}\right.$$
$$\left.\times\frac{\left(\omega - \omega_0 - \sum_{\alpha}n_\alpha\omega_1^{\alpha} - \sum_{\beta}k_\beta\omega_2^{\beta} - j\omega_3^{\gamma}\right)T_2 + i}{1 + \left(\omega - \omega_0 - \sum_{\alpha}n_\alpha\omega_1^{\alpha} - \sum_{\beta}k_\beta\omega_2^{\beta} - j\omega_3^{\gamma}\right)^2 T_2^2}\exp\left[i\left(\sum_{\alpha'}n_{\alpha'}\omega_1^{\alpha'} - \sum_{\alpha}n_\alpha\omega_1^{\alpha} - \sum_{\beta}k_\beta\omega_2^{\beta} - j\omega_3^{\gamma}\right)t\right]\right\}$$

where $J_{n_\alpha}(\Omega_1^{\alpha}/\omega_1^{\alpha})$, $J_{n_{\alpha'}}(\Omega_1^{\alpha'}/\omega_1^{\alpha'})$, and $J_{k_\beta}(\Omega_2^{\beta}/\omega_2^{\beta})$ are the Bessel functions of the first kind and Σ' denotes the summation over three indices n_α, $n_{\alpha'}$, and k_β from $-\infty$ to ∞. Here α and α' are integers ranging from 1 to p, β runs over the integral values from 1 to q, and γ over those from 1 to r, where p, q, and r denote the number of the field, frequency, and amplitude modulations, respectively.

Equation [11] is the general formula for an ensemble of mutually-noninteracting spin systems in the presence of the multiple-modulation fields simultaneously applied; this describes sideband structures induced by arbitrary combinations of multiple modulations. Naturally, eq. [11] contains the terms corresponding to the various combination bands characterized by

$$\sum_{\alpha}n_\alpha\omega_1^{\alpha},\ \sum_{\beta}k_\beta\omega_2^{\beta},\quad \text{and}\quad \pm\omega_3^{\gamma}$$

whose intensity distributions can be predicted through the Bessel functions using the experimentally-given modulation indices, $\Omega_1^{\alpha}/\omega_1^{\alpha}$, $\Omega_2^{\beta}/\omega_2^{\beta}$, etc.

C. The Bloch equation approach

We now describe the behavior of magnetization of an ensemble of spin systems in the presence of multiple-modulation fields in terms of the phenomenological Bloch equation

$$[12]\quad \frac{d\boldsymbol{M}}{dt} = \gamma_e(\boldsymbol{M}\wedge\boldsymbol{H}) - \frac{M_x\boldsymbol{i} + M_y\boldsymbol{j}}{T_2} - \frac{M_z - M_0}{T_1}\boldsymbol{k}$$

which is referred to the laboratory frame defined by the unit vectors, $\boldsymbol{i}$, $\boldsymbol{j}$, and $\boldsymbol{k}$. The resultant magnetic field $\boldsymbol{H}$ is given by

$$[13]\quad \boldsymbol{H} = \boldsymbol{H}_0 + \boldsymbol{H}'(t) = H_0\boldsymbol{k} + \boldsymbol{H}'(t)$$

where $\boldsymbol{H}_0$ is the static magnetic field applied along $\boldsymbol{k}(\|z)$ and $\boldsymbol{H}'(t)$ is the time-dependent radiation field given by eq. [1].

Substituting eqs. [1] and [13] into [12], we obtain the components of the Bloch equation for the magnetization:

$$[14]\quad dM_x/dt = \gamma_e\left[M_y\left(H_0 + \sum_{\alpha}H_1^{\alpha}\cos\omega_1^{\alpha}t\right) - M_zH'\left(1 + \sum_{\gamma}\Omega_3^{\gamma}\cos\omega_3^{\gamma}t\right)\sin\left\{\omega t - \sum_{\beta}(\Omega_2^{\beta}/\omega_2^{\beta})\sin\omega_2^{\beta}t\right\}\right] - M_x/T_2$$

$$[15]\quad dM_y/dt = \gamma_e\left[M_zH'\left(1 + \sum_{\gamma}\Omega_3^{\gamma}\cos\omega_3^{\gamma}t\right)\cos\left\{\omega t - \sum_{\beta}(\Omega_2^{\beta}/\omega_2^{\beta})\sin\omega_2^{\beta}t\right\} - M_x\left(H_0 + \sum_{\alpha}H_1^{\alpha}\cos\omega_1^{\alpha}t\right)\right] - M_y/T_2$$

$$[16]\quad dM_z/dt = \gamma_e\left[M_xH'\left(1 + \sum_{\gamma}\Omega_3^{\gamma}\cos\omega_3^{\gamma}t\right)\sin\left\{\omega t - \sum_{\beta}(\Omega_2^{\beta}/\omega_2^{\beta})\sin\omega_2^{\beta}t\right\}\right.$$
$$\left. - M_yH'\left(1 + \sum_{\gamma}\Omega_3^{\gamma}\cos\omega_3^{\gamma}t\right)\cos\left\{\omega t - \sum_{\beta}(\Omega_2^{\beta}/\omega_2^{\beta})\sin\omega_2^{\beta}t\right\}\right] - (M_z - M_0)/T_1$$

where M_0 denotes the magnetization in thermal equilibrium, T_1 the longitudinal relaxation time, and T_2 the transverse relaxation time. From eqs. [14] and [15], we obtain the differential equation for the transverse magnetization $M_+ = M_x + iM_y$,

$$[17]\quad dM_+/dt + \left[-i\left(\omega_0 + \sum_{\alpha}\Omega_1^{\alpha}\cos\omega_1^{\alpha}t\right) + 1/T_2\right]M_+ = i\gamma_eH'\left(1 + \sum_{\gamma}\Omega_3^{\gamma}\cos\omega_3^{\gamma}t\right)M_z\exp\left[i\left\{\omega t - \sum_{\beta}(\Omega_2^{\beta}/\omega_2^{\beta})\sin\omega_2^{\beta}t\right\}\right]$$

where $\omega_0 = -\gamma_e H_0$. For a sufficiently small radiation field satisfying $|\gamma_e H'| \ll 1/T_1$, viz., for negligible saturation, we may replace M_z by M_0 in eq. [17]. Equation [17] is then mathematically equivalent to eq. [8] derived in the preceding section except for the multiplying constant factor on the right-hand side. Therefore, under negligible saturation the solution for the Bloch equation should have the same form as that for eq. [11] derived by the density matrix formalism.

III. Effect of amplitude modulation on the equivalence of field and frequency modulations

It is widely known that in the absence of frequency modulation the transverse magnetization is written, in terms of the rotating frame with an rf frequency ω, as $M_x + iM_y = (\tilde{M}_x + i\tilde{M}_y)\exp(i\omega t)$. Radio frequency detection is normally carried out with reference to an rf voltage proportional to $\exp(i\omega t)$ which is supplied either as a permanent leakage voltage from the driving rf field when the rf bridge, the cross-coil system, or the resonant cavity is unbalanced, or as a reference voltage with a well-defined phase when the bridge or its equivalent is completely balanced. The stationary components $\tilde{M}_x$ and $-(\gamma_e/|\gamma_e|)\tilde{M}_y$ then give the dispersion and absorption modes, respectively. Analogously, in the presence of amplitude and frequency modulations, the rf-detected signal is given by the stationary components with reference to the *amplitude- and frequency-modulated* rf voltage which is in this case the driving rf field. Since we have shown in the preceding section that $\sigma_{ba}(t)$ is mathematically equivalent to $M_+ = M_x + iM_y$ for negligible saturation, we can write the rf-detected signal as

$$[18]\quad \tilde{\sigma}_{ba}(t) = \sigma_{ba}\left\{1 + \sum_{j=\pm1}\sum_{\gamma}\frac{\Omega_3^\gamma}{2}\exp[i(-j\omega_3^\gamma)t]\right\}\exp\left[-i\left\{\omega t - \sum_{\beta}(\Omega_2^\beta/\omega_2^\beta)\sin\omega_2^\beta t\right\}\right]$$

Using eqs. [11] and [18], and the identity

$$[19]\quad \exp(i\omega t) = \exp\left[i\left\{\omega t - \sum_{\beta}(\Omega_2^\beta/\omega_2^\beta)\sin\omega_2^\beta t\right\}\right]\sum_{k_\beta}\prod_{\beta}J_{k_\beta}(\Omega_2^\beta/\omega_2^\beta)\exp(ik_\beta\omega_2^\beta t)$$

we obtain as the stationary component of the reduced density matrix corresponding to $\tilde{M}_x$ and $-(\gamma_e/|\gamma_e|)\tilde{M}_y$

$$\begin{aligned}[20]\quad \tilde{\sigma}_{ba}(t) = (q\,d\omega_0 T_2)&\left\{1 + \sum_{j=\pm1}\sum_{\gamma}\frac{\Omega_3^\gamma}{2}\exp[i(-j\omega_3^\gamma)t]\right\}\sum{}'\prod_{\alpha}J_{n_\alpha}(\Omega_1^\alpha/\omega_1^\alpha)\prod_{\alpha'}J_{n_{\alpha'}}(\Omega_1^{\alpha'}/\omega_1^{\alpha'})\prod_{\beta}J_{k_\beta}(\Omega_2^\beta/\omega_2^\beta)\prod_{\beta'}J_{k_{\beta'}}(\Omega_2^{\beta'}/\omega_2^{\beta'})\\
&\times\left\{\frac{\left(\omega-\omega_0-\sum_\alpha n_\alpha\omega_1^\alpha-\sum_\beta k_\beta\omega_2^\beta\right)T_2+i}{1+\left(\omega-\omega_0-\sum_\alpha n_\alpha\omega_1^\alpha-\sum_\beta k_\beta\omega_2^\beta\right)^2T_2^2}\exp\left[i\left(\sum_{\alpha'}n_{\alpha'}\omega_1^{\alpha'}-\sum_\alpha n_\alpha\omega_1^\alpha+\sum_{\beta'}k_{\beta'}\omega_2^{\beta'}-\sum_\beta k_\beta\omega_2^\beta\right)t\right]\right.\\
&+\sum_{j=\pm1}\sum_\gamma\frac{\Omega_3^\gamma}{2}\frac{\left(\omega-\omega_0-\sum_\alpha n_\alpha\omega_1^\alpha-\sum_\beta k_\beta\omega_2^\beta-j\omega_3^\gamma\right)T_2+i}{1+\left(\omega-\omega_0-\sum_\alpha n_\alpha\omega_1^\alpha-\sum_\beta k_\beta\omega_2^\beta-j\omega_3^\gamma\right)^2T_2^2}\\
&\left.\times\exp\left[i\left(\sum_{\alpha'}n_{\alpha'}\omega_1^{\alpha'}-\sum_\alpha n_\alpha\omega_1^\alpha+\sum_{\beta'}k_{\beta'}\omega_2^{\beta'}-\sum_\beta k_\beta\omega_2^\beta-j\omega_3^\gamma\right)t\right]\right\}\end{aligned}$$

where Σ' now denotes the summation over the indices n_α, $n_{\alpha'}$, k_β, and $k_{\beta'}$ ($\alpha, \alpha' = 1, 2, \ldots, p$; $\beta, \beta' = 1, 2, \ldots, q$) from $-\infty$ to ∞. The real and imaginary parts of $\tilde{\sigma}_{ba}(t)$ correspond to the dispersion and absorption modes, respectively.[2] They contain a.c. components which are further phase-sensitively detected with reference to the modulation frequencies or to their harmonics, yielding sideband structures. The d.c. component also yields different sideband structures.

Equation [20] shows that the effects of the field and frequency modulations appear equivalently not only in the first term in the parentheses of the right-hand side but also in the second term which arises from the amplitude modulation. Thus the problem of their equivalence mentioned before can be answered in a more generalized way: *for sideband production, the field and frequency modulations are equivalent even in the presence of amplitude modulation.*

IV. Special cases of multiple modulation

It can be shown that the general expression eq. [11], or equivalently eq. [20], completely reproduces the formulas reported so far by several authors (4–9, 11). We deal with two particular cases here as applications of the general formula of multiple-modulation effects.

A. Multiple amplitude modulation

This modulation scheme has not been studied so far. Ignoring other modulation effects in eq. [20], we find for the rf-detected signal due to the r-tuple amplitude modulation with the frequencies ω_3^γ ($\gamma = 1, 2, \ldots, r$)

[2]"Dispersion" and "absorption" modes indicate here the phase relation on the rf-detection and do not mean the lineshapes characteristic of the original Bloch equation.

Can. J. Chem. Downloaded from www.nrcresearchpress.com by 122.72.124.2 on 09/07/12
For personal use only.

$$[21]\quad \bar{\sigma}_{ba}(t) = (q\,\mathrm{d}\omega_0 T_2)\left\{1 + \sum_{j=\pm 1}\sum_{\gamma}\frac{\Omega_3^{\gamma}}{2}\exp\left[i(-j\omega_3^{\gamma})t\right]\right\}\left\{\frac{(\omega-\omega_0)T_2 + i}{1+(\omega-\omega_0)^2T_2^2} + \sum_{j=\pm 1}\sum_{\gamma}\frac{\Omega_3^{\gamma}}{2}\frac{(\omega-\omega_0-j\omega_3^{\gamma})T_2 + i}{1+(\omega-\omega_0-j\omega_3^{\gamma})^2T_2^2}\exp\left[i(-j\omega_3^{\gamma})t\right]\right\}$$

The sideband structure observed after the phase-sensitive detection at ω_3^{γ} is given by the coefficient of $\exp(\pm i\omega_3^{\gamma}t)$ including the phase where the real and imaginary parts correspond, respectively, to the dispersion and absorption modes. Thus eq. [21] shows that the sideband is composed solely of the two first bands at $\omega_0 \pm \omega_3^{\gamma}$ for each γ in addition to the center band at ω_0. Furthermore, their intensity is simply proportional to the degree Ω_3^{γ} of the γ-th amplitude modulation. These simple modulation effects contrast with those of the field modulation and/or frequency modulation in which various overtones and/or combination bands with complex intensities appear in the sideband structures. In view of the complexity resulting from other modulation schemes the multiple amplitude modulation has its own right because of its extreme simplicity. An application of this modulation scheme will be presented elsewhere.

B. Double field modulation

For this modulation scheme eq. [20] reduces to

$$[22]\quad \bar{\sigma}_{ba}(t) = (q\,\mathrm{d}\omega_0 T_2)\sum{}'\, J_{n_1}(\Omega_1/\omega_1)J_{n_2}(\Omega_2/\omega_2)J_{n_1'}(\Omega_1/\omega_1)J_{n_2'}(\Omega_2/\omega_2)\,\frac{(\omega-\omega_0-n_1\omega_1-n_2\omega_2)T_2 + i}{1+(\omega-\omega_0-n_1\omega_1-n_2\omega_2)^2T_2^2} \times \exp\left[i(n_1'\omega_1 + n_2'\omega_2 - n_1\omega_1 - n_2\omega_2)t\right]$$

where Σ' denotes the summation over the indices n_1, n_1', n_2, and n_2' from $-\infty$ to ∞. For brevity, we use Ω_α and ω_α instead of Ω_1^α and ω_1^α in eq. [20], neglecting the subscript for field modulation. Evidently, sideband structures produced by the double field modulation are much more complex than those by single field modulation as shown in eq. [22] which involves a linear combination of the products of the four Bessel functions.

If the absorption mode is selected for the rf-detection, the detected signal is given by the imaginary part of eq. [22]:

$$[23]\quad I_m[\bar{\sigma}_{ba}(t)] = (q\,\mathrm{d}\omega_0 T_2)\sum{}'\, J_{n_1}(\beta_1)J_{n_1'}(\beta_1)J_{n_2}(\beta_2)J_{n_2'}(\beta_2)\rho(\omega-\omega_0-n_1\omega_1-n_2\omega_2)[\cos\{(n_1'-n_1)\omega_1 + (n_2'-n_2)\omega_2\}t + T_2(\omega-\omega_0-n_1\omega_1-n_2\omega_2)\sin\{(n_1'-n_1)\omega_1 + (n_2'-n_2)\omega_2\}t]$$

where $\beta_1 = \Omega_1/\omega_1$, $\beta_2 = \Omega_2/\omega_2$, and $\rho(x) = (1 + x^2T_2^2)^{-1}$. Equation [23] derived as a special case agrees, except for the symbols and the trivial proportional constants, with eq. [61] in ref. 9 and eq. [1] in ref. 11 which have been derived by Miyagawa *et al.* for double field modulation using the first-order time-dependent perturbation theory.

One of the potential applications of the sideband production by the double field modulation is to measure simultaneously accurate amplitudes of two different rf radiation fields in TRIPLE experiments, in which measurement of the rf field strengths at the same site is important for studying spin dynamics. Although the basic principle of the measurement is an extension of that in ENDOR experiments proposed by Miyagawa *et al.* (8, 9) the complete analysis of the double field modulation effect and the sideband structure is much more complicated. Details of the analysis and the experimental examination will be published shortly.

V. Conclusion

A general description of multiple modulation in terms of the density matrix and the phenomenological Bloch equation has led to the general formula predicting the multiple-modulation effects and the sideband structure in the case of negligible saturation. This formula reveals, as an answer to the controversy reported previously (6, 7), that for sideband production the field and frequency modulations are equivalent even in the presence of the amplitude modulation. It is shown that multiple amplitude modulation produces far simpler sideband structures than any other modulation scheme. Application to the double field modulation has led to the formula equivalent to those derived previously by the time-dependent perturbation theory (9, 11).

Acknowledgements

The authors wish to thank Professor I. Miyagawa of the University of Alabama for valuable comments on the manuscript. The present work was supported by the Grant-in-Aid for Science research and for Special Project Research from the Ministry of Education, Science and Culture.

1. R. Karplus. Phys. Rev. **73**, 1027 (1948).
2. B. Smaller. Phys. Rev. **83**, 812 (1951).
3. J. D. Macomber and J. S. Waugh. Phys. Rev. A, **140**, 1949 (1965).
4. W. A. Anderson. Phys. Rev. **102**, 151 (1956).
5. O. Haworth and R. E. Richards. Prog. Nucl. Magn. Reson. Spectrosc. **1**, 1 (1966).
6. Y. W. Kim. J. Magn. Reson. **46**, 193 (1982).
7. A. Dulčić and B. Rakvin. J. Magn. Reson. **52**, 323 (1983).
8. I. Miyagawa, Y. Hayashi, and Y. Kotake. J. Magn. Reson. **25**, 183 (1977).
9. T. Islam and I. Miyagawa. J. Magn. Reson. **51**, 383 (1983).
10. H. Sakamoto, S. Kita, T. Takui, and K. Itoh. 21st ESR Symposium, Tsukuba. 1982. p. 140.
11. B. Rakvin, T. Islam, and I. Miyagawa. Phys. Rev. Lett. **50**, 1313 (1983).
12. B. Rakvin. Chem. Phys. Lett. **109**, 280 (1984); M. Peric, B. Rakvin, and A. Dulčić. J. Chem. Phys. **82**, 1079 (1985).
13. A. Abragam. The principles of nuclear magnetism. Oxford Univ. Press, London. 1961. p. 522.

Can. J. Chem. Downloaded from www.nrcresearchpress.com by 122.72.124.2 on 09/07/12
For personal use only.

Appendix

In order to perform the general treatment of modulation, one should take into account the phases of its individual frequency components, since these phases do not generally coincide. Introduction of the phases, however, does not affect the discussion in the text. Hence, we have omitted them to simplify the expressions. In this Appendix, we make a brief comment on their role in multiple modulation.

If we introduce the phases θ_1^α, θ_2^β, and θ_3^γ, respectively, for the field, frequency, and amplitude modulations. Equations [1] and [8] are rewritten as

$$[A1]\quad \boldsymbol{H}'(t) = H'\left[\boldsymbol{x}\left\{1 + \sum_{\gamma=1}^{r} \Omega_3^\gamma \cos(\omega_3^\gamma t + \theta_3^\gamma)\right\} \cos\left\{\omega t - \sum_{\beta=1}^{q} (\Omega_2^\beta/\omega_2^\beta) \sin(\omega_2^\beta t + \theta_2^\beta)\right\}\right.$$
$$\left. + \boldsymbol{y}\left\{1 + \sum_{\gamma=1}^{r} \Omega_3^\gamma \cos(\omega_3^\gamma t + \theta_3^\gamma)\right\} \sin\left\{\omega t - \sum_{\beta=1}^{q} (\Omega_2^\beta/\omega_2^\beta) \sin(\omega_2^\beta t + \theta_2^\beta)\right\}\right] + \boldsymbol{z}\left\{\sum_{\alpha=1}^{p} H_1^\alpha \cos(\omega_1^\alpha t + \theta_1^\alpha)\right\}$$

$$[A2]\quad \mathrm{d}\sigma_{ba}/\mathrm{d}t + \left[-i\left\{\omega_0 + \sum_{\alpha} \Omega_1^\alpha \cos(\omega_1^\alpha t + \theta_1^\alpha)\right\} + 1/T_2\right]\sigma_{ba} = iq\,\mathrm{d}\omega_0\left[1 + \sum_{\gamma} \Omega_3^\gamma \cos(\omega_3^\gamma t + \theta_3^\gamma)\right]$$
$$\times \exp\left[i\left\{\omega t - \sum_{\beta} (\Omega_2^\beta/\omega_2^\beta) \sin(\omega_2^\beta t + \theta_2^\beta)\right\}\right]$$

The Bloch equation equivalent to eq. [A2] can be derived by the same procedure as in the text. Equation [A2] can also be analytically solved to give

$$[A3]\quad \sigma_{ba}(t) = (q\,\mathrm{d}\omega_0 T_2)\exp(i\omega t)\sum{}' \prod_{\alpha} J_{n_\alpha}(\Omega_1^\alpha/\omega_1^\alpha) \prod_{\alpha'} J_{n_{\alpha'}}(\Omega_1^{\alpha'}/\omega_1^{\alpha'}) \prod_{\beta} J_{k_\beta}(\Omega_2^\beta/\omega_2^\beta)$$
$$\times \left\{\frac{\left(\omega - \omega_0 - \sum_{\alpha} n_\alpha\omega_1^\alpha - \sum_{\beta} k_\beta\omega_2^\beta\right)T_2 + i}{1 + \left(\omega - \omega_0 - \sum_{\alpha} n_\alpha\omega_1^\alpha - \sum_{\beta} k_\beta\omega_2^\beta\right)^2 T_2^2} \exp\left[i\left\{\left(\sum_{\alpha'} n_{\alpha'}\omega_1^{\alpha'} - \sum_{\alpha} n_\alpha\omega_1^\alpha - \sum_{\beta} k_\beta\omega_2^\beta\right)t\right.\right.\right.$$
$$\left.\left.\left. + \left(\sum_{\alpha'} n_{\alpha'}\theta_1^{\alpha'} - \sum_{\alpha} n_\alpha\theta_1^\alpha - \sum_{\beta} k_\beta\theta_2^\beta\right)\right\}\right] + \sum_{j=+1} \sum_{\gamma} \frac{\Omega_3^\gamma}{2} \frac{\left(\omega - \omega_0 - \sum_{\alpha} n_\alpha\omega_1^\alpha - \sum_{\beta} k_\beta\omega_2^\beta - j\omega_3^\gamma\right)T_2 + i}{1 + \left(\omega - \omega_0 - \sum_{\alpha} n_\alpha\omega_1^\alpha - \sum_{\beta} k_\beta\omega_2^\beta - j\omega_3^\gamma\right)^2 T_2^2}$$
$$\times \exp\left[i\left\{\left(\sum_{\alpha'} n_{\alpha'}\omega_1^{\alpha'} - \sum_{\alpha} n_\alpha\omega_1^\alpha - \sum_{\beta} k_\beta\omega_2^\beta - j\omega_3^\gamma\right)t + \left(\sum_{\alpha'} n_{\alpha'}\theta_1^{\alpha'} - \sum_{\alpha} n_\alpha\theta_1^\alpha - \sum_{\beta} k_\beta\theta_2^\beta - j\theta_3^\gamma\right)\right\}\right]\Bigg\}$$

Equation [A3] is the most general expression for σ_{ba} because of the inclusion of the modulation phases. It can be seen that the phases appear in the form of $\exp i[\Omega(n_\alpha, n_{\alpha'}, k_\beta, j)t + \Phi(n_\alpha, n_{\alpha'}, k_\beta, j)]$, viz., they contribute only to the total phase shift Φ added to the periodic time-dependent term Ωt in the exponent. Suppose we make a phase-sensitive detection with reference to a particular frequency component $\Omega(n_\alpha, n_{\alpha'}, k_\beta, j) = \Omega_0$. The observed sideband then consists of the lines arising from all the terms with Ω_0 in eq. [A3]. These terms, however, have the same total phase shift because the coefficients of θ_1^α, θ_2^β, and θ_3^γ are identical with those of ω_1^α, ω_2^β, and ω_3^γ, respectively. Therefore, the role of the phases in multiple modulation is simply to change the optimum condition of phase adjustment in phase-sensitive detection of a sideband spectrum as in the case of single modulation.

Can. J. Chem. Downloaded from www.nrcresearchpress.com by 122.72.124.2 on 09/07/12
For personal use only.

Molecular recognition. VIII.[1] The binding of the β-D-galactopyranosyl residue of the Lewis b human blood group determinant by the lectin IV of *Griffonia simplicifolia* and by a monoclonal anti-Lewis b antibody. Evidence for intramolecular hydrogen bonding

RAYMOND U. LEMIEUX,[2] RÉMY CROMER,[3] AND ULRIKE SPOHR[4]

Department of Chemistry, University of Alberta, Edmonton, Alta., Canada T6G 2G2

Received May 25, 1988

RAYMOND U. LEMIEUX, RÉMY CROMER, and ULRIKE SPOHR. Can. J. Chem. **66**, 3083 (1988).

The 3b-deoxy, 4b-deoxy, 6b-deoxy, 6b-deoxy-6b-fluoro, 6b-chloro-6b-deoxy, and the 5b-des-hydroxymethyl derivatives of the Lewis b (αLFuc^d(1→2)βDGal^b(1→3)[αLFuc^c(1→4)]βDGlcNAc^a-OMe) human blood group determinant were synthesized in order to examine the involvement of the βDGal b unit in the binding of the Le^b-OMe tetrasaccharide both by the lectin IV of *Griffonia simplicifolia* and a hybridoma monoclonal anti-Le^b antibody. The replacement of the CH_2OH-5b group by hydrogen resulted in very weak binding by both the proteins, but the 6b-deoxy derivative was bound nearly as strongly as the parent compound in the case of the lectin but nine times more strongly in the case of the antibody. The 6b-fluoride was slightly more strongly bound than the 6b-deoxy derivative by both the proteins. On the other hand, the 6b-chloride was bound three times more strongly by the lectin but three times more weakly by the antibody than the 6b-deoxy derivative. The thermodynamic parameters for the binding of the 6b-deoxy derivative by the lectin as compared to those for Le^b-OMe confirmed that OH-6b interacts within the combining site of the complex. The results appear to require that for both proteins the CH_2OH-5b group becomes involved in nonpolar interactions within the combining site. It seems probable that OH-6b is accepted intramolecularly hydrogen bonded to O-5b in the case of the lectin but to OH-4b in the case of the antibody. The involvement of OH-3b, OH-4b, and OH-4c as the key polar grouping for the binding of Le^b-OMe by the lectin and of OH-3b and OH-2d in the case of the antibody was reported previously.

RAYMOND U. LEMIEUX, RÉMY CROMER et ULRIKE SPOHR. Can. J. Chem. **66**, 3083 (1988).

On a synthétisé les dérivés déoxy-3b, déoxy-4b, déoxy-6b, déoxy-6b-fluoro-6b, chloro-6b-déoxy-6b et des-hydroxyméthyl-5b du déterminant du groupe sanguin humain de type b de Lewis (αLFuc^d(1→2)βDGal^b(1→3)[αLFuc^c(1→4)]βDGlcNAc^a-OMe), dans le but de déterminer l'implication de l'unité b β-Gal dans le type de liaison du tétrasaccharide Le^b-OMe avec la léctine IV du *Griffonia simplicifolia* et avec un anticorps anti-Le^b monoclone hydrome. Le remplacement du groupe CH_2OH-5b par l'hydrogène a pour conséquence l'établissement d'un lien très faible avec les deux protéines; mais pour le dérivé déoxy-6b la liaison est presqu'aussi forte que celle du composé dont il dérive dans le cas de la léctine et neuf fois plus forte dans le cas de l'anticorps. La liaison du fluorure-6b avec les deux protéines est légèrement plus forte que celle du dérivé déoxy-6b. Par ailleurs, le chlorure-6b est lié trois fois plus fortement avec la léctine mais trois fois plus faiblement avec l'anticorps comparativement au dérivé déoxy-6b. Les paramètres thermodynamiques de la liaison du dérivé déoxy-6b avec la léctine comparés à ceux du Le^b-OMe confirment que le OH-6b interagit à l'intérieur du site de combinaison du complexe. Les résultats semblent indiquer que les deux protéines sont impliquées dans des interactions nonpolaires à l'intérieur du site de combinaison. Il existe probablement des liaisons hydrogènes intramoléculaires entre le groupe OH-6b et le O-5b dans le cas de la léctine mais ces liaisons hydrogènes impliqueraient cependant le groupe OH-4b dans le cas de l'anticorps. On a déjà rapporté l'implication des groupes OH-3b, OH-4b et OH-4c comme groupes polaires principaux dans le type de liaison du Le^b-OMe avec la léctine et de groupes OH-3b et OH-2d dans leur liaison avec l'anticorps.

[Traduit par la revue]

Introduction

The specific, non-covalent binding of oligosaccharides by antibodies and lectins in dilute aqueous solution is a remarkable phenomenon of great biological significance. Our approach to investigate the dominant forces for complex formation involves binding studies using a variety of synthetic oligosaccharides both as inhibitors in radioimmunoassays and as substrates when following changes in ultraviolet absorption that accompany the binding reactions (1–9). The latter technique has allowed the determination of thermodynamic parameters (2, 3, 6). To achieve information on the participation of the polar hydroxyl groups in the binding reactions, all possible monodeoxy derivatives are synthesized and, usually, also certain deoxy-halogeno compounds.

All the complexation reactions studied to date have been found to be enthalpy driven with a countervailing decrease in entropy (2, 3, 6). In all likelihood, the main reasons for the decreases in entropy are the need to order conformationally labile polypeptide chains to form the combining site, and the immobilization of the substrate within the complex including the structuring of water molecules.

In most of the cases so far studied, the binding has involved a cluster of two to three hydroxyl groups of the oligosaccharide in a polar interaction within the combining site. These clusters, termed the "key polar groupings" (10), are found at the edges of lipophilic surfaces that enter into nonpolar interactions with complementary counterparts of the protein combining sites. The key polar interactions are essential to the binding since modifications of the polar groupings that are involved produce essentially inactive compounds. In several instances, the key grouping is made up of hydroxyl groups stemming from different sugar units. However, its formation by hydroxyl groups from only one sugar unit, as in the substrates for the lectin I of *Ulex europaeus* (3) and the monoclonal anti-I antibody (1), has also been observed. The polar grouping may be involved in a highly specific interaction with charged groups of the receptor protein, and binding energies greater than 2.5

[1]Paper VII in this series is ref. 9.

[2]Author to whom correspondence may be addressed.

[3]University of Alberta Postdoctoral Fellow, 1986–1988.

[4]Research Associate, 1984–1988.

Can. J. Chem. Downloaded from www.nrcresearchpress.com by 122.72.124.2 on 09/07/12
For personal use only.

Can. J. Chem. Downloaded from www.nrcresearchpress.com by 122.72.124.2 on 09/07/12
For personal use only.

kcal/mol are lost on removing one of these hydroxyl groups (11). It remains to be established whether this loss in binding strength arises from a loss of the polar interaction that had involved the hydroxyl group or from the creation of a hydrophobic region that interacts unfavorably with the polar groups of the "gate" to the receptor site. In other words, it is possible that the key polar interactions are more concerned with guiding specificity than with the stability of the complex. More specific evidence in this regard is forthcoming from X-ray analyses of single crystals both for the lectin IV of *Griffonia simplicifolia*, and for its complexes with the Lewis b determinant and several of its derivatives (12).

We have often observed that the replacement of a hydroxyl group by hydrogen has no significant effect on the extent of the binding. This result could indicate that the hydroxyl group is not involved in the complexation. However, we have now found that although a structural change caused little change in free energy, the enthalpy and entropy terms may be profoundly affected (6). In some cases, deoxygenation or halogen substitution significantly strengthens the binding. In these instances, the decreases in entropy are much smaller and, therefore, the complexations appear to involve increased liberation of structured water molecules from hydrophobic environments in both the substrate and the protein. Such situations were found in studies of monoclonal anti-Le^b (4) and anti-B (5) antibodies and the lectin I of *Ulex europaeus* (3, 7) and it was proposed that these hydoxyl groups are intramolecularly hydrogen bonded for acceptance of the various oligosaccharides into nonpolar regions of the protein combining sites. Presumably, the hydroxyl group that becomes intramolecularly hydrogen bonded was previously bound by water and the return of these water molecules to bulk does not cause as great an increase in entropy as the liberation of water from about the deoxy derivative.

Fersht *et al.* (11) have suggested that the binding of tyrosyl adenylate may involve very weak hydrogen bonds with uncharged groups of the protein. We have preferred the intramolecular hydrogen bond proposal (13) because the improved binding resulting from deoxygenation of a hydroxyl group has occurred only when the hydroxyl group was sterically well disposed for intramolecular hydrogen bonding with a nearby proton-accepting atom.

This communication describes the synthesis of derivatives of the Lewis b blood group determinant modified in the βDGal unit and their use as probes for mapping the combining sites of the lectin IV of *Griffonia simplicifolia* (2, 9) and a monoclonal anti-Le^b antibody (4). The combining sites of these two Le^b-active proteins are different, since the anti-Le^b antibody distinguishes between the Le^b and Y (αLFuc(1→2)βDGal (1→4)[αLFuc(1→3)]βDGlcNAc) blood group determinants (4) whereas the lectin does not (2, 9). Furthermore, the key polar grouping in the binding by the lectin is formed by OH-3b and OH-4b of the βDGal unit and OH-4c of the αLFuc(1→4) unit of the Le^b tetrasaccharide (2), whereas in the case of the monoclonal antibody, the key polar group is provided by OH-3b of the βDGal unit and OH-2d of the αLFuc(1→2) unit (4).

We have previously reported that the 6b-deoxy derivatives **40** of the Lewis-b tetrasaccharide (**41**) is nearly as strongly bound by the lectin as is the parent compound. The possibility therefore existed that the determinant was accepted into the combining site with OH-6b intramolecularly hydrogen bonded to O-5b as displayed in **41***a*. Since, in water, the formation of the intramolecular hydrogen bond shown in **41***a* is not likely extensive, the energy required for its formation may importantly

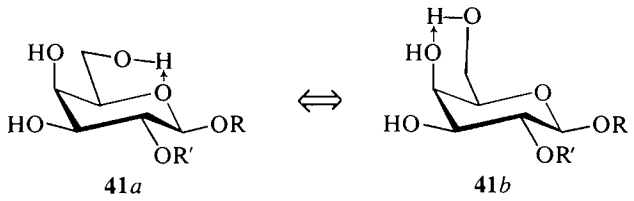

41*a* ⇔ **41***b*

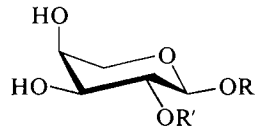

37

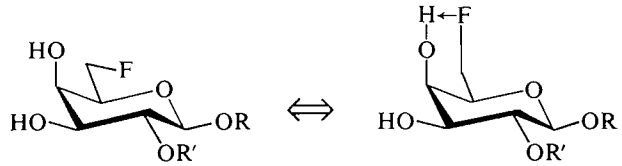

38*a* ⇔ **38***b*

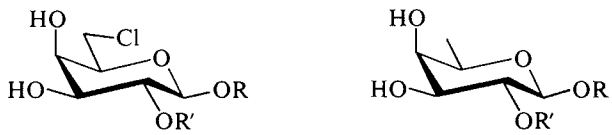

39 **40**

R = -3-[αLFuc(1 → 4)]βDGlcNAc-OMe
R′ = αLFuc-

oppose complexation. The fluoride atom of the 6b-fluoride **38** will be hydrogen bonded to water and, therefore, should be accepted into a hydrophobic region of the combining site as the conformer **38***a* about as readily as **41**. On the other hand, the 6b-chloride **39** would be expected to be a superior inhibitor of the lectin–antigen interaction since the chloromethyl group is certainly more hydrophobic than the fluoromethyl group. Also, the chloromethyl group should offer better complementarity with the combining site than would the small methyl group of **40**. The situation could be expected to be quite different for binding by the anti-Le^b antibody, since in this case the 6b-deoxy derivative **40** was bound 18 times[5] more strongly than the parent (**41**) (4). It was proposed that the high activity displayed by **40** was related to the release of the need to form the conformer **41***b*, which, in spite of the intramolecular hydrogen bond, is known to be highly unstable. Should the OH-6b group be involved in the binding, substantial complementarity would be absent in binding the des-hydroxymethyl derivative **37** by either the lectin or the antibody.

Discussion

A. Synthesis

As displayed in Scheme 1, the disaccharide **8**, which has free hydroxyl groups at positions 4a and 2b, was prepared as a precursor for the synthesis of the 4b-deoxy-Le^b tetrasaccharide **11**. The first step was to synthesize the orthoester **2** from the glycosyl bromide **1** (14) using standard conditions (15). Treatment of **2** with acetyl bromide in the presence of tetraethylammonium bromide (16) then provided the glycosyl

[5]As will be seen later in this communication, we now find the binding to be nine times stronger. This finding does not materially affect the previous interpretation. The cause of the discrepancy remains unknown.

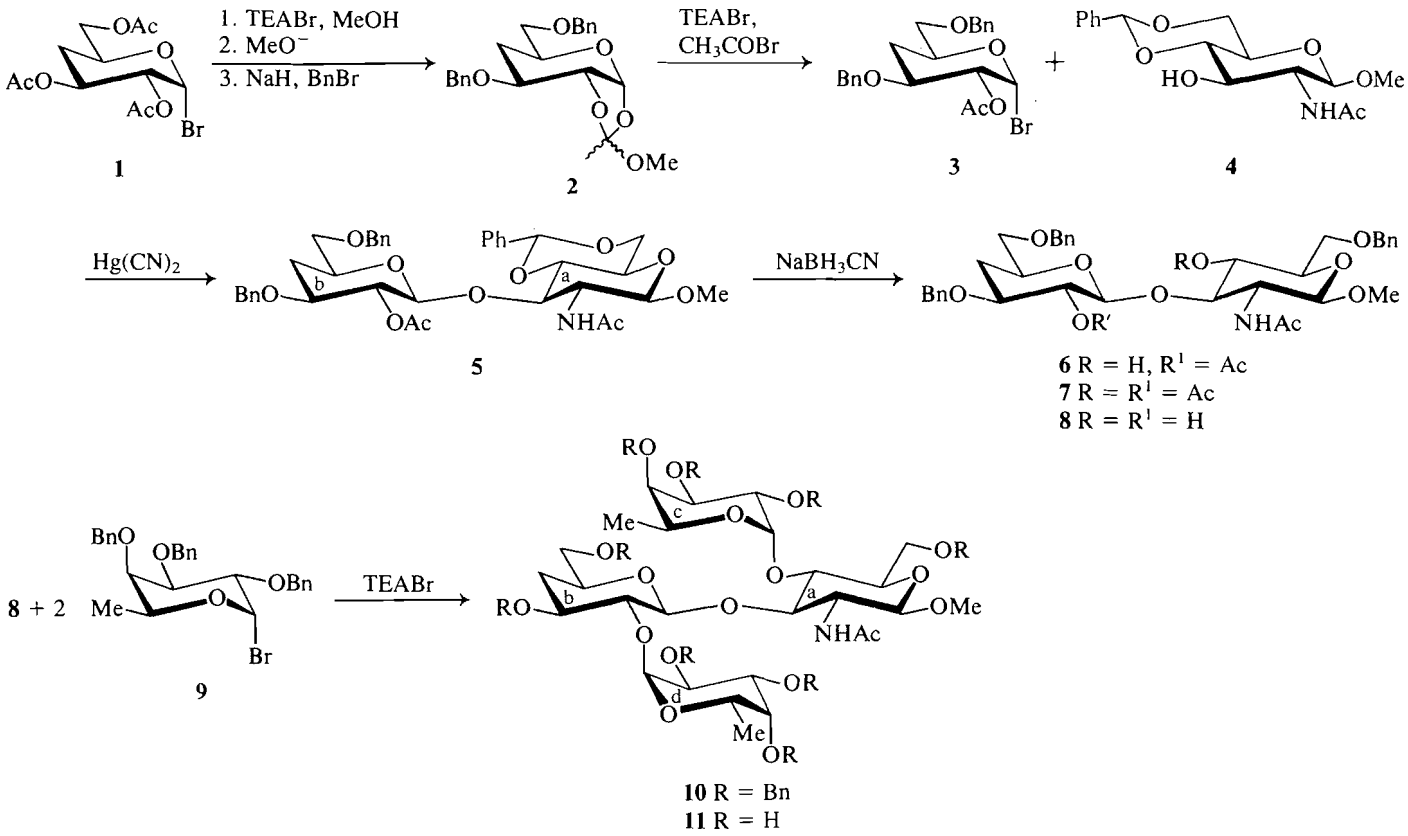

SCHEME 1. Synthesis of 4b-deoxy-Le^b-OMe (**11**).

bromide **3**. Condensation of **3** with the known alcohol **4** (17), under Helferich conditions (18) at room temperature, provided the crystalline disaccharide **5** in 80% yield. To deblock the 4a position (for subsequent fucosylation reaction) while keeping the 6a position protected, the benzylidene ring in **5** was reductively cleaved with sodium cyanoborohydride/hydrogen chloride as described by Garegg *et al.* (19). The resulting alcohol **6** was obtained crystalline in 93% yield and also characterized as its acetate **7**. The ^{1}H nmr spectrum fully supported the assigned structure. Zemplen deacetylation of **6** then provided the diol **8**, which was di-α-L-fucosylated under halide-ion-catalyzed conditions (20) using the fucosyl bromide **9** (21). The benzyl substituted tetrasaccharide **10** was isolated in 64% yield and subjected to catalytic hydrogenolysis over palladium-on-carbon to provide the 4b-deoxy-Le^b derivative **11** in 84% yield. The identity of the compound and its high purity were confirmed by ^{1}H and ^{13}C nmr spectroscopy (see Tables 1 and 2).

The preparation of the 3b-deoxy-Le^b tetrasaccharide (**16**) is outlined in Scheme 2. The precursor disaccharide **12** (P. Bird, O. Hindsgaul, and R. U. Lemieux, unpublished results) was prepared by reaction of methyl 2-acetamido-4,6-*O*-benzylidene-2-deoxy-β-D-glucopyranoside (**4**) with 2,4,6-tri-*O*-acetyl-3-deoxy-α-D-*xylo*-hexopyranosyl bromide (22) under Helferich conditions using mercuric cyanide in toluene–nitromethane (1:1) (83% yield), followed by reductive opening of the benzylidene ring with sodium cyanoborohydride/hydrochloric acid (19). Compound **12** was de-*O*-acetylated and the product was treated in *N*,*N*-dimethylformamide with α,α-dimethoxytoluene in the presence of *p*-toluenesulfonic acid (23). The crystalline 4b,6b-*O*-benzylidene derivative **13** was obtained and then acetylated to form **14**. The ^{1}H nmr spectrum of the diacetate **14** fully supported the structural assignment. Difucosylation of **13** with the benzylated fucosyl bromide **9** under halide-ion-catalyzed conditions then provided **15** in 84% yield. Hydrogenolysis in the presence of palladium-on-carbon afforded the desired 3b-deoxy-Le^b tetrasaccharide **16** in 83% yield.

To examine the possible involvement of the CH_2OH-5b group of the Le^b tetrasaccharide in its complexations with the lectin IV of *Griffonia simplicifolia* and the monoclonal anti-Le^b antibody, the L-Ara derivative **37** was synthesized as outlined in Scheme 3. Glycosylation of **4** (Scheme 1) with tri-*O*-acetyl-β-L-arabinopyranosyl bromide (**17**) (24) under Helferich conditions produced the β-linked disaccharide **21** in 62% yield. Reductive cleavage of the benzylidene ring of **21**, using sodium cyanoborohydride/hydrogen chloride (19), converted the benzylidene group to 6a-*O*-benzyl and liberated the hydroxyl at position 4a to thereby afford **24**. Zemplen deacetylation of **24** then provided methyl 2-acetamido-3-*O*-(α-L-arabinopyranosyl)-6-*O*-benzyl-2-deoxy-β-D-glucopyranoside, which was benzylidenated (23) to yield **28** as a mixture of diastereoisomeric 3b,4b-*O*-benzylidene derivatives. The free hydroxyl groups at positions 4a and 2b of **28** were then difucosylated to form the blocked tetrasaccharide **33** (76% yield). Removal of the benzyl and benzylidene groups by hydrogenolysis over palladium-on-carbon then provided the 5b-des-hydroxymethyl derivative **37** of the Le^b glycoside (**41**).

To study the involvement of OH-6b of Le^b-OMe (**41**) in the binding reactions, the 6b-deoxy-6b-fluoro-, 6b-chloro-6b-deoxy-, and 6b-deoxy-Le^b derivatives (**38**, **39**, and **40**, respectively), were synthesized following routes similar to that described for the synthesis of **37** (Scheme 3). Alcohol **4** was glycosylated using both 6-deoxy-6-fluoro-glycosyl bromide

Can. J. Chem. Downloaded from www.nrcresearchpress.com by 122.72.124.2 on 09/07/12
For personal use only.

Can. J. Chem. Downloaded from www.nrcresearchpress.com by 122.72.124.2 on 09/07/12
For personal use only.

TABLE 1. Comparison of ^{1}H nmr chemical shifts (ppm) and coupling constants (Hz) for the Le^b blood group determinant (αLFuc)(1→2)βDGal(1→3)-[αLFuc(1→4)]βDGlcNAc-OMe) (9) and related structures[a]

		Derivatives of Le^b-OMe					
	Le^b-OMe (ref. 9)	3b-Deoxy (**16**)	4b-Deoxy (**11**)	6b-Deoxy (**40**)	6b-Deoxy-6b-fluoro (**38**)	6b-Chloro-6b-deoxy (**39**)	5b-Des-hydroxymethylene (**37**)
b-unit							
H-1 ($J_{1,2}$)	4.64 (7.8)	4.69 (7.7)	4.64 (7.8)	4.59 (8.0)	4.67 (7.8)	4.66 (7.8)	4.57 (7.8)
H-2 ($J_{2,3}$)	3.59 (9.3)	3.66 (12.0)	3.23 (9.0)	3.55 (9.5)	3.61 (9.5)	3.60 (9.5)	3.60 (9.5)
H-3 ($J_{3,4}$)	3.79	1.71 (2.7)[b]	3.90 (5.5)	3.78 (3.5)	3.81	3.80 (3.6)	3.80
H-4 ($J_{4,5}$)	3.85	3.98	1.97 (1.0)[c]	3.68 (<1.0)	3.92	3.96 (<1.0)	3.85[d]
H-5 ($J_{5,6}$)	3.57	3.61	3.58	3.62 (6.5)	3.81 (4.5)[e]	*	3.56[f]
H-6 ($J_{6,6'}$)	3.77[d]	*	3.63[d]	1.23 (Me)	4.65 (9.8)[e]	*	—
H-6′ ($J_{5,6'}$)	3.72[d]	*	3.63[d]	—	4.58 (7.3)[e]	*	—
		Differences in chemical shift ($\delta - \delta_{Le^b_{OMe}}$) ppm					
βDGlcNAc a-unit							
H-1 ($J_{1,2}$)	4.32 (8.3)	0.02	0.0	−0.02	−0.02	−0.01	0.0
H-2 ($J_{2,3}$)	3.81 (10.3)	0.0	0.0	−0.02	−0.01	−0.01	−0.02
H-3 ($J_{3,4}$)	4.12 (9.3)	−0.02	−0.03	−0.09	−0.02	−0.02	−0.15
H-4 ($J_{4,5}$)	3.69 (9.5)	0.0	0.0	−0.02	−0.01	−0.02	0.1
H-5 ($J_{5,6}$)	3.53 (1.8)	0.1	0.0	−0.02	−0.01	0.01	−0.04
H-6 ($J_{6,6'}$)	3.98 (12.0)	0.01	0.01	0.0	0.0	0.0	0.0
H-6′ ($J_{5,6'}$)	3.85 (4.0)	0.0	0.0	0.0	0.01	0.01	0.0
CH_3O	3.48	0.0	0.0	−0.01	−0.01	0.0	−0.01
CH_3CO	2.07	−0.02	−0.01	−0.03	−0.01	−0.02	−0.02
αLFuc c-unit							
H-1 ($J_{1,2}$)	5.01 (3.8)	0.0	0.02	−0.01	−0.01	−0.01	0.01
H-2 ($J_{2,3}$)	3.80 (10.0)	−0.01	0.0	−0.03	−0.03	−0.03	−0.02
H-3 ($J_{3,4}$)	3.92 (3.3)	−0.02	−0.01	0.07	−0.01	0.01	*
H-4 ($J_{4,5}$)	3.81 (<1.0)	−0.05	−0.04	0.03	0.0	0.02	−0.01
H-5 ($J_{5,6}$)	4.84 (6.5)	0.06	−0.01	0.05	0.01	0.03	−0.05
CH_3-6	1.27	−0.05	0.01	−0.02	−0.02	−0.02	−0.01
αLFuc d-unit							
H-1 ($J_{1,2}$)	5.14 (3.8)	−0.33	0.02	0.0	0.01	0.0	0.0
H-2	3.73	−0.01	0.0	−0.01	0.01	0.02	0.0
H-3	3.73	−0.01[d]	*	*	0.01[d]	0.04[d]	*
H-4 ($J_{4,5}$)	3.75 (<1.0)	0.0	0.0	−0.01	0.04	0.05	0.04
H-5 ($J_{5,6}$)	4.34 (6.5)	−0.01	0.02	0.0	0.0	0.0	−0.02
CH_3-6	1.27	−0.02	−0.01	−0.02	−0.02	−0.02	−0.02

[a]Measured at 360 MHz and 295 K using 0.04 M solutions in D_2O with acetone at 2.225 ppm as internal reference. The assignments were based on homonuclear decoupling and homonuclear shift-correlated 2-D experiments (COSY) and expected to be within ±0.01 ppm except for those marked with *d*, which are within ±0.03 ppm.

[b]H-3eq 2.23 ppm, $J_{2,3eq}$ 5.0 Hz, $J_{3eq,3ax}$ 14.0 Hz, $J_{3eq,4}$ 3.3 Hz.

[c]H-4ax 1.22 ppm, $J_{4eq,4ax}$ 12.5 Hz.

[d]Expected to be within ±0.03 ppm.

[e]$J_{5,F}$ 15.0 Hz, $J_{6,F}$ 45.5 Hz, $J_{6',F}$ 48.0 Hz.

[f]H-5eq 3.85[d] ppm, $J_{5eq,5ax}$ 13.0 Hz.

*Could not be assigned.

Can. J. Chem. Downloaded from www.nrcresearchpress.com by 122.72.124.2 on 09/07/12
For personal use only.

TABLE 2. Comparison of ^{13}C nmr chemical shifts for the Le^b blood group determinant (αLFuc(1→2)βDGal(1→3)[αLFuc(1→4)]βDGlcNAc-OMe) (9) and related structures[a]

	δ, ppm	Differences in chemical shifts ($\delta - \delta_{Le^bOMe}$), ppm					
		Derivatives of Le^b-OMe					
	Le^b-OMe (ref. 9)	3b-Deoxy (**16**)	4b-Deoxy (**11**)	6b-Deoxy (**40**)	6b-Deoxy-6b-fluoro (**38**)	6b-Chloro-6b-deoxy (**39**)	5b-Des-hydroxymethylene (**37**)
βDGlcNAc a-unit							
C-1	103.52	−0.11	−0.08	0.03	0.02	−0.02	0.03
C-2	56.35	0.08	0.04	0.01	−0.02	0.01	−0.08
C-3	75.63	−0.02	0.08	0.16	0.13	0.31	0.26
C-4	73.12	0.18	−0.02[b]	−0.03	−0.12	−0.17[b]	−0.24[b]
C-5	76.33	0.02	−0.02	0.10	−0.06	−0.09	−0.03
C-6	60.60	0.0	0.0	0.05	−0.18	−0.18	−0.13
$CH_3(CO)$	23.07	0.04	0.0	−0.01	−0.03	−0.02	−0.04
CO	174.45	0.04	0.0	−0.05	0.08	0.07	0.09
CH_3O	58.02	−0.01	−0.01	−0.02	0.03	0.04	0.05
b-unit							
C-1	101.44	1.6	−0.05	−0.08	−0.01	−0.03	0.59
C-2	77.39	−5.56	4.18	−0.17	−0.24	−0.32	−0.01
C-3	74.55	−39.28	−2.28	0.2	−0.26	−0.21	−0.41
C-4	69.62	−3.41	−33.55	2.64	−0.54	−0.33[c]	−0.2
C-5	75.63	2.95	−2.26[b]	−4.66	−2.2	−0.62	−8.73
C-6	62.38	0.26	2.71	−45.81	21.61[d]	−19.0	—
αLFuc c-unit							
C-1	98.67	0.05	0.15	−0.06	0.0	−0.07	0.02
C-2	68.73	0.0[b]	−0.04	0.1	0.04	0.07	0.05
C-3	70.01	0.0	0.0	−0.1	−0.08	−0.07	−0.15
C-4	72.87[b]	−0.01[c]	−0.06[c]	0.05[b]	0.01[b]	0.04[b]	0.01[b]
C-5	67.80	−0.09	−0.27	−0.05	0.01	−0.02	0.07
C-6	16.21	0.07	0.19	0.0	−0.02	−0.04	0.06
αLFuc d-unit							
C-1	100.42	−3.0	0.22	−0.01	0.03	0.01	0.07
C-2	69.18	−0.39[b]	0.03	0.01	−0.08	−0.09[c]	−0.07
C-3	70.35	−0.07	−0.04	0.0	−0.09	−0.12	−0.06
C-4	72.82[b]	0.12[c]	0.13[c]	0.0[b]	−0.04[b]	−0.04[b]	−0.05[b]
C-5	67.06	0.12	0.06	−0.02	0.04	0.04	0.05
C-6	16.09	−0.01	0.01	0.0	0.01	0.0	0.03

[a]0.05 M solutions in D_2O with dioxane as internal standard at 67.4 ppm were measured at 100 and 75 MHz at 295 K. The assignments were made by inspection using model compounds (26).

[b,c]The corresponding assignments of the chemical shifts are tentative and may be reversed.

[d]$J_{C6,F}$ 166 Hz, $J_{C5,F}$ 20 Hz, $J_{C4,F}$ 8 Hz.

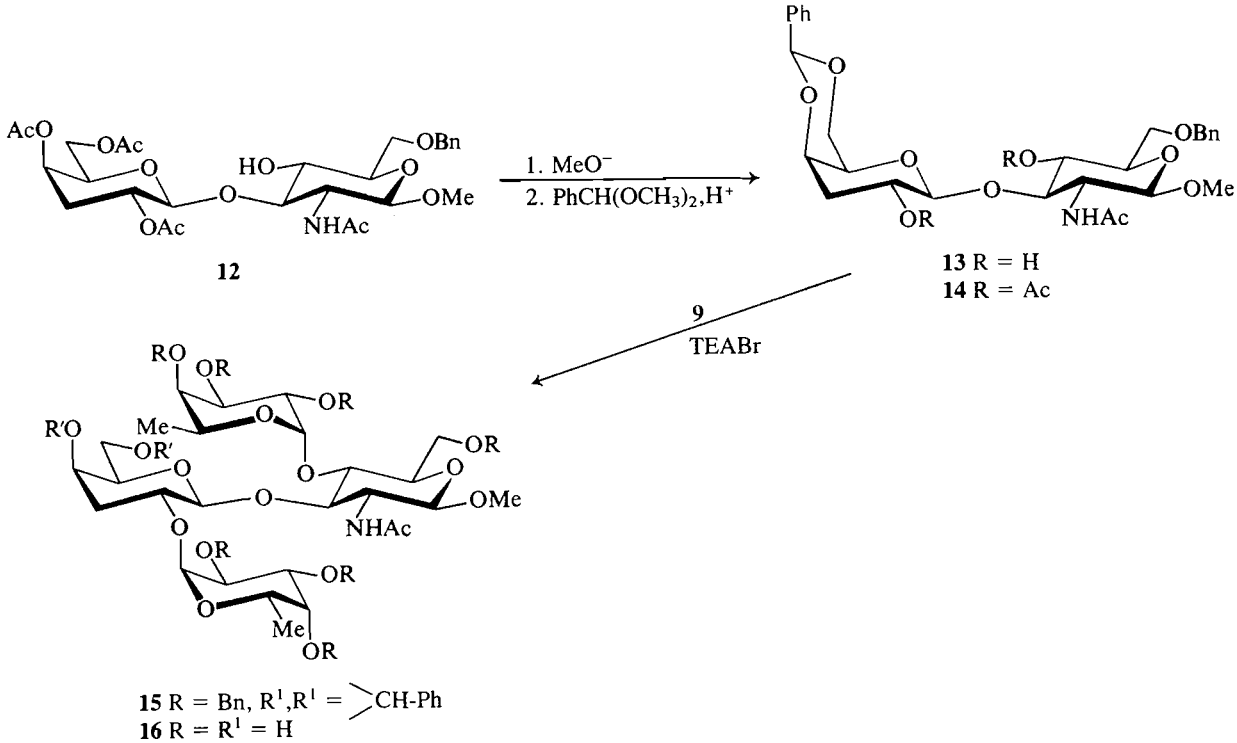

SCHEME 2. Synthesis of 3b-deoxy-Le^b-OMe (**16**).

(**18**) (25) and the 6-chloro-6-deoxy-glycosyl bromide (**20**) under Helferich conditions to provide the disaccharides **22** and **23** in yields of 49 and 31%, respectively. Reductive opening of the benzylidene ring, as for **21**, provided the alcohols **25** and **26**. Similarly, the 6b-deoxy disaccharide **27** had been prepared (S. Narasimhan, P. Bird, O. Hindsgaul, and R. U. Lemieux, unpublished results). Conventional deacetylation of **25**, **26**, and **27** followed by benzylidenation afforded the precursor diols **29**, **30**, and **31** as diastereoisomeric mixtures in yields of 94, 77, and 75%. Structural proof was obtained by the ^{1}H nmr spectra of the corresponding di-*O*-acetates **29***a*, **30***a*, and **32** (see Experimental). Difucosylation of the diols **29**, **30**, and **31** furnished the blocked tetrasaccharides **34**, **35**, and **36** (66, 80, 80%). Hydrogenolytic debenzylation and debenzylidenation then led to the deblocked Le^b derivatives **38**, **39**, and **40**. The ^{1}H and ^{13}C nmr spectra are in complete agreement with the structural assignments (Tables 1 and 2).

B. Structural and conformational assignments

The ^{1}H and ^{13}C nmr parameters for Le^b-OMe and the various monodeoxy (**11**, **16**, **40**) and deoxy-halogeno (**38**, **39**) derivatives are reported in Tables 1 and 2 together with the 5b-des-hydroxymethyl derivative (**37**). The data clearly agree with the various structural assignments. A consideration of the conformational preferences for the modified determinants is required since it is intended to compare the energetics of the binding of the various compounds both by the lectin and by the antibody. Should the structural changes cause appreciable change in conformational preference, then the changes would have to be considered in any effort to interpret the relative potency.

Although the conformational preferences ϕ/ψ = 55°/10°, 55°/25°, 45°/15° about the glycosidic bonds involving the βDGal^b(1→3), αLFuc^c(1→4), and αLFuc^d(1→2) units, respectively, have been reported (27), we wish to review the salient points and to indicate how the conclusions then reached were reinforced by recent developments. In this regard, the ^{1}H chemical shifts for the reference glycoside, methyl α-L-fucopyranoside, measured under the conditions reported in Table 1 are reported in Table 3 since it was possible to assign the signals for the hydrogens with greater confidence and accuracy than was possible at 270 MHz (28).

As seen in Table 3, H-5c of the Le^b tetrasaccharide is deshielded by 0.80 ppm relative to H-5 of the αLFuc-OMe. This strong, specific interunit deshielding by O-3a and O-5b, first noted for the Lewis a trisaccharide (29), provided sufficient evidence for the conformational preference of the Lewis a portion of the tetrasaccharide. This conclusion was anticipated by HSEA calculation (30) and confirmed by nuclear Overhauser enhancement (nOe) studies (9). This orientation for the αLFuc c unit projects H-1c between the H-4a and the CH_2OH-5a groups of the βDGlcNAc unit and, therefore, should be somewhat deshielded relative to H-1 of methyl α-L-fucopyranoside. In fact (Table 3), the deshielding is by 0.24 ppm. Examination of the chemical shifts, reported in Table 1, for the hydrogens of the αLFuc c unit shows that the specific interunit deshieldings for the H-1c atom of the various derivatives of Le^b-OMe are essentially constant and the same as that for Le^b-OMe. This situation also applies to the chemical shifts for H-5c. The slight deshielding of this atom noted for the 3b (**16**) and 6b (**11**) deoxy derivatives is even greater than for Le^b-OMe and suggests even greater preference for the conformational assignment. Therefore, the chemical changes in the βDGal b unit do not appreciably affect the orientation of the c-fucose unit.

The ^{1}H nmr data show that the various modifications of the b unit also caused no significant change in the conformational preference of the d unit. As seen from Table 3, both H-1d and H-5d of Le^b-OMe experience specific interunit deshielding effects. In the case of H-1d, the deshielding of 0.37 ppm is assigned to a strong nonbonded interaction with O-3b. This

Can. J. Chem. Downloaded from www.nrcresearchpress.com by 122.72.124.2 on 09/07/12
For personal use only.

Can. J. Chem. Downloaded from www.nrcresearchpress.com by 122.72.124.2 on 09/07/12
For personal use only.

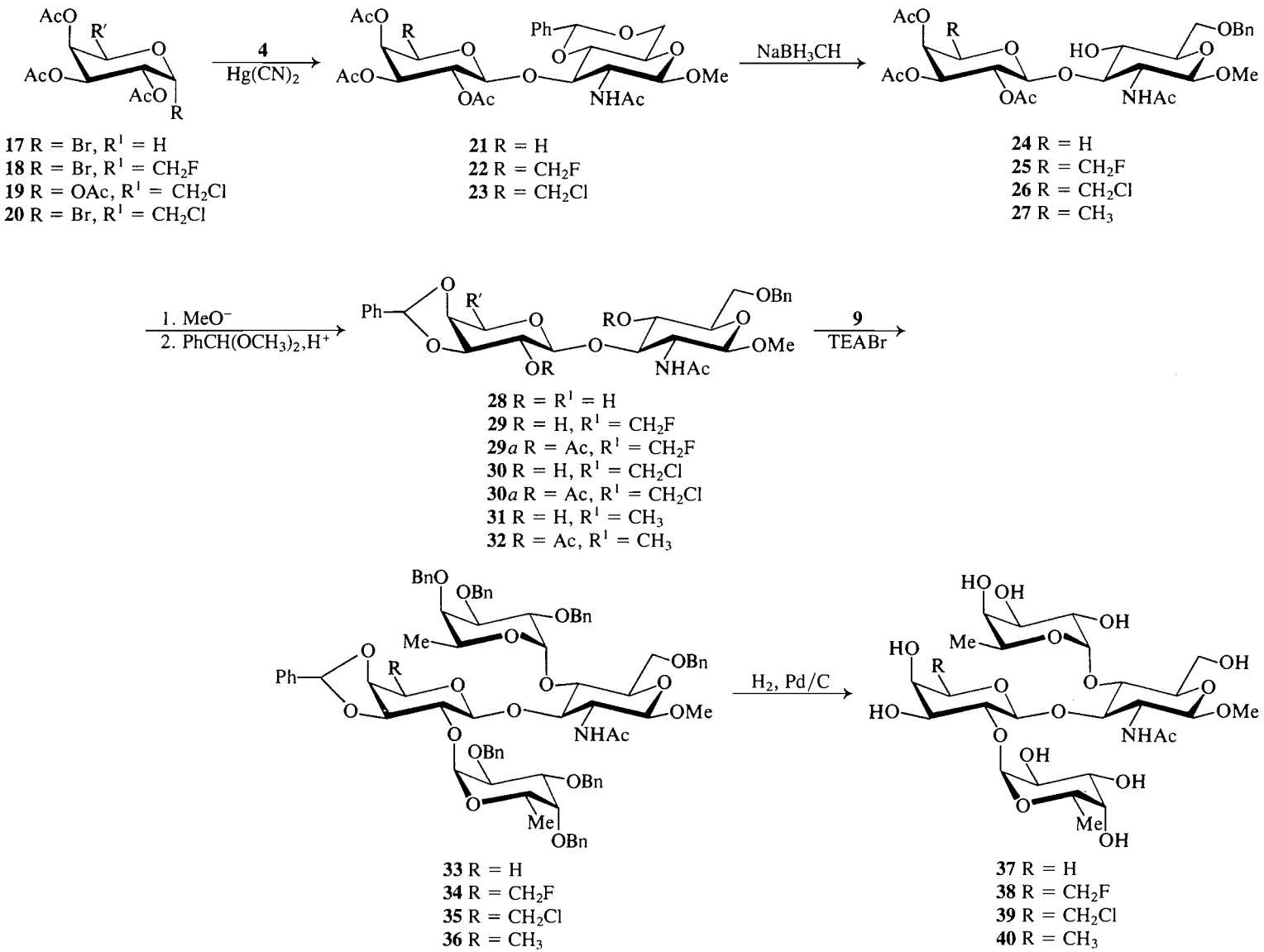

SCHEME 3. Synthesis of derivatives of Le^b-OMe involving alterations at the 5b position.

TABLE 3. Comparison of the ^1H nmr chemical shifts for the ring hydrogens and the methyl groups of the αLFuc units in the Le^b-OMe tetrasaccharide with those of methyl α-L-fucopyranoside

	$\delta_{\alpha LFuc\text{-}OMe}$, ppm	$\delta_{Le^b\text{-}\alpha LFuc\text{-}OMe}$, ppm	
		c unit	d unit
H-1	4.77	0.24	0.37
H-2	3.77	0.03	−0.04
H-3	3.82	0.10	−0.09
H-4	3.78	0.03	−0.03
H-5	4.04	0.80	0.30
CH_3-6	1.22	0.05	0.05
OMe	3.39		

result agrees with the greater than 0.3-ppm interunit deshielding that Lemieux and Bock (31) found to be characteristic for the anomeric protons of certain α-glycopyranosides and assigned to nonbonded interaction with an equatorial oxygen in the aglycon. It was not surprising, therefore, to find that the signal for H-1d of 3b-deoxy-Le^b-OMe (**16**) is 0.33 ppm to higher field than that for Le^b-OMe. On the basis of this orientation for the d unit, H-5d should be in very near van der Waals contact with O-3a and therefore deshielded as compared to H-5 of αLFuc-OMe. The nOe data (9) agree with this conformational preference, which is that predicted by HSEA calculation. Consequently, the immunochemical data, including those for the 5b-des-hydroxymethyl derivative (**37**) (Tables 4, 5, and 6) will be considered on the basis of the HSEA conformer. The orientations of the OH-groups shown in Fig. 1 are all arbitrary but may be those in best accord with the binding studies.

The ^{13}C nmr chemical shifts reported in Table 2 are considered to be in good general accord with the conclusions reached above, on the basis of the ^1H nmr, as to the conformational preference. Nevertheless, the occurrence of chemical shift differences of as great as ±0.2 ppm for the carbon atoms of the βDGlcNAc[a], αLFuc[c], and αLFuc[d] units on making changes in the βDGal[b] unit are noteworthy. We expect that these arise from very slight changes in the hybridization (30) of the carbon atoms as the result of changes in the solvation shells caused by the chemical change.

R.U.L. takes umbrage from the statement (32) that we have assigned single conformations to oligosaccharides in solution. This is, of course, preposterous and was never done. Furthermore, it was disappointing that our paper on the conformational preference of the B blood group determinant (27) and the inference of the finding on the A determinant was ignored. Also, this publication (27) is our definitive paper on HSEA molecular modelling and this fact should not be obscured. What we do believe is that, as stated in our first publication on HSEA calculation (30) and reinforced in the more recent papers (27, 33), the *exo*-anomeric effect appears sufficiently strong to both narrow and deepen the potential energy well occupied by the preferred conformer to the extent that the nOe data well reflect the conformational preference indicated by the specific interunit deshielding effects. Why the HSEA conformer is often in fine agreement with the nmr data is surely of interest. However, we wish to reiterate that, although we have normally found this to be the case when D_2O was the solvent, there exists no reason to expect that it should be so. In the case of maltosides, the HSEA conformer is that suggested as most favorable by the nmr data when the solvent is D_2O but not when it is DMSO-d_6 (34).

C. *Immunochemical studies*

Our initial studies of the binding of the Lewis b determinant by the lectin IV of *Griffonia simplicifolia* allowed the conclusion that the β side of the tetrasaccharide (namely, the side of the core βD-Gal unit over which the two αLFuc units are extended) is extensively involved in the complexation reaction (2). Since the replacement of OH-6b of the βDGal unit by hydrogen had little effect on the strength of the association, the possibility existed that this hydroxyl group remained in contact with water and that the binding was restricted to the β side as displayed on the left in Fig. 1. However, we have now shown that the lipophilic surfaces that are presented by oligosaccharides may become extensively involved when bound both by antibodies (1, 4, 5, 8) and lectins (2, 3) and it was to be noted (2) that the α side[6] of the Le^b tetrasaccharide is extensively lipophilic in character. Consequently, the involvement of this α side seemed likely, especially since the OH-6b can be intramolecularly hydrogen bonded to O-5b (5). Thus, the hydroxyl group could more readily be accepted into a lipophilic cleft involving contact with both sides of the tetrasaccharide, as is depicted in Fig. 1.

That OH-6b is in fact involved in the binding was established by the thermodynamic data presented in Table 4. It is seen that in contrast to the complexation of the 6a-deoxy derivative of Le^b-OMe (9), the binding of the 6b-deoxy compound **40** involves thermodynamic parameters that differ very substantially from those for the Le^b-OMe tetrasaccharide. The differential change in enthalpy of 4.6 kcal/mol is well outside experimental error and clearly implicates OH-6b as directly involved in the complex. The decrease in entropy involved in the binding of **40** is 14.9 entropy units less than that for Le^b-OMe. The most obvious explanation would be that the binding of **40** involves a greater release of ordered water because of the greater hydrophobicity about the CH_3-5b group. On this basis, the OH-6b is accepted into a hydrophobic cleft presented by the lectin. The decrease in the change in enthalpy observed for **40** can be assigned, at least in part, to the loss in complementarity.

The importance of complementarity is well demonstrated by the observation that replacement of the CH_3-5b group of the 6b-deoxy-Le^b-OMe (**40**) by hydrogen provides a very weakly bound compound (**37**). As seen in Table 5, the differential change in free energy for compounds **40** and **37** amounts to 2.3 kcal/mol. The complementarity lost on preparing the 6b-deoxy compound **40** was somewhat restored on introducing a fluorine atom since the 6b-deoxy-6b-fluoro compound **38** is twice more potent an inhibitor than is **40**. The strong binding of the fluoride **38** cannot be attributed to a strictly hydrophobic effect since the fluorine atom is known to be somewhat hydrophilic in character. Also, the high activity of **38** precludes the possibility that OH-6b of Le^b-OMe becomes hydrogen bonded to the combining site as a proton donor. That OH-6b is actually merely involved as a space-filling group appears supported by the fact that the 6b-chloro-6b-deoxy derivative **39** is twice as potent an inhibitor as the parent Le^b-OMe compound and three times more potent than the 6b-deoxy compound (**40**). Thus, it appears most probable that OH-6b is accepted as hydrogen bonded to O-5b. The answer to this problem will be available when the X-ray structure for the lectin-Le^b-OMe complex is determined (12).

Table 6 reports the effects of changes in the βDGal b unit of

[6]Note that this side of the βDGal unit was mistakenly identified as the β side in our previous publication.

Can. J. Chem. Downloaded from www.nrcresearchpress.com by 122.72.124.2 on 09/07/12
For personal use only.

TABLE 4. Thermodynamic parameters[a] for the binding of the Le^b-, 6a-deoxy-Le^b-, and 6b-deoxy-Le^b-OMe tetrasaccharides by the lectin IV of *Griffonia simplicifolia* (6)

	$K_{Assoc.}$[b] $\times 10^{-4}$	ΔH^0, kcal mol^{-1}	ΔS^0, cal mol^{-1} K^{-1}	$T\Delta S^0$, kcal mol^{-1}	$\Delta G^{0,b}$ kcal mol^{-1}
Le^b-OMe	4.4	−13.3	−23.3	−7.0	−6.3
6a-Deoxy-Le^b-OMe (ref. 9)	3.9	−13.1	−22.8	−6.8	−6.3
6b-Deoxy-Le^b-OMe (**40**)	4.1	−8.7	−8.4	−2.5	−6.2

[a]From changes in ultraviolet absorption in the temperature range 9–44°C (2).
[b]At 298 K.

TABLE 5. Inhibition of the binding of an artificial $(Le^b)_{19}$-BSA ^{125}I-antigen by the lectin IV of *Griffonia simplicifolia* in a solid-phase radioimmunoassay (2)

Compound	50% Inhibition, μmol L^{-1}	Relative potency	$\Delta\Delta G^0$, kcal mol^{-1}
Le^b-OMe	44[a]	100	0
5b-Des-hydroxymethylene-Le^b-OMe (**37**)	3200[b]	0.01	2.5
6b-Deoxy-Le^b-OMe (**40**)	64	69	0.2
6b-Deoxy-6b-fluoro-Le^b-OMe (**38**)	38	116	−0.1
6b-Chloro-6b-deoxy-Le^b-OMe (**39**)	23	191	−0.4
3b-Deoxy-Le^b-OMe (**16**)	Inactive (2)	—	—
4b-Deoxy-Le^b-OMe (**11**)	Inactive (2)	—	—

[a]Previously 100.
[b]By extrapolation.

TABLE 6. Inhibition of the binding of an artificial $(Le^b)_{1\text{-}2}$-BSA ^{125}I-antigen by a monoclonal anti-Le^b antibody in a solid-phase radioimmunoassay (4)

Compound	50% Inhibition, μmol L^{-1}	Relative potency	$\Delta\Delta G^0$, kcal mol^{-1}
Le^b-OMe	217[a]	100	0
5b-Des-hydroxymethylene-Le^b-OMe (**37**)	2230	10	1.4
6b-Deoxy-Le^b-OMe (**40**)	25	870	−1.3
6b-Deoxy-6b-fluoro-Le^b-OMe (**38**)	17	1280	−1.5
6b-Chloro-6b-deoxy-Le^b-OMe (**39**)	67	320	−0.7
3b-Deoxy-Le^b-OMe (**16**)	Inactive (4)	—	—
4b-Deoxy-Le^b-OMe (**11**)	1584 (4)	12	1.3

[a]Previously 189.

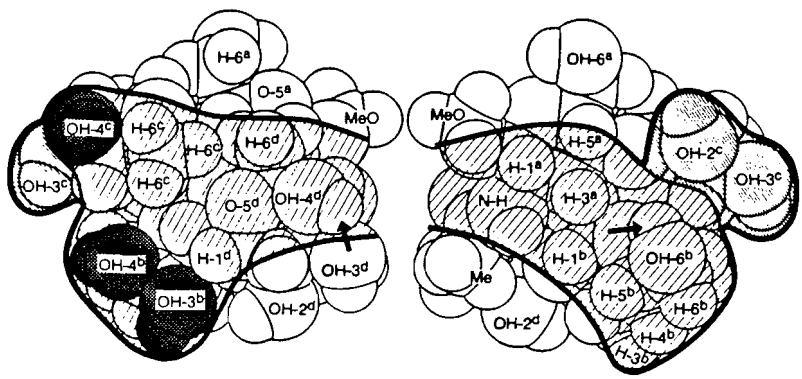

FIG. 1. Revised proposal for the binding of the Lewis b methyl tetrasaccharide by the lectin IV of *Griffonia simplicifolia* (2). The key polar grouping is presented by the cross-hatched hydroxyl groups. It is suggested that OH-4^d and OH-6^b are intramolecularly hydrogen bonded in order to participate in the binding of the lightly hatched surface in a lipophilic cleft. The regions left clear are known (9) to remain in contact with the water. The more darkly hatched OH-2^c and OH-3^c are considered to be engaged in peripheral interactions at the interface of the protein, the tetrasaccharide, and water.

Can. J. Chem. Downloaded from www.nrcresearchpress.com by 122.72.124.2 on 09/07/12
For personal use only.

Can. J. Chem. Downloaded from www.nrcresearchpress.com by 122.72.124.2 on 09/07/12
For personal use only.

Le^b-OMe on binding by the monoclonal anti-Le^b antibody. It was previously reported that OH-3b, along with OH-2d of the αLFuc(1→2) unit, provides the key polar interaction (4). As seen in Table 6, replacement of OH-4b by hydrogen strongly reduced the potency of the compound as an inhibitor of the binding of the Le^b-artificial antigen. As previously mentioned, the 6b-deoxy is much more strongly bound by the antibody than is Le^b-OMe and this result was attributed to the necessity of OH-6b being oriented as in conformer **41***b*. If so, OH-4b is required as the proton acceptor for the intramolecular hydrogen bond (OH-6b ← OH-4b).

The *syn*-axial-like relationship between OH-4b and OH-6b shown in **41***b* is surely energetically unfavorable (35). Consequently, for this orientation to occur there must exist an especially strong driving force to have the CH_2OH-5b group accepted into a hydrophobic environment. Indeed, this appears to be the case since, as seen in Table 6, the inhibition provided by the 6b-deoxy derivative **40** is nine times stronger. This high activity does not appear to be mainly related to the creation of a hydrophobic effect since the 6b-deoxy-6b-fluoro derivative **38** is even more potent (13 times more). This greater potency may arise because **38** can adopt conformation **38***b* more readily than Le^b-OMe can adopt **41***b*. Also, **38***b* should provide greater complementarity than does the 6b-deoxy derivative **40**.

It must be expected that prohibitive energy would be required for the chlorine atom of 6-chloro-6-deoxy-Le^b-OMe (**39**) to adopt the −Cl/O-5 conformation, and thereby come into a *syn*-axial-like interaction with the OH-4b hydroxyl. On the other hand, the combining site could adjust to allow acceptance of **39** in the +Cl/O-5 conformation. Especially, the strong binding of the chloride **39**, i.e., one third that of the 6b-deoxy derivative **40** but 3 times greater than Le^b-OMe, indicates that the CH_2OH-5b group is accepted at the bottom of a lipophilic cleft. If so, the replacement of this large group by hydrogen would lead to a large loss in complementarity and, therefore, the product **37** should be quite inactive. In fact, as seen in Table 6, the compound proved to be a poor inhibitor but only 10 times less potent than Le^b-OMe. As seen above, in the case of the lectin IV of *Griffonia simplicifolia*, **37** was inactive. The stronger binding of **37** by the anti-Le^b antibody is not surprising when it is considered that the driving force for complexation is so great that it can force the OH-6b group into an energetically unfavorable orientation for acceptance into the combining site. Presumably, the same strong driving force can act on **37** and force complex formation in spite of the loss in complementarity. In this regard, it is interesting to note that our probing studies indicate that the monoclonal anti-Le^b antibody accepts Le^b-OMe along an unusually large lipophilic surface (4). As previously suggested (10), it appears that it is the interaction between the complementary lipophilic surfaces that provides the main driving force for the complexation reaction.

Experimental

General methods

The ^{1}H nmr spectra were measured at 300, 360, and 400 MHz (Bruker AM 300, WM 360, and WH 400) with tetramethylsilane as internal standard for $CDCl_3$ solutions. Reference standard for D_2O solutions was acetone (2.225 ppm). The ^{13}C nmr spectra were recorded at 100 and 75 MHz (Bruker WH 400 and AM 300) using D_2O as solvent and 1,4-dioxane (67.4 ppm) as internal standard. Optical rotations were measured at room temperature (23 ± 1°C) in a 1-dm cell on a Perkin Elmer 241 polarimeter. Thin-layer chromatograms were performed on precoated plates of silica gel (60-F 254, E. Merck, Darmstadt) and visualized by spraying with 10% sulfuric acid in ethanol followed by heating. For column chromatography, silica gel 60 (230–400 mesh, E. Merck, Darmstadt) and distilled solvents were used. Solvents and reagents were purified and dried according to standard procedures. Melting points are uncorrected.

*2,3,6-Tri-*O*-acetyl-4-deoxy-α-*D*-*xylo*-hexopyranosyl bromide (**1**) (14)*

A solution of 45% (w/v) hydrogen bromide in glacial acetic acid (20 mL) was added to a solution of 1,2,3,6-tetra-*O*-acetyl-4-deoxy-D-*xylo*-hexopyranose (14) (1.3 g, 3.9 mmol) in dichloromethane (20 mL) with ice-bath cooling. The mixture was kept for 45 min at ice-bath temperature and was then diluted with dichloromethane and poured into ice-water. The organic layer was successively washed with water, aqueous sodium hydrogen carbonate, and water. Drying with sodium sulfate, evaporation, and drying of the residual material in an oil-pump vacuum provided crystalline bromide **1** (1.31 g, 95%); mp 77–79°C (lit. (14) mp 83–84°C (light petroleum)); $[\alpha]_D$ +197° (*c* 0.4, chloroform); ^{1}H nmr ($CDCl_3$) δ: 6.66 (d, 1H, H-1, $J_{1,2}$ 3.8 Hz), 5.39 (ddd, 1H, H-3, $J_{2,3}$ 9.5 Hz, $J_{3,4eq}$ 5.5 Hz, $J_{3,4ax}$ 11.5 Hz), 4.78 (dd, 1H, H-2), 4.38 (m, 1H, H-5, $J_{4eq,5}$ 2.0 Hz, $J_{4ax,5}$ 12.0 Hz, $J_{5,6}$ 4.5 Hz), 4.18 (d, 2H, H_2-6), 2.29 (ddd, 1H, H-4eq, $J_{4eq,4ax}$ 13.0 Hz), 2.12, 2.10, 2.07 (3s, each 3H, $3CH_3COC$), 1.70 (q, 1H, H-4ax).

*3,6-Di-*O*-benzyl-4-deoxy-1,2-*O*-(1-methoxyethylidene)-α-*D*-xylo-hexopyranose (**2**)*

A mixture of the acetylated bromo sugar **1** (14) (1.31 g, 3.71 mmol), tetraethylammonium bromide (1.2 g, 5.71 mmol), *sym*-collidine (1.52 mL), methanol (0.83 mL), and 4 Å molecular sieves (3 g) in nitromethane (13 mL) was stirred at room temperature for 10 h. It was then diluted with dichloromethane, filtered, and the solution washed with water prior to evaporation to dryness. The oily residue was treated with methanolic 0.17 N sodium methoxide (19.5 mL) for 45 min, evaporated, and dried in an oil-pump vacuum. The resulting material was dissolved in *N*,*N*-dimethylformamide (32 mL), sodium hydride (780 mg, approximately 50% dispersion in oil) was added, and the mixture kept at ice-bath temperature for 30 min. After the addition of benzyl bromide (1.56 mL, 13.1 mmol), it was stirred for another 30 min before pouring the mixture into ice-water. Extraction with dichloromethane, drying, and evaporation left an oily residue, the purification of which was achieved by chromatography on a column of silica gel (hexane–triethylamine 33:1, hexane – ethyl acetate – triethylamine 3:1:0.12) providing syrupy **2** (1.08 g, 73%). The ^{1}H nmr of this product showed it to consist of >90% of the main isomer. Repeated chromatography of a small sample gave the pure, slower migrating main isomer that was characterized; $[\alpha]_D$ +15.5°, $[\alpha]_{365}$ +45.4° (*c* 0.5, chloroform); ^{1}H nmr ($CDCl_3$) δ: 7.4–7.2 (m, 10H, 2Ph), 5.81 (d, 1H, H-1, $J_{1,2}$ 5.0 Hz), 4.71 and 4.63 (AB, 2H, CH_2Ph, J_{AB} 12.0 Hz), 4.59 (s, 2H, CH_2Ph), 4.26 (t, 1H, H-2, $J_{2,3}$ 5.0 Hz), 4.05 (m, 1H, H-5, $J_{4eq,5}$ 3.5 Hz, $J_{4ax,5}$ 9.5 Hz, $J_{5,6}$ 5.0 Hz), 3.8 (ddd, 1H, H-3, $J_{3,4eq}$ 6.0 Hz, $J_{3,4ax}$ 8.0 Hz), 3.68–3.47 (m, 2H, H-6, H-6′), 3.30 (s, 3H, CH_3O), 2.01 (ddd, 1H, H-4eq, $J_{4eq,4ax}$ 14.0 Hz), 1.68 (ddd, 1H, overlapped by CH_3C, H-4ax), 1.62 (s, 3H, CH_3C). *Anal.* calcd. for $C_{23}H_{28}O_6$: C 68.98, H 7.05; found: C 69.61, H 7.07.

*2-*O*-Acetyl-3,6-di-*O*-benzyl-4-deoxy-α-*D*-xylo-hexopyranosyl bromide (**3**)*

Acetyl bromide (300 μL, 4.06 mmol) was added to a mixture of compound **2** (840 mg, 2.10 mmol), tetraethylammonium bromide (210 mg, 1.0 mmol), and 4 Å molecular sieves (3 g) in dichloromethane (8 mL). The mixture was stirred for 45 min at room temperature, then decanted from the sieves and poured into a stirred mixture of aqueous sodium hydrogen carbonate, ice, and dichloromethane. The organic layer was washed with water, dried, and evaporated to leave **3** (880 mg, 93%) as a syrup; ^{1}H nmr ($CDCl_3$) δ: 7.4–7.2 (m, 10H, 2Ph), 6.72 (d, 1H, H-1, $J_{1,2}$ 3.5 Hz), 4.7 (dd, 1H, H-2, $J_{2,3}$ 9.5 Hz), 4.67 (s, 2H, CH_2Ph), 4.57 (s, 2H, CH_2Ph), 4.25 (m, 1H, H-5, $J_{4ax,5}$ 12.0 Hz, $J_{4eq,5}$ 2.5 Hz), 4.06 (ddd, 1H, H-3, $J_{3,4ax}$ 12.0 Hz, $J_{3,4eq}$ 5.0 Hz), 3.75–3.4 (m, 2H, H-6, H-6′), 2.22 (ddd, 1H, H-4eq, $J_{4eq,4ax}$ 13.0 Hz), 2.12 (s, 3H, CH_3O), 1.77 (q, 1H, H-4ax).

Can. J. Chem. Downloaded from www.nrcresearchpress.com by 122.72.124.2 on 09/07/12
For personal use only.

Methyl 2-acetamido-3-O-(2-O-acetyl-3,6-di-O-benzyl-4-deoxy-β-D-xylo-hexopyranosyl)-4,6-O-benzylidene-2-deoxy-β-D-glucopyranoside (5)

A mixture of methyl 2-acetamido-4,6-*O*-benzylidene-2-deoxy-β-D-glucopyranoside (**4**) (17) (480 mg, 1.48 mmol), mercuric cyanide (725 mg, 2.87 mmol), powdered calcium sulfate (500 mg), and 4 Å molecular sieves (1 g) in a mixture of toluene and nitromethane (1:1, 40 mL) was stirred under nitrogen, and a solution of bromide **3** (1.96 mmol) in toluene–nitromethane (1:1, 6 mL) was added. The completion of the reaction was indicated by tlc 20 min after the addition. The reaction mixture was filtered, and poured into a mixture of aqueous sodium hydrogen carbonate and dichloromethane. The organic layer was washed with water, dried, and evaporated. The crude reaction product was chromatographed on a column on silica gel (ethyl acetate, dichloromethane – 7% methanol) to provide pure crystalline **5** (825 mg, 80%). The analytical sample was recrystallized from dichloromethane – ethyl acetate; mp 205–207°C; $[\alpha]_D$ +9.6°, $[\alpha]_{365}$ +41° (*c* 0.5, chloroform); ^{1}H nmr ($CDCl_3$) δ: 7.5–7.2 (m, 15H, 3 Ph), 5.84 (d, 1H, NH, $J_{NH,2a}$ 7.0 Hz), 5.44 (s, 1H, C*H*Ph), 5.12 (d, 1H, H-1a, $J_{1a,2a}$ 8.5 Hz), 4.82 (dd, 1H, H-2b, $J_{1b,2b}$ 8.0 Hz, $J_{2b,3b}$ 9.0 Hz), 4.60 (d, overlapped by CH_2Ph and H-3a, H-1b), ~4.59 and 4.42 (AB, 2H, CH_2Ph, J_{AB} 12.0 Hz), 4.59 (t, overlapped by CH_2Ph and H-1b, H-3a, $J_{2a,3a} \sim J_{3a,4a}$ 9.0 Hz), 4.45 and 4.41 (AB, 2H, CH_2Ph, J_{AB} 12.0 Hz), 4.30 (dd, 1H, H-6a, $J_{6a,6a'}$ 10.5 Hz, $J_{6a,5a}$ 5.0 Hz), 3.71 (t, 1H, H-6a', $J_{6a',5a}$ 10.0 Hz), 3.67 (t, 1H, H-4a, $J_{4a,5a}$ 9.0 Hz), 3.52 (m, overlapped by CH_3O and H-3b, H-5a), 3.50 (s, 3H, CH_3O), 3.49 (overlapped by CH_3O and H-5a, H-3b, $J_{3b,4beq}$ 5.0 Hz), ~3.45–3.35 (m, H-6b, H-6b'), ~3.36 (m, H-5b), 3.04 (m, 1H, H-2a), 2.09 (ddd, 1H, H-4beq, $J_{4beq,4bax}$ 13.0 Hz, $J_{4beq,5b}$ 1.0 Hz), 1.96 (s, 6H, CH_3COOC, CH_3CONH), 1.46 (q, 1H, H-4bax, $J_{4bax,3b}$ 12.0 Hz, $J_{4bax,5b}$ 12.0 Hz). *Anal.* calcd. for $C_{38}H_{45}NO_{11}$: C 65.98, H 6.56, N 2.03; found: C 65.98, H 6.52, N 2.00.

Methyl 2-acetamido-3-O-(2-O-acetyl-3,6-di-O-benzyl-4-deoxy-β-D-xylo-hexopyranosyl)-6-O-benzyl-2-deoxy-β-D-glucopyranoside (6)

A mixture of compound **5** (685 mg, 0.99 mmol), sodium cyanoborohydride (1.8 g), 3 Å molecular sieves (3 g), and a few crystals of methyl orange in tetrahydrofuran (33 mL) was stirred at 0°C under nitrogen. Diethyl ether saturated with hydrogen chloride was added until the colour of the indicator turned red and gas evolution occurred. After hydrogen evolution ceased, tlc showed the reaction to be complete. The mixture was diluted with dichloromethane and poured into aqueous sodium hydrogen carbonate solution. The organic layer was washed with water, dried, and evaporated. Deionization with Amberlite MBl and column chromatography (silica gel, dichloromethane – 5% methanol) provided crystalline compound **6** (640 mg, 93%). The analytical sample was recrystallized from dichloromethane – ethyl acetate; mp 163–164°C; $[\alpha]_D$ +18.9° (*c* 0.9, chloroform); ^{1}H nmr ($CDCl_3$) δ: 7.4–7.2 (m, 15H, 3Ph), 5.69 (d, 1H, NH, $J_{2a,NH}$ 7.0 Hz), 4.89 (dd, 1H, H-2b, $J_{1b,2b}$ 7.5 Hz, $J_{2b,3b}$ 9.0 Hz), 4.85 (d, 1H, H-1a, $J_{1a,2a}$ 8.0 Hz), 4.62 and 4.46 (AB, 2H, CH_2Ph, J_{AB} 12.0 Hz), 4.60 (s, 2H, CH_2Ph), 4.53 and 4.50 (AB, 2H, CH_2Ph, J_{AB} 12.0 Hz), 4.41 (s, 1H, OH), 4.40 (d, 1H, H-1b), 4.33 (dd, 1H, H-3a, $J_{2a,3a}$ 10.0 Hz, $J_{3a,4a}$ 9.0 Hz), 3.49 (s, overlapped, CH_3O), 3.01 (m, 1H, H-2a), 2.10 (ddd, overlapped by CH_3CO, 1H, H-4beq, $J_{4beq,4bax}$ 13.0 Hz, $J_{3b,4beq}$ 5.0 Hz, $J_{4beq,5b}$ 1.0 Hz), 2.06, 1.96 (each s, each 3H, CH_3COOC, CH_3CONH), 1.52 (q, 1H, H-4bax, $J_{4bax,3b}$ 12.0 Hz, $J_{4bax,5b}$ 12.0 Hz). *Anal.* calcd. for $C_{38}H_{47}NO_{11}$: C 65.79, H 6.83, N 2.02; found: C 65.73, H 6.88, N 1.98.

Methyl 2-acetamido-4-O-acetyl-3-O-(2-O-acetyl-3,6-di-O-benzyl-4-deoxy-β-D-xylo-hexopyranosyl)-6-O-benzyl-2-deoxy-β-D-glucopyranoside (7)

A solution of compound **6** (30 mg, 0.04 mmol) in pyridine (1 mL) and acetic anhydride (0.5 mL) was kept at room temperature for 5 h. The mixture was poured into ice-water, extracted with dichloromethane, and evaporated. The resulting material was recrystallized from dichloromethane – ethyl acetate – hexane to provide the diacetate **7** (23 mg, 72%); mp 126–127°C, $[\alpha]_D$ +17° (*c* 0.4, chloroform); ^{1}H nmr ($CDCl_3$) δ: 7.4–7.2 (m, 15H, 3Ph), 5.85 (d, 1H, NH, $J_{2a,NH}$ 7.5 Hz), 4.89 (t, 1H, H-4a, $J_{3a,4a} \sim J_{4a,5a}$ 9.0 Hz), 4.81 (d, 1H, H-1a, $J_{1a,2a}$ 7.5 Hz), 4.76 (dd, 1H, H-2b, $J_{2b,3b}$ 9.0 Hz, $J_{1b,2b}$ 7.5 Hz), 4.60 and 4.44 (AB, 2H, CH_2Ph, J_{AB} 12.0 Hz), 4.52, 4.50 (2s, 4H, CH_2Ph), 4.42 (d, 1H, H-1b), 4.33 (t, 1H, H-3a, $J_{2a,3a}$ 8.0 Hz), 3.68 (m, 1H, H-5a), ~3.54 (m, H-3b, overlapped), 3.48 (s, CH_3O), 3.31 (m, 1H, H-2a), 2.13 (ddd, 1H, H-4beq, $J_{3b,4beq}$ 5.0 Hz, $J_{4beq,4bax}$ 13.0 Hz, $J_{4beq,5b}$ 1.0 Hz), 2.05, 1.92, 1.90 (each s, each 3H, $2CH_3COOC$, CH_3CONH), 1.5 (q, 1H, H-4bax, $J_{4bax,3b}$ 12.0 Hz, $J_{4bax,5b}$ 12.0 Hz). *Anal.* calcd. for $C_{40}H_{49}NO_{12}$: C 65.29, H 6.71, N 1.90; found: C 65.12, H 6.69, N 1.93.

Methyl 2-acetamido-6-O-benzyl-2-deoxy-3-O-(3,6-di-O-benzyl-4-deoxy-β-D-xylo-hexopyranosyl)-β-D-glucopyranoside (8)

Compound **6** (480 mg, 0.69 mmol) was treated with 0.17 N sodium methoxide in methanol (9 mL) for 16 h. The solution was made neutral with Amberlite IRC 50 H^+, evaporated to dryness, and the resulting product passed through a column of silica gel (dichloromethane – 7% methanol) to provide crystalline **8** (405 mg, 90%). Recrystallization from methanol gave the analytical sample; mp 170–172°C; $[\alpha]_D$ −4.5°, $[\alpha]_{365}$ −9.1° (*c* 1.1, chloroform); ^{1}H nmr ($CDCl_3$) δ: 7.4–7.2 (m, 15H, 3Ph), 6.07 (d, 1H, NH, $J_{2a,NH}$ 7.0 Hz), 4.72 (d, 1H, H-1a, $J_{1a,2a}$ 8.5 Hz), 4.66 and 4.65 (AB, 2H, CH_2Ph, J_{AB} 12.0 Hz), 4.67 (s, 2H, CH_2Ph), 4.56 and 4.51 (AB, 2H, CH_2Ph, J_{AB} 12.0 Hz), 4.24 (d, 1H, H-1b, $J_{1b,2b}$ 7.0 Hz), 4.07 (dd, 1H, H-3a, $J_{2a,3a}$ 9.0 Hz, $J_{3a,4a}$ 10.0 Hz), 3.54 (s, CH_3O), 3.41 (m, 1H, H-2a), 1.98 (s, CH_3CONH), ~1.98 (overlapped, H-4beq), 1.39 (q, 1H, H-4bax, $J_{4bax,4beq}$ 13.0 Hz, $J_{4bax,3b}$ 12.0 Hx, $J_{4bax,5b}$ 12.0 Hz). *Anal.* calcd. for $C_{36}H_{45}NO_{10}$: C 66.34, H 6.96, N 2.15; found: C 66.45, H 6.99, N 1.94.

2,3,4-Tri-O-benzyl-α-L-fucopyranosyl bromide (9) (21)

Bromide **9** was prepared freshly before use from 2,3,4-tri-*O*-benzyl-L-fucopyranose as described in ref. 9.

Methyl 2-acetamido-6-O-benzyl-2-deoxy-3-O-[3,6-di-O-benzyl-4-deoxy-2-O-(2,3,4-tri-O-benzyl-α-L-fucopyranosyl)-β-D-xylo-hexopyranosyl]-4-O-(2,3,4-tri-O-benzyl-α-L-fucopyranosyl)-β-D-glucopyranoside (10)

Bromide **9** (1.3 g, 2.99 mmol) dissolved in dichloromethane (3 mL) was added to a mixture of diol **8** (320 mg, 0.49 mmol), tetraethylammonium bromide (250 mg, 1.19 mmol), and 4 Å molecular sieves (3 g) in dichloromethane (3 mL) and *N*,*N*-dimethylformamide (0.9 mL). The mixture was kept stirring under nitrogen for 4 days, then methanol was added (0.5 mL) and stirring continued for a further 2 h. It was diluted with dichloromethane, filtered through a pad of Celite, washed with aqueous sodium hydrogen carbonate and water, dried, and evaporated. Purification was effected by column chromatography (silica gel, hexane – ethyl acetate 3:1, dichloromethane – ethyl acetate 2:1) to provide the title compound **10** (467 mg, 64%) as a white foam; $[\alpha]_D$ −75.4° (*c* 0.9, chloroform); ^{1}H nmr ($CDCl_3$) δ: 7.45–7.15 (m, 45H, 9Ph), 6.36 (d, 1H, NH, $J_{NH,2a}$ 8.5 Hz), 5.76 (d, 1H, H-1d, $J_{1d,2d}$ 3.5 Hz), 5.12 (d, 1H, H-1c, $J_{1c,2c}$ 3.5 Hz), 3.31 (s, 3H, CH_3O), 2.23 (ddd, 1H, H-4beq, $J_{4beq,4bax}$ 13.0 Hz, $J_{4beq,5b}$ 1.5 Hz, $J_{4beq,3b}$ 4.0 Hz), 1.66 (s, 3H, CH_3CONH), 1.41 (q, 1H, H-4bax, $J_{4bax,5b}$ 12.0 Hz, $J_{4bax,3b}$ 12.0 Hz), 1.14 (d, 6H, H_3-6c, H_3-6d, $J_{5c,6c} = J_{5d,6d}$ 6.5 Hz). *Anal.* calcd. for $C_{90}H_{101}NO_{18}$: C 72.80, H 6.86, N 0.94; found: C 72.51, H 6.78, N 0.97.

Methyl 2-acetamido-2-deoxy-3-O-[4-deoxy-2-O-(α-L-fucopyranosyl)-β-D-xylo-hexopyranosyl]-4-O-(α-L-fucopyranosyl)-β-D-glucopyranoside (11)

Compound **10** (288 mg, 0.19 mmol) in ethanol (9 mL) was hydrogenated over 5% palladium-on-carbon (288 mg) for 2 days at 100 psi (1 psi = 6.9 kPa). The catalyst was removed by filtration, the solvent evaporated and the resulting material precipitated from methanol – ethyl acetate to provide pure **13** (109.2 mg, 84%); $[\alpha]_D$ −131.7° (*c* 0.6, water). The ^{1}H and ^{13}C nmr data are reported in Tables 1 and 2.

Can. J. Chem. Downloaded from www.nrcresearchpress.com by 122.72.124.2 on 09/07/12
For personal use only.

*Methyl 2-acetamido-6-O-benzyl-3-O-(4,6-O-benzylidene-3-deoxy-β-D-xylo-hexopyranosyl)-2-deoxy-β-D-glucopyranoside (**13**)*

The triacetate **12** (600 mg, 1.00 mmol) was treated with methanolic 0.2 N sodium methoxide solution (13 mL) for 5 h. Deionization with Amberlite MB1, followed by evaporation to dryness, left a crystalline solid (374 mg), which was dissolved in acetonitrile (12 mL). α,α-Dimethoxytoluene (270 μL, 1.80 mmol) and *p*-toluenesulfonic acid monohydrate (20 mg) were added. A few minutes after the addition, the reaction product started to crystallize from the mixture and tlc indicated the reaction to be complete. A few drops of triethylamine were added and the mixture was kept in the fridge for 2 h before it was filtered to provide pure **13** (323 mg). Preparative tlc (dichloromethane – 7% methanol) of the mother liquor afforded an additional amount of **13** (48 mg, total yield 66%). The analytical sample was prepared by recrystallization from ethanol. No sharp melting point, but decomposition >240°C; $[\alpha]_D$ −56.7° (*c* 0.3, chloroform); ^{1}H nmr ($CDCl_3$, 1% dimethyl-d_6 sulfoxide) δ: 7.66 (d, 1H, NH, $J_{NH,2a}$ 7.5 Hz), 7.55–7.24 (m, 10H, 2Ph), 5.53 (s, 1H, C*H*Ph), 4.96 (d, 1H, H-1a, $J_{1a,2a}$ 8.5 Hz), 4.63 and 4.61 (AB, 2H, CH_2Ph, J_{AB} 12.0 Hz), 4.34 (d, 1H, OH-2b, $J_{OH,2b}$ 2.0 Hz), 4.23 (d, 1H, H-1b, $J_{1b,2b}$ 8.0 Hz), 3.99 (dd, 1H, H-3a, $J_{2a,3a}$ 10.0 Hz, $J_{3a,4a}$ 8.5 Hz), 3.90 (dd, 1H, H-6d, $J_{6b,6b'}$ 11.5 Hz, $J_{6b,5b}$ 1.5 Hz), 3.81 (m, 1H, H-2b), 3.69 (dd, 1H, H-6a, $J_{6a,6a'}$ 11.0 Hz, $J_{6a,5a}$ 5.5 Hz), 3.55 (s, overlapped, CH_3O), 3.22 (m, 1H, H-2a), 2.33 (ddd, 1H, H-3beq, $J_{3beq,3bax}$ 13.5 Hz, $J_{2b,3beq}$ 5.0 Hz, $J_{3beq,4b}$ 2.5 Hz), 1.97 (s, 3H, CH_3CONH), 1.68 (ddd, 1H, H-3bax, $J_{2b,3bax}$ 12.0 Hz, $J_{3bax,4b}$ 3.5 Hz). *Anal.* calcd. for $C_{29}H_{37}NO_{10}$: C 62.24, H 6.66, N 2.50; found: C 61.94, H 6.69, N 2.80.

*Methyl 2-acetamido-4-O-acetyl-3-O-(2-O-acetyl-4,6-O-benzylidene-3-deoxy-β-D-xylo-hexopyranosyl)-6-O-benzyl-2-deoxy-β-D-glucopyranoside (**14**)*

A solution of the diol **13** (40 mg, 0.07 mmol) in pyridine (0.8 mL) and acetic anhydride (0.4 mL) was kept at room temperature for 2 h. The usual work-up, followed by recrystallization of the resulting material from ethanol, provided the di-*O*-acetate **14** (36.0 mg, 79%); mp 119–120°C, $[\alpha]_D$ +2.8°, $[\alpha]_{365}$ +25° (*c* 0.6, chloroform); ^{1}H nmr ($CDCl_3$) δ: 7.55–7.25 (m, 10H, 2Ph), 5.80 (d, 1H, NH, $J_{NH,2a}$ 7.0 Hz), 5.47 (s, 1H, C*H*Ph), 5.00 (d, 1H, H-1a, $J_{1a,2a}$ 8.0 Hz), 4.94 (t, 1H, H-4a, $J_{3a,4a} \sim J_{4a,5a}$ 9.0 Hz), 4.86 (ddd, 1H, H-2b, $J_{1b,2b}$ 8.5 Hz, $J_{2b,3beq}$ 5.0 Hz, $J_{2b,3bax}$ 11.5 Hz), 4.56 and 4.53 (AB, 2H, CH_2Ph, J_{AB} 12.0 Hz), 4.51 (t, 1H, H-3a, $J_{2a,3a}$ 9.0 Hz), 4.25 (dd, 1H, H-6b, $J_{6b,6b'}$ 12.0 Hz, $J_{6b,5b}$ < 1.0 Hz), 4.05 (dd, overlapped by H-4b, H-6b', $J_{6b',5b}$ 1.5 Hz), 4.03 (br s, 1H, H-4b), 3.76 (m, 1H, H-5a, $J_{6a,5a}$ 2.5 Hz, $J_{6a',5a}$ 5.5 Hz), ~3.65, ~3.59 (m, 2H, H-6a, H-6a', $J_{6a,6a'}$ 10.5 Hz), 3.55 (s, 3H, CH_3O), 3.49 (br s, 1H, H-5b), 3.20 (m, 1H, H-2a), 2.50 (ddd, 1H, H-3beq, $J_{3beq,3bax}$ 13.5 Hz, $J_{3beq,4b}$ 2.5 Hz), 2.05, 2.04, 2.02 (3s, each 3H, 2CH_3COOC, CH_3CONH), 1.65 (ddd, 1H, H-3bax, $J_{3bax,4b}$ 3.5 Hz). *Anal.* calcd. for $C_{33}H_{41}NO_{12}$: C 61.58, H 6.42, N 2.18; found: C 61.59, H 6.53, N 2.31.

*Methyl 2-acetamido-6-O-benzyl-3-O-[4,6-O-benzylidene-3-deoxy-2-O-(2,3,4-tri-O-benzyl-α-L-fucopyranosyl)-β-D-xylo-hexopyranosyl]-2-deoxy-4-O-(2,3,4-tri-O-benzyl-α-L-fucopyranosyl)-β-D-glucopyranoside (**15**)*

A solution of bromide **9** (2.76 mmol) in dichloromethane (2.5 mL) was added to a stirred mixture of diol **13** (250 mg, 0.45 mmol), tetraethylammonium bromide (200 mg, 0.95 mmol), 4 Å molecular sieves (3 g) in dichloromethane (3 mL), and *N*,*N*-dimethylformamide (0.8 mL). After stirring for 24 h, the mixture was processed conventionally and separated on a column of silica gel using hexane – ethyl acetate (3:1) and dichloromethane – ethyl acetate (2:1) as eluents. The title compound **15** was obtained as a foam in 84% yield (524 mg); $[\alpha]_D$ −61.7° (*c* 0.6, chloroform); ^{1}H nmr δ: 7.55–7.15 (m, 40H, 8Ph), 6.26 (d, 1H, NH, $J_{2a,NH}$ 7.0 Hz), 5.56 (s, 1H, C*H*Ph), 5.09 (d, 1H, H-1c, $J_{1c,2c}$ 3.5 Hz), 3.44 (s, 3H, CH_3O), 3.09 (m, 1H, H-2a), 2.56 (m, 1H, H-3beq, $J_{3beq,3bax}$ 13.0 Hz), 1.74 (s, 3H, CH_3CONH), 1.56 (m, 1H, H-3bax, $J_{3bax,2b}$ 11.0 Hz, $J_{3bax,4b}$ 2.5 Hz), 1.15, 1.00 (each d, each 3H, H_3-6c, H_3-6d, $J_{5c,6c} = J_{5d,6d}$ 6.5 Hz). *Anal.* calcd. for $C_{83}H_{93}NO_{18}$: C 71.58, H 6.73, N 1.01; found: C 71.55, H 6.74, N 1.35.

*Methyl 2-acetamido-2-deoxy-3-O-[3-deoxy-2-O-(α-L-fucopyranosyl)-β-D-xylo-hexopyranosyl]-4-O-(α-L-fucopyranosyl)-β-D-glucopyranoside (**16**)*

The tetrasaccharide **15** (400 mg, 0.29 mmol) was hydrogenated for 3 days in the presence of 5% palladium-on-carbon as described for the preparation of compound **11**. The hydrogenation product was precipitated twice from methanol – ethyl acetate to provide pure **16** (160.2 mg, 83%); $[\alpha]_D$ −149.8° (*c* 0.9, water). The ^{1}H and ^{13}C nmr data are reported in Tables 1 and 2.

*2,3,4-Tri-O-acetyl-β-L-arabinopyranosyl bromide (**17**) (24)*

Bromide **17** was prepared from 1,2,3,4-tetra-*O*-acetyl-L-arabinopyranose (36) (3 g, 9.4 mmol) as described for the preparation of bromide **1**.

*2,3,4-Tri-O-acetyl-6-deoxy-6-fluoro-α-D-galactopyranosyl bromide (**18**) (25)*

Bromide **18** was prepared from 1,2,3,4-tetra-*O*-acetyl-6-deoxy-6-fluoro-D-galactopyranose (25) (1.7 g, 5.06 mmol) as described for the preparation of bromide **1**. Conventional work-up provided **18** (1.64 g, 88%) as a white powder; $[\alpha]_D$ −195.6° (*c* 0.4, chloroform); ^{1}H nmr ($CDCl_3$) δ: 6.72 (d, 1H, H-1, $J_{1,2}$ 4.0 Hz), 5.58 (br d, 1H, H-4, $J_{4,3}$ 3.5 Hz), 5.42 (dd, 1H, H-3, $J_{3,2}$ 10.5 Hz), 5.07 (dd, 1H, H-2), 4.60–4.32 (m, 3H, H-5, H-6, H-6'), 2.15, 2.12, and 2.02 (3s, each 3H, CH_3COOC). *Anal.* calcd. for $C_{12}H_{16}BrFO_7$: C 38.83, H 4.36; found: C 39.56, H 4.36.

*1,2,3,4-Tetra-O-acetyl-6-chloro-6-deoxy-D-galactopyranose (**19**)*

A mixture of 6-chloro-6-deoxy-D-galactose (37) (1.7 g, 8.56 mmol) in pyridine (50 mL) and acetic anhydride (8.3 mL) was kept at room temperature for 24 h. Conventional work-up provided the tetraacetate **19** (3 g, 96%) as a yellowish syrup in an α:β ratio of 0.75:1; ^{1}H nmr ($CDCl_3$) δ: 6.37 (d, 0.43H, H-1α, $J_{1,2}$ 3.0 Hz), 5.71 (d, 0.57H, H-1β, $J_{1,2}$ 8.5 Hz), 5.66, 5.59 (2 dd, 0.43H, H-4α, 0.57H, H-4β, $J_{4,3}$ 3.5 Hz, $J_{4,5}$ 1.5 Hz), 5.40–5.30 (m, 1.43H, H-2α, H-2β, H-3α, at 5.32), 5.11 (dd, 0.57H, H-3β, $J_{3,2}$ 10.5 Hz, $J_{3,4}$ 3.5 Hz), 4.27, 4.02 (2 ddd, 0.43H, H-5α, 0.57H, H-5β, $J_{5,6}$ 8.0 Hz, $J_{5,6'}$ 6.0 Hz, $J_{5,4}$ 1.5 Hz), 3.7–3.4 (2H, H-6α, H-6'α, H-6β, H-6'β), 2.18, 2.175, 2.015, 2.01 (4s, each 1.29H, 4CH_3COO from α isomer), 2.19, 2.13, 2.05, 2.005 (4s, each 1.71H, 4CH_3COO from β isomer). *Anal.* calcd. for $C_{14}H_{19}ClO_9$: C 45.83, H 5.22, Cl 9.67; found: C 46.01, H 5.22, Cl 9.43.

*2,3,4-Tri-O-acetyl-6-chloro-6-deoxy-α-D-galactopyranosyl bromide (**20**)*

Tetraacetate **19** (2.71 g, 7.39 mmol) was converted into bromide **20** as described for the preparation of compound **1**. Usual work-up provided **20** (2.67 g, 93%) as a syrup; ^{1}H nmr ($CDCl_3$) δ: 6.69 (d, 1H, H-1, $J_{1,2}$ 4.0 Hz), 5.66 (dd, 1H, H-4, $J_{4,3}$ 3.0 Hz, $J_{4,5}$ 1.0 Hz), 5.42 (dd, 1H, H-3, $J_{3,2}$ 10.5 Hz), 5.04 (dd, 1H, H-2), 4.43 (br t, 1H, H-5, $J_{5,6} = J_{5,6'}$ 7.0 Hz), 3.53 (m, 2H, H-6, H-6'), 2.20, 2.12, 2.05 (3s, each 3H, CH_3COO).

*Methyl 2-acetamido-4,6-O-benzylidene-2-deoxy-3-O-(2,3,4-tri-O-acetyl-α-L-arabinopyranosyl)-β-D-glucopyranoside (**21**)*

Alcohol **4** (1.76 g, 5.44 mmol) was reacted with 2,3,4-tri-*O*-acetyl-β-L-arabinopyranosyl bromide (24) **17** (2.77 g, 8.16 mmol) for 22 h at 40°C following the procedure used for the preparation of disaccharide **5**. Further processing of the reaction mixture in the usual way, followed by crystallization of the crude product from dichloromethane – ethyl acetate, afforded the title compound **21** (1.96 g, 62%); mp 203–204°C; $[\alpha]_D$ +4.4° (*c* 1.0, chloroform); ^{1}H nmr ($CDCl_3$) δ: 7.50–7.35 (m, 5H, Ph), 5.77 (d, 1H, NH, $J_{NH,2a}$ 7.0 Hz), 5.51 (s, 1H, C*H*Ph), 5.13 (m, 1H, H-4b), 5.07 (dd, 1H, H-2b, $J_{2b,3b}$ 8.5 Hz, $J_{2b,1b}$ 6.0 Hz), 5.03 (d, 1H, H-1a, $J_{1a,2a}$ 8.0 Hz), 4.93 (dd, 1H, H-3b, $J_{3b,4b}$ 3.5 Hz), 4.67 (d, 1H, H-1b), 4.59 (dd, 1H, H-3a, $J_{3a,4a}$ 10.0 Hz, $J_{3a,2a}$ 9.0 Hz), 4.35 (dd, 1H, H-6aeq, $J_{6aeq,6aax}$ 10.0 Hz, $J_{6aeq,5a}$ 4.5 Hz), 3.92 (dd, 1H,

Can. J. Chem. Downloaded from www.nrcresearchpress.com by 122.72.124.2 on 09/07/12
For personal use only.

H-5beq, $J_{5beq,5bax}$ 12.5 Hz, $J_{5beq,4b}$ 4.5 Hz), 3.78 (t, 1H, H-6aax, $J_{6aax,5a}$ 10.0 Hz), 3.64 (t, 1H, H-4a, $J_{4a,5a}$ 9.0 Hz), 3.55 (ddd, 1H, H-5a), 3.50 (s, 3H, CH_3O), 3.24 (dd, 1H, H-5bax, $J_{5bax,4b}$ 2.5 Hz), 3.10 (br td, 1H, H-2a), 2.10, 2.05, 2.01, 2.00 (4s, each 3H, $3CH_3COOC$, CH_3CONH). *Anal.* calcd. for $C_{27}H_{35}NO_{13}$: C 55.76, H 6.06, N 2.41; found: C 55.40, H 6.06, N 2.40.

Methyl 2-acetamido-4,6-O-benzylidene-2-deoxy-3-O-(2,3,4-tri-O-acetyl-6-deoxy-6-fluoro-β-D-galactopyranosyl)-β-D-glucopyranoside (22)

Compound **4** (1.1 g, 3.4 mmol) was reacted with bromide **18** (1.6 g, 4.3 mmol) at 50°C for 21 h as described for the preparation of disaccharide **5**. The resulting solid product was recrystallized from dichloromethane–ether to provide the pure disaccharide **22** (0.99 g, 1.62 mmol). More material (0.13 g, total yield 49%) was obtained by chromatography of the mother liquor on a column of silica gel (dichloromethane – 2% methanol); mp 233.5–234.5°C; $[\alpha]_D$ +10° (*c* 0.2, chloroform); ^{1}H nmr ($CDCl_3$) δ: 7.50–7.35 (m, 5H, Ph), 5.73 (d, 1H, NH, $J_{NH,2a}$ 7.0 Hz), 5.51 (s, 1H, C*H*Ph), 5.29 (dd, 1H, H-4b, $J_{4b,3b}$ 3.5 Hz, $J_{4b,5b}$ 1.0 Hz), 5.16 (dd, 1H, H-2b, $J_{2b,3b}$ 10.5 Hz, $J_{2b,1b}$ 8.0 Hz), 5.08 (d, 1H, H-1a, $J_{1a,2a}$ 8.5 Hz), 4.89 (dd, 1H, H-3b), 4.80 (d, 1H, H-1b), 4.70 (dd, 1H, H-3a, $J_{3a,2a}$ 10.0 Hz, $J_{3a,4a}$ 9.0 Hz), 4.33 (dd, 1H, H-6aeq, $J_{6aax,6aeq}$ 10.5 Hz, $J_{6aeq,5a}$ 5.0 Hz), 4.31 (ddd, 1H, H-6b, $J_{6b,F}$ ~ 47 Hz, $J_{6b,6b'}$ 9.5 Hz, $J_{6b,5b}$ 6.5 Hz), 4.27 (ddd, 1H, H-6b′, $J_{6b',F}$ ~ 47 Hz, $J_{6b',5b}$ 5.0 Hz), 3.79 (t, 1H, H-6aax, $J_{6aax,5a}$ 10.5 Hz), 3.72 (t, 1H, H-4a, $J_{4a,5a}$ 9.0 Hz), 3.61–3.50 (m, 2H, H-5a, H-5b), 3.50 (s, 3H, CH_3O), 3.05 (ddd, 1H, H-2a), 2.11, 2.03, 2.01, 1.96 (4s, each 3H, $3CH_3COOC$, CH_3CONH). CI ms (NH_3), *m/z*: 614 (2.9, $[MH]^+$), 582 (10, $[M - OMe]^+$).

Methyl 2-acetamido-4,6-O-benzylidene-2-deoxy-3-O-(2,3,4-tri-O-acetyl-6-chloro-6-deoxy-β-D-galactopyranosyl)-β-D-glucopyranoside (23)

The disaccharide **23** was prepared from alcohol **4** (586 mg, 1.8 mmol) by reaction with bromide **20** (891 mg, 2.3 mmol) at 45°C for 60 h following the procedure used for the synthesis of compound **5**. The crude reaction product was chromatographed on a column of silica gel (dichloromethane – 2% methanol) and recrystallized from dichloromethane–hexane to provide the title compound **23** (350 mg, 31%); mp 180°C; $[\alpha]_D$ +2.5° (*c* 0.8, chloroform); ^{1}H nmr ($CDCl_3$) δ: 7.50–7.40 (m, 5H, Ph), 5.71 (d, 1H, NH, $J_{NH,2a}$ 7.0 Hz), 5.52 (s, 1H, C*H*Ph), 5.40 (dd, 1H, H-4b, $J_{4b,3b}$ 3.5 Hz, $J_{4b,5b}$ 1.0 Hz), 5.13 (dd, 1H, H-2b, $J_{2b,3b}$ 10.5 Hz, $J_{2b,1b}$ 8.0 Hz), 5.08 (d, 1H, H-1a, $J_{1a,2a}$ 8.5 Hz), 4.91 (dd, 1H, H-3b), 4.77 (d, 1H, H-1b), 4.70 (dd, 1H, H-3a, $J_{3a,2a}$ 10.0 Hz, $J_{3a,4a}$ 9.0 Hz), 4.34 (dd, 1H, H-6aeq, $J_{6aeq,6aax}$ 10.5 Hz, $J_{6aeq,5a}$ 5.0 Hz), 3.78 (t, 1H, H-6aax, $J_{6aax,5a}$ 10.5 Hz), 3.69 (t, 1H, H-4a, $J_{4a,5a}$ 9.0 Hz), 3.58 (br ddd, 1H, H-5a), 3.51 (s, 3H, CH_3O), 3.47 (br t, 1H, H-5b, $J_{5b,6b}$ ~ $J_{5b,6b'}$ 7.0 Hz), 3.34–3.27 (m, 2H, H-6b and H-6b′), 3.05 (ddd, 1H, H-2a), 2.13, 2.02, 2.01 and 1.96 (4s, each 3H, $3CH_3COOC$, CH_3CONH). *Anal.* calcd. for $C_{28}H_{36}ClNO_{13}$: C 53.37, H 5.76, Cl 5.63, N 2.22; found: C 53.33, H 5.89, Cl 5.42, N 2.14.

Methyl 2-acetamido-6-O-benzyl-2-deoxy-3-O-(2,3,4-tri-O-acetyl-α-L-arabinopyranosyl)-β-D-glucopyranoside (24)

Compound **21** (1.70 g, 2.13 mmol) was reacted with sodium cyanoborohydride (4.11 g, 65 mmol) as described for the preparation of disaccharide **6**. Purification of the reaction product was achieved by column chromatography (dichloromethane – 5% methanol) and recrystallization from methanol–ether to provide **24** in 85% yield (1.45 g); mp 158°C; $[\alpha]_D$ +19.0° (*c* 0.5, chloroform); ^{1}H nmr ($CDCl_3$) δ: 7.35–7.30 (m, 5H, Ph), 5.63 (d, 1H, NH, $J_{NH,2a}$ 7.5 Hz), 5.26 (m, 1H, H-4b), 5.21 (dd, 1H, H-2b, $J_{2b,3b}$ 10.0 Hz, $J_{2b,1b}$ 7.5 Hz), 5.03 (dd, 1H, H-3b, $J_{3b,4b}$ 3.5 Hz), 4.76 (d, 1H, H-1a, $J_{1a,2a}$ 8.0 Hz), 4.62 (s, 2H, CH_2Ph), 4.48 (d, 1H, H-1b), 4.33 (br dd, 1H, H-3a, $J_{3a,2a}$ 10.0 Hz, $J_{3a,4a}$ 8.0 Hz), 4.05 (dd, 1H, H-5beq, $J_{5beq,5bax}$ 13.0 Hz, $J_{5beq,4b}$ 2.5 Hz), 3.51 (br s, 4H, with CH_3O), 3.11 (br td, 1H, H-2a), 2.14 and 2.10 (2s, each 3H, $2CH_3CO$), 2.01 (s, 6H, $2CH_3CO$). *Anal.* calcd. for $C_{28}H_{39}NO_{13}$: C 55.57, H 6.35, N 2.40; found: C 55.19, H 6.38, N 2.29.

Methyl 2-acetamido-6-O-benzyl-2-deoxy-3-O-(2,3,4-tri-O-acetyl-6-deoxy-6-fluoro-β-D-galactopyranosyl)-β-D-glucopyranoside (25)

Compound **25** was prepared from disaccharide **22** (1.0 g, 1.64 mmol) by reaction with sodium cyanoborohydride (2.3 g) as described for the preparation of compound **6**. Chromatography of the crude reaction product on a column of silica gel (dichloromethane – 2% methanol) and recrystallization from chloroform–ether provided the title compound **25** (663 mg, 66%); mp 144–145°C; $[\alpha]_D$ +6.9° (*c* 0.5, chloroform); ^{1}H nmr ($CDCl_3$) δ: 7.40–7.25 (m, 5H, Ph), 5.82 (d, 1H, NH, $J_{NH,2a}$ 8.0 Hz), 5.41 (br dd, 1H, H-4b, $J_{4b,3b}$ 3.5 Hz, $J_{4b,5b}$ 1.0 Hz), 5.24 (dd, 1H, H-2b, $J_{2b,3b}$ 10.0 Hz, $J_{2b,1b}$ 8.0 Hz), 5.03 (dd, 1H, H-3b), 4.74 (d, 1H, H-1a, $J_{1a,2a}$ 8.0 Hz), 4.63 (d, 1H, H-1b), 4.61 (s, 2H, CH_2Ph), ~4.45 (m, 2H, H-6b and H6b′, $J_{6,F}$ ~ $J_{6'F}$ ~ 45 Hz), 4.36 (1H, H-3a, overlapped by H-6b, H-6b′), 4.08 (m, 1H, H-5b), 3.87 (br d, 1H, H-6a, $J_{6a,6a'}$ 11.0 Hz, $J_{6a,5a}$ ~ 1.0 Hz), 3.73 (m, 2H, H-5a and OH-4a), 3.55–3.48 (m, 5H, H-6a′, H-4a, with CH_3O at 3.50), 3.17 (td, 1H, H-2a, $J_{2a,3a}$ 10.0 Hz), 2.15, 2.10, 2.03, 2.00 (4s, each 3H, 3 CH_3COOC, CH_3CONH). *Anal.* calcd. for $C_{28}H_{38}FNO_{18}$: C 54.63, H 6.22, N 2.28; found: C 54.30, H 6.23, N 2.45.

Methyl 2-acetamido-6-O-benzyl-2-deoxy-3-O-(2,3,4-tri-O-acetyl-6-chloro-6-deoxy-β-D-galactopyranosyl)-β-D-glucopyranoside (26)

Compound **26** was synthesized from disaccharide **23** (450 mg, 0.7 mmol) following the procedure used for the preparation of compound **6**. Chromatographic purification on a column of silica gel (dichloromethane – 2% methanol) and recrystallization from chloroform–ether afforded pure **26** (300 mg, 76%); mp 174–175°C; $[\alpha]_D$ +7.5° (*c* 0.2, chloroform); ^{1}H nmr ($CDCl_3$) δ: 7.35–7.30 (m, 5H, Ph), 5.79 (d, 1H, NH, $J_{NH,2a}$ 8.0 Hz), 5.48 (dd, 1H, H-4b, $J_{4b,3b}$ 3.5 Hz, $J_{4b,5b}$ 1.0 Hz), 5.22 (dd, 1H, H-2b, $J_{2b,3b}$ 10.5 Hz, $J_{2b,1b}$ 8.0 Hz), 5.01 (dd, 1H, H-3b), 4.78 (d, 1H, H-1a, $J_{1a,2a}$ 8.0 Hz), 4.61 (d, 1H, H-1b), 4.61 (s, 2H, CH_2Ph), 4.39 (m, 1H, H-3a), 3.95 (br t, 1H, H-5b, $J_{5b,6b}$ ~ $J_{5b,6b'}$ ~ 7.0 Hz), 3.87 (br d, 1H, H-6a, $J_{6a,6a'}$ 11.0 Hz), 3.75–3.45 (m, 9H, with CH_3O at 3.50), 3.11 (td, 1H, H-2a, $J_{2a,3a}$ 9.0 Hz), 2.16, 2.08, 2.02, 1.99 (4s, each 3H, $3CH_3COOC$, CH_3CONH). FAB ms, *m/z*: 654 (4.1, $[M + Na]^+$), 632 (2.0, $[M + H]^+$), 631 (0.2, M^+), 601 (2.2, $[M - OMe + H]^+$), 600 (6.8 $[M - OMe]^+$). An analytical sample was acetylated following standard conditions (pyridine, acetic anhydride). The resulting methyl 2-acetamido-4-*O*-acetyl-6-*O*-benzyl-2-deoxy-3-*O*-(2,3,4-tri-*O*-acetyl-6-chloro-6-deoxy-β-D-galactopyranosyl)-β-D-glucopyranoside was characterized by ^{1}H nmr spectroscopy: ^{1}H nmr ($CDCl_3$) δ: 7.40–7.30 (m, 5H, Ph), 5.72 (d, 1H, NH, $J_{NH,2a}$ 7.5 Hz), 5.48 (dd, 1H, H-4b, $J_{4b,3b}$ 3.5 Hz, $J_{4b,5b}$ 1.0 Hz), 5.08 (dd, 1H, H-2b, $J_{2b,3b}$ 10.5 Hz, $J_{2b,1b}$ 7.5 Hz), 4.98 (dd, 1H, H-3b), 4.94 (t, 1H, H-4a, $J_{4a,3a}$ = $J_{4a,5a}$ 9.0 Hz), 4.80 (d, 1H, H-1a, $J_{1a,2a}$ 7.5 Hz), 4.59 (d, 1H, H-1b), 4.54 (s, 2H, CH_2Ph), 4.41 (t, 1H, H-3a, $J_{3a,2a}$ 9.0 Hz), 3.81 (dt, 1H, H-5b, $J_{5b,6b}$ ~ $J_{5b,6b'}$ ~ 7.0 Hz), 3.71 (ddd, 1H, H-5a, $J_{5a,4a}$ 9.0 Hz, $J_{5a,6a}$ 6.0 Hz, $J_{5a,6a'}$ 3.0 Hz), 3.60–3.40 (m, 7H, H-6a, H-6a′, H-6b, H-6b′, with CH_3O at 3.49), 3.32 (td, 1H, H-2a), 2.15, 2.06, 2.02 (3s, each 3H, $3CH_3CO$), 1.97 (s, 6H, $2CH_3CO$).

Methyl 2-acetamido-6-O-benzyl-3-O-(3,4-O-benzylidene-α-L-arabinopyranosyl)-2-deoxy-β-D-glucopyranoside (28)

A solution of compound **24** (1.44 g, 2.47 mmol) in methanolic 0.05 N sodium methoxide (30 mL) was kept under argon for 5 h. After neutralization with Amberlite IRC 50 H^+ and evaporation to dryness, the residual powder was dissolved in *N*,*N*-dimethylformamide (5 mL) and acetonitrile (30 mL) and then treated with *p*-toluenesulfonic acid (100 mg, 5.26 mmol) and α,α-dimethoxytoluene (1.25 mL, 8.1 mmol) at room temperature for 1 day. The mixture was neutralized with triethylamine and evaporated to dryness. Purification was achieved by column chromatography on silica gel (dichloromethane – 4% methanol) to provide compound **28** (1.08 g, 77%) as a mixture of two diastereoisomers. A fraction containing the slower migrating isomer was evaporated and the residual material recrystallized from chloroform–ether and characterized; mp 174.5°C; $[\alpha]_D$ +22.5° (*c* 0.9,

chloroform); ^{1}H nmr ($CDCl_3$) δ: 7.60–7.20 (m, 10H, 2Ph), 6.25 (br d, 1H, NH), 5.95 (s, 1H, C*H*Ph), 4.66 (d, 1H, H-1a, $J_{1a,2a}$ 8.5 Hz), 4.60 (s, 2H, CH_2Ph), 4.35 (dd, 1H, H-5beq, $J_{5beq,5bax}$ 13.5 Hz, $J_{5beq,4b}$ 2.0 Hz), 4.00 (dd, 1H, H-3a, $J_{3a,2a}$ 10.0 Hz, $J_{3a,4a}$ 8.0 Hz), 3.55–3.44 (m, 5H, with CH_3O at 3.49), 3.39 (td, 1H, H-2a, $J_{2a,NH}$ 8.5 Hz), 1.98 (s, 3H, CH_3CONH). *Anal.* calcd. for $C_{28}H_{35}NO_{10}$: C 61.64, H 6.47, N 2.57; found: C 61.43, H 6.32, N 2.77.

*Methyl 2-acetamido-6-*O*-benzyl-3-*O*-(3,4-*O*-benzylidene-6-deoxy-6-fluoro-β-*D*-galactopyranosyl)-2-deoxy-β-*D*-gluco-pyranoside (**29**)*

Compound **25** (625 mg, 1 mmol) was deacetylated and benzylidenated as described for the preparation of diol **28**. Purification and partial separation of the two diastereoisomers of **29** was effected by column chromatography on silica gel (dichloromethane – 4% methanol). Total yield 94% (540 mg). A pure fraction of the more polar isomer was evaporated and the compound crystallized from dichloromethane – ethyl acetate – hexane; mp 184.5–185.5°C; $[\alpha]_D$ +10.9° (*c* 0.7, chloroform); ^{1}H nmr ($CDCl_3$) δ: 7.50–7.25 (m, 10H, 2Ph), 6.52 (d, 1H, NH, $J_{NH,2a}$ 8.0 Hz), 5.86 (s, 1H, C*H*Ph), 4.69 (m, 2H, H-6b, H-6b′, $J_{6b,F} \sim J_{6b',F} \sim$ 45 Hz), 4.60 (d, 1H, H-1a, $J_{1a,2a}$ 8.5 Hz), 4.29 (d, 1H, H-1b, $J_{1b,2b}$ 8.5 Hz), 3.73–3.45 (m, 8H, with CH_3O at 3.45), 1.94 (s, 3H, CH_3CONH). *Anal.* calcd. for $C_{29}H_{36}FNO_{10}$: C 60.30, H 6.28, N 2.42; found: C 60.06, H 6.25, N 2.48. An analytical sample of methyl 2-acetamido-4-*O*-acetyl-3-*O*-(2-*O*-acetyl-3,4-*O*-benzylidene-6-deoxy-6-fluoro-β-D-galactopyranosyl)-6-*O*-benzyl-2-deoxy-β-D-glucopyranoside (**29***a*) was prepared from the slower migrating isomer of diol **29** by acetylation (pyridine, acetic anhydride); ^{1}H nmr ($CDCl_3$) δ: 7.57–7.25 (m, 10H, 2Ph), 7.82 (s, 1H, C*H*Ph), 7.79 (d, NH, $J_{NH,2a}$ 7.5 Hz), 4.94 (t, 1H, H-2b, $J_{2b,3b} \sim J_{2b,1b}$ 6.5 Hz), 4.94 (t, 1H, H-4a, $J_{4a,3a} \sim J_{4a,5a}$ 9.5 Hz), 4.89 (d, 1H, H-1a, $J_{1a,2a}$ 7.5 Hz), 4.67 (d, 1H, H-1b, overlapped by H-6b and H-6b′), ~4.63 (m, 2H, H-6b, H-6b′, $J_{6b,F} \sim J_{6b',F} \sim$ 45 Hz), 4.53 (s, 2H, CH_2Ph, overlapped by H-6b and H-6b′), 4.45 (t, 1H, H-3a, $J_{3a,2a}$ 9.5 Hz), 4.36 (t, 1H, H-3b, $J_{3b,4b}$ 6.5 Hz), 4.25 (dd, 1H, H-4b, $J_{4b,5b}$ 2.5 Hz), 4.12 (dddd, 1H, H-5b, $J_{5b,F}$ 14.0 Hz, $J_{5b,6b}$ 7.0 Hz, $J_{5b,6b'}$ 5.0 Hz), 3.70 (ddd, 1H, H-5a, $J_{5a,6a}$ 5.5 Hz, $J_{5a,6a'}$ 3.5 Hz), 3.61–3.51 (m, 2H, H-6a, H-6a′), 3.50 (s, 3H, CH_3O), 3.15 (td, 1H, H-2a), 2.10, 2.0, 1.93 (3s, each 3H, $2CH_3COO$, CH_3CONH).

*Methyl 2-acetamido-6-*O*-benzyl-3-*O*-(3,4-*O*-benzylidene-6-chloro-6-deoxy-β-*D*-galactopyranosyl)-2-deoxy-β-*D*-glucopyranoside (**30**)*

Diol **30** was prepared from tri-*O*-acetate **26** (300 mg, 0.47 mmol) by deacetylation and subsequent benzylidenation as described for the preparation of compound **28**. Chromatographic purification on a column of silica gel (dichloromethane – 3% methanol) provided **30** (217 mg, 77%) as a diastereoisomeric mixture. A pure fraction of the less polar isomer was evaporated and the resulting material crystallized from chloroform–ether–hexane; mp 151–152°C; $[\alpha]_D$ +27.9° (*c* 0.3, chloroform); ^{1}H nmr ($CDCl_3$) δ: 7.44–7.24 (m, 1H, 2Ph), 6.10 (s, 1H, C*H*Ph), 6.04 (d, 1H, NH, $J_{NH,2a}$ 8.0 Hz), 4.62 (d, 1H, H-1a, $J_{1a,2a}$ 8.5 Hz), 4.58 (s, 2H, CH_2Ph), 4.42 (dd, 1OH, H-3b, $J_{3b,2b}$ 7.5 Hz, $J_{3b,4b}$ 5.5 Hz), 4.29 (d, 1H, H-1b, $J_{1b,2b}$ 8.5 Hz), 4.15 (dd, 1H, H-4b, $J_{4b,5b}$ 2.0 Hz), 4.04 (s, 1H, OH), 3.51 (s, 3H, CH_3O), 2.04 (s, 3H, CH_3CONH). *Anal.* calcd. for $C_{29}H_{36}ClNO_{10}$: C 58.63, H 6.11, N 2.36; found: C 58.24, H 6.11, N 2.66. An analytical sample of this isomer was acetylated conventionally (pyridine, acetic anhydride) to provide methyl 2-acetamido-4-*O*-acetyl-3-*O*-(2-*O*-acetyl-3,4-*O*-benzylidene-6-chloro-6-deoxy-β-D-galactopyranosyl)-6-*O*-benzyl-2-deoxy-β-D-glucopyranoside (**30***a*); ^{1}H nmr ($CDCl_3$) δ: 7.50–7.30 (m, 10H, 2Ph), 6.17 (s, 1H, C*H*Ph), 5.85 (d, 1H, NH, $J_{NH,2a}$ 7.5 Hz), 5.04 (t, 1H, H-2b, $J_{2b,1b} \sim J_{2b,3b}$ ~6.0 Hz), 5.00 (t, 1H, H-4a, $J_{4a,3a} = J_{4a,5a}$ 9.0 Hz), 4.96 (d, 1H, H-1a, $J_{1a,2a}$ 7.5 Hz), 4.64 (d, 1H, H-1b), 4.55 (s, 2H, CH_2Ph), 4.48 (t, 1H, H-3b, $J_{3b,4b}$ 6.0 Hz), 4.48 (t, 1H, H-3a, $J_{3a,2a}$ 9.0 Hz), 4.36 (dd, 1H, H-4b, $J_{4b,3b}$ 6.0 Hz, $J_{4b,5b}$ 2.0 Hz), 3.86 (dt, 1H, H-5b, $J_{5b,6b} \sim J_{5b,6b'} \sim$7.0 Hz), 3.80–3.66 and 3.60–3.56 (m, 5H, H-6b, H-6b′, H-6a, H-6a′, H-5a), 3.50 (s, 3H, CH_3O), 3.21 (td, 1H, H-2a), 2.21 (s, 3H, CH_3CO), 2.00 (s, 6H, $2CH_3CO$).

*Methyl 2-acetamido-6-*O*-benzyl-3-*O*-(3,4-*O*-benzylidene-6-deoxy-β-*D*-galactopyranosyl)-2-deoxy-β-*D*-glucopyranoside (**31**)*

The tri-*O*-acetate **27** (250 mg, 0.42 mmol) was converted into compound **31** by deacetylation and subsequent benzylidenation as described for the preparation of compound **28**. The resulting material was applied to a column of silica gel (dichloromethane – ethyl acetate 1:1, dichloromethane – 5% methanol) to provide solid **31** (175 mg, 75%). The ^{1}H nmr spectrum indicated the product to be a 1:1 mixture of *S* and *R* isomers of the 3,4-*O*-benzylidene acetal; $[\alpha]_D$ +2.1°, $[\alpha]_{365}$ +17.9° (*c* 0.5, dichloromethane); ^{1}H nmr ($CDCl_3$) δ: 7.5–7.2 (m, 10H, 2Ph), 6.62, 6.50 (each d, each 0.5H, NH, $J_{NH,2a}$ 7.5 Hz), 6.18, 5.90 (each s, each 0.5H, C*H*Ph), 4.72, 4.69 (each d, each 0.5H, H-1a, $J_{1a,2a}$ 8.5 Hz), 4.22, 4.21 (each d, each 0.5H, H-1b, $J_{1b,2b}$ 7.5 Hz), 3.50 (s, CH_3O), 2.01, 1.98 (2s, each 1.5H, CH_3CONH), 1.45, 1.40 (2d, each 1.5H, H3-6b, $J_{5b,6b}$ 6.5 Hz).

*Methyl 2-acetamido-4-*O*-acetyl-3-*O*-(2-*O*-acetyl-3,4-*O*-benzylidene-6-deoxy-β-*D*-galactopyranosyl)-6-*O*-benzyl-2-deoxy-β-*D*-glucopyranoside (**32**)*

A solution of diol **31** (25 mg, 0.05 mmol) in pyridine (0.6 mL) and acetic anhydride (0.3 mL) was kept at room temperature overnight. After work-up and evaporation to dryness, the reaction products was separated by preparative tlc (dichloromethane – 5% methanol, developed three times). Elution of the faster moving band provided one diastereoisomer (10.2 mg, 35.5%) as a solid; ^{1}H nmr ($CDCl_3$) δ: 7.55–7.25 (m, 10H, 2Ph), 6.16 (s, 1H, C*H*Ph), 5.89 (s, 1H, NH, $J_{NH,2a}$ 7.0 Hz), 4.99 (t, overlapped, 1H, H-2b, $J_{1b,2b}$ 6.5 Hz, $J_{2b,3b}$ 6.0 Hz), 4.99 (d, 1H, H-1a, $J_{1a,2a}$ 7.5 Hz), 4.97 (t, 1H, H-4a, $J_{3a,4a} = J_{4a,5a}$ 9.0 Hz), 4.56 (s, 2H, CH_2Ph), 4.53 (d, 1H, H-1b), 4.46 (t, 1H, H-3a, $J_{2a,3a}$ 9.0 Hz), 4.44 (t, 1H, H-3b, $J_{3b,4b}$ 6.0 Hz), 4.06 (dd, 1H, H-4b, $J_{4b,5b}$ 2.0 Hz), 3.80 (dq, 1H, H-5b, $J_{5b,6b}$ 6.5 Hz), 3.74 (m, 1H, H-5a), 3.63–3.54 (m, 2H, H-6a, H-6a′), 3.52 (s, 3H, CH_3O), 3.17 (m, 1H, H-2a), 2.12 (s, 3H, CH_3CO), 2.04 (s, 6H, $2CH_3CO$), 1.39 (d, 3H, H3-6b).

The lower band provided the solid second isomer (10.2 mg, 35.5%); ^{1}H nmr ($CDCl_3$) δ: 7.6–7.25 (m, 10H, 2Ph), 5.80 (s, 1H, C*H*Ph, overlapped by NH), 5.82 (d, 1H, NH, $J_{NH,2a}$ 7.0 Hz), 4.92 (t, 1H, H-4a, $J_{3a,4a} = J_{4a,5a}$ 9.0 Hz), 4.90 (d, overlapped by H-4a, 1H, H-1a, $J_{1a,2a}$ 7.5 Hz), 4.86 (t, 1H, H-2b, $J_{1b,2b}$ 7.0 Hz, $J_{2b,3b}$ 6.5 Hz), 4.58 (d, 1H, H-1b), 4.56 (s, 2H, CH_2Ph), 4.43 (t, 1H, H-3a, $J_{2a,3a}$ 9.0 Hz), 4.29 (t, 1H, H-3b, $J_{3b,4b}$ 6.5 Hz), 4.08 (dd, 1H, H-4b, $J_{4b,5b}$ 2.0 Hz), 3.92 (dq, 1H, H-5b, $J_{5b,6b}$ 6.5 Hz), 3.72 (m, 1H, H-5a), ~3.61, 3.66 (m, 2H, H-6a, H-6a′), 3.51 (s, 3H, CH_3O), 3.15 (m, 1H, H-2a), 2.09, 2.03, 1.97 (3s, each 3H, $2CH_3COOC$, CH_3CONH), 1.42 (d, 3H, H3-6b).

*Methyl 2-acetamido-6-*O*-benzyl-3-*O*-[3,4-*O*-benzylidene-2-*O*-(2,3,4-tri-*O*-benzyl-α-L-fucopyranosyl)-α-L-arabino-pyranosyl]-2-deoxy-4-*O*-(2,3,4-tri-*O*-benzyl-α-L-fuco-pyranosyl)-β-D-glucopyranoside (**33**)*

A solution of bromide **9** (5.8 mmol) in dichloromethane (5 mL) was added to a mixture of diol **28** (500 mg, 0.92 mmol), tetraethylammonium bromide (210 mg, 1 mmol), 4 Å molecular sieves (3 g) in dichloromethane (4 mL), and *N*,*N*-dimethylformamide (1 mL). The mixture was stirred for 40 h and then processed as described for the preparation of compound **10**. Column chromatography on silica gel (hexane – ethyl acetate 1:1, dichloromethane – ethyl acetate 3:1) afforded compound **33** (962 mg, 76%) as a mixture of two diastereoisomers. A pure fraction of the more polar isomer was characterized as a gum; $[\alpha]_D$ −65.5° (*c* 0.8, chloroform); ^{1}H nmr ($CDCl_3$) δ: 7.55–7.20 (m, 40H, 8 Ph), 6.14 (d, 1H, NH, $J_{NH,2a}$ 8.5 Hz), 5.93 (s, 1H, C*H*Ph), 5.51 (d, 1H, H-1d, $J_{1d,2d}$ 3.5 Hz), 5.02 (d, 1H, H-1c, $J_{1c,2c}$ 3.5 Hz), 3.32 (s, 3H, CH_3O), 1.67 (s, 3H, CH_3CONH), 1.10, 0.95 (2d, each 3H, H3-6c, H3-6d, $J_{5c,6c} = J_{5d,6d}$ 6.5 Hz). *Anal.* calcd. for $C_{82}H_{91}NO_{18}$: C 71.44, H 6.65, N 1.02; found: C 70.97, H 6.82, N 0.72.

Can. J. Chem. Downloaded from www.nrcresearchpress.com by 122.72.124.2 on 09/07/12
For personal use only.

Can. J. Chem. Downloaded from www.nrcresearchpress.com by 122.72.124.2 on 09/07/12
For personal use only.

Methyl 2-acetamido-6-O-benzyl-3-O-[3,4-O-benzylidene-6-deoxy-6-fluoro-2-O-(2,3,4-tri-O-benzyl-α-L-fucopyranosyl)-β-D-galactopyranosyl]-2-deoxy-4-O-(2,3,4-tri-O-benzyl-α-L-fucopyranosyl)-β-D-glucopyranoside (34)

Diol **29** (475 mg, 0.82 mmol) was reacted with bromide **9** (4.13 mmol) for 30 h according to the preparation of compound **10**. The crude product was applied to a column of silica gel (hexane – ethyl acetate, 1:1, dichloromethane – ethyl acetate, 3:1) to provide the title compound **34** (767 mg, 66%) as a mixture of two diastereoisomers. The slower migrating isomer was characterized. $[\alpha]_D$ −64.7° (*c* 0.6, chloroform); ^{1}H nmr ($CDCl_3$) δ: 7.43–7.20 (m, 40H, 8Ph), 6.40 (d, 1H, NH, $J_{NH,2a}$ 8.0 Hz), 5.99 (s, 1H, C*H*Ph), 5.52 (d, 1H, H-1d, $J_{1d,2d}$ 4.0 Hz), 5.11 (d, 1H, H-1c, $J_{1c,2c}$ 4.0 Hz), 3.29 (s, 3H, CH_3O), 1.65 (s, 3H, CH_3CONH), 1.13 (d, 6H, H3-6c, H3-6d, $J_{5c,6c} = J_{5d,6d}$ 6.5 Hz). *Anal.* calcd. for $C_{83}H_{92}FNO_{18}$: C 70.67, H 6.57, N 1.00; found: C 70.36, H 6.63, N 0.95.

Methyl 2-acetamido-6-O-benzyl-3-O-[3,4-O-benzylidene-6-chloro-6-deoxy-2-O-(2,3,4-tri-O-benzyl-α-L-fucopyranosyl)-β-D-galactopyranosyl]-2-deoxy-4-O-(2,3,4-tri-O-benzyl-α-L-fucopyranosyl)-β-D-glucopyranoside (35)

The tetrasaccharide **35** was prepared from diol **30** (235 mg, 0.40 mmol) and bromide **9** (3 mmol) as described for the preparation of compound **10**. Usual work-up after 42 h, followed by chromatography on a column of silica gel (hexane – ethyl acetate 1:1, dichloromethane – ethyl acetate 3:1) provided **35** as a mixture of two diastereoisomers (572 mg, 80%); $[\alpha]_D$ −60.2° (*c* 1.0, chloroform); ^{1}H nmr ($CDCl_3$) δ: 7.50–7.20 (m, 40H, 8Ph), 6.39, 6.31 (2d, 1H, NH, $J_{NH,2a}$ 8.0 Hz), 6.00, 5.91 (2s, 1H, C*H*Ph), 5.52, 5.50 (2d, 1H, H-1d, $J_{1d,2d}$ 4.0 Hz), 5.09, 5.04 (2d, 1H, H-1c, $J_{1c,2c}$ 4.0 Hz), 3.28, 3.27 (2s, 3H, CH_3O), 1.70, 1.65 (2s, 3H, CH_3CONH), 1.11, 1.08 1(2d, each 3H, H3-6c, H3-6d, $J_{6c,5c} = J_{6d,5d}$ 6.5 Hz). *Anal.* calcd. for $C_{83}H_{92}ClNO_{18}$: C 69.85, H 6.50, N 0.98, Cl 2.48; found: C 69.73, H 6.74, N 0.75, Cl 2.50.

Methyl 2-acetamido-6-O-benzyl-3-O-[3,4-O-benzylidene-6-deoxy-2-O-(2,3,4-tri-O-benzyl-α-L-fucopyranosyl)-β-D-galacto-pyranosyl]-2-deoxy-4-O-(2,3,4-tri-O-benzyl-α-L-fucopyranosyl)-β-D-glucopyranoside (36)

Bromide **9** (0.81 mmol) was reacted with diol **31** (140 mg, 0.25 mmol) as described for the preparation of compound **10**. After stirring for 20 h, more bromide **9** (0.57 mmol) was added and stirring continued for a further 20 h. Conventional processing and purification on a column of silica gel using hexane – ethyl acetate 1:1 as eluent provided the title compound **36** (279 mg, 80%) as a diastereoisomeric mixture; $[\alpha]_D$ −82.5° (*c* 0.7, dichloromethane); ^{1}H nmr ($CDCl_3$) δ: 7.55–7.21 (m, 40H, 8Ph), 6.38, 6.31 (each d, each 0.5H, NH, $J_{NH,2a}$ 7.5 Hz), 6.00, 5.92 (each s, each 0.5H, C*H*Ph), 5.57, 5.55 (each d, each 0.5H, H-1d, $J_{1d,2d}$ 3.5 Hz), 5.10, 5.04 (each d, each 0.5H, H-1c, $J_{1c,2c}$ 3.5 Hz), 3.34 (s, 3H, CH_3O), 1.68, 1.64 (each s, each 1.5H, CH_3CONH), 1.35, 1.32, 1.154, 1.148, 1.08, 0.92 (each d, each 1.5H, H3-6b, H3-6c, H3-6d, $J_{5b,6b} = J_{5c,6c} = J_{5d,6d}$ 6.5 Hz). *Anal.* calcd. for $C_{83}H_{93}NO_{18}$: C 71.58, H 6.73, N 1.01; found: C 71.57, H 6.74, N 0.81.

Methyl 2-acetamido-2-deoxy-4-O-(α-L-fucopyranosyl)-3-O-[2-O-(α-L-fucopyranosyl)-α-L-arabinopyranosyl]-β-D-glucopyranoside (37)

Compound **33** (200 mg, 0.15 mmol) was hydrogenated for 10 days over 10% palladium-on-carbon (100 mg) as described for the preparation of **11**. After filtration and evaporation, the crude product was applied to a column of Sephadex LH 20 and eluted with ethanol–water 1:1. Tetrasaccharide **37** was obtained as a light white powder (45 mg, 47%) after freeze-drying an aqueous solution; $[\alpha]_D$ −147.4° (*c* 0.4, water). The ^{1}H and ^{13}C nmr data are reported in Tables 1 and 2.

Methyl 2-acetamido-2-deoxy-3-O-[6-deoxy-6-fluoro-2-O-(α-L-fucopyranosyl)-β-D-galactopyranosyl]-4-O-(α-L-fucopyranosyl)-β-D-glucopyranoside (38)

A mixture of compound **34** (160 mg, 0.11 mmol) and 20% palladium hydroxide-on-carbon (160 mg) was hydrogenated for 22 h in the usual way. The reaction mixture was then treated as described for compound **37** and afforded the tetrasaccharide **38** (74 mg, 95%) as a light white powder; $[\alpha]_D$ −141.0° (*c* 0.4, water). The ^{1}H and ^{13}C nmr data are reported in Tables 1 and 2; ^{19}F nmr (367 MHz, D_2O, $CFCl_3$ as external standard set at 0) δ: −230.25 (ddd, F-6d, $J_{F,H6b}$ 47.8 Hz, $J_{F,H6b'}$ 45.5 Hz, $J_{F,H5b}$ 15.0 Hz).

Methyl 2-acetamido-3-O-[6-chloro-6-deoxy-2-O-(α-L-fuco-pyranosyl)-β-D-galactopyranosyl]-2-deoxy-4-O-(α-L-fuco-pyranosyl)-β-D-glucopyranoside (39)

Hydrogenolysis of compound **35** (150 mg, 0.1 mmol) was done over 10% palladium-on-carbon (75 mg) for 8 days in the usual way. The reaction mixture was then processed as described for **37** and afforded the title compound **39** (35 mg, 47%) as a light white powder; $[\alpha]_D$ −132.0° (*c* 0.5, water). The ^{1}H and ^{13}C nmr data are reported in Tables 1 and 2.

Methyl 2-acetamido-2-deoxy-3-O-[6-deoxy-2-O-(α-L-fucopyranosyl)-β-D-galactopyranosyl]-4-O-(α-L-fucopyranosyl)-β-D-gluco-pyranoside (40)

Compound **36** (200 mg, 0.14 mmol) was hydrogenated for 3 days over 5% palladium-on-carbon in the usual way. Precipitation of the resulting material from methanol – ethyl acetate provided the tetrasaccharide **40** (76 mg, 79%); $[\alpha]_D$ −129.4° (*c* 0.4, water). The ^{1}H and ^{13}C nmr data are reported in Tables 1 and 2.

Acknowledgements

This research was supported by the Natural Sciences and Engineering Research Council of Canada (Grant A-172 to R.U.L.) and by a special grant to R.U.L. from the Alberta Heritage Foundation for Medical Research. The donation of the anti-Lewis b antibody by Chembiomed Ltd. is gratefully acknowledged.

1. R. U. LEMIEUX, T. C. WONG, J. LIAO, and E. A. KABAT. Mol. Immunol. **21**, 751 (1984).
2. U. SPOHR, O. HINDSGAUL, and R. U. LEMIEUX. Can. J. Chem. **63**, 2644 (1985).
3. O. HINDSGAUL, D. P. KHARE, M. BACH, and R. U. LEMIEUX. Can. J. Chem. **63**, 2653 (1985).
4. U. SPOHR, N. MORISHIMA, O. HINDSGAUL, and R. U. LEMIEUX. Can. J. Chem. **63**, 2659 (1985).
5. R. U. LEMIEUX, A. P. VENOT, U. SPOHR, P. BIRD, G. MANDAL, N. MORISHIMA, O. HINDSGAUL, and D. R. BUNDLE. Can. J. Chem. **63**, 2664 (1985).
6. U. SPOHR, M. BACH, and R. U. LEMIEUX. Thermodynamic parameters for the binding of the Lewis b tetrasaccharide by the lectin IV of *Griffonia Simplicifolia*. Abstracts of the XIIIth International Carbohydrate Symposium, August 10–15, 1986. Ithaca, NY p. 353.
7. E. PETRAKOVA, U. SPOHR, M. BACH, and R. U. LEMIEUX. Intramolecular hydrogen bonding in the binding of the H type 2-trisaccharide by the lectin I of *Ulex Europaeus*. Abstracts of th XIIIth International Carbohydrate Symposium, August 10–15. 1986. Ithaca, NY. p. 346.
8. R. U. LEMIEUX, O. HINDSGAUL, P. BIRD, S. NARASIMHAN, and W. W. YOUNG, JR. Carbohydr. Res. **178**, 293 (1988).
9. U. SPOHR and R. U. LEMIEUX. Carbohydr. Res. **174**, 211 (1988).
10. R. U. LEMIEUX. The hydrated polar-group 'gate' effect on the specificity and strength of the binding of oligosaccharides by protein receptor sites. Proceedings of the VIIth International Symposium on Medicinal Chemistry, August 27–31, 1984. Uppsala, Sweden. Vol. 1. pp. 329–351.
11. A. R. FERSHT, J.-P. SHI, J. KNILL-JONES, D. M. LOWE, A. J. WILKINSON, D. M. BLOW, P. BRICK, P. CARTER, M. M. Y. WAYE, and G. WINTER. Nature, **314**, 235 (1985).

12. M. VANDONSELAAR, L. T. J. DELBAERE, U. SPOHR, and R. U. LEMIEUX. J. Biol. Chem. **262**, 10 848 (1987).
13. R. U. LEMIEUX, P. H. BOULLANGER, D. R. BUNDLE, D. A. BAKER, A. NAGPURKAR, and A. VENOT. Nouv. J. Chim. **2**, 321 (1978).
14. E. J. HEDGLEY, W. G. OVEREND, and R. A. C. RENNIE. J. Chem. Soc. 4701 (1963); L. VEGH and E. HARDEGGER. Helv. Chim. Acta, **56**, 2079 (1973).
15. H. B. BOREN, G. EKBORG, K. EKLIND, P. J. GAREGG, Å. PILOTTI, and C. G. SWAHN. Acta Chem. Scand. **27**, 2639 (1973).
16. O. HINDSGAUL, T. NORBERG, J. LEPENDU, and R. U. LEMIEUX. Carbohyd. Res. **109**, 109 (1982).
17. W. ROTH and W. PIGMAN. J. Am. Chem. Soc. **82**, 4608 (1960); J. CONCHIE and G. A. LEVVY. Methods Carbohydr. Chem. **2**, 332 (1963); M. FUJINAGA and Y. MATSUSHIMA. Bull. Chem. Soc. Jpn. **39**, 185 (1966).
18. B. HELFERICH and K.-F. WEDEMEYER. Ann. **563**, 139 (1949).
19. P. J. GAREGG and H. HULTBERG. Carbohydr. Res. **93**, C10–C11 (1981); P. J. GAREGG, H. HULTBERG, and S. WALLIN. Carbohydr. Res. **108**, 97 (1982).
20. R. U. LEMIEUX, K. B. HENDRIKS, R. V. STICK, and K. JAMES. J. Am. Chem. Soc. **97**, 4056 (1975).
21. M. DEJTER-JUSZYNSKI and H. M. FLOWERS. Carbohydr. Res. **18**, 219 (1971).
22. T. M. K. CHIU, K. A. WATANABE, and J. J. FOX. Carbohydr. Res. **32**, 211 (1974).
23. M. E. EVANS. Carbohydr. Res. **21**, 473 (1972); Methods Carbohydr. Chem. **8**, 313 (1980).
24. J. MEISENHEIMER and H. JUNG. Ber. **60**, 1462 (1927); M. GEHRKE and F. X. AICHNER. Ber. **60**, 918 (1927).
25. P. W. KENT and J. R. WRIGHT. Carbohydr. Res. **22**, 193 (1972).
26. K. BOCK and C. PEDERSEN. Adv. Carbohydr. Chem. Biochem. **41**, 27 (1983).
27. H. THØGERSEN, R. U. LEMIEUX, K. BOCK, and B. MEYER. Can. J. Chem. **60**, 44 (1982).
28. R. U. LEMIEUX and K. BOCK. Jpn. J. Antibiot. **32**, Suppl., S-163 (1979).
29. R. U. LEMIEUX, D. R. BUNDLE, and D. A. BAKER. J. Am. Chem. Soc. **97**, 4076 (1975).
30. R. U. LEMIEUX, K. BOCK, L. T. J. DELBAERE, S. KOTO, and V. S. RAO. Can. J. Chem. **58**, 631 (1980).
31. R. U. LEMIEUX and K. BOCK. Arch. Biochem. Biophys. **221**, 125 (1983).
32. C. A. BUSH, Z.-Y. YAN, and B. N. N. RAO. J. Am. Chem. Soc. **108**, 6168 (1986); Z.-Y. YAN, B. N. N. RAO, and C. A. BUSH. J. Am. Chem. Soc. **109**, 7663 (1987).
33. J. P. PRALY and R. U. LEMIEUX. Can. J. Chem. **65**, 213 (1987).
34. E. ALVARADO. Ph.D. thesis, University of Alberta, 1987.
35. S. J. ANGYAL and D. J. MCHUGH. Chem. Ind. (London), 1147 (1956).
36. C. S. HUDSON and J. K. DALE. J. Am. Chem. Soc. **40**, 992 (1918).
37. K. R. WOOD, D. F. FISHER, and P. W. KENT. J. Chem. Soc. (London) C, 1994 (1966).

Can. J. Chem. Downloaded from www.nrcresearchpress.com by 122.72.124.2 on 09/07/12
For personal use only.

A comparative study of gas phase aromatic desilylation and detertbutylation by charged electrophiles

FULVIO CACACE,[1] M. ELISA CRESTONI, GIULIA DE PETRIS, AND SIMONETTA FORNARINI
Università di Roma "La Sapienza", P.le A.Moro, 5, 00185 Rome, Italy

AND

FELICE GRANDINETTI
Istituto di Chimica nucleare, Area della Ricerca del C.N.R. di Roma, 00016 Monterotondo Stazione, Rome, Italy

Received May 14, 1988

FULVIO CACACE, M. ELISA CRESTONI, GIULIA DE PETRIS, SIMONETTA FORNARINI, and FELICE GRANDINETTI. Can. J. Chem. **66**, 3099 (1988).

Aromatic desilylation and detertbutylation by CH_5^+, $C_2H_5^+$, $i\text{-}C_3H_7^+$, and $t\text{-}C_4H_9^+$ ions have been studied in the gas phase by mass spectrometric and radiolytic techniques. The higher rate of desilylation than of dealkylation is traced to the step involving the formation of *ipso* arenium ions, protonated at the ring carbon bearing the $SiMe_3$ or the CMe_3 substituent. The latter has been shown by *ab initio* calculations at the SCF STO-3G level to selectively depress the basicity of the *ipso* position, hence the stability of the corresponding arenium ion relative to its protomers, e.g. the basicity of the *ipso* position of $PhCMe_3$ is lower by ca. 11 kcal mol^{-1} than of the *para* position. The $SiMe_3$ group has no comparable effect, very close basicities being computed for the *para* and the *ipso* position of $PhSiMe_3$. The different effects of the CMe_3 and $SiMe_3$ groups are traced to electronic and steric factors.

FULVIO CACACE, M. ELISA CRESTONI, GIULIA DE PETRIS, SIMONETTA FORNARINI et FELICE GRANDINETTI. Can. J. Chem. **66**, 3099 (1988).

Opérant en phase gazeuse et faisant appel à des techniques de spectrométrie de masse et de radiolyse, on a étudié les réactions de dé-*tert*-butylation et de désilylation aromatiques par les ions CH_5^+, $C_2H_5^+$, $i\text{-}C_3H_7^+$, et $tert\text{-}C_4H_9^+$. Le fait que la vitesse de désilylation est plus rapide que celle de la déalkylation est attribué à l'étape impliquant la formation des ions ipso arénium qui sont protonés au niveau du cycle carboné portant les substituants $SiMe_3$ ou CMe_3. Faisant appel à des calculs ab initio, en champ auto-cohérent, au niveau STO-3G, on a démontré que, par rapport à ses protomères, le dernier abaisse la basicité de la position *ipso* et, par conséquent, la stabilité de l'ion arénium correspondant; par exemple, la basicité de la position *ipso* du $PhCMe_3$ est environ 11 kcal mol^{-1} plus faible que celle de la position *para*. Le groupement $SiMe_3$ n'a pas d'effet semblable et les calculs fournissent des valeurs très comparables pour les positions *para* et *ipso* du $PhSiMe_3$. On attribue les effets différents des groupements CMe_3 et $SiMe_3$ à des facteurs électronique et stérique.

[Traduit par la revue]

Introduction

Electrophilic cleavage of aryl–silicon bonds, observed as early as in 1901 (1), has been characterized by the systematic work of Eaborn (2, 3) as a typical aromatic substitution, whose rate-determining step is the formation of the *ipso* σ complex.

We report here extension of the work to the gas phase by an integrated approach based on the coordinated application of mass spectrometric, radiolytic, and computational techniques (4). The same approach has recently allowed us to demonstrate the first example of the inverse process, the direct aromatic substitution by $SiMe_3^+$ (5, 6), unprecedented in solution, nor previously characterized in the gas phase.

In order to provide a proper perspective, and in view of the close correlations between carbon and silicon chemistry, a parallel investigation has been carried out of gas-phase aromatic detertbutylation, the subject of earlier detailed studies by chemical ionization mass spectrometry (CIMS) in the low-pressure range (7, 9).

Results

Radiolytic reactions

The *absolute* yields, measured by the G_{+M} values of the products, i.e. by the number of molecules formed per 100 eV, are reported for several representative systems in Table 1. Such absolute values are affected by large uncertainties, estimated around ±30%, owing to the severe problems associated with absolute dosimetric measurements, while *relative* yields can be determined with far better accuracy. To circumvent the problem, the experiments have been based on the competition of the unlabelled substrate of interest with a reference substrate, $p\text{-}CD_3\text{-}C_6H_4\text{-}t\text{-}C_4H_9$, whose products can easily be discriminated from their light isotopomers by GC/MS. Attack of the $C_nH_5^+$ (n = 1, 2) and $i\text{-}C_3H_7^+$ ions on *t*-butyltoluenes (TBT) and trimethylsilyltoluenes (TST) promotes several competing processes, i.e. (*i*) replacement of the XMe_3 group (X = C, Si) by H or by an alkyl group, Et or *i*-Pr, (*ii*) protonation-induced isomerization, and (*iii*) alkylation of the substrate without XMe_3 loss. Desilylation and detertbutylation are major reaction channels, whose ionic character is suggested by the presence of a radical scavenger (O_2) in the system, by the decrease of their yields caused by addition of nucleophiles that intercept ionic reactants and intermediates, and by the direct observation of the latter, in the CH_4 and C_3H_8 CI spectra of TBT and TST isomers (*vide infra*). A comparison between the relative rate of XMe_3 loss from TBT and TST substrates is reported in Table 2, showing that the reactivity of the latter is generally higher, the difference becoming quite large in passing from $C_nH_5^+$ to the milder $i\text{-}C_3H_7^+$ cation. With one exception, *m*-TST in CH_4, isomeric substrates fit into a regular pattern, their reactivity following the order *ortho* ≃ *para* > *meta*.

The addition of gaseous nucleophiles has mechanistically informative effects, illustrated in Table 1 in the case of MeOH and of NEt_3. While both additives depress the *absolute* yields by intercepting $C_nH_5^+$ and $i\text{-}C_3H_7^+$ ions, MeOH *enhances*, while NEt_3 strongly *reduces*, the predominance of desilylation over detertbutylation.

Table 3 provides a more detailed illustration of the reactions

[1]To whom correspondence should be addressed.

Printed in Canada / Imprimé au Canada

Can. J. Chem. Downloaded from www.nrcresearchpress.com by 122.72.124.2 on 09/07/12
For personal use only.

Can. J. Chem. Downloaded from www.nrcresearchpress.com by 122.72.124.2 on 09/07/12
For personal use only.

TABLE 1. Competitive desilylation and detertbutylation by gaseous cations

Bulk gas	Additives	System composition (Torr)[a] CD_3-*t*-Bu	CH_3-Y	Absolute yields of products (G_{+M})[b] $PhCH_3$	$PhCD_3$	R-CH_3	R-CD_3
CH_4: 700		0.40	Y=*o*-*t*-Bu :0.46	0.68	0.58	R=Et: 0.21	0.18
95		0.50	*o*-*t*-Bu :0.50	1.02	0.78	0.35	0.30
700		0.39	*m*-*t*-Bu :0.47	0.40	0.57	0.19	0.13
140		0.47	*m*-*t*-Bu :0.48	0.67	0.87	0.32	0.38
700		0.46	*o*-$SiMe_3$:0.18	0.96	1.73	0.16	0.22
700		0.49	*p*-$SiMe_3$:0.55	1.19	0.39	0.28	0.18
700		0.49	*p*-$SiMe_3$:0.55	1.19	0.39	0.28	0.18
700		0.38	*m*-$SiMe_3$:0.39	0.98	0.28	0.25	0.10
130		0.44	*m*-$SiMe_3$:0.41	0.78	0.23	0.18	0.14
700	MeOH: 2.7	1.70	*m*-$SiMe_3$:1.40	0.51	0.16	0.032	0.026
700	NEt_3: 0.96	2.04	*m*-$SiMe_3$:1.49	0.49	0.52	0.054	0.065
C_3H_8: 720		0.50	*o*-*t*-Bu :0.45	0.055	0.030	R=*i*-Pr: 0.054	0.066
100		0.46	*o*-*t*-Bu :0.44	0.10	0.026	0.22	0.13
700		0.58	*m*-*t*-Bu :0.48	0.002	0.004	0.014	0.030
100		0.25	*m*-*t*-Bu :0.26	0.019	0.019	0.12	0.11
700		1.02	*o*-$SiMe_3$:1.01	1.58	0.018	1.98	0.09
100		1.04	*o*-$SiMe_3$:0.93	2.27	0.038	1.40	0.21
700		0.68	*p*-$SiMe_3$:0.53	1.87	0.018	2.05	0.11
100		0.48	*p*-$SiMe_3$:0.39	2.15	0.026	1.26	0.15
700		0.41	*m*-$SiMe_3$:0.41	1.02	0.054	2.22	0.14
130		0.79	*m*-$SiMe_3$:0.60	0.10	—	3.21	0.51
710	MeOH (2.2)	1.17	*m*-$SiMe_3$:1.13	0.26	0.003	0.48	0.024
710	NEt_3 (0.78)	1.87	*m*-$SiMe_3$:1.45	0.25	0.001	0.49	0.033

[a]All systems contained O_2 (10 Torr).
[b]See text.

TABLE 2. Relative rate of substitution of the XMe_3 group of *t*-butyl- and trimethylsilyl-toluenes by gaseous electrophiles

Substrate	Relative reactivity (k/k_r)[a] H for XMe_3	R′ for XMe_3	overall[f]
o-*t*-Butyltoluene[b]	1.0	1.0[d]	1.0
m-*t*-Butyltoluene[b]	0.6	1.2[d]	0.7
p-*t*-Butyltoluene[b]	1.0	1.0[d]	1.0
o-Trimethylsilyltoluene[b]	1.4	1.9[d]	1.5
m-Trimethylsilyltoluene[b]	3.4	2.4[d]	3.2
p-Trimethylsilyltoluene[b]	2.7	1.4[d]	2.3
o-*t*-Butyltoluene[c]	2.0	0.9[e]	1.3
m-*t*-Butyltoluene[c]	0.6	0.6[e]	0.6
p-*t*-Butyltoluene[c]	1.0	1.0[e]	1.0
o-Trimethylsilyltoluene[c]	88.0	22.0[e]	33.0
m-Trimethylsilyltoluene[c]	19.0	16.0[e]	17.0
p-Trimethylsilyltoluene[c]	113.0	24.0[e]	29.0

[a]*p*-*t*-Butyltoluene has been used as the reference substrate.
[b]In CH_4 at 700 Torr, 37°C.
[c]In C_3H_8 at 700 Torr, 37°C.
[d]R′ = Et.
[e]R′ = *i*-C_3H_7.
[f]Standard deviation ca. 10%.

promoted by the $C_nH_5^+$ attack on the TBT isomers. Consistent with the results in Table 1, the absolute yields of the proto-detertbutylation process are comparatively *lower* from *m*-TBT, while the extent of ethyldetertbutylation is approximately the same from the three isomers. The composition of the products shows that the Et group is not necessarily, nor even predominantly, found in the position formerly occupied by the *t*-Bu group, e.g. only 13% *p*-ethyltoluene is formed from *p*-TBT. Only in the case of *o*-TBT the isomerization process is significant, causing the shift of the *t*-Bu group mainly to the *para* position. The isomeric composition of the products from the replacement of the XMe_3 group of *p*-CH_3-C_6H_4-XMe_3 substrates by Et and *i*-C_3H_7 groups under different experimental conditions is reported in Table 4. The isomeric composition of cymenes from *p*-TBT and *p*-TST is considerably different and strongly dependent on the pressure, particularly in C_3H_8.

Alkylation of the substrate without loss of the XMe_3 group is significant only in the case of the TBT isomers. The orientation, illustrated in Table 5 for R = *i*-C_3H_7, reflects the operation of steric factors that hinder substitution ortho to the *t*-Bu group, as noted in earlier studies (10). The same factors are conceivably responsible for the migration of the *t*-Bu group that occurs, if to a limited extent, in the alkylation of *m*- and *p*-TBT.

Mass spectrometric evidence

The CH_4 CI spectra of TSB and of TST isomers are characterized by predominant loss of $SiMe_3^+$. In passing to milder Brønsted acids, the CI spectra of TSB, recorded in C_3H_8 and *i*-C_4H_{10} at a pressure of ca. 0.5 Torr, while significantly dependent on the source temperature, display most of the ionic intermediates whose formation is suggested by the radiolytic results. Thus, the C_3H_8 CI spectrum of TSB at 120°C is characterized by an abundant $SiMe_3^+$ peak at m/e = 73, and by its adduct with TSB, the $C_6H_5(SiMe_3)_2^+$ ion at m/e = 223. The $(M + H)^+$ adduct at m/e = 151 is detectable, albeit in low (<5%) abundances, while no isopropylated adducts could be detected.

Two typical *i*-C_4H_{10} CI spectra of TSB, recorded at 0.5 Torr at two different temperatures, are reported in Fig. 1. The *t*-butylated adduct at m/e = 207 is the base peak at 40°C,

TABLE 3. Reaction of isomeric *t*-butyltoluenes with $C_nH_5^+$ ions (n = 1,2) in methane

System composition[a] (Torr)				Absolute yields of products (G_M)[b]		
Substrate		CH_4	NMe_3	PhMe	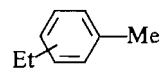	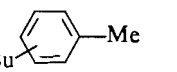
o-*t*-Butyltoluene	: 0.58	700		1.4	0.35 (*o*:35, *m*:30, *p*:35)	0.32 (*m*:32, *p*:68)
	: 0.36	700	1.0	0.46	0.12 (*o*:36, *m*:28, *p*:36)	0.07 (*m*:23, *p*:77)
	: 0.40	700	2.0	0.24	0.08 (*o*:39, *m*:27, *p*:34)	0.03 (*m*:20, *p*:80)
	: 0.50	720		1.6	0.30 (*o*:38, *m*:29, *p*:33)	0.21 (*m*:31, *p*:69)
m-*t*-Butyltoluene	: 0.47	700		0.51	0.35 (*o*:44, *m*:27, *p*:29)	0.03
p-*t*-Butyltoluene	: 0.51	700		1.0	0.33 (*o*:51, *m*:36, *p*:13)	0.03

[a]All systems contained O_2 (10 Torr).
[b]See text.

TABLE 4. Isomeric composition of alkyldetertbutylated and alkyldesilylated products

Substrate	CH_4		C_3H_8	
	700 Torr	100 Torr	700 Torr	100 Torr
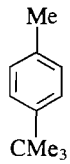	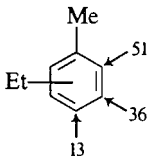	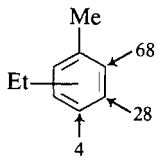	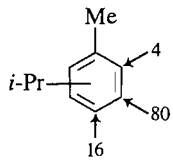	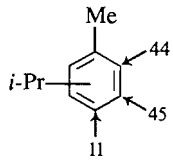
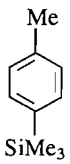			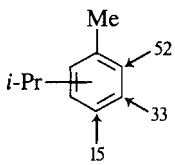	

TABLE 5. Isomeric composition of products from the isopropylation of *t*-butyltoluenes in C_3H_8 at 700 Torr[a]

o-*t*-Butyltoluene	*m*-*t*-Butyltoluene		*p*-*t*-butyltoluene	
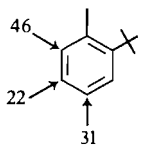	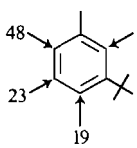	(98%)	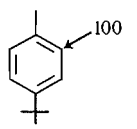	(92%)
	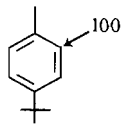	(2%)	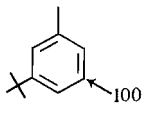	(8%)

[a]Standard deviation of the data ca. 10%.

accompanied by much lower abundances of the $(M + H)^+$ adduct at m/e = 151 and of $SiMe_3^+$. The latter becomes increasingly more significant as the source temperature is raised, becoming the most abundant peak at 100°C. The CH_4, C_3H_8, and i-C_4H_{10} CI spectra of the TST isomers are qualitatively similar to those of TSB.

As to *t*-butylbenzene (TBB) and the TBT isomers, their CI spectra have previously been reported (8, 11). The CH_4 spectra are dominated by the loss of t-Bu^+, while the protonated adduct is but a minor peak, accounting for less than 1% of the total ionization in CH_4 at 185°C, 0.5 Torr (8).

Metastable ion spectrometry

Despite the low abundances of protonated adducts in the CH_4 CI spectra of TBT and TST isomers, the study of their metastable decomposition has provided useful information. The intensity ratios of the metastable peaks from protonated TBT isomers are the same and show the same dependence on the CH_4 pressure. The transitions investigated include elimination of CH_3 from the XM_3 group (transition **I**) and of neutral toluene (transition **II**) from the $(M + H)^+$ ion.

The kinetic energy release data, i.e. the $T_{0.22}$, $T_{0.5}$, and $\langle T \rangle$ values, as well as the shape coefficient (12), are reported in Table 6, together with those of protonated TST isomers. The intensity ratios of the metastable peaks from the latter are the same, within the experimental error, irrespective of the particular isomer concerned, although the spectra are in general less reproducible than those of the TBT isomers, and as sensitive to pressure changes.

Furthermore, the low abundance of the protonated adducts from TST isomers restricts quantitative study to transition **I**. A comparison of the metastable decomposition **I** of the $(M + H)^+$ adducts from TBT isomers (ions *a*) and from TST isomers (ions *b*) reveals significant differences, both in the peaks shape and in the average kinetic energy release, $\langle T \rangle$. The metastable peaks from ions *a* (Fig. 2*a*) are not of pure Gaussian shape, being characterized by $n \neq 2$, although the difference (<0.4) is insufficient (12) to detect two competing fragmentation pathways. Their $\langle T \rangle$ values cluster around 50 meV, and increase in passing from the *meta* to the *ortho* and to the *para* isomer,

Can. J. Chem. Downloaded from www.nrcresearchpress.com by 122.72.124.2 on 09/07/12
For personal use only.

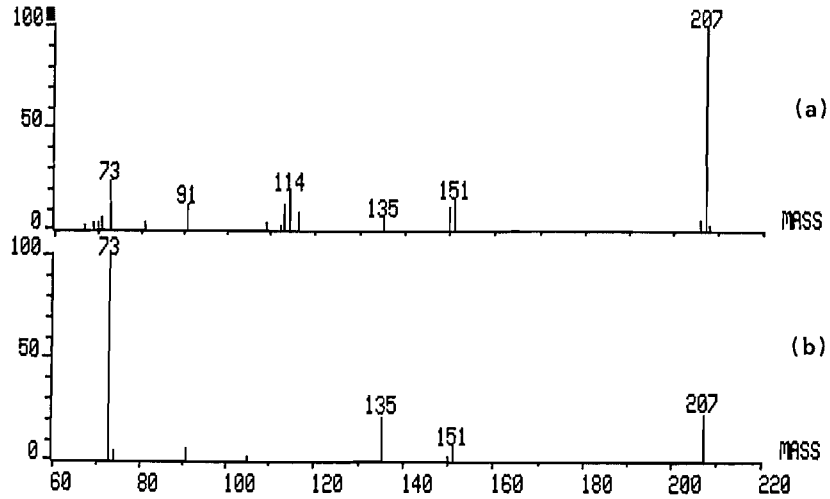

FIG. 1. Isobutane CI spectra of TSB recorded at a source temperature of 40°C (*a*) and 100°C (*b*). The spectra have been truncated below mass 60, in order to eliminate the abundant protonating reactant, the ion $t\text{-}C_4H_9^+$ at $m/e = 57$. The peak at $m/e = 91$ corresponds to the $Me_3SiOH_2^+$ adduct from the reaction of $SiMe_3^+$ with adventitious water in the ion source.

TABLE 6. Kinetic energy release in metastable decomposition of protonated *t*-butyltoluenes and trimethylsilyltoluenes[a]

Substrate	Transition	$T_{0.22}$	$\langle T \rangle$	$T_{0.5}$	n^c
o-TBT	**I**	62.5±0.7	48.8±1.4	22.6±0.7	1.61±0.14
	II	16.6±0.7	16.2±1.2	7.5±0.1	2.00±0.2
m-TBT	**I**	56.8±0.4	47.1±0.4	21.8±0.2	1.72±0.18
p-TBT	**I**	68.0±2.1	55.1±4.8	25.5±2.4	1.58±0.07
	I[b]	66 ±1.0	50.5±2.4	23.4±1.2	1.59±0.06
	II	16.8±0.8	17.0±0.4	7.8±0.4	2.3 ±0.07
o-TST	**I**	38.0±0.8	40.4±1.2	18.7±0.6	2.03±0.10
m-TST	**I**	38.0±1.0	40.4±1.2	18.5±0.7	2.10±0.05
p-TST	**I**	39.5±0.8	39.1±1.0	18.1±0.5	2.06±0.09

[a]Protonation by $C_nH_5^+$ ions in CH_4 at 0.5 Torr, 180°C. *T* values given in meV.
[b]Data concerning $p\text{-}CD_3C_6H_4\text{-}t\text{-}Bu$.
[c]For the definition and the calculation of shape parameters cf.ref.12.

which, interestingly, fails to reflect any enhanced steric compression in the $(M + H)^+$ ion from *o*-TBT.

On the other hand, ions *b* give pure Gaussian-type metastable peaks (Fig. 2*b*) and a lower $\langle T \rangle$ value, ca. 40 meV, that is the same, within experimental errors, for all TST isomers.

Fragmentation **II** of ions *a* into neutral toluene and $t\text{-}Bu^+$ is characterized by pure Gaussian-type peaks ($n = 2$) and by the same value of $\langle T \rangle$, ca. 16 meV for the isomers investigated, *o*- and *p*-TBT.

Discussion

The reactants

The primary charged reactants are obtained both in CI mass spectrometry and in the radiolytic experiments from the ionization of the bulk gas. Methane, propane and isobutane give respectively $C_nH_5^+$ ($n = 1, 2$), $i\text{-}C_3H_7^+$ and $t\text{-}C_4H_9^+$, with G_{+M} values ranging from 2.9 to 3.3 as established by extensive radiolytic and mass spectrometric studies (13, 14). The ions undergo many unreactive collisions with the parent molecules, and can be regarded as fully thermalized before encountering an aromatic molecule. The heats of formation of the gaseous ions are the following: CH_5^+:216, $C_2H_5^+$:216, $i\text{-}C_3H_7^+$:191, $t\text{-}C_4H_9^+$:166 kcal mol^{-1} (unless specified otherwise, all thermochemical data have been taken from ref. 15).

The ionic reactions and their energetics

The processes promoted by the attack of the primary ionic reactants AH^+ ($A = CH_4, C_2H_4, C_3H_6, i\text{-}C_4H_8$) on the aromatic substrates are schematically represented in Scheme 1, where *a* denotes species containing the *t*-Bu group, and *b* those containing the $SiMe_3$ group.

Fruitful mechanistic discussion presupposes reasonably detailed information on the energetics of the processes and of the species involved, especially of key ionic intermediates. While many such ions have directly been detected by CI mass spectrometry, their energetics are frequently unknown and sometimes experimentally inaccessible, e.g. in the case of the *ipso* adducts **2** and **5** (in this example, and throughout the discussion, the term *ipso* refers exclusively to species protonated, or alkylated, at the ring carbon bearing the XMe_3 group). The problem is compounded by the lack of reliable data on *neutral* organosilicon compounds, whose combustion calorimetry is notoriously unreliable (16).

The above difficulties have prompted recourse to computa-

Can. J. Chem. Downloaded from www.nrcresearchpress.com by 122.72.124.2 on 09/07/12
For personal use only.

TABLE 7. Proton affinities of substituted benzenes relative to proton affinity of benzene

Molecule	Site of protonation	PA (kcal mol^{-1})	Technique, ref.
Benzene	1	181.3	Experimental, 15
Toluene	1	181.6	SCF, STO-3G, 18
	4	189.8	Experimental, 15
t-Butylbenzene	1	182.4	SCF, STO-3G, this work
	4	193.0	Experimental, 15
Trimethylsilylbenzene	1	193.2	SCF, STO-3G, this work
	4	193.2	SCF, STO-3G, this work

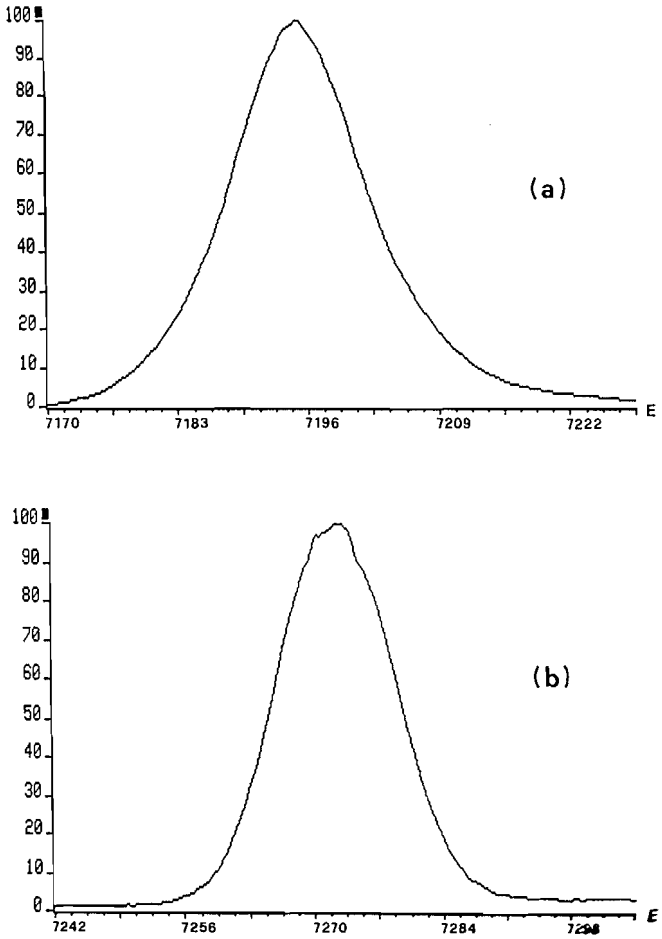

FIG. 2. Shape of the peaks from the unimolecular CH_3 loss from protonated *o*-TBT (*a*) and protonated *o*-TSB (*b*).

tional methods, whose results, suitably calibrated against experimental data and referred to a proton affinity (PA) of 181.3 kcal mol^{-1} of benzene (15), are reported in Table 7.

The computed values, in conjunction with the available experimental (15, 17) and theoretical (18) results, can be used to derive reasonably accurate estimates of the energetics of the processes of interest, reported in Table 8.

The result most significant to the present discussion is the different effect of the *t*-Bu and of the $SiMe_3$ groups on the basicity of the *ipso* position. In fact, while position 1 of TBB is less basic than position 4 by as much as 10.6 kcal mol^{-1}, positions 1 and 4 of TSB have nearly the same basicity. Another mechanistically significant result is the different stability of the **2***a* ions containing, respectively, a Me group in the meta and in the para position. As a consequence, unimolecular dissociation [3A] of the latter ion is *more endothermic* by ca. 9 kcal mol^{-1}.

As a final bonus, the STO-3G calculation allows calculation of the heat of formation of neutral TSB, whose experimentally measured value is uncertain. Combination of the experimental heat of formation of **2***a*, R = H (17), with the calculated PA value leads to a heat of formation of $PhSiMe_3$ of −26.6 kcal mol^{-1} that compares well with a value of −25 kcal mol^{-1} estimated according to the additivity approach, based on the heat of formation of $SiMe_4$ (16).

Protonation-induced detertbutylation and desilylation

The arguments planted earlier provide a satisfactory rationale for the mass spectrometric results, accounting, in particular, for the striking difference between the CI spectra obtained using isobutane, rather than methane or propane, as the reactant gas. In fact, owing to the inefficiency of collisional deactivation under CI conditions, most of the energy released in step 1 is stored in ions **1** and **2**, available to promote **1** → **2** isomerization and eventually loss of XMe_3^+ from ions **2**, a process favoured by the low pressure and the relatively high temperature of the CI ion source. This is the case of the reactions promoted by the $C_nH_5^+$ ions from CH_4, and by the i-$C_3H_7^+$ ions from C_3H_8, whose exothermicity exceeds the endothermicity of dissociation [3A], as shown in Table 8.

On the other hand, protonation by t-$C_4H_9^+$ is endothermic, or insufficiently exothermic, to allow XMe_3^+ loss from ions **2**, which accounts for the predominant formation of alkylated adducts, peculiar of the isobutane CI spectra.

The mechanistic picture is more complex in the radiolytic systems, where collisional deactivation is highly efficient, and the reactions can be assumed to obey thermal kinetics.

The paramount mechanistic feature of the radiolytic experiments, i.e. the higher rate of protolytic desilylation than of de-*t*-butylation, can reflect, in principle, operation of different factors, including: (*i*) the higher protonation rate of silylated substrates, (*ii*) the faster removal of $SiMe_3^+$ from **2***b* than of t-Bu^+ from **2***a* ions, (*iii*) the higher steady-state concentration of the *ipso*-protonated ions **2***b* than of **2***a*.

From the current theories of ion–molecule interactions, e.g. the ADO model, and from the kinetic data available on exothermic proton transfer reactions (19), the rate of protonation of silylated and *t*-butylated substrates is expected to be very close, and any difference largely inadequate to account for the higher rate of desilylation, particularly predominant in the C_3H_8 systems.

Factor (*ii*) can safely be discounted in the case of desilylation, that has been shown (5, 6) to be a fast process promoted by

Can. J. Chem. Downloaded from www.nrcresearchpress.com by 122.72.124.2 on 09/07/12
For personal use only.

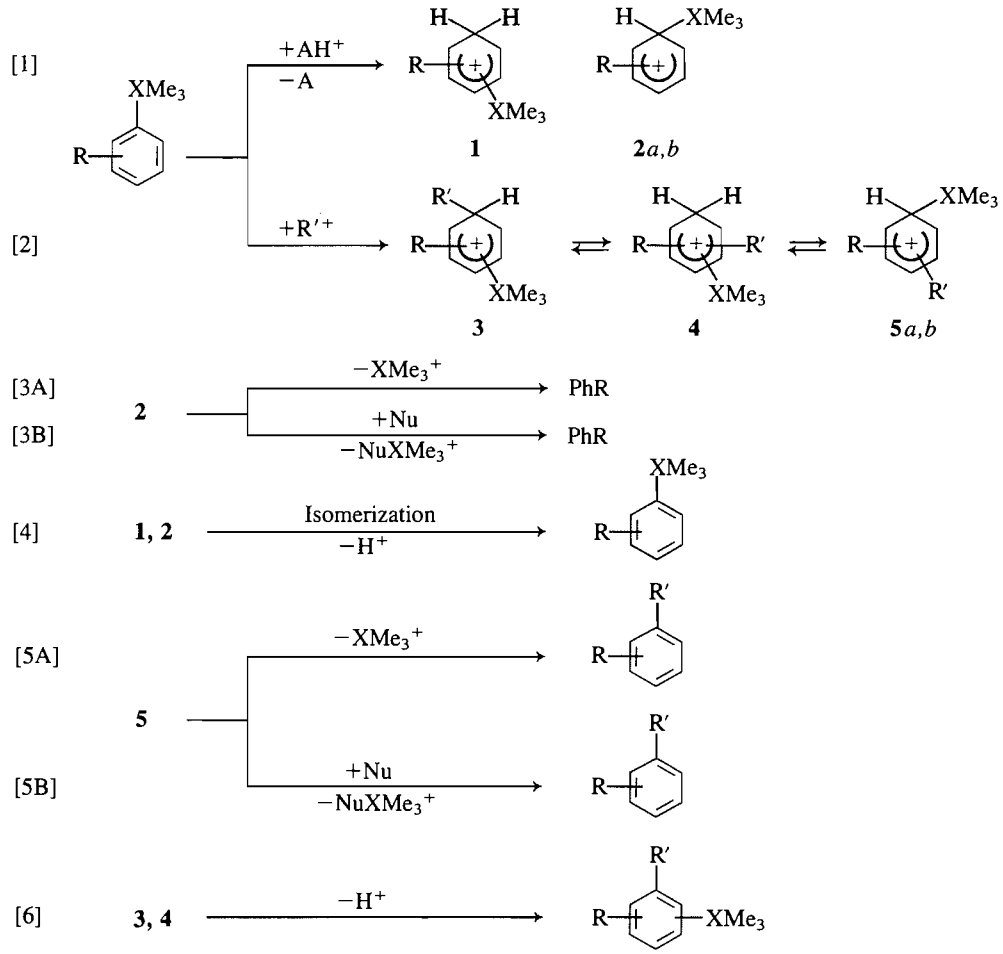

SCHEME 1. Simplified scheme of the reactions promoted by the attack of AH^+ ions on the aromatic substrates.

oxygenated nucleophiles, either deliberately added, or formed in the radiolysis (H_2O, CH_2O, etc.), while gaseous NEt_3 promotes deprotonation, rather than desilylation of **2***b*. Such findings are consistent with the present results, in particular with the contrasting effects of added MeOH and NEt_3 on the desilylation rate.

The same conclusion can reasonably be extended to ions **2***a*, whose dealkylation rate *increases* in passing from *m*- to *p*-TBT. This trend is hardly consistent with a kinetically significant role of the dealkylation step, either occurring unimolecularly [3A] or promoted by nucleophiles [3B]. In fact, the activation energy of [3A] can be regarded as the sum of the two terms, the endothermicity of the dissociation and the activation energy of the reverse reaction, i.e. t-Bu^+ addition to toluene. Combination of such terms leads to a *lower* activation barrier for the unimolecular dealkylation of ion **2***a* containing a Me group in the position *meta*, rather than *para*, to the *ipso* carbon. In fact, the endothermicity of [3A] is higher by ca. 9 kcal mol^{-1} when ion **2***a* contains a Me group in the *para*, rather than in the *meta* position, while the activation energy of the reverse process, *t*-butylation of toluene, changes only by ca. 2 kcal mol^{-1} in passing from the *meta* to *para* positions, as deducted from intramolecular selectivity data (20). The role of the bimolecular process [3B], even in low-pressure systems, is independently supported by CI studies (9).

The same trend is expected for process [3B], e.g. t-Bu^+ transfer to H_2O from **2***a* ions is energetically allowed only when the Me group is in the *meta* position (Table 8). In summary, the overall dealkylation rate, if assumed to depend on steps [3A] or [3B], should *decrease* in passing from *m*-TBT to the *ortho* and *para* isomers, which conflicts with the experimental trend.

In passing, it is interesting to note that metastable loss of t-Bu^+ from protonated *o*-TBT does not involve a larger kinetic energy release than from protonated *p*-TBT, despite the large steric strain due to the *ortho* relation of the two alkyl groups (21). This is hardly surprising, in view of the intricate way the Me and *t*-Bu groups are entangled in *o*-TBT, as shown by conformational studies in solution (22). Under such conditions, according to the so-called "dynamic gearing" effect, the *t*-Bu group, receding from the ring plane as a result of *ipso* protonation and in the way to leave as a free t-Bu^+ ion, can be expected to possess, if anything, excess vibrational and especially rotational, rather than translational, energy.

The role of ipso *protonation*

Having disposed of other alternatives, it is appropriate to inquire whether the observed reactivity pattern reflects the abundance of the *ipso* adduct **2** in the population of interconverting (23*a*)[2] isomeric ions formed from the attack of AH^+, e.g.

[2]Low barriers to intraannular H^+ shifts in gaseous naphtalenium ions have recently been calculated by Filger and Grützmacher (23*b*) despite the fact that their MINDO approach notoriously overestimates the energy of the correspondent transition states.

Can. J. Chem. Downloaded from www.nrcresearchpress.com by 122.72.124.2 on 09/07/12
For personal use only.

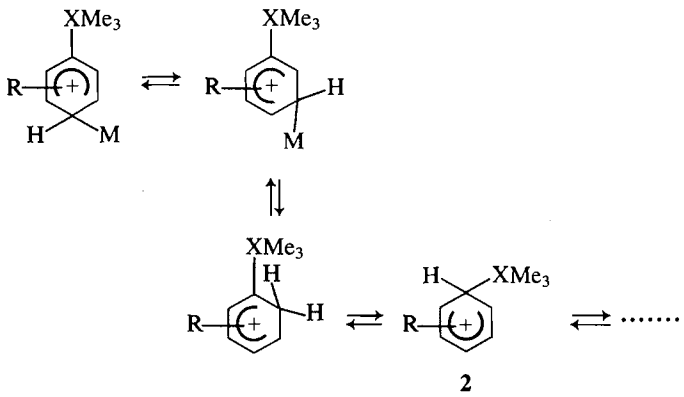

2

Clearly, a major role is played by the basicity of the *ipso* carbon relative to those of the other ring positions. If the PA of the *ipso* carbon is comparatively low, formation of **2** is hampered by unfavourable energetics, and its isomerization into more stable arenium ions is accelerated, thus reducing its steady-state concentration, hence the rate of XMe_3^+ removal via [3B]. A mechanistic model based on the different relative basicity of the *ipso* position of **2***a* and **2***b* accounts satisfactorily for the major experimental features. The SCF STO-3G results show, in the first place, that *t*-Bu group, unlike $SiMe_3$, *selectively* depresses the PA of the *ipso* position, which provides a straightforward explanation of the lower efficiency of protodetertbutylation. Secondly, the kinetic consequences of the (modest) stability differences among isomeric arenium ions can be expected to be particularly relevant when the latter are formed with a limited excess of internal energy. This accounts for the enhanced desilylation/detertbutylation ratio when the reactions are promoted by $i\text{-}C_3H_7^+$, a much milder acid than $C_nH_5^+$, as apparent from Table 8. Finally, the relative detertbutylation rate of TBT isomers, that increases in the order *meta* < *para* ≃ *ortho*, finds a reasonable explanation.

In fact, the basicity of the *ipso* position of *m*-TBT is not appreciably enhanced by the Me group, which instead increases the *ipso* PA of *o*- and *p*-TBT, hence the stability of the corresponding **2***a* ions. This accounts for the lowest relative rate of dealkylation of *m*-TBT. While the stabilizing effect of the Me group is comparable in the **2***a* ions from *p*- and *o*-TBT, formation of the *ipso*-protonated adduct from the latter is expected to be accelerated by the relief of the steric compression of coplanar Me and *t*-Bu groups (22).

The preceding discussion is based on the assumption that energetic factors, concerning in particular the relative stability of the protomers from reaction [1], control the kinetics of their isomerization, which is mechanistically relevant. In fact, since initial protonation largely occurs at sites other than the *ipso* position, the rate of formation of **2**, hence of XMe_3^+ loss, depends on the barriers to H^+ migration to the *ipso* carbon. Admittedly, purely energetics arguments bear only on the endothermicity of the process, whose *total* barrier includes an additional, unknown term, that corresponds to the activation energy of the inverse reaction. Accurate evaluation of the latter term is extremely difficult, especially in the case of *ipso*-protonated species. However, the published data show that the activation energies proper, i.e. not arising from unfavourable energetics, for intraannular H^+ migration in gaseous arenium ions are generally remarkably low (23), and their differences can hardly be expected to affect the relative heights of the total barriers predictable on energetic grounds. Thus, the total barrier to the significantly endothermic H^+ shift to the *ipso* carbon of $PhCMe_3$ can reasonably be estimated to be higher than the barrier to the thermoneutral, but otherwise analogous, process in protonated $PhSiMe_3$. The approximate character of such interpretation seems tolerable if restricted to purely comparative purposes, especially since in this framework the experimental observations, including the relative dealkylation rates of TBT isomers, find a satisfactory accommodation.

TABLE 8. Energies of relevant ionic processes[a]

AH^+	Product	R	$\Delta H°$ (kcal mol^{-1})
	[1] $AH^+ + R\text{-}C_6H_4XMe_3 \rightarrow A + \mathbf{2}$		
CH_5^+	**2***a*	H	−49.3
	2*a*	*p*-Me	−58.9
	2*b*	H	−61.2
	2*b*	*p*-Me	−69.7
$C_2H_5^+$	**2***a*	H	−19.8
	2*a*	*p*-Me	−28.3
	2*b*	H	−30.6
	2*b*	*p*-Me	−39.1
$i\text{-}C_3H_7^+$	**2***a*	H	−2.8
	2*a*	*p*-Me	−11.4
	2*b*	H	−13.6
	2*b*	*p*-Me	−22.2
$t\text{-}C_4H_9^+$	**2***a*	H	+13.5
	2*a*	*p*-Me	+5.0
	2*b*	H	+2.7
	2*b*	*p*-Me	−5.8

Reactant	R	$\Delta H°$ (kcal mol^{-1})
	[3A] $\mathbf{2} \rightarrow PhR + XMe_3^+$	
2*a*	H	+7.4
2*a*	*p*-Me	+16.5
2*a*	*m*-Me	+7.4
2*b*	H	+23.9[b]
2*b*	*p*-Me	+26.6[b]

Reactant	R	Nu	$\Delta H°$ (kcal mol^{-1})
	[3B] $\mathbf{2} + Nu \rightarrow PhR + NuXMe_3^+$		
2*a*	*p*-Me	H_2O	+5.5
2*a*	*m*-Me	H_2O	−3.6
2*a*	*p*-Me	MeOH	−6.5
2*b*	*p*-Me	H_2O	−6.5
2*b*	*p*-Me	MeOH	−12.6[b]

[a] $\Delta H°$ values based on the STO-3G results from this work and from ref. 18, combined with the available experimental data, refs. 15 and 17.

[b] Calculated directly from the thermochemical data from ref. 17.

Alkylation-promoted detertbutylation and desilylation

The composition of the products, where the alkyl group R′ is not exclusively, nor predominantly, bound to the carbon formerly bearing the XMe_3 group, suggests initial attack to any activated ring position, followed by H^+, and possibly R'^+ shifts, eventually leading to the *ipso* protonated ions **5**, that undergo XMe_3^+ removal via process [5B]. While there are close similarities with the scheme suggested for protolytic reactions, the situation is more complicated in several respects. First, the

Can. J. Chem. Downloaded from www.nrcresearchpress.com by 122.72.124.2 on 09/07/12
For personal use only.

Can. J. Chem. Downloaded from www.nrcresearchpress.com by 122.72.124.2 on 09/07/12
For personal use only.

exothermicity of the alkylation is generally higher than of protonation, which enhances the rearrangement of the primary arenium ions and tends to level the reactivity of different substrates. Secondly, the stability of ions **5** reflects the cumulative effects of *two* substituents, the Me and the R′ groups, whose interplay depends on their respective positions.

Finally, the influence of isomerization process (4) and of the alkylation process (6) must be taken into account. In view of the complex nature of the problem, the discussion is limited to a few salient aspects.

The exothermic (24) addition of $i\text{-}C_3H_7^+$ to *p*-TST in C_3H_8 at 700 Torr is invariably followed by desilylation, yielding a mixture of cymenes whose composition, illustrated in Table 4, reflects the selectivity of the initial electrophilic attack. Clearly, H^+ shifts to the *ipso* position, whose basicity is not selectivity depressed by the $SiMe_3$ group, are energetically accessible to the arenium ions from [2], irrespective of the position of the $i\text{-}C_3H_7$ group, i.e. independently of the stabilization of **5***b* provided by R′ when bound to the *ortho* positions.

Comparison with the comparably exothermic addition of $i\text{-}C_3H_7^+$ to *p*-TBT, occurring under the same conditions, is informative. Owing to the selective depression by the *t*-Bu group of the basicity of the *ipso* carbon, its protonation via H^+ intramolecular shifts is energetically allowed only by the combined activating effects of *two* substituents, i.e. the *ortho* $i\text{-}C_3H_7$ and the *para* Me groups. This accounts for the predominant (80%) formation of *m*-cymene (Table 4). When alkylation occurs *meta* to the *ipso* carbon, the basicity of the latter is not appreciably enhanced by the $i\text{-}C_3H_7$ group, which makes formation of **5***a* energetically unfavourable. This depresses the rate of detertbutylation [5], allowing alkylation [6] to occur, but, significantly, only from the *meta* to the *t*-Bu group (Table 4). Such interpretation is supported by the pressure dependence of the products composition. At 100 Torr, collisional deactivation is less efficient, and the higher internal energy of the arenium ions from the exothermic addition (2) makes formation of **5***a*, and subsequent detertbutylation, much less dependent on the specific position attacked by $i\text{-}C_3H_7^+$. As a consequence, loss of $t\text{-}Bu^+$ becomes predominant and, significantly, the relative yield of *o*-cymene undergoes a tenfold increase with respect to that measured at 700 Torr.

The same considerations apply to alkylation by $C_2H_5^+$ in methane, that displays the same typical composition of the detertbutylation products, and the same dependence on the CH_4 pressure, although the higher exothermicity of ethylation tends to depress the selectivity of the process with respect to isopropylation.

Conclusions

The salient result of the present study is the higher efficiency of desilylation than of detertbutylation of aromatic substrates following the attack of charged electrophiles. Such a finding extends to the gas phase a trend well established in solution, where facile aromatic desilylation is exploited as a synthetic tool (2).

Several lines of evidence identify the key difference between $SiMe_3$ and the *t*-Bu groups with their different effects on the basicity of the *ipso* carbon, hence on the stability of **2** and **2***b* relative to the respective isomers protonated at other positions.

Such a difference can be traced, in part, to electronic factors, since silicon, less electronegative than carbon, has a significant inductive effect and the $SiMe_3$ group is known to stabilize a β positive center, hence the mesomeric structures of the *ipso*

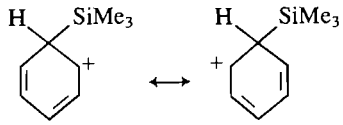

arenium ion **2***b*. The present study suggests operation of an additional steric factor that stabilizes **2***b* with respect to **2***a*. In the course of the SCF STO-3G calculations it has been noted that the aromatic ring of **2***a* (R = H) cannot be assumed to be rigorously planar, probably due to the significant steric repulsion between the bulky *t*-Bu substituent and the aromatic π system, that causes a destabilizing deformation of the latter. The greater length of the C—Si bond, 1.88 Å vs. 1.54 Å of the C—C bond, reduces the effective bulk of $SiMe_3$, hence the steric destabilization of **2***b*, which accounts, in part, for the fact that the PA of the *ipso* carbon bearing the $SiMe_3$ substituent is very close to the PA of the para position.

Experimental

Materials

The gases, CH_4, C_3H_8, $i\text{-}C_4H_{10}$, O_2, NMe_3, were obtained from Matheson Gas Products Inc., with a stated purity of at least 99.9 mol%, and were used without further purification. The ethyltoluenes and cymenes used as substrates or chromatographic standards were obtained from commercial sources. The TBT and TST isomers were prepared from the corresponding Grignard reagents, obtained from the appropriate bromo- or iodo-toluenes, and *t*-butyl bromide or trimethylsilyl methanesulphonate. The analogous reaction involving *p*-bromo-*t*-butylbenzene and CD_3I was used to prepare labeled *p*-TBT, used as a reference competitive substrate in the radiolytic reactions. The crude products from the synthesis were purified by preparative GC, using a 4-m column, packed with Carbowax 20M (10% w/w) and KOH (2% w/w) on Supelcoport, repeating the operation until analytical GC of the purified samples failed to detect traces of unwanted impurities, in particular of PhMe. The identity of the products was confirmed by NMR and mass spectrometry.

Radiolytic reactions

The gaseous samples were prepared using a greaseless vacuum line according to established procedures (25), by introducing the desired amounts of the reactants into carefully evacuated and outgassed 250-mL Pyrex vassels, equipped with fragile tips, that were cooled to −196°C and sealed-off. After thorough mixing of the reactants, the vessels were irradiated at 37°C to a total dose of 1.8×10^4 Gy, at a dose rate of ca. 6×10^3 Gy h^{-1}, in a 220 Gammacell from Nuclear Canada Ltd. The irradiated vessels were cooled to LN_2 temperature, their break-seal opened, and the contents, dissolved into ethyl acetate, analyzed by GC, using Perkin-Elmer Sigma 1 and Sigma 3 and Hewlett-Packard 5700 A chromatographs, equipped with FID and PID detectors. The products were identified by comparison of their capacity factors with those of authentic standards, using the following columns: (*i*) a 2-m long glass column, packed with SP 1000 (1% w/w) on Carbopack C, (*ii*) a 2-m long stainless steel column, packed with SP 2100 silicone fluid, deactivated with Carbowax 20 M. The yields of the products were deduced from the areas of the corresponding elution peaks, corrected for the individual response of the detector used, employing the internal-standard calibration method. In most cases, the identity of the products was confirmed by GC/MS, using a quadrupole HP 5985 A spectrometer and a HP 5970B mass selective GC detector from Hewlett-Packard. The same technique was used to measure the relative yields of $PhCH_3$ and $PhCD_3$ from the competitive reactions where methyl-d_3 *p*-TBT was used as the reference substrate.

CI and MIKE spectra

The CI spectra were recorded with the Hewlett-Packard 5985A quadrupole instrument, or a ZAB-2F magnetic spectrometer from VG-Micromass Ltd. Typical operating conditions of the latter instrument were as follows: reactant gas pressure 0.3 Torr, emission current

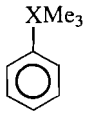

I*a,b*

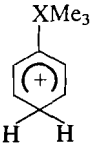

II*a,b*

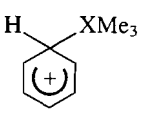

III*a,b*

1 mA, electron energy 50 eV, repeller potential 0 V, source temperature 180°C. The MIKE spectra were recorded as the average of 200 to 300 consecutive scans, at an energy resolution of 8 000 with a main-beam width of 1 eV.

Ab initio calculations

Standard quantum mechanical calculations were performed on the following species where *a* denotes X = C, *b* X = Si. The calculations were carried out, using a VM-CMS version of the Gaussian 80 package of programs (26), on an IBM 3090 computer. Geometry optimizations were carried out at the STO-3G level (27), and, limited to species *a*, single points were computed at the 4-31G level (28). Geometrical structures were considered to be optimized when the components of the gradient were less than 4.5×10^{-4} hartree/bohr, or hartree/rad^{-1}. The optimization at the SCF STO-3G level was carried out within the following constraints: (*i*) aromatic ring was assumed to be planar; (*ii*) C_s symmetry was assumed, with a plane perpendicular to the aromatic ring passing through the C_6—C_1—X—C_9 atoms; (*iii*) all C—H distances in the XMe_3 groups were considered to be identical.

Within the above constraints, stationary points were found corresponding to all species except **III***a* and **III***b*, that were not stationary on the energy surface. Analysis of the gradient vectors showed that for the latter species it is not correct to assume that the aromatic ring is rigorously planar. Single-point STO-3G calculations were carried out in correspondence of such corrugate situations, whose results showed that deformation of the aromatic ring has a great influence on gradient vectors, but does not appreciably affect total energies ($\Delta E < 10^{-3}$ au). Owing to the exceedingly high cost of the calculations required to achieve stationary points, such approximation was regarded as tolerable, and no further investigations of these regions of the potential energy surfaces were performed.

Acknowledgements

The authors are indebted to the Italian Ministero della Pubblica Istruzione and to National Research Council (CNR) for financial support.

1. F. S. Kipping and L. L. Loyd. J. Chem. Soc. 449 (1901).
2. C. Eaborn. J. Organomet. Chem. **100**, 43 (1975).
3. W. P. Weber. Silicon reagents in organic synthesis. Springer-Verlag, Berlin, 1983. p. 114 and references therein.
4. F. Cacace. Structure/reactivity and thermochemistry of ions. *Edited by* P. Ausloos and S. G. Lias. D. Riedel, Dordrecht. 1987. p. 467.
5. S. Fornarini. J. Org. Chem. **53**, 1314 (1988).
6. F. Cacace, M. E. Crestoni, S. Fornarini, and R. Gabrielli. Int. J. Mass Spectrom. Ion Processes, **84**, 17 (1988).
7. A. J. Harrison, P.-H. Lin and H.-W. Leung. Adv. Mass Spectrom. **7**, 1394 (1978).
8. M. S. B. Munson and F. H. Field. J. Am. Chem. Soc. **89**, 1047 (1979).
9. D. K. Sen Sharma, S. Ikuta, and P. Kebarle. Can. J. Chem. **60**, 2325 (1982).
10. F. Cacace, G. Ciranni, and P. Giacomello. J. Am. Chem. Soc. **103**, 1513 (1981).
11. J. A. Herman and A. G. Harrison. Org. Mass Spectrom. **16**, 423 (1981).
12. J. L. Holmes and J. K. Terlow. Org. Mass Spectrom. **15**, 383 (1981).
13. P. Ausloos, S. G. Lias, and R. Gorden, Jr. J. Chem. Phys. **39**, 3941 (1963).
14. S. G. Lias, R. E. Rebbert, and P. Ausloos. J. Am. Chem. Soc. **92**, 6430 (1970).
15. S. G. Lias, J. F. Liebman, and R. D. Levin. J. Phys. Chem. Ref. Data, **13**, 695 (1984).
16. J. D. Cox and G. Pilcher. Thermochemistry of organic and organometallic compounds. Academic Press, London. 1970.
17. A. C. M. Wojtyniak and J. A. Stone. Int. J. Mass Spectrom. Ion Processes, **71**, 59 (1986).
18. J. L. Devlin, III, J. F. Wolf, R. W. Taft, and W. J. Hehre. J. Am. Chem. Soc. **97**, 1990 (1975).
19. D. H. Aue and M. T. Bowers. Gas phase ion chemistry. Vol. 2. *Edited by* M. T. Bowers. Academic Press, New York. 1979. p. 2.
20. F. Cacace and P. Giacomello. J. Am. Chem. Soc. **95**, 5851 (1973).
21. H. C. Brown and L. Domash. J. Am. Chem. Soc. **78**, 5384 (1956).
22. H. Pearson. J. Chem. Soc. Chem. Commun. 912 (1975) and references therein.
23. (*a*) R. S. Mason, M. T. Fernandez, and K. R. Jennings. J. Chem. Soc. Faraday Trans. 2, **83**, 159 (1987) and references therein; (*b*) U. Filger and H.-F. Grützmacher. Int. J. Mass Spectrom. Ion Processes, **83**, 93 (1988); **83**, 111 (1988).
24. M. Attinà, F. Cacace, G. Ciranni, and P. Giacomello. J. Am. Chem. Soc. **99**, 2611 (1977).
25. F. Cacace. Acc. Chem. Res. **21**, 215 (1988).
26. J. S. Brinkley, R. A. Whiteside, R. Krishnan, R. Seeger, D. J. De Frees, H. B. Schlegel, S. Topiol, L. R. Rahn, and J. A. Pople. QCPE, **13**, 406 (1981).
27. W. J. Hehre, R. F. Stewart, and J. A. Pople. J. Chem. Phys. **51**, 2657 (1969).
28. R. Ditchfield, W. J. Hehre, and J. A. Pople. J. Chem. Phys. **54**, 724 (1971).

Can. J. Chem. Downloaded from www.nrcresearchpress.com by 122.72.124.2 on 09/07/12
For personal use only.

The chemistry of thujone. XII.[1] The synthesis of pyrethroid analogues via chiral cyclopropanation

ADAM BECALSKI, WILLIAM R. CULLEN, MICHAEL D. FRYZUK, GEORG HERB, BRIAN R. JAMES, JAMES P. KUTNEY,[2] KRYSTYNA PIOTROWSKA, AND DIANNE TAPIOLAS

Department of Chemistry, 2036 Main Mall, University of British Columbia, Vancouver, B.C., Canada V6T 1Y6

Received June 1, 1988

ADAM BECALSKI, WILLIAM R. CULLEN, MICHAEL D. FRYZUK, GEORG HERB, BRIAN R. JAMES, JAMES P. KUTNEY, KRYSTYNA PIOTROWSKA, and DIANNE TAPIOLAS. Can. J. Chem. **66**, 3108 (1988).

An extensive study involving achiral and chiral cyclopropanation of various isoprenoid units derived from the monoterpene thujone is presented. Carbenoid intermediates generated from ethyl and L-menthyl diazoacetates and various achiral and chiral copper catalysts are employed to achieve the desired cyclopropanation reaction. It is shown that high levels of enantiomeric excess can be achieved, particularly when L-menthyl diazoacetate and a chiral catalyst are employed. The resultant products are then converted to pyrethroid-like analogues.

ADAM BECALSKI, WILLIAM R. CULLEN, MICHAEL D. FRYZUK, GEORG HERB, BRIAN R. JAMES, JAMES P. KUTNEY, KRYSTYNA PIOTROWSKA et DIANNE TAPIOLAS. Can. J. Chem. **66**, 3108 (1988).

On présente une étude approfondie sur la cyclopropanation chirale et achirale de diverses unités isopropénoïdes provenant de la thujone. Dans le but de réaliser les cyclopropanations désirées, on a utilisé des carbénoïdes intermédiaires générés à partir des diazoacétates d'éthyle et de L-menthyle, en présence de divers catalyseurs chiraux et achiraux à base de cuivre. On montre qu'il est possible d'obtenir un grand excès d'énantiomère, particulièrement lorsqu'on utilise le diazoacétate de L-menthyle en présence d'un catalyseur achiral. On a réalisé la transformation des produits obtenus en dérivés du type pyréthroïde.

[Traduit par la revue]

Introduction

Pyrethroid-type insecticides comprise a highly important family of compounds with a wide diversity of application in the agricultural industry. Enormous efforts in various laboratories have provided a wide variety of structure–function relationships, and studies continue to potentiate activity while maintaining the well-established features of low mammalian toxicity. In the previous publication (2) in this series, we described utilization of thujone (**1**) in the synthesis of racemic analogs of pyrethroid insecticides. As biological activity of pyrethroid insecticides is closely related to the chirality of the cyclopropane ring (3), we set out to prepare optically active analogs to possibly maximize their insecticidal potency and to compare these data with the biological activity of the corresponding racemic material available from the earlier study.

Scheme 1 summarizes the overall sequence employed. The starting material, the methyl ester of *E*-α-thujaketonic acid (**4**), was synthesized with modification of the earlier described procedure (2). Via previously established methodology, α-thujaketonic acid **2**, obtained by the permanganate oxidation of **1**, was converted to the isopropenyl derivative **3** by Wittig reaction using methyltriphenylphosphonium bromide and potassium *tert*-butoxide in tetrahydrofuran. Conversion of **3** to **4** was achieved by thermal rearrangement of **3** to *E*-β-thujaketonic acid followed by esterification by CH_2N_2.

It had been shown earlier (2) that selective cyclopropanation of **4**, employing ethyl diazoacetate and copper sulfate, could be achieved with exclusive attack of the generated carbene occurring at the more reactive non-conjugated double bond. To achieve a potential entry into the chiral series, two diazoacetic esters, namely, ethyl diazoacetate and L-menthyl diazoacetate, prepared according to the literature procedure (4, 5) were employed along with five different copper catalysts. Two of these catalysts (A, B) were achiral while three continued a chiral ligand (C, D, E) (Scheme 2).

Cyclopropanation of the double bond by carbenoid addition is known to be promoted by catalysts containing various metals (6–9), e.g., ruthenium, palladium, rhodium, cobalt. We chose copper catalysts since they give high yields (10–12), and are inexpensive. Furthermore, Aratani *et al.* (10, 11, 13) had demonstrated successful chiral cyclopropanation of olefinic systems with high enantiomeric excess in the resultant cyclopropane analogues. In particular, catalysts C and D (Scheme 2) seemed well suited for our study.

Catalysts C and D have opposite configurations at the asymmetric centre and have different carbon chain lengths in the aryl ether group. Catalyst D with the butoxyaryl ether moiety is a free flowing powder while catalyst C with a C_8 unit is a very sticky gum and more difficult to handle.

Catalyst E, which gave excellent optical yields during cyclopropanation of styrene (14), was also included in the study for purposes of comparison.

Catalysts C and E were prepared according to the published literature procedures (13, 15). Catalyst D was obtained as a gift from Dr. Aratani while catalyst B was synthesized by condensation of salicylaldehyde with 2-aminoethanol and subsequent treatment of the resulting imine with NaOH and copper acetate.

The results of the various cyclopropanation experiments employing **4** as substrate, under varying conditions of temperature, solvent, and catalyst, are summarized in Table 1.

The ratio of the *trans* (see **6***a* and **6***b*) to *cis* isomers (**5***a* and **5***b*) was determined by hplc using a reverse phase C_{18} silica column and a mixture of water/methanol (10:90) as an eluent. In the case of experiment 5, gas–liquid chromatography was employed for analysis of the reaction products.

Determination of enantiomeric excess (e.e.) was done by ^1H nmr using a europium shift reagent. To illustrate the methodology, some detail of the procedure for the calculation of e.e. in the case of the diesters **5***a* and **6***a* and the keto-esters **11***a* and **12***a* is presented. In each case 10 mg of compound was dissolved in $CDCl_3$ and shift reagent was added portionwise (~10–15 mg) until optimal separation of the relevant signals of the enantiomers present was observed in the nmr spectrum. It

[1]For Part XI, see ref. 1.

[2]Author to whom correspondence may be addressed.

Can. J. Chem. Downloaded from www.nrcresearchpress.com by 122.72.124.2 on 09/07/12
For personal use only.

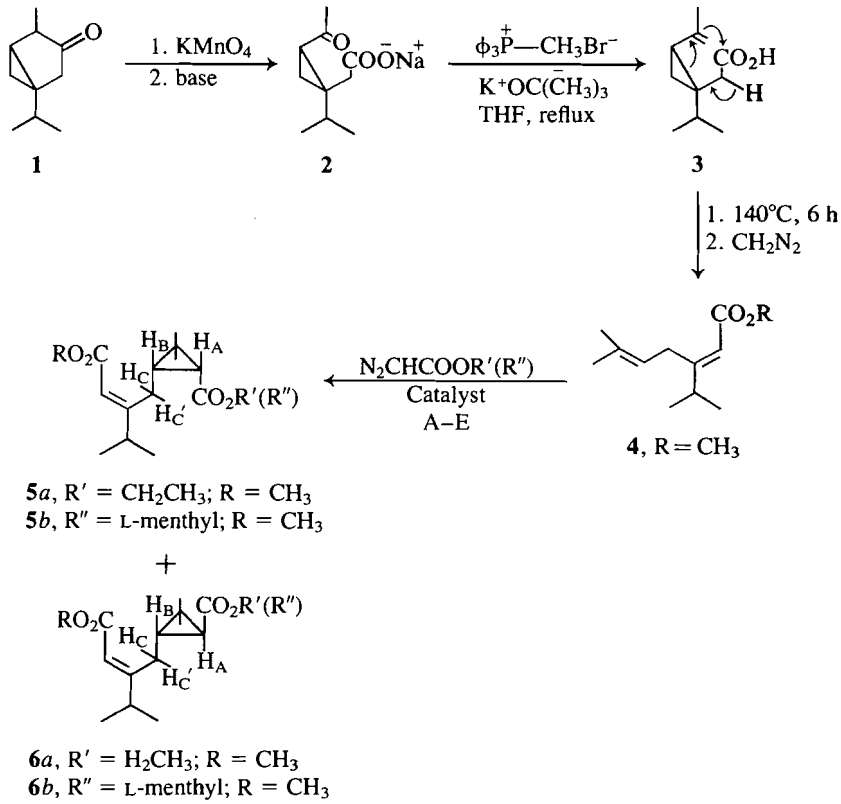

SCHEME 1

was shown (see Table 2) that different proton signals were shifted within the spectra of the different compounds, but these could be unambiguously analyzed for determination of enantiomeric excess present in the various reaction product mixtures.

As seen from Table 1, chemical yields vary only slightly in spite of considerable differences in the chemical structure of the catalysts.

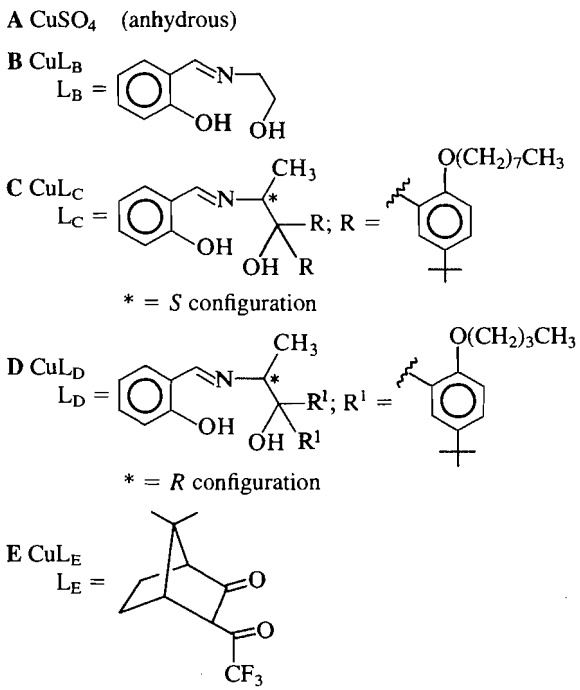

SCHEME 2. Catalysts employed in cyclopropanation reaction.

In the case of achiral catalyst B, formation of the *trans* isomer **6** is favored over the *cis* isomer **5**. When the chiral catalysts C and D are employed, the *cis*/*trans* ratio of products is influenced by the ratio of ethyl diazoacetate to olefin (see experiments 1–4, Table 1) while with catalyst E, the ratio of reacting diazo compound and olefin appears to play no dominant role (see experiments 6 and 7, Table 1).

With respect to enantiomeric excess (e.e.) in *both* the *cis* and *trans* series obtained from chiral cyclopropanation of **4** with catalysts C and D, an excess of diazo ester is detrimental. For example, comparison of the results obtained with catalyst D (experiments 1 and 2, Table 1) reveals that a much higher e.e. value is obtained (78% versus 13.5% in the *cis* series) when a *low* ratio of diazo compound to substrate olefin is employed. A similar result is observed with catalyst C (experiments 3 and 4, Table 1). However, with catalyst E this effect is less pronounced.

It was reported (9) that use of "bulky" diazoacetates instead of alkyl diazoacetate in the cyclopropanation reaction results in increased optical yields of products.

Catalytic methods for metal carbene transformations have been extensively studied in various laboratories and excellent recent reviews (16, 17) are available. The mechanism of cyclopropanation using such methods has been presented with different models depending on the nature of the olefin and catalysts employed. Our results can be well explained by using the model of the cyclopropanation reaction as proposed by Aratani (18). Scheme 3 illustrates such a reaction mediated by catalyst C. The structure of the actual catalyst responsible for the asymmetric induction is proposed as a mononuclear cuprous complex such as **7**, in which copper carries a tetrahedral configuration and one of the four coordination sites is left vacant. Alkyl diazoacetate will attack the vacant site of **7** from the less hindered side (back side of the plane) to give the

Can. J. Chem. Downloaded from www.nrcresearchpress.com by 122.72.124.2 on 09/07/12
For personal use only.

TABLE 1. Results of cyclopropanation experiments employing **4** as substrate

Expt. no.	Catalyst used	Catalyst configuration	Reaction temperature (°C)	Chemical yield (%)	Ratio[c] *trans*/*cis* **6**/**5**	Enantiomeric/diastereomeric[e] excess		Molar ratio		
						cis	*trans*	$N_2CHCOOOR$[g] substrate	Substrate catalyst	$N_2CHCOOOR$ catalyst
1	D	*R*	40[b]	88	1.78	13.5	3	18.7[f]	50	
2	D	*R*	40[a]	70	0.60	78	17	0.1		50
3	C	*S*	40[b]	86	1.53	25	9	22[f]	33	
4	C	*S*	40[a]	71	0.59	80	29	0.1		50
5	C	*S*	35[b]	70	0.79[d]	>95	>95	0.1		50
6	E		40[b]	68	1.63	<2	<2	13[f]	50	
7	E		40[a]	72	1.80	11	12	0.1		50
8	A		100[a]	72.5	2.05	n/a	n/a	7.9[f]	2.7	
9	B		Reflux[b]	69	1.86	n/a	n/a	5.5[f]	4.5	
10	B		100[a]	73	1.74	n/a	n/a	6.6[f]	23	
11	B		40[b]	90	1.95	n/a	n/a	23[f]	4.5	

[a]Neat substrate employed.
[b]Cyclohexane as solvent employed.
[c]Determined by hplc*.
[d]Determined by gc.
[e]Determined by nmr employing a chiral shift reagent**.
[f]$N_2CHCOOEt$ was added until tlc showed total consumption of starting material.
[g]R = Et except Expt. no. 5 where R = L-menthyl.
*Waters Radial Pak (8 MM)C_{18}, 10% H_2O in MeOH, flow rate 2 mL/min., R.T. of **6***a*: 3.5 min, **5***a*: 4 min.
** Tris[3-(heptafluoropropylhydroxymethylene)-(+)-camphorato] europium.
Catalysts C and E give products which are dextrorotatory; Catalyst D gives levorotatory products.

TABLE 2. Effect of europium shift reagents on selected ^1H nmr signals

Compound no.	Groups in which ^1H nmr signals were used for determination of e.e.	Chemical shift before addition of the shift reagent (ppm)	Chemical shift after addition of the shift reagent (ppm)
5*a*	Methyl group in the ethyl ester moiety	1.25	2.14; 2.26
6*a*	Methyl group in the methyl ester moiety	3.70	4.17; 4.24
11*a*	Methyl group in the cyclopropane ring	1.14	2.58; 2.67
12*a*	Methylene group in the ethyl ester moiety	4.25	5.50; 5.75

carbon–copper complex **8**. Subsequent attack of the olefin **4** occurs again from the back side of the plane and will afford a mixture of metallocyclobutanes **9** and **10**, which then undergo rearrangement to form products **5** and **6** with regeneration of the active catalyst.

In the case of achiral catalyst B, formation of the *trans* isomer **6** is favored since its derivation, via the metallocyclobutane intermediate **10** (R = H, Scheme 3), is energetically preferred due to less severe steric interactions between R^1 and the ester group. These groups are in a *cis* relationship in **9** and in a more favorable *trans* relationship in **10**.

On the other hand, the *cis* isomer **5** should be favored over **6** when the chiral catalysts C and D are employed. In these cases, the steric interactions between R^1 and bulky R groups become most important. Such interactions are more severe in the metallocyclobutane intermediate **10** than in **9**. It should be noted that the rationalizations presented here assume that the product distribution follows the relative ground state stabilities of the two diastereomers, i.e., the most stable diastereomer generates the major enantiomeric product; this may not necessarily be so, and there are examples in asymmetric catalysis where the energetically *least* favoured form of two diastereomers leads to the major enantiomer in the product (25).

During the course of the cyclopropanation reaction, the molecule of carbene liberated from the diazoacetate ester can add to the double bond of **4** to form products **5** and **6** *or*, alternatively, can undergo a process of dimerization.

Indeed when an excess of diazoacetate ester is employed, the dimerization of carbene molecules and the formation of fumaric and maleic acid diesters (FDE and MDE respectively) becomes an important process. It is known that such molecules can coordinate strongly with copper (19, 20). It is therefore possible that the change in the *trans*/*cis* ratio, as observed in experiments 3 and 4, for example, may be a result of coordination of the catalyst or the resultant intermediate by FDE and (or) MDE.

When catalyst E is employed, the Aratani type model (intermediates **9** or **10**) is not applicable and the *trans* isomer **6** is formed as a major product regardless of the amount of diazo ester employed.

Enantiomeric/diastereomeric excess of compounds **5** and **6** varies a great deal depending on the nature of the catalyst and the reaction conditions. In our opinion, the huge difference in e.e. in experiments 1–5 is associated with the varied degree of coordination of the copper(I) atom by FDE and (or) MDE formed during the process of collapse of the metallocyclobutanes with resultant different geometry in the end product.

In previous studies done by Aratani's group, it was shown (18) that catalyst C gave slightly better optical yields of products than did catalyst D. It is a matter of interest to note that, in our

Can. J. Chem. Downloaded from www.nrcresearchpress.com by 122.72.124.2 on 09/07/12
For personal use only.

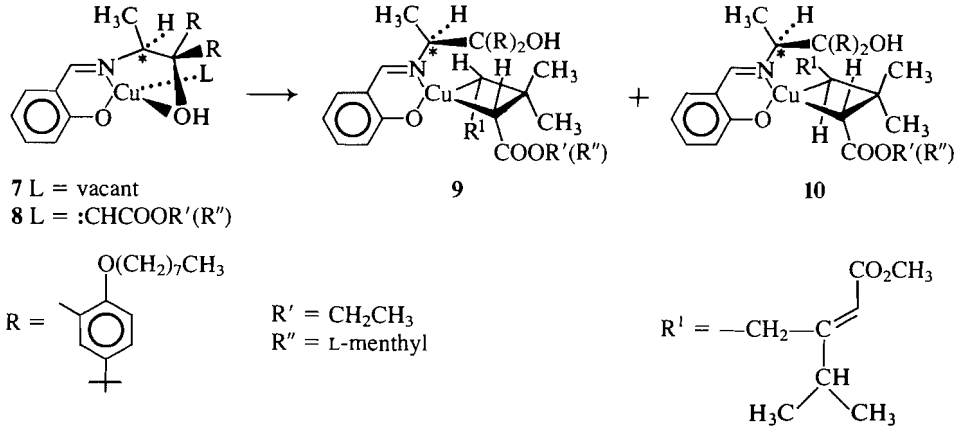

SCHEME 3

experiment, catalyst C is also superior except in the case of the *cis* isomer **5***a* when excess of olefin **4** is used.

To achieve efficient chirality transfer from metallocyclobutanes **9** and **10** to the products, thus achieving high optical purity of **5** and **6**, formation of products of dimerization should be minimized (21).

Catalyst E was used for cyclopropanation of terminal olefins and an enantiomeric excess close to 100% was achieved (14). In our experiments, where the reaction was carried out with a substituted ethylene derivative, the surprisingly low e.e. suggests that this catalyst is very sensitive to the steric hindrance at the -C=C- bond.

In summary, the chiral esters produced in the course of the above described cyclopropanation reactions give entry to the family of chiral compounds shown in Scheme 4.

Diesters **5** and **6** were ozonized to afford ketones **11** and **12**. Separation of the *cis* and *trans* series and subsequent determination of enantiomeric and (or) diastereomeric excess could be achieved at either the diester *or* keto-ester stage.

In the case of the ethyl series, **5***a* and **6***a* were separated by preparative hplc on a silica column but purification can also be achieved by employment of C_{18} reverse phase columns and the use of a mixture of methanol and water (7:3) as eluent.

However, it is far more convenient to separate the corresponding ketones **11***a* and **12***a* after ozonolysis of the mixture of **5***a* and **6***a*, and work-up with zinc and acetic acid. In the case of the menthyl series, it is more practical to separate the mixture of **5***b* and **6***b* instead of **11***b* and **12***b*.

Ketones **11***b* and **12***b* were obtained by ozonolysis of esters **5***b* and **6***b* and reduction of the ozonide by dimethyl sulfide.

In the ethyl series, ketones **11***a* and **12***a* were reduced with sodium borohydride to afford, respectively, diastereomeric mixtures of alcohols **13** and **14**.

These alcohols were converted to olefins **17–22** via tosylation and subsequent elimination of *p*-toluenesulfonic acid under basic conditions.

Although synthesis of olefins **17**, **19**, **21** and **18**, **20**, **22** can be carried out in a "one-pot" process (for example, by heating the corresponding alcohols with TsCl in pyridine), it is more convenient to isolate the intermediate tosylates, as the tosyl group undergoes nucleophilic substitution by chloride anion in the course of the reaction and the corresponding chloride formed further complicates separation of the olefinic products.

In general, the intermediate tosyl derivatives **15** and **16** were prepared from alcohols **13** and **14** by the action of TsCl in CH_2Cl_2 in the presence of dimethylaminopyridine (DMAP).

The elimination reaction to afford the olefinic products was carried out using pyridine and 1,8-diazabicyclo[5.4.0]undec-7-ene (DBU) (22). When DBU was used as a base, yields were lower than those obtained when pyridine was the base employed. One-pot conversion of alcohols **13** and **14** to olefins via tosylate with DBU as a base also gave lower yields since the corresponding chlorides, formed as by-products, do not eliminate HCl at temperatures low enough to preserve the cyclopropyl ring in the resultant olefins.

Some attempts to increase yields of olefins **17** and **18**, which resemble more closely the natural pyrethroids, were made.

Using previously described reaction conditions (23, 24) ($(n\text{Bu})_4\text{NBr}$, 2,6-lutidine in acetone), which favor an elimination of TsOH toward formation of Saytzeff type products, we observed an increased yield of olefins **17** and **18** when compared to the reaction in which pyridine was used as a base.

Numerous attempts were made to separate, on a preparative scale, mixtures of the isomeric olefins **17**, **19**, **21** and **18**, **20**, **22** by means of chromatographic methods. Various combinations of solvents used with SiO_2, C_{18}-reverse phase hplc, or SiO_2 columns impregnated with $AgNO_3$ gave unsatisfactory results. Results obtained by utilizing analytical hplc suggest that such preparative separation will be very difficult. However, chromatography on SiO_2 columns impregnated with 15% $AgNO_3$ using an aromatic solvent (toluene) as an eluent gave partial resolution of the mixtures. We also showed that olefin **21** can be separated from olefins **17** and **19** by hplc on C_{18}-reverse phase columns using a mixture of methanol/water (80:20).

The resultant chiral cyclopropane analogues, as described above, will be evaluated for their potential in the agrochemical industry.

Experimental

Ultraviolet spectra were recorded on a Cary 15 spectrophotometer. Infrared spectra were recorded on a Perkin–Elmer 1710 spectrophotometer. The ^{1}H nmr spectra were recorded on one of the following instruments: Varian XI-300, Bruker WP-80, or Bruker WH-400 MHz. Deuteriochloroform was used as a solvent with TMS as internal standard. Mass spectra were recorded using a KRATOS MS50 apparatus. $[\alpha]_D$ measurements were made on a Perkin–Elmer 141 polarimeter. Microanalyses were carried out by Mr. P. Borda, Microanalytical Laboratory, University of British Columbia. Ethyl diazoacetate, chiral shift reagents, and 3-(trifluoroacetyl)-*d*-camphor were purchased from Aldrich. Anhydrous $CuSO_4$ was obtained from BDH. Starting materials were prepared according to the literature: L-menthyl diazoacetate (4, 5), catalyst C (13), catalyst E (14), *E*-β-thujaketonic acid methyl ester (2). Ligand for catalyst B was

Can. J. Chem. Downloaded from www.nrcresearchpress.com by 122.72.124.2 on 09/07/12
For personal use only.

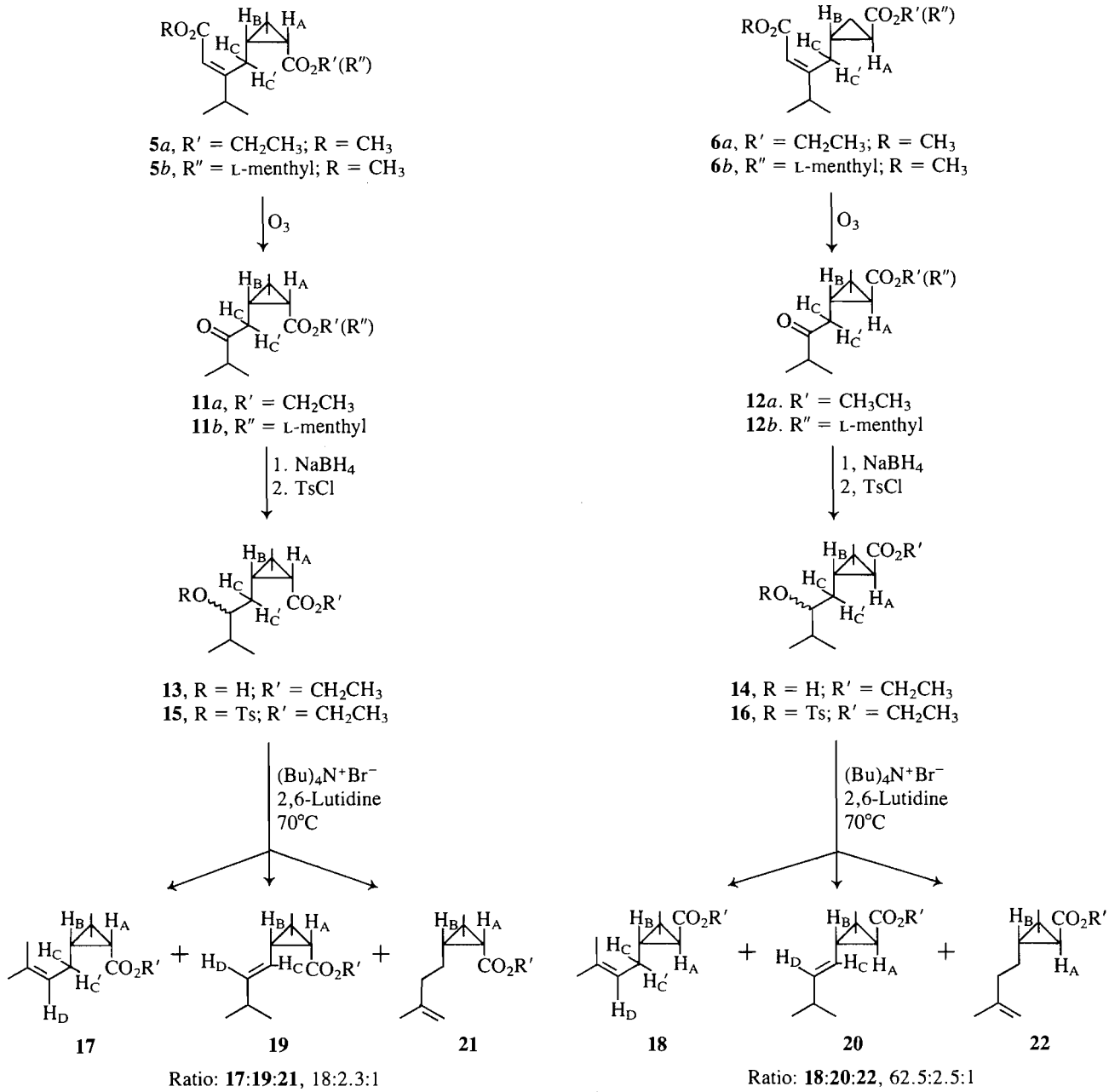

SCHEME 4

prepared from salicylaldehyde and 2-aminoethanol. Catalyst D was obtained from Dr. T. Aratani.

Isopropenyl derivative **3**

The sodium salt of isopropenyl acid **2** (14.4 g, 0.07 mol) was added to the suspension of the Wittig reagent prepared from triphenylmethylphosphonium bromide (50 g, 0.14 mol) and potassium *tert*-butoxide (16.8 g, 0.15 mol) in 1 L of THF and the resultant mixture was stirred under reflux for 20 h. After cooling, THF was removed *in vacuo*, and the residue was dissolved in a minimum amount of water and washed with ether. The aqueous layer was acidified with 10% hydrochloric acid and extracted with ether. This extract was washed with water, dried over Na_2SO_4, and concentrated *in vacuo* to give **3** (11.3 g, 89% yield).

Diesters **5**a *and* **6**a, **5**b *and* **6**b

See Table 1 for details.

Experiment 1

The solution of catalyst D (0.06 g, 0.092 mmol) and ester **4** (0.9 g, 4.6 mmol) in cyclohexane (4 mL) was heated to 75–80°C with vigorous stirring under an argon atmosphere and a few drops of the solution of ethyl diazoacetate (9 mL, 9.81 g, 86 mmol) in cyclohexane (9 mL) were added to initiate the reaction evidenced by evolution of nitrogen. Then the temperature was lowered to 40°C and the remainder of the solution of ethyl diazoacetate was added dropwise over a period of 8 h. After evaporation of solvent, the bulk of diethyl fumarate and diethyl maleate produced as by-products was removed by distillation (bulb-to-bulb, 40–50°C, 0.05 Torr; 1 Torr = 133.3 Pa). The remaining residual oil (3 g) was chromatographed on neutral alumina (500 g) using a mixture of toluene and ethyl acetate (40:1) as eluent to afford a mixture of **5***a* and **6***a* (1.17 g, 88%). Separation of *cis* **5***a* and *trans* **5***b* isomers was achieved by preparative hplc on the Waters Prep 500 instrument using two silica gel cartridges in series and 2% ethyl acetate in hexane as eluent to yield (*i*) pure *cis* isomer **5***a* (0.33 g), retention time ~75 min, bp ~60°C (bulb-to-bulb, 0.03 Torr); ir ν_{max} (neat): 1718, 1641, 1191, 1165 cm^{-1}; ^1H nmr δ: 5.7 (1H, s, =CH-), 4.1 (2H, m, CH_3CH_2COO-), 3.7 (3H, s, CH_3COO), 3.05 (1H, dd, $H_{C'}$, $J_{C'B}$ = 6.0 Hz), 2.9 (1H, dd, $H_{C'}$, $J_{CC'}$ = 13.7, J_{CB} = 6.0 Hz), 2.35 (1H, septet,

Can. J. Chem. Downloaded from www.nrcresearchpress.com by 122.72.124.2 on 09/07/12
For personal use only.

$(CH_3)_2CH$, J = 6.0 Hz), 1.5 (1H, d, H_A, J_{AB} = 8.6 Hz), 1.25 (4H, m, CH_3CH_2COO + H_B), 1.15 (6H, s, CH_3 cyclopropyl), 1.05 (6H, m, $(CH_3)_2CH$); ms m/z: 282 (M^+), 250, 237, 205, 153 (100). *Anal.* calcd. for $C_{16}H_{26}O_4$: C 68.05, H 9.28; found: C 67.95, H 9.33; (*ii*) pure *trans* isomer **6***a* (0.496 g), retention time ~90 min, bp ~60°C (bulb-to-bulb, 0.03 Torr); ir ν_{max} (neat): 1720, 1642, 1230, 1175 cm^{-1}; ^1H nmr δ: 5.7 (1H, s, =CH-), 4.1 (2H, m, CH_3CH_2COO-), 3.7 (3H, s, CH_3COO-), 2.9 (1H, dd, $H_{C'}$, $J_{C'B}$ = 6.0 Hz), 2.75 (1H, dd, $H_{C'}$, $J_{CC'}$ = 14.0, J_{CB} = 8.0 Hz), 2.5 (1H, septet, $(CH_3)_2CH$-, J = 6.0 Hz), 1.5 (1H, m, H_B), 1.35 (1H, d, H_A, J_{AB} = 6.0 Hz), 1.25 (9H, m, CH_3 cyclopropyl + CH_3CH_2COO-), 1.1 (6H, m, $(CH_3)_2CH$-); ms m/z: 282 (M^+), 250, 237, 205, 153 (100). *Anal.* calcd. for $C_{16}H_{26}O_4$: C 68.05, H 9.28; found: C 68.23, H 9.19; and (*iii*) a mixed fraction of **5***a* and **6***a* (0.26 g).

Experiment 2

The solution of catalyst D (0.04 g, 0.06 mmol) in 2 g of the ester **4** was heated with vigorous stirring to 75–80°C under an argon atmosphere and a few drops of the solution of ethyl diazoacetate (0.33 mL, 0.34 g, 3 mmol) in 3.9 g of **4** (total amount of the ester **4** employed in this reaction was 5.9 g, 30 mmol) was added to initiate the reaction evidenced by evolution of nitrogen. Then the temperature of the reaction was lowered to 40°C and the remainder of the solution of ethyl diazoacetate in **4** was added dropwise over a period of 8 h. The product of the reaction was separated from the excess of the substrate by column chromatography on silicia gel (500 g, 230–400 mesh), using a mixture of hexanes/ethyl acetate (80:1) as eluent. The mixture of **5***a* and **6***a* obtained (0.620 g, 70%) was separated by hplc, as described in experiment 1, to give pure **5***a* (0.32 g), pure **6***a* (0.19 g), and a mixed fraction (0.057 g).

Experiment 3

Procedure: As in experiment 1.
Work-up: As in experiment 1.

Experiment 4

Procedure: As in experiment 2.
Work-up: As in experiment 2.

Experiment 5

The solution of catalyst C (0.0966 g, 0.13 mmol) in the ester **4** (12.5 g, 63.8 mmol) was heated to 75°C and a dew drops of the solution of L-menthyl diazoacetate (1.43 g, 6.38 mmol) in cyclohexane (3 mL) was added with stirring to initiate the reaction evidenced by foaming and evolution of nitrogen. Then the temperature of the reaction was lowered to 40°C and the remainder of the solution of L-menthyl diazoacetate in cyclohexane was added dropwise at a rate of approximately 1 drop per 1–2 min. Subsequently, the reaction was heated to 80°C for 5 min and cooled to room temperature. Then the solvent was removed and the crude product was chromatographed on silica gel 60 (230–400 mesh) using toluene as eluent. Further separation and purification of the *cis*/*trans* products was achieved by repeated chromatography on silica gel 60 G (tlc grade) using toluene as eluent to give (*i*) pure *cis* isomer **5***b* (630 mg); bp ~120°C (bulb-to-bulb, 0.03 Torr); ir ν_{max} (neat): 1719, 1640, 1459, 1168 cm^{-1}; uv λ_{max} (MeOH): 223 (ε 16 265) nm; ^1H nmr δ: 5.70 (1H, br s), 4.68 (1H, ddd, J = 10.8, 4.4 Hz), 3.70 (3H, s), 3.10 (1H, dd, J = 13.8, 5.9 Hz), 2.90 (1H, dd, J = 13.8, 6.5 Hz), 2.31 (1H, septet, J = 7.0 Hz), 2.2–1.84 (2H, m), 1.68 (2H, m), 1.45 (1H, d, J = 8.6 Hz), 1.48 (1H, m), 1.36 (1H, m), 1.24 (3H, s), 1.16 (3H, s), 1.07 (3H, d, J = 6.8 Hz), 1.06 (3H, d, J = 6.8 Hz), 0.90 (6H, d, J= 7.0 Hz), 0.78 (3H, d, J = 7.0 Hz); ms m/z: 392 (M^+), 254, 236, 153 (100). *Exact Mass* (hrms) calcd. for $C_{24}H_{40}O_4$: 392.2926; found: 392.2926. *Anal.* calcd. for $C_{24}H_{40}O_4$: C 73.54, H 10.29; found: C 73.70, H 10.30; (*iii*) pure *trans* isomer **6***b* (510 mg); bp ~120°C (bulb-to-bulb, 0.03 Torr); ir ν_{max} (neat): 1719, 1641, 1460, 1170 cm^{-1}; uv λ_{max} MeOH): 220 (ε 15 360) nm; ^1H nmr δ: 5.68 (1H, br s), 4.66 (1H, ddd, J = 10.8, 10.8, 4.4 Hz), 3.68 (3H, s), 2.94 (1H, dd, J = 13.8, 5.4 Hz), 2.68 (1H, dd, J = 13.8, 8.9 Hz), 2.48 (1H, septet, J = 7.0 Hz), 1.94 (1H, m), 1.83 (1H, d, septet, J = 2.5, 6.9 Hz), 1.65 (2H, m), 1.48 (2H, m), 1.33 (1H, d, J = 5.4 Hz), 1.23 (3H, s), 1.19 (3H, s), 1.08 (3H, d, J = 6.9 Hz), 1.07 (3H, d, J = 6.9 Hz), 0.88 (3H, d, J = 7.0 Hz), 0.87 (3H, d, J = 7.0 Hz), 0.72 (3H, d, J = 6.9 Hz); ms m/z: 392 (M^+), 254, 222, 177, 153 (100). *Exact Mass* (hrms) calcd. for $C_{24}H_{40}O_4$: 392.2926; found: 392.2928. *Anal.* calcd. for $C_{24}H_{40}O_4$: C 73.54, H 10.29; found: C 73.70, H 10.35; and (*iii*) a mixed fraction of **5***b* and **6***b* (612 mg).

Experiment 6

Procedure: As in experiment 1, but temperature of the reaction was kept constant at 40°C throughout the entire experiment.
Work-up: As in experiment 1.

Experiment 7

Procedure: As in experiment 2, but temperature of the reaction was kept constant at 40°C throughout the entire experiment.
Work-up: As in experiment 2.

Experiment 8

The mixture of catalyst A ($CuSO_4$, 0.6 g, 3.8 mmol) and the ester **4** (2 g, 10.3 mmol) was heated to 100°C and then ethyl diazoacetate (neat, 9.28 g, 8.5 mL, 81 mmol) was added dropwise with stirring over a period of 8 h. The resulting oil was diluted with dichloromethane, filtered, and worked up further as in experiment 1.

Experiment 9

To the refluxing mixture of catalyst B (0.52 g, 2.3 mmol) and the ester **4** (2 g, 10.3 mmol) in cyclohexane (10 mL), ethyl diazoacetate (6.5 g, 6 mL, 56.6 mmol) was added dropwise over a period of 8 h. The resulting reaction mixture was worked up as in experiment 1.

Experiment 10

Procedure: As in experiment 8.
Work-up: As in experiment 1.

Experiment 11

Procedure: As in experiment 1.
Work-up: As in experiment 1.

Ketones **11**a *and* **12**a

A solution of a mixture of **5***a* and **6***a* (ratio **5***a*:**6***a* ≈ 2:1) (4.5 g) in dichloromethane (150 mL) was treated at −78°C with an excess of ozone for 30 min. Excess of ozone was removed by passing argon through the solution at −78°C and then the solution was allowed to warm to −20°C. At this temperature, 80% acetic acid (50 mL) and zinc powder (15 g) were added and the mixture was stirred at 0°C for 2 h and left overnight at 4°C. Then the solids were filtered off from the reaction mixture, and the filtrate was washed with water and saturated $NaHCO_3$, dried with Na_2SO_4, and concentrated *in vacuo*. Chromatography on silica gel (tlc grade), using a mixture of hexanes/ethyl acetate (20:1) as eluent, gave the isomeric ketones **11***a* (1.1 g, 92%); bp ~80°C (bulb-to-bulb, 0.03 Torr); ir ν_{max} (neat): 1720, 1172, 1136 cm^{-1}; ^1H nmr δ: 4.1 (2H, q, CH_3CH_2COO, J = 7.0 Hz), 2.9 (2H, dd, H_C + $H_{C'}$, $J_{CC'}$ = 18.0 Hz), 2.61 (1H, s, $(CH_3)_2CH$, J = 7.0 Hz), 1.54 (1H, d, H_A, J_{AB} = 8.9 Hz), 1.42 (1H, m, H_B, J_{BC} = 7.0, $J_{BC'}$ = 7.0 Hz), 1.3–1.18 (6H, m, CH_3 cyclopropyl + CH_3CH_2COO), 1.14 (3H, s, CH_3 cyclopropyl), 1.08 (6H, m, $(CH_3)_2CH$); ms m/z: 226 (M^+), 208, 180, 71 (100). *Anal.* calcd. for $C_{13}H_{22}O_3$: C 68.99, H 9.80; found: C 69.30, H 9.81; and **12***a* (2.4 g quant), bp ~90°C (bulb-to-bulb, 0.03 Torr); ir ν_{max} (neat): 1720, 1200, 1168 cm^{-1}; ^1H nmr δ: 4.1 (2H, m, CH_3CH_2COO), 2.7–2.58 (2H, m, $H_{C'}$, J_{BC} = 8.0, $J_{CC'}$ = 17.0 Hz), 1.64 (1H, m, H_B), 1.25 (6H, m, CH_3CH_2COO + CH_3 cyclopropyl), 1.23 (1H, d, H_A, J_{AB} = 5.5 Hz), 1.08 (9H, m, $(CH_3)_2CH$ + CH_3 cyclopropyl); ms m/z: 226 (M^+), 208, 180, 71 (100). *Anal.* calcd. for $C_{13}H_{22}O_3$: C 68.99, H 9.80; found: C 69.07, H 9.64.

Ketone **11**b

A solution of **5***b* (0.128 g) in dichloromethane (20 mL) was treated at −78°C with an excess of ozone for 30 min. Excess of ozone was removed by passing nitrogen through the solution at −78°C. Then dimethyl sulphide (10 molar excess) was added and the solution was allowed to warm up to room temperature and left overnight (14 h). The solvent was removed *in vacuo* and the crude reaction mixture was chromatographed on silica gel 60 G (tlc grade) to afford pure **11***b* (86 mg, 84% yield); bp ~140°C (bulb-to-bulb, 0.03 Torr); ir ν_{max} (neat):

Can. J. Chem. Downloaded from www.nrcresearchpress.com by 122.72.124.2 on 09/07/12
For personal use only.

Can. J. Chem. Downloaded from www.nrcresearchpress.com by 122.72.124.2 on 09/07/12
For personal use only.

1718, 1460, 1388, 1173 cm^{-1}; ^1H nmr δ: 4.66 (1H, ddd, J = 10.8, 10.8, 4.4 Hz), 2.97 (2H, dd, J = 7.1, 2.0 Hz), 2.64 (1H, septet, J = 7.1 Hz), 1.90 (2H, m), 1.69 (2H, m), 1.55 (1H, d, J = 8.6 Hz), 1.50–1.15 (3H, m), 1.25 (3H, s), 1.16 (3H, s), 1.13 (3H, d, J = 7.1 Hz), 1.12 (3H, d, J = 7.1 Hz), 0.92 (6H, d, J = 6.8 Hz), 0.78 (3H, d, J = 7.0 Hz); ms m/z: 336 (M^+), 321, 198, 180, 110, 83, 71 (100). *Exact Mass* (hrms) calcd. for $C_{21}H_{36}O_3$: 336.2665; found: 336.2659. *Anal.* calcd. for $C_{21}H_{36}O_3$: C 75.00, H 10.71; found: C 75.12, H 10.70.

Ketone **12b**

6*b* (0.1 g) was ozonized as above, to give pure **12***b* (81 mg, 91% yield); bp ~140°C (bulb-to-bulb, 0.03 Torr); ir ν_{max} (neat): 1713, 1459, 1201, 1169 cm^{-1}; ^1H nmr δ: 4.70 (1H, ddd, J = 10.8, 10.8, 4.4 Hz), 2.66 (1H, dd, J = 16.1, 6.1 Hz), 2.65 (1H, septet, J = 6.8 Hz), 2.41 (1H, dd, J = 16.1, 6.9 Hz), 1.99 (1H, m), 1.85 (1H, d, septet, J = 2.5, 6.8 Hz), 1.15 (4H, m), 1.23 (3H, s), 1.11 (6H, s and d, J = 6.8 Hz), 1.10 (3H, d, J = 6.8 Hz), 0.90 (6H, d, J = 6.8 Hz), 0.76 (3H, d, J = 6.5 Hz); ms m/z: 336 (M^+), 293, 262, 251, 198, 180, 110, 83 (100). *Exact Mass* (hrms) calcd. for $C_{21}H_{36}O_3$: 336.2665; found: 336.2640. *Anal.* calcd. for $C_{21}H_{36}O_3$: C 75.00, H 10.71; found: C 74.91, H 10.90.

Alcohol **13**

Reduction of **11***a* (0.64 g) with sodium borohydride (0.64 g) in ethanol (15 mL) for 30 min at 0°C gave alcohol **13** (0.61 g, 94%); ir ν_{max} (neat): 1725, 1134, 1093 cm^{-1}; ^1H nmr δ: 4.1 (2H, m, CH_3CH_2COO), 3.4 and 3.3 (1H, bs, $CH(OH)$), 1.9 (1H, m, $(CH_3)_2CH$), 1.7–1.25 (5H, m, H_A + H_B + H_C + $H_{C'}$ + OH), 1.25–1.15 (9H, CH_3CH_2COO + 2 × CH_3 cyclopropyl), 0.9 (6H, m, $(CH_3)_2CH$), most signals were doubled due to the presence of diastereoisomers; ms m/z: 210 ($M^+ - H_2O$), 182, 167, 139, 82 (100). *Exact Mass* (hrms) calcd.: 210.1620; found: 210.1616. *Anal.* calcd. for $C_{13}H_{24}O_3$: C 68.38, H 10.59; found: C 68.45, H 10.49.

Alcohol **14**

Reduction of **12***a* (0.64 g) with sodium borohydride (0.64 g) in ethanol (15 mL) for 30 min at 0°C gave alcohol **14** (0.59 g, 91%); ir ν_{max} (neat): 1724, 1202, 1165 cm^{-1}, ^1H nmr δ: 4.1 (2H, m, CH_3CH_2COO), 3.45 (1H, m, $CH(OH)$), 1.73–1.5 (3H, m, OH + $(CH_3)_2CH$, H_B), 1.5–1.35 (2H, m, H_C, $H_{C'}$), 1.3–1.1 (10H, m, CH_3CH_2COO + 2 × CH_3 cyclopropyl, H_A), 0.9 (6H, m, $(CH_3)_2CH$); ms m/z: 210 ($M^+ - H_2O$), 183, 143, 113, 55 (100). *Exact Mass* (hrms) calcd.: 210.1620; found: 210.1627. *Anal.* calcd. for $C_{13}H_{24}O_3$: C 68.38, H 10.59; found: C 68.60, H 10.59.

Tosylate **15**

p-Toluenesulphonyl chloride (0.17 g, 1.32 mmol) was added to the cool solution (ice bath) of the alcohol **13** (0.1 g, 0.44 mmol) and 4-dimethylaminopyridine (DMAP, 0.430 g, 3.52 mmol) in dichloromethane (2 mL) and stirred at 20°C under an argon atmosphere for 20 h. Then the solution was poured into ice, and extracted with dichloromethane. The organic layer was washed twice with cold 5% HCl and dried over Na_2SO_4 and $NaHCO_3$. Evaporation of the solvent yielded tosylate **15** (0.145 g, 87%), which was used in the next step without further purification; tlc gave one spot at R_f 0.4, hexanes/ethyl acetate 10:1; ^1H nmr δ: 7.7–7.2 (4H, m, ϕ), 3.55–3.40 (1H, m, C*H*OTs), 2.45 (3H, d, CH_3-ϕ). Most signals were doubled due to the presence of two diastereoisomers.

Tosylate **16**

The tosylate **16** was synthesized from the alcohol **14** following the procedure described above for tosylate **15**; ^1H nmr δ: 7.2–7.8 (4H, m, ϕ), 3.6 (1H, m, C*H*OTs), 2.5 (3H, s, CH_3-ϕ).

Olefins **17**, **19**, **21**

Tosylate **15** (0.150 g) was heated in dry pyridine (1 mL) at 110°C for 6 h. The mixture was cooled, poured into ice water, and extracted with ether. The extract was washed with cold 5% hydrochloride acid, dried over Na_2SO_4 and $NaHCO_3$, and concentrated *in vacuo*. The residual oil was chromatographed on a silica gel column using a mixture of hexanes/ethyl acetate (100:1) as eluent. After evaporation of the solvent, a mixture of **17**, **19**, and **21** (0.067 g, 81%) was obtained as a colorless oil. (Ratio of olefins by ^1H nmr, 10:3.2:1.) This oil was chromatographed on a silica gel column impregnated with $AgNO_3$ (15%) using a mixture of hexanes/toluene (1:3) as eluent. Fractions enriched in each olefin were collected and analysed by ^1H nmr and gc/hrma.

Olefins **17**, **19**, **21.** *Alternative preparation*

Tosylate **15** (0.57 g, 1.5 mmol), $(n\text{Bu})_4\text{NBr}$ (0.49 g, 1.5 mmol), and 2,6-lutidine (0.6 mL, 5 mmol) in anhydrous acetone (10 mL) were heated in a closed vessel at 70°C for 2 days. After the work-up, a mizture of olefins **17**, **19**, **21** (0.267 g, 89%, ratio 18:2.3:1) was obtained and separated as above.

Olefin **17**: ^1H nmr δ: 5.1 (1H, m, H_D), 4.1 (2H, m, CH_3CH_2COO), 2.3 (2H, m, H_C + $H_{C'}$), 1.65 (6H, ds, $(CH_3)_2$=C), 1.4 (1H, d, H_A, J_{AB} = 9.0 Hz), 1.25 (3H, t, CH_3CH_2COO), 1.22 (3H, s, CH_3 cyclopropyl), 1.2 (1H, m, H_B), 1.16 (3H, s, CH_3 cyclopropyl). *Exact Mass* (hrms) calcd.: 210.1620; found: 210.1637.

Olefin **19**: ^1H nmr δ: 5.68 (1H, dd, H_C, J_{CD} = 16.1, J_{CB} = 9.0 Hz), 5.57 (1H, dd, H_D, J = 6.2 Hz), 0.95 (6H, dd, $(CH_3)_2CH$). *Exact Mass* calcd.: 210.1620; found: 210.1619.

Olefin **21**: ^1H nmr δ: 4.7 (2H, m, CH_2=), 4.1 (2H, m, CH_3CH_2-COO), 2.0 (2H, m, CH_2), 1.8 (2H, m, CH_2), 1.72 (3H, s, CH_3—C=), 1.4 (1H, d, H_A, J_{AB} = 9.0 Hz), 1.25 (3H, t, CH_3CH_2COO), 1.23 (3H, s, CH_3 cyclopropyl), 1.2 (1H, m, H_B), 1.14 (3H, s, CH_3 cyclopropyl). *Exact Mass* (hrms) calcd.: 210.1620; found: 210.1642.

Olefins **18**, **20**, **22**

The olefins **18**, **20**, **22** were prepared following both procedures described above for the olefins **17**, **19**, **21**. When tosylate **16** was heated in pyridine, 87% yield was obtained (ratio of olefins 48:5:1). In reaction with $(n\text{Bu})_4\text{NBr}$ and lutidine, 93% yield was obtained (ratio of olefins 62.5:2.5:1). After separations on silica gel columns impregnated with $AgNO_3$ as above, fractions enriched in each olefin were collected and analysed by ^1H nmr and gc/hrms.

Olefin **18**: ^1H nmr δ: 5.1 (1H, m, -CH=), 4.1 (2H, m, CH_3CH_2-COO), 2.1 (2H, m, H_{3C} + $H_{C'}$), 1.68 (3H, s, CH_3—C=), 1.58 (3H, s, CH_3—C=), 1.35 (1H, m, $H_{B'}$, $J_{CB} \approx J_{C'B}$ = 7.6 Hz), 1.25 (3H, t, CH_3CH_2COO), 1.20 (3H, s, CH_3 cyclopropyl), 1.18 (1H, d, H_A, J_{AB} = 7.0 Hz), 1.15 (3H, s, CH_3 cyclopropyl). *Exact Mass* (hrms) calcd.: 210.1620; found: 210.1655.

Olefin **20**: ^1H nmr δ: 5.65 (1H, dd, H_D, J = 6.6, J_{CD} = 15.0 Hz), 5.10 (1H, dd, H_C, J_{BC} = 7.5 Hz), 4.1 (2H, m, CH_3CH_2COO), 2.25 (1H, m, $(CH_3)_2CH$), J = 6.6 Hz), 2.0 (1H, m, H_B), 1.45 (1H, d, H_A, J_{AB} = 5.3 Hz), 1.25 (3H, t, CH_3CH_2COO), 1.22 (3H, s, CH_3 cyclopropyl), 1.15 (3H, s, CH_3 cyclopropyl), 0.35 (6H, d, $(CH_3)_2CH$, J = 6.8 Hz). *Exact Mass* (hrms) calcd.: 210.1620; found: 210.1599.

Olefin **22**: ^1H nmr δ: 4.67 (2H, m, =CH_2). *Exact Mass* (hrms) calcd.: 210.1620; found: 210.1627.

Acknowledgements

Financial aid from the Natural Sciences and Engineering Research Council of Canada is gratefully acknowledged. We also wish to thank Dr. T. Aratani, Central Research Laboratory, Sumitomo Chemical Co., Ltd., Osaka, Japan, for providing a sample of catalyst D.

1. J. P. KUTNEY and A. K. SINGH. Can. J. Chem. **62**, 2813 (1984).
2. J. P. KUTNEY, J. M. CHOUDHURY, J. M. DECESARE, H. JACOBS, A. K. SINGH, and B. R. WORTH. Can. J. Chem. **59**, 3162 (1981).
3. M. ELLIOTT, A. W. FARNHAM, N. F. JANES, P. M. NEEDHAM, and D. A. PULMAN. A.C.S. Symposium Series No. 2, 80 (1974).
4. K. HARADA and T. HAYAKAWA. Bull. Chem. Soc. Jpn. **37**, 191 (1964).
5. N. TAKAMURA, T. MIZOGUCHI, K. KOGA, and S. YAMADA. Tetrahedron, **31**, 227 (1975).

6. A. J. ANCIAUX, A. DEMONCEAU, A. F. NOELS, R. WARIN, A. J. HUBERT, and P. TEYSSIE. Tetrahedron, **39**, 2169 (1983).
7. A. NAKAMURA, A. KONISHI, Y. TATSUMO, and S. OTSUKA. J. Am. Chem. Soc. **100**, 3993 (1978).
8. M. P. DOYLE, R. L. DOROW, W. L. BUCHRO, J. H. GRIFFIN, W. H. TAMBLYN, and M. L. TRUDELL. Organometallics, **3**, 44 (1984).
9. A. J. ANCIAUX, A. J. HUBERT, A. F. NOELS, N. PETINIOT, and P. TEYSSIE. J. Org. Chem. **45**, 695 (1980).
10. T. ARATANI, Y. YONEYOSHI, and T. NAGASE. Tetrahedron Lett. **18**, 2599 (1977).
11. T. ARATANI, Y. YONEYOSHI, and T. NAGASE. Tetrahedron Lett. **23**, 685 (1982).
12. H. FRITSCHI, U. LEUETENEGGER, and A. PFALZ. Angew. Chem. Int. Ed. Engl. **25**, 1005 (1986).
13. T. ARATANI, Y. YONEYOSHI, and T. NAGASE. Tetrahedron Lett. **16**, 1707 (1975).
14. S. A. MATLIN, W. J. LOUGH, L. CHAN, D. M. H. ABRAM, and Z. ZHOU. J. Chem. Soc. Chem. Commun. 1038 (1985).
15. T. SHIGEMATSU, M. MATSUI, Y. SASAKI, and M. SAKURADA. Bull. Inst. Chem. Res. Kyoto Univ. **59**, 335 (1976).
16. M. P. DOYLE. Chem. Rev. **86**, 919 (1986).
17. G. MAAS. Top Curr. Chem. **137**, 75 (1987).
18. T. ARATANI. Pure Appl. Chem. **57**, 1838 (1985).
19. D. L. REGER and M. D. DUKES. J. Organomet. Chem. **113**, 173 (1976).
20. H. W. QUINN and J. H. TASI. Adv. Inorg. Chem. Radiochem. **12**, 217 (1969).
21. M. P. DOYLE, D. VAN LEUSEN, and W. H. TAMBLYN. Synthesis, 787 (1981).
22. P. WOLKOFF. J. Org. Chem. **47**, 1977 (1982).
23. I. N. FEIT, I. K. BREGER, A. M. CAPOBIANCO, T. W. COOKE, and L. F. GITLIN. J. Am. Chem. Soc. **97**, 2477 (1975).
24. P. J. LLOYD and A. J. PARKER. Tetrahedron Lett. **12**, 637 (1971).
25. B. BOSNICH (*Editor*). Asymmetric catalysis. Martinus Nijhoff Publishers, Dordrecht, The Netherlands. 1986. Chap. 1.

Can. J. Chem. Downloaded from www.nrcresearchpress.com by 122.72.124.2 on 09/07/12
For personal use only.

Diastereoselective alkylation of glycinates. 4.[1] The role of the metal cation and additives

JOHN M. MCINTOSH AND KENNETH C. CASSIDY
Department of Chemistry and Biochemistry, University of Windsor, Windsor, Ont., Canada N9B 3P4

Received April 7, 1988

JOHN M. MCINTOSH and KENNETH C. CASSIDY. Can. J. Chem. **66**, 3116 (1988).

The alkylation of the sodium, potassium, zinc, and zirconium enolates of the *R*-camphor imine of *tert*-butyl glycinate have been examined and the stereochemical results compared with those obtained with the lithium enolate. No difference was noted for the sodium enolate but inferior chemical yields and stereoselectivities were obtained with the potassium enolate, perhaps due to its increased ionic character. Substituting TMEDA for HMPA in these reactions led in all but one case to reduced stereoselectivities. The results support and are interpreted in terms of the π-metal association model previously proposed.

JOHN M. MCINTOSH et KENNETH C. CASSIDY. Can. J. Chem. **66**, 3116 (1988).

On a étudié l'alkylation des énolates de sodium, de potassium, de zinc et de zirconium de l'imine du glycinate de *tert*-butyl du *R*-camphre et on a comparé les résultats stéréochimiques observés avec ceux obtenus avec l'énolate de lithium. On n'a noté aucune différence pour l'énolate de sodium; toutefois, on a obtenu des rendements chimiques et des stéréosélectivités inférieurs avec l'énolate de potassium et ces résultats sont peut-être dus à son plus grand caractère ionique. La substitution, dans ces réactions, du TMEDA par du HMPA provoque dans tous les cas, excepté un, une réduction des stéréosélectivités. Les résultats obtenus sont en accord avec et ils sont interprétés en fonction du modèle d'association π–métal qui a été proposé antérieurement.

[Traduit par la revue]

Can. J. Chem. Downloaded from www.nrcresearchpress.com by 122.72.124.2 on 09/07/12
For personal use only.

Introduction

Recently we presented the results of the alkylation of the *R*-camphor imine of *tert*-butyl glycinate (**1**) with a variety of alkylating agents and showed that the stereochemical results can be nicely rationalized on the basis of electronic and steric effects (1–3). In particular, when π unsaturation is present in the electrophile in a position where it may interact with the enolate system, dramatically increased diastereoselectivities (de's) were observed. It was unclear, however, whether this effect was due to association of the electrophile π system with the π system of the enolate or with the coordination sphere of the metal cation of the enolate, which, in all cases, was lithium. Information on this point can be obtained by determining the effect of changing the metal cation on the stereoselectivity and yield of the reactions. In contrast to aldol reactions (4), this type of information is not routinely available for alkylation reactions. In a recent comprehensive review, Evans (5) classified one of the effects that controls alkylation stereoselectivity as "chelate-enforced chirality transfer" and gave a limited number of examples of the use of cations other than lithium. He also noted that chelation control in the alkylation of some amino acid derivatives is speculative because of the lack of information on enolate geometry. In our case, this uncertainty is absent since the C10 methyl group of camphor demands that the enolate have the *E* configuration. In this paper, the results of changing the metal cation are reported, as is the effect of changing the additive from HMPA (hexamethylphosphoramide) to TMEDA (tetramethylethylenediamine). The results are interpreted in terms of the reaction mechanism and the origin of the observed π effect.

A. Effect of the metal ion (Table 1)

In all cases reported to date, the enolate **2***a* was generated using one equivalent of LDA (lithium diisopropylamide) in THF solution and thus one equivalent of diisopropylamine (DIPA) was present during the alkylation reaction. Previous results had shown that one equivalent of HMPA was required to achieve satisfactory chemical yields, but that two equivalents had a deleterious effect on the de's obtained (2). Identical effects were obtained when this additive was introduced either prior to addition of the electrophile or coincident with it. These conditions will be referred to hereafter as "standard conditions". In either case, the enolate **2***a* was a homogeneous yellow solution.

When NaH was reacted with **1**, no reaction occurred unless a proton transfer reagent was added. To make the conditions as comparable as possible to those of the potassium enolate, one equivalent of *tert*-butyl alcohol was used. A homogeneous solution of **2***b* was obtained, which, upon alkylation with either allyl or benzyl bromide in the presence of HMPA, afforded **3** or **4** respectively. Both the chemical yield and diastereomeric

TABLE 1. Dependence of stereochemistry and yields of products on metal ion in presence of HMPA

Enolate	Electrophile	Product	Yield[a,c]	%de
2*a*	Allyl bromide	**3**	89	76[b]
	BnBr	**4**	80	>98[b]
	^{i}PrI	**5**	20[80]	67[d]
	^{i}PrI	**5**	86[g]	65
2*b*	Allyl bromide	**3**	72	72
	BnBr	**4**	89	>98
2*b*′	Allyl bromide	**3**	75	71
	BnBr	**4**	80	>98
	^{i}PrI	**5**	60[g]	67
2*c*	Allyl bromide	**3**	36[50]	67
	BnBr	**4**	54[67]	66
	BnBr	**4**	55[68][e]	60
	BnBr	**4**	65[f]	65
	^{i}PrI	**5**	8[19][g]	68
2*d*	Allyl bromide	**3**	24[75]	73
	BnBr	**4**	30[73]	>98
2*e*	Allyl bromide	**3**	41[67]	82
	BnBr	**4**	32[45]	>98

[a]All reactions done at −78°C for 1–2 h.
[b]Reported in ref. 2.
[c]Square brackets denote yields based on unrecovered starting material.
[d]Reported in ref. 1.
[e]Two equivalents of HMPA were used.
[f]Reaction run at −100°C.
[g]Reaction run at −20°C.

[1]For part 3, see ref. 1.

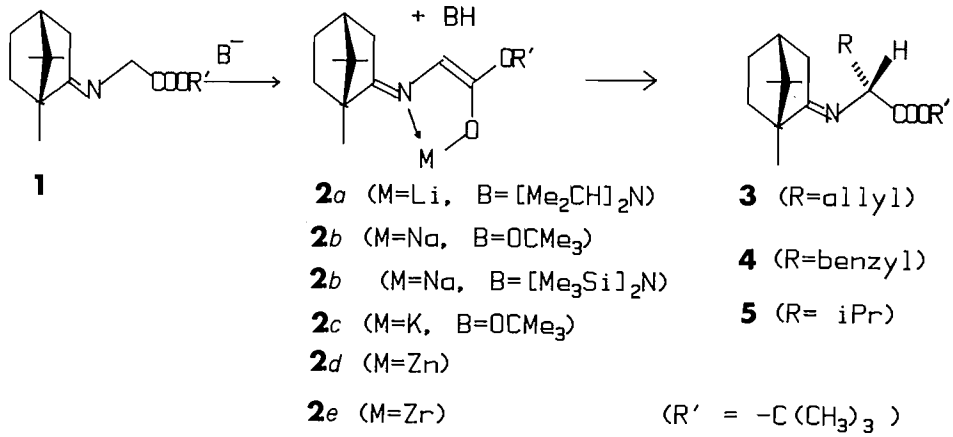

SCHEME 1

excesses obtained as determined by 300 MHz ^{1}H nmr measurements were indistinguishable from those obtained using enolate **2***a*. To better duplicate the reaction conditions used in the alkylation of **2***a*, the reactions were repeated using sodium hexamethyldisilazide as the base. The reactions of enolate **2***b*′ generated in this manner showed identical behavior to **2***a* and **2***b* (Table 1). Seebach and co-workers (6) have shown that the conjugate acid of the base used can have a significant effect on reactions of the enolate. The similarity of the reactions of **2***b* and **2***b*′ is reassuring.

The physical nature of enolate **2***c*, which was prepared using KO^{t}Bu, depended strongly on the temperature of its generation. At −20°C a precipitate formed immediately, which could not be stirred magnetically unless two equivalents of HMPA were added. When one equivalent of HMPA was added *simultaneously* with the base, a stirrable, but very turbid, heterogeneous mixture resulted. When enolate **2***c* was generated at −78°C in the presence of one equivalent of HMPA, a yellow-orange solution was formed, which persisted for approximately 15 min, at which time a precipitate formed. The process was not reversible. Enolate formation at −100°C, again in the presence of HMPA, gave a stable yellow-orange solution of enolate **2***c*. Alkylation of **2***c* generated at any of the above temperatures with allyl or benzyl bromide gave indentical results. (Alkylation with isopropyl iodide required a temperature of −20°C and therefore was necessarily conducted on the suspended enolate.) In every case, the chemical yield was low and the de values obtained with those electrophiles for which π association has been invoked (allyl and benzyl bromides) (1, 2) were severely reduced while that for isopropyl iodide, where no such association is possible, was unaffected.

The Zn^{2+} enolate (**2***d*) was prepared by exchanging Zn for Li at −78°C. When **2***d* was alkylated, poor chemical yields were obtained but the diastereoselectivities were comparable with those obtained under standard conditions. Finally, when enolate **2***a* was treated with one equivalent of Cp_2ZrCl_2 followed by either allyl or benzyl bromide, **3** and **4** were obtained. The de of the benzylated product **4** was unchanged whereas that of **3** increased slightly to 82%.

B. Effect of the additive

When one equivalent of TMEDA, a bidentate ligand, was used in place of HMPA with enolates **2***a*, **2***b*′, or **2***c*, alkylation with allyl or benzyl bromides or isopropyl iodide gave the results shown in Table 2. In the case of enolate **2***a* a severe reduction in the chemical yield and diastereoselectivity was observed for all three electrophiles, whereas very little effect was noted when enolates **2***b*′ and **2***c* were used.

TABLE 2. Stereochemistry and yields of products using TMEDA as additive

Enolate	Electrophile	Product	Yield[a,b]	%de
2*a*	Allyl bromide	**3**	56[72]	69
	BnBr	**4**	45[62]	82
	^{i}PrI	**5**	4[18][c]	57
2*b*′	Allyl bromide	**3**	72	73
	BnBr	**4**	84	>98
	^{i}PrI	**5**	60[c]	64
2*c*	Allyl bromide	**3**	45[62]	66
	BnBr	**4**	35[54]	70
	BnBr	**4**	54[67][d]	70
	^{i}PrI	**5**	43[63][c]	69

[a]All reactions done at −78°C for 1–2 h.
[b]Square brackets denote yields based on unrecovered starting material.
[c]Reaction run at −20°C.
[d]Reaction run at −100°C.

Discussion

In the generation of enolates **2***b* and **2***c*, one equivalent of *tert*-butyl alcohol is generated. The corresponding conjugate acid formed in the Li case is diisopropylamine, which is also present in both **2***d* and **2***e*. The fact that the chemical yields and diastereomeric excesses obtained using **2***b* did not diminish significantly suggests that the presence of *tert*-butyl alcohol is, in itself, not deleterious and therefore not responsible for the reduced yields using **2***c*. Further support for this conclusion can be found in a comparison of the alkylations of enolates **2***b* and **2***b*′.

The solubility phenomenon described for enolate **2***c* is ascribed to aggregation effects. As initially generated, the enolate is monomeric and soluble. As the temperature increases, the rate of combination into insoluble aggregates increases, aided by the more ionic character of potassium. It may be that the enolate has changed to an extended one from which reduced de's might be expected. However, the low yield and selectivity obtained using **2***c* cannot be ascribed to the physical state of the enolate since, at −100°C, the homogeneous solution of **2***c* gave the same results as the heterogeneous mixture at −20°C and, also, alkylation with isopropyl iodide gave the same stereoselectivity as obtained with enolate **2***a*. The

Can. J. Chem. Downloaded from www.nrcresearchpress.com by 122.72.124.2 on 09/07/12
For personal use only.

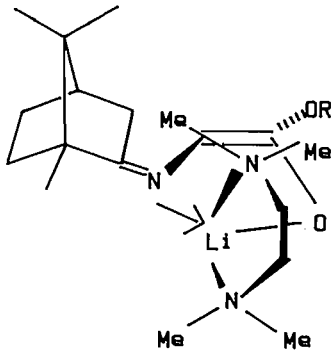

FIG. 1

use of two equivalents of HMPA in the reaction of **2***c* with benzyl bromide did not lead to significantly reduced de's. This stands in contrast to the results obtained with enolate **2***a*. Thus it seems that the aggregation state of enolate **2***c* may be responsible for the reduced chemical yields but not the lowered stereochemistry of the reaction.

The effect of the additive is especially interesting. As previously noted, whereas one equivalent of HMPA is required for acceptable yields in the alkylation of **2***a*, two equivalents significantly reduce the stereoselectivity. Lithium is known to be tetracoordinate in a tetrahedral geometry. Also, it is generally accepted that electronic forces operating beyond the first coordination sphere are weak and that alkali metal cations are seldom complexed by neutral ligands unless chelation can occur (7). Thus, coordinated HMPA in the lithium enolate should be much more easily displaced than should TMEDA. Complexation with TMEDA as shown in Fig. 1 should add significant steric bulk on both the *re* and *si* faces of the planar enolate system, making π association much less favorable and reducing the stereoselectivity of the reaction. Coordination to sodium should be even weaker and it appears that here HMPA and TMEDA are comparable. Both allow the interaction that leads to the enhanced stereoselectivity. When potassium is the counterion, the selectivity is reduced to a level that seems independent of the amount and nature of the additive. It is significant that this level of chiral induction is that observed with bulky aliphatic halides where no association of the kind invoked in our previous papers can occur. Of all the metal cations used in this study, potassium should be the most weakly complexing. The observed significant reduction in stereoselectivity suggests that the effect responsible for the correlation of diastereoselectivity with π unsaturation is π–metal, not π–π, coordination.

It should be noted also that the metal cations used in this study differ considerably in their atomic radii. It is possible that as the radius of the metal atom in the cyclic enolate increases, the metallocycle may begin to deviate significantly from planarity. The approach of the electrophile may then be along a path that does not efficiently discriminate between the *re* and *si* faces.

In summary, the following appear to rationalize the results. In the absence of a *chelating* additive and using enolate **2***a*, or using enolate **2***b* with either type of additive, an essentially covalent cyclic enolate ion of the type previously envisaged (Scheme 1) is formed. The function of HMPA in these cases may be to deaggregate the enolate (8). However, with the exception of the coordination of TMEDA to lithium, the coordination of any additive with the remaining two coordination sites on lithium or sodium must be so weak that little impediment to the association of the electrophile with the metal is present. The presence of TMEDA with lithium leads to an effective coordination that imposes larger steric requirements on the *re* face (and may destroy the cyclic nature of the enolate) and reduces the asymmetric induction.

When potassium is used, sufficient ionic character is imparted to the enolate to favor its aggregation and render it essentially insoluble in the organic medium. Even the presence of HMPA cannot prevent this, and the metallocycle structure of the enolate may have been destroyed. In the zinc and zirconium cases, strong cyclic chelation and π–metal association would be expected and the observed de's support this contention.

Experimental

The preparation of **1**, the general details for the formation and alkylation of enolate **2***a*, and the determination of the diastereomeric excesses (de's) have been published previously (1). The preparation and alkylation of enolates **2***b*-**2***e* are given below. The experiments using TMEDA as the additive were performed in an exactly analogous manner, substituting it for HMPA.

Enolate 2b

To a cold mixture of **1** (1.0 g, 3.77 mmol) and 1.1 equiv. of oil-free sodium hydride in 5 mL of dry THF was added 1 equiv. of *tert*-butyl alcohol under nitrogen. The mixture was stirred at 0°C for 0.5 h to afford a clear yellow solution of **2***b*. The solution was cooled to −78°C and a THF solution containing 1 equiv. of each of the alkylating agent and HMPA was added dropwise. After 1 h, the reaction was quenched at −78°C and work-up and purification were effected as previously reported (1). The results are shown in Table 1.

Enolate 2b′

A cold solution of **1** (1.0 g, 3.77 mmol) and 1 equiv. of HMPA in 5 mL of dry THF were added dropwise with stirring to 3.8 mL of a solution of sodium hexamethyldisilazide (1 M in THF). The solution was cooled to −78°C and alkylated as described above for enolate **2***b*.

Enolate 2c

To a cold solution of 0.43 g (3.8 mmol) of potassium *tert*-butoxide in 5 mL of dry THF was added a solution of **1** (1.0 g, 3.77 mmol) at −20°C in the same solvent. Immediate precipitation of the enolate caused the solidification of the mixture. It required the addition of 2 equiv. of HMPA to provide a heterogeneous but stirrable mixture that could be alkylated. If 1 equiv. of HMPA was added to the base *simultaneously* with **1**, a tractable slurry was obtained, which was cooled to −78°C and alkylated in the usual way. The results are given in Table 1.

Generation of the enolate at −78°C in the presence of 1 equiv. HMPA afforded **2***c* as a yellow-orange solution that precipitated after ca. 15 min. When enolate formation was carried out at −100°C, the enolate remained in solution.

Enolate 2d

To a solution of **2***a* in the THF generated in the usual way was added 1 equiv. of solution of anhydrous $ZnCl_2$ in ether. After stirring for 30 min, the solution had changed from orange to yellow. The solution was cooled to −78°C and the alkylation performed in the usual manner. The results are given in Table 1.

Enolate 2e

To a solution of **2***a* in dry, degassed THF was added a THF solution of 1 equiv. of Cp_2ZrCl_2 at −78°C under nitrogen. The color of the solution changed from orange to a dark red-brown. Alkylation and work-up were performed in the standard manner. The results are given in Table 1.

Acknowledgements

The financial assistance of the Natural Sciences and Engineering Research Council of Canada in the form of operating grants and an equipment grant for the purchase of the NMR facility made this work possible and is most gratefully acknowledged.

Can. J. Chem. Downloaded from www.nrcresearchpress.com by 122.72.124.2 on 09/07/12
For personal use only.

1. J. M. McINTOSH, K. C. CASSIDY, R. K. LEAVITT, P. MISHRA, J. E. DRAKE, and R. CHADHA. J. Org. Chem. **53**, 1954 (1988).
2. J. M. McINTOSH and P. MISHRA. Can. J. Chem. **64**, 726 (1985).
3. J. M. McINTOSH and R. K. LEAVITT. Tetrahedron Lett. **27**, 3839 (1986).
4. C. H. HEATHCOCK. *In* Asymmetric synthesis. Vol. 3. *Edited by* J. D. Morrison. Academic Press, New York, NY. 1984. p. 111.
5. D. A. EVANS. *In* Asymmetric synthesis. Vol 3. *Edited by* J. D. Morrison. Academic Press, New York, NY. 1984. p. 1.
6. T. LAUBE, J. D. DUNITZ, and D. SEEBACH. Helv. Chim. Acta, **68**, 1373 (1985).
7. A. J. LAYTON, R. S. NYHOLM, A. K. BANNERJEE, D. E. FENTON, C. N. LESTAS, and M. R. TRUTER. J. Chem. Soc. (A), 1984 (1970).
8. R. AMSTUTZ, W. B. SCHWEIZER, D. SEEBACH, and J. DUNITZ. Helv. Chim. Acta, **64**, 2617 (1981), and references cited therein.

Can. J. Chem. Downloaded from www.nrcresearchpress.com by 122.72.124.2 on 09/07/12
For personal use only.

The chemistry of platinum hydrides. Part XXX.[1] The chemical and structural effects of steric overcrowding in the compounds *cis*- and *trans*-H[R_3Sn]Pt(PCy_3)$_2$, R = Ph, Cl

HOWARD C. CLARK,[2] GEORGE FERGUSON, MARK J. HAMPDEN-SMITH,[3] HEINZ RUEGGER, AND BARBARA L. RUHL

Guelph-Waterloo Centre for Graduate Work in Chemistry, Guelph Campus, University of Guelph, Guelph, Ont., Canada N1G 2W1

Received April 21, 1988

HOWARD C. CLARK, GEORGE FERGUSON, MARK J. HAMPDEN-SMITH, HEINZ RUEGGER, and BARBARA L. RUHL. Can. J. Chem. **66**, 3120 (1988).

The reaction of $Pt^0(PCy_3)_2$ with triphenyltin hydride yields *cis*-H(Ph_3Sn)Pt(PCy_3)$_2$ as the initial product; isomerization to the *trans* isomer is accelerated by light, heat, and the presence of free phosphine. Both isomers have been characterized by multinuclear nmr spectroscopy; in particular, the $^{31}P\{^1H\}$ spectra in solution are correlated with the solid state CP/MAS ^{31}P nmr spectra and the crystal structure. The crystal structures of *trans*-H(X_3Sn)Pt(PCy_3)$_2$ X = Ph or Cl have been determined and the nature of the distortions produced by steric overcrowding is identified and discussed.

HOWARD C. CLARK, GEORGE FERGUSON, MARK J. HAMPDEN-SMITH, HEINZ RUEGGER et BARBARA L. RUHL. Can. J. Chem. **66**, 3120 (1988).

Le composé $Pt^0(PCy_3)_2$ réagit avec l'hydrure de triphénylétain pour donner le composé H(Ph_3Sn)Pt(PCy_3)$_2$ *cis* comme produit initial; la lumière, la chaleur et la présence de phosphine libre accélèrent l'isomérisation en isomère *trans*. On a caractérisé les deux isomères par spectroscopie de rmn à noyaux multiples. On a déterminé, en particulier, les rapports existants entre les spectres du $^{31}P\{^1H\}$ en solution, les spectres RMN de ^{31}P CP/MAS à l'état solide et la structure cristalline. On a déterminé les structures cristallines du composé H(X_3Sn)Pt(PCy_3)$_2$, X = Ph ou Cl et on a identifié la nature des distorsions produites par l'encombrement.

[Traduit par la revue]

Introduction

Compounds containing platinum(II)–tin(IV) bonds have been extensively investigated (1) largely because many of these systems function as effective homogeneous hydrogenation catalysts. A large number of such compounds have been fully characterized and a variety of preparative methods are available (2–6). A common method involves oxidative addition of organotin compounds to zerovalent tertiary phosphine complexes of Pt(II) (5), e.g.

[1] $(PPh_3)_2Pt(C_2H_4) + R^1R^2R^3R^4Sn \rightarrow R^1[R^2R^3R^4Sn]Pt(PPh_3)_2 + C_2H_4$

By this method, Pidcock and co-workers (5, 6) have prepared both *cis* and *trans* isomers of compounds $R^1[R^2R^3R^4Sn]$-$Pt(PPh_3)_2$ where R^{1-4} are alkyl, aryl, or halide, and where the nature of the group (R^1) transferred from tin to platinum depends on the nature of the various substituents on tin (R^1–R^4). Thus, the tin substrates $SnPh_4$, $SnPh_3Cl$, $SnPh_2Cl_2$, $SnMe_4$, and $SnMe_3Cl$ react with Pt(0) species via Sn—C bond cleavage, whereas $SnPhCl_3$, $SnMe_2Cl_2$, and $SnCl_4$ react via Sn—Cl bond cleavage. In such reactions, the *cis*-stereochemistry predominates when Sn—C cleavage occurs, but small amounts of *trans*-isomers are observed when Sn—Cl bond scission occurs. In these systems, a number of reaction pathways are possible; attempts to observe radical intermediates by esr spectroscopy were unsuccessful, perhaps surprising in view of the extensive radical chemistry of organotin compounds.

Previously, it was reported from this laboratory (3) that triphenyltin hydride reacts with a variety of bis(tertiaryphosphine) platinum(II) dihydrides to form bis-tin-, mono-tin-, or no tin- platinum products apparently depending on the steric bulk of the tertiary phosphine ligands. No tin–platinum product was isolated from the reaction of $HSnPH_3$ and $Pt^0(PCy_3)_2$ over a period of 1 h. More recently, however, we found[4] that $HSiPh_3$ reacts with $Pt^0(PCy_3)_2$ to form exclusively *cis*-H(Ph_3Si)Pt(PCy_3)$_2$ which could be quantitatively isomerized to the *trans* analogue by exposure to uv light. Clearly, the course of these reactions is influenced by the steric crowding at the platinum centre; indeed, given the steric bulk of the tricyclohexylphosphine ligand and of —SnX_3, these molecules must be severely distorted. We have therefore examined in more detail the reaction of $HSnPh_3$ with $Pt^0(PCy_3)_2$ to gain some better understanding of these reactions and have also determined the crystal structures of two molecules *trans*-H(SnX_3)Pt(PCy_3)$_2$, X = Ph or Cl, as a means of observing the steric overcrowding.

Experimental

All reactions were carried out using Schlenck apparati and techniques or adaptations of them, utilizing a dry nitrogen atmosphere and dry solvent. Our general preparative techniques have previously been described (7). Elemental analyses were carried out by Guelph Chemical laboratories.

(I) Preparation of trans-*H[Ph_3Sn]Pt(PCy_3)$_2$*

(i) From $HSnPh_3$ and $^0Pt(PCy_3)_2$

trans-$(PCy_3)_2PtCl_2$ (530 mg, 0.64 mmol) was reduced with sodium naphthalide according to the literature method (8). To the pale yellow hexane extract containing $Pt(PCy_3)_2$, 250 mg (0.71 mmol) of $HSnPh_3$ was added dropwise. The solution darkened slightly and after 3 h of stirring some white precipitate had been formed. The stirring was continued for a further 12 h, during which some of the white precipitate redissolved. The solution was filtered to yield 324 mg of a white solid, found to be *trans*-H[Ph_3Sn]Pt(PCy_3)$_2$ by ^1H and ^{31}P nmr spectroscopy

[1]For Part XXIX, see ref. 26.

[2]Present address: Department of Chemistry, Dalhousie University, Halifax, N.S., Canada B3H 4H6.

[3]Present address: Department of Chemistry, Indiana University, Bloomington, IN, USA.

[4]H. C. Clark and M. J. Hampden-Smith. Unpublished results.

Can. J. Chem. Downloaded from www.nrcresearchpress.com by 122.72.124.2 on 09/07/12
For personal use only.

Can. J. Chem. Downloaded from www.nrcresearchpress.com by 122.72.124.2 on 09/07/12
For personal use only.

(see data below). Evaporation of the solvent from the supernatant, followed by washing with two 3 mL portions of cold *n*-pentane, led to isolation of a further portion of the *trans*-product (185 mg) to give an overall yield of 509 mg (0.46 mmol.), 72% based on $(PCy_3)_2PtCl_2$. *trans*-$H[Ph_3Sn]Pt(PCy_3)_2$ calculated for $C_{54}H_{82}P_2SnPt$: C 58.57, H 7.46; found: C 59.32, H 7.29. mp 158–162°C dec. ν(Pt—H) = 2050 cm^{-1}. Single crystals of *trans*-$H[Ph_3Sn]Pt(PCy_3)_2$ were grown by vapour diffusion between a benzene solution of the complex and external ethanol.

(ii) From $O_2Pt(PCy_3)_2$

$(PCy_3)_2PtO_2$ (97 mg, 0.12 mmol) was dissolved in 5 mL of benzene and an excess (100 μL) of Ph_3SnH was added. An immediate evolution of gas was observed and the solution was stirred for 1 h. The solvent was removed and the residue washed with two 4 mL portions of cold *n*-pentane to yield 115 mg of *trans*-$H[Ph_3Sn]Pt(PCy_3)_2$ (84.4%).

In an attempt to observe intermediates in this reaction, an nmr tube was charged with a known weight of $(PCy_3)_2PtO_2$ dissolved in 0.5 mL of $CDCl_3$. The solution was cooled to −60°C in the magnet and a ^{31}P nmr spectrum of the starting material was obtained at this temperature. One half of the stoichiometric amount of Ph_3SnH was added at −76°C and the tube quickly shaken and replaced into the cold magnet. On subsequent warming to −10°C, the ^{31}P nmr spectra taken at 10°C intervals revealed only the presence of starting material ($(PCy_3)_2PtO_2$) and final product (*trans*-$H[Ph_3Sn]Pt(PCy_3)_2$). No other phosphorus resonances were observed.

(II) Preparation of cis-*$H[Ph_3Sn]Pt(PCy_3)_2$*

trans-$Cl_2Pt(PCy_3)_2$ (1.00 g, 1.2 mmol) was reduced with 2 equiv. of sodium naphthalide and the hexane extract was transferred to a darkened Schlenk flask. $HSnPh_3$ was added (155 μL, 0.21 g, 0.6 mmol) and the solution was vigorously stirred in the dark for 3 h. During this period, a fine white precipitate formed which was separated by filtration. The white solid was found to be *cis*-$H[Ph_3Sn]Pt(PCy_3)_2$ (0.6243 g, 0.56 mmol) (93.3% yield based on $HSnPh_3$) by ^1H and ^{31}P nmr spectroscopy. The second equivalent of $HSnPh_3$ was added to the supernatant in room light and resulted in an immediate precipitation and yellowing of the solution. The mixture was stirred for a further 12 h (in room light), after which time the precipitate had redissolved. The solvent was reduced to a quarter of its original volume and the pale yellow solid filtered. This solid was found to be *trans*-$H[Ph_3Sn]Pt(PCy_3)_2$ by (^1H and ^{31}P nmr spectroscopy) (0.3422 g, 0.31 mmol). Total yield of *cis*- and *trans*-$H[Ph_3Sn]Pt(PCy_3)_2$ based on *trans*-$Cl_2Pt(PCy_3)_2$ starting material, 72.5%. *cis*-$H[Ph_3Sn]Pt(PCy_3)_2$: *Anal.* calcd. for $C_{54}H_{82}P_2SnPt$: C 58.78, H 7.46; found: C 58.84, H 7.76. Melting point 147–149°C dec. ν(Pt—H) = 2033 cm^{-1}.

(III) Preparation of trans-*$H[Cl_3Sn]Pt(PCy_3)_2$*

trans-$HClPt(PCy_3)_2$ (108 mg, 0.02 mmol) was dissolved in 15 mL of benzene and 50 mg (0.26 mmol) of $SnCl_2$ were added. The mixture was vigorously stirred as 0.2 mL of water was added to dissolve the tin(II) chloride. After stirring for 2 h the solution was filtered and the solvent was removed *in vacuo*. The white solid obtained was crystallized from a benzene/hexane mixture to give 208 mg (0.21 mmol) of *trans*-$H[Cl_3Sn]Pt(PCy_3)_2$, characterized by nmr spectroscopy, a yield of 92.1%, mp 183–186°C (dec), ν(Pt—H) 2115 cm^{-1}.

(IV) Nuclear magnetic resonance data

(*a*) Solution ^1H and ^{31}P nmr spectra were recorded on either Bruker AM 250 or WH400 nmr instruments. ^1H nmr spectra were referenced either to protio impurity of deuterated solvents, or to tetramethylsilane (TMS). ^{31}P nmr were referenced to external trimethylphosphate, and shifts were reported using the high frequency positive sign convention relative to phosphoric acid. The stereochemistry of *bis*-phosphine platinum(II) hydride species can readily be assigned from a partially proton-coupled ^{31}P nmr spectrum. In this experiment, the alkyl phosphine protons are decoupled at low decoupler power leaving the coupling of the hydride ligand essentially intact. The ^{31}P resonance of a phosphine ligand *trans* to a hydride ligand exhibits the large $J_{H—Pt_{trans}}$ of the order of 150 Hz while the value of $J_{H—P_{cis}}$ commonly lies in the range 20–35 Hz.

(*b*) The ^{31}P CP-MAS nmr spectra was acquired at 81.0 MHz on a Bruker CXP-200 instrument equipped with the standard CP-MAS probe, using the standard cross polarisation pulse program, PENMR.PPG. The Hartman–Hahn condition was set as described elsewhere (9). The magic angle was set by observing the ^{79}Br resonance of KBr and adjusting the angle to give maximum intensity to the spinning side bands. Typical acquisition parameters were as follows: spin rate, 3.5 to 4.0 kHz; 90° pulse, 6.0 μs; contact time, 0.5 ms; spectral width, 20 kHz centered on 0 ppm with respect to external 85% H_3PO_4; data table, 0.5 to 1K zero filled to 4K before Fourier transformation; recycle time, 10 s.

For the compounds prepared above, the following nmr data were recorded:

For *trans*-$H[Ph_3Sn]Pt(PCy_3)_2$: ^1H nmr (in C_6D_6): δ(hydride) = −5.84 ppm, $J_{H—P}$ = 13, $^1J_{H—Pt}$ = 918, $^2J_{H—Sn}$ = 698 Hz; ^{31}P nmr (in C_6D_6): δP = 43.3 ppm; $J_{P—Pt}$ = 2627, $J_{Sn—P}$ = 14.5; ^{119}Sn nmr (in C_6D_6): δSn = −21.8 ppm, $J_{Sn—Pt}$ = 9680 Hz.

For *cis*-$H[Ph_3Sn]Pt(PCy_3)_2$: ^1H nmr (in C_6D_6): δ(hydride) = −5.00 ppm, $^{cis}J_{H—P}$ = 18, $^{trans}J_{H—P}$ = 143, $J_{H—Sn}$ = 26, $J_{H—Pt}$ = 638 Hz; ^{31}P nmr (in C_6D_6): δP_A (*trans* to Sn) = 43.5, δP_B = 41.8, $J_{P_A—P_B}$ = 5, $J_{P_A—Pt}$ = 2568, $J_{P_B—Pt}$ = 2738, $J_{P_A—^{117}Sn}$ = 1750, $J_{P_A—^{119}Sn}$ = 1753, $J_{P_B—Sn}$ = 138 Hz.

For *trans*-$H[Cl_3Sn]Pt(PCy_3)_2$: ^{31}P nmr (in C_6D_6): δP = 44.5 ppm, $J_{P—Pt}$ = 2485, ^{119}Sn nmr (in C_6D_6): δSn = 134 ppm, $J_{^{119}Sn—H}$ = 752, $J_{Sn—P}$ = 11 242. ^1H nmr (in C_6D_6): δ(hydride) = −10.96 ppm (broad); $J_{H—Pt}$ = 1337.3 Hz. Solid State ^{31}P nmr data: for *trans*-$H[Ph_3Sn]Pt(PCy_3)_2$; δP_A = 40.0, δP_B = 44.3, $J_{P—P}$ = 354, $J_{P_A—Pt}$ = 2531, $J_{P_B—Pt}$ = 2683 Hz; for *trans*-$H[Cl_3Sn]Pt(PCy_3)_2$: δP ~41.3 ppm, $J_{P—Pt}$ = 2506 Hz.

(V) ^{31}P nmr tube experiments on cis/trans *isomerization*

These experiments were conducted in 5 mm nmr tubes by dissolving accurately weighed portions (25–35 mg) of solid in 0.5 mL of the appropriate solvent. The limit of solubility of *cis*-$H[Ph_3Sn]Pt(PCy_3)_2$ in benzene-d_6 is approximately 40 mg/0.6 mL (0.072 molar). The *trans*-isomer is very soluble, being even slightly soluble in *n*-hexane. Isomerization reactions, which were followed "in the dark" were run in the magnet (generally overnight) and spectra were recorded at various intervals. Temperatures were calibrated against methanol or ethylene glycol standard, where appropriate.

(VI) X-ray structure determinations for trans-*$H[Ph_3Sn]Pt(PCy_3)_2$ (I) and* trans-*$H[Cl_3Sn]Pt(PCy_3)_2$ (II)*

General crystallographic details for both molecules are given in Table 1. Accurate cell data were obtained by a least-squares treatment of the setting angles (25 for **I**, 12 for **II**) of reflections with θ between 10 and 15°, measured with graphite monochromatized Mo-Kα radiation, on a CAD4 diffractometer for **I** and on a Hilger & Watts Y290 four-circle diffractometer for **II**. The systematic absences for **I** (0*k*0) absent if $k = 2n + 1$) allow the space group to be $P2_1$ or $P2_1/m$; the former was chosen and confirmed by the successful analysis. Molecule **II** is triclinic; space group $P\bar{1}$ was assumed amd established by the analysis.

Both structures were solved via the heavy-atom method, and refined by full-matrix least-squares calculations (using SDP-Plus ref. 10 for **I** and SHELX ref. 11 for **II**). At intermediate stages in the analyses, difference maps revealed maxima in positions consistent with the expected locations of the phenyl and cyclohexyl hydrogen atoms; ripples at the Pt atoms precluded location of the hydrogen at these sites. The hydrogen atoms were then allowed for in geometrically idealised locations (C—H 1.08 A) and included but not refined in the final rounds of calculations in which all non-hydrogen atoms were allowed anisotropic motion. Molecule **I** occurs in the polar space group $P2_1$; at an intermediate stage in the analysis, calculations with the opposite hand gave R = 0.051, whereas the chosen model had R = 0.039. Refinement was then continued until convergence with this model. Final difference maps had no chemically significant features. Weights in the refinement were based on counting statistics with $w = 1/(\sigma - {}^2F_o + pF_o^2)$; scattering factors and anomalous dispersion correction factors were from ref. 12.

TABLE 1. Crystal data and data collection parameters

Formula	$C_{54}H_{82}P_2PtSn$ (**I**)	$C_{36}H_{67}Cl_3P_2PtSn$ (**II**)
M_r	1107.0	982.0
Crystal size, mm	$0.05 \times 0.18 \times 0.30$	$0.15 \times 0.13 \times 0.48$
Space group	$P2_1$, monoclinic	$\bar{P}1$, triclinic
a, Å	10.468(3)	9.485(1)
b, Å	18.627(6)	11.983(2)
c, Å	13.553(3)	21.921(3)
α, deg	90	108.52(1)
β, deg	105.62(2)	104.92(1)
γ, deg	90	93.66(1)
V, Å^3	2545(2)	2254(1)
Z	2	2
D_{calc}, g cm^{-3}	1.44	1.45
F (000)	1128	984
λ(MoKα), cm^{-1}	33.6	39.6
Transmission factors	0.60 to 0.86	—
Scan type	ω/2–θ	ω/2–θ
Scan width, deg	0.60	0.60
Collection range, θ°	2–25	2–20
Unique data	4859	4177
Unique data with $I > 3\sigma(I)$	3889	2987
Parameters refined	522	388
Final R value	0.028	0.058
Final $R_w = (\Sigma w^2/\Sigma wF_o^2)^{1/2}$	0.034	0.076
Largest coordinate shift/error ratio in last cycle	0.03	0.10
p value in weight	0.05	0.04

Refinement details are in Table 1. Tables 2 and 3 contain final fractional coordinates. Principal dimensions for **I** and **II** are given in Table 4. Tables of calculated hydrogen coordinates, all bond lengths and angles, anisotropic thermal parameters and structure factor listings are available as supplementary material.[5] Views of the molecules prepared with the aid of Ortep (ref. 13) are in Figs. 3 and 4.

Results and discussion

Addition of a 50% excess of the stoichiometric amount of $HSnPh_3$ to a hexane solution of $Pt^0(PCy_3)_2$ led to precipitation of analytically pure *trans*-$H[Ph_3Sn]Pt(PCy_3)_2$ over a period of 15 h at room temperature.

$$[2]\quad Pt^0(PCy_3)_2 + \text{excess } HSnPh_3 \xrightarrow{15\text{ h}} \textit{trans}\text{-}H[Ph_3Sn]Pt(PCy_3)_2$$

Evaporation of the solvent *in vacuo* led to recovery of a further portion of *trans*-$H[Ph_3Sn]Pt(PCy_3)_2$ after washing with cold pentane. This organotinplatinum species was characterized by a variety of spectroscopic methods and the structure was determined by X-ray crystallography.

The analogous trichlorostannate complex, *trans*-$H[Cl_3Sn]$-$Pt(PCy_3)_2$, was prepared by the following reaction:

$$[3]\quad \textit{trans}\text{-}HClPt(PCy_3)_2 + SnCl_2 \rightarrow \textit{trans}\text{-}H[Cl_3Sn]Pt(PCy_3)_2$$

By comparison with previous results[6] concerning the oxidative addition of organosilicon hydrides to $Pt^0(PCy_3)_2$, in which products of *cis* geometry were generally obtained, we were surprised to isolate a product of *trans* stereochemistry for the case of $HSnPh_3$. Formation of a *trans* product may arise from a reaction pathway involving a free radical mechanism or by isomerization of an unstable *cis* intermediate, amongst others. We have previously observed such a spontaneous *cis*→*trans*-isomerization process for *cis*-$H[Cl_3Si]Pt(PCy_3)_2$.[6] Using ^{31}P nmr spectroscopy to monitor reactions between $HSnPh_3$ and $Pt^0(PCy_3)_2$, we were able to observe formation of *cis*-$H[Ph_3Sn]$-$Pt(PCy_3)_2$, as an intermediate species. Over a period of

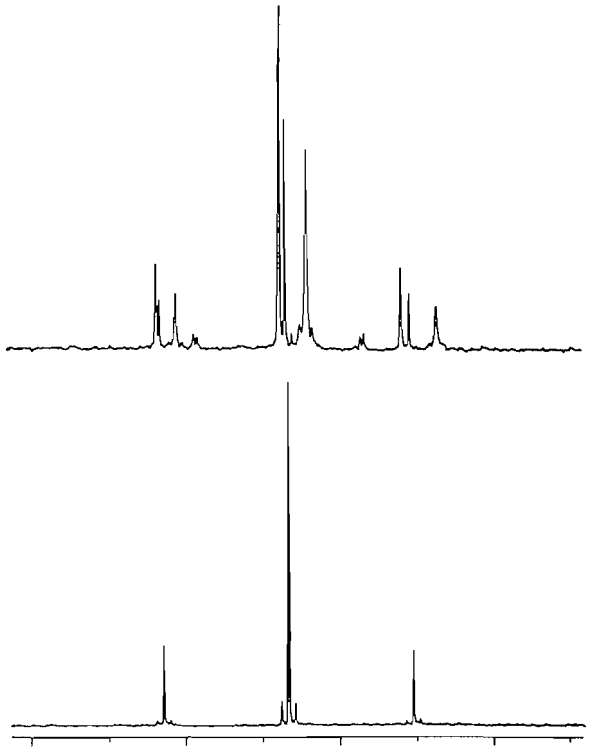

FIG. 1. $^{31}P\{^1H\}$ nmr spectra of (*a*) *cis*-$H[Ph_3Sn]Pt(PCy_3)_2$ and (*b*) after heating for 30 min at 60°C to form *trans*-$H[Ph_3Sn]Pt(PCy_3)_2$.

[5]A complete set of material may be purchased from the Depository of Unpublished Data, CISTI, National Research Council of Canada, Ottawa, Ont., Canada K1A 0S2.

[6]H. C. Clark, and M. J. Hampden-Smith. Unpublished results.

Can. J. Chem. Downloaded from www.nrcresearchpress.com by 122.72.124.2 on 09/07/12
For personal use only.

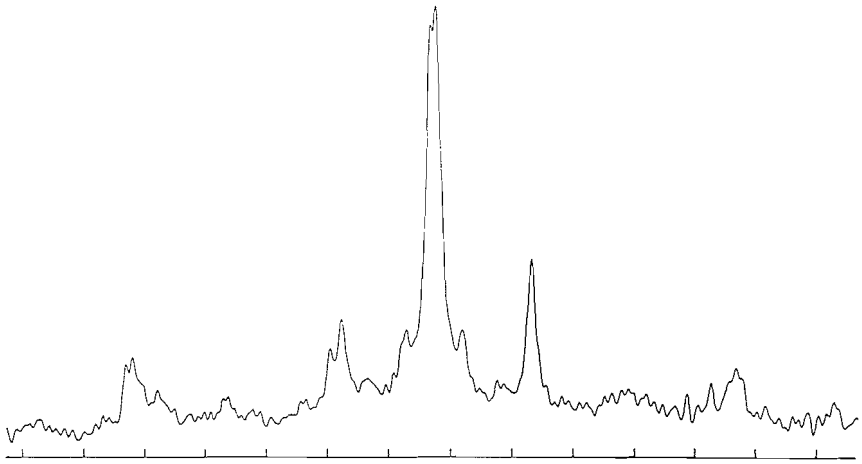

FIG. 2. Solid state CP/MAS ^{31}P nmr spectrum of *trans*-$H[Ph_3Sn]Pt(PCy_3)_2$.

Can. J. Chem. Downloaded from www.nrcresearchpress.com by 122.72.124.2 on 09/07/12
For personal use only.

approximately 4 h at room temperature, the *cis* isomer completely rearranged to its *trans* analogue in these solutions. The *cis* isomer could also be observed on addition of half an equivalent of $HSnPh_3$ to a benzene solution of $(PCy_3)_2Pt(C_2H_4)$ at room temperature and was found to be stable in these solutions. The isolation of only the *trans* analogue from mixtures of excess $HSnPh_3$ and $Pt^0(PCy_3)_2$ is therefore thought to be due to isomerization caused either by one, or a combination, of the following factors; the presence of free PCy_3;[7] excess $HSnPh_3$ which after double oxidative addition to form a platinum(IV) intermediate could eliminate to form preferentially the *trans* isomer; or exposure to light. There are a number of precedents for each of these possibilities. The catalytic *cis–trans* isomerization of Pt(II) phosphine complexes caused by the presence of free phosphine is well known (16). With regard to the second possibility, there is both physical and chemical evidence for the formation of platinum(IV) intermediates in such reactions. Physical evidence, for example, comes from the direct observation of platinum(IV) intermediates by low temperature ^{31}P nmr spectroscopy during the reaction of various silanes with *trans*-$H_2Pt(PCy_3)_2$ (17) while chemical evidence derived from the mixtures of products obtained on addition of $HSnPh_3$, to *trans*-$H[CN(CH_2)_2]Pt(PCy_3)_2$. We have also found that irradiation of the complexes *cis*-$H[Ph_3Si]Pt(PCy_3)_2$ with a weak uv light source is very effective for quantitative isomerization of the *trans* analogues.

On addition of half the stoichiometric amount of $HSnPh_3$ to a hexane solution of $Pt^0(PCy_3)_2$ and stirring for 3 h *in the dark*, a white precipitate was formed. The ^1H and ^{31}P nmr spectra of this white solid showed it to be *cis*-$H[Ph_3Sn]Pt(PCy_3)_2$ and it was found to be analytically pure.

[4] $Pt^0(PCy_3)_2 + HSnPh_3 \rightarrow$ *cis*-$H[Ph_3Sn]Pt(PCy_3)_2$

Addition of the remaining one half equivalent of $HSnPh_3$ to the filtrate led to an immediate precipitation and a yellowing of the solution over a period of 12 h. *cis*-$H[Ph_3Sn]Pt(PCy_3)_2$ does not exhibit either of the fluxional processes observed for its silyl analogue at room temperature. However, on warming to $\geq 50°C$, the ^1H nmr resonance of the hydride ligand exhibits a similar lineshape to that of the complex *cis*-$H[Ph_3Si]Pt(PCy_3)_2$, characteristic of an exchange of ligand position with retention of P—H spin correlation. By comparison with the results obtained for some chelating diphosphine silyl platinum hydrides for which the same fluxional process was observed, we infer that for *cis*-$H[Ph_3Sn]Pt(PCy_3)_2$ the ligand position exchange process involves exchange of the tin and hydride ligands rather than the phosphine ligands. We also note that the corresponding lineshapes in the ^1H nmr spectra of *cis*-$H[Ph_3Si]Pt(PCy_3)_2$ and *cis*-$H[Ph_3Sn]Pt(PCy_3)_2$ occur at $+10$ and $+70°C$, respectively, which implies that a higher energy barrier to site exchange exists for the tin species compared to its silicon analogue. Attempts to observe the platinum(0) species, $Pt^0(PCy_3)_2$, in solutions of *cis*-$H[Ph_3Sn]Pt(PCy_3)_2$ at $+60°C$ by ^{31}P nmr spectroscopy in analogy to the oxidative addition – reductive elimination equilibrium observed for the silyl analogue according to eq. [5] have been unfruitful.

[5] *cis*-$H[Ph_3Si]Pt(PCy_3)_2 \rightleftharpoons Pt^0(PCy_3)_2 + HSiPh_3$

At temperatures greater than $+60°C$, the thermal isomerization of the *cis* species is too rapid to explore this phenomenon further. The possibility that at still higher temperatures, a Pt^{II}–Pt^0 equilibrium exists therefore cannot be precluded. On standing at room temperature in normal light, benzene solutions of pure *cis*-$H[Ph_3Sn]Pt(PCy_3)_2$ isomerize to the *trans* species over a period of about 20 h. On heating to $+60°C$ for less than 0.5 h in the dark, the *cis* isomer is completely transformed into the *trans* derivative as shown by the ^{31}P nmr spectra of Fig. 1. The *cis* → *trans* isomerization is not reversible; this is hardly surprising considering the anticipated severe steric interactions between the ligands of the *cis* isomer. In contrast, it is noteworthy that solutions of the silicon analogue, *cis*-$H[Ph_3Si]Pt(PCy_3)_2$ show no observable isomerization at temperature of up to $+60°C$.

This marked contrast between the apparent thermally allowed *cis*-to-*trans* isomerization of the tin derivative compared to the thermal stability of its *cis*-silyl analogue has led us to examine the mechanism of the isomerization reactions in more detail. In the case of *cis*-$H[Ph_3Sn]Pt(PCy_3)_2$, we can presumably exclude an ionic dissociative mechanism due to a lack of ionizable ligands. The presence of free phoshine may either accelerate or retard the rate of isomerization depending on the mechanism of the process.

We have made the following observations from ^{31}P nmr spectroscopy: (*i*) At room temperature, the addition of 1 equiv. of free PCy_3 to a benzene solution of analytically pure *cis*-

[7] Reduction of *trans*-$(Cy_3P)_2PtCl_2$ with sodium napthelide results in the production of substantial quantities of free PCy_3 as well as $Pt^0(PCy_3)_2$. We have found that increased yields of the platinum (0) species may be obtained by addition of 10–50% mole excess of PCy_3 to the *trans*-$(Cy_3P)_2PtCl_2$ mixture before reduction.

Can. J. Chem. Downloaded from www.nrcresearchpress.com by 122.72.124.2 on 09/07/12
For personal use only.

TABLE 2. Positional parameters and their estimated standard deviations

Atom	x	y	z	B (Å^2)
Pt	0.91811(3)	0.75[a]	0.76193(2)	2.421(5)
Sn	0.74966(6)	0.64168(3)	0.70494(4)	2.57(1)
P1	0.9553(2)	0.7670(1)	0.6043(2)	2.52(5)
P2	0.9158(2)	0.7707(1)	0.9275(2)	2.89(5)
C11	1.0013(9)	0.6849(5)	0.5432(7)	3.3(2)
C12	1.0673(10)	0.6953(6)	0.4557(8)	4.1(2)
C13	1.0871(12)	0.6223(7)	0.4075(8)	5.6(3)
C14	1.1685(11)	0.5717(6)	0.4879(8)	4.7(3)
C15	1.1062(11)	0.5613(6)	0.5752(8)	4.4(3)
C16	1.0847(8)	0.6330(5)	0.6236(7)	3.1(2)
C21	0.8018(9)	0.8006(5)	0.5114(7)	3.3(2)
C22	0.7230(9)	0.8516(6)	0.5610(7)	3.5(2)
C23	0.5925(10)	0.8725(6)	0.4888(9)	5.0(3)
C24	0.6076(11)	0.9028(6)	0.3881(9)	4.7(3)
C25	0.6852(11)	0.8529(7)	0.3394(8)	5.3(3)
C26	0.8204(11)	0.8339(6)	0.4124(7)	4.5(3)
C31	1.0884(9)	0.8316(5)	0.6021(7)	2.8(2)
C32	1.2247(10)	0.8058(5)	0.6688(8)	3.7(2)
C33	1.3378(10)	0.8568(7)	0.6654(9)	5.0(3)
C34	1.3087(12)	0.9316(6)	0.6968(11)	5.9(3)
C35	1.1748(11)	0.9588(5)	0.6290(8)	4.0(2)
C36	1.0630(10)	0.9083(5)	0.6337(7)	3.3(2)
C41	0.8339(10)	0.7072(5)	0.9968(7)	3.2(2)
C42	0.8851(11)	0.6314(6)	1.0024(8)	4.5(3)
C43	0.7971(14)	0.5802(6)	1.0435(9)	5.7(3)
C44	0.7854(15)	0.6050(7)	1.1466(8)	6.6(3)
C45	0.7409(13)	0.6805(7)	1.1461(8)	6.4(3)
C46	0.8266(12)	0.7305(7)	1.1042(8)	5.4(3)
C51	0.8318(9)	0.8576(5)	0.9371(7)	3.5(2)
C52	0.8680(12)	0.9187(6)	0.8718(9)	4.8(3)
C53	0.8055(14)	0.9899(6)	0.8900(11)	6.5(4)
C54	0.6607(15)	0.9832(7)	0.8692(11)	7.7(4)
C55	0.6189(12)	0.9225(8)	0.9269(10)	6.5(3)
C56	0.6817(11)	0.8510(7)	0.9103(9)	4.9(3)
C61	1.0872(9)	0.7788(6)	1.0139(7)	4.2(2)
C62	1.1767(12)	0.7208(7)	0.9904(8)	5.0(3)
C63	1.3157(12)	0.7218(8)	1.0668(10)	6.8(4)
C64	1.3804(13)	0.7913(10)	1.0726(11)	8.8(4)
C65	1.2886(13)	0.8514(10)	1.0900(12)	8.8(5)
C66	1.1529(11)	0.8528(7)	1.0146(9)	5.3(3)
C71	0.5892(8)	0.6200(5)	0.7752(6)	2.7(2)
C72	0.5124(10)	0.6743(6)	0.7978(7)	3.7(2)
C73	0.4064(11)	0.6606(7)	0.8379(8)	5.4(3)
C74	0.3771(10)	0.5909(7)	0.8575(8)	4.8(3)
C75	0.4531(12)	0.5359(7)	0.8381(8)	5.2(3)
C76	0.5567(11)	0.5493(6)	0.7971(8)	4.3(3)
C81	0.8342(9)	0.5341(5)	0.7115(7)	3.2(2)
C82	0.7653(11)	0.4778(5)	0.6549(7)	3.9(2)
C83	0.8171(13)	0.4091(6)	0.6624(8)	5.4(3)
C84	0.9398(14)	0.3950(6)	0.7258(9)	6.2(3)
C85	1.0075(12)	0.4484(7)	0.7818(8)	5.3(3)
C86	0.9590(11)	0.5177(6)	0.7764(8)	4.4(3)
C91	0.6224(8)	0.6426(5)	0.5479(6)	3.0(2)
C92	0.5062(10)	0.6817(6)	0.5249(8)	4.1(2)
C93	0.4262(10)	0.6886(7)	0.4240(10)	5.7(3)
C94	0.4654(13)	0.6541(7)	0.3432(9)	6.1(3)
C95	0.5768(13)	0.6147(6)	0.3665(8)	5.4(3)
C96	0.6568(13)	0.6077(5)	0.4664(7)	3.7(2)

[a]The y-coordinate of Pt was fixed to define the origin.

TABLE 3. Positional parameters and estimated standard deviations[a]

Atom	x	y	z
Pt	0.01385(11)	0.10840(9)	0.28464(5)
Sn	−0.16971(19)	0.26059(15)	0.29634(9)
CL1	−0.2174(8)	0.3560(6)	0.4002(4)
CL2	−0.4221(8)	0.2199(7)	0.2290(4)
CL3	−0.1071(8)	0.4352(6)	0.2720(4)
P1	0.1917(7)	0.2034(5)	0.3860(3)
P2	−0.0924(7)	−0.0206(5)	0.1750(3)
C11	0.2956(24)	0.3458(17)	0.3921(12)
C12	0.2379(28)	0.4587(20)	0.4298(13)
C13	0.3327(30)	0.5705(20)	0.4312(14)
C14	0.3429(30)	0.5701(23)	0.3646(15)
C15	0.3882(33)	0.4587(20)	0.3271(14)
C16	0.2982(29)	0.3463(20)	0.3233(12)
C21	0.1242(25)	0.2328(20)	0.4600(11)
C22	0.0073(27)	0.1369(21)	0.4562(12)
C23	−0.0549(31)	0.1782(23)	0.5170(14)
C24	0.0621(31)	0.2134(24)	0.5824(13)
C25	0.1861(34)	0.3059(24)	0.5885(14)
C26	0.2518(27)	0.2664(22)	0.5292(11)
C31	0.3465(26)	0.1120(20)	0.3985(12)
C32	0.4388(27)	0.1089(26)	0.3501(14)
C33	0.5594(30)	0.0318(28)	0.3623(17)
C34	0.4998(34)	−0.0916(26)	0.3582(16)
C35	0.4181(40)	−0.0846(30)	0.4045(18)
C36	0.2906(34)	−0.0088(21)	0.3970(15)
C41	−0.2987(22)	−0.0513(21)	0.1381(11)
C42	−0.3614(26)	−0.1101(23)	0.0637(13)
C43	−0.5246(28)	−0.1132(29)	0.0429(15)
C44	−0.5989(29)	−0.1717(28)	0.0795(15)
C45	−0.5404(28)	−0.1180(27)	0.1526(16)
C46	−0.3718(27)	−0.1123(24)	0.1745(13)
C51	−0.0209(28)	−0.1648(20)	0.1636(12)
C52	−0.0395(34)	−0.2220(24)	0.2138(17)
C53	0.0592(39)	−0.3176(26)	0.2154(19)
C54	0.0206(39)	−0.4082(26)	0.1408(19)
C55	0.0341(40)	−0.3508(24)	0.0907(19)
C56	−0.0533(35)	−0.2522(26)	0.0945(16)
C61	−0.0265(25)	0.0438(20)	0.1181(11)
C62	−0.0897(30)	0.1605(24)	0.1199(13)
C63	−0.0358(32)	0.2178(26)	0.0752(13)
C64	0.1295(33)	0.2404(28)	0.0956(16)
C65	0.1959(31)	0.1294(25)	0.0952(13)
C66	0.1459(25)	0.0737(22)	0.1411(12)

[a]Anisotropically refined atoms are given in the form of the isotropic equivalent thermal parameter defined as: $(4/3)[a^2B(1,1) + b^2B(2,2) + c^2B(3,3) + ab(\cos\gamma)B(1,2) + ac(\cos\beta) \times B(1,3) + bc(\cos\alpha)B(2,3)]$.

$H[Ph_3Sn]Pt(PCy_3)_2$ does not significantly alter the rate of isomerization compared to a benzene solution of pure *cis*-$H[Ph_3Sn]Pt(PCy_3)_2$ of similar concentration in the dark. The *cis* isomer is essentially unchanged after 20 h in C_6D_6 solution in the dark. (*ii*) The isomerization is faster in $CDCl_3$ (complete within 15 h) than C_6D_6 in the dark, and is accelerated at higher temperatures (in $CDCl_3$ completely isomerized in 2.5 h at 313 K in the dark). (*iii*) Addition of 1 equiv. of $HSnPh_3$ to benzene solutions of *cis*-$H[Ph_3Sn]Pt(PCy_3)_2$ resulted in a slight increase in the rate of isomerization. (*iv*) Changing the concentration of solutions of *cis*-$H[Ph_3Sn]Pt(PCy_3)_2$ did not alter the rate of isomerization, and so *inter*molecular mechanisms may be precluded. (*v*) A $CDCl_3$ solution of *cis*-$H[Ph_3Sn]Pt(PCy_3)_2$ exposed to room light had completely isomerized within (i.e. in less than) 5 h. (*vi*) Addition of 1 equiv. of PCy_3 to a $CDCl_3$ solution of the *cis* isomer of similar concentration as (*i*) at 313 K led to complete isomerization within 10 min.

On the preparative scale, a hexane solution containing a mixture of $Pt^0(PCy_3)_2$, excess $HSnPh_3$, and PCy_3 results in isolation of the *trans* isomer alone over a period of only 15 h. Since the observations (*i*), (*ii*), and (*iii*) above, all of which were followed by ^{31}P nmr spectroscopy, were made in the dark,

Can. J. Chem. Downloaded from www.nrcresearchpress.com by 122.72.124.2 on 09/07/12
For personal use only.

TABLE 4. Principal dimensions for (**I**) $H[Ph_3Sn]Pt(PCy_3)_2$ and (**II**) $H[ClySn]Pt(PCy_3)_2$

I		II	
Atoms	Distance (Å)	Atoms	Distance (Å)
Pt—Sn	2.6539(6)	Pt—Sn	2.600(2)
Pt—P1	2.294(2)	Pt—P1	2.302(5)
Pt—P2	2.283(2)	Pt—P2	2.319(5)
Sn—C71	2.180(10)	Sn—CL1	2.375(8)
Sn—C81	2.183(9)	Sn—CL2	2.392(7)
Sn—C91	2.186(8)	Sn—CL3	2.394(9)
P1—C11	1.863(10)	P1—C11	1.86(2)
P1—C21	1.862(9)	P1—C21	1.83(3)
P1—C31	1.847(9)	P1—C31	1.90(3)
P2—C41	1.857(11)	P2—C41	1.88(2)
P2—C51	1.864(10)	P2—C51	1.86(3)
P2—C61	1.866(9)	P2—C61	1.87(3)

I		II	
Bonds	Angle (deg)	Bonds	Angle (deg)
Sn—Pt—P1	95.75(5)	Sn—Pt—P1	98.2(2)
Sn—Pt—P2	103.44(6)	Sn—Pt—P2	101.8(2)
P1—Pt—P2	160.24(8)	P1—Pt—P2	159.0(2)
Pt—Sn—C71	122.9(2)	Pt—Sn—CL1	122.0(2)
Pt—Sn—C81	117.1(2)	Pt—Sn—CL2	124.4(2)
Pt—Sn—C91	117.4(3)	Pt—Sn—CL3	115.4(2)
C71—Sn—C81	99.4(4)	CL1—Sn—CL2	95.6(3)
C71—Sn—C91	95.0(3)	CL1—Sn—CL3	98.1(3)
C81—Sn—C91	100.5(3)	CL2—Sn—CL3	95.2(3)
Pt—P1—C11	115.4(3)	Pt—P1—C11	114.4(8)
Pt—P1—C21	110.2(3)	Pt—P1—C21	114.7(7)
Pt—P1—C31	115.0(3)	Pt—P1—C31	110.9(6)
C11—P1—C21	104.7(4)	C11—P1—C21	107.8(10)
C11—P1—C31	103.9(4)	C11—P1—C31	101.3(11)
C21—P1—C31	106.7(4)	C21—P1—C31	106.6(12)
Pt—P2—C41	121.2(3)	Pt—P2—C41	119.9(7)
Pt—P2—C51	110.2(3)	Pt—P2—C51	109.7(7)
Pt—P2—C61	111.6(3)	Pt—P2—C61	107.8(6)
C41—P2—C51	103.2(5)	C41—P2—C51	109.2(11)
C41—P2—C61	103.4(4)	C41—P2—C61	103.8(11)
C51—P2—C61	106.1(5)	C51—P2—C61	105.5(12)

Mean cyclohexyl C—C 1.52 Å Mean cyclohexyl C—C 1.52 Å
Mean aromatic C—C 1.38 Å

we also investigated the effect of exposure to light on solutions of *cis*-$H[Ph_3Sn]Pt(PCy_3)_2$. From these observations, it seems likely that the presence of light is responsible for the *cis*-to-*trans* isomerization in the preparative scale reaction rather than excess PCy_3 or $HSnPh_3$ at room temperature. However, from (*v*) above, it appears that the presence of free phosphine would accelerate rather than retard the isomerization process. The increase in rate with added phosphine implies intermediacy of a 5-coordinate species rather than prior phosphine dissociation (in which case added phosphine would reduce the rate of isomerization). The observation that the rate of isomerization is faster in a polar solvent than a non-polar solvent, (*iii*), is rather surprising since it was expected that the polar solvent would stabilize the more polar *cis* isomer.

Addition of a large excess of $HSnPh_3$ to a benzene solution of $(PCy_3)_2PtO_2$ resulted in a vigorous gas evolution and the ^1H and ^{31}P nmr spectra of the product showed it to be *trans*-$H[Ph_3Sn]Pt(PCy_3)_2$.

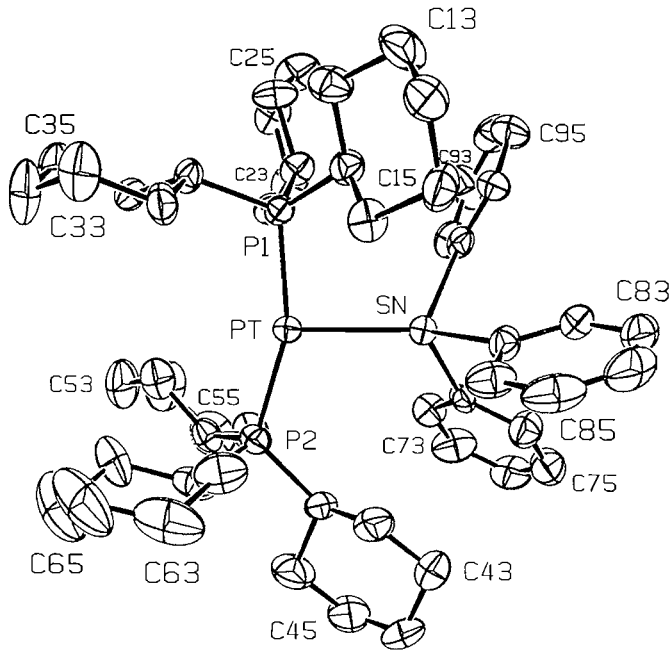

FIG. 3. A view of $H[Ph_3Sn]Pt(PCy_3)_2$ showing the crystallographic numbering scheme. Ellipsoids are at the 50% level.

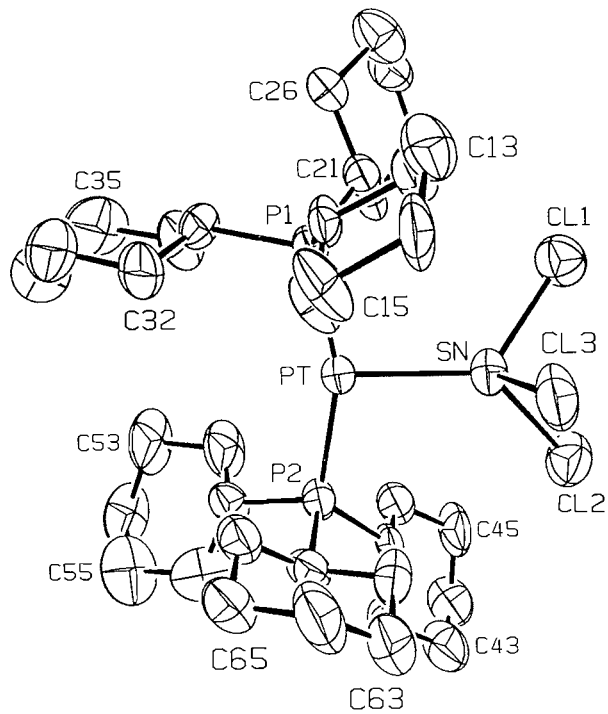

FIG. 4. A view of $H[Cl_3Sn]Pt(PCy_3)_2$ showing the crystallographic numbering scheme. Ellipsoids are at the 50% level.

[6] $(Cy_3P)_2PtO_2$ + excess $HSnPh_3 \rightarrow$ *trans*-$H[Ph_3Sn]Pt(PCy_2)_2 + O_2$

This reaction is extremely rapid at room temperature, and attempts to observe any intermediates by low temperature (−60°C) ^{31}P nmr spectroscopy in benzene and chloroform solutions were unfruitful. If the reaction proceeds via an oxidative addition – reductive elimination process, involving initial *cis* coordination of the $HSnPh_3$ moiety to platinum, elimination of dioxygen, followed by formation of a product with *trans* geometry due to severe inter-ligand repulsions

Can. J. Chem. Downloaded from www.nrcresearchpress.com by 122.72.124.2 on 09/07/12
For personal use only.

(particularly between the two PCy_3 ligands) will most likely occur. If initial coordination of $HSnPh_3$ to the dioxygen complex is slow, but elimination of the O_2 is fast, the concentration of any intermediate will be too small to observe. Since no other products have been observed in this reaction,[8] and since it would be expected that the liberated oxygen would trap any intermediate tin radicals, a radical mechanism is unlikely but not completely excluded. A mechanism involving prior dissociation of a phosphine ligand (or oxygen molecule) is also possible provided the concentration of the free phosphine (or $Pt^0(PCy_3)_2$) is too small to be observed by ^{31}P nmr spectroscopy.

The ^{119}Sn nmr spectrum of *trans*-$H[Ph_3Sn]Pt(PCy_3)_2$ (proton coupled) was observed as a doublet of triplets with ^{195}Pt satellites centered at −21.8 ppm. The $^{119}Sn—^{195}Pt$ coupling constant of 9 680 Hz is somewhat smaller than those reported (18) for other compounds (e.g. 12 686 Hz for *cis*-$Ph[Ph_3Sn]Pt(PPh_3)_2$), and probably indicates the presence of a long tin–platinum bond caused by a combination of the high *trans* influence of the hydride ligand and severe steric interactions between the tin ligand and the PCy_3 ligands (see later). In the ^{119}Sn nmr spectrum of *trans*-$H[Cl_3Sn]Pt(PCy_3)_2$, the corresponding hydride resonance in the ^1H nmr spectrum and the ^{31}P nmr resonances were all broad at room temperature, probably due to one of the fluxional processes well known for such M—$SnCl_3$ derivatives. The value of $J_{Sn—Pt}$ of 11 242 Hz is smaller than other analogous compounds,[9] and is probably due to the high *trans* influence of the hydride ligand.

In this laboratory, it has previously been observed (19) that for compounds of *cis* geometry, e.g. *cis*-$(PPh_3)_2PtCl_2$, the single line (with platinum 195 satellites) observed in the solution ^{31}P nmr spectrum occurs as two distinct resonances in the solid state CP/MAS ^{31}P nmr spectrum due to the different environments of the two magnetically different phosphorus nuclei as shown by X-ray structural analysis (20). For the *trans* derivatives, however, only a single line (with platinum 195 satellites) was observed in the solid state ^{31}P nmr spectra. Similar results have recently been reported (21) for both palladium and platinum compounds, $(R_3P)_2MCl_2$. For the case of both *trans*-$H[R_3Sn]Pt(PCy_3)_2$, R = Ph or Cl, the single resonance observed in solution for the two magnetically equivalent phosphorus nuclei of each complex appeared as an AB spin system (with platinum 195 satellites) in the solid state ^{31}P nmr spectrum with the characteristic large $^2J_{P—P_{trans}}$ coupling of approximately 350 Hz (see Fig. 2).

Severe distortion of the intensities of the AB pattern are apparent, probably due to the similarity in shielding of both phosphorus nuclei. The non-equivalence of the phosphorus nuclei in these solid state ^{31}P nmr spectra can readily be appreciated by reference to the crystal structures of **I** and **II**. Also, the *small* difference in shielding of the ^{31}P nuclei in the solid state may be understood since the inequivalence is caused by different orientations of cyclohexyl rings. Recently, we have observed[9] that for other species such as *trans*-$Cl(X_3Si)Pt(PCy_3)_2$, where inequivalence of the ^{31}P nuclei is caused by spatial proximity to an electron-rich centre (i.e. chloride), there is a much more *distinct* difference in shielding. In some cases a chemical shift difference of over 15 ppm was observed.

Attempts to observe non-equivalence of the phosphorus nuclei of *trans*-$H[Ph_3Sn]Pt(PCy_3)_2$ in solution at low temperature (−90°C) by ^{31}P nmr spectroscopy could not be conducted due to the low solubility at this temperature.

In the solution $^{31}P\{^1H\}$ nmr spectrum of *cis*-$H[Ph_3Sn]Pt(PCy_3)_2$, the ^{31}P resonance of the PCy_3 ligand *trans* to the hydride is extensively broadened at room temperature. This feature is believed to be due to restricted rotation of this phosphine ligand about the Pt—P bond since it is "sandwiched" between two other sterically demanding ligands. A similar phenomenon was also observed for the *cis*-$H[R_3Si]Pt(PCy_3)_2$ analogues in which R = *ortho*- or *meta*-substituted benzyl. This broadening is field-dependent, these resonances being more broadened (in ppm) at higher field (S.F. = 161.9) than lower field (S.F. = 100.23 MHz) consistent with the above interpretation.

X-ray crystallographic characterization of both *trans*-$H[Ph_3Sn]Pt(PCy_3)_2$ and *trans*-$H[Cl_3Sn]Pt(PCy_3)_2$ were carried out in order to establish a positive basis for the non-equivalence of the phosphorus nuclei in the solid state ^{31}P nmr; to compare the relative "ligand volumes" of —$SnPh_3$ and —$SnCl_3$ ligands and to examine the ligand interactions in these compounds.

(i) trans-*$H[Ph_3Sn]Pt(PCy_3)_2$ (**I**)*

Allowing for location of the hydride ligand, the Pt atom has distorted square-planar geometry; the Pt atom is 0.082 Å out of the P_2Sn plane and the P—Pt—P angle is reduced to 160.24 (8)° (see Fig. 3) in order to accommodate the bulky $SnPh_3$ ligand. This angle is smaller than that of *trans*-$H[H_3Si]Pt(PCy_3)_2$ (166°) (17) but larger than the values for both *trans*-$[H(Ph_3P)Pt(PCy_3)_2]^+PF_6^-$ (155.2°) (22) and *trans*-$[H(PCy_2Ph)Pt(PCy_3)_2]^+PF_6^-$ (142.7°) (23). The Pt—P bond distances of 2.294(2) and 2.283(2) Å are significantly shorter than the sum of the covalent radii of Pt and P but comparable to those of other Pt(II)—phosphine complexes. The long Sn—Pt bond (2.6539(6 Å) reduces the steric interactions between the ligands to some extent and no doubt results from the *trans* influence of the hydride ligand. The tetrahedral geometry about tin is distorted with all Pt—Sn—C angles greater than the tetrahedral angle, in particular, the Pt—Sn—C(71) angle of 122.9(2)°. The geometry about the phosphorus ligands is also distorted, especially that of P2 where Pt—P(2)—C(41) = 121.2(3)°. The cyclohexyl rings of the phosphine ligands adopt a staggered conformation with respect to each other and also with respect to the phenyl rings of the triphenyltin ligand. All cyclohexyl rings possess a chair conformation and there are no significant *inter*molecular non-bonded contacts. However, there are a number of intramolecular non-bonded contacts between cyclohexyl hydrogens and platinum. The shortest interactions are between platinum and H222 (2.85 Å), H162 (2.99 Å) and H621 (3.03 Å), although these H...Pt distances are not as short as those observed in the species $Pd(PPt_tBu_2)_2$ (ca. 2.7 Å) (24). We have observed[9] a similar interaction between an *ortho*-phenyl hydrogen and platinum in the X-ray crystal structure of *trans*-$Cl(PhCl_2Si]Pt(PCy_3)_2$ (H...Pt = 2.94 Å) in which the square planar geometry about platinum is severely distorted. In the present case, however, the proposed H...Pt interaction does not cause significant distortion of the structure as would be apparent for example in the angles about carbon atoms C21, C11, or C61.

[8]The aromatic region of the ^1H nmr spectra gives a good indication of the purity of the tin containing species. The *ortho* phenyl protons of —$SnPh_3$ exhibit a three bond coupling to ^{119}Sn and occur at a characteristic shift position, e.g. 8.2 ppm, $^3J_{Sn—H}$ = for *cis*-$H[Ph_3Sn]Pt(PCy_3)_2$ and 7.57 ppm, $^3J_{Sn—H}$ = for $HSnPh_3$ (C_6D_6 solution).

[9]H. C. Clark, M. J. Hampden-Smith, E. Ferguson, and H. Raegger. Unpublished results.

(ii) trans-*H[Cl$_3$Sn]Pt(PCy$_3$)$_2$ (II)*

In this complex (Fig. 4) as in **I**, the Pt atom has distorted square-planar geometry; the Pt atom is 0.114 Å from the P_2Sn plane and the P—Pt—P is reduced to 159.0(2)°.

The Pt—Sn distance (2.600(2) Å) in this complex is shorter than that in **I**; it was anticipated that the Pt—Sn bond of **II** would be significantly shorter than that in **I** due to the increased electronegativity of the substituents on tin, as judged, for example by a comparison of $J_{H—Pt}$ values. The Pt—P bonds of **II** are slightly longer than those of **I**, an effect expected based on previous studies in which evidence was found for a *cis*-influence opposite in effect to the *trans*-influence in square planar complexes. Thus the —$SnCl_3$ ligand of **II** is expected to produce a shortening of the Pt—H bond compared to the $SnPh_3$ ligand of **I**, while the Pt—P bonds will be expected to be longer for **II** on the basis of the different *cis*-influence of the tin ligands. However, the observed Pt—P bond lengthening may also have some steric origin. Again, for **II** there are some intramolecular H...Pt interactions from hydrogens of the cyclohexyl rings; the shortest distances are 3.05 (H162), 3.02 (H522), and 2.97 Å (H662). As in the case of **I**, there is little if any distortion of the angles at adjacent carbon atoms indicating no significant Pt...H bonding interaction. Comparison of these interactions in **I** and **II** show that they all arise from hydrogen atoms attached to β-carbons of the cyclohexyl rings and it seems likely they arise from the forced spatial proximity due to the relative orientations and conformations of the cyclohexyl rings themselves.

While there is a marked similarity between the structures of **I** and **II** (Fig. 4), the most notable difference is the relative orientation of the two PCy_3 ligands labelled P2. Furthermore, if the angle P—Pt—P is taken as indicative of the bulk of the tin substituents, then the similarity in the values for $SnPh_3$ (160.2°) and $SnCl_3$ (159°) shows that the "coordinative" volume required by these two ligands *at the metal centre* is virtually identical (assuming the same D(Pt—Sn)). This is contrary to expectations based on both cone angle measurements (i.e. PCl_3 compared to PPh_3) and electronic effects.

Comparison of these structures indicates that bulky ligands, X, in the species *trans*-$HXPt(PCy_3)_2$ whose existence cannot be predicted on the basis of cone angle values, are accommodated by (25): (*i*) a significant reduction in the P—Pt—P angle; (*ii*) lengthening of the P—Pt bonds; and (*iii*) severe distortion of the Pt—P—C angles in the PCy_3 substituents. It is significant that these distortions occur while the planarity of the complex is apparently maintained, and also that the value of the Pt—P bond lengths do not exceed the sum of the covalent radii in either of these compounds. This may well be further evidence for π-back-bonding from phosphorus to platinum.

Acknowledgements

We are grateful for the continued financial support (to H.C.C. and G.F.) from the Natural Sciences and Engineering Research Council of Canada, and for the loan of platinum compounds from Johnson Mattley Ltd.

1. C. MASTER. Homogeneous transition metal catalysis. Chapman Hall, London. 1981.
2. C. EABORN, A. PIDCOCK, and B. RATCLIFF. J. Organomet. Chem. **66**, 23 (1974).
3. H. C. CLARK, A. B. GOEL, and C. BILLARD. J. Organomet. Chem. **182**, 431 (1979).
4. A. ALBINATI, P. C. PREGOSIN, and H. RUEGGER. Inorg. Chem. **23**, 3223 (1984).
5. G. BUTLER, C. EABORN, and A. PIDCOCK. J. Organomet. Chem. **185**, 367 (1980).
6. G. BUTLER, C. EABORN, and A. PIDCOCK. J. Organomet. Chem. **181**, 47 (1979).
7. H. C. CLARK, G. FERGUSON, A. B. GOEL, E. G. JANZEN, H. RUEGGER, P. Y. SIEW, and C. S. WONG. J. Am. Chem. Soc. **108**, 6961 (1986).
8. D. SHRIVER, *(Editor)*. Inorganic syntheses. Vol. XIX. McGraw-Hill, New York. 1979. p. 105.
9. T. ALLMAN and R. E. LENKINSKI. Inorg. Chem. **25**, 3202 (1986).
10. B. FRENZ AND ASSOCIATES INC. SDP-Plus. College Station, Texas 77840, and Enraf-Nonius, Delft, Holland. 1983.
11. G. M. SHELDRICK. SHELX-a program for crystal structure analysis. Cambridge, England. 1976.
12. International tables for X-ray crystallography. Vol. IV. Kynoch Press, Birmingham. 1974.
13. C. K. JOHNSON. ORTEPII Report ORNL-5138 Oak Ridge National Laboratory, TN. 1976.
14. The study of kinetics and mechanisms of reactions of transition metal complexes. R. G. Wilkins, Allyn and Bacon. 1974. Chap. 7. p. 352.
15. E. A. V. EBSWORTH, V. M. MARGARIAN, F. J. S. REID, and R. O. GOULD. J. Chem. Soc. Dalton Trans. 1167 (1978).
16. S. CARR, R. CAULTON, and D. DAKTOMCEKS. J. Organomet. Chem. **249**, 327 (1983).
17. H. C. CLARK, J. A. DAVIES, C. A. FYFE, P. J. HAYNES, and R. E. WASYLISHEN. J. Am. Chem. Soc. **105**, 6577 (1983); Organometallics, **2** 177 (1983); L. BEMI, H. C. CLARK, J. A. DAVIES, C. A. FYFE, and R. E. WASYLISHEN. J. Am. Chem. Soc. **104**, 438 (1982).
18. G. K. ANDERSON, H. C. CLARK, J. A. DAVIES, G. FERGUSON, and M. PARVEZ. J. Cryst. Spectrosc. Res. **12**, 449 (1982).
19. J. H. NELSON, J. A. RAHN, and W. H. BEARDEN. Inorg. Chem. **26**, 2192 (1987).
20. H. C. CLARK, M. J. DYMARSKI, and J. D. OLIVER. J. Organomet. Chem. **154**, C40 (1978).
21. G. FERGUSON, B. RUHL, and M. J. HAMPDEN-SMITH. Abstracts, American Crystallography Association Meeting, Hamilton, Ont., Canada. June 1986.
22. M. MATSAMOTO, H. YOSHIDA, N. NAKATSU, T. YOSHIDA, and S. OTSUKA. J. Am. Chem. Soc. **96**, 3322 (1974).
23. H. C. CLARK and M. J. HAMPDEN-SMITH. Coord. Chem. Rev. **79**, 229 (1987).
24. H. C. CLARK and M. J. HAMPDEN-SMITH. Organometallics. To be published.

Can. J. Chem. Downloaded from www.nrcresearchpress.com by 122.72.124.2 on 09/07/12
For personal use only.

Configurationally dependent hydroxyl group effects on ^{13}C nuclear magnetic resonance chemical shifts of olefinic carbons in cyclic six-membered allylic alcohols

TEODORO S. KAUFMAN[1]

Instituto de Química Orgánica de Síntesis (CONICET-UNR), Facultad de Ciencias Bioquímicas y Farmacéuticas, Casilla de Correo 991, 2000 Rosario, Argentina

Received June 29, 1987

TEODORO S. KAUFMAN. Can. J. Chem. **66**, 3128 (1988).

The differences in chemical shifts of olefinic carbons, $\Delta\delta(sp^2)$, of pseudoequatorial and pseudoaxial six-membered allylic alcohols were correlated with the $\Delta\delta(sp^2)$ values of their parent olefins. The results obtained reflect configurationally dependent substituent effects, the magnitude of which could be used for the stereochemical assignment of the hydroxyl group in these compounds.

TEODORO S. KAUFMAN. Can. J. Chem. **66**, 3128 (1988).

On a établi une corrélation entre les différences de déplacements chimiques des carbones oléfiniques, $\Delta\delta(sp^2)$, des alcools allyliques à six chaînons pseudoaxial et pseudoéquatorial et les valeurs des $\Delta\delta(sp^2)$ des oléfines apparentées. Les résultats obtenus sont le reflet d'effets de substituants dépendant de la configuration dont l'amplitude pourrait être utilisée pour l'attribution stéréochimique du groupement hydroxyle de ces composés.

[Traduit par la revue]

Can. J. Chem. Downloaded from www.nrcresearchpress.com by 122.72.124.2 on 09/07/12
For personal use only.

Introduction

The assignment of ^{13}C nmr chemical shifts from substituent effects and the interpretation of their variations obviously require a precise knowledge of these effects. Generally, these perturbations depend not only on the nature of the carbon frame to which the substituent is bonded, but also on the geometry of the molecule (electronic and steric effects).

The analyses of the ^{13}C nmr chemical shifts of selected model molecules in various classes of organic compounds have proved to be of great diagnostic and prognostic value in the elucidation of unknown structures. Cyclic six-membered allylic alcohols as a class, although common in organic synthesis as well as in the field of natural products (1, 2), are of special interest since they display ^{13}C nmr chemical shifts that are often difficult to predict and interpret, particularly in relation to the geometrical features of the molecule.

There are some scattered references in the literature to ^{13}C nmr studies of allylic alcohols (3–5) but, surprisingly, no systematic and comprehensive study is available concerning the role of the hydroxyl group on the chemical shifts of olefinic carbons.

Our aim was to investigate the chemical shift variations of the olefinic carbons in cyclic six-membered allylic alcohols as a function of the substituent orientation, and hence to try to delineate further the factors that influence these ^{13}C nmr chemical shifts.

During previous studies (6), it was shown that classifying allylic alcohols into pseudoaxial (the dihedral angle between the oxygen, the carbinyl carbon, and the olefinic carbon atoms approaches ±90°) and pseudoequatorial (the value of the same dihedral angle is in the range of ±30°) was more useful for studying hydroxyl group–double bond interactions in this class of compounds than the classification defined in ref. 7, which is based on the conformational class of the hydroxyl group.

A set of 33 allylic alcohols and their related olefins, corresponding to different chemical families, namely, steroids, mono-, bi-, and tri-cyclic terpenoids, was constructed using information available from the current literature (6, 8–10). The values of the ^{13}C nmr resonances and substituent-induced chemical shift differences of these alcohols and parent olefins are listed in Table 1.

The unequivocal assignments of the hydroxyl group orientation (Table 1) were made with the aid of Dreiding models, by measuring the dihedral angle formed by the oxygen, the carbinyl carbon atom, and both olefinic carbons. When data belonging to both epimers in an epimeric pair of alcohols were available (**1***b*–**1***c*, **2***b*–**2***c*, **3***b*–**3***c*, **4***b*–**4***c*, **5***b*–**5***c*, **6***b*–**6***c*,

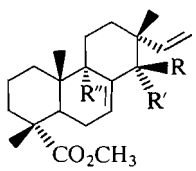

	R	R′	R″
1*a*	H	H	H
1*b*	H	OH	H
1*c*	OH	H	H
1*d*	H	H	OH

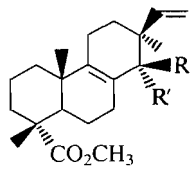

	R	R′
2*a*	H	H
2*b*	H	OH
2*c*	OH	H

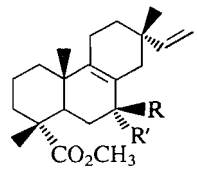

	R	R′
3*a*	H	H
3*b*	H	OH
3*c*	OH	H

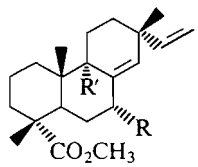

	R	R′
4*a*	H	H
4*b*	OH	H
4*c*	H	OH

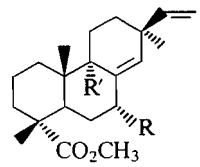

	R	R′
5*a*	H	H
5*b*	OH	H
5*c*	H	OH

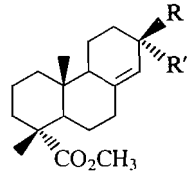

	R	R′
6*a*	H	H
6*b*	H	OH
6*c*	OH	H

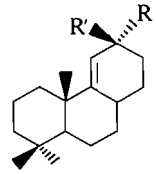

	R	R′
7*a*	H	H
7*b*	H	OH
7*c*	OH	H

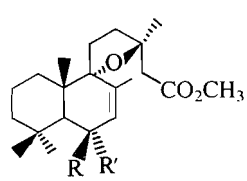

	R	R′
8*a*	H	H
8*b*	H	OH
8*c*	OH	H

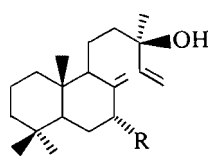

9*a* R = H
9*b* R = OH

[1]Present address: Department of Medicinal Chemistry, University of Mississippi, University, MS 38677, U.S.A.

TABLE 1. The ^{13}C nmr chemical shifts of allylic alcohols,[a] and substituent effects of the hydroxyl group

Compound	γ-Carbon	β-Carbon	Δδ(γ)	Δδ(β)	Δδ(sp^2)	Alcohol[b]
1*a*	121.2	135.6			−14.4	
1*b*	126.9	136.4	5.7	0.8	−9.5	pa
1*c*	118.7	136.5	−2.5	0.9	−17.8	pe
1*d*	125.2	136.1	4.0	0.5	−10.9	pa
2*a*	136.1	124.6			11.5	
2*b*	140.3	127.8	4.2	3.2	12.5	pe
2*c*	140.2	126.9	4.1	2.3	13.3	pa
3*a*	136.6	124.7			11.9	
3*b*	141.1	127.3	4.5	2.6	13.8	pa
3*c*	140.7	127.6	4.1	2.9	13.1	pe
4*a*	128.8	136.4			−7.6	
4*b*	134.0	139.2	5.2	2.8	−5.2	pa
4*c*	132.3	137.9	3.5	1.5	−4.8	pa
5*a*	128.5	138.0			−9.5	
5*b*	133.6	140.6	5.1	2.6	−7.0	pa
5*c*	131.5	138.5	3.0	0.5	−7.0	pa
6*a*	138.5	121.4			17.1	
6*b*	140.3	126.1	1.8	4.7	14.1	pe
6*c*	143.9	122.9	5.4	1.5	21.0	pa
7*a*	151.5	114.3			37.2	
7*b*	153.1	119.3	1.6	5.0	33.8	pe
7*c*	155.2	117.4	3.7	3.1	37.8	pa
8*a*	134.8	126.5			8.3	
8*b*	136.6	130.4	1.8	3.9	6.2	pe
8*c*	137.0	128.3	2.2	1.8	8.7	pa
9*a*	106.3	148.6			−42.3	
9*b*	109.5	149.5	3.2	0.9	−40.0	pa
10*a*	107.3	148.5			−41.2	
10*b*	104.2	150.5	−3.1	2.0	−46.3	pe
11*a*	125.6	125.7			−0.1	
11*b*	130.4	127.9	4.8	2.2	2.5	pa
12*a*	144.7	118.8			25.9	
12*b*	147.3	123.2	2.6	4.4	24.1	pe
13*a*	135.5	124.5			11.0	
13*b*	137.9	128.8	2.4	4.3	9.1	pe
14*a*	142.4	126.1			16.4	
14*b*	147.9	128.1	5.5	2.0	19.8	pa
14*c*	144.2	127.9	1.8	1.8	16.3	pe
14*d*	147.2	134.1			13.1	
14*e*	151.2	136.2	4.0	2.1	15.0	pa
15*a*	108.9	146.1			−37.2	
15*b*	106.1	150.1	−2.8	4.0	−44.0	pe
16*a*	132.2	128.8			−3.4	
16*b*	136.5	130.6	4.3	1.8	−5.9	pe
16*c*	135.0	131.2	2.8	2.4	−3.8	pa
17*a*	109.4	128.8			−19.4	
17*b*	111.7	135.2	2.3	6.4	−23.5	pe
18*a*	143.8	135.2			8.6	
18*b*	143.0	134.9	−0.8	−0.3	8.1	pe
19*a*	140.6	109.3			31.3	
19*b*	140.4	106.5	−0.2	−2.8	33.9	pa
19*c*	140.1	105.3			34.8	
19*d*	142.7	106.9	2.6	1.6	35.8	pa
20*a*	141.6	105.3			36.3	
20*b*	142.9	106.5	1.3	1.2	36.4	pa

[a]In ppm, downfield from internal TMS. Resonances were taken from refs. 6, 8, 9, and 10.
[b]Hydroxyl group: pa = pseudoaxial, pe = pseudoequatorial.

7*b*–**7***c*, **8***b*–**8***c*, **14***b*–**14***c*, and **16***b*–**16***c*), assignments were confirmed by the use of the empirical rule proposed in ref. 6.

Analysis of the data showed that the changes in the γ carbon atom resonances of the olefins due to the introduction of a hydroxyl group in the allylic position (Δδ(γ)), although representing mainly downfield shifts (4), did not appear to be related to the orientation of the allylic substituent. The same trend was observed during the examination of hydroxyl effects of pseudoaxial and pseudoequatorial alcohols on chemical shift differenes of the β carbon atoms (Δδ(β)). Particularly worth

Can. J. Chem. Downloaded from www.nrcresearchpress.com by 122.72.124.2 on 09/07/12
For personal use only.

Can. J. Chem. Downloaded from www.nrcresearchpress.com by 122.72.124.2 on 09/07/12
For personal use only.

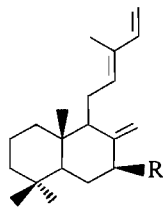

10*a* R = H
10*b* R = OH

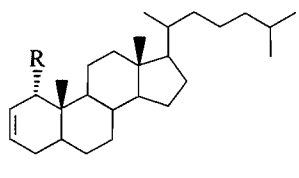

11*a* R = H
11*b* R = OH

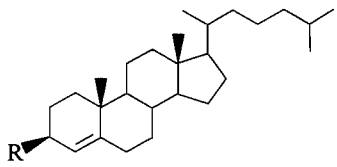

12*a* R = H
12*b* R = OH

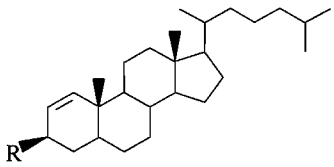

13*a* R = H
13*b* R = OH

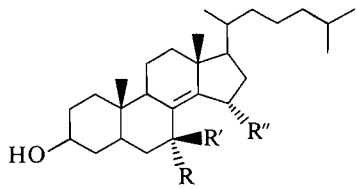

	R	R′	R″
14*a*	H	H	H
14*b*	OH	H	H
14*c*	H	OH	H
14*d*	H	H	OH
14*e*	OH	H	OH

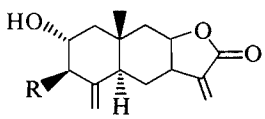

15*a* R = H
15*b* R = OH

noting was the relationship among the pairs of epimeric alcohols derived from the compounds **2***a* and **3***a*, which did not agree with the proposal of Delmont *et al.* that relates the $\Delta\delta(\gamma)$ value with the alcohol configuration (4).

It seemed reasonable to suppose that these results could be a consequence of the superposition of several effects simultaneously acting on both olefinic carbons. Evidence for strengthening this line of reasoning might be obtained if a correlation

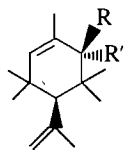

	R	R′
16*a*	H	H
16*b*	H	OH
16*c*	OH	H

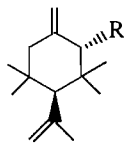

17*a* R = H
17*b* R = OH

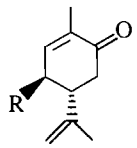

18*a* R = H
18*b* R = OH

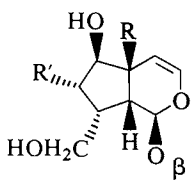

β Glucose

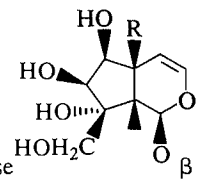

β Glucose

	R	R′
19*a*	H	OH
19*b*	OH	OH
19*c*	H	H
19*d*	OH	H

20*a* R = H
20*b* R = OH

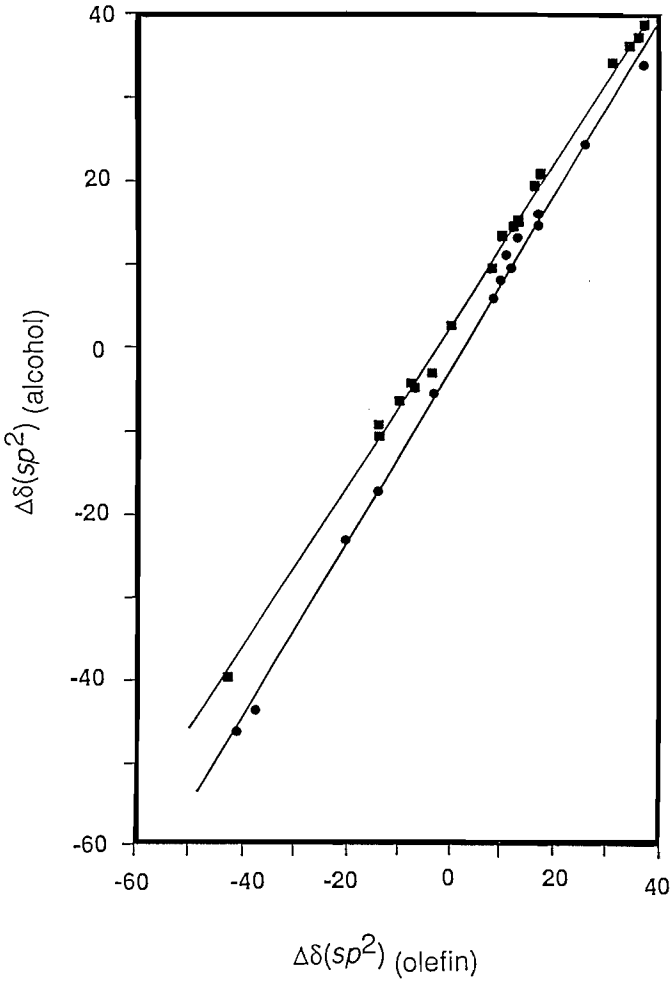

FIG. 1. Plot of $\Delta\delta(sp^2)_{(alcohol)}$ vs. $\Delta\delta(sp^2)_{(olefin)}$. (●) Pseudoequatorial alcohols; (■) pseudoaxial alcohols.

between parameters representing both sp^2 carbon atoms in the allylic alcohols and the parent olefins could be found.

Based on trends in chemical shift variations of the sp^2 carbons previously reported by Eggert and Djerassi (11), we have recently proposed a new empirical parameter called $\Delta\delta(sp^2)$, defined as the difference between the chemical shifts of the γsp^2 and βsp^2 carbon atoms relative to the hydroxyl group (eq. [1]). We have also demonstrated the usefulness of this parameter for the determination of the hydroxyl group stereochemistry in each member of a given pair of epimeric allylic alcohols (6).

$$[1] \quad \Delta\delta(sp^2) = \delta\gamma sp^2C - \delta\beta sp^2C$$

Considering that $\Delta\delta(sp^2)$, a measure of the difference of the perturbations exerted on both sp^2 carbon atoms, would take the olefin moiety as a unit, the $\Delta\delta(sp^2)$ values of alcohols and olefins were tested for linear regression by the least-squares method. The data, which are plotted in Fig. 1, adhered to eq. [2]; the complete sets of parameters for both straight lines, representing the behavior of pseudoaxial and pseudoequatorial allylic alcohols, are collected in Table 2.

$$[2] \quad \Delta\delta(sp^2)_{(alcohol)} = K + S\cdot\Delta\delta(sp^2)_{(olefin)}$$

It is interesting to note that the data displayed in Table 1 show a smooth progression from large negative $\Delta\delta(sp^2)$ values corresponding to alcohols bearing an unsubstituted γ carbon atom (**9***b*, **15***b*), to large positive values for compounds having

TABLE 2. Allylic alcohols vs. related olefins. Correlation parameters

Parameter	K^a	S^b	r^c	p^d	sd[e]	n^f
Alcohol:						
Pseudoaxial	2.29 (±0.30)	0.97 (±0.01)	0.9982	<0.001	1.21	19
Pseudoequatorial	−2.46 (±0.48)	1.06 (±0.02)	0.9975	<0.001	1.65	14

[a]Zero ordinate.
[b]Slope.
[c]Correlation coefficient.
[d]Significance level.
[e]Root-mean-square deviation between calculated and observed resonances.
[f]Number of data points.

the hydroxyl group in the allylic position referred to an enol acetal double bond (**19***b*, **20***b*), in a range of 80 ppm.

Several other observations may be pointed out from these straight lines. The surprisingly precise correlations obtained by plotting the $\Delta\delta(sp^2)$ data contrast with the apparent independence of $\Delta\delta(\gamma)$ and $\Delta\delta(\beta)$ from substituent orientation, thus allowing a first approximation – complete description of each alcohol–olefin relationship by using only two parameters, namely K and S.

The zero ordinates, K, may be interpreted as the $\Delta\delta(sp^2)$ variations produced when a hydroxyl group replaces a pseudoequatorial or pseudoaxial hydrogen atom in the allylic position of an olefin, in which both sp^2 carbons display the same chemical shift.

On the other hand, S, the slope of the straight lines, describes the sensitivity of the olefinic carbons to changes in their chemical shift difference when the hydrogen–hydroxyl substitution is done.

Because the slopes are statistically different ($p < 0.05$), the observed differences in $\Delta\delta(sp^2)$ associated with pseudoaxial and pseudoequatorial alcohols depend on both K and S values. These linear relationships with slopes other than 1.0 suggest a constant relative enhancement or attenuation of $\Delta\delta(sp^2)_{(\text{alcohol})}$ in relation to $\Delta\delta(sp^2)_{(\text{olefin})}$, depending on the stereochemistry of the alcohol.

From the relative magnitudes of K and S, it is observable that the system presents a high activity associated with a first phenomenon (related to K), accompanied by a weak sensitivity associated with a second phenomenon (connected to S).

The above findings are indicative that at least two different, although simultaneously operating, mechanisms would be required to justify them. They are concordant with previous reports (12) ascribing these effects to geometry-dependent trough-space and trough-bond interactions between the oxygen lone pair and the olefin π-electrons.

The sets of additive parameters listed in Table 2 and the $\Delta\delta(sp^2)$ value of an olefin, when applied to eq. [2], allow the estimation of $\Delta\delta(sp^2)$ for the related pseudoequatorial or pseudoaxial allylic alcohols, providing a tool for the hydroxyl group stereochemical assignment by comparison of the resonances of the olefinic carbons of the alcohol with those of the parent olefin.

Almost all the geometric environments of the hydroxyl group are represented in this series, which includes 10 pairs of epimers, heterocyclic rings, double bonds bearing oxygen or sp^2 carbons in the homoallylic position, and tertiary alcohols. The fact that the hydroxyl group exerts essentially the same effect in different environments may be indicative that the transmission of the effect of this particular substituent is independent of the presence of the others.

Thus, the above observations seem to be general for cyclic six-membered allylic alcohols, and the estimated parameters S and K (Table 2), which appear to be independent of the double bond substitution pattern or substituents interacting with the olefinic carbon atoms, avoid the need of additional parameters to account for the effects of these factors (3, 4).

Acknowledgements

T.S.K. is grateful to CONICET (Consejo Nacional de Investigaciones Científicas y Técnicas) and UNR (Universidad Nacional de Rosario) for their financial support and a fellowship. Thanks are due to Edmundo A. Rúveda and Manuel González Sierra for helpful discussions.

1. D. W. BROOKS, H. S. BEVINAKATTI, E. KENNEDY, and J. HATTAWAY, J. Org. Chem. **50**, 628 (1985).
2. A. F. THOMAS, W. THOMMEN, and J. BECKER. Helv. Chim. Acta, **64**, 161 (1981).
3. H. BROWER and J. B. STOTHERS. Can. J. Chem. **50**: 1361 (1972).
4. B. DELMONT, M. TARAN, J. VALADE, M. PETRAUD, and B. BARBE. Org. Magn. Reson. **17**, 207 (1981).
5. Y. SENDA, J.-I. ISHIYAMA, and S. IMAIZUMI. Tetrahedron Lett. 1805 (1978).
6. T. S. KAUFMAN, M. P. MISCHNE, M. GONZALEZ-SIERRA, and E. A. RUVEDA. Can. J. Chem. **64**, 2331 (1986), and references cited therein.
7. IUPAC Commission on Nomenclature of Organic Chemistry. Pure Appl. Chem. **45**, 13 (1976).
8. F. W. WHERLI and T. NISHIDA. Fortschr. Chem. Org. Naturst. **36**, 1 (1978).
9. M. MIYASHITA, T. SUZUKI, and A. YOSHIKOSHI, J. Org. Chem,. **50**, 3377 (1985).
10. E. DAVINI, C. IAVARONE, and C. TROGOLO. J. Org. Chem. **48**, 2854 (1983).
11. H. EGGERT and C. DJERASSI. J. Org. Chem. **46**, 5399 (1981).
12. J.-I. ISHIYAMA, Y. SENDA, and S. IMAIZUMI. J. Chem. Soc. Perkin Trans. **2**, 71 (1982).

Can. J. Chem. Downloaded from www.nrcresearchpress.com by 122.72.124.2 on 09/07/12
For personal use only.

Ionic conductivity and solid phase transitions in Na_2SO_4–Cs_2SO_4 system

KEVIN G. MACDONALD,[1] CHARLES MACLEAN,[2] AND E. A. SECCO[3]
Chemistry Department, St. Francis Xavier University, Antigonish, N.S., Canada B2G 1C0

Received May 20, 1988

KEVIN G. MACDONALD, CHARLES MACLEAN, and E. A. SECCO. Can. J. Chem. **66**, 3132 (1988).

The ac conductivity and DSC calorimetry data reveal interesting solid state interactions and solid phase transition behavior in the Na_2SO_4–Cs_2SO_4 binary system. The $\beta \rightarrow \alpha$ solid transition of $NaCsSO_4$ is reported for the first time. These data indicate preferential reaction between Cs_2SO_4 and the high temperature phase I of Na_2SO_4, exemplifying the Hedvall effect, to form the compound $NaCsSO_4$ which further interacts with excess Na_2SO_4 or excess Cs_2SO_4 to form 1:1 association complexes, viz. $NaCsSO_4$:Na_2SO_4 and $NaCsSO_4$:Cs_2SO_4. These complexes appear to dissociate at low temperatures reminiscent of spinodal-type decomposition behavior. The reaction enthalpies of $NaCsSO_4$, $\beta \rightarrow \alpha$ transition of $NaCsSO_4$ and complex associations are reported.

The report contains two unexpected results: (*i*) a subdued higher ionic conductivity relative to its Rb_2SO_4 analogue and (*ii*) a conductivity drop accompanying the high temperature phase transition which is in strong contrast to all the other Na_2SO_4 – mixed alkali compositions.

KEVIN G. MACDONALD, CHARLES MACLEAN et E. A. SECCO. Can. J. Chem. **66**, 3132 (1988).

Les données de conductivité ca et de calorimétrie DSC se rapportant au système binaire Na_2SO_4–Cs_2SO_4 révèlent des interactions intéressantes dans l'état solide et des transitions de phase solide. On rapporte pour la première fois la transition $\beta \rightarrow \alpha$ du $NaCsSO_4$ à l'état solide. Ces données indiquent une réaction préférentielle entre le Cs_2SO_4 et la phase I à haute température du Na_2SO_4, mettant en évidence l'effect Hedvall, pour former le composé $NaCsSO_4$ qui par la suite interagit avec le Na_2SO_4 ou le Cs_2SO_4 en excès pour former des complexes d'association 1:1, par exemple $NaCsSO_4$–Na_2SO_4 et $NaCsSO_4$–Cs_2SO_4. Ces complexes semblent se décomposer à basses températures ce qui appelle un comportement de type spinodal. On rapporte les enthalpies de réaction du $NaCsSO_4$, de la transition $\beta \rightarrow \alpha$ du $NaCsSO_4$ et des complexes d'association.

Cette étude comporte deux résultats inattendus: (*i*) une plus grande conductivité ionique douce par rapport à son analogue Rb_2SO_4 et (*ii*) une chute de conductivité accompagnant la transition à haute température qui contraste beaucoup avec celle de tous les autres complexes métal alcalin–Na_2SO_4.

[Traduit par la revue]

Can. J. Chem. Downloaded from www.nrcresearchpress.com by 122.72.124.2 on 09/07/12
For personal use only.

Introduction

Na_2SO_4 exhibits a sharp jump in ionic conductivity by a factor of 10 as it transforms to the high temperature phase Na_2SO_4(I). The phase transition is accompanied by a volume expansion of ~4%. Based on this volume expansion we reported recently on the mixed alkali and mixed anion effects of Na^+ ion conductivity (1). The enhanced ionic conductivity by a factor of 40 in $Na/RbSO_4$ compositions was attributed to lattice expansion, ceteris paribus, effected by the larger ionic radius Rb^+ incorporated in the Na^+ sublattice of Na_2SO_4. The lattice expansion within structural limits provides more "free" or "unoccupied" volume which facilitates inter-site mobility via a percolation-type or jump diffusion transport mechanism. This interpretation prompted us to pursue the effect of the still larger ionic radius Cs^+, $r_{Cs^+} = 181$ pm versus $r_{Rb^+} = 166$ pm, in the Na^+ sublattice. This paper presents ac electrical conductivity data and phase transition behavior along with transition enthalpies over the complete composition range in the Na_2SO_4–Cs_2SO_4 system.

Experimental procedure

The two compounds used were supplied by Alfa Products (Thiokol/Ventron Division, Danvers, MA) with the specified grade, Na_2SO_4 ultrapure and Cs_2SO_4 99.999$^+$%. All samples were prepared by fusing in air the requisite composition mixture of the respective compounds, previously well ground manually, at 50–75 K above its reported melting point (2) in a platinum crucible. There was no discernible weight loss after fusion. The fused product in each case appeared as a solid solution/reaction product and confirmed by its DTA effects. Except for the previously unreported transition at 395°C our recorded DTA effects up to 625°C are in qualitative agreement with the phase diagram (2).

Electrical conductivity measurements were made on compressed (force of 1.2×10^4 kg) polycrystalline sample in a stainless steel conductivity cell. The experimental procedure for these measurements as described earlier (1, 3), maintained the sample, whose surfaces were coated with graphite, by a spring-loaded support between stainless steel leads using two polished Pt discs as electrodes. Temperature was monitored within ±1 K by a standardized chromel–alumel thermocouple with a Keithley digital multimeter.

Thermal analyses of the samples were done on a DuPont 1090B Thermal Analyzer equipped with Disk Memory and Data Analyzer. Calorimetry measurements were carried out using gold pans with a differential scanning calorimeter DSC cell. The transition temperature T_t and transition enthalpy ΔH_t were obtained on samples up to 550°C in a flowing N_2 (ultrapure) atmosphere with ignited A_2O_3 as reference material.

Results and discussion

Ionic conductivity

The ionic conductivity, σ, in a solid phase is a composite quantity, $\sigma = nqu$ where n is the number of carriers of charge, q per unit volume, and u is the mobility of these charged carriers. The dependence of the ionic conductivity on temperature usually follows an Arrhenius-type expression,

$$[1] \quad \sigma T = \sigma_0 \exp(-Q_c/RT) = nq^2\lambda^2\gamma\nu/k \exp(-Q_c/RT)$$

the result of combining the Nernst–Einstein relation $\sigma/D = nq^2/kT$ and the diffusion equation $D = D_0 \exp(-Q_c/RT)$ where $D_0 = n\lambda^2\gamma\nu$. In this equation ν is the jump frequency, λ the inter-site distance, γ the inter-site geometric constant, and Q_c the apparent activation energy for mobility of the specific ion, k and R are fundamental constants.

[1]American Chemical Society – Petroleum Research Fund Scholar.
[2]Natural Sciences and Engineering Research Council of Canada Undergraduate Summer Research Award Holder.
[3]To whom correspondence should be addressed.

Can. J. Chem. Downloaded from www.nrcresearchpress.com by 122.72.124.2 on 09/07/12
For personal use only.

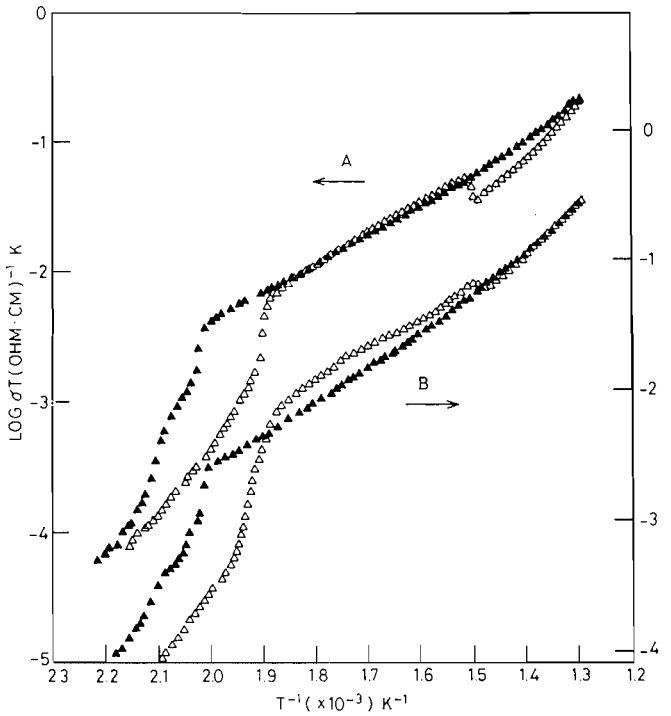

FIG. 1. Plots of log σT versus $(T/\mathrm{K})^{-1}$ of 3:1 mole ratio Na_2SO_4:Cs_2SO_4; *A* annealed at 500°C, *B* unannealed, △ heating, ▲ cooling.

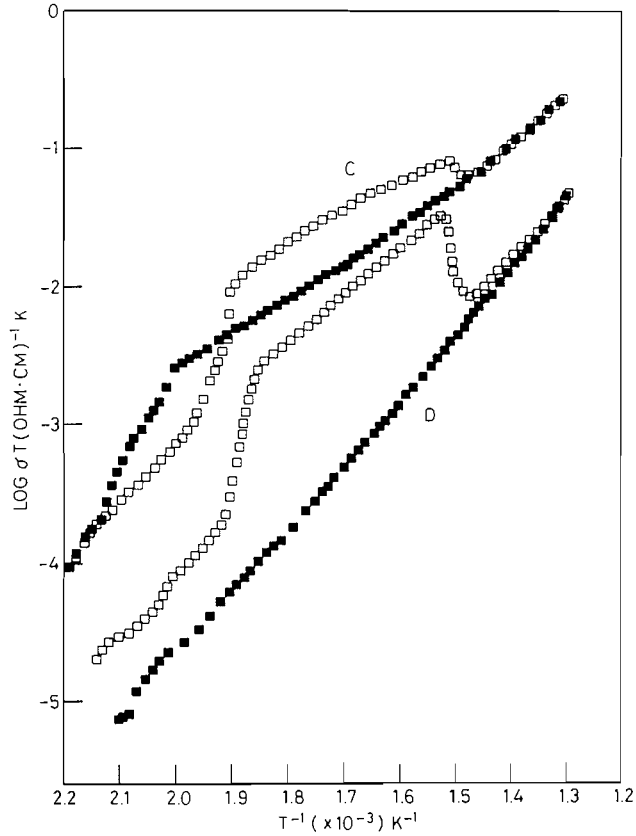

FIG. 2. Plots of log σT versus $(T/\mathrm{K})^{-1}$ of 1:1 mole ratio Na_2SO_4:Cs_2SO_4; *C* unannealed, *D* annealed at 500°C, □ heating, ■ cooling.

On the basis of eq. [1] typical heat and cool mode plots of log σT versus $(T/\mathrm{K})^{-1}$ representing Na_2SO_4-rich composition, 1:1 compound, and Cs_2SO_4-rich composition are presented. In Fig. 1 are given the plots for the 3:1 Na_2SO_4:Cs_2SO_4 samples: annealed in air at 500°C disc, *A*, and unannealed disc, *B*. Figure 2 gives the plots for the 1:1 Na_2SO_4:Cs_2SO_4, unannealed disc, *C* and annealed disc, *D*; Fig. 3 presents the plots for the 1:3 Na_2SO_4:Cs_2SO_4 unannealed disc. Figure 4 shows plots for unannealed discs, 9:1 Na_2SO_4:Cs_2SO_4, *F* and 1:9 Na_2SO_4:Cs_2SO_4, *G*.

The log σT (1 kHz) values at constant temperature of 282°C as a function of Cs^+:Na_2SO_4 composition are plotted in Fig. 5. The conductivity versus composition parallels the pattern for the Rb^+:Na_2SO_4 system at lower σ values. The Cs^+:Na_2SO_4 system is assumed to be hexagonal Na_2SO_4(I) phase incorporating Cs^+ in the cation sublattice. The activation energy values Q_c for the Na_2SO_4-rich compositions remain essentially constant at 44 ± 3 kJ/mol in excellent agreement with values for the Rb/Na_2SO_4 and Na_2SO_4/MoO_4 systems (1). Any additional "free" volume provided by the larger Cs^+ ion relative to Rb^+ ion does not effect a proportionate increase in Na^+ conductivity. This result suggests limits to the quest ion-free volume hypothesis.

All log σT versus T^{-1} plots of annealed and unannealed discs for Cs/Na_2SO_4 compositions up to 1:4 exhibit the normal positive conductivity response to the phase transition at 250 ± 10°C usually associated with the Na_2SO_4 III → I transition. Its appearance in the 1:1 compound $NaCsSO_4$ and Cs_2SO_4-rich compositions suggests break-down of the compound on cooling. On the other hand all log σT versus T^{-1} plots for Cs/Na_2SO_4 compositions between 1:4 and 4:1 show the unusual negative conductivity response to the new phase transition at 400 ± 5°C attributed to the compound $NaCsSO_4$. The normal hysteresis ΔT = 30°C for the 250°C transition is observed but the extended hysteresis ΔT = 140°C only appears

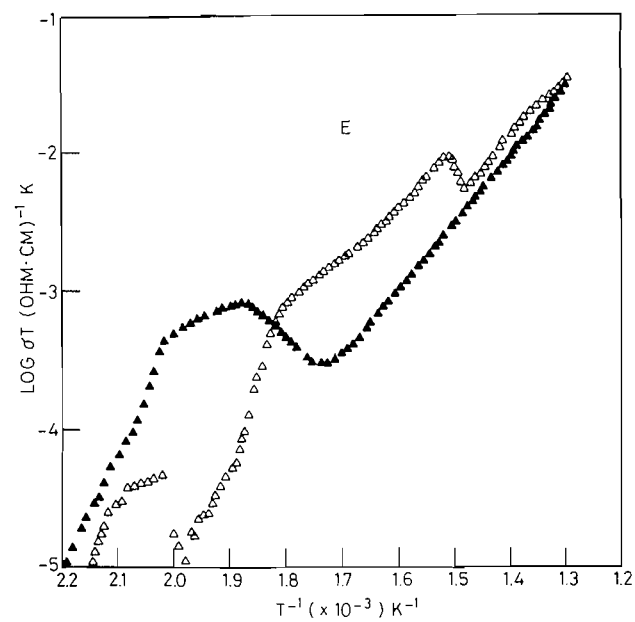

FIG. 3. Plots of log σT versus $(T/\mathrm{K})^{-1}$ of 1:3 mole ratio Na_2SO_4:Cs_2SO_4, △ heating, ▲ cooling.

for Cs/Na_2SO_4 compositions between 2:1 and 4:1 mole ratios. Annealing of the Na_2SO_4-rich samples at ~500°C prior to conductivity measurements had a negligible effect on σ and Q_c values. However, anneal of compound $NaCsSO_4$ lowered σ values and raised Q_c values. Furthermore, the Na_2SO_4 I → III

Can. J. Chem. Downloaded from www.nrcresearchpress.com by 122.72.124.2 on 09/07/12
For personal use only.

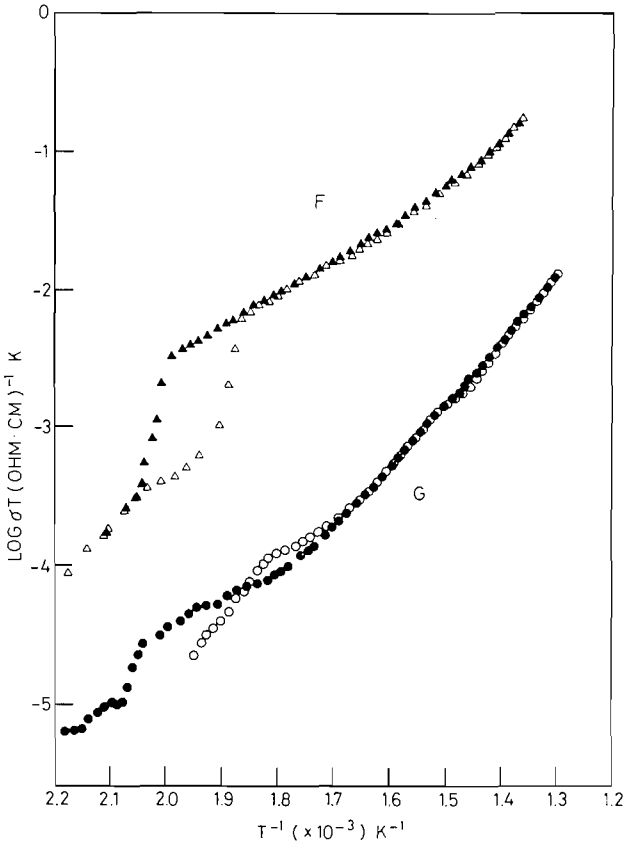

FIG. 4. Plots of log σT versus $(T/K)^{-1}$ of Na_2SO_4:Cs_2SO_4 in mole ratio 9:1, F, △ heating and ▲ cooling; 1:9, G ○ heating and ● cooling.

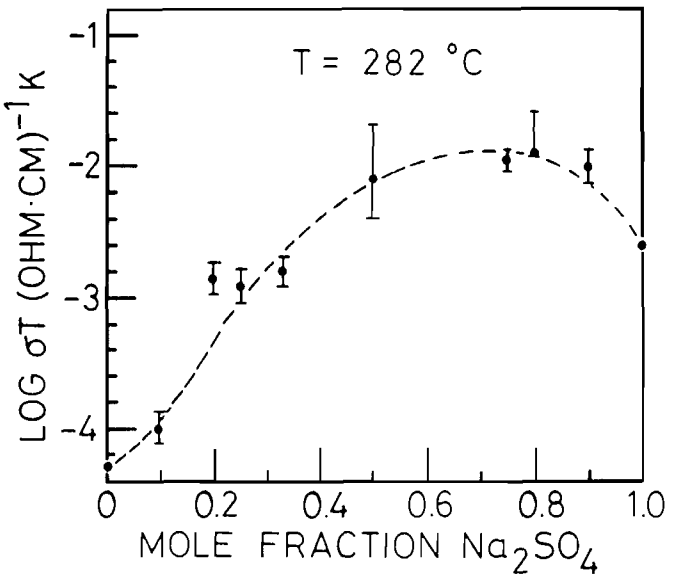

FIG. 5. Plot of log σT versus mole fraction Na_2SO_4 at 282°C.

transition at 250°C is absent on cooling the annealed $NaCsSO_4$ disc.

The negative conductivity effect accompanying the 400°C phase transition parallels the $Pm3m \rightarrow Fm3m$ transition of CsCl (4, 5), the V → III single crystal of Na_2SO_4 (6), the β → α transition of Na_2WO_4 (7), the Ag_2SO_4–K_2SO_4 compositions (8) and the glass transition of $Na_4UO_2(SO_4)_3$ (9). Similar conductivity behavior occurs in melting AgI (10–12) and Na_2UBr_6 (5, 13). All systems exhibit an abrupt conductivity

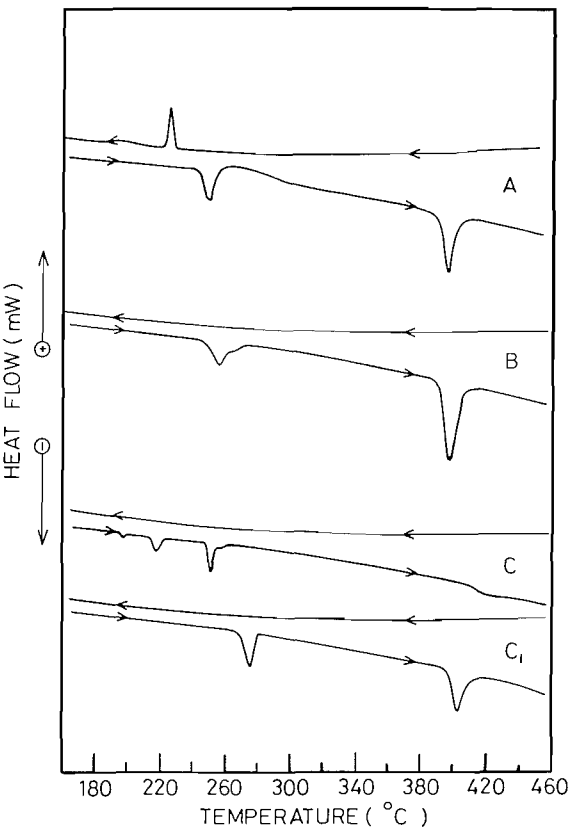

FIG. 6. Differential scanning calorimetry traces of Na_2SO_4:Cs_2SO_4 in mole ratios 3:1, A; 1:1, B; 1:3, C and C_1, first heat–cool cycle and second heat–cool cycle, respectively.

drop. Bogacz *et al.* (13) attributed Na_2UBr_6 behavior to melting of its anionic sublattice according to Ubbelohde's theory of independent melting of sublattices (14). Buerger (15) proposed a mechanism of dilatation for the $Pm3m \rightarrow Fm3m$ transformation in CsCl. The Na_2WO_4 result was interpreted as a switch over from intrinsic to extrinsic charge carrier, i.e. from Na^+ ions to Na^+ vacancies. The most striking structural characteristic accompanying the phase transition where a positive conductivity effect, i.e. conductivity jump, is observed as in solid AgI is the availability of substantially more than one site per conducting cation. On this same basis one can visualize a negative conductivity effect, i.e. conductivity drop, as observed in the above-cited cases, to be the result of a restriction in the number of sites, that is, a drop in the ratio of sites per mobile cation. Our interpretation for these cases, therefore, is a simple structural rearrangement of the whole lattice effecting a constriction of an open framework, rather than a melting of a specific sublattice. This restriction will affect ν, γ, and λ of eq. [1] to lower the overall ionic conductivity. The jump or drop in ionic conductivity during a solid phase transition as in $NaRbSO_4$ and $NaCsSO_4$ systems, respectively, represent the response of systems to perturbation, which can be used to probe and analyze the dynamics of molecular motions during lattice restructuring as in relaxation methods. However, attempts to develop theoretical models to adequately describe fast-ion conduction in the presence of a lattice phase transition have met with very limited, if any, success (16–18).

Differential scanning calorimetry

Figure 6 presents consistently typical heat and cool DSC traces for Na_2SO_4-rich, A, $NaCsSO_4$, B, and Cs_2SO_4-rich, C and C_1, compositions. Two thermal effects are evident in the

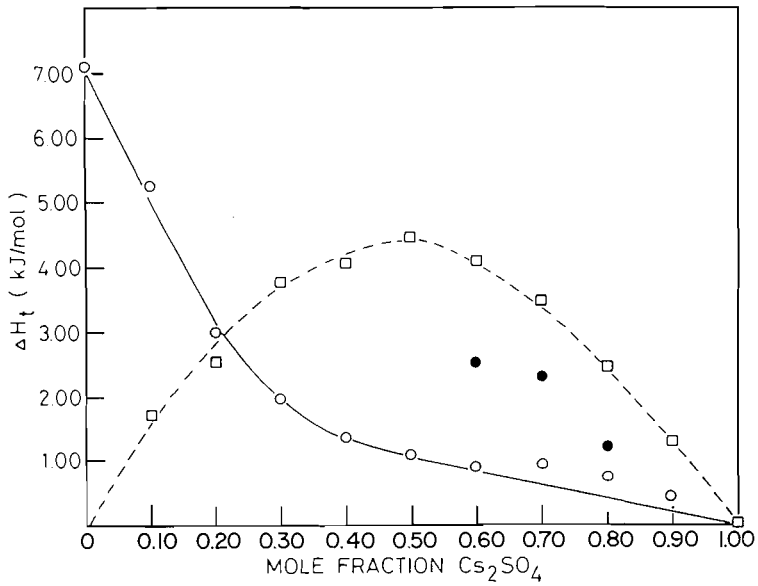

FIG. 7. Plots of ΔH values versus mole fraction Cs_2SO_4 for various thermal processes: ○, ΔH_2 from Table 1; □, ΔH_2 from Table 2; ●, 275°C endotherm on second heating.

TABLE 1. Enthalpy values (kJ/mol) for transition at 250°C[a]

Mole fraction Na_2SO_4	ΔH_1	ΔH_2	ΔH^E_{250}	ΔH_3	ΔH_4
1.00	7.03	7.03	—	—	—
0.90	6.33	5.25	1.08	0.48	0.60
0.80	5.62	3.00	2.62	0.96	1.66
0.70	4.92	2.00	2.92	1.44	1.48
0.60	4.22	1.40	2.82	1.93	0.89
0.50	3.52	1.10	2.42	—	—
0.40	2.81	0.90	1.91	1.93	—
0.30	2.11	0.85	1.26	1.44	—
0.20	1.46	0.55	0.91	0.96	—
0.10	0.70	0.45	0.25	0.48	—

[a] ΔH_1, expected enthalpy for fraction of Na_2SO_4 III → I transition using 7.03 kJ/mol for Na_2SO_4; ΔH_2, experimentally observed enthalpy for the composition cited; $\Delta H^E_{250} = \Delta H_1 - \Delta H_2$; ΔH_3, calculated enthalpy for fraction of $NaCsSO_4$ formed using 2.42 kJ/mol for pure $NaCsSO_4$; ΔH_4, enthalpy calculated for the association complex between β-$NaCsSO_4$ and excess Na_2SO_4.

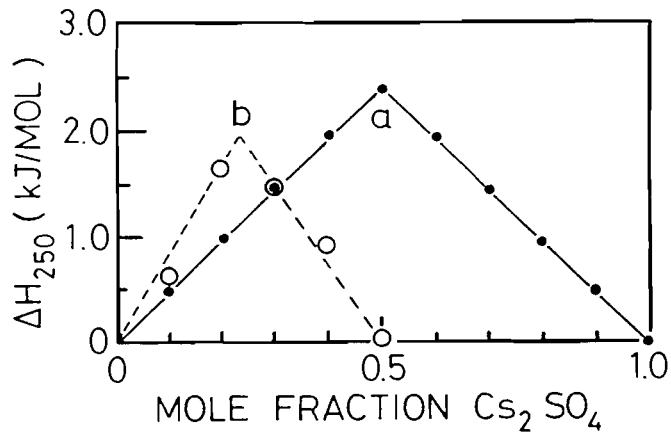

FIG. 8. Plots of ΔH values versus mole fraction Cs_2SO_4 for processes occurring at 250°C: plot *a*, ΔH_3; plot *b*, ΔH_4 from Table 1.

heat mode (*i*) a 255°C endotherm previously identified with the III → I transitions in Na_2SO_4 and (*ii*) a 395°C endotherm associated with a transition in $NaCsSO_4$. These T_t values are in excellent agreement with the conductivity data T_t values. The conspicuous absence of the 395°C exotherm in all cool traces suggests the existence of metastable states; only the reversible I → III transition in Na_2SO_4-rich compositions appears in the cool mode. The Cs_2SO_4-rich compositions show interesting behavior: only the characteristic endotherms of Na_2SO_4 at 210 and 255°C appear on the first heat-cool cycle, *C*. The second heating produces the endotherms at 275 and 395°C, C_1.

In Fig. 7 is given the transition enthalpy ΔH_t dependence on mole fraction of Cs_2SO_4. The 395°C endotherm maximum ΔH_t value occurs at 1:1 mole ratio, i.e. $NaCsSO_4$. However ΔH values for the 245°C peak of Na_2SO_4 exhibit accelerated decline relative to its fractional presence. The presence of Na_2SO_4 in the Cs_2SO_4 excess region, i.e. $x_{Cs_2SO_4} = 0.9$, suggests instability of $NaCsSO_4$ at low temperatures. The ΔH_t value for pure Na_2SO_4 given in Fig. 7 is for the III → I transition (6). Also the ΔH_t values for the 395°C peak associated with $NaCsSO_4$ show an accelerated rise relative to its fractional presence. The filled circles representing values obtained for the 275°C endotherm on the second heating of the Cs_2SO_4-rich compositions, Fig. 6 trace C_1, are found to fall on a straight line between pure Na_2SO_4 and pure Cs_2SO_4 values. The interpretation proposed for this behavior of Cs_2SO_4-rich compositions is another phase transition since Cs_2SO_4 has exhibited sporadic trimorphism instead of the usual dimorphism (2).

Assigning ΔH^E_{250} to the sum value of enthalpy to form $NaCsSO_4$ and the enthalpy of the association complex involving $NaCsSO_4$ and excess Na_2SO_4 I, we obtain the values in Table 1 which are plotted in Fig. 8. These data indicate preferential reaction of Cs_2SO_4 with Na_2SO_4 I, rather than Na_2SO_4 III, exemplifying the Hedvall effect (19). The maximum ΔH for complex association near $x_{Cs_2SO_4} = 0.25$ suggests a 1:1 complex, i.e. $NaCsSO_4$:Na_2SO_4. No complex association between $NaCsSO_4$ and excess Cs_2SO_4 is evident at 250°C.

The thermal effect at 400°C is attributed to the combined solid phase transition β → α in $NaCsSO_4$ and complex association of α-$NaCsSO_4$ with excess Na_2SO_4 or excess Cs_2SO_4. Taking ΔH_2 to be the sum of the enthalpy for the β → α transition and the complex association enthalpy the values in Table 2 are

Can. J. Chem. Downloaded from www.nrcresearchpress.com by 122.72.124.2 on 09/07/12
For personal use only.

TABLE 2. Enthalpy values (kJ/mol) for transition at 400°C[a]

Mole fraction Na_2SO_4	ΔH_1	ΔH_2	ΔH^E_{400}
1.00	—	—	—
0.90	0.89	1.60	0.71
0.80	1.78	2.90	1.12
0.70	2.67	3.75	1.08
0.60	3.57	4.10	0.53
0.50	4.45	4.45	0
0.40	3.57	4.10	0.53
0.30	2.67	3.50	0.83
0.20	1.78	2.50	0.72
0.10	0.89	1.25	0.36

[a]ΔH_1, expected enthalpy for the fraction of $NaCsSO_4$ $\beta \rightarrow \alpha$ transition using 4.45 kJ/mol for pure $NaCsSO_4$; ΔH_2, experimentally observed enthalpy for the composition cited; ΔH^E_{400}, enthalpy calculated for the association complex between α-$NaCsSO_4$ and excess Na_2SO_4 or excess Cs_2SO_4.

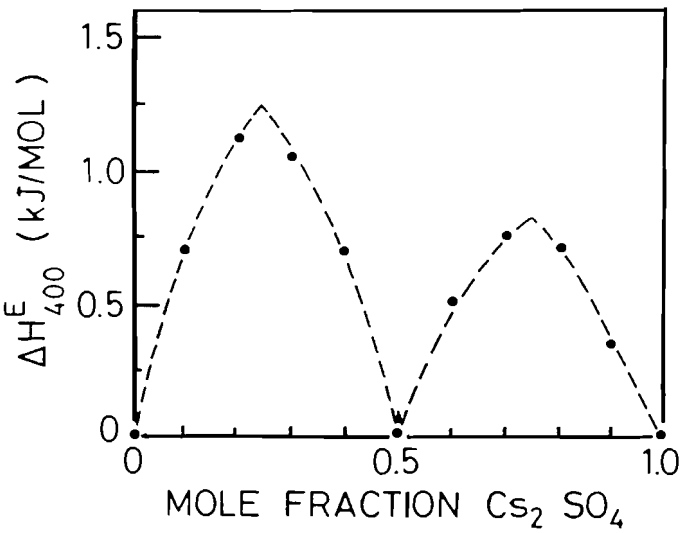

FIG. 9. Plot of ΔH^E_{400} versus mole fraction Cs_2SO_4 from Table 2.

obtained and plotted in Fig. 9. The maximum near $x_{Cs_2SO_4} = 0.25$ confirms the existence of the complex $NaCsSO_4$:Na_2SO_4 and the maximum near $x_{Cs_2SO_4} = 0.75$ suggests the existence of the complex $NaCsSO_4$:Cs_2SO_4.

The ac conductivity and DSC calorimetry data show the reaction products from Na_2SO_4 and Cs_2SO_4 to be relatively unstable. The conductivity drop associated with the I → III Na_2SO_4 transition is evident on cooling the compressed disc of $NaCsSO_4$ but no evidence of this transition appears on the cool mode DSC trace of the uncompressed sample. Furthermore, the presence of the III → I transition on the second heat mode DSC trace indicates behavior reminiscent of spinodal-type decomposition. The observation of V → III transition along with the III → I transition of Na_2SO_4 in the Cs_2SO_4-rich compositions, Fig. 6 trace *C*, suggests the stabilising action by Cs_2SO_4 where pure polycrystalline Na_2SO_4 can persist in metastable phase III for many months. The sporadic behavior and lack of reproducibility of some properties have been noted earlier for the Na_2SO_4–Cs_2SO_4 system (2). The spread and the lack of reproducibility in the conductivity data as evident in Fig. 5 is in strong contrast to the Na_2SO_4–Rb_2SO_4 system. Our observation on complex association is qualitatively consistent with solid solution in the Cs_2SO_4-rich region of the reported phase diagram (2) but the enthalpic effect at 400°C involving $NaCsSO_4$ is reported for the first time.

Acknowledgement

The support for this study, funded by the American Chemical Society – Petroleum Research Fund Grant #17536-B5 and the University Council of Research, is gratefully acknowledged.

1. U. M. GUNDUSHARMA and E. A. SECCO. Can. J. Chem. **65**, 1205 (1987).
2. V. E. PLYUSHCHEV, R. G. SAMUSEVA, and I. F. POLETAEV. Zh. Neorgan. Khim. **7**, 860 (1962); Russ. J. Inorg. Chem. (Engl. Transl.) **7**, 444 (1961).
3. M. NATARAJAN and E. A. SECCO. Can. J. Chem. **52**, 712 (1974).
4. J. ARENDS and H. NIJBDER. Phys. Status Solidi (a) **26**, 537 (1968).
5. Y. FOUQUE, M. GAUNE-ESCARD, W. SZCZEPANIAK, and A. BOGACZ. J. Chim. Phys. **75**, 360 (1978).
6. R. MacL. MURRAY and E. A. SECCO. Can. J. Chem. **56**, 2616 (1978).
7. H. T. CAHEN, P. H. BOTTELBERGHS, and G. H. J. BROERS. Mat. Res. Bull. **12**, 693 (1977).
8. M. S. KUMARI and E. A. SECCO. Can. J. Chem. **63**, 234 (1985).
9. U. M. GUNDUSHARMA and E. A. SECCO. To be published.
10. C. TUBANDT and E. LORENZ. Z. Phys. Chem. **87**, 513 (1914).
11. K. SHAHI. Phys. Status Solidi (a) **41**, 11 (1977).
12. A. KVIST and A. M. JOSEFSON. Z. Naturfor. **23a**, 625 (1968).
13. A. BOGACZ, W. SZCZEPANIAK, J-P. BROS, Y. FOUQUE, and M. GAUNE-ESCARD. J. Chem. Soc. Faraday Trans. 1 **80**, 2935 (1984).
14. A. R. UBBELOHDE. The molten state of matter. John Wiley, New York. 1978.
15. (*a*) M. J. BUERGER. Phase transformation in solids. *Edited by* R. Smoluchowski, J. E. Mayer, and W. A. Weyl. John Wiley, New York. 1951; (*b*) M. J. BUERGER. Fortschr. Miner. **39**, 9 (1961).
16. D. BINGHAM and C. H. BURTON. Phys. Status Solidi (*b*) **130**, 483 (1985).
17. W. J. PARDEE and G. D. MAHAN. J. Solid State Chem. **15**, 310 (1975).
18. (*a*) L. LAM and A. BUNDE. Z. Phys. B**30**, 65 (1978); (*b*) A. BUNDE. Z. Phys. B**36**, 251 (1980).
19. C. N. RAO and K. J. RAO. Phase transitions in solids. McGraw-Hill Inc., New York. 1978. p. 13 and references therein.

Can. J. Chem. Downloaded from www.nrcresearchpress.com by 122.72.124.2 on 09/07/12
For personal use only.

Correlation of ^{31}P nuclear magnetic resonance chemical shifts in aryl phosphinates with Hammett substituent constants: Inductive versus resonance interactions and relevance to p_π–d_π bonding

E. J. DUNN, J. G. PURDON, AND R. A. B. BANNARD

Chemical Detection and Decontamination Section, Protective Sciences Division, Defence Research Establishment Ottawa, Ottawa, Ont., Canada K1A 0Z4

AND

K. ALBRIGHT AND E. BUNCEL[1]

Department of Chemistry, Queen's University, Kingston, Ont., Canada K7L 3N6

Received June 2, 1988

E. J. DUNN, J. G. PURDON, R. A. B. BANNARD, K. ALBRIGHT, and E. BUNCEL. Can. J. Chem. **66**, 3137 (1988).

Substituent-induced chemical shifts and coupling constants in the ^{31}P, ^{13}C, and ^{1}H nuclear magnetic resonance spectra of *meta*- and *para*-substituted phenyl dimethylphosphinates (**1**), methylphenylphosphinates (**2**), and diphenylphosphinates (**3**) have been determined in $CDCl_3$ solvent. For all three series, a correlation of $\delta\,^{31}P$ with Hammett–Taft σ^0 (or σ) constants is preferred over σ^- on the basis of the correlation coefficient and standard deviations of the slope and intercept values. Electron-withdrawing substituents induce downfield shifts in $\delta\,^{31}P$, in contrast to the inverse trends observed for structurally related series of oxyphosphorus acids and their derivatives. It is proposed that electron-withdrawing substituents act to deplete the electron density on the aryl oxygen, thereby weakening a p_π–d_π bonding interaction between the aryl oxygen and phosphorus. The resultants loss of *d*-orbital density on phosphorus causes a downfield shift in $\delta\,^{31}P$ in each of the phosphinate series. Phenyl substituents attached directly to phosphorus in series **2** and **3** increase the phosphoryl p_π–d_π back-bonding interactions, either through inductive or resonance effects, which leads to shielding of the phosphorus atom, overriding the anticipated downfield shift through inductive electron withdrawal of the phenyl substituents in series **2** and **3**, relative to the methyls in series **1**. Trends in Hammett ρ values for the plots of $\delta\,^{31}P$ and $\delta\,^{13}C$ versus σ^0 and differences in the shielding of ^{13}C and ^{1}H nuclei of the methyl attached to phosphorus in series **1** and **2** suggest that the phenyl groups may interact in π bonding with the phosphorus atom through a resonance interaction.

E. J. DUNN, J. G. PURDON, R. A. B. BANNARD, K. ALBRIGHT et E. BUNCEL. Can. J. Chem. **66**, 3137 (1988).

Opérant dans le $CDCl_3$, on a déterminé les déplacements chimiques induits par les substituants ainsi que les constantes de couplage observés dans les spectres de résonance magnétique nucléaire du ^{31}P, du ^{13}C et du ^{1}H des diméthyl- (**1**), méthylphényl- (**2**) et diphényl- (**3**) phosphinates de phényles substitués en *méta* et en *para*. Dans les trois séries, on a établi une corrélation entre les valeurs des $\delta\,^{31}P$ et les constantes σ^0 (ou σ) de Hammett–Taft qui est meilleure que celle avec les constantes σ^- si l'on se base sur le coefficient de corrélation ainsi que sur les déviations standard de la courbe et les valeurs à l'origine. Les $\delta\,^{31}P$ sont déplacés vers les bas champs par les substituants électro-affinitaires et cet effet est l'inverse de celui que est observé avec les acides oxyphosphorés (ainsi que leurs dérivés) qui leur sont apparentés d'un point de vue structural. On suggère que les substituants électro-affinitaires agissent de façon à réduire la densité électronique sur l'oxygène de l'aryle et à provoquer un affaiblissement de l'interaction liante p_π–d_π entre l'oxygène de l'aryle et le phosphore. Dans chacune des séries de phosphinates, les $\delta\,^{31}P$ sont déplacés vers les bas champs par la diminution de la densité de l'orbitale *d* du phosphore que en résulte. Les substituants phényles qui sont attachés directement au phosphore dans les séries **2** et **3** augmentent les interactions de liaison en retour p_π–d_π, soit par des effets inductifs ou de résonance, et ils provoquent un blindage de l'atome de phosphore qui fait disparaître les déplacement vers les bas champs que l'on peut anticiper sur la base des substituants électro-affinitaires des séries **2** et **3** par rapport aux groupements méthyles de la série **1**. Les tendances dans les valeurs de ρ des courbes des valeurs de $\delta\,^{31}P$ et de $\delta\,^{13}C$ vs. σ^0 ainsi que dans les différences dans les blindages des noyaux de ^{13}C et de ^{1}H des groupements méthyles attachés au phosphore des séries **1** et **2** suggèrent que les groupements phényles peuvent interagir dans les liaisons π avec l'atome de phosphore par le biais d'une interaction de résonance.

[Traduit par la revue]

A unified theory of factors affecting chemical shifts and coupling constants is still in the developing stages for ^{31}P nmr (1, 2). Thus, relatively few studies of directly attached or remote substituent effects on $\delta\,^{31}P$, or of coupling constants to nuclei other than H, have been undertaken. Following the summaries of Gorenstein (1) and of Letcher and van Wazer (3), several factors have been identified as contributing to ^{31}P chemical shifts. These factors include hybridization of the phosphorus atom, electronegativity of attached ligands, π-bonding overlap, and σ-bonding angles (1–3).

An interesting observation has been made that, in series of structurally related P(V) esters and their derivatives, including substituted phenylphosphonic difluorides (4), ethyl α-diethylphosphonocinnamates, α-diethylphosphonocinnamonitriles (5), arylphosphonic dichlorides (6), phenylphosphonic acids (7), and alkyl phenyl phenylphosphonates (8), what may be termed an *inverse* chemical shift trend is observed; electron-withdrawing substituents act to shield the phosphorus nucleus. In a recent study (9), however, electron-withdrawing substituents on the ester phenyl ring of substituted phenyl diphenylphosphinates were shown to cause a *normal* or downfield shift in $\delta\,^{31}P$, as would be predicted for ^{13}C or ^{1}H. As well, ^{31}P chemical shifts were shown to correlate with Hammett σ or Hammett–Taft σ^0 substituent constants (9).

We have now extended the previous study to include the substituted phenyl dimethylphosphinates (series **1**) and substituted phenyl methylphenylphosphinates (series **2**). These series provide a useful extension of the previously studied phenyl

[1]Author to whom correspondence may be addressed.

Can. J. Chem. Downloaded from www.nrcresearchpress.com by 122.72.124.2 on 09/07/12
For personal use only.

diphenylphosphinate series (**3**), in regard to nmr spectral parameters (chemical shifts, coupling constants), as well as chemical reactivities (10).

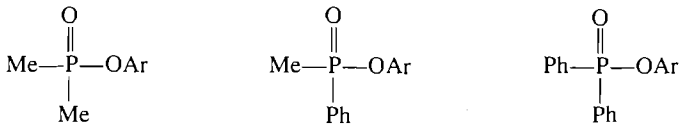

1 **2** **3**

In instances of *inverse* chemical shift trends, it has been argued that electron-withdrawing substituents act, inductively or through resonance, to decrease electron density around the phosphorus nucleus, thereby contracting the phosphorus *d* orbitals and increasing the phosphoryl P—O p_π–d_π bonding overlap to favour **4***b* over **4***a* and thus enhance the shielding of the phosphorus nucleus. It is noteworthy, however, that as a result of MO calculations, Schmidt and Gordon (11) have recently argued that the doubly bonded structure **4***b* is inappropriate, at least for phosphine oxide, and that structures of this type are more correctly represented by canonical forms **4***a* and **4***c*, with **4***a* being the dominant form:

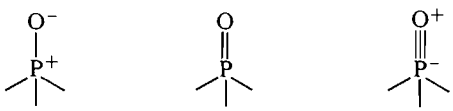

4*a* **4***b* **4***c*

Moreover, the calculations indicate that increasing the electronegativity of the ligands attached to the phosphorus atom increases the contribution of the triply bonded structure (**4***c*) as a result of increased π back-bonding to the phosphorus atom (11). The partial triple bond of the phosphoryl group in phosphine oxide may be described as consisting of one σ bond and two mutually perpendicular, half π bonds formed by p_π–d_π overlap (12).

More recently, Streitwieser and co-workers (13, 14) have shown by *ab initio* MO calculations that, for H_3PO and $H_3PCH_2^-$, there is only a small degree of π back-bonding from O (or C) to P. It was also found that in compounds such as $H_2PO_2^-$, $H_2POCH_2^-$, $H_2P(CH_2)_2^-$, and PO_3^- there appears to be almost no allylic conjugation, suggesting that these bonds are best described as being very highly polar (e.g., $^-O—PH_2^+—O^-$).

The interaction between ligands attached to the phosphorus atom and the extent of π back-bonding is evident from studies of the gas-phase protonation of phosphine oxides and phosphoramides (15). It is shown that protonation of the phosphoryl oxygen causes a lengthening of the bonds of the attached ligands, due to a decrease in π back-bonding. Thus it is reasonable that the electronegativity of the attached ligands will have an effect on the extent of the π back-bonding in the phosphoryl group.

The measurement of the ^{31}P nmr chemical shifts in these types of compounds should yield direct evidence of differences in electron density on phosphorus as a result of changes in substituents either attached directly to or remote from the phosphorus atom. The observation of normal or inverse chemical shifts in a given system is therefore pertinent. To the best of our knowledge, the only other instance of a *normal* chemical shift trend in compounds of the type $R_2P(O)X$ has been reported by Schmidpeter and Brecht (16) for the series of phosphinyl derivatives **5**, where the varied substituent was directly attached to the phosphorus atom. $\delta^{31}P$ was found to correlate linearly with Hammett σ substituent constants, and electron-donating moieties (X) were found to increase shielding of the phosphorus nucleus. The diamagnetic shielding from increased electron density on phosphorus was thought to override all other factors in determining chemical shift trends for these compounds. Notably, all of the substituents studied possessed lone pairs of electrons capable of π back-bonding to phosphorus, making it difficult to assess whether the observed trend was due to diamagnetic shielding alone or to increased *d*-orbital occupancy on phosphorus as well.

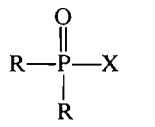

R = alkyl, aryl
X = O^-, NH_2, NMe_2, NHMe, OH, OMe, OEt, S^-, SMe, F, Cl, Br

5

In somewhat related studies with the $Ph_3P{=}NAr$ series, Bödeker *et al.* (17) and Pomerantz *et al.* (18) found normal chemical shift trends for *meta* and *para* substituents on the *N*-phenylimino moiety of the (*N*-phenylimino)triphenylphosphoranes. The latter workers found both chemical shifts (^{31}P, ^{13}C, ^{15}N) and one-bond phosphorus–carbon coupling constants ($^1J(PC)$), to correlate well with Hammett σ^- constants.

Antti Manninen (8) has reported on ^{31}P chemical shifts of derivatives of oxalates of 2-(*N*,*N*-dimethylamino)ethyl phenyl phenylphosphinates with both phenyl and phenoxy groups substituted in the *para* position. An inverse correlation of $\delta^{31}P$ vs. σ^0 was observed with substituents on the phenyl ring. No clear correlation with substituents on the phenoxy group was demonstrated, perhaps due to the limited range of substituents studied.

In light of the apparently anomalous effect of substituents on ^{31}P nmr chemical shifts, as described above, there is a need for further study into the factors that determine substituent-induced chemical shifts in phosphorus-containing compounds. Chemical shift (^{31}P, ^{13}C, ^1H) and coupling constant ($^1J(PC)$, $^2J(PH)$) data may provide additional information concerning the factors that determine chemical shifts for tetrahedral phosphorus and also factors pertaining to bonding and electronic effects in these families of compounds.

Results and discussion

Correlation of ^{31}P chemical shifts with substituent constants σ, σ^0, *and* σ^-

As stated in the introduction, in contrast to chemical shift trends observed in the majority of P(V) compounds, the series **3** was found to exhibit downfield shifts for electron-withdrawing substituents on the ester phenyl ring (9). This observation was interpreted (9) in terms of changes in the p_π–d_π overlap of the P—OAr bond. It was argued that electron-withdrawing substituents on the ester phenyl ring of **3** would act to deplete electron density on the aryl oxygen, resulting in a decrease in p_π–d_π interaction between phosphorus and the aryl oxygen. The results of the present work on series **1** and **2** allow for a comparison of the role of directly attached phenyl substituents in phosphorus bonding and provide further support for our arguments concerning p_π–d_π P—OAr bonding in these families of compounds.

^{31}P chemical shifts for the phosphinate esters **1**, **2**, and **3** are given in Table 1 along with Hammett σ, Hammett–Taft σ^0 and σ^- constants, and correlations. Correlation of $\delta^{31}P$ data to σ^0

Can. J. Chem. Downloaded from www.nrcresearchpress.com by 122.72.124.2 on 09/07/12
For personal use only.

TABLE 1. ^{31}P chemical shifts of the substituted phenyl dimethylphosphinates (**1**), methylphenylphosphinates (**2**), and diphenylphosphinates (**3**) in $CDCl_3$ solution, relative to 85% H_3PO_4 (external) reference; correlations of $\delta^{31}P$ with σ, σ^0, and σ^-

	$\delta^{31}P$ (ppm)					
Substituent	**1**	**2**	**3**	σ	σ^0	σ^-
4-MeO	—	42.374	30.80	−0.27	−0.17	—
4-Me	52.444	41.984	30.52	−0.16	−0.12	—
H	53.527	42.186	30.85	0	0	0
4-Br	54.083	43.158	31.74	0.23	0.26	—
4-Ac	54.159	43.437	31.87	0.50	0.46	0.84
4-CF_3	—	—	32.17	0.55	0.53	0.68
4-CN	—	—	32.89	0.66	0.69	0.88
3-NO_2	56.299	44.818	33.23	0.71	0.70	—
4-NO_2	55.561	44.738	33.10	0.78	0.82	1.24

	Correlation of $\delta^{31}P$ with σ, σ^0, and σ^-								
	1			**2**			**3**		
Parameter	σ	σ^0	σ^-	σ	σ^0	σ^-	σ	σ^0	σ^-
Hammett ρ	3.37	3.45	—	3.07	3.18	1.98	2.80	2.89	1.84
Correlation coeff. (r)	0.933	0.932	—	0.976	0.985	0.887	0.968	0.979	0.883

was generally preferred, on the basis of correlation coefficients (r) and standard deviations in slope and y-intercept, over σ and σ^-. However, the difference in correlation between σ and σ^0 does not appear statistically significant for any of the three series. Correlation to σ^0 was preferred, however, in related studies (7, 9). The correlation to σ^0 may be expected on the basis of the structural similarities of the phosphinates to the standard series of compounds defining σ^0 (19). The plot of $\delta^{31}P$ versus σ^0 is shown in Fig. 1 for the series, **1**, **2**, and **3**.

The correlation between $\delta^{31}P$ and σ^0 may be explained by considering the resonance structures **6** and **6***a* where R^1, R^2 = Me or Ph:

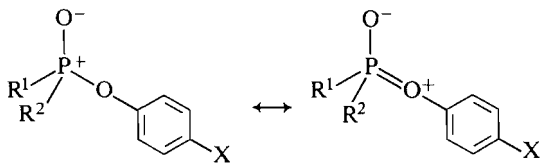

6 **6***a*

The resonance structure **6***a* results from donation of an electron pair in a *p* orbital on the phenoxy oxygen to a *d* orbital of the partially positive phosphorus atom (**6**). Electron-donating substituents (X) would enhance the contribution of resonance structure **6***a*, thereby resulting in increased *d*-orbital occupancy and hence increased shielding of the phosphorus nucleus. Conversely, decreased contribution from **6***a* would result from electron-withdrawing substituents on the phenoxy ring, leading to a decrease in electron density (deshielding) around the phosphorus atom.

The interesting observation follows, from the trends in the ^{31}P chemical shifts in the three families of compounds, that the phosphorus atom in the dimethylphosphinates (**1**) is deshielded relative to the methylphenylphosphinates (**2**) and the diphenylphosphinates (**3**), despite the fact that methyl substituents are inductively more electron donating than phenyl substituents. It is also seen (Fig. 1) that the magnitude of the slope, ρ, decreases upon phenyl for methyl substitution, i.e., along the series **1** → **2** → **3** (ρ values are 3.45, 3.18, and 2.89 respectively, see Table 1).

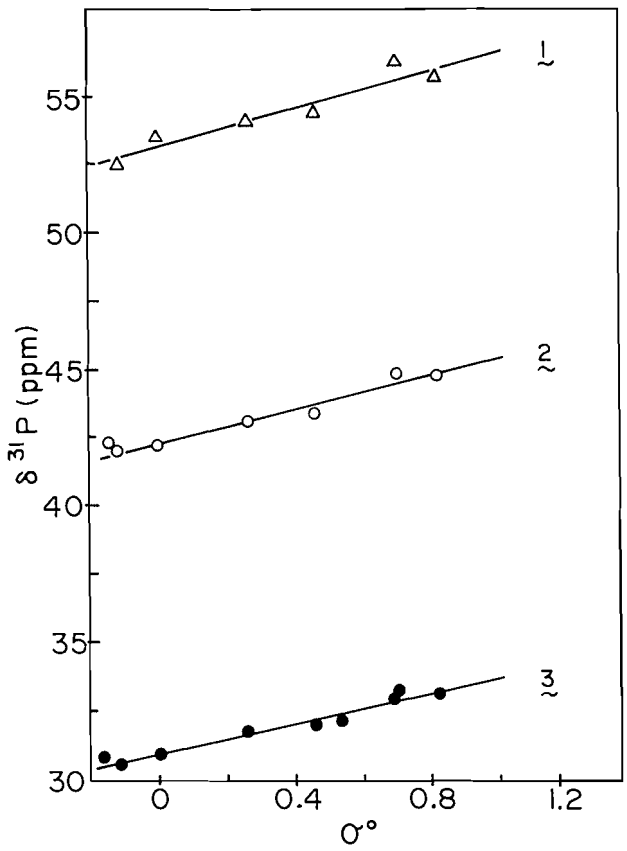

FIG. 1. Plot of $\delta^{31}P$ for phosphinate series **1**, **2**, and **3** versus Hammett–Taft σ^0 substituent constants.

Substitution of Me for Ph causes a large shielding effect around the phosphorus nucleus. For example, the difference in

Can. J. Chem. Downloaded from www.nrcresearchpress.com by 122.72.124.2 on 09/07/12
For personal use only.

Can. J. Chem. Downloaded from www.nrcresearchpress.com by 122.72.124.2 on 09/07/12
For personal use only.

^{31}P chemical shifts for *p*-nitrophenyl diphenylphosphinate (**3***a*) and *p*-nitrophenyl dimethylphosphinate (**1***a*) is 22.5 ppm. The difference in chemical shift between the 4-NO_2 and 4-Me substituted compounds in series **1**, **2**, and **3** is, at most, 3.2 ppm. Therefore, the large increase in shielding of the phosphorus atom observed in series **3** (compared to **2** and **1**), as a result of the attached phenyl groups, may make changes in $\delta^{31}P$ less sensitive to smaller electron differences in the substituents attached to the phenoxy group.

The observed shielding effect of the phenyl groups, compared to the methyl groups, can be described in two ways. First, the phenyl rings inductively withdraw electrons from the phosphorus atom, which in turn increases the p_π–d_π back-bonding interaction of the phosphoryl oxygen, i.e., increased resonance contribution of **4***c* over **4***a*. Secondly, the *p* orbitals of the phenyl rings may be able to overlap with the *d* orbitals around the phosphorus atom through a resonance interaction.

Thus, whereas for series **1** only structures **6** and **6***a* ($R^1 = R^2$ = Me) are possible, for series **2** and **3** the phenyl groups may be involved via **6***b* and **6***c* as well. Contributions from **6***b* and **6***c* could be greater for the series **3** ($R^1 = R^2$ = Ph), where two phenyl groups are attached to phosphorus, relative to series **2**. For series **2** and **3**, the resulting effect of greater contribution by structures **6***b* and **6***c* may be to moderate the effects of the substituents in the ester moiety through electron withdrawal/donation of substituents via structures **6***a*, which would lead to smaller ρ values.

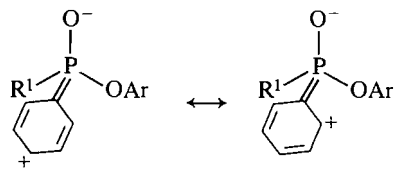

6*b* **6***c*

Hence electron-withdrawing substituents on the ester phenyl ring may act to weaken a π interaction of type **6***a* between the ester oxygen and phosphorus atom. In series **3**, and to a lesser extent series **2**, such weakening may be compensated for by increasing proportions of canonical forms **6***b* and **6***c*. In series **1**, however, there is no compensating effect by phenyl substituents, and the effect of the aryl oxygen–phosphorus π-bond weakening is seen to be greater, as reflected in the larger ρ values.

Correlation of ^{13}C and ^{1}H chemical shifts with the Hammett–Taft substituent constant σ^0

$\delta^{13}C$ and $\delta^{1}H$ values for the methyl moieties of series **1** and **2** are given in Table 2. On plotting the methyl $\delta^{13}C$ and $\delta^{1}H$ values in Table 2 versus σ^0 constants, a downfield shift in $\delta^{13}C$ and $\delta^{1}H$ is found with increasing electron-withdrawing ability of the ester phenyl substituents for **1** and **2**, as illustrated in Fig. 2 for $\delta^{13}C$. It is also seen that $\delta^{13}C$ and $\delta^{1}H$ for the methylphenylphosphinates (**2**) occur downfield of their dimethyl (**1**) counterparts.

The above observation of electron-withdrawing substituents on the phenoxy group inducing downfield shifts in $\delta^{13}C$ and $\delta^{1}H$ indicates that these substituents act to inductively withdraw electron density from the phosphorus atom and consequently from the attached methyl group. The higher resonance frequencies of series **1** as compared to **2** further implicate phenyl substituents in inductive electron withdrawal (relative to methyl substituents) from the phosphorus atom.

TABLE 2. ^{1}H and ^{13}C chemical shifts for the methyl substituents attached to phosphorus and ^{2}J(PH) and ^{1}J(PC) coupling constants for (*a*) the substituted phenyl dimethylphosphinate series (**1***a*–**1***f*) and (*b*) the substituted phenyl methylphenylphosphinate series (**2***a*–**2***f*), in $CDCl_3$ (shifts in ppm are quoted downfield of TMS, *J* is given in Hz)

(*a*)

Substituent	$\delta^{1}H$	$\delta^{13}C$	^{2}J(PH)	^{1}J(PC)
4-Me (**3***f*)	1.626	15.68	13.90	95.86
H (**3***e*)	1.634	15.61	13.98	94.91
4-Cl (**3***d*)	1.649	15.67	13.97	94.51
4-Ac (**3***c*)	1.688	15.96	13.96	94.00
3-NO_2 (**3***b*)	1.717	16.00	13.91	93.90
4-NO_2 (**3***a*)	1.732	16.13	13.80	94.08

(*b*)

Substituent	$\delta^{1}H$	$\delta^{13}C$	^{2}J(PH)	^{1}J(PC)
4-Me (**2***f*)	1.830	16.00	14.35	102.46
H (**2***e*)	1.850	16.01	14.41	101.71
4-Cl (**2***d*)	1.862	16.06	14.47	101.87
4-Ac (**2***c*)	1.902	16.30	14.50	102.42
3-NO_2 (**2***b*)	1.940	16.20	14.56	101.36
4-NO_2 (**2***a*)	1.944	16.35	14.57	102.20

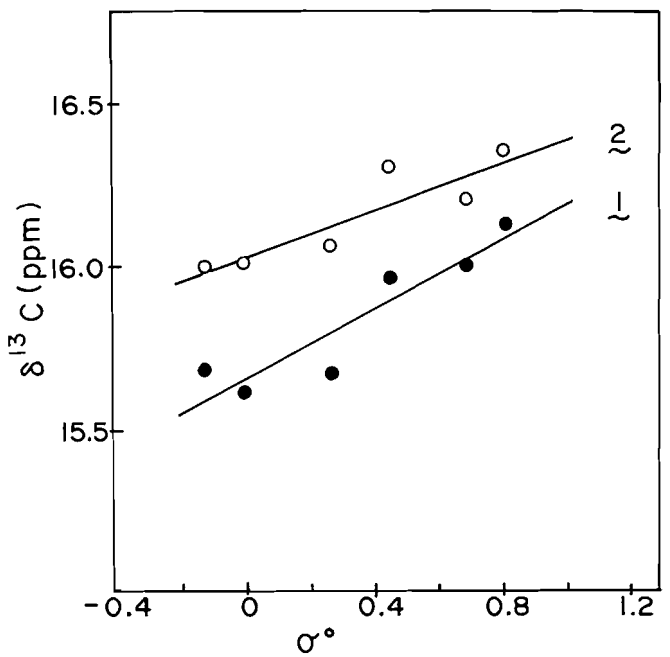

FIG. 2. Plot of $\delta^{13}C$ for the phosphorus-attached methyl group of series **1** and **2** esters versus Hammett–Taft σ^0 substituent constants.

The Hammett slope (ρ) may be taken as a measure of the sensitivity of phosphorus $\delta^{31}P$ and methyl $\delta^{13}C$ and $\delta^{1}H$ to substituent changes on the ester phenyl ring. The lower ρ values found for series **2** as compared with series **1** for both ^{13}C and ^{1}H are consistent with the argument for moderating effects of ester substituent changes by phenyl groups either through mesomeric forms **6***b* and **6***c* or by increased p_π–d_π back-bonding of the phosphoryl oxygen as a result of the inductive effect of the phenyl rings.

TABLE 3. Physical properties and elemental analyses of substituted phenyl methylphenylphosphinates, series **2**

Substituent		Melting point (°C)	Analysis					
			Calcd.			Found		
			C	H	N	C	H	N
4-NO_2	(**2***a*)	86–87 (86–87)[a]	—	—	—	—	—	—
3-NO_2	(**2***b*)	58	56.32	4.36	5.05	55.95	4.31	5.06
4-$COCH_3$	(**2***c*)	81–82	65.69	5.51	—	65.49	5.49	—
4-Cl	(**2***d*)	76–77	58.55	4.54	—	58.55	4.59	—
H	(**2***e*)	56–58 (bp 151–153)[b]	—	—	—	—	—	—
4-Me	(**2***f*)	66–67	66.29	6.14	—	68.12	6.06	—

[a]Reference 23.
[b]Reference 24.

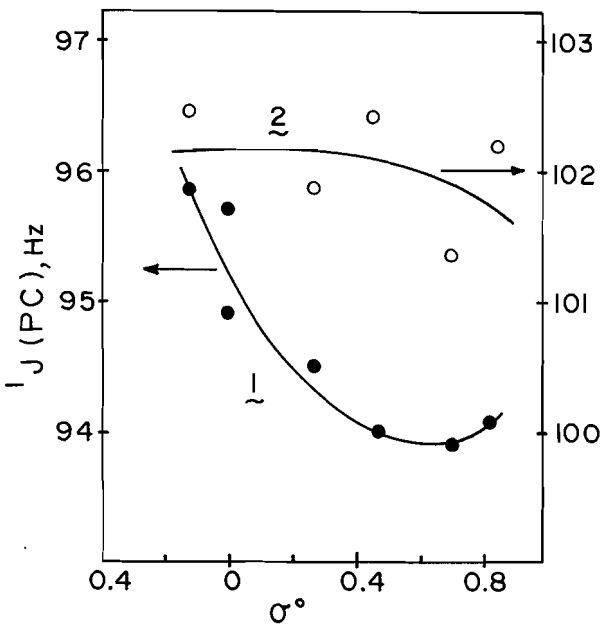

FIG. 3. Comparison of ^1J(PC) values for the methyl carbons of series **1** and **2**, plotted against Hammett–Taft σ^0 substituent constants. Series **1**, left-hand scale (●); series **2**, right-hand scale (○).

Correlation of one-bond P–C coupling constants (^{1}J(PC)) and two-bond P–H coupling constants (^{2}J(PH)) with σ^0

Plotted in Fig. 3 are the one-bond phosphorus – methyl carbon coupling constants ^1J (PC) for series **1** and **2** versus the σ^0 substituent constants (data in Table 2). ^1J(PC) values for series **2** remain approximately constant at ca. 102 Hz throughout the series. Series **1**, on the other hand, exhibits a decrease in ^1J(PC) from 95.86 Hz for **1***f* to ca. 93.90 Hz for **1***b*. ^2J(PH) coupling constants in series **1** assume approximately constant values of ca. 13.9 Hz, while in series **2** the values remain at ca. 14.5 Hz.

Duangthai and Webb (20), using calculations at the INDO level, have recently shown ^1J(PC) to be positive and completely dominated by the Fermi contact term for pentavalent phosphorus compounds, as is believed to be the case for ^1J(PC) and ^1J(PO) (21). Hence the magnitude of ^1J(PC) may be taken as a measure of the *s*-orbital density of the phosphorus – methyl carbon bond in **1** and **2**. If it is also assumed that the hybridization of the methyl carbon does not change noticeably within series **1** and **2**, then changes in ^1J(PC) are determined primarily by the hybridization of the phosphorus atom.

It follows from the above argument that the larger ^1J(PC) values for series **2** indicate that phosphorus in series **2** is involved in more extensive π bonding than in **1**. Thus, the relatively constant ^1J(PC) values found for series **2** can be taken to indicate that hybridization of the phosphorus atom does not change significantly within the series **2**, yet in series **1** hybridization is seen to change significantly. This observation may be explained in two ways. First, in series **2**, the larger phenyl group may present a steric barrier to significant C—P—C bond angle compression. This is not consistent with our previous arguments based on chemical shifts, since the sensitivity of the ^{31}P or methyl ^{13}C and ^{1}H nuclei to ester substituent changes is not expected to be lessened by a steric barrier to bond angle changes. Alternatively, the phenyl moiety of series **2** may enhance the p_π–d_π interaction of the phosphoryl oxygen with the phosphorus atom through contribution of structures such as **4***c*, **6***b*, and **6***c*. This interpretation is also consistent with the observation that the phosphoryl oxygen coupling constant ^1J(PO)) for $F_3P{=}O$ is much greater than in $H_3P{=}O$ (21).

Conclusions

An analysis of the ^{31}P chemical shift information for the series **1–3** shows that electron-withdrawing substituents on the ester phenyl ring of these phosphinates contribute to a deshielding of the ^{31}P nucleus, whereas directly attached phenyls act to shield the phosphorus nucleus, by promoting a p_π–d_π interaction of the phosphoryl oxygen with phosphorus and possibly by p_π–d_π overlap between the phenyl ring and phosphorus. The shielding effect brought about by a greater p_π–d_π interaction overrides the effect of inductive electron withdrawal by the phenyl group. The theory of Letcher and van Wazer (22) suggests that the difference in direct substituent effects may be due either to a change in π-bond overlap, or to the larger σ-bond angle in the methylphenyl series (**2**). Both of these arguments appear possible in light of the evidence presented.

Electron-withdrawing substituents on the ester phenyl ring may act, either inductively or through resonance, to deplete electron density on the aryl oxygen and thereby decrease a P—OAr p_π–d_π bonding interaction. The resultant decrease in *d*-orbital density induces a downfield shift in δ^{31}P. Phenyl moieties attached to phosphorus in **2** and **3** may moderate the effects of phenyl-ester substituent changes, either inductively or

Can. J. Chem. Downloaded from www.nrcresearchpress.com by 122.72.124.2 on 09/07/12
For personal use only.

through canonical structures **6***b* and **6***c*. Resonance donation of the type **4***c*, **6***b*, and **6***c* increases *d*-orbital occupancy on phosphorus (hence shielding the ^{31}P nucleus), overriding the effects of inductive electron withdrawal by phenyl substituents. Thus, differences in phosphorus *d*-orbital density in series **1–3** appear to play a major role in determining shielding of the ^{31}P nucleus in these series of compounds.

Experimental

Nuclear magnetic resonance spectra

All spectra were recorded on a Bruker AM400 nmr spectrometer. The 400-MHz ^{1}H and 101-MHz ^{13}C spectra were obtained in 5 mm o.d. nmr tubes in $CDCl_3$ solution with 0.5% tetramethylsilane (TMS) as internal reference. The ^{13}C nmr spectra were run in the ^{1}H-decoupled mode. The 162-MHz ^{31}P spectra were obtained in the PWRGATHT (^{1}H decoupled) mode on 0.1 M $CDCl_3$ solutions in 10 mm o.d. tubes and are quoted downfield with respect to 85% H_3PO_4 external reference.

Preparation of phosphinates

Substituted phenyl diphenylphosphinates were obtained from a previous study (9). Substituted phenyl dimethylphosphinates were prepared according to the method of Douglas and Williams (23). Substituted phenyl methylphenylphosphinates were prepared from the phosphinic chloride as described for **2***a* below as a representative example.

4-Nitrophenyl methylphenylphosphinate (**2***a*) was prepared by modification of the method of Raevskii *et al.* (24). To 3.10 g (0.022 mol) of 4-nitrophenol in a 50-mL solution of diethyl ether or benzene contained in a 100-mL 2-necked round-bottom flask under N_2 were added, in order, 3.25 mL (0.023 mol) of triethylamine and 3.96 g (0.022 mol) of methylphenylphosphinic chloride by syringe. The resulting yellow suspension was stirred at room temperature for 1 day, filtered under N_2 in a dry box to remove precipitated triethylamine hydrochloride, and concentrated on a rotary evaporator under reduced pressure, leaving behind a dark yellow oil. Acetone was added to triturate any methylphenylphosphinic acid; the resulting suspension was dried over $MgSO_4$ and filtered. Acetone was removed by rotoevaporation and the resulting partially crystalline mass was crystallized from ca. 20 mL of anhydrous diethyl ether by addition of petroleum ether (35/60) at room temperature. The product **2***a* was recrystallized twice from carbon tetrachloride.

Physical properties of the esters are provided in Table 3. Elemental analysis is included for compounds not previously reported. Melting points are uncorrected.

Acknowledgement

This research was supported by the Defence Research Establishment, Ottawa, Department of National Defence.

1. D. G. Gorenstein. *In* Phosphorus-31 NMR, Principles and applications. *Edited by* D. G. Gorenstein. Academic Press, New York, NY. 1984.
2. D. J. Craik. Annu. Rep. NMR Spectros. **15**, 1 (1983).
3. J. H. Letcher and J. R. Van Wazer. Top. Phosphorus Chem. **5**, 75 (1967).
4. L. L. Szafraniec. Org. Magn. Reson. **6**, 565 (1974).
5. C. N. Robinson and C. D. Slater. J. Org. Chem. **52**, 2011 (1987).
6. R. C. Grabiak, J. A. Miles, and G. M. Schwenzer. Phosphorus Sulfur, **9**, 197 (1980).
7. C. C. Mitsch, L. D. Freedman, and C. G. Moreland. J. Magn. Reson. **3**, 446 (1970).
8. P. Antti Manninen. Acta Chem. Scand. (B), **35**, 13 (1981).
9. S. Hoz, E. J. Dunn, E. Buncel, R. A. B. Bannard, and J. G. Purdon. Phosphorus Sulfur, **24**, 321 (1985).
10. E. Buncel, E. J. Dunn, R. A. B. Bannard, and J. G. Purdon. J. Chem. Soc. Chem. Commun. 162 (1984).
11. M. W. Schmidt and M. S. Gordon. J. Am. Chem. Soc. **107**, 1922 (1985).
12. W. Kutzelnigg. Angew. Chem. Int. Ed. Engl. **23**, 272 (1984).
13. A. Streitwieser, A. Rajca, R. S. McDowell, and R. Glaser. J. Am. Chem. Soc. **109**, 4184 (1987).
14. A. Rajca, J. E. Rice, A. Streitwieser, and H. F. Schaefer. J. Am. Chem. Soc. **109**, 4189 (1987).
15. J. C. Bollinger, R. Houriet, C. W. Kern D. Perret, J. Weber, and T. Yvernault. J. Chem. Soc. **107**, 5352 (1985).
16. A. Schmidpeter and H. Brecht. Angew. Chem. Int. Ed. Engl. **6**, 945 (1967).
17. J. Bödeker, P. Köckritz, H. Köppel, and R. Radeglia. J. Prakt. Chem. **322**, 735 (1980).
18. M. Pomerantz, D. S. Marynick, K. Rajeshwar, W-N. Chou, L. Throckmorton, E.W. Tsai, P.C.Y. Chen, and T. Cain. J. Org. Chem. **51**, 1223 (1986); M. Pomerantz, B. T. Ziemnicka, Z. M. Merchant, W-N. Chou, W. B. Perkins, and S. Bittner. J. Org. Chem. **50**, 1757 (1985).
19. R. W. Taft, Jr. J. Phys. Chem. **64**, 1805 (1960).
20. S. Duangthai and G. A. Webb. Org. Magn. Reson. **21**, 125 (1983).
21. G. A. Gray and T. A. Albright. J. Am. Chem. Soc. **99**, 3243 (1977).
22. J. H. Letcher and J. R. Van Wazer. J. Chem. Phys. **44**, 815 (1966).
23. K. T. Douglas and A. Williams. J. Chem. Soc. Perkin Trans. **2**, 515 (1976).
24. O. A. Raevskii, F. G. Khalitov, and M. A. Pudovik. Izv. Akad. Nauk SSSR, Ser. Khim. (English Transl.), **11**, 2595 (1971).

Can. J. Chem. Downloaded from www.nrcresearchpress.com by 122.72.124.2 on 09/07/12
For personal use only.

Diels–Alder reactions of 2-carbomethoxy-2-cyclohexen-1-one[1]

HSING-JANG LIU, TENG KO NGOOI, AND ERIC N. C. BROWNE[2]
Department of Chemistry, The University of Alberta, Edmonton, Alta., Canada T6G 2G2

Received June 21, 1988

HSING-JANG LIU, TENG KO NGOOI, and ERIC N. C. BROWNE. Can. J. Chem. **66**, 3143 (1988).

Under stannic chloride catalysis, 2-carbomethoxy-2-cyclohexen-1-one (**5**) was found to undergo Diels–Alder reaction with a variety of dienes to give directly the *cis*-1-octalone system possessing a functionalized substituent at the angular position. With unsymmetrically substituted dienes, the adducts were those predicted on the basis of the normal rules (*ortho* and *para*) governing the orientation of Diels–Alder addition. In cases where differing secondary orbital overlap would affect the stereochemistry of the adducts, the major isomer in each case was that produced by secondary overlap of the diene with the ester carbonyl rather than the ketone carbonyl, presumably due in part to a steric effect. The degree of stereoselectivity was further shown to be dependent upon both the reaction temperature and the diene used and was generally enhanced when the reaction was carried out at lower temperatures or when a bulkier diene was involved.

HSING-JANG LIU, TENG KO NGOOI et ERIC N. C. BROWNE. Can. J. Chem. **66**, 3143 (1988).

On a trouvé que, sous l'influence d'une catalyse par le chlorure stannique, la carbométhoxy-2 cyclohexène-2 one-1 (**5**) subit des réactions de Diels–Alder avec un grand nombre de dienes pour conduire directement au système de l'octalone-1-*cis* possédant un substituant fonctionnalisé en position angulaire. Lorsqu'on effectue la réaction avec des dienes qui ne sont pas substitués d'une façon symétrique, les adduits sont ceux que l'on peut prévoir en se basant sur les règles normales (*ortho* et *para*) régissant l'orientation de l'addition de Diels–Alder. Dans les cas où un recouvrement d'orbitales secondaires différent peut affecter la stéréochimie des adduits, l'isomère principal obtenu est toujours celui provenant du recouvrement secondaire du diène avec le carbonyle de l'ester plutôt qu'avec le carbonyle de la cétone; ce résultat est vraisemblablement dû à un effet stérique. On a démontré que le degré de stéréosélectivité dépend aussi de la température de la réaction ainsi que du diène utilisé; on a remarqué qu'il augmente généralement lorsqu'on opère à des températures plus basses ou lorsqu'un diène plus encombré est impliqué.
[Traduit par la revue]

Introduction

The poor results of attempts to achieve cycloadditions to cyclohexenones are well known in the field of Diels–Alder reactions (1–4). The catalytic effect of Lewis acids on Diels–Alder additions to α,β-unsaturated carbonyl compounds (5–8) was discovered long before it was applied to simple cyclic enones. Furthermore, while catalysis has made available a variety of adducts of cyclohexenones substituted on the dienophilic double bond,[3] cycloadditions to unsubstituted cyclohexenone continue to give poor results.

Wenkert and co-workers (9, 11–22) made an extensive study to systematize the Diels–Alder additions of a variety of simple cyclic enones. Liu and Browne (23–28) carried out an extensive study of the Diels–Alder reactions of 4,4-dimethyl-2-cyclohexen-1-one (**1**) and its derivatives **2**, **3**, and **4**. They observed improved rates and yields by the introduction of an additional electron-withdrawing group into the dienophilic moiety (as in **3**) as predicted by the Alder rule (29, 30). That study also indicates the potential of using different Lewis acid catalysts to effect different regiochemical outcomes in the reaction of isoprene with the dienone **3** (25).

Although conjugated cyclohexenones having an additional electron-withdrawing group attached to the dienophilic double bond have been observed to display improved dienophilicity in Diels–Alder reactions, few studies using such cyclohexenone derivatives have been reported. The compounds that were studied include examples substituted either at the α-carbon (24, 26, 28, 31) or the β-carbon (32–34) of the cyclohexenone. In the former case all of the enones explored were geminally substituted at the γ-carbon, blocking the facile enolization

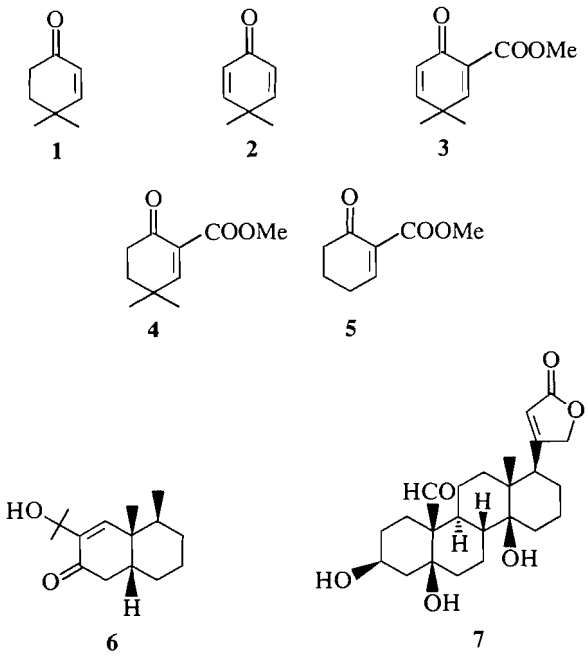

1 2 3 4 5 6 7

towards that center. In spite of their broader synthetic utility, cycloadditions of enolizable analogs of cyclohexenone that have an electron-withdrawing α-substituent had not been reported prior to our first communication of this work (10).

We have examined the dienophilicity of 2-carbomethoxy-2-cyclohexen-1-one (**5**). The results as well as the structural assignments and mechanistic significance of the study will be discussed. A total synthesis of petasitolone (**6**) has been achieved (35) by a Diels–Alder addition to **5**. The use of enone ester **5** in a key Diels–Alder reaction for a synthetic study of the cardenolide strophanthidin (**7**) is under study in these laboratories (36).

[1]Taken in part from the Ph.D. thesis of T. K. Ngooi, The University of Alberta, 1984.

[2]Present Address: Wyeth–Ayerst Research, 1025 Laurentian Blvd., St. Laurent, P.Q., Canada H4R 1J6.

[3]For a bibliography see footnote 8 in ref. 9 and notes 3 and 4 in ref. 10.

Can. J. Chem. Downloaded from www.nrcresearchpress.com by 122.72.124.2 on 09/07/12
For personal use only.

Can. J. Chem. Downloaded from www.nrcresearchpress.com by 122.72.124.2 on 09/07/12
For personal use only.

Results and discussion[4]

The effective preparation of 2-carbomethoxy-2-cyclohexen-1-one (**5**) has only recently been achieved since mild conditions for the carbon–carbon double bond formation have become available.[5] It could be prepared according to the two-step procedure of Reich *et al.* (40) or according to the method developed by Liotta *et al.* (41). We preferred the latter procedure for its simplicity and reproducibility. The starting 2-carbomethoxycyclohexanone (**8**) was treated with phenylselenenyl chloride pyridine complex (42) in methylene chloride. After an aqueous acid extraction of the reaction mixture to remove pyridine, the resulting selenide was oxidized with a solution of 30% aqueous hydrogen peroxide to give the required enone ester **5** in quantitative yield.

The enone ester **5** thus obtained was found to enolize and decompose rapidly,[6] but it was of good quality by ^{1}Hmr analysis. Attempts to distill this material led to reduced yield and it was more expedient to use the "crude" enone ester **5** in the Diels–Alder reaction without purification. A variety of conditions were initially examined for the Diels–Alder reaction of **5**. Thermal conditions did not give synthetically useful yields of adducts.[7] For example, when freshly prepared enone ester **5** was heated with 2,3-dimethyl-1,3-butadiene in benzene the adduct **9** was obtained in only 6% yield. Even with a more reactive diene the yields of adducts were not significantly improved. Thus reaction of enone ester **5** with 2-trimethylsilyloxy-1,3-butadiene (**10**) (44) carried out over a range of temperatures (20–120°C) gave at best 8% yield of the keto ester **11** after hydrolysis. A

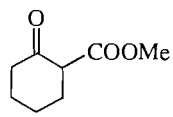

8

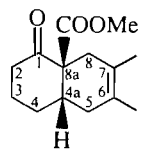

9

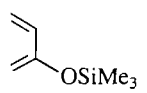

10

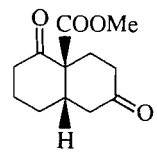

11

preliminary study indicated that various Lewis acids could be used to catalyze the Diels–Alder reaction of enone ester **5**. The results are summarized in Table 1. Stannic chloride usually gave the best yields of adducts and so, for further exploration of the scope of the Diels–Alder reactions of enone ester **5**, it was chosen as the Lewis acid catalyst. The results of this broader study are summarized in Table 2.

In general, the additions to **5** proceeded without operational difficulty and in moderate to good overall yield from **8** taking into account the 3 or 4 steps (selenation, oxidative elimination, cycloaddition, and, for the silyl enol ether derivatives, hydrolysis) required in the transformation. The structures of the adducts were established from their spectroscopic properties including ^{1}Hmr decoupling experiments, spectroscopic and chemical correlation with known compounds, and by degradation techniques previously developed in this laboratory (25–27). The usual orientational and stereochemical rules of Diels–Alder addition (27, 29, 45) were followed.

Structural assignments

Several of the adducts of **5** shown in Table 2 required more detailed analysis to unambiguously establish their structures. The chemical transformations used in the assignment of structures are summarized in Scheme 1. Ring junction stereochemistry was typically assigned on the basis of the *cis* principle (4, 27, 29, 45). In support of this general assignment, a reduction product **26** derived from **14**, **19**, or **22** was converted to the *cis*-fused natural product petasitolone **6** (35). We will discuss the regiochemical and stereochemical assignments of each group of adducts in turn.

The expected product of Diels–Alder reaction of **5** with 2-trimethylsilyloxy-1,3-butadiene **10** would have structure **11** after hydrolytic cleavage of the initially formed silyl enol ether **30**. Evidence in support of the regiochemical assignment was obtained from the high-field (400 MHz) ^{1}Hmr spectrum. A one-proton signal appeared at δ 3.11 with three coupling constants of 14, 7.0, and 3.5 Hz. This signal was assigned to the methine proton at the ring junction. The signal was coupled to a doublet at δ 2.29 (J = 7.0 Hz),[8] which integrated for two protons and was assigned to the methylene protons at C-5.[9] Clearly, these data are consistent with structure **11**. The regioisomeric adduct **31** would show no vicinal coupling to the ring junction proton for the methylene protons at C-8. Instead it would show a geminally coupled doublet for each proton, or a two-proton singlet if they were magnetically equivalent.

It is known that the Diels–Alder reaction with 2-substituted dienes can lead to regioisomeric mixtures of products (29, 45) or even complete orientational reversal (25). Therefore, it was important to prove that the addition of isoprene to enone ester **5** gave **12** and not the regioisomeric keto ester **29**. This simple structural proof has been detailed in a previous report (46).

Preliminary analysis of the spectral data indicated that the structure of the adduct of cyclopentadiene was either **13** or **32**. Conformational analysis showed that the keto ester **13** would have conformation **13***a*, in which a long-range *W*-coupling between the proton at C-4a and one of the protons on C-9 (H_x) would be expected in the ^{1}Hmr spectrum. On the other hand, in **32***a* no such *W*-coupling would be possible. Decoupling experiments of all isolable signals in the ^{1}Hmr spectrum led to assignment of all the protons on the bicyclo[2.2.1]heptene ring system of the adduct. The signal for the C-4a proton appeared at δ 2.52, with coupling constants of 12, 7.0, and 2.0 Hz, while the signal at δ 1.42 was assigned to the H_x proton on C-9. This

[4]For a preliminary communication see ref. 10.

[5]Although the corresponding ethyl ester was reported much earlier (37–39), the methods required were laborious or extreme.

[6]To slow decomposition and enolization, the crude oil was stored in a clean dry flask that had been pretreated with aqueous NH_4OH before drying. Usually freshly prepared **5** was used.

[7]A recent communication (43) reports successful thermal cycloaddition of a complex silyloxy diene to **5** (62% yield) in a synthetic strategy where acid catalysis would be incompatible with the required survival of the resulting silyl enol ether adduct.

[8]This coupling was confirmed by irradiation of the signal at δ 3.11, which caused the signal at δ 2.29 to collapse to a singlet. Conversely, a doublet of doublets was observed at δ 3.11 on irradiation of the signal at δ 2.29.

[9]These two methylene protons have the same chemical shift in $CDCl_3$; however, when the ^{1}Hmr spectrum was run in deuterobenzene these same two protons showed different chemical shifts at δ 1.91 and 1.80. The signal at δ 1.91 showed coupling constants of 14.5, 5.5, and 1.0 Hz, while the signal at δ 1.80 gave coupling constants of 14.5, 8.5, and 1.5 Hz.

TABLE 1. Effect of different Lewis acid catalysts on Diels–Alder reactions of enone ester **5**[a]

Entry	Diene (10 equiv.)	Catalyst (0.5 equiv.)	Time (h)	Product	% Yield from **8**
1		$Et_2O{\cdot}BF_3$	3	**9**	38
		$SnCl_4$	1.5	**9**	61
		$FeCl_3$	1.5	**9**	42
2		$SnCl_4$	1.5	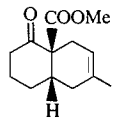 **12**	61
		$FeCl_3$	2	**12**	46

[a]All reactions were run at 0°C using ether as the solvent.

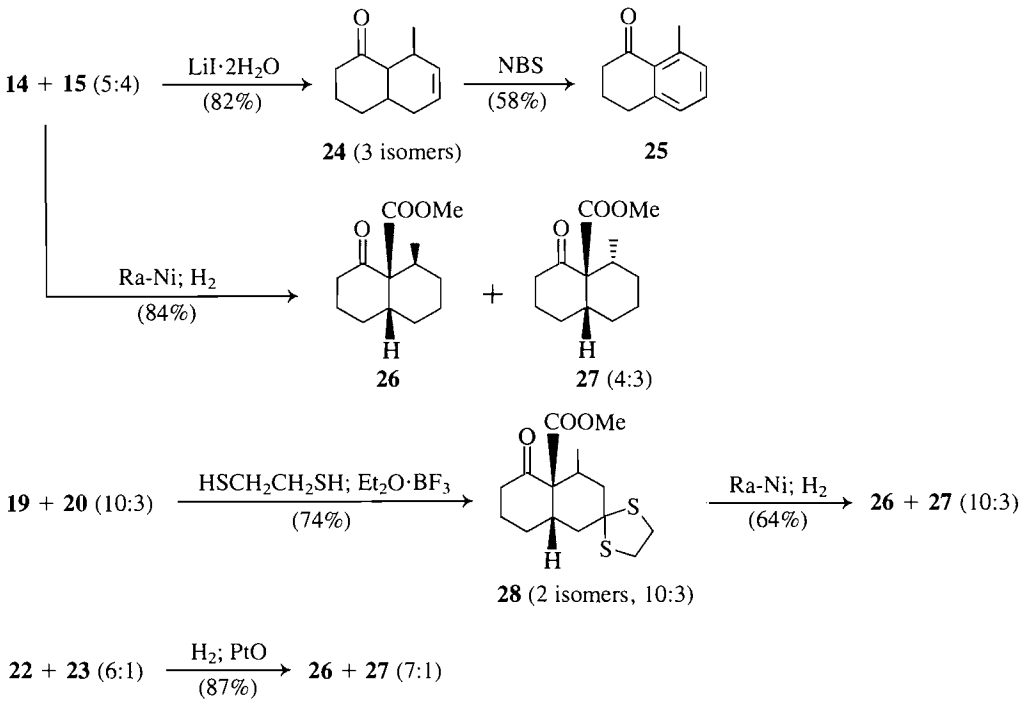

SCHEME 1. Transformations of adducts, **14**, **15**, **19**, **20**, **22**, and **23**.

latter signal had coupling constants of 9.0, 2.0, and 1.0 Hz. Irradiation of the signal at δ 1.42 led to simplification of the signal at δ 2.52 to a doublet of doublets with coupling constants of 12 and 7.0 Hz. Conversely, irradiation of the signal at δ 2.52 led to the disappearance of the 2.0-Hz coupling constant for the signal at δ 1.42. This demonstrated coupling between the C-4a and C-9 H_x protons confirmed the assignment of structure **13** to the adduct.

To conclusively determine the regiochemistry of the addition of *trans*-piperylene, the 5:4 mixture of Diels–Alder adducts was converted to the corresponding aryl ketone derivative (Scheme 1) by the established method (25, 27, 46). Decarbomethoxylation of the mixture of adducts **14** and **15** by treatment with lithium iodide dihydrate in refluxing 2,4,6-collidine (40, 47) gave a mixture of three ketones **24**. The mixture of ketones was dehydrogenated with *N*-bromosuccinimide in refluxing carbon tetrachloride (48) to give a single aryl ketone in 58% yield. The aryl methyl signal in the ^{1}Hmr spectrum appeared as a singlet at δ 2.65. The absence of any signal above δ 7.30 as well as the presence of the *peri*-deshielded (49) aryl methyl signal indicated the assignment of structure **25** for the aryl ketone. The Diels–Alder adducts must then possess the regiochemistry shown in structures **14** and **15**.

The determination of the major epimer of the product mixture was made by chemical correlation of the major adduct to the known (35) compound **33**. The mixture of adducts was

Can. J. Chem. Downloaded from www.nrcresearchpress.com by 122.72.124.2 on 09/07/12
For personal use only.

TABLE 2. Stannic chloride catalyzed Diels–Alder reactions of enone ester **5**[a]

Entry	Diene (equiv.)	Temperature (°C)	Time (h)[b]	Products (ratio)[c]	% Yield from **8**
1	(10)	0	1.5	**9**	61
2	**10** (5)	0	4	**11**[d]	27
3	(10)	0	6	**12**	61
4	(11)	−25	3	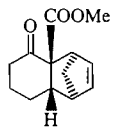 **13**	29
5	(10)	0	5	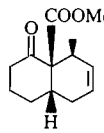 + 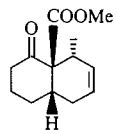 **14** **15** (5:4)	28
		−25	6	**14** + **15** (5:3)	34
		−78	6	**14** + **15** (5:3)	34
6	(3)	0	3	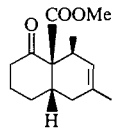 + 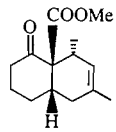 **16** **17** (2:1)	33
		−35	3	**16** + **17** (6:1)	34
		−78	3	**16** + **17** (13:1)	37
7	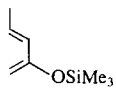 **18** (3)	−30	5	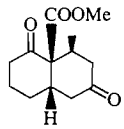 + 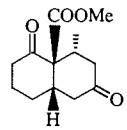 **19** **20** (10:3)[d]	45
	(5)	−50[e]	6	**19** **20** (7:1)[d]	46
8	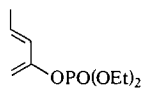 (1.5)	−30	6	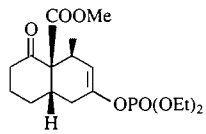 + 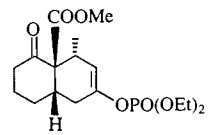 **21** **22** **23** (6:1)	66
		−78	6	**22** + **23** (6:1)	45

[a]Reactions were carried out in ether except where otherwise stated.

[b]Since the reactions are not easily monitored while in progress, they were not examined for completion prior to quenching and work-up. Minimum times for completion and optimum yield were not determined.

[c]Ratios were determined by ^{1}Hmr integration.

[d]Hydrolytic cleavage of the silyl enol ether occurred during the work-up.

[e]This reaction was carried out in ether–dichloromethane (1:1).

hydrogenated with Raney nickel to give the chromatographically separable keto esters **26** and **27** in 84% total yield. The structure of the major keto ester **26** was confirmed by its conversion (35) in four steps to ketone **33**. This conclusively established the structure of the major Diels–Alder adduct of *trans*-piperylene as **14**. The minor adduct must have epimeric structure **15**.

At this stage it is useful to introduce several features of the ^{1}Hmr spectrum of the adducts **14** and **15** that were useful in determining the C-8 stereochemistry of the adducts in this

Can. J. Chem. Downloaded from www.nrcresearchpress.com by 122.72.124.2 on 09/07/12
For personal use only.

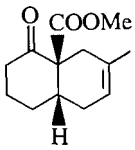

29

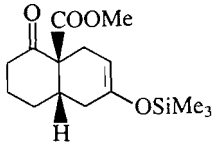

30

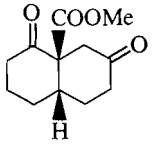

31

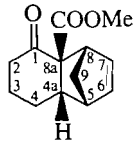

32

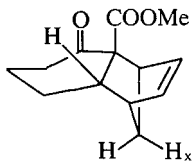

13*a*

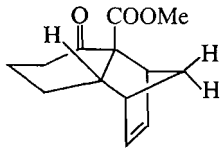

32*a*

series. The secondary methyl group of **15** appeared at δ 1.17, strongly deshielded relative to the secondary methyl of **14** (δ 0.83). Conversely, the allylic methine proton at C-8 of **14** appeared at δ 2.92, strongly deshielded relative to the allylic methine proton at C-8 of **15** (δ 2.49).[10] These observations were attributed to deshielding of the C-8 proton or methyl, which is *trans* to the angular carbomethoxyl group in the adduct, by the ketone carbonyl. Consideration of the conformations of these adducts showed that adduct **15** would have possible conformations **15***a* and **15***b*, in which the preferred conformation **15***b* would have the C-8 methyl in the deshielding zone of the ketone carbonyl. Adduct **14** would have possible conformations **14***a* and **14**b, in which the preferred conformation **14***b* would have the C-8 proton in the deshielding zone of the ketone carbonyl. These ^{1}Hmr results have been consistently observed in similar decalin derivatives. For instance, in the ketone **34** (9), the secondary methyl group appears at δ 1.15, deshielded relative to the corresponding methyl group of **35** at δ 0.75. Similarly, in ketone **36** (27) the allylic methine proton on C-8 shows a signal at δ 3.06, strongly deshielded relative to the C-8 proton of **37** (δ 2.34), while the C-8 methyl of **37** appears at δ 1.38, shifted downfield relative to the corresponding methyl of **36** at δ 1.04.

Attempts to determine the regiochemistry of the Diels–Alder adducts of *trans*-2-methyl-1,3-pentadiene by the decarbomethoxylation–aromatization sequence (*vide supra*) were not successful. The other examples in the study (Table 2) indicated that the *ortho* and *para* rules were consistently followed and from these results we presume that the addition of *trans*-2-methyl-1,3-pentadiene to **5** followed the usual rules to give the C-8 epimeric keto esters **16** and **17**.

As indicated above, the ^{1}Hmr data were used to determine the C-8 stereochemistry of the keto esters **16** and **17**. In the spectrum of the 2:1 mixture of epimers, the allylic methine proton at C-8 of the major adduct appeared at δ 2.83, strongly deshielded relative to the C-8 proton of the minor adduct (δ 2.40),[11] while the C-8 methyl of the minor adduct appeared at δ 1.08, deshielded relative to the C-8 methyl of the major adduct (δ 0.73). These data confirmed the assignment of structure **16** to the major adduct and the C-8 epimeric structure **17** to the minor adduct.

The stereoselectivity in favor of keto ester **16** was improved by the use of a lower reaction temperature. At −30°C enone ester **5** reacted with *trans*-2-methyl-1,3-pentadiene under stannic chloride catalysis to give a 6:1 mixture of Diels–Alder adducts **16** and **17** respectively in 34% total yield. At even lower reaction temperature (− 78°C) the Diels–Alder reaction proceeded to give excellent 13:1 stereoselectivity in favor of **16**; however, the total yield of adducts was again only 37%.

trans-2-Trimethylsilyloxy-1,3-pentadiene (**18**) was prepared by the general method of Ohfune and Tomita (50) by trimethylsilyl chloride trapping of the enolate formed from *trans*-3-penten-2-one with lithium diisopropylamide at −78°C. The addition of **18** to enone ester **5** gave an inseparable mixture of Diels–Alder adducts tentatively identified as the C-8 epimeric diketones **19** and **20**.[12] Treatment of the mixture of adducts with 1,2-ethanedithiol and boron trifluoride etherate in methylene chloride at 0°C for 30 min furnished the mixture of thioketals **28**. Desulfurization of the thioketals **28** was accomplished with Raney nickel in refluxing ethanol. After chromatographic separation two products were obtained in a ratio of 10:3 and in a combined yield of 64%. The major product was identical to the saturated keto ester **26** previously obtained from **14** and the minor product was identical to the keto ester **27** derived from **15**. This transformation unambiguously established the structures of the Diels–Alder adducts as the epimeric diketones **19** and **20**, and that **19** was the major isomer. At a lower temperature (−50°C) the selectivity in favor of adduct **19** was increased to 7:1 (35).

Enone ester **5** reacted with *trans*-2-diethylphosphoryloxy-1,3-pentadiene (**21**)[13] at −30°C (35) to give a 6:1 mixture of adducts in 66% yield. These Diels–Alder adducts were also unambiguously identified (35) as the epimeric enol phosphates **22** and **23** by their transformation to the previously obtained chromatographically separable keto esters **26** and **27**, by hydrogenolysis of the mixture of adducts using platinum oxide as the catalyst (53, 54).

When the Diels–Alder reaction of **5** with **21** was carried out at −78°C, a similar stereoselectivity (6:1) in favor of **22** was observed; however, the yield was lower (45%). The use of methylene chloride as the solvent did not lead to any improvement in the result. For example, when the addition was run at −30°C in methylene chloride, a 6:1 ratio of **22** to **23** was again obtained in 50% yield.

endo *Selectivities of the additions*

Enone ester **5** has two dienophilic components, namely, the α,β-unsaturated ketone and the α,β-unsaturated ester moieties. Ordinarily, it would not be necessary to distinguish these two moieties except in cases where the *endo* rule applies. The factors determining which dienophilic moiety would control the reaction pathway are expected to be a function of the secondary

[10]The assignments for the allylic methine protons at C-8 (δ 2.92 and 2.49) were confirmed by the observation of significant sharpening of the signals upon irradiation of the adjacent methyl protons (δ 0.83 and 1.17).

[11]The assignments for the allylic methine protons at C-8 (δ 2.83 and 2.40) were confirmed by the observation of significant sharpening of the signals upon irradiation of the adjacent methyl protons (δ 0.73 and 1.08).

[12]Hydrolysis of the labile silyl enol ether of the initially formed Diels–Alder adducts occurred during the work-up.

[13]For a broader discussion of the Diels–Alder reactions of **21** and a related dienyl phosphate see refs. 51 and 52.

Can. J. Chem. Downloaded from www.nrcresearchpress.com by 122.72.124.2 on 09/07/12
For personal use only.

Can. J. Chem. Downloaded from www.nrcresearchpress.com by 122.72.124.2 on 09/07/12
For personal use only.

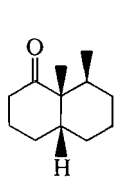

33

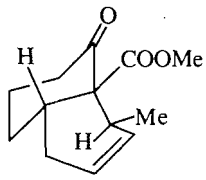

14*a*

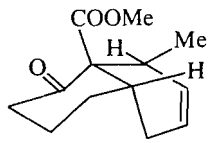

14*b*

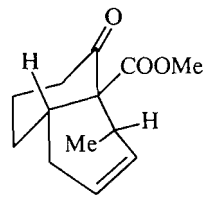

15*a*

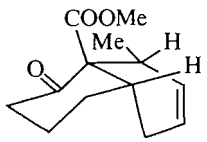

15*b*

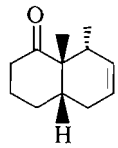

34

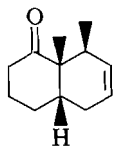

35

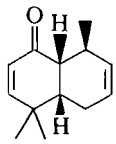

36

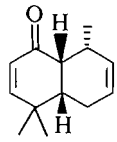

37

orbital overlap with the diene (27, 55). Additions of 1-substituted dienes to enone ester **5** gave predominantly the product resulting from addition with secondary overlap with the ester group ("ester-*endo*" transition state **B**) rather than with the ketone carbonyl ("keto-*endo*" transition state **A**).[14]

The bias in favor of transition state **B** may be of combined electronic and steric origins. The electronic effect promoted by a catalyst complexing more effectively with the ester group of the enone ester **5** would favor ester-*endo* addition via transition state **B** to give the various major adducts (**13**, **14**, **16**, **19**, and **22**). Addition via transition state **A** would encounter steric interaction between the diene and the nonreacting centers of the cyclohexenone ring of the dienophile. The presence of this steric effect was substantiated by the increased predominance of ester-*endo* adducts in cases where a bulky substituent was used at the C-3 position of the 1-substituted diene.

The formation of two C-8 epimeric adducts **14** and **15** in a ratio of 5:4 by addition of *trans*-piperylene to **5** at 0°C clearly was the result of addition via the two different transition states **14B** and **15A** respectively. The preferential formation of the adduct **14** can be attributed in part to a destabilization of transition state **15A** by steric interaction between the diene and the nonreacting centers of the cyclohexenone ring of the dienophile.[15] Addition via transition state **14B** would not encounter such a steric interaction.

This steric effect was evidently larger for the addition of *trans*-2-methyl-1,3-pentadiene. A larger product ratio (**16**:**17** = 2:1) was observed in favor of ester-*endo* addition via transition state **16B** to give the adduct **16**. Clearly, in the keto-*endo* addition via the competing transition state **17A**, a greater steric interaction would be encountered between the more bulky diene and the nonreacting centers of the ring of the dienophile.

The cases of *trans*-2-trimethylsilyloxy-1,3-pentadiene (**18**) and *trans*-2-diethylphosphoryloxy-1,3-pentadiene (**21**) again showed very good stereoselectivities in favor of the ester-*endo* adducts (**19** and **22**) resulting from additions via transition states **19B** and **22B** with significantly less addition via the sterically less favourable transition states **20A** and **23A**.

The addition of cyclopentadiene is also noteworthy. Its addition to enone ester **5** gave only the adduct **13** arising from ester-*endo* addition to **5**. Conformational analysis of the possible transition states revealed that in **36A** a severe steric interaction would be encountered between both the C-2 and C-3 protons of the diene and the nonreacting centers of the cyclohexenone ring of the dienophile. On the other hand, in **13B**, the methylene protons on C-5 of cyclopentadiene would be nearer the center of the cyclohexenone ring than to the nonreacting centers of the ring and would experience less steric interaction.

At lower reaction temperatures the stereoselectivity in favor of the ester-*endo* addition should be greater and this expectation was confirmed. For instance, in the case of *trans*-2-methyl-1,3-pentadiene, the stereoselectivity improved to 6:1 in favor of adduct **16** at −30°C compared to 2:1 at 0°C. This stereoselectivity was even greater at −78°C where a product ratio of 13:1 in favor of the ester-*endo* adduct **16** was obtained.

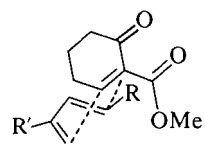

A (keto-*endo* orientation)

15A R = CH_3, R′ = H
17A R = R′ = CH_3
20A R = CH_3, R′ = OSi $(Me)_3$
23A R = CH_3, R′ = OPO $(OEt)_2$

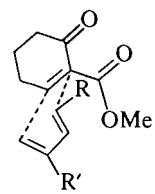

B (ester-*endo* orientation)

14B R = CH_3, R′ = H
16B R = R′ = CH_3
19B R = CH_3, R′ = $OSi(Me)_3$
22B R = CH_3, R′ = OPO $(OEt)_2$

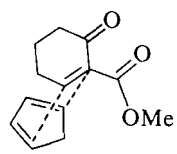

36A

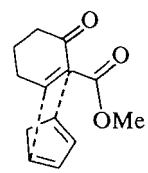

13B

Conclusions

In conclusion, the development of enone ester **5** as a dienophile makes available a new method for the rapid construction of angularly substituted *cis*-decalin derivatives. The angular carbomethoxyl group of the resulting *cis*-decalin derivatives can either be removed or used as a reactive site for further elaboration of the adducts. Furthermore, the stereochemical outcome of the addition of 1-substituted dienes to **5** is opposite to that observed for the Lewis acid catalysed Diels–Alder additions to 2-cyclohexenone and 2-methyl-2-cyclohexenone. Thus the two processes are complementary in stereochemical control.

Experimental

General

Melting points were determined on a Kofler hot stage apparatus and are uncorrected. Elemental analyses were performed by the microana-

[14]We have adopted the terms keto-*endo* and ester-*endo* to distinguish transition states, orientations, and adducts that have, or result from, secondary orbital overlap with a particular functional group (here ketone and ester respectively) in cases where the *endo* rule of Diels–Alder addition applies. See introduction to ref. 27.

[15]A similar explanation has been offered to account for the relatively poor dienophilicity of cyclohexenones (4) and also to account for an orientational reversal in violation of the *para* rule in the Diels–Alder reaction (26, 27).

Can. J. Chem. Downloaded from www.nrcresearchpress.com by 122.72.124.2 on 09/07/12
For personal use only.

lytical laboratory of this department. Infrared (ir) spectra were recorded on a Perkin–Elmer model 457 or Nicolet 7-199 FT-IR spectrophotometer and, except where otherwise stated, were obtained on solutions in carbon tetrachloride. Proton nuclear magnetic resonance (^{1}Hmr) spectra were recorded on a Varian HA-100, HA-100/Digilab, Bruker WH-200 or WH-400 spectrometer, and, except where otherwise stated, were obtained on solutions in deuterochloroform with tetramethylsilane as internal reference. Carbon-13 nuclear magnetic resonance (^{13}Cmr) spectra were recorded on a Bruker HFX-90/Nicolet 1085 system, Bruker WH-200 or WH-400 spectrometer, and were obtained on solutions in deuterochloroform using tetramethylsilane as internal reference. The following abbreviations are used: s = singlet, d = doublet, t = triplet, q = quartet, and m = multiplet. Mass spectra (ms) were recorded using A.E.I. model MS9, MS12, or MS50 mass spectrometers. Unless otherwise stated, anhydrous magnesium sulfate was used for drying organic solutions. Crystalline samples were recrystallized and liquid samples were subjected to Kuhgelrohr distillation before submitting for elemental analysis. Flash chromatography (56) was routinely used for purification and separation of product mixtures.

Materials

Benzene, ether, tetrahydrofuran, and 1,2-dimethoxyethane were freshly distilled over lithium aluminum hydride. *n*-Hexane was purified by simple distillation for use in chromatographic purifications. Anhydrous stannic chloride was purchased from A. G. Fluka and used without further purification. Nitrogen or argon was passed through a purification train of Fieser's solution (57), saturated aqueous lead acetate, concentrated sulfuric acid, and potassium hydroxide pellets. Enone ester **5** was prepared from 2-carbomethoxycyclohexanone according to the reported procedures (40, 41). 2-Trimethylsilyloxy-1,3-butadiene (**10**) was prepared according to the procedure of Conia (44, 58). 1,3-Cyclopentadiene was prepared by thermal cracking of dicyclopentadiene and was used immediately after the distillation.

*General conditions for the Diels–Alder reaction of enone ester **5** using different Lewis acids (Table 1)*

Enone ester **5** (1.0 equiv.) and the diene (2,3-dimethylbutadiene or isoprene; 10 equiv.) were dissolved in ether at 0°C. The Lewis acid (boron trifluoride etherate, ferric chloride, or stannic chloride; 0.5 equiv.) was added. After stirring under an atmosphere of argon for 1.5–3 h as indicated, saturated aqueous sodium bicarbonate was added and the resulting mixture was extracted with methylene chloride. The organic extracts were dried, filtered, and concentrated. Purification of the residue by flash chromatography gave the product **9** or **12**. The results are summarized in Table 1.

*8aβ-Carbomethoxy-6,7-dimethyl-3,4,4aβ,5,8,8a-hexahydro-1(2H)-naphthalenone (**9**)*[16]

To a solution of enone ester **5** (531 mg, 3.45 mmol) and 2,3-dimethyl-1,3-butadiene (2.8 g, 34.4 mmol) in ether (10 mL) at 0°C and under an atmosphere of argon was added anhydrous stannic chloride (0.44 g, 1.70 mmol). After stirring for 1.5 h at 0°C, saturated aqueous sodium bicarbonate (50 mL) was added and the resulting mixture was filtered through Celite. The filtrate was extracted with methylene chloride and the organic extracts were washed with water, dried, filtered, and concentrated. Purification of the residue by flash chromatography on silica gel, eluting with 8% ethyl acetate in petroleum ether, gave keto ester **9** (499 mg, 61% yield), which crystallized on standing. Recrystallization from ether/*n*-hexane gave white crystals of pure keto ester **9**: mp 69–70°C; ir: 1743 (ester C=O) and 1717 (ketone C=O) cm^{-1}; ^{1}Hmr δ: 3.72 (s, 3H, -COOCH$_3$) and 1.64 (br s, 6H, 2 × -CH$_3$); ^{13}Cmr δ: 208.0, 172.8, 123.1, 121.7, 61.7, 52.2, 38.1, 37.6, 33.9, 33.5, 26.9, 23.9, 18.9, and 18.5; ms M$^+$: 236.1414 (calcd. for $C_{14}H_{20}O_3$: 236.1413). *Anal.* calcd. for $C_{14}H_{20}O_3$: C 71.16, H 8.53; found: C 71.02, H 8.58.

[16]The stereochemical designations and all other chemical names used in this section denote relative stereochemistry. All compounds used and obtained were racemic.

*8aβ-Carbomethoxy-2,3,4,4aβ,5,8,8a-octahydro-1,6-naphthalenedione (**11**)*

To a solution of enone ester **5** (568 mg, 3.69 mmol) and 2-trimethylsilyloxy-1,3-butadiene (**10**) (2.8 g, 18.5 mmol) in ether (20 mL) at 0°C and under an atmosphere of argon was added anhydrous stannic chloride (479 mg, 1.84 mmol). After stirring for 4 h water was added and the resulting mixture was extracted with methylene chloride. The organic extracts were combined, dried, filtered, and concentrated. Flash chromatography of the residue on silica gel, eluting with 20% ethyl acetate in petroleum ether, gave diketone **11** (212 mg, 27% yield). Recrystallization from ether/petroleum ether gave white crystals of pure **11**: mp 87–88°C; ir: 1736 (ester C=O) and 1714 (ketone C=O) cm^{-1}; ^{1}Hmr δ: 3.82 (s, 3H, -COOCH$_3$), 3.11 (ddd, 1H, J = 14 Hz, J' = 7.0 Hz, J'' = 3.5 Hz, C-4a H), and 2.29 (d, 2H, J = 7.0 Hz, 2 × C-5 H); ^{13}Cmr δ: 209, 206, 171, 60, 52, 43, 42, 38, 37, 29, 27, and 23; ms M$^+$: 224.1049 (calcd. for $C_{12}H_{16}O_4$: 224.1049). *Anal.* calcd. for $C_{12}H_{16}O_4$: C 64.27, H 7.19; found: C 64.13, H 7.18.

*8aβ-Carbomethoxy-5,8α-methano-3,4,4aβ,5,8,8a-hexahydro-1(2H)-naphthalenone (**13**)*

To a solution of enone ester **5** (428 mg, 2.78 mmol) and 1,3-cyclopentadiene (2.0 g, 30.3 mmol) in ether (20 mL) at −25°C and under an atmosphere of argon was added anhydrous stannic chloride (360 mg, 1.38 mmol). After stirring for 3 h water was added and the resulting mixture was extracted with chloroform. The organic extracts were washed with water, dried, filtered, and concentrated. Column chromatography of the residue on silica gel, eluting with 5–10% ether in petroleum ether, gave an impure fraction containing the adduct **13**. A second purification by column chromatography on neutral alumina (grade III), eluting with 20% ethyl acetate in petroleum ether, gave pure adduct **13** (174 mg, 29% yield). Recrystallization from *n*-hexane gave white crystals of pure **13**: mp 91–93°C; ir: 1730 (ester C=O) and 1709 (ketone C=O) cm^{-1}; ^{1}Hmr δ: 6.31 (dd, 1H, J = 5.5 Hz, J' = 3.0 Hz, C-6 H), 6.00 (dd, 1H, J = 5.5 Hz, J' = 3.0 Hz, C-7 H), 3.67 (s, 3H, -COOCH$_3$), 3.63 (m, 1H, C-8 H), 2.60 (m, 1H, C-5 H), 2.52 (ddd, 1H, J = 12 Hz, J' = 7.0 Hz, J'' = 2.0 Hz, C-4a H), and 1.42 (ddd, 1H, J = 9.0 Hz, J' = 2.0 Hz, J'' = 1.0 Hz, bridge -CH*H*-); ^{13}Cmr δ: 208.8, 171.1, 139.5, 138.8, 81.7, 52.5, 48.4, 47.5, 46.8, 45.9, 38.4, and 29.0; ms M$^+$: 220.1098 (calcd. for $C_{13}H_{16}O_3$: 220.1100).

*8aβ-Carbomethoxy-8β-methyl-3,4,4aβ,5,8,8a-hexahydro-1(2H)-naphthalenone (**14**) and 8aβ-carbomethoxy-8α-methyl-3,4,4aβ,5,8,8a-hexahydro-1(2H)-naphthalenone (**15**)*

(a) By Diels–Alder reaction at 0°C

To a solution of enone ester **5** (453, 2.94 mmol) and *trans*-piperylene (2.0 g, 29.4 mmol) in ether (20 mL) at 0°C and under an atmosphere of argon was added anhydrous stannic chloride (374 mg, 1.44 mmol). After stirring for 5 h water was added and the resulting mixture was extracted with methylene chloride. The organic extracts were washed with water, dried, filtered, and concentrated. Column chromatography of the residue on silica gel, eluting with 1–5% ether in petroleum ether, gave an impure mixture of adducts **14** and **15**. Further purification by column chromatography on neutral alumina (Woelm III), eluting with 10% ethyl acetate in petroleum ether, gave a mixture of pure adducts **14** and **15** (182 mg; 28% yield). The ^{1}Hmr spectrum of the mixture showed two sets of signals in an integral ratio of 5:4. One set, assigned to the major adduct **14**, showed signals at δ: 5.32 (m, 2H, -CH=CH-), 3.72 (s, 3H, -COOCH$_3$), 2.92 (m, 1H, -C*H*—CH$_3$), and 0.83 (d, 3H, J = 7.0 Hz, -CH—C*H*$_3$). The other set, assigned to the minor adduct **15**, showed signals at δ: 5.63 (m, 2H, -CH=CH-), 3.78 (s, 3H, -COOCH$_3$), 2.49 (m, 1H, -C*H*—CH$_3$), and 1.17 (d, 3H, -CH—C*H*$_3$). The mixture also showed the following spectral data: ir (film): 1743 (ester C=O) and 1717 (ketone C=O) cm^{-1}; ms M$^+$: 222.1256 (calcd. for $C_{13}H_{18}O_3$: 222.1256).

(b) By Diels–Alder reaction at −30°C

To a solution of enone ester **5** (331 mg, 2.15 mmol) and *trans*-piperylene (1.5 g, 22.0 mmol) in ether (10 mL) at −30°C and under an atmosphere of nitrogen was added anhydrous stannic chloride

Can. J. Chem. Downloaded from www.nrcresearchpress.com by 122.72.124.2 on 09/07/12
For personal use only.

(2.86 mg, 1.09 mmol). After stirring for 6 h the reaction mixture was warmed to room temperature. Water was added and the resulting mixture was extracted with methylene chloride. The organic extracts were dried, filtered, and concentrated. Column chromatography of the residue on neutral alumina (grade III), eluting with 10% ethyl acetate in petroleum ether, gave an impure mixture of adducts **14** and **15**. A second chromatographic purification on neutral alumina (Woelm III), eluting with 10% ethyl acetate in petroleum ether, gave a pure 5:3 mixture (by ^{1}Hmr integration) of adducts **14** and **15** (164 mg, 34% yield).

(c) By Diels–Alder reaction at −78°C

To a solution of enone ester **5** (408 mg, 2.65 mmol) and *trans*-piperylene (1.8 g, 26.5 mmol) in ether (15 mL) at −78°C and under an atmosphere of nitrogen was added anhydrous stannic chloride (352 mg, 1.35 mmol). After stirring for 6 h the reaction mixture was warmed to room temperature. Water was added and the resulting mixture was extracted with methylene chloride. The organic extracts were combined, dried, filtered, and concentrated. Column chromatography of the residue on neutral alumina (Woelm III) gave an impure mixture of adducts **14** and **15**. A second purification on neutral alumina (Woelm III), eluting with 10% ethyl acetate in petroleum ether, gave a pure 5:3 mixture (by ^{1}Hmr integration) of adducts **14** and **15** (200 mg, 34% yield).

6-Methyl-3,4,4aβ,5,8,8a-hexahydro-1(2H)-naphthalenone, mixture of ketones 24

Finely divided anhydrous lithium iodide (101 mg, 0.74 mmol) was suspended in 2,4,6-collidine (5 mL) with vigorous stirring. Water (27 mg, 1.51 mmol) was added and the suspension dissolved on vigorous stirring. A 5:4 mixture of keto esters **14** and **15** (84 mg, 0.38 mmol) was added to the lithium iodide dihydrate solution. The mixture was heated to reflux for 1.5 h under an atmosphere of nitrogen. The reaction mixture was cooled to room temperature, poured into ice-cold aqueous 1.0 N hydrochloric acid, and extracted with methylene chloride. The extracts were washed with aqueous 1.0 N hydrochloric acid and water, dried, filtered, and concentrated. Flash chromatography of the residue on silica gel, eluting with a solution of 5% ether in petroleum ether, gave a mixture of three ketones **24** (51 mg, 82% yield). The mixture showed the following spectral data: ir (film): 1712 (ketone) cm^{-1}; ^{1}Hmr δ: 1.00, 0.99, 0.98 (each d, total 3H, each J = 7.0 Hz, -CH_3) and 5.56 (complex, total 2H, -CH=CH-); ms M$^+$: 164.1198 (calcd. for $C_{11}H_{16}O$: 164.1201).

8-Methyl-3,4-dihydro-1(2H)-naphthalenone (25)

A mixture of ketones **24** (51 mg, 0.31 mmol) was dissolved in carbon tetrachloride (10 mL). Benzoyl peroxide (5 mg, 0.02 mmol) and *N*-bromosuccinimide (110 mg, 0.62 mmol) were added. The reaction mixture was heated to reflux for 10 h under an atmosphere of nitrogen and cooled to room temperature. Filtration and concentration gave an oily residue, which was purified by flash chromatography on silica gel. Elution with 10% ether in petroleum ether gave aryl ketone **25** (29 mg, 58% yield): ir (film): 1690 (C=O) cm^{-1}; ^{1}Hmr δ: 7.30 (m, 2H, 2 × Ar-H), 7.10 (d, 1H, J = 7.0 Hz, Ar-H), 2.95 (t, 2H, J = 6.0 Hz, -CH_2CO-), 2.65 (t, 2H, J = 7.0 Hz, -CH_2C=), 2.63 (s, 3H, -CH_3), and 2.50 (m, 2H, -$CH_2CH_2CH_2$); ms M$^+$: 160.0891 (calcd. for $C_{11}H_{12}O$: 160.0888).

8aβ-Carbomethoxy-8β-methyl-3,4,4aβ,5,6,7,8,8a-octahydro-1(2H)-naphthalenone (26) and 8aβ-carbomethoxy-8α-methyl-3,4,4aβ,5,6,7,8,8a-octahydro-1(2H)-naphthalenone (27)

(a) From mixture of Diels–Alder adducts 14 and 15

A 5:4 mixture of Diels–Alder adducts **14** and **15** (540 mg, 2.43 mmol) and Raney nickel (grade W-2, ca. 5.0 g) were stirred together in ethanol (15 mL). After 7 h the reaction mixture was filtered and the organic filtrate was concentrated. Column chromatography of the residue on silica gel, eluting with 1% ethyl acetate in petroleum ether, gave pure keto ester **27** (198 mg; 36% yield) as a colorless oil: ir (neat): 1739 (ester C=O) and 1712 (ketone C=O) cm^{-1}; ^{1}Hmr δ: 3.79, (s, 3H, -$COOCH_3$) and 1.18 (d, 3H, J = 7.0 Hz, -$CHCH_3$); ms M$^+$: 224.1410 (calcd. for $C_{13}H_{20}O_3$: 224.1407). Continued elution gave the isomeric keto ester **26** (263 mg, 48% yield), which crystallized on standing: mp 37–39°C; ir: 1740 (ester C=O) and 1714 (ketone C=O) cm^{-1}; ^{1}Hmr δ: 3.72, (s, 3H, -$COOCH_3$) and 0.86 (d, 3H, J = 7.0 Hz, -$CHCH_3$); ms M$^+$: 224.1411 (calcd. for $C_{13}H_{20}O_3$: 224.1407). *Anal.* calcd. for $C_{13}H_{20}O_3$: C 69.91, H 8.99; found: C 69.77, H 9.01.

(b) From thioketals 28

To a solution of a 10:3 mixture of thioketals **28** (31 mg, 0.09 mmol) in dry ethanol (5.0 mL) was added Raney nickel (grade W-2, ca. 0.5 g) under an atmosphere of nitrogen. The mixture was heated to reflux for 5 h and then cooled to room temperature, filtered, and concentrated to give a light yellow oil, which was purified by column chromatography on silica gel. Elution with 2% ether in petroleum ether gave the minor keto ester **27** (3.0 mg, 14% yield). Continued elution gave the major keto ester **26** (11 mg, 50% yield).

8aβ-Carbomethoxy-6,8β-dimethyl-3,4,4aβ,5,8,8a-hexahydro-1(2H)-naphthalenone (16) and 8aβ-carbomethoxy-6,8α-dimethyl-3,4,4aβ,5,8,8a-hexahydro-1(2H)-naphthalenone (17)

(a) By Diels–Alder reaction at 0°C

To a solution of enone ester **5** (505 mg, 3.28) in ether (10 mL), at 0°C and under an atmosphere of argon, were sequentially added *trans*-2-methyl-1,3-pentadiene (808 mg, 9.85 mmol) and anhydrous stannic chloride (427 mg, 1.64 mmol). After stirring for 3 h water was added and the resulting mixture was extracted with methylene chloride. The organic extracts were dried, filtered, and concentrated. Column chromatography of the residue on silica gel, eluting with 5–10% ethyl acetate in petroleum ether, gave an impure mixture of adducts **16** and **17**. A second purification by flash chromatography, eluting with 6% ethyl acetate in petroleum ether, gave a mixture of pure adducts **16** and **17** (255 mg, 33% yield). The ^{1}Hmr spectrum of the mixture showed two sets of signals in an integral ratio of 2:1. One set was assigned to the major keto ester **16**: δ: 5.25 (m, 1H, =CH—), 3.63 (s, 3H, -$COOCH_3$), 2.83 (m, 1H, -C*H*—CH_3), and 0.73 (d, 3H, J = 7.0 Hz, -CH—CH_3). The other set was assigned to the minor keto ester **17**: δ: 5.15 (m, 1H, =CH—), 3.70 (s, 3H, -$COOCH_3$), 2.40 (m, 2H, -C*H*—CH_3), and 1.08 (d, 3H, J = 7.0 Hz, -CH—CH_3). The mixture also showed the following spectral data; ir (neat): 1740 (C=O ester) and 1716 (C=O ketone) cm^{-1}; ms M$^+$: 236.1413 (calcd. for $C_{14}H_{20}O_3$: 235.1413).

(b) By Diels–Alder reaction at −35°C

Enone ester **5** (574 mg, 3.73 mmol) and *trans*-2-methyl-1,3-pentadiene (0.92 g, 11.2 mmol) were placed in ether (10 mL) and cooled to −35°C. Anhydrous stannic chloride (485 mg, 1.86 mmol) was added. After stirring under an atmosphere of argon for 3 h the reaction mixture was warmed to room temperature. Water was added and the resulting mixture was extracted with methylene chloride. The combined organic extracts were dried, filtered, and concentrated. Column chromatography of the residue on silica gel, eluting with 5% ethyl acetate in petroleum ether, gave an impure mixture of adducts **16** and **17**. A second chromatographic purification on neutral alumina (Woelm III), eluting with 50% ether in petroleum ether, gave a 6:1 mixture (by ^{1}Hmr integration) of adducts **16** and **17** (299 mg, 34% yield).

(c) By Diels–Alder reaction at −78°C

To a solution of enone ester **5** (238 mg, 1.54 mmol) in ether (8 mL), at −78°C and under an atmosphere of argon, were sequentially added *trans*-2-methyl-1,3-pentadiene (380, 4.64 mmol) and anhydrous stannic chloride (201 mg, 0.77 mmol). After stirring for 6 h the reaction mixture was warmed to room temperature. Water was added and the resulting mixture was extracted with methylene chloride. The combined organic extracts were dried, filtered, and concentrated. Column chromatography of the residue on neutral alumina (Woelm III), eluting with 20–50% ether in petroleum ether, gave an impure mixture of adducts **16** and **17**. A second chromatographic purification on neutral alumina (Woelm III), eluting with 50% ether in petroleum ether, gave a 13:1 mixture (by ^{1}Hmr integration) of adducts **16** and **17** (136 mg, 37% yield). Fractional recrystallization of the mixture from ether/petroleum ether gave white crystals of pure **16**: mp 110–111°C; ^{1}Hmr δ: 5.24

(m, 1H, =CH—), 3.64 (s, 3H, -$COOCH_3$), 2.82 (m, 1H, -C*H*—CH_3), and 0.73 (d, 3H, J = 7.0 Hz, -CH—CH_3).

trans-2-*Trimethylsilyloxy-1,3-pentadiene (**18**)*

At −78°C and under an atmosphere of argon, *n*-butyllithium (56.7 mL of 1.5 M solution in *n*-hexane, 85.0 mmol) was added to a solution containing diisopropylamine (8.59 g, 84.9 mmol) in tetrahydrofuran (40 mL). After stirring for 15 min, a solution of *trans*-3-penten-2-one (6.48 g, 77.0 mmol) in tetrahydrofuran (20 mL) was added dropwise over 10 min through a pressure equalizing dropping funnel. After another 20 min, chlorotrimethylsilane (16.8 g, 154 mmol) was rapidly added. The resulting solution was allowed to warm to room temperature. *n*-Pentane was added to the reaction mixture and the resulting solution was washed with ice-cold distilled water (400 mL). The organic layer was dried, filtered, and concentrated. The residue was fractionally distilled under vacuum, collecting the fraction distilling at 56–62°C (16 Torr; 1 Torr = 133.3 Pa). The resulting colourless oil was the required diene **18** (6.7 g, 54% yield); ir: 2960, 1569, 1507, 1256, and 1048 cm^{-1}; ^{1}Hmr δ: 5.88, 5.30 (both m, total 2H, -CH=CH-), 4.07 (br s, 2H, =CH_2), 1.80 (m, 3H, =CH—CH_3), and 0.18 (s, 9H, -$Si(CH_3)_3$); ms M^+: 156.0968 (calcd. for $C_8H_{16}OSi$: 156.0971).

*8aβ-Carbomethoxy-8β-methyl-2,3,4,4aβ,5,7,8,8a-octahydro-1,6-naphthalenedione (**19**) and 8aβ-carbomethoxy-8α-methyl-2,3,4,4aβ,5,7,8,8a-octahydro-1,6-naphthalenedione (**20**)*

Enone ester **5** (179 mg, 1.16 mmol) was dissolved in ether (5 mL) and cooled to −30°C. *trans*-2-Trimethylsilyloxy-1,3-pentadiene (**18**) (560 mg, 3.59 mmol) and anhydrous stannic chloride (151 mg, 0.58 mmol) were sequentially added. After stirring at −30°C under an atmosphere of nitrogen for 4.5 h, the reaction mixture was warmed to room temperature and water was added. The resulting mixture was extracted with methylene chloride. The organic extracts were combined, dried, filtered, and concentrated and the crude residue was purified by flash chromatography. Elution with 10% ethyl acetate in petroleum ether gave a mixture of keto esters **19** and **20** (86 mg, 45% yield). The ^{1}Hmr spectrum of the mixture showed two sets of signals in an integral ratio of 10:3. The major set, assigned to **19**, showed signals at δ 3.73 (s, 3H, -$COOCH_3$) and 0.90 (d, J = 7.0 Hz, -CH—CH_3). The minor set, assigned to **20**, showed signals at δ 3.82 (s, 3H, -$COOCH_3$) and 1.15 (d, 3H, -CH—CH_3). The mixture of keto esters **19** and **20** also showed the following spectral data: ir: 1740 (ester C=O) and 1714 (ketone C=O) cm^{-1}; ms M^+: 238.1205 (calcd. for $C_{13}H_{22}O_4$: 238.1205).

6,6-Ethylenedithio-8aβ-carbomethoxy-3,4,4aβ,5,6,7,8,8a-octahydro-1(2H)-naphthalenone, mixture of thioketals 28

To a solution of a 10:3 mixture of **19** and **20** (171 mg, 0.72 mmol) in methylene chloride (5 mL) at 0°C were sequentially added 1,2-ethanedithiol (339 mg, 3.60 mmol) and boron trifluoride etherate (112 mg, 0.79 mmol). After stirring under an atmosphere of argon for 25 min, ice-cold 2.0 N aqueous sodium hydroxide solution was added and the resulting mixture was extracted with methylene chloride. The organic extracts were washed with water, dried, filtered, and concentrated. Column chromatography of the residue on silica gel, eluting with 20% ether in *n*-hexane, gave a 10:3 mixture of thioketals **28** (137 mg, 74% yield, based on consumed starting material). The ^{1}Hmr spectrum showed two sets of signals in an integral ratio of 10:3 and showed signals at δ: 3.80, 3.74 (each s, total 3H, -$COOCH_3$), 3.30 (complex, 4H, -SCH_2CH_2S-), 1.10, 1.02 (each d, total 3H, each J = 7.5 Hz, -CH—CH_3). The following spectral data were also recorded for the mixture of thioketals **28**: ir (film): 1740 (ester C=O) and 1713 (ketone C=O) cm^{-1}; ms M^+: 314.1008 (calcd. for $C_{15}H_{22}O_3S_2$: 314.1010). Continued elution gave a mixture of diketones **19** and **20** (31 mg, 18% recovery).

Acknowledgements

We are grateful to the Natural Sciences and Engineering Research Council of Canada and the University of Alberta for financial support, and to the Alberta Heritage Foundation for Medical Research for a Studentship to T.K.N.

1. P. D. Bartlett and G. F. Woods. J. Am. Chem. Soc. **62**, 2933 (1940).
2. M. D. Soffer, G. E. Günay, O. Korman, and M. B. Adams. Tetrahedron Lett. 389 (1963).
3. M. D. Soffer and G. E. Günay. Tetrahedron Lett. 1355 (1965).
4. J. G. Martin and R. K. Hill. Chem. Rev. **61**, 537 (1961).
5. P. Yates and P. Eaton. J. Am. Chem. Soc. **82**, 4436 (1960).
6. G. I. Fray and R. Robinson. J. Am. Chem. Soc. **83**, 249 (1961).
7. T. Inukai and M. Kasai. J. Org. Chem. **30**, 3567 (1965).
8. P. Laszlo and J. Lucchetti. Actual. Chim. 42 (1984).
9. F. Fringuelli, F. Pizzo, A. Taticchi, T. D. J. Halls, and E. Wenkert. J. Org. Chem. **47**, 5056 (1982).
10. H. J. Liu and T. K. Ngooi. Synth. Commun. **12**, 715 (1982).
11. F. Fringuelli, F. Pizzo, A. Taticchi, and E. Wenkert. Synth. Commun. **9**, 391 (1979).
12. F. Fringuelli, L. Minuti, F. Pizzo, A. Taticchi, T. D. J. Halls, and E. Wenkert. J. Org. Chem. **48**, 1810 (1983).
13. F. Fringuelli, F. Pizzo, A. Taticchi, and E. Wenkert. J. Org. Chem. **48**, 2802 (1983).
14. F. Fringuelli, F. Pizzo, A. Taticchi, V. F. Ferreira, E. L. Michelotti, B. Porter, and E. Wenkert. J. Org. Chem. **50**, 890 (1985).
15. E. C. Angell, F. Fringuelli, L. Minuti, F. Pizzo, B. Porter, A. Taticchi, and E. Wenkert. J. Org. Chem. **50**, 4686 (1985).
16. E. C. Angell, F. Fringuelli, T. D. J. Halls, F. Pizzo, B. Porter, A. Taticchi, A. P. Tourris, and E. Wenkert. J. Org. Chem. **50**, 4691 (1985).
17. E. C. Angell, F. Fringuelli, F. Pizzo, B. Porter, A. Tatticchi, and E. Wenkert. J. Org. Chem. **50**, 4696 (1985).
18. F. Fringuelli, F. Pizzo, A. Taticchi, and E. Wenkert. Synth. Commun. **16**, 245 (1986).
19. E. C. Angell, F. Fringuelli, F. Pizzo, B. Porter, A. Taticchi, and E. Wenkert. J. Org. Chem. **51**, 2642 (1986).
20. E. C. Angell, F. Fringuelli, L. Minuti, F. Pizzo, B. Porter, A. Taticchi, and E. Wenkert. J. Org. Chem. **51**, 2649 (1986).
21. E. C. Angell, F. Fringuelli, L. Minuti, F. Pizzo, A. Taticchi, and E. Wenkert. J. Org. Chem. **51**, 5177 (1986).
22. E. C. Angell, F. Fringuelli, F. Pizzo, A. Taticchi, and E. Wenkert. J. Org. Chem. **53**, 1424 (1988).
23. E. N. C. Browne. Ph. D. thesis. The University of Alberta, 1980.
24. H. J. Liu and E. N. C. Browne. Tetrahedron Lett. 2929 (1977).
25. H. J. Liu and E. N. C. Browne. Can. J. Chem. **59**, 601 (1981).
26. H. J. Liu and E. N. C. Browne. Can. J. Chem. **57**, 377 (1979).
27. H. J. Liu and E. N. C. Browne. Can. J. Chem. **65**, 1262 (1987).
28. H. J. Liu, E. N. C. Browne, and S. Y. Chew. Can. J. Chem. **66**, 2345 (1988).
29. J. Saver. Angew. Chem. Int. Ed. Engl. **6**, 16 (1967).
30. N. T. Anh, E. Canadell, and O. Eisenstein. Tetrahedron. **34**, 2283 (1978).
31. D. Liotta, M. Saindane, and C. Barnum. J. Am. Chem. Soc. **103**, 3225 (1981).
32. S. Torii, T. Kanitomi, and T. Okamoto. Bull. Chem. Soc. Jpn. **52**, 2640 (1979).
33. E. Piers and T. W. Hall. Can. J. Chem. **58**, 2613 (1980).
34. E. J. Corey and H. Estreiches. Tetrahedron Lett. **22**, 603 (1981).
35. H. J. Liu and T. K. Ngooi. Can. J. Chem. **62**, 2676 (1984).
36. T. K. Ngooi. Ph.D. thesis. The University of Alberta, 1984.
37. J. E. Brenner. J. Org. Chem. **26**, 22 (1961).
38. M. Edelson and E. I. Becker. J. Am. Chem. Soc. **80**, 908 (1958).
39. C. W. T. Hussey and A. R. Pinder. J. Chem. Soc. 1517 (1962).
40. H. J. Reich, J. M. Renga, and I. L. Reich. J. Am. Chem. Soc. **97**, 5434 (1975).
41. D. Liotta, C. Barnum, R. Puleo, G. Zima, C. Bayer, and H. S. Kezar. J. Org. Chem. **46**, 2970 (1981).

Can. J. Chem. Downloaded from www.nrcresearchpress.com by 122.72.124.2 on 09/07/12
For personal use only.

42. G. ZIMA and D. LIOTTA. Synth. Commun. **9**, 697 (1979).
43. J. ORBAN and J. V. TURNER. Tetrahedron Lett. **24**, 2697 (1983).
44. C. GIRARD, P. ARNICE, J. P. BARNIER, and J. M. CONIA. Tetrahedron Lett. 3329 (1974).
45. A. S. ONISHCHENKO. Diene synthesis. Israel Program for Scientific Translation, Jerusalem. 1964.
46. J. DAS, Z. VALENTA, H. J. LIU, and T. K. NGOOI. Can. J. Chem. **62**, 481 (1984).
47. F. ELSINGER. Org. Synth. **45**, 7 (1965).
48. R. A. BARNES. J. Am. Chem. Soc. **70**, 145 (1948).
49. L. M. JACKMAN and S. STERNHELL. Applications of nuclear magnetic resonance spectroscopy in organic chemistry. 2nd ed. Pergamon Press, Oxford, England. 1969.
50. Y. OHFUNE and M. TOMITA. J. Am. Chem. Soc. **104**, 3511 (1982).
51. H. J. LIU and W. M. FENG. Synth. Commun. **16**, 1485 (1986).
52. H. J. LIU and W. M. FENG. Synth. Commun. **17**, 1777 (1987).
53. A. JUNG and R. ENGEL. J. Org. Chem. **40**, 3652 (1975).
54. R. M. COATES, S. K. SHAH, and R. W. MASON. J. Am. Chem. Soc. **101**, 6765 (1979).
55. D. GINSBURG. Tetrahedron, **39**, 2095 (1983).
56. C. STILL, M. KAHN, and A. MITRA. J. Org. Chem. **43**, 2923 (1978).
57. L. F. FIESER and M. FIESER. Reagents for organic synthesis. Vol. 1. Wiley and Sons, Inc., New York, NY. 1967.
58. M. E. JUNG, C. A. MCCOMBS, Y. TAKEDA, and Y. G. PAN. J. Am. Chem. Soc. **103**, 6677 (1981).

Can. J. Chem. Downloaded from www.nrcresearchpress.com by 122.72.124.2 on 09/07/12
For personal use only.

Ionic reorientations and phase transition in solid IF_6AsF_6[1]

SHMUEL ALBERT
Department of Chemistry, University of Illinois, Urbana, IL 61801, U.S.A. and Department of Radiology, Beth Israel Medical Center, New York, NY 10003, U.S.A.

AND

JOHN A. RIPMEESTER
Department of Chemistry, University of Illinois, Urbana, IL 61801, U.S.A. and Chemistry Division, National Research Council of Canada, Ottawa, Ont., Canada K1A 0R6

Received April 25, 1988

SHMUEL ALBERT and JOHN A. RIPMEESTER. Can. J. Chem. **66**, 3153 (1988).

^{19}F static and rotating frame spin–lattice relaxation times (T_1 and $T_{1\rho}$) as well as broadline NMR studies have been carried out on solid IF_6AsF_6 between 213 and 393 K. From the T_1– and $T_{1\rho}$–temperature behaviour, we inferred a phase transition at 350(±2) K and a supercooled high temperature phase. In both phases the second moments are consistent with a model where both IF_6^+ and AsF_6^- reorient about random axes. The T_1 and $T_{1\rho}$ data in the low temperature phase can be interpreted in terms of a single frequency factor $\tau_0 = 3.15(\pm0.2) \times 10^{-16}$ s and activation energy $E_a = 10.4(\pm0.4)$ kcal/mol for both cation and anion reorientation. At the temperature of the phase transition the ionic-reorientational frequencies become faster by ~ 2 orders of magnitude. In the high temperature phase T_1 and $T_{1\rho}$ are essentially independent of temperature which may be associated with a spin–rotation relaxation mechanism.

SHMUEL ALBERT et JOHN A. RIPMEESTER. Can. J. Chem. **66**, 3153 (1988).

Opérant à des températures allant de 213 à 393 K, on a déterminé les temps de relaxation spin–réseau statiques et de rotation du ^{19}F (T_1 et $T_{1\rho}$) et on a effectué des études rmn à bandes larges sur le IF_6AsF_6. En se basant sur le comportement des valeurs de T_1 et $T_{1\rho}$ en fonction de la température, on en a déduit qu'il existe une phase de transition à 350(±2) K ainsi qu'une phase à une température de surfusion. Dans chacune de ces phases, les moments secondaires sont en accord avec un modèle dans lequel les deux ions IF_6^+ ainsi que AsF_6^- se réorientent autour d'axes au hasard. On peut interpréter les données relatives aux T_1 et $T_{1\rho}$ de la phase à basse température en fonction d'un facteur de fréquence unique, $\tau_0 = 3{,}15(\pm0{,}2) \times 10^{-16}$ s et une énergie d'activation $E_a = 10{,}4(\pm0{,}4)$ kcal/mol pour les réorientations tant du cation que de l'anion. A la température de la transition de phase, les fréquences de la réorientation ionique augmentent par un facteur d'environ 100. Dans la phase à haute température, les valeurs de T_1 et $T_{1\rho}$ sont essentiellement indépendantes de la température qui pourrait être associée avec un mécanisme de relaxation spin–rotation.

[Traduit par la revue]

Introduction

The solid formed when AsF_5 reacts with IF_7 has been formulated as an ionic adduct consisting of discrete IF_6^+ and AsF_6^- ions (1, 2). Subsequent infrared, Raman, and powder X-ray studies (3, 4) have substantiated this suggestion. The ^{75}As NMR spectrum (5) of $IF_6^+AsF_6^-$ demonstrated that AsF_6^- ion is a regular octahedron in the room temperature solid. Mössbauer (6) and ^{127}I NMR (5) studies have shown that the IF_6^+ ion has octahedral symmetry. The room temperature crystal structure of $IF_6^+AsF_6^-$ is cubic, space group $Pa3$, with four formula units per unit cell, and a unit cell constant of 9.4935 ± 0.0005 Å (3). Magnetic field and temperature dependent ^{19}F broadline NMR studies (7) of IF_6AsF_6 have been carried out and have yielded information regarding chemical shift parameters and ionic mobility in the solid state.

To obtain further information on the cation and anion motions as well as the interactions in solid IF_6AsF_6, we have studied the temperature dependence of its ^{19}F static and rotating frame spin–lattice relaxation times, T_1 and $T_{1\rho}$, respectively. We also measured the limiting high temperature ^{19}F second moments and reevaluated them in terms of a motional model, chemical shift parameters, and ^{19}F–^{127}I indirect coupling constant.

Experimental

IF_6AsF_6 was prepared by condensing AsF_5 (Ozark Mahoning Co., Tulsa, OK) and IF_7 (Alfa Inorganic, Inc., Beverly, MA) in a cold trap using a Pyrex vacuum system. The solid mixture was allowed to react by first warming to the melting point of AsF_5, then to ~0°C. Excess reagent was removed by pumping at ~60°C. Further purification of the product was not necessary, as the 1:1 adduct is the only product (4). Portions of the solid were transferred under dry conditions to Pyrex sample tubes which were subsequently evacuated.

The ^{19}F T_1 and $T_{1\rho}$ of IF_6AsF_6 were measured between 213 and 394 K at a radio frequency of 25.3 MHz. For the $T_{1\rho}$ measurements a rf field amplitude of 9 G was utilized. The apparatus and techniques used for the measurements have been described previously (8). Broad line ^{19}F NMR spectra were recorded as first derivative of the absorption line at a frequency of 56.4 MHz. The measurements ranged between 295 K and ~360 K. The ^{19}F second moments were determined by conventional integration methods including modulation amplitude correction (8).

Results and discussion

Low temperature phase

Second moment

A line narrowing region was identified between 205 and 235 K in the plot of the ^{19}F second moment vs. temperature reported by Barr and Dunell (7). The limiting low temperature second moment data (77 to 200 K) have been interpreted in terms of a static structure (7). This is consistent with our analysis and calculations. We studied the ^{19}F NMR spectra above the line narrowing region between 295 and ~360 K, the limiting high temperature. Our second moment measured at 56.4 MHz was 2.94 ± 0.2 G^2 at 341 K. Considering the frequency of measurement our line shape and second moment are in good agreement with the experimental results of Barr and Dunell (7).

The limiting high temperature second moment, M_2, can be interpreted as a sum of the following three contributions:

[1]NRCC No. 29524.

Printed in Canada / Imprimé au Canada

Can. J. Chem. Downloaded from www.nrcresearchpress.com by 122.72.124.2 on 09/07/12
For personal use only.

Can. J. Chem. Downloaded from www.nrcresearchpress.com by 122.72.124.2 on 09/07/12
For personal use only.

[1] $M_2 = M_D + M_{IC} + M_{CS}$

where the various contributions to the ^{19}F second moment are due to: M_D, nuclear dipolar interactions partially averaged by motions of the IF_6 and AsF_6 octahedra (field independent); M_{IC}, indirect $^{127}I-^{19}F$ coupling (field independent); and M_{CS}, chemical shift difference between cationic and anionic fluorines (field dependent).

It is assumed here that the chemical shift anisotropy is averaged out by the motion.

Let us evaluate each of these second moment contributions. M_D is determined by the type of motion for which we propose a simple model. If we assume that both IF_6^+ and AsF_6^- groups reorient in a random manner such as to average out all intramolecular nuclear dipolar interactions we can calculate the second moment by taking all the fluorine nuclei to be at their respective ionic centers. Using the Van Fleck (9) second moment expression and counting contributions from ^{19}F, ^{75}As, and ^{127}I nuclei, we calculate M_D to be 1.43 G^2. It was found from solution NMR studies (10) that the $^{127}I-^{19}F$ indirect coupling is quite strong, the coupling constant being 2730 ± 15 Hz. This will contribute significantly to the field-independent ^{19}F second moment of IF_6AsF_6. This is supported by the indication that the IF_6^+ component of the spectrum has a greater line width than that of the AsF_6^- component. The second moment contribution due to indirect coupling is given by (11)

[2] $M_{IC} = (1/3)S(S+1)\sum_k A_{ik}^2$

where A_{ik} is the coupling constant between nuclei i and k expressed in gauss. Taking account only of the six $^{127}I-^{19}F$ couplings and the aforementioned coupling constant of 2730 Hz we find a M_{IC} of 0.68 G^2. We note that this is a maximum contribution for M_{IC}, as it depends on the ^{19}F spin state lifetimes. The ^{19}F spin exchange time depends on the $^{19}F-^{19}F$ dipolar interactions, and will be significantly longer in the presence of random intramolecular motion, than under rigid lattice conditions. Contributions from $^{75}As-^{19}F$ couplings are negligible.

A chemical shift difference of 143 ± 15 ppm was found (7) between the IF_6^+ and the AsF_6^- fluorines of IF_6AsF_6. This chemical shift difference yields a second moment contribution, M_{CS}, of 1.02 ± 0.2 G^2 at 56.4 MHz. The total calculated second moment, M_2, at this frequency becomes 3.13 ± 0.2 G^2, in good agreement with our experimental value of 2.94 ± 0.2 G^2.

If we extrapolate the field dependent second moment data of Barr and Dunell (7) to zero field, a field-independent second moment of ~1.9 G^2 is obtained. This value is in agreement with the field independent second moment that is determined to be 2.11 G^2 from the first two terms of eq. [1]. This implies that our motional model and analysis are consistent with the experimental results of ref. 7. Barr and Dunell (7) suggested that the 1.9 G^2 field-independent second moment corresponds to a situation where both ions reorient about more than one axis with the AsF_6^- motions more extensive than the IF_6^+ motions. However, the calculated second moments do not support this suggestion.

Spin–lattice relaxation times

The static and rotating frame ^{19}F spin–lattice relaxation times for IF_6AsF_6 are shown in Fig. 1 as semilog plots vs. inverse temperature. Both relaxation processes show exponential behavior. From the lowest temperature of measurement, T_1 and

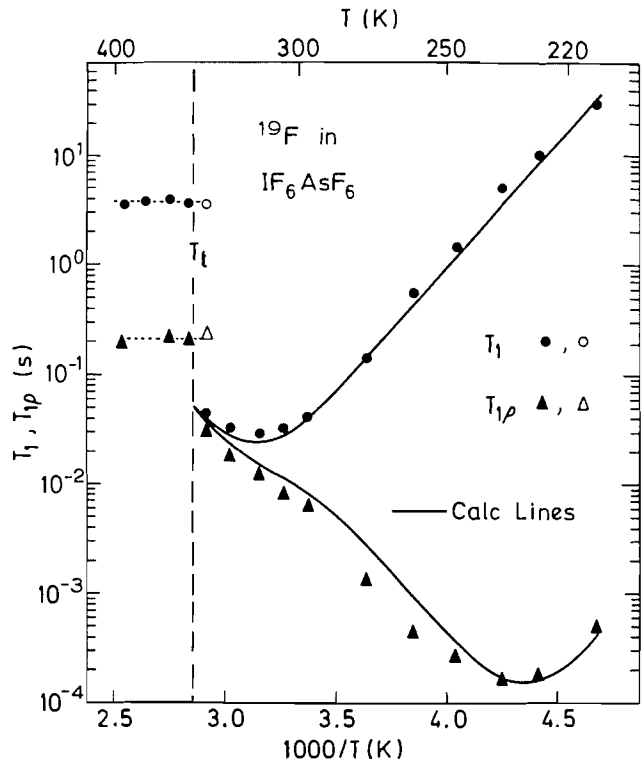

FIG. 1. A semilog plot of the ^{19}F static and rotating frame spin–lattice relaxation times, T_1 and $T_{1\rho}$, respectively, versus the inverse temperature measured at a frequency of 25.3 MHz in solid IF_6AsF_6. τ is the proposed phase transition temperature 350(±2) K. The open circle and triangle are measured in the supercooled high temperature phase. The solid curves were calculated by means of eqs. [3]–[14] as explained in the text.

$T_{1\rho}$ decrease with increasing temperature. Minima of 2.9(±0.2) × 10^{-2} and 1.6(±0.12) × 10^{-4} s are found at temperatures of 316 and 233 K for T_1 and $T_{1\rho}$, respectively. There is a discontinuity in these parameters at 350(±2) K, which we presume to be due to a phase transition.

In the low temperature phase of IF_6AsF_6 the dominant ^{19}F spin–lattice relaxation mechanism will be the modulation of the nuclear dipolar interactions by the random spherical reorientations of the IF_6^+ and AsF_6^- ions. The main contribution is from $^{19}F-^{19}F$ dipolar interactions (T_1^{FF}, $T_{1\rho}^{FF}$) and there will also be smaller contributions from $^{19}F-^{127}I$ (T_1^{FI}, $T_{1\rho}^{FI}$) and $^{19}F-^{75}As$ (T_1^{FAs}, $T_{1\rho}^{FAs}$) nuclear dipolar interactions as well as from the averaging of the chemical shift anisotropy [$(T_1)_{CSA}$, $(T_{1\rho})_{CSA}$]. We assume that the expression for T_1 can be written as a sum of these four individual contributions.

[3] $(T_1)^{-1} = (T_1^{FF})^{-1} + (T_1^{FI})^{-1} + (T_1^{FAs})^{-1} + (T_1)_{CSA}^{-1}$

According to BPP theory (12)

[4] $(T_1^{FF})^{-1} = \frac{2}{3}\gamma_F^2 \Delta M_{FF} g(\omega_F, \tau_c)$

where

[5] $g(\omega_F, \tau_c) = \tau_c/(1 + \omega_F^2\tau_c^2) + 4\tau_c/(1 + 4\omega_F^2\tau_c^2)$

In a similar vein we may write for the heteronuclear dipolar interactions (11) which give rise to the T_1^{FI} and T_1^{FAs} contributions:

[6] $(T_1^{FI})^{-1} = \frac{1}{2}\gamma_F^2 \Delta M_{FI} g(\omega_{FI}, \tau_c)$

where

$$[7]\quad g(\omega_{Fl}, \tau_c) = \tau_c/(1 + (\omega_F - \omega_l)^2\tau_c^2) + 3\tau_c/(1 + \omega_F^2\tau_c^2) + 6\tau_c/(1 + (\omega_F + \omega_l)^2\tau_c^2)$$

and $[T_1^{FAs}]^{-1}$ is obtained by substituting I for As. ΔM_{FF}, ΔM_{Fl}, and ΔM_{FAs} are the fractions of the fluorine dipolar second moment "averaged out" by the random motions of the IF_6^+ and AsF_6^- ions. The other symbols have their usual meaning. The chemical shift anisotropy contribution is given by (13)

$$[8]\quad (T_1)_{CSA}^{-1} = \frac{1}{15}\gamma_F^2 H_0^2 \Delta\sigma^2[\tau_c/(1 + \omega_F^2\tau_c^2)]$$

Similarly, $T_{1\rho}$ will be given by a sum of four contributions:

$$[9]\quad (T_{1\rho})^{-1} = (T_{1\rho}^{FF})^{-1} + (T_{1\rho}^{Fl})^{-1} + (T_{1\rho}^{FAs})^{-1} + (T_{1\rho})_{CSA}^{-1}$$

Assuming a weak collision limit we have for the nuclear dipolar interaction (14, 15)

$$[10]\quad (T_{1\rho}^{FF})^{-1} = \tfrac{2}{3}\gamma_F^2 \Delta M_{Fl} g_\rho(\omega_F, \tau_c, \omega_1)$$

$$[11]\quad (T_{1\rho}^{Fl})^{-1} = \tfrac{1}{4}\gamma_F^2 \Delta M_{Fl} g_\rho(\omega_{Fl}, \tau_c, \omega_1)$$

and $(T_{1\rho}^{FAs})^{-1}$ is obtained by substituting I for As. The spectral density functions are

$$[12]\quad g_\rho(\omega_F, \tau_c, \omega_1) = \tfrac{5}{2}\tau_c/(1 + \omega_F^2\tau_c^2) + \tau_c/(1 + 4\omega_F^2\tau_c^2) + \tfrac{3}{2}\tau_c/(1 + 4\omega_1^2\tau_c^2)$$

$$[13]\quad g_\rho(\omega_{Fl}, \tau_c, \omega_1) = 4\tau_c/(1 + \omega_1^2\tau_c^2) + \tau_c/[1 + (\omega_F - \omega_l)^2\tau_c^2] + 3\tau_c/(1 + \omega_F^2\tau_c^2) + 6\tau_c/(1 + \omega_1^2\tau_c^2) + 6\tau_c/[1 + (\omega_F^2 + \omega_l)^2\tau_c^2]$$

and $\omega_1 = \gamma H_1$.

The chemical shift anisotropy contribution is (13)

$$[14]\quad (T_{1\rho})_{CSA}^{-1} = \frac{1}{45}\gamma_F^2 H_0^2 \Delta\sigma^2[3\tau_c/(1 + \omega_F^2\tau_c^2) + 4\tau_c/(1 + \omega_1^2\tau_c^2)]$$

From the ^{19}F T_1 and $T_{1\rho}$ (Fig. 1) and second moment (ref. 7) variations with temperature it appears that the motions of both ions can be described by a single correlation time. We assume simple Arrhenius behaviour for the correlation time in terms of an inverse frequency factor, τ_0, and an activation energy, E_a, according to $\tau_c = \tau_0 \exp(E_a/RT)$. From the temperature of the T_1 minimum and the low temperature straight line portion of the semilog T_1 plot we derive values for $\tau_0 = 3.15(\pm0.2) \times 10^{-16}$ s and $E_a = 10.4(\pm0.4)$ kcal/mol. From our second moment calculations as well as Barr and Dunell's (7) we find ΔM_{FF}, ΔM_{Fl}, and ΔM_{FAs} to be 5.18, 0.95, and 0.38 G^2, respectively. An average value of the chemical shift anisotropy for the two ions of $\Delta\sigma = 333 \pm 20$ ppm, obtained by Barr and Dunell (7), was employed in the calculations of the CSA contribution to the spin–lattice relaxation times. Using these parameters and eqs. [3]–[14] we calculated the T_1 and $T_{1\rho}$ curves shown as solid lines in Fig. 1. There are some discrepancies between the calculated lines and the experimental data points at the T_1 minimum and at the high temperature side of $T_{1\rho}$ curve. To a good degree our T_1 and $T_{1\rho}$ data are consistent with the same motional parameters for both AsF_6^- and IF_6^+ ion reorientations. This is not surprising if we consider the crystal structure determined for IF_6AsF_6 at room temperature. The anions and cations are almost of equal size (considering the I—F and As—F bond lengths of ~ 1.85 Å and ~ 1.77 Å, respectively) and are arranged in an essentially close packed arrangement with six cations surrounding an anion and vice versa. The anions and cations will thus be in quite close contact, so that motions of one will affect the other. This implies that there is some degree of correlation between the motions of IF_6^+ and AsF_6^-. Correlation effects have not been taken into account in our simple motional model and this may explain the discrepancies between the calculated lines and experimental data points of Fig. 1.

Phase transition and high temperature phase

On heating IF_6AsF_6 samples from room temperature, a discontinuity in the ^{19}F T_1 and $T_{1\rho}$ behaviour was observed at 350(±2) K. The respective changes in T_1 and $T_{1\rho}$ are two and one order of magnitude. On cooling the samples from a temperature above the discontinuity point, no change in the relaxation times was noted until we reached a temperature of 329(±2) K, where both T_1 and $T_{1\rho}$ returned to their original values of the heating cycle. From this behaviour we conclude that a phase transition occurs at a temperature of 350(±2) K and that the high temperature phase supercools down to 329(±2) K. It is pertinent to point out that significant hysteresis of the phase transition temperature has also been found for $KAsF_6$ (29°C) (20) and $KSbF_6$ (38°C) (22). The T_1 and $T_{1\rho}$ times measured in the normal region of stability of the high temperature phase are shown in Fig. 1 to the left of the vertical dashed line. The T_1 and $T_{1\rho}$ measurements in the supercooled high temperature phase are presented in Fig. 1 as open circles and triangles and are consistent with the other T_1 and $T_{1\rho}$ data points in this phase.

On going through the phase transition, the line shape does not change. We measured the ^{19}F second moment as 56.4 MHz and a value of 3.32(±0.3) G^2 was obtained at 354 K, slightly larger than the second moment of 2.94(±0.2) G^2 observed in the low temperature phase. The signal-to-noise ratio attainable in this temperature region was poorer than that in the low temperature phase in accordance with the longer T_1 values. No new motions appear at the phase transition. The slightly larger second moment the high temperature phase may simply reflect the difference in the crystal structure between the high and low temperature phases, such as a change from one cubic structure to another cubic structure. The measured second moment in the high temperature phase is in good agreement with our calculated second moment of 3.13(±0.2) G^2. Accordingly, the high temperature phase is consistent with the simple motional model where both IF_6^+ and AsF_6^- reorient about random axes. The frequency of reorientation of the ions has increased by ~ 2 orders of magnitude on going from the low to the high temperature phase.

In the high temperature phase and its supercooled region the ^{19}F T_1 and $T_{1\rho}$ are essentially independent of temperature. T_1 is relatively long (~4 s) while $T_{1\rho}$ is shorter by a factor of ~20 (~0.2 s). This behaviour of T_1 and $T_{1\rho}$ can be interpreted in terms of an additional relaxation mechanism that becomes effective in the high temperature phase, with the net T_1 and $T_{1\rho}$ due to the dipolar and the additional mechanism essentially temperature independent. A possible relaxation mechanism is spin–rotation (16, 17). The fast reorientations of the octahedral IF_6^+ and AsF_6^- ions in the high temperature phase of IF_6AsF_6 may well be associated with spin–rotation relaxation. Similar behaviour of ^{19}F T_1 was found in the high temperature phases of

Can. J. Chem. Downloaded from www.nrcresearchpress.com by 122.72.124.2 on 09/07/12
For personal use only.

$CsPF_6$, $RbPF_6$, and NH_4PF_6 where fast reorientations of PF_6^- ions take place (18, 19). It is of interest to note that spin–rotation relaxation also has been proposed for the high temperature phase of $KAsF_6$ as T_1 was found to decrease with increasing temperature (20). On the other hand, relaxation of the slightly larger SbF_6^- ions in the sodium and potassium salts could be explained by using dipole–dipole interactions only (21).

1. F. SEEL and O. DETMER. Angew. Chem. **70**, 163 (1958).
2. F. SEEL and O. DETMER. Z. Anorg. Allg. Chem. **301**, 113 (1959).
3. S. P. BEATON. Ph.D. thesis, University of British Columbia. Vancouver, B.C. 1966.
4. K. O. CHRISTE and W. SAWODNY. Inorg. Chem. **6**, 1783 (1967).
5. J. F. HON and K. O. CHRISTE. J. Chem. Phys. **52**, 1960 (1970).
6. S. BUKSHPAN, J. SORIANO, and J. SHAMIR. Chem. Phys. Lett. **4**, 241 (1969).
7. M. R. BARR and B. A. DUNELL. Can. J. Chem. **48**, 895 (1970).
8. S. ALBERT, H. S. GUTOWSKY, and J. A. RIPMEESTER. J. Chem. Phys. **56**, 2844 (1972).
9. J. H. VAN VLECK. Phys. Rev. **74**, 1168 (1948).
10. M. BROWNSTEIN and H. SELIG. Inorg. Chem. **11**, 657 (1972).
11. A. ABRAGAM. The principles of nuclear magnetism. University Press. Oxford. 1961.
12. N. BLOEMBERGEN, E. M. PURCELL, and R. V. POUND. Phys. Rev. **73**, 679 (1948).
13. J. S. BLICHARSKI. Z. Naturforschg. **27a**, 1456 (1972).
14. D. C. LOOK and I. J LOWE. J. Chem. Phys. **44**, 2995 (1966).
15. D. E. O'REILLY, E. M. PETERSON, and T. TSANG. Phys. Rev. **160**, 333 (1967).
16. R. BLINC and G. LAHAJNAR. Phys. Rev. Lett. **19**, 685 (1967).
17. M. O. NORRIS, J. G. STRANGE, J. G. POWLES, M. RHODES, K. MARSDEN, and K. KRYNICKI. J. Phys. **2**, 422 (1968); **2**, 445 (1968).
18. H. S. GUTOWSKY and S. ALBERT. J. Chem. Phys. **58**, 5446 (1973).
19. S. ALBERT and H. S. GUTOWSKY. J. Chem. Phys. **59**, 3585 (1973).
20. L. K. E. NIEMELÄ. Ann. Univ. Turku. Ser. A1, **162**, 99 (1973).
21. L. K. E. NIEMELÄ and O. A. VESANEN. Chem. Phys. Lett. **32**, 507 (1975).
22. A. M. HEYNS and E. C. REYNHARDT. J. Phys. Chem. Solids, **42**, 461 (1981).

Can. J. Chem. Downloaded from www.nrcresearchpress.com by 122.72.124.2 on 09/07/12
For personal use only.

LEED and AES studies of chemisorption resulting from low exposures of C_2H_4, CO, and PH_3 to the (0001) surface of zirconium

J. R. LOU, P. C. WONG, AND K. A. R. MITCHELL

Department of Chemistry, University of British Columbia, 2036 Main Mall, Vancouver, B.C., Canada V6T 1Y6

Received March 30, 1988

J. R. LOU, P. C. WONG, and K. A. R. MITCHELL. Can. J. Chem. **66**, 3157 (1988).

Low-energy electron diffraction (LEED) and Auger electron spectroscopy (AES) have been used to study for the first time the chemisorption systems formed on the (0001) surface of zirconium by exposing to C_2H_4, CO, and PH_3 in the one to ten Langmuir regime. The adsorptions are done at room temperature, but there is subsequent heating to optimize the surface ordering. The main observations are as follows: (*i*) after heating C_2H_4-covered surfaces to effect hydrogen desorption, the remaining carbon can form two different ordered (1×1)-C structures; (*ii*) CO forms both (2×2)- and (1×1)-type structures; (*iii*) the temperature at which the bulk diffusion of oxygen becomes significant, as determined by AES, is about 40°C greater on a CO-treated surface than for an O_2-treated Zr(0001) surface; and (*iv*) heating a PH_3-covered surface can yield a weakly-ordered (3×3)-P structure. The observation (*iv*) contrasts with that for the analogous surface prepared previously with H_2S; the poorly developed (3×3)-P surface structure results from the fact that the temperatures required for surface ordering overlap with those which yield a loss of phosphorus from the surface region.

J. R. LOU, P. C. WONG et K. A. R. MITCHELL. Can. J. Chem. **66**, 3157 (1988).

Faisant appel à la diffraction électronique de faible énergie (LEED) et à la spectroscopie électronique de Auger (AES), on a étudié pour la première fois les systèmes de chemisorption formés à la surface (0001) du zirconium exposé au C_2H_4, au CO et au PH_3 dans l'un des dix régimes de Langmuir. On a réalisé les adsorptions à la température ambiante avec un chauffage subséquent pour optimiser l'ordonnance la surface. Les principales observations sont les suivantes : (*i*) après le chauffage des surfaces couvertes de C_2H_4, pour affecter la désorption de l'hydrogène, les atomes de carbone restants peuvent former deux différentes structures ordonnées de type (1×1)-C; (*ii*) le CO forme deux structures de type (2×2) et (1×1); (*iii*) la température à laquelle le gros de la diffusion de l'oxygène devient significative, telle que déterminée par AES, est plus élevée d'environ 40°C pour une surface traitée au CO que pour une surface de Zr(0001) traitée à l'oxygène et (*iv*) une surface couverte de PH_2 peut donner une structure P de type (3×3) faiblement ordonnée. L'observation (*iv*) contraste avec celle relative à la surface analogue préparée antérieurement avec du H_2S. La structure P de type (3×3) faiblement développée résulte du fait que la température requise pour l'agencement de la surface rejoint celles qui conduisent à une perte de phosphore à partir de la surface.

[Traduit par la revue]

Can. J. Chem. Downloaded from www.nrcresearchpress.com by 122.72.124.2 on 09/07/12
For personal use only.

1. Introduction

Currently only very limited information is available for the structural details of well-characterized surfaces of hexagonal close packed metals after chemisorption with common reactive gas molecules. We have accordingly been undertaking a project to investigate the structural chemistry of the (0001) surface of zirconium with low-energy electron diffraction (LEED) (1–3), motivated both by some interesting early observations for the corresponding surface of titanium (4, 5) and by the general technological importance of the surface chemistry of zirconium (6, 7). Our interest in the Zr(0001) surface concentrates on the structures resulting from chemisorption, that is with coverages of the order of a monolayer formed by exposures to less than 10 Langmuir (1 L = 10^{-6} Torr s) of reactive gas.

The present paper describes the use of Auger electron spectroscopy (AES) and qualitative LEED for characterizing chemisorption systems formed by exposing a Zr(0001) surface at room temperature to C_2H_4, CO, and PH_3. It aims to provide a basis for future structural analyses, although here comparisons are made both with previous studies of the chemisorption of O_2 (2, 8), N_2 (3), and H_2S (9) on Zr(0001), and with relevant investigations for reactive adsorption on polycrystalline samples of this metal (10–13).

2. Experimental

The apparatus and cleaning procedures used were as described previously from this laboratory for a LEED crystallographic analysis for the clean Zr(0001) surface (14). Each adsorption study was made on a surface which showed a sharp (1×1) LEED pattern, with hexagonal symmetry at normal incidence, and for which no contaminants were apparent with AES measured by a cylindrical mirror analyzer. The exposures were made at room temperature, although commonly further heating was necessary to order the surface regions sufficiently for undertaking structural analyses with a diffraction technique. The experiments used high purity gases which were directed to the Zr(0001) surface via a nozzle. For various exposures of the adsorbing gas, the relative amounts of adsorbed species were assessed with appropriate Auger peak height ratios; specifically R_C, R_O, and R_P

$$R_C = A_{270}/A_{92}, \quad R_O = A_{510}/A_{92}, \quad R_P = A_{120}/A_{92}$$

for carbon, oxygen, and phosphorus respectively. In these defining equations A_{270}, A_{92}, A_{510}, and A_{120} are the Auger peak heights, respectively, for C at 270 eV, Zr at 92 eV, O at 510 eV, and overlapping P and Zr signals at 120 eV. In addition, since there are indications that the Zr Auger peak at 147 eV can be sensitive to adsorbates including hydrogen (9), we also used the peak height ratio

$$R_{Zr} = A_{147}/A_{92}$$

as a further surface monitor.

Quantitative assessments of LEED patterns, with regard to either diffracted beam intensity-versus-energy ($I(E)$) curves or spot profile analyses, were measured with a video LEED analyzer as described previously (15). After each adsorption experiment, the sample surface was cleaned by Ar^+ bombardment and re-ordered by raising the temperature to 600°C followed by immediate cooling (heating and cooling rates are approximately 1°C s^{-1}). All heating operations referred to here were done by flashing in this way to the stated temperature. The cleaned zirconium surface is characterized with $R_C = 0.00$, $R_O = 0.00$, $R_P = 0.74$, and $R_{Zr} = 1.40$.

3. Results and discussion

3.1. C_2H_4 adsorption

Exposure of a clean, ordered Zr(0001) surface to about 1 L of C_2H_4 at room temperature yielded a diffuse (1×1) LEED

Can. J. Chem. Downloaded from www.nrcresearchpress.com by 122.72.124.2 on 09/07/12
For personal use only.

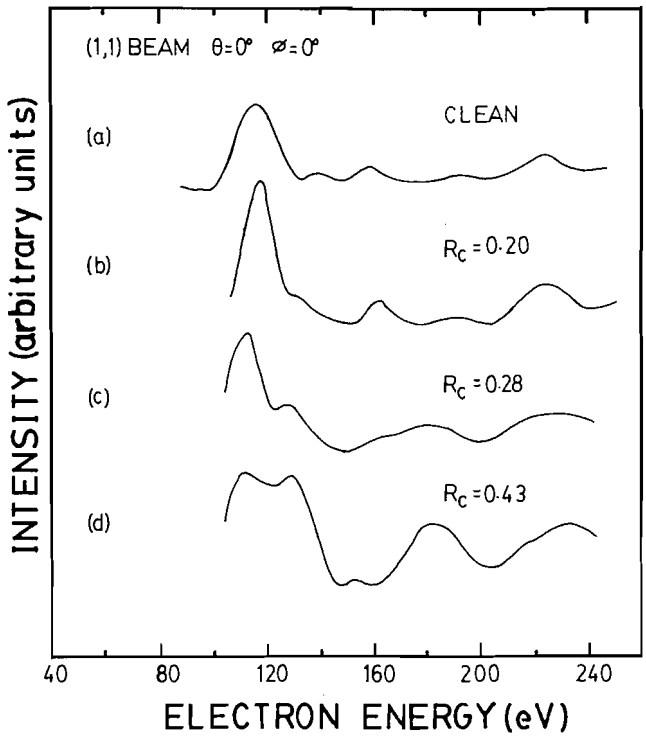

FIG. 1. Intensity-versus-energy curves for normal incidence measured for the (1,1) beam from: (*a*) clean Zr(0001); (*b*) Zr(0001)–(1×1)-C with $R_C = 0.20$ from C_2H_4 adsorption; (*c*) as (*b*) except $R_C = 0.28$; (*d*) as (*b*) except $R_C = 0.43$.

pattern with high background, and the AES results are summarized with $R_C = 0.20$ and $R_{Zr} = 1.20$. However, the latter changed to 1.34 upon heating to 400°C, an observation which, in conjunction with our previous report for H_2S chemisorption on Zr(0001) (9) and observations by Lin and Gilbert (13), appears to be associated with hydrogen desorption. With further brief heating to 470°C, a very sharp (1×1) LEED pattern was observed on cooling to room temperature; for this surface R_C and R_{Zr} remained at 0.20 and 1.34, respectively. Upon heating to above 600°C both R_C and R_{Zr} returned to the clean surface values, observations that we take to indicate the completion of hydrogen desorption and carbon diffusion to the bulk.

Similar observations were made for surfaces with a range of R_C values, which were varied according to the extent of the initial C_2H_4 exposure. Careful visual observations of the intensity distribution in the sharp (1×1) LEED patterns at normal incidence were compared with that of the clean Zr(0001) surface. As R_C was increased from zero, a new feature was established at $R_C = 0.20$, namely a bright region for the (1,1) beam between 132 and 136 eV. This differs from the clean surface where the (1,1) beam is dim for that particular energy range. This contrast is also apparent in the measured LEED $I(E)$ curves, as shown in Fig. 1.

The data in Fig. 2 give a suggestive indication from AES of carbon and hydrogen migration from the surface region. They apply to a C_2H_4-treated Zr(0001) surface for which R_C and R_{Zr} initially equal 0.33 (referred to as R_C^{init}) and 1.15, respectively; this surface was heated to a temperature T and then cooled back to room temperature for measuring the new Auger peak-height ratios (R_C^T and R_{Zr}^T). Two plots of the normalized carbon and zirconium ratios (R_C^T/R_C^{init} and $R_{Zr}^T/1.40$) obtained for successively increasing T are shown in Fig. 2. The first break in $R_{Zr}^T/1.40$ (Fig. 2(*b*)) at around 400°C appears to be associated with the desorption of hydrogen, while the second starting at 490°C results from carbon diffusion into the bulk (see Fig. 2(*a*)). The latter observation provides the basis for the choice noted above of heating to 470°C to encourage surface carbon ordering. The temperature at which the bulk diffusion of carbon becomes appreciable, according to Fig. 2, is approximately 50 and 250°C higher than the corresponding values found previously for nitrogen (3) and oxygen (8), respectively, when measured under comparable conditions.

The evolution of $I(E)$ curves from Zr(0001) surfaces which show (1×1) LEED patterns, and have increasing amounts of bonded carbon, was studied to $R_C = 0.43$, and representative curves for the (1,1) beam are given in Fig. 1. Changes from the clean surface are quite subtle until $R_C = 0.20$, but we believe that value corresponds to a well-defined (1×1)-C surface, whose structure is currently under investigation with LEED crystallography. Bigger changes occur as R_C increases beyond 0.20. With reference to the $I(E)$ curves in Fig. 1, the intensity

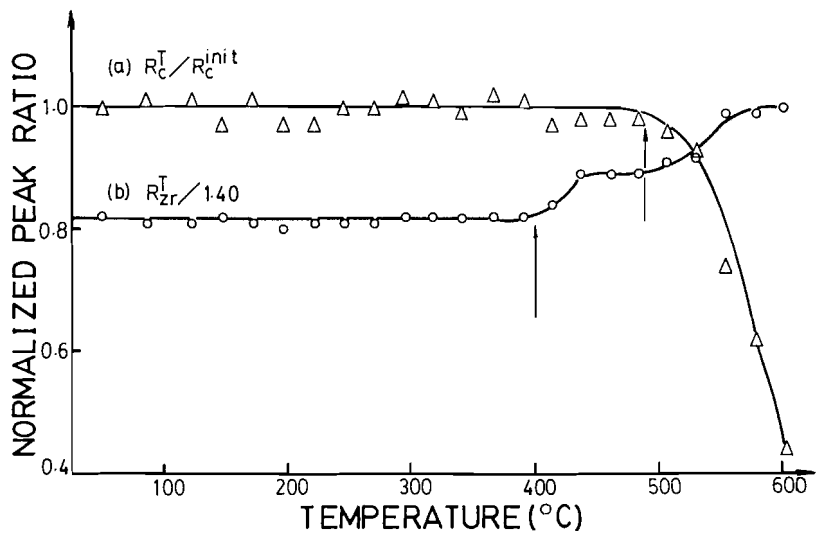

FIG. 2. Normalized Auger peak-height ratios (*a*) R_C^T/R_C^{init} and (*b*) $R_{Zr}^T/1.40$ as a function of temperature for C_2H_4 adsorbed on Zr(0001). The initial coverage corresponds to $R_C^{init} = 0.33$ and $R_{Zr}^{init} = 1.15$.

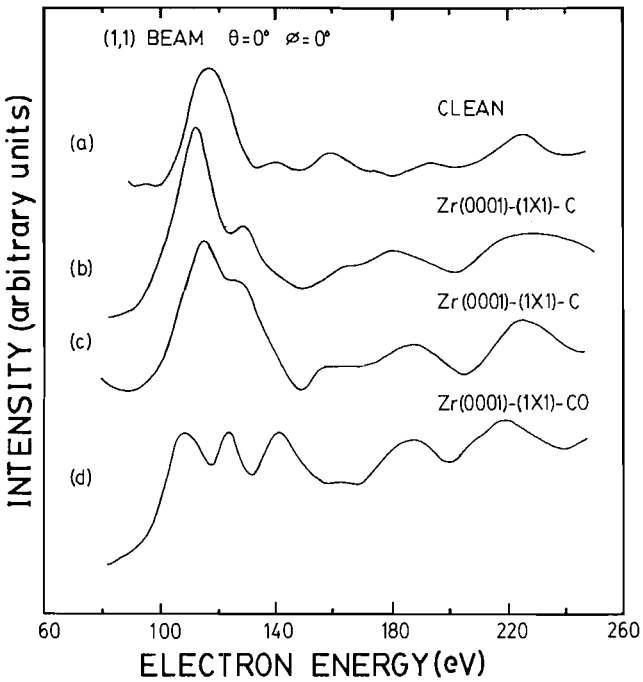

FIG. 3. Intensity-versus-energy curves for normal incidence measured for the (1,1) beam from: (*a*) clean Zr(0001); (*b*) Zr(0001)–(1×1)-C with $R_C = 0.28$ from C_2H_4 adsorption after heating; (*c*) Zr(0001)–(1×1)-C with $R_C = 0.26$ from CO adsorption after heating; (*d*) Zr(0001)–(1×1)-CO with $R_C = 0.44$ and $R_O = 0.18$.

of the carbon peak around 136 eV increases very significantly, while the peak which is at 118 eV for $R_C < 0.20$ shifts to lower energy and is reduced to 112 eV for $R_C = 0.43$. This evolution suggests a further (higher-coverage) (1×1)-C structure, although we have not studied this adsorption system beyond $R_C = 0.43$ and so we do not know whether that value completes the second structure. Nevertheless, it does correspond to a carbon coverage approximately twice that of the first (lower-coverage) (1×1)-C structure. The $I(E)$ curves measured for the intermediate coverages (e.g. $R_C = 0.28$) can be well reproduced by appropriately weighted mixtures of the curves for $R_C = 0.20$ and $R_C = 0.43$. That suggests the surfaces with intermediate coverages are made up of lower-coverage and higher-coverage (1×1) domains. By contrast, the $I(E)$ curves for $R_C = 0.28$ are not well modelled by mixtures of $I(E)$ curves for the clean and $R_C = 0.43$ surfaces, an observation which provides further support for $R_C = 0.20$ defining a completed (1×1)-C structure.

3.2. *CO adsorption*

Exposure of a clean, ordered Zr(0001) surface to about 1 L of CO at room temperature gave adsorption of both atomic constituents ($R_C = 0.28$, $R_O = 0.10$), but no extra LEED beams were immediately detectable. However, a poorly developed (2×2) pattern was observed on heating to 240°C, although on heating to 300°C the surface became depleted of oxygen and showed a sharp (1×1) LEED pattern. With greater initial exposures to CO only (1×1) patterns were found, and these patterns were best established after heating to 270°C. The $I(E)$ curve measured from such a Zr(0001)–(1×1)-CO surface ($R_C = 0.44$, $R_O = 0.18$) for the (1,1) beam at normal incidence is included in Fig. 3. This curve differs from the corresponding curves measured from either clean Zr(0001) or from the (1×1)-C structures; indeed it is also not adequately reproduced by weighted averages of measured curves from the (1×1)-O and (1×1)-C structures, and therefore it appears to identify a new ordered surface.

The onset of the effective surface depletion of both carbon and oxygen was assessed by following R_C and R_O values at room temperature after heating to progressively higher temperatures as described in 3.1. The data in Fig. 4 apply to a surface which was initially characterized with $R_C = 0.36$, $R_O = 0.18$; there is an initial depletion at around 120°C which appears to be associated with CO desorption (10). By contrast the bulk diffusion of oxygen and carbon becomes significant near to 270 and 490°C, respectively; interestingly the former value is increased by about 40°C over that measured previously for the Zr(0001)–O system (8), thereby suggesting the presence of some attractive C...O interactions within the surface region.

When the temperature of an ordered CO-treated (1×1) surface with $R_C = 0.44$, $R_O = 0.18$ is raised to 485°C and immediately cooled, it yields a surface which is characterized by $R_C = 0.26$, $R_O = 0.00$ and shows a sharp (1×1)-C LEED pattern. The $I(E)$ curves for this surface preparation can be

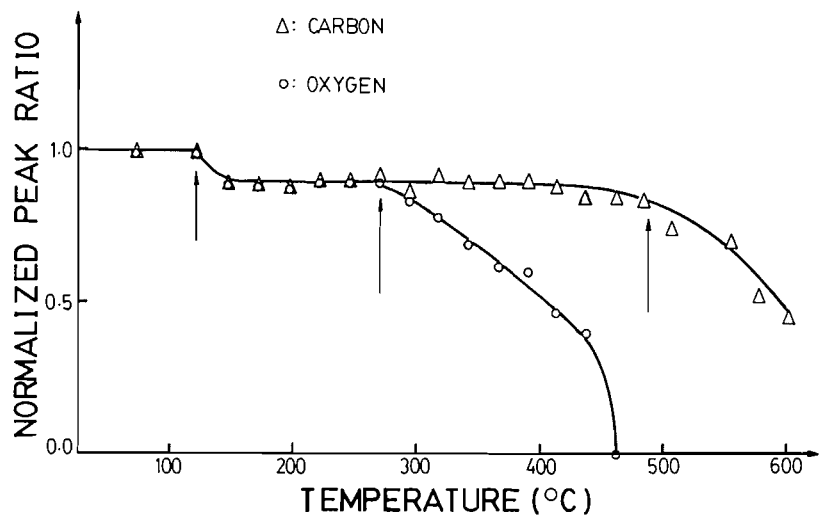

FIG. 4. Normalized Auger peak-height ratios as a function of temperature for both carbon and oxygen. The initial surface of Zr(0001) is characterized with $R_C = 0.36$ and $R_O = 0.18$ after exposure to CO.

Can. J. Chem. Downloaded from www.nrcresearchpress.com by 122.72.124.2 on 09/07/12
For personal use only.

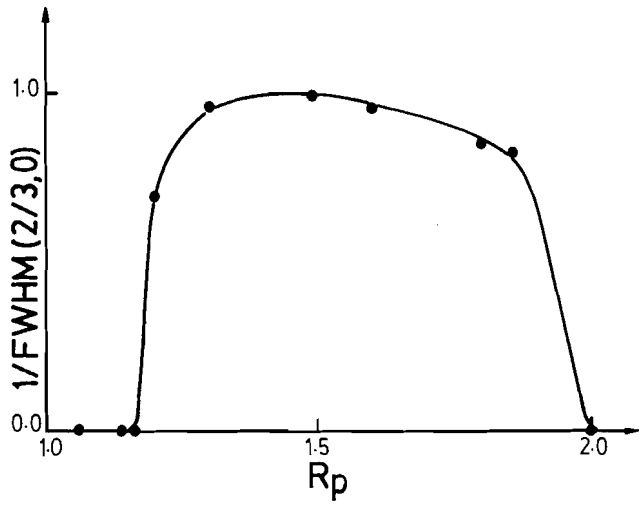

FIG. 5. Variation for a Zr(0001)–(3×3)-P surface of normalized 1/FWHM for the (2/3,0) beam at 92 eV as a function of phosphorus coverage resulting from increasing exposures to PH_3.

similar to those prepared from the adsorption of C_2H_4 as indicated in Fig. 3. When the surface with $R_C = 0.26$, $R_O = 0.00$ was re-exposed to oxygen, heated to 240°C, and cooled to room temperature, a faint (2×2) LEED pattern could be recovered. Since there is no evidence for carbon (Section 3.1), like nitrogen (3), forming a (2×2)-type structure on Zr(0001), it is natural to associate the existence of (2×2) patterns formed from CO adsorption especially with the presence of oxygen. Previous work has shown that oxygen forms (2×2)-type LEED patterns on Zr(0001) over the range of R_O values from 0.09 to 0.23 (8). Incidentally both (2×2) and (1×1) LEED patterns have also been observed with CO adsorption at Ti(0001) (16). Further, since oxygen has a strong tendency to form underlayer structures at both the (0001) surfaces of zirconium (2) and titanium (17), it is possible that the carbon plus oxygen structures involve oxygen beneath the carbon layer. Nevertheless the reverse is also possible (18); clearly this is a topic for further investigation with LEED crystallography and other structural probes.

3.3 PH_3 adsorption

AES shows that PH_3 readily adsorbs at room temperature on clean ordered Zr(0001) surfaces, although only diffuse (1×1) LEED patterns are found for exposures in the range 1–10 L. An initial empirical testing indicated that surfaces with $R_P > 2.0$ need heating to 555°C in order to get (3×3)-P LEED patterns on cooling back to room temperature, by which stage R_P is typically reduced to between 1.3 and 1.6. Such patterns were still found to be diffuse, and, unlike our experience with H_2S (9), it was not possible to measure $I(E)$ curves over a sufficiently useful energy range. Nevertheless some initial indications of the ordering process could be obtained by measuring the spot profiles with our video LEED analyzer. Figure 5 reports measurements of the reciprocal of beam width (defined as full-width at half-maximum (FWHM) height) for the (2/3,0) beam at 92 eV as a function of R_P. After each exposure to PH_3, the sample was heated to 555°C and cooled to room temperature before measuring R_P and 1/FWHM. Variation of the beam widths reflect variation in the size of the ordered regions that contribute to the (3×3) structure; specifically, larger values of 1/FWHM correspond to larger ordered regions (19).

Figure 6 reports measurements made with a PH_3-treated surface, for which the initial R_P value was 2.5. This assesses conditions both for phosphorus depletion from the surface region, as well as for the formation of (3×3) LEED patterns (the information in Fig. 6(*b*) complements that in Fig. 5). The initial depletion at around 100°C probably relates to PH_3 desorption, although the larger depletion in R_P which starts at 360°C may be associated with the desorption of hydrogen (either free or in combination with phosphorus). The latter step, judging by the 1/FWHM curves in Fig. 6(*b*), appears to initiate the (3×3)-P ordering which starts at around 420°C, although by 480°C there is a further phosphorus loss. In principle the latter could involve either bulk diffusion or desorption from the surface. Given that a similar effect is not observed for sulphur below 600°C (9), and that atomic phosphorus has a comparatively high bonding capability, the phosphorus loss starting at 480°C possibly relates to the desorption of species like P_4 or P_2 from the surface. Certainly this phosphorus loss, from whichever mechanism, acts in opposition to the formation

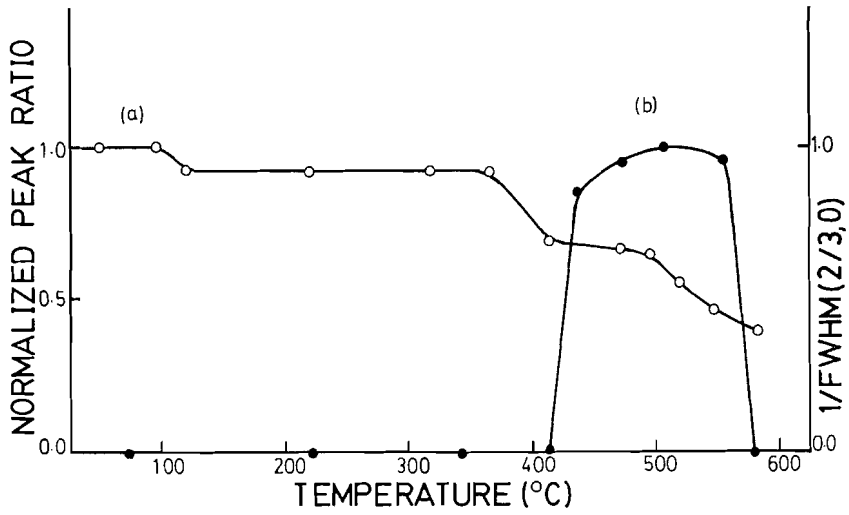

FIG. 6. (*a*) Normalized Auger peak-height ratio for phosphorus as a function of temperature. The initial Zr(0001) surface has been exposed to sufficient PH_3 to make the R_P value equal to 2.5. (*b*) Variation of normalized 1/FWHM for the (2/3,0) beam in the (3×3) LEED pattern at 92 eV for the same conditions as in (*a*).

Can. J. Chem. Downloaded from www.nrcresearchpress.com by 122.72.124.2 on 09/07/12
For personal use only.

of well-ordered (3×3)-P surface structures, although Fig. 6 does suggest that the latter may be optimized by heating at around 470°C. Also, for forming ordered structures, there may be advantages in introducing phosphorus to the Zr(0001) surface from a pure source rather than from PH_3. Such possibilities are to be investigated in further studies.

4. Concluding remarks

This paper reports the first study of the interaction between a clean and ordered (0001) surface of zirconium and the adsorbing gases C_2H_4, CO, and PH_3. All exposures are of the order of one L, and the emphasis is particularly to provide background information prior to making structural analyses with LEED crystallography. For this purpose it is important to identify optimal procedures for surface preparation, and this is done by following changes with exposure and heating in both AES and qualitative LEED patterns. An assumption is that the trends in Auger peak height ratios follow variations in surface concentrations, although strictly that requires the shape of the basic Auger peak to be constant (20). That peak shape effects (21) can occur is included in the assumption that some changes (e.g. in R_{Zr}) follow changes in hydrogen concentration. The desorption of hydrogen from polycrystalline zirconium at around 400°C has previously been recognized mass spectrometrically (13), and that emphasizes that additional characterization procedures (e.g. thermal desorption spectroscopy) would have been helpful for identifying desorbing species in the present work.

The reduced tendency for carbon to migrate below the Zr(0001) surface compared with nitrogen and oxygen reinforces previous estimates of bulk diffusion coefficients made by Foord *et al.* (10). The evolution of $I(E)$ curves after carbon adsorption suggests the existence of three successive (1×1) surfaces (including the clean surface), a feature that has not to our knowledge been reported previously. Another new structure designated Zr(0001)–(1×1)-C+O may involve underlayer oxygen, although we were not able to draw conclusions for the corresponding (2×2)-type structure. The poorly defined Zr(0001)–(3×3)-P surface recognized here likely has the same basic structure as that of the better ordered Zr(0001)–(3×3)-S system prepared previously (9). However, the ready loss of phosphorus from the former, compared with sulphur in its structure, apparently indicates that the limit to good ordering is set by ease of desorption, a condition which in turn may suggest that the surface structure is based on a phosphorus overlayer, rather than a phosphide-type (i.e. mixed Zr–P) region. Such clues are important in setting priorities for approaching the expensive multiple-scattering calculations required in the LEED structural analyses, especially for Zr(0001)–(3×3)-S.

Acknowledgements

We gratefully acknowledge the support of this research provided by the Natural Sciences and Engineering Research Council of Canada. Also we thank Y. K. Wu for her help and advice in the earlier stages of this work.

1. K. C. Hui, R. H. Milne, K. A. R. Mitchell, W. T. Moore, and M. Y. Zhou. Solid State Commun. **56**, 83 (1985).
2. P. C. Wong, K. C. Hui, B. K. Zhong, and K. A. R. Mitchell. Solid State Commun. **62**, 293 (1987).
3. P. C. Wong and K. A. R. Mitchell. Surface Sci. **187**, L599 (1987).
4. H. D. Shih, F. Jona, D. W. Jepsen, and P. M. Marcus. Surface Sci. **60**, 445 (1976).
5. H. D. Shih, F. Jona, D. W. Jepsen, and P. M. Marcus. Phys. Rev. B, **15**, 5550 (1977); **15**, 5561 (1977).
6. G. L. Miller. Zirconium. Butterworths, London. 1957.
7. J. H. Scheml and H. S. Rosenbaum (*Editors*). Zirconium in nuclear applications. American Society for Testing and Materials, Special Technical Publ. 551, Philadelphia, 1973.
8. P. C. Wong and K. A. R. Mitchell. Can. J. Phys. **65**, 464 (1987).
9. P. C. Wong and K. A. R. Mitchell. Can. J. Chem. **64**, 2409 (1986).
10. J. S. Foord, P. J. Goddard, and R. M. Lambert. Surface Sci. **94**, 339 (1980).
11. G. B. Hoflund, D. F. Cox, and R. E. Gilbert. J. Vac. Sci. Technol. A, **1**, 1837 (1983).
12. G. B. Hoflund, D. A. Asbury, D. F. Cox, and R. E. Gilbert. Appl. Surface Sci. **22/23**, 252 (1985).
13. J. M. Lin and R. E. Gilbert. Appl. Surface Sci. **18**, 315 (1984).
14. W. T. Moore, P. R. Watson, D. C. Frost, and K. A. R. Mitchell. J. Phys. C, **12**, L887 (1979).
15. P. C. Wong, M. Y. Zhou, K. C. Hui, and K. A. R. Mitchell. Surface Sci. **163**, 172 (1985).
16. H. D. Shih, F. Jona, D. W. Jepsen, and P. M. Marcus. J. Vac. Sci. Technol. **15**, 596 (1978).
17. R. L. Strong and J. L. Erskine. J. Vac. Sci. Technol. A, **3**, 1428 (1985).
18. G. B. Hoflund, G. R. Corallo, D. A. Asbury, and R. E. Gilbert. J. Vac. Sci. Technol. A, **5**, 1120 (1987).
19. D. G. Welkie and M. G. Lagally. Thin Solid Films, **93**, 219 (1982).
20. R. E. Weber and A. L. Johnson. J. Appl. Phys. **40**, 314 (1969).
21. D. E. Ramaker. Appl. Surface Sci. **21**, 243 (1985).

Can. J. Chem. Downloaded from www.nrcresearchpress.com by 122.72.124.2 on 09/07/12
For personal use only.

Cyclopalladation of trimesitylarsine. The X-ray crystal structure for $[Pd(Asmes_2C_6H_2(CH_3)_2CH_2)Cl(PPh_3)]$

ELMER C. ALYEA,[1] GEORGE FERGUSON,[1] JOHN MALITO, AND BARBARA L. RUHL

Guelph-Waterloo Centre for Graduate Work in Chemistry, Guelph Campus, Department of Chemistry and Biochemistry, University of Guelph, Guelph, Ont., Canada N1G 2W1

Received May 13, 1988

ELMER C. ALYEA, GEORGE FERGUSON, JOHN MALITO, and BARBARA L. RUHL. Can. J. Chem. **66**, 3162 (1988).

The bulky trimesitylarsine ligand, $As(mes)_3$, undergoes facile cyclopalladation to yield the dimeric complex, $[Pd(Asmes_2C_6H_2(CH_3)_2CH_2)Cl]_2$, characterized by microanalysis, IR and ^1H NMR spectroscopy. This complex is very stable but readily undergoes bridge-cleavage reactions with tertiary phosphine ligands having ligand cone angles less than 170°. The crystal structure for the PPh_3 bridge-cleavage product is reported. This complex, $[Pd(Asmes_2C_6H_2(CH_3)_2CH_2)Cl(PPh_3)]$ is monoclinic, space group $P2_1/c$ with $a = 20.469(2)$, $b = 12.702(2)$, $c = 15.401(4)$ Å, $\beta = 98.46(1)°$, $V = 3961$ Å^3, $Z = 4$, $R = 0.0284$ and $R_w = 0.0305$. The Pd geometry is distorted square-planar with principal dimensions, Pd—Cl 2.395(1), Pd—P 2.318(1), Pd—C 2.056(3), and Pd—As 2.437(1) Å; As—Pd—Cl 96.5(1), Cl—Pd—P 90.9(1), P—Pd—C 93.7(1), As—Pd—C 78.9(1), As—Pd—P 172.6(1), and Cl—Pd—C 171.7(1)°. The average C—P—C angle (104.3(1)°) is smaller than expected and is rationalized on the basis of steric effects operative within the complex.

ELMER C. ALYEA, GEORGE FERGUSON, JOHN MALITO et BARBARA L. RUHL. Can. J. Chem. **66**, 3162 (1988).

Le ligand encombrant trimésitylarsine, $As(mes)_3$, subit une cyclopalladation facile conduisant au complexe dimère, $[Pd(Asmes_2C_6H_2(CH_3)_2CH_2)Cl]_2$, qui a été caractérisé par des microanalyses et par spectroscopie IR et RMN du ^1H. Ce complexe est très stable; toutefois, mis en présence de ligands phosphines tertiaires comportant des angles du cône de ligand inférieurs à 170°, il subit facilement des réactions de clivage de pont. On a déterminé la structure cristalline du produit obtenu par clivage de pont à l'aide de la PPh_3. Ce complexe, $[Pd(Asmes_2C_6H_2(CH_3)_2CH_2)Cl(PPh_3)]$, est monoclinique, groupe d'espace $P2_1/c$, avec $a = 20{,}469(2)$, $b = 12{,}702(2)$ et $c = 15{,}401(4)$ Å, $\beta = 98{,}46(1)°$, $V = 3961$ Å^3, $Z = 4$, $R = 0{,}0284$ et $R_w = 0{,}0305$. La géométrie du Pd est du type plan carré déformé et les principales dimensions du cristal sont : Pd—Cl 2,395(1), Pd—P 2,318(1), Pd—C 2,056(3) et Pd—As 2,437(1) Å; As—Pd—Cl 96,5(1), Cl—Pd—P 90,9(1), P—Pd—C 93,7(1), As—Pd—C 78,9(1), As—Pd—P 172,6(1) et Cl—Pd—C 171,7(1)°. L'angle C—P—C moyen (104,3(1)°) est plus faible que prévu et on rationalise ce fait sur la base d'effets stériques opérant à l'intérieur du complexe.

[Traduit par la revue]

Introduction

Tertiary phosphine complexes of the platinum group metals have proven valuable as homogeneous catalysts (1). Integral to the design and development of these catalysts are studies related to ligand modification affecting either or both the steric and electronic properties of the ligand in question. It has now become very clear that as the overall bulk of a tertiary phosphine ligand is increased, steric factors begin to play a dominating role often leading to new and unexpected effects (1*b*, 2, 3). For example, bulky phosphine ligands tend to promote internal metallation reactions (3, 4).

Trimesitylphosphine ($P(mes)_3$) is at the upper limit for phosphine steric bulk (2, 5) and shows transition metal chemistry dominated by steric factors (6) as does the trimesitylarsine analogue, $As(mes)_3$ (6*b*, 7). Both these ligands readily undergo relatively facile cyclopalladation and cycloplatination (8) and despite literature trends (3, 4), in each case, the former is the more facile of the two processes (8). These observations for $As(mes)_3$ are somewhat surprising in view of the limited examples of cyclometallated arsine complexes (9). Furthermore, in those cases involving platinum group metals (9, 10), only cycloplatination is observed.

We have pursued this cyclometallation chemistry of $As(mes)_3$ and in this paper, we present details for the synthesis and characterization of the stable complex, $[Pd(Asmes_2C_6H_2(CH_3)_2CH_2)Cl]_2$. We have placed special emphasis on the monomeric species produced by bridge-cleavage reactions and in particular the complex, $[Pd(Asmes_2C_6H_2(CH_3)_2CH_2)Cl(PPh_3)]$. The X-ray crystal determination for this complex appears to be the first such analysis for a cyclometallated arsine ligand.

Experimental

General

Trimesitylarsine was prepared by literature methods (11). Palladium dichloride (Johnson, Matthey and Mallory Ltd.) was used to prepare $PdCl_2(CH_3CN)_2$ by literature methods (12). All reactions were carried out under a dinitrogen atmosphere using standard Schlenk line techniques with solvents purified by standard methods.

Physical methods

Elemental analyses were performed by MHW laboratories, Phoenix, Arizona. Melting points were determined on a Gallenkamp Melting Point apparatus in unsealed capillary tubes and calibrated against a series of melting point standards. Infrared spectra (500–180 cm^{-1}) were recorded as Nujol mulls between polyethylene plates on a Perkin-Elmer 180 spectrophotometer. ^1H and ^{31}P NMR spectra were acquired on a Bruker WH-400 spectrometer operating in the pulsed FT mode at 400.13 and 161.98 MHz, respectively, at 297 K. Nuclear magnetic resonance samples were prepared in $CDCl_3$ with TMS and 80% H_3PO_4 as internal (^1H) and external (^{31}P) standards, respectively. Chemical shifts downfield of positions observed for the standards are considered positive.

Synthesis

$[Pd(Asmes_2C_6H_2(CH_3)_2CH_2)Cl]_2$

A mixture of $PdCl_2(CH_3CN)_2$ (0.080 g, 0.31 mmol) and $As(mes)_3$ (0.260 g, 0.60 mmol) in benzene (55.0 cm^3) was refluxed (20 h),

[1]To whom correspondence may be addressed.

Can. J. Chem. Downloaded from www.nrcresearchpress.com by 122.72.124.2 on 09/07/12
For personal use only.

TABLE 1. Details of refinement for $C_{45}H_{47}AsClPPd$

Range of θ	2–27°
Range of indices	*h* 0 to 26
	k 0 to 16
	l −19 to 19
Reflections measured	9552
Unique reflections	8634
Reflections with $I > 3\sigma(I)$	5862
Crystal size	0.10 × 0.30 × 0.63 mm
Range of transmission coefficients	0.648 to 0.869
R	0.0284
R_w	0.0305
Number of variables	386
Maxima in final difference map	0.74 e Å^{-3} at Pd

cooled, concentrated (to 10 cm^3), and *n*-hexane was added. Overnight refrigeration afforded a yellow precipitate which was isolated and recrystallized from chloroform/petroleum ether (BP 30–60°C) (1:3 v/v) to give yellow needles which were washed with cold petroleum ether and dried *in vacuo*, yield 0.16 g (94%). *Anal.* calcd. for $[Pd(Asmes_2C_6H_2(CH_3)_2CH_2)Cl]_2$: C 56.56, H 5.63; found: C 56.42, H 5.71. MP: 252–253°C (dec.).

$[Pd(Asmes_2C_6H_2(CH_3)_2CH_2)Cl(PPh_3)]$

A mixture of the dimer (0.11 g, 0.10 mmol) and triphenylphosphine (0.05 g, 0.20 mmol) was refluxed in benzene (50.0 cm^3, 1.5 h), cooled, concentrated (to 10 cm^3), and poured onto a silica-gel column (Baker 60–200 mesh, $CHCl_3/C_6H_6$, 1:1 v/v). The yellow fraction collected was reduced to dryness, washed with cold petroleum ether, and dried *in vacuo*, yield 0.14 g (84%). *Anal.* calcd. for $[Pd(Asmes_2C_6H_2(CH_3)_2CH_2)Cl(PPh_3)]$: C 64.68, H 5.67; found: C 64.51, H 5.77. MP: 238–241°C (to colourless, then black liquid).

X-ray crystallography

$[Pd(Asmes_2C_6H_2(CH_3)_2CH_2)Cl(PPh_3)]$

Pale yellow plates suitable for X-ray diffraction were grown by slow precipitation from chloroform/*n*-hexane (1:4 v/v) at ambient temperatures in the dark. Crystal data are as follows:

$C_{45}H_{47}AsClPPd$ $M = 835.6$

Monoclinic, $a = 20.469(2)$, $b = 12.702(2)$, $c = 15.401(4)$ Å, $\beta = 98.46(1)°$, $V = 3961$ Å, $Z = 4$, $D_c = 1.475$ g cm^{-3}, $F(000) = 1712$; MoK_α radiation, $\lambda = 0.71073$ Å, $\mu = 14.7$ cm^{-1}, space group $P2_1/c$ (from systematic absences $h0l$, $l = 2n + 1$, $0k0$, $k = 2n + 1$).

Accurate cell dimensions and crystal orientation matrix were determined on a CAD4 diffractometer by a least-squares treatment of 25 reflections with θ in the range 10–15° and an intensity data set collected to θ = 27° (see Table 1 for details). The data were corrected for Lorentz, polarization, and absorption effects and the structure solved via the Patterson heavy-atom method. Refinement was by full-matrix least-squares calculations, initially with isotropic and finally with anisotropic thermal parameters. At an intermediate stage in the refinement, a difference map showed maxima in positions consistent with the expected locations of all hydrogen atoms. In the final rounds of calculations, the hydrogen atoms were positioned on geometrical grounds (C—H 0.95 Å) and included (as riding atoms) in the structure factor calculations. A final difference map had no chemically significant features. Weights in the refinement process were derived from the counting statistics. Scattering factors and anomalous dispersion corrections were taken from refs. 13 and 14. Final fractional coordinates are given in Table 2 and details of molecular geometry are given in Table 3. All other data tables (hydrogen coordinates, thermal parameters, mean planes, structure factors) have been deposited. An ORTEP diagram of the molecule showing the crystallographic numbering scheme is in Fig. 1.

Results and discussion[2]

Cyclopalladation of $As(mes)_3$ seems to proceed in a similar but much slower manner than cyclopalladation of $P(mes)_3$ (8) to give the chlorobridged structure suggested by our ^1H NMR and IR data.

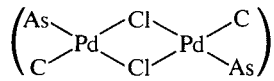

As^C = $Asmes_2C_6H_2(CH_3)_2CH_2$

The far-infrared spectrum shows two bands (280 and 252 cm^{-1}) assignable to the two "vibrational modes" of the bridging Pd—Cl bonds shown and there is no evidence for terminal Pd—Cl bonds. Two higher energy bands (365 and 350 cm^{-1}) have been assigned to Pd—As bonding modes. The *trans-anti* geometry shown is assigned on the basis of stereochemical arguments and solvent (8*c*) and X-ray (8*d*) studies of the related palladium and platinum complexes of $P(mes)_3$.

In comparison to the ^1H NMR spectrum for free $As(mes)_3$ (a, b, c: δ 2.12, 2.24, 6.77 ppm, relative integration 18:9:6), the spectrum for $[Pd(As\hat{}C)Cl]_2$ (a′, b′, b, a, a″, c″, c′, c: δ 1.81, 2.25, 2.34, 2.38, 3.41, 6.56, 6.74, 6.78 ppm, relative integration 3:3:6:12:2:1:1:4) indicates two types of mesitylene ring. The two proton peak at δ 3.41 ppm is diagnostic of orthometallation and the assignments made are based upon the labelling scheme given below.

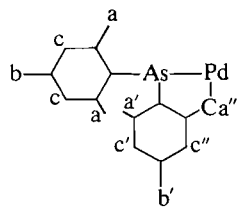

We saw no evidence for formation of the 1:2 monomeric $[Pd(As(mes)_3)_2Cl_2]$ species reported earlier by other workers (15) but the 1:1 dimeric species, $[Pd(As(mes)_3)Cl_2]_2$, is observed (8*a*). This latter species undergoes facile cyclopalladation to form the more stable chlorobridged complex $[Pd(As\hat{}C)Cl]_2$. Solutions of the cyclopalladated complex are unaffected by treatment with O_2 or HX (X = H, F, Cl).

The bulky phosphine ligands, $P(t\text{-}Bu)_3$ and $P(mes)_3$ (θ = 182 and 212°, respectively) (2) will not cleave the $PdCl_2Pd$ bridge unit of $[Pd(As\hat{}C)Cl]_2$ even under rigorous reaction conditions while $P(o\text{-}tol)_3$ (θ = 194°) (2) does react with the dimer but leads to a complicated product mixture. Reaction with the less bulky PPh_3 however, leads clearly to the isolable bridge-cleavage product *trans*-$[Pd(As\hat{}C)Cl(PPh_3)]$.

The latter complex is also a stable compound in the solid state but will revert to the parent dimer over a period of weeks if left standing in solution. The far-infrared spectrum shows only one ν(Pd—Cl) band of relatively low energy at 275 cm^{-1}, consistent with this bond being *trans* to the Pd—C bond. The higher energy bands (365 and 349 cm^{-1}) attributable to Pd—As stretching modes have not shifted significantly relative to positions observed for $[Pd(As\hat{}C)Cl]_2$. The ^1H NMR spectrum (a′, b′, b, a, a″, a″, c″, c′, c: δ 1.81, 2.12, 2.28, 2.42, 2.61, 2.63, 6.11, 6.49, 6.85 ppm, relative integration

[2]A complete set of data may be purchased from the Depository of Unpublished Data, CISTI, National Research Council of Canada, Ottawa, Ont., Canada K1A 0S2.

Can. J. Chem. Downloaded from www.nrcresearchpress.com by 122.72.124.2 on 09/07/12
For personal use only.

Can. J. Chem. Downloaded from www.nrcresearchpress.com by 122.72.124.2 on 09/07/12
For personal use only.

TABLE 2. Final fractional coordinates for $C_{45}H_{47}AsClPPd$ (Pd, As, Cl, P × 10^5, C × 10^4) with esd values in parentheses

Atom	x	y	z
Pd	21066(1)	20379(2)	3939(1)
As	31212(1)	10155(2)	4743(2)
Cl	15289(4)	8254(6)	11986(6)
P	12120(4)	31767(6)	2280(5)
C(11)	3735(1)	2195(2)	617(2)
C(12)	3400(1)	3117(2)	333(2)
C(13)	3727(2)	4077(3)	487(2)
C(14)	4365(2)	4141(3)	931(2)
C(15)	4680(2)	3199(3)	1204(2)
C(16)	4387(2)	2219(3)	1049(2)
C(17)	2707(1)	3077(2)	−141(2)
C(18)	4702(2)	5183(3)	1123(3)
C(19)	4772(2)	1247(3)	1347(3)
C(21)	3366(1)	111(2)	1505(2)
C(22)	3602(2)	−942(2)	1489(2)
C(23)	3647(2)	−1507(2)	2263(2)
C(24)	3485(2)	−1114(3)	3036(2)
C(25)	3298(2)	−75(3)	3044(2)
C(26)	3240(1)	557(2)	2302(2)
C(27)	3837(2)	−1428(3)	707(2)
C(28)	3513(2)	−1785(3)	3855(2)
C(29)	3055(2)	1688(3)	2410(2)
C(31)	3144(1)	274(2)	−643(2)
C(32)	2632(2)	−455(2)	−876(2)
C(33)	2521(2)	−853(3)	−1726(2)
C(34)	2900(2)	−552(3)	−2355(2)
C(35)	3402(2)	128(3)	−2111(2)
C(36)	3546(2)	554(3)	−1266(2)
C(37)	2183(2)	−835(3)	−246(3)
C(38)	2737(2)	−954(4)	−3289(3)
C(39)	4142(2)	1269(3)	−1087(2)
C(41)	420(1)	2666(2)	−331(2)
C(42)	82(2)	3136(3)	−1077(2)
C(43)	−506(2)	2714(3)	−1479(3)
C(44)	−759(2)	1824(3)	−1150(3)
C(45)	−437(2)	1361(3)	−415(3)
C(46)	150(2)	1773(3)	−4(2)
C(51)	1036(1)	3581(2)	1306(2)
C(52)	419(2)	3937(3)	1440(2)
C(53)	305(2)	4241(3)	2265(2)
C(54)	805(2)	4188(3)	2963(2)
C(55)	1412(2)	3832(3)	2848(2)
C(56)	1533(2)	3539(2)	2014(2)
C(61)	1322(1)	4402(2)	−352(2)
C(62)	1476(1)	4358(2)	−1206(2)
C(63)	1581(2)	5261(3)	−1656(2)
C(64)	1543(2)	6226(3)	−1261(2)
C(65)	1388(2)	6283(3)	−423(2)
C(66)	1279(1)	5378(2)	32(2)

TABLE 3. Principal bond lengths (Å) and bond angles (deg) for $C_{45}H_{47}AsClPPd$ with esd values in parentheses

Bond	Length
Pd—As	2.437(1)
Pd—Cl	2.395(1)
Pd—P	2.318(1)
Pd—C(17)	2.056(3)
As—C(11)	1.946(3)
As—C(21)	1.963(3)
As—C(31)	1.968(3)
P—C(41)	1.837(3)
P—C(51)	1.824(3)
P—C(61)	1.823(3)

Bonds	Angle	Bonds	Angle
As—Pd—Cl	96.5(1)	C(41)—P—C(51)	104.3(1)
As—Pd—P	172.6(1)	C(41)—P—C(61)	103.6(1)
As—Pd—C(17)	78.9(1)	C(51)—P—C(61)	105.1(1)
Cl—Pd—P	90.9(1)	Pd—P—C(41)	117.4(1)
Cl—Pd—C(17)	171.7(1)	Pd—P—C(51)	109.5(1)
P—Pd—C(17)	93.7(1)	Pd—P—C(61)	115.7(1)
Pd—As—C(11)	97.3(1)	As—C(11)—C(12)	109.4(2)
Pd—As—C(21)	117.9(1)	As—C(11)—C(16)	128.6(2)
Pd—As—C(31)	109.9(1)	As—C(21)—C(22)	125.6(2)
C(11)—As—C(21)	106.0(1)	As—C(21)—C(26)	114.3(2)
C(11)—As—C(31)	111.6(1)	As—C(31)—C(32)	115.1(2)
C(21)—As—C(31)	113.0(1)	As—C(31)—C(36)	124.7(2)
Pd—C(17)—C(12)	114.0(2)		

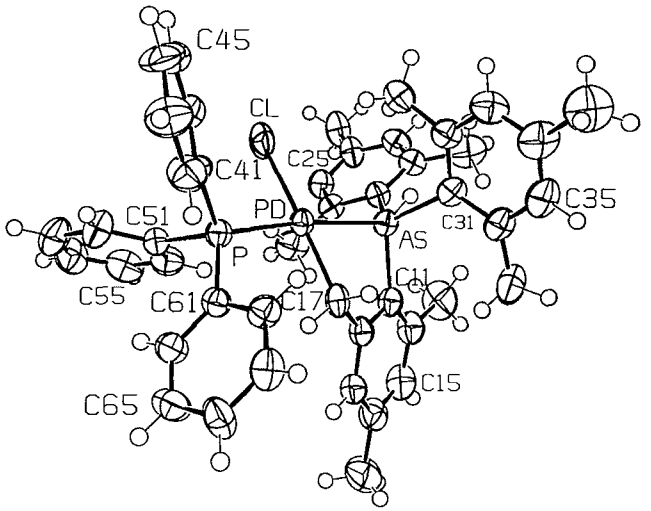

FIG. 1. A view of the [Pd(As—C)Cl(PPh_3)] complex with 50% probability ellipsoids and an indication of the numbering scheme. Phenyl ring carbons are numbered C*i*1–C*i*6 (*i* = 1–6); methyl carbons are numbered C*i*7–C*i*9 (*i* = 1–3).

3:3:6:12:1:1:1:1:4) shows the appropriate resonances due to bound PPh_3 (δ 7.63–7.58 ppm, relative integration 15). The two protons on the metallated carbon are now magnetically nonequivalent, perhaps due to the steric effects of the relatively bulky PPh_3 moiety present in a position *cis* to this carbon. Relative to the parent dimer, protons on the nonmetallated and metallated mesityl rings are more deshielded and shielded, respectively. This perhaps suggests a Pd—As bond which shortens at the expense of a lengthening Pd—C bond. That the latter should happen is reasonable since upon bridge-cleavage, the metallated carbon finds itself *trans* to a terminal rather than bridging Pd—Cl bond. Also, a steric effect induced by proximity of the relatively bulky PPh_3 ligand might be a factor here. Nevertheless, the *trans*-influence of PPh_3 is higher than that of a chloro group and one should expect an overall lengthening of the Pd—As bond upon cleavage. Unfortunately, the ν(Pd—As) positions measured for the monomer and dimer are virtually the same and do not allow a decision about which factor is dominant.

The Pd geometry in *trans*-[Pd(As⌒C)Cl(PPh_3)] (Fig. 1) is close to square-planar geometry. Deviations from the plane

defined by atoms P, Cl, As, and C(17) are P 0.063, Cl −0.055, As 0.066, C(17) −0.074, and Pd 0.067 Å. Atoms As and P have distorted tetrahedral coordination. For the As^C moiety, the average C—C ring (1.391(5) Å) and C—C methyl (1.509(5) Å) bond distances and corresponding bond angles are virtually identical to those observed for free $As(mes)_3$ (16).

The Pd—P bond length (2.318(1) Å) is shorter than those reported for *trans*-$[PdCl_2(PPh_3)_2]$ (2.337(1) Å) (17) or $[PdCl_2(PPh_3)_2]\cdot(1/2)p\text{-}C_6H_4Cl_2$ (2.349(1) Å) (18) and at the lower end of the range for *trans*-$[PdCl_2(PR_3)_2]$ complexes (2.310(5)–2.388(16) Å) (19). The average P—C bond length (1.828(3) Å), however, is exactly the same as that measured for noncoordinated PPh_3 (20) but longer than that observed for *trans*-$[PdCl_2(PPh_3)_2]$ (1.816(2) Å; range is 1.810(1)–1.820(1) Å) (17). It is worth noting that the As—C(11) bond distance (1.946(3) Å) of the metallated ring is shorter than either the As—C(21) or As—C(31) bonds and is shorter than that observed for the As—C bond distance in free $As(mes)_3$ (average 1.976(5) Å) (16). The Pd—As bond distance (2.437(1) Å) appears to be longer than that measured for the Pd—As bond distance in *trans*-$[PdCl_2(AsPh_3)_2]$, which is reported as 2.42 Å (21). Finally, the Pd—Cl bond (2.395(1) Å) is longer than those measured for other related systems (2.267(9)–2.326(4) Å) (17–19), in accord with our infrared data (see above).

The maximum cone angle measured for PPh_3 in *trans*-$[Pd(As^C)Cl(PPh_3)]$ is 154° which is comparable to a predicted value of 145° (2) in view of the different modes of measurement and the environmental dependence of ligand cone angles in general (22). In any case, the changes in C—P—C bond angles give more reliable information as to the effects of steric environment on coordinating PPh_3. The average C—P—C angle should increase upon coordination from the value (102.6°) (20) in free PPh_3 toward the ideal tetrahedral angle (109.5°). Instead, it is found to be 104.3(1)° which is smaller than the average C—P—C angle (105.0(1)°; range 104.0(1)–106.3(1)°) measured in the less sterically hindered *trans*-$[PdCl_2(PPh_3)_2]$ (17). Thus, the opening of the C—P—C angles in PPh_3 upon coordination in the bridge-cleavage of $[Pd(As^C)Cl]_2$ is effectively constrained by the crowded environment about Pd(II).

Acknowledgements

Financial support from NSERC of Canada to E.C.A. and G.F. and from Imperial Oil of Canada Ltd. to J.M. is gratefully acknowledged. Dr. S. Dias is thanked for performing some initial reactions of $As(mes)_3$ with $PdCl_2$.

1. (*a*) G. W. PARSHALL. Homogeneous catalysis. John Wiley and Sons Inc., New York. 1980; (*b*) E. C. ALYEA and D. W. MEEK (*Editors*). Adv. Chem. Ser. **196**, 1-421 (1982); (*c*) L. H. PIGNOLET. Homogeneous catalysis with metal phosphine complexes. Plenum Press, New York. 1983.
2. C. A. TOLMAN. Chem. Rev. **77**, 313 (1977).
3. B. L. SHAW. J. Organomet. Chem. **200**, 307 (1980).
4. (*a*) J. DEHAND and M. PFEFFER. Coord. Chem. Rev. **18**, 327 (1976); (*b*) M. I. BRUCE. Angew. Chem. Int. Ed. Engl. **16**, 73 (1977); (*c*) I. OMAE. Coord. Chem. Rev. **32**, 235 (1980).
5. J. F. BLOUNT, C. A. MARYANOFF, and K. MISLOW. Tetrahedron Lett. **11**, 913 (1975).
6. (*a*) E. C. ALYEA, S. A. DIAS, G. FERGUSON, and M. PARVEZ. Inorg. Chim. Acta, **37**, 45 (1977); (*b*) E. C. ALYEA, S. A. DIAS, and S. STEVENS. Inorg. Chim. Acta Lett. **44**, 207 (1980); (*c*) E. C. ALYEA, G. FERGUSON, and A. SOMOGYVARI. Inorg. Chem. **21**, 1369 (1982); (*d*) E. C. ALYEA, S. A. DIAS, G. FERGUSON, and P. Y. SIEW. Croat. Chem. Acta, **57**, 457 (1984); (*e*) E. C. ALYEA, G. FERGUSON, J. MALITO, and B. L. RUHL. Inorg. Chem. **24**, 3719 (1985).
7. E. C. ALYEA, S. A. DIAS, G. FERGUSON, and P. Y. SIEW. Can. J. Chem. **61**, 257 (1983).
8. (*a*) S. A. DIAS and E. C. ALYEA. Trans. Met. Chem. **4**, 205 (1979); (*b*) E. C. ALYEA and J. MALITO. J. Organomet. Chem. **340**, 119 (1988); (*c*) E. C. ALYEA and J. MALITO. Inorg. Chim. Acta Lett. **144**, 155 (1988); (*d*) E. C. ALYEA, G. FERGUSON, J. MALITO, and B. L. RUHL. Organometallics. In press.
9. (*a*) R. L. BENNETT, M. I. BRUCE, and F. G. A. STONE. J. Organomet. Chem. **94**, 65 (1975); (*b*) B. L. SHAW and R. E. STAINBANK. J. Chem. Soc. Dalton Trans. 2394 (1973); (*c*) J. M. DUFF, B. E. MANN, B. L. SHAW, and B. TURTLE. J. Chem. Soc. Dalton Trans. 139 (1974).
10. R. L. BENNETT, M. I. BRUCE, and F. G. A. STONE. J. Organomet. Chem. **38**, 325 (1972).
11. B. I. STEPANOV, E. N. KARPOVA, and A. I. BOKANOV. J. Gen. Chem. U.S.S.R. **39**, 1514 (1969).
12. J. R. DOYLE, P. E. SLADE, and H. B. JONASSEN. Inorg. Synth. **6**, 216 (1960).
13. D. T. CROMER and J. T. WABER. International tables for X-ray crystallography. Vol. IV. The Kynoch Press, Birmingham, England. 1974. Table 2.2B.
14. J. A. IBERS and W. C. HAMILTON. Acta Crystallogr. **17**, 781 (1964).
15. D. NEGOIU and V. SERBAN. Universitatea Buccaresti Analele Chimie, **18**, 55 (1969); Chem. Abstr. **77**, 62127 (1970).
16. A. N. SOBOLEV, I. P. ROMM, N. YU CHERNIKOVA, V. K. BELSKY, and E. N. GUR'YANOVA. J. Organomet. Chem. **219**, 35 (1981).
17. G. FERGUSON, R. MCCRINDLE, A. J. MCALEES, and M. PARVEZ. Acta Crystallogr. B**38**, 2679 (1982).
18. Y. KITANO, Y. KINOSHITA, R. NAKAMURA, and T. ASHIDA. Acta Crystallogr. C**39**, 1015 (1983).
19. (*a*) N. A. AL-SALEM, W. S. MCDONALD, R. MARKHAM, M. C. NORTON, and B. L. SHAW. J. Chem. Soc. Dalton Trans. 59 (1980); (*b*) F. BACHECHI, L. ZAMBONELLI, and L. M. VENANZI. Helv. Chim. Acta, **60**, 2815 (1977); (*c*) K. KAN, K. MIKI, Y. KAI, N. YASUOKA, and N. KASAI. Bull. Chem. Soc. Jpn. **51**, 733 (1978); (*d*) W. S. MCDONALD. Acta Crystallogr. B**35**, 3051 (1979); (*e*) N. C. TAYLOR, S. E. JACOBSON, and A. J. CARTY. Inorg. Chem. **14**, 2648 (1975).
20. J. J. DALY. J. Chem. Soc. 3799 (1964).
21. S. T. MALINOVSKII, I. F. BURSHTEIN, and T. I. MALINOVSKII. Izu. Akad. Nauk Mold. SSR, Ser. Fiz-Tekh. Mat. Nauk, **1**, 45 (1975); Chem. Abstr. **91**, 149719c (1975).
22. (*a*) A. IMMIRZI and A. MUSCO. Inorg. Chim. Acta, **25**, L41 (1977); (*b*) G. FERGUSON, P. J. ROBERTS, E. C. ALYEA, and M. KAHN. Inorg. Chem. **17**, 2965 (1978).

Can. J. Chem. Downloaded from www.nrcresearchpress.com by 122.72.124.2 on 09/07/12
For personal use only.

On the calculation of atomization energies of organic molecules in the Xα local spin density approximation

S. FLISZÁR, S. RIOUX, AND J. ANDZELM
Département de Chimie, Université de Montréal, C.P. 6128, Succ. A, Montréal (Qué.), Canada H3C 3J7

C. MINICHINO
Istituto di Chimica, Università della Basilicata Via N. Sauro 85, Potenza, Italia I-85100

AND

E. C. VAUTHIER
Département de recherches physiques, L.A. 04.0071, Université Pierre et Marie Curie, 4 Place Jussieu, 75230, Paris, France

Received April 15, 1988

S. FLISZÁR, S. RIOUX, J. ANDZELM, C. MINICHINO, and E. C. VAUTHIER. Can. J. Chem. **66**, 3166 (1988).

The atomization energies of selected alkanes, alkyl radicals, and amines are deduced from Xα local spin density calculations of E, the total energy of a molecule in its potential minimum. Both the exchange-correlation energy, $\alpha(\partial E/\partial\alpha)$, and $\partial E/\partial\alpha$ itself obey, in a first approximation, simple atom-by-atom additivity rules. The appropriate α's for use in Xα(LSD) calculations of organic molecules thus appear as weighted averages and depend on the particular composition of each molecule. The at least approximate validity of this averaging procedure is illustrated by the accuracy of calculated atomization energies.

S. FLISZÁR, S. RIOUX, J. ANDZELM, C. MINICHINO et E. C. VAUTHIER. Can. J. Chem. **66**, 3166 (1988).

On a déduit les énergies d'atomisation d'une série d'alcanes, de radicaux alkyles et d'amines à partir des calculs de E, l'énergie totale d'une molécule à son minimum de potentiel, basés sur la densité locale de spin Xα. L'énergie totale de corrélation-échange $\alpha(\partial E/\partial\alpha)$ et $\partial E/\partial\alpha$ lui-même suivent, en première approximation une simple règle d'additivité atome-par-atome. Les valeurs appropriées de α utilisées dans les calculs de Xα(LSD) des molécules organiques sont des moyennes pondérées et dépendent de la composition particulière de chaque molécule. La précision des énergies d'atomisation calculées illustre pour le moins la validité approximative de cette procédure.

[Traduit par la revue]

Introduction

By far the most useful non-empirical alternatives to configuration interaction calculations are the methods rooted in density functional theory (DFT) (1, 2). Building on their success in numerous applications to inorganic chemistry (3), an area where the familiar wave function methods rapidly sink under the burden of formidable computational demands, we examine here the applicability of DFT to the "simpler" organic systems, particularly to the study of their atomization energies, keeping in mind that any presently known density functional approach involves approximations. The tests are meaningful in that they are conducted at a very demanding level, that approaching experimental accuracy.

Here we use the local spin density (LSD) approximation (4) and expand the molecular orbitals as a linear combination of gaussian type orbitals (LCGTO) for solving the LSD equations. The specific form of the latter depends on the treatment of exchange and correlation in electron-gas calculations. The Xα approach yields the following exchange energy (2, 5)

$$E_{X\alpha} = -\frac{3}{4}\alpha\left(\frac{81}{8\pi}\right)^{1/3}\int\rho(1)^{4/3}\mathrm{d}v_1$$

where α is treated as a variable parameter. The tentative hypothesis is that the LCGTO-Xα(LSD) method basically meets the required demands of accuracy. In other words, we assume that the energy should be right if α is properly selected.

This is where the problem lies. Ever since the appearance of the Xα method, the way of selecting α has been a fundamental problem. In this work we focus attention on this particular topic. On the basis of regularities which are observed for exchange-correlation energies, we develop a recipe permitting valid estimates of α and, thus, an assessment of the possibilities offered by LCGTO-Xα(LSD) calculations. Momentarily we concentrate on the description of this recipe and illustrate our approach with results obtained for a representative collection of saturated hydrocarbons, alkyl radicals, and amines. Extensions to other systems are contemplated at a later stage, e.g., to organic molecules containing oxygen.

The calculations are made for molecules at 0 K when all the atoms are stationary in their equilibrium positions. The total ground state energy is then

$$[1]\quad E = \sum_i E_i^{\mathrm{atom}} - \Delta E_a^*$$

where E_i^{atom} is the ground state energy of the isolated atom i and ΔE_a^* the atomization energy of that molecule. E is the target of our LCGTO-Xα(LSD) calculations. ΔE_a^* is convenient for comparisons with experimental results.

The evaluation of ΔE_a^* and E from experimental data

The energy of an isolated atom, E^{atom}, is taken (with the appropriate change in sign) as the sum of its ionization potentials. With the conversion factor 1 hartree = 27.2106 eV, we obtain from the tabulation given by Moore (6) $E_C^{\mathrm{atom}} = -37.8558$, $E_N^{\mathrm{atom}} = -54.6121$, and $E_H^{\mathrm{atom}} = -0.5$ au. These energies are used in calculations of E, eq. [1], together with the appropriate experimental ΔE_a^* results. The latter are deduced from eq. [2] (7)

$$[2]\quad \Delta E_a^* = \sum_i n_i[\Delta H_f^0(A_i) - \tfrac{5}{2}RT] + \mathrm{ZPE} + (H_T - H_0) - \Delta H_f^0$$

where ΔH_f^0 is the standard enthalpy of formation of the molecule in the gas phase and $\Delta H_f^0(A_i)$ that of the isolated atom A_i, with n_i = number of atoms A_i found in the molecule. We have used (8) $\Delta H_f^0(H) = 52.09$, $\Delta H_f^0(C) = 170.89$, and $\Delta H_f^0(N) = 113.0$ kcal atg^{-1}. ZPE is the zero point energy of the molecule (usually evaluated in the harmonic oscillator

Printed in Canada / Imprimé au Canada

Can. J. Chem. Downloaded from www.nrcresearchpress.com by 122.72.124.2 on 09/07/12
For personal use only.

approximation) and $(H_T - H_0)$ its heat content. Most of the ZPE + $(H_T - H_0)$ and ΔE_a^* results considered in this work are conveniently tabulated elsewhere (7, 9, 10). The most important source of errors accompanying the evaluation of ΔE_a^* and, thus, of E originates in the experimental uncertainty associated with ΔH_f^0. Possible errors associated with ZPE + $(H_T - H_0)$ are expected (10) not to exceed ~0.2 kcal mol^{-1}.

Outline of LCGTO-Xα(LSD) calculations (11, 12)

The calculations were performed using the program developed by Dunlap, Connolly, and Sabin (12). Huzinaga's $(9s5p)$ basis (13) was used for carbon and nitrogen. Hydrogen was described by a $(5s)$ basis obtained from Dunning's $(3s)$ basis set (14). In this Xα method it is necessary to fit the charge density and the exchange potentials to sets of auxiliary Hermite gaussian functions. The Xα exchange potentials were fitted to the auxiliary functions following the criterion given by Dunlap *et al.* (12), i.e.,

$$\int \rho(\widetilde{\rho^{1/3}})d\tau = \int (\widetilde{\rho^{1/3}})^4 d\tau$$

where the tilde represents a fitted quantity. The sampling points for the exchange potentials were determined by taking each tenth point of the Herman–Skillman radial mesh (15) and an angular mesh consisting of the twelve vertices of a regular icosahedron (16). The selected auxiliary functions were $(9s5p3d)$ for carbon and nitrogen and $(5s5p)$ for hydrogen. Two s-type bond-centered auxiliary functions were also used, as suggested by Dunlap *et al.* (12).

The final value obtained for E, the energy of a molecule, obviously depends on α, where $\partial E/\partial\alpha = \partial E_{X\alpha}/\partial\alpha$ and

$$[3] \quad \frac{\partial E}{\partial \alpha} = \frac{E_{X\alpha}}{\alpha}$$

Now we turn our attention to this important point.

The selection of α

Slater's original treatment (17) of the exchange potential amounts to taking $\alpha = 1$ but Gáspár (5) and later Kohn and Sham (2) showed that $\alpha = 2/3$ is more appropriate. The more recent treatment of the exchange-correlation potential by Gáspár and Nagy (18) represents a generalization of the Slater and Gáspár–Kohn–Sham approaches and contains those as special cases. The theoretical α's deduced by Gáspár and Nagy are intermediate between 2/3 and 1. They offer a justification for the value $\alpha \simeq 0.7$ advocated by Baerends and Ros (19) for molecular calculations. For the calculation of accurate atomization energies, however, "approximate" α values are clearly insufficient because even a relatively minor error, $\Delta\alpha$, accompanying the selection of α results in a sizeable error, $\Delta\alpha(\partial E/\partial\alpha) = \Delta\alpha(E_{X\alpha}/\alpha)$, in the evaluation of E.

With this idea in mind, we examine first the α values which would duplicate the experimental energies, eq. [1]. Second, we examine the possibility of constructing these α's in a simple manner on the basis of structural features. Our approach is illustrated by means of a representative collection of molecules. Table 1 indicates (*i*) their total energies, E, obtained from eqs. [1] and [2] and the appropriate experimental data, (*ii*) the α values which duplicate these energies, and (*iii*) the corresponding $\partial E/\partial\alpha$ results, eq. [3]. Experimental geometries were used throughout the LCGTO-Xα(LSD) calculations of the alkanes and amines but additional verifications have indicated that equally consistent results can be obtained with the systematic use of theoretical (STO-3G and 4-31G) geometries. The geometries of the radicals were derived from 4-31G computations. For each molecule we have calculated the total Xα(LSD) energy using an initial guess, α^0, for α. This yields an approximate value of E, namely $E^0 = E^0(\alpha^0)$. Next, we have estimated an improved α value, $\alpha = \alpha^0 + \Delta\alpha$, using the experimental E of Table 1 and the formula

$$[4] \quad E = E^0 + \Delta\alpha(\partial E/\partial\alpha)$$

and repeated the procedure until convergence was attained. In practice, with a little experience as regards the initial guess, two calculations suffice. We tentatively proceed with the idea that, under proper circumstances, Xα-LSD calculation effectively mimic correlated calculations, although there is presently no formal justification for this contention.

The α's obtained for the individual molecules listed in Table 1 differ significantly from one another. Indeed, a recalculation using one single α value for the alkanes and the alkyl radicals, namely the best possible one, 0.778, leads to sizeable errors,

TABLE 1. Experimental energies (hartree) and corresponding α and $\partial E/\partial\alpha$ values of selected molecules[a]

Molecule	E	α	$\partial E/\partial\alpha$
Methane	−40.5239	0.781456	−8.8724
Ethane	−79.8439	0.779431	−16.8329
Propane	−119.1675	0.778775	−24.7737
Butane	−158.4919	0.778374	−32.6977
Isobutane	−158.4944	0.778420	−32.8057
Pentane	−197.8163	0.778257	−40.6647
Neopentane	−197.8223	0.778250	−40.7891
Cyclopropane	−117.9236	0.777459	−23.8986
Cyclobutane	−157.2503	0.777488	−31.8998
Cyclopentane	−196.6066	0.777323	−39.9270
Cyclohexane	−235.9408	0.777466	−47.7890
Spiropentane	−195.3208	0.776547	−38.9909
Methyl·	−39.8465	0.780721	−8.3612
Ethyl·	−79.1721	0.778869	−16.3537
Propyl·	−118.4967	0.778313	−24.3458
Isobutyl·	−157.8248	0.777880	−32.3452
tert-Butyl·	−157.8342	0.778009	−32.3452
Cyclopropyl·	−117.2432	0.776944	−23.4430
Cyclopropylcarbinyl·	−156.5838	0.776824	−31.4424
Cyclobutyl·	−156.5841	0.777180	−31.4127
Ammonia	−56.5858	0.776920	−10.4256
Methylamine	−95.8945	0.776901	−18.3777
Ethylamine	−135.2187	0.776944	−26.3533
Dimethylamine	−135.2077	0.776917	−26.3424
Isopropylamine	−174.5482	0.776945	−34.3344
tert-Butylamine	−213.8778	0.776949	−42.3198
Diethylamine	−213.8587	0.776940	−42.3038
Azirane	−133.9696	0.775816	−25.4346
Pyrrolidine	−212.6500	0.776112	−41.4130
Piperidine	−251.9848	0.776270	−49.4130

[a]The energy of spiropentane was calculated from eqs. [1] and [2] using ZPE + $(H_T - H_0)$ = 73.56 kcal mol^{-1}, obtained in the harmonic oscillator approximation from experimental frequencies (20) and ΔH_f^0 = 44.25 kcal mol^{-1} selected by Cox and Pilcher (21). The appropriate ΔE_a^* energies for the other alkanes (7) and selected alkyl radical (9) were given earlier. In addition, we have used ΔH_f^0 = 51.1 ± 1.6 (cyclopropylcarbinyl radical) (22) and 51.2 ± 1.0 kcal mol^{-1} (cyclobutyl radical) (23); their ZPE + $(H_T - H_0)$ energies were estimated at 61.26 and 61.55 kcal mol^{-1}, respectively, by subtracting 8.85 kcal mol^{-1} from the ZPE + $(H_T - H_0)$ values of the corresponding hydrocarbons, following an empirical rule described elsewhere (9). For the nitrogen compounds we have used standard ΔH_f^0 results (21) and reported values for the ZPE + $(H_T - H_0)$ energies (10). The experimental geometry (24) of azirane was used, whereas those of piperidine and pyrrolidine are calculated (STO-3G) values.

Can. J. Chem. Downloaded from www.nrcresearchpress.com by 122.72.124.2 on 09/07/12
For personal use only.

Can. J. Chem. Downloaded from www.nrcresearchpress.com by 122.72.124.2 on 09/07/12
For personal use only.

TABLE 2. A comparison between $\partial E/\partial\alpha$ and $\alpha(\partial E/\partial\alpha)$ given by eqs. [5] and [6], respectively, and their Xα(LSD) counterparts

Molecule	$(\partial E/\partial\alpha)$, a.u.		$\alpha(\partial E/\partial\alpha)$, a.u.	
	Eq. [5]	Xα(LSD)	Eq. [6]	Xα(LSD)
Methane	−8.85	−8.87	−6.91	−6.93
Ethane	−16.82	−16.83	−13.11	−13.12
Propane	−24.79	−24.77	−19.30	−19.29
Butane	−32.76	−32.70	−25.50	−25.45
Isobutane	−32.76	−32.81	−25.50	−25.54
Pentane	−40.73	−40.66	−31.70	−31.65
Neopentane	−40.73	−40.79	−31.70	−31.74
Cyclopropane	−23.92	−23.90	−18.59	−18.58
Cyclobutane	−31.89	−31.90	−24.79	−24.80
Cyclopentane	−39.86	−39.93	−30.99	−31.04
Cyclohexane	−47.83	−47.79	−37.18	−37.15
Spiropentane	−38.99	−38.99	−30.28	−30.28
Methyl·	−8.41	−8.36	−6.56	−6.53
Ethyl·	−16.38	−16.35	−12.75	−12.74
Propyl·	−24.35	−24.35	−18.95	−18.95
Isobutyl·	−32.33	−32.35	−25.15	−25.16
tert-Butyl·	−32.33	−32.35	−25.15	−25.16
Cyclopropyl·	−23.48	−23.44	−18.24	−18.21
Cyclopropylcarbinyl·	−31.45	−31.44	−24.44	−24.43
Cyclobutyl·	−31.45	−31.41	−24.44	−24.41
Ammonia	−10.42	−10.43	−8.08	−8.10
Methylamine	−18.39	−18.38	−14.28	−14.28
Ethylamine	−26.36	−26.35	−20.48	−20.48
Dimethylamine	−26.36	−26.34	−20.48	−20.47
Isopropylamine	−34.33	−34.33	−26.68	−26.68
tert-Butylamine	−42.30	−42.32	−32.87	−32.88
Diethylamine	−42.30	−42.30	−32.87	−32.87
Azirane	−25.49	−25.43	−19.76	−19.73
Pyrrolidine	−41.43	−41.41	−32.17	−32.14
Piperidine	−49.40	−49.41	−38.37	−38.36

averaging 13.5 kcal mol^{-1} for the alkanes and 10.7 kcal mol^{-1} for the radicals. Clearly, we have to account for the variations of α in these classes of compounds, even though they may seem small at first sight. For the aliphatic amines, in contrast, one singla α value could do, namely α = 0.776936 (average error = 0.23 kcal mol^{-1}).

Inspection of the results (Table 1) indicates that the $\partial E/\partial\alpha$ derivatives linearly depend on the numbers of atoms of each species found in the molecule. In writing

$$[5]\quad \frac{\partial E}{\partial\alpha} = \sum_i n_i\left(\frac{\partial E_i}{\partial\alpha}\right)$$

we express the idea that $\partial E/\partial\alpha$ is, at least to a good approximation, the sum of individual atomic contributions, $\partial E_i/\partial\alpha$. Equation [5] is, indeed, satisfied with $\partial E_H/\partial\alpha = -0.437$, $\partial E_C/\partial\alpha = -7.098$, and $\partial E_N/\partial\alpha = -9.105$ au (Table 2). In addition, it appears that our exchange-correlation energies, $\alpha(\partial E/\partial\alpha)$, are also linearly related to the n_i's, i.e.,

$$[6]\quad \alpha\left(\frac{\partial E}{\partial\alpha}\right) = \sum_i n_i\alpha_i\left(\frac{\partial E_i}{\partial\alpha}\right)$$

where each $\alpha_i(\partial E_i/\partial\alpha)$ plays the role of a local "atomic" contribution to $\alpha(\partial E/\partial\alpha)$, that of atom i, α_i being the corresponding "atomic" α. The genuine Xα-LSD results are well given by eq. [6] with $\alpha_H(\partial E_H/\partial\alpha) = -0.357$, $\alpha_C(\partial E_C/\partial\alpha) = -5.484$, and $\alpha_N(\partial E_N/\partial\alpha) = -7.011$ au (Table 2). Briefly, both $\partial E/\partial\alpha$ and $\alpha(\partial E/\partial\alpha)$ satisfy, in a first approximation, simple atom-by-atom additivity rules. As a consequence, it

TABLE 3. Predicted α values and a comparison of the corresponding Xα(LSD) atomization energies with their thermochemical counterparts[a]

Molecule	α	ΔE_a^*, kcal mol^{-1}	
		Xα(LSD)	Thermochem.
Methane	0.781263	418.17	419.24
Ethane	0.779446	710.69	710.54
Propane	0.778797	1004.42	1004.08
Butane	0.778465	1300.00	1298.15
Isobutane	0.778465	1300.63	1299.70
Pentane	0.778262	1592.31	1592.18
Neopentane	0.778262	1596.25	1595.94
Cyclopropane	0.777429	850.58	851.0
Cyclobutane	0.777429	1145.35	1146.5
Cyclopentane	0.777429	1462.25	1460.6
Cyclohexane	0.777429	1759.71	1760.80
Spiropentane	0.776559	1281.53	1281.23
Methyl·	0.780699	307.77	307.89
Ethyl·	0.778922	603.28	602.73
Propyl·	0.778309	896.82	896.88
Isobutyl·	0.777998	1195.66	1193.26
tert-Butyl·	0.777998	1198.94	1199.16
Cyclopropyl·	0.776912	737.36	737.83
Cyclopropylcarbinyl·	0.776947	1044.46	1042.04
Cyclobutyl·	0.776947	1037.63	1042.23
Ammonia	0.776900	297.18	297.26
Methylamine	0.776925	581.72	581.45
Ethylamine	0.776934	875.22	875.38
Dimethylamine	0.776934	868.77	868.47
Isopropylamine	0.776939	1172.50	1172.62
tert-Butylamine	0.776943	1469.77	1469.94
Diethylamine	0.776943	1458.03	1457.96
Azirane	0.775604	715.71	719.09
Pyrrolidine	0.776124	1327.32	1327.01
Piperidine	0.776259	1627.25	1627.60

[a]The ΔE_a^* values are indicated with a precision which is in many cases not warranted by our actual knowledge, particularly as regards the radicals (9). They are used here primarily to facilitate recalculations without being continually bothered by rounding-off errors. None of the conclusions reached in this paper critically depends on the precision of the data given here.

follows that

$$[7]\quad \alpha = \frac{\sum_i n_i\alpha_i(\partial E_i/\partial\alpha)}{\sum_i n_i(\partial E_i/\partial\alpha)}$$

showing that the molecular α can be understood as a weighted average governed by the composition of the molecule. We shall now test eq. [7] for its appropriateness as a source of sufficiently accurate α's for use in Xα(LSD) calculations of molecular energies.

Results

Here we examine the average molecular α's deduced from eq. [7]. These are used in LCAO-Xα(LSD) computations of E. The latter, in turn, give access to ΔE_a^*, eq. [1]. The theoretical atomization energies thus obtained, using 1 hartree = 627.51 kcal mol^{-1}, are compared in Table 3 with their experimental counterparts, eq. [2]. The $\partial E_i/\partial\alpha$ values for use in eq. [7] are those indicated earlier, as they were derived from eq. [5].

A statistical data analysis indicates that $\alpha_H = 0.816235$ and $\alpha_C = 0.772651$ minimize the errors of the ΔE_a^*'s computed for the hydrocarbons. The average deviation is 0.78 kcal mol^{-1}. For the radicals and the amines we have proceeded with the

TABLE 4. A comparison between theoretical and experimental strain energies[a]

Molecule	Strain energy, kcal mol^{-1}	
	Xα(LSD)	Exptl.
Cyclohexane	0	0
Cyclopentane	4.2	6.7
Cyclobutane	27.8	27.4
Cyclopropane	29.3	29.4
Spiropentane	59.2	60.2
Piperidine	0	0
Pyrrolidine	6.8	7.1
Azirane	31.7	28.1

[a]The "model" ΔE_a^* values with reference to cyclohexane (with zero strain energy) are deduced from $(1/6)\Delta E_a^*$ of cyclohexane times the number of CH_2 groups in the cycle. Strain energy is defined in each case as the difference between the "model" ΔE_a^* and the corresponding genuine value. For spiropentane we have estimated the contribution of the quaternary carbon from spiro [5,5]undecane (7), $\Delta E_a^* = 3102.24$ kcal mol^{-1}, less 10 cyclohexane-like CH_2 groups, at 167.57 kcal mol^{-1}. The "model" ΔE_a^* of spiropentane is obtained by adding 4 cyclohexane-like CH_2 contributions to that of the quaternary carbon and the strain energy is defined as above with respect to the genuine ΔE_a^*.

same α_H and α_C parameters plus, in a first approach, $\alpha_{C\cdot} = 0.773103$ (for the radical C atom) and $\alpha_N = 0.770076$ for nitrogen. The average deviations, 2.57 and 2.95 kcal mol^{-1} for the radicals and the amines, respectively, are acceptable considering that with $\partial E/\partial\alpha$ values ranging from -8 to -40 au an error of 0.001 in the estimate of α translates into a ~5–25 kcal mol^{-1} error for ΔE_a^*. A reevaluation of the results, however, reveals a regular trend in the errors made for the aliphatic amines, from a too small ΔE_a^* for NH_3 (by 6.76 kcal mol^{-1}) to a too large ΔE_a^* for $C_4H_9NH_2$ (by $\sim 2.7 \pm 0.1$ kcal mol^{-1}). This observation prompted us to examine the possibility that the parameters determined for the hydrocarbons are perhaps not exactly transferable to other classes of compounds. This may be so on physical grounds or only appear that way as a result of approximations involved in the present form and use of Xα(LSD) theory, not to forget possible superposition errors like those discussed for conventional *ab initio* calculations of ammonia and alkylamines (25) and, more generally, for computations involving hydrogen basis sets which are not adequately balanced (26). In either event, it requires only a modest correction in order to achieve a significant improvement of the results. Using now $\alpha_{C\cdot} = 0.774589$ and $\alpha_N = 0.771777$ in eq. [7], as well as the α_H and α_C values of the alkanes, we multiply the α's thus obtained by 0.99951 (radicals) or 0.999392 (amines). The averages of the errors which are now normally distributed, meaning that they do not follow any trend with molecular size, drop to 1.35 and 0.17 kcal mol^{-1} for the radicals and the aliphatic amines, respectively (Table 3). This fine-tuning is visibly important if we desire to approach experimental results as closely as possible. On the other hand, considering the smallness of the required correction, it is also clear that eq. [7] basically represents a valid approximation for α.

A good insight is offered by the cycloalkanes C_3H_6 to C_6H_{12}. Their thermochemical stabilities reflect an important destabilizing effect, the strain energy, accompanying the shrinking of a ring. Because all these cycloalkanes have the same composition, $(CH_2)_n$, they also have the same α, eq. [7], for use in our Xα(LSD) calculations. The quality of the results (Table 4) strongly suggests that the very strained cyclopropane and the strain-free cyclohexane are, indeed, to be treated in precisely the same manner in applications of eq. [7]. This, of course, implies the persistence, even in highly strained systems, of simple additivity as far as exchange-correlation energies are concerned. A similar conclusion holds true for the nitrogen-containing small cycles.

Conclusions

Postulating that the local spin density approximation in its present LCGTO-Xα(LSD) form effectively mimics correlated calculations[1] the results obtained for a variety of organic systems indicate that, as a rule, α differs from molecule to molecule. Inspection of the results reveals that both the exchange-correlation term, $\alpha(\partial E/\partial\alpha)$, and $(\partial E/\partial\alpha)$ itself behave, at least to a good approximation, as additive properties in that they are linearly dependent on the number of atoms of each chemical species found in a molecule. As a consequence, the appropriate α's for use in Xα(LSD) calculations appear as weighted averages depending on the composition of the molecules under scrutiny. These average α's, constructed from theoretical $\alpha(\partial E/\partial\alpha)$ and $(\partial E/\partial\alpha)$ values obtained for a representative collection of molecules, lead to satisfactory evaluations of atomization energies, thus demonstrating the at least approximate validity of our averaging procedure.[2] Numerical analyses reveal that the agreement between calculated and experimental atomization energies can be further improved if the average α's deduced for the alkyl radicals and the amines are systematically reduced by 0.049 and 0.061%, respectively. A formal justification for these corrections cannot be given but their very smallness suggests that our averaging procedure is basically efficient. The deviations between calculated and experimental results are, indeed, remarkably small (0.85 kcal mol^{-1} on the average) in situations where an error of 0.001 in the evaluation of α translates into a 5–30 kcal mol^{-1} error in atomization energy. It seems thus reasonable to hope that the present results may serve as useful guidelines in the search for accurate theoretical derivations of α in molecular systems, perhaps along the lines developed by Gáspár and Nagy which represent an important step in that direction.

Acknowledgements

We wish to express our gratitude to Professor D. Salahub for helpful discussions. The financial support given by the Natural Sciences and Engineering Research Council of Canada is gratefully acknowledged. We also express our gratitude to DRET for financial assistance to one of us (E.C.V.).

[1]The Xα approach in itself contains only the exchange term, but the present Xα(LSD) calculations are meant to include correlation as well. For an alternate way of effectively incorporating correlation in LSD, see ref. 27.

[2]The use of the familiar exchange parameters α_{HF} given by Schwarz (28), i.e., 0.77725 for H and 0.75928 for C, obtained from an adjustment of the statistical total energies to the Hartree–Fock total energies of the isolated atoms, is not appropriate. They do, indeed, lead to large discrepancies depending on molecular size, ranging from ~104 (CH_4) to ~486 kcal mol^{-1} (C_6H_{12}). The results can be empirically improved if the average molecular α's obtained from these atomic parameters are systematically multiplied by 1.02162, but the average error still remains large, ~8 kcal mol^{-1}.

Can. J. Chem. Downloaded from www.nrcresearchpress.com by 122.72.124.2 on 09/07/12
For personal use only.

1. P. HOHENBERG and W. KOHN. Phys. Rev. **136**, B864 (1964).
2. W. KOHN and L. J. SHAM. Phys. Rev. **140**, A1133 (1965).
3. D. R. SALAHUB. Adv. Chem. Phys. **69**, 447 (1987); J. P. DAHL and J. AVERY (*Editors*). Local density approximations in quantum chemistry and solid state physics. Plenum, New York. 1984; S. LUNDQVIST and N. H. MARCH (*Editors*). Theory of the inhomogeneous electron gas. Plenum, New York. 1983.
4. U. VON BARTH and L. HEDIN. J. Phys. C.: Solid State Phys. **5**, 1629 (1972).
5. R. GÁSPÁR. Acta Phys. Acad. Sci. Hung. **3**, 263 (1954).
6. C. E. MOORE. Nat. Stand. Ref. Data Ser. (US Nat. Bur. Stand.) NSRD-NBS **34**, 1 (1970).
7. S. FLISZÁR. Charge distributions and chemical effects. Springer-Verlag, New York. 1983.
8. D. R. STULL and G. C. SINKE. Adv. Chem. Ser. **18**, (1956).
9. S. FLISZÁR and C. MINICHINO. Can. J. Chem. **65**, 2495 (1987).
10. S. FLISZÁR, F. POLIQUIN, I. BĂDILESCU, and E. VAUTHIER. Can. J. Chem. **66**, 300 (1988).
11. H. SAMBE and R. H. FELTON. J. Chem. Phys. **62**, 1122 (1975).
12. B. I. DUNLAP, J. W. D. CONNOLLY, and J. R. SABIN. J. Chem. Phys. **71**, 3386 (1979); **71**, 4993 (1979).
13. S. HUZINAGA. J. Chem. Phys. **42**, 1293 (1965).
14. T. H. DUNNING. J. Chem. Phys. **55**, 716 (1970).
15. F. HERMAN and S. SKILLMAN. Atomic structure calculations. Prentice-Hall, Englewood Cliffs, NJ. 1963.
16. A. H. STROUD. Approximate calculation of multiple integrals. Prentice-Hall, Englewood Cliffs, NJ. 1971.
17. J. C. SLATER. Phys. Rev. **81**, 385 (1951); J. C. SLATER. Adv. Quantum Chem. **6**, 1 (1972); J. C. SLATER. The self-consistent field for molecules and solids. Vol. 4. McGraw-Hill, New York. 1974.
18. R. GÁSPÁR and Á. NAGY. Theor. Chim. Acta, **72**, 393 (1987); Á. NAGY. Int. J. Quantum Chem. **31**, 269 (1987); R. GÁSPÁR. Acta Phys. **35**, 213 (1974).
19. E. J. BAERENDS and P. ROS. Chem. Phys. **2**, 52 (1973).
20. G. R. BURNS and D. G. MCGAVIN. Appl. Spectrosc. **26**, 540 (1972).
21. J. D. COX and G. PILCHER. Thermochemistry of organic and organometallic compounds. Academic Press, New York. 1970.
22. D. F. MCMILLEN, D. M. GOLDEN, and S. W. BENSON. Int. J. Chem. Kinet. **3**, 359 (1971).
23. K. C. FERGUSON and E. WHITTLE. Trans. Faraday Soc. **67**, 2618 (1971).
24. A. KOMORNICKI, F. PAUZAT, and Y. ELLINGER. J. Phys. Chem. **87**, 3847 (1983).
25. G. DEL RE, S. FLISZÁR, M. COMEAU, and C. MIJOULE. Can. J. Chem. **63**, 1487 (1985).
26. W. KOLOS. Theor. Chim. Acta, **54**, 187 (1980); W. A. SOKALSKI. J. Chem. Phys. **77**, 4529 (1982); J. G. M. VAN DUIJNEVELDT-VAN DE RIJDT and F. B. VAN DUIJNEVELDT. J. Mol. Struct. Theochem. **89**, 185 (1982).
27. H. STOLL, E. GOLKA, and H. PREUSS. Theoret. Chim. Acta, **55**, 29 (1980).
28. K. SCHWARZ. Phys. Rev. B**5**, 2466 (1972).

Can. J. Chem. Downloaded from www.nrcresearchpress.com by 122.72.124.2 on 09/07/12
For personal use only.

Excess partial molar enthalpies of water in water–*tert*-butanol mixtures

YOSHIKATA KOGA

Department of Chemistry, University of British Columbia, Vancouver, B.C., Canada V6T 1Y6

This paper is dedicated to Professor Charles A. McDowell on the occasion of his seventieth birthday

Received May 19, 1988

YOSHIKATA KOGA. Can. J. Chem. **66**, 3171 (1988).

The excess partial molar enthalpies of H_2O, $H_m^E(H_2O)$, in water–*tert*-butanol mixtures were measured at 30.00, 36.75, and 40.45°. Using the values of H_m^E(TBA) of the previous work (Y. Koga, Can. J. Chem. **66**, 1187 (1988)), the excess (integral) molar enthalpies of the solution, H_m^E, were calculated at 30.00°C, and compared with the literature values. The comparison was satisfactory. From the literature values of the excess free energy, the chemical potentials of each component were evaluated for the range, $x_{TBA} > 0.1$. With the measured values of the excess partial molar enthalpies, the excess partial molar entropies were also calculated. These partial molar thermodynamic quantities and their dependence on temperature and composition clearly support the following views: (*1*) in the intermediate region, $0.1 < x_{TBA} < 0.5$, the system is very close to a critical demixing, and (*2*) in the TBA-rich region, $x_{TBA} > 0.6$, TBA molecules in the solution are in almost the same environment as in the pure liquid, while H_2O molecules lose the hydrogen bond network completely and are dispersed in the TBA liquid structure.

YOSHIKATA KOGA. Can. J. Chem. **66**, 3171 (1988).

On a mesuré les enthalpies molaires partielles en excès du H_2O, $H_m^E(H_2O)$, dans des mélanges eau–*tert*-butanol à 30,00, 36,75 et 40,45°C. Utilisant les valeurs du H_m^E(TBA) de travaux antérieurs (Y. Koga, J. Can. Chem. **66**, 1187 (1988)), on a calculé les enthalpies molaires (intégral) en excès à 30,00°C, du H_m^E en solution et on les a comparées aux valeurs existantes. La comparaison s'est révélée satisfaisante. A partir des valeurs d'énergie libre répertoriées dans la littérature, on a évalué les potentiels chimiques de chaque composante dans l'intervalle de $x_{TBA} > 0,1$. On a également calculé les entropies molaires en excès à partir des valeurs mesurées des enthalpies molaires partielles en excès. Ces quantités thermodynamiques partielles en excès, leurs relations avec la température et la composition confirment nettement les faits suivants : (*1*) dans la région intermédiaire, $0,1 < x_{TBA} < 0,5$, le système est très près de la démixion critique, et (*2*) dans la région riche en TBA, $x_{TBA} > 0,6$, les molécules de TBA en solution sont à peu près dans le même environnement que dans le liquide pur; par ailleurs, les molécules de H_2O perdent complètement le réseau de liaisons hydrogènes et se dispersent dans la structure du TBA.

[Traduit par la revue]

Introduction

In the previous papers (called paper I (1) and II (2) hereinafter), results were reported on the excess partial molar enthalpies of *tert*-butanol (TBA) in TBA–H_2O mixtures, H_m^E(TBA). While this system had been investigated previously (3, 4), it was the first time that the *partial* molar enthalpies were measured directly for the TBA–water mixtures. Generally, evaluation of these quantities is possible by differentiating the existing values of excess (integral) molar enthalpies, H_m^E. One difficulty is, however, that differentiation magnifies errors and uncertainties, and the resulting values of the partial molar enthalpies are not accurate enough for detailed discussion. Indeed, the importance and usefulness of directly measured excess partial molar enthalpies have been demonstrated some time ago for ethanol–water and methanol–water mixtures (23). Thus it was chosen to measure the excess partial molar enthalpies directly for TBA–water mixtures in papers I (1) and II (2).

The results of papers I and II provided more direct information on the nature of solute–solvent and solute–solute interactions, and indicated clearly that there were two distinct regions bounded at about $x_{TBA} = 0.07$. The values of H_m^E(TBA) at $x_{TBA} \approx 0$ and the temperature dependence showed that TBA molecules not only form hydrogen bonds towards H_2O molecules for an enthalpy gain but also induce more hydrogen bondings among the solvent H_2O molecules for an equally, if not more, substantial enthalpy gain. The latter effect has been termed "iceberg formation", or in a more recent terminology, "structure enhancement of the solvent" (5–8). It was pointed out in paper II that such an effect was long range. At $x_{TBA} \approx 0.001$, the value of H_m^E(TBA) becomes less negative than that at a lower concentration, indicating that the solute–solute interaction is apparently repulsive. This suggests that already at this concentration TBA molecules have more enthalpic difficulty in settling into the solution, i.e. the structure enhancement by a previously settled TBA molecule spans a long range. If TBA molecules are distributed randomly among H_2O molecules without any preferential association, a TBA molecule is surrounded by $(1 - x_{TBA})/x_{TBA}$ molecules of H_2O, about 1000 molecules in this case at $x_{TBA} = 0.001$. Assuming that such H_2O molecules surround in a spherical fashion, the radius, n_r, in terms of number of molecule, would be about 6, $[(4/3)\pi 6^3 = 904]$.

As x_{TBA} increases and the TBA–TBA distance, $2n_r$, becomes smaller, the apparent solute–solute repulsion increases sharply to a threshold, beyond which such an apparent enthalpic repulsion diminishes rapidly to almost zero. As to the number, k, of H_2O molecules surrounding a TBA molecule in the form of $TBA(H_2O)_k$, the above threshold values corresponded to k = 16, 20, and 23 at 26.90, 45.17, and 59.49°C, respectively (2), in comparison with k = 15–19, 21, and 21–25 for 17.5, 24, and 63°C obtained from light scattering measurements (9, 10).

In the second region, $x_{TBA} > 0.1$, the values of H_m^E(TBA) become small with almost no dependence on composition and temperature, suggesting that the environment of TBA molecules in the solution is almost the same as that in pure TBA liquid. This is not inconsistent with closeness to a probable critical demixing, as pointed out previously (11–13).

In the present work, the excess partial molar enthalpies of H_2O in the solution, $H_m^E(H_2O)$, were measured directly at 30.00, 36.75, and 40.45°C. It was not expected that the values of $H_m^E(H_2O)$ and their dependence on composition and temperature might add any qualitatively newer insight into the nature of this solution, since H_m^E(TBA) and $H_m^E(H_2O)$ are

Can. J. Chem. Downloaded from www.nrcresearchpress.com by 122.72.124.2 on 09/07/12
For personal use only.

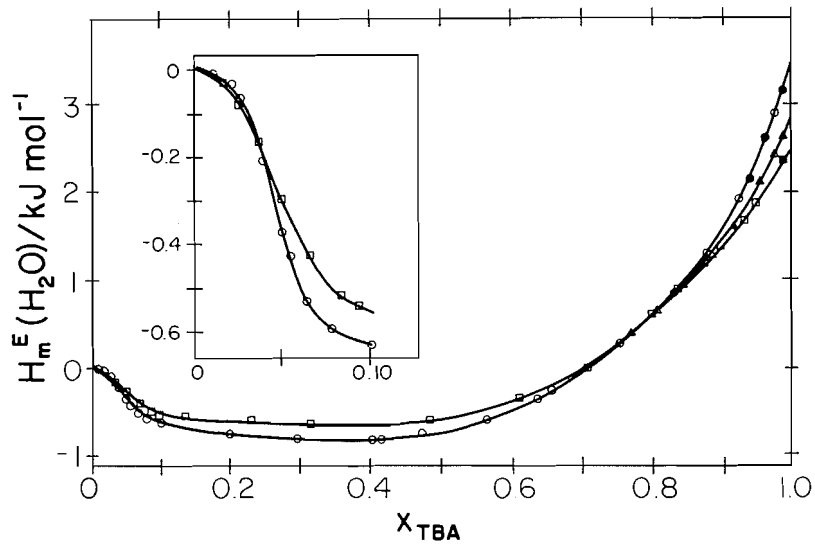

FIG. 1. The excess partial molar enthalpies of H_2O against the mole fraction. ●,○, 30.00°C; ▲,△, 36.75°C; ■,□, 40.45°C. Filled symbols, $\Delta n_{H_2O} = 0.03$ mol; open symbols, $\Delta n_{H_2O} = 0.05$ mol.

not independent, being related by the Gibbs–Duhem relation. However, the values of the measured $H_m^E(H_2O)$ together with those of $H_m^E(TBA)$ in papers I and II enable an accurate evaluation of the excess (integral) molar enthalpies, which will then be compared directly with the literature values (14, 15). This was the original purpose of the present work. It turned out, however, that the measured values of $H_m^E(H_2O)$ show a clearly different behaviour in another, the third region, $x_{TBA} > 0.6$, as will be shown below. Furthermore, an unexpectedly clearer indication was obtained for a precursor of a critical demixing in the intermediate range, $0.1 < x_{TBA} < 0.5$ when the chemical potentials were calculated from the existing excess molar free energy data (15) for the purpose of estimating the excess partial molar entropies. This will also be discussed below.

Experimental

The excess partial molar enthalpies were measured by means of an LKB Bromma 8700 precision calorimetry system, following the same procedure as described elsewhere (1, 2, 22). The results were calculated as $H_m^E(H_2O) = \Delta H/\Delta n_{H_2O}$, where ΔH is the enthalpy change of the mixture of about 100 mL due to the addition of a small amount of H_2O, Δn_{H_2O} (~0.05 mol). The above relation, $H_m^E(H_2O) = \Delta H/\Delta n_{H_2O}$, is correct if Δn_{H_2O} is sufficiently small in comparison with the total amount of the mixture. In the worst situation, i.e. at $x_{TBA} \approx 1$, where the total amount of the mixture is about 1 mol, several runs were performed with a reduced amount of H_2O increment (~0.03 mol). As shown below (Fig. 1), the data points with the two different sets of increments appear to lie on the smooth curve within the experimental error. This indicates that $\Delta n_{H_2O} = 0.05$ mol is sufficiently small for the entire concentration range. The experimental error in $H_m^E(H_2O)$ was estimated to be ± 0.015 kJ mol^{-1}.

Result and discussion

The measured values of $H_m^E(H_2O)$ are listed in Table 1 and plotted in Fig. 1. As is apparent from the figure, there is the third region, $x_{TBA} > 0.6$, where the composition dependence is different from those in the water-rich region, $x_{TBA} < 0.07$, and the intermediate region, $0.1 < x_{TBA} < 0.5$. The difference between the latter two regions was conspicuous in the composition dependence of $H_m^E(TBA)$, but the difference of the third TBA-rich region from the second intermediate region was not quite apparent in papers I and II. The excess partial molar heat capacities of H_2O, $C_p^E(H_2O)$, were calculated as $\{H_m^E(H_2O, T_1) - H_m^E(H_2O, T_2)\}/(T_1 - T_2)$ and listed in Table 2. Towards $x_{TBA} \approx 1$, the value of $H_m^E(H_2O)$ is positive, and the absolute values of $C_p^E(H_2O)$ are of the same magnitude as the heat capacity of pure H_2O with the negative sign. These may suggest that H_2O loses its hydrogen bond network completely and mixes into the solution as a single molecule. This point will be touched upon later, using the calculated excess partial molar entropies of TBA and H_2O.

Now that the values of $H_m^E(H_2O)$ and those of $H_m^E(TBA)$ at 30.00°C (2) are available, the excess (integral) molar enthalpies, H_m^E, of this solution are calculated and plotted in Fig. 2 together with the literature values (14, 15). The comparison appears satisfactory, and hence confidence can be placed on the values of $H_m^E(TBA)$ (1, 2) and those of $H_m^E(H_2O)$.

If the excess partial molar free energies of TBA and H_2O are available, the excess partial molar entropies can now be calculated. The latter quantities may shed more light on the nature of the solution. Kenttamaa *et al.* have measured among other quantities the isothermal vapour pressures of the mixtures (14). Their data, however, are spotty in terms of composition and temperature. Quitzsch *et al.* obtained isobars (16), while Okamoto *et al.* (17) measured the freezing points in a water-rich region ($x_{TBA} < 0.02$) and determined the second virial coefficient of the excess free energy. With only the second virial coefficient at 25°C, however, the excess free energies can be calculated accurately only in the very water-rich region, $x_{TBA} < 0.003$ (18). Thus all these data need various corrections to be applied before they become useful for the present purpose. On the other hand, Westmeier (15) reviewed in 1977 all the available data and compiled the best values of the excess molar free energies, G_m^E, at every 10 K from 273.15 to 373.15 K and from $x_{TBA} = 0.1$ to 0.9.

It is therefore elected to calculate the excess partial molar free energies, $G_m^E(H_2O)$ and $G_m^E(TBA)$, at 303.15 K from Westmeier's values of G_m^E for $0.1 < x_{TBA} < 0.9$. This will inevitably leave out the most interesting region, $x_{TBA} < 0.07$. More complete data are necessary for further discussion in that region.

Can. J. Chem. Downloaded from www.nrcresearchpress.com by 122.72.124.2 on 09/07/12
For personal use only.

Can. J. Chem. Downloaded from www.nrcresearchpress.com by 122.72.124.2 on 09/07/12
For personal use only.

TABLE 1. Excess partial molar enthalpies of H_2O

x_{H_2O}	x_{TBA}	$H_m^E(H_2O)$/kJ mol^{-1}
	T = 30.00°C	
0.01406	0.98594	3.170
0.02501	0.97499	2.914
0.03904	0.96096	2.620
0.05842	0.94158	2.150
0.07618	0.92382	1.939
0.1243	0.8757	1.295
0.1671	0.8329	0.840
0.2457	0.7543	0.262
0.3411	0.6589	−0.265
0.3648	0.6352	−0.364
0.4345	0.5655	−0.586
0.5280	0.4720	−0.751
0.5866	0.4134	−0.799
0.5919	0.4081	−0.807
0.5975	0.4025	−0.808
0.7049	0.2951	−0.793
0.8021	0.1979	−0.753
0.8985	0.1015	−0.626
0.9227	0.0773	−0.594
0.9353	0.0647	−0.528
0.9446	0.0554	−0.421
0.9489	0.0511	−0.369
0.9612	0.0388	−0.210
0.9666	0.0334	−0.125
0.9717	0.0283	−0.063
0.9778	0.0222	−0.031
0.9826	0.0174	−0.028
0.9892	0.0108	−0.005
	T = 36.75°C	
0.01339	0.98661	2.663
0.02462	0.97538	2.431
0.04663	0.95337	2.145
0.07346	0.92654	1.659
0.08581	0.91419	1.615
0.11735	0.88265	1.278
0.1574	0.8426	0.929
0.1958	0.8042	0.633
0.2313	0.7687	0.390
	T = 40.45°C	
0.01733	0.98267	2.386
0.05387	0.94613	1.866
0.07409	0.92591	1.675
0.1027	0.8973	1.372
0.1263	0.8737	1.194
0.1663	0.8337	0.863
0.2024	0.7976	0.598
0.2924	0.7076	−0.023
0.3901	0.6099	−0.363
0.5167	0.4833	−0.601
0.6847	0.3153	−0.644
0.7720	0.2280	−0.598
0.8646	0.1354	−0.530
0.9064	0.0936	−0.539
0.9161	0.0839	−0.517
0.9324	0.0676	−0.421
0.9503	0.0497	−0.295
0.9632	0.0368	−0.163
0.9756	0.0244	−0.078
0.9838	0.0162	−0.027

TABLE 2. Excess partial molar heat capacities of H_2O

		$C_p^E(H_2O)$/J K^{-1} mol^{-1}		
x_{H_2O}	x_{TBA}	30.00–36.75°C	36.75–40.45°C	30.00–40.45°C
0.0	1.0	−100.7	−81.1	−93.8
0.02	0.98	−75.6	−62.0	−70.7
0.05	0.95	−45.9	−40.5	−44.0
0.075	0.925	−38.5	−13.5	−29.7
0.125	0.875			−9.7
0.2	0.8			0.0
0.25	0.75			0.2
0.375	0.625			0.7
0.525	0.475			1.4
0.625	0.375			1.5
0.7	0.3			1.5
0.8	0.2			1.3
0.9	0.1			0.7
0.92	0.08			0.9
0.95	0.05			0.6
0.96	0.04			0.0
0.975	0.025			−0.2
0.985	0.015			−0.1
1.0	0.0			0.0

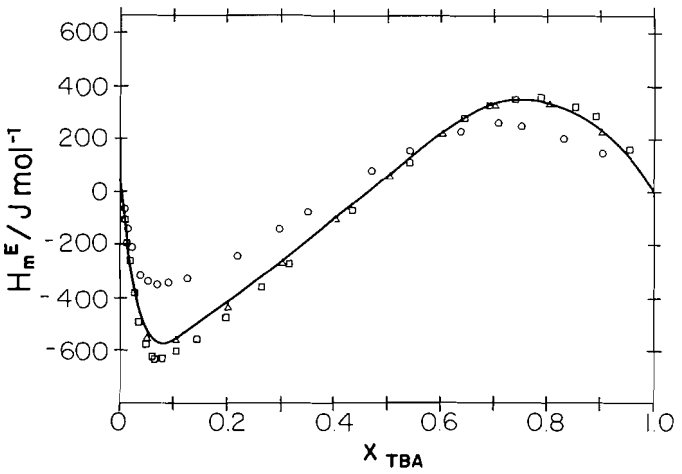

FIG. 2. The excess (integral) molar enthalpies against the mole fraction. △, Westmeier, 30°C, ref. 15; □, Kenttamaa, 26°C, ref. 14; ○, Kenttamaa, 40°C, ref. 14; smooth curve, 30.00°C, this work.

The values of G_m^E appear to vary smoothly and nearly symmetrically with composition (15). It may therefore be possible to curve-fit the following equation (19) to these data points,

$$[1] \quad G_m^E = x_{TBA}(1 - x_{TBA})\sum_j a_j(1 - 2x_{TBA})^{j-1}$$

Equation [1] serves only as an empirical formula, from which the excess partial molar free energy, $G_m^E(i)$, and the chemical potential, μ_i, (i = H_2O or TBA) can be calculated algebraically.

$$[2] \quad G_m^E(i) = G_m^E + (1 - x_i)(\partial G_m^E/\partial x_i)$$

and

$$[3] \quad \mu_i = G_m^E(i) + RT \ln x_i$$

where i = H_2O or TBA. The chemical potential for the standard states at x_i = 1.0 are taken to be zero hereinafter. The excess

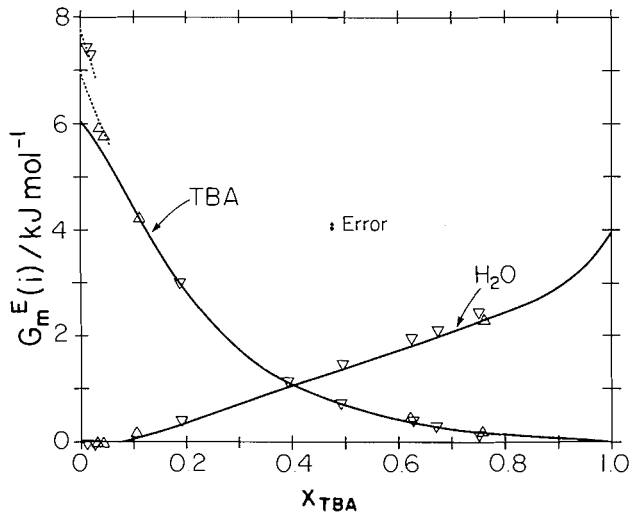

FIG. 3. The excess partial molar free energies against the mole fraction, 30.00°C. △, Kenttamaa, 25°C, ref. 14; ▽, Kenttamaa, 50°C, ref. 14; Dotted lines are drawn using the second virial coefficients of Perron *et al.*, ref. 20; solid lines are calculated using Westmeier's data, ref. 15. See text.

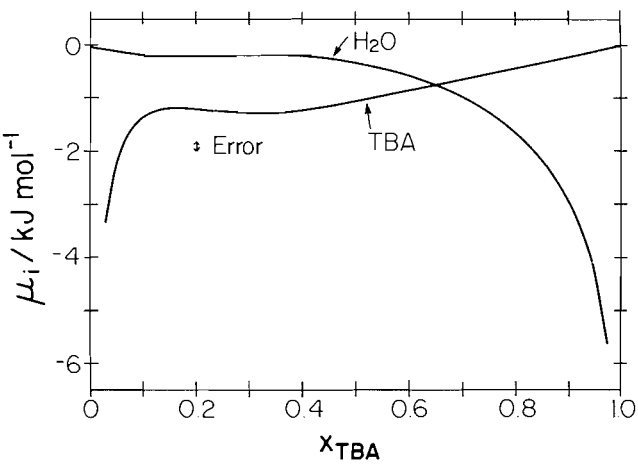

FIG. 4. Chemical potentials of TBA and H_2O against mole fraction, at 30.00°C, calculated using Westmeier's data, ref. 15. See text.

partial molar entropies, $S_m^E(i)$, are then calculated as

$$[4] \quad S_m^E(i) = \{H_m^E(i) - G_m^E(i)\}/T$$

Note in passing that, since the chemical potentials for the standard states, $x_i = 1.0$, are taken to be zero, μ_i, $G_m^E(i)$, and $S_m^E(i)$ can be written with the activity coefficients γ_i as,

$$[4b] \quad \mu_i = RT \ln x_i\gamma_i$$

$$[4c] \quad G_m^E(i) = RT \ln \gamma_i$$

and

$$[4d] \quad S_m^E(i) = -R \ln \gamma_i - RT(\partial \ln \gamma_i/\partial T)$$

Equation [1] with six terms was least-square-fitted to the data of G_m^E at 303.15 K (15). While the uncertainty of the data is quoted as ±150 J mol^{-1}, the fitted values were all within ±10 J mol^{-1} of the data. With the six coefficients of eq. [1] thus obtained, $G_m^E(i)$, μ_i, and $S_m^E(i)$ (i = H_2O or TBA) were calculated by eqs. [2], [3], and [4] and plotted in Figs. 3, 4, and 5, respectively.

In Fig. 3 are also plotted Kenttamaa's data at 25 and 50°C (14). The dotted lines at $x_{TBA} \approx 0$ are drawn using the appropriate values for the second virial coefficient taken from Perron *et al.* (20) for 25 and 50°C. As was suspected, eq. [1] with six terms is not satisfactory in the first region, $x_{TBA} < 0.07$. For further discussion in that region, more complete data for the excess partial molar free energy are necessary.

Figure 4 shows plots of chemical potential against composition. A striking feature is that in the range $0.15 < x_{TBA} < 0.4$, μ_{TBA} behaves as a three-valued function in x_{TBA} for a single value of μ_{TBA}. Although such a variation in μ_{TBA} is about the same magnitude as the estimated uncertainty, it is an indication of a phase separation, if genuine. It is, however, most likely to be an artifact due to a subtle incorrectness in the curvature of eq. [1] with the six terms in this range, since the measured concentration fluctuations are finite in the same range (9, 21). Namely, the structure factor at the zero momentum transfer, $S_{xx}(0)$, and the concentration fluctuations, $N\langle(\Delta x_i)^2\rangle$, are related to the derivative of the chemical potential as

$$[5] \quad S_{xx}(0) = N\langle(\Delta x_i)^2\rangle = RT(1 - x_i)/(\partial\mu_i/\partial x_i)$$

In Fig. 6, the values of $S_{xx}(0)$ measured by means of light scattering (9) and those obtained by small angle X-ray scattering (21) are shown together with the curve calculated by using eqs. [1], [3], and [5]. If there is a phase separation, the measured values of $S_{xx}(0)$ should be infinity. While a more complete set of data of $S_{xx}(0)$ or μ_i in this range is necessary, it seems safe to say that $S_{xx}(0)$ is large but finite. This means that μ_i is nearly but not constant in this range, suggesting closeness to a critical demixing.

Figure 5 shows the excess partial molar entropies, $S_m^E(i)$, calculated by eq. [4]. The partial molar enthalpies, $H_m^E(i)$, are also replotted. Since the data for $G_m^E(i)$ and hence those of $S_m^E(i)$ are not reliable in the first region, $x_{TBA} < 0.1$, nothing new is said about that region from the figure. For the second region, $0.1 < x_{TBA} < 0.5$, all that can be deduced from Fig. 5 have been more directly pointed out from Figs. 4 and 6. Thus the solution in this region at 30°C under the atmospheric pressure is very close to a critical demixing. In the third region, $x_{TBA} > 0.6$, the values of S_m^E(TBA) (not including the term, $-R \ln x_{TBA}$) stays zero (<1 J K^{-1} mol^{-1}) and those of H_m^E(TBA) are also nearly zero (<1 kJ mol^{-1}) with a small concentration dependence. These facts suggest that an additional TBA molecule in the solution in this composition range always settles in the environment that is almost exactly the same as in the pure liquid of TBA. On the other hand, as pointed out earlier, the values of $H_m^E(H_2O)$ and the temperature as well as the composition dependences seem to suggest that H_2O molecules lose the hydrogen bond network and are dispersed among TBA molecules as a single molecule, with a repulsion from TBA and a resulting attraction from H_2O molecules. H_2O molecules are still dispersed due to the gain in the ideal mixing entropy up to $x_{TBA} \approx 0.5$. The non-ideal part of the partial molar entropy, $S_m^E(H_2O)$, is also small (<7 J K^{-1} mol^{-1}) and almost constant as shown in Fig. 5, indicating an almost regular solution behaviour. When the concentration of H_2O increases to $x_{TBA} \approx 0.5$, the H_2O–H_2O attraction causes H_2O clusters to form possibly $TBA(H_2O)_k$ and in the second region the situation very close to a phase separation, between TBA and $TBA(H_2O)_k$, sets in.

While all these views presented here are not entirely new (3, 4), the present work provides some additional data to support such views within a limited power of the thermodynamic

Can. J. Chem. Downloaded from www.nrcresearchpress.com by 122.72.124.2 on 09/07/12
For personal use only.

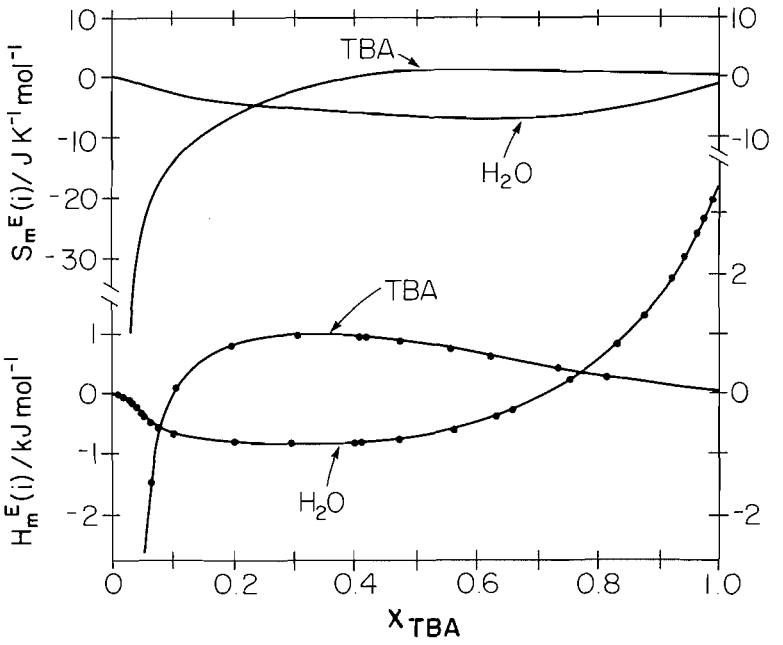

FIG. 5. Excess partial molar entropies and enthalpies of TBA and H_2O against mole fraction, at 30.00°C.

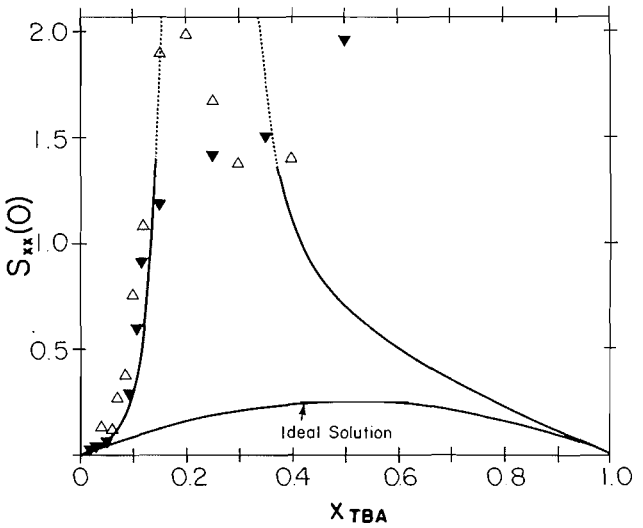

FIG. 6. Concentration fluctuations against mole fraction. △, Koga, 27°C, ref. 21; ▼, Iwasaki, 24°C, ref. 9; solid line is calculated for 30.00°C. See text.

quantities. Although much has been known about this solution, it appears still worthwhile to measure accurately the quantities that are proportional to the higher order derivatives of the free energy, in particular chemical potential and concentration fluctuations. Eventually it may become possible to formulate the free energy of this solution as a function of the mole fraction based on a physically reasonable model.

Acknowledgements

I would like to thank Professors D. H. Dolphin and L. G. Harrison for allowing me to use their facilities and many departmental colleagues for lending chemicals and incidentals. This paper is dedicated to University Professor C. A. McDowell on the occasion of his 70th birthday. I had a lucky encounter with him 23 years ago in the lobby of City Center Hotel, Tokyo, as a result of which I have come to U.B.C.

1. Y. KOGA. Can. J. Chem. **64**, 206 (1986).
2. Y. KOGA. Can. J. Chem. **66**, 1187 (1988).
3. F. FRANKS and D. J. G. IVES. Q. Rev. **20**, 1 (1966).
4. F. FRANKS and J. E. DESNOYERS. *In* Water science review 1. *Edited by* F. Franks, Cambridge University Press, Cambridge. 1985. p. 171.
5. H. UEDAIRA and J. KIDA. Nippon Kagaku Kaishi, 539 (1982).
6. T. M. BENDER and R. PECORA. J. Phys. Chem. **90**, 1700 (1986).
7. K. NAKANISHI, K. IKARI, S. OKAZAKI, and H. TOUHARA. J. Chem. Phys. **80**, 1656 (1984).
8. H. TANAKA, K. NAKANISHI, and H. TOUHARA. J. Chem. Phys. **81**, 4065 (1984).
9. K. IWASAKI and T. FUJIYAMA. J. Phys. Chem. **81**, 1908 (1977).
10. K. IWASAKI and T. FUJIYAMA. J. Phys. Chem. **83**, 463 (1979).
11. G. W. EULISS and C. M. SORENSEN. J. Chem. Phys. **80**, 4767 (1984).
12. M. F. VUKS and L. V. SHURAPOVA. Opt. Commun. **11**, 150 (1972).
13. N. ITO, T. KATO, and T. FUJIYAMA. Bull. Chem. Soc. Jpn. **54**, 2573 (1981).
14. J. KENTTAMAA, E. TOMMILA, and M. MARTTI. Ann. Acad. Sci. Fenn. A II. **93**, 2 (1959).
15. S. WESTMEIER. Chem. Techn. **29**, 218 (1977).
16. K. QUITZSCH, R. KOPP, W. RENKER, and G. GEISELER. Z. Physik. Chem. (Leipzig). **237**, 256 (1968).
17. B. Y. OKAMOTO, R. H. WOOD, and P. T. THOMPSON. J. Chem. Soc. Faraday Trans. I, **74**, 1990 (1978).
18. J. E. DESNOYERS, C. OSTIGUY, and G. PERRON. J. Chem. Educ. **55**, 137 (1981).
19. E. A. GUGGENHEIM. Trans. Faraday Soc. **33**, 151 (1939).
20. G. PERRON and J. E. DESNOYERS. J. Chem. Thermodyn. **13**, 1105 (1981).
21. Y. KOGA. Chem. Phys. Lett. **111**, 176 (1984).
22. Y. KOGA. J. Chem. Thermodyn. **19**, 571 (1987).
23. G. L. BERTRAND, F. J. MILLERO, C.-H. WU, and L. G. HEPLER. J. Phys. Chem. **70**, 699 (1966).

Can. J. Chem. Downloaded from www.nrcresearchpress.com by 122.72.124.2 on 09/07/12
For personal use only.

Gold(I) dimers. The synthesis and reactions of [*tert*-BuC≡CAu(dmpm—P)], and the crystal and molecular structures of $[Au_2(\mu\text{-dmpm})_2]X_2\cdot 2H_2O$, X = Cl, I

N. C. PAYNE,[1] R. J. PUDDEPHATT,[1] R. RAVINDRANATH, AND I. TREURNICHT

Chemistry Department, University of Western Ontario, London, Ont., Canada N6A 5B7

Received June 27, 1988

N. C. PAYNE, R. J. PUDDEPHATT, R. RAVINDRANATH, and I. TREURNICHT. Can. J. Chem. **66**, 3176 (1988).

Acetylide complexes of formula [*tert*-BuC≡CAu($R_2PCH_2PR_2$)], R = CH_3 (**6***a*) and C_6H_5 (**6***b*), have been prepared, and characterized by spectroscopic methods. These complexes undergo a fluxional process involving a three-coordinate Au(I) centre. Complex **6***a* dimerizes by a first-order process in chlorinated solvents, with substitution of the acetylide ligand by chloride ion, to form $[Au_2(\mu\text{-dmpm})_2]Cl_2\cdot 2H_2O$ (**7***a*). The crystal and molecular structures of **7***a* and the iodide salt **7***b* have been determined by single crystal X-ray diffraction methods. Both crystallize in the triclinic space group $P\bar{1}$ with $Z = 1$; unit cell dimensions are $a = 7.962(1)$, $b = 9.987(1)$, $c = 7.895(1)$ Å, $\alpha = 90.11$, $\beta = 109.13(1)$, and $\gamma = 112.84(1)°$ for **7***a*; $a = 8.243(1)$, $b = 9.057(1)$, $c = 8.167(1)$ Å, $\alpha = 90.23$, $\beta = 110.33(1)$, and $\gamma = 89.92(1)°$ for **7***b*. The analyses refined to final agreement factors on F of $R = 0.035$ based on 3225 unique reflections with $I > 3\sigma(I)$ for **7***a*, and $R = 0.030$ based on 2971 unique reflections with $I > 3\sigma(I)$ for **7***b*. The structures are closely related, with the cations containing an eight-membered centrosymmetric ring formed by the Au(I) centres and the bridging dmpm ligands. The Au...Au′ distances are 3.014(1) and 3.019(1) Å in **7***a* and **7***b*, respectively. In the solid state, the halide ions bridge the two Au centres, and, together with the water molecules, form a network of hydrogen bonds running at an angle of 104° to the eight-membered $Au_2P_4C_2$ rings.

N. C. PAYNE, R. J. PUDDEPHATT, R. RAVINDRANATH et I. TREURNICHT. Can. J. Chem. **66**, 3176 (1988).

On a préparé les complexes d'acétylure de formule [*tert*-BuC≡CAu($R_2PCH_2PR_2$)], dans lesquels R = CH_3 (**6***a*) et C_6H_5 (**6***b*), et on les a caractérisés par des méthodes spectroscopiques. Ces complexes subissent un processus de fluxion impliquant les centres tri-coordonnés Au(I). Dans les solvants chlorés, le complexe **6***a* se dimérise par un processus du premier ordre impliquant une substitution du ligand acétylure par l'ion chlorure et la formation de $[Au_2(\mu\text{-dmpm})_2]Cl_2\cdot 2H_2O$ (**7***a*). Faisant appel à des méthodes de diffraction des rayons-X sur un cristal unique, on a déterminé les structures tant cristallines que moléculaires des composés **7***a* ainsi que **7***b*. Chacun cristallise dans le groupe d'espace triclinique $P\bar{1}$ avec $Z = 1$; les dimensions de la maille sont $a = 7{,}962(1)$, $b = 9{,}987(1)$ et $c = 7{,}895(1)$ Å, $\alpha = 90{,}11$, $\beta = 109{,}13(1)$ et $\tau = 112{,}84(1)°$ pour **7***a* et $a = 8{,}243(1)$, $b = 9{,}057(1)$ et $c = 8{,}167(1)$ Å, $\alpha = 90{,}23$, $\beta = 110{,}33(1)$ et $\tau = 89{,}92(1)°$ pour **7***b*. Les structures ont été affinées sur F jusqu'à une valeur de $R = 0{,}035$ pour 3225 réflexions uniques avec $I > 3\sigma(I)$ pour **7***a* et jusqu'à une valeur de $R = 0{,}030$ pour 2971 réflexions uniques avec $I \geq 3\sigma(I)$ pour **7***b*. Les structures sont très apparentées alors que les cations contiennent un cycle centro-symétrique à huit chaînons formé par les centres Au(I) et les ligands dmpm qui forment le pont. Les distances Au...Au′ sont respectivement de 3,014(1) et 3,019(1) Å pour les composés **7***a* et **7***b*. A l'état solide, les ions halogénures forment un pont entre les deux centres Au et, avec les molécules d'eau, ils forment un réseau de liaisons hydrogènes avec un angle de 104° avec les cycles à huit chaînons de $Au_2P_4C_2$.

[Traduit par la revue]

Introduction

Diphosphine ligands such as $CH_2(PR_2)_2$ (R = Ph, dppm; R = Me, dmpm), $CH_2{=}C(PPh_2)_2$ (vdpp) $EtOCH_2CH(PPh_2)_2$ (edpp), or $CH_2CH_2C(PPh_2)_2$ (cdpp) are commonly used to bind two metal centres in close proximity (1–5). An interesting feature of the coordination chemistry of gold(I) with these ligands is the tendency of gold to adopt coordination number three in some cases. Known structures with dppm and related ligands are **1**–**4** (2–5).

In these complexes, the gold–halogen bonds are long and presumably weak but are still strong enough to give considerable distortion of the PAuP angle away from the normal 180° found for two-coordinate gold(I) and to have a major effect on the ^{197}Au Mössbauer parameters (2–5). In complexes **1** and **4** both gold(I) centres are three-coordinate, but the former has only terminal halides and is neutral while the latter has a bridging halide and is cationic. Complexes **2** and **3** each have one three-coordinate and one two-coordinate gold(I) centre, but in **2** the chloride ligand is approximately perpendicular to the eight-membered $Au_2P_4C_2$ ring whereas in **3** the chloride is approximately coplanar with this ring. In some cases, the structural changes are caused by subtle changes in the diphosphine ligand (e.g. **1***a*, **1***b*, **4**) (2–5). The reasons for the structures being different are not known, but the energy differences are small and the unsymmetrical complexes **2** and **3** are fluxional in solution (2–4).

We were interested in studying how the coordinating ability of the ligand X and the steric bulk of the diphosphine ligand affected the structures of complexes of the formula $\{AuX(R_2PCH_2PR_2)\}_n$ and chose to investigate the complexes with the ligand $Me_2PCH_2PMe_2$, dmpm, which is less bulky than the phenyl substituted ligands dppm, vdpp, and cdpp. Despite this lower steric effect, there was a report that the gold(I) chloride derivative possessed the ionic structure $[Au_2(\mu\text{-dmpm})_2]Cl_2$ (6) and this was confirmed during the course of the present work by an X-ray structure determination (structure **5** with very long Au..Cl distances) (7).

Experimental

^{1}H (200 MHz) and $^{31}P\{^1H\}$ NMR (121.4 MHz) were recorded using a Varian XL200 and Varian XL300 spectrometer. Chemical shifts are quoted with respect to TMS and H_3PO_4, respectively. Infrared spectra were recorded on a Bruker IR/32 FTIR spectrometer, and FAB mass spectra were recorded on a Finnigan MAT 8230 mass spectrometer. Elemental analyses were carried out by Guelph Chemical Laboratories, Guelph, Ontario. All experiments were carried out under a dry, oxygen-free dinitrogen atmosphere.

[Au(C≡C′Bu)(dmpm—P)]

To a yellow suspension of [AuC≡C′Bu] (0.350 g, 1.259 mmol) in acetone (10 mL) was added dmpm (0.1712 g, 1.257 mmol). An instant colour change from a yellow suspension to a white powder was

[1]To whom correspondence should be addressed.

Can. J. Chem. Downloaded from www.nrcresearchpress.com by 122.72.124.2 on 09/07/12
For personal use only.

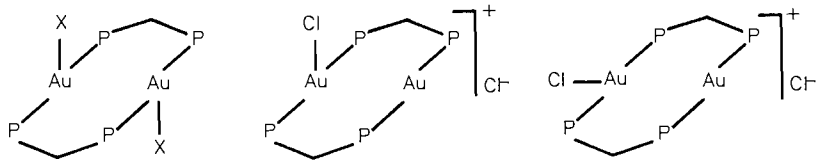

1a, PP=dppm, X=Cl
1b, PP=dppm, X=Br
1c, PP=vdpp, X=Cl

2, PP=cdpp

3, PP=edpp

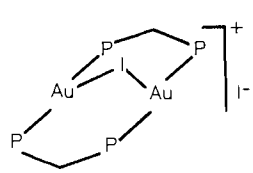

4, PP=dppm

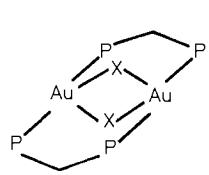

5, PP=dmpm, X=Cl

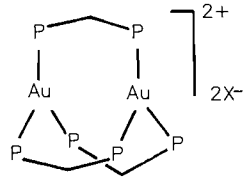

8, PP=dmpm

observed. The solution was stirred for 2 h. The white solid was filtered, dried under vacuum, and identified as [Au(C≡C^{t}Bu)(dmpm—P)]. Yield: 72%. MP: 165°C (dec); ir (Nujol): ν_{max} 2100 cm^{-1} [ν(C≡C)]; ^{1}H NMR in $CDCl_3$ at 20°C: δ1.19 (s, 9H, *t-Bu*); 1.77 (br.s, 12H, *Me*P); 2.93 (s, 2H, PCH_2P); ^{31}P{^{1}H} NMR: δ3.8 (br.s, P). ^{1}H NMR in CD_2Cl_2 at −80°C: δ1.08 (s, 9H, *t-Bu*); 1.70 and 1.88 (br.s, each 6H, *Me*P); 3.1 (m, 2H, PCH_2P). *Anal.* calcd. for $C_{11}H_{23}AuP_2$: C 31.9; H 5.60; found: C 29.8, H 5.47. Mass spectrometry: calcd. for $C_{11}H_{23}AuP_2$: *m/e* = 414; found *m/e* = 414; 333 (Parent − C≡C^{t}Bu).

[Au(C≡C'Bu)(dppm—P)]

[AuC≡C^{t}Bu] (0.2563 g, 0.922 mmol) was suspended in CH_2Cl_2 (3 mL). To this was added dppm (0.3543 g, 0.922 mmol) in CH_2Cl_2 (5 mL). After 3 h stirring, the product was precipitated by slow addition of pentane. The product was washed with diethyl ether and dried under vacuum. Yield: 68%. MP: 99°C (dec); ^{1}H NMR in CD_2Cl_2 at 20°C: δ1.25 (s, 9H, *t-Bu*); 3.25 (br.s, 2H, PCH_2P); 7.31 to 7.51 (m, 20H, PC$_6H_5$); ^{31}P{^{1}H} NMR at 20°C: —Au—P^a P^b; δ29.35 (br. s, P^a); −27.20 (br.s, P^b). Mass spectrometry calcd. for $C_{30}H_{29}AuP_2$: *m/e* = 662; found: *m/e* = 662; 384 (P − AuC≡C^{t}Bu); 278 (Parent − dppm).

[Au$_2$(μ-dmpm)$_2$]Cl$_2$·2H$_2$O

This complex was obtained by two different procedures. (*a*) To a yellow suspension of [AuC≡C*t*—Bu] (0.345 g, 1.241 mmol) in CH_2Cl_2 (10 mL) was added dmpm (0.169 g, 1.241 mmol). Immediately the solution turned milky. The solution was stirred for 3 h. On slow evaporation of solvent, colourless crystals were obtained and were characterized as [Au$_2$(μ-dmpm)$_2$]Cl$_2$·2H$_2$O. Yield: 75%. MP: 228°C (dec); ^{1}H NMR in CD_2Cl_2 at 20°C: δ1.84 (m, ^2J(PH) + ^4J(PH) = 7, 24H, *Me*P); 2.98 (quintuplet, ^2J(PH) + ^4J(PH) = 10, 4H, PCH_2P); ^{31}P{^{1}H} NMR at 20°C: δ5.6 (s, *P*). *Anal.* calcd. for $C_{10}H_{32}Au_2Cl_2O_2P_4$: C 15.53, H 4.17; found: C 15.94, H 3.85. (*b*) To a solution of [AuCl(SMe$_2$)] (0.305 g, 1.037 mmol) in CH_2Cl_2 (6 mL) was added dmpm (0.1412 g, 1.037 mmol) and the mixture was stirred for 3 h. On removal of solvents, a white solid was isolated. Yield: 70%. *Anal.* calcd. for $C_{10}H_{32}Au_2Cl_2O_2P_4$: C 15.53, H 4.17; found: C 15.30, H 3.96.

[Au$_2$(μ-dmpm)$_2$]I$_2$·2H$_2$O

A solution of NaI (0.051 g, 0.3402 mmol) in acetone (5 mL) was added to a suspension of [AuCl(SMe$_2$)] (0.1028 g, 0.3490 mmol) dissolved in acetone (5 mL). The contents were stirred at −78°C for 0.5 h. [AuI(SMe$_2$)] was then filtered into a Schlenck tube containing dmpm (0.049 g, 0.3602 mmol) and the contents were stirred at −78°C for 3 h. A pale yellow solid turning white on exposure to air was isolated. The product was washed with cyclohexane and dried under vacuum. Recrystallization in water gave colourless crystals. Yield: 60%. MP: 233°C (dec); ^{1}H NMR in CD_2Cl_2 at 20°C: δ1.71 (s, 24H, *Me*P); 2.44 (br.m, ^2J(PH) + ^4J(PH) = 8, 4H, PCH_2P); ^{31}P{^{1}H} NMR at 20°C: δ − 7.8 (s, *P*). *Anal.* calcd. for $C_{10}H_{32}Au_2I_2O_2P_4$: C 12.56, H 3.37; found: C 12.61, H 3.08. Mass spectrometry: *m/e* = 793 [P − (I, 2H$_2$O)], 657 [P − (dmpm, I)].

[Au$_2$(μ-dmpm)$_3$]Cl$_2$

To a solution of [AuCl(SMe$_2$)] (0.5114 g, 1.736 mmol) in CH_2Cl_2 (10 mL) was added dmpm (0.3544 g, 2.604 mmol). The contents were stirred for 3 h. A yellow solid was obtained which was filtered and dried under vacuum. Yield: 69%. ^{1}H NMR in CD_2Cl_2 at 20°C: δ1.76 (m, ^2J(PH) + ^4J(PH) = 8, 36H, *Me*P); 2.97 (br.m, ^2J(PH) + ^4J(PH) = 12, 6H, PCH_2P). ^{31}P{^{1}H} NMR at 20°C: δ3.24 (s, Au*P*). *Anal.* calcd. for $C_{15}H_{42}Au_2Cl_2P_6$: C 20.63, H, 4.85; found: C 20.30, H 4.86.

[Au$_2$(μ-dmpm)$_3$]I$_2$

The work-up procedure was similar to that of [Au$_2$(μ-dmpm)$_2$]I$_2$. The stoichiometries of the reagents used were as follows: NaI (0.0698 g, 0.4565 mmol). [AuCl(SMe$_2$)] (0.1029 g, 0.3493 mmol) and dmpm (0.0701 g, 0.5146 mmol). Yield: 73%. MP: 290°C (dec). ^{1}H NMR in CD_2Cl_2 at 20°C: δ1.71 (s, 36H, *Me*P); 2.40 (br.s, 6H, PCH_2P): ^{31}P{^{1}H} NMR at 20°C: δ − 8.5 (s, Au*P*). *Anal.* calcd. for $C_{15}H_{42}Au_2I_2P_6$: C 17.06, H 4.01; found: C 16.79, H 4.00.

Kinetic studies

The reaction kinetics of the conversion of the acetylide product **6***a* to chloride product **7***a* was followed by monitoring the decay of the MLCT band of **6***a*. [AuC≡C*t*—Bu(dmpm—P)] (0.0083 g, 2 × 10^{-5} *M*) was dissolved in $CHCl_3$ (10 mL) and was transferred to a 1 cm cuvette and placed in a cell compartment, thermostated at 25°C. The absorbance (at λ = 282 nm) was recorded at 20 min intervals for 5 h. Computer treatment of the data showed good first-order kinetics, with the rate constant, $k = 7.9 \times 10^{-5}$ s^{-1}.

X-ray data collection and reduction

Clear, colourless, bladed crystals of **7***a* were obtained by slow diffusion of pentane into a chloroform solution at room temperature. A preliminary photographic examination, employing Weissenberg and precession techniques, showed no symmetry other than triclinic. The crystal density was determined by neutral buoyancy in mixtures of $CHBr_3$ and CH_2Cl_2, and crystal data are summarized in Table 1.

The structure determination of **7***a* was undertaken first. Cell constants and an orientation matrix were refined from the angular settings at ±2θ for carefully centred high angle reflections (8). ω-Scans of intense low angle reflections indicated a satisfactory crystal quality (9). Intensity data were collected in two shells, employing variable scan rates within a maximum time per datum of 90 s in order to optimize counting statistics. Background estimates were made by extending the scan by 25% on each side. A Zr foil attenuator was used for extremely strong reflections. Four standard reflections were

Can. J. Chem. Downloaded from www.nrcresearchpress.com by 122.72.124.2 on 09/07/12
For personal use only.

Can. J. Chem. Downloaded from www.nrcresearchpress.com by 122.72.124.2 on 09/07/12
For personal use only.

TABLE 1. Summary of X-ray structure determinations

Crystal data	7*a*	7*b*
Compound, formula weight	$Au_2Cl_2O_2P_4C_{10}H_{32}$, 773.10	$Au_2I_2O_2P_4C_{10}H_{32}$, 956.00
Crystal system, space group	Triclinic, $P\bar{1}$ (No. 2)	
Temperature (°C)	23	
Cell dimensions		
a (Å)	7.962(1)	8.243(1)
b (Å)	9.987(1)	9.057(1)
c (Å)	7.895(1)	8.167(1)
α (deg)	90.11(1)	90.23(1)
β (deg)	109.13(1)	110.33(1)
γ (deg)	112.84(1)	89.92(1)
Cell volume (Å^3), *Z*	540.6(3), 1	571.6(3), 1
Density (g cm^{-3}), obsd; calcd	2.283(2), 2.375	2.718(2), 2.777
Experimental details		
Diffractometer, monochromator	Enraf-Nonius CAD4F, graphite	
Radiation, wavelength (Å)	Mo, λ(Kα mean) 0.71073	
Crystal-detector (mm), t.o.a. (deg)	205, 2.5	
Aperture (mm), vertical; horizontal	4.0; 6.0 + 0.35 tan θ	
Centering reflection; θ range	20; $30.0 < 2\theta < 40.0$	20; $30.0 < 2\theta < 40.0$
Data collection		
Approximate crystal dimensions (mm)	0.25 × 0.12 × 0.42	0.32 × 0.09 × 0.14
Crystal volume (mm^3); number of faces	5.53×10^{-3}; 8	3.08×10^{-3}; 9
Face indices	100, {010}, {101}, {1$\bar{1}$0}, and 001	$\bar{1}$20, {100}, {010}, {001}, and {10$\bar{1}$}
ω-Scan widths, before, after	0.11 0.11	
Scan mode, width (deg)	ω–2θ, 0.7 + 0.35 tan θ	
Index and θ ranges	$-12 \leq h \leq 12$ $-15 \leq k \leq 15$ $0 \leq l \leq 12$ $0 \leq \theta \leq 33°$	$-12 \leq h \leq 12$ $-13 \leq k \leq 13$ $0 \leq l \leq 12$ $0 \leq \theta \leq 32.5°$
Scan speed (deg min^{-1})	3.3 to 0.9	3.3 to 1.0
Maximum time per datum, total time	90 s, 92.9 h	90 s, 98.1 h
Standard reflections	$\bar{1}$02, 100, 010, 001	$\bar{1}$01, 100, 010, 001
Monitor frequency, % variance	180 m, 1.6	180 m, 2.3
Number of data, standards collected	4311, 132	4383, 148
Data processing		
Corrections	Lorentz, polarization and monochromator polarization	
Decay, absorption corrections	None; Gaussian	None; Gaussian
Absorption coefficient (cm^{-1}); grid size	140.74, 12 × 8 × 20	157.47, 22 × 6 × 10
Transmission, maximum, minimum	0.283, 0.112	0.857, 0.109
R(*F*) for average, before, after	0.009, 0.014	0.011, 0.011
Number of unique data, significance	$3225 > 3\sigma$	$2971 > 3\sigma$
Structure refinement		
Number of observations, variables	3225, 92	2971, 92
Final model; R_1 and R_2	0.035, 0.047	0.030, 0.054
Top residual (e Å^{-3}), coordinates	3.45 (0.791 0.889 0.082)	1.80 (0.791 0.305 0.291)

monitored regularly. ω-Scans were again recorded after 4311 data had been collected, and, together with the standard reflections, showed no evidence for crystal deterioration.

The data were processed using the Enraf-Nonius Structure Determination Package, Version 3.0 (10), running on a PDP 11/23+ computer. Standard deviations were assigned on the basis of counting statistics, a starting value of 0.04 was chosen for *p* (11), and an absorption correction was applied (12). The equivalent reflections were averaged. In all, 3225 unique data with $I > 3\sigma(I)$ were available for solution and refinement.

Clear, colourless, bladed crystals of 7*b* were obtained by recrystallization from water solutions. Preliminary photography showed the crystals to belong to triclinic system. The crystal density was determined by neutral buoyancy in mixtures of $CHBr_3$ and 1,2-$C_2H_4Br_2$. Data collection and reduction procedure was similar to that for structure 7*a*. Again, no significant crystal deterioration occurred, and 2971 unique data with $I > 3\sigma(I)$ were available for the analysis. Full details for both studies are presented in Table 1.

Solution and refinement of the structures

7*a*: A statistical analysis of the data using the *N*(*Z*) test (13) suggested that the space group was *P*1. The positional parameters of the Au and P atoms were obtained from a three-dimensional Patterson synthesis. A series of least-square refinements and difference Fourier syntheses were used to locate the remaining six non-H atoms. At this stage it became apparent that the cation possessed a centre of symmetry, so the analysis was continued in space group $P\bar{1}$, with the cation placed on the centre at (0,0,0). Refinement of atomic parameters was by full-matrix least-squares techniques on *F*, minimizing the function $\Sigma w(|F_o| - |F_c|)^{1/2}$, where F_o and F_c are the observed and calculated structure factor amplitudes and *w*, the weighting factor, is given by $w = 4F_o/\sigma^2(F_o^2)$. Scattering factors for neutral, non-H atoms

TABLE 2. Atomic positional ($\times 10^4$) and thermal ($\times 10^3$) parameters

Atom	x	y	z	U_{eq}*(Å^2)
Compound **7***a*				
Au	1392.2(2)	161.0(2)	−976.8(2)	30.10(4)
Cl	3461(3)	2454(2)	3132(3)	64.3(6)
P(1)	864(2)	2089(1)	−2283(2)	27.0(3)
P(2)	−2102(2)	1682(1)	−401(2)	27.5(3)
O	2589(8)	5302(7)	3607(9)	80(2)
C(1)	−790(10)	1624(9)	−4624(9)	58(2)
C(2)	3048(8)	3613(6)	−2300(9)	49(2)
C(3)	−120(6)	2934(5)	−1039(6)	28(1)
C(4)	−2520(7)	2921(6)	937(8)	41(1)
C(5)	−4271(7)	938(7)	−2450(8)	41(1)
Compound **7***b*				
Au	5919.6(3)	−192.7(3)	−1294.7(3)	36.55(5)
I	2275.5(7)	−2615.8(7)	−2120.7(8)	58.0(2)
P(1)	2433(2)	2095(2)	−312(2)	34.5(4)
P(2)	4299(2)	1668(2)	−3008(2)	33.3(4)
O	1196(22)	−4976(15)	−5766(22)	189(8)
C(1)	2216(11)	3671(10)	955(11)	57(2)
C(2)	268(11)	1655(13)	−1646(13)	62(3)
C(3)	3446(8)	2941(7)	−1758(8)	37(1)
C(4)	5412(10)	2964(10)	−3965(11)	59(2)
C(5)	2451(10)	1048(10)	−4808(9)	50(2)

*$U_{eq} = \frac{1}{3}\Sigma_i\Sigma_j U_{ij}\, a_i^*\, a_j^*\, \mathbf{a}_i\cdot\mathbf{a}_j$.

were taken from ref. 14, and the real components of anomalous dispersion were included for all atoms (14). Agreement factors $R_1 = \Sigma(||F_o| - |F_c||)/\Sigma|F_o| = 0.094$ and $R_2 = (\Sigma w(||F_o| - |F_c||)^2/\Sigma w|F_o|) = 0.129$ were achieved.

The 14 H atoms were located in a difference Fourier synthesis with peaks ranging from 1.4(2) to 0.7(2) e Å^{-3}, and included in ideal positions (C—H = 0.95 Å, sp^3 hybridization) in calculations of F_c, but were not refined. Positions for the methyl hydrogen atoms were optimized by a least-squares routine. The scattering factor values were taken from Stewart *et al.* (15). The hydrogen atoms on the water molecule were clearly visible in a difference Fourier, see Fig. 3. For the final cycles, positional and anisotropic thermal parameters were refined for all non-H atoms, and H atom positions were recalculated after each cycle. The model converged (3225 unique reflections for which $I > 3\sigma(I)$, 92 variables) with agreement factors $R_1 = 0.035$ and $R_2 = 0.047$.

In the final cycle no parameter shift exceeded 0.01 of its estimated standard deviation, and, with a p value of 0.06, the error in an observation of unit weight was 1.28 e. A total difference Fourier synthesis showed that the highest peak, with an electron density of 3.4(1) e Å^{-3} is situated 0.88 Å from the Au atom. A statistical analysis of R_1 and R_2 in terms of $|F_o|$, $\lambda^{-1}\sin\theta$, and classes of indices showed no unusual trends. There was no secondary extinction. Final positional and U equivalent thermal parameters for the non-H atoms are presented in Table 2. H atom parameters, anisotropic thermal parameters, selected torsion angles, weighted least-square planes, and structure amplitudes have been deposited.[2]

7*b*

Space group $P\bar{1}$ was assumed. The positional parameters of the Au atom were obtained from a three-dimensional Patterson synthesis, and the remaining eight non-H atoms were located from a series of least-squares refinements and difference Fourier syntheses. The 12 methyl H atoms were located with electron densities varying from 1.1(3) to 0.5(3) e Å^{-3}, and their idealized contributions included in the calculation of F_c; those on the water molecule could not be found. The refinement of 92 variables with 2971 unique observations ($I > 3\sigma(I)$) converged at $R_1 = 0.030$ and $R_2 = 0.054$. In the final cycle all parameter shifts were less than 0.01σ, and, with a p value of 0.06, the error in an observation of unit weight was 1.38 e. The highest peak in a difference Fourier synthesis is of electron density 1.8(1) e Å^{-3} is at a distance of 0.72 Å from the I atom. A statistical analysis of the structure factors showed no unusual trends. Final positional parameters of non-H atoms are given in Table 2. Hydrogen atom parameters, anisotropic thermal parameters, selected torsion angles and weighted least-squares planes, and structure factor amplitudes have been deposited.[2]

Results and discussion

The complexes [t-BuC≡CAuPR$_2$CH$_2$PR$_2$]

The above complexes **6***a*, R = Me and **6***b*, R = Ph were prepared by reaction of AuC≡C*t*—Bu with an equimolar amount of the corresponding diphosphine ligand. They were readily characterized by elemental analysis and mass spectroscopy and the structures were defined by the ^{1}H and ^{31}P NMR spectra. Both **6***a* and **6***b* gave a parent ion in the mass spectrum.

The complexes contain monodentate diphosphine ligands as shown by the variable temperature NMR spectra. Thus, complex **6***a* gave two *Me*P resonances in the low temperature ^{1}H NMR spectrum and **6***b* gave two ^{31}P resonances in the low temperature ^{31}P NMR spectrum. In the former case, the two resonances coalesced to a single resonance at room temperature indicating fluxionality according to eq. [1], but coalescences did not occur for **6***b* indicating slower fluxionality. The ^{31}P NMR chemical shifts for **6***b* were +29.4 ppm and −27.2 ppm, characteristic of coordinated and free phosphine atoms, respectively. Hence, in complexes **6**, it is clear that gold(I) is two-coordinate and that three-coordination occurs only in the transition state for exchange as shown in eq. [1]. Similar fluxionality of dppm ligands has been observed previously (16, 17), and monodentate phosphines also undergo exchange in gold(I) complexes, for example, the exchange of free and coordinated PMe_3 in [MeAuPMe$_3$] with PMe_3 (18).

[2]Hydrogen atom parameters, anisotropic thermal parameters, selected torsion angles and weighted least-squares planes, and structure amplitude tables for **7***a* and **7***b* may be purchased from the Depository of Unpublished Data, CISTI, National Research Council of Canada, Ottawa, Ont., Canada K1A 0S2.

Can. J. Chem. Downloaded from www.nrcresearchpress.com by 122.72.124.2 on 09/07/12
For personal use only.

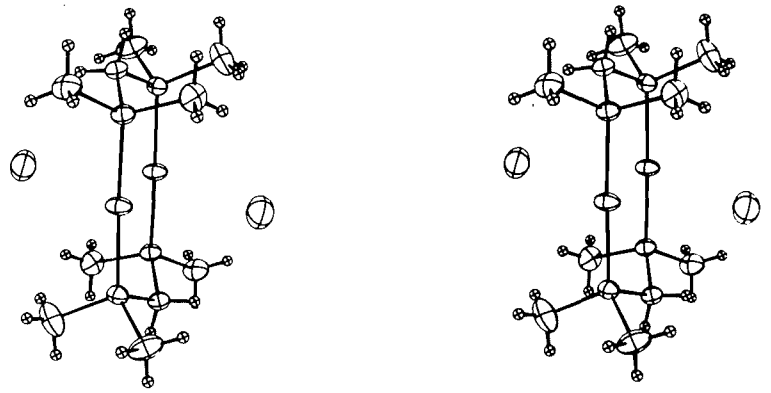

FIG. 1. A stereoview of the salt in **7***a*.

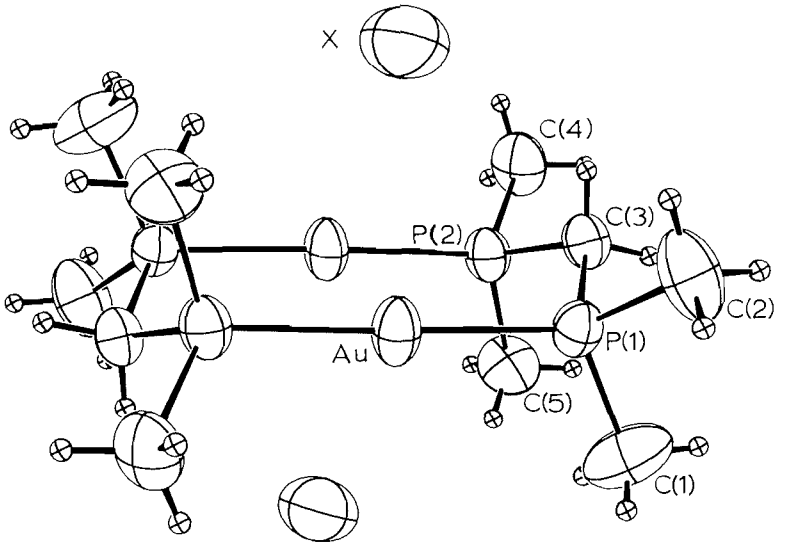

FIG. 2. A perspective view of the cation **7***a*, giving the atom numbering scheme. Atoms are drawn as 50% probability thermal ellipsoids.

[1]

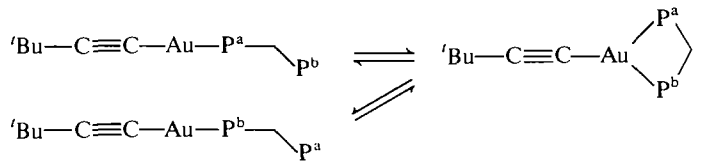

The complexes $[Au_2(\mu\text{-dmpm})_2]^{2+}$ and $[Au_2(\mu\text{-dmpm})_3]^{2+}$

The complex $[Au_2(\mu\text{-dmpm})_2]Cl_2$, **7***a*, was formed when complex **6***a* was recrystallized slowly from the chlorinated solvents $CHCl_3$ or CH_2Cl_2. Thus, although the gold–acetylide bond is usually considered strong (19), it is readily cleaved in these complexes. In $CHCl_3$ at 25°C the reaction was first order in the concentration of **6***a*, with an observed first order rate constant of 7.9×10^{-5} s^{-1}.

The complex **7***a* was prepared more rationally by reaction of $[AuCl(SMe_2)]$ with one equivalent of dmpm and, when recrystallized from $CHCl_3$/*n*-pentane, it formed the hydrate $[Au_2(\mu\text{-dmpm})_2]Cl_2 \cdot 2H_2O$, **7***a*. Similarly the iodide derivative was prepared from $[AuI(SMe_2)]$, made *in situ*, with dmpm and again it formed a hydrate $[Au_2(\mu\text{-dmpm})_2]I_2 \cdot 2H_2O$, **7***b*, when recrystallized from water. The structures of **7***a* and **7***b* were determined by X-ray diffraction methods.

Reaction of $[AuCl(SMe_2)]$ with either 1.5 or 2 equiv. of dmpm gave the yellow complex $[Au_2(\mu\text{-dmpm})_3]Cl_2$, **8**. This was obtained analytically pure and gave single resonances in the NMR spectra due to CH_3P, CH_2P_2, and ^{31}P groups, indicating a symmetrical structure. Slow crystallization of this complex **8** led to partial loss of dmpm and formation of $[Au_2(\mu\text{-dmpm})_2]Cl_2$ which is much paler yellow in colour. Hence an X-ray structure of **8** could not be obtained. However, the X-ray structure of the corresponding tetrafluoroborate salt, $[Au_2(\mu\text{-dmpm})_3](BF_4)_2$, has recently been reported (20).

Coordination number four is possible in gold(I) complexes (21) but there was no interaction of $[Au_2(\mu\text{-dmpm})_3]^{2+}$ with excess dmpm and, together with the observation that dissociation of dmpm from **8** occurs readily, this suggests that this binuclear system has little tendency to exceed coordination number three. In contrast, the isoelectronic $[Pt_2(\mu\text{-dmpm})_3]$ readily adds one or two triphenylphosphine ligands to give four-coordinate platinum (0) centres (22).

There are many examples of transition-metal binuclear complexes of the sterically less demanding dmpm ligand which

Can. J. Chem. Downloaded from www.nrcresearchpress.com by 122.72.124.2 on 09/07/12
For personal use only.

Can. J. Chem. Downloaded from www.nrcresearchpress.com by 122.72.124.2 on 09/07/12
For personal use only.

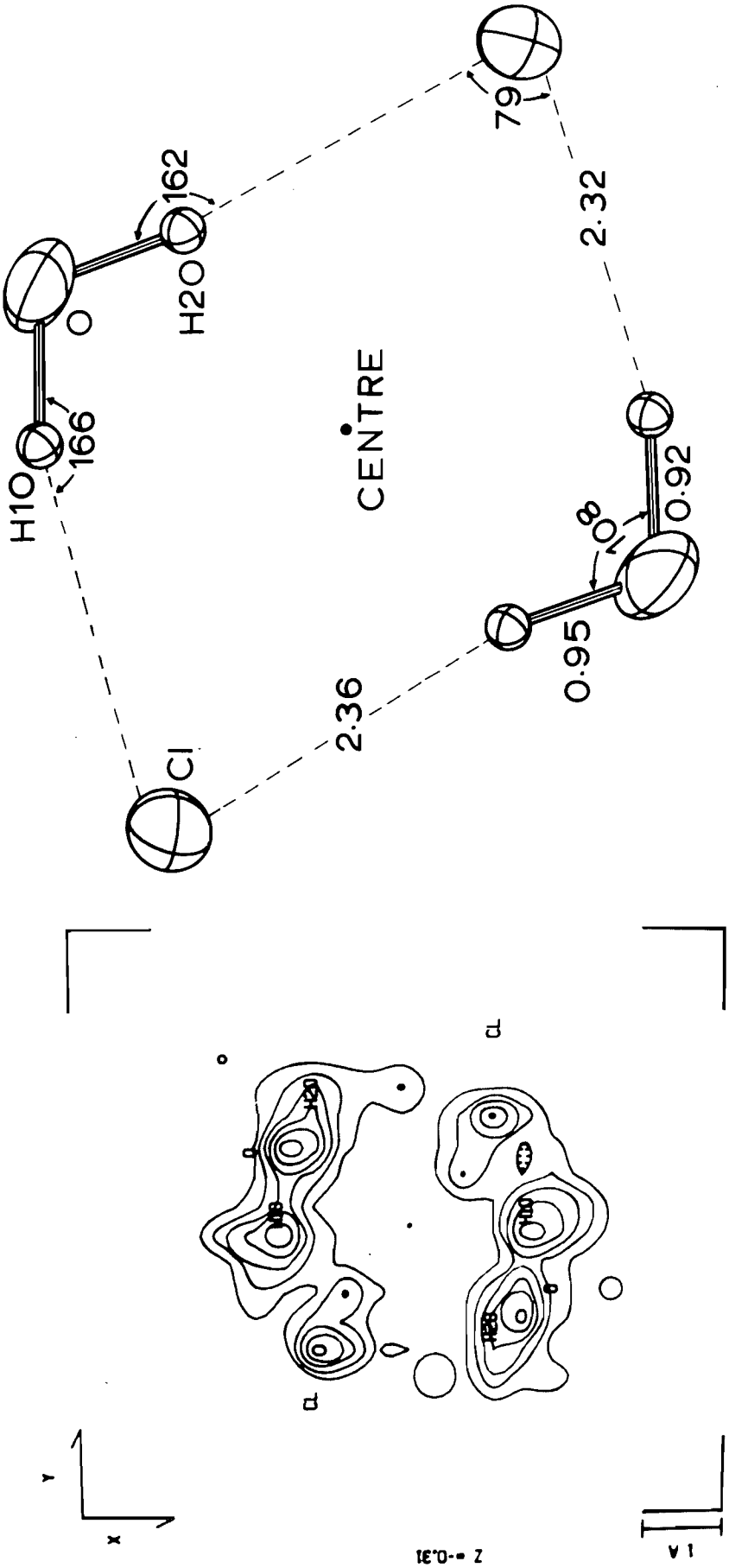

FIG. 3. A difference Fourier contour map of *7a* showing the presence of hydrogen atoms on the water molecule (left), and the hydrogen bonding scheme (right).

Can. J. Chem. Downloaded from www.nrcresearchpress.com by 122.72.124.2 on 09/07/12
For personal use only.

have been characterised by crystallographic methods (7, 20, 22–29). Each of them displays a different kind of molecular structure.

The crystal structures of compounds **7***a* and **7***b* consist of discrete $[Au_2(\mu\text{-dmpm})_2]^{2+}$ cations and two halide anions. The anions are located above and below the eight-membered ring formed by two gold atoms and the atoms of the bidentate ligands of the cation. A perspective view of the complex cation is presented in Fig. 2. Although the structures appear to be identical, the salts are not isomorphous. Each formula unit of the gold dimer in the crystal lattice is associated with two molecules of water of crystallization. The crystal structure contains polymeric chains made of discrete molecules linked together by hydrogen bonds formed between water molecules and the halide anions.

In the solid state the cationic dimers **7***a* and **7***b* have an exact C_i symmetry, the mid-point of the Au → Au′ vector coinciding with a crystallographic centre of inversion. The $Au_2P_4C_2$ ring adopts a chair conformation. In both structures, the metal atoms are spanned by two bridging dmpm ligands in a mutually *trans* arrangement. The Au...Au separations, 3.0143(3) Å in **7***a* and 3.0190(4) Å in **7***b*, fall well outside the range considered typical for Au—Au single bonds (ca. 2.757–2.780 Å) (30). However, the P...P bite distances of 3.084(2) Å in **7***a* and 3.116(3) Å in **7***b* are slightly larger than the Au...Au distance, suggesting a weak metal–metal interaction. The Au—P bond lengths in **7***a* and **7***b* are indistinguishable, averaging 2.302(2) Å. The halide anions are located approximately normal to the Au_2P_4 plane as indicated by the P—Au—X angles (see Table 3). The closest distances of approach between the gold atoms and the halide anions are 3.467(2), 3.534(2) Å in **7***a* and 3.590(1), 3.678(1) Å in **7***b*, clearly indicating that the interaction is essentially ionic, with little covalent character. In the analogous chloride, bromide and iodide dppm complexes, there is at least one covalently bonded halide atom with Au—Cl = 2.771(4)–2.963(4) Å in compounds **1**–**3** and Au—I = 3.127(3)–3.196(2) Å in **4** (2, 5). Each of the two water molecules forms two hydrogen bonds to chloride ions of two neighbouring unit cells.

It is interesting to speculate on the reasons for the different structures **1**–**5** being adopted by such similar complexes. It has been suggested that the Au_2dppm_2 ring, and the other rings with phenyl substituents on phosphorus, must twist (giving non-linear PAuP groups) in order to reduce steric hindrance between phenyl substituents and that this favours halide coordination above the $Au_2P_4C_2$ ring. Thus, steric effects would be responsible for the greater tendency of the halide to coordinate in dppm compared to dmpm complexes (7). However, this argument is contrary to the more general trend that increased steric hindrance usually leads to *lower* coordination numbers. In addition, there are now more structures which do not conform to the expected pattern; for example, in **3** the halide is coordinated in the plane of the $Au_2P_4C_2$ ring rather than above the ring (2–5). Therefore, it is more probable that the lower tendency of halide to coordinate in the dmpm compared to dppm complexes is primarily an electronic effect. However, since the energy differences between the different structural forms **1**–**5** are low, this conclusion is tentative. By examination of structures **1**–**5**, it is easy to see how either intramolecular or intermolecular halide exchange could occur easily in these complexes, as shown experimentally in several cases (2–5). Thus, interconversion of structures **1** and **5** leads to exchange of halide between gold centres while both halides remain weakly coordinated. Similarly, interconversion between structures **2**, **3**, and **4** leads to fluxionality while only one halide is coordinated throughout. Finally, conversion of **1** or **5** to **2**, **3**, or **4**, involving halide dissociation, would lead to intermolecular halide exchange.

TABLE 3. Selected bond distances (Å) and angles (deg)

	Distance	
Bond*	**7***a*, X = Cl	**7***b* X = I
Au—Au′	3.0143(3)	3.0190(4)
P(1)—P(2)	3.084(2)	3.116(3)
Au—X	3.467(2)	3.5903(7)
Au—X′	3.543(2)	3.6780(6)
Au—P(1)	2.302(1)	2.303(2)
Au—P(2)	2.303(1)	2.301(2)
P(1)—C(1)	1.813(6)	1.804(9)
P(1)—C(2)	1.817(6)	1.783(8)
P(1)—C(3)	1.819(6)	1.837(8)
P(2)—C(3)	1.817(5)	1.831(7)
P(2)—C(4)	1.817(7)	1.83(1)
P(2)—C(5)	1.822(5)	1.798(7)
X—O	3.227(8)	3.512(16)
X—O′	3.277(5)	3.532(15)
	Angle (deg)	
Bonds*	**7***a*, X = Cl	**7***b* X = I
P(1)—Au—P(2)	176.80(3)	177.42(7)
Au—P(1)—C(1)	115.2(3)	116.7(4)
Au—P(1)—C(2)	114.8(2)	114.9(3)
Au—P(1)—C(3)	111.6(2)	111.8(2)
Au—P(2)—C(3)	112.2(2)	112.1(2)
Au—P(2)—C(4)	117.1(2)	117.5(3)
Au—P(2)—C(5)	111.4(2)	114.7(3)
X—Au—X′	129.01(6)	130.93(2)
X—Au—P(1)	86.33(5)	86.44(4)
X—Au—P(2)	91.91(5)	93.64(4)
X′—Au—P(1)	95.13(4)	94.66(4)
X′—Au—P(2)	88.05(4)	87.24(4)
P(1)—C(3)—P(2)	116.1(2)	116.3(4)
Au—X—Au′	50.99(2)	49.07(1)
O—X—O′	76.5(2)	44.7(5)
X—O—X′	103.5(2)	135.3(6)

*X′ is related to X by the centre at (0, 0, 0).

Acknowledgment

We thank the Natural Sciences and Engineering Research Council of Canada for financial support of this work, through grants to N.C.P. and R.J.P., and the University for a Visa bursary to R.R.

1. R. J. PUDDEPHATT. Chem. Soc. Rev. 99 (1983).
2. H. SCHMIDBAUR, A. WOHLLEBEN, U. SCHUBERT, A. FRANK, and G. HUTTNER. Chem. Ber. **110**, 2951 (1977).
3. H. SCHMIDBAUR, TH. POLLOK, R. HERR, F. E. WAGNER, R. BAU, J. RIEDE, and G. MÜLLER. Organometallics, **5**, 566 (1986).
4. H. SCHMIDBAUR, R. HERR, G. MÜLLER, and J. RIEDE. Organometallics, **4**, 1208 (1985).
5. J. SHAIN and J. P. FACKLER JR. Inorg. Chim. Acta, **131**, 157 (1987).
6. W. LUDWIG and W. MEYER. Helv. Chim. Acta, **65**, 934 (1982).

7. J. KOZELKA, H. R. OSWALD, and E. DUBLER. Acta Crystallogr. C**42**, 1007 (1986).
8. Enraf-Nonius CAD4 operators manual. Enraf-Nonius Delft: Delft, The Netherlands. 1984.
9. T. C. FURNAS (*Editor*). Single crystal orienter instruction manual. G.E. Co., Milwaukee, WI. 1966.
10. Enraf-Nonius structure determination package. SDP-Plus, Version 3.0. 1985.
11. W. R. BUSING and H. A. LEVY. J. Chem. Phys. **26**, 563 (1957).
12. P. COPPENS, L. LEISEROWITZ, and D. RABINOVICH. Acta Crystallogr. **18**, 1035 (1965).
13. E. R. HOWELLS, D. C. PHILLIPS, and D. ROGERS. Acta Crystallogr. **3**, 210 (1950).
14. International tables for X-ray crystallography. Vol. A. D. Reidel, Boston 1983, International tables for X-ray crystallography. Vol. IV. Kynoch, Birmingham, England. 1974.
15. R. F. STEWART, E. R. DAVIDSON, and W. T. SIMPSON. J. Chem. Phys. **42**, 3175 (1965).
16. M. P. BROWN, J. R. FISHER, R. H. HILL, R. J. PUDDEPHATT, and K. R. SEDDON. Inorg. Chem. **20**, 3516 (1983).
17. P. A. W. DEAN, J. J. VITTAL, and R. S. SRIVASTAVA. Can. J. Chem. **65**, 2628 (1987).
18. A. SHIOTANI, H.-F. KLEIN, and H. SCHMIDBAUR. J. Am. Chem. Soc. **93**, 1555 (1971); H. SCHMIDBAUR, A. SHIOTANI, and H.-F. KLEIN. Chem. Ber. **104**, 2831 (1971).
19. R. J. PUDDEPHATT. *In* Comprehensive organometallic chemistry. *Edited by* G. Wilkinson, F. G. A. Stone, and E. W. Abel. Pergamon, Oxford. 1982. Chap. 15.
20. W. BENSCH, M. PRELATI, and W. LUDWIG. J. Chem. Soc. Chem. Commun. 1762 (1986).
21. R. J. PUDDEPHATT. *In* Comprehensive coordination chemistry. *Edited by* G. Wilkinson, R. D. Gillard, and J. A. McCleverty. Pergamon, Oxford. 1987. Chap. 55.
22. S. S. M. LING, I. R. JOBE, LJ. MANOJLOVIC-MUIR, K. W. MUIR, and R. J. PUDDEPHATT. J. Chem. Soc. Chem. Commun. 566 (1985).
23. LJ. MANOJLOVIC-MUIR, S. S. M. LING, and R. J. PUDDEPHATT. J. Chem. Soc. Dalton Trans. 151 (1986).
24. H. H. KARSCH and U. SCHUBERT. Z. Naturforsch. Teil. B, **37**, 186 (1982).
25. S. S. M. LING, R. J. PUDDEPHATT, LJ. MANOJLOVIC-MUIR, and K. W. MUIR. Inorg. Chim. Acta, **77**, L95 (1983).
26. LJ. MANOJLOVIC-MUIR, K. W. MUIR, A. A. FREW, S. S. M. LING, M. A. THOMSON, and R. J. PUDDEPHATT. Organometallics, **3**, 1637 (1984).
27. M. L. KULBERG and C. P. KUBIAK. Organometallics, **3**, 632 (1984).
28. S. S. M. LING, N. C. PAYNE, and R. J. PUDDEPHATT. Organometallics, **4**, 1546 (1985).
29. H. H. KARSCH and B. M. MILEWSKI-MAHRLA. Angew. Chem. Int. Ed. Engl. **20**, 814 (1981).
30. D. M. P. MINGOS. Gold Bull. **17(1)**, 5 (1984).

Can. J. Chem. Downloaded from www.nrcresearchpress.com by 122.72.124.2 on 09/07/12
For personal use only.

Polarimetric and nuclear magnetic resonance studies of the complexation of mercury by thiols

MOHAMED M. SHOUKRY,[1] BRUCE V. CHEESMAN, AND DALLAS L. RABENSTEIN[2]
Department of Chemistry, University of Alberta, Edmonton, Alta., Canada T6G 2G2

Received February 11, 1988

MOHAMED M. SHOUKRY, BRUCE V. CHEESMAN, and DALLAS L. RABENSTEIN. Can. J. Chem. **66**, 3184 (1988).

The complexation of Hg(II) by glutathione has been studied by polarimetry under conditions of excess ligand with the objective of characterizing formation of the 3:1 complex, Hg(glutathione)$_3$. The optical rotatory power of solutions containing glutathione only and of solutions containing glutathione and Hg(II) at ratios of 2:1, 2.5:1, 3:1, and 4:1 was measured as a function of pH. Acid dissociation constants for the ammonium and thiol groups of glutathione and for the two ammonium groups of Hg(glutathione)$_2$ and the formation constant of the 3:1 complex (Hg(glutathione)$_2$ + glutathione $\rightleftarrows$ Hg(glutathione)$_3$) were determined from the pH dependence of the optical rotatory power. The value obtained for the formation constant, $K_f = 1.5 \times 10^3$, indicates that binding of the third ligand to form Hg(glutathione)$_3$ is much weaker than binding of the first two glutathione ligands. However, calculations indicate that binding is sufficiently strong that a significant fraction of Hg(II) is present as Hg(glutathione)$_3$ under physiological conditions. Equilibrium constants were also determined by polarimetry and by ^{13}C nuclear magnetic resonance for the displacement of one thiolate ligand by another (RSHgSR + R′SH $\rightleftarrows$ RSHgSR′ + RSH; RSHgSR′ + R′SH $\rightleftarrows$ R′SHgSR′ + RSH). The results indicate that, at pH 5.5 and at physiological pH, the relative stability increases in the order Hg(glutathione)$_2$ < Hg(penicillamine)$_2$ < Hg(mercaptoethylamine)$_2$. However, when competitive protonation of free ligand is accounted for, it is shown that the intrinsic stability of the complexes increases in the order Hg(penicillamine)$_2$ < Hg(mercaptoethylamine)$_2$ < Hg(glutathione)$_2$, which parallels the order of the Brønsted basicity of the thiolate ligands.

MOHAMED M. SHOUKRY, BRUCE V. CHEESMAN et DALLAS L. RABENSTEIN. Can. J. Chem. **66**, 3184 (1988).

Faisant appel à la polarimétrie et opérant dans des conditions impliquant un excès de ligand, on a étudié la complexion du Hg(II) par le glutathion dans le but de caractériser la formation du complexe 3:1, Hg(glutathion)$_3$. On a mesuré la variation, en fonction du pH, du pouvoir rotatoire optique de solutions ne contenant que du glutathion ainsi que de solutions contenant du glutathion et du Hg(II) à des rapports de 2:1, 2.5:1, 3:1 et 4:1. En se basant sur la relation entre le pouvoir rotatoire optique et le pH, on a déterminé les constantes de dissociation acide des groupements ammonium et thiol du glutathion ainsi que des deux groupements ammonium du complexe Hg(glutathion)$_2$ de même que la constante de formation du complexe 3:1 (Hg(glutathion)$_2$ + glutathion $\rightleftarrows$ Hg(glutathion)$_3$). La valeur obtenue pour la constante de formation, $K_f = 1{,}5 \times 10^3$, indique que la liaison du troisième ligand pour former le complexe Hg(glutathion)$_3$ est beaucoup plus facile que les liaisons des deux premiers ligands glutathion. Toutefois, des calculs indiquent que la liaison est suffisamment forte pour qu'un fraction importante du Hg(II) soit présent sous la forme Hg(glutathion)$_3$, dans des conditions physiologiques. Faisant appel à la polarimétrie ainsi que la résonance magnétique nucléaire du ^{13}C, on a aussi déterminé les constantes d'équilibre pour le déplacement d'un ligand thiolate par un autre (RSHgSR + R′SH $\rightleftarrows$ RSHgSR′ + RSH; RSHgSR′ + R′SH $\rightleftarrows$ R′SHgSR′ + RSH). Les résultats indiquent que, à un pH de 5,5 ainsi qu'au pH physiologique, les stabilités relatives augmentent dans l'ordre Hg(glutathion)$_2$ < Hg(pénicillamine)$_2$ < Hg(mercaptoéthylamine)$_2$. Toutefois, on démontre que, lorsqu'on tient compte de la protonation compétitive du ligand libre, la stabilité intrinsèque des complexes augmente dans l'ordre Hg(pénicillamine)$_2$ < Hg(mercaptoéthylamine)$_2$ < Hg(glutathion)$_2$ qui est parallèle à l'ordre de la basicité selon Brønsted des ligands thiolates.

[Traduit par la revue]

Introduction

Mercury(II) forms extremely stable, linear two-coordinate complexes with sulfhydryl-containing ligands (1–6). For example, stability constants for the Hg(glutathione)$_2$ and Hg(cysteine)$_2$ complexes at physiological pH and 25°C are reported to be 9×10^{40} and 2×10^{40} respectively (1). However, even though the thermodynamic stability of Hg(II)–thiol complexes is high, Hg(II)–thiol binding is labile, with the Hg(II) exchanging among thiol ligands. Consequently, in biological systems, Hg(II) exchanges among the multitude of thiol groups it encounters, with some ultimately combining with thiol groups of enzymes and other molecules that are dependent on free thiol groups for their activity.

In a recent ^{13}C nmr study of the kinetics of Hg(II) – thiol ligand exchange, we obtained evidence for the formation at physiological pH of complexes having the stoichiometry Hg(thiol)$_3$ when the thiol:Hg(II) ratio is greater than 2:1 (7).

[1] $$RS^- + RSHgSR \rightleftarrows Hg(SR)_3$$

$$K_f = \frac{[Hg(SR)_3^-]}{[RS^-][Hg(SR)_2]}$$

We proposed that the rapid exchange of thiol between the free and Hg(thiol)$_2$ forms proceeds via a mechanism involving Hg(thiol)$_3$ complexes. Even though the complexation of Hg(II) by sulfhydryl-containing amino acids and peptides has been the subject of a number of studies, including potentiometric studies with ligand:Hg(II) ratios greater than 2:1 (1, 4–6), this is apparently the first report of complexes of the stoichiometry Hg(thiol)$_3$ with sulfhydryl-containing amino acids and peptides.

Because of the potential importance of Hg(thiol)$_3$ complexes in accounting for the mobility of Hg(II) in biological systems, we have investigated the formation of the 3:1 complex with the sulfhydryl-containing tripeptide glutathione (GSH) by an independent technique, polarimetry. Glutathione was chosen for this study because it has been established previously that Hg(II) in human erythrocytes is complexed predominantly by glutathione (8), and GSH has been implicated in numerous other studies of the toxicology of Hg(II) (9–12).

We also report on the use of polarimetry to measure

[1]Present address: Department of Chemistry, Faculty of Science, The United Arab Emirates University, Al-Ain, United Arab Emirates.
[2]Address correspondence to this author at: Department of Chemistry, University of California, Riverside, CA 92521, U.S.A.

Can. J. Chem. Downloaded from www.nrcresearchpress.com by 122.72.124.2 on 09/07/12
For personal use only.

equilibrium constants for the displacement of one thiol ligand by another.

[2] $RSHgSR + R'SH \leftrightarrows RSHgSR' + RSH$

$$K_1 = \frac{[RSHgSR'][RSH]}{[RSHgSR][R'SH]}$$

[3] $RSHgSR' + R'SH \rightleftarrows R'SHgSR' + RSH$

$$K_2 = \frac{[R'SHgSR'][RSH]}{[RSHgSR'][R'SH]}$$

[4] $RSHgSR + 2R'SH \rightleftarrows R'SHgSR' + 2RSH$

$$K_d = K_1K_2 = \frac{[R'SHgSR'][RSH]^2}{[RSHgSR][R'SH]^2}$$

Because of the extremely high stability of $Hg(thiol)_2$ complexes, it is difficult to measure accurate values for their stability constants. However, if displacement constants K_1 and K_2 can be measured, they will provide the relative affinity of various thiol ligands for Hg(II). Such information is of interest, e.g., in determining the relationship, if any, between the stabilities of Hg(II)–ligand complexes and the effectiveness of the ligands as therapeutic antidotes for mercury poisoning. Equilibrium constants were determined for the displacement of glutathione by penicillamine and for the displacement of penicillamine by mercaptoethylamine (cysteamine). Equilibrium constants for the displacement of glutathione by penicillamine were also determined by ^{13}C nmr spectroscopy for comparison with the polarimetric results.

Experimental

Glutathione, D-penicillamine, and mercaptoethylamine hydrochloride (Sigma) were used as received. All thiols were stored under an inert atmosphere below 4°C. Solutions of Hg(II) were prepared from analytical grade mercuric nitrate (J. T. Baker Chemical Co.). 1,4-Dioxane and D_2O were from BDH Chemicals Ltd. and Stohler Isotope Chemicals, respectively.

All solutions used in the polarimetric studies were prepared in water that had been purified by distilling it twice and then passing it through a Barnstead D8902 ultrapure mixed-bed ion-exchange resin. The solvent was deoxygenated by bubbling with nitrogen or argon before addition of thiol, to minimize oxidation by dissolved oxygen. Inert gas was also bubbled through the solutions during adjustment of pH and, in the nmr experiments, nmr tubes were flushed with gas before transfer of an aliquot of solution to the tube. In the polarimetric experiments to characterize the $Hg(glutathione)_3$ complex, 50 mL of solution containing 0.10 M glutathione, 0.3 M $NaNO_3$, and either 0.025, 0.0333, 0.040, or 0.050 M $Hg(NO_3)_2$ was prepared from solid glutathione and $NaNO_3$ and stock $Hg(NO_3)_2$ solution. The pH was initially adjusted to ~6 and then increased by adding ~10 M NaOH as the optical rotation was measured, as described below. In the polarimetric experiments to measure displacement equilibrium constants, 50 mL of solution containing 0.015 M $Hg(glutathione)_2$ or 0.015 M $Hg(penicillamine)_2$ and 0.3 M $NaNO_3$ were prepared from $Hg(NO_3)_2$ stock solution and solid $NaNO_3$ and glutathione or penicillamine. The pH was adjusted to 5.5 ± 0.1, and the optical rotation was measured as 0.491 M penicillamine was added to the $Hg(glutathione)_2$ solution and as 0.492 M mercaptoethylamine was added to the $Hg(penicillamine)_2$ solution. The penicillamine and mercaptoethylamine titrant solutions were prepared immediately before use. The pH was kept at 5.5 ± 0.1 during the titration by addition of ~10 M NaOH or HCl as necessary.

In the ^{13}C nmr experiments, a solvent mixture consisting of 5% D_2O/95% H_2O was used. Solid penicillamine was added to a pH 6.0 solution containing 0.10 M $Hg(glutathione)_2$ and 0.3 M KNO_3. Solution preparation was done in a water-jacketed titration cell at 25.0 ± 0.1°C. The cell was covered with a tightly fitting plastic lid with holes for glass and reference electrodes, a micropipet delivery tube, and argon inlet and outlet tubes. After each addition of penicillamine, the pH was adjusted to 6.0, and a sample was withdrawn for nmr measurements.

For the nmr experiments, pH measurements were made with an Orion model 701A pH meter equipped with a Phillips glass electrode (GAT 130) and a Phillips glass sleeve double junction Ag/AgCl reference electrode (R44/2-SD/12). For the polarimetric experiments, pH measurements were made with a Fisher Accumet 620 pH meter equipped with an Ingold combination electrode. The pH meters were calibrated with freshly prepared N.B.S. standard solutions having pH values of 4.008 (phthalate) and 6.865 (phosphate).

Polarimetric measurements were made with a Perkin–Elmer model 141 polarimeter using the 589-nm line of the sodium lamp. The polarimeter was calibrated using solutions of sucrose. The precision of the measurements is estimated to be ±0.002 degrees of arc. A water-jacketed cell of 100 mm length and 5 mL total volume was used. The solutions were contained in a water-jacketed titration cell (25.0 ± 0.1°C), which was connected to the polarimetric cell via Teflon tubing. Solution was transferred from the titration cell to the polarimetric cell and back to the titration cell through the Teflon tubing with a 10-mL syringe that was connected to one of the two Teflon transfer lines with a liquid chromatography sample injection loop. The pH of the solution was adjusted in the titration cell, and then the solution was circulated through the polarimetric cell with the syringe. Titrant was added with a 1-mL Mettler DV11 autoburette.

The ^{13}C nmr measurements were made at 90.56 MHz and 25°C on a Bruker WM-360 spectrometer. Sample temperature was maintained at 25°C by collecting free induction decays under conditions of inverse gated decoupling (nOe suppressed) with chilled air blowing over the sample tube in the probe to minimize sample heating. ^{13}C chemical shifts were measured relative to internal 1,4-dioxane, but are reported relative to tetramethylsilane (TMS). The resonance for 1,4-dioxane is at 67.40 ppm to high frequency from TMS.

Results and discussion

Characterization of Hg(glutathione)$_3$

The optical rotatory power (α_{obs}) of solutions containing 0.10 *M* GSH (A), 0.05 *M* $Hg(NO_3)_2$ and 0.10 *M* GSH (B), and 0.025 *M* $Hg(NO_3)_2$ and 0.10 *M* GSH (C) is plotted as a function of pH in Fig. 1. Since Hg(II) has a strong tendency to form linear, two-coordinate complexes with thiol ligands (1, 3–6), curve B in Fig. 1 corresponds to the optical rotatory power for the complex $Hg(glutathione)_2$. Curve D is the predicted optical rotatory power vs. pH for solution C if only the 2:1 complex and free GSH were present. At pH ~ 6, the predicted and observed curves are similar, indicating that these are the only species at this pH. However, at higher pH, α_{obs} is different from $\alpha_{predicted}$, which indicates the formation of other Hg(II)–GSH complexes. A similar variation was observed between experimental and predicted ^{13}C chemical shifts for GSH in solutions having GSH:Hg(II) ratios greater than 2:1 at pH > 6 (7). From studies in which the ^{13}C chemical shifts were measured as a function of the Hg(II):GSH ratio at constant pH, it was shown that the differences are due to formation of the 3:1 complex, $Hg(glutathione)_3$. Evidence for the formation of $Hg(SR)_3^-$ complexes, where R represents methyl and *tert*-butyl groups, in solution has also been obtained from vibrational spectroscopic studies (13). In another study, the crystalline mononuclear, three-coordinate mercury(II) thiolate $[NBu^n_4][Hg(SPh)_3]$ was prepared and its crystal structure determined (14).

The formation constant for $Hg(glutathione)_3$ was determined from the data in Figs. 1 and 2. First, however, the acid dissociation constants for GSH and $Hg(glutathione)_2$ were determined from the data in Curves A and B of Fig. 1. For GSH, the thiol and ammonium groups are titrated in the pH range

Can. J. Chem. Downloaded from www.nrcresearchpress.com by 122.72.124.2 on 09/07/12
For personal use only.

Can. J. Chem. Downloaded from www.nrcresearchpress.com by 122.72.124.2 on 09/07/12
For personal use only.

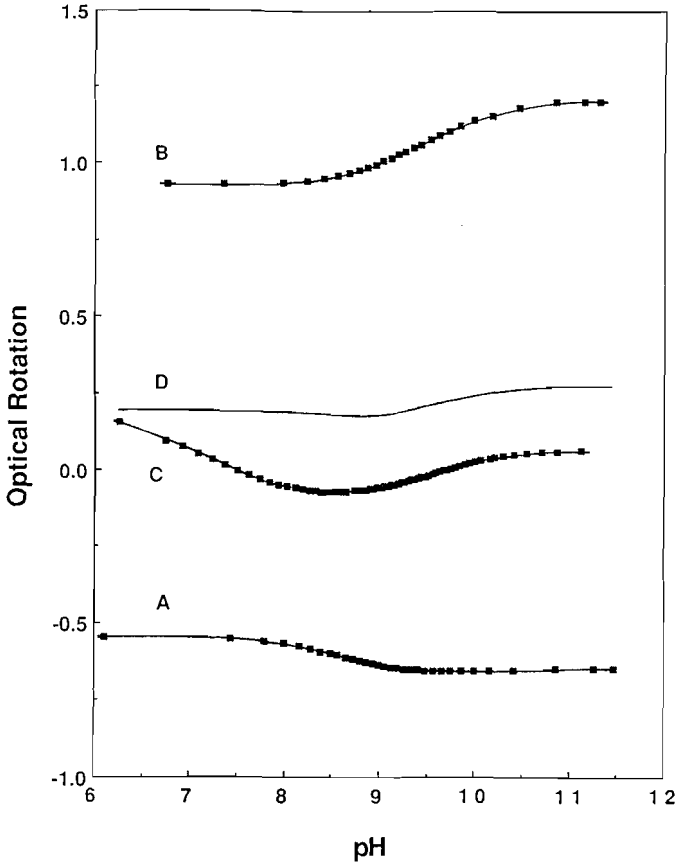

FIG. 1. pH dependence of the optical rotation of solutions containing (A) 0.100 M GSH, (B) 0.05 M $Hg(NO_3)_2$ and 0.100 M GSH, and (C) 0.025 M $Hg(NO_3)_2$ and 0.100 M GSH. Curve D represents the optical rotation expected for solution C if only free GSH and $Hg(glutathione)_2$ were present. The solid curves through the experimental points in A–C are theoretical curves calculated with acid dissociation and formation constants determined in this study.

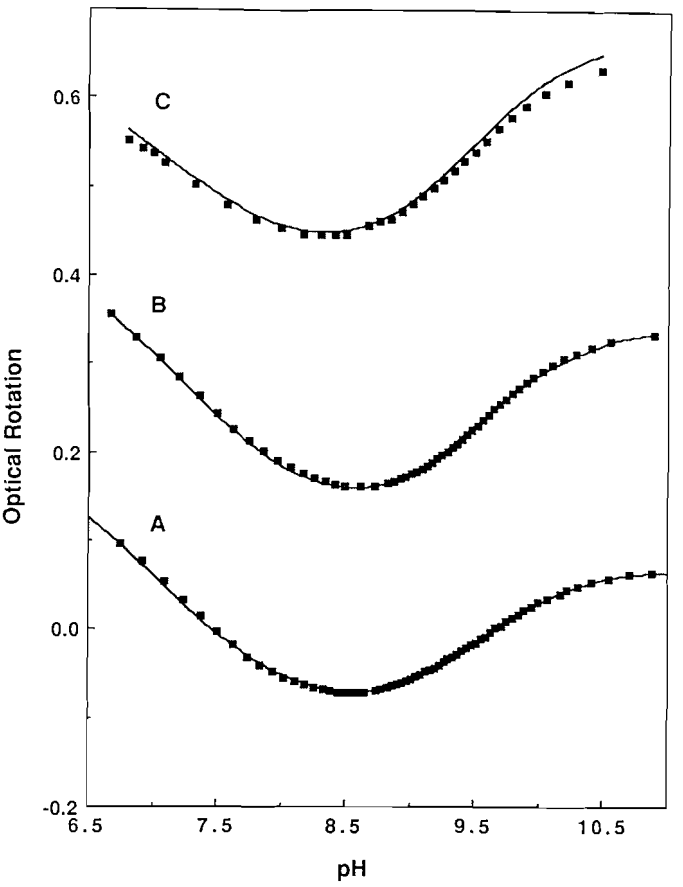

FIG. 2. pH dependence of the optical rotation of solutions containing (A) 0.025 M $Hg(NO_3)_2$ and 0.100 M GSH, (B) 0.0333 M $Hg(NO_3)_2$ and 0.100 M GSH, and (C) 0.04 M $Hg(NO_3)_2$ and 0.100 M GSH. The solid curves are theoretical curves calculated with the acid dissociation and formation constants determined in this study.

shown in Fig. 1, as given by eqs. [5] and [6],

[5] $H_2A^- \rightleftarrows H^+ + HA^{2-}$

$$K_3 = \frac{[H^+][HA^{2-}]}{[H_2A^-]}$$

[6] $HA^{2-} \rightleftarrows H^+ + A^{3-}$

$$K_4 = \frac{[H^+][A^{3-}]}{[HA^{2-}]}$$

where H_3A represents the triprotonated form of GSH. The contribution of each species to the total rotation, α_{obs}, at a given pH is the product of its concentration and its molar optical rotatory power:

[7] $$\alpha_{obs} = \alpha_A[A^{3-}] + \alpha_{HA}[HA^{2-}] + \alpha_{H_2A}[H_2A^-]$$

where α_A, α_{HA}, and α_{H_2A} are the molar optical rotatory powers of the species indicated. Substitution of eqs. [5] and [6] into [7] leads to:

[8] $$\alpha_{obs} = \frac{\alpha_A K_3 K_4 + \alpha_{HA} K_3[H^+] + \alpha_{H_2A}[H^+]^2}{[H^+]^2 + K_3[H^+] + K_3K_4}[GSH]_{total}$$

Since H_2A^- and A^{3-} are the only species present at pH 6–7 and pH > 11 respectively, values of $\alpha_{H_2A} = -5.431$ and $\alpha_A = -6.481$ deg·L·mol^{-1} were calculated directly from α_{obs} at these pH values. K_3, K_4, and α_{HA} were then determined by fitting the α_{obs} vs. pH data for GSH to eq. [8] using the nonlinear least-squares computer program KINET (15). The values obtained are $\alpha_{HA} = -6.691$ deg·L·mol^{-1}, $pK_3 = 8.58$, and $pK_4 = 9.54$. The solid line through the experimental points for GSH in Fig. 1 is the optical rotatory power vs. pH predicted using these parameters. The average values from three experiments are $pK_3 = 8.60 \pm 0.02$ and $pK_4 = 9.56 \pm 0.06$; these values are in excellent agreement with values determined by other techniques (16–18).

The optical rotatory power of the solution containing Hg(glutathione)$_2$ is pH dependent due to titration of the free ammonium group of each thiolate-coordinated ligand, as defined by eqs. [9] and [10].

[9] $Hg(AH)_2^{2-} \rightleftarrows H^+ + Hg(AH)(A)^{3-}$

$$K_5 = \frac{[H^+][Hg(AH)(A)^{3-}]}{Hg(AH)_2^{2-}}$$

[10] $Hg(AH)(A)^{3-} \rightleftarrows H^+ + Hg(A)_2^{4-}$

$$K_6 = \frac{[H^+][Hg(A)_2^{4-}]}{[Hg(AH)(A)^{3-}]}$$

where $Hg(AH)_2^{2-}$ represents the form of the complex with both amine groups protonated, etc. pK_5 and pK_6 were determined from the data in curve B of Fig. 1. Because the two ammonium

Can. J. Chem. Downloaded from www.nrcresearchpress.com by 122.72.124.2 on 09/07/12
For personal use only.

groups are quite distant from each other in $Hg(AH)_2^{2-}$, each group is assumed to dissociate independently of the other and to have an acid dissociation constant that is independent of the protonation state of the other group. Thus, the macroscopic constants K_5 and K_6 are assumed to equal $2K_{NH_3^+}$ and $K_{NH_3^+}/2$ respectively, where $K_{NH_3^+}$ is the dissociation constant for the ammonium group. Substitution of these equations for K_5 and K_6 into the equation analogous to eq. [8] for $Hg(SG)_2$ gives an equation for α_{obs} in terms of $K_{NH_3^+}$ and the molar optical rotatory powers of $Hg(AH)_2^{2-}$, $Hg(AH)(A)^{3-}$, and $Hg(A)_2^{4-}$. Since $Hg(AH)_2^{2-}$ and $Hg(A)_2^{4-}$ are the only species present at pH 6–7 and pH > 11, respectively, values of $\alpha_{Ag(AH)_2} = 18.66$ deg·L·mol^{-1} and $\alpha_{Hg(A)_2} = 24.20$ deg·L·mol^{-1} were calculated directly from the α_{obs} vs. pH data at these pHs. Values of 9.34 and 20.94 deg·L·mol^{-1} were obtained for $pK_{NH_3^+}$ and $\alpha_{Hg(HA)(A)^{3-}}$ respectively from a nonlinear least-squares fit of the data in Fig. 1B. The solid line through the experimental points in Fig. 1B is the theoretical curve predicted with these parameters. The average value obtained for $pK_{NH_3^+}$ from three experiments is 9.33 ± 0.06. Values calculated for pK_5 and pK_6 from this value for $pK_{NH_3^+}$ are 9.03 and 9.63 respectively.

To determine the formation constant for the 3:1 complex, the optical rotatory power was measured as a function of pH for solutions containing GSH and Hg(II) at ratios of 2.5:1, 3:1, and 4:1 (Fig. 2). For these solution conditions, α_{obs} is given by eq. [11].

$$[11]\quad \alpha_{obs} = \sum_{i=0}^{2} \alpha_{H_iA}[H_iA] + \sum_{i=0}^{2} \alpha_{Hg(A)_2H_i}[Hg(A)_2H_i] + \sum_{i=0}^{3} \alpha_{Hg(A)_3H_i}[Hg(A)_3H_i]$$

The formation constant for $Hg(A)_3^{7-}$, defined by eq. [12],

$$[12]\quad A^{3-} + Hg(A)_2^{4-} \rightleftarrows Hg(A)_3^{7-}$$

$$K_{f3} = \frac{[Hg(A)_3^{7-}]}{[A^{3-}][Hg(A)_2^{4-}]}$$

was determined by fitting the data in Fig. 2 to an equation that gives α_{obs} in terms of the acid dissociation constants for H_3A, $Hg(AH)_2^{2-}$, and $Hg(AH)_3^{4-}$, the formation constant for $Hg(A)_3^{7-}$, the pH, and the total concentrations of Hg(II) and glutathione.[3] The equation was derived by appropriate substitutions into eq. [11]. Because the three $-NH_3^+$ groups of $Hg(AH)_3^{4-}$ are quite distant from each other and from the site of complexation, the acidity of each $-NH_3^+$ group was assumed to be independent of the protonation states of the other $-NH_3^+$ groups. The three macroscopic acid dissociation constants used for $Hg(AH)_3^{4-}$ in the formation constant calculations were calculated using the value determined above for $pK_{NH_3^+}$ for the $Hg(AH)_2^{2-}$ complex and the equations $K_7 = [H^+][Hg(A)(AH)_2^{5-}]/[Hg(AH)_3^{4-}] = 3K_{NH_3^+}$; $K_8 = [H^+][Hg(A)_2(AH)^{6-}]/[Hg(A)(AH)_2^{5-}] = K_{NH_3^+}$; and $K_9 = [H^+][HgA_3^{7-}]/[Hg(A)_2(AH)^{6-}] = K_{NH_3^+}/3$. The values obtained by fitting simultaneously the data from the three separate experiments in Fig. 2 using nonlinear least-squares methods are: $\log K_{f3} = 3.18 \pm 0.02$, $\alpha_{Hg(AH)_3} = 1.63 \pm 0.07$, $\alpha_{Hg(A)(AH)_2} = 3.74 \pm 0.11$, $\alpha_{Hg(A)_2(AH)} = 6.14 \pm 0.14$, and $\alpha_{HgA_3} = 9.17 \pm 0.08$. The value obtained for $\log K_{f3}$ is in excellent agreement with the average value of 3.23 obtained from ^{13}C nmr chemical shift data (7).

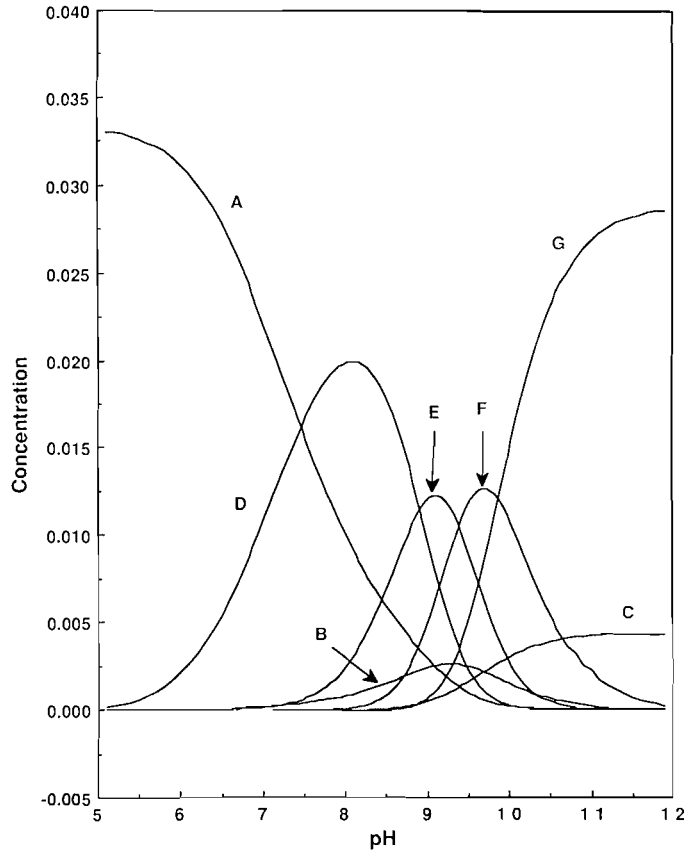

FIG. 3. pH dependence of the distribution of Hg(II) among its various complexes in a solution containing 0.0333 M $Hg(NO_3)_2$ and 0.100 M GSH. The curves were calculated using acid dissociation and formation constants determined in this study. The complexes are: (A) $Hg(AH)_2^{2-}$; (B) $Hg(A)(AH)^{3-}$; (C) HgA_2^{4-}; (D) $Hg(AH)_3^{4-}$; (E) $Hg(A)(AH)_2^{5-}$; (F) $Hg(A)_2(AH)^{6-}$; (G) HgA_3^{7-}.

Figure 3 shows the distribution of Hg(II) among its various complexes with GSH in a solution containing 0.100 M GSH and 0.0333 M Hg(II) (the conditions for curve C of Fig. 1). These curves were calculated using the formation constants and acid dissociation constants determined in this study and show that even though the formation constant for addition of the third ligand is much less than that for the formation of $Hg(AH)_2^{2-}$ (9×10^{40}) (1), it is large enough that a major fraction of the Hg(II) is present in the various 3:1 complexes. It is also of interest to use these results to predict the extent to which the 3:1 complexes will form in vivo. As an example, in human erythrocytes, where the GSH concentration is $\sim 2.2 \times 10^{-3}$ M and the pH ~ 7.4 (19), ~10% of the Hg(II) is predicted to be present as the $Hg(AH)_3^{4-}$ complex at total Hg(II) concentrations in the range 1×10^{-4} to 1×10^{-6} M. Thus, these results predict that, even at the somewhat lower GSH concentrations present in biological systems, a significant fraction of the Hg(II) will be present in the 3:1 complexed form. GSH has been identified as a major binding site for Hg(II) in intact human erythrocytes and has also been implicated in studies of the toxicology of Hg(II) (9–12).

[3]Equations used to determine the formation constant of $Hg(A)_3^{7-}$, the acid dissociation constants of $Hg(AH)_3^{4-}$, and the optical rotatory powers of $Hg(A)_3^{7-}$, $Hg(A)_2(HA)^{6-}$, $Hg(A)(AH)_2^{5-}$, and $Hg(AH)_3^{4-}$ may be purchased from the Depository of Unpublished Data, CISTI, National Research Council of Canada, Ottawa, Ont., Canada K1A 0S2.

Can. J. Chem. Downloaded from www.nrcresearchpress.com by 122.72.124.2 on 09/07/12
For personal use only.

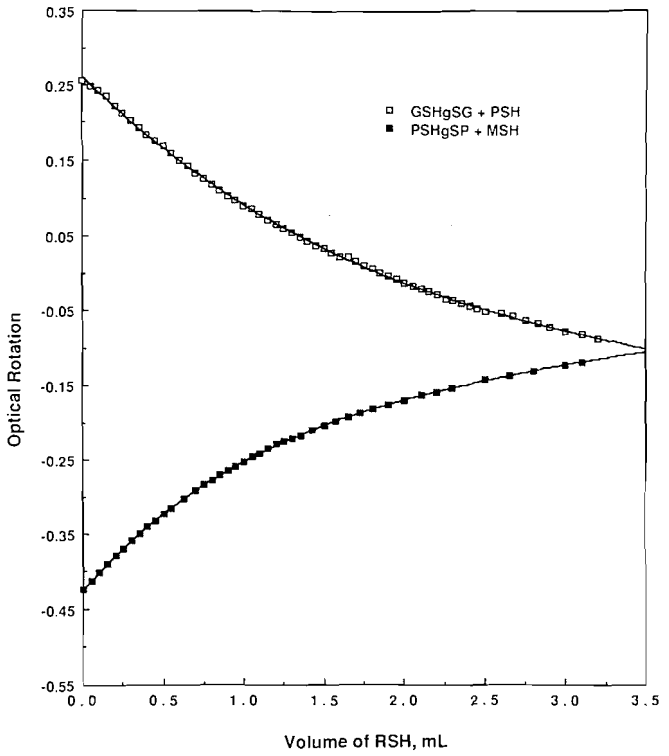

FIG. 4. The optical rotation of (A) a solution containing initially 0.015 M $Hg(NO_3)_2$ and 0.030 M GSH as a function of the volume of added 0.491 M penicillamine and (B) a solution containing 0.015 M $Hg(NO_3)_2$ and 0.030 M PSH as a function of the concentration of added 0.493 M mercaptoethylamine. Both solutions were kept at a constant pH of 5.5. The initial volume was 50 mL for both experiments. The solid curves through the experimental points are theoretical curves calculated using the displacement equilibrium constants determined in this study.

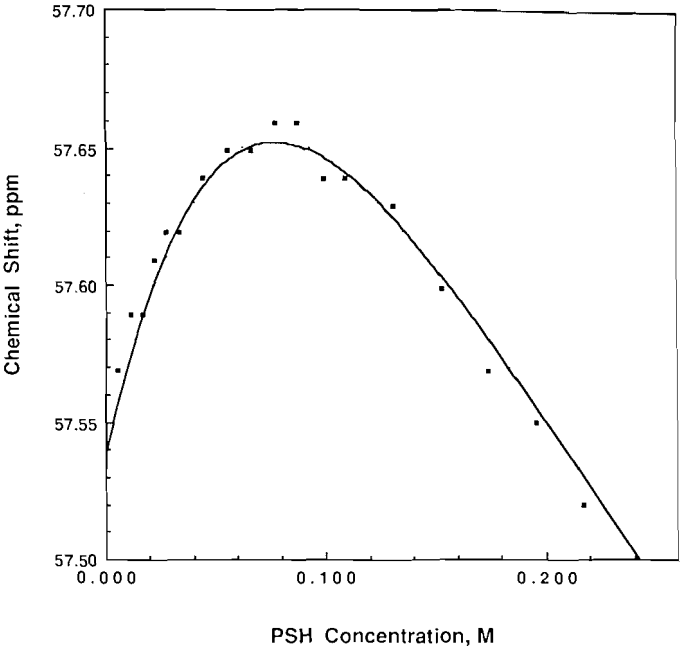

FIG. 5. The chemical shift of the C_α carbon of the cysteinyl residue of GSH in a solution containing 0.100 M $Hg(NO_3)_2$ and 0.200 M GSH as a function of the concentration of added penicillamine at pH 6. The solid curve is a theoretical curve calculated using the displacement constants determined from the ^{13}C chemical shift data.

Displacement equilibrium constants

To investigate the feasibility of using polarimetry to measure equilibrium constants for the displacement of complexed thiol ligand by free thiol ligand, as described by eqs. [2]–[4], the optical rotatory power was measured as solutions containing $Hg(SR)_2$ were titrated at constant pH with R′SH. Figure 4 shows results for (A) the titration at pH 5.5 of a solution containing 0.015 M Hg(glutathione)$_2$ with 0.491 M penicillamine and (B) the titration at pH 5.5 of a solution containing 0.015 M Hg(penicillamine)$_2$ with 0.493 M mercaptoethylamine. A pH of 5.5 was used since the results in curve C of Fig. 1 indicate there is little tendency to form the 3:1 complex at this pH. At pH 5.5, free ligands are in the amino and thiolate protonated forms, the amino groups of the complexed ligands are protonated, and carboxylic acid groups of the free and complexed ligands are deprotonated.

The observed optical rotation is described by eq. [13]:

$$[13]\quad \alpha_{obs} = \alpha_{RSHgSR}[RSHgSR] + \alpha_{RSHgSR'}[RSHgSR'] + \alpha_{R'SHgSR'}[R'SHgSR'] + \alpha_{RSH}[RSH] + \alpha_{R'SH}[R'SH]$$

Displacement equilibrium constants K_1 and K_2 (eqs. [2] and [3]) were determined by fitting the data in Fig. 4 to eq. [13] using nonlinear least-squares curve-fitting methods. The values used for α_{RSHgSR}, $\alpha_{R'SHgSR'}$, α_{RSH}, and $\alpha_{R'SH}$ in the curve fitting were calculated directly from α_{obs} measured for solutions containing only these species. The curve-fitting procedure involved first estimating values for equilibrium constants K_1 and K_2 (eqs. [2] and [3]) and $\alpha_{RSHgSR'}$. Then, using equations derived by combining the mass balance equations and the displacement equilibria, the concentrations of RSHgSR, RSHgSR′, R′SHgSR′, RSH, and R′SH were calculated using the estimated values for K_1 and K_2, and α_{obs} was predicted using these concentrations, the measured α values for RSHgSR, R′SHgSR′, RSH, and R′SH, and the estimated value for $\alpha_{RSHgSR'}$ at each added R′SH concentration. Using the nonlinear least-squares program KINET (15), the estimates for K_1, K_2, and $\alpha_{RSHgSR'}$ were then refined and the procedure repeated until the best fit between α_{obs} and $\alpha_{predicted}$ was obtained, as judged by the sum of the squares of the residuals.

The equilibrium constants obtained for the displacement of GSH by penicillamine using the data in Fig. 4A are $K_1 = 2.4 \pm 0.1$ and $K_2 = 0.41 \pm 0.01$. The solid curve through the experimental points in Fig. 4A is the predicted curve calculated using these parameters. The results obtained from a second experiment on the same system are $K_1 = 2.7 \pm 0.3$ and $K_2 = 0.47 \pm 0.03$. The equilibrium constants for the displacement of penicillamine by mercaptoethylamine ($\alpha_{R'SH}$ and $\alpha_{R'SHgSR'} = 0$) using the data in Fig. 4B are $K_1 = 4.4 \pm 0.03$ and $K_2 = 0.27 \pm 0.02$. The solid curve through the experimental points in Fig. 4B is the predicted curve calculated using these parameters.

To verify the results obtained by polarimetry, the equilibrium constants for the displacement of GSH by penicillamine were also determined by ^{13}C nmr spectroscopy. The chemical shifts of the ^{13}C resonances for GSH in pH 6.0 solutions containing 0.20 M GSH, 0.10 M $Hg(NO_3)_2$, and various concentrations of penicillamine were measured as a function of the penicillamine concentration. The exchange of glutathione among the various complexed and free forms is fast on the ^{13}C nmr time scale (20), and thus single, exchange-averaged resonances are observed for each of the carbons of glutathione. The chemical shift of the exchange-averaged resonance for the C_α carbon of the

cysteinyl residue of glutathione is plotted as a function of the penicillamine concentration in Fig. 5.

The exchange-averaged chemical shift for the Cys-C_β or Cys-C_α resonances is the weighted average of the chemical shifts of the various GSH species present, as described by eq. [14]:

$$[14] \quad \delta_{obs} = \delta_{RSHgSR} f_{RSHgSR} + \delta_{RSHgSR'} f_{RSHgSR'} + \delta_{RSH} f_{RSH}$$

where δ_{obs} is the observed chemical shift, RSH and R'SH represent GSH and penicillamine, respectively, and δ_{RSHgSR}, f_{RSHgSR}, etc. represent the chemical shifts and the fractional concentrations of GSH in the forms indicated by the subscripts. The displacement equilibrium constants were evaluated by non-linear least-squares curve fitting using a procedure analogous to that described above for their evaluation from polarimetric data. The values calculated from the chemical shift data for the Cys-C_α carbon are $K_1 = 2.1 \pm 0.1$ and $K_2 = 0.40 \pm 0.01$. The equilibrium constants were also calculated from the chemical shift data for the Cys-C_β carbon; the results are $K_1 = 2.0 \pm 0.1$ and $K_2 = 0.31 \pm 0.06$. The values determined by ^{13}C nmr are in good agreement with those determined by polarimetry.

The equilibrium constant for the complete displacement of one thiol ligand by another, K_d (eq. [4]), is the product of K_1 and K_2. Thus, for the displacement of GSH by penicillamine, $K_d = 1.12$, and for the displacement of penicillamine by mercaptoethylamine, $K_d = 1.19$. These equilibrium constants indicate that the relative stabilities of the $Hg(SR)_2$ complexes at pH 5.5 are in the order Hg(mercaptoethylamine)$_2$ > Hg(penicillamine)$_2$ > $Hg(GSH)_2$. Since the protonation states of the amino and thiol groups of the free ligands and the amino groups of the complexed ligands are essentially identical at pH 5.5 and 7.4, this also is the order of relative stabilities at physiological pH. The greater stability of Hg(penicillamine)$_2$ compared to that of Hg(glutathione)$_2$ is consistent with the effectiveness of penicillamine as a therapeutic antidote for mercury poisoning (21).

At pH 5.5, the free ligands are in the thiol form. Thus, to compare the intrinsic stabilities of the various complexes, it is necessary to account for the competitive protonation of the thiolate group (eq. [15]) since it is the thiolate form of the ligand that is complexed.

$$[15] \quad \begin{array}{ccc} RSHgSR + 2R'S^- & \rightleftarrows & R'SHgSR' + 2RS^- \\ \updownarrow H^+ & & \updownarrow H^+ \\ 2R'SH & & 2RSH \end{array}$$

$$K_d' = \frac{[R'SHgSR'][RS^-]^2}{[RSHgSR][R'S^-]^2}$$

Thus, the equilibrium constants determined above are conditional equilibrium constants for pH 5.5. Using values of pK_{SH} = 8.97, 8.05, and 8.37 for the microscopic acid dissociation constants of GSH, penicillamine, and mercaptoethylamine, respectively (18, 22, 23), K_d' is calculated to be 0.0162 for the displacement of GSH by penicillamine and 5.19 for the displacement of penicillamine by mercaptoethylamine. Thus, the relative order of intrinsic stability is Hg(glutathione)$_2$ > Hg(mercaptoethylamine)$_2$ > Hg(penicillamine)$_2$, which parallels the order of the Brønsted basicity of the thiolate ligands. Methylmercury(II) complexes of thiolate ligands show the same correlation between formation constant and Brønsted basicity of the thiolate ligand (22).

Acknowledgements

This research was supported by the Natural Sciences and Engineering Research Council of Canada and the University of Alberta.

1. W. Stricks and I. M. Kolthoff. J. Am. Chem. Soc. **75**, 5673 (1953).
2. W. L. Hughes. Ann. N.Y. Acad. Sci. **65**, 454 (1957).
3. A. J. Carty and S. F. Malone. *In* The biogeochemistry of mercury in the environment. *Edited by* J. O. Nriagu. Elsevier/North Holland Biomedical Press, New York, NY. 1979. pp. 433–479.
4. W. E. Van der Linden and C. Beers. Anal. Chim. Acta, **68**, 143 (1973).
5. J. S. Casas and M. M. Jones. J. Inorg. Nucl. Chem. **42**, 99 (1980).
6. R. Strand, W. Lund, and J. Aaseth. J. Inorg. Biochem. **19**, 301 (1983).
7. B. V. Cheesman, A. P. Arnold, and D. L. Rabenstein. J. Am. Chem. Soc. **110**, 6359 (1988).
8. D. L. Rabenstein and A. A. Isab. Biochem. Biophys. Acta, **721**, 374 (1982).
9. N. Ballatori and T. W. Clarkson. Science, **216**, 61 (1982).
10. N. Ballatori and T. W. Clarkson. Biochem. Pharmacol. **33**, 1087 (1984).
11. N. Ballatori and T. W. Clarkson. Biochem. Pharmacol. **33**, 1093 (1984).
12. N. Ballatori and T. W. Clarkson. Fundam. Appl. Toxicol. **5**, 816 (1985).
13. G. A. Bowmaker, I. G. Dance, B. C. Dobson, and D. A. Rogers. Aust. J. Chem. **37**, 1607 (1984).
14. G. Christou, K. Folting, and J. C. Huffman. Polyhedron, **3**, 1247 (1984).
15. J. L. Dye and V. A. Nicely. J. Chem. Educ. **48**, 443 (1971).
16. R. B. Martin and J. T. Edsall. Bull. Soc. Chim. Biol. **40**, 1763 (1958).
17. D. D. Perrin and A. E. Watt. Biochim. Biophys. Acta, **230**, 96 (1971).
18. D. L. Rabenstein. J. Am. Chem. Soc. **95**, 2797 (1973).
19. S. Natelson and E. A. Natelson. Principles of applied clinical chemistry. Plenum Press, New York, NY. 1978. p. 36.
20. B. J. Fuhr and D. L. Rabenstein. J. Am. Chem. Soc. **95**, 6944 (1973).
21. W. Stopford. *In* The biogeochemistry of mercury in the environment. *Edited by* J. O. Nriagu. Elsevier/North Holland Biomedical Press, New York, NY. 1979. pp. 368–397.
22. R. S. Reid and D. L. Rabenstein. Can. J. Chem. **59**, 1505 (1981).
23. A. P. Arnold, K. S. Tan, and D. L. Rabenstein. Inorg. Chem. **25**, 2433 (1986).

Can. J. Chem. Downloaded from www.nrcresearchpress.com by 122.72.124.2 on 09/07/12
For personal use only.

Peter Smith and Jill Suzanne Robertson. Electron paramagnetic resonance study of the reactions of the spin trap 3,5-dibromo-4-nitrosobenzenesulfonate. Can. J. Chem. **66**, 1153 (1988).

Page 1158, reference 29, insert "J." before "Chem. Soc."

Table 4. For radical **39**, the listed α-, β-, and γ-H(CH) splitting constants and *g*-value should be replaced by "20.25(2)", "26.17(2)", "1.56(3)", and "2.00323(2)", respectively. For radical **40**, the β-H(CH) splitting constant listed as "20.07(3)[d]" should be replaced by "18.46(2)[d], 22.68(4)[e]", and the listed δ-H(CH) splitting constant and the *g*-value should be replaced by "1.53(2)" and "2.00325(2)", respectively. The text in footnote *d* should be replaced by "β-CH_2OH group." and a new footnote, *e*, reading "β-CH_3 group." should be added.

Can. J. Chem. Downloaded from www.nrcresearchpress.com by 122.72.124.2 on 09/07/12
For personal use only.